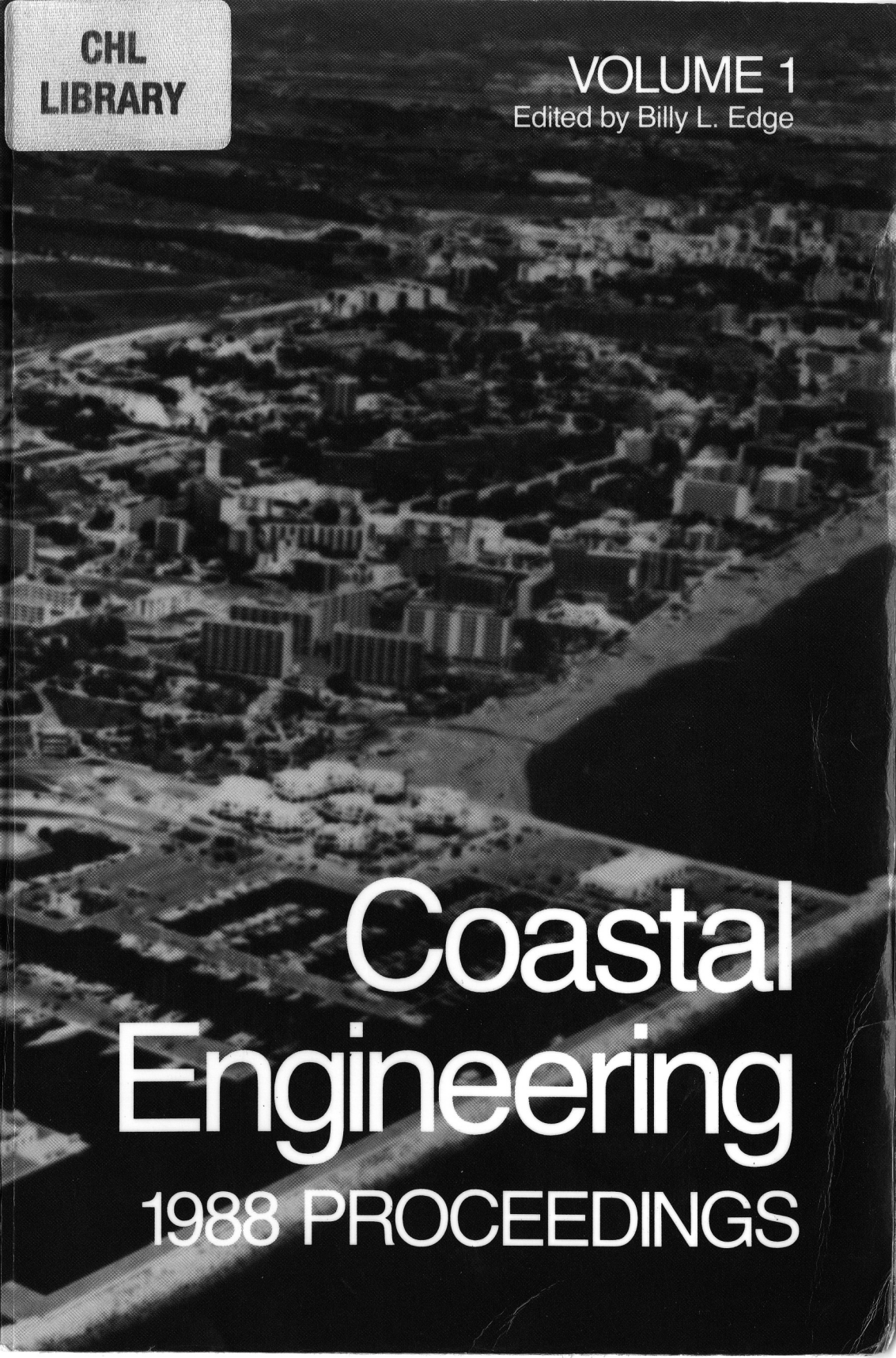


**CHL
LIBRARY**

VOLUME 1
Edited by Billy L. Edge

An aerial, black and white photograph of a coastal city. The city is densely packed with buildings and streets, extending to a large body of water in the foreground. The water is dark and calm. The city's layout is somewhat irregular, with buildings of various sizes and shapes. The overall scene is captured from a high angle, looking down on the city and the water.

**Coastal
Engineering**
1988 PROCEEDINGS

Twenty-first Coastal Engineering Conference

Proceedings of the International Conference
VOLUME 1

June 20-25, 1988
Costa del Sol-Malaga, Spain

Conference held under the auspices of the
Coastal Engineering Research Council of the
American Society of Civil Engineers

Organized by the Colegio de Ingenieros de
Camino, Canales y Puertos de Espana

and cosponsored by the
Directorate General for Ports and Coasts of the
Spanish Ministry of Public Works
Polytechnical Universities of
Madrid, Barcelona, Santander,
and Valencia

Edited by Billy L. Edge



Published by the
American Society of Civil Engineers
345 East 47th Street
New York, New York 10017-2398



ABSTRACT

This book contains over 220 papers presented at the 21st International Conference on Coastal Engineering. The book is divided into six parts: theoretical and observed wave characteristics; coastal processes and sediment transport; coastal structures and related problems; coastal, estuarine and environmental problems; case studies; and ship motions. The individual papers include such topics as the effects of wind, waves, storms and currents, erosion, sedimentation, and beach nourishment. Special emphasis is given to case studies of completed engineering projects. With the inclusion of both the theoretical and the practical, these papers provide the civil engineer with a broad range of information on coastal engineering.

The Society is not responsible for any statements made or opinions expressed in its publications.

Authorization to photocopy material for internal or personal use under circumstances not falling within the fair use provisions of the Copyright Act is granted by ASCE to libraries and other users registered with the Copyright Clearance Center (CCC) Transactional Reporting Service, provided that the base fee of \$1.00 per article plus \$.15 per page is paid directly to CCC, 27 Congress Street, Salem, MA 01970. The identification for ASCE Books is 0-87262/88. \$1 + .15. Requests for special permission or bulk copying should be addressed to Reprints/Permissions Department.

Copyright © 1989 by the American Society of Civil Engineers.

All Rights Reserved.

ISBN 0-87262-687-3

ISSN 0893-8717

Manufactured in the United States of America.

FOREWORD

The 21st International Conference on Coastal Engineering was held in Malaga, Spain. The 21st ICCE, like the ones before it, was well organized with the primary objective being to share scientific and engineering information and to provide a forum for interaction with other engineers and scientists working similar problems. The time and efforts contributed to that objective were extensive and the results have proven that the planning is a vital part of each conference. All who attended the 21st ICCE will agree that it was a tremendous success in many ways.

Since the conference was held, Dean Morrough P. O'Brien died. Dean O'Brien has been a very familiar person to all who have attended these conferences in the past. His direction and motivation developed the International Coastal Conferences into the very successful forum we now have. For over thirty years, Dean O'Brien served as Chairman of the Council on Wave Research and subsequently the Coastal Engineering Research Council. The importance of his contributions to the Coastal Engineering profession are detailed in the "In Memorium" which is included in this volume. This volume is dedicated to Dean O'Brien for his long standing interest in coastal processes, for his dedication to development of solutions of real problems and for his untiring efforts in the development of this area of engineering.

The papers in the "Proceedings" have been prepared by the authors who made presentations at the 21st International Conference on Coastal Engineering. The authors were asked to make the presentations and submit final papers based upon review of the abstracts which were submitted well in advance of the conference. These abstracts were reviewed by a committee of four professionals active in this field, including representation from the local organizing committee. The papers included in this volume are eligible for discussion in the *Journal of the Waterway Port, Coastal, and Ocean Division* of the ASCE. All papers are eligible for ASCE awards.

Venues for the upcoming conferences are listed below:

- 22nd Delft, The Netherlands, 1990
- 23rd Venice, Italy, 1992
- 24th Kobe, Japan, 1994
- 25th USA, 1996

Countries desiring to host a future conference should contact the Secretary of the Coastal Engineering Research Council to receive information about submitting a proposal.

Billy L. Edge, Secretary
Coastal Engineering Research Council
American Society of Civil Engineers

ACKNOWLEDGMENTS

Committee of Honour

President: King Juan Carlos I

Members:

The President of the Government.
The Minister for Foreign Affairs.
The Minister for Public Works and Urbanism.
The President of the Autonomous Community of Andalusia.
The Government Representative in the Autonomous Community of Andalusia.
The Mayor of Málaga.
The Secretary of State for International Cooperation and with Ibero-America.
The Counselor for Public Works of the Autonomous Community of Andalusia.
The Civil Governor of Málaga.
The President of the Provincial Government of Málaga.
The Director General for Ports and Coasts.
The Director General of Centro de Estudios y Experimentación de Obras Públicas.
The President of Colegio Nacional de Ingenieros de Caminos, Canales Y Puertos.

Organizing Committee

President:

Dr. D. Fernando Palao Taboada.

Executive Secretary:

Prof. Dr. José Luis Juan-Aracil.

Members:

Prof. Dr. D. Felipe Martínez Martínez.
Dra. D.^a Milagros Couchoud Gregori.
Dr. D. Rafael Aznar Garrigues.
D. José Trigueros Rodrigo.

Techno-Scientific Committee

Prof. Dr. D. Pedro Suárez Bores.
Prof. Dr. D. Javier Díez González.
Prof. Dr. D. Agustín Sánchez Arcilla.
Prof. Dr. D. Miguel Losada Rodríguez.
Prof. Dr. D. José R. Medina Folgado.
Prof. Dr. D. Felipe Martínez Martínez.

Coastal Engineering Research Council

Chairman:

Prof. Robert L. Wiegel.

Vice Chairman:

Prof. Orville T. Magoon.

Secretary:

Dr. Billy L. Edge.

Members:

Prof. Eco W. Bijker.
Prof. Robert G. Dean.
Dr. Douglas N. Foster.
Prof. Kyoshi Horikawa.
Ronald M. Noble.
Thorndike Saville, Jr.
Prof. Leonardo Zeevaert.



IN MEMORIAM MORROUGH PARKER O'BRIEN

Morrrough Parker O'Brien died Thursday, the 28th of July, 1988, in Cuernavaca, Mexico. He was 85. Long the leader in coastal engineering, his wisdom and counsel will be greatly missed by all who have been privileged to work with him. He is survived by his wife Mary; a son, Morrrough, of Boulder, Colorado; and a daughter, Shiela, of Berkeley, California.

He was born in Hammond, Indiana, on 21 September, 1902. He received a B.S. in Civil Engineering from Massachusetts Institute of Technology in 1925. He did graduate work at Purdue University, 1925-27, and in 1927-28, as a Freeman Scholar, at the Technische Hochschule in Danzig and The Royal College of Engineering in Stockholm. He received three honorary degrees: the D.Sc. from Northwestern University; the D.Eng. from Purdue University; and the LL.D. from the University of California.

O'Brien engaged in three fundamentally different careers. His academic career as Professor and Dean of Engineering at the University of California, Berkeley, spanned the years 1928-59. A second career was his pioneering work in the development of coastal engineering which, while it had some impact on the research programs at Berkeley, was unrelated to his academic pursuits. His third career was his service from 1949 until his death on an annual retainer to General Electric Company.

O'Brien's academic steps were:

<i>Mechanical Engineering:</i>	
Assistant Professor	1928-31
Associate Professor	1931-36
Professor	1936-43
Chairman	1937-43
<i>Department of Engineering: Chairman</i>	1943-59
<i>Professor of Engineering:</i>	1943-59
<i>Dean, College of Engineering:</i>	1943-59
<i>Retired</i>	June 30, 1959

Ernest O. Lawrence and Robert J. Oppenheimer were appointed assistant professors in the same year as O'Brien, and the three became good friends. These associations greatly influenced his views regarding the importance of research in a modern engineering school. During his tenure as Dean of the College of Engineering at Berkeley he led the development of the College to its top-ranked status in many engineering disciplines. He was widely regarded as a powerful and perceptive leader in engineering education, understanding that modern engineering education had to be improved by a systems approach: good students are attracted to good faculty; good faculty are active in research in the outside world; good graduate students are needed to work with the faculty on research. The University furthers the interaction of students, faculty and society by the establishment of an external advisory council, and of such research units as the Institute of Traffic and Transportation Engineering

and the University-wide Water Resources Center, both of these, incidentally, begun at UC with O'Brien's help. UC President Emeritus Clark Kerr, who had served as Chancellor when O'Brien was Dean, remembered him as "the mighty Mike" and the "builder of the College of Engineering and a builder of Berkeley" during the symposium held in O'Brien's honor in March 1987 (see *Shore & Beach*, July/October 1987).

O'Brien received a number of honors from the University. O'Brien Hall, which houses the Hydraulic Laboratory and the Water Resources Center Archives, was named after him. The portrait of O'Brien reproduced with this article hangs in the entry hall of this building. He was awarded the Doctor of Laws degree. In April 1988 he was awarded the Clark Kerr Award, given by the Academic Senate to "an individual considered to have made an extraordinary and distinguished contribution to the advancement of higher education." This Award, presented by Kerr himself, was particularly notable in that it was given to O'Brien as one of four leaders "who played pivotal roles in building the academic strength of the campus." A photo of the presentation is reproduced below. Dean O'Brien was also awarded the Lamme Award for excellence in teaching by the American Society of Engineering Education.

O'Brien continued to be active in university education after his retirement from the University of California, working with Massachusetts Institute of Technology, Harvard University, and Purdue University. From 1968 on he was a part-time consultant and Professor of Coastal Engineering at the University of Florida, participating in many research projects in collaboration with Professor Robert G. Dean.

O'Brien was the founder of modern coastal engineering. He wrote a number of papers on the subject which have had a lasting influence. He was appointed Civil Engineer for the U.S. Army Board on Sand Movement and Beach Erosion in 1929, and initiated research by this board on coastal engineering. In 1930 he made field studies along the coasts of Washington, Oregon and California, and wrote a detailed seven-volume report on the results of his observations. A landmark paper on the relationship between tidal prism and entrance area was one of the results of these studies. He summarized many of his observations and thoughts on beach processes and the effects of structures on beaches in his paper "The Coast of California as a Beach Erosion Laboratory" (*Shore & Beach*, July 1936). In 1938 he was appointed a member of the Beach Erosion Board, U.S. Army Corps of Engineers, and served on it until it was abolished in 1963. He was then appointed to its successor, the Coastal Engineering Research Board, serving there from 1963 until 1978, a total of forty years on the two boards.

The years of World War II were extremely busy for O'Brien, serving as Chairman of the Mechanical Engineering Department until 1943 when he was appointed both Dean of the College of Engineering and also Chairman of the Department of Engineering. He was Executive Engineer of the Radiation Laboratory under Professor E.O. Lawrence in 1942-43. O'Brien was asked by Lawrence and General Groves, the Manhattan Project Director, to recruit an engineering team to design the production facilities at Oak Ridge for the electromagnetic system. O'Brien said that probably the most important thing he did in his life was to convince them that there was not time to build a competent staff, that they should hire companies with an established engineering staff to do the job. He was in charge of the Statewide University of California Engineering Science and Management War Training program, 1940-44, when the program registered 46,000 students who worked under 1,800

instructors. He worked for the U.S. Navy Bureau of Ships on underwater sound, on cavitation generated by submarine propellers (the results of this research were immediately implemented by submariners), and on the design and operation of amphibious craft. He also worked with Professor H.U. Sverdrup of the Scripps Institution of Oceanography on the forecasting of waves, and he directed a program of field and laboratory studies of landing craft for the Bureau.

In 1950 he and Professor Joe W. Johnson started what are now known as the International Conferences on Coastal Engineering. The first of these was held in Long Beach, California, under the auspices of the University Engineering Extension, each paper being by invitation. The most recent of these conferences was held in Torremolinos, Spain, in June 1988 when more than five hundred abstracts were submitted for consideration and fewer than half could be accommodated (O'Brien served on the Technical Papers Review Committee).

O'Brien had a strong public service orientation. He was a member of the Army Scientific Advisory Panel, 1954–65, serving as its chairman, 1961–65; a member of the Defense Science Board, 1961–65; member of the Board of the National Science Foundation (a Presidential appointment), 1958–60; and he served on numerous committees of the National Research Council.

He was active in professional societies. He was elected honorary member of the American Society of Civil Engineers (1976), the American Society of Mechanical Engineers (1979), and the Japan Society of Civil Engineers (1988). He was elected to membership in the National Academy of Engineering in 1969.

O'Brien was a leader in several fields of engineering, including pumps and air compressors. The compressor design for the first American axial flow jet engine was laid out exactly in accordance with the method presented in the paper by O'Brien and Folsom entitled "The Design of Propeller Pumps and Fans." It was incorporated in what became the J47 engine with a production run of thousands. He was elected to the General Electric Company Propulsion Hall of Fame in 1984.

In March 1987, the *Symposium to Honor Morrrough P. O'Brien—Working Solutions: Shore and Beach* was held at the University of California at Berkeley. The State University of New York at Stony Brook established the M.P. O'Brien Fellowships in 1987. The American Shore and Beach Preservation (O'Brien served as its president from 1978 to 1983) is establishing the *Morrrough P. O'Brien Award for Outstanding Achievement in Shore and Beach Preservation*.

Robert L. Wiegel

Joe W. Johnson

CONTENTS

COASTAL ENGINEERING TRENDS AND RESEARCH NEEDS	I
<i>R.L. Wiegel</i>	

PART I THEORETICAL AND OBSERVED WAVE CHARACTERISTICS

Chapter 1	
NONLINEAR DIFFRACTION BY A VERTICAL CYLINDER	17
<i>D.L. Kriebel</i>	
Chapter 2	
WAVE-CURRENT INTERACTION IN HARBOURS	32
<i>J.K. Kostense, M.W. Dingemans and P. van den Bosch</i>	
Chapter 3	
OBSERVATION OF DIRECTIONAL WAVE SPECTRA AND REFLECTION COEFFICIENT OF BREAKWATER IN A HARBOR	47
<i>T. Ohshimo, K. Kondo and T. Sekimoto</i>	
Chapter 4	
DIRECTIONAL SPECTRUM ESTIMATION FROM A BAYESIAN APPROACH	62
<i>N. Hashimoto and K. Kobune</i>	
Chapter 5	
LONGSHORE CURRENTS FORCING AT A BARRED BEACH	77
<i>D.J. Whitford and E.B. Thornton</i>	
Chapter 6	
NUMERICAL COMPARISON OF WAVE SYNTHESIS METHODS	91
<i>M.D. Miles and E.R. Funke</i>	
Chapter 7	
ON THE TRANSFORMATION OF WAVE STATISTICS DUE TO SHOALING	106
<i>E.P.D. Mansard, E.R. Funke, J.S. Readshaw and R.K. Girard</i>	
Chapter 8	
WAVE FIELD BEHIND THE PERMEABLE DETACHED BREAKWATER	121
<i>S-H. Ou, S-Y. Tzang and T-W. Hsu</i>	

Chapter 9		
INCOMING AND OUTGOING WAVE INTERACTIONS ON BEACHES	136	
		<i>R.V.S.N. Tatavarti, D.A. Huntley and A.J. Bowen</i>
Chapter 10		
WAVE RUN-UP ON A NATURAL BEACH	151	
		<i>M. Takezawa, M. Mizuguchi, S. Hotta and S. Kubota</i>
Chapter 11		
CHARACTERISTICS OF DIFFUSION AND AERATION DUE TO WAVE ACTION NEAR PERMEABLE BREAKWATERS	166	
		<i>H. Murakami and Y. Hosoi</i>
Chapter 12		
GENERALIZED WAVE THEORY FOR SLOPING BED	181	
		<i>D.H. Swart and J.B. Crowley</i>
Chapter 13		
WAVE GROUPS ON WAVE RECORDS MEASURED ALONG SPANISH SHORES	204	
		<i>A. Maron</i>
Chapter 14		
ARE SOLITARY WAVES THE LIMITING WAVES IN LONG WAVE RUNUP?	219	
		<i>C.E. Synolakis</i>
Chapter 15		
COHERENT EDDIES INDUCED BY BREAKERS ON A SLOPING BED	234	
		<i>N. Matsunaga, K. Takehara and Y. Awaya</i>
Chapter 16		
WIDE-ANGLE WATER WAVE MODELS USING FOURIER METHOD	246	
		<i>R.A. Dalrymple and K.D. Suh</i>
Chapter 17		
WAVE CLIMATE OFF RIO DE JANEIRO	261	
		<i>M.H.S. de Souza and C.E.P. Ribeiro</i>
Chapter 18		
AN EXPERIMENTAL STUDY OF HARBOR RESONANCE PHENOMENA	270	
		<i>F.M. Martínez and V.S. Naverac</i>

Chapter 19		
DEVELOPMENT AND APPLICATION OF A MATHEMATICAL MODEL OF WAVE ACTION ON STEEP SLOPES	281	
		<i>N.W.H. Allsop, J.V. Smallman and R.V. Stephens</i>
Chapter 20		
ABOUT THE ENERGY DISSIPATION OVER BARRED BEACHES ...	292	
		<i>J. Oelerich and H-H. Dette</i>
Chapter 21		
TRUNCATION ORDER OF FOURIER WAVE THEORY	307	
		<i>R.J. Sobey</i>
Chapter 22		
DIRECTIONAL SEA STATE NEAR THE ISLAND OF SYLT	322	
		<i>D. Schade and K.-F. Daemrich</i>
Chapter 23		
REDUCTION OF WAVE OVERTOPPING BY THE USE OF ARTIFICIAL REEFS	335	
		<i>T. Sawaragi, I. Deguchi and S-K. Park</i>
Chapter 24		
EFFECT OF BOUSSINESQ EQUATIONS ON WAVE SPECTRA PROPAGATION	350	
		<i>J.P. Sierra, A.S. Arcilla, J.J. Egozcue and J.L. Monso</i>
Chapter 25		
THE INFLUENCE OF CURRENTS ON WAVE ATTENUATION	363	
		<i>R.R. Simons, A.J. Grass, and A. Kyriacou</i>
Chapter 26		
SOME CHARACTERISTICS OF BREAKING WAVES	377	
		<i>F. Raichlen and P. Papanicolaou</i>
Chapter 27		
NUMERICAL MODELING OF WAVE DEFORMATION WITH A CURRENT	393	
		<i>S. Ohnaka, A. Watanabe and M. Isobe</i>
Chapter 28		
THEORETICAL MODEL FOR NEARSHORE CIRCULATIONS	408	
		<i>M. Sasaki, A. Ozaki and H. Saeki</i>

Chapter 29		
THE MEASURED PROPERTIES OF IRREGULAR WAVE BREAKING AND WAVE HEIGHT CHANGE AFTER BREAKING ON THE SLOPE		419
	<i>A. Seyama and A. Kimura</i>	
Chapter 30		
VERIFICATION OF NUMERICAL WAVE PROPAGATION MODELS IN TIDAL INLETS		433
	<i>J.A. Vogel, A.C. Radder and J.H. de Reus</i>	
Chapter 31		
KINEMATICS AND RETURN FLOW IN A CLOSED WAVE FLUME		448
	<i>J.D. Ramsden and J.H. Nath</i>	
Chapter 32		
A HYDRODYNAMIC MODEL FOR COMPUTER AIDED HARBOUR ENGINEERING		463
	<i>J.L. Monso, A.S.-Arcilla and J.P. Sierra</i>	
Chapter 33		
VERTICAL VARIATION OF UNDERTOW IN THE SURF ZONE		478
	<i>A. Okayasu, T. Shibayama and K. Horikawa</i>	
Chapter 34		
SPECTRAL WAVE ATTENUATION BY BOTTOM FRICTION: THEORY		492
	<i>O.S. Madsen, Y-K. Poon and H.C. Graber</i>	
Chapter 35		
SUBGRID MODELLING IN DEPTH INTEGRATED FLOWS		505
	<i>P.A. Madsen, M. Rughjerg and I.R. Warren</i>	
Chapter 36		
PROPAGATION OF WIND WAVES ON TIDES		512
	<i>H.L. Tolman</i>	
Chapter 37		
ON JOINT DISTRIBUTION OF WAVE HEIGHTS AND PERIODS		524
	<i>M. Isobe</i>	
Chapter 38		
FIELD MEASUREMENT OF WAVE SET-UP		539
	<i>G.A. Davis and P. Nielsen</i>	

Chapter 39		
ON THE MAXIMUM RUNUP OF CNOIDAL WAVES		553
	<i>C.E. Synolakis and M.K. Deb</i>	
Chapter 40		
THE WAMS MODEL APPLIED TO THE MEDITERRANEAN SEA ...		566
	<i>L. Cavaleri, L. Bertotti, J.E. De Luis and P. Lionello</i>	
Chapter 41		
A NUMERICAL MODEL OF WAVE DEFORMATION		
IN SURF ZONE		578
	<i>A. Watanabe and M. Dibajnia</i>	
Chapter 42		
COUPLING STOKES AND CNOIDAL WAVE THEORIES IN A		
NONLINEAR REFRACTION MODEL		588
	<i>T.A. Hardy and N.C. Kraus</i>	
Chapter 43		
WAVES IN TURNING WINDS		602
	<i>G.Ph. van Vledder and L.H. Holthuijsen</i>	
Chapter 44		
TRANSFORMATION OF SHALLOW WATER SPECTRA		612
	<i>G. Bendykowska and G. Werner</i>	
Chapter 45		
SOLITARY WAVES PASSING OVER SUBMERGED BREAKWATER		624
	<i>M. Cooker and H. Peregrine</i>	
Chapter 46		
LABORATORY EXPERIMENTS ON THE INFLUENCE OF WIND ON		
NEARSHORE WAVE BREAKING		632
	<i>S.L. Douglass and J.R. Weggel</i>	
Chapter 47		
WAVE RUN-UP PREDICTION VS. MODEL TEST RESULTS:		
A COMPARISON		644
	<i>P.E. Gadd, V. Manikian and J.L. Machemehl</i>	
Chapter 48		
STATISTICAL PROPERTIES OF THE MAXIMUM RUN OF		
IRREGULAR SEA WAVES		655
	<i>A. Kimura</i>	

Chapter 49		
SOME RESULTS FROM THE LABRADOR SEA EXTREME WAVES EXPERIMENT		667
	<i>S.P. Kjeldsen, H.E. Krogstad and R.B. Olsen</i>	
Chapter 50		
ON THE PARTITION OF HORIZONTAL MOMENTUM BETWEEN VELOCITY AND PRESSURE COMPONENTS THROUGH THE TRANSITION REGION OF BREAKING WAVES		682
	<i>D.R. Basco and T. Yamashita</i>	
Chapter 51		
A DIRECTIONAL PREDICTION MODEL OF WAVES WITH VARIABLE WIND		698
	<i>J.R. Acinas</i>	
Chapter 52		
THREE DIMENSIONAL FLOW PROFILES ON LITTORAL BEACHES		705
	<i>I.A. Svendsen and R.S. Lorenz</i>	
Chapter 53		
GRAIN-GRAIN INTERACTION IN OSCILLATING SHEETFLOW		718
	<i>W.T. Bakker, W.G.M. van Kesteren and Z.H. Yu</i>	
Chapter 54		
NONLINEAR EFFECTS ON FOCUSED WATER WAVES		732
	<i>D.H. Peregrine, D. Skyner, M. Stiassnie and N. Dodd</i>	
Chapter 55		
OSCILLATORY BOTTOM BOUNDARY LAYER BY LOW-REYNOLDS NUMBER TURBULENCE MODEL		743
	<i>T. Asano, H. Godo and Y. Iwagaki</i>	
Chapter 56		
ON THE OCCURRENCE OF ABNORMAL STORMS AND ITS IMPLICATIONS ON DESIGN PARAMETERS (STATISTICAL ANALYSIS OF SAME)		756
	<i>O.J. Jensen and P. Klinting</i>	
Chapter 57		
WAVE OVERTOPPING ON RUBBLE MOUND BREAKWATERS		770
	<i>P. Aminti and L. Franco</i>	
Chapter 58		
REFLECTIONS FROM COASTAL STRUCTURES		782
	<i>N.W.H. Allsop and S.S.L. Hettiarachchi</i>	

Chapter 59		
SEAWALL OVERTOPPING MODEL		795
	<i>J.P. Ahrens and M.S. Heimbaugh</i>	
Chapter 60		
CLOSED-FORM SOLUTIONS FOR THE PROBABILITY DENSITY OF WAVE HEIGHT IN THE SURF ZONE		807
	<i>W.R. Dally and R.G. Dean</i>	
Chapter 61		
DESIGN WAVES AND THEIR PROBABILITY DENSITY FUNCTIONS		822
	<i>J. Rossouw</i>	
Chapter 62		
REALIZABLE WAVE PARAMETERS IN A LABORATORY FLUME ..		835
	<i>E.R. Funke, E.P.D. Mansard and G. Dai</i>	
Chapter 63		
SPECTRAL WAVE ATTENUATION BY BOTTOM FRICTION: EXPERIMENTS		849
	<i>O.S. Madsen and M.M. Rosengaus</i>	
Chapter 64		
A BAROTROPIC 3D-MODEL FOR THE STUDY OF CURRENTS AROUND THE ATLANTIC COAST OF THE IBERIAN PENINSULA ..		858
	<i>I. Rodriguez, J. Krohn and J.O. Backhaus</i>	
Chapter 65		
KINEMATICS OF BREAKING WAVES IN COASTAL REGIONS		871
	<i>W.J. Easson, M.W.P. Griffiths and C.A. Greated</i>	
Chapter 66		
WAVE GROUP ANALYSIS BY THE HILBERT TRANSFORM		884
	<i>R.T. Hudspeth and J.R. Medina</i>	
Chapter 67		
ON THE METHODOLOGY OF SELECTING DESIGN WAVE HEIGHT		899
	<i>Y. Goda</i>	
Chapter 68		
UNSTEADY FLOW AROUND A VERTICAL CIRCULAR CYLINDER IN A WAVE		914
	<i>K. Hayashi and T. Shigemura</i>	
Chapter 69		
A STEADY-STATE WAVE MODEL FOR COASTAL APPLICATIONS		929
	<i>D.T. Resio</i>	

Chapter 70		
COMPARISONS OF NUMERICAL RANDOM WAVE SIMULATORS ..	941	
		<i>J.R. Medina and C.R. Sanchez-Carratala</i>
Chapter 71		
STORM STATISTICS IN THE NORTH SEA	956	
		<i>B.A. Salih, R. Burrows and R.G. Tickell</i>
Chapter 72		
STATUS OF U.S.A. OCEAN ENERGY RECOVERY ACTIVITIES	971	
		<i>Y.C. Kim, L. Lewis, M.E. McCormick and L.S. Slotta</i>
Chapter 73		
LONG WAVES IN A SPANISH HARBOUR	984	
		<i>Jose C. Suntas López and G.G. Pina</i>
Chapter 74		
DYNAMIC WAVE SETUP	999	
		<i>J-M. Lo</i>
Chapter 75		
PORE PRESSURE INDUCED BY WIND WAVES IN SAND BED	1011	
		<i>S.R. Massel and L. Kaczmarek</i>
Chapter 76		
PROBABILITY OF WAVE BREAKING IN THREE-DIMENSIONAL SEAS	1020	
		<i>D. Mather, M.W.G. Snook, C.A. Greated, W.J. Easson and I.G. Bryden</i>
Chapter 77		
A NEW PARAMETER FOR WAVE BREAKING WITH OPPOSING CURRENT ON SLOPING SEA BED	1035	
		<i>S. Sakai, K.-I. Hirayama, and H. Saeki</i>
Chapter 78		
WHAT IS THE SLOPE OF EQUILIBRIUM RANGE IN THE FREQUENCY SPECTRUM OF WIND WAVES?	1045	
		<i>P.C. Liu</i>
Chapter 79		
SURF BEAT GENERATION ON A MILD-SLOPE BEACH	1058	
		<i>H.A. Schaffer and I.A. Svendsen</i>
Chapter 80		
SOLITARY WAVE TRANSMISSION THROUGH POROUS BREAKWATERS	1073	
		<i>C. Vidal, M.A. Losada, R. Medina and J. Rubic</i>

Chapter 81		
TIME-DEPENDENT WAVE SHEAR STRESS		1084
	<i>S. Vongvisessomjai</i>	

Chapter 82		
A PARAMETERIC HURRICANE WAVE PREDICTION MODEL		1098
	<i>I.R. Young</i>	

Chapter 83		
A NUMERICAL MODEL OF NEARSHORE CURRENTS DUE TO IRREGULAR WAVES		1113
	<i>M. Yamaguchi</i>	

PART II
COASTAL PROCESSES AND SEDIMENT TRANSPORT

Chapter 84		
NON-UNIFORM SUSPENDED SEDIMENTS UNDER WAVES		1129
	<i>A. Armanini and P. Ruol</i>	

Chapter 85		
INITIAL MOTION IN COMBINED WAVE AND CURRENT FLOWS ..		1140
	<i>J.S. Lee-Young and J.F.A. Sleath</i>	

Chapter 86		
STUDY OF SHELF WAVES VS. SAND DRIFT IN NW COAST OF TAIWAN		1152
	<i>H-S. Hou</i>	

Chapter 87		
SWASH OSCILLATION AND RESULTING SEDIMENT MOVEMENT		1167
	<i>N. Kobayashi, M.S. Strzelecki and A. Wurjanto</i>	

Chapter 88		
TOWARD AN IMPROVED EMPIRICAL FORMULA FOR LONGSHORE SAND TRANSPORT		1182
	<i>N.C. Kraus, K.J. Gingerich and J.D. Rosati</i>	

Chapter 89		
GENERIC TREATMENT OF DUNE EROSION FOR 100-YEAR EVENT		1197
	<i>R.J. Hallermeier and P.E. Rhodes</i>	

Chapter 90		
CALCULATION OF ON-OFFSHORE SAND MOVEMENT AND WAVE DEFORMATION ON TWO-DIMENSIONAL WAVE-CURRENT COEXISTENT SYSTEM		1212
	<i>K. Kinose, S. Okushima and M. Tsuru</i>	

Chapter 91		
MOVABLE-BED EXPERIMENTS OF SHANTOU HARBOR	1227
	<i>Huang Jianwei</i>	
Chapter 92		
ENVIRONMENTAL CONTROLS ON LITTORAL SAND TRANSPORT		1238
	<i>P.D. Komar</i>	
Chapter 93		
PREDICTIVE MODEL FOR DAILY CHANGES OF SHORELINE	1253
	<i>K. Katoh and S-i. Yanagishima</i>	
Chapter 94		
PROTOTYPE APPLICATIONS OF A GENERALIZED SHORELINE CHANGE NUMERICAL MODEL	1265
	<i>H. Hanson, M.B. Gravens and N.C. Kraus</i>	
Chapter 95		
INCEPTION OF SAND MOTION AROUND A LARGE OBSTACLE	...	1280
	<i>H. Katsui and T. Toue</i>	
Chapter 96		
BEACH PROFILE CHANGE: MORPHOLOGY, TRANSPORT RATE, AND NUMERICAL SIMULATION	1295
	<i>M. Larson, N.C. Kraus and T. Sunamura</i>	
Chapter 97		
LOCAL SCOUR AROUND CYLINDRICAL PILES DUE TO WAVES AND CURRENTS COMBINED	1310
	<i>Y. Kawata and Y. Tsuchiya</i>	
Chapter 98		
STUDIES FOR VILLAJYOYA'S BEACH REGENERATION (SPAIN)		1323
	<i>J.L. Campello Chorro, V.J. de Esteban Chapapria, J. Aguilar Herrando and J.J. Diez Gonzalez</i>	
Chapter 99		
COASTAL PROCESSES IN GUARDAMAR BAY (SPAIN)	1330
	<i>V.J. de Esteban Chapapria, J.J. Diez Gonzalez, M. Arenillas Parra, and R. Cortes Gimeno</i>	
Chapter 100		
TRACERS OF SAND MOVEMENT ON THE OREGON COAST	1338
	<i>K.E. Clemens and P.D. Komar</i>	
Chapter 101		
PROBABILISTIC ANALYSIS OF SEAFLOOR LIQUEFACTION	1352
	<i>R. Blazquez and F.M. Martinez</i>	

Chapter 102		
EROSION AROUND A PILE DUE TO CURRENT AND BREAKING WAVES		1368
	<i>E.W. Bijker and C.A. de Bruyn</i>	
Chapter 103		
IMPROVED LONGSHORE SAND TRANSPORT EVALUATION		1382
	<i>A.S.-Arcilla, A. Vdaor and J. Pous</i>	
Chapter 104		
LONGSHORE CURRENT AND TRANSPORT ACROSS NON-SINGULAR EQUILIBRIUM BEACH PROFILES		1396
	<i>K.R. Bodge</i>	
Chapter 105		
DESIGN OF POCKET BEACHES. THE SPANISH CASE		1411
	<i>J.M. Berenguer and J. Enriquez</i>	
Chapter 106		
DUNE EROSION AND SEDIMENT PROFILE DUE TO WAVE UPRUSH		1426
	<i>T.A. Fenaish, M.F. Overton and J.S. Fisher</i>	
Chapter 107		
BARCELÓNA'S LITTORAL REGENERATION LOOKING FORWARD TO THE OLYMPIC GAMES. NUMERICAL MODEL		1437
	<i>V. Negro Valdecantos and M. Quecedo Gutierrez</i>	
Chapter 108		
WAVE-INDUCED FLOW AND NEARSHORE SUSPENDED SEDIMENT		1452
	<i>J.C. Doering and A.J. Bowen</i>	
Chapter 109		
WAVE-INDUCED BREAKOUT OF HALF-BURIED MARINE PIPES ..		1464
	<i>M.A. Foda, A.W-K Law and J. Y-H Chang</i>	
Chapter 110		
PERCHED BEACH PROFILE RESPONSE TO WAVE ACTION		1482
	<i>R.M. Sorensen and N.J. Beil</i>	
Chapter 111		
EFFECTS OF A VERTICAL SEAWALL ON PROFILE RESPONSE		1493
	<i>M.R. Barnett and H. Wang</i>	
Chapter 112		
BED RESPONSE TO FAIRWEATHER AND STORM FLOW ON THE SHOREFACE		1508
	<i>M.O. Green, J.D. Boon, J.H. List and L.D. Wright</i>	

Chapter 113		
PHASE-LOCKING OF MODES IN THE NEARSHORE:		
FIELD EVIDENCE	1522	
		<i>J. Haines and A.J. Bowen</i>
Chapter 114		
BEACH PROFILE CHANGE UNDER VARYING WAVE CLIMATES ..	1535	
		<i>Y. Kai, R. Rushu and W. Liang</i>
Chapter 115		
REPRODUCTION MODEL OF BEACH CHANGE		
BY STORM WAVES	1544	
		<i>M. Ito and Y. Tsuchiya</i>
Chapter 116		
REALISTIC ECONOMIC BENEFITS FROM BEACH NOURISHMENT	1558	
		<i>R.G. Dean</i>
Chapter 117		
EFFECTS OF STRUCTURE ON DEPOSITION OF DISCHARGED		
SEDIMENT AROUND RIVERMOUTH	1573	
		<i>I. Deguchi and T. Sawaragi</i>
Chapter 118		
DUNE STABILIZATION WITH A SAND/GEL COMPOSITE SYSTEM	1588	
		<i>M.H. Auerbach, G.W. Borden and B.L. Edge</i>
Chapter 119		
LITTORAL DRIFT MODEL FOR NATURAL ENVIRONMENTS	1603	
		<i>R. Deigaard, J. Fredsow, I.B. Hedegaard, J.A. Zyserman and O.H. Anderson</i>
Chapter 120		
CARIBBEAN BEACH-FACE SLOPES AND EQUILIBRIUM PROFILES	1618	
		<i>J.D. Boon and M.O. Green</i>
Chapter 121		
BEACH PROFILE CHARACTERISTICS DUE TO THE		
INCLINED WAVES	1631	
		<i>T-W. Hsu and S-H. Ou</i>
Chapter 122		
SEDIMENT SUSPENSION DUE TO LARGE SCALE EDDIES IN THE		
SURF ZONE	1646	
		<i>K. Nadaoka, S. Ueno and T. Igarashi</i>

Chapter 123		
SUSPENDED SEDIMENT CONCENTRATION IN THE SURF ZONE . . .	1661	
		<i>M. Ifuku and T. Kakinuma</i>
Chapter 124		
VALIDATION OF CROSS-SHORE TRANSPORT FORMULATIONS . . .	1676	
		<i>R.J. Seymour and D. Castel</i>
Chapter 125		
A QUASI-3D MATHEMATICAL MODEL OF COASTAL MORPHOLOGY	1689	
		<i>H.J. de Vriend and J.S. Ribberink</i>
Chapter 126		
VERTICAL VARIABILITY OF COASTAL SEDIMENT TRANSPORT . . .	1704	
		<i>R.B. Zeidler</i>
Chapter 127		
ABOUT THE INFLUENCE OF EROSION VOLUME ON CROSS-SHORE MOVEMENT AT PROTOTYPE SCALE	1721	
		<i>K. Uliczka and H.H. Dette</i>
Chapter 128		
SEDIMENT TRANSPORT ON NEARLY-PRISMATIC BEACHES	1736	
		<i>M.J.F. Stive and J.A. Roelvink</i>
Chapter 129		
SAND RIPPLE GEOMETRY AND SAND TRANSPORT MECHANISM DUE TO IRREGULAR OSCILLATORY FLOWS	1748	
		<i>S. Sato and K. Horikawa</i>
Chapter 130		
THE DYNAMIC RESPONSE OF SHINGLE BEACHES TO RANDOM WAVES	1763	
		<i>K.A. Powell</i>
Chapter 131		
ESTIMATES OF CROSS-SHORE BEDLOAD AND BED CHANGES . . .	1774	
		<i>Z. Pruszek and R.B. Zeidler</i>
Chapter 132		
SECULAR CHANGE IN TIDAL FLAT HEIGHTS	1788	
		<i>W. Siefert</i>
Chapter 133		
BED LOAD TRANSPORT DUE TO NON-LINEAR WAVE MOTION . . .	1803	
		<i>H. Tanaka</i>

Chapter 134		
PHYSICAL MODELLING OF BEACH EROSION AND LITTORAL DRIFT		1818
	<i>O.J. Sayao and R.B. Nairn</i>	
Chapter 135		
FIELD CALCULATION OF WAVE ENERGY DISSIPATION AND RELATED BEACH PROFILE		1833
	<i>J.R. Tallent, T. Yamashita and Y. Tsuchiya</i>	
Chapter 136		
EFFECTS OF ENERGY LOSS NEAR BED SURFACE ON WAVE-INDUCED PORE PRESSURE IN SAND LAYER		1842
	<i>Y.-H. Maeno</i>	
Chapter 137		
SIMULATION MODELING OF DUNE EROSION		1857
	<i>M.F. Overton and J.S. Fisher</i>	
Chapter 138		
THE CRITERION OF RIPPLE FORMATION BY WAVE ACTION		1868
	<i>Y. Tsuchiya and M. Banno</i>	
Chapter 139		
EXTREME EROSION EVENT ON AN ARTIFICIAL BEACH		1882
	<i>J.P. Moller and D.H. Swart</i>	
Chapter 140		
A MODEL FOR BREACH GROWTH IN A DIKE-BURST		1897
	<i>P.J. Visser</i>	
Chapter 141		
SHORELINE AT JETTY DUE TO CYCLIC AND RANDOM WAVES ..		1911
	<i>T.L. Walton, P.L-F. Liu and E.B. Hands</i>	
Chapter 142		
CHARACTERISTICS OF SHINGLE BEACHES WITH REFERENCE TO CHRISTCHURCH BAY, S. ENGLAND		1922
	<i>R. Nicholls and N. Webber</i>	
Chapter 143		
PREDICTION OF 3-D BEACH CHANGES ON THE FUJI COAST		1937
	<i>H. Ohishi, T. Uda, Y. Murakami and M. Watanabe</i>	
Chapter 144		
TOWARDS MODELLING COASTAL SEDIMENT TRANSPORT		1952
	<i>P. Nielsen</i>	

Chapter 145	LONGSHORE SEDIMENT TRANSPORT RATE VS. CROSS-SHORE DISTRIBUTION OF SEDIMENT GRAIN SIZES	1959
	<i>C.I. Moutzouris</i>	

Chapter 146	THE THEORICAL TEMPORAL STRUCTURE OF THE LONGSHORE CURRENTS	1974
	<i>J. Aguilar and J.J. Diez</i>	

PART III
COASTAL STRUCTURES AND RELATED PROBLEMS

Chapter 147	GENTLE SLOPE SEAWALLS COVERED WITH ARMOUR UNITS ...	1983
	<i>O. Toyoshima</i>	

Chapter 148	ON BERM BREAKWATERS	1997
	<i>A. Torum, S. Naess, A. Instanes and S. Vold</i>	

Chapter 149	NUMERICAL MODEL OF BREAKWATER WAVE FLOWS	2013
	<i>A.C. Thompson</i>	

Chapter 150	STATISTICAL ANALYSIS OF DETACHED BREAKWATERS IN JAPAN	2028
	<i>T. Uda</i>	

Chapter 151	DESIGN ASPECTS OF BLOCK REVETMENTS	2043
	<i>K.W. Pilarczyk</i>	

Chapter 152	RELIABILITY ANALYSIS OF RUBBLE-MOUND BREAKWATERS ...	2053
	<i>K. Mizumura, M. Yamamoto, T. Endo and N. Shiraishi</i>	

Chapter 153	RELIABILITY BASED DESIGN OF RUBBLE-MOUND BREAKWATER	2063
	<i>M. Yamamoto, K. Mizumura, T. Endo and N. Shiraishi</i>	

Chapter 154	STABILITY AND STRUCTURAL BEHAVIOUR OF STRENGTH IMPROVED DOLOSSE	2075
	<i>J.A. Zwamborn, D.J.P. Scholtz and H. Claassens</i>	

Chapter 155		
SEAWALLS AND SHORELINE PROTECTION	2090	
		<i>J. van de Graaff and E.W. Bijker</i>
Chapter 156		
QUALITY AND DURABILITY OF CONCRETE ARMOUR UNITS	2102	
		<i>L. Van Damme, L. Taerwe, R. Dedeyne and J. De Rouck</i>
Chapter 157		
LARGE VERIFICATION TESTS ON ROCK SLOPE STABILITY	2116	
		<i>J.W. van der Meer and K.W. Pilarczyk</i>
Chapter 158		
ANALYSIS OF 42-TON DOLOS MOTIONS AT CRESCENT CITY	2129	
		<i>T.R. Kendall</i>
Chapter 159		
WAVE FORCE ON BREAKWATERS WITH CONCRETE BLOCK MOUND	2144	
		<i>M. Hattori, K. Inagaki, Y. Noguchi and T. Endo</i>
Chapter 160		
BLOCK REVETMENT DESIGN WITH PHYS. AND NUM. MODELS	2159	
		<i>A. Bezuijen, J. Wouters and C. Laustrup</i>
Chapter 161		
FULL-SCALE WAVE ATTACK OF UNIFORM SLOPING SEA DYKES	2174	
		<i>A. Fuhrboter and U. Sparboom</i>
Chapter 162		
FLOATING BREAKWATER RESPONSE TO WAVE ACTION	2189	
		<i>M. Isaacson and R. Byres</i>
Chapter 163		
SIMULATION OF WAVE FORCES ON A HORIZONTAL CYLINDER	2201	
		<i>S. Tsuzuki, K. Horikawa and A. Watanabe</i>
Chapter 164		
WATER WAVE SCATTERING BY ROWS OF CIRCULAR CYLINDERS	2216	
		<i>R.A. Dalrymple, S.N. Seo and P.A. Martin</i>
Chapter 165		
WAVE TRANSMISSION THROUGH A DOUBLE-ROW PILE BREAKWATER	2229	
		<i>J.B. Herbich and B. Douglas</i>

Chapter 166		
GEOHYDRAULIC INVESTIGATIONS OF RUBBLE MOUND BREAKWATERS		2242
	<i>W. Burger, H. Oumeraci and H.W. Partenscky</i>	
Chapter 167		
IRREGULAR WAVE LOADING ON A CONICAL STRUCTURE		2257
	<i>W.W. Jamieson, E.P.D. Mansard and G.R. Mogridge</i>	
Chapter 168		
EXPERIMENTAL STUDY OF IMMersed PLATES USED AS BREAKWATERS		2272
	<i>A. Drouin and Y. Ouellet</i>	
Chapter 169		
ON 3-DIMENSIONAL STABILITY OF RESHAPING BREAKWATERS		2284
	<i>H.F. Burcharth and P. Frigaard</i>	
Chapter 170		
ASSESSING THE EFFECT OF ARMOURSTONE SHAPE AND WEAR		2299
	<i>J.-P. Latham and A.B. Poole</i>	
Chapter 171		
WAVE UPLIFT FORCES ON PLATFORMS WITH ENERGY ABSORBERS		2313
	<i>J.-J. Lee and C.P. Lai</i>	
Chapter 172		
A NEW TYPE OF BREAKWATER UTILIZING AIR COMPRESSIBILITY		2326
	<i>M. Ikeno, N. Shimoda and K. Iwata</i>	
Chapter 173		
WAVE-INDUCED SHOCK PRESSURES UNDER REAL SEA STATE CONDITIONS		2340
	<i>J. Grüne</i>	
Chapter 174		
MEASUREMENTS OF FORCES ON DOLOS ARMOR UNITS AT PROTOTYPE SCALE		2355
	<i>G.L. Howell</i>	
Chapter 175		
“DOUBLE U BLOCK” AND “IBLOCK”—THE ARMOUR BLOCKS OF TWO NEW TYPES		2370
	<i>S.W. Twu, S.C. Lin and S.G. Chang</i>	

Chapter 176		
ARMOUR UNIT STRUCTURAL RESPONSE—A PARAMETRIC STUDY		2385
	<i>C.D. Anglin, W.F. Baird, E.P.D. Mansard, R.D. Scott and D.J. Turcke</i>	
Chapter 177		
ARTICULATED CONCRETE MAT SLOPE PROTECTION		2400
	<i>C.B. Leidersdorf, P.E. Gadd and W.G. McDougal</i>	
Chapter 178		
DESIGN AND CONSTRUCTION OF BERM TYPE BREAKWATERS		2416
	<i>Committee on Rubble Mound Structures D. Treadwell, Chairman</i>	
Chapter 179		
SIMPLIFIED MODELS FOR MEASURING ARMOUR UNIT FORCES		2418
	<i>R.D. Scott, D.J. Turcke, C.D. Anglin and W.F. Baird</i>	
Chapter 180		
WAVE FORCE ON CURTAIN-WALL-TYPE BREAKWATER DUE TO OBLIQUELY INCIDENT WAVES		2430
	<i>T. Sekimoto, K. Kondo and T. Ohshimo</i>	
Chapter 181		
STRUCTURAL RESPONSE OF DOLOS IN WAVES		2445
	<i>J.W. Tedesco, P.B. McGill, J.A. Melby and W.G. McDougal</i>	
Chapter 182		
LONG TERM EXPERIENCE WITH SEAWALLS ON AN EXPOSED COAST		2455
	<i>O.T. Magoon, J.L. Pope, R.L. Sloan and D.D. Treadwell</i>	
Chapter 183		
DYNAMIC STUDIES ON CAISSON-TYPE BREAKWATERS		2469
	<i>Gao Ming, Dai Guanying and Yang Jihua</i>	
Chapter 184		
WAVE FORCES ON ARMOR BLOCKS		2479
	<i>M.A. Losada, R. Medina and M. Alejo</i>	
Chapter 185		
HYDRODYNAMIC CHARACTERISTICS OF WAVE-POWER-EXTRACTING CAISSON BREAKWATER		2489
	<i>S. Takahashi</i>	

Chapter 186		
DYNAMIC FORCES DUE TO WAVES BREAKING AT VERTICAL COASTAL STRUCTURES		2504
	<i>H.-W. Partenscky</i>	

PART IV
COASTAL, ESTUARINE AND ENVIRONMENTAL PROBLEMS

Chapter 187		
MIXING OF THERMAL DISCHARGES IN COASTAL WATERS		2521
	<i>N.M. Ismail, R.L. Wiegel, P.J. Ryan and S.W. Tu</i>	

Chapter 188		
STOCHASTIC ANALYSIS OF OFFSHORE CURRENTS		2536
	<i>M.K. Ochi and R.I. McMillen</i>	

Chapter 189		
ENTRAINMENT DUE TO MEAN FLOW IN TWO-LAYERED FLUID		2550
	<i>M. Ura and N. Matsunaga</i>	

Chapter 190		
BOUNDARY CONDITIONS IN FINITE ELEMENT MODELING OF STRATIFIED COASTAL CIRCULATION		2561
	<i>G.C. Christodoulou and G.D. Economou</i>	

Chapter 191		
A MODELING SYSTEM FOR COASTAL OIL SPILL RISK ANALYSIS		2574
	<i>S-K. Liu and J.J. Leendertse</i>	

Chapter 192		
BORE FRONT MODELING IN TERMS OF BURGERS EQUATION AND ITS NUMERICAL CALCULATION METHOD		2589
	<i>T. Yamashita, Y. Tsuchiya and D.R. Basco</i>	

Chapter 193		
NEARSHORE CIRCULATIONS ON A WAVY COAST		2603
	<i>M-C. Lin and S-Y. Hwang</i>	

Chapter 194		
STUDY ON THE VARIATIONS OF AN EUTROPHIC ECOSYSTEM FROM THE SPANISH MEDITERRANEAN LITTORAL: DATA TO HAVE IN MIND IN THE N		2615
	<i>E. Soler T., J.G. del Rio and J.J. Diez</i>	

Chapter 195		
FLUSHING BEHAVIOR OF A COASTAL MARINA		2626
	<i>R.A. Schwartz and J. Imberger</i>	

Chapter 196		
STEEP SLOPE SEAWATER SUPPLY PIPELINE	2641	
		<i>L.F. Lewis, J. Van Ryzin and L. Vega</i>
Chapter 197		
COASTAL AND ESTUARINE HYDRODYNAMIC MODELING IN CURVILINEAR GRIDS	2655	
		<i>Y.P. Sheng, T.S. Wu and P.F. Wang</i>
Chapter 198		
HYDRAULIC ASPECTS OF WETLAND DESIGN	2666	
		<i>J.R. Walker, A. Bertolotti, R.E. Flick and C.R. Feldmeth</i>
Chapter 199		
A COMPARISON BETWEEN GERMAN AND NORTH AMERICAN TIDAL INLETS	2681	
		<i>R. Dieckmann, M. Osterthun and H.W. Partenscky</i>
Chapter 200		
FLOW DEPENDENCY OF BOTTOMSTRESSES IN TIDAL MODELS	2692	
		<i>J.J. Leendertse and A. Langerak</i>
Chapter 201		
NUMERICAL MODELLING OF SUSPENDED SEDIMENT TRANSPORT IN THE LOIRE ESTUARY	2707	
		<i>C. Teisson and D. Fritsch</i>
PART V		
CASE STUDIES OF SOLUTIONS TO COASTAL ENGINEERING PROBLEMS		
Chapter 202		
ENGINEERING STUDY FOR A NEW SEAWATER INTAKE SYSTEM	2723	
		<i>B.L. Edge and R.S. Schlueter</i>
Chapter 203		
ACCRETION—EROSION IN THE BEACHES OF THE CANARY ISLANDS (SPAIN)	2738	
		<i>J.M. Martinez</i>
Chapter 204		
SUBMARINE SIPHONS FOR ATHENS SEWERAGE SYSTEM	2753	
		<i>Y. Eisenberg, Th. C. Gofas, R.A. Fasano and F.S. Hinds</i>
Chapter 205		
QUANTIFICATION OF SAND TRANSPORT AND SAND BYPASSING AT SOUTH LAKE WORTH INLET, PALM BEACH COUNTY, FLORIDA	2772	
		<i>J.S. Yeend and D.J. Hatheway</i>

Chapter 206		
THE BEACH OF VINAROS. ITS ORIGIN, EVOLUTION AND FUTURE		2784
	<i>J.S. Peris and J.J.D. Gonzalez</i>	
Chapter 207		
STABILIZATION OF COAST BY CONSTRUCTION OF HEADLANDS ON THE KASHIMANADA COAST, JAPAN		2791
	<i>T. Uda, M. Sumiya and H. Sakuramoto</i>	
Chapter 208		
RESULTS FROM THE ATLANTIC CITY, NJ BEACH NOURISHMENT MONITORING PROGRAM		2806
	<i>R.M. Sorensen, S.L. Douglass and J.R. Weggel</i>	
Chapter 209		
BERM BREAKWATER FAILURE AT ST. PAUL HARBOR, ALASKA		2818
	<i>J. Weckmann and G.M. Watts</i>	
Chapter 210		
COASTAL GENESIS		2825
	<i>J.H. de Vroeg, E.S.P. Smit and W.T. Bakker</i>	
Chapter 211		
ARTIFICIAL BEACH UNITS ON LAKE MICHIGAN		2840
	<i>K.J. MacIntosh and C.D. Anglin</i>	
Chapter 212		
THE BEACH REHABILITATION PROJECT AT OSTEND-BELGIUM ..		2855
	<i>R. Simoen, H. Verslype, D. Vandenbossche</i>	
Chapter 213		
AN ENGINEERING STUDY OF OCEAN CITY'S BEACHES, NEW JERSEY, USA		2867
	<i>J.R. Weggel, S.L. Douglass and R.M. Sorensen</i>	
Chapter 214		
SHORE PROTECTION OF KAOHSIUNG HARBOR OUTER BREAKWATER		2882
	<i>S-D. Kuo</i>	
Chapter 215		
RIA DE FOZ: SOLUTION FOR A HARBOUR AND COASTAL PROBLEM		2896
	<i>J.J. Diez Gonzalez, V.A. Escobar Paredes and J. Aquila Herrando</i>	

PART VI
SHIP MOTIONS

Chapter 216	
WAVE-INDUCED SHIP MOTIONS IN HARBOUR APPROACH CHANNELS	2911
<i>A.C. van Wyk and J.A. Zwamborn</i>	
Chapter 217	
DYNAMIC BEHAVIOR OF A MOORING BUOY INSTALLED IN OPEN SHORE	2923
<i>T. Shigemura and K. Hayashi</i>	
Chapter 218	
THE FUNDAMENTAL STUDY TO REDUCE THE SETTLED AREA OF THE FISH AGGREGATION DEVICES ON THE SEA FLOOR THROWN FROM A SHIP	2937
<i>Y. Matsumi and A. Seyama</i>	
Chapter 219	
THE TIME DOMAIN ANALYSIS ON MOORED SHIP MOTIONS	2952
<i>M. Kubo, N. Shimoda and S. Okamoto</i>	
Chapter 220	
FENDER SELECTION CRITERIA	2966
<i>F. Vasco Costa</i>	
Chapter 221	
UTILIZATION OF MOORED VESSELS IN HYDRAULIC MODELS OF HARBORS	2979
<i>R. Guarga, E. Goldsztejn and F. Puntigliano</i>	
Chapter 222	
A NUMERICAL WAVE PREDICTION MODEL FOR PERSONAL COMPUTERS	2991
<i>David J. Schwab</i>	
SUBJECT INDEX	2999
AUTHOR INDEX	3005

COASTAL ENGINEERING TRENDS AND RESEARCH NEEDS

by

Robert L. Wiegel, Hon. Mem. ASCE

Abstract: The most important coastal engineering trend is the increasing demand for its application, worldwide, owing to the growing use of, and expansion of, the coastal zone. This requires research and development in: coastal zone management, including coastal erosion management; recreational use of the coastal zone; extension of coastal engineering to works in deeper water, data collection; change in relative mean sea level; construction equipment and methods; analysis, computation and hydraulic models; field experiments; waste disposal in nearshore waters; beach nourishment and detached breakwaters. The research must be expanded now. Long term funding is required, rather than the more common "start and stop" funding. Coastal engineering is one of the most difficult branches of civil engineering, as the environmental loading on structures by waves, currents and winds is always dynamic, as is the geomorphology of the beaches and nearshore regions. Furthermore, there are substantial scale effects so that full-scale field experiments are needed. It is urgent to increase the involvement of coastal engineers and scientists in meetings which include the general public, elected officials, and appointed city, county, state and federal officials and public works personnel, and to encourage interactions if better coastal works are to be designed, constructed, and operated for the public benefit.

Introduction

What is coastal engineering? In the preface to the proceedings of the first conference on coastal engineering, organized by J.W. Johnson and Morrough P. O'Brien in 1950, O'Brien states:

"A word about the term 'Coastal Engineering' is perhaps in order here. It is not a new or separate branch of engineering and there is no implication intended that a new breed of engineer, and a new society is in the making, Coastal Engineering is primarily a branch of Civil Engineering which leans heavily on the sciences of oceanography, meteorology, fluid mechanics, electronics, structural mechanics, and others. However, it is also true that the design of coastal works does involve many criteria which are foreign to other phases of civil

1 Professor Emeritus of Civil Engineering, University of California, Berkeley, California 94720. Chairman, ASCE Coastal Engineering Research Council.

engineering and the novices in this field should proceed with caution. Along the coastlines of the world, numerous engineering works in various stages of disintegration testify to the futility and wastefulness of disregarding the tremendous destructive forces of the sea. Far worse than the destruction of insubstantial coastal works has been the damage to adjacent shorelines caused by structures planned in ignorance of, and occasionally in disregard of, the shoreline processes operative in the area."

There is increasing worldwide demand for coastal engineering, owing to growing use of the coastal zone. One increasing demand is for recreation; this together with other uses, requires coastal zone management. Some uses and some areas needing research and development are (Wiegel, 1987):

- Increasing Demand for Coastal Engineering
- Recreational Use of the Coastal Zone
- Coastal Zone Management
- Extension to Works in Deeper Water
- Data Collection
- Field Experiments
- Analysis, Computation, and Hydraulic Models
- Waste Disposal in Nearshore Waters
- Beach Nourishment, Seawalls and Detached Breakwaters
- Change in Relative Mean Sea Level
- Construction Equipment and Methods

An Ad Hoc Committee for the Civil and Environmental Engineering Division of NSF, Natural Hazards and Research Needs in Coastal and Ocean Engineering, studied some of these areas and made recommendations for research in their report (1984). A committee of the National Research Council is presently assessing options for coastal erosion zone management for incorporation into the National Flood Insurance Program (NFIP) of the Federal Emergency Management Administration (FEMA). These two studies emphasize the interest in coastal engineering research needs. In addition, in the article "Restoring the Shore," by Virginia Fairweather (1987), she states:

"A recent Congressional Office of Technology Assessment report underscores the need for research on coastal solutions, concluding that 'so little is known about these natural processes (shoreline erosion) that public works improvements often are undertaken with insufficient understanding to ensure structural longevity.'"

The present paper is an update and modification of a position paper prepared by the author for use in the ASCE Conference on Civil Engineering Research Needs in the 21st. Century, held in Williamsburg, Virginia, 11-14 November 1987.

Increasing Demand for Coastal Engineering

A major reason for the increase in demand for coastal engineering is the expanding use of the coastal zone. People like to live on the coast, tourists like to visit the coast, ocean shipping is increasing, recreational uses (such as boating, bathing in the surf, walking along the shore, surfing, or just sitting on a beach) are growing, coastal fisheries are important, and there is an increasing use of nearshore waters for the disposal of large quantities of man's non-toxic wastes (including power plant waste heat and airport noise).

Another reason for the increase in demand is the developing awareness of the complexity of some problems, and the desire to do a better job. The Marine Board, National Research Council (1981), study of problems and opportunities in the design of entrances to ports and harbors is used as an example of this; it could be generalized to other activities. They state the most important problems requiring resolution to be:

- "• Improved and validated models for the prediction of horizontal and vertical ship movements in the particular conditions of harbor entrances;
- Use of systems analysis in the design of harbor entrance;
- Reliable and economical measurement, reduction, presentation, and storage of environmental data;
- Cost-effective models of the physical environment for prediction of natural conditions and forces, and changes caused by human activity;
- Improved procedures for prediction of shoaling rates and patterns, including development and verification of appropriate field methodologies;
- Improved entrance-channel design and operating criteria;
- Development of accepted standards and uniform methods for measuring and assessing navigability of harbor entrances;
- Quantitative definition of the needs of mariners;
- Review and reform of decision making processes for port and harbor projects, and
- Evaluation of the importance of natural resources for balanced decisions about harbor siting and related matters, and increased attention to the restoration of natural habitats."

Nearly 500 million yd³ of material are dredged each year in the U.S.A. to create and maintain navigable waterways and harbors (National Research Council, Marine Board, 1987). Alternatives to dredging will be a major opportunity in the 21st century. The 1987 Marine Board report on sedimentation control concludes that each harbor, channel and turning basin is unique, and must be studied and treated separately, investigating 3 options: 1) stopping the sediment before it reaches the site; 2) keeping the material in suspension as it passes through the site; 3) diverting the sediment flow away from the site.

The relationship between coastal engineering and port engineering is close, and one should consider how trends in port engineering affect coastal engineering, and vice versa. As pointed out in a recent PIANC Working Group report (1986), the traditional freighter has almost disappeared from the seas, with a substantial amount of the replacement being by very large container and roll-on/roll-off ships. These often require deeper navigation channels, and major changes in shoreside arrangements. Redevelopment of urban waterfronts results, often with emphasis on needs for recreation and tourists; interest in this is such that there is now an annual conference in the U.S.A. on "Urban Waterfronts." These factors result in more demand for coastal engineering and coastal zone management.

Recreational Use of the Coastal Zone

In southern California, the attendance in 1984 at state, county and city beaches was approximately 126.5 million (POD, 1985). About 43 million tourists visited Spain in 1985, most of whom spent all, or part of their time on the coast. It has been estimated that in Japan the use of beaches would increase from 110 million in 1975 to 220 million by 1990 (Nakayama et al., 1982). Rockaway Beach, on the Atlantic Coast of New York City, has an estimated 24 million "annual uses" (Nersesian, 1977). About 30 million tourists visit Florida each year, with most of them making use of the state's beaches (Wiegel, 1988). In some areas, tourists visiting beaches are responsible for a major segment of local jobs and income, and some countries are trying to increase tourist use of their coasts. For the general benefit of the world's economy, and the well-being of its people, it is necessary for highly industrialized countries to shift some emphasis from internal industrial production to the recreational use of coasts in other countries, and in doing so, transfer to them funds that are required for their development.

One trend that will continue into the 21st century, derivative of recreational use, is increasing use of beach nourishment; this is considered in a separate section. Another trend is the construction of outfall sewers into deeper water, farther seaward of beaches. An example is the outfall sewer for Honolulu, Hawaii, which together with an advanced primary treatment plant, "has completely cleaned up nearshore pollution, and no longer threaten beach areas" (Miyamira et al., 1979).

Growth of recreational boating is substantial, and the shortage of small boat harbors and/or marinas is often the limiting factor in the expansion of boating. Often these require the construction of breakwaters or jetties, which affect the contiguous coast.

Coastal Zone Management, Including Coastal Erosion Control Management

One factor mentioned by O'Brien, damage to adjacent shorelines caused on occasions by structures constructed for other purposes, is one of the reasons for the trend in the increasing use of coastal zone management; its growth is phenomenal (Wiegel, 1987). In the 1970's, the U.S. Congress passed the Coastal Zone Management Act, a national policy "to preserve, protect, develop, and where possible, to restore or enhance, the resources of the Nation's coastal zone for this and succeeding generations." As a result, many coastal states developed coastal management plans.

An important part of coastal zone management is public education, and this is done successfully in different ways, on different scales. One example is the conference "Beach Erosion, A Regional Alternative," held in Santa Barbara, California on 24-26 October 1985. It was sponsored and organized by the California Chapter of the American Shore and Beach Preservation Association and the Santa Barbara-Ventura County Erosion Control Group. Presentations were made by engineers, scientists, lawyers, planners, elected and appointed city, county and state officials and legislators. Another example is the symposium "Beach Preservation Technology 88: Problems and Advancements in Beach Nourishment," in Gainesville, Florida on 24-25 March 1988, arranged by the Florida Shore & Beach Preservation Association, in which there was a similar mix of backgrounds. Many of the general public attended, and participated in both of these meetings. This type of activity must be expanded.

Other countries have coastal zone management plans and agencies. The Queensland, Australia, Beach Protection Authority was established in 1968, with the legislation changed substantially in 1984 (QBPA, 1985). The Authority "...deals with management of the whole of the Queensland coast and its main function is to provide advice to Local Authorities, Harbour Boards and River Improvement Trusts which are responsible for implementing coastal management programmes, whether these programmes relate to beaches, rock foreshores, sand flats, estuaries or river banks in tidal areas."

Japan, in 1956, enacted their Coastal Law, and they have implemented three 5-year Seashore Protection Projects (1st. 5-year plan, 1970-74; 2nd 5-year plan, 1976-80; 3rd. 5-year plan, 1981-85) (Nakayama et al., 1982). Japan has 34,000 km of coast, with about 16,000 km requiring protection of which almost 8,700 km is already protected by seawalls, etc. Denmark has a shore protection plan. Other countries are developing national coastal erosion management plans. Egypt is developing a plan for the Nile Delta, which is eroding considerably along much of its boundary with the Mediterranean Sea (Diephuis et al., 1983). The plan has been prepared under the Shore Protection Authority of Egypt, with the cooperation of the UNDP (Kadib et al., 1986). Malaysia completed their national coastal erosion study in 1986; it will be a major input to their coastal zone management plan (Nathan and McAlister, 1987). Sri Lanka is working on a plan (Amarasinghe et al., 1987).

Extension of Coastal Engineering to Works in Deeper Water

Economies of deep draft bulk carriers has led to more dredging in many ports, to building artificial harbors in relatively deep water, and to offshore terminals.

A serious problem occurred in breakwaters in deep water, subjected to large waves, which used large concrete armor units. As pointed out by O'Brien, the internal stresses in the units increase with size (weight/cross-sectional area $W/L^2 = D$), so there is little reserve strength in large units, and extensive failures occurred (Godden, 1981; Edge et al., 1982). Engineers are studying how to improve our ability to design and construct better breakwaters in deep water at exposed locations, both rubblemound and caisson types; this must be accelerated.

The disposal of wastes using outfalls constructed farther offshore into deeper water is growing. An outfall extending into water 240 feet deep was built offshore Honolulu, Hawaii (Miyamira et al., 1979). The recently completed San Francisco outfall (Murphy and Eisenberg, 1985), extends 23,400 feet offshore, into water 80 feet deep, with a capacity of 450 million gallons per day. It crosses one of the world's major active earthquake fault zones, the San Andreas. A similar ocean outfall is being planned for Taipei, R.O.C. The submarine siphons for the ocean disposal system of the Athens, Greece, sewerage system have recently been completed, and this is also in a semically active region (Eisenberg et al., 1988). Research is needed on the design of ballast for such pipelines.

Data Collection

Long-term management plans should be based on, or incorporate provisions for detailed studies of extended regions, which include data collection and analysis. This is being done in Queensland, Australia, and in Japan. Egypt is studying the Nile Delta, which is eroding owing to the shortage of sediment supplied to the coast by the Nile River due to the Aswan High Dam and the low dams located a few miles upstream from each of the two mouths of the Nile. As the transport of sand is in an easterly direction along the southeastern coast of the Mediterranean Sea, from Alexandria, past Sinai, to Haifa, Israel, the effects are extensive. Field studies have been made, and are being made of the waves, currents, sediment characteristics, beach profiles, sediment transport, etc., along the Nile Delta as an input to their plan. Terms of reference for the development of a plan for the Nile Delta was prepared by Diephaus, Mobarek, Saville and Wiegel (1983). The recommended work has been completed, and a report made to the Egyptian Government (Kadib et al., 1987). In California, the US Army Corps of Engineers (Los Angeles District, 1983) is making a long-term study "...to provide coastal data and information to planners and decision-makers so that better and more informed decisions can be made regarding the restoration and maintenance of the 1,100-mile California coastline."

Although the number of wave measuring programs is increasing, almost no measurements are being made routinely of surf and nearshore currents, and almost no measurements are being made of directional spectra; these data are needed, and must be long term to provide an adequate time series for statistical analysis. Hindcast wave data are used to supplement measurements, or as a substitute for measurements if not available. Weather data, available from about 1900, can be used as input. This type of work should be expanded.

There is much interest in making measurements in the ocean. In April 1986 the International Conference on Measuring Techniques of Hydraulic Phenomena in Offshore, Coastal & Inland Waters was held in England. It was concluded that better methods of making routine measurements for coastal engineering use must be developed. Presently the Marine Board, National Research Council, has a Committee on Coastal Engineering Measurement Systems to assess operational needs and research requirements for making coastal measurements for engineering purposes.

Field Experiments

The trend to conducting field experiments is slow, owing to their high costs. Examples of three experiments are: 1) Oceanside, CA, sand bypassing system (Diemer, 1987); 2) Crescent City, CA, instrumented 42-ton dolos concrete armor units (Kendall et al., 1986; Wood et al., 1986); 3) floating breakwater, Friday Harbor, WA (England, 1986). The performance of comprehensive field experiments must be expanded, such as the wave, current and beach 1980 ARSLOE and 1986 SUPERDUCK experiments at Duck, NC, and the thermal power plant coastal cooling water tests reported by Wiegel and Doyle (1987).

Many citations are given to the 'Bruun Rule.' The author has always had misgivings about this rule, as there are examples of sand moving from offshore onto beaches (for a recent study, see Williams and Meisburger, 1987). Dean (1987) has reexamined this 'rule,' and concludes that there are conditions under which sand will move onto beaches. Field studies of this problem must be made.

Analysis, Computation and Hydraulic Models

A major trend in coastal engineering is the continuing development of our ability to analyse problems in the sciences mentioned in O'Brien's statement on coastal engineering, including growth in the use of computers to obtain numerical solutions. Great advances have been made in our capabilities to analyse problems using analytical and numerical techniques, but there is still need for hydraulic models to check theory, and to study coastal projects in which the details are very complicated (see, for example, Wiegel and Doyle, 1987).

Waste Disposal in Nearshore Water

Nearshore ocean water is a convenient sink for the disposal of non-toxic wastes. In many coastal locations untreated wastes flow into the ocean, at a very low cost. This is no longer permitted in many locations, and the trend, sometimes an over-reaction, is to expensive outfalls extending perhaps more than four miles offshore into water as much as 200 feet deep. Treatment plants may be a part of the system. Research is being done on mixing processes of buoyant fluid discharge in the ocean, and on environmental conditions. A few references have already been given to major ocean outfall installations. Studies of the effect of effluent discharged into the nearshore waters are of great importance in the planning of ocean outfalls. The most extensive and long-term study of the effects of municipal waste discharge on marine life and human health is being done off southern California (Bascom, 1984); a long-term study of the disposal of waste heat in a local region, is described by Wiegel and Doyle (1987). These types of studies are needed for other regions.

Beach Nourishment, Seawalls and Detached Breakwaters

With increasing recreational use of beaches, there is a trend to the placement of sand on beaches in erosional areas, and also in some areas where no beaches exist. Sand bypassing at harbor entrances is an example. Since construction of the

jetties at the entrance of small boat harbor at Santa Cruz, California, sand has accumulated upcoast from the west jetty. This protects bluffs that were eroding badly before the construction, and buildings on the bluffs. The sand trapped upcoast and in the harbor entrance was not moving downcoast. The entrance became unusable, and had to be dredged, with the sand being deposited downcoast, to nourish those beaches. Similar conditions exist at Santa Barbara and at Oxnard, California, at Durban, South Africa, at Carrara, Italy, and at other sites. Sand bypassing and beach nourishment is a well-established coastal erosion management tool, and its use should increase in the next century. A little of the history of the subject, together with some conceptual and design considerations, and recommendations for needed research was presented by the author (Wiegel, 1988) at a recent symposium on this subject. It is very clear from existing studies that we should not waste sand in harbor dredging projects by dumping it in deep water. The importance of the detrimental effect of dumping sand in water too deep for it to be moved onto a beach by natural processes can be illustrated by a calculation by Dean (1988). He estimates that on the east coast of Florida more than 40 million cubic meters of sand have been dumped in deep water. Assuming an average simplified beach profile extending to offshore "closure", he calculated that this quantity is the equivalent of an additional 8 meters of beach width along the entire 640 km length of the east coast of Florida.

A symposium on beach nourishment was held in Gainesville, Florida on 24-25 March 1988, sponsored by the Florida Shore & Beach Preservation Association, the proceedings of which will be published. This has been referred as earlier in the present paper.

In high population density coastal areas it can be economical to dredge sand from offshore, from harbor entrances, from inshore regions, and place it on the shore to build a wide beach. Examples are Miami Beach, Florida (10.5 miles of beach, with 14 million yd³ of sand placed, by 1980, for \$64 million); Rockaway Beach, New York (completed in late 1977, 6.2 miles of beach, about 6-2/3 million yd³ of sand placed, for about \$14.3 million); Waikiki, Hawaii; 8.5 million cubic meters dredged from offshore and placed along 8 km of beach near Zeebrugge, Belgium; Durban, South Africa; Singapore; 141,000 cubic meters at Walland, England with 31,000 cubic meters annual replenishment; Gold Coast, Queensland, Australia (2.4 million cubic meters). Beach nourishment in Japan is extensive. About 108 million yd³ in about 60 different projects was placed in southern California between 1919 and 1978 (Herron, 1980). A new look is needed of the economics of using large bulk carriers to transport sand from relatively distant sources to densely populated areas where the value of beaches is great.

In a recent study of four large volume beach nourishment projects, Egense and Sonu (1987) conclude:

"At the present stage of technology, beach nourishment is more art than science. Although many uncertainties continue to characterize the design and construction procedures, opportunities for establishing rational guidelines appear available from careful re-analysis of past and on-going projects. The importance of implementing comprehensive, long-term monitoring programs and performing more in-depth comparative studies cannot be over emphasized".

"As a general guideline within the limited scope of this study, it can be stated that compartmentalization of a project beach has the single most important effect on the retention of the placed fill. It may be about time to question the wisdom of using beach nourishment without additional measures to enhance fill retention on beaches that have little or no compartmentalization".

Detailed monitoring of beach nourishment projects is needed. Chapman (1980) reports on the monitoring of a 2.4 million m³ project at Gold Coast, Australia. Over 400 profiles were measured from the backshore to a point of zero change in the inshore zone, and 38 tons of tracer was injected into the dredge line at a controlled rate. They found that the sand moved in slugs and there was poor correlation between the subaerial beach width and the sand prism volume, including the inshore region. This is an example of what is needed by coastal engineers to improve their capability to design this type of project.

Much misinformation is spoken and written about how seawalls and revetments function. The statement is often made that they "cause beach erosion." This is unproven at best, and wrong at worst. Very few people build seawalls unless their property is already subject to erosion. The seawall is blamed for the erosion which occurs in an already eroding location (O'Brien and Johnson, 1980; Wiegel, 1987). Prior to making a decision on whether or not to use a seawall, the papers of Krauss (1987), Dean (1986; 1988), and Grigg and Tait (1987) should be studied. More field studies should be made of the effects, if any, of seawalls not normally exposed to wave action.

In some places the use of a seawall or revetment, constructed between the nourishment project and the buildings and infrastructure, should be considered as backup protection during a particularly severe winter in which much of the sand may be moved offshore or alongshore. The structure can be covered by sand, with dune grass and other vegetation planted in the sand (Wiegel, 1988).

Detached breakwaters for coastal protection are used extensively in some countries and their use is growing. More than 2,300 detached breakwaters are in Japan; the number grew exponentially between 1962 and 1982 (from 205 to 2,305) (Toyoshima, 1982). The writer has looked at many detached breakwaters in Italy, Monaco, Spain, Singapore, Israel, and the USA. Many have functioned well, but they sometimes cause erosion downcoast if there is a net littoral drift. In some circumstances they may fill too much, causing other problems. They are an excellent coastal erosion control tool, but their design requires a detailed site study of waves, currents, sediment supply, and sediment transport.

Change in Relative Mean Sea Level

A change in relative mean sea level is expected in the next century, owing to rising eustatic mean sea level (resulting partly from the "greenhouse effect"), land subsidence from both geophysical and human activity, and other processes. These changes would require major coastal engineering work. Much information useful to coastal engineers is in the report of the U.S. National Research Council Marine Board's Committee on Engineering Implications of Changes in Relative Mean Sea Level (1987). Two of their recommendations are:

"The committee concluded that the most appropriate present engineering strategy is not to adopt one particular sea level rise scenario, but instead to be aware of the probability of increasing sea level and to keep all response options open. In many engineering projects, it may be desirable to carry out sensitivity calculations, using specific sea level rise scenarios. If a particular structure is ill-suited for retrofitting, it will undoubtedly be appropriate to allow for an acceleration of sea level rise in the initial design. Sea level change during a structure's design service life should be considered along with other factors, but a change does not present such essentially new problems as to require new techniques of analysis."

"The committee's recommendations highlight the need for continuing and increased scientific study of the rates and causes of sea level change and the development of a sound basis for forecasting these changes. Efforts to understand coastal processes and the effects of sea level rise on engineering projects should also be expanded considerably."

Construction Equipment and Methods

There has been a great advance in our ability to construct and install large complex structures in deeper water farther offshore than previously. The value of offshore oil and gas in the 1970's and early 1980's was so huge that considerable money was made available to engineers for developing this capability. Equipment is available which can work in the open sea, together with well-trained experienced people to operate them (Gerwick, 1986). Much of this equipment can be used for the construction of coastal engineering works, such as pipelines for disposal in the ocean of non-toxic wastes (municipal wastes, power plant cooling water), breakwaters for deep water ports, offshore special purpose terminals, manmade islands for airports and industrial facilities, beach nourishment projects, and marinas.

References

Ad Hoc Committee for the Civil and Environmental Engineering Division of the National Science Foundation, *Natural Hazards and Research Needs in Coastal and Ocean Engineering*, report to the US National Science Foundation and the Office of Naval Research, John H. Nath and Robert G. Dean, editors, November 1984, 62 pp.

Amarasinghe, S.R. and H.J.M. Wickremeratne, "The Coastal Engineer as an Initiator of Coastal Zone Management Programmes--Sri Lanka Case Study," *1987 Proceedings of Coastal and Port Engineering in Developing Countries*, Vol. I, edited by Nanjing Hydraulic Research Institute, China Ocean Press, China, pp. 61-68.

Bascom, Willard (editor), *Southern California Coastal Water Research Project Biennial Report, 1983-1984*, Southern California Coastal Water Research Project, 646 West Pacific Coast Highway, Long Beach, California 90806, 1984, 332 pp.

Chapman, David M., "Beach Nourishment as a Management Tool," *Proc. 17th Coastal Engineering Conference, March 23-28, 1980, Sydney, Australia*, ASCE, pp. 1636-1649

Dean, R.G., "Coastal Armoring: Effects, Principles and Mitigation," *Twentieth Coastal Engineering Conference: Proceedings of the International Conference, November 9-14, 1986, Taipei, Taiwan*, ASCE, Vol. III, Chapter 135, pp. 1843-1857.

Dean, R.G., "Additional Sediment Input to the Nearshore Region," *Shore & Beach*, Vol. 55, Nos. 3-4, July - October 1987, pp. 76-81.

Dean, R.G., "Sediment Interaction at Modified Coastal Inlets: Processes and Policies," *Symposium on Hydrodynamics and Sediment Dynamics of Tidal Inlets, Woods Hole, Massachusetts, December 1986* (in press), 1988, 38 pp.

Diemer, Douglas J., "Oceanside Experimental Sand Bypass," *Proceedings: West Coastal Regional Coastal Design Conference, 7-8 November 1985, Oakland, California*, US Army Corps of Engineers, Coastal Eng. Res. Center, WES, Vicksburg, MS, 1986, pp. 193-217.

Diephuis, J.R.H.R., I. Mobarek, T. Saville, Jr. and R.L. Wiegel, *Project EGY/83/003--Master Plan for Coastal Protection: First Meeting of the International Advisory Panel Inception Report*, Shore Protection Authority, Ministry of Irrigation, Egypt, 1983, 58 pp.

Edge, Billy L., W.F. Baird, J.M. Caldwell, V. Fairweather, O.T. Magoon, and D.D. Treadwell, *Failure of the Breakwater at Port Sines, Portugal*, ASCE, 1982, 278 pp.

Egense, Anders K. and Choule J. Sonu, "Assessment of Beach Nourishment Methodologies," *Coastal Zone '87: Proceedings of the Fifth Symposium on Coastal and Ocean Management, Seattle, Washington, May 26-29, 1987*, ASCE, Vol. 4, pp. 4421-4433.

Eisenberg, Y., Th C. Gofas, R.A. Fasano and F.S. Hindes, "Submarine Siphons for Athens Sewerage System," *Abstract Book: 21st. International Conference on Coastal Engineering, Torremolinos, Spain, 20-25 June 1988*, ASCE, Paper No. 224, pp. 438-439.

England, George G., "Testing and Analysis of a Floating Breakwater," *Proceedings: West Coast Regional Coastal Design Conference, 7-8 November, Oakland, California*, US Army Corps of Engineers, Coastal Eng. Res. Center, WES, Vicksburg, MS, 1986, pp. 233-249.

Fairweather, Virginia, "Restoring the Shore," *Civil Engineering*, Vol. 57, No. 9, September 1987, pp. 74-77.

Gerwick, Ben C., Jr., *Construction of Offshore Structures*, John Wiley & Sons, 1986, 552 pp.

Godden, W.G., "Breakwater Modeling Problems," Extension Course *Recent Developments in Ocean Engineering*, University of California, Berkeley, CA, 24-27 Feb. 1981, 16 pp.

Griggs, Gary B. and James F. Tait, "The Effects of Coastal Protection Structures on Beaches," Department of Earth Sciences and Institute of Marine Sciences, University of California, Santa Cruz, California, manuscript of paper to be presented later, sent to R.L. Wiegel by Professor Griggs on 10 December 1987, 37 pp.

Herron, W.J., "Artificial Beaches in Southern California," *Shore & Beach*, Vol. 48, No. 1, Jan. 1980, pp. 3-12.

Kadib, al, A. Shak, A. Mazen, and M.K. Nadar, "Shore Protection Plan for the Nile Delta Coastline," *Twentieth Coastal Engineering Conference: Proceedings of the International Conference, November 9-14, 1986, Taipei, Taiwan*, ASCE, Vol. III, Chapter 186, pp. 2530-2544.

Kendall, T.R., G.L. Howell, and T. Denes, "Prototype Measurement of the Structural Response of Dolos Armor Units," *Proceedings: West Coast Regional Coastal Design Conference, 7-9 November 1985, Oakland, California*, US Army Corps of Engineers, Coastal Eng. Res. Center, WES, Vicksburg, MS, 1986, pp. 288-299.

Kraus, Nicholas C., "The Effects of Seawalls on the Beach: A Literature Review," *Proceedings: Coastal Sediments '87, New Orleans, LA, May 12-14, 1987*, ASCE, 14 pp.

Miyamira, W.S. and ST. Yamanaka, Jr., "Honolulu Sewage Plant Pioneers Advanced Primary Treatment, Has Deepest Ocean Outfall," *Civil Engineering*, Vol. 49, No. 6, 1979, pp. 76-77.

Murphy, G.J. and Y. Eisenberg, "San Francisco Outfall: The Champs?," *Civil Engineering*, Vol. 55, No. 12, December 1985, pp. 58-61.

Nakayama, Yasuyuki, Shinji Kataoka, and Kouhei Obara, "Construction of Artificial Beaches in Japan," *Civil Engineering in Japan*, Vol. 21, 1982, pp. 100-113.

Nathan, Robert A. and Ian J. McAlister, "Study Methodology for the Malaysian National Coastal Erosion Study," *1987 Proceedings of Coastal & Port Engineering in Developing Countries*, Vol. I, edited by Nanjing Hydraulic Research Institute, China Ocean Press, China, pp. 255-268.

National Research Council, *Problems and Opportunities in the Design of Entrances to Ports and Harbors: Proceedings of a Symposium, August 13-15, 1980, Fort Belvoir, Virginia*, Marine Board, Panel on Harbor/Port Entrance Design, National Academy Press, Washington, D.C., 1981, 177 pp.

National Research Council, *Sedimentation Control to Reduce Maintenance Dredging of Navigational Facilities in Estuaries: Report and Symposium Proceedings*, Marine Board, Committee on Sedimentation Control to Reduce Maintenance Dredging in Estuaries, National Academy Press, Washington, D.C., 1987, 342 pp.

National Research Council, *Understanding and Responding to Sea Level Rise*, Marine Board, Committee on Engineering Implications of Changes in Relative Mean Sea Level, National Academy Press, Washington, D.C., 1987, 148 pp.

Nersesian, G.K., "Beach Fill Design and Placement at Rockaway Beach, N.Y., Using Offshore Ocean Borrow Sources," *Coastal Sediments '77, Charleston, SC, Nov. 1977*, ASCE, pp. 228-247.

O'Brien, Morrough, P. and J.W. Johnson, "Structures and Sandy Beaches," *Coastal Zone '80, Hollywood Beach, Florida, November 17-20, 1980*, ASCE, Vol. IV, pp. 2718-2740.

PIANC Working Group, *Development of Modern Marine Terminals*, August 1986, 41 pp.

POD, Inc., *Socioeconomic Data Summary: Southern California Shoreline*, prepared for the US Army, Corps of Engineers, Los Angeles District, Coast of California Storm and Tidal Waves Study, Ref. No. CCSTWS 85-6, December 1985, 195 pp.

Queensland Beach Protection Authority, *Beach Protection Authority Queensland Annual Report 1985*, Queensland, Australia, 1985, 48 pp.

Toyoshima, Osamu, "Variation of Foreshore due to Detached Breakwaters," *Proc. 18th Coastal Engineering Conference, November 14-19, 1982, Cape Town, Rep. South Africa*, ASCE, pp. 1873-1892.

US Army, Corps of Engineers, Los Angeles District, *Coast of California Storm and Tidal Waves Study: Plan of Study*, September 1983, 25 pp.

Wiegel, R.L., "Trends in Coastal Engineering Management," *Shore & Beach*, Vol. 55, No. 1, January 1987, pp. 3-11.

Wiegel, R.L. and M.J. Doyle, Jr., "Cooling by Ocean Water: Model/Field Comparison," *Shore & Beach*, Vol. 55, Nos. 2 and 3, July and October 1987, pp. 38-53.

Wiegel, R.L., "Keynote Address: Some Notes on Beach Nourishment," presented at the symposium *Beach Preservation Technology 88: Problems and Advancements in Beach Nourishment*, Gainesville, Florida, 24-25 March 1988, Florida Shore & Beach Preservation Association, 20 pp. (in press).

Wiegel, R.L., Trends in Coastal Engineering," *1987 Proceedings of Coastal & Port Engineering in Developing Countries*, Vol. 1, Edited by Nanjing Hydraulic Research Institute, China Ocean Press, pp. 46-58.

Williams, S.J. and E.P. Meisburger, "Sand Sources for the Transgressive Barrier Coast of Long Island, New York: Evidence for Landward Transport of Shelf Sediments," *Coastal Sediments '87: New Orleans, LA, May 12-14, 1987*, ASCE, pp. 1517-1532.

Wood, W.L., G.L. Howell, and R.A. Cole, "Crescent City Dolos Project," *Proceedings of the 43rd Meeting of the Coastal Engineering Research Board*, US Army Corps of Engineers, Coastal Eng. Res. Center, WES, Vicksburg, MS, 1985, pp. 114-136.



San Sebastian—Guipuzcoa

PART I

WAVES

Playa y costa en Punta Fagelda—Pontevedera



CHAPTER 1

NONLINEAR DIFFRACTION BY A VERTICAL CYLINDER

David L. Kriebel *

ABSTRACT

A theoretical solution is developed for the interaction of second-order Stokes waves with a large vertical circular cylinder in water of finite depth. The solution is obtained in terms of the velocity potential such that any kinematic or dynamic quantity of interest may be derived, consistent to the second perturbation order. In this study, the second-order wave field around the cylinder is determined, showing the modification of the incident Stokes waves by wave-wave and wave-structure interactions, both in the reflection-dominated up-wave region and in the diffraction-dominated down-wave region. The theory is then compared to experimental data for wave runup and rundown amplitudes on the cylinder as well as for wave crest and trough envelopes in the up-wave and down-wave regions.

INTRODUCTION

Over the past 15 years, numerous theories have been proposed for the problem of the interaction of second-order Stokes waves with a fixed vertical circular cylinder. The first-order problem - the linear diffraction theory - was solved by MacCamy and Fuchs (1954); however, the second-order problem has proven more difficult to solve and, at present, none of the proposed solution is universally accepted. A review of all previous theories for the nonlinear diffraction problem is beyond the scope of this paper. Some of the most recent second-order diffraction theories for a vertical cylinder include those of Chen and Hudspeth (1982), Hunt and Williams (1982), Rahman and Heaps (1983), and Sabuncu and Gören (1985), while Garrison (1978) presents a nonlinear diffraction theory for arbitrary fixed or floating bodies.

The goals of this paper are to review a theory for the second-order diffraction problem developed recently by the author and to present examples of the resulting second-order free surface and nonlinear wave runup. These features of the nonlinear free surface are found to differ significantly from the linear solution, unlike the second-order wave forces which most theories predict are only slightly larger than the forces derived from linear diffraction theory. Interestingly, few of the previous theories have considered second-order free surface features, despite the fact that the second-order free surface contains fundamental nonlinear effects for a very simple geometry that has been widely used in offshore construction.

* Ocean Engineering Program, United States Naval Academy, Annapolis, MD 21402

THEORETICAL DEVELOPMENT

The problem under consideration consists of a fixed, vertical cylinder of radius, a , in water of uniform depth, d , subjected to nonlinear periodic waves of height, H , propagating in the positive x direction as shown in Figure 1. It is assumed that the fluid is irrotational and incompressible such that a potential-flow solution may be obtained in terms of the velocity potential, $\Phi(r, \theta, z, t)$. This potential must then satisfy the Laplace equation plus appropriate kinematic and dynamic boundary conditions at the bottom, at the free surface, at the cylinder, and in the far field.

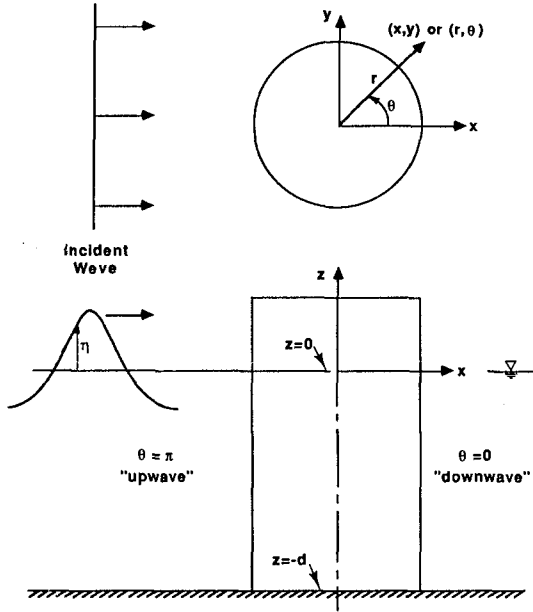


Figure 1. Definition sketch.

Due to the complexity of the nonlinear boundary value problem, an approximate solution is sought through a perturbation expansion in which the velocity potential and the free surface elevation are expressed in series form as

$$\begin{aligned}\Phi &= \Phi_1 + \Phi_2 + \dots \\ \eta &= \eta_1 + \eta_2 + \dots\end{aligned}\quad (1)$$

where the first-order term has a linear dependence on the wave steepness, kH , while the second-order term has a dependence like $(kH)^2$, where k is the linear wavenumber. In addition, the free surface boundary conditions are expanded in a Taylor series about the still water level, $z = 0$. As a result, separate boundary value problems are obtained for each term in the perturbation expansion, Φ_1 and Φ_2 .

At first-order, the solution must be obtained for the linear boundary value problem, which may be expressed as

$$\nabla^2 \Phi_1 = 0 \quad (2a)$$

$$\Phi_{1z} = 0 \quad \text{on } z = -d \quad (2b)$$

$$\Phi_{1tt} + g\Phi_{1z} = 0 \quad \text{on } z = 0 \quad (2c)$$

$$\Phi_{1r} = 0 \quad \text{on } r = a \quad (2d)$$

$$\lim_{r \rightarrow \infty} r^{1/2} (\Phi_{1r}^* - ik\Phi_1^*) = 0 \quad (2e)$$

where the combined free surface boundary condition, (2c), is particularly important since it governs the wavenumbers of the linear solution and since it changes dramatically at second-order. The general solution for this linear diffraction problem has been given by MacCamy and Fuchs (1954) as the real part of

$$\Phi_1 = -\frac{igH}{2\sigma} \frac{\cosh k(d+z)}{\cosh kd} \sum_{n=0}^{\infty} \beta_n \left[J_n(kr) - \frac{J'_n(ka)}{H'_n(ka)} H_n(kr) \right] \cos n\theta e^{-i\sigma t} \quad (3)$$

where $\beta_n = (2 - \delta_{n0}) i^n$ and where δ_{n0} is the Kronecker delta function. In (3), the infinite series of Bessel functions $J_n(kr)$ represents linear incident plane waves while the Hankel functions $H_n(kr)$ represent outwardly-propagating linear scattered waves.

At second-order, the governing boundary value problem is considerably more complicated due to nonlinear forcing terms which appear in the free surface boundary condition. The second-order boundary value problem may be given by

$$\nabla^2 \Phi_2 = 0 \quad (4a)$$

$$\Phi_{2z} = 0 \quad \text{on } z = -d \quad (4b)$$

$$\Phi_{2tt} + g\Phi_{2z} = \frac{1}{g} \Phi_{1t} [\Phi_{1ttz} + g\Phi_{1zz}] \quad (4c)$$

$$-2 \left[\Phi_{1r} \Phi_{1rt} + \frac{1}{r^2} \Phi_{1\theta} \Phi_{1\theta t} + \Phi_{1z} \Phi_{1zt} \right] \quad \text{on } z = 0$$

$$\Phi_{2r} = 0 \quad \text{on } r = a \quad (4d)$$

and a form of the radiation condition, which is not well-posed for the second order problem. Because of the quadratic forcing terms on the right side of (4c), the second-order boundary value problem is nonhomogeneous. The second-order solution is therefore expected to have both particular solutions, which represent forced wave motions due to nonlinearity in the free surface boundary condition, as well as complementary or homogeneous solutions, which represent free scattered wave motions at second-order.

By substituting the first-order solution in (3) into the second-order free surface boundary condition in (4c), it is found that the quadratic forcing is periodic and oscillates at twice the frequency of the linear waves. The quadratic forcing is also an even function of θ , such that (4c) may be rewritten in series form as

$$\Phi_{2tt} + g\Phi_{2z} = -i \frac{(gkH)^2}{8\sigma} \sum_{n=0}^{\infty} [f_n^{II}(r) + f_n^{IS}(r) + f_n^{SS}(r)] \cos n\theta e^{-i2\sigma t} \quad (5)$$

Expressions for the radial functions $f_n^{II}(r)$, $f_n^{IS}(r)$, and $f_n^{SS}(r)$ are given by Hunt and Williams (1982), Sabuncu and Gören (1985), or Kriebel (1987), where each term represents a distinct nonlinear product term from the first order incident and scattered waves.

In (5), the f_n^{II} term represents plane-wave forcing which leads to the expected second-order plane-wave component at wavenumber $2k$, as found in the usual Stokes second-order wave theory. This term would exist at second-order even if no cylinder were present and is the result of nonlinear self-interactions of the first-order incident waves. The remaining forcing terms, f_n^{IS} and f_n^{SS} , are the result of nonlinear cross-interactions of the first-order incident and scattered waves and nonlinear self-interactions of the first-order scattered waves, respectively. These forcing terms behave much like a non-uniform pressure field applied to the free surface and they generate additional cylindrical standing and outwardly progressive waves at second-order.

The solution for the second-order velocity potential may be obtained by separating the potential Φ_2 into particular solutions, Φ_2^P , and complementary or homogeneous solutions, Φ_2^H , as

$$\Phi_2 = \Phi_2^P + \Phi_2^H \quad (6)$$

Based on (5), the particular solution may be further separated as

$$\Phi_2^P = \Phi_{2P}^{II} + \Phi_{2P}^{IS} + \Phi_{2P}^{SS} \quad (7)$$

The component, Φ_{2P}^{II} , then represents the forced wave motion generated by the f_n^{II} forcing, which is the usual Stokes plane wave component given by the real part of

$$\Phi_{2P}^{II} = -i \frac{3g(kH)^2}{8\sigma} \frac{(\tanh^2 kd - 1)}{(2k \tanh 2kd - k_2 \tanh k_2d)} \frac{\cosh 2k(d+z)}{\cosh 2kd} \sum_{n=0}^{\infty} \beta_n J_n(2kr) \cos n\theta e^{-i2\sigma t} \quad (8)$$

The wavenumber k_2 is the characteristic free wavenumber for the second-order problem and satisfies the second-order dispersion relationship

$$4\sigma^2 = gk_2 \tanh k_2d \quad (9)$$

which can be obtained from the homogeneous form of the free surface boundary condition in (4c) or (5). It is found that k_2 approaches $4k$ in deep water but approaches $2k$ in shallow water, where Φ_{2P}^{II} becomes infinite due to resonant forcing in the free surface boundary condition, as is well known.

In the same way, other forced wave components exist in the "incident" wave field due to the remaining f_n^{IS} and f_n^{SS} forcing terms. The solution for these second-order forced waves is found in closed integral form based on a source distribution method, which may be formalized by application of either Green's theorem or through use of Hankel transforms. In this analysis, the solution is first obtained for an isolated point source of pressure oscillating on the free surface. This result is then generalized by integrating over the free surface in r and θ , to account for the distribution of the actual quadratic forcing found in the second-order free surface boundary condition. The solution follows that of Wehausen and Laitone (1960) for an arbitrary pressure distribution on the free surface; and, the resulting velocity potential due to the distributed forcing terms, f_n^{IS} and f_n^{SS} , may be shown to be given by

$$\begin{aligned} \Phi_{2P}^{IS} + \Phi_{2P}^{SS} = & -i \frac{g(kH)^2}{8\sigma k} \sum_{n=0}^{\infty} \cos n\theta \left[i2\pi \frac{k_2 \cosh k_2d \cosh k_2(d+z)}{k \sinh 2k_2d + 2k_2d} J_n(k_2r) D_n(k_2) \right. \\ & \left. + PV \int_0^{\infty} \frac{\kappa \cosh \kappa(d+z)}{k \cosh \kappa d (\kappa \tanh \kappa d - k_2 \tanh k_2d)} J_n(\kappa r) D_n(\kappa) d\kappa \right] e^{-i2\sigma t} \end{aligned} \quad (10)$$

where "PV" represents a Principal Value integral and where $D_n(\kappa)$ represents a wavenumber spectrum for cylindrical wave motions based on a Hankel transform as

$$D_n(\kappa) = \int_a^\infty r' [f_n^{IS}(r') + f_n^{SS}(r')] J_n(\kappa r') dr' \quad (11)$$

In the solution given by (10), the principal value integral represents standing wave motions based on a continuum of wavenumbers that are required to fit the complicated free surface boundary condition arising from the quadratic forcing. Away from the cylinder, however, only the second-order free wavenumber, k_2 , is important and the integral term yields a cylindrical standing wave in the far field. From the source distribution method, the wave motions generated by any point source must satisfy the Sommerfeld radiation condition and yield outwardly propagating wave motions far from each source. Therefore, the additional term in the solution (10), represented by the component containing $J_n(k_2 r)$, is required so that the entire solution satisfies a form of the radiation condition.

The complicated forced-radiated waves given in (10), together with the incident bound second-harmonic given in (8), satisfy the nonlinear free surface boundary condition but do not satisfy the no-flow condition on the cylinder boundary by themselves. By allowing these waves to interact with the cylinder, second-order scattered waves must exist which are given by the complementary or homogeneous solutions in (6). These solutions must satisfy the Laplace equation, the bottom boundary condition, the Sommerfeld radiation condition, and the homogeneous form of the free surface boundary condition; and, they may be found from the general set of eigenfunction solutions for cylindrical waves as given by Dean and Dalrymple (1984) as

$$\begin{aligned} \Phi_2^H = & \sum_{n=0} a_{n0} \cosh k_2(d+z) H_n(k_2 r) \cos n\theta \\ & + \sum_{n=0} \sum_{j=1} a_{nj} \cos \kappa_{2j}(d+z) K_n(\kappa_{2j} r) \cos n\theta e^{-i2\sigma t} \end{aligned} \quad (12)$$

From the homogeneous form of the second-order free surface boundary condition, two second-order dispersion relationships result which specify the wavenumbers k_2 and κ_{2j} . For outwardly propagating second-order free waves

$$4\sigma^2 = gk_2 \tanh k_2 d \quad (13)$$

which was given in (9); while for the standing or evanescent wave modes, the wavenumbers are given by

$$4\sigma^2 = -g\kappa_{2j} \tan \kappa_{2j} d \quad (14)$$

which has infinitely many positive roots, κ_{2j} , given by

$$(j - \frac{1}{2})\pi \leq \kappa_{2j} h \leq j\pi$$

The homogeneous solutions therefore consist of outwardly radiating second-order free waves as well as local standing waves, i.e. evanescent modes, both of which are determined to within a set of unknown constants. The unknown coefficients, a_{n0} and a_{nj} , are then determined by satisfying the no-flow condition on the cylinder. This is accomplished with the same procedure that is used to obtain the first-order scattered wave solution, based on the orthogonality properties of $\cosh k_2(d+z)$ and $\cos \kappa_{2j}(d+z)$. The method is straightforward but lengthy; thus, it will not be given in detail in this paper.

The final solution at second-order is completely specified by combining the particular solutions in (8) and (10) with the complementary solutions obtained from (12) after evaluating the unknown coefficients. The solution for the second-order velocity potential is derived in detail by Kriebel (1987) and may ultimately be expressed in closed integral form as

$$\begin{aligned}
 \Phi_2 = & -i \frac{g(kH)^2}{2k\sigma} \sum_{n=0}^{\infty} \cos n\theta \\
 & \cdot \left[C_1 \cosh 2k(d+z)\beta_n J_n(2kr) - C_{10} C_0 \cosh k_2(d+z)\beta_n \frac{J'_n(2ka)}{H'_n(k_2a)} H_n(k_2r) \right. \\
 & \quad \left. - \sum_{j=1}^{\infty} C_{1j} C_j \cos \kappa_{2j}(d+z)\beta_n \frac{J'_n(2ka)}{K'_n(\kappa_{2j}a)} K_n(\kappa_{2j}r) \right] \\
 & + \left[PV \int_0^{\infty} \frac{C_2}{k} \cosh \kappa(d+z) J_n(\kappa r) d\kappa - C_0 I_{20} \cosh k_2(d+z) \frac{H_n(k_2r)}{k H'_n(k_2a)} \right. \\
 & \quad \left. - \sum_{j=1}^{\infty} C_j I_{2j} \cos \kappa_{2j}(d+z) \frac{K_n(\kappa_{2j}r)}{k K'_n(\kappa_{2j}a)} \right. \\
 & \quad \left. + C_3 C_0 \cosh k_2(d+z) \left[J_n(k_2r) - \frac{J'_n(k_2a)}{H'_n(k_2a)} H_n(k_2r) \right] \right] e^{-i2\sigma t}
 \end{aligned} \tag{15}$$

where the nondimensional coefficients are defined as

$$\begin{aligned}
 C_0 &= \frac{\cosh k_2 d}{\sinh 2k_2 d + 2k_2 d} & C_j &= \frac{\cos \kappa_{2j} d}{\sin 2\kappa_{2j} d + 2\kappa_{2j} d} \\
 C_1 &= \frac{3}{4} \frac{k(\tanh^2 kd - 1)}{\cosh 2kd(2k \tanh 2kd - k_2 \tanh k_2 d)} \\
 C_{10} &= 6 \frac{k^2(\tanh^2 kd - 1)}{4k^2 - k_2^2} & C_{1j} &= 6 \frac{k^2(\tanh^2 kd - 1)}{4k^2 + \kappa_{2j}^2} \\
 C_2 &= \frac{1}{4} \frac{\kappa D_n(\kappa)}{\cosh \kappa d(\kappa \tanh \kappa d - k_2 \tanh k_2 d)} \\
 I_{20} &= \int_0^{\infty} \frac{\kappa^2 D_n(\kappa) J'_n(\kappa a)}{(\kappa^2 - k_2^2)} d\kappa & I_{2j} &= \int_0^{\infty} \frac{\kappa^2 D_n(\kappa) J'_n(\kappa a)}{(\kappa^2 + \kappa_{2j}^2)} d\kappa \\
 C_3 &= \frac{i\pi}{2} \frac{k_2}{k} D_n(k_2)
 \end{aligned}$$

In the solution given by (15), terms enclosed in the first bracket on the right hand side represent: (1) the forced Stokes plane wave component at wavenumber $2k$ and (2) the free cylindrical wave motion due to the scattering of this Stokes plane wave from the cylinder. These terms are found to be identical to a portion of the solution proposed by Chen and Hudspeth (1982), derived using the method of Green's functions. Terms in the second bracket then represent: (1) the remaining forced-radiated wave motion due to other nonlinear wave-wave interactions as well as (2) free scattered waves due to the interaction of these forced-radiated waves with the cylinder. Although derived in an independent way, the solution for these forced wave motions in (10) is identical to that proposed by Garrison (1979), also through application of Green's theorem, as Garrison's Green's function for the free surface potential can be reduced analytically to that given by (10) for a circular cylinder. Garrison then obtains the scattered wave solutions numerically in terms of a second Green's function and an unknown source distribution on the cylinder. The scattered wave motions in the proposed solution are obtained in closed-form based on the complete set of eigenfunction solutions for the homogeneous boundary value problem.

SOLUTION FOR NONLINEAR FREE SURFACE

The first and second-order velocity potentials are substituted into the dynamic free surface boundary condition to evaluate the form of the free surface around the cylinder. Based on the perturbation expansion technique, Φ and η are expanded in power series form, and the dynamic free surface boundary condition is then expanded in a Taylor series about the still water level, $z = 0$. The resulting expression for the water surface, consistent to the second perturbation order, may then be obtained as

$$\eta_1 + \eta_2 = -\frac{1}{g}\Phi_{1t} - \frac{1}{g}\Phi_{2t} - \frac{1}{g^2}\Phi_{1t}\Phi_{1tz} - \frac{1}{2g}\left[\Phi_{1r}^2 + \frac{1}{r^2}\Phi_{1\theta}^2 + \Phi_{1z}^2\right] \quad (16)$$

The resulting wave field, based on the right side of (16), is found to include: (1) linear incident and scattered waves, (2) second-order components from the second-order velocity potential, and (3) second-order components derived from nonlinear product terms of the first-order wave field. These last quadratic terms are found to include both steady components as well as components that oscillate at twice the frequency of the linear waves. All terms may be obtained from a straightforward substitution of the velocity potentials in (3) and (15) into (16); however, the results are quite lengthy and include several double-summations. The interested reader may refer to Kriebel (1987) for details.

In Figures 2 and 3, contours of wave crest amplitudes around the cylinder are shown for the linear and nonlinear diffraction solutions respectively. An example of the predicted wave crest and trough envelopes along the x-axis, as well as around the circumference of the cylinder, is then shown in Figure 4, where second-order mean water levels are also shown. In each figure, results are normalized by the incident wave amplitude and are given for a reference case where $ka = 1.0$, $kd = 1.57$, and where $kH = 0.5$. It is noted, however, that while the nonlinear solution in (15) and in Figure 3 is a function of kH , the nondimensional linear solution in (3) and in Figure 2 is not a function of the wave steepness.

In the up-wave region, the linear scattered wave opposes the linear incident wave to form a partial standing wave system. Second-order components generally increase the crest heights in the antinodes while reducing trough amplitudes. It is found, however, that terms from the second-order velocity potential in (10) are mostly out-of-phase with the linear solution and tend to decrease crest heights while other second-order components are in-phase and lead to the expected increase in crest heights. The nonlinear increase in crest heights is most pronounced on the up-wave cylinder boundary, where runup amplitudes are significantly increased relative to linear theory. Spatially varying mean water levels are also found which are the cylindrical analog to the "corrugated" mean water levels associated with standing waves in front of a vertical plane barrier. These components are superimposed upon the usual uniform set-down associated with the two-dimensional Stokes wave theory.

In the down-wave region, linear incident and scattered waves propagate in generally the same direction and do not generate strong quadratic interactions compared to the up-wave region. At second-order, however, scattered free waves and diffracted waves from the up-wave region propagate away from the cylinder in the down-wave region. These waves are superimposed on the linear waves and their bound second harmonics to produce spatially varying crest and trough envelopes, analogous to those produced by the superposition of first- and second-order free and forced waves in a wave flume. These interactions vary in both r and θ such that significant diffraction patterns are obtained with localized areas of constructive and destructive wave interactions. One result of these interactions is that there is also significant recovery of the wave crest amplitude immediately behind the cylinder at second-order, something that is not predicted by the first-order diffraction theory.

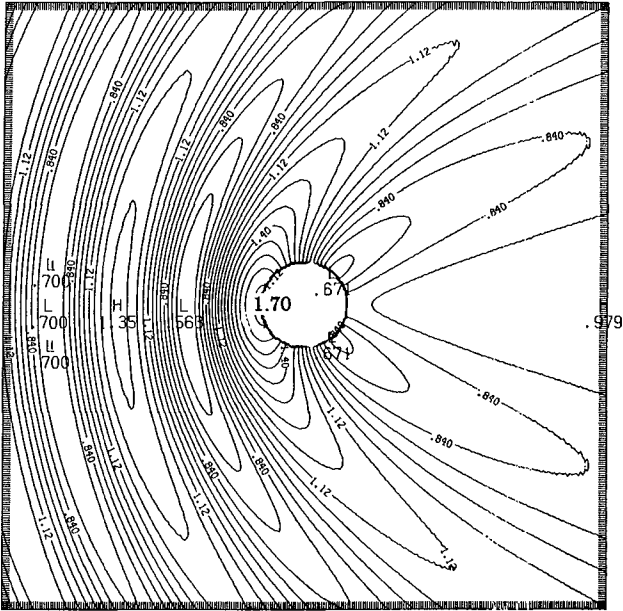


Figure 2. Wave crest amplitude contours for linear diffraction theory, for example case with $ka = 1.0$ and $kd = 1.57$.

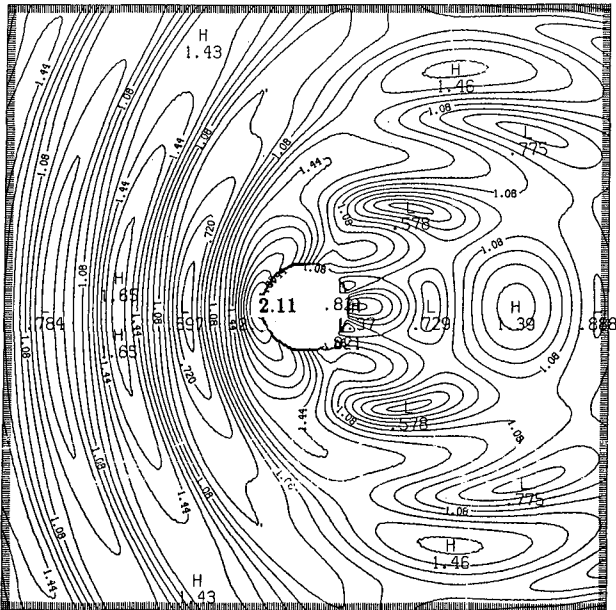


Figure 3. Wave crest amplitude contours for nonlinear diffraction theory, for example case with $ka = 1.0$, $kd = 1.57$, and $kH = 0.5$.

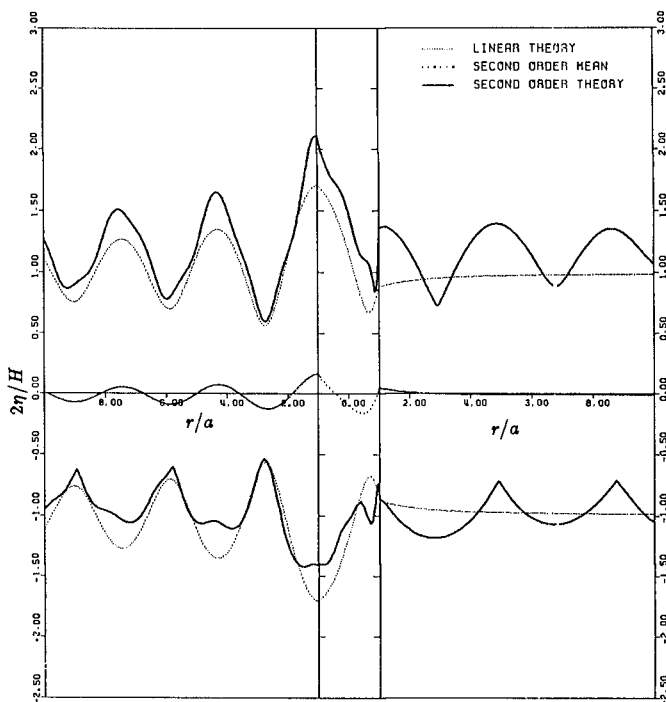


Figure 4. Wave crest and trough envelopes along x-axis, for example case with $ka = 1.0$, $kd = 1.57$, and $kH = 0.5$.

EXPERIMENTAL VERIFICATION

The second-order diffraction theory is verified through comparison to laboratory data for: (1) wave runup and rundown envelopes around the circumference of the cylinder and (2) wave crest and trough envelopes along the x-axis out to a distance of 5 times the cylinder radius. The experiments were conducted in the directional wave basin at the University of Florida Coastal and Oceanographic Engineering Laboratory. The water depth was maintained at 45.0 centimeters with a cylinder radius of 16.25 centimeters, such that a constant depth-to-radius ratio of 2.77 was used for all experiments.

The experiments were conducted with monochromatic long-crested waves and a total of 22 experiments were carried out covering a broad range of the nondimensional parameters. Relative cylinder sizes remained in the diffraction regime with ka values from 0.271 to 0.917. Relative water depths remained in the intermediate depth regime kd values from 0.75 to 2.536. Values of the wave steepness were selected such that Stokes theory would remain convergent, although some waves with very high steepness were also tested; kH values ranged from 0.085 to 0.806. Stokes second-order theory is formally expected to be appropriate for only 8 of the 22 experiments, while higher order wave theories would be most appropriate for the remaining conditions.

Wave runup data were obtained by video-taping the water surface on the circumference of the cylinder as waves passed a grid painted on the outside of the cylinder. Data analysis included selecting a 20 to 30 second period of steady state conditions and then averaging the wave crest runup and trough rundown for 10 waves every 15 degrees around the cylinder. For 12 of the experiments a video record was also made of waves passing a "photopole" array, which consisted simply of 10 thin vertical rods placed in a linear array along the x axis as depicted in Figure 5. The photopole data consists of the wave crest and trough envelopes at each pole location, averaged over 10 waves. The photopole experiments were conducted separately from the runup experiments so that the presence of the poles would not disrupt the other measurements.

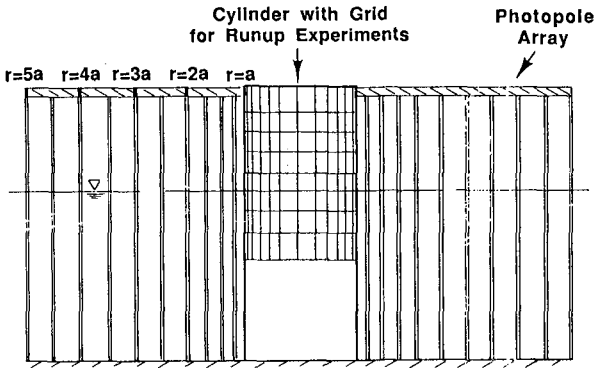


Figure 5. Experimental set up showing photopole array along x -axis.

Examples of the first- and second-order theories compared to laboratory wave runup and rundown data are shown in Figures 6 through 8. Based on a comparison of the data to linear theory, several general conclusions may be reached. Maximum wave runup at the front of the cylinder is greater than that predicted by linear theory in all cases and the runup distribution is poorly predicted by the linear theory. At the rear of the cylinder, the wave crest amplitude is also greater than that predicted by linear theory in all cases. Finally, the rundown amplitudes in the front and rear of the cylinder are not as large as predicted by linear theory.

In contrast, the nonlinear diffraction theory provides much better agreement for runup distributions and maxima. From Figure 6, for the smallest relative cylinder size and depth tested, the measured runup profile is almost exactly predicted over all angular positions by the second-order theory, even though this wave steepness is just at the limit of validity of Stokes theory where cnoidal theory may be more appropriate. The rundown envelope is well-predicted only over the rear half of the cylinder in this case.

For larger values of ka and kd , second-order predictions for wave runup distributions are in good agreement with the data for conditions where Stokes second-order theory is expected to be valid. At higher values of kH , however, like that shown in Figure 7, the nonlinear theory predicts substantially larger runup than linear theory but still tends to underpredict the maximum runup. The rundown envelope is predicted fairly well at front and rear, however, the large trough amplitudes predicted near 75° are not displayed in the data, exact for waves of low steepness.

In Figure 8, the runup and rundown envelopes are predicted very accurately, this time even for a condition where Stokes 3rd or higher order theories are most appropriate and where the wave steepness is at nearly 70 percent of the theoretical breaking steepness. In this case, both the maximum runup at the front and at the rear are predicted almost exactly. The rundown distribution is also well-predicted over the leading half of the cylinder, but again is not well-predicted along the sides of the cylinder.

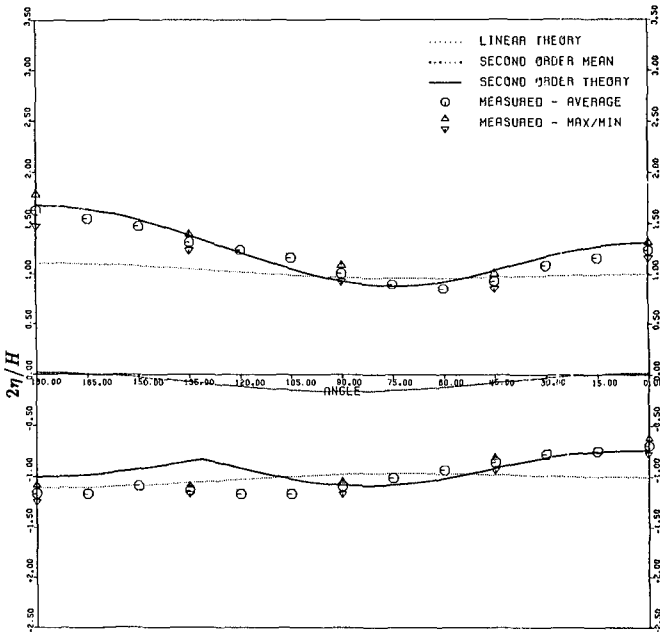


Figure 6. Example of wave runup distribution for $ka = 0.271$, $kd = 0.750$, and $kH = 0.215$.

In Table 1, the measured maximum crest runup is compared to both linear and nonlinear diffraction theories for all experiments. The results indicate that the maximum runup exceeds that predicted by linear theory by 13 to 83 percent and by 44 percent on average for the experimental data set. In contrast, the second-order theory overpredicts the maximum runup by 1 to 5 percent for the first set of conditions, predicts the measured runup to within 0 to 22 percent for most cases, and underpredicts by more than 40 percent for only two tests where the steepness was near breaking. In general, the data exceeds the nonlinear theory by 11 percent on average and by only 8 percent if the two conditions near breaking are excluded.

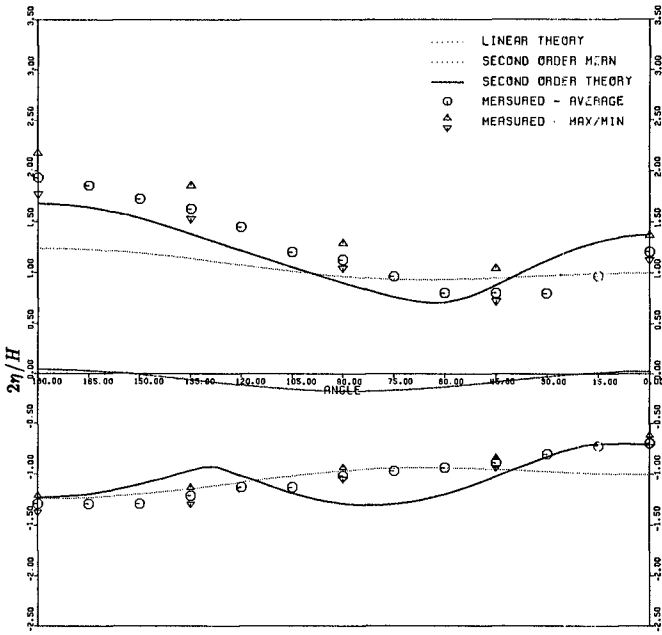


Figure 7. Example of wave runup distribution for $ka = 0.374$, $kd = 1.036$, and $kH = 0.286$.

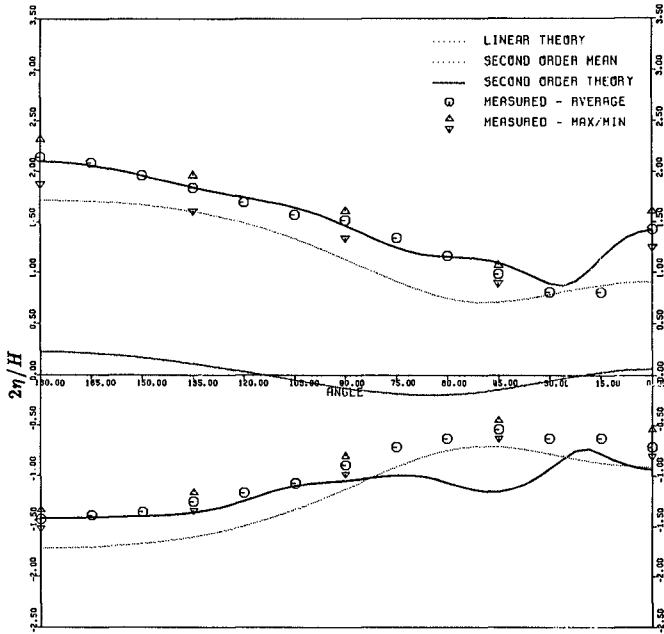


Figure 8. Example of wave runup distribution for $ka = 0.917$, $kd = 2.536$, and $kH = 0.631$.

Table 1. Experimental results for maximum wave runup

ka	kd	kH	% Diff.	
			Linear	Nonlinear
0.271	0.750	0.132	27	-2
		0.178	36	-5
		0.215	48	-1
0.308	0.853	0.085	16	1
		0.137	33	5
		0.182	45	6
		0.250	65	13
0.374	1.036	0.296	78	13
		0.122	13	0
		0.205	36	15
		0.286	56	19
0.481	1.332	0.385	69	16
		0.402	76	18
		0.186	13	7
		0.317	20	4
0.631	1.745	0.438	35	9
		0.530	80	40
		0.683	61	22
0.684	1.894	0.391	18	5
0.917	2.536	0.572	43	22
		0.631	25	0
		0.806	83	43

Examples of the photopole experiments are presented in Figures 9 and 10. The visual observations of the wave crest and trough envelopes are compared to the first and second-order theoretical solutions, which have been extended out to $r = 10a$ to give a better indication of the overall scattering and diffraction patterns along the x axis. In general, the photopole data seem to verify the general features of the wave envelopes predicted by the second-order theory. For the smaller cylinder size, in Figure 9, the second-order scattered waves lead to additional nodes and antinodes in the up-wave region compared to linear theory. The photopole data confirm the positions and magnitudes of these maxima and minima for both the wave crest and trough on the up-wave side. On the down-wave side, the second-order wave components do not produce significant modulations in the envelopes; and, to within measurement accuracy, the data verify this theoretical prediction as well.

The data in Figure 10, for the largest cylinder size tested, show that both the predicted and measured envelopes are similar to the linear envelope except that the crest elevations are increased while troughs are reduced. No secondary maxima are predicted in the envelopes, in contrast to the results at smaller values of ka . On the down-wave side, significant spatial modulation is predicted for this case. Data from the crest envelopes provide a rough verification of these nonlinear diffraction effects, as the presence and approximate spacing of the predicted envelope maxima and minima are confirmed, although the measured envelopes are more poorly defined.

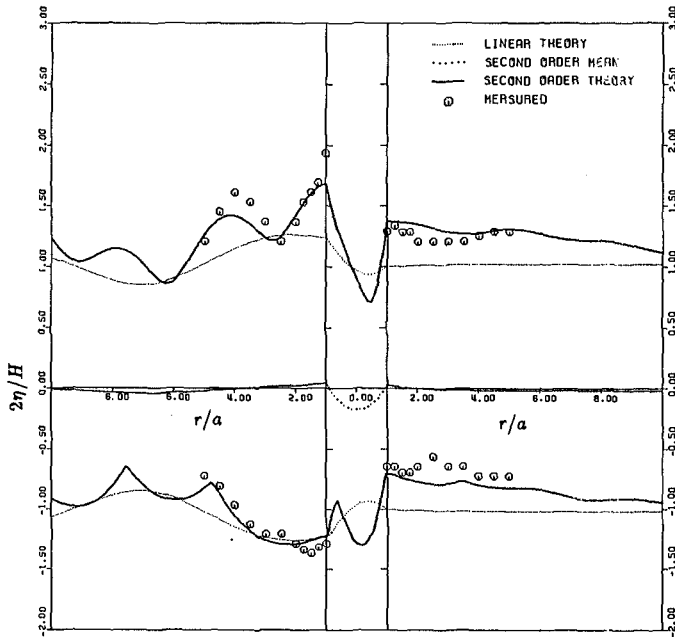


Figure 9. Example of wave envelopes along x-axis for $ka = 0.374$, $kd = 1.036$, and $kH = 0.286$.

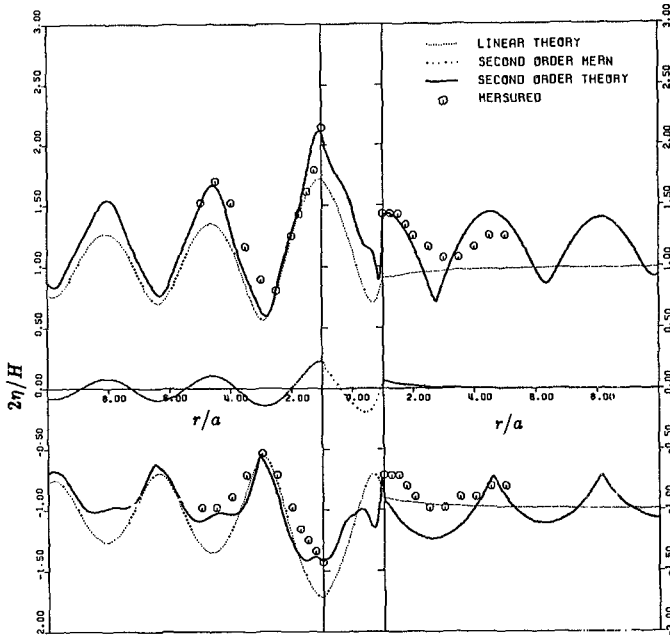


Figure 10. Example of wave envelopes along x-axis for $ka = 0.917$, $kd = 2.536$, and $kH = 0.631$.

CONCLUSIONS

The proposed second-order diffraction theory seems to rigorously account for nonlinear wave components including second-order forced waves due to nonlinearities in the free surface boundary condition as well as second-order free waves due to the nonlinear scattering process. Based on comparisons to laboratory data, the theory is then found to realistically predict the nonlinear characteristics of the wave field surrounding the cylinder. A comparison of the theory to previously proposed nonlinear diffraction theories shows substantial agreement in portions of the solution, but not in the entire solution, with the theories of Chen and Hudspeth (1982) and Garrison (1979). Finally, the proposed second-order theory seems to be valid for the same relative depth and wave steepness conditions for which the usual Stokes plane wave theory is valid.

ACKNOWLEDGEMENTS

The author is grateful to Robert G. Dean and the Coastal and Oceanographic Engineering Department of the University of Florida for support on this project.

REFERENCES

- Chen, M.C., and Hudspeth, R.T., 1982, "Nonlinear Diffraction by Eigenfunction Expansion," *J. Waterway, Port, Coastal and Ocean Div.*, ASCE, Vol. 108, No. WW3.
- Dean, R.G., and Dalrymple, R.A., 1984, *Water Wave Mechanics for Engineers and Scientists*, Prentice-Hall, Englewood Cliffs, New Jersey.
- Garrison, C. J., 1979, "The Consistent Second-Order Theory of Wave/Structure Interaction," Naval Postgraduate School, Tech. Rpt. No. NPS-69-79-010, Monterey.
- Hunt, J.N., and Williams, A.N., 1982, "Nonlinear Diffraction of Stokes Water Waves by a Circular Cylinder for Arbitrary Uniform Depth," *J. de Mécanique Théorique et Appliquée*, Vol. 1, No. 3.
- Kriebel, D.L., 1987, "A Second-Order Diffraction Theory for Wave Runup and Wave Forces on a Vertical Circular Cylinder," Coastal and Ocean. Engr. Dept., Rpt. TR-072, University of Florida.
- MacCamy, R.C., and Fuchs, R.A., 1954, "Wave Forces on Piles: A Diffraction Theory," U.S. Army Corps of Eng., *Beach Erosion Board*, Tech. Mem. No. 69.
- Rahman, M., and Heaps, H.S., 1983, "Wave Forces on Offshore Structures: Nonlinear Wave Diffraction by Large Cylinders," *J. Phys. Ocean.*, Vol. 13.
- Sabuncu, T., and Gören, O., 1985, "Second-Order Vertical and Horizontal Wave Forces on a Circular Dock," *Ocean Engr.*, Vol. 12, No. 4.
- Wehausen, J. V., and Laitone, E.V., 1960, "Surface Waves," In *Encyclopedia of Physics*, ed. S. Flugge, Springer-Verlag, Berlin, Vol. IX.

CHAPTER 2

WAVE-CURRENT INTERACTION IN HARBOURS

Jan K. Kostense, Maarten W. Dingemans and Peter Van den Bosch *

ABSTRACT

A finite element model has been developed to study the effect of currents on the wave propagation in and around arbitrarily shaped harbours of variable depth. The model solves an elliptic mild-slope type of equation for time-harmonic waves, and thus circumvents the limitations of existing models for wave-current interaction in coastal areas, which apply a parabolic approximation. Numerical examples are presented, both for schematized cases, as the effect of "rip currents" on normal incident waves on a sloping beach, and for a realistic geometry.

1. INTRODUCTION

An effective tool to study the wave penetration into harbours of variable depth and arbitrary shape is the mild-slope equation as originally derived by Berkhoff (1972). The equation describes the combined effect of bottom refraction and diffraction on the propagation of linear gravity waves. Booij (1981) suggested how to extend the equation to account for dissipative effects. To solve the full elliptic equation, Kostense et al. (1986) presented a finite-element model, which has been implemented with several types of boundary conditions, such as partial reflection, and combined reflection and transmission. They experimentally verified their model for a complex harbour geometry, and showed that it can be successfully applied, for instance to study the dissipative effects of bottom friction and permeable breakwaters on harbour resonances. The implementation of wave breaking in the model is described by De Girolamo, Kostense and Dingemans (1988), while the numerical solution methods are discussed by Hurdle, Kostense and Van den Bosch (1989). The

* Delft Hydraulics, P.O. Box 152, 8300 AD Emmeloord, the Netherlands

model has been implemented on two different supercomputers, viz. a Cray XMP and a NEC SX/2. Taking advantage of its vector-processors, the system of equations is solved quite efficiently, enabling computations of relatively large areas.

Radder (1979) introduced a parabolic approximation of the mild-slope equation and thus converted a boundary value problem into an initial value problem. The nature of the parabolic approximation is such that diffraction and reflection are neglected in the computational main-wave propagation direction. Since then, this technique was widely applied to study the wave propagation in coastal areas, especially after Booij (1981) introduced an extended equation accounting for the effect of varying currents. Kirby (1984) showed that Booij used an improper form of the dynamic free surface boundary condition, and derived an improved equation.

Apart from coastal regions, currents may also have a noticeable effect on the wave penetration into harbours, especially if they are situated in tidal inlets, in estuaries, near in- and outlets of power plants, etc. Until now this effect could not be incorporated in numerical studies, as parabolic methods inhibit reflections opposite to the main direction of wave propagation. Therefore, the finite element model presented by Kostense et al. (1986) has been modified to solve the equation as derived by Kirby (1984). The model has been given in section 2 and the necessary iteration procedure for the wave direction has been described in section 3. To illustrate the effectiveness of the model, in section 4 a series of computations is discussed, both for schematized cases, and for a realistic geometry.

2. THE EXTENDED MILD-SLOPE EQUATION

For irrotational wave motion, the velocity potential $\Phi(\vec{x}, z, t)$ is written as

$$\Phi(\vec{x}, z, t) = f(z, h) \phi(\vec{x}, t) \quad \text{with} \quad (1)$$

$$f(z, h) = \frac{\cosh[k(h+z)]}{\cosh kh} \quad (2)$$

With an ambient current field $\vec{U}(\vec{x})$ the time-dependent mild-slope

equation results as (Kirby, 1984)

$$\frac{D^2\phi}{Dt^2} + (\nabla \cdot \vec{U}) \frac{D\phi}{Dt} + \phi \frac{D}{Dt} (\nabla \cdot \vec{U}) - \nabla \cdot (cc_g \nabla \phi) + (\omega_r^2 - k^2 cc_g) \phi = 0, \quad (3)$$

where c , c_g and k represent the phase velocity ω_r/k , the group velocity $d\omega_r/dk$, and the wave number $|\vec{k}|$, respectively, ∇ is the two-dimensional gradient operator, and further

$$\frac{D}{Dt} \equiv \frac{\partial}{\partial t} + \vec{U} \cdot \nabla, \quad (4)$$

$$\omega_r = \omega - \vec{k} \cdot \vec{U}, \quad \text{and} \quad \omega_r^2 = gk \tanh kh. \quad (5a, b)$$

Introducing time-harmonic motion,

$$\phi(\vec{x}, t) = \text{Re} \left\{ \psi(\vec{x}) e^{-i\omega t} \right\}, \quad (6)$$

there results

$$\frac{\partial}{\partial x_i} \left[cc_g \frac{\partial \psi}{\partial x_i} - U_i U_j \frac{\partial \psi}{\partial x_j} \right] + 2i\omega U_j \frac{\partial \psi}{\partial x_j} + \left(k^2 cc_g + \omega^2 - \omega_r^2 + i\omega \nabla \cdot \vec{U} \right) \psi = 0. \quad (7)$$

The equation solved in the finite element model is obtained from Eq. (7) by assuming currents which are small compared to the group velocity, and thus neglecting the quadratic term in U . Furthermore, at the right-hand side of the equation the dissipation term is added (see also Hurdle et al., 1989):

$$\frac{\partial}{\partial x_j} \left[cc_g \frac{\partial \psi}{\partial x_j} \right] + 2i\omega U_j \frac{\partial \psi}{\partial x_j} + \left(k^2 cc_g + \omega^2 - \omega_r^2 + i\omega \nabla \cdot \vec{U} \right) \psi = -i\omega_r W \psi. \quad (8)$$

The equation is solved by means of standard finite element techniques, using triangular elements with linear interpolation functions.

3. ITERATION PROCEDURE FOR CURRENT EFFECT

As the relative wave frequency, ω_r , is dependent on the unknown direction of \vec{k} , Eq. (8) can be solved only in an iterative manner. To elucidate the iteration procedure and its underlying assumptions, the case of a traveling wave is considered:

$$\psi(\vec{x}) = b(\vec{x}) e^{iS(\vec{x})} . \quad (9)$$

Inserting this expression into Eq. (8) results into an energy transport equation and the eikonal equation:

$$(\nabla S)^2 = k^2 + \frac{\nabla c c_g}{c c_g} \cdot \frac{\nabla b}{b} + \frac{\nabla^2 b}{b} + \frac{1}{c c_g} \left[(\omega - \vec{U} \cdot \nabla S)^2 - \omega_r^2 \right] . \quad (10)$$

Since the phase function of ϕ reads $\chi(\vec{x}, t) = S(\vec{x}) - \omega t$, the wave number vector as resulting from the (extended) mild-slope equation can be obtained as

$$\vec{\kappa} = \nabla \chi = \nabla S . \quad (11)$$

It is stressed that the absolute value, k , of the initial wave number results as a constant due to the separation of variables in Eq. (1), which splits off the vertical structure from the wave propagation space. Equation (10) shows that in the wave propagation space the absolute value of the wave number vector κ is different from k due to the effects of bottom slope (through $\nabla c c_g / c c_g$), of diffraction (through $(\nabla^2 b)/b$), and of currents. The unknown direction of $\vec{\kappa}$ in the Doppler-shift equation (5a) is now approximated by the resulting direction of $\vec{\kappa}$, resulting from the former iteration step.

The iteration procedure runs as follows. For the first step the relative wave frequency ω_r in Eq. (5a) is obtained assuming either $\vec{U} = 0$, or a direction of $\vec{\kappa}$ equal to the incident wave direction. Then Eq. (8) yields the solution ψ_0 and the wave number vector

$$\vec{\kappa}_0 = \nabla S = \text{Im} \left(\frac{\nabla \psi_0}{\psi_0} \right) . \quad (12)$$

For the second step the direction of $\vec{\kappa}_0$ is used as an estimate for the direction of $\vec{\kappa}$ in Eq. (5a)

$$\omega_r = \omega - \left(\frac{\vec{\kappa}_0}{\kappa_0} k \right) \cdot \vec{U} , \quad (13)$$

from which, together with the dispersion relation (5b), ω_r and k can be solved and substituted into the mild-slope equation. Now the solution

ψ_1 , which yields from the second step, is used to determine $\vec{\kappa}_1$ and ω_r from expressions similar to Eqs. 12 and 13. From hereon the iteration process continues till a certain accuracy is achieved. To determine whether the stopping criterion is met, the procedure is essentially the same as applied for problems involving dissipation, where the magnitude of W is dependent on the local wave potential, see also Kostense et al. (1986) and De Girolamo et al. (1988). The number of occurrences for which the successive iterations of ψ_n differ more than some relative amount from ψ_{n-1} are counted. This is carried out separately for the real and the imaginary part for each of the mesh points:

$$\text{if } \left| \frac{\text{Re}(\psi_n) - \text{Re}(\psi_{n-1})}{\text{Re}(\psi_n)} \right| > \epsilon \text{ then } N_{\circ} = N_{\circ} + 1$$

and also

$$\text{if } \left| \frac{\text{Im}(\psi_n) - \text{Im}(\psi_{n-1})}{\text{Im}(\psi_n)} \right| > \epsilon \text{ then } N_{\circ} = N_{\circ} + 1$$

Here ϵ is a predetermined accuracy of a few percents. With N_{\circ} occurrences at a total of N mesh points, the iteration is stopped when $N_{\circ}/N < 0.01$. Because the real and the imaginary parts are counted separately, deviations may occur in less than 0.5 % of the mesh points. To obtain reliable estimates of $\nabla\psi$ in Eq. 12, a minimum number of about 12 mesh elements per wave length is required. This condition is essentially the same as for bottom friction computations, which also involve the assessment of $\nabla\psi$, see Kostense et al (1986). Fulfilling this condition, usually about 5 iterations appear to be adequate to obtain reliable results of wave-current computations.

4.0 NUMERICAL EXAMPLES

As numerical examples have been selected wave propagation over a rip current, over a vortex ring and, as an example of a realistic geometry, wave penetration in the Malamocco inlet to the Venice Lagoon.

Rip current

To demonstrate the application of the model to wave-current interactions, computations were performed on the effect of a rip current

on the propagation of normally incident waves on a plane beach with a slope of 1/50, a problem that was originally studied by Arthur (1950). The velocity field is given by

$$U_x = -3.60 \left[2 - \left(\frac{y}{76.2} \right)^2 \right] F \left(\frac{y}{76.2} \right) \int_0^{\frac{x}{7.62}} F(\sigma) d\sigma$$

$$U_y = 0.4731 y F \left(\frac{y}{76.2} \right) F \left(\frac{x}{7.62} \right)$$

with

$$F(\sigma) = (1/\sqrt{2\pi}) \exp(-\sigma^2/2)$$

and is illustrated in Fig. 1. This Figure also shows Arthur's results for a wave period of 8 seconds. These results were obtained with the ray approximation method, which allows for refraction and shoaling only and thus yields unlimited wave heights where the rays cross each other.

Fig. 2 shows two wave height distributions - without and with the effect of wave breaking - obtained from the finite element model. For these computations a grid of 74,003 nodes was used. For nonbreaking and breaking conditions, the computations required 5 and 8 iterations, respectively. The conditions are the same as applied by Arthur. To quantify the effect of wave breaking the formulation given by Battjes and Janssen (1978) has been used, see De Girolamo et al. (1988). Comparing both wave height distributions, the inclusion of wave breaking appears to yield more stable results.

It should be noted that the results in Fig.2 could have been approximated satisfactory by parabolic models, see e.g. Kirby (1983). The reason to perform these computations was to show that nowadays supercomputers enables one to cope with relatively large areas, to which one would have been compelled by the presence of any reflective constructions, such as groynes.

Vortex ring

The model has also been applied to study the wave propagation over a vortex ring in constant water depth. Examples of the occurrence of

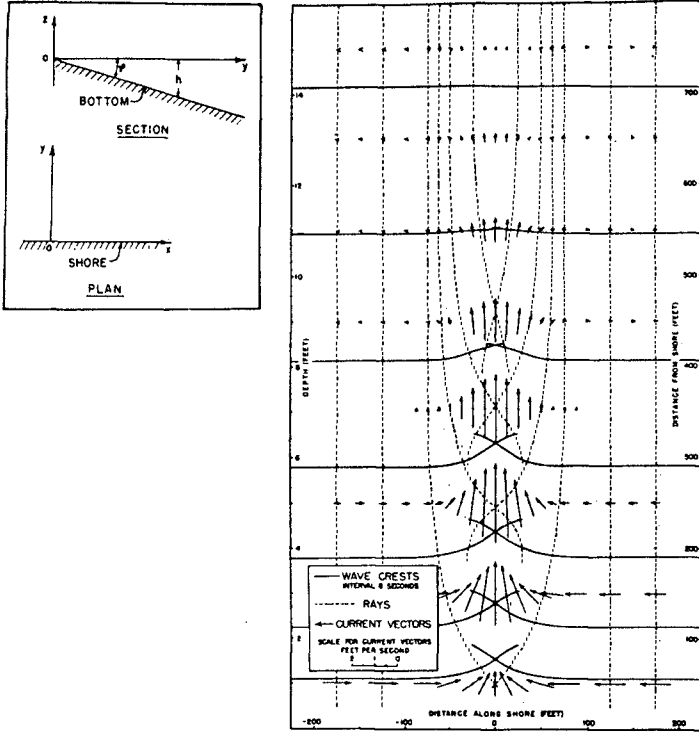
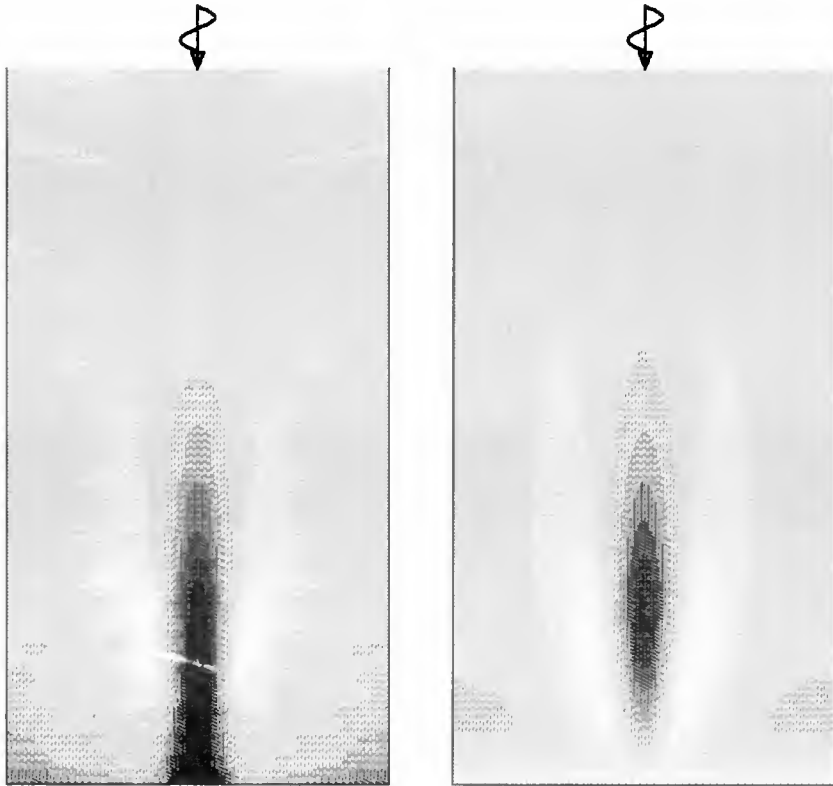
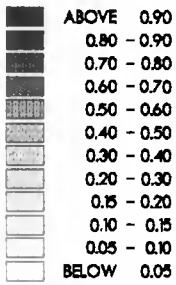


Figure 1 Typical rip current, from Arthur (1950)



without breaking

with breaking



$H_s = 0.20 \text{ m}$

$T = 8.0 \text{ s}$

Wave height in m

Figure 2 Rip current; wave height distributions without and with breaking

vortex rings in nature are the Gulf stream warm-core rings and the large-scale vortices along the Norwegian coast. The finite element grid, which was used for this study consisted of 114,661 nodes, representing a circular area with a diameter of 5 km. The shape of the current velocity distribution is essentially the same as applied by Yoon (1987): the radial velocity component $V_r = 0$ and the tangential velocity given by

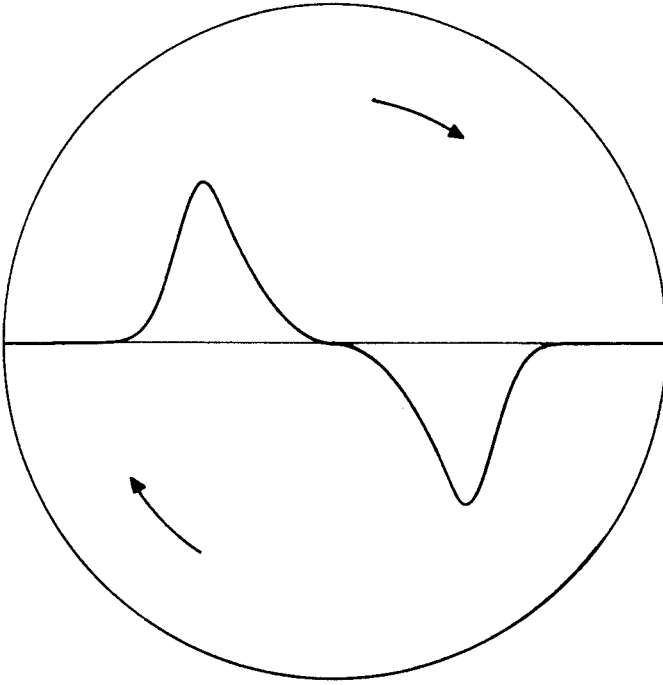
$$V_{\theta} = C_1 \left(\frac{r}{R_1} \right)^N \quad \text{for } r \leq R_1, \text{ and}$$

$$V_{\theta} = C_2 \exp \left[- \left(\frac{R_2 - r}{R_3} \right)^2 \right] \quad \text{for } r > R_1.$$

The maximum velocity C_2 occurs along the circle $r = R_2$. For the numerical computation the coefficients were taken to be $C_1 = 0.9$ m/s, $C_2 = 1.0$ m/s, $R_1 = 900$ m, $R_2 = 1000$ m, $R_3 = 300$ m and $N = 2$. Fig. 3 shows the current velocity distribution, which rotates clockwise. For a water depth of 100 m, a wave period of 10 seconds and an incident wave height of 1.0 m the wave height distribution resulting from a computation without dissipation is shown in Fig. 4. The computation required 7 iterations. In the lower part of the graph the wave directions diverge due to current refraction, resulting in low waves. This area is bounded by a caustic line, where the refracted waves interact with the undisturbed ones. Diffraction in lateral direction precludes unlimited wave heights along this line. The consecutive caustic lines in the upper part of the graph originate from converging wave directions.

Malamocco inlet to the Venice Lagoon

An example from engineering practice of the effect of an ambient current is the wave penetration of the Malamocco inlet to the Venice Lagoon, which was computed as part of the project to develop a flood defence system for Venice. The schematization of the inlet and the bottom topography, as well as a representative ebb current field, are illustrated in Fig. 5. The computational grid comprised 249,088 nodes. The wave field was computed for a water level of CD + 0.80 m, representing mean sea level, and for waves incident from a bearing of 137° N with a height of 1.8 m and a period of 8 seconds.



$$V_r = 0$$

$$V_\theta = C_5 \left[\frac{r}{R_1} \right]^N \quad \text{for } r < R_1$$

$$V_\theta = C_6 \exp \left[-\left(\frac{R_2 - r}{R_3} \right)^2 \right] \quad \text{for } r \geq R_1$$

with:

$$C_5 = 0.9 \text{ m/s}$$

$$C_6 = 1.0 \text{ m/s}$$

$$R_1 = 900 \text{ m}$$

$$R_2 = 1000 \text{ m}$$

$$R_3 = 300 \text{ m}$$

$$N = 2$$

Figure 3 Vortex ring; current velocity profile

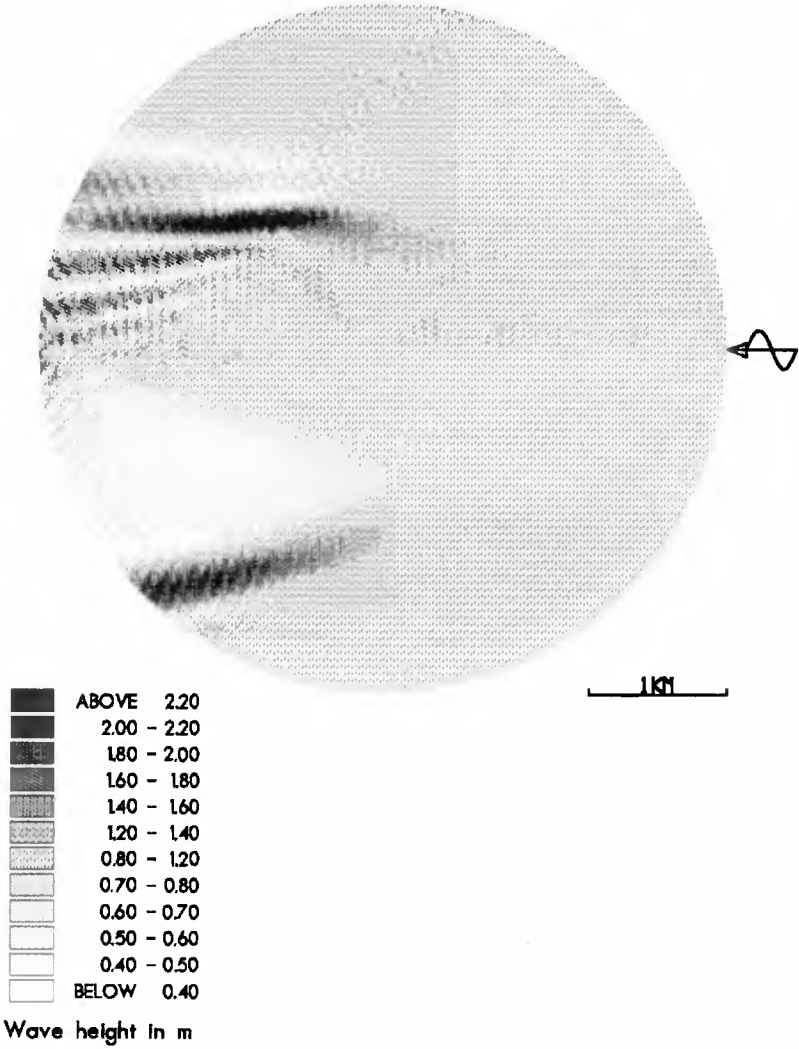


Figure 4 Vortex ring; wave height distribution

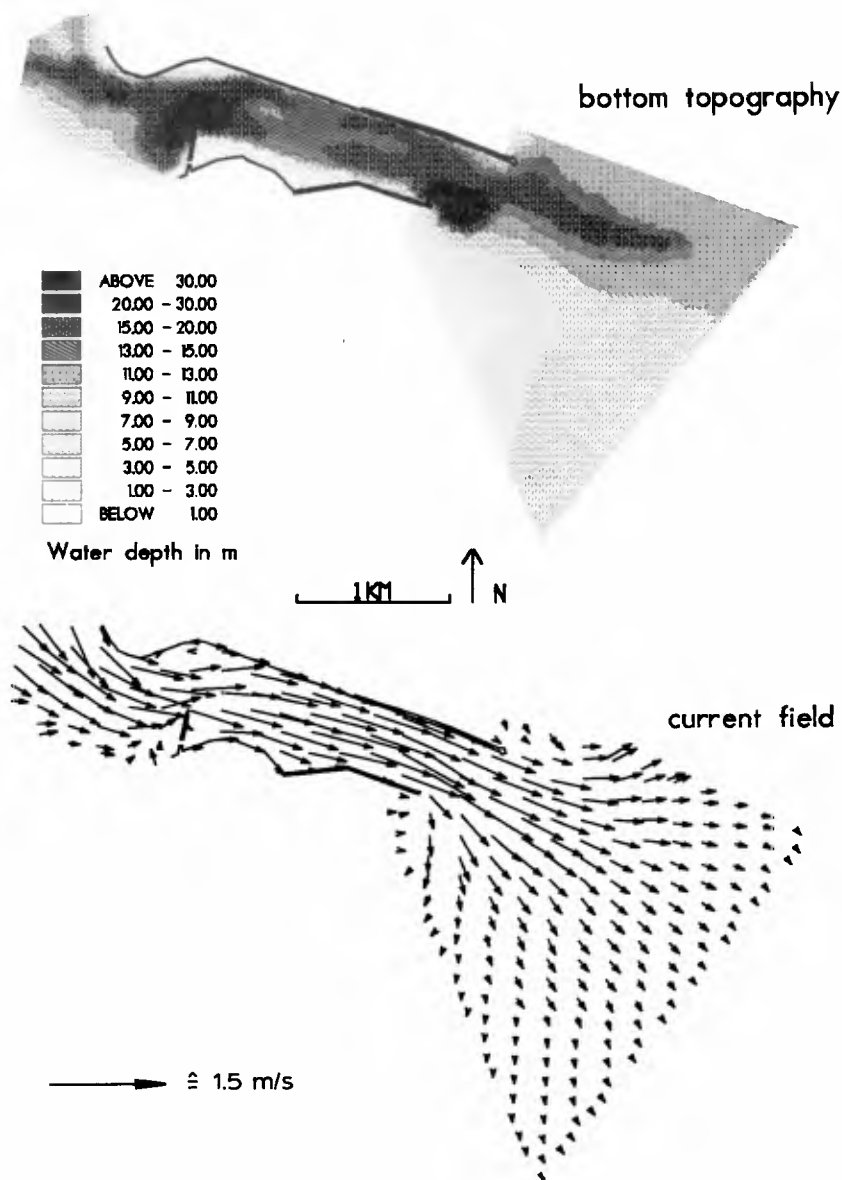


Figure 5 Malamocco inlet to the Venice lagoon area; bathymetry and typical ebb currents

The results, with and without current, are shown in Figure 6. The wave height distribution for the no current case shows a focussing of energy along the south side of the entrance channel due to so-called channel refraction. This also results in a reduction of the wave height in the channel region. The inclusion of the ebb current in the computation results in a significant increase in penetration of the inlet. This is due to the effects of current refraction, which offset the effects of bottom refraction on the south slope of the channel. The computation with current required 4 iterations and was executed on a NEC SX/2. The required CPU time was 42 minutes at a performance of 250 Mflop/s.

5. DISCUSSION

The effect of ambient currents on wave propagation in and around harbours and coastal regions with reflective boundaries can be determined by means of a finite element model solving an extended mild-slope equation. Contrary to the original mild-slope equation for bottom refraction and diffraction only, the extended equation should be solved in an iterative way, as beforehand the wave direction in the computational region is unknown. Apart from the strength of the currents, the number of iterations depends on the number of elements per wave length. For stability reasons a minimum number of about 12 elements per characteristic wave length is required to obtain accurate estimates of the gradient of the velocity potential. This number is essentially the same as applied for the dissipative effects of bottom dissipation, see Kostense et al. (1986). For non-iterative computations without currents and dissipation the number of elements is determined by the desired accuracy; for engineering purposes usually about 8 elements per characteristic wave length are applied.

The presented numerical examples show that the extended model successfully integrates the effects of diffraction, bottom refraction, current refraction, reflection and dissipation. Moreover, it is shown that even relatively weak currents may have a significant influence on the wave propagation.

6. ACKNOWLEDGEMENT

The case study results shown in Fig.6 were established within the scope

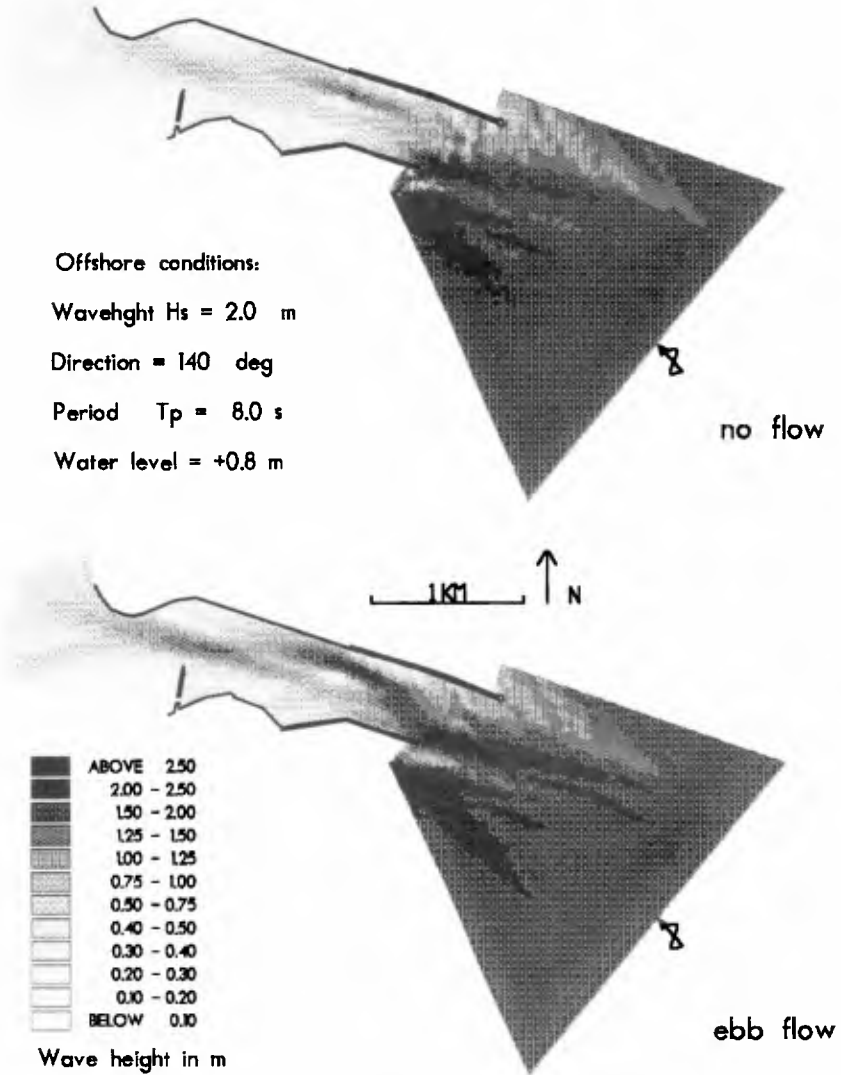


Figure 6 Malamocco inlet to the Venice lagoon area; effect of an ambient current field on the wave height distribution

of a study of the wave behaviour at the Venice Lagoon inlets, which study was commissioned to Delft Hydraulics by Consorzio VENEZIA NUOVA.

7. REFERENCES

- Arthur, R.S., 1950: Refraction of shallow water waves: the combined effect of currents and underwater topography; *Trans. Am. Geoph. Union*, Vol. 31, No. 4, pp. 549-552.
- Battjes, J.A. and Janssen, J.P.F.M., 1978: Energy loss and set-up due to breaking of random waves; *Proc. 16th Int. Conf. Coastal Engng.*, Hamburg, pp. 569-587.
- Berkhoff, J.C.W., 1972: Computation of combined refraction-diffraction; *Proc. 13th Int. Conf. Coastal Engng.*, Vancouver, pp. 471-490.
- Booij, N., 1981: Gravity waves on water with non-uniform depth and current; *Communications on Hydraulics*, Dept. of Civil Engng., Delft Univ. of Techn., Rep. no. 81-1.
- De Girolamo, P., Kostense, J.K. and Dingemans, M.W., 1988: Inclusion of wave breaking in a mild-slope model; in *Proc. Int. Conf. Computer Modelling in Ocean Engng.*, Venice.
- Hurdle, D.P., Kostense, J.K. and Van den Bosch, P., 1989: Mild-slope model for the wave behaviour in and around harbours and coastal structures in areas of variable depth and flow conditions; *Proc. 2nd Int. Symp. Water Modelling and Measurement*, Harrogate, England.
- Kirby, J.T., 1983: Propagation of weakly-nonlinear surface water waves in regions with varying depth and current; *Univ. Delaware, Newark, U.S.A.*, Research rep. no. CE-83-37
- Kirby, J.T., 1984: A note on linear surface wave-current interaction over slowly varying topography; *J. Geophys. Res.*, Vol. 89, No. C1, pp. 745-747.
- Kostense, J.K., Meijer, K.L., Dingemans, M.W., Mynett, A.E. and Van den Bosch, P., 1986: Wave energy dissipation in arbitrarily shaped harbours of variable depth; *Proc. 20th Int. Conf. Coastal Engng.*, Taipei, pp. 2002-2016.
- Radder, A.C., 1979: On the parabolic equation method for water wave propagation; *J. Fluid Mech.*, Vol. 95, No. 1, pp. 159-176.
- Yoon, S.B., 1987: Propagation of shallow-water waves over slowly varying depth and currents; thesis Cornell Univ., U.S.A.

CHAPTER 3

OBSERVATION OF DIRECTIONAL WAVE SPECTRA AND REFLECTION COEFFICIENT OF BREAKWATER IN A HARBOR

by

Tetsunori Ohshimo*, Kosuke Kondo**, and Tsunehiro Sekimoto*

ABSTRACT

Field investigations were performed in order to show the effect of wave diffraction by breakwaters through directional wave spectra measurements in a harbor, and to estimate the reflection coefficient by resolving the incident and reflected wave energy in front of a composite type breakwater. Combinations of an ultrasonic wave gage (USW) and an electromagnetic current meter (EMC) were used to measure the synchronized data of the water surface elevation and two horizontal velocities. The EMLM (Extended Maximum Likelihood Method) was applied for the calculation of the directional wave spectrum, and the modified EMLM for an incident and reflection wave field was applied for the estimation of the reflection coefficient. Through the estimated directional wave spectra, the effect of wave diffraction by breakwaters were discussed and the reflection coefficient was estimated at about 0.9. As a result, the applicability of the field investigation method and the modified EMLM were verified.

1. INTRODUCTION

In the design of maritime structures it is necessary to estimate not only the characteristic height and period parameters but also the random nature of sea waves. To describe the irregularity of sea waves with different frequencies and directions, the concept of directional wave spectrum is of great importance, since the directional wave spectrum employs both the frequency and the wave direction. It is basically possible to determine the directional wave spectrum of random sea waves by use of various methods and instruments. As there have been recent remarkable advances in the theories for estimating the directional wave spectrum, many field investigations have also been performed.

Among the methods for computation of directional spectrum, the Maximum Likelihood Method (MLM) is known to yield the highest directional resolution. However, it is applicable only to wave gage array measurements. So, Isobe, Kondo,

* Engineer, Design and Engineering Department, Penta-Ocean Construction Co., Ltd., 2-2-8 Koraku, Bunkyo-ku, Tokyo, 112 Japan.

** Principal Engineer, Design and Engineering Department, Penta-Ocean Construction Co., Ltd., 2-2-8 Koraku, Bunkyo-ku, Tokyo, 112 Japan.

and Horikawa (1984) extended the MLM to mixed arrays and named it the Extended Maximum Likelihood Method (EMLM). For the estimation of the directional spectrum by the EMLM, a set of data records of various wave properties at one point is sufficient. Moreover, at sites where wave transformation such as that due to refraction and diffraction is significant, the EMLM makes it possible to obtain the local directional wave spectrum. But the EMLM is not applied for the estimation of the directional wave spectrum near the reflection line, because the phase lag between the incident and reflected waves is not random. It is necessary to consider the fixed phase relation of each pair of incident and reflected wave components. So, the EMLM is modified for calculating the directional spectrum in the wave reflection system similar to the relation between the MLM and the MMLM (Isobe and Kondo, 1984). This method is termed the EMLM-2. It is possible to estimate the reflection coefficient of a vertical wall type breakwater by using the EMLM-2. This method to find the reflection coefficient of prototype structures is much easier than the other methods, because of one-point measurement.

The object of this study is to elucidate the diffracting characteristics through the change of the directional wave spectra calculated by the EMLM, and to estimate the reflection coefficient by analyzing the directional wave spectra by the EMLM-2.

2. FIELD INVESTIGATION

2.1 Site Location and Period of Investigation

The field investigations were carried out in the eastern shore of the Japan Sea at Kashiwazaki, Niigata prefecture, Japan, from January through February, 1986. A location map of the investigation site is shown in figure 1. As geographical features, Sado island and Noto peninsula lie north and west of the study area, respectively. So the dominant wave directions during storm are almost limited from northwest to west.

2.2 Harbor Layout and Field Investigation Program

Figure 2 explains the harbor layout and positions of the instrument combination of a wave gage and a current meter. The Harbor layout is a complex shape in order to keep the harbor tranquil, prevent retention of coastal sediment, allow free flow of water, and so on. Therefore, the wave transformation due to diffraction in the harbor is fairly intricate.

The field investigation program consisted of :

- 1) measurements of incident waves at location free from the effects of breakwaters (point P0);
- 2) measurements of waves diffracted by breakwaters (point P1, P3, and P4); and
- 3) measurements of diffracted and reflected waves in front of the south breakwater (point P2).

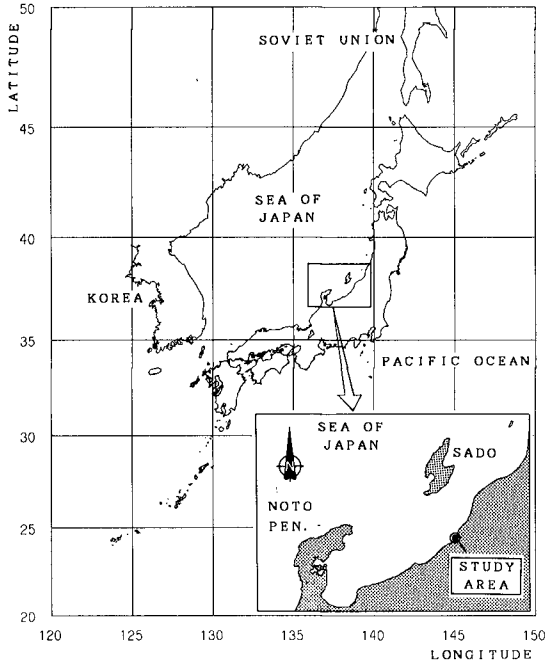


Figure 1 Location map of the investigation site

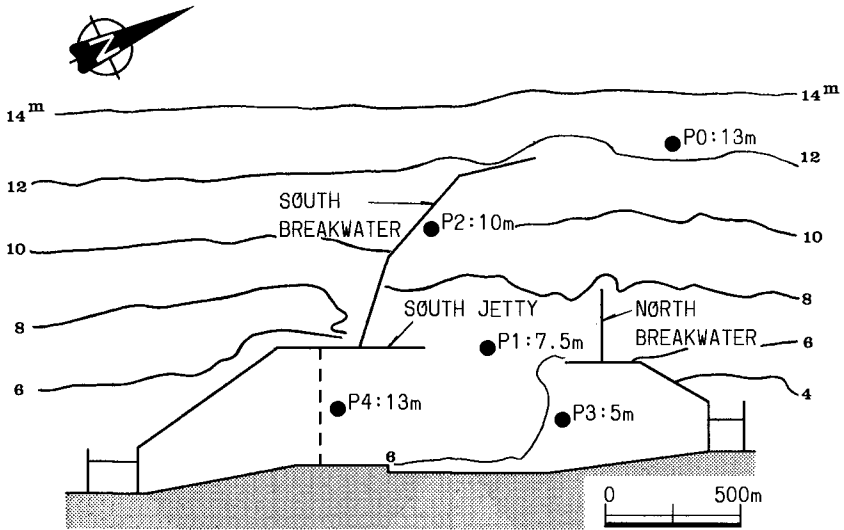


Figure 2 Harbor layout and positions of measuring point

In the third set of measurements, the distance between point P2 and the south breakwater was calculated beforehand, because the accuracy in estimating the directional wave spectra and the reflection coefficient changes depended upon the ratio of distance between the instruments and the breakwater (X) to wave length (L).

Schematic profile of the south breakwater, which is a composite type breakwater without wave energy dissipation, is given in figure 3. This figure also shows the location of point P2 where the instruments were installed at the distance of 32.0 m away from the south breakwater.

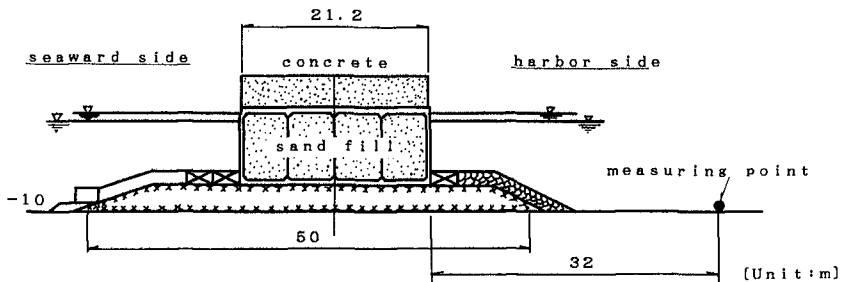


Figure 3 Schematic profile of the south breakwater

2.3 Measuring Instruments and Data Sampling Mode

Combinations of the ultrasonic wave gage (USW) and the electromagnetic current meter (EMC) were located on the bottom of the sea. The distance between USW and EMC is about 1.0 m and timing is synchronized through an electrical cable link. Therefore this measuring system is considered "one-point measuring" in terms of field scale.

USW acts as a reversed echo sounder to measure the surface elevation and EMC measures the two components of the horizontal water particle velocity at orthogonal angles. Data is measured for approximately 9 minutes every 2 hours, containing 1022 samples with an interval of 0.5 second, and stored on cassette tape inside the instrument.

3. METHOD OF DATA PROCESSING

3.1 Statistical Analysis

Both the USW and EMC data sometimes contained more noise spikes than were acceptable for statistical analysis. The data records were therefore semi-automatically corrected on a graphics terminal, which allowed an immediate visual check of corrections. All data were analyzed statistically, including the calculation of significant wave height and period by the zero-up-crossing method, principal wave direction and current velocity, etc.

3.2 Directional Spectrum Analysis

In the analysis of the directional spectrum with no reflected waves, that is, at positions P0, P1, and P3, the EMLM was applied for the calculation of the directional wave spectrum. In the analysis of the directional wave spectrum in the wave reflection system, however, the fixed phase relation of each pair of incident and reflected wave components should be considered. Therefore, the EMLM was modified to estimate the directional wave spectrum and the reflection coefficient in an incident and reflected wave field, according to the relation between the MLM and the MMLM (Isobe and Kondo, 1984). A directional wave spectrum and a reflection coefficient can be estimated as follows:

$$\hat{S}(k, \sigma) = \alpha \left[\sum_{m,n} \phi_{mn}^{-1} \cdot \{ H_m^*(k, \sigma) \exp(-ikx_m) + r H_m^*(k_r, \sigma) \exp(-ikx_{mr}) \} \right. \\ \left. \times \{ H_n(k, \sigma) \exp(ikx_n) + r H_n(k_r, \sigma) \exp(ikx_{nr}) \} \right]^{-1} \quad (1)$$

$$r = - \frac{\sum_{m,n} \phi_{mn}^{-1} \{ H_m^*(k, \sigma) \cdot H_n(k_r, \sigma) \cdot \exp\{ik(x_{nr} - x_m)\} + H_m^*(k_r, \sigma) \cdot H_n(k, \sigma) \cdot \exp\{ik(x_n - x_{mr})\} \}}{2 \sum_{m,n} \phi_{mn}^{-1} H_m^*(k_r, \sigma) \cdot H_n(k_r, \sigma) \cdot \exp\{ik(x_{nr} - x_{mr})\}} \quad (2)$$

where k is the wavenumber vector, σ is the angular frequency. $\hat{S}(k, \sigma)$ means the estimated wavenumber-frequency spectrum. r denotes the reflection coefficient. $\phi_{mn}(\sigma)$ is the cross-power spectrum of the water surface and horizontal velocity variations at point x_m and point x_n . H is the transfer function and $*$ denotes the complex conjugate. α is a proportionality constant which can be determined from the relationship between the wavenumber-frequency spectrum and the power spectrum. When the reflection coefficient r equals zero, it completely coincides with that for the EMLM. The present method is termed the EMLM-2.

3.3 Numerical Simulation of EMLM-2

Applying the MMLM for estimating the directional wave spectrum in an incident and reflected wave field, the resolution power of the directional wave spectrum depends on the number and the arrangement of wave gages. In general, the resolution power increases with increasing number of wave gages, and spurious spectral peaks appear if the nearest wave gage is located farther than about $0.2L$ from the reflection line (L : wave-length). Therefore, in the analysis of the directional wave spectrum, using the EMLM-2, it is considered that the resolution power of the directional wave spectrum also depends on the number and arrangement of instruments.

Numerical simulations were performed to example the validity of the EMLM-2. The procedure for the numerical simulation is as follows:

- 1) Specify a functional form for the directional spectrum,

$S(k, \sigma)$, and reflection coefficient, r . Here, the Mitsuyasu-type directional distribution expressed by equation (3) was used. The reflection coefficient was assumed constant for every directional component of waves.

$$S(k, \sigma) = \cos^{2s} \{ (\theta - \theta_0) / 2 \} \quad (3)$$

where θ_0 is a principal wave direction and s is a parameter respecting the degree of directional energy concentration.

- 2) Calculate $\phi_{mn}(\sigma)$ for all given components using the relationship between the cross-power spectrum and the directional wave spectrum in an incident and reflected wave field, which is expressed by equation (4).

$$\begin{aligned} \phi_{mn}(\sigma) = & \int_k S(k, \sigma) \\ & \times \{ \exp(ikx_m) + r \exp(ikx_{mr}) \} \\ & \times \{ \exp(-ikx_n) + r \exp(-ikx_{nr}) \} dk \end{aligned} \quad (4)$$

- 3) Estimate the directional energy distribution from equation (1) and compare to the given one.

Figure 4 shows the definition sketch of an incident and reflected wave field for numerical simulation. X is the distance between the measuring point and the reflective wall, and θ is the wave direction. In this simulation the calculation conditions were set as the typical conditions in this field investigation. For example, the wave period was 8 seconds, the degree of energy concentration was 100, the wave direction was 60 degrees from perpendicular to the breakwater and the given reflection coefficient was 0.90. The number of measuring component was 3 and the distance between USW and EMC was 0.0 m.

Moreover the distance between the reflection line and measuring point, X , is an important parameter to keep the accuracy of estimating the directional wave spectrum and the reflection coefficient. So the three ratio of the distance, X , and wave length, L , that is, $X/L=0.2, 0.5$, and 1.0 were set for the conditions of numerical simulations.

Figure 5 shows examples of the numerical simulation, and R_s and R_p are the estimated reflection coefficients by use of the methods mentioning in 4.4. When $X/L=0.2$, the resolution power is highest and the estimated reflection coefficient also agrees with the given one. When $X/L=0.5$, the estimated reflection coefficient also agrees with the given one, though the resolution power goes down a little and spurious peaks appear around 270 degrees. When $X/L=1.0$, the resolution power goes down considerably and the

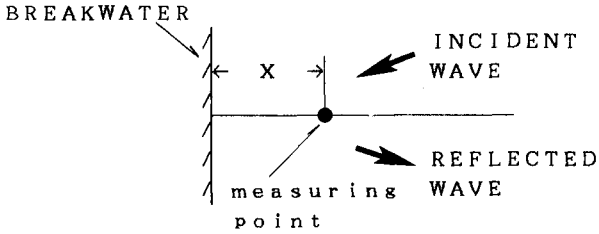


Figure 4 Definition sketch of an incident and reflected wave

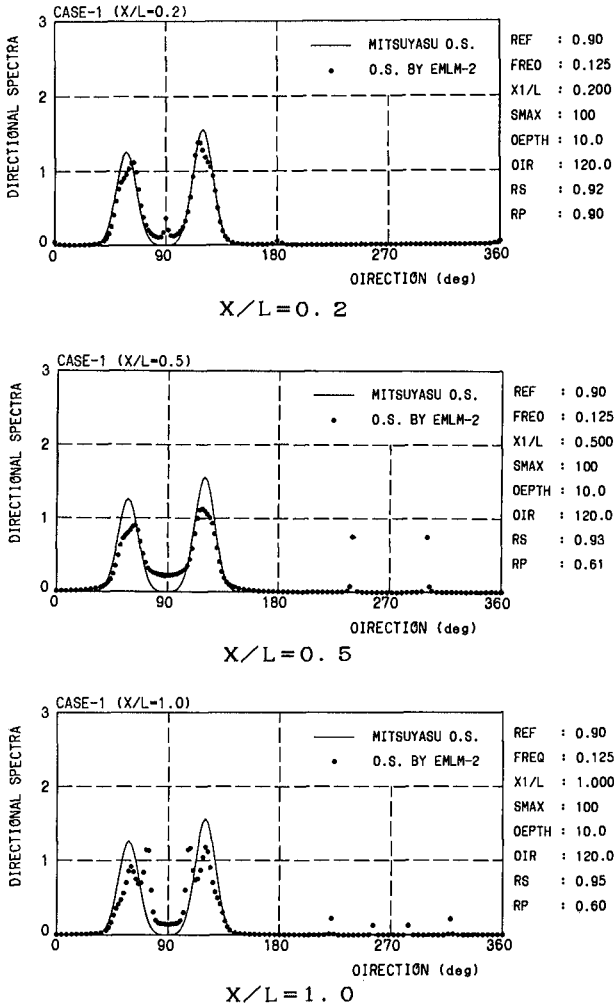


Figure 5 Examples of numerical simulation

estimated reflection coefficient does not agree with the given one.

So, if the measuring point is located far from the reflection line, the resolution power goes down and spurious peaks appear in the estimated spectrum. It is necessary that X/L should be set less than 0.2 in order to keep the accuracy of estimating both the directional wave spectrum and the reflection coefficient, and that X/L should be set less than about 0.5 in order to keep the accuracy of estimating the reflection coefficient.

4. RESULTS

4.1 Wave Conditions

The wave conditions such as significant wave height, significant wave period and principal wave direction during the observation periods are shown in figure 6. As the significant wave heights were always more than 1.0 m, sometimes reaching 2.0 m to 3.0 m, the wave climate was very rough during the period of investigation. The most prevalent significant wave period was about 6 s to 8 s, though it seems that the wave periods become longer in accordance with the increase of wave height. The wave directions clearly changed from west to north in accordance with the increase of wave height. This change of the wave direction followed a move of a low atmospheric pressure.

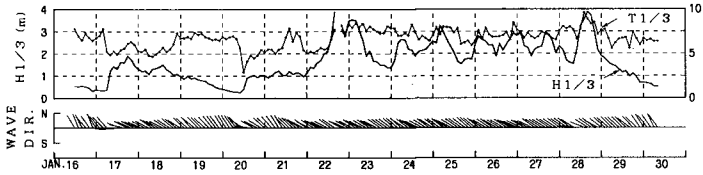
4.2 Wave Characteristics in a Harbor

Figure 7 shows the relationship between the incident wave direction and the ratio of incident and diffracted wave heights, and compares the diffracted wave direction to the incident wave direction. Symbols are field data and the solid line is the results of numerical simulation in respect of harbor tranquility (Kondo, Shimizu, and Yamada, 1987).

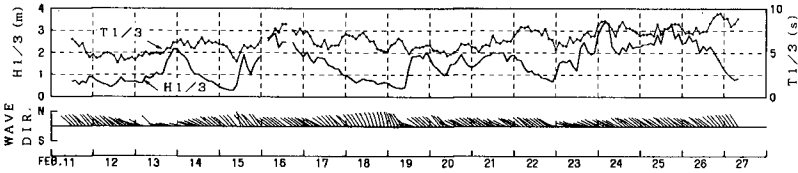
In numerical simulation, the incident directional wave spectrum was considered of a combination of the Bretschneider-Mitsuyasu-type frequency spectrum and the Mitsuyasu-type directional distribution, instead of the observed directional wave spectrum. The other input conditions were typically determined in consideration of mean wave climate during investigations, that is, the significant wave period of 7 s and the degree of energy concentration, S_{max} , of 25, were chosen.

As regards the rate of significant wave heights, field data exhibits the gradual increase according to the change of incident wave direction from west to northwest because of the shelter of the south breakwater.

Comparing between two wave directions at position P0 and P1, the characteristic of the diffracted wave by the south breakwater is obviously recognized. That is to say, when the incident wave directions are west to northwest, the diffracted wave directions are constantly northwest which is

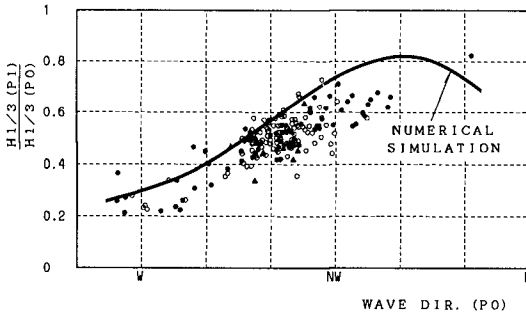


(a) 1st investigation period

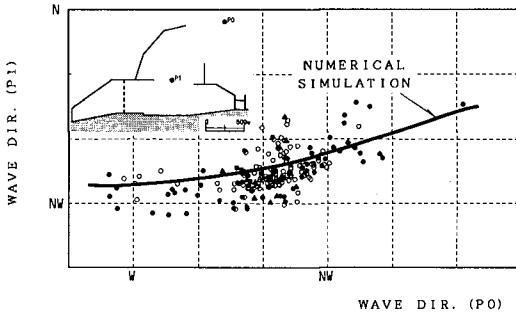


(b) 2nd investigation period

Figure 6 Wave conditions during the observation periods



(a) Ratio of the incident and diffracted wave height



(b) Comparison of the incident and diffracted wave direction

Figure 7 Wave characteristics in a harbor

a straight line direction from the tip of the south breakwater to the measuring point. When the incident wave directions are northwest to north, the diffracted wave directions change in accordance with the incident one. The results of numerical simulation show good agreement with field data.

4.3 Change of Directional Wave spectra due to Diffraction

In order to estimate the effect of wave diffraction due to the south breakwater through the directional wave spectra, the directional wave spectra were computed for three different incident wave direction data sets as shown in table 1.

Table 1 Cases for estimating the directional wave spectrum

CASE NO.	DATE	WAVE DIRECTION	H _{1/3} (m)	T _{1/3} (s)
1	1/17 12:00	W (N96° W)	1.31	4.9
2	1/22 12:00	WNW (N64° W)	2.09	5.6
3	1/15 12:00	NNW (N14° W)	1.30	5.0

Examples of the estimated directional wave spectrum are shown in figure 8. Each figure consists of the directional energy distribution contour (central part), the frequency spectra (upper part) and the directional spreading function (righthand part), estimated using the EMLM. The upper three figures are the results at position P0. The lower three figures are the results at position P1.

When the incident wave direction is west, the south breakwater causes a change between the two directional wave spectra as follows.

- 1) The directional peak of incident wave changes to a straight line direction from the tip of the south breakwater in the sheltered area.
- 2) The degree of energy concentration of the directional spreading function in the sheltered area becomes higher than that of the incident wave.
- 3) The frequency power spectrum at sheltered area is different from that at incident area, and the significant wave period changes shorter in the sheltered area. This is because the wave energy included between 0.15 Hz and 0.18 Hz frequency band is more sheltered than that included between 0.21 Hz and 0.24 Hz frequency band.

On the other hand, when the incident wave direction is north-north-west, the two directional wave spectra are almost similar. In this case the south breakwater hardly influences the change of the directional wave spectrum in the sheltered area.

When the incident wave direction is west-north-west that is intermediate direction between the above-mentioned two cases, the change of two directional wave spectra also shows the intermediary characteristics.

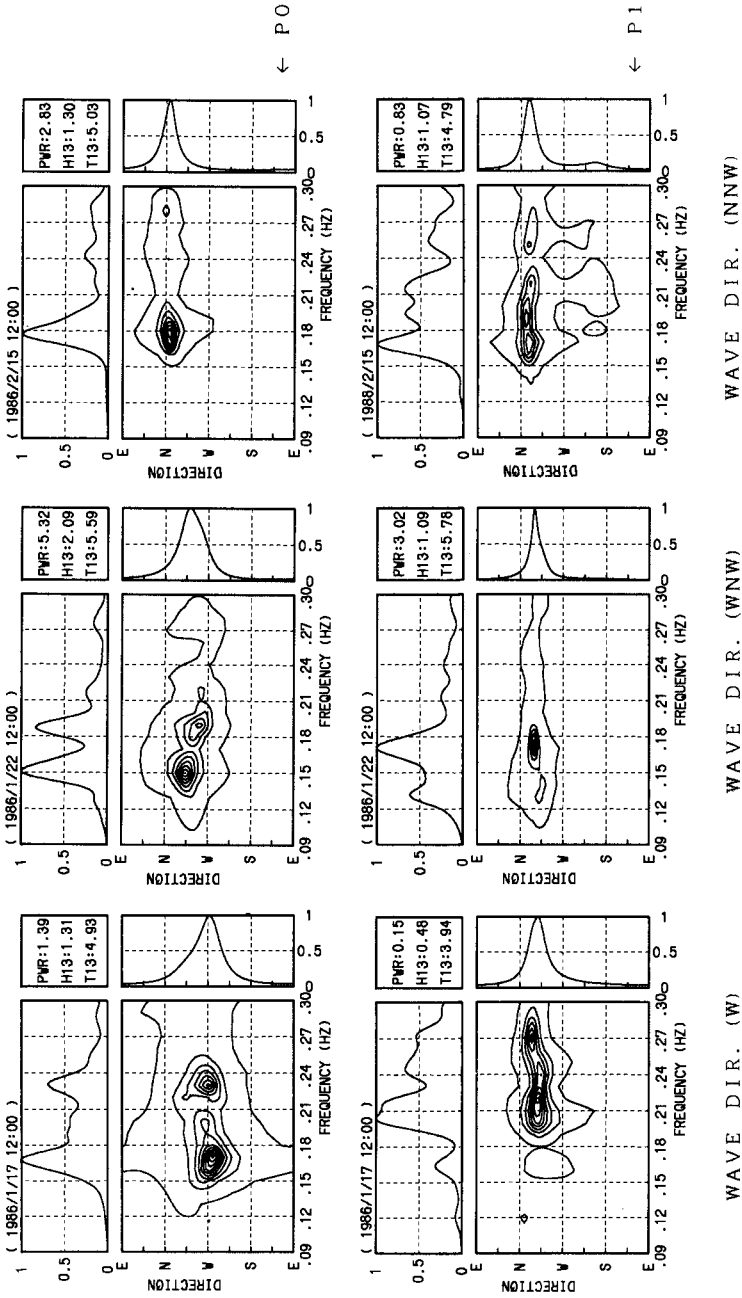


Figure 8 Examples of the estimated directional wave spectrum by the EMLM at positions P0 and P1

Figure 9 shows the three directional wave spectra at positions, P0, P1, and P3, in order to understand the effect of wave diffraction by breakwaters more than ever. In the incident directional wave spectrum, the swell and wind wave co-exist, but two wave directions are different, that is, the swell direction with 0.12 Hz to 0.15 Hz frequency is north-west, and the wind wave direction with 0.18 Hz to 0.24 Hz frequency is west. The frequency power of the swell is lower than that of the wind wave at position P0. But at position P1, the frequency power of the swell becomes higher than that of the wind wave. This tendency is more clear at position P3 which is sheltered by both the south breakwater and the north jetty, therefore, the swell only enters into the interior of the harbor.

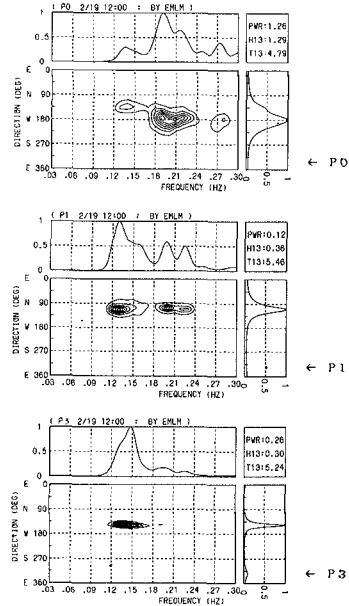


Figure 9
Examples of the estimated wave spectrum

4.4 Reflection Coefficient and Directional Wave Spectra

(1) Reflection Coefficient

In estimating the reflection coefficient, there are the following two methods. Equation (2) gives an estimation of the reflection coefficient (R_s) for each frequency and for each direction. The second method (R_p) is to adopt the square root of the ratio between the integrated reflected and incident wave energy.

The estimated reflection coefficient by the second method are shown in table 2. In accordance with the results of the numerical simulation, the integrated reflected and incident wave energy between 0.03 Hz and 0.15 Hz was only used for estimating the reflection coefficient, in order to keep the accuracy of estimation. Thus, ten cases including higher wave energy in the frequency range of 0.03 Hz to 0.15 Hz were chosen.

The reflection coefficient shows rather stable values between 0.75 and 0.99 with a mean value of 0.86. Judging from approximate values (0.7-1.0) of the reflection coefficients for a vertical wall as reported in various sources (Goda, 1985), this value is valid.

- (2) Directional wave spectra in incident and reflected wave field.

Figure 10 shows examples of the estimated directional wave spectrum at position, P2, that is, in front of the south breakwater. The EMLM-2 was applied for estimation. 0 degree means that the wave direction is perpendicular to the south breakwater, and 90 degrees is parallel to the south breakwater. The wave direction is defined anti-clockwise. The estimated directional wave spectra have two peaks in symmetrical positions. The direction of the first peak is about 65 degrees, and that of second peak is about 115 degrees.

Judging from the harbor layout, it is understood that the first peak corresponds to the incident wave which come from the tip of the south breakwater, the second peak corresponds to the reflected wave which are set as mirror images of the incident wave at south breakwater. The directional peaks of the incident and reflected waves are sufficiently separated to permit use of the EMLM-2 for estimating the directional wave spectrum.

The peaks between 180 degrees and 360 degrees are, however, regarded as spurious peaks in consideration of the harbor layout and the results of numerical simulation.

Figure 11 shows example of the directional wave spectrum at position, P2, for the same data set with Figure 10, by use of the EMLM. There are also the directional peaks of the incident and reflected wave in this result, whereas the resolution power is lower than the result of the EMLM-2.

5. CONCLUSIONS

The wave measurements were carried out by means of combinations of a wave gage and a current meter. The field data was processed to estimate the directional wave spectra by the EMLM and the EMLM-2, which is the modified EMLM for calculating the directional wave spectrum in an incident and reflected wave system. The effect of diffraction by breakwaters were discussed through the transformation of the directional wave spectra, and the reflection coefficient of the composite type breakwater, without wave energy dissipation, was estimated at a mean value of 0.86. As a result, the applicability of the field investigation method and the EMLM-2 were verified.

ACKNOWLEDGEMENTS

The authors wish to thank Mr. S. Imai of Tokyo Electric Power Co., Inc., and Mr. M. Nakamura of Tokyo Electric Power Service Co., Ltd., for their kind support. We would also thank Associate Professor M. Isobe of University of Tokyo for his useful suggestion.

Table 2 Reflection coefficient of the south breakwater

NO.	DATE	H1/3 (m)	T1/3 (s)	REFLECTION COEFFICIENT
1	1/28 20:00	0.92	4.95	0.84
2	1/28 18:00	0.91	4.34	0.99
3	1/23 6:00	0.87	5.35	0.77
4	1/26 8:00	0.85	4.88	0.96
5	1/24 6:00	0.83	5.29	0.88
6	1/26 2:00	0.82	4.38	0.81
7	1/26 6:00	0.81	4.63	0.89
8	1/24 8:00	0.80	5.14	0.75
9	1/25 8:00	0.80	4.57	0.89
10	1/25 4:00	0.78	4.71	0.78

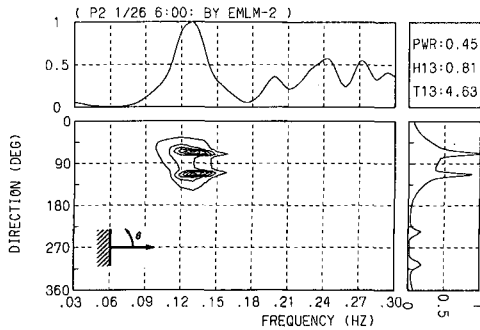


Figure 10 Example of the estimated direction wave spectrum in front of the south breakwater by EMLM-2

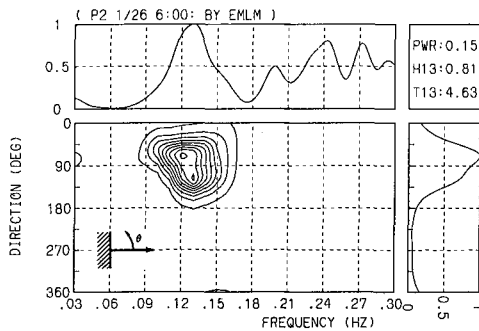


Figure 11 Example of the estimated directional wave spectrum in front of the south breakwater by EMLM

REFERENCES

- 1) Goda, Y. (1985): Random Seas and Design of Maritime Structures, University of Tokyo Press, 323p.
- 2) Isobe, M. and K. Kondo (1984): Method for Estimating Directional Wave Spectrum in Incident and Reflected Wave Field, Proc. 19th Int. Conf. Coastal Eng., Houston, pp.467-483.
- 3) Isobe, M., Kondo, K., and Horikawa, K. (1984): Extension of MLM for Estimating Directional Wave Spectrum, Proc. Symposium on Description and Modeling of Directional Seas, Copenhagen, Paper No. A-6, 15p.
- 4) Kobune, K. and N. Hashimoto (1986): Estimation Directional Spectra from the Maximum Entropy Principle, Proc. 5th International Offshore Mechanics and Arctic Engineering Symposium, Vol.I, ASME, Tokyo, pp.72-79.
- 5) Kondo, K., Akama, M., and Isobe, M. (1986): Measurement of Reflection Coefficient of Seawall in Omura Bay, Proc. 20th Int. Conf. Coastal Eng., Taipei, pp. 1987-2001.
- 6) Kondo, K. and J.P.A. de Koning (1986): Comparison Sea Measurements by an Orbital following Buoy and a Combination of a Wave Gage and a Current Meter, Proc. 5th International Offshore Mechanics and Arctic Engineering Symposium, Vol.I, ASME, Tokyo, pp.51-58.
- 7) Kondo, K., Shimizu, T., and Yamada, K. (1987): Green Function Method for Calculation of Directional Wave Spectrum in a Harbor, Proc. 34th Japanese Conf. on Coastal Eng., pp. 106 - 110, (in Japanese).

CHAPTER 4

DIRECTIONAL SPECTRUM ESTIMATION

FROM A BAYESIAN APPROACH

Noriaki Hashimoto* and Koji Kobune**

ABSTRACT

A new directional spectral estimation method using a Bayesian approach is proposed. The proposed method is examined for numerical simulation data, and the validity of the method is discussed. Some examples of the directional spectra estimated from field observation data attained at an offshore oil rig utilizing seven wave probes are also shown in this report. The major conclusions of the report are : (1) The proposed method can be applied for more than four arbitrarily mixed instrument array measurements. (2) It has a higher resolution power than other existing methods for estimating directional spectrum. (3) It is a better method for estimating directional spectra from the cross-power spectra contaminated with estimation errors. (4) It is more adaptable to reformulation of the estimation equations as the study of structures of directional spectrum progresses.

1. INTRODUCTION

Directional spectra are the fundamental properties of ocean waves expressing the energy distribution as a function of the wave frequency and direction of wave propagation. Many efforts have been made to estimate directional spectra on the bases of point measurements utilizing various wave probes, and several methods have been proposed to improve the directional resolution of the estimation.

These methods are based on a mathematical relationship between the directional spectrum and the cross-power spectra. The cross-power spectra are computed from time series records of various wave properties. In practice, wave records are often contaminated with noises. This leads to errors in the cross-power spectral estimation. Thus, the estimate of the directional spectrum is often biased by the noises and errors associated with the observed cross-power spectra.

However, no current methods take into account the existence of such errors. The directional spectrum is estimated only to satisfy the above mentioned relationship with the observed cross-power spectra, and this may be one of the causes that estimates of the directional spectrum sometimes result in poorly conditioned shape, i.e. negative values or zigzags, for instance.

* Senior Research Engineer, Marine Hydrodynamics Division.

**Chief, Marine Observation Laboratory, Marine Hydrodynamics Division.
Port and Harbour Research Institute, Ministry of Transport,
1-1, Nagase 3chome, Yokosuka, 239, Japan

The same type of problems are seen in the field of the regression analysis problems where the number of the parameters to be estimated is large compared with the sample size. In order to overcome these difficulties, Akaike(1980) introduced a Bayesian model which better approximates the sample data, and which is compatible with an a priori condition subsistent in the phenomenon to be analyzed.

The estimation of the directional spectrum can be considered as a regression analysis problem to find the most suitable model from limited data. Therefore, the Bayesian approach should be useful to obtain the most reasonable model (directional spreading function) which best approximates the sample data (cross-power spectra) and which also conforms to the subsistent nature of the physical phenomenon, i.e., continuous and smooth variation of its value. This is accomplished by maximizing the likelihood of the model with a priori condition that the directional spreading function varies smoothly over the wave direction.

In the practical computation, another parameter which is called a hyperparameter, is introduced to consider the balance of the two requirements imposed on the model : to maximize the likelihood of the model and to maintain the smoothness of the model. In order to select the most suitable value of the hyperparameter for the given cross-power spectra, the ABIC (Akaike's Bayesian Information Criterion, 1980) is also introduced as a criterion to determine the most suitable model.

The proposed method is examined by numerical simulations, and its application to a practical directional wave analysis is also presented with the data recently recorded on an offshore oil rig at a water depth of 150 meters.

2. FUNDAMENTAL EQUATIONS RELATED TO DIRECTIONAL SPECTRUM

The relationship between the cross-power spectrum for a pair of arbitrary wave properties and the directional spectrum is introduced by Isobe et al.(1984) as the following equation :

$$\begin{aligned} \Phi_{mn}(f) = \int_0^{2\pi} H_m(f, \theta) H_n^*(f, \theta) [\cos \{k(x_{mn} \cos \theta + y_{mn} \sin \theta)\} \\ - i \sin \{k(x_{mn} \cos \theta + y_{mn} \sin \theta)\}] S(f, \theta) d\theta \end{aligned} \quad (1)$$

where f is the frequency, k is the wave number, θ is the wave propagation direction, $\Phi_{mn}(f)$ is the cross-power spectrum between the m -th and the n -th wave properties, $H_m(f, \theta)$ is the transfer function from the water surface elevation to the m -th wave property, i is the imaginary unit, $x_{mn} = x_n - x_m$, $y_{mn} = y_n - y_m$, (x_m, y_m) is the location of the wave probe for the m -th wave property, $S(f, \theta)$ is the directional spectrum and the superscript * denotes the complex conjugate.

The directional spectrum $S(f, \theta)$ is often expressed as a product of the frequency spectrum and the directional spreading function.

$$S(f, \theta) = S(f) G(\theta|f) \quad (2)$$

where, $S(f)$ is the frequency spectrum and $G(\theta|f)$ is the directional spreading function. The directional spreading function takes non-negative values and satisfies the following relationship.

Table 1 Transfer function from small amplitude wave theory

MEASURED QUANTITY	SYMBOL	$h(k, \sigma)$	α	β
Water surface elevation	η	1	0	0
Excess pressure	p	$\rho g \frac{\cosh kz}{\cosh kd}$	0	0
Vertical water surface velocity	η_t	$-i\sigma$	0	0
Vertical water surface acceleration	η_{tt}	$-\sigma^2$	0	0
Surface slope (x)	η_x	ik	1	0
Surface slope (y)	η_y	ik	0	1
Water particle velocity (x)	u	$\sigma \frac{\cosh kz}{\sinh kd}$	1	0
Water particle velocity (y)	v	$\sigma \frac{\cosh kz}{\sinh kd}$	0	1
Water particle velocity (z)	w	$-i\sigma \frac{\sinh kz}{\sinh kd}$	0	0

k : wave number, σ : angular frequency, d : water depth, z : elevation from the bottom, ρ : fluid density, g : gravitational acceleration.

$$\int_0^{2\pi} G(\theta|f) d\theta = 1 \quad (3)$$

The transfer function $H_m(f, \theta)$ in Eq.(1) is generally expressed in the form

$$H_m(f, \theta) = h_m(f) \cos^{\alpha_m \theta} \sin^{\beta_m \theta} \quad (4)$$

where the function h_m and the parameter α_m and β_m in Eq.(4) are shown in Table 1.

Equations (1) are the fundamental equations for the estimation of the directional spectrum on the basis of the simultaneous measurements of various wave properties. If the function $S(f, \theta)$ which satisfies Eq.(1) and which takes only non-negative values is obtained, the function is called a directional spectrum.

3. ESTIMATION OF DIRECTIONAL SPECTRUM FROM THE BAYESIAN APPROACH

The directional spreading function takes values greater than or equal to zero, but in this section, the function is treated as a function which always takes positive values only.

Firstly, it is assumed that the directional spreading function is expressed as a piecewise-constant function over the directional range from 0 to 2π ($K\Delta\theta=2\pi$). This assumption is commonly employed in the numerical computation of random waves.

Since $G(\theta|f) > 0$, and let

$$\ln G(\theta_k|f) = x_k(f), \quad (k=1, \dots, K) \tag{5}$$

the directional spreading function is approximated by the following equation.

$$G(\theta|f) = \prod_{k=1}^K \exp\{x_k(f)\} I_k(\theta) \tag{6}$$

where,

$$I_k(\theta) = \begin{cases} 1 & : (k-1)\Delta\theta \leq \theta < k\Delta\theta \\ 0 & : \text{otherwise,} \quad (k=1, \dots, K) \end{cases} \tag{7}$$

Substituting Eq.(6) into Eq.(1) and after some manipulation, the following equation is obtained considering the errors $\epsilon_{mn}(f)$ of the cross-power spectra.

$$\phi_i(f) = \sum_{k=1}^K \alpha_{ik}(f) \exp\{x_k(f)\} + \epsilon_i(f) \quad (i=1, \dots, 2N) \tag{8}$$

where, the subscripts $i=1$ to N denote real parts and $i=N+1$ to $2N$ denote imaginary parts of the complex numbers ϕ_i , $\alpha_{i,k}$ and ϵ_i ,

$$N = M \times (M+1) / 2; \quad M: \text{Number of the wave probes} \tag{9}$$

$$\alpha_{i,k}(f) = \Delta\theta H_m(f, \theta_k) H_n^*(f, \theta_k) [\cos\{k(x_{mn} \cos \theta_k + y_{mn} \sin \theta_k) - i \sin\{k(x_{mn} \cos \theta_k + y_{mn} \sin \theta_k)\} / \sqrt{\Phi_{mm}(f)\Phi_{nn}(f)}] \tag{10}$$

$$\phi_i(f) = \Phi_{mn}(f) / \{S(f) \sqrt{\Phi_{mm}(f)\Phi_{nn}(f)}\} \tag{11}$$

$$\epsilon_i(f) = \epsilon_{mn}(f) / \sqrt{\Phi_{mm}(f)\Phi_{nn}(f)} \tag{12}$$

In Eq.(8), though ϕ_i , $\alpha_{i,k}$ and ϵ_i are the functions of the frequency f , f is omitted to simplify the expression hereafter.

When ϕ_i ($i=1, 2, \dots, 2N$) are given and ϵ_i ($i=1, \dots, 2N$) are assumed to be independent from each other and have the probability of their occurrence expressed by the normal distribution having the mean 0 and the variance σ^2 , the likelihood function of x_k ($k=1, \dots, K$) and σ^2 is given by Eq.(13).

$$L(x_1, \dots, x_K; \sigma^2) = \frac{1}{(2\pi\sigma^2)^{2N}} \exp\left[-\frac{1}{2\sigma^2} \sum_{i=1}^{2N} \left\{ \phi_i - \sum_{k=1}^K \alpha_{i,k} \exp(x_k) \right\}^2\right] \tag{13}$$

In the derivation of the equations mentioned above, the directional spreading function $G(\theta|f)$ is expressed by a piecewise constant function and the correlation between the wave energy falling on each segment of θ has not yet been taken into account considering the background of the linear wave theory. However, it is not unreal to assume that the energy distribution over the wave directions is discontinuous. Therefore, the additional condition must be added. As the simplest additional condition, the following condition is added by assuming that the second order difference of $\{x_k\}$ are close to zero for $k=1, \dots, K$. That is,

$$\sum_{k=1}^K \{x_k - 2x_{k-1} + x_{k-2}\}^2 \quad (x_0 = x_K, x_{-1} = x_{K-1}) \quad (14)$$

becomes smaller as the estimate of the directional spreading function $G(\theta | f)$ becomes smoother.

The estimate of x_k maximizing the likelihood (Eq.(13)) and minimizing the above mentioned quantity are determined as the estimates which maximize the following quantity :

$$\ln L(x_1, \dots, x_K; \sigma^2) - \frac{u^2}{2\sigma^2} \sum_{k=1}^K (x_k - 2x_{k-1} + x_{k-2})^2 \quad (15)$$

where, u^2 is a hyperparameter.

The maximization of Eq.(15) is achieved by maximizing the following exponential function having the power expressed by Eq.(15).

$$L(x_1, \dots, x_K; \sigma^2) \exp\left\{-\frac{u^2}{2\sigma^2} \sum_{k=1}^K (x_k - 2x_{k-1} + x_{k-2})^2\right\} \quad (16)$$

When normalized, the second term can be regarded as a following distribution of $\mathbf{x} = (x_1, \dots, x_K)$.

$$p(\mathbf{x} | u^2, \sigma^2) = \left(\frac{u}{\sqrt{2\pi}\sigma}\right)^K \exp\left\{-\frac{u^2}{2\sigma^2} \sum_{k=1}^K (x_k - 2x_{k-1} + x_{k-2})^2\right\} \quad (17)$$

In Bayesian statistics, the distribution $p(\mathbf{y} | \mathbf{x})$, which is called the posterior distribution, is proportional to the likelihood $L(\mathbf{y} | \mathbf{x})$ and the distribution $p(\mathbf{y})$, which is called the prior distribution, as follows.

$$p(\mathbf{y} | \mathbf{x}) \propto L(\mathbf{y} | \mathbf{x}) p(\mathbf{y}) \quad (18)$$

Thus, the distribution of Eq.(17) corresponds to the prior distribution in Bayesian statistics. The estimate of \mathbf{x} obtained by maximizing Eq.(16) is regarded as the mode of the posterior distribution of $p_{\text{post}}(\mathbf{x} | u^2, \sigma^2)$.

If the value of u is given, the value of \mathbf{x} which maximizes Eq.(18) are determined by minimizing Eq.(19), regardless of the values of σ^2 .

$$\sum_{i=1}^{2N} \left\{ \phi_i - \sum_{k=1}^K \alpha_{i,k} \exp(x_k) \right\}^2 + u^2 \left\{ \sum_{k=1}^K (x_k - 2x_{k-1} + x_{k-2})^2 \right\} \quad (19)$$

The most suitable values of the hyperparameter u^2 and the variance σ^2 are determined so that the following ABIC is minimum.

$$\text{ABIC} = -2 \ln \int L(\mathbf{x}, \sigma^2) p(\mathbf{x} | u^2, \sigma^2) d\mathbf{x} \quad (20)$$

4. NUMERICAL COMPUTATION OF DIRECTIONAL SPECTRUM

In order to estimate the directional spectrum by means of the Bayesian approach, the minimization of Eq.(19) and the integration and the minimization of Eq.(20) must be performed. The following is the summary of the procedure of the computation presented by Ishiguro (1985) and Sakamoto (1985).

- 1) For a proper value of hyperparameter u and initial values x_0 of x , compute the estimate of \hat{x} by means of the least square method utilizing Eq.(21).

$$J(x) \cong |\hat{A}x - \hat{B}|^2 + u^2 |Dx|^2 \tag{21}$$

where,

$$\hat{A} = AE(x_0) \tag{22}$$

$$\hat{B} = B - AF(x_0) + AE(x_0)x_0 \tag{23}$$

$$A = \begin{bmatrix} \alpha_{1,1}, & \dots, & \alpha_{1,K} \\ \vdots & & \vdots \\ \alpha_{2N,1}, & \dots, & \alpha_{2N,K} \end{bmatrix} \tag{24}$$

$$B = (\phi_1, \dots, \phi_{2N})^t \tag{25}$$

$$D = \begin{bmatrix} 1 & 0 & 0 & \dots & 0 & 1 & -2 \\ -2 & 1 & 0 & \dots & 0 & 0 & 1 \\ 1 & -2 & 1 & \dots & 0 & 0 & 0 \\ \vdots & \vdots & \vdots & \ddots & \vdots & \vdots & \vdots \\ 0 & 0 & 0 & \dots & 1 & -2 & 1 \end{bmatrix} \tag{26}$$

$$E(x) = \begin{bmatrix} \exp(x_1) & 0 & \dots & 0 \\ 0 & \exp(x_2) & \dots & 0 \\ \vdots & \vdots & \ddots & \vdots \\ 0 & 0 & \dots & \exp(x_K) \end{bmatrix} \tag{27}$$

$$F(x) = \{\exp(x_1), \dots, \exp(x_K)\}^t \tag{28}$$

That is, for a certain initial value x_0 , the values of x_1 are computed by means of the least square method utilizing Eq.(21) through Eq.(23). Substituting these x_1 for the initial x_0 in Eq.(22) to Eq.(23), and repeating the same process, we obtain the another set of x_2 . Iterating these process until the values of x converges to \hat{x} , the estimate of \hat{x} is obtained for the given value of u^2 .

- 2) Compute the ABIC by Eq.(29) for the given u and the estimate of \hat{x} obtained above.

$$ABIC = 2N \ln(2\pi) + 2N + 2N \ln(\hat{\sigma}^2) - K \ln(u^2) + \ln\{\det(\hat{A}^t \hat{A} + u^2 D^t D)\} \tag{29}$$

where,

$$\hat{\sigma}^2 = \frac{1}{2N} \{|\hat{A}\hat{x} - \hat{B}|^2 + u^2 |D\hat{x}|^2\} \tag{30}$$

and \hat{A} and \hat{B} are the coefficient matrix renewed in Eq.(22) and (23), which are computed for the least square estimate \hat{x} .

- 3) Changing the value of u , repeat the process of 1) and 2).
- 4) From various estimates of \hat{x} obtained through the process 1) through 3), choose the values \hat{u}^2 and $\hat{\sigma}^2$ as well as the estimate \hat{x} which yield the minimum ABIC as the final estimate of x as the estimate of the directional spreading function.

In the computation of the estimate of the directional spreading function mentioned above, the initial values of x_0 are given uniformly ($x_i = \ln(1/2\pi)$). The iteration of Eq.(21) is terminated when the standard deviation of the difference between the values of x_n of n-th step and that of the previous step is smaller than or equal to 10^{-3} , i.e., $|\sigma_n| \leq 10^{-3}$.

In addition, the hyperparameter which minimizes the ABIC is found by the method of trial and error. The value of the hyperparameter is given by utilizing Eq.(31) with the value of m changing in a sequential manner.

$$u = ab^m \quad (m=1, 2, \dots) \quad (31)$$

The derivation of the Eq.(21) through Eq.(30) and the details of the computation is given in Hashimoto et al.,(1987).

5. EXAMINATION OF THE ESTIMATION METHOD BY NUMERICAL SIMULATION

5.1 procedure of numerical simulation

Numerical simulations were performed to examine the validity of the proposed method. The procedure is the same as the one used for examining the EMLM (Isobe et al.,1984).

The directional spectrum is expressed as a product of the directional spreading function and the frequency spectrum and is computed frequency by frequency. Hence, in this section, a directional spreading function for an arbitrarily chosen frequency is examined. The practical procedure of the numerical simulation is as follows.

- 1) The directional spreading functions to be employed in the examination are Mitsuyasu-type ones which are given by Eq.(32).

$$G(\theta) = \sum_i \alpha_i \cos^2 S_i \left(\frac{\theta - \theta_i}{2} \right) \quad (32)$$

where α_i is the proportionality coefficient and is given so that Eq.(32) satisfies Eq.(3). For the simulation of a uni-directional sea, the directional spreading function is given by Eq.(32) with $i=1$ only. On the other hand, for a bi-directional sea, two different wave groups having different values of α_i, S_i, θ_i ($i=1, 2$) are superimposed.

- 2) The cross-power spectra are computed for the directional spreading function given by process 1) utilizing Eq(1).
- 3) On the basis of the cross-power spectra obtained above, the directional spreading function is estimated by means of the methods mentioned in the previous section. The estimate of the

directional spreading function is compared with the input directional spreading function, i.e. the one given by Eq.(32).

In addition, the directional spreading functions are also estimated by the EMLM for the comparison of those given by the Bayesian approach.

5.2 Examination of the estimation method

The results of the simulations are shown in Fig.1 for the three types of arrays of wave probes. The same wave condition is employed for all the arrays : wind waves characterized by $S=10$ coming in the direction $\theta_1=0^\circ$ and a swell characterized by $S=100$ coming in the direction $\theta_2=100^\circ$ coexist, and the ratio of the peak spectral density of the two wave groups is $a_1/a_2=0.5$. In addition, the distance between the wave probes D is given as $D/L=0.2$ (L is the wave length of the component wave to be examined) for all the arrays. The solid lines denoted by TRUE in Fig.1 show the input directional spreading function, and the lines denoted by BDM shows the estimate of the directional spreading function given by the Bayesian directional spectral estimation method (which is called BDM hereafter). The ordinate of Fig.1 is normalized utilizing the peak value of the TRUE directional spreading function for respective cases as reference value.

It is observed in Fig.1 by comparing the estimates of the directional spreading functions result from Type-1 through Type-3 that as the number of wave probes increases, the directional resolution shown by the BDM and the EMLM is improved. In particular, the BDM for Type-2 and Type-3 are almost the same as the TRUE. On the other hand, though the EMLM seems to be closer to the TRUE than the BDM for Type-1 layout, the EMLM yields an erroneous peak inbetween the two peaks exhibited by the TRUE for Type-2 layout. The EMLM is considerably improved for Type-3 in comparison with the estimate for Type-2, but the resolution is inferior to that of the BDM. For the wave probe arrays consisting more than or equal to four probes, it is seen that the BDM shows a better directional resolution than that of the EMLM.

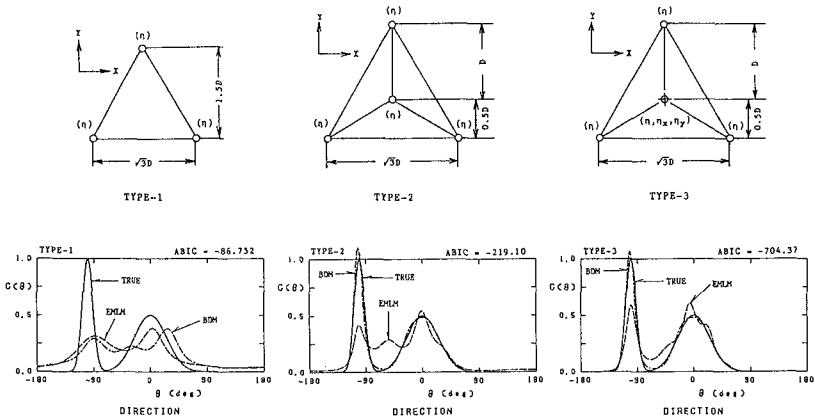


Fig.1 Directional spreading functions estimated from various types of probe arrays

For Type-1 layout, only three wave probes are utilized to measure the directional seas, the BDM does not find a suitable statistical model to explain directional seas. The reason is supposed that three independent wave properties are the minimum data to analyze the directional spectrum, and so it is impossible to estimate the errors introduced in Eq.(8).

The effect of the errors contained in the cross-power spectral estimates is illustrated in Fig.2 for six different magnitudes of errors. The probe array employed is Type-2. The values of r in the figure show the ratio of the magnitude of the errors added to the cross-power spectra and the absolute values of the cross-power spectrum. In the computation, the same magnitude of errors is equally added to all the four wave properties.

It is noted that as the magnitude of error increases, the information of the directional spectrum carried by the cross-power spectra become more biased. In fact, as seen in Fig.2, the estimates of the BDM become flatter as the magnitudes of errors increases. On the other hand, when the cross-power spectra contain larger errors, the EMLM estimates erroneous peaks and sometimes fails to yield a smooth and continuous estimates of directional spreading function. However, in these cases, the BDM detects the directional peaks properly, though it underestimates the peak values. Thus, the BDM seems to be very robust method against the errors.

6. FIELD DATA ANALYSIS

6.1 Facilities of directional wave measurement

The new method for the estimation of directional spectrum on the bases of the Bayesian approach mentioned above is applied to the analysis of the wave records acquired at an offshore oil rig 42 km off the Iwaki coast (Northeastern coast of the main island of Japan, see Fig.3). The Onahama Port Construction Office (OPCO), the Second Port Construction Bureau, Ministry of Transport, is conducting a multi-element measurement of ocean waves at this location. Figure 4 shows

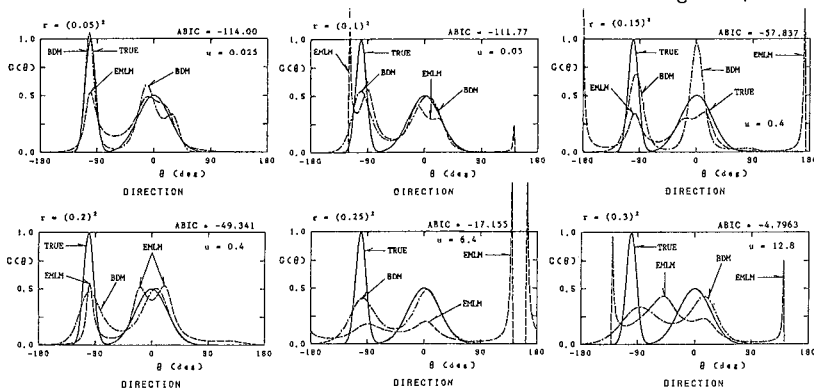


Fig.2 Effect of noise in cross-power spectra on the estimates of directional spreading functions

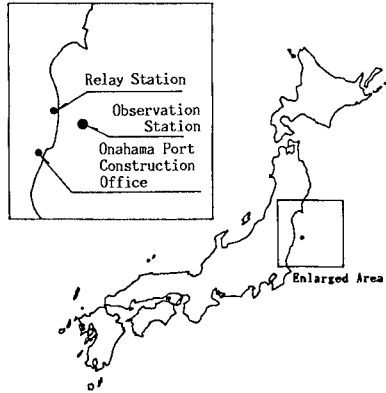


Fig.3 Location of the observation station

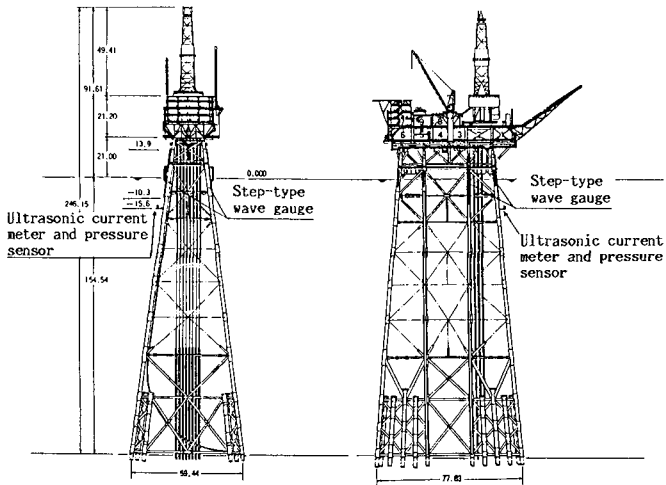


Fig.4 Offshore oil rig and the location of wave probes

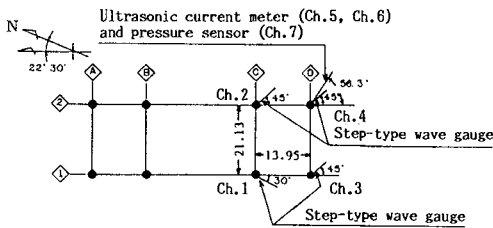


Fig.5 Wave probe array

the oil rig where four step type wave gauges and a two-axis directional current meter with a pressure sensor are installed on its legs as shown in Fig.5. The location of the rig is $37^{\circ} 17' 49''$ N and $141^{\circ} 27' 47''$ E, in a water depth of 155m below C.D.L.

The simultaneous measurement of 7 elements is performed for 20 minutes at a time interval of two hours. The wave records as well as the wind records are immediately transmitted by a radio telemetering system to a nearby coastal relay station for landline transmission to the OPCO.

The time series wave data are recorded on a digital magnetic tape. Data are also analyzed immediately following each observation using a mini-computer of the OPCO for real time information such as significant wave height, wave period and mean wave direction, etc. The EMLM is employed for the real time directional analysis at the office. The directional wave analysis presented herein is performed at the Port and Harbour Research Institute using the wave data recorded on the magnetic tapes.

6.2 Field data analysis

The time series wave records analyzed here were obtained during the passage of Typhoon No.17 from September 29 to 30 in 1986. At 12:00 on September 30, the maximum significant wave height ($H_{1/3} = 6.20\text{m}$) and period ($T_{1/3} = 12.5\text{s}$) was recorded. Figure 6 is the weather maps of these two days.

Figure 7 shows the time variation of the directional spectrum estimated on the basis of the 7-element wave records by the BDM for every four hours from 16:00 on Sept. 29 to 20:00 on Sept. 30. Up to 4:00 on Sept. 30, bi-directional seas are observed: swell comes from the south and the wind generated waves come from the east-southeast at the same time. After 8:00 on the 30th, the directional spectra are uni-directional. During the passage of Typhoon No. 17, the significant wave height shows two maxima. One was observed at 2:00 on the 30th, when the spectral density of the swell reaches its maximum. The other peak significant wave height was observed at 12:00 on the 30th and it was the highest during these two days. It should be noted that the directional spreading of the directional spectra observed at 12:00 and later are constricted at the peak frequency, i.e., the concentration of the spectral density is highest at the peak frequency and becomes lower as the frequency deviates from the peak frequency. This is the same characteristics shown in the directional spreading function proposed by Mitsuyasu et al.(1975).

Examples of the directional spectra for various types of probe arrays estimated by the BDM and the EMLM are compared in Fig.8. The left figures are the estimates given by the BDM and the right figures are those by the EMLM. The major difference between the estimates given by the two different methods is that those given by the BDM show higher spectral peak than those given by the EMLM. Though the BDM yields almost the same shape of the directional spectral estimates for various types of probe arrays, the EMLM yields the different shape of the estimates depending on the arrangement and the number of wave sensors.

On the basis of these results, we conclude that the estimates of the directional spectra show considerably different shapes depending

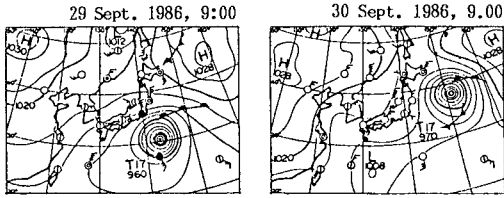


Fig.6 Weather maps of Typhoon No.17

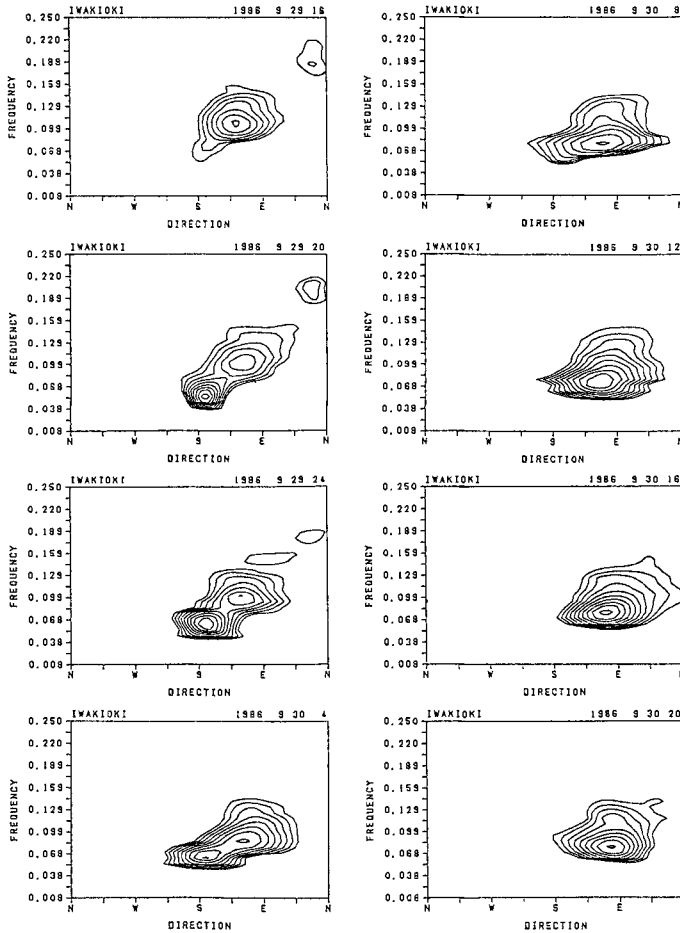
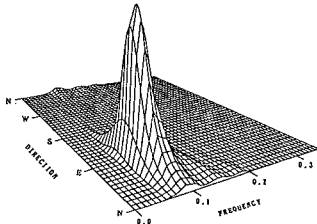
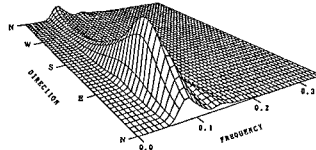


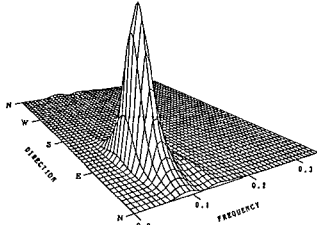
Fig.7 Time Variation of the directional spectrum
(estimated by the BDM from 7-element measurement)



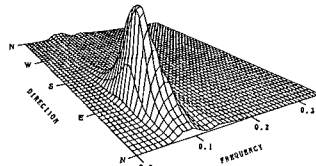
(1) Input Channel : Ch.1,2,3,4,5,6,7 (BDM)



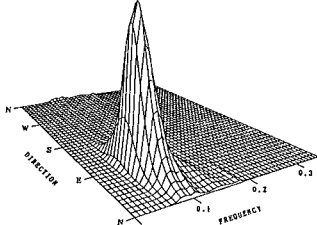
(1) Input Channel : Ch.1,2,3,4,5,6,7 (EMLM)



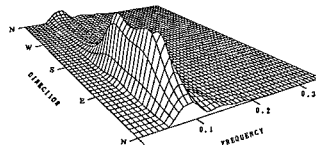
(2) Input Channel : Ch.1,5,6,7 (BDM)



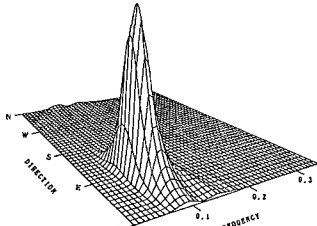
(2) Input Channel : Ch.1,5,6,7 (EMLM)



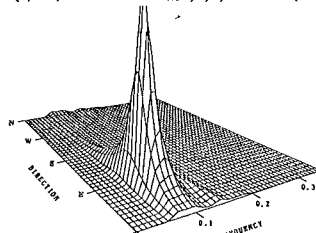
(3) Input Channel : Ch.2,5,6,7 (BDM)



(3) Input Channel : Ch.2,5,6,7 (EMLM)



(4) Input Channel : Ch.2,3,5,6 (BDM)



(4) Input Channel : Ch.2,3,5,6 (EMLM)

Fig.8 Examples of the directional spectra for various types of probe array estimated by the BDM and the EMLM

on the method for the directional spectral estimation. Therefore, many wave properties must be measured, and the estimation method utilized must be examined for a detailed analysis of the directional spectrum.

6. CONCLUSIONS

The following major conclusions sum up the study:

- 1) The proposed Bayesian Directional Spectral Estimation Method (BDM) can be applied for the directional wave analysis on the basis of an arbitrary wave probes. However, the method needs wave records consisting of at least four elements of wave properties. When only three elements are measured, the Extended Maximum Likelihood Method (EMLM) and the Maximum Entropy Principle Method (MEP : Kobune and Hashimoto ; 1986) are recommended.
- 2) When four or more wave probes are employed in the observation, the BDM is the preferred analytical approach. The directional resolution exhibited by the BDM in this circumstance is greater than those shown by the EMLM or other existing methods.
- 3) The BDM is fairly sound against the noises contained in the estimates of the cross-power spectra. As the rate of the noise over the cross-power spectra increases, the estimate given by the BDM becomes flatter than the true directional spectrum. This BDM tendency emerges as the method tends to rely on the a priori condition (smooth and continuous), whenever the given information (cross-power spectra) is not reliable enough. When the cross-power spectra contain large errors, the EMLM fails to yield reasonable estimates, while the BDM can detect the directional peak where the true directional spectrum shows its peak density.
- 4) Estimates of the directional spectrum vary widely depending on the method employed for the directional wave analysis, number of elements of wave properties to be analyzed and the layout of the probes. Though the directions where the directional spectrum shows its peak density can be detected from the directional wave analysis on the basis of three or four element measurement, it is necessary to measure directional waves with many probes to detail the shape of the directional spectrum. For field observation, especially in deep sea, simultaneous measurements of many wave properties are very difficult for technical and financial reasons. However, the BDM is a very powerful method for the directional wave analysis in laboratories.
- 5) In the present paper, as an a priori condition, the simplest condition is introduced to characterize the inherent nature of the directional spectrum. This is necessary, as the BDM relies heavily on the a priori condition when the given information is insufficient, to delineate the directional spectrum. However, when research reveals more detail in the structure of ocean directional waves, the method can be improved by adopting the newly attained knowledge as the a priori condition. Thus, the BDM is more adaptable to reformulation of the estimation equations as the study of structures of directional wave spectrum progresses.

REFERENCES

- 1) Akaike, H. (1980) : Likelihood and Bayes procedure, Bayesian statistics (Bernardo, J.M., De Groot, M.H., Lindley, D.U. and Smith, A.F.M. eds) University Press, Valencia, pp.143-166.
- 2) Hashimoto, N., K.Kobune and Y.Kameyama (1987): Estimation of directional spectrum using the Bayesian Approach, and its Application to Field Data Analysis, Rept. of P.H.R.I., Vol. 26, No. 5, pp.57-100.
- 3) Ishigoro, M. (1985) : On the use of multiparameter models in statistical measurement technique, Doctorial Dissertation, Tokyo Univ.
- 4) Isobe, M., K.Kondo and K. Horikawa (1984): Extension of MLM for estimating directional wave spectrum, Proc. Sympo. on Description and Modelling of Directional Seas, Paper No.A-6, 15p.
- 5) Kobune, K. and N.Hashimoto (1986): Estimation of directional spectra from the Maximum Entropy Principle, Proc. 5th int. Offshore Mechanics and Arctic Engineering (OMAE) Sympo., Tokyo, pp.80-85.
- 6) Mitsuyasu, H., et al. (1975) : Observation of the directional spectrum of ocean waves using a cloverleaf buoy, Jour. Physical Oceanography, Vol.5, pp.750-760.
- 7) Sakamoto, Y. (1985): Categorical data analysis by AIC and ABIC, Kyoritsu Publishing Co. Ltd., 221p. (in Japanese)

CHAPTER 5

Longshore Current Forcing at a Barred Beach

D.J. Whitford¹ and E.B. Thornton², Member ASCE

1. Introduction

A local alongshore momentum balance was measured at various locations across a barred surf zone during the SUPERDUCK experiment held at the U.S. Army Corps of Engineers, CERC Field Research Facility (FRF), DUCK, N.C., U.S.A. on October 16, 1986. A mobile sled was instrumented to measure the various terms in the alongshore momentum equation. Numerically orienting the instrumentation perpendicular to the local bottom contours, the alongshore momentum balance simplifies to:

$$\frac{\partial M_y}{\partial t} + \frac{\partial S_{yx}^T}{\partial x} = \tau_y^n - \tau_y^b \quad (1)$$

where the terms represent (left to right) the temporal change of the time-averaged, depth-integrated mean momentum per unit area in the alongshore direction (M_y) due to both steady (\bar{M}_y) and unsteady (M_y') flow, the cross-shore gradient of the total alongshore momentum flux, surface wind stress, and bottom shear stress.

Three vertically and horizontally separated Marsh-McBirney bi-directional electromagnetic current meters, a Paroscientific digiquartz pressure sensor, and a single-point R.M. Young wind monitor, all mounted on a moveable sled, were used to measure current, wave and wind conditions in the surf zone. Spatially-dependent bed shear stress coefficients were determined as residuals from the alongshore momentum balance.

2. Experimental Site

The FRF site is located along a 100-km unbroken stretch of barrier island formation known as North Carolina's "Outer Banks." There are no littoral barriers to perturbate incoming wave trains along the entire reach of shoreline. The site has a tidal range of 0.5 to 2.0 m and regular offshore bathymetry. On October 16, the beach had a mean foreshore slope of 0.06, a single alongshore linear bar system, and a mean slope of 0.02 offshore of the

¹Fleet Numerical Oceanography Center, Monterey, CA, 93943 U.S.A.; formerly of Naval Postgraduate School, Monterey, CA, 93943, U.S.A.
²Naval Postgraduate School, Monterey, CA, 93943 U.S.A.

bar.

Sled instrumentation and deployment were described in Martens and Thornton (1987). Current meters were mounted at approximately 0.5 m, 1.0 m, and 1.5 m above the sled bottom. A Paroscientific digiquartz pressure sensor was used to infer surface elevation and mean water depth.

Daily bathymetric profiles of the experiment site were accurately measured with a Zeiss Elta-2 laser surveying system which sighted on the FRF Coastal Research Amphibious Buggy (CRAB) as it methodically traversed the experiment area. Precise orientation of the sled was achieved to within 0.5° using the laser surveying system to triangulate on two reflective prisms mounted approximately 2 m apart on a mast spreader above the sled.

Sled sensor measurements were acquired during 9 transects of the surf zone over a 7-day period. This paper discusses only a single transect accomplished on 16 October, as the additional transects are currently undergoing analysis. Wind speeds measured at 10 m elevation ranged from 10 to 12 ms⁻¹ and offshore H_{mo} ranged from 1.4 to 1.6 m. The transect consisted of 5 positions across the surf zone - outside the surf zone, at the point of maximum wave breaking, immediately before the bar, on top the bar, and in the bar-trough. Data were acquired at each position for approximately 35 minutes.

3. Momentum Balance Term Formulation

a. Temporal variability of mean longshore currents - Mean alongshore momentum is formulated from:

$$M_y = \overline{M_y} + M_y' = \rho V D + \int_{-h}^{\eta} \rho v' dz \quad (2)$$

where ρ is water density, V and v' are the mean and fluctuating components of the longshore current, D is the mean water depth, η is sea surface elevation and the over-bar denotes time averaging. Finite differencing in time was examined by varying the time step from 1-22 minutes, with and without a running mean.

b. Cross-shore gradient of alongshore momentum flux - Alongshore momentum flux (or radiation stress) is calculated using a linear wave theory transfer function:

$$S_{yx}(f) = |H(f)|^2 C_{uv}(f) \quad (3)$$

$$|H(f)|^2 = \frac{\rho[\sinh(2kh) + 2kh]}{4k[\cosh^2 k(h + z_m)]}$$

where C_{uv} is the co-spectrum of the current velocity components (u, v), f is frequency, k is wavenumber, h is mean water depth, and z_m is the measurement depth. Finite differencing in space is taken over the horizontal

distance between sled run positions, varying between 13-51 m. S_{yx}^T is the summation of $S_{yx}(f)$ over the sea-swell frequency band (0.06-0.44 Hz).

c. Surface wind stress -The alongshore component of surface wind stress (τ_y^N), hereafter referred to as simply 'surface wind stress', is calculated using the drag coefficient method (also called the bulk coefficient method):

$$\tau_y^N = \rho_a C_{d10} |U_{10}| U_{10y} \quad (4)$$

where ρ_a is air density, C_{d10} is a stability-dependent atmospheric drag coefficient for an elevation of 10 m, and U_{10} and U_{10y} are the total and alongshore components of wind speed measured by the sled anemometer, with atmospheric stability conversion to $z = 10$ m. During the SUPERDUCK experiment, Sethu Raman et al. (1987) calculated wind stress (τ^N) by the eddy correlation method using a three-component Gill anemometer. The wind speed measurements were acquired for $z_m = 18.7$ m at the seaward end of the FRF pier. This location was outside the surf zone and approximately 400 m from the sled transect area. Relative humidity, air, and sea surface temperature were also measured at the seaward end of the FRF pier. Atmospheric friction velocity (u_*) and the Monin-Obukhov length (L) were assumed spatially constant over both the surf zone and the end of the FRF pier. Onshore winds and unstable atmospheric conditions were predominant during the sled transect. A stability-dependent drag coefficient for the end of the FRF pier at a height of 10 m was calculated using:

$$u_* = (\tau^N / \rho_a)^{1/2} \quad (5)$$

$$U_{10} = U_{zm} - \frac{u_*}{\kappa} \left[\ln \frac{z_m}{10} + \psi_m \left(\frac{10}{L} \right) - \psi_m \left(\frac{z_m}{L} \right) \right] \quad (6)$$

$$C_{d10} = \tau^N / [\rho_a (U_{10} - U_0)^2] \quad (7)$$

where $\kappa = 0.4$ is von Karman's constant, ψ_m is an integral diabatic term for momentum, U_0 is the mean current (assumed negligible at the end of the FRF pier), and L is determined from the Businger et al. (1971) iterative approach. The increased surface roughness of a surf zone may be conservatively likened to the chaotic seas observed in advance of a cold front. Swell generated behind the cold front can travel through the front and interact with waves generated ahead of the front and propagating parallel to the front. This interaction results in a chaotic sea of larger, steeper waves and enhanced wave breaking. From a composite of wind stress measurements taken from multiple chaotic sea cases found in advance of storm fronts, the atmospheric drag coefficient was found to be increased by approximately 33% over that expected for non-chaotic seas of equal windspeed (Davidson et al., 1988a, 1988b). Atmospheric drag coefficients for the surf zone are therefore increased by

33% over that determined for the end of the FRF pier. Surf zone surface wind stress is then calculated from eqn. (4) and (6), where the C_{d10} and U_{10} are for the sled location. The substitution of $U_{10}-U_0$ for U_{10} in eqn. (4) for the surf zone surface wind stress made negligible difference.

d. Bottom shear stress - Bottom (or bed) shear stress is determined as the residual in eqn. (1). A bed shear stress coefficient (C_f) is then determined from:

$$C_f = \frac{\tau_b}{[\rho(u^2 + v^2)^{1/2}v]} \quad (8)$$

4. Sled Operation

The sled was deployed in an area of straight-and-parallel isobaths. The sled was towed offshore by the FRF's CRAB and dragged onshore with a tethered chain by a heavy-duty forklift. The sled's position and orientation were determined from laser surveys acquired at the beginning and end of each data run, with additional positioning surveys acquired during the run itself. Prior to sled deployment, a portable Zeiss laser ranging system was used to precisely determine the sled instruments' three-dimensional coordinates with respect to the sled prisms' three-dimensional coordinates. Laser surveys of the sled mast prisms during sled deployment provided precise location, sled pitch angle, and sled yaw angle to correct the sensor data with respect to the local horizontal and vertical. A mean bathymetric isobath orientation is determined by applying a least-squares regression fit to the bathymetric data. The sensors are then oriented with respect to this mean bathymetric isobath to determine cross-shore and longshore currents. Breaking waves were visually identified and electronically marked on the data tapes. The analog data were PCM encoded at the sled, telemetered ashore, decoded, and recorded on 9-track magnetic tape. The data were digitized at 8 Hz, demeaned and spectrally analyzed using Fast Fourier Transforms and ensemble averaging.

5. Data Analysis

Since S_{yx} is conserved outside the surf zone, any $S_{yx}(f)$ difference between the current meters measured outside the surf zone is assumed to be attributable to incorrect current meter alignment with respect to each other and the sled. Therefore, the rear current meter was numerically rotated until its $S_{yx}(f)$ coincided with the front current meter $S_{yx}(f)$. This 2.86° rotation was assumed to account for the alignment error and was fixed for the remaining data runs inside the surf zone.

Current meter calibration was conducted in flow tanks by different laboratories before and after the experiment. Current meter gain agreed within $\pm 3\%$ and current meter offset differed by only 0.01 - 0.04 ms^{-1} .

Homogeneity of surf zone currents is investigated by

overlying the bathymetry contours on both the mean current vectors determined at each sled run position and the mean current vectors determined from the fixed-bed current meters of an alongshore array (Figure 1). All current vectors have the same general direction and magnitude relative to their cross-shore position. No evidence of rip currents were seen visually during the sled transect nor are rip currents detected in Figure 1. Homogeneity of the surf zone current regime is therefore assumed for 16 October.

Stationarity is investigated by examination of S_{yx}^T calculated from measurements outside the surf zone acquired from a fixed-bed pressure and velocity sensor designated 'south tripod.' Sequential 34.1-minute spectra are calculated and resultant S_{yx}^T versus time are compared to the sled run transect times (Figure 2). In shallow water, $S_{xy} = \rho h \text{cov}_{uv}$. Ninety-five percent confidence limits for S_{yx}^T in Figure 2 are based on the Fisher-Z transformation (Miller and Freund, 1985):

$$Z = \frac{1}{2} \ln \left[\frac{1+r}{1-r} \right] \quad (9)$$

where the correlation coefficient (r) is

$$r = \frac{\text{cov}_{uv}}{\sigma_u \sigma_v} \quad (10)$$

and σ_u , σ_v are the standard deviations of u and v , and the covariance is calculated by integrating the co-spectrum of u , v . The Fisher-Z statistic is a value of a random variable having approximately a normal distribution. Unfortunately the 'south tripod' gage was not recording for the entire time of the transect. Therefore, stationarity is confirmed only for the first two runs of the transect and is assumed for the last three runs.

Relative contributions of wave forcing ($\partial S_{yx}^T / \partial x$), wind forcing (τ_y^n), and temporal variability of mean momentum ($\partial M_y / \partial t$) to the total momentum balance are determined by first defining their total contribution (TOT) as the cumulative sum of their absolute values:

$$\text{TOT} = \left| \frac{\partial S_{yx}^T}{\partial x} \right| + \left| \tau_y^n \right| + \left| \frac{\partial M_y}{\partial t} \right| \quad (11)$$

Their individual relative contributions (rc) are then determined by dividing by the total contribution:

$$\text{wave}_{rc} = \frac{\left| \frac{\partial S_{yx}^T}{\partial x} \right|}{\text{TOT}} \quad (12)$$

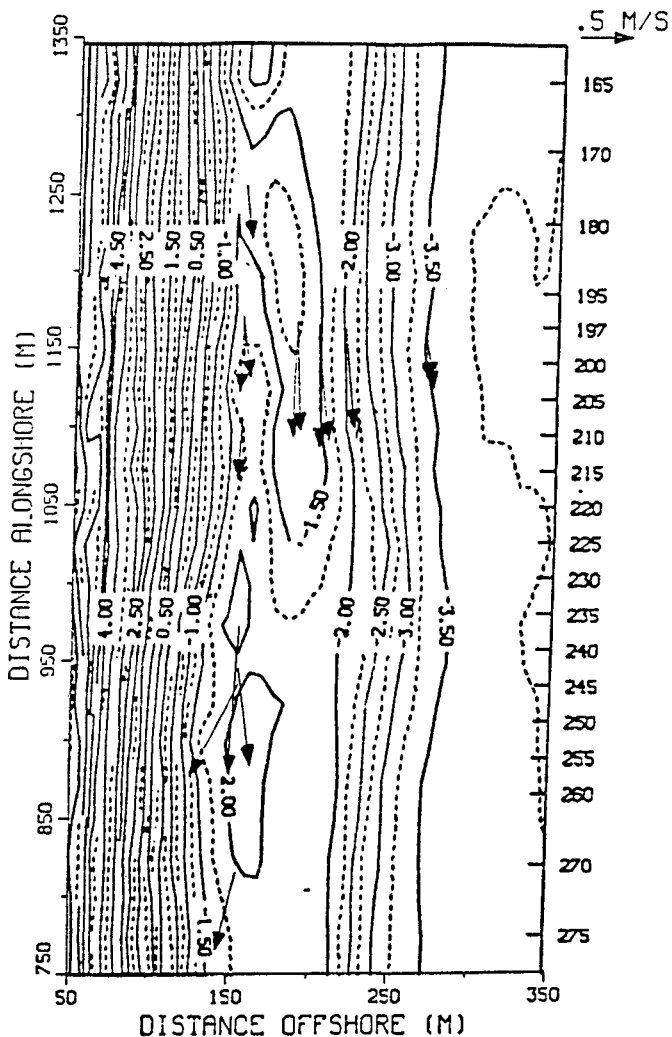


Figure 1. Sled and alongshore array mean current vectors for 16 October 1986 overlaid on bathymetry. Velocity scale is at upper right.

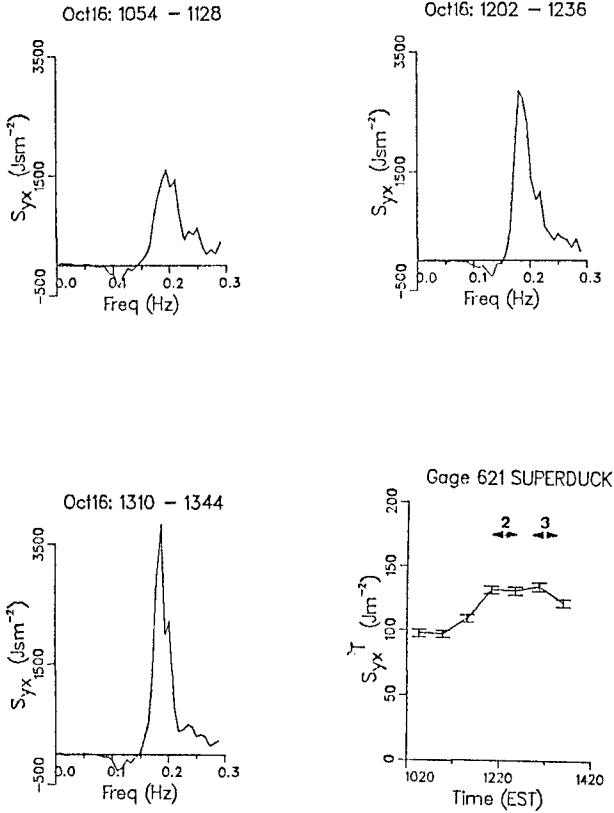


Figure 2. Offshore S_{yx} spectra and S_{yx}^T from 'puv' gage 621 for October 1986. Three representative S_{yx} spectra are shown. Numbers on S_{yx}^T figure indicate data runs. Intervals are 95% Fisher-Z confidence.

$$\text{wind}_{rc} = \frac{|\tau_y|}{TOT} \quad (13)$$

$$\frac{\partial M_y}{\partial t}_{rc} = \frac{\left| \frac{\partial M_y}{\partial t} \right|}{TOT} \quad (14)$$

An error analysis was conducted to place error bounds on the bed shear stress coefficients. Errors considered were beach angle orientation error, measurement error, finite differencing error, and an estimate of unquantified errors.

6. Results

Measured data and calculated results for all five data runs on 16 October are listed in Table 1. Three-dimensional portrayal of the mean current structure across the bar is illustrated in Figure 3. Current vectors represent 34.1-minute means and the numbers label data run locations. The short dotted lines above each run location indicate the mean water level (MWL) for each run and the long dashed line indicates mean sea level. The different arrowheads represent the three different current meter heights above the bed. Runs 16-4 and 16-5 had only two current meters totally submerged due to their shallow locations. The onset of breaking occurs between Runs 16-2 and 16-3.

Mean alongshore current [$0(1.0 \text{ ms}^{-1})$] dominates over the mean cross-shore current [$0(0.1 \text{ ms}^{-1})$]. Significant spatial variability is observed across the bar with strongest flow just before the bar and weakest flow in the trough and outside the breaker zone. The spatial distribution of the longshore current is of the same order as that found by Thornton and Guza (1986) for a planar beach, and thus the bar appears not to exert any major perturbation on the spatial variability of the flow from the trough to offshore. No measurements were taken inside the foreshore breakers where an additional peak (although of smaller magnitude) in mean longshore current would be expected. The substantial flow in the trough may be due to an along-shore pressure gradient (which was not measured) or turbulent mixing, since there was essentially no wave breaking occurring inside the trough between Runs 16-5 and 16-6. The current outside the breaker zone may be attributable to turbulent mixing. Offshore flow near the bed is noted for Runs 16-4 through 16-6. The vertical distribution of alongshore and cross-shore velocities is compared to normalized water depth (Figure 4). Current measurements for a single run are connected, with the numbers indicating the chronological run order (i.e., number 1 is run 16-2). Nearly depth-uniform flow is seen for the mean alongshore current, with a slight increase in velocity near the surface. A logarithmic velocity profile between current meter heights (0.5-1.5 m) was not found. However the data does not preclude a logarithmic profile over a different height

TABLE 1. Field experiment conditions on 16 October 1986

	Data Runs				
	16-2	16-3	16-4	16-5	16-6
1. Start time (E.S.T)	<u>1222</u>	<u>1318</u>	<u>1406</u>	<u>1449</u>	<u>1536</u>
2. h (m)	3.33	1.89	1.51	1.54	1.91
3. H_{rms} (m)	0.98	0.80	0.57	0.52	0.49
4. H_{m0} (m) from FRF gage 630	1.59	1.53	1.46	1.41	1.35
5. 1α	19°	15°	12°	19°	10°
6. $2Q(\%)$	0	12	5	3	1
7. S_{yx}^T (Jm^{-2})	250.5	151.0	57.2	48.0	25.9
8. U_{10} (ms^{-1})	12.3	11.4	10.9	10.2	10.0
9. 3θ	030°	027°	025°	026°	026°
10. 4C_f	0.003 ± 0.0010	0.004 ± 0.0010	0.001 ± 0.0006	0.001 ± 0.0003	0.002 ± 0.0003
11. x-coord (m)	269.3	218.8	201.1	188.1	154.6
12. y-coord (m)	1157.4	1162.3	1165.2	1166.6	1170.4
13. cross-shore current (ms^{-1}):					
upper	0.09	0.12	-0.26	-0.25	-0.03
mid	0.04	0.10	0.03	-0.02	0.03
lower	0.08	0.09	0.12	0.05	0.08
14. longshore current (ms^{-1}):					
upper	-0.53	-1.09	-0.95	-0.91	-0.75
mid	-0.44	-0.98	-1.21	-1.13	-0.64
lower	-0.44	-0.99	-1.16	-1.07	-0.60
15. relative contributions (%) to momentum balance					
$\partial S_{yx}^T / \partial x$	87	95	77	70	81
$\frac{\eta}{\tau_y}$	8	3	19	18	2
$\partial M_y / \partial t$	4	2	3	12	17
16. $C_d(10^{-3})$	1.5	1.6	1.6	1.8	1.9

1. Wave incident angle relative to beach normal
2. Percent of waves which are breaking
3. Wind direction relative to true north
4. The C_f value noted is for the distance between the run indicated and the next run shoreward.
5. Peak frequency in both the η and S_{yx} spectra for all runs was 0.19 Hz

SUPERDUCK
 16 Oct 86
 Profile 197

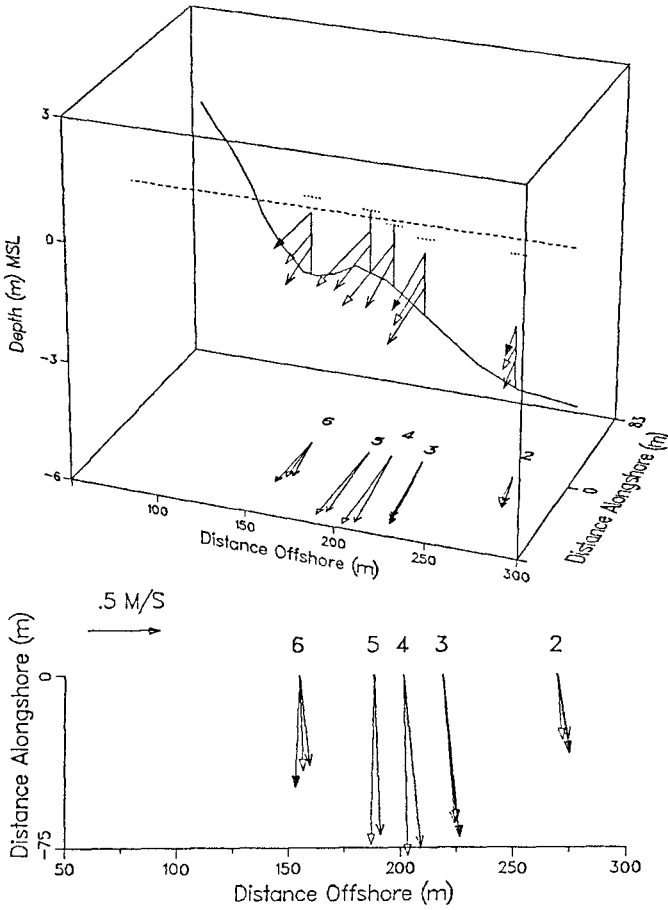


Figure 3. Mean current structure across the bar on 16 October 1986. Numbers represent data runs, short dotted lines are MWL's, and distance alongshore is arbitrary.

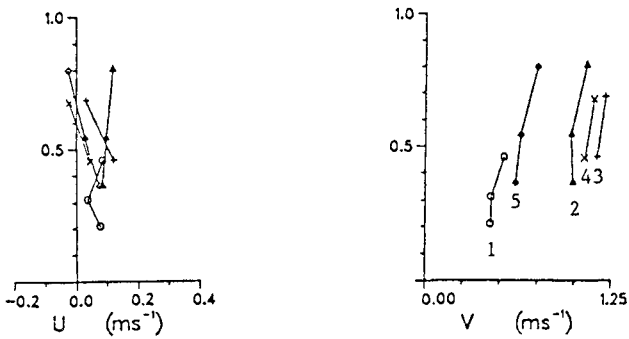


Figure 4. Mean cross-shore U and alongshore velocity V profiles versus normalized water depth for 16 October. Numbers on V profile indicate chronological sequence of data runs (e.g., 1 is Run 16-2).

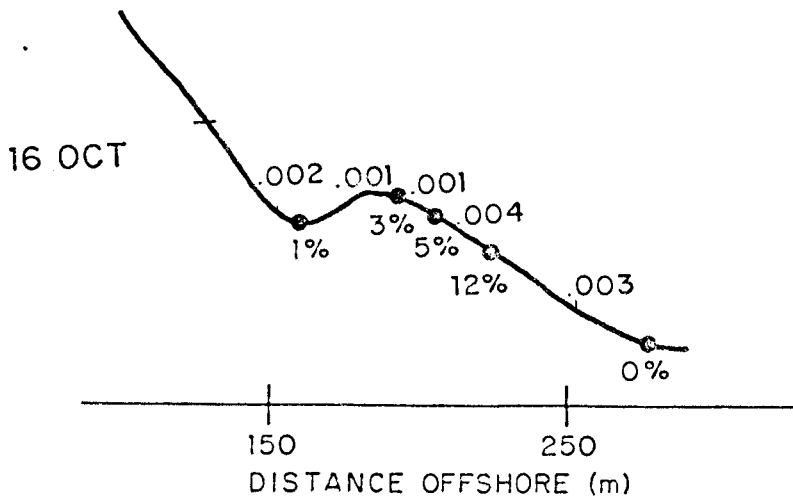


Figure 5. Bed shear stress coefficients (C_f) and percent breaking wave (Q) values as a function of offshore distance (C_f is above and Q is below the profile line).

interval (e.g., 0.0-1.0 m). The mean cross-shore flow exhibits a tendency for onshore flow in the upper third of the water column and offshore flow in the lower third of the water column.

The mean momentum due to the waves (M_y') was found to be less than an order of magnitude of the mean momentum due to the steady flow (M_y). Varying the time step for the temporal term (as discussed in paragraph 3a) made negligible difference, therefore Δt was arbitrarily assigned as 64 seconds.

Spatially-variable bed shear stress coefficients, calculated for the distance between run positions, and the percentage of waves which were breaking at each run position are indicated above and below the bathymetric profile in Figure 5. The bed shear stress coefficients are of $O(10^{-3})$ and are of the same order of magnitude as the model-fitted C_f values determined by Thornton and Guza (1986) using a non-linear formulation for bed shear stress. Spatial variability is indicated with higher C_f values offshore the bar and lower C_f values immediately before and on the bar. Grant et al. (1984) showed that C_f is increased by a factor of 2-3 due to the combined effect of waves and currents, therefore the shoreward decreasing C_f may be attributed to the shoreward decreasing surface wave action.

A surprising result was the low percentage of waves which were visually identified and marked as breaking waves. Visual identification of breaking was defined as when "white water" was observed passing the sled mast. For example, Run 16-3 was visually positioned in the surf zone at the point of maximum breaking (i.e., where the breaking wave heights were largest and therefore the maximum wave dissipation was occurring), yet only 12% of the waves were identified as breaking. Subsequent runs exhibited even less breaking wave occurrences.

The relative contribution of the radiation stress gradient to the momentum balance is observed to be highest at the two locations of maximum wave breaking - just before the bar (Run 16-3) and near the foreshore (Run 16-6). Surface wind stress' relative contribution doubles to nearly 20% in the trough, where wave breaking is reduced. The relative contribution of the temporal term increases shoreward from approximately 3% to a maximum of nearly 20% in the trough, perhaps due to the effect of infra-gravity waves and decreased wave breaking.

7. Summary

A local alongshore momentum balance is calculated from measurements of pressure, current, and wind acquired during a single transect of a barred beach during the SUPERDUCK experiment. Large incident wave angles (10° - 19°), combined with a highly accurate laser surveying system, signifi-

cantly reduced S_{yx} angular sensitivity which had plagued previous nearshore investigations and precluded accurate S_{yx} calculations. Surface wind stress is calculated using a stability-dependent atmospheric drag coefficient determined from wind stress measurements acquired during the field experiment. A three-dimensional depiction of surf zone currents indicates nearly depth-uniform mean alongshore flow with a slight increase in alongshore flow near the surface. Mean cross-shore flow indicates a tendency for onshore flow in the upper water column with offshore flow in the lower water column. Significant spatial variability of the alongshore flow is observed with maximum flow immediately offshore the bar. Spatial variability of the bed shear stress coefficient is observed with larger values offshore the bar (0.003-0.004) and lower values on the bar and in the trough (0.001). Relative contributions of wind forcing and the temporal term to the alongshore momentum balance are less than 10% offshore of the bar, where wave forcing was largest. However, relative contributions of wind forcing and the temporal term both approach 20% on the bar and in the trough. For this data set, wind forcing and the temporal term were not negligible terms in the momentum balance for locations on the bar and in the trough.

The information presented is the result of a single transect of the barred beach. A much more definitive conclusion should be reached after analysis of the remaining 8 transects of SUPERDUCK data.

8. Acknowledgments

Support for this field investigation and analysis was received from ONR under Contract NR 388-114. The staff of the U.S. Army Corps of Engineers, CERC Field Research Facility, Duck, N.C., assembled the sled and installed and maintained the offshore sensors and data acquisition system for the SUPERDUCK experiment.

9. References

- Businger, J. A., J. C. Wyngard, and Y. Izumi, 1971: Flux profile relationships in the atmospheric surface layer. J. Atmos. Sci., 28, 181-189.
- Davidson, K. L., P. J. Boyle, S. R. Fellbaum, and J. R. Mundy, 1988a: Atmospheric surface and mixed layer properties observed from ships in FASINEX. Proc. 7th A.M.S. Conf. on Air-Sea Interaction, 161-165.
- Davidson, K. L., W. J. Shaw, and W. G. Large, 1988b: Wind stress results from multi-platform and multi-sensor measurements in FASINEX. Proc. 7th AMS Conf. on Air-sea Interaction, Anaheim, CA, 132-136.
- Grant, W. D., A. J. Williams, III, and S. M. Glenn, 1984: Bottom stress estimates and their prediction on the northern California continental shelf during CODE-1: The

importance of wave current interaction. J. Phys. Oceanogr., 14, 506-507.

Martens, D. E. and E. B. Thornton, 1987: Nearshore zone monitoring system. Proc. Coastal Hydrodynamics Conf., ASCE, 579-588.

Miller, I. and J. E. Freund, 1985: Probability and Statistics for Engineers. 2nd ed., Prentice Hall, Inc., Englewood Cliffs, N.J., 530 pp.

Sethu Raman, S., M. J. Kang, C. E. Long, and J. M. Hubertz, 1987: SUPERDUCK Marine Meteorological Experiment, Data Summary Report, Vol. I (Mean Values) and Vol II, (Turbulence Parameters). U.S. Army Corps of Engineers, Coastal Engr. Rsch. Ctr., Waterways Experiment Station, Vicksburg, MS., (preliminary report, not yet published).

Thornton, E.B. and R.T. Guza, 1986: Surf zone longshore currents and random waves: field data and models. J. Phys. Oceanogr., 16(7), 1165-1178.

CHAPTER 6

NUMERICAL COMPARISON OF WAVE SYNTHESIS METHODS

M.D. Miles¹ and E.R. Funke¹

ABSTRACT

A numerical comparison study is carried out on a variety of methods for synthesizing pseudo-random Gaussian wave records for laboratory wave generation. Three nonharmonic superposition methods and three time domain filtering procedures are compared to a harmonic FFT technique. The synthesis methods are evaluated on the basis of a statistical analysis of 16 standard wave parameters obtained from a set of 200 wave records. Second order group-bounded long wave components are also investigated.

INTRODUCTION

Numerically synthesized wave records are commonly used to drive wave machines in laboratory basins in order to produce reasonably realistic simulations of the wind generated seas found in nature. A variety of numerical techniques have been used as described in Funke and Mansard (1987). These are all based on the assumption that natural seas can be modelled as a stationary, ergodic, Gaussian random process. Although this assumption becomes questionable in extreme wave conditions, linear synthesis methods have generally proven to be practical tools in many coastal and ocean engineering applications. The relative advantages and limitations of various linear simulation models are discussed in Medina et al. (1985).

Some methods are popular because they are believed to be superior representations of a natural sea state due to their ability to generate arbitrarily long non-repeating wave records with continuous rather than discrete spectra. Others are promoted on the basis of computational efficiency. FFT techniques can efficiently handle a large number of frequencies and are also very convenient for operations such as phase propagation and transfer function compensation. A potential disadvantage of the FFT approach is that it imposes the restriction that all components must be harmonically related. As a consequence, FFT wave records are always cyclic in contrast to nonharmonic methods. Since any constraint in a synthesis procedure may have an effect on the statistical

¹ Hydraulics Laboratory, National Research Council,
Ottawa, Ont., Canada, K1A 0R6

properties of the wave records, it was decided to carry out a numerical study to compare a standard FFT method with six different nonharmonic wave synthesis procedures.

The synthesis methods were compared by performing a statistical analysis of 16 basic wave parameters obtained from frequency and time domain analysis of a set of wave records generated by each method. Two different target spectral density functions were used and 200 independent wave records were computed for each wave spectrum and synthesis method. In order to cover both broad and narrow spectra, a Pierson-Moskowitz (PM) spectrum and a JONSWAP spectrum with $\gamma = 7$ were chosen as the two target spectral densities. Each target spectrum had a peak frequency of 0.55 Hz which is a typical frequency for model basin applications. The synthesized wave records had a duration of 200 seconds (model scale). The peak frequency and record length were chosen to be compatible with a previous study comparing different FFT synthesis methods (Mansard and Funke, 1986). At a scale of 1:36, the duration of the synthesized wave records corresponds to the 20 minute length which is typical of most full scale wave records. Each wave record thus contained approximately 100 wave cycles.

The synthesized wave records were analyzed for the following parameters:

- (1) FPD = peak frequency by the Delft method.
- (2) QP = Goda peakedness factor.
- (3) HMO = estimate of significant wave height = $4\sqrt{m_0}$.
- (4) m_1 = first spectral moment.
- (5) m_2 = second spectral moment.
- (6) m_3 = third spectral moment.
- (7) H13D = zero downcrossing significant wave height.
- (8) HMAXD = maximum zero downcrossing wave height.
- (9) HMAXD/H13D = ratio of maximum and significant zero downcrossing wave heights.
- (10) SZ[HSIG] = average steepness of the significant waves.
- (11) SCF[HSIG] = average crest front steepness of the significant waves.
- (12) MYH[HSIG] = average horizontal asymmetry factor of the significant waves.
- (13) RL[HAV] = average run length of a group for waves greater than the average wave height.
- (14) TRN[HAV] = average length of a total run for waves greater than the average wave height.
- (15) RL[HSIG] = average run length of a group for the significant waves.
- (16) TRN[HSIG] = average length of a total run for the significant waves.

Parameters 1-12 are defined in the "List of Sea State Parameters" published by the IAHR Working Group on Wave Generation and Analysis in January, 1986. The run length parameters (13-16) are defined in Goda (1976).

In order to give particular attention to the possibility that nonharmonic simulations may be necessary in order to correctly represent the long wave content, a shallow water depth of 0.5 m was assumed for which the theoretical group-bounded long wave components were calculated using the

methods described in Barthel et al. (1983). Since wave grouping is greater for narrower spectra, only the JONSWAP target spectrum was used for this part of the study. The length of the wave records was also increased from 200 to 400 seconds because of the low frequencies involved. The standard deviation, maximum and minimum elevations and average period were calculated for the long wave components.

A separate investigation was also carried out to determine how well typical wave records synthesized by the nonharmonic methods could be approximated by an equivalent FFT-based harmonic representation.

WAVE SYNTHESIS METHODS

Method M1:

The first nonharmonic technique used was the equal amplitude component superposition method (Borgman, 1969). In this procedure, the frequency density varies with spectral amplitude as shown in Figure 1. Although the wave records were actually synthesized with 200 components, only 66 components have been shown in Figure 1 for clarity. Each of the wave simulation methods was checked by computing the average measured wave spectrum for all 200 synthesized wave records and plotting this together with the target spectrum. The results for method M1 are shown in Figure 2. It can be

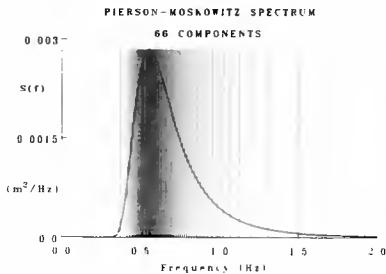


Fig.1 Method M1
Frequency Comb

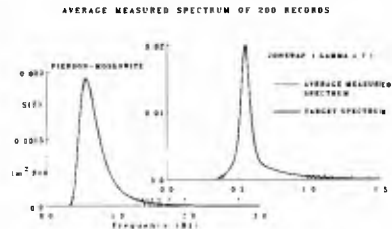


Fig.2 Average Spectra of
Method M1 Records

seen that the method gives a very close fit over the main part of each spectrum but the lack of frequency density is evident in the high frequency tail above 1 Hz. This effect could be reduced by increasing the number of components but the computation time becomes prohibitive. In order to provide a uniform basis for comparison, it was decided to use 200 components for all of the nonharmonic superposition procedures in accordance with the recommended value for Method M2.

Method M2:

The second nonharmonic method used was the deterministic spectral amplitude technique defined in Goda (1970). This procedure uses a random distribution of frequencies whose average spacing increases with frequency. The amplitude of each component is set to a value such that the energy of the component is equal to the area of the target spectrum over the frequency band to be represented by the component. The phase of each component is selected at random from a uniform

distribution. Method M2 thus has deterministic amplitude combined with random frequency and phase.

Method M3:

The third nonharmonic superposition technique was the random amplitude and frequency method. This is essentially a modified version of the Random Fourier Coefficient FFT technique with randomized instead of harmonic frequencies. The frequency range is first partitioned into N intervals of constant width. A final set of N frequencies is then obtained by selecting one frequency at random from a uniform distribution over each interval. This method thus has random amplitude, frequency and phase.

Method M4:

The fourth nonharmonic method was the filtering of pseudo-random Gaussian white noise in the time domain using a linear nonrecursive filter. This method has the advantage that filters can be designed very quickly to match any desired target spectrum. It is necessary to use rather long filters in order to obtain a close fit to the target spectrum, however. Consequently, this method is not computationally efficient for generating large numbers of wave records.

The average measured spectra for the 200 wave records synthesized by this method are shown in Figure 3. It can be seen that a very close match was obtained for both target spectra. However, this required fairly long filters with 300 points for the PM spectrum and 1000 points for the JONSWAP.

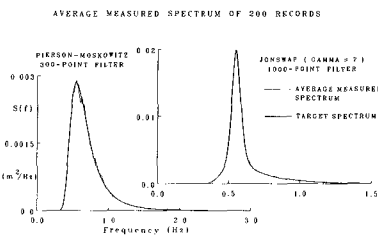


Fig.3 Average Spectra of Method M4 Records

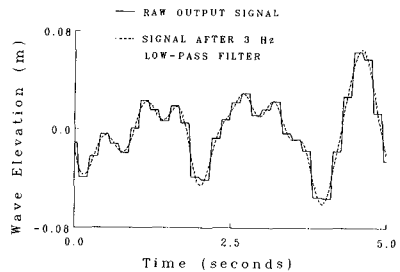


Fig.4 Typical Method M5 Wave Record

Method M5:

The fifth nonharmonic technique used was the filtered binary noise method which is also known as the Wallingford method (Fryer et al., 1973). This method is based on a digital pseudo-random binary noise generator which is implemented by means of a 65-bit shift register. The desired spectral shape is obtained by using a digital filter which computes a weighted sum of pairs of bits from the shift register. Although the shift register contains binary noise, the output signal is approximately Gaussian because of the summation process of the digital filter. This method is normally implemented in hardware but it was simulated in software for the present study. Figure 4 shows the raw output signal and the signal after low-pass filtering.

The average measured spectra for the 200 wave records generated by this method are shown in Figure 5. An excellent fit is obtained for the PM case but the peak of the average measured JONSWAP spectrum is somewhat lower and wider than the target. This is probably due to the fact that only 16 digital filter components are available to define the main part of the spectrum which is somewhat marginal for this narrow-band situation.

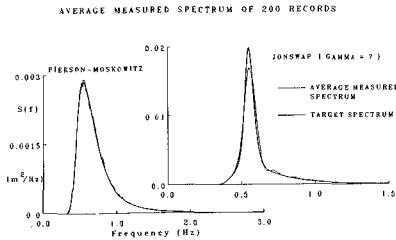


Fig.5 Average Spectra of Method M5 Records

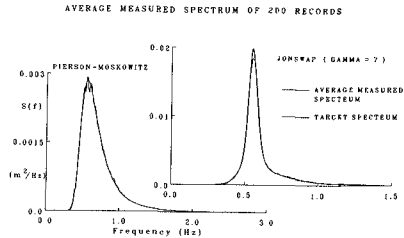


Fig.6 Average Spectra of Method M6 Records

Method M6:

The sixth nonharmonic method investigated was the Autoregressive Moving Average or ARMA filter method. In this technique, Gaussian white noise is filtered in the time domain using an ARMA filter whose coefficients are selected to obtain the desired target spectrum. The use of ARMA filters for wave synthesis is discussed in Samii and Vandiver (1984) and Medina et al. (1985). ARMA filters are the most general class of linear digital filters. Their main disadvantage is that they are rather difficult to design for any given spectral shape. Once the ARMA coefficients have been determined, however, they are much more efficient than the nonrecursive filters used in method M4 because the number of terms required is much smaller.

A good fit to the PM spectrum was obtained with an ARMA(15,15) filter but it was necessary to use an ARMA(21,21) filter to fit the JONSWAP spectrum. The average measured spectra for this method are shown in Figure 6. The PM fit is excellent. The JONSWAP fit is also very good although the peak of the average measured spectrum is slightly lower than the target.

Method M7:

There are two basic FFT methods which are commonly used for wave synthesis. These are the Random Phase (RP) method and the Random Fourier Coefficient (RFC) method (Funke and Mansard, 1987). The RP method is spectrally deterministic whereas the RFC method is not. It was decided to use the RFC method for this study so that the statistical variability of the synthesized wave records would be commensurate with that of natural wave records of similar duration.

2048 frequency components were used with a frequency spacing of 0.005 Hz for the 200-second records. This resulted

in 4096-point wave records with $\Delta t = 0.0488$ seconds. The 400-second records for the long wave investigation were synthesized with $\Delta f = 0.0025$ Hz and $\Delta t = 0.0977$ seconds.

WAVE PARAMETER STATISTICS

Each set of 200 wave records synthesized by a particular method for a given target spectrum was analyzed in order to obtain values for the wave parameters defined previously. This resulted in a set of 200 independent samples for each parameter. A basic statistical analysis was then carried out on each set of parameter values in order to compare the performance of the different synthesis methods.

The resulting wave parameter statistics are plotted for comparison in Figures 7 and 8 for the PM and JONSWAP spectra respectively. The 90% confidence intervals have been calculated on the basis of a Gaussian distribution. The results of a Chi-squared goodness-of-fit test indicate that most of the parameters do have Gaussian distributions. HMAXD, HMAXD/H13D and the four run length parameters were found to be non-Gaussian, however. Consequently, the confidence intervals for these parameters must be considered as rough estimates only.

The filtered Gaussian white noise methods M4 and M6 do not impose any constraints on the basic assumption that the sea can be modelled as a stationary Gaussian process. Consequently, these methods would be expected to generate the most realistic wave records. Method M4 was selected as the primary benchmark against which the other methods were evaluated, because the nonrecursive filters were able to match the target spectra with greater precision than the ARMA filters used in method M6.

It can be seen from Figures 7 and 8 that there is generally good agreement on the mean values of the wave parameters obtained by the various synthesis methods. One exception is the third spectral moment where method M1 is biased slightly high and method M5 is biased slightly low. This occurs for both the PM and JONSWAP spectra and is probably caused by a lack of frequency density in the high frequency tail. The mean value of HMAXD is also slightly lower for method M5 compared to the other methods.

There are considerable differences in the standard deviations of certain parameters. Since methods M1 and M2 are spectrally deterministic, it is not surprising that the standard deviations of the spectral parameters and H13D are much smaller for these methods. The standard deviations of the wave steepness parameters are also somewhat smaller, but the variability of the other time domain parameters is not strongly influenced by the fact that methods M1 and M2 are spectrally deterministic.

One interesting feature of the results is that method M3 has substantially larger standard deviations than the other methods for all of the spectral parameters and also for H13D, SZ and SCF. This effect is most noticeable in QP for the PM spectrum where the mean is also biased high. Since method M3 is simply a randomized frequency version of the FFT method, it was suspected that this effect might be caused by an

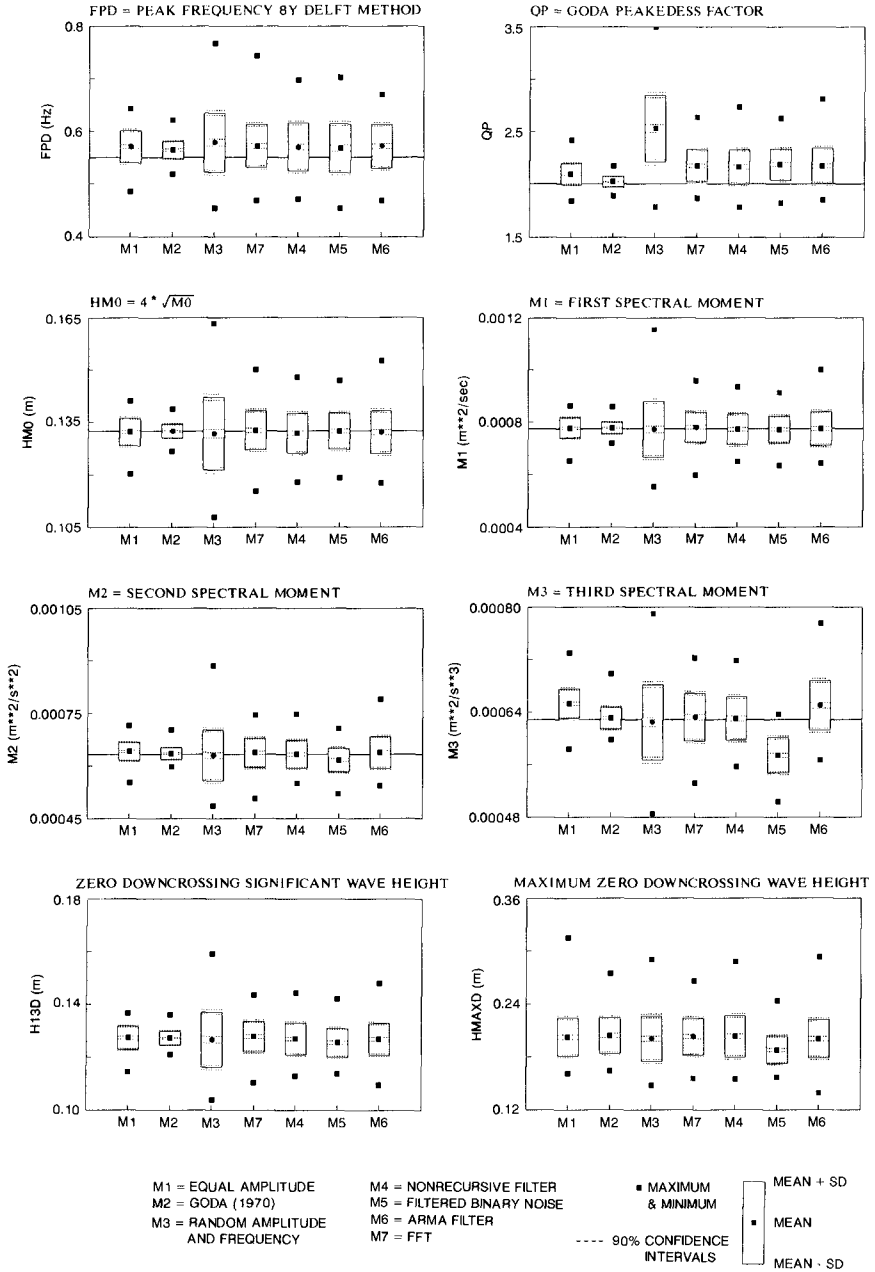


Fig.7a Wave Parameter Statistics for PM Spectrum

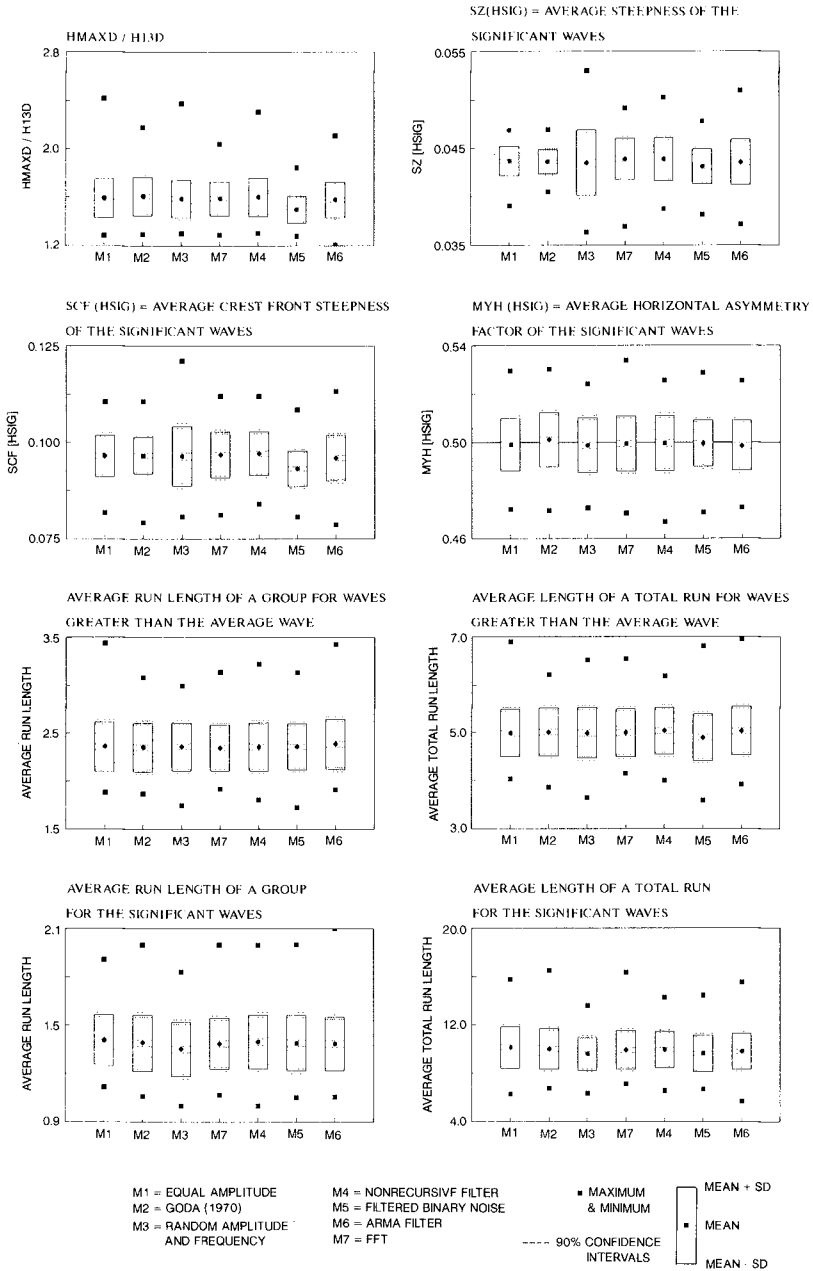


Fig.7b Wave Parameter Statistics for PM Spectrum

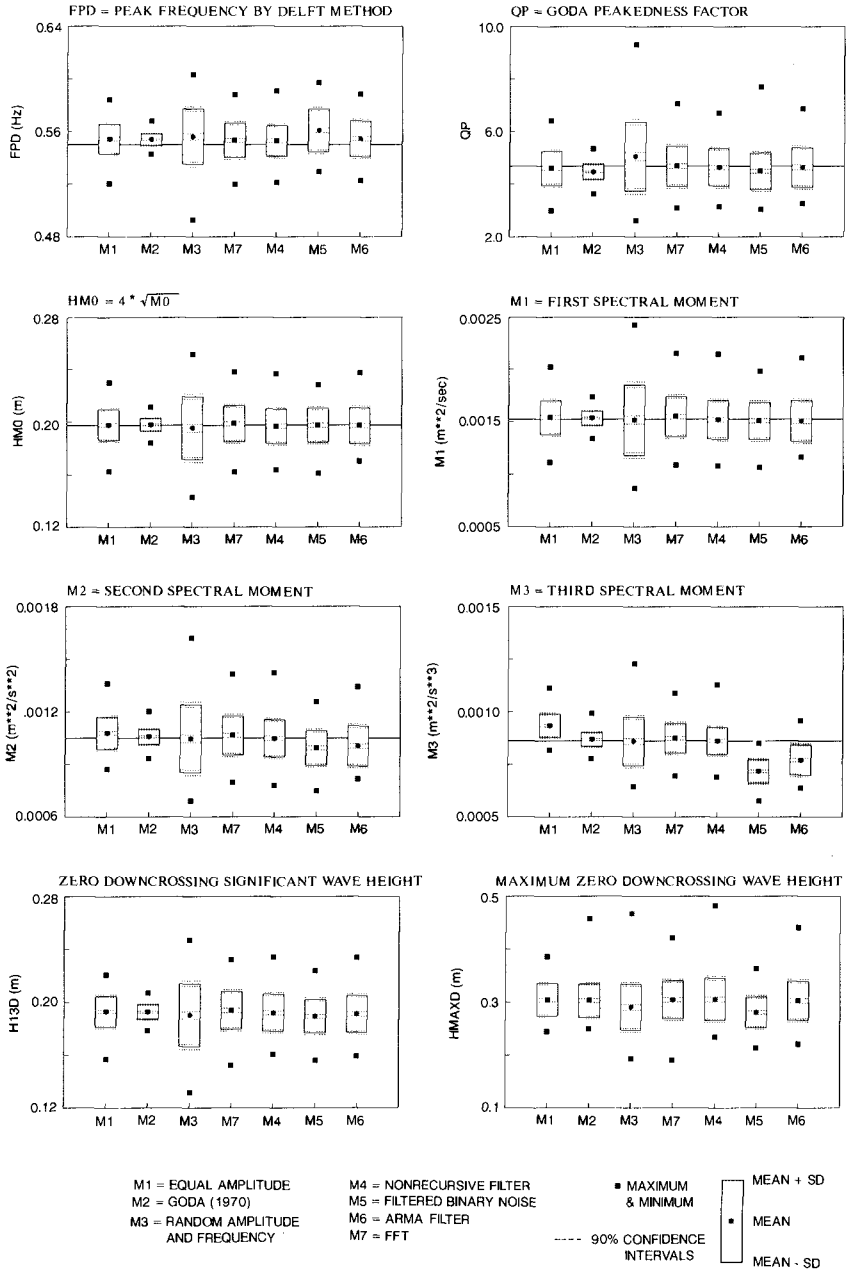


Fig.8a Wave Parameter Statistics for JONSWAP Spectrum

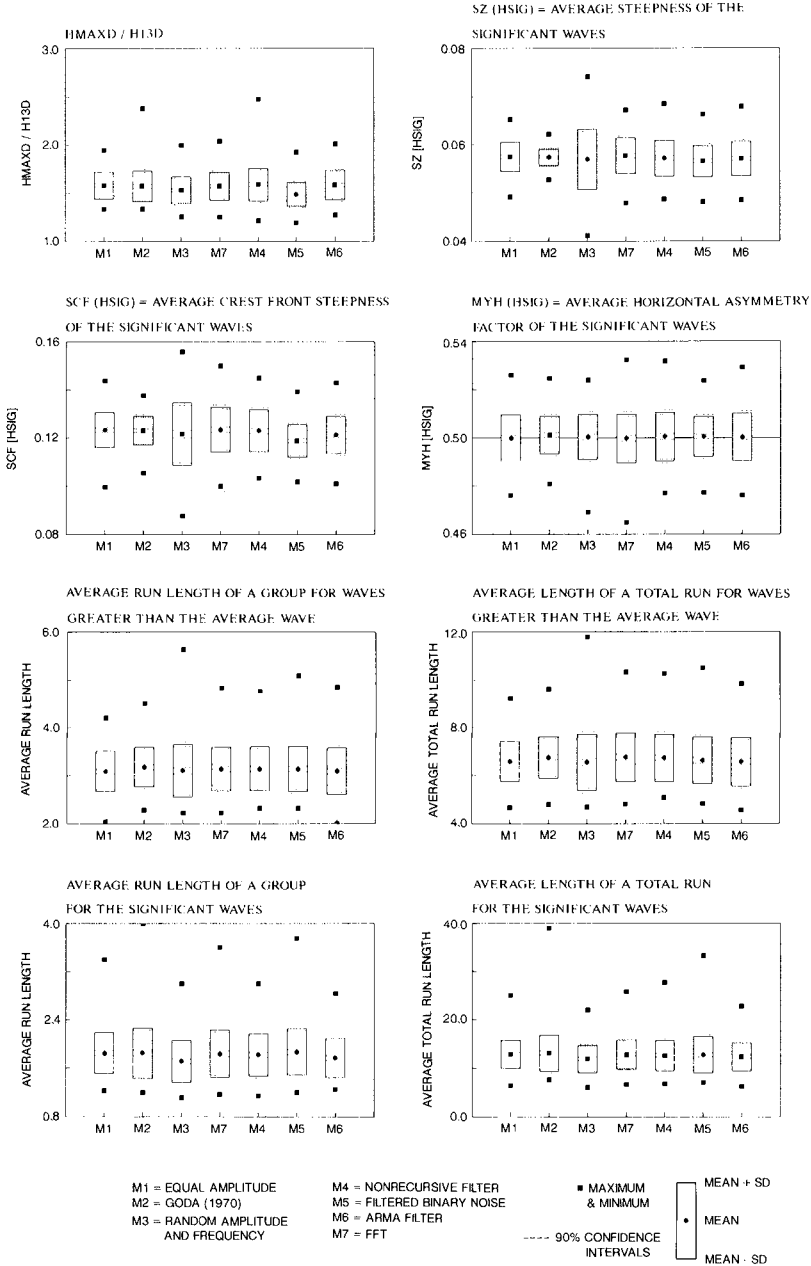


Fig.8b Wave Parameter Statistics for JONSWAP Spectrum

insufficient number of frequencies. A second set of wave records was therefore generated by method M3 with the number of frequencies increased from 200 to 600. This resulted in standard deviations which were similar to the other synthesis methods. For example, the mean value of QP was reduced from 2.53 to 2.24 and the standard deviation was reduced from 0.320 to 0.226 for the PM spectrum case.

Comparing the results of methods M4 and M7 in particular, it can be seen that there is very good agreement in both mean values and standard deviations for all wave parameters tested. The differences are generally small and well within the 90% confidence intervals in most cases. Although the standard deviation of HMAXD for method M7 is slightly smaller than that for method M4, the difference is probably not large enough to be significant. It must also be noted that the confidence intervals shown may not be very accurate since HMAXD is non-Gaussian.

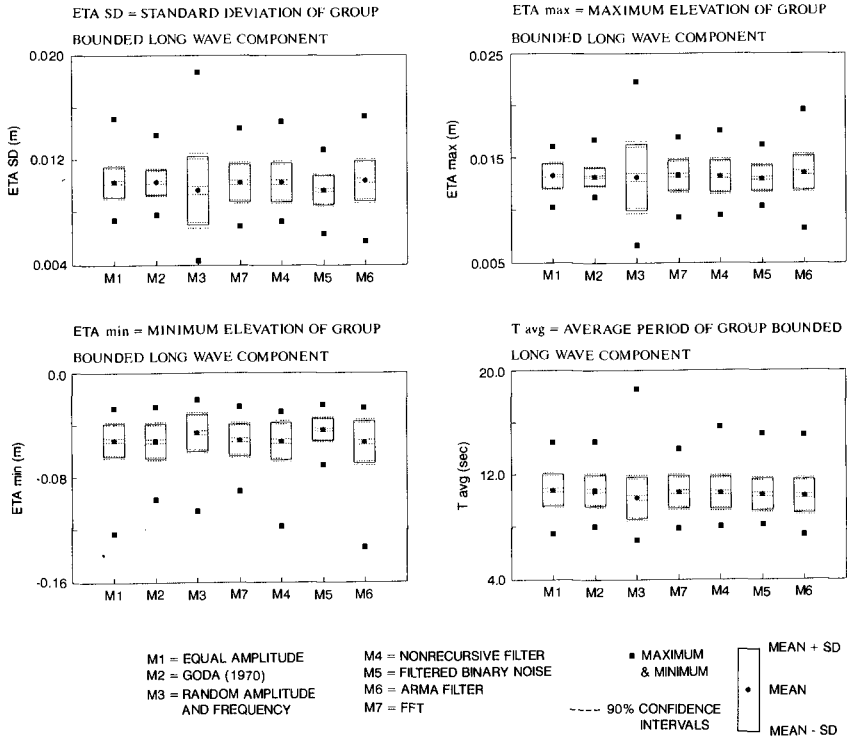


Fig.9 Long Wave Parameter Statistics for JONSWAP spectrum

The results of the statistical analysis of the 4 long wave parameters are shown in Figure 9. Methods M1 and M2 have smaller variability than the others for both the standard deviation and the maximum elevation of the group bounded long wave component. Method M3 has larger variability than the

other methods for these parameters. In all cases, however, there is very good agreement between methods M7 and M4 for the mean values and standard deviations of the long wave parameters.

FFT APPROXIMATIONS OF NONHARMONIC WAVE RECORDS

A separate part of this study was to determine how well an FFT synthesized wave record could approximate typical wave records generated by the nonharmonic methods. It is well known that any continuous waveform of finite duration can be represented exactly by a Fourier series expansion. This result has limited practical value, however, since an infinite number of components with infinite bandwidth are required. Furthermore, Fourier representations are always cyclic whereas nonharmonic wave records are not. Consequently, Fourier representations of such records must generally cope with an implicit discontinuity. A further constraint imposed by most FFT algorithms is that the number of points in the Fourier time series must be an integer power of 2.

In order to deal with these problems, an iterative procedure was developed which can generate a very accurate FFT approximation to any arbitrary discrete time series of M points. The FFT approximation has N points where N is an integer power of 2 which is less than $2M$. The original M -point time series is first resampled at N points by simple linear interpolation. An initial set of Fourier coefficients is obtained by an FFT transform. These coefficients are then multiplied by Lanczos smoothing factors in order to minimize any Gibbs phenomenon oscillations associated with the implicit discontinuity in the original record. The initial FFT approximation is then obtained by an inverse FFT.

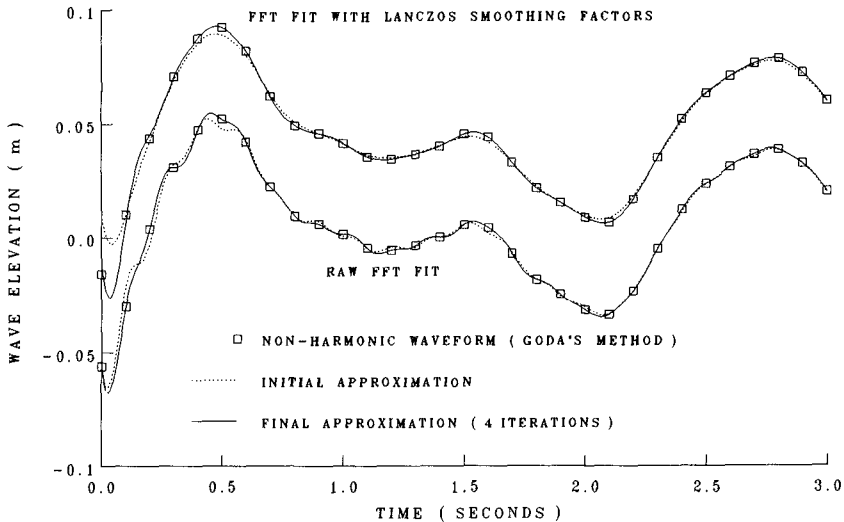


Fig. 10 FFT Approximations to a Method M2 Record

The initial FFT approximation is then resampled back to the original M time points by linear interpolation and subtracted from the original record to obtain a residual M -point record. The entire process is then applied to the residual record and repeated for 3 or 4 iterations until the amplitude of the residual record becomes sufficiently small.

An example of this procedure is shown in Figure 10 for the case of a nonharmonic wave record synthesized by method M2 (Goda's method). The lower pair of curves shows the result obtained without including the Lanczos smoothing factors. The Gibbs oscillations are quite evident. It can be seen from the upper pair of curves that the Lanczos factors do an excellent job of suppressing these oscillations and the final FFT representation is a very good approximation of the original nonharmonic wave record. The only noticeable difference is a small negative peak at the beginning caused by the cyclic property of the FFT. Such effects are very localized, however, and a very close fit is obtained over the main part of the record. It should also be noted that this example was selected with a large discontinuity to emphasize this aspect whereas records are normally selected on zero crossing boundaries to minimize these effects. Three more FFT approximations of nonharmonic wave records are plotted in Figure 11. These results clearly demonstrate that the use of an FFT synthesis technique does not impose any significant constraints on the types of waveforms which can be represented.

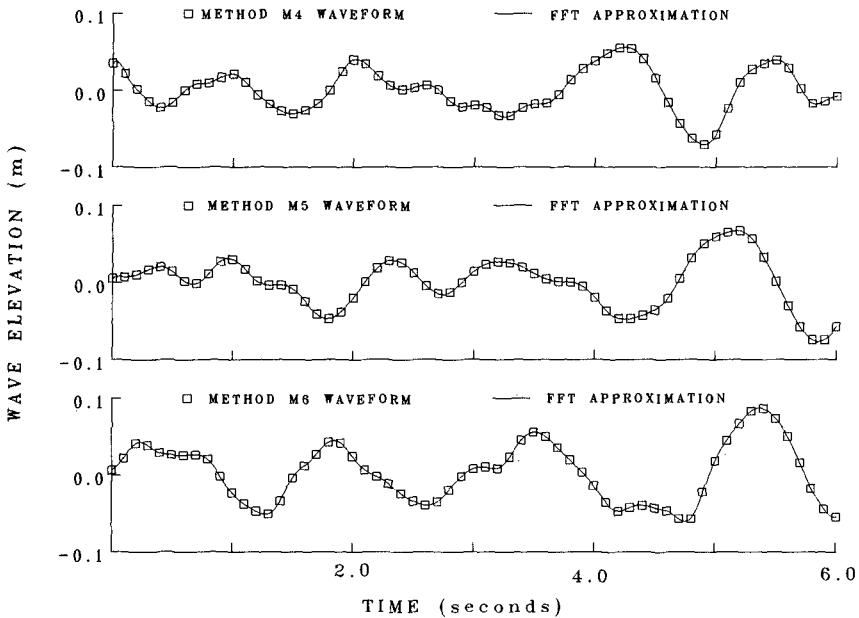


Fig.11 FFT Representation of 3 Nonharmonic Records.

DISCUSSION AND CONCLUSIONS

Methods M4 - M7 all produced very similar standard deviations for the wave parameters tested. As expected, methods M1 and M2 produced smaller standard deviations for the spectral parameters since they are spectrally deterministic in contrast to the other methods. Method M3 generally gave larger wave parameter variability than the other methods when 200 frequencies were used but the variability was similar to the other methods when the number of frequencies was increased to 600.

The nonrecursive filtered white noise method M4 should produce the most realistic wave records because it imposes no constraints on the basic assumption of a stationary Gaussian process and it provides a closer spectral fit than the ARMA filter method. There are no significant differences in either the mean values or the standard deviations of the wave parameters produced by the FFT method M7 and those produced by method M4. It is therefore concluded that the use of FFT synthesis methods does produce realistic Gaussian wave records provided that the maximum number of frequencies is used for the required record length. In other words, the FFT wave records will be realistic if $\Delta f = 1/(\text{record length})$ so that the wave records are never actually recycled.

The nonharmonic superposition methods can generate very long non-repetitive wave records with a relatively small number of frequencies compared to FFT techniques. However, the results from method M3 demonstrate that the use of nonharmonic frequencies cannot compensate for a lack of frequency density. The number of nonharmonic frequencies over the main spectral band must be at least as large as those in an FFT representation in order to obtain correct short-term variability of certain wave parameters.

It has been shown that any discrete time domain wave record generated by a nonharmonic synthesis method can be approximated by an equivalent FFT time series with no significant residual error. Thus, the use of an FFT representation per se does not impose any practical limitations on the types of waveforms which can be produced. It is sometimes claimed that filtered noise methods are superior to FFT techniques because they have continuous rather than discrete spectra. An FFT approximation to a filtered white noise record will have Gaussian Fourier coefficients so this is simply an alternate implementation of the RFC method. Since the time domain wave records are virtually identical, a finite length record generated by a filtered noise method cannot be considered to have a more continuous spectrum than a record of the same length generated by the RFC FFT technique.

In summary, all of the synthesis methods investigated can be used in principle to generate realistic Gaussian wave records but spectrally nondeterministic procedures are necessary for correct short term variability. The choice of a method is thus largely a matter of computational efficiency and convenience. The ARMA filter and FFT methods were found to be 20 to 30 times faster than the nonharmonic superposition methods. The ARMA filter technique is slightly faster than the FFT but the design of ARMA filters is

somewhat difficult and time consuming. In most applications, the convenience of FFT techniques will usually outweigh the marginal speed benefit of the ARMA filter approach.

REFERENCES

Barthel, V., E.P.D. Mansard, S.E. Sand and F.C. Vis, "Group Bounded Long Waves in Physical Models", *Ocean Engineering*, Vol. 10, No. 4, 1983.

Borgman, L.E., "Ocean Wave Simulation for Engineering Design", *J. Waterways and Harbors Div., ASCE*, Vol. 95, No. WW4, 1969, pp. 557-583.

Fryer, D.K., G. Gilbert and M.J. Wilkie, "A Wave Spectrum Synthesizer", *J. Hydraulic Res.*, Vol. 11, No. 3, 1973.

Funke, E.R. and E.P.D. Mansard, "A Rationale for the Use of the Deterministic Approach to Laboratory Wave Generation", *IAHR Seminar on Wave Generation and Analysis in Laboratory Basins, Lausanne, 1987.*

Goda, Y., "Numerical Experiments on Wave Statistics with Spectral Simulation", *Rpt. of Port & Harbour Res. Inst.*, Vol. 9, No. 3, 1970.

Goda, Y., "On Wave Groups", *BOSS Conference, Trondheim, 1976.*

IAHR (1986), "List of Sea State Parameters", *Joint Publication by the IAHR Section on Maritime Hydraulics and PIANC, Supplement to Bulletin no 52, General Secretariat of PIANC, Brussels, Belgium.*

Mansard, E.P.D. and E.R. Funke, "On the Statistical Variability of Wave Parameters", *National Research Council Canada Tech. Rpt. 26604, 1986.*

Medina, J.R., J. Aguilar and J.J. Diez, "Distortions Associated with Random Sea Simulators", *ASCE J. Waterway, Port, Coastal & Ocean Eng.*, Vol. 111, No. 4, 1985.

Samii, K. and J.K. Vandiver, "A Numerically Efficient Technique for the Simulation of Random Wave Forces on Offshore Structures", *Paper 4811, 16th Offshore Technology Conference, Houston, 1984.*

CHAPTER 7

ON THE TRANSFORMATION OF WAVE STATISTICS DUE TO SHOALING

E.P.D. Mansard¹, E.R. Funke¹, J.S. Readshaw² & R.K. Girard¹

ABSTRACT

The results of a 1:40 scale physical model investigation into the shoaling process are described. The model simulated a nearly constant slope of 1:40 with wave measurements made at a depth of approximately 25 and 9 m. Two hundred individual tests were undertaken, with four offshore significant wave heights as the only test variant. The results indicate that the most severe nearshore wave conditions do not occur with the worst offshore conditions. There is evidence of a significant increase in low frequency wave energy in the nearshore zone.

INTRODUCTION

For the laboratory design of coastal structures in depth-limited situations, it is customary to simulate a pre-specified sea state in the offshore region of a model and let the shoaling take its natural course on a bathymetry similar to that found in nature. The final design of the structure is then related to that offshore sea state and its probability of occurrence. Coastal engineers usually design their structures to withstand 1 in 100 year storm conditions.

The transformation of wave statistics due to shoaling has been an active field of research for a number of years. However, the complex physics of this phenomenon is not thoroughly understood. An extensive series of model investigations were carried out recently, for the purpose of gaining a better understanding of this phenomenon. This study included only one bathymetry and only one offshore water depth. Only one spectral shape with only one peak frequency was used. Waves were only recorded at two locations. In this sense, the investigation was simply a case study.

This research was motivated by the discovery of certain unexplained inconsistencies during a commercial model study. It was therefore undertaken to obtain a better insight into

¹ Hydraulics Laboratory, National Research Council
Ottawa, Ont., Canada, K1A 0R6

² W.F. Baird Associates Ltd., 38 Antares Drive,
Ottawa, Ont, Canada, K2E 7V2

the shoaling phenomenon and to quantify the wave parameter statistics that may result from shoaling. Some of the results have previously been reported by Readshaw et al (1987). Further results are presented here. Therefore, this paper complements the information contained in Readshaw et al (1987) and is intended to provide the basis for further comprehensive research.

The model investigation has shown that, for a given offshore sea state described solely by the variance spectral density, the severity of the nearshore wave climate can be grossly misjudged. Although this research has led to several useful conclusions, which are stated below, it must be expected that other test conditions for wave period, water depth, bathymetry and perhaps wave direction may lead to different results than those reported here. Nevertheless, it is believed that the conditions for this investigation are typical and the results will give a general indication of what may be expected for other situations.

EXPERIMENTAL SET-UP AND TEST WAVE CONDITIONS

Figure 1 shows a sketch of the experimental set-up. Waves were allowed to shoal from a depth of approximately 25.2 m (full scale units) to a depth of 8.6 m, where a breakwater was to be constructed. For convenience, the deeper region will be referred to here as the offshore zone and the other as the nearshore zone. The bathymetry that was used in this study had a nearly constant slope of approximately 1:40. This corresponded to the conditions in nature after which the study was modelled. The scale factor of the model was 1:40.

Waves were generated from numerically synthesized data derived from a JONSWAP spectral density with a peak period of 16.6 s and a γ value of 3.3. The method of wave synthesis was the "Random Complex Spectrum" method³ described by Funke & Mansard (1984). This method of synthesis creates wave trains from a Gaussian distributed white noise complex spectrum which is filtered by the specified target spectrum. It is known that it produces wave trains which mimic the variability of the natural sea state. Fifty different time series of 20 minute duration (full scale) were synthesized from a common JONSWAP target spectrum. Each of these was rescaled in four different ways, creating therefore four different sets of wave generator command signals, one for each offshore significant wave height of 4.8 m, 6.3 m, 7.8 m and 9.3 m. The rescaling was adjusted for each individual wave record to ensure that the desired variance was achieved near the wave board. As a result, 200 command signals were synthesized originating from a common spectral shape with common peak frequency, but differing only in their variance. Each set contained therefore 50 time series which were identical to those in the other sets in every respect except the amplitude scale. This is an important point, because the only parameter which was varied for the purpose of this study was the offshore significant wave height H_{m0} .

³ Miles and Funke (1988) refer to this method as the "Random Fourier Coefficient" method. A description of its statistical characteristics is also provided in their publication.

ANALYSIS OF WAVE DATA

All wave data was subjected to spectral density and zero-crossing analysis. From the spectral density the following parameters were obtained:

- f_{pD} - the peak frequency according to the Delft method (IAHR List of Sea State Parameters, 1986). It was computed as the centroid of the part of the spectrum which is delimited by its first and its last crossing of a threshold that is 80% of the spectral peak value.
- H_{m0} - the estimate of the significant wave height which was computed as $4 \cdot \sqrt{m_0}$, where m_0 was obtained by integration of the spectral density from $0 < f < 0.5$ Hz. This corresponded, in this case, to an upper limit of $8.5f_p$ and was for all practical purposes an upper limit of infinity. For reasons to be explained later, this parameter was also evaluated for the integration limits of $0.03 < f < 0.5$ and $0.03 < f < 0.15$ Hz.
- $m_{0,LW}$ - the variance of the long waves which was computed by numerical integration of the spectral density from $0 < f < 0.03$ Hz. This corresponded, in this case, to an upper limit of $0.5f_p$.

From zero crossing analysis the following parameters were obtained:

- $H_{1/3}$ - the significant wave height, computed as the average of the highest one-third of all zero down and zero up-crossing waves.
- $H_{1/10}$ - the average one-tenth of all wave heights from zero down and zero up-crossing analysis.
- $H_{1/20}$ - the average one-twentieth of all wave heights from zero down and zero up-crossing analysis.
- H_{max} - the larger of the maximum zero up- or down-crossing wave.
- $\bar{S}_{H1/3,d}$ the average steepness of the significant waves. This is the average of the ratios of wave heights and wave lengths for those waves which belong to the highest one-third of all zero down-crossing waves.

RESULTS AND DISCUSSION

The results presented here correspond to waves measured at the two locations shown in the Figure 1. Four pairs of example wave records, as measured by the two probes, are shown in Figure 2. It will be noticed that the offshore wave record is given below the corresponding nearshore wave record for each of the four significant wave heights given in this example. Closer comparison between the four offshore wave records will reveal that they originate from the same time history which was scaled to yield the desired wave heights $H_{m0} = 4.8, 6.3, 7.8$ and 9.3 m. Evidently, for the higher wave heights, the offshore wave crests become more accentuated and some distortions occur because of breaking. Nevertheless, except for scaling, the inputs to the four tests were the

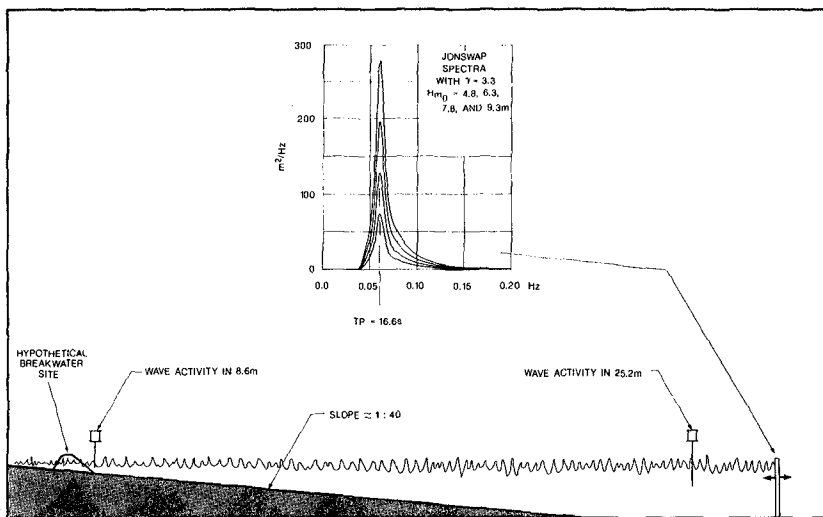


FIGURE 1
DEFINITION SKETCH OF THE EXPERIMENTAL SET-UP

same and hence this figure illustrates the influence of just the variance of the offshore wave activity on the transformation of wave profiles from deep to shallow water.

The nearshore wave records in Figure 2 were synchronized to the offshore wave trains. The arrows in the wave records point approximately to corresponding points in the two recordings, making allowance for the propagation delay. From observations during the tests, it was apparent that the wave trains on the left hand side of the figure describe the shoaling situation before breaking in the nearshore zone, whereas the right hand wave records illustrate the nearshore post-breaking state.

Figure 2 shows, as one would expect, that the nearshore wave profiles have sharper crests and flatter troughs when compared to the nearly sinusoidal profiles in deep water. Even for the lowest significant wave height, it is difficult to identify a similarity between the nearshore and the corresponding offshore wave record. However, with some stretch of the imagination, one can see a correspondence between wave groups. But, for the largest significant wave height, all meaningful relationship seems to have vanished. It can be speculated that, as the variance of the offshore sea state increases, the individual nearshore wave profiles steepen up much more quickly during shoaling and become unstable. This results then in the breaking of waves and their subsequent reconstitution before they reach the hypothetical breakwater site.

Another interesting observation is the skewness of waves in the nearshore zone. This is more pronounced for large offshore wave heights. It is speculated that this is the result

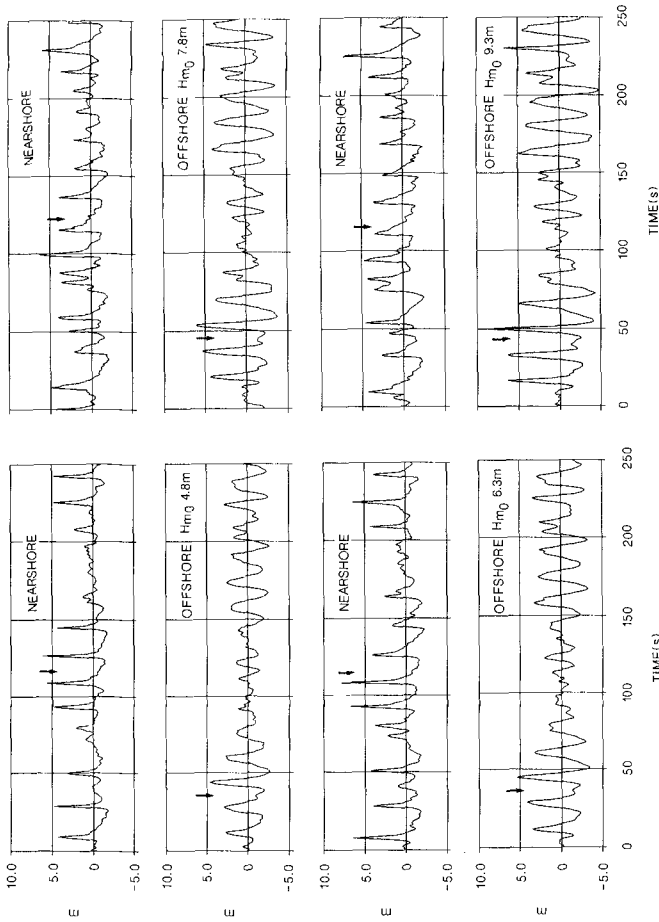


FIGURE 2
 SAMPLE TIME SERIES MEASURED BY THE TWO PROBES
 FOR THE FOUR SIGNIFICANT WAVE HEIGHTS (H_{m0})
 OF THE TARGET SPECTRUM

of an interaction between the shoaling waves and the return currents from the beach.

The spectral densities of the eight wave trains in Figure 2 are shown in Figure 3 with each corresponding pair of spectra for a nearshore and an offshore case superimposed on the same graph. From this it can be seen that, in spite of a substantial increase in the variance of the offshore sea state, there is not an equivalent increase in the variance in the nearshore sea state, evidently because of energy loss due to breaking. On the other hand, as a result of shoaling, the nearshore spectra indicate a significant increase in the variance for the low frequency range (i.e. $0 < f < 0.03\text{Hz}$). It can also be noted, that the peak frequencies of the nearshore spectra tend to be lower than those of the offshore spectra. This frequency shift can be partly attributed to possible transfer of energy from high to low frequencies during the

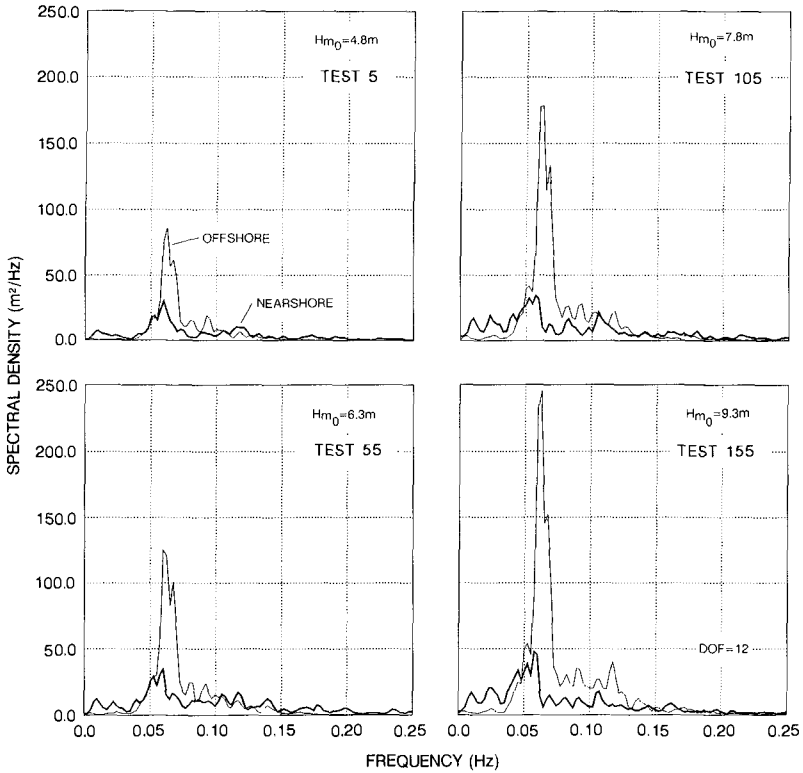


FIGURE 3
 SPECTRAL TRANSFORMATION ON A 1:40 SLOPE
 FOR THE FOUR SIGNIFICANT WAVE HEIGHTS (H_{m0})
 OF THE TARGET SPECTRUM

breaking process. In general, the nearshore spectra are much broader than their offshore origins.

Figure 4 shows the results of the analysis for the offshore significant wave height of 9.8 m. The time series given in this figure, are the various wave parameters from the fifty offshore and nearshore wave records placed in sequential order.

It can be seen from this figure, that there is no significant correlation between offshore and nearshore wave parameters. Except for the peak frequency and the long wave energy, the variability of wave parameters is approximately the same. It is also evident that there is generally a significant increase in long wave energy as a result of

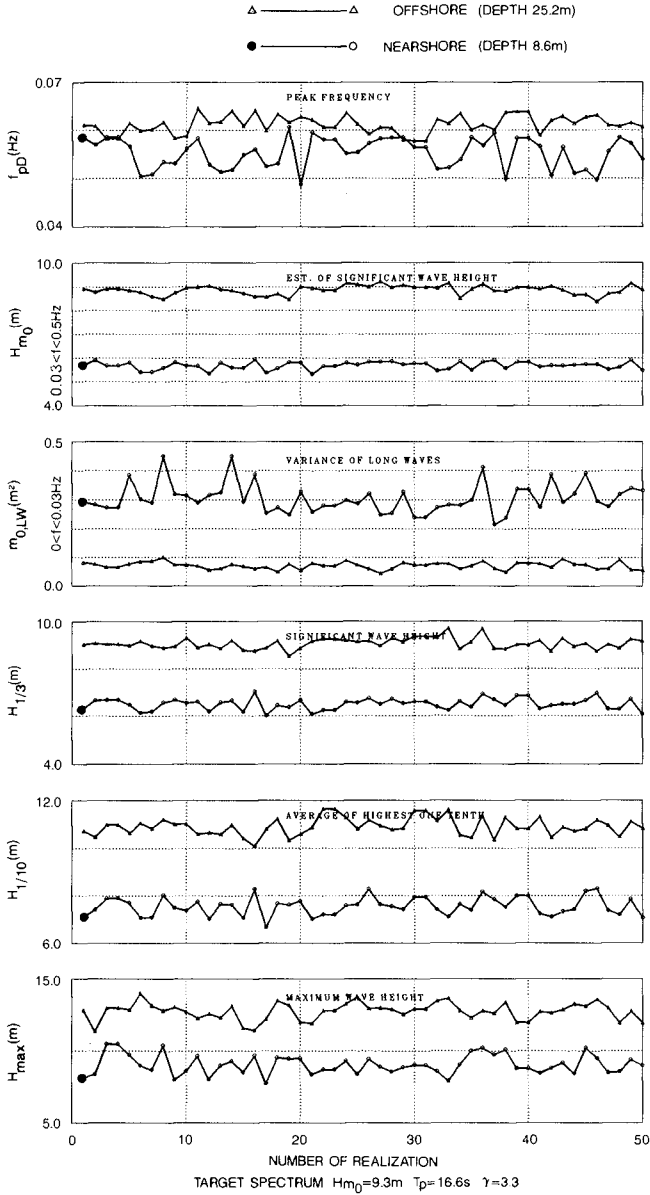


FIGURE 4
 SELECTED WAVE PARAMETERS , OFFSHORE AND NEARSHORE ,
 FOR 50 DIFFERENT REALIZATIONS OF THE TIME SERIES

shoaling. Although the command signals to the wave machine were rescaled to eliminate the variability of the offshore significant wave height, it is apparent that at the probe location 11 m from the wave board some variability has re-established itself. This is partly due to breaking and non-linear effects.

NON-LINEARITIES

The Laplace equation with proper boundary conditions is most often used for describing waves. Solutions of this equation can be obtained by the perturbation technique and waves are therefore of infinite order. However, for most practical applications, the first order solution to this equation is found to be quite satisfactory. But in shallow water, where the boundary conditions are principally non-linear, this equation would have to be solved to a higher order and, during this, two important phenomena will appear. These are the bounded sub- and the super-harmonics (Mansard et al 1988). The wave components resulting from these non-linearities travel with velocities bound to their fundamentals, while other components satisfy the linear dispersion relation. Barthel et al(1983) and Sand & Mansard(1986) show that classical first order wave generation theory does not properly satisfy the boundary conditions needed for the correct reproduction of these waves and therefore some spurious components of similar frequencies will appear in the simulations. This theory can be used to estimate the frequencies and their amplitudes as a consequence of shallow water boundary conditions, and permits therefore the prediction of spectral distortions.

Figure 5 shows two arbitrarily selected sample spectra measured by the first probe when using the target spectrum with a significant wave height $H_{m0} = 7.8$ m. On the left hand side of this figure, a comparison is shown between the expected spectral density for this particular realization and the one which was actually measured. The expected spectral density corresponds here to the one synthesized by the random complex spectrum, which is of course based on linear superposition of frequency components. It can be seen from this figure, that the measured energy content in the two frequency ranges of $0 < f < 0.03$ Hz and $0.1 < f < 0.5$ Hz are distinctly higher than expected. However, by applying second order wave and wave generation theory to the prediction of the wave spectra at this site, the agreement with the measured spectra is much improved as is shown on the right side of Figure 5.

RELATIONSHIP BETWEEN OFFSHORE AND NEARSHORE WAVE PARAMETERS

Examples of the relationship between offshore and nearshore wave heights are illustrated in Figures 6 and 7 for the four different offshore wave height parameters. In these illustrations a nearshore wave height parameter is plotted against the same offshore parameter.

In order to reduce the variability of wave height estimates as computed from 20 minute long records, the data were also analyzed by joining them first into blocks of 3 and 6 to give 1 and 2 hour averages of wave parameters. Figures 6 and 7 provide therefore the results for each of four different wave height parameters, calculated for three different averages.

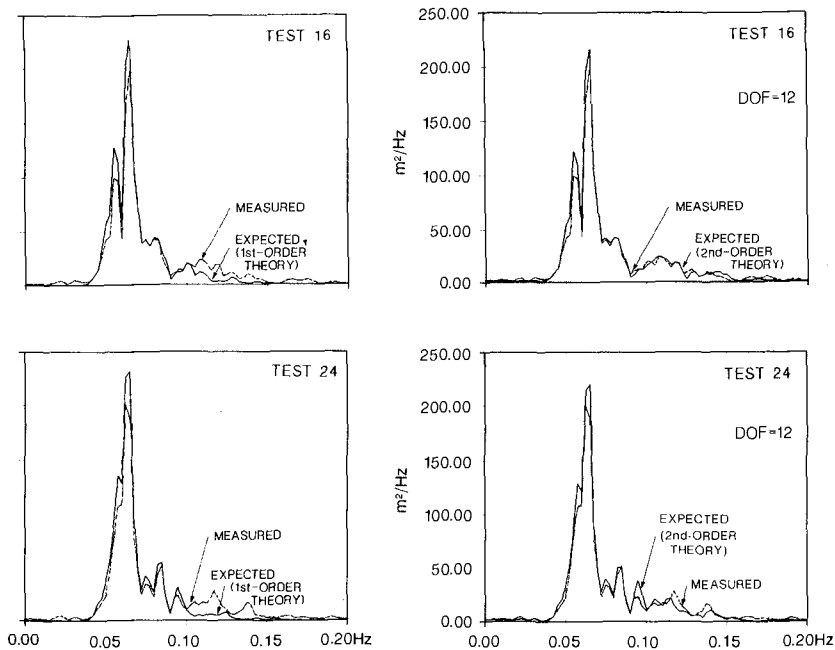


FIGURE 5
NON-LINEAR PREDICTION OF WAVE SPECTRA

$H_{m0}=7.8\text{m}$ $T_p=16.6\text{s}$ $h=25.2\text{m}$

DISTANCE FROM PADDLE = 11m

As one would expect, it can be seen from these results that the variability does decrease with increasing record lengths. The 2 hour averages illustrate quite clearly the general trend in the shoaling process. It will be seen that the nearshore wave heights do not increase with increasing offshore wave height. There is also an indication that for three of these parameters there is a slight reverse trend in as much as the nearshore wave height seems to decrease for very large offshore wave heights.

Figure 8 presents the data in a different mode. Following a statistical analysis of nearshore wave height parameters obtained from 20 min records, the extrema, the average as well as the average +1 and -1 standard deviation were plotted against the offshore significant wave height H_{m0} . This was also done for the variance of the long waves and the steepness of the significant waves.

RELATIONSHIP BETWEEN FREQUENCY AND TIME DOMAIN ESTIMATION OF SIGNIFICANT WAVE HEIGHT

In deep water, the significant wave heights derived either by zero crossing analysis or by spectral density analysis are

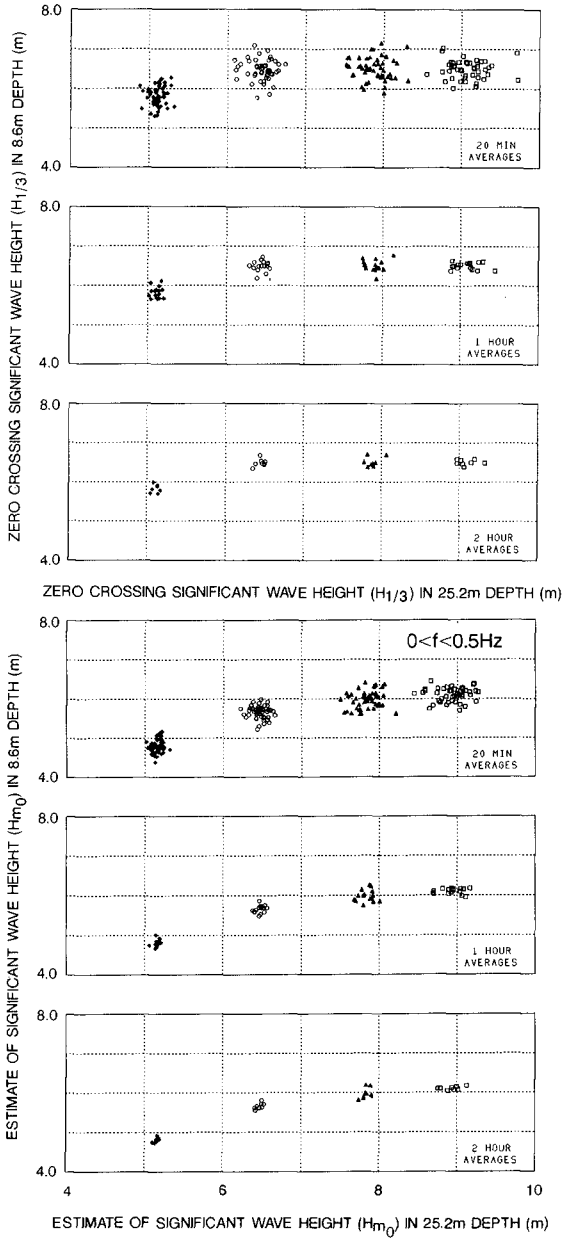


FIGURE 6
VARIABILITY OF SIGNIFICANT WAVE HEIGHTS

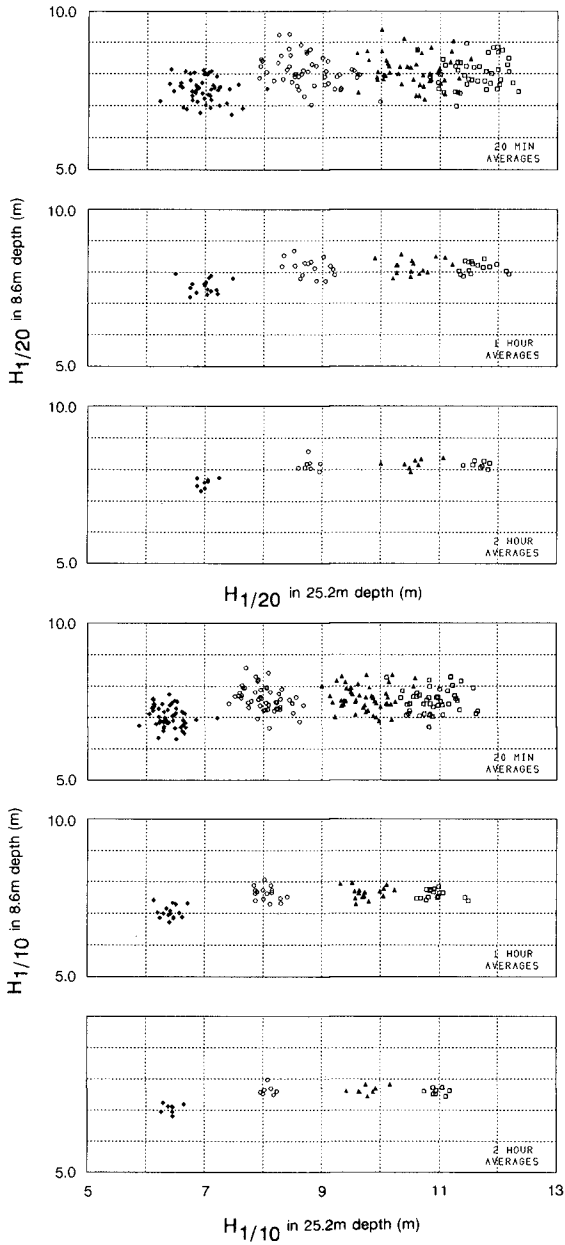


FIGURE 7
 VARIABILITY OF $H_{1/10}$ AND $H_{1/20}$

proportional to each other. This is because deep water waves are, for all practical purposes, Gaussian in character. However, in the nearshore zone, this assumption is not valid and the estimation formula for the significant wave height, $H_{1/3} \approx 4 \cdot \sqrt{m_0}$ no longer applies. There is also a real difficulty in deciding over what band of frequencies the spectral moment m_0 should be evaluated, because the nearshore spectrum contains significant energy below and above the original first order spectrum.

The left side of Figure 9 gives the average over 50 wave records of the ratio between the two nearshore significant wave heights, one as computed from zero crossing and the other as estimated from spectral analysis. For the latter, the variance of the nearshore sea state was computed with three different bandwidths, i.e.:

- $0 < f < 0.5$ Hz, which for all practical purposes, covers the range from 0 to ∞ ,
- $0.03 < f < 0.5$ Hz, which excludes the long wave frequency range, and
- $0.03 < f < 0.15$ Hz, which represents the typical first order frequencies contained between $0.5f_p < f < 2.5f_p$.

The reasons for choosing these integration limits are as follows. Waverider buoys cannot give outputs for wave periods longer than 30 seconds. Therefore, wave data recorded by them do not contain meaningful energy in the low frequency band. Furthermore, because of communication interference, it is generally presumed that spectral energy beyond $f > 2.5f_p$ must be considered background noise. By applying the same limits to this data collected in the laboratory, which are usually imposed implicitly or explicitly on natural wave data, Figure 9 may serve a useful purpose in the interpretation of some wave spectra recorded in nature.

The right hand side of Figure 9 gives the shoaling coefficient as a function of the offshore wave height. This coefficient is computed as the ratio of the average nearshore to the average offshore wave height. Once again, various estimates of the significant wave height are displayed. In case of the significant wave height estimated from spectral integration, this is done with the three different cut-off frequencies.

CONCLUSIONS AND RECOMMENDATIONS

For the conditions which prevailed during the test series, the study concluded that:

- The significant wave height in the nearshore zone derived from zero-crossing analysis is generally larger than the nearshore significant wave height estimated from the zeroth spectral moment function (see also Thompson & Vincent 1985). This is apparent from Figure 9.
- A particular nearshore wave height can be realized by a wide range of offshore sea states. This information is contained in Figure 8.
- It is possible for the nearshore zero-crossing significant wave height to be larger than the offshore significant wave

height. This is the case here for the group of offshore wave heights of 4.8 m, as shown in Figure 9.

- On the average, it may be predicted that the worst nearshore wave conditions may not be produced by the worst offshore sea states. The offshore wave conditions of moderate wave height may lead to the worst nearshore significant wave heights. In this case the worst conditions arise probably at an offshore wave height of 7.8 m (c.f. Figures 6 and 7).
- As a result of the shoaling process, there is a significant increase of long wave energy in the nearshore zone. Figures 3 and 8 attest to this.
- The nearshore spectra tend to have a larger peak period than the corresponding offshore spectra. Otherwise, there is no simple relationship between offshore and nearshore peak periods. This is indicated in Figure 3.

The results presented so far illustrate the fact that for a given offshore sea state a large combination of nearshore sea states, some severe and some less severe, can be obtained. This is a consequence of statistical variability, and it implies that in every model study of depth limited situations one cannot be absolutely sure that the worst nearshore wave conditions have been simulated for a specified offshore sea state. One obvious solution to this problem is to simulate very long wave records in physical model studies. However, this may become expensive and time consuming since design optimization of a given structure usually requires many repetitions of the same test conditions in order to optimize several design parameters.

To overcome this difficulty, the technique currently used at the Hydraulics Laboratory of the NRCC, consists of first determining experimentally the worst nearshore wave climate by testing a large number of time domain realizations for each offshore sea state. This can be done by building a structure, say a preliminary design of a breakwater, at the projected site and then by identifying which of the time domain realizations results in the maximum number of breaking waves impacting on the structure. If this approach is not practical, the various nearshore wave records obtained during the preliminary tests can be subjected to frequency and time domain analyses. For example, at the NRCC Hydraulics Laboratory the following nearshore wave parameters are computed:

- the estimate of the significant wave height, H_{m0} ,
- the variance of long waves, $m_{0,LW}$,
- the zero crossing significant wave height, $H_{1/3}$,
- the average of the highest 1/10th zero crossing waves, $H_{1/10}$,
- the average crest front steepness of the significant waves, $\bar{S}_{H1/3}$, and
- the Groupiness factor value, GF.

Those offshore time series which give consistently the worst nearshore wave conditions for most of these six parameters are then selected as being the most suitable for the design study.

None of the above techniques are entirely satisfactory because the decisions made during this approach are very

subjective and are often based on intuition. It is speculated that there is no single wave parameter, but rather a combination of several parameters which may form a relevant criterion in the selection process. Furthermore, every structure is different and may therefore require different criteria for testing.

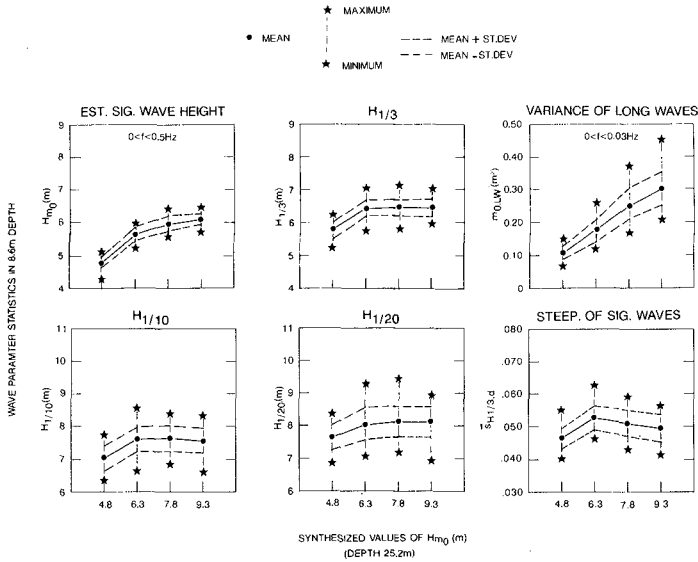


FIGURE 8
EFFECT OF OFFSHORE WAVE HEIGHTS ON NEARSHORE WAVE STATISTICS

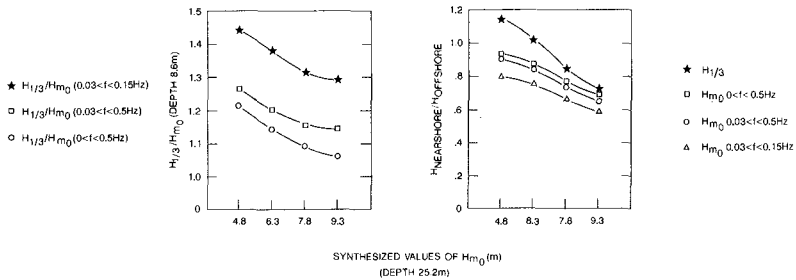


FIGURE 9
EFFECT OF OFFSHORE WAVE HEIGHTS ON THE RATIO OF NEARSHORE $H_{1/3}/H_{m0}$ AND ON THE SHOALING COEFFICIENT

Evidently, the best approach is to strive towards a better understanding of the relevance of various wave parameters, such as grouping, crest front steepness etc., to the stability of a structure and to establish their relationship to the offshore sea state through a better understanding of the shoaling mechanism. However, because of the complexity of the problem, a major research effort with international cooperation will undoubtedly be required.

Last, but not least, it should be apparent from information contained in Figure 8, that the distribution functions for the probability of occurrence of offshore wave parameters require a transformation in order to estimate from them the return period of a nearshore design wave. It can be seen, for example, that a nearshore significant wave height of, say, 6.5 m can be produced by all offshore sea states with significant wave heights equal to or greater than 6.3 m. This fact alone places a new perspective on the design of coastal structures.

REFERENCES

- BARTHEL, V., E.P.D. MANSARD, S.E. SAND and F.C. VIS, "Group Bounded Long Waves in Physical Models". Ocean Engineering, vol. 10, no. 4. 1983.
- FUNKE, E.R. and E.P.D. MANSARD, "The NRCC 'Random' Wave Generation Package", NRCC Hydraulics Laboratory Technical Report TR-HY-002, 1984
- IAHR (1986), "List of Sea State Parameters", Joint Publication by the IAHR Section on Maritime Hydraulics and PIANC, Supplement to Bulletin no. 52, General Secretariat of PIANC, Brussels, Belgium.
- MANSARD, E.P.D. and V. BARTHEL, "Shoaling Properties of Bounded Long Waves", Proc. 19th ICCE, Houston, USA, 1984.
- MANSARD, E.P.D., S.E. SAND and P. KLINTING, "Sub and Super Harmonics in Natural Waves", Journal of Offshore Mechanics and Arctic Engineering, vol. 110, Aug. 1988.
- MILES, M.D. and E.R. FUNKE, "Numerical Comparison of Wave Synthesis Methods", Proc. 21st ICCE, Malaga, Spain, June 1988.
- READSHAW, J.S., W.F. BAIRD and E.P.D. MANSARD, "Shallow Water Wave Generation: An Engineering Perspective", Proc. IAHR Seminar on Wave Analysis and Generation in Laboratory Basins, 22nd IAHR Congress, Lausanne, Switzerland, Sep. 1987, pp 397-410.
- SAND, S.E. and E.P.D. MANSARD, "Description and Reproduction of Higher Harmonic Waves", National Research Council Canada, Hydraulics Laboratory Technical Report TR-HY-012, NRC no. 25339, January 1986.
- THOMPSON, E.F. and C.L. VINCENT, "Significant Wave Height for Shallow Water Design", Journal of Waterway, Port, Coastal and Ocean Eng., vol. 111, no. 5, 1985.

CHAPTER 8

WAVE FIELD BEHIND THE PERMEABLE DETACHED BREAKWATER

Shan-Hwei Ou¹ Shiaw-Yih Tzang² and Tai-Wen Hsu²

ABSTRACT

Based on the concept of linear superposition, the model for combined wave refraction and diffraction developed by Liu et al. is extended to the situation of permeable detached breakwaters in a slowly varying water depth. Two cases are investigated which include a semi-infinite permeable breakwater and a single permeable breakwater. Laboratory results with a particular transmission coefficient in a wave basin are used to compare with the theoretical results. Fair agreements are found.

1. INTRODUCTION

The use of detached breakwaters as a countermeasure against beach erosion is ever increasing in the past. In practice, most of the breakwaters are constructed with the armor units so that waves can transmit through the breakwaters. The wave field behind permeable detached breakwaters has not yet been fully understood because of the complicated phenomena induced by the breakwater and the bottom topography.

Hotta (1978) proposed a wave superposition model around the permeable breakwaters due to the wave diffraction. The cases studied by Hotta are in a constant water depth with normal incident waves. Due to the fact that the water depth

1. Professor, Ph.D., Department of Hydraulics & Ocean Engineering, National Cheng Kung Univ., Tainan, Taiwan 70101, Rep. of China.

2. Graduate Student, ditto.

is changing in the field, the wave diffraction must be calculated under the consideration of wave refraction. The purpose of this study is to attempt to clarify the wave height distribution behind permeable detached breakwaters in a slowly varying water depth with obliquely incident water waves.

The applicability of linear superposition of combined refraction-diffraction wave field proposed by Liu, Lozano and Pantazaras (1979) has been verified by Ou and Tzang (1986) for impermeable detached breakwaters. This paper uses the same approach for the study of wave height distribution behind permeable breakwaters. Numerical examples are given and a series of experiments are conducted in a wave basin to compare the results.

2. REFRACTION-DIFFRACTION EQUATIONS

The wave patterns near a detached breakwater have been studied in the past decade by the combined effects of refraction due to slowly varying water depth and diffraction by the breakwater. Much progress have been achieved in both extending the applicability of the theoretical framework and saving the computer time and storage in numerical scheme (Liu and Mei, 1976; Liu et al. 1979; Tsay and Liu, 1982; Isobe, 1986). In this section we briefly summarize the combined refraction-diffraction equations developed by Liu et al. (1979) and Liu (1982) for the impermeable detached breakwater. These equations will be used in the following section for the derivation of wave superposition behind permeable detached breakwater.

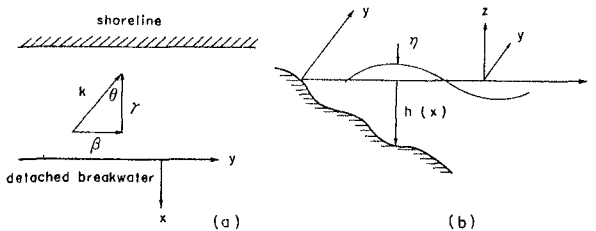


Fig. 1 Definition sketch and coordinate system

Considering small amplitude incident waves with the incident wave amplitude a_0 , and the radian frequency ω and the angle of incidence θ_0 as shown in the coordinate system of Fig. 1, the leading order asymptotic solutions for the free surface displacement η and the velocity potential ϕ can be expressed as follows:

$$\eta(x, y, t) = \gamma' A(x) [G(\mathbb{H})e^{iS} + G(\bar{\mathbb{H}})e^{i\bar{S}}] e^{-i\omega t} \dots\dots\dots(1)$$

$$\phi(x, y, t) = - \frac{ig \eta(x, y, t)}{\omega} \frac{\cosh k(z+h)}{\cosh kh} \dots\dots\dots(2)$$

where

$$\begin{aligned} \gamma' &= \pi^{-1/2} \exp(-i\pi/4) \\ G(\zeta) &= \int_{-\infty}^{\zeta} e^{i\sigma^2} d\sigma \dots\dots\dots(3) \end{aligned}$$

and $A(x)$ represents the shoaling and refraction factor as expressed by Nielsen (1982) in explicit form as

$$\begin{aligned} A(x) &= a_0 \sqrt{\cos \theta_0} \left[1 - \frac{2\pi h}{L_0} \left(1 - \frac{h}{L_0} \right)^2 \sin^2 \theta_0 \right]^{-0.25} \left(\frac{8\pi h}{L_0} \right)^{-0.25} \\ &\quad \exp\left(\frac{\pi h}{2L_0} \right) \dots\dots\dots(4) \end{aligned}$$

$G(\zeta)$ can be written in terms of the well known Fresnel integrals as

$$G(\zeta) = \left(\frac{\pi}{2} \right)^{1/2} \left\{ \left[\frac{1}{2} + C(\zeta^2) \right] + i \left[\frac{1}{2} + S(\zeta^2) \right] \right\} \dots\dots\dots(5)$$

where

$$\begin{aligned} C(\zeta^2) &= \frac{1}{\sqrt{2\pi}} \int_0^{\zeta^2} \frac{\cos \tau}{\tau^{1/2}} d\tau \\ S(\zeta^2) &= \frac{1}{\sqrt{2\pi}} \int_0^{\zeta^2} \frac{\sin \tau}{\tau^{1/2}} d\tau \dots\dots\dots(6) \end{aligned}$$

The arguments of the function $G(\zeta)$ in Eq. (1) are defined as

$$\mathbb{H}^2 = R - S, \quad \bar{\mathbb{H}}^2 = R - \bar{S} \dots\dots\dots(7)$$

where S, \bar{S}, R are the phase functions of the incident waves, the reflected waves and the radiated waves generated by an oscillatory point source at the tip of the breakwater, respectively. The value of \mathbb{H} is negative inside the shadow

region and is positive elsewhere. On the other hand, \bar{H} is positive in the reflection region and is negative elsewhere. The phase functions are expressed as follows:

$$S = - \int_0^x k \cos \theta \, dx + K_0 y \quad \dots\dots\dots(8)$$

$$\bar{S} = \int_0^x k \cos \theta \, dx + K_0 y \quad \dots\dots\dots(9)$$

$$R = - \int_0^x k \cos \theta \, dx + K_t y \quad \dots\dots\dots(10)$$

with

$$K_0 = k \sin \theta = k_0 \sin \theta_0 \quad \dots\dots\dots(11)$$

$$K_t = k \sin \theta = k_t \sin \theta_t \quad \dots\dots\dots(12)$$

where k_t and θ_t are the wave number and the initial angle of incidence of a radiated wave ray at the tip of the breakwater, respectively.

3. WAVE SUPERPOSITION

Based on the concepts of Hotta (1978), the wave height distributions behind permeable detached breakwater in a slowly varying water depth are established by extending the solutions developed by Liu et al. (1979). Substituting Eq. (5) into Eq. (1), the free surface displacement η can be expressed as follow:

$$\eta_D = \frac{A(x)}{\sqrt{2}} e^{-i(\frac{\pi}{4} + \omega t)} \{ [(\frac{1}{2} + c_1) + i(\frac{1}{2} + s_1)] e^{iS} + [(\frac{1}{2} + c_2) + i(\frac{1}{2} + s_2)] e^{i\bar{S}} \} \quad \dots\dots\dots(13)$$

where c_1, s_1 and c_2, s_2 are the Fresnel integrals for the incident waves and reflected waves, respectively. The subscript D refers to diffraction.

For brevity, the basic assumptions for this paper is the same as Ou and Tzang (1986). According to the definition of \bar{H} and \bar{H} , and from Eqs. (5) and (6), we define $G(\zeta)$ for clarity as follow:

$$G(-\zeta) = \left(\frac{\pi}{2}\right)^{1/2} \left\{ \left[\frac{1}{2} - C(\zeta^2) \right] + i \left[\frac{1}{2} - S(\zeta^2) \right] \right\} \dots\dots\dots(14)$$

A Semi-infinite Permeable Detached Breakwater

According to Hotta's (1978) concepts, the waves behind permeable breakwater consist of two main parts: diffracted

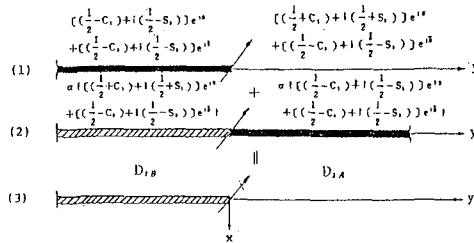


Fig. 2 Refraction-Diffraction function for a semi-infinite permeable breakwater

waves from impermeable breakwater and transmitted wave through permeable breakwater. As shown in Fig. 2, a permeable breakwater is placed parallel to the shoreline from y=0 to y=-∞. Waves in region A (incident region) and region B (diffraction region) are assumed to be the superposition of diffracted waves (Fig.2-(1)) and transmitted waves (Fig. 2-(2)). The free surface displacement in region A is

$$\eta = \gamma' A(x) [G(\bar{H}) e^{iS} + G(-\bar{H}) e^{i\bar{S}}] e^{-i\omega t} + \alpha \gamma' A(x) [G(-\bar{H}) e^{iS} + G(-\bar{H}) e^{i\bar{S}}] e^{-i\omega t} \dots\dots\dots(15)$$

where α is the transmission coefficient of permeable breakwater. From Eqs. (3), (5) and (14), we have

$$\eta = \frac{1}{\sqrt{2}} A(x) |D_{1A}(x, y)| e^{-i(\omega t + \pi/4)} \dots\dots\dots(16)$$

where $D_{1A}(x, y)$ is the refraction-diffraction function and subscript A refers to region A. Hence, $D_{1A}(x, y)$ in its final form is:

$$D_{1A}(x, y) = \left\{ \left[\frac{1+\alpha}{2} + (1-\alpha) C_1 \right] \cos S - \left[\frac{1+\alpha}{2} + (1-\alpha) \right. \right.$$

$$\begin{aligned}
 & S_1 \} \sin S + \left[\frac{1+\alpha}{2} - (1+\alpha)C_2 \right] \cos \bar{S} - \left[\frac{1+\alpha}{2} \right. \\
 & \left. - (1+\alpha)S_2 \right] \sin \bar{S} \} + i \left\{ \left[\frac{1+\alpha}{2} + (1-\alpha)C_1 \right] \right. \\
 & \left. \sin S + \left[\frac{1+\alpha}{2} + (1-\alpha)S_1 \right] \cos S + \left[\frac{1+\alpha}{2} - \right. \right. \\
 & \left. \left. (1+\alpha)C_2 \right] \sin \bar{S} + \left[\frac{1+\alpha}{2} - (1+\alpha)S_2 \right] \cos \bar{S} \right\} \dots (17)
 \end{aligned}$$

Similarly, we can derive $D_1(x,y)$ in region B in the same manner (see Tzang (1986) for details). Taking α equal to zero, the final equations agree with the solutions for a impermeable breakwater.

A Single Permeable Detached Breakwater

For a single impermeable detached breakwater, Ou and Tzang (1986) has developed a solution for the wave height distribution. When the breakwater is permeable, the waves behind the breakwater are assumed to be the superposition of the waves arising from an impermeable breakwater and the waves multiplied by α passing through a gap as described by Ou and Tzang (1986), as shown in Fig. 3. The free surface displacement based on the above assumption is as

$$\eta = \eta_s + \alpha \eta_g \dots \dots \dots (18)$$

The subscript s denotes a single impermeable detached breakwater, g denotes a single gap in a long breakwater.

Now we should consider the coordinate system first. The origin of the coordinate is located at the center of the breakwater. As described in the last section, we have

$$\begin{aligned}
 D_{2A}(x,y) = & \left\{ \left[\frac{1+\alpha}{2} + (1-\alpha)C_{1r} \right] \cos \left(S_r - \frac{\pi}{4} \right) \right. \\
 & - \left[\frac{1+\alpha}{2} + (1-\alpha)S_{1r} \right] \sin \left(S_r - \frac{\pi}{4} \right) + \left[\frac{1+\alpha}{2} \right. \\
 & \left. - (1+\alpha)C_{2r} \right] \cos \left(\bar{S}_r - \frac{\pi}{4} \right) - \left[\frac{1+\alpha}{2} - (1+\alpha)S_{2r} \right] \\
 & \left. \sin \left(\bar{S}_r - \frac{\pi}{4} \right) + \left[\frac{1+\alpha}{2} - (1-\alpha)C_{1t} \right] \cos \left(S_t - \frac{\pi}{4} \right) \right\}
 \end{aligned}$$

$$\begin{aligned}
 & - \left[\frac{1+\alpha}{2} - (1-\alpha) S_{1i} \right] \sin \left(\bar{S}_i - \frac{\pi}{4} \right) + \left[\frac{1+\alpha}{2} \right. \\
 & \left. - (1+\alpha) C_{2i} \right] \cos \left(\bar{S}_i - \frac{\pi}{4} \right) - \left[\frac{1+\alpha}{2} - (1+\alpha) S_{2i} \right] \\
 & \sin \left(\bar{S}_i - \frac{\pi}{4} \right) - \alpha \sqrt{2} \cos S_0 \} + i \left\{ \left[\frac{1+\alpha}{2} + (1-\alpha) C_{1r} \right] \right. \\
 & \left. \sin \left(S_r - \frac{\pi}{4} \right) + \left[\frac{1+\alpha}{2} + (1-\alpha) S_{1r} \right] \cos \left(S_r - \frac{\pi}{4} \right) \right. \\
 & \left. + \left[\frac{1+\alpha}{2} - (1+\alpha) C_{2r} \right] \sin \left(\bar{S}_r - \frac{\pi}{4} \right) + \left[\frac{1+\alpha}{2} \right. \right. \\
 & \left. \left. - (1+\alpha) S_{2r} \right] \cos \left(\bar{S}_r - \frac{\pi}{4} \right) + \left[\frac{1+\alpha}{2} - (1-\alpha) \right. \right. \\
 & \left. \left. C_{1i} \right] \sin \left(S_i - \frac{\pi}{4} \right) + \left[\frac{1+\alpha}{2} - (1-\alpha) S_{1i} \right] \right. \\
 & \left. \cos \left(S_i - \frac{\pi}{4} \right) + \left[\frac{1+\alpha}{2} - (1+\alpha) C_{2i} \right] \sin \left(\bar{S}_i - \frac{\pi}{4} \right) \right. \\
 & \left. + \left[\frac{1+\alpha}{2} - (1+\alpha) S_{2i} \right] \cos \left(\bar{S}_i - \frac{\pi}{4} \right) - \alpha \sqrt{2} \sin S_0 \right\} \dots (19)
 \end{aligned}$$

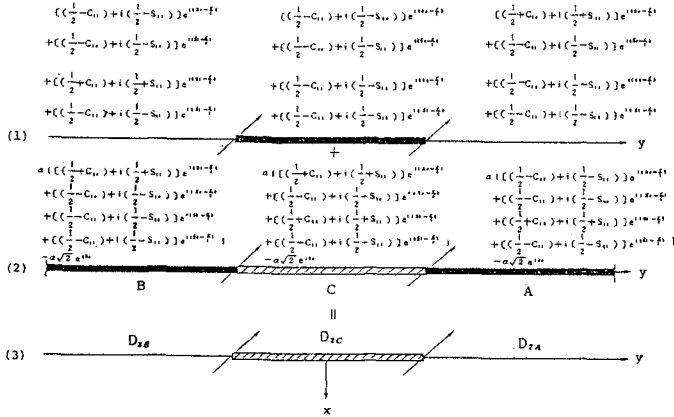


Fig. 3 Refraction-Diffraction function for a single detached permeable breakwater

where the subscripts r and ℓ denote the effects of the tip located on the right hand side and left hand side of the origin, respectively. Subscript o denotes the case without the appearance of the breakwater. Similarly, we can also derive $D_2(x,y)$ in region B (diffraction region) and in region

C (incident region) in a similar manner (see Tzang (1986) for details). Taking α equal to zero, the final equations also agree with the solutions developed by Ou and Tzang(1986) for a single impermeable detached breakwater.

4. NUMERICAL RESULTS

In this section simple numerical results are given. Computations for different values of transmission coefficient are given.

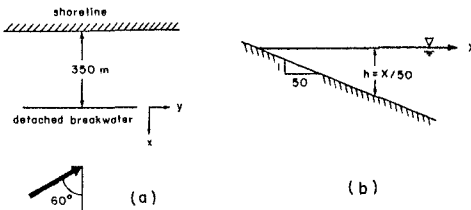


Fig. 4 Definition sketch for the detached breakwater

As shown in Fig. 4, the geometry chosen is as follows. The beach has a uniform slope $1/50$ in the x direction. The water depth of the location of breakwater is fixed at $h_R=7m$. The semi-infinite permeable breakwater is placed from $y=0$ to $y=-\infty$. The length of the single permeable detached breakwater is $L_B=700m$; the wave period $T=10$ sec arrives with a 60° inclination. Diagrams with $\alpha=0, 0.3, 0.5$ along two different cross sections ($h=5m$ and $h=3m$) are given. The treatment of the phase function R are described by Ou and Tzang (1986). The mesh size in the section is $10m$.

In Fig. 5, since the semi-infinite breakwater is permeable, the normalized wave height distributions on diffraction region are no more smoothly decreasing away from the tip. The wave height distributions oscillate with the same phase and the mean wave height increases as α varies from 0 to 0.5. On the contrary, the distributions become more smooth as α increases on incident region. In Fig. 6, for a single permeable detached breakwater, waves behind the breakwater are affected by waves diffracted from the two tips of the breakwater and by waves transmitted through the permeable breakwater. On diffraction region, the wave height distributions

oscillate more regularly but with bigger amplitude when breakwater is permeable. In incident region, the maximum wave height somewhat decreases as α increases, but the wave

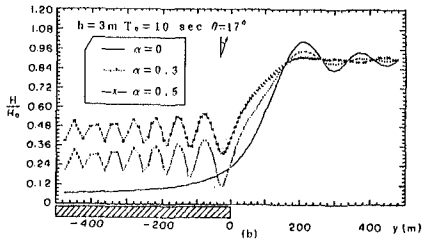
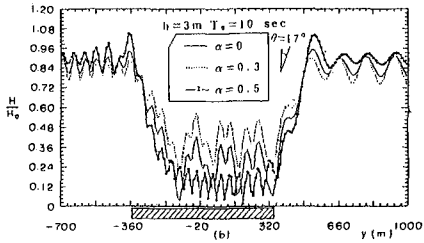
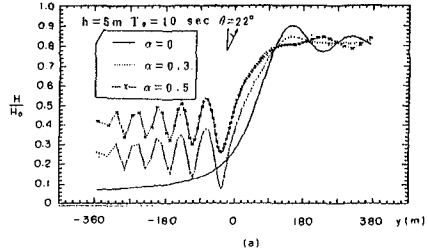
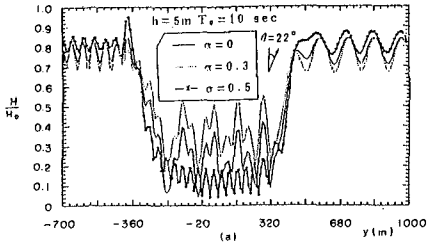


Fig. 5 wave height distribution for a semi-infinite breakwater with various values of transmission coefficient ($T_0=10\text{sec}$)

Fig.6 Wave height distribution for a single detached breakwater with various values of transmission coefficient ($T_0=10\text{sec}$)

height distributions oscillate without the tendency of attenuation. This is more obvious on the downwave side than on the upwave side. From the numerical results above, it is seen that as the transmission coefficient α increases, the transmitted waves through the permeable breakwater play a more important role in the wave field behind breakwaters.

5. LABORATORY EXPERIMENTS.

To verify the solutions for waves behind permeable breakwaters, a series of careful experiments are performed in a wave basin (16m×12m). The detail discussion of the laboratory experiments is given by Tzang (1986). A brief summary of the experimental setup is given herein.

As shown in Fig. 7, a plane beach with 1/20 slope is

installed in otherwise constant water depth of 0.4m. The permeable detached breakwater, made of plywood and lumber filled with armor units, as shown in Fig. 8, has a length of 3m for single detached breakwater. Waves are generated by a 9m long flap-type wave maker, which is mobile for changing the direction of wave propagation. Four wave gauges were used to measure the wave height. One is used for the incident wave information in constant water depth. The others are used for the diffracted wave amplitude behind the breakwater. The sections chosen are located at 0.5, 1.0, 1.5, 2.0 m from the breakwater ($h = 15, 12.5, 10, 7.5$ cm, respectively). All 4 gauges were recorded simultaneously along one section, and then to other section. The distance among the three gauges was 25cm. The transmission coefficient α of the permeable breakwater is tested preliminarily in a wave tank. The wave tank is lined up by guidewalls with 3m width in the wave basin. For the incident wave height $H_0=3$ cm and wave period $T=1$ sec, the experimented value of α equals 0.3. The test conditions are given in Table 1.

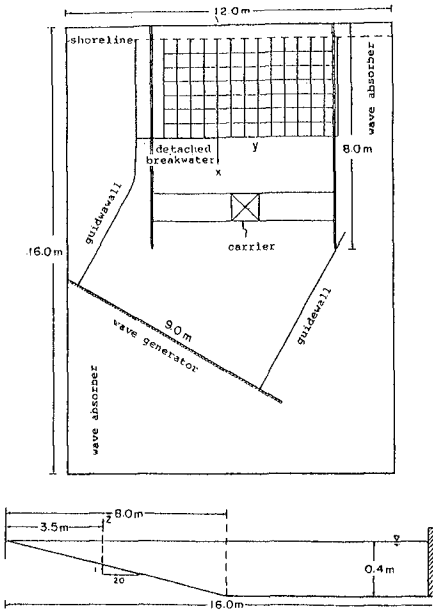


Fig. 7 Sketch of wave basin

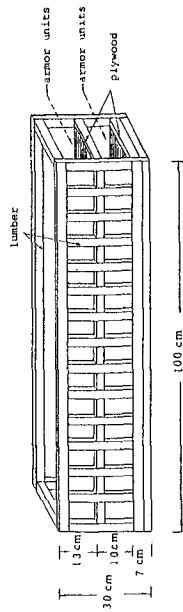


Fig. 8 Sketch of permeable breakwater

Table 1. List of Tests Conditions

α	θ_0 (deg.)	BREAKWATER TYPE	BREAKWATER LENGTH (m)	T(sec)	H_0 (cm)
0.3	0°	semi-infinite		1.0	3
				0.8	
		a single detached	3	1.0	
				0.8	
	30°	semi-infinite		1.0	
				0.8	
		a single detached	3	1.0	
				0.8	

Experimental data, obtained by Tzang (1986), behind permeable breakwater for $T=1.0$ sec only are replotted here in Fig. 9 to Fig. 12. In each figure the distributions of wave height are shown for four sections, $h=15, 12.5, 10, 7.5$ cm. Theoretical curves are also included for comparison. In Fig. 9 and Fig. 10 the wave height distribution on diffraction region of semi-infinite permeable breakwater are not attenuating but oscillating. On incident region, the theory usually underpredicts the experimental data. The agreement between theoretical solutions for $\alpha=0.3$ and experimental data in Fig. 10 is reasonably good. But the scattering of the experimental data in Fig. 9 is rather significant. This could be caused by the reflection from the breakwater. In Fig. 11 and Fig. 12 the overall agreements between theoretical solutions and experimental data are quite good except on the incident region far from the origin. This could be partially influenced by the boundaries of the wave basin and partially attributed to the existence of circulations of current (Liu and Mei, 1976). Also, wave reflected from the breakwater will influence the incident waves so as to cause the scattering of the experimental data. This is more obviously for normal incidence ($\theta_0=0^\circ$) than for oblique incidence ($\theta_0=30^\circ$).

6. CONCLUSIONS

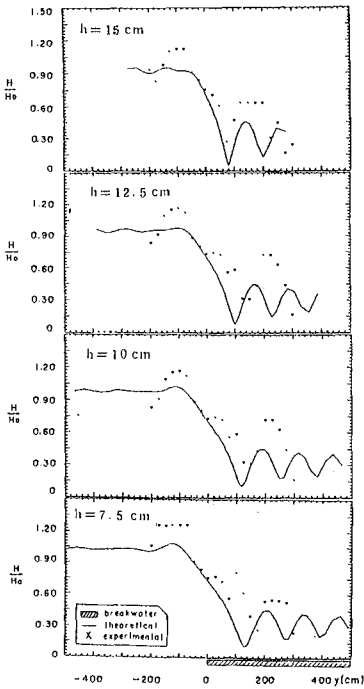


Fig. 9 Comparisons between theoretical results of wave height and experimental data ($T_0 = 1.0 \text{ sec}, \theta_0 = 0^\circ, \alpha = 0.3$): a semi-infinite permeable breakwater

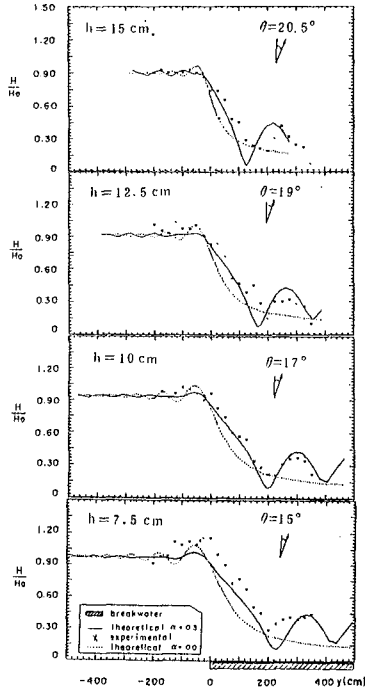


Fig. 10 Comparisons between theoretical results of wave height and experimental data ($T_0 = 1.0 \text{ sec}, \theta_0 = 30^\circ, \alpha = 0.3$): a semi-infinite permeable breakwater

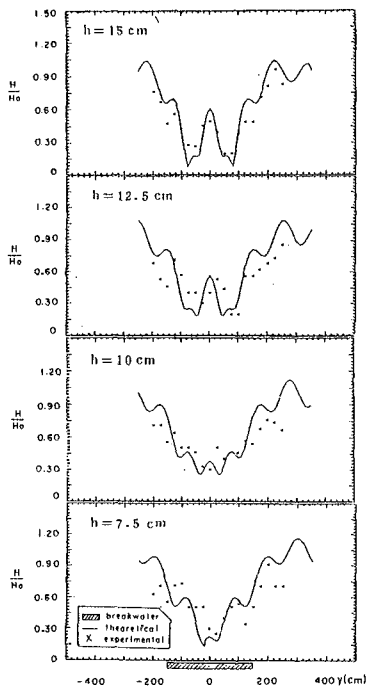


Fig. 11 Comparisons between theoretical results of wave height and experimental data ($T_0=1.0$ sec, $\theta_0=0^\circ$, $\alpha=0.3$): a single detached permeable breakwater

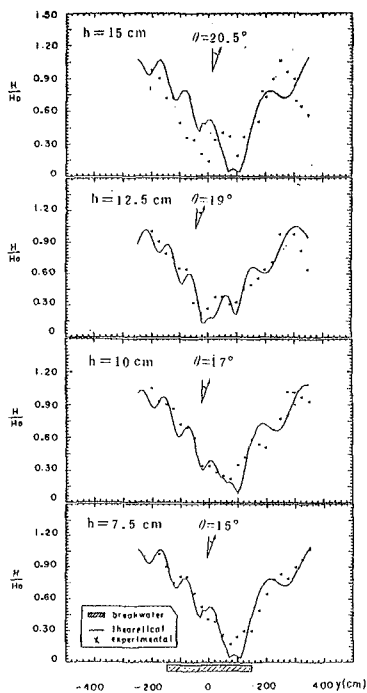


Fig. 12 Comparisons between theoretical results of wave height and experimental data ($T_0 = 1.0$ sec, $\theta_0 = 30^\circ$, $\alpha = 0.3$): a single detached permeable breakwater

By employing Hotta's (1978) concepts and extending the asymptotic solutions developed by Liu et al. (1979), we have obtained a simple description of wave height distributions behind permeable detached breakwaters. It is seen that the transmission coefficient α , the wave period T , and the incident angle are all contributed to the wave height variation. Large values of the transmission coefficient α will increase the mean wave height distribution on diffraction region but will not change its phase. It is also shown that, for a larger value of α , the transmitted waves play a more important role than the diffracted waves. The solutions developed in this paper have been reasonably verified by laboratory experiments except on the incident region far from the origin.

REFERENCES

1. Hotta, S., Wave height distribution around permeable breakwater, Proc. 16th Conf. on Coastal Eng., 695-714, ASCE, Hamburg, Germany, 1978.
2. Isobe, M., A parabolic refraction-diffraction equation in the ray-front coordinate system, Proc. 20th Conf. on Coastal Eng., ASCE, Taipei, Republic of China, 1986 (in press).
3. Liu, P. L-F., Combined refraction and diffraction: Comparison between theory and experiments, J. Geophys. Res., 87, 5723-5730, 1982.
4. Liu, P. L-F., C.J. Lozano and N. Pantazaras, An asymptotic theory of combined wave refraction and diffraction, Appl. Ocean Res., 1(3), 137-146, 1979.
5. Liu, P. L-F. and C.C. Mei, Water motion on a beach in the presence of a breakwater, 1, waves, J. Geophys. Res., 81, 3079-3084, 1976.
6. Nielsen, P., Explicit formulae for practical wave calculations, Coastal Eng., 6, 389-398, 1982.
7. Ou, S.H. and S.Y. Tzang, Wave patterns behind the detached breakwater, Proc. of Annual Meeting of the Chinese Institute of Civil & Hydraulic Eng., 315-336, 1986.
8. Tsay, T. -K. and P. L-F. Liu, Numerical solution of

waterwave refraction and diffraction problems in the parabolic approximation, *J. Geophys. Res.*, 87, 7932-7940, 1982.

9. Tzang, S.Y., The study of wave patterns behind permeable breakwaters, M.S. Thesis, Dept. of Hydraulics & Ocean Eng., National Cheng Kung Univ., Tainan, Taiwan, Rep. of China, 1986.

CHAPTER 9

INCOMING AND OUTGOING WAVE INTERACTIONS ON BEACHES

Rao V.S.N.Tatavarti*, David A.Huntley†, and Anthony J.Bowen*

A technique to decompose colocated random field measurements of wave elevation and current velocity into incoming (shoreward propagating) and outgoing (seaward propagating) components is presented. This decomposition technique, which is less sensitive to noise, enables us to determine the frequency dependent reflection coefficients and also the relative phase between the incoming and outgoing waves. The method is applied to C^2S^2 and NSTS data sets, from beaches with wide ranging characteristics and wave regimes. The results demonstrate the selective nature of beach absorption/reflection characteristics but are inconclusive in terms of a proper parameterization of reflections on natural beaches.

Introduction

Since the pioneering work of Miche (1951) coastal engineers have generally relied on empirical formulations to determine the reflectivity of a nearshore structure or a natural beach. These formulations, being based on monochromatic wave theories for planar beaches, were primarily designed to yield bulk reflection coefficients. In reality, however, we are faced with a spectrum of incident waves and complicated beach topographies, thus questioning the validity of bulk reflection coefficients. According to Miche's theory the reflected wave height is determined by the maximum wave steepness possible for a non breaking wave on a beach of linear slope. Therefore Miche's hypothesis suggests that there is a f^{-2} dependence of the reflection coefficient R , for monochromatic waves, where f is the wave frequency. This strong frequency dependence suggests that the use of a single bulk reflection coefficient for a spectrum of incident waves will be unsatisfactory. Carrier and Greenspan (1958) suggested that very small reflection coefficients are characteristic of natural beaches for waves of all but the very smallest amplitudes and that standing waves play no important role on such beaches. On the contrary there is ample evidence that standing waves are important on natural beaches (Suhayda,1974; Huntley, 1976; Holman, 1981; Guza and Thornton, 1982; Wright *et al.*, 1982; Bowen and Huntley, 1984; Elgar and Guza,1985) and that steeper beaches are reflective (Wright and Short, 1984).

As beaches have been used in hydraulic laboratories for over a century, it is but natural to focus attention on the laboratory investigations for more information on wave reflections. However, it is surprising to note that these investigations are ambiguous due to a lack of consensus in defining the critical parameters affecting the determination of reflection coefficient, leading to differences in results (Battjes, 1974; Guza and Bowen, 1976) and confusion in understanding the physics. This confusion reflects the difficulty in obtaining reliable measurements of the wave reflections. Moreover there is an additional difficulty of extending these results obtained on the basis of monochromatic wave theories to a spectrum of incident waves naturally found on beaches.

Field investigations of low frequency waves have yielded equally confusing results. Munk (1949) and Tucker (1950) implied that there is a small nonlinear long wave correction under shoreward propagating wave groups and a larger seaward propagating long

* Dept. of Oceanography, Dalhousie University, Halifax B3H 4J1, Canada.

† Institute of Marine Studies, Plymouth Polytechnic, Drake Circus, Plymouth PL4 8AA, U.K.

frequency wave released at breakpoint. In contradiction, Hasselman *et al.* (1963) presented evidence that shoreward propagating nonlinearly forced motion is larger than the seaward propagating component. Suhayda (1974) however, suggested that the incoming and outgoing components are of roughly equal magnitudes indicating that the concept of standing waves is important. The foregoing demonstrates the need to decompose random wave observations into incoming and outgoing components not only to understand clearly the nearshore wave dynamics and resulting sediment transport process but also to quantify the frequency dependent reflection coefficients.

The more recent studies on wave reflections utilize various analytical techniques to resolve a composite wave field into incident and reflected waves using measurements from wave sensors at adjacent locations (Thornton and Calhoun, 1972; Goda and Suzuki, 1976; Isobe and Kondo, 1984; Kim, 1985; Mansard and Funke, 1987).

The technique which is currently used by hydraulic laboratories for separating the incident and reflected spectra from the measured standing wave system in a laboratory is that of Goda and Suzuki (1976). The basic assumptions in this technique are that an irregular sea state can be described as a linear superposition of an infinite number of discrete frequency components, each with their own frequency, amplitude and phase, and that each frequency component travels with its own individual celerity described by the linear dispersion relationship. The technique consists of simultaneous measurements of the composite waves (superposition of incident and reflected) at two or three known positions in a line parallel to the direction of wave propagation. Fourier analysis of these measurements then provides the amplitudes and phases of the frequency components constituting the irregular sea state, on the basis of which the incident and reflected components can be resolved.

Although the technique is applicable to both regular and irregular trains of waves, the resolution into incident and reflected components is effective only outside the condition of the wave sensor spacing being an even integer of half wave length. In other words the resolution technique is strongly affected by the location of the sensors and the spacing between them. Also any nonlinear wave interaction affects the accuracy of the resolution technique.

Isobe and Kondo (1984) utilize the maximum likelihood method to measure the directional wave spectrum in a reflective system and determine the reflection coefficient of a structure in a directional sea. As the resolution power of the maximum likelihood method for a directional wave spectrum depends on the number and arrangement of wave sensors, this methodology cannot be applied where sufficient number of sensors are not deployed and also where the optimal arrangement of sensors is not made. A more serious limitation is the inaccuracy in computing reflectivities due to changing wave conditions with wave frequency and the wave direction.

Kim (1985) attempted to estimate the reflection coefficient of a natural beach by computing a cross correlation function for a wave field consisting of incoming and outgoing waves and comparing it with observed spatial correlation functions. The shallow water wave orbital velocities measured at two locations by current meters can be expressed as a combination of incoming and outgoing components. By analytically deriving an expression for the cross correlation function between the two measurements from the expressions for the combined wave fields at two locations, Kim suggests that cross correlation peaks appear at time lags associated with incoming and outgoing waves. Kim's study provides evidence for the existence of standing waves and seagoing waves at the expected time lags and allows a rough estimation of the relative magnitudes of incident and reflected waves. However, the major disadvantage of using the cross correlation function is that no frequency information can be obtained.

The most recent study on the problem of determining the reflection characteristics of test structures in laboratories was carried out independently by nine laboratories of the IAHR working group (Mansard and Funke, 1987). As the principle used to compute reflection coefficients is based essentially on Goda and Suzuki's theory, there are limitations in obtaining the true reflections. Mansard and Funke (1987), comparing results from various laboratory experiments under similar conditions using the same techniques, conclude that the estimated reflective properties of impervious sloped beaches vary appreciably between different laboratories.

The usual way of addressing the problem of wave reflection from beaches seems inevitably to imply perfect reflection, a direct consequence of the assumed form of the offshore wave field and the conservation of mechanical energy (Carrier and Greenspan, 1958; Meyer and Taylor, 1972). Energy considerations show that wave absorption must be associated with the degradation of mechanical energy through wave breaking. However, in practice it is not possible to make a direct determination of the energy absorption, so this has to be inferred from observations of the wave field. Also there are no rigorous theoretical models to describe the physics of wave breaking on beaches and it is customary to treat breaking as a specific event for each identifiable wave (some recent exceptions to this line of thought are Guza and Thornton, 1982; Symonds *et al.*, 1982, where random waves are considered). Hence we focussed our attention on field measurements in attempting to decompose a random wave field into incoming and outgoing components. Tataavarti and Huntley (1987) and Tataavarti (1987) demonstrate a number of different techniques attempted in order to compute frequency dependent reflections from field measurements and also highlight various advantages and limitations associated with each technique.

Over the past twenty years there has been a very significant increase in the number of field measurements of wave elevations and currents in the nearshore region. It has become customary in recent years to deploy colocated elevation and current meters in the field. Therefore, we decided to estimate frequency dependent reflections utilizing colocated elevation and current measurements.

Data For Analysis

Data collected as part of the C²S² program on two maritime Canadian beaches at Pointe Sapin, New Brunswick, Stanhope Lane, P.E.I.; and NSTS data from Leadbetter beach at Santa Barbara, California (U.S.A) have been used to test the theoretical formulation. Measurements of the flow field were made using colocated Marsh- McBirney electromagnetic current meters and pressure transducers. Each current meter, measuring the two orthogonal axes of the flow with a response time of 0.2 *secs*, was aligned to measure the onshore/offshore and the alongshore components of the flow. The pressure transducers were designed to measure the wave elevation. The field environments comprise plane and barred beaches with wide ranging wave conditions (Table 1). Pointe Sapin (PS62) beach has a mild slope with a steep foreshore. Stanhope Lane (ST12) is a barred beach. Leadbetter (LB7, LB3) beach has a relatively steep slope (Fig.1).

Prior to the decomposition, corrections were made for the filter characteristics of the current meter electronics, the current meter axes have been aligned towards the predominant wave direction and the time series Fourier decomposed into frequency components and each Fourier amplitude multiplied by $(\tanh kh/\omega)$ factor, where k is the wave number, h the water depth and ω the radian frequency. The resulting Fourier amplitudes and the Fourier decomposed phases have been inverse Fourier transformed into the time domain. The output time series of the current measurements (\hat{u}) now have units of meters, consistent with the units of elevation measurements.

TABLE 1

Run/Beach	Offshore Dist. from Shoreline (m)	Depth (m)	Beach slope	$H_s(m)$	$T_p(sec)$	$\langle v \rangle^2 / \langle u \rangle^2$	Beach Profile
PS62 (Pointe Sapin)	58.0	1.95	0.05	0.90	8.4	0.034	concave
ST12 (Stanhope)	175.0	1.8	0.02*	0.87	5.6	0.323	Barred
LB7 (Leadbetter)	20.5	1.8	0.064	0.67	15.6	0.048	planar
LB3 (Leadbetter)	50.0	3.0	0.064	0.64	15.6	0.055	planar

*approximate slope

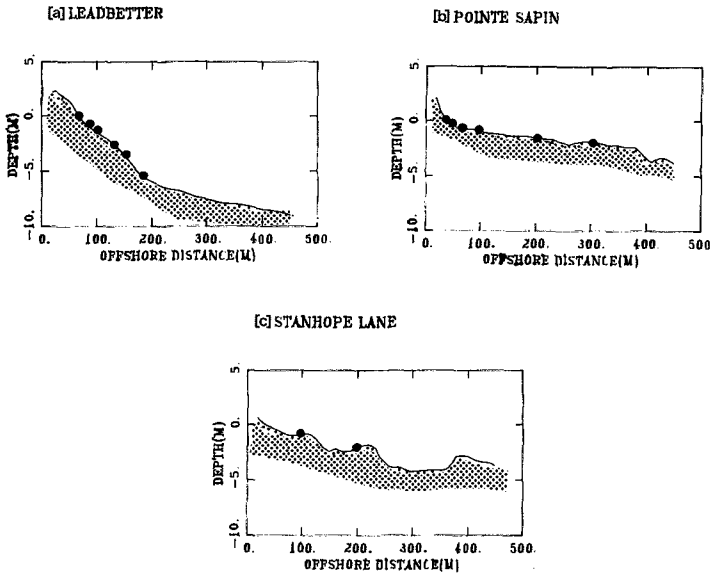


Figure 1. Beach profiles and relative locations of the instrument stations for (a) Leadbetter, California (U.S.A), (b) Pointe Sapin, New Brunswick (Canada) and (c) Stanhope Lane, P.E.I., (Canada).

Incoming and Outgoing Waves: Time Domain Analysis

Utilizing the linear wave theory, the velocity potential Φ_{io} of near normal incidence shallow water waves may be expressed as a linear superposition of incoming (shoreward propagating) and outgoing waves (seaward propagating) over a flat bottom as follows,

$$\Phi_{i_o} = \frac{g}{\omega} [a \sin(kx - \omega t + \phi_i) + b \sin(kx + \omega t + \phi_o)] \quad (1)$$

where a and b are the amplitudes associated with incoming and outgoing waves respectively, ϕ_i and ϕ_o are the relative phases of incoming and outgoing waves respectively, x is the cross shore coordinate, positive onshore.

If we transform the cross shore velocity ($u = \frac{\partial \Phi_{i_o}}{\partial x}$) into elevation ($\eta = -g^{-1} \frac{\partial \Phi_{i_o}}{\partial t}$) using linear wave theory, then we can express the sum and difference series of elevation and the transformed velocity as incoming and outgoing components,

$$\frac{(\eta + \hat{u})}{2} = a \cos(kx - \omega t + \phi_i) \quad (2)$$

$$\frac{(\eta - \hat{u})}{2} = b \cos(kx + \omega t + \phi_o) \quad (3)$$

where \hat{u} is the transformed u .

Defining the ratio of the amplitude of the outgoing wave to that of the incoming wave as the reflection coefficient R we have

$$R = \left[\frac{\langle (\eta - \hat{u})^2 \rangle}{\langle (\eta + \hat{u})^2 \rangle} \right]^{\frac{1}{2}} \quad (4)$$

where $\langle \rangle$ denotes ensemble averaging. Thus, after obtaining the incoming and outgoing wave series the frequency dependent reflection coefficient can be determined using standard spectral techniques.

Guza *et al.* (1984) have shown that colocated elevation and current meters can be used to decompose measured waves into incoming and outgoing components based on the aforementioned theory. However, there is an important problem associated with this method of estimating the frequency dependent reflection coefficient. A close examination of the coherence estimates of η and u time series and the estimated frequency dependent reflection coefficient plots (Fig.2a and 2b) of the Stanhope Lane data set shows that the reflection plot is almost a mirror image of the coherence plot. At low coherences the reflection coefficient tends to unity. Clearly, if η and u are incoherent, their sum and difference time series, as in equations (2) and (3), will have the same variance so that the apparent reflection coefficient will tend to 1.0. Therefore there is a need to reduce the noise dependence of the reflection coefficient estimates. This led us to search for alternate techniques to decompose the field measurements into incoming and outgoing components.

Incoming and Outgoing Waves: Frequency Domain Analysis

Studies by Oppenheim and Lim (1981) have focussed on the importance of phase in signals. The phase between two signals, computed using the cross spectrum, is only related to the coherent part of the two series and hence should be independent of noise. So spectral phase information obtained from the η and u measurements may be used to obtain incoming and outgoing components and hence determine the frequency dependent reflection coefficients. As discussed in Tatavarti and Huntley (1987) this would require modelling waves over complex topographies naturally occurring on beaches. This is a significant complication. However, in principle one can avoid the necessity for modelling waves over complex topography by calculating, from the time series of η and u at a single location, the gain between the two series in addition to the phase.

Let us now express the time series of colocated measurements of wave elevation and on-offshore current velocity in terms of a modulation function and a carrier function.

$$\eta(x, t) = \Re \{ A(\psi) e^{i\omega t} \} \quad (5)$$

$$\hat{u}(x, t) = \Re \{ B(\psi) e^{i(\omega t + \theta(\psi))} \} \quad (6)$$

where $\eta(x, t)$, is the time series measurement of elevation (m) at an offshore location x , from shoreline.

$\hat{u}(x, t)$, is the time series measurement of the on-offshore velocity at an offshore location x , from the shoreline, normalized such that it has the units of elevation (m).

$A(\psi)$ and $B(\psi)$, are the slowly varying amplitude modulation functions associated with the time series of $\eta(x, t)$ and $\hat{u}(x, t)$ measurements, in which ψ is a function of beach slope, local wave amplitude, wave number and wave frequency.

$\theta(\psi)$ is the phase difference associated with the two time series measurements.

$e^{i\omega t}$, is the carrier wave in which ω is the radian frequency.

In practice the ensemble averaging is often estimated by a frequency band averaging, whose equivalence is supported by the ergodicity hypothesis. Therefore, from a spectral perspective we can rewrite the variance of the incoming waves and the variance of the outgoing waves respectively as per equations (2) and (3) as

$$E_{in}(\omega) = \tilde{A}^2(\omega) + \tilde{B}^2(\omega) + 2\tilde{A}(\omega)\tilde{B}(\omega) \cos \theta_{\eta\hat{u}}(\omega) \quad (7)$$

$$E_{out}(\omega) = \tilde{A}^2(\omega) + \tilde{B}^2(\omega) - 2\tilde{A}(\omega)\tilde{B}(\omega) \cos \theta_{\eta\hat{u}}(\omega) \quad (8)$$

where \tilde{A} and \tilde{B} are the average estimates of A and B over a realization (record length in practice). Writing the gain function as $G(\omega) = \frac{\tilde{A}(\omega)}{\tilde{B}(\omega)}$, we express the frequency dependent reflection coefficient $R(\omega)$ as

$$R^2(\omega) = \left[\frac{1 + G^2(\omega) - 2G(\omega) \cos \theta_{\eta\hat{u}}(\omega)}{1 + G^2(\omega) + 2G(\omega) \cos \theta_{\eta\hat{u}}(\omega)} \right] \quad (9)$$

Equation (9) therefore gives the frequency dependent reflection coefficient in terms of the gain and the phase relationships between η and u measurements.

The phase between two signals, computed using the cross spectrum, is only related to the coherent part of the two time series and hence should be independent of noise. *Hence the key to this method of estimating $R(\omega)$ is to find an estimator for gain, $G(\omega)$, which is insensitive to noise in both η and u measurements.*

Generally, in spectral analysis, the time series of one parameter is designated as a base series and coherence and phase relationships are computed between this series and those of other parameters. There are a number of problems associated with the use of base series. For example, when different waves are present in the same frequency band, there is considerable difficulty in interpreting the cross spectrum data as there is no way of determining how many wave structures are present and what is the relative contribution of each wave type to the variance spectra. Also the use of base series produces a bias in favour of the base series, when computing wave amplitudes. If the coherence between various parameters and the base series is not large, this can result in considerable distortion in the pattern of wave amplitudes. Moreover this does not exploit the information contained in the cross spectra between parameters other than the base series. In order to avoid these problems we resorted to the complex eigenvector analysis suggested by Wallace and Dickinson (1972), where the vector time series is expressed as a linear combination of eigenvectors of the cross spectrum

matrix for frequency bands of interest. To increase the statistical confidence in E.O.F. analysis the colocated alongshore velocity (v) time series is also considered.

Employing complex empirical orthogonal function analysis to reduce noise sensitivity it is possible to determine the reflection coefficients from a spectral perspective utilizing the relation

$$\hat{R}(\omega) = \left[\frac{1 + \hat{G}^2(\omega) - 2\hat{G}(\omega) \cos \hat{\theta}_{\eta\hat{u}}(\omega)}{1 + \hat{G}^2(\omega) + 2\hat{G}(\omega) \cos \hat{\theta}_{\eta\hat{u}}(\omega)} \right]^{1/2} \quad (10)$$

where $\hat{G}(\omega)$ is the gain function, the ratio of the amplitude of the principal mode of the elevation to the amplitude of the principal mode of the on-offshore velocity at that frequency $\hat{\theta}_{\eta\hat{u}}(\omega)$ is the phase difference between the principal modes of pressure and on-offshore velocity.

Figure 2c shows the estimated (using equation 9) frequency dependent reflection coefficients for the Stanhope Lane data set. A comparison of Fig. 2b and Fig. 2c demonstrates the significance of estimating reflection coefficients by the frequency domain analysis as opposed to that using the time domain analysis.

Determination Of The Phase Between Incoming and Outgoing Waves

Let us assume that the signal which a sensor measures at any time t , is a linear superposition of incoming wave and outgoing wave signals. One can always represent the incoming and outgoing wave signals as products of the modulation function and a carrier function. As in the previous section, let us consider a harmonic carrier system ($e^{i\omega t}$),

$$S(x, t) = \Re \{ A(\psi)e^{i\omega t} \} = A_{in}(\psi) \cos \omega t + A_{out}(\psi) \cos(\omega t + \phi(\psi)) \quad (11)$$

where $S(x, t)$ is the signal the sensor measures at time t and location x .

$A_{in}(\psi)$ and $A_{out}(\psi)$ are the slowly varying amplitude modulation functions associated with incoming and outgoing wave signals, in which ψ is a function of beach slope, wave amplitude, wave number and wave frequency.

$\cos \omega t$ is the carrier function for the incoming wave signal

$\cos(\omega t + \phi(\psi))$ is the carrier function for the outgoing wave signal

$\phi(\psi)$ is the phase difference associated with the incoming and outgoing wave signals.

Hence, colocated pressure(elevation) and on-offshore current velocity measurements may be expressed as linear superpositions of incoming and outgoing signals,

$$\eta(x, t) = A_{in}(\psi) \cos \omega t + R(\psi)A_{in}(\psi) \cos(\omega t + \phi(\psi)) \quad (12)$$

$$\hat{u}(x, t) = B_{in}(\psi) \cos \omega t - R(\psi)B_{in}(\psi) \cos(\omega t + \phi(\psi)) \quad (13)$$

where $A(\psi)$ and $B(\psi)$ are the slowly varying amplitudes associated with $\eta(x, t)$ and $\hat{u}(x, t)$ measurements

$R(\psi)$ is the ratio of the outgoing to the incoming wave amplitudes, which can be approximated by the average value of the reflection coefficient for a given realization, usually the length of the record, estimated using equation (10)

Utilizing spectral techniques to compute Fourier coefficients, co spectrum, quad spectrum and phase spectrum the following expression for the phase associated with incoming and outgoing components is obtained,

$$\tan \phi(\omega) = \frac{2\hat{G}(\omega)}{1 - \hat{G}^2(\omega)} \sin \hat{\theta}_{\eta\hat{u}}(\omega) \quad (14)$$

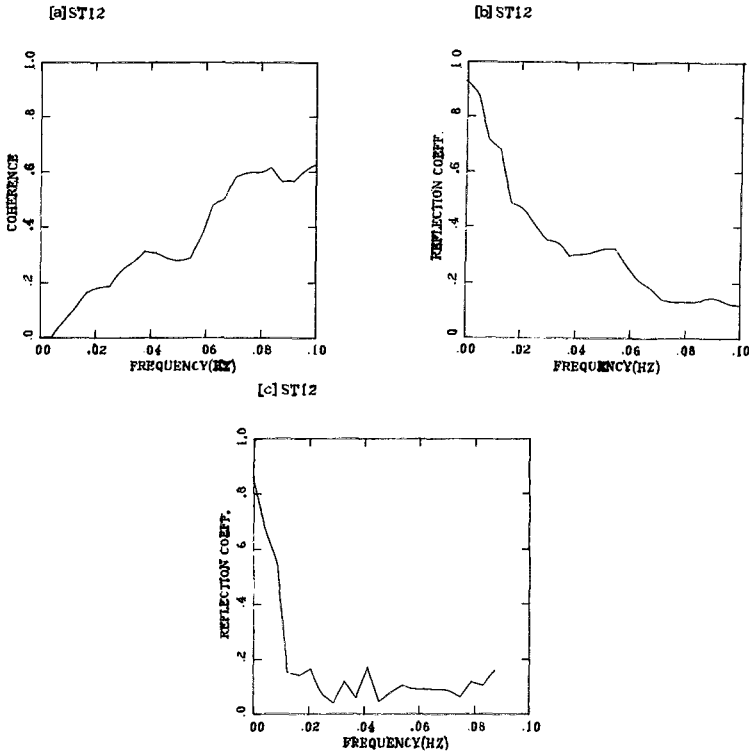


Figure 2. (a) Cross spectral coherence between the wave elevation η and the on/offshore velocity u for Stanhope Lane data (ST12). (b) Reflection coefficient as a function of the frequency using time domain analysis and (c) frequency domain analysis for the same data.

Decomposition Of Random Waves Into Incoming and Outgoing Components

Once the magnitude of the reflection, $R(\omega)$, and the phase associated with reflection, $\phi(\omega)$, are computed it becomes trivial to decompose the random wave field into incoming and outgoing components.

One can express the composite variance that any sensor measurement yields as

$$E(\omega) = A_{in}^2(\omega) + R^2(\omega)A_{in}^2(\omega) + 2A_{in}^2(\omega)R(\omega) \cos \phi(\omega) \tag{15}$$

In other words, the composite variance is the summation of the incoming variance, the outgoing variance and twice the co spectrum of incoming and outgoing components. Therefore, the incoming variance is given by

$$E_{in}(\omega) = \frac{E(\omega)}{\{1 + R^2(\omega) + 2R(\omega) \cos \phi(\omega)\}} \tag{16}$$

and the outgoing variance is given by

$$E_{out}(\omega) = \frac{E(\omega)}{\{1 + R^{-2}(\omega) + 2R^{-1}(\omega) \cos \phi(\omega)\}} \tag{17}$$

If the measured auto-spectral phase of the elevation sensor (computed by spectral analysis techniques) is denoted by θ_η , then assuming that the measured phase is actually a linear superposition of the incoming ($\phi_{\eta i}$) and the outgoing ($\phi_{\eta o}$) phases, it can be shown that

$$\phi_{\eta i}(\omega) = \theta_\eta(\omega) - \tan^{-1} \left[\frac{R(\omega) \sin \phi(\omega)}{1 + R(\omega) \cos \phi(\omega)} \right] \quad (18)$$

and

$$\phi_{\eta o}(\omega) = \phi(\omega) + \phi_{\eta i}(\omega) \quad (19)$$

Using equations (16), (17), (18) and (19) and employing inverse Fourier transform techniques the random series, i.e., the measured time series, can be decomposed into incoming time series and outgoing time series as shown in Figure 3.

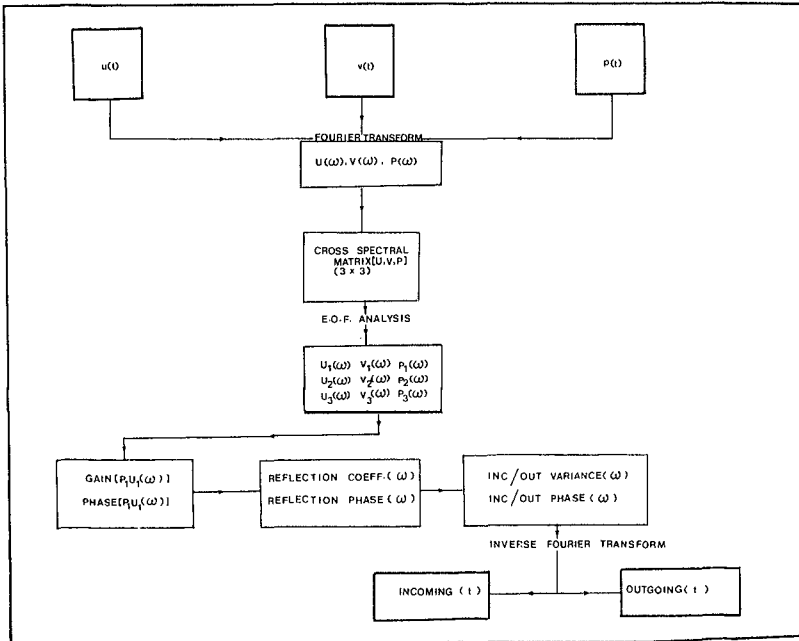


Figure 3. Flow chart demonstrating the technique employed to decompose random waves into incoming and outgoing components.

Observations and Discussion

Standing waves can either exist as leaky modes or trapped modes. Leaky modes are the two dimensional waves with the fluid motion normal to the shore and uniform alongshore. The trapped modes are the three dimensional edge waves trapped in the nearshore by refraction and periodic alongshore, with both shore normal and shore parallel components. The present technique of decomposition only considers the leaky waves. A review of the pertinent literature points out the difficulties previous researchers (Huntley, 1976; Holman

et al., 1978; Oltman-Shay and Guza, 1987) faced in distinguishing between the edge waves and leaky waves, even with observations from cross shore and longshore arrays of instruments located in the nearshore region. This is clearly indicative of how formidable, if not intractable, the problem of distinguishing edge waves from leaky waves can be. Utilizing the fact that the key distinction between edge waves and leaky waves lies in their directions of progress, with edge waves propagating alongshore and leaky waves propagating primarily on-offshore, the energy levels in the cross shore (u) and the alongshore (v) components of velocity measurement should provide an indication of the presence or absence of edge waves. The ratio of the energy in the v component to that of the u component of the horizontal velocity being larger in the presence of edge waves than in the presence of near normal incidence leaky waves alone. The ratios of variances [$\langle v^2 \rangle / \langle u^2 \rangle$] in Table 1 suggest that Pointe Sapin and Leadbetter beach data may not be seriously contaminated by edge wave motions. For Stanhope Lane beach data, however, the ratio is indicative of a significant contribution of energy from low mode edge waves.

Figure 4 shows the reflection coefficient estimates as functions of frequency for the different beaches. The most prominent feature that stands out in Fig. 4 is that the low frequency waves are strongly reflective while the wind wave frequencies are progressive onshore. This is consistent with earlier studies by Suhayda (1974), Huntley (1976), Bowen (1980), Holman (1981), Wright *et al.* (1982), Guza and Thornton (1982), Bowen and Huntley (1984), and Elgar and Guza (1985); who suggested that low frequency energy occurs in the form of cross shore leaky waves. The similar frequency dependent reflection coefficient plots for the data from different locations on the Leadbetter beach suggests the insignificant role of edge wave motions in these measurements and demonstrates the ability of this technique to minimize the influence of noise.

Figure 5 shows the relative phase between incoming and outgoing waves as a function of the frequency. For any incoming wave the outgoing wave can either be i) the reflected component, ii) any wave generated by some mechanism (for example, Symonds *et al.*, 1982) inside the zone between the sensor and the shoreline or iii) a combination of both. The more or less linear phase with frequency observed in Fig. 5 suggests that the outgoing waves are mostly the reflected waves. The linear phase is also consistent with the nondispersive time lag (considering only low frequencies) associated with a shoreline reflection for Pointe Sapin and Leadbetter beaches. Stanhope Lane beach of course, being a barred beach, further complicates the interpretation of the incoming/outgoing phase difference because of the distinct possibility of multiple reflectors (Tatavarti, 1987).

Figure 6 shows the decomposed incoming and outgoing spectra against the measured elevation spectra. As one would expect *a priori*, the outgoing variance is significantly smaller than the incoming variance, except in the low frequency region. It is clear that the low frequency outgoing energy is statistically significant. This feature has also been indicated in the frequency dependent reflection coefficient plots. Thus the primary region of interest for decomposition seems to be the low frequency band of the wave spectra.

The ability to decompose the observed wave field into incoming and outgoing components suggests that one can quantify the relative magnitudes of the incoming and outgoing components and determine whether the outgoing long wave is a simple reflection of the incoming long wave. Of future interest would be the question of the origin of the outgoing long waves. If the outgoing long waves are simple reflections of the incoming long waves then at what location on the beach are these waves being reflected? *i.e.*, Is there any particular region on the beach topography which effectively reflects the long waves?

Figure 7a shows the smoothed reflection coefficient as a function of the wave frequency for data from different beaches (Pointe Sapin, Stanhope Lane, Leadbetter) and at different locations on the same beach (Leadbetter). It is clear that the barred beach data set (ST12)

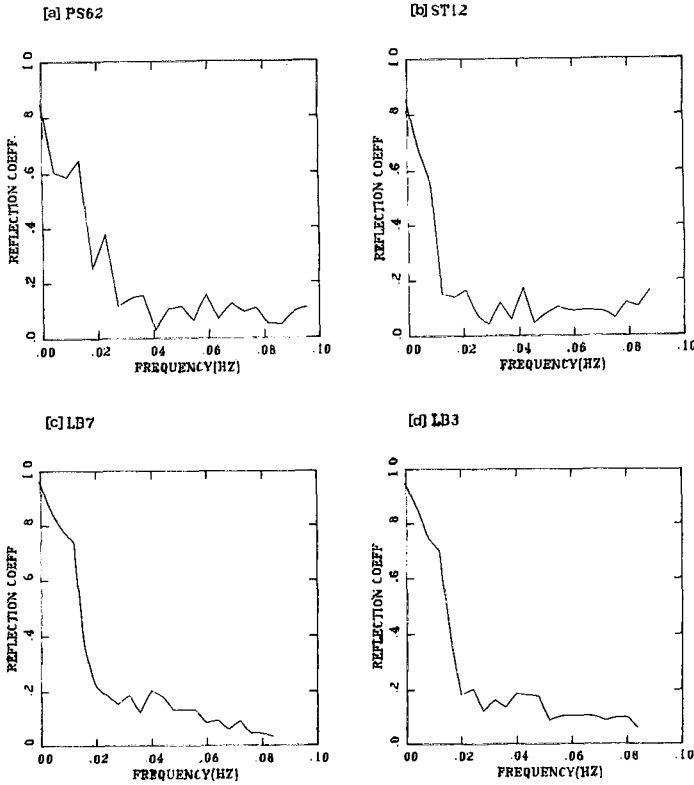


Figure 4. Frequency dependent reflection coefficient estimates obtained using equation (14) for (a) Pointe Sapin data set (PS62), (b) Stanhope lane data set (ST12), (c) Leadbetter data sets (LB7) and (d) LB3.

shows remarkably different characteristics from the planar beaches suggesting the influence of the beach slope on the reflection coefficient estimates. Figure 7b shows the reflection coefficients for data from different beaches and at different locations as a function of the Iribarren number ($\epsilon = \frac{2a_o \omega^2}{g \tan^2 \beta}$). From Fig. 7b it is evident that inclusion of the beach slope did bring the reflection curve of ST12 data set towards the general trend shown by the other data sets. However, the inclusion of the record average wave amplitude for a_o , in the case of Leadbetter data set has not reduced the scatter in the curves. It is not clear whether to use a frequency band averaged amplitude or a representative record averaged amplitude for a_o in the expression for ϵ . A frequency band averaged amplitude would be meaningless if the waves in that frequency band are breaking. This problem of extending the monochromatic wave results to a spectrum of incident waves naturally found on beaches is a general one for which no satisfactory solution exists.

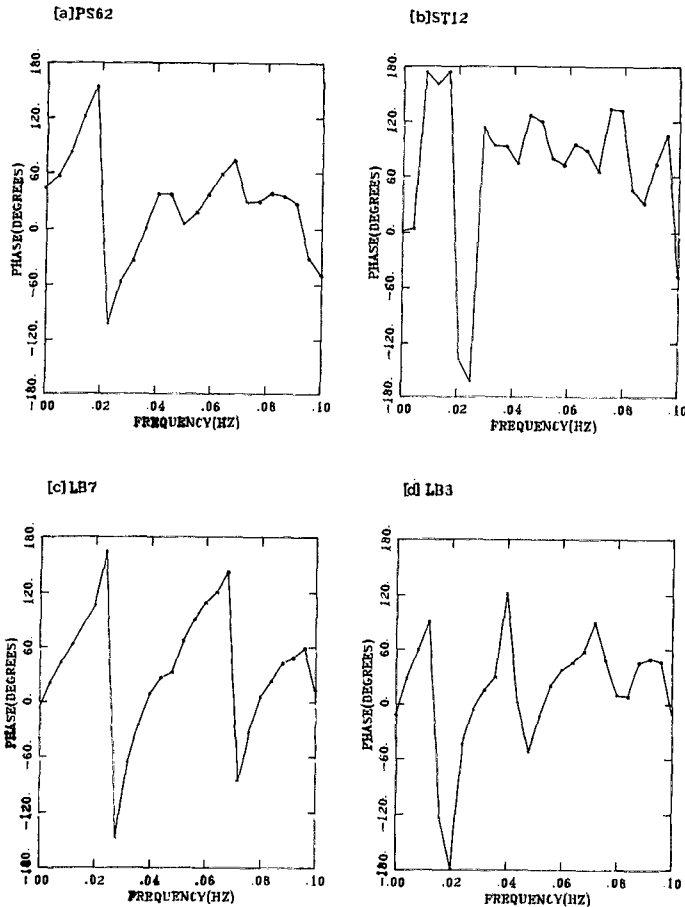


Figure 5. Relative phase between incoming and outgoing waves as a function of the frequency obtained using Equations (19) and (20) for (a) Pointe Sapin data set (PS62), (b) Stanhope Lane data set (ST12), (c) Leadbetter data sets (LB7) and (d) LB3.

Conclusions

- i) Use of colocated velocity and elevation measurements avoids the resolution problem associated with the more common method of spatially separated sensors.
- ii) Our technique minimizes the influence of noise, which tends to drive the reflection coefficient towards unity.
- iii) The technique also gives the relative phase between incoming and outgoing waves and leads to decomposition of the original time series into time series of incoming and outgoing waves.
- iv) Results from different beach sites and different wave conditions confirm that the re-

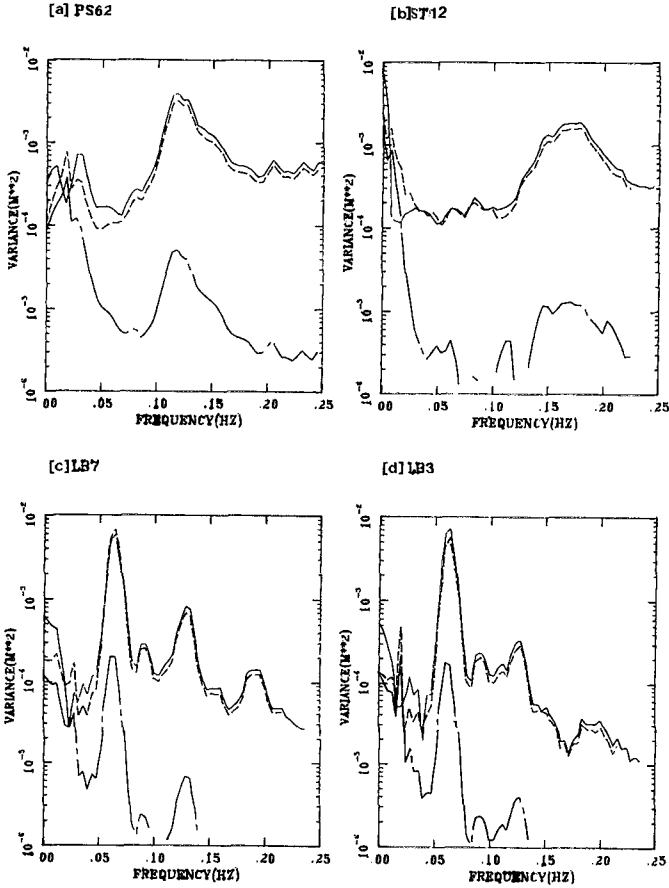


Figure 6. The measured elevation spectrum (solid line) and the decomposed incoming (short broken line) and outgoing (long broken line) for runs (a) PS62, (b) ST12, (c) LB7 and (d) LB3, d.o.f.=95.

flection coefficient is high at low frequencies but usually becomes very small at high frequencies.

- v) The shape of the frequency dependent reflection coefficient appears to depend strongly on the shoreface beach slope, but the influence of wave amplitude is less clear.

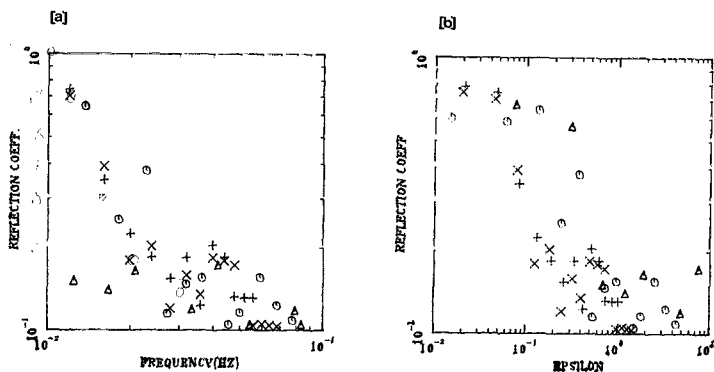


Figure 7. (a) Reflection coefficient as a function of the frequency for run PS62 (o), ST12 (Δ), LB7 (+), LB3 (x). (b) Reflection coefficient as a function of the non dimensional number ϵ for run PS62 (o), ST12 (Δ), LB7 (+), LB3 (x).

References

1. Battjes, J.A. (1974). Surf Similarity, *Proc. of the 14th Conf on Coastal Engineering*, Vol. I, A.S.C.E., pp. 466-480, New York.
2. Bowen, A.J. (1980). Simple models of nearshore sedimentation: beach profiles and longshore bars. In: S.B. McCann (ed.), *The Coastline of Canada*, Geol. Surv. Can., pap. 80-10, pp. 1-11, Ottawa.
3. Bowen, A.J. and D.A. Huntley (1984). Waves, long waves and nearshore morphology, *Marine Geology*, 60, pp. 1-13.
4. Carrier, G.F. and H.P. Greenspan (1958). Water waves of finite amplitude on a sloping beach, *J. Fluid Mech.*, 4(1), pp. 97-109.
5. Elgar, S. and R.T. Guza (1985). Shoaling gravity waves: comparisons between field observations, linear theory and a nonlinear model, *J. Fluid Mech.*, 158, pp. 47-70.
6. Goda, Y. and S. Suzuki (1976). Estimation of incident and reflected waves in random wave experiments, *Proc. 15th Conf. on Coastal Engg.*, Vol. II, A.S.C.E., pp. 828-848, Honolulu.
7. Guza, R.T. and A.J. Bowen (1976). Resonant interactions for waves breaking on a beach, *Proc. 15th Conf. on Coastal Engg.*, Vol. I, A.S.C.E., pp. 560-579, Honolulu.
8. Guza, R.T. and E.B. Thornton (1982). Swash oscillations on a natural beach, *J. Geophys. Res.*, 87, pp. 483-491.
9. Guza, R.T., E.B. Thornton, and R.A. Holman (1984). Swash on steep and shallow beaches, *Proc. 19th Conf. on Coastal Engg.*, Vol. II, A.S.C.E., pp. 708-723, Houston.
10. Hasselmann, K., W.H. Munk, and G.J.F. MacDonald (1963). Bispectra of Ocean Waves, In: M. Rosenblatt (ed.), *Time Series Analysis*, John Wiley Sons, p. 125, New York.
11. Holman, R.A. D.A. Huntley and A.J. Bowen (1978). Infragravity waves in storm conditions, *Proc. 16th Conf. on Coastal Engg.*, Vol. I, A.S.C.E., pp. 268-284.
12. Holman, R.A. (1981). Infragravity energy in the surf zone, *J. Geophys. Res.*, 86, pp. 6442-6450.
13. Huntley, D.A. (1976). Long period wave motion on a natural beach, *J. Geophys. Res.*,

- 81, pp. 6441-6449.
14. Isobe, M. and K. Kondo (1984). Method for estimating directional wave spectrum in incident and reflected wavefield, *Proc. 19th Conf. on Coastal Engg.*, Vol. I, A.S.C.E., pp. 467-483, San Francisco.
 15. Kim, C.S. (1985). Field Observations of wave groups and long waves on sloping beaches, unpublished M.Sc. thesis, Dalhousie University, pp. 151, Halifax, Canada.
 16. Mansard, E.P.D. and E.R. Funke (1987). Experimental and analytical techniques in wave dynamics — A comparative study, *Proc. IAHR SEMINAR*, Lausanne, Switzerland.
 17. Meyer, R.E. and A.D. Taylor (1972). Run up on beaches. In *Waves on beaches and resulting sediment transport*, ed. R.E. Meyer, Academic Press, pp. 357-411, New York.
 18. Miche, M. (1951). Le Pouvoir réfléchissant des ouvrages Maritimes exposés à l'action de la houle, *Annales des Ponts et chaussées*, Vol. 121, pp. 2285-319.
 19. Munk, W.H. (1949). Surf Beats, *EOS Trans.*, A.G.U., Vol. 30, pp. 849-854.
 20. Oltman-Shay, J. and R.T. Guza (1987). Infragravity edge wave observations on two California beaches, *J. Phy. Oceanogr.*, Vol. 17, pp. 644-663.
 21. Phillips, O.M. (1980). *The dynamics of the upper ocean*, Cambridge University Press, 336pp., New York.
 22. Suhayda, J.N. (1974). Standing waves on beaches, *J. Geophys. Res.*, 79, pp. 3065-3071.
 23. Symonds, G., D.A. Huntley and A.J. Bowen (1982). Two dimensional surf beat: Long wave generation by a time varying break points, *J. Geophys Res.*, 87, pp. 492-498.
 24. Tatavarti, Rao V.S.N. (1987). Decomposition of random wave energy on beaches, *Proc. Dock and Harbour Engg.*, Madras, India.
 25. Tatavarti, Rao V.S.N. and D.A. Huntley (1987). Wave reflections at Beaches, *Proc. Canadian Coastal Conf.*, pp. 241-256, Quebec City, Canada.
 26. Thornton, E.B. and R.J. Calhoun (1972). Spectral resolution of breakwater reflected waves, *J. Waterways, Harbours, Ports and Coast. Engg.*, Vol. 98, No. WW4, pp. 443-460.
 27. Tucker, M.J. (1950). Sea waves of 1 to 5 minute period, *Proc. Roy. Soc. Lon.*, A202, pp. 2981-2987.
 28. Wallace, J.M. and R.E. Dickinson (1972). Empirical orthogonal representation of time series in the frequency domain, Part I: Theoretical considerations, *J. App. Meteorology*, Vol. 11, No. 6, pp. 887-892.
 29. Wright, L.D., R.T. Guza and A.D. Short (1982). Dynamics of high energy dissipative surf zone, *Marine Geology*, 45, pp. 45-62.
 30. Wright, L.D. and A.D. Short (1984). Morphodynamic variability of surf zones and beaches: A synthesis, *Marine Geology*, 56, pp. 93-118.

CHAPTER 10

WAVE RUN-UP ON A NATURAL BEACH

Mitsuo Takezawa¹, Masaru Mizuguchi²

Shintaro Hotta³ and Susumu Kubota⁴

ABSTRACT

The swash oscillation, waves and water particle velocity in the surf zone were measured by using 16 mm memo-motion cameras and electromagnetic current meters. It was inferred that incident waves form two-dimensional standing waves with the anti-node in the swash slope. Separation of the incident waves and reflected waves was attempted with good results using small amplitude long wave theory. Reflection coefficient of individual waves ranged between 0.3 and 1.0. The joint distribution of wave heights and periods in the swash oscillation exhibited different distribution from that in and outside the surf zone. This indicates that simple application of wave to wave transformation model fails in the swash zone.

1. INTRODUCTION

The understanding of wave dynamics in the swash zone on natural beaches is important for understanding beach erosion, designing coastal structures, estimating beach deformation after construction of structures, and so on. However, the properties of swash waves are not well understood. Clarification of the wave characteristics is difficult because field observation of waves in the swash zone are difficult to perform. Only a few measurements are reported (Guza and Thornton, 1982; Mizuguchi, 1984; Holman and Sallenger, 1985).

-
- 1 Dr. Eng., Professor, Dept. of Civil Eng., College of Science and Technology, Nihon University, Kanda-surugadai 1-8-14, Chiyoda-ku, Tokyo, 101 Japan
 - 2 Dr. Eng., Associate Professor, Dept. of Civil Eng., School of Science and Technology, Chuo University, Kasuga 1-13-27, Bunkyo-ku, Tokyo 112 Japan
 - 3 Dr. Eng., Associate Professor, Dept. of Civil Eng., Nihon University
 - 4 Research Associate, Dept. of Civil Eng., Nihon University

For measurement of waves in the swash zone, the visual method, in which the water surface profile is recorded by camera or video movie camera, and the electrical method, in which resistance-type or capacitance-type wave gages are employed with some modification for the limited use, have been employed (Holman and Guza, 1984). The authors here use both methods for measuring waves in the swash zone, with improvements, and have developed a technique that combines the two method together.

The method developed is an electrical technique utilizing a capacitance-type wave gages, a wave run-up meter, stretched parallel to and about 2 cm above the sand surface, and monitoring of the water surface at marker sticks installed in the swash zone using video-movie cameras or 16mm memo-motion cameras. An advantage of this method is that the record can be supplemented with data form the cameras when the run-up meter malfunctioned.

Field observations were carried out at three different locations Chigasaki, Oarai, and Hasaki Beaches. The field experiment conducted at Chigasaki Beach (facing the Pacific Ocean and located about 50 km southwest of Tokyo) was a preliminary one, and only limited results were obtained as shown in the Conference ABSTRACT. Based on the experience gained in the preliminary experiment, the measuring method was improved and successfully employed in observations at Oarai and Hasaki Beaches. The purpose of present paper is to describe the measuring method, the analysis procedures applied to the data, and their results. More data were obtained than presented in this paper. Only the results fom at Oarai Beach will be described and discussed in this paper. These data were obtained using a remote sensing photographic technique utilizing synchronized 16 mm memo-motion cameras which film the water surface on marker sticks at a fixed time interval.

II FIELD OBSERVATION

Field observation was carried out on July 29, 1987, at Oarai Beach located about 200 km north of Tokyo and facing the Pacific Ocean (Fig. 1). Oarai Beach is bounded by a harbor at its northern end. Groins were constructed for protecting the harbor from contamination by intruding sand from the south. Sand accumulats at the southside of groins and erosion is occurring in an area approximately 2 km south of the largest groin. The observation site was located approximately 1.8 km south of the largest groin (see Fig. 1).

Figure 2 shows the sea bottom topography, and arrangement of instrumentation. In the swash zone vertical target sticks made of iron bar, painted white, were installed normal to the shoreline at an interval of 50 cm (see Fig. 3). A total of 41 sticks were installed covering the entire swash zone.

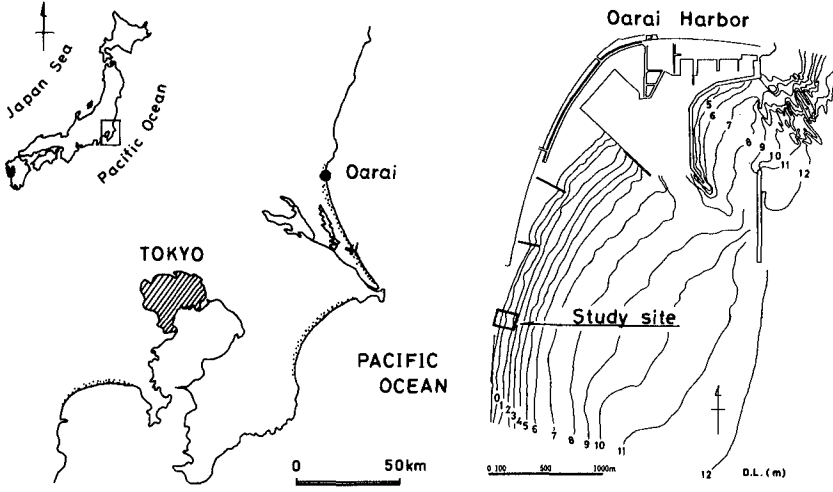


Fig. 1 Location map of field site.

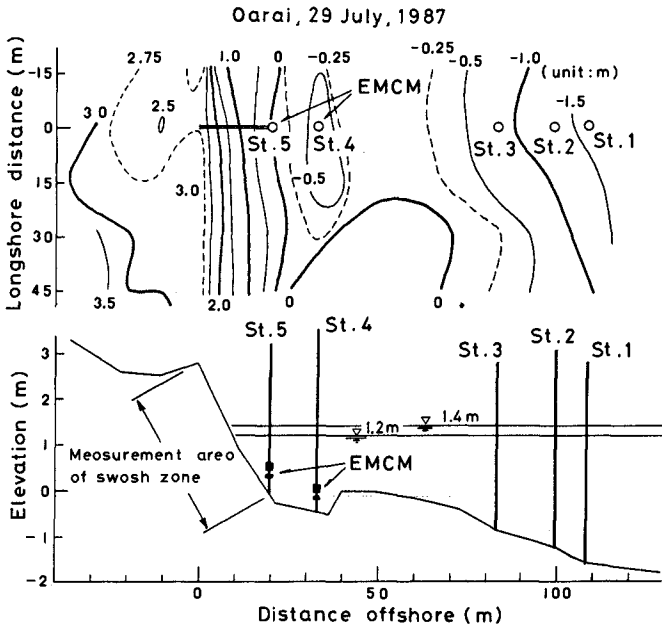


Fig. 2 Beach profile, plan, and arrangement of instrumentation.

A scaffold for photographing waves from the side was erected at the midpoint of the swash zone approximately 40 m south of the stick array. Swash oscillations of the water surface along the array were photographed by two pairs of 16 mm cameras placed on the scaffold. Each camera pair photographed a 10 m section of the swash zone. Five target poles (St. 1 to St. 5 in Fig. 2) were also installed for wave measurement. The sea water surface movement at the poles were recorded by two pairs of cameras mounted on another scaffold constructed on berm. All four pairs of 16 mm cameras were synchronized. The shooting interval was 0.2 s.

A run-up meter was also employed to measure the swash oscillation. The run-up meter was essentially a capacitance-type wave gage, but the measuring range was modified for run-up measurements. The capacitance wire was installed parallel to, and about 50 cm north from, the stick array. The wire was held at a constant height of 2 cm above the sand surface by supporting rods installed at an interval of 2 m. As it was crucial to keep the fixed space of 2 cm during the observation, a couple of man was engaged in for adjusting the height of supporting devices of the capacitance wire. A capacitance-type wave gage and a two-component electromagnetic current meter (EMCM) were attached to filming target poles at St. 4 and St. 5. Photograph 1 shows the stick array and the run-up meter.

The data collection was started at 16:10 and ended at 17:50, giving a 100 min. experiment duration. During the experiment the tide rose about 20 cm. Average breaking wave height and period by visual observation were 1 m and 12 s. Average breaker line was located between Sts. 2 and 3. The type of breaker was plunging and the wave direction was almost normal to the shoreline.

Output of the electrical instrument was recorded on an open-reel digital data recorder. The data sampling interval was 0.2 s. Synchronization between the camera system and data recorder was done by hand. The time lag between both data series was 0.4 s.

Sand in the swash zone was collected at four locations along the array. Sieve analysis indicated the sand was well-sorted with a median diameter of 0.43 to 0.52 mm, sorting coefficients of 1.20 to 1.32, and skewness of 0.92 to 1.11.

III RESULTS AND DISCUSSION

The measuring instruments worked well throughout the experiment except for a capacitance-type wave gage attached to St. 4 which experienced mechanical trouble after installation. The tape was directly loaded onto a main-frame computer and data were transferred to disk for analysis. The data of the 16 mm photographs were first transferred to a personal computer floppy disk using a 16 mm film

analyzer and an ultrasonic digitizer graph pen system. The data were then transferred to computer disk for convenient analysis. The water edge of the swash zone in the 16mm film was read as the horizontal distance from a reference point. Then the distance was transferred to a vertical distance by assuming the swash zone face was a compound slope consisting of three straight slopes (Fig. 3). The swash oscillation was also measured by the run-up meter. A comparison of data by 16 mm film and by the run-up meter showed the same results as already reported by Halman and Guza(1984). The wave data by 16 mm cameras and by electromagnetic current meters are used in this paper.

3.1 Raw Data

Figure 4 shows a portion of sea water surface records from St. 1 through St. 5 and the swash oscillation. We can easily recognize the crests of primary individual waves (Mizuguchi, 1982) at each measurement point. However, at St. 4 and St. 5, in the surf zone, there small waves appear, which are not observed at St. 1. These waves were generated mainly due to breaking. In addition we could clearly observe small outgoing waves by viewing the film. Some of small waves recorded at St. 4 and St. 5 are these reflected waves.

Figure 5 shows power spectral density functions of the sea water surface variation at St. 1 and St. 5, and the swash oscillation. The main power, which lies in the range from 0.03 Hz to 0.2 Hz ($0.03 \text{ Hz} < f < 0.2 \text{ Hz}$, where f is frequency.), decreases considerably from St. 1 to St. 5. However, power in the high frequency range at St.5 increases almost five times that observed at St. 1. This change of power spectral function, which means energy transfer from the peak frequency range to the higher frequency range, is due to the wave breaking. Power in the high frequency range of swash oscillation reduces down to almost the same magnitude of that at St. 1 and power in the frequency range lower than about 0.2 Hz increases greatly. This implies that the low frequency waves form standing waves which have an anti-node in the swash zone. At St. 5, peaks and deep depressions in the power density function alternately appear. However this alternate change of power is not observed in the swash oscillations. Figure 6 shows the cross spectral density function between the sea surface elevation and the on-offshore component of water particle velocity at St. 4. An abrupt fall in coherence and a sudden change in phase function at corresponding frequencies are characteristic features of two-dimensional standing waves (Hotta, Mizuguchi and Isobe, 1981). No significant power was found in the longshore velocity.

The gradient of power density function in the saturated range at the high frequency side of the peak follows -3 power of the frequency (f^{-3}) at the outside of the breaker zone (Sawaragi and Iwata, 1980) and follows -4 power of frequency (f^{-4}) inside the surf zone, as reported by Mizuguchi(1984), and Mase and Iwagaki(1984).

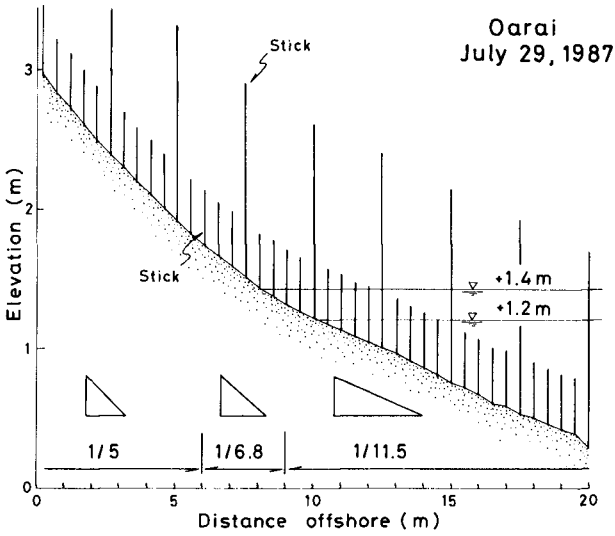


Fig. 3 Assumed compound slope for swash zone.

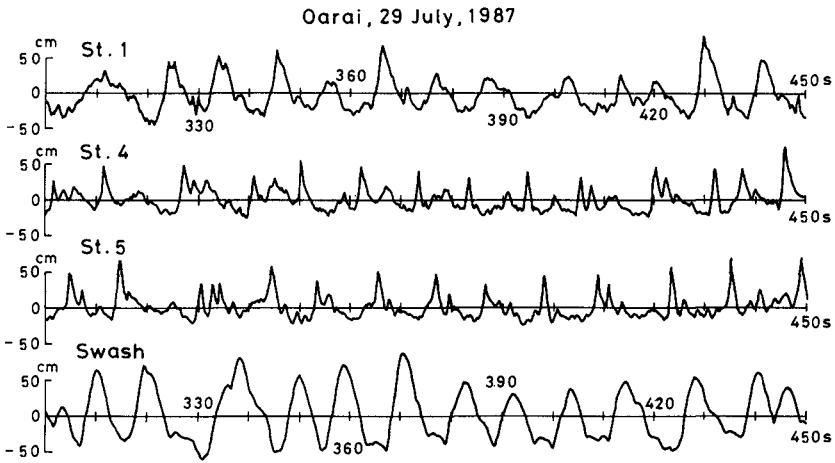


Fig. 4 Example of raw data.

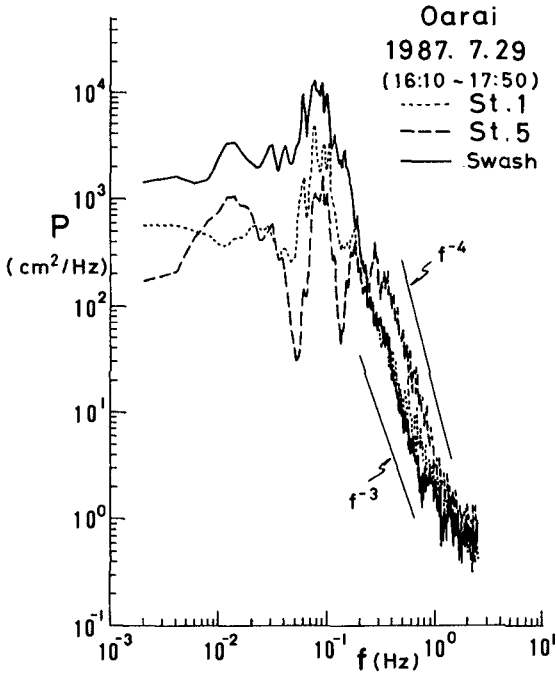


Fig. 5 Power spectral density functions.

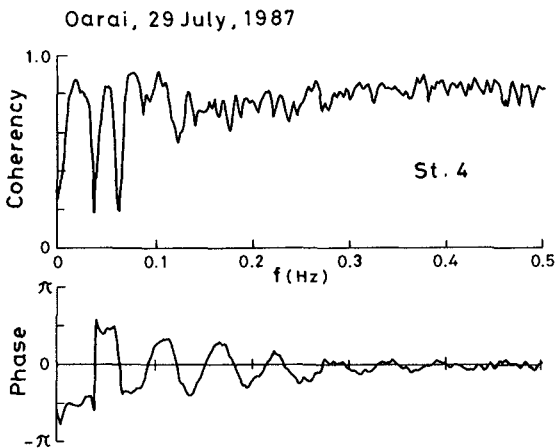


Fig. 6 Cross spectra between surface elevation and on-offshore component of water particle velocity at St. 4.

3.2 Wave Height and Period Distribution

For the study of waves, the wave-to-wave method by zero-crossing analysis was employed. The zero-crossing method was applied to raw data, data that a mean sea water level trend due to the tide was identified with the assumption of a parabolic curve, and tide trend was removed (Hereafter referred to as adjusted data), data that were then processed a high pass filter with cut off frequency of 0.045 Hz (Hereafter referred to as filtered data). The filter utilized is given in Fig. 6 of Mizuguchi (1982). Before discussing the results, we note the accuracy of wave data. Wave data obtained by means of 16mm cameras contain error of ± 2 cm in elevation. Therefore, waves lower than 6 cm in height were ignored in analysis (see Hotta and Mizuguchi, 1980).

Figure 7 shows the distributions of wave height and period defined by zero-down crossing method for raw, adjusted, and filtered data at St. 1, St. 4, and the swash oscillation. The number of big waves having large height and long period decreases and the number of small waves having relatively small height and short period increases in order when moving from to raw, adjusted, and filtered data. This can be explained by the effect of the tide and long period fluctuations of the sea water surface on the waves in the nearshore zone. The removal of the tidal trend and the long period fluctuations of sea water surface results in an increase in the number of waves defined by the zero crossing method. Figure 8 compares the wave height distribution of the filtered data by the zero-up and the zero-down crossing methods. Figure 9 shows the joint distribution of wave height and period for the filtered data. Table 1 gives statistically representative waves of the filtered data by zero-down crossing method.

Station 1 is located in the outside of the breaker zone and St. 4 is located in the surf zone. Typical features of wave height and period in the nearshore zone are presented in Figs. 8 and 9. It is seen that the marginal distributions of wave height and period outside of breaker zone is quite similar to the Rayleigh distribution, though the peak shifts to the smaller side. The marginal distributions of the wave height becomes bi-modal and the joint distribution exhibits two maxima in the surf zone. This tendency is particularly strong if waves are defined by the zero-down crossing method (Hotta, Mizuguchi and Isobe, 1982).

It appears that the wave height and period of the swash oscillation is similar to the Gaussian distribution about the mean wave height. However, detailed examination of the joint distribution indicates that the marginal distributions of the wave height and period become bi-modal, and the joint distribution exhibits two maxima if the waves are defined by the zero-up crossing method. This means that big waves often are preceded by relatively small waves in the

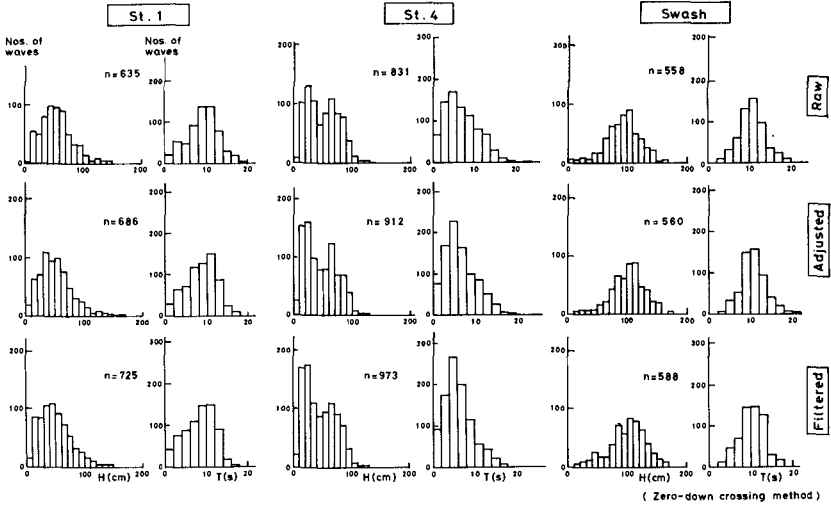


Fig. 7 Wave height and period distribution.

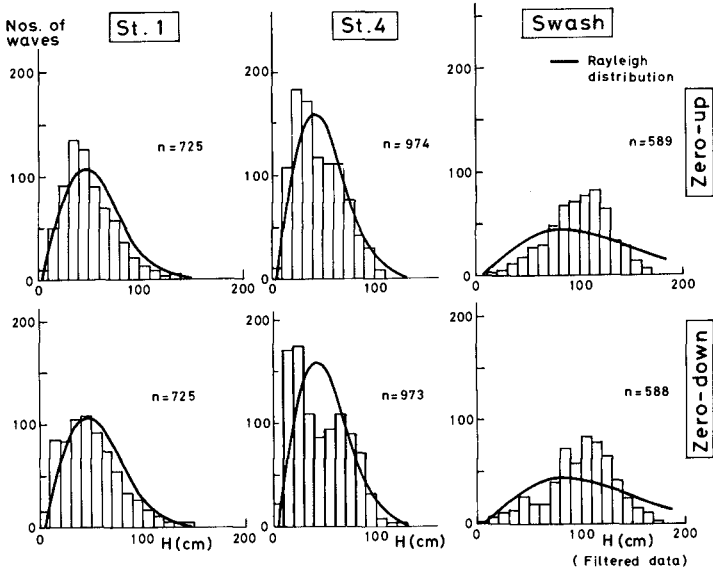


Fig. 8 Comparison of wave height distribution by zero-up and zero-down crossing method.

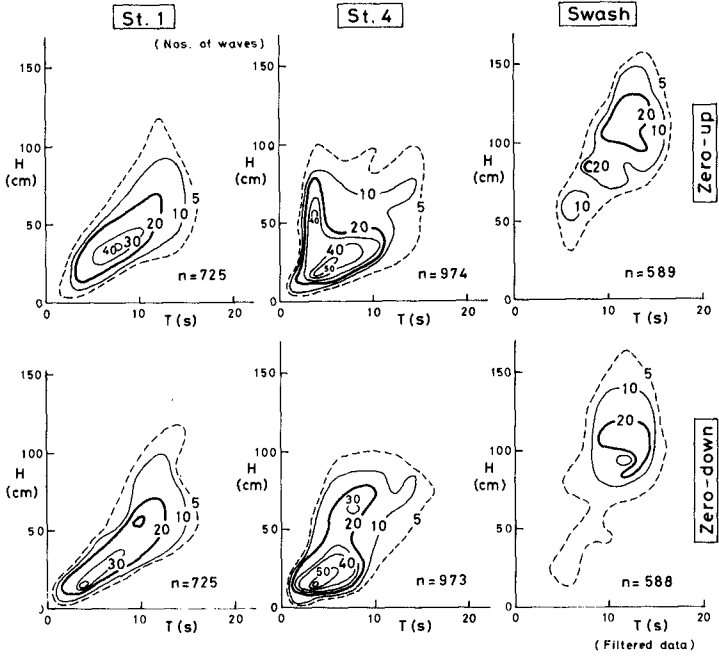


Fig. 9 Joint distribution of wave high and period.
Oarai, 29 July, 1987

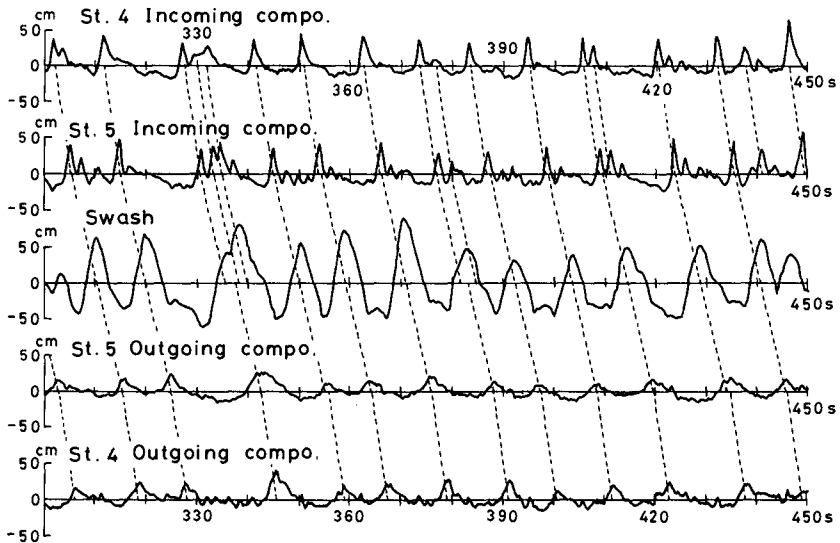


Fig. 10 Example of resolved incident and reflected waves.

swash zone. It is often observed that a larger wave following a smaller preceding wave travels faster, catches up, and passes the preceding wave when the wave is running up on the swash slope.

3.3 Reflected Waves

In section 3.1, indications that waves in the inner surf zone form two dimensional standing waves, during this experiment were given. Separation of incident waves and reflected waves was tried. After Guza, Thornton and Holman (1984), the linear small amplitude long wave theory was applied. That is

$$\eta_{IN}(t) = (\eta + \alpha (h/g)^{1/2} u) / 2 \dots\dots\dots (1)$$

$$\eta_{OUT}(t) = (\eta - \alpha (h/g)^{1/2} u) / 2 \dots\dots\dots (2)$$

where η_{IN} and η_{OUT} are the water surface elevation of incident and reflected waves, u is the on-offshore component of water particle velocity, g is the acceleration due to gravity, h is the water depth and α is a constant. The constant α theoretically takes the value of unity. However the data contained some experimental error. Therefore using the power value in cross spectral analysis between η and u , the most suitable value of α was selected in order to accomplish the separation.

Figure 10 shows examples of the result. The period of the record shown in Fig. 10 corresponds to that in Fig.4. The upper two plots give the separated incident waves at St. 4 and St. 5. The lower two plots give the reflected waves. The middle plot is the swash oscillations (run-up waves) in the swash zone. The broken lines in Fig.10 identify individual waves. Figure 10 shows that incident and reflected waves propagate with the same celerity between two measuring stations. Figure 11 shows the cross-correlation functions between incident and reflected waves. The maximum correlation coefficients are found at a time lag of 10.2 s at St. 5 and 16.4 s at St. 4. The wave celerity between St. 4 and St. 5 estimated from the above two values agreed well with that calculated from the linear small amplitude long wave theory, taking the average value of water depth between St. 4 and St. 5. Figure 11 also shows that a wave group consisting of two or three individual waves is combined into a single wave in the swash zone and is reflected to the offshore. This is popularly observed at natural beaches.

Finally reflection coefficient of individual waves, defined by a ratio between reflected wave height and incident wave height (H_{OUT}/H_{IN}), was examined. Reflection of irregular waves on natural beaches have been dealt with in the frequency domain. However, reflection on a foreshore slope is the result of run-up and run-down of each individual waves. The reflection coefficients in the time

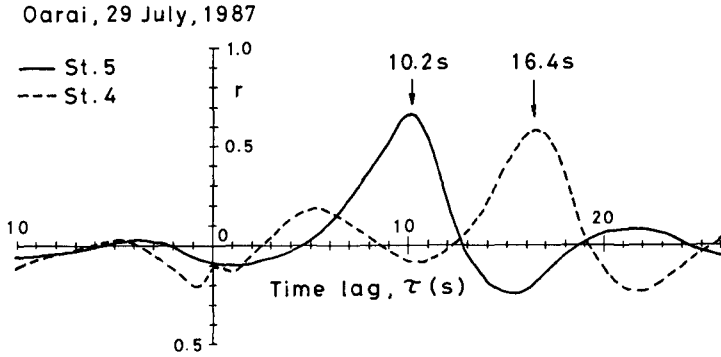


Fig. 11 Cross-correlation function between incident and reflected waves

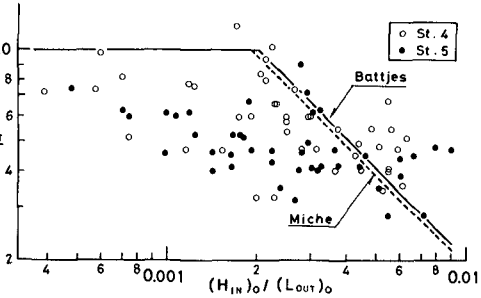
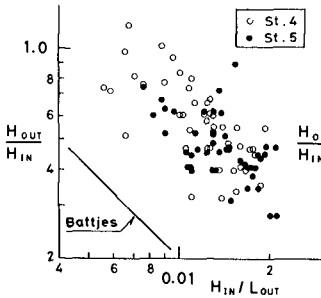


Fig. 12 Relationship between reflection coefficient and wave steepness.

Fig. 13 Relationship between reflection coefficient and wave steepness in deep water.

Table 1 Statistically representative waves.

Oarai, 29 July, 1987

Station number	Depth h (cm)	Nos. of waves	Wave height					Wave period			
			H_{rms} (cm)	H_{mean} (cm)	H_{max} (cm)	$H_{1/10}$ (cm)	$H_{1/3}$ (cm)	T_{mean} (s)	T_{max} (s)	$T_{1/10}$ (s)	$T_{1/3}$ (s)
St. 1	292	725	59	51	187	114	85	8.3	12.2	11.3	10.9
St. 2	256	762	62	53	207	122	90	7.8	9.1	10.9	10.6
St. 3	220	712	68	57	195	139	98	8.4	10.3	10.8	10.6
St. 4	175	973	53	46	128	93	77	6.2	7.3	9.1	8.5
St. 5	139	1178	50	44	151	91	72	5.1	8.3	8.1	7.3
Swash	0	588	104	99	175	152	133	10.2	10.9	11.3	11.1

(filtered data, zero-down crossing method)

domain is only an artifice, for which it is difficult to attach any physical meaning.

Figure 12 shows a plot of reflection coefficients against the local wave steepness, defined by the ratio between the incident wave height to the shallow water wave length calculated from the reflected wave period. The solid curve in Fig.12 gives the result of reflection coefficient obtained by Battjes (1974) for the regular waves with beach gradient of one-seventh ($\tan \beta = 1/7$). There is a tendency that reflection coefficients are inversely proportional to the local wave steepness as found in the case of regular waves. However values of ratio in irregular waves are much greater than those given by Battjes (1974). This is because the wave height and period were measured in the deeper offshore area in the laboratory experiment, which support Battjes' formula. The reflection coefficients at St. 4 are generally greater than those at St. 5. Physically it is reasonable that the reflection coefficient at St. 5 should be greater than that at St.4 since St. 5 is located nearer to the shoreline. The opposite result in Fig. 12 may result from the fact that the incident waves at St. 5 had sharp peaks due to nonlinear shoaling. The mean reflection coefficient defined by the ratio of rms value of water surface elevations of reflected waves to that of incident waves is 0.67 at St. 4 and 0.93 at St. 5.

Figure 13 shows a plot of reflection coefficients against the deep water wave steepness. The solid curve denotes Battjes' criterion and the broken curve gives Miche's criterion (Miche, 1951, or Horikawa, 1978). Considerable scatter of data makes it difficult to draw conclusions from Fig. 13 except that the magnitude of reflection coefficient of individual waves in irregular waves is comparable to those for corresponding regular waves.

IV CONCLUDING REMARKS

Field data of swash motion of good quality is obtained by a photographic method. Wave data in and outside of the surf zone were measured simultaneously. Analysis in the frequency domain shows that most of the power in the inner surf zone is of standing waves. However wave to wave analysis is better to describe the waves both in the surf zone and in the swash zone.

Zero-crossing methods are applied to define the individual waves. It is revealed that the number of waves changes considerably when waves propagates from outside the surf zone through the surf zone to the swash zone. This indicates that simple wave to wave method fails to describe the transformation of waves.

Joint distribution of height and period of swash oscillation is obtained. Marginal distributions of wave height as well as period is

similar to Gaussian distribution. Physical interpretation of these facts are left in future. It, however, can be pointed out that nearly constant power in the low frequency range in the swash spectrum might be related to the shape of distribution.

Incident waves and reflected waves are decomposed by using measured surface elevation and cross-shore velocity under the assumption of the linear long wave theory. The decomposed surface elevation profiles show it possible to identify incident waves (or groups of incident waves) and the corresponding outgoing (reflected) waves. Crude estimate of reflection coefficients of these individual waves is attempted. The values are inversely proportional to the local wave steepness in the inner surf zone, and of the same magnitude as those given by Miche formula for monochromatic waves, though the data scatter is rather large.

Reflected waves can be seen as those generated in the swash zone by the incoming waves. It will be a next problem to find out the relationships among the incoming waves, the swash oscillation and the outgoing waves. The problem would be best treated in the physical time domain.

ACKNOWLEDGEMENT

We would like to express our appreciation to the our university students who supported the field work and digitized the films. Without their help we could not have carried out this field research. We gratefully acknowledge the assistance of Dr. S. A. Hughes of the Coastal Engineering Research Center, WES, in the preparation of the manuscript.

REFERENCES

- Battjes, J. A. (1974): Surf similarity, Proc. 14th Coastal Eng. Conf., pp.446-480.
- Guza, R. T. and E. B. Thornton(1982): Swash oscillation on a natural beach, J. Geophys. Res., Vol. 87. No. C1, pp.483-491.
- Guza, R. T., E. B. Thornton and R. A. Holman(1984): Swash on steep and shallow beaches, Proc. 19th Coastal Eng. Conf., pp.708-723.
- Holman, R. A. and R. T. Guza(1984): Measuring runup on natural beaches, Coastal Eng., Vol. 8, pp.129-140.
- Holman, R. A. and A. H. Sallenger(1985): Setup and swash on a natural beach, J. Geophys. Res., Vol. 90. No. C1, pp.945-953.

- Horikawa, K.(1978): Coastal Engineering---An Introduction to Ocean Engineering---, Univ. of Tokyo Press, Tokyo, 402p.
- Hotta, S. and M. Mizuguchi(1980): A field study of waves in the surf zone, Coastal Eng. in Japan, Vol. 23, pp.59-79.
- Hotta, S., M. Mizuguchi and M. Isobe(1981): Observations of long period waves in the nearshore zone, Coastal Eng. in Japan,
- Hotta, S., M. Mizuguchi and M. Isobe(1982): A field study of waves in the nearshore zone, Proc. 18th Coastal Eng. Conf., pp.38-57.
- Mase, H. and Y. Iwagaki(1984): Run-up of random waves on gentle slopes, Proc. 19th Coastal Eng. Conf., pp.593-609.
- Miche, R.(1951): le pouvoir reflechissant des ouvrages maritime exposes a l'action de la houle, Annales Ponts et Chaussees, 121^e Annee, pp.285-319.
- Mizuguchi, M.(1982): Individual wave analysis of irregular wave deformation in the nearshore zone, Proc. 18th Coastal Eng. Conf., pp.485-504.
- Mizuguchi, M.(1984): Swash on a natural beach, Proc. 19th Coastal Eng. Conf., pp.678-694.
- Sawaragi, T. and K. Iwata(1980): Wave power spectrum slope on high frequency range in shallow water surf, Coastal Eng. in Japan, Vol. 23, pp.91-99.



Photo 1 Run-up meter and stick array.

CHAPTER 11

Characteristics of Diffusion and Aeration due to Wave Action near Permeable Breakwaters

Hitoshi MURAKAMI* and Yoshihiko HOSOI**

Abstract

This paper deals with the effect of wave action on the water purification near a permeable breakwater. When determining standards for water purification, three indexes are usually taken into account: the diffusion coefficient, the concentration reflection ratio and the reaeration coefficient.

In our study, the values of the diffusion coefficients K_x near the breakwater ranged from about $10^{-1} \text{ cm}^2/\text{sec}$ to $7 \times 10 \text{ cm}^2/\text{sec}$. The effect of aeration caused by setting up a permeable breakwater was limited to within a distance of only one wave length at either side of the breakwater. As a result, values of the reaeration coefficients were then estimated to be in the order of $10^{-5} - 10^{-4}/\text{sec}$.

1. Introduction

In recent years, many legitimate plans for harbor and coastal zone developments have been proposed in succession, e.g, the construction of an artificial island, respective steam and wave force power stations etc. Breakwaters which would protect these facilities must therefore be built in increasing numbers.

However, in response to the recent social demand for better environmental conditions, we are also aware that greater efforts should be made to prevent water pollution in these harbor areas.

* Professor, Technical College, The University of Tokushima, Minami-
jyosanjima, Tokushima, 770, Japan.

** Associate Professor, Technical college, The University of Tokushima.

As a result, the need to design a multipurpose breakwater is required. This means a breakwater effective not only for the reduction of incident wave energy but also for water purification through a permeable wall. The hydraulic characteristics of various kinds of permeable breakwater models have already been investigated both theoretically and experimentally. We also have discussed the effective cross section geometry of the vertical slit-type breakwater from viewpoints of both the hydraulic and water exchange discharge due to the wave action (Murakami et al., 1986).

In addition we may expect a diffusion and aeration function for a permeable breakwater, because of waves which break causing water turbulence along the permeable wall. Although we observed this function, a satisfactory discussion could not be presented in the preceding study.

The purpose of this study is to examine the effect of the vertical slit-type breakwater on water purification paying special attention to the functions of diffusion and aeration.

2. Diffusion Characteristics

2.1 Experimental apparatus and procedure

Models of the vertical slit-type breakwater in this study are shown in Fig.1. A wave tank equipped with a flap-type wave generator at one end and measuring $15\text{m} \times 18\text{cm} \times 30\text{cm}$ was used. The models were placed at a distance of 10m from the wave generator. The water depth h and the wave period T were kept at a constant of 15cm and 0.75sec, respectively. Consequently the wave length L was 75cm. Incident wave steepness H/L was maintained at a value of 0.02.

In the diffusion experiment, a drop of methylene-blue solution was directly introduced as a tracer at the point located one wave length L from the front wall of the breakwater as shown in Fig.2. Periodical changes in concentration of the tracer were measured at two points, one at $L/3$ and the other at $2L/3$. Tests were performed on both the seaward and shoreward side of the breakwater.

Experimental conditions on the diffusion of the contaminant are represented in Table.1.

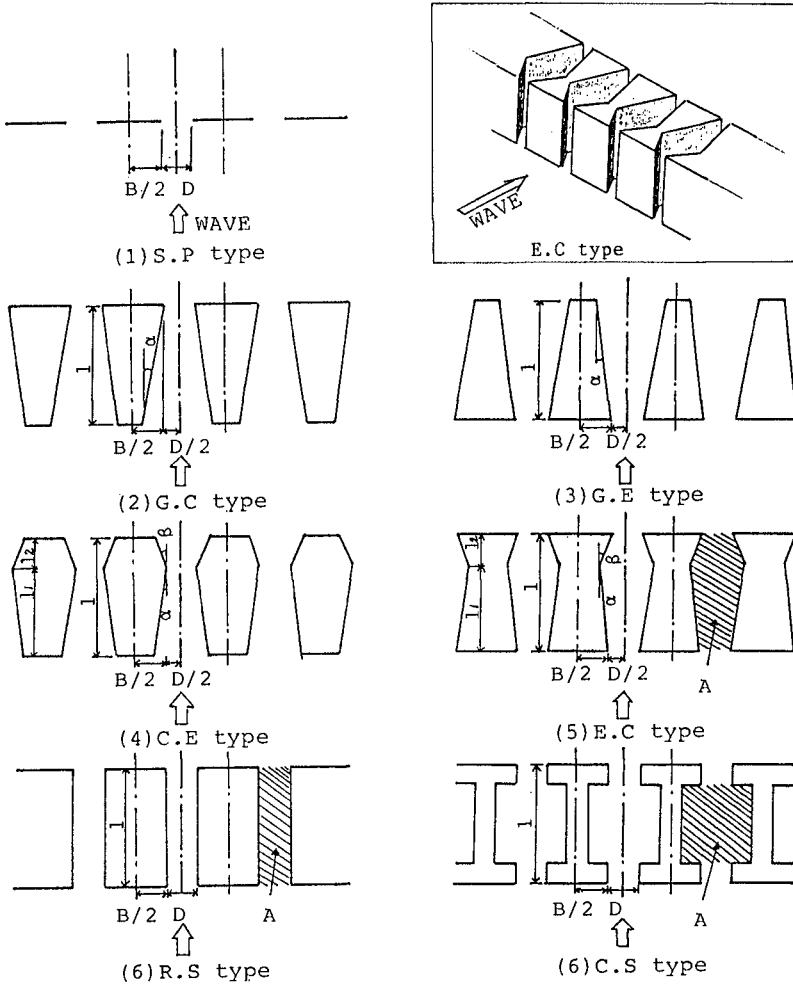


Fig.1 Horizontal cross sections of vertical slit-type breakwaters

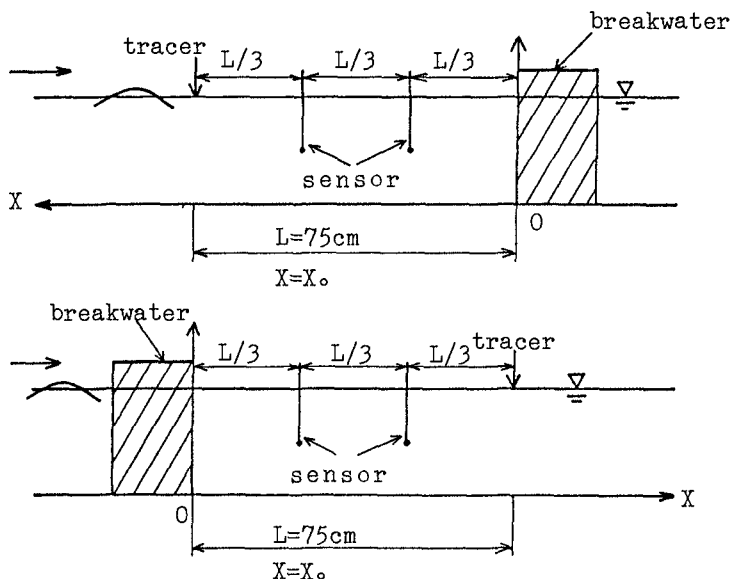


Fig.2 Definition sketch and coordinate system

2.2 Analysis method on diffusion characteristics

The diffusion of a tracer near a permeable wall in a relatively narrow wave tank can be assumed to be a one dimensional diffusion phenomenon.

The diffusion equation on the concentration of tracer C with time factor t and in a given space x is given as follows,

$$\frac{\partial C}{\partial t} = K_x \frac{\partial^2 C}{\partial X^2} \tag{1}$$

where K_x is the one dimensional diffusion coefficient. When the tracer material is introduced at the point x, the solution in Eq.(1) is easily obtained at an arbitrary point x under the following initial and boundary conditions,

$$\left. \begin{aligned} C(0,0) &= \infty \\ C(x,\infty) &= 0 \\ \int_{-\infty}^{\infty} C(x,t) dx &= M \end{aligned} \right\} \tag{2}$$

$$\begin{aligned}
 C(x,t) &= \frac{M}{2\sqrt{\pi K_x t}} \left\{ \exp\left\{-\frac{(x-x_0)^2}{4K_x t}\right\} + r \exp\left\{-\frac{(x+x_0)^2}{4K_x t}\right\} \right\} & x > 0 \\
 C(x,t) &= \frac{M}{2\sqrt{\pi K_x t}} (1-r) \exp\left\{-\frac{(x-x_0)^2}{4K_x t}\right\} & x < 0
 \end{aligned} \quad (3)$$

where M is the mass of the introduced tracer material, r represents the concentration reflection ratio due to the existence of a breakwater, $r=1$ indicates the impermeability of the breakwater and $r=0$ signifies that no breakwater has been installed. Thus we can consider r as an index representing the water quality exchange through the permeable wall. We can clarify the diffusion mechanism from Eq.(2) only if the values of the diffusion coefficient K_x and r are to be correctly estimated. By using the simplex method, we derived values for K_x and r , in which the calculated values of the tracer concentration in Eq.(2) most resembled the observed values of the concentration.

As a result of estimating K_x and r by using the simplex method, we obtain the most approximate curve to the experimental values as seen in Fig.3.

Values of K_x and r for each experiment are shown in Table.2. The lack of values for K_x and r in Table.2 means that unrealistic values for both had been obtained during the course of analysis.

2.3 Consideration of K_x and r

From Table 2, it became evident that values of the diffusion coefficient near a breakwater fall in the range of $10^{-1} \text{cm}^2/\text{sec}$ to $7 \times 10 \text{cm}^2/\text{sec}$. Generally speaking, the value of K_x is greater on the seaward side of a breakwater compared to that of the shoreward side; the value in GC and CE type breakwaters obtained particularly large values.

We would like to discuss the characteristics of K_x and r in more detail. We can only conjecture that the diffusion characteristics near a breakwater will be effected by the turbulence caused by an opening in a permeable wall. The rate of wave energy dissipation at the opening of this wall ε is expressed as follows;

$$\varepsilon = 1 - r_R^2 - r_T^2 \quad (4)$$

Table.1 Experimental conditions
 $T=0.75\text{sec}, h=15\text{cm}, h/L=0.20, H/L=0.02$

No.	TYPE	$\mu = D/(D+B)$	$l=l_1+l_2(\text{cm})$	$l_1/(l_1+l_2)$	$\alpha (^{\circ})$	$\beta (^{\circ})$	$A(\text{cm}^2)$
1 2 3	S.P	0.0625 0.125 0.25	0				
4 5 6	G.C 1	0.0625 0.125 0.25	9.4		19		
7 8 9	G.C 2	0.0625 0.125 0.25	18.8				
10 11 12	G.E 1	0.0625 0.125 0.25	9.4		19		
13 14 15	G.E 2	0.0625 0.125 0.25	18.8				
16 17 18 19	C.E 1	0.125	9.4	0.25	20 40 20 40	20 20 40 40	
20 21 22 23	C.E 2			0.75	20 20 40 40	20 40 20 40	
24 25 26 27	E.C 1	0.125	9.4	0.25	20 40 46 68	7 16 20 40	30.08 40.42 45.12 77.08
28 29 30 31	E.C 2			0.75	7 16 20 40	20 40 46 68	30.08 40.42 45.12 77.08
32	R.S	0.125	9.4		0	0	
33	C.S	0.125	9.4				77.08

Table.2 Values of diffusion coefficient Kx and concentration reflection ratio r

No.	TYPE	Kx ($*10\text{cm}^2/\text{S}$)		r	
		Seaward	Shoreward	Seaward	Shoreward
1	S.P	1.43	1.69	0.42	0.34
2		3.45	2.31	0.41	0.63
3					
4	G.C 1		0.41		0.52
5					
6		6.30	2.64	0.94	0.57
7	G.C 2	5.08	0.59	0.68	0.04
8		3.65	1.08	0.62	0.27
9			3.95		0.83
10	G.E 1	0.47	0.23	0.07	0.14
11		1.15		0.29	
12		3.23	1.03	0.79	0.51
13	G.E 2		1.06		0.30
14			2.45		0.56
15		0.48	3.97	0.72	0.84
16	C.E 1	6.10	0.27	0.94	0.46
17		3.93	3.08	0.76	0.80
18		3.32	0.34	0.39	0.69
19		2.47	3.66	0.56	0.82
20	C.E 2				
21		2.76	0.25	0.78	0.37
22		6.85		0.96	
23			0.46		0.11
24	E.C 1		1.34		0.69
25		0.78	1.22	0.02	0.69
26					
27		7.00	2.38	0.77	0.56
28	E.C 2	0.65	3.94	0.20	0.83
29		3.04	0.65	0.80	0.52
30		1.70	0.47	0.53	0.05
31		1.44	2.04		0.75
32	R.S	3.04	2.03	0.58	0.45

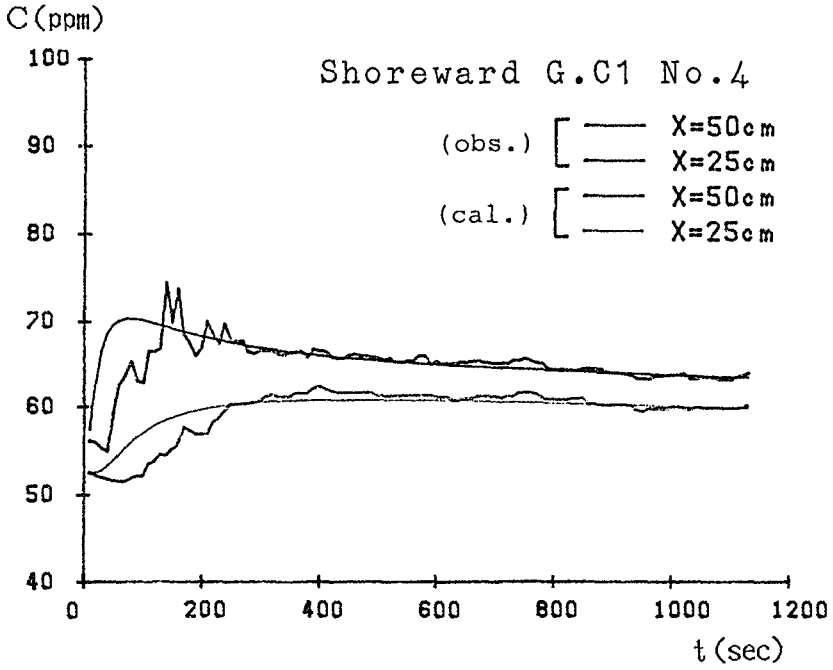


Fig.3 Concentration change of tracer

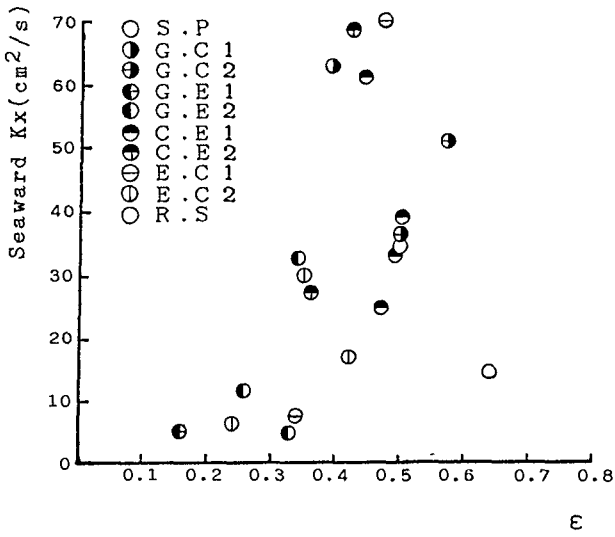


Fig.4 Dependence of diffusion coefficient of the seaward side on energy dissipation rate

where r_R is the reflection coefficient which is defined by the ratio of the reflection wave height H_R to the incident wave height H_I and r_T is the transmission coefficient H_T/H_I (H_T : transmission wave height).

Fig.4 shows the relationship between Kx on the seaward side of the breakwater and the rate of wave energy dissipation ϵ . Here, we notice a tendency emerge, where values of Kx increase concomitantly with an increase in the value of ϵ .

Likewise, on the shoreward side of the breakwater, the values of Kx increase with the increase in the value of the transmission coefficient r_T as shown in Fig.5. Under the condition where the constant value of the incident wave steepness at the wall opening is larger, values of Kx on both seaward and shoreward sides are greater as shown in Fig.6. In Fig.6 the opening ratio is defined by $D/D+B$ as shown too in Fig.1.

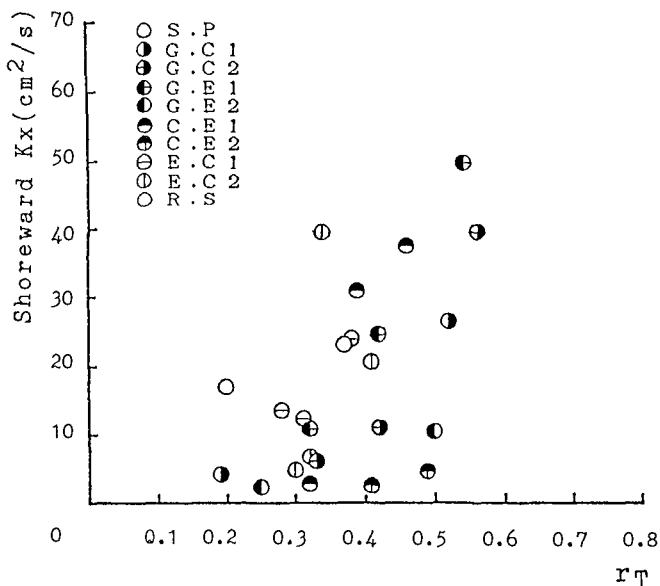


Fig.5 Dependence of diffusion coefficient of the shoreward side on wave transmission coefficient

We may infer that the effect due to the existence of a breakwater on the diffusion coefficient will be limited to a small area close to the breakwater.

Next, let us consider the characteristics of the concentration reflection ratio r .

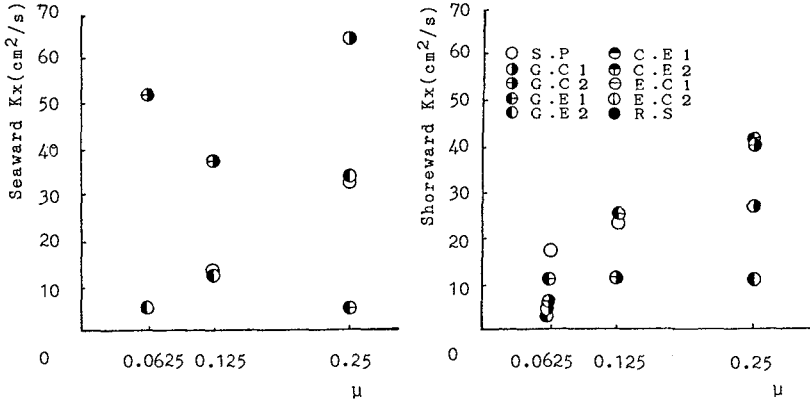


Fig.6 Dependence of diffusion coefficient on opening ratio of permeable wall

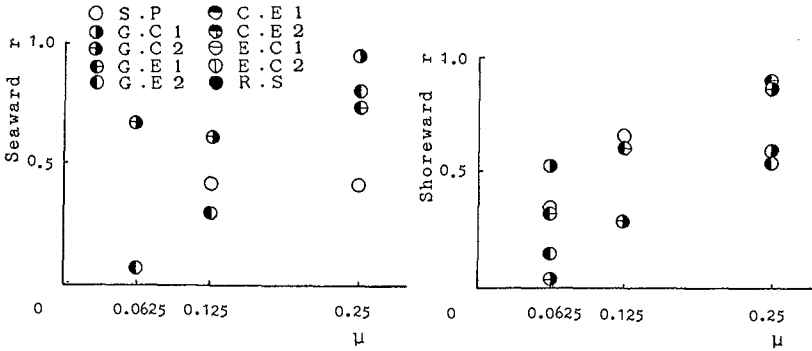


Fig.7 Dependence of concentration reflection ratio on opening ratio of permeable wall

Fig.7 shows the relationship between r on both sides of the breakwater and the opening ratio μ . As the opening ratio μ increases, values of r will similarly increase on both sides. This means that if a large opening in the permeable wall occurs, the contaminant near the breakwater will easily flow back with less dilution, regardless of its initial location. According to this inference, as the concentration reflection ratio r on the shoreward side is larger, the diffusion function on the seaward side must decrease, because the contaminant on one side can not easily flow out through the opening to the opposite side of the breakwater. The tendency in Fig.8 supports this suggestion.

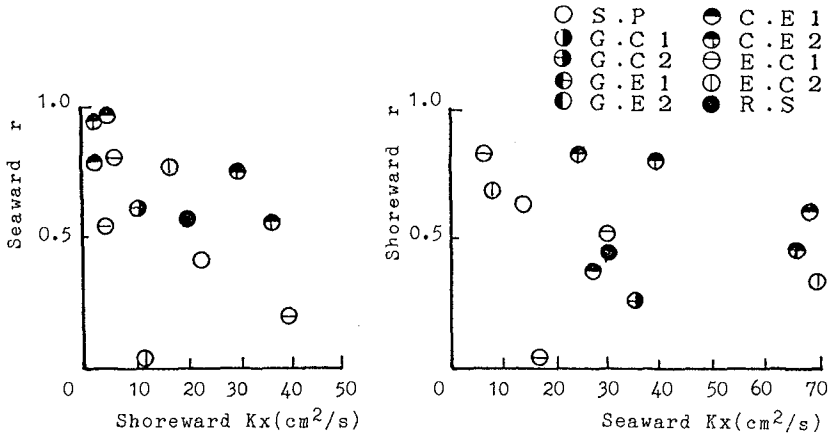


Fig.8 Relationship between concentration reflection ratio and diffusivity of the opposite side

3. Reaeration Characteristics

3.1 Experimental apparatus and procedure

The experiment on reaeration was carried out in the same wave tank and the same breakwater models were used as in the diffusion experiment. The range of the incident wave steepness H/L was extended from $H/L=0.01$ to 0.05 . After the concentration of dissolved oxygen in the wave tank was compulsorily reduced by sodium sulfite, a wave was generated for one hour to observe the concentration change of the dissolved oxygen. The concentration of the oxygen was measured at time intervals of 15 minutes and values of concentration change for each location were estimated at 50cm apart from each other. The origin of these observation points was situated in the rear wall of the breakwater and is represented by zero on the abscissa.

Fig.9 shows some examples of spatial concentration distribution of the dissolved oxygen over certain periods of time for four breakwater types. The region containing the minus sign in these figures represents the seaward side of the breakwater. The abbreviation P.I on the right hand side of the lower figure stands for an impermeable plate, in this case the concentration change depends only on the aeration caused by the standing wave. Apart from this exception, the concentration of dissolved oxygen increases remarkably with time in the restricted area near to the breakwater.

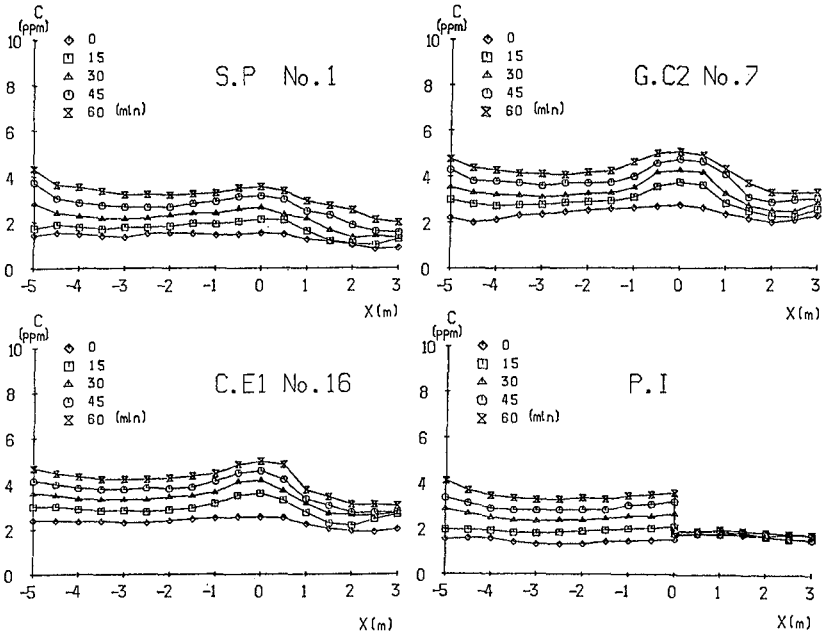


Fig.9 Spatial concentration distribution of dissolved oxygen near breakwater

3.2 Reaeration Coefficient

We shall explain the mechanism of reaeration briefly. Reaeration compensates for the deficiency in oxygen levels through the water surface exposed to the atmosphere. As shown in Fig.9, reaeration efficiency near the breakwater is greater than that in other areas. The mass conservation equation relating to the dissolved oxygen can be written as follows:

$$\frac{dC}{dt} = K_L \frac{A_S}{V} (C_S - C) \quad (5)$$

where C and C_S represent the dissolved oxygen concentration and its saturation value respectively. K_L indicates the mass transfer coefficient, A_S and V are surface area and water volume respectively.

The reaeration coefficient k_2 which represents "the aerateability", is defined as follows.

$$k_2 = K_L \frac{A_S}{V} \quad (6)$$

Then Eq.(5) is rewritten

$$\frac{dC}{dt} = k_2 (C_S - C) \quad (7)$$

Eq.(7) is solved as follows:

$$\ln \left(\frac{C - C_S}{C_0 - C} \right) = - k_2 t \quad (8)$$

From Eq.(8), we can easily arrive at the reaeration coefficient k_2 , if there has been a change of concentration in the dissolved oxygen over a certain period of time as seen in the experiment, where C_0 represents the initial concentration of dissolved oxygen.

3.3 Consideration of k_2

The reaeration coefficient k_2 at each observation point was measured; concentration changes in the dissolved oxygen can be calculated from Eq.(8) as mentioned above. We examined first the effect on the reaeration by setting up the breakwater as follows: we isolated the effective region identifiable by its pronounced convex shape from the remaining spatial distribution of the dissolved oxygen as shown in Fig.9. We next calculated the value of k_2 for each section. Finally, we estimated the value of k_2 from the following procedure,

$$k_2 = \frac{\sum_i k_{2i} V_i}{\sum_i V_i} \quad (9)$$

where k_{2i} is i -th the value of k_2 and V_i is the volume of the i -th section.

Fig.10 shows the relationship between the reaeration coefficient k_2 and the wave steepness H/L . Generally, values of k_2 will only increase with the growth of the incident wave height because the wave length remains at a constant ($L = 75\text{cm}$) for all experiments. Furthermore, values of k_2 are seen to be larger as the breakwater width l becomes wider.

Consequently, the values of k_2 are in the range of $10^{-5} - 10^{-4}$ 1/sec. We have already decided on the equation to predict the reaeration coefficient by breaking waves on the uniform sloping bed (Hosoi et al., 1986). If we apply the equation to this experimental condition, we obtain values for k_2 approaching 10^{-3} 1/sec. This

logically implies that the effect of the slit-type breakwaters on aeration is about 1/10 less than that of the uniform slope bed.

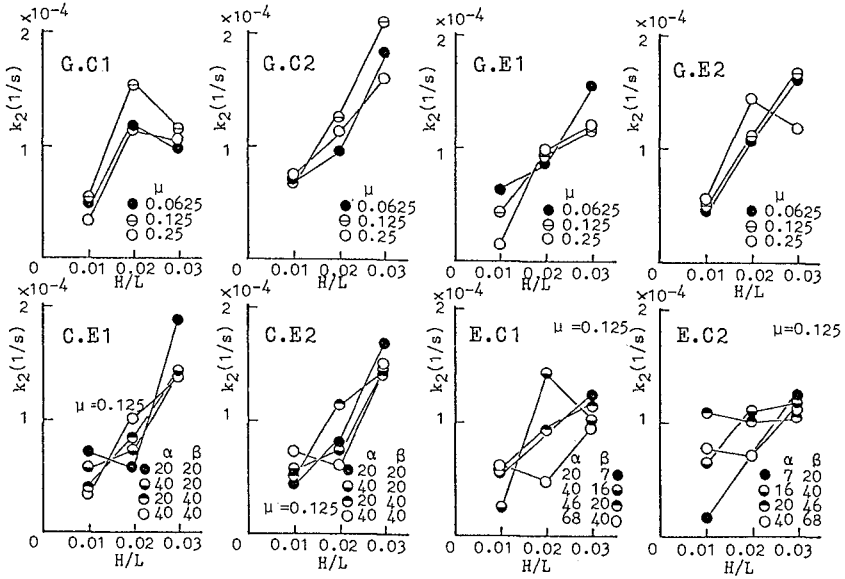


Fig.10 Relationship between reaeration coefficient and incident wave steepness

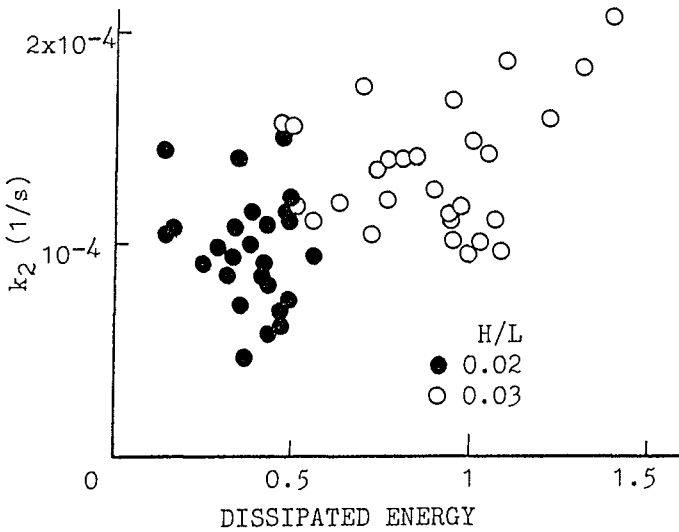


Fig.11 Relationship between reaeration coefficient and dissipated energy

Fig.11 represents the relationship between the value of k_2 and the amount of the dissipated energy at the permeable wall. In this figure the dissipated energy is standardized by the amount of the incident energy of a wave measuring $H=1.5\text{cm}$, which is similar to one of the wave conditions already experienced. We can then deduce that aeration through the water surface near the breakwater depends on the energy dissipation caused by turbulence regardless of other factors such as the shape of the opening in the breakwater.

4. Conclusion

The characteristics of the diffusion and aeration near a permeable breakwater due to the wave action were discussed.

Results are summarized as follows.

- 1) The diffusion coefficients near the breakwater on the seaward and shoreward sides were estimated in the range of $10^{-1} - 7 \times 10 \text{cm}^2/\text{sec}$.
- 2) The mechanism of the water quality exchange through a permeable wall can be explained by using the concentration reflection ratio r .
- 3) The reaeration coefficients near the breakwater were estimated at values in the order of $10^{-5} - 10^{-4} 1/\text{sec}$. These values corresponded to a mean $1/10$ the value of the breaking wave on the uniform slope bed. Furthermore, the value of the reaeration coefficient increased with the increase of the incident wave height and wave energy dissipation caused by turbulence near the breakwater.

Acknowledgement

The authors would like to acknowledge the assistance of Mr.Yuji Amino who contributed his efforts to the accomplishment of the many experiments.

Reference

- 1) Hosoi.Y and H.Murakami: Effects of breaking waves on dissolved oxygen and organic matter, Proc. of 20th Conf. on Coastal Engng., pp.2498-2512,1986.
- 2) Murakami,H. and Y.Hosoi: Analysis of permeable breakwaters, Proc. of 20th Conf.on Coastal Engng., pp.2104-2118, 1986.

CHAPTER 12

Generalized Wave Theory for a Sloping Bed

D H Swart* and J B Crowley**

ABSTRACT This paper discusses the development from first principles of a first-order solution for non-breaking waves on a gently sloping bottom. The theory is derived in a similar fashion as was done by Swart and Loubser (1978) for vocoidal waves on a horizontal bottom. The resulting covocoidal theory was compared to an extensive data set for waves over a sloping bottom (Nelson, 1981) and is tested for analytical validity. It adheres exactly to continuity and the kinematic free surface boundary condition, and shows comparable errors in the dynamic free surface boundary condition to that found for the better, general horizontal bed wave theories.

1. BACKGROUND

In the past decade increasing emphasis has been placed in nearshore and coastal dynamics studies on the measurement in the field of wave and current motions, infragravity activity, suspended sediment loads and associated shoreline changes. These studies have demonstrated that periodic motions in the nearshore, non-breaking wave area are extremely non-linear. It has been shown that various time-independent wave properties such as the maximum horizontal orbital velocity at the bed and the transfer function between incident energy flux and longshore currents, are predicted reasonably well by using linear wave theory (e.g. Le Mehaute et al, 1968 and various recent references). However, time-dependent properties such as wave shape and orbital excursion are non-linear due to the shallow relative depth and asymmetrical due to the sloping bottom.

Elegant computer models are being developed to predict cross-shore wave-driven movement (Baillard, 1982, Stive, 1986). These models rely on an accurate prediction of wave-driven mass transport, and for this purpose use higher moments derived from orbital velocities predicted with Stokesian wave theories. Swart and Loubser (1979) already showed that this mass transport is a function of the non-adherence of these theories to the continuity

*Programme Manager, Coastal Processes and Management Advice, EMA, CSIR, Box 320, Stellenbosch, Republic of South Africa

**Coastal Processes and Management Advice, EMA, CSIR, Box 320, Stellenbosch, Republic of South Africa.

equation. In this respect the cross-shore transport theories would be improved by using a better higher-order wave theory, although this would admittedly increase the computational effort involved. Swart (1978) derived a variable-order cosinusoidal wave theory, the so-called vocoidal wave theory, from first principles. Swart and Loubser (1979) showed that as far as both experimental and analytical validity are concerned, vocoidal theory is comparable to the best other commonly used wave theories. Swart (1982) developed a higher-order Fourier analysis which allows the extraction of vocoidal component waves from a wave spectrum instead of sinusoidal or cosinusoidal waves as in a usual Fourier analysis. Swart (1987) reported on nearshore wave data, gathered in shallow water just outside the breaker zone. In as yet unreported analyses of the data, Swart found deviations from the observed spectra, which can be shown to be consistent with asymmetries associated with the waves shoaling on a sloping bed.

The purpose of the study reported on herein was therefore to investigate the possibility to generalise vocoidal theory to make it applicable for waves shoaling over mildly sloping bottoms. If this can be achieved, it would be possible to without excessive computer effort establish a technique to extract the non-symmetrical, higher-order wave shapes in shallow water and to predict orbital motions and higher moments thereof with greater accuracy than with the Stokesian theories. The potential to improve wave force calculations with asymmetrical waves would also be worth pursuing.

Section 2 reviews the method of derivation of the new theory, after which the analytical and experimental validity of the theory is reviewed in Sections 3 and 4. Section 5 contains a summary of conclusions.

2. DERIVATION

A very similar approach was followed for the development of the generalised vocoidal theory than was followed for the original derivation of vocoidal water wave theory on a horizontal bed. In the following the general assumptions, the governing equations, the boundary conditions and the derivation are given with regular reference to the horizontal bed derivation.

General assumptions

For the derivation of a generalised water wave theory the following general assumptions are made:

- * only non-breaking waves are considered;
- * the water movement is two-dimensional;
- * the flow is frictionless;
- * the fluid density is invariant in time and space,

- that is, the fluid is incompressible and homogeneous;
- * surface tension effects are neglected;
 - * the sea bed is mildly sloping, that is, it exhibits a slow variation in water depth in the direction of wave propagation;
 - * the wave motion is periodic and the slope is mild enough for relationship (1) below to be approximately valid.

$$\frac{d\theta(x,t)}{dt} = \frac{\partial\theta(x,t)}{\partial t} + c \frac{\partial\theta(x,t)}{\partial x} \quad \dots(1)$$

In expression (1) $\theta(x,t)$ is any time or space-dependent parameter, t denotes time, x is the distance in the direction of wave travel, and c denotes wave celerity. The second-last assumption above, namely, that of a mildly-sloping bed, implies in reality that it is assumed that the bed slope is mild enough to assume that the governing equations are not affected by the sloping bed. The only way in which the formulation used for the derivation of the theory is affected is via the boundary conditions at the sea bed which will be discussed in more detail below.

Governing equations

The three basic equations which govern the water wave problem are the equation for the conservation of fluid mass, the equations of motion and the expression for the rotationality of a fluid particle.

Continuity equation

In the case of an incompressible, homogeneous fluid in the two-dimensional situation, the continuity equation can be written as

$$\frac{\partial u}{\partial x} + \frac{\partial w}{\partial z} = 0 \quad \dots(2)$$

where z = vertical dimension positive upwards from the bed and u and w are velocity components in the x and z directions.

Equations of motion

For a frictionless fluid the two-dimensional equations of motion are:

x - direction:

$$\frac{1}{\rho} \frac{\partial \Phi}{\partial x} + \frac{\partial u}{\partial t} + u \frac{\partial u}{\partial x} + w \frac{\partial u}{\partial z} = 0 \quad \dots(3)$$

z - direction:

$$g + \frac{1}{\rho} \frac{\partial p}{\partial z} + \frac{\partial w}{\partial t} + u \frac{\partial w}{\partial x} + \frac{\partial w}{\partial z} = 0 \quad \dots(4)$$

where p = pressure and ρ is fluid density.

Angular velocity

$$R = \frac{1}{2} \left(\frac{\partial w}{\partial x} - \frac{\partial u}{\partial z} \right) \quad \dots(5)$$

It should be noted that if equation (5) should point to a net rotation, this is purely the result of the mathematical manipulation. It can be used to derive rotational wave theories without considering how much such a type of flow i.e. frictionless, "rotational" flow could originate. It was shown, however, in e.g. the vortical theory (Swart 1978) that such an approach is advantageous in the development of the theory whilst the net rotation which results is in fact negligible (see Bleach, 1982).

Boundary conditions

The following three boundary conditions are used:

Kinematic bed boundary condition (KBBC)

$$w(x; z=0) = u(x; z=0) \tan \alpha \quad \dots(6)$$

(see Figure 1 for axis-notation)

Kinematic free-surface boundary condition (KFSBC):

$$w(x; z=d+\eta) - u(x; z=d+\eta) \frac{\partial \eta}{\partial x} = \frac{\partial \eta}{\partial t} \quad \dots(7)$$

where η = is the surface elevation, measured relative to the mean water level.

Dynamic free-surface boundary condition (DFSBC)

$$p(x; z=d+\eta) = 0 \quad \dots(8a)$$

Owing to the fact that the free surface is a streamline, one can use Bernoulli's equation for irrotational flow to transform equation (8) to:

$$Q = \frac{\eta}{d} + \frac{1}{2gd} \left[\{u(x; z=d+\eta) - c\}^2 + \{w(x; z=d+\eta)\}^2 \right] - \frac{c^2}{2gd} \quad \dots(8b)$$

where Q is the constant total energy along the free surface.

Further qualitative assumptions

Nelson (1981) specifically found that the various

parameters related to what could be termed bulk properties such as wave celerity and potential energy are virtually unaffected by the slope, whereas time - (or space -) dependent parameters are strongly affected. On the basis of the vocoidal horizontal bed solution and the various results obtained by Nelson (1981) specific, qualitative assumptions were made in addition to those already outlined above.

Swart (1979) assumed that the wave profile on a horizontal bed is qualitatively given by:

$$\frac{\eta}{H} = \text{voc}(P, X) - \eta_{*t} \quad \dots(9)$$

where $\text{voc}(P, X)$ = the vocoidal function = variable-order-cosinusoidal function

$$= \{\cos^2(\pi X)\}^P \quad \dots(10)$$

X = dimensionless time = t/T ; η_{*t} = dimensionless (with respect to wave height) trough depth and P is the wave profile parameter. The only assumption made regarding P is that it is equal to or greater than unity.

Analogously, it is assumed that the following qualitative definition is representative of **surface elevation** for a sloping bed:

$$\frac{\eta}{H} = h_\alpha \{\text{voc}(P, X) - \eta_{*t}\} + 0.5r_\alpha \{\text{cov}(P, X)(1 + \cos(\pi X)) - (1 - \eta_{*t})\} \quad \dots(11)$$

where $\text{cov}(P, X)$ is the newly defined "covocoidal" function given by

$$\text{cov}(P, X) = 1 - \text{voc}(P, X) \quad \dots(12)$$

and η_{*t} is defined in equation (9).

The parameters h_α and r_α are unknowns to be determined from the solution to the continuity equation, equations of motion and the surface and sea bed boundary conditions. It is assumed that P , the vocoidal wave profile parameter, has the same value as in the horizontal bed solution.

It can be seen that this equation for wave shape (equation 11) has the horizontal bed solution as a special case when $r_\alpha = 0$ and $h_\alpha = 1$.

The horizontal orbital velocity u is given by:

$$u/c = \frac{\eta}{H} \frac{M(X)k \cosh\{M(X)kz\}}{\sinh\{M(X)k(d+\eta)\}} + \frac{q_\alpha}{c(d+\eta)} \quad \dots(13)$$

where $M(X)$ is the vocoidal orbital velocity parameter and q_α is the mass flow due to a sloping sea bed. When $q_\alpha = 0$ this equation is the same as that used by Swart (1979) in the derivation of vocoidal theory.

It will be shown below that the effect of slope on the variation of $M(X)$ with X is such that the values of this parameter as obtained for a horizontal bed solution are not valid on a sloping bed.

It is assumed that the wave celerity c is defined by the same equation as for the horizontal bed vocoidal solution.

$$\frac{c^2}{gd} = \frac{1}{kd} \tanh(Nkd) \quad \dots(14)$$

This "assumption" was checked as part of finding a solution to the wave boundary value problem and was found to be valid as a first approximation (see Figure 2).

In solving for the wave boundary value problem as defined by equations (2) to (8b), the unknowns to be quantified are h_α and r_α (in equation 11) and $M(X)$ and q_α (in equation 13).

Solution for wave profile parameters r_α and h_α

The DFSBC is used to solve for the optimum ratio r_α/h_α . The rms value of the deviation over the wave profile ($0 < X < 1$) from the mean value of the Bernoulli constant Q (equation 8b) at the free surface, determines to what extent the theory adheres to the DFSBC, i.e.

$$E(\text{DFSBC}) = \frac{1}{4l} \left\{ \sum_{j=1}^{4l} (Q - \bar{Q})^2 \right\} \quad \dots(15)$$

where Q is given by equation 8b and \bar{Q} is the mean value of Q in the area $0 < X < 1$.

The value of q_α in the horizontal orbital velocity component is obtained from the continuity equation and the kinematic boundary conditions, namely,

$$\frac{q_\alpha}{c(d+\eta)} = \frac{\lambda}{d} \int_0^1 \left(\frac{u_s}{c} - \frac{u_b}{c} \right) \tan \alpha \, dX \quad \dots(16)$$

which also yields an expression for w , namely:

$$w = w(X) + w_{\text{mass}} + u \tan \alpha \quad \dots(17)$$

In the above subscripts "s" and "b" refer to "surface" and

"bed" respectively. In equation (17) $w(X)$ represents the cyclic vertical orbital velocity as given in the Appendix, with the qualification that the derivatives of η and $M(X)$ are derivatives of these values for waves on a slope. Furthermore w_{mass} is the component of the vertical orbital velocity which is due to the mass transport q_α . It can from the continuity equation be shown to be equal to

$$w_{\text{mass}} = \frac{q_\alpha}{d} \left(\frac{H}{\lambda}\right) (z/d) \frac{\partial(\eta/H)}{\partial X} (1+\eta/d)^{-2} \quad \dots(18)$$

The method of solution now involves finding that ratio of r_α/h_α for which the variation of $E(\text{DFSBC})$ is minimized. The following initial conditions were used:

$$T_c = 1, 2, 3, 4, 5, 10, 20, 30, 40, 50, 60.$$

$$H/d = 0.01, 0.02, 0.05, 0.10, 0.20, 0.50, 1.0.$$

$$\tan\alpha = 0.001, 0.002, 0.005, 0.01, 0.02, 0.05, 0.10, 0.20.$$

The numerical results for r_α/h_α were shown by inspection to be functions of H/d , T_c and $\tan\alpha$.

$$r_\alpha/h_\alpha = G(H/d, T_c, H/d) \quad \dots(19)$$

The detailed curve-fitted expressions for r_α/h_α are given in Table I.

The absolute values of r_α and h_α are determined by the fact that

$$\eta_c - \eta_t = H \quad \dots(20)$$

where subscripts c and t refer to "crest" and "trough" respectively. η_c and η_t are known in terms of r_α and h_α . Tables IIa and IIb show typical values of r_α and h_α .

Solution for orbital velocity parameters $M(X)$ and q_α

The orbital velocity parameter $M(X)$ is found by rewriting the particle rotation R (equation 5) through substitution of the appropriate expressions for u and w . In the same way as was done by Swart (1979) the orbital velocity parameter was found by defining

$$M(X) = R_M M_1(X) \quad \dots(21)$$

where $M_1(X)$ is the first-order, i.e. small amplitude, approximation of $M(X)$ and R_M is the correction which has

to be made to negate the small-amplitude assumption. It is assumed that the expression for R_M in the Appendix is also valid for the covocoidal theory. The value of $M_1(X)$ is found from the small-amplitude, covocoidal version of equation 5, that is

$$\frac{\partial^2(\eta/H)}{\partial X^2} + 4\pi^2(\eta/H) M_1^2(X) = 0 \quad \dots(22)$$

It can be shown (Swart, 1988) that at the wave crest ($X=0$) the values of M_1 for covocoidal and vocoidal theory are related, namely

$$M_{1c}(\text{covoc}) = (h_\alpha - r_\alpha)^{0.5} M_{1c}(\text{voc}) \quad \dots(23)$$

$M_1(\text{covoc})$ is called $M_{c1\alpha}$ herein.

Swart (1988) solved for $M_1(X)$ from equation (22) for a range of initial conditions, namely

$$\begin{aligned} T_C &= 1, 2, 3, 4, 5, 10, 20, 30, 40, 50, 60 \\ h/d &= 0, 01, 0.02, 0.05, 0.10, 0.2, 0.5, 1.0 \\ r_\alpha/h_\alpha &= 0.01, 0.02, 0.05, 0.10, 0.20, 0.40 \end{aligned}$$

Figure 3 shows a typical variation of $M_1(X)$ for covocoidal theory in comparison with $M_1(X)$ for vocoidal theory on a horizontal bed. The value of $M_1(X)$ at $x = 0.5$ was called $M_{t1\alpha}$ and was established from the numerical results for the whole range of initial conditions to be

$$M_{t1\alpha} = g_1(T_C) g_2(r_\alpha/h_\alpha) \quad \dots(24)$$

Curve-fitted expressions $M_{t1\alpha}$ given in Table III.

It is straightforward to find a solution for q_α . Equation (16) was integrated numerically using the Rombert integration method for a range of initial conditions:

$$\begin{aligned} T_C &= 5, 10, 20, 30, 40, 50, 60 \\ H/d &= 0.1, 0.2, 0.5, 1.0 \\ \tan\alpha &= 0.01, 0.02, 0.05, 0.10 \end{aligned}$$

By means of curve-fitting an expression was found from the numerical results for the mass transport velocity:

$$\frac{q_\alpha}{c(d+\eta)} = R(H/d, T_C, \tan\alpha) \quad \dots(25)$$

The nature of the function R is given in Table IV.

This concludes the derivation of covocoidal theory.

3. ANALYTICAL VALIDITY

As part of the validation of vocoidal water wave theory for a horizontal bed Swart and Loubser (1979) performed an analytical validity study in which the adherence of vocoidal theory to the original governing equations and boundary conditions was compared with that for twelve other commonly used water wave theories, namely, linear Airy theory, Stokes II and V, three different gravity cnoidal theories, Dean's stream function theory, two different rotational cnoidal theories and three different approximated wave theories. The two free surface boundary conditions and the adherence to the continuity equation were computed for each of the theories for a wide range of initial conditions.

Vocoidal theory adheres exactly to the kinematic free surface boundary condition and the continuity equation. Swart and Loubser (1979) showed that the error in the DFSBC was for a range of non-linearities covering all non-breaking waves either the lowest of all theories tested or not statistically different from the theory with the lowest error at the 95 per cent confidence level, for non-linearity values exceeding 260, which cover intermediate and shallow water conditions.

In exactly the same manner as was done in the Swart and Loubser study the error in the DFSBC was computed at 41 equidistant points over one wave period for covocoidal theory and a mean error calculated in subsets which were chosen to represent waves of roughly equal non-linearity, i.e. which had approximately equal wave shapes. The results were compared with those for vocoidal theory in the earlier study and it was concluded that although covocoidal theory exhibits errors in the DFSBC which grow marginally bigger as slope increases (see Figure 4), the covocoidal theory still had such small errors in the DFSBC that it did not differ significantly at the 95 per cent confidence level from vocoidal theory, which as stated above was shown to be amongst the best theories in the Swart and Loubser (1979) study as far as adherence to the DFSBC is concerned (see Figure 4). It is therefore concluded that the theory has a sufficiently sound basis to serve as a good first approximation of waves on a sloping bed.

4. EXPERIMENTAL VALIDITY

Experimental validation studies for wave theories have traditionally used laboratory data (Le Mehaute *et al*, 1968; Swart and Loubser, 1979 and Hattori 1986). Good full-scale data are nowadays being gathered in the field and in mega-flumes. Due to the fact that such data are usually for random waves, it is not simple to establish

the exact cause(s) of correspondence or non-correspondences of theory to data.

Nelson (1981) performed an extensive set of experiments for slopes from horizontal to 1 in 10, to test the effect of bed slope on wave profile parameters and wave celerity. His celerity data yield results totally compatible with the theoretical predictions in Figure 2. Figure 5 defines the wave profile parameters tested. Using the same range of initial conditions (H/d , T_c , $\tan\alpha$) as in the Nelson study, theoretical predictions of the parameters defined in Figure 5 were made. The resulting correspondences between Nelson's measured data and the theoretical predictions in this study are shown in Figure 6. It can be concluded that good, qualitative correspondence is achieved, although there are some quantitative divergences. Nevertheless, wave shape changes on beds of different slope are predicted well as a first approximation.

Swart and Loubser (1979) showed that vocoidal theory was consistently the best predictor of the thirteen theories tested as far as the prediction of horizontal orbital velocity is concerned. No good data exists to test systematically the effect of increasing bottom slope on the orbital velocity. Four orbital velocity data sets were selected from the Swart and Loubser study which have roughly similar initial wave conditions (H/d , T_c) and for which the bed slope varies between 0 and 1 in 20. Although the covocoidal orbital velocity shows some improvement over vocoidal theory, particularly as far as the variation of orbital velocity under the wave trough with distance from the bed is concerned, the improvement expected in the absolute value of the orbital velocity did not materialise (see Figure 7). Nevertheless, the overall correspondence with the data is satisfactory. To improve the inconclusiveness as far as orbital velocity prediction is concerned, emphasis should be placed on gathering high quality orbital velocity data, preferably in the field to eliminate the introduction of spurious mass transport, for a range of bed slopes.

5. CONCLUSIONS

- A new wave theory, the so-called covocoidal wave theory, was derived from first principles and is valid for all non-breaking waves on a mildly sloping bottom.
- No simplifying assumptions were made and the finite amplitude condition was preserved. Some approximation was, however, introduced because the numerical results were represented by means of curve-fitted expressions to facilitate easier application.

- The **analytical validity** of the theory was established to be as good as or better than the better, commonly-used horizontal bed wave theories, by virtue of the fact that the theory adheres exactly to the KFSBC and to continuity and has a minimised error in the DFSBC which was shown to not differ statistically from vocoidal theory (for $\tan\alpha=0$) at the 95 per cent confidence level.
- **Experimental validity** was established primarily by comparison of theoretical predictions with an extensive data set collected by Nelson (1981) to establish the effect of bottom slope on wave profile parameters and wave celerity. Indications on the prediction of orbital velocity are inconclusive due to the lack of appropriate data.
- The new **covocoidal theory** can serve as basis for the study of a variety of wave processes on a sloping bed outside the breaker zone.

REFERENCES

- BAILLARD, J. A. (1982) Modelling on-offshore sediment transport in the surf zone; Proceedings, 18th ICCE, Cape Town.
- BLEACH, G.P. (1982) Integral properties for vocoidal theory and applications, proceedings, 18th ICCE, Cape Town.
- HATTORI, M. (1986) Experimental study on the validity range of various wave theories; Proceedings, 20th ICCE, Taipei.
- Le MEHAUTE, B., DIVOKY, D, and LIN, A (1968) Shallow water waves: a comparison of theories and experiments; Proceedings, 11th ICCE, pp 86-107.
- STIVE, M.J.F. (1986) A model for cross-shore sediment transport; Proceedings, 20th ICCE, Taipei.
- SWART, D.H. (1978) Vocoidal water wave theory, Volume 1: Derivation; CSIR Research Report 357, 138pp.
- SWART, D.H. and LOUBSER, C.C. (1978) Vocoidal waves for all non-breaking waves; Proceedings, 16th ICCE, Hamburg
- SWART, D. H. and LOUBSER, C.C. (1979) Vocoidal water wave theory, Volume 2: Verification; CSIR Research Report 360, 130pp.
- SWART, D.H. (1982) The nature and analysis of random waves in shallow water. CSIR Research Report 388/1 and 2; 58pp.
- SWART, D.H. (1987) CAESAR: Coastal area environmental and sediment applied research: Surf zone experiments in South Africa; Proceedings, Workshop on Surf Zone Measurements SOGREAH, Grenoble, France.
- SWART, D.H. (1988) First-order solution for water waves on a sloping bottom; to be submitted.

TABLE I: Equations for determination of r_a and h_a

G_a	$= 0.16 (H/d)^{0.77}$...(I. 1)
G_b	$= 5 \tan \alpha$...(I. 2)
G_c	$= 0.15 (H/d)^{0.5}$...(I. 3)
G_d	$= 0.28 (H/d)^{-0.42} + 1.6$...(I. 4)
G_e	$= 1 + \{ \ln [2.04 (H/d)^{-1/16}] \}^{1.0}$...(I. 5)
G_f	$= G_e \exp[-G_d \exp(-G_c T_c)]$...(I. 6)
G_g	$= 0.48 (1 - \exp(-48H/d))$...(I. 7)
G_h	$= G_f G_g$...(I. 8)
G_i	$= 1 - \exp(-22(\tan \alpha)^{0.5})$...(I. 9)
G_j	$= (G_h - G_a) G_i$...(I. 10)
G_k	$= G_j + G_a G_b$...(I. 11)
G_l	$= 0.03 \ln(\tan \alpha) + 0.275$...(I. 12)
G_m	$= 0.424 + 0.0128(\tan \alpha)^{-0.6}$...(I. 13)
G_n	$= \begin{matrix} 1 & \text{for } H/d < 0.5 \\ G_l (H/d - 0.5) G_m - 0.1 & \text{for } H/d > 0.5 \end{matrix}$	
If $G_n > 1$	then $G_n = 1$(I. 14)
r_a/h_a	$= G_k G_n$...(I. 15)
F_a	$= 0.66 + 0.065(\ln P)^{0.5}$...(I. 16)
F_b	$= 1 + 1.375P^{-F_a}$...(I. 17)
F_e	$= -0.92(\ln P)^{0.25} + 1.82$...(I. 18)
F_d	$= 1 + 0.2584 \exp(-0.353(P-1)^{F_e})$...(I. 19)
$r_a + h_a$	$= 1 + F_b (r_a/h_a)^{F_d}$...(I. 20)
r_a and h_a are then found from equations (I. 15) and (I. 20)		

TABLE IIa: Typical values for r_{α}

	.01	.02	.05	.10	.20	.50	1.00
1.0	.01	.0061	.0153	.0296	.0325		
	.02	.0068	.0168	.0325	.0362		
	.05	.0077	.0186	.0362	.0417		
	.10	.0089	.0207	.0404	.0468		
2.0	.01	.0067	.0167	.0333	.0386	.0345	
	.02	.0074	.0183	.0365	.0428	.0392	
	.05	.0083	.0202	.0403	.0485	.0477	
	.10	.0095	.0223	.0446	.0557	.0598	
5.0	.01	.0084	.0213	.0456	.0589	.0650	.0634
	.02	.0092	.0233	.0498	.0647	.0722	.0727
	.05	.0102	.0253	.0541	.0714	.0821	.0899
	.10	.0115	.0275	.0585	.0789	.0942	.1153
10.0	.01	.0117	.0302	.0697	.0991	.1244	.1531
	.02	.0127	.0329	.0758	.1082	.1364	.1695
	.05	.0139	.0353	.0813	.1169	.1494	.1909
	.10	.0151	.0375	.0860	.1250	.1630	.2172
20.0	.01	.0198	.0526	.1294	.1904	.2406	.2810
	.02	.0215	.0570	.1403	.2065	.2613	.3066
	.05	.0231	.0604	.1485	.2192	.2789	.3327
	.10	.0243	.0628	.1538	.2280	.2929	.3586
50.0	.01	.0579	.1470	.3161	.3954	.4097	.3697
	.02	.0625	.1586	.3410	.4266	.4426	.4017
	.05	.0656	.1661	.3571	.4475	.4669	.4312
	.10	.0672	.1693	.3636	.4574	.4816	.4573

TABLE IIb: Typical values for h_{α}

	.01	.02	.05	.10	.20	.50	1.00
1.0	.01	.9978	.9971	.9987	.9994		
	.02	.9977	.9971	.9994	1.0003		
	.05	.9975	.9972	1.0002	1.0018		
	.10	.9974	.9974	1.0014	1.0040		
2.0	.01	.9977	.9971	.9995	1.0008	.9997	
	.02	.9976	.9972	1.0003	1.0020	1.0010	
	.05	.9974	.9974	1.0013	1.0038	1.0035	
	.10	.9973	.9976	1.0026	1.0064	1.0079	
5.0	.01	.9974	.9974	1.0023	1.0063	1.0077	1.0066
	.02	.9973	.9976	1.0037	1.0084	1.0104	1.0096
	.05	.9972	.9979	1.0051	1.0111	1.0144	1.0159
	.10	.9971	.9982	1.0067	1.0142	1.0198	1.0261
10.0	.01	.9970	.9983	1.0092	1.0196	1.0256	1.0216
	.02	.9970	.9988	1.0116	1.0233	1.0298	1.0247
	.05	.9969	.9993	1.0137	1.0269	1.0343	1.0289
	.10	.9969	.9998	1.0157	1.0304	1.0391	1.0339
20.0	.01	.9970	1.0033	1.0250	1.0291	1.0225	1.0081
	.02	.9971	1.0046	1.0282	1.0323	1.0248	1.0090
	.05	.9972	1.0057	1.0308	1.0348	1.0267	1.0099
	.10	.9973	1.0065	1.0324	1.0365	1.0282	1.0108
50.0	.01	1.0053	1.0175	1.0210	1.0132	1.0059	.9999
	.02	1.0062	1.0193	1.0228	1.0144	1.0064	1.0001
	.05	1.0069	1.0205	1.0239	1.0151	1.0069	1.0003
	.10	1.0072	1.0210	1.0244	1.0154	1.0071	1.0005

TABLE III: Equations for determination of K_{c1a}

q_a	= K_{c1a} (from equation (24) for $M/d = 0.1$)	... (III.1)
q_b	= $1.63 q_a T_c^{-1.44}$... (III.2)
q_c	= $0.21 q_a$... (III.3)
If $q_b > q_c$ then $q_b = q_c$... (III.4)
q_d	= $v \left(\frac{v_a}{h_a} \right)^{0.5}$... (III.5)
q_e	= $\exp[-4.3(P_1-1)]$... (III.6)
where P_1 is defined in the Appendix		
q_f	= $q_b q_d$... (III.7)
If $q_f < q_e$ then $q_f = q_e$... (III.8)
K_{c1a}	= q_f	... (III.9)

TABLE IV: Equations for determination of $q_{\infty}/(c(d+a))$

R_a	= $0.9(1 - \exp(-0.528 T_c^{R_b}))$... (IV.1)
R_b	= $0.26 - 0.14 \cos(0.05 \cdot T_c)$ (for $T_c < 20$) 0.40 (for $T_c > 20$)	... (IV.2)
R_c	= $R_d (M/H_b) + R_e (M/H_b)^2 + R_f (M/H_b)^3$... (IV.3)
R_d	= $0.795 (1 - \exp(-0.044 T_c))$... (IV.4)
R_e	= $0.45 + 0.75 (\cos^2(0.005 \cdot T_c))^2 - 0.0043 T_c$... (IV.5)
R_f	= $-0.75 (\cos^3(0.005 \cdot T_c/200))^2 - 0.13$	
R_g	= $1 - \exp(-0.046 T_c)$... (IV.6)
R_h	= $12 \times 10^{-3} (M/H_b) - 10 \times 10^{-3} (M/H_b)^{1.5}$... (IV.7)
R_i	= $R_h R_g$... (IV.8)
R_j	= $16.12 + \ln(\tan \alpha + 10^{-2})$... (IV.9)
R_k	= $R_i R_j$... (IV.10)
R_l	= $R_c R_d / (R_d + R_g + R_f)$... (IV.11)
R_m	= $R_l - R_k$... (IV.12)
$\frac{q_{\infty}}{c(d+a)}$	= $R_m \tan \alpha$... (IV.13)

APPENDIX A: Expressions for wave profile, orbital velocity and celerity parameters in Vocoidal theory (Swart, 1978 and Swart, 1988)

Wave profile parameter

$$\eta/H = \text{voc}(F, X) - \eta_{st} \quad \dots (A.1)$$

$$\text{voc}(F, X) = H \left[\cos^2 \left(\frac{\pi}{X} \right) \right]^F \quad \dots (A.2)$$

$$\eta_{st} = (\pi F)^{-0.5} \{ 1 - (8F)^{-1} + (8F)^{-2} - (8F)^{-3} \} \quad \dots (A.3)$$

$$F = R_p F_1 \quad \dots (A.4)$$

$$R_p = R_{p1} - (R_{p1} - 2) \exp \left(\frac{b}{d_1} \right) \quad \dots (A.5)$$

$$R_{p1} = 1 + 0.0021 (P_{11} - 1) + 6.09 \times 10^{-7} (P_{11} - 1)^{2.56} \quad \dots (A.6)$$

$$b = -0.0916 + 2.718 \times 10^{-3} P_{11} \quad \dots (A.7)$$

$$P_1 = \begin{cases} P_{13} & \text{for } F_g < -1.1 \\ P_{13} + 5 (P_{12} - P_{13}) (F_g + 1.1) & \text{for } -1.1 < F_g < -0.9 \\ P_{12} & \text{for } F_g > -0.9 \end{cases} \quad \dots (A.8)$$

$$P_{13} = \begin{cases} P_{10} & \text{for } P_{11} < P_{10} \\ P_{11} & \text{for } P_{11} > P_{10} \end{cases} \quad \dots (A.9)$$

$$P_{10} = 1 + 0.05 U_c \quad \dots (A.10)$$

$$U_c = \left(\frac{H}{d} \right) \left(\frac{\lambda}{d} \right)^2 \quad \dots (A.11)$$

$$P_{11} = a_1 + b_1 U_c \quad \dots (A.12)$$

$$a_1 = -0.133 - 1.767 \left(\frac{H}{d} \right) + 0.00248 \exp \left(8.33 \left(\frac{H}{d} \right) \right) \quad \dots (A.13)$$

$$b_1 = 0.1672 - 0.112 \left(\frac{H}{d} \right) \quad \dots (A.14)$$

$$P_{12} = 1.03 F_g + 9 + 3.33 \exp \{ -0.109(11 + F_g) \} \quad \dots (A.15)$$

$$P_1 = 1 \text{ when } F_g < -11 \text{ or when } P_1 < 1 \text{ according to the above.}$$

$$F_g = (U_c - U_{co}) / \theta \quad \dots (A.16)$$

$$U_{co} = 63 + 90 \left(\frac{H}{d} \right)^{-0.28} \quad \dots (A.17)$$

$$\theta = \begin{cases} 1.01 \exp \left\{ 3.31 \left(\frac{H}{d} \right) \right\} & \text{for } H/d \geq 0.505 \\ 5.38 & \text{for } H/d < 0.505 \end{cases} \quad \dots (A.18)$$

$$P_{11} = P_1 \text{ where } \frac{\lambda}{d} = 50 \text{ and } H/d = H/d \quad \dots (A.19)$$

Orbital velocity parameter

$$\frac{u}{c} = \frac{u(X) k \cosh \left[\frac{H(X) k z}{d+h} \right]}{\sinh \left[\frac{H(X) k (d+h)}{d+h} \right]} \quad \dots (A.20)$$

$$H(X) = \begin{cases} (M_c - M_t) \left[\cos \left(\frac{\pi}{2} \right) \right] + M_t & \text{for } r_1 P_1 < 0.5 \\ M_c \operatorname{voc} (r_1 P_1, X) & \text{for } r_1 P_1 \geq 0.5 \\ M_c & \text{for } P = 1 \end{cases} \quad \dots (A.21)$$

$$r_1 = 0.4 (1 - P_1^{-0.5}) \quad \dots (A.22)$$

$$M_c = R_H M_{c1} \quad \dots (A.23)$$

$$M_{c1} = \begin{cases} [P/(2 n_{oc1})]^{0.5} & \text{for } H/d \leq 0.7 \\ [P_1/(2 n_{oc1})]^{0.5} & \text{for } H/d > 0.7 \\ & H/d=0.7 \end{cases} \quad \dots (A.24)$$

$$R_H = \begin{cases} \frac{0.54}{1 + 6.7 \left(\frac{H}{d} \right)} + 0.46 & \text{for } \frac{H}{d} \leq 0.7 \\ 0.667 & \text{for } \frac{H}{d} > 0.7 \end{cases} \quad \dots (A.25)$$

$$M_t = R_H \exp \{ -4.2 (P_1 - 1) \} \quad \dots (A.26)$$

Wave celerity parameter

$$\frac{c^2}{gd} = \left(\frac{1}{k d} \right) \tanh k d \quad \dots (A.27)$$

$$N = \begin{cases} R_n N_1 & \text{for } R_n N_1 < 1 + n_c/d \\ 1 + n_c/d & \text{for } R_n N_1 > 1 + n_c/d \end{cases} \quad \dots (A.28)$$

$$R_n = \begin{cases} 0.67 f_a + 0.938 & \text{for } f_a > 0.093 \\ 1 & \text{for } f_a < 0.093 \end{cases} \quad \dots (A.29)$$

$$f_a = \left(\frac{H}{d} \right) \left(\frac{1}{d} \right)^{-0.25} \quad \dots (A.30)$$

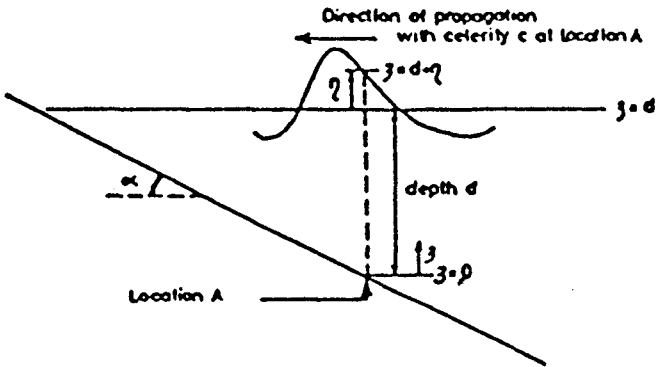
$$N_1 = \begin{cases} 1 + 0.19 f_b^{4.5} & \text{for } f_b < 0.72 \\ 0.72 f_b + 0.6 & \text{for } f_b > 0.72 \end{cases} \quad \dots (A.31)$$

$$f_b = \left(\frac{H}{d} \right) \left(\frac{1}{d} \right)^{0.1} \quad \dots (A.32)$$

$$n_c = H + n_t \quad \dots (A.33)$$

$$n_t = -n_{oc} H \quad \dots (A.34)$$

SPATIAL VIEW



**TEMPORAL VIEW
at Location A**

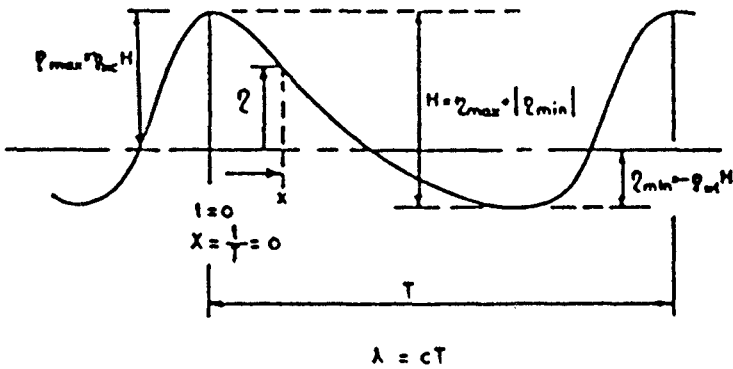


Figure 1: Axis-notation for development of generalised vocoidal theory on a sloping bottom.

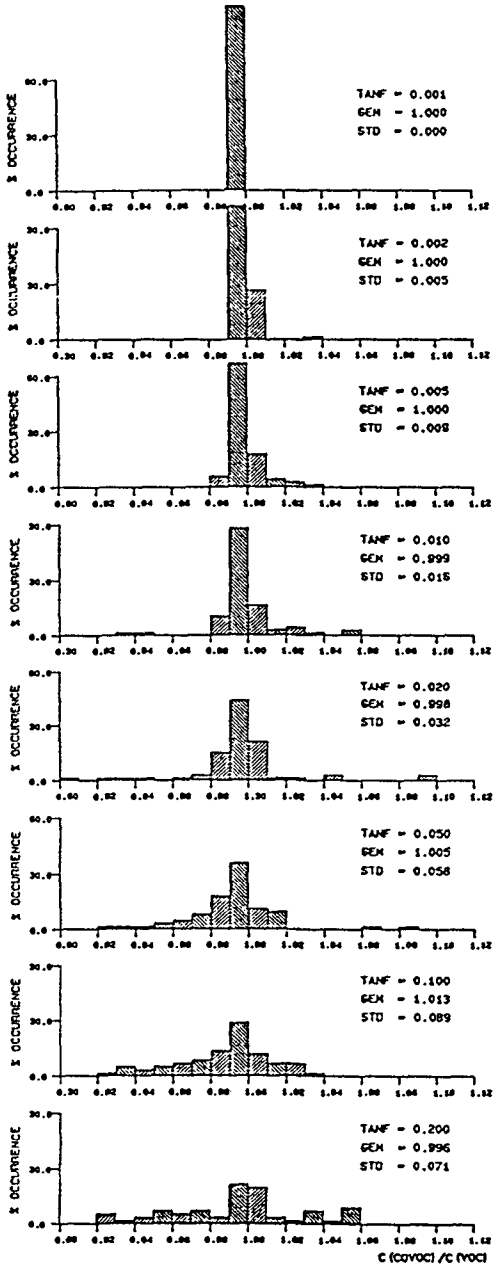


Figure 2: Distribution of the ratio of c^2/gd for a sloping bed to that for a horizontal bed for a slope of 1 in 5 and a range of initial conditions.

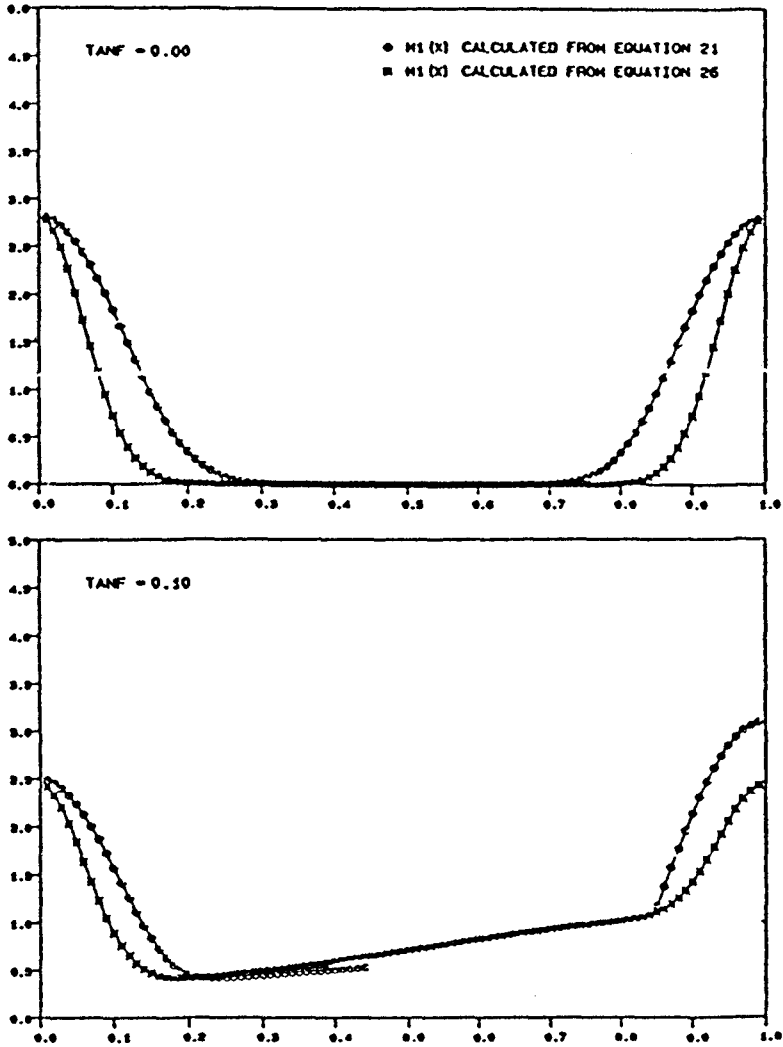


Figure 3: Typical, predicted variation of the orbital velocity parameter $M_1(X)$ for a horizontal bed and for a slope of 1 in 10 for waves with $H/d = 0.5$ and $T_c = 20$.

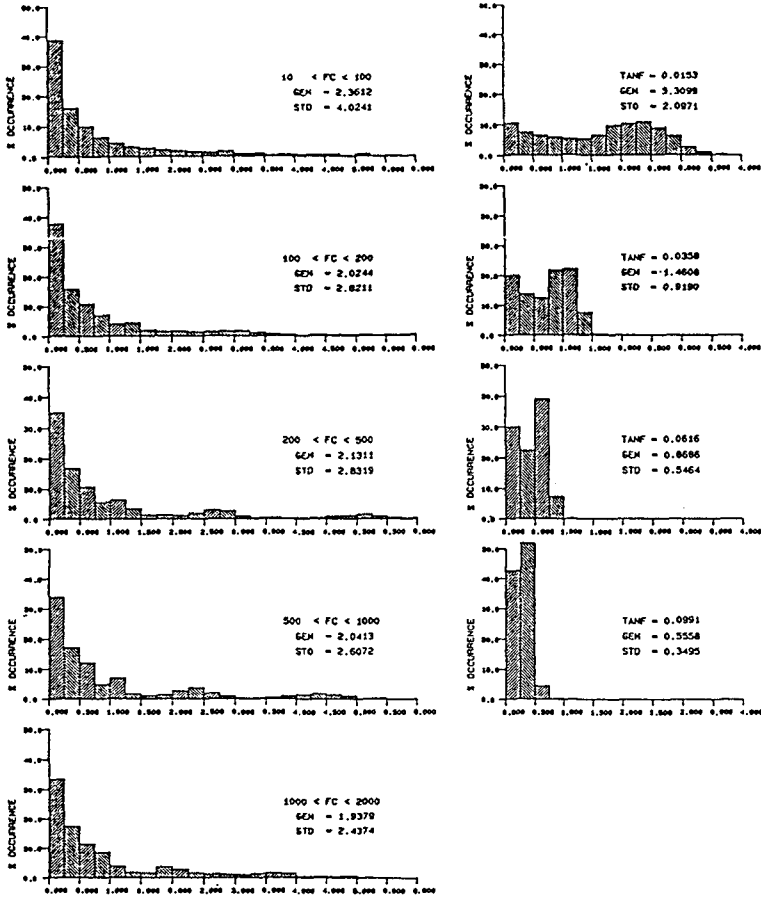


Figure 4: The error in the DFSBC for covocoidal theory for $\tan \alpha = 0.1$, and for vovoidal theory on a horizontal bed, for a range of nonlinearity parameter values.

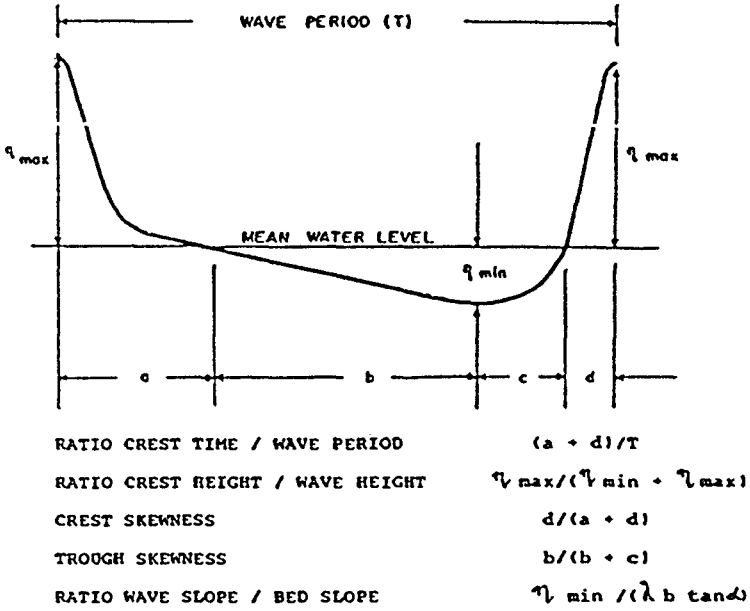


Figure 5: Definition sketch for wave parameters.

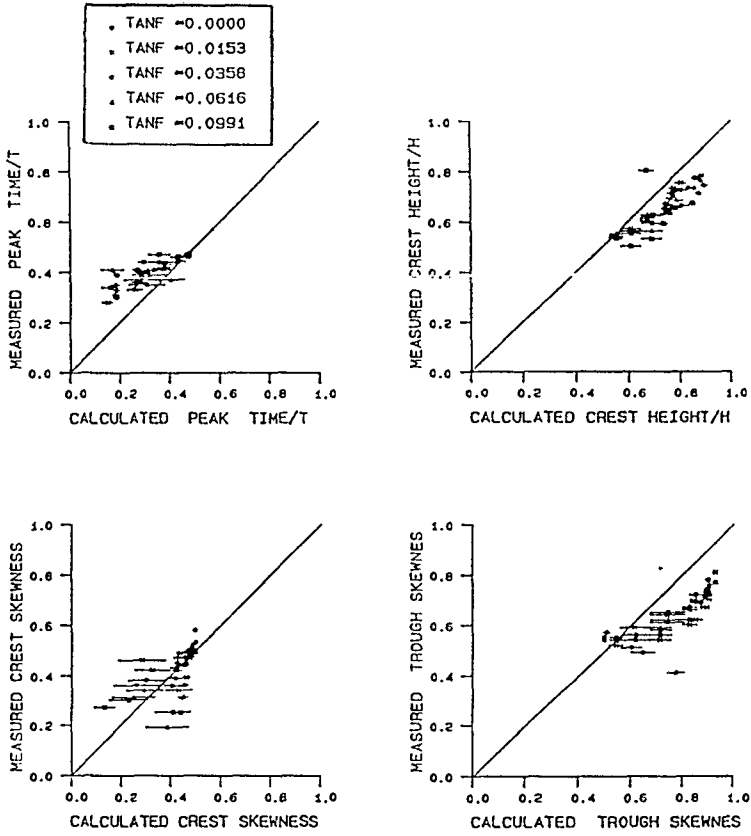


Figure 6: Comparison of predicted and observed wave parameters according to definitions in Figure 5 for a range of nonlinearity parameter values and bed slopes.

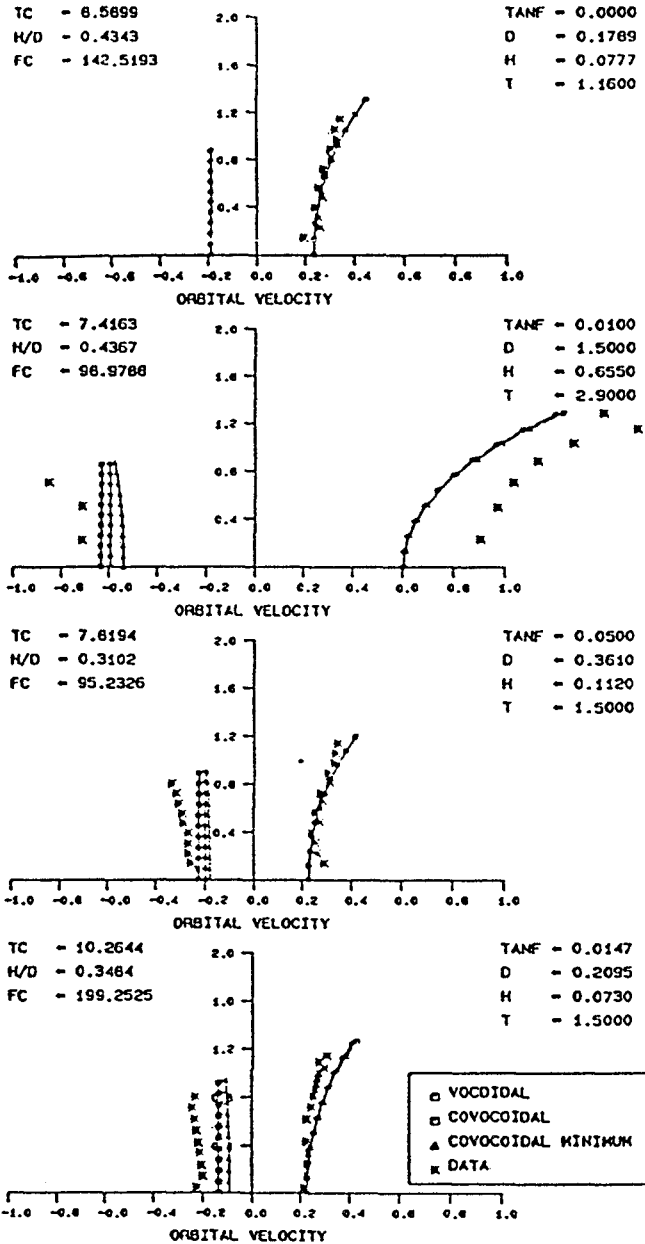


Figure 7: Comparison of predicted and observed horizontal orbital velocities under the wave crest for a range of bottom slopes and $F_c \sim 100$; $T_c \sim 8$, $H/d \sim 0.4$.

CHAPTER 13

Wave Groups on Wave Records Measured Along Spanish Shores

Adolfo Marón *

Abstract

A large amount of wave records measured at four different locations of the Spanish shores have been analysed from the point of view of wave group formation. The influence of wave climate and depth on the results is studied. The results are compared with existing theories for runs of waves, SIWEH and envelope functions. Characteristics of extreme groups are also considered

1 Introduction

It is generally recognized the importance that the presence of wave groups can have in the behaviour of coastal and offshore structures and consequently many studies have been carried out trying to determine the grouping characteristics of ocean waves.

As a consequence of these studies, different theories have been proposed to explain the formation of groups among wind generated waves. These theories try to relate the groupiness characteristics observed in the waves with other better known wave properties (spectral parameters, zero crossing statistics and others).

All of them could be divided into two main groups: those which defend that the formation of groups can be explained by pure linear interactions and those which propose the contrary. No definitive conclusion has been reached yet (Marón, 1986).

Among the linear methods we have selected those corresponding to the statistics of runs of high waves (Goda, 1976 and Kimura, 1980), the SIWEH function (Funke & Mansard, 1980) and the envelope theory (Longuet-Higgins, 1984) as well as different modifications introduced by several authors. Most of the studies have deal with simulated records and only a few have analysed measured records and generally not in a systematic basis.

For this study we have implemented a computer program which calculates all the parameters for wave groupiness proposed in the previously mentioned works as well as others relating to extreme events which we think that can be of

(*) Programa de Clima Marítimo y Banco de Datos Oceanográficos. P^a de la Castellana n^o 16 - 5^a Dcha. 28046 Madrid Spain. Tel: 34.1.431 28 99

interest in design. This program was run on a large amount of wave records measured in four different locations of the Spanish shores by means of moored waverider buoys.

We intended in this way to evaluate the ability of the different theories to predict the observed results. At the same time we tried to see if the groupiness characteristics were affected directly by local maritime climate factors or in the contrary they only depend on spectral and/or statistical wave properties independently of site.

Finally, one of the buoys was moored in relatively shallow waters and therefore it can give us some indication on how shoaling could affect the group behaviour.

2 Description of wave data

The main characteristics of the four buoys used in the analysis are presented in Table I.

TABLE I
MAIN BUOY CHARACTERISTICS

Buoy	Net	Sea	Depth	No. of points	No. of records
BILBAO	REMRO	Cantabric	50	5120	2605
CARTAGEMA	REMRO	Mediterranean	70	5120	4420
SEVILLA-3	Special	Gulf of Cadiz	10	*	613
SEVILLA-4	Special	Gulf of Cádiz	38	*	1327

* Variable for each record between 675 to 1500.

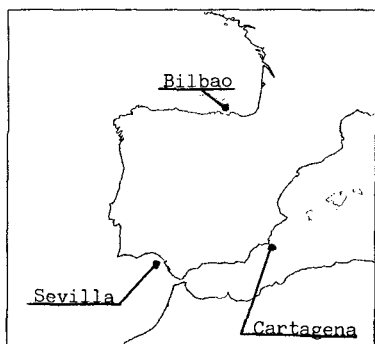


Fig. 1.- Buoy locations

Their locations can be seen in figure 1. Two of the buoys belong to the REMRO Net (Spanish Net for Wave Recording and Measurement) owned by the Spanish Port and Shore Authority. The other two buoys were deployed by the Sevilla Harbour Authority for a special campaign. The records from the first two buoys are specially adequate for group analysis because of their long length of 5120 points at a sampling rate of 2 Hz.

Regretfully the other two sets of records are of very short and variable length which increases the variance and the uncertainty in the results. Although they are not the best buoys for group analysis, they were the only available

case of two buoys in different depths but at very near positions.

The BILBAO buoy is located in a place characterized by strong storms and frequent presence of long swell coming from the North Atlantic. The CARTAGENA buoy is located in the Mediterranean Sea and therefore the waves are shorter and steeper than in the previous one, also the possibilities of swell are very reduced. The two SEVILLA buoys are moored in the Atlantic Ocean but due to their positions, they are protected from most of the swell and bigger storms.

A quality control program has been applied to all the records in the study. Any record considered incorrect or suspected to be so was rejected for the analysis. A correction to allow for the transfer function of the buoy electronics was applied to the records. This transfer function affects mainly the phases of the Fourier components of the wave record and therefore it can have a great influence in the results as far as groupiness is concerned.

3 Statistics of runs of high waves

The length of a run of high waves (R) is the number of consecutive waves that are higher than a given threshold. The corresponding length of group (L) is the number of consecutive waves from the beginning of a run to the beginning of the next one. The wave height is defined by the zero upcrossing method rejecting waves lower than 10% of the standard deviation or shorter than one second.

Goda (1976), assuming no correlation between consecutive wave heights, proposed the following distributions for R and L:

$$R(i) = Pr(R = i) = P_0^{i-1} Q_0 \quad L(i) = Pr(L = i) = \frac{P_0 Q_0}{P_0 - Q_0} (P_0^{i-1} - Q_0^{i-1})$$

where P_0 and Q_0 are the exceedence and nonexceedence probabilities for the given threshold. As a consequence the respective mean values are given by:

$$R = \frac{1}{Q_0} \quad L = \frac{1}{P_0} + \frac{1}{Q_0}$$

The exceedence probabilities can be estimated theoretically by assuming a Rayleigh distribution for the wave heights.

As an example, figure 2 compares these theoretical results with the measured mean distributions for R and L for the threshold at the mean wave height and for records with wave height correlations below 0.1 and between 0.4 and 0.5. Here and in the following the curves give the theoretical values, the solid dots are the results for BILBAO, the open

dots the results for CARTAGENA, the solid squares are those of SEVILLA-3 and the open squares those of SEVILLA-4.

Mean distribution of runs & groups for hmean

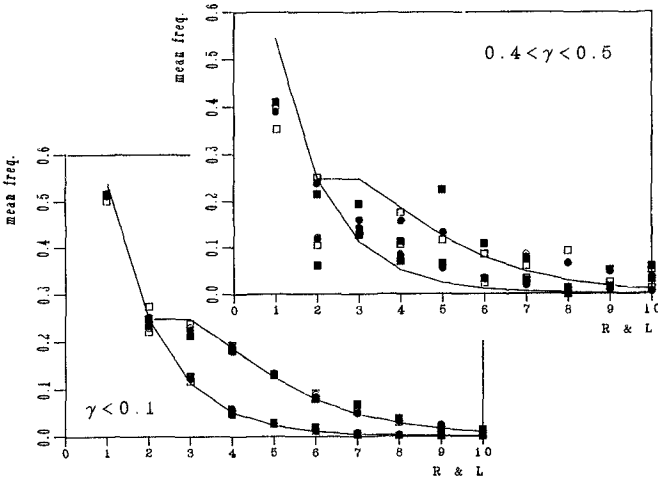


Fig.2.- Mean distributions of group and run length, compared with Goda's theory.

It can be seen that the theory is quite good for records with low or no correlations but the lengths are underpredicted for records with high correlations, results which are coincident with those from other authors. The comparisons when other thresholds are considered are very similar.

It should be kept in mind that these and the following results are in general accompanied by a big dispersion about the mean, specially for the shorter records of the SEVILLA buoys, but these dispersions are not considered in this study for simplicity.

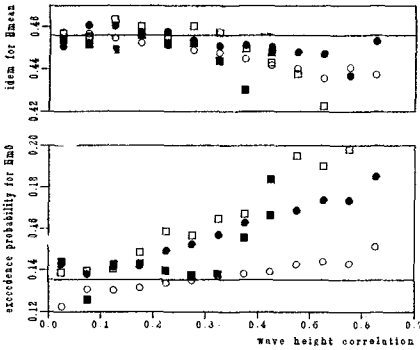
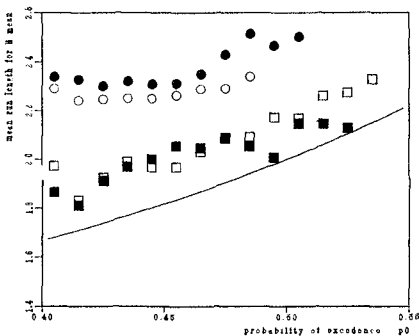


Fig.3.- Probability of exceedence as a function of wave height correlation, compared with Rayleigh distribution.

The differences with the theory for records with high correlations could be due to the simplifying assumptions but also to the fact observed in the records that the Rayleigh distribution is not completely correct when the correlation be-



tween successive wave heights is high. In figure 3, it can be seen that the exceedence probabilities are overpredicted for the mean height and underpredicted for the significant wave height at high correlation values.

Fig.4. Mean run and group length.

Anyway, figure 4 indicates that the errors in Goda's formulation can not be explained by this feature because the results are far from the theory even when the probabilities estimated from the records are used. This is specially true for the BILBAO and CARTAGENA buoys which happens to be the ones measuring higher correlations.

Kimura (1980) introduced the correlation between successive wave heights in the formulation, resulting in the following equations:

$$R(i) = (1 - P_{22})P_{22}^{i-1} \qquad L(i) = (1 - P_{11})(1 - P_{22}) \frac{P_{11}^{i-1} - P_{22}^{i-1}}{P_{11} - P_{22}}$$

Here the probabilities P11 and P22 are defined as:

$$P_{11} = Pr(H_i \leq H_0 | H_{i-1} \leq H_0) \qquad P_{22} = Pr(H_i > H_0 | H_{i-1} > H_0)$$

and H_0 is the threshold considered. These probabilities can be calculated assuming a two dimensional Rayleigh distribution for the joint distribution of successive wave heights. This distribution depends on a shape parameter k which can be related to the statistical or spectral properties of the records in different ways. In this study three different formulations have been investigated: Uhlenbeck (1943) equation relating the correlation between successive wave heights and the shape parameter, Longuet-Higgins (1984) relation between k and the spectral shape and Battjes (1983) equation based in the correlation between the squares of the wave heights. The comparisons between them have shown some superiority for the first approach in predicting the results although the differences are not very important. In the following the first equation is used.

Figures 5 and 6 compare Kimura's theory with the measurements for two different thresholds. Here two theoretical curves are plotted for each distribution, corresponding to the lower and upper bound of the

correlation. The agreement is very good except for the SEVILLA's buoys at high correlation but this is due to the fact that only a small number of records has been found with this correlation values and therefore the statistical variability is very high.

Mean distribution of runs & groups for hmean

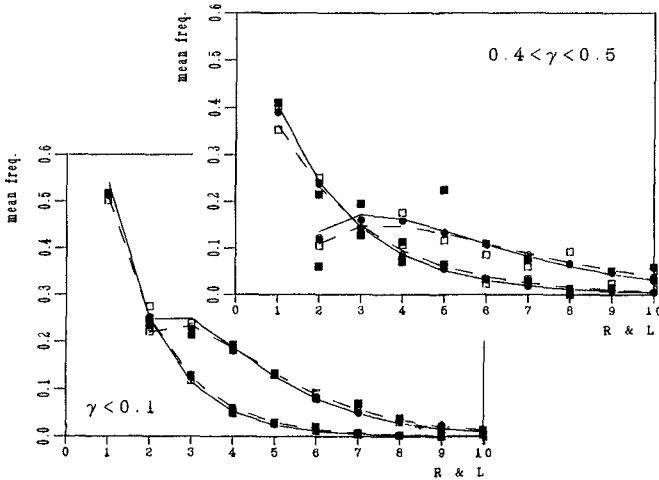


Fig.5.- Mean distributions of group and run length for Hmean, compared with Kimura's theory. Upper plot is for high correlation and lower plot is for low correlation values.

Mean distribution of runs & groups for hm0

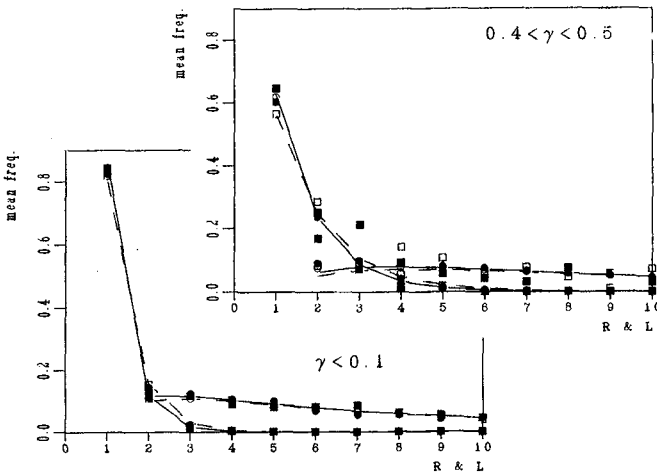


Fig.6.- Same as figure 5 but for Hm0.

The mean run and group length can be calculated from the given distributions:

$$\bar{R} = \frac{1}{1 - P_{22}}$$

$$L = \frac{1}{1 - P_{11}} + \frac{1}{1 - P_{22}}$$

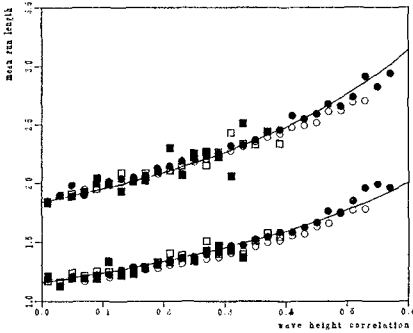


Fig.7.- Mean run length compared with Kimura's theory. Upper curve is for H_{m0} and lower if for H_{mean} .

These are compared with the results in figures 7 and 8. The agreement is very good except for a small overprediction of the mean group length at the significant level. This could be due to an overprediction of P_{11} at this level. The error is in any case below 10%.

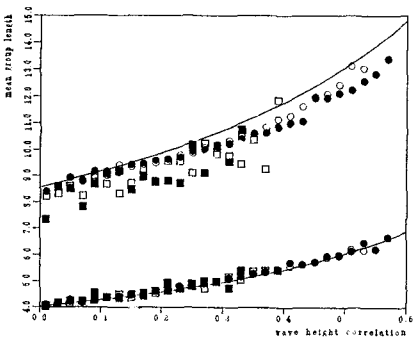


Fig.8.- Mean group length compared with Kimura's theory. Lower curve is for H_{mean} and upper is for H_{m0} .

Ewing (1973) gave another formulation for the mean run length based in the envelope theory and whose main result can be written as:

$$\bar{R} = \sqrt{\frac{m_2}{2\pi\mu_2}} \frac{2\sqrt{m_0}}{H_0}$$

where the m_i are the spectral moments of order i , μ_2 is the second order central moment of the spectrum and H_0 is the threshold level. Here the length of run is counted in a continuous basis and should be corrected for discrete counting in order to be comparable with the zero crossing measurements. This can be done by using the following relationship:

$$\bar{R} = \frac{1}{1 - \exp(-\frac{1}{\bar{R}})}$$

From the previous equation an asymptotic expression valid for narrow banded spectra can be found:

$$\bar{R} = Q_p \sqrt{\frac{2m_0}{H_0}}$$

$$Q_p = \frac{2}{m_0^2} \int_0^\infty f S(f)^2 df$$

Where Q_p is the peakedness parameter proposed by Goda.

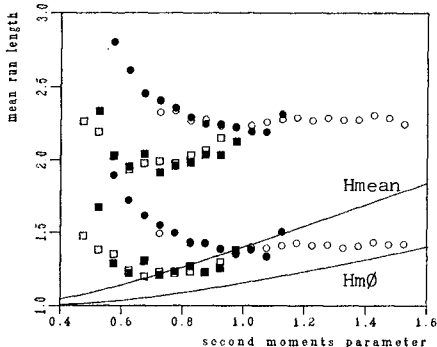


Fig. 9.- Comparison with Ewing's equation

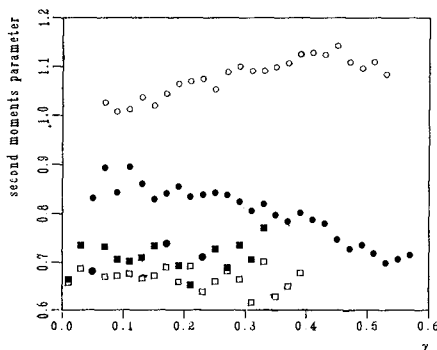


Fig. 10.- Ewing's parameter vs. correlation.

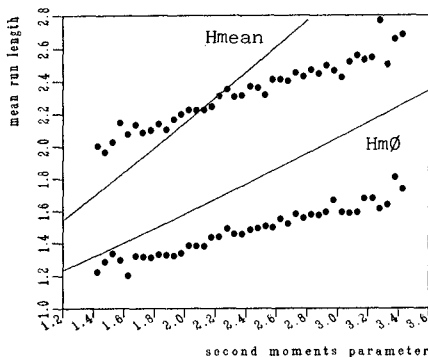


Fig. 11.- As figure 9 but for filtered records.

Figure 9 gives the measured values plotted against the first factor of Ewing's equation. The results compare very bad with the theory and are quite different for each buoy. This can be explained by the fact that the parameter considered is uncorrelated with the wave height correlation as can be seen in figure 10. Another evidence of this is that if one computes this factor for a Jonswap spectrum the result is independent of the peak enhancement factor while it is clear that more peaked spectra give longer runs.

If one filters the records (see the envelope section later in the paper) the correlation between the measurements and Ewing's factor is much better but still far from the theory (figure 11).

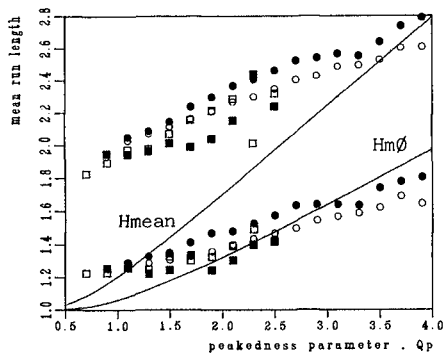


Fig.12.- Comparison with Ewing's asymptotic equation.

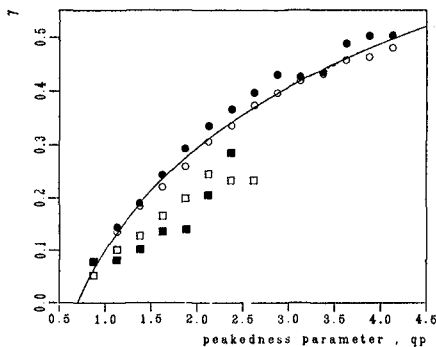


Fig.13.- Relationship between Q_p and correlation.

This is specially so for the BILBAO and CARTAGENA buoys which are the more reliable ones. The relation for these two buoys can be approximated by:

$$y = 0.28 \ln Q_p + 0.10$$

4 Analysis of SIWEH function

Funke & Mansard (1980) proposed the SIWEH function (Smoothed Instantaneous Wave Energy History) as a mean to recognize the presence of groups in the wave records. This function is obtained by convoluting the square of the signal with a triangular window of a width equal to the spectral peak period. In the present study the convolution is actually made in the frequency domain.

The same authors have proposed two parameters obtained from the SIWEH in order to characterize the group formation.

The asymptotic equation gives acceptable results only for high values of Q_p (figure 12). Here the Q_p calculated from the raw spectra have been corrected to account for the bias in the estimator (dividing by 2). It seems from the results that Ewing's theory will only be valid for spectra narrower than those found in nature.

Anyway, the peakedness parameter is a good indicator of groupiness as can be deduced from figure 13, where a good relationship is observed between it and the wave height correlation.

They are the groupiness factor and the mean SIWEH period which are given by:

$$GF = \frac{1}{m_0} \sqrt{\frac{1}{T_0} \int_0^{T_0} [E(t) - \bar{E}]^2 dt}$$

$$T_{SIWEH} = \frac{1}{T_p} \frac{1}{N_0} \sum_{i=1}^{N_0} T_{Si}$$

where $E(t)$ is the SIWEH function, \bar{E} its mean value, t_0 is the length of the records, T_p is the spectral peak period, N_0 is the number of zero upcrossings of the SIWEH and T_{Si} are the corresponding zero upcrossing periods.

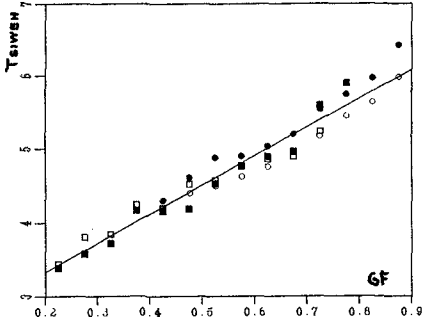


Fig.14.- SIWEH period/groupiness factor.

Figure 14 presents the observed relation between these two parameters. The result is the same for the four buoys and can be approximated by the straight line:

$$T_{SIWEH} = 3.92GF + 2.55$$

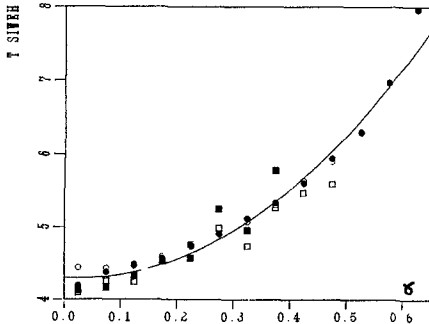


Fig.15.- SIWEH period/correlation.

Also the mean period of the SIWEH is related to the wave height correlation (figure 15) in a similar way for the four buoys which can be approximated by:

$$T_{SIWEH} = 8.7\gamma^2 - 0.45\gamma + 4.3$$

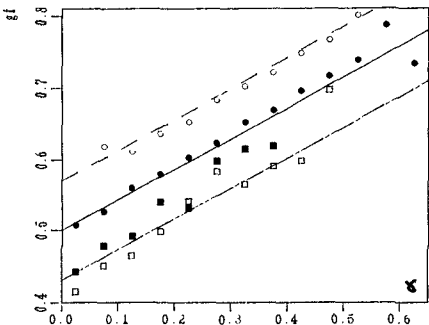


Fig.16.- Groupiness factor/correlation.

On the contrary, figure 16 indicates that the relationship between the groupiness factor and the correlation varies with the buoy considered. This relation approximates straight lines with the same slope but different inter-

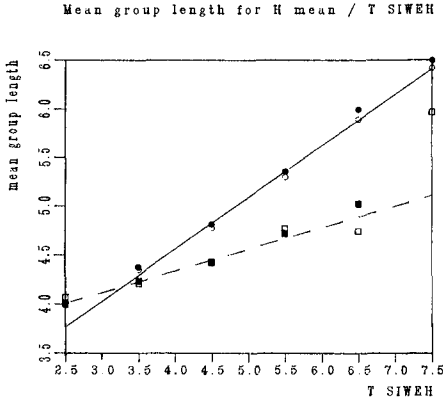


Fig.17.- SIWEH period/mean group Length.

Figure 17 indicates that a linear relation exists between these two quantities but again it depends on the buoy considered. The two SEVILLA buoys behave exactly in the same way and the same happens with BILBAO and CARTAGENA buoys.

5 The envelope function

The envelope of all the records has been computed by using the complex pre-envelope function. Following a recommendation by Longuet-Higgins (1978) the same has been made for filtered records obtained by suppressing all the frequencies in the raw signal below .5 the spectral peak frequency and above 1.5 the same frequency.

In the first place we looked at the effect of this filtering in the characteristics of the signal and we observed that while the total variance is only slightly reduced and other spectral and statistical parameters are not significantly changed, the spectral width suffers a drastic change.

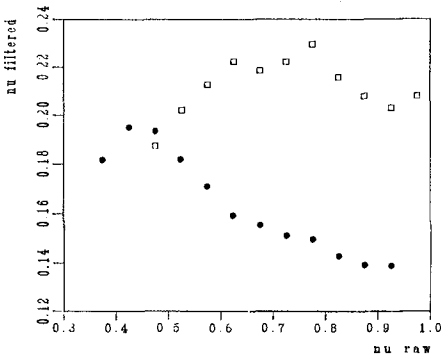


Fig.18.- Comparison between the bandwidth after and before filtering.

cepts for each buoy. Only the two SEVILLA buoys present a similar behaviour.

The mean SIWEH period is an indication of the length of group and therefore should be related to the mean length of groups obtained in the previous paragraph.

This will result in completely different group behaviours as predicted by the envelope theory. In figure 18 the bandwidth (measured by ν , defined later) after filtering is compared with the raw record value.

Both bandwidths are uncorrelated or even negatively correlated for the BILBAO buoy.

A level crossing analysis of the envelope has been performed at different levels. From it a mean run and group length can be computed. The theory predicts their values as given by:

$$\bar{R} = \frac{1}{\sqrt{2\pi}} \sqrt{\frac{1+\nu^2}{\nu}} \frac{2\sqrt{m_0}}{H_0} \quad \bar{L} = \frac{1}{\sqrt{2\pi}} \sqrt{\frac{1+\nu^2}{\nu}} \frac{2\sqrt{m_0}}{H_0} \exp\left(\frac{H_0^2}{8m_0}\right)$$

Here H_0 is two times the level considered and ν is a measure of the spectral bandwidth given by:

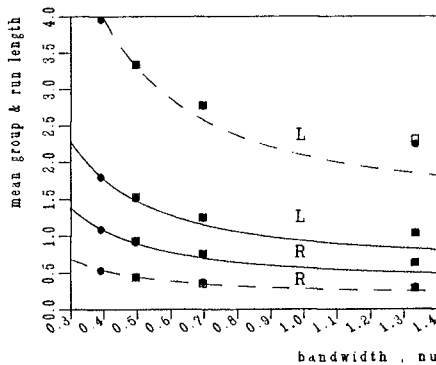


Fig.19.- Envelope results for raw records.

$$\nu = \sqrt{\frac{m_2 m_0}{m_1^2} - 1}$$

The results obtained for the raw and filtered records can be seen in figures 19 and 20. The continuous lines correspond to the level which is near the mean height and the dashed lines are for which is the significant height. The measurements agree very well with the theory except maybe in some cases for the SEVILLA buoys but this could be most probably due to the statistical variability. Only the mean group length at the significant level seems to be overestimated by the theory for this two buoys.

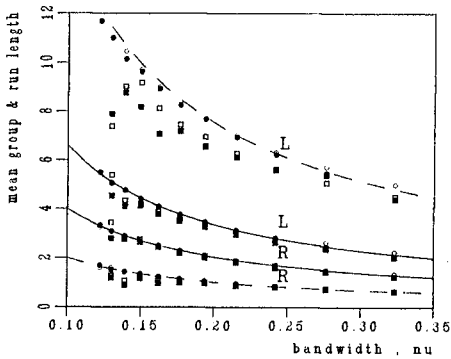
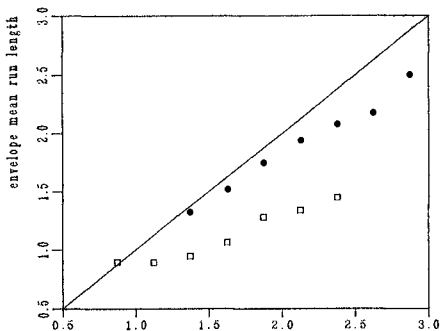


Fig.20.- Envelope results for filtered records.

A comparison of the results obtained with this procedure and those corresponding to the zero crossing

analysis was made. It was found that no relation is apparent between both results when the raw records are considered but



some correspondence is found if the filtered record envelopes are considered (figure 21) although it depends on the buoy selected. This fact seems to support the need of the filtering for the envelope analysis.

Fig.21.- Envelope/zero-crossing run length.

6 Longest group and run

Assuming that the kimura's distribution is correct, one can easily compute the theoretical distribution of the longest run and group in a record. These will be dependent on the number of runs present in the record and therefore on the mean group length and mean wave period for records of a fixed length.

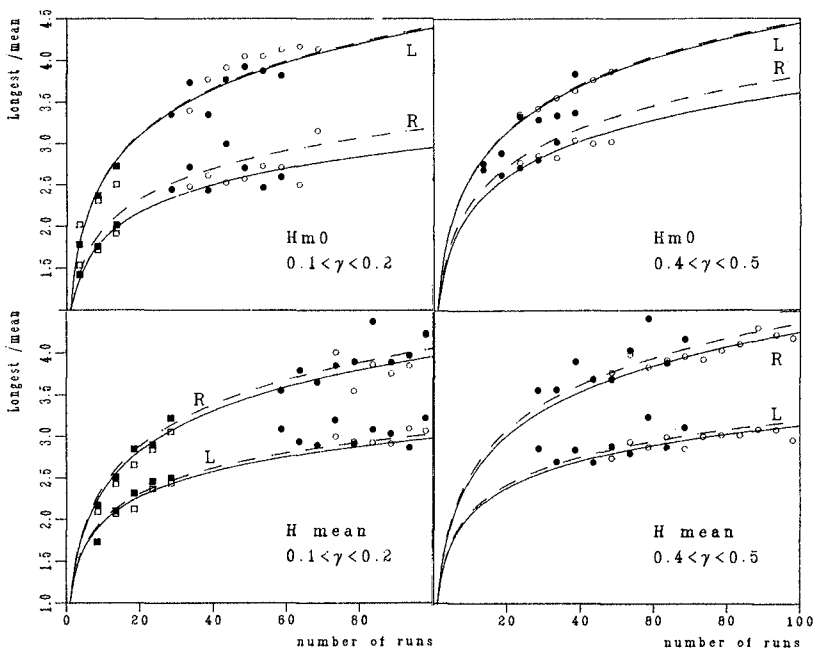


Fig.22.- Longest group and run for Hmean and Hm \emptyset and different correlations.

From these distributions the expected values can be estimated. Figure 22 presents the results obtained for the means of the longest run and group adimensionalized by the respective means compared with the values predicted by the theory. Two threshold levels have been considered. The theoretical values have been numerically approximated on the computer because no closed form was found for the resulting expressions. As the distribution depends on the wave correlation, the records have been grouped into classes of correlation and two cases are presented in the figure representative of low and high correlations. The two theoretical curves correspond to the lower and higher values of each class.

The agreement with the theory is quite good although the observed scattering is somewhat higher than in the previous results, but this is always to be expected when dealing with extreme order statistics.

7 Conclusions

- * The theory developed by kimura predicts very well the group behaviour of waves. The correlation between successive wave heights seems to be the best indicator of groupiness. Some discrepancies are found between the observations and the Rayleigh distribution for wave heights.
- * The formalations proposed by Ewing are not correct for the range of values observed in nature.
- * The groupiness factor and mean period of the SIWEH are good indicators of group characteristics but the results depend in some cases on the buoy considered and this is probably due to differences in the wave correlations at the different sites. Therefore, it seems that some information on groupiness is lost with these parameters.
- * The envelope theory performs quite well. A previous filtering of the signal seems to be needed in order to get results coherent with other analysis methods.
- * No significant difference was found between the buoys that could not be explained by differences in the correlation and therefore it can be concluded that the group formation is independent of the local maritime climate and depth variation for the depths considered here.

8 Acknowledgments

I want to thank professor H. Rye for introducing me in this field. This research is part of the work carried out by the "Programa de Clima Marítimo y Banco de Datos Oceanográficos" of the Spanish Authority of Ports and Shores.

9 References

FUNKE, E.R. and E.P.D. MANSARD. On the synthesis of realistic sea states. Proceedings 17th International Conference on Coastal Engineering, vol. 3, pp 2974-2991, 1980.

GODA, Y. On wave groups. Proceedings B.O.S.S., pp 115-127, 1976.

KIMURA, A. Statistical properties of random wave groups Proceedings 17th International Conference on Coastal Engineering, 1980.

LONGUET-HIGGINS, M.S. Statistical properties of wave groups in a random sea. Phil. Trans. of the Royal Society of London, A312, pp. 4117-4155, 1978.

MARON, A. Análisis de la formación de grupos de olas. (Analysis of wave group formation). Pub. Programa de Clima Marítimo, no. 9, 1986.

MEDINA, J.R. and R.T. HUDSPETH. Sea states defined by wave height/period functions. Proceedings of IAHR seminar on Wave Analysis and Generation in Laboratory Basins, pp. 249-260, Lausanne, 1987.

RYE, H Ocean wave groups. Ph. D. Thesis. Division of Marine Hydrodynamics, University of Trondheim, 1982.

CHAPTER 14

Are solitary waves the limiting waves in long wave runup ?

Costas Emmanuel Synolakis †, A.M., ASCE

This is a study of the maximum runup of single long waves on plane beaches. Laboratory data are presented that suggest that solitary waves attain the higher runup distances than other single long waves with identical generation characteristics, such as energy or momentum. These results suggest that solitary waves may provide a limiting condition for long wave runup on plane beaches.

1. Introduction.

The problem of determining the runup and reflection of long single waves usually arises in the study of the coastal effects of tsunamis. Tsunamis are long water waves of small steepness generated by impulsive geophysical events on the ocean floor or at the coastline. Solitary waves and cnoidal waves are believed to model important aspects of the coastal effects of tsunamis well and in the past twenty years there has been a large number of analytical, numerical and laboratory investigations studying the runup of solitary waves. There has been comparatively less attention paid to the runup of cnoidal waves. However, consensus has emerged that one suitable physical model for this process is the formalism of a long wave propagating over constant depth and encountering a sloping beach.

A comprehensive review of these results may be found in Synolakis (1986, 1987, 1988), where some basic questions—such as the analytical substantiation of empirical relationships—have been resolved. However a basic question still persists and it refers to the actual shape of tsunamis in nature which are rarely Boussinesq-solitary wave-like or cnoidal wave like. Therefore most analytical results have only been used to calibrate numerical codes which solve the equations of motion with more “realistic” and “tsunami-like” profiles and actual topographies.

Unfortunately there is little knowledge as to what constitutes a “realistic” tsunami profile for specifying boundary or initial conditions in numerical solutions. No data exist on the surface elevation of a tsunami at generation and little data exist on the elevation of tsunamis far from the source, although this is likely to change with the field implementation of the THRUSH program (Bernard, 1988).

† Assistant Professor, School of Engineering, University of Southern California, Los Angeles, California 90089-0242

The question then arises of whether it is useful to develop numerical schemes correct to many orders of approximation when realistic initial or boundary data do not exist. One could argue that the details of the wave at generation may not be very important in the eventual propagation process and the coastal effects; it is well established that long waves fission after sufficient propagation distances into series of solitary waves. However, then the process can be described relatively well analytically.

In this paper, I will report some preliminary data that address this question in particular. I will describe a series of laboratory experiments which suggest that although the details of the wave at generation are important in estimating the coastal effects at finite distances, it is possible to use solitary wave theory to obtain a limiting condition for long wave runup.

2. Basic phenomenology and dimensional analysis.

Consider the two-dimensional topography consisting of a constant depth region of depth d encountering a plane sloping beach of angle β . This is the model most frequently used in calibrating numerical codes and it is only appropriate to check its sensitivity to different initial conditions. The topography is shown in figure 1.

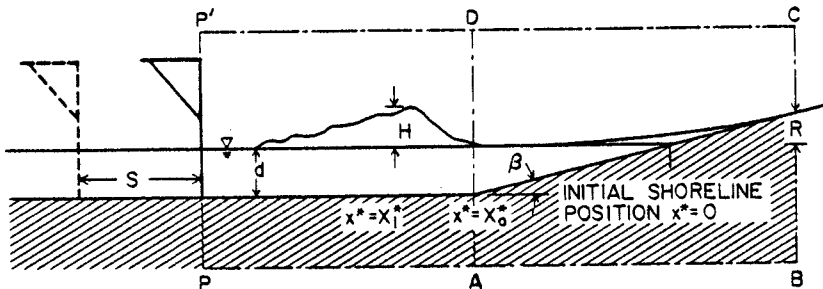


Figure 1. A definition sketch for long wave runup.

Waves will be generated with a vertical plate moving horizontally along the path $x = \xi(t)$, $0 < t < T$, and where T is the generation time. The origin of the coordinate system is at the initial position of the wavemaker and x increases seaward. The problem can be stated as finding the maximum runup R that a wave motion generated with trajectory $\xi(t)$ at a distance L from the generator in a fluid of depth d , density ρ and viscosity μ will attain on a sloping beach of angle β . It is

assumed that the flow boundary is hydrodynamically smooth. The following table lists the independent and dependent variables. The appropriate units are included in parentheses.

DIMENSIONAL ANALYSIS †

R	is the maximum runup	(L),
d	is the depth of the constant depth region,	(L),
T	is the characteristic generation time	(T),
S	is the stroke of the generator	(L),
L	is the propagation distance	(L),
β	is the angle of the sloping beach	(-),
g	is the acceleration of gravity	(L/T^2),
ρ	is the density of the fluid	(M/L^3),
and		
μ	is the viscosity of the fluid	(M/LT).

In dimensional terms, one can write

$$\mathbf{R} = \mathcal{F}(d, \mathbf{S}, \mathbf{T}, \rho, \mu, L, g, \beta). \quad (1)$$

If the equations of motion were solvable for arbitrary plate trajectories, specification of the independent variables on the right hand side of equation (1) would be sufficient to define the runup exactly. Unfortunately, no analytical or numerical methods exist to calculate the evolution of a wave through breaking to its maximum runup and it is necessary to conduct laboratory experiments to determine the functional form of \mathcal{F} .

Buckingham's π -theorem suggests that six independent groups can be constructed. The following is one possible grouping of variables ‡,

$$\frac{\mathbf{R}}{d} = \mathcal{F}\left(\beta, \frac{(\mathbf{S}/\mathbf{T})d}{\mu/\rho}, \frac{\mathbf{S}}{\mathbf{T}\sqrt{gd}}, \mathbf{T}\sqrt{\frac{g}{d}}, \frac{L}{d}\right). \quad (2)$$

† In this list, I have replaced the trajectory time history $\xi(t)$ with the maximum stroke \mathbf{S} and the generation time \mathbf{T} . During the experiments, $\xi(t)$ will be varied and \mathbf{S} and \mathbf{T} will be kept constant to determine the effect of the details of the trajectory.

‡ As is customary, the variable have been assembled in dimensionless groups that have the form of standard fluid mechanics parameters such as the Reynolds number $Re = (\mathbf{S}/\mathbf{T})d/(\mu/\rho)$ and the Froude number $Fr = \mathbf{S}/(\mathbf{T}\sqrt{gd})$.

For fixed propagation distances L , inviscid flow $\mu = 0$, and fixed slopes β , this list reduces to †

$$\frac{\mathbf{R}}{d} = \mathcal{F} \left(\frac{\mathbf{S}}{\mathbf{T}\sqrt{gd}}, \mathbf{T}\sqrt{\frac{g}{d}} \right). \quad (3)$$

One can now speculate on the possible form of the function \mathcal{F} . For a given depth, and given generation number $Fr = \mathbf{S}/(\mathbf{T}\sqrt{gd})$, as the generation time $\mathbf{T}\sqrt{g/d}$ increases the normalized runup \mathbf{R}/d should increase, because then the stroke increases in proportion and higher waves are generated. However, this increase should not be observed for very large generation times because then the waves become unstable, break at generation and fission to smaller waves. It is likely that for each given value of the generation number, there exists some limiting generation time beyond which no further increases in runup would be possible. This would imply runup saturation and it would provide a limiting condition for long wave runup.

Whether this speculation is correct and whether different $\xi_1(t) \dots \xi_n(t)$ with identical $\mathbf{S}/(\mathbf{T}\sqrt{gd})$ and $\mathbf{T}\sqrt{g/d}$ result in different \mathbf{R}/d is unknown and will be explored in the next sections.

3. Experimental results.

Experiments were conducted in the 40m wave tank facility of the W.M. Keck laboratories of the California Institute of Technology. The facility is equipped with a programmable hydraulic wave generator and a wave measuring system. A ramp of slope 1 : 19.85 was installed at one end of the tank to model a uniformly sloping beach. The ramp surface was made of anodized aluminum panels and it was hydrodynamically smooth over the range of flows studied.

The experimental procedure is described in detail elsewhere (Synolakis, 1986, 1987). The experiments consisted of specifying a normalized plate trajectory shape $\xi(t)/d$ and of then varying \mathbf{S} and \mathbf{T} and of measuring \mathbf{R} until a sufficiently large data set was generated to draw some preliminary conclusions.

3.1 Ramp trajectory. Type R waves.

The simplest possible plate motion is a ramp trajectory defined by

$$\begin{aligned} \xi(t) &= \left(\frac{\mathbf{S}}{\mathbf{T}}\right)t, \quad 0 < t < \mathbf{T}, \\ \xi(t) &= 0, \quad t > \mathbf{T}. \end{aligned} \quad (4)$$

† I have resisted the temptation to use an Irribaren like parameter in this analysis. This type of long waves change substantially as they propagate over constant depth and it is difficult to define the wave steepness consistently. If further analysis is desired, a tabulation of the data may be found in Synolakis (1986).

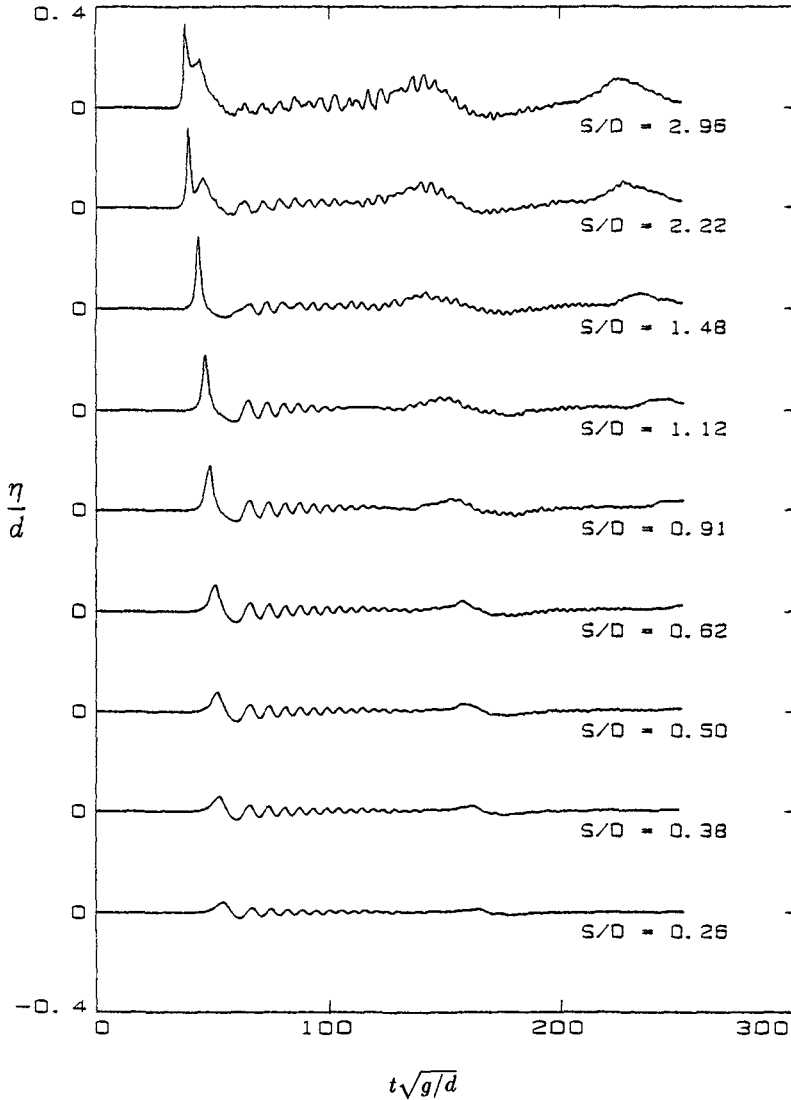


Figure 2 The wave hierarchy generated with a ramp trajectory with generation time $T\sqrt{g/d} = 7.2$ and different strokes. The profiles were measured at approximately 20 depths away from the wave generator. The profiles are not synchronized in time and their relative positions do not necessarily reflect differences in propagation speeds.

In this case the entire wave generation process is described by three parameters only, the depth, the stroke and the generation time. For identification purposes in the subsequent discussion, these waves will be referred to as type R waves.

The experiments covered a range of depths from 12.60 to 20.24cm, a range of dimensionless times $T\sqrt{g/d}$ from 3.481 to 15.747 and a range of generation numbers $S/(T\sqrt{gd})$ from 0.034 to 0.846. Small generation numbers ($S/(T\sqrt{gd}) < 0.11$) resulted in waves that never broke and in small runup heights ($R/d < 0.22$) larger generation numbers ($S/(T\sqrt{gd}) < 0.37$) resulted in waves that broke as they climbed up the beach and in larger runup heights ($R/d < 0.80$). Larger numbers ($Fr < 0.65$) produced waves that broke before reaching the beach, reformed and then broke again as they climbed up the beach. Relatively large generation numbers ($Fr < 0.84$) produced waves that were generated broken and propagated broken without ever reforming. These waves were essentially bores of finite volume and they had the highest runup distances $R/d \approx 1$. Further increases in the generation number did not result in larger runup; there was runup saturation.

Figure 2 presents the surface elevation time history of one series of such waves generated with similar generation times but with generation numbers differing by an order of magnitude. All waves shown assume the shape of a leading solitary wave followed by an oscillatory tail. The second hump seen at about 100 dimensionless time units behind the leading wave is the reflected wave generated by the beach.

The relationship of the runup of the waves generated with a ramp motion (4) with the generation number is presented in figure 3. All the wave shown are waves that broke only as they climbed up the slope. As expected, the relative runup increases with the generation number. Also as anticipated, for fixed generation numbers, the relative runup increases with the generation time.

3.2 Solitary wave-like trajectory. Type S waves.

In this set of experiments waves were generated using different solitary wave-like trajectories. A solitary wave trajectory is a plate motion that produces a solitary wave of given H/d at a given depth d . This trajectory is the solution of the equation

$$\xi(t) = \frac{H}{kd} \tanh k(ct - \xi(t)), \quad (5)$$

where $k = \sqrt{(3/4)H/d^3}$ and $c = \sqrt{g(H+d)}$ (Goring, 1978).

The correct stroke and generation times for solitary waves are $S = \sqrt{(16/3)Hd}$ and $T = (2/kc)(3.80 + H/d)$. † If different values are specified, then the generator

† It has been verified *ibid* and in Synolakis (1986, 1987) that these values produce true Boussinesq solitary waves $\forall 0.08 < H/d < 0.68$. However, depending on the response of the generation system fine tuning may be necessary to obtain perfectly clean waves. Specifically, T may have to be adjusted by 5%.

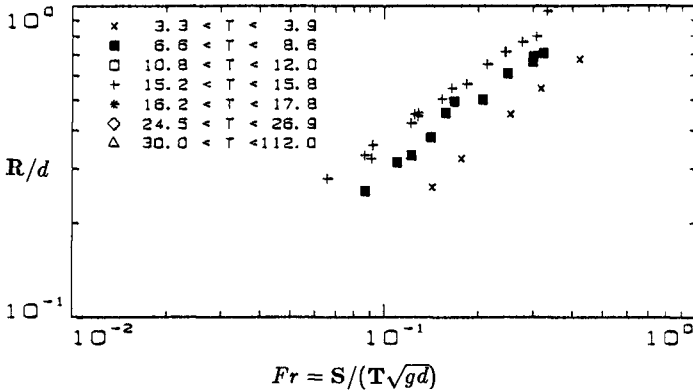


Figure 3 The variation of the normalized runup with the generation number. Type R waves. All waves shown break only as they climb up the beach.

produces a single long wave followed by an oscillatory tail. A *solitary wave-like* trajectory is a solution of (5) but with different S and T than for solitary waves.

Figure 4 shows one wave hierarchy that is produced when the generation time is kept constant at $T = 15.0$ and the generation number is varied. These waves were generated at depths ranging from $d = 11.74\text{cm}$ to $d = 25.53\text{cm}$. Waves generated with $S/d < 0.7$ are nonbreaking, while waves produced with $S/d > 2.0$ are breaking/reforming waves or bores.

Many other similar hierarchies were generated. The experiments covered a range of dimensionless times $T\sqrt{g/d}$ from 3.388 to 55.966 and a range of generation numbers $S/(T\sqrt{g/d})$ from 0.01 to 1.10. Small generation numbers ($S/(T\sqrt{g/d}) < 0.10$) resulted in waves that never broke and in small runup heights ($R/d < 0.22$) while larger generation numbers ($S/(T\sqrt{g/d}) < 0.40$) resulted in waves that broke as they climbed up the beach and in larger runup heights ($R/d < 0.75$). Larger numbers ($Fr < 0.70$) produced waves that broke before reaching the beach, reformed and then broke again as they climbed up the beach. Relatively large generation numbers ($Fr < 0.80$) produced waves that were generated broken and propagated broken without ever reforming. These waves attained the highest runup distances $R/d \approx 1$. It is really surprising how well these values correspond to the values obtained with the ramp trajectory in section 3.1. Runup saturation was again observed; increasing the generation number beyond $Fr = 0.80$ did not result into higher runup heights.

Figure 5 presents the variation of the runup of the waves generated with the

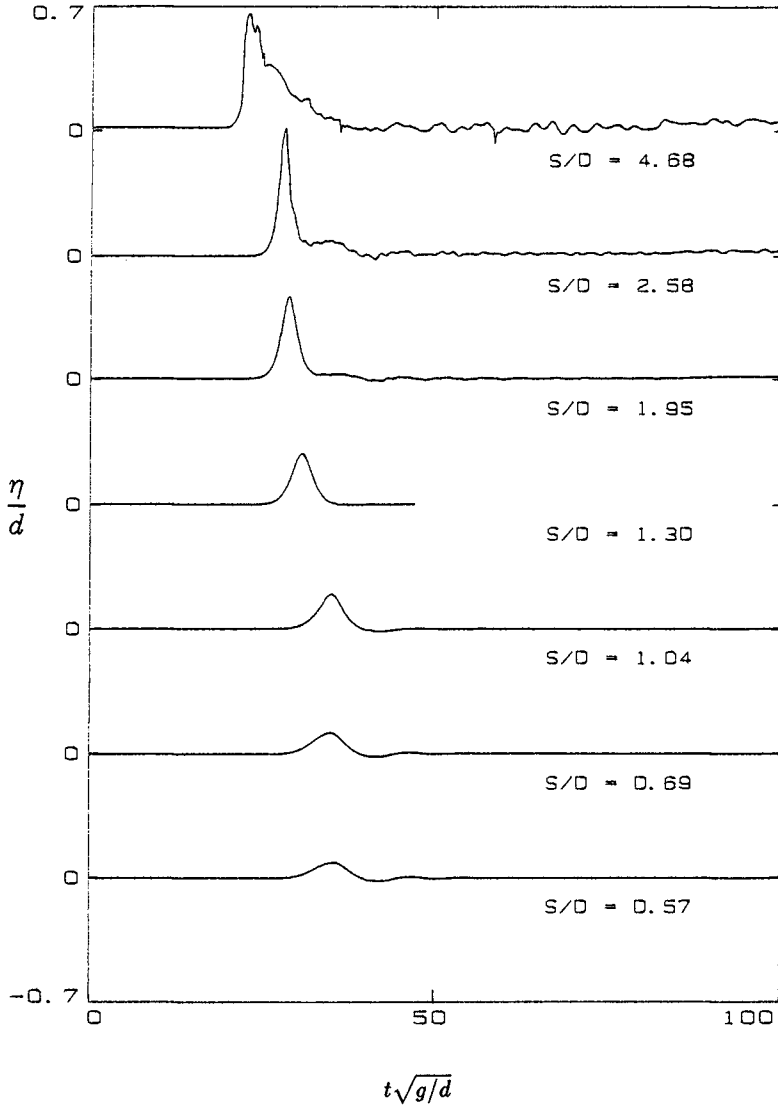


Figure 4 The wave hierarchy generated with a ramp trajectory with generation time $T\sqrt{g/d} = 7.2$ and different strokes. The profiles were measured at approximately 20 depths away from the wave generator. The profiles are not synchronized in time and their relative positions do not necessarily reflect differences in propagation speeds.

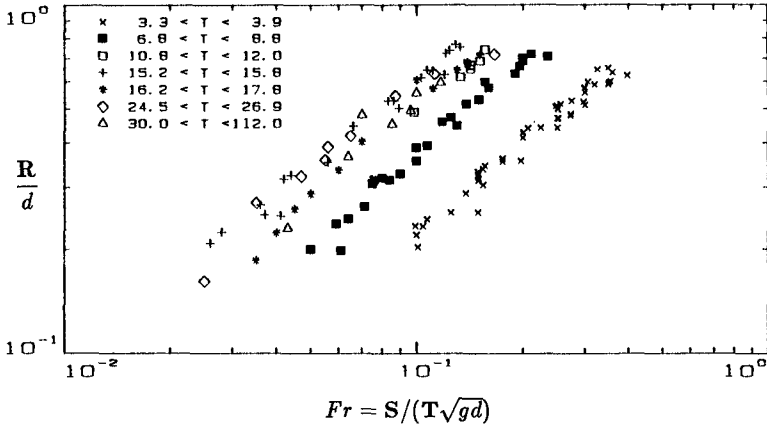


Figure 5 The variation of the normalized runup with the generation number. Type S waves. All waves shown break only as they climb up the beach.

solitary wave-like motion, i.e., equation (5) with the generation number.

3.3 Comparison with solitary waves.

It is interesting to compare the data described in section (3.1) and (3.2) with data for Boussinesq solitary waves. A comprehensive study of solitary wave runup has been presented in Synolakis (1987,1987). Figure 6 presents the variation of the normalized runup with the generation number for type R waves, type S waves and for solitary waves. It appears that for a given generation number and regardless of the generation time and the trajectory used, the solitary waves always attain the highest runup distances. This observation hints that solitary waves may indeed be a limiting condition, at least in single long wave runup.

It is important to note that bores of finite volume produce normalized runup distances than are even higher than those produced by solitary waves. This is anticipated and it is not contradictory to the previous discussion; it is not possible to create a solitary wave that is simultaneously a bore. The highest generation number that produces a solitary wave is $Fr = 0.189$. On the other hand it is possible to create bores with generation numbers as high as $Fr = 0.85$. Even then, there is saturation and further increases in the generation number cannot produce higher runup.

These three observations, the fact that details of the plate motion are important in determining the runup, the fact that solitary waves provide a limiting condition

for the runup of long waves that break on the beach and the fact that the bore runup is saturated, suggest that there might exist some dimensionless number such that solitary waves assume the highest value of this number. This question will be explored next.

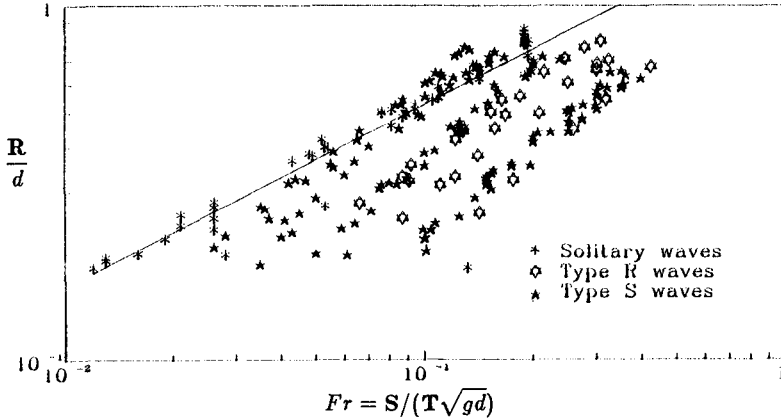


Figure 6 The variation of the normalized runup with the the generation number. Breaking type R, S waves and solitary waves. The solid line is the line of best fit for the solitary wave data and it is given by $R/d = 1.739Fr^{0.518}$.

4. The runup number.

In attempting to determine a single parameter to describe the process, it is instructive to consider the kinematic analogy of a material particle moving up a frictionless inclined plane. Suppose that a particle of mass m starts climbing up a ramp of slope $\tan\beta$ with horizontal momentum mV . As the particle climbs up, the component of the body force in its direction of motion acts to reduce its momentum. Newton's law implies that $dV/dt = -g \sin\beta$. The maximum elevation the particle will reach is $R = V^2/2g$. The same result can be arrived at by using an energy argument. It is therefore likely that two important motion invariants are the particle's energy and momentum.

The kinematic analogy cannot be carried further; as a wave climbs up a beach reflection continuously reduces its momentum, while wave breaking dissipates its energy. Friction dissipates both momentum and energy. However, it is well known that these processes are slowly acting in extremely long waves such as tsunamis. I will therefore proceed to derive momentum and energy scales that can be used in the derivation of motion invariants.

Consider a single long wave with horizontal momentum M_x per unit mass and per unit width incident upon the sloping beach. The wave attains a maximum

runup height R . The basic variables are R, g, M_x and they can produce only one group, $Rg^{\frac{1}{2}}/M_x^{\frac{2}{3}}$. If one uses the kinetic energy per unit mass and per unit depth as an independent variable, dimensional analysis suggests the group $Rg^{\frac{1}{2}}/\mathcal{E}^{\frac{1}{2}}$. †

The horizontal momentum per unit width and per unit mass is given by $M_x = \int_{\mathcal{V}} u_x d\mathcal{V}$ where \mathcal{V} is the volume occupied by the wave and u_x is the horizontal velocity. To calculate this integral detailed amplitude and velocity data are needed. However since the wavemaker displaces a volume Sd per unit width and since S/T is a measure of the velocity imparted to the motion, an estimate of the momentum of the wave motion is S^2d/T . This leads to a dimensionless momentum invariant $\mathcal{R} = Rg^{\frac{1}{2}}/(S^2d/T)^{\frac{2}{3}}$. This parameter will be referred to as the runup number.

To determine whether this parameter is motion invariant, it is necessary to examine its variation with other independent parameters. Repeating the dimensional analysis of section 2 one obtains

$$\mathcal{R} = \frac{Rg^{\frac{1}{2}}}{(S^2d/T)^{\frac{2}{3}}} = \mathcal{F}\left(\beta, \frac{(S/T)d}{\mu/\rho}, \frac{S}{T\sqrt{gd}}, \frac{S}{d}\right). \quad (6)$$

Figure 7 presents the variation of the runup number with three of the parameters in equation (6) for type R waves. With the exception of bores of finite volume, the runup number does seem to vary very little. Figure 8 presents the variation of the runup number for type S waves. The runup number variation is greater than it is for type R waves; still it only ranges from $\mathcal{R} = 0.8$ to $\mathcal{R} = 1.2$.

Figure 9 presents the runup number variation with the generation number for all wave types previously described. ‡ The figure suggests that the runup number might not be a true motion invariant, in the sense that it varies from $\mathcal{R} = 0.7$ to $\mathcal{R} = 1.3$. (However, the scatter seen is within the margin of experimental error.) More important, the figure also suggests that solitary waves have the highest runup number $\mathcal{R} = 1.30$, implying that indeed solitary waves may provide a limiting condition for wave runup.

† From this point on, I will discuss the influence of the momentum of generation only. The analysis presented in Synolakis (1986) suggests that the motion invariant derived from the momentum describes the process further better than the motion invariant derived from energy.

‡ Figure 9 also includes data for type P waves, which are waves generated with a parabolic trajectory. In the interest of brevity these waves are not in discussed in detail here. Refer to Synolakis (1986) for tables of data and for a description of the experiments.

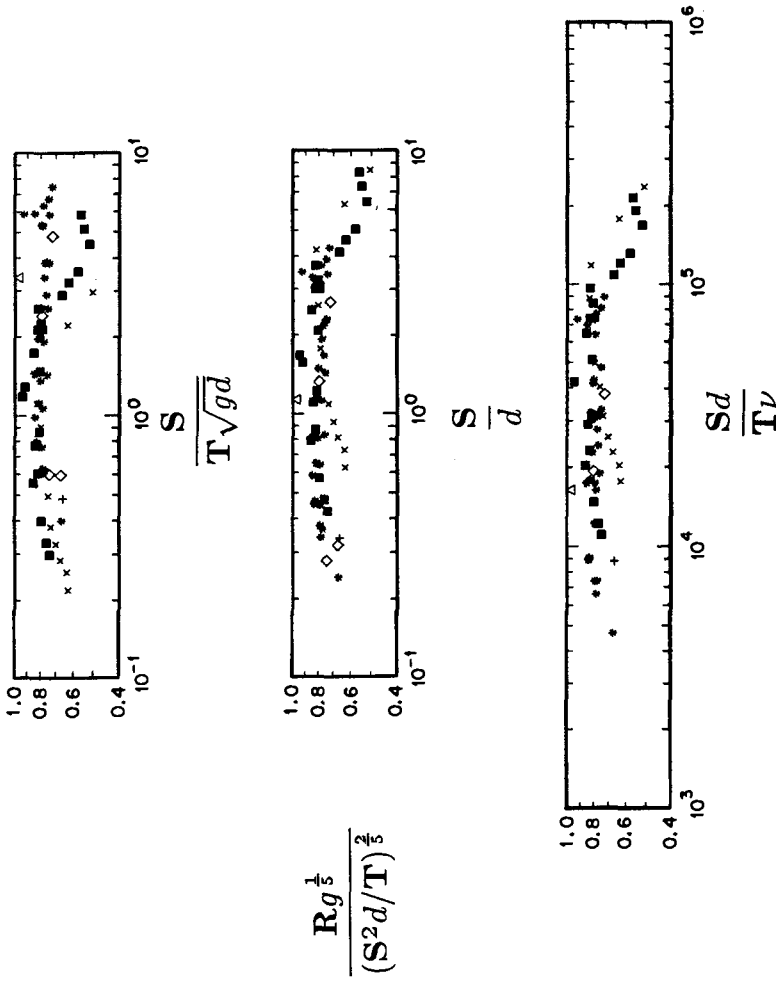


Figure 7 The variation of the runup number with the generation number (a), with the normalized stroke (b) and with the Reynolds number (c). Type R nonbreaking, breaking, breaking/reforming and bores of finite volume.

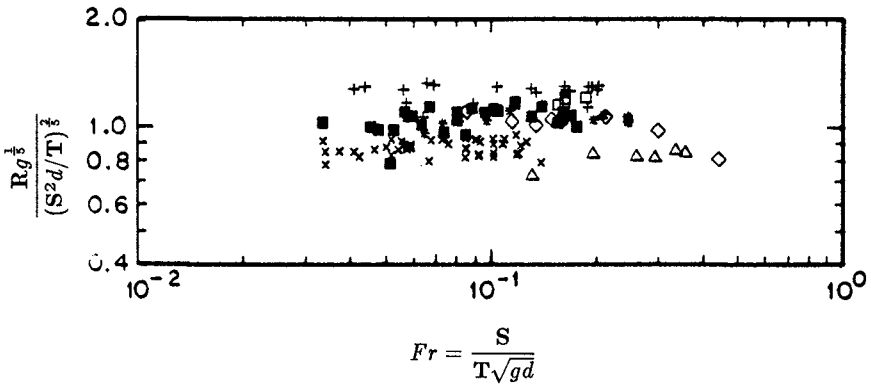
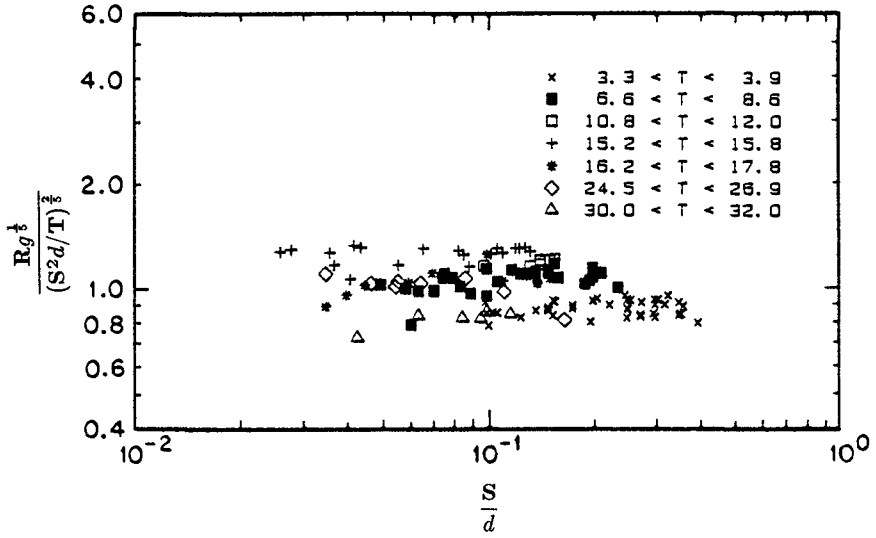


Figure 8 The variation of the runup number with the stroke (a) and with the generation number (b). Type S breaking waves.

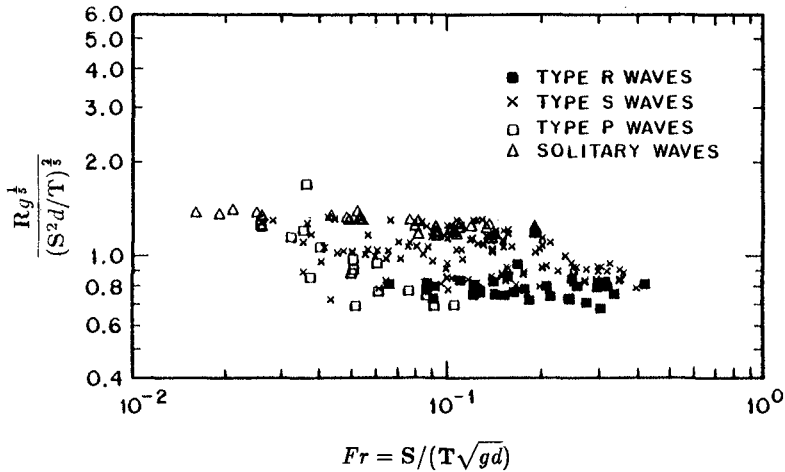


Figure 9 The variation of the runup number with the generation number. Type R, S, P waves and solitary waves.

5. Discussion.

The data presented clearly demonstrate that solitary waves are a limiting condition for wave runup on a sloping beach. For a given generation number the solitary waves attain the highest runup distances regardless of the generation times and trajectory type. Also solitary waves have the highest runup number of all long waves described in this study. One can only speculate why this should be the case.

Arbitrary plate motions produce either single long waves that may be non-breaking, breaking, or bores followed by an oscillatory train or solitary waves. It is reasonable to expect that the runup of a wavetrain will be primarily affected by the runup of the leading wave that emerges from the wavetrain. † The momentum of this wave is less than the momentum that was imparted to the fluid during wave generation. Had all the momentum at generation been used to produce a solitary wave, then this wave would have a larger waveheight and it would attain higher runup distances than the leading wave emerging from a long wavetrain with the same momentum.

This is a very exciting result. It implies that it might be possible to determine

† This analysis is consistent with nonlinear dispersive theory that predicts that any long wavetrain of positive volume will fission into a series of solitons given a sufficiently large propagation distance.

the highest possible runup distance that a wave motion of a given momentum distribution may attain by simply calculating the runup of the solitary wave generated with the same total momentum. Whether this result is true for natural beaches † and whether it is true for three-dimensional topographies remains to be established. However it does suggest that it might be possible to obtain reliable predictions of the coastal effects of tsunamis using solitary wave theory.

6. Conclusions.

There are three major conclusions based on the data on the 1 : 19.85 beach.

- 1) On a given beach, there are maximum runup values that a wave may attain depending on its breaking character, i.e., whether a wave is nonbreaking, breaking, breaking/reforming or a bore of finite volume.
- 2) The generation characteristics of a long wave determine its runup at finite propagation distances. In particular if the momentum scale is estimated using the generation time and stroke, the resulting dimensionless group, the runup number, might be a motion invariant. The runup number for the 1 : 19.85 beach is given by

$$\mathcal{R} = \frac{Rg^{\frac{1}{5}}}{(S^2d/T)^{\frac{2}{5}}} = 1.023 \pm 0.3.$$

The exact value of the generation number depends weakly on the generation time.

- 3) Breaking solitary waves have the highest possible runup number among all other single long waves, thereby providing a limiting condition for long wave runup.

Acknowledgements This research was supported by a grant from the Faculty Research and Innovations Fund of the University of Southern California and by the Alexander Onassis Public Benefit Foundation and by a grant of the National Science Foundation managed by Fred Raichlen of the California Institute of Technology.

References

- Bernard, E.N. et al 1988 *EoS* **69**, 24, 659–661.
 Guza, R.T. and Thornton, E.B. 1982 *J. Geoph. Res.* **87**, 483–491.
 Huntley D.A., Guza, R.T., and Bowen A.J. 1977 *J. Geoph. Res.*, **82**, 18, 2577–2581.
 Synolakis, C.E. 1986, *The runup of long waves* Ph.D. Thesis, California Institute of Technology, Pasadena, CA, 228pp.
 Synolakis, C.E. 1987 *J. Fluid Mech.*, **185**, 523–545.
 Synolakis, C.E. 1988 *Qu. Appl. Math.*, **XLVI**, 105–107.
 Synolakis, C.E., Deb M.K. and Skjelbreia, E.J. 1988 *Phys. Fluids*, **31**, 1–4.

† Even though this discussion implies runup saturation, there is little evidence ((Huntley et al, 1977, Guza and Thornton, 1982) that there is runup saturation in periodic waves up natural beaches.

CHAPTER 15

Coherent Eddies Induced by Breakers on a Sloping Bed

Nobuhiro Matsunaga* , Kosei Takehara** and Yoichi Awaya***

Abstract

The separation of boundary layer occurs periodically near a breaking point when incident waves climbing up a sloping bed are about to break. Not the breaker but the separation forms an unsteady coherent eddy, which suspends a large amount of bed material. A row of steady vortices has been found along the water surface of an offshore zone. Its formation is due to the shear instability between shoreward steady flow induced near the bed and offshore steady flow near the water surface. Moving in the offshore direction, the steady vortices repeat amalgamation each other and increase their intervals at the order of mean water depth. They decay after reaching to the region where the shear rate is not enough between the two steady flows. This shear instability may be excited by the periodic separation of boundary layer.

1. Introduction

Recently, the velocity in nearshore zone has been measured vigorously through field and laboratory investigations in order to reveal the mechanism of suspension and sediment transport or to understand the process of water exchange between nearshore zone and offshore. Many researchers (e.g., Mizuguchi, 1986 ; Okayasu, et al., 1986) have the idea that turbulence by breakers lifts up much bed material, and their attention has focused on coherent eddies in surf zone. Miller (1976) showed the formation of breaker vortices on basis of the pattern of entrained air bubbles. Kaneko(1985) confirmed their formation by tracing the paths of polystyrene beads. Nadaoka(1986) has suggested the existence of oblique eddies from bubble patterns. However, the question that the flow drawn schematically by him forms truly in surf zone will remain until it becomes clear that the ensemble-averaged behavior of individual tracers has such a coherent, rotational structure.

* Research Associate, Dept. Civil Engineering, Kyushu University, Fukuoka 812, Japan.

** Graduate Student, Dept. Civil Engineering, Kyushu University, Fukuoka 812, Japan.

*** Professor, Dept. Civil Engineering, Kyushu University, Fukuoka 812, Japan.

We often observe that a large amount of bed material has been already rolled up at the breaking point when incident waves are about to break. The purposes of this paper are to reveal experimentally the mechanism of this suspension and to show the qualitative characteristics of a vortex train induced in an offshore zone, which has been supposed to be irrotational flow region.

2. Experimental Methods

Figure 1 shows schematically an experimental apparatus. The wave tank was 12 m long, 0.4 m deep and 0.15 m wide. It was made of transparent acrylic plates and equipped with a sloping bed. Two-dimensional regular waves were formed by oscillating a flap. The behaviors of flow were observed near a breaking point and in offshore zone.

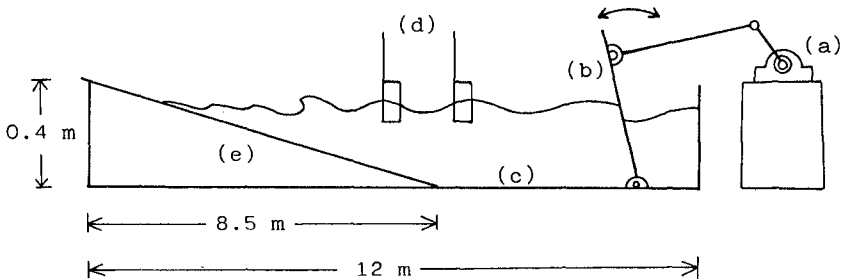


Figure 1. Experimental apparatus.

(a) Motor; (b) wave generator; (c) wave tank;
(d) wave gauges; (e) sloping bed.

Near the breaking point, turbulent flow by a plunging breaker was investigated by means of both velocity measurement and flow visualization. The slope θ of the bed was 0.056 and the wave period T was 1.3 s. Figure 2 shows the measuring points and the level of wave crest. The points P.P. and B.P. indicate the plunging point and breaking point, respectively. The velocity measurement was carried out by using a single-component Lazer-Doppler velocimeter of forward scattered fringe mode. Therefore, the horizontal and vertical velocities had to be measured separately under the same hydraulic conditions. Two capacitance-type wave gauges were used for the measurement of wave profiles. One was placed right above the measuring point of velocity and the other was fixed at an offshore position. Signals from the L.D.V. and wave gauges were recorded simultaneously by a data recorder. They were digitized; the sampling time and number were 8/1000 s and 16,384, respectively. Flow patterns were visualized by using granules of aniline blue, condensed milk and saw dust as a tracer.

The flow in offshore zone was observed only by means of flow visualization. The value of θ was 0.043. The period T ranged from 0.55 to 2.0 s. Granules of aniline blue were used as a tracer and were scattered on the water surface of

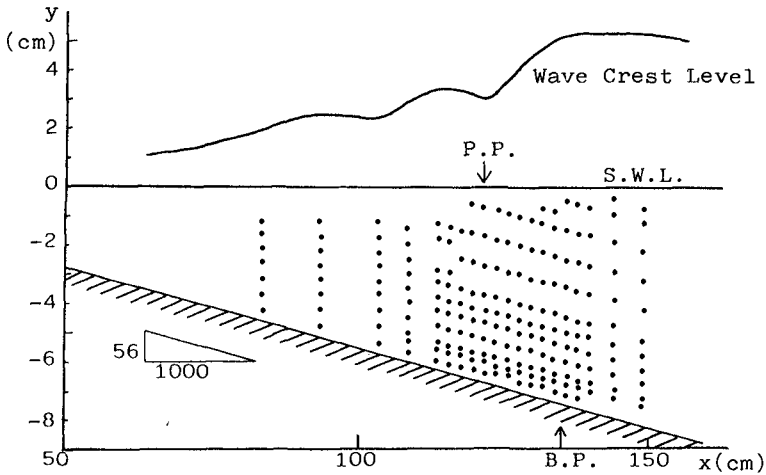
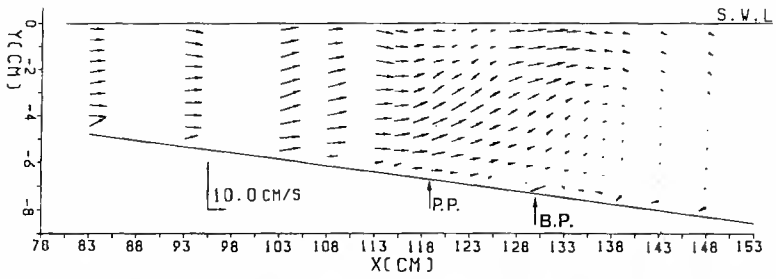


Figure 2. Measuring points and wave crest level. (P.P. indicates the punging point and B.P. the breaking point.)

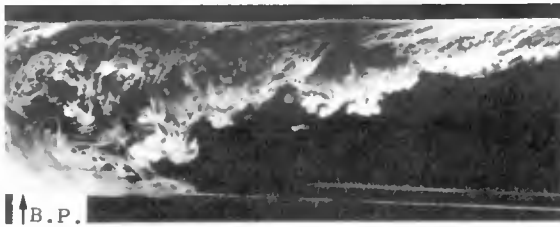
the offshore zone. All the flow patterns were photographed instantaneously through a side wall of the tank by using a 35mm camera, which was at rest with respect to it. The offshore side is on the right in all these photos.

3. Results and discussion

Figures 3(a) to (d) show the patterns of secondary steady flow induced near the breaking point. Mean velocity vectors are drawn in figure 3(a). The steady flow rises at the breaking point and runs along the water surface. Shoreward steady flow forms along the boundary layer of the offshore zone (e.g., Longuet-Higgins 1953). It is therefore seen that the breaking point is a separation point of the steady flow. Figure 3(b) shows a lift-up pattern of condensed milk immediately after the start of oscillation. The tracer was precipitated beforehand near the breaking point. Here, t is the time elapsed since the start of oscillation and T the wave period. A large amount of the tracer is lifted up at the breaking point without running down along the bed of the offshore zone, and it is transported along the water surface. This pattern agrees well with that shown in figure 3(a). Figure 3(c) was taken when $t/T = 92$. A row of vortices with the clockwise rotation is seen in the offshore zone. The formation mechanism and formation region of this vortex train will be discussed later in detail. Figure 3(d) is a close-up view of the boundary layer separation. Aniline blue dye was used as a tracer. The dye dropped on the bed of the offshore zone is transported onshore by the shoreward steady flow



(a)



(b)



(c)



(d)

Figure 3. Steady flow patterns induced near the breaking point. (Arrow (1) indicates the separation of boundary layer and arrow (2) the trace of dye along the bed.)

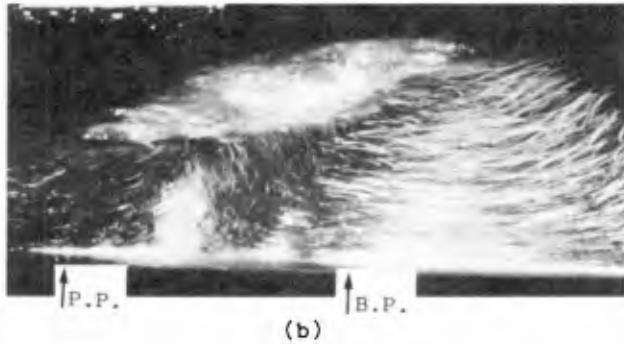
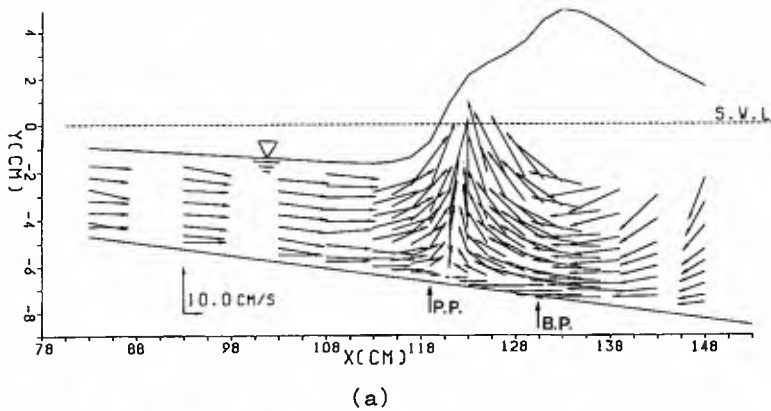


Figure 4. Velocity and flow patterns when an incident wave is about to break. Scale bar is 10 cm.

along the boundary layer, and separates at the breaking point just before breaking. It should be noted that the run-up of tracer along the bed is not observed in surf zone owing to the separation. This visualized result supports also the pattern shown in figure 3(a).

Figure 4(a) shows the ensemble-averaged velocity pattern at a phase just before breaking. Strong upward orbital motion is seen at the front of wave crest. Figure 4(b) is taken at almost the same phase as figure 4(a). Saw dust is lifted up owing to both the separation of boundary layer and the orbital motion.

Figure 5(a) is the ensemble-averaged velocity pattern at a phase immediately after breaking. Arrow (1) indicates a flow pattern induced by plunging. It should be emphasized that the flow does not form a complete rotational pattern since its direction is shoreward near both the bed and water surface. Arrow (2) indicates a vortical pattern with the clockwise rotation. The formation of this coherent eddy is closely related to the separation of boundary layer. From these reasons, therefore, it may properly be called the 'backwash vortex', which was found by one of the authors(1979, 1981). Figure 5(b) shows an instantaneous

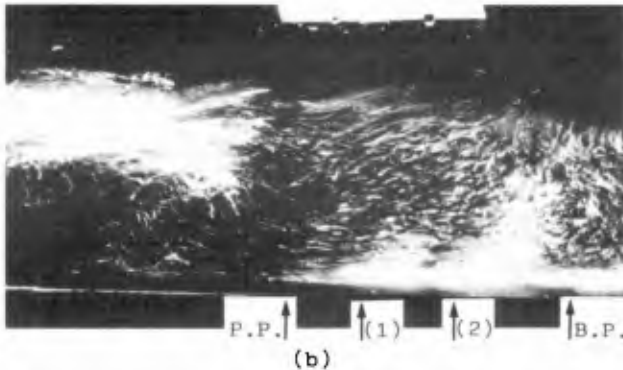
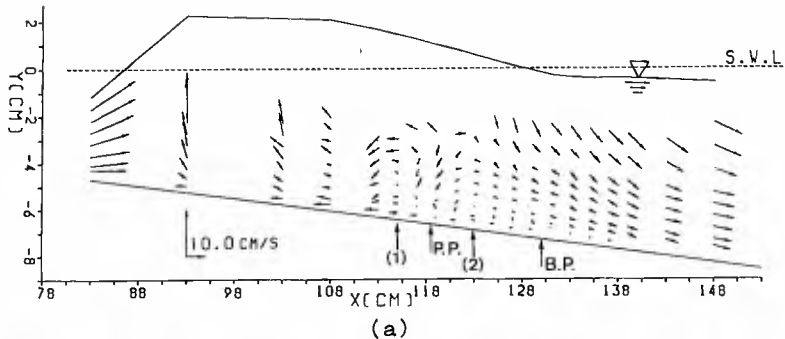
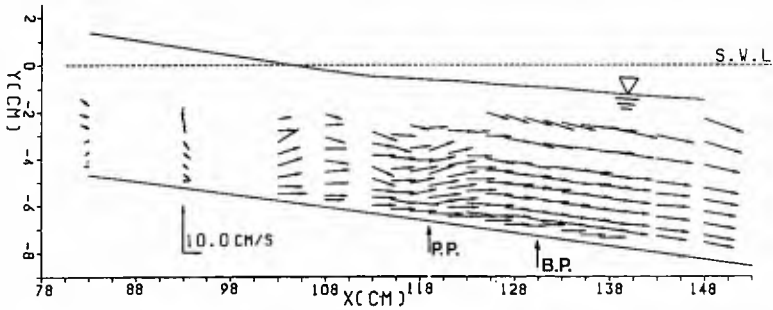


Figure 5. Velocity and flow patterns immediately after breaking. Scale bar is 10 cm.

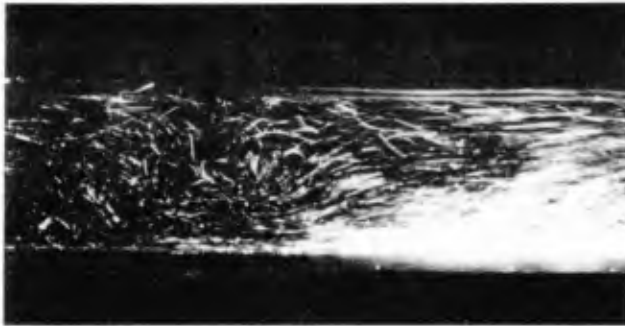
flow pattern at almost the same phase as that of figure 5(a). Two lift-ups of saw dust are seen as indicated by arrows (1) and (2). The lift-up shown by arrow (1) seems to be due to plunging breaker. On the other hand, considering that the suspension shown by arrow (2) has the clockwise rotation and forms near the breaking point every wave period, we can guess that it is generated by the backwash vortex.

Figures 6(a) and (b) show velocity and flow patterns, respectively, when a wave trough passes through the breaking point. Both the patterns agree well and the coherent suspensions have been already wiped out by the orbital motion.

Now, let us discuss about the vortex train appearing in offshore zone. Figure 7 shows a steady flow pattern induced along the water surface of offshore zone. The breaking point was at 0.68 m shoreward from the position E and the intervals between adjacent positions was 0.5 m. A wavy flow pattern is seen in the top photo. Between the positions D and B, the wavy pattern develops to a row of vortices with the clockwise rotation. Their intervals increase with the increase of water depth. As shown in the bottom photo,



(a)



(b)

Figure 6. Velocity and flow patterns when a wave trough passes through the breaking point.

the vortical pattern disappears in the region seaward from B. In the following discussion, this vortex will be called an 'offshore vortex'.

In figures 8(a) to (f), the process is shown in which the intervals of offshore vortices increase in the seaward direction. Here, t is the time passed from the photographing of figure 8(a). Let us focus attention on the two offshore vortices indicated by the arrows. Moving in the seaward direction, the two vortices approach gradually each other as shown in figures 8(b) to (d). Figure 8(e) shows that they have become one offshore vortex after their amalgamation. In figure 8(f), we can see the offshore vortices rearranged at the intervals of the order of mean water depth.

Let us consider about the formation region of the offshore vortex train. It may be expressed by the following function.

$$\text{Formation region} = f(h, L, H, T, C, g)$$

Here, h is the mean water depth, L the wavelength, H the wave height, T the wave period, C the phase velocity of incident waves and g the acceleration of gravity. In this



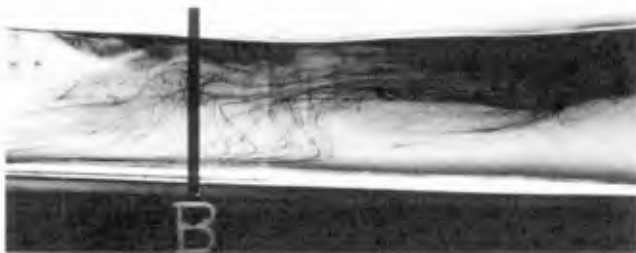
(a)



(b)

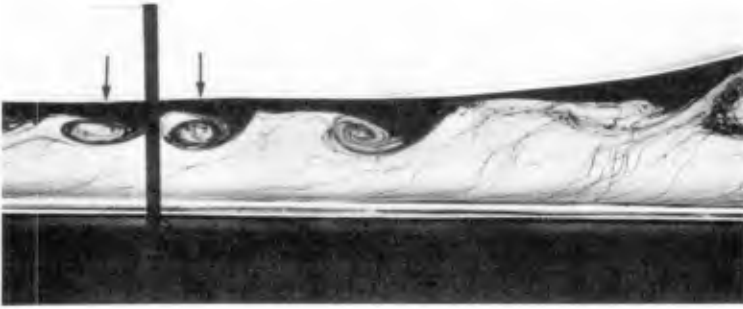


(c)

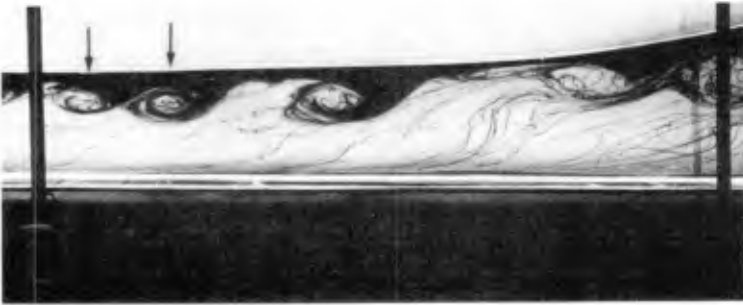


(d)

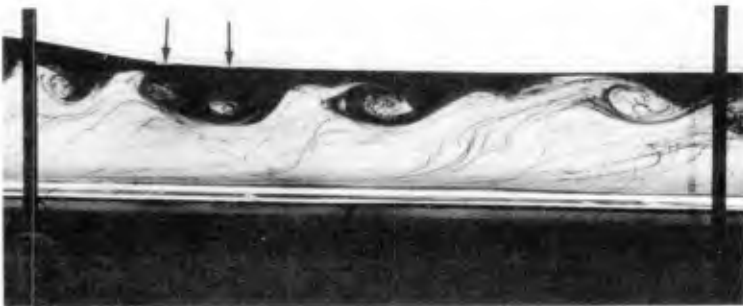
Figure 7. Local patterns of a vortex train in offshore zone. (The mean water depths are 7.9 cm at E, 10 cm at D, 12 cm at C and 14 cm at B.)



(a)



(b)

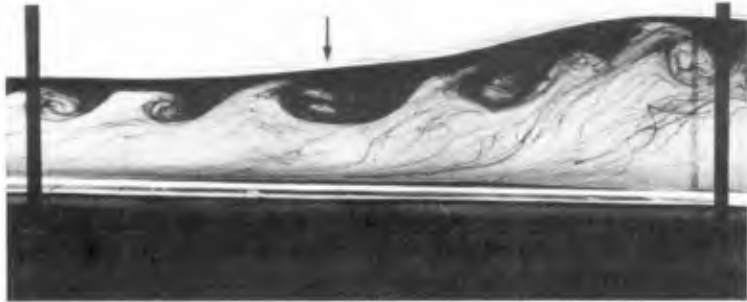


(c)

Figure 8. (a)-(c). For caption see next page.



(d)



(e)



(f)

Figure 8. Increase-process of intervals of offshore vortices. The interval between D and C is 0.5 m.

(a) $t/T=0$; (b) $t/T=12$; (c) $t/T=23$;
(d) $t/T=26$; (e) $t/T=30$; (f) $t/T=38$.

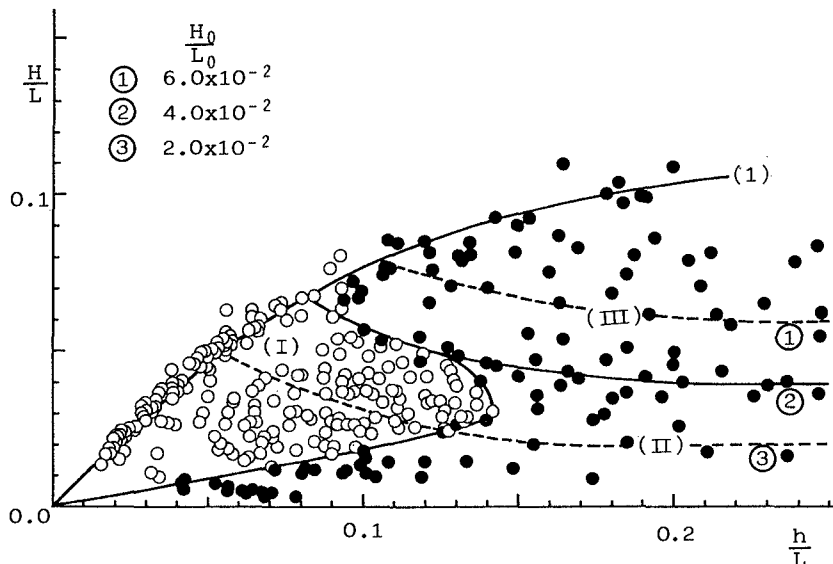


Figure 9. Formation region of offshore vortices.

expression, it has been assumed that the bed slope and the kinematic viscosity of fluid are constant. If the relation of $C = L/T$ and the dispersion relation are taken into account, the function is simplified as $g(h, L, H, g)$. Therefore, non-dimensional quantities to describe the formation region become h/L and H/L .

In figure 9, the formation region is examined by plotting H/L against h/L . The parameter H_0/L_0 is the steepness of deep water waves. The open circles indicate the formation of offshore vortices and the solid circles mean that the vortices are not observed. Regions (I), (II) and (III) are bounded by the solid lines. Line (1) expresses an empirical relationship between wave height and mean water depth at breaking points. Region (I) is the formation region of the vortex train. Region (II) indicates the region where the offshore vortices decay as shown in the bottom photo of figure 7. In region (III), no laminar vortical pattern is observed because of the strong diffusion due to high steepness of waves.

Figure 10 shows schematically the flow patterns induced in the offshore zone on the basis of the qualitative results mentioned above. The backwash vortex forms periodically near the breaking point owing to the separation of boundary layer. In the offshore zone, the train of offshore vortices develops in the seaward direction from the breaking point. Its formation is due to the shear instability between the shoreward and seaward steady flows, which are indicated by the arrows. This instability may be excited by the periodic separation. The offshore vortices increase their intervals as they move in the seaward direction. However, they decay after reaching to the region where the shear rate is not enough between the two steady flows.

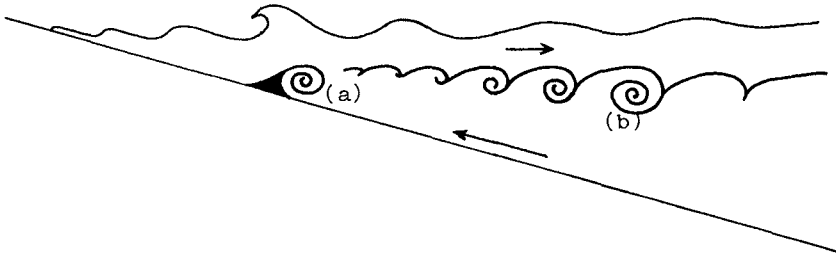


Figure 10. Schematic diagram of coherent eddies induced by breakers.
(a) backwash vortex; (b) offshore vortices.

In conclusion, the authors suggest that the separation of boundary layer near the breaking point and the offshore vortex train would be very important in the process of near-shore sediment transport.

Acknowledgments

We would like to express our sincere thanks to Dr. T. Komatsu of Kyushu University and Professors H. Honji of Kyushu University and P. D. Komar of Oregon State University for valuable suggestions. A grant from the foundation 'Hattori-Hokokai' is also acknowledged.

References

- Kaneko, A. (1985). Formation of beach cusps in a wave tank. *Coastal Eng.*, 9, 81-98.
- Longuet-Higgins, M. S. (1953). Mass transport in water waves, *Philosophical Transaction of the Royal Society*, London, England, Series A, 535-581.
- Matsunaga, N and H. Honji (1980). The backwash vortex. *J. Fluid Mech.* 99, 813-815.
- Matsunaga, N. and H. Honji (1983). The steady and unsteady backwash vortices. *J. Fluid Mech.*, 135, 189-197.
- Miller, R. L. (1976). Role of vortices in surf zone prediction: sedimentation and wave forces. In R. A. Davis Jr. and R. L. Ethington (Editor), *Beach and Nearshore Sedimentation*. Soc. Econ. Paleontol. Mineral. Spec. Publ. 24, 81-98.
- Mizuguchi, M. (1986). Experimental study on kinematics and dynamics of wave breaking. *Proc. 20th Conf. on Coastal Eng.*, 1, 589-603.
- Nadaoka, K. (1986). A fundamental study on shoaling and velocity field structure of water waves in the nearshore zone. Technical Report, No. 36, Department of Civil Engineering, Tokyo Institute of Technology.
- Okayasu, A., T. Shibayama and N. Mimura (1986). Velocity field under plunging waves. *Proc. 20th Conf. on Coastal Eng.*, 1, 660-674.

CHAPTER 16

Wide-Angle Water Wave Models Using Fourier Method

Robert A. Dalrymple,¹ Member, ASCE
Kyung Duck Suh,² Associate Member, ASCE

Abstract: Two Fourier models for the propagation of surface waves are reported, which are theoretically valid for angles of propagation up to $\pm 90^\circ$ with respect to normal incidence. This is a great improvement in comparison with the present parabolic models. The first model is based on the assumption of straight and parallel depth contours, and the second one is the extension to the case of irregular bathymetry.

1 Introduction

The parabolic equation method has proven to be a convenient and rapid method for modelling the propagation of surface waves over water of varying depths, including such important phenomena as refraction and diffraction, e.g. Radder (1979), Booij (1981), Kirby & Dalrymple (1983), Liu & Tsay (1984). The small-angle approximation of this method, however, leads to errors if the wave direction deviates largely from the assumed propagation direction like the waves diffracted behind a breakwater, for example.

Very recently Dalrymple & Kirby (1988) developed a wave propagation model valid for angles of propagation up to 90° with respect to the assumed propagation direction (positive x direction in this paper), based on the assumption that the depth contours are straight and parallel in the y direction. This model was extended to the case of irregular bathymetry by Dalrymple *et al* (1988). In Dalrymple & Kirby, the incident wave train at $x = 0$ is decomposed into directional modes, or an angular spectrum, by taking the Fourier transform of the wave train in the y direction, and each directional mode propagates in the x direction only undergoing refraction and shoaling. In Dalrymple *et al*, however, bottom irregularities are shown to interact with nonzero directional modes and to force the evolution of other directional modes, even if they are initially of zero magnitude. In this paper, these two models are briefly summarized and various examples are presented.

2 Linear Fourier model – Straight and parallel contours

The mild-slope equation developed by Birkhoff (1972) can be written, on a beach with straight and parallel (in the y direction) depth contours, as

$$(CC_g\Phi_x)_x + CC_g\Phi_{yy} + k^2CC_g\Phi = 0 \quad (1)$$

¹Prof., Dept. of Civ. Engrg., Univ. of Delaware, Newark, DE 19716.

²Res. Asst., Dept. of Civ. Engrg., Univ. of Delaware, Newark, DE 19716.

where C and C_g are the phase and group velocities, respectively, k is the wavenumber, and $\Phi(x, y)$ is the free surface elevation obtained by dropping the harmonic time dependence. The Fourier transform of the above equation in the y direction leads to the decomposition of the potential into directional modes

$$(CC_g \hat{\Phi}_x)_x + (k^2 - \lambda^2)CC_g \hat{\Phi} = 0 \tag{2}$$

where the caret denotes a variable in the Fourier space and λ is the continuous Fourier parameter.

Splitting the potential into the forward propagating and backscattered potentials and neglecting the assumed small backscattered wave (see Dalrymple & Kirby (1988) for details), the propagation model for the forward propagating wave (denoted by the superscript +) is obtained as

$$\hat{\Phi}_x^+ = i\sqrt{k^2 - \lambda^2} \hat{\Phi}^+ - \frac{[CC_g \sqrt{k^2 - \lambda^2}]_x}{2CC_g \sqrt{k^2 - \lambda^2}} \hat{\Phi}^+. \tag{3}$$

This equation can be solved analytically to give the solution

$$\hat{\Phi}^+(x, \lambda) = \hat{\Phi}^+(0, \lambda) \left[\frac{(CC_g)_o \sqrt{k_o^2 - \lambda^2}}{CC_g \sqrt{k^2 - \lambda^2}} \right]^{1/2} e^{i \int \sqrt{k^2 - \lambda^2} dx} \tag{4}$$

where the subscript o indicates initial conditions at $x = 0$. The bracketed term contains the shoaling and refraction coefficients associated with gradual water depth changes (e.g. Dean & Dalrymple (1984)).

Under the assumption that the model domain is laterally periodic, the problem can be approximated in the discrete Fourier space. The domain is discretized in the y direction by N equidistant points, with spacing $\Delta y = \ell / (N - 1)$ where ℓ is the width of the domain. The velocity potential $\Phi^+(x, y)$, numerically defined only on these points, can be transformed into discrete Fourier modes by

$$\hat{\Phi}^+(x, n) = \frac{1}{N} \sum_{j=0}^{N-1} \Phi^+(x, j\Delta y) e^{-in\lambda j\Delta y}, \quad n = 0, \pm 1, \dots, \pm \left(\frac{N}{2} - 1\right), -\frac{N}{2}. \tag{5}$$

The inversion formula is

$$\Phi^+(x, j\Delta y) = \sum_n \hat{\Phi}^+(x, n) e^{in\lambda j\Delta y}, \quad j = 0, 1, \dots, (N - 1) \tag{6}$$

where

$$\lambda = \frac{2\pi}{N\Delta y} \tag{7}$$

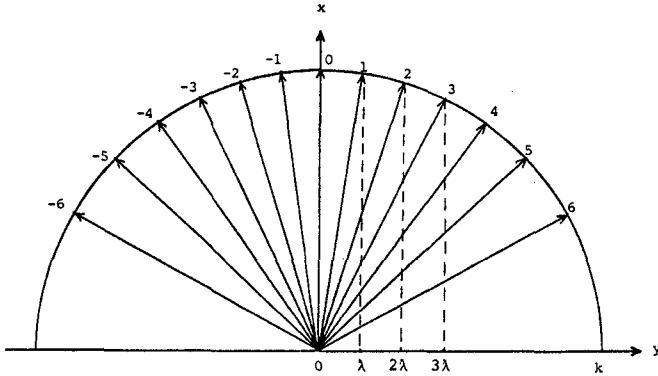


Figure 1: Diagram of the Fourier decomposition of the wave field on a row with an angular spectrum (with lateral wavenumbers, $n\lambda$, $n = 0, \pm 1, \pm 2, \dots$).

which is different from the continuous Fourier parameter λ used before. Subsequently, λ is defined by (7) if it is used in the discrete Fourier space. These transforms can be performed efficiently by using a fast Fourier transform (FFT for short) with $N = 2^p$ where p is a positive integer. Now the equation (4) can be expressed, in the discrete Fourier space, as

$$\hat{\Phi}^+(x, n) = \hat{\Phi}^+(0, n) \left[\frac{(CC_g)_o \sqrt{k_o^2 - (n\lambda)^2}}{CC_g \sqrt{k^2 - (n\lambda)^2}} \right]^{1/2} e^{i \int \sqrt{k^2 - (n\lambda)^2} dx}, \tag{8}$$

$$n = 0, \pm 1, \pm 2, \dots, \pm \left(\frac{N}{2} - 1 \right), -\frac{N}{2}.$$

Here $\hat{\Phi}^+(x, n)$ denotes the directional modes of the wave field on a row, each has the direction depicted in Fig. 1. As $n\lambda$ exceeds k in magnitude, $\sqrt{k^2 - (n\lambda)^2}$, the wavenumber in the x direction, becomes imaginary, indicating evanescent modes which decay exponentially in the propagation direction. Usually the evanescent modes have negligible amplitude with sufficiently large N , so only the progressive modes are carried in the computation.

2.1 Periodic gaps in breakwaters

For periodic gaps of width $2a$ in breakwaters, the initial condition is given by the Kirchoff condition on Φ_x^\pm along the breakwater, i.e.

$$\Phi_x^+(0, y) = \begin{cases} e^{i\lambda_o y}, & |y| < a \\ 0, & |y| > a \end{cases} \tag{9}$$

where λ_o is the projection of the wavenumber in the y direction at $x = 0$, that is, $\lambda_o = k_o \sin \theta_o$, where θ_o is the incident wave angle, and the origin of the coordinates is located at

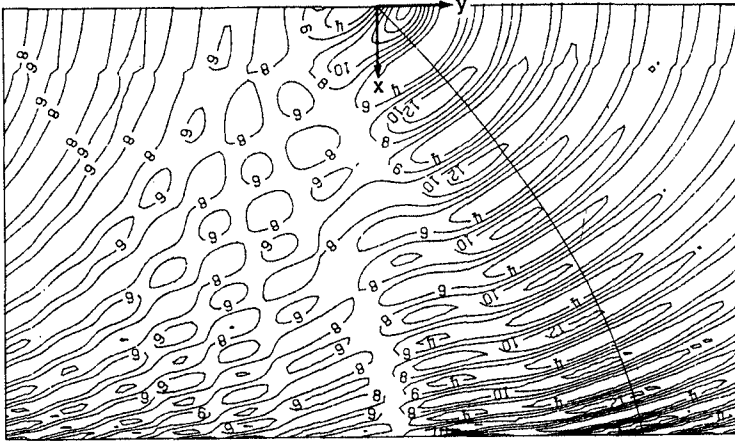


Figure 2: Instantaneous wave field behind periodic breakwater gaps on a sloping beach. The line denotes a wave ray, emanating from the center of one of the gaps. Depicted area is $405.75 \times 692.48 \text{ m}$. (reprinted with permission of Cambridge University Press)

the center of one of the gaps. $\hat{\Phi}_x^+(0, n)$ is obtained by an FFT of (9), and then $\hat{\Phi}^+(0, n)$ is computed by

$$\hat{\Phi}_x^+(0, n) = i\sqrt{k_o^2 - (n\lambda)^2} \hat{\Phi}^+(0, n) \tag{10}$$

which is the reduced form of (3) on constant depth. Finally $\Phi^+(0, y)$ is obtained by an inverse FFT of $\hat{\Phi}^+(0, n)$.

The breakwater gap shown in Fig. 2 is backed by a plane sloping beach with a slope $h_x = 0.0308k_o h_o$ where $h_o = 10 \text{ m}$ is the water depth at the location of breakwater. The gap has a width of 100 m . The incident wave field has a 9 sec wave period and a 45° angle of incidence. $N = 128$ and $\Delta x = \Delta y = 5 \text{ m}$. In Fig. 2, the instantaneous wave field on the sloping beach is shown. The influence of wave refraction is clear with the maximum of the diffraction pattern turning towards the shoreline normal. The influence of the periodic boundary conditions is also apparent as the waves from the upwave gap have intruded into the figure, yielding a short-crested sea state near the middle of the figure. The wave ray shown in the figure was determined independently using the method outlined in Mei (1983). The diffracting wave train follows the wave ray very well.

2.2 Intersecting waves past a breakwater

The specification of the incident wave field can be quite general. As a simple example, two synchronous wave trains of 9 sec period are assumed to be incident on a breakwater (386 m in length, lying on the y axis) at $\pm 30^\circ$ to each side of the x axis, creating a short-crested sea state in the absence of the breakwater, as shown in Fig. 3. Behind the breakwater, centered in the middle of the y axis, the two shadow zones cast by the two wave trains

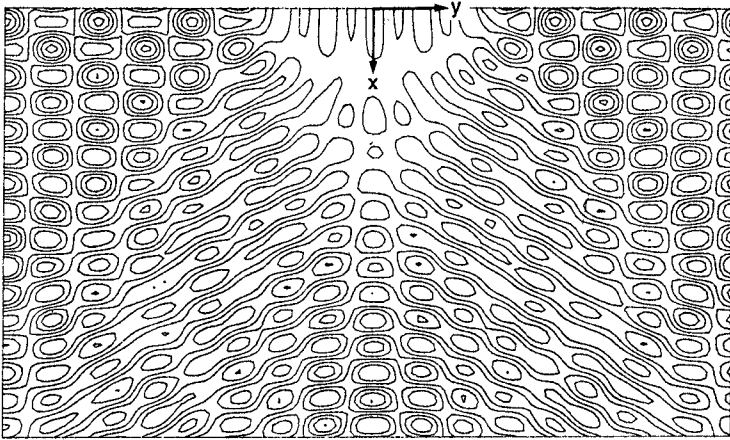


Figure 3: Instantaneous wave field behind an offshore breakwater created by two intersecting wave trains. The breakwater length is 386 m and the displayed area is 1016 m wide. (reprinted with permission of Cambridge University Press)

result in a long-crested sea state in these zones, as only one of the wave trains is blocked by the breakwater.

Extension to a truly directional sea state composed of many frequencies is straightforward. It is a matter of superposing the requisite number of wave trains with different frequencies and appropriate random phases, since for each frequency the evolution of the directional spectrum is computed in the present model.

3 Nonlinear Fourier model on irregular bathymetry

The governing equation is again taken to be the mild-slope equation

$$\nabla \cdot (CC_g \nabla \Phi) + k^2 CC_g \Phi = 0. \quad (11)$$

The wavenumber k is related to the wave angular frequency ω and the local water depth h by the linear dispersion relationship

$$\omega^2 = gk \tanh kh \quad (12)$$

where g is gravity. This relation is modified later to incorporate nonlinearity in the model.

Using the definitions of $p(x, y) = CC_g$ and $\phi = \sqrt{p} \Phi$ as in Radder (1979), the mild-slope equation becomes an Helmholtz equation

$$\nabla^2 \phi + k_c^2 \phi = 0 \quad (13)$$

where

$$k_c^2 = k^2 - \frac{\nabla^2 \sqrt{p}}{\sqrt{p}}. \tag{14}$$

For the convenience of later splitting of the solution, we define a laterally averaged wavenumber, \bar{k} , as

$$\bar{k}^2 = \frac{1}{\ell} \int_0^\ell k_c^2 dy \tag{15}$$

so that

$$k_c^2 = \bar{k}^2 (1 - \nu^2) \tag{16}$$

where

$$\nu^2 = 1 - \frac{k_c^2}{\bar{k}^2} \tag{17}$$

whose magnitude is usually much smaller than unity if the topography does not deviate drastically from straight and parallel contours. Note that \bar{k}^2 is a function of x only and the variability of depth in the y direction is contained in $\nu^2(x, y)$. Substituting (16) into (13) gives

$$\nabla^2 \phi + \bar{k}^2 \phi - \bar{k}^2 \nu^2 \phi = 0. \tag{18}$$

The Fourier transform of (18) in the y direction leads to the equations for directional modes

$$\hat{\phi}_{xx} + (\bar{k}^2 - \lambda^2) \hat{\phi} - \bar{k}^2 F(\nu^2 \phi) = 0. \tag{19}$$

Note that the Fourier transform of $(\nu^2 \phi)$ involves ϕ in the real space. Again splitting the potential and neglecting the backscattered wave, the propagation model for the forward propagating wave is obtained as

$$\hat{\phi}_x^\pm = i\sqrt{\bar{k}^2 - \lambda^2} \hat{\phi}^\pm - \frac{[\sqrt{\bar{k}^2 - \lambda^2}]_x}{2\sqrt{\bar{k}^2 - \lambda^2}} \hat{\phi}^\pm - \frac{i\bar{k}^2 F(\nu^2 \phi^\pm)}{2\sqrt{\bar{k}^2 - \lambda^2}}. \tag{20}$$

The second term on the right side represents the shoaling/refraction of each wave mode on the laterally averaged depths. The $F(\nu^2 \phi^\pm)$ term represents the interaction between

surface wave and the lateral bottom variation, which will be examined in detail later in this section. For straight and parallel bottom contours, this term vanishes and the above equation reduces to (3).

In the discrete Fourier space, (20) can be approximated as

$$\hat{\phi}_x^+ = i\sqrt{k^2 - (n\lambda)^2} \hat{\phi}^+ - \frac{\left[\sqrt{k^2 - (n\lambda)^2} \right]_x}{2\sqrt{k^2 - (n\lambda)^2}} \hat{\phi}^+ - \frac{i\bar{k}^2 F_n(\nu^2 \phi^+)}{2\sqrt{k^2 - (n\lambda)^2}}, \quad (21)$$

$$n = 0, \pm 1, \pm 2, \dots, \pm\left(\frac{N}{2} - 1\right), -\frac{N}{2}$$

associated with the discrete Fourier transforms (5) and (6). F_n denotes the n^{th} Fourier component. The above equation represents N first-order ordinary differential equations in x , which are solved by a fourth-order Runge-Kutta method. The details of finite differencing and stability analysis of the numerical method are referred to Dalrymple *et al* (1988). The numerical procedure involves calculating the Fourier modes by marching along the x direction. However, $F_n(\nu^2 \phi^+)$ in the last term in (21) should be calculated in the real domain, so, at each step, recourse to the real domain by the inverse FFT is needed.

The Fourier model (21) is linear since it is based on the linear mild-slope equation (11). In order to incorporate nonlinearity in the model, an empirical nonlinear dispersion relation proposed by Kirby & Dalrymple (1986) is used, which approximates the wavenumber for a solitary wave in shallow water and, in deep water, provides the wavenumber corresponding to the Stokes third-order theory, given by

$$\omega^2 = gk[1 + f_1(ka)^2 D] \tanh[kh + f_2(ka)] \quad (22)$$

where a is the local wave amplitude and

$$f_1(kh) = \tanh^5 kh, \quad (23)$$

$$f_2(kh) = \left[\frac{kh}{\sinh kh} \right]^4, \quad (24)$$

$$D = \frac{\cosh 4kh + 8 - 2 \tanh^2 kh}{8 \sinh^4 kh}. \quad (25)$$

The calculation of the wavenumber k using (22) needs iteration because of the dependence of the wavenumber on wave height. Thus, first we perform the computation with the wavenumber given by the linear dispersion relation (12). Using the calculated wave height, then, the wavenumber is corrected by the nonlinear dispersion relation (22). This procedure is repeated until convergence is achieved.

3.1 Interaction between surface wave modes and the bottom variation

The term $F_n(\nu^2 \phi^+)$ in (21) represents the interaction between the directional wave modes and the lateral bottom variation, which can force the evolution of the various directional

modes, even if they are initially of zero magnitude. In order to examine this mechanism, we express $F_n(\nu^2\phi^+)$, in terms of periodic convolution, as

$$F_n(\nu^2\phi^+) = \frac{1}{N} \sum_{m=0}^{N-1} \hat{\nu}^2(x, m\lambda) \hat{\phi}^+(x, (n-m)\lambda) \quad (26)$$

where $\hat{\nu}^2(x, m\lambda)$, $m = 0$ to $N - 1$, is the discrete Fourier series obtained by the Fourier transform of $\nu^2(x, y)$ in the y direction. This equation states that the m^{th} bottom mode $\hat{\nu}^2(x, m\lambda)$ triggers the $(n - m)^{\text{th}}$ wave mode to evolve the n^{th} wave mode.

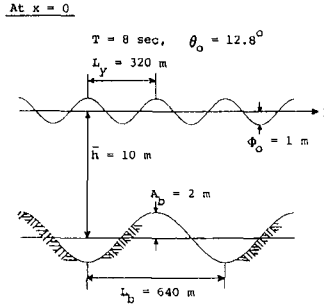


Figure 4: Bottom geometry and the initial condition of the wave field for the example of wave propagation over a bathymetry consisting of laterally periodic ridges and troughs.

In order to illustrate this more explicitly, we have applied the model to a monochromatic wave train travelling over a bed whose depth is constant in the x direction but varies sinusoidally in the y direction, creating transverse bottom ridges. These ridges begin at $x = 0$. In this particular example, the second term on the right side in (21) vanishes. The mean water depth is 10 m and the wavelength and amplitude of the bed are 640 m and 2 m, respectively, as shown in Fig. 4. At $x = 0$, a plane wave of 8 sec period and 1 m amplitude enters the domain at an incident angle of 12.8°. We have taken $\Delta x = 5$ m and $\Delta y = 10$ m to make a grid of 500 × 128 rows over 2,500 × 1,280 m model area, so that the wave mode at $x = 0$, $\hat{\phi}^+(0, n\lambda)$, is nonzero for $n = 4$ and zero for all other modes, while the bottom mode $\hat{\nu}^2(x, m\lambda)$ are appreciable for $m = 2, 4, 6, (N - 6), (N - 4), (N - 2)$ and are negligibly small for all other modes as shown in Fig. 5. At the first step, these bottom modes interact with $\hat{\phi}^+(0, 4\lambda)$ to generate the wave modes of $n = 6, 8, 10, -2, 0, 2$, respectively, which were initially of zero magnitude. Note that in an FFT, the following changes are made: $\hat{\nu}^2(x, (N - m)\lambda) = \hat{\nu}^2(x, -m\lambda)$. The mechanism for the subsequent generation of new directional modes is very complicated. Note that only the even-number modes are generated in this particular example.

Figs. 6 (a)–(d) show the amplitude spectra of the progressive modes at different sections. The wave field at $x = 0$ (Fig. 6 (a)) is described by single wave mode, $\hat{\phi}^+(0, 4\lambda)$, which is propagating at 12.8° to the x axis. The generation of new modes near the initial condition is shown in Figs. 6 (b)–(c), and the broad spectrum at $x = 2,500$ m is shown in Fig. 6 (d). Again observe that the odd-number modes are never generated.

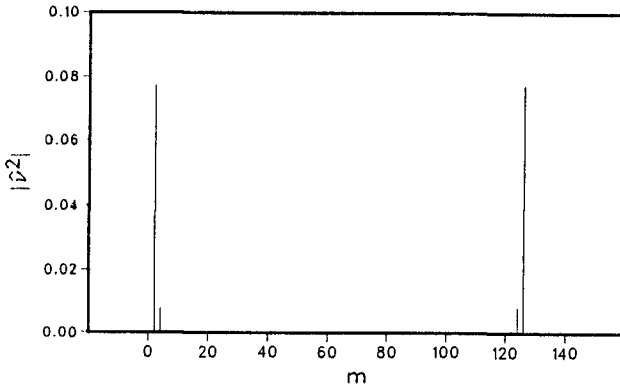


Figure 5: Amplitude spectrum of the bottom modes $\hat{\nu}^2(x, m\lambda)$ for the periodic bathymetry shown in Fig. 4. Note that $\hat{\nu}^2(x, m\lambda)$ is different from the depth mode $\hat{h}(x, m\lambda)$ which gives nonzero values for $m = 2$ and $N - 2$ and zero for all other values of m .

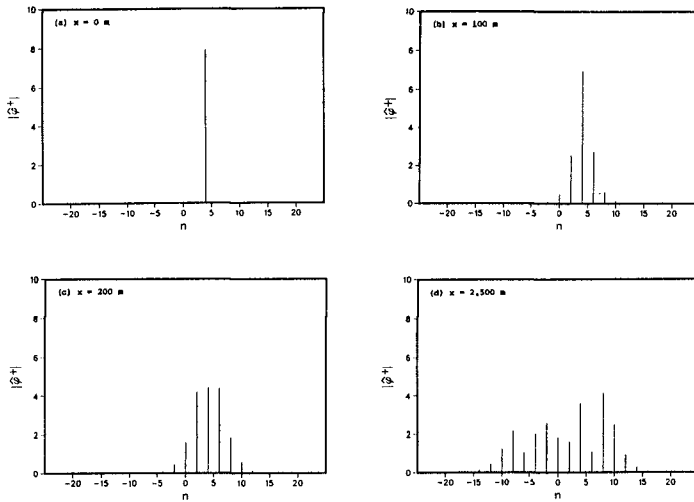


Figure 6: Evolution of the amplitude spectra of the progressive modes at different sections.

Another interesting result in this example is the wave trapping over the ridge as shown in Fig. 7, which is the contour map of the instantaneous free surface elevation at intervals of 0.5 m. The waves passing over the central ridge are focused near $x = 700\text{ m}$, $y = 720\text{ m}$ and turn back to the left. Mei (1983) has discussed this problem based on ray theory. Some of the rays determined by the Mei's method are drawn in Fig. 7. The rays 1, 2 and 8, counting from the left, travel over the wavy bed without being trapped. The rays 3 to 7,

however, are trapped. For these rays computation was stopped at the turning points, where the ray model blows up, but the extrapolation of these rays can explain the wave trapping phenomenon over the ridge in this example.

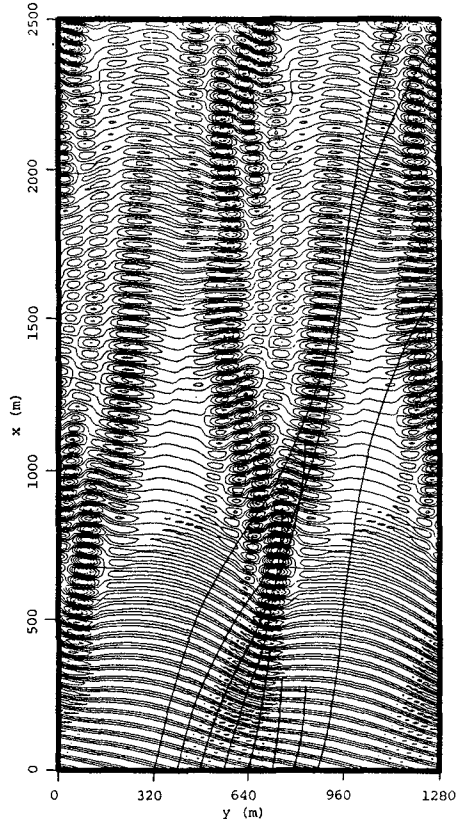


Figure 7: Instantaneous wave field over periodic ridges and troughs. The lines denote wave rays emanating from $x = 0$ at 12.8° angle of incidence at intervals of 80 m .

3.2 Wave focusing behind a circular shoal

For the purpose of testing the model for the prediction of wave deformation on an irregular bathymetry, we have chosen the experiment reported by Ito & Tanimoto (1972).

The experimental bathymetry consists of a circular shoal resting on a flat bottom $h_1 = 0.15\text{ m}$ as shown in Fig. 8. The water depths in the shoal region are described by

$$h = h_2 + 0.15625[(x - 1.2)^2 + (y - 1.2)^2] \quad (27)$$

where $h_2 = 0.05 \text{ m}$ is the depth at the shoal crest. A monochromatic wave train with the wave height 1.04 cm and the wave period 0.511 sec enters the domain at $\theta_o = 0^\circ$.

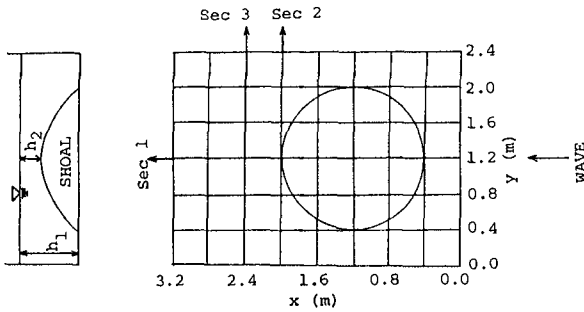


Figure 8: Geometry of the computational domain for the experiment by Ito & Tanimoto (1972).

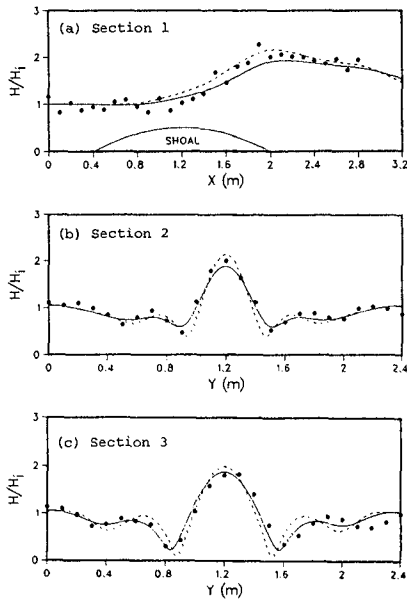


Figure 9: Comparison of the model results against the experimental data by Ito & Tanimoto (1972) in terms of normalized wave height with respect to incident wave height. ● = Experiment, - - - = Linear model, — = Nonlinear model.

For the three different sections indicated in Fig. 8, data from the experiment of Ito & Tanimoto are available. Comparison with the model results along these sections are shown in Figs. 9 (a)–(c) in terms of normalized wave height with respect to the incident wave height. In each figure, linear and nonlinear model results are indicated by dashed and solid lines, respectively, while black dots indicate measured data points. Nonlinear effects reduce the wave heights along the centerline of wave focusing and broaden the region of focused wave so that the diffraction fringes are displaced away from the centerline. Along the centerline (Fig. 9 (a)), data fall between the predictions of the two models, with the nonlinear model slightly underpredicting the data. On section 2 where the cusped caustic is fully developed, again it is difficult to judge which model predicts the data better. However, on section 3 where the wave has passed through the caustic cusp, the nonlinear model predictions and the data points are in much better agreement than the linear model.

Through the above example we have verified that our model is a reasonably good predictor of the wave field development on an irregular bathymetry where the effects of refraction, diffraction and nonlinearity are equally significant. However, that example is not sufficient for showing the ability of the model for a large angle of incidence. The next example we have chosen for this purpose is for the same wave and bottom geometry as those in the above example but different angle of incidence. Due to the axisymmetry of the circular shoal, the wave focusing pattern behind the shoal should be independent of the angle of incidence, if the model predicts it 'correctly'.

The contours of wave height normalized with respect to the incident wave height are shown in Figs. 10 (a) and (b) for $\theta_o = 0^\circ$ and $\theta_o = 45^\circ$, respectively. The right half of the domain in the case of $\theta_o = 45^\circ$ is the extension of the flat bottom. The results of a linear parabolic model are also shown in Fig. 10 (a) as dotted lines for $\theta_o = 0^\circ$ and in Fig. 10 (c) for $\theta_o = 45^\circ$. The difference between the present model and the parabolic one is not significant for $\theta_o = 0^\circ$ even though the entire wave focusing pattern in the parabolic model is shifted slightly backward compared with that in the present model. For $\theta_o = 45^\circ$, however, the parabolic model gives large distortion of the wave focusing pattern. Especially the center line of wave focusing rotates by about 12.5° towards the positive x direction. For the present model, some images of the shoal appear periodically in the y direction and the upper left corner is contaminated by the effects of the upwave shoal. Over the shoal, the asymmetric distortion to the focusing pattern at $\theta_o = 45^\circ$ is apparent. However, the overall wave focusing pattern behind the shoal at $\theta_o = 45^\circ$ is very similar to that at $\theta_o = 0^\circ$, showing that the model works reasonably well for a large angle of incidence.

The height of the shoal in the above example is $2/3$ of the water depth on the flat bottom, indicating an unreasonably high shoal considering the normal situation in real cases. Dalrymple *et al* (1988) have tested the model for shallower shoals and showed that the bigger the shoal height, the bigger the asymmetric distortion to the focusing pattern for the same angle of incidence. They also have presented a simple theoretical analysis regarding the accuracy of the model in terms of lateral depth variation and wave propagation angle, concluding that in order for the present model to be accurate for a large angle of incidence, the lateral depth variation should be small.

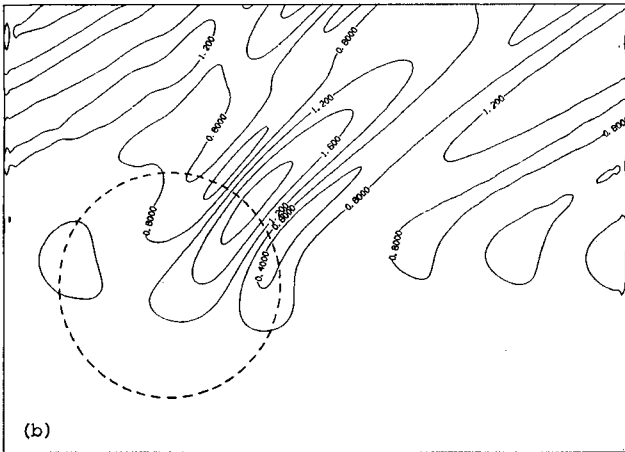
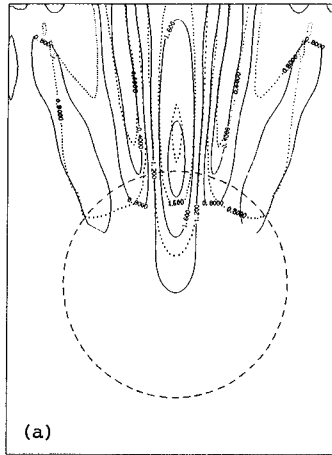


Figure 10: For caption see next page.

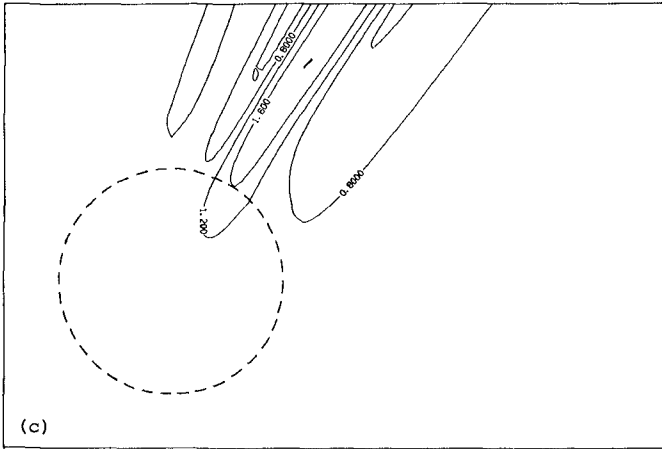


Figure 10: Wave focusing pattern behind the circular shoal used in the experiment by Ito & Tanimoto (1972). Contours indicate wave height normalized with respect to incident wave height. (a) $\theta_o = 0^\circ$ (— = Present model, = Parabolic model), (b) $\theta_o = 45^\circ$ (Present model), (c) $\theta_o = 45^\circ$ (Parabolic model).

4 Conclusion and discussion

Two wide-angle water wave propagation models using the spectral Fourier method have been reported, one for straight and parallel depth contours and the other for irregular bathymetry. In both of the models, the wave field at the initial row ($x = 0$) is Fourier decomposed into directional modes and the evolution of each mode due to bottom variation is calculated by marching along the x direction; finally, the real wave field is recovered by taking the inverse Fourier transform in the y direction.

All the examples presented are for a monochromatic wave train or two intersecting waves. As demonstrated in the example of two intersecting waves past a breakwater, a directional wave with single frequency can be modelled easily by the present models. If the steady state is assumed so that the interaction among the waves with different frequencies is neglected, the extension of the models to the random directional wave field can be made by superposing the requisite number of waves with different frequencies, with appropriate phases.

Nonlinearity was included in the model by correcting the wavenumbers iteratively using the nonlinear dispersion relationship, (22). Wave-current interaction also could be included by using the following dispersion relationship

$$\sigma = \omega + \vec{k} \cdot \vec{U} \tag{28}$$

where $\sigma = 2\pi/T$ is newly defined as the angular frequency, ω is given by (22), and \vec{U} is the depth-mean current vector which is assumed to be known.

Acknowledgement

This work is partly a result of research sponsored by NOAA Office of Sea Grant, Department of Commerce, under Grant No. NA86AADSG040. The U.S. Government is authorized to produce and distribute reprints for governmental purposes, notwithstanding any copyright notation that may appear herein.

References

- Berkhoff, J.C.W. 1972. Computation of combined refraction-diffraction. *Proc. 13th Int. Conf. Coastal Eng.*, ASCE, Vancouver. 471-490.
- Booij, N. 1981. Gravity waves on water with non-uniform depth and current. *Rep. 81-1*, Dept. of Civil Eng., Delft Univ. of Tech.
- Dalrymple, R.A. & Kirby, J.T. 1988. Models for very wide-angle water waves and wave diffraction. *J. Fluid Mech.* 192. 33-50.
- Dalrymple, R.A., Suh, K.D., Kirby, J.T. & Chae, J.W. 1988. Models for very wide-angle water waves and wave diffraction. Part 2. Irregular bathymetry. *J. Fluid Mech.* (in review)
- Dean, R.G. & Dalrymple, R.A. 1984. *Water wave mechanics for engineers and scientists*. Englewood Cliffs: Prentice-Hall. 353pp.
- Ito, Y. & Tanimoto, K. 1972. A method of numerical analysis of wave propagation: Application to wave diffraction and refraction. *Proc. 13th Int. Conf. Coastal Eng.*, ASCE, Vancouver. 503-522.
- Kirby, J.T. & Dalrymple, R.A. 1983. A parabolic equation for the combined refraction-diffraction of Stokes waves by mildly varying topography. *J. Fluid Mech.* 136. 453-466.
- Kirby, J.T. & Dalrymple, R.A. 1986. An approximate model for nonlinear dispersion in monochromatic wave propagation models. *Coastal Eng.* 9. 545-561.
- Liu, P.L.-F. & Tsay, T.-K. 1984. Refraction-diffraction model for weakly nonlinear water waves. *J. Fluid Mech.* 141. 265-274.
- Mei, C.C. 1983. *The applied dynamics of ocean surface waves*. New York: Wiley-Interscience. 740pp.
- Radder, A.C. 1979. On the parabolic equation method for water-wave propagation. *J. Fluid Mech.* 95. 159-176.

CHAPTER 17

Wave Climate off Rio de Janeiro

Maria Helena Severo de Souza*
Carlos Eduardo Parente Ribeiro**

ABSTRACT

The objective of this work is to understand the evolution and main features of the wave climate in the offshore area off Rio de Janeiro State - Brazil, using point measurements. Several spectral models are compared with the data and criteria based on Jonswap and Mitsuyasu relationships are established to identify situations of combined sea and swell from different directions. The Toba model is used to get friction wind values from the spectra for comparison with measured winds. After understanding the main features of the wave climate and using visual observations for wave direction and the spectral information, a distribution of average energy vs direction is calculated.

1. INTRODUCTION

The offshore area northern off Rio de Janeiro State (fig. 1a) is a big oil production region known as Campos basin. In some locations oil is being exploited in water depths of 400 meters, among the largest in the world and new promising fields shall be exploited above 1000 meters. The design and operation of structures and other oceanic systems for such depths is being a big challenge for ocean engineers and the knowledge of environmental conditions is of paramount importance. Wave data is still scarce in the area mainly that concerned with directional spectra.

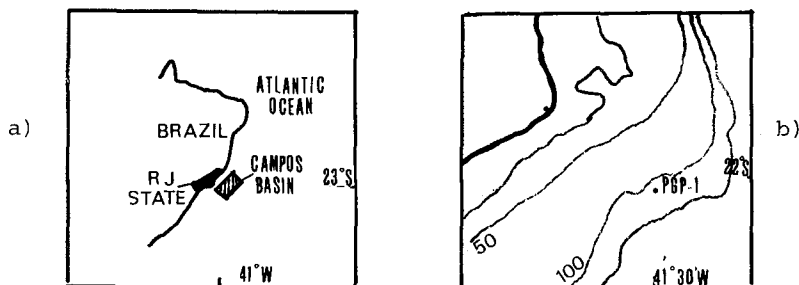


Figure 1.a) The Campos basin; b) Offshore plataform PGP-1

*- Researcher, Brazilian Navy Hydrographic Institute

** Associate Professor, COPPE - Federal University of R. de Janeiro. Brazil.

The weather in the basin is dominated by the presence of a tropical anticyclone and periodically visited by cold fronts and polar masses coming from the south.

This work is an attempt to describe the evolution and main features of the wave climate from point measurements and visual wave direction observations. Several criteria are established for the identification of the different situations most of them of combined seas and swell.

2. DATA ACQUISITION AND ANALYSIS

The wave and wind data used in this work was acquired from May 1984 to June 1985 in an offshore platform in the Campos basin (PGP-1) located as shown in fig.1b. The related information is resumed below.

Wave staff:	discrete resistive - magnetic coupling
measurement period:	26.09 minutes
measurement interval:	3 hours
wave direction:	visual observation
wind sensor:	cup anemometer and vane
local depth:	130 mts
FFT analysing period:	17,06 minutes
sampling frequency:	1 Hz
number o samples:	1024
degrees of freedom:	50

Two wavestaffs were used and according to the wave direction the best record was selected.

3. A BRIEF METEOROLOGICAL PICTURE OF THE AREA

The region is deeply influenced by the South Atlantic anticyclone. A typical good weather chart is shown in fig.3a. NE moderate winds and relatively large fetches are common at these times. Polar masses coming from the South reach periodically the region.

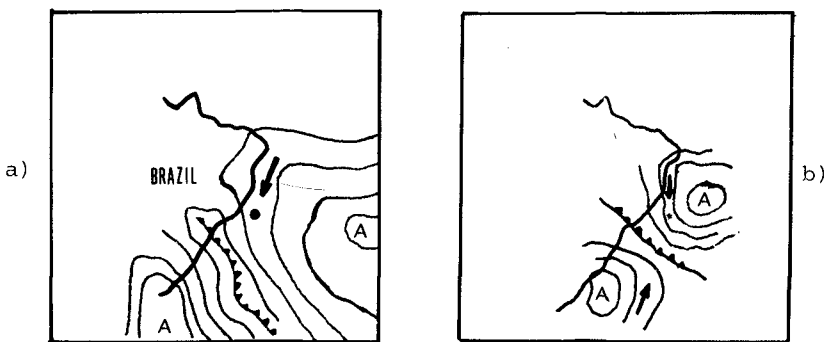


Figure 3. a) good weather; b) cold front approaching

The wind changes successively from NE to NW and to SW. With strong SW winds and large fetches, big swells and rough seas occur in the area. Fig.4 shows the cold front approaching, producing a strong, limited fetch, NW wind. After the passage of the cold front, SE winds can blow for hours and even days producing big swells in the region. Fig. 4 illustrates this situation.

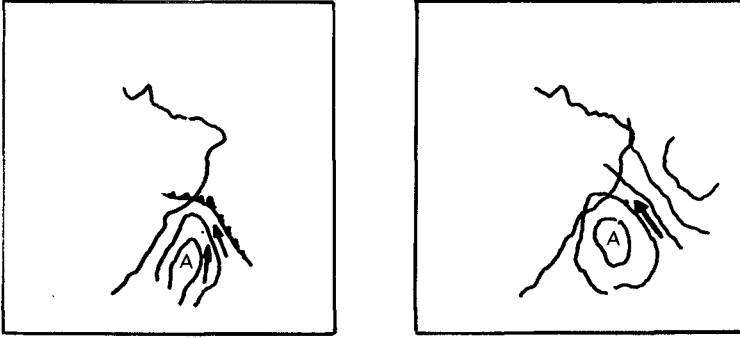


Figure 4. cold front passing over Campos basin

4. SPECTRAL MODELS

The meteorological situations can produce a combination of sea and swell from several directions; by fitting spectral models to the data we try to identify these different contributions in order to have a better understanding of the wave climate.

4.1. THE PIERSON-MOSKOWITZ MODEL (PM)

The PM model for well developed seas, proposed in 1964, is used here to indicate a limiting value for the nondimensional peak frequency. Below this value one considers a developed sea and the presence of swell. The formulation is:

$$S(f) = \alpha g^2 (2\pi)^{-4} f^{-5} \exp [-5/4 (f/f_m)^4] , \text{ where:}$$

$$\alpha = 8.1 \times 10^{-3} - \text{Phillips constant;}$$

$$f_m = (2\pi)^{-1} (4 \beta/5)^{1/4} g (U_{19.5})^{-1} - \text{peak frequency;}$$

$$U_{19.5} = \text{wind at 19.5 mts ; } \beta = 0.74$$

$$\tilde{f}_m = f_m U/g - \text{non dimensional frequency}$$

$$\tilde{f}_m = 0.14 \text{ for } U_{19.5} \text{ and } \tilde{f}_m = 0.13 \text{ for } U_{10}$$

4.2. THE JONSWAP (J) MODEL

For fetch limited seas Hasselmann et alli (1973) proposed the JONSWAP model named after an experiment in the North Sea; This model fits a spectrum to the wave data. The formulation is:

$$S(f) = \alpha g^2 (2\pi)^{-4} \exp[-5/4 (f/f_m^2)^{-4}] \gamma \exp[-(f-f_m)^2 / 2\sigma^2 f_m^2] \quad [1]$$

α = scale factor; f_m = peak frequency; γ = scale factor

σ = shape factor

A shape parameter λ is defined as: $\lambda = E f_m^4 / \alpha g^2$ [2]

E = Energy of the spectrum ; α is calculated by:

$$\alpha = (0.65 f_m)^{-1} \int_{1.35 f_m}^{2 f_m} (2\pi)^4 f^5 g^2 \exp[5/4 (f/f_m)^4] S(f) df \quad [3]$$

γ is calculated from α and $S(f)$:

$$\gamma = S(f_m) (2\pi)^4 f_m^5 e^{(5/4)} (\alpha g^2)^{-1} \quad [4]$$

Hasselmann and alli (1976) have shown that for developing seas λ has an average value of 1.3×10^{-4} with a small scatter.

Considering that E and f_m are parameters measured with confidence if the data quality is good. We decide to compare the value of α obtained from relation [3], called now α' , with the one from relation [2] called now α_h .

If there is only a local sea in the area the values of α' and α_h must be very close. If there is a swell mixed with a local sea α' is bigger than α_h . In some situations a peak in the high frequency region due to a mixture of two seas may cause $\alpha_h > \alpha'$. Fig. 5 illustrates these situations.

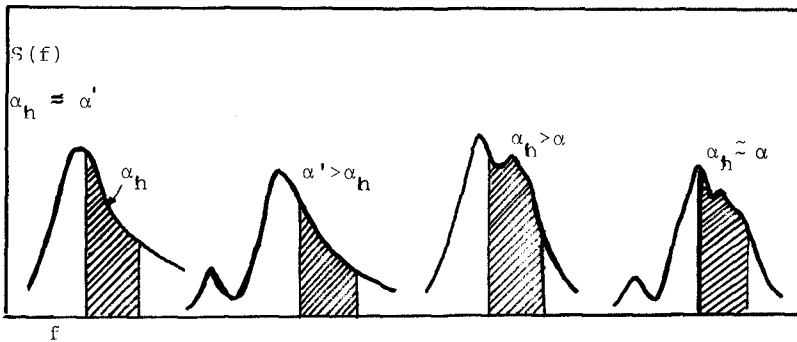


Figure 5. α' and α_h for different situations

In the last example d) we may have a compensation caused by the two effects and both values can remain very close. This comparison of α_h and α' was used to help in the selection of pure and combined seas. See Souza (1988).

4.3. JONSWAP AND MITSUYASU RELATIONSHIPS

Several nondimensional parameters are used in the data modelling:

$$\tilde{f}_m = f_m U_{10}/g = \text{non dimensional peak frequency}$$

$$\tilde{E} = E g^2/4 ; \tilde{F} = F g/U_{10}^2$$

where F is the fetch, E the energy of the spectrum, f_m the peak frequency and U_{10} the wind at 10 mts.

Hasselmann proposed (1976) the following relationships between these parameters:

$$\tilde{f}_m = 2.84 \times \tilde{F}^{-0.3} \quad [5]$$

$$\alpha = 6.62 \times 10^{-2} \tilde{F}^{-0.2} \quad [6] \quad \alpha = 3.3 \times 10^{-2} \tilde{f}_m^{2/3} \quad [7]$$

$$\tilde{E} = 5.3 \times 10^{-6} \tilde{f}_m^{-10/3} \quad [8]$$

Mitsuyasu (1980) after experiments in bays and lakes suggested:

$$gE^{1/2}/u_*^2 = 1.31 \times 10^{-2} (gF/u_*^2)^{0.5} \quad \text{and}$$

$$f_m u_*/g = (g F/u_*^2)^2$$

where u_* is the friction wind

Using $u_* = CD U_{10}$ and CD , the drag coefficient, as 1.6×10^{-3} he arrived to the following relationships:

$$\tilde{E}^{1/2} = 5.24 \times 10^{-4} \tilde{F}^{1/2} \quad [9] \quad \tilde{f}_m = 2.92 \times \tilde{F}^{-1/3} \quad [10]$$

$$\tilde{E} = 6.84 \times 10^{-6} \tilde{f}_m^{-3} \quad [11]$$

The dimensional form of [11] is $E f_m^3 = 6.84 \times 10^{-6} g u_e^2$. Using E and f from the data an effective wind (U_e) can be calculated for the area. Differences between the two formulations can be explained by the use of different values for CD (J uses 1.0×10^{-3}).

4.4. THE TOBA MOEEL

The wind was measured at 40 mts. In order to improve the wind values and have more confidence when using the relationships for the nondimensional parameters, we used the model proposed by Toba (1978) for the high frequency part of the spectrum, to calculate u_* and U_{10} . The formulation is:

$$S(f) = \alpha' (2\pi)^{-3} g u_* f^{-4} \quad \text{for } f > f_m \quad [12]$$

$$\alpha' = 8.7 \times 10^{-2} \quad (\text{value suggested by Mitsuyasu (1980)})$$

u_* is calculated from:

$$u_* = (0.8 f_m)^{-1} \int_{1.2 f_m}^{2 f_m} (\alpha' g)^{-1} S(f) (2\pi)^3 f^4 df \quad [13]$$

From u_* we calculate U_{10} using $u_* = CD U_{10}$. For the calculation of CD we used the formula proposed by Garratt (1977) based in another one by Charnock adapted for an interval for U between 4 and 21 m/s.

$$CO \times 10^{-3} = 0.75 + 0.067 u_* \quad [14]$$

We can correct U_{10} to 40 meters by:

$$U_{40} = U_{10} (1 + (1/0.4) \sqrt{CO} \ln(40/10)) \quad [15]$$

and compare with the measured wind V_{40}

5. RESULTS AND DISCUSSIONS

5.1. CALCULATED PARAMETERS

The following parameters were calculated for each record: f_m (peak frequency), E (energy) H_s (- significant wave), u_* , $f_m^* = f_m u_*/g$, f_m , $E^* = E g / u_*$, F , U_{10} - wind at 10m from u_* , CO , V_{10} - measured wind reduced to 10m, α' , α and.

5.2. WIND CALCULATIONS AND COMPARISONS

For sea states free of swell, produced by local winds over small fetches it was possible to compare the wind at 10m calculated from u_* (U_{10}) with the wind at the same height (V_{10}) reduced from the wind measured at 40m (V_{40}). Table 1 below shows values of U_{10} , V_{10} , U_e and CO for situations of local winds and small fetches. The agreement is considered good, the differences being due to innacurate values of CO , innadequacy of the correction formula or even poor quality wind measurements.

V10	U10	Ue	CD	V10	U10	Ue	CD
14.5	14.4	14.0	1.7	12.1	14.4	13.8	1.7
13.3	15.0	15.4	1.8	12.9	14.5	16.9	1.7
13.4	15.0	16.9	1.8	12.0	15.2	17.9	1.8
12.2	13.6	-	1.7	11.2	14.3	17.8	1.7
12.0	16.9	-	1.9	13.4	14.7	14.5	1.7
15.5	17.4	-	1.9	13.4	13.1	14.5	1.6
13.3	16.6	-	1.9	13.4	12.7	13.6	1.6
9.1	12.0	13.3	1.5	16.0	13.6	13.1	1.7
13.4	14.5	14.7	1.7	10,8	14.4	15.9	1.7
14.3	14.8	16.2	1.7	11.7	12.2	13.6	1.6
12,9	13.7	12.4	1.7	9.0	12.3	13.3	1.6

Table 2 - Wind Comparisons

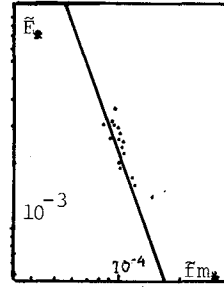


Figure 7. F_m^* vs F

Using relation [11] from Mitsuyasu we can evaluate the quality of the u^* values as shown in fig.7 above. The data points refer to situations without swell.

5.3 - COMPARISONS OF α with f_m and \tilde{F}

Fig. 8 shows plots of α vs f_m , α vs \tilde{F} and γ vs \tilde{F} for the selected situations. The basic criterium for this selection is α' close to α_h

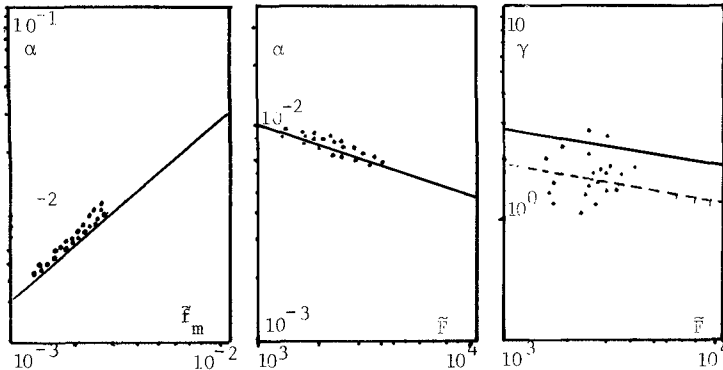


Figure 8. Comparison between parameters

5.4. CRITERIA FOR SELECTION OF SEA STATES

The following criteria were used to identify the different sea states in the area:

- a) fetch limited seas: high values of u^* , f_m^* and α_h ; α_h close to α' .
- b) developed seas: $f_m < 0.13$; u^* values indicating local sea and sufficient wind duration.
- c) swell (unimodal): no local wind; low values of f_m^* , α_h and α'
- d) fetch limited sea and swell: $\alpha' \gg \alpha_h$; high values of f_m^* .

5.5. ENERGY DISTRIBUTION

Using visual observations and establishing several criteria to separate different combinations of sea and swell it was possible to calculate a daily average of energy distribution per 22.5 degrees sector for every month. A computer program was written to compare values of α' and α_h and with this information and taking into account the peak frequency value to verify the quality of the visual observations and also the make a partition of the energy between the sectors. Table 2 below show this result.

MONTH	000	022	045	067	090	112	135	157	180	202	225	247	270	292	315	337
JUN	1	2	8	15	0	14	142	135	14	14	21	0	10	7	0	38
JUL	5	62	65	45	72	35	80	124	130	320	63	12	5	0	5	0
AUG	11	74	46	36	0	5	0	35	147	364	0	0	0	0	0	0
SEP	0	8	20	33	67	37	28	54	97	49	4	2	1	0	1	6
OCT	0	13	13	12	18	16	45	67	78	64	63	1	0	0	0	0
NOV	3	0	19	78	51	3	25	33	20	20	0	0	0	0	0	0
DEC	17	55	27	11	27	45	11	43	45	64	8	14	0	0	0	0
JAN	13	73	46	2	0	0	11	22	25	26	5	1	2	3	2	4
FEV	14	28	49	10	9	13	14	31	32	25	0	5	0	0	0	0
MAR	10	9	22	20	17	27	6	72	77	69	35	0	0	0	0	1
APR	2	19	10	6	54	18	42	94	100	76	0	0	0	1	0	0
MAY	5	8	38	24	15	24	12	91	110	98	2	3	8	2	0	4

Table 2 - Energy distribution - daily average in kw-hr per sector.

6. CONCLUSIONS

The techniques presented in this work made possible to characterize the main features of the wave climate in the Campos basin based on wave data from point measurements.

The comparison of α_h and α' and the calculation of U_{10} from u_* produced good results and made possible an automatic identification of different sea states.

The South Atlantic anticyclone has an strong influence in the wave climate of the basin. The good weather prevails most of the time with NE winds and a combination of velocity and fetch in such a way that peak periods are always less than 7.5 seconds.

When the cold front is approaching the intensification of the NE wind is associated with small fetches so that again the peak period remains under 7.5 seconds.

The cold front bring strong SW winds and large fetches producing rough seas and peak periods between 11 and 15 seconds. When the front passes can produce SE winds with moderate fetches. A swell from SE occurs very often with

the NE wind blowing again and closing the cycle.

7. BIBLIOGRAFY

- GARRATT, J.R. (1977) - "Review of drag coefficients over oceans and continents". Mon. Weath. Rev. U.S. Dep. Agric., 105, pp. 915-929.
- HASSELMANN, K. et al. (1973) - "Measurements of Wind-Wave Growth and Swell Decay during the Joint North Sea Wave Project (JONSWAP)". Dtsch. Hydrog. Inst.
- HASSELMANN, K. et al. (1976) - "A Parametric Wave Prediction Model". J. Phys. Oceanogr. 6, pp. 200-228
- MITSUYASU, H. et al. (1980) - "Observation of the Power Spectrum of Ocean Waves Using a Cloverleaf Buoy". J. Phys. Oceanogr. 10, No. 2, pp. 286-296
- TOBA, Y. (1978) - "Stochastic form of the growth of wind waves in a single-parameter representation with physical implications". J. Phys. Oceanogr. 8, No. 3, pp. 494-507
- SOUZA, M.H.S. (1988) - "Caracterização do Clima de Ondas ao norte do Estado do Rio de Janeiro" - In portuguese- MSc. Thesis - COPPE/UFRJ.

CHAPTER 18

AN EXPERIMENTAL STUDY OF HARBOUR RESONANCE PHENOMENA

F.M.Martinez *
V.S.Naverac **

An extensive series of experiments has been carried out at the laboratory in order to study rectangular harbour oscillation excited by incident long waves. Attention is focused on the effect of head loss entrance on resonant response attenuation. A "gross" quadratic hydraulic head loss coefficient is defined and information about it, resulting from tests, is provided. Experimental conditions used in this piece of work seem to be realistic under suitable scaling for Northern Spain harbours.

Introduction

It is a well known fact that long period waves induce harbour oscillations and can cause severe problems to moored ships: breakage of mooring lines, hazards in berthing and cargo handling and possibly an eventual leaving of the berth, damaged fenders and so on.

Resonance of harbours has attracted the attention of researchers and has been successfully studied by means of both mathematical and physical models including the cases of inviscid and real fluid. If real fluid effects are ignored a narrowing of the harbour entrance leads to an enhancement in harbour surging ("harbour paradox", Miles and Munk (1961)).

Previous studies have shown the importance of frictional loss at the harbour entrance (Fukuuchi and Ito (1966), Ito (1970), Horikawa and Nishimura (1970), etc) and the effectiveness of energy dissipation due to friction at the bottom, Kostense et al (1986), in order to influence the peak amplitude, particularly at the first mode of resonance.

This piece of work, where abstraction is made about the long wave origin, includes results, analysis and comparison of different test carried out at the laboratory on two rectangular harbour models excited by incident regular long waves. Attention is focused on

* Director

** Head of Physical Models Division
Centro de Estudios de Puertos y Costas, CEDEX
Antonio López, 81, 28026 Madrid, SPAIN

definition, evaluation and providing some information about a quadratic hydraulic "gross" head loss coefficient by using, under some special experimental conditions, a significant reference velocity.

Although numerical models predict the natural frequencies and the corresponding oscillation modes there is an increasing need for realistic values of amplitudes and as a consequence more experimental information is also needed about head loss or friction coefficient values.

Other previous experimental works (Horikawa and Ishimura (1970), Lee (1971), Lee and Raichlen (1972), Giles and Lee (1975), etc.) considered the case of a total reflective coast. In this study, the imposed conditions ignore the reflected waves from the coast in the same way as a harbour with breakwaters protruding seaward from a dissipative beach. This hypothesis was used by Iribarren (1958) studying the resonance phenomena in the Spanish Basque Country harbours.

Although the first mode of resonance has only been tested the proposed "gross" coefficient could be relied on to apply to Helmholtz or pumping mode.

Lee (1971) and (1972) provides a comprehensive summary about experimental research in this field.

Some experimental works aimed at solving real problems have been carried out by different researchers: Wegell and Sorensen (1980), etc.

Remarks about the theory

a) Effect of a sudden constriction. Usual approach.

From continuity, energy and momentum equations applied between two sections at each side of a sudden constriction, outside the eddy zone, we may write:

$$\Delta\eta = \frac{k}{2g} u|u| + \frac{L}{g} \frac{\partial u}{\partial t} \quad (1)$$

Mei (1983), where

$\Delta\eta$ = free surface elevation difference
 u = velocity
 k = head loss coefficient
 L = length coefficient

If apparent inertia term is neglected equation (1) becomes:

$$\Delta\eta = \frac{k}{2g} u|u| \quad (2)$$

The quadratic friction term makes the problem non linear and the so-called equivalent linearization may be applied if the response is dominated by the first harmonic:

$$\Delta \eta = C u \quad (3)$$

$C =$ equivalent friction coefficient

Ito (1970) and Horikawa and Nishimura (1970) developed a theoretical model which incorporated formula (2) by using an estimated constant K proved to be reliable from Ofunato Bay results against tsunami.

b) Located head loss

In non-oscillatory flows the head loss at a sudden constriction may be written:

$$\Delta H = K \frac{V^2}{2g}$$

where

$\Delta H =$ head loss (specific energy difference)
 $V =$ reference velocity
 $K =$ coefficient attached to V

$K = K(\text{Re, geometry})$
 $\text{Re} =$ flow Reynolds number
 if the flow is highly turbulent
 $K = K(\text{geometry})$

In highly turbulent oscillatory flows:

$K = K(\text{geometry, oscillatory, Strouhal or Keulegan - Carpenter, etc., flow numbers})$

Proposed analysis

The present analysis, aimed at yielding reasonable global predictions, is rather different from the usual ones and can be formulated as following:

Assuming that ΔH is the water surface elevation difference, with and without constriction at the entrance, at the back wall section inside the rectangular harbour, we may write:

$$\Delta H = K \frac{V^2}{2g} \quad (5)$$

under the hypothesis that head loss balances at the harbour entrance the joint effect of surface elevation, radiation and reflection difference. Measuring ΔH and taking an appropriate and significant reference velocity V , a "gross" quadratic head loss coefficient K , can be estimated, which is indicative of constriction effectiveness and useful to practical applications.

- K estimation

Let : a = the outside amplitude (a=h/2; h=long wave height)
 f_0 = the amplification factor at resonance without constriction
 f_i = the amplification factor at resonance with constriction i

The amplification factor is defined as the ratio of the maximum wave height occurring in the harbour model to the wave height measured outside. For the first mode of resonance, the maximum wave height occurred along the back wall of the model. (f_0 and f_i are referred to maximum amplitude inside the harbour).

Thus: $\Delta H = f_0 a - f_i a = (f_0 - f_i) a$

putting $v = \sqrt{2gf_i a}$ (from Bernouilli/Torricelli law)

and invoking (6), we have:

$$K = \frac{f_0}{f_i} - 1$$

Bearing in mind that the amplification factor is a function of amplitude and other variables.

The effectiveness of constriction can also be simply evaluated by means of:

$$E = \frac{(f_0 - f_i)^a}{f_0^a} = 1 - \frac{f_i}{f_0} = 1 - \frac{1}{K} \quad (8)$$

Experimental apparatus

A series of experiments, aimed at f and K evaluation, was conducted at the laboratory in a rectangular wave basin 0.5 m deep, 5 m. wide and 18 m. long. The hydraulic piston wave generator was located at one end of the basin.

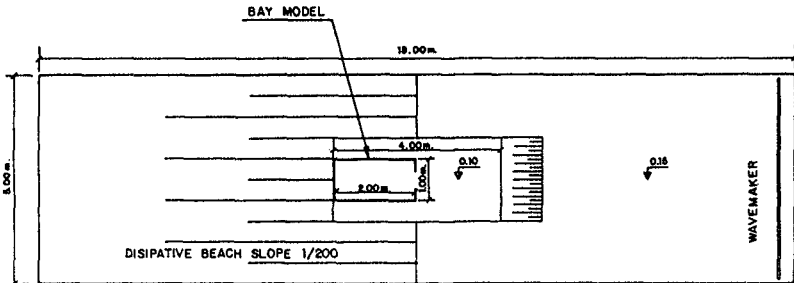


Fig. 1.- Wave basin. Plan view

A 5:1000 beach was built opposite the wavemaker in order to minimize wave reflections. Regular waves were generated with amplitudes (height) between 3 and 8 mm. and frequencies in the range 0.150-0,05 Hz. Two rectangular harbour models were used:

- Model A (2m. long, 1m. wide, 0.1m. deep)
- Model B (2m. long, 0.5 m. wide, 0.1m. deep)

Constrictions at the model entrance were made by using sharp edge elements as breakwaters. Effective wave absorbers (coconut fiber blankets and metallic wire filters) were placed to minimize reflections. Water surface levels were recorded, inside and outside the harbour basin model, when resonance had reached stationary conditions, by using resistive gauges placed to provide information about different conditions (open sea without model, standing waves, partially reflected waves, etc.).

Flow Reynolds number values guaranteed turbulence development in the models. Long wave requirements were fulfilled.

Extrapolation to real conditions is assumed to be made by using Froude similarity, without or with slight scale distortion

Results and analysis

Figures 2 to 5, similar to those of other authors, summarize some results corresponding to the present experiments in the case of centered entrance.

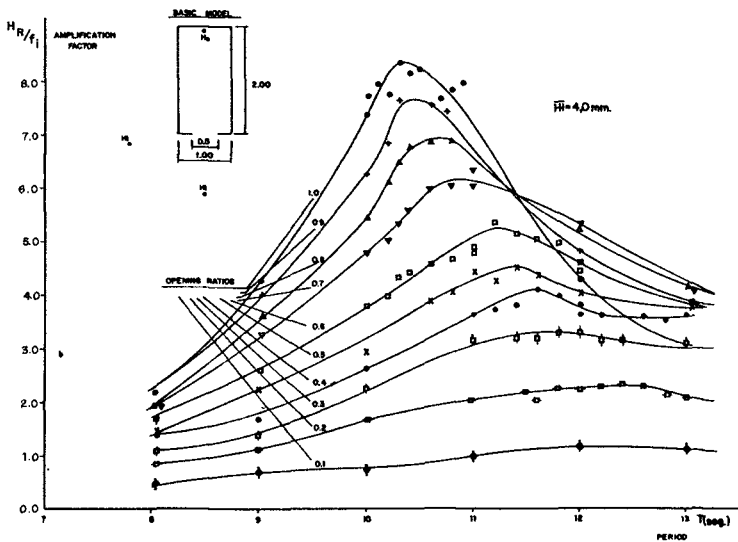


Fig. 2.- f versus T curves. Model A. Pure wave 4mm.

The amplification factor versus period bell-shaped curves, corresponding to several opening ratios, show clearly the peak response attenuation, inside the harbour, due to entrance friction. Separation of horizontal flows at each end of the entrance was very noticeable in the experimental work.

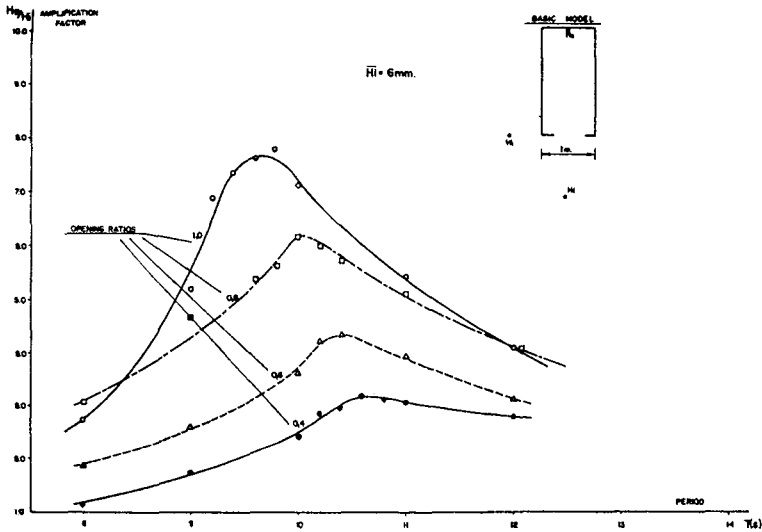


Fig. 3.- f versus T curves. Model A. Pure wave 6mm.

Amplification factor and resonant period depend upon the opening ratio, on harbour and entrance geometries and on oscillatory flow characteristics.

Bell-shaped curve "steepness" depends on the outside amplitude and on the harbour geometry. Small outside amplitudes lead to an increase in curve "steepness", larger ones lead to smoother curves. Note that increasing the amplitude leads to a decrease in f .

In the range of present experimental conditions, nearly fifty percent of peak amplitude reduction inside the harbour can be achieved with fifty percent of entrance aperture ratio.

As was previously pointed out, amplification factor depends upon the harbour geometry. Increasing the harbour ratio (width/length) leads to a decrease in amplification factor and viceversa.

From test results it can be concluded that the reduction of resonant peaks by entrance loss is more pronounced for larger amplitude and narrower entrance.

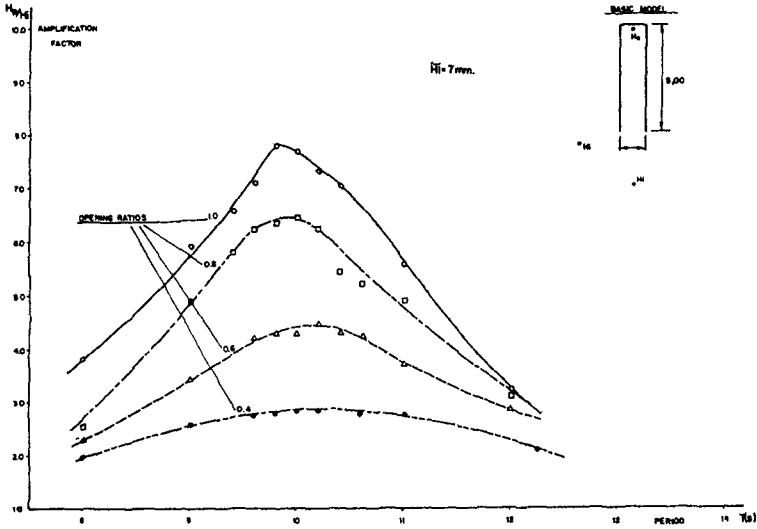


Fig. 4.- f versus T curves. Model B. Pure wave 7 mm.

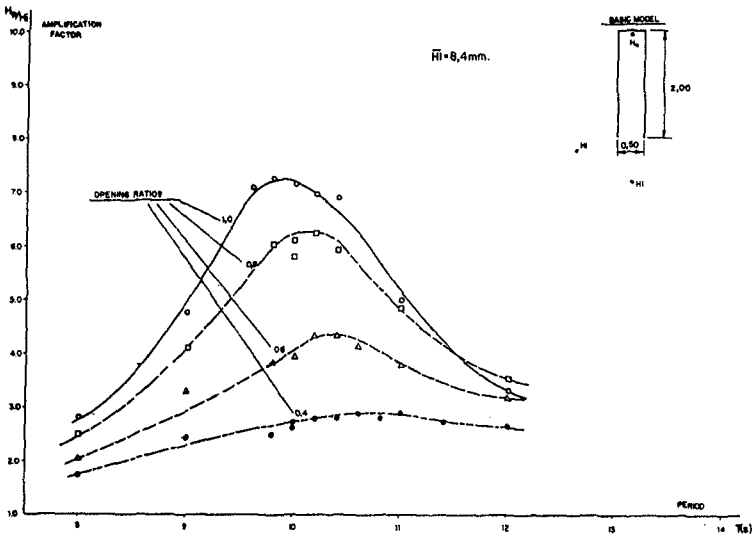


Fig. 5.- f versus T curves. Model B. Pure wave 8mm.

The observed displacement of resonance peak period as a consequence of entrance constriction enables us to find out that it is important to take into account the range of frequencies where head loss is effective, otherwise some kind of harbour paradox may result.

From test data, "gross" head loss coefficient values were estimated by using (6).

Figure 6 shows K values versus opening ratio curves, corresponding to two outside amplitudes considered to be appropriated for Cantábrico sea conditions.

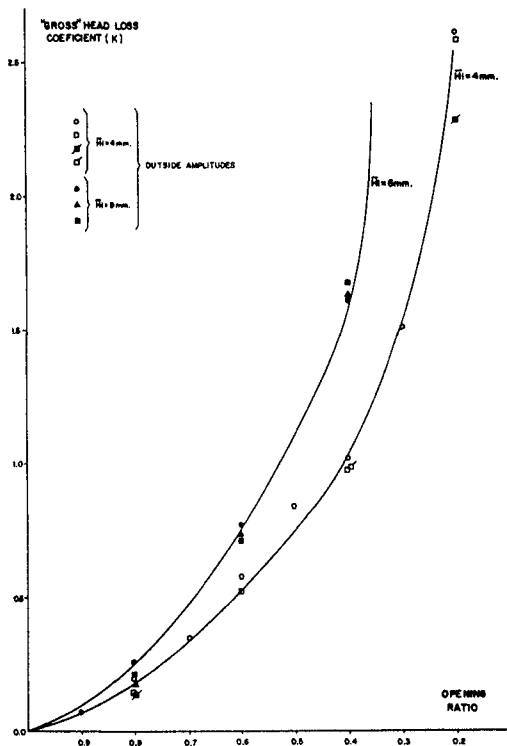


Fig.-6 K versus aperture ratio curves.

With present experiment results, the "gross" head loss coefficient K proved to be practically independent of harbour geometry, (Width/length) ratio; K strongly depended on the outside amplitude.

In general, K may depend, for highly turbulent flows, on the Strouhal, or Keulegan - Carpenter, number and on geometry of breakwater-tips, not considered in this piece of work.

Fig. 7 correlates amplification factor values under different hypothesis related to measured outside amplitude: open sea or pure wave (basin without harbour model), partially reflected and radiated wave and standing wave with harbour entrance blocked off.

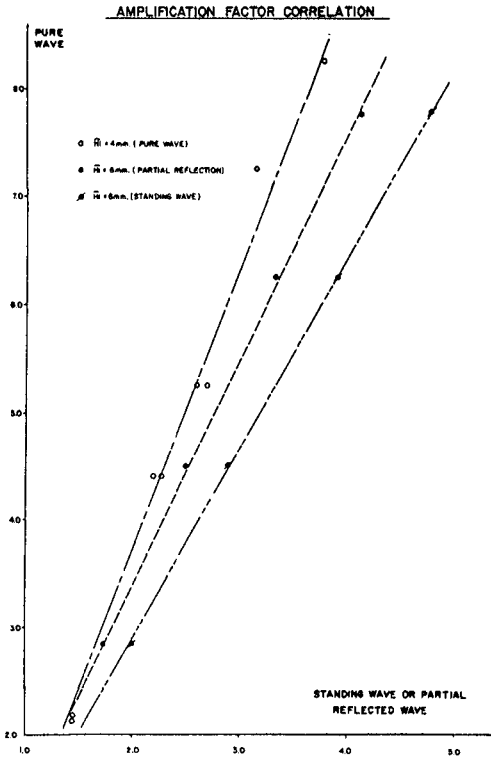


Fig. 7.- f correlations.

From test data, calculations were made in order to evaluate the harbour effective length: distance from the harbour back wall to node of the standing wave near the harbour mouth. Comparison with theoretical length resulting from asymptotic formulas, for the fundamental mode, enables us to point out that lower opening ratios require severe modifications of f_3 , Miles and Munk (1961), function, adequate for inviscid fluid conditions or hypothesis. Asymptotic formula overestimates effective length for lower apertures. A linear approximation fits rather well with test results.

Summary and conclusions

Experiments were conducted at the laboratory in order to measure the importance and effectiveness of friction loss at the harbour entrance. Two rectangular harbour models with several opening ratios were used.

Entrance head loss practically eliminates the first mode (quarter wave mode) of resonance as was pointed out earlier.

A "gross" head loss coefficient K , including the joint effect of reflection, transmission, radiation and friction differences, is defined and evaluated under some special experimental conditions by using a significant reference velocity.

Curves amplification factor versus period or equivalent magnitude, deduced from tests, have shown that it is important to take into account the range or periods where constriction is effective, if not undesirable "harbour paradox" effects may result.

K values, under different assumptions are provided.

K values and bell-shaped curves (f versus T) have shown to be dependent on oscillatory flow characteristics. The influence of oscillatory numbers needs to be investigated.

Basin dimensions, water depth, long wave characteristics and other experimental conditions could be extrapolated to harbours in Northern Spain by using suitable scales.

Research was limited to first mode of resonance; analysis carried out seems to be appropriate to Helmholtz or pumping mode.

f_3 , Miles and Munk (1961) function, overestimates effective length for severe constrictions where real fluid effects are important.

REFERENCES

- Fukuuchi, H. and Ito Y.: On the effect of breakwaters against tsunami. Proc. 10th Conf. on Coastal Engineering Tokyo - 1966.
- Horikawa, K., Nishimura H.: On the function of tsunami breakwaters. Coastal Engineering in Japan. Vol 13. 1970.
- Iribarren R., Nogales C. and Fernández P.: Onda de resaca en los puertos. Ensayos de resonancia en modelos reducidos. Revista de Obras Públicas. Feb. 1958.

- Ito, Y.: Head loss at Tsunami Breakwater Opening. Proc. 12th Conference on Coastal Eng. Washington D.C. 1970.
- Kostense J.K. et al: Wave energy dissipation in arbitrary harbours of variable depth. Proc. 20th Conference on Coastal Eng. Taipei. 1986.
- Lee J. Wave induced oscillations in harbors of arbitrary geometry. Journal of Fluid Mech. (1971) Vol. 45, part. 2 pp 375-394.
- Lee J. and Raichlen F.: Oscillations in harbours with connected basins. Journal of Waterways, Harbours and Coast Div. ASCE Aug. 1972.
- Mei Ch.: The applied dynamics of ocean surface waves J.Wiley 1983.
- Miles, J. and Munk, W.: Harbor Paradox, Jour. Waterways and Harbors Div., Proc. ASCE, Vol 87, No WW3, 1961.
- Miles J.W. and Y.K.Lee: (1975). Helmholtz resonance of harbors. J. Fluid Mech. 67. 445-464.
- Weggel J.R. and Sorensen R. Surging in the Shark River boat basin - Ports'80.

CHAPTER 19

Development and Application of a Mathematical Model of Wave Action on Steep Slopes

N W H Allsop*
J V Smallman@
R V Stephens+

Abstract

This paper summaries the initial stages in the development of a mathematical model of wave action on slopes. The model calculates water surface elevation and depth averaged velocity on the slope, and uses this data to estimate the level of wave run-up. The model has been validated by comparing its results with those from similar models, and from a physical model. Examples are presented of these comparisons, which were found to be in good agreement in most cases.

1 Introduction

A mathematical model has been developed to estimate wave induced flows on sloping faces of breakwaters, coastal revetments and seawalls. Of particular interest is the application of the model to slopes armoured with high porosity single layer armour units. The model calculates instantaneous surface elevations and uprush/downrush velocities for waves normally incident to a slope. The nature of the armour layer is described in terms of an empirical roughness coefficient which must be calibrated against flume measurements and, if possible, also against prototype measurements. Part of a field measurement programme on a breakwater in Jersey has recently been completed, see Stephens (1988), and it is anticipated that its results will be used to calibrate the mathematical model in the near future.

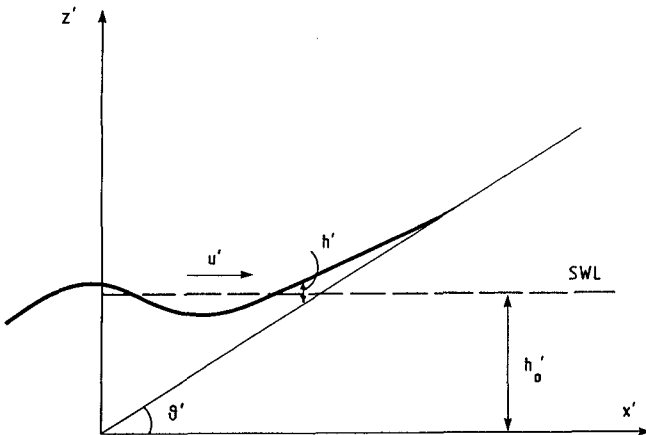
The mathematical model once calibrated will be of value in preliminary assessment of hydraulic characteristics of an armoured slope. It is envisaged that one of its applications will be in examining various options prior to more extensive physical model testing. The use of this numerical model, together with physical modelling techniques, may lead to considerable improvements in efficiency and cost over the alternative of simply testing a number of potential designs in a physical model.

* Principal Scientific Officer, Coastal Structures Section
@ Senior Scientific Officer, Ports and Harbours Section
+ Higher Scientific Officer, Coastal Structures Section
Maritime Engineering Department, Hydraulics Research,
Wallingford, OX10 8BA, England.

2 Description of the mathematical model

The basic technique used in the mathematical model is to solve numerically the non-linear shallow water wave equations. Boundary conditions allow reflection and run-up at a steep slope to be incorporated. The set of equations which are solved contain a term to describe frictional dissipation on a rough slope. The model is based on a method originally developed for beach slopes which is reported in Hibbard & Peregrine (1970) and Packwood & Peregrine (1981). Clearly many structural slopes will be considerably steeper than typical beach slopes, and the extension of the original method to include steeper slopes has been described by Kobayashi et al (1987) and is also addressed in a companion paper by Thompson (1988).

The layout and co-ordinate system used in the mathematical model are shown in Figure 1. It should be noted that the x' co-ordinate is taken to be positive in the landward direction, with $x' = 0$ at the toe of the slope. The z' co-ordinate is taken to be positive upwards with $z' = 0$ at the toe of the slope. The water depth is denoted by h' and the depth averaged velocity by u' . The local angle of the slope is θ' . The structure slope, s' is defined by $\frac{ds'}{dx'} = \theta'$. The slope is assumed horizontal for $x' < 0$.



Incident wave amplitude a' , period T'

Figure 1 Mathematical model layout

The incident wave train is specified at the toe of the slope, where the water depth below SWL is given by h_0 . It is assumed that the slope is impermeable, waves are non-breaking and that no overtopping occurs. Vertical pressure is taken to be hydrostatic and the vertical fluid acceleration is assumed to be negligible. This is a reasonable assumption for a relatively mild slope, i.e. $\tan \theta' \ll 1$.

The governing equations may then be expressed in dimensionless form as:-

$$\frac{\partial h}{\partial t} + \frac{\partial}{\partial x} (hu) = 0 \quad (1)$$

$$\frac{\partial}{\partial t} (hu) + \frac{\partial}{\partial x} (hu^2 + \frac{1}{2}h^2) = -\theta h - f|u|u \quad (2)$$

where

$$h = h'/a', \quad u = u'/(ga')^{\frac{1}{2}}$$

$$t = t'/T', \quad x = x'/T'(ga')^{\frac{1}{2}},$$

$$\theta = T'(g/a')^{\frac{1}{2}} \tan \theta' \quad \text{and} \quad f = \frac{1}{2}T'(g/a')^{\frac{1}{2}}f'.$$

here f' is an empirically determined constant friction factor associated with the slope, a' is the incident wave amplitude and T' is the incident wave period. For all the mathematical model tests described in this paper the incident wave train is taken to be sinusoidal.

In addition to the governing equations, initial and boundary conditions also need to be specified. At time $t = 0$ the fluid is assumed undisturbed giving initial conditions

$$h = h_0 - s, \quad u = 0 \quad \text{at} \quad t = 0, \quad x > 0$$

The seaward boundary condition is derived from a characteristics based argument in which it is assumed that waves reflected from the structure do not modify the incident wave. The derivation of the seaward boundary condition used in the model is described in Reardsley et al (1988). At the landward boundary it is assumed that both the water depth on the slope and its velocity are zero at the leading edge of the wave.

The governing equations (1) and (2) are presently solved using a Lax Wendroff finite difference scheme. This has the advantage of being relatively easy to apply, and is numerically stable provided the Courant condition,

$$(gh_0)^{\frac{1}{2}} \frac{\Delta t}{\Delta x} < 1 \quad ,$$

where Δt and Δx are the time and space steps, is satisfied. This scheme has been found to provide a reasonably efficient and robust method for solving the differential equations for waves of moderate steepness. For steeper waves there will be inaccuracies introduced by using this finite difference scheme, and the adoption of an alternative method will be necessary. The alternatives which have been examined so far are all Roe type schemes, see Priestley (1987), which are widely used in aerodynamic problems. The results from early

tests with these schemes appear promising, and work is currently underway to investigate them further.

3 Calibration and validation of the mathematical model

Similar mathematical models to the one described here have been developed by both Kobayashi et al (1987) and Thompson (1988). Therefore a starting point in validating the model is to compare its results with those available from similar models. In addition, a series of physical model tests were carried out at Hydraulics Research to allow comparisons to be made between the mathematical model results and those from a physical model.

3.1 Comparisons with other mathematical models

On comparing the results from the present model with those of Thompson very good agreement was achieved both for the surface elevations and velocities calculated by the model. In general the differences between the two sets of model results was less than 5%. The outcome of these comparisons is discussed further in Beardsley et al (1988).

The results from the present model were also compared with one of the cases given in Kobayashi et al (1987). Both models use a similar form of the equations and boundary conditions, and the same finite difference scheme. The only significant difference between them will be in the numerical implementation and the accuracy of the computer on which the models are run.

The present model was run for the case $\theta = 6.0$, $h_0 = 5.8$, $\sigma \equiv T' \left(\frac{g}{h} \right)^{1/2} = 15$ and $Ur = 4.5$. It should be noted that these are all dimensionless variables, and that therefore the results are also given in terms of dimensionless values h and u . In fact the angle θ given here is equivalent to a slope of 1:2.5. The results from the two model tests are compared in Figures 2 and 3 in terms of the dimensionless elevations and velocity. The present model was run using a dimensionless time step $\Delta t = 0.0025$ and dimensionless space step $\Delta x = 0.01$; these satisfy the stability constraint. The results were plotted after 5, 5.25, 5.5 and 5.75 wave periods had elapsed.

It can be seen that the predicted elevations between the two models are in close agreement, but that in general Kobayashi's model gives velocities which are higher in magnitude. This discrepancy is probably due to the different time steps which were used in running the models. Kobayashi uses 2000 time steps per wave period whereas in the present model a maximum of 400 per wave period were used. Some early runs of the present model were actually made with 250 time steps per wave period and increasing to 400 was found to have no significant effect on the velocity profiles. It is therefore likely that the discrepancies can only be due to machine rounding errors, which will have a small but cumulative effect on the solution.

3.2 Comparison with physical models

Tests were conducted in the 'Deep Wave Flume' facility at Hydraulics Research. A smooth impermeable slope was constructed at a gradient of 1:2. The flume bed profile seaward of the test slope was at a gradient of 1:50. In all of the tests the static water level was

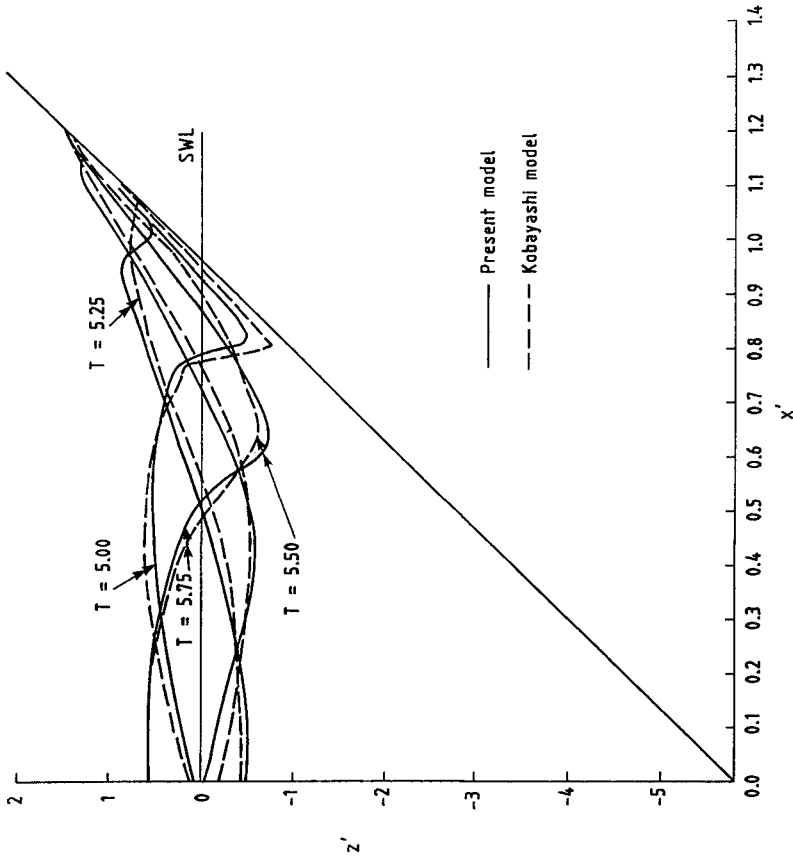


Figure 2 Comparison of model elevation with those of Kobayashi

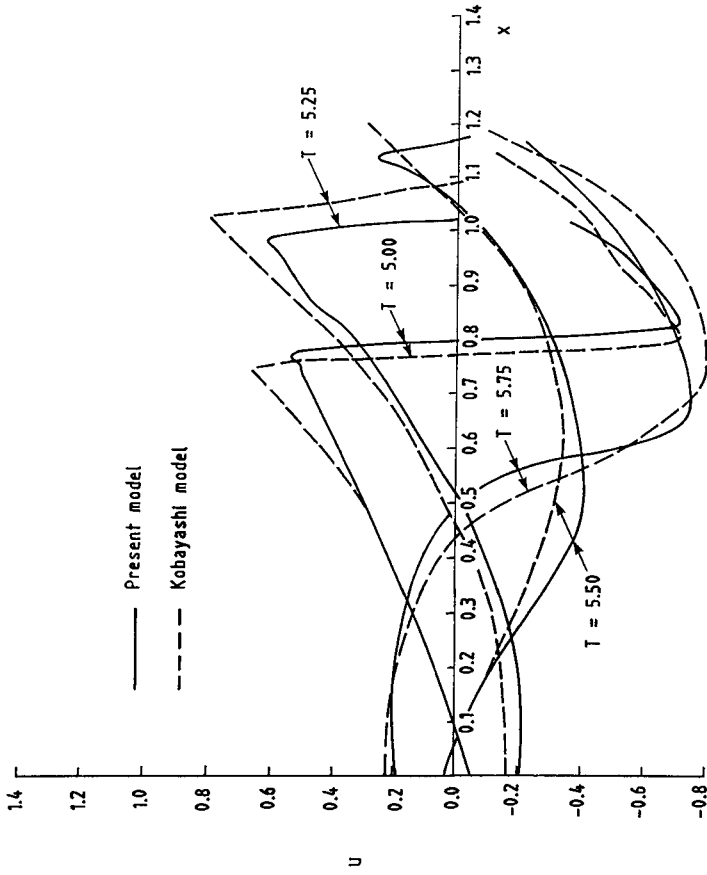


Figure 3 Comparison of model velocities with those of Kobayashi

set to be 0.3 metres above the toe of the 1:2 slope. A series of parallel vertical wave probes were positioned at regular intervals up the slope (see Fig 4) to measure instantaneous surface elevation. Measurements were also made of wave run-up and reflection, and the tests were recorded using a video camera.

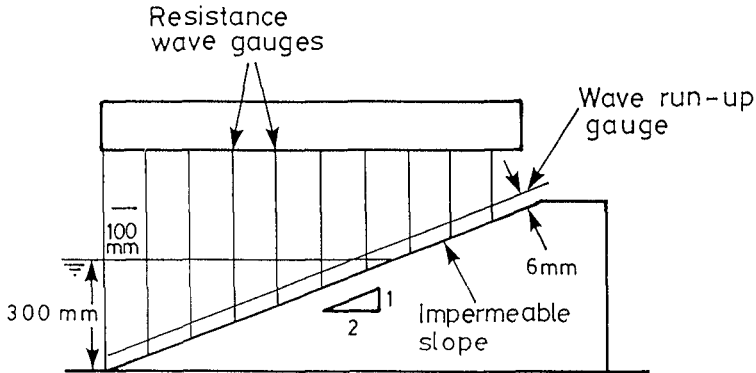


Figure 4 Layout for physical model tests

Two sets of tests were run; the first for the smooth, impermeable slope; and the second for the same slope covered with a single layer of Shed armour units. In each instance, short sequences of regular waves were run for a variety of combinations of wave height and period. The philosophy behind running these tests was that they should be used to provide calibration data for the mathematical model.

To run the mathematical model a friction factor f' needs to be specified. For this model f' is regarded as a calibration factor which needs to be determined experimentally. Once a value of f' has been determined for the particular slope characteristics, it would then be used for all subsequent tests with slopes of that type.

As a starting point in the calibration the mathematical model was set up to represent the experimental layout. The first case to be examined used a wave amplitude of 0.043m and a wave period of 2.0s at the seaward boundary. These incident conditions were taken from the results of a reflection analysis performed in the physical model at an equivalent position. The model was run using a time step of 0.0075s and a space increment of 0.018m; these satisfy the stability constraint.

For this first case a variety of friction factors were used in the mathematical model. After each run a visual comparison of the

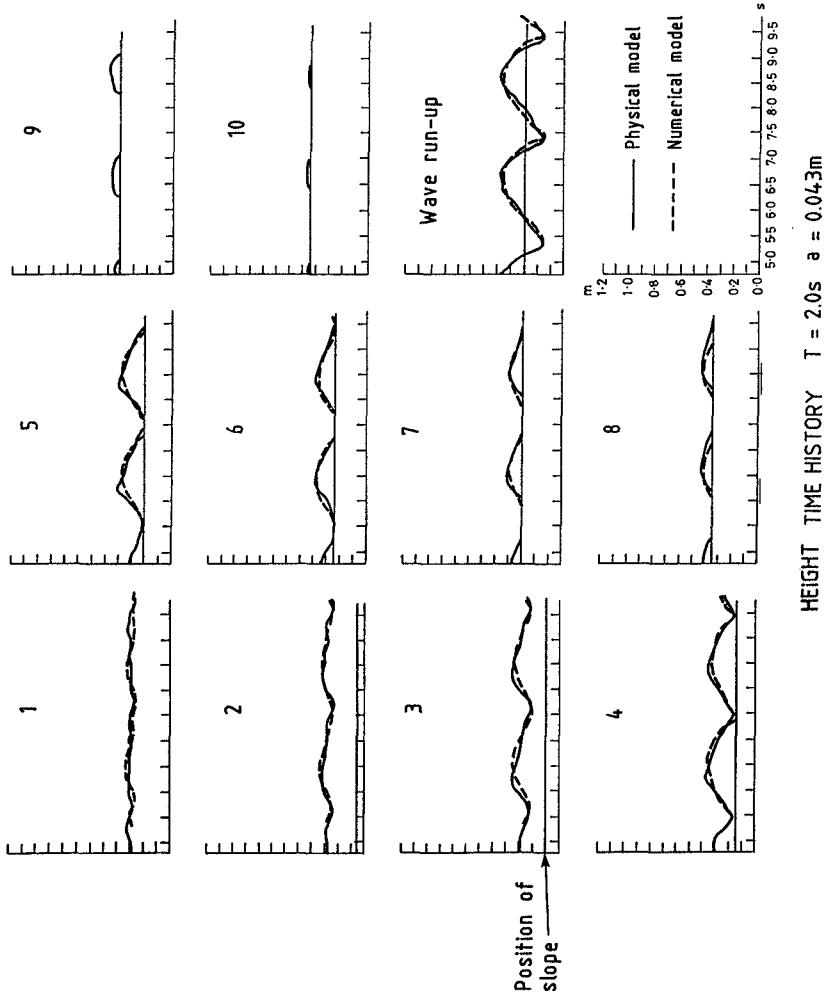


Figure 5 Comparison of elevations for physical and numerical models

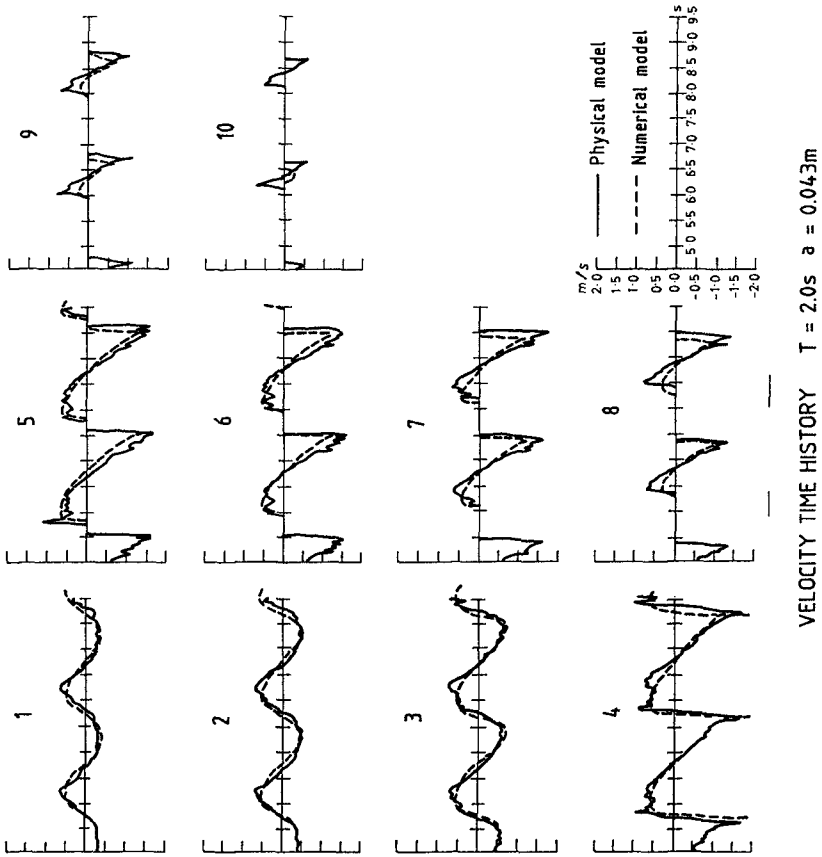


Figure 6 Comparison of velocities for physical and numerical models

elevation and velocity time histories at positions corresponding to the location of the wave probes in the physical model were made. Good agreement was achieved using a friction factor of 0.01. The comparisons for this case are shown in Figures 5 and 6, where results are plotted for each of the probe positions shown in Figure 4. It can be seen from Figure 5 that the elevations predicted by the mathematical model are in good agreement with those from the physical model. The agreement between the velocities (Figure 6) is not as good as for the elevations, but is reasonable with the same specific trends being displayed.

The next stage in the calibration process is to make similar comparisons for other wave conditions which were tested in the physical model. However, rather than relying on a visual comparison to assess the best choice of friction factor, the maximum run-up levels and velocities at probe positions will be examined. Analysis of results obtained using this method is still in progress, but they appear to be promising, and give confidence that the mathematical model can be developed and used further to represent wave action on rough slopes.

4 Conclusions

The non-linear shallow water equations have been adapted to calculate wave action on steep slopes. A number of numerical techniques have been investigated, and initial comparisons made with physical model tests. The results from the mathematical model appear to give a reasonable representation of the hydrodynamic processes. Clearly, further research is needed to develop the model and extend and improve its range of applicability. However, the results reported here indicate that the model will eventually be a useful tool for the engineer involved in the design of coastal structures.

5 Acknowledgements

The work described in this paper forms part of the research carried out for the Single Layer Armour Unit Research Club in the Maritime Engineering Department of Hydraulics Research. The authors would like to thank Mr Andrew Beardsley and Mr Barry Edwards of Brunel University for their assistance.

6 References

1. Beardsley A, Smallman J V & Stephens R V. "Single Layer Armour Research Club: Development of a mathematical model of wave action on slopes - recent progress". Report IT 318 (restricted) Hydraulics Research, Wallingford, July 1988.
2. Hibberd S & Peregrine D H. "Surf and run-up on a beach: a uniform bore". *Journal of Fluid Mechanics*, Vol 95, Part 2, pp 323-345, 1979.
3. Kobayashi N, Otta A K & Roy I. "Wave reflection and run-up on rough slopes". *Journal of Waterway Port Coastal and Ocean Engineering*. American Society of Civil Engineers. Vol 113 No 3 pp 282-298, May 1987.

4. Packwood A R & Peregrine D H. "Surf and run-up on beaches: models of viscous effects". Report No AM-81-07, School of Mathematics, University of Bristol, UK 1981.
5. Priestley A. "Roe type schemes for the 2-D shallow water equations". Internal Report, Mathematics Department, Reading University, 1987.
6. Stephens R V. "Single Layer Armour Research Club: Field Work on La Collette breakwater, Jersey, January-May 1988". Report IT 237 (restricted), Hydraulics Research, Wallingford, September 1988.
7. Thompson A C. "Numerical Model of Breakwater wave-flows". Paper submitted to 21st International Conference on Coastal Engineering Malaga, 1988.

CHAPTER 20

ABOUT THE ENERGY DISSIPATION OVER BARRED BEACHES

by

Johannes Oelerich 1) and Hans-Henning Dette 2)

Abstract:

Since wave energy dissipation in the surf zone is a stochastic process closed mathematical formulations cannot be expected. The dissipation was computed using several analytical and/or empirical approaches and compared with prototype measurements in the Big Wave Flume (GWK) in Hannover as well as with field measurements from the west coast of the Island of Sylt/North Sea. Generally good agreements were found for moderate energy dissipation conditions (spilling-breaker), whereas in the case of plunging breakers, however, the fitting is not solved satisfactory.

1. Introduction

Due to the stochastic nature of energy dissipation in the surf zone, closed mathematical solutions for the given sea state in the nearshore zone cannot be expected. It is therefore the task to idealize the problem and/or to apply empirical approaches based on laboratory- and/or in-situ measurements of waves in the area of interest.

Laboratory investigations were carried out in the Big Wave Flume (GWK) and in-situ measurements at the Island of Sylt in order to obtain data representing spilling- and plunging breaker conditions for comparison with the results from selected decay models.

2.1 Empirical Wave Height Decay Formulations

Two empirical approaches have been selected for computational tests. HORIKAWA/KUO(1966) derived from laboratory tests the following formulation for the determination of wave height decay:

1) research engineer 2) senior research engineer

Leichtweiß-Institut für Wasserbau, Department of Coastal Engineering, Technical University of Braunschweig, Beethovenstr. 51a, 3300 Braunschweig, West-Germany

$$\frac{H_i}{d_i} = 0.5 + 0.3 \cdot \exp\left(-0.11 \cdot \frac{x_i}{m \cdot x_b}\right) \quad (1)$$

H_i = wave height at x_i in [m]
 d_i = water depth [m]
 x_i = distance shoreward from break-point [m]
 i = arbitrary location index
 x_b = distance of shoreline to break-point [m]

This approach was modified by ANDERSON/FREDSØE(1983) for plane slopes. The coefficients were adapted to spilling-breakers as they do occur along the westcoast of Jütland/-Denmark:

$$\frac{H_i}{d_i} = 0.35 + 0.65 \cdot \exp\left(-0.12 \cdot \frac{x_i}{H_b}\right) \quad (2)$$

H_b = wave height at the break-point [m]

In case of partial wave breaking over a bar TUCKER et al.(1983) found that waves restabilize themselves at:

$$\frac{H_i}{d_i} = 0.5 \quad (3)$$

2.2 Analytical Wave Height Decay Formulations

Three analytical approaches were applied for describing wave height decay of periodic waves. DALLY et al.(1984) have developed an approach based on energy conservation law:

$$\frac{H_i}{H_b} = \left[\left(\frac{h_i}{h_b} \right)^{\left(\frac{K}{m_i} - 0.5 \right)} \cdot \left(1 - \alpha_i \right) - \alpha_i \cdot \left(\frac{h_i}{h_b} \right)^2 \right]^{0.5} \quad (4)$$

$$\alpha_i = \frac{(K \cdot \Upsilon)^2}{m_i \cdot \left(2.5 - \frac{K}{m_i} \right)} \cdot \left(\frac{h_b}{H_b} \right)^2$$

h_i = water depth at still water level [m]
 h_b = still water level at the breakpoint [m]
 m_i = beach slope at location x_i [-]
 K = waveheight decay factor [-]
 Υ = waveheight stabilization factor [-]

BATTJES(1986) published an approach based on the analogy of energy dissipation of a spilling breaker to the energy dissipation in a bore:

$$\frac{H_i}{H_b} = \left[\left(1 - \frac{4}{9} \cdot k \right) \cdot \left(\frac{d_i}{d_b} \right) + \frac{4}{9} \cdot \left(\frac{d_i}{d_b} \right)^{-3.5} \right]^{-0.25} \quad (5)$$

$$k = 2 \cdot B \cdot \Upsilon \cdot \frac{1}{m_i \cdot T_m} \cdot \left(\frac{d_b}{g} \right)^{0.5}$$

$$\gamma = 0.7 + 5 \cdot m_i \quad (0.01 \leq m_i \leq 0.1)$$

B = dimensionless coefficient [-]
 d_b = water depth at the breakpoint [m]
 T_m = mean wave period [s]

STIVE (1984) derived a formula based on the same analogy but added an energy dissipation factor A_e for better adaptation:

$$\frac{H_i}{H_b} = \left[\left(1 - \frac{4}{3} \cdot \sigma \right) \cdot \left(\frac{d_i}{d_b} \right)^{0.25} + \sigma \cdot \frac{4}{3} \cdot \left(\frac{d_i}{d_b} \right)^{0.5} \right]^{-1} \quad (6)$$

$$\sigma = \left(\frac{1}{2 \cdot \pi} \cdot \frac{H_b}{d_b} \right)^{0.5} \cdot A_e \cdot \zeta_b^{-1} \quad \zeta_b = m_b \cdot \left(\frac{H_b}{L_o} \right)^{-0.5} \leq 0.4$$

$$A_e = 2 \cdot \tanh(5 \cdot \zeta_o) \quad \zeta_o = m_b \cdot \left(\frac{H_o}{L_o} \right)^{-0.5} \leq 0.5$$

H_o = deep water wave height [m]
 L_o = deep water wave length [m]
 m_b = bottom slope at the break-point [-]

Another five approaches have been selected to take as well wave height distribution as water level set-up/set-down into account.

Based on linear wave theory wave height is calculated:

$$\frac{H_i}{H_o} = \left[\frac{1 + \frac{4\pi d_o}{L_o}}{\sinh\left(\frac{4\pi d_o}{L_o}\right)} \cdot \frac{2\pi}{L_i} \right]^{0.5} \cdot \frac{\sinh\left(\frac{4\pi d_i}{L_i}\right) + \frac{4\pi d_i}{L_i}}{\sinh\left(\frac{4\pi d_i}{L_i}\right)} \cdot \frac{2\pi}{L_o} \quad (7)$$

set-up/set-down offshore the break-point:

$$\eta_i = -\frac{1}{8} \cdot H_o^2 \cdot \frac{2\pi}{L_o} \cdot \frac{\coth^2\left(\frac{4\pi d_i}{L_i}\right)}{\sinh\left(\frac{4\pi d_i}{L_i}\right) + \frac{4\pi d_i}{L_i}} \quad (8)$$

set-up/set-down inside the breaker-zone:

$$\eta_i = \frac{3 \cdot \gamma_b^2}{3 + 3 \cdot \gamma_b^2} \cdot (h_b - h_i) + \eta_b \quad (9)$$

$$\gamma_b = \frac{H_b}{d_b} = 0.78$$

η_i = deviation from still water level (set-up/set-down) [m]
 η_b = set-up/set-down at the breakpoint [m]

L_i = wave length [m]

Wave height decay formulations of DALLY et. al. (1984) are mentioned above. The set-up/set-down is calculated by:

$$\eta_i = \eta_{i-1} - \frac{3}{16} \cdot \frac{1}{d_i} \cdot (H_i^2 - H_{i-1}^2) \quad (10)$$

At barred coastlines waves restabilizes at:

$$\frac{H}{d} = \alpha \quad (11)$$

$\alpha = 0.35$ - moderate beach slopes

$\alpha = 0.48$ - steep beach slopes

IZUMIYA/HORIKAWA (1978) calculated wave height and wave set-up/set-down from energy dissipation rate due to wave breaking and bottom friction. There expressions are:

$$H_i = \left(\frac{8 \cdot E_i}{\rho \cdot g} \right)^{0.5} \quad (12)$$

$$E_i = E_{i-1} \cdot \frac{C_{gi-1}}{C_{gi}} - \frac{X_i - X_{i-1}}{C_{gi}} \cdot \left[\alpha_1 \cdot \left(\frac{2k_i d_i}{\sinh(2k_i d_i)} \right)^{1.5} + \alpha_2 \cdot \left[\left[\frac{E_i}{\rho \cdot g \cdot d_i} \cdot \left(\frac{1}{2} + \frac{k_i d_i}{\sinh(2k_i d_i)} \right) - \alpha_3 \right]^{0.5} \cdot \left(\frac{2k_i d_i}{\sinh(2k_i d_i)} \right)^{0.5} \right] \right] \cdot \frac{E_i^{1.5}}{\rho^{0.5} \cdot d_i^{1.5}}$$

$$k_i = \frac{4 \cdot \pi^2}{T_m^2 \cdot g \cdot \tanh(k_i \cdot d_i)}$$

$$C_{gi} = \frac{1}{2} \cdot \left[\frac{g}{\frac{2\pi d_i}{L_i}} \cdot \tanh\left(\frac{2\pi d_i}{L_i}\right) \right] \cdot \left[\frac{1 + \frac{2\pi d_i}{L_i}}{\sinh\left(\frac{2\pi d_i}{L_i}\right)} \right]$$

E_i = wave energy [kWs/m²]

$c_{g i}$ = group velocity [m/s]

k_i = wave number $2\pi/L$ [-]

α_1 = bottom roughness coefficient = 0.01 - 0.03

α_2 = wave breaking coefficient = 10

α_3 = wave breaking coefficient = $0.9 \cdot 10^{-2}$

The water level deviation is calculated based on radiation stress theory:

$$\eta_i = \eta_{i-1} - \frac{S_{xxi} - S_{xxi-1}}{\rho \cdot g \cdot d_i} \quad (13)$$

$$S_{xxi} = \left(\frac{1}{2} + \frac{2k_i d_i}{\sinh(2k_i d_i)} \right) \cdot E_i$$

S_{xxi} = radiation stress [kWs/m²]

The break-point is defined as a critical relative wave-height due to a critical energy:

$$\left(\frac{H}{d}\right)_{crit} = 0.17 \cdot \frac{L_o}{d} \cdot \left[1 - \exp \left[-1.5 \cdot \frac{\pi d}{L_o} \cdot (1 + 15 \cdot m)^{1.33} \right] \right] \quad (14)$$

BATTJES/JANSSEN (1978) calculated the energy dissipation rate for RALEIGH distributed waves:

$$H_{rmsi} = \left(\frac{8 \cdot E_i}{\rho \cdot g} \right)^{0.5} \quad (15)$$

$$E_i = E_{i-1} \cdot \frac{C_{gi-1}}{C_{gi}} - \frac{\alpha}{8} \cdot \frac{1}{T_m} \cdot \frac{0.88^2}{C_{gi}} \cdot \left[\frac{Q_{bi}}{k_i^2} \cdot \tanh^2(k_i \cdot d_i) + \frac{Q_{bi-1}}{k_{i-1}^2} \cdot \tanh^2(k_{i-1} \cdot d_{i-1}) \right] \cdot (x_i - x_{i-1})$$

$$\frac{1 - Q_{bi}}{\ln(Q_{bi})} = \frac{H_{rmsi}^2}{H_b^2}$$

H_{rmsi} = root-mean-square-wave-height [m]
 Q_{bi} = probability of broken- or breaking waves [-]
 α = 1.0

The wave set-up is calculated due to radiation stress theory mentioned above.

The approach of GERRITSEN (1980) is similar to BATTJES/-JANSSEN(1978) (eqn.15) but assumes the waves as WEILBULL distributed:

$$\frac{1 - Q_{bi}}{((1+0.71) \cdot (Q_{bi}-1)^2) \cdot \ln(Q_{bi})} = \frac{H_{rmsi}^2}{H_b^2}$$

The energy dissipation formula was modified for the WEILBULL distribution as follows:

$$E_i = E_{i-1} \cdot \frac{C_{gi-1}}{C_{gi}} - \left[\frac{2}{3} \cdot \alpha_1 \cdot \frac{\rho}{\pi} \cdot \left(\frac{\pi \cdot H_{rmsi}}{T_m \cdot \sinh(k_i d_i)} \right)^3 + Q_{bi} \cdot \frac{\alpha_2}{5.66} \cdot \rho \cdot g \cdot \frac{2\pi}{T_m} \cdot H_{rmsi}^2 \right] \cdot (x_i - x_{i-1}) \cdot C_{gi}$$

α_1 = bottom friction coefficient = 0.1 - 0.5
 α_2 = wave breaking coefficient = 0.1 - 0.36

The energy dissipation thus can be calculated in correspondence with the decay of wave height for different nearshore profiles and wave conditions.

3. Applications of Wave Height Decay on a natural Profile in Full Scale Experiments

In the Big Wave Flume (GWK) full scale experiments over natural beach profiles with sand ($D_{50} = 220 \mu m$) have been carried out under a wide range of wave-, beach- and profile conditions.

3.1 Wave Height Decay of individual Waves

The wave height decay from the breakpoint up to the uprush zone was recorded by means of video registrations of breaking wave trains through a grid at one of the tank walls and analysed for nearly 100 successive waves. The waves have been characterized by the breaker parameter β (FÜHRBÖTER(1976)) (see Fig. 2).

Fig. 1 shows the measured and computed wave height decay in the surf zone for a spilling breaker (above) and a plunging breaker (below).

The comparison of computed values with measured data is illustrated in Fig. 2. in terms of the difference in wave height ΔH and the standard deviation $\sigma(\Delta H)$. For DALLY et al. (1984) and BATTJES(1986) the parameters K , Γ , and B have been adapted to the individual wave heights in order to minimize the differences ΔH . Table 1 shows the results of the parameters as functions of H_b/d_b and breaker parameter β .

3.2 Energy Dissipation of irregular Wave Trains in Full-Scale Experiments

Dissipation of wave energy profile changes are caused until a morphologic equilibrium is reached. For investigations during such profile transformation processes the wave heights were measured by resistance wave gauges at 10 locations at intervals of 10 m along the beach profile for regular waves as well as irregular waves.

The results of statistical analysis are presented in Fig. 3. for each wave gauge as follows:

- deviation from SWL η (set-up/set-down)
- dimensionless probability density function $p(H/H_m)$
- statistical wave height parameters H_m , $H_{1/3}$, H_{max}

The results of spectral analysis are shown in Fig. 4 for each wave wire:

- spectral density function presented as block diagram
- spectral parameters H_s , $T_{m0,2}$, and band width parameter ν

The computed wave heights and set-up, respectively, of the models described in section 2. are plotted together with wave height parameter H_m and deviations for the initial wave parameters of the reference wave gauge and the actual profile from SWL as obtained from measured data (see Fig. 5).

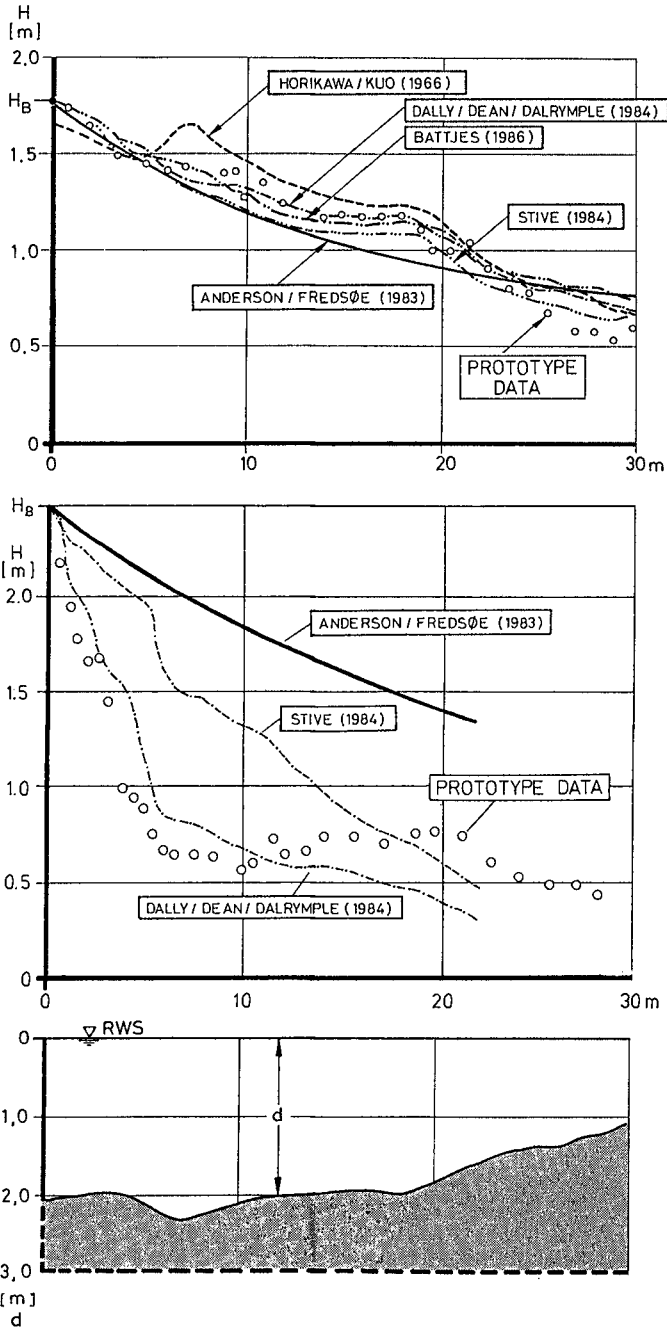


Fig. 1: Comparison between measured data (GWK) and wave-height calculations by empirical and analytical wave decay models for a spilling breaker (above) and an extreme plunging breaker (below) at a natural profile.

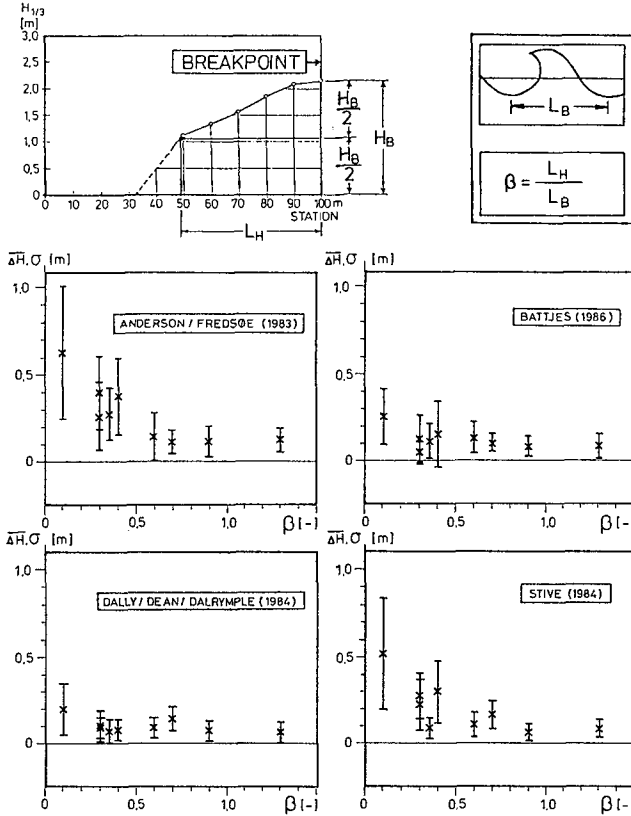


Fig. 2: Mean differences between measured and computed wave heights ΔH and standard deviations $\sigma(\Delta H)$ as function of the breaker parameter β .

INDIVIDUAL BREAKING WAVES		BIG WAVE FLUME HANNOVER			
Breaker-type	Wave-Parameter		Energy-Dissipation-Parameter		
	β [-]	H_b/d_b [-]	DALLY et. al. K [-]	BATTJES γ [-]	BATTJES B [-]
extreme plunging plunging spilling	0.1-0.2	1.4-1.8	0.5 -1.0	0.5	5.0-20.
	0.2-0.7	0.7-1.4	0.2 -0.3	0.35-0.5	1.0-10.
	0.7-1.4	0.7-1.1	0.2	0.35-0.5	1.0- 2.
	H_0/gT^2 [-]	H_b/d_b [-]	K [-]	γ [-]	B [-]
	0.0025	1.2-1.8	0.35-1.0	0.5	5.0-20.0
	0.0035	0.8-1.1	0.15-0.35	0.3 -0.5	1.0-10.0
	0.0070	0.7-1.1	0.15-0.35	0.25-0.35	1.0-10.0
	0.0110	0.7-0.9	0.2 -0.25	0.35	1.0

Table 1: Variations of parameters K and γ for DALLY et. al. and B for BATTJES' models to minimize the differences between measured data and computed values.

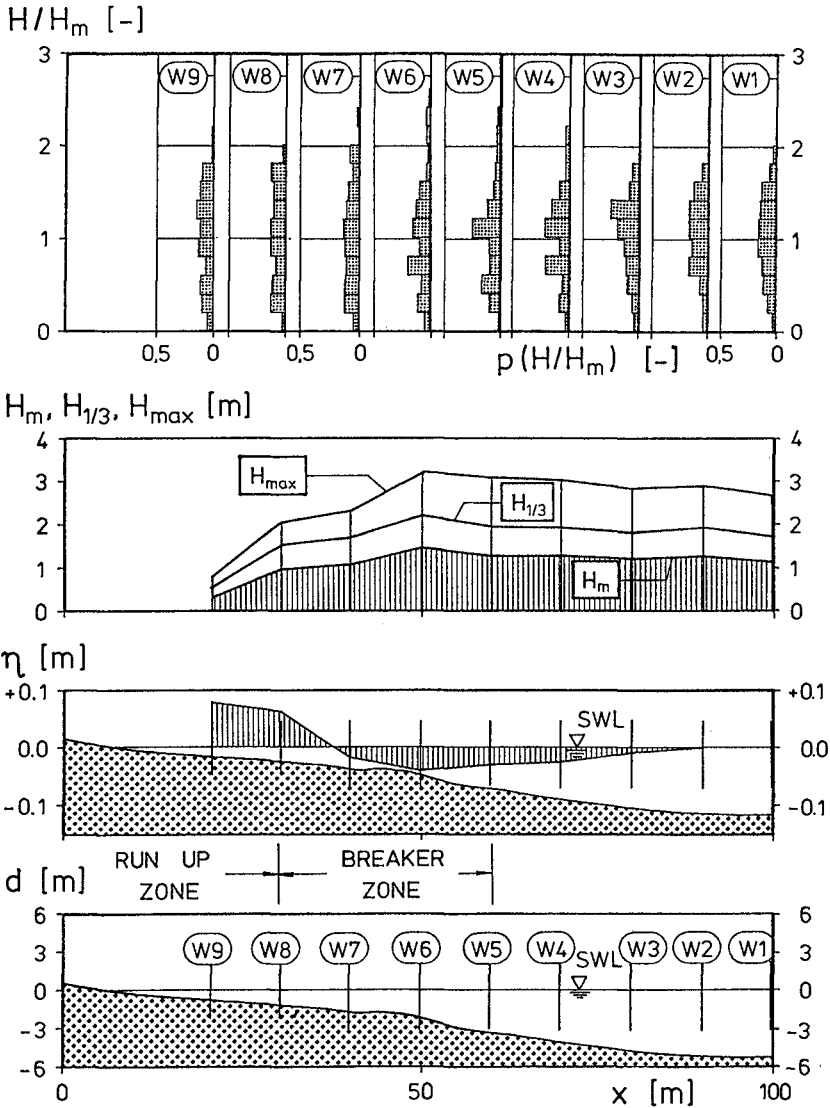


Fig. 3: The results of statistical analysis for a spectrum of $H_s = 1.5$ m and $T_p = 6.0$ s

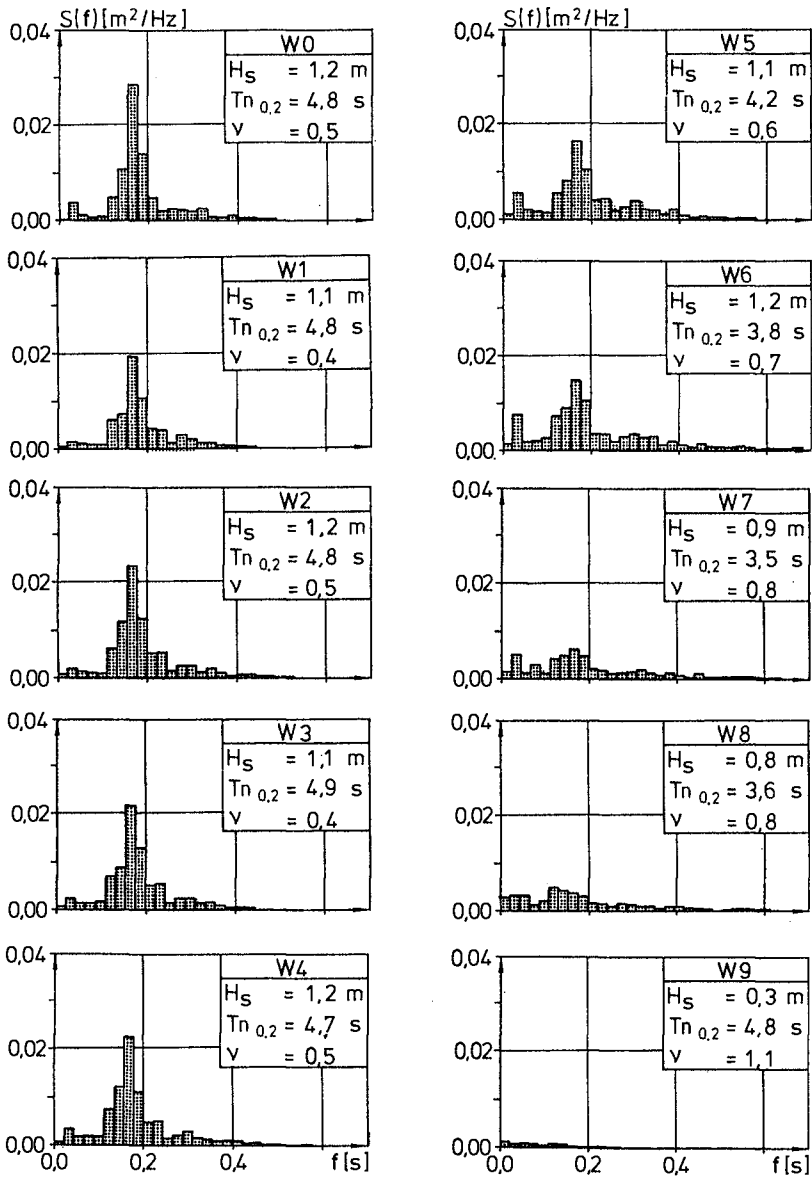


Fig. 4: The results of spectral analysis for a wave spectrum of $H_s = 1.5$ m, $T_p = 6.0$ s, where n_0 and n_2 denotes the spectral moments

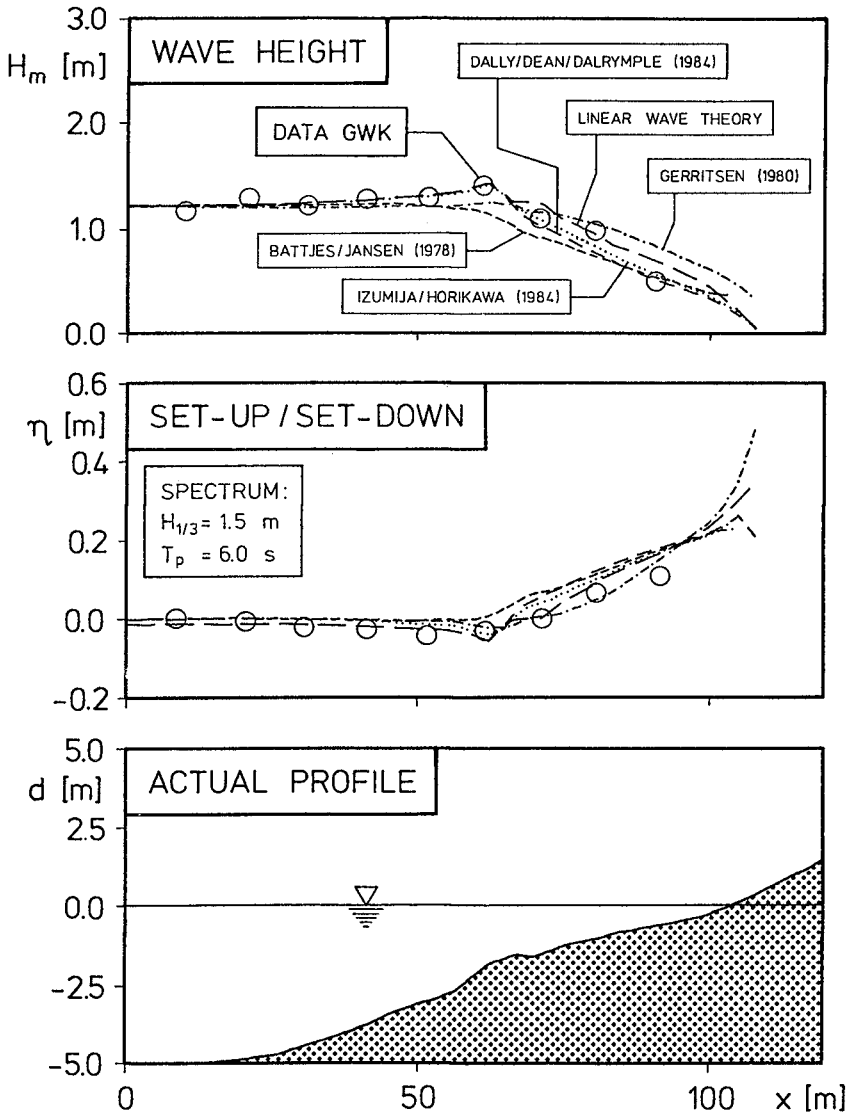


Fig. 5: Comparison of computed and measured values for a spectrum of $H_s = 1.5$ m, $T_p = 6.0$ s across the profile.

The above results, Fig 4, show, that (I) the energy density spectrum shows dissipation of wave energy in the breaker zone in direction of wave approach, $\Delta n_0 = 95 \%$, (II) the peak of the energy spectrum is reduced and, (III) the transformation of incident wave energy to lower and higher frequency contributions i.e. higher frequency oscillations and in the surf zone disintegration of waves and turbulence.

The statistical analysis of wave heights and comparison with selected wave height decay models show fairly good agreement between computed values and measured data, even for the more simple models predicting only regular waves (Fig.3 and Fig 5).

The comparison of measured and computed water level deviations shows slight underprediction of set-down and significant overprediction of set-up in the surf zone for the examples (Fig. 3 and Fig. 5).

3.3 Energy Dissipation of Waves in Field Investigations

Measurements of wave height have been recently started in a profile perpendicular to the shoreline at the west-coast of the island of Sylt (North Sea) near the village of Rantum with a typical nearshore bar- and trough topography. Using as initial values the measured data from a wave rider buoy offshore (10 m-depth) wave heights and set-up/set-down were computed by the models described in section 2.4 and compared with wave height measurements inside the surf zone.

Fig. 6 shows time series of measured and computed data for a storm event in february 1988 with offshore wave heights up to $H_s = 4.0$ m.

3.4 Application to a 2-Dimensional Nearshore Topography

A wave refraction model based on the wave ray method was adapted to the study site by implementation of a breaker criterium (WEGGEL(1972)), a wave height decay model (ANDERSON/FREDSØE (1983)) and a criterion of wave height stabilization (TUCKER et al. (1983)).

The topography of the investigation area was taken into account up to the MSL-10.0 m depth contour line. Fig. 7 shows as an example areas of wave height exceedance in the nearshore topography, the breakpoints (●) and points of restabilization (o) for incident wave parameters of $H = 6.0$ m , $T = 10.0$ s and the direction of wave approach perpendicular to the shore.

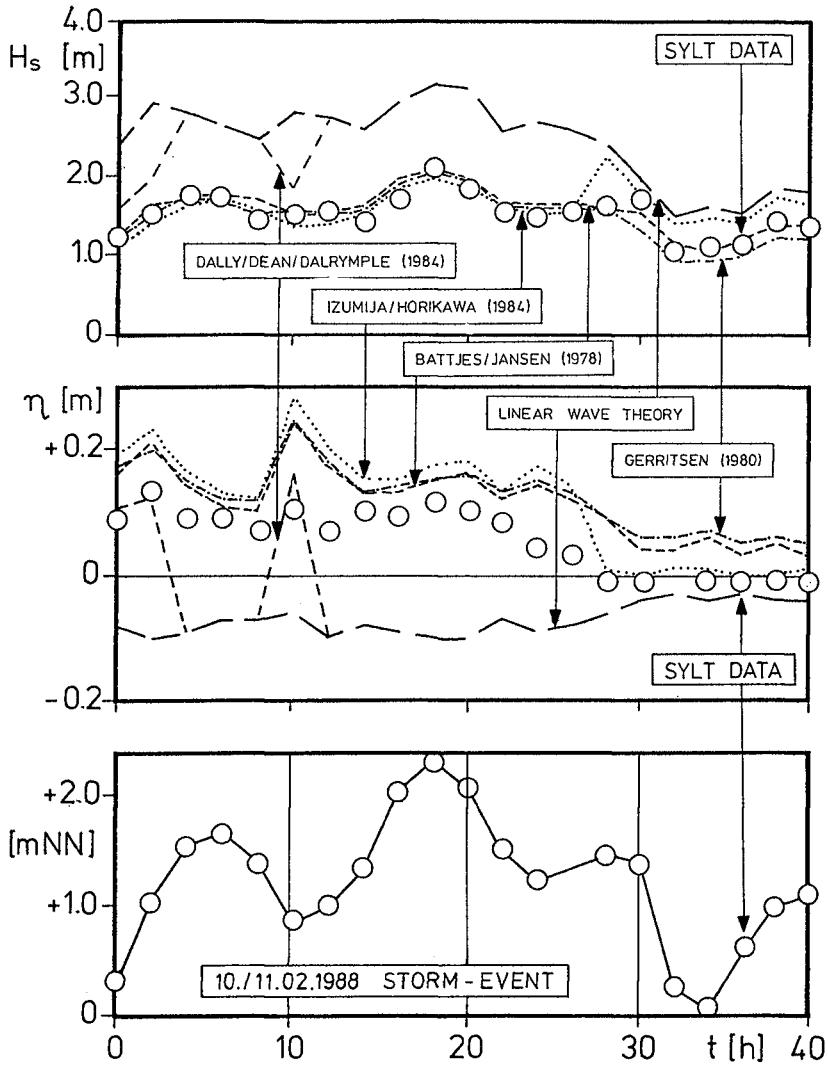


Fig. 6: Comparison of computed values and measured data for a storm event at the west coast of the Island of Sylt/North Sea

The contour lines of equal wave height indicates the effect of morphological elements as the bar (breaker zone) and the gap in the bar (wave energy intake into the trough region).

First comparisons of measured wave heights and computed wave heights show generally fairly good agreement but in some cases significant differences arise due to the inadequacy of the energy dissipation formulation. Therefore it is the task to combine one of the more sophisticated models mentioned in section 2. with the refraction model in order to obtain better agreement between computed and measured wave parameters.

4. Discussion

Measurements in the Big Wave Flume (GWK) and at the west coast of the Island of Sylt have been carried out with respect to energy dissipation due to breaking waves. The wave height decay of individual waves and of irregular wave trains were analysed and compared with empirical and analytical models which partly take the effects of wave height distribution into account to predict the wave height variation and wave set-up/set-down over a profile.

For individual waves good agreements were found for moderate energy dissipation conditions (spilling breakers). The energy dissipation of plunging breakers, however, is not satisfactory described.

The application to a nearshore site with rough and varying topography is still under investigation. The models tested with full scale experiment data were found to predict wave height decay quite well for the 1-dimensional case.

For the rough varying bar and trough profile at the west coast of Sylt significant differences were found due to the different treatments of regular waves, irregular waves and the breakpoint formulation.

The models will be tested in combination with a refraction model to obtain a suitable description of wave energy dissipation in a 2-dimensional topography.

5. Acknowledgments

The authors are indebted to the Deutsche Forschungsgemeinschaft (DFG) and the German Ministry of Research and Technology (BMFT) for their sponsorship of the Big Wave Flume experiments and the research-projekt " Optimization of Coastal Protection at the Island of Sylt ".

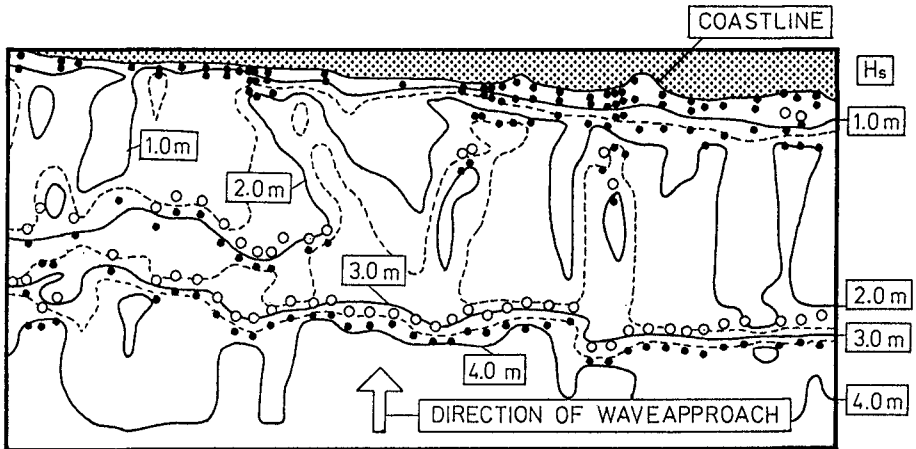


Fig. 7: Contour lines of wave height exceedance, break-points (●) and points of wave restabilization (○) for wave parameters $H = 6.0$ m, $T = 10.0$ s, $\theta = 270$ degrees

6. References

- ANDERSEN, O.H./FREDSØE, J. " Transport of Suspended Sediment along the Coast ", Inst. Hydrodyn. and Hydraulic Eng., Techn. Univ. Danmark, Progr. Rep. 59, 1983
- BATTJES, J.A. " Energy Dissipation in Breaking Solitary and Periodic Waves ", Comm. on Hydraulic and Geotech. Eng., Dec. 1986
- BATTJES, J.A./JANSSEN, J.P.F.H. " Energy Loss and Setup due to Breaking of Random Waves ", Proc. 16th Intern. Conf. on Coast. Eng., Vol.1, pp 569-587, Hamburg, W.-Germany, 1978
- DALLY, W.R./DEAN, R.G./DALRYMPLE, R.A. " A Model for Breaker Decay on Beaches ", Proc. 19th Intern. Conf. on Coast. Eng., Vol.1, pp 82-98, Houston, U.S.A., 1984
- FÜHRBÖTER, A. " Einige Ergebnisse aus Naturuntersuchungen in Brandungszonen ", Mittl. des Leichtweiß-Instituts für Wasserbau, Techn. Univ. Braunschweig, Heft 40, 1974
- GERRITSEN, F. " Wave Attenuation and Wave Set-up on a Coastal Reef ", Proc. 17th Intern. Conf. on Coast. Eng., Vol.1, pp 444-461, Sydney, Australia, 1980
- HORIKAWA, K./KUO, C.T. " A Study of Wave Transformation Inside the Surf Zone ", Proc. 10th Intern. Conf. on Coast. Eng., pp 217-233, 1966
- IZUMIYA, T./HORIKAWA, K. " Wave Energy Equation Applicable In- and Outside the Surf Zone ", Coastal Eng. in Japan, 1984
- STIVE, M.J.F. " Energy Dissipation in Waves Breaking on Gentle Slopes ", Coastal Eng. Journal, Vol.8, 1984
- TUCKER, J./CARR, A.R./PITT, E.G. " The Effect of an Offshore Bank in Attenuating Waves ", Coastal Eng. Journal, Vol.7, 1983
- WEGGEL, J.R. " Maximum Breaker Height ", Journ. of the Waterw., Harbour, and Coastal Eng. Div., ASCE, Vol.15, 1972

CHAPTER 21

TRUNCATION ORDER OF FOURIER WAVE THEORY

Rodney J. Sobey¹, M.ASCE

Specific consideration is given to the dependence of Fourier wave solutions on both truncation order and the number of free surface nodes. Solution dependence is quantified by a comprehensive set of numerical experiments over a typical range of wave height, water depth, truncation order and overspecification values. Integral error measures include the rms free surface boundary condition errors and a slope error that identifies non-physical positive slope segments in the wave profile between crest and trough. Summary error diagrams are presented as a guide to the adoption of suitable truncation orders and overspecification for Fourier solutions. The truncation order is the crucial parameter but there is measurable advantage is some small overspecification.

INTRODUCTION

Fourier wave theory has proved to be a robust steady wave theory for almost the complete range of wave heights, water depths and uniform currents experienced in practice. It is a hybrid analytical/numerical theory. The analytical aspects are relatively straightforward though not entirely without difficulties. The numerical part of the solution however is distinctly nontrivial. It involves the simultaneous solution of a large number of implicit nonlinear algebraic equations in a large number of unknowns. This is recognized as an extremely difficult problem in numerical analysis for which a successful solution algorithm depends critically on the analytical formulation of the problem and on the physical nature of the solution. For waves of small to moderate height in relatively deep water, successful solutions do not appear to be difficult to obtain. For higher waves in deep water and especially waves of moderate to large height in shallow water, changes in the physical nature of the solution significantly complicate the achievement of a successful solution. So much so in fact that it becomes appropriate to consider just what is a successful solution. The complexity of the numerical solution procedure has tended to distract attention from this rather more fundamental question, namely, whether an achievable numerical solution can be equated with a reasonable physical solution of a particular steady wave problem.

STEADY WAVE THEORY

Progressive waves of permanent form are steady in a frame of reference moving at the phase speed C . Accordingly, it is convenient to adopt a steady and moving x,z reference frame that is located at the mean water level (MWL) and moves at speed C with the wave crest, rather than an unsteady and fixed X,Z reference frame. The field solution is described by the stream function $\psi(x,z)$. Assuming that the flow is incompressible and irrotational, the field equation representing mass and momentum conservation is the Laplace equation

¹ Professor, Hydraulic and Coastal Group, Department of Civil Engineering, University of California at Berkeley, Berkeley, CA 94720

$$\frac{\partial^2 \Psi}{\partial x^2} + \frac{\partial^2 \Psi}{\partial z^2} = 0 \quad (1)$$

where the velocity components (u,w) are $(\partial\Psi/\partial z, -\partial\Psi/\partial x)$.

This field equation is subject to the following boundary conditions:

(1) Bottom boundary condition, representing no flow through the horizontal bed, is

$$\Psi(x, -h) = 0 \quad \text{at } z = -h \quad (2)$$

(2) Kinematic free-surface boundary condition (KFSBC), representing no flow through the free surface, is

$$\Psi(x, \eta) = -Q \quad \text{at } z = \eta(x) \quad (3)$$

where $\eta(x)$ is the free surface and $-Q$ is the constant volume flow rate per unit width under the steady wave. Q is positive and this flow is in the negative x direction.

(3) Dynamic free surface boundary condition (DFSBC), representing constant atmospheric pressure on the free surface, is

$$\frac{1}{2} \left(\frac{\partial \Psi}{\partial x} \right)^2 + \frac{1}{2} \left(\frac{\partial \Psi}{\partial z} \right)^2 + g\eta = R \quad \text{at } z = \eta(x) \quad (4)$$

where g is the gravitational acceleration and R the Bernoulli constant.

(4) Wave is periodic.

$$\Psi(x + L, z) = \Psi(x, z) \quad (5)$$

where $L (= 2\pi/k)$ is the wave length and k is the wave number

Given parameters defining a steady wave solution are generally the wave height H , the water depth h , the wave period $T (= 2\pi/\omega)$ and either the coflowing Eulerian current C_E or the wave-averaged mass transport velocity or Stokes drift C_S . The wave height is defined as

$$H = \eta(x=0) - \eta(x=L/2) \quad (6)$$

and mass conservation requires an invariant MWL such that

$$\int_0^{L/2} \eta(x) dx = 0 \quad (7)$$

The speed C of the moving and steady reference frame is related to the fixed and unsteady reference frame by the dispersion relationship. Where C_E is known, the dispersion relationship is

$$C = \frac{L}{T} = \bar{u} + C_E \quad (8)$$

where \bar{u} is the mean fluid speed at any z wholly within the fluid. The Stokes drift is then defined as

$$C = \frac{L}{T} = \frac{Q}{h} + C_S \quad (9)$$

Where C_S is known, Equation 9 is the dispersion relationship and Equation 8 is the definition equation for C_E .

FOURIER WAVE THEORY

The solution for the stream function is represented by a truncated Fourier series

$$\Psi(x, z) = -\bar{u}z + \frac{g^2}{\omega^3} \sum_{j=1}^N B_j \frac{\sinh jk(h+z)}{\cosh jkh} \cos jkx \quad (10)$$

where the B_j are the dimensionless Fourier coefficients, of which there are N . This representation of the stream function automatically satisfies the field equation, the kinematic bottom boundary condition and the periodic lateral boundary conditions. The Fourier coefficients are chosen numerically to satisfy the free surface boundary conditions, the finite truncation order N being the only necessary assumption in the analytical formulation of Fourier wave theory.

The unknown variables in a Fourier wave solution are k, \bar{u}, C_E or C_S, Q, R , the η_m for $m=0(1)M$ and B_j for $j=1(1)N$, of which there are $M+N+6$ in total. The $\eta_m = \eta(x_m)$ are water surface nodes, where the $x_m = (m-1)\pi/kM$ are uniformly distributed in x from crest to trough.

The problem formulation provides $2M+6$ implicit algebraic equations in these $M+N+6$ unknowns, each equation being cast in the form

$$f_i(k, \bar{u}, C_E \text{ or } C_S, Q, R, \eta_m, B_j) = 0 \quad (11)$$

The equations define the wave height

$$f_1 = \eta_0 - \eta_M - H \quad (12)$$

the mean water level

$$f_2 = \frac{1}{2M} \left(\eta_0 + 2 \sum_{m=1}^{M-1} \eta_m + \eta_M \right) \quad (13)$$

the Eulerian current

$$f_3 = \frac{2\pi/k}{T} - \bar{u} - C_E \quad (14)$$

the Stokes drift

$$f_4 = \frac{2\pi/k}{T} - \frac{Q}{h} - C_S \quad (15)$$

the kinematic free surface boundary condition (KFSBC) at each of the $M+1$ free surface nodes

$$f_{5+2m} = \Psi(x_m, \eta_m) + Q \quad (16)$$

and the dynamic free surface boundary condition (DFSBC) also at each of the free surface nodes

$$f_{6+2m} = \frac{1}{2} \left[\frac{\partial \Psi(x_m, \eta_m)}{\partial x} \right]^2 + \frac{1}{2} \left[\frac{\partial \Psi(x_m, \eta_m)}{\partial z} \right]^2 + g \eta_m - R \quad (17)$$

Note in particular the use of the trapezoidal rule in Equation 13 for the MWL. This is an exact result for the continuous integral in Equation 7 where $\eta(x)$ is represented by a truncated Fourier series, as is implied by Equation 10.

The problem is uniquely defined for $M = N$ and overspecified for $M > N$. The solution of a set of $2N+6$ simultaneous implicit algebraic equations in $2N+6$ unknowns is a familiar problem in numerical analysis for which successful algorithms are generally variations on the Newton-Raphson method. A set of $2N+6$ simultaneous implicit algebraic equations in $M+N+6$ unknowns, where $M > N$, is an equally familiar problem in numerical analysis in the context of nonlinear optimization. A solution is established by seeking a minimum value for an objective function of the $M+N+6$ unknowns. A familiar algorithm is the least squares method where the objective function is the sum of squares of the left hand sides of the $2M+6$ equations.

$$O(k, \bar{u}, C_E \text{ or } C_S, Q, R, \eta_m, B_j) = f_1^2 + f_2^2 + \dots + f_{2M+6}^2 \quad (18)$$

Such an algorithm is equally successful for $M = N$ where the objective function would be expected to be zero. In practice, this involves little sacrifice in computational efficiency and none in solution precision and is accordingly a convenient choice of algorithm for the present purposes.

The choice of numerical solution algorithm should not influence the solution and the present computations have exclusively adopted the IMSL subroutine ZXSSQ, which is a finite-difference Levenberg-Marquardt algorithm with strict descent in double precision. This algorithm is mature, routinely successful and commonly available. Given that a solution exists, there are two potential difficulties with any optimization algorithm. The first is the difference in physical dimensions and relative magnitudes of the dependent variables. This has been minimized by redefining the variables and the implicit algebraic equations in dimensionless form, here in terms of ω and g . Subse-

quently, all constants and variables are non-dimensional, simply achieved by setting $\omega = g = \rho = 1$. A second difficulty is the potential existence of multiple solutions, especially the odd harmonics which are legitimate mathematical solutions of the gravity wave problem as formulated. This problem can be avoided, for example, by the choice of an initial estimate of the complete solution from Airy wave theory at a fraction of the given wave height. The wave height is then progressively increased towards the given wave height, with an initial estimate at each subsequent step being provided by a Taylor series expansion in H about the converged solution at the previous height step. A fraction sequence of 0.01, 0.02, 0.05, 0.1, 0.2, 0.5, 1.0 has been employed, with two steps normally sufficient in very deep water, four in transitional water and all seven in extremely shallow water.

Whether a solution exists at all is a further potential difficulty and there are two aspects here that require attention. The first is the truncation order N of the Fourier series. Steep crest and flat trough profiles typical of shallow water waves require many more Fourier terms than the more closely sinusoidal wave profiles in deep water. The theoretical slope discontinuity at the crest of limit waves would require an infinite truncation order and can not be accommodated by Fourier wave theory; in practice however, adequate solutions can be achieved very close to this limit. The second aspect is whether or not a solution does indeed exist and here the problem formulation is remarkably prophetic and robust. Convergence is just not achieved for the present formulation, despite the mathematical possibility of a minimum of the objective function, at combinations of dependent variables that are not physically possible. This is an especially encouraging aspect of the problem formulation and the numerical solution, considering the extreme multi-dimensionality of the problem and the considerable potential for spurious solutions.

Previous formulations of Fourier wave theory (Dean 1965 & 1974, Dalrymple 1974, Chaplin 1980, Rienecker & Fenton 1981) have been reviewed in detail elsewhere (Sobey 1988) and compared with the present generalized formulation. Differences are more apparent than real. The Dean, Dalrymple and Chaplin algorithms lack some flexibility in excluding Stokes second definition of phase speed. The present algorithm is a modification (normalized by known wave frequency rather than unknown wave number) and generalization (M can be greater than N) of the Fenton (1983) version of the Rienecker and Fenton formulation. All algorithms were shown to provide essentially identical results with Stokes first definition of phase speed for wave height up to at least 90% of the breaking wave height. The slope discontinuity for limit waves requires an infinite Fourier series which is beyond the capabilities of a truncated Fourier series. Substantially increasing the truncation order (Chaplin uses $N=51$ at 90% of breaking wave height) improves fidelity for near-limit waves but finite machine precision rapidly limits the utility of this approach. Numerical solutions for nominally limit waves at finite truncation orders by Dean (1974) have been shown to be spurious solutions by Chaplin (1980), as they do not capture the dual-valued nature of integral properties of near-limit waves.

Given the essentially complete agreement among Fourier wave theory formulations for small to moderately extreme wave heights, the present generalized formulation can be utilized in an analysis of solution characteristics in the reasonable expectation that the results will be applicable also to alternative formulations. Limit waves can not be accommodated by any Fourier formulation and will not be included in the analysis, which will focus on small (Dean case A at 25% of empirical breaking wave height) and moderately extreme (Dean case C at 75% of empirical breaking wave height) waves.

ERROR MEASURES

Fourier wave theory has but two assumptions, the truncation order N and the number of water surface steps $M+1$. Given that M must be greater than or equal to N for closure, it is convenient to define the overspecification $MN = M - N$. Both N and MN influence the fidelity of the solution and, being the only assumptions of the theory, there is considerable value in documenting the numerical solution dependence on both parameters. The influence of truncation order is implicit in most published solutions,

with adopted N values increasing from small to high waves and especially from deep to shallow water. The influence of MN is rather less obvious. Dean and Dalrymple do not record M , beyond a statement to the effect that M is large. Chaplin apparently uses $M=200$ but Rienecker and Fenton use $M=N$, i.e. $MN=0$. In principle and frequently in practice, numerical solutions are achievable for all $N \geq 1$ and all $MN > 0$. Spurious solutions may result from inappropriate choices of both N and MN . The truncation order is broadly analogous to order of an analytical waves theory such as Stokes or cnoidal; it should not be too small but what is large enough? Similarly, what is an appropriate value for MN ? It is implicit in the Dean, Dalrymple and Chaplin formulations that a "large" value of MN is essential for solution fidelity. How large is "large"? Some guidance in answering these questions can be provided from the analysis of numerical solutions over a range of N and MN values.

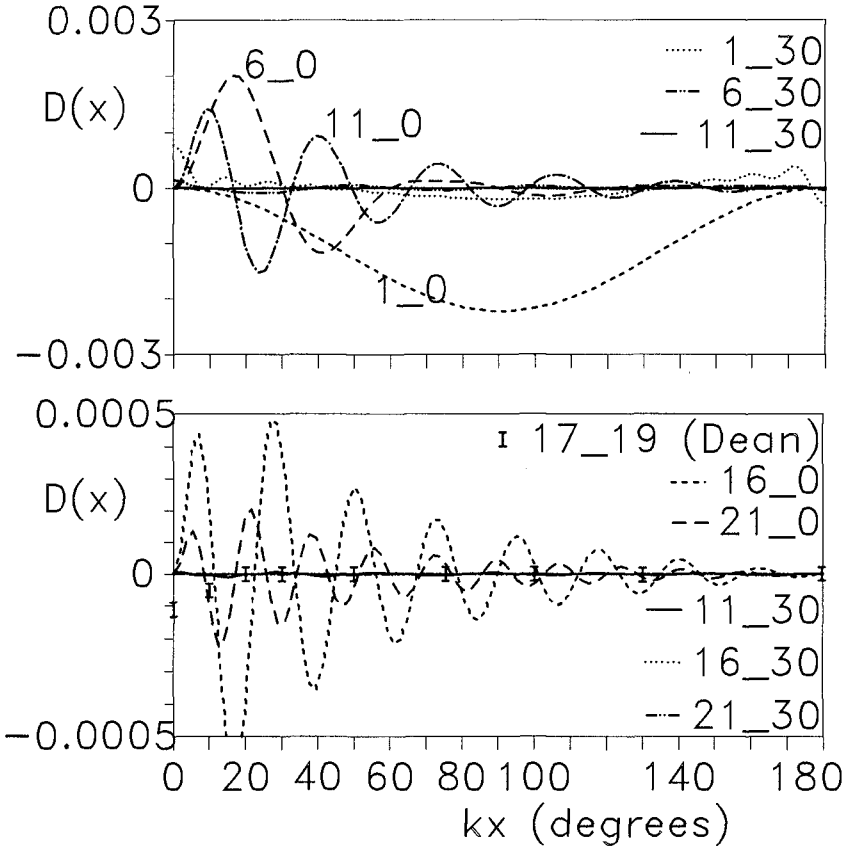


Figure 1 DFSBC Error Traces for Case 3C

Error measures must be defined to assist in this analysis. Two appropriate objective criteria follow naturally from the problem formulation, where only the free surface boundary conditions are not satisfied exactly. The residual error in the KFSBC is

$$K(x) = \psi(x, n) + Q \quad (19)$$

Similarly, the residual error in the DFSBC is

$$D(x) = \frac{1}{2} \left(\frac{\partial \psi}{\partial x} \right)^2 + \frac{1}{2} \left(\frac{\partial \psi}{\partial z} \right)^2 + g\eta - R \tag{20}$$

These error traces oscillate about zero in a manner typical of truncated Fourier series. The Fourier solution satisfies these boundary conditions at discrete, uniformly spaced surface nodes, not along the entire free surface. This is illustrated in Figure 1 for Dean Case 3C ($\omega^2 h/g = 2\pi/100$; $\omega^2 H/g = 0.03657$, $C_n = 0$) for $D(x)$ over a range of N and MN , each profile being based on 100 points between crest and trough. The truncation order influences these traces directly, there being exactly N oscillatory cycles per wavelength. For $MN = 0$, the zero crossings of the error traces identify the locations of the free surface nodes. Overspecification MN influences the phasing and amplitude of these traces, generally decreasing the amplitude of the oscillation, except where the truncation order is ridiculously small ($N = 1$). The principal advantage of overspecification would appear to be the change in the phasing of the error traces; the free surface nodes are moved from the natural zero-crossings of the N -term finite Fourier series and the amplitude of the trace oscillations is damped significantly in consequence. The markers on Figure 1 are the published Dean (1974) solution (where $N=17$, $MN=36n-17$, n being an unrecorded integer). These errors are given to only one significant figure and are indicated by error bands, but are nonetheless entirely consistent with the present results. The phase reversal is apparently a consequence of the different numerical optimization algorithms and is not believed to be significant. In all cases except the trivial $N = 1$, the trace amplitude is a maximum at the crest and decays rapidly in magnitude towards the trough.

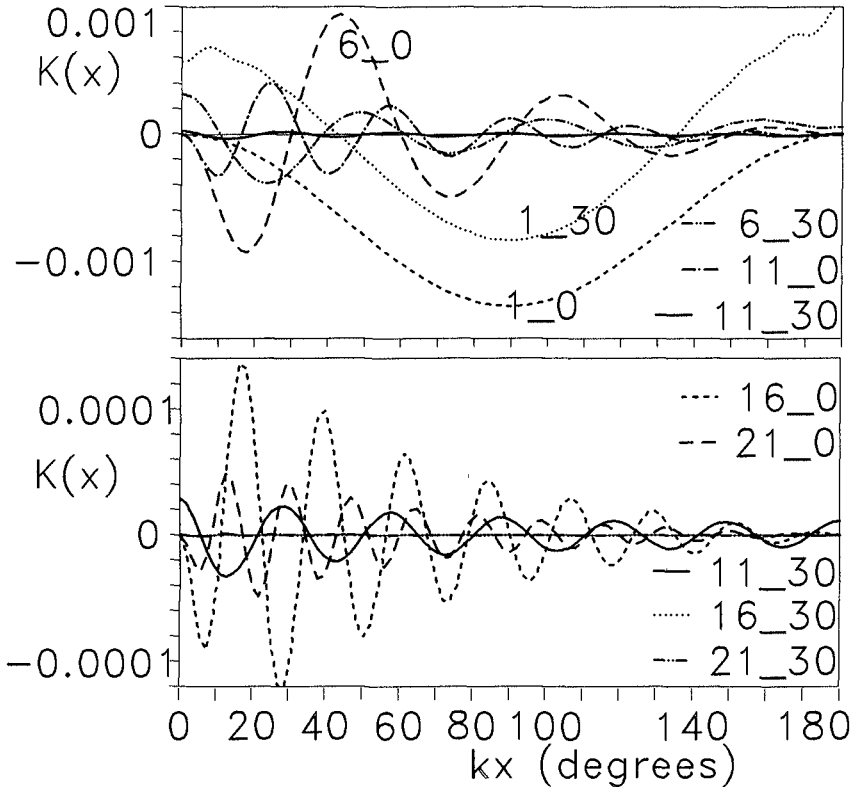


Figure 2 KFSBC Error Traces for Case 3C

The KFSBC error trace $K(x)$ behaves similarly and is shown in Figure 2 for the same Dean case 3C solutions as in Figure 1. Dean (1965, 1974) defines the KFSBC errors as $dn/dx - u/w$, which is not directly comparable with Equation 19. It is emphasized in the Dean (1965, 1974) formulation of Fourier wave theory that the KFSBC is exactly satisfied but this is a misleading statement (Sobey 1988). Dean has adopted a multi-step solution algorithm that decouples the KFSBC from the balance of the problem formulation and assumes that k , R , Q and the B_j coefficients are given parameters, equated to the most recent estimates from earlier steps in the iterative algorithm. This is a significantly weaker statement that cannot be categorized as exact. KFSBC errors as defined by Equation 19 will remain.

Single number measures of these boundary condition error traces are conveniently provided by the root-mean-square values (Dean 1974), as

$$\epsilon_{KFSBC} = \frac{1}{J+1} \sum_{j=0}^J K^2(x_j) \quad (21)$$

and

$$\epsilon_{DFSBC} = \frac{1}{J+1} \sum_{j=0}^J D^2(x_j) \quad (22)$$

where the x_j are evenly spaced between crest and trough and J should significantly exceed M ; $J=100$ was adopted throughout. Note however that these error measures will be artificially small if J is chosen to correspond with the surface nodes, e.g. $J = M = N$.

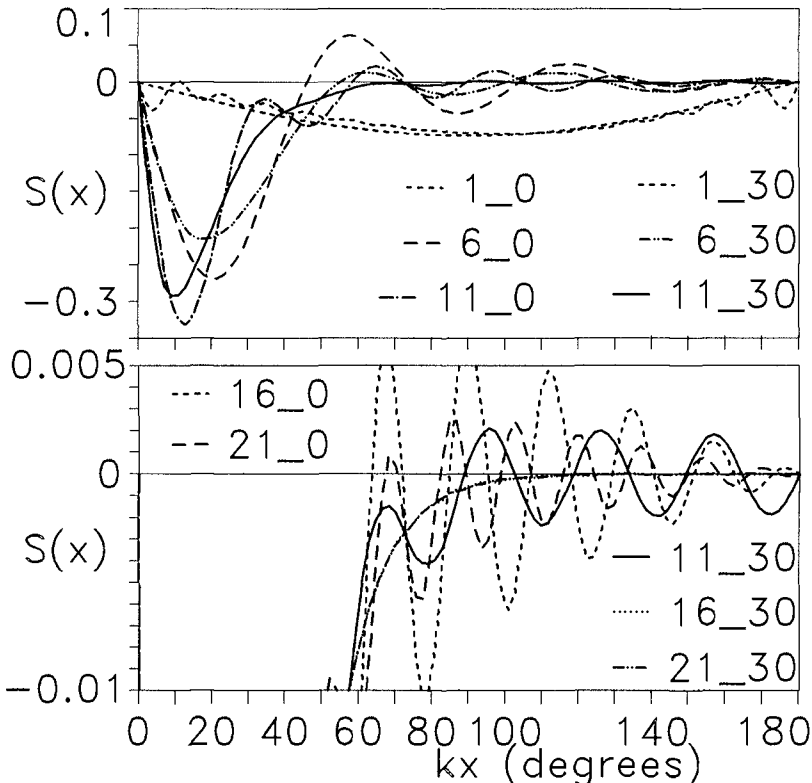


Figure 3 Slope Traces for Case 3C

The influence of the truncation order is implicit in the free surface boundary condition errors which provide a measure of a satisfactory numerical solution but not an especially direct measure of just what is a satisfactory physical solution. The direct influence of truncation order is rather more apparent from specific consideration of the truncated Fourier series approximation. Fourier series approximations to near sinusoidal profiles are quite trivial but the sharpening of the crest profile and flattening of the trough profile, that is experienced for higher waves in deep water and almost all waves in shallower water, requires a rapidly increasing truncation order. Insufficient Fourier terms will result in the Gibbs phenomenon and non-physical profile oscillations. In principle, a physical wave profile should be monotonically decreasing from crest to trough; the profile slope $S(x) = d\eta/dx$ should never be positive. Figure 3 shows water surface slope traces for the same Dean case 3C solutions as in Figures 1 and 2, except that the Dean tabulated solution does not provide this information. The slope traces assist in identifying profile oscillations in the long flat trough profiles. Where the truncation order is insufficient, the slope traces oscillate above and below the zero level. These slope traces are especially sensitive to truncation order and overspecification and an additional error measure is provided by the positive area under the slope traces

$$\epsilon_{Slope} = \int_0^{L/2} \left[\frac{d\eta}{dx} \right]_{+} dx \quad (23)$$

the + subscript indicating the inclusion of only those segments of the profile where $d\eta/dx \geq 0$. Physically satisfactory solutions should have a zero slope error.

Collectively, the KFSBC, DFSBC and water surface slope errors provide a reasonably comprehensive measure of the analytical veracity of a Fourier wave solution. In addition, the slope errors provide an excellent indication of the physical suitability of a computed solution.

NUMERICAL EXPERIMENTS

Any Fourier wave solution is in principle dependent on three physical parameters wave height $\omega^2 H/g$, water depth $\omega^2 h/g$, and current $\omega C_v/g$ or $\omega C_s/g$ and on two numerical parameters truncation order N and overspecification MN . The three integral error measures defined above are then dependent on these five parameters. The details would be available from a comprehensive range of numerical. Each of these solutions is computationally intensive and exhaustively covering this five parameter space would be a massive computational task. A representative yet still reasonably comprehensive set of solutions were undertaken, based essentially on Dean case C at 75% of an empirical depth-dependent breaking wave height and $\omega C_v/g = 0$. Water depth $\omega^2 h/g$ values included Dean cases 3 ($\omega^2 h/g = 2\pi/100$), 4 ($2\pi/50$), 5 ($2\pi/20$), 6 ($2\pi/10$), 7 ($2\pi/5$), 8 (π) and 10 (4π). Case A solutions at 25% of an empirical depth-dependent breaking wave height were also computed for depth cases 3, 6 and 10. For each of these ten wave height - water depth combinations, solutions were computed for truncation orders $N = 1(5)21$ and overspecification $MN = 0(10)30$; MN extended from 0(10)50 for cases 3C, 4C and 7C. A total of 230 separate Fourier wave solutions were completed, which collectively provide an overall perspective on the N and MN dependence throughout the practical range of wave height and water depth values.

For each Dean case there are 20 or 30 separate solutions and results are conveniently presented as three dimensional bar charts for each dimensionless integral error measure and each Dean case. Even so there are 30 such plots and only selected examples can be included. The previous discussion has highlighted Dean case 3C and Figures 4, 5 and 6 show the corresponding integral error plots for the DFSBC, the KFSBC and the slope. As an aide to interpretation, these dimensionless plots are all to the same scale. They are truncated at 10^{-6} , a convenient number that does not absolutely identify a successful solution but is strongly suggestive of one.

Figure 4 for the DFSBC shows a dependence on both truncation order and overspecification as anticipated by Figure 1. For $MN = 0$, there is a steady decrease in the rms error with increasing truncation order. Increasing overspecification has an immediate influence in significantly decreasing the rms error; further increases in MN have limited influence. The nature of this presentation however is rather deceptive of the computational effort involved. Computational effort is directly related to $(2M + 6)^2$, where $M = N + MN$. Designating computational effort as E^2 , truncation order and overspecification are related as

$$N + MN = E - 6 \quad (24)$$

which can be represented on Figure 4 as straight line lines intersecting both the N and MN axes at the same numerical values. The dashed lines on the base plane of Figure 4 indicate lines of equal computational effort, which put the combined influence of both N and MN in better perspective. As perhaps expected, the rms error is rather more directly related to computational effort (i.e. $N + MN$) than to either N or MN separately. Increasing MN alone may lead to a spurious result as the rms error very rapidly reaches a plateau level. Increasing N alone however leads to a consistent decrease in the rms error. It is apparent that truncation order is the crucial parameter. Overspecification can provide some measurable advantages but arguably no more (and potentially much less) than an equivalent increase in the truncation order to achieve the same computational effort.

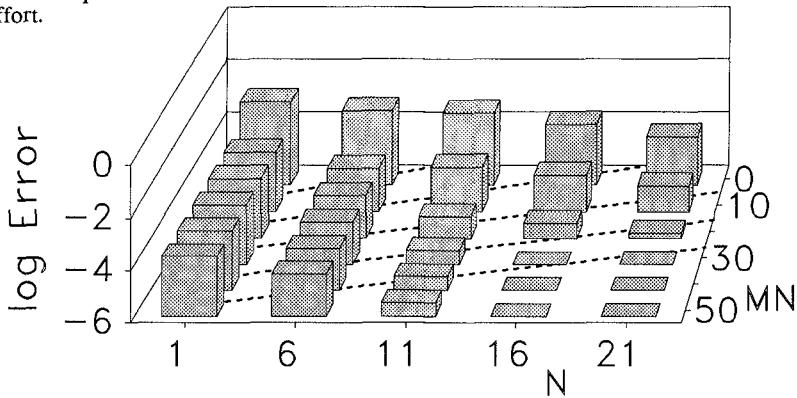


Figure 4 Rms DFSBC Error for Case 3C

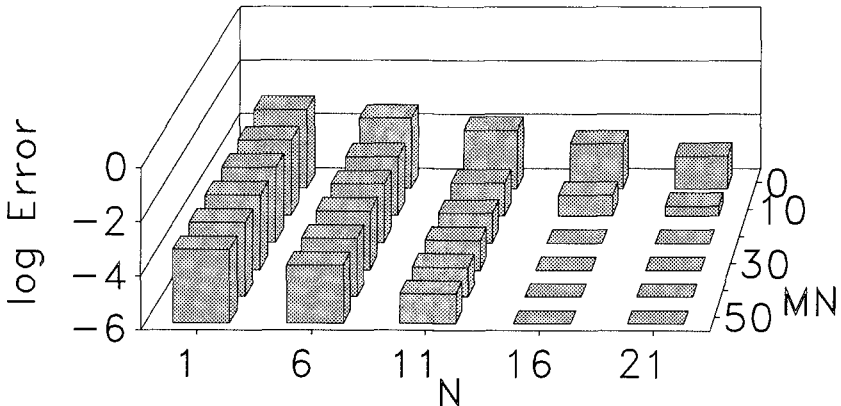


Figure 5 Rms KFSBC Error for Case 3C

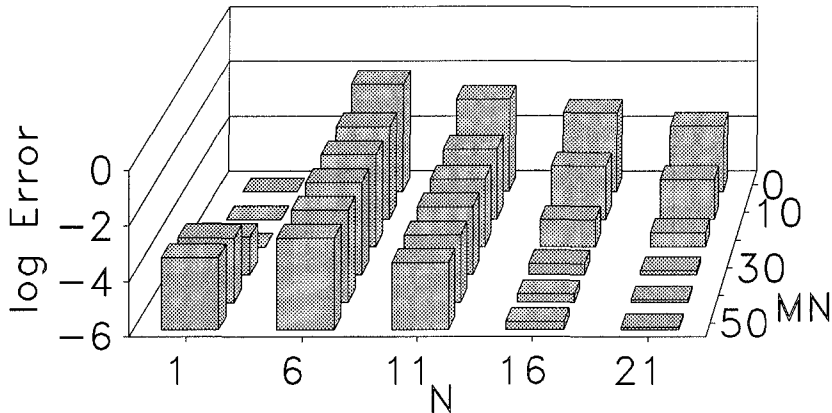


Figure 6 Slope Error for Case 3C

Figure 5 for the KFSBC shows a very similar trend as does Figure 6 for the water surface slope. The base levels at $N = 1$ are clearly spurious solutions; they predict a near-sinusoidal wave as is apparent from the equivalent slope traces in Figure 3. The overall picture presented by each of the three integral error plot is very similar, but there is one essential difference however. The rms errors in the free surface boundary conditions must approach zero asymptotically, whereas the slope error may suddenly jump to zero at finite values of the rms boundary errors. At the 10^{-6} level, oscillations in the trough profile at barely perceptibly and certainly define a pragmatic solution. Higher cutoff levels may in fact be acceptable. It would appear nonetheless that the slope summary plot provides a useful measure of an acceptable solution, both mathematically and physically.

Space limitations preclude presentation of all the summary plots. Sufficient detail is provided by one of the rms error plot (say DFSBC) together with the slope plot. Figure 7 shows these error plots for Dean case 3A ($\omega^2 h/g = 2\pi/100$; $\omega^2 H/g = 0.01224$, $C_p = 0$) at 25% of the empirical breaking wave height. The significantly lower wave height is much less demanding of the Fourier wave theory and the 10^{-6} base levels are rapidly achieved for both the rms DFSBC error and the slope error.

Figure 8 through 14 shows the summary plots for Dean cases 4C, 5C, 6A, 6C, 7C, 8C and 10C respectively. These plots clearly demonstrate the relative ease with which acceptable solutions are achieved in deeper water. Case 4C (Figure 8) follows a very similar trend to Case 3C but profile steepness is not quite as extreme in the slightly deeper water and the 10^{-6} base level is reached with somewhat less computational effort. Case 5C (Figure 9), 6C (Figure 11) and 7C (Figure 12) continue this trend, slope errors becoming rapidly less problematic. In fact, slope errors appear not to be a serious problem in deeper water. A comparison of Case 6A (Figure 10) and Case 6C (Figure 11) once again demonstrates the relative ease with which Fourier solutions are achieved at lower wave heights.

The Case 8C (Figure 13) summary plot continues these trends in very deep water, except that the DFSBC (and also the KFSBC which is not included) errors reveal an additional problem at $N = 21$, $MN = 0$. The Case 10C solution (Figure 14) follows the same trend but not the Case 10A solution (not included). Perusal of the solution details reveals that this apparent problem is a consequence of finite compiler and machine precision. The Fourier coefficients become very small very rapidly in deep water and the higher coefficients are typically fifteen orders of magnitude smaller than the leading B_1 coefficient. This confronts the capabilities of double precision arithmetic (REAL*8 variables in Fortran), although this is both compiler and machine dependent. In such a

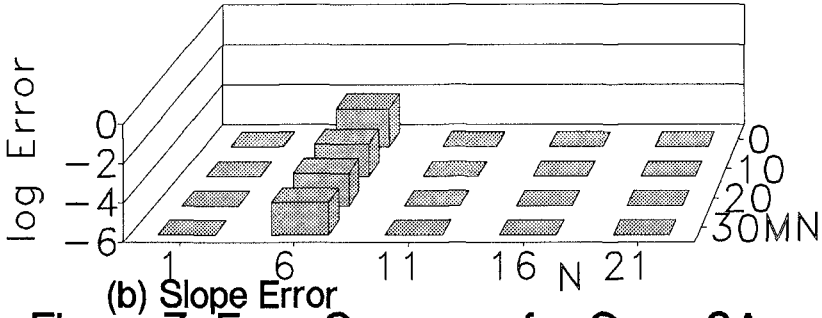
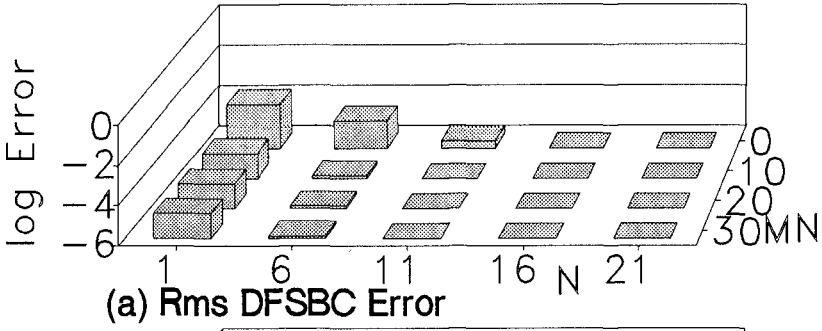


Figure 7 Error Summary for Case 3A

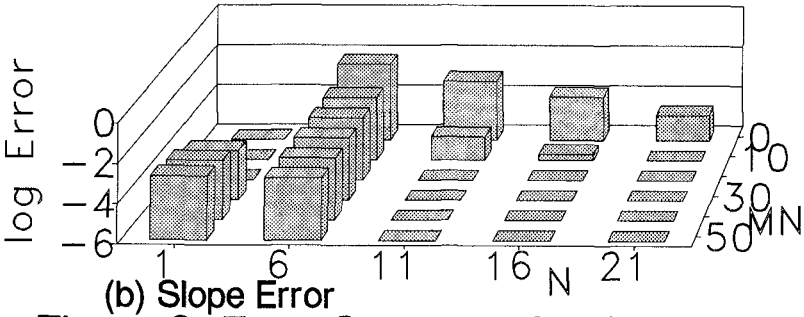
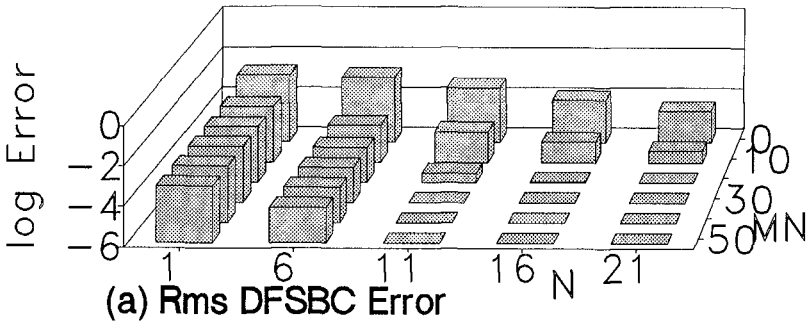


Figure 8 Error Summary for Case 4C

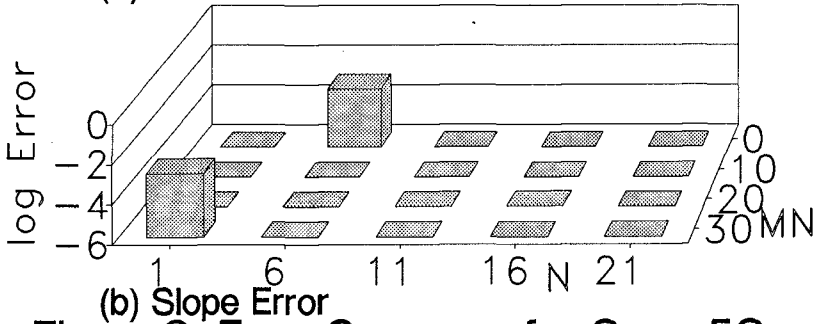
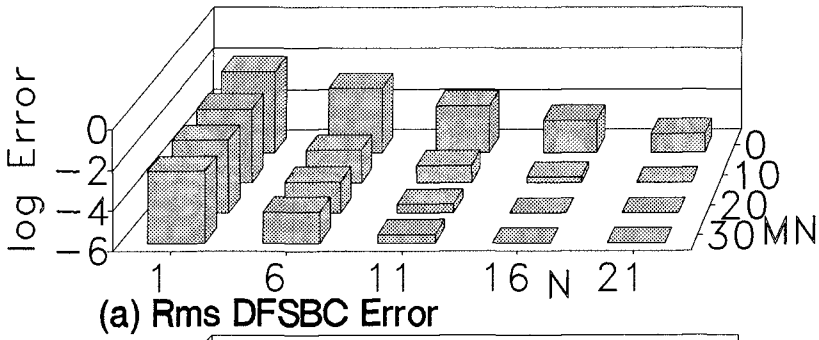


Figure 9 Error Summary for Case 5C

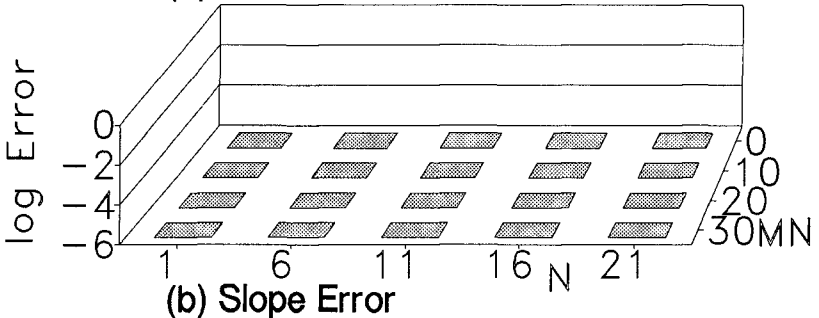
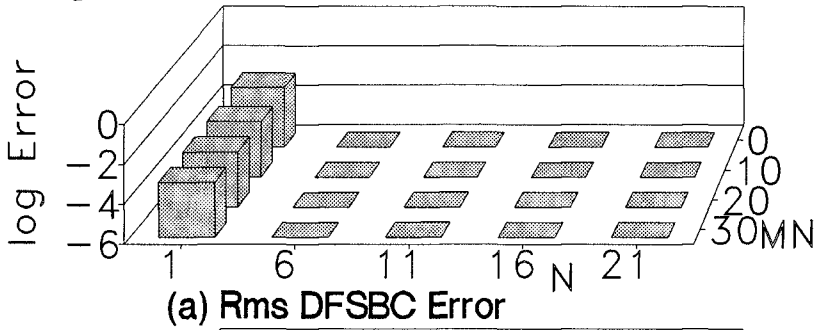


Figure 10 Error Summary for Case 6A

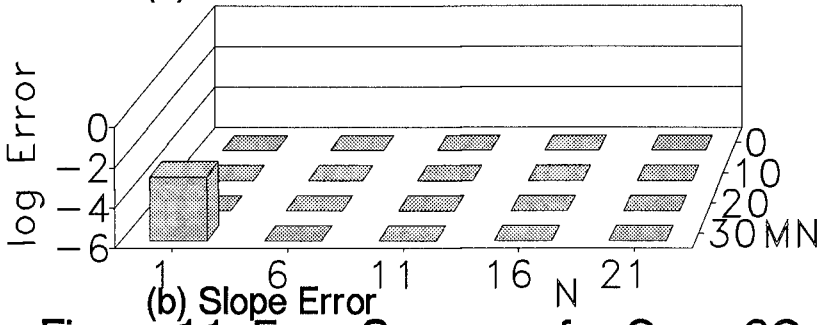
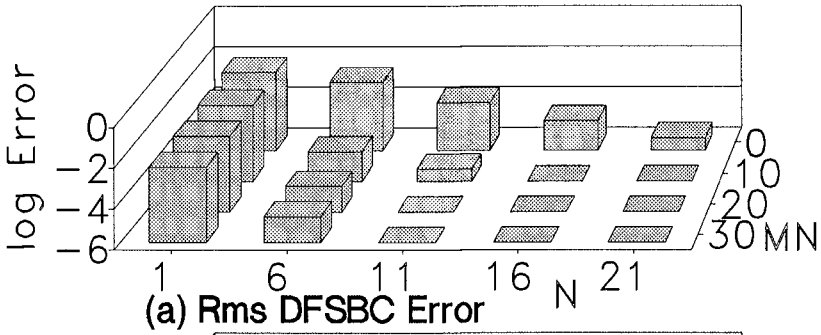


Figure 11 Error Summary for Case 6C

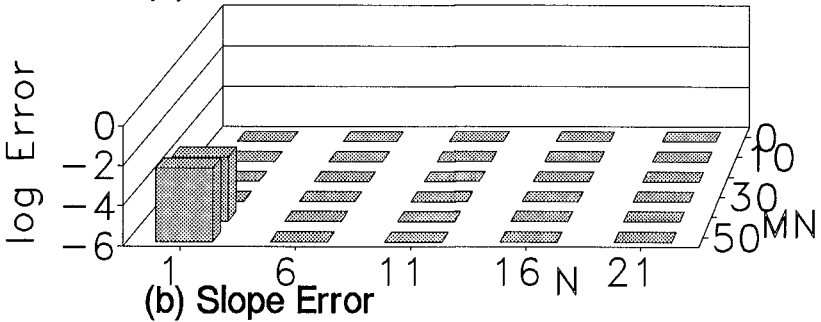
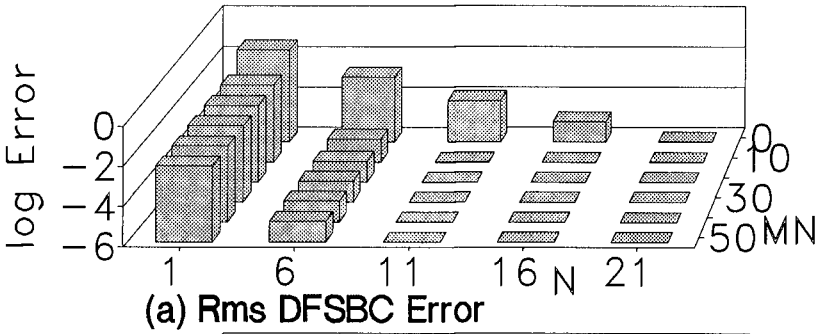


Figure 12 Error Summary for Case 7C

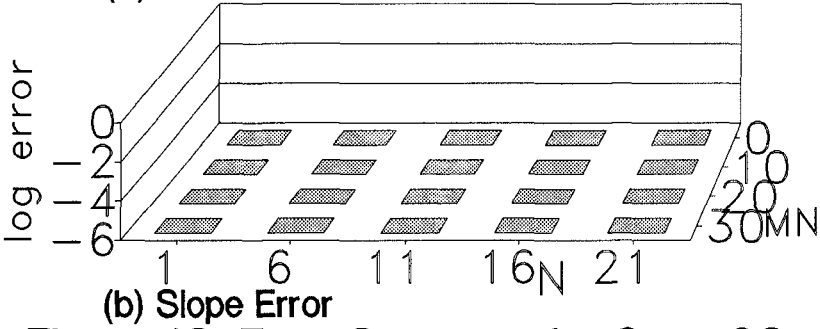
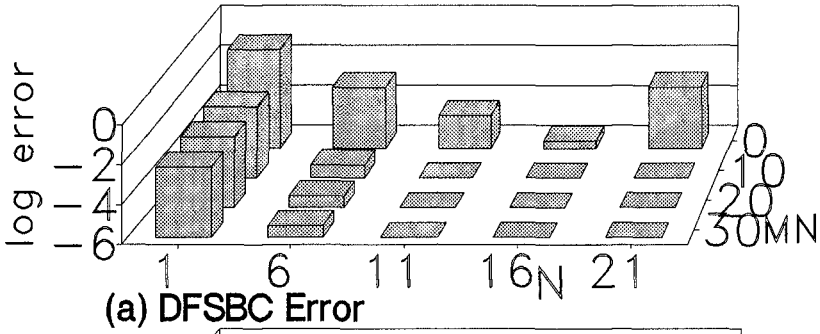


Figure 13 Error Summary for Case 8C

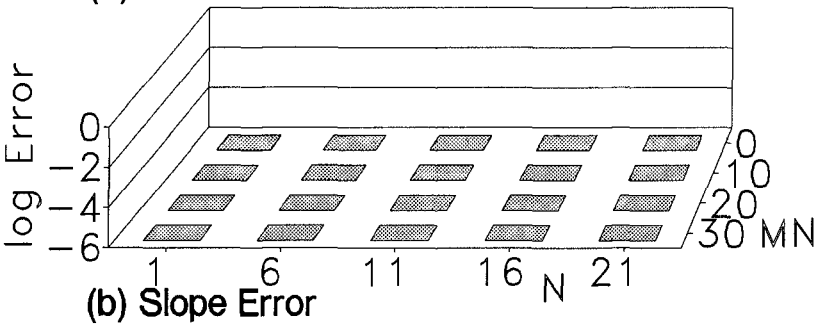
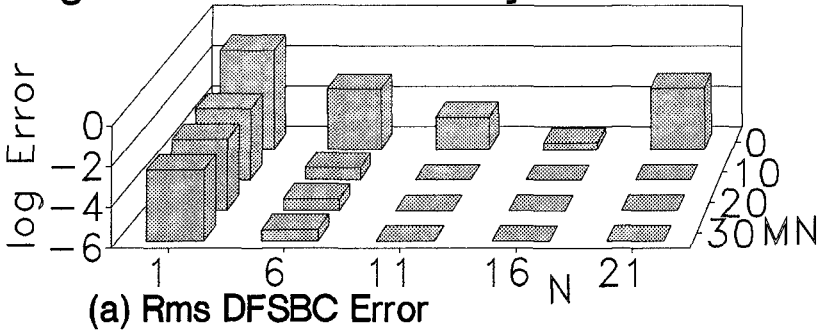


Figure 14 Error Summary for Case 10C

case it is possible to adopt too high a truncation order, very much the reverse of the more serious problems in shallower water. A truncation order of 21 is unnecessary in deep water.

In the application of analytical wave theories such as Stokes and cnoidal, the choice of an appropriate order is a matter of engineering judgement, and depends upon the nature of the physical problem, the required precision of the computation and sometimes on overriding regulatory requirements. The choice of truncation order and overspecification for Fourier wave theory is similarly a matter of engineering judgement and it is not appropriate to nominate specific values. The consequences of a particular choice however can be evaluated from the range of summary plots presented that have been presented.

CONCLUSIONS

Each Fourier wave solution is nominally dependent of three physical parameters, wave height $\omega^2 H/g$, water depth $\omega^2 h/g$, and current $\omega C_v/g$ or $\omega C_s/g$ and on two numerical parameters truncation order N and overspecification MN . Specific attention has been given to the solution dependence on N and MN and to the distinction between a successful numerical solution and a successful physical solution.

Some 230 separate Fourier wave solutions have been completed over a wide parameter range representative of field conditions. Trends are summarized in terms of three integral error measures, the rms DFSBC and rms KFSBC errors, which are measures of a successful numerical solution, and a slope error, which is a measure of a successful physical solution. A dimensionless cutoff level of 10^{-6} has been adopted to identify a successful solution. Precision is shown to be closely related to computational effort ($N + MN$) but the truncation order N is the dominant parameter. There is some minor advantage in a little over specification but significant overspecification does not enhance precision.

A range of summary error plots should assist in the rational assignment of truncation order and possible overspecification for Fourier wave solutions.

REFERENCES

- Chaplin, J.R. (1980) "Developments of stream-function wave theory". Coastal Engineering, 3, 179-205.
- Dalrymple, R.A. (1974) "A finite amplitude wave on a linear shear current". Journal of Geophysical Research, 79, 4498-4504.
- Dean, R.G. (1965) "Stream function representation of nonlinear ocean waves". Journal of Geophysical Research, 70, 4561-4572.
- Dean, R.G. (1974) "Evaluation and development of water wave theories for engineering application". U.S. Army Coastal Engineering Research Center, Report SR-1, 2 volumes.
- Fenton, J.D. (1983) "The numerical solution of steady water wave problems". Manuscript.
- Rienecker, M.M. and Fenton, J.D. (1981) "A Fourier approximation method for steady water waves". Journal of Fluid Mechanics, 104, 119-137.
- Sobey, R.J. (1988) "Variations on Fourier wave theory". Manuscript under review.

CHAPTER 22

DIRECTIONAL SEA STATE NEAR THE ISLAND OF SYLT

by

Daniel Schade ¹⁾, Karl-Friedrich Daemrich ²⁾

Abstract

In the scope of a joint research program dealing with erosion problems of the island of Sylt in the North Sea, wave measurements with two pitch-and-roll buoys are carried out in order to obtain more detailed information on the sea state with regard to wave dependent morphological processes.

The instrumentation is described. Results from the directional analysis of closely spaced buoys are compared, showing good agreement in significant parameters and in distributions in the frequency range. Differences between wave and wind directions are discussed. A method of separating double peak spectra by fitting theoretical shallow water spectra to the measured energy density distributions is presented.

1. Introduction and scope of investigations

The island of Sylt is one of the North Frisian Islands, located in the southeastern part of the North Sea (fig.1). The main dimensions are about 40 km in north-south direction and 1 to 4 km in east-west direction, except the central part. The main wave directions are from the west, striking the islands broadside.

1) Dipl.-Ing., Research Engineer

2) Dr.-Ing., Senior Research Engineer

both

Franzius-Institut, University of Hannover, Nienburgerstr. 4
D-3000 Hannover 1, F.R.G.

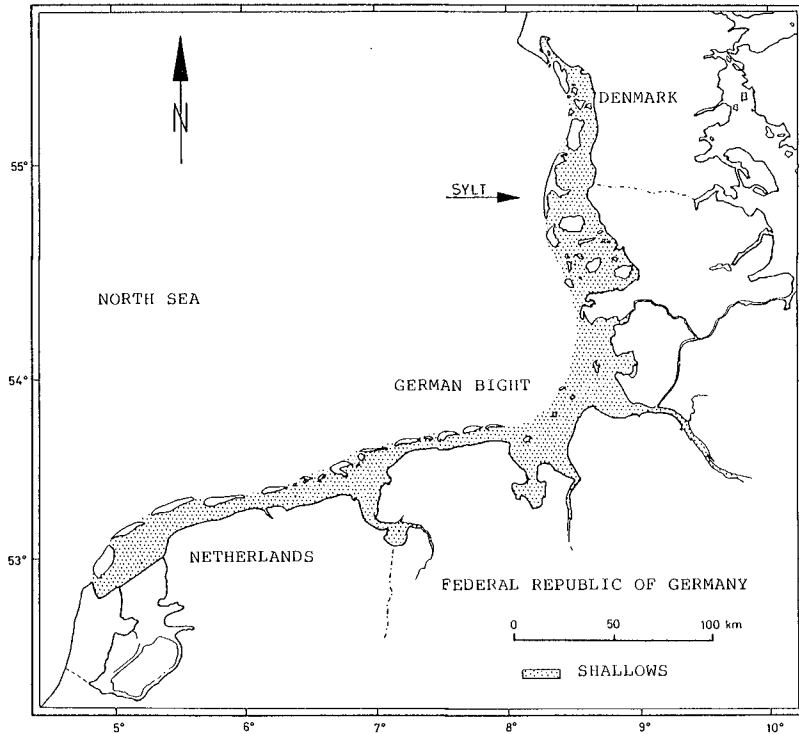


Fig.1:
Location of the island of Sylt in the North Sea

Due to the exposed site of the island the erosion has been a serious problem for centuries. This could not be stopped even with intensified shore protection works, e.g. the construction of groynes and revetments started in 1865 and by beach nourishments since 1972. During the last 35 years the island lost an area of about 2.50 km^2 equivalent to a quantity of some $50 \cdot 10^6 \text{ m}^3$ material.

In 1985 a joint research program was created to deal with the problems of the island and work towards an optimization of coast protection measures. Scientists from various German universities and the Amt für Land- und Wasserwirtschaft Husum (local technical authority) are participating in this project.

One part of this research program realized by the Franzius-Institut is to carry out measurements with two pitch-and-roll buoys in order to obtain directional wave spectra.

The main task of these measurements is to provide more detailed information on the sea state as a basis and reference for the wave related investigations within this

research program. Especially the directional information, essentially important for the judgement of longshore sediment transport processes, was not available up to now and had to be estimated on the basis of wind information.

In this contribution the following topics are treated:

- description of the instrumentation
- comparison of results from closely spaced Wavec buoys
- comparison of wind versus wave direction
- treatment of double peak spectra.

2. Instrumentation

For the investigations it was decided to procure the Datawell wave direction measuring system (fig.2). The buoy has a total weight of 700 kg, its diameter is 2.50 m. The mooring system consists of a mooring cross, 30 m rubbercord with a safety line (maximum load 8 t) and a 2 t heavy chain as an anchor weight.

The buoy measures vertical acceleration (heave) and pitch and roll angles against buoy defined x- and y- directions.

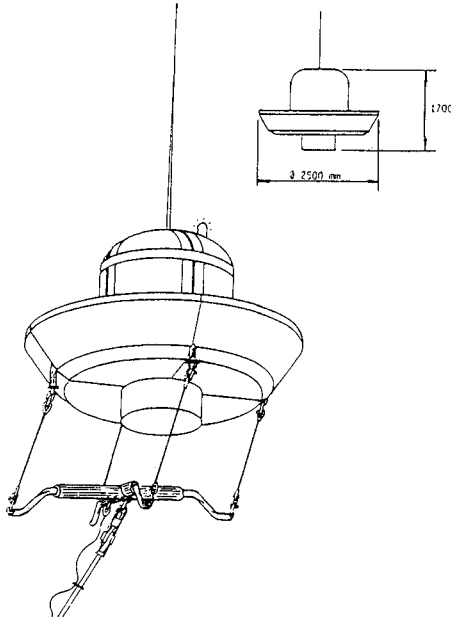


Fig.2:
Wavec pitch-and-roll buoy

The land station on Sylt consists of a Direc receiving station, a HP85 deskcomputer and a HP winchester disc for each buoy. The data are decoded and analysed by the Direc and then plotted and stored by the HP85 and the winchester disc. In the standard mode every 4 hours a 30 min series of data are processed and stored. The main computer in Hannover, 400 km southwards, is connected by telephone data line for

- transmission of the measured data
- function control
- change of the measuring mode.

For the processing of the measured time series, the Datawell standard package is used to calculate

- energy density spectrum
- mean direction for each frequency
- beam width of directional distribution

according to the methods established by LONGUET-HIGGINS et al. (1963).

3. Comparison of results from closely spaced buoys

It was decided to have one buoy at a permanent position as a basis and reference for the long term wave statistics. The second buoy is assigned for measurements in areas of special investigations along the island, but also for investigations of variations of the sea state, including shoaling and refraction. In a first measurement series, the buoys were located for a period of about 7 month in a distance of less than 1000 m (water depth of about 13 m below MSL) for the assessment of the reliability of the measuring system and the homogeneity of the wave field.

Significant parameters

$$\begin{aligned}
 H_S - \text{significant wave height} &= H_{m_0} = 4 \cdot \sqrt{m_0} \\
 & m_0 = \int_0^{\infty} S(f) \cdot df \\
 T_Z - \text{significant wave period} &= T_{0,2} = \sqrt{\frac{m_0}{m_2}} \\
 & m_2 = \int_0^{\infty} S(f) \cdot f^2 \cdot df \\
 \bar{\theta} - \text{overall mean direction} &= \frac{1}{m_0} \cdot \int_0^{\infty} S(f) \cdot \theta_m(f) \cdot df
 \end{aligned}$$

were calculated and the results for October 1987 compared in fig.3 as scatter diagrams.

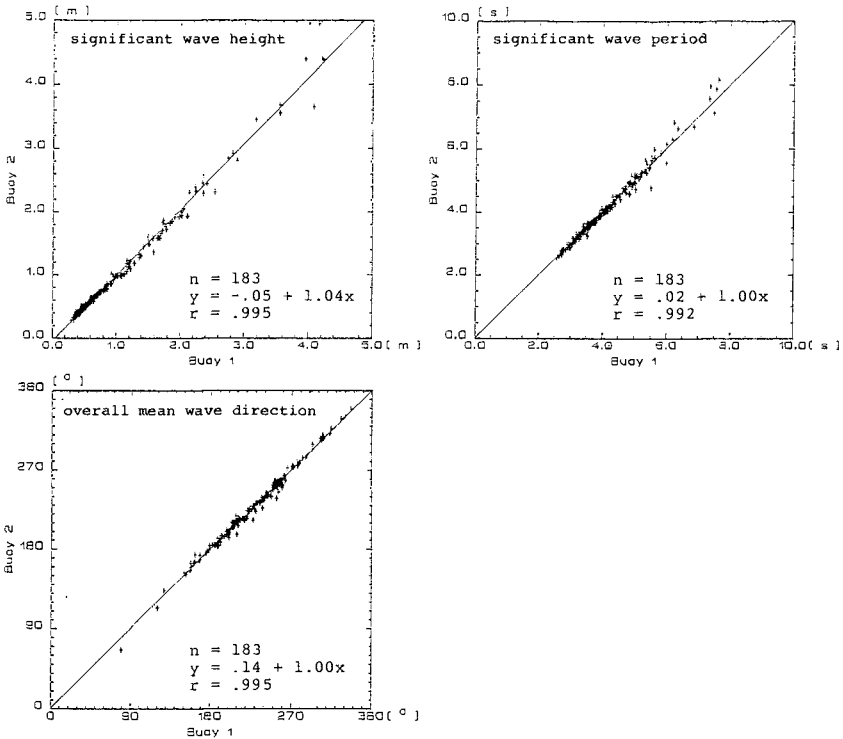


Fig.3:

Comparison of two closely spaced buoys, October 1987
linear regression

-significant wave height H_s [m]
-significant wave period T_z [s]
-overall mean wave direction $\bar{\theta}$ [°]

From the figures a good agreement can be seen. The correlation coefficient for all significant parameters is near to one.

In addition, the distribution in the whole frequency range was compared. Two examples are plotted, one with nearly identical significant parameters (fig.4) and one with some differences in the parameters (fig.5). In both cases the deviations are not too serious.

These results are in accordance with data presented by other authors (e.g. v.d.VLUGT, 1984).

4. Comparison of wind versus wave direction

One main part of this research program is to get better directional information and to check this against the wind direction, which was the up to now deepwater reference for the calculation of sediment transport rates.

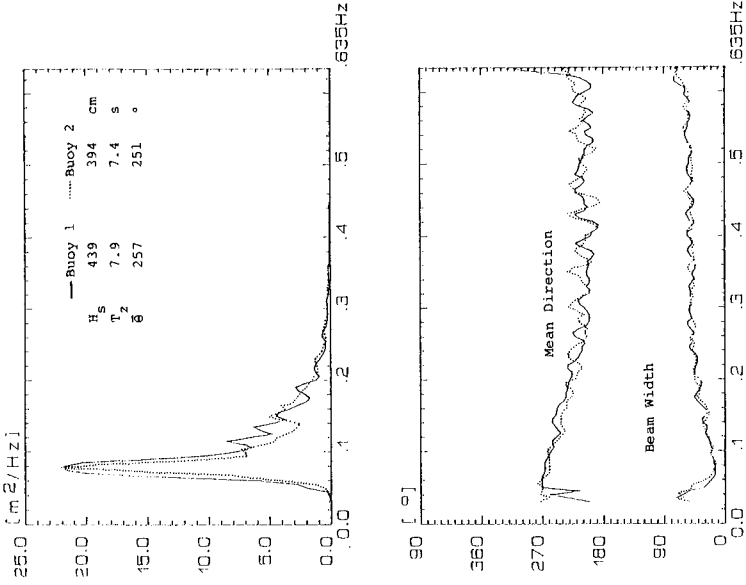


Fig.5:

Comparison of directional spectra of two closely spaced buoys (16.10.1987 15.30)

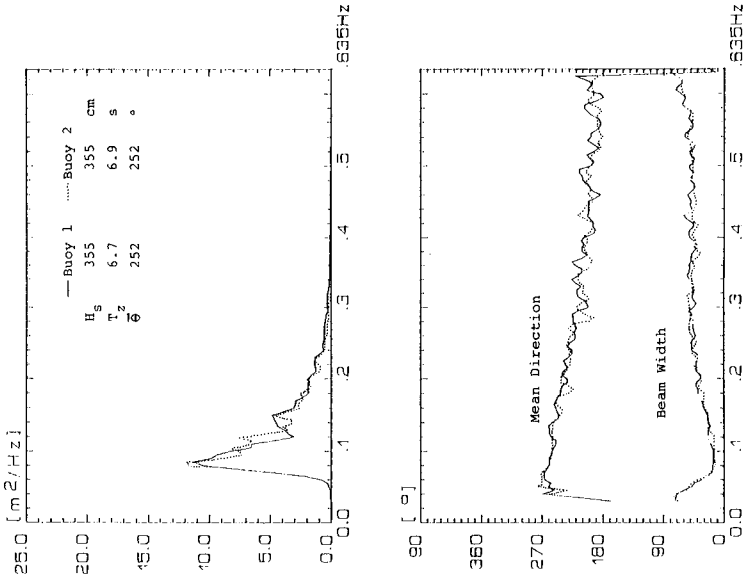


Fig.4:

Comparison of directional spectra of two closely spaced buoys (16.10.1987, 19.00)

The wave and wind direction, together with the wave height and the wind speeds are compiled in monthly plots. In fig.6 the data for October 1987 are shown.

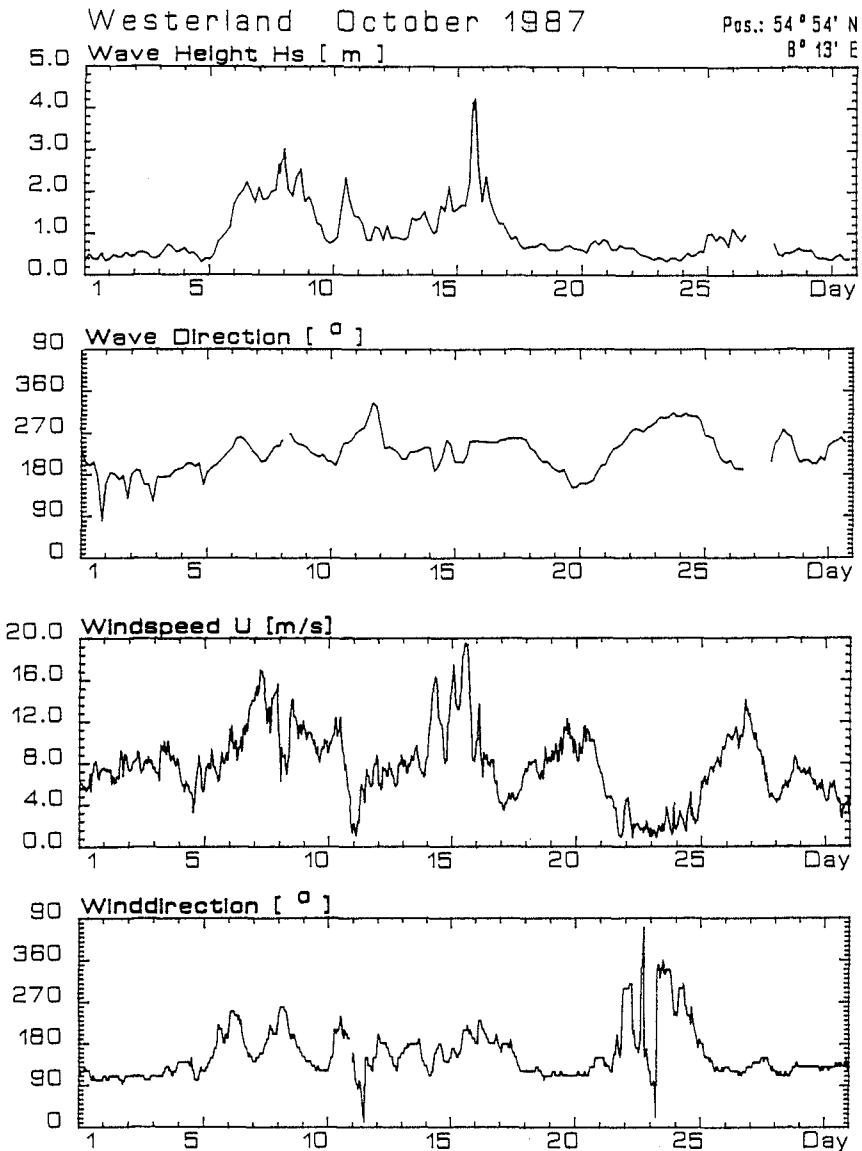


Fig.6:
Compilation of wave and wind parameters, October 1987

It is the general tendency, that fluctuations in wind direction are accompanied by minor fluctuations in wave direction. For easterly wind directions, i.e. wind from the land, no significant relationship can be expected, due to the still existing swell and wave heights below 0.5 m.

To investigate typical deviations, the wave directions were plotted directly against the wind directions for the period November 1987 to March 1988 (fig.7 a-c). The plot was restricted to events with westerly wave directions

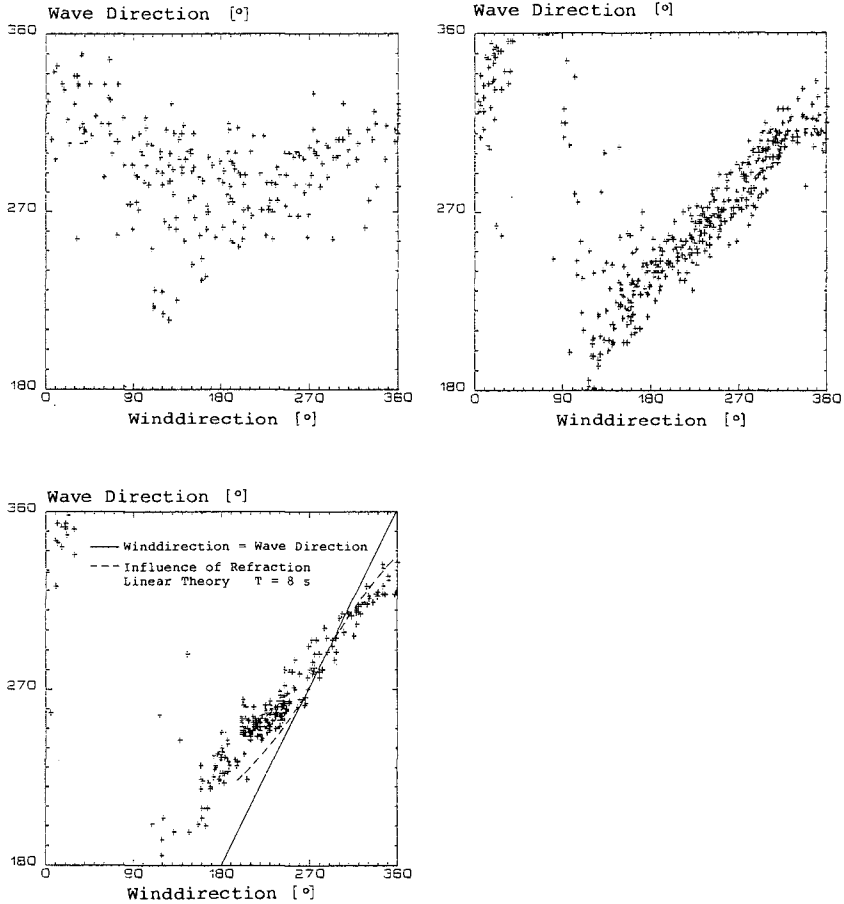


Fig.7:
Comparison of wind and wave direction
November 1987 - March 1988

a)	$u < 5$ m/s	n = 281
b)	$5 \text{ m/s} < u < 10$ m/s	n = 430
c)	$10 \text{ m/s} < u$	n = 288

between 180° to 360° . Besides that, a distinction was made between different groups of wind speeds (wind speeds and pertinent wind directions are 4 h averages of data preceding the wave measurements). Fig 7a shows a wide scatter, among others due to a great variety of wind direction at low wind speeds. In fig. 7b (wind speeds between 5 m/s and 10 m/s) a general tendency already appears in outlines, but still some remarkable scatter is left, due to influences from former events. In fig 7c the comparison is shown for wind speeds of more than 10 m/s. A distinct relation of the wave direction to the wind direction is now obvious.

Refraction influences were estimated with a regular wave model on the basis of linear wave theory, assuming parallel depth contours (strand orthogonal: 273° south part of the island, 290° north part of the island). According to the measurements, for wind speeds around 10 m/s a characteristic wave period of $T = 8$ s was used as input parameter. The result is plotted in fig. 7c for comparison (dotted line). Although the tendency of the results corresponds with the general trend of the deviation, this is not sufficient for application in design methods. A better agreement is expected from more sophisticated refraction models and considering results from measurements in deeper water with the second buoy.

5. Treatment of double peak spectra

It occurs, due to changing wind conditions, that a swell is superposed by a new generated wind sea. In the frequency domain, this may result in double peak spectra. The calculation of overall significant sea state parameters seems not to be sufficient in these cases (example see fig.8).

One way to identify these spectra and to separate for further working with significant wave parameters is to fit theoretical spectra, e.g. of the JONSWAP type, to the measured energy density distributions.

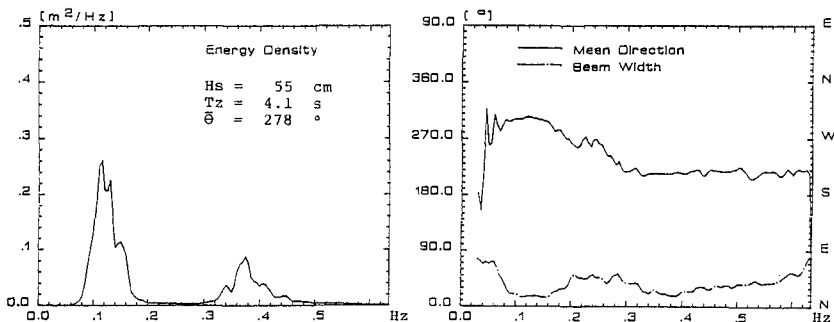


Fig.8:
Double peak spectrum 08.01.1987 00.30

As the JONSWAP shape is valid for deep water conditions, whereas the location of measurement is in a water depth of about 13 m below MSL, shallow water influences should be considered. To estimate the shape of the shallow water spectrum, the self similarity criteria as published by BOUWS et al. (1985), meanwhile well known as TMA shallow water spectrum (fig.9), were utilized.

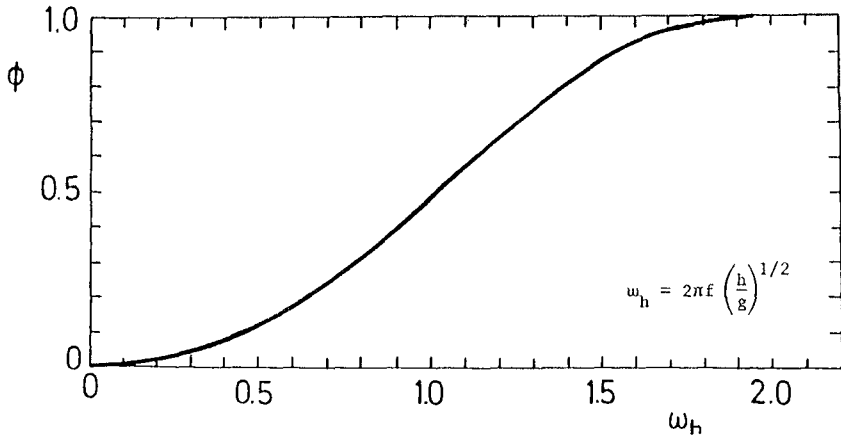


Fig.9:
KITAIGORODSKII et al.'s ϕ as a function of ω_h
(after BOUWS et al. 1985)

By this method, it is possible to calculate a shallow water spectrum from a deepwater JONSWAP spectrum, using a transformation factor, which is a function of water depth and frequency. Using the TMA spectrum for the pertinent water depth a relatively good approximation to the measured spectrum was achieved (fig.10) by varying the PHILLIPS constant α and the peak enhancement factor γ . There is still some scatter, but the difference in significant wave heights is less than 5% in this example (4.5 m measured to 4.6 m calculated).

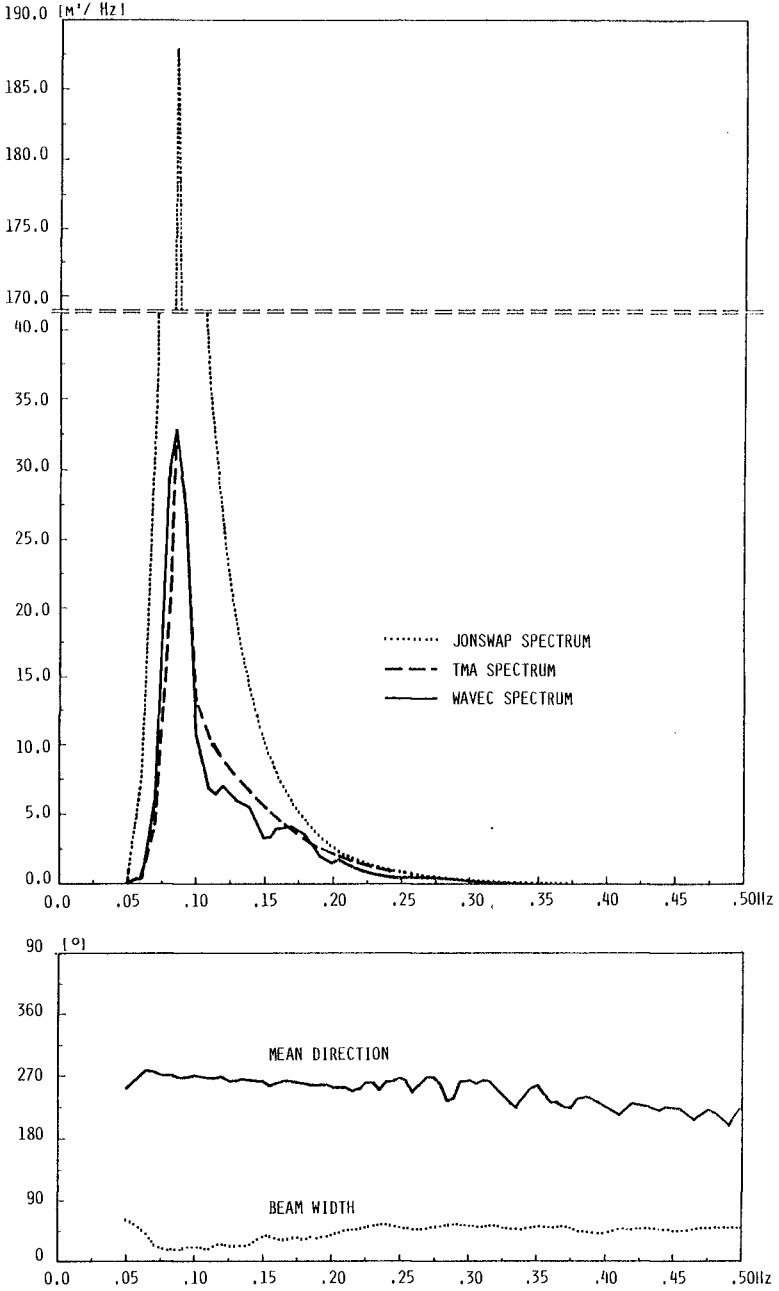


Fig.10:
Measured spectrum 10.2.1988 19.30 and pertinent TMA spectrum

For the separation and parameterization of a double peak spectrum, first the spectrum part with the lowest peak frequency is fitted by means of a TMA spectrum. The remaining part of the spectrum is then fitted by using the peak frequency of the second peak and the pertinent energy density reduced by the energy of the first spectrum at this frequency (example see fig.11).

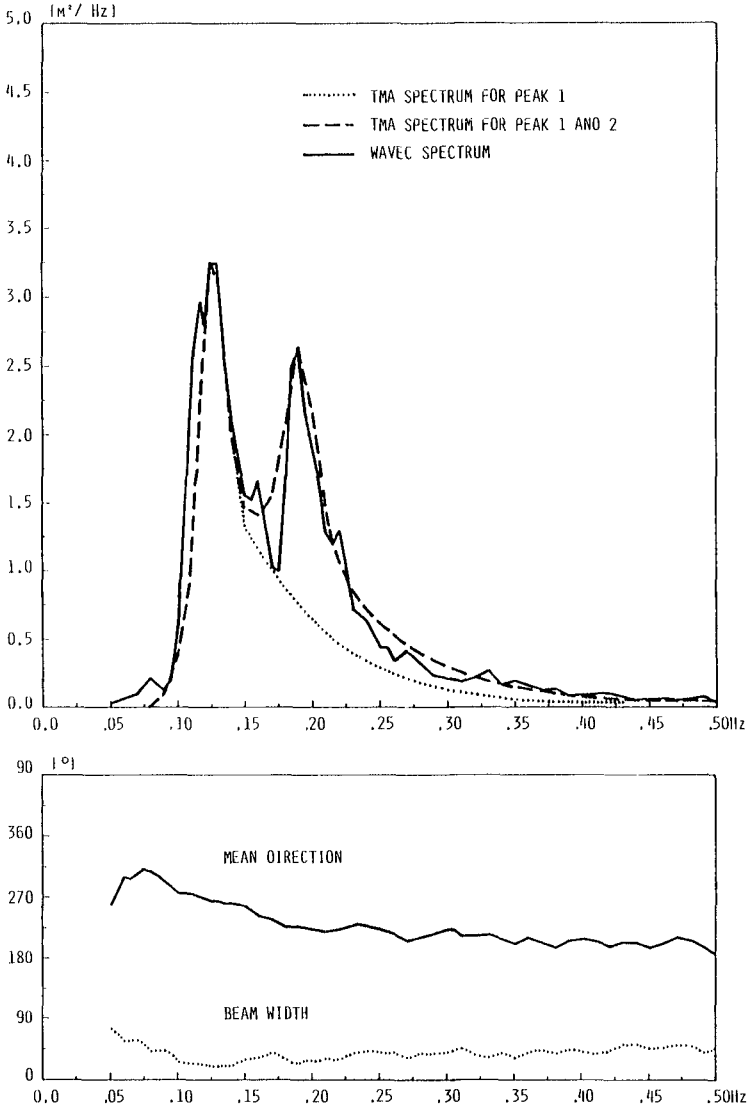


Fig.11:

Double peak spectrum 7.10.1987 16.30 and fitted TMA spectra

Using this parameterization approximate average wave directions could be calculated for each wave field. The wave parameters of the resulting TMA spectrum compared with the measured spectrum are as follows:

	H_s	T_z	T_p	$\bar{\theta}$
	m	s	s	°
measured spectrum	1.98	5.00	8.00	243
TMA 1	1.53		8.00	248
TMA 2	1.19		5.26	223

Fitting double peak spectra by this method has to be seen as a first attempt. In the scope of the project it is used to determine more reliable wave parameters for the estimation of longshore transport rates, e.g. by the CERC formula.

Assuming that both wave fields can be treated independently, two transport rates can be calculated and compared with the rate calculated from the overall parameters of the original spectrum. On a yearly basis $5.2 \cdot 10^6 \text{ m}^3$ are estimated from the first part of the spectrum (lower frequencies) and $2.4 \cdot 10^6 \text{ m}^3$ from the second part. The calculation with the overall parameters results in $9.8 \cdot 10^6 \text{ m}^3$. This is equivalent to a difference of about 25%.

6. Acknowledgement

The authors like to acknowledge the financial support by the Bundesminister für Forschung und Technologie and the Minister für Ernährung, Landwirtschaft, Forsten und Fischerei des Landes Schleswig-Holstein. The assistance by the Amt für Land- und Wasserwirtschaft Husum is highly appreciated.

7. References

- BOUWS, E.; GÜNTHER, H.; ROSENTHAL, W. and VINCENT, C.L.: Similarity of the wind wave spectrum in finite depth water. Journal of Geophysical Research, Vol. 90 p. 975-986, 1986.
- LONGUET-HIGGINS, M.S.; CARTWRIGHT, D.E. and SMITH, N.D.: Observations of the directional spectrum of sea waves using the motions of a floating buoy. Ocean Wave Spectra, Prentice-Hall, p. 111-136, 1963.
- Van der VLUGT, A.J.M.: Experiences with the wavec buoy. Description and Modelling of Directional Seas, Copenhagen, Paper no. A3, 1984.

CHAPTER 23

REDUCTION OF WAVE OVERTOPPING RATE BY THE USE OF ARTIFICIAL REEFS

by

Toru Sawaragi*, Ichiro Deguchi** and San-Kil Park***

ABSTRACT

A wave overtopping rate from a sea dike of various toe depths is formulated based on a weir model in an unidirectional flow. To evaluate the wave overtopping rate from a seadike on an artificial reef by the weir model, a numerical procedure for predicting wave transformations including the effect of forced wave breaking on the reef is constructed. After confirming the applicability of the model through experiments with regular and irregular waves, the effect of artificial reef on wave overtopping is discussed. So-called individual wave analysis method is shown to be applicable to the wave overtopping caused by irregular waves.

INTRODUCTION

To cope with the wave overtopping from existing seawalls and seadikes, various kinds of wave energy dissipating structures such as an offshore detached breakwater, armor blocks and so on have been used. The highest priority has been given to the wave energy dissipating function of these structures and utilization and the view of the coast have been left out of considerations.

In Japan, recently, an artificial reef has been widely constructed as a multi-purposed coastal structure to control coastal erosion, to reduce wave overtopping and to utilize coastal zone to the best advantage. The artificial reef usually consists of a submerged breakwater with broad crown width and an artificially nourished beach behind it.

*Professor and **Associate Professor, Dept. of Civil Engineering, Osaka University, Osaka, Japan

***Assistant Professor, Dept. of Civil Engineering, Pusan University, Pusan, Korea

The main function of the artificial reef is to make incident waves break forcibly and reduce wave energy in the nearshore zone.

The primary objective of this study is to investigate the effects of artificial reef on the reduction of wave overtopping rate from the vertical seadikes when the artificial reef is constructed in front of it.

The wave overtopping rate from the sea walls and seadikes on an uniformly sloping beach has been studied under various conditions. Most results of these studies are analyzed by using wave conditions in deep water and crest elevations from the still water (e.g. Goda(1985) and CERC(1984)). Therefore, the effects of artificial reef on wave overtopping can not be discussed based on these results because the incident waves in front of the seadikes are greatly altered by the reef.

In this study, the authors apply the weir model, in which wave heights in front of the seadike and the crest elevation of the seadikes from the mean water level are directly taken into account, to investigate the effect of the reef on wave overtopping. To utilize the model, it is necessary to evaluate wave conditions in front of the seadike. The authors also construct a numerical model for a prediction of wave transformation on the reef.

After confirming the applicability of the proposed model through experiments with regular and irregular waves, the effects of the artificial reef on the reduction of wave overtopping are discussed. A block diagram of this study is shown in Fig. 1.

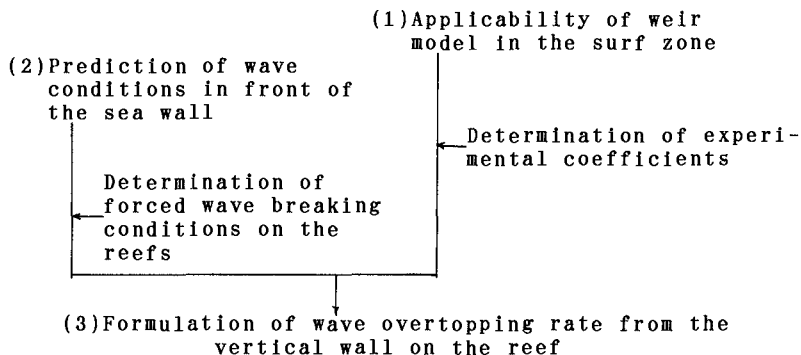


Fig.1 A block diagram of the study

APPLICABILITY OF WEIR MODEL IN THE BREAKER ZONE AND DETERMINATION OF EXPERIMENTAL CONSTANTS OF THE MODEL

The weir model was originally proposed by Kikkawa et al. (1967) to estimate wave overtopping rate from the seadike in the region where the water depth at the foot of seadike is deep enough for the incident waves to form clapotis without breaking. They gave the following expressions for the wave overtopping rate on the basis of weir discharge in the uni-directional flow:

$$Q = \frac{4\sqrt{2g}}{3} m K^{3/2} H_i^{3/2} \int_{t_1/T}^{t_2/T} \left[F(t/T) - \frac{H_c}{KH_i} \right]^{3/2} d(t/T) \quad (1)$$

where Q is the wave overtopping rate per unit time and unit width of the seadike, H_i is the incident wave height in front of the seadike, H_c is the crest height from the mean water level, η_{max} is the maximum elevation of the surface in front of the seadike, t_1 and t_2 are the times when the surface elevation becomes H_c and $F(t/T)$ is the non-dimensional time variation of the surface elevation, $\eta(t)$, defined by $F(t) = \eta(t)/\eta_{max}$, $K = \eta_{max}/H_i$, Z_0 is the crest height from the still water level. m is the discharge coefficient; in this study we assume that m will take the value about 0.5 according to Kikkawa et al. (1967). A definition sketch of wave overtopping together with notations used in this paper is shown in Fig.2.

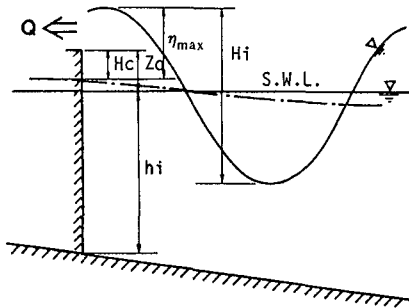


Fig.2 Definition sketch of wave overtopping

To evaluate wave overtopping rate by this model, the following three quantities must be given: the ratio of maximum surface elevation and incident wave height, K , the non-dimensional time variation of the surface displacement, $F(t/T)$, and the incident wave height, H_i . In this study, we redefine η_{max} and H_c as the maximum surface elevation and the crest height of the seadikes from the mean water level as shown in Fig.2 to refine the model. Therefore, besides those three quantities the mean water level, $\bar{\eta}$, is also required.

If we can find universal expression for K and $F(t/T)$, it

becomes possible to estimate wave overtopping rate based on the weir model (Eq.(1)) provided that the incident wave height, H_i , and the mean water level in front of the seadike, $\bar{\eta}$, are given. However, it is surely a hopeless work to formulate the non-dimensional time variation of the surface displacement, $F(t/T)$, within the breaker zone.

In this study, we first calculated the value of K from Eq.(1) by using the experimental results of wave overtopping rate conducted by many researchers (Ishihara et al.(1960), Inoue et al.(1972), Kikkawa et al.(1967), Tominaga et al.(1970) and Inoue(1973)). Then, we conducted close investigations of the value of K by assuming that $F(t/T)$ varies sinusoidally.

The results are shown in Fig.3. The upper part of the figure indicates the results obtained in the cases where clapotis without breaking were formed in front of the seadike. That is the depth at the foot of the seadike was deep. The lower part of the figure shows the results in the cases where seadikes were located in the breaker zone. In the cases where no information about H_i and $\bar{\eta}$ was given, these values were estimated numerically, the detailed procedure for which is described in the following section.

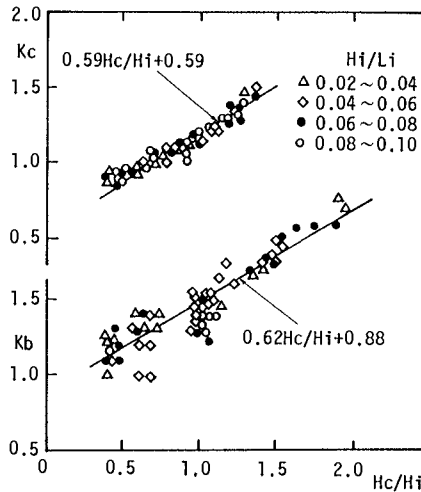


Fig.3 K vs. H_c/H_i

The value of K in the clapotis region is uniquely determined by H_c/H_i and not depend on H_i/L_i where L_i is the wave length in front of the seadikes. This agrees with the results which have already pointed out by Tsuchiya et al.(1970). The solid line in the figure is the regression of K in the clapotis region. Hereafter we refer K in this region as K_c , which is

expressed by

$$K_c = 0.59H_c/H_i + 0.59 \quad (2)$$

The value of K in the breaker zone also increase with the increase of H_c/H_i and does not depend on H_i/L_i . However, some scatter can be seen when compared with K 's value in the clapotis region.

Figure 4 illustrates examples of variation of K 's value in the breaker zone with the relative location of seadikes to the wave break point to investigate the reason of the scatter of K 's value in the breaker zone (Park et al. (1987)). X_i in the horizontal axis is the relative distance between the location of seadikes and wave breaking point and is taken positive onshorewards. L_b is the wave length at the wave breaking point.

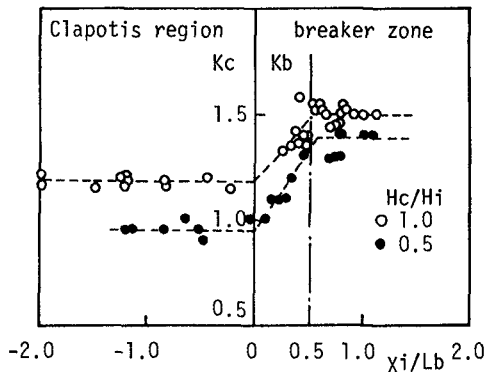


Fig.4 Variation of K with X_i/L_b

From this figure, it is found that K is constant in the region of $X_i/L_b < 0$ and $X_i/L_b > 0.5$. However, in the region of $0 < X_i/L_b < 0.5$, K increases with the increase of X_i/L_b .

The authors (Sawaragi et al. (1986)) have already pointed out that when the vertical wall is located in the region of $X_i/L_b < 0$, that is offshore of the wave breaking point, clapotis without breaking forms in front of the wall. When it is located in the region of $X_i/L_b > 0.6$, waves after breaking attack it. When the vertical wall is located in the region between $0 < X_i/L_b < 0.6$, clapotis with breaking at the loop forms. The variation of K 's value with the change of X_i/L_b appears in Fig.4 coincides with these situation of wave fields in front of the seadikes. However, the reason for the increase of K 's value in the region of $0 < X_i/L_b < 0.5$ is not found out.

A solid line in the lower part of Fig.3 is the regression line of K calculated in the cases where $X_i/L_b > 0.5$. Here-

after, we refer K in this region as K_b , which is given by

$$K_b = 0.62H_c/H_i + 0.88 \quad (3)$$

The value of K in the region where $0 < X_i/L_b < 0.5$ becomes a function of X_i/L_b and can be evaluated by

$$K = 2(K_b - K_c)(X_i/L_b) + K_c \quad (4)$$

NUMERICAL MODEL FOR THE PREDICTION OF WAVE TRANSFORMATION ON THE REEF

A series of experiments was carried out to investigate wave transformation including forced wave breaking on the reef. Based on the experimental results, numerical model for predicting wave transformation on the reef was constructed.

1) Two-dimensional experiments of the wave transformation on an artificial reef

Experiments were carried in a wave tank of 30m long, 0.7m wide and 0.9m high. An artificial reef made of polywood was placed on a model beach with a slope of 1/30. The slope of artificial reef was determined at 1/30 as suggested in the manual on the utilization of sandy beach (Port and Harbor Bureau (1979)). The offshore slope of the reef was 1/2. A sketch of the artificial reef used in the experiments is given in Fig.5 together with the notation used in the following descriptions.

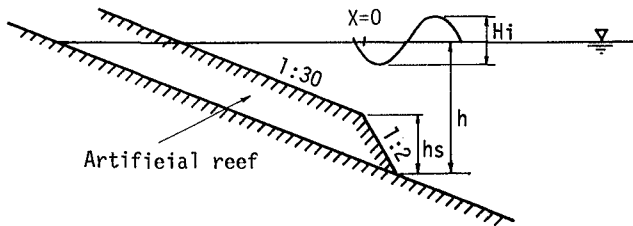


Fig.5 Sketch of artificial reef used in the experiments

A water depth at a toe of the reef, h , was kept constant at 10cm and reefs of different relative heights ($h_s/h = 0.25, 0.55$ and 0.75) were used. Periods of experimental waves were $T = 0.8s, 1.1s$ and $1.4s$. Wave heights at the toe of the reef, H_i , were adjusted to be $H_i/h = 0.5, 0.5^*, 0.75, 0.75^*$ and 0.9 where $*$ indicates the case where waves had broken before they reached the toe of the reef. All the waves which reached the toe of the reef without breaking broke forcibly

on the offshore slope of the reef. A breaker type of these waves was a typical plunger.

Water surface elevations were measured with six capacitance type wave gauges at an interval of 5 to 10cm around the artificial reef. The analogue output signals were digitized at a time interval of 1/20s. Mean water levels and wave heights were calculated from these digital data. A reflection coefficient was also calculated by the method proposed by Goda(1985) to be 0.15 at the maximum.

2) Condition for forced wave breaking on an artificial reef
 When waves reach an artificial reef, they break owing to an abrupt change in water depth. In this section, the condition for wave breaking on the artificial reef is investigated by applying Goda's breaking criterion(Goda(1985), which explicitly takes into account the effect of bottom slope:

$$H_b/L_o = A[1 - \exp(-1.5(1 + 15 \tan^4 \theta) \pi h_b/L_o)] \quad (5)$$

where H_b and h_b are the wave height and the water depth at the breaking point, L_o is the deep water wave length, $\tan \theta$ is the bottom slope and A is the coefficient which will take the value between 0.12 to 0.18 for the waves that break on an uniformly sloping beach.

The applicability of Eq.(5) to the wave breaking on the artificial reef was examined by evaluating the coefficient A in Eq.(5) from measured H_b and h_b , where $\tan \theta$ was assumed to be the slope of the artificial reef(1/30). The results are shown in Fig.6. Open circles in the figure indicate the cases of offshore breaking; in these cases, the value of A shows almost constant(0.18). However, when waves break on the reef, A 's value increases with the relative height of the reef, h_s/h , as shown by closed circles in the figure. It is also seen that the value of A decreases with increasing relative water depth at the toe of the reef, h/L_o .

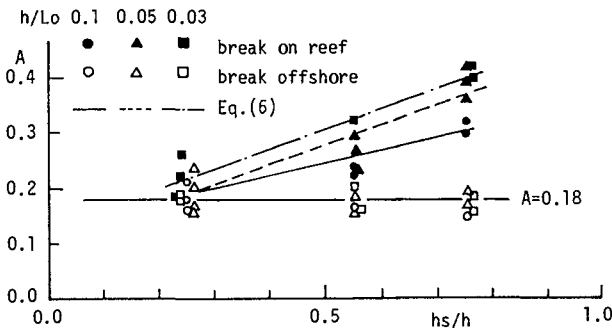


Fig.6 Relation between A and h_s/h

From these results, the following approximate expression is obtained under the condition of $0.25 < h_s/h < 0.75$ and $0.03 < h/Lo < 0.10$:

$$A = (-2.18h/Lo + 0.45) h/h + 0.1.7 + 0.21h/Lo \quad (6)$$

The values of A estimated from Eq.(6) are also shown in Fig.6.

3) Applicability of the bore model to the prediction of wave attenuation on an artificial reef

Some examples of wave height distributions measured in the experiments are shown in Figs.7 to 9 for the case of $T=1.1s$ and $h/Lo=0.05$. Figures 7 and 8 correspond to the cases where incident waves broke on the offshore slope of the reef or on the reef. Figure 9 represents the case where incident waves broke off the reef. In these figures, (a),(b) and (c) indicate the cases of $h_s/h=0.25, 0.55$ and 0.75 , respectively.

The decay of wave height after breaking in the figures becomes more rapid when the reef is higher regardless of the value of H_i/h .

The authors applied the bore model to predicting the wave height and mean water level on the reef. The wave height in the offshore region was calculated by using the shoaling coefficient formulated by Shuto(1974). The wave height within the breaker zone was estimated from the bore model with the energy dissipation rate proposed by Mase et al. (1982). In the calculation, equations of energy flux conservation and time and vertically averaged momentum flux and mass flux conservations were reduced to a system of difference equations and solved iteratively until the stable solutions are obtained.

The grid spacing was taken at $1/400$ to $1/800$ of the incident wave length to determine the breaking point exactly from Eqs.(5) and (6).

Calculated wave heights are shown by the solid lines in Figs.7 to 9. In the cases that the reef is relatively low ($h_s/h=0.55$), predicted wave heights agree well with the measured wave heights. When the reef is relatively high ($h_s/h=0.75$), the wave heights after breaking is slightly underestimated.

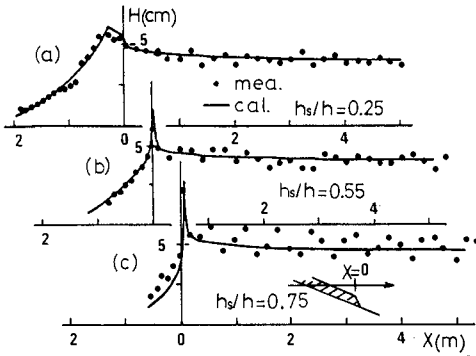


Fig.7 Wave height distributions on the reef ($H_i/h=0.5$)

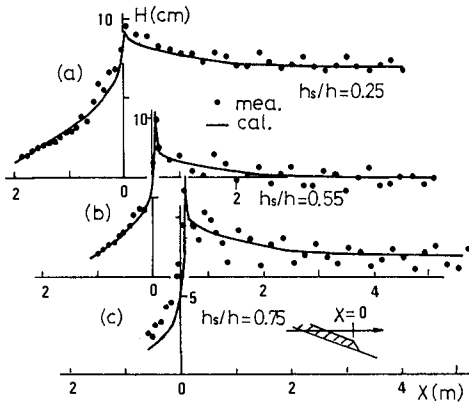


Fig.8 Wave height distributions on the reef ($H_i/h=0.9$)

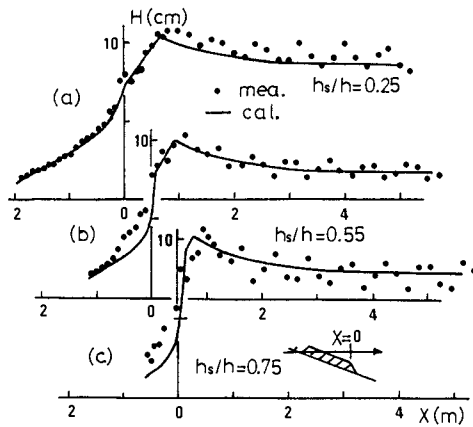


Fig.9 Wave height distributions on the reef ($H_i/h=0.75$)

WAVE OVERTOPPING RATE FROM THE SEADIKE ON THE REEF

Now, we can finally obtain all information to predict wave overtopping rate from the vertical seadike on the artificial reef. In this chapter, the applicability of proposed procedure for predicting wave overtopping rate on the reef is examined through experiments.

Experiments were carried out in the same wave tank as used in the experiments of wave transformations. Horizontal reefs set on the model beach with the slope of 1/30 was used and wave overtopping rate from the seadikes on various locations on the reef were measured. A water depth on the reef, h , was varied between 4cm to 8cm and experimental waves of deep water wave heights, H_o , and periods, T , between 7cm to 11cm and 1.0s to 1.5s were used. Whereas, the height of the reef, h_s , was kept constant (10cm).

Total number of experimental runs was 150 in which the relative crown height of the seadike, H_c/H_i , covered 0.3 to 2.0. The location of seadike, X_i/L_i , was varied from 0.0 to 3.0, where X_i is the distance between the shoulder of the reef and the seadike and L_i is the length of incident waves on the reef. In all the cases, all the incident waves broke forcibly on the shoulder of the reef.

Fig.10 shows the comparison between measured and calculated non-dimensional wave overtopping rate, q ,

$$q = \frac{Q}{\sqrt{g}L_iH_i} \quad (7)$$

Solid lines in the figure illustrate q estimated by Eq.(2).

From the figure, it is found that measured wave overtopping rate decreases rapidly with the increase of H_c/H_i . It is also seen that predicted q covers upper limit of measured q and increases a little with H_i/L_i .

This implies that our procedure for the prediction of wave overtopping rate from the seadike on the reef is adequate.

EFFECT OF THE ARTIFICIAL REEF ON WAVE OVERTOPPING

The applicability of our model to the wave overtopping by the irregular waves is examined by conducting experiments on the assumption of actual state. Further, the effect of artificial reef constructed in front of existing seadikes on wave overtopping in the irregular field is also discussed.

The experiments were conducted in the same wave tank as used in the former two experiments. The slope of model artificial reef was 1/30. The length of the reef, B , was 0.5, 1.0, 1.5 and 2.0m and the height of the reef, h_s , was 4.5 and 7.0cm.

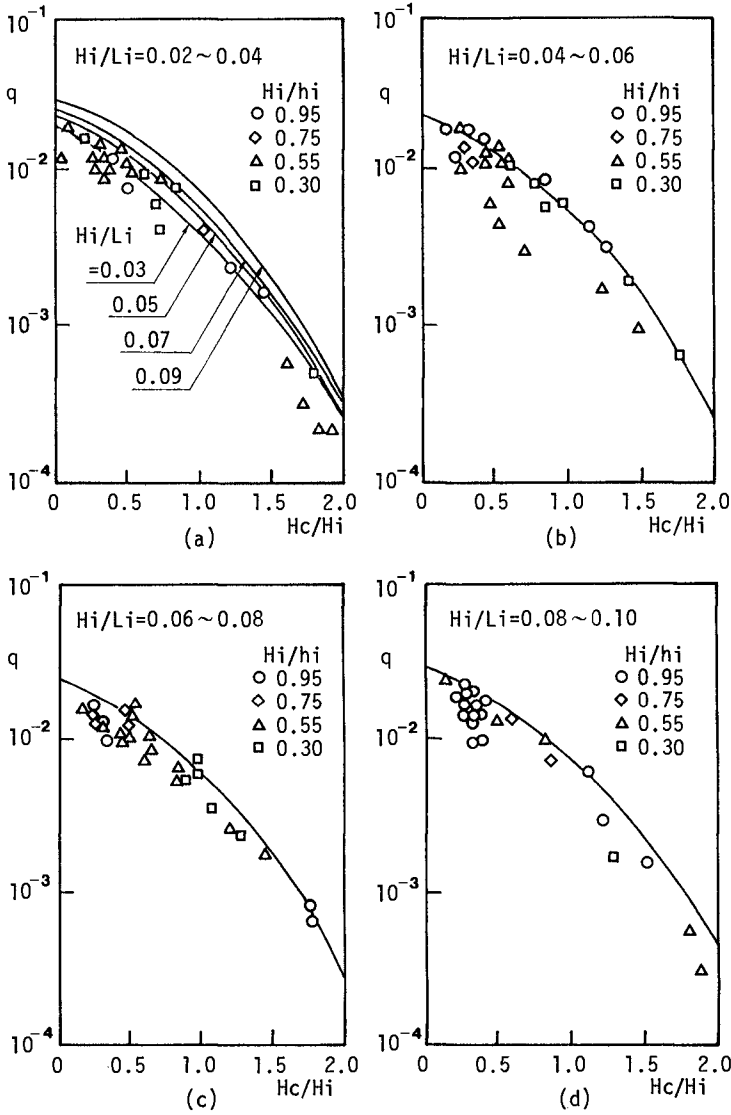


Fig.10 Non-dimensional wave overtopping rate from the
seadike on the reef

Experimental waves generated numerically to have Pierson-Moskowitz spectrum were used. Significant wave period, T_s , was 1.21s and significant wave heights, H_{s0} , in deep water were 8cm in the case of $h_s=4.5$ cm and 9.3cm in the case of $h_s=7$ cm. The crown height of the seadike, Z_0 , from the sill water level was adjusted to be $Z_0/H_{s0}=0.5-0.6$.

To predict wave overtopping rate by irregular waves, so-called "individual wave analysis method" is applied. That is, each volume of wave overtopping, q_k , brought about by individual waves which are defined by the zero-up-cross method in the irregular wave train is calculated from Eq.(2). Then, the time averaged wave overtopping rate, \bar{Q} , is estimated by summing up, q_k , as given by Eq.(8).

$$\bar{Q} = \left[\sum_k^N (q_k \sqrt{g H_k^2 L_k T_k}) \right] / \left(\sum_k^N T_k \right) \quad (8)$$

where N is the number of waves reached at the seadikes during the measurement of wave overtopping, H_k , L_k and T_k are the height, the length and the period of k -th wave. The value of q_k in Eq.(8) indicates the predicted volume of wave overtopping caused by k -th wave.

The individual wave analysis method for irregular wave transformation on the reef is applied on the assumption that there is no interaction between individual zero-up-crossing waves. This kind of analyses of irregular wave transformation on uniformly sloping beach have already been carried out by Mase et al.(1982).

As mentioned before, wave overtopping rate depends on both H_c/H_i and H_i/L_i , the joint distribution of wave height and period was given as a boundary condition at the offshore of the reef. To determine wave breaking points of individual waves, Eqs.(5) and (6) are used. Based on these results, q_k caused by each waves is calculated by using empirical expression of K (Eqs.(2)-(4)).

Fig.12 shows the comparison between measured and predicted time averaged wave overtopping rate on the reef by irregular waves. From the figure, we can judge that our model can also be applicable to the wave overtopping from the seadike on the reef by irregular waves.

Finally, Fig.13 indicates the effect of the length of the artificial reef on the reduction of wave overtopping. The vertical axis is normalized time averaged wave overtopping rate \bar{q} ($=\bar{Q}/\sqrt{gH_{s1}^2 L_{s1}}$) and the horizontal axis is the non-dimensional length of the artificial reef, B/L_{s1} , where H_{s1} and L_{s1} are the significant wave height and length in front of the seadike. From the figure, it can be seen that \bar{q} decreases rapidly in the region of $B/L_{s1} < 0.8$ and becomes almost constant beyond that range of B/L_{s1} .

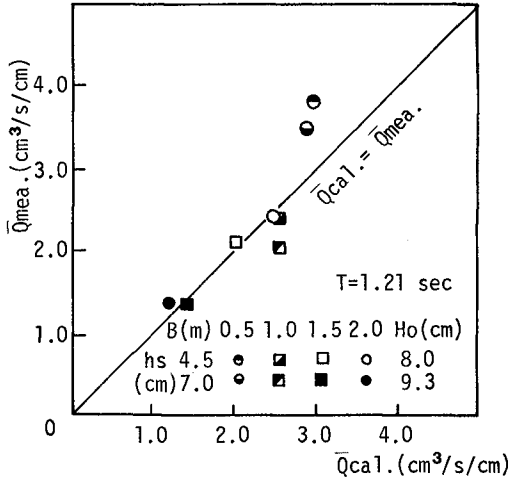


Fig.12 Comparison of measured and estimated time averaged wave overtopping rate on the reef by irregular

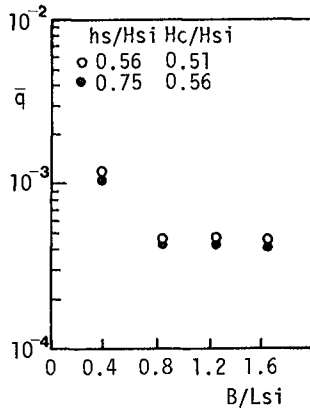


Fig.13 Non-dimensional wave overtopping rate vs. non-dimensional length of artificial reef

When the artificial reef was constructed in front of the seadike, relatively large waves in the irregular wave train broke forcibly and number of higher waves of the wave train which reached in front of the seadike decreased. Character-

ristics of the incident waves and dimensions of the reef determine the maximum waves which can transmit on the reef without breaking. However, the number of the waves which broke forcibly on the reef decreased with the increase of the length of the reef because the depth at the shoulder of the reef became deep. In such cases, the effects of the artificial reef appears in the point that it merely decreases the depth at the foot of the seadike.

This is the implication of the change of \bar{q} shown in Fig.13. In the case shown in Fig.13, it can be said that the effective length of the artificial reef to break large waves significantly corresponds to $0.8 \cdot L_{si}$.

CONCLUDING REMARKS

A procedure for estimating a wave overtopping rate from a seadike on an artificial reef is proposed based on a weir model in an unidirectional flow by assuming that the surface displacement in front of the seadike varies sinusoidally. In the procedure, the crown height and the maximum surface elevation from the mean water level and the incident wave height in front of the seadike are required to calculate the wave overtopping rate.

Among these, an empirical expression for the ratio of the maximum surface elevation to the incident wave height is given as an increasing function of the ratio of the crown height to the incident wave height. The incident wave height and mean water level in front of the seadike can be estimated numerically by using empirical criterion for the forced wave breaking on the reef proposed in the study.

So-called "individual wave analysis method" is applicable for the estimation of the wave overtopping rate in the irregular wave field.

It is also found that when the height of the reef in front of the seadike is given, a proper length of the reef exists to reduce the wave overtopping.

REFERENCES

- Coastal Engineering Research Center(1984) : Shore Protection Manual, Vol.II.
- Goda,Y.(1985) : Random seas and design of maritime structures, Univ. of Tokyo Press, 323p.
- Inoue,M. and T.Kikuoka(1972) : Effect of bottom topography in front of the seadike on wave overtopping, Proc. 19th Japanese Conf. on Coastal Eng., pp.283-288(in Japanese).
- Inoue,M.(1973) : Mechanism of wave overtopping, Proc. 20th Japanese Conf. on Coastal Eng., pp.107-112(in Japanese).
- Ishihara,T., Y.Iwagaki and H.Mitsui(1960) : Wave overtopping on seawalls, Coastal Engineering in Japan, Vol.3, pp.53-62.
- Kikkawa,H., H.Shiigai and F.Khono(1967) : Fundamental study on wave overtopping on seawall, 14th Japanese Conf. on Coastal Engineering, pp.118-122(in Japanese).
- Mase,H. and Y.Iwagaki(1982) : Wave heights distribution and wave grouping in surf zone, Proc. 18th ICCE, pp.58-76.
- Park,S.G., T.Sawaragi, I.Deguchi and Y.Inoue(1987) : Effects of zonal protection system on the reduction of wave overtopping rate, Proc. 34th Japanese Conf. of Coastal Eng., pp.526-530(in Japanese).
- Port and Harbor Bureau, Min. of Transport, Japan(1979) : Manual of the construction of artificial reefs, 110p(in Japanese).
- Sawaragi,T., I.Deguchi and G.P.Hong(1986) : Effect of rubble mound foundation of composite type breakwater on reduction of reflection, Proc. 5th APD-LAHR, pp.361-378.
- Shuto,N.(1974): Nonlinear long wave in a channel of variable section, Coastal Eng. in Japan, Vol.17, pp.1-12.
- Tominaga,M. and H.Hashimoto(1970) : Wave overtopping on seadike due to irregular waves, Proc. 18th Japanese Conf. on Coastal Eng., pp.265-268(in Japanese).
- Tsuchiya,Y., M.Yamaguchi(1970) : Characteristics of standing waves with wave overtopping, Proc. 17th Japanese Conf. on Coastal Eng., pp.79-84(in Japanese).

CHAPTER 24

EFFECT OF BOUSSINESQ EQUATIONS ON WAVE SPECTRA PROPAGATION

J.P.Sierra, A.S.Arcilla*, J.J.Egozcue** and J.L.Monso**

ABSTRACT

A 2-D numerical model has been developed to simulate wave propagation prior to breaking. This non linear hydrodynamic model works in connection with various spectral analysis routines. This paper intends to study the propagation effects on the wave time-series and on the corresponding spectral density functions in order to gain insight on both the spectral description of waves and irregular wave propagation.

1.- INTRODUCTION

Flow properties in coastal areas are of great importance in Maritime Engineering, for the solution of numerous problems such as the desing of offshore and coastal structures, shore evolution analysis, ship motions etc. For all of these subjects, a detailed knowledge of the shallow water wave heigth and propagation direction are required. State of art wave propagation models are usually either linear or unidirectional (in the input).

However, in order to enable the characterizacion of desing wave conditions, the use of two parameters as wave height and period is not enough. Wave randomness must be considered, since the assumption of unidirectional and monochromatic waves, can lead to unacceptable results from the Maritime Engineering standpoint.

One of the best ways to describe the wave irregularity is through a spectral density function, which is able to condense easily all the information involved in a wave time-series, with different frequencies and wave heights. If the possibility of waves travelling in different directions is considered, the estimation of the directional spectrum will be necessary, in order to achieve a full description of the wave characteristics.

Although spectral analysis has been widely used for several decades, a non linear model has been seldom coupled with spectral models.

In this paper a 2-D numerical non linear model for the simulation of wave propagation prior to breaking is described. In this model, both regular and irregular wave trains can be used. The propagation effects on the wave time-series and on the spectral density function are studied, in order to gain insight on both the spectral description of waves and irregular wave propagation.

* Maritime Eng.Lab., Catalonia University of Techn. in Barcelona. Spain.

** Department of Numerical Methods., Catalonia Univ. of Techn. in Barcelona.

2.- WAVE PROPAGATION

The numerical model is based on Boussinesq-type equations, in which the vertical velocity of the fluid particles is supposed to increase linearly from zero at the bed to a maximum magnitude at the free surface. The Boussinesq equations are formulated in terms of vertically-integrated mass and momentum conservation laws and are obtained with a perturbation technique (S.Arcilla and Monso, 1985), yielding the following expressions (Peregrine, 1967).

- Continuity equation

$$\frac{\partial H}{\partial t} + \frac{\partial p}{\partial x} + \frac{\partial q}{\partial y} = 0 \tag{1}$$

- x-momentum equation

$$\begin{aligned} \frac{\partial p}{\partial t} + \frac{\partial}{\partial x} \left(\frac{p^2}{H} \right) + \frac{\partial}{\partial y} \left(\frac{p \cdot q}{H} \right) + gH \frac{\partial(H-h)}{\partial x} = \\ \frac{Hh}{2} \left[\frac{\partial^3 \left(\frac{hp}{H} \right)}{\partial t \partial x^2} + \frac{\partial^3 \left(\frac{hq}{H} \right)}{\partial t \partial x \partial y} \right] - \frac{h^2 H}{6} \left[\frac{\partial^3 \left(\frac{p}{H} \right)}{\partial t \partial x^2} + \frac{\partial^3 \left(\frac{q}{H} \right)}{\partial t \partial x \partial y} \right] \end{aligned} \tag{2}$$

-y-momentum equation

$$\begin{aligned} \frac{\partial q}{\partial t} + \frac{\partial}{\partial x} \left(\frac{p \cdot q}{H} \right) + \frac{\partial}{\partial y} \left(\frac{q^2}{H} \right) + gH \frac{\partial(H-h)}{\partial y} = \\ \frac{Hh}{2} \left[\frac{\partial^3 \left(\frac{hp}{H} \right)}{\partial t \partial x \partial y} + \frac{\partial^3 \left(\frac{hq}{H} \right)}{\partial t \partial y^2} \right] - \frac{h^2 H}{6} \left[\frac{\partial^3 \left(\frac{p}{H} \right)}{\partial t \partial x \partial y} + \frac{\partial^3 \left(\frac{q}{H} \right)}{\partial t \partial y^2} \right] \end{aligned} \tag{3}$$

Where $H = h + \eta$

h is the still water depth

η is the free surface elevation

$p = \int_{-h}^{\eta} u \cdot dz$ is the mass flux along the x axe.

$q = \int_{-h}^{\eta} v \cdot dz$ is the mass flux along the y axe

u, v are the particle velocities along the x,y, axes.

Other terms can be easily included in these momentum equations, (S.Arcilla and Monso, 1986). With these additional terms, (e.g.Coriolis acceleration, wind friction, turbulent viscosity or bottom friction) a large number of physical phenomena can be adequately reproduced by the model.

The momentum conservation laws are highly non linear differential equations, and they include a third order derivative term, which is due to the existence of a constant vertical acceleration.

The vertical integration of equations (1),(2) and (3) reduces the problem from three to two independent dimensions. These equations are suitable for a wide range

of wave lengths. In particular, short wind waves in shallow water provide an acceptable ratio of water depth to wave length except for the shortest waves. These waves can be thus considered as long waves, and their propagation can be correctly simulated by the model.

The behaviour of different kinds of waves can be characterized by Ursell's parameter (UR).

$$UR = \eta \frac{L^2}{h^3} \quad (4)$$

Boussinesq equations ($UR = O(1)$) degenerate into de linear long-wave equations ($UR \ll 1$) or the Airy equations ($UR \gg 1$) with certain additional errors (S. Arcilla et al., 1985). This means that a single model, based on Boussinesq-type equations may be used to cover the whole range of physical problems (provided the associated errors are acceptable). When waves are of finite amplitude, the ratio h/L is small and breaking does not occur.

Considering different terms of the momentum equations and varying initial and boundary conditions, it is possible to reproduce a wide variety of physical phenomena such as Kelvin waves, storm surges, solitary waves, refraction, reflexion, diffraction, bottom friction, etc.

The equations are solved by means of an implicit centered finite-differences technique with variables defined on a space staggered rectangular grid. A double-sweep algorithm (Abbott and Ionescu, 1967) is invoked for solving the system avoiding large and expensive matrix inversion operations.

The truncation errors are of second order in time and space, i.e. $T.E. = O(\Delta x^2, \Delta y^2, \Delta t^2)$. The numerical scheme is conditionally stable and convergent. The propagation model is valid and yields reasonable results when $h/L < 0.2$. This means that the model can be applied in shallow or intermediate water depth but not in deep water.

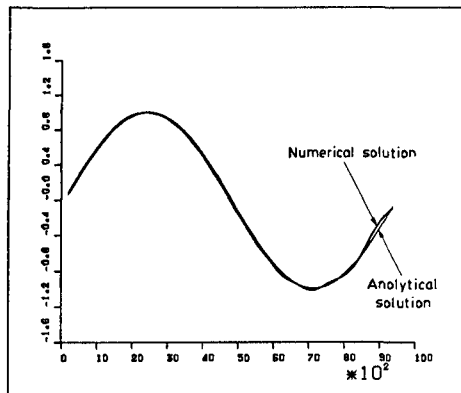


Figure 1. Sinusoidal long wave propagation

In open boundaries, an absorbing-reflecting boundary condition (S. Arcilla et al., 1986) is used. In this way, the multiple reflections due to innerly reflected waves are avoided, because these reflected waves are allowed to escape the domain unhampered.

The model was first calibrated in its linear version. Here, the momentum equations only include the local acceleration and the linear part of the pressure gradient term.

Figure 1 shows the application of the model for a sinusoidal long wave propagation. The characteristics of the discretization were $\Delta x = 200 \text{ m.}$, $\Delta y = 200 \text{ m.}$ and $\Delta t = 5 \text{ s.}$

The wave parameters were : Wave amplitude $a=1 \text{ m.}$, wave period $T=300 \text{ s.}$, wave length $L=9389 \text{ m.}$ and the depth was $h=100 \text{ m.}$

The figure shows a good agreement between the numerical model results and the analytical solution.

Another test was made for sinusoidal short waves in shallow water. The characteristics of the discretization were $\Delta x = 3 \text{ m.}$, $\Delta y = 3 \text{ m.}$ and $\Delta t = 1 \text{ s.}$

and the wave parameters were Wave amplitude $a=1 \text{ m.}$, wave period $T=18 \text{ s.}$, wave length $L=125 \text{ m.}$ in a depth of $h=5 \text{ m.}$

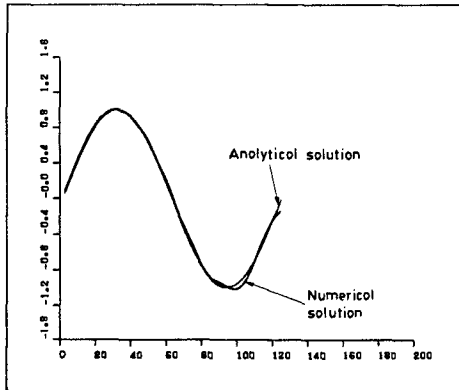


Figure 2. Sinusoidal short wave in shallow water propagation

Figure 2 shows that as the wave progresses the quality of the results decreases, although the fit between numerical and theoretical solutions is relatively acceptable. The poor quality of the results is obviously due to the fact that linear theory is not valid in shallow water.

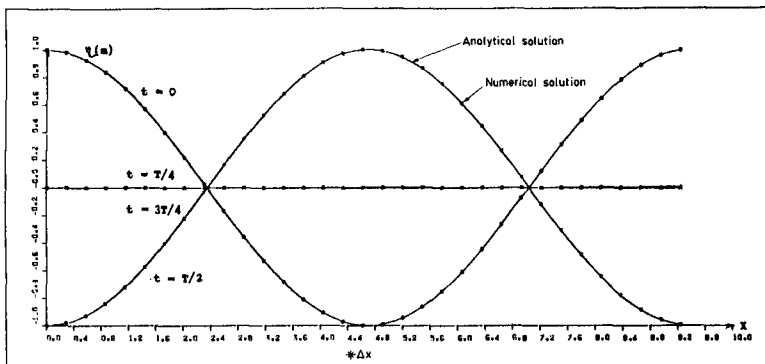


Figure 3. Reflection of a sinusoidal wave

Once the model had been tested for wave propagation, tests were made for reflecting waves, comparing computed results with the theoretical solution. Figure 3 shows the reflection of a sinusoidal wave on a vertical wall with constant water depth, forming a stationary wave.

The discretization and wave characteristics are the same as in the example showed in figure 1. The fit at different instants of time, between numerical and analytical results is excellent.

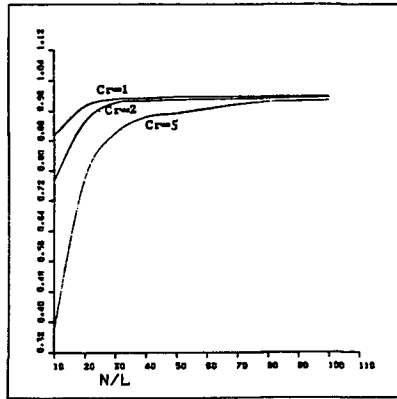


Figure 4. Illustration of model accuracy for different Courant numbers

Finally, phase and amplitude portrait errors were analysed. As an example, figure 4 shows the ratio of numerical celerity to theoretical celerity vs the number of points per wave length for different Courant numbers. It is seen that, for $Cr=1$, an acceptable accuracy is obtained with values of $N/L > 20$. When the Courant number increases, it is difficult to get a similar accuracy though more points per wave length are used.

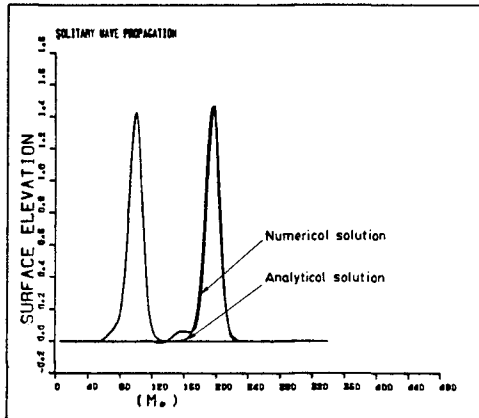


Figure 5. Solitary wave propagation

After the linear version was calibrated, the non linear model was tested with cnoidal wave theoretical solutions, using equations (1), (2) and (3). The analytical solution of these equations, that exclude frictional stresses, Coriolis accelerations and similar terms, is the solitary wave. Figure 5 demonstrates the good fit between

numerical and theoretical results after 24 seconds. The discretization characteristics were $\Delta x = 2.5 \text{ m}$, $\Delta y = 2.5 \text{ m}$. and $\Delta t = 0.25 \text{ s}$.

and the wave parameters were wave height $H_0 = 1.5 \text{ m}$, depth $h = 5 \text{ m}$.

3.- SPECTRAL MODELS

In scalar spectral analysis, numerous models exist for time series generation and processing. These models are based on different techniques and may be divided in two groups:

- Conventional methods, based on the Fast Fourier Transform (FFT) algorithm (Cooley and Tukey, 1965).

-Parametric methods, involving autoregressive (AR) and autoregressive-moving average (ARMA) models.

Every technique presents several advantages and inconvenients with respect to the others. Therefore, the selection in every case of the most suitable algorithm will be necessary. For improving the use of design spectra in Maritime Engineering, several pattern spectra have been introduced in last decades. These spectra depend on various parameters. Fitting the parameters to the local conditions, a representative spectrum is obtained. The Pierson-Moskowitz spectrum (Pierson and Moskowitz, 1964) and the JONSWAP spectrum (Hasselmann et al.,1973) are the most well-known ones. However, the two formulations are only accepted in deep water. In shallow water, the use of suitable spectra as TMA spectrum (Bouws et al.,1983) is needed.

An example of the use of scalar spectral analysis techniques, in which the time series is generated from a JONSWAP spectrum through an ARMA(8,1) model, is showed in figure 6. The parameters of the JONSWAP spectrum were $\sigma_u = 0.07$, $\sigma_b = 0.09$, $\alpha = 0.03$, $\gamma = 3.3$ and $\omega_m = 0.18$

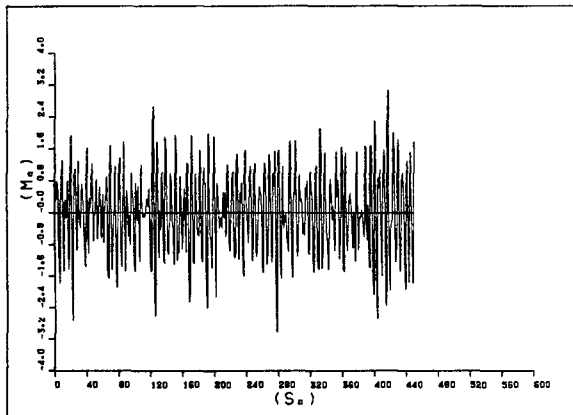


Figure 6. Time series generated from a JONSWAP spectrum

In figure 7, three spectra are plotted. They belong to the initial JONSWAP spectrum, the theoretical spectrum calculated from the autocorrelation function corresponding the JONSWAP, and the spectrum evaluated from the time series simulated. The agreement between the three spectra is remarkable, showing the validity of the time series generation technique.

On the other hand, the determination of the directional spectral density function $S(\omega, \theta)$ is made by recasting the function as

$$S(\omega, \theta) = S(\omega) \cdot D(\omega, \theta) \quad (5)$$

with

$$\int_0^{2\pi} D(\omega, \theta) \cdot d\theta = 1 \quad (6)$$

where $S(\omega)$ is the scalar spectral density function, computed using one of the aforementioned methods, and $D(\omega, \theta)$ is the directional spreading function. A convenient approximation to this function may be obtained by expanding $D(\omega, \theta)$ as a Fourier series as

$$D(\omega, \theta) = \frac{1}{\pi} \left[\frac{1}{2} + \sum_{n=1}^{\infty} (a_n \cdot \cos n\theta + b_n \cdot \sin n\theta) \right] \quad (7)$$

a_k, b_k are Fourier coefficients

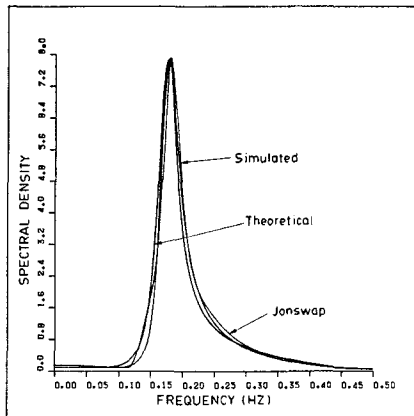


Figure 7. Spectral density functions of the time series generated

Measurement of directional waves in Nature are rather difficult. For this purpose, the pitch-roll buoy is one of the most extended instruments nowadays. This device provides three time series corresponding to the free surface elevation $\eta(t)$, and the wave slopes in two perpendicular directions $\eta_x(t)$, $\eta_y(t)$. Having time series of three canals, just the two first Fourier coefficients can be computed only.

For the estimate of the directional spectrum, the way to be followed involves three steps :

- i) Determination of the cross spectra between the time series
- ii) Computation of the Fourier coefficients for different frequencies.

iii) Interpolation of the directional spectrum. This last step may be carried out by two ways. The first is fitting the directional spectrum to prefixed distribution functions. The second is the rational interpolation through AR and ARMA models. The latter was tested with 10 directional wave records obtained in the North Sea the 1-12-1983 and provided by the Programa de Clima Marítimo of the Ministry of Public Works (MOPU) in Spain. These time series were recorded at intervals

of 3 hours on a well developed sea with a wind direction of $250 - 260^\circ$ for the first series. The wind direction changes to 0° in the tenth series, producing a change in the wave direction for the high frequencies.

Figures 8 and 9 show the wind and wave mean direction for the first and the tenth records.

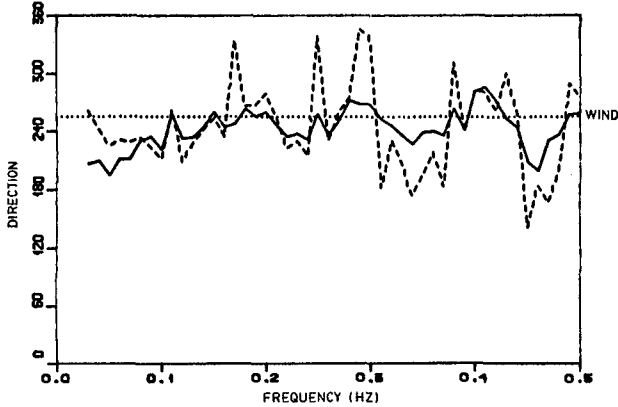


Figure 8. Wind and wave mean direction. Series 1

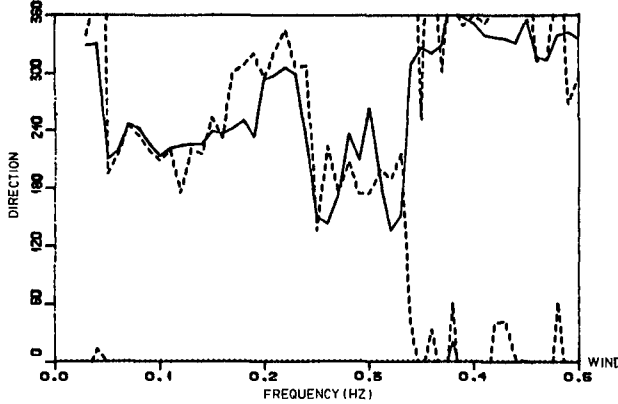


Figure 9. Wind and wave mean direction. Series 10

The directional spectra from these records (with three time series $\eta(t)$, $\eta_x(t)$, $\eta_y(t)$ in every record), were determined using rational interpolation through AR and ARMA models. In figures 10 and 11, the directional spectrum modes, i.e. the predominant directions, for every frequency are plotted. The results show a good reproduction of the mean direction in the directional spectra calculated.

The use of rational interpolation gives an additional advantage, since it is very easy to reverse the procedure and given a directional spectrum to generate a record. This record will be composed of three time series corresponding to the free surface elevation $\eta(t)$ and other two parameters, such as the wave slopes $\eta_x(t)$, $\eta_y(t)$. Nevertheless, these two parameters may be replaced for others if the transference function is changed.

4.- WAVE TIME-SERIES PROPAGATION

As it has been showed in section 2, the present model reproduces closely the different phenomena involved in the regular wave trains propagation. In the case of irregular waves, it would be necessary to determine each parameter from the field data or calibrate them with physical models. Both possibilities, are out of the scope of this work. Because of the difficulty of handling large wave records, the authors have assumed their representation by means of the spectral density function. Therefore, when random waves are used, the calibration of the model is done assuming the invariability of the spectrum when waves travel on a constant deep area and without obstacles that could interfere their propagation.

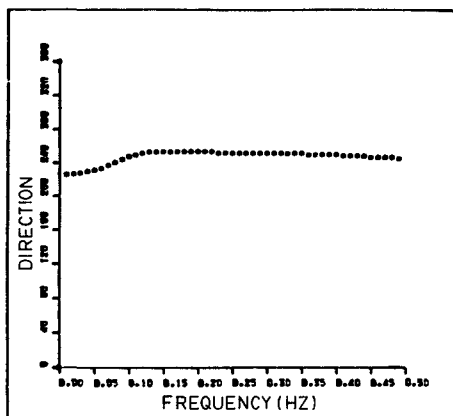


Figure 10. Predominant directions in directional spectrum. Series 1

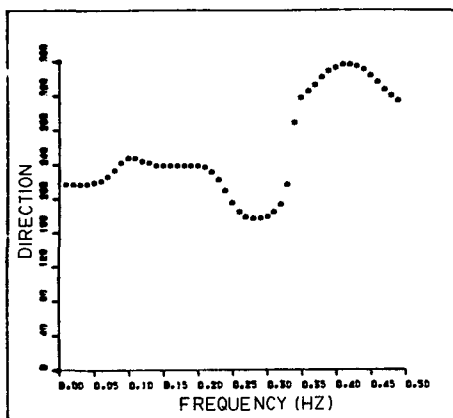


Figure 11. Predominant directions in directional spectrum. Series 10

A time series generated by means of one of the aforementioned techniques was propagated using the Boussinesq model, over a fluid domain with horizontal bottom and with a depth of 5 m. The result was another time series. As the visual comparison between the two time series is very difficult, their characteristics have been confronted computing the spectral density functions, that are showed in figure 12. The plots of these functions are practically identical and therefore it implies that the numerical model reproduces accurately the irregular wave propagation, over a horizontal bottom.

Another case analysed was the refraction of irregular wave over an uniform slope. Figure 13 presents the spectral density functions of the time series before and after the refraction. In this plot it is shown that the peak period is the same, but refraction produces a secondary peak with a frequency that is nearly twice the peak frequency. Then refraction produces a transference of energy towards higher frequencies, keeping the peak period but decreasing the mean period.

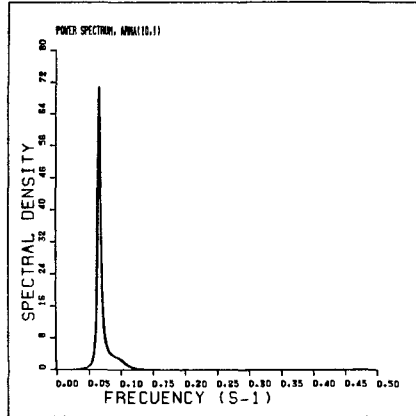


Figure 12. Spectra of the generated and propagated time series

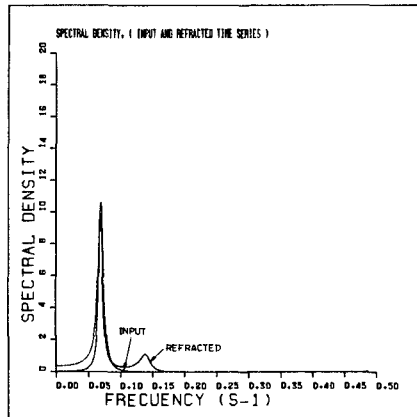


Figure 13. Spectral density functions of the initial and refracted time series

Moreover the study of the diffraction of irregular waves was carried out. In this study, a linearized version of the numerical model was employed. In figure 14, the fluid domain is illustrated. The boundary with the gap is a vertical wall. The other boundaries are open, to avoid reflections. In the points A,B,C, and D, the free surface elevation was recorded. When the time series were obtained, the spectral density functions were determined and compared with the spectral density function of the initial time series, as it is showed in figure 15. The analysis of these figures shows logical results because the greater the distance to the gap is, the smaller the area comprised below $S(\omega)$ is, i.e. the energy of the spectrum decreases when the point is far away. On the other hand, the peak frequency does not change after diffraction in all points inside the fluid domain, though this circumstance can be due to the use of a linearized version of the propagation model.

Finally, a real example has been analysed. Here, the lay-out and the bathymetry are the ones corresponding to a Spanish harbour. Figure 16a represents the input wave spectrum used at the entrance of the harbour. This spectrum has been derived from field measurements.

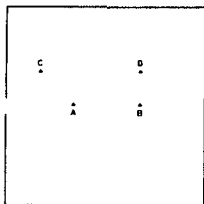


Figure 14. Diffraction study. Fluid domain.

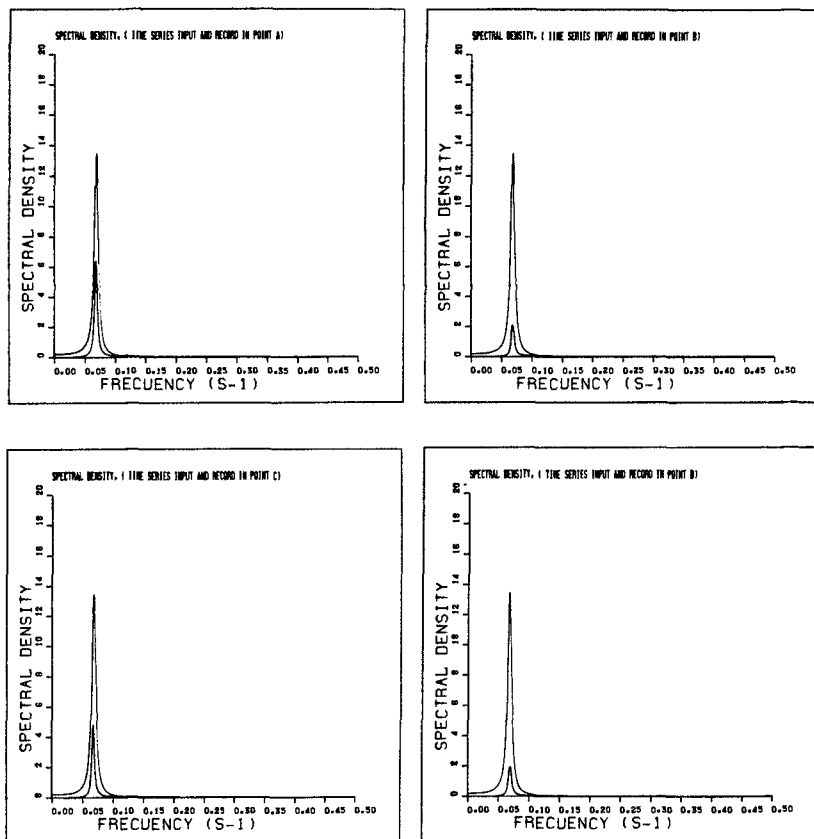


Figure 15. Spectral density function before and after diffraction.

Figure 16b shows the result of carrying out an ARMA spectral process of the surface elevation time series, obtained after a run of the propagation model, inside a basin of the harbour. This output wave spectrum has a secondary peak in the origin. Since the spectrum has been plotted with 100 points, the secondary peak means that a long wave with a period up to 200 seconds is present in the time series recorded by the numerical model inside the basin. Actually similar wave conditions to those of the numerical simulation gave way to the record of long waves with a period of 240 seconds in the same basin. Therefore, the propagation model allows simulating and discovering long wave phenomena in real cases.

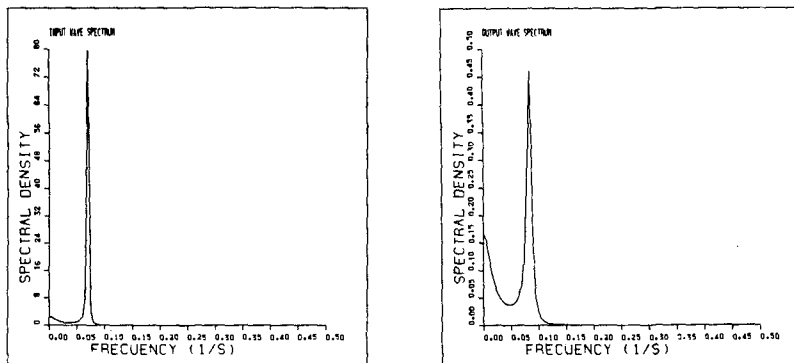


Figure 16. Input and output wave spectrum.

5. CONCLUSIONS AND FUTURE PERSPECTIVES

The main conclusions of this paper are

- The wave propagation numerical model simulates accurately the propagation of regular and irregular waves in a wide range of conditions. The model behaviour has proved to be satisfactory for the usual values of the control parameters. The main exception is the breaker zone, in which the wave height is an important fraction of the water depth. However, the third order (truncation error) scheme which is now being developed, is expected to provide improved results in these cases.

- With a given $S(\omega)$, a time series $\eta(t)$ can be simulated. This signal can be used as a model input. After the run of the propagation model, the result will be another time series $\eta^*(t)$, which conveniently processed will give way to another spectral density function $S^*(\omega)$.

- With a given directional spectrum $S(\omega, \theta)$, a record with three time series ($\eta(t)$, $\eta_x(t)$, $\eta_y(t)$ for example) can be simulated, and conversely, three time series let the directional spectrum to be obtained. Up till now, the propagation model does not accept three time series as input, though it can yield these three signals as output. The efforts are now concentrated in getting the directional wave as the input of the model. In this case, a $S(\omega, \theta)$ could be the incoming one to the model, and another directional spectrum $S^*(\omega, \theta)$ could be the outgoing one.

- Numerical simulation with Boussinesq equations is an useful tool for the spectral determination and the analysis of the spectral evolution in shallow water when waves are travelling. The model has been applied successfully to real cases. With the coupling between the Boussinesq model and the spectral techniques developed in this paper, it is possible to obtain a more compact and coherent

information on irregular wave propagation in coastal zones, bays and harbours, taking into account non-linear propagation effects.

6.- REFERENCES

- ABBOTT, M.B. and F. IONESCU (1967). "On the numerical computation of nearly-horizontal flows". J. Hyd. Res. Vol. 5
- ARCILLA, A.S. y J.L.MONSO (1985). "Modelado numérico del flujo en zonas costeras". Dirección General de Puertos y Costas, MOPU. Programa de Clima Marítimo n.7
- ARCILLA, A.S. and J.L.MONSO (1986). "Numerical modelling of Coastal Flow". Proceedings of the International Conference of Computer Techniques of Environmental Studies. Los Angeles, U.S.A.
- ARCILLA, A.S., J.L. MONSO y J.P. SIERRA (1986) "Modelo numérico no lineal de ondas de superficie libre". Dirección General de Puertos y Costas, MOPU. Programa de Clima Marítimo. n.17.
- BOUWS, E. et al. (1983). "A similarity based spectral form for limite deep water: wave growth relationships for the entire depth TMA spectral form". International Association for Hydraulic Research Conference, Moscow.
- COOLEY, J.W. and J.W. TUKEY (1965). "An algorithm for machine calculation of complex Fourier Series". Mathematics of computation, vol.19
- HASSELMAN, K. et al. (1973). "Measurements of wind-wave growth and swell decay during the Joint North Sea Wave Project (JONSWAP)". Deust. Hydrogr. Z., Suppl. A, 8 n. 12
- PEREGRINE, D.H. (1967). "Long waves on a beach". J. Fluid Mechanics. Vol. 27
- PIERSON, W.J. and L. MOSKOWITZ (1964)."A proposed spectral form for fully developed wind seas based on the similarity theory of S.A. Kitaigorodskii". J. Geophys. Res. 69
- URSELL, F. (1953) "The long wave paradox in the theory of gravity waves". Proc. Camb. Phil. Sec. Vol. 49.

CHAPTER 25

The Influence of Currents on Wave Attenuation

Richard R. Simons 1
Anthony J. Grass 2
Andreas Kyriacou 3

Measurements have been made of wave height decay in a rough bottomed flume for waves alone and for waves combined with 3 following currents. Tests have also been carried out to quantify energy dissipation at the sidewalls under these conditions. Results show that waves attenuate less rapidly when propagating on a following current, with a corresponding reduction in wave-current friction factor. A simple method is suggested by which wave attenuation in the presence of following and opposing currents can be predicted.

Introduction

Coastal Engineering is dependent on a detailed knowledge of wave climate for the design of coastal structures and defences, and in the prediction of sediment transport. An important step in obtaining this information is to transform available offshore wave data for application to coastal conditions. This procedure has to take into account shoaling, depth refraction, diffraction, frictional energy losses, and the action of currents. Apart from additional refraction, currents have two other important effects on waves. The first is that as the waves propagate onto a region of flowing water they experience a change in wave length, height, and orbital velocity distribution. These changes are local and to some extent reversible. The second effect is that the shear stress at the seabed, and hence the rate of wave energy dissipation, is altered significantly. This causes a permanent change which propagates with the waves until they break on the shore.

A number of papers describing field observations (i.e. Battjes, 1982) have commented that wave heights often increase when waves are propagating on a following current, and, conversely, that they decrease in the presence of an

¹Lecturer, Civil Engineering Dept, University College London
England

²Reader, Civil Engineering Dept, University College London
England

³Research Assistant, University College London England

opposing current. At first sight, these effects are anomalous in that all theories of "local" wave-current interaction predict that the stretching effect of a following current on waves reduces their height. However, a possible explanation is provided by the results of Kemp and Simons (1983), who found that attenuation rates go down if waves propagate with a following current, but that attenuation increases when waves move onto an opposing current. Data showing similar trends have also been published by Brevik and Aas (1980) and Asano et al (1984).

The purpose of the research described in this paper is to provide more experimental data for the precise determination of wave attenuation and boundary shear stresses under combined waves and currents, and to suggest a simple method by which the observed results can be predicted for any particular relative current strength in terms of a wave-current friction factor.

Experiments

The main set of tests were performed in a flume 610mm wide and 30m long, with a still water depth of 300mm. The sides of the flume were of smoothly painted wood, incorporating glass windows at regular intervals. The bed was evenly covered with a single layer of 10mm angular limestone chippings, producing a Nikuradse roughness of approximately 25mm, close to that found in the work of Kemp and Simons (1983). These large roughness elements had a critical velocity in excess of 1m/s, and thus remained immobile without the need to be glued down under any of the conditions considered in the present study.

Waves were generated by a flap-type paddle supported from above and pivoted about a point below bed level. This arrangement allowed the recirculating current flow to pass beneath the paddle within the existing channel cross section, although it was found necessary to install a duct to carry the flow downstream of the paddle before combining the current with the waves. An 0.5m length of chicken wire acted as an excellent filter for unwanted waves and turbulence in this region. At the far end, the beach was constructed of a light metal framework covered with 25mm thick permeable sheets of a woven nylon. It sloped at 6° to the horizontal.

Preliminary velocity measurements were made with a propeller meter at positions along and across the flume to determine the influence of secondary flow cells, sidewall boundary layers, and the developing bottom boundary layer. These tests were carried out for the currents alone and for combined waves and currents, taking care to reject unreliable measurements in regions where the flow was subject to reversal. The detailed velocity field was measured at a section midway along the test length of the flume using a single channel laser Doppler anemometer (LDA). This provided mean velocities, turbulence intensities, and orbital velocities at up to 30 points through the vertical, the measurements being concentrated in the highly turbulent nearbed layer. The

distribution of Reynolds stress was obtained from a two-channel LDA and used to establish the mean bed shear stress.

Wave attenuation and changes in mean water level were measured by resistance type wave probes traversed in 100mm steps through four 2m blocks spaced out along a 22m length of the flume. This made it possible to identify the pattern of reflected waves and to fit an exponential decay curve through the underlying incident wave heights.

The tests were conducted in a water depth of 300mm, using wave periods of 0.7s and 1.0s; such waves fall into the "intermediate" classification, with D/L of 0.40 and 0.22 respectively. Four wave heights were investigated for each period, giving bed orbital velocities in the range 10mm/s to 70mm/s. Scaled against the large bed roughness used in these tests, the relative bed orbital amplitude, a/k_s , was generally less than unity. Four different current conditions were considered in combination with these waves, namely, no current, and following currents with mean-over-depth velocities of 75mm/s, 190mm/s and 250mm/s. The test parameters are set out in Table 1.

Results

Hydrodynamics:

Before considering the effects of currents on the wave surface properties, it is worth noting that the hydrodynamics of the combined waves and currents were very much as found in preceding studies of a similar nature (i.e. Brevik and Aas, 1980; Kemp and Simons, 1983). For each of the three steady currents, the mean velocity profiles showed that there was a clearly identifiable logarithmic region whose slope was increased by the superposition of waves of increasing height. This implied an increase in mean bed shear stress, and also of apparent bed roughness calculated from the z_0 zero velocity intercept, when waves were added. A comparison between these results and the predictions of a number of mathematical models has recently been presented by Simons et al, (1988). It should be noted that the results were based on von Karman's constants in the range 0.33 to 0.35. These values of κ , significantly less than the classical figure of 0.4, were calculated from bed shear stresses derived from the direct Reynolds stress measurements.

With the waves propagating through still water, without any current, orbital velocities were closely described by 2nd order Stokes wave theory down to the edge of a very thin boundary layer, reflecting the low a/k_s ratios under consideration. However, the addition of a turbulent current produced a significant increase in wave boundary layer thickness - see figure 1. Reynolds stresses were also changed under the combined flow conditions: whereas for the currents alone there was a linear decrease from the maximum value at the bed out to the edge of the boundary layer, when the waves were added $\overline{u'v'}$ actually decreased in the nearbed region, producing a maximum at the outer edge of the

RUN	H (mm)	L (mm)	u_b (mm/s)	a/k_s	u (mm/s)	α m^{-1}
T=0.7s						
RDWA1	15.5	755	9	0.06	0	11.8
RDWA2	19.3	760	11	0.07	0	11.2
RDWA3	22.5	760	10	0.06	0	10.8
RDWA4	23.0	760	10	0.06	0	11.5
T=1.0s						
RIWA1	19.2	1352	32	0.28	0	7.6
RIWA2	31.1	1388	47	0.42	0	7.5
RIWA3	40.3	1380	63	0.56	0	9.6
RIWA4	50.7	1380	78	0.69	0	10.6
T=0.7s						
RDWCW1	14.1	847	11	0.06	81	8.1
RDWCW2	18.4	847	13	0.08	81	8.6
RDWCW3	21.1	847	14	0.09	81	8.8
RDWCW4	22.6	847	17	0.11	81	8.2
T=1.0s						
RIWCW1	19.6	1512	25	0.20	70	6.4
RIWCW2	29.5	1512	39	0.31	77	5.8
RIWCW3	38.5	1512	58	0.59	74	7.8
RIWCW4	50.5	1512	71	0.72	74	8.3
T=0.7s						
RDWCM1	11.8	1000	12	0.06	191	2.9
RDWCM2	15.0	1000	15	0.08	195	2.2
RDWCM3	17.2	1000	16	0.08	192	1.4
RDWCM4	18.2	1000	15	0.08	197	4.8
T=1.0s						
RIWCM1	13.5	1664	23	0.17	194	3.7
RIWCM2	22.7	1664	35	0.26	197	5.4
RIWCM3	30.5	1664	47	0.35	197	6.0
RIWCM4	40.7	1668	61	0.45	197	6.5
T=0.7s						
RDWCS1	9.9	1065	13	0.05	253	3.2
RDWCS2	12.9	1065	15	0.06	252	4.1
RDWCS3	15.1	1065	16	0.06	252	3.9
RDWCS4	16.3	1065	15	0.06	250	3.2
T=1.0s						
RIWCS1	12.0	1751	21	0.11	250	5.9
RIWCS2	20.1	1751	34	0.18	253	6.2
RIWCS3	27.7	1751	44	0.24	251	6.9
RIWCS4	36.9	1751	56	0.30	247	6.2

Table 1: Test Parameters and Observed Attenuation Coefficients.

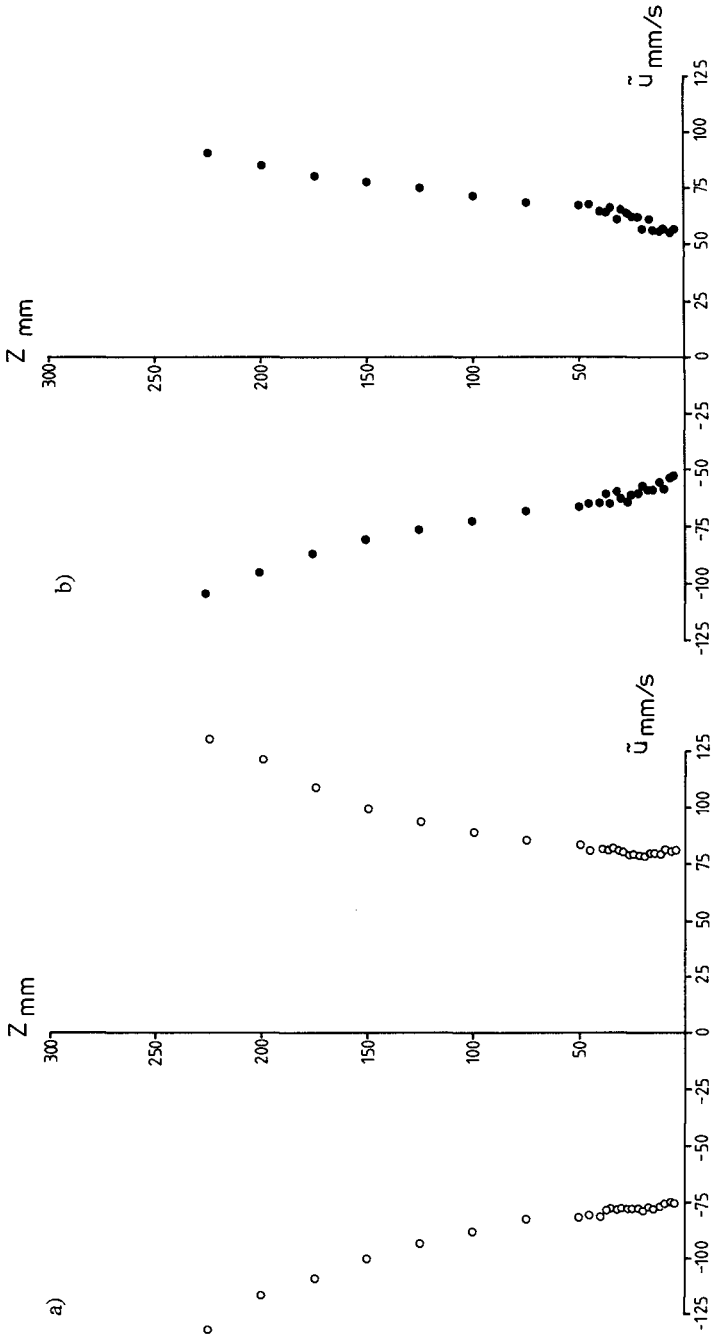


Fig 1: Vertical Distribution of Wave-induced Orbital Velocity
 Amplitudes: a) Waves alone (Run RIWA4);
 b) Waves with current (Run RIWCS4).

logarithmic layer, some 35mm above the bed.

Sidewall Tests:

The objective of the main test programme was to investigate the rate of attenuation of waves propagating over a following current, and to compare the results with those from waves in still water. The tests were carried out in a relatively narrow laboratory flume, and in order for the results to be applicable to real sea conditions it was necessary to take into account the energy dissipation at the flume sidewalls. For the case of waves alone in a smooth walled channel, Hunt (1952) presented a theory apportioning dissipation between bed and sidewalls for any chosen aspect ratio. Wave height decay was shown to be exponential, in the form: $H = H_0 e^{-\alpha x}$, with the attenuation coefficient, α , given as:

$$\alpha = \frac{k}{B} \sqrt{\left(\frac{TV}{\pi}\right) \left(\frac{Bk + \sinh 2kD}{2kD + \sinh 2kD}\right)}$$

Here, B is the channel width, D the depth of water, and k the wave number, $2\pi/L$. A similar empirical formula based on dimensional analysis was later suggested by Treloar and Brebner (1970). However, the application of theories of this type to the case of combined waves and currents has not before been considered. Thus it was decided to carry out a short series of tests to quantify the influence of the sidewalls under the present conditions, and to establish whether the Hunt theory formed the basis for an appropriate correction technique.

A temporary vertical wall of plate glass was installed over a 6m length of the flume, parallel to one of the sidewalls and such as to leave a closely uniform gap of just 10mm. Waves propagating in 300mm of water through this narrow channel attenuated rapidly, due almost entirely to frictional dissipation at the sidewalls. Figure 2 shows a typical exponential decay of wave heights for one of the tests with no current present, indicating that the Hunt theory predicts the attenuation coefficient to well within 15%, although with a consistent trend to underpredict. The modified form developed by Treloar and Brebner produced values even lower. Similar results were found when the tests were repeated with the gap reset to 20mm.

For the tests in combined waves and currents, it was impossible in such a narrow channel to reproduce the detailed characteristics of the stronger currents found in the full-width flume, although acceptable correlation was achieved with the weaker current mean velocity. Despite the reflected wave pattern being amplified by the addition of the current, the results from these tests (figure 3) showed that the sidewall attenuation was reduced by approximately 15% from that for the waves alone. In this case, taking the sidewall contribution from the corresponding wave alone tests to be between 35% and 50% of the total dissipation, use of the wave alone sidewall correction produced an error of 6%. For the

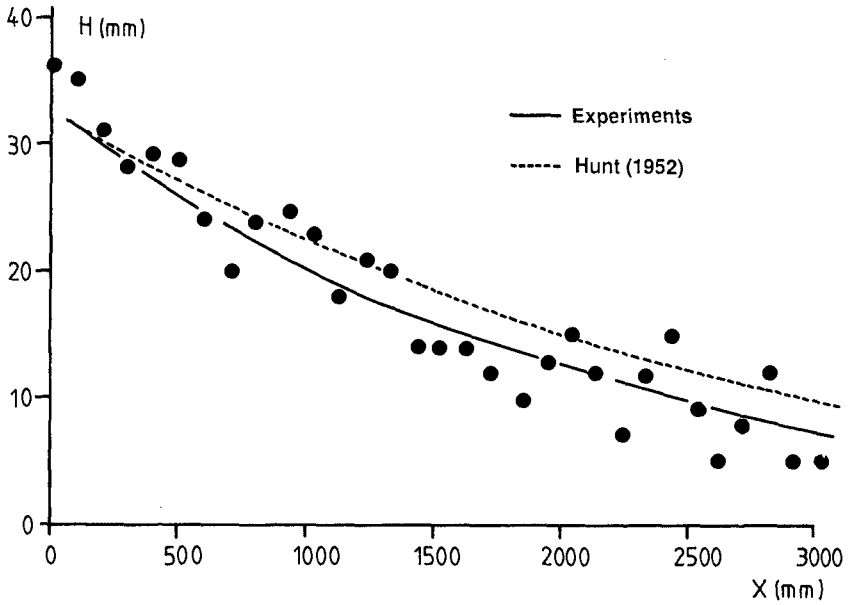


Fig.2: Wave Decay under the Influence of Smooth Sidewalls:
 $T = 0.7s$; $D = 300mm$; $u = 0$; gap = 10mm.

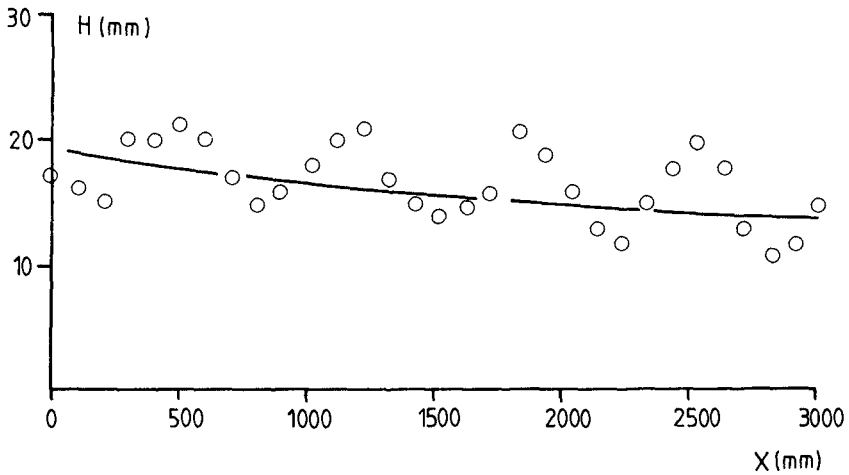


Fig.3: Wave Decay under the Influence of Smooth Sidewalls:
 $T = 1.0s$; $D = 300mm$; $u = 70mm/s$; gap = 20mm.

present work, this was felt to be acceptable.

Attenuation:

Results from the main tests in the 610mm wide flume showed that wave heights reduced exponentially along the flume both with and without currents flowing. However, attenuation coefficients were found to decrease systematically when following currents of increasing strength were superimposed (figure 4). The same effect was found both for the waves of 0.7s and 1.0s period, and it confirmed the earlier observations of Kemp and Simons (1983), who had furthermore reported that attenuation increased when an opposing current was introduced. These observations, made in a fixed frame of reference, are relevant to those predicting wave heights under real sea conditions. However, even when expressed in terms of wave height loss per wave length, or of loss of wave action (wave energy divided by relative angular frequency), there was still a clear trend for the currents to reduce the rate of change in all the tests carried out. The possibility was examined that the changes in wave height might be the result of variations in mean velocity profile over the 22m test length of the flume rather than of modified energy dissipation. However, the preliminary velocity measurements showed that any influence of the developing boundary layer, and in particular a gradual increase in surface velocity, would tend to increase apparent attenuation and hence oppose the observed effect.

In order to simplify the presentation of the results, it was decided to follow the method first proposed by Jonsson (1966) and reassessed by Brevik and Aas (1980), and to express the attenuation rates in terms of a wave-current friction factor, f_{wc} , assumed constant through the wave cycle. Neglecting the phase difference between the flow in the oscillatory boundary layer and that in the outer region, the bed shear stress is related to f_{wc} as follows:

$$\tau_{wc} = 1/2 \rho f_{wc} |\bar{u} + u_b| \cdot (\bar{u} + u_b)$$

where \bar{u} is the depth averaged mean velocity and u_b the amplitude of the oscillatory wave-induced velocity, taken to be sinusoidal, just above the wave boundary layer. Assuming that the flow is not current dominated, the Momentum Equation,

$$dF/dx + \tau_{wc} = 0, \quad (1)$$

with $F = 1/8 \rho g H^2 (2c_{gr}/c - 1/2) + \rho D u^2 + 1/2 \rho g D^2$

and $c_{gr} = c_{ga} - u$ then becomes:

$$1/4 \rho g H \frac{dH}{dx} (2c_{gr}/c - 1/2) + \rho g D \frac{dD}{dx} + 1/2 \rho f_{wc} |\bar{u} + u_b| \cdot (\bar{u} + u_b) = 0 \quad (2)$$

The averaged Energy Equation can be treated in a similar way to give:

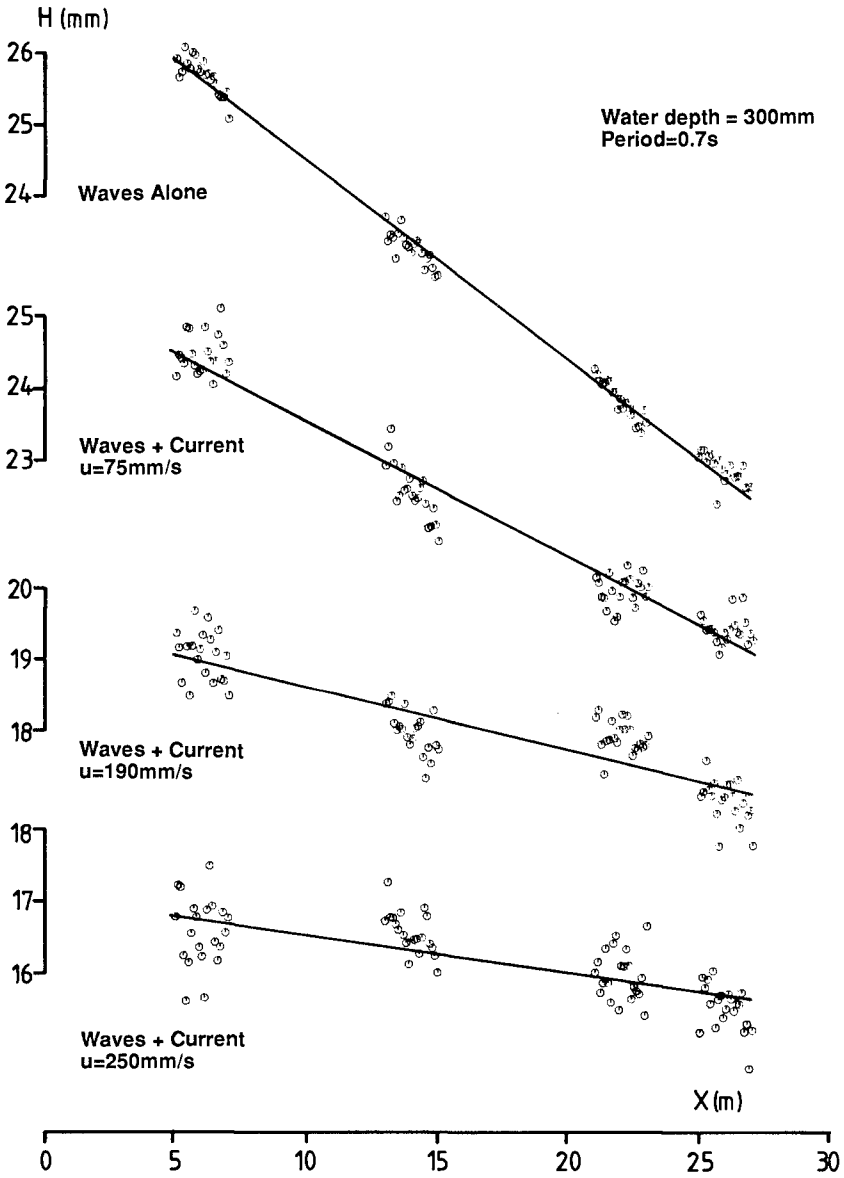


Fig.4: Wave Height Attenuation along the Main Test Flume.

$$\frac{1}{4} \rho g H (c_{gr} + 2c_{gr}/c + 1/2) u + \rho g D u \frac{dD}{dx} + \frac{1}{2} \rho f_{WC} |\mu + u_b \cos \omega t|^3 = 0 \quad (3)$$

Eliminating the water surface slope dD/dx between (1) and (2), we are left with a relationship between wave height attenuation and f_{WC} in the form:

$$f_{WC} = \frac{gH/2\beta (c_{gr} + u) dH/dx}{|\mu + u_b \cos \omega t| \cdot (u + u_b \cos \omega t)} \quad (4)$$

$$\text{where } \beta = \frac{u \cdot |\mu + u_b \cos \omega t| \cdot (u + u_b \cos \omega t)}{|\mu + u_b \cos \omega t|^3} \quad (5)$$

It must be emphasised that this derivation relies on the assumptions of 1st order waves, a time-invariant friction factor, significant wave action relative to the current strength, neglect of phase shifts between orbital velocities and bed shear stress, and a uniform mean velocity profile.

Considering first the results for waves alone, it was found that the friction factor continued to increase for the smaller waves as the bed orbital amplitude was reduced - see figure 5. Values agreed closely with the expression given by Jonsson (1966), and also with the trends predicted by Kajiwara (1968) and Kamphuis (1975). In contrast, the addition of following currents caused a steady decrease in friction factor as the current strength was increased, with f_{WC} for very low bed orbital amplitudes tending towards the value of 0.01 determined from the current only tests. However, this behaviour became less pronounced for the larger waves ($a/k_s > 1$). Figure 5 also includes the results from the tests of Kemp and Simons (1983) where the current opposed the waves. It is interesting to note that in this case, despite the increase in observed attenuation rates when the currents were added, the corresponding friction factors were actually less than those for waves alone. This apparent anomaly was caused by the reduction in absolute wave group velocity in (4) proving more significant than the increase in attenuation dH/dx . The ratio of current strength to wave orbital velocity (u/u_b) for these tests was similar to that for the weakest following current series in the present tests, and the values of f_{WC} produced by these two very different sets of conditions agreed remarkably well with each other. This suggests that the variation in f_{WC} with relative bed orbital excursion can be characterised by a series of curves, each representing a particular relative current strength. A similar set of curves can also be generated if f_{WC} is plotted against Reynolds number (as in figure 6).

While at first sight it might seem surprising that friction factors should decrease as current strength is increased, the effect is predicted qualitatively by mathematical models of wave-current interaction such as Christoffersen and Jonsson (1985). Friction factors calculated from these models fall off from the wave alone curve for values of a/k_s less than 30, although not to such an extent as observed in the present study. The values of f_{WC} so calculated are also insensitive to the direction of the current, whether it propagates with or

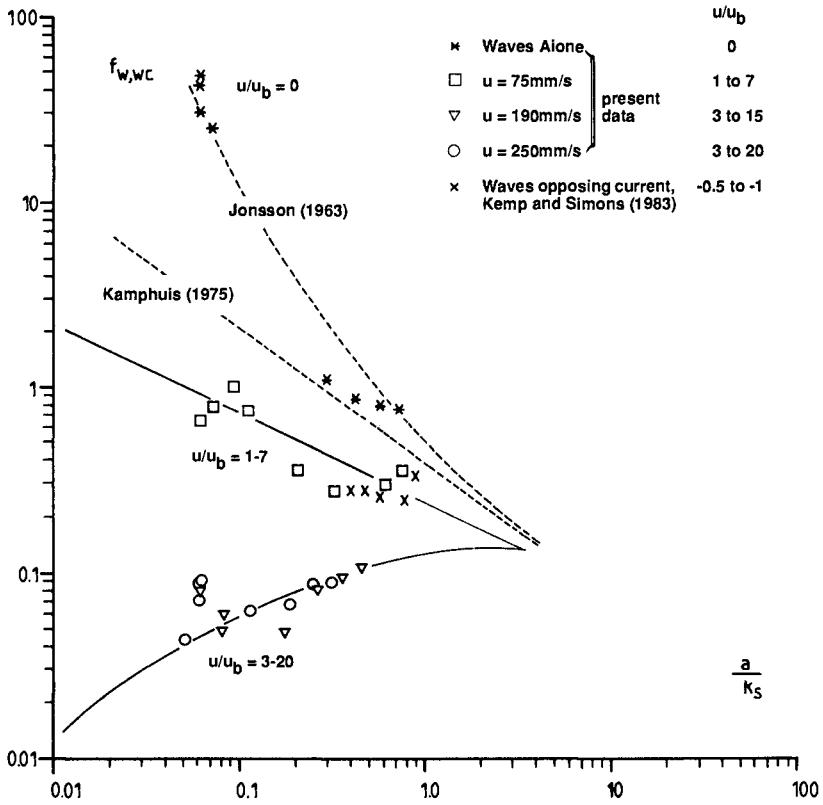


Fig.5: Variation of Friction Factor, $f_{w,WC}$, with relative bed orbital amplitude, a/k_s , for different current strengths.

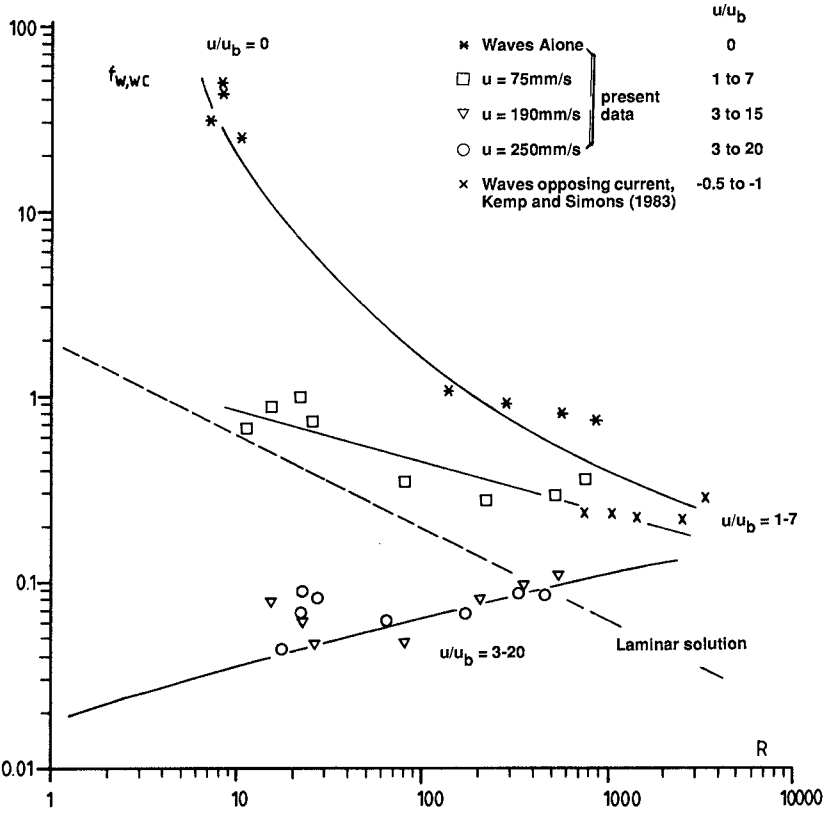


Fig.6: Variation of Friction Factor, $f_{w,WC}$, with Oscillatory Reynolds Number, $a u_b/\nu$.

against the waves, once again agreeing with the present observations.

Conclusions

An estimate of wave height attenuation for combined wave and current flows can be obtained for given bed roughness, relative current strength, and relative bed orbital excursion either by use of an empirical friction factor diagram or from one of the many mathematical models for wave-current interaction. A possible procedure might be as follows:

1. Calculate β from (5);
2. Derive f_{wc} from Christoffersen and Jonsson (1985);
3. Use Eqn.(4) to calculate dH/dx , and hence derive the attenuation coefficient α .

For a following current, the attenuation will be reduced with increasing current strength, but for the opposing current case the attenuation might increase or decrease, depending on the relative changes in f_{wc} and $(c_{gr} + u)$. A decrease is likely only if the current is very strong relative to the wave group velocity, with the possibility in the extreme case of a negative attenuation rate, growth in wave height, and eventual breaking.

Acknowledgements

The authors are grateful to Hydraulics Research Ltd, Wallingford for generously providing the facilities for these experiments, also to the Science and Engineering Research Council for their support of the work.

References

- Asano T., Nakagawi M. and Iwagaki Y. 1986 Changes in current properties due to wave superimposing. Proc. 20th Int. Conf. on Coastal Engng, Ch.70, pp.925-939.
- Battjes J.A. 1982 A case study of wave height variations due to currents in a tidal entrance. Coastal Engng., 6, pp.47-57.
- Brevik Iand Aas B. 1980 Flume experiments on waves and currents: rippled beds. Coastal Engineering, 3, pp.149-177.
- Christoffersen J.B. and Jonsson I.G. 1985 Bed friction and dissipation in a combined current and wave motion. Ocean Engng, 12, No.5, pp.387-423.
- Hunt J.N. 1952 Viscous damping of waves over an inclined bed in a channel of finite width. La Houille Blanche, Dec.1952, p.836.
- Jonsson I.G. 1966 The friction factor for a current with superimposed waves. Prog. Rep. 11, Coastal Engng. Lab.,

Tech. Univ. Denmark.

Kajiura K. 1968 A model of the bottom boundary layer in water waves. Bull. Earth Res. Inst., 46, pp.75-123.

Kamphuis J.W. 1975 Friction factors under oscillatory waves. J. Waterways, Harb., Coastal Engng, 101(WW2), pp.135-144.

Kemp P.H. and Simons R.R. 1983 The interaction of waves and a turbulent current: waves propagating against the current. J. Fluid Mech., 130, pp.73-89.

Simons R.R., Kyriacou A., Soulsby R.L. and Davies A.G. 1988 Predicting the nearbed turbulent flow in waves and currents. Proc. IAHR Symp. on Math. Modelling of Sed. Trans. in Coastal Zone, Copenhagen, pp.33-47.

Treloar P.D. and Brebner A. 1970 Energy losses under wave action. Proc. 12th Int. Conf. on Coastal Engng, pp.257-267.

CHAPTER 26

Some Characteristics of Breaking Waves by

Fredric Raichlen¹ and Panos Papanicolaou²

INTRODUCTION

In recent years there has been a surge in coastal engineering research devoted to various aspects of breaking waves including their kinematics at and after breaking. For a review of certain aspects of this field the interested reader is referred to Peregrine (1983) and Battjes (1988); in this discussion only certain publications pertinent to this investigation will be mentioned briefly.

With the advent of laser-Doppler velocimetry (LDV) a number of investigators have measured the internal velocities of waves both before, at, and after breaking. For example, Nadaoka (1986) measured the velocities in the shoaling region under periodic breaking shallow water waves. This extensive study of the nearshore regions resulted in vector diagrams which described very well several spatial aspects of the flow shoreward of breaking. Skjelbreia (1987) also used LDV techniques to define the kinematic characteristics of breaking solitary waves. Measurements were made of the water particle velocities under spilling and plunging breaking waves both very near breaking and after breaking, close to the water surface and to the bottom. A high degree of reproducibility was possible with the laboratory wave generation system used so experiments were conducted at different locations with essentially the same wave; this will be discussed more fully later. Skjelbreia (1987) also presented vector diagrams of the velocities under plunging and spilling solitary breakers. These measurements when compared to those of Nadaoka (1986) raise several questions regarding similarities and differences between breaking oscillatory waves and waves of translation. In addition to detailed kinematic measurements, a macroscopic view of shoaling solitary waves was also taken by Skjelbreia (1987) yielding results on the variation of the wave height with distance both before and after breaking. Although there has been a considerable amount of work along these lines in the past, observations of the changes in the wave at and after breaking are still quite useful in developing an overall understanding of the breaking process.

Other investigators have presented experimental and analytical studies dealing with waves in the regions at and just after breaking. For example, Horikawa and Kuo (1966) presented the results of experiments on the change in height of periodic waves after breaking. They, Dally et al (1984), and others used these data to compare to analytical approaches to this problem with some degree of success. Svendsen et al (1978) and Svendsen (1984) also gave attention to the decrease in wave height which was associated with wave breaking and the subsequent propagation of the broken wave. Svendsen et al (1978) have defined several different regions after breaking to describe the wave characteristics in the surf zone: an outer region where there is a rapid change in wave shape, an inner region where changes are slow and the front part of the wave resembles a periodic bore, and the region of runup of the wave on the beach. The concept of the

¹Professor of Civil Engr., W.M.Keck Lab of Hydr. and Water Res., California Institute of Tech., Pasadena, CA 91125 USA

²Post-Grad. Res. Engr. UC San Diego, Dept. of AMES/INLS, B-010, La Jolla, CA 92093, USA

changing wave shape as an important aspect of the decrease of wave height after breaking was discussed by Svendsen (1984). In this connection it was suggested by him that a smaller percentage of the decrease in wave height after breaking is due to energy dissipation associated with the roller formation at breaking (and the concomitant turbulence generated) compared to that due to the change in the shape of the wave, i.e., the general collapse of the wave with distance after breaking. Svendsen (1984) applied estimates of the roller size measured by Duncan (1981), who formed a breaker behind a towed hydrofoil, to the question of the energy dissipation in a breaking wave; this will be discussed more fully later.

For some years simplified solitary wave models have been used for estimates of the characteristics of periodic breaking waves. In this paper several characteristics of breaking solitary and cnoidal waves will be discussed and contrasted to assist in evaluating the adequacy of such models. In that regard, of interest were the change in wave height and wave shape with distance and the growth and decay with distance of the roller generated at breaking for these two types of waves. The latter was given attention because of the relation between the roller characteristics and the vorticity generated in the post breaking region by the wave at breaking. For both solitary and cnoidal waves some comparisons will be made between the characteristics of spilling and plunging breakers. Experiments were conducted in the laboratory using breaking solitary and cnoidal waves with the data collected from detailed visual observations. Thus, a comparison of these waves will be made in a macroscopic context only. The experimental equipment and techniques used will be presented first followed by the presentation and the discussion of the results.

EXPERIMENTAL EQUIPMENT

A tilting wave tank was used for all experiments; the tank is 39.6 m long, 1.1 m wide, and 0.61 m deep and is constructed with glass sidewalls throughout and a stainless steel bottom which is plane to within about ± 1.0 mm. The tank is supported at a central hinge point with two motorized jacks upstream and two downstream, geared to operate together thereby permitting a continuous adjustment of slope from horizontal to a maximum slope of about 1:50. The supports for a bulkhead wave generator located at one end of the tank are an integral part of the wave tank structure and tilts with the tank; in this manner waves can be produced on a slope and caused to break at predetermined locations.

The generator is driven by an electro-hydraulic servo-system with the voltage time history determined so the velocity of the wave plate, at a given time, matches the water particle velocity of the wave as it propagates away from the plate. This wave generation technique has been described by Goring and Raichlen (1980). An iterative procedure can be used to compensate for the dynamics of the mechanical hydraulic system; see Skjelbreia (1987). The general characteristics of solitary waves generated in this tank when horizontal have been described by Lee, Skjelbreia, and Raichlen (1982); and a description of the cnoidal waves and their kinematics generated with the tank horizontal has been given by Raichlen and Lee (1984). As mentioned earlier, to produce breaking waves the wave tank was tilted and both solitary and cnoidal waves wave breaking could be induced at pre-determined locations by modifying the characteristics of the wave plate trajectory, i.e., the relative wave height at the point of generation: (H_0/h_0) , where H is the wave height, h is the depth, and the subscript $_0$ indicates the location is at the wave generator.

It was found by Skjelbreia (1987) that just prior to and at wave breaking, wire resistance wave gages normally used to define the free surface were inaccurate when the free surface changed rapidly with time. Problems using this type of gage increased after breaking when air is entrained. It was apparent that observations made using high speed motion picture techniques would eliminate such questions regarding the gage response and the effect of the variation of the electrical conductance of the air-water mixture. Therefore, the wave shape and wave heights were obtained from the frame-by-frame analysis of projected images of the wave obtained from high speed motion pictures. The 16 mm. camera which was used can operate at film speeds which can be continuously adjusted up

to a maximum of 500 frames per second with adjustable shutter speeds to 1/4000 sec. Timing marks every 1/100 sec. are automatically imaged on the film frames. The camera and the necessary lights were mounted to a carriage which could be moved along precision rails mounted to the walls of the tank. The carriage was moved manually so that the breaking region of the wave was approximately centered in each film frame. This was relatively easy even though the wave speed decreased as the wave approached the shoreline. There was probably an error of about ± 1 mm using this technique due to the meniscus which formed on the sidewall of the tank.

An estimate of the size of the roller on the front face of the breaker was made also using the individual frames of the high speed motion pictures. The cross sectional area of the *bubble mass* was used as a measure of the roller size, and its cross section area was estimated from the projection of the *bubble mass* on the sidewall of the tank as seen in the individual film frames. Only the *bubble mass* seen on the front face of the wave was used for this definition; bubbles appearing further back in the wave were not included in this defined area. Several aspects of this measurement will be discussed more fully later.

RESULTS AND DISCUSSION OF RESULTS

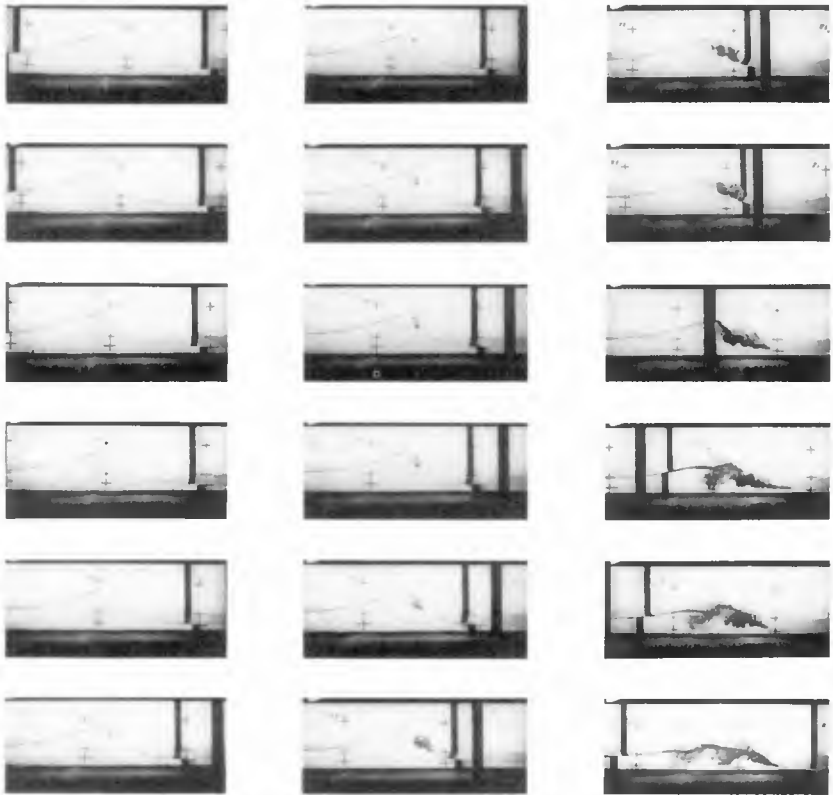
It is instructive, before discussing the more quantitative aspects of wave breaking obtained from the experiments conducted, to view certain features of breaking in a qualitative sense. This can be done from sequences of frames of selected high speed motion pictures taken in the course of the experiments.

A series of frames taken from a 300 frame per second high speed movie of a breaking solitary wave are presented in Figure 1. The solitary wave was generated in the wave tank which was sloped at 0.0191 m/m with a water depth at the wave generator of 43.25 cm; the experiment is denoted as Experiment P-1. In each frame the bottom of the tank can be seen along with the vertical members which support the glass sidewalls. The numbers in each frame indicate distance in meters measured from one end of the tank, and the horizontal bars superposed on the short vertical ones define the still water level for the experiments. (The lowest line corresponds to the still water level for this group of experiments.) The distance between crosses is 50 cm.; for convenience a bar-scale is shown at the bottom of the figure. For reference, the mean position of the wave machine is at Station 37.71 m.

In Figure 1 the sequence of breaking for a plunging breaker can be followed from the position just at breaking (shown in the upper lefthand frame at tank station 22.12 m.) to the post breaking position (shown in the lower righthand frame). Breaking is defined as occurring when the face of the wave in the crest region becomes vertical shortly before overturning takes place. This definition was used for both plunging and spilling breakers. The depth at breaking is: $h_b = 13.50$ cm. and the wave height at breaking is: $H_b = 16.50$ cm as obtained directly from the frame. As one views the sequence of frames, the overturning of the crest and the subsequent formation of the jet just after breaking can be seen as the wave crest approaches $x = 22$ m. The wave propagates shoreward about one breaking depth before the jet impinges with splashup on the front face of the wave. (See the third frame in the center row of photographs.) At that point the wave begins to collapse and change shape while generating the roller on the front face of the wave. The process of the "folding" of the air into the wave can be seen easily. As the wave propagates shoreward it appears to travel through the *bubble mass* as can be seen in the last few photographs of the sequence. The vortical motion so generated can be seen easily. It should be noted that the total distance the wave has travelled in the complete sequence of photographs shown is only about 1.5 m. or about 12 breaking depths.

A qualitative comparison between a breaking solitary wave and a breaking cnoidal wave can be made by reviewing the series of photographs presented in Figure 2. The left-hand column of frames is for the plunging breaking solitary wave which was shown in Figure 1 (Experiment P-1) with the relative distance shoreward of breaking indicated beneath each frame. The right-hand column corresponds to a plunging breaking cnoidal wave (Experiment ACN-4) with the relative shoreward distance from breaking also shown

SOLITARY (EXPERIMENT: P1)


 $S = 0.0191 \text{ m/m}$

SCALE:

 $h_b = 13.50 \text{ cm}$
 $H_b = 16.50 \text{ cm}$
 $x_b = 22.12 \text{ m}$

Figure 1 Photographs of a Breaking Solitary Wave, Experiment P1,
 $S = 0.0191 \text{ m/m}$.

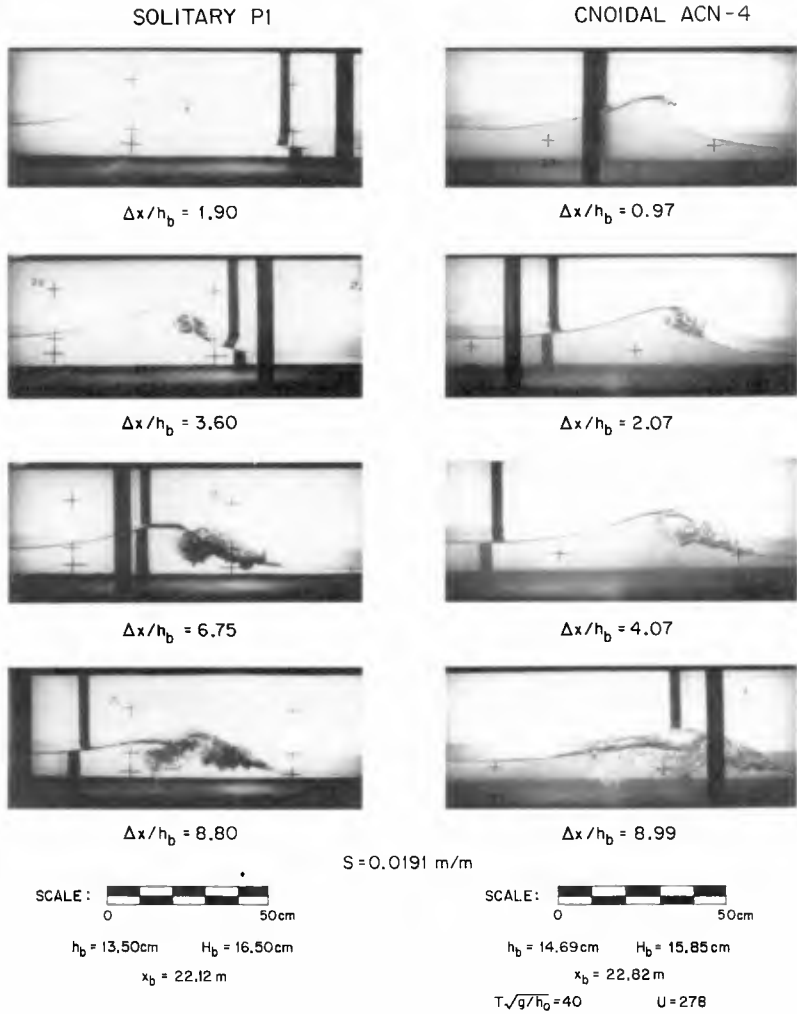


Figure 2 Photographs of a Breaking Solitary Wave (Exp. P1) and a Breaking Cnoidal Wave (Exp. ACN-4).

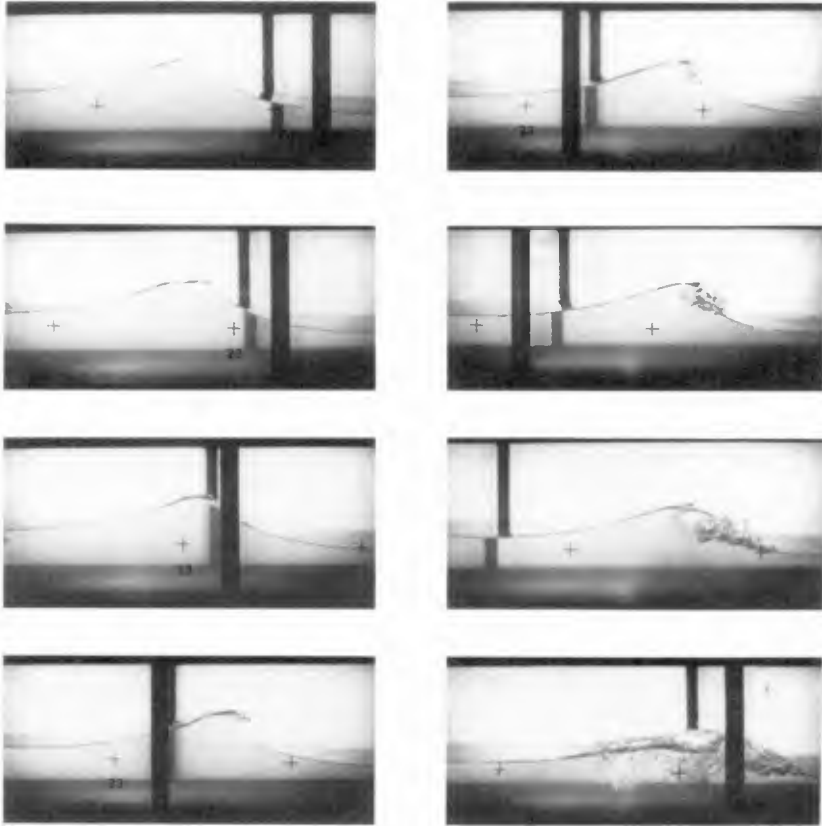
below each frame. In all cases where the results for the cnoidal waves are shown, the photographs and data are for the fourth wave in the wave train. This wave was used as it is far enough back in the wave train so that it appears fully developed and yet not so far back that it would be affected by the reflections from the wave generator of waves which are reflected from the slope. In both cases the flume slope was 0.0191 m/m which is the steepest the wave tank can be tilted. Again the crosses are spaced 50 cm. apart and are located at the still water level; a bar-scale is shown for each sequence of photographs. The cnoidal wave has an Ursell Number at the point of generation which is about 278. (The Ursell Number at the wave generator is defined as: $(HL^2/h^3)_0$, where H is the wave height, h is the water depth, L is the computed wave length.) With that in mind, it is seen, perhaps as would be expected, there are striking similarities between these two types of breaking waves. The solitary wave shows the classic profile of a plunging wave whereas the cnoidal wave shown just to the right, for the locations chosen, shows the jet as it is being ejected from the crest. The shape of the jet appears to be more complex than that for the solitary wave. Certain of the differences observed between the solitary and the cnoidal waves are probably due, for the cnoidal case, to the influence of the prior breaking waves. As waves break they leave behind a turbulent field which, along with the effect of the offshore current generated by the runup and rundown of the waves at the shoreline, must influence the breaking of subsequent waves in the train. Nevertheless, after breaking occurs, the shape of the waves as they propagate shoreward are similar for the two cases. This suggests that the post breaking region is strongly controlled by the details of the flow at the crest during the overturning process. This is probably reasonably similar for the cases shown indicating that the details of the initial wave, i.e., solitary or cnoidal, probably are not too important in this regard.

In Figures 3 and 4, photographs are presented showing the breaking of cnoidal waves with Ursell Numbers, at generation, of 278 and 98.3, respectively, with the wave tank sloped at 0.0191 m/m. In a general way the photographs are similar for both the breaking and post breaking regions. The irregularities near the crest in the second photograph on the left in Figure 3 may be an indication of a wave propagating offshore generated at the shoreline by the runup-rundown process. Further into the sequence it is seen that the broken wave travels through the vortices generated during the breaking process, e.g., see the last photographs of the two sequences. The depth to which the bubbles generated at the water surface during the breaking process penetrate when the wave is greater than ten breaking depths shoreward of the breaking location is somewhat surprising in these figures, as well as in Figure 1 for the solitary wave. (Similar effects have been observed by Nadaoka (1986).) A series of photographs is presented in Figure 4 for the cnoidal wave with an Ursell Number of 98.3 when breaking in the tank with a bottom slope of 0.0191 m/m. There is little difference in the overall features seen in the photographs for similar distances shoreward of breaking for the waves shown in Figures 3 and 4 suggesting that the processes among the three waves: the solitary wave and the two cnoidal waves for the same bottom slope are similar.

The variation of the relative wave height at breaking, $(H/h)_b$, with the bottom slope, S , for the solitary waves and the cnoidal waves which were tested is presented in Figure 5. Plotted next to each data point is the relative wave height at generation: H_0/h_0 . In this figure the nondimensional parameter: $T(g/h_0)^{1/2}$ is used to define the two different cnoidal waves which were used; Table 1 shows the experimental conditions for these cnoidal waves. The slopes were chosen to generate a range of breaking waves from spilling to plunging. The spilling wave occurs at a slope of 0.0061 m/m with a gradual change to plunging at a slope of 0.0191 m/m. This figure demonstrates that the differences between spilling and plunging breakers are not distinct; perhaps they are more related to the *intensity* of the overturning jet associated with breaking rather than major differences in the waves themselves. The interested reader is directed to Papanicolaou and Raichlen (1987) for a discussion of certain of these aspects for the solitary wave.

In Figure 5 self-similarity at breaking for the solitary wave is demonstrated by the three data points shown for a tank slope of 0.0126 m/m. For that case the relative breaking height is essentially the same, independent of the generation conditions. The

CNOIDAL ACN-4



$S = 0.0191 \text{ m/m}$

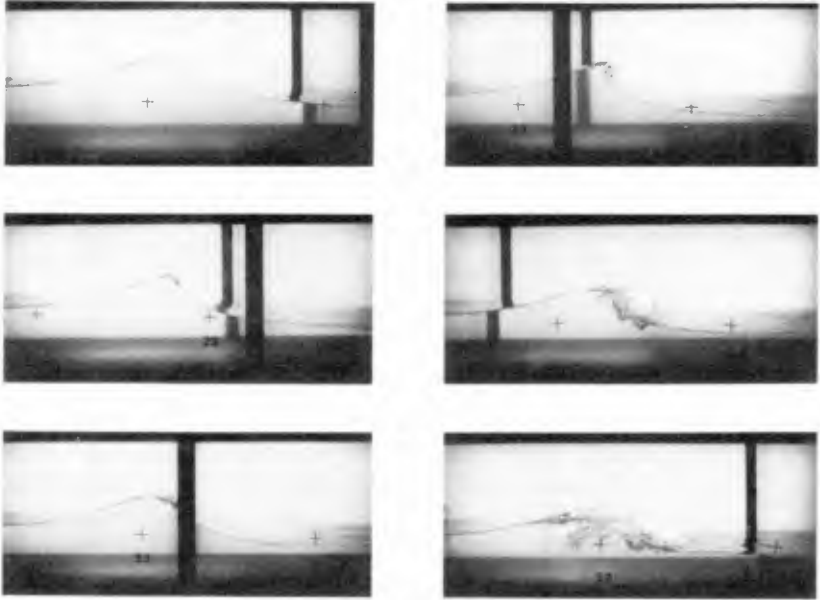
SCALE:  0 50cm

$h_b = 14.69 \text{ cm}$ $H_b = 15.85 \text{ cm}$ $x_b = 22.82 \text{ m}$

At Generation: $T\sqrt{g/h_0} = 40$ $U = 278$

Figure 3 Photographs of a Breaking Cnoidal Wave (Exp. ACN-4).

CNOIDAL ACN-2


 $S = 0.0191 \text{ m/m}$

SCALE :  0 50 cm

 $h_b = 15.05 \text{ cm}$ $H_b = 14.59 \text{ cm}$ $x_b = 23.03 \text{ m}$

At Generation: $T\sqrt{g/h_0} = 25$ $U = 98.3$

Figure 4 Photographs of a Breaking Cnoidal Wave (Exp. ACN-2).

water depth at the location of the wave generator was the same for the three different experiments, hence, the waves break at different locations. An experimental curve is shown for the solitary wave which, if extrapolated, tends to a value of relative height at breaking of about 0.8 for a horizontal bed. The data for the cnoidal waves vary in a similar manner with slope as the corresponding data for the solitary waves. Thus, there appears to be a strong similarity in the trends of relative breaking height with increasing slope for solitary and cnoidal breaking waves. The differences observed between the relative breaking heights of solitary and cnoidal waves for the same slopes are probably related to the influence of the prior breaking waves on the observed wave in the train, i.e., the fourth wave.

Table 1 Experimental Conditions for Cnoidal Waves

Experiment No.	S (m/m)	T(g/h ₀)	(HL ² /h ³) ₀
ACN4	0.0191	40	278.
ACN2	0.0191	25	98.3
ACN7-1,2	0.0061	40	706.
ACN6-1	0.0061	25	263.

In Figure 6 the variation of the breaking wave heights for the cnoidal waves is shown (normalized by the breaking solitary wave height) as a function of the generation Ursell Number for each of two different wave tank slopes. It is interesting to see that the effect of slope does not appear significant for these data even though at the smaller slope the breaking wave is essentially a spilling wave and at the larger slope it is a plunging wave (see Figures 3 and 4).

The variation of the relative wave height, H/H_b , with distance shoreward of breaking, $\Delta x = (x - x_b)$, is presented in a nondimensional manner in Figures 7 and 8 for waves breaking on a slope of 0.0191 m/m and 0.0061 m/m, respectively. (The location of the point of observation is denoted as x and the location of the breaking position is x_b .) For each tank slope, data are shown for solitary and cnoidal waves with different non-dimensional generation times. It should be mentioned, after breaking the wave height defined corresponds to the height for the portion of the wave which appears to have little air entrained. If, for example, one refers to the last frame presented in Figure 4, it is seen that the height of the roller (or *bubble mass*) is somewhat greater than that corresponding to the clearer region behind; the height used in Figure 7 corresponds to the latter. As seen in Figures 7 and 8, and also best shown in the photographs presented in Figure 2, both the cnoidal and the solitary waves propagate some distance shoreward of breaking with little effect on the wave height. This is in accord with the observations of Galvin (1968), (1969); the Shore Protection Manual of the U.S. Army Corps of Engineers (1984) follows these observations and recommends that the post-breaking distance during which the wave height changes only slightly be defined as: $(\Delta x/h_b) = (4 - 9.25S)(H/h)_b$. For the solitary wave of Figure 7 the distance computed from this expression is about 4.7.

Figure 7 shows that, for the solitary wave, at a location of about five breaking depths the rate of change of the wave height with distance begins to increase. For the two cnoidal waves, i.e., $U = 98.3$ and 278, there is a more rapid decrease in relative wave height with distance shoreward of $\Delta x/h_b = 3$ than for the solitary wave. This is probably due to the influence of the preceding waves on the breaking process. This can be seen easily in Table 2 where the exponent, n , in the expression: $(H/H_b) \sim (\Delta x/h_b)^n$ is presented for the various experiments for $4 < \Delta x/h_b < 8$. Thus, these data indicate an increase in the energy dissipation in the post breaking region of periodic waves compared to solitary waves. The data shown in Figure 7 for the region of $7 < \Delta x/h_b < 15$ shows a relatively constant relative wave height of about $H/H_b = 0.5$. This is the beginning of the region where a bore is formed and the wave height changes more slowly. Horikawa and Kuo (1966) show, in this bore region, that the wave height relative to the local water depth

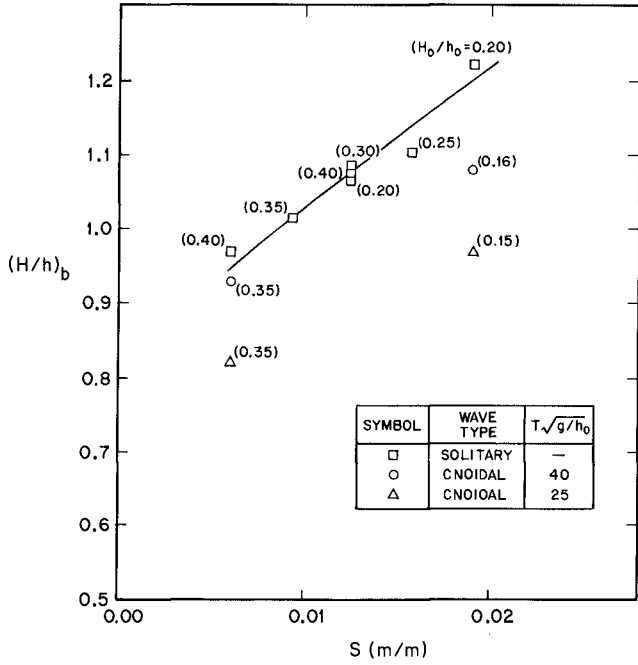


Figure 5 Variation of Relative Height at Breaking with Bottom Slope.

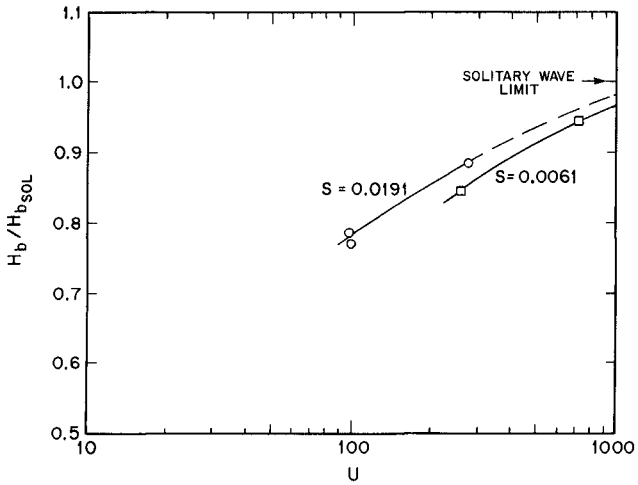


Figure 6 Variation of Relative Height and Breaking with Ursell Number at Generation.

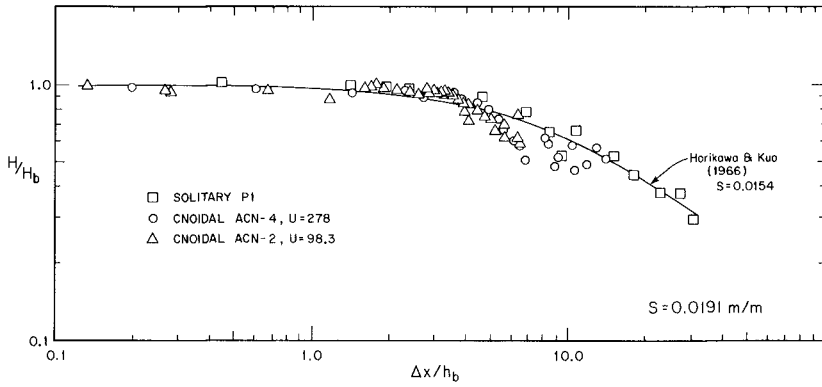


Figure 7 Variation of Relative Height after Breaking with Relative Distance ($S = 0.0191 \text{ m/m}$).

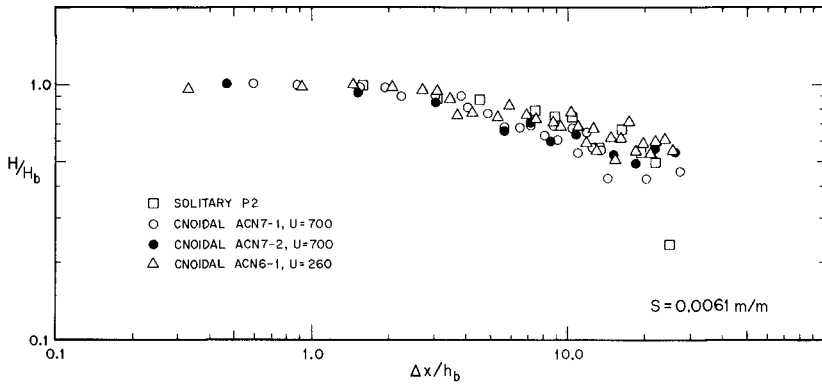


Figure 8 Variation of Relative Height after Breaking with Relative Distance ($S = 0.0061 \text{ m/m}$).

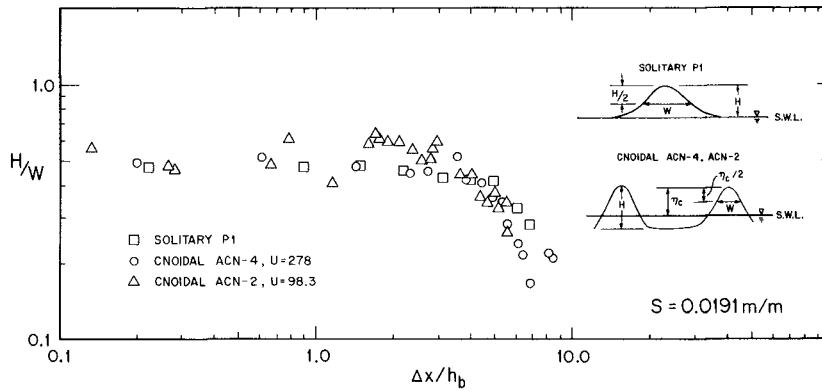


Figure 9 Variation of Aspect Ratio of Wave after Breaking with Relative Distance ($S = 0.0191 \text{ m/m}$).

asymptotically approaches a constant value of between 0.35 and 0.4 for certain of their experiments. A curve is presented which corresponds to the experimental data from

Table 2 The Exponent n for the Various Experiments

Experiment Number	n
P1	- 0.621
ACN4	- 1.01
ACN2	- 0.769
SP2	- 0.521
ACN7-1,2	- 0.398
ACN6	- 0.382

Horikawa and Kuo (1966) for periodic waves breaking on a slope of 0.0154 for the region of data from these experiments. (Similar data have been presented by Svendsen et al (1978) for periodic waves breaking on a slope of 0.0292.)

In Figure 8 the variation of relative wave height with distance is presented for a solitary wave and for two cnoidal waves with Ursell Numbers of about 700 and 260 breaking on a bottom slope of 0.0061 m/m. Instead of the plunging waves in Figure 7, the waves break as spilling breakers. The first observation is that for $\Delta x/h_b \geq 3$ the rate of decrease in the relative wave height is less for the spilling breaker than it is for the plunging breaker. This has been shown, with reference to the exponent, n , in Table 2. In fact, for the spilling breaker the relative change in wave height with distance shoreward of breaking is *similar* for the solitary and two cnoidal waves shown; actually the rates are somewhat less for the cnoidal waves as compared to the solitary wave. For the spilling waves the relative wave height becomes approximately constant at about $H/H_b = 0.5$ to 0.6 for: $15 \leq \Delta x/h_b \leq 25$ which, similar to the plunging wave case, is where the broken waves become bores and propagate shoreward with a smaller change in relative height. The consistency of the data acquisition and analysis is shown by the agreement of the data for Experiments ACN 7-1 and ACN 7-2 conducted at separate times with the same experimental conditions. It is interesting to observe that the rate of change of relative wave height with distance for the spilling and plunging solitary waves shown in Figures 7 and 8 are similar.

It was realized from reviewing the motion pictures that the change in wave height in the initial region after breaking was related also to the change in the wave shape in addition to the effects of energy dissipation. However, the effects of energy dissipation must not be too great in the region just after breaking, since in that region the overturning crest associated with the breaking process has not had time to fully generate the vortical motion observed further shoreward of breaking. To explore this with the data available from the current experiments, an aspect ratio of the wave was used which was defined as the ratio of the wave height, H , to the width of the wave, W , measured one half of the distance from the still water level to the crest. The variation of H/W with relative distance from breaking, $\Delta x/h_b$, is presented in Figure 9 for plunging breaking solitary and cnoidal waves. (A definition sketch for the width, W , is shown in the inset.) For this slope, i.e., $S = 0.0191$ m/m, the Ursell Numbers for the two cnoidal waves are 98.3 and 278, respectively. In the region from breaking to about two breaking depths shoreward of breaking the aspect ratio is relatively constant and equal to between about 0.5 and 0.6 for both the solitary and the cnoidal waves. There is a relatively gradual decrease in H/W for the solitary wave when $2 \leq \Delta x/h_b \leq 5$; for $\Delta x/h_b > 5$ the aspect ratio decreases more rapidly. In the case of the two cnoidal waves similar changes take place. If the variation of the aspect ratio with distance for this rapidly changing region is expressed as: $(H/W) \sim (\Delta x/h_b)^n$; the exponent n for experiments: P1, ACN4, and ACN2 are - 1.285, - 1.43, and - 1.17, respectively. Within the errors involved in the definition of the aspect ratio, it appears that the decrease in the aspect ratio with distance in this rapidly changing region is

similar for each of the three different waves.

Svendsen (1984) and Duncan (1981) have given attention to the size of the roller generated during the breaking process. Measurements were reported by Duncan (1981) using a breaker which was generated by a towed hydrofoil. These results were used by Svendsen (1984) to estimate the percentage of energy dissipated from breaking through the region referred to by him as the transition region. However, the experiments reported by Duncan (1981) were essentially steady ones, i.e., the hydrofoil moved at a constant velocity, whereas the wave breaking process is highly unsteady.

As mentioned in the previous section, the variation in roller size was determined in this study as a function of distance from breaking using the high speed motion pictures taken with the camera following the wave. The roller area was defined using the projection on the side of the wave tank of the area of the *bubble mass* which travels on the front face of the breaker. Obviously this technique can only provide an estimate of the roller area, but if it is done consistently, a comparison of this area can be made among the different types of waves used in these experiments. Examples of these projected areas can be seen easily in the photographs presented in Figures 1 through 4. There is some lateral variation to the *bubble mass*, as can be seen in the frame corresponding to $\Delta x/h_b = 8.99$ in Figure 2, so the technique used yields simply an *estimate* of the roller size. This is a crude measurement of the roller area, but at the very least it provides one other way by which the breaking process of solitary and cnoidal waves can be compared.

In Figure 10 the variation of the cross section area of the *bubble mass* normalized by the square of the breaking wave height, A/H_b^2 , is presented as a function of the relative distance shoreward of breaking, $\Delta x/h_b$, for a plunging solitary wave and two cnoidal waves breaking in the wave tank sloped to 0.0191 m/m. It is seen that, for the cases shown, the maximum value of the relative area is close to unity. The average value of the normalized roller area reported by Duncan (1981) from his steady experiments was: $A/H_b^2 = 0.86$. The *bubble mass* area ratio reaches a maximum between about seven and ten breaking depths shoreward of breaking. (The interested reader is directed to Papanicolaou and Raichlen (1987) for more detailed information on *bubble mass* areas for solitary waves.) Referring back to Figure 7, for the cnoidal waves, the maximum appears to be reached *after* the wave height has decreased at its maximum rate to the observed *plateau* in height. As would be expected, the area of the bubble mass increases significantly over the distance that the height is changing the most, i.e., for: $3 < \Delta x/h_b < 8$ the relative roller area increases by a factor of ten. The data for the solitary waves and the cnoidal waves with Ursell Numbers of 98.3 and 278 are quite similar in trend and in the maximum relative bubble areas.

The growth of the roller, i.e., the *bubble mass*, for spilling breakers was investigated also, and the results are presented in Figure 11. With the wave tank sloped to 0.0061 m/m both the solitary wave and the two cnoidal waves broke as spilling breakers where the overturning at the crest was observable but certainly not as dramatic as for the waves breaking on the steeper slope. The data from two different experiments for the same conditions, i.e., $U = 700$, are in good agreement indicating that comparisons of *bubble mass* areas made among the different waves are reasonable. In comparing the relative roller area for the solitary wave to that observed for the cnoidal waves it was found that there was very little difference in the trend of the data. The relative areas grew from about 0.1 to a maximum for: $2 < \Delta x/h_b < 10$. However, unlike the plunging breakers, the maximum relative areas are somewhat different. They range from about 0.5 to 0.6 for the cnoidal waves to 0.8 for the solitary waves. Although this may be within the range of the accuracy of the data reduction, it is also possible (and reasonable) that the rate of growth of the roller is slower for the spilling breaker compared to the plunging breaker. Thus, assuming this area is related to the associated energy dissipation, Figures 10 and 11 support the generally held hypothesis that the energy dissipation for spilling breakers is less than that for plunging breakers. This also agrees with the observations made in comparing Figures 7 and 8 for the change in relative wave height after breaking.

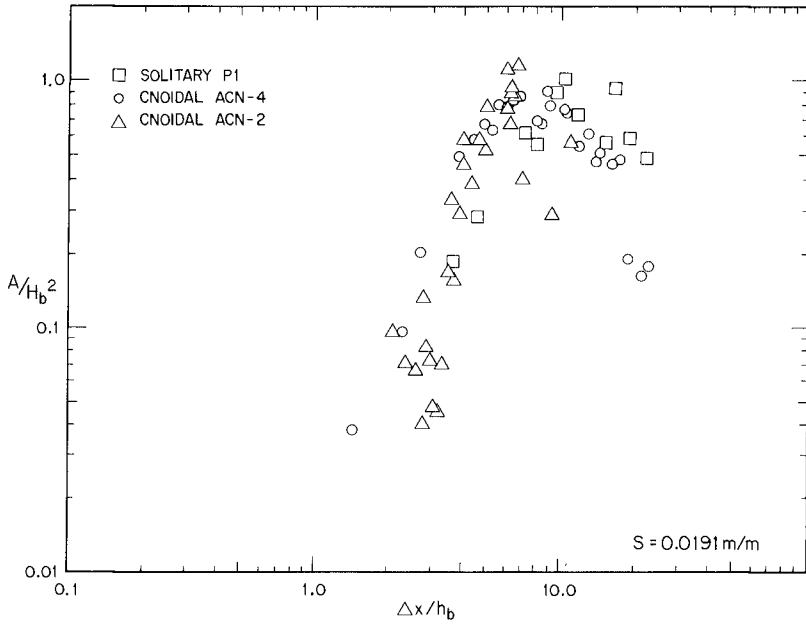


Figure 10 Variation of Relative Bubble Mass after Breaking with Relative Distance ($S = 0.0191 \text{ m/m}$).

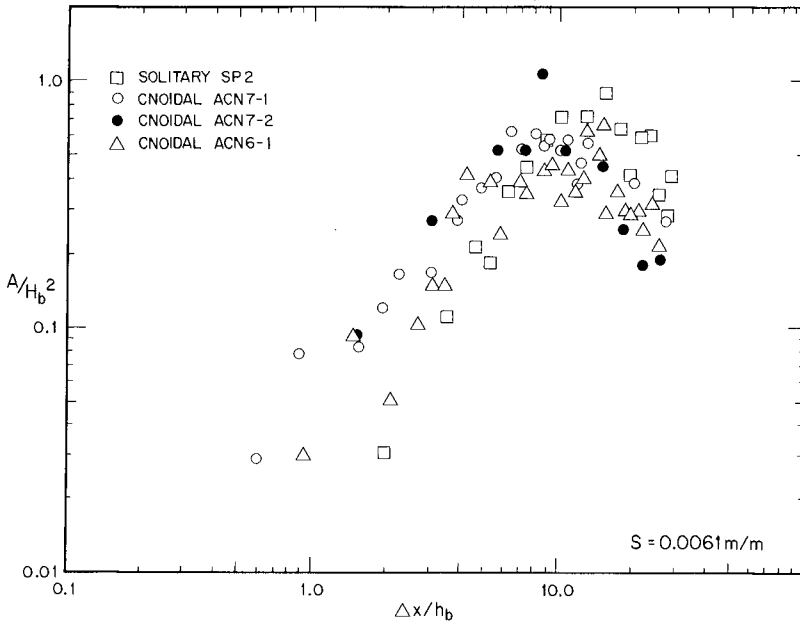


Figure 11 Variation of Relative Bubble Mass after Breaking with Relative Distance ($S = 0.0061 \text{ m/m}$).

Conclusions

The following major conclusions may be drawn from this study:

1. The data for breaking solitary and cnoidal waves each show plunging waves differ from spilling waves primarily in the *rate* of change of the properties investigated, not in overall characteristics.
2. The relative breaking height $(H/h)_b$, for the solitary and cnoidal waves tested, increases with slope and for a given slope the relative breaking wave height is a maximum for solitary waves compared to the cnoidal waves.
3. The breaking of a solitary wave which is between a spilling and a plunging breaker is self-similar.
4. There is a region of three to five depths shoreward from breaking where the wave height is relatively unchanged, followed by a region of three to five breaking depths over which major changes in wave height and shape take place. It was apparent from the data that the changes in height for the cnoidal waves with distance after breaking was significantly greater for the plunging waves compared to the spilling waves. The comparable changes for the solitary waves (plunging and spilling) were similar.
5. The aspect ratio of the wave, H/W , changes in a manner similar to the height. For the plunging case, for which this was defined, the decrease of the aspect ratio in the rapidly changing region was similar for the solitary and the two cnoidal waves.
6. The *bubble mass* on the front face of the wave grows from zero, reaches a maximum, and decreases; the maximum relative size of the mass expressed as A/H_b^2 is of the order of unity.
7. Solitary and cnoidal waves exhibit reasonably similar changes in wave height and *bubble mass* for each type of breaking wave investigated (spilling or plunging) indicating that effects on the waves of breaking for these translatory and oscillatory waves may be similar.

Acknowledgement

The writers appreciate the support of the National Science Foundation through Grant : MSM-8311374 and by the Miriam and Omar J. Lillevang Fund at Caltech.

References

- Battjes, J.A., "Surf-Zone Dynamics", Ann. Rev. Fluid Mech., 20:257-93, 1988
- Dally W.B., Dean, R.G., and Dalrymple, R.A., "Modeling Wave Transformation in the Surf Zone", Misc. Paper CERC-84-8, Coastal Engineering Research Center, Waterways Exp. Sta., 1984
- Duncan, J.H., "An Experimental Investigation of Breaking Waves Produced by a Towed Hydrofoil", Proc.R.Soc.Lond., A377, 331-348, 1981
- Galvin, C.J., Jr., "Breaker Type Classification on Three Laboratory Beaches", Journ. of Geophysical Res., Vol. 73, No. 12, 1968
- Galvin, C.J., Jr., "Breaker Travel and Choice of Design Wave", Journ. of Waterways and Harbors Div., ASCE, WW2, 1969
- Goring, D.G. and Raichlen, F., "The Generation of Long Waves in the Laboratory", Proc. of the Seventeenth Coastal Engineering Conf., Sidney, Australia, 1980

- Horikawa, K. and Kuo, C-T, "A Study on Wave Transformation Inside the Surf Zone", Proc of the Tenth Conf. on Coastal Engr., Tokyo, Japan, 1966
- Lee, J.-J., Skjelbreia, J.E., and Raichlen, F., "Measurement of Velocities in Solitary Waves", Journ.of Waterways, Ports, Coastal and Ocean Div., ASCE, Vol. 108, No. WW2, pp.200-218, May 1982
- Nadaoka, K., "A Fundamental Study on Shoaling and Velocity Field Structure of Water Waves in the Nearshore Zone", Tech. Rpt. No. 36, Dept. of Civil Engr. Tokyo Institute of Technology, 1986
- Papanicolaou, P. and Raichlen, F., "Wave Characteristics in the Surf Zone", Coastal Hydrodynamics, ASCE, University of Delaware, 1987
- Peregrine, D.H., "Breaking Waves on Beaches", Ann. Rev.Fluid Mech., 15:149-78, 1983
- Peregrine, D.H. and Svendsen, I.A., "Spilling Breakers, Bores, and Hydraulic Jumps", Proc. of the Sixteenth Coastal Engr. Conf., Hamburg, Germany, 1978
- Raichlen, F. and Lee, J.-J., "The Interaction of Small and Finite Amplitude Long Waves and Currents", Proc. of the Nineteenth Conf. on Coastal Engr., Houston, Texas, 1984
- Shore Protection Manual, Coastal Engr. Res. Center, U.S.Army Corps of Engrs., 1984
- Skjelbreia, J.E., "Observations of Breaking Waves on Sloping Bottoms by Use of Laser Doppler Velocimetry", Report No. KH-R-48, W.M.Keck Laboratory of Hydraulics and Water Resources, Calif. Inst. of Tech., 1987
- Svendsen, I.A., "Wave Heights and Set-Up in a Surf Zone", Coastal Engineering, Vol. 8, 1984
- Svensen, I.A., Madsen, P.Å., and Hansen, J.B., "Wave Characteristics in the Surf Zone", Proc. of the Sixteenth Coastal Engr. Conf., Hamburg, Germany, 1978

CHAPTER 27

Numerical Modeling of Wave Deformation with a Current

Susumu OHNAKA*, Akira WATANABE** and Masahiko ISOBE***

ABSTRACT

A numerical computation method for a wave field coexisting with a current is presented to study wave-current interaction on a slowly varying bottom topography. Derivation is given for a new set of time-dependent mild-slope equations extended to a wave and current coexisting field, which can deal with wave deformation due to combined refraction, diffraction, reflection and breaking as well as to wave-current interaction. Discussion is made on the numerical computation schemes, boundary conditions and breaking conditions. Some examples of the numerical computations are shown for wave and current coexisting fields.

1. INTRODUCTION

Many efforts have been devoted to the evaluation of wave deformation in the shallow water region with numerical models. The mild-slope equation has been presented and used by Berkhoff (1972) to study combined wave refraction and diffraction on a slowly varying bottom topography. Watanabe and Maruyama (1986) have proposed a time-dependent version of the mild-slope equation, which can be more easily solved numerically and can deal with not only the combined refraction, diffraction and reflection but also wave breaking and decay in the surf zone.

In these equations, however, wave-current interaction is ignored. Coastal and nearshore currents such as rip current, longshore current and river discharge flow affect the wave deformation and therefore it is important to estimate the wave-current interaction in order to accurately predict the nearshore waves and currents and the resultant sediment transport.

* Research Engineer, Technical Research Institute, Toa Corporation, 1-3, Anzen-cyo, Tsurumi-ku, Yokohama, 230 Japan

** Professor, Department of Civil Engineering, Univ. of Tokyo, Hongo 7-3-1, Bunkyo-ku, Tokyo, 113 Japan

*** Associate Professor, ditto

For a wave field coexisting with a varying current, three kinds of wave equations and models have been proposed by Booij (1981), Liu (1983) and Kirby (1984), respectively. All these three models employ elliptic-type differential equations which are in general difficult to numerically solve. Hence these models are often approximated by parabolic equations, and then they are not applicable to the wave field including significant reflection due to structures.

In the present study, a new set of the time-dependent mild-slope equations extended to a wave and current coexisting field is derived and the numerical computation method is discussed. Some results of the computation are compared with analytical solutions and experimental results. The model is also applied to computing waves and currents under practical conditions including the presence of structures with consideration of the wave-current interaction.

2. DERIVATION OF GOVERNING EQUATIONS

The mild-slope equation presented by Berkhoff (1972) is the second-order partial differential equation. On the other hand, the time-dependent mild-slope equations proposed by Watanabe and Maruyama (1986) consist of two first-order equations, which are obtained by separating the original mild-slope equation in terms of the water surface elevation and the flow rate. They also include a term for the energy dissipation due to breaking. The numerical computation is conducted for every time-step, and it is easy to deal with boundary conditions in general and to calculate local wave direction needed for introducing partially reflective boundaries and for solving the dispersion relation in a wave and current coexisting field.

As mentioned before, three kinds of elliptic equations have been proposed for a wave and current coexisting field. Among them, the equation proposed by Kirby (1984), which exactly satisfies the conservation equation of wave action, is given by

$$\frac{D^2\phi}{Dt^2} + (\nabla \cdot U) \frac{D\phi}{Dt} - \nabla \cdot (C \cdot C_g \nabla \phi) + (\sigma^2 - k^2 C \cdot C_g) \phi = 0 \quad (1)$$

where $D/Dt = \partial/\partial t + U \cdot \nabla$, ∇ is the horizontal gradient operator, ϕ the complex velocity potential at the mean water level, U the steady current velocity vector, σ the intrinsic angular frequency, k the wave number vector, and C and C_g the phase and group velocity vectors calculated with σ , which is determined from

$$\omega = \sigma + k \cdot U, \quad \sigma^2 = gk \tanh kh \quad (2)$$

where ω is the apparent angular frequency, h the water depth, and g the acceleration due to gravity. The velocity potential at an elevation z will be given by

$$\Phi(x, z, t) = \phi(x, t) f(z) \tag{3}$$

where $f(z)$ is the vertical distribution function represented by

$$f(z) = \cosh k(h+z) / \cosh kh \tag{4}$$

Now we separate Eq. (1) into two equations expressed in terms of the surface elevation ζ and the flow rate vector Q instead of ϕ . The flow rate vector Q is defined by

$$Q = \int_{-h}^0 \nabla \phi \, dz \tag{5}$$

Substituting Eqs. (3) and (4) into Eq. (5), we obtain

$$Q = C^2 \nabla \phi / g \tag{6}$$

On the other hand, the kinematic boundary condition at the water surface including the convection term due to a steady current requires

$$\zeta = - (1/g) D\phi / Dt \tag{7}$$

Here the complex velocity potential ϕ is expressed in terms of the amplitude and the phase as

$$\phi = \phi(x) e^{i\psi} \tag{8}$$

where $\psi = k \cdot x - \omega t$ is the phase function. When we ignore change in the amplitude of the velocity potential as compared with change in the phase, $D\phi / Dt$ is represented as

$$D\phi / Dt = -i\sigma\phi \tag{9}$$

Substitution of Eq. (9) into Eq. (7) yields the following expression of the surface elevation ζ in terms of ϕ :

$$\zeta = i(\sigma/g) \phi \tag{10}$$

Substituting Eq. (10) into Eq. (5) and differentiating with t , we obtain

$$\partial Q / \partial t + \omega C^2 \nabla(\zeta / \sigma) = 0 \tag{11}$$

On the other hand, using Eqs. (7) and (9), ϕ is expressed as

$$\phi = (g / \sigma \omega) \partial \zeta / \partial t \tag{12}$$

Substituting Eqs. (6), (7) and (12) into Eq. (1), we obtain

$$m \partial \zeta / \partial t + \nabla \cdot (U \zeta) + \nabla \cdot (n Q) = 0, \tag{13}$$

$$m = 1 + (\sigma / \omega) (n - 1), \quad n = C_g / C$$

Equations (11) and (13) are time-dependent mild-slope equations extended to a wave and current coexisting field. If we set the steady current

velocity vector $U = 0$, these equations reduce to the ones proposed by Watanabe and Maruyama (1986), though the latter include an additional term for the energy dissipation due to breaking.

3. NUMERICAL COMPUTATION METHOD

Equations (11) and (13) are solved by using a finite difference method. A study area is divided into grid cells and a staggered mesh scheme is employed as shown in Fig. 1. Successive computation is conducted alternately for the flow rate Q and for the water surface elevation ζ . If the convection term due to the steady current in Eq. (13) is neglected, Eqs. (11) and (13) can be easily solved by using an explicit finite difference scheme. However, when this terms is included as needed for general wave and current coexisting systems, some problems appear in numerical computations, such as numerical diffusion and unphysical reflection from the boundaries. In order to determine the most appropriate one among various finite difference schemes, we consider a one-dimensional wave and current field. The following notation is used.

$$\zeta_i^j = \zeta(i\Delta x, j\Delta t) \tag{14}$$

$$Q_i^j = Q\{(i+1/2)\Delta x, (j+1/2)\Delta t\} \tag{15}$$

namely the subscript i denotes the spatial point and the superscript j denotes the time-step. Equations (11) and (13) for the one-dimensional case are discretized to yield

$$m_i \frac{\zeta_i^{j+1} - \zeta_i^j}{\Delta t} + \frac{\delta(U\zeta)}{\delta x} + \frac{n_i Q_i^j - n_{i-1} Q_{i-1}^j}{\Delta x} = 0 \tag{16}$$

$$\frac{Q_i^{j+1} - Q_i^j}{\Delta t} + \omega C_i^2 \frac{(\zeta/o)_{i+1}^j - (\zeta/o)_i^j}{\Delta x} = 0 \tag{17}$$

where $m_i = 1 + (\sigma_i / \omega) (n_i - 1)$. In Eq. (17), the flow rate Q_i^{j+1} can be calculated explicitly since the surface elevations ζ_{i+1}^j and ζ_i^j are known values. The problem is how to discretize the convection term $\delta(U\zeta) / \delta x$ in Eq. (16).

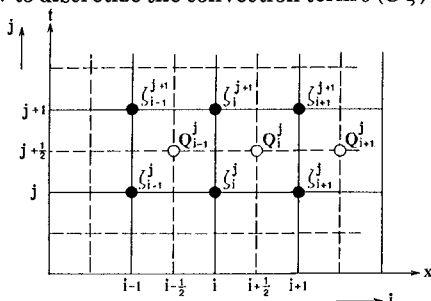


Fig. 1 Staggered mesh scheme.

Table 1 Difference schemes for the convection term.

type	scheme for $\delta(U\zeta)/\delta x$	grid model	numerical diffusion term
implicit type	$\frac{1}{2} \left(\frac{\zeta_{i+1}^{j+1} - \zeta_i^{j+1}}{\Delta x} + \frac{\zeta_{i+1}^j - \zeta_i^j}{\Delta x} \right)$ $U \geq 0$		$-\frac{U}{2} \Delta x \frac{\partial^2 \zeta}{\partial x^2}$
	$\frac{1}{2} \left(\frac{\zeta_{i+1}^{j+1} - \zeta_{i-1}^{j+1}}{\Delta x} + \frac{\zeta_{i+1}^j - \zeta_{i-1}^j}{\Delta x} \right)$ $U < 0$		
II	$\frac{1}{2} \left(\frac{\zeta_{i+1}^{j+1} - \zeta_{i-1}^{j+1}}{2 \Delta x} + \frac{\zeta_{i+1}^j - \zeta_{i-1}^j}{2 \Delta x} \right)$		_____
explicit type	$\frac{\zeta_{i+1}^j - \zeta_i^j}{\Delta x} \quad U \geq 0$		$-\frac{U}{2} \Delta x \left(1 - \frac{U \Delta t}{a \Delta x} \right) \frac{\partial^2 \zeta}{\partial x^2} + \frac{U}{a} \Delta t$ $+ \frac{\partial^2 (nQx)}{\partial x^2} \frac{\Delta t}{2} \frac{\partial^2 (nQx)}{\partial x \partial t}$
	$\frac{\zeta_{i+1}^j - \zeta_{i-1}^j}{\Delta x} \quad U < 0$		
	$\frac{\zeta_{i+1}^{j+1} - \zeta_{i-1}^{j+1}}{2 \Delta x}$		
V	$\frac{\zeta_{i+1/2}^{j+1/2} - \zeta_{i-1/2}^{j+1/2}}{\Delta x}$ $\zeta_{i+1/2}^{j+1/2} = (\zeta_{i+1}^{j+1} + \zeta_{i,1}^j) / 2$ $\zeta_{i-1/2}^{j+1/2} = (\zeta_{i-1}^{j+1} + \zeta_i^j) / 2$		_____

First we use two types of the modified Euler method, which is of an implicit scheme. Type I in Table 1 is an up-wind difference scheme. With this scheme, however, a numerical diffusion term shown in Table 1 is added to Eq. (16). Such a diffusion term doesn't appear when a central difference scheme (Type II) is used. Types I and II are of implicit type, and therefore it will be hard to extend them to computations of two-dimensional wave fields.

Next we discuss explicit difference scheme. Type III is an up-wind difference scheme and Type IV is a central difference scheme. With either of these schemes, however, a numerical diffusion term is added to Eq. (16) as shown in Table 1. This problem is solved by adopting the Alternating Direction Explicit (A. D. E.) method as presented as Type V in Table 1. In this scheme a value at a point $(i-1)$ at a time-step (j) is replaced with the value calculated at the time-step $(j+1)$ just before. By using this method, Eq. (16) can be solved explicitly without numerical diffusion.

Now the treatment of nonreflective boundary condition is discussed. For the equations proposed by Watanabe and Maruyama (1986), which include no convection term due to currents, the nonreflective boundary condition is given by the flow rate. Namely the flow rate at a point x on

the boundary at time t , Q_x^t , is calculated by the flow rate at the inner point $x - \Delta x$ at time $t - \tau$, $Q_{x-\Delta x}^{t-\tau}$. If this boundary condition given by the

flow rate is used in the calculation for a wave and current coexisting field, the surface elevation at the point $x + \Delta x/2$ is needed in order to evaluate the convection term in Eq. (16) with the scheme of Type V. This point is, however, located outside the calculation region, and therefore we must give the convection term along the boundary by backward difference scheme. Using this scheme, the second term in Eq. (16) is evaluated at the point $x - \Delta x/2$, whereas the third term is evaluated at the point x . The difference of the evaluation points causes unphysical reflection from the boundary.

In order to evaluate these terms at the same point, the calculation region is extended up to the point $x + \Delta x/2$ and the boundary condition is given by the surface elevation ζ instead of the flow rate Q , as shown in Fig. 2. The surface elevation at the point $x + \Delta x/2$ on the boundary at time t is given by the one at the inner point $x - \Delta x/2$, at the time $t - \tau$, using a characteristic line $C + U$, as :

$$\zeta_{x+\Delta x/2}^t = \zeta_{x-\Delta x/2}^{t-\tau} \tag{18}$$

where τ is defined by

$$\tau = \Delta x / (C + U) \tag{19}$$

By using this boundary condition, the surface elevation at the point $x + \Delta x/2$ on the boundary is given independently of the difference scheme. Surface elevations at inner points are given by A. D. E. difference scheme, which can evaluate the second and third terms in Eq. (16) at the same point, and consequently we can avoid unphysical reflection.

For the two-dimensional case, τ is calculated from the next equation instead of Eq. (19).

$$\tau = \Delta x \cos a_n / (C + U) \tag{20}$$

where a_n is the direction angle of the incident wave component measured from the normal line to the boundary.

By applying this procedure to a nonreflective boundary, the offshore open boundary condition is set in terms of the surface elevation as

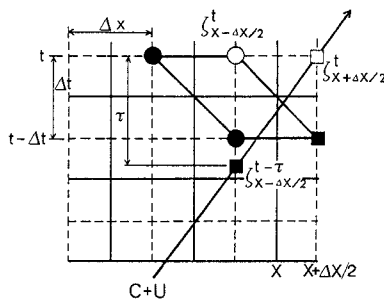


Fig. 2 Nonreflective boundary condition.

$$\zeta^t(x_0, y_0) = a_i \sin(kx_0 + ky_0 - \omega t) + \zeta_R^{t-\tau}(x_0 + \Delta x, y_0)$$

$$\zeta_R^{t-\tau}(x_0 + \Delta x, y_0) = \zeta^{t-\tau}(x_0 + \Delta x, y_0) - a_i \sin\{k(x_0 + \Delta x) + ky_0 - \omega t\}$$
(21)

where a_i is the incident wave amplitude.

4. RESULTS OF NUMERICAL COMPUTATION

To examine the applicability of these equations and method, numerical computations have been performed for two cases of wave deformation due to a current only.

The first case is a one-dimensional wave and current field as shown in Fig. 3. Figure 4 shows the wave height change in the shoreward direction in the steady state. In this figure H is the wave height, C the wave celerity and subscript o denotes quantities at the location where no current exists. The wave heights change corresponding to the current intensity and direction. Waves freely pass through the nonreflective boundary, and no unphysical reflection appears.

Figure 5 shows time histories of the surface elevation at the boundary. The wave amplitudes and the arrival time to the boundary change according to the difference of currents.

The numerical computation results are compared with the analytical solutions in Fig. 6. Solid lines show the analytical solutions given by the wave action conservation equation, and solid circles show the numerical solutions. The numerical solutions agree quite well with the analytical solutions. On the other hand, if we neglect the scalar product $k \cdot U$ in the dispersion relation, computations become easier particularly for a two-dimensional case. However if we set $\sigma = \omega$, both the numerical and analytical solutions deviate far from the true analytical solutions. From these results, it is confirmed that the scalar product $k \cdot U$ in the dispersion relation cannot be neglected for a wave and current coexisting system.

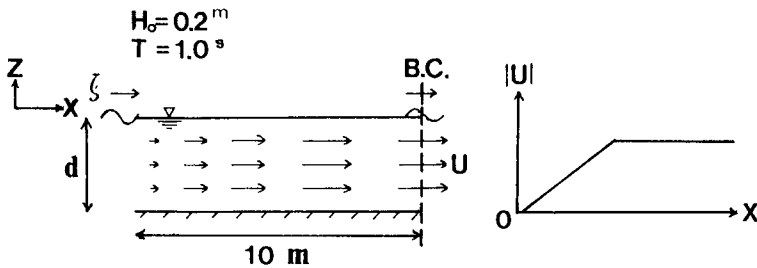


Fig. 3 Calculation condition for a one-dimensional wave and current field.

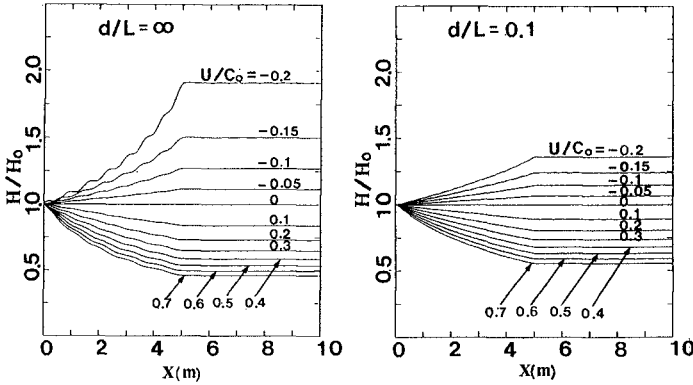


Fig. 4 Wave height change due to a current.

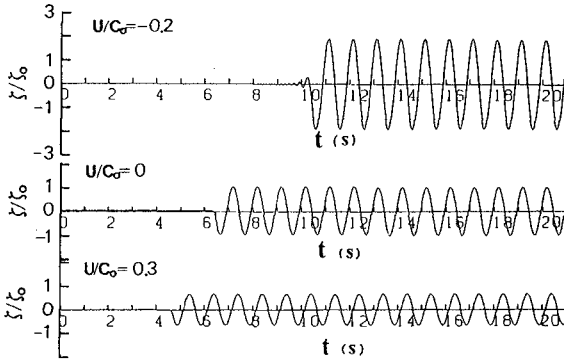


Fig. 5 Time history of the surface elevation at the boundary.

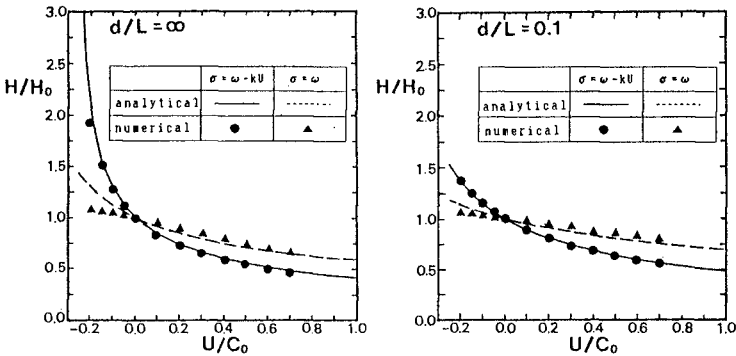


Fig. 6 Comparisons between numerical and analytical solutions of the wave height change due to a current.

The second case is for the wave refraction due to a current. The steady current is assumed to change in the x-direction only and waves are incident obliquely into the constant depth region as shown in Fig. 7. In this calculation, for the wave direction needed for solving the dispersion relation, the analytical solution given by Longuet-Higgins (1961) is adopted. The numerical solutions for the wave height and direction are compared with the analytical solutions in Fig. 8. Here the wave direction in the numerical calculation has been obtained from the principal direction of the flow rate vector. The numerical results agree well with the analytical solutions.

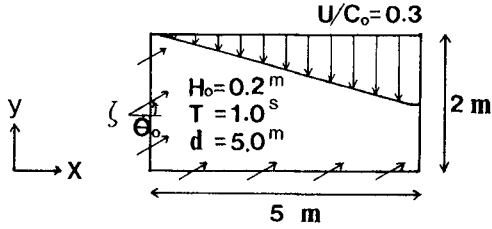


Fig. 7 Calculation condition for wave refraction due to a current.

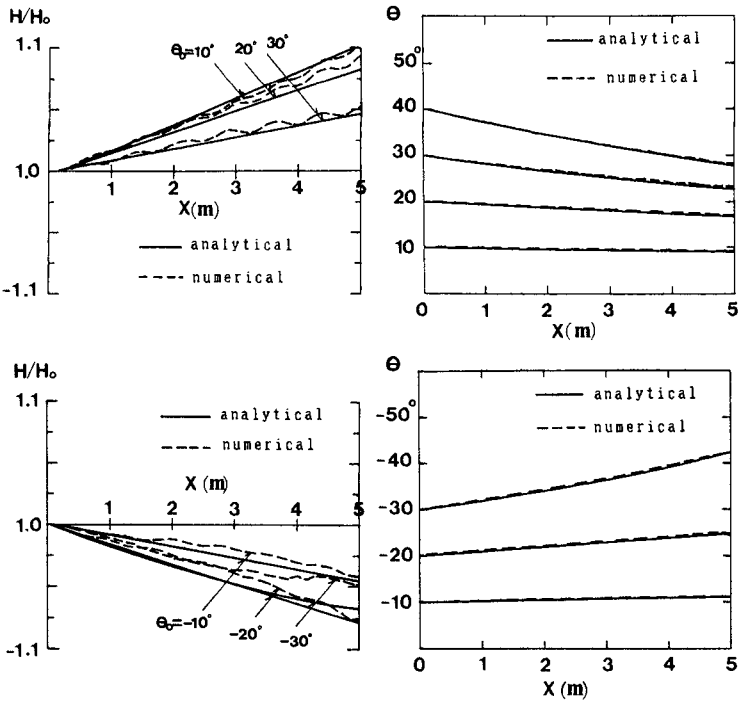


Fig. 8 Comparisons between numerical and analytical solutions of the wave height and direction.

5. DETERMINATION OF THE BREAKER LINE AND WAVES IN THE SURF ZONE

First we discuss the determination of the location of the breaker line which is very important to properly predict nearshore wave and current fields.

Goda (1970) has presented a breaker index diagram which is expressed in terms of the ratio of the depth at the breaking point h_b to the equivalent deepwater wave height H_0' as a function of the deepwater wave steepness H_0'/L_0 and the bottom slope s . This diagram can be used to evaluate the location of the breaking point of a single wave train. On the other hand, Watanabe *et al.* (1984) have proposed another breaker index diagram using the ratio of the amplitude of horizontal water particle velocity to the wave celerity at the breaking point, u_b / C_b , in order to extend to a composite wave field. This can be obtained from the Goda's breaker index diagram by converting the governing parameter from h_b / H_0' to u_b / C_b with a linear wave theory. It will be applicable even to a wave and current coexisting system when a moving coordinate relative to the current is adopted.

In order to examine the applicability of this breaker index, a series of laboratory experiments have been carried out on the breaking of waves on a current with the same or the adverse direction. Using the breaking depth h_b obtained from the experimental results, the horizontal water particle velocity amplitude u_b at the mean water level and the wave celerity C_b are calculated with a linear wave theory as

$$u_b = (H_b / 2) \sigma \cosh kh_b / \sinh kh_b \quad (22)$$

$$C_b = \sigma / k \quad (23)$$

where the wave number k and the angular frequency σ are calculated from the dispersion relation for a wave and current coexisting system as the values relative to the current. The breaker height H_b is calculated from the incident wave height H_i considering the bottom and side wall friction as

$$E_i(C_i + U_i) / \sigma_i = E_b(C_b + U_b) / \sigma_b - \Delta E / \omega \quad (24)$$

$$E = (1/8) \rho g H^2$$

where U is the mean velocity of the current, subscripts i and b denote quantities at the locations where the incident wave height and the breaking point are respectively given, and ΔE denotes the energy dissipation rate due to the bottom and side wall friction, which is calculated with the friction law from a wave and current coexisting system presented by Tanaka and Shuto (1981).

Using Eqs. (22) and (23), the ratio of the horizontal water particle

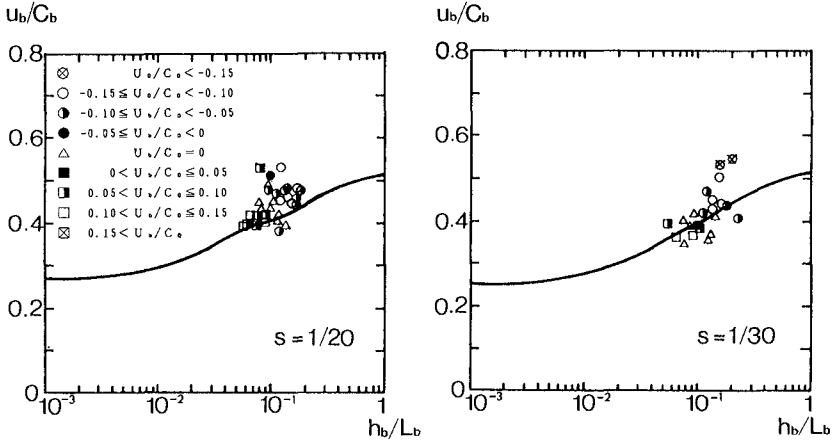


Fig. 9 Comparisons between the breaker index and experimental results for wave and current coexisting fields.

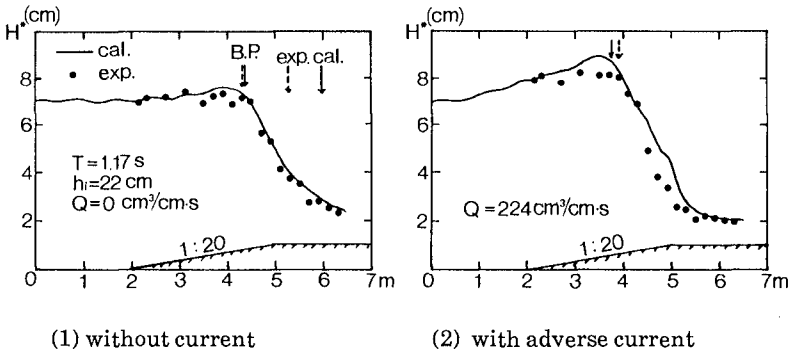


Fig. 10 Cross-shore distributions of the wave height.

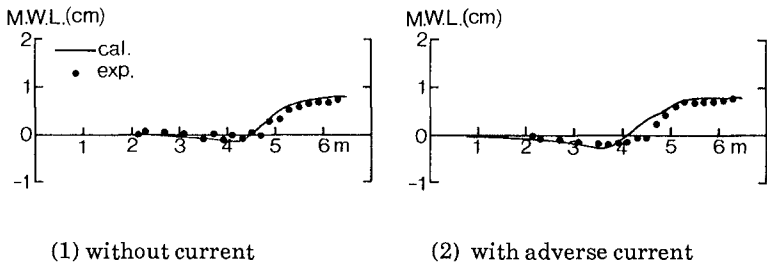


Fig. 11 Cross-shore distributions of the mean water level.

velocity to the wave celerity, u_b / C_b , is calculated. The relation between this ratio and the relative water depth at the breaking point, h_b / L_b , is compared with the breaker index proposed by Watanabe *et al.* (1984) in Fig. 9, where the bottom slope s is 1/20 and 1/30, respectively. Different symbols are used for the experimental results according to the ratio of the steady current velocity at the breaking point to the wave celerity at the deepwater. For the cases of a strong adverse direction current, the experimental results show larger values of u_b / C_b than the breaker index. This will be attributed to the acceleration of breaking, which is ignored in Eq. (24), due to the turbulence transported toward the offshore by the current. As a whole, the experimental results agree fairly well with the breaker index. Hence this breaker index is applicable with a sufficient accuracy to a wave and current coexisting field.

Using the time-dependent mild-slope equations proposed in this study together with the above breaker index, numerical computations have been conducted for the location of the breaking point and the deformation of waves coexisting with a current on a uniformly sloping beach. For the computation of wave decay in the surf zone, the dissipation term proposed by Watanabe *et al.* (1988) has been added to Eq. (11).

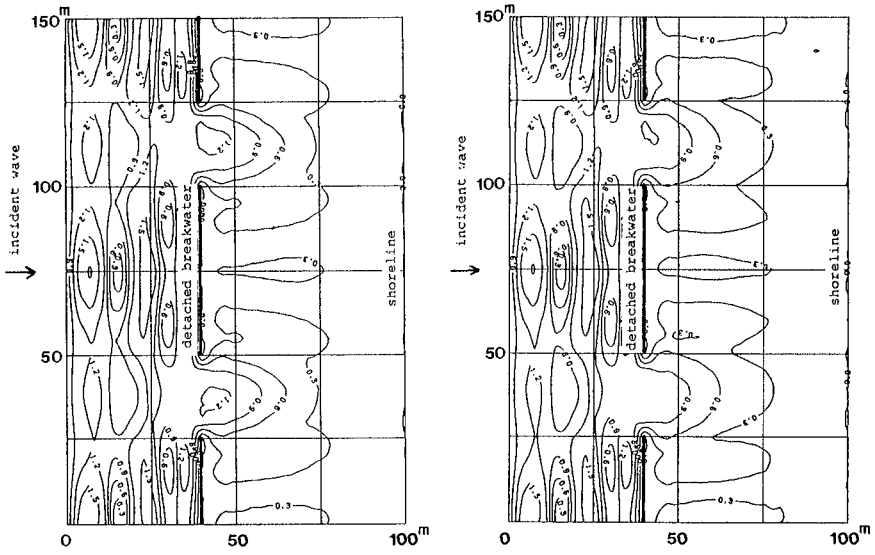
Figure 10 shows the comparisons of the computed and the experimental result of the wave height distributions. The left figure is for a case of no current, while the right figure is for an adverse current with the flow rate of 224 cm³/cm/s. The experimental values are represented by the wave heights calculated from the root mean square of the measured surface elevation as $H^* = 2 \sqrt{2} \eta_{rms}$. The computed and the measured locations of the breaking point (B.P.) shows a good agreement regardless of the presence of currents. The wave height distributions also show a good overall agreement between the computations and the model. A slight overestimation of the wave height for the case of an adverse current is caused owing to the ignorance of the turbulence transported into the offshore across the breaking point by the current.

The comparisons of the mean water level between the computations and the measurements are shown in Fig. 11. The computed values agree well with the experimental results.

6. EXAMPLES OF THE NUMERICAL COMPUTATION FOR A PLANAR TWO-DIMENSIONAL CASE

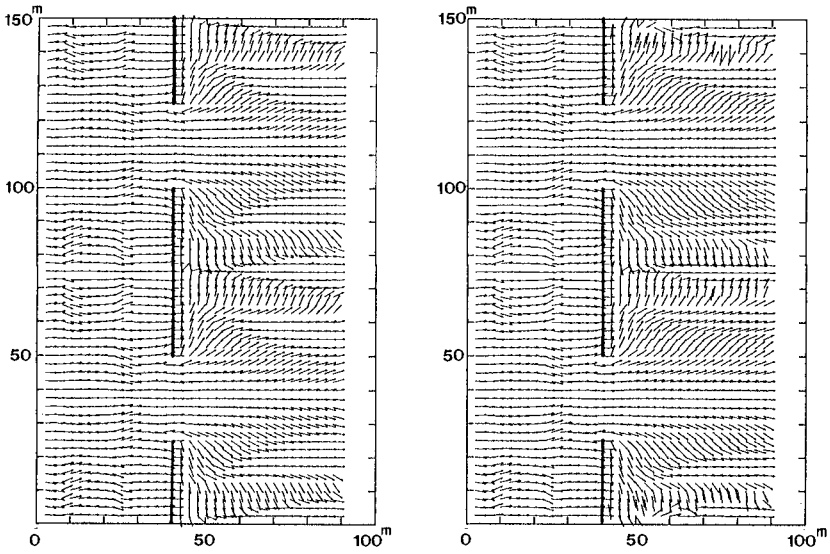
The present numerical model has been applied to computing a wave field around detached breakwaters on a sloping beach. The detached breakwaters are placed at a water depth of 3 m and the bottom slope is 1/20. Waves are incident normal to the detached breakwaters and the contour lines, and the incident wave height and period are 3.0 m and 5.7 s.

In this computation including wave decay due to breaking, the wave height should become 0 along the shoreline, and therefore the shoreline boundary condition is set as



(1) without wave current interaction (2) with wave current interaction

Fig. 12 Distributions of the wave height.



(1) without wave current interaction (2) with wave current interaction

Fig. 13 Distributions of the wave direction.

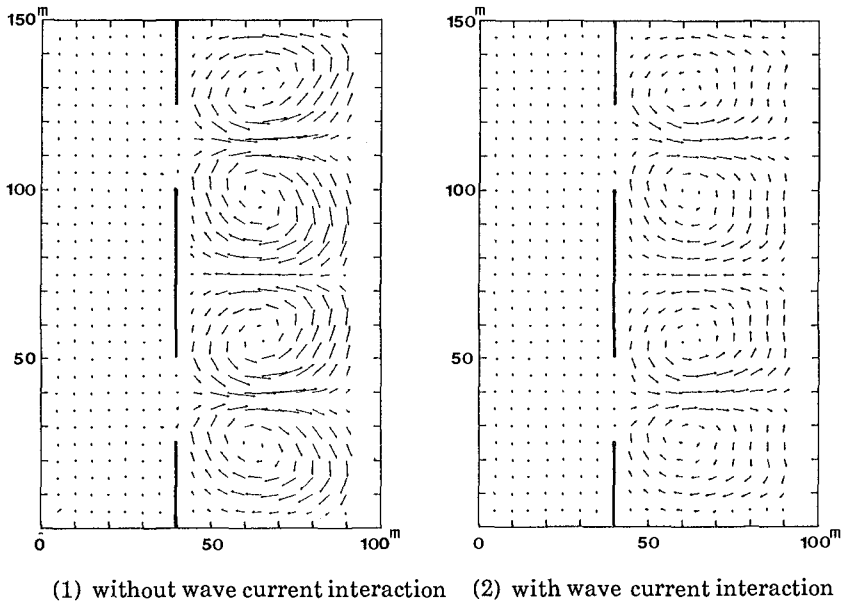


Fig. 14 Distributions of nearshore currents.

$$\zeta'(x_0, y_0) = 0 \quad (25)$$

Along the side boundaries, perfect reflection of waves and no-slip of mean currents are assumed.

Figure 12 shows distributions of the wave height with and without wave-current interaction: the figure on the left hand-side is the result without wave-current that with wave-current interaction. The change of the wave height can be observed when wave-current interaction is taken into consideration.

Distributions of the wave direction for both cases are shown in Fig. 13. Refraction due to the nearshore current is well observed near the shoreline.

Figure 14 show distributions of the nearshore current for both cases. Reduction of current can be observed when wave-current interaction is included.

7. CONCLUSIONS

A new set of time-dependent mild-slope equations has been derived for a wave and current coexisting field, and numerical computational method has been presented. Validity of this model has been demonstrated by comparisons of numerical results with analytical and experimental results. Then it has

been found that the breaker index expressed by the ratio of the water particle velocity to the wave celerity is applicable to a wave and current coexisting system. Finally this model has been applied to general two-dimensional wave and current fields and it has been found that wave-current interaction plays an important role in nearshore waves and currents.

REFERENCES

- 1) Berkhoff, J.C.W. (1972) : Computation of combined refraction-diffraction, Proc. 13th Coastal Eng. Conf. , ASCE, pp. 471-490.
- 2) Booij, N. (1981) : Gravity waves on water with non-uniform depth and current, Communications on Hydraulics, No. 81-1, Dept. of Civil Eng. , Delft Univ. of Tech. , p. 131
- 3) Goda, Y. (1970) : A synthesis of breaker indices, Proc. of the Japan Society of Civil Eng. , No. 180, pp. 39-49.
- 4) Kirby, J. T. (1984) : A note on linear surface wave-current interaction over slowly varying topography, J. Geophys. Res. , Vol. 89, No. C1, pp. 745-747.
- 5) Liu, P. L. F. (1983) : Wave-current interactions on slowly varying topography, J. Geophys. Res. , Vol. 88, No. C7, pp.4421-4426.
- 6) Longuet-Higgins, M. S. and R. W. Steward (1961) : The changes in amplitude of short gravity waves on steady non-uniform currents, J. fluid Mech. , Vol. 10, pp. 529-549.
- 7) Tanaka, M. and N. Shuto (1981) : Friction coefficient for a wave-current coexistent system. Coastal Eng. in Japan, Vol. 24, pp. 105-128.
- 8) Watanabe, A. , T. Hara and K. Horikawa (1984) : Study on breaking condition for compound wave trains, Coastal Eng. in Japan, Vol. 27, pp.71-82.
- 9) Watanabe, A. and K. Maruyama (1986) : Numerical modeling of nearshore wave field under combined refraction, diffraction and breaking, Coastal Eng. in Japan, Vol. 29, pp. 19-39.
- 10) Watanabe, A. and M. Dibajnia (1988) : A numerical model of wave deformation in surf zone, Proc. 21st Coastal Eng. Conf. , ASCE, (in print)

CHAPTER 28

THEORETICAL MODEL FOR NEARSHORE CIRCULATIONS

Mikio Sasaki * M. JSCE
Akira Ozaki ** M. JSCE
Hiroshi Saeki *** M. JSCE

Abstract

The dynamics of nearshore circulations is investigated using mass, momentum and energy conservation equations with bottom friction, lateral mixing and wave-current interaction. By means of introducing a perturbation expansion for the mean variables, the first-order solutions are found in the surf and offshore zones according to the boundary conditions at the coast.

It is found that: (1) The rip velocity attains a maximum value in the offshore region near the break point as Yr^* becomes larger. (2) The longshore velocities become higher in the surf zone and lower in the offshore region with increasing Yr^* . (3) The rip and longshore velocities in the surf zone become relatively smaller due to the effects of the bottom friction, and that the rip and longshore velocities in the surf zone become smaller due to the wave-current interaction.

1. INTRODUCTION

Nearshore currents play an important role in the transportation of sediments and sea water in nearshore areas, and so several theoretical studies with respect to nearshore circulations have been presented. However many researchers take only bottom friction into account to avoid the mathematical complexities resulting from the lateral mixing, then the results obtained theoretically suggests that the lateral mixing should be included in more detailed analysis. The turbulent viscosity as well as wave-current interaction is important in flow field of nearshore circulations. In order to consider nearshore circulations

* Associate Professor, Hachinohe Institute of
Technology, Myo, Hachinohe 031, Japan
** Professor, Hokkaido Institute of Technology,
Teine, Sapporo, Japan
*** Professor, Hokkaido University, Kita 8 Nishi 13,
Sapporo, Japan

at the actual condition, it is necessary to have more realistic model for the dynamics of rip current circulation. In present paper, theoretical model including the bottom friction, the wave-current interaction and the lateral mixing is proposed.

According to Ozaki, Sasaki and Usui(1977), an important parameter on the dynamics of rip currents caused by normally incident waves in the symmetrical cellular(Harris,1967) is the nondimensional rip spacing Yr^* , where $Yr^*=Yr/X_B$, Yr = the rip spacing, X_B =the width of the surf zone. When the value of Yr^* is small, rip current circulation is confined to a very small region near the shore, and as the value of Yr^* becomes larger, rip currents flow rapidly from the surf zone to a large region where extends several surf zone widths offshore, and the rip currents grow intenser and narrower. The wave number and wave energy density are affected by the currents like the free jet. The wave-current interaction in nearshore circulations is important for the dynamics of rip currents.

2. BASIC FORMULATION

The beach considered here is of linear plane shape alongshore and of uniform slope offshore; the water depth, h , in the absence of waves is given by $h=sx$, where x is a distance in offshore direction normal to the shore line and s is the bottom slope. The waves are normally incident and break at a uniform distance from the shoreline at $x=x_B$ the breaker line. The fluid motion of currents is steady. The motion of water is described by Eqs.(1) and (2) in terms of the mean surface elevation ζ and the vertically averaged horizontal velocity components u and v in offshore and longshore directions,

$$ud=-\partial F/\partial y \quad vd=\partial F/\partial x \quad d=h+\zeta \quad (1)$$

$$u_j \frac{\partial u_i}{\partial x_j} + \frac{1}{\rho d} \frac{\partial S_{ij}}{\partial x_j} + g \frac{\partial \zeta}{\partial x_i} + \frac{B_i}{\rho d} - \frac{1}{\rho} \frac{\partial}{\partial x_j} (T_{ij}) = 0 \quad (2)$$

where d =the total mean depth, F =the transport stream function, S_{ij} =the radiation stress, T_{ij} =the effective stress, including effects of non-uniform velocity distribution, B_i =the bottom shear stress, and ρ is the fluid density. The steady state conservation of wave energy equation is

$$\frac{\partial}{\partial x_j} [(u_j + C_j)E] + S_{ij} \frac{\partial u_i}{\partial x_j} = -D \quad (3)$$

where $C_j = -(gd)^{1/2} + u, v$ is the velocity of the waves, E =the wave energy density and D =an energy dissipation function.

The radiation stress S_{ij} , the bottom shear stress B_i and the lateral stress T_{ij} can be written as follows:

$$S_{xx} = \frac{3}{2}E \quad S_{yy} = \frac{1}{2}E \quad S_{xy} = S_{yx} = 0 \quad (4)$$

$$B_x = 2fu \quad B_y = fv \quad f = \rho C_f \bar{u} / \pi \quad (5)$$

$$\bar{u} = \frac{1}{2} \frac{H}{d} \sqrt{gd} (x \leq x_B), \frac{1}{2} \frac{H_B}{d_B} \sqrt{gd_B} (x \geq x_B)$$

$$\frac{1}{\rho} T_{ij} = \nu t \left(\frac{\partial u_i}{\partial x_j} + \frac{\partial v_j}{\partial x_i} \right) - \frac{2}{3} K \delta_{ij} \quad (6)$$

$$\nu t = \mu \frac{ET}{\rho d} (x \leq x_B), \quad \mu \frac{E_B T}{\rho d_B} (x > x_B)$$

where H = the wave height, H_B = the breaking wave height, d_B = the breaking depth, νt = the eddy viscosity, T = the wave period, $E_B = \rho g H_B^2 / 8$, μ = a coefficient (≈ 0.5) and K = the turbulent kinetic energy. We assume that K can be modelled as a function of the energy dissipation rate D/ρ using the breaking-waves approximation (Wind and Vreugdenhil (1986))

$$K = (D/\rho)^{2/3} \quad (7)$$

The dissipation term D plays an important role in the energy balance. We assume that

$$D = \sqrt{gd} u' u_w \quad |u'| \propto |u_w| \quad (8)$$

where u' and u_w are the turbulence and the wave orbital velocity. Then, using the shallow water long wave approximation, the energy dissipation D is given by

$$D = q \sqrt{gd} \frac{E}{d} \quad (9)$$

where q = the dissipation factor. In the absence of the currents q is found by substituting Eq. (9) into the surf zone energy equation:

$$q = \frac{5}{2} m \quad m = \partial d_0 / \partial x \quad d_0 = h + \zeta_0 \quad (10)$$

where ζ_0 represents the wave set-up in an equilibrium state.

Small perturbations are imposed on the steady state, and the variables are expressed as

$$\begin{aligned} E &= E_0(x) + \epsilon E_1(x, y) \\ \zeta &= \zeta_0(x) + \epsilon \zeta_1(x, y) \\ F &= \epsilon F_1(x, y) \end{aligned} \quad (11)$$

$$D = D_0(x) + \epsilon D_1(x, y)$$

where ϵ is a small ordering parameter.

3. FIRST-ORDER SOLUTIONS

The energy dissipation to the first order becomes, by using the relation shown in Eq.(9),

$$D_1 = q_1 \sqrt{gd} \frac{E_1}{d} \quad (12)$$

Then the dissipation factor q_1 can be written as

$$q_1 = \frac{5}{2} m \left(\frac{d}{d\beta} \right) \quad (x \leq x\beta) \quad , \quad \frac{5}{2} m \left(\frac{d\beta}{d} \right) \quad (x \geq x\beta) \quad (13)$$

where the first expression is modified partly from Eq.(10) due to the necessity of keeping the solution bounded at the shoreline, and the offshore expression corresponds to the expression in the surf zone.

In deriving Eqs.(12) and (13) we have assumed $\zeta_0 \ll d_0$. The radiation stress S_{ij} can be expressed as

$$S_{xx} = \frac{3}{2} (E_0 + \epsilon E_1) \quad S_{yy} = \frac{1}{2} (E_0 + \epsilon E_1) \quad (14)$$

Dimensionless variables are introduced as follows:

$$\begin{aligned} \xi &= \frac{d}{d\beta} = \frac{X}{X\beta} & X &= x + x\beta & d &= mX & \eta &= \frac{Y}{Yr} \\ \zeta_1^* &= \frac{\zeta_1}{d\beta} & E_0^* &= \frac{E_0}{E\beta} & E_1^* &= \frac{E_1}{E\beta} \\ F^* &= \frac{F}{(u_0 d\beta X\beta)} & u_0 &= \sqrt{gd\beta} & u^* &= \frac{u}{u_0} & v^* &= \frac{v}{v_0} \end{aligned} \quad (15)$$

Making nondimensional form of Eqs.(1)-(3) and then eliminating the nondimensional perturbation energy E_1^* from a equation obtained by taking the curl of Eq.(2), finally, we find that, for the nondimensional stream function F^* only,

$$L(F^*) = 0 \quad (16)$$

where the differential operator L is defined as

$$L = L_1 \left(\frac{\xi^{3/2}}{q^*} L_2 \right) - \frac{5}{2} \xi^2 L_2 - C_4 L_1 \left(\frac{L_3}{q^*} \right) \quad (17)$$

where

$$L_1 = \xi \frac{\partial}{\partial \xi} + \frac{1}{2}$$

$$\begin{aligned}
L_2 = & \left(\frac{\partial^2}{\partial \xi^2} - \frac{\partial^2}{\partial \eta^2} \right) \left(v^* \left(\frac{1}{\xi} \frac{\partial^2}{\partial \xi^2} - \frac{1}{\xi} \frac{\partial}{\partial \xi} - \frac{1}{\xi} \frac{\partial^2}{\partial \eta^2} \right) \right) \\
& + \frac{\partial}{\partial \xi} \left(2 v^* \left(2 \frac{1}{\xi} \frac{\partial}{\partial \xi} - \frac{1}{\xi^2} \right) \right) \frac{\partial^2}{\partial \eta^2} \\
& - C_5 \left(\frac{C^*}{\xi} \frac{\partial^2}{\partial \xi^2} + \frac{\partial}{\partial \xi} \left(\frac{C^*}{\xi} \right) \frac{\partial}{\partial \xi} + 2 \frac{C^*}{\xi} \frac{\partial^2}{\partial \eta^2} \right) \\
L_3 = & \left(2E^*_0 \frac{1}{\xi} \frac{\partial}{\partial \xi} - \frac{7}{2} E^*_0 \frac{1}{\xi^2} + 2 \frac{\partial E^*_0}{\partial \xi} \frac{1}{\xi} \right) \frac{\partial^2}{\partial \eta^2} \\
q^*_1 = & \xi^{1/2} \quad (\xi \leq 1), \quad \xi^{-3/2} \quad (\xi \geq 1) \\
E^*_0 = & \xi^2 \quad (\xi \leq 1), \quad \xi^{-1/2} \quad (\xi \geq 1) \\
C^* = & \xi^{-1/2} \quad (\xi \leq 1), \quad \xi^{-1} \quad (\xi \geq 1) \\
v^*_t = & \xi \quad (\xi \leq 1), \quad 1 \quad (\xi \geq 1) \\
C_4 = & (\mu T \sqrt{g/d_{13}})^{-1} \\
C_5 = & (4/\mu \pi \gamma^2) (C_f/m) (\ln T \sqrt{g/d_{13}})^{-1}
\end{aligned} \tag{18}$$

where C_4 and C_5 are the nondimensional parameter representing the relative importance of the interaction and the bottom friction, and γ is the ratio of the waveheight to the local mean depth in the surf zone.

Equation (16) is to be solved subject to the following boundary conditions:

$$u^* = v^* = F^* = 0 \quad \text{at} \quad \xi = 0 \tag{19}$$

$$u^* = v^* = F^* = 0 \quad \text{at} \quad \xi \rightarrow \infty \tag{20}$$

$$(u^*_i)_{in} = (u^*_i)_{off} \quad \text{at} \quad \xi = 1 \tag{21}$$

$$\left(\frac{\partial u^*_i}{\partial \xi} \right)_{in} = \left(\frac{\partial u^*_i}{\partial \xi} \right)_{off} \quad \text{at} \quad \xi = 1$$

We introduce a function given by

$$F^*(\xi, \eta) = \phi(\xi) \text{sink} \eta \tag{22}$$

where $k = 2\pi/Yr^*$, Yr^* is the nondimensional rip spacing. The solution in the surf zone to Eq.(16) is written as a series of power of :

$$\phi = \sum_{m=0}^{\infty} a_m \xi^{\rho + \frac{m}{2}} \quad (23)$$

The roots of the indicial equation are $\rho = 0, 2, 2, 5/2, 3$. The first, second and third roots are dropped through Eq.(19). Hence the solution bounded at the shoreline in the surf zone is found as

$$\phi^*(\xi) = A_{S1} X_1(\xi) + A_{S2} X_2(\xi) \quad (24)$$

where

$$X_1 = \sum_{m=0}^{\infty} a_m \xi^{\rho_1 + \frac{m}{2}} \quad (a_0 = 1, \rho_1 = 3)$$

$$X_2 = \sum_{m=0}^{\infty} \frac{\partial}{\partial \rho} (a_m \xi^{\rho + \frac{m}{2}}) \Big|_{\rho = \rho_2} \quad (a_0 = \rho - 5/2, \rho_2 = 5/2)$$

$$\sum_{i=0}^{10} f_i(\rho + \frac{m-i}{2}) a_{m-i} = 0$$

$$f_0(a) = a(a-2)^2(a-\frac{5}{2})(a-3)$$

$$f_1(a) = -C_5 a(a-2)(a-\frac{5}{2})$$

$$f_2(a) = -\frac{5}{2} a(a-2)^2(a-3)$$

$$f_3(a) = \frac{5}{2} C_5 a(a-\frac{5}{2}) \quad (25)$$

$$f_4(a) = -2k^2 \{ a(a-1)^2 + \frac{3}{4} a - \frac{1}{2} \}$$

$$f_5(a) = k^2 a \{ 2C_4(a + \frac{1}{4}) + 2C_5 \}$$

$$f_6(a) = \frac{5}{2} k^2 (2a^2 - 3a + 2)$$

$$f_7(a) = -5C_5 k^2$$

$$f_8(a) = k^4(a + \frac{3}{2}) \quad f_9(a) = 0 \quad f_{10}(a) = -\frac{5}{2} k^4$$

where A_{S1} and A_{S2} are constants of integration.

In the deep-water region, we can consider the case of water of infinite depth, i.e. $\xi = \infty$. Hence the operator L given by Eq.(17) is rewritten as

$$L = \xi^4 \left(\frac{\partial}{\partial \xi} \left(\frac{\partial^2}{\partial \xi^2} + \frac{\partial^2}{\partial \eta^2} \right) \right) \left(\frac{\partial^2}{\partial \xi^2} + \frac{\partial^2}{\partial \eta^2} \right) \quad (26)$$

Using the general solution of Eq.(26), the approximate solution to Eq.(16) in the offshore region is found according to the boundary condition Eq.(20) as

$$\phi(\xi) = A_{01} e^{-k\xi} + A_{02} \xi e^{-k\xi} \quad (27)$$

where A_{01} and A_{02} are a constants of integration.

The fluid motion of the currents must be continuous at the breaker line as shown in Eq.(21). However three constants of the four constants, A_{S1} , A_{S2} , A_{01} and A_{02} , are determined through the matching condition, then, we introduce normalized velocities as follows:

$$U^* = \frac{u^*(\xi, \eta)}{u_1^*} \quad V^* = \frac{v^*(\xi, \eta)}{u_1^*} \quad (28)$$

where

$$u_1^* = u^*(\xi, \eta) \Big|_{\xi=1, \eta=0} \quad (29)$$

4. DISCUSSION

The normalized rip and longshore velocities, U^* and V^* , are shown in Figure 1. The Figure 1(a) suggests that the rip velocity attains a maximum value in the offshore region near the break point as Yr^* becomes larger. This results are in good agreement with laboratory experiments of Ozaki et al(1977) and Sasaki(1985). Figure 1(b) shows that the longshore velocities become higher in the surf zone and lower in the offshore region with increasing Yr^* . It is also found that the derivative of the longshore velocity is continuous at the breaker line. The solutions in the surf and offshore regions, Eqs.(24) and (27), are adequate in each zone including the neighbourhood of the break point.

Figure 2 shows the normalized rip and longshore velocities in case of $Yr^*=4$ and $C_4=1$ with respect to $C_5=0$ and 2. C_5 denotes the ratio of the bottom friction term to the lateral mixing term, and it means the relative effects of the bottom friction. Then, as shown in Figure 2, the rip and longshore velocities in the surf zone become relatively smaller due to the effects of the bottom friction.

Figure 3 shows the profiles of the normalized rip and longshore velocities in case of $Yr^*=4$ and $C_5=1.0$ with respect to $C_4=0.5, 1.0$ and 2.0. As above mentioned, C_4 means the effects of energy coupling between currents waves. Then, the figure demonstrates that the rip and longshore velocities in the surf zone become smaller due to the wave-current interaction.

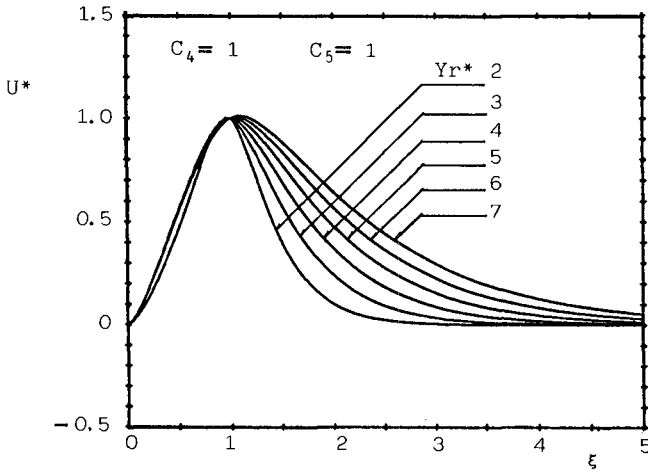


Fig.1(a) The normalized rip velocity U^* .

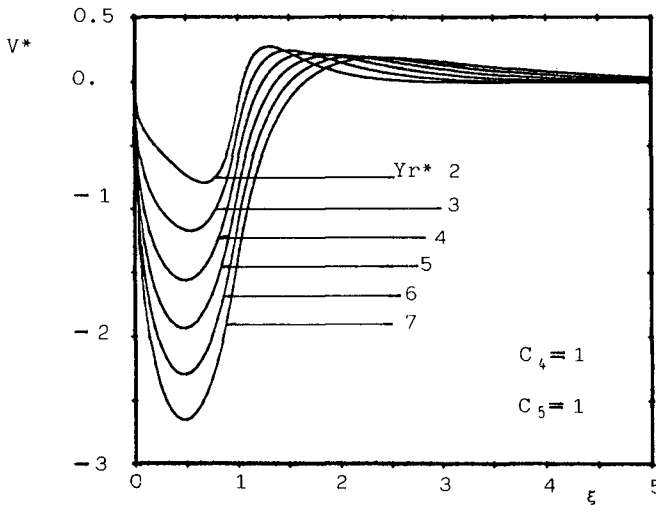


Fig.1(b) The normalized longshore velocity V^* .

Figure 1 Profiles of the normalized rip and longshore velocities, U^* and V^* .

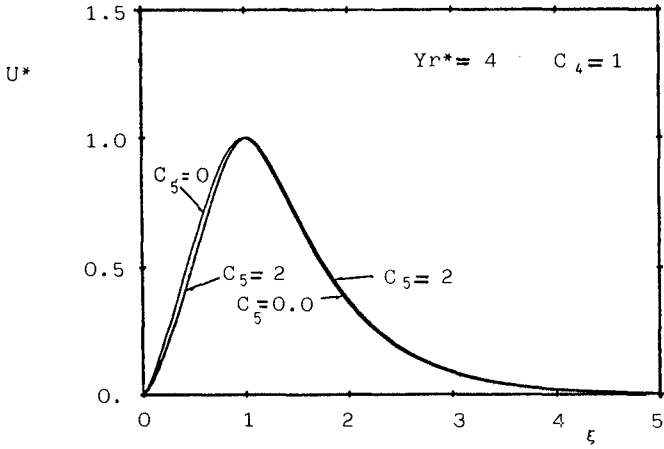


Fig.2(a) The normalized rip velocity with/without the effect of the bottom friction.

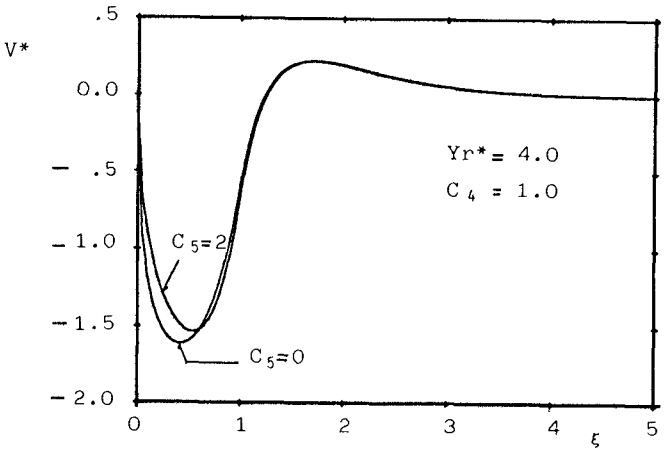


Fig.2(b) The normalized longshore velocity with/without the bottom friction.

Figure 2 Profiles of the normalized velocity for typical two conditions of the bottom friction.

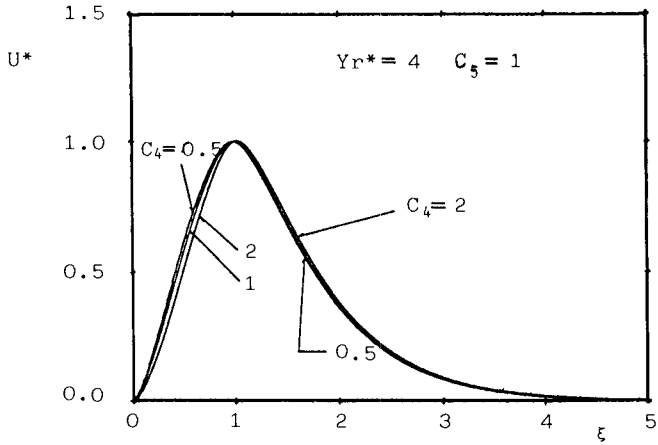


Fig.3(a) The normalized rip velocity.

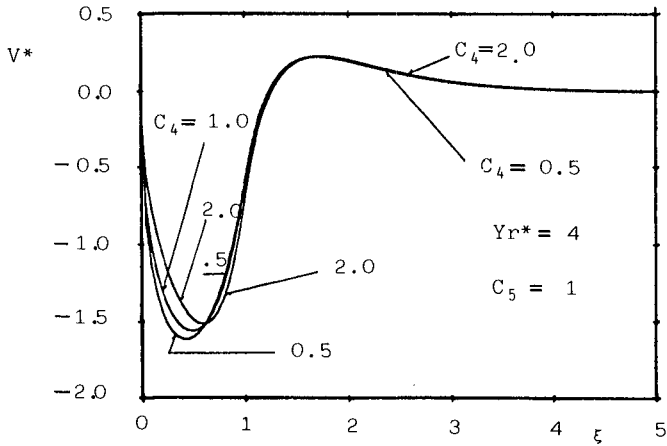


Fig.3(b) The normalized longshore velocity.

Figure 3 Profiles of the normalized velocity for various conditions of the wave-current interaction.

5. CONCLUSIONS

We have extended the theory of rip currents to include the bottom friction, the wave-current interaction and the lateral mixing. By means of introducing a perturbation expansion for the mean variables, the first-order solutions are found in the surf and offshore zones according to the boundary conditions at the coast. In present model the continuity at the breaker line in the derivative of the longshore velocity keeps for the first time. The several results in this investigation conform with results of observations reported by Ozaki et al(1977) and Sasaki(1985).

REFERENCES

- 1) Bowen, A.J., Rip currents, J. Geophy. Res., Vol.78, No.12, pp.1937-1943, 1969
- 2) Dalrymple, R.A., and Lozano, C.J., Wave-current interaction models for rip currents, J. Geophy. Res., Vol.83, No.C12, pp. 6063-6071, 1978
- 3) Iwata, N., Rip current spacing, J. Oceanogr. Soc. Jap., Vol.32, pp.1-10, 1976
- 4) LeBlond, P.H., and C.L. Tang, On energy coupling between waves and rip currents, J. Geophy. Res., Vol.79, pp.No.6, pp. 811-816, 1974
- 5) Ozaki, A., Sasaki, M. and Usui, Y., Study on rip currents, Coastal Eng. in Japan, Vol.20, pp.147-158, 1977
- 6) Sasaki, M., Velocity profiles in nearshore circulation current, Coastal Eng. in Japan, Vol.28, pp.125-136, 1985
- 7) Wind, H.G. and C.B. Vreugdenhil, Rip-current generation near structures, J. Fluid Mech., Vol.171, pp.459-476, 1986

CHAPTER 29

THE MEASURED PROPERTIES OF IRREGULAR WAVE BREAKING AND WAVE HEIGHT CHANGE AFTER BREAKING ON THE SLOPE

by Akira Seyama* and Akira Kimura**

ABSTRACT

Wave height change of the zero-down-cross waves on uniform slopes were examined experimentally. The properties of shoaling, breaking and decay after breaking for a total of about 4,000 irregular waves of the Pierson-Moskowitz type on 4 different slopes (1/10, 1/20, 1/30 and 1/50) were investigated. The shoaling property of the zero-down-cross waves can be approximated by the linear wave theory. However, the properties of breaking and decay after breaking differ considerably from those for periodic waves. The wave height water depth ratio (H/d) at the breaking point for the zero-down-cross waves is about 30% smaller than that for periodic waves on average despite the slopes. Wave height decay after breaking also differs from that for periodic waves and can be classified into three regions, i.e. shoaling, plunging and bore regions. Experimental equations for the breaking condition and wave height change after breaking are proposed in the study. A new definition of water depth for the zero-crossing wave analysis which can reduce the fluctuation in the plotted data is also proposed.

1. INTRODUCTION

Several models for irregular wave propagation in a surf zone have already been proposed by researchers such as Collins(1970), Battjes(1972), Kuo and Kuo(1972) and Goda(1975a). However, these models attempt to build a theory combining the theoretical or experimental properties of periodic waves i.e. breaking condition, energy dissipation, wave set-up and -down, etc. There have been few models which apply only the properties of the zero-(down or up)-crossing waves to complete the theory. There is a group of researchers, on the other hand, who have studied about the dynamic properties of irregular waves determined by the wave by wave method. The present author(1977), Isobe et al.(1980) and Sawaragi et al. (1980), for example, have examined experimentally the breaking properties of zero-crossing waves and showed that the averaged breaking wave height water depth ratio for zero-crossing irregular waves is smaller than that for periodic wave. This study also attempts to investigate the dynamic properties of zero-crossing irregular waves, especially their shoaling, breaking and decay after breaking, and tries to establish experimental equations for these properties.

* Prof. and ** Associate Prof. Tottori Univ., Koyama, Tottori, Japan

2. EXPERIMENTS

The wave tank used was a 29m long, 0.5m wide and 0.75m deep glass sided tank. At one end of this wave tank, a hydro-electric type irregular wave generator was set up (Kimura et al., 1987). At the other end, a uniform slope was installed. The slopes investigated were 1/10, 1/20, 1/30 and 1/50. The wave profile was measured by wave gauges installed with an equal interval on the slope, and also taken by two video cameras from the side of the wave tank. The data recorder and the video-cameras were synchronized using a clock unit. The spectra of the irregular waves were of the Pierson-Moskowitz type with different peak frequencies from $f_p=0.7\text{Hz}$ to 1.0 Hz . The experiments for breaking, shoaling and decay after breaking were carried out separately. Individual measurements were carried out for about 1 hour. The wave profiles recorded by the wave gauges were discretized and stored in floppy discs. The records taken by the video cameras were read off using a function of the super-impose unit in a micro-computer system and stored also in floppy discs. Throughout this study, wave height was determined by the zero-down-cross method for the wave profile in the time domain.

3. BREAKING

The picture taken by the video-camera and the coordinates were super-imposed on the CRT(Cathode-Ray-Tube) of the micro-computer. Reading the video-tape frame by frame the vertical line is drawn on the CRT at the breaking point of the wave which broke within the sights of the video-cameras. Moving the video-tape back and forth, the times when the wave profile crossed the still water level at the vertical line and the maximum and minimum water levels within the zero-down-cross intervals at this line were read off on the CRT. The wave height and period can be, therefore, determined as if there were a wave gauge just at the breaking point. For further investigations, the zero-up-cross wave definition method was also applied for the same wave. The definition of breaking applied in this study was that of Stokes' i.e. the instance when a water particle start to come out from its crest. Sometimes temporal white forms were observed around wave crests which were left behind the wave movement. Those were not considered to be breaking in this study.

Table-1 Experimental conditions

Case	Slope	f_p (Hz)	$H_{1/3}$ (cm)	$T_{1/3}$ (s)	Data Total
1	1/10	0.7,0.9	8.2,8.0	1.33,1.01	800
2	1/20	0.7,1.0	8.2,7.9	1.33,0.95	1010
3	1/30	0.8	7.5	1.11	1004
4	1/50	0.8	7.5	1.11	1007

Table-1 shows the slope, peak frequency, significant wave height and period, and total number of waves investigated. Figure 1 shows the energy spectra of the wave profiles measured at the horizontal part ($h=45\text{cm}$) of the wave tank ($f_p=0.7\text{Hz}$ and 0.9Hz ; $\tan\theta=1/10$). Since the saw shape pattern on the spectrum, which is inherent when reflected and incident waves are composed, is not prominent, the reflection coefficient of the slope may be negligibly small.

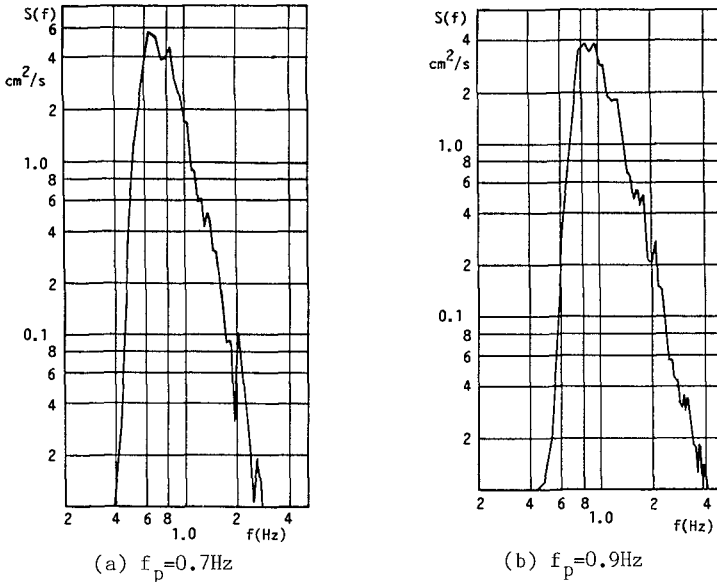


Fig.1 Power spectra

Figures 2 (a), (b), (c) and (d) show the relation between the relative wave height (H_b/h_b) and relative water depth (h_b/L_0) at the breaking point, in which H_b and h_b are wave height and water depth at the breaking point respectively and L_0 is the deep water wave length. The solid lines in individual figures show the breaking condition for the periodic waves (Goda,1970). The fluctuation of the plotted data in individual figure is considerably large, especially in figure (a). The major reason for the large fluctuations may exist in the insufficient definition of irregular wave properties in the analysis. Several researchers have investigated the effects of additional wave parameters. Herbers (1984), Sawaragi et al.(1980) and Isobe et al.(1980), for example, examined the effect of local wave profile or irregularity of the former and latter waves. The present authors also investigated these effects (some are very difficult in practical application), but no significant property which can reduce the fluctuation has been detected. Therefore, no more wave properties other than those determined by the ordinary zero-down-cross method are applied in this study except for the newly introduced definition for water depth.

3.1 A new definition of water depth

Figure 3 shows applications of the zero-down-cross method for two different waves. If the wave height H and period T for these two waves are the same, and if no additional property such as wave crest height, for example, is used, these waves are considered to be the same in the ordinary definition. In this study, to distinguish the difference between these waves without any additional properties to those used in Fig.2, water depth is determined as,

$$d = h + (a_c - a_t) / 2 \tag{1}$$

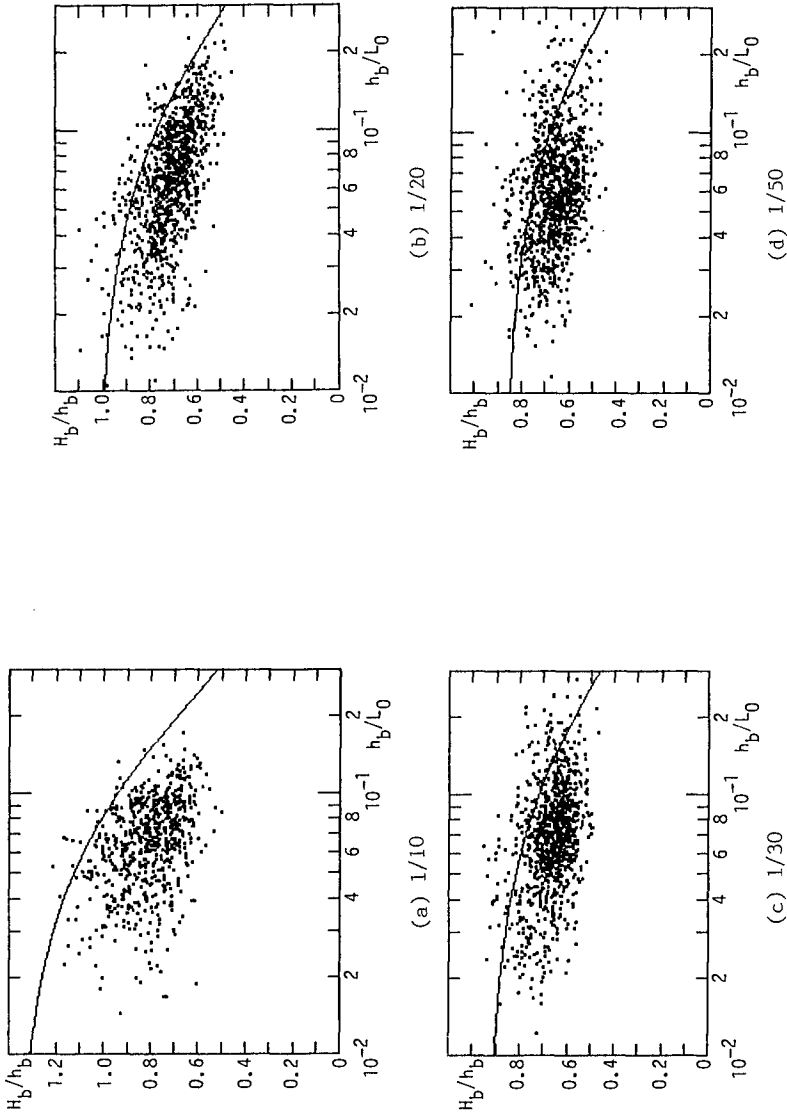


Fig.2 $H_b/h_b \sim h_b/L_0$ (ordinary definition for the water depth)

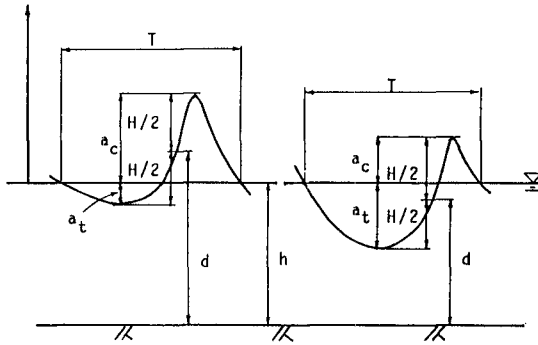


Fig.3 Definition of water depth d and h

in which a_c and a_t are the zero-crossing crest height and trough excursion (positive) respectively.

The data used in Fig.2 are reanalysed using the new definition of water depth in Fig.4. Considerable reductions in scattering are achieved for all cases. The reductions are prominent when the slope is mild. The solid lines in the figures are the experimental equations proposed in this study.

3.2 The breaking condition for irregular waves

Two types of breaking conditions for periodic waves have been proposed, which apply (1) the critical wave steepness and (2) the critical wave height water depth ratio respectively. Since the present experiments were carried out in the region $d_b/L_0 > 0.01$, the formulation following the former condition (1) was applied in this study. Following Goda's formulation for periodic waves (1970), we assume the breaking condition in the form,

$$H_b/d_b = A \{ 1 - \exp [-B \pi (d_b/L_0)(1+15 \tan^4 \theta)] \} (L_0/d_b) + C \quad (2)$$

in which θ is an angle of slope, and $A=1.7$, $B=1.5$ and $C=0$. In Goda's equation water depth is measured from the bottom to the still water level. Applying the least square method for the data in Fig.4, optimum values for A, B and C were calculated as follows.

$$H_b/d_b = 0.16 \{ 1 - \exp [-0.8 \pi (d_b/L_0)(1+15 \tan^4 \theta)] \} (L_0/d_b) - 0.96 \tan \theta + 0.2 \quad (3)$$

The solid lines in Fig 5 (and in Fig.4) show the experimental equations (eq.3) and the broken lines are Goda's breaking condition for periodic waves. Since the difference between the equations for the 1/30 and 1/50 slopes is very small and the equation for the 1/50 slope agrees well with the measurement on the 1/60 slope by Kuo and Kuo (1972) ($H_b/h_b=0.63$), the equation for 1/50 may be applicable for further mild slopes as in the case for periodic waves (Goda,1970).

The above equations were introduced using experimental data in the range $0.01 < d_b/L_0 < 0.3$, the application of these equations may be restricted to waves within the above range.

The breaking types were also investigated. However, no recognized

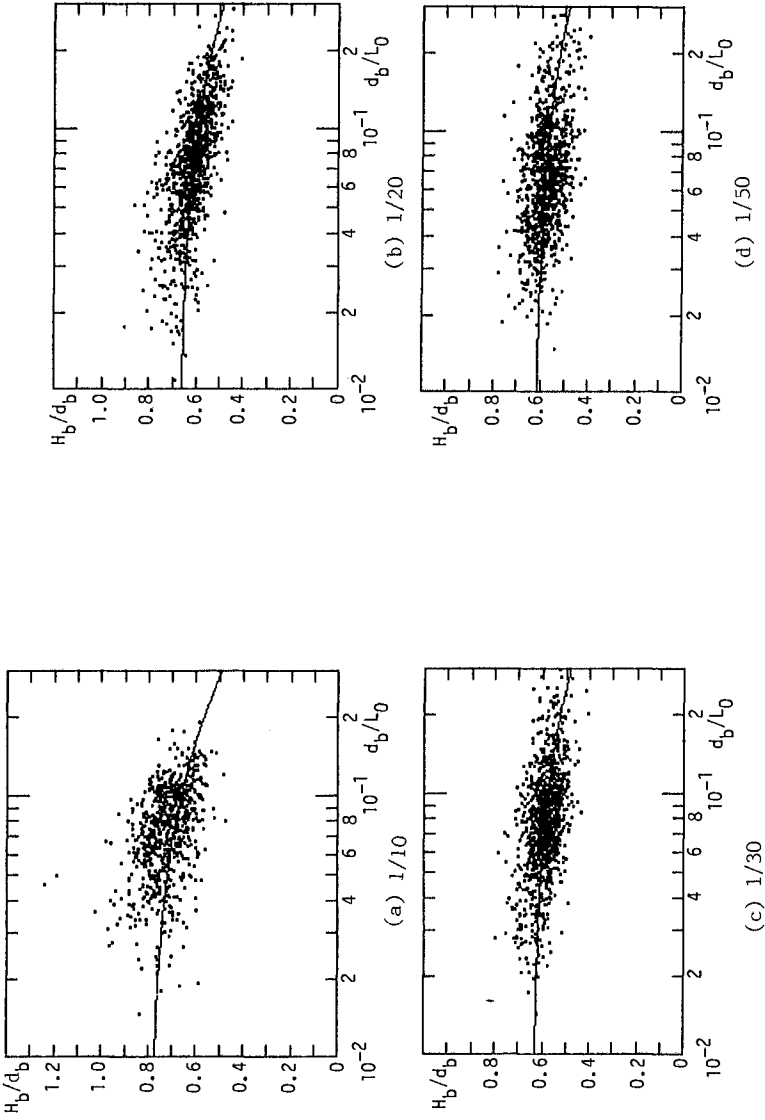


Fig.4 $H_b/d_b \sim d_b/L_0$ (new definition for the water depth)

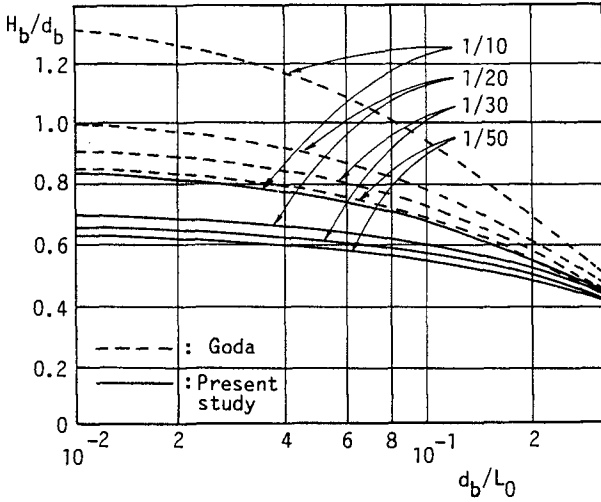


Fig.5 Experimental equations (eq.3; solid lines)

property was found other than the property that the portion of plunging breaker increases with an increasing angle of the slope. The clarifications with other factors such as the surf-similarity parameter were not successful.

4. WAVE SHOALING

The measurement system applied was almost the same as that explained in the former section. Wave gauges were shifted to the offshore-side on the slope. The breaking point of waves were read off, at first, from the pictures recorded in the video-tapes. The corresponding zero-down-cross wave heights and periods at the wave gauge points were calculated from the wave profiles stored in the floppy discs. The figures in Fig.6 show the relation between the measured wave height and relative water depth d/L_0 on the slope of (a) 1/10, (b) 1/20, (c) 1/30 and (d) 1/50 respectively, in which H_0' and L_0 are wave height and period in deep water conditions, which were calculated substituting the wave height and period, measured by the most off-shore side wave gauge, in the small amplitude wave theory. In individual figures, data of about 1000 waves are plotted. The solid lines are the shoaling coefficient K_s of the small amplitude wave theory. Since the scatterings in the data are considerably large, the averaged relations of the above properties were compared with the theory. The figures in Fig.7 show the averaged relation between H/H_0' and d/L_0 . The circles are the averages of about 100, which distribute around them, and plotted individual mean positions. The vertical line attached to each circle shows the range of its standard deviation. The top figure (a) is for the data of $0.015 < H_0'/L_0 < 0.025$. The solid line shows the shoaling coefficient of the linear wave theory and the chain line also shows the coefficient of Shuto's theory (1974) which is introduced on the basis of the K-dV equation. The dotted line is the breaking condition for irregular waves newly proposed in section 3. The breaking condition for the 1/30 slope is representatively shown in the figure. Other breaking conditions for different slopes are very close to this line. The middle (b) and bottom

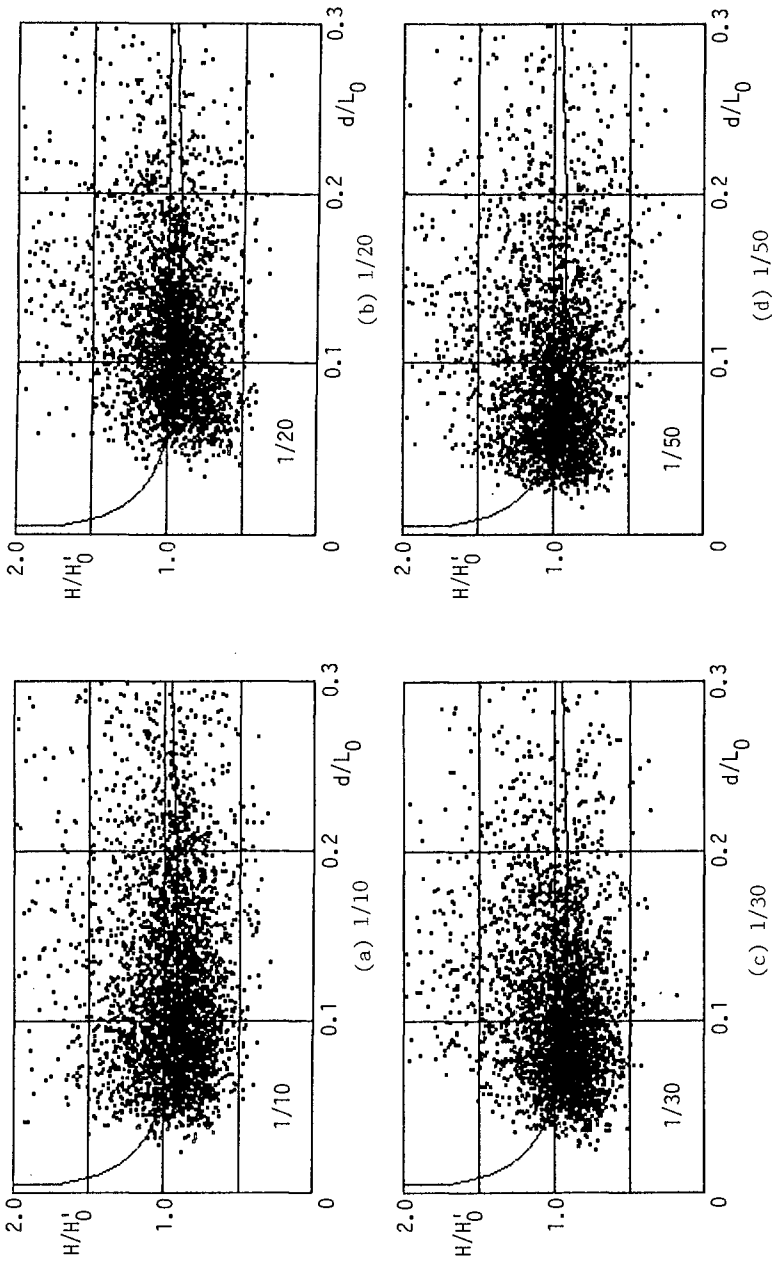


Fig. 6 $H/H_0' \sim d/L_0$

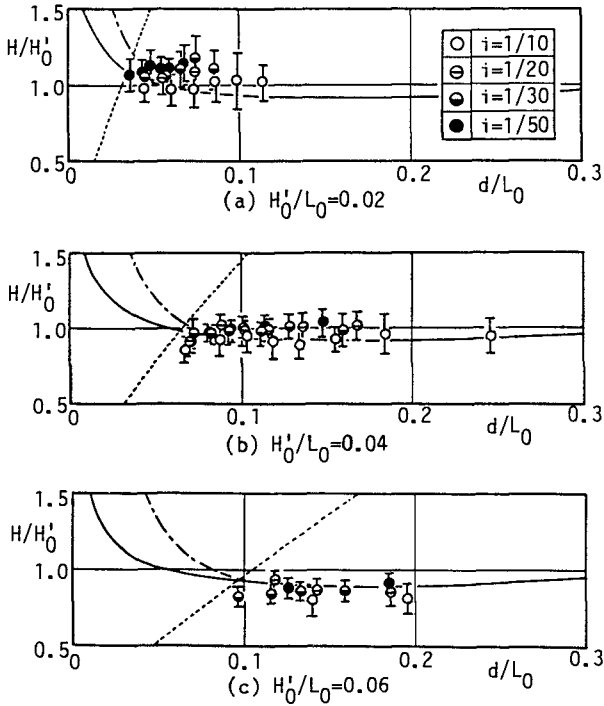
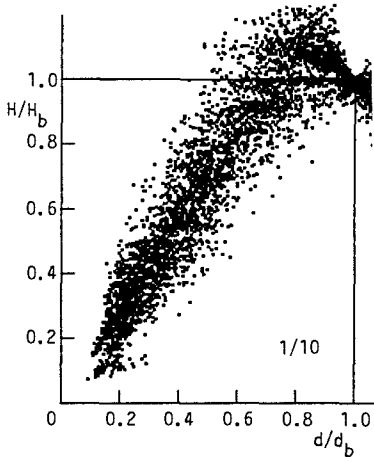
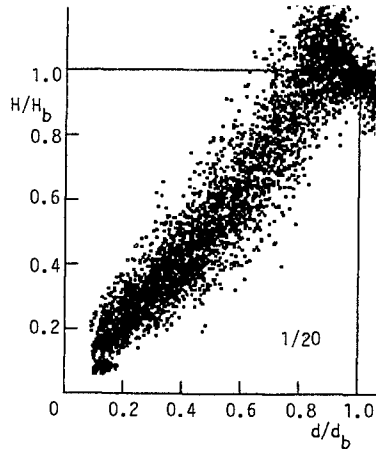


Fig.7 Averaged relations between H/H_0' and d/L_0

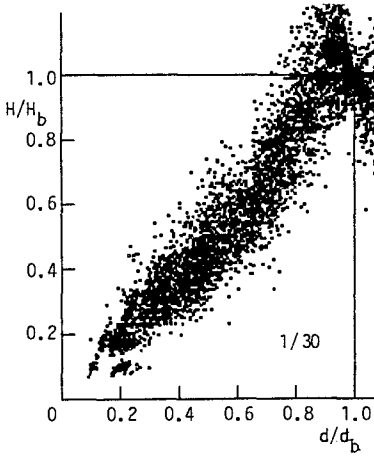
(c) figures are for the data of $0.035 < H_0'/L_0 < 0.045$ and $0.055 < H_0'/L_0 < 0.065$ respectively. The dotted lines are also the new breaking conditions for the slope of 1/30. No averaged data is plotted left of the dotted lines despite the slopes and H_0'/L_0 . For all slopes, a decreasing nature of plotted data with increasing wave steepness is observed. Furthermore data on the mild slope are slightly larger than those on the steep slope, especially in figure (a). However, the differences between the data and the theory are small (about 10% of the linear wave theory at most). Wave steepness may give a small effect on K_s . Especially, in the case of middle figure (b) ($H_0'/L_0 = 0.04$), in which the major portion of the data is included in this study, agreement between data and the theory is good despite the slope. The nonlinearity in the wave height change is compared with Shuto's theory in this study. His theory branches from the linear wave theory at Urcell number 30. The nonlinearity in the wave shoaling becomes, therefore, prominent from this point. However, the branch point and the intersections between the new breaking condition and solid and chain lines are very close to each other. This means that irregular waves break and start to decay before the difference between the linear and non-linear wave theories becomes prominent. For the waves with small steepness, however, the interval between the branch point and intersections becomes wider. For example, the distance is wider in figure (a) than in (c). However, the steepness of a significant wave in a fully developed sea condition distributes around 0.03 (Goda, 1975b). Thus, we may conclude that the shoaling property of the zero-down-



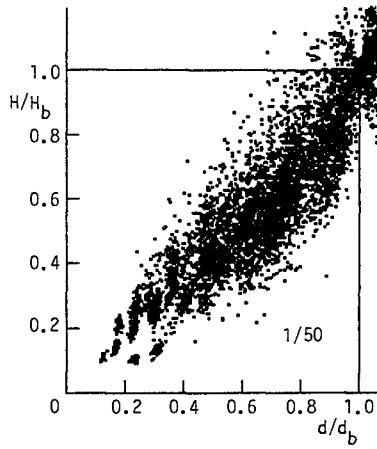
(a) 1/10



(b) 1/20



(c) 1/30



(d) 1/50

Fig.8 Wave height change after breaking

cross waves can be approximated by the linear wave theory as far as the present definition of wave breaking is applied and where the sea condition is a fully developed one. However, for waves with a smaller steepness than $H_0'/L_0=0.01$ the non-linear property in the shoaling may not be neglected in a very small region of d/L_0 . New investigations on the wave shoaling for zero-down-cross waves may be necessary.

5. WAVE HEIGHT DECAY AFTER BREAKING

The same measurement system as used in the former sections was applied in the experiments, although the whole system was shifted onto the shore side on the slope. The breaking points, at first, were read off from the picture recorded in the video-tape. The corresponding zero-down-cross wave heights and periods at the wave gauge points were also read off from the wave profiles stored in the floppy discs. The figures in Fig.8 show the wave height after breaking on the slope of (a) 1/10, (b) 1/20 (c) 1/30 and (d) 1/50, in which H_b and d_b are the wave height and water depth at the breaking point. Measured wave height decay of about 1000 are plotted in individual figures. The new definition of water depth also had a significant effect in reducing the scattering of the plotted data. To examine the mean tendency in detail, the data of every 0.1 interval of d/d_b were averaged and plotted in their mean position. Figure 9 shows the averaged relation between H/H_b and d/d_b on the slope of 1/30. The plotted data increase even after the breaking point. This is mainly due to the definition applied in this study since no practical energy dissipation takes place and wave height keeps increasing nature until it reaches the plunging point. There have been many studies which have adopted the maximum wave height to be the breaking wave height. However, this definition is difficult for practical measurements and the wave property at this point has not been clarified yet.

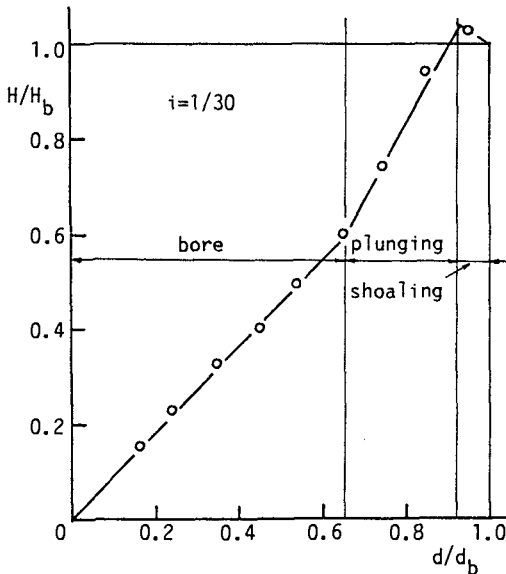


Fig.9 Averaged relation between H/H_b and d/d_b (1/30)

After reaching its maximum, the wave height starts to decay. The mean relations between H/H_b and d/d_b shore-side from this point are not uniform but have bends in all cases at around $d/d_b < 0.6$. Around the bend, the appearance of stable bores were observed in the experiments. Therefore, the process after breaking is divided into three different regions in this study. They are the shoaling region (from the breaking point to the point of maximum wave height), the plunging region (from the point of maximum wave height to the bend) and the bore region (from the bend to the shore). Although, the shoaling region reduces with decreasing slope angle, the data lies on straight lines approximately in individual regions despite the slopes. The wave height changes in these regions are approximated by straight lines in this study. Figures 10 (a) 1/10 and (b) 1/30 show the approximated regression lines for different wave steepnesses classified in the figure. Wave steepness brings a difference in the regression lines. This property is prominent in figure (a), but reduces in (b) considerably and becomes negligibly small in the case of 1/50 (although the figure is not shown in here). As explained in section 4, zero-down-cross wave steepnesses distribute around 0.03 when the sea condition is a fully developed one. In the region between $H_0'/L_0 = 0.01$ and 0.06, the difference in wave height change with respect to the steepness is small even in the case of 1/10. Therefore we may conclude that the effect of wave steepness on the wave height change after breaking is small if the sea condition is a fully developed one. Figure 11 shows the regression lines and averaged data for all cases. The regression lines are given by the equation,

$$H/H_b = A (d/d_b) + B \quad (4)$$

in which A and B are the constants given as follows in individual regions. (Subscripts S,P and B show that the values are for the shoaling, plunging and bore regions respectively.)

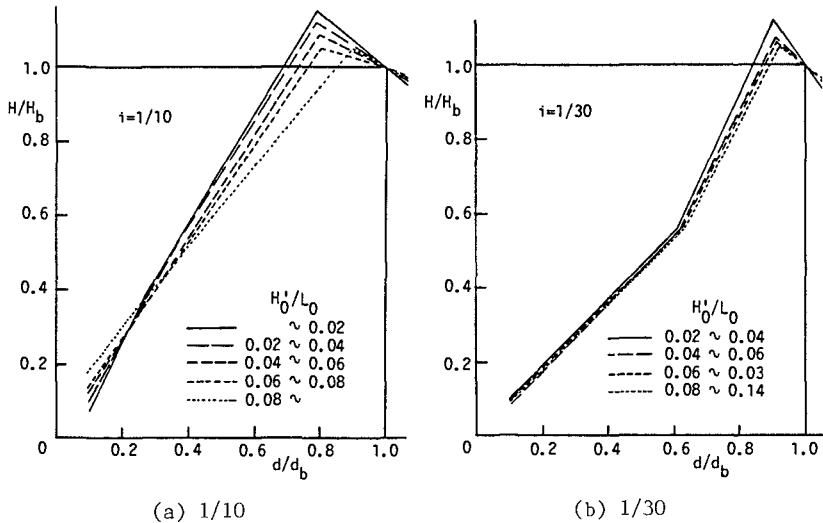


Fig.10 Effect of the wave steepness

Shoaling region:

$$A_S = -0.01 \tan \theta - 0.37$$

$$B_S = 1.0 - A_S \tag{5}$$

Plunging region: ($(H/H_b)_{\text{bore}}$, $(d/d_b)_{\text{bore}}$; see eq.(9))

$$A_P = 1.65 \exp(-2.3 \tan \theta)$$

$$B_P = (H/H_b)_{\text{bore}} - A_P (d/d_b)_{\text{bore}} \tag{6}$$

Bore region:

$$A_B = 0.72 \exp(6.11 \tan \theta)$$

$$B_B = 0.02 \tag{7}$$

The water depth and the wave height at the boundary between the shoaling and plunging regions (waves reach their maximum around this point) are given by

$$(d/d_b)_{\text{peak}} = (B_P - B_S) / (A_S - A_P)$$

$$(H/H_b)_{\text{peak}} = (A_P B_S - A_S B_P) / (A_P - A_S) \tag{8}$$

The water depth and wave height at the bend (the bore appears around this point) are given by

$$(H/H_b)_{\text{bore}} = 0.67 \exp(-3.1 \tan \theta)$$

$$(d/d_b)_{\text{bore}} = \{ (H/H_b)_{\text{bore}} - B_B \} / A_B \tag{9}$$

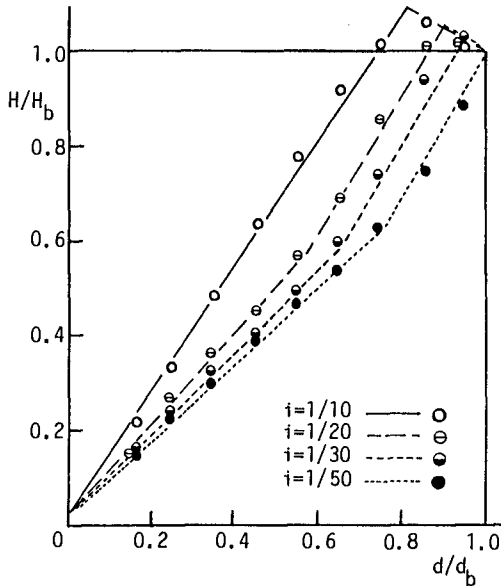


Fig.11 Regression lines for the wave height change after breaking

In the definition of eq.(5), data from a slightly offshore-side of the breaking point are applied in the calculation. On the shore-side of the breaking point, wave height change is affected by the mean water level change such as wave set-up and surf beat. The new definition applied in this study therefore determines the water depth as a sum of the still water depth and the (long period) mean water level displacement(s), consequently those effects of the (long period) mean water level changes are not included in these equations. In the practical application of these equations, the long period water level changes (Goda,1975b) should be introduced, although their properties are not investigated in this study.

6. CONCLUDING REMARKS.

The properties of zero-down-cross irregular waves on uniform slopes are examined experimentally. About 4,000 irregular waves of the Pierson-Moskowitz spectrum are analyzed in the study. The followings results were obtained:

- (1) The shoaling characteristics can be approximated by the linear wave theory.
- (2) H_p/d_b is about 30% smaller than that for periodic waves.
- (3) The process after breaking can be divided into three regions i.e. the shoaling, plunging and bore regions.
- (4) The experimental equations throughout the process are given.
- (5) A new definition of water depth which can largely reduce the fluctuation in the plotted data is proposed.

ACKNOWLEDGMENT: The authors wish to express their thanks to Mr T. Goto for his help in the experiment.

REFERENCES

- Battjes, J.A. (1972): Set-up due to irregular waves, Proc., 13rd ICCE, pp.1993-2004.
- Collins, J.I.(1970): Probabilities of breaking wave characteristics, Proc., 12nd ICCE, pp.399-414.
- Goda, Y. (1970): Analysis on the breaker index, Proc. JSCE, No.180, pp.39-49.
- Goda, Y. (1975a): Deformation of irregular waves due to depth-controlled wave breaking, Report of PHRI, Vol.14, No.3, pp.59-106.
- Goda, Y. and Y. Suzuki(1975b): Computation of refraction and diffraction of sea waves with Mitsuyasu's directional spectral, Tech. Note of PHRI, No.230, 45p.
- Herbers, T.H.C.(1984): The breaking of windwaves in deep water, Report No.8-84, Delft Univ. of Tech., Dept. of Civil Engg.
- Isobe, M, H. Nishimura and T. E(1980): Experimental study on irregular wave breaking, Proc. 27th JCCE, pp.139-142.
- Iwagaki, Y., A. Kimura and N. Kishida (1977): Breaking characteristics of random waves on the sloping beach, Proc. 24th JCCE, pp.102-106.
- Kimura, A. and T. Kimura(1987): Low price random signal processor with high efficiency numerical filters, Proc. 1AHR seminar, pp.435-446.
- Kuo and Kuo (1972): Change in irregular wave height and its probability distribution due to breaking, Proc., 19th JCCE, pp.137-142.
- Sawaragi, T, K. Iwata and T. Ishii(1980): Experimental study on irregular wave breaking, Proc. 27th JCCE, pp.139-142.
- Shuto, N. (1974): Deformation of non-linear long wave, Proc, 21st JCCE, pp.57-63.

CHAPTER 30

Verification of numerical wave propagation models in tidal inlets

J.A. VOGEL, A.C. RADDER AND J.H. DE REUS*

The performance of two numerical wave propagation models has been investigated by comparison with field data. The first model is a refraction-diffraction model based on the parabolic equation method. The second is a refraction model based on the wave action equation, using a regular grid. Two field situations, viz. a tidal inlet and a river estuary along the Dutch coast, were used to determine the influence of the local wind on waves behind an island and a breaker zone. It may be concluded from the results of the computations and measurements that a much better agreement is obtained when wave growth due to wind is properly accounted for in the numerical models. In complicated coastal areas the models perform well for both engineering and research purposes.

1. INTRODUCTION

Sea waves approaching coastal regions can be influenced by a number of physical processes: shoaling, refraction by depth and current variations, diffraction, nonlinear effects, energy dissipation by wave breaking and bottom friction, and wave growth due to wind. In order to estimate inshore wave conditions from wave data available offshore, shallow water wave models should be able to account for these effects. Usually, numerical 2D shallow water wave propagation models include propagation and dissipation processes, while the influence of the local wind is often neglected (see e.g. Martin et al., 1987; Vincent and Carrie, 1988). For regions behind an island (c.q. peninsula) or a breaker zone the input from the local wind may be appreciable, and this effect cannot be accounted for by, e.g., taking a lower value of the friction factor. The purpose of this study is to verify two numerical models in this respect, with wave measurements in two field situations.

*senior researchers, Rijkswaterstaat, Tidal Waters Division,
P.O.Box 20904, 2500 EX The Hague, The Netherlands

2. SHALLOW WATER WAVE MODELS

The performance of two shallow water wave models has been investigated:

- The model CREDIZ, which is based on the parabolic approximation of the mild-slope equation (Radder, 1979; Dingemans et al., 1984; Dingemans 1985).
- the model HISWA, which is based on refraction computations using a regular grid (Holthuijsen and Booij, 1986; Holthuijsen et al., 1988)

A mathematical formulation of these models is given below.

2.1 THE MODEL CREDIZ

The parabolic model CREDIZ describes the propagation of waves in coastal areas with non-uniform depth and current, in particular where both refraction and diffraction effects are important. The model is based on the following equation for monochromatic wave motion (for more details, see Dingemans, 1985):

$$(1) \quad \nabla \cdot (cc_g \nabla \varphi) + (k^2 cc_g + i\sigma(W + \nabla \cdot \vec{U}))\varphi = 0$$

where \vec{U} is the (steady) current-velocity vector, ∇ is the horizontal gradient operator ($\partial/\partial x$, $\partial/\partial y$), $\varphi(x, y)$ is the complex wave potential function, k the wave number, c and c_g the phase- and group velocity, σ the relative angular frequency, $i = \sqrt{-1}$ the imaginary unit, and W a dissipation coefficient, to be specified later on.

The absolute (ω) and relative (σ) frequencies are related by:

$$(2) \quad \omega = \sigma + \vec{k} \cdot \vec{U}$$

where σ is given by the linear dispersion relation:

$$(3) \quad \sigma^2 = gk \tanh kh$$

with g the acceleration of gravity and h the local depth.

In the parabolic approximation the assumption is made that the waves propagate mainly into a specific direction, say x .

Defining the operator M by $M = \frac{\partial}{\partial y}(\beta \frac{\partial}{\partial y})$ with $\beta = cc_g$

the parabolic approximation to equation (1) is given by:

$$(4) \quad \frac{\partial}{\partial x}(\sqrt{\beta k} \varphi + \frac{p_1}{k \sqrt{\beta k}} M \varphi) - i(k \sqrt{\beta k} \varphi + \frac{p_2}{\sqrt{\beta k}} M \varphi) +$$

$$+\frac{\sigma}{2\sqrt{\beta k}}(W + \nabla \cdot \vec{U})\varphi = 0$$

The coefficients p_1 and p_2 result from the approximation of pseudo-operators by differential operators and are related by:

$$(5) \quad p_2 = p_1 + \frac{1}{2}, \quad 0 \leq p_1 \leq \frac{1}{2} \quad (\text{optimal : } p_1 = \frac{1}{4})$$

As the wave-number vector \vec{k} in (2) is not exactly known beforehand, the relative frequency σ is approximated by:

$$\sigma = \omega - r k U_x$$

in which r is a reduction factor expressing the fact that the waves do not exactly follow the x-direction ($0 \leq r \leq 1$; standard value: $r = 0.9$).

The energy-dissipation term $W\varphi$ in equation (4) accounts for the effects of wave breaking, bottom friction and wave growth due to wind:

$$(6) \quad W\varphi = (W_b + W_f + W_g)\varphi$$

The dissipation function W_b due to wave breaking is computed according to the method of Battjes and Janssen (1978); see also Battjes and Stive (1985). For the dissipation function W_f due to bottom friction the method of Putnam and Johnson (1949) is used.

The effect of wave growth by wind is simulated by the (negative) dissipation term W_g :

$$(7) \quad W_g = -\frac{2c_g}{H_s} \frac{dH_s}{dx}$$

where $H_s = 2a$ is the significant wave height and a the wave amplitude. To compute the gradient dH_s/dx in (7), the growth curve of Krylov/Wilson is used (cf. Holthuisen, 1980; Krylov et al.,1976; Wilson, 1965):

$$(8) \quad \tilde{H}_s = \beta [1 - 1 / (1 + \alpha \sqrt{\tilde{x}})^2]$$

with $\tilde{H}_s = gH_s / V_x^2$, $\tilde{x} = gx / V_x^2$,
 V_x = component of wind speed in x-direction,
 α, β = coefficients ($\alpha \approx 0.006$, $\beta \approx 0.256$).

It is noted that the growth curve (8) is based on a parametric description of the wave spectrum; the effect of wave growth is assumed to be local, while

the period of the waves (due to the restriction to monochromatic waves) is assumed to be constant, equal to the peak period of the spectrum. Therefore, a spectral decomposition is not allowed when (8) is used.

The influence of the wave amplitude a on the propagation velocity is taken into account by setting the local depth h in the dispersion relation (3) equal to: $h = d + p_v a$ where d is the actual mean water depth and p_v is an adjustable parameter (standard value: 1). In the shallow water limit the celerity c of a solitary wave is obtained for $p_v = 1$, while in the deep water limit the linear expression for c is recovered.

The parabolic differential equation (4) can be solved in finite difference form, using a two-level, implicit numerical scheme on a rectangular grid. When dissipative physical effects are included (through the term $W\varphi$), the difference equations are linearized in a special way to ensure stability: in the case of $W < 0$, a positive diffusion is introduced in the (fully implicit) numerical scheme, in order to prevent non-linear instabilities in the early stage of wave growth due to wind. In practice, fairly accurate solutions have been obtained for values of grid spacings Δx and Δy according to: $\Delta x/L \leq 1/4$; $\Delta y/L \leq 1/6$, where $L = 2\pi/k$ is the local wave length.

The solution of equation (4) requires as initial conditions the amplitude, period and direction of the incident wave field; along the lateral boundaries, the wave field is generally not known, and an approximate boundary condition (reflecting or partially absorbing) may be applied. However, for instance in case of strong wave-current interactions, these conditions give not the right description; therefore, the computational grid should be chosen sufficiently large, to avoid disturbances of the wave field in the region of interest.

2.2 THE MODEL HISWA

The model HISWA accounts for refractive propagation of shortcrested waves over arbitrary bottom topography and current fields. The model is based on the action balance equation:

$$(9) \quad \frac{\partial A}{\partial t} + x_i \frac{\partial A}{\partial x_i} + \dot{k}_i \frac{\partial A}{\partial k_i} = T$$

where $A(\vec{k}, \vec{x}, t)$ denotes the wave action density, $x_i \equiv \frac{dx_i}{dt} = \frac{\partial \Omega}{\partial k_i}$ is the group velocity and $\dot{k}_i \equiv \frac{dk_i}{dt} = -\frac{\partial \Omega}{\partial x_i}$ is the rate of change of wave number due to refraction. The right hand side denotes the local change of action density, e.g. by dissipation. The dispersion relation is given as $\omega = \Omega(\vec{k}, \vec{x}, t)$, see (2) and (3). For simplicity we assume in this derivation that there is no ambient current; see Dingemans et al. (1986) for the current case. In the model the simplifying assumption of stationarity, i.e. no explicit dependence on time, is made. Then

Ω is a Hamiltonian for the vectorfield (x_i, k_i) . Transforming from (\vec{k}, \vec{x}) -space to the $(\vec{x}, \omega, \vartheta)$ -space with ϑ the wave direction and introducing the absolute energy density \tilde{E} by $\tilde{E} = A\omega$, one obtains after integration over ω between 0 and ∞ :

$$(10) \quad \frac{\partial}{\partial x} [\omega^A \cdot A^{(o)} \cdot \bar{c}_g \cos\vartheta] + \frac{\partial}{\partial y} [\omega^A \cdot A^{(o)} \cdot \bar{c}_g \sin\vartheta] + \frac{\partial}{\partial \vartheta} [\omega^A \cdot A^{(o)} \cdot \bar{c}_\vartheta] = T_1$$

where the mean quantities ω^A , $A^{(o)}$, \bar{c}_g and \bar{c}_ϑ are defined by:
 $A^{(o)}(x, y, \vartheta) = \int_0^\infty A(x, y, \omega, \vartheta) d\omega$; $\omega^A(x, y, \vartheta) = \frac{1}{A^{(o)}} \int_0^\infty \omega A d\omega$;
 $E^{(o)} = \omega^A \cdot A^{(o)}$; $\bar{c}_g = \frac{1}{E^{(o)}} \int_0^\infty \tilde{E} \cdot c_g d\omega$; $\bar{c}_\vartheta = \frac{1}{E^{(o)}} \int_0^\infty \tilde{E} (c_g - \frac{c}{2}) \frac{1}{h} \frac{\partial h}{\partial n} d\omega$;
 $T_1 = \int_0^\infty \omega T d\omega$; $c_g = \frac{\partial \Omega}{\partial k}$; $c = \frac{\omega}{k}$; $\vec{n} = (-\sin\vartheta, \cos\vartheta)$.

Using Leibniz' rule and rewriting the result, a second equation is obtained:

$$(11) \quad \frac{\partial}{\partial x} [A^{(o)} \cdot \bar{c}_g \cos\vartheta] + \frac{\partial}{\partial y} [A^{(o)} \cdot \bar{c}_g \sin\vartheta] + \frac{\partial}{\partial \vartheta} [A^{(o)} \cdot \bar{c}_\vartheta] = \frac{1}{\omega^A} [T_1 - A^{(o)} \cdot \bar{c}_{g,i} \cdot \frac{\partial \omega^A}{\partial x_i}]$$

Equation (10) and (11) are the basic equations for HISWA. The source term T_1 is implemented as $(\omega^A/\sigma^A) \cdot S^{(o)}$, where $S^{(o)}$ denotes the local chance of energy and $\bar{c}_{g,i} \cdot \frac{\partial \omega^A}{\partial x_i}$ is interpreted as the change of the frequency ω^A , which is prescribed as a function S_ω of the local data.

The source terms $S^{(o)}$ and S_ω represent the effects of wave breaking, bottom friction, wind wave generation, and wave blocking on an opposing current. The dissipation due to wave breaking and bottom friction is modelled by the same methods as used in the CREDIZ model. The formulation is extended to random waves with directional distribution by assuming that the dissipation per direction is proportional to the energy density at that direction. The formulation of the source term for wave generation by wind is based on available expressions giving the total energy and the frequency averaged over the whole spectrum, as functions of fetch and wind speed. Details can be found in Holthuijsen et al. (1988).

The first order partial differential equations (10, 11) can be solved on a regular grid in (x,y,ϑ) -space, with the x-direction parallel to the main direction of the wave field. In the present version of the model, a leapfrog finite difference scheme is used, together with appropriate boundary conditions. As initial conditions, the wave height, period, direction and spreading (or the directional spectrum) of the incident wave field are required.

3. COMPARISON WITH FIELD MEASUREMENTS

The present verification study concerns two field situations:

- the tidal inlet of Texel,
- the estuary of Haringvliet.

Results of the comparison are presented below.

3.1 THE TIDAL INLET OF TEXEL.

This is a strait connecting an ebb tidal delta at the North Sea side with the area of interest, the Wadden Sea, at the other side (see fig. 1). The entrance of the inlet is sheltered by a shoal, which is flooded only during very high tide. The effect of the local wind is thus dominant, while the influence of the tidal current is of secondary importance.

Wave data are available from five locations, of which we used three in this paper:

EIERLAND, located offshore in the North Sea, to provide the input wave conditions for the models;

BOLLEN and MALZWIN, located in the Wadden Sea, to verify the numerical models.

Apart from the wavestaff at MALZWIN, waverider buoys were employed at the measurement locations. Measurements were selected from the period 11 October 1981 to 11 March 1982, using the criteria:

- wind direction ranging from 220° to 300° (\pm SW to NW);
- wind speed higher than 6 m/s.

In table 1 thirteen selected cases are shown which provide the input wave parameters measured at the offshore buoy. In each case, the tidal current is represented by one of four characteristic stages: maximum ebb, slack tide ebb-flood, maximum flood, slack tide flood-ebb (see figs. 2 - 5). The wave direction of the incident wave field is assumed to be equal to the wind direction, given in table 1.

The bottom topography is represented by a depth array of 136×104 grid points, with a spacing of 250 m. At the same grid points, the components of the current velocities are given. Further details can be found in: den Adel (1988). The results of the computations of the models are compared with the measurements in table 1, and a scatter plot is given in fig. 10.

From the computations we draw the conclusions:

- the influence of the local wind is most important in this area: when wave growth due to wind is not accounted for, the computed wave height reduces to values less than a few percent of the incident wave height. This is mainly due to -besides breaking on the shoal- diffraction of wave energy in the Wadden Sea: swell decays here rapidly.
- the influence of the tidal current (with velocities up to 1.5 m/s) can be appreciable: differences of more than 50% may be found, comparing cases

with and without current; in the maximum-ebb case nr. 13, a tunneling of waves does occur (see figs. 6, 7 and 8, 9).

- the influence of the waves on the North Sea is very small; only during maximum-ebb-flow and if the waves come from the South-East more than a few percent of the input wave height remains at the Wadden Sea.
- the change in significant wave period plays a role: at lower periods, the wave-current interaction is stronger, while refraction by depth and bottom friction are weaker. This partially explains the differences in the results of the model computations.

Remarks

1. The present version of the model HISWA does not perform well in case of very small directional distribution; therefore, the model should be used with care when swell-components are present in the wave field.
2. The model CREDIZ shows a sensitive dependence of the side-boundary conditions of the computational grid, in case of strong tidal currents crossing these boundaries; care should be taken that the wave field in the area of interest is not disturbed, by choosing the computational grid sufficiently large.

3.2 THE ESTUARY OF HARINGVLIET.

This area is characterized by a shoal called Hinderplaat which falls partly dry during low tide, a region with nearly straight isobaths offshore the shoal, and a complicated bottom geometry inshore (see fig. 11). In the vicinity of the shoal, wave breaking is the predominant physical process; after this breaking, the wind may enhance the wave height appreciably along a distance of a few miles behind the shoal.

Wave data are available from a measurement campaign during the autumn of 1982 (for details, see Dingemans, 1983; Dingemans et al. 1984). Recently, this data set has been used extensively to test the performance of numerical shallow water wave models (Martin et al. 1987; Vincent and Carrie, 1988). However, energy input from the wind is not included in these models.

In order to test the effect of the local wind, the storm situation of 14 - 15 October 1982 was selected. For a fair comparison with previous CREDIZ results, the same cases as described by Dingemans (1983) were used, with the same input parameters (e.g. the 1981 - bottom topography, consisting of 88 x 117 grid points with spacing of 250 m, and a bottom friction factor $f = 0.005$ instead of the more appropriate 0.01). Further input conditions were:

- wind direction ranging from 300° to 320° ;
- wind speed ranging from 12.9 to 16.5 m/s;
- peak period ranging from 7.1 to 8.3 s (at the Wavec buoy).

The results of the computations are shown in table 2, where the relative error δ is defined by $\delta = (H_s - H_{sm})/H_{sm}$. For each of the six cases, the bias b and the rms-deviation ϵ_{rms} are given in table 3.

By definition, $b = \sum (H_s - H_{sm}) / \sum H_{sm}$;

$$\epsilon_{rms} = [n^{-1} \sum (H_s - H_{sm})^2]^{1/2} / [n^{-1} \sum H_{sm}].$$

The following conclusions may be inferred:

- the model CREDIZ (and, to a lesser extent, also HISWA) performs much better when wave growth due to wind is properly accounted for, especially at low water levels.
- while HISWA performs well at E-75, the wave-staff far behind the shoal, CREDIZ still gives too low values of H_s there; this is probably due to the effect of directional spreading of the wave field, and the transfer of energy between spectral components, resulting in a lowering of the significant wave period, and less dissipation due to bottom friction.
- the computed wave height at WR4, just behind the Hinderplaat, is still too low for low water levels; this is probably due to (local) set-up of the mean water level by waves, which effect is not included in the models.
- at the other locations (mainly at WR5 and WR6), the process of spectral saturation (white-capping) is of importance. This process is simulated in the models by the dissipation method of Battjes and Janssen (1978) for random breaking waves, where breaking is caused also by exceedence of steepness.

4. CONCLUSIONS

A verification study of two wave propagation models has been made, using field data in which the influence of the local wind is significant. In spite of the distinct differences between the models (e.g. CREDIZ is a monochromatic model including diffractive effects, while HISWA is a variable frequency model with directional spreading effects), both models perform equally well in complicated coastal areas. (For specific conclusions, see §3.1 and §3.2).

There remains the problem to describe in a more fundamental way changes in wave frequency, especially in shallow water (for instance, by the undular bore model; see Dingemans and Battjes, these Proceedings). This is important when the models are used in sediment transport studies.

Acknowledgements.

The authors would like to thank J.D. den Adel, J. Hoekema, A.W. Hokke, D. Knoester, T. Louters and A.M. Walburg for assistance in the computations, R.C.M. Ariaans and A.P. Roskam for supplying the field data.

Table 1. Comparison of significant wave heights and periods, Texel.

case nr.	water level (m)	tidal stage	wind speed (m/s)	wind direction (°)	incident wave EIERLAND		wave height (m)		wave period (s)		location	
					Hs(m)	Ts(m)	meas.	CREDIZ	HISWA	meas.		HISWA
1	0.49	ebb-flood	8	250	1.38	6.1	0.15	0.26	0.23	3.7	3.6	BOLLEN
2	0.20	,,	18	270	4.41	10.0	0.86	0.55	0.84	3.8	3.9	,,
3	0.50	,,	18	270	4.41	10.0	0.88	0.74	0.82	3.5	4.0	,,
4	0.52	max. flood	7	280	1.92	9.1	0.14	0.19	0.15	3.6	4.5	,,
5	1.00	,,	9	240	1.35	6.0	0.20	0.27	0.21	4.0	4.0	,,
6	0.87	flood-ebb	7	230	1.12	6.4	0.15	0.15	0.30	3.7	2.6	,,
7	0.12	,,	8	280	1.81	8.2	0.27	0.29	0.26	3.4	2.9	,,
8	1.73	,,	15	280	4.24	9.6	0.64	0.52	0.33	3.6	4.8	MALZWIN
9	1.49	,,	15	280	4.24	9.6	0.55	0.51	0.33	4.2	4.6	,,
10	-0.18	max. ebb	6	290	1.01	6.2	0.30	0.17	0.15	2.8	3.3	BOLLEN
11	-0.62	,,	9	300	1.69	7.7	0.21	0.29	0.35	3.4	2.6	,,
12	-0.48	,,	9	220	2.28	7.0	0.51	0.28	0.32	3.3	5.3	,,
13	-0.43	,,	11	230	2.24	7.7	0.36	0.38	0.38	4.7	4.7	,,

Table 2. Comparison of significant wave heights, Haringvliet.

date and time	water level	location	measurement H _{sm}	GREDIZ (new)		HISWA (new)	
				H _s	δ(%)	H _s	δ(%)
82 10 14 17:00	-0.10	Wa	2.58	2.58	0	2.58	0
		WR1	2.34	2.55	+9	2.58	+10
		WR2	2.21	2.31	+5	2.34	+6
		WR3	2.21	2.23	+1	2.30	+4
		WR4	0.40	0.29	-27	0.28	-30
		WR5	0.66	0.76	+15	0.89	+35
		WR6	1.16	1.29	+11	1.22	+5
82 10 14 20:00	0.20	E-75	0.61	0.52	-15	0.58	-5
		Wa	3.06	3.06	0	3.06	0
		WR1	2.65	2.98	+12	3.05	+15
		WR2	2.38	2.57	+8	2.56	+8
		WR3	2.45	2.48	+1	2.50	+2
		WR4	0.48	0.33	-31	0.36	-25
		WR5	0.75	0.89	+19	1.00	+33
82 10 14 22:00	0.85	WR6	1.20	1.39	+16	1.32	+10
		E-75	0.74	0.46	-38	0.64	-14
		Wa	3.23	3.23	0	3.23	0
		WR1	2.90	3.18	+10	3.24	+12
		WR2	2.53	2.85	+13	2.83	+12
		WR3	2.70	2.74	+1	2.77	+3
		WR4	0.62	0.52	-16	0.65	+5
		WR5	1.05	1.17	+11	1.21	+15
		WR6	1.60	1.61	+1	1.56	-3
		E-75	0.94	0.78	-17	0.86	-9

Table 2. Continued

date and time	water level	location	measurement H _{sm}	GREDIZ (new)		HISWA (new)	
				H _s	δ(%)	H _s	δ(%)
82 10 14 23:00	1.70	Wa	3.54	3.54	0	3.54	0
		WR1	3.10	3.40	+10	3.54	+14
		WR2	2.63	3.11	+18	3.16	+20
		WR3	2.72	3.04	+12	3.11	+14
		WR4	0.72	0.79	+10	0.99	+38
		WR5	1.45	1.50	+3	1.53	+6
82 10 15 02:00	1.50	WR6	1.86	1.88	+1	1.88	+1
		E-75	1.08	0.99	-8	1.10	+2
		Wa	2.89	2.89		2.89	0
		WR1	2.68	2.82	+5	2.86	+7
		WR2	2.75	2.70	-2	2.83	+3
		WR3	2.68	2.74	+2	2.81	+5
		WR4	0.70	0.76	+9	0.88	+26
82 10 15 04:00	0.45	WR5	1.15	1.39	+21	1.40	+22
		WR6	1.95	1.63	-16	1.75	-10
		E-75	0.88	0.46	-48	1.05	+19
		Wa	2.72	2.72	0	2.72	0
		WR1	2.49	2.63	+6	2.72	+9
		WR2	2.41	2.43	+1	2.53	+5
		WR3	2.56	2.44	-5	2.49	-3
		WR4	0.44	0.30	-32	0.44	0
		WR5	0.70	0.99	+41	1.05	+50
		WR6	1.35	1.32	-2	1.40	+4
		E-75	0.63	0.50	-21	0.72	+14

Table 3. Bias and rms-deviation (%); Haringvliet.

time	water level (m)	CREDIZ, <u>old</u> *)		CREDIZ, <u>new</u>		HISWA, <u>new</u>	
		b	ϵ_{rms}	b	ϵ_{rms}	b	ϵ_{rms}
17.00	- 0.10	- 1.5	19.2	+ 3.8	8.8	+ 6.3	10.8
20.00	0.20	- 2.4	26.1	+ 4.2	13.7	+ 7.3	13.5
22.00	0.85	+ 1.9	16.5	+ 4.1	10.3	+ 6.3	10.6
23.00	1.70	+ 6.9	12.4	+ 8.5	12.9	+12.9	16.4
02.00	1.50	- 3.2	15.3	- 2.3	12.5	+ 6.2	9.7
04.00	0.45	+ 0.5	13.4	+ 0.3	9.9	+ 7.3	11.3

*) Cf. Dingemans et al. (1984)

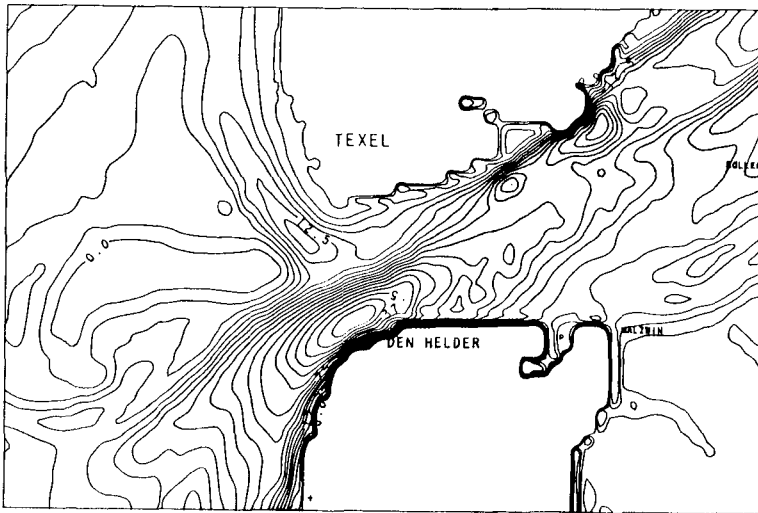


Fig. 1 Bottom contours, tidal inlet of Texel.

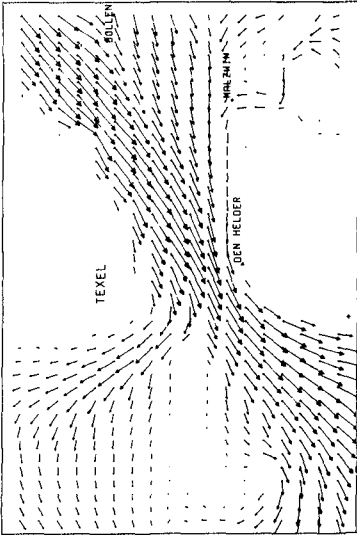


Fig. 2 Maximum ebb current.

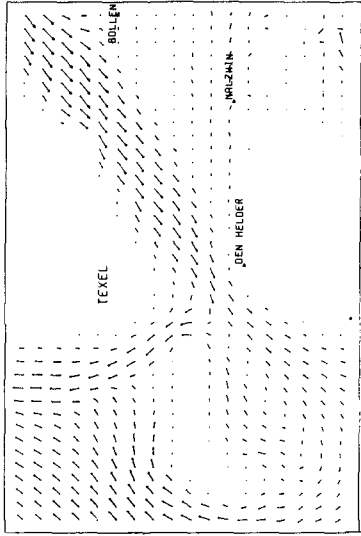


Fig. 3 Slack tide ebb-flood current.

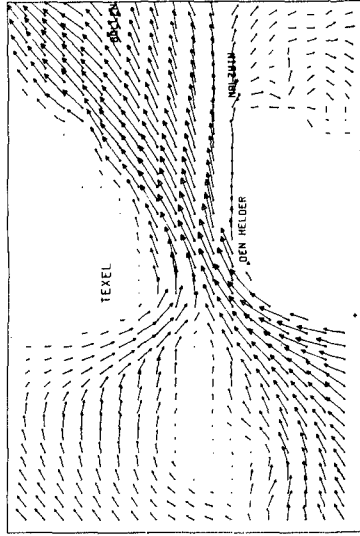


Fig. 4 Maximum flood current.

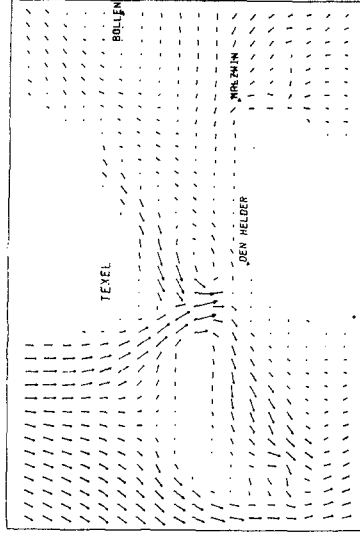


Fig. 5 Slack tide flood-ebb current.

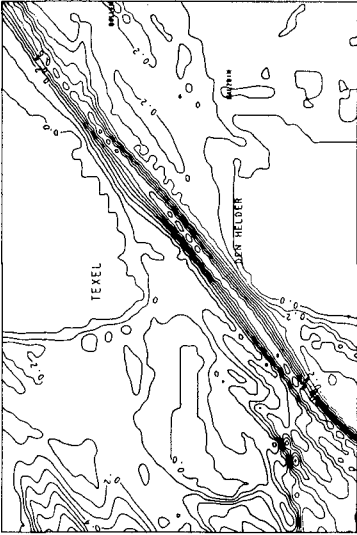


Fig. 6 Isolines of amplitude (CREDIZ), max. ebb current.

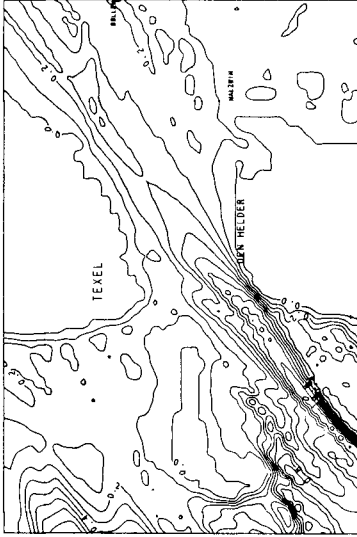


Fig. 7 Isolines of amplitude (CREDIZ), no current.

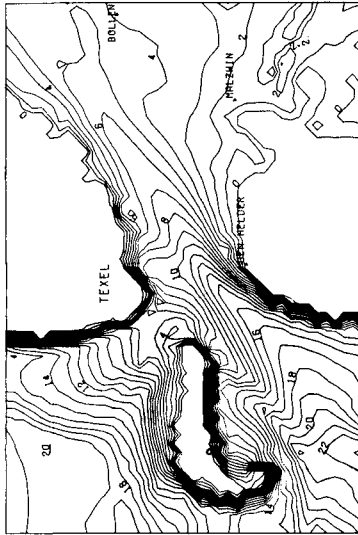


Fig. 8 Isolines of wave height (HISWA), max. ebb current.

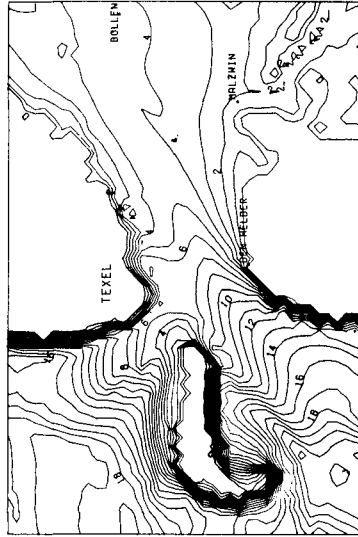


Fig. 9 Isolines of wave height (HISWA), no current.

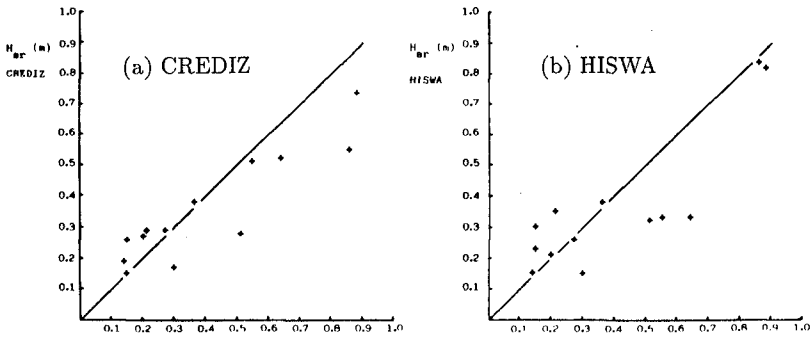


fig. 10 Comparison of measured and computed wave heights.

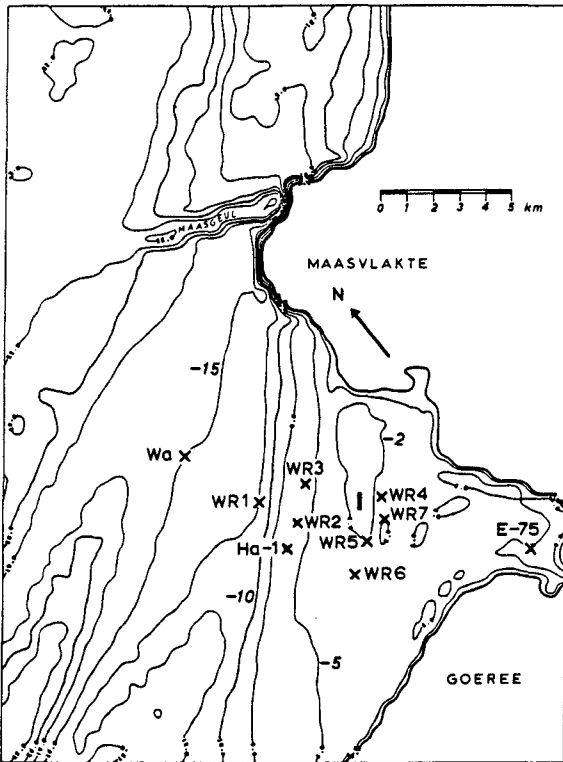


Fig. 11 Bottom contours, estuary of Haringvliet.

REFERENCES

- Adel, J.D. den, *Verificatie van de numerieke golfvoortplantingsmodellen CREDIZ en HISWA bij het zeegat van Texel*, Rijkswaterstaat, Report GWAO 88.044 (in Dutch) (1988).
- Battjes, J.A. and Janssen, J.P.F.M., *Energy loss and set-up due to breaking of random waves*, Proc. 16th Coastal Eng. Conf. ASCE, Hamburg, 569 - 587 (1978).
- Battjes, J.A. and Stive, M.J.F., *Calibration and verification of a dissipation model for random breaking waves*, J. Geophys. Res. 90 (C5), 9159 - 9167 (1985).
- Dingemans, M.W., *Verification of numerical wave propagation models with field measurements. CREDIZ verification Haringvliet*, Delft Hydraulics Lab., Report W 488 (1983).
- Dingemans, M.W., *Surface wave propagation over an uneven bottom. Evaluation of two-dimensional horizontal wave propagation models*, Delft Hydraulics Lab., Report W 301, part 5 (1985).
- Dingemans, M.W.; Stive, M.J.F.; Kuik, A.J.; Radder, A.C. and Booij, N., *Field and Laboratory verification of the wave propagation model CREDIZ*, Proc. 19th Coastal Eng. Conf. ASCE, Houston, 1178 - 1191 (1984).
- Dingemans, M.W.; Stive, M.J.F.; Bosman, J.; De Vriend, H.J. and Vogel, J.A., *Directional nearshore wave propagation and induced currents*, Proc. 20th Coastal Eng. Conf. ASCE, Taipei, 1092 - 1106 (1986).
- Holthuijsen, L.H., *Methoden voor golfvoorspelling (in Dutch)*, Technische Adviescommissie voor de Waterkeringen (1980).
- Holthuijsen, L.H. and Booij, N., *A grid model for shallow water waves*, Proc. 20th Coastal Eng. Conf. ASCE, Taipei, 261 - 270 (1986).
- Holthuijsen, L.H.; Booij, N. and Herbers, T.H.C., *A prediction model for stationary, short-crested waves in shallow water with ambient currents*, Coastal Engineering, in preparation (1988).
- Krylov, Yu.M. Strelakov, S.S. and Tsyplukhin, V.F., *Vetrovye volny i ich vozdejstvie na sooruzewija (wind waves and their impact on structures). In Russian*, Hydrometeoizdat, Leningrad (1976).
- Martin, C.J.; Dalrymple, R.A. and Miller, M.C., *A verification procedure for wave propagation models*, Modelling the Offshore Environment, Proc. of an international conference, Society for Underwater Technology, London. Chap. 13, 181 - 202 (1987).
- Putnam, J.A. and Johnson, J.W., *The dissipation of wave energy by bottom friction*, Transactions Am. Geophys. Union, 30, 67 - 74 (1949).
- Radder, A.C., *On the parabolic equation method for water wave propagation*, J. Fluid Mech. 95, 159 - 176 (1979).
- Vincent, C.E. and Carrie, A., *Evaluation of an energy propagation wave refraction model*, Continental Shelf Res. 8 (3), 287 - 305 (1988).
- Wilson, B.W., *Numerical prediction of ocean waves in the North Atlantic for December, 1959*, Deutsche Hydrographische Zeitschrift, 18 (3), 114 - 130 (1965).

CHAPTER 31

KINEMATICS AND RETURN FLOW IN A CLOSED WAVE FLUME

Jerald D. Ramsden¹, AM. ASCE

John H. Nath², F. ASCE

ABSTRACT

Stokes (1847) showed that finite amplitude progressing waves cause a net drift of fluid, in the direction of wave motion, which occurs in the upper portion of the water column. In a closed wave flume this drift must be accompanied by a return flow toward the wave generator to satisfy the conservation of mass. This study presents Eulerian velocity and water surface measurements soon after the onset of wave motion from 12 locations in a large scale flume. Waves with $.67 \leq kh \leq 2.29$ and $.09 \leq H/h \leq .39$ were produced in a water depth of 3.5 meters. Superimposing the return flow theory of Kim (1984) with seventh order stream function theory is shown to improve the velocity predictions. The measured return flows are a function of time and depth and agree with Kim's theory as a first approximation. The mean water surface set-down agrees with the theory of Brevik (1979) except for the nearly deep water waves.

INTRODUCTION

Periodic progressing gravity waves confined in a closed wave flume cause a longitudinal circulation to develop. This circulation is driven by mass transport [Stokes (1847)] in the direction of wave propagation and results in a return flow toward the wave generator. The circulation in closed flumes has been extensively studied

¹Graduate Student, W. M. Keck Laboratory, California Institute of Technology, Pasadena, CA

²Professor Emeritus, Department of Civil Engineering, Oregon State University, Corvallis, OR.

in Lagrangian coordinates while few Eulerian measurements have been published. Many studies of the Eulerian water particle velocities and wave force measurements on fixed structures are carried out in closed wave flumes. Measurements from these studies will include the effects of the circulation. The free waves, beach reflections, wind, flume geometry, and the initial conditions may also differ between the wave flume and the ocean.

Studies in flumes are often conducted within a few or several waves after the onset of wave motion to minimize reflections and oscillations characteristic of the flume geometry. The objective of this study is to characterize the behavior of the return flow during this time period.

Two distinct methods have been used to predict the return flow. In one method, inviscid wave theory is used to compute a volume flux due to mass transport. Then a steady uniform return flow (R_c) is superimposed on the wave theory, such that the volume flux due to the return flow cancels the flux from the mass transport. This method was used on stream function wave theory by Dalrymple (1976) and on Stokes' second through fifth order wave theories by Kim (1984). The other was pioneered by Longuet-Higgins (1953) who solved the 'conduction equation' assuming a viscous fluid. He obtained an explicit solution for the circulation in a closed two dimensional flume. The conduction solution predicts parabolic return flow profiles over depth in contrast to the uniform return flow assumed with the inviscid theory. Return flows predicted from inviscid theory should provide reasonable results for flow outside the boundary layers during the first several waves as discussed by Longuet-Higgins (1953) and as shown in this paper. Longuet-Higgins' method provides reasonable predictions near the bottom boundary layer [Russel and Osorio (1958)] and throughout the water column when the wave motion has continued for several hundred wave periods [Bullock and Short (1985)].

To the authors' knowledge only Nath (1978) and Kim (1984) have published Eulerian return flow measurements which were collected soon after the start of wave motion. Both of these authors used the same flume, water depth, and approximately the same wave conditions as used in this study. Both their results contained considerable variability. Due to this variability, Kim found that Longuet-Higgins method and the one developed by him based on

Stokes fifth order wave theory yeild similar errors when compared with both their measurements.

THEORY

As discussed by Longuet-Higgins (1953), when the wave motion starts, the flow is everywhere irrotational except in the boundary layers along the flume walls, the bottom, and the free surface. The boundary layer thickness δ along the flume bottom is approximately $(2\nu/\omega)^{1/2}$, where ω is the angular frequency of the wave motion and ν is the kinematic viscosity of water. For the conditions of this study, δ is on the order of a few millimeters. If the boundary layer thickness on the sides and surface is of this same order, then approximately two tenths of one percent of the flume cross section lies within the boundary layers. Thus, inviscid wave theory should adequately predict the mass transport volume flux and the return flow within the first several wave periods.

The results of Kim's (1984) return current model [see also Kim, Hudspeth, and Sulisz (1986)] based on Stokes second and fifth order wave theories are presented in Figure 1, where T is the wave period, h the water depth, H the wave height, $L_o = gT^2/2\pi$ the deep water wave length where g is the gravitational constant, $C_o = L_o/T$ the deep water wave celerity, and R_c the theoretical return flow. His model, based on the assumption that the return flow is steady and uniform, is the first to include the contribution from the free waves. The fifth order return flow theory is used throughout this paper.

Kim, Hudspeth, and Sulisz (1986) showed that a complete second order solution of the wavemaker boundary value problem requires a time independent potential in addition to the Stokes wave, a free wave, and a series of evanescent waves which were treated earlier by others. The evanescent waves decay with distance from the wave generator and do not propagate. Figure 1 is only valid beyond 3 water depths from the wave generator where the evanescent waves have decayed to a negligible value. The free wave is forced at twice the wave generator frequency. Since the free wave obeys its own dispersion relation, it propagates slower than the Stokes wave which causes the waveform to be nonpermanent along the flume [Buhr Hansen and Svendsen (1974)].

In this study seventh order stream function wave theory is linearly superimposed with Kim's return flow theory. Studies by Chandler and Hinwood (1982) and Dalrymple (1976) indicate that

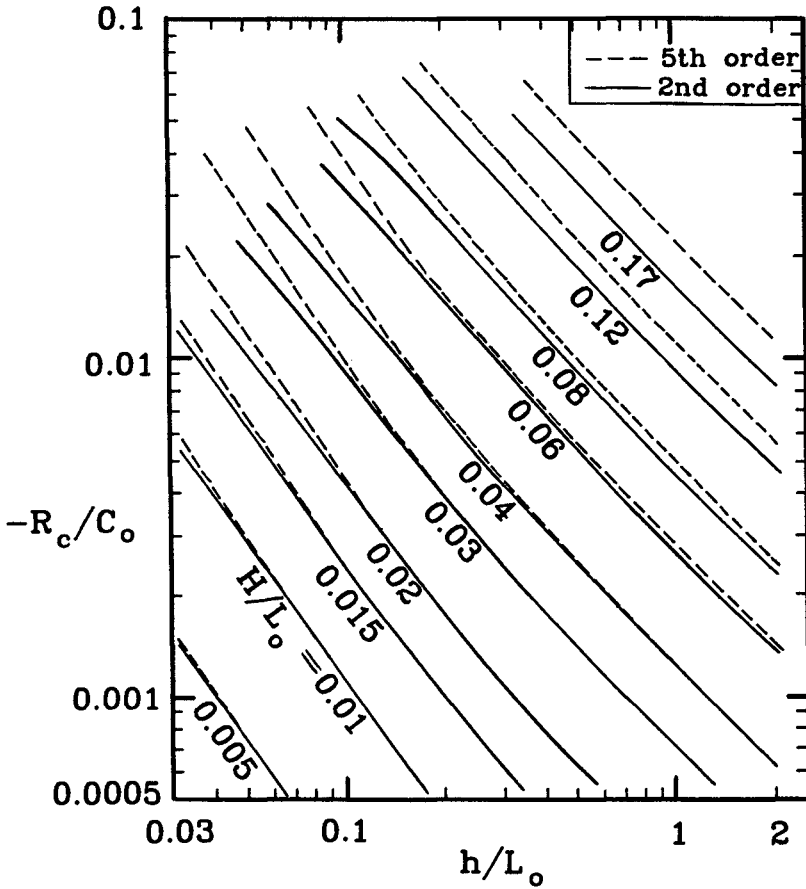


Figure 1: Return current in a closed wave flume for a flap type wave-maker computed from Stokes wave theory [adapted from Kim(1984)].

small currents, like those due to the return flow, can be linearly superimposed with wave theory since the nonlinear interaction effects are quite small.

From the concept of the radiation stress, Longuet-Higgins and Stewart (1964) showed that waves propagating into still water may cause a change in the mean water surface elevation. The mean water levels in this study are compared with a theory presented by Brevik (1979). He derived an expression for the water surface set-down under a packet of waves propagating in water of a constant

depth. The wave packet was assumed to have a Gaussian wave height distribution in space and a narrow banded wave number spectrum.

EXPERIMENT

The wave kinematics were measured in the O. Howard Hinsdale Wave Research Laboratory wave flume (Fig. 2.) during February 1985. The flume is 3.94 m. wide, 96.5 m. long, and has walls of smooth concrete. The wave board is hinged at the flume bottom and driven in a sinusoidal motion by a hydraulic piston.

Four Marsh McBirney Model 711 current meters were used to measure the horizontal and vertical velocities. They operate on the principle of Faraday's law of electromagnetic induction. Each probe is a 2.5 cm. diameter cylinder with a length of 25 cm. and senses the velocities in a plane perpendicular to its axis. Over the frequency range of interest in this study, 0.0 to 2.0 Hz., the current meter electronics behave as a linear first order filter, Ramsden (1987). Both axes of each meter were calibrated using two independent methods which gave complimentary results.

The water particle velocities were measured in twelve locations for each wave condition. The water depth was 3.77 m at the test section during all the measurements. The 25 wave conditions were repeated three times with the meters in different arrangements. Figure 2 shows the three stations where the measurements were collected. Two current meters were placed on each side of the flume for arrangement no. 1 and no. 2. For meter arrangement no. 3 all the current meters were placed on the same side of the flume with two at station no. 1 and two at station no. 3. Three of the current meters were mounted .33 meters from the flume wall while the other was .98 meters from the wall. All the measurements were collected within $-.74 \leq z/h \leq -.04$, where z is the vertical coordinate with its origin at the water surface and directed positive upward.

The wave conditions were obtained by using five different wave generator strokes for each of five wave periods. The wave periods were 2.5, 3.7, 4.6, 5.3, and 6.0 seconds. The stroke was set to obtain wave heights ranging between .33 m. to the maximum possible height for each wave period. The maximum wave heights ranged from 1.07 meters at $T=2.5$ sec., up to 1.37 m. at $T=3.7$ sec., then down to .94 m. for the 6.0 sec. waves. The water surface profile (η) was measured with sonic wave profilers at the center of the flume

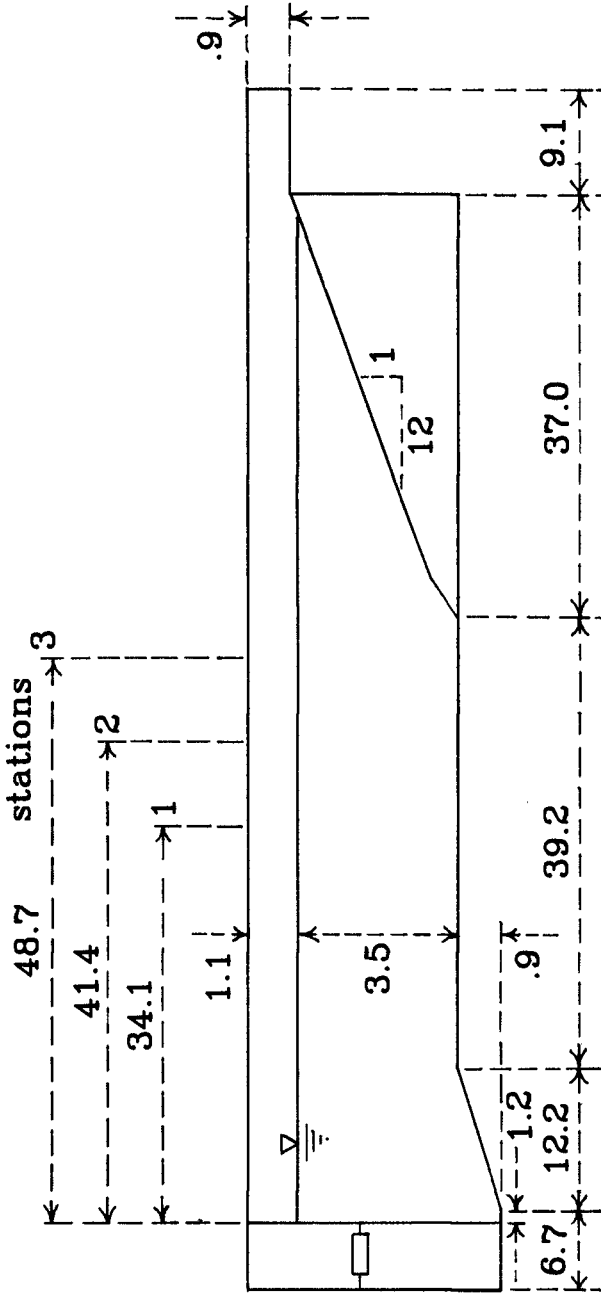


Figure 2: The wave flume at the O. Howard Hinsdale Wave Research Laboratory on the Oregon State University Campus (all dimensions are in meters).

in each cross section containing current meters. The measurements were collected for 14 wave periods beginning with the initial wave disturbance at the current meter locations. The data were recorded digitally at 256 samples per wave period. Before the wave generator was started, 256 samples were collected which are averaged to establish the still water level and the velocity reference. For some of the runs during the first current meter arrangement, an additional block of 14 wave periods of data was collected while letting the wave generator run continuously. This second data block began from 30 sec. to 120 sec. after the end of the first data block.

RESULTS

Out of 525 velocity records 439 were clean and consistent. For the other 86 records there were some problems which included very noisy or erratic reference measurements, voltage jumps during sampling, and some runs where one or two of the meters gave no response.

Figures 3a through 3c show a comparison of the horizontal velocity measurements vs. theory under the wave peak (positive velocities) and trough (negative velocities). Measurements from the maximum wave heights obtained at each wave period are shown. The questionable measurement in Fig. 3a is from a current meter that was intermittently submerged and gave quite low velocities, relative to the other measurements, for the 2.5 sec. waves. This may reveal a minimum amount of submergence time for the model 711 to record the actual velocity when placed above the wave trough. The questionable measurements in Figures 3b and 3c are from a current meter which was working intermittently.

Figure 3a shows velocity profiles at the crest and the trough of a fairly deep water wave. The data from this study and those from Kobune (1978) and Jensen (1978) agree quite well even though they were collected at widely different times and with different types of current meters. Jensen and Kobune used a water depth of 3.35 m. instead of the 3.50 m. of this study.

The measurements follow the theoretical trends quite well although there is some variability which tends to increase with the wave length. This variability is most likely due to both the free waves and the beach reflections. Nath measured the beach reflections with the same flume geometry in 1982. He found the reflection coefficient to be independent of the wave height and to range from

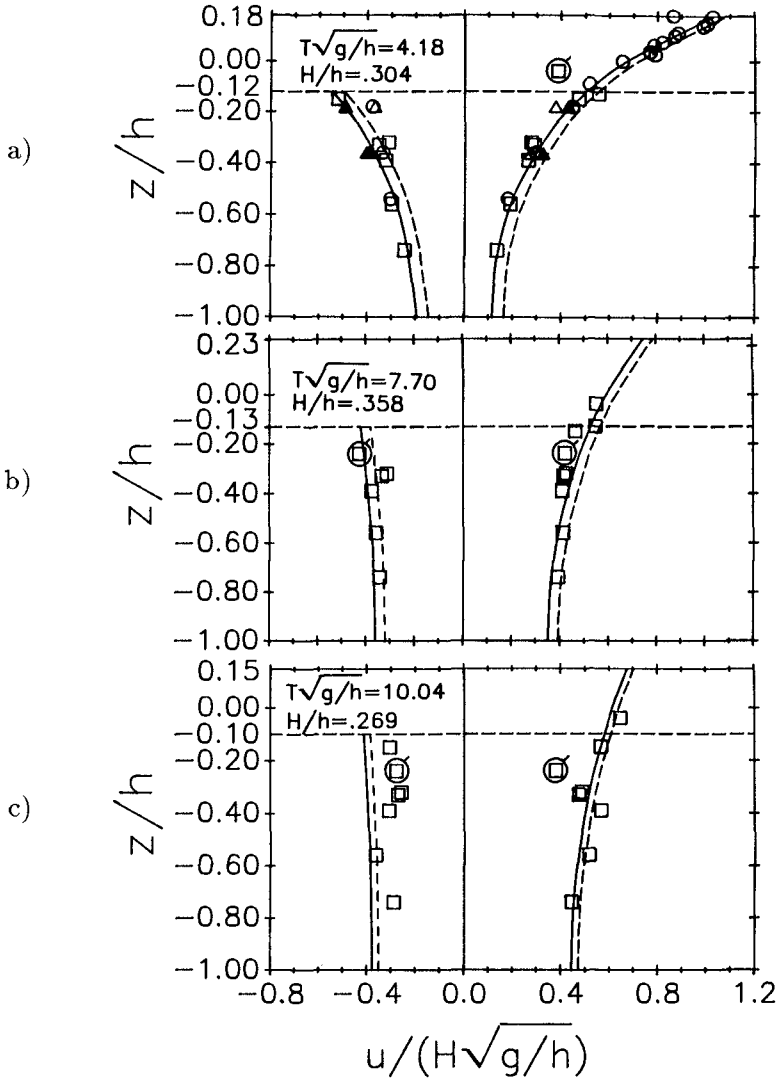


Figure 3: Nondimensional horizontal velocity under the wave crest and trough vs. relative depth. Figures 4a, b, and c show the results of Ramsden (\square) electromagnetic current meters, (—) stream function theory, (---) stream function theory with return flow theory, and (\circ) questionable measurements. Figure 4a also shows the measurements of Jensen (1978) (\circ) propellor meter and Kobune (1978) (\blacktriangle) hot film anemometer, (\triangle) propellor meter.

5% to 10% for the 2.5 sec. to 6. sec. waves, respectively. The free waves may be about as large as the second order Stokes wave as shown by Buhr Hansen and Svendsen (1974). The data of this study and that of Bullock and Short (1985) showed that the amplitude of the second harmonic of η is typically 10%, and at most 25%, of the fundamental harmonic. The second harmonics of 25% most likely include a contribution from both the free wave and the Stokes wave. Thus, the free wave is probably at most 12% of the Stokes first harmonic. Since the free and reflected waves travel in opposite directions, their effect on the horizontal velocity will be the largest where the crest of one coincides with the trough of the other. With a reflection of 10% and a free wave of 12% this effect should be limited to $\pm 22\%$ of the Stokes first harmonic. To correct the theory for the reflection and the free wave, one must know their amplitude as well as their phase relative to the Stokes wave.

Since the free wave celerity is smaller than the Stokes wave celerity, one can compute the time lag between the leading edge of the two wave groups for any location along the flume. For station 1 the lag between the groups is 7.5 and .9 Stokes wave periods for the 2.5 sec. and 6. sec. waves, respectively. Since the measured velocities plotted in Fig. 3 are from about the fourth wave, the results in Fig. 3a from this study were most likely obtained before arrival of the free wave. Since the free waves have not arrived and the reflections are about 5%, the agreement between measurements and predictions is very close. As the wave length increases one should expect more variability in the measurements, due to the free and reflected waves, as shown in Figures 3b and 3c.

In Fig. 3a the ratio of the return flow to the maximum velocity increases with increasing depth due to the attenuation of the water wave velocity. As a result, the return flow reaches 26% of the maximum measured velocity at a relative depth of $z/h = -.74$. From all the measurements in this study, the stream function theory modified for the return flow predicted the maximum measured velocities within $\pm 15\%$ during 85% of the runs. A few measurements were from 30% to 50% less than predicted, however most of these were associated with questionable current meter response.

The mean wave profile ($\bar{\eta}$) and the return flow (\bar{u}) are shown for the largest 2.5 sec. wave and 5.3 sec. wave in Figures 4a and 4b, respectively. The mean values were computed at specific points in

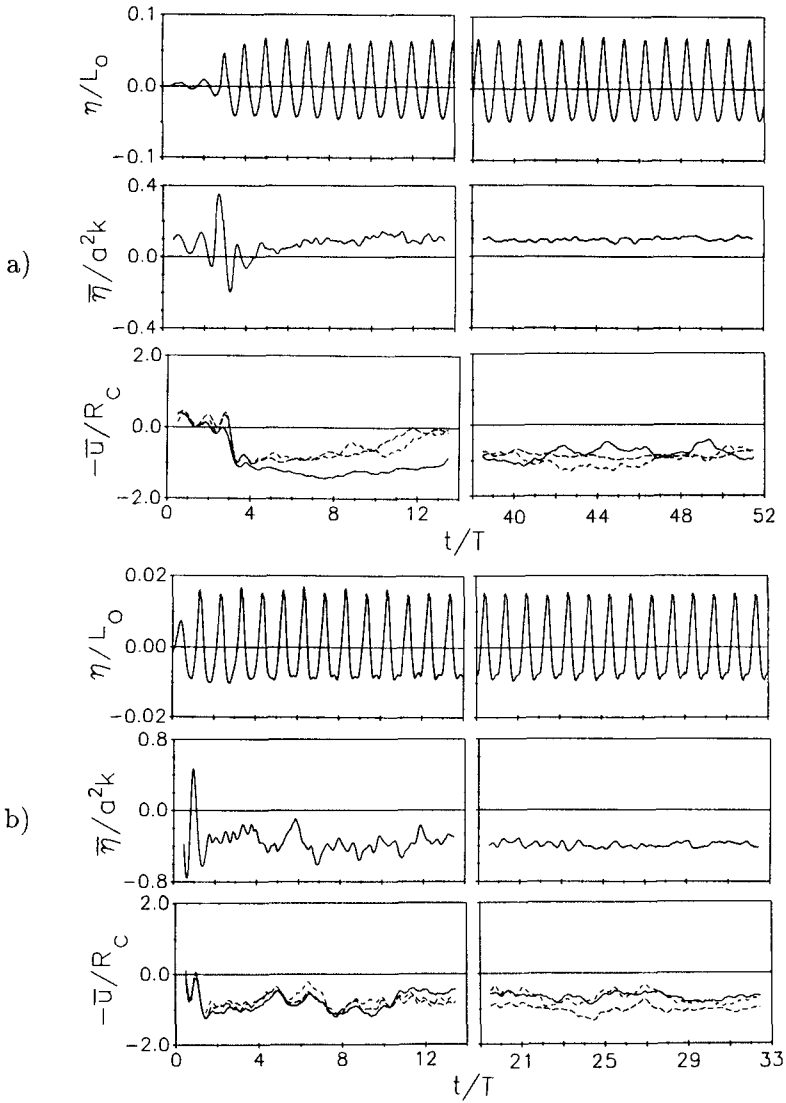


Figure 4: Nondimensional water surface profile, mean water surface, and return flow vs. time. Wave conditions: (a) $T=2.5$ sec. ($T\sqrt{g/h} = 4.18$), $H=1.07$ m. ($H/h = .304$); and (b) $T=5.3$ sec. ($T\sqrt{g/h} = 8.87$), $H=1.07$ m. For $-\bar{u}/R_c$ the various lines correspond to (—) $z/h = -0.74$, (---) $z/h = -0.33$, and (- - -) $z/h = -0.32$.

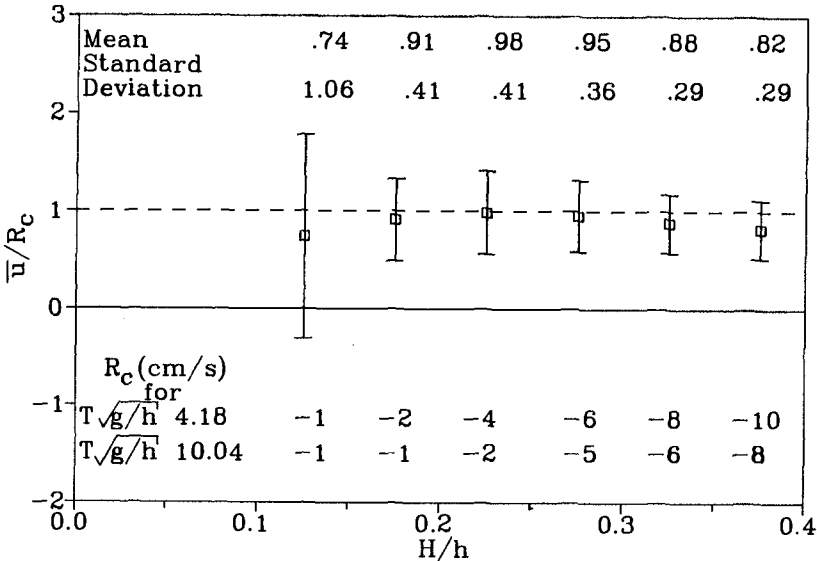


Figure 5: Mean and standard deviation of the normalized return flow vs. the relative wave height for all the runs. In the bottom of the figure the theoretical return flow is shown at each wave height for the 2.5 sec. and 6. sec. waves.

time by averaging the record over a wave period which is centered at that point. This average is then computed at 32 points per wave period over the entire record. The water surface profile is shown on the top of each figure and the time scale is reference to the start of the measurements. The break in the time scale represents the amount of time elapsed between the two blocks of data.

For the nearly deep water wave (Fig. 4a), the return flow at relative depths of $-.33$ and $-.32$ show a gradual rize to zero during the first data block, while settling to nearly constant values in the second block. This was characteristic of the 2.5, 3.7, and 4.6 sec. waves, although the unsteadiness in the first data block was quite variable from one run to another. Figure 4b is characteristic of the 5.3 and 6. sec. waves, where the return flow is fairly stable from the start except for a subharmonic response which may be due to long waves excited at these wave periods.

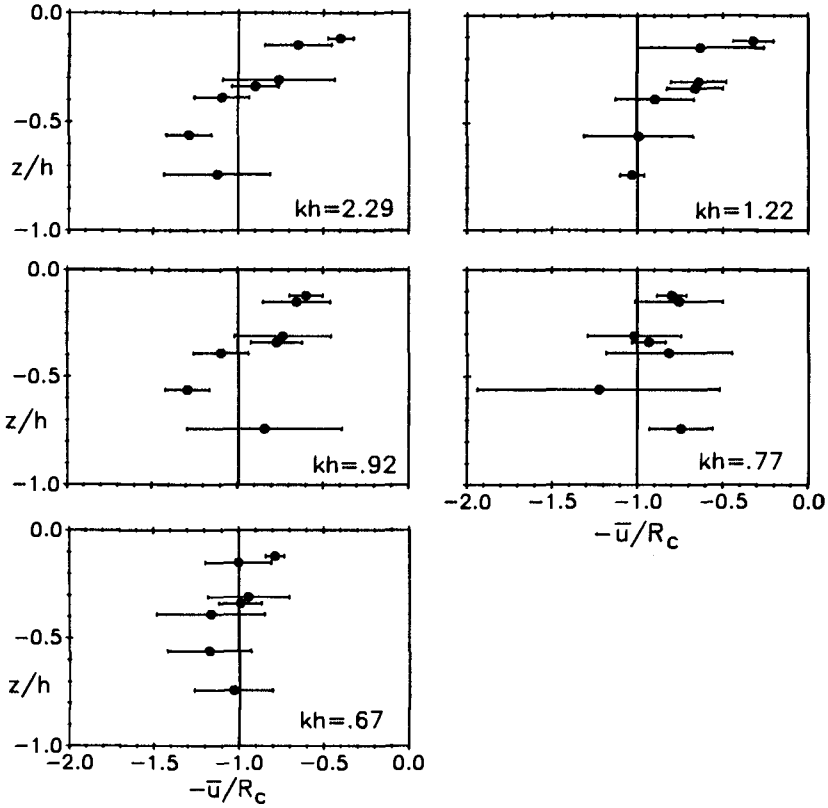


Figure 6: Mean and standard deviation of the nondimensional return flow, averaged over the wave height, vs. the relative depth for each wave period.

Surprisingly, $\bar{\eta}$ was positive for all the 2.5 second waves (Fig. 4a) and the smallest 3.7 sec. wave. For all the other wave conditions (Fig. 4b) $\bar{\eta}$ was negative in accordance with the theory of Brevik (1979) which always predicts a negative $\bar{\eta}$. For the shorter waves, $\bar{\eta}$ tended to stabilize much more rapidly and had no large jumps like that in (Fig. 4b) at $t/T=5$ which were characteristic of the longer waves records. In Figure 4b the η record shows the time lag between the free and Stokes waves, since the hump in the wave

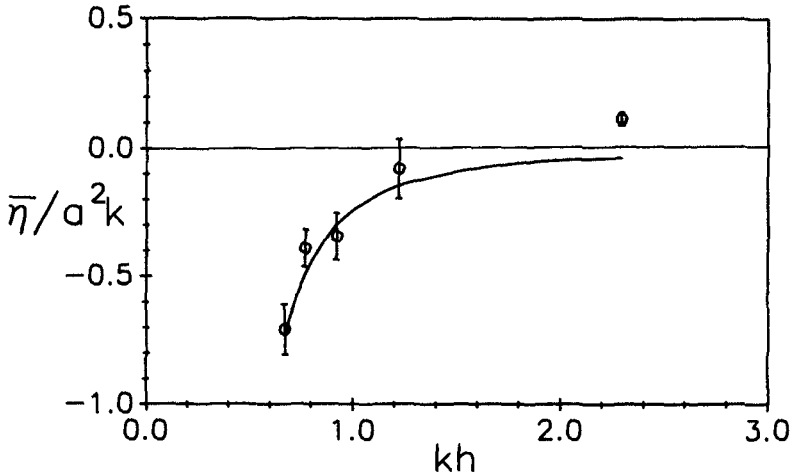


Figure 7: Mean water surface set-down vs. kh . The mean and standard deviation of the measurements are compared with the theory of Brevik (1979) which is shown as a solid line.

trough takes a few wave periods to develop.

Figure 5 shows \bar{u}/R_c vs. the relative wave height for all the runs. The data were grouped according to the wave period. The measured horizontal velocity was averaged over eight waves to compute \bar{u} . The average was started at about the third wave of constant height. This figure shows that on the average, Kim's theory predicts the return flows within about 18%. The smallest return flows had large variability which may be due to the numerical sensitivity of dividing two small numbers, and it may indicate a lower limit of the current meters sensitivity.

The values of $-\bar{u}/R_c$, averaged over the wave heights at each vertical location are shown for each wave period in Figure 6. The measured return flow was computed as in Figure 5. There is considerable vertical structure to the return flow which tends to diminish as the wave period increases. Due to this structure, Kim's theory overpredicts the return flow above $z/h = -0.4$, while it tends to underpredict the return flow below this level. It may be that if one could extend this trend, the return flow would become zero somewhere near the mean water surface and would be positive above

that point, becoming zero again at the wave crest elevation.

Figure 7 shows the normalized wave set-down plotted against kh . The mean water surface elevations were computed by averaging the last eight waves of the first 14 wave period data block. The measurements follow Brevik's (1979) theory closely for the longer waves, but as the wave length becomes smaller his theory tends to zero while the measurements show a wave set-up.

CONCLUSIONS

There is a return flow under large amplitude waves. For the conditions of this study Kim's theory is a good first approximation except very near the mean water surface. Including Kim's return flow model with stream function wave theory improves the agreement between the measured and predicted velocities. The return flow is a function of time and depth. Brevik's theory predicts the water surface set-down closely except for the nearly deep water waves. No dependence of the return flow or the water surface set-down with horizontal position could be determined from these data.

REFERENCES

- Brevik, I. (1979). "Remarks on set-down for wave groups and wave-current systems." *Coastal Engrg.*, 2, 313-326.
- Bullock, G.N., and Short, I. (1985). "Water particle velocities in regular waves." *J. of Waterway, Port, Coastal and Ocean Div.*, ASCE, 111(02), 189-200.
- Buhr Hansen, J., and Svendsen, Ib A. (1974). "Laboratory generation of waves of constant form." *Proc. 14th Conf. Coastal Engrg.*, 1, 321-339.
- Chandler, B.D., and Hinwood, J.B. (1982). "Combined wave-current forces on horizontal cylinders." *Proc. 18th Conf. Coastal Engrg.*, 3, 2171-2188.
- Dalrymple, R.A. (1976). "Wave-induced mass transport in water waves." *J. of Waterway, Port, Coastal and Ocean Div.*, ASCE, 102(02), 255-264.

- Jensen, R.E. (1978). "Finite amplitude deep water waves: a comparison of theoretical and experimental kinematics and dynamics." Masters Thesis, Department of Civil Engineering, Oregon State University, Corvallis, OR, U.S.A.
- Kim, T.I. (1984). "Mass transport in laboratory water wave flumes." Doctoral Thesis, Department of Civil Engineering, Oregon State University, Corvallis, OR, U.S.A.
- Kim, T.I., Hudspeth, R.T., and Sulisz, W. (1986). "Circulation kinematics in nonlinear laboratory waves." *Proc. 20th Conf. Coastal Engrg.*, 1, 381-395.
- Kobune, K. (1978). "Random wave velocity field from periodic theory." Masters Thesis, Department of Civil Engineering, Oregon State University, Corvallis, OR, U.S.A.
- Longuet-Higgins, M.S. (1953). "Mass transport in water waves." *Philosophical Transactions of the Royal Society of London*, Series A, 245(903), 535-581.
- Longuet-Higgins, M.S., and Stewart, R.W. (1964). "Radiation stresses in water waves; a physical discussion, with applications." *Deep-Sea Research*, 11, 529-562.
- Nath, J.H., (1978). "Drift speed of bouys in waves." *Proc. 16th Conf. Coastal Engrg.*, 3, 859-873.
- Ramsden, J.D. (1987). "Kinematics and return flow in a closed wave flume." Masters Thesis, Department of Civil Engineering, Oregon State University, Corvallis, OR, U.S.A.
- Russell, R.C.H., and Osorio, J.D.C. (1958). "An experimental investigation of drift profiles in a closed channel." *Proc. 6th Conf. Coastal Engrg.*, Council on Wave Research, ASCE, 171-193.
- Stokes, G.G. (1847). "On the theory of oscillatory waves." *Transactions of the Cambridge Philosophical Society*, London, England, 8:441-455.

CHAPTER 32

A HYDRODYNAMIC MODEL FOR COMPUTER AIDED HARBOUR ENGINEERING

J.L. Monsó*, A.S.- Arcilla* and J.P. Sierra*

Abstract

Coastal Hydrodynamic analyses are basic for the planning and assessment of activities in that area. An important application of these analyses is harbour lay-out and location. In this paper, hydrodynamic results of a numerical model based on Boussinesq-type equations are presented in the issue of Computer Aided Harbour Engineering. This model achieves overall second-order accuracy and has efficient modules of pre- and post-processing of information. The model has been used as a CAD tool for the planning and design of Spanish harbours. Its flexibility and economy of operation allow the model to be used, in the future, as a module of a global expert system for CAD harbour lay-out. This global expert system will provide a fully automatic design process. The output of this system will consist in the final optimized harbour configuration, considering all imposed constraints and requirements.

1. Introduction

Computer-aided harbour engineering has become a subject of considerable economic importance. The inputs for the design process are an initial harbour geometry, expected environmental conditions and a set of lay-out design specifications. Hydrodynamic descriptions of wave propagation, sea level oscillations and associated currents are provided by numerical 2-D models, usually based on shallow water Boussinesq-type equations. Analyses of obtained results are now performed by an expert engineer. From here, the appropriate modifications in geometry are carried out by an iterative process until a final optimized configuration is reached.

In this paper both the numerical model describing the flow and the expert system designing the optimal lay-out configuration (in lieu of the engineer) are presented. The first one is being used for commercial applications while the second one is under development. Nevertheless, the general structure of the system has already been defined.

2. Hydrodynamic Model Equations

The model is based on Boussinesq-type shallow-water equations.
*Maritime Engineering Laboratory.
Universidad Politécnica de Catalunya. Barcelona, Spain.

quations. They are similar to the Airy equations but include an additional term due to the vertical acceleration effect which, in turn, induces a non-hydrostatic pressure distribution. Alternatively, these equations include frequency-dispersion effects to the leading order.

The governing equations are obtained applying a perturbation technique to the vertically integrated continuity and momentum equations (Peregrine, 1967). From the perturbation analysis different sets of equations may be obtained for various orders of approximation. It is important to point out that the various long-wave equations available are always simplifications of the actual problem (prototype) with a degree of approximation depending on the physical characteristics of the phenomenon considered. These mean, in turn, different truncation errors that may be evaluated in terms of dimensionless parameters, ϵ and σ .

$$\epsilon \equiv \frac{\eta}{h} \quad (1)$$

$$\sigma \equiv \frac{h}{L} \quad (2)$$

in which η is the free-surface elevation, h is the water depth and L is a typical wave length. These parameters define the URSELL parameter, which characterizes the relative importance of nonlinearity and dispersion.

$$Ur = \epsilon/\sigma^2 \quad (3)$$

Most of the hydrodynamic conditions that can be found inside of a harbour are due (associated) to short-waves with $Ur = O(1)$, i.e. $\epsilon = O(\sigma^2)$. In such cases, Boussinesq equations result from the vertical integration of mass and momentum conservation equations, with an associated error of $O(\epsilon^2)$ or more generally $O(\epsilon^2, \epsilon^2, \epsilon^4)$.

The set of non-linear differential equations to be discretized are similar to the ones used by other authors (Abbot, 1981), (Hauguel, 1980) and have been developed with detail elsewhere (S.-Arcilla and Monsó, 1985). The following simplifying hypotheses are required in the derivation:

1. Newtonian, isotropic and incompressible fluid.
2. Slowly varying bottom topography.
3. Water depth is always small with respect to the wave length (i.e. $\sigma^2 \ll 1$).

The main variables of the problem (velocities, pressure and free-surface elevation) are expressed as power series:

$$f = f_0 + \epsilon f_1 + \epsilon^2 f_2 + \dots \quad (4)$$

in which f is any of these variables with the exception of vertical velocities that are written as:

$$\omega = \sigma(\omega_0 + \epsilon\omega_1 + \epsilon^2\omega_2 + \dots) \quad (5)$$

The resulting vertically integrated equations are:

1. Mass conservation:

$$\frac{\partial \eta}{\partial t} + \nabla \vec{Q} = 0 \tag{6}$$

2. Momentum conservation:

$$\frac{\partial \vec{Q}}{\partial t} + \frac{Q}{H} \nabla \vec{Q} + (\vec{Q} \nabla) \frac{\vec{Q}}{H} + gH \nabla \eta = \frac{1}{2} Hh \frac{\partial}{\partial t} \nabla (\nabla_h \vec{Q}) - \frac{1}{6} Hh^2 \cdot \frac{\partial}{\partial t} \nabla (\nabla \frac{\vec{Q}}{H}) \tag{7}$$

in which:

$$\vec{Q} = (p, q) \tag{8}$$

$$p = \int_{-h}^{\eta} u dz \tag{9}$$

$$q = \int_{-h}^{\eta} v dz \tag{10}$$

$$H = \eta + h \tag{11}$$

$$\nabla = (\partial / \partial x, \partial / \partial y) \tag{12}$$

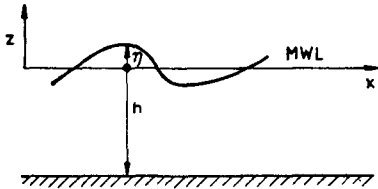


Fig.1: Definition sketch.

To simplify the resulting expressions, terms due to Coriolis forces, wind and bottom stresses, atmospheric pressure gradients, etc. have not been included in the equations. These terms do not introduce significant additional difficulties from the point of view of the numerical solution and shall not, therefore, be here considered.

The linear long-wave equations are easily derived from (6) and (7) and may be written as:

$$\frac{\partial \eta}{\partial t} + \nabla \vec{Q} = 0 \tag{13}$$

$$\frac{\partial \vec{Q}}{\partial t} + gh \nabla \eta = 0 \tag{14}$$

These lower order relation can be used for manipulating the third-derivative terms as demonstrated by (Long, 1964).

3. Hydrodynamic Model Numerical Solution

3.1. Discretization

The system of partial differential equations (6) and (7) can be discretized by means of an Abbot-type alternating di-

rection implicit finite-differences scheme.

The resulting algorithm is centred both in space and time and is solved by means of a double sweeping technique along both coordinate axes x and y . This technique allows the solution of the implicit equations without having to resort to matrix inversion operations, always cumbersome and time consuming.

This scheme is consistent with the original system of differential equations and it may also be shown to be conditionally stable and convergent (S.-Arcilla and Monsó, 1986). The overall truncation error is now of second order and can be improved to third-order with suitable correction terms added to the difference equations and appropriate centering of the convective and Boussinesq terms (Abbott, 1984). Time centering can be achieved by adequate averaging in time and accumulation of information in intermediate levels, as e.g. in (Abbott, 1973) and (S.-Arcilla and Monsó, 1986). An additional trick to improve centering of derivatives is what is usually known as "side-feeding". With this technique inconsistent approximations are introduced in the fractional (auxiliary) time steps that balance themselves to centered and consistent approximations when viewed over a complete time cycle.

Side-feeding is a device by which we can make use of information produced in the immediately preceding sweep to improve the approximation of cross-derivatives.

The right way of doing it is to reverse the sense of column and row computations so that the most up-to-date information comes from different directions in the individual stages (sweeps). This balances the inconsistency in space-derivative approximations when using values in different time levels. An alternative approach is to use quasi-Newton approximation techniques to achieve second-order discrete schemes compatible with the algorithmic structure.

3.2. Solution algorithm

In the Abbott-Ionescu type of schemes (1968) 4 discretized equations are employed. The first group of 2 equations (continuity and x -momentum) is solved with a double sweep along the x -axis in which p is raised a full Δt timestep while information on η is accumulated in an intermediate time-level. As pointed out in some previous papers η^{n+1} is only an intermediate value of a dependent variable in the fractional step scheme and is not representative of a true water level at time $(n+1/2)\Delta t$. In the second half time-step, η is raised from $t + \Delta t/2$ to $t + \Delta t$, while q is raised a full Δt , using the second group of two equations, continuity and y -momentum, with a double sweeping along the y -axis. The corresponding accumulation information is schematized in fig.2 and the staggered disposition of the problem variables is showed in fig. 3.

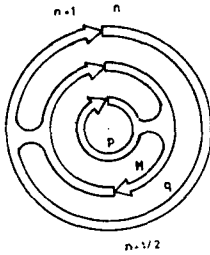


Fig. 2: "Clock diagram" representing the accumulation of information in the scheme using an intermediate time-level.

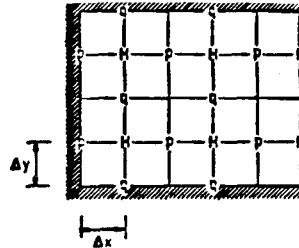


Fig. 3: Staggered spatial disposition of the problem variables (H, p, q) once both horizontal and vertical sweeps have been completed.

The full non-linear version of the scheme, however, requires η , p, q values at every nodal point. This is obtained by means of either consistent 2nd-order interpolation or additional double-sweeps.

One step further is a side-feeding scheme, advancing from time level n to time level n+1 by means of a fourfold division of the time step with the following algorithmic structure:

1. Sweep in y direction, laid down with decreasing x.
2. Sweep in x direction, laid down with decreasing y.
3. Sweep in x direction, laid down with increasing y.
4. Sweep in y direction, laid down with increasing x.

In this scheme side feeding is introduced to improve centering in the cross-derivative terms. These terms remain centered when viewed over a complete timestep, while making extensive use of "falsification" in each of the individual stages.

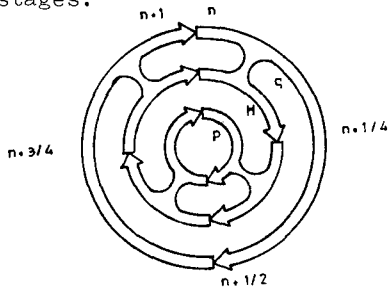


Fig. 4: "Clock diagram" representing the accumulation of information in the scheme using 3 intermediate time-levels.

In figure 4 we represent the information accumulating properties of this scheme adapted from the one presented in (Abbott, 1988).

Close to the boundaries, application of side-feeding presents essentially the same problems as other alternative computations of convective, cross momentum and Boussinesq terms. Information on all dependent variables η , p, q at the boundaries is needed but not always known. To solve

this problem, estimates of the variables have to be provided. Extrapolation can always be used, but may introduce 1st. order truncation error that can spread all over the domain and even introduce unstable components.

Another source of error present in these schemes is the inappropriate centering of the coefficients in the discretized equations. The difficulty arises when their form is not algorithmically compatible with the employed tri-diagonal al-

gorithmic structures (i.e. they cannot be directly introduced without resorting to iteration).

Furthermore, if one looks for a higher accuracy, it is necessary to add correction terms to obtain third order truncation errors because 2nd order differences introduce an error which is of the same order and type as terms in the momentum equation (Boussinesq terms) describing vertical acceleration.

An order-of magnitude analysis has shown that the third order correction terms corresponding to convective, cross-derivatives and Boussinesq terms are much smaller than other terms.

Apart from the numerical schemes, already presented, we are now implementing an "implicit leap-frog" scheme which is both space and time staggered. Here, from the mass conservation law (4), four discretized equations are obtained. If side feeding is considered as well, 8 discretized equations have to be solved. For the linear 2-D case those 4 equations (excluding side-feeding) are the following:

$$\frac{1}{\Delta t} (\eta_{j,k}^{n+1/2} - \eta_{j,k}^{n-1/2}) + \frac{1}{4\Delta x} (P_{j+1,k}^{n+1} - P_{j-1,k}^{n+1} + P_{j+1,k}^{n-1} - P_{j-1,k}^{n-1}) + \frac{1}{2\Delta y} (q_{j,k+1}^n - q_{j,k-1}^n) = 0 \tag{15}$$

$$\frac{1}{2\Delta t} (P_{j,k}^{n+1} - P_{j,k}^{n-1}) + \frac{gh}{4\Delta x} (\eta_{j+1,k}^{n+1/2} - \eta_{j-1,k}^{n+1/2} + \eta_{j+1,k}^{n-1/2} - \eta_{j-1,k}^{n-1/2}) = 0 \tag{16}$$

$$\frac{1}{\Delta t} (\eta_{j,k}^{n+3/2} - \eta_{j,k}^{n+1/2}) + \frac{1}{2\Delta x} (P_{j+1,k}^{n+1} - P_{j-1,k}^{n+1}) + \frac{1}{4\Delta y} (q_{j,k+1}^{n+2} - q_{j,k-1}^{n+2} + q_{j,k+1}^n - q_{j,k-1}^n) = 0 \tag{17}$$

$$\frac{1}{2\Delta t} (q_{j,k}^{n+2} - q_{j,k}^n) + \frac{gh}{4\Delta y} (\eta_{j,k+1}^{n+3/2} - \eta_{j,k-1}^{n+3/2} + \eta_{j,k+1}^{n+1/2} - \eta_{j,k-1}^{n+1/2}) = 0 \tag{18}$$

In Fig. 5 the clock diagram of this time is shown.

The advantages of this algorithm with respect to classical ADI schemes are:
 1. Symmetric treatment of all variables respect to x and y axes, i.e. total isotropy.

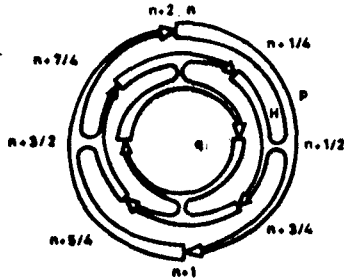


Fig.5: "Clock diagram" of the implicit space - time staggered algorithm

2. Splitted discretized mass equations staggered in space and time.
3. Better time-centering of H, as used in the coefficients.
4. No fractioned step correction on the continuity equation is needed to obtain better performance.
5. Easier implementation of open boundary conditions.

The main disadvantage is that all variables are calculated at different time levels, but this is not a severe limitation.

3.3. Boundary conditions

The number of boundary conditions required by the hyperbolic system presented in the previous section is determined by the number of characteristic lines (in 1-D) or surfaces (in 2-D) defined in the considered area (Daubert and Graffe, 1967). The conditions must also define a well-posed problem and allow the exit of waves generated inside the domain.

In recent literature (Verboom et al., 1983) there have been several references to weakly reflecting boundary conditions developed for the 1-D linear hyperbolic equations. These conditions are based on the Riemann invariants for the 1-D case, but are not a good approximation to the physical problem when waves are either not planar or obliquely incident to the open boundary. The use of weakly reflecting conditions in the aforementioned cases induce a non-physical reflection, even though far from boundary the results may be still acceptable. This explains the satisfactory engineering performances of many existing models, in spite of the limitations of their formulation for boundary conditions.

(A.S.-Arcilla and J.L. Monsó, 1986) presented a new approach to treat open boundaries. This new condition allows a reduction of the degree of spurious reflection which, in turn, means an improved accuracy of the model results. In this paper an improvement to the latter approach is proposed. It is based on a linear superposition of the in- and out-going mass-flux vectors, \vec{Q} and free-surface elevations, η , on the open boundary line. This may be written as:

$$(p, q) \equiv \vec{Q} = \vec{Q}_i + \vec{Q}_s \equiv (p_i + p_s, q_i + q_s) \quad (19)$$

in which

i, s: sub-indexes denoting incident (ingoing) and reflected (out-going) waves respectively.

$$\eta = \eta_i + \eta_s \quad (20)$$

The "in-going" values of the variables are known from the specified boundary conditions, and the three additional equations still required to solve the problem are the mass, x-momentum and y-momentum conservation laws.

3.4. Calibration

The presented numerical models have been first calibrated in linearized versions. The non-linear models have been subsequently tested with solitary and cnoidal waves which are analytical solutions of the differential equations when no frictional stresses, Coriolis forces, etc. are considered. Phase and amplitude errors were likewise studied for these non-linear versions, finding excellent results except for the case in which the wave height was an important part of the water depth (i.e. near wave breaking). A sample result is shown in figure 6.

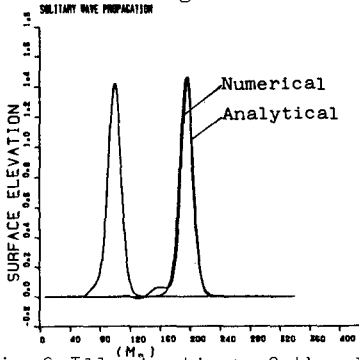


Fig.6: Illustration of the differences obtained with analytical and non-linear equations for 1D wave propagation along a canal of uniform depth.

Once the models had been calibrated with the standard type of boundary conditions, specific tests were designed to ascertain the performance of the open boundary condition described above. One of the most severe test-cases is a square domain with four open sides in which the direction of wave incidence coincides with one of the diagonals. An illustration of the results obtained for this case appears in figure 7. The contour-lines of the disturbed free-surface are, as should be, nearly parallel and perpendicular oriented to the wave propagation direction.

4. Expert System

Artificial Intelligence and Expert Systems (E.S.) are a relatively recent advance in civil engineering. The scope of E.S. projects is usually defined by experts rather than by knowledge engineers. For this reason there is still much work to be done by experts in this field.

With such a system access to high-level expertise can be made readily available to project engineers. This reduces overall costs and eliminates time-delays produced as a result of the expert's prior commitments. From an operational standpoint, immediate access to expert knowledge can significantly reduce non-productive times for labour. Moreover, the capability of the programme to incorporate feed-back information from the engineers can be used to improve its performance.

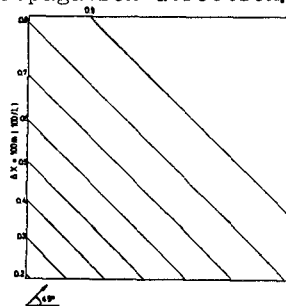


Fig.7: Contour-lines of the disturbed free surface for a square domain with 4 open sides and oblique wave incidence.

The basic structure of these programmes consists in a knowledge base and an inference mechanism. In the E.S. we are developing, the knowledge representation method is based on production rules. These rules consist in a set of conditions (such as width of harbour entrance, orientation of breakers, depths, etc.) and a set of actions (such as harbour lay-out and bathymetry modifications, etc.). When all conditions in a particular rule are true, the corresponding actions are executed. The conditions are contained in the "IF" part of the rule and the actions in the "THEN" part. Because human experts are not always certain about these rules, conditions and actions may incorporate some associated uncertainty factors. This allows a more realistic representation of the expert's knowledge, based on this degree of confidence in each rule.

The inference mechanism consists of two different methods, viz. forward-chaining and backward-chaining. In both forms the program acquires information either in the form of a question to the engineer or by means of accessing other programs and data bases.

In backward-chaining systems, the program possesses a built-in method to guess an initial solution, i.e. it assumes one particular harbour lay-out configuration. The system then attempts to prove that the assumption is correct, by requiring confirmation of all the prerequisite conditions for this particular lay-out to the expert engineer or by using its own inference capabilities. If the solution is disproved, the program chooses a different possible lay-out configuration and proceeds to test this new solution in the same manner.

In a forward-chaining system, the program has no "a-priori" knowledge of possible harbour lay-outs. It uses the acquired information to evaluate the tree of possibilities, as it progresses through the solution procedure. Information is gathered until the list of possible causes of problems has been narrowed down as much as possible. The reasoning progresses from an initial to a final state, in which the program has reached its goal.

We have selected a backward-chaining strategy, more suitable for our case, because we usually start from an initial lay-out, either imposed by the client or proposed by the expert engineer. This try-and-error or back-tracking technique is usually followed in most design processes. However, it is obvious that the aim of CAD researchers must be the completion of the forward-chaining system applied to harbour lay-out design. This strategy would give an optimal geometric configuration of the harbour with respect to the rules supplied with a minimum of subjective influences.

It is also possible to use a mixed strategy combining both forward-chaining and backward-chaining approaches. The main advantage of this strategy is that the engineer only needs to supply data which are relevant for the problem considered.

In current state-of-art, numerical models are used only in a post-design phase, to evaluate the performance of a final lay-out design, which will be modified only if the obtained results are unacceptable. Because of the time and cost required for a new lay-out analysis, numerical models are used primarily for verification, rather than for feedback or iterative-design improvements.

Our proposed global expert system has the following characteristics:

1. The entire modeling process is carried out on the computer using a combination of interactive and automatized modeling procedures.
2. Expert knowledge is used in the modeling software to increase the level of automatization and to aid the engineer in making better decisions.
3. The engineer is relieved of the need to make rudimentary calculations.
4. The engineer can always ask why the programmed modeling rules pretend to model a particular geometric configuration of the harbour.

The result will be not only a drastic reduction in the time and effort required, but also an improved reliability in the designing process.

5. Engineering Applications

In this section, results from an existing numerical model for wave propagation, based on Boussinesq-type shallow-water equations are presented in the context of harbour lay-out. This model is the basis for the improvements herein proposed.

The first case presented belongs to the wave propagation analysis carried out to design the new lay-out of the Bilbo Harbour in the North Coast of Spain.

The main aim of the study was to improve the hydrodynamic design of the harbour lay-out. The overall plan dimensions were approximately 7 Km. x 5 Km. which required more than 10^5 grid-points in the discretization.

The inputs for the runs were irregular time-series of free-surface elevations generated from a Jonswap spectral density function. This simulated wave record was made to enter the domain from different directions through the open boundary.

Figures 8 and 9 depict the contours of equal variance for two different geometries of the Bilbo Harbour. It is easy to understand now these and similar results may be used to estimate the lay-out design.

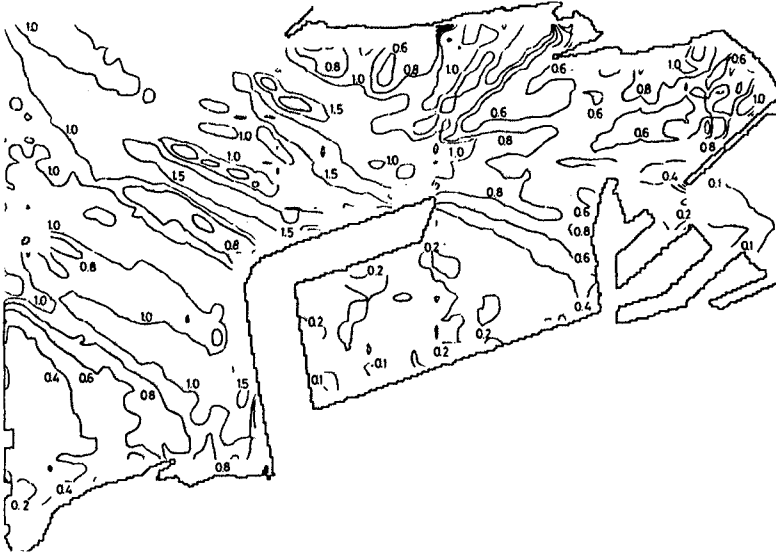


Fig.8: Isolines of variance for the wave propagation problem in the new Bilbo Harbour (Superport).



Fig.9: Isolines of variance for the wave propagation problem in the new Bilbo Harbour (Superport).

The second example presented is an application of the system to design the entrance of a harbour in the Catalonia Coast. After some variations in entrance geometry and wave climate conditions, a final optimized configuration was obtained. Figures 10 and 11 show two possible lay-outs.

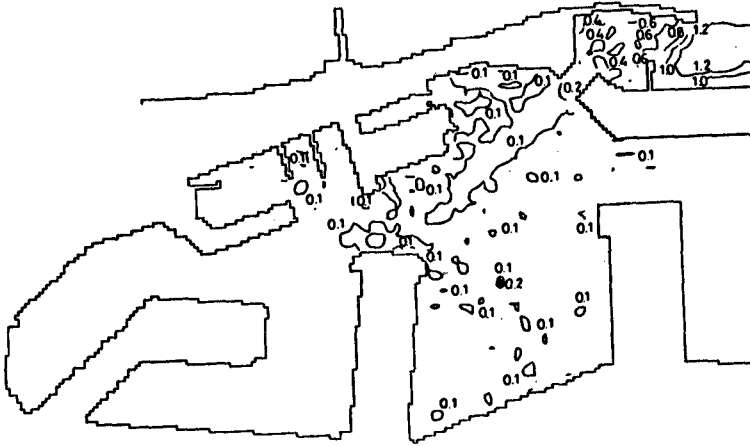


Fig.10: Equal variance contour-lines and entrance lay-out for the second example presented.

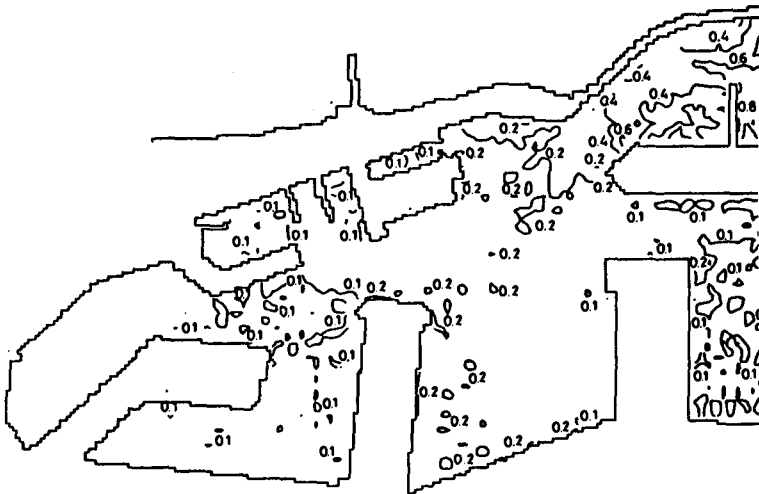


Fig.11: Equal variance contour lines and entrance lay-out for the second example presented.

The last case presented is an application of the system to design the lay-out of a marina at the Canary Islands, Spain. In this example we had to design the width and depth of the canal, including the entrance configuration, so as to obtain a better overall performance from a hydrodynamic standpoint (i.e. to provide shelter) without interfering with the set of operational constraints imposed. Some sample results corresponding to different entrance lay-outs are shown in figures 12 and 13.

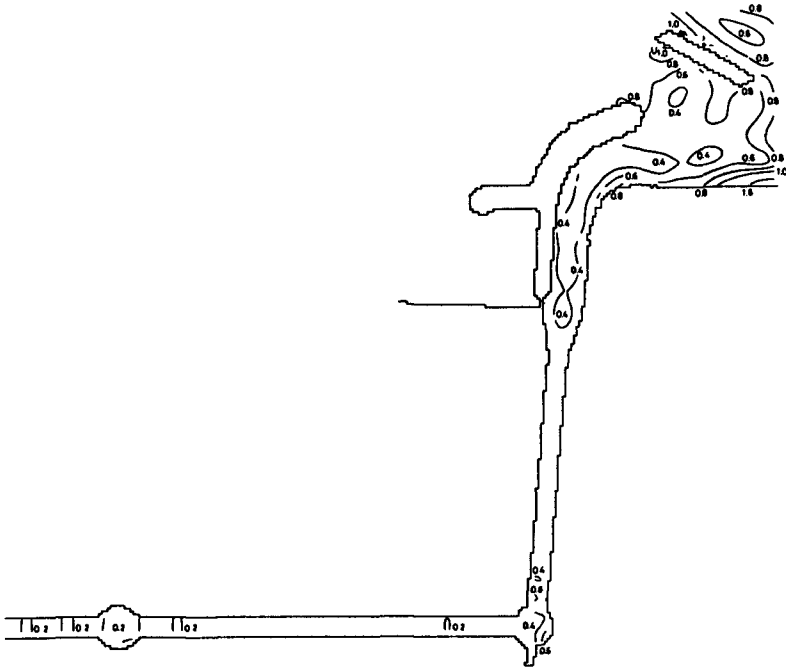


Fig.12: Marina lay-out and variance isolines

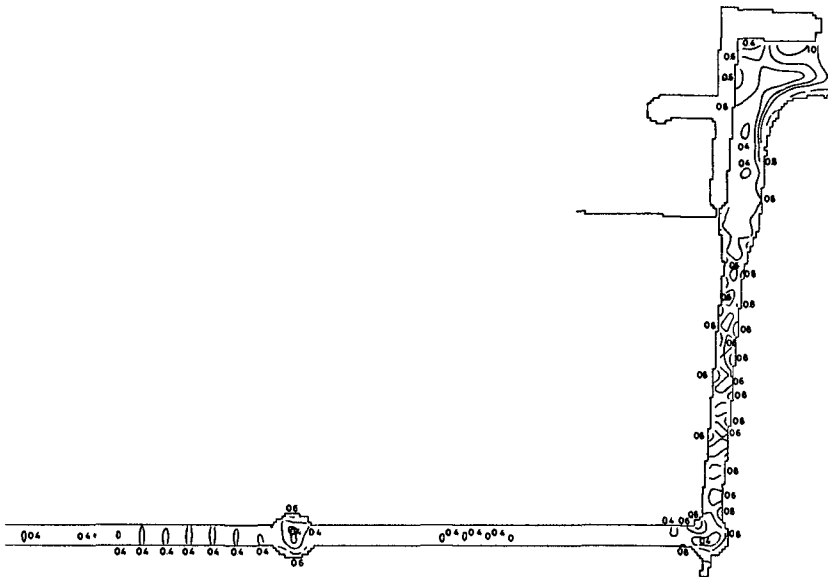


Fig.13: Marina lay-out and variance isolines

6. Conclusions

In this paper, a CAD expert system for harbour lay-out is presented. The system is based in previous experience acquired by the use of hydrodynamic numerical models for wave-current propagation. Some of the obtained results have been presented together with a new, improved numerical scheme.

The most important conclusions are the following:

1. A new ADI scheme has been presented combining the virtues of the leapfrog-scheme with the efficiency of ADI schemes. In this algorithm all the variables are evaluated at different time-levels. This allows a better centering of the discretized mass conservation equations together with a total isotropy of performance.
2. The proposed open boundary condition provides an improvement over former weakly reflecting conditions. This, in turn, means a higher degree of accuracy in the simulations.
3. A new third order scheme, which is now being developed is expected to provide improved results with finite amplitude wind waves in which the wave height is an important part of the water depth. This means a reduction of the number of mesh points, for the same truncation error.
4. The use of a numerical model, based on Boussinesq-type equations, as a module of a global expert system both from technical and economical standpoint will make it possible to obtain an improved design for harbour layouts.

References

- Abbott, M.B. and Ionescu, F (1968). On numerical computation of nearly-horizontal flows. *Jnl. Hyd. Res.*, 5.
- Abbott, M.B. (1979). *Computational Hydraulics: Elements of the theory of free-surface flows*. Pitman.
- Abbott, M.B., McCowan, A and Warren, I.R. (1981). Numerical modeling of free-surface flows that are 2-D in plan. *Transport models for inland and coastal waters*. Academic Press.
- Abbott, M.B., Damsgaard, A. and Rodenhuis, G.S.(1983). S 21 Jupiter, a design system for 2-D nearly-horizontal flows. *Jnl. Hyd. Resources*. Vol. 11.
- Abbott, M.B. McCowan, A.D. and Warren, I.R. (1984). Accuracy of short-wave numerical models. *Jnl. of Hydraulic Eng.* Vol. 110, n° 10.
- Daubert, A. and Graffe, O. (1967) Quelques aspects des écoulements presque horizontaux à deux dimensions en plan et non permanents. *La Houille Blanche*. vol. 22 n° 8.

Hauguel, A. (1980). Adaptation of tidal numerical models to shallow waters wave problems. Proc. 17th. I.C.C.E., Sydney, Australia.

Long, R.R. (1964). The initial value problems for long waves of finite amplitude. Jnl. Fluid Mech. Vol. 20. Part. 1

Peregrine, D.H. (1967). Long waves on a beach. Jnl. of Fluid Mech. Vol. 27, Part. 4.

S.- Arcilla, A. and Monsó, J.L. (1985). Modelado numérico del flujo en la zona costera. Dirección Gral. de Puertos y Costas. Programa de Clima Marítimo. MOPU, Pub. nº 7.

S.- Arcilla, A., Monsó, J.L. and Sierra, J.P. (1986). Modelado numérico no lineal de ondas de superficie libre. Dirección Gral. de Puertos y Costas. Programa de Clima Marítimo. Pub. 17.

S.- Arcilla, A. and Monsó, J.L.(1986). Numerical grid generation in coastal hydrodynamics. Proc. Int. Conf. Numerical Grid Gen. in Fluid Mech. Landshut, W.G.

S.- Arcilla, A. and Monsó, J.L. (1986) Numerical modeling of coastal flow. Proc. Envirosoft'86. Los Angeles, U.S.A.

S.- Arcilla et al. (1988). Numerical modeling of surf-zone dynamics. Progress report 2nd. part. (In preparation).

Verboom, G.K., Stelling, G.S. and Officer, M.J.(1983). Boundary conditions for the shallow water equations. Eng. App. of Comp. Hyd. I. Pitman.

CHAPTER 33

VERTICAL VARIATION OF UNDERTOW IN THE SURF ZONE

Akio Okayasu^{*}, Tomoya Shibayama^{**} and Kiyoshi Horikawa^{***}
S.M. JSCE M. JSCE, A.M. ASCE M. JSCE, F. ASCE

ABSTRACT

In order to establish a model of the vertical distribution of the undertow, laboratory experiments were performed on uniform slopes of 1/20 and 1/30. The turbulent velocity in the surf zone including the area close to the bottom was measured by using a two-component laser doppler velocimeter. The distributions of the mean Reynolds stress and the mean eddy viscosity coefficient were calculated. Based on the experimental results, a model to predict the vertical profile of the undertow was presented.

1. INTRODUCTION

The velocity field in the surf zone is of great importance in the coastal engineering problems. In order to predict the sediment transport rate or the wave attenuation rate in the surf zone, it is necessary to estimate the velocity distribution with high accuracy. Especially, the prediction of the velocity near the bottom is necessary for the evaluation of both of the sediment transport rate and the bottom friction factor. In this study, we focus our attention on the evaluation of the undertow in the inner region of the surf zone.

The existence of the undertow was first observed by Bagnold (1940). After that, some researches of the undertow were carried out with laboratory measurements [see e.g. Hansen and Svendsen (1984)]. Recently, Svendsen (1984) presented a model for estimating the vertical distribution of the undertow applying the eddy viscosity model. He used a boundary condition in which the mass transport velocity on the bottom was given by the Stokes wave theory. Tsuchiya et al.(1988) gave the boundary condition at the trough level.

* Graduate Student, Dept. of Civil Eng., Univ. of Tokyo, Bunkyo-ku, Tokyo, 113 JAPAN

** Associate Professor, Dept. of Civil Eng., Yokohama National Univ., Hodogaya-ku, Yokohama, 240 JAPAN

*** Professor Emeritus, Univ. of Tokyo; Professor, Dept. of Civil Eng., Saitama Univ., Urawa, Saitama, 338 JAPAN

Okayasu et al.(1986) also presented a model which had a slip condition on the bottom. Nadaoka and Hirose (1986) evaluated the diffusion coefficient in the surf zone. They also discussed the vertical distribution of the steady current on the basis of the distribution of the mean vorticity.

However, the above mentioned studies may have a problem in formulating the velocity field near the bottom, and therefore they may not accurately evaluate the velocity distribution near the bottom or the bottom shear stress. From this point of view, Svendsen (1988) theoretically evolved his model taking the bottom boundary layer into account, but the applicability is still unknown. One reason for that is the lack of the velocity data near the bottom.

In the present study, laboratory experiments on constant slopes were performed under various regular wave conditions. The velocity field in the surf zone including the area close to the bottom was measured by a two-component laser doppler velocimeter. The first objective of the present study is to evaluate the distributions of the mean Reynolds stress and the mean eddy viscosity coefficient in the surf zone based on the experimental results. The second objective is to present a model for estimating the vertical distribution of the steady current below the trough level which is valid through the inner region of the surf zone including near the bottom.

2 EXPERIMENT

2.1 Experimental Arrangements

Ten experiments were performed on 1/20 and 1/30 constant slopes of smooth beds for various incident waves. The flume was 23m long and 0.8m wide and had a partition at the center for the sake of keeping the phenomena to be two-dimensional. In Case 5, plastic mirrors were placed on the bottom to prevent reflected laser beams from disturbing the signal. This was proved to be successful in getting velocity data with high S/N (signal to noise) ratio. The still water

Table 1 Experimental condition

Case	slope	T (s)	H_i (cm)	H_0/L_0	x_b (cm)	x_p (cm)
1		2.00	8.50	0.0139	-270	-220
2		2.00	5.63	0.0092	-200	-165
3	1/20	1.17	9.87	0.0502	-275	spilling
4		0.91	6.69	0.0542	-200	spilling
5		1.50	7.48	0.0230	-250	-200
6		1.61	8.80	0.0232	-410	spilling
7		1.97	6.17	0.0104	-290	-230
8	1/30	1.96	8.22	0.0140	-410	spilling
9		1.12	8.26	0.0457	-350	spilling
10		1.23	6.05	0.0279	-290	spilling

depths in the offshore regions were 40.0cm (39.5cm in Case 5). The experimental condition is listed in Table 1.

In the table, T is the wave period, H_i the wave height in the offshore region of the constant depth, H_0/L_0 the deep-water wave steepness, x_b the wave breaking point, x_p the wave plunging point. The x -axis and z -axis were set to be shoreward and vertically upward, respectively. The origin of the co-ordinates was the shoreline at the still water level.

An arrangement of the measuring points which was rough in the horizontal direction and close in the vertical direction was adopted for the purpose of detailed measurements of the undertow profiles. The measuring points were arranged along 6 or 7 vertical measuring lines in every case except Case 5. The arrangement of Case 5 will be mentioned later. The first measuring line was set on the wave breaking point. The second line was located on the plunging point in case of plunging breakers, or the intermediate point between lines 1 and 3 for spilling breakers. From the third line, the measuring lines were arranged in the inner regions where the surface rollers developed well. The lowest measuring points in each measuring line are 1mm above the bottom in case of 1/20 slope, and for the cases of 1/30 slope they are 2mm above the bottom. The vertical distance of those points were 1-20mm and the highest points are near the mean water levels. For example, the arrangement of Case 1 is shown in Fig.1.

In Case 5, the measuring points were taken only close to the bottom to investigate the detail of the bottom boundary layer in the surf zone. Nine measuring lines were allocated every 40cm of distance from the offshore side of the breaking point to the still water shoreline. The measuring points were arranged 1, 2, 3, 5, 10 and 20mm above the bottom along each line.

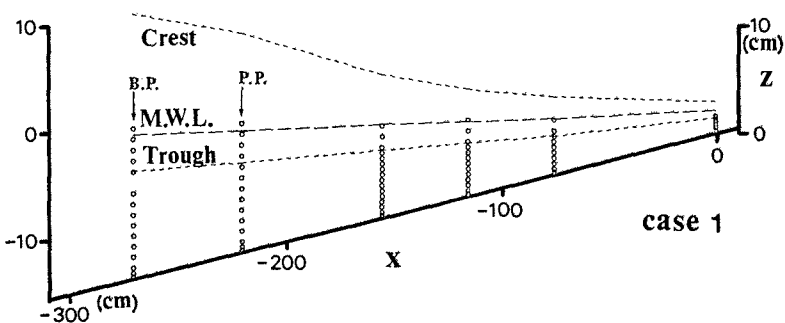


Fig.1 Arrangement of the measuring points for Case 1.

2.2 Data Processing and Analysis

A two-component laser doppler velocimeter was used to measure the time history of two-dimensional velocity vector lying on the xz -plane. The velocity data were sampled every 10ms and were converted into digital data over 100 wave periods. The data of the water surface elevation over the measuring point were also taken simultaneously by using a capacitance-type wave gage.

The ensemble mean (equi-phase-mean) value of velocity which is expressed by u in x -direction or w in z -direction was calculated as the average of the velocity at the same phase of every wave. The steady current was calculated from those ensemble mean values. The turbulence component denoted by u' or w' was determined as the deviation from the ensemble mean value. The Reynolds stress was calculated from the turbulence. The mean Reynolds stress $-\rho\overline{u'w'}$ was obtained by averaging the Reynolds stress over one wave period, where ρ is the water density. From the steady current and the mean Reynolds stress, the mean eddy viscosity coefficient ν_t was calculated by using the eddy viscosity model.

2.3 Experimental Results

Figure 2 gives an example of the steady current distribution for Case 2. It can be seen that the undertow profile in the inner region is significantly different from that around the breaking point. Figure 3 is the steady current of Case 5. In the inner region the velocity at the elevation of 1mm above the bottom indicates large value in the offshore direction, while it still directs onshore at the plunging point. This is because the oscillatory bottom boundary layer in the inner region does not develop well due to the agitation of the turbulence from the upper layer. The

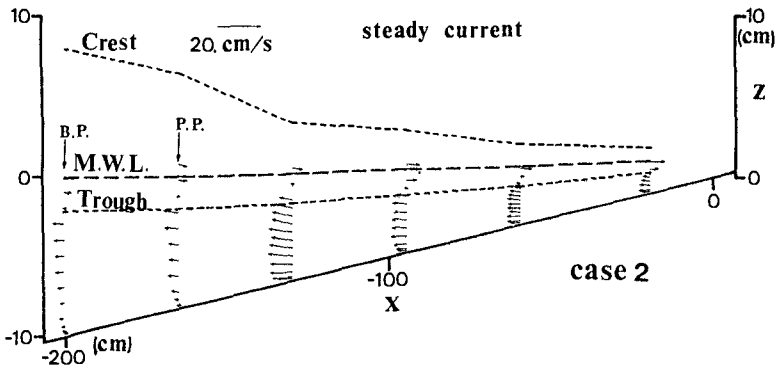


Fig.2 Distribution of the steady currents for Case 2.

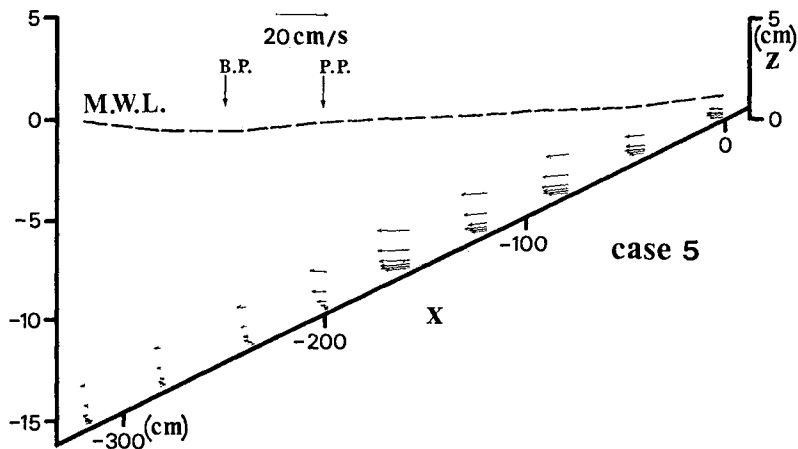


Fig.3 Distribution of the steady currents for Case 5.

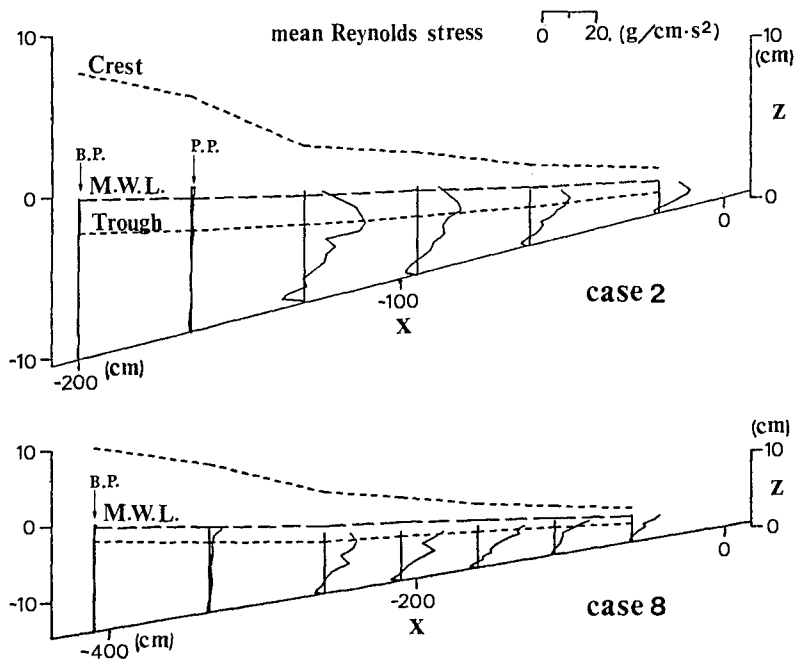


Fig.4 Distributions of the mean Reynolds stress for Cases 2 and 8.

influence by the bottom to the steady current can be seen up to 3mm above the bottom there.

Figure 4 shows the distributions of the mean Reynolds stress of Cases 2 and 8. The distributions of the mean eddy viscosity coefficient of those cases are given in Fig.5. In the figures, it can be seen that both of them decrease linearly from the trough level to the bottom in the inner region. On the bottom, the value of the mean eddy viscosity coefficient is very small compared with that at the trough level. This should corresponds to the fact that the turbulence produced by the large vortex on the front face of the wave crests is far larger than that generated near the bottom. But with respect to the mean Reynolds stress, it is observed that the offshoreward directed shear stress is too large to be neglected. Some researches were done with the assumption that the mean eddy viscosity is independent of the vertical coordinate [e.g. Svendsen and Hansen (1988) or Tsuchiya et al.(1988)], but the result of this study is not consistent with that assumption.

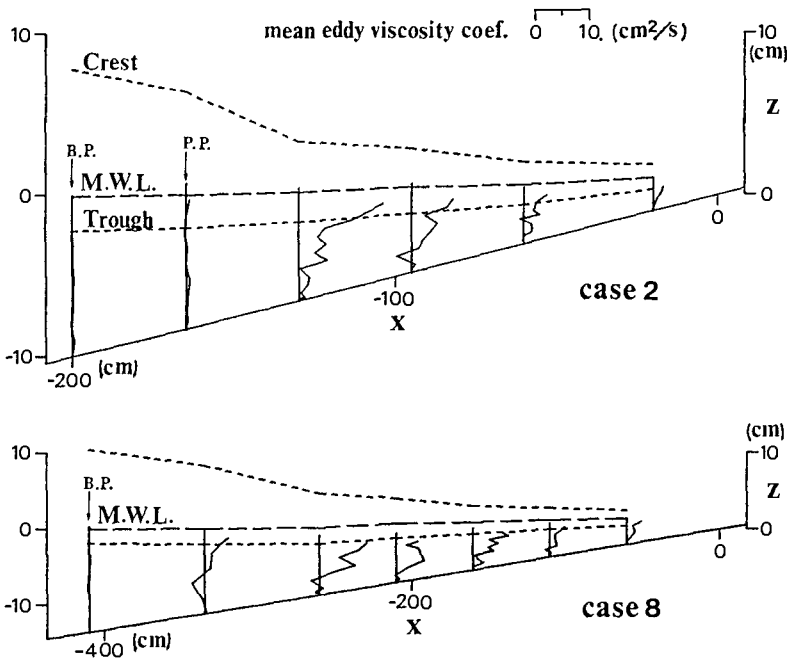


Fig.5 Distributions of the mean eddy viscosity coefficient for Cases 2 and 8.

3 MODELING OF UNDERTOW

3.1 On-offshore Variation of Vertically Averaged Undertow

It can be considered that the mass flux by the breaking waves in the inner region consists of two components, the mass flux by the wave motion and that by the large vortex formed just in front of the wave crest. That means, the vertically averaged value of the undertow can be separated into two parts which are the contribution U_S from the wave component and U_r from the onshore mass flux by the large vortex [Okayasu et al.(1986)].

U_S can be calculated from the wave profile by using the stream function method of Dean (1965). As the calculation by the stream function method is done with the assumption of no shear stress on the bottom, the velocity very close to the bottom should not agree with the actual velocity. However, it would not be a problem when we discuss about the vertically averaged on-offshore steady current because the oscillatory bottom boundary layer by the wave motion is much thinner than that of the steady current.

On the other hand, U_r in the inner region can be estimated by the square of the local wave height H as Svendsen (1984) did, and it does not depend on the incident wave condition. The onshore mass flux by the large vortex can be expressed as

$$M_r = \frac{AH^2}{T}, \quad (1)$$

where A is a constant. And U_r can be obtained by dividing M_r by the trough level d_t as

$$U_r = - \frac{AH^2}{d_t T}. \quad (2)$$

The calculated value U_c of the vertically averaged undertow in the inner region is

$$U_c = U_S + U_r = U_S - \frac{AH^2}{d_t T}. \quad (3)$$

In the equation, we used the value

$$A = 2.3, \quad (4)$$

in all cases based on the laboratory data. In order to decide A , the value

$$A' = - (U_m - U_S) \frac{d_t T}{H^2}, \quad (5)$$

was calculated for each measuring line except Case 5, where U_m is the vertically averaged value of the measured undertow. Next we averaged A' of all measuring lines in the inner region, and took the average again for all cases. The influence of the bottom slope to the constant A could not be

revealed by the experiments.

The comparison between the calculated value U_c and measured value U_m for Case 2 is shown in Fig.6. Here we set A equal to be 0 from the breaking point to the plunging point then changed the value linearly in the distance to the inner region. The value A was 2.3 in the inner region.

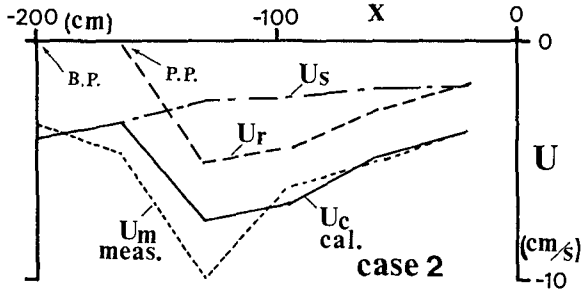


Fig.6 Comparison between the measured and the calculated value of the vertically averaged undertow for Case 2.

3.2 Modeling of Vertical Distributions of Mean Reynolds Stress and Mean Eddy Viscosity

Based on the experimental results mentioned in Section 2.3, the vertical distributions of the mean Reynolds stress and the mean eddy viscosity coefficient can be assumed as linear functions of the vertical elevation z . This assumption is different from that used by Svendsen and Hansen (1988) or Tsuchiya et al.(1988). Figure 7 shows this

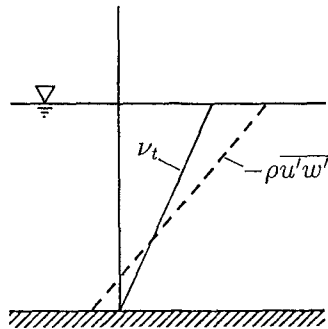


Fig.7 Assumed distributions of the mean Reynolds stress and the mean eddy viscosity coefficient.

model. The constants in the model were investigated as follows.

First, the coefficients of the linear functions for the measuring lines 4 and 5 were obtained for all cases by using the regression analysis. Then the coefficients were non-dimensionalized by using the water density ρ , the celerity c and the trough depth d_t as the representative values. At last, the averages of the measuring lines 4 and 5 were taken. Using these parameters, the linear functions was expressed as

$$-\rho \overline{u^T w^T} = \alpha_1 \rho \frac{c^2}{d_t} z' + \beta_1 \rho c^2, \quad (6)$$

$$v_t = \alpha_2 c z' + \beta_2 c d_t, \quad (7)$$

where α_1 , β_1 , α_2 and β_2 are dimensionless parameters and z' is the vertical elevation from the bottom. The wave celerity is expressed as

$$c = \sqrt{g (d_t + H)}, \quad (8)$$

on the basis of the solitary wave theory, where g is the gravity acceleration. Table 2 is the list of the dimensionless parameters.

Table 2 Dimensionless parameters for the distribution of $-\rho \overline{u^T w^T}$ and v_t

Case	slope	α_1	β_1	α_2	β_2	γ_2
1		0.0024	-0.00058	0.015	-0.00042	0.015
2		0.0027	-0.00062	0.015	-0.0015	0.014
3	1/20	0.0020	-0.00026	0.0098	0.0013	0.011
4		0.0022	-0.00016	0.015	0.0015	0.016
Ave. of 1/20		0.0023	-0.00041	0.014	0.00022	0.014
6		0.0018	-0.00036	0.010	0.000066	0.010
7		0.0015	-0.00024	0.017	-0.00052	0.016
8	1/30	0.0019	-0.00036	0.011	-0.00043	0.010
9		0.0013	-0.00024	0.0091	-0.00010	0.0081
10		0.0011	-0.00016	0.0046	0.00042	0.0050
Ave. of 1/30		0.0015	-0.00027	0.010	-0.00011	0.0099

In the table, the parameter β_2 is the dimensionless value of v_t on the bottom ($z' = 0$) and γ_2 is the value at the trough level ($z' = d_t$). We can find that β_2 is far smaller than γ_2 and it is consistent with the experimental result. Therefore, it should be possible to take $v_t = 0$ on the bottom. Equation (7) can be approximated as

$$v_t = \alpha_2 c z'. \quad (9)$$

In each bottom slope, the variance of the parameters is so small that the parameters can be regarded as constants. Hence the averaged values are taken for each slope.

Considering the influence of the bottom slope $\tan\beta$, we simply express the parameters as

$$\begin{aligned}\alpha_1 &= 0.046 \tan\beta , \\ \beta_1 &= -0.008 \tan\beta , \\ \alpha_2 &= 0.30 \tan\beta .\end{aligned}\tag{10}$$

Substituting Eq.(10) into Eqs.(6) and (9), we obtain the equations for the distributions of the mean Reynolds stress and the mean eddy viscosity coefficient as

$$-\rho \overline{u'w'} = 0.046 \tan\beta \rho \frac{c^2}{d_t} z' - 0.008 \tan\beta \rho c^2 ,\tag{11}$$

$$v_t = 0.30 \tan\beta c z' .\tag{12}$$

3.4 Vertical Variation of Undertow

By using the eddy viscosity model, the relation between the mean shear stress $\bar{\tau}$ acting on the horizontal plane and the steady current U in x -direction is expressed as

$$\bar{\tau} = \rho v_t \frac{\partial U}{\partial z} .\tag{13}$$

Transforming $\bar{\tau}$ to $-\rho \overline{u'w'}$ and considering Eq.(6), we obtain the equation

$$\frac{1}{\rho} \frac{\partial \bar{\tau}}{\partial z} = \frac{\partial}{\partial z} \left\{ v_t \frac{\partial U}{\partial z} \right\} \equiv C_1 ,\tag{14}$$

where C_1 is a constant. And from the Eq.(9), v_t can be expressed as

$$v_t = C_2 z' ,\tag{15}$$

where C_2 is also a constant. If using z' instead of z , we get

$$\frac{\partial}{\partial z'} \left\{ z' \frac{\partial U}{\partial z'} \right\} = \frac{C_1}{C_2} ,\tag{16}$$

from Eq.(14). This equation can be integrated by using integral constants C_3 and C_4 as

$$U = C_3 \ln z' + C_4 + \frac{C_1}{C_2} z' .\tag{17}$$

It can be considered that the third term of the right hand side of Eq.(17) directly expresses the "shear effect" termed by Nadaoka and Hirose (1986). C_1 and C_2 can be decided as

$$C_1 = 0.046 \tan\beta \frac{c^2}{d_t} ,\tag{18}$$

$$C_2 = 0.30 \tan\beta c ,\tag{19}$$

from Eqs.(11) and (12). The boundary condition at the trough level is given by using Eq.(13) as

$$\left. \frac{\partial U}{\partial z'} \right|_{d_t} = \frac{1}{\rho} \left. \frac{\bar{\tau}}{v_t} \right|_{d_t} = \frac{0.038 \tan \beta c^2}{C_2 d_t} . \quad (20)$$

Substituting Eq.(20) into the first derivation of Eq.(17) which is

$$\frac{\partial U}{\partial z'} = \frac{C_3}{z'} + \frac{C_1}{C_2} , \quad (21)$$

we obtain

$$C_3 = \left[\frac{0.038 \tan \beta c^2}{C_2 d_t} - \frac{C_1}{C_2} \right] d_t = -0.027c . \quad (22)$$

Furthermore, By using the relation

$$\begin{aligned} U_c &= \frac{1}{d_t} \int_0^{d_t} U dz' \\ &= C_3 (\ln d_t - 1) + C_4 + \frac{1}{2} \frac{C_1}{C_2} d_t , \end{aligned} \quad (23)$$

the constant C_4 is given as

$$C_4 = U_c + C_3 (1 - \ln d_t) - \frac{1}{2} \frac{C_1}{C_2} d_t . \quad (24)$$

From the equations above, the vertical distribution of the undertow can be obtained as

$$\begin{aligned} U &= U_c + C_3 \left(\ln \frac{z'}{d_t} + 1 \right) + \frac{C_1}{C_2} \left(z' - \frac{d_t}{2} \right) \\ &= -0.027c \ln \frac{z'}{d_t} + 0.15c \frac{z'}{d_t} - 0.10c + U_c . \end{aligned} \quad (25)$$

In the equation, the bottom steepness $\tan \beta$ does not appear.

4. COMPARISONS WITH THE EXPERIMENTAL RESULTS

Using Eq.(25), we can evaluate the undertow profile from the time history of the wave profile at that point. Figure 8 gives the comparisons between the measured and the calculated undertow profiles for the measuring lines 3 and 5 of 1/20 slope by using Eq.(25). In the figure, a dimensionless value which is obtained by dividing U by the absolute value of U_c is taken for the horizontal coordinate, and the vertical coordinate is z'/d_t . The positions of the measuring lines are indicated by x/x_b . The comparisons for the 1/30 slope are also shown in Fig.9.

The nondimensional parameters which determine the each constant in Eq.(25) are invariant through the all cases and

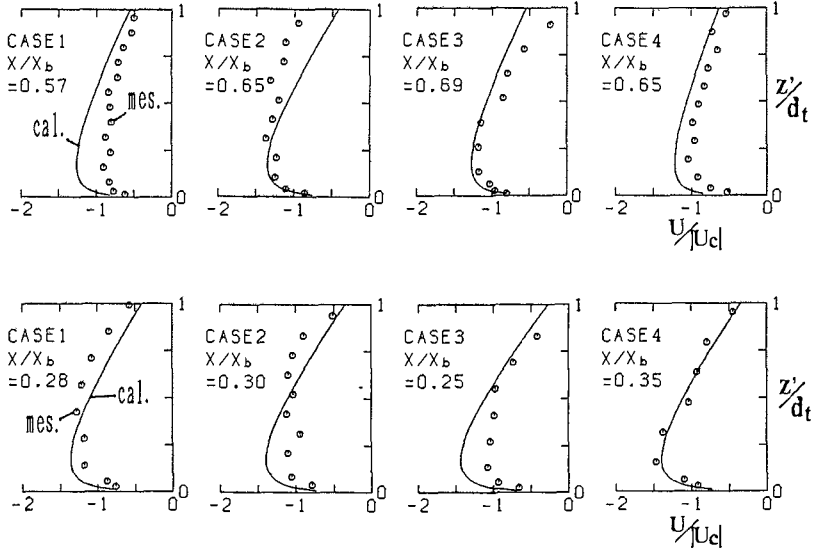


Fig.8 Comparisons between the measured and the calculated undertow profiles for the 1/20 slope.

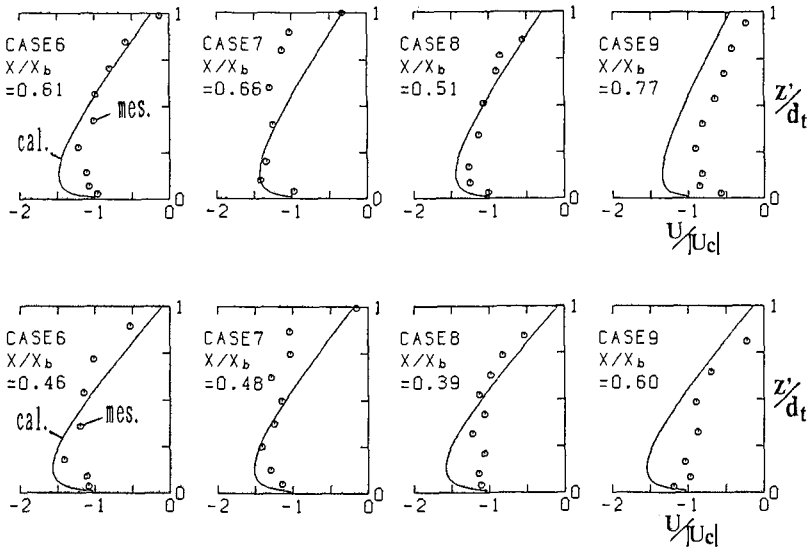


Fig.9 Comparisons between the measured and the calculated undertow profiles for the 1/30 slope.

the agreement between the measured and calculated values is good. However, in general the gradient of the calculated values are a little smaller than the measured values in the upper regions, that means the further investigation for estimating C_1 and C_2 in Eq.(25) is required.

Figure 10 shows the comparisons when we apply Eq.(25) to Case 5 of the 1/20 slope. The agreement is well especially in the area close to the bottom. It can be said that the model is usable for evaluating the steady current distribution close to the bottom in various conditions.

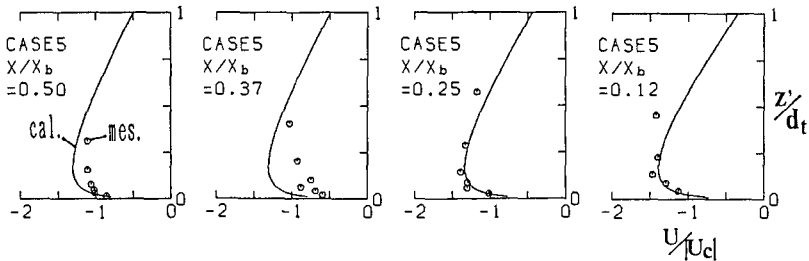


Fig.10 Comparisons between the measured and the calculated undertow profiles for Case 5.

5. CONCLUDING REMARKS

The velocity distribution in the surf zone on 1/20 and 1/30 constant slopes was measured in detail by using a two-component laser doppler velocimeter. The distributions of the steady current, the mean Reynolds stress and the mean eddy viscosity coefficient were evaluated. A model was proposed to estimate the vertical distribution of the undertow in the inner region, especially close to the bottom.

The conclusions are as follows.

(1) The mean Reynolds stress and the mean eddy viscosity coefficient in the inner region can be regarded as linear functions of the vertical elevation. The offshore directed mean shear stress on the bottom is so large that it can not be neglected. The nondimensional parameters which express the linear distribution can be expressed in terms of the bottom slope.

(2) The vertically averaged on-offshore steady current can be evaluated from the sum of two components: the first component is resulted from the wave component and the second one from the large vortex formed just in front of the wave crest. The second component can be evaluated by the square of the local wave height.

(3) The vertical distribution of the undertow in the inner region of the surf zone can be estimated by using Eq.(25). The calculated undertow profiles agree well with the measured values near the bottom. However, further investigations are required for the accurate evaluation around the trough level.

REFERENCES

- Bagnold, R.A. (1940) : Beach formation by waves; some model experiments in a wave tank. *J. Institute Civil Eng.*, Vol.15, pp.27-52.
- Dean, R.G. (1965) : Stream function representation of nonlinear ocean wave, *J. Geophysical Res.*, Vol.70, No.18, pp.4561-4572.
- Hansen, J.B. and I.A. Svendsen (1984) : A theoretical and experimental study of undertow, *Proc. 19th ICCE.*, pp.2246-2262.
- Nadaoka, K. and F. Hirose (1986) : A modeling of water particle dispersion under breaking waves in the surf zone, *Proc. 33rd Japanese Conf. Coastal Eng.*, pp.26-30. (in Japanese)
- Okayasu, A., T. Shibayama and N. Mimura (1986) : Velocity field under plunging waves, *Proc. of 20th ICCE.*, pp.660-674.
- Svendsen, I.A. (1984) : Mass flux and undertow in a surf zone, *Coastal Eng.*, Vol.8, pp.347-365
- Svendsen, I.A. and J.B. Hansen (1988) : Cross-shore currents in surf zone modeling, *Coastal Eng.*, Vol.12, pp.23-42.
- Tsuchiya, Y., T. Yamashita and M. Uemoto (1988) : A model of undertow in the surf zone, *Coastal Eng. in Japan*, Vol.30, No.2, pp.63-73.

CHAPTER 34

Spectral Wave Attenuation by Bottom Friction: Theory

Ole Secher Madsen¹, Ying-Keung Poon², and Hans C. Graber³

ABSTRACT

Based on the linearized form of the boundary layer equations and a simple eddy viscosity formulation of shear stress, the turbulent bottom boundary layer flow is obtained for a wave motion specified by its directional spectrum. Closure is obtained by requiring the solution to reduce, in the limit, to that of a simple harmonic wave. The resulting dissipation is obtained in spectral form with a single friction factor determined from knowledge of the bottom roughness and an equivalent monochromatic wave having the same root-mean-square near-bottom orbital velocity and excursion amplitude as the specified wave spectrum. The total spectral dissipation rate is obtained by integration and compared with the average dissipation obtained from a model considering the statistics of individual waves defined by their maximum orbital velocity and zero-crossing period. The agreement between the two different evaluations of total spectral dissipation supports the validity of the spectral dissipation model.

INTRODUCTION

As waves propagate into water of finite depth the presence of a bottom manifests itself in various ways, e.g., causing shoaling, depth-refraction, and dissipation of energy. In the present context of wave attenuation by bottom friction the most important manifestation of the bottom is the establishment of a bottom boundary layer in the immediate vicinity of the bottom. Within this wave boundary layer, of thickness a few cm, the flow is strongly sheared, generally turbulent, and associated with significant dissipation of energy.

Several models for turbulent wave boundary layer flows and associated energy dissipation have been developed, e.g., Putnam and Johnson (1949), Kajiura (1964, 1968), and Jonsson (1966), to mention a few of the earliest contributions. According to these (and later contributions) the

1 Professor of Civil Engineering, R. M. Parsons Laboratory, MIT, Cambridge, MA 02139, USA

2 Graduate student, R. M. Parsons Laboratory, MIT

3 Assistant Scientist, Woods Hole Oceanographic Institution, Woods Hole, MA 02543, USA

attenuation of periodic waves in constant but finite water depth, h , may be expressed formally through the conservation of wave energy equation

$$\frac{\partial E}{\partial t} + \frac{\partial E_f}{\partial x} = -E_d \quad (1)$$

where, according to linear wave theory,

$$\begin{aligned} E &= \frac{1}{2} \rho g a^2 \\ E_f &= c_g E = \frac{1}{2} \left[1 + \frac{2kh}{\sinh 2kh} \right] \frac{\omega}{k} E \\ \omega^2 &= kg \tanh kh \end{aligned} \quad (2)$$

and the average rate of energy dissipation by bottom friction is obtained from

$$E_d = \langle \tau_b u_{\infty} \rangle \simeq \frac{1}{4} \rho f_w u_{br} u_b^2 \quad (3)$$

in which f_w is the wave friction factor (Jonsson, 1966), $u_b = (a\omega/\sinh kh)$ is the near-bottom maximum orbital velocity, and $u_{br} = (8/3\pi)u_b$. Use of Eqs. (1) through (3) allows evaluation of the wave attenuation due to bottom friction to be performed from knowledge of the periodic wave characteristics--amplitude $a = H/2$ and radian frequency $\omega = 2\pi/T$ --and the bottom roughness. For practical applications, however, real waves are not periodic and the question arises which wave amplitude (wave height) and period to choose to represent the random wave field.

An alternative approach was taken by Hasselmann and Collins (1968) who evaluated the average rate of dissipation from $\langle \tau_b u_{\infty} \rangle$ treating $\tau_b = \frac{1}{2} \rho f_w |u_{\infty}| u_{\infty}$ and u_{∞} as random variables defined by the directional spectrum of u_{∞} , the near-bottom orbital velocity. A simplified version of their analysis, corresponding to the use of Eqs. (1) through (3) for each wave component with u_{br} being the orbital velocity having the same root-mean-square value as the specified spectrum, was later proposed and used by Collins (1972) to evaluate the spectral attenuation of waves due to bottom friction. While overcoming the problem of which equivalent periodic wave to choose to represent the wave spectrum, the Hasselmann-Collins approach does not provide information on how the friction factor is related to bottom roughness. Thus the friction factor, f_w , becomes a parameter to be fitted by comparison of model predictions and observations, e.g., Hsiao and Shemdin (1978).

To overcome the problem associated with available models for the prediction of attenuation of waves by bottom friction, we start from the linear equation governing the bottom boundary layer flow. A simple, time-invariant eddy viscosity formulation is used to express the turbulent shear stress and a solution for the boundary layer flow is obtained for a wave motion specified by its directional spectrum. The problem is closed by requiring the spectral representation of the bottom shear stress to reduce the known solution, e.g., Grant and Madsen (1979, 1986), in the limit of a single periodic wave. In this manner theoretical justification is obtained for the application of Eqs. (1) through (3) for each spectral wave component with u_{br}

as specified by Collins (1972). However, in contrast to Collins's study the present analysis also results in a relationship for the friction factor, f_w , in terms of spectral wave characteristics--represented by an equivalent periodic wave having the same root-mean-square near-bottom orbital velocity and excursion amplitude--and the bottom roughness.

Integration of the spectral wave dissipation model over all frequencies produces an expression for the total average dissipation rate associated with a wave motion specified by its frequency spectrum. This estimate of the average dissipation rate is compared with that obtained from a model which considers the joint probability of near-bottom orbital velocity and zero-crossing period derived from the near-bottom orbital velocity spectrum following Longuet-Higgins (1983). Besides resulting in comparable estimates of total average dissipation, thereby supporting the validity of the spectral dissipation model, the total dissipation rate is expressed in terms of representative surface wave characteristics, root-mean-square wave height and significant period, which greatly facilitates the approximate computation of wave attenuation by bottom friction.

SPECTRAL DISSIPATION MODEL

Governing Equation

We start by adopting the linearized boundary layer approximation for the flow above a horizontal bottom located at $z = 0$, i.e.,

$$\frac{\partial \vec{u}}{\partial t} = -\nabla(p/\rho) + \frac{\partial(\vec{\tau}/\rho)}{\partial z} \quad (4)$$

in which $\vec{u} = (u, v)$ and $\vec{\tau}$ are the velocity and shear stress, respectively, ∇ is the horizontal (x, y) gradient operator, and ρ is the fluid density. Realizing that the shear stress vanishes while the velocity approaches its free stream value as $z \rightarrow \infty$, we have

$$\frac{\partial \vec{u}_\infty}{\partial t} = -\nabla(p/\rho) \quad (5)$$

For small values of z , i.e., as the solid boundary is approached, the no-slip condition requires the velocity to approach zero. Thus, we obtain as $z \rightarrow 0$

$$\frac{\partial(\vec{\tau}/\rho)}{\partial z} = -\frac{\partial \vec{u}_\infty}{\partial t} = \nabla(p/\rho) \quad (6)$$

which, by integration from $z = "0"$, where $\vec{\tau} = \vec{\tau}_b$, to $z = 0^+$ yields

$$\vec{\tau} = \vec{\tau}_b - \int_{"0"}^{0^+} \rho \frac{\partial \vec{u}_\infty}{\partial t} dz \simeq \vec{\tau}_b \quad (7)$$

i.e., a constant shear stress equal to the boundary shear stress within a region close to the solid boundary

($z \leq 0^+$). In this context it should be pointed out that "constant" refers to the spatial not the temporal variation, since τ_b clearly will vary with time.

Thus in a region very close to the solid bottom the "law of the wall" is valid. In analogy with steady turbulent flows over a rough wall we therefore expect a logarithmic velocity profile for $z \leq 0^+$. This requirement is met if we express the shear stress through the concept of a vertical turbulent eddy viscosity, ν_t , which varies linearly with distance from the bottom, i.e., if we take

$$\tau/\rho = \nu_t \frac{\partial \vec{u}}{\partial z} = \kappa u_{*r} z \frac{\partial \vec{u}}{\partial z} \quad (8)$$

Strictly speaking we should carry the dynamic analogy with steady turbulent flows further by requiring the friction velocity u_{*r} to be $\sqrt{(\tau_b/\rho)}$ with τ_b denoting the time-varying magnitude of the bottom shear stress. However, Trowbridge and Madsen (1984a, b) considered this complication, in the context of periodic wave boundary layers, and concluded that a time-invariant eddy viscosity suffices so long as the boundary layer analysis is limited to first order in wave steepness as is the case here. For this reason we adopt the expression for the turbulent shear stress given by Eq. (8) with u_{*r} denoting a time-invariant representative friction velocity.

Incorporating Eqs. (5) and (8) in (4) and realizing that $u_\infty \neq u_\infty(z)$ we obtain

$$\frac{\partial(\vec{u} - \vec{u}_\infty)}{\partial t} = \frac{\partial}{\partial z} \left[\kappa u_{*r} z \frac{\partial(\vec{u} - \vec{u}_\infty)}{\partial z} \right] \quad (9)$$

governing the turbulent flow within the bottom boundary layer.

Solution

To solve the governing equation we specify the free stream velocity as that associated with a directional wave spectrum, i.e.,

$$\vec{u}_\infty = \sum_n \sum_m u_{b,nm} (\cos \theta_m, \sin \theta_m) e^{i\omega_n t} \quad (10)$$

in which n and m denote summation over frequencies and directions, respectively. With this representation of u_∞ the velocity amplitudes $u_{b,nm}$ are related to the near-bottom orbital velocity spectrum and to the directional surface amplitude spectrum through

$$u_{b,nm} = \sqrt{2S_{u_b}(\omega_n, \theta_m) d\theta d\omega} = \frac{\omega_n}{\sinh k_h h} \sqrt{2S_\eta(\omega_n, \theta_m) d\theta d\omega} \quad (11)$$

in which ω_n and k_n are related through the linear dispersion relationship, Eq. (2).

The linearity of Eq. (9) combined with the assumed time-invariant representative friction velocity suggests a solution of the form

$$\vec{u} = \sum_n \sum_m u_{nm} (\cos \theta_m, \sin \theta_m) e^{i\omega_n t} \quad (12)$$

in which $u_{nm} = u_{nm}(z)$ represents the complex velocity component amplitudes and only the real part of Eq. (12) constitutes the solution sought.

Introducing Eqs. (10) and (12) in (9) we obtain the equation for each velocity component

$$\frac{d}{d\zeta_n} \left[\zeta_n \frac{d\tilde{u}_{nm}}{d\zeta_n} \right] - i\tilde{u}_{nm} = 0 \quad (13)$$

in which

$$\begin{aligned} \tilde{u}_{nm} &= u_{nm} - u_{b,nm} \\ \zeta_n &= z\omega_n / (\kappa u_{*r}) \end{aligned} \quad (14)$$

The boundary conditions to be satisfied by each component are

$$\begin{aligned} \tilde{u}_{nm} &\rightarrow 0 & \text{as} & \zeta_n \rightarrow \infty \\ \tilde{u}_{nm} &= -u_{b,nm} & \text{for} & \zeta_n = \zeta_{n0} = z_0\omega_n / (\kappa u_{*r}) \end{aligned} \quad (15)$$

where, once again, we have drawn upon the analogy with steady turbulent flows over a rough boundary by requiring the no-slip condition to be satisfied at $z = z_0 = k_b/30$, where k_b is the equivalent Nikuradse sand grain roughness of the bottom.

The solution to Eq. (13) subject to the boundary conditions stated in Eq. (15) may be written in terms of Kelvin functions of zeroth order (e.g., Hildebrand, 1976)

$$\tilde{u}_{nm} = - \frac{\text{ker}2\sqrt{\zeta_n} + i \text{kei}2\sqrt{\zeta_n}}{\text{ker}2\sqrt{\zeta_{n0}} + i \text{kei}2\sqrt{\zeta_{n0}}} u_{b,nm} \quad (16)$$

Invoking the limiting form of Kelvin functions for small values of their arguments (Abramowitz and Stegun, 1972, Ch. 9) we obtain from Eqs. (12), (14), and (16)

$$|\vec{u}_{nm}| = \frac{u_{b,nm}}{\left[\left[\ln \frac{\kappa u_{*r}}{z_0 \omega_n} - 1.15 \right]^2 + \left[\frac{\pi}{2} \right]^2 \right]^{1/2}} \ln \frac{z}{z_0} \cos(\omega_n t + \phi_n) \quad (17)$$

where

$$\tan \phi_n = \frac{\pi/2}{\ln \frac{\kappa u_{*r}}{z_0 \omega_n} - 1.15} \quad (18)$$

valid for small z .

Closure

While a solution for the turbulent flow in the wave boundary layer has been obtained, this solution involves the representative friction velocity u_{*r} which is yet to be

specified. From the expression for the bottom shear stress, Eq. (8), we obtain with the velocity solution given by Eq. (17)

$$\begin{aligned} \frac{1}{\rho} \tau_{b, nm} &= \lim_{z \rightarrow 0} \left[\kappa u_{*r} z \frac{\partial u_{nm}}{\partial z} \right] \\ &= \frac{\kappa u_{*r}}{\left[\left[\ln \frac{\kappa u_{*r}}{z_0 \omega_n} - 1.15 \right]^2 + \left[\frac{\pi}{2} \right]^2 \right]^{1/2}} u_{b, nm} \end{aligned} \quad (19)$$

Now, in deriving the asymptotic form of u_{nm} as given by Eq. (17) it was assumed that $\zeta_{n0} = z_0 \omega_n / (\kappa u_{*r}) \ll 1$. The proportionality factor between the bottom stress component amplitude, $\tau_{b, nm} / \rho$, and the orbital velocity component amplitude, $u_{b, nm}$, given by Eq. (19) is therefore dominated by the first term in the denominator, which in turn is a weak function of ω_n . We may therefore replace ω_n in Eq. (19) by a constant representative radian frequency, ω_r , and consider the ratio of bottom shear stress and orbital velocity amplitudes to be constant. With these approximations the bottom shear stress spectrum is given in terms of the near-bottom orbital velocity spectrum by

$$S_{\tau_b}(\omega, \theta) = \left[\frac{\rho \kappa u_{*r}}{\ln \frac{\kappa u_{*r}}{z_0 \omega_r} - 1.15} \right]^2 S_{u_b}(\omega, \theta) \quad (20)$$

Integration of Eq. (20) over all frequencies and directions and denoting

$$\begin{aligned} (\tau_{br} / \rho)^2 &= 2 \iint S_{\tau_b / \rho}(\omega, \theta) d\omega d\theta \\ u_{br}^2 &= 2 \iint S_{u_b}(\omega, \theta) d\omega d\theta \end{aligned} \quad (21)$$

we obtain the following relationship

$$\tau_{br} = \frac{\rho \kappa u_{*r}}{\ln \frac{\kappa u_{*r}}{z_0 \omega_r} - 1.15} u_{br} \quad (22)$$

which, given the approximation made in the present analysis, is identical to the result obtained for a periodic wave motion (Grant and Madsen, 1986) when we take

$$u_{*r} = \sqrt{\tau_{br} / \rho} = \sqrt{f_{wr} / 2} u_{br} \quad (23)$$

In fact, Eq. (23) may be introduced in Eq. (22) to obtain an equation for the wave friction factor similar to that originally proposed by Jonsson (1966)

$$\frac{1}{4\sqrt{f_{wr}}} + \log_{10} \frac{1}{4\sqrt{f_{wr}}} = \log_{10} \frac{A_{br}}{k_b} - 0.17 \quad (24)$$

with $k_b = 30z_0$ denoting the equivalent bottom roughness and

$$A_{br}^2 = \left[\frac{u_{br}}{u_r} \right]^2 = 2 \iint \omega^{-2} S_{u_b}(\omega, \theta) d\omega d\theta \quad (25)$$

denoting the near-bottom orbital excursion amplitude of an equivalent periodic wave having the same root-mean-square near-bottom orbital velocity and excursion amplitude as the specified directional wave spectrum. While Eq. (24) is limited to small relative roughness, i.e., large values of A_{br}/k_b , the general formula given by Grant and Madsen (1979) may be used for large relative roughness values.

Spectral Dissipation and Wave Attenuation

Following Kajiura (1968) the average rate of dissipation of wave energy in the bottom boundary layer is given by Eq. (3), $\langle \tau_b u_\infty \rangle$. Expressed in terms of the spectral components of τ_b , Eq. (19), and u_∞ , Eq. (10), including random phase consideration for components of the same frequency, results in

$$\begin{aligned} E_{d,nm} &= \langle \tau_{b,nm} u_{\infty,nm} \rangle = \frac{1}{2} f_{wr} \rho u_{br} u_{b,nm}^2 \langle \cos(\omega_n t + \phi_n) \cos(\omega_n t) \rangle \\ &= \frac{1}{4} f_{wr} \rho u_{br} u_{b,nm}^2 \end{aligned} \quad (26)$$

in which the phase difference between bottom shear stress and free stream velocity--amounting to a $\cos \phi_n$ factor--is neglected to be consistent with previous approximations.

Rewriting the dissipation rate given by Eq. (26) by making use of Eq. (11), we may formally express the conservation of wave energy equation in spectral terms as

$$\begin{aligned} \frac{D(S_\eta(\omega, \theta))}{Dt} &= - \frac{1}{\rho g} E_d(\omega, \theta) = - \frac{1}{2g} f_{wr} u_{br} S_{u_b}(\omega, \theta) \\ &= - \frac{1}{2g} f_{wr} u_{br} \left[\frac{\omega}{\sinh kh} \right]^2 S_\eta(\omega, \theta) \end{aligned} \quad (27)$$

with u_{br} given by Eq. (21) and f_{wr} obtained from knowledge of the equivalent Nikuradse sand grain roughness of the bottom and an equivalent periodic wave having the same root-mean-square orbital velocity and excursion amplitude as the specified directional wave spectrum.

EVALUATION OF TOTAL DISSIPATION

Spectral Model

From the model of spectral dissipation derived in the preceding section we may obtain the average rate of dissipation of energy for the entire wave field by integration of $E_d(\omega, \theta)$, given by Eq. (27), over frequency and direction. Performing this integration and recalling the definition of u_{br} , Eq. (21), the total average dissipation rate may be expressed as

$$E_{d1} = \iint E_d(\omega, \theta) d\omega d\theta = \frac{1}{4} \rho f_{wr} u_{br}^3 \quad (28)$$

While quite simple in appearance, the evaluation of Eq. (21) is somewhat cumbersome since it requires evaluation of quantities that depend on spectral characteristics of the near bottom orbital motion. It would be far simpler if the total average dissipation rate were expressed in terms of wave characteristics derived from the surface amplitude spectrum. We therefore define a characteristic periodic wave with the same root-mean-square amplitude as the wave motion specified by its directional spectrum, i.e.,

$$a_c^2 = 2 \iint S_\eta(\omega, \theta) d\omega d\theta \quad (29)$$

and a period defined by

$$\omega_c = \frac{2\pi}{T_c} = \frac{m_1}{m_0} \quad (30)$$

where m_j denotes the j 'th spectral moment

$$m_j = \iint \omega^j S_\eta(\omega, \theta) d\omega d\theta \quad (31)$$

Denoting the near-bottom velocity associated with this characteristic wave by u_{bc} we have

$$u_{bc} = \frac{a_c \omega_c}{\sinh k_c h} = A_{bc} \omega_c \quad (32)$$

where $k_c = 2\pi/L_c$ is the wave number corresponding to the characteristic wave period, i.e.,

$$\omega_c^2 = k_c g \tanh k_c h \quad (33)$$

Introducing the characteristic wave parameters in the expression for the energy dissipation, Eq. (28), we obtain

$$E_{d1} = \left\{ \frac{f_{wr}}{f_{wc}} \left[\frac{u_{br}}{u_{bc}} \right]^3 \right\} \frac{1}{4} \rho f_{wc} u_{bc}^3 = C_1 E_{dc} \quad (34)$$

where E_{dc} is the average rate of dissipation predicted for the characteristic equivalent periodic wave defined by Eqs. (29) and (30).

Values of C_1 have been computed for JONSWAP spectra with different peak-enhancement values ($\gamma = 1, 3.3, 7$) in different water depths, defined by h/L_c , for a range of different relative bottom roughness, A_{bc}/k_b . The results, shown in Figure 1 as dashed curves, indicate that the value of C_1 depends on spectral peakedness and relative water depth with C_1 increasing as the spectrum becomes broader ($\gamma = 1$) and as the relative depth increases. This behavior reflects the increased importance of the low-frequency part of the surface amplitude spectrum in determining the near-bottom orbital velocity characteristics. Within the range of relative bottom roughness tested, $1 \leq A_{bc}/k_b \leq 1000$, the resulting value of C_1 was found to be essentially independent of this parameter.

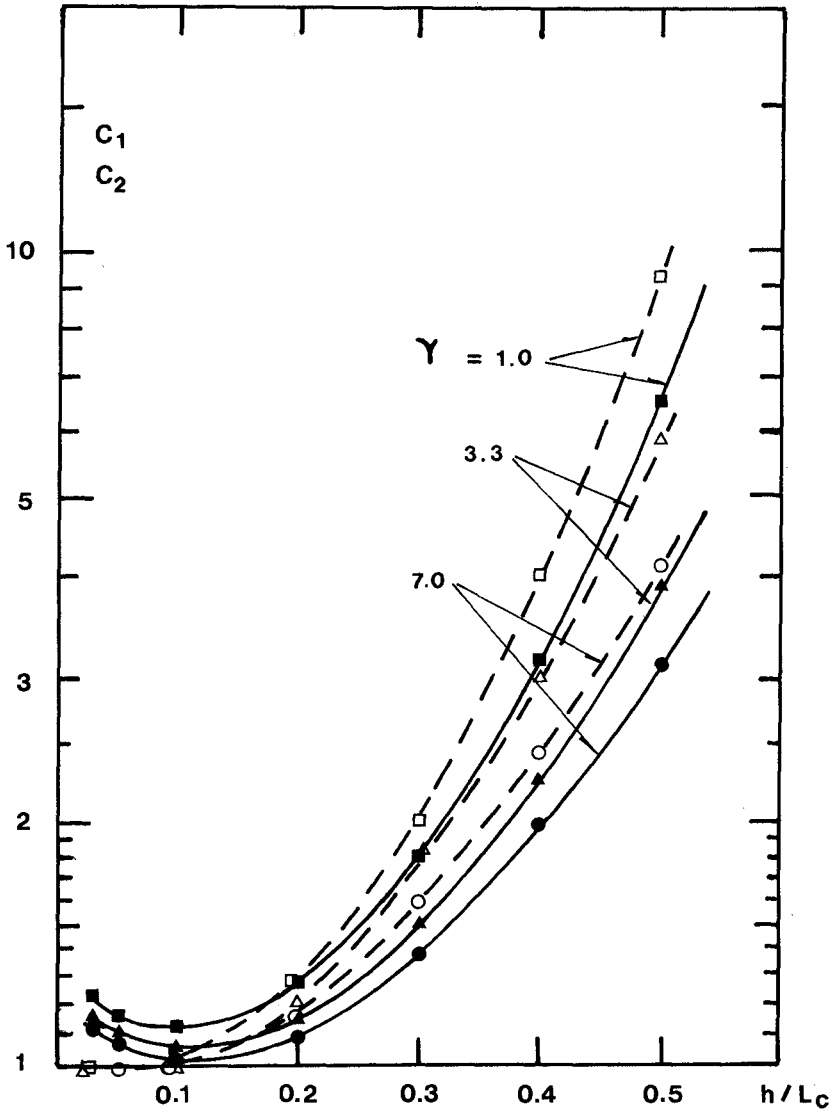


Figure 1. Variation of constants C_1 , Eq. (34), and C_2 Eq. (42), for the evaluation of total bottom dissipation for a random wave field with relative water depth h/L_c and spectral peakedness γ .

Individual Wave Model

Longuet-Higgins (1983) derived the joint probability distribution of zero-crossing wave heights and periods for a narrow banded surface spectrum. Replacing the surface amplitude spectrum by the near-bottom orbital velocity spectrum

$$S_{u_b}(\omega) = \left[\frac{\omega}{\sinh kh} \right]^2 S_{\eta}(\omega) \quad (35)$$

the formulae derived by Longuet-Higgins (1983) may be adopted directly to obtain the joint probability of maximum near-bottom orbital velocity and period

$$p(R, \tau) = \frac{2}{\nu\sqrt{\pi}} \left[\frac{R^2}{\tau^2} \right] e^{-R^2[1+(1-1/\tau)^2/\nu^2]} \cdot L(\nu) \quad (36)$$

where

$$R = \frac{u_b}{\sqrt{2M_0}} = \frac{u_b}{u_{br}}$$

$$\tau = \frac{M_1}{2\pi M_0} T = \frac{T}{T_1} \quad (37)$$

denote the normalized maximum orbital velocity, u_b , and period, T , respectively, and

$$1/L(\nu) = [1 + (1 + \nu^2)^{-1/2}]/2$$

$$\nu^2 = \frac{M_0 M_2 - M_1^2}{M_1^2} \quad (38)$$

with M_j denoting the j -th moment of the near-bottom orbital velocity spectrum

$$M_j = \int \omega^j S_{u_b}(\omega) d\omega \quad (39)$$

Assuming each individual wave, defined by u_b and T , to be simple harmonic a friction factor f_w can be calculated for each wave from knowledge of the bottom roughness. Thus, the dissipation of energy associated with a single wave, D , may be written as the product of the average dissipation rate, cf Eq. (26), and the wave period T , i.e.,

$$D = \frac{1}{4} \rho f_w u_b^3 \cdot T = \left[\frac{u_{br}}{u_{bc}} \right]^3 \left[\frac{f_w}{f_{wc}} \left(\frac{u_b}{u_{br}} \right) \frac{3T}{T_1} \right] \frac{1}{4} \rho f_{wc} u_{bc}^3 T_1$$

$$= \left[\frac{u_{br}}{u_{bc}} \right]^2 \left[\frac{f_w}{f_{wc}} R^3 \tau \right] \frac{1}{4} \rho f_{wc} u_{bc}^3 T_1 \quad (40)$$

To obtain the average rate of energy dissipation we sum the contribution of N individual random waves and divide by the time necessary for N waves to pass. This time is NT_2 , where

$$T_2 = 2\pi \left[\frac{M_0}{M_2} \right]^{1/2} \quad (41)$$

is the mean zero-crossing period of the near-bottom waves. Since the number of waves within an area around u_b (or R) and T (or τ) relative to the total number of waves is given by the joint probability density function, Eq. (36), we obtain the average rate of energy dissipation from

$$E_{d2} = \left[\frac{[u_{br}]^3 T_1}{[u_{bc}] T_2} \int_0^\infty \int_0^\infty \frac{f_w R^3 \tau P(R, \tau) dR d\tau}{f_{wc}} \right] E_{dc} = C_2 E_{dc} \quad (42)$$

Again we take the JONSWAP spectrum with $\gamma = 1, 3.3,$ and 7 for the surface amplitude spectrum, transform it into a near-bottom orbital velocity spectrum for different values of h/L_c , and evaluate the constant C_2 in Eq. (42) for a range of relative bottom roughness, $1 \leq A_{bc}/k_b \leq 1000$. Again, the value of C_2 was found insensitive to the value of relative bottom roughness while varying, as shown by the full lines in Figure 1, with relative water depth and spectral peakedness, in much the same manner as found for C_1 .

Over the important range of relative water depths where bottom frictional attenuation is expected to be most pronounced, $h/L_c < 0.25$, the excellent agreement between C_1 and C_2 supports the validity of the simple model for spectral wave dissipation derived here.

SUMMARY AND CONCLUSIONS

Based on a simple formulation of the turbulent flow in a bottom boundary layer a solution is obtained corresponding to a wave motion specified by its near-bottom orbital velocity spectrum. From the solution the spectral wave dissipation is obtained in the form

$$E_d(\omega, \theta) = \frac{1}{2} \rho f_{wr} u_{br} S_{u_b}(\omega, \theta)$$

in which

$$u_{br} = \sqrt{2 \iint S_{u_b}(\omega, \theta) d\omega d\theta}$$

and f_{wr} may be obtained from any of the many available wave friction factor relationships from knowledge of the equivalent Nikuradse roughness of the bottom, k_b , for an equivalent periodic wave of near-bottom orbital velocity u_{br} and radian frequency, ω_r , defined by

$$A_{br} = \sqrt{2 \iint \omega^{-2} S_{u_b}(\omega, \theta) d\omega d\theta} = u_{br}/\omega_r$$

In passing it is noted that the analysis of turbulent wave-current bottom boundary layers, e.g., Grant and Madsen (1979, 1986), may be extended to waves specified by their directional spectrum by an identical procedure to the one employed here for a pure wave bottom boundary layer. The

result of such an analysis, Madsen (in prep.), shows that available theories for wave-current interaction, which assume a periodic wave motion, may be used also to approximate waves specified by their directional spectrum when the spectral wave is represented by the equivalent periodic wave, defined by u_{br} and A_{br} , propagating in the mean wave direction.

In the important range of intermediate to shallow water depths, the total average dissipation rate predicted by the spectral model is shown to agree with the prediction afforded by a model which considers the statistics of individual waves, defined by their near-bottom orbital velocity characteristics. Besides supporting the validity of the spectral dissipation model the formulae and the results presented in Figure 1 for the overall dissipation experienced by random waves may serve as a simple tool for the prediction of wave attenuation by bottom friction. This use of the results presented here is facilitated by the average dissipation rate experienced by random waves being expressed in terms of a characteristic equivalent periodic wave defined in terms of the surface amplitude spectrum. In this context it should be noted that the characteristic equivalent wave is defined with the root-mean-square wave height, not the significant wave height!

The practical limitation of the present results is that they require a priori knowledge of the bottom roughness, k_b . Experimental results directed towards overcoming this limitation are presented in a companion paper by Madsen and Rosengaus (1988).

ACKNOWLEDGMENTS

The research presented here was supported by the U.S. Department of Commerce National Atmospheric and Oceanic Administration's Office of Sea Grant under Grant NA86AA-D-SG089, by the Office of Naval Research under Grant N00014-86-K-0325, and by Standard Oil Production Company through its support of CSEOE. The expert typing skills of Read Schusky are also acknowledged.

REFERENCES

- Abramowitz, M., I. A. Stegun. 1972. Handbook of mathematical functions. National Bureau of Standards Applied Math Series, No. 55, pp 379-509.
- Collins, J. I. 1972. Prediction of shallow-water spectra. J. Geophys. Res. 77:2693-2707.
- Grant, W. D., O. S. Madsen. 1979. Combined wave and current interaction with a rough bottom. J. Geophys Res. 84(C4):1797-1808.
- Grant, W. D., O. S. Madsen. 1986. The continental-shelf bottom layer. Ann. Rev. Fluid Mech. 18:265-305.
- Hasselmann, K., J. I. Collins. 1968. Spectral dissipation of finite-depth gravity waves due to turbulent bottom friction. J. Marine Res. 26:1-12.

- Hildebrand, F. 1976. Advanced calculus for applications. 2d ed., Prentice Hall.
- Hsiao, S. V., and O. H. Shemdin. 1978. Bottom dissipation in finite-depth waves. Proc, 16th Coastal Engineering Conf., ASCE, 434-448.
- Jonsson, I. G. 1966. Wave boundary layers and friction factors. Proc, 10th Coastal Engineering Conf., ASCE, 127-148.
- Kajiura, K. 1964. On the bottom friction in an oscillatory current. Bulletin of the Earthquake Research Institute 42:147-174.
- Kajiura, K. 1968. A model of the bottom boundary layer in water waves. Bulletin of the Earthquake Research Institute 46:75-123.
- Longuet-Higgins, M. S. 1983. On the joint distribution of wave periods and amplitudes in a random wave field. Proc. of the Royal Society, London A389:241-258.
- Madsen, O. S., M. M. Rosengaus. 1988. Spectral wave attenuation by bottom friction: Experiments. Proc. 21st Coastal Engineering Conf., ASCE.
- Putnam, J. A., J. W. Johnson. 1949. The dissipation of wave energy by bottom friction. Trans. Am. Geophys. Union. 30:67-74.
- Trowbridge, J., O. S. Madsen. 1984a. Turbulent wave boundary layers: 1, Model formulation and first-order solution. J. Geophys. Res. 89(C5):7989-7997.
- Trowbridge, J., O. S. Madsen. 1984b. Turbulent wave boundary layers: 2, Second-order theory and mass transport. J. Geophys. Res. 89(C5):7999-8007.

CHAPTER 35

Subgrid Modelling in Depth Integrated Flows

by

P.A. Madsen, M. Rugbjerg and I.R. Warren

Introduction

Hydrodynamic simulations in coastal engineering studies are still most commonly carried out using two-dimensional vertically integrated mathematical models. As yet, three-dimensional models are too expensive to be put into general use. However, the tendency with 2-D models is to use finer and finer resolution so that it becomes necessary to include approximations to some 3-D phenomena.

It has been shown by many authors that simulations of large scale eddies can be quite realistic in 2-D models (c.f. Abbott et al. 1985).

Basically there exists two different mechanisms of circulation generation. The first one is based on a balance between horizontally and grid-resolved momentum transfers and the bed resistance - i.e. a balance between the convective momentum terms and the bottom shear stress.

The second one is due to momentum transfers that are not resolved at the grid scale but appears instead as horizontally distributed shear stresses.

In many practical situations the circulations will be governed by the first mechanism.

This is the case if the diameter of the circulation and the grid size is much larger than the water depth. In this situation the eddies are friction dominated so that the effect of sub-grid eddy viscosity is limited.

In this case 2-D models are known to produce very realistic results and several comparisons with measurements have been reported in the literature.

However, when $\Delta x \leq h$ then the eddy viscosity becomes the most important parameter determining the flow pattern. In this case the modelling operation must proceed more cau-

Danish Hydraulic Institute
5, Agern Alle, DK-2970 Hoersholm, Denamrk

tiously and a proper closure of the equations must be made in order to describe the effective shear stresses in the momentum equations.

Effective Stresses

The effective stresses arise in the momentum equations via various filtering processes.

The commonly recognized filtering processes are:

<u>Scale 1:</u> Filter out the random molecular motion	}	→	molecular diffusion
		→	viscosity
<u>Scale 2:</u> Filter out the turbulent motion below a <u>given</u> scale	}	→	turbulent diffusion
		→	eddy-viscosity
<u>Scale 3:</u> Depth averaging to filter out the vertical velocity profile for 2-D models	}	→	dispersion
		→	bed & surface shear stresses
		→	horizontal ("effective") shear stresses

It is generally accepted that the eddy terms due to the processes at scale 1 and 2 are negligible relative to scale 3. The effect of the depth-averaging of the velocity profile was taken care of by Elder (1959) who used a logarithmic profile to derive the following expression for the eddy viscosity,

$$E = K_v \cdot h \cdot u^* \quad , \quad K_v \approx 6$$

where

$$u^* \equiv \sqrt{\frac{\tau}{\rho}} = \sqrt{g} \cdot \frac{u}{C} \quad , \quad C = \text{chezy number}$$

However, field measurements and modelling generally show that Elder's coefficient is several orders of magnitude too small. This is illustrated by table 1 in which calibrated eddy coefficients are compared to Elder's expression for 4 different model applications.

Case	h m	u m/s	u* m/s	Δx m	Δt s	E calib. m ² /s	6·hu* m ² /s
A	8	0.7	0.05	50	30	2-5	2.4
B	20	1.0	0.1	500	300	40-50	12
C	30	0.5	0.03	6000	600	≈500	5.4
D	1000	0.1	0.003	30000	900	>6000	18

Table 1 Comparison between Elder's eddy coefficient and calibrated coefficients.

In most classical texts, the development of the equations for nearly-horizontal flow stop at scale 3. However it turns out that for application to numerical modelling it is necessary to extend the filtering process to scale 4, that of the model resolution:

Scale 4:	}	→	→
Horizontal averaging over the model grid size Δx			

When Δx and h are of the same order of magnitude then the processes at both scales 3 and 4 must be considered.

Many modellers attempt to account for the processes at scale 4 by increasing the coefficient, K_v , in Elder's formula, $K_v hu^*$, but this is a mistake.

Since the purpose of the eddy viscosity is to represent sub-grid processes it is natural to relate the length scale to Δx and the time scale to Δt . Hence the eddy viscosity at scale 4 could be considered in one of the following forms:

$$K_1 \cdot \frac{\Delta x^2}{\Delta t} \quad , \quad K_2 \cdot \Delta x \cdot u \quad , \quad K_3 \cdot \Delta t \cdot u^2$$

In table 2 the 3 different forms of the eddy viscosity for scale 4 have been compared to calibrated results in 5 different situations.

Case	h (m)	u (m/s)	Δx (m)	Δt (s)	$E_{cal.}$ (m^2/s)	K_1	K_2	K_3
A	8	0.7	50	30	1-5	0.06-0.01	0.14-0.03	0.34-0.07
B	20	1.0	500	300	40-50	0.06	0.10	0.17
C	30	0.5	6000	600	≈ 500	0.008	0.17	3.3
D	40	1.0	20	10	1-3	0.075-0.025	0.15-0.05	0.30-0.10
E	1000	0.1	30000	900	≈ 6000	0.006	2.0	667

Table 2 Eddy coefficients of scale 4.

The form $K_2 \cdot \Delta \cdot u$ appears to be promising since K_2 is almost constant in the 5 different cases.

A more advanced approach is the Smagorinski type of eddy viscosity which depends on horizontal gradients of the depth-averaged flow velocity. This approach will be introduced in the following section.

Smagorinski Eddy Viscosity

The Smagorinsky sub-grid model has been widely used and is generally believed to be correct for homogeneous, isotropic turbulence. Various authors have extended this

model to inhomogeneous or anisotropic turbulence, e.g. close to a wall (Schuman, 1975) and to the viscous sub-layer in the boundary layer (Moin and Kim 1982).

The flow equation after filtering out turbulence below the scale Δ , is commonly written

$$\frac{\partial u_i}{\partial t} + \frac{\partial u_i u_j}{\partial x_j} = -\frac{1}{\rho} \frac{\partial P}{\partial x_i} + F_i + \frac{\partial}{\partial x_j} (E \cdot S_{ij}) \quad (1)$$

where $i, j = 1, 2, 3$

u = filtered velocity vector
 P = pressure
 F_i = body forces
 E^i = turbulent eddy viscosity

$$S_{ij} = \frac{1}{2} \left(\frac{\partial u_i}{\partial x_j} + \frac{\partial u_j}{\partial x_i} \right) \quad (2)$$

The Smagorinsky sub-grid eddy viscosity takes on the form (cf. Leslie, 1982)

$$E = l^2 (S_{ij} S_{ji})^{\frac{1}{2}} \quad (3)$$

The mixing length l is determined by

$$l = C_s \cdot \Delta x \quad (4)$$

It has been shown by Lilly (1965) and Leonard (1974) that the resultant energy cascade i.e. the dissipation of the large scales is consistent with the Kolmogorov power spectrum and the constant C_s is dependent only on Kolmogorov's universal constant.^s Lilly (1965) used the value $C_s = 0.1825$.

In order to extend the Smagorinsky model to 2-D free surface flow, it is necessary to integrate the flow equations over the vertical.

By analogy to the 3-D form we get,

2-D modelling:

$$\frac{\partial U}{\partial t} - \left[\frac{\partial}{\partial x} (E \cdot \frac{\partial U}{\partial x}) + \frac{1}{2} \frac{\partial}{\partial y} (E (\frac{\partial U}{\partial y} + \frac{\partial V}{\partial x})) \right] \quad (5)$$

where

$$E = l^2 \cdot \left[\left(\frac{\partial U}{\partial x} \right)^2 + \left(\frac{\partial V}{\partial y} \right)^2 + \frac{1}{2} \left(\frac{\partial U}{\partial y} + \frac{\partial V}{\partial x} \right)^2 \right]^{\frac{1}{2}} \quad (6)$$

i.e. the local velocities have simply been replaced by the depth-averaged velocities U and V .

The mixing length is still determined from Eq. (4) but it must be expected that the value of the empirical constant C_s will differ from the values established in 3-D modelling. From the first applications of the model it appears that C_s should be found in the interval 0.4 to 0.8.

Results

Some results from the application of the model to Haraldsund in the Faroe Islands are shown in Figs. 1 and 2. Water depths in the area are up to 60 m while the grid size is only 20 m, so it is certain that bed friction is not the governing factor in the size and intensity of the eddies produced by the model. In such a case, dispersive terms such as those introduced by eddy viscosity should be necessary to produce a realistic flow pattern and have a major effect on the eddies, as is seen in Figs. 1 and 2.

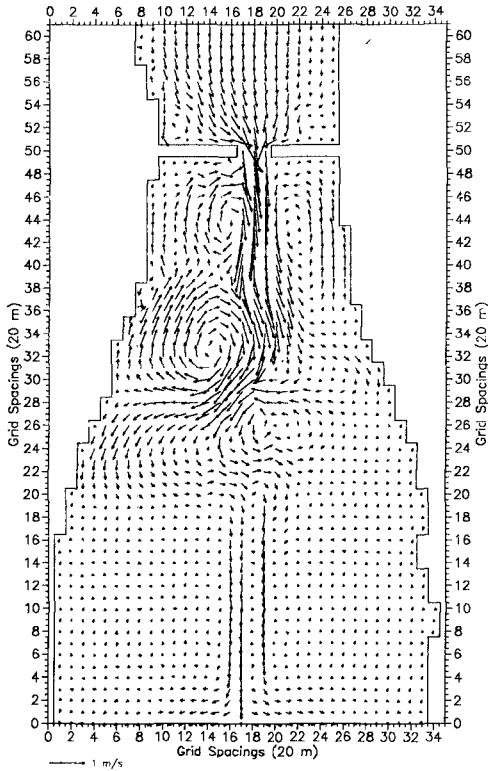


Fig. 1 No eddy viscosity.
Manning Number = 32.

With Zero eddy viscosity a quite unrealistic flow pattern is produced, Fig. 1. In Fig. 2, the results at the same time with $C_s = 0.75$ are much more plausible.

With $C_s = 0.75$, eddy viscosities of 1-2 m^2/s were computed by the Smagorinsky model in regions of maximum velocity gradient, and these are of the correct order of magnitude. Finally, it is reported that the results were very sensitive to the value of C_s . In this and other studies, it seems that $C_s = 0.40$ to 0.80 produces realistic results.

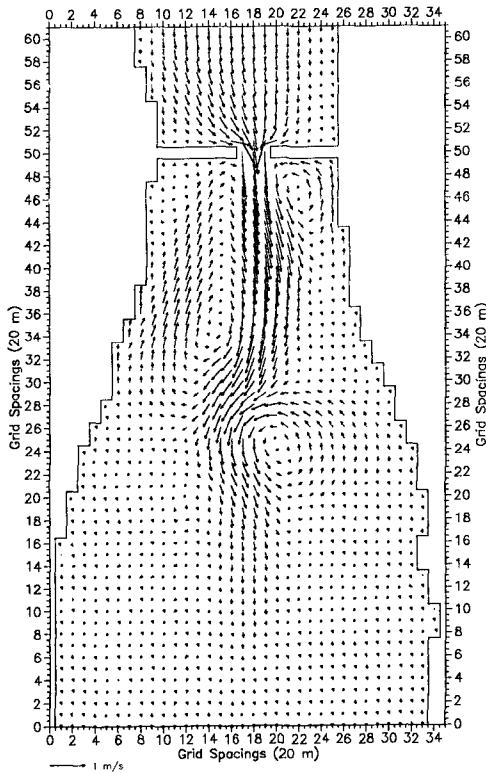


Fig. 2 Smagorinsky eddy, $C_s = 0.75$.
Manning Number = 32.5

References

Abbott, M.B., Larsen J. and Tao Jianhua: "Modelling circulations in depth-integrated flows. Part 1: The accumulation of the evidence". Journal of Hydraulic Research, Vol. 23, 1985. No. 4.

Elder, J.W. (1959): The dispersion of a marked fluid in a turbulent shear flow. *Journal of Fluid Mechanics*, 5 pp 544-560.

Leonard, A. (1974): Energy cascade in large-eddy simulations of turbulent fluid flows. *Adv. in Geophysics*, A, 18, pp 237-248.

Leslie, D.C. (1982): Simulation methods for turbulent flows". In *Numerical Methods for Fluid Dynamics*. Ed: Morton K.W. and Baines, M.J., Academic Press, pp. 63-80.

Moin, Parviz and Kim, John (1982): "Numerical investigation of turbulent channel flow". *J. Fluid Mech.*, vol. 118, pp. 341-377.

Schumann, U. (1975): "Subgrid scale model for finite difference simulations of turbulent flows in plane channels and annuli". *J. Comput. Phys.*, vol. 18, pp. 376-404.

CHAPTER 36

PROPAGATION OF WIND WAVES ON TIDES

Hendrik L. Tolman *

abstract

Effects of instationary depths and currents in tides on shelf seas on wind wave propagation are investigated using two numerical models in two academical situations representing shelf sea conditions. It is shown that changes in absolute frequency, which are induced by the instationarity of depth and current, are significant in contrast to what is usually assumed. If these changes are neglected large and unpredictable errors may occur in calculated changes of wavenumber and amplitude.

INTRODUCTION

In the present study the influence of instationary depths and currents on wind generated surface gravity waves, in particular on their propagation, is investigated.

Instationary depths and currents occur when the travel time of waves through some area is of the same order of magnitude as the time scale of the variations in the depth and current field or larger. This is for instance the case for wind waves traveling on tides in shelf seas such as the North Sea. The potential importance of wave-current interactions in such instationary conditions can be illustrated with a measured modulation of significant wave height in the southern North Sea (figure 1), which has the same period as the tide. Since the tidal range is only about 5% of the average depth, current variations (in space and time) rather than depth variations are expected to be responsible for the observed wave height modulations of up to 50 %.

Interactions between waves and currents, in particular the influence of currents on waves, have been studied extensively in the last decades. The importance of these interactions is generally recognized and the subject is treated in many textbooks, e.g. Whitham (1974), Phillips (1977), Mei (1983), review papers, e.g. Peregrine (1976) and

* Delft University of Technology, Department of Civil Engineering,
P.O. box 5048, 2600 GA, Delft, The Netherlands

reports, e.g. Peregrine and Jonsson (1983). However, wave-current interactions are usually considered in small scale (coastal) areas where depths and currents are treated as non-homogeneous and stationary. In such cases the absolute frequency ω of a periodic wave remains constant in space and time. This implies that the number of incoming waves equals the number of outgoing waves (per unit time) for a fixed area. This invariance of absolute frequency is exploited in numerical wave propagation models for stationary depths and currents, e.g. Tayfun et al. (1976) and in calculations of spectral wave transformations due to stationary currents, e.g. Hedges et al. (1985).

In instationary conditions the absolute frequency does not remain constant during propagation as indicated by theory (e.g. Whitham, 1974, his page 383) and observations (Barber, 1949). The governing equations are well known (e.g. Whitham (1974), Mei (1983)). Nevertheless, a constant absolute frequency has been assumed in several models for large scale (and therefore usually instationary) depth and current fields, e.g. Burrows and Hedges (1985), even when it is stated explicitly that depth and current are instationary, e.g. Chen and Wang (1983). Although the subject of instationary wave-current interactions is properly treated in several other publications, e.g. Unna (1941), Barber (1949), Longuet-Higgins and Stewart (1960) and Christoffersen (1982), none of these papers deals explicitly with the influence of the change of absolute frequency on wave-current interactions.

In the present paper the equations for wave propagation on instationary depths and currents and the corresponding changes in wave parameters are summarized. Furthermore interactions are calculated for two academic cases using numerical models. To illustrate the effects of instationarity of depth and current, in particular the change of absolute frequency, calculations are performed for monochromatic waves in a simple one-dimensional geometry. To illustrate such effects in a more realistic situation, calculations are performed for irregular waves in a more complex two-dimensional geometry. For the latter calculations a discrete spectral two-dimensional wave propagation model is used.

H_S (m)

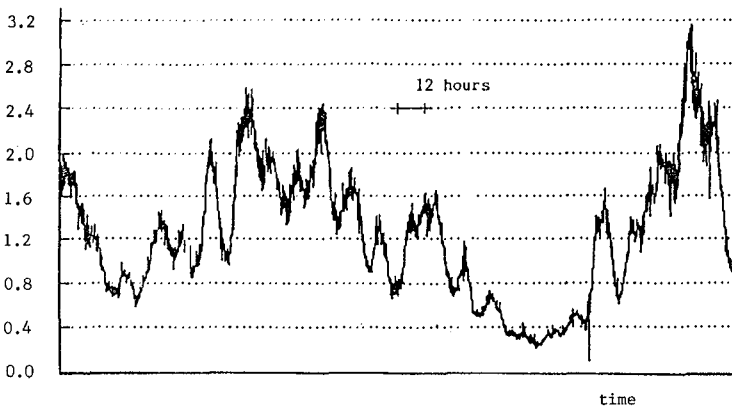


Fig. 1 Measured significant wave heights H_S at the southern North Sea, platform Euro-0, 50 km west of the entrance to the port of Rotterdam, water depth 26 m. Illustration provided by the Ministry of Public Works and Transportation, The Netherlands.

WAVE PROPAGATION ON INSTATIONARY MEDIA

To describe variations in waves due to variations in currents and depths, linear surface gravity waves propagating on a two-dimensional instationary and inhomogeneous depth and current field are considered. Waves are in general characterized with wavenumber (k), absolute frequency (ω), direction (θ) and some amplitude parameter. For monochromatic waves this is the amplitude (a) of the harmonic wave and for short-crested irregular waves this is a two-dimensional spectrum, e.g. the action density spectrum N as a function of ω and θ . If waves on currents are considered, it is convenient to make a distinction between a frame of reference fixed to the bottom, in which the wave frequency is the absolute frequency ω , and a frame of reference moving with the local current velocity \underline{U} , in which the wave frequency is the intrinsic frequency σ . The absolute frequency ω , the intrinsic frequency σ and the wavenumber k are interrelated by the Doppler equation (1) and the dispersion relation (2),

$$\omega = \sigma + \underline{k} \cdot \underline{U} \quad (1)$$

$$\sigma = \{ gk \tanh(kd) \}^{\frac{1}{2}} \quad (2)$$

where \underline{k} is the wavenumber vector, defined by k and θ , g is the acceleration of gravity and d is the water depth.

In the following a Lagrangian viewpoint is taken in which wave energy is followed during propagation. In a frame of reference moving with the local current velocity \underline{U} the propagation velocity of wave energy c_g (direction θ) is given by the linear theory as :

$$c_g = \frac{\partial \sigma}{\partial k} = \frac{\sigma}{k} n \quad (3)$$

in which

$$n = \frac{1}{2} + \frac{kd}{\sinh 2kd} \quad (4)$$

In the fixed frame the propagation velocity of the energy (\underline{c}_w) is (e.g. Phillips, 1977) :

$$\underline{c}_w = \underline{c}_g + \underline{U} \quad (5)$$

The corresponding rates of change in absolute frequency ω , intrinsic frequency σ , wavenumber k and direction θ (denoted as $d\omega/dt$, $d\sigma/dt$, dk/dt and $d\theta/dt$ respectively) can be determined using equations (1), (2) and the conservation of waves $\partial k/\partial t + \partial \omega/\partial x = 0$ (e.g. Whitham (1974), his page 11). These rates of change are (e.g. Christoffersen (1982), Mei (1983), his page 96) :

$$\frac{d\omega}{dt} = \frac{\partial \sigma}{\partial d} \frac{\partial d}{\partial t} + \underline{k} \cdot \frac{\partial \underline{U}}{\partial t} \quad (6)$$

$$\frac{dk}{dt} = - \frac{\partial \sigma}{\partial d} \frac{\partial d}{\partial s} - \underline{k} \cdot \frac{\partial \underline{U}}{\partial s} \quad (7)$$

$$\frac{d\sigma}{dt} = \frac{\partial \sigma}{\partial d} \left(\frac{\partial d}{\partial t} + \underline{U} \cdot \nabla d \right) - c_g \underline{k} \cdot \frac{\partial \underline{U}}{\partial s} \quad (8)$$

$$\frac{d\theta}{dt} = - \frac{1}{k} \frac{\partial \sigma}{\partial d} \frac{\partial d}{\partial m} - \frac{\underline{k}}{k} \cdot \frac{\partial \underline{U}}{\partial m} \quad (9)$$

in which s is a coordinate in the direction θ , m a coordinate perpendicular to s and ∇ the differential operator in space. The operator d/dt is defined as :

$$\frac{d}{dt} \equiv \frac{\partial}{\partial t} + \underline{c}_w \cdot \nabla \quad (10)$$

The calculation of wave amplitudes for propagation over currents in absence of energy sources and sinks (wave generation and dissipation e.g. by wind) is based on the conservation of action (e.g. Whitham 1974, Phillips, 1977). The formulation of the action conservation for monochromatic waves differs from that for irregular waves. For monochromatic waves the (Eulerian) action conservation equation is written as :

$$\frac{\partial A}{\partial t} + \nabla \cdot (\underline{c}_w A) = 0 \quad (11)$$

where wave action density A is related to energy density E and amplitude a :

$$A = E/\sigma \quad (12)$$

$$E = \frac{1}{2} \rho g a^2 \quad (13)$$

For short-crested irregular waves the action conservation equation is written as :

$$\frac{\partial N}{\partial t} + \nabla \cdot (\underline{c}_w N) + \frac{\partial}{\partial \theta} (c_\theta N) + \frac{\partial}{\partial \omega} (c_\omega N) = 0 \quad (14)$$

where the action density spectrum $N(\omega, \theta)$ (action per unit surface, frequency and direction) is related to the energy density spectrum $F(\omega, \theta)$:

$$N(\omega, \theta) = F(\omega, \theta) / \sigma \quad (15)$$

As amplitude parameter of the irregular waves the significant wave height H_S is used, which is calculated from the energy density spectrum as

$$H_S = 4.0 \left(\iint F(\omega, \theta) d\omega d\theta \right)^{\frac{1}{2}} / \rho g \quad (16)$$

The first term in equation (14) represents the local variation in time, which is balanced by the other terms which represent different forms of convection. The first of these represents convection in space (including shoaling), where c_w is given as in equation (5). It corresponds to the second term in equation (11) for monochromatic waves. The third term in equation (14) represents refraction where c_θ equals $d\theta/dt$ as given in equation (9). These first three terms are quite common for models which consider only stationary propagation conditions. The fourth term is unique for instationary depths and currents. It represents transport of action over the spectral frequencies, which corresponds to the change of absolute frequency in a monochromatic case. Its formulation is analogous to the above spectral representation of refraction, where the change of wave direction is represented by transport of action over the spectral directions. The propagation velocity c_w equals $d\omega/dt$ as given in equation (6).

Based on equation (6), which is formulated in terms of time derivatives, the importance of the instationarity can be expressed in terms of the (relative) change of absolute frequency $\Delta\omega/\omega$. Likewise, the importance of the inhomogeneity can be expressed in the (relative) change of wavenumber $\Delta k/k$, based on equation (7). The ratio between the relative change in absolute frequency $\Delta\omega/\omega$ and the relative change in wavenumber $\Delta k/k$ can therefore be used to assess the importance of the instationarity compared to the importance of the inhomogeneity.

MONOCHROMATIC ONE-DIMENSIONAL SITUATION

To illustrate the influence of instationary depth and current variations on waves, consider monochromatic waves in a one-dimensional geometry. The current field (representing a tide) consists of a one-dimensional long wave over a constant bottom level. The tide propagates in the positive x-direction and its characteristics are described as :

$$d(x,t) = d_0 + A_d \sin \chi(x,t) \quad (17)$$

$$U(x,t) = A_U \sin \chi(x,t) \quad (18)$$

$$\chi(x,t) = Kx - \Omega t \quad (19)$$

$$c_t = \Omega/K = (gd_0)^{\frac{1}{2}} \quad (20)$$

$$A_U/A_d = (g/d_0)^{\frac{1}{2}} \quad (21)$$

In these equations χ is the tidal phase, c_t is the propagation velocity of the tide, K and Ω are the wavenumber and frequency of tide and A_U and A_d are the current and depth amplitude respectively (current velocity constant over depth).

The calculations for the above situation are carried out as follows. Absolute frequency ω as a function of x and t is calculated by simultaneous integration of $dx/dt = c_w$ and $d\omega/dt$ as given by (6), starting at a situation with $\chi = 0$ (no current, suffix o). Using ω , d and U the parameters needed for this integration (k and c_g) can be calculated using equations (1) through (4). As it can be shown that for the considered situation ω , k , A etc. vary with x and t through χ only, action density A is stationary in a frame of reference which moves with the propagation velocity of the tide c_t . Using this property, the action conservation equation (11) can be rewritten as :

$$\frac{\partial}{\partial x} ((c_w - c_t) A) = 0 \quad (22)$$

so that the relative action density A/A_0 can be calculated as :

$$\frac{A}{A_0} = \frac{c_{w,o} - c_t}{c_w - c_t} \quad (23)$$

The wave energy and amplitude are subsequently calculated from the relative action density using equations (23), (12) and (13).

Figure 2 (solid lines) shows the results of calculations for conditions roughly representing the M_2 tide in the southern North Sea ($\omega_0 = 2\pi/10$ rad/s, period of the tide = 12 h, $d_0 = 25$ m, $A_d = 1$ m resulting in $AJ = 0.63$ m/s). Calculated values of wave parameters are basically a function of the phase χ of the tide, but they are presented in figure 2 as they appear at a fixed location as a function of time. This transformation from phase χ to time t is easily performed using equations (19) and (20). This figure shows variations in the normalized absolute frequency (ω/ω_0) which cannot be neglected compared to variations in the normalized wavenumber (k/k_0). Consequently both in stationarity and inhomogeneity are important for the situation considered. Similar results were obtained for tide and waves traveling in opposite directions and for other depths, wave frequencies and depth and current oscillation amplitudes.

If the change in absolute frequency is neglected ($d\omega/dt = 0$, dashed lines in figure 2), large errors in calculated wavenumbers and amplitudes occur. If tide and waves travel in opposite directions (c_t and c_w with opposite signs, not shown here), such an approach overestimates the change of wavenumber by a factor of 2 or more. For tide and waves traveling in the same direction (figure 2) the situation is even worse as the predicted sign of the variation of the wavenumber is always wrong; the thus predicted variation of the amplitude also shows large errors which can include wrong signs.

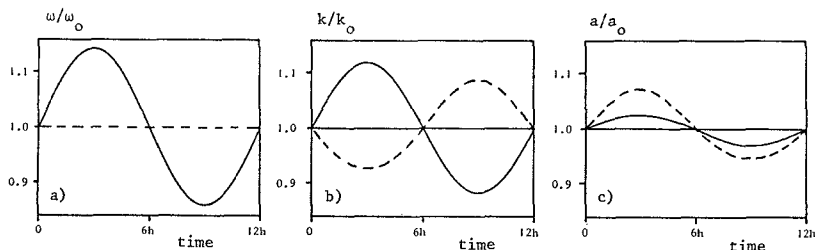


Fig. 2 Results of calculations with simple one-dimensional model for monochromatic waves, tidal period 12 h, $\omega_0 = 2\pi/10$ rad/s, $d_0 = 25$ m, $A_d = 1$ m and $AJ = 0.63$ m/s. — $d\omega/dt$ given by equation 6, - - - $d\omega/dt = 0$ a) normalized absolute frequency ω/ω_0 b) normalized wavenumber k/k_0 c) normalized amplitude a/a_0 .

SPECTRAL TWO-DIMENSIONAL SITUATION

Wave-current interactions in more realistic situations should be determined using a spectral approach based on equation (14). In the following the spectral development of a wave field is calculated using a numerical model in which equation (14) is approximated using a finite difference approach. The model will be described elsewhere. It suffices to say that it is approximately second order accurate in all five dimensions (\underline{x} , ω , θ , t).

Again a situation is considered which roughly represents the M_2 tide in the North Sea (figure 3). The area ($500 \times 750 \text{ km}^2$) is discretized using a square grid with spatial increments of 25 km. The action density spectrum is discretized with 24 directions (directional increment 15°) and 18 frequencies ranging from 0.05 Hz to 0.30 Hz (exponential distribution). The time step in the integration is 15 min. Current and depth fields are calculated using a two-dimensional depth integrated current model, which includes Coriolis forces (Coriolis parameter constant as for 53° N) and bottom friction (Chezy coefficient $C = 18 \log(-120 d_0)$). A periodic surface elevation with amplitude of 0.25 m and a period of 12 h was applied to the open boundary to

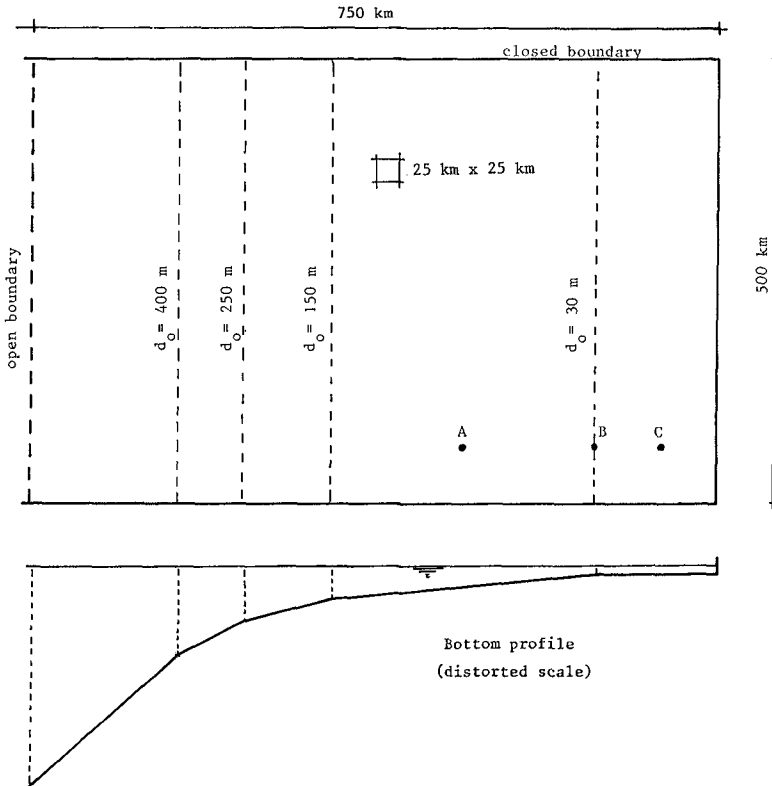


Fig. 3 Layout of academical shelf sea as used in the spectral two-dimensional calculations

simulate the M_2 tide. The resulting tide travels counterclockwise through the area considered with resulting maximum current velocities as shown in figure 4. A stationary energy density spectrum was imposed at the open boundary. The mean wave direction is perpendicular to the boundary. The spectral shape is that of a Gaussian distribution over the frequencies and $\cos^2(\theta)$ over the directions (average frequency 0.1 Hz, frequency spread 0.015 Hz). After a few days of simulation depth, current and wave spectra are periodic with an oscillation period of 12 hours. All results presented next refer to the periodic solution.

Figure 5 shows the spatial distribution of the range of local variation in time of some spectral parameters (e.g. $H_{S,max} - H_{S,min}$). These parameter values are normalized with their local value averaged over the tidal period (suffix a, e.g. $H_{S,a}$). Presented are : a) mean absolute frequency defined as

$$\bar{\omega} = \frac{\iint \omega F(\omega, \theta) d\omega d\theta}{\iint F(\omega, \theta) d\omega d\theta} \quad (24)$$

b) mean wavenumber, defined as

$$\bar{k} = \frac{\iint k F(\omega, \theta) d\omega d\theta}{\iint F(\omega, \theta) d\omega d\theta} \quad (25)$$

and c) significant wave height, see equation (16).

To illustrate the behaviour in time of several wave parameters and the nature of the errors which are made if the change in absolute frequency is neglected, results are given in figure 6 for three locations in the area with large variations in wave parameters (figures 3 and 5). They have been selected to illustrate the phase lags between the local current velocity and e.g. the variation of wavenumber. These lags vary with location, which indicates that it is a cumulative effect, not a local one.

Essentially the above calculations with the two-dimensional model have to be repeated with $d\omega/dt = 0$ to determine the errors then made.

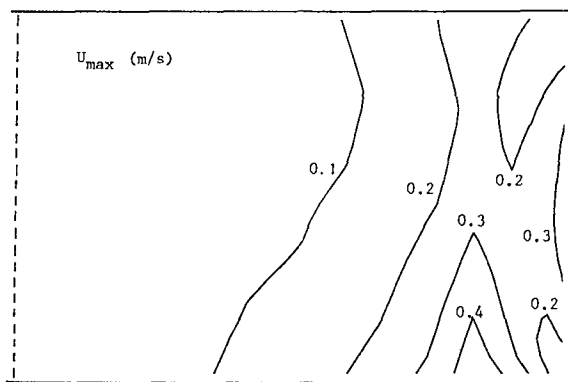


Fig. 4 Maximum current velocities of M_2 tide in shelf sea of fig. 3.

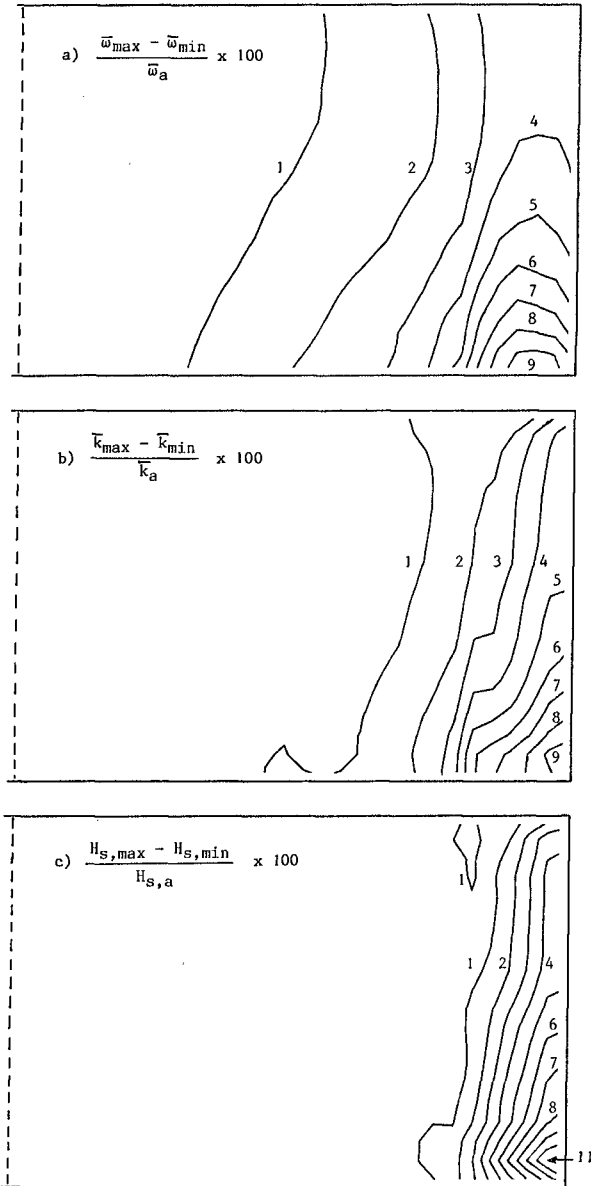


Fig. 5 Normalized ranges of variation of a) absolute frequency $\bar{\omega}/\bar{\omega}_a$ b) wavenumber \bar{k}/\bar{k}_a and c) significant wave height $H_s/H_{s,a}$ for spectral two-dimensional calculations (distribution over area of figure 3).

As these calculations are quite expensive (approximately 1.5 hours CPU time on an IBM 3083-JX1) they have not been performed. However, the mean absolute frequency now (approximately) equals the stationary mean absolute frequency at the input boundary $\bar{\omega}_b$. Furthermore the (input) spectrum is extremely narrow banded and can therefore be described with a single wavenumber \bar{k} and frequency $\bar{\omega}$ which approximately satisfy equations (1) and (2). Thus the wavenumber as obtained when the absolute frequency is assumed to be constant can be estimated using equations (1) and (2) with $\bar{\omega} = \bar{\omega}_b$, $k = \bar{k}$ and $\underline{k} \cdot \underline{U} = \bar{k}U'$ where U' is the current velocity in the mean propagation direction of the waves. For the calculation of action density and significant waveheight, which includes integrating equation (14), no simple approximation is available. The solid lines in figure 6 represent results of the two-dimensional calculations (including frequency shifts) and the dashed lines represent the approximate solutions as obtained when the change in absolute frequency is neglected.

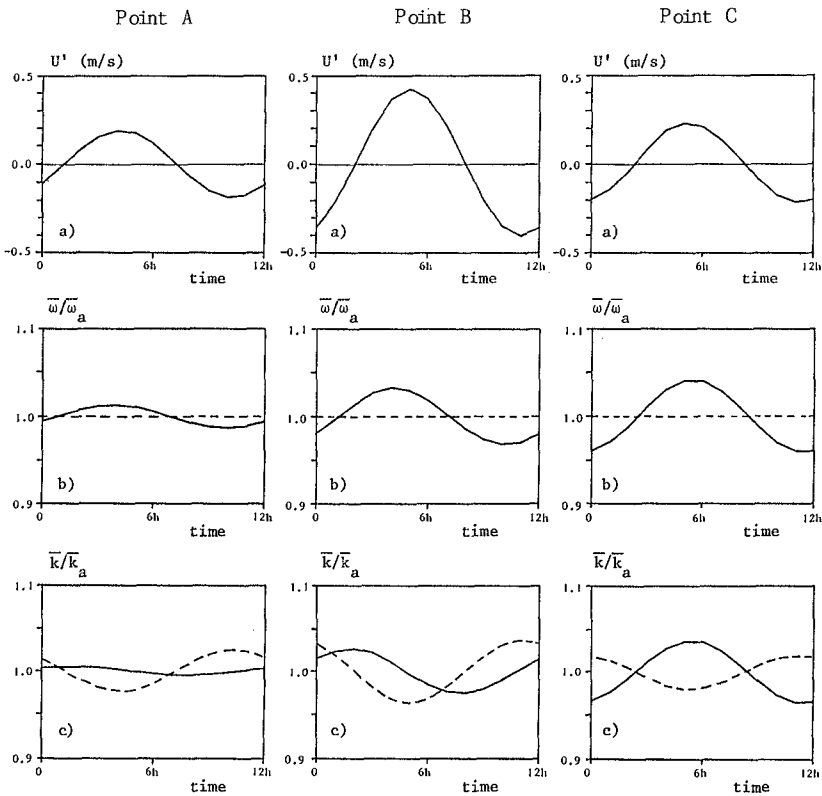


Fig. 6 Parameter values for points A, B, and C of figure 3 as a function of time, — $d\omega/dt$ according to equation 6 (in-stationary), - - - $d\omega/dt = 0$ (quasi-stationary) : a) Current velocity in propagation direction of waves U' , b) normalized absolute frequency $\bar{\omega}/\bar{\omega}_a$ and c) normalized wavenumber \bar{k}/\bar{k}_a .

DISCUSSION

The results of calculations for monochromatic waves in the one-dimensional case (figure 2) clearly show the influence of instationarity of depth and current on changes in absolute frequency, wavenumber and wave amplitude. In particular the change in absolute frequency is significant. Its normalized change is of the same order of magnitude as the normalized change in wavenumber or larger. This indicates that in this case instationarity is at least as important as inhomogeneity.

The results of calculations with the spectral two-dimensional wave propagation model for the academical shelf sea of figure 3 confirm these findings. Figure 5 a) shows that variations in absolute frequency are not negligible, specially in shallow water areas with relatively strong currents (see figure 4). Again normalized changes of absolute frequency (figure 5a) are of the same order of magnitude as normalized changes of wavenumber (figure 5b), indicating the importance of instationarity. Finally variations in significant wave height (figure 5c) are significant.

If the absolute frequency is assumed to be constant ($d\omega/dt = 0$), large errors occur in the predicted change of wavenumber, both in the one- and two-dimensional situations considered. Similar errors are expected to occur for the significant waveheight in the two-dimensional situation. They do occur for the change of amplitude in the one-dimensional situation. Unfortunately such errors cannot be estimated from calculations based on the assumption of constant absolute frequency, as will be shown next. In instationary conditions the change of wave parameters depends on the (local) change of absolute frequency. This change in turn depends on depth and current conditions along the propagation path of the wave energy. Due to these accumulated effects the local current is not correlated with the local wave parameters such as the wavenumber (see solid lines of figure 6 a and c). If the shift in absolute frequency is neglected, the cumulative effects disappear and the local current and variations in e.g. wavenumber depend on local parameters only (see dashed lines in figure 6c). As the cumulative effects can usually not be estimated from local parameters only, errors thus made cannot be estimated.

Wave-current interactions not only affect propagation but also generation and dissipation. Therefore work is in progress to add these interactions to the above two-dimensional model. This model will be used to determine the influence of tide and storm surge induced wave-current interactions in the North sea. A description of this model and results of this continued effort will be published elsewhere.

CONCLUSIONS

In this study it is shown that instationary depth and current fields such as tides in shelf seas induce significant variations of the absolute frequency of (wind) waves. These variations are not only induced by local depth and current variations but also by the structure of the depth and current field in space and time. The commonly used quasi-stationary approach, in which the absolute frequency is assumed to remain constant during propagation, can lead to significant errors in the calculated variations in wavenumber and amplitude at least for the fairly typical shelf sea conditions considered in this study.

Acknowledgements

The author acknowledges with pleasure the Dutch Ministry of Public Works and Transportation for supplying figure 1 and L.H. Holthuijsen, J.A. Battjes and P. Visser of the Delft University of Technology for their valuable discussion and reviewing early drafts of this paper.

References

- Barber, N.F., 1949: Behaviour of waves on tidal streams. Proc. Roy. Soc. London, A, **198**, 81-93
- Burrows R. and T.S. Hedges, 1985: The influence of currents on ocean wave climates, Coastal Engineering, **9**, 247-260
- Chen, Y.H. and H. Wang, 1983: Numerical model for nonstationary shallow water wave spectral transformations, J. Geophys. Res., **88 C14**, 9851-9863
- Christoffersen, J.B., 1982: Current depth refraction of dissipative water waves, Institute of Hydrodynamics and Hydraulic Engineering, Technical University of Denmark, Series paper no. 30
- Hedges, T.S., K. Anastasiou and D. Gabriel, 1985 Interaction of random waves and currents, Journal of the Waterway, Port, Coastal and Ocean Eng., ASCE, **111**, 275-288
- Longuet-Higgins, M.S. and R.W. Stewart, 1960: Changes in the form of short gravity waves on long waves and tidal currents, J. Fluid Mech., **8**, 565-583
- Mei, C.C., 1983: The applied dynamics of ocean surface waves, Wiley
- Peregrine, D.H., 1976: Interaction of water waves and currents, Advances in applied mechanics, **16**, 9-117
- Peregrine, D.H. and I.G. Jonsson, 1983: Interaction of waves and currents, Miscellaneous report no. 83-6, CERC, U.S. Army Corps of Engineers
- Phillips, O.M., 1977: The dynamics of the upper ocean, 2nd edition, Cambridge University Press
- Tayfun, M.A., R.A. Dalrymple and C.Y. Yang, 1976: Random wave-current interaction in water of varying depth, Ocean Engineering, **3**, 403-420
- Unna, P.J.H., 1941: White horses, Nature, **148**, 226-227
- Whitham, G.B., 1974: Linear and nonlinear waves, Wiley

CHAPTER 37

ON JOINT DISTRIBUTION OF WAVE HEIGHTS AND DIRECTIONS

Masahiko Isebe*; M. JSCE, M. ASCE

In the individual wave analysis of short-crested irregular waves, the wave direction of an individual wave is an important quantity as well as the wave height and period. In this paper, the joint probability density of the wave height and direction is derived theoretically on the assumption of a narrow-banded frequency spectrum. A field experiment was carried out to examine the validity of the theory. The measured joint distribution agreed well with that predicted by the theory.

1. INTRODUCTION

It is of great importance to describe random sea states with sufficient accuracy. Two major methodologies in the analysis of irregular waves are the spectral analysis and individual wave analysis.

In the spectral analysis, irregular waves are regarded as a superposition of component regular waves with various frequencies and directions. From the expected values of the component wave energies, an energy spectrum is defined. Based on the concept of superposition, this analysis method is especially valid as applied to linear phenomena.

On the other hand, in the individual wave analysis, an irregular wave train is decomposed into successive individual waves defined by a zero-crossing method or others. An individual wave is usually regarded as a part of a regular wave train with the same height, period and direction. Hence, various properties of the individual wave such as the surface profile, water particle velocity and pressure can be calculated by applying a nonlinear regular wave theory. This method may not be appropriate in deep water because waves are dispersive and hence an individual wave cannot be independent of the adjoining individual waves. However, in shallow water where wave dispersion is not so rapid, we can even make a nonlinear analysis

* Associate Professor, Department of Civil Engineering, University of Tokyo, Bunkyo-ku, Tokyo 113, Japan

employing this analysis procedure.

Irregular waves are either uni-directional or multi-directional, in other terms, long-crested or short-crested. In the spectral analysis of long-crested irregular waves, the frequency spectrum is defined as the energy density with respect to frequency, and used to describe the characteristics of the wave field. On the other hand, in the individual wave analysis of long-crested irregular waves, the distribution of wave heights or the joint distribution of wave heights and periods is used. For short-crested irregular waves, the spectral analysis is made by introducing the directional spectrum which represents the energy density with respect to frequency and direction. Much effort has been devoted through theoretical and experimental works to extend basic and practical knowledge in these categories. However, the individual wave analysis of short-crested irregular waves, in which the distribution of directions should also be discussed, remains to be developed. If a theory is established in this category, it will be of practical use because it will allow to evaluate the nonlinear actions of short-crested irregular waves such as wave forces and sediment transport.

The main purpose of this study is to derive a joint probability density of wave height and direction. The envelope functions of the water surface elevation and the two components of horizontal water particle velocity are introduced to define the wave height and direction, on the assumption that the frequency spectrum is narrow-banded. Among possible definitions of wave direction of an individual wave, a definition similar to the mean direction is employed. Examples of the joint density are depicted. The present theory is examined through comparison with the result of a field experiment.

2. THEORY

2.1 Envelope Functions

Wave direction may be defined in many ways. Among them, the propagation direction of the wave crest, the direction of the surface slope, and the direction of the water particle velocity are promising candidates from a practical point of view. In the present study, the two components of horizontal water particle velocity as well as the water surface fluctuation are used for the definition. This will make it more easy to apply the result to the evaluation of wave force, sediment transport, breaking criterion, and others. In addition, the theory can easily be examined by field experiments.

Short-crested irregular waves consist of an infinite number of component waves with various periods and directions. Let the i 'th component of frequency be f_i and the j 'th component of direction θ_j , then the time series of the water surface elevation, η , at the location, (x, y) , and the two components, u and v , of horizontal water particle velocity in the x - and y - direction can be expressed as

$$\left. \begin{aligned} \eta(t) &= \sum_{i=1}^{\infty} \sum_{j=1}^{\infty} c_{ij} \cos \phi_{ij} \\ u(t) &= \sum_{i=1}^{\infty} \sum_{j=1}^{\infty} \hat{H}_i \cos \theta_j \cdot c_{ij} \cos \phi_{ij} \\ v(t) &= \sum_{i=1}^{\infty} \sum_{j=1}^{\infty} \hat{H}_i \sin \theta_j \cdot c_{ij} \cos \phi_{ij} \end{aligned} \right\} \quad (1)$$

$$\phi_{ij} = k_i(x \cos \theta_j + y \sin \theta_j) - 2\pi f_i t - \varepsilon_{ij} \quad (2)$$

$$\hat{H}_i = 2\pi f_i \frac{\cosh k_i z}{\sinh k_i h} \quad (3)$$

where c_{ij} and ε_{ij} , respectively, denote the amplitude and phase angle of component waves which represent the frequency range Δf_i and direction range $\Delta \theta_j$. The quantity h is the water depth, z the elevation from the bottom, k_i the wave number determined from f_i by the dispersion relation, and t the time. From the definition, the amplitude is related to the directional spectrum, $S(f, \theta)$, as

$$\langle c_{ij}^2 \rangle / 2 = S(f_i, \theta_j) \Delta f_i \Delta \theta_j \quad (4)$$

where $\langle \rangle$ denotes the expected value. The phase angle, ε_{ij} , has a uniform distribution between 0 to 2π .

Here, we assume that the frequency spectrum is narrow-banded. Then f_i can be expressed as the sum of the mean frequency, \bar{f} , and a small deviation, f'_i :

$$f_i = \bar{f} + f'_i \quad (5)$$

On substituting Eqs. (2) and (5) into Eq. (1) and with use of the additional formulas of the trigonometric functions, the following expressions can be obtained:

$$\left. \begin{aligned} \eta(t) &= \eta_0 \cos 2\pi \bar{f} t + \eta_s \sin 2\pi \bar{f} t \\ u(t) &= u_c \cos 2\pi \bar{f} t + u_s \sin 2\pi \bar{f} t \\ v(t) &= v_c \cos 2\pi \bar{f} t + v_s \sin 2\pi \bar{f} t \end{aligned} \right\} \quad (6)$$

where η_0 , u_c , v_c , etc. are slowly-varying envelope functions defined by

$$\left. \begin{aligned} \eta_0 &= \sum_{i=1}^{\infty} \sum_{j=1}^{\infty} c_{ij} \cos \phi'_{ij} \\ u_c &= \sum_{i=1}^{\infty} \sum_{j=1}^{\infty} \hat{H}_i \cos \theta_j \cdot c_{ij} \cos \phi'_{ij} \\ v_c &= \sum_{i=1}^{\infty} \sum_{j=1}^{\infty} \hat{H}_i \sin \theta_j \cdot c_{ij} \cos \phi'_{ij} \end{aligned} \right\} \quad (7)$$

$$\phi'_{ij} = k_i(x \cos \theta_j + y \sin \theta_j) - 2\pi f'_i t - \varepsilon_{ij} \quad (8)$$

The envelope functions, η_s , u_s and v_s , are defined by substituting $\cos \phi'_{ij}$ by $\sin \phi'_{ij}$ on the right hand side of Eq. (7).

In Longuet-Higgins (1952), the probability density of wave height was determined from the envelope function of the water surface elevation. In the present study, the six envelope functions, η_c , η_s , u_c , u_s , v_c and v_s , determine the wave height and phase lags among the water surface fluctuation and the two components of horizontal water particle velocity of an individual wave. Hence, the joint density of these quantities determines the joint density of the wave height and direction of an individual wave.

The quantity, ϵ_{ij} , and hence ϕ'_{ij} are uniformly distributed random quantities. By applying the central limit theorem to Eq. (7) and the corresponding equations for η_s , u_s and v_s , all the six quantities are found to have normal distributions. Therefore, the joint density can be determined from the moments up to the second order. The moments of the first order, which are the mean values, vanish from the definition. The moments of the second order, which are variances and covariances, are expressed from Eqs. (1) and (7) as follows:

$$\left. \begin{aligned} \langle \eta_c^2 \rangle &= \langle \eta_s^2 \rangle = \langle \eta^2 \rangle \equiv m_{00}, & \langle \eta_c u_c \rangle &= \langle \eta_s u_s \rangle = \langle \eta u \rangle \equiv m_{10} \\ \langle u_c^2 \rangle &= \langle u_s^2 \rangle = \langle u^2 \rangle \equiv m_{20}, & \langle \eta_c v_c \rangle &= \langle \eta_s v_s \rangle = \langle \eta v \rangle \equiv m_{01} \\ \langle v_c^2 \rangle &= \langle v_s^2 \rangle = \langle v^2 \rangle \equiv m_{02}, & \langle u_c v_c \rangle &= \langle u_s v_s \rangle = \langle uv \rangle \equiv m_{11} \end{aligned} \right\} \quad (9)$$

The covariances for the combination of the subscripts, c and s , such as $\langle \eta_c \eta_s \rangle$ vanish, which means they are independent of each other. With a definition, $(\eta_c, u_c, v_c, \eta_s, u_s, v_s) = (\xi_1, \xi_2, \xi_3, \xi_4, \xi_5, \xi_6)$, the covariance matrix, M , is summarized as

$$M = [\langle \xi_i \xi_j \rangle] = \begin{bmatrix} M_3 & 0 \\ 0 & M_3 \end{bmatrix} \quad (10)$$

$$M_3 = \begin{bmatrix} m_{00} & m_{10} & m_{01} \\ m_{10} & m_{20} & m_{11} \\ m_{01} & m_{11} & m_{02} \end{bmatrix} \quad (11)$$

In general, the multi-dimensional normal distribution is written as

$$p(\xi_1, \xi_2, \dots, \xi_n) = \frac{1}{(2\pi)^{n/2} \sqrt{|M|}} \exp \left[-\frac{1}{2} \left(\sum_{i=1}^n \sum_{j=1}^n \xi_i M_{ij}^{-1} \xi_j \right) \right] \quad (12)$$

(Rice, 1944). From Eqs. (10) and (11)

$$|M| = (m_{00} m_{20} m_{02} A)^2 \quad (13)$$

$$M^{-1} = \frac{1}{A} \begin{bmatrix} M'_3 & 0 \\ 0 & M'_3 \end{bmatrix} \quad (14)$$

$$M'_3 = \begin{bmatrix} \frac{1-r_{11}^2}{m_{00}} & -\frac{r_{10}-r_{01}r_{11}}{\sqrt{m_{00}m_{20}}} & -\frac{r_{01}-r_{10}r_{11}}{\sqrt{m_{00}m_{02}}} \\ -\frac{r_{10}-r_{01}r_{11}}{\sqrt{m_{00}m_{20}}} & \frac{1-r_{01}^2}{m_{20}} & -\frac{r_{11}-r_{10}r_{01}}{\sqrt{m_{20}m_{02}}} \\ -\frac{r_{01}-r_{10}r_{11}}{\sqrt{m_{00}m_{02}}} & -\frac{r_{11}-r_{10}r_{01}}{\sqrt{m_{20}m_{02}}} & \frac{1-r_{10}^2}{m_{02}} \end{bmatrix} \quad (15)$$

where

$$A = 1 + 2r_{10}r_{01}r_{11} - r_{10}^2 - r_{01}^2 - r_{11}^2 \quad (16)$$

$$r_{10} = m_{10}/\sqrt{m_{00}m_{20}} \quad (17)$$

$$r_{01} = m_{01}/\sqrt{m_{00}m_{02}} \quad (18)$$

$$r_{11} = m_{11}/\sqrt{m_{20}m_{02}} \quad (19)$$

and hence Eq. (12) becomes

$$\begin{aligned} & p(\eta_c, u_c, v_c, \eta_s, u_s, v_s) \\ &= \frac{1}{(2\pi)^3 m_{00} m_{20} m_{02} A} \\ & \times \exp \left[-\frac{1}{2A} \left\{ (1-r_{11}^2) \frac{\eta_c^2 + \eta_s^2}{m_{00}} + (1-r_{01}^2) \frac{u_c^2 + u_s^2}{m_{20}} \right. \right. \\ & \quad + (1-r_{10}^2) \frac{v_c^2 + v_s^2}{m_{02}} - 2(r_{10}-r_{01}r_{11}) \frac{\eta_c u_c + \eta_s u_s}{\sqrt{m_{00}m_{20}}} \\ & \quad \left. \left. - 2(r_{01}-r_{10}r_{11}) \frac{\eta_c v_c + \eta_s v_s}{\sqrt{m_{00}m_{02}}} - 2(r_{11}-r_{10}r_{01}) \frac{u_c v_c + u_s v_s}{\sqrt{m_{20}m_{02}}} \right\} \right] \quad (20) \end{aligned}$$

Here, we take the x -axis in the principal wave direction. Then $m_{11}=0$, and hence $r_{11}=0$. Furthermore, non-dimensional variables are introduced by

$$\begin{aligned} N_c &= \eta_c/\sqrt{m_{00}}, & U_c &= u_c/\sqrt{m_{20}}, & V_c &= v_c/\sqrt{m_{02}} \\ N_s &= \eta_s/\sqrt{m_{00}}, & U_s &= u_s/\sqrt{m_{20}}, & V_s &= v_s/\sqrt{m_{02}} \end{aligned} \quad (21)$$

Since

$$\begin{aligned} & d\eta_c du_c dv_c d\eta_s du_s dv_s \\ &= m_{00} m_{20} m_{02} dN_c dU_c dV_c dN_s dU_s dV_s \end{aligned} \quad (22)$$

Eq. (20) becomes

$$\begin{aligned} & p(N_c, U_c, V_c, N_s, U_s, V_s) \\ &= \frac{1}{(2\pi)^3 A} \exp \left[-\frac{1}{2A} \left\{ N_c^2 + N_s^2 + (1-r_{01}^2)(U_c^2 + U_s^2) + (1-r_{10}^2)(V_c^2 + V_s^2) \right. \right. \\ & \quad \left. \left. - 2r_{10}(N_c U_c + N_s U_s) - 2r_{01}(N_c V_c + N_s V_s) + 2r_{10}r_{01}(U_c V_c + U_s V_s) \right\} \right] \quad (23) \end{aligned}$$

where from Eq. (16) with $r_{11}=0$

$$A = 1 - r_{i0}^2 - r_{o1}^2 \tag{24}$$

2.2 Change of Reference Phase

From the cos and sin components of the envelope functions, the amplitudes and phase angles of the water surface fluctuation and particle velocity of an individual wave can be determined. To take the phase angle, δ , of the water surface elevation as a reference phase, we shift the phases of the three wave properties by δ :

$$\begin{aligned} N_o &= N_p \cos \delta, & U_c &= U_p \cos \delta - U_q \sin \delta, & V_c &= V_p \cos \delta - V_q \sin \delta \\ N_s &= N_p \sin \delta, & U_s &= U_p \sin \delta + U_q \cos \delta, & V_s &= V_p \sin \delta + V_q \cos \delta \end{aligned} \tag{25}$$

where the subscript, p , denotes the component which is in phase with the water surface fluctuation, and the subscript, q , the component which is 90° out of the phase. The above transformation of variables implies

$$dN_o dU_c dV_c dN_s dU_s dV_s = N_p dN_p d\delta dU_p dU_q dV_p dV_q \tag{26}$$

Hence, Eq. (23) is transformed as

$$\begin{aligned} & p(N_p, \delta, U_p, U_q, V_p, V_q) \\ &= \frac{N_p}{(2\pi)^3 A} \exp \left[-\frac{1}{2A} \{ N_p^2 + (1 - r_{o1}^2)(U_p^2 + U_q^2) + (1 - r_{i0}^2)(V_p^2 + V_q^2) \right. \\ & \quad \left. - 2r_{i0}N_pU_p - 2r_{o1}N_pV_p + 2r_{i0}r_{o1}(U_pV_p + U_qV_q) \} \right] \end{aligned} \tag{27}$$

Since the right hand side of the above equation is independent of δ , $p(N_p, U_p, U_q, V_p, V_q)$ can be obtained by simply multiplying it by 2π .

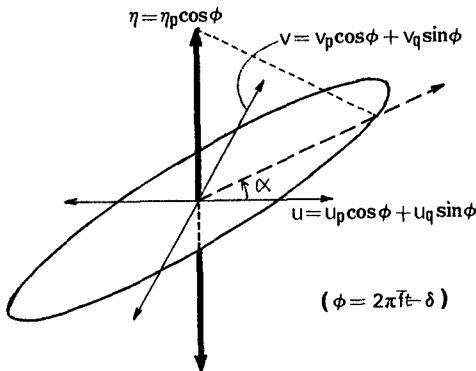


Fig. 1 The path lines of the water surface elevation and the vector of the horizontal water particle velocity.

Figure 1 depicts the physical meaning of the above parameters. The parameters are shown in dimensional form as η_p , u_p , u_q , v_p and v_q . In general, the water surface elevation oscillates sinusoidally and the velocity vector, (u, v) , moves along an ellipse. The principal axis of the ellipse represents the velocity vector at the time of its maximum magnitude. Its direction does not necessarily coincide with the direction of the water particle velocity at the time of the maximum water surface elevation. The former one corresponds to the principal wave direction since it is the direction of the principal axis. The latter one corresponds to the mean wave direction since it is defined from the ratio of the two components of water particle velocity which are in phase with the water surface fluctuation. These two directions are candidates of the definition of the individual wave direction. The appropriate definition depends on the problem in which the distribution is used. In this study, the definition similar to the mean direction is employed for the sake of simplicity.

Since the wave direction is independent of U_q and V_q in this definition, Eq. (27) is integrated with respect to U_q and V_q to yield

$$p(N_p, U_p, V_p) = \frac{N_p}{2\pi\sqrt{A}} \exp \left[-\frac{1}{2A} \{N_p^2 + (1-r_{01}^2)U_p^2 + (1-r_{10}^2)V_p^2 - 2r_{10}N_pU_p - 2r_{01}N_pV_p + 2r_{10}r_{01}U_pV_p\} \right] \quad (28)$$

2.3 Joint Density of Wave Height and Direction

Since the wave direction is defined by $\alpha = \tan^{-1}(v_p/u_p)$ in the present study, (U_p, V_p) are transformed to the polar coordinates, (W, α) :

$$U_p = W \cos \alpha, \quad V_p = (W/\gamma) \sin \alpha \quad (29)$$

where γ is the correction factor which compensates the distortion resulted through the non-dimensionalization. This is expressed from Eq. (21) by

$$\gamma = \sqrt{m_{02}/m_{20}} \quad (30)$$

Thus γ is found to be the long-crestedness parameter. From Eq. (29)

$$dU_p dV_p = (W/\gamma) dW d\alpha \quad (31)$$

Hence, Eq. (28) becomes

$$\begin{aligned}
 p(N_p, W, \alpha) &= \frac{N_p W}{2\pi\sqrt{D}\gamma} \exp \left[-\frac{1}{2D} \left\{ N_p^2 + (1-r_{01}^2)W^2 \cos^2 \alpha + (1-r_{10}^2)W^2 \frac{\sin^2 \alpha}{\gamma^2} \right. \right. \\
 &\quad \left. \left. - 2r_{10}N_p W \cos \alpha - 2r_{01}N_p W \frac{\sin \alpha}{\gamma} + 2r_{10}r_{01}W^2 \cos \alpha \frac{\sin \alpha}{\gamma} \right\} \right] \quad (32)
 \end{aligned}$$

Since N_p and α are the non-dimensional amplitude (half wave height) and direction of an individual wave, the joint probability density of wave height and direction can be obtained by integrating the above equation from 0 to ∞ with respect to W . This can be done by using the following relationship:

$$\begin{aligned}
 &\int_0^\infty W \exp \left[-\frac{1}{2D} (aW^2 - 2bN_p W) \right] dW \\
 &= \frac{D}{a} + \frac{\sqrt{D} b N_p}{a^{3/2}} \exp \left[\frac{1}{2D} \frac{b^2 N_p^2}{a} \right] \sqrt{\frac{\pi}{2}} \left(1 + \operatorname{erf} \left(\frac{b N_p}{\sqrt{D a}} \right) \right) \quad (33)
 \end{aligned}$$

where erf denotes the error function defined by

$$\operatorname{erf}(\zeta) = \sqrt{\frac{2}{\pi}} \int_0^\zeta \exp \left(-\frac{\zeta'^2}{2} \right) d\zeta' \quad (34)$$

The result of the integration is as follows:

$$\begin{aligned}
 p(N_p, \alpha) &= \frac{1}{2\pi\gamma} \left\{ \frac{\sqrt{D}}{a} N_p \exp \left[-\frac{N_p^2}{2D} \right] \right. \\
 &\quad \left. + \frac{b}{a^{3/2}} N_p^2 \exp \left[-\frac{1}{2} \frac{c}{a} N_p^2 \right] \sqrt{\frac{\pi}{2}} \left(1 + \operatorname{erf} \left(\frac{b N_p}{\sqrt{D a}} \right) \right) \right\} \quad (35)
 \end{aligned}$$

where

$$\left. \begin{aligned}
 a &= (1-r_{01}^2) \cos^2 \alpha + 2r_{10}r_{01} \cos \alpha \frac{\sin \alpha}{\gamma} + (1-r_{10}^2) \frac{\sin^2 \alpha}{\gamma^2} \\
 b &= r_{10} \cos \alpha + r_{01} \frac{\sin \alpha}{\gamma} \\
 c &= \cos^2 \alpha + \frac{\sin^2 \alpha}{\gamma^2}
 \end{aligned} \right\} \quad (36)$$

We see from the above result that the joint probability density, $p(N_p, \alpha)$, of wave amplitude and direction can completely be determined from r_{10} , r_{01} and γ . Figure 2 shows some examples of the joint density.

When the directional distribution is narrow and symmetrical, $r_{10} \rightarrow 1$ and $r_{01} = 0$. Then Eq. (35) is simplified as

$$p(N_p, \alpha) = \frac{1}{\sqrt{2\pi}\gamma} \frac{N_p^2}{\cos^2 \alpha} \exp \left[-\frac{1}{2} \left(1 + \frac{\tan^2 \alpha}{\gamma^2} \right) N_p^2 \right] \quad (\cos \alpha > 0) \quad (37)$$

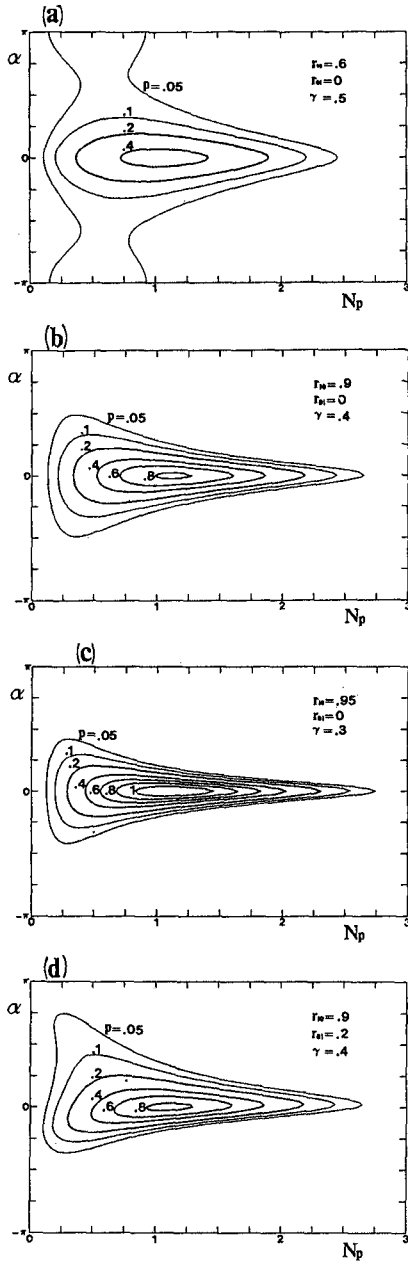


Fig. 2 Examples of the joint probability density of wave height and direction.

In this case, the mean wave height, $2\bar{N}_p(\alpha)$, for a fixed wave direction defined by

$$2\bar{N}_p(\alpha) = 2 \int_0^\infty N_p p(N_p, \alpha) dN_p / \int_0^\infty p(N_p, \alpha) dN_p \tag{38}$$

can be obtained analytically as

$$2\bar{N}_p(\alpha) = 8 / \sqrt{2\pi \left(1 + \frac{\tan^2 \alpha}{\gamma^2}\right)} \tag{39}$$

This shows that the mean wave height decreases as the direction shifts away from the principal direction.

2.4 Joint Density of Two Components of Water Particle Velocity

In this section, we derive the joint probability density, $p(U_p, V_p)$, of the two components of water particle velocity at the time of maximum water surface elevation. For this purpose, we have only to integrate Eq. (28) from 0 to ∞ with respect to N_p . By using Eq. (33) in the derivation, the following result can be obtained:

$$p(U_p, V_p) = \frac{1}{2\pi} \left[\sqrt{A} \exp \left[-\frac{1}{2A} \{ (1-r_{01}^2)U_p^2 + 2r_{10}r_{01}U_pV_p + (1-r_{10}^2)V_p^2 \} \right] + (r_{10}U_p + r_{01}V_p) \exp \left[-\frac{1}{2}(U_p^2 + V_p^2) \right] \times \sqrt{\frac{\pi}{2}} \left(1 + \operatorname{erf} \left(\frac{r_{10}U_p + r_{01}V_p}{\sqrt{A}} \right) \right) \right] \tag{40}$$

Hence, it can be seen that $p(U_p, V_p)$ is determined from only r_{10} and r_{01} . However, γ is necessary to compensate the distortion in the non-dimensionalization. By using the same method as that of Cartwright and Longuet-Higgins (1956), the probability density of the quantities at the time of the maximum water surface elevation can more directly be derived without introducing envelope functions. Through this derivation, Eq. (40) can be obtained without the assumption of a narrow-banded frequency spectrum.

Figure 3 depicts examples of $p(U_p, V_p)$. The probability for U_p to take a negative value decreases as r_{10} increases.

For a symmetrical wave field, in which the principal direction coincides with the mean direction, $r_{01}=0$. Then, Eq. (40) becomes

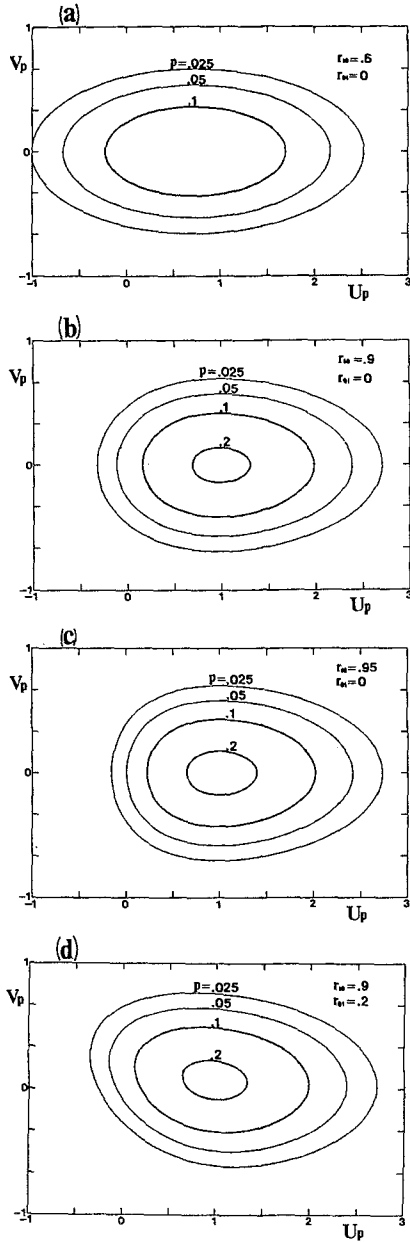


Fig. 3 Joint distribution of the two components of water particle velocity at the time of the maximum water surface elevation.

$$p(U_p, V_p) = \frac{1}{\sqrt{2\pi}} \left[\begin{aligned} &\sqrt{1-r_{10}^2} \exp\left[-\frac{U_p^2}{2(1-r_{10}^2)}\right] \\ &+ r_{10} U_p \exp\left[-\frac{U_p^2}{2}\right] \\ &\times \sqrt{\frac{\pi}{2}} \left(1 + \operatorname{erf}\left(\frac{r_{10} U_p}{\sqrt{1-r_{10}^2}}\right)\right) \end{aligned} \right] \times \frac{1}{\sqrt{2\pi}} \exp\left[-\frac{V_p^2}{2}\right] \quad (41)$$

This indicates that U_p and V_p are independent of each other. The root-mean-square values of these parameters are

$$(U_p)_{\text{rms}} = 1 + r_{10}^2 \quad (42)$$

$$(V_p)_{\text{rms}} = 1 \quad (43)$$

Furthermore, in the limit of $r_{10} \rightarrow 1$, Eq. (41) becomes

$$p(U_p, V_p) = U_p \exp\left[-\frac{U_p^2}{2}\right] \times \frac{1}{\sqrt{2\pi}} \exp\left[-\frac{V_p^2}{2}\right] \quad (44)$$

which shows U_p has a Rayleigh distribution and V_p has a normal distribution. The average magnitude of the water particle velocity for a fixed direction can be calculated as

$$\bar{W}(\alpha) = \int_0^\infty W p(W, \alpha) dW / \int_0^\infty p(W, \alpha) dW \quad (45)$$

With the same assumption that gives Eq. (44), the following explicit expression can be obtained:

$$\bar{W}(\alpha) = 2 \sqrt{\frac{\pi}{2} \left(\cos^2 \alpha + \frac{\sin^2 \alpha}{r^2} \right)} \quad (46)$$

3. FIELD EXPERIMENT

3.1 Procedure

A field experiment was carried out near Oarai Port in Ibaraki prefecture, Japan, on August 28, 1985. The port which is shown in Fig. 4 faces to the Pacific Ocean. The primary purpose of the experiment is to measure the spatial distribution of directional spectra resulted from the diffraction due to an offshore breakwater. A set of an ultrasonic wave gage and an electro-magnetic current meter was used to measure simultaneously the water surface elevation and the two components of horizontal water particle velocity near the bottom, from which the directional spectrum at the measuring location was calculated. Among four sets of instruments used, three are fixed all day at No. 0, 4 and 8 in the figure, and the other one was moved to measure the directional spectra at No. 1, 2, 3, 5, 6 and 7. The sampling interval is 0.5s and the

duration of one record is 17min. 3s. In the figure, the distribution of significant wave heights and principal and mean wave directions is shown. The details of the result are found in Izumiya et al. (1986).

The location No. 0 at which the water depth is about 13m is for measuring the incident wave condition. This is the only location at which the recorded data is long enough to calculate two-dimensional joint distributions. Data for 22 hours, and hence 75 records are available there. Since high-frequency waves generated by fishing boats appeared in the data, a numerical band-pass filter which passes the components with the frequency between 0.056 to 0.19Hz was employed. This makes the band width of the data narrower than that of the incident waves. The average significant wave height and period are 62cm and 9.4s, respectively. The variance coefficients, i.e. the ratios of the standard deviations and average values, are 0.088 and 0.033 for the significant wave height and period, respectively, which allows to regard the wave field as steady. However, to reduce the effect of variation of wave field, the average values for each record are used for normalizing individual wave properties in the record. The total number of waves is 7343, and the average values, γ , r_{10} and r_{01} , for the 75 records are 0.31, 0.95 and 0.00, respectively.

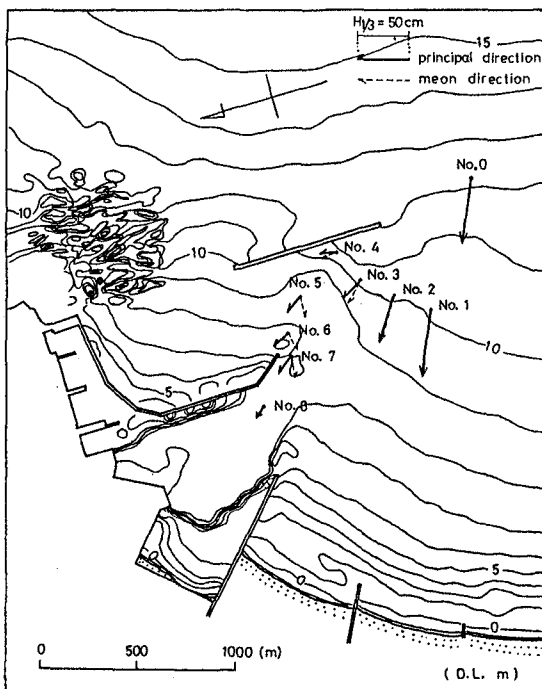


Fig. 4 Observation site.

3.2 Result

Figure 5 compares the predicted and measured joint probability densities of wave height and period. The distance from the origin and the angle from the horizontal axis represent the non-dimensional height and wave direction, respectively. The wave height is non-dimensionalized by the average wave height. Solid and dot lines denote contour lines of the joint density predicted by the present theory. The numbers in a matrix form show the measured values. The values are multiplied by 100. The agreement between the theory and experiment is quite good.

Figure 6 compares the measured and predicted joint probability densities of the two components of horizontal water particle velocity at the time of maximum water surface elevation. As well as in Fig. 5, contour lines represent the theoretical prediction and numbers represent the experimental result. They agree well with each other.

4. CONCLUSION

In the present study, the joint probability density of wave height and direction is derived from the envelope functions of the water surface elevation and the two components of horizontal water particle velocity. In the derivation, the frequency spectrum is assumed to be narrow-banded, and the wave direction of an individual wave is defined similarly to the mean direction. The result is expressed in explicit forms which contain only the long-crestedness parameter and the correlation coefficients between the water surface elevation and the two components of horizontal water particle velocity.

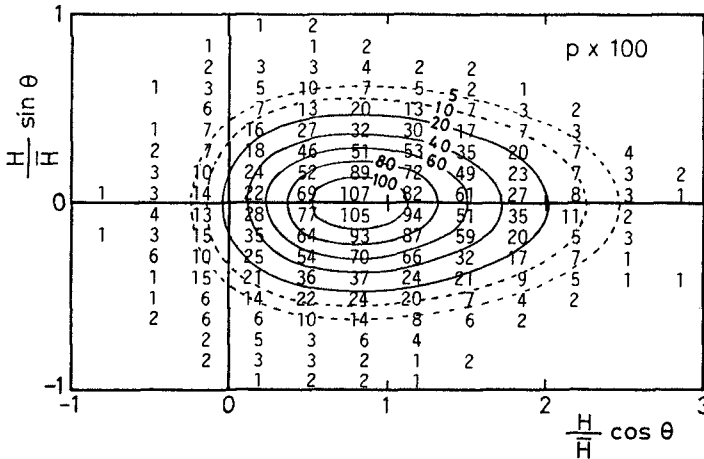


Fig. 5 Comparison between the predicted and measured joint probability densities of wave height and period.

The validity of the present theory is examined by a field experiment. The measured and predicted joint probability densities agree well with each other. Since the numerical band-pass filter used for eliminating ship waves makes the frequency spectrum narrow-banded, the theory remains to be examined for a wide range of sea conditions.

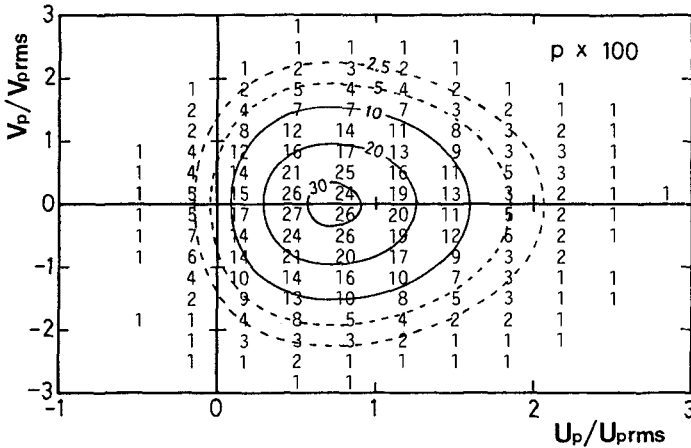


Fig. 6 Comparison between the measured and predicted joint probability densities of the two components of horizontal water particle velocity at the time of the maximum water surface elevation.

REFERENCES

- 1) Cartwright, D. E. and M. S. Longuet-Higgins (1956): The statistical distribution of the maxima of a random function, Proc. Roy. Soc. London, Ser. A, vol. 237, pp. 212-232.
- 2) Izumiya, T., M. Isobe, T. Shimizu and T. Ohshimo (1986): Field measurement of directional spectra around a breakwater, Proc. 33rd Japanese Conf. on Coastal Eng., pp. 129-133 (in Japanese).
- 3) Longuet-Higgins, M. S. (1952): On the statistical distribution of the heights of sea waves, J. Mar. Res., Vol. 11, pp. 245-266.
- 4) Rice, S. O. (1944): Mathematical analysis of random noise, Bell Syst. Tech. J., Vol. 23, pp. 282-332.

CHAPTER 38

FIELD MEASUREMENT OF WAVE SET-UP

By Gregory A. Davis* and Peter Nielsen**

Abstract

A new, efficient and cheap method is described for obtaining field measurements of surf zone mean water levels. The method applies manometer tubes rather than the traditional pressure transducers. Together with simple stilling well measurements of the water table the results obtained from manometer tubes demonstrate for the first time a complete mean water level profile, from offshore of the break-point to the back-beach region.

While some previous studies have provided information about the average position of the waterline, the present study is the first to provide comprehensive field data on the position of the shoreline defined as the intersection of the mean water surface and the sand. The difference between average position of the waterline and the shoreline is not trivial.

1. Introduction

1.1 Concepts and Definitions

When waves break on a beach the water line moves back and forth with the arrival of individual waves. Its instantaneous co-ordinates are x_w and z_w . Correspondingly, the average position of the water line defines \bar{z}_w (see Figure 1).

When the local surface elevation $\eta(x,t)$ is averaged over a time span much longer than the wave and surf beat periods but shorter than the tidal period the result is the local mean water level $\bar{\eta}(x)$ which traces mean water surface MWS.

The still water level SWL is the level of the still water surface (i.e. the sea surface in the hypothetical situation of no waves). For practical purposes, the SWL can be taken as the mean water level at infinite depth: $SWL = \bar{\eta}(\infty)$.

* Geomarine Pty Ltd, 426 Wilson Street, Darlington, Australia 2008

** New South Wales Department of Public Works, Coast and Rivers Branch, 140 Phillip Street, Sydney, Australia 2000

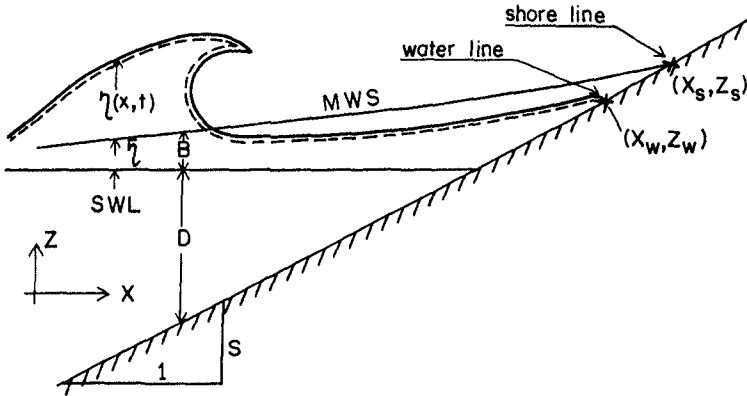


Figure 1: Definition diagram for instantaneous water surface parameters, mean water surface and shore line.

The local setup (and setdown) $B(x)$ is defined as the local super-elevation of the mean water surface above the SWL.

Tides, barometric pressure fluctuations, and changes in wave height cause variations to the mean water surface $\bar{\eta}(x)$ on time scales ranging from a few hours to a few days.

The shoreline and hence the shoreline elevation $z_s (= \bar{\eta}_s)$ and the shoreline setup B_s are defined by the intersection of the mean water surface and the beach.

For the intersection between the still water surface and the beach, we shall use the term Still water shoreline SWS.

Note that the shoreline MWL is in general different from the average runup level.

Field measurements of z_w can be obtained with capacitance runup meters (e.g. Guza and Thornton, 1981) or with down-looking cameras (e.g. Holman and Sallenger 1985), and the amount of field data on z_w is large, while field measurements of $\bar{\eta}$ are virtually non-existent. On the other hand, theoretical models are generally aimed at $\bar{\eta}$ because it is more easily tractable by theory than is \bar{z}_w .

The continuation of the mean water surface landward of the shoreline is the water table, which is the surface where the mean pore water pressure is zero. The local level of the water table $\bar{h}(x)$ is thus the level of the free surface in a suitably responsive stilling well.

There are practical difficulties in measuring mean water levels in the surf and swash zones and until now no detailed field measurements have been made of a wave set up profile. A couple of studies (Guza and Thornton 1981, Holman & Sallenger 1985) reported field measurements of the mean elevation of the water line, but this is different from the set up as defined above.

2. Previous Setup Observations

The phenomenon of super-elevated water level at the shoreline on a natural beach is important for a number of reasons. The run up component is important in determining design set-backs and crest-levels for shoreline structures and vulnerability of shoreline protection and natural dunes. The set up component is important to the dynamics of near-shore currents such as undertow, rip currents and longshore currents arising from longshore variations of wave height.

Holman and Sallenger, (1985) report that the study of wave setup was prompted by the hurricane that hit the East Coast of the USA in 1938. Observations of the hurricane event showed a discrepancy of one metre in shoreline elevation between two nearby locations. One location was the relatively exposed area of Narragansett Pier, where wave energy was dissipated as surf. The other location was the relatively calm waters of Newport. Subsequent model tests by Savage (1957) and Saville (1961) verified the existence of wave set-up.

The earliest field measurement of wave set up are reported by R. Dorrestein (1961). He made field observations of set up at various locations across the surf zone. He set up his experimental apparatus at Fernandina Beach on the Atlantic Coast of Florida. He used a pier extending into the sea from a straight beach on which two tide gauges were installed to give offshore water level. On the beach near the shoreline adjacent to the pier, four to six transparent plastic tubes were inserted into the beach to act as stilling wells. The water level in the swash and run up zone could be recorded by filming floats in the plastic tubes.

The experimental method is flawed, however, because the data sampling period of 72 secs is not long enough to average out the effects of surf beat.

Guza and Thornton (1981) used a combination of offshore pressure transducers and a runup gauge in the swash zone to gain information about the shape of the mean water surface. There are two main difficulties with their approach. Firstly, the average position of the water line which is measured by the runup gauge is not related in a simple way to the shoreline setup (Guza and Thornton assumed they were identical) and the absolute levels of the offshore pressure sensors had to be inferred because surveying was impossible.

Holman and Sallenger (1985) applied a similar approach to that of Guza and Thornton, only the resistance runup gauge was replaced by down-looking cameras. Again the average position of the water line was misinterpreted as being equal to the shoreline position.

The present approach differs from the latter two in that the measured quantity is the mean water level and from these measurements the shoreline is found directly as the intersection between the MWS and the beach. Also, the manometer tubes have the great practical advantage over pressure transducers that the elevation of the seaward ends need not be known.

3. Field Measurements

3.1 Field Site

Field measurements of wave set-up were performed at Dee Why beach, an open coastal beach located about 5 km north of Sydney, New South Wales, Australia. The beach faces the south east which is the dominant direction of the swell from the Tasman Sea (see Figure 2).

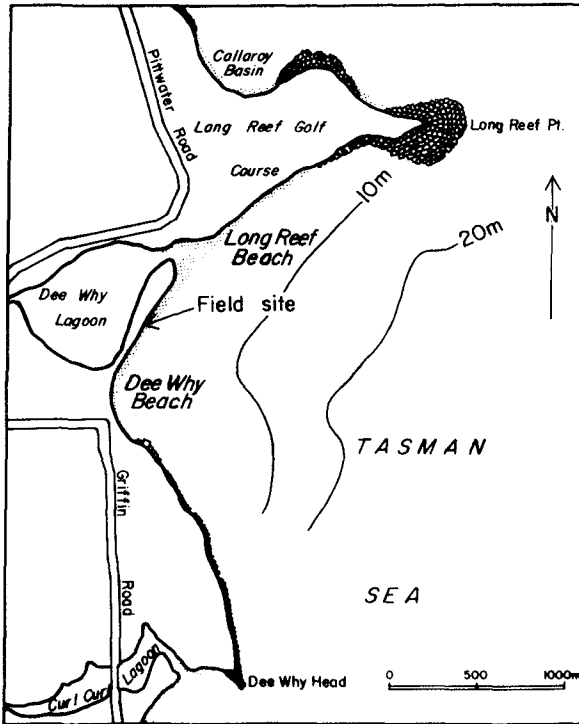


Figure 2: Location diagram for the field site at Dee Why Beach, Sydney, Australia.

The sand grain size varies somewhat across the profile, being coarsest in the swash zone. A sample taken on 17th November 1987 from the swash zone had the following size characteristics: $d_{50} = 0.30\text{mm}$; $d_{10} = 0.13\text{mm}$; $d_{90} = 0.95\text{mm}$.

Topographically, the beach varies between a rip current topography, with rip spacings of a few hundred metres under high energy conditions, and a steep reflective topography with regular beach cusps after extended periods of calm weather.

A sample of surveyed beach profiles are shown in Figure 3 which shows that the profile envelope corresponding to the field data is quite wide.

Offshore wave height data was provided by two Waverider Buoys, one located in deep water offshore of Botany Bay, 20 km to the south and one directly offshore from the field site.

Tide level data was provided by the Fort Denison Tide Gauge, located inside Sydney Harbour.

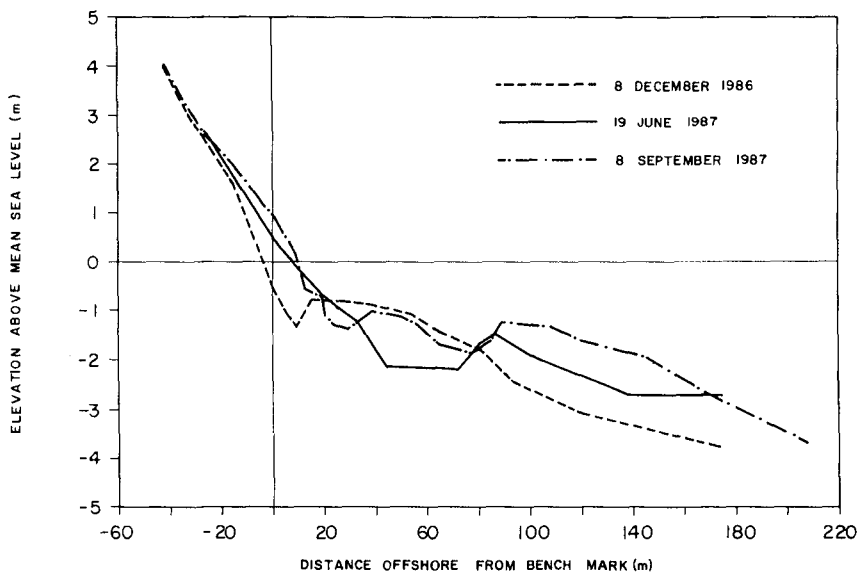


Figure 3: Selected surveys of the line along which the mean water level measurements were made. The setup data was collected between December 1986, and September 1987.

3.2 Field Equipment

The basis of the success of the method described here is the use of simple and reliable equipment. In essence, hydrostatic pressure at different points across the surf zone was "translated" through rigid plastic tubes to a central array of riser tubes. The plastic tubes "damped" the response of the system in such a way as to effectively filter out individual waves and surf-beat, leaving the mean water surface over a period of a few minutes (this process being further enhanced by taking a number of observations over a couple of minutes and averaging them).

The equipment comprising the offshore water level "sensors" consists of a stabilising steel chain, and a bundle of plastic tubes of different lengths, deployed permanently (in this case for over one year) across the surf zone. The longest rigid plastic tube extended 204 metres seaward of the bench mark, which is a stilling well positioned close to the average shoreline (see Figure 4).

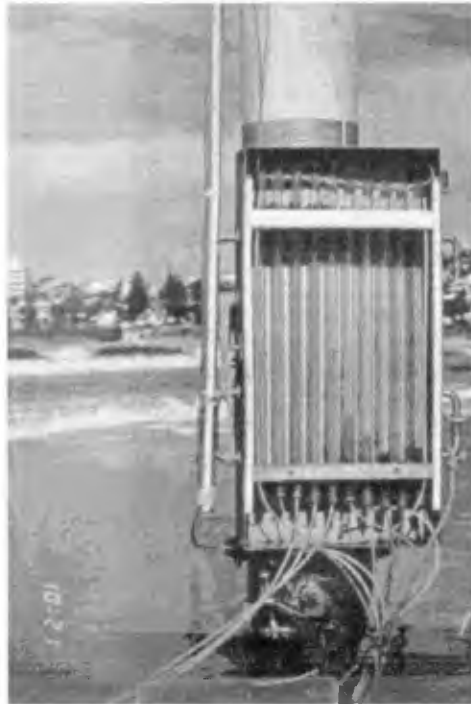


Figure 4: The "barometer" mounted on the stilling well which served as a bench mark for the surveys for reference it can be compared with the schematic representation in Figure 5.

In order to roughly maintain the same damping effect within the array of tubes of differing length, the inner diameter of the longer tubes was chosen to be 6mm while the shorter ones were 4mm. In hindsight these dimensions must be said to have been well chosen, except perhaps for the longest tube, which ought to have had an i.d. of 8mm in order to obtain optimal response characteristics.

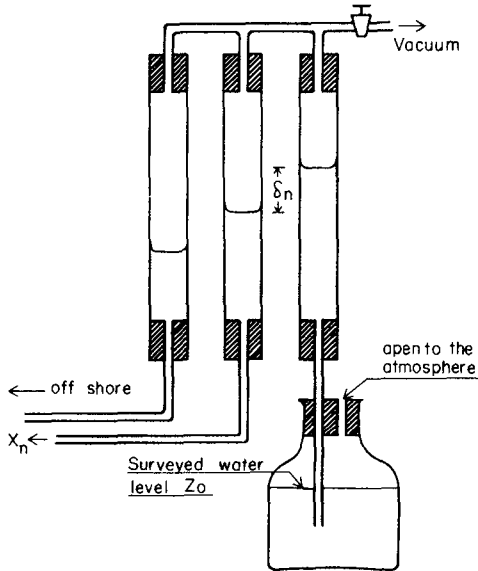


Figure 5: Schematic diagram of the apparatus used for measuring water table levels and hence, setup.

Deployment of the tubes had to be undertaken with some care to ensure no damage occurred to the tubes. All tension was taken by the steel chain, not the plastic tubes.

The tubes, once deployed, were left permanently on site. It is important that the tubes are permanently submerged so that any air bubbles in the system dissolve over time. Air bubbles would contaminate the readings of the system by offsetting the water levels in the riser tubes.

It is also important that the tubes are firmly anchored or buried in the sand so that movements (acceleration) of the tubes are avoided. Such movements would otherwise generate oscillations of the riser tube water levels.

All the tubes were laid out on the beach and bundled together with electrical cable ties. The bundle in turn was tied to a long length of 6mm steel chain. The steel chain was about 10m longer than the longest tube and had a large steel mass attached to the seaward end to help in anchoring. The landward end was fixed to a steel well in the swash zone. This steel well was permanently on site. It was about 300mm o.d., with 6mm thick walls.

The seaward ends of the plastic tubes were covered by geotechnical filter cloth, in order to prevent the intrusion of sand. The landward ends were capped and stowed inside the steel well.

The whole length (some 200m) of bundled up plastic tubes and steel chain was then man-handled out to waist-deep water, and from there a powerful boat dragged the seaward end of the chain out shore-normal from the beach until it was straight and then dropped it. Needless to say, reasonably calm seas and low tide were necessary for this operation.

A few days after deployment, the tubes and the steel chain had been covered by sand and only occasionally did sections of the tubes become exposed due to local erosion.

At the shoreward end, at the steel well in the swash zone, was mounted the "barometer box" (see Figure 4). This heavy steel box was fixed sturdily to the beach well on the day of an experiment at low tide. The permanently deployed plastic tubes had their shoreward ends uncapped and each was connected to the bottom of a vertical glass riser tube, i.d. 22mm, mounted in the barometer box.

The glass tubes were closed to the atmosphere and in turn inter-connected at their tops, so that the air pressures inside were at all times identical (see Figure 5).

An extra glass tube was connected to a reservoir bottle (about 2 litre capacity) partially filled with water to known (surveyed) level, open to the atmosphere, to provide an absolute reference level.

3.3 Experimental Procedure

The system is partially evacuated by sucking by mouth on a vent tube in the riser tube array. This is in order to bring the water levels in the tubes up above the sand to a level where they can be observed. Dye was introduced into the riser tubes to enhance contrast in the photographic observations.

After an initial settling down period of about 20 minutes, recordings were made every half hour throughout a half-tidal cycle, generally starting at low tide and finishing at high tide. With tidal ranges of up to 1.9m and the profile not being linear, this led to considerable variation in the effective beach profile through each field day.

Recordings were made by photographing the vertical glass tubes and the rulers on either side of them, 3 to 5 times with a 20 to 30 second interval, in order to average out traces of surf beat. A "data-back" camera was used so that accurate time was logged with each photograph.

Actual measurements were made by reading the slides off a micro-fiche reader, and adjusting the observed levels in the riser tubes by the absolute water level in the reservoir.

3.4 Water Table Measurements

Water table heights were measured in a series of simple stilling wells installed at four to eight metre intervals along the test traverse of Dee Why Beach.

The wells consisted of plastic pipes of 2.5 to 5 centimetre i.d., capped at the bottom end with geotechnical filter cloth to prevent the intrusion of sand.

The bottom of each well was sunk to a few tens of centimetres below the lowest position of the water table, and the well tops were surveyed.

Measurements of the water levels in the wells were made every half hour with a Geotechnical Instruments "Dip Meter". This is essentially a measuring tape with a conductivity sensor at the end, enabling measurements of the distance between well top and water surface to the nearest centimetre.

The "Dip Meter" measurements were aimed at the details of the water table shape between the shoreline and the runup limit, and the region immediately shoreward thereof. Complementary long term measurements were obtained with a MACE datalogger recording from a Druck pressure sensor inside the permanent stilling well, about 27 metres landward of the average shoreline. Pressure readings were taken every ten minutes for a period of four weeks.

The main purpose of these measurements was to obtain quantitative information about the influence through runup infiltration, of incoming wave height on the average water table height.

4. Study Results

4.1 Setup Profiles

Figure 6 shows a time series of measurements taken at twenty second intervals over about four minutes. A surf beat crest is visible in the readings from the two shortest tubes (3m and 7m) at time 90 seconds. The suppression of the reservoir tube at the same time is also forced by the surf beat. The standard deviations are 2.0 centimetres for the reservoir tube and 0.7 centimetres for the most dynamic offshore tube leading to a combined standard deviation of at most, 2.7 centimetres.

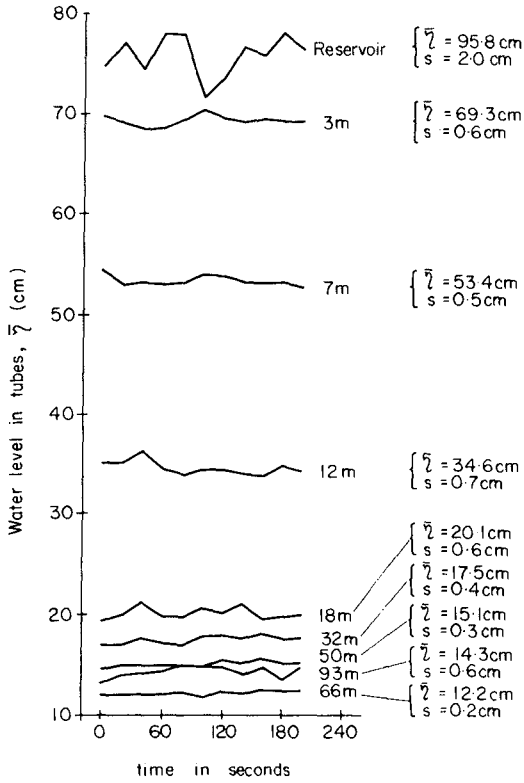


Figure 6: A time series of water level readings at 8 stations taken on 3rd June 1987. Numbers on the curves indicate the distance offshore of the open end. The two shortest tubes show a surf beat peak at $t=90s$, and correspondingly, the reservoir tube is suppressed at the same time.

A total of 120 setup profiles from 11 field days were obtained during the present study.

As an example, a sequence of setup profiles measured on 8th September 1987 are shown in Figure 7.

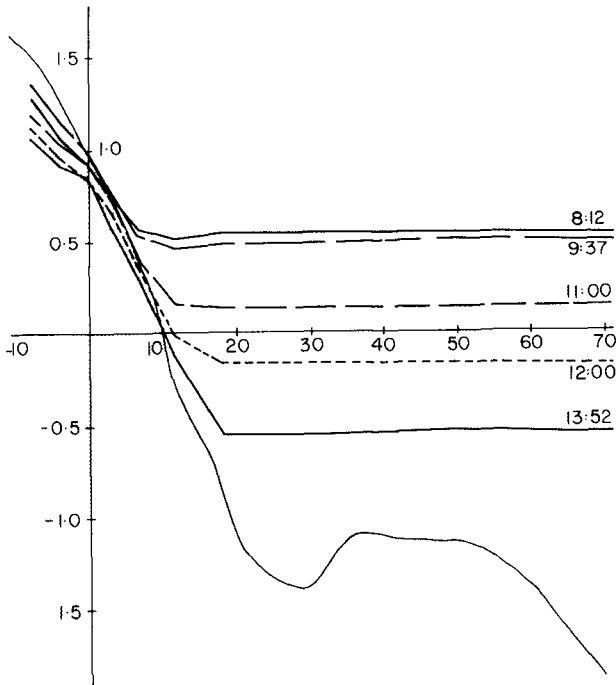


Figure 7: A series of setup profiles measured at Dee Why Beach on 8th September 1987. The offshore RMS wave height (H_{Orms}) ranged from 0.69 to 0.82 metres during these tests.

All the data from one field day (4th August 1987) are shown in Figure 8. The setup is plotted in dimensionless form (B/H_{Orms}) versus the likewise dimensionless total depth $(D+B)/H_{Orms}$. For comparison, the predicted setup according to Bowen et al (1968), with $\lambda = 0.5$, is also shown.

The setup at the still water shoreline B_{SWS} can be found from the intersection of the line "D=0" with the data. We see that B_{SWS} corresponds rather closely to the predicted value, while the setup is less than predicted seaward of SWSL and much larger than predicted between SWSL and the shoreline. The smaller values at the seaward end can at least partly be explained by wave height variability. For a more detailed discussion see Nielsen et al (1988).

The measured shape of the mean water surface between the still water line and the shoreline shows clearly that the simple model of Bowen et al (1968) does not apply in this area. This was foreseen by Bowen et al.

Quantitatively the data show that (within the data range) the shoreline setup was approximately 40% of the offshore wave height, which is about twice the predicted value from Bowen et al's model with reasonable choices of the wave height to depth ratio.

The data of the present study (reported in full by Nielsen et al, 1988) provide a considerable amount of information, which could serve as a guide line for the development of new models.

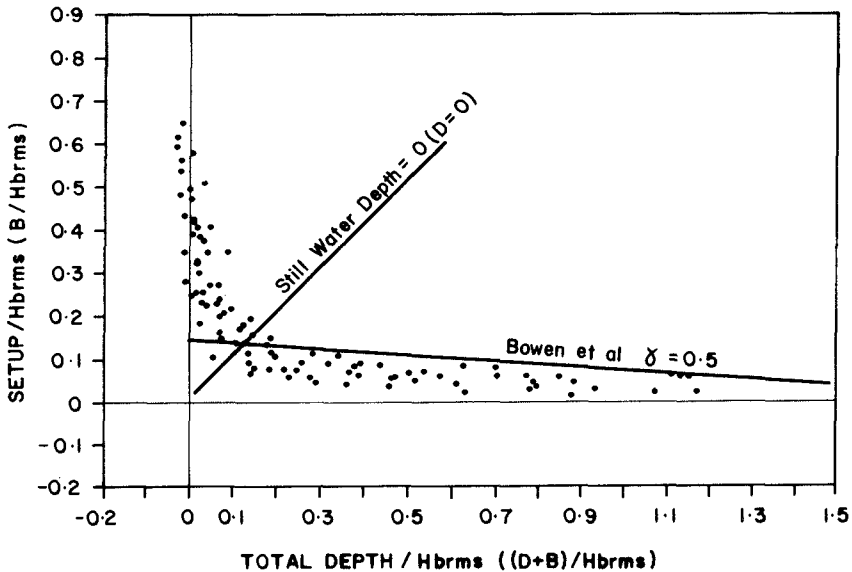


Figure 8: Dimensionless setup versus dimensionless total depth. Measurements from 4th August 1987.

4.2 Water-Table Profiles

The results of the integrated study shows that the input of a sinusoidal tide leads to a water table wave which is considerably skewed and on average, super-elevated above the mean shoreline level. This skewing and super-elevation originate mainly from the asymmetry (or non-linearity) of the boundary condition at the shoreline. A simple analytical model for this process is presented by Nielsen et al (1988).

Apart from the tidal fluctuations, the water table will move in response to wave height changes. The effects of these changes on the water table are twofold; firstly, the setup of the shoreline and secondly, a contribution to infiltration from runoff. The nature of this interaction is discussed in detail by Nielsen et al, 1988.

5. Merits and Further Potential of the Method

The main advantages of the method are as follows:-

- No need to level offshore components. The surf is a very harsh environment in which to work. Once the gear is deployed, no surveying of "sensors" is required.
- The equipment is simple and robust. Even in the high wave-energy environment of Dec Why Beach, the gear performed without major fault for over one year, surviving numerous storm events.
- No electronic components. Delicate calibrations and considerations of "drift" not required.
- Low cost. All of the components are readily available and inexpensive.

Further application of the method would be in studies of hydraulic behaviour of river entrances, and also in the study of the behaviour of rips on coastal beaches. A further application may be to study the phenomenon of surf-beat.

Possible improvements to the system may include the following:-

- Instead of using the relatively thin rigid plastic tubes to provide an (uncontrolled) damping of the response of the system, it may be better to deploy larger i.d. tubes and add the capacity to dampen response (by a "choke" mechanism, say) at the manometer box. In this way, all the tubes may be "calibrated" to have similar response characteristics.

The benefits of this may be a better ability to observe water level phenomena that vary within shorter or longer time scales, say for example surf beat instead of wave set-up.

- Use more than one line of tubes to provide a three-dimensional observation of water levels in the surf zone. This would enable the study of rips and rip feeder currents.

6. Conclusion

Manometer tubes of lengths up to two hundred metres have been applied successfully for measuring mean water levels in highly dynamic surf zones. The obtained accuracy was of the order ± 3 centimetres, but to obtain such accuracy it is essential that the tubes are permanently deployed with most of the length kept below the average water level. Then air bubbles will tend to dissolve with time and partial burying of the tubes in the sand will prevent movements due to waves and currents. Such movements could otherwise cause disturbing oscillations of the manometer water surface levels.

The technique has enabled the collection of a unique data base on wave setup and it has great potential for direct measurement of the water level gradients which drive rip currents and rip feeder currents.

7. References

- Holman, R. A. and Sallenger, A. H. (1985) : Set-Up and Swash on a Natural Beach Journal of Geophysical Research, Vol.90, No.C1, pp 945-953.
- Dorresteijn, R. (1961): Wave Setup on a Beach. Proc. 2nd Tech. Conf. Hurricanes, pp 230-237.
- Guza, R.T. and Thornton, E.B. (1981): Wave Setup on a Natural Beach. Journal of Geophysical Research, Vol 86, No.C5, pp 4133-4137.
- Nielsen, P. (1988) : Wave Setup : A Field Study, Journal of Geophysical Research, Vol 93.
- Nielsen, P., Elias, G., Davis, G. and Winterbourne, J. (1988) : Wave setup and the Water Table in Sandy Beaches. T.M. 88/1, Public Works Department, Coast and Rivers Branch, Sydney.
- Savage, R.P. (1957) : Model tests for Hurricane Protection Project Bull U.S. Corps of Engineers, Beach Erosion Board.
- Saville, T (1961) : Experimental Determination of Wave Setup. Proc. 2nd Tech. Conf. on Hurricanes, Miami Beach, pp 242-252.

CHAPTER 39

On the maximum runup of cnoidal waves.

Costas Emmanuel Synolakis †, A.M., ASCE and Manas Kumar Deb ‡.

This is a study of the maximum runup of cnoidal waves on plane beaches. An approximate theory is described for determining the maximum runup of non-breaking cnoidal waves. It is shown that the linear and nonlinear theory predict mathematically identical maximum runup heights. An asymptotic result is derived for the maximum runup of solitary waves, which are one limiting form of cnoidal waves. A series of laboratory experiments is described to support the theory. Other numerical results are presented that suggest that the runup of cnoidal waves is significantly higher than the runup of monochromatic waves with the same waveheight and wavelength. Preliminary laboratory data are also presented which suggest that, for certain cnoidal waves, the maximum runup is not a monotonically varying function of the normalized wavelength.

1. Introduction

The problem of determining the runup and reflection of cnoidal waves on plane beaches usually arises in the study of the coastal effects of tsunamis. Tsunamis are long water waves of small steepness generated by impulsive geophysical events on the ocean floor or at the coastline. Cnoidal waves are believed to model important aspects of the coastal effects of tsunamis well.

The process of long wave generation and propagation is now well understood. The process of long wave runup and reflection is not. However, there is consensus that one suitable physical model for this process is the formalism of a long wave propagating over constant depth and encountering a sloping beach. The studies of long wave runup have concentrated either on solitary waves or on monochromatic waves, i.e., at the two extremes of cnoidal waves. (For a comprehensive review of studies on solitary wave runup see Synolakis (1986).) To date, there appear to have been only three studies on cnoidal wave runup, one unpublished study by Pedersen and Gjevik (1983), the study of Ohyama (1987) – in Japanese – and the study of Synolakis et al (1988).

† Assistant Professor, School of Engineering, University of Southern California, Los Angeles, California 90089-0242

‡ Graduate Research Assistant, School of Engineering, University of Southern California, Los Angeles, California 90089-0242

Despite the quality of the analytical work, fundamental unresolved questions about the runup of long waves still persist. For example, in the study of solitary waves, the empirical relationship between the normalized runup and the normalized wave height that has been established in the classic laboratory investigations of Hall and Watts (1955) remained, until recently, unexplained. The results of the available numerical solutions have not been confirmed with detailed surface profiles from laboratory data, and, as a consequence, there is little conclusive information about the relative importance of dispersion and nonlinearity during runup. Until Synolakis (1987), there was no realization of the differences in the runup behaviour of breaking and nonbreaking long waves, and this had led to comparisons between numerical data for nonbreaking waves with laboratory data for breaking waves. There is still little understanding of the criteria that determine whether a wave breaks during runup or rundown, or of the reflection process. Compared to recent advances in understanding periodic wave runup on natural beaches, (Huntley et al 1977, Guza and Thornton, 1982 and Holman, 1986) the state of the art in cnoidal runup has been very limiting.

In the present study an exact solution to an approximate theory is described for determining the runup of long waves up plane beaches. The basic solution details and the evolution of the amplitude for solitary waves have been presented in Synolakis (1987). Some results for cnoidal waves have been presented in Synolakis et al (1988). In this paper we will summarize the predictions of the linear and nonlinear theory and we will show that the linear and nonlinear theory predict mathematically identical maximum runup heights. We will summarize the asymptotic results that lead to the runup law presented *ibid* and we will present numerical results for the runup of cnoidal waves. These results hint on a rich and unexpected behavior in the runup of long waves.

2. Basic equations and solutions

Consider a topography consisting of a plane sloping beach of angle β , as shown in figure 1. The origin of the coordinate system is at the initial position of the shoreline and x increases seaward. The topography $\tilde{h}_0(\tilde{x})$ is described as follows :

$$\tilde{h}_0(\tilde{x}) = \tilde{x} \tan \beta \text{ when } \tilde{x} \leq d \cot \beta \text{ and } \tilde{h}_0(\tilde{x}) = d \text{ when } \tilde{x} > d \cot \beta. \quad (1)$$

d is the undisturbed water depth in the constant depth region. Dimensionless variables are introduced as follows : $\tilde{x} = xd$, $\tilde{H} = Hd$, $\tilde{\eta} = \eta d$, $\tilde{h}_0 = h_0 d$, $\tilde{u} = u\sqrt{gd}$, and $\tilde{t} = t\sqrt{d/g}$. Consider a propagation problem described by the shallow water wave equations:

$$h_t + (hu)_x = 0, \quad (2a)$$

$$u_t + uu_x + \eta_x = 0, \quad (2b)$$

where $h(x) = h_0(x) + \eta(x, t)$.

2.1 Linear theory

The system of equations (2) can be linearized by retaining the first order terms only, resulting into $\eta_{tt} - (\eta_x h_0)_x = 0$. When $h_0(x) = x \tan \beta$, a well known solution of this equation is $\eta(x, t) = B(k, \beta) J_0(2k\sqrt{x \cot \beta}) e^{-ikct}$, where B is the amplification factor, k is the wavenumber and $c = 1$. Keller and Keller (1964) presented another steady state solution for the combined topography defined by (1). For an incident wave of the form $\eta(x, t) = A_i e^{-i(x+ct)}$, they determined the amplification factor $B(k, \beta, A_i) = 2e^{-ik \cot \beta} A_i / [J_0(2k \cot \beta) - iJ_1(2k \cot \beta)]$.

Since the governing equation is linear and homogenous, any standing wave solutions can be used to obtain travelling wave solutions by linear superposition. For example, when the incident wave is of the form $\eta(X_0, t) = \int_{-\infty}^{\infty} \Phi(k) e^{-ikct} dk$, then the wave transmitted to the beach is given by :

$$\eta(x, t) = 2 \int_{-\infty}^{\infty} \Phi(k) \frac{J_0(2k\sqrt{xX_0}) e^{-ik(X_0+ct)}}{J_0(2kX_0) - iJ_1(2kX_0)} dk, \tag{3}$$

where $X_0 = \cot \beta$. This solution is only valid when $x \geq 0$. To obtain the details of the solution when $x < 0$ one must solve the nonlinear set (2).

2.2 Nonlinear theory

To solve the nonlinear set (2) for the sloping beach case, $h_0(x) = x \tan \beta$, Carrier and Greenspan (1958) introduced the following hodograph transformation,

$$x = \cot \beta \left(\frac{\sigma^2}{16} - \frac{\psi_\lambda}{4} + \frac{u^2}{2} \right), \quad t = \cot \beta \left(\frac{\psi_\sigma}{\sigma} - \frac{\lambda}{2} \right)$$

$$u = \frac{\psi_\sigma}{\sigma}, \quad \text{and} \quad \eta = \frac{\psi_\lambda}{4} - \frac{u^2}{2}. \tag{4}$$

This change of variables reduces the set of equations (2) to a single linear equation,

$$(\sigma \psi_\sigma)_\sigma = \sigma \psi_{\lambda\lambda}. \tag{5}$$

The transformation is such that in the hodograph plane, i.e., the (σ, λ) space, the shoreline is always at $\sigma = 0$; this can be deduced easily by setting $\sigma = 0$ in (4); then $x = -\eta \cot \beta$, which is an equality only valid at the shoreline tip.

Equation (5) can be solved with standard methods. Defining the Fourier transform of $\psi(\sigma, \lambda)$ as $\Psi(\sigma, \tilde{k}) = \int_{-\infty}^{\infty} \psi(\sigma, \lambda) e^{-i\lambda \tilde{k}} d\lambda$, and, if $\Psi(\sigma_0, \tilde{k}) = F(\tilde{k})$, then the bounded solution at $\sigma = 0$ and $\sigma = \infty$ takes the form :

$$\psi(\sigma, \lambda) = \frac{1}{2\pi} \int_{-\infty}^{\infty} F(\tilde{k}) \frac{J_0(\tilde{k}\sigma)}{J_0(\tilde{k}\sigma_0)} e^{i\tilde{k}\lambda} d\tilde{k}. \tag{6a}$$

If an initial condition is available instead, one may use Hankel transform methods (Carrier (1966)).

The process of specifying explicitly an initial or a boundary condition to equation (5) is nontrivial. Even if initial or a boundary data are available in the (x, t) space, the process of deriving the equivalent conditions in the (σ, λ) space is very complex. These difficulties have restricted the use of the Carrier and Greenspan formalism and this is rather unfortunate, because some of the problems described can be circumvented. (Carrier, 1966.) Another method has been described by Synolakis (1986, 1987) to specify a boundary condition *including reflection*. We will summarize it here.

2.3 Approximate solution of the nonlinear theory

Carrier (1966) pointed out that far from the shoreline nonlinear effects are small. The transformation equations can then be simplified by neglecting terms $\sim O(u^2)$. To the same order, $\psi_\lambda \ll \frac{\sigma^2}{16}$ and $\frac{\psi_\sigma}{\sigma} \ll \frac{\lambda}{2}$. Using these approximations the transformation equations (4) reduce to $u = \frac{\psi_\sigma}{\sigma}$, $\eta = \frac{\psi_\lambda}{4}$, $x = \frac{\sigma^2}{16} \cot \beta$ and $t = -\frac{\lambda}{2} \cot \beta$. These equations are uncoupled and allow direct transition from the (σ, λ) space to the (x, t) space.

One method for specifying a boundary condition in the physical space is to use the solution of the equivalent linear problem, as given by equation (3), at the seaward boundary, where $x = X_0 = \cot \beta$, i.e., the point $\sigma = \sigma_0 = 4$ in the (σ, λ) space. Then equations (4) imply that $\eta(X_0, t) = \frac{1}{4} \psi_\lambda(4, \lambda)$. The boundary condition $F(\vec{k})$ in the (σ, λ) space is determined from (3) by repeated application of the Fourier integral theorem. Assuming that $\psi(\sigma_0, \lambda) \rightarrow 0$ as $\lambda \rightarrow \pm\infty$, then the solution of equation (5) follows,

$$\psi(\sigma, \lambda) = -\frac{16i}{X_0} \int_{-\infty}^{\infty} \frac{\Phi(\kappa)}{\kappa} \frac{J_0\left(\frac{\sigma\kappa X_0}{2}\right) e^{-i\kappa X_0(1-\frac{\lambda}{2})}}{J_0(2\kappa X_0) - iJ_1(2\kappa X_0)} d\kappa. \quad (6b)$$

3. Comparison of the linear and of the nonlinear theory

The maximum runup according to the linear theory is the maximum value attained by the wave amplitude at the initial position of the shoreline, i.e., at $x = 0$, or

$$\eta(0, t) = 2 \int_{-\infty}^{\infty} \frac{\Phi(k) e^{-ik(X_0+ct)}}{J_0(2kX_0) - iJ_1(2kX_0)} dk. \quad (7)$$

In the nonlinear theory the maximum runup is given by the maximum value of the amplitude at the shoreline $\eta(x_s, \lambda)$. (x_s is the x -coordinate of the shoreline and it corresponds to $\sigma = 0$.) Using (4), one obtains that :

$$\eta(x_s, t) = \frac{\psi_\lambda}{4} - \frac{u_s^2}{2} = 2 \int_{-\infty}^{\infty} \frac{\Phi(\kappa) e^{-i\kappa X_0(1-\frac{\lambda}{2})}}{J_0(2\kappa X_0) - iJ_1(2\kappa X_0)} d\kappa - \frac{u_s^2}{2}; \quad (8)$$

$u_s = dx_s/dt$ is the velocity of the shoreline tip. At the point of maximum runup u_s becomes zero. Setting $u_s = 0$ and $\sigma = 0$ in the transformation equations (4) reduces the transformation equations to $u = 0$, $\eta = \frac{\psi_\lambda}{4}$, $x = -\eta \cot \beta$, and $t = -\frac{\lambda}{2} \cot \beta$. Substitution of these values in equation (8) reduces it to equation (7), proving that the maximum runup predicted by the linear theory is identical to the maximum runup predicted by the nonlinear theory. At the minimum rundown point the shoreline tip attains zero velocity also, and the same argument applies again. This result was first noted by Carrier (1971) in a problem where reflection was negligible. As shown by Synolakis (1987) it is valid in general, even when reflection is important. It is largely unexpected, because the linear and nonlinear theory differ most at the initial position of the shoreline.

4. The cnoidal wave solutions

Cnoidal waves are exact periodic solutions of the KdV equation $\eta_t + (1 + \frac{3}{2}\eta)\eta_x + \frac{1}{6}\eta_{xxx} = 0$. A cnoidal wave propagating over constant depth is given by Svendsen (1974) as

$$\eta(x, t) = y_t - 1 + H \operatorname{cn}^2(2K(\frac{x}{L} + \frac{t}{T})|m). \tag{9}$$

y_t is the distance of the trough from the bottom, and H, L and T are the dimensionless wave height, wavelength and period respectively. $K(m)$ is the first elliptic integral and m is the elliptic parameter. If one defines the Ursell number as $U = HL^2$, then $U = (16/3)mK^2$. The function $\operatorname{cn}(z|m)$ is the Jacobian elliptic function and it is given by Abramowitz and Stegun (1972) as:

$$\operatorname{cn}(z|m) = \frac{2\pi}{\sqrt{m}K} \sum_{i=0}^{\infty} \frac{q^{i+\frac{1}{2}}}{1+q^{2i+1}} \cos[(2n+1)\frac{\pi z}{2K}]$$

$q = e^{-\pi K'/K}$, and K and K' are the real and imaginary quarter periods of the elliptic functions respectively. Cnoidal waves have two important limiting cases. As $m \rightarrow 1$, it can be shown that

$$\eta(x, t) = H \operatorname{sech}^2 \sqrt{\frac{3}{4}H}(x + ct). \tag{10}$$

$c = \sqrt{1+H}$ is the wave celerity. Equation (10) is the Boussinesq profile for a solitary wave. As $m \rightarrow 0$, then

$$\eta(x, t) = \frac{H}{2} \cos 2\pi(\frac{x}{L} + \frac{t}{T}),$$

the profile of a monochromatic periodic wave. For comparison, figure 1 shows a cnoidal wave, a solitary wave and a sinusoidal wave with the same normalized height H propagating over constant depth. The cnoidal and sinusoidal waves also have the same wavelength L .

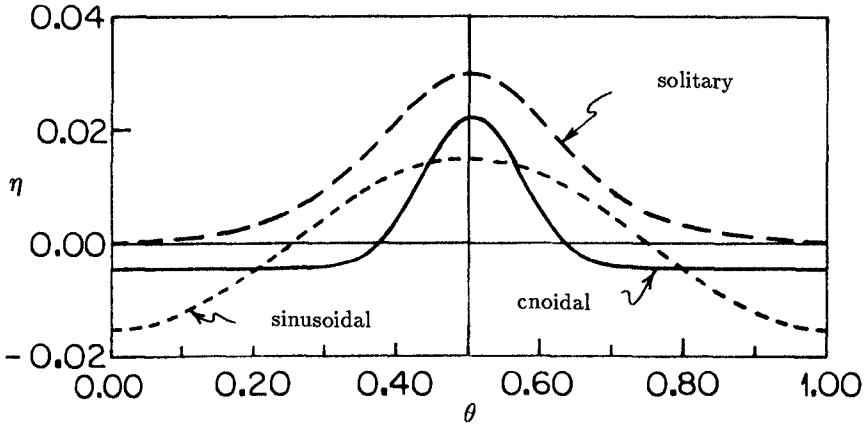


Figure 1 The amplitude profile of a solitary wave ($\eta = H\text{sech}^2\theta$), a sinusoidal wave ($\eta = \frac{H}{2} \cos \theta$) and a cnoidal wave ($\eta = y_t - 1 + H\text{cn}^2(2K\theta|m)$) with the same $H = 0.027$ propagating over constant depth as a function of the dimensionless phase θ . The cnoidal wave and the sinusoidal wave also have the same wavelength L .

The results of the previous section will now be applied to derive a result for the maximum runup of cnoidal waves climbing up a sloping beach.

4.1 The solitary wave solution

A solitary wave centered at $x = X_1$ at $t = 0$ has the following surface profile $\eta(x, 0) = \frac{H}{d} \text{sech}^2\gamma(x - X_1)$, where $\gamma = \sqrt{3H/4d}$. The function $\Phi(k)$ associated with this profile is derived in the appendix. It is given by $\Phi(k) = (2/3)k\text{cosech}(\alpha k)e^{ikX_1}$ where $\alpha = \pi/2\gamma$. Substituting $\Phi(k)$ into equation (7) and defining as $R(t)$ the dimensionless surface elevation at the initial position of the shoreline, then

$$R(t) = \frac{4}{3} \int_{-\infty}^{\infty} k\text{cosech}(\alpha k) \frac{e^{ik(X_1 - X_0 - ct)}}{J_0(2kX_0) - iJ_1(2kX_0)} dk. \tag{11}$$

This integral can be calculated with standard methods of applied mathematics; its convergence and evaluation is discussed in Synolakis (1987,1988). The integration result is :

$$R(t) = 8H \sum_{n=1}^{\infty} \frac{(-1)^{n+1} n e^{-2\gamma(X_1 - X_0 - ct)n}}{I_0(4\gamma X_0 n) + I_1(4\gamma X_0 n)}. \tag{12}$$

The series can be simplified further by using the asymptotic form for large arguments of the modified Bessel functions. When $4X_0\gamma \gg 1$, then :

$$R(t) = 8\sqrt{\pi X_0} H (3H)^{\frac{1}{4}} \sum_{n=1}^{\infty} (-1)^{n+1} n^{\frac{3}{2}} e^{-2\gamma(X_1 + X_0 - ct)n}. \tag{13}$$

This form of the solution is particularly helpful for calculating the maximum runup. The series in (12) is of the form $\sum_{n=1}^{\infty} (-1)^{n+1} n^{3/2} \chi^n$; its maximum value occurs at $\chi = 0.481$. This value defines the time $t_{max} = (1/c)[X_1 - X_0 - 0.366/\gamma]$ when the wave reaches its maximum runup, and the value of the series at t_{max} is $s_{max} = 0.15173$. Defining as \mathbf{R} the maximum value of $R(t)$ and evaluating the term $8\sqrt{\pi\sqrt{3}s_{max}}$, then the following expression results for the maximum runup :

$$\mathbf{R} = 2.831\sqrt{\cot\beta}(H)^{\frac{5}{4}}. \tag{14}$$

The term *the runup law* has been coined for this equation. It is formally valid when the series converges and when $4X_0\gamma \gg 1$, i.e., $\sqrt{H} \gg 0.288 \tan\beta$.

4.2 Validity of the solution

The solution described is valid for functions $\Phi(k)$ such that the Jacobian of the transformation (4) is never equal to zero. The Jacobian becomes zero when the surface slope $\partial\eta/\partial x$ becomes infinite. In the physical plane this point is usually interpreted as the point of wave breaking.

The Jacobian of the Carrier and Greenspan transformation is $\mathbf{J} = c(t_\sigma^2 - t_\lambda^2)$. Taking the limit as $\sigma \rightarrow 0$, then $\mathbf{J} \rightarrow (u_\lambda - \frac{1}{2})^2$. Using the formalism used in calculating the runup integral (Eq. 11), one can show analytically that the limiting H when $u_\lambda - \frac{1}{2}$ goes through zero, as :

$$H = 0.8183(\cot\beta)^{-\frac{10}{3}}. \tag{15a}$$

This is a weaker restriction than that presented in Pedersen and Gjevik (1983), who reported that waves break when

$$H > 0.479(\cot\beta)^{-\frac{10}{3}}. \tag{15b}$$

However, there are two basic differences between the two results. The Gjevik and Pedersen criterion (15) indicates the limiting H when a solitary wave breaks during the backwash. Equation (15b) indicates when a wave first breaks during runup. Also, the Gjevik and Pedersen result (15b) was derived by using the sinusoidal wave profile that best fits the Boussinesq profile, while equation (15a) is based on the actual Boussinesq profile (Eq. 10).

4.3 Maximum runup

Although it has long been known that breaking and nonbreaking periodic waves follow different runup variations, this behaviour has never been recognized in single-wave runup. In Synolakis (1987), data was presented that demonstrated conclusively that two different runup regimes exist, one for breaking and one for non-breaking solitary waves.

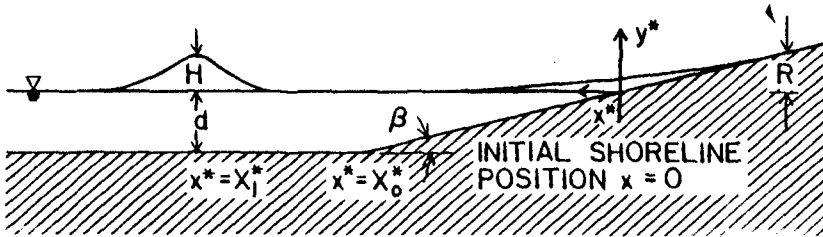


Figure 2a. A definition sketch for solitary wave runup.

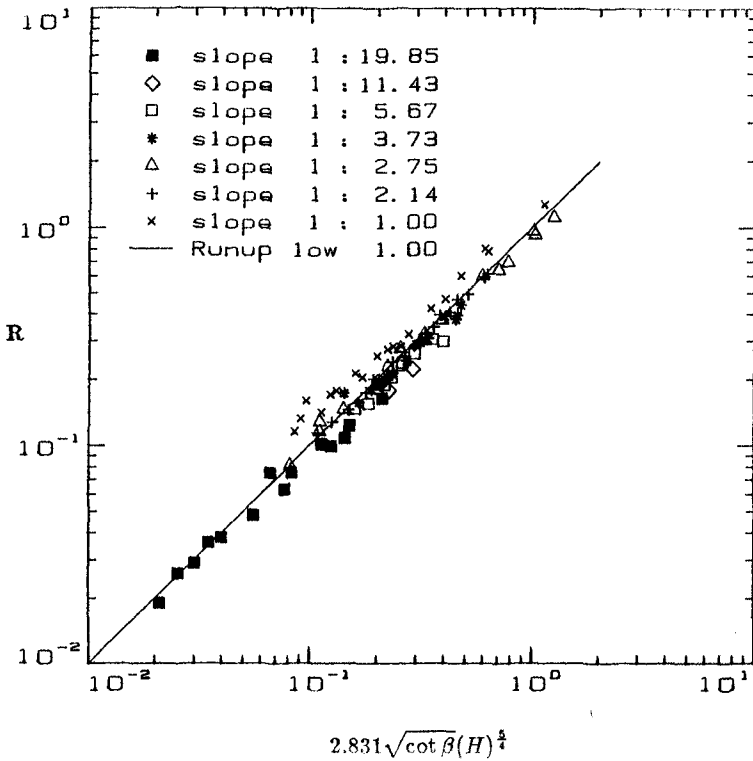


Figure 2b. The normalized runup R of solitary waves of height H climbing up different beaches of slope $1 : \cot \beta$ plotted against the runup law (Eq. 13). All data refer to nonbreaking waves and they were derived in the laboratory. The data for the slopes $1 : 11.47, 1 : 5.67, 1 : 3.73, 1 : 2.14,$ and $1 : 1.00$ are from Hall and Watts (1953), the data for the $1 : 2.75$ slope are from Pedersen and Gjevnik (1983), and the data for the $1 : 19.85$ slope are from Synolakis (1987).

To verify this observation for other beaches, the runup law has been compared *ibid* with laboratory data. Comparisons of analytical results with laboratory data such as those of Hall and Watts (1953) are not as straightforward as often assumed. That study includes both breaking and nonbreaking wave data without identifying them as such, and therefore the empirical relationships derived there may not be directly applicable when determining the runup of nonbreaking waves. To perform a posteriori identification of the Hall and Watts data, the breaking criterion (Eq 15) was used, and the identified nonbreaking wave data are presented in figure 2b. The abscissa is the runup law (Eq. 14), and the ordinate is the maximum runup. The asymptotic result does appear to model the laboratory data very well. No data are presented for slopes smaller than 1:20, because no such data are yet available; on a 1:100 slope, the highest nonbreaking wave is a wave with $H \approx 0.003$.

4.4 The cnoidal wave solution

Consider an incoming cnoidal wave of the form (9). In this case the method of choice for the solution is a Fourier–Bessel series. The solution proceeds in a manner similar to the development in section 4.2.

The complete expression for a cnoidal wave is given by

$$\begin{aligned} \eta(x, t) = & y_t - 1 \\ & + \frac{2\pi^2 H}{mK^2} \sum_{i=0}^{\infty} \sum_{j=0}^{\infty} \frac{q^{i+j+1}}{(1+q^{2i+1})(1+q^{2j+1})} \cos 2\pi(i+j+1)\left(\frac{x}{L} - \frac{t}{T}\right) \\ & + \frac{2\pi^2 H}{MK^2} \sum_{n=0}^{\infty} \sum_{m=0}^{\infty} \frac{q^{m+n+1}}{(1+q^{2n+1})(1+q^{2m+1})} \cos 2\pi(m-n)\left(\frac{x}{L} - \frac{t}{T}\right). \end{aligned} \quad (16)$$

Using the Keller and Keller (1964), and, after some algebra, we obtain the wave transmitted to the beach and eventually the wave amplitude at the initial shoreline :

$$\begin{aligned} \eta(0, t) = & y_t - 1 \tag{17} \\ & + \frac{4\pi^2 H}{mK^2} \sum_{i=0}^{\infty} \sum_{j=0}^{\infty} \frac{q^{i+j+1}}{(1+q^{2i+1})(1+q^{2j+1})} \frac{\cos[\phi - k_{ij}(\cot \beta + c_0 t)]}{\sqrt{J_0^2(2k_{ij} \cot \beta) + J_1^2(2k_{ij} \cot \beta)}} \\ & + \frac{4\pi^2 H}{mK^2} \sum_{i=0}^{\infty} \sum_{j=0}^{\infty} \frac{q^{i+j+1}}{(1+q^{2i+1})(1+q^{2j+1})} \frac{\cos[\phi' - k'_{ij}(\cot \beta + c_0 t)]}{\sqrt{J_0^2(2k'_{ij} \cot \beta) + J_1^2(2k'_{ij} \cot \beta)}}. \end{aligned}$$

$k_{ij} = 2\pi(i+j+1)/L$, $k'_{ij} = 2\pi(i-j)/L$, $\phi = \arctan[\frac{J_1(2k_{ij} \cot \beta)}{J_0(2k_{ij} \cot \beta)}]$ and $\phi' = \arctan[\frac{J_1(2k'_{ij} \cot \beta)}{J_0(2k'_{ij} \cot \beta)}]$. Since $\cot \beta \geq 1$, the arguments of the Bessel functions are either zero or much larger than one, and the Bessel functions can be replaced by

their asymptotic forms for large arguments. Simplifying (17) we obtain,

$$\begin{aligned} \eta(0, t) \approx y_t - 1 &+ \frac{4\pi^2 H}{mK^2} \sqrt{\frac{2\pi}{L} \cot \beta} \sum_{i=0}^{\infty} \sum_{j=0}^{\infty} \frac{\sqrt{(i+j+1)} q^{i+j+1}}{(1+q^{2i+1})(1+q^{2j+1})} \cos\left[\frac{2\pi}{L}(i+j+1)(\cot \beta - c_0 t) - \frac{\pi}{4}\right] \\ &+ \frac{4\pi^2 H}{mK^2} \sqrt{\frac{2\pi}{L} \cot \beta} \sum_{\substack{i=0 \\ i \neq j}}^{\infty} \sum_{j=0}^{\infty} \frac{\sqrt{|i-j|} q^{i+j+1}}{(1+q^{2i+1})(1+q^{2j+1})} \cos\left[\frac{2\pi}{L}(i-j)(\cot \beta - c_0 t) - \frac{\pi}{4}\right] \\ &+ \frac{2\pi^2 H}{mK^2} \sum_{i=0}^{\infty} \frac{q^{2i+1}}{(1+q^{2i+1})^2}. \end{aligned} \quad (18)$$

As $m \rightarrow 0$, it is possible to simplify this expression. However, since it is necessary to determine the behavior $\forall m$, we proceed with a direct evaluation of the series in Eq (18).

Figure 3 shows the maximum relative runup of cnoidal waves R/H with the same H as a function of the dimensionless wavelength L up three different sloping beaches. The figure suggests that the runup of a cnoidal wave is substantially higher than the runup of the monochromatic wave with the same height and wavelength. It is also seen that there exists a minimum in the functional variation of the cnoidal wave runup with the wavelength. This minimum is more pronounced in the runup variation of the larger waves, in Figures 3(b) and 3(c).

All the waves in figure 3 are nonbreaking. The linear theory cannot provide directly a breaking criterion. To determine when waves start to break, the Jacobian of the Carrier and Greenspan transformation was monitored continuously as described in Synolakis (1986). The implication is that these results are valid for waves climbing up very steep beaches or for very long waves. Most natural beaches are gently sloping, and it is not obvious if similar differences exist. However, Figure 3 does suggest that the common practice of choosing the dominant frequency of an incoming wave-spectrum and using the runup of the monochromatic wave with that dominant frequency for calculating wave runup may not be entirely appropriate when the incoming wave energy is dominated by low frequency swell.

To investigate if this behavior can be demonstrated in the laboratory, a series of preliminary experiments were conducted in the 40m wave tank of the Keck Laboratory of Hydraulics and Water Resources of the California Institute of Technology. At a distance of 20m from the wave generator a sloping beach of 45° angle was installed. The wave generation system and the generation algorithm is described in detail by Skjelbreia (1987).

The results of the laboratory experiments for the climb of cnoidal waves of $H = 0.1$ up a 45° beach are shown in Figure 3. The relative runup is shown to decrease and then increase again as the wavelength increases. This is as the theory suggests.

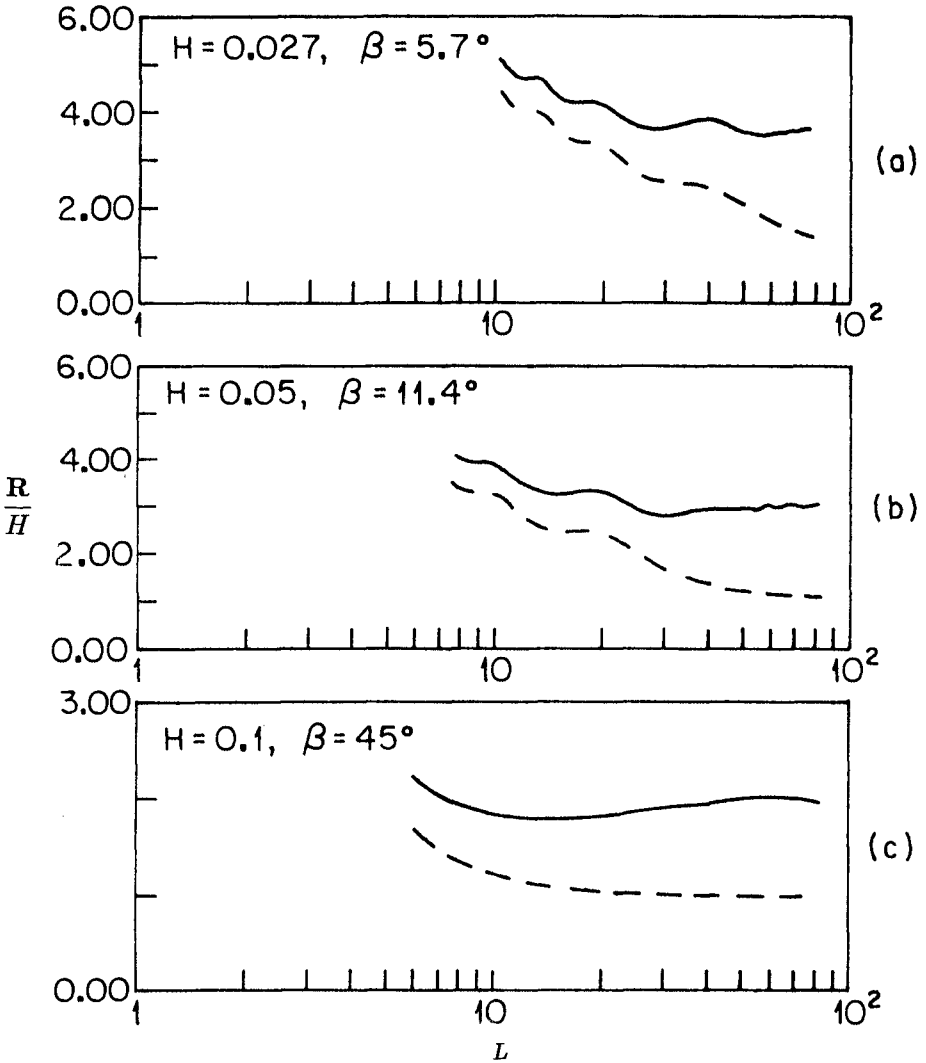


Figure 3 The maximum relative runup of sinusoidal waves (dashed lines) and the maximum relative runup of cnoidal waves (solid lines) with the same height H up three sloping beaches as a function of the dimensionless wavelength. (a) $H = 0.027, \beta = 5.7^\circ$; (b) $H = 0.05, \beta = 11.3^\circ$; (c) $H = 0.1, \beta = 45^\circ$. Nonbreaking waves.

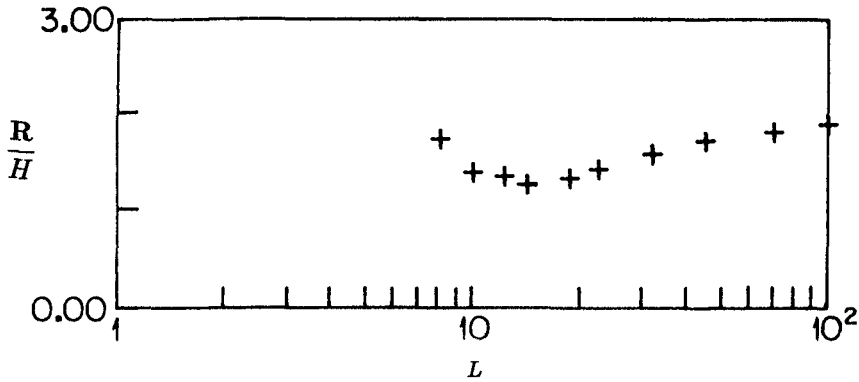


Figure 4. The maximum relative runup of nonbreaking cnoidal waves with $H = 0.1$ up a 45° beach as a function of the normalized wavelength. Laboratory data after Synolakis et al (1988).

This behavior is not entirely unexpected. The current paradigm in wave runup predicts that the relative runup decreases as the wave-steepness decreases, i.e., as the wavelength increases Ahrens and Titus (1985). On the other hand, there is empirical evidence (ibid) that as the nonlinearity of a given wave increases, the relative runup increases as the wavelength increases. (This is an intuitively pleasing behavior for cnoidal waves; as the nonlinearity increases and the wave has an increasing portion of its volume above the mean water level, the relative runup is expected to increase.) Figure 3(c) and Figure 4 suggest that both descriptions are correct, over different ranges of the wavelength.

We suggest two explanations why this behavior has been previously unrecognized. One, most existing runup data have been obtained from laboratory studies with monochromatic waves, where the effects of nonlinearity are difficult to quantify. Two, since most empirical runup relationships are based on synthesis of laboratory data from many different runup investigations, it is likely that any anomalies in the functional variations were attributed to differences in the quality of the data.

5. Conclusions

In summary, our analysis suggests the following conclusions.

1) The runup of nonbreaking waves predicted by nonlinear theory is mathematically identical to the runup predicted by linear theory for waves climbing up plane beaches.

2. The runup of solitary waves is described well by the runup law,

$$R = 2.831\sqrt{\cot\beta(H)}^{\frac{5}{4}}.$$

3. Different criteria apply for wave breaking during runup and rundown.

4. The runup of cnoidal waves is significantly higher than the runup of the equivalent monochromatic waves.

5. The runup variation of cnoidal waves is not a monotonically increasing or decreasing function of the wave steepness.

Acknowledgements This research was supported by a grant from the National Science Foundation (managed by Fred Raichlen of CIT) and by the Faculty Research and Innovations Fund of the University of Southern California. Additional funding was provided by a grant from the Alexander Onassis Public Benefit Foundation.

References

- Abramowitz, M. and Stegun, I.A. 1972 *Handbook of Mathematical Functions*, Natl. Bur. Stands., Washington, D.C., p575.
- Ahrens, J.P. and Titus, M.F. 1985 *JWW, Proc. ASCE*, **111**, 1, 128-133.
- Carrier, G. F. 1966 *J. Fluid Mech.* **24**, 641-659.
- Carrier, G.F. 1971 Proc. of the 6th Summer Seminar on Applied Mathematics, RPI, Troy, NY, 1970. AMS.
- Carrier, G.F. and Greenspan, H.P. 1958 *J. Fluid Mech.* **17**, 97-110.
- Guza, R.T. and Thornton, E.B. 1982 *J. Geoph. Res.*, **87**, 483-491.
- Hall, J.V. and Watts, J.W. 1953 TM 33, BEB, USArmy Corps Eng., 14 pp.
- Holman, R.A. 1986 *Coastal Engineering*, **9**, 527-544.
- Huntley, D.A., Guza, R.T., and Bowen, A.J. 1977 *J. Geoph. Res.*, **82**, 2577-2581.
- Keller, J.B. and Keller, H.B. 1964 ONR Research Report Contract No NONR-3828(00), Dept. of the Navy, Washington, D.C.. 40 pp.
- Pedersen, G. and Gjevik, B. 1983 *J. Fluid Mech.* **135**, 283-299. This is a paper on solitary waves. The cnoidal wave paper is unpublished.
- Ohyama, T. 1987 *Proc. JSCE* **381**, II-7, 189-198. (*In Japanese.*)
- Skjelbreia, J.E. 1987 *Observations of breaking waves on beaches by use of laser doppler velocimetry* Ph.D. Thesis, California Institute of Technology, Pasadena, CA, 160pp.
- Synolakis, C.E. 1986, *The runup of long waves* Ph.D. Thesis, California Institute of Technology, Pasadena, CA, 228pp.
- Synolakis, C.E. 1987 *J. Fluid Mech.*, **185**, 523-545.
- Synolakis, C.E. 1988 *Qu. Appl. Math.*, **XLVI**, 105-107.
- Synolakis, C.E., Deb M.K. and Skjelbreia, E.J. 1988 *Phys. Fluids*, **31**, 1-4.
- Svendsen, I.A. 1974 *Cnoidal waves over gently sloping bottom*. Inst. Hydr. Hydr. Eng., Techn. Univ. Denmark, Ser. Pap. 6, Lyngby, Denmark, 181pp.

CHAPTER 40

THE WAMS MODEL APPLIED TO THE MEDITERRANEAN SEA

Luigi Cavaleri*, Luciana Bertotti*,
Jose E. De Luis** and Piero Lionello*

Summary

The application of an advanced third generation wave model to the Mediterranean Sea is described. The model is based on the physical description of the wind wave evolution, avoiding any shortcoming in the estimate of the single terms that contribute to the energy budget. The capability of the model to respond to any meteorological situation is illustrated by applying it to a severe storm occurred in January 1987. The results show that the crucial point for the final accuracy lies in the correct evaluation of the wind field.

Introduction

The SWAMP study (SWAMP, 1985), intercomparing the results of ten different wave models for some well defined tests, made clear that, for any drastic improvement in the field to arise, a completely new approach to the problem was to be taken. In particular any shortcoming in the description of the wind wave evolution had to be released, and the problem had to be

- * Istituto per lo Studio della Dinamica delle Grandi Masse, C.N.R., San Polo 1364, 30125 Venice, Italy.
- ** Programa de Clima Maritimo, D.G.P. y C., MOPU, P^a de la Castellana no. 16, 5^o Dcha., 28046 Madrid, Spain.

approached only on a physical basis. Being beyond the capability of any single group, the task was faced by a whole team of modellers. The result is the so-called "third generation WAM wave model" (WAMDI-Group, 1988).

While most of the WAM group interest was in the large oceans, we have focused our attention on the Mediterranean Sea. This is a quite interesting basin, with a rather complicated meteorology. Occasional very heavy storms are present, which, from the point of view of a modeller aiming at a detailed study, have the advantage of being free of any distant swell eventually affecting the local results. In the following sections we give a brief description of the model, of its implementation in the basin, and we discuss the implications of the results.

The WAM Model

The WAM model, or WAMS, in its shallow water version used for the Mediterranean Sea, is based on the numerical integration of the energy balance equation. It is assumed that wave conditions at a given time t and location ϕ and λ (ϕ = latitude, λ = longitude) are represented by the two-dimensional spectrum $F(f, \theta, \phi, \lambda, t)$, f and θ being the frequency and direction that characterize the single wave component. The evolution of $F()$ on the spherical earth is governed by the transport equation

$$(1) \quad \frac{\partial F}{\partial t} + (\cos \phi)^{-1} \frac{\partial}{\partial \phi} (\dot{\phi} \cos \phi F) + \frac{\partial}{\partial \lambda} (\dot{\lambda} F) + \frac{\partial}{\partial \theta} (\dot{\theta} F) = S$$

where S represents the local source function and the dots represent derivatives with respect to time.

Specifically

$$(2) \quad \dot{\phi} = v R^{-1} \cos \theta$$

$$(3) \quad \lambda = v \sin \theta (R \omega \sin \phi)^{-1}$$

$$(4) \quad \dot{\theta} = v \sin \theta \tan \phi R^{-1}$$

Here v is the group velocity and R is the radius of the earth.

The left side of the energy balance equation represents the kinematics of wind waves, i.e. the advection, and its solution is purely a mathematical problem. The physics of waves, the dynamics of the problem, is on the right side term S that is considered as composed of three parts

$$(5) \quad S = S_{in} + S_{nl} + (S_{br} + S_{bf})_{dis}$$

S_{in} represents the input of energy from the wind based on the Miles process,

$$S_{in} = \beta F$$

where the expression for β is adopted from Snyder et al. (1981). With respect to the original expression the model uses a slightly modified version of β based on the friction velocity U_* . It is given by Komen et al. (1984) as

$$(6) \quad \beta = \max \left(0, 0.25 \frac{\rho_a}{\rho_w} \left(2.8 \frac{U_*}{c} \cos \theta_w - 1 \right) \right) \cdot \sigma$$

($\sigma = 2\pi f$, ρ_a , ρ_w = air and water density, c = water

phase velocity, Θ_w = angle between wind and wave direction).

S_{nl} represents the nonlinear conservative energy exchanges between all the possible quadruplets of wave components that satisfy given resonance conditions. Requiring enormous computer power for its evaluation, the evaluation of S_{nl} has been brought within the actual operational capabilities by the discrete interaction operator parametrization proposed by Hasselmann et al. (1985).

The accuracy of the procedure has been proved by direct comparison against the full calculation results done for different spectral shapes. In shallow water the nonlinear exchanges are corrected by a scaling factor evaluated according to Harterich and Hasselmann (1980). The involved approximation is within acceptably small limits in the range $kd > 0.8$ (k is wave number, d is depth).

S_{dis} represents the dissipation processes, and it can be conveniently split into whitecapping and bottom interaction processes. Whitecapping or breaking is the only relevant dissipation term in deep water. For its evaluation the model uses a modified version of the expression proposed by Komen et al. (1984) given as

$$(7) \quad S_{br}^d = -2.35 \cdot 10^{-5} \tilde{\omega} \left(\frac{\omega}{\tilde{\omega}} \right)^2 \left(\frac{\tilde{\alpha}}{\tilde{\alpha}_{PM}} \right)^2 F$$

The tilde represents a slight approximation to the exact values as, for stability reasons, mean circular frequency $\tilde{\omega}$ is obtained as the inverse of the mean period. Specifically

$$(8) \quad \tilde{\omega} = E \omega^4 / g^2$$

$$(9) \quad \hat{\alpha}_{PM} = 3.02 \cdot 10^{-3}$$

E is the overall energy, g the acceleration of gravity.

The only bottom dissipation process permanently considered in the model is bottom friction. The bottom friction is expressed by

$$(10) \quad S_{bf} = - \frac{\Gamma}{g^2} \frac{\sigma^2}{\sinh^2 kd} F$$

a parametrized expression deduced from the JONSWAP study (Hasselmann et al., 1973, henceforth referred to as J) with the constant $\Gamma = 0.038 \text{ m s}$.

Equation (1) includes the long distance refraction of wave train associated with the great circle path. For shallow water this term, given by (4), is augmented to include the refraction due to the variation of water depth.

In the actual version the model considers 25 frequencies in geometric progression ($f_1 = 0.0418 \text{ hz}$, $f_{n+1} = 1.1 f_n$), and 12 directional bands with 30 degree resolution. Beyond the upper frequency limits ($F_{25} = 0.4114 \text{ hz}$) the spectrum is completed with a f^{-4} tail.

WAM Implementation in the Mediterranean Sea

Two grids, with different resolution, have been used to represent the geometry of the basin, respectively with 0.25 and 0.50 degree resolution. In this paper we describe the former, applied to the western Mediterranean Sea.

The grid is shown in Fig. 1. It covers the area from Gibraltar till Bengasi at the right end of the Sirte Gulf. The 0.25 degree resolution corresponds to

20-24 km in longitude and 28 km in latitude. This is largely enough to describe with good accuracy the geometry of the coasts. Obviously, if detailed studies were to be carried out at a single location, a nested high resolution model should be used. We point out how this implementation requires almost as many points as the global model at the three degree resolution described by the WAMD1-Group (1988).

The advection and integration time steps have both been fixed at 15 minutes. The outputs are available at 3-hour intervals. All these are optional quantities. In the actual form the model requires 5 minutes of CPU on a CRAY X-MP48 for each day of simulation.

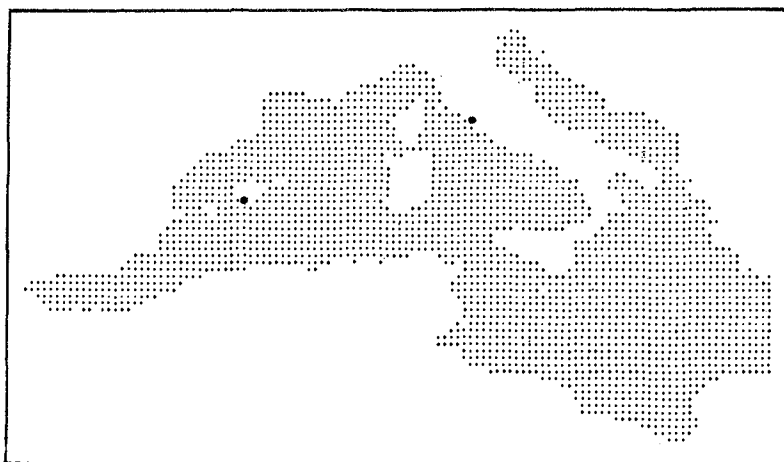


Figure 1. Grid covering the western Mediterranean Sea
The resolution is 0.25 degree. Dots indicate
wave recording positions.

Wind Fields

Two main sources of wind fields are available for the Mediterranean Sea, the European Centre for Medium Range Weather Forecasts (ECMWF) and the British

Meteorological Office (BMO). the latter has been used for the hindcast here reported.

The BMO runs a global model within which a high resolution nested model is used to describe in detail the wind over Europe. In this area, and in particular over the Mediterranean Sea, the wind is provided at the knots of a geographic grid with 0.9375 degree resolution in longitude and 0.75 degree for latitude. This corresponds to a step size of 70-80 km. The wind is available at 1-hour intervals, and it is linearly interpolated in longitude and latitude to provide the wind fields in correspondence of the WAM grid. At the same time, prior to the use by the wave model, the wind is transformed into wind stress according to the formula

$$U_*^2 = c_D U^2$$

where c_D is a friction coefficient that is again a function of U given by (WAMDI-Group, 1988)

$$c_D = \max(1.2875, 0.8 + 0.065 U) 10^{-5}$$

Severe Events of 10-15 January 1987

Several major storms have been hindcasted and compared with measured data. The results show in general the very good performance of the WAM model, even in basins with complicated geometry as the Mediterranean Sea. As an example we report here the results for a period of severe events that took place in the first fortnight of January 1987. Between 10 and 15 January two sequential storms entered the western Mediterranean producing heavy sea conditions twice at a short interval. Fig. 2 reports the wave fields (significant wave height H_S , in meters) for 03 and 21 UT of 11 January.

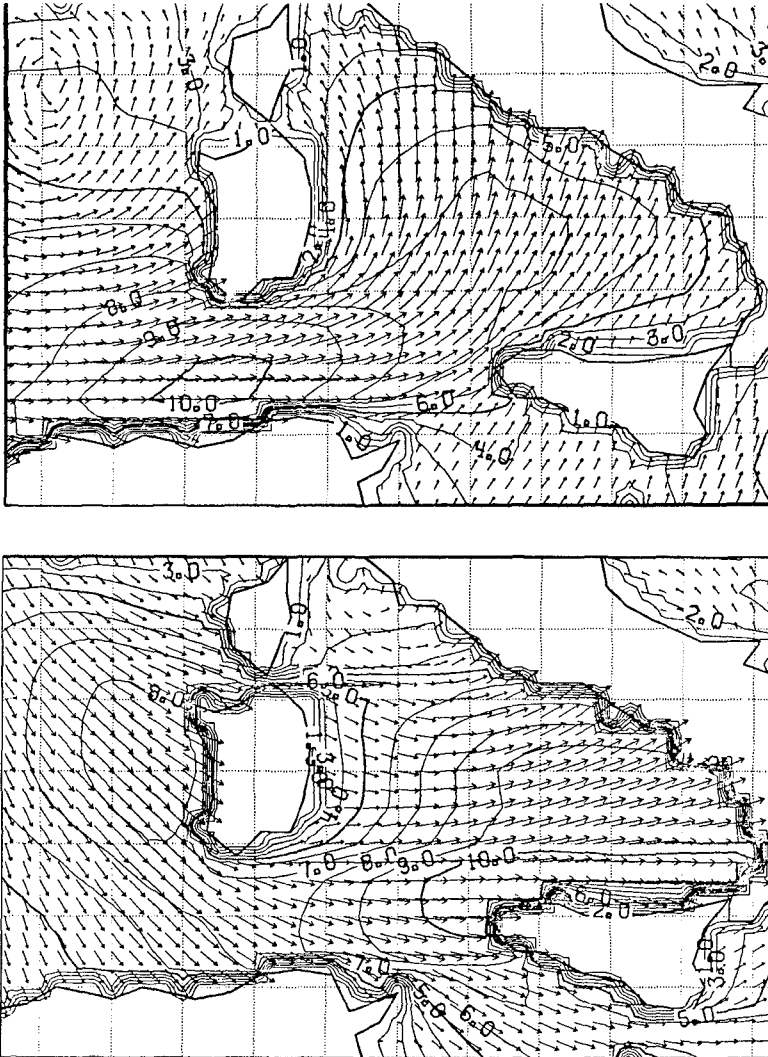


Figure 2. Wave fields for 03 and 21 UT of 11 January 1987.

Several wave measuring stations were active during this period. Anyhow most of them are of little use because of short fetch or secluded locations. The two main sources of information came in this case from Palma de Mallorca, in the Balearic Islands, and Montalto di Castro on the west coast of Italy marked by dots in Fig. 1. At both stations a Waverider buoy was operating, and the records were taken for 20 minutes at 3-hour intervals. Fig. 3 shows the H_s comparison between model and experimental data at Palma for the period 8-15 January. Both the storms are well reproduced, particularly in the growing stage, the decay being anticipated a few hours by the hindcast. This is likely, as from direct inspection of the maps, to be strictly dependent on the input wind fields.

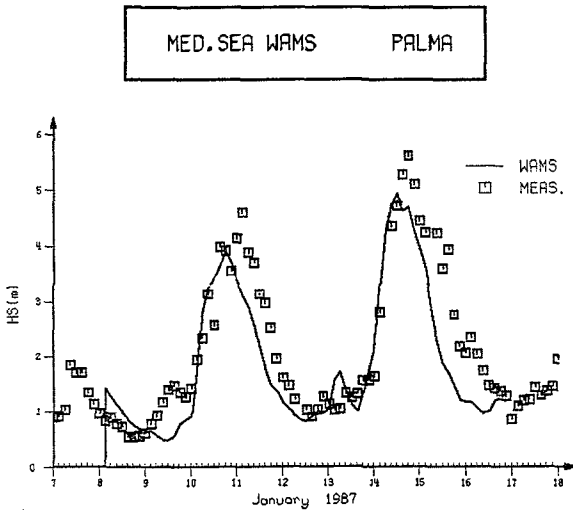


Figure 3. Model results versus experimental data at Palma de Mallorca (see Fig. 1).

Fig. 4 shows four sequential 2-dimensional spectra at Palma out of the model. The arrow in each figure represents the direction of the local and actual wind (the modulus is shown in the lower righthand corner, 1.0 corresponding to about 18 m/s). Ten levels of energy, scaled on the peak value, are shown. The three complete circles are at 0.05, 0.10 and 0.20 hz frequency.

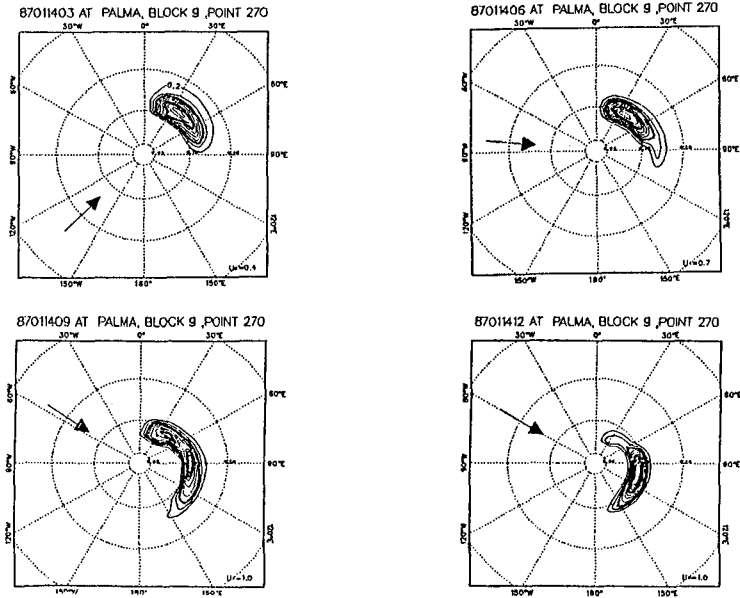


Figure 4. Four sequential 2-dimensional spectra at Palma de Mallorca on 14 January 1987.

The sequence is simultaneous to the passage of the cold front. The wind is firstly from the southwest, ahead of the front, and a well developed 3 meter sea is present in the same direction. While the front is passing (next map of 06 UT) a local wind sea begins to develop in the new wind direction, then quite evident in

the next spectrum of 09 UT. The swell to the northeast is still very strong. A few hours later, at 12 UT, a major storm has developed in the new direction, with H_s up to almost 6 meters, and only a slight swell still propagating to the northeast.

Fig. 5 shows the H_s history at Montalto. On the general trend the storm is well reproduced, but the experimental field showed wild oscillations only partially reproduced in the hindcast. Supported also by evidence of the local wind record, we believe this to be due to oscillations of the wind field largely smoothed by the atmospheric model.

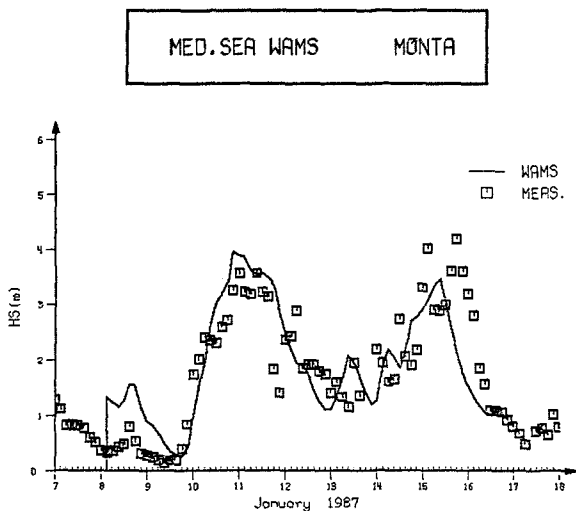


Figure 5. Model results versus experimental data at Montalto di Castro (see Fig. 1).

Conclusion

The main advantage of a physical approach to wind wave description is that the resulting model has no limitation, and it can be reliably applied to any meteorological situation also in basins with very complicated geometry. Together with the ones reported by the WAMDI-Group (1988), the results we have obtained confirm the above statement and the validity of the approach. On the other hand the sensitivity of the results to limited variations of the wind field transfer the problem to the meteorological input. The correct definition of the surface field in the Mediterranean Sea is not an easy task, as proved by detailed tests carried out by Dell'Osso (1984) for the Alpex experiment. It is our feeling that, for the full exploitations of the WAM model capabilities, high resolution local wind models are required to provide correct input in the area of interest.

Acknowledgements

The wave data have been provided for Palma by the Programa de Clima Maritimo, D.G.P. y C., MOPU, Madrid, Spain, and for Montalto by Ente Nazionale Energia Elettrica, ENEL-CRIS, Venice, Italy. We acknowledge their kindness on providing the data.

References

- Dell'Osso, L., 1984. High-resolution experiments with the ECMWF model: a case study, *Monthly Weather Review*, Vol. 112, No. 9, pp. 1853-1883.
- SWAMP Group, 1985. *Ocean Wave Modelling*, Plenum Press, NY, 256 pp.
- WAMDI-Group, 1988. The WAM model - a third generation ocean wave prediction model, accepted for publication in *JPO*.

CHAPTER 41

A NUMERICAL MODEL OF WAVE DEFORMATION IN SURF ZONE

Akira WATANABE* and Mohammad DIBAJNIA**

Abstract

A numerical model is presented for nearshore wave deformation due to shoaling and breaking, and to decay and recovery in the surf zone. The model is based on a set of time-dependent mild slope equations including a term of wave energy dissipation caused by breaking. Its applicability is demonstrated by comparisons between the computations and the measurements of cross-shore distributions of the wave height and potential energy over typical beach configurations.

1. INTRODUCTION

Upon arriving at the nearshore zone, waves come to play an important role in various coastal processes. It is in this area that the waves undergo some drastic changes due to shoaling, diffraction, refraction and breaking, and that they gain the ability to affect sea bottom configuration, to damage man-made structures or to cause difficulties in the handling of ships. A conventional approach to describing nearshore waves is through using the wave energy equation. Although the method has been widely employed in coastal engineering, it is not a general one in the sense that reflection, refraction and diffraction of the waves should be separately calculated. In addition in case of boundaries with complicated geometry, the method faces severe computational difficulties. A more general and new approach is available through using the mild-slope equation first derived by Berkhoff (1972). The equation, expressed in an elliptic form, describes waves under combined diffraction and refraction on a slowly varying bottom. Its solution, however, often involves

* Dr. Eng., Professor, Dept. of Civil Eng., Univ. of Tokyo, Hongo 7, Bunkyo-ku, Tokyo, 113 Japan.

** M. E., Postgraduate student, ditto.

considerable computational trouble, and the treatment of boundary conditions is in general difficult. To overcome these difficulties, simplified parabolic forms of this equation have been derived, which reduce the computation involved, but instead we cannot easily deal with reflected waves in general. Watanabe and Maruyama (1986) have proposed a set of time-dependent mild-slope equations, which has the advantages of reduced computation time as compared with the elliptic form equation and of simpler treatment of boundary conditions for open boundaries as well as for boundaries with arbitrary reflectivity. In addition, their model incorporates wave breaking and decay in the surf zone. However its validity has not yet been fully examined.

The time-dependent mild-slope equations will be applied in the present paper to computing cross-shore change in a one-dimensional wave field; namely, deformation of waves with normal incidence on a straight parallel-contour coast. The selection of such simple conditions will avoid the involvement of wave diffraction and refraction, and enable us to study in details about the wave deformation due to breaking. The formulation for energy dissipation in the previous study will be modified to more properly express the wave decay and recovery processes. Some numerical computations through the new equations will be conducted on cross-shore distributions of the wave height and potential energy over three kinds of typical beach configurations, and compared with the experimental data.

2. Time-Dependent Mild-Slope Equations for Waves in the Surf Zone

Watanabe and Maruyama (1986) have presented a set of the time-dependent mild-slope equations and a numerical model for nearshore waves under combined refraction, diffraction, and breaking. This model is applied here to a cross-shore one-dimensional wave field, and is improved for the behavior in the surf zone.

The equations are expressed in terms of the water surface elevation ζ and the flow rate Q into the cross-shore direction as:

$$\frac{\partial Q}{\partial t} + c^2 \frac{\partial \zeta}{\partial x} + f_D Q = 0 \quad (1)$$

$$\frac{\partial \zeta}{\partial t} + \frac{1}{n} \frac{\partial (nQ)}{\partial x} = 0 \quad (2)$$

where t is time, x is the horizontal coordinate normal to the shoreline, c is the phase velocity, and

$$Q = \int_{-h}^0 u \, dt, \quad n = \frac{1}{2} \left(1 + \frac{2kh}{\sinh 2kh} \right) \quad (3)$$

in which u is the x -component of the orbital velocity, h is the water depth, and k is the wave number. Equations (1) and (2) may be regarded as vertically integrated equations of motion and of continuity, respectively. In Eq. (1), f_D is the energy dissipation factor, and has been expressed by Watanabe and Maruyama (1986) as:

$$f_D = \alpha_D \tan\beta \sqrt{\frac{g}{h} \left(\frac{Q_m}{Q_r} - 1 \right)} \quad (4)$$

where $\tan\beta$ is a representative bottom slope around the breaking point, Q_m is the amplitude of Q , and Q_r is the flow rate amplitude of the broken waves recovered in an area of uniform depth of h and expressed as $Q_r = \gamma' \sqrt{gh^3}$. Values of 2.5 and 0.25 have been proposed by them for the coefficients, α and γ' , respectively. The dissipation factor, f_D , is set equal to zero outside the surf zone and in any region in which $Q_m < Q_r$. Under this condition, $f_D = 0$, Eqs. (1) and (2) reduce to the mild-slope equation proposed by Berkhoff (1972).

In order to improve the behavior of the model for the wave decay and recovery processes, we now redetermine the expression for the energy dissipation factor f_D . A proper modeling of wave transformation in the surf zone depends strongly on appropriate evaluation of this factor. Several models for wave motion in the surf zone have been proposed. A brief summary of the works up to the present is given by Horikawa (1988). However, the wave breaking process and the subsequent breaking-induced turbulence have not yet been fully clarified and much remains to be done. In the present work a semi-empirical general expression for f_D is given through using some new concepts and experimental results.

If we assume purely progressive waves, combination of Eqs. (1) and (2) yield the following wave energy equation.

$$\frac{d}{dx} (E c_g) = -n f_D E \quad (5)$$

where E is the wave energy density per unit horizontal area, and c_g is the group velocity. Now assuming long waves over a uniformly sloping beach and a constant ratio of the wave height to the water depth, we obtain the following expression for f_D from Eq. (5).

$$f_D = \alpha_D \tan\beta \sqrt{\frac{g}{h}} \quad (6)$$

For a general bottom topography, Eq. (6) needs some modification. To do this we should introduce two parameters. The first one is the amplitude of the wave-induced flow rate inside the surf zone of a uniformly sloping beach, which will be denoted by Q_s . According to experimental data (Isobe, 1986), Q_s can be safely formulated as:

$$Q_s = \gamma_s c h, \quad \gamma_s = 0.4 (0.57 + 5.3 \tan\beta) \quad (7)$$

For the second parameter, we will adopt the flow rate of recovered waves in a similar way to Watanabe and Maruyama (1986). Let us assume waves coming into an area of uniform depth h after breaking as shown in Fig. 1. It is well known that upon arriving at this area, broken waves start to recover and after a certain distance shown as the transient zone, they will find a stable form and will no more lose their energy. Considering the experimental results (Maruyama & Shimizu, 1986), the amplitude of the flow rate of recovered waves, Q_r , can be expressed as:

$$Q_r = \gamma_r c h, \quad \gamma_r = 0.4 (a / h)_b \quad (8)$$

where $(a/h)_b$ is the ratio of the wave amplitude to the water depth at the breaking point.

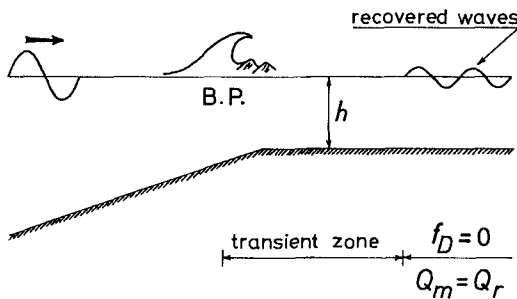


Figure 1 Wave recovery zone with constant depth.

The fact that the value of f_D should become equal to zero for recovered waves suggests that at any water depth, the value of Q_r may be regarded as the critical flow rate below which there is no dissipation of energy. Therefore we assume the following form of expression for f_D .

$$f_D = A (Q_m - Q_r)^m \quad (9)$$

where at any depth Q_m is the amplitude of the actual flow rate and Q_r is the flow rate amplitude of the broken waves virtually recovered in the same constant depth. The power m should be less than unity in order to get a finite distance to recovery. The proportionality constant A can be determined by requiring that when $Q_m = Q_s$

then the value of f_D should be equal to that for uniform slope, i.e. Eq. (4). Assuming $m = 1/2$ for simplicity we finally obtain Eq. (10) for general bottom topography.

$$f_D = \alpha_D \tan \beta \sqrt{\frac{g}{h} \left(\frac{Q_m - Q_r}{Q_r - Q_s} \right)} \quad (10)$$

The location of the breaking point is calculated with the generalized breaker index diagram proposed by Watanabe *et al.* (1984). Change in the mean water elevation is evaluated through the distribution of radiation stresses, which are calculated from time histories of ζ and Q by using the formulas presented by Watanabe and Maruyama (1986).

3. Boundary Conditions

For the computation of a cross-shore one-dimensional wave field, there are two boundaries: the offshore boundary and the shoreline boundary.

The offshore boundary where incident waves are prescribed is treated as an open boundary in order to let the reflected waves, if any, to go out of the region freely. For this, assuming a locally constant depth region at the offshore, we express the boundary condition in terms of the water surface elevation as:

$$\zeta(x_0) = \zeta(x_0 + \Delta x) + a_1 \{ \sin(kx_0 - \sigma t) - \sin[k(x_0 + \Delta x) - \sigma(t - \tau)] \} \quad (11)$$

where $\tau = \Delta x / c_0$, Δx is the grid length in the finite difference scheme, a_1 and σ are the amplitude and angular frequency of the incident waves, respectively, the subscript 0 denotes quantities at the offshore boundary and the x -axis is taken shoreward.

At the shoreline, previous computations have usually assumed a hypothetical constant depth region to avoid infinity in the value of wave height. However, the solution of the time-dependent mild-slope equations gives a time history of wave propagation so that the breaking point can be determined contemporarily with the computation of wave propagation and the wave height will decay thereafter. This makes it possible to impose the shoreline boundary condition simply as $Q = 0$. The receding of the shoreline due to change in the mean water level is also included using a moving boundary technique.

4. Results and Discussion

The nearshore wave model based on Eqs. (1), (2), and (7) to (10) is here applied to computing wave deformation for three kinds of typical beach profiles: uniform slope,

step-type, and bar-type. The equations are solved by a finite difference method with a staggered mesh scheme.

The results are compared with measurements reported by Nagayama (1983) in Figs. 2 to 4, where H is the wave height, E_p is the potential energy, ρ is the water density, and the x -axis is taken here in the offshore direction with the origin at the shoreline in still

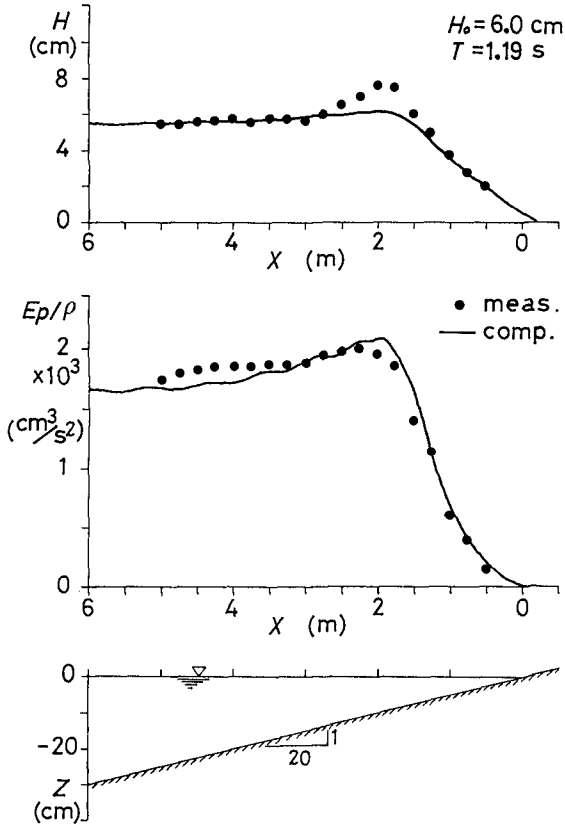


Figure 2 Wave height and potential energy on a uniform slope.

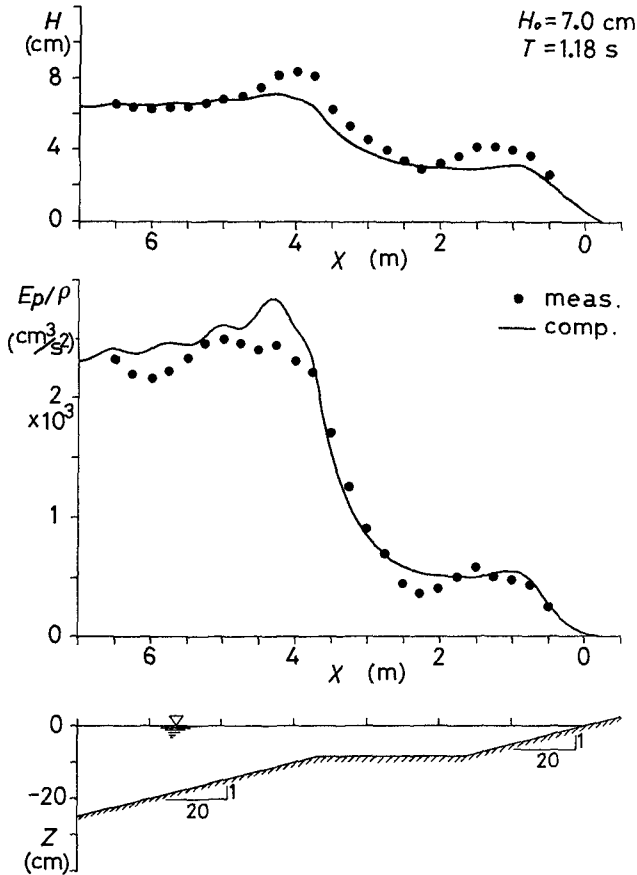


Figure 3 Wave height and potential energy on a step-type beach.

water. The potential energy in the measurements has been evaluated from the mean square values of $\zeta(t)$ at each location.

The wave decay, recovery, and secondary breaking are well reproduced in the computations. Although the wave height is slightly underestimated around the breaking

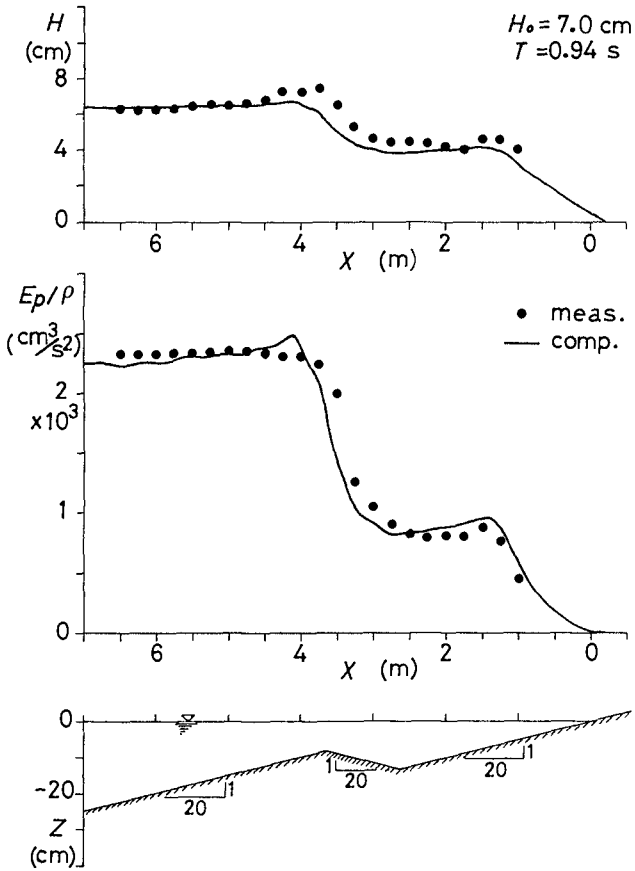


Figure 4 Wave height and potential energy on a bar-type beach.

point as is anticipated whenever linear theories are used, the distributions of the potential energy which represents overall intensity of the wave motion over one wave period are very well estimated. The small disagreement in the potential energy on the step-type beach before the first breaking point is attributed to the generation of cross waves in the wave channel.

Figure 5 shows the cross-shore variations of some other quantities calculated for the case of the bar-type beach. Figure 5(a) gives the variations of the energy dissipation factor f_D and of the energy dissipation rate per unit mass $n f_D E / \rho$. It is seen that after the first breaking the energy dissipation becomes zero as the water depth behind the bar increases and it is kept as zero until the secondary breaking occurs. In Fig. 5(b) the variation of the mean water level is shown. Unfortunately experimental data of the mean water level change are not available. However, considering the results for wave energy, we can expect that the wave set-up/down are well predicted, as we have found in further applications of the model. Figure 5(c) shows the variations of the flow rate amplitude Q_m and Q_r .

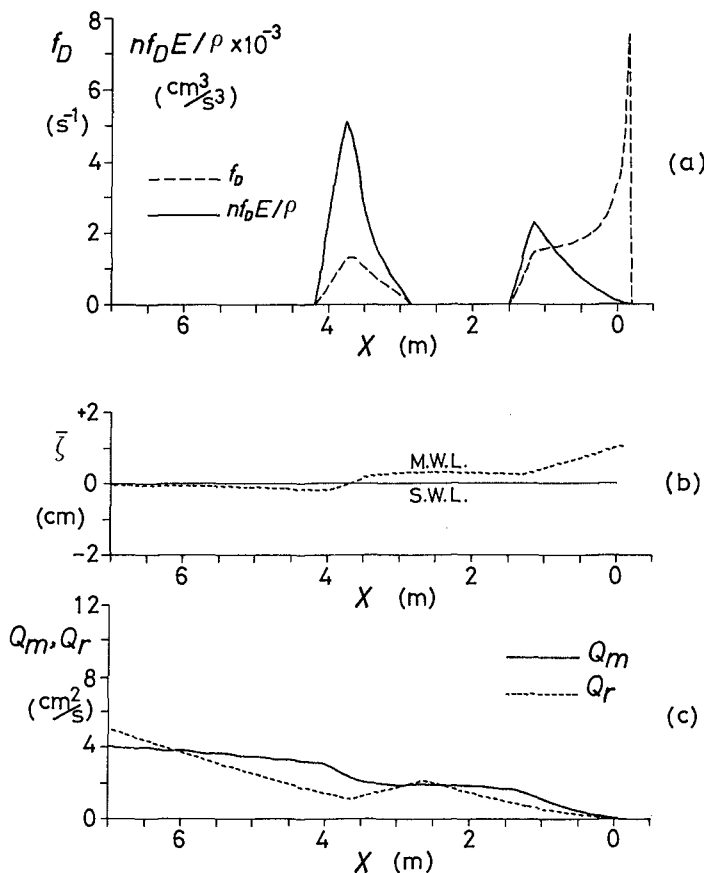


Figure 5 Energy dissipation factor, dissipation rate, mean water level and flow rate amplitude.

5. Concluding Remarks

A numerical model for nearshore waves based on the time-dependent mild-slope equations have been presented, with modification of the term for the energy dissipation due to breaking. It has been shown that the model can reproduce very well cross-shore wave deformation due to shoaling, breaking, decay, and recovery.

Generalization of the present model to two-dimensional wave fields will be rather straightforward and easy to conduct in a similar way to that described by Watanabe and Maruyama (1986). The two-dimensional model thus obtained will be applicable to computing wave deformation due not only to shoaling, breaking and recovery but also to refraction and diffraction.

References

- Berkhoff, J.C.W. (1972): Computation of combined refraction-diffraction, *Proc. 13th Coastal Eng. Conf.*, ASCE, pp.471-490.
- Horikawa, K. (ed.) (1988): *Nearshore Dynamics and Coastal Processes*, Univ. of Tokyo Press, 522pp.
- Isobe, M. (1987): A parabolic equation model for transformation of irregular waves due to refraction, diffraction and breaking, *Coastal Eng. in Japan.*, JSCE., Vol. 30, NO. 1, pp. 33-47.
- Maruyama, K. and T. Shimizu (1986): Simulation model for wave deformation considering interaction of waves and a beach, *Proc. 33rd Japanese Conf. on Coastal Eng.*, pp. 109-113. (in Japanese)
- Nagayama, S. (1983): Study on the change of wave height and energy in the surf zone, *Bachelor thesis*, Yokohama National Univ., 80pp. (in Japanese)
- Watanabe, A., T. Hara and K. Horikawa (1984): Study on breaking condition for compound wave trains, *Coastal Eng. in Japan*, JSCE, Vol. 27, pp. 71-82.
- Watanabe, A. and K. Maruyama (1986) Numerical modeling of nearshore wave field under combined refraction, diffraction and breaking, *Coastal Eng. in Japan*, JSCE, Vol. 29, pp. 19-39.

CHAPTER 42

COUPLING STOKES AND CNOIDAL WAVE THEORIES IN A NONLINEAR REFRACTION MODEL

Thomas A. Hardy¹, A.M. ASCE
Nicholas C. Kraus², M. ASCE

ABSTRACT

An efficient numerical model is presented for calculating the refraction and shoaling of finite-amplitude waves over an irregular sea bottom. The model uses third-order Stokes wave theory in relatively deep water and second-order cnoidal wave theory in relatively shallow water. It can also be run using combinations of lower-order wave theories, including a pure linear wave mode. The problem of the connection of Stokes and cnoidal theories is investigated, and it is found that the use of second-order rather than first-order cnoidal theory greatly reduces the connection discontinuity. Calculations are compared with physical model measurements of the height and direction of waves passing over an elliptical shoal. The finite-amplitude wave model gives better qualitative and quantitative agreement with the measurements than the linear model.

INTRODUCTION

Wave transformation models are commonly used in coastal engineering projects to provide nearshore wave height and direction. This information is needed at specified grid locations for input into nearshore circulation and shoreline change numerical models. Often, multiple simulations over a wide geographical area are required. Small-amplitude (linear) wave theory is the basis for almost all wave transformation models presently in engineering use. It is well known that finite-amplitude (nonlinear) wave theories predict greater shoaling and less refraction than does small-amplitude theory, and the nearshore wave properties predicted by nonlinear theories are expected to provide an improved description of real waves transforming in shallow water. However, the dual requirements of accuracy (finite-amplitude theories) and efficiency (minimal computer CPU time) have been thought to be contradictory. Also, finite-amplitude wave transformation models have proven complicated and difficult to develop.

There are three main challenges in developing a finite-amplitude wave refraction model. First, if computationally intensive, numerically based wave theories are to be avoided, two perturbation theories are necessary, Stokes for deeper water and cnoidal for shallower water. Mutually consistent solutions are essential, and expressions must be available for secondary quantities such as wave energy flux. Second, efficient and accurate calculation of cnoidal wave theory is necessary. Finally, the connection between

(1) Department of Civil and Systems Engineering, James Cook University, Townsville, Queensland, Australia 4811, (2) Senior Research Scientist, Coastal Engineering Research Center, U.S. Army Engineer Waterways Experiment Station, P.O. Box 631, Vicksburg, MS, USA 39180-0631

the two theories has to be optimized. The purpose of this paper is to present a numerical model which accurately and efficiently calculates finite-amplitude wave refraction over an irregular sea bottom. The outputs of the model are wave height and wave direction at each grid node for a steady state monochromatic wave. The model is intended for engineering use where a number of simulations are required and information is desired over a large area of open-ocean coast.

LITERATURE REVIEW

Two of the earlier efforts in the study of finite-amplitude wave transformation treated shoaling of cnoidal waves. Svendsen and Brink-Kjaer (1973) connected first-order cnoidal theory with linear theory to develop a wave shoaling equation. They imposed the requirement of a matching energy flux to connect the two theories. Svendsen and Buhr-Hansen (1977) continued the study of shoaling by altering the connection to allow a discontinuity in energy flux but maintaining a matching wave height between linear theory for deeper water and first-order cnoidal theory for shallower water. The theories were connected at $d/L_0 = 0.1$, where d is depth and L_0 is the linear deepwater wavelength. Cnoidal theory predicted greater shoaling than linear theory and there was good agreement with laboratory measurements of wave height.

The first finite-amplitude refraction model for an irregular bathymetry was presented by Chu (1975). He used a combination of third-order Stokes and first-order cnoidal wave theories. He avoided the need of an expression for energy flux for cnoidal theory by using the flux from the hyperbolic wave theory of Iwagaki (1968) for the calculation of wave shoaling. Ray tracing was used to calculate refraction. The connection between Stokes and cnoidal theories was at a critical Ursell number, U_c , given by

$$U_c = 7.5 + 25\frac{H}{d} \quad (1)$$

where H is wave height. Stokes theory was used if the Ursell number,

$$U = \frac{HL^2}{d^3} \quad (2)$$

was less than U_c and cnoidal theory used if $U > U_c$, where L is wavelength

A finite-amplitude refraction model applicable to straight and parallel bottom contours was developed by Skovgaard and Petersen (1977). The model employed first-order cnoidal theory, and the authors suggested that it should be connected to a linear model if $U > 15$ and $d/L_0 < 0.1$ by matching energy flux at the connection. Headland and Chu (1985) built upon the above-mentioned work of Svendsen and Brink-Kjaer and Svendsen and Buhr-Hansen, to develop a refraction model for nonplane bathymetry using ray tracing techniques. They reported that problems in the connection between linear and first-order cnoidal theories, as well as inefficiencies in the calculation of cnoidal wave properties, required further research. Oh and Grosch (1985) presented a refraction model which was based on third-order Stokes theory and used ray tracing methods. However, they incorrectly applied the model to shallow water, outside the region of validity of Stokes theory (Kraus, Cialone, and Hardy, 1987a).

Dalrymple (1988) presented a model with a solution scheme similar to the one presented in this paper and previous work by the authors (Cialone and Kraus, 1987; Hardy and Kraus, 1987; and Kraus, Cialone, and Hardy, 1987). Wave-current interaction was included, but the use of finite-amplitude theory was inconsistent. Wavelength was calculated using third-order Stokes theory with an empirical correction applied to allow calculation in shallow water. However, the finite-amplitude effect on wave shoaling was incorrectly represented since a mixture of linear and nonlinear theories was used in the calculation of wave energy flux.

NUMERICAL MODEL

The model presented in this paper is based on derivations of third-order Stokes theory and second-order cnoidal theory of Isobe and Kraus (1983a, 1983b). These derivations are consistent in definitions and solution technique; both specify the second definition of Stokes (zero mass flux) to determine the wave celerity.

The model builds on separate refraction models for Stokes waves (Cialone and Kraus, 1987) and cnoidal waves (Hardy and Kraus, 1987). Expressions for energy flux which are necessary for wave height calculations and the basic solution mechanics were developed in these previous efforts. The present model, called NLWAVE for Non-Linear WAVE model, refines a preliminary version (Kraus, Cialone, and Hardy, 1987b) by adopting an improved finite difference scheme and optimizing the connection between the component theories.

The difficulty in the calculation of cnoidal quantities has been a deterrent to the practical application of cnoidal wave theory. Subroutines in computer libraries and formulae found in mathematics handbooks for the calculation of needed elliptic functions cannot be directly used in cnoidal wave theory. The result has often been inefficient and inaccurate calculations. NLWAVE uses the method developed by Isobe (1985) for first-order cnoidal theory and extended to expressions for second-order cnoidal theory by Hardy and Kraus (1987). The procedure allows the efficient and accurate calculation of cnoidal wave properties.

The model uses a compact and direct technique for the calculation of wave refraction, which was introduced for linear waves by Noda *et al.* (1974). This scheme allows the determination of wave properties at predetermined grid locations and thus offers a distinct advantage over wave ray tracing methods which require interpolation to provide information at grid points.

The solution technique can be divided into three parts. First, wavelength is calculated using the dispersion relationship of the appropriate wave theory (third-order Stokes or second-order cnoidal). Second, wave angle is determined using the equation for the irrotationality of wave number, which can be written as

$$\nabla \times \nabla k = 0$$

or

$$\frac{\partial}{\partial x} \left(\frac{\sin \alpha}{L} \right) - \frac{\partial}{\partial y} \left(\frac{\cos \alpha}{L} \right) = 0 \quad (3)$$

where k is wave number, α is wave angle, and the directions x and y are as defined in Figure 1. And third, energy flux, F , and thus wave height, H , are determined from a conservation of energy flux equation given as

$$\nabla \cdot \vec{F} = 0$$

or

$$\frac{\partial}{\partial x} (F \cos \alpha) + \frac{\partial}{\partial y} (F \sin \alpha) = 0 \tag{4}$$

where

$$H \propto \sqrt{F} \tag{5}$$

Energy flux expressions for Stokes and cnoidal wave theories used in NLWAVE were derived in Cialone and Kraus (1987) and Hardy and Kraus (1987) .

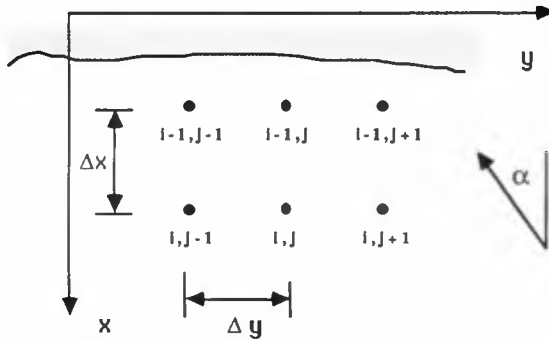


Figure 1. Numerical Model Grid

Equations 3 and 4 are solved on a rectilinear grid (Figure 1) using a finite difference scheme. The desired wave properties are functions of wave height, H , wave period, T , and water depth, d . The depth is specified at each grid point and does not change during a simulation. Outer boundary information for H and T is given. This input can either be placed directly at the outer boundary, or deepwater values can be transformed to the outer boundary of the grid assuming straight and parallel bottom contours. The solution scheme marches towards shore (in the $-x$ direction) one row ($i = \text{constant}$) at a time. Each row is swept in the $+y$ direction. Since wave properties are functions of wave height in a finite-amplitude wave theory, iteration is required on each row. The dispersion relationship, the irrotationality of wave number (Equation 3), and the divergence of energy flux equation (Equation 4) are solved for L , α , and F , respectively, using an updated value of wave height. Iteration continues until a convergence criterion defined as a percentage change in the calculated quantity (0.1%) is satisfied. Usually, only two or three and at most six iterations have been found to be necessary .

A simple criterion ($H_b = 0.8d$) is used to determine the height of breaking waves, H_b . Although the model is not intended to describe waves in the surf zone, if depth-limited wave breaking is indicated at a node, then energy flux is reevaluated at the node using the height of the breaking wave. The simulation continues until the wave has broken at all columns across the simulated area.

Equations 3 and 4 can be represented as

$$\frac{\partial A}{\partial x} + \frac{\partial B}{\partial y} = 0 \quad (6)$$

where A and B symbolically represent the quantities in Equations 3 and 4. The finite difference form of Equation 6 is

$$\frac{A_{i,j} - A_{i-1,j}}{\Delta x} + \frac{1}{2\Delta y} \left[(1-a)(B_{i-1,j+1} - B_{i-1,j-1}) + a(B_{i,j+1} - B_{i,j-1}) \right] = 0 \quad (7)$$

where Δx and Δy are the grid spacings, and i and j denote the x and y directions, respectively (Figure 1). A weighting coefficient, a , allows adjustment of the finite difference scheme between explicit and implicit versions. If $a = 0.0$, then the scheme is fully implicit; if $a = 1.0$, it is explicit. A value of $a = 0.5$ is recommended, since this results in the solution with the highest accuracy. This scheme will be labeled ATCS or average time central space, where x is "time like." The ATCS scheme is implicit since it involves unknown values ($j+1, i-1$) as the row ($i-1$) is being calculated (Figure 1). However, the usual penalty of iteration to solve the implicit scheme does not degrade model efficiency since iteration is required for the finite-amplitude solution. Only rarely does the implicit nature of the solution scheme cause an additional iteration, so the difference in execution time between explicit and implicit versions of the model is negligible.

The lateral boundary conditions imposed are the simplest possible; boundary values of α , H , and F are assigned values of their nearest neighboring node on row $i-1$. Tests have shown that the results on the interior of the grid are insensitive to these lateral boundary conditions. However, the lateral boundaries should be placed away from the main areas of interest and not in regions of steep gradients in the bathymetry. A shoreward boundary is not needed as the solution marches towards the shore, and reflections are neglected.

Connection Between Stokes and Cnoidal Components

As has been mentioned previously, neither Stokes nor cnoidal wave theory is valid over the whole range of depths from deep water to the breaking point, and the connection between quantities calculated by the two theories is not always smooth. The range of validity of a particular theory depends somewhat on the derivation of that theory. However, following the review in Kraus, Cialone, and Hardy (1987a), the Ursell number (Equation 2) can be used as a practical validity criterion. In general, Stokes theory is valid for $U < 25$ and cnoidal theory is valid for $U > 10$. Therefore, there is a region of overlap, $10 < U < 25$, where connection between the two theories should be possible.

Since neither third-order Stokes theory nor second-order cnoidal theory is an exact solution to the wave boundary value problem, it is to be expected that the two theories calculate slightly different values of the desired wave parameters (L , α , F) given the same inputs (H , T , d). The differences between the Stokes and cnoidal calculations of

the first two of the parameters, L and α are negligible, as they were found to be less than 1% in numerous tests. However, the differences in calculation of F can be substantial, and this can cause a significant discontinuity in the wave height at the connection node.

Treatment of this problem requires some considerations external to the wave theories. At first thought it might appear best to maintain energy flux across the connection. If the Stokes-determined value of the energy flux is input into the cnoidal calculations of wave height, the resulting wave height is sometimes significantly different from the wave height calculated by Stokes theory. Instead, we chose to follow the lead of Svendsen and Buhr Hansen (1977) and match wave height at the connection. The reasoning is that wave height is a fundamental quantity in the wave theories, whereas energy flux is a secondary or calculated quantity. It is therefore considered more appropriate to maintain the fundamental quantity and allow the energy flux and other secondary quantities to vary. It could be argued that this procedure violates energy conservation. However, repeating from above, neither theory is exact; neither calculates the "true" energy flux. Therefore, we argue that maintaining the primary variables is the most consistent approach and the best way to conserve energy.

At the start of our research into a suitable connection criterion, it was anticipated that it would be a difficult task, perhaps requiring a complex empirical formula to optimize the connection. However, it soon became apparent that the use of second-order cnoidal theory resolved most of the difficulties that previous researchers had encountered using first-order cnoidal theory. To examine the connection, simulations were conducted for a plane beach case. At each of four deepwater wave steepnesses ($H_0/L_0 = 0.005, 0.01, 0.02, 0.03$), four separate connection criteria were tested ($U = 10, 15, 20, 25$). These 16 tests were conducted for the model configured in third-order Stokes/second-order cnoidal mode, as well as in linear/first-order cnoidal mode. At the connection point between the component theories, the percentage change in F was determined as:

$$\% \text{ change} = \frac{F_{\text{cn}} - F_{\text{st}}}{F_{\text{st}}} \quad (8)$$

The subscripts "st" and "cn" denote the Stokes and cnoidal calculated energy fluxes, respectively.

The results presented in Table 1 show a notable improvement for the nonlinear model. In addition, tests using linear/second-order cnoidal and third-order Stokes/first-order cnoidal modes indicated that the improvement in connection was due principally to the use of a higher-order cnoidal theory.

The results in Table 1 indicate that the connection point should be set at $U = 25$, where the discontinuity between energy flux calculated from third-order Stokes and second-order cnoidal theories varies with wave steepness and ranges from -0.25% to -3.7%. In contrast, the difference for the linear/first-order cnoidal combination at $U = 25$ ranges from 8.9% to 24%.

Figure 2 shows the effect of varying the connection criterion. The two curves in this figure correspond to connection at $U = 10$ and $U = 25$ for shoaling on a plane beach using NLWAVE in nonlinear mode, with beach slope of 1/50 and the deepwater wave steepness of 0.03. If the model is switched to second-order cnoidal theory at $U = 10$, the upward trend in wave height that was predicted in deeper water by third-order Stokes theory is reversed. There is a reduction in wave height before resuming the upward trend in much shallower water. However, if the connection is made at $U = 25$, cnoidal theory much more smoothly continues the upward trend in wave height predicted by Stokes theory.

H_0/L_0	U			
	10	15	20	25
.005	-2.4	-1.4	-0.70	-0.25
.01	-4.8	-2.9	-1.7	-.55
.02	-10	-6.3	-3.9	-2.0
.03	-16	-10	-6.5	-3.7

(a) 3rd-order Stokes/2nd-order cnoidal

H_0/L_0	U			
	10	15	20	25
.005	18	14	11	8.9
.01	25	20	16	13
.02	36	28	23	20
.03	44	35	29	24

(b) Linear/1st-order cnoidal

TABLE 1. Percentage Change in Energy Flux at Connection

As a wave begins to be influenced by the bottom as it travels from deep water, there is a slight reduction in wave height due to shoaling before beginning a more rapid increase in height as the water becomes shallower. Stokes wave theory predicts that the region of minimum wave height lies in deeper water, outside the connection region, whereas for cnoidal wave theory, the region of minimum wave height lies inside the connection zone. This phenomenon is clearly visible in Figure 2. Fortunately, the use of second-order cnoidal theory and the selection of the $U = 25$ as the connection criterion greatly reduce the connection discontinuity without the need for empirical corrections.

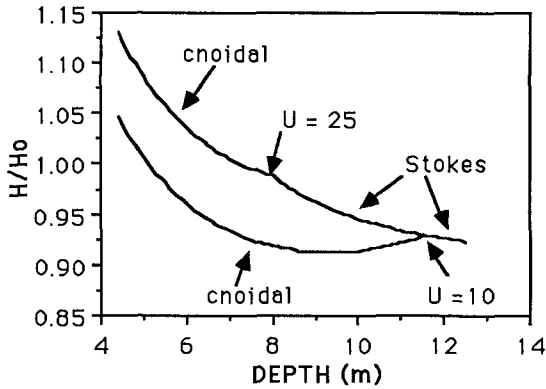


Figure 2. Connection Comparison. $H_0/L_0 = 0.03$

The adopted connection procedure is as follows: as an iteration is completed at a node on the row $i-1$, the Ursell number is checked against the connection criterion. If $U > 25$ and if the quantities at the node have been calculated using Stokes theory, then the wave height that has been calculated from Stokes theory is used to recalculate L , α , and F using cnoidal theory. These values are then used to carry the solution forward towards the breaker zone. The Ursell number is checked after each iteration for each node on a row and if at a row closer to shore, $U < 25$ at a cnoidal point, then the model switches back to Stokes by using the cnoidal H to calculate a Stokes L , α , and F . The model is designed for application to irregular sea bottoms, so a mixture of Stokes and cnoidal calculation nodes is possible on a row (alongshore). Also, along a column (on-offshore), the scheme can switch from Stokes to cnoidal and back to Stokes as often as is dictated by the bathymetry.

ELLIPTICAL SHOAL TESTS

The cnoidal and Stokes refraction routines performed well in extensive tests with laboratory measurements of wave shoaling and analytical results. These tests have been reported in Cialone and Kraus (1987), Hardy and Kraus (1987), and Kraus, Cialone, and Hardy (1987) and will not be discussed here. In the present paper we examine model prediction by comparing with laboratory measurements of waves focusing over an elliptical shoal.

NLWAVE does not have the capability to model diffractive effects; therefore, it is intended for use in open coast situations where the bathymetry is not complex. As a stringent test of the connection procedure and behavior of the full refraction and shoaling prediction of the model, simulations were conducted for an elliptical shoal. Even though the model is not recommended for application to such bathymetry, it was thought that testing of the model at its limits would be informative. A plan view of the shoal is given in Figure 3. The shoal had a major radius of 13 ft (3.96 m), a minor radius of 10 ft (3.05 m), and a maximum height over the otherwise flat bottom of the basin of 1.0 ft (0.305 m). The water depth was 1.5 ft (0.46 m) in the flat bottom region of the basin.

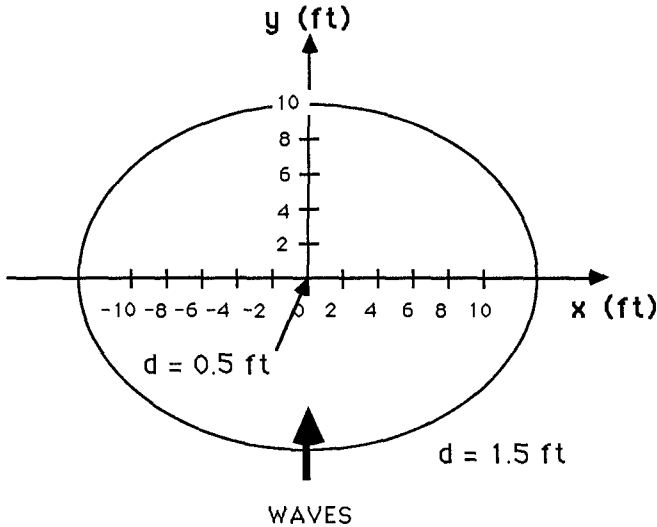


Figure 3. Plan View of Physical Model Basin

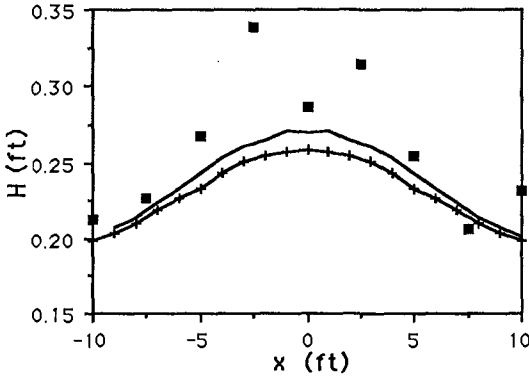
Data from physical model tests over this shoal were made available from the US Army Engineer's Coastal Engineering Research Center (Vincent and Briggs, in press). Two of the physical model tests of monochromatic waves were simulated by both linear and nonlinear versions of NLWAVE. The two tests were as follows:

TEST	H	T
M1I	2.54 in. (6.5 cm)	1.3 s
M2I	1.75 in. (4.4 cm)	1.3 s

The specified wave heights were measured in the flat portion of the basin in front of the shoal. For wave height, results from M1I and M2I are shown in Figure 4 and 5, respectively. The results are for sections parallel to the major axis of the shoal and normal to the initial direction of wave propagation, along $y = 0$ ft (Figures 4a and 5a), and $y = 10$ ft (Figure 4b and 5b).

For the present work, wave directions were measured carefully from photographs of wave crests taken during the physical model tests. Results for test M2I are compared with both linear and nonlinear models along $y = 0$ ft (Figure 6a) and $y = 5$ ft (Figure 6b).

As expected, the numerical results are symmetrical about the centerline of the shoal ($x = 0$ ft). Refraction focused increasing amounts of energy toward the centerline as the wave propagated behind the shoal; therefore, wave heights and wave angles near the centerline increased. The finite-amplitude effect on refraction is clearly evident. Along $y = 0$ ft (Figures 4a, 5a, and 6a), the linear model predicts smaller wave heights and larger wave angles than does the nonlinear model. Here, shoaling dominated, and the nonlinear theories predict greater wave heights due to shoaling. Along $y = 10$ ft (Figures 4b and 5b), the linear model predicts greater wave heights along the centerline. Here, refractive effects dominated, and the greater angle changes predicted by linear theory (Figure 6) concentrated more energy towards the centerline.

(a) $y = 0$ ft

LEGEND

- Finite-amp.
- + Small-amp.
- Measured

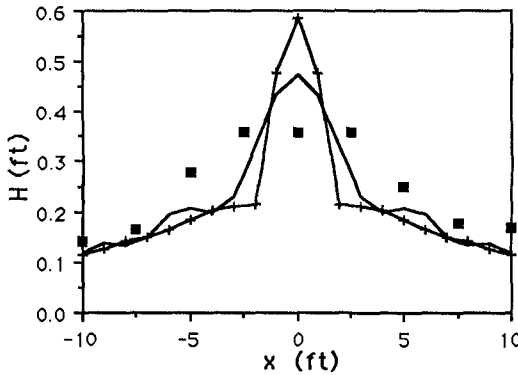
(b) $y = 10$ ft

Figure 4. Wave Height, Test M11

There is considerable scatter in the wave heights measured in the physical model tests along $y = 0$ ft (Figures 4a and 5a). This was presumably caused by irregularities in the bottom of the basin, nonuniform wave formation at the generator, or wave reflection from the sides and ends of the basin. The finite-amplitude model shows closer agreement with the physical model results than the small-amplitude model. Closer agreement between numerical and physical models is shown along $y = 10$ ft (Figure 4b and 5b). However, the numerical model results show a greater concentration of energy towards the centerline than do the physical model results. This was expected since the numerical model has no diffractive capability. Wave heights calculated by the finite-amplitude model again show better agreement with the measured wave heights than does the linear model.

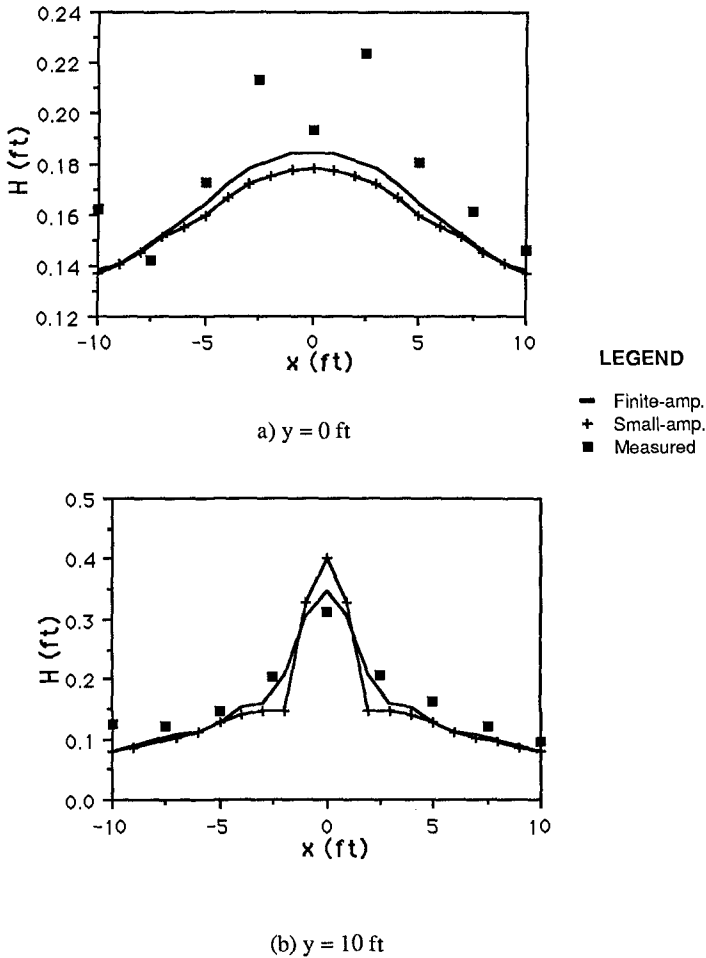


Figure 5. Wave Height, Test M2I

Noda *et al.* (1974) showed that the solution technique (irrotationality of wave number, conservation of energy) forming the basis of NLWAVE is equivalent to ray tracing. A model using ray tracing techniques would form a caustic behind the shoal and fail because an infinite wave height would be calculated. The model presented in this paper also fails behind the shoal, but the failure is manifested differently. As energy is diverted from the edge of the shoal and directed towards the middle, a negative energy flux is calculated at a node and the wave height becomes undefined. In linear mode the model fails at $y = 11$ ft, whereas in nonlinear mode it continues until $y = 13$ ft. To allow the model to continue calculation behind the shoal, smoothing was added to the finite difference scheme by replacing $A_{i,j}$ in Equation 7 by a three-point average given by

$$A_{i,j} = w A_{i,j+1} + (1-2w)A_{i,j} + w A_{i,j-1} \tag{9}$$

The smoothing adds dissipation to the finite difference solution and reduces both the rate of angle change and the concentration of energy towards the center of the grid. Although this mimics diffraction, the amount of smoothing needed to approximate the diffractive effects would vary with the bathymetry. With $w = 0.167$, the nonlinear mode did not fail, but the linear mode still failed at $y = 15$ ft. No smoothing was incorporated in the model for the results shown in Figures 4, 5, and 6 ($w = 0$). Simulations over less severe bathymetry do not need smoothing to continue calculations to the breaking zone. For the realistic bathymetry for which the model is intended, it is not anticipated that smoothing will be necessary.

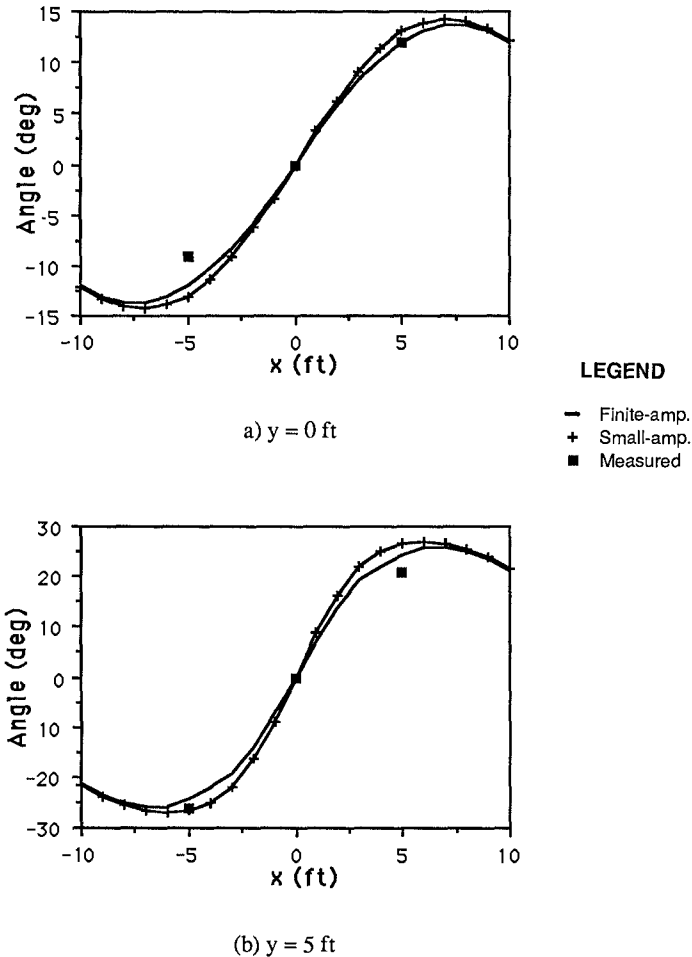


Figure 6. Wave Angle, Test M2I

CONCLUSIONS

A numerical model which efficiently and accurately calculates the shoaling and refraction of finite-amplitude waves over a nonplane bathymetry has been presented. The model can use any combination of Stokes and cnoidal wave theories up to a third-order Stokes and second-order cnoidal combination. The component theories are connected by maintaining wave height at the point of connection. By connecting third-order Stokes and second-order cnoidal wave theories at $U = 25$, the discontinuities which have been reported by previous researchers are minimized. It is concluded that the use of a higher-order cnoidal wave theory is the main factor in the reduction of these discontinuities.

In a test which exercised the model beyond its intended purpose, the numerical solution produced stable and symmetrical results. The nonlinear model provided quantitatively and qualitatively better results than the linear model in reproducing wave height and direction measured in a laboratory experiment.

The difficult and time-consuming work associated with a higher-order refraction model lies in its development. Although the nonlinear model requires approximately 2.5 times as much computer execution time than is required in linear mode, simulation times are small so that the difference can be neglected. On a VAX 750 computer the nonlinear model takes less than three minutes CPU time for a 100 x 100 cell grid.

ACKNOWLEDGEMENTS

This study was partially supported by the work unit "Surf Zone Sediment Transport Processes," under the Shore Protection and Restoration Program of the U. S. Army Corps of Engineers at the Waterways Experiment Station's Coastal Engineering Research Center. The work of T.A.H. was conducted under contract no. R & D 5963-EN-09 through the U. S. Army Research, Development, and Standardization Group - U.K. Permission was granted by the Office, Chief of Engineers to publish this information.

REFERENCES

- Chu, H-L. 1974. "Numerical Model for Wave Refraction By Finite-Amplitude Wave Theories," Proceedings of the Symposium on Modeling Techniques (Modeling '75) ASCE, pp. 1082-1100.
- Cialone, M. A., and Kraus, N. C. 1987. "A Numerical Model for the Shoaling and Refraction of Third-Order Stokes Waves Over an Irregular Bottom," Misc. Paper CERC-87-10, US Army Eng. Waterways Experiment Station, Coastal Engineering Research Center, 195 pp.
- Dalrymple, R. A. 1988. "Model for Refraction of Water Waves," J. of Waterways, Port, Coastal, and Ocean Engineering, Vol. 114, No. 4, pp. 423-435.
- Hardy, T. A., and Kraus, N. C. 1987. "A Numerical Model for the Shoaling and Refraction of Second-Order Cnoidal Waves Over an Irregular Bottom," Misc. Paper CERC-87-9, US Army Eng. Waterways Experiment Station, Coastal Engineering Research Center, 198 pp.
- Headland, J. R., and Chu, H-L. 1985. "A Numerical Model for Refraction of Linear and Cnoidal Waves", Proceedings of 19th Coastal Engineering Conference, ASCE, pp. 1118-1131.
- Isobe, M. 1985. "Calculation and Application of First- Order Cnoidal Wave Theory," Coastal Engineering, Vol. 9, pp. 309-325.

Isobe, M., and Kraus, N. C. 1983a. "Derivation of a Third- Order Stokes Wave Theory," Hydraulic Lab. Report No. YNU-HY- 83-1, Dept. of Civil Eng., Yokohama National Univ., 37 pp.

Isobe, M., and Kraus, N. C. 1983b. "Derivation of a Second- Order Cnoidal Wave Theory," Hydraulic Lab. Report No. YNU- HY-83-2, Dept. of Civil Eng., Yokohama National Univ., 43 pp.

Iwagaki, Y. 1968. "Hyperbolic Waves and Their Shoaling, "Coastal Engineering in Japan, Vol. II, pp. 1 - 12.

Kraus, N. C., Cialone, M. A., and Hardy, T. A. 1987a. Discussion of "Numerical Study of Finite Amplitude Wave Refraction," By I. S. Oh and C. E. Grosch, J. of Waterways, Port, Coastal, and Ocean Engineering, Vol. 113, No. 2, pp. 199-201.

Kraus, N. C., Cialone, M. A., and Hardy, T. A. 1987b. "Numerical Model of Finite-Amplitude Wave Refraction,"Proceedings of Coastal Hydrodynamics, R. A. Dalrymple, ed. ASCE, pp. 46-59.

Noda, E. K., Sonu, C. J., Rupert, V. C., and Collins, J. I. 1974. "Nearshore Circulation Under Sea Breeze Conditions and Wave-Current Interactions in the Surf Zone," Tech. Report No. 4, Tetra Tech, Inc., Pasadena, Ca.

Oh, I. S., and Grosch, C. E. 1985. "Numerical Study of Finite Amplitude Wave Refraction," J. of Waterways, Port, Coastal, and Ocean Engineering, Vol. 111, No. 1, pp. 78-95.

Skovgaard, O., and Petersen, M. H. 1977. "Refraction of Cnoidal Waves," Coastal Engineering, Vol. 1, pp. 43-61.

Svendsen, I. A., and Brink-Kjaer, O. 1973. "Shoaling of Cnoidal Waves," Proceedings of 13th Coastal Engineering Conference, ASCE, pp. 365-382.

Svendsen, I. A., and Buhr-Hansen, J. 1977. "The Wave Height Variation For Regular Waves in Shoaling Water," Coastal Engineering, Vol. 1, pp. 261-284.

Vincent, C. L., and Briggs, M. J. In press. "Refraction- Diffraction of Irregular Waves Over a Mound," J. of Waterway, Port, Coastal, and Ocean Engineering.

CHAPTER 43

WAVES IN TURNING WIND FIELDS

G.Ph. van Vledder *) **)

L.H. Holthuijsen *)

Abstract

A numerical model to compute to a high degree of accuracy nonlinear wave-wave interactions of wind generated waves supplemented with formulations of wind generation and white-capping, has been used to estimate qualitatively and quantitatively the effect of these physical processes on the directional response of waves in a turning wind field. After a sudden shift in wind direction the wave spectrum develops a secondary peak in the new wind direction. The initial peak of the spectrum either merges fairly quickly with this new peak or it slowly disappears, depending on the magnitude of the directional wind shift. The turning of the mean wave direction towards the new wind direction is caused by wind generation. The processes of nonlinear wave-wave interactions and white-capping tend to slow down the turning rate induced by the wind generation. The net turning rate of the mean wave direction in the model is twice as slow as in observations acquired in the central and southern North Sea.

Introduction

The directional characteristics of waves at sea are still poorly understood due to the scarcity of observations and the operational problems with wave models that properly represent the physics of waves in a wind field. In both aspects significant developments have taken place in the last few years. Instrumentation to observe wave directions is available on an acceptable operational basis and computers and numerical techniques are now available that permit a limited degree of experiments with the indicated type of wave models.

In the present study the EXACT-NL model of Hasselmann and Hasselmann (1985) is used to quantitatively determine the contributions of generation, dissipation and

*) Delft University of Technology, P.O.Box 5048, 2600 GA Delft, the Netherlands.

**) now at Delft Hydraulics, P.O.Box 152, 8300 AD Emmeloord, the Netherlands.

nonlinear wave-wave interactions to the variation of the mean wave direction in a turning wind field. The results are compared with observations in the North Sea which have been treated to separate the effects just mentioned from the effects of wave propagation.

Numerical computations

The EXACT-NL model is a discrete spectral wave model which has been developed by Hasselmann and Hasselmann (1985) to determine numerically to a high degree of accuracy the rather complicated nonlinear wave-wave interactions formulated by Hasselmann (1968). These computations have been supplemented with formulations from the literature for wind generation and white-capping. For a description of the model reference is made to Hasselmann and Hasselmann (1985) and Van Vledder and Weber (1988). In the EXACT-NL model the evolution of a homogeneous wave field is described by the energy balance equation:

$$\frac{\partial E}{\partial t} = S = S_{in} + S_{ds} + S_{nl} \quad (1)$$

in which E is the two-dimensional variance density spectrum $E(f, \theta)$ and S_{in} , S_{ds} and S_{nl} are the source terms representing the effect of wind input, dissipation by white-capping and nonlinear wave-wave interactions. The model is applied in six situations where a constant, spatially homogeneous wind suddenly turns to a 'new' directions after which the wind direction is constant again. The wind shifts considered are: 30°, 60° and 90° in combination with a constant wind speed U of 10 and 20 m/s. All computations start with a relatively young sea and the waves grow until the peak frequency has dropped to twice the Pierson-Moskowitz frequency at which time the wind direction shifts to the 'new' wind direction.

The mean wave direction θ_0 is defined as in the routine analysis of pitch-and-roll buoys (e.g Kuik et al., 1988):

$$\theta_0 = \arctan \left(\frac{b}{a} \right) \quad (2)$$

in which

$$a = \int_0^{2\pi} \int_0^{\infty} \cos(\theta) E(f, \theta) df d\theta \quad (3)$$

and

$$b = \int_0^{2\pi} \int_0^{\infty} \sin(\theta) E(f, \theta) df d\theta \quad (4)$$

The response of the mean wave direction in turning towards the new wind direction is found to occur in a manner somewhat similar to that of a relaxation process.

Therefore, the rate of change of the mean wave direction is quantified by means of a time scale τ of a relaxation model:

$$\frac{\partial \theta_0}{\partial t} = \frac{1}{\tau} \sin(\theta_w - \theta_0) \quad (5)$$

in which θ_w is the wind direction.

It can be shown by applying the definition operator of mean direction (see equation 2) to the energy balance equation (1), that:

$$\tau = \frac{\cos(\theta_s) \int_0^{2\pi} \int_0^{\infty} \cos(\theta) E(f, \theta) df d\theta}{\cos(\theta_0) \int_0^{2\pi} \int_0^{\infty} \cos(\theta) S(f, \theta) df d\theta} \frac{\sin(\theta_w - \theta_0)}{\sin(\theta_s - \theta_0)} \quad (6)$$

in which θ_s is the mean direction of the total source function $S(f, \theta)$.

The contributions of the above mentioned physical processes to this response are available in the model results as a function of time in the form of spectral source functions. Visual inspection of these provide a qualitative insight in the effect of the various processes. To quantitatively determine the effect of each source term a time scale per source term is introduced in a way similar to that of the time scale of the relaxation model (5), i.e. replace in equation (6) $S(f, \theta)$ by the source term considered. The rationale of this is that upon applying the definition operator of mean direction to the energy balance equation (1), the time scale τ of the relaxation model (5) is related to the time scales per source term as:

$$\frac{1}{\tau} = \frac{1}{\tau_{in}} + \frac{1}{\tau_{ds}} + \frac{1}{\tau_{nl}} \quad (7)$$

The time scales of the response of the mean wave direction (τ) and of the source terms (τ_{in} , τ_{ds} and τ_{nl}) are determined with their definition based on equation (6) from the computed spectra and source functions.

Observations

Observations have been carried out in the central and southern North Sea with a WAVEC pitch-and-roll buoy at two locations near the offshore platforms AUK and K13 (geographic locations 56.39 N, 2.05 E and 53.22 N, 3.22 E respectively). The directional behaviour of the waves in these observations are obviously affected by the inhomogeneity of the wave field. These effects are estimated with the results of an operational hindcast model (the WINCH model, Eide et al., 1986) and the observations are corrected accordingly. The time scales of the response of the mean

wave direction are subsequently determined with a finite difference treatment of the time series of the observed mean wave direction.

To account for effects of measurement errors and to correct for propagation effects, the wave, wind and model data have been selected rather carefully to retain high quality data (e.g. good correspondence between observations and hindcast results). Consequently only five of the fifteen hundred observations were accepted for further analysis.

Results

An example of the response of the two-dimensional spectrum is given in Fig. 1. An example of the various acting and counter-acting energy fluxes (source terms) is given in Fig. 2. The spectrum and the source functions are given for the situation in which the wind shifts suddenly over 90° (constant wind speed of 20 m/s). The illustrated situation is taken half-way through the turning of the wave spectrum towards the new wind direction. The mean wave direction at this moment is 50.3° and the spectrum has developed a secondary peak in the new wind direction (panel a). The wind input source function in this case is located around the new wind direction and turns the spectrum towards this direction (panel b). The dissipation source function is located at the high frequencies while skewed towards the new wind direction thus counteracting (the contribution is negative) the effect of the wind input somewhat (panel c). The nonlinear wave-wave interaction transfers energy from the newly generated high-frequency energy towards the old low-frequency energy in the old direction (panels d and e, for the positive and negative parts of this source function respectively) thus also counteracting the effect of the wind input.

A review of all model results (not shown here) indicates that after a shift in wind direction the wave spectrum always develops a new peak at high frequencies in the new wind direction, resulting in a bi-modal spectrum. However, the spectrum assumes a uni-modal shape rapidly when the wind shift is small or moderate. In a situation with a large wind shift (more than 60 degrees, say) the spectral shape remains bi-modal for a long period of time. In both cases the wind generates energy in the high frequencies in the new wind direction. In the case with a small or moderate wind shift the nonlinear wave-wave interactions siphon part of this new, high-frequency energy away towards lower frequencies in the 'old' wind direction. This, together with the rapid fusion of the two peaks due to their proximity, prevents the continued growth of a distinctly separate high-frequency peak. In the situation with a large wind shift the nonlinear interactions between the high-frequency energy in the new wind direction and the low-frequency energy in the old wind direction is almost nonexistent which provides the high-frequency peak with the opportunity to develop more or less independently from the peak in the old wind direction.

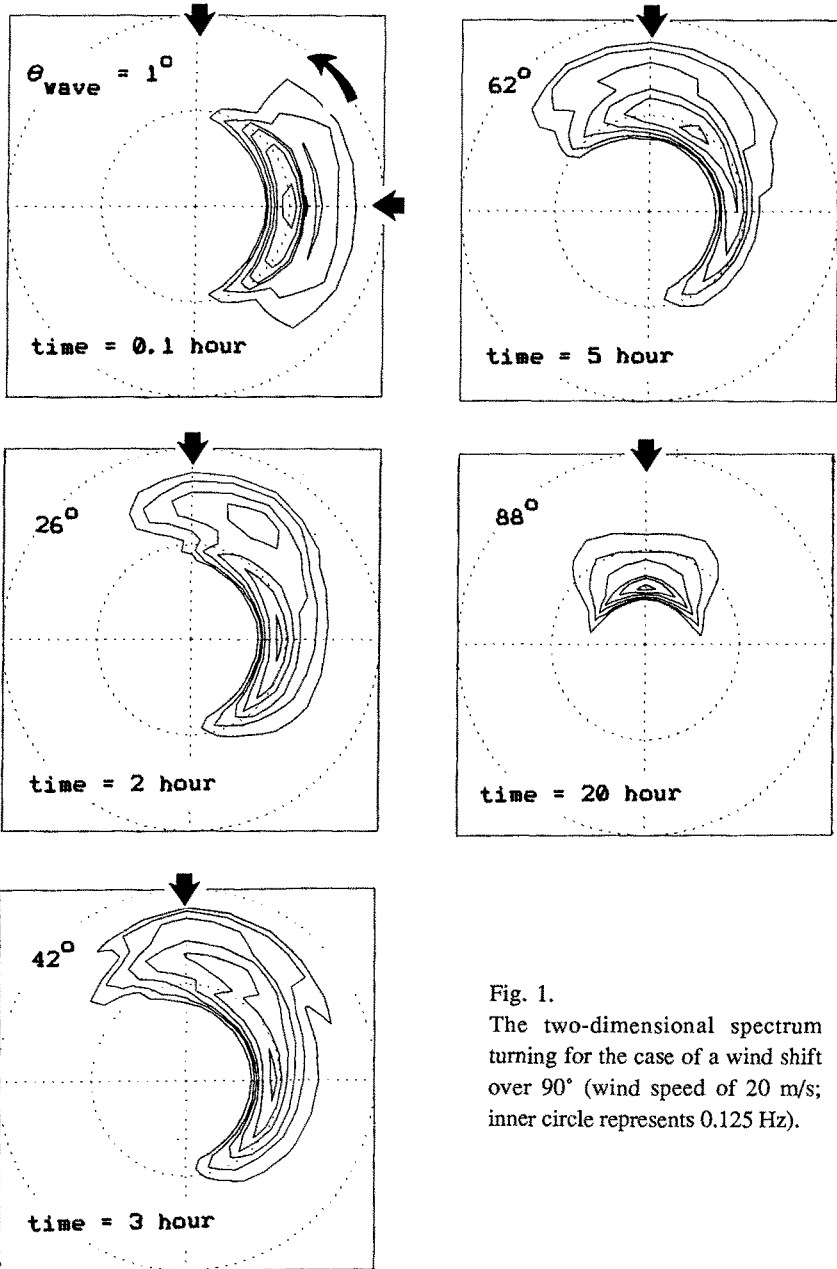
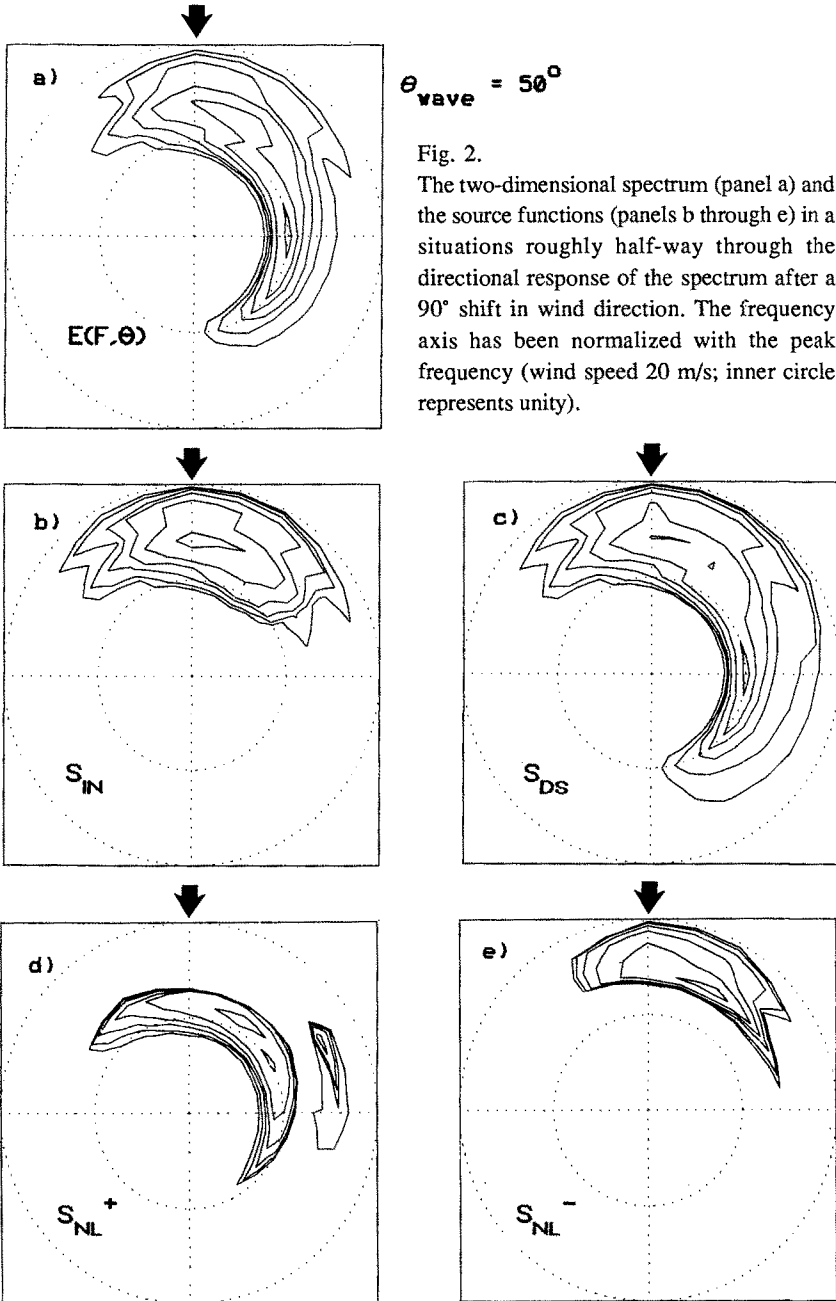


Fig. 1.
 The two-dimensional spectrum turning for the case of a wind shift over 90° (wind speed of 20 m/s; inner circle represents 0.125 Hz).



To generalize the computational results and to compare these results with information from the literature, the time scale estimates are normalized using the friction velocity U_* and the gravitational acceleration g . They are given as a function of growth stage, represented by the nondimensional peak frequency ν_* :

$$\tau_* = \tau g/U_* \quad (8)$$

and

$$\nu_* = f_p U_*/g \quad (9)$$

in which f_p is the peak frequency of the spectrum. Where necessary in the following U_* is determined from the wind speed at 10 m elevation (U_{10}) with the drag coefficient from Wu (1982).

The results of the time scale estimates obtained from the numerical computations and the observations are given in Fig. 3. It appears that the time scale increases with the stage of development of the waves (the response becomes slower as ν_* decreases). A similar increase in time scale is found in the observations. However, the time scales obtained from the observations are about a factor 2 lower than those obtained from the computations. One possible reason for this discrepancy is the severity of the selection of the wave measurements, which perhaps eliminates large time scales.

Comparison with literature

The time scale estimates are compared in Fig. 4 with the results of computations by Young et al. (1987), the results of observations (Hasselmann et al., 1980 and Allender et al., 1983) and with results of Günther et al. (1981) and Holthuijsen et al. (1987) who both parameterized the energy balance equation to estimate the time scales.

The dimensionless time scale τ_* obtained by all these investigators (except Holthuijsen et al., 1987) are only weakly dependent on ν_* , in contrast to the time scales obtained in this study (both the numerical and observational results). The difference between the results of Young et al. (1987) and of the present study (both based on the EXACT-NL model) can be explained by the fact that Young et al. (1987) assumed a constant time scale during the directional response in each case, whereas in the present study the time scale was allowed to vary. The results of Holthuijsen et al. (1987) are generally somewhat closer to those of Young et al. (1987). Holthuijsen et al. (1987) predict the rapid increase in time scale for waves approaching the fully developed stage ($\nu_* = \nu_{*,PM}$).

Relatively large differences occur between the computational results of the present study and the observational results of Hasselmann et al. (1980) and Allender et al. (1983) (as interpreted by Holthuijsen et al., 1987). For the most part ($\nu_* > 0.075$, say), these observed time scales are about a factor 2 to 5 higher than those of the

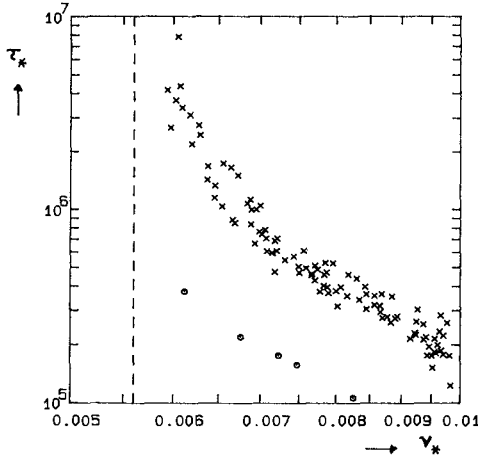


Fig. 3. Nondimensional time scale estimates τ_* as a function of growth stage ν_* . The results of the computations and observations are indicated with the symbols (x) and (o) respectively. Computations refer to the cases of a sudden wind shift of 30°, 60° and 90° and to the wind speeds $U = 10$ and 20 m/s. The dashed vertical line at $\nu_* = \nu_{*,PM}$ indicates the non-dimensional Pierson-Moskowitz frequency (fully developed waves).

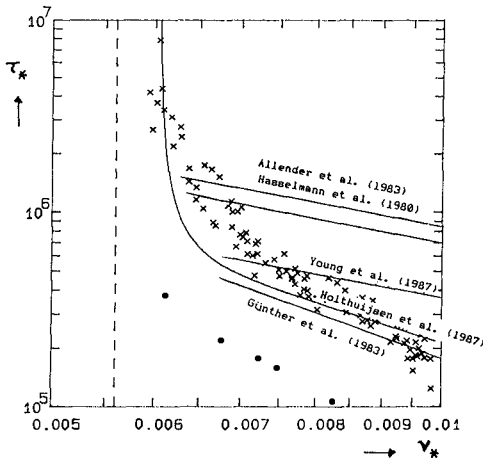


Fig. 4. Time scale estimates obtained from the model computations (x) and from the observations of the present study (o) and time scale estimates in the literature (—).

computations. This difference is possibly due to the nature of the selection procedure followed for these observations. A reanalysis of part of these observations (based on illustrations 7 and 8 in Hasselmann et al., 1980) shows that, when the same selection criteria are used as in the present study (except those related to the hindcast data and not corrected for propagation effects), the remaining observed time scales of Hasselmann et al. (1980) are on the average about a factor 3 lower than the original ones.

Conclusions

Numerical calculations with an advanced wave model (Hasselmann and Hasselmann, 1985) show that the response of the mean direction of waves in a turning wave field is primarily due to the effect of wind generation. This effect is counteracted to some degree by white-capping and nonlinear wave-wave interactions. For comparison with these model results, time scales of directional wave response have been estimated from observations in the southern and central North Sea. Both the model results and the observations indicate that the time scales increase with increasing growth state. However, the observed time scales are a factor of two smaller than the model time scales.

References

- Allender, J.H., J. Albrecht and G. Hamilton, 1983: Observations of directional relaxation of wind sea spectra. *J. Phys. Oceanogr.*, Vol. 13, 8, 1519–1525.
- Eide, L.E., M. Reistad and J. Guddal, 1986: A comparison of hindcast studies with a coupled discrete wave model and a coupled hybrid wave model. *Proc. Int. Workshop on Wave Hindcasting and Forecasting*, Halifax, Nova Scotia, Sept. 23–26, Environmental Studies Revolving Funds, Report Series No. 065, Ottawa, pp. 153–159.
- Günther, H., W. Rosenthal and M. Dunkel: The response of surface gravity waves to changing wind direction. *J. Phys. Oceanogr.*, Vol. 11, 5, 718–728.
- Hasselmann, D.E., M. Dunkel and J.A. Ewing, 1980: Directional wave spectra observed during JONSWAP 1973, *J. Phys. Oceanogr.*, Vol. 10, 8, 1264–1280.
- Hasselmann, K., 1968: Weak-interaction theory of ocean waves. In 'Basic developments in Fluid Dynamics', Vol. 2, 117–182, Ed. M. Holt, Academic Press. N.Y. London.
- Hasselmann, S. and K. Hasselmann, 1981: A symmetrical method of computing the nonlinear transfer in a gravity wave spectrum. *Hab. Geophys. Einzelschr.*, Max Planck Institut für Meteorologie a.d. Universität Hamburg, Ser. A, Wiss. Abh. 52.
- Hasselmann, S. and K. Hasselmann, 1985: The wave model EXACT–NL, in: *Ocean Wave Modeling*, Plenum Press, New York, pp. 249–251.
- Holthuijsen, L.H., A.J. Kuik and E. Mosselman, 1987: The response of wave direction to changing wind direction. *J. Phys. Oceanogr.*, Vol. 17, 7, 845–853.

- Kuik, A.J., G.Ph. van Vledder and L.H. Holthuijsen, 1988: Proposed method for the routine analysis of pitch-and-roll buoy wave data. *J. Phys. Oceanogr.*, Vol. 18, 7, 1020–1034.
- Van Vledder, G.Ph. and S.L. Weber, 1988: Guide for the program EXACT–NL, Report No. 20, Max Planck Institut für Meteorologie, Hamburg.
- Wu, J. 1982: Wind-stress coefficients over sea surface from breeze to hurricane. *J. Geophys. Res.*, Vol. 87, No. C12, 11, 9704–9706.
- Young, I.R., S. Hasselmann and K. Hasselmann, 1987: Computations of the response of a wave spectrum to a sudden change in wind direction. *J. Phys. Oceanogr.*, Vol. 17, 9, 1317–1338.

CHAPTER 44

TRANSFORMATION OF SHALLOW WATER WAVE SPECTRA

Genowefa BENDYKOWSKA¹. Gosta WERNER².

ABSTRACT

Investigations are presented on some effects of non-linearity in the motion of shallow water wave spectra. The waves were generated mechanically in a laboratory wave flume with fixed bottom. Essential differences with the linear dispersion relation are found, showing vanishing dispersivity of higher frequency spectral components in strongly nonlinear spectra. The mean frequency increases with decreasing water depth. The relation of the peak frequency to the mean frequency varied in the experiments from 0.9 to 0.5, for deep to shallow water wave spectra respectively.

1. INTRODUCTION

Two following spectral characteristics are analysed

- the dispersion relation of spectral components in shallow water conditions
- changes of the relation between the mean and peak frequencies of wave spectra, propagating over sloping bottom.

The experiments were performed with mechanically generated irregular wave trains, propagating in one direction, over a fixed bed. In these conditions the waves were not affected by the wind and wind generated currents / as it is in laboratory when waves are generated by wind / and did not depend on the angular energy spread nor changes of bottom topography / that always influences the wave motion in field conditions /.

The relationship between the wave number k and the frequency ω , known as the dispersion relation:

$$\omega^2 = gk \tanh kh$$

is widely used and proves a powerful tool in analysing regular wave. However several laboratory/Romamonijariosa 1976, Mitsuyasu et al. 1979 and field Massel, 1980 / measurements on irregular wave trains, show a deviation

-
1. Ph.D., Institute of Hydroengineering Polish Academy of Sciences, Kościarska 7 80-328 Gdańsk, Poland
 2. Eng. Royal Institute of Technology, S-100 44 Stockholm Sweden

of the dispersion relation from the theoretical one, especially for higher frequencies. Experimental results on wave pressure attenuation Naguszewski et al. 1985 show the same qualitative differences with the commonly used theoretical description, which includes the dispersion relation, given above.

Several theoretical studies have been published, which take into account the influence on the dispersion relation of various aspects of the nonlinearity of a random wave field /Crawford et al. 1981, Huang and Tung 1977, Massel and Chybicki 1983, Masuda et al. 1979 /. All these studies concerned deep water wave conditions.

The results of this study prove an essential departure from the linear dispersion relation of low and high frequency spectral components in a broad range of tested shallow water spectra.

It is often assumed, that for a given wave train, propagating over shallowing water, the peak frequency ω_p and the mean frequency $\bar{\omega}$ do not change with depth and the relation $\omega_p/\bar{\omega} = 0.7 - 0.8$ remains constant through the surf zone / Massel 1980 /. Goda 1987, reports results of a broad statistical analysis of deep water wave trains, simulated according to JONSWAP and WALLOPS spectra, where a strong dependence of $\omega_p/\bar{\omega}$ from the spectral width is proved. Different values of the enhancement factor $\gamma = 1 - 20$ in JONSWAP formula followed changes of $\omega_p/\bar{\omega} = 0.74 - 0.91$; different values of $m = 3 - 20$ in WALLOPS formula gave $\omega_p/\bar{\omega} = 0.58 - 0.95$.

In the following a strong dependence is found of the mean frequency from the relative water depth. These changes follow the changes of the shape (width) of the spectrum and the appearance of secondary peaks at smaller depths.

2. EXPERIMENTS. INPUT SPECTRUM

- Two sets of experiments were performed -
- one - concerned with the measurements of the dispersion relation of spectral components in shallow water wave spectra
 - the second - concerned with measurements of wave spectra over sloping bottom, to study the transformation of spectral parameters on shallowing water depths

The wave flume of dimensions 15 m x 0.305 m x 0.62 m was build of glass. A programmable wave maker of flap type was monitored by a punched tape, read at discrete intervals of 0.02 s. The water surface elevations were measured by means of resistance gauges. Analog records were taken and stored on a tape recorder. The tape recordings were converted into digital data with sampling interval 0.05 - 0.1 s and transmitted to a computer.

In the measurements of the dispersion relation four gauges, spaced equally at 0.1 m, were mounted over the horizontal bottom of the flume. The beach at the end of

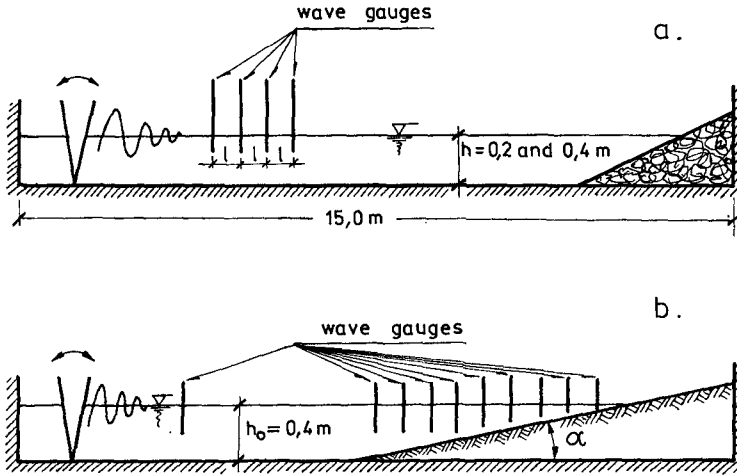


Fig. 1 Experimental scheme

the flume was a porous structure of slope 1 : 10. In the second part of the investigations an array of eleven gauges was used: one - over the deep water section and ten at sections of decreasing depth / fig. 1 /.

JONSWAP energy spectrum was generated / of peak enhancement factor $\gamma = 1$ and 6 / consisting of 100 spectral components. The frequency of these components were distributed within cut-off frequencies

$$\omega_{\min} = 0.5 \omega_p \quad , \quad \omega_{\max} = 2.5 \omega_p$$

The frequencies of the spectral components were random values in intervals $\Delta \omega_i = \omega_i - \omega_{i-1}$ determined by the Goda's formula

$$\omega_i = \omega_{i-1} \cdot d \quad , \quad d = \left(\frac{\omega_{\max}}{\omega_1} \right)^{\frac{1}{98}}$$

Phase angles of the components were random within $(0, 2\pi)$

3. DISPERSION RELATION OF THE SPECTRAL COMPONENTS IN SHALLOW WATER WAVE SPECTRA.

3.1 Range of the study.

Usual technique of cross spectral analysis was applied to two simultaneous records, taken at known distances. Wave numbers $k(\omega_i)$ and celerities $C(\omega_i)$ of the spectral components were determined. Only cases of coherence coefficient ≥ 0.8 were analysed. To describe the degree of nonlinearity of the wave spectrum a modified Stokes number was used, as a function of the parameters of the peak spectral component:

$$S = \left(\frac{2\pi}{k_p} \right)^2 \frac{H_s}{h^3} \quad , \quad H_s = 4\sqrt{m_0}$$

The effects of nonlinearity were examined by varying the peak frequency of 7 tested wave spectra in the range: $2.45 \leq \omega_p \leq 7.98$ [rad/s] at two water depths $h = 0.2$ m and 0.4 m. The Stokes' numbers varied between 0.75 and 45.2

3.2 Results

Examples of measured results are given in fig. 2 - 5. On fig. 2 three spectra are shown, measured at water depth 0.2 m

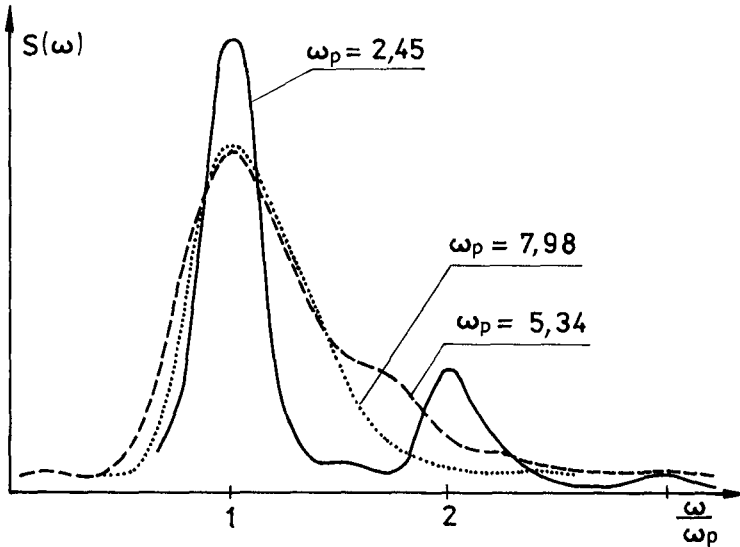


Fig. 2 Energy spectra measured. $h = 0.2$ m

The spectrum of peak frequency $\omega_p = 7.98$ rad/s has a shape very close to that of the input spectrum. The spectrum of the lowest peak frequency $\omega_p = 2.45$ rad/s proves, that the deep water input spectrum transformed in this shallow water conditions into a two-peaks spectrum. The second peak, appearing at $2\omega_p$, is certainly due to bounded waves, that of second order Stokes type.

In fig. 3 some measured results of the wave frequency ω against the wave number k in comparison with the theoretical curve $\omega^2 = gk \tanh kh$ are plotted. All measured results indicate, that the prediction of the linear theory are true only in the vicinity of the peak frequency. The measured curves level out in the bands of $2\omega_p$ and $3\omega_p$. As the tested wave systems were not linear, both free and bounded harmonics existed in the motion. The dominating components are those of the peak frequency, thus also their harmonics travel faster, than free waves of the same frequency. If so, the decrease of the wave numbers of the components $2\omega_p$ and $3\omega_p$ would be explained.

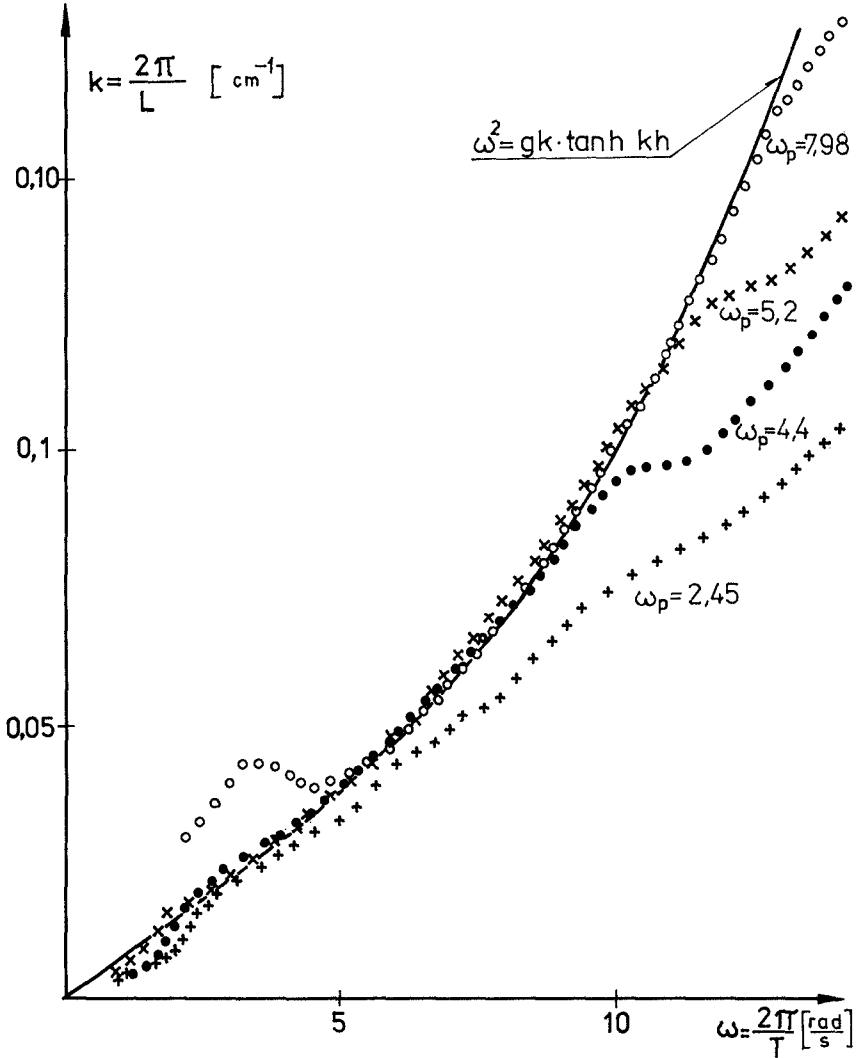


Fig. 3 Comparison of theoretical and measured dispersion relation. $h = 0.2$ m.

In fig. 4 the line $C(\omega)/C_0(\omega) = 1$ is the theoretical relation. All spectral components of $\omega > 1.5 \omega_p$ in all tested cases travel at higher velocities, than the theoretical. The presence of bounded waves is one explanation. Another one is, that in the range $\omega > 2.5 \omega_p$ no free wave components are generated, so only bounded and interaction waves of that frequencies exist in the wave train, both propagating faster than free waves. In the range $\omega < \omega_p$

the measured components phase velocity is either higher / high Stokes' number / or lower / low Stokes' number / than predicts the theory. A similar result was found by Crawford et al, 1981, in their numerical study. The relationship in fig. 5 shows most evidently the influence of the nonlinearity of the motion on the dispersive behaviour of the spectral components. For cases of higher Stokes' numbers the dispersivity of components of $\omega > \omega_p$ vanishes and all these components travel at the velocity of the peak frequency component.

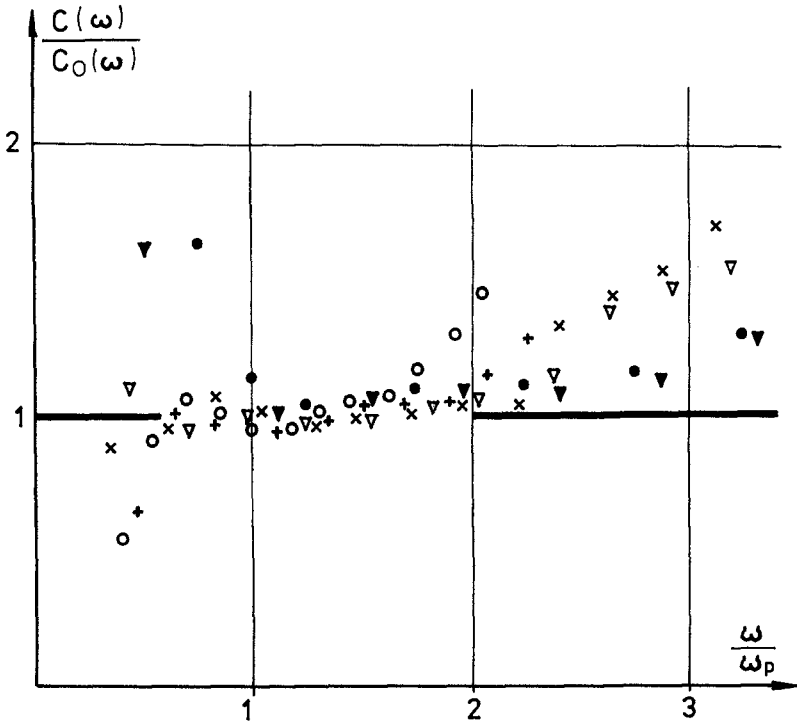


Fig. 4 Measured component phase velocity normalised by its theoretical value. $h = 0.2$ m.

- Legend:
- $\omega_p = 2.45$ rad/s, $S = 45$
 - ▼ $\omega_p = 2.76$ rad/s, $S = 42$
 - ▽ $\omega_p = 4.40$ rad/s, $S = 25$
 - x $\omega_p = 5.34$ rad/s, $S = 9.8$
 - + $\omega_p = 6.74$ rad/s, $S = 6.4$
 - o $\omega_p = 7.98$ rad/s, $S = 3.73$

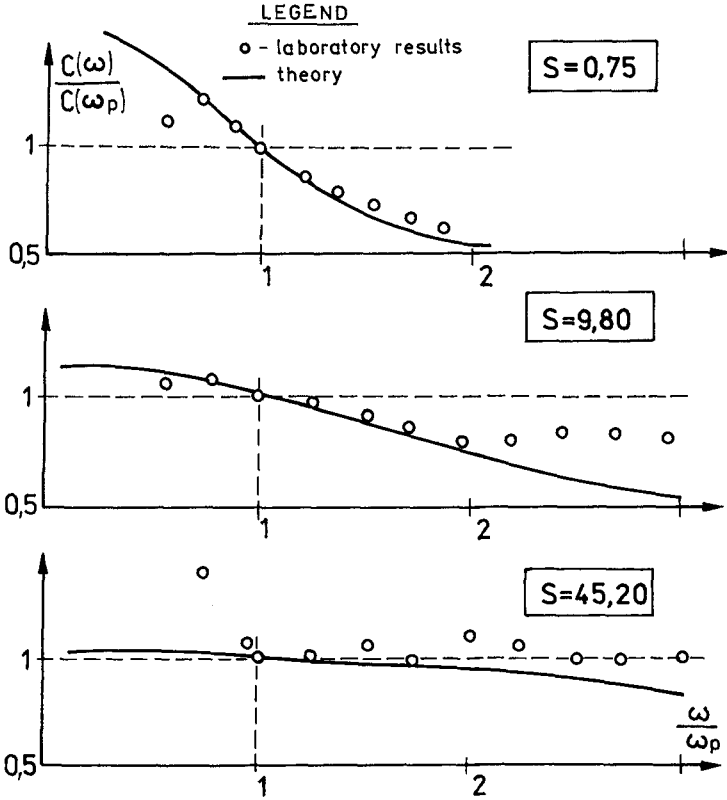


Fig. 5 Measured component phase velocity normalised by the peak component phase velocity.

4. SPECTRAL CHARACTERISTICS OF WAVE SPECTRA OVER SLOPING BOTTOM.

4.1. Range of the study.

The experiments were performed for four different wave spectra of peak frequencies $\omega_p = 6,25, 7,87$ and $12,56$ while two wave trains of different energies were tested for $\omega_p = 7,87$ rad/s. Wave spectra were measured over two slopes $\gamma = 0,04$ and $0,06$ with $h = 0,4$ m in the deep water section of the flume. The mean frequencies and the width of the spectra were determined from spectral analysis:

$$\bar{\omega}^2 = \frac{m_2}{m_0} , \quad \varepsilon^2 = 1 - \frac{m_2}{m_0 \cdot m_4} , \quad m_n = \int_0^\infty \omega^n S(\omega) d\omega$$

4.2 Results.

Results, concerning the changes of the mean frequency of the spectrum, when propagating from deep water $\bar{\omega}_0$ / over decreasing depth $\bar{\omega}$ / are shown in fig 6. Results, obtained for both tested slopes are plotted together. They prove an increase of the mean frequency when the water depth decreases.

Changes of the relation between the peak ω_p and the mean frequency $\bar{\omega}$ of the spectrum as a function of the relative water depth $k_{p_0} \cdot h$ (k_{p_0} - wave number of the deep water peak frequency component $k_{p_0} = \omega_p^2/g$) are given in fig. 7. The peak frequency didn't change from deep water $/h = 0.4m/$ up to the shallowest water depth $/h = 0.05 m/$, except the case of highest peak frequency tested $/\omega_p = 12.56 \text{ rad/s} /$, when a shift of about 10 % toward the lower frequency band occurred for both tested slopes. The relation $\omega_p/\bar{\omega}$ varies from 0.9 on deep water, to 0.5 for very small relative depth. Those changes are due to the changes of the shape of the spectrum. The values of the spectral width given in table 1 show a consequent increase of ϵ^2 with decreasing water depth. An example of energy spectra measured at different water depth presented on fig. 8, explains, that the

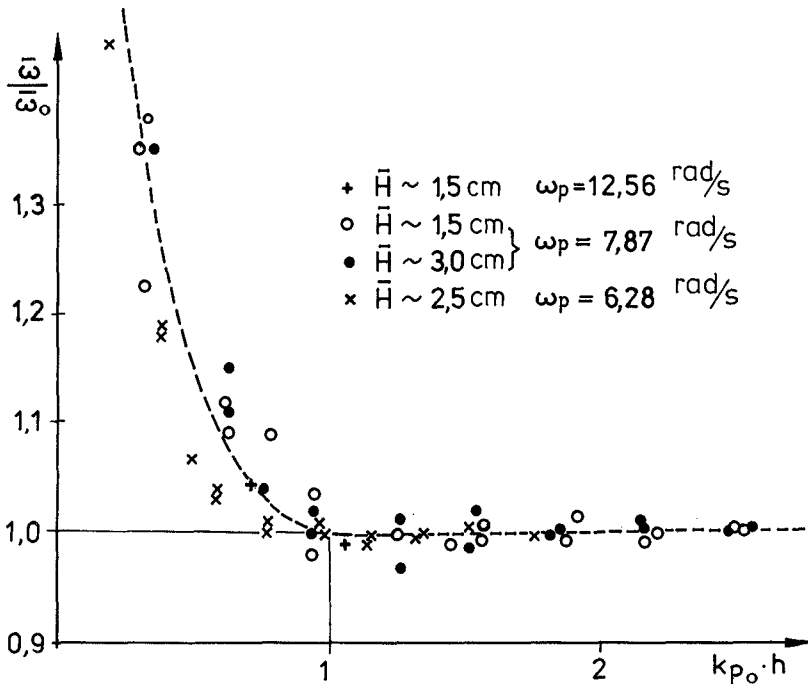


Fig. 6 Changes of mean frequency. Experimental results. $\gamma = 0.04$ and 0.06

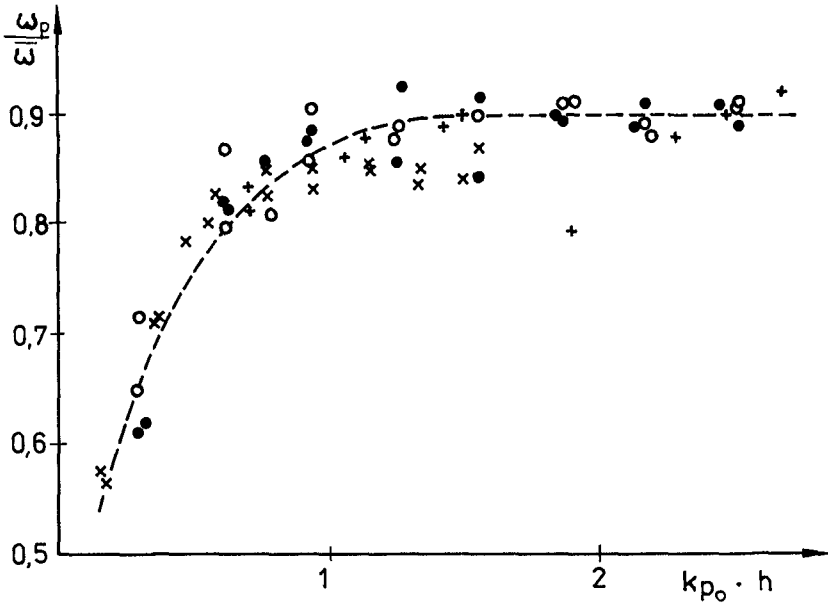


Fig. 7 Relation of peak the frequency to the mean frequency. Experimental results. $\gamma = 0.04$ and 0.06 . Legend as on fig. 6

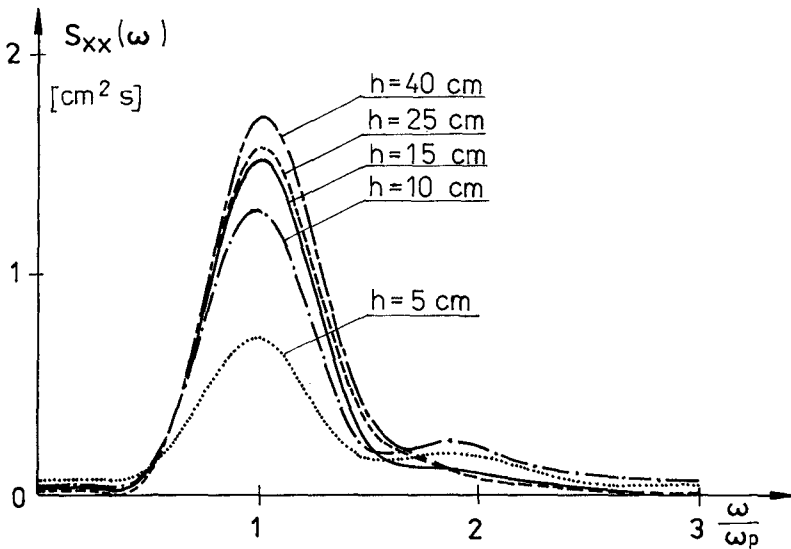


Fig. 8 Changes of energy spectra over sloping bottom $\gamma = 0.06$, $\omega_p = 6.28$ rad/s.

increase of the spectral width is due to the increasing nonlinearity of the wave motion on smaller depth / see fig. 2 for comparison /.

Fig. 9 shows a comparison of the experimental curve with field data measured in the coastal zone of the Black Sea. The measurements were done at six wave conditions, of peak frequencies varying between 0.72 to 1.59 rad/s, at depths 1.5 - 3 m. It should be mentioned, that for the field data the mean frequency was determined as $\bar{\omega} = \frac{2k_p}{T_z}$, where T_z is the average zero-up crossing period.

Table 1. Spectrum width parameter measured in the experiments

slope	ω_{p0} rad/s	ξ^2	
		h = 40 cm	h = 5 cm
0.06	12.56	0.210	0.379
	7.87	0.329	0.403
	7.87	0.393	0.631
	6.28	0.338	0.628
0.04	12.56	0.228	0.403
	7.87	0.382	0.560
	7.87	0.417	0.573
	6.28	0.437	0.639

5. CONCLUDING REMARKS.

- The relative water depth of the peak frequency component $k_p \cdot h$ proves to be good measure of the nonlinearity of a shallow water wave spectrum. Presence of bounded harmonics and waves of interaction between free spectral components are supposed to account for all shallow water effects observed in the experiments.
- An essential departure from the theoretical dispersion relation is proved in the experiments. The spectral components of the peak frequency band follow the relation in all tested cases. Components of frequency $\omega > \omega_p$ propagate faster, than predicted theoretically and for strongly nonlinear wave trains the dispersivity of those components almost vanishes. Components of frequency $\omega < \omega_p$ propagate either slower / moderate nonlinearity / or faster / strong nonlinearity /, than predicts the theory.
- The mean frequency $\bar{\omega}$ increases with decreasing water depth / $k_p \cdot h < 1$ /. The relation between the peak and the mean frequencies decreases with decreasing relative water depth in a range $0.5 < \omega_p / \bar{\omega} < 0.9$.
- The spectral characteristics of the peak frequency components are the most reliable parameters in a simple estimation of a spectrum. The parameter of the mean frequency / zero-crossing period / has a poor physical meaning in shallow water wave spectra.

- The very simple laboratory model, applied in this experiment, proves a good tool in studying general features of shallow water wave spectra. The comparison with other field data and results of different laboratory technics and numerical simulations / Crawford et al. 1981, Goda 1987, Mitsuyasu et al. 1979, Ramamonijarisoa 1976 / gives a satisfactory qualitative agreement.

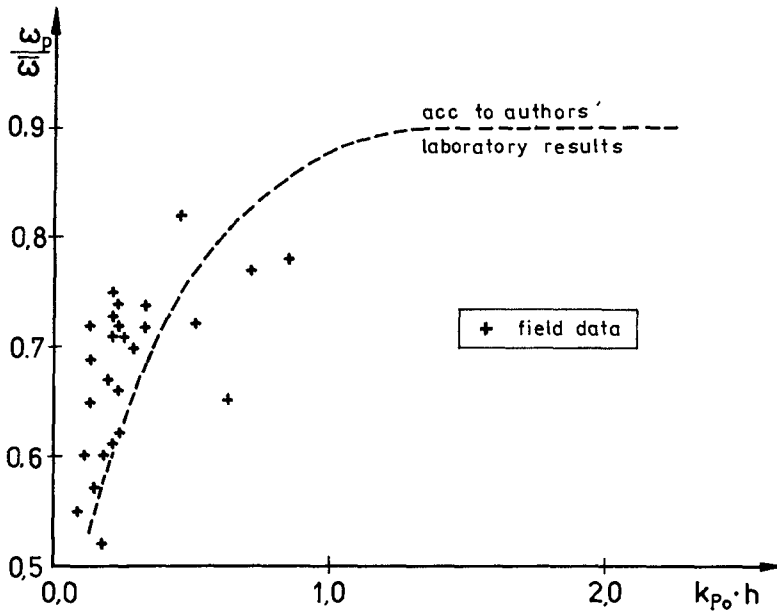


Fig. 9 Field data compared with experimental curve.

Bibliography

- Crawford D.R., Lake B.M., Saffman P.G., Yuan H.C., 1981 "Effects of Nonlinearity and Spectral Bandwidth on the Dispersion Relation and Component Phase Speeds of Surface Gravity Waves". J.Fl.Mech. vol. 112 pp. 1-32.
- Goda Y., 1987 "Statistical variability of Sea State Parameters as a Function of Wave Spectrum". JAHR Seminar Maritime Hydraulics Section, XXIII Congress Lausanne. pp. 237 - 248.
- Huang N.E., Tung C.C., 1977 "The influence of the Directional Energy Distribution on the Nonlinear Dispersion Relation in a Random Gravity Wave Field" Journal of Phys. Ocenogr. vol. 7 pp. 403 - 414.

- Massel St., 1980, "Some statistical properties of wind waves in the coastal zone".
Hydrotechnical Trans. vol. 41
pp. 57 - 62.
- Massel St., Chybicki W., 1983 "Nonlinear dispersion relation for wind waves at limited water depth. Theoretical analysis" / in polish /.
Studia i Materialy Oceanolog. KBM, nr 40 pp. 47 - 71.
- Masuda A., Kuo Y.Y., Mitsuyasu H. 1979 "On the Dispersion Relation of Random Gravity Waves. Part 1. Theoretical Framework".
J. of Fluid Mech. vol. 92, p. 4,
pp. 717 - 730.
- Mitsuyasu H., Kuo Y.Y., Masuda A., 1979 "On the Dispersion Relation of Random Gravity Waves. Part. 2. An Experiment".
J. of Fluid Mech. vol. 92, p. 4
pp. 743 - 749.
- Ramamonjarisca A., Coantic M., 1976, "Loi experimentale de dispersion des vagues par le vent sur une faible longueur d'action"
C.R.Acad. Sc. Paris, B282, pp. 111-114.

CHAPTER 45

Solitary waves passing over submerged breakwaters

Mark Cooker *
Howell Peregrine †

Abstract:

A method is described for the computation of the two-dimensional unsteady motion of a solitary wave passing over submerged breakwaters. Far from the breakwater the fluid is assumed static and the sea bed is level. The fluid motion is assumed to be irrotational, incompressible and inviscid. The exact boundary conditions at the free surface and the impermeable bed are satisfied. Laplace's equation for the velocity potential is solved using a boundary integral method.

Numerical results are reported which show the variety of ways in which solitary waves are distorted when they encounter submerged breakwaters.

This work is part of a program of study to provide more understanding of the hydrodynamics of steep waves when they encounter coastal structures. We have developed a computer program which models the motion of waves in 2D, irrotational, inviscid flows. The method is not restricted to any particular free surface motion but we choose here to examine solitary waves. This class of waves includes the largest 2D irrotational, inviscid wave which can steadily propagate on a fixed depth. Solitary waves are everywhere elevated above the undisturbed water level, so it was thought likely that these model the waves most damaging to structures. We can accurately reproduce solitary waves with heights up to 96% of the highest wave.

The numerical method employs a boundary integral technique to solve Laplace's equation for the velocity potential. Bernoulli's equation is used as one boundary condition at the free surface. We ignore surface tension, and take the atmospheric pressure above the liquid surface to be constant. The second boundary condition is to assume that fluid particles on the free surface stay on the surface. All rigid boundaries are assumed to be impermeable. Details of the method are given by Dold & Peregrine (1986).

The method is accurate, stable and efficient. A solitary wave of height 0.5 of the depth can propagate over a horizontal distance of 50 depths with less than 0.1% change in height. The method does not suffer from "sawtooth" instabilities.

The program can be run on an IBM-compatible AT personal computer: in 60 minutes elapsed time we can calculate the motion of a wave passing over a breakwater.

The method also uses conformal mappings to transform flow domains

*Research Assistant †Professor of Applied Maths
School of Maths, University of Bristol,
Bristol BS8 1TW, England.

with irregular beds into regions with a flat horizontal bed. This is done to make Laplace's equation easier to solve. For the examples used here the conformal mapping has a bottom comprising a semicircle (radius R) on an otherwise flat horizontal bed. See figure 1.

The solitary wave is started with its crest far enough from the semicircle for the wave to be unaffected by it in the first few time steps. The wave moves left towards the cylinder. The initial data describing an incident solitary wave is calculated using the method of Tanaka (1986).

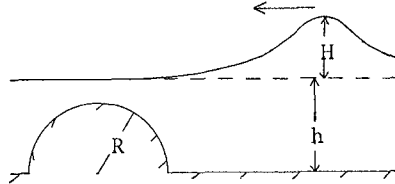


Figure 1 : Solitary wave approaching submerged semicircular breakwater.

Let the undisturbed fluid depth $h = 1$. Then H , the incident wave height, and cylinder radius R , are dimensionless parameters. The $H - R$ parameter space is surprisingly rich: see figure 2. We expected all waves to steepen and break on the cylinder, but this only happens for the largest waves ($H > 0.6$) and the largest cylinders ($R > 0.8$) and even these extreme waves tend to break downstream of the breakwater.

Small cylinders ($R < 0.5$) cause very large, linearly unstable waves ($H > 0.8$) to eventually break, long after they have passed over the breakwater. See figure 3. Tanaka et al. (1987) show that unstable solitary waves do not necessarily break. The growth in time of the breakwater instability closely follows that discussed by Tanaka et al. (1987). Waves with height $H < 0.77$ develop a train of small dispersive waves in their wake, after they have passed over the breakwater when $R < 0.4$. See figure 4.

A very common but unexpected phenomenon occurs for many waves for cylinders with radius in the range 0.5 to 0.9. As the wave approaches the cylinder a second crest grows on the opposite side of the obstacle. The second crest grows and soon dominates the first which meanwhile decays. The new crest propagates away from the cylinder. This exchange of crests across the cylinder is reminiscent of a large solitary wave catching up a smaller one. See figure 5.

Most surprising of all are those waves of height between 0.3 and 0.6, passing over cylinders of radius 0.7 to 0.9. The wave passes over the breakwater and having cleared it a second, stationary wave forms above the left-hand margin of the breakwater. This second wave steepens enough to break over backwards, onto the cylinder. See figure 6.

For the example shown in figure 6 if we increase R from 0.7 to 0.8 the transmitted wave breaks forward before the second wave breaks backward. See figure 7. We are unable to continue the computations beyond the time at which a wave breaks, but experiments have indicated that breaking can occur for both of the waves. The breaking is simultaneous when $R=0.77$ for $H = 0.58$.

Wave tank experiments at Santander University in Spain by C ezar Vidal confirm the backwards breaker. Some measurements of depth as a function of time, at fixed stations, also agree well with prediction.

Figure 6 also illustrates the instantaneous streamlines of the flow. The pressure contours can also be found and the total force on the cylinder determined. For example when $H = 0.8$ and $R = 0.9$

the wave breaks on top of the cylinder. See figures 8 and 9. The horizontal and vertical components of hydrodynamic force on the breakwater as the wave approaches are plotted in figure 10. The maximum horizontal component of force occurs during the wave's approach and well before breaking. Both of the maxima in horizontal and vertical components of force are about as large as the hydrostatic force.

This shows how waves can exert large dynamical forces on submerged coastal structures.

Figures 11 and 12 show a sequence of profiles of a solitary wave of height 0.8 breaking on a shoal of elliptical profile. The bed is reminiscent of a gently shelving beach and our method has predicted the classical plunging breaker. The pressure distribution is plotted in figure 13, at a time soon after the front face of the wave has become vertical. The large pressure gradients normal to the front face of the wave and parallel to the bed remind us of the strength of the sea.

REFERENCES

- DOLD, J.W., D.H.PEREGRINE, 1986, Water-wave modulation, Proc.20th Internat.Conf. Coastal Engng. Taipei, A.S.C.E., 1, 163-175.
- TANAKA, M. 1986, The stability of solitary waves, Phys. of Fluids, 29, 650-655.
- TANAKA, M., J.W.DOLD, M.LEWY, & D.H.PEREGRINE, 1987, Instability and breaking of a solitary wave, J. Fluid Mech., 185, 235-248.

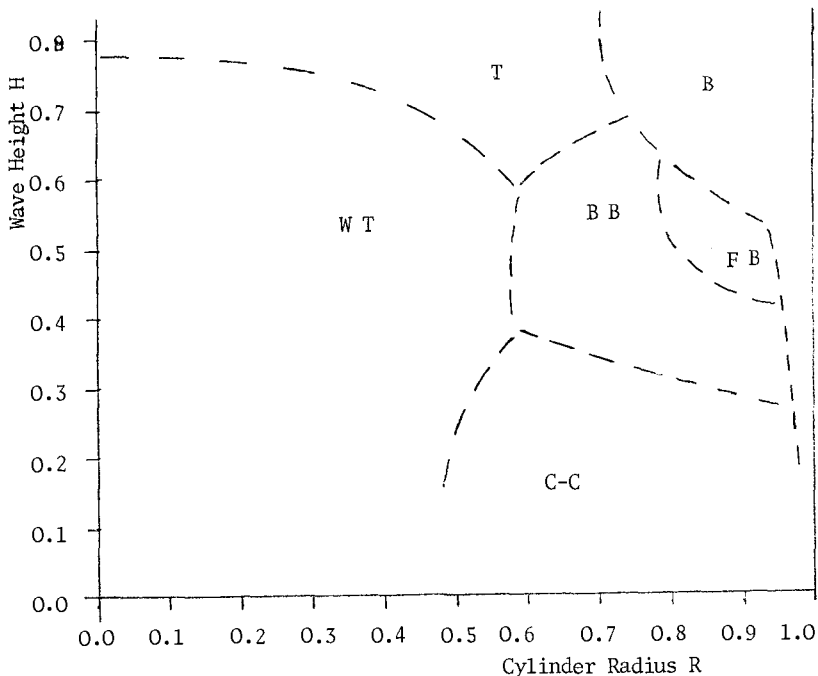


Figure 2 : B: Breaking at cylinder. B B: Backward breaking.
C-C: Crest interchange across cylinder. F B: Forward breaking.
T: Tanaka-type instability. W T: Wave train behind transmitted wave.

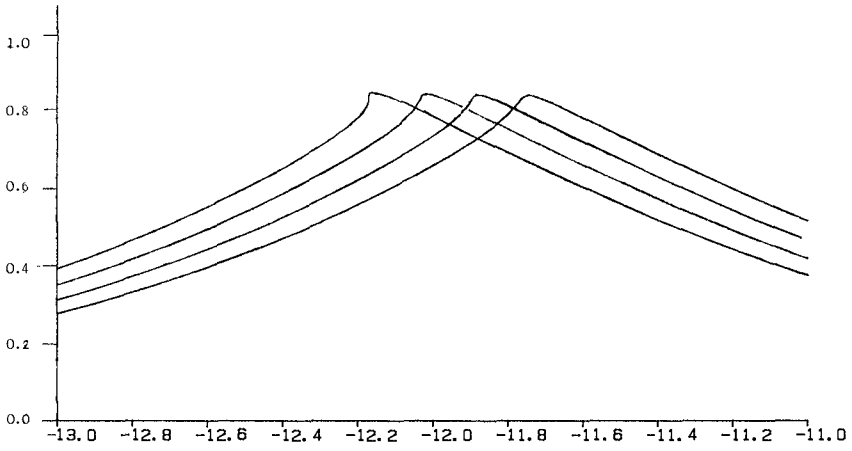


Figure 3: $H = 0.8$, $R = 0.3$. Breaking far downstream of cylinder. Natural scaling.

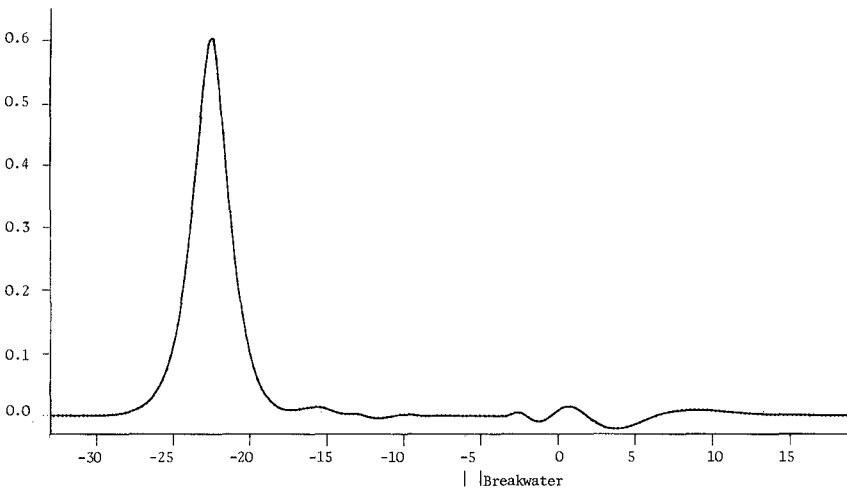


Figure 4: $H = 0.6$, $R = 0.5$. Dispersive waves trailing transmitted wave. Note right-travelling reflected waves. Vertical exaggeration = 40.

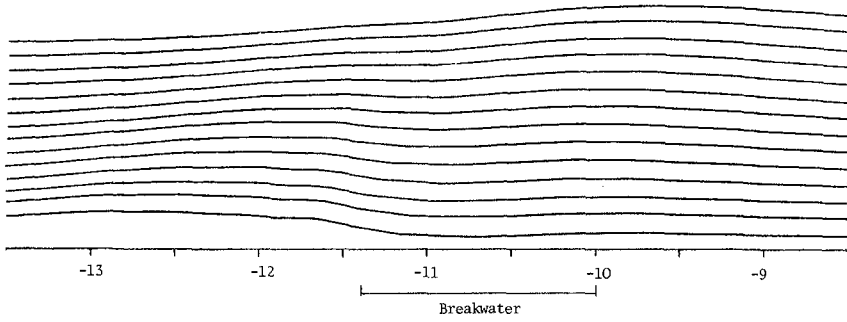


Figure 5: $H = 0.22$, $R = 0.7$. Exchange of crests across breakwater. Times 9, 9.2, ... 9.6. Natural scaling.

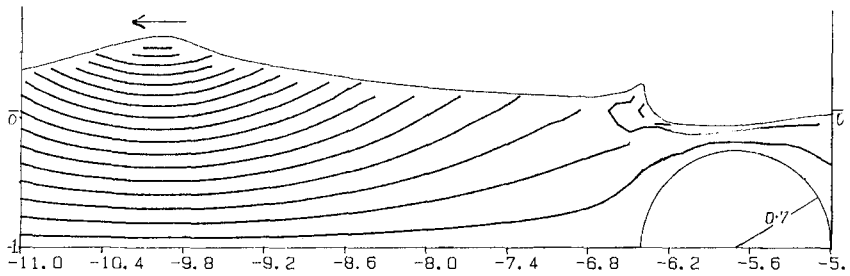


Figure 6: The backwards breaker for $H = 0.46$ and $R = 0.7$. The instantaneous streamlines are also shown. Natural scaling.

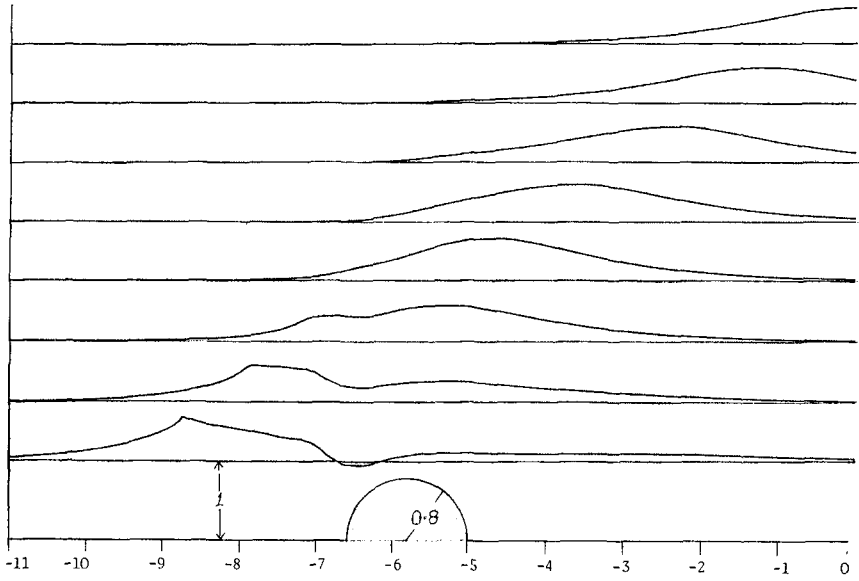


Figure 7: $H = 0.46$, $R = 0.8$. Wave breaks forward, downstream of cylinder. Times 0, 1, ..., 7.

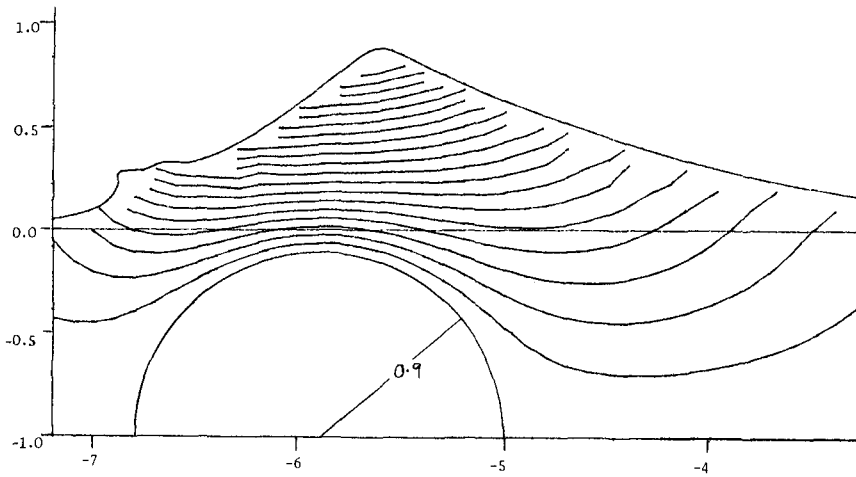


Figure 8: $H = 0.8$, $R = 0.9$. Instantaneous streamlines. Natural scaling.

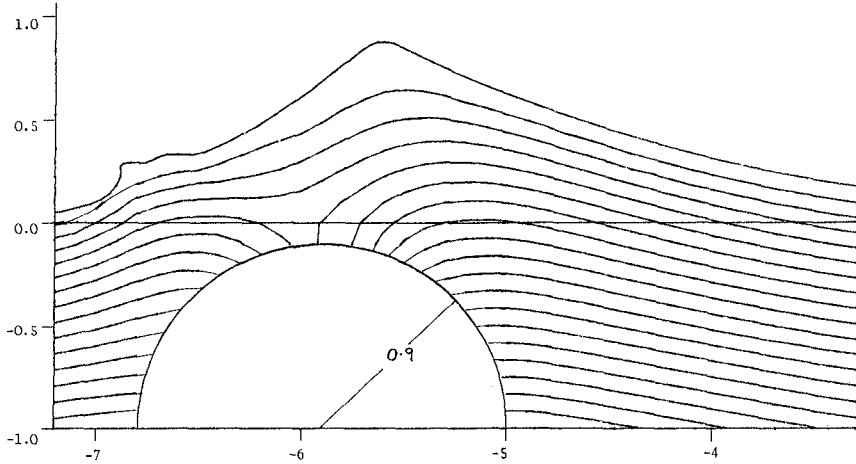


Figure 9: $H = 0.8$, $R = 0.9$. Pressure contours. Natural scaling.

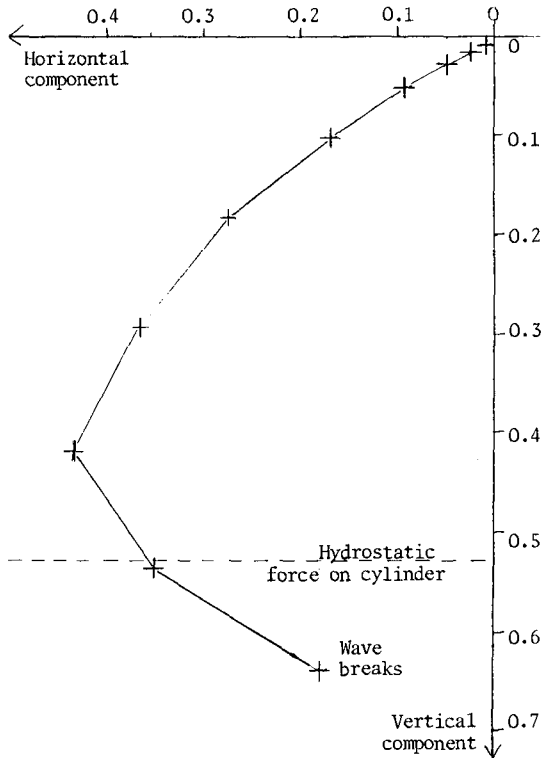


Figure 10: The dynamic force on a cylinder $H = 0.8$, $R = 0.9$. Times 0, 0.5, ..., 4.5.

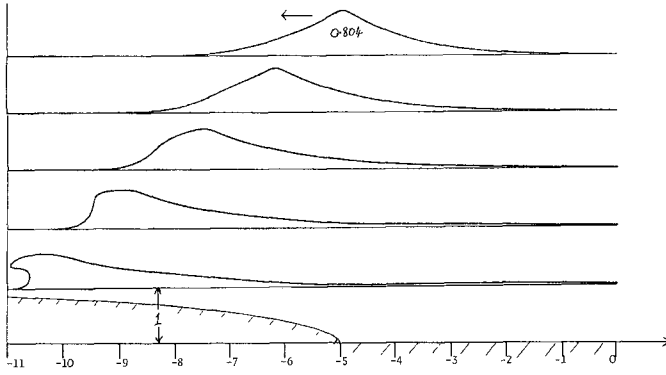


Figure 11: Wave breaking on an elliptical shoal where minimum depth is 0.1, $H = 0.8$. Times 4, 5, 6, 7, 8. Natural scaling.

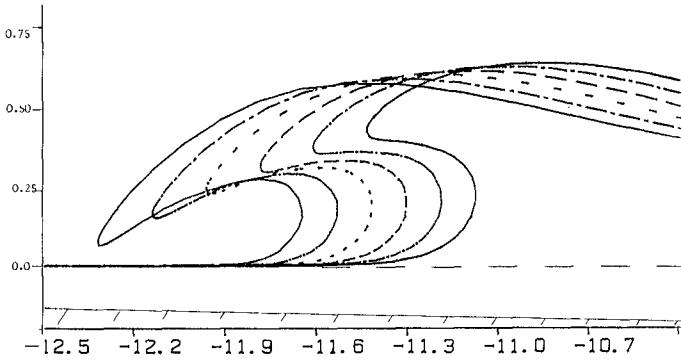


Figure 12: $H = 0.8$. Elliptical shoal. Times 8.0, 8.1, ..., 8.5. Natural scaling. Continuation of figure 11.

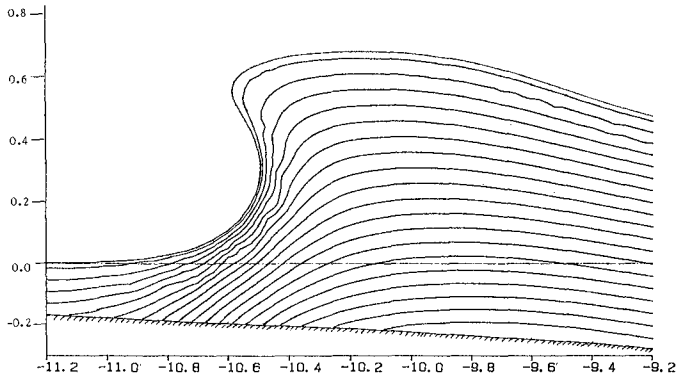


Figure 13: As figure 11. Pressure contours at time 7.5. Natural scaling.

CHAPTER 46

LABORATORY EXPERIMENTS ON THE INFLUENCE OF WIND ON NEARSHORE WAVE BREAKING

Scott L. Douglass, A.M. ASCE ¹

J. Richard Weggel, F. ASCE ²

ABSTRACT

The influence of wind on nearshore breaking waves was investigated in a laboratory wave tank. Breaker location, geometry, and type depended upon the wind acting on the wave as it broke. Onshore winds tended to cause waves to break earlier, in deeper water, and to spill; offshore winds tended to cause waves to break later, in shallower water, and to plunge. A change in wind direction from offshore to onshore increased the surf zone width by up to 100%. Wind's effect was greatest for waves which were near the transition between breaker types in the absence of wind. For onshore winds, it was observed that micro-scale breaking can initiate spilling breaking by providing a perturbation on the crest of the underlying wave as it shoals.

INTRODUCTION

The most common breaker types on the open ocean coast are spilling and plunging. Spilling breakers are characterized by white-water at the crest which tumbles down the wave face until the entire wave face is a wall of tumbling white water. Plunging breakers are characterized by an unbroken wave face which steepens until it is vertical and then continues to curl over to form a surfer's "tube" before it plunges down on the base of the

(1) Sen. Proj. Engr., Pare Engr. Corp., 8 Blackstone Valley Pl., Lincoln, RI, 02865, USA; formerly Grad. Stud., Drexel Univ.

(2) Professor, Civil & Arch. Engr. Dept., Drexel Univ., 32nd & Chesnut Sts., Philadelphia, PA, 19104, USA

wave face. Collapsing and surging waves, the other two breaker types, are more common on coastal structures and relatively steep beaches. These descriptive breaker types are subjective and the transition from one type to another is not always distinct.

It is well known that wave forces on structures can be extremely sensitive to breaker type. Plunging breakers can cause extremely high, short duration forces when a pocket of air is trapped between the wave face and the structure. It is also known that currents and sediment transport in the surf zone depend on breaker type and surf zone width. Breaker type has an effect on the wave height decay, energy decay, and turbulence across the surf zone, important factors in modeling surf zone dynamics.

Existing models of breaker type (Patrick & Wiegel, 1955; Galvin, 1968; Battjes, 1974) consider two independent dimensionless variables, the wave steepness and the beach slope. Battjes combines these variables in the surf similarity parameter and shows that nearshore breaker type and mechanics can be determined by ranges of the parameter.

There is little mention in the literature of the influence of wind on nearshore breaking waves. Three authors mention the effect in passing without agreement as to its importance. Walker (1974) states that offshore winds tend to cause breakers to plunge and that the optimum wind for surfing (surfers prefer plunging breakers) is a ten knot offshore wind. Walker reached this conclusion on the basis of his observations and a survey of recreational surfers. Kinsman (1965) mentions that an offshore wind is "conducive to the formation of plunging breakers," and that onshore winds contribute to producing spilling breakers. Kinsman goes on in jest that an offshore wind is a reason for graduate students at the University of Hawaii to cut class and go surfing. Peregrine (1983) states that wind effects on wave breaking are probably slight for moderate wind speeds. Neither Kinsman nor Peregrine discuss a basis for their statements.

Although the influence of wind on wave breaking has not been investigated and has rarely even been mentioned in the coastal engineering literature, it is well known by fishermen, surfers, lifeguards and others who spend much time in the surf. The first author has often observed an influence of wind on wave breaking along the southern New Jersey shore. The wind shift from a light land breeze to a sea breeze which occurs many summer days changes the breakers from plungers to spillers. A thunderstorm which quickly changes the wind direction from a sea breeze to a land breeze can dramatically change the breaker type from spilling to plunging within seconds.

This investigation was conducted to fill a gap in the knowledge about the effect of local wind on the nearshore, depth-limited breaking of individual waves. The primary objective was to qualitatively and quantitatively determine what effects winds have on breaking and to investigate the physical explanation of the phenomenon.

EXPERIMENTAL FACILITIES

Experiments on the influence of wind on shoaling breakers were conducted in the glass wave tank at Drexel University. The tank is 35 m long, 0.76 m deep and 0.91 m wide. The tank has glass walls and a glass bottom with aluminum supports spaced every 1.52 m along its length. At one end of the tank is a piston-type wave generator capable of generating monochromatic waves.

A plywood beach and splitter wall were installed beginning 17 m from the wave generator. The splitter wall was located midway across the breadth of the tank and divided the tank into two sections (see Figure 1). On one side of the splitter wall, a rigid 1:25 sloping plywood beach was constructed. On the other side of the splitter wall were the two-by-four bracing for the beach and a wave-absorbing pile of rubble at the far end from the wavemaker. All the seams between the splitter wall and beach and beach and glass walls were sealed.

A plywood cover roof was constructed over the beach section of the flume and a variable-speed, bi-directional fan was installed on the upper end of the beach above the level of wave runup. All the seams in the roof section were sealed with duct tape. This arrangement allowed wind to be blown offshore or drawn onshore over the beach section. A honeycomb was placed in the airflow one meter from the fan. A bell-shaped mouth piece was constructed at the open end of the covered beach section to allow smooth entry of the onshore wind.

EXPERIMENTAL PROCEDURES

Video recording was the primary method of measuring the location of the water surface in the shoaling and breaking waves. A thin, black 2 cm x 2 cm grid on clear plexiglass sheets was attached to the front glass sidewall. During video recording, the room was darkened and the water was lit from below the waterline with lights clipped on the outside of the glass sidewall. This

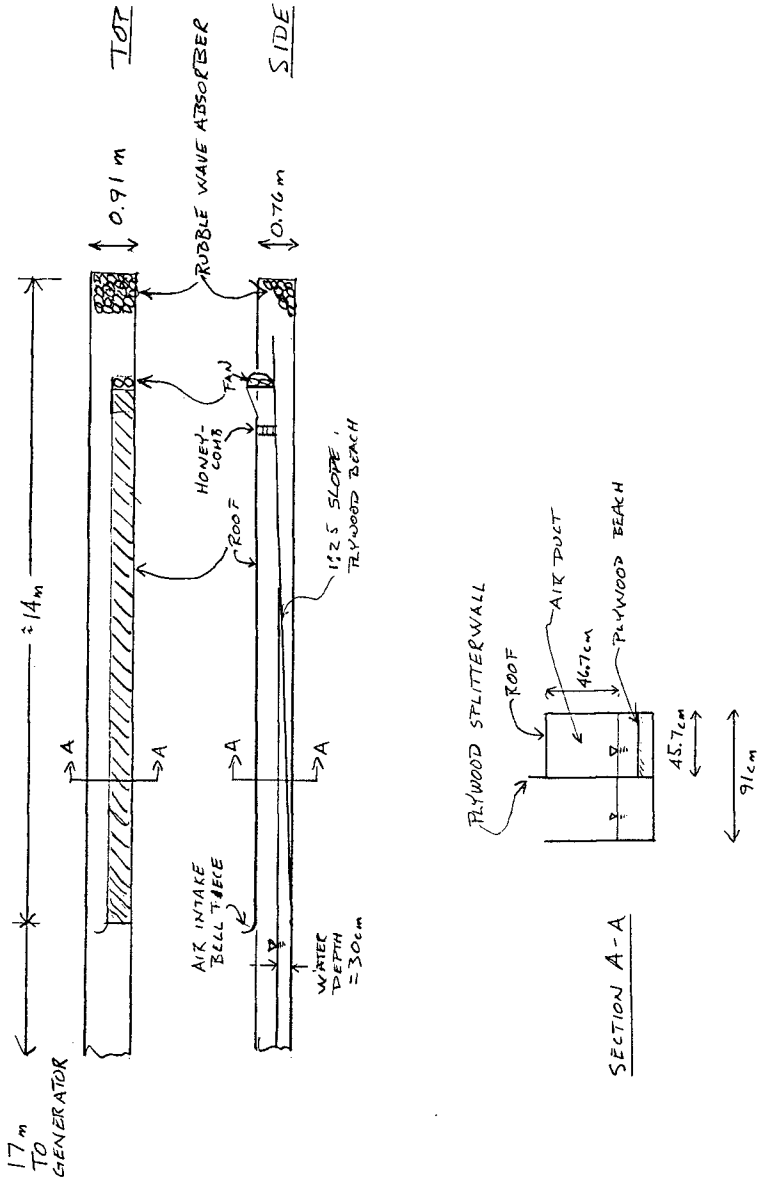


Figure 1. Wave tank schematic

avoided glare and reflection problems from the plexiglass and glass and allowed the water surface to be easily seen through the grid and against the white splitter wall. The recording was done with two goals in mind:

- 1) to measure the variation in water surface elevation in space at an instant in time (i.e. a snapshot of the water surface elevation),
- 2) to measure the variation of water surface elevation in time at a specific location along the beach (i.e. a wave gage).

The video tapes were viewed on a professional video editing system with stop-action, frame-by-frame advance, frame counting capability, and a high resolution video screen. Water surface elevation vs. time and elevation vs. distance information were manually viewed during data reduction.

Windspeeds were measured using a pitot tube and micro-manometer. The pitot tube was extended through the plywood cover roof down into the air duct above the beach section.

WAVE AND WIND CONDITIONS TESTED

The range of experimental conditions were selected to produce spilling breaker conditions and plunging breaker conditions when there was no wind. Three different wave conditions; designated S, I, and P; were selected. Wave "S" broke in a spilling manner in the absence of wind. Wave "I" (for Intermediate) was chosen to be as close to the limit between the two breaker types as possible. It was chosen by holding the piston stroke length constant and varying the motor speed until the breaker type switched. The stop action of the video showed that the breaker type varied across the wave tank. The front one-third of the wave (the third adjacent to the glass sidewall) was spilling but along the rest of the wave crest a small jet was visible. A slightly steeper wave spilled evenly across the entire beach and a slightly less steep wave plunged evenly across the entire beach. This cross-tank variation in breaker type was used as an indicator of the midpoint of the demarcation between breaker types. Wave "P" was of very low steepness and clearly plunged.

Wind direction was defined as follows: wind in the direction of wave propagation, i.e. a sea breeze, was called onshore wind; wind in the opposite direction of wave propagation, i.e. a land breeze, was called offshore

wind. The sign convention adopted was onshore winds positive and offshore winds negative.

Thirteen different sets of tests were run using the three wave conditions and the five wind conditions. The test conditions are summarized in Table 1. The low windspeeds were approximately of the same magnitude as the wave celerities. The high windspeeds were approximately twice the wave celerities. Wave steepnesses (H/L) and wave celerities are as calculated in the flat portion of the tank.

RESULTS

Breaker Type

Table 2 shows the changes in breaker type due to wind (S-spilling, P-plunging). Wind changed the breaker type for both waves "I" and "S". In the absence of wind, wave "I" was intermediate between spilling and plunging. With an onshore wind the breaker distinctly spilled. With an offshore wind the breaker distinctly plunged. Wave "S", which spilled in the absence of wind, plunged with an offshore wind. Wind did not effect the breaker type for wave "P" which was always plunging. Wind had little effect whatsoever on wave "P".

Breaker Location and Width of Surf Zone

The change in breaker location was one of the most visually obvious effects of wind on wave breaking. Breaking was defined as the moment the front face became vertical or started to entrain air. The change in surf zone width (defined as the horizontal distance from the breaker location to the intersection of the still water level and the beach) as a function of the ratio of wind velocity, U , to wave celerity, C , is shown in Figure 2. Acceleration due to gravity, g , and wave period, T , are used to non-dimensionalize the breaker depth, d . For wave "I", the surf zone width was 43% narrower with the high offshore wind than with no wind. The change in wind direction from high offshore to high onshore about doubled the surf zone width. For wave "S", the changes were not as large but were still significant. For wave "P", the change in breaker location was much smaller.

Breaker Height to Depth Ratio

The influence of wind on the breaker height to depth ratio is shown in Figure 3. Most of the influence of wind on breaker height to depth ratio is due to wind's effect on breaker depth (Figure 4). The effect of wind on

Table 1. Test Conditions

WIND CONDITION	TEST CONDITIONS		
	WAVE CONDITION		
	"S" H/L = 0.025 SPILLING	"I" 0.019 SPILLING/ PLUNGING	"P" 0.004 PLUNGING
HIGH ONSHORE	████	████	████
LOW ONSHORE	████	████	
NO WIND	████	████	████
LOW OFFSHORE	████	████	
HIGH OFFSHORE	████	████	████

Table 2. Change in breaker type due to wind.

INFLUENCE OF WIND ON BREAKER TYPE

WIND CONDITION	WAVE CONDITION		
	"S"	"I"	"P"
HIGH ONSHORE	S	S	P
LOW ONSHORE	S	S	-
NO WIND	S	S/P	P
LOW OFFSHORE	P	P	-
HIGH OFFSHORE	P	P	P

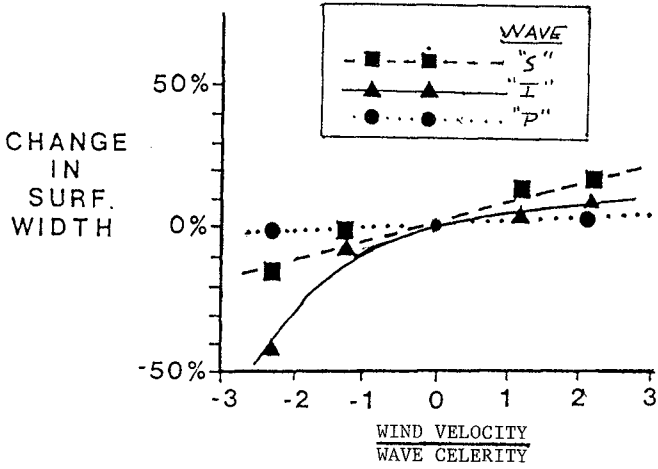


Figure 2. Effect of wind on surf zone width.

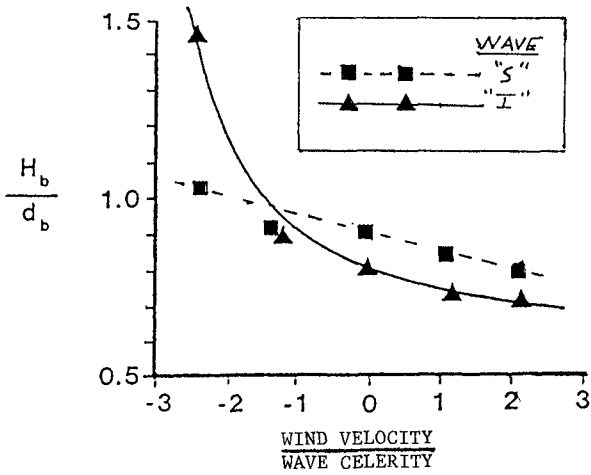


Figure 3. Effect of wind on breaker height to depth ratio.

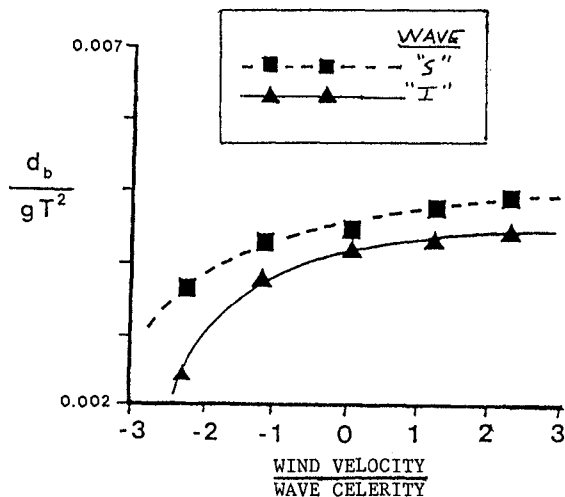


Figure 4. Effect of wind on breaker depth.

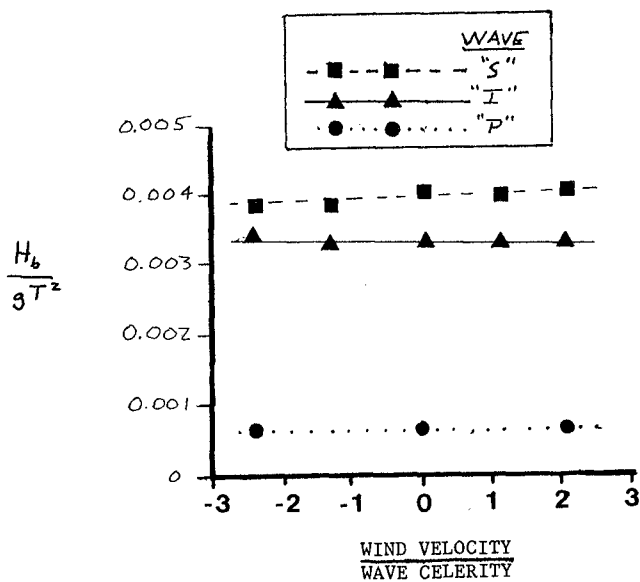


Figure 5. Effect of wind on breaker height.

breaker height (Figure 5) is only 5 to 10%. Height was defined as crest to trough height at the point of breaking. Depth was defined as the vertical distance from the still water level to the bottom. Set-down and wind's effect on set-down were found to be smaller than the experimental error introduced by the resolution of the video procedure.

The above results show that wind's influence on breaking was greatest for waves which were near the transition between breaker types in the absence of wind, waves "1" and "S". Wave "P" had such a low steepness it was closer to the transition to collapsing/surging than to the transition to spilling. It was barely effected by the wind.

DISCUSSION

The recent numerical studies of breaking waves using potential flow theories (see New, et al., 1985) supplemented by observations (Basco, 1985) have led to the concept that both plunging and spilling breaking are due to the same hydrodynamic instability. The difference between spilling and plunging waves is the size of the jet. This study does not contradict this concept but shows that the approach to such breaking may be physically unstable to perturbations such as wind shear.

The video recordings of the onshore wind tests for waves "S" and "1" showed that the spilling breakers were initiated by a micro-scale breaking wave. Micro-scale breaking waves occur on the crests of the underlying longer waves due to the shearing effect of the wind (Phillips, 1977). Most of these micro-scale breakers are short-lived but as the primary underlying wave shoals, eventually one of the micro-scale breakers is the instability which triggers spilling of the primary wave. Thus, it appears that the wind effect is enough to trigger the initiation of breaking for waves which are approaching but not yet at the point of breaking in the absence of wind. Spilling breaking occurred farther offshore as the onshore wind speed was increased.

The mechanisms responsible for the influence of an offshore wind on breaking waves appear to be a reduction in shoaling combined with surface wind drag and perhaps wind pressure differences. Wind drag prevents small instabilities from tumbling forward down the wave face. Once a jet begins to form, the shear layer is probably of little importance since it is thin compared with the thickness of the jet. By that point, the water surface is vertical on the front face and the distribution of

pressure due to the wind can play a more significant role. It was found that the offshore wind effectively retarded the last stages of wave shoaling. This explains the waves propagating farther inshore before breaking. The reduced wave height at a specific location on the beach may be due to interactions between the offshore-propagating, wind-driven ripples and the primary wave. The reduced wave height implies a lower steepness which would tend toward a plunging breaker for a fixed beach slope.

SUMMARY

Laboratory studies show that breaker location, type, and geometry depend critically upon the wind acting on the wave as it breaks. Onshore winds tend to cause waves to break earlier, in deeper water, and to spill. Offshore winds tend to cause waves to break later, in shallower water and to plunge.

REFERENCES

- Basco, D.R., "A Qualitative Description of Wave Breaking," *Journal of Waterway, Port, Coastal and Ocean Engineering*, American Society of Civil Engineers, vol. 111, no. 2, pp. 171-188, March, 1985.
- Battjes, J.A., "A Computation of Set-Up, Longshore Currents, Run-Up and Overtopping Due to Wind-Generated Waves," Ph.D. Dissertation, Delft University of Technology, The Netherlands, July, 1974.
- Galvin, C.J. Jr., "Breaker Type Classification on Three Laboratory Beaches," *Journal of Geophysical Research*, vol. 73, no. 12, pp. 3651-3659, June 15, 1968.
- Kinsman, B., Wind Waves: Their Generation and Propagation on the Ocean Surface, Prentice-Hall, Englewood Cliffs, N.J., 1965.
- New, A.L., McIver, P. and Peregrine, D.H., "Computation of Overtopping Waves," *Journal of Fluid Mechanics*, vol. 150, pp. 233-251, 1985.
- Patrick, D.A., and Wiegel, R.L., "Amphibian Tractors in the Surf," *Proceedings of the First Conference on Ships and Waves*, Council in Wave Research and Society of Naval Architects and Marine Engineers, 1955. (see Wiegel, Oceanographical Engineering, 1964)

Peregrine, D.H., "Breaking Waves on Beaches," Annual Review of Fluid Mechanics, vol. 15, pp. 149-78, 1983.

Phillips, O.M., The Dynamics of the Upper Ocean, Cambridge University Press, Cambridge, Great Britian, 2nd. edition, 1977.

Walker, J.R., "Recreational Surf Parameters," Look Laboratory, University of Hawaii, Technical Report No. 30, February, 1974.

CHAPTER 47

WAVE RUN-UP PREDICTION VS. MODEL TEST RESULTS: A COMPARISON

PETER E. GADD¹
VICTOR MANIKIAN²
JERRY L. MACHEMEHL³

ABSTRACT

Large-scale physical model test measurements of wave run-up are compared with wave run-up prediction derived from the Shore Protection Manual (SPM). Noteworthy discrepancies between the results of these two methods have been identified that include substantial overestimation of wave run-up elevations using the SPM approach, and computation of roughness coefficient values that vary as a function of wave steepness. The slope armors tested in the study at model scales of 1:3 and 1:4 include linked concrete matting and overlapped gravel-filled fabric bags.

INTRODUCTION

Accurate prediction of wave run-up elevation is an important element in the design of coastal and offshore structures. Should the design process result in a run-up elevation prediction that is too low, serious flooding of the structure work surface may result. Conversely, if the predicted wave run-up is too high, the cost of the structure will be unnecessarily expensive due to the implementation of fill quantities and slope armor that are not truly required. The methods available to predict wave run-up on a particular structure include empirical techniques, such as those set forth in the Shore Protection Manual (U.S. Army Corps of Engineers, 1984), and the performance of a physical model to simulate wave run-up for the structure and oceanographic conditions under study.

-
1. Principal, Coastal Frontiers Corporation, Altadena, California, U.S.A.
 2. Staff Civil Engineer, Arco Alaska, Inc., Anchorage, Alaska, U.S.A.
 3. Professor, Texas A & M University, College Station, Texas, U.S.A.

In recent years, we have collected large-scale physical model data of breaking wave run-up. This data can be used to determine the accuracy with which empirical prediction techniques match results from the large-scale modelling efforts.

The objective of this presentation is two-fold:

1) To provide a direct comparison of large-scale physical model study results of wave run-up to estimated values generated from conventional wave run-up prediction techniques as presented in the Shore Protection Manual.

2) To provide large-scale wave run-up values for two relatively obscure shore protection armors--large overlapped gravel-filled bags and linked concrete block matting. These armor types have proven to be useful in providing protection against moderate wave impact at project sites where more substantial materials (quarystone, large concrete units) are unavailable and/or uneconomical.

LARGE-SCALE WAVE RUN-UP DATA

Figure 1 provides a definition sketch for the wave run-up process. A wave exhibiting an unrefracted deepwater wave height and wavelength (H_0' and L_0) and period (T), impacts a slope having an inclination angle (θ) in a still water depth (d_s). The height of wave run-up (R) on the slope of the structure is measured as a vertical elevation above the still water line (SWL).

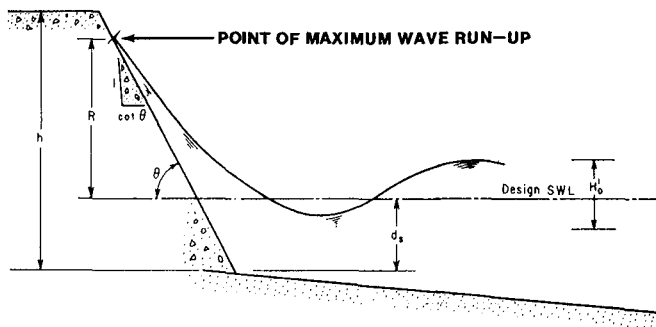


FIGURE 1: WAVE RUN-UP DEFINITION SKETCH

The model tests summarized herein were performed at the Oregon State Wave Research Facility, Corvallis, Oregon, U.S.A., in February-March, 1984. The wave tank is 104 m (340 ft) in length, 3.7 m (12 ft) wide, and the water depth was varied to accurately simulate the 2.5 - 5.2 m (8 - 17 ft) water depth range that was expected to exist at the prototype location. The size of the wave

tank allowed the model tests to be conducted at scales of 1:3 and 1:4. Wave heights under study ranged from prototype values of 1.5 - 3.0 m (5 - 10 ft). While both monochromatic and irregular wave trains were studied during the course of the model test program, only the results of the monochromatic breaking wave tests are reported herein. The range of values of the Surf Similarity Parameter ($= \tan\theta (H/L_0)^{-1/2}$) exhibited by the waves in this study was 1.1 - 3.5, corresponding primarily to plunging and collapsing breakers.

Wave height in the model test was measured using an acoustic water level profiler secured above the wave tank. A graduated tape was firmly affixed to the slope allowing the investigator to carefully observe the position of the still water level prior to testing, and the elevation of wave run-up. Conventional surveying of the slope allowed a correlation to be developed between each value noted from the graduated tape and the corresponding elevation relative to the still water level.

Slope armors that were tested in the model study included linked concrete matting of two different types, and large gravel-filled fabric bags (prototype bag weight = 6,000 kg (13,200 pounds)). These armor types have been extensively used in the Alaskan Arctic offshore, the site of the structure under consideration (Gadd, 1988; Leidersdorf, 1988). In addition, gravel bags and concrete matting have been studied and utilized in moderate wave climates in more temperate areas of the world (Breteler, *et al.*, 1988; Heerten, *et al.*, 1988; for example), where more durable armor types are unavailable, too costly, or inappropriate due to the temporary nature of the slope protection required.

The concrete mat exhibits a very smooth slope surface, interrupted only by the regular voids at the spaces between adjacent blocks. The gravel bag slopes exhibit a substantial bag overlap of 50% of the bag length. The resulting slope is "stair-stepped", a cross-section that is effective in dissipating wave run-up. Both armors studied were placed on permeable filter fabric overlying a smooth gravel slope inclined at an angle of 1V:3H (18.4° from horizontal).

CONVENTIONAL WAVE RUN-UP PREDICTION

In the absence of physical model study data collected for a particular structure and ocean environment, the coastal engineer must rely on predictive techniques developed for more generalized structures and oceanographic conditions. While numerous methods exist world-wide for this engineering task, perhaps the most popular means in the United States is the use of the wave run-up diagrams presented in the Shore Protection Manual (SPM). The basis for the methods presented in the

SPM are the numerous model tests of wave run-up undertaken by the U.S. Beach Erosion Board in the 1950's. These studies dealt only with the idealized conditions of monochromatic waves impacting structures in which the slopes were planar, smooth, and impermeable. The majority of these model tests can be considered to have been performed at "small scale" (typically, model scales of 1:17 or 1:30 were employed) (Saville, 1987).

Wave run-up prediction taken from the SPM curves requires computation of the wave steepness parameter, H_o'/gT^2 . The value of the wave run-up elevation, R , for a particular structure slope angle and wave steepness parameter is given in the SPM for relative depth values, d_s/H_o' , of 0.0, 0.45, 0.8, 2.0, and ≥ 3.0 . The family of curves given for a relative depth ≥ 3.0 is shown in Figure 2. As dictated by the SPM, wave run-up values taken from these curves require modification to account for scale effect and slope roughness and permeability prior to establishing the predicted run-up value.

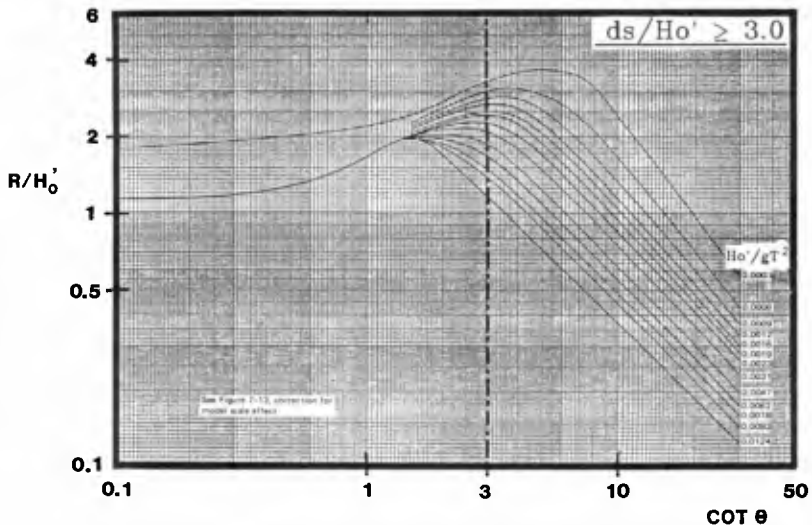


FIGURE 2: EXAMPLE OF SPM RUN-UP CURVES

The scale effect correction prescribed for use in the SPM is presented in Figure 3. This relationship that indicates an increasing scale effect with increasing structure slope was developed using limited test data collected at three values of structure slope: 1:3, 1:6, and 1:15. A description of the large-scale testing and the rationale supporting the selection of this scale effect correction has been recently presented by Saville (1987).

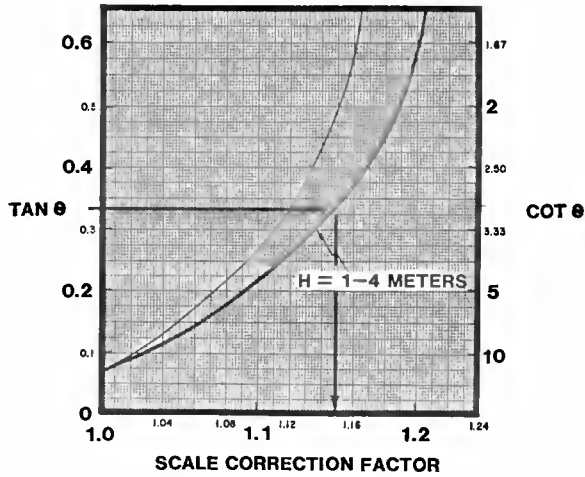


FIGURE 3: SPM RUN-UP CORRECTION FOR SCALE EFFECTS

The wave run-up reduction from the SPM curves necessitated by slope roughness and permeability is expressed by the "roughness coefficient", r . Based on research by Battjes (1974), the SPM specifies an individual value of " r " for a variety of armor types, as indicated in Table 1. As is evident, the maximum value of run-up coefficient for a permeable slope is 0.9, given for concrete blocks. For highly permeable quarystone slope armor, the SPM suggests that the roughness coefficient can be as low as 0.45. While no value is given in the SPM for gravel bag armor, we presume that the value given for rounded quarystone ($r = 0.60 - 0.65$) is most appropriate for use in the comparison presented herein.

TABLE 1: ROUGHNESS COEFFICIENTS FOR VARIOUS ARMORS

Slope Surface Characteristics	Placement	r
Smooth, impermeable	-----	1.00
Concrete blocks	Fitted	0.90
Basalt blocks	Fitted	0.85 to 0.90
Gobi blocks	Fitted	0.85 to 0.90
Grass	-----	0.85 to 0.90
One layer of quarystone (impermeable foundation)	Random	0.80
Quarystone	Fitted	0.75 to 0.80
Rounded quarystone	Random	0.60 to 0.65
Three layers of quarystone (impermeable foundation)	Random	0.60 to 0.65
Quarystone	Random	0.50 to 0.55
Concrete armor units (~ 50 percent void ratio)	Random	0.45 to 0.50

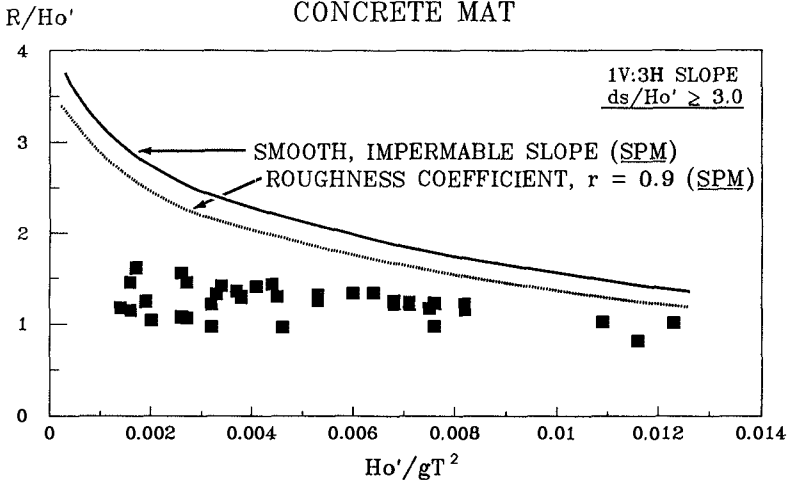
COMPARISON OF RESULTS

A number of figures have been prepared to illustrate the comparison between the predicted run-up values as determined by the SPM techniques and the actual data measured in the physical model study performed at scales of 1:3 and 1:4. As is the case in the SPM, the relative run-up (R/H_o') is plotted against the wave steepness parameter, H_o'/gT^2 . All of the data collected represents the single side slope value of 1V:3H (18.4° from horizontal).

Concrete Mat Armor

Figure 4 shows the wave run-up diagram for linked concrete mat armor and a relative depth, d_s/H_o' , greater than or equal to 3.0. The solid curve indicates the smooth slope SPM prediction with the scale effect correction applied. A constant roughness coefficient, $r = 0.9$, is applied to the smooth slope curve to yield the dotted curve which represents the SPM run-up prediction for concrete mat armor. As is evident, the measured data lies below the predicted curve. As the wave steepness parameter, H_o'/gT^2 , decreases, the discrepancy increases between the SPM prediction and the measured data. Indeed, for small values of wave steepness parameter, the SPM technique overpredicts the wave run-up elevation by nearly 100% relative to the model test data.

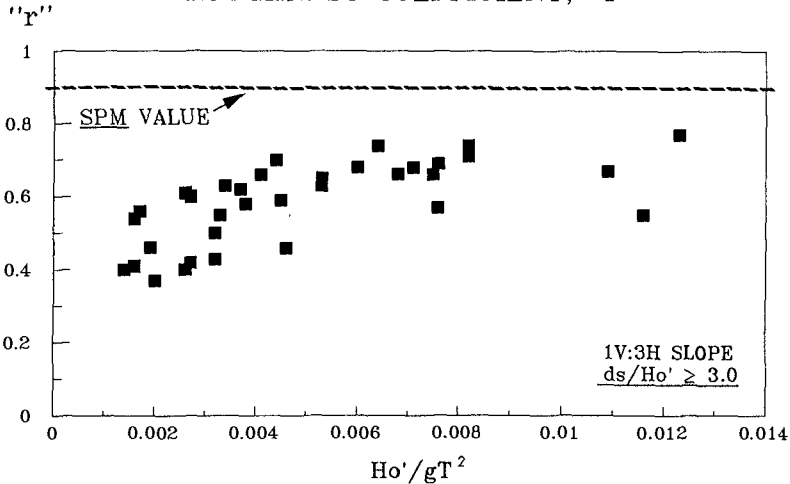
FIGURE 4:
WAVE RUN-UP
CONCRETE MAT



A determination of the measured roughness coefficient, r , for each data point has been plotted as a function of wave steepness parameter in Figure 5. While the SPM methods suggest a constant "r" value of 0.9 for

the concrete mat, the data indicates that the value of "r" varies from 0.4 to 0.8 over the range of wave steepness that was tested. While scatter does exist in the data, it seems clear that the SPM overpredicts wave run-up relative to the data measured, and the roughness coefficient, "r", increases with increasing wave steepness.

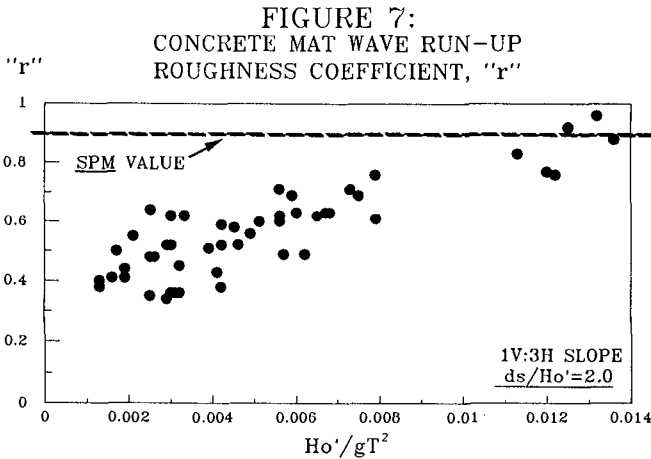
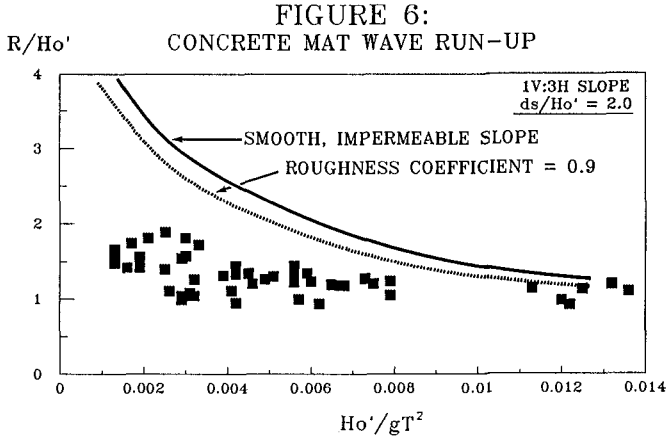
FIGURE 5:
CONCRETE MAT
ROUGHNESS COEFFICIENT, "r"



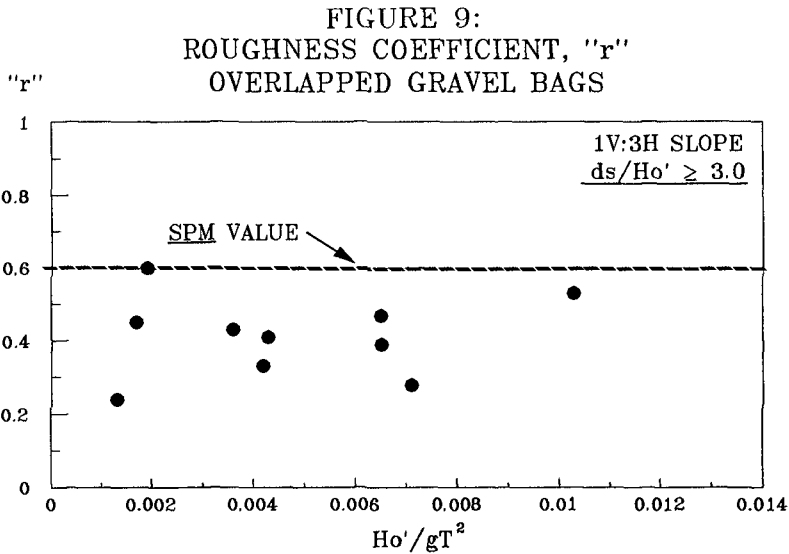
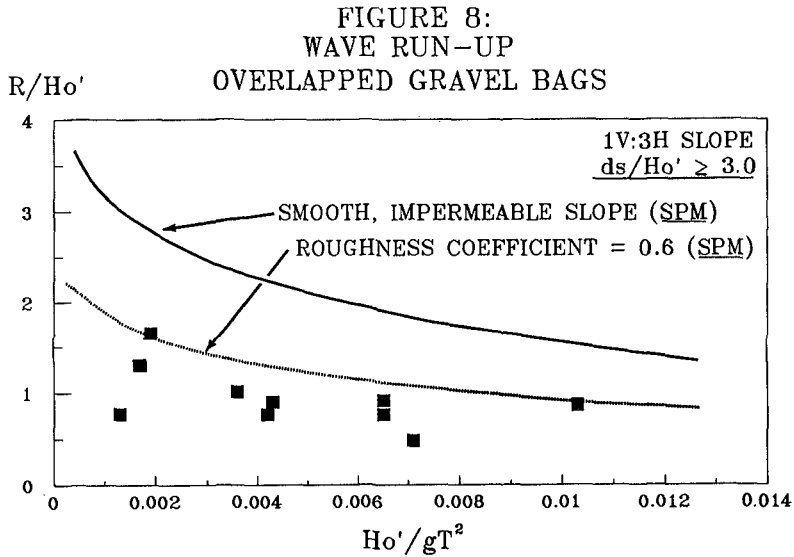
Figures 6 and 7 are presented to show wave run-up and roughness coefficient characteristics for the concrete mat armor for relative depths, d_s/H_o' , of approximately 2.0. While both the predicted wave run-up and the measured data are marginally larger for this case, a similar trend is indicated as that noted previously for the value of relative depth, d_s/H_o' , ≥ 3.0 . In this case, the value of the roughness coefficient, r, suggested by the SPM ($r = 0.9$) fits the data for values of the wave steepness parameter, H_o'/gT^2 , that exceed 0.011. Below this value, however, "r" decreases to as low as about 0.4.

Overlapped Gravel Bags

For gravel bag armor, similar trends exist as those noted previously for concrete mat armor. To predict wave run-up using the SPM approach, we have selected a roughness coefficient value of 0.60 from the SPM to typify the gravel bag slope. Due to the irregular nature of the gravel bag armor, a greater degree of data scatter is indicated than that seen previously for the concrete



mat. In Figure 8, for the relative depth value, $d_s/H_o' \geq 3.0$, most of the data falls below the SPM prediction, although the trend of the data appears to suggest that the SPM methods represent an upper bound for the model test results. Figure 9 indicates that the roughness coefficient value for this case appears to be less dependent on wave steepness with a constant value of 0.45 being applicable. Should a greater degree of conservatism be desired, a value of "r" of 0.60 is a reasonable choice.



As shown in Figure 10, in which the relative depth value is approximately 2.0, the gravel bag slope again indicates overprediction of wave run-up using the SPM methods, however, the functional dependence on wave steepness is not clearly defined. A constant value of "r" of 0.50 seems to be applicable to gravel bag slopes for this relative depth value, as shown in Figure 11.

FIGURE 10:
WAVE RUN-UP
OVERLAPPED GRAVEL BAGS

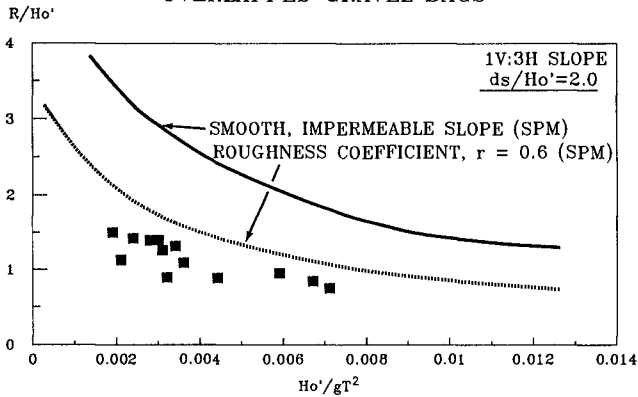
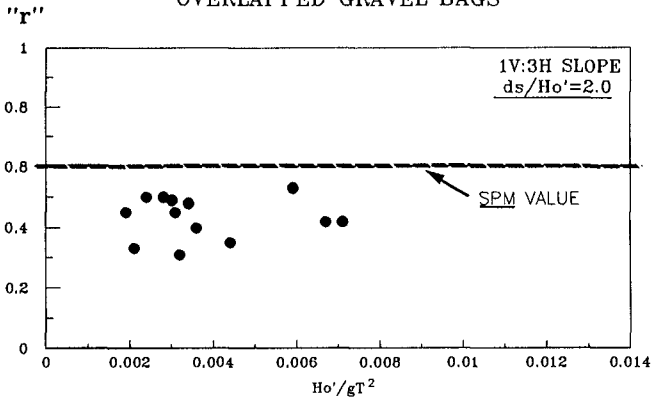


FIGURE 11:
ROUGHNESS COEFFICIENT, "r"
OVERLAPPED GRAVEL BAGS



CONCLUSIONS

For two specific slope armor types, overlapped gravel bags and linked concrete matting, comparison of measured data from large-scale physical model studies with wave run-up prediction methods presented in the SPM suggests the following:

- 1) The SPM predictive methods overpredict wave run-up. Particularly in the case of concrete mat slope protection, the degree of discrepancy between the results of the SPM methods and the measured data appears to be dependent on the wave steepness. For small values of the wave steepness parameter, H_o'/gT^2 , the measured data is on the order of one-half of the predicted value.

- 2) For concrete mat armor, a variable roughness coefficient, "r", is indicated. The value of "r" varies from about 0.4 for $H_o'/gT^2 = 0.002$, to 0.9 for $H_o'/gT^2 = 0.13$.
- 3) Because no value of roughness coefficient for overlapped gravel bags is given in the SPM, it is not possible to precisely judge the predictive accuracy of the SPM for this armor type. Use of an "r" value of 0.6 (suggested by the SPM for rounded quarystone) slightly overpredicts wave run-up for gravel bag armor. The discrepancy between the predicted and measured run-up values is not as great as that noted for concrete mat armor. Unlike the results of the concrete mat research, the roughness coefficient for gravel bags does not appear to be strongly dependent on wave steepness. Selection of a constant roughness coefficient of 0.5 - 0.6 for overlapped gravel bag armor seems appropriate over the range of our experimental data.

REFERENCES

- Battjes, J.A., 1974, "Wave Run-up and Overtopping", Technical Advisory Committee on Protection Against Inundation, Rijkswaterstaat, The Hague, Netherlands.
- Breteler, M.K., A.M. Burger, L. Banach, and A. Bezuijen, 1988, "Analytical Design Method for Block Revetments", 21st International Coastal Engineering Conference, Abstracts Book, p. 159-160.
- Gadd, P.E., 1988, "Sand Bag Slope Protection: Design, Construction, and Performance", in Arctic Coastal Processes and Slope Protection Design, A Monograph by the American Society of Civil Engineers, A.T. Chen and C.B. Leidersdorf, Eds., p. 145-165.
- Heerten, G., S. Kohlase, F. Saathoff, L.A. Jackson, and S.A. Cant, 1988, "Geotextiles in Coast Protection: Examples of Project-Oriented Solutions", 21st International Coastal Engineering Conference, Abstracts Book, p. 349-350.
- Leidersdorf, C.B., 1988, "Concrete Mat Slope Protection for Arctic Applications", in Arctic Coastal Processes and Slope Protection Design, A Monograph by the American Society of Civil Engineers, A.T. Chen and C.B. Leidersdorf, Eds., p. 166-189.
- Saville, T., Jr., 1987, "Early Large-Scale Experiments on Wave Run-up", Shore and Beach, Journal of the American Shore and Beach Preservation Association, Volume 55, Nos. 3-4, p. 101-108.
- U.S. Army Corps of Engineers, 1984, Shore Protection Manual, 2 Volumes, Coastal Engineering Research Center.

CHAPTER 48

STATISTICAL PROPERTIES OF THE MAXIMUM RUN OF IRREGULAR SEA WAVES

by Akira Kimura

ABSTRACT

The probability distribution of the maximum run of irregular wave height is introduced theoretically. Probability distributions for the 2nd maximum, 3rd maximum and further maximum runs are also introduced. Their statistical properties, including the means and their confidence regions, are applied to the verification of experiments with irregular waves in the realization of a "severe sea state" in the test.

1. INTRODUCTION

The importance of bringing the statistical nature of irregular sea waves into the design concepts of coastal structures has been widely recognized. Hydraulic tests with irregular waves in a wave tank have become one of the standard techniques to investigate dynamic properties of coastal and ocean structures. Simulation and generation techniques of irregular sea waves have been developed and applied for this purpose.

The group nature of irregular sea waves, on the other hand, has been clarified recently. Since there is a correlation between consecutive wave heights (and period), high waves (or low waves) tend to arrive in groups. This means that high waves tend to arrive intermittently in groups and that there are long durations between them, in which low waves consecutively arrive. Irregular wave simulation techniques are mainly directed to simulate the averaged properties of irregular sea waves, i.e. wave spectrum, probability distribution for wave height and period, etc. A long term steady state for these properties is designed to be simulated in the techniques except for the simulation of definite wave profiles. However, those properties measured in a short duration are not always guaranteed to be the same as the designed ones but rather distribute around them statistically. Therefore, hydraulic tests which are carried out in durations in which no high wave run arrives may bring about an under-estimation of wave effects. Insufficient estimation from the test, especially under-estimation, may induce deficiencies in the design for prototype structures. Model tests always have a possibility of missing the temporal "severe sea state" if the test is not sufficiently long. However, there have, in fact, been no established criterion used in

Associate Prof. Tottori Univ., Koyama Minami 4-101, Tottori, Japan

the verification of test results regarding whether the severe sea state is realized during the test. In addition to ordinary criteria, then, a new criterion which can be a measure for the temporal state of irregular sea waves becomes necessary and the property of the high wave group, especially its maximum value, may be suitable for this. This study aims at clarifying the statistical properties of the maximum run of high waves which may be a good measure for the temporal "severe sea state". The statistical properties of the 2nd maximum, 3rd maximum, and further maximum runs of high waves are also clarified and confidence regions for their means are given and explained in the examination of the effectiveness of the model test in this study.

2. PROBABILITY DISTRIBUTION OF THE MAXIMUM RUN OF HIGH WAVES

The author has introduced the probability distribution of the maximum run of high waves to apply for "short term overtopping" (Kimura, 1984). It can be summarized as follows:

Assuming the time series of wave height to be the Markov chain, the probability distribution of a run of waves which exceed the threshold wave height (h_t) consecutively is given as (Kimura, 1980)

$$P_1(\ell) = p^{\ell-1}(1-p) \quad (1)$$

in which p is given by

$$p = \frac{\int_{h_t}^{\infty} \int_{h_t}^{\infty} P_0(h_1, h_2) dh_1 dh_2}{\int_{h_t}^{\infty} Q_0(h_1) dh_1} \quad (2)$$

P_0 is the two dimensional Rayleigh distribution while Q_0 is the Rayleigh distribution. These are given as follows (wave height is normalized by the mean wave height throughout this study):

$$P_0(h_1, h_2) = h_1 h_2 / A \cdot I_0(h_1 h_2 \rho / A) \exp\{-(h_1^2 + h_2^2) / \pi A\} \quad (3)$$

$$Q_0(h_1) = \pi h_1 / 2 \exp(-\pi h_1^2 / 4) \quad (4)$$

$$A = 4 / \pi^2 - \rho^2 \quad (5)$$

in which I_0 is the modified Bessel function of the 1st kind, and ρ is a correlation parameter between consecutive wave heights. This has the following relation with a correlation coefficient of consecutive wave heights.

$$\gamma_h = \{E(\pi \rho / 2) - (1/2)(1 - \pi^2 \rho^2 / 4)K(\pi \rho / 2) - \pi / 4\} / (1 - \pi / 4) \quad (6)$$

K and E are the complete elliptic integrals of the 1st and 2nd kinds, respectively.

The probability distribution of the maximum run in a population of high wave runs of size N is introduced as follows:

The probability that the run is equal to or smaller than $\ell - 1$ is given

as

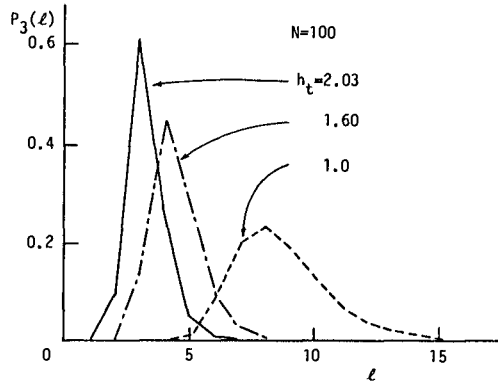
$$P_2(\ell) = \sum_{\ell'=1}^{\ell-1} p^{\ell'-1} (1-p) = (1-p)^{\ell-1} \quad (7)$$

Therefore, all runs in the population are equal to or smaller than $\ell - 1$ giving $(1-p)^{\ell-1} N$, assuming all runs to be independent. On the other hand, the probability that at least one or more runs in the population are equal to or greater than ℓ is given as $1 - (1-p)^{\ell-1} N$. In the same way, the probability that at least one or more runs are equal to or greater than $\ell + 1$ is given as $1 - (1-p)^{\ell} N$. The probability that the maximum run becomes ℓ is, therefore, given as

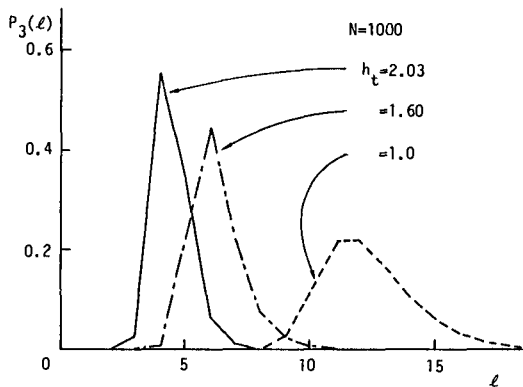
$$P_3(\ell) = (1-p)^{\ell} N - (1-p)^{\ell-1} N = \exp\{N \cdot \ln(1-p)^{\ell}\} - \exp\{N \cdot \ln(1-p)^{\ell-1}\} \quad (8)$$

in which \ln is the natural logarithm.

Equation (8) is shown in Fig.1; (a) $N=100$ and (b) $N=1,000$. The 1/10 maximum wave (solid line), the significant wave (chain line) and the mean wave (broken line) heights are used for h_t respectively.



(a) $N=100$



(b) $N=1000$

Fig.1 Probability distribution of the maximum run of high waves

Example 1 (duration and number of runs)

Giving a duration and wave properties, the probability distribution of the maximum run of high wave is given as follows:

An expected number of high wave runs N within a duration D is given by

$$N = D / \ell_t T_m \quad (9)$$

in which ℓ_t is a mean of the total run (recurrence interval of the runs) of high waves and T_m is a mean wave period. We assume here a steady sea state, its spectrum to be the Pierson-Moskowitz type (for simplicity this spectrum is used throughout this study; the spectrum gives affect on the correlation parameter ρ in eq.3, Battjes and van Vledder,1984), $h_t=1.6$ (significant wave height) and $T_m=10s$. The averaged value of the total run is given by (Kimura,1980),

$$\ell_t = 1/(1-p') + 1/(1-p) \quad (10)$$

in which p is given by eq.(2) and p' is given by

$$p' = \frac{\int_0^{h_t} \int_0^{h_t} P_0(h_1, h_2) dh_1 dh_2}{\int_0^{h_t} Q_0(h_1) dh_1} \quad (11)$$

Substituting $\rho=0.247$ (Pierson-Moskowitz spectrum; Kimura,1980) and $h_t=1.6$, we obtain $\ell_t=10.2$. The expected number of high wave runs is calculated as

$$N = D / 10.2 \times 10 \quad (12)$$

If we use 1 week for the duration ($D=604800s$) we obtain $N=5929$. Substituting values of p and N into eq.(8), we obtain the probability distribution of the maximum run of wave height ($h >$ significant wave height) which appears once a week. The relations between h_t and ℓ_t for the representative wave heights are listed in Table-1.

Table-1 h_t and ℓ_t

h_t	ℓ_t
1.0 (H_{mean})	4.7
1.60 ($H_{1/3}$)	10.2
2.03 ($H_{1/10}$)	30.1

3. MEAN OF THE MAXIMUM RUN OF HIGH WAVES

From eq.(8), the mean of the maximum run is introduced as

$$\sum_{i=1}^N N^C_i \frac{(-1)^{i+1}}{1-p^i} \quad (13)$$

Since this equation is difficult to carry out in practice when N and i are large, the following approximation is applied (Longuet-Higgins,

1952).

Applying ℓ_0 , which is given by the equation $N \cdot p^{\ell_0} = 1$, $(1-p^\ell)^N$ in eq.(8) is written as

$$(1-p^\ell)^N = (1-p^{\ell - \ell_0} / N)^N$$

Since $p < 1$, for large values of N the above equation reduces to

$$(1-p^{\ell - \ell_0} / N)^N \approx \exp(-p^{\ell'}) \tag{14}$$

in which $\ell' = \ell - \ell_0$

and $\ell_0 = -\ln(N) / \ln(p)$ (15)

The general form of eq.(14) is shown in Fig.2 (solid line). If N is sufficiently large, eq.(14) asymptotically approaches to

$$\exp(-p^{\ell'}) \approx \begin{cases} 0 & \ell' < \ell_*' \\ 1 & \ell' > \ell_*' \end{cases} \tag{16}$$

in which ℓ_*' is a point which makes equal the upper and lower shadowed portions between eq.(14) and eq.(16) (Fig.2),

$$\begin{aligned} \ell_*' &= \int_0^\infty 1 - \exp(-p^{\ell'}) d\ell' - \int_{-\infty}^0 \exp(-p^{\ell'}) d\ell' \\ &= -\gamma / \ln(p) \end{aligned} \tag{17}$$

in which γ is Euler's constant ($= 0.5772\dots$). In the same way, $(1-p^{\ell-1})^N$ in eq.(8) is given approximately as

$$(1-p^{\ell-1} / N)^N \approx \exp(-p^{\ell'-1}) \approx \begin{cases} 0 & \ell' < \ell_*'+1 \\ 1 & \ell' > \ell_*'+1 \end{cases} \tag{18}$$

From the definition, the mean of the maximum run is given as

$$\ell_{1*} = \sum_{\ell=1}^\infty \ell P_3(\ell) \tag{19}$$

From eqs.(16) and (18),

$$\ell_{1*} = \sum_{\ell = \ell_0 + \ell_*'}^{\ell_0 + \ell_*' + 1} \ell \tag{20}$$

Since $\ell_0 + \ell_*'$ is not an integer in general, ℓ_{1*} is the integer between $\ell_0 + \ell_*'$ and $\ell_0 + \ell_*' + 1$. Extending the definition for ℓ into real numbers and approximating the probability of ℓ between $\ell_0 + \ell_*'$ and $\ell_0 + \ell_*' + 1$ with eqs.(16) and (18), we obtain an expected mean of the maximum run as

$$\ell_{1*} = \ell_0 + \ell_*' + 1/2 = -(\ln(N) + \gamma) / \ln(p) + 1/2 \tag{21}$$

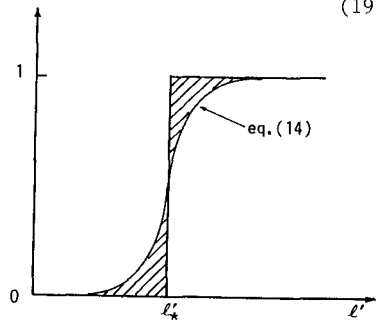


Fig.2 Approximation of eq.(14)

If we apply eq.(1) for the probability of ℓ in the same interval instead, we obtain,

$$\ell_{1*} = \ell_0 + \ell_*' + \int_{\ell_0 + \ell_*'}^{\ell_0 + \ell_*' + 1} \ell p^{\ell-1} (1-p) d\ell / \int_{\ell_0 + \ell_*'}^{\ell_0 + \ell_*' + 1} p^{\ell-1} (1-p) d\ell$$

$$= -(\ln(N) + \gamma) / \ln(p) - 1/\ln(p) + p/(p-1) \tag{22}$$

Figure 3 shows the relation between ℓ_{1*} and N. The approximation of eq.(22) is used in the calculation.

Example 2 (mean of the maximum run)

If we use the same conditions applied in Example 1 ($h_t=1.6$; significant wave height, $T_m=10s$), the expected mean of the maximum runs during 1 day, 1 week and 1 month are calculated as follows.

Table-2 D,N and ℓ_{1*}

duration	number of waves	number of runs	maximum run (eq.22)
1 day	8640	847	6.0
1 week	60480	5929	7.5
1 month	259200	25412	8.6

The number of runs is given by dividing the number of waves by the mean of the total run (10.2; $h_t=1.6$).

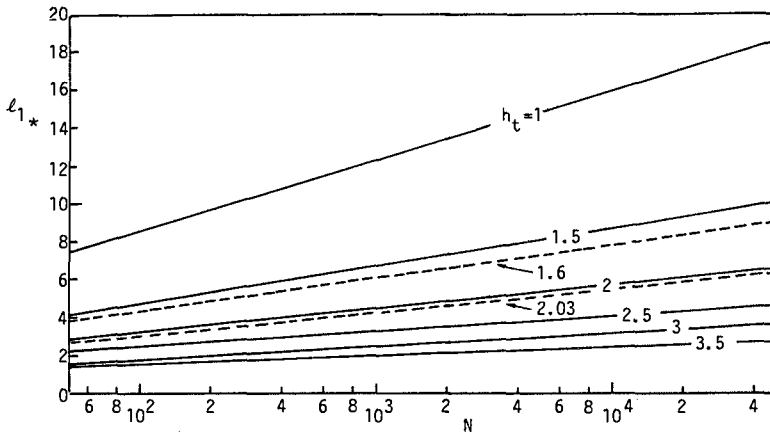


Fig.3 Expected mean of the maximum run

4. VERIFICATION OF THE EXPERIMENTAL RESULT

As explained in the introduction, high waves tend to arrive in groups. Therefore, if a short duration for the model test is applied, the possibility of missing high wave runs during the test may be large. Since a high wave or its group may actually have the greatest effect on coastal structures, the reliability of the model test is highly affected by the frequency of high waves and high wave runs which appear during the test. If a long duration is applied for the test, the statistical properties of the high wave run can be investigated by the ordinary theory (Kimura, 1980). However, if a short duration is applied, the verification of the test is difficult due to an insufficient number of runs. When tests with 100 irregular waves are carried out, for example, we can investigate the ordinary properties such as the power spectrum, wave height distribution, etc. However, it may be difficult to investigate the results regarding the severity of the sea state for the model, since only 10 (roughly) high wave runs are expected if we apply the significant wave height for h_t . In this section, for verification of the efficiency of the model test which is short in duration, the ordered statistics of the run of high waves are investigated.

In the population of N independent high wave runs of $h > h_t$, the probability that i runs are equal to or greater than ℓ and that the other $N-i$ runs are equal to or smaller than $\ell-1$ is given as

$$P_G(\ell)^i \cdot P_L(\ell)^{N-i} \quad (23)$$

in which P_G and P_L are the probabilities that a run is greater than or equal to ℓ and equal to or smaller than $\ell-1$ respectively,

$$\begin{aligned} P_G(\ell) &= \sum_{\ell'=1}^{\infty} p^{\ell'-1} (1-p)^{p^{\ell-1}} \\ P_L(\ell) &= \sum_{\ell'=1}^{\ell-1} p^{\ell'-1} (1-p)^{(1-p)^{\ell-1}} \end{aligned} \quad (24)$$

There are $N C_i$ combinations to select i runs among N runs. Therefore, the probability that all i runs selected are equal to or greater than ℓ and that the remaining $N-i$ runs are equal to or smaller than $\ell-1$ is given as

$$N C_i \cdot P_G(\ell)^i \cdot P_L(\ell)^{N-i} \quad (25)$$

The probability that at least $n+1$ ($n=1,2,$) runs are equal to or greater than ℓ is given as

$$1 - \sum_{i=0}^n N C_i \cdot P_G(\ell)^i \cdot P_L(\ell)^{N-i} \quad (26)$$

In the same way, the probability that at least $n+1$ runs are equal to or greater than $\ell+1$ is given as

$$1 - \sum_{i=0}^n N C_i \cdot P_G(\ell+1)^i \cdot P_L(\ell+1)^{N-i} \quad (27)$$

Consequently, the probability that the $(n+1)$ -th maximum run ($n=1,2, \dots$) equals to ℓ is given as

$$P_{n+1}(\ell) = \sum_{i=0}^n N C_i \{ p^i \ell (1-p)^\ell \}^{N-i} p^{i(\ell-1)} (1-p)^{\ell-1} \}^{N-i} \quad (28)$$

The distribution function of P_{n+1} is given as

$$F_{n+1}(\ell) = \sum_{i=0}^n N C_i \cdot p^i \ell (1-p)^\ell \}^{N-i} \quad (29)$$

(The above equations also hold for $n=0$; maximum run.)

Applying the same approximation as in eqs.(16) and (18), the mean of the $(n+1)$ -th maximum run ($n=1,2, \dots$) is given as

$$\ell_{(n+1)*} = \ell_{1*} - \sum_{i=1}^n N C_i \left\{ \sum_{\ell=\ell_{1*}}^{\infty} \left(\frac{p^\ell}{1-p^\ell} \right)^i \right\} \quad (30)$$

($n \geq 1$)

in which ℓ_{1*} is given by eq.(21) or (22). The definition for ℓ is extended into real numbers again in this equation. The summation with respect to ℓ is taken for the values at $\ell = \ell_{1*}, \ell_{1*+1}, \ell_{1*+2}$, and so on.

If measured values of $\ell_{(n+1)*}$ ($n=1,2,3, \dots$) fall within a significant part of the distribution (eq.28), the experimental data may be judged to be statistically significant. When we apply the 95%* or the 99%* confidence intervals, we may consider the data to be statistically significant if $\ell_{(n+1)*}$ falls within the intervals between $\ell_{(n+1)*-} - \ell_c$ and $\ell_{(n+1)*+} + \ell_c$. ℓ_c is a half of the confidence interval for the given confidence coefficient and is given by solving eq.(29) implicitly .

* (traditional standards are adopted, i.e. 95% and 99%.)

$$\left| \sum_{i=0}^n N C_i p^i \ell (1-p)^\ell \}^{N-i} \right| \begin{matrix} \ell_{(n+1)*+} + \ell_c \\ \ell_{(n+1)*-} - \ell_c \end{matrix} = 0.95 \text{ or } 0.99 \quad (31)$$

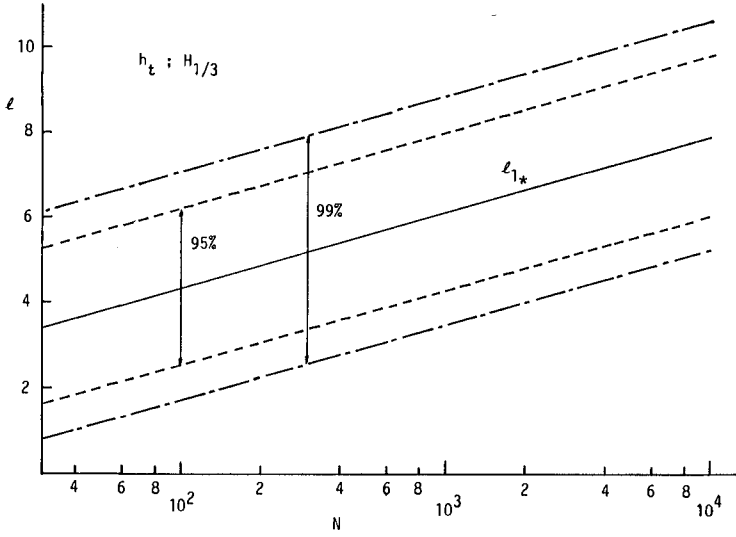
($n=0,1,2, \dots$)

To have an exact value for ℓ_c in the above equation, the definition for ℓ has to be extended into the real numbers.

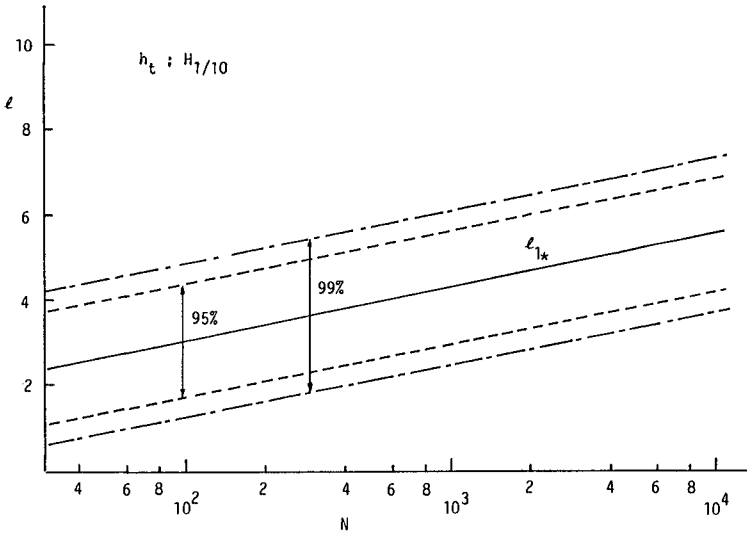
Figures 4 (a) and (b) show the changes in the confidence regions of the maximum run with respect to N when (a) the significant wave height and (b) the 1/10 maximum wave height are used for h_t respectively. The dotted line is for the 95% and the chain line is for the 99% confidence regions respectively. Figures 5 (a) and (b) show the changes in the confidence regions of the maximum run with respect to h_t when (a) $N=50$ and (b) $N=500$ are used respectively.

Example 3 (statistically significant run)

When $N=100$ and $h_t=1.6$, we can see from Fig.4(a) that the number of the maximum run in the data must fall between 3 and 6 if we apply the 95% confidence interval or 2 and 7 for the 99% confidence interval.

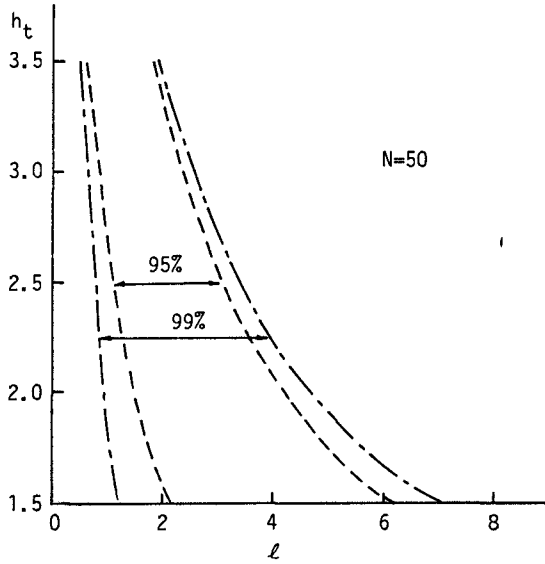


(a) $h=1.60$

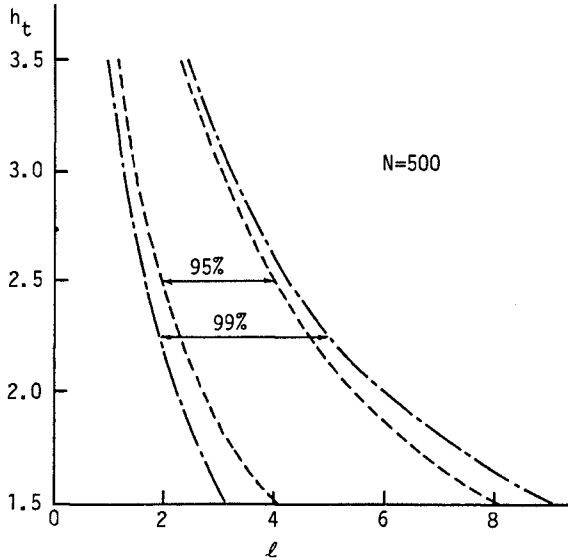


(b) $h=2.03$

Fig.4 Change in the confidence regions (maximum run)



(a) $N=50$



(b) $N=500$

Fig.5 Change in the confidence regions (maximum run)

Table-3 Measured runs of wave height in a numerical simulation ($h \geq 1$)

length	total	frequency	eq.(1)
1	22	0.44	0.467
2	10	0.20	0.249
3	6	0.12	0.133
4	3	0.06	0.071
5	4	0.08	0.038
6	1	0.02	0.020
7	0	0	0.011
8	3	0.06	0.006
9	1	0.02	0.003

Example 4 (verification of the experiment)

Table-3 shows the measured runs of wave height which exceed the mean wave height ($h_t=1$) obtained in the numerical simulation of the Pierson-Moskowitz spectrum. Figure 6 shows the comparison of data and the theoretical probability distribution of the run (eq.1). The agreement between the data and eq.(1) in the region $\ell \leq 4$ is fairly good. However, the verification of eq.(1) in the region $\ell \geq 5$ is difficult due to the fluctuation of data. This is mainly due to the insufficient amount of data. Instead of making a long measurement to obtain a sufficient amount of data, the following verification for the data is possible applying the ordered statistics explained so far. White circles in Fig.7 show the run of wave height in descending order from its 1st through 6th maximum values which are listed in Table-3. Two solid curves show the limit for the 95% confidence region given by eq.(31). Judging from the figure, the distribution has a statistical bias to the larger side.

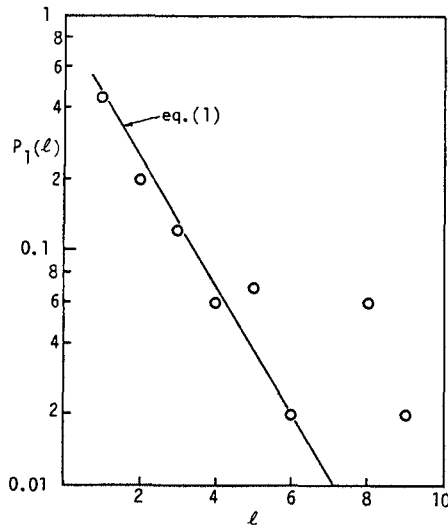


Fig.6 Probability distribution of the run of high waves ($h \geq 1$)

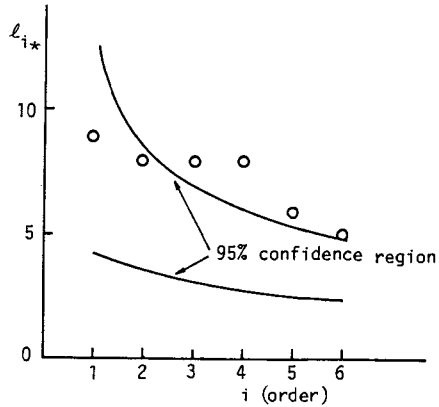


Fig.7 Ordered maximum runs and the limit for the 95% confidence regions

5. SUMMARY AND REMARKS

The probability distribution of the maximum run of wave height for the irregular sea waves is introduced theoretically. The mean of the run and its approximations are also introduced and the changes with respect to the number of runs for different h_t are shown in the figure. The probability distributions for the 2nd maximum, 3rd maximum and further maximum runs and their mean values are also introduced. The confidence regions for the above means are introduced, although the definition for l is extended into real numbers and the traditional confidence coefficients of 95% and 99% are applied. (We may have to introduce confidence coefficients which are effective in coastal engineering problems.)

REFERENCES

- Battjes, J.A. and G. Ph. van Vledder (1984): Verification of Kimura's theory for wave group statistics, Proc. 19th ICCE, pp.642-648.
- Kimura, A. (1980): Statistical properties of random wave groups, Proc. 17th ICCE, pp.2955-2973.
- Kimura, A. and A. Seyama (1984): Statistical properties of short-term overtopping, Proc. 19th ICCE, pp.532-546.
- Longuet-Higgins, M.S. (1952): On the statistical distributions of the heights of sea waves, Jour. Marine Res., Vol. IX, No.3, pp.245-266.

CHAPTER 49

SOME RESULTS FROM THE LABRADOR SEA EXTREME WAVES EXPERIMENT

Søren Peter Kjeldsen¹⁾
Harald Elias Krogstad²⁾
Richard Bjarne Olsen²⁾

ABSTRACT

The Labrador Sea Extreme Waves Experiment (LEWEX), is an international basic research programme concerned with full-scale measurements, analysis, modelling and simulation in test basins of 3-dimensional seas. The research is carried out in order to assess the significance of 3-dimensional sea states in engineering applications. The first phase of the programme full scale wave measurements in the North Atlantic Ocean was performed at a site and time that had a high probability of encountering severe sea states.

The present publication shows examples of measured bi-modal directional sea spectra obtained with the WAVESCAN buoy and directional sea spectra measured with an airborne Synthetic Aperture Radar (SAR). Directional spectra of gravity waves are obtained with the SAR both in open waters and below an ice cover. Further work is needed in order to verify SAR-measurements with in-situ observations. In-situ measured directional spectra are also compared with hindcast spectra from the 3G-WAM model. Hindcast significant wave heights were found to be lower than the in-situ measurements.

1. INTRODUCTION

The Labrador Sea Extreme Waves Experiment (LEWEX) is a large scale international research programme currently underway with participation from United States, Canada, Norway, Netherlands, France, West Germany, Spain and the United Kingdom. LEWEX is supported by a total of 17 research institutions from these countries, and has a variety of resources available for its activities (see BALES, BEAL and FREEMAN, 1987). The first phase of the LEWEX-programme full scale sea trials was successfully performed 9-27 March 1987. Fig. 1 shows the location of the experiment offshore the great banks of Newfoundland along with the positions of vessels, aircrafts and

-
- 1) MARINTEK, Norwegian Marine Technology Research Institute A/S, P.O.Box 4125, N-7002 Trondheim, Norway
 - 2) OCEANOR, Oceanographic Company of Norway A/S, P.O.Box 2905 Tempe, N-7002 Trondheim, Norway

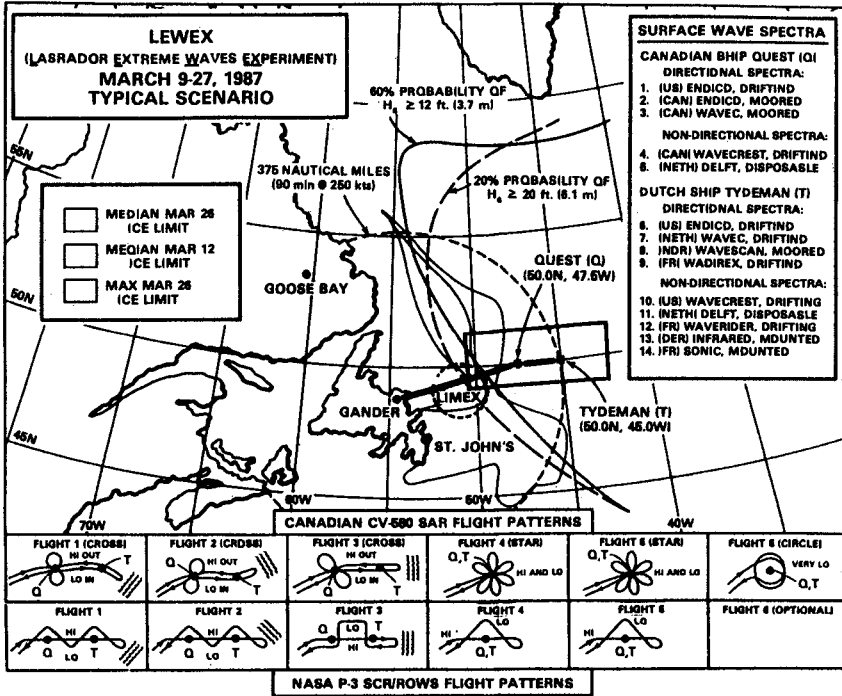


Fig. 1 LEWEX (Labrador Extreme Waves Experiment) March 9-27, 1987, typical scenario. Measurements of directional wave spectra were made with buoys as listed in the upper right corner and with the following airborne instruments: Synthetic aperture radar SAR, Surface Contour radar SCR, Radar Ocean wave spectrometer ROWS. (From BALES, BEAL and FREEMAN 1987).

participating in-situ and airborne instruments for directional wave measurements. Field measurements were supplemented with 9 numerical wave models developed for forecast and hindcast purposes. Two of these are global models. The LEWEX field activities were coordinated with a large marginal ice zone experiment LIMEX (Labrador Ice Margin Experiment) see (BHOGAL et al., 1987). Altogether, nearly 350 people have been involved in the planning, preparation and field work associated with these two experiments. The field experiment is now being followed up with a comprehensive data analysis, comparison of results as well as a reconstruction of selected measured sea states in the advanced 3-dimensional Ocean Wave Basin at MARINTEK, Norway.

The present paper which contains only a limited number of examples of results, shows directional bi-modal sea states obtained with the WAVESCAN buoy and examples of directional spectra obtained with SAR in open waters and below ice-covers. Finally, the paper contains a comparison between the 3G-WAM model and in-situ measurements for a bi-modal sea state.

2. SCOPE AND OBJECTIVES OF LEWEX

The major aim of the LEWEX-project is to evaluate the applicability and usefulness of directional wave data for engineering design. The largest responses in terms of motion of floating structures and associated sea loads are not always encountered in the most extreme sea state (see BALES, 1987). It turns out that less severe crossing seas in some cases lead to larger responses. Bi- and tri-modal directional seas were fairly common during LEWEX and even four modes were observed in a few cases. However, none of these sea states represent really heavy seas.

The performance of the various wave directional instruments under such complicated conditions is not well known. Therefore, one of the main scientific objectives of the LEWEX project is to recommend/identify new procedures where existing techniques of measurement or analysis are inadequate. A series of measurement systems for directional seas were used during the experiment:

- Moored oceanographic buoys: ENDECO, WAVESCAN, WAVEC.
- Freely floating oceanographic buoys, WAVEC, WADIREX, ENDECO.
- Shipborne navigation radar connected to a bow-mounted wave gauge.
- The NASA Surface Contour Radar (SCR).
- The NASA Radar Ocean Wave Spectrometer (ROWS).
- The CCRS' C-band Synthetic Aperture Radar (SAR).

In addition, a large number of drifting buoys were deployed for measurements of one-dimensional frequency spectra. From the measurements it was possible to determine the capability of the airborne remote sensing radars (SCR, SAR and ROWS) for estimation of the directional wave properties over a variety of sea states.

A second major aim of the LEWEX-project is to compare various idealized wave models and operational wave forecasts with observations. In particular, the LEWEX analysis intend to assess the relative performance of the recently developed "third-generation" (3G-WAM) wind wave model against earlier first and second generation

models. The 3G-WAM model incorporates superior physics over all of its predecessors at the expense of a significant increase in computational demands. The 3G-WAM model is most likely to exhibit its superiority in a complex, rapidly-changing sea state, as may occur associated with a major storm or frontal passage. No less than 9 operational wave forecast models have been run in hindcast mode for the LEWEX measurement period using common wind fields. One is thus able to assess the adequacy of directional wave estimates derived from various first, second and third generation wave forecast models in realistic complex sea states, and in situations for which a pre-existing wave field is likely to influence new wave growth. A final important objective of LEWEX is to examine the penetration of waves into the ice pack in cooperation with the Labrador Ice Margin Experiment, LIMEX, as shown in section 4.

3. EXAMPLES OF RESULTS - IN-SITU DIRECTIONAL WAVE MEASUREMENTS

The WAVESCAN metocean data acquisition buoy is shown in Fig. 2. It was first deployed from "Tydeman" at (50.0°N, 45.0°W) on 14 March 0345Z, see Fig 1. The water depth at the site was 3955 m. The buoy remained in this position until 18 March 2110Z. The buoy was then recovered and moved to (50.0°N, 47.5°W) where it remained from 19 March 0950Z to 20 March 1835Z. The buoy was finally deployed using a drag anchor for two periods between the 23 and 25 March. Data was recorded every 90 minutes throughout the experiment. During such operations, the buoy is checked daily by means of the ARGOS surveillance system. A pre-selected set of wave and meteorological parameters as well as various housekeeping data are transmitted to shore via ARGOS.

The directional analysis is carried out on the time series after the pitch/roll series have been rotated into the north-east reference system using the wave compass series. A Fast Fourier Transform is carried out on each of the time series and the resulting discrete Fourier transform of the heave series is compensated for by the manufacturer's transfer function. Similarly, the discrete Fourier transforms of the slope series are corrected for the buoy's hydro-mechanical behaviour which exhibits a response similar to a forced linear oscillator with eigenfrequency, f_0 , and damping ratio, λ . For WAVESCAN, $f_0 = 0.43$ Hz and $\lambda = 0.11$. The nine possible auto- and cross-spectra are computed from 2048 data point/1Hz time series and smoothed using a moving average over 16 adjacent frequencies giving spectral estimates with 32 degrees of freedom. The directional wave spectrum may be expressed as:

$$E(\theta, f) = S(f) D(\theta, f) \quad (1)$$

where S is the one-dimensional frequency spectrum and D is the directional distribution:

$$D(\theta, f) = \frac{1}{2\pi} + \frac{1}{\pi} \sum_{n=1}^{\infty} \{a_n(f) \cos n\theta + b_n(f) \sin n\theta\}, \quad (2)$$

and $\int_0^{2\pi} D(f, \theta) d\theta = 1$. The Fourier coefficients a_1 , b_1 , a_2 and b_2

Measured Variable	Sensor Type and Manufact.	Measuring Technique	Sensor Location	Range	Accuracy
Waves: Heave Pitch Roll	Datwell Hippy 40 or 120	Double integrated accel. Signal Magnetic inclinometer	Near the buoy's COB	± 10 m $\pm 90^\circ$ $\pm 90^\circ$ ± 10 m/s ²	$< 3.0\%$ $< 0.5\%$ $< 0.5\%$ $< 3.0\%$
Wind direction	Wind vane	Vector averaged over a 10 min.	3.7 m above sea level	0-360°	$\pm 4^\circ$
Wind Speed	Cup Anemometer B&G MOD 152	Vector averaged over a 10 min.	3.7 m above sea level	0-90 knots	$\pm 4\%$
Pressure	Monolithic AEB80 ANE		3.7 m above sea level	920-1070 mbar	± 0.5 mbar
Air temperature	Platinum		3.7 m above sea level	-40°C - +45°C	$\pm 0.4^\circ$
Sea temperature	Thermistor Aandersaa 1229		0.3 m above sea level	-4°C - +30°C	$\pm 0.2^\circ$
Compass	Fluxgate	Fluxgate DIGICOURSE 101E		0° - 360°	$\pm 1^\circ$
Internal Temperature		Transducer LM 235		-40°C - +125°C	$\pm 1^\circ$

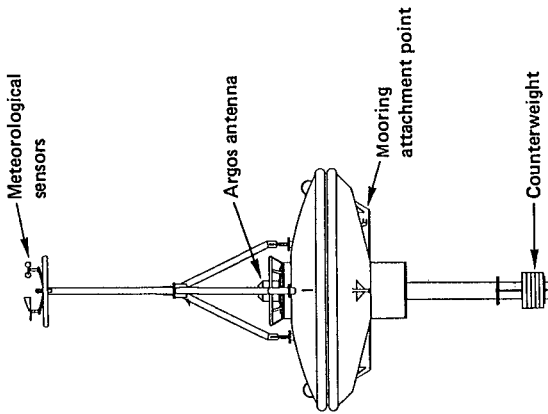


Fig. 2 The WAVECAN metocean data acquisition buoy with instrumentation. (From KROGSTAD 1987).

are defined as follows (LONG, 1980):

$$a_1 = Q_{HE}/(C_{HH}(C_{EE} + C_{NN}))^{1/2} \quad (3)$$

$$b_1 = Q_{HN}/(C_{HH}(C_{EE} + C_{NN}))^{1/2} \quad (4)$$

$$a_2 = (C_{EE}-C_{NN})/(C_{EE}+C_{NN}) \quad (5)$$

$$b_2 = 2C_{EN}/(C_{EE} + C_{NN}) \quad (6)$$

In these relations, C denotes the co-spectrum and Q the quad-spectrum and the indices H heave, N slope in northerly direction and E slope in easterly direction. The main directional parameters are mean wave direction, $\theta_1(f) = \arctan(b_1/a_1)$, and circular standard deviation $\sigma_1 = 2(1-(a_1^2 + b_1^2))^{1/2}$.

A full directional estimate $D(\theta, f)$ based on a_1 , b_1 , a_2 and b_2 is the maximum entropy (MEM) spectral estimate (LYGRE and KROGSTAD, 1986):

$$D(\theta, f) = \frac{1}{2\pi} \left(1 - \phi_1 c_1^* - \phi_2 c_2^* \right) / \left(1 - \phi_1 e^{-i\theta} - \phi_2 e^{-2i\theta} \right)^2 \quad (7)$$

where

$$\phi_1 = (c_1 - c_2 c_1^*) / (1 - |c_1|^2) \quad (8)$$

$$\phi_2 = c_2 - c_1 \phi_1, \quad (9)$$

$$c_1 = a_1 + ib_1 \quad (10)$$

$$c_2 = a_2 + ib_2 \quad (11)$$

c^* is the complex conjugate of c . An example of a bi-modal wave number spectrum is shown in Fig. 3. The outer circle corresponds to a wave number, $k=2\pi/L=0.01m^{-1}$, while the inner circle corresponds to $k=0.005m^{-1}$. The energy scale is linear. The plot is oriented with North at the top and shows the direction towards which the waves are travelling. The observed wind direction is indicated with an arrow. The directional spectrum shows one wave system travelling towards the north in alignment with the prevailing wind direction and another system coming in as a swell and travelling nearly perpendicular to the first system towards west. The corresponding one dimensional frequency spectrum is shown to the right. The one-dimensional spectrum is not, however, bi-modal and the superiority and necessity of a complete directional resolution is clearly demonstrated.

Fig. 4 shows the development of two swell systems with nearly opposing directions at (50°N, 47.5°W). The time interval between the displayed spectra is 1.5 hour. Finally, Fig. 5 shows an example of directional sea spectra collected in the Gulf stream where wave-current refraction will be important. These measurements were obtained at (43°N, 55°W) where a very strong current shear was detected. At this position the cold Labrador current coming from the north

WAVESCAN/LEWEX Rec. 30, 870315/2359GMT
 $H_m0 = 2.9\text{m}$, $T_p = 9.3\text{s}$, $W.sp. = 5.7\text{m/s}$

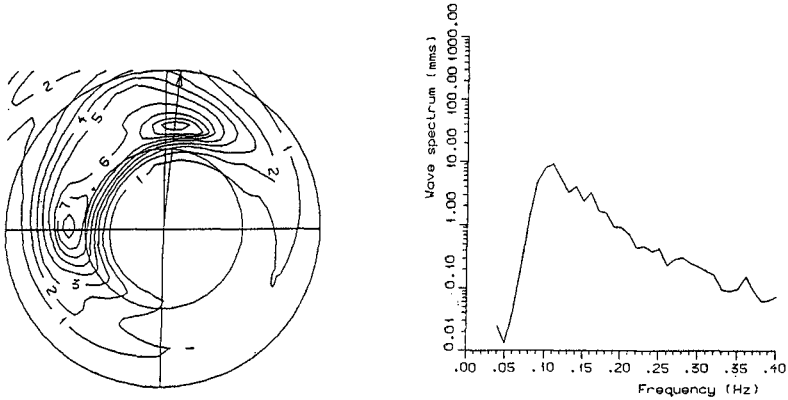


Fig. 3 Left, example of bi-modal directional wavenumber spectrum measured at grid point 1, on 16th March at 0000Z. Outer circle $k=0.01\text{m}^{-1}$, inner circle $k=0.005\text{m}^{-1}$. Right, the corresponding one dimensional frequency spectrum.

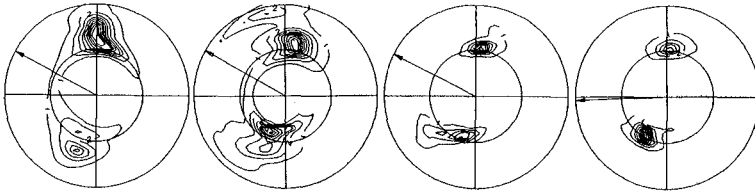


Fig. 4 Examples of development of two swell systems with nearly opposing directions at grid point 2, on 20th March at 0600Z, 0730Z, 0900Z, 1030Z.

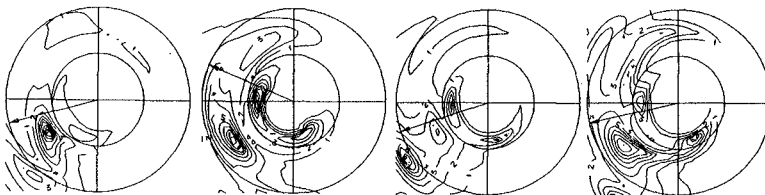


Fig. 5 Examples of wave-current refraction of the directional sea spectrum observed in the current shear in the Labrador current and the Gulf Stream at 55°W , 43°N , on 24th March at 0600Z, 0730Z, 0900Z, 1030Z.

east encounters the warm Gulf Stream coming from the south west. In this case the buoy was operated with a drag anchor and moved through the current shear. At least 3 individual wave systems can be identified in the observed directional spectra. Propagation of swell from this area may be influenced by strong currents. Such an influence shall be taken into account in wave models.

4. EXAMPLES OF RESULTS FROM THE C-BAND SAR

Part of Canada's participation in the LEWEX experiment was to fly an airborne Synthetic Aperture Radar (SAR), belonging to the Canada Centre for Remote Sensing. The radar operates in the C-band, and is designed, among other things, for research work related to the European ERS-1 and Canadian RADARSAT satellites, planned to be launched in 1990 and 1994, respectively. The CCRS Convair 580 C-band SAR was flown operationally for the first time during LEWEX. It is a digitally controlled radar, with a digital recording system, and a sophisticated real time processor. Motion compensation is carried out in real time, using output from the inertial navigation system to control the antenna drive and to perform digital corrections to the in-phase and quadrature data before processing and recording. In addition to recording the real time processed data, raw signal data may also be recorded, allowing post-flight ground processing. A more detailed description may be found in (LIVINGSTONE et al. 1987).

The SAR was flown on 6 dedicated wave flights during the experimental period, in addition to 4 ice mapping flights for LIMEX, which took place further west in the same period. Fig. 6 (left) shows an image from the first flight on March 13 during the transit from Gander to "Quest"'s location, when waves were observed to propagate from the open water into the ice. Although we do not have ground truth data for this location, the image provides a very interesting situation for studying mechanisms of SAR imaging of ocean surface waves. SAR imaging of oceans waves is widely discussed in the literature, and a full understanding of all the mechanisms leading to SAR detection of ocean waves has not been reached at present. The imaging of waves propagating azimuthally, or along-track, is a particular point of discussion. The effects of scene motion may be divided into coherent and non-coherent classes. The most important coherent effects include velocity bunching, acceleration defocus and coherence time limitations. Non-coherent effects include scanning distortion and look mis-registration. It is important to understand the scene motion effects when interpreting SAR imagery and information, such as directional wave spectra. More detailed discussions may be found in the literature, e.g, (RANEY 1985), (RUFENACH and ALPERS 1981), ALPERS, ROSS and RUFENACH (1981), (RANEY and VACHON (1988), (HASSELMAN et. al. 1985). One of the limiting factors in imaging azimuthally travelling waves is the maximum available scene coherence time. This is often determined by estimating the target decorrelation time scale. For open water, where Bragg scattering is the dominant mechanism this is dominated by the wavelengths of the order of cm for C-band. For ice covered waters, however, the Bragg length waves are effectively filtered out and other back-scatter mechanisms dominate, providing the opportunity to study other effects, such as the velocity bunching mechanism and the look-misregistration.

Fig. 6 (left) shows a SAR scene from the marginal ice zone recorded 13th of March. The waves are propagating from the open water into the ice. Mechanisms contributing to the modulation of the image intensity could primarily be either tilt modulation or velocity bunching, or a combination of both. However, if we consider the variation of cross-section with incidence angle, this varies continuously from near nadir to more than 70 degrees. In the image, the average of this variation is compensated for, along with range and antenna pattern effects, through a real-time Sensitivity Time Control (STC). Removing the incidence angle component of the correction, averaging an ice covered portion of the image in the azimuth direction, and scaling the resulting curve with scatterometer data also acquired from the CV-580 during the experiment, we end up with a cross-section variation with incidence angle of 0.24 dB/degree in the midswath. In the same part of the image, wave image contrast was measured to 8.3 dB. Combining these two figures, we find that if tilt modulation were to be the only mechanism contributing to the wave imaging, a significant wave height of 20 m would be required, which is far higher than any wave observation reported in the area on this day. Ocean Data Gathering Program (ODGP) wave model forecasts actually predicted 3.4 m significant wave height. Velocity-bunching models in the literature (e.g. ALPERS and RUFENACH 1979) predict very narrow peaks in wave pattern image intensity. In examining the image, we find that the wave pattern in the ice, indeed has this character. The open water wave pattern, however, is somewhat broader but this could also be due to reduced resolution caused by scene coherence time limitations. Propagation of wave energy below the ice cover shall be considered in further developments of wave models.

Fig. 6 (right) shows examples of image spectra computed from the 512x512 pixel squares, at near, mid and far range for waves in ice and waves in open water. SAR image spectra will always be symmetric and the interpretation of wave direction has to rely on in-situ measurements or hindcasts. The circles correspond to wavelengths $L = 50, 100$ and 200 m. The spectra from the ice-covered regions are notably more complex than the open water spectra which indicate a single dominant wave system in all 3 cases. This system is also apparent in the ice spectra, but in these there are also additional contributions. In particular, the near and mid-range cases indicate a shorter wavelength component at a different propagation angle, which is not evident in the open water spectra. The reason for the latter may be scene coherence time limitations. Alternatively, this mode may be an artifact of velocity bunching when imaging waves with a relatively slow platform velocity and the geometry of this example. Theoretical work is currently being carried out in order to examine this effect more closely (VACHON, 1988). An intercomparison of SAR and WAVESCAN spectra where the latter are modified for scanning distortion is reported in (KROGSTAD and OLSEN 1988).

5. COMPARISON WITH 3-G WAM MODEL

The third generation (3-G) WAM-model is a wave model developed by an international team of ocean wave scientist. The model takes the non-linear transfer between wave frequencies due to resonant four-wave interactions fully into account and is based on ideas

LEWEX March 13, 1987

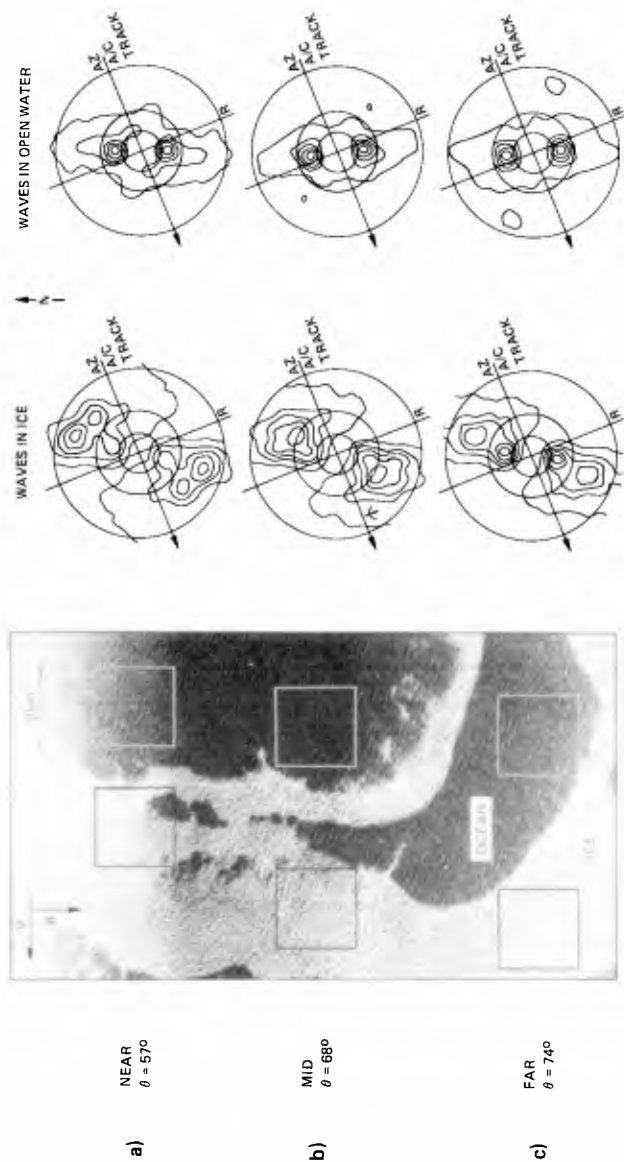


Fig. 6 Left: Real time SAR image of the ice margin obtained on March 13th. The six sub areas indicated were subjected to spectral analysis with the results appearing to the right. V is the aircraft vector, R is the range dimension, and θ is the angle of incidence. Right: SAR image spectra of the near, mid-, and far range subscenes extracted from the image. The contours of the spectra represent 10%, 30%, 50%, 70% and 90% of the peak spectral energy present. Circles correspond to wavelengths 50, 100 and 200 m.

developed at the Max Planck Institute for Meteorology (HASSELMANN et al. 1988). It is now operational at the European Centre for Medium-Range Weather Forecasts (ECMWF) and produces daily directional wave spectra over the entire globe. The model has been programmed in such a way that it can be interfaced with different wind field sources. In the LEWEX analysis a common wind field is used for all 9 wave models. However, in the present publication an alternative choice is made namely ECMWF-wind fields. The LEWEX-experiment is one of the opportunities that is available for calibration and tuning of the 3-G WAM model. Fig. 7 shows an example of hindcasted significant wave heights for the North Atlantic during the LEWEX-experiment. The position of the WAVESCAN buoy is also shown. On 16 March at 1200Z, a large storm with significant wave heights up to 10 m is present about 1130 nautical miles southwest of the WAVESCAN buoy and swell from the storm is propagating towards the buoy. Fig. 8 shows examples of directional spectra hindcasted with the 3-G WAM model and the corresponding directional spectra measured with the buoy. The directional spectra are shown in a plot with a logarithmic frequency scale. The circles correspond to frequency $f = 0.05, 0.10$ and 0.20 Hz. The wave energy scale is linear with constant contour. Wave direction is defined as the direction towards the waves are travelling. The wind direction is indicated by arrow.

On 16 March at 0600Z, the wind is weak and from SE. A swell is evident from the same direction. By 1200Z, the wind has increased and veered to NE. A secondary swell is now propagating out of the Labrador Basin travelling towards SE. At 1800Z a new wind-driven sea is evident, superimposed upon the two previously existing wave systems. This tri-modal sea is predicted by the 3G-WAM model, but the model overestimates the energy content in the swell travelling towards NW. On the 17th March the wind gradually turns to SE and SW, and increases again, see Fig. 9. There is a good qualitative agreement between measured and hindcasted spectra for this complex bimodal sea, although, the hindcast spectra appear to overestimate the SW swell travelling towards NE. The timing of the swell is important. The 16th at 0600Z the hindcast swell has not yet arrived at the buoy. It arrives by 1200Z and from that time there is a good qualitative agreement between bi-modal measured and hindcast directional spectra. There is also good agreement for the case shown on the 17th March. However, the hindcast significant wave heights are biased, and 20-30% lower in these examples than in the measurements. Further analysis and comparisons are ongoing.

6. CONCLUSIONS

1. - Results from the LEWEX-experiment indicate that some of the most important parameters for a proper description of directional sea states are the number of individual sea systems contained in the directional sea and their relative orientation. It is expected that directional spectra to be used in the future for engineering design will be more complex, and thus closer to realistic sea states. Thus, the demand that ocean basins be able to simulate more realistic directional sea states for engineering applications, will increase. A swell-corrupted wind sea is a quite common situation, as the LEWEX full scale directional wave measurements show.

SIGNIFICANT WAVE HEIGHT
March 16, 1987 at 12GMT

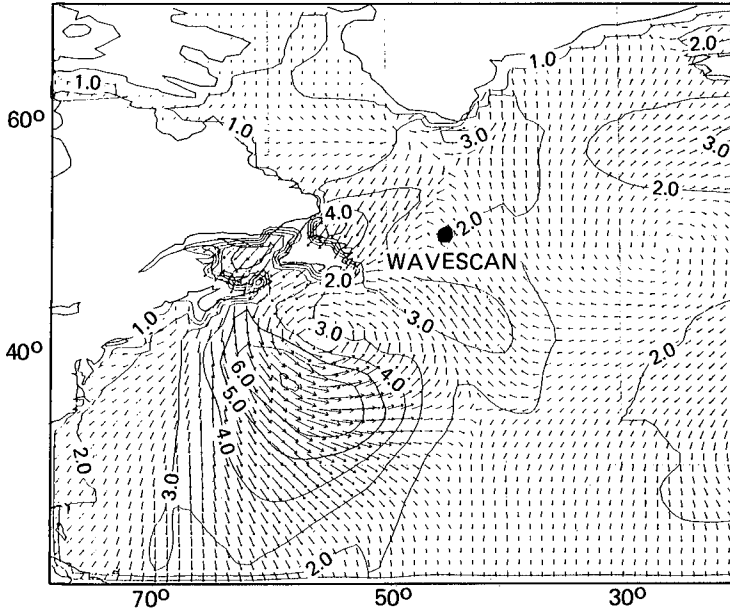


Fig. 7 Hindcast of wave height fields for the North Atlantic made by the 3G-WAM model driven by ECMWF wind fields. The contours are of wave height in meters and the arrows point in the mean wave direction. The location of the WAVESCAN buoy is shown. (From ZAMBRESKY 1988).

WAVESCAN/LEWEX Rec. 34, 870516/0559GMT WAVESCAN/LEWEX Rec. 38, 870516/1159GMT WAVESCAN/LEWEX Rec. 42, 870516/1759GMT

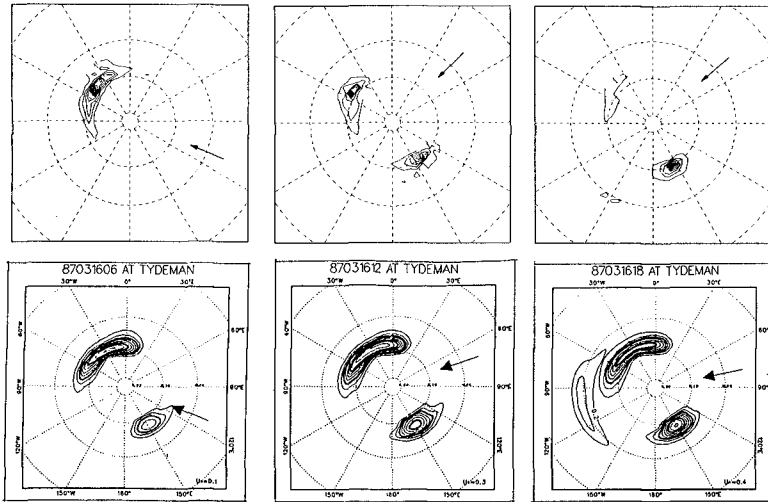


Fig. 8 Above: Directional spectra measured with WAVESCAN for 16th March 0600Z, 1200Z, 1800Z. Below: Hindcast directional spectra from the 3G-WAM Model (From ZAMBRESKY 1988).

WAVESCAN/LEWEX Rec. 54, 870517/1159GMT WAVESCAN/LEWEX Rec. 58, 870517/1759GMT WAVESCAN/LEWEX Rec. 62, 870517/2359GMT

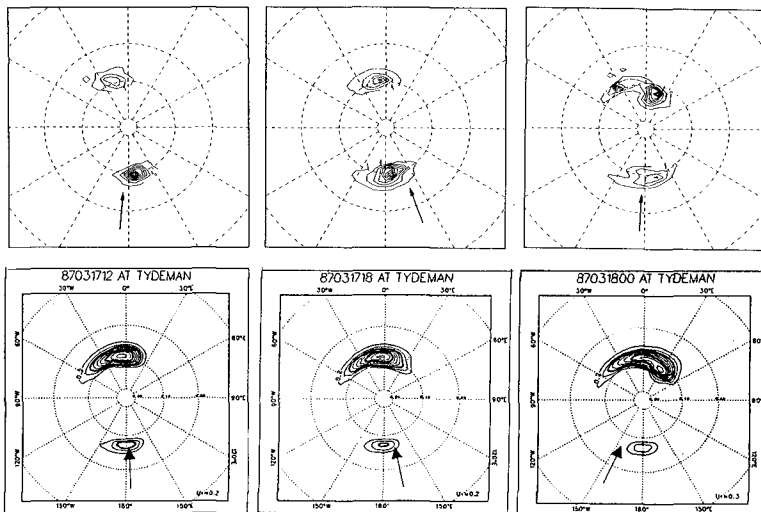


Fig. 9 Above: Directional spectra measured with WAVESCAN for 17th March 1200Z, 1800Z and 18th March 0000Z. Below: Hindcast directional spectra from the 3G-WAM Model (From ZAMBRESKY 1988).

2. - Validation of the capability of airborne and spaceborne (shuttle) SAR, SCR and ROWS to detect directional distributions of ocean gravity waves will be an important aspect of the LEWEX-programme. A method is suggested by (KROGSTAD and OLSEN 1988) for modifying in-situ data to provide spectra which are equivalent to those expected from an ideal airborne scanning instrument. Still much validation of results is needed in this area. In the future it is foreseen that global orbiting space shuttles and satellites will provide us with a large quantity of directional sea spectra covering all sea areas of the world. Such data should be assimilated into wave forecasting models.

3. - Significant wave heights hindcast with the 3G-WAM model were found to be 20-30% lower than in-situ measurements and measured swell components were somewhat delayed in time. Accuracy of wave forecasts/hindcasts will depend on accuracy of the chosen input wind fields.

4. - Propagation of wave energy below the ice cover shall be considered in further developments of wave models.

5. - Propagation of swell in this part of the North Atlantic may be influenced by strong currents, and such an influence shall be taken into account in wave models.

7. ACKNOWLEDGEMENTS

The LEWEX-project is organized within NATO as a multi-lateral scientific research programme. Two working groups are responsible for the performance of the LEWEX-project. These are RSG-1 and RSG-2. A list of participating scientists is found in (BALES, BEAL and FREEMAN 1987).

8. REFERENCES

- ALPERS, W.R. and RUFENACH, C.L., 1979: "The effect of Orbital Motions on Synthetic Aperture Radar Imagery of Ocean Waves" *IEEE Transactions on Antennas and Propagation*, Vol. AP-27 (5) pp. 685-690.
- ALPERS, W.R., ROSS, D.B. and RUFENACH, C.L., 1981: "On the Detectability of Ocean Surface Waves by Real and Synthetic Aperture Radar". *J. Geoph. Res.* Vol. 86 (C7) pp. 6481-6498.
- BALES, S.L., BEAL, R.C., FREEMAN, N.G., 1987: "LEWEX-Science Plan". DTNSRDS. Bethesda, Maryland, USA.
- BALES, S.L., 1987: "Practical Seakeeping Using Directional Wave Spectra" in *Symposium on Measuring Ocean Waves from Space* Johns Hopkins APL Technical Digest, Vol 8 No. 1 January - March 1987. The Johns Hopkins University Applied Physics Laboratory. Laurel, Maryland, USA.
- BHOGAL, A.S., ARGUS, S.A., FREEMAN, N.G., 1987: "LIMEX/LEWEX Operations informations". Canada Centre for Remote Sensing, Ottawa, Canada, January 1987.
- HASSELMAN, K., RANEY, R.K., PLANT, W.J. ALPERS, W.R., SHUCHMAN, R.A., LYZENGA, D.R., RUFENACH, C.L. and TUCKER, M.J., 1985: "Theory of Synthetic Aperture radar Ocean Imaging". *A MARSEN View. J. Geoph. Res.* Vol. 90 (C3). pp 4659-4686.
- HASSELMANN, S., HASSELMANN, K., BAUER, E., JANSSEN, P.A.E.M., KOMEN, G.J., BERTROTTI, L., LIONELLO, P., GUILLAUME, A., CARDONE, V.C., GREENWOOD, M., REISTAD, M., ZAMBRESKY, L., and EWING, J.A., 1988: "The WAM model - a third generation ocean wave prediction model", submitted to *J. Phys. Ocean.*
- KROGSTAD, H.E., 1987: "Wave Data Collected by WAVESCAN during the Labrador Sea Extreme Waves Experiment (LEWEX)", Rep.no. 87.111, OCEANOR, Oceanographic Company of Norway, Trondheim, Norway.
- KROGSTAD, H.E., OLSEN, R.B., 1988: "An Intercomparison of SAR and Buoy Directional Wave Spectra from LEWEX". To be presented at IGARSS'88 - International Geoscience and Remote Sensing Symposium, Edinburgh, Scotland 1988.
- LIVINGSTONE, C.L., GRAY, A.L., HAWKINS, R.K., DEANE, R.A., HALBERTSMA, J.G. and OLSEN, R.B., 1987: "CCRS C-band Airborne Radar - System Description and Test Results". Presented at the 11th Canadian Symposium on Remote Sensing.
- LONG, R.B., 1980: "The Statistical Evaluation of Directional Spectrum Estimates Derived from Pitch/Roll Data". *J. Phys. Ocean.* 10, pp. 944-52.
- LYGRE, A. and KROGSTAD, H.E., 1986: "Maximum Entropy Estimation of the Directional Distribution in Ocean Wave Spectra", *J. Phys. Ocean.* 16, pp. 2052-2059.
- RANEY, R.K., 1985: "Theory and Measure of Certain Image Norms in SAR". *IEEE Transactions of Geoscience and Remote Sensing*, Vol. GE-23 (3), pp 343-348.
- RANEY, R.K. and VACHON, P.W., 1988: "SAR Imaging of Ocean Waves from an Airborne Platform: Focus and Tracking Issues". Submitted to *J. Geoph. Res.*
- RUFENACH, C.L. and ALPERS, W.R., 1981: "Imaging Ocean Waves by Synthetic Aperture Radars with Long Integration Times". *IEEE Transactions on Antennas and Propagation* Vol. AP-29 (3) pp. 422-428.
- VACHON, P.W., 1988. Canada Centre for Remote Sensing, Ottawa, Canada. (Personal communication).
- ZAMBRESKY, L.F., 1988. GKSS Forschungszentrum Geesthacht, Federal Republic of Germany, currently at European Centre for Medium-Range Weather Forecasts. (Personal communication).

CHAPTER 50

On the Partition of Horizontal Momentum Between Velocity and Pressure Components Through the Transition Region of Breaking Waves

David R. Basco¹ and Takao Yamashita²

Abstract

When a water wave breaks, it undergoes a complicated interchange of total, depth integrated horizontal momentum between that part due to the velocity field and the part that can be assigned to the pressure distribution beneath the surface. This partition of total momentum for a strong, plunging breaker is described by a relatively crude model in which the horizontal velocity profile (over the vertical) is schematized in two layers and the pressure distribution is related to a hydrostatic distribution for the given water depth. An example calculation at four locations across the breaking transition region on a plane beach is utilized to demonstrate the principles of the model. The limitations of the approach which assumes momentum conservation in a reference frame moving with the wave celerity defined at the wave crest are presented, but await verification. The ultimate goal is a relatively simple model to predict the transition width of breaking waves (spillers, plungers and intermediate types) for plain and bar-trough beaches.

1.0 Introduction

Svendsen (1984) defined the wave breaking transition region as the distance from the break point (vertical free surface) to the transition point where the time-mean water surface changes from relatively level to an increasing slope (wave set-up). Figure 1 displays these two end points along with the plunge point (pp) and an intermediate point (ip) which shall be discussed later. At the transition point (tp), the bore-like wave with surface roller area (A) encompasses a trapped mass of fluid which is transported within the inner, surf-zone region on plane beaches.

A qualitative description of the transition region was presented by Basco (1985). The overturning, plunging jet pushes on the trough fluid ahead like a wave paddle to create the surface roller but is left behind as it generates a new, bore-like wave with completely new wave kinematics. A simple, empirically based transition zone model designed to match the Svendsen (1984) inner-region model was then presented by Basco and Yamashita (1986) at the 20th ICGE in Taiwan. The surface

¹Professor of Civil Engineering and Director of Coastal Engineering Institute, Old Dominion University, Norfolk, VA 23529-0242

²Instructor, Disaster Prevention Research Institute, Kyoto University Kyoto 611, Japan

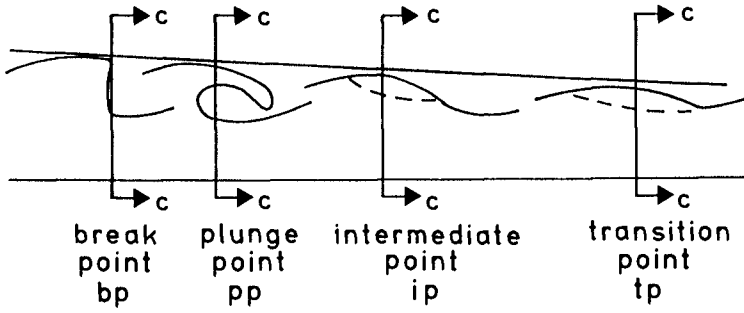


Fig. 1 Schematic of Transition and Four Key Locations

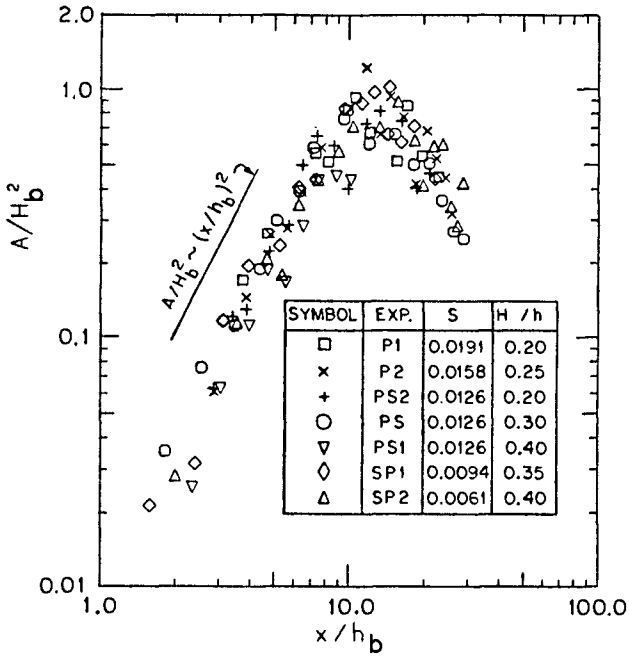


Fig. 2 Growth of Surface Roller Area With Distance From Break Point (after Papanicolaou and Raichlen, 1987)

roller area $A(x)$ was speculated to increase linearly from zero at the plunge point to a value equal to $0.9 H^2$ at the transition point as suggested by Svendsen (1984). Fig. 2 from experimental data by Papanicolaou and Raichlen (1987) suggests that $A(x)$ varies nonlinearly as the squared distance from the plunge point to the place where $A \sim 0.9 H_b^2$. It is not clear however that these researchers used the same definition of surface roller area, A as first suggested by Svendsen (1984).

This paper extends these previous efforts by developing a quantitative model for the horizontal, total depth integrated momentum as partitioned between the momentum flux due to the velocity and the pressure induced momentum component. This is done in a reference frame moving with the wave celerity defined by the wave crest. Total, vertically integrated, horizontal momentum is conserved in this system.

Section 2 presents the general theory and discusses the limitations of the approach. Theoretical expressions are derived in Section 3 for the four locations in Fig. 1 and a general expression is formulated for any location. An example computation to demonstrate the plausibility of the formulations is then presented in Section 4. The paper concentrates on strong plunging breakers on a plane beach with the goal to develop relatively simple ways to predict the transition width. And, eventually to also model the transition width on a bar-trough profile where the surface roller grows and then decays rapidly as the wave "reforms" in the trough.

2.0 Theoretical Considerations

2.1 Steady Flow Momentum Balance. The vertically integrated, total horizontal momentum (m) per unit width and unit mass density (ρ) can be found from

$$m = \int_0^h \left[u^2(z) + \frac{1}{\rho} p(z) \right] dz \quad (1)$$

where z is the vertical coordinate from the floor ($z = 0$) to the free surface ($z = h$) and $u(z)$, $p(z)$ are the horizontal velocity and pressure distributions beneath the surface, respectively. From standard definitions of the volumetric flow rate per unit width (q), momentum correction coefficient (α), and a pressure correction coefficient (a) relative to hydrostatic pressure (e.g., see Chow, 1959, p. 32) this can be written

$$m = \alpha \left[\frac{q^2}{h} \right] + a \left[\frac{1}{2} \rho g h^3 \right] \quad (2)$$

or

$$m = m_v + m_p \quad (3)$$

so that total momentum is partitioned between the momentum flux part (m_v) and the pressure component (m_p). Four initial conditions are required to define m , namely the water depth (h), velocity magnitude ($v = q/h$), velocity profile (α) and pressure distribution (a).

For the classical hydraulic jump (Belanger, 1849), a uniform velocity profile ($\alpha = 1$) and hydrostatic pressure distribution ($a = 1$) are assumed both upstream and downstream of the surface roller. This reduces the problem to only two initial conditions and two unknowns so that together with the conservation of mass, a unique solution (the so-called sequent-depth equation) is possible for the downstream conditions. Madsen and Svendsen (1983) utilized a theoretical velocity profile for the flow reversal with depth through the surface roller and an empirical, vertical turbulent momentum exchange coefficient to theoretically derive the jump profile and jump length. Basco and Yamashita (1986, Fig. 6, p. 956) used this theory to present the partition of $m_v(x)$ and $m_p(x)$ across the jump. The surface roller, flow reversal causes $\alpha \gg 1.0$ through the jump and results in nonlinear distributions of $m_v(x)$ and $m_p(x)$ components even though $a(x) = 1$ is taken as a first approximation.

2.2 Unsteady Flow Momentum Conservation. The integral, control volume definition of linear momentum conservation for unsteady flow can be written in vector terminology (\vec{V} is the vector velocity field)

$$\int_V \frac{\partial(\rho \vec{V})}{\partial t} dV + \int_s (\rho \vec{V}) \vec{V} \cdot d\vec{s} = \Sigma \vec{F} \quad (4)$$

the first term (LHS) is the unsteady flow contribution over the control volume (V) and the second is the momentum flux through the control surface (s). The RHS is the sum of all external forces (F) responsible for the changes taking place on the LHS.

In this paper, we make the unproven assumption that the unsteady, time-derivative term on the LHS is small relative to the other terms in the momentum balance. Therefore we neglect the time-derivative term in this paper. For a breaking/broken water wave with dominant flow direction parallel to the bottom, the momentum balance in this direction is then given by Eqn (1) if we also neglect the boundary shear stress. And, if we operate in a moving coordinate system.

2.3 Non-accelerating Coordinate System. We can perform a Galilean transformation of our momentum conservation equation by moving our control volume at constant speed, i.e., by using a non-accelerating coordinate system. To remain phase locked with the wave crest we can use the wave propagation celerity as defined by the crest.

In this paper, we make the experimentally demonstrated assumption that the breaking/broken wave celerity through the transition region is approximately constant (see e.g., Basco, 1985, Fig. 4, p. 175).

2.4 Time-averaged Momentum Balance. Time-averaging Eqn (1) and then subtracting the hydrostatic pressure force measured from the mean water surface ($\bar{\eta}$) for a water wave produces the wave-induced momentum thrust or radiation stress. Across the transition region, by definition, $\bar{\eta}$ is constant so that if we again neglect the bottom shear stress, the radiation stress must also be constant based on the time-averaged momentum balance. One way for this to occur is for each phase-locked section of the breaking/broken wave moving through the transition to have constant total momentum. This gives added confidence to our assumptions cited above.

3.0 Transition Region Theory

3.1 Definitions. Consider the velocity profile $u(z)$ beneath a breaking wave as shown in Fig. 3 relative to a fixed reference frame. We schematize the velocity distribution into two major segments; (1) a crest region velocity $V_c(x)$ and (2) a trough region velocity $V_t(x)$ that act over $b(x)$ and $d(x)$, respectively. Note that one key feature of wave breaking is that the crest region and trough region absolute* velocities are in opposite directions.

It is useful to define the following dimensionless ratios using the wave crest celerity (c) as the reference velocity:

$$\lambda = \frac{V_c}{c} \quad (5)$$

$$\xi = \frac{|V_t|}{V_c} \quad (6)$$

therefore

$$\lambda\xi = \frac{|V_t|}{c} \quad (7)$$

The wave crest celerity for shallow water wave breaking is approximately

$$c^2 \approx gh_c \quad (8)$$

where h_c is the total water depth at the wave crest.

3.2 Moving Reference Momentum Balance. The counterpart of Eqn (1) for a control volume moving with speed (c) is

$$m^* = \int_0^h \left\{ [u(z) + c]^2 + \frac{1}{\rho} p(z) \right\} dz \quad (9)$$

or

$$m^* = m_v^* + m_p^* \quad (10)$$

where now total relative momentum (m^*) is partitioned into relative velocity (m_v^*) and pressure (m_p^*) components.

3.3 Schematized Transition - Strong Plunging Breaker. Using the qualitative model and ideas presented in Basco (1985), we schematically depict the velocity and pressure distributions for a strong, plunging breaker on a plane beach in Fig. 4. The crest velocity begins to exceed the wave celerity ($\lambda \geq 1$) at the break point and continuity results in $\lambda \gg 1$ at the plunge point for a strong plunging jet. At this point, the surface roller begins to form ($A \geq 0$) and grows in size as the plunging jet slows down ($\lambda < 1$) and exchanges its momentum through turbulent shear stresses with the trough fluid below. The overturning jet of a

*Absolute when referenced to a fixed (Eulerian) observer.

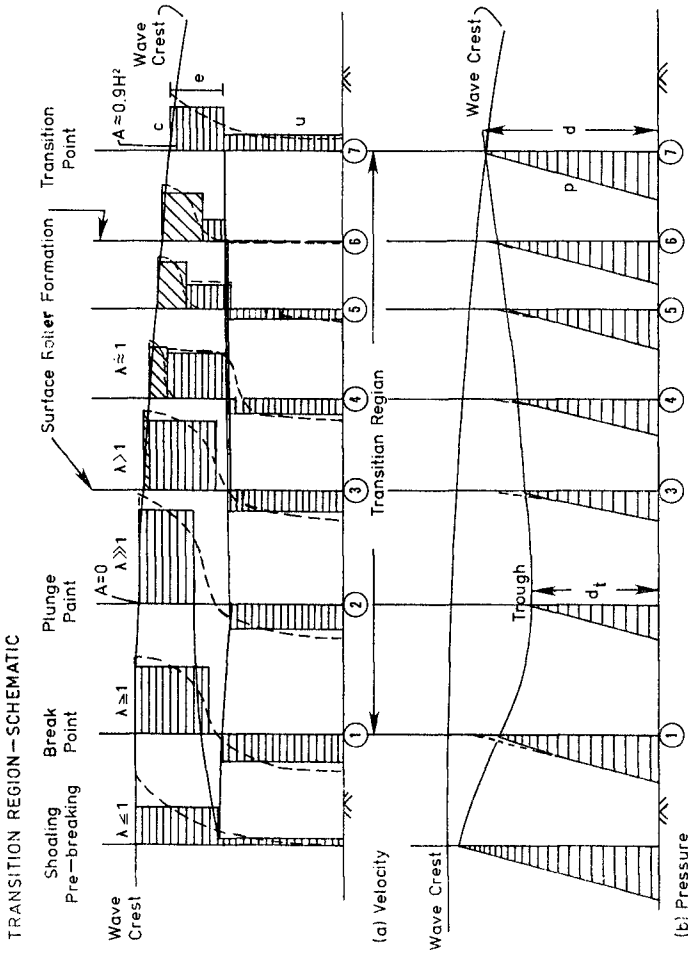
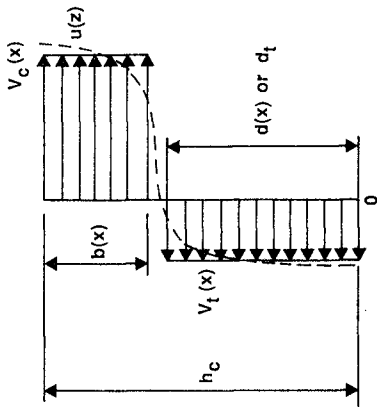


Fig. 4 Schematized Velocity and Pressure Distributions Across Transition Region (following qualitative model of Basco, 1985)



Define

$$\lambda \equiv \frac{V_c}{C}$$

$$\lambda \xi \equiv \frac{|V_t|}{C}$$

$$\xi \equiv \frac{|V_t|}{V_c}$$

$$C^2 = gh_c$$

Fig. 3 Schematized Horizontal Velocity Distribution Beneath Crest Region of Breaking Wave

breaking wave can be seen to perform two primary tasks in the transition region, namely:

- (1) to create a surface roller, with trapped mass of fluid that propagates with the wave celerity, and
- (2) to reverse the direction of the trough velocity from that opposing the crest, to that in the same direction as the particles in the surface roller.

At the transition point, or end of the transition region, the velocity profile beneath the crest is that of a propagating bore (Svendsen, 1984).

The corresponding pressure distribution changes are also shown in Fig. 4. Streamline curvature causes the pressure to remain less than hydrostatic ($a < 1$) through the break point. The pressure within the plunging jet is essentially zero if we assume it behaves as a free jet so that the pressure falls to essentially that approximated by hydrostatic pressure in the trough fluid. The pressure distribution then rises again to reach full hydrostatic pressure ($a = 1$) at the transition point.

These schematic ideas are translated into quantifiable relations at four representative locations within the transition region.

(i) Break Point (bp)

Fig. 5 depicts the absolute velocity structure ($\xi < 1$) and assuming $\lambda = 1$ ($V_c = c$), the velocity distribution for an observer moving with the wave crest, i.e., the relative velocity is also shown acting over the depths indicated. The velocity momentum (m_v^*) is then given by

$$m_v^* = (V_t + c)^2 d_t = [(\lambda\xi)c + c]^2 d_t = c^2(\lambda\xi + 1)^2 d_t \quad (11)$$

and is taken here to act over the depth (d_t) which is essentially the trough depth for a strong plunging breaker. Using Eqn (8) for c^2 and multiplying by unity (h_c/h_c) gives

$$m_v^* = \left[\frac{dt}{h} \right] (\lambda\xi + 1)^2 gh_c^2 \quad (12)$$

The first two terms in parentheses are dimensionless so that the last term (gh_c^2) gives the physical scale to the momentum and/or can be used to normalize the equation.

The pressure related momentum is simply

$$m_p^* = (a) \left[\frac{1}{2} gh_c^2 \right] \quad (13)$$

so that the total, relative momentum at the break point (m_{bp}^*) becomes

$$m_{bp}^* = \left[\left[\frac{dt}{h} \right] (\lambda\xi + 1)^2 + \frac{1}{2} a \right] gh_c^2 \quad (14)$$

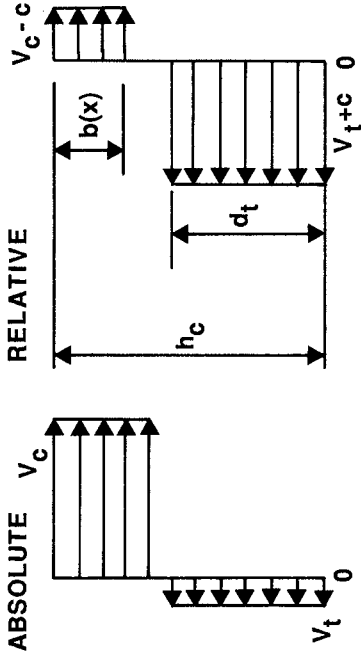


Fig. 6 Plunge Point - Absolute and Relative Velocities

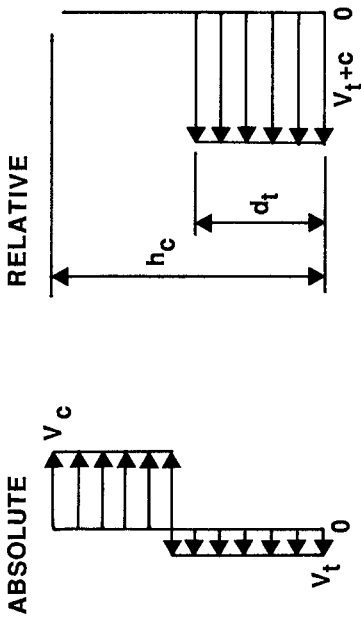


Fig. 5 Break Point - Absolute and Relative Velocities

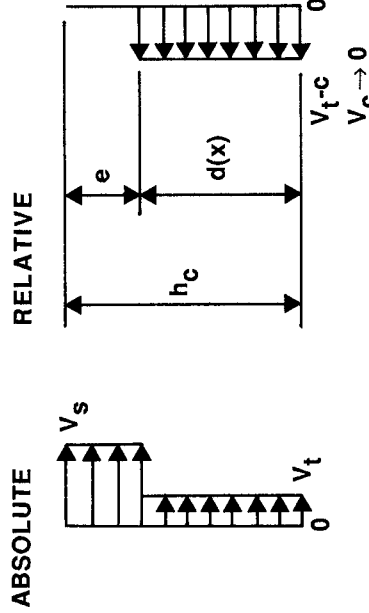


Fig. 8 Transition Point - Absolute and Relative Velocities

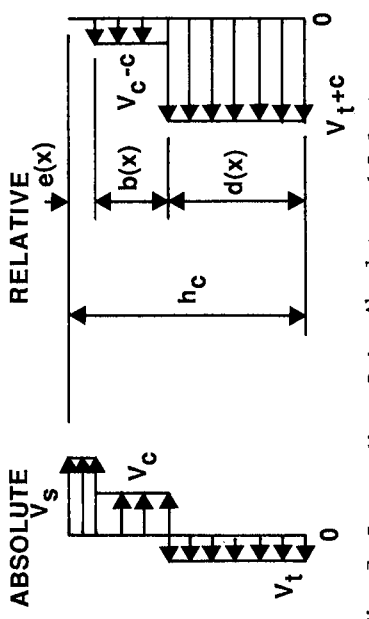


Fig. 7 Intermediate Point - Absolute and Relative Velocities

Four quantities must be specified [(d_t/h_c) , ξ , a , and h_c] to define m_{bp}^* if we assume $\lambda = 1$ at the break point.

Using the trough relative Froude number (F_t^*) as a measure of the strength of the breaking wave defined as (Stive, 1984)

$$(F_t^*)^2 = \frac{(V_t + c)^2}{gd_t} \quad (15)$$

this becomes at the break point

$$(F_t^*)^2 = (\lambda\xi + 1) \left[\frac{h_c}{d_t} \right]^{1/2} \quad (16)$$

or combining Eqn (12) and (16) we have

$$(F_t^*)^2 = \frac{m_v^*}{gh_c^2} \left[\frac{h_c}{d_t} \right]^2 \quad (17)$$

so that we need only two quantities (d_t/h_c and ξ) to specify the incoming relative Froude number if we again take $\lambda = 1$ at the wave breaking point.

(ii) Plunge Point (pp)

Now, $\lambda > 1$ ($V_c > c$) and again taking $\xi < 1$ as depicted in Fig. 6 with V_c acting over a contracted, free jet width $b(x)$ with $p = 0$ gives

$$m_v^* = \left[\frac{d_t}{h_c} (\lambda\xi + 1)^2 + \frac{b(x)}{h_c} (\lambda - 1)^2 \right] gh_c^2 \quad (18)$$

with the plunging jet now contributing to the relative momentum as given by the second term within the brackets.

With the pressure zero in the overturning jet, the pressure momentum coefficient a becomes

$$a = \frac{1/2gd_t^2}{1/2gh_c^2} = \left[\frac{d_t}{h_c} \right]^2 \quad (19)$$

if we assume the streamlines within the trough are relatively flat to create a hydrostatic pressure distribution. This then results in

$$m_p^* = \left[\frac{1}{2} \left[\frac{d_t}{h_c} \right]^2 \right] gh_c^2 \quad (20)$$

when the wave crest height h_c is used as reference. Combining gives for total relative momentum at the plunge point (m_{pp}^*)

$$m_{pp}^* = \left[\left[\frac{d_t}{h_c} \right] (\lambda\xi + 1)^2 + \frac{b(x)}{h_c} (\lambda - 1)^2 + \frac{1}{2} \left[\frac{d_t}{h_c} \right]^2 \right] gh_c^2 \quad (21)$$

Comparing Eqn (14) at the break point and (21) we see that if total, relative momentum is conserved, and when the first term within the brackets also remains relatively unchanged, then the added momentum of the overturning jet is balanced by the decreased pressure momentum within the trough. Four quantities [d_t/h_c , b/h_c , λ , and h_c] must again be specified to calculate m_{pp}^* if we now also assume that ξ remains the same as at the break point.

(iii) Transition Point (tp)

Now lets move to the end of the transition region and consider the transition point (t_p) as depicted in Fig. 8. We here define the velocity in the trapped surface roller as V_s to distinguish it from that within the plunging jet (V_c) that is slowing down and being left behind [$\lambda \rightarrow 0$, $b \rightarrow 0$]. The surface roller area (A) grows as shown in Fig. 2 and consequently so does the thickness of the trapped surface roller (e).

The relative velocity momentum becomes

$$m_v^* = \left[\frac{d(x)}{h_c} (\lambda\xi - 1)^2 \right] gh_c^2 \quad (22)$$

and the fact that the trough velocity V_t is now in the same direction as the wave celerity produces the negative sign within the bracketed term. This translates into a decrease in relative importance in the velocity component of the total momentum.

The pressure component must therefore increase and we take $a = 1$ to give full hydrostatic pressure as a first approximation, or

$$m_p^* = \frac{1}{2} gh_c^2 \quad (23)$$

so that the total relative momentum at the transition point (m_{tp}^*) becomes

$$m_{tp}^* = \left[\frac{d}{h_c} (\lambda\xi - 1)^2 + \frac{1}{2} \right] gh_c^2 \quad (24)$$

We again need four quantities [d/h_c (or e/h_c), λ , ξ and h_c] to compute m_{tp}^* .

(iv) Intermediate Point (ip)

This is obviously the most complicated region between the plunge and transition points (see Fig. 4). The plunging jet velocity slows down ($V_c < c$) as the surface roller moving with the phase speed ($V_s = c$) expands from $e = 0$ at the plunge point to e at the transition point where $A = 0.9 H_b^2$. The most important physical factor is the reversal in direction of V_t so that the $(\lambda\xi + 1)$ term becomes $(\lambda\xi - 1)$. Also V_t acts over an expanding width $d(x)$ as $b(x) \rightarrow 0$ which is a consequence of the turbulent mixing between the jet and trough fluids. Fig. 7 depicts both absolute and relative velocity distributions at an intermediate point where the trough velocity is still opposing the wave celerity. In general, the velocity momentum can be written

$$m_v^* = \left[\frac{d(x)}{h_c} (\lambda \xi \pm 1)^2 + \frac{b(x)}{h_c} (\lambda - 1)^2 \right] g h_c^2 \quad (25)$$

and the pressure momentum

$$m_p^* = \left[\frac{1}{2} a \right] g h_c^2 \quad (26)$$

so that the total relative momentum at an intermediate position becomes

$$m_{ip}^* = \left[\frac{d(x)}{h_c} (\lambda \xi \pm 1)^2 + \frac{b(x)}{h_c} (\lambda - 1)^2 + \frac{1}{2} a \right] g h_c^2 \quad (27)$$

Eqn (27) reduces Eqn (14) at the break point, to Eqn (21) at the plunge point and to Eqn (24) at the transition point when the appropriate assumptions are made. Consequently it is also the general expression for total relative momentum anywhere within the transition region.

In general, six quantities [d/h_c , λ , ξ , b/h_c , a , h_c] are needed to use Eqn (27). Two additional expressions can be $e(x)$ as related to $A(x)$ and some relation for $b(x) \rightarrow 0$ in the overturning jet along with the fact that $e(x) + b(x) + d(x) = h_c$.

4.0 An Example Computation

Consider a strong plunging breaker on a plane beach with crest height h_c of 13.5 ft (4.1m) at the instant of breaking. The water depth in the trough, immediately ahead is about one-half this depth ($d_t/h_c = 0.5$) and the trough velocity is about 20% of the crest velocity ($\xi = 0.2$, Stive, 1984). The situation is schematized in Fig. 9 and summarized in Table I. Assume also that at the instant of breaking (front wave face is vertical) the streamline curvature is such that the pressure coefficient a is 0.6. Using Eqn. (14), the relative velocity momentum, m_v^* is calculated to be $4221 \text{ ft}^3/\text{sec}^2$ ($120 \text{ m}^3/\text{s}^2$) and the pressure momentum, m_p^* is $1759 \text{ ft}^3/\text{sec}^2$ ($49 \text{ m}^3/\text{s}^2$) resulting in a total relative momentum, m^* of $5980 \text{ ft}^3/\text{sec}^2$ ($169 \text{ m}^3/\text{sec}^2$). In other words, the total momentum is about $6000 \text{ ft}^3/\text{sec}^2$ of which the initial partition at breaking results in 71 percent due to velocity and 29 percent due to pressure.

From Eqn (16), the relative trough Froude number, F_t^* is 1.7. This value would indicate a strong plunging breaker (spilling breakers have much lower values) but a weak bore or hydraulic jump. The fluid flow in the trough in the relative, moving coordinate system is supercritical.

As the wave overturns, the crest height (h_c) decreases. The example shows h_c values (col 3) of 13.1 ft (4.0m) at the plunge point, 12.7 ft (3.9 m) at the intermediate point, and 12.3 ft (3.7m) at the transition point or end of the transition region. These values were estimated for this example although they also could have been calculated if the total relative momentum m^* was assumed constant at $6000 \text{ ft}^3/\text{sec}^2$.

The example shows that using these h_c values and the other given conditions which are all plausible and or referenced magnitudes, that

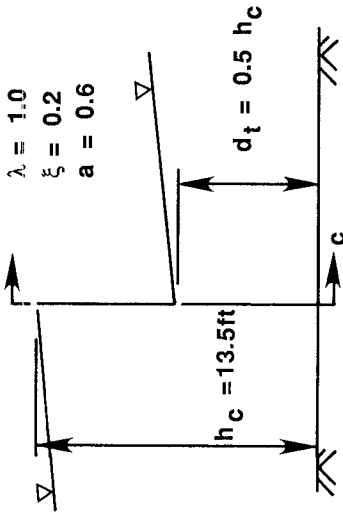


Fig. 9 Break Point - Given Conditions

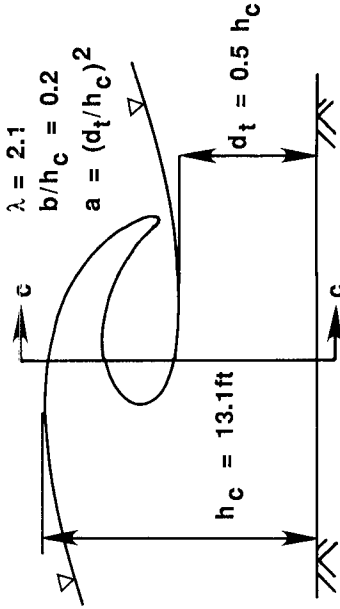


Fig. 10 Plunge Point - Given Conditions

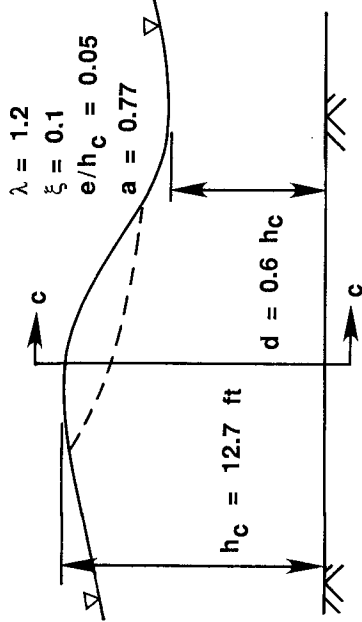


Fig. 11 Intermediate Point - Given Conditions

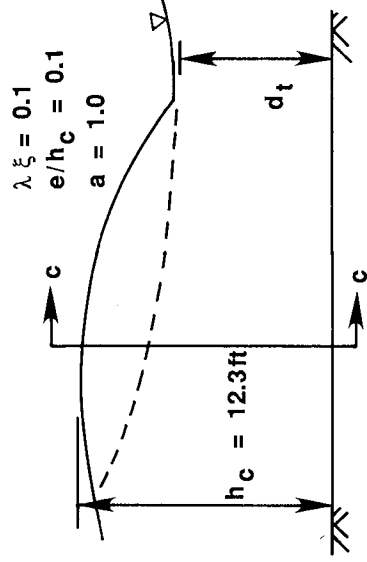


Fig. 12 Transition Point - Given Conditions

Table I - An Example Computation for Strong, Plunging Breaker on Plane Beach

Location Fig. (Equation) Nos.	Given Conditions [reference]					$m^* \text{ ft}^3/\text{sec}^2$			$m^* p$	m^*	Remarks	
	h_c ft (m)	d/h_c	d	b/h_c or e/h_c	a	$d \frac{-(\lambda \pm 1)}{h_c}$ (m^3/s^2)	$b \frac{-(\lambda - 1)}{h_c}$ (percent of m^*)	Total $m^* \lambda^2$ (percent of m^*)	$\frac{1}{2} \rho g h_c^2$ (percent of m^*)	Total Relative Momentum (m^3/s^2)		
(1)	(2) (3)	(4)	(5)	(6)	(7)	(8)	(9)	(10)	(11)	(12)	(13)	(14)
Break Point Eqn (14)	5,9 13.5 (4.1)	0.5 (trough)	1.0 (assume)	0.2 [9]	- 0.6	4221 (120)	0	4221 (71%)	1759 (29%)	5980 (169)	Velocity Dominates	
Plunge Point Eqn (21)	6,10 13.1 (4.0)	0.5 (trough)	2.1 [5,6]	$\lambda \xi$ same as b_p	d_t^2/h_c	3975 (113)	1325 (22%)	5300 (88.5%)	690 (11.5%)	5990 (170)	Velocity Nearly 90% of Total	
Inter. Point Eqn (27)	7,11 12.7 (3.9)	0.6	1.2	0.1 (0.05)	0.77	3905 (111)	73 (2%)	3978 (66.6%)	1998 (33.4%)	5976 (169)		
Transition Point Eqn (24)	8,12 12.3 (3.7)	-	$\lambda \xi = 0.1$ [9]	0.1 [10] (assume)	1.0 (assume)	3553 (101)	0	3553 (59%)	2433 (41%)	5986 (169)	Velocity Still Dominates But to Less Extent	

the partition of momentum changes through the transition. At the plunge point, we have taken the value of $\lambda\xi$ the same as at the break point but increased λ to over 2 as demonstrated numerically by Cokelet (1976) and experimentally by Kjeldsen (1984). The result is more velocity momentum with m_v^* now being $5300 \text{ ft}^3/\text{sec}^2$ ($150 \text{ m}^3/\text{s}^2$) or almost 89 percent of the total. And, a full 22 percent of the total is found in the jet momentum. The pressure component drops to only $960 \text{ ft}^3/\text{sec}^2$ ($20 \text{ m}^3/\text{sec}^2$) which is 11 percent of the total m^* of $5990 \text{ ft}^3/\text{sec}^2$ ($170 \text{ m}^3/\text{s}^2$).

At the intermediate section, the pressure begins to recover with m_p^* now $1998 \text{ ft}^3/\text{sec}^2$ ($57 \text{ m}^3/\text{s}^2$) or 33.4 percent. The velocity momentum, m_v^* has dropped to $3978 \text{ ft}^3/\text{sec}^2$ ($113 \text{ m}^3/\text{s}^2$) or 66.6 percent and of this amount, only $73 \text{ ft}^3/\text{sec}^2$ ($2 \text{ m}^3/\text{sec}^2$) remains in the crest region due to the plunging jet. Clearly, the original, plunging jet momentum is decaying and being left behind.

At the end of the transition region, the pressure component (m_p^*) has now risen to $2433 \text{ ft}^3/\text{sec}^2$ ($69 \text{ m}^3/\text{s}^2$) or 41% of the total which is the highest across the entire region. Conversely, the relative velocity momentum, m_v^* is the lowest [$3553 \text{ ft}^3/\text{sec}^2$, ($101 \text{ m}^3/\text{s}^2$), 59 percent] since all the particles beneath the crest are now traveling in the same direction as the wave. The given conditions employed in these calculations were aided by experimental data found in Stive (1988) and Svendsen (1984). At the end of the transition region, the relative velocity momentum still dominates the pressure component but to a far lesser extent.

5.0 Summary

All of these values are summarized in Fig. 13 for the four "points" across the transition region. Smooth curves have been drawn in to demonstrate the momentum partition trends for this example. These results, although a delicate balance and sensitive to the individual values used for each given condition at each section, can be looked upon as somewhat indicative of the general trends that must be present, namely:

- (i) the velocity dominates in all cases and is largest at the plunge point of a strong, plunging breaker;
- (ii) the trough velocity is the key variable, and the physical processes present to reverse its direction dominate the transition region; and
- (iii) the pressure is secondary in all cases and is smallest at the plunge point, then recovers to attain its greatest influence at the end of the transition region.

For a strong, plunging breaker on a plane beach and within the limitations and assumptions made throughout, we have developed a crude, quantitative model of the relative momentum and its partition. The role of the plunging jet momentum is to (1) form a surface roller and (2) reverse the trough flow direction over the trough depth. It becomes quite apparent that the relative strengths of the plunging jet momentum and the trough momentum control the time and hence spacial extent over which this transition process takes place. At one extreme is a relatively rapid, short transition as in this example for the strong

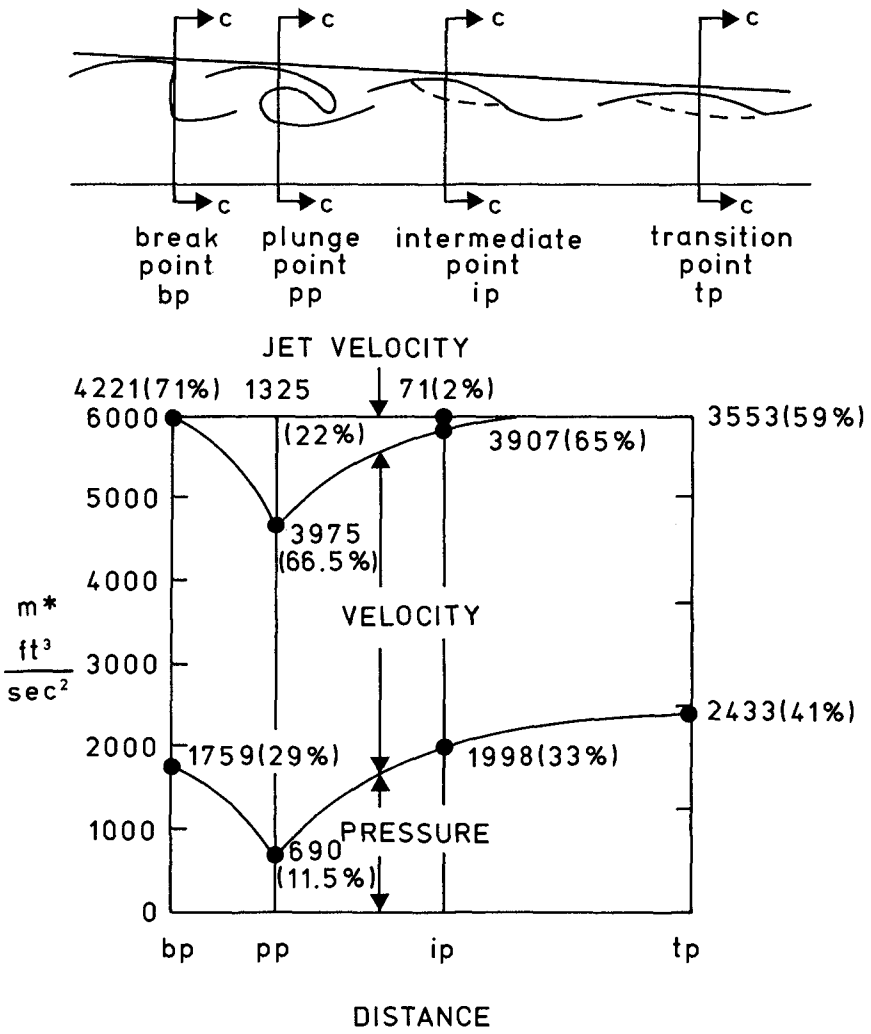


Fig. 13 Summary of Example Computation Across Transition Region

plunger.

The opposite extreme is a weak spilling breaker. The small overturning jet at the crest is still present but barely discernable. It's role remains the same but the transition requires a wide distance for the full surface roller to form and for the trough flow to be reversed over the entire vertical depth.

However, in both extremes, the strength of the trough velocity is believed to be the key variable. In nature, at some beaches, we can simultaneously observe waves breaking on relatively plane sections, waves breaking on bars and reforming in the deeper trough regions and waves breaking in the swash zone right on the beach. In all cases, the strength of the return flow in the trough appears to control the entire process. Consequently, it is felt that future numerical and experimental research (both laboratory and field) on breaking waves should give greater emphasis to defining the character of the trough flow.

References

1. Basco, D.R., (1985) "A Qualitative Description of Wave Breaking", Journ WW, ASCE, Vol. III, No. 2, Mar., pp. 171-188.
2. Basco, D.R. and T. Yamashita (1986), "Toward A Simple Model of the Wave Breaking Transition Region in Surf Zones", Proceedings, 20th ICCE, Taiwan, Vol. II, pp. 955-970.
3. Chow, V.T. (1959), Open-Channel Hydraulics, McGraw-Hill, N.Y.
4. Cokelet, E.O. (1978), "The Plunging Jet of a Breaking Wave", Euromech 102 (Breaking Waves: Surf and Run-Up on Beaches), Univ. of Bristol, England, July
5. Kjeldsen, S.P. (1984), "The Experimental Verification of Numerical Models of Plunging Breakers", 19th ICCE Proceedings, Vol. I, pp. 15-30.
6. Madsen, P.A. and I.A. Svendsen (1983), "Turbulent Bores and Hydraulic Jumps", Journal Fluid Mechanics, Vol. 129, pp. 1-25.
7. Papanicolaou, P. and F. Raichlen (1987), "Wave Characteristic in the Surf Zone", Proceedings Coastal Hydrodynamics 87, ASCE, NY, p. 765-780.
8. Stive, M.J.F. (1980), "Velocity and Pressure Field of Spilling Breakers", Proceedings, ICCE, 17th, pp. 547-566.
9. Svendsen, I.A. (1984), "Wave Heights and Set-Up in a Surf Zone", Coastal Engineering, Vol. 8, pp. 303-329.

CHAPTER 51

A DIRECTIONAL PREDICTION MODEL OF WAVES WITH VARIABLE WIND

Juan R. Acinas

ABSTRACT.- A model of the response of the direction of the waves to changing winds is presented. First the theoretical results that associate an average direction of energy propagation to every wave component is introduced. From this model, numerical results are presented both by simulations of ideal wind veering situations and compared with field data taken from pitch and roll buoys.

1. INTRODUCTION

The wave generation as a response to action of wind variable in intensity and direction is still an open problem, where either the theoretical models or the numerical methods used for its forecasting and hindcasting require a proper validation based on strictly controlled wind and wave measurements.

This communication presents a theoretical model of the directional wave response, as well as numerical examples in ideal conditions and comparisons with field data taken from the Norwegian ODAP project.

The model allows us to associate an average direction of energy propagation to every spectral component, so that with a little additional computational effort we get a wave prediction method with analogous precision in the two dimensions of the spectrum; frequency and direction.

Numerical results are presented illustrating the general behaviour of the wave directional relaxation. The data available to the author backs up these results.

Civil Engineer, Asesor Tecnico, Centro de Estudios y Experimentacion de Obras Publicas, c/ Alfonso XII, 3, 28014 Madrid, Spain.
Tel.: 34 91 4682400, Telex: 45022 CEDEX-E

2. MODEL

The global mean direction Ω of the wave spectral density function $S(f,\theta) = S(f) \cdot D(f,\theta)$ due to the wind action depends on: The boundary and initial values of the wave field, the change in the directional shape of S , and the direct action of the wind. This effect has, in turn, two components; the energy contribution E_{Δ} , and the change in its directional distribution, J.R.Acinas (1987).

In this communication only the directional variation due to the energy E_{Δ} , is taken into account as a consequence of the wind action in a homogeneous wave field. Starting from the energy balance equations and the global average direction of the wave:

$$dS(f,\theta)/dt = G(f,\theta) \equiv \text{Source Function} \quad (1)$$

$$\Omega = \arctan \left(\int_0^{2\pi} \sin\theta \cdot S \cdot df \cdot d\theta / \int_0^{2\pi} \cos\theta \cdot S \cdot df \cdot d\theta \right) \quad (2)$$

Differentiating equation (2) and after some manipulations involving (1) and (2) the result is:

$$\frac{d\Omega}{dt} = \frac{-DI}{A^2 + B^2} \cdot \frac{1}{E} \cdot \frac{dE_{\Delta}}{dt} \quad (3)$$

with: $DI = (A_{\Delta}B - B_{\Delta}A)\cos\epsilon - (A_{\Delta}A + B_{\Delta}B)\sin\epsilon$
 A, B and A_{Δ}, B_{Δ} first order direction estimators of the total wave energy, E , and of the wind contribution, E_{Δ} .
 $A = \iint \cos\theta D(f,\theta) df d\theta$; $B = \iint \sin\theta D df d\theta$
 $S = (\theta_u - \Omega)$; $E = \iint S(f,\theta) df d\theta$

If we centre $D(f,\theta)$ around Ω , we obtain in general

$$\frac{d\Omega}{dt} = \left(\frac{A_{\Delta}}{A} \cdot \sin\epsilon + \frac{B_{\Delta}}{A} \cdot \cos\epsilon \right) \cdot \frac{1}{E} \cdot \frac{dE_{\Delta}}{dt} \quad (4)$$

and doing the same with the energy contribution, E_{Δ} we have

$$\frac{d\Omega}{dt} = \frac{A_{\Delta}}{A} \sin \delta \cdot \frac{1}{E} \cdot \frac{dE_{\Delta}}{dt} \quad (5)$$

If we consider, for example, spectral evolution according to the JONSWAP study, we obtain the global average direction of the wave (based on parameters which characterise its growth) by:

$$\frac{d\Omega}{dt} = \frac{A_{\Delta}}{A} \sin \delta \cdot \frac{E_{\Delta}}{E} \cdot \left(-4 \cdot \frac{dL f_P}{dt} + \frac{dL \alpha}{dt} + \frac{dLP}{dt} \right)_{\Delta} \quad (6)$$

with: $P = P(\gamma, \sigma) = \int_0^{\infty} x^{-5} \exp(-1.25/x^4) \cdot \gamma^y dx$
 $y = \exp(-((x-1)/\sigma)^2 / 2)$

The response of the wave direction Ω_c , of a spectral band (f_1, f_2) represented by the frequency, f_c and energy component E_c is similarly given by:

$$\frac{d\Omega_c}{dt} = \frac{A_{\Delta c}}{A_c} \sin \delta \cdot \frac{1}{E_c} \cdot \frac{dE_{\Delta c}}{dt} \quad (7)$$

Systematic application of this formulation is the basis of the development of a directional wave prediction model in which each spectral component has an associated mean direction of energetic propagation.

3. RESULTS

The model is illustrated both by simulations under ideal wind-veering situations (Figs. 1 and 2), and compared with measurements from the ODAP data analyzed by T. Audunson et al. (1981), Fig. 3.

Initial wind and wave conditions are assumed to be homogeneous and are used as input to a parametrical wave prediction model, (Acinas 1981).

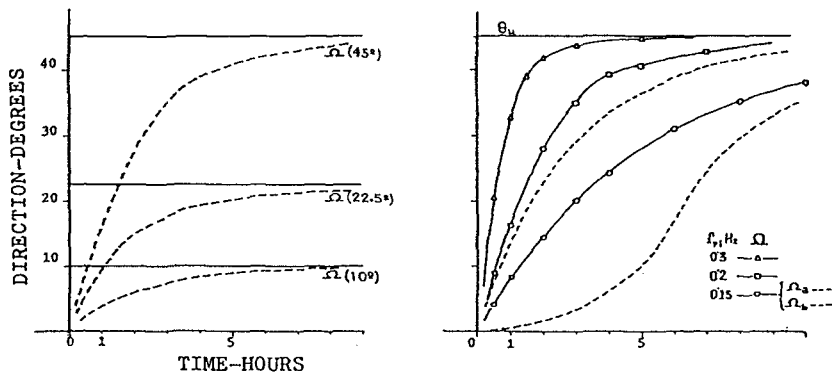


Fig.1 Response of wave direction to a sudden change $\Delta\theta_u$, in wind direction. Wind velocity U , constant.

- a) Global mean wave direction response Ω , to $\Delta\theta_u = 10^\circ, 22.5^\circ$ and 45° . Initial peak frequency $f_{pi} = 0.2\text{Hz}$.
- b) As in a) but for $\Delta\theta_u = 45^\circ$ and $f_{pi} = .15, .2, \text{ and } .3\text{Hz}$. Response $\Omega_a(3/2f_p)$ and $\Omega_b(2/3f_p)$; $f_{pi} = 0.15\text{Hz}$.

Computation is carried out along characteristic lines and for easier comparison of results, $A_\Delta/A = 3.5$ has been used for all cases. This number comes from an empirical best fit with the ODAP data.

Inspection of the equations and results shows the following behaviour:

a) For the same initial wave field, the veering rate of Ω grows according to $\Delta\theta_u$.

b) For the same variation $\Delta\theta_u$, Ω grows faster with the largest f_p of the initial state.

c) For a given wave field, the direction Ω_a , of the high frequencies, $f_a > f_p$, responds in a quasi-instantaneous way to the variations of θ_u , and at a faster rate than the global direction.

On the other hand, low frequencies $f_b < f_p$ show a temporal delay in the response with lower response rate than the global direction.

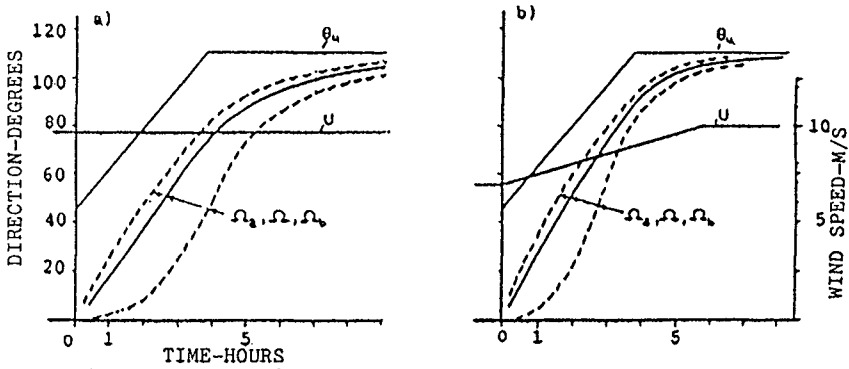


Fig.2 Response of global, high and low frequency directions Ω , Ω_a and Ω_b , to changing wind (U, θ_w); $f_{pi} = .2\text{Hz}$.

a) (U constant, θ_w variable) b) (U variable, θ_w variable)

d) As the wave field grows towards FDW (fully developed wave spectrum) levels, the direction at all frequencies tends to align with that of the wind.

These results are in analogous with the theoretical-experimental results suggested previously by several authors; D.E. Hasselmann et al. (1980), H.Gunther et al (1981), T.Audunson et al (1981), J.H.Allender et al (1983).

From the ODAP data available to the author (Fig. 3.a) the prediction model has been evaluated for the period in which there is a growing sea, so that we can expect quasi-homogeneous conditions. A rapidly growing wind dominates this period. The results are given in Fig. 3.b.

4. CONCLUSIONS

The response of wave directions, due only to the energy variation, under changing wind direction conditions can be summarized according to our results in three stages:

1^a) The high frequencies respond quasi-instantaneously, and quickly adjust to wind direction then remaining saturated in energy.

During this first stage the low frequencies do not react to the change in wind direction. This may be explained because its energy E_{Δ} , does not increased.

2^a) The low frequencies then begin to increase in energy, with a subsequent very rapid variation in its direction Ωb , that is very strong and has an inflexion point.

3^a) On approaching FDW for a given wind all the components tend asymptotically to the wind direction in the same way.

These three stages can be totally or partially completed, but are always in order and with the same characteristics. This behaviour is clear both in the measurements as well as in the numerical calculations for the ideal situations (Figs. 1 and 2).

It is worth mentioning that the theoretical directional model does fit well to the available data (Fig. 3).

As a consequence, it's logical to begin to use the directional results of the model in the engineering evaluations of wave forecasting and hindcasting.

The directional measurements currently available are very limited. An international data base is therefore proposed which would greatly assist future theoretical work.

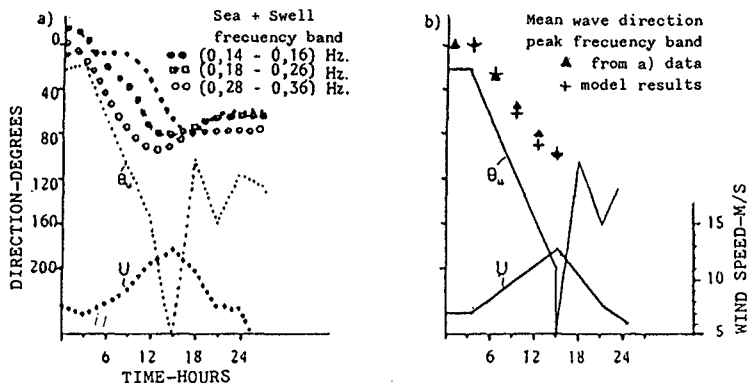


Fig.3 Response of wave direction Ω , to a changing wind (U, θ).

- a) Analysis of field observations by T. Audunson, S. Barstow and H. Krogstad, 1981.
- b) Input (U, θ) values and numerical present results $\Omega(t)$ compared with the response obtained from a) field data.

REFERENCES

- Acinas J.R. 1981. Previsión del oleaje en los grandes puertos del Cantábrico MOPU.
1987. Relación direccional oleaje-viento. Análisis teórico. CEDEX en edición.
- Allender J.H., J. Albrecht and G. Hamilton 1983. Observation of directional relaxation of wind sea spectra. J. of Physical Oceanography, vol 13.
- Audunson T., S.F. Barstow and H.E. Krogstad 1981. Analysis of wave directionality from H.P.R. Buoy operated Offshore Norway. Wave wind direct. Paris 1981.
- Holthuisen L.H., B. Monsselman and A.J. Kuik 1984. A model for the response of wave directions to changes in wind direction. Symp. on description and modelling of directional seas. T.U. Denmark.

CHAPTER 52

THREE DIMENSIONAL FLOW PROFILES ON LITTORAL BEACHES

Ib A. Svendsen, M.ASCE¹ and Rene S. Lorenz²

ABSTRACT: The problem of combined cross-shore and longshore currents generated by waves in and around a surf zone is considered in its full three-dimensional formulation. The equations for the two current components are decoupled and it is found that for a cylindrical coast with no longshore variations the longshore current variation with depth and distance from the shoreline satisfies a Poisson equation. This equation is solved by a perturbation method and it is shown that the longshore velocities are always larger than the velocities found by classical theory. In the simple uncoupled case, the full 3-D current profile is constructed by combining the results with cross-shore velocities determined in previous publications. Also, the total velocities are larger than velocities found from simple depth averaged models.

1. INTRODUCTION

The present paper deals with the variation over depth of the magnitude and direction of the wave induced mean currents on a beach.

In the past, the dept variation of wave induced currents have been studied for the purely two-dimensional case of cross-shore flow with particular aim at the seaward going undertow (among the latest contributions may be mentioned Stive & Wind (1986) and Svendsen & Hansen (1988)).

Longshore currents have mostly been analyzed in the simplified case of a long beach with straight bottom contours and no flow variations in the longshore direction. The first contributions date back nearly 20 years (Bowen, 1969; Thornton, 1970; Longuet-Higgins, 1970), and numerous works have been published on the topic since then. They all, however, consider depth integrated equations only, and therefore can only determine a sort of depth averaged value of the longshore current velocity.

Some contributions have claimed three dimensionality for the current description without actually being so. There is also a quasi-3D model inspired by river hydraulics was recently suggested by deVriend & Stive (1987) (essentially the same as Stive & deVriend, 1987). They divide the current motion into a primary part which has the direction and depth averaged magnitude of the net discharge; and a secondary flow which has zero depth mean, goes in the direction of the wave energy flux, and is generated by the wave motion. Further, the secondary current is assumed small relative to the primary current. As an example, however, the undertow is generated by the waves and has

¹Prof., Dept. of Civil Engrg., Univ. of Delaware, Newark, DE 19716 USA (Mail address for this paper).

²Research Engineer, Lic Engineering, Vimmelskafdet 47, 4, 1161 Copenhagen K, Denmark.

zero depth mean and hence would be a secondary current according to their definition. On the other hand, it will usually be significant in comparison to net flux current and for obliquely incident waves it will not be in the direction of the wave energy flux. Another example, the longshore current does not seem to fit into the idea that the secondary currents generated by the waves have zero depth mean. Thus the assumptions of de Vriend and Stive (1987) do not seem to cover those two important examples of wave generated currents.

In the present paper we shall take a very much different approach to the problem of three dimensional nearshore circulation and particularly discuss two aspects. One is the variation over depth of the longshore (as well as the cross-shore) currents. The other is the variation of the combined cross-shore and longshore flow. The discussion will be centered around the basic assumptions and the physical aspects of the solution. Readers are referred to Svendsen and Lorenz (1988) for some of the detailed derivations omitted here.

The starting point is taken from the three dimensional Reynolds' equations derived in the above mentioned reference for a combination of waves and wave induced currents in an environment with turbulence produced by primarily wave breaking. Although those equations are fairly general we concentrate the discussion here on the situation of a long straight coastline since some of the essential features of the combination of cross and longshore currents also appear in that canonical situation.

2. THE BASIC ASSUMPTIONS AND THE EQUATIONS USED

The flow situation on a beach corresponds to a combination of a turbulent, oscillatory (wave) motion and a current. In particular inside the breaker point the turbulence generated by the wave breaking will be very intensive.

The equations governing the wave induced currents can be derived from the general Navier-Stokes equations by transformations that correspond to turbulent (or ensemble) averaging (leading to Reynolds type equations) and to averaging over a wave period (corresponding to the equations derived by Whitham (1962) and Longuet-Higgins and Steward (1960,61)).

In accordance with the above description, the total velocity $\vec{u} = (u, v, w)$ is divided into three components by the relations

$$\left. \begin{aligned} u &= U + u_w + u' \\ v &= V + v_w + v' \\ w &= w_w + w' \end{aligned} \right\} \quad (2.1)$$

Here index w indicates oscillatory (wave) components, ' turbulent quantities. We use $\bar{\quad}$ to indicate ensemble averaging, which means that $\bar{u}' = \bar{v}' = \bar{w}' = 0$. Similarly, $\overline{\quad}$ denotes averaging over a wave period so that $\overline{u_w} = \overline{v_w} = \overline{w_w} = 0$ below trough level.

By the above mentioned averaging processes and eliminating the pressure by integrating the vertical component of the momentum flux we arrive at the following two equations for U and V, the horizontal current components.

$$\begin{aligned} \frac{\partial U}{\partial t} + \frac{\partial U^2}{\partial x} + \frac{\partial UV}{\partial y} + \frac{\partial (\overline{u_w^2} - \overline{w_w^2})}{\partial x} + \frac{\partial \overline{u_w v_w}}{\partial y} + \frac{\partial \overline{u_w w_w}}{\partial z} \\ = - \frac{\partial b}{\partial x} - \frac{\partial (\overline{u'^2} - \overline{w'^2})}{\partial x} - \frac{\partial \overline{u' v'}}{\partial y} - \frac{\partial \overline{u' w'}}{\partial z} \end{aligned} \quad (2.2)$$

and

$$\frac{\partial V}{\partial t} + \frac{\partial V^2}{\partial y} + \frac{\partial UV}{\partial x} + \frac{\partial(\overline{v_w^2} - \overline{w_w^2})}{\partial y} + \frac{\partial \overline{u_w v_w}}{\partial x} + \frac{\partial \overline{v_w w_w}}{\partial z} \\ - - g \frac{\partial b}{\partial y} - \frac{\overline{\partial v'^2 - w'^2}}{\partial y} - \frac{\overline{\partial u' v'}}{\partial x} - \frac{\overline{\partial v' w'}}{\partial z} \quad (2.3)$$

Eqs. (2.2) and (2.3) are in principle the momentum equations governing the wave induced current motion and it is those equations that are examined further in the following. They differ from the usual depth averaged equations in that they are not integrated in the vertical direction. Thus U, V are in general functions of x, y and z. The equations are only valid below trough level.

In order to solve these equations for U, V it is necessary

- to assume that the terms with index w representing the wave motion are determined by some wave theory or by measurements.
- to model in terms of quantities determined otherwise the turbulent normal and tangential stresses.

In the present context, we do not loose any of the effects we want to examine by using a simple time-independent eddy viscosity model for the turbulence. Besides, this has been shown for the cross shore flow to yield very reliable results (see e.g. the earlier quoted references and Svendsen et al. (1987)). Hence we let

$$\left. \begin{aligned} \overline{u' v'} \quad , \quad \overline{v' w'} &= -\nu_t \left[\frac{\partial V}{\partial x} \quad , \quad \frac{\partial V}{\partial z} \right] \\ \overline{u' w'} &= -\nu_t \frac{\partial U}{\partial z} \end{aligned} \right\} \quad (2.4)$$

in which we have already introduced the simplification of uniform flow conditions in the longshore direction ($\partial/\partial y = 0$). We also neglect the turbulent normal stresses.

3. THE FLOW PROFILES ON A CYLINDRICAL COAST WITH NO LONGSHORE VARIATIONS

This canonical case corresponds to letting $\partial/\partial y = 0$ in both (2.2) and (2.3) which yields equations amenable to analytical solution without the essential features of the flow are lost. We also limit our considerations to time independent current patterns. Hence the equations we consider for further simplification are the following

$$\frac{\partial}{\partial x} \left[U^2 + gb + (\overline{u_w^2} - \overline{w_w^2}) \right] + \frac{\partial \overline{u_w w_w}}{\partial z} = - \frac{\partial(\overline{u'^2 - w'^2})}{\partial x} + \frac{\partial}{\partial z} \left[\nu_t \frac{\partial U}{\partial z} \right] \quad (3.1)$$

and

$$\frac{\partial}{\partial x} \left[UV + \overline{u_w v_w} \right] + \frac{\partial \overline{v_w w_w}}{\partial z} = \frac{\partial}{\partial x} \left[\nu_t \frac{\partial V}{\partial x} \right] + \frac{\partial}{\partial z} \left[\nu_t \frac{\partial V}{\partial z} \right] \quad (3.2)$$

where also (2.4) has been substituted.

The Cross-Shore Motion

With suitable additional simplification (3.1) becomes the equation solved in the literature for undertow. Several of those simplifications were analyzed by Stive & Wind (1982) and Svendsen et al. (1987), using measurements to calculate the magnitude of the $\overline{w_w^2}$,

the $\overline{u'^2} - \overline{w'^2}$ and U^2 terms. Although the U^2 term is found not to be quite negligible, the measurements used by Svendsen et al. (1987) show that the dominating driving term in (3.1) is the $\partial b / \partial x$ - term. $\partial \overline{u_w^2} / \partial x$ is only 10-20% of that and the other terms are even smaller.

The measurements also show that $\overline{u_w^2}$ is remarkably constant over depth, a fact that has been further confirmed by later, yet unpublished, laboratory results.

The $\partial \overline{u_w w_w} / \partial z$ term has also been neglected in all previous investigations. It represents the net horizontal shear stress on a fluid particle generated by the oscillatory wave component. For constant depth wave theories (such as the linear wave theory which is often used for the wave contributions) this term is identically zero (except in the boundary layer). On a sloping bottom we have no wave theory from which we can evaluate the term. Simple estimates suggest, however, that the term is substantially smaller than $\partial \overline{u_w^2} / \partial x$. Hence in spite of the principal importance of the $\partial \overline{u_w w_w} / \partial z$ term in deriving the depth integrated version of the equations, it is a good approximation locally to disregard this term in the equation for cross-shore currents.

With the assumed constant eddy viscosity and with the driving term

$$\alpha_1 = \frac{\partial}{\partial x} \left[gb + \overline{u_w^2} - \overline{w_w^2} + U^2 \right] \quad (3.3)$$

uniform over depth the solution for the undertow may be written

$$U = \frac{1}{2} \frac{\alpha_1}{\nu_t} \zeta^2 + \frac{A_1}{\nu_t} \zeta + U_b \quad (3.4)$$

where A_1 is an integration parameter related to the mean bottom friction. U_b is the bottom value of the undertow profile if extended to the bottom without consideration of the bottom boundary layer. For a closer discussion of evaluation of A_1 and U_b reference is made to Svendsen & Hansen (1988).

The Longshore Motion

The longshore motion is given by (3.2). The additional simplification needed to make this equation solvable is related to the UV-term. This term represents the effect which the undertow has on the longshore current. Although this effect may locally be appreciable it can readily be shown that averaged over depth the contribution will be almost nil. In order to proceed we choose here to neglect the term. Then (3.2) reduces to

$$\frac{\partial}{\partial x} \left[\nu_t \frac{\partial V}{\partial x} \right] + \frac{\partial}{\partial z} \left[\nu_t \frac{\partial V}{\partial z} \right] = \frac{\partial \overline{u_w v_w}}{\partial x} + \frac{\partial \overline{v_w w_w}}{\partial z} \quad (3.5.)$$

Since the right hand side is considered known, this is a Poisson equation for the variation of the longshore current velocity V over depth and cross shore directions.

It may be noticed that the effect of neglecting the UV-term is that the equation for the longshore current becomes independent of the solution for the cross-shore current. Similarly, in the general case of arbitrary bottom topography this would have freed the cross shore current from dependence of the longshore current solution.

Eq. (3.5) may also be written

$$\nabla(\nu_t \nabla V) = g_{xy}$$

where

$$g_{xy} = \frac{\partial}{\partial x} \left(\overline{u_w v_w} \right) + \frac{\partial}{\partial z} \left(\overline{v_w w_w} \right)$$

4. SOLUTION FOR THE LONGSHORE CURRENT VARIATION WITH x AND z

It turns out that by physically realistic assumptions about magnitude of the terms in (3.5) and the boundary condition at the bottom (3.5) can be solved by a perturbation technique which as the first approximation has the classical solution for depth averaged longshore current velocity.

First we notice that since (3.5) is an elliptic equation it requires boundary conditions along the full boundary.

The forcing term $g(x,y)$ will only be non-zero shoreward of the transition point, x_t (Svendsen, 1984). Hence, at x_t , g_{xy} is discontinuous and matching of solutions must be arranged as in traditional longshore current solutions with depth independent velocities.

Eq. (3.5) is only valid below wave trough level. Therefore another boundary condition is that at the trough level

$$\tau_{zy} = \rho \nu_t \frac{\partial V}{\partial z} = \frac{\partial}{\partial x} S_{xy,s} \quad \text{at } x = \eta_t \quad (4.1)$$

where $S_{xy,s}$ is the radiation stress contribution above trough level, and η_t is the wave trough level. This boundary condition is introduced into the mathematical formulation by combining it with the requirement that (3.5) be satisfied at all z below trough level to yield the depth integrated momentum balance which becomes

$$\frac{\partial}{\partial x} \int_{-h_0}^b \rho \nu_t \frac{\partial V(x,z)}{\partial x} dz - \tau_{yb} = \frac{\partial S_{xy}}{\partial x} \quad (4.2)$$

For V independent of z this expression reduces to the well known

$$\frac{\partial}{\partial x} \left(\rho \nu_t h \frac{\partial V}{\partial x} \right) - \tau_{yb} = \frac{\partial S_{xy}}{\partial x} \quad (4.3)$$

which is the equation normally solved for longshore currents.

The most important boundary condition, however, is at the bottom. Here we have an oscillatory boundary layer in which the turbulent eddy viscosity can be assumed much smaller than above (Svendsen et al., 1987). In contrast to cross-shore flow, however, the bottom shear stress is the (exterior) force resisting the driving radiation stress gradient. In this context the horizontal turbulent mixing--represented by the $\partial/\partial x(\nu_t \partial V/\partial x)$ term--only redistribute the radiation stress contributions from one place to another, and the

integral of all radiation stresses from sea to shore must equal S_{xy} at the breaker point.

The boundary layer at the bottom will yield a relationship between the bottom velocity V_b and the bottom shear stress $\tau_{y,b}$, and we assume that this relationship can be represented by a generalization of the expression derived by Svendsen & Hansen (1988)

$$\tau_{y,b} = \left(\rho \nu_t \frac{\partial V}{\partial z} \right) = \frac{1}{2} \rho f_w u_{wb} V_b \quad (4.4)$$

where f_w is the friction factor for waves only, u_{wb} the oscillatory particle velocity in the wave direction. It is emphasized that although this expression formally may resemble the frequently used relationships between bottom shear stress and depth mean velocity (4.4) is actually based on the elaborate wave current boundary layer theory by Christoffersen & Jonsson (1983).

The turbulent mixing term cannot be neglected even in a first approximation since that would change the degree of the differential operator in the x-direction and radically change the nature of the x variation of V (Longuet-Higgins, 1970).

With the turbulence mixing as a modifying term, however, the longshore flow is very much a balance between the driving radiation stress gradient and the resisting τ_{zy} shear stress. Thus, if we for a moment assumed the right hand side of (3.5) and the turbulent mixing were uniformly distributed over depth then τ_{zy} would vary linearly over depth, with the largest values at the bottom. The small viscosity inside the bottom boundary layer and much larger value above therefore means that by far the largest velocity gradients will occur within the bottom boundary layer. Or, in other words, the velocity outside the boundary layer will only show a moderate variation in comparison to the variation inside the boundary layer.

Mathematically this can be expressed by assuming that the first approximation to the longshore current velocity is independent of z . Thus we assume a perturbation expansion of the form

$$\left. \begin{aligned} V &= V_0(x) + \epsilon V_1(x, z) + \dots \\ \tau_{yb} &= \tau_0(x) + \epsilon \tau_1(x) + \dots \\ V_b &= V_{b0} + \epsilon V_{b1} + \dots \end{aligned} \right\} \quad (4.5)$$

In order to obtain a consistent modification of the equations (3.5), (4.2) and (4.4) a scaling is required which introduces the assumption that the width of the surf zone $x_s - x_t$ is $\ll h_t$ where h_t is the depth at the transition point x_t . It is also utilized that

$$\frac{f_w}{\nu_t} h_t \sqrt{gh_t} = O(s_x^2) \quad (4.6)$$

where $s_x = \epsilon^{1/2}$ is a characteristic value of the bottom slope. With

$$X = -s_x x \quad ; \quad Z = z \quad ; \quad \epsilon = s_x^2 \ll 1$$

the modified equations become

$$\epsilon \frac{\partial}{\partial X} \left[\nu_t \frac{\partial V}{\partial X} \right] + \frac{\partial}{\partial Z} \left[\nu_t \frac{\partial V}{\partial Z} \right] = -\epsilon g_{xy} / s_x^2 \quad (3.5a)$$

$$\frac{\tau_0}{\rho\nu_t} = \left(\frac{\partial V}{\partial z} \right)_{-h_0} = \epsilon \frac{1}{2} \frac{f_w}{\nu_t s_x^2} u_{wb} V_b \quad (4.4a)$$

and

$$\epsilon \frac{\partial}{\partial X} \int_{-h_0}^b \rho\nu_t \frac{\partial V}{\partial X} dz - \tau_{yb} = \frac{\epsilon}{s_x^2} \frac{\partial S_{xy}}{\partial x} \quad (4.2a)$$

The first order approximation shows that since $V_0 = V_0(x)$ outside the boundary layer we get $\tau_0 = 0$.

The system also yields $V_{b0} = V_0$ and hence

$$\frac{\tau_1}{\rho\nu_t} = \frac{1}{2} \frac{f_w}{\nu_t s_x^2} u_{wb} V_0 = \left(\frac{\partial V_1}{\partial z} \right)_{-h_0} \quad (4.7)$$

V_0 is then determined from (4.2), and since V_0 is independent of z (4.2) takes the form of (4.3)

$$\frac{\partial}{\partial X} \left(\rho\nu_t h \frac{\partial V_{b0}}{\partial X} \right) - \tau_1 = \frac{1}{s_x^2} \frac{\partial S_{xy}}{\partial x} \quad (4.8)$$

where τ_1 is given by (4.7).

Thus we have found that the first approximation V_0 to the longshore velocity V is determined exactly by the equation which has so far been used in the literature for depth averaged longshore current velocities. V_{b0} , however, is not the depth averaged value of V as we shall see shortly.

Carrying the computations through to second order we find that

$$\begin{aligned} V(x,z) &= V_0 + \epsilon V_1 \\ &= V_{b0} + \epsilon V_{b1} + \frac{1}{2} \left(g_{xy} - \frac{\partial}{\partial x} \left(\nu_t \frac{\partial V_0}{\partial x} \right) \right) (z+h_0)^2 \\ &\quad + \frac{f_w}{2\nu_t} u_{wb} V_{b0}(z+h_0) \end{aligned} \quad (4.9)$$

Here V_{b1} can be determined from the differential equation

$$\frac{\partial}{\partial X} \left(\nu_t h \frac{\partial V_{b1}}{\partial X} \right) - \frac{1}{2} \rho f_w u_{wb} V_{b1} = -F(x) \quad (4.10)$$

where $F(x)$ is a known function of x determined from the first order solution. One important observation here is that (4.9) shows that the depth average of V is always larger than V_{b0} , $V_{b0} = V_0$ is in fact the smallest velocity in the profile.

The results also show that there is a correction V_{b1} to the bottom velocity V_{b0} found by the traditional longshore current equation (4.8). This correction is entirely due to the fact that in (4.8) we

use V_0 to evaluate the turbulent mixing, not V . Since V_{b1} will normally be a small term, we may get a good approximation to V by neglecting V_{b1} . That yields

$$V(x, z) \approx V_{b0} + \frac{1}{2} \frac{g'_{xy}}{\nu_t} (z+h_0)^2 + \frac{f_w}{2\nu_t} u_{wb} V_{b0}(z+h_0) \quad (4.11)$$

where

$$g'_{xy} = g_{xy} - \frac{\partial}{\partial x} \left[\nu_t \frac{\partial V_{b0}}{\partial x} \right] \quad (4.12)$$

5. NUMERICAL RESULTS FOR THE LOCAL LONGSHORE CURRENT VELOCITY PROFILE

For both V_0 and V_1 , a full solution for the local profile requires that we solve the differential equations (4.8) and (4.10) for V_{b0} and V_{b1} , respectively. Properly done this also implies determination of the wave height variation across the surf zone to establish the variation of S_{xy} .

To illustrate the nature of the results, however, let us neglect the effect of the turbulent mixing and concentrate on the local velocity profiles only. This implies that $g'_{xy} = g_{xy}$ in (4.11).

Using Svendsen's (1984) description of the surf zone waves with a shape factor $B_0 = \eta^2/H^2$ to account for the breakers we get

$$\overline{u_w w_w} = g \left(\frac{H}{h} \right)^2 h B_0 \frac{c^2}{gh} \sin \alpha \cos \alpha$$

where α is the angle of incidence for the waves. Approximating the $\partial \overline{v_w w_w} / \partial z$ term in a way that satisfies the known requirements for that term (for details see Svendsen & Lorenz, 1988) then yields

$$g_{xy} = \frac{5}{2} \left(\frac{H}{h} \right)^2 B_0 \frac{c^2}{gh} \frac{\partial h}{\partial x} \sin \alpha \cos \alpha$$

and

$$\frac{\partial S_{xy}}{\partial x} = \rho gh \frac{\partial h}{\partial x} \left(\frac{H}{h} \right)^2 \left[\frac{5}{2} B_0 + 3 \frac{A}{H^2} \frac{h}{L} \right] \sin \alpha \cos \alpha$$

where the second term originates from the shear stress created at wave trough level by the surface roller. A is the roller area and L the wave length.

Fig. 1 shows some examples of velocity profiles obtained by using the following values of the parameters.

Phase velocity	$c = \sqrt{gh}$
Bottom friction coefficient	$f_w = 2 \cdot 10^{-2}$
Breaker shape	$B_0 = \eta^2/H^2 = 0.08$
Roller contribution	$\frac{Ah}{H^2 L} = 0.09$
Eddy viscosity	$\nu_t/h\sqrt{gh} = 0.015$

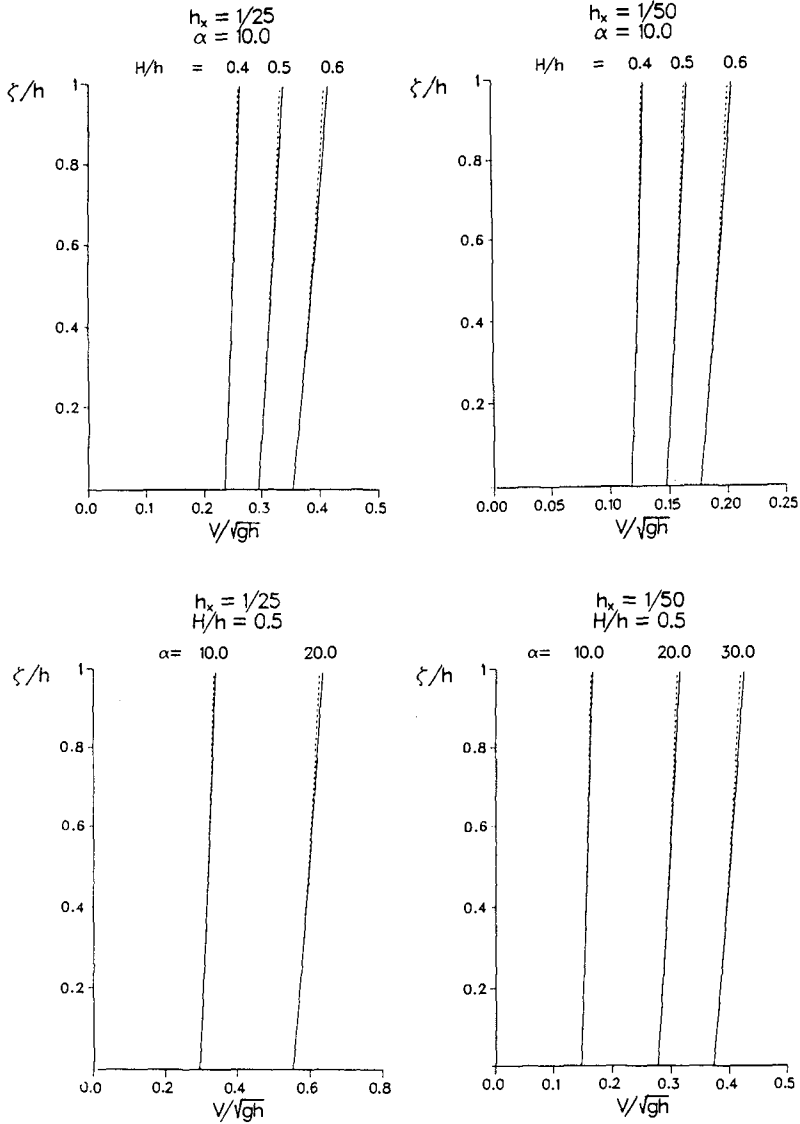


FIG. 1. Examples of longshore current profiles for different angles of incidence α , bottom slopes h_x and wave height to water depth H/h . No horizontal mixing.

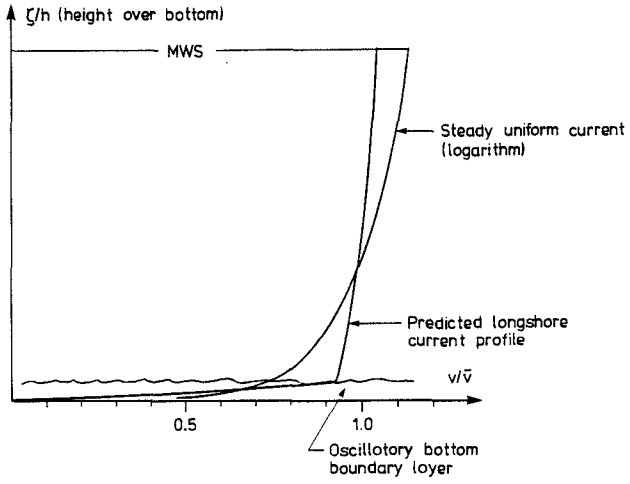
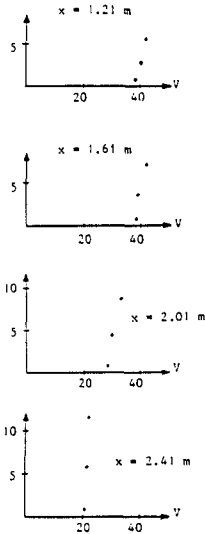


FIG. 2. A comparison between a longshore current profile and a logarithmic profile as in a river.

Beach at $x = 0$ m



Breaking point at $x = 2.51$ m

Fig. 3. Measurements of longshore velocities at three different elevations above the bed (from Visser, 1984).

The absence of turbulent mixing makes the calculated velocities larger than real. The important conclusion, however, is that the velocity profiles are very different from the logarithmic profile sometimes assumed in analogy with open channel flow. Fig. 2 shows a comparison between the two profiles. In fact the assumption of a uniform velocity over depth would be much closer to the real velocities than would a logarithmic profile. It also implies that the near-bottom velocities are significantly larger than for a logarithmic profile.

It may be emphasized that since the classical longshore current velocity found e.g. by Louguet-Higgins corresponds to $V = V_{b0}$, the real velocities will always be 10-20% larger than those found by classical theory.

Fig. 3 shows measurements of longshore currents in the surf zone at three different elevations above the bottom (from Visser, 1984). We see that the nature of the variation of depth is qualitatively in agreement with the theoretical profiles shown in Fig. 1.

6. COMBINED LONGSHORE AND CROSS-SHORE VELOCITY PROFILE

In the simplified case described here of no coupling between the cross-shore and the longshore current (the UV term in (3.2)) the total 3D velocity profile can be constructed by a simple vector addition of the cross-shore and the longshore velocity profiles determined independently. Such a 3D profile is shown in Fig. 4.

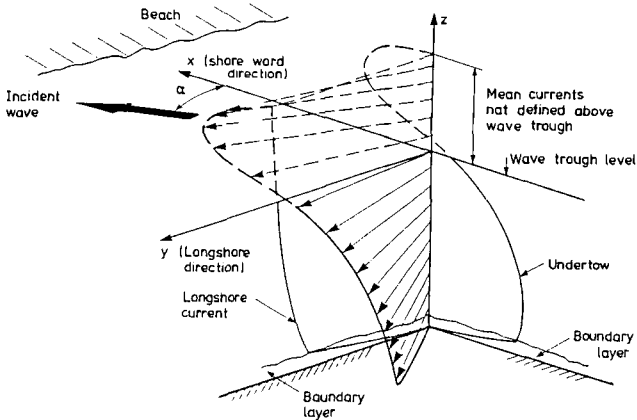


FIG. 4. The full 3-D current velocity profile as it occurs in a situation with both an undertow and a longshore current.

The result shows features that are of significant importance for the sediment transport on a coast.

From the knowledge of the fact that a strong undertow will be present in a surf zone even with no net cross shore current, we know that there is a tendency that sediments are being carried seaward by the current. The 3D profile, however, shows that close to the bottom the current direction may actually deviate 45° or more from the depth mean current vector which in this case is purely along-shore.

Moreover, if e.g. the longshore and crossshore bottom current velocities are of equal magnitude the total current velocity is 40% larger than given by a depth averaged model. Hence it can be quite misleading to use depth averaged models to predict bottom currents in the surf zone.

The predictions of the described 3D velocity profile are qualitatively confirmed by the tracer sediment observations by Ingle (1966). Fig. 5 shows a summary of his results.

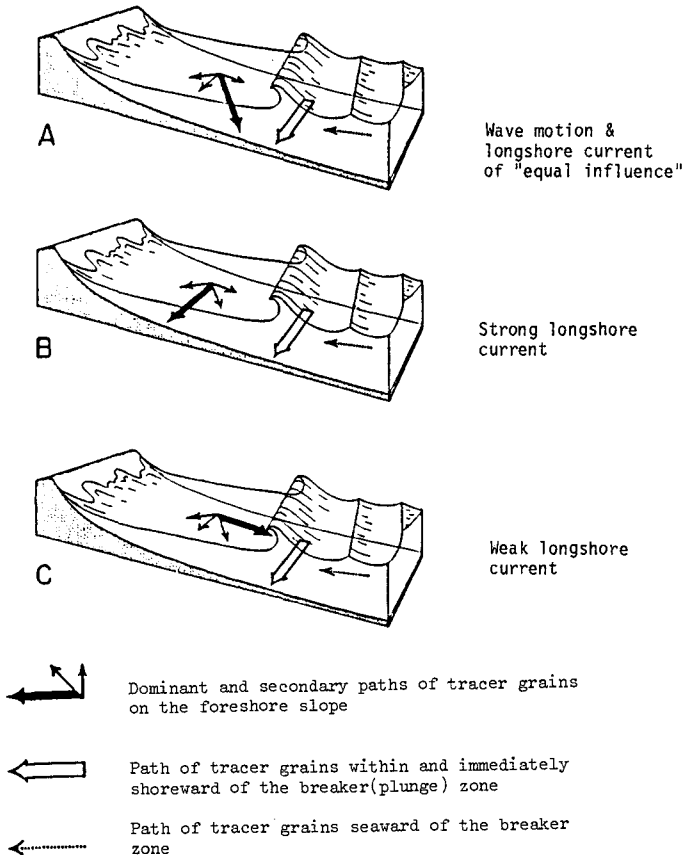


FIG. 5. Sediment movements in and near the surf zone. Summary of tracer observations by Ingle (1966).

6. REFERENCES

- Bowen, A.J. (1969). "The Generation of Longshore Currents on a Plane Beach," *J. Mar. Res.*, **27**, 206-215.
- Christoffersen, J.B. and I.G. Jonsson (1985). "Bed Friction and Dissipation on a Combined Current and Wave Motion," *Ocean Eng.*, **12**, 5, 387-423.
- DeVriend, H.J. and M.J.F. Stive (1987). "Quasi-3D Modelling of

- Nearshore Currents," Coast. Eng., 11, 5/6, 565-602.
- Ingle, J.C. (1966). "The Movement of Beach Sand," Elsevier, Amst., Developments in Sedimentology, 5, 221 pp.
- Longuet-Higgins, M.S. (1970). "Longshore Currents Generated by Obliquely Incident Sea Waves - 1&2," J. Geophys. Res., 75, 6778-6789 & 6790-6801.
- Longuet-Higgins, M.S. and R.W. Stewart (1961). "The Changes in Amplitude of short Cravity Waves on Steady Non-Uniform Currents," J. Fluid Mech., 10, 529-549.
- Longuet-Higgins, M.S. & R.W. Stewart (1960). "Changes in the Form of Short Cravity Waves on Long Waves and Tidal Currents," J. Fluid Mech., 8, 565-583.
- Stive, M.J.F. and H.J. DeVriend (1987). "Quasi-3D Nearshore current Modelling: Wave-Induced Secondary Current," Proceeding ASCE Conf. Coastal Hydrodynamics, Delaware, 356-370.
- Stive, M.J.F. and H.C. Wind (1986). "Cross-Shore Mean Flow in the Surf Zone," Coast. Eng., 10, 325-340.
- Stive, M.J.F. and H.C. Wind (1982). "A Study of Radiation Stress and Set-Up in the Nearshore Region," Coast. Eng., 6, 1, 1-26.
- Svendsen, I.A. and R.S. Lorenz (1988). "Three Dimensional Velocity Profiles in Combined Undertow and Longshore Currents," to appear in Coastal Eng..
- Svendsen, I.A. and J.B. Hansen (1988). "Cross Shore Currents in Surf Zone Modelling," Coast. Eng., 12, 1, 43-62.
- Svendsen, I.A., H.A. Schäffer and J.B. Hansen (1987). "The Interaction Between the Undertow and the Boundary Layer Flow on a Beach," J. Geophys. Res., 92, C11, 11845-11856.
- Svendsen, I.A. (1984). "Wave Heights and Set-Up in a Surf Zone," Coastal Eng., 8, 4, 303-329.
- Thornton, E.C. (1970). "Variation of Longshore Current Across the Surf Zone," Proc. 12th Int'l. Conf. on Coast. Eng., Washington, D.C., Ch. 18, 291-308.
- Visser, P.J. (1984). "A Mathematical Model of Uniform Longshore Currents and the Comparison with Laboratory Data," Delft Univ. Tech., fluid Mech. Lab. Rep., 84-2.
- Whitham, C.B. (1962). "Mass, Momentum and Energy Flux in Water Waves," J. Fluid Mech., 12, 135-147.

CHAPTER 53

GRAIN-GRAIN INTERACTION IN OSCILLATING SHEETFLOW

W.T. Bakker¹⁾, W.G.M. van Kesteren²⁾ and Z.H. Yu³⁾

ABSTRACT

Viscous grain-grain interaction is an important aspect of the dynamics of oscillating sheetflow. This interaction between sand grains has been investigated qualitatively in a pulsating water tunnel. Furthermore, experiments concerning the interaction between neutrally buoyant spheres in a Couette flow have been carried out at a scale of 100:1 in a new developed ring shear apparatus, called "Carrousel."

With respect to the dynamics of sheetflow, in-situ measuring devices for the sand concentration in the sheetflow ("Harp") and the bed load ("Swan") has been developed; some preliminary results are shown.

For sand grains, the intrusion depth of sheetflow appears to be of the order of several mm. On high speed video recordings no lateral mixing between grain layers can be observed; for this some physical explanation is given. This supports the modelling of the sheetflow mechanism as moving grain layers.

1. INTRODUCTION.

For a good understanding of coastal behaviour and for accurate coastal field models, knowledge about sheetflow is indispensable.

From theoretical investigations (for instance Lofquist (1978), Mogridge (1972), Nielsen (1979) and Van Kesteren (1982)) and from visual observations from Dingle and Inman (1976) the impression arises that for normal beach sands ($D_{50} \approx 200 \mu\text{m}$) sheetflow occurs, when orbital velocities surpass an order of magnitude of 1 m/s. Fig. 1 shows visual observations of Yu (1987) made along the Dutch coast.

The impression exists, that generally sheetflow occurs at the seaward side of breaker bars and in the uprush zone.

This paper contains more a progress report on sheetflow studies than clear-cut solutions. It has to be seen in the context with former papers on the same subject (Bakker and Van Kesteren (1986) and (1987)) and with papers on near-bottom velocities (Bakker and Van Doorn (1978) and Van

¹⁾ Coastal Specialist, Tidal Waters Department Rijkswaterstaat; Principal Scientific Officer Delft University of Technology. Delft, The Netherlands.

²⁾ Project Engineer Delft Hydraulics.

³⁾ Researcher Forschungsstelle Küste Norderney.

Kesteren and Bakker (1984)), which finally are due to merge into an integrated model for the sediment transport under sheetflow conditions. The recent research is concentrated on two subjects, which are considered the main bottle-necks with respect to the solution of the sheetflow problem: the transmission of the shear stress from the turbulent boundary water layer to the sheetflow (treated in a preliminary way in Bakker and Van Kesteren (1987)) and grain-grain interaction, which is the subject of the present paper. First the preliminary results of new laboratory experiments in the Large Pulsating Water Tunnel of Delft Hydraulics (ch. 2.1) and in the Carrousel of Delft University of Technology (ch. 2.2) are presented, as well as the results of some measurements in nature (ch. 2.3). Furthermore, some theoretical considerations with respect to the importance of lift forces on grains in a high concentrated granular shear flow are given (ch. 3). Chapter 4 gives the conclusions.

2. EXPERIMENTS.

2.1. PULSATING WATER TUNNEL.

In order to observe the sheetflow mechanism into detail some tests on sand with a mean diameter of $220 \mu\text{m}$ were performed in the Large Pulsating Watertunnel of Delft Hydraulics. The occurrence of sheetflow was observed in a harmonically oscillating flow with a period of 6 s and a maximum velocity of 1.6 m/s.

The behaviour of the sand near and in the bed was recorded with high-speed video (200 and 400 frames/s) (see photo 1). The camera was focussed on an area of $5 \times 7 \text{ mm}$ and $10 \times 14 \text{ mm}$ respectively. Although the velocities within this area exceeded 1 m/s the position of the top and bottom of the sheetflow layer remained constant within a range of only a few grain diameters.

Fig. 2 shows an example of particle velocities within an area of $10 \times 14 \text{ mm}$; the velocities are obtained from two sequential frames (time interval 5 ms) using the frame-freezing and overlay technique of the high-speed video equipment. Fig. 3 shows velocity distributions measured in this way at 6 equal time intervals of $1/10$ of the wave period.

When the velocity distributions are compared with the velocity just outside the turbulent boundary layer (arrows in top of fig. 3) a very significant phase lag of more than 45 dgr. can be observed. This is consonant with the phaselag between shear stresses and velocities in the turbulent boundary layer (see Bakker and Van Kesteren (1986) and Horikawa et al. (1982)).

In fig. 4 the intrusion depth (i.e. the depth of the point of zero velocity) during half a wave period is shown. The maximum depth occurred before the time of maximum velocity outside the turbulent boundary layer ($t = .2T$). A phase lag of the same order was found by Horikawa et al. (1982).

The observations revealed the following important features of the sheetflow mechanism:

- * No lateral mixing can be observed, even at high shear-rates (500 s^{-1}); this supports the modelling the sheetflow mechanism as moving grainlayers.
- * As the name of the flow already indicates, the subsequent erosion of grain layers occurs in the way of the mobilisation of sheets of the paperfile in a foto-copier.

- * The deposition of moving grains at the time of current reversal occurred uniformly in horizontal direction in a very short time (10 - 20 ms); because of the high concentration settlement can occur without much vertical motion.
- * All over the wave period but especially at the time of current reversal a density wave within the sheetflow layer can be observed. These waves might indicate that, in accordance with Bakker and Van Kesteren (1986), the transfer and dissipation of the turbulent shear stress in the sheetflow layer takes place by the means of viscous waves generated by the turbulent pressure wave caused by burst-phenomena in the boundary layer acting on the top of the sheetflow-layer.

2.2. CARROUSEL.

At the Delft University of Technology the grain - grain interaction is investigated by using a grain ring shear apparatus called Carrousel. Fig. 5 shows a plan view; photo 2 shows the set-up.

In the annular space between two concentric cylindrical walls ($\phi = 1062$ mm. resp. $\phi = 1198$ mm.) and a bottom and a top ring, a mixture of polypropene spheres ($\phi=14$ mm, $\rho=870$ kg/m³), immersed in oil with the same density is contained. The viscosity of the oil is 10^{-4} m²/s at 18°C. The top ring can be adjusted with respect to its height. Four rings of half spheres are glued on both rings in a regular pattern (vide photo 3)

This mixture is sheared by rotating the top ring with velocities up to 4 m/s while the bottom ring is fixed.

Fig. 5b shows the way of measuring the forces on the bottom ring with 3 "gallow"-shaped metal bearings, provided with strain gauges.

Thus grain-grain interaction can be investigated at a scale 100:1.

The apparatus is in the stage of calibration; some first results are shown in photo 4a,b,c, which will be discussed in ch.3 .

2.3. MEASUREMENTS IN NATURE.

In cooperation with the Forschungsstelle Küste at Norderney (Dr.H.Niemeyer) a measurement project "Lohengrin" has started, involving the development of two measuring instruments, a "Harp" and a "Swan". The Swan (vide photo 5) is dug into the sand (fig. 6) only its tail and neck rise above.

It feeds itself through its tail; the sediment comes to rest in its body and the water is discharged through its beak; the amount of it is measured with a flow meter (e).

When the current reverses, a repercussion valve (f) in the beak hinders an internal flow reversal.

Distance between tail and beak is so designed, that the own frequency of the water in the instrument allows an equal velocity in the entrance as in the sheetflow layer. The height of the opening in the tail can be adjusted; normally it is 12 mm. Also the height of the tail itself can be adjusted by a diver; it is essential, that it remains on the same level as the sand bottom.

Up to now, average concentrations over a height of 12 mm of 4 to 34 gr/l were measured (Yu (1987)). However, still more calibration should be done.

A very simple prototype of this instrument has been developed in 1983 by the first author and prof. dr.H.Krock of the Look Laboratory in Hawaii; since then it has been tested and developed by the third author along

Dutch beaches and in the laboratory for Fluid Mechanics of Delft University of Technology (Yu (1987)) and, at present, in Norderney.

A second instrument in developing stage, to be tested at the Forschungsstelle Küste, is the Harp.

It consists of 3 concentration probes, sensing at a different level in the sheetflow (fig. 7). The probes are mounted in upward direction on a lower bar under the sand, which is connected to a frame, consisting of 2 poles driven into the beach sand and an upperbar between. The whole lower bar can be lifted, as it is connected with screws to the upper bar of the frame.

The concentration probes consist each of 4 electrodes of 1 mm. protruding from a probe head of 10 x 2 mm (fig. 8). A 2 kHz AC is generated between the outer electrodes and the voltage difference (electrical resistance) between the inner electrodes is measured.

Fig. 9 gives the calibration curve between the relative resistance and the volumetric concentration (from Mastbergen and Bezuijen (1988)).

Fig.10a,b shows the situation in Norderney where the instruments are tested, in the swash zone between the groyne fields D and E.

Up to present, no three-level measurements are available; fig.11 and 12 show measurements resulting from 1 sensor.

In fig.11 showing concentration versus time, one probe is driven into the bottom, thus giving a concentration of about 50%, but still reacting on the waves. At arrow "A" the probe is lifted over 2 mm. The lifting causes a hole (lower concentration) which fills up quickly again. After some waves the whole bottom lowers obviously, thus causing a low concentration at the instrument. Now wave motion causes an increase in concentration.

After ca. 15 seconds the old situation is restored, more or less and later on again the concentration decreases. Lifting the probe again 2 mm (arrow B) leads to analogous results, however now with a lower mean concentration. The next lifting of the probe (arrow C) brings it out of the sheetflow area. Now only accidentally high concentrations occur.

The local range of the sheetflow layer (from maximum concentration up to suspended load concentrations) thus shows to be of the order of 6 mm.

Fig.12 shows an interrelation between sheetflow concentration and orbital velocities measured ca. 20 cm. above the bottom. Here the probe is kept stationary at a rather high level.

There is shown respectively: the concentration, the cross-shore and longshore component of an electromagnetic current meter and the wave height, measured with a pressure meter. Averaged concentrations of about 3% are found.

3. THEORETICAL ASPECTS.

Little grains love physical law and order. This is confirmed by observations during preliminary tests in the grain Carrousel (photo 4a,b,c). When the distance between the upper and bottom ring is decreased, the neutrally buoyant spheres do not only center themselves between the rings, but also show a preference for equally mutual distance and for the same orbit, situated halfway the outer ring of spheres glued on the steel rings and the adjacent ring of spheres.

Sometimes a rebel grain, deviating too much from neutral buoyancy, disturbs the order causing some rattling in the Carrousel, but mostly the order is restored quickly.

The number of 'free' grains in the tests was half the number of glued grains on one ring.

Experimentally and theoretically, the centering force has been investigated by quite a school of investigators, from which will be mentioned : Halow and Wills (1970), Vasseur and Cox (1976) and Ho and Leal (1974).

The last two papers deal with theory concerning a neutrally buoyant sphere in a Couette flow between two (flat) plates. The first one gives as well theory as experimental results concerning radial migration of a sphere in the annular region between two concentric cylinders, of which the outer one was in rest and the inner one was rotating. The theoretical considerations of the last two papers seem more adequate than the ones of Halow and Wills (1970), as a confined space is considered, where Halow and Wills use Saffman's theory (1965), valid for Couette flow in an unconfined space.

From Vasseur and Cox (1976) a velocity \dot{x} of a neutrally buoyant sphere in the vicinity of the central position can be derived, equal to:

$$\dot{x} = - \frac{x r^3 S^2}{3.5 h \nu} \quad (1)$$

where x is the deviation from the central position, h is the distance between the plates, r is the radius of the sphere, S is the vertical velocity gradient and ν is the kinematic viscosity of the fluid.

Reading (1) as a differential equation (neglecting the inertia of the grain itself), one finds for the 'neperian' time T_e , in which the distance to the central position reduces with a factor e :

$$T_e = 3.5 \frac{h \nu}{r^3 S^2} \quad (2)$$

Neperian times T_e of 4 and 9500 s, found in this way for two experiments of Halow and Wills (1970), (their fig. 4 and 5) are not inconsistent with their results. For the Carrousel experiments neperian times of 0.3 s or less are found.

For natural grains (for instance a velocity gradient $S = \Delta u / \Delta z = 100 \text{ s}^{-1}$ (velocity difference Δu of 0.5 m/s over a layer thickness Δz of 0.05 m); $r = 10^{-4}$ m, $h/r = 4$, $\nu = 10^{-6} \text{ m}^2/\text{s}$ one finds $T_e = 0.14 \text{ s}$).

Deriving the maximum lift velocity from Vasseur and Cox (1976) and using (1) one finds the order of magnitude of 1 mm/s, i.e. small with respect to the unhindered settling velocity of grains, but essential when using mechanism, exposed in by Bakker and Van Kesteren (1986).

However, the self-centering capacity of grains did not show to be so dominant, that a total layer of grains in the Carrousel pops into position (i.e. in an experiment similar to that shown in photo 6, but with a higher concentration of grains).

The reason for this (too much density differences?) is subject of future research.

4. CONCLUSIONS.

As well in the field as in the laboratory (Pulsating Water Tunnel) the result of Horikawa et al. (1982), that the intrusion depth of sheetflow is of the order of several mm has been confirmed.

High Speed Video recording reveals that layers of grains shear with respect to each other, without lateral mixing. Theoretically, shearing grain layers in a viscous medium should show the tendency to centering themselves with respect to adjacent layers. This effect is also observed

in tests with neutrally-buoyant grains sheared in a ring shear apparatus (Carrousel). This self centering effect can be explained by lift forces caused by inertia of the fluid surrounding the grains.

ACKNOWLEDGMENTS.

The authors acknowledge the support from the Forschungsstelle Küste, Norderney (Dr. G. Luck, Dr. H. Künz and Dr. H. Niemeier) and their consent of publishing about the measurements at Norderney.

The Carrousel would never have delivered results without the designing of ir. H. Havinga, the construction by mr. Groeneveld and the experiments carried out by mr. W. Klomp (all Delft University of Technology).

Hi-Speed video was made possible by courtesy of mr. Reinders of Reinka B.V.

REFERENCES.

- Ahilan, R.V. and Sleath, J.F.A. (1983), Wave induced bed load transport, Proc. Symp. on Seabed Mechanics (IUTAM and IUGG), Newcastle upon Tyne, pp. 183-190.
- Bakker, W.T. and Van Doorn, Th. (1978), Near-bottom velocities in waves with a current, Proc. 16th Conf. on Coastal Eng. Hamburg, pp. 1394-1414.
- Bakker, W.T. and Van Kesteren, W.G.M. (1986), The dynamics of oscillating sheetflow, Proc. 20th Conf. on Coastal Eng. Taipeh.
- Bakker, W.T. and Van Kesteren, W.G.M. (1987), Oscillating sheetflow in the turbulent boundary layer, Euromech. 215 Genua.
- Dingler, J.R. and Inman, D.L. (1976), Wave formed ripples in near shore sands, Proc. 15th Conf. on Coastal Eng., ch. 123, pp. 2109-2126.
- Halow, J.S. and Wills, G.B. (1970), Radial migration of spherical particles in Couette systems, AICH.E. Jnl. 16, nr.2, pp. 281-286.
- Ho, B.P. and Leal, L.G. (1974), Inertial migration of rigid spheres in two-dimensional unidirectional flows, Jnl. of Fluid Mech. vol. 65, pp 365-400.
- Horikawa, K., Watanaba, A. and Katori, S. (1982), Sediment transport under sheetflow condition, Proc. 18th Conf. on Coastal Eng. Cape Town.
- Mastbergen, D.R. and Bezuijen, A. (1988), Sand-water mixture flow, Dumping of sand below sealevel, Delft Hydraulics, Report Z261.
- Mogridge, G.R. et al. (1972), Experiments on bed form generating by wave action, Proc. 13th. Conf. on Coastal Eng., pp. 1123-1142.
- Lofquist, K.E.B. (1978), Sandripple growth in an oscillatory flow water-tunnel, U.S. Corps of Eng. Techn. Paper 78-5.
- Nielsen, P. (1979), Some basic concepts of wave sediment transport, Techn. Univ. of Danmark, Inst. of Hydrodyn. and Hydraulic Eng., Lingby, series paper 20.
- Saffman, P.G. (1965), The lift on a small sphere in a slow shear flow, Jnl. of Fluid Mech. vol. 22, pp. 385. and vol. 31 (1968).
- Kesteren, W.G.M. van (1982), Survey of the phenomenon sheetflow, in "Notes on sheetflow", Rijkswaterstaat advisory department at flushing, study report WWKZ-82.V014.
- Kesteren, W.G.M. van and Bakker, W.T. (1984), Near-bottom velocities in waves with a current; analytical and numerical computations, Proc. 19th Conf. on Coastal Eng. Houston.
- Vasseur, P. and Cox, R.G., The lateral migration of spherical particles in two dimensional shear flows, J. Fluid Mech. vol. 78, pp. 385.

Yu, Z.H. (1987), Research on the Bed Load Transport Meter for in-situ measurement under sheetflow conditions, Technical University Delft, Department of Civil Eng (in Dutch).

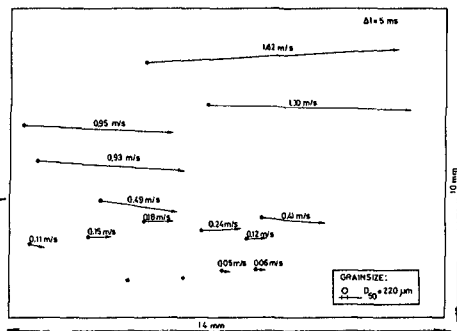
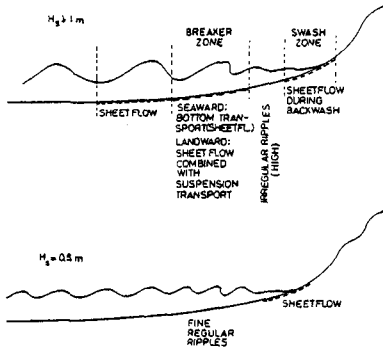


Fig. 1 Visual observations concerning sand transport mechanisms along Dutch coast. Tunnel

Fig. 2 Particle velocities within sheetflow layer measured in the the Delft Hydraulics Pulsating Water

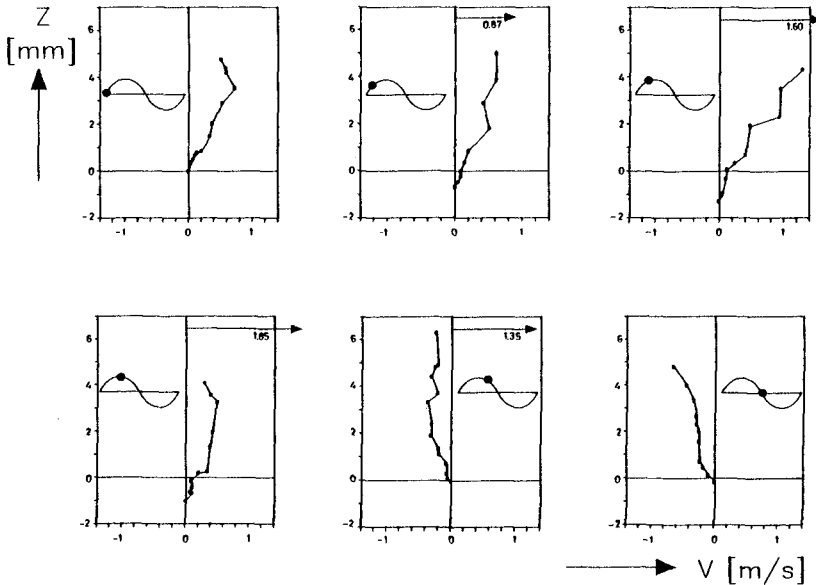


Fig. 3 Velocity distributions in sheetflow layer at 6 successive times (arrows indicate water velocities, measured above the boundary layer).

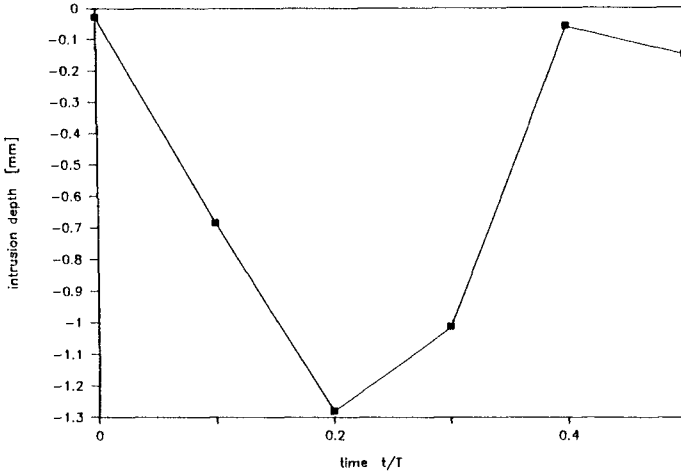


Fig. 4 Intrusion depth as function of time.

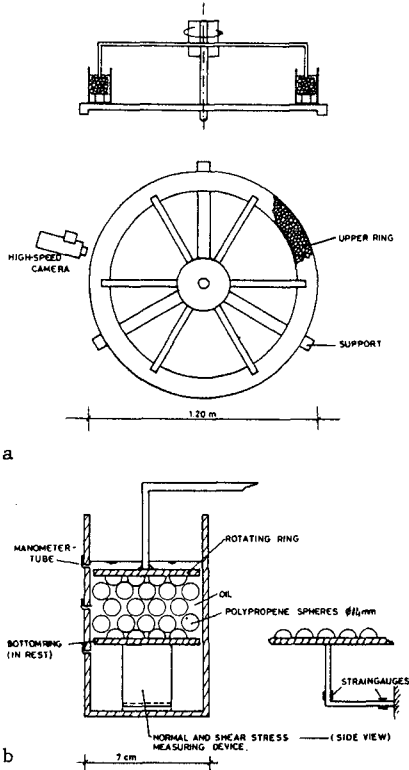


Fig. 5 Carrousel; a) cross-section and top-view, b) detail cross-section.

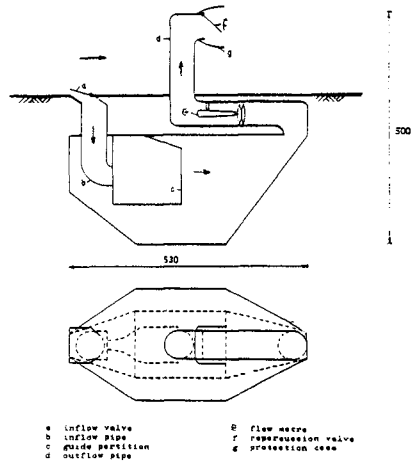


Fig. 6 Cross-section Swan.

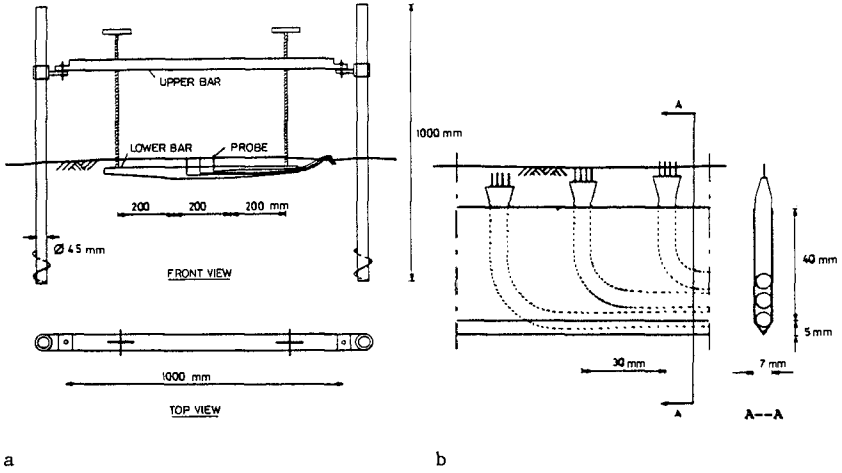


Fig. 7 The "Harp"; a) front- and top-view, b) detail position probes on lower bar.

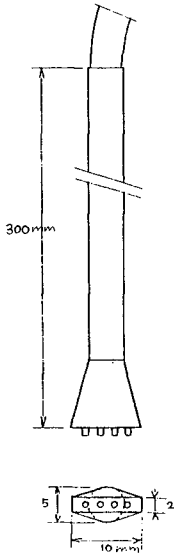


Fig. 8 Detail probe used in "Harp" (electrical conductivity meter, developed by Delft Hydraulics).

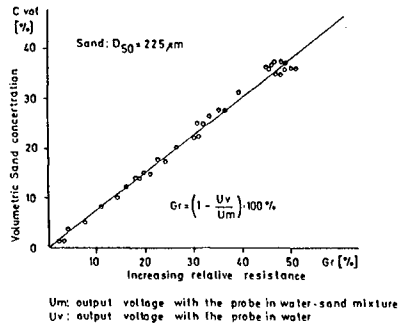
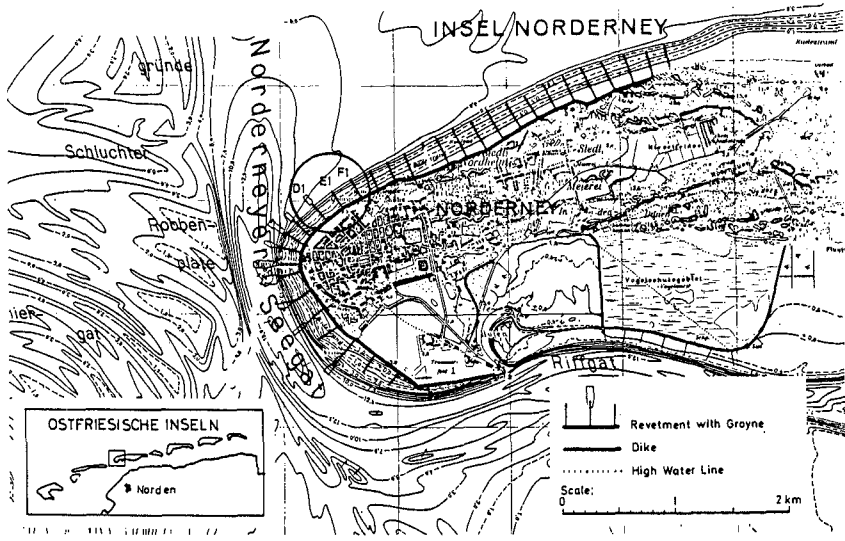
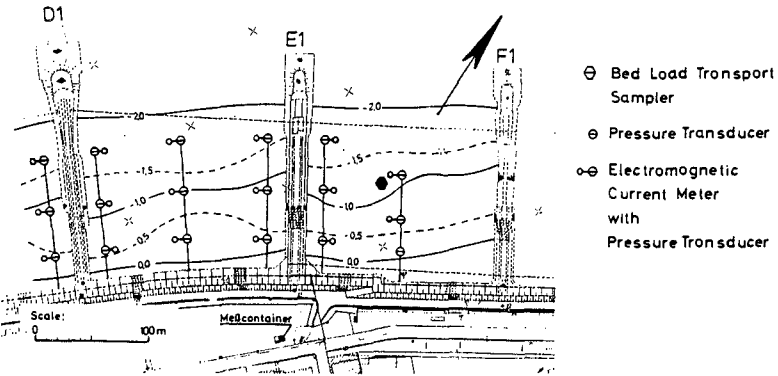


Fig. 9 Relation between measured increase of relative resistance and volumetric concentration.



a



b

Fig.10 Measuring site of the Forschungsstelle Küste at Norderney.

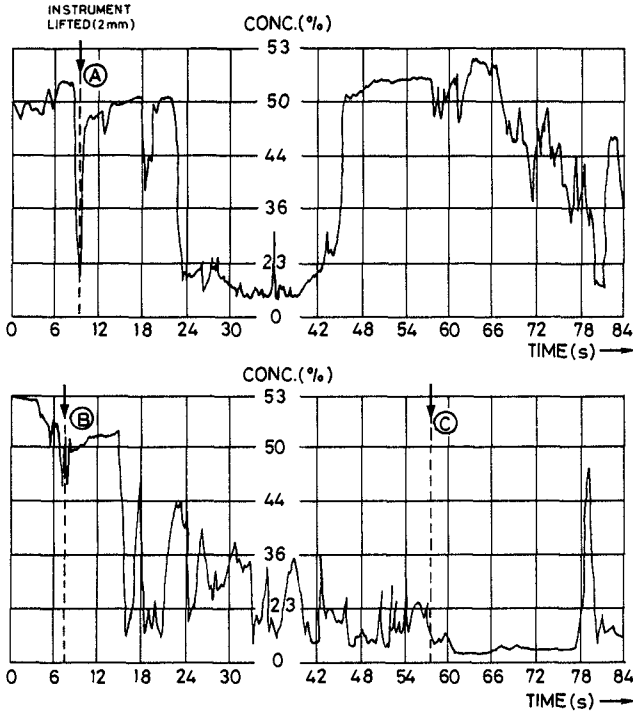


Fig.11 Concentration measurement Norderney, 11 december 1987 (swash zone).

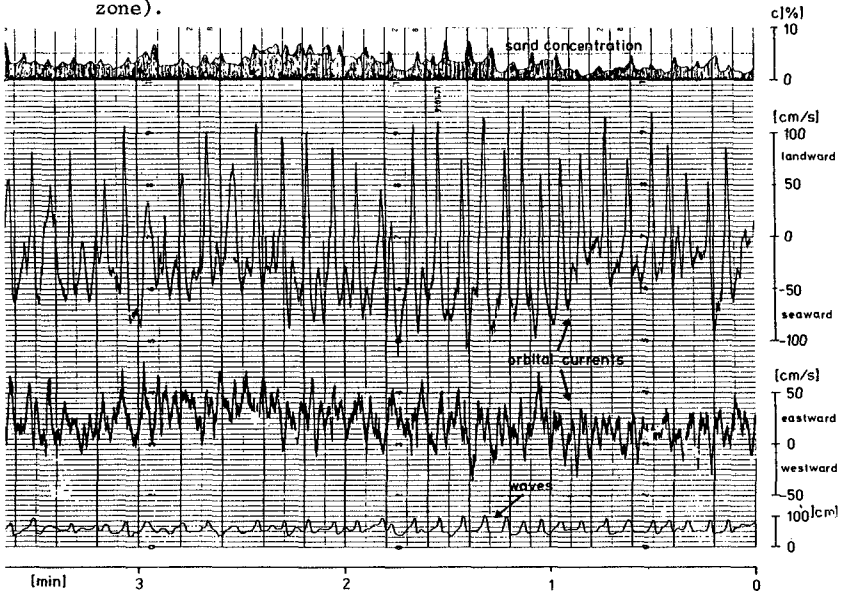


Fig.12 Concentration measurement Norderney, 16 june 1988 (waterdepth \approx 1.2 m.)



Photo 1 Set-up High Speed Video at Delft Hydraulics Pulsating Water Tunnel.

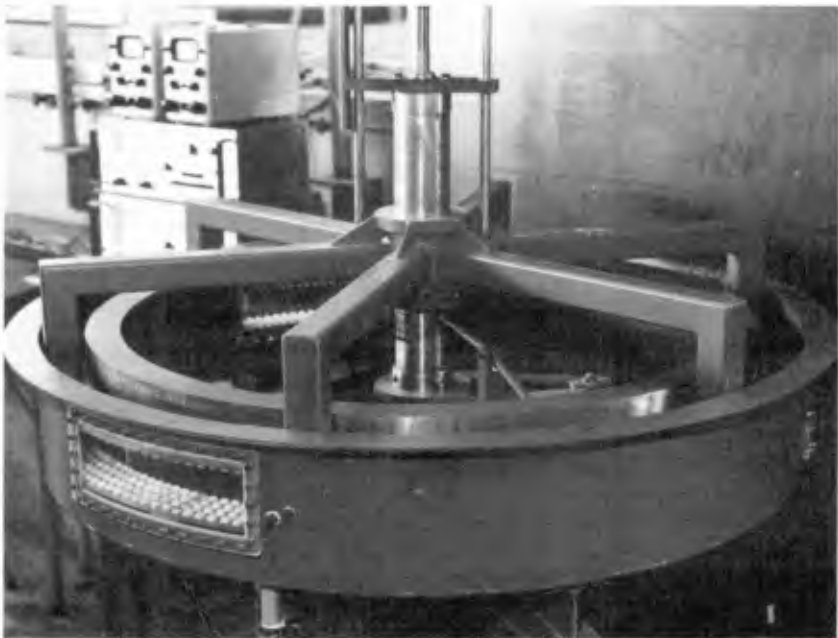


Photo 2 Set-up grain ring shear apparatus "Carrousel".



Photo 3 Detail Carrousel: 4 rings of half spheres are glued on the top and bottom ring.

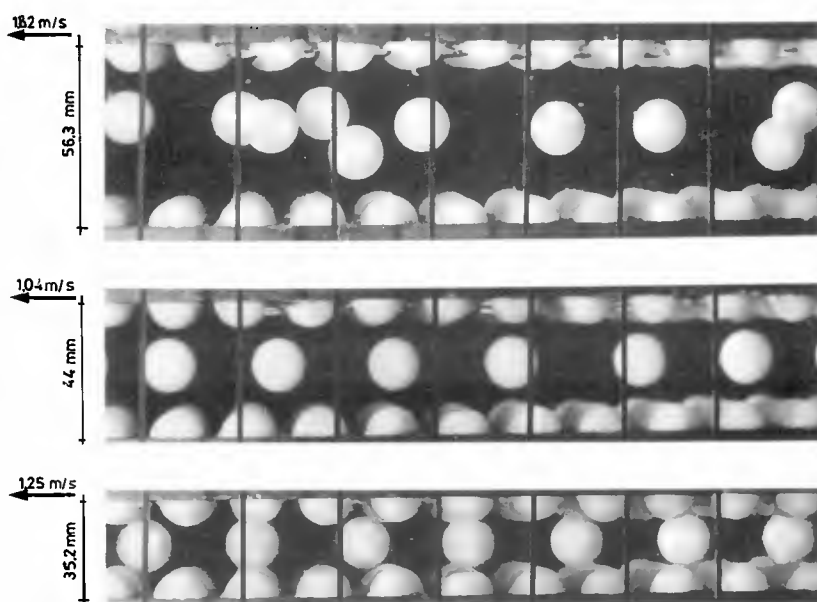


Photo 4 Neutrally buoyant spheres in Couette-flow in the Carrousel showing self-centering capacity.



Photo 5 Swan.

CHAPTER 54

Nonlinear effects on focussed water waves

by

D.H.Peregrine*, D.Skyner[†], M.Stiassnie[‡] & N.Dodd**

Abstract

A brief account is given of theory and experiments for water wave focussing. The theory uses weakly nonlinear wave modulation theory, that is the nonlinear Schrödinger equation, summarises earlier theoretical papers and augments them with numerical results. Experiments were performed to compare with theory. The limited comparison shown here indicates that the theory gives satisfactory results even for waves close to breaking. Both the numerical and experimental results indicate the importance of linear diffraction when waves are focussed. The relevance of diffraction is easily assessed, and is likely to dominate in many coastal examples of weak focussing.

Introduction

In practical examples of water-wave refraction, ray diagrams frequently show rays crossing. Often the initial ray intersections involve only a few rays with no well defined structure apparent. Any crossing of rays is an indication that the ray-theory approximations have become invalid, and a greater density of rays will normally reveal a focussing of rays near the initial crossing point. In practice simple smoothing or averaging methods are sometimes used to calculate wave heights. Where these have no rational basis there is always an uncertainty about possible steep waves due to focussing being missed.

Diffraction effects need to be included in order to obtain accurate solutions near a focus. In addition, if waves are steep nonlinear effects are significant. This paper reports on theoretical and experimental work.

* Professor of Applied Mathematics, Bristol University, School of Mathematics, University Walk, Bristol BS8 1TW England.

**Research Student, address as above.

† Research Assistant, Wave Power Project, Edinburgh University, Kings Bldgs, Edinburgh EH9 3JZ, Scotland

‡ Assoc.Prof. of Civil Engng., Technion, Haifa, Israel.

Model examples

In order to clarify ideas we consider two simple cases. In each case we suppose that waves have already suffered refraction due to propagation over a shoaling area or through non uniform currents which focus them but that the waves now propagate toward a focus over water of uniform depth. The focussing portion of the wave front is taken to be circular subtending an angle $2a$ at the focus which is at a distance f . The rest of the wave front is taken to be straight. In case (a) waves away from the focussing region are taken to be parallel to the central ray through the focus, and in case (b) they are taken to be smooth straight extensions of the circular arc; see figure 1.

In case (a) there are no further ray crossings until well beyond the focus and study can be directed to wave amplitudes in the focal region. In case (b) waves from both sides continue to cross behind the focus and wave amplitudes can be expected to be at least twice those of the original wave train, and any exception near the focus is of interest.

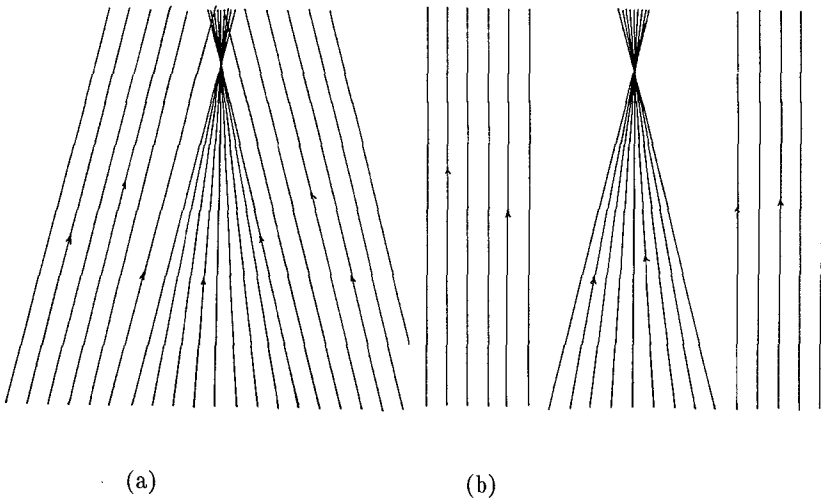


Figure 1 Two examples of wave focussing (a) where the focussing region is not influenced by the wave front on each side of the initial focussing wave. (b) where the waves each side of the focussing wave meet close to the focussing region.

Linear waves

Since solutions of the linear wave equation may be superposed, the initial conditions may be broken down into sub-problems: two semi-infinite plane waves with their attendant diffraction and the focussing arc. The latter is of the greater interest since the half-plane waves correspond to Sommerfeld's solution for diffraction by a semi-infinite barrier. Exact solutions of the linear problem are easily created by adding plane-wave solutions. We have used one particular example to represent a focussing arc. It is a set of N plane waves of equal amplitude and equal angular spacing in the range $(-\alpha, \alpha)$ all in phase at the focus. We call this example F and it is taken to be illustrative of the case shown in figure 1(a).

It is easy to compute solutions for example F corresponding to the focus having differing angles 2α of incoming waves and different distances, f , from an initial line. The effects of diffraction show for $\alpha = 15^\circ$ and a focal distance $f = 10L$, (L is wavelength), this exact solution shows an increase of amplitude over the initial conditions of only 20%. This small increase is due to diffraction counter balancing the focussing effects. On the other hand initial conditions with the same value of α but larger values of f do lead to focussing with enhancement of wave amplitude, so that it might approach the estimate of $2\alpha(2f/L)^{\frac{1}{2}}$ given, in different notation, by Peregrine (1986).

The effects of diffraction scale with the Fresnel number

$$N = a^2 f / L.$$

The example given above, with $N = 0.7$, is chosen since it represents a balance between diffraction and focussing. For large N , focussing is dominant. In any specific example it is easy to calculate N and assess diffraction. For example, if waves have a wavelength of 80 metres and part of the wave front of angle 20° , i.e. $\alpha = 10^\circ = 0.174$ radius, focusses at a distance of 2000 metres, then $N = 0.76$, which implies strong diffractive effects

Nonlinear waves

A major effect of nonlinearity on refraction is wave defocussing. Some aspects of this are described in Peregrine (1983, 1985 and 1986) for examples where Stokes's wave theory is a good approximation for periodic waves, i.e. not too shallow water. From a practical point of view this defocussing is reassuring since the nonlinear effects are reducing maximum amplitudes. However, unlike linear waves, theory shows that the effects of the waves bounding the waves that focus cannot be treated by simple superposition of solutions.

For the configuration of figure 1(a) the bounding waves do not contribute significantly more energy to the focussing region, in fact they act to spread the disturbance of the wave front more rapidly, since nonlinear effects lead to a "splitting" of linear rays (Peregrine, 1983).

More care is needed when assessing the effects of converging waves such as in figure 1(b). Here linear theory indicates that behind the focussing region the bounding waves contribute twice the initial amplitude as they are superposed. On the other hand for small angles, 2α , between these waves the nonlinear theory indicates formation of a 'wave jump'. Such jumps were identified by Yue and Mei (1980) and

further studied by Peregrine (1983). They give rise to a "Mach stem" type of interaction between the two wave fields. The height of the Mach-stem may be greater or less than twice the height of the incident waves as may be seen from careful study of figures 3 and 4 in Peregrine (1983). One figure is for deep water waves, the other for solitary waves ("Wedge angle" on these figures should be identified with α here).

In the above-mentioned figures amplifications as high as four times the incident waves appear possible. Such amplifications have not been observed in experiments and there are indications that diffraction effects may limit all or most of these excessive amplifications especially in deeper water. For solitary waves the maximum amplification observed by Melville (1980) in experiments on Mach stem reflection was no greater than twice, but Funakoshi's (1980, 1981) computations with the Boussinesq equations do include an example with an amplification of nearly three times.

Numerical solutions

The linear superposition of waves described above, gives an exact linear solution has been compared with solutions of a linear parabolic equation,

$$2ikA_y = A_{xx}$$

for wave amplitude $A(x,y)$ where surface elevation is $\eta = Ae^{iky - \omega t}$, k is the wavenumber and y is in the direction from the initial line to the focus. As expected good agreement was obtained up to $\alpha = 30^\circ$ the maximum value considered.

Nonlinear solutions were found by numerically integrating the nonlinear Schrödinger equation

$$2ikA_y = A_{xx} - K|A|^2A,$$

as described by Yue and Mei (1980). Some computation was with a simple implicit finite difference scheme, but for most computations a substantially more efficient high-order explicit scheme due to Dold is used. Integration time on a multi-user VAX computer is of the order one minute elapsed time, so results are readily available for any choice of parameters. Figure 2 shows an example corresponding to the case in figure 1(b) depicting the wide focussing region and bordering wave jumps with modulations as described by Peregrine (1983). A useful way of interpreting this type of example is that the focussing part of the wave contributes an extra width to the Mach-stem regions the bounding plane waves would create on their own. However, there are further aspects of this area which are to be described in a more complete account in preparation. For comparison figure 3 shows a linear solution for the same initial conditions.

Experimental measurements

Experiments corresponding to the examples described above were carried out in the Wide Wave Tank at Edinburgh University. This tank has 75 wave paddles each one foot (30cm) wide. A line of 24 wave gauges were used to measure wave height. Any chosen wave pattern was repeated 16 times, on each occasion being moved along by one paddle. In this way a set of 24×16 wave measurements were made without changing equipment position. Under computer control this gave a whole range of experimental results at different steepnesses, and focussing distances with both the wave patterns indicated in figure 1.

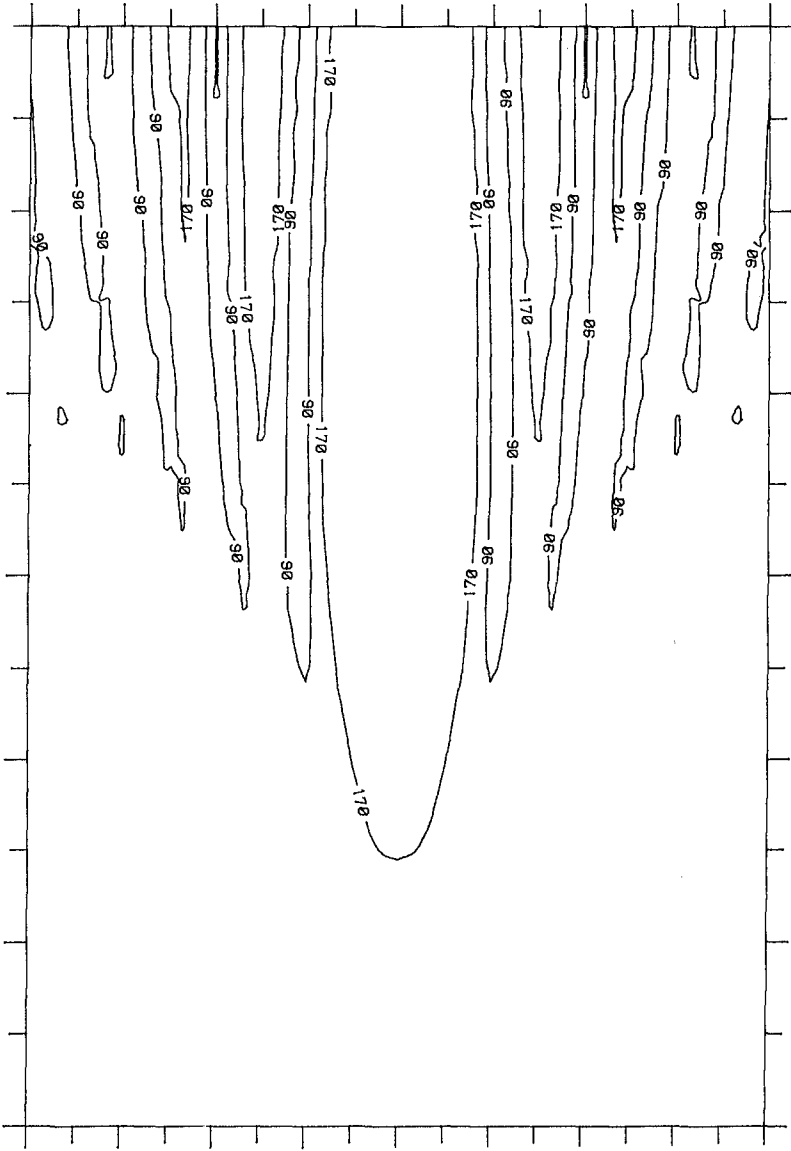


Figure 2 A contour plot of a numerical solution for the amplitude of a wave, like that in figure 1(b), with uniform initial steepness $ak = 0.2$, $H/L = 0.06$. This shows the very wide focussing region and the modulated wave jumps at each side. Contours are at 10%, 90% and 170% of the initial amplitude.

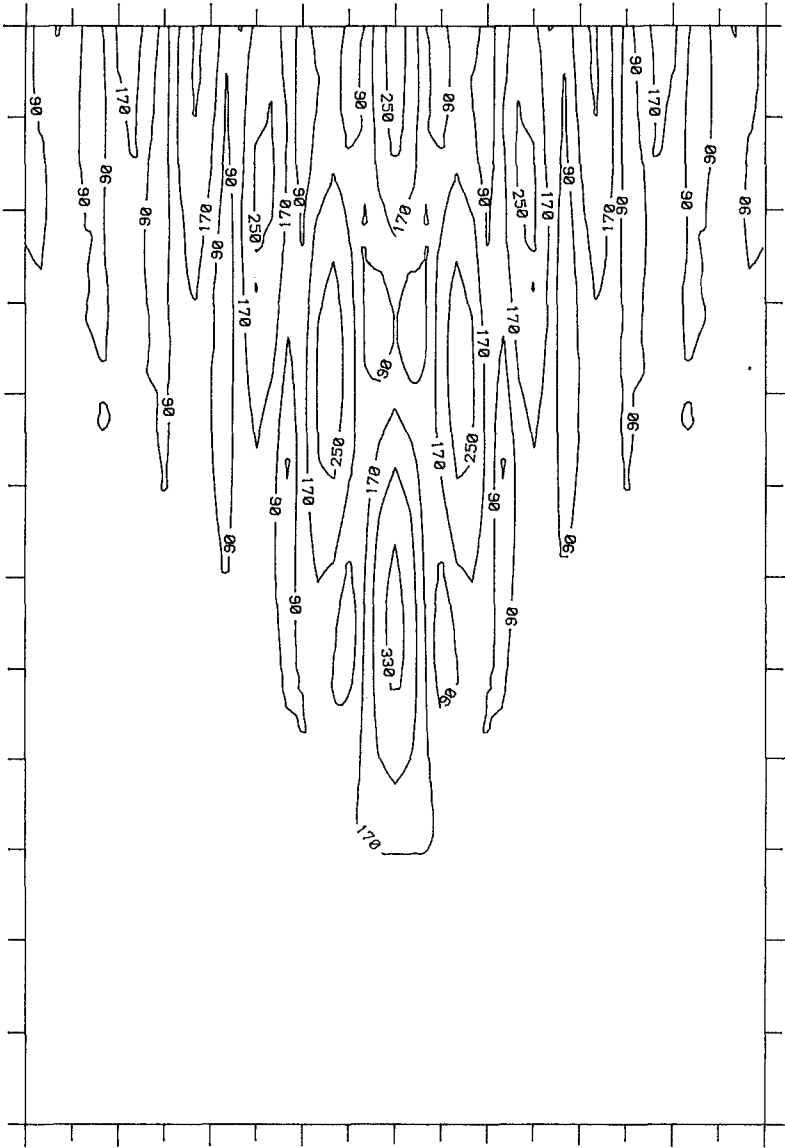


Figure 3 The linear theory solution equivalent to figure 2. Contour intervals are the same, but also include 250% and 330% of the initial amplitude, which are not reached in figure 2

In figure 4(a) we show, experimentally measured wave amplitudes for example F. The amplitude of the measured Fourier component at the forcing frequency is shown. This is compared in figure 4(b) with the corresponding linear solution, and the amplitude is clearly much greater than in the experiment. The nonlinear solution in figure 4(c) is much closer to the experimental values. However, there are small scale features in the experiment which suggest the spatial modulation one may expect from a reflected waves. The numerical integration was continued "beyond" the end of the tank where it was reduced by a reflection coefficient corresponding to that measured for plane waves, 0.05 in this case, and the resulting reflected wave added to the wave field of figure 4(c) with the result shown in figure 4(d). A superposition of figures 4(a) and (d) given in figure 5 shows that although there are some differences agreement is satisfactory in many details.

It would be surprising if there were no discrepancy since the nonlinear Schrödinger equation describes weakly nonlinear waves and in this particular experiment the maximum wave steepness is 85% of the steepness of the steepest steadily propagating wave.

Conclusions

Experiment and theory for wave focussing are in good quantitative agreement once reflection from the end of the tank is allowed for. In some experiments waves just reached breaking steepness.

Nonlinear defocussing of water waves is confirmed, but the importance of linear diffraction in defocussing has also been noted and this can be dominant in practical cases.

The experimental tank length is insufficient for wave jumps to be studied but the results give confidence in the equations describing their existence, even for waves close to breaking.

A definitive report of this work is in preparation. The support of the U.K. Science and Engineering Research Council is gratefully acknowledged, and we thank Professor S. Salter for the use of the Wide Wave Tank at Edinburgh University.

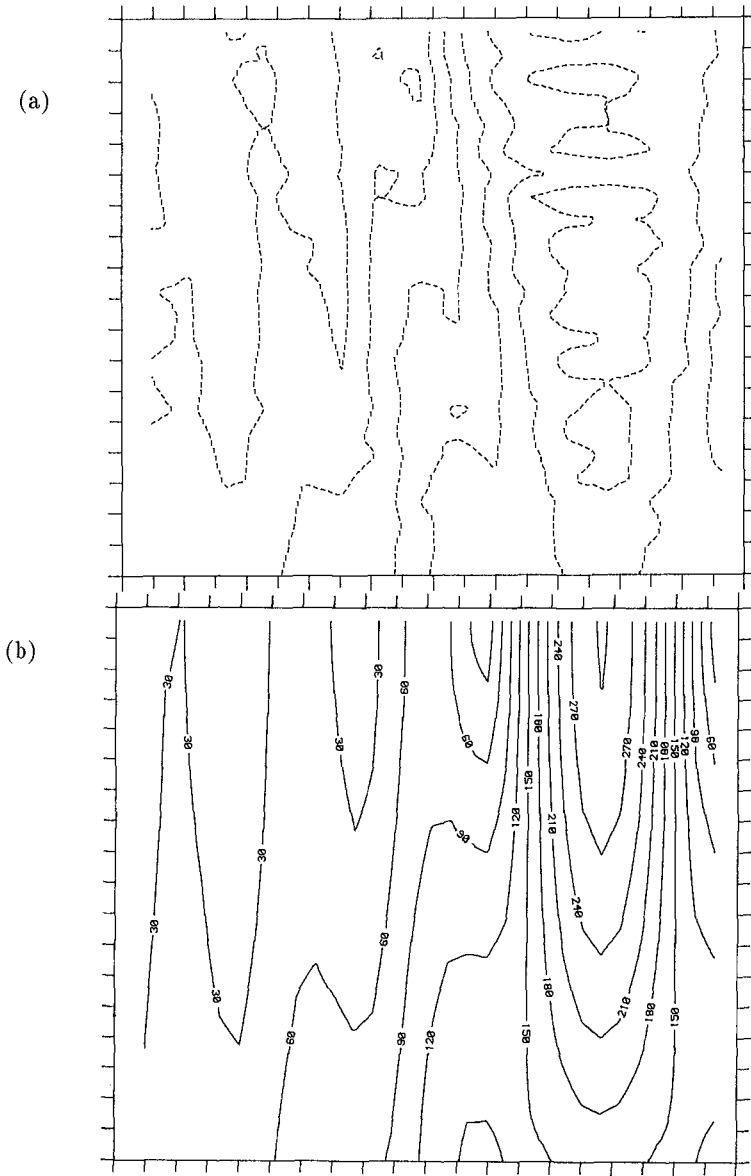


Figure 4 Contour plots of wave amplitude in the region of experimental measurements for the wave pattern of example F with initial maximum steepness of $ak = 0.2$, $H/L = 0.06$. Contours at intervals of 30% of initial amplitude. (a) experiment (b) linear theory.

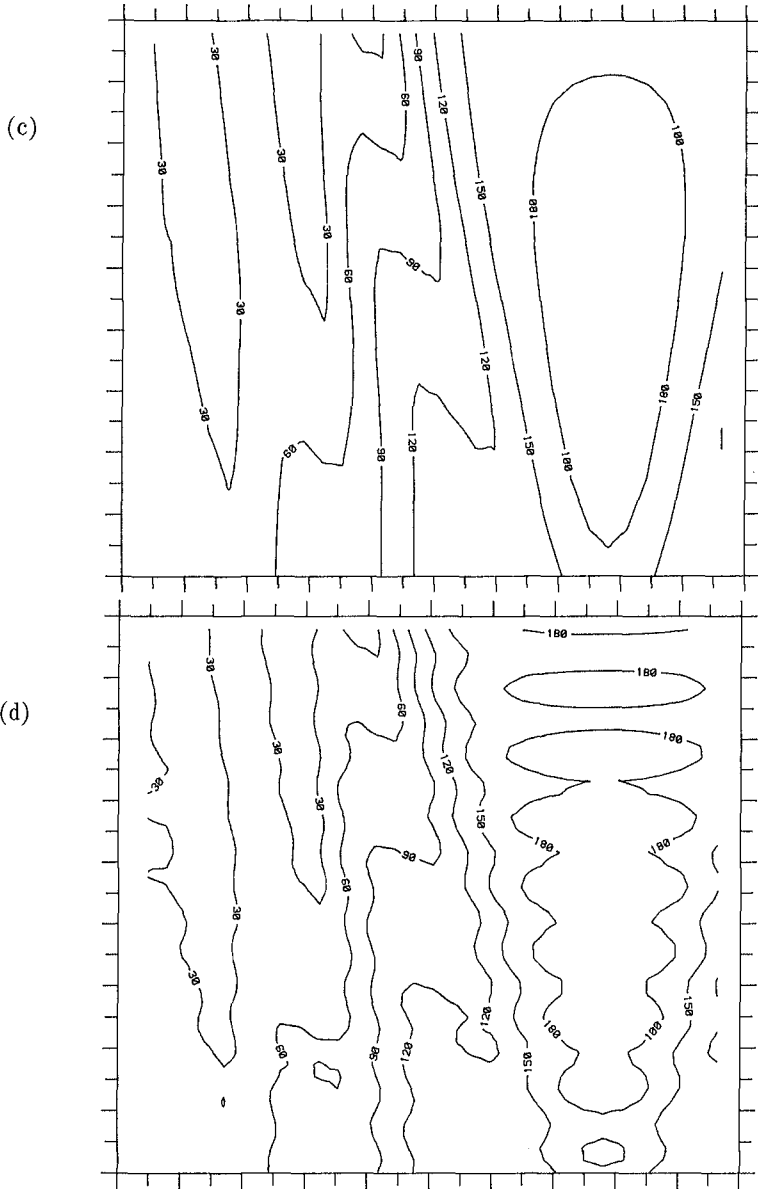


Figure 4 Contour plots of wave amplitude in the region of experimental measurements for the wave pattern of example F with initial maximum steepness of $ak = 0.2$, $H/L = 0.06$. Contours at intervals of 30% of initial amplitude. (c) nonlinear theory (d) nonlinear theory plus 5% reflection.

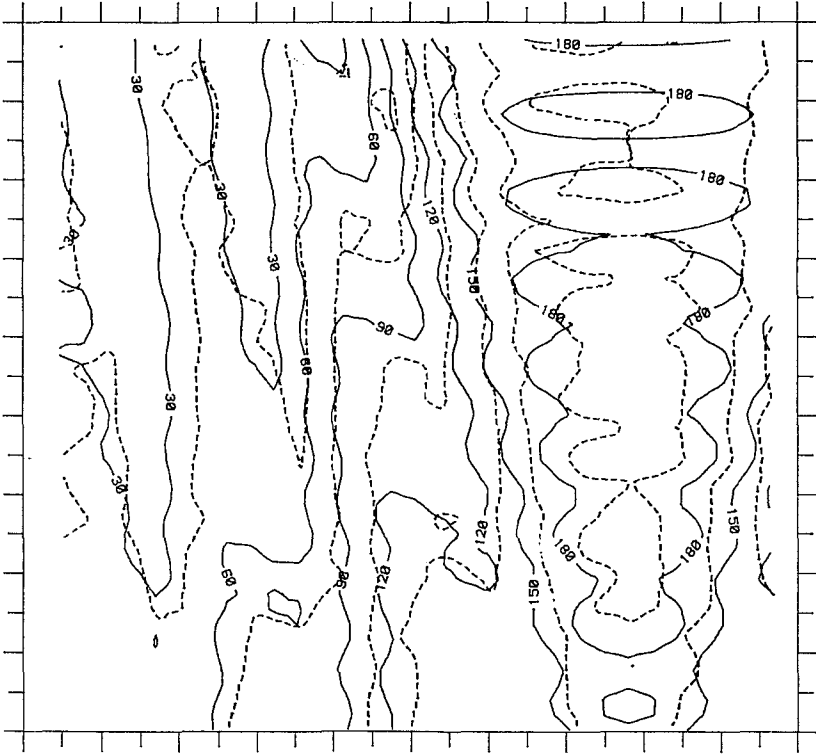


Figure 5 Figures 4(a) and 4(d) superimposed.
The broken lines are the experimental contours.

References

- FUNAKOSHI, M. (1980) Reflection of obliquely incident solitary waves, *J.Phys.Soc.Japan* **49**, 2371-2379.
- FUNAKOSHI, M. (1981) On the time evolution of a solitary wave reflected by an oblique wall, *Rep.Res.Inst.Appl.Mech., Kyushu Univ.* **29**, 91, 79-93.
- MELVILLE, W.K. (1980) On the Mach reflexion of a solitary waves, *J.Fluid Mech.* **98**, 285-297.
- PEREGRINE, D.H. (1983) Wave jumps and caustics in the propagation of finite-amplitude water waves, *J.Fluid.Mech* **136**, 435-452.
- PEREGRINE, D.H. (1985) Water waves and their development in space and time. *Proc.Roy.Soc.London* **400**,1-18.
- PEREGRINE, D.H. (1986) Approximate equations for water-wave focussing, *Proc.20th Internat.Conf. on Coastal Engng.*
- YUE, D.K.P. and MEI, C.C. (1980) Forward diffraction of Stokes waves by a thin wedge, *J.Fluid Mech.*, **99**, 33-52.

CHAPTER 55

OSCILLATORY BOTTOM BOUNDARY LAYER BY LOW-REYNOLDS NUMBER

TURBULENCE MODEL

TOSHIYUKI ASANO¹⁾

HITOMI GODO²⁾

YUICHI IWAGAKI³⁾

ABSTRACT

Characteristics of mean velocity and turbulence properties in oscillatory bottom boundary layers are investigated with low-Reynolds number turbulence model. Since this model is capable to describe the flow field close to the bottom, special attentions are paid on the characteristics of the viscous sublayer. Several interesting results, which coincide with or differ from existing knowledge on steady bottom boundary layers, are presented in particular on the mean velocity profile, turbulent viscosity coefficient and growth of the viscous sublayer.

I. INTRODUCTION

Existing studies for turbulent transport phenomena in coastal processes are mainly based on the eddy viscosity concept. However, it has been recognized that the predictive ability of eddy viscosity models is severely limited. Recently, as the computer technology has been advancing, applications of turbulent transport models to oscillatory flow have received special interest. At present, $k-\epsilon$ model is regarded as the most widely tested and the most applicable two equation model, in which two partial differential equations are used to describe turbulent kinematic energy k and its dissipation rate ϵ .

A few researchers have investigated the applicability of the $k-\epsilon$ model to oscillatory boundary layers (Cousteix et al., 1979; Hayashi and Shinoda, 1979; Shen, 1984), most of these studies dealing only with a high Reynolds number version of the $k-\epsilon$ model. Such a model is no longer applicable to the near bottom region, where the local isotropic condition is not satisfied. Besides, in oscillatory flow, the velocity is so small when the flow direction changes that the turbulence is not always intensive throughout a full period. From above reasons, a $k-\epsilon$ model which accounts for low-Reynolds number effects should be applied to oscillatory turbulent boundary layers.

1) Dr. Eng., Research Associate, Dept. of Civil Eng., Kyoto Univ. Sakyo-ku, Kyoto, 606, JAPAN

2) M. Eng., Ministry of Construction (Formerly Post-graduate Student, Kyoto Univ.), JAPAN

3) Dr. Eng., Professor, Dept. of Civil Eng., Meijo Univ., Tenpaku-ku, Nagoya, 468, JAPAN

This study examines the applicability of a $k-\epsilon$ model of low-Reynolds number version to oscillatory boundary layers. From the results obtained, characteristics of both the mean velocity and turbulence are discussed. Furthermore, since the model describes the flow field close to the bottom, comprehensive investigations have been made on the characteristics of the viscous sublayer. The growth of the viscous sublayer under the flow acceleration is investigated in relation to a phenomenon of 're-laminarization' in an accelerated uni-directional flow.

II. $k-\epsilon$ MODEL FOR LOW-REYNOLDS NUMBERS

In order to predict the flow within a viscous sublayer close to the bottom, Jones and Launder (1972, a) have introduced the following extra terms into the standard $k-\epsilon$ model: (1) terms to represent viscous diffusion of k and ϵ , and (2) terms to account for the non-isotropic dissipation process. Furthermore, they have modified some coefficients in the $k-\epsilon$ equations into functions of the turbulence Reynolds number R_T , which is defined with k , ϵ and kinematic viscosity ν as follows:

$$R_T = k^2 / \nu \epsilon \quad (1)$$

For a steady flow, the wall function method (Rodi, 1978) is often used as an alternative to the direct consideration of viscous sublayer properties. In this method the boundary conditions at the bottom are replaced by those immediately outside the viscous sublayer based on empirical laws under the local turbulence equilibrium condition. The method, however, is not applicable to an oscillatory flow since the rate of turbulence generation does not coincide with that of its dissipation at each phase. One of the merits of the low-Reynolds number $k-\epsilon$ model is that all the variables at the bottom can be set to be zero without invoking any empirical knowledge.

III OUTLINE OF THE ANALYSIS

(1) Basic equations

The oscillatory boundary layer equation is given as follows:

$$\frac{\partial(u - u_p)}{\partial t} = -\frac{\partial \overline{u'w'}}{\partial z} + \nu \frac{\partial^2 u}{\partial z^2} \quad (2)$$

where x and z axes are taken along and normal to the flat bottom respectively, t is the time, u is the mean velocity in the boundary layer, u_p is the mean velocity at the outer edge of the boundary layer, and u' and w' are the fluctuating velocity components. The Reynolds stress $-\rho \overline{u'w'}$ is expressed as a product of mean rate of strain $\partial u / \partial z$ and turbulent viscosity ν_T .

$$-\overline{u'w'} = \nu_T \frac{\partial u}{\partial z} \quad (3)$$

The turbulent viscosity ν_T is determined by local values of turbulent kinematic energy k and its dissipation rate ϵ .

$$\nu_T = c_\mu f_\mu k^2 / \epsilon \quad (4)$$

According to Jones and Launder's model (1972,a), the following equations are adopted for k and ϵ .

$$\frac{\partial k}{\partial t} = \frac{\partial}{\partial z} \left[\left(\nu + \frac{\nu_T}{\sigma_k} \right) \frac{\partial k}{\partial z} \right] - \overline{u'w'} \frac{\partial u}{\partial z} - \epsilon - \underbrace{2\nu \left(\frac{\partial k^{1/2}}{\partial z} \right)^2}_{\text{underlined}} \quad (5)$$

$$\frac{\partial \epsilon}{\partial t} = \frac{\partial}{\partial z} \left\{ \left(\nu + \frac{\nu_T}{\sigma_\epsilon} \right) \frac{\partial \epsilon}{\partial z} \right\} - c_1 f_1 \frac{\epsilon}{k} \overline{u'w'} \frac{\partial u}{\partial z} - c_2 f_2 \frac{\epsilon^2}{k} + \underbrace{2\nu \nu_T \left(\frac{\partial^2 u}{\partial z^2} \right)^2}_{\text{underlined}} \quad (6)$$

The underlined terms are included to account for low-Reynolds number effects. After Jones and Launder, the coefficients in Eqs.(4) ~ (6) are given as follows:

$$\left. \begin{aligned} c_\mu &= 0.09, & c_1 &= 1.55, & c_2 &= 2.0, \\ \sigma_k &= 1.0, & \sigma_\epsilon &= 1.3 \end{aligned} \right\} \quad (7)$$

The following expressions proposed by Jones and Launder for f_1 , f_2 , f_μ are also adopted.

$$\left. \begin{aligned} f_1 &= 1.0 \\ f_2 &= 1.0 - 0.3 \exp(-R_T^2) \\ f_\mu &= \exp\{-2.5/(1+R_T/50)\} \end{aligned} \right\} \quad (8)$$

These are a lot of arguments (Hanjalic and Launder, 1976 ; Hosoda and Yokoshi, 1986) concerning the values of the coefficients in Eq. (7) and the functional forms in Eq.(8) even for steady flows. Another problem may arise in applying the values and functional forms proposed for steady flows to oscillatory flows. However, they have been confirmed to be universal at least for various types of steady flow. Furthermore, as seen from Eq.(1), the turbulent Reynolds number R_T varies spatially and temporally with k and ϵ , and it is expected that the vaiations of f_2 and f_μ express the temporal variations of the oscillatory flow properties.

(2) Non-dimensional description of basic equations

To obtain non - dimensional forms of the basic equations, the following variables are introduced:

$$\left. \begin{aligned} \bar{u}_r &= (u - u_p) / \hat{u}_p, & z_r &= z / \delta, & t_r &= \omega t, \\ \tau_r &= -\overline{u'w'} / \hat{u}_p^2, & k_r &= k / \left(\frac{1}{2} \hat{u}_p^2 \right), & \epsilon_r &= \epsilon / \left(\frac{1}{2} \omega \hat{u}_p^2 \right) \end{aligned} \right\} \quad (9)$$

where \hat{u}_p is the velocity amplitude immediately outside the boundary layer, ω is the angular frequency of the oscillatory flow, $\delta = \sqrt{\nu/\omega}$ is related to Stokes length. Now, the system of the equations to be analysed here is as follows:

$$\frac{\partial \bar{u}_r}{\partial t_r} = R^{1/2} \frac{\partial \tau_r}{\partial z_r} + \frac{\partial^2 \bar{u}_r}{\partial z_r^2} \quad (10)$$

$$\tau_r = \frac{1}{2} R^{1/2} c_\mu f_\nu \frac{k_r^2}{\epsilon_r} \frac{\partial \bar{u}_r}{\partial z_r} \quad (11)$$

$$\begin{aligned} \frac{\partial k_r}{\partial t_r} = \frac{\partial}{\partial z_r} & \left\{ \left(1 + \frac{1}{2} R \frac{c_\mu}{\sigma_k} f_\nu \frac{k_r^2}{\epsilon_r} \right) \frac{\partial k_r}{\partial z_r} \right\} \\ & + 2 R^{1/2} \tau_r \frac{\partial \bar{u}_r}{\partial z_r} - \epsilon_r - 2 \left(\frac{\partial k_r^{1/2}}{\partial z_r} \right)^2 \end{aligned} \quad (12)$$

$$\begin{aligned} \frac{\partial \epsilon_r}{\partial t_r} = \frac{\partial}{\partial z_r} & \left\{ \left(1 + \frac{1}{2} R \frac{c_\mu}{\sigma_\epsilon} f_\nu \frac{k_r^2}{\epsilon_r} \right) \frac{\partial \epsilon_r}{\partial z_r} \right\} \\ & + 2 R^{1/2} c_1 f_1 \frac{\epsilon_r}{k_r} \tau_r \frac{\partial \bar{u}_r}{\partial z_r} - c_2 f_2 \frac{\epsilon_r^2}{k_r} \\ & + 2 R c_\mu f_\nu \frac{k_r^2}{\epsilon_r} \left(\frac{\partial^2 \bar{u}_r}{\partial z_r^2} \right)^2 \end{aligned} \quad (13)$$

where R is the Reynolds number defined as follows:

$$R = \frac{(\widehat{u}_p)^2}{\omega \delta} = \frac{\widehat{u}_p a}{\nu} \quad (14)$$

where a is the orbital amplitude at the bottom.

By using low Reynolds number k - ϵ model, the bottom boundary condition is described in the following simple way.

$$\bar{u}_r = -\cos t_r, \quad k_r = 0, \quad \epsilon_r = 0, \quad \text{at } z_r = 0 \quad (15)$$

The upper boundary condition is described as follows.

$$\frac{\partial \bar{u}_r}{\partial z_r} = 0, \quad \frac{\partial k_r}{\partial z_r} = 0, \quad \frac{\partial \epsilon_r}{\partial z_r} = 0, \quad \text{at } z_r = 1 \quad (16)$$

(3) Computational Technique

The vertical grid spacing Δz was determined at $D/600$ (D : the height where shear stress becomes negligible) to obtain sufficient number of grid points in the viscous sublayer. The system of the basic equations (10)~(13) was solved by the Crank-Nicolson implicit scheme. The time increment Δt was $T/2160$. The calculation was continued until the variables at a phase in successive cycles converge. The conditions of calculations are listed in Table 1.

Table 1 Conditions of calculations.

	\widehat{u}_p (cm/sec)	T (sec)	D (cm)	R
CASE-I	30.0	9.8	4.0	1.40×10^5
CASE-II	30.0	15.0	4.0	2.15×10^5
CASE-III	40.0	9.8	5.0	2.50×10^5
CASE-IV	49.9	9.8	7.0	3.87×10^5
CASE-V	49.9	15.0	7.0	5.93×10^5

IV. RESULTS AND DISCUSSION

(1) Mean velocity and turbulence properties

Figure 1 shows profiles of the non-dimensional mean velocity u_R , Reynolds stress τ_R , turbulent energy k_R and its dissipation rate ϵ_R for every $\pi/6$ phase. In Fig.1 and following all figures, the height z is normalized by D ($z_R'=z/D$) instead of δ ($z_R'=z/\delta$). It is found in the results at the phases 0 and π that the heights where the mean velocity reaches its maximum increase with the Reynolds number R ; that is, the velocity gradient decreases with R .

Figure 2 depicts variations of these quantities with phase. The peak values of τ_R , k_R and ϵ_R becomes larger as R increases. The phase lags of the maxima of τ_R , k_R and ϵ_R behind the maxima of the outer velocity decrease with increase in R . It should be noted that the phase of the total shear stress $-\rho\overline{u'w'}+\rho\nu\partial u/\partial z$ close to the bottom goes ahead of the phase of the outer velocity although the phase of the Reynolds stress $-\rho\overline{u'w'}$ lags behind it.

Profiles of the mean velocity u_R are given in Figure 3, where the ordinate is taken in the logarithmic scale. The figure also shows the positions of the outer edge of the viscous sublayer D_L and the overlapped layer d estimated on the basis of Kajiwara's (1968) theory. It is observed in the profiles around the phase 0 and π that the mean velocity shows linear variation in the region $z_R'<D_L/D$, and log-linear variation in the region $D_L/D<z_R'<d/D$. These properties are consistent with the general findings in steady unidirectional flow. Such properties however are not so obvious for the other phases.

(2) Turbulent viscosity coefficient

Figure 4 shows the profiles of the turbulent viscosity coefficient ν_T , which is calculated by the local instantaneous values of k and ϵ shown in Eq.(4). It is found that ν_T increases almost linearly in the region close to the bottom; the phase averaged value of ν_T is almost constant in the region of $0.1<z_R'<0.4$; ν_T decreases with the height in the outer region $z_R'>0.4$.

(3) Transport process of turbulent energy

Figure 5 shows the turbulent energy balance in the oscillatory boundary layer for CASE-I. The symbols Dif, P, ϵ and Ni in the figure denote the turbulence diffusion(1st term of R.H.S. of Eq.(12)), production(2nd term), dissipation(3rd term) and non-isotropic part of the dissipation near the bottom(4th term).

The turbulence production P does not balance with the dissipation ϵ at each phase. The heights for peak values of P and ϵ appear in the range of $z_R'=0.015\sim 0.025$, and the variation of the heights coincide fairly well with the variation of the height of the outer edge of the viscous sublayer which is shown in Figure 6 later. The diffusion term Dif is positive in the region corresponding to the viscous sublayer. The non-isotropic dissipation term Ni takes negative values in the viscous sublayer and tends to zero outside the region.

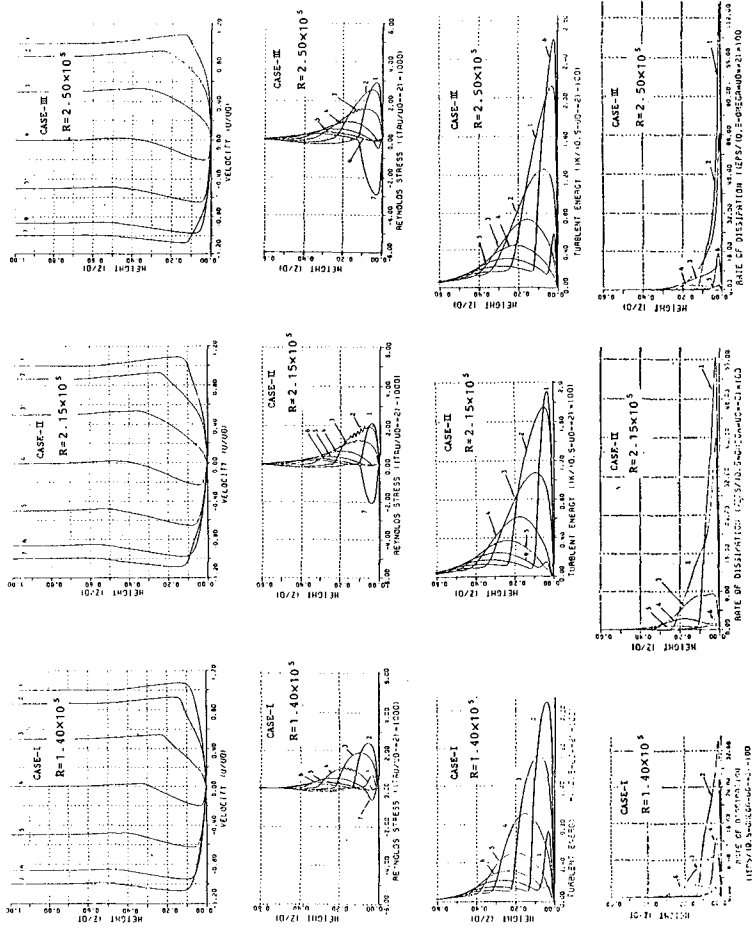


Fig. 1 Profiles of non-dimensional mean velocity u_r (top), Reynolds stress τ_r (2nd), turbulent energy ϵ_r (3rd) and turbulent energy dissipation rate ϵ_r (bottom).

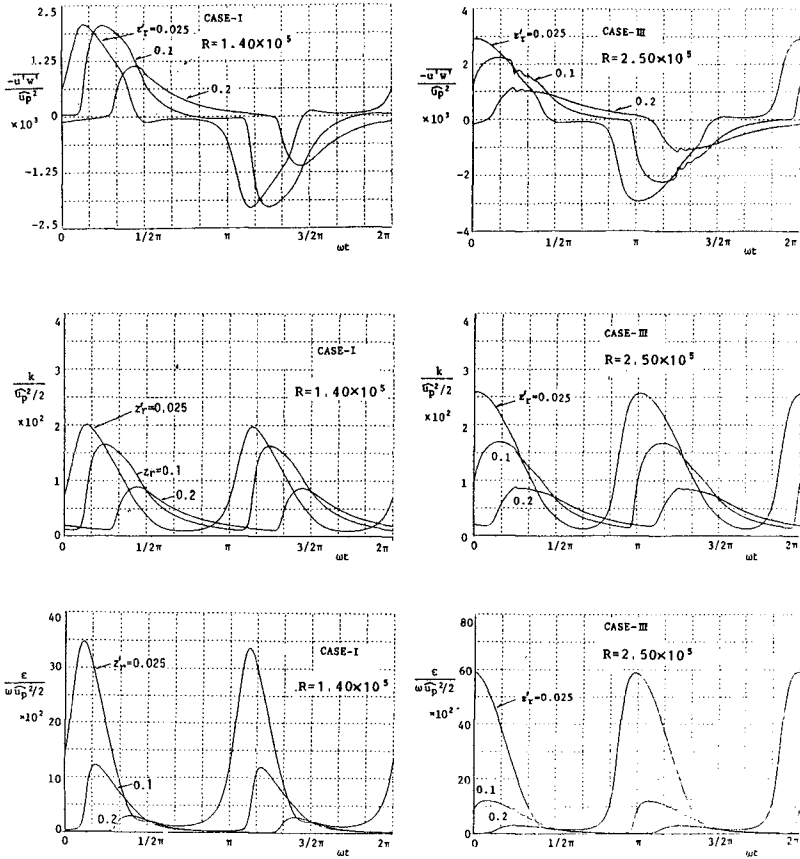


Fig.2 Phase variations of Reynolds stress τ_r (top), turbulent energy k_r (middle) and turbulent energy dissipation rate ϵ_r (bottom).

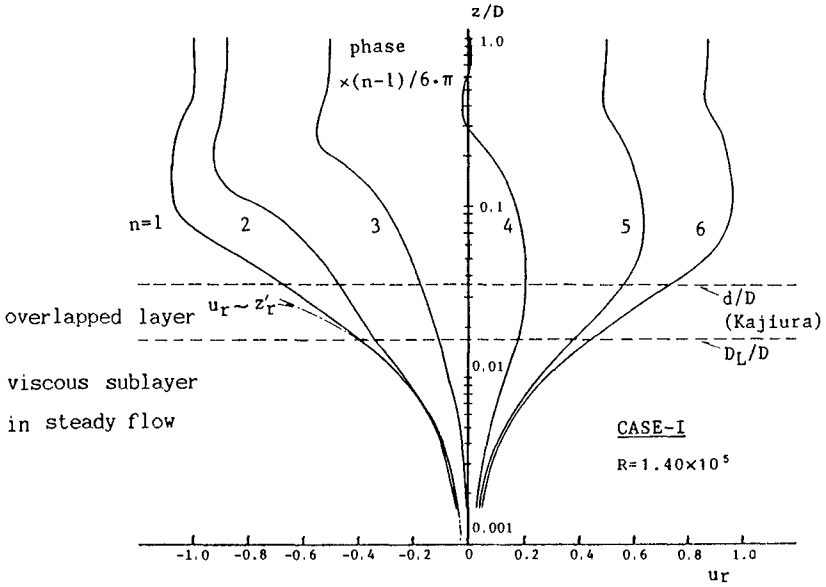


Fig.3 Profiles of mean velocity.

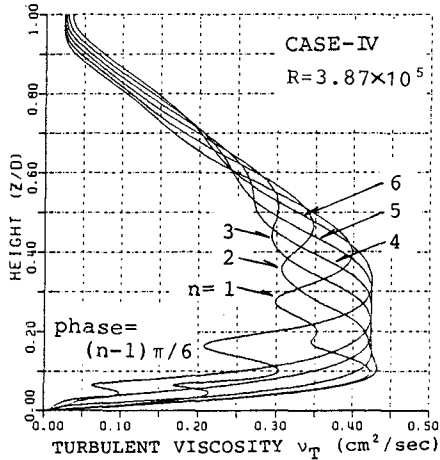


Fig.4 Profiles of turbulent viscosity v_T .

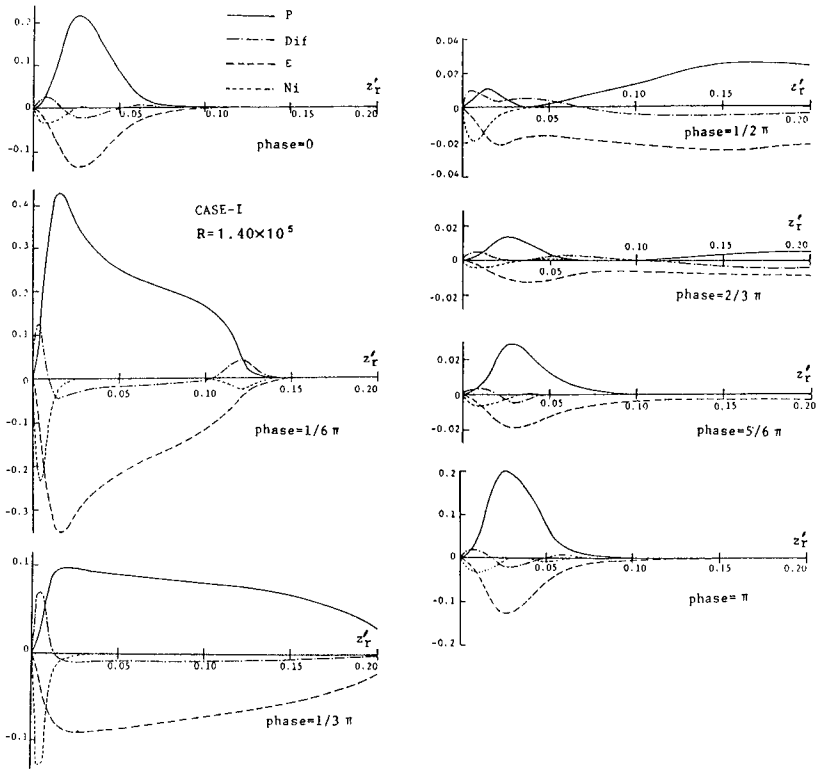


Fig.5 Turbulent energy balance near the bottom.

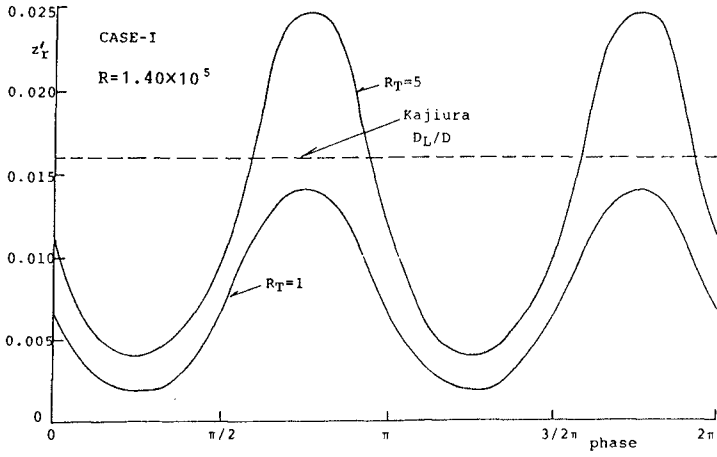


Fig.6 Variations of the height of viscous sublayer with phase.

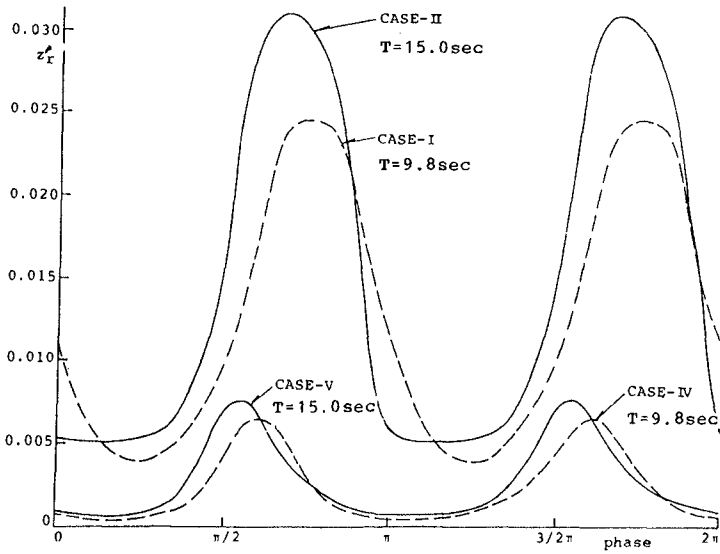


Fig.7 Variations of the height of viscous sublayer with phase (at the height where $R_T=5$).

(4) Variation of the height of viscous sublayer

In Kajiura's(1968) theory, the height of the viscous sublayer is assumed to be invariant regardless of phase. However, it is found from the following consideration that the height varies with the phase.

The total shear stress τ_A consists of the viscous and the turbulent shear stresses.

$$\tau_A = \rho(\nu + \nu_T) \frac{\partial u}{\partial z} \quad (17)$$

From Eqs.(1) and (4), ν_T is expressed as a function of the turbulent Reynolds number R_T :

$$\nu_T = c_\nu f_\nu \nu R_T \quad (18)$$

Consequently, the ratio of the viscous shear stress to the total shear stress is a function of R_T . The viscous shear stress occupies 95.7% of the total shear stress when $R_T=5$, and 99.2% when $R_T=1$. If the outer edge of the viscous sublayer is defined as a position where R_T equals 5, the phase averaged height coincides well with that estimated from Kajiura's theory for all cases of the present calculations. The coincidence is not surprising because both this model and Kajiura's theory are based on same experimental knowledge on steady bottom boundary layers.

Figure 6 shows variations of the heights where R_T equals 5 and 1. It is concluded that the thickness of the viscous sublayer varies with the phase and reaches the maximum slightly after the occurrence of the maximum acceleration. In other words, the turbulent energy becomes minimum at the accelerating phases. This is analogous to the re-laminarization in accelerated unidirectional flow(Jones and Launder, 1972b). For an oscillatory pipe flow, Hino et al.(1976) have found experimentally the recovery of a laminar flow condition in the accelerating phases.

Figure 7 shows the variations of the height where R_T equals 5. Comparisons of cases I and II and of cases IV and V, in which cases the velocity amplitudes are same and the oscillation periods are different, show that the maximum thickness of the viscous sublayer increases as the oscillation period increases. In a steady accelerated flow, the thickness of the viscous sublayer increases with the flow acceleration(Jones and Launder, 1972b), whereas the results in Fig. 7 show the opposite feature that the viscous sublayer becomes thicker under smaller flow acceleration. Such difference is attributed to the time required for turbulent energy decay. In the case of short-period oscillating flow, the duration of small flow velocity is not enough for the turbulent energy to attenuate. It can be concluded that the duration of turbulence decaying is a more predominant factor than the effect of flow acceleration for the growth of the viscous sublayer.

V. CONCLUSIONS

1) The variations of the mean velocity and turbulence quantities depending on the Reynolds number have been investigated. The velocity gradients at the phases 0 and π close to the bottom decrease with the Reynolds number. The phase lags of the turbulence quantities behind the outer velocity decrease with increase in the Reynolds number.

2) At the phases around 0 and π , the mean velocity varies in proportion to the height from the bottom in the viscous sublayer and shows the logarithmic variation in the overlapped layer. These are consistent with the general findings in steady flow. However, for the other phases such properties are not so obvious.

3) The turbulence viscosity coefficient increases in proportion to the height in the region close to the bottom, then keeps almost constant in the region $0.1 < z_r' < 0.4$, and decreases with the height in the outer flow region.

4) The thickness of the viscous sublayer varies with phases of an oscillatory flow and becomes maximum when the flow accelerates. The thickness increases with the oscillation period, meanwhile it increases with the flow acceleration in accelerated unidirectional flow.

REFERENCES

- Cousteix, J., A. Desopper and R. Houdeville (1979) : Structure and development of a turbulent boundary layer in an oscillatory external flow, Turbulent Shear flow, Vol. 1 , Springer-Verlag, pp.154-171.
- Hanjalic, K. and B.E. Launder (1976) : Contribution toward a Reynolds-Stress closure for low-Reynolds number turbulence, J. Fluid Mech., Vol.74, pp.593-610.
- Hayashi, T. and K. Shinoda (1979) : Basic study on the turbulent oscillatory boundary layer, Proc. of 23th Japanese Conf. on Hydraulics, pp.41-48.
- Hino, M., M. Sawamoto and S. Takasu (1976) : Experiments on transition to turbulence in an oscillatory pipe flow, J. Fluid Mech., Vol.75, Part 2, pp.193-207.
- Hoshoda, H. and S. Yokoshi (1986) : Representation of the dissipation term of ϵ -equation in the case of low turbulent Reynolds number, Proc. of 30th Japanese Conf. on Hydraulics, pp.517-522 (in Japanese).
- Jones, W. P. and B. E. Launder (1972,a) : The prediction of laminarization with a two-equation model of turbulence, J. Heat Mass Transfer, Vol.15, pp.301-314.
- Jones, W. P. and B. E. Launder (1972,b) : Some properties of sink-flow turbulent boundary layers, J. Fluid Mech., Vol. 56, pp.337-351.

Kajiura, K. (1968) : A model of the bottom boundary layer in water waves, Bull. Earthq. Res. Inst., Vol.46, pp.75-123.

Rodi, W. (1978) : Turbulence models and their application in hydraulics, a state of the art review, Univ. Kurlsruhe, SFB 80/T/127, p.140.

Sheng, Y. P. (1984) : A turbulent transport model of coastal processes , Proc. of 19th Inter. Conf. of Coastal Eng., pp.2380-2396.

CHAPTER 56

On the Occurrence of Abnormal Storms and Its Implications on Design Parameters (Statistical Analysis of Same)

Ole Juul Jensen* & P. Klinting**

Abstract

The assessment of design parameters has a fundamental importance for port planning and design of coastal structures. Special emphasis has to be put on the importance of the occurrence of abnormal storms. The authors' experience from investigations of port projects has revealed that on many sites it is storms with unusual tracks or otherwise unusual behaviour that are determinant for the design events. This experience is documented by two case stories. The importance of unusual weather systems is discussed and statistical methods for investigation of such phenomena are discussed.

1. Introduction

The design parameters for ports and coastal structures are usually established by statistical analysis of environmental data on extreme events from measurements or hindcast or a combination of these methods.

Traditionally statistical analysis is based on the application of a probability distribution such as: Gumbel, Exponential or Weibull etc. The theory of statistical distributions requires that the data to be introduced in the statistical analysis all belong to the same stochastic/statistical population. This is usually assumed to be the case if for example the data originate from wave measurements at a specific site.

On some sites, it is, however, evident that two wave regimes occur. This is for example the case for the coasts of the Indian Ocean where both normal monsoon waves and tropical storm waves occur. The two types of waves have clearly

*) Ole Juul Jensen, Head Ports and Marine Structures Department, Danish Hydraulic Institute, Agern Allé 5, DK-2970 Hørsholm, Denmark.

***) Per Klinting, Senior Hydraulic Engineer, Danish Hydraulic Institute, Agern Allé 5, DK-2970 Hørsholm, Denmark.

different origin and may thus be expected to be of different populations as has been documented by many studies. For such sites, it has since long been known by coastal engineers that it is necessary to separate the two regimes of waves when performing statistical analyses. Experience shows that two regimes of storms or storms leading to two statistical populations may also occur on sites exposed to cyclones. (Examples will be presented from Europe and North Africa).

2. Statistical Method for Analysis of Storms

In Ref. /6/, Rosbjerg et al. present the so-called POT-estimation of Extreme Sea States. The POT-method, i.e. peak-over-threshold, considers the distribution of peaks (for example wave heights, H_s) over a preselected threshold level. The following description is an extract from Ref. /6/.

The appropriate threshold is introduced and the recorded wave heights below this level are deleted, the remaining data constitute a partial duration series. This series is likely to represent independent storm events provided that the threshold is reasonably selected. Within each storm the peak value is used for further analysis. The POT-method focus on the relevant statistical variable for extreme events. A basic requirement of further analysis is that selected peaks are independent and identically distributed (i.e. that in any period of time there is the same probability of occurrence of a given wave height. Since for example the waves in the winter and summer season are quite different, it is normally most accurate to separate the two seasons and to consider the waves for example in the winter season, on the Northern Hemisphere October to March, both months included (about 180 days).

Denote either the storm peak itself or some suitable transformation by H'_s and the threshold level by h_* , the distribution function F for H'_s is then introduced as

$$P\{H'_s \leq h \mid H'_s > h_*\} = F(h) \quad (1)$$

Further assume that the occurrence of wave peaks takes place according to a Poisson process with a seasonally varying intensity. This implies that the number of storms per year follows a Poisson distribution with the parameter equal to the integral of the intensity over a year. If this quantity is denoted by λ , the expected number of storms in t years with wave peaks greater than an arbitrary level $h (> h_*)$ becomes

$$v_h = \lambda t (1 - F(h)) \quad (2)$$

The T-year event, h_T , is now defined as the level which, on the average, will be exceeded once per T years. Since this situation corresponds to $v_h = 1$ for $t = T$, the T-year event is obtained by solving Eq. (2) under these conditions leading to

$$h_T = F^{-1} \left(1 - \frac{1}{\lambda T} \right) \quad (3)$$

By use of the above mentioned assumptions implying that the number of storms with wave peaks greater than h in t years follows a Poisson distribution with ν_h as parameter, the distribution for the maximum value of H'_s in t years, $H'_{s \max, t}$ becomes

$$P \{ H'_{s \max, t} \leq h \} = e^{-\nu_h} = e^{-\lambda t (1-F(h))} \quad (4)$$

Now denote by R the probability (the risk) that the level $h_{R, L}$ will be exceeded once or more during a time period of L years (for example the lifetime of the structure). Accordingly, the left hand side of Eq. (4) equals $1-R$ for $t = L$, and a relation between R , L and the corresponding value of T can then be obtained by solving the equation for $h_{L, R}$ and equalizing the expression with Eq. (3). Hereby the following relationship is obtained

$$R = 1 - e^{-L/T} \quad (5)$$

In case of exponentially distributed wave peak exceedances i.e.

$$F(h) = 1 - e^{-\frac{h-h_*}{\alpha}} \quad (6)$$

where the parameter α is equal to the expected value of the exceedances above the threshold value h_* , the expression for the T -year event becomes particularly simple. Combining Eqs. (3) and (6) results in

$$h_T = h_* + \alpha \ln \lambda T \quad (7)$$

which can be used in order to exemplify an approximate method for calculating the standard error of the T -year estimate. In Ref. /6/ it is shown that the approximate standard error of T -year estimate can be written

$$\hat{s}_T = \frac{\alpha}{\sqrt{\lambda}} \left(1 + (\ln \lambda T)^2 \right)^{\frac{1}{2}} \quad (8)$$

It is important to notice that the POT-approach is not limited to the exponential distribution assumption applied above. If another type of distribution, (e.g. lognormal or gamma) is justified, a similar procedure can be applied leading to revised expressions for the standard error of the T -year estimate. For other types of statistical distributions special care should be taken when the threshold level is selected.

3. Storms Caused by Cyclones

In many parts of the world including Europe and the Mediterranean, the severe storms are of the cyclone-type, being roughly circular low-pressure areas with a diameter that may range from hundreds to perhaps two thousand kilometers.

Most storms are associated with cold and warm fronts separating different air masses, but storms also occur when depressions form within the same air mass. The most severe cyclones are normally generated in the Atlantic Ocean east of New Foundland (Ref. /2/) and travel eastwards over the Atlantic Ocean to Europe and the Mediterranean following typical tracks as seen in Fig. 1. These cyclones occur due to unstable waves on the polar front and are therefore always associated with fronts separating different air masses with a difference in temperature. Besides these "Atlantic Cyclones" other cyclones affect Europe and the Mediterranean. Cyclones are sometimes generated on the southwest or southeast side of a cyclone, so-called secondary lows, which sometimes develop into major cyclones (Donn, Ref. /3/).

Many "Atlantic Cyclones" reach the Mediterranean, but in addition cyclones are also generated locally. Ref. /8/ presents an attempt to characterize cyclones in the western Mediterranean after their generation area and track characteristics. The most well known "local" Mediterranean cyclones are those generated within or near the Gulf of Genoa. They usually move southeast across the Tyrrhenian Sea. Fig. 2 from Ref. /5/ shows typical tracks of depressions affecting the western Mediterranean.

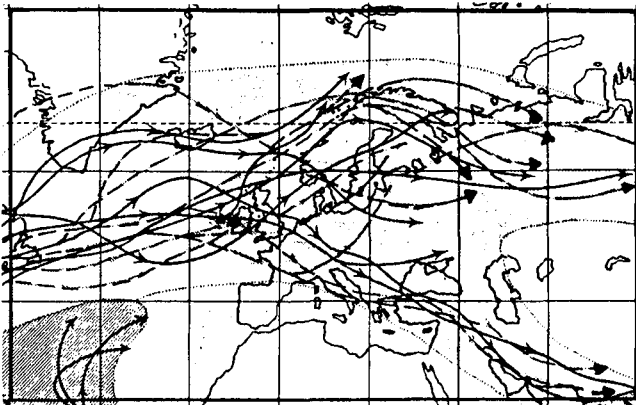


Figure 1. Typical tracks of Atlantic cyclones, Ref. /2/.

When making data analyses of wind velocities, wave heights, or water levels it is assumed that the cyclone generated physical data belong to the same statistical popula-

tion. It is the authors' practical experience that in many cases the assumption of all data originating from the same homogeneous data population may be questioned. On some sites, it appears that the most extreme events are due to abnormal cyclone storm tracks leading to unusual weather situations and extreme wind, wave or water level conditions.

When dealing with sites with more than one statistical population of storm waves, it is necessary to separate the analyses into two distributions. A serious problem often arises in this respect, as although there may be sufficient data for the estimate of the distribution for the "normal" waves, the data available for the determination of the parameters of the unusual or abnormal waves will normally be very scarce as shown in the following examples from case studies.

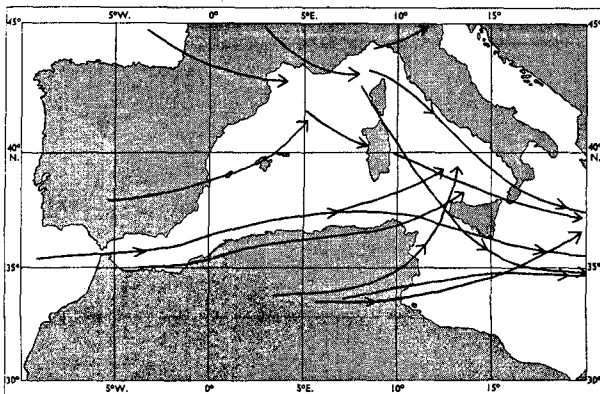


Figure 2. Typical tracks of depressions affecting the Mediterranean.

4. Examples of Abnormal Storm Events

4.1 The Western Part of the Mediterranean (the Coast of Algeria)

The most severe storm situations in the western Mediterranean area are due to Atlantic cyclones entering the Mediterranean after passage of the southern part of France (see Fig. 1 and 2). The cyclones usually follow a track towards ESE passing Italy and propagating further eastwards over Greece and Turkey. For the most severe of this type of cyclones the waves can be relatively high in the western Mediterranean, but due to the relatively fast propagation time of 30-50 km/h the duration of high winds is generally short and hence storms are not fully utilizing the geographical fetch. It appears, however, that the cyclones/depressions causing the largest waves especially on the central and western part of the Algerian coast (see example from the Oran/Arzew area) follow less frequent tracks which are more southerly than the typical patterns described above. Some-

times the cyclones even become stationary as will be seen in some of the following examples.

Based on local information, literature, available measurements and hindcast results from numerical hindcast models, the storms in Table 1 have been found to be among the most severe in the last say 50-60 years. Table 1 shows results of numerical hindcast studies as well.

Table 1. Extreme storms selected for analysis. (Western Mediterranean).

Storm No.	Date/year	Offshore Waves H_s (m)			
		a)Arzew/Oran area	Betw. a&b	b)Alger Betw.b&c	c) Algeria/Tunesian Border
i	1934, Feb.1-5	4.3		4.8	8.6*
ii	1965, Jan.5-6	5.8**	8.4*	7.2	4.1
iii	1967, Dec.10-12	7.3	7.6	6.6	9.3*
iv	1969, Nov.30-Dec.2	3.4	5.8	5.3	9.6*
v	1979, Dec.19-23		Wave height not known		
vi.	1980, Dec.27-29	7.0*			

* Maximum value found by hindcast study.

** Wave measurements near Port of Oran, $H_s = 5.5$ m.

- i. The Feb. 1934 storm caused the failure of Jetée Mustapha in Port d'Alger, Ref. /9/ & /10/ in Port of Oran displacement of several blocks on the main breakwater, wave direction NNE. (Note highest waves towards east in Algeria). Wave direction observed, NNE.
- ii. In Port Oran, about 200 blocks displaced. Wave height measured by LCHF, France, at $H_s = 5.5$ m.
- iii. In Port of Oran, damage to the wave wall in several points and some blocks displaced from the armour layer. Wave direction NNE.
- v. Many blocks (in the order of 150) displaced on the main breakwater in Port of Oran, wave direction NNE.
- vi. Failure of the new breakwater in Port d'Arzew el Djedid and damage on other ports in Algeria and Morocco. Wave direction at Arzew/Oran, NNE.

The tracks of all these storms have been analysed and the results are shown in Fig. 3. Figs. 4 and 5 show examples of the results of numerical hindcast studies of the 1967 and 1986 storms.

All the storms are caused by depressions with rather unusual tracks. The centres of the depressions arrived in all cases at or very close to the Algerian Coast. The configuration of the wind field being almost circular with the wind blowing anti-clockwise results in a curved fetch larger than the apparent geographical fetch, see Fig. 4.

It is further interesting to notice that although they all exhibit this common feature, the tracks are all very different. It appears that the tracks of the depressions to a large extent are unpredictable i.e. the atmospheric air flow is highly irregular and once the depressions deviate from their normal track their propagation becomes extremely

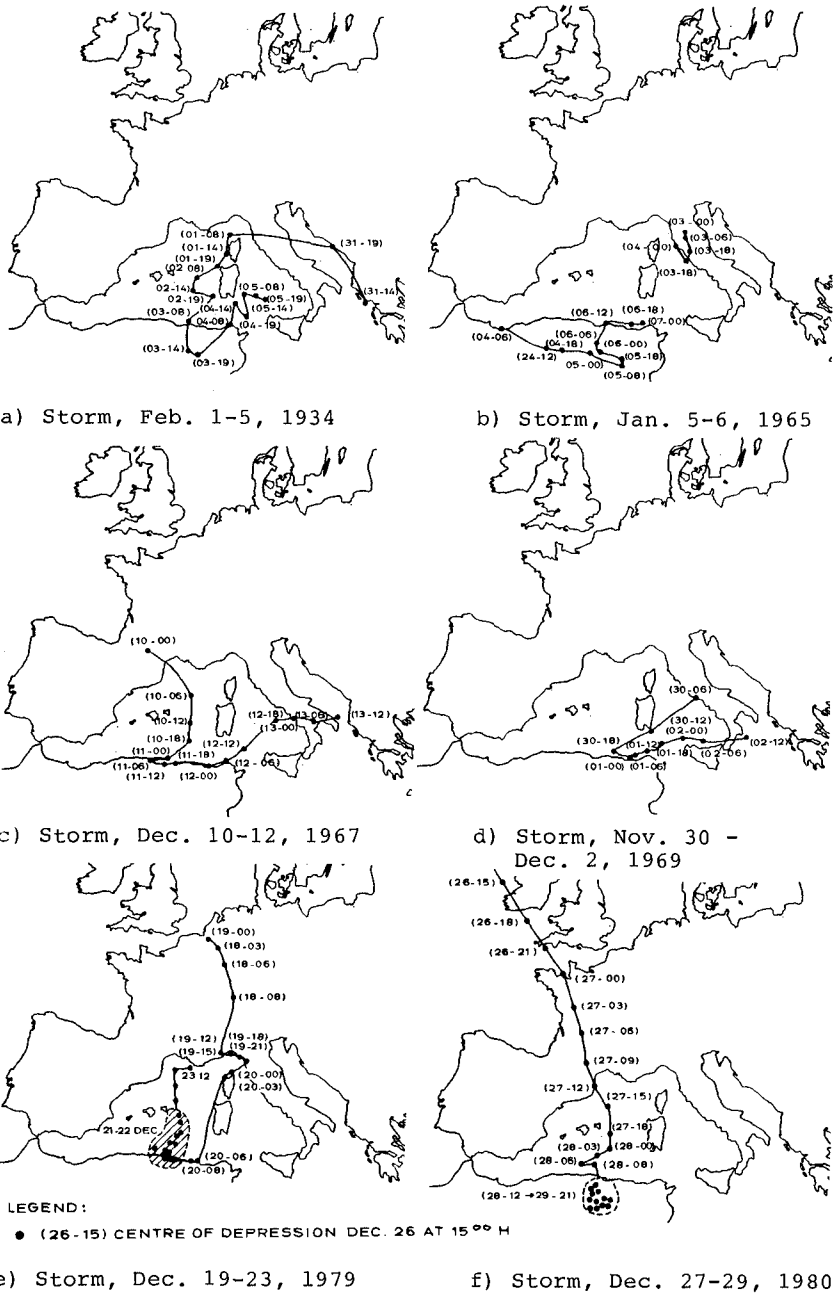


Figure 3. Tracks of cyclones for selected storms over the Mediterranean.

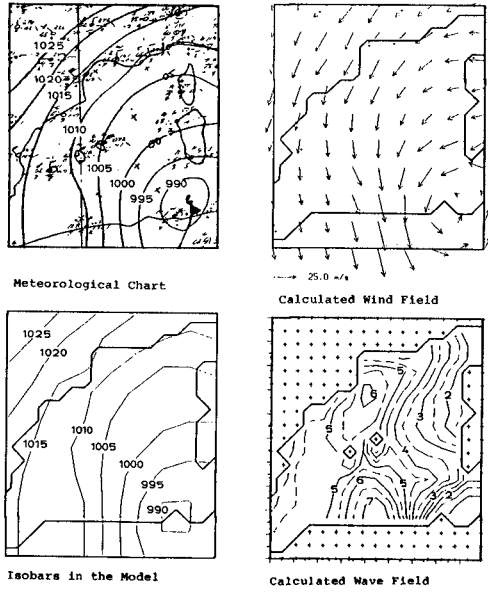


Figure 4. Example of hindcast results of storm on Dec. 10-12, 1967. Situation in the Western Mediterranean on Dec. 12 at 00GMT.

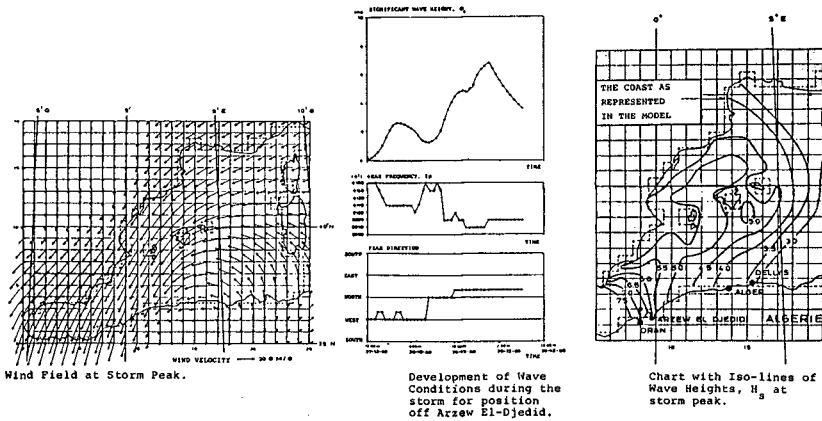


Figure 5. Example of hindcast results of storm on Dec. 27-29, 1980 from Ref. /1/.

complex.

The wave data available from the western part of Algeria show that the storms belong to two populations and further that all the most severe storms occur from NNE and further that they are rather rare. Those storms are associated with the abnormal depressions as seen in Fig. 3.

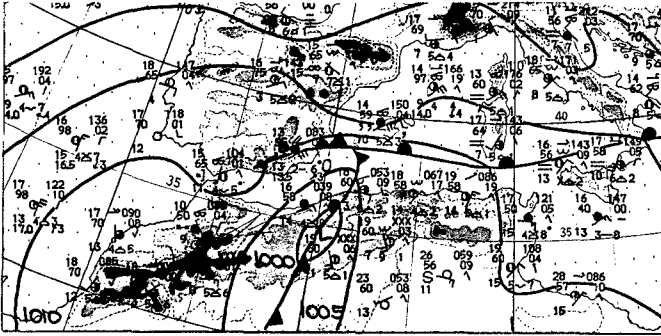


Figure 6. Weather situation May 1, 1976.

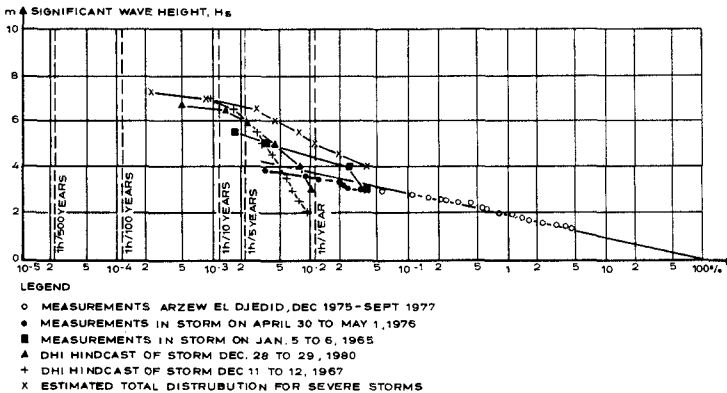


Figure 7. Wave statistics for Arzew El Djedid.

This may be proven by a wave statistics for Arzew El Djedid in the western Algeria. The statistics come partly from wave measurements in the period December 1975 to September 1977 and from the hindcast study shown in Table 1. The most severe storm in the measuring period was due to a low pressure originating from the Gulf of Cadiz (Type B2 in Ref. /8/ propagating straight eastwards through the Strait of Gibraltar (see typical storm tracks in Fig. 2). The situation at the peak of the storm appears on the weather map in Fig. 6. The center of the depression is near the site,

but the fetch to the north is disturbed by the presence of a front running west to east. The statistics appears in Fig. 7. Wave measurements were not available in a form allowing for a POT-analysis. The available data were therefore plotted on logarithmic paper.

It is clear from the statistics that the "normal" wave conditions covered by the measurements did not include any severe storms from NNE of the more stationary type shown in Fig. 3. The statistics for these storms lie above the statistics of the normal storms and two distinct populations of storms are identified although the upper one is not well defined. In this case it is seen to be highly risky to base the long term statistics on two years of measurements where only one regime (population) of the storms occurring on that site is included.

4.2 Extreme Waves from SE in the Faroe Islands

The main harbour in the Faroe Islands is Torshavn. This harbour is exposed to waves from SSE and NE. Torshavn is partly sheltered by the island of Nolsoe, see Fig. 8, which shows the position of Torshavn and of the wave recording station, East, mentioned in the following.

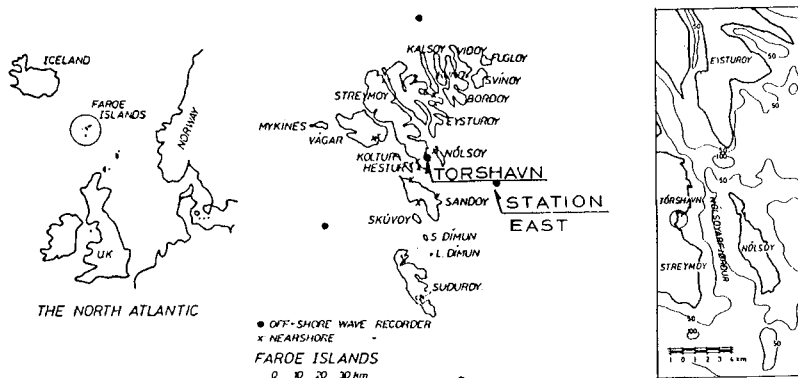


Figure 8. Location of Torshavn.

The design storms occur from SSE and they are associated with the occurrence of unusual depressions, unusual not with respect to the storm track but in the sense that they become stationary. The two most severe storms from SSE since 1930 occurred on Jan. 15-19, 1972, and on Jan. 21-22, 1984. Both storms created very large waves from SSE due to a depression over Ireland that could not move eastwards because of blocking high pressure over Norway. The depression consequently became stationary.

In Figs. 9 & 10 the weather situation for the two storms is described by weather maps.

A detailed survey of the weather maps of storms from SSE in the period 1930 to 1972 has revealed that no other storms in this period are as severe. The two storms caused offshore waves in the order of $H_s = 11$ m. In the storm of Jan. 21-22, 1984, the waves were measured at $H_s = 11.3$ m at the peak. A desk hindcast study using the SMB-method has shown that the third and fourth most severe storm since 1930 occurred in 1959 ($H_s \sim 9.5$ m) and 1941 ($H_s \sim 9.0$ m). Both storms were of the same type as 1972 and 1984, but with lower wind velocity. In Fig. 11 a POT analysis of measurements from station East is shown for the period Oct. 1980 to April 1987. The threshold level used is $H_s = 5.0$ m.

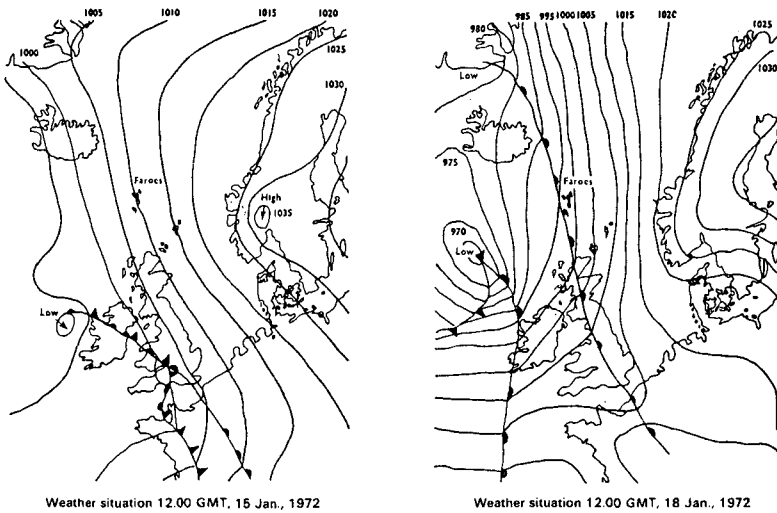


Figure 9. Weather maps of 1972 storm.

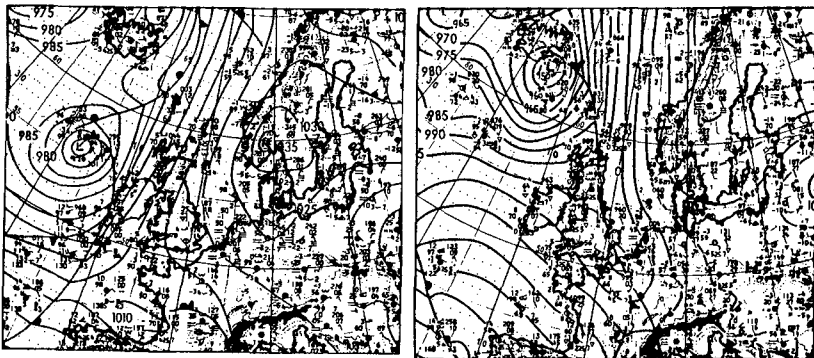


Figure 10. Weather maps of 1984 storm.

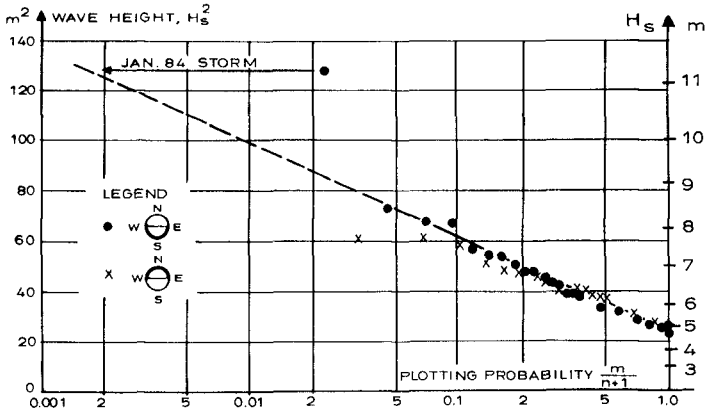


Figure 11. POT analysis of wave measurements. Station East.

It is seen that the data for "northern" and "southern" directions are following the distribution except the storm of January 1984, which falls well above the rest of the distribution. In order to see whether the distribution is actually a double distribution composed of two distributions the available information on the storms has been plotted in Fig. 12 where the abscissa has been changed to show the number of storms per year instead of the probability. The storms in question appear in Table 2. In this presentation the two severe storms of 1972 & 1984 are still above the distribution of measured data while the two storms of 1941 & 1959 are below.

Table 2 Ranking of the four most severe storms.

Ranking	Storm	H_s (m)	Return Period years $\frac{n+1}{m}$	Probability of Occurrence per year $\frac{m}{n+1}$
1	1984	11.3	59	0.017
2	1972	11.0	29	0.034
3	1959	9.5	19	0.05
4	1941	9.0	14	0.07

It is seen that also in this analysis the wave data indicate two distributions. The analyses were performed under the assumption that the wave climate has not changed in the period 1930 to 1987, while from other sources there are certain indications from the Northern Atlantic and the North Sea that the wind and waves have been more severe in the last 10-15 years.

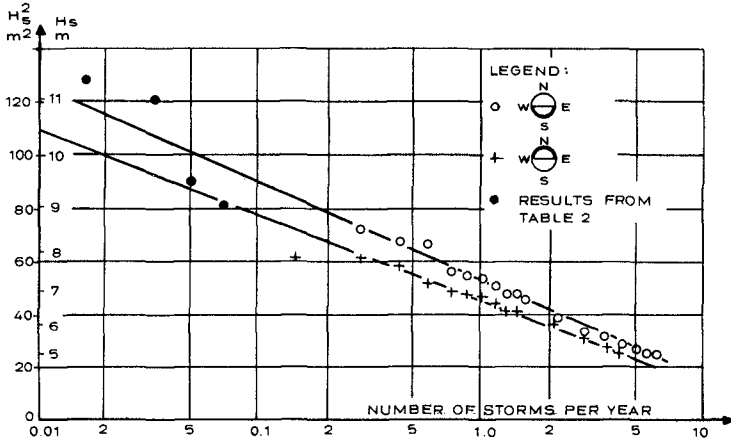


Figure 12. Statistics of number of storms per year.

5. Conclusions

The paper has shown that the occurrence of storms and high waves and water levels at many sites is highly complex and that it can be risky to assume all data belonging to one statistical population.

It is consequently the hope that the paper will encourage meteorologists and coastal engineers to embark on detailed co-operation for improving the understanding of the occurrence of abnormal storm events in order to provide more reliable assessments of extreme design events. The above are only a few examples of sites where mixed distributions occur. It is the author's feeling that on many sites, the same is the case.

The meteorological data bases that are set up these years and the advanced wave hindcast techniques on numerical models now available enable more profound studies to determine more accurate design data for man made marine and maritime structures and for assessing the risk for existing installations. The paper has shown the necessity for such investigations.

6. Acknowledgement

The authors would like to express their appreciation to the Laboratoire d'Etudes Maritimes (LEM) for cooperation on hydraulic studies for Algerian Projects and to the Faroe Islands Harbour Authorities (Landsverkfrødingurin) for providing data and making the POT-analysis of wave data from Station East at Faroe Islands.

7. References

- /1/ Abdelbaki A. & Juul Jensen (1983). Study of Provisional Repair of the Breakwater in Port d'Arzew-El-Djedid, Algeria. Conf. on Coastal and Port Eng. in Developing Countries, Colombo, 1983.
- /2/ Bartholomew J. (1963). The Edinburgh World Atlas. The Geographical Institute, Edinburgh.
- /3/ Donn, W.L. Meteorology. Third Edition.
- /4/ Langvad S. & Sørensen T. Extension of Torshavn Breakwaters (incl. discussions). Institution of Civ. Eng. U.K. Proceedings, Part 1, Vol. 58, 1975.
- /5/ Mediterranean Pilot Vol. I. Ninth Edition 1963. Published by the Hydrographer of the Navy, U.K. Mc. Graw-Hill Book Company.
- /6/ Rosbjerg, D. and Knudsen J. POT-estimation of Extreme Sea States and the Benefit of Using Wind Data. Proceedings of the NATO Advanced Study Institute on Statistical Extremes and Applications. Vimeiro, Portugal, Aug./Sept. 1983.
- /7/ Thomsen J. (1987). Application of the Faroese Wave and Current Measuring Project to Harbour Projects. Baltic Conf. on Design Const. and Maintenance of Harbour Structures, Norrköping, Sweden, Sept. 1987.
- */8/ Climates of Northern and Western Europe. World Survey of Climatology Volume 5. Edited by C.C. Wallén. Elsevier Publishing Company, 1970
- /9/ Renaud, P.J.M.
Port of Algiers: The Mustapha Jetty I. The Dock and Harbour Authority, Feb. 1936.
- /10/ Renaud, P.J.M.
Port of Algiers: The Mustapha Jetty II. The Dock and Harbour Authority, March 1936.

CHAPTER 57

WAVE OVERTOPPING ON RUBBLE MOUND BREAKWATERS

Pierluigi Aminti *

Leopoldo Franco **

ABSTRACT

The paper gives the results of an extensive series of hydraulic model tests carried out in a random wave flume, in order to study the effects on wave overtopping of the main geometric parameters of a typical rubble mound breakwater with crown wall. The results have been compared with those from other studies and analyzed with different methods. Generalized design diagrams and formulae for the prediction of overtopping discharges are finally given for a large number of popular breakwater configurations.

1. INTRODUCTION AND BACKGROUND

Wave overtopping is one of the most important hydraulic processes affecting the design of a breakwater, especially when a crown wall protects a quay or a reclamation. However, most research work on breakwaters just deals with the hydraulic stability and structural response of the primary armour. Still too limited information is available to the engineers for predicting the overtopping discharges and then checking against well established admissible values. In particular no reliable methods allow the fundamental design selection of the breakwater crest elevation and configuration to be effective against wave overtopping.

Model tests have often been carried out with regular waves, with consequent underestimation of the overtopping rates, which are mainly governed by the highest waves in the train.

Even the current prediction method given by the Shore Protection Manual (SPM, 1984) is based on early tests with monochromatic waves. In this method the overtopping discharge is given by a formula

* Associate Professor of Marine Civil Engineering, University of Florence, Via S.Marta 3, Florence, Italy

** Associate Professor of Coastal Engineering, Polytechnic of Milan, Piazza Leonardo da Vinci 32, Milan, Italy

related to the potential runup on a corresponding infinite slope. Then many problems arise as pointed out by Ahrens and Heimbaugh (1986). Moreover it should be observed that the runup computations themselves may be wrong. In fact in the SPM the runup on a rough slope is linearly related, by a simple reduction factor, to the runup on the equivalent smooth slope, while extensive random wave model tests reported by Allsop, Franco and Hawkes (1985) have shown a quite different behaviour of the two types of slopes for variable Iribarren numbers.

Some simplified theoretical approaches for the evaluation of overtopping discharge have been proposed by various Japanese researchers and recently by Jensen and Juhl (1987). These Authors also report on the very few existing field measurements carried out in Denmark and in Japan, which seem to agree with model test results when the experiments are conducted with irregular waves.

The Japanese prototype measurements reported by Fukuda, Uno and Irie (1974) were also used to provide the only available rough and conservative guidelines for acceptable overtopping discharges or intensities. In general, according to them, inconvenience for persons or vehicles (passing 3 m behind the crown wall) arise when the mean overtopping discharge per unit length of breakwater $\frac{Q}{3}$ reaches about 10^{-6} m³/s m, while danger occurs if Q exceeds $2 \cdot 10^{-5}$ m³/s m. These apparently low figures account for the fact that the danger levels are actually determined by the single largest overtopping waves which, due to the high irregularity of the physical phenomenon, can produce peak intensities a few hundreds times greater than the average intensity.

Most information is still obtained from laboratory work, which however often concerns seawalls in shallow water, such as the random wave investigations performed by Owen (1980) and by Ahrens and Heimbaugh (1986).

With reference to rubble mound breakwaters in relatively deep water, Jensen (1984) collected results from irregular wave model tests carried out at DHI for several different projects (some including the wind effect too); the set of graphs, later reanalyzed by Jensen and Juhl (1987), is useful but limited to the specific geometries and conditions of the tested breakwaters.

The lack of reliable and complete design guidelines then stimulated the Authors to begin in 1986 a systematic experimental research program: the preliminary results given by Aminti and Franco (1987) are now supplemented by numerous additional tests with new configurations, whose results are presented here in a more effective and general form.

At the final preparation of this paper it was possible to examine the results of a similar basic research program conducted at HR, Wallingford by Bradbury and Allsop (1988). They studied the effect on overtopping discharge of various crown wall and armour crest configurations with smooth and rock armoured slopes at a fixed angle (1:2). The satisfactory comparison of the hydraulic performance of the similar structures then suggested a consistent and general form of analysis and presentation of the experimental data, as shown in par. 3.

2. TEST EQUIPMENT AND PROCEDURE

The model tests were conducted in the 48 m long, 0.80 m wide and 0.80 m deep wave flume of the Florence University's hydraulic laboratory. The flume is equipped with an oleodynamically actuated piston-type wavemaker, with a random wave input signal obtained by filtering a white noise (Aminti, Liberatore and Petti, 1984).

A Jonswap type spectrum was reproduced with a significant wave height $H_s = H_{1/3,u} = 0.136$ m and a mean period $T = \bar{T} = 1.33$ s, measured by capacitive gages at the model structure location before its construction, having an absorbing beach at the end of the flume.

The water depth at the model section was 0.40 m (with a constant foreshore gradient of 1/50) to ensure non-breaking wave conditions before the structure. The duration of each test, twice repeated, was 10 minutes (one hour prototype). A 1:36 Froude undistorted scale was in fact used.

Only one random wave condition was considered in order to reduce the number of tests to the manageable figure of 270 and focus the attention to the influence of breakwater geometry and construction.

The typical model test section is shown in fig.1. The usual composition of the relatively impermeable core and of the filter layer were not changed, while the other structural parameters affecting the overtopping performance were varied as follows, in order to simulate the most popular prototype configurations (for symbols see fig.1):

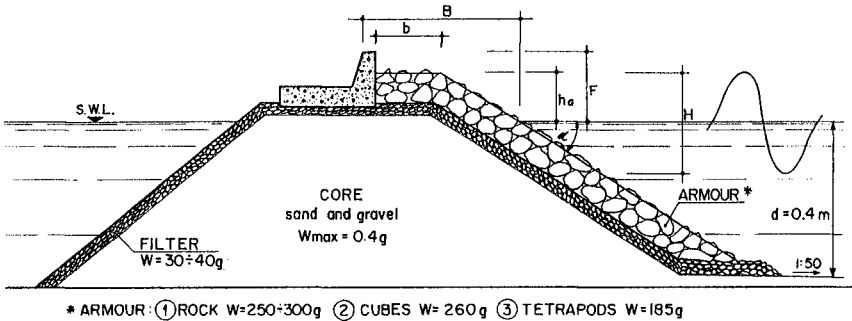


FIG.1: Typical model test section with notation of geometric parameters

- 1 - Relative crown wall freeboard (to S.W.L.): $F/H = 0.60+2.00$
- 2 - Relative armour crest height (to S.W.L.): $h_a/H_s = 0.60, 0.75, 1.05$
- 3 - Relative armour crest berm width: $b/H_s = 1.10, 1.85, 2.60$
- 4 - Seaward slope angle: $\cot \alpha = 1.33, 1.50, 2.00$
- 5 - Type of armour unit: rock, cube, tetrapod

It should be noted that:

- F and h_a are not totally independent, being $F/h_a \geq 1.0$ in all tests;
- the three ratios b/H_s approximately correspond to horizontal armour crest berms of 3-5-7 units respectively;
- the armour units had random placement with the typical recommended

densities and their weights determined as to guarantee stability under the test conditions;

- the parameter B/H_s , which represents the breakwater width, is dependent on b , h_s^a and $\cotg\alpha$ and varies between 1.9 and 4.7;
- due to the marginal influence of the slope angle the analysis was then restricted to the extreme values of $\cotg\alpha = 1.33$ and 2.00 (slopes $3/4$ and $1/2$).

In each tests the following measurements were taken:

- a) number of overtopping waves (visually counted)
- b) average overtopping discharge (collected in a graduated cylinder through a 0.1 m wide prismatic pipe placed behind the crown wall)
- c) jet falling distance (visualized by the water quantities contained in five consecutive trays).

However, the latter measurements were not considered accurate enough to derive reliable quantitative results, also bearing in mind the neglected wind effect and the incorrectly scaled simulation of the air-drop interaction. It was just possible to observe qualitatively the same exponential decay found by Jensen and Juhl (1987).

In consideration of the practical design needs the attention was concentrated on the model measured overtopping discharges Q ($m^3/m s$) averaged over the time interval for one metre of breakwater length.

3. PRESENTATION OF MODEL TEST RESULTS

An open question is the selection of the proper parameters for the presentation of the experimental data. The above mentioned Authors use different dimensionless frameworks (and often different symbols) to generalize the relationship between the overtopping discharge Q and the crown wall freeboard F , which is the most relevant geometric factor.

A significant summary of this variety of coefficients is given in tab.1. In Jensen and Juhl (1987) the parameter Q was not even made dimensionless, because of the difficulty in deriving a unique universal factor (the previously used factor QT_m/B^2 is no more regarded correct).

Even the proposed empirical relationships are not consistent and generally have one of these two different forms:

$$Q^* = A \exp(-BF^*) \quad (1)$$

$$Q^* = A (F^*)^{-B} \quad (2)$$

where Q^* and F^* are the dimensionless discharge and freeboard, A and B best fit coefficients.

The data obtained from the present tests was therefore analyzed using a variety of methods. In general a higher correlation was obtained with equation (2), as shown by the linear regressions of the logarithms of Q^* and F^* (in agreement with Bradbury and Allsop, 1988).

The dimensionless parameters which are regarded most effective and of simplest practical use are Q^* ($=Q/g T_m H_s$) and F/H_s . However, due to the unique wave test condition, all graphs have been drawn with double scales/parameters for both the discharge (Q and Q^*) and the freeboard F/H_s and $F^* = (F/T_m \sqrt{g H_s}) \cdot (F/H_s)$ in order to make an easier comparison with the recent data of Bradbury and Allsop (1988) and to

AUTHOR	DIMENSIONLESS DISCHARGE Q*	DIMENSIONLESS FREEBOARD F*
Owen (1980)	$\frac{\bar{Q}}{\bar{T} g H_s}$	$R^* = \frac{R_c}{\bar{T} \sqrt{g H_s}}$
Jensen (1984)	$\frac{Q T_z}{B^2}$	$\frac{H_s}{\Delta h}$
Ahrens and Heimbaugh (1986)	$\frac{Q}{\sqrt{g H_{mo}^3}}$	$F' = \frac{F}{(H_{mo}^2 L_p)^{1/3}}$
Bradbury and Allsop (1988)	$\frac{\bar{Q}}{T_m g H_s}$	$F^* = \frac{R_c}{T_m \sqrt{g H_s}} \cdot \frac{R_c}{H_s}$
Sawaragi, Deguchi Park (ICCE, 1988)	$\frac{\bar{Q}}{\sqrt{g L H^2}}$	$\frac{H_c}{H}$
Note: $R_c = H_c = \Delta h = F =$ crown wall freeboard		

TAB.1: Summary of representative overtopping parameters proposed by various Authors

facilitate their general design use.

The large number of tested variables allows the plotting of several diagrams outlining the influence of each variable with different configurations. Due to space limitations it was decided to plot all data within six graphs for fixed armour type and slope angle, thus emphasizing the most relevant effects of variable freeboards and armour berm widths (figs. 2 A-B, 3 A-B, 4 A-B).

Then, the marginal influences of variable armour type or slope angle (for fixed berm widths) can be both shown by just one representative typical diagram (fig. 5 A-B). For a better analysis of the effect of the armour type, the configuration with minimum path to be run by the overtopping wave was selected ($b/H_s = 1.1$, slope 3/4). Similarly the influence of the slope could be better detected for the configuration with shortest berm and most controlled armour units (tetrapods).

It should be noted that the data scatter is partly due to the different values of h_a tested for the same F. However all regression lines have very high correlation coefficients, with a minimum of 0.89.

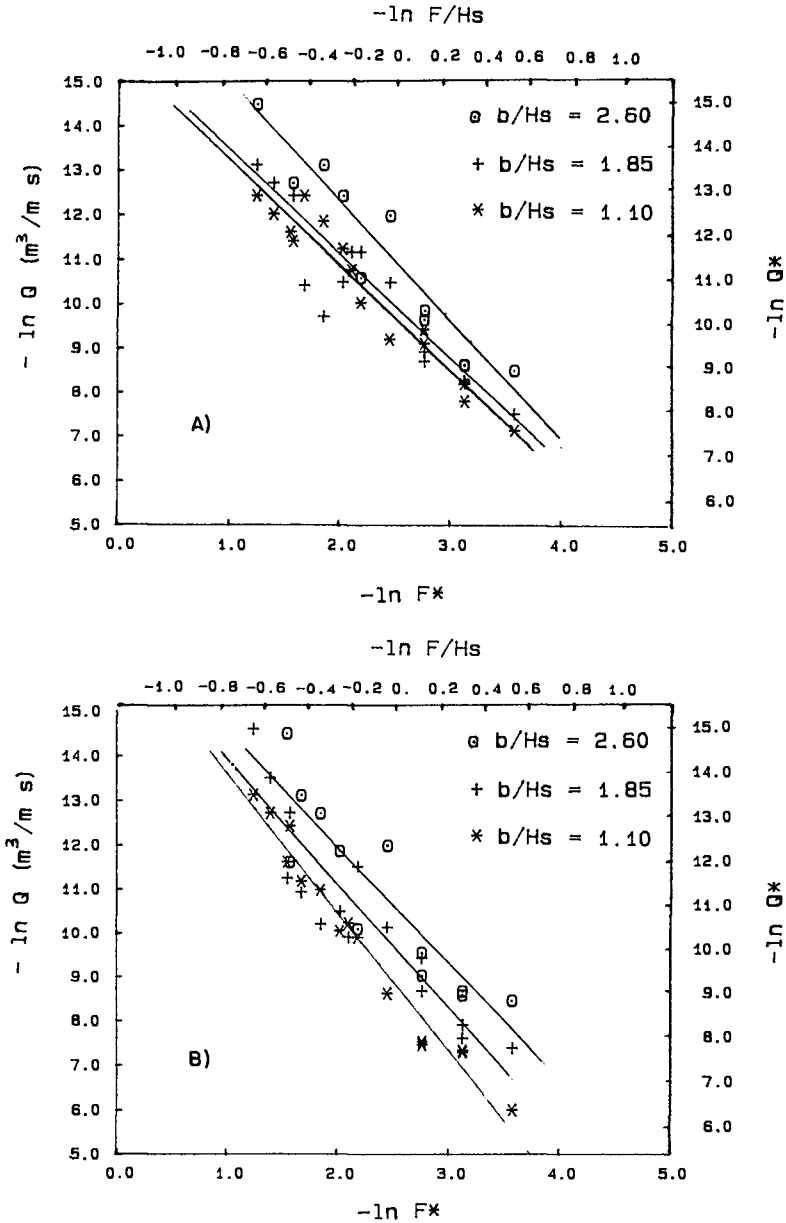


FIG.2: Effect of freeboard and armour crest berm width on overtopping discharge. Test results for rock armor: A)slope 1/2,B)slope 3/4

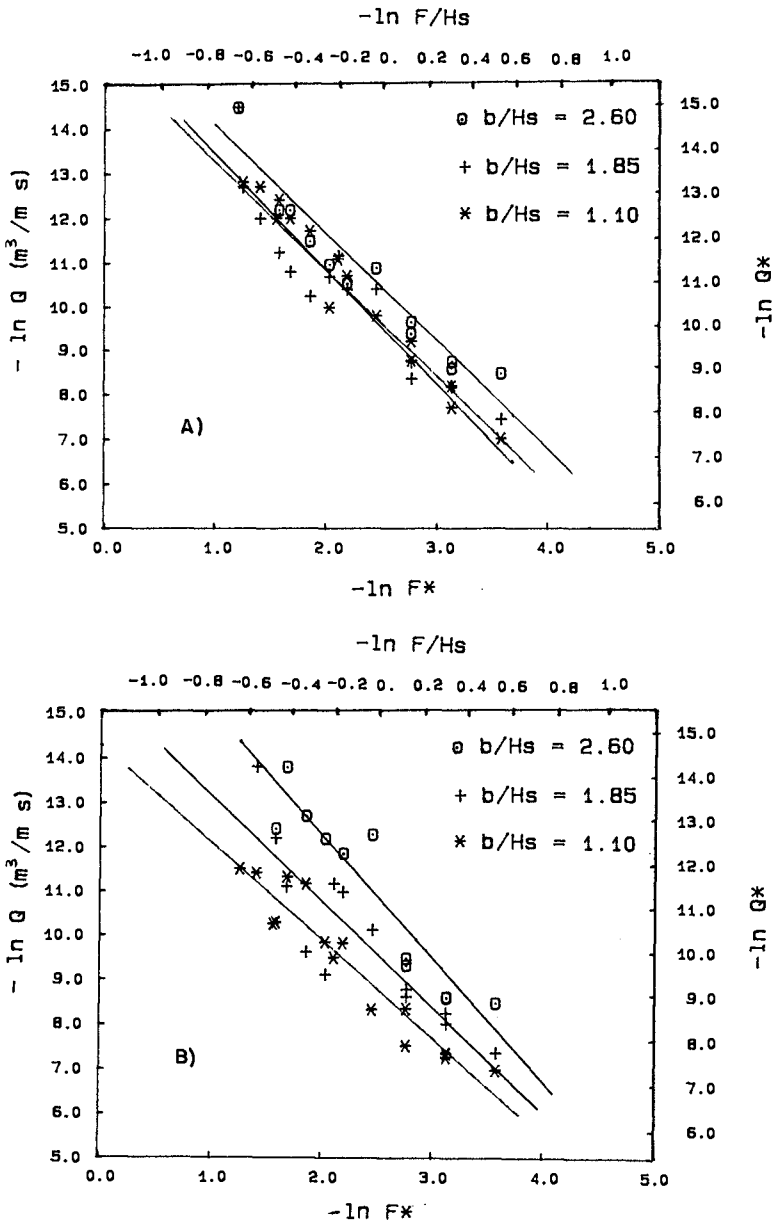


FIG.3: Effect of freeboard and armour crest berm width on overtopping discharge. Test results for cubes: A) slope 1/2, B) slope 3/4

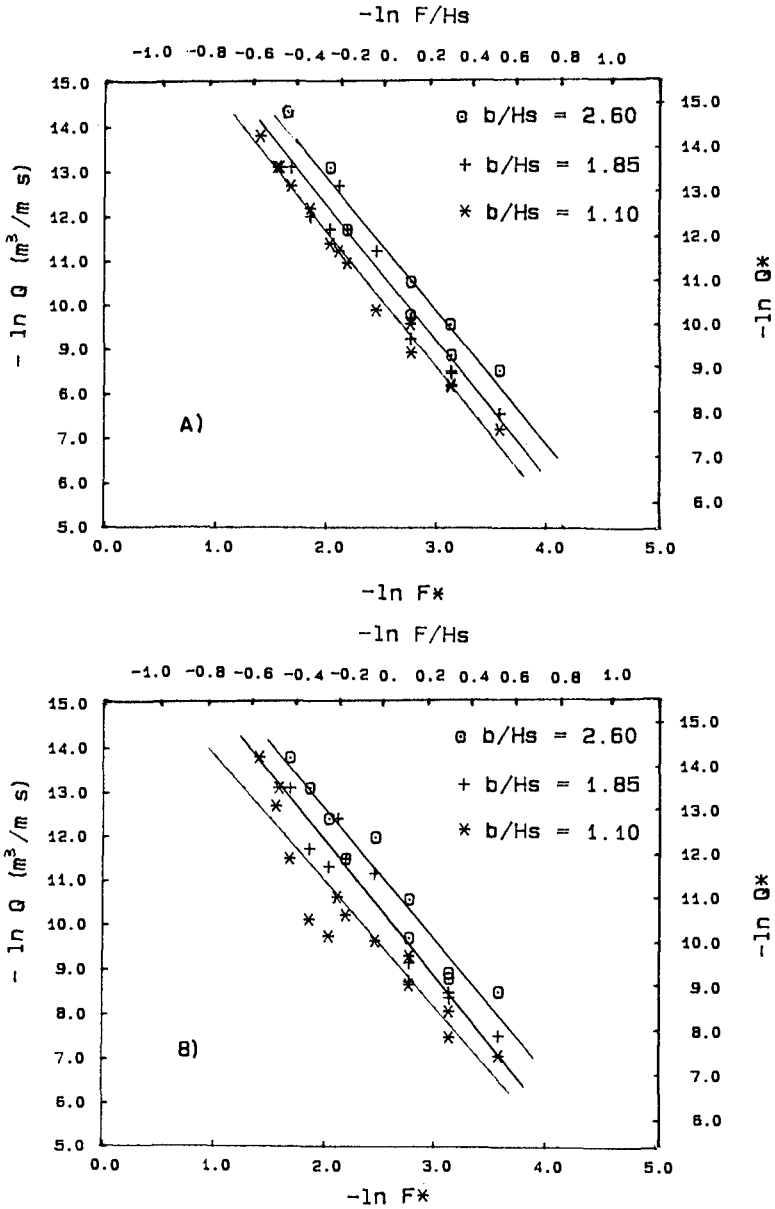


FIG.4: Effect of freeboard and armour crest berm width on overtopping discharge. Test results for tetrapods: A)slope 1/2, B)slope 3/4

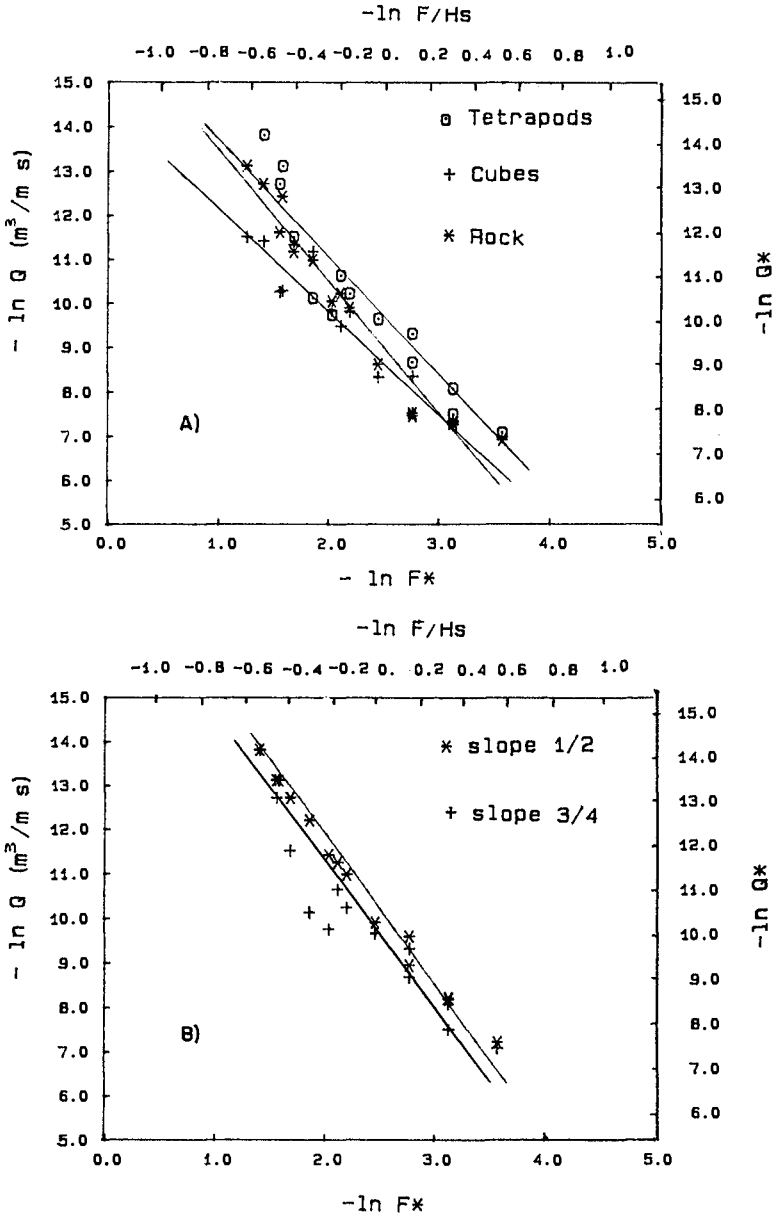


FIG.5: A) Effect of freeboard and armour type on overtopping discharge. Test results for slope 3/4 and $b/H_s = 1.1$
 B) Effect of freeboard and slope angle on overtopping discharge. Test results for tetrapod armour and $b/H_s = 1.1$

In tab.2 the empirical coefficients A and B obtained for the various test section are listed.

ARMOUR	SLOPE	b/H _s	A	B	R ²
ROCK	1/2	1.10	1.67 10 ⁻⁸	2.41	0.97
		1.85	1.85 10 ⁻⁷	2.30	0.92
		2.60	2.27 10 ⁻⁸	2.68	0.95
ROCK	3/4	1.10	5.05 10 ⁻⁸	3.10	0.98
		1.85	6.83 10 ⁻⁸	2.65	0.92
		2.60	3.07 10 ⁻⁸	2.69	0.95
CUBES	1/2	1.10	8.33 10 ⁻⁸	2.64	0.98
		1.85	1.52 10 ⁻⁷	2.43	0.94
		2.60	8.35 10 ⁻⁷	2.38	0.96
CUBES	3/4	1.10	6.16 10 ⁻⁷	2.20	0.95
		1.85	1.68 10 ⁻⁷	2.42	0.89
		2.60	1.86 10 ⁻⁸	2.82	0.93
TETRAPODS	1/2	1.10	1.88 10 ⁻⁸	3.08	0.99
		1.85	1.13 10 ⁻⁸	3.80	0.97
		2.60	1.07 10 ⁻⁸	2.86	0.96
TETRAPODS	3/4	1.10	5.59 10 ⁻⁸	2.81	0.94
		1.85	1.68 10 ⁻⁸	3.02	0.96
		2.60	9.23 10 ⁻⁹	2.98	0.97

TAB.2: Summary of empirical coefficients

The analysis of the plotted results leads to the following main observations:

- 1) Increasing the freeboard of the vertical wall (F) has the greatest effect in reducing the overtopping discharge (according to a power law).
- 2) Increasing the armour crest berm width (b) also produces a reduction of discharge, which is more evident and consistent with steeper slopes and with tetrapod armour units.
- 3) Shallower slopes (1:2) can also reduce overtopping, probably due to the longer rough path; this slope-effect is confirmed by the results from Jensen and Juhl (1987) and is more evident with narrow armour berms.
- 4) Tetrapods have a slightly better hydraulic performance than rock and cubes; the rock armour seems to give less overtopping discharges than cubes except for extreme events.
- 5) Increasing the armour crest elevation (h_a) often results in a reduction of discharge, but the trend is not clearly defined and no plot is therefore given.

It can be observed that in order to satisfy the existing safety guidelines proposed by Fukuda, Uno and Irie (1974), within the test

conditions, the relative crown wall freeboard F/H_s generally ranges between 1.0 and 1.4. The conservative nature of these guidelines may be compensated by the neglected effects of onshore winds, oblique wave attack and by scale effects.

It was possible to check just a few test results against data points for similar conditions reported by Jensen and Juhl (1987) in their figures 12-13: the measured discharges compare quite well.

A fair agreement can also be found with the results obtained by Bradbury and Allsop (1988), although the overtopping prediction seems to give slightly larger values than those reported for their most similar configurations n.8 and 10. Moreover their assumption of slope 1/2 being the worst case is contradicted by the present test results.

Finally another regression analysis was carried out with all data, in order to relate the overtopping discharge Q to the percentage of overtopping waves P . Again the best fit was given by an equation of the form $Q = C P^D$ (C , D empirical coefficients): the discharge increases rapidly as the number of overtopping waves increases. However the data scatter and the limits of tested conditions don't allow the derivation of a useful relationship of general validity.

4. CONCLUSIONS

The results of several random wave model tests for variable configurations of breakwater superstructure have shown the influence of various geometric parameters on the overtopping discharge and allowed the presentation of a set of graphs useful for preliminary design purposes.

The prediction model providing the best description of the overtopping performance is based on an equation of the form $Q^* = A (F^*)^{-B}$, where the dimensionless discharge Q^* rapidly increases with decreasing relative crown wall freeboard F^* .

However, representative universal dimensionless factors are still to be defined. Other geometric parameters have shown a significant effect on the overtopping, especially the width of the armour crest berm. The change of seaward slope angle also has some influence, while different armour types have a quite similar behaviour (within the test conditions). The inclusion of these effects into a more complex comprehensive factor might be possible when more tests will be conducted with different wave conditions (wave periods in particular), and by combining the data from various Authors.

It is then hoped that a normalization of definitions and symbols of the typical breakwater geometric parameters will be agreed internationally, as recently done by IAHR-PIANC for the wave parameters.

Further work should also be addressed to the definition of more accurate, detailed and universal design criteria, i.e. admissible overtopping discharges for different degrees and destinations of the protection. More measurements of individual overtopping discharges should be carried out both in model and prototype conditions, together with the assessment of their consequences on variable targets.

REFERENCES

- AHRENS J.P. and HEIMBAUGH M.S. (1986): Irregular wave overtopping of seawalls, Proc. Conf. IEEE Oceans '86, Washington
- ALLSOP N.W.H., FRANCO L., HAWKES P.J. (1985): Probability distribution and levels of wave runup on armoured rubble slopes, Int. Conference on Numerical and Hydraulic Modelling of Ports and Harbours, Birmingham
- AMINTI P., LIBERATORE G., PETTI M. (1984): Generatore di moto ondoso irregolare: l'esperienza del laboratorio idraulico del dipartimento di ingegneria civile di Firenze, XIX Convegno di Idraulica, Pavia
- AMINTI P., FRANCO L. (1987): Indagine sperimentale sulla tracimazione di onde irregolari su dighe a scogliera, Congresso AIPCN sez. Italiana, Ravenna
- BRADBURY A.P. and ALLSOP N.W.H. (1988): Hydraulic effects of breakwater crown walls, BREAKWATERS '88 Conference, ICE, Eastbourne
- C.E.R.C. (1984): Shore Protection Manual, Washington
- FUKUDA N., UNO T., IRIE I. (1974): Field observations of wave overtopping of wave absorbing revetment, Coastal Eng. in Japan, 17
- JENSEN O.J. (1984): A monograph on rubble mound breakwaters, Book published by Danish Hydraulic Institute, Horsholm
- JENSEN O.J., JUHL J. (1987): Wave overtopping on breakwaters and sea dikes. 2° Conf. Coastal and Port Eng. in Developing Countries, Beijing
- OWEN M.W. (1980): Design of seawalls allowing for wave overtopping, Report EX924, Hydraulics Research, Wallingford

CHAPTER 58

Reflections from coastal structures

N W H Allsop+
S S L Hettiarachchi*

Abstract

Wave reflections at and within a coastal harbour may make a significant contribution to wave disturbance in the harbour. Reflected waves may lead to danger to vessels navigating close to structures, and may reduce the availability of berths within the harbour. Wave reflections may also increase local scour or general reduction in sea bed levels.

In the design of breakwaters, sea walls, and coastal revetments, it is therefore important to estimate and compare the reflection performance of alternative structure types. In the use of numerical models of wave motion within harbours, it is essential to define realistically the reflection properties of each boundary. This paper presents results from a study of the reflection performance of a wide range of structures used in coastal and harbour engineering.

1 Introduction

The importance of wave reflection from coastal and harbour structures has historically been given relatively little weight in the design of harbours or of coastal protection schemes, despite the problems that may arise from the cumulative increase in wave energy. Typically, increased wave action due to reflections may lead to:

- a) danger in navigating vessels through steep seas arising from the interaction of incident and reflected wave trains, this often occurs at harbour entrances;
- b) increased berth down-time within the harbour arising from unacceptable vessel motions during loading or unloading;
- c) damage to vessels, moorings, or fenders, arising from increased mooring forces;
- d) increased wave velocities, and hence shear stresses, at the structure toe, leading to potentially greater local scour or sea bed erosion.

This paper summarises results from a study of the reflection performance characteristics of a wide range of structure types used in

+ Principal Scientific Officer, Coastal Structures Section,
Hydraulics Research, Wallingford, OX10 8BA, UK.

* Lecturer, Department of Civil Engineering, University of Moratuwa,
Moratuwa, Sri Lanka.

coastal and harbour engineering. The report on that study (Ref 1) discusses the design and use of wave absorbing structures, and derives values of empirical coefficients for the prediction of reflection performance in random waves. Some of the results of that study have been employed in the derivation of appropriate boundary conditions for the numerical modelling of wave disturbance in harbours (Ref 2).

2 Wave absorbing structures

Coastal structures devised to absorb or dissipate wave energy may be considered under three main categories:

- a) non-porous, slopes;
- b) armoured, porous, slopes;
- c) porous vertical face or faces.

Each of these structure types will dissipate some proportion of the incident wave energy and will generally reflect the greatest part of the remainder. At the extremes the reflection performance of such structures may be compared either with that of a vertical wall, for which the proportion reflected approaches unity, or with a gently sloping yet porous beach for which the energy reflected approaches zero.

A number of different mechanisms may be employed to absorb or dissipate wave energy. These will depend upon the properties of both the structure, and of the incident waves. A number of empirical methods have been developed to aid the identification of wave behaviour at such a structure. Of these a single parameter of particular relevance to wave action on sloping structures is the Iribarren number, I_r , sometimes known as the surf similarity parameter, introduced by Battjes. For regular waves:

$$I_r = \tan \alpha / (H/L_0)^{1/2} \quad (1)$$

On non-porous rough slopes wave run-up and reflections are generally similar to those on the equivalent smooth face, but with some further energy dissipation due to the greater frictional and turbulent losses.

The behaviour of waves at an armoured rubble slope is different in that a significant depth of porosity in the armour and under-layers, and perhaps the core, is available for energy dissipation. Much of the incident wave energy may be converted to flows over and within the armour and under-layers, thence being dissipated in turbulence within the voids. Some of this energy may be converted to pumping water into the mound, particularly under long period waves when the phreatic surface inside a rubble mound may be considerably elevated. Energy from such flows will be substantially lost in frictional flow within the porous rock layers.

The advantages of vertical face structures over those with sloping faces lie in the efficient use of space, economy of material, and the ability to moor vessels alongside. These factors are of considerable importance to the harbour engineer. Problems due to the reflections from solid vertical faces suggest a number of alternative forms of construction. Porous vertical walls must dissipate wave energy in a gradual manner to avoid undue reflections. Significant

energy absorption will require a reasonable depth of structure in relation to the incident wave length. Examples of types of structures to do this include:

- a) cribwork or gabion walls;
- b) piled wave screens;
- c) perforated caissons; and
- d) stacked voided blockwork.

Each of these structure types offer some considerable advantage over sloping face structures in the greater utilisation of the harbour area. In general, however only the last three types (b)-(d) are likely to be used in harbours.

The simplest wave absorbing vertical walls used in harbours are single or multiple wave screens. These may be formed of closely spaced elements such as steel or timber piles, concrete or timber planks, or other pre-cast concrete elements. In a single screen porosities, n_a , of around 5-20% will commonly be used. The screen elements are generally supported on a steel or timber pile structure. This may allow the provision of two or more screens on the same structure. Examples of the design and/or construction of single or double wave screens are described by Gardner et al (Ref 3), and Hutchinson & Raudkivi (Ref 4).

A single screen alone will absorb or dissipate relatively little of the incident wave energy. Most will be either reflected or transmitted. Certain arrangements of two or more screens may be devised to yield acceptable levels of reflection, whilst restricting wave transmission.

The simplest multiple screen in general use incorporates a perforated front screen separated from a solid rear screen by a spacing B . For B equal to around 0.25 of the local wavelength L_s , waves transmitted through the front screen will reflect off the rear screen to return to the front screen exactly out of phase with the next wave. The resulting interference leads to a significant dissipation of wave energy between the two screens, and hence yields particularly low reflections. For wavelengths other than the optimum of $4B$, the reflection performance will be less good. By judicious choice of screen porosity n_a , and screen spacing B , acceptable reflection performance may be obtained over a reasonable range of wavelengths, or wave periods.

Similar principles may be used in the design of pre-cast concrete caissons with a perforated front face. Such caissons will incorporate at least two chambers: one open to wave-induced flows; the other filled with sand or concrete to ensure adequate resistance to sliding or overturning. The front face may be perforated by horizontal or vertical slots, or by circular holes. The perforations may extend only part depth and/or vary in spacing with depth. The size and shape of the void chamber may vary, as may its complexity.

Some of the hydraulic characteristics of the wave-absorbing caisson can be obtained on a smaller scale by the use of voided concrete blocks. These may be stacked vertically to form breakwaters, sea walls, or in some instances quay walls. A variety of these blocks have been developed, and most have been widely patented. Examples of stacked voided blocks are:

Igloo	Perforcell
Neptune	Pilock
Cross-hollow	Trium
Warock	Diaer
Monobar	Tine
Arc	H. W.

3 Calculation of reflection performance

The prediction of the level of reflected wave energy has been investigated using both theoretical and of experimental studies. Methods to allow predictions reflection performance have been identified using three main approaches:

- a) empirical equations;
- b) mathematical modelling;
- c) graphical presentation of model test results.

Empirical equations and coefficients have been developed from the results of hydraulic model tests. Most of the available literature is based on studies with regular waves and often assumes the validity of linear wave theory. Apart from some model tests pertaining to particular structures, few detailed studies have been performed using random waves. The following general empirical equations have been presented:

$$C_r = f (a Ir^b) \quad (2)$$

$$C_r = a Ir / (Ir + b) \quad (3)$$

$$C_r = a Ir^2 / (Ir^2 + b) \quad (4)$$

$$C_r = a (1 - \exp (-bIr)) \quad (5)$$

where a and b are empirical coefficients.

For random waves, the significant wave height, H_g , and the wave length corresponding to the period of peak energy density, L_p , are used to define a modified Iribarren number Ir' :

$$Ir' = \tan \alpha / (2\pi H_g / g T_p^2)^{\frac{1}{2}} \quad (5)$$

Smooth slopes

Much of the most useful information for the prediction of wave reflection from non-porous sloping structures is presented by Seelig & Ahrens, a summary of which was later given by Seelig (Refs 5 and 6). For simple smooth slopes Seelig advocates the use of equation 4 with values of a = 1.0 and b = 5.5, giving:

$$C_r = \frac{1.0 Ir^2}{Ir^2 + 5.5} \quad (6)$$

Seelig also compares the use of equation 4 with coefficients a = 1.0 and b = 6.2 for a smooth slope, with measured data, and the other empirical equations, Figure 1.

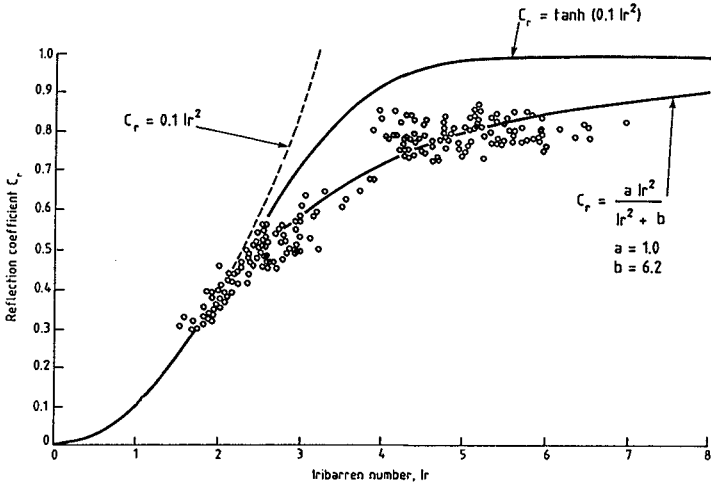


Fig 1 Reflection performance of smooth slopes, after Seelig

Results from earlier studies at Hydraulics Research have been re-analysed. Measurements were made of random wave reflections from smooth slopes of 1:1.33, 1:1.5 and 1:2.0. For conditions within the range $3 < Ir' < 6$, prediction equation 4 with $Ir = Ir'$, and empirical coefficients $a = 1.08$ and $b = 5.7$, provides a good fit to the experimental data:

$$C_r = \frac{1.08 Ir'^2}{Ir'^2 + 5.7} \tag{7}$$

These results are illustrated in Figure 2. It is noted that the predicted values for C_r using these coefficients and the modified Iribarren number, Ir' , are slightly greater than those recommended by Seelig.

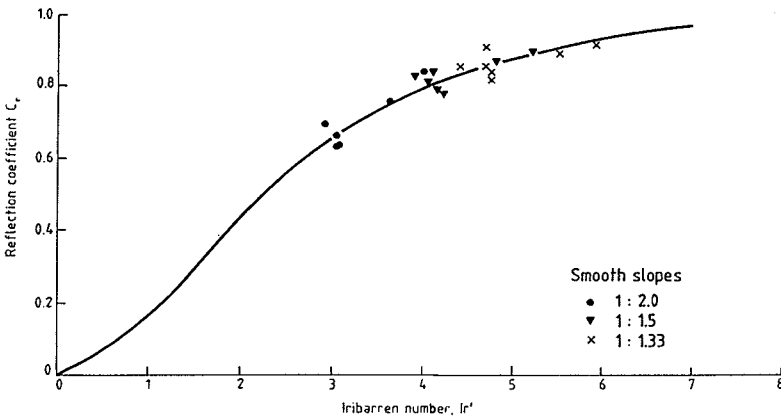


Fig 2 Reflection performance of smooth slopes under random waves

Rough slopes

The reduction in the reflection coefficient due to the placement of rockfill on the surface of an otherwise impervious structure has been investigated by Seelig and Ahrens. For a revetment with layers of armour rock, they recommend values of empirical coefficients to correct predicted reflection coefficients for smooth sloping surfaces using equation 4.

Porous sloping structures

Generally rubble breakwaters, sea walls and revetments will dissipate significantly more wave energy than the equivalent non-porous slope. The principal structure parameters governing this are the armour, underlayer, and core porosities, permeabilities, and available void volume.

For rock armoured structures, Seelig argues that the calculation method based upon the use of equation 4 may be further extended by defining $a = a_1 a_2 a_3$, where the empirical coefficients a_1 , a_2 , and a_3 take account of relative water depth, thickness of armour and underlayer, and relative armour size. The method is based on successive modifications to the expression for smooth slopes. Alternatively, Seelig suggests that quick and conservative estimates may be made by using equation 4 with $a = 0.6$, $b = 6.6$.

Concrete armour

A sea wall or breakwater armoured with concrete armour units will exhibit a reflection performance that is essentially similar to that of the equivalent rock armoured slope. Some types of concrete armour unit are more open and permeable to wave action than rock armouring, and reduced reflections may therefore be expected. Conversely bulky armour units such as cubes have sometimes been placed very closely with low armour layer porosity, and hence higher reflections will result than might be predicted.

Measurements of the reflection performance of laboratory slopes armoured with concrete armour units have been re-analysed for this study. The results are presented in Figures 3-6 as values of reflection coefficient C_r against Iribarren number Ir , or Ir' for random waves. Empirical equations of the form of equation 4 have been fitted to the data and the results are summarised below:-

Armour	Wave	Range of slope angles	Range of Ir or Ir'	Coefficients in equation 4	
				a	b
Dolos	Regular	1.5-3.0	$1.5 < Ir < 5.5$	0.56	10.0
Cobs	Regular	1.33-2.5	$1.5 < Ir < 4.5$	0.50	6.54
Tetrapods or Stabits	Random	1.33-2.0	$2.5 < Ir' < 6.0$	0.48	9.62
Sheds or Diodes	Random	1.33-2.0	$3.0 < Ir' < 6.0$	0.49	7.94

An alternative use of either rock or concrete armouring is in a mound placed against a vertical wall. Such protection will significantly reduce the reflections, as well as protecting the wall from wave impact. Rock or concrete armour may also reduce

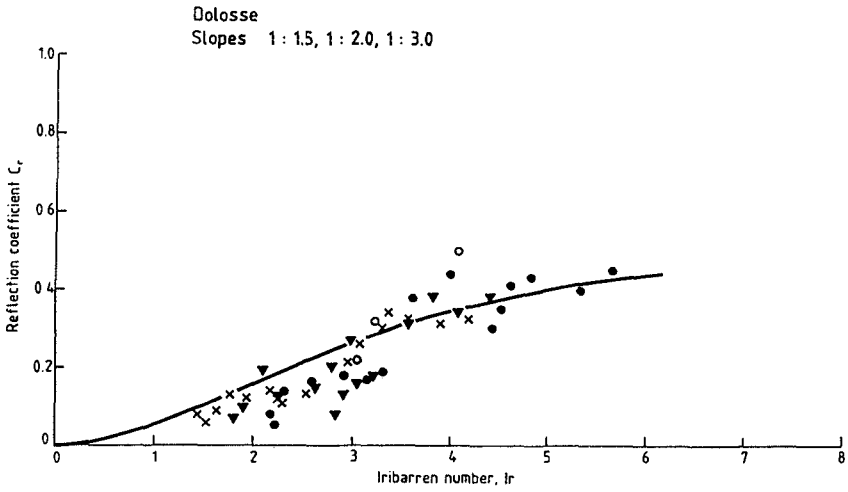


Fig 3 Reflection performance of Dolos armoured slopes, regular waves

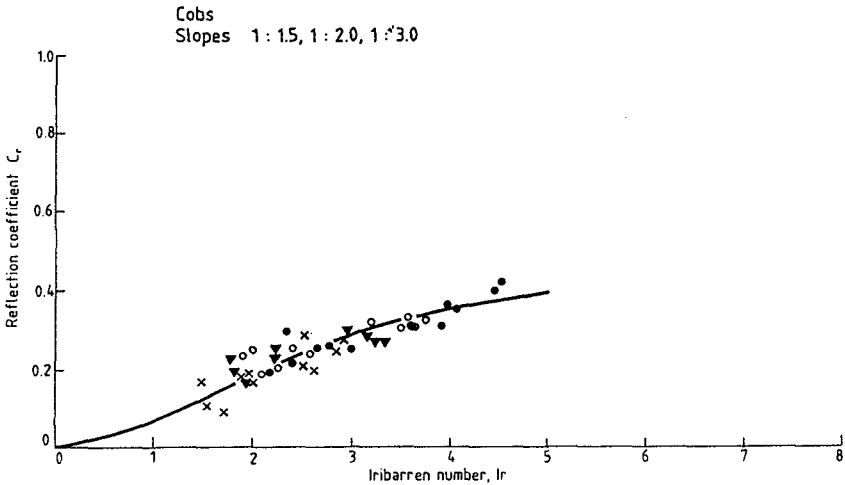


Fig 4 Reflection performance of Cob armoured slopes, regular waves

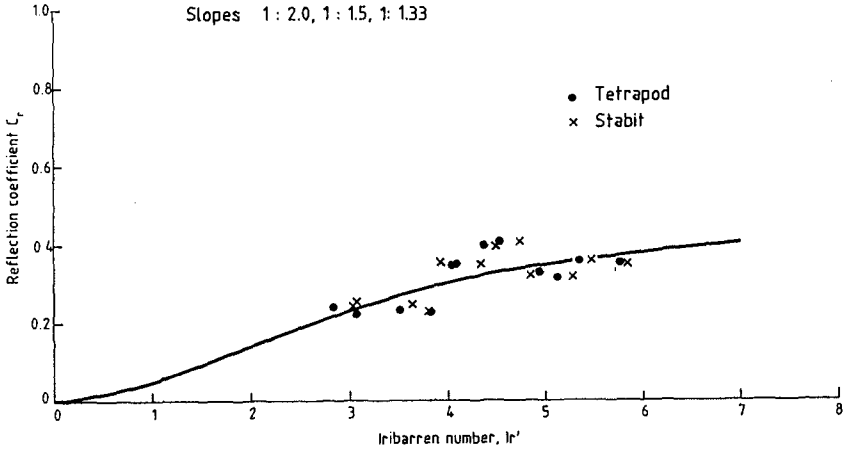


Fig 5 Reflection performance of Tetrapod or Stabit armoured slopes, random waves

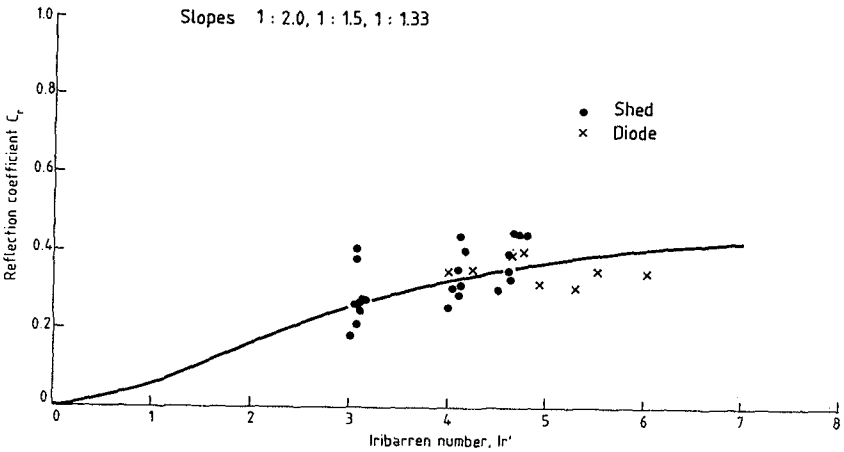


Fig 6 Reflection performance of Shed or Diode armoured slopes, random waves

overtopping. An example of protection to an existing sea wall was discussed at a seminar (Ref 7). Measurements of reflections for three sections are presented in Figure 7. The existing wall, section 1, has high reflections. At low water levels, wave breaking in front of the wall has reduced the reflections to around 0.65. At the higher water levels C_r approaches 0.9. The reflection performance of the alternative rock protection, sections 2 and 3, varies with water level, and particularly with the relative position of the berm formed by the crest of the rock protection. For those water levels close to the crest level of the rock the reflection coefficient reaches minimum values with C_r around 0.20-0.30. When the waves reflect from the armour slope the performance deteriorates slightly with C_r generally nearer 0.4.

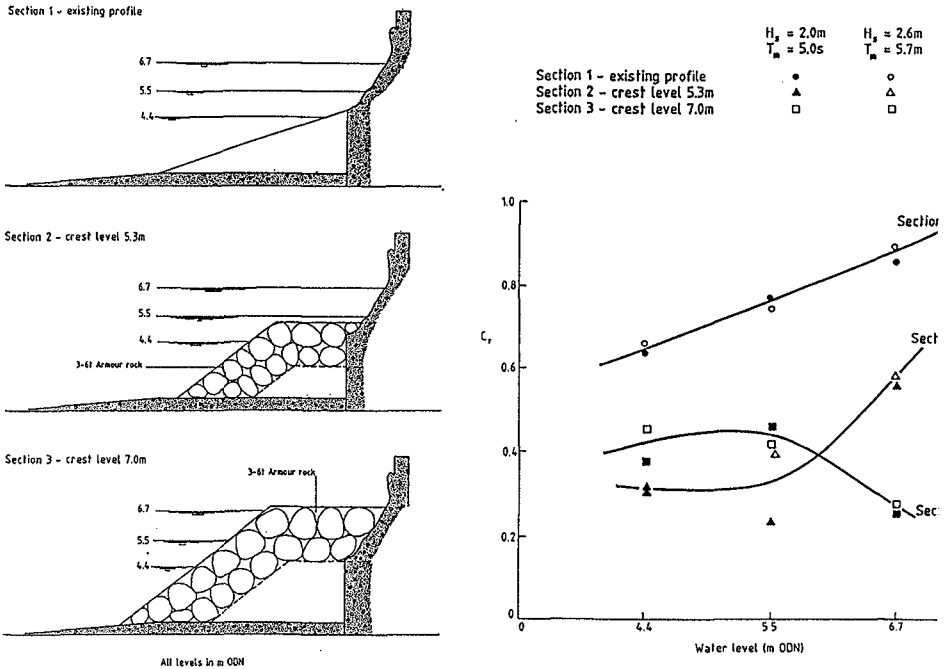


Fig 7 Performance of rock protection to existing wall

Vertically faced structures

Pervious wave screens or pile arrays have been much studied by researchers concerned with wave energy transmission, dissipation, and reflection. Results from model tests for single wave screens have been presented previously by Kakuno (Ref 8) and Allsop & Kalmus (Ref 9). Example summaries of their results are shown in Figure 8.

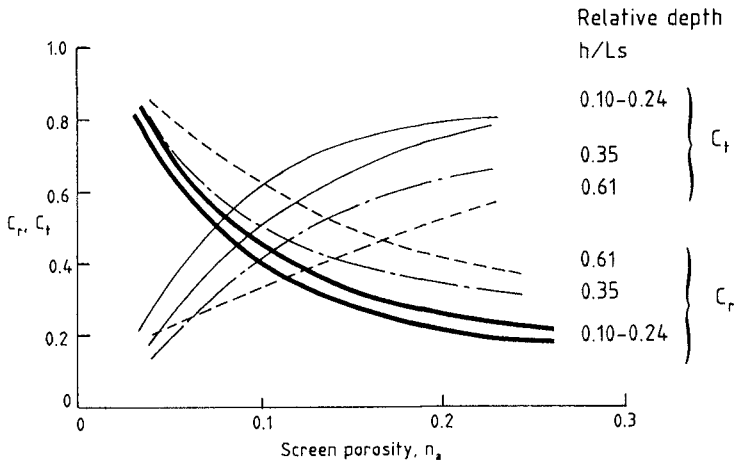


Fig 8 Reflection and transmission for single wave screens

In many instances in coastal and harbour engineering, wave-absorbing structures such as quays or sea walls are built with a solid rear face. The performance of the double wave screen used by Gardiner et al (Ref 3) at Plymouth has been described by Allsop & Kalmus (Ref 9). A simple summary of the effects of front screen porosity, n_a , screen spacing, B , and local wave length, h_s , on the reflection performance is shown in Figure 9. These results, derived from measurements in random waves, seem to indicate that the optimum performance is given by a front screen of porosity, n_a between 0.15 and 0.25. At the lower end of this band the range of wavelengths that give low reflections, say $C_r < 0.4$, is significantly wider than for a screen of porosity around 0.3.

It should be noted that a full description of the processes of wave reflections from a structure would require details of the reflection coefficient function with frequency, of the effects of wave breaking, particularly in shifting energy over frequencies, of the phase shift at reflection, and of the effects of oblique wave/structure interactions. The methods presented in this study therefore represent a considerable simplification of the processes involved. The reader is therefore advised to use the results with some care and circumspection.

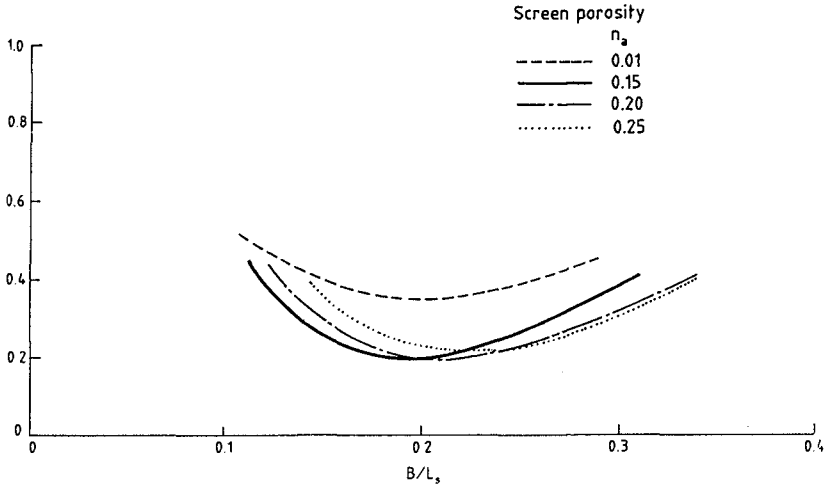
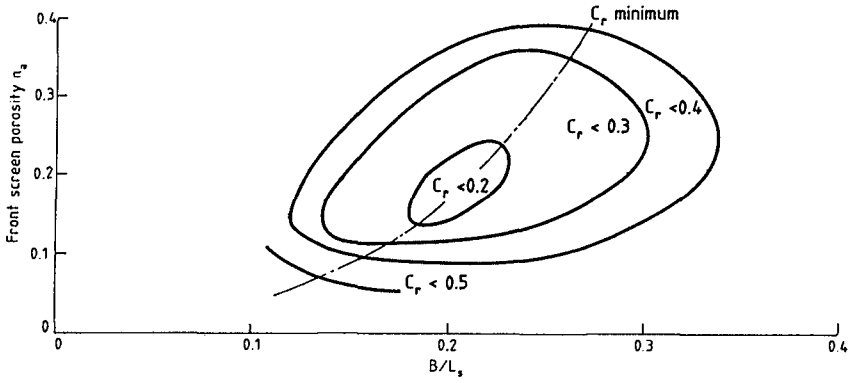


Fig 9 Wave reflection performance of wave screen with impermeable rear wall

4 Conclusions and recommendations

The reflection performance of a range of structure types have been examined and quantified. A general empirical expression of form advanced by Seelig has been used to describe the reflection characteristics of permeable or impermeable slopes. Results from random wave model tests have given values for the empirical expression for permeable slopes armoured with Dolos, Tetrapod, Stabit, Cob, Shed, and Diode, units, and for smooth impermeable slopes. During this study it was not however possible to quantify the reflection performance of rock-armoured slopes under random waves. It was therefore recommended that a systematic series of random wave model tests be conducted to quantify the effect of structure slope, armour size, armour thickness, and berm configuration on wave reflections. (These tests have been conducted, summer 1988, and will be described in a future report, Reference 10).

Vertically faced structures offer the harbour designer potential space saving and enhanced use over structures with sloping faces. This study has reviewed the reflection performance of a range of caisson and voided block systems. This paper has summarised the reflection performance of single and double wave screens under random waves.

5 Acknowledgements

This paper summarises work conducted by Hydraulics Research for the British Overseas Development Administration. Dr Hettiarachchi was on study leave from the University of Moratuwa, and was supported by a bursary from Hydraulics Research during the period of this work.

6 References

- 1 Allsop N W H & Hettiarachchi S S L. "Wave reflections in harbours: design, construction and performance of wave absorbing structures". Report OD89, Hydraulics Research, Wallingford, April 1987.
- 2 Jones D V & Smallman J V. "Wave reflections in Caribbean harbours: studies for Port Castries, St Lucia". Report OD94, Hydraulics Research, Wallingford, March 1987.
- 3 Gardner J D, Fleming C A & Townsend I H. "The design of a slotted vertical screen breakwater" Proc 20th Coastal Engineering Conference, Taipei, November 1986.
- 4 Hutchinson P S & Raudkivi A J. "Case history of a spaced pile breakwater at Half Moon bay marina, Auckland, New Zealand" Proc 19th Coastal Eng Conf, Houston, September 1984.
- 5 Seelig W N & Ahrens J P. "Estimation of wave reflection and energy dissipation coefficients for beaches, revetments and breakwaters." CERC Technical Paper 81-1, Fort Belvoir, February 1981.
- 6 Seelig W N. "Wave reflection from coastal structure." Proc Conf Coastal Structures '83, ASCE, Arlington, 1983.

- 7 Allsop N W H, Powell K A & Bradbury A P (Editors). "The use of rock in coastal structures." Summary of a seminar, Hydraulics Research, Wallingford, January 1986.
- 8 Kakuno S. "Reflection and transmission of waves through vertical slit type structures". Proc Coastal Structures 83, ASCE, Arlington, March 1983.
- 9 Allsop N W H & Kalmus D C. "Plymouth marine events base: performance of wave screens" Report EX 1327, Hydraulics Research, Wallingford, July 1985.
- 10 Allsop N W H & Channell A R. "Wave reflections in harbours: The reflection performance of rock armoured structures in random waves". Report OD102, Hydraulics Research, Wallingford, in preparation, autumn 1988.

7 NOTATION

A, B	Empirical coefficients
a, b	"
B	Structure width, in direction normal to face
C_1, C_2, C_i	Empirical or shape coefficients
C_r	Coefficient of reflection, defined $H_r/H_i = (E_r/E_i)^{\frac{1}{2}}$
D	Particle size or typical dimension
D_n	Nominal particle diameter
E_i	Incident wave energy
E_r	Reflected wave energy
g	Gravitational acceleration
H	Wave height, from trough to crest
H_o	Offshore wave height, unaffected by shallow water processes
H_s	Significant wave height, average of highest one-third of wave heights
h	Water depth
Ir	Iribarren or surf similarity number
Ir'	Modified Iribarren number
L	Wave length, in the direction of propagation
L_o	Deep water or offshore wave length, $gT^2/2\pi$
n	Porosity, usually taken as n_v
n_a	Area porosity, proportion of unobstructed area in a screen
S_i	Incident spectral energy density
S_r	Reflected spectral energy density
s	Wave steepness, H/L_o
s_p	Steepness of peak period, $2\pi H_s/g T_p^2$
T_p	Wave period
T_m	Mean wave period
T_p'	Spectral peak period, inverse of peak frequency
W	Armour unit weight
W_{50}	Median armour unit weight
α	Structure front slope angle
β	Angle of wave attack

CHAPTER 59

SEAWALL OVERTOPPING MODEL

John P. Ahrens, Aff. M.¹ and Martha S. Heimbaugh, A.M.,² ASCE

ABSTRACT

Results from an extensive series of laboratory tests of irregular wave overtopping for a number of seawall and seawall/revetment configurations is presented. Data for 13 configurations has been collected and grouped into 7 data sets representing relatively similar geometrical characteristics. All data sets showed an approximately exponential relationship between the overtopping rate and a dimensionless freeboard parameter which is the ratio of the seawall freeboard to the local wave severity. This finding logically led to the development of three progressively more complex overtopping models. The models provide a relatively simple way to estimate overtopping rates and an objective way to evaluate the hydraulic performance of seawalls/revetments. Advantages and disadvantages of the models are discussed and their ability to predict overtopping rates is compared.

INTRODUCTION

Wave runup and overtopping are two of the most important factors influencing the design of coastal structures. Current methods to predict overtopping rates, such as given in the Shore Protection Manual (SPM, 1984), rely on a data base composed of laboratory tests using monochromatic waves. In addition, problems arise in using the SPM method because of uncertainty in choosing proper overtopping coefficients and treating wave runup as an independent variable. Studies have been conducted which indicate that the SPM method can, for some circumstances, under predict overtopping rates (Douglass, 1986) and for other circumstances greatly over predicts the rates (Gadd, et al. 1985). When these over estimates or underestimates of overtopping rates might be expected is unclear. Recent laboratory work using irregular waves has produced an alternative to the SPM method of calculating overtopping rates.

Data for 13 different seawall and seawall/revetment configurations has been collected and collated into 7 representative data sets. Examination of these data sets revealed that all had the common property that the overtopping rate could be expressed as an exponential function of a dimensionless freeboard parameter. This characteristic

¹Oceanographer, Coastal Engineering Research Center, U.S. Army Engineer Waterways Experiment Station, P.O. Box 631, Vicksburg, MS 39180

²Civil Engineer, Coastal Engineering Research Center, U.S. Army Engineer Waterways Experiment Station, P.O. Box 631, Vicksburg, MS 39180

held regardless of whether the overtopping rate was expressed as a dimensional or dimensionless variable. Similar findings have been reported by Owen (1982) and Jensen and Juhl (1987). This paper will develop three exponential overtopping models which represent a logical extension of the general relation. Each model has characteristics which are useful and the advantages and disadvantages of each model will be discussed. A criteria for comparing the models will be presented and their ability to predict overtopping rates will be compared.

DATA COLLECTION

Laboratory tests were conducted in the Coastal Engineering Research Center's (CERC) 45.73m long, 0.91m wide, and 0.91m deep wave tank and the 76.20m long, 3.35m wide, and 1.83m deep wave tank. All tests used irregular waves generated by computer controlled, hydraulically actuated, piston type wave boards.

Data sets were compiled from three separate CERC studies. One study tested three seawall/revetment configurations which have been proposed to protect the historic lighthouse at Cape Hatteras, North Carolina (Grace and Carver 1985). A second study tested a number of seawall/revetment configurations proposed to improve the performance of existing seawalls at Roughans Point, Massachusetts, (Ahrens, et al. 1986). The third study tested a seawall proposed to protect Virginia Beach, Virginia, (Heimbaugh, et al. 1988). Research funds were used to extend the range of conditions tested to allow the development of more general relationships.

Each test consisted of approximately 30 minutes of irregular wave generation during which wave conditions were measured using resistance type wave gages. Incident and reflected wave spectra were resolved using the method of Goda and Suzuki (1976). Water was allowed to pass over the seawalls and collected in a calibrated container. Elevations in the container were measured with a point gage before and after each test. Figure 1 shows simple profiles of each seawall/revetment configuration used to compile the seven data sets, and Table 1 summarizes test conditions for each data set. More detailed descriptions of test conditions and testing procedures can be found in references cited above.

METHOD OF ANALYSIS AND FINDINGS

One of the most important findings to date is the development of an effective dimensionless freeboard parameter, denoted F' . F' can consolidate all of the overtopping data for similar structure configurations into a single, well defined trend. F' is defined

$$F' = \frac{F}{\left(H_{mo}^2 L_p \right)^{1/3}} \quad (1)$$

where F , the freeboard, is the average vertical distance from the mean local water level to the crest of the seawall, H_{mo} is the energy based zero-moment wave height either measured near the structure (data sets 1 through 6) and assumed to be representative of H_{mo} at the toe of the seawall/revetment, or measured at the toe (data set 7). L_p is the Airy wave length calculated using the nominal T_p (data sets 1 through 6) and the water depth at the

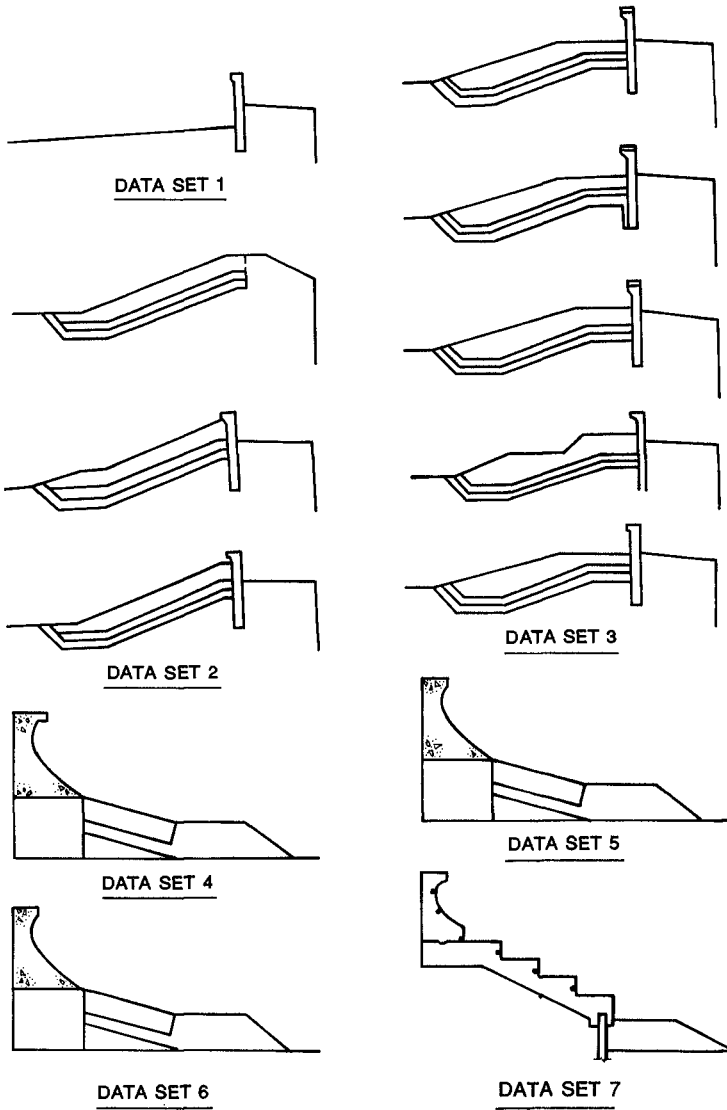


Figure 1. Simple geometric profiles used in each data set

Table 1
Seawall Test Conditions Summary Table

Data Set No.	Description	Model Scale	Wave Tank Dimensions	Spectrum Type	Offshore Slope Near Structure	Range of			Water Depth at Wave Board, m
						Nominal T_p sec	H_{mo} cm	d_s cm	
1	Roughans Point Seawall Configuration 1 Vertical wall w/recurved parapet No revetment	1:16	0.91x0.91x76.20m	JONSWAP	1:100	1.25-3.0	4.77-16.81	16.92-22.30	0.619-0.648
2	Roughans Point Seawall/Revetment Configurations 2,3,10 Seawall w/high revetment	1:16	0.91x0.91x76.20m	JONSWAP	1:100	1.25-3.0	7.20-17.47	22.23-28.28	0.576-0.662
3	Roughans Point Seawall/Revetment Configurations 4,5,6,7,8 Seawall w/bermed revetment and wall caps of 0.3 and 0.6m	1:16	0.91x0.91x76.20m	JONSWAP	1:100	1.25-3.0	8.88-16.39	23.28-28.38	0.624-0.655
4	Cape Hatteras Type Seawall Seawall/Revetment Configuration 1 Severe Recurve	1:16	0.91x0.91x76.20m	JONSWAP	1:100	1.25-3.0	9.32-17.16	19.99-23.26	0.639-0.672
5	Cape Hatteras Type Seawall Seawall/Revetment Configuration 2 Moderate Recurve	1:16	0.91x0.91x76.20m	JONSWAP	1:100	1.25-3.0	9.13-16.42	18.99-23.36	0.626-0.673
6	Cape Hatteras Type Seawall Seawall/Revetment Configuration 3 Vertical Wall	1:16	0.91x0.91x76.20	JONSWAP	1:100	1.25-3.0	8.96-19.26	18.50-22.68	0.623-0.665
7	Virginia Beach Seawall Seawall/riprap Stepped wall with recurved parapet	1:19	3.35x1.83x76.20m	TMA-shallow water	1:16 and 1:100	1.15-2.98	3.42-10.01	9.80-14.07	0.713-0.747

structure toe, d_s , or the measured T_p (data set 7), where T_p is the period of peak energy density of the wave spectrum. The nominal T_p used in data sets 1 through 6 was an assumed period based on the known peak period generated at the wave board and T_p for data set 7 was the measured peak period using a three gage Goda array.

The relative freeboard, F' , is the ratio of the freeboard to the severity of the local wave conditions. For energy based wave conditions the severity seems to be better characterized by variables containing L_D than by just H_{mo} (Ahrens 1987). The overtopping parameter F' is efficient since it contains in one term information about the water level, structure height, and wave conditions. During a test series on a seawall/revetment configuration, as wave conditions become more severe, a point is reached where details of the structure's geometry seem to have little influence on the overtopping rate. This point occurs when a combination of a high water level and large waves causes the structure to be virtually swamped or inundated by wave action. Inundation occurs when $F' < 0.3$.

Three exponential models have been found useful in estimating overtopping rates and evaluating the performance of seawalls and seawall/revetment configurations. The models in order of increasing complexity are:

$$\text{Model 1, } Q = Q_o \exp (C_1 F') \quad (2)$$

$$\text{Model 2, } Q' = Q'_o \exp (C_1 F') \quad (3)$$

$$\text{Model 3, } Q' = Q'_o \exp (C_1 F' + C_2 X_2) \quad (4)$$

where Q is the overtopping rate in cubic meters per second per meter length of seawall crest and Q' is the dimensionless overtopping rate given by

$$Q' = \frac{Q}{\sqrt{g H_{mo}^3}} \quad (5)$$

where g is the acceleration of gravity. Q_o is an overtopping coefficient having the same units as Q . Overtopping coefficients Q'_o , C_1 , and C_2 are dimensionless coefficients determined by regression analysis. The term " X_2 " in Model 3 can be any one of several dimensionless variables which improve the predictive ability of Model 3 over Model 2.

During regression analysis of the data a weight function was used to reflect the greater importance of tests which produced high overtopping rates. The weight function used is defined as

$$\text{weight function} = \text{Int} (Q \times 100) + 1 \quad (6)$$

where, Int, indicates that the quantity in parenthesis is a truncated integer and Q is the overtopping rate in English units, i.e. $\text{ft}^3/\text{ft-sec}$, converted to prototype values. Taking the logarithm of the models in order to linearize them and determine overtopping coefficients tends to decrease the relative influence of tests with high overtopping rates. In addition, tests with low rates have a higher percent error associated with measuring the overtopping volume. The weight function given by Equation 6 is an attempt to balance these undesirable effects on the regression process.

Each of the models has certain advantages and disadvantages which will be illustrated using data set 1 (Table 1) as an example. Figure 2 shows a detailed profile of the seawall configuration for data set 1. The seawall is basically a vertical wall without a fronting revetment and a small recurve at the crest (see Ahrens, et al. 1986

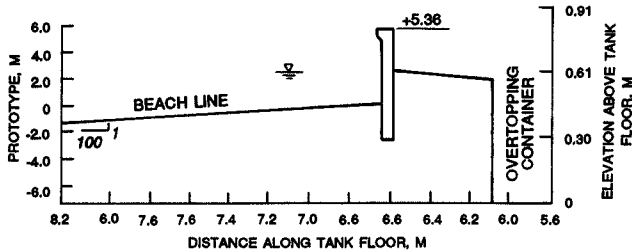


Figure 2. Data set 1 seawall configuration

for further details). Figures 3a through 3c compare predicted versus observed overtopping rates using Models 1 through 3 for predicted values, respectively. Figures 4a through 4c show the observed and predicted values of Q or Q' as a function of F' for Models 1 through 3, respectively. In Figure 4c a horizontal line indicates an overtopping rate of $0.05 \text{ m}^3 / \text{m-sec}$ which represents the approximate upper limit of overtopping for structure safety, Goda (1987). Figure 4c illustrates an advantage of Model 1, overtopping is given in dimensional units which can be directly related to potential flooding, levels of damage, or levels of danger, such as discussed by Fukuda et al. (1974) and tabulated in Owen (1982).

By intercomparing Figures 3a, 3b, and 3c, it can be seen that Model 3 is best at predicting Q . The same conclusion is reached using the correlation coefficients for data set 1 given in Table 2. This finding would be expected since Model 3 has the second variable, X_2 , which improves the prediction based on just F' . Table 2 shows that the secondary variable for data set 1 is F'/d_B . Considerable trial and error effort went into the selection of the secondary variable for each data set. In Table 2 the secondary variable which worked best with F' in predicting Q' is listed by data set. In four of the seven data sets the most important second independent variable to use with F' is the wave steepness parameter,

$$x_2 = \left(\frac{H_{mo}}{L_o} \right)^{1/2}$$

where,

$$L_o = \frac{g T^2}{2\pi}$$

The influence of steepness in predicting Q' indicates that surf conditions and their affect on potential runup are quite important to the overtopping process on some structures. For data sets 4 and 6 the influence of the rubble berm in front of the wall is important and the secondary variables reflect this fact. The secondary variables which improve the prediction of Q' for data sets 4 and 6 are W_B/L_p and H_{mo}/d_B respectively, where W_B is the width of the berm and d_B is the water depth over the berm. Review of the data and test conditions suggest that when the water depth over the berm is small the berm depth is quite important, e.g. data set 6, but a relatively modest

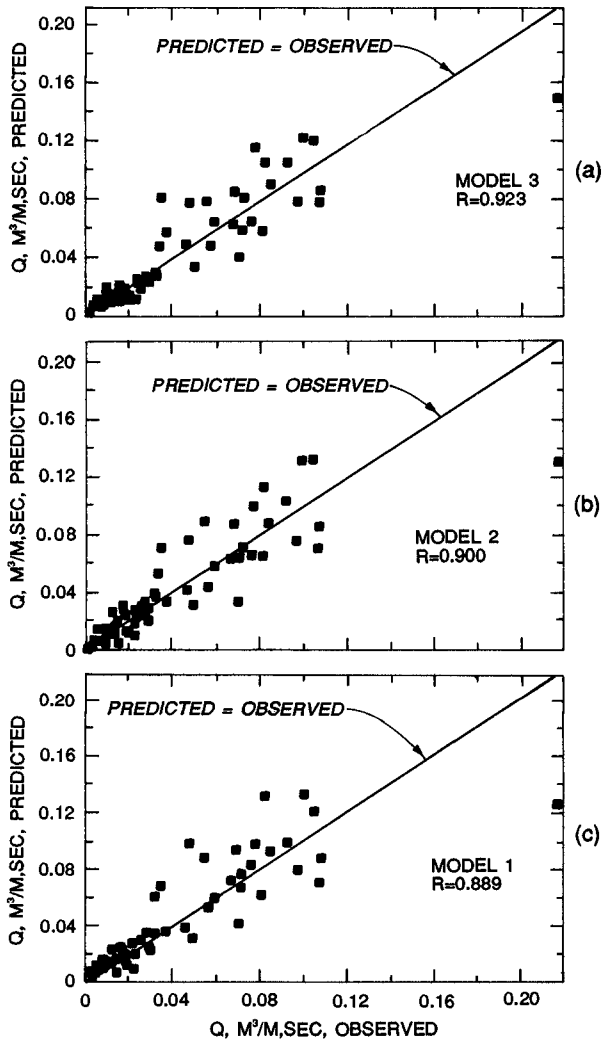


Figure 3. Predicted versus observed overtopping rates, Models 1-3

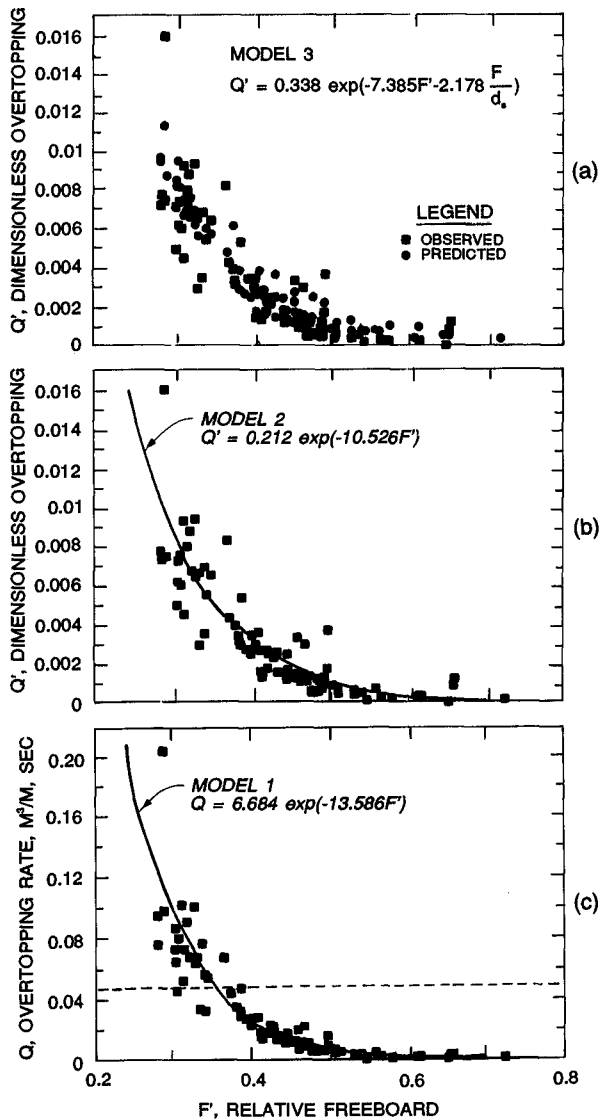


Figure 4. Observed and predicted values of Q and Q' as a function of F'

Table 2
Seawall Revetment Summary Chart*

Data Set No.	Model	Regression Coefficient	Overtopping Variables	No. of Observations	Correlation Coefficient (Q pred. vs Q obs.)	A'_q
1	1	71.952 -13.586	Q_o F^2	89	0.889	
	2	0.212 -10.526	Q_o' F^2		0.90	0.0008564
	3	0.338 -7.385 -2.178	Q_o' F^2 F/d_s		0.923	
2	1	32.357 -13.091	Q_o F^2	118	0.777	
	2	0.1472 -11.138	Q_o' F^2		0.789	0.0004677
	3	0.308 -10.732 -6.629	Q_o' F^2 $(H_{mo}/L_o)^{1/2}$		0.794	
3	1	58.71 -16.723	Q_o F^2	111	0.825	
	2	0.279 -14.885	Q_o' F^2		0.811	.0002155
	3	1 -14.371 -11.411	$(H_{mo}/L_o)^{1/2}$		0.841	
4	1	394.625 -20.676	Q_o F^2	62	0.93	
	2	1 -17.555	Q_o' F^2		0.915	.000294
	3	1 -12.69 -20.87	Q_o' F^2 W_b/L_p		0.943	
5	1	93.251 -14.749	Q_o F^2	57	0.953	
	2	0.332 -12.414	Q_o' F^2		0.934	.0006454
	3	0.541 -11.702 -5.771	Q_o' F^2 $(H_{mo}/L_o)^{1/2}$		0.947	
6	1	8.798 -6.334	Q_o F^2	37	0.771	
	2	0.0232 -3.791	Q_o' F^2		0.615	.0019625
	3	1 -7.558 -1.366	Q_o' F^2 H_{mo}/D_B		0.918	
7	1	253.93 -18.26	Q_o F^2	68	0.927	
	2	0.348 -11.232	Q_o' F^2		0.923	.0010659
	3	1 -11.174 -10.664	Q_o' F^2 $(H_{mo}/L_o)^{1/2}$		0.948	

*NOTE Q_o in Model 1 is dimensional while Models 2 and 3 are dimensionless.

increase in water depth causes the width of the berm to be the more important characteristic, e.g. data set 4. In some instances it was not clear why one choice of a secondary variable was better than another choice. Since the secondary variables are partly dependent on the conditions tested the model 3 approach should not be regarded as producing an overly general formula.

In Table 2 a correlation coefficient is given for each model for each data set. This coefficient is the correlation between the predicted and observed dimensional overtopping rates. Using this correlation coefficient provides a fair way to compare the effectiveness of the three models. For some data sets Model 2 has a lower correlation coefficient than Model 1, which suggest that the method of normalizing Q was not optimum for that data set. In one case, data set 5, Model 1 even had a higher correlation coefficient than model 3. It is assumed that normalizing Q interfered with the surprisingly high correlation between Q and F' . Of course, it was necessary to normalize Q the same way for all data sets in order to make comparisons. Quite a few different ways to normalize Q were tried. Ideally it would be advantageous to normalize Q using wave condition variables H_{m0} , L_p , and T_p and use characteristics of the geometry of the seawall/revetment and water depth to formulate the dimensionless independent variables. Attempts to develop an effective overtopping prediction method based on separating wave and structure variables was unsuccessful. Experience from this study indicates that there does not seem to be a conspicuously superior way to normalize Q ; this finding is consistent with those of Jensen and Juhl (1987).

Inspection of Table 2 indicates that Model 3 does a substantially better job predicting overtopping rates for data sets 1, 4, 5, 6, and 7 than for data sets 2 and 3. Data sets 2 and 3 were the only ones with the correlation between predicted and observed overtopping rates less than 0.90. Data sets 2 and 3 were also the only data sets where tests of seawall/revetment configurations with slightly different geometries were lumped together. In all of the other data sets the wave heights, wave periods, and water depths were varied but there were no changes in the geometry of the structure. The conclusion is that small changes in geometry of a seawall/revetment configuration can have an important influence on the overtopping rate but is difficult to properly account for the change in a simple overtopping model. This finding is consistent with Owen (1980) who tabulates different overtopping coefficients for each different profile tested of embankment type seawalls, Jensen and Juhl (1987) who show different overtopping curves for each breakwater and sea dike tested, and Bradbury and Allsop (1988) who tabulate different overtopping coefficients for each breakwater crown wall configuration tested.

One of the useful characteristics of model 2 is that it can be easily used to generate a hydraulic inefficiency coefficient, A'_q , for a seawall/revetment configuration. A'_q is defined as the area under the curve, such as shown in Figure 4b, between $F' = 0.30$ and infinity. The lower limit of integration has been set at the approximate value of F' where wave inundation of the structure becomes the dominant mode of overtopping. Symbolically we have

$$A'_q = Q'_o \int_{0.30}^{\infty} \exp(C_1 F') dF' = -\frac{Q'_o}{C_1} \exp(0.30 C_1)$$

Values of A'_q are given in Table 2. Generally the ranking of the structures using A'_q seems logical with some small surprises. The stepped seawall with a moderate recurve, data set 7, seems to perform below expectations. When the data sets based on seawalls with recurved parapets are examined, data sets 4, 5, and 7, the vertical scale of the recurves for data sets 4 and 5 are larger in relation to the incident H_{mo} than the recurve for data set 7. It may be that the recurves used for data sets 3 and 4 are more effective than the one used for data set 7, partly because they represent a larger discontinuity to the runup flow, even though they are partly submerged at high water levels. Table 3 summarizes the relevant information on discontinuity effects for recurved parapets on seawalls for heavy overtopping conditions and long period waves. Ranking seawalls on the basis of A'_q values also indicates that the small curve at the crest of the wall tested for data set 1 is effective despite its small size.

Table 3. Discontinuity effects for recurved parapets on seawalls for heavy overtopping conditions, $F' = 0.30$, and long waves, $T_p = 3.0$ sec

Data Set	d_s for a High Water Level cm	Freeboard cm	Vertical Height of Recurved cm	H_{mo} for Heavy Overtop cm	Discontinuity/ H_{mo}
4	23.1	13.5	21.3	14.3	1.49
5	23.1	12.9	20.8	13.4	1.55
7	14.0	9.6	9.1	9.7	0.94

SUMMARY AND CONCLUSION

Results from an extensive series of laboratory tests of irregular wave overtopping of a number of seawall and seawall/revetment configurations are presented. Overtopping rates were found to be strongly dependent on a dimensionless freeboard parameter, F' , which is the ratio of the freeboard to a measure of the local wave severity, Equation 1. There is an approximately exponential relation between Q and F' which logically leads to the development of three progressively more complex overtopping models, Equations 2, 3, and 4. The primary purpose of the models is to predict overtopping rates but they are also useful for evaluating various strategies to reduce overtopping and ranking the hydraulic performance of the structures. Model 3 is the most complex and usually makes the best estimates of overtopping rates, however, no completely satisfactory approach has been developed which will provide a good generalized overtopping model for a variety of seawall and seawall/revetment configurations.

ACKNOWLEDGEMENTS

The support of the Office, Chief of Engineers, Civil Works Research and Development Program for granting permission to publish this paper is greatly appreciated.

REFERENCES

Ahrens, J. P., Heimbaugh, M. S., and Davidson, D. D. "Irregular Wave Overtopping of Seawall/Revetment Configurations, Roughans Point, Massachusetts, Waterways Experiment Station, Corps of Engineers, Technical Report CERC-86-7, Vicksburg, MS, Sep. 1986.

Ahrens, J. P., "Characteristics of Reef Breakwaters," Technical Report CERC-87-17, U.S. Army Engineer Waterways Experiment Station, Vicksburg, MS. Dec. 1987.

Bradbury, A. P., and Allsop, N.W.H., "Hydraulic Effects of Breakwater Crown Walls," 3rd International Conference, ICE, Eastbourne, England, May 1988.

Douglass, S. L., "Review and Comparison of Methods for Estimating Irregular Wave Overtopping Rates," Technical Report CERC-86-12, U.S. Army Engineer Waterways Experiment Station, Vicksburg, MS., Dec 1986.

Fukuda, N., Uno, T., and Irei, I., "Field Observations of Wave Overtopping of Wave Absorbing Revetment," Coastal Engineering in Japan, Vol 17, 1974.

Gadd, P. E., Machemehl, J. L., and Maniban, V., "Comparison of Wave Overtopping Prediction to Measurements from Large-Scale Model Tests," Proceedings of Artic '85, San Francisco, California, April 1985.

Goda, Y. and Suzuki, Y., "Estimation of Incident and Reflected Waves in Random Wave Experiments," Proceedings 15th Coastal Engineering Conference, Honolulu, Hawaii, 1976.

Goda, Y., "Random Seas and Design of Maritime Structures," University of Tokyo Press 1985.

Grace, P. J. and Carver, R. D., "Seawall and Revetment Stability Study, Cape Hatteras Lighthouse, North Carolina," Technical Report CERC-85-12, U.S. Army Engineer Waterways Experiment Station, Vicksburg, MS. 1985.

Heimbaugh, M. S., Grace, P. J., Ahrens, J. P., and Davidson, D. D., "Coastal Engineering Studies in Support of Virginia Beach, Virginia, Beach Erosion Control and Hurricane Protection Project," Waterways Experiment Station, Corps of Engineers, Technical Report CERC-88-1, Vicksburg, MS., March 1988.

Jensen, O. J. and Juhl, J., "Wave Overtopping on Breakwaters and Sea Dikes," International Conference on Coastal and Port Engineering in Developing Countries, Beijing, China, Sept. 1987.

Owen, M. W., "Design of Seawalls Allowing for Wave Overtopping," Report No. EX 924, Hydraulics Research Station, Wallingford, England, June 1980.

Owen, M. W., "The Hydraulic Design of Seawall Profiles," Proceedings ICE Conference on Shoreline Protection, Southampton, Sept. 1982 also Published Thomas Telford Ltd, London, 1983.

Shore Protection Manual, 4th Ed., U.S. Army Engineer Waterways Experiment Station, Coastal Engineering Research Center, U.S. Government Printing Office, Washington, D.C. 1984.

CHAPTER 60

Closed-Form Solutions for the Probability Density of Wave Height in the Surf Zone

William R. Dally¹, M.ASCE and Robert G. Dean², M.ASCE

Abstract

By invoking the assumption that in the surf zone, random waves behave as a collection of individual regular waves, two closed-form solutions for the probability density function of wave height on planar beaches are derived. The first uses shallow water linear theory for wave shoaling, assumes a uniform incipient condition, and prescribes breaking with a regular wave model that includes both bottom slope and wave steepness effects on the rate of decay. In the second model, the shallow water assumption is removed, and a distribution in wave period (incipient condition) is included. Preliminary results indicate that the models exhibit much of the behavior noted for random wave transformation reported in the literature, including bottom slope and wave steepness effects on the shape of the probability density function.

Introduction

The probability density function (pdf) for wave height in the surf zone is a subject of distinct import, as the transformation of random waves due to shoaling and breaking is the primary driving force in beach dynamics. Figure 1 contains histograms of wave height, H , non-dimensionalized by the local average height, \bar{H} , observed at different times at the same location in the inner surf zone during the DUCK '85 field experiment, as reported in Ebersole and Hughes (1987). Note that the general shape of the pdf varies significantly, depending on incident wave characteristics and tide elevation. It is stressed that the pdf does not appear to have a typical shape, at least one that is easily recognized.

Most previous efforts to model the transformation of random waves along a beach transect, e.g. Collins (1970), Kuo and Kuo (1975), Goda (1975), Battjes and Janssen (1978), and Thornton and Guza (1983), start with the Rayleigh distribution outside the surf zone, and rely on the assumption that the height of an individual wave is directly proportional to the local water depth in order to represent energy dissipation due to breaking; i.e.,

¹Florida Institute of Technology, Oceanography and Ocean Engineering, 150 W. University Blvd., Melbourne, Florida 32901, U.S.A.

²Coastal and Oceanographic Engineering Department, 336 Weil Hall, University of Florida, Gainesville, Florida 32611, U.S.A.

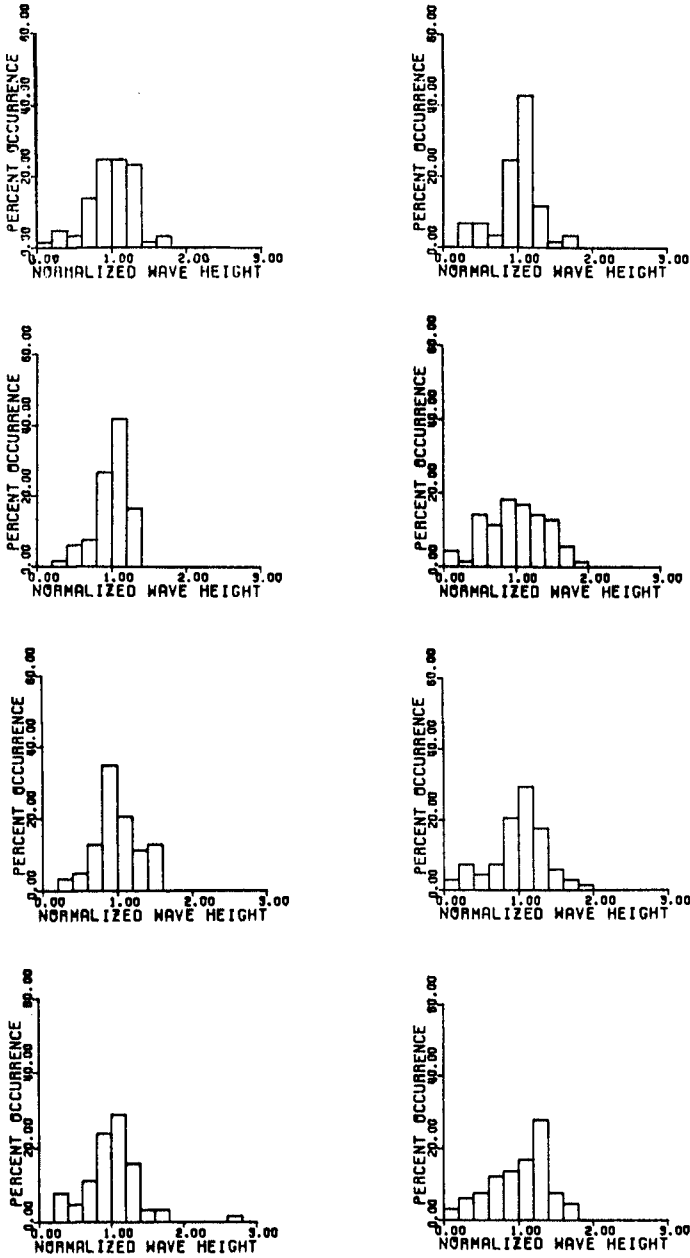


Figure 1 - Sample histograms of dimensionless wave height (H/\bar{H}) observed at the same location (pole#6) during DUCK'85 field experiment. Data reported in Ebersole and Hughes (1987). Waves were identified using the zero-down-cross technique.

$$H = \gamma h \quad (1)$$

where h is water depth and γ is a coefficient whose behavior must be parameterized empirically. As described by Collins (1970), this results in a pdf shape that at its upper limit contains a spike of finite area - a shape not supported by data. Kuo and Kuo (1975), Goda (1975), and Thornton and Guza (1983) remove this behavior with various ad hoc treatments that require additional empirical fitting. However, adopting a single basic shape for the pdf a priori results in only limited agreement to the wide variety of histograms found in reliable field data, as evidenced by Figure 1.

Mase and Iwagaki (1982) and Dally and Dean (1986) approach the problem in basically the same manner as Collins (1970), but employ models more realistic than (1) for describing the decay of individual waves. Because the pdf is allowed to transform "naturally", i.e. no typical shape is adopted a priori, better agreement with observed histograms is attained. While γ in (1) has been parameterized in terms of bottom slope and deepwater wave steepness, the expressions for decay of individual waves adopted by Mase and Iwagaki (1982) and Dally and Dean (1986) include the effect of bottom slope and wave steepness on the shape of the decay profile. That is, they model the observational fact that the gradient in wave height is rarely uniform across a beach of uniform slope (see Horikawa and Kuo, 1966). In result, for random waves the observed dependence of the transformation of both the pdf and statistically representative waves (e.g. H_{rms} and $H_{1/3}$) on beach slope and mean wave steepness, as discussed in Thornton, Wu and Guza (1984) and Sallenger and Holman (1985), is more faithfully represented. Both of these models require numerical solution which, although suitable and practical for engineering application, does not facilitate study of the general behavior of the pdf. The purpose of this paper is to present two closed-form solutions which will hopefully serve to better edify the problem of random wave transformation, and provide a theoretical foundation for future work in stochastic modeling of surf zone dynamics and design of engineering projects.

Closed-Form Solution #1

The first closed form solution is the subject of an upcoming paper by one of the authors (Dally, 1988), in which its derivation, analysis of the behavior of the solution, and comparison to field data are described in detail. Consequently, only a brief overview is presented below.

As an initial condition, we adopt the Rayleigh pdf for wave height, truncate it at some realistically large wave height, and assume no waves are breaking, i.e.,

$$\begin{aligned} \text{pdf}(H_1) &= \frac{2H_1}{H_{rms1}} \exp \left[-\frac{H_1^2}{H_{rms1}^2} \right] & H_1 \leq \gamma h_1 \\ &= 0 & H_1 > \gamma h_1 \end{aligned} \quad (2)$$

where the subscript "1" denotes initial conditions. Set-up is not included, and in this first solution γ is assumed constant.

The area lost above the truncation point, Ω_t , is equal to

$$\Omega_t = \int_{\gamma h_1}^{\infty} \text{pdf}(H_1) dH_1 = \exp -(\gamma h_1 / H_{\text{rms}1})^2 \quad (3)$$

which shows that starting in water much deeper than the root mean square wave height will make Ω_t negligible. Otherwise, the pdf should be normalized by dividing by the quantity $(1 - \Omega_t)$. The random variable H_1 is now transformed to local wave height H due to either shoaling or breaking, as a function of the local water depth, h .

Shoaling waves - It is now assumed that linear shallow water wave theory is valid, so that from Green's Law

$$H_1 = H (h/h_1)^{1/4} \quad (4)$$

Calculating the Jacobian and performing a standard transformation of random variable yields

$$\text{pdf}(H)_{\text{sh}} = \frac{2H}{H_{\text{rms}1}} (h/h_1)^{1/2} \exp\left[-\frac{H^2}{H_{\text{rms}1}^2} (h/h_1)^{1/2}\right] \quad (5)$$

where subscript "sh" denotes the pdf for shoaling waves. This distribution, which still has a Rayleigh shape, must be truncated at the largest wave height that can occur at the local water depth, i.e., $H \leq \gamma h$. If the random variable is non-dimensionalized by the initial root mean square height, $H_{\text{rms}1}$, we obtain

$$\text{pdf}(A)_{\text{sh}} = 2A \hat{h}^{1/2} \exp(-A^2 \hat{h}^{1/2}) \quad A \leq A_{\text{max}} \quad (6)$$

where $A = H/H_{\text{rms}1}$, $A_{\text{max}} = \gamma h/H_{\text{rms}1}$, and $\hat{h} = h/h_1$.

Breaking waves - The probability density function of wave height for broken waves is derived in a similar manner, but in two steps. The random variable H_1 is first transformed to h_b , the water depth at which incipient breaking is attained, by applying Green's Law

$$H_1 = \gamma h_b^{5/4} h_1^{-1/4} \quad (7)$$

To transform from h_b to H , we utilize the analytical solution to the model of Dally, Dean, and Dalrymple (1985) for regular waves breaking on a planar beach (neglecting set-up). When inverted this solution becomes

$$h_b = \left[\frac{H^2 + \alpha h^2}{(\gamma^2 + \alpha) h^{(K/m-1/2)}} \right]^{1/(5/2-K/m)} \quad (8)$$

where

$$\alpha = \frac{(K/m)\Gamma^2}{(5/2 - K/m)} \quad (9)$$

m is beach slope, K is the decay coefficient (~ 0.17), and Γ the stable wave factor (~ 0.50). Performing the transformation and again nondimensionalizing by H_{rms1}, the portion of the pdf due to broken waves is

$$\text{pdf}(A)_{br} = \frac{5 A \hat{h}^{(1/2-K/m)} B^{K/m}}{|(5/2 - K/m)|(\gamma^2 + \alpha)} \exp\left[-\left(\frac{\gamma h_1}{H_{rms1}}\right)^2 B^{5/2}\right]; A_{min} \leq A \leq A_{max} \tag{10}$$

$$\text{where } B = \left[\frac{\left(\frac{H_{rms1}}{h_1}\right)^2 A^2 + \alpha \hat{h}^2}{(\gamma^2 + \alpha) \hat{h}^{(K/m-1/2)}} \right]^{1/(5/2-K/m)} \tag{11}$$

This distribution must be truncated not only at the upper limit A_{max} = γh/H_{rms1}, but also at the lower bound given by the breaking wave height that corresponds to the largest wave of the original pdf(H₁). By applying the original solution for regular waves we find

$$A_{min} = \left[\hat{h}^{(K/m-1/2)} (\gamma^2 + \alpha) - \alpha \hat{h}^2 \right]^{1/2} (h_1/H_{rms1}) \tag{12}$$

If γ and m are such that the decay profiles are convex, A_{max} and A_{min} switch.

The expressions (6) and (10) are plotted in Figure 2a for a beach slope m = 1/80 and γ = 0.78, in Figure 2b for m = 1/50 and γ = 1.0, and in Figure 2c for m = 1/20 and γ = 1.2. Note that for the mild beach slope, as one moves into the surf zone, area is taken from the shoaling pdf and "piled up" at the lower breaking wave heights of the breaking pdf and not the upper limiting wave height, as is the case for the steep beach and was assumed by Collins (1970). This is in at least qualitative agreement with field data, as demonstrated by the observations of Ebersole and Hughes (1987). The apparent discontinuity in the model pdf at the lower limit of the breaking portion also appears in this data set, as is shown in Figure 1. However, the model does tend to overpredict the amount of this abrupt jump in the pdf; plus, observed histograms display a slightly more gradual decline over the upper range of wave height, as opposed to the truncation assumed by the model. These characteristics in the model result from neglecting the mechanisms present in nature which smooth the pdf, such as surf beat and a varying height to depth ratio at incipient breaking. The numerical solution of Dally and Dean (1986) and Dally (1987) includes both of these effects. In the next closed form solution to be presented however, it is only practicable to address the variation in the incipient breaker condition.

Closed-Form Solution #2

To improve upon the first solution, in the following the shallow water assumption is removed and the incipient condition varies according to a general form for available empirical expressions, e.g. Moore (1982), which is a hybrid of Weggel (1972) and Komar and Gaughan (1972):

$$\gamma = b(m) - a(m) \left[\frac{0.36}{(2\pi)^{4/5}} \left(\frac{H_o}{L_o}\right)^{4/5} \right] \tag{13}$$

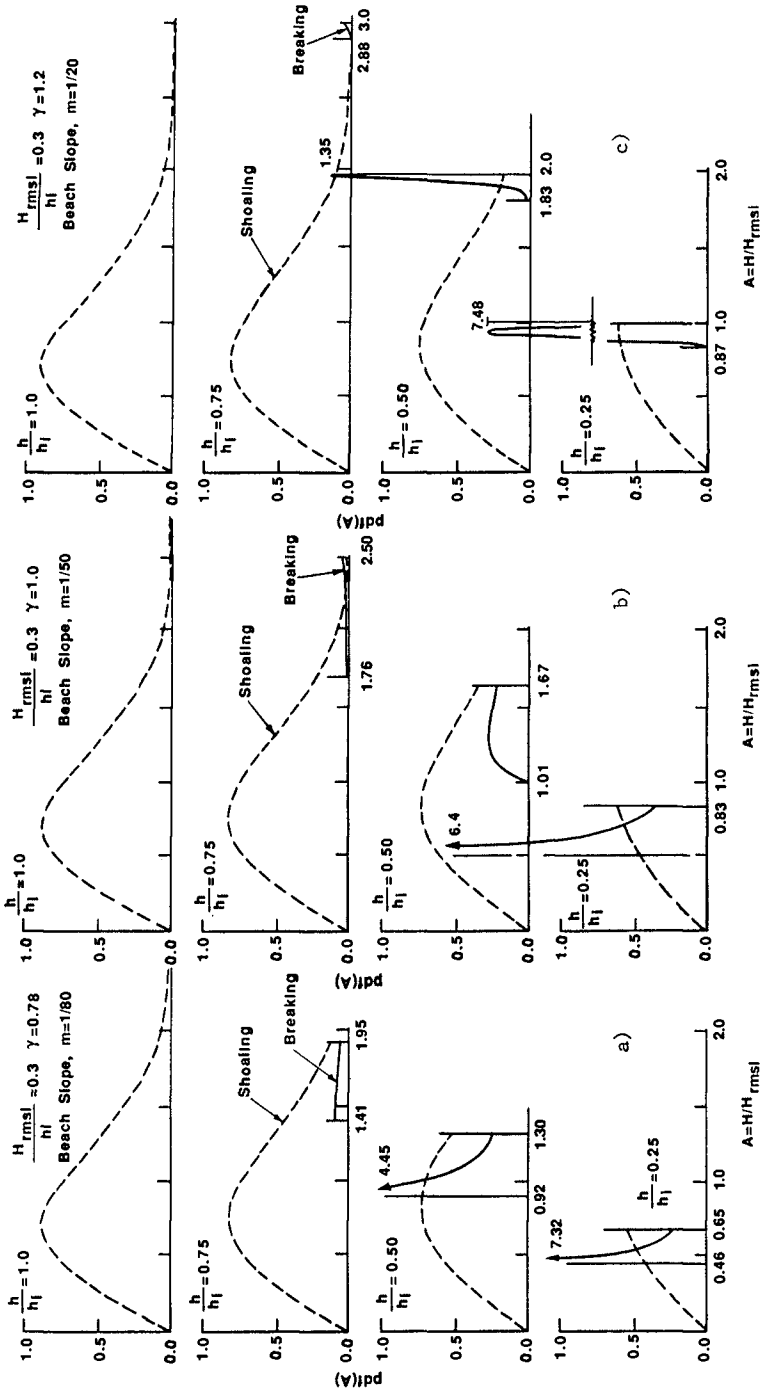


Figure 2 - Transformation of the pdf of wave height across the surf zone according to solution #1, (6) and (10).
 a) beach slope $m=1/80$, incident condition $\gamma = 0.78$; b) $m=1/50, \gamma = 1.0$; c) $m=1/20, \gamma = 1.2$.

where

$$a(m) \approx 43.8(1.0 - e^{-19 m}) \quad (14)$$

$$b(m) \approx 1.56/(1.0 + e^{-19.5m}) \quad (15)$$

L is wave length and the subscript "o" denotes deepwater conditions.

These improvements require knowledge of the distribution of wave period, and so we will conduct a series of transformations of a joint pdf in two random variables. In the final step the second random variable is integrated out to obtain the marginal pdf of shoaling and breaking wave heights. It is noted that the formulation presented below is identical in basis to one solved numerically in Dally and Dean (1986).

The initial condition is taken to be the joint probability density function for wave height and period in deep water as derived by Longuet-Higgins (1983), which is

$$\text{pdf}(R_o, \tau) = C_1 \frac{R_o^2}{\tau^2} \exp\left\{-R_o^2\left[1 + \frac{1}{v^2}\left(1 - \frac{1}{\tau}\right)^2\right]\right\} \quad (16)$$

$$\text{where} \quad R_o = H_o/H_{rmso} = H_o/\sqrt{8a_0} \quad (17)$$

$$\text{and} \quad \tau = T/\bar{T} = T \frac{a_1}{2\pi a_0} \quad (18)$$

T and \bar{T} are wave period and average wave period, a_0 is the area under the measured spectral density function in deep water, and a_1 is the first moment of this area. The coefficient C_1 is given by

$$C_1 = \frac{4}{\sqrt{\pi} v} \left[1 + (1 + v^2)^{-1/2}\right]^{-1} \quad (19)$$

and v is the band-width parameter determined by the first three moments of the spectrum

$$v = \left[\frac{a_0 a_2}{(a_1)^2} - 1\right]^{1/2} \quad (20)$$

Shoaling waves - Although the transformation could be performed in one step, for better tractability, the pdf for shoaling waves will be developed in two steps. The first is to transform τ to deepwater relative depth, D_o

$$D_o = k_o h = \frac{(2\pi)^2}{gT^2} h \quad (21)$$

and so

$$\tau = \frac{2\pi}{T} \left(\frac{h}{gD_o} \right)^{1/2} \quad (22)$$

and the joint pdf is transformed to

$$\text{pdf}(R_o, D_o) = \frac{C_1}{2} R_o^2 \frac{T}{2\pi} \left(\frac{g}{hD_o} \right)^{1/2} \exp(-R_o^2 \left\{ 1 + \frac{1}{\sqrt{2}} \left[1 - \frac{T}{2\pi} \left(\frac{gD_o}{h} \right)^{1/2} \right]^2 \right\}) \quad (23)$$

The second step is to transform the deepwater wave height to the local shoaling wave height. By applying conservation of energy flux and invoking linear wave theory yields

$$R_o^2 \frac{gT}{4\pi} = R^2 \left[\frac{g \tanh kh + gkh(1 - \tanh^2 kh)}{2(gk \tanh kh)^{1/2}} \right] \quad (24)$$

From the dispersion relation and adopting the notation $D = kh$, (24) reduces to

$$R_o^2 = R^2 \left[\frac{D_o + D^2 - D_o^2}{D} \right] \quad (25)$$

An approximate solution to the dispersion relation given by Hunt (1979) is

$$D^2 = D_o^2 + \frac{D_o}{1 + \sum_{n=1}^{\infty} d_n D_o^n} \quad (26)$$

in the present notation (d_n are provided constants), and (25) can now be expressed explicitly in terms of D_o

$$R_o = R \left\{ \frac{1 + 1/(1 + \Sigma)}{[1 + 1/D_o(1 + \Sigma)]^{1/2}} \right\}^{1/2} \quad (27)$$

where Σ denotes the summation in (26). Finally, the joint probability density function of shoaling wave height and deepwater relative depth is produced

$$\text{pdf}(R, D_o)_{sh} = \frac{C_1}{2} \bar{D}_o^{-1/2} D_o^{-1/2} \left\{ \right\}^{3/2} R^2 \exp(-R^2 \left\{ \right\} \left[1 + \frac{1}{\sqrt{2}} \left[1 - \left(\frac{D_o}{\bar{D}_o} \right)^{1/2} \right]^2 \right\}) \quad (28)$$

in which $\left\{ \right\}$ denotes the expression within the braces of (27) and

$$\bar{D}_o = \bar{k}_o h = \frac{2\pi}{L_o} h = 2\pi \frac{H_{rmso}}{L_o} \frac{h}{H_{rmso}} = 2\pi \bar{S}_o \hat{h} \quad (29)$$

\bar{S}_o is mean deepwater wave steepness and \hat{h} is dimensionless water depth.

The marginal pdf for dimensionless shoaling wave height is found by integrating between proper limits (numerically) with respect to deep-water relative depth D_o . These limits are defined by the incipient breaking condition, which is a function of deepwater steepness and bottom slope. This function can be expressed in a general form which encompasses most of the empirical relationships for γ available in the literature:

$$S_o = H_o/L_o = \frac{D_o R_o}{2\pi h} = [F(m, \gamma)]^p \tag{30}$$

As an example, for γ given by (13)

$$F = \left[\frac{b(m) - \gamma (2\pi)^{4/5}}{a(m)} \right] \tag{31}$$

and

$$p = 5/4 \tag{32}$$

The essence of the problem at hand is, given the local water depth and choosing a wave height of interest, what is the deepwater relative depth of the single wave that is at incipient breaking, if such a wave exists. If it does exist, all waves of that height but with smaller relative depth are still shoaling, while all waves of that height but greater relative depth are already breaking. Thus to determine the marginal pdf of shoaling wave height, the joint pdf(R, D_o)_{sh} is integrated according to

$$mpdf(R)_{sh} = \int_0^{D_{oI}} pdf(R, D_o)_{sh} dD_o \tag{33}$$

where D_{oI} is the deepwater relative depth of the wave with height R at incipient breaking. D_{oI} must be calculated numerically as is described in Dally (1987).

Breaking waves - Four steps will be required to derive the pdf of wave height due to breaking, represented conceptually by

$$\begin{aligned} pdf(H_o, T) &\Rightarrow pdf\left(H_o, \frac{H_o}{L_o}\right) \Rightarrow pdf(H_o, \gamma) \Rightarrow pdf(h_b, \gamma) \\ &\Rightarrow pdf(H, \gamma)_{br} ; mpdf(H)_{br} = \int_{\gamma_1}^{\gamma_2} pdf(H, \gamma)_{br} d\gamma \end{aligned} \tag{34}$$

Again starting with (16) and applying

$$\tau = \left(\frac{R_o}{S_o} \frac{H_{rmso}}{L_o}\right)^{1/2} = \left(\frac{R_o}{S_o} \bar{S}_o\right)^{1/2} \tag{35}$$

we obtain

$$\text{pdf}(R_o, S_o) = \frac{C_1}{2} \frac{R_o^{3/2}}{S_o^{1/2}} (\bar{S}_o)^{-1/2} \exp(-R_o^2 \{1 + \frac{1}{\nu^2} [1 - (\frac{R_o}{\bar{S}_o})^{-1/2}]^2\}) \quad (36)$$

In the second step, (30) is employed so that

$$\text{pdf}(R_o, \gamma) = \frac{C_1}{2} (\bar{S}_o)^{-1/2} R_o^{3/2} p_F^{(P/2-1)} |\partial F / \partial \gamma| \cdot \exp(-R_o^2 \{1 + \frac{1}{\nu^2} [1 - (\frac{R_o}{F^P} \bar{S}_o)^{-1/2}]^2\}) \quad (37)$$

We now apply conservation of energy flux between the deepwater wave and the same wave at incipient breaking (which is in shallow water)

$$\frac{R_o^2 L_o^{1/2} \sqrt{g}}{2\sqrt{2\pi}} = R_b^2 \sqrt{gh_b} = \frac{\gamma^2 h_b^2}{H_{rmso}^2} \sqrt{gh_b} \quad (38)$$

Rearranging and applying (30) yields

$$R_o = \hat{h}_b (8\pi)^{1/5} \gamma^{4/5} [F(m, \gamma)]^{P/5} \quad (39)$$

where $\hat{h}_b = h_b / H_{rmso}$, and the joint pdf of \hat{h}_b and γ is determined

$$\text{pdf}(\hat{h}_b, \gamma) = \frac{C_1}{2} (\bar{S}_o)^{-1/2} (8\pi)^{1/2} \gamma^2 p_F^{(P-1)} |\partial F / \partial \gamma| \hat{h}_b^{3/2} \cdot \exp(-\hat{h}_b^2 (8\pi)^{2/5} \gamma^{8/5} F^{2P/5} \{1 + \frac{1}{\nu^2} [1 - (\frac{\hat{h}_b (8\pi)^{1/5} \gamma^{4/5} \bar{S}_o}{F^{4P/5}})^{-1/2}]^2\}) \quad (40)$$

The final transformation again utilizes the inverted analytic solution for wave decay on planar beaches (8) which in the present dimensionless notation is

$$\hat{h}_b = \left[\frac{R^2 + \alpha \hat{h}^2}{\hat{h}^{(K/m-1/2)} (\gamma^2 + \alpha)} \right]^{1/5} \frac{1}{5/2 - K/m} \quad (41)$$

Finally, the joint pdf of R and γ for breaking waves is

$$\begin{aligned}
 \text{pdf}(R, \gamma)_{br} &= \frac{C_1}{2} (\bar{S}_o)^{-1/2} (8\pi)^{1/2} \gamma^2_p F^{(p-1)} \left| \frac{\partial F}{\partial \gamma} \right| \left[\left(\frac{K/m}{5/2 - K/m} \right) \right. \\
 &\quad \cdot \frac{1}{|5/2 - K/m|} \frac{2R}{h^{(K/m-1/2)} (\gamma^2 + \alpha)} \\
 &\quad \cdot \exp(-[\left(\frac{2}{5/2 - K/m} \right) (8\pi)^{2/5} \gamma^{8/5} F^{2p/5} \\
 &\quad \left. \left\{ 1 + \frac{1}{\sqrt{2}} \left[1 - \left(\frac{1}{F^{4p/5}} \frac{1}{[\left(\frac{1}{5/2 - K/m} (8\pi)^{1/5} \gamma^{4/5} \bar{S}_o \right)^{-1/2} \right]^2} \right) \right] \right\} \right] \Bigg)
 \end{aligned}
 \tag{42}$$

where [] denotes the quantity in the brackets of (41). The region of integration for γ and the numerical procedure followed are described in detail in Dally (1987). Example results for the marginal pdf(R) are displayed in Figures 3a, 3b, and 4. Note that in Figure 3 the closed form solution for breaking on the 1/20 slope has been smoothed, and that the discontinuity at the upper bound of the pdf has been eliminated. For mild beach slopes, the anomaly in the lower range of values for breaking waves displayed by the first model (Figure 2a) still exists as shown in Figure 4 for a beach slope of 1/80.

To test the sensitivity of the model to the expression chosen to dictate incipient breaking, that given by Singamsetti and Wind (1980),

$$\gamma = 0.568 m^{0.107} \left(\frac{H_o}{L} \right)^{-0.237}
 \tag{43}$$

is also applied and results for the same conditions as Figure 3a are displayed in Figure 5. This breaker criterion allows more range in values of γ than (13), perhaps more than is actually found in nature and in fact has no upper limit. This is responsible for the broad and flat shape of the pdf for broken waves, and the upper tail of the pdf for shoaling waves as compared to Figure 3a.

Discussion and Conclusions

Due to space limitations, direct comparison of the models to observed histograms cannot be presented here. However, in Dally (1988) solution #1 is compared to the field data of Ebersole and Hughes (1987), while Dally and Dean (1986) and Dally (1987), applying to complex topography the same formulation as developed for solution #2, compared direct numerical solutions to the field data of Hotta and Mizuguchi (1980, 1986). The model comparisons are quite reasonable, and faithfully represent major features of the shape of observed histograms as the surf zone is traversed. As hoped, allowing for a variation in γ in solution #2 does improve agreement, especially across the range of higher wave heights. As previously noted, the models do tend to overpredict measured values near the mean wave height for mild beach slopes - behavior

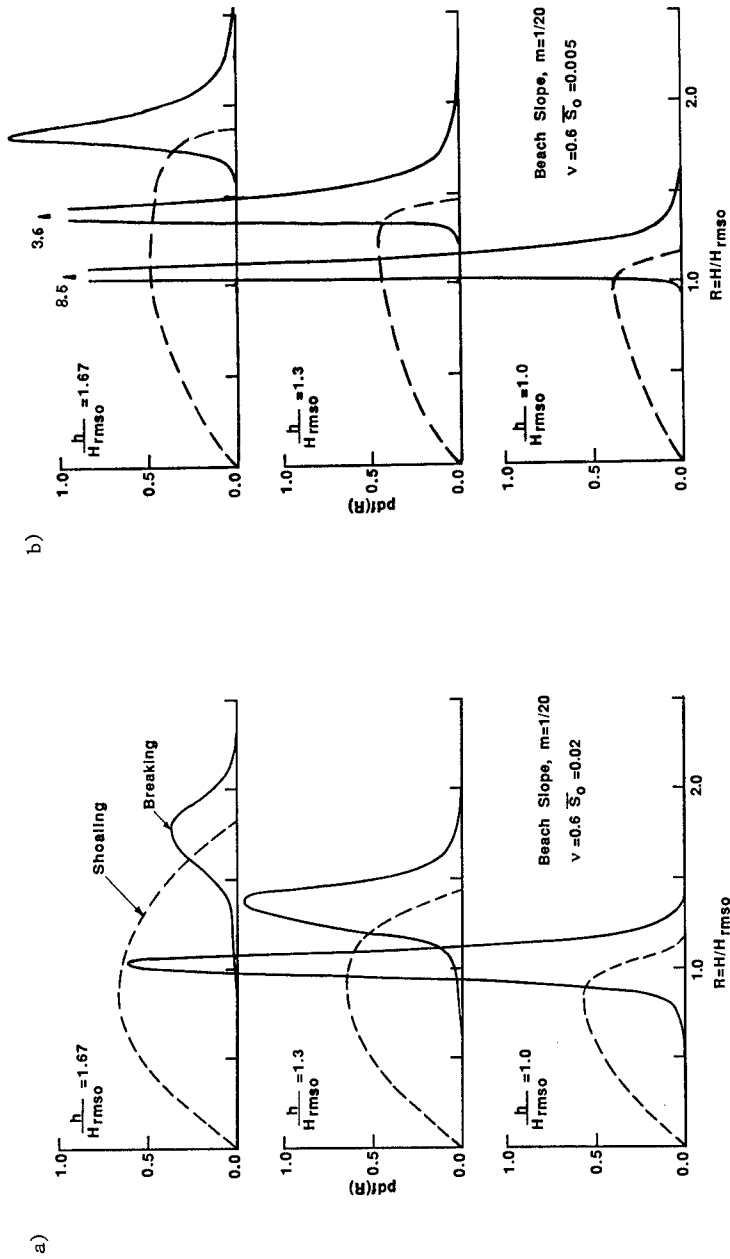


Figure 3 - Transformation of the pdf of wave height across the surf zone according to solution #2, (28) and (42) for beach slope $m=1/20$. a) mean deepwater steepness $S_0=0.02$; b) $S_0=0.005$.

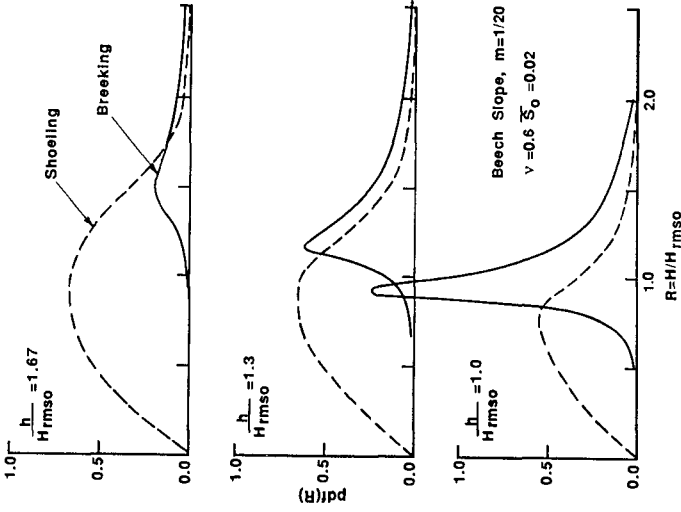


Figure 5 - Transformation of the pdf of wave height across the surf zone according to solution #2, (28) and (42), for beech slope $m=1/20$. Incipient condition of Singamsetti and Wind (1980), (43), utilized.

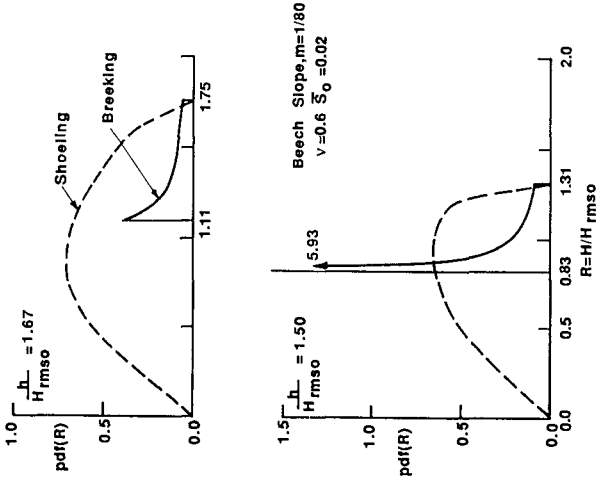


Figure 4 - Transformation of the pdf of wave height across the surf zone according to solution #2, (28) and (42), for beech slope $m=1/80$.

most likely due to neglecting surf beat. Comparison of the transformation of statistically representative waves H_{rms} , $H_{1/3}$ and $H_{1/10}$ as predicted by the second formulation are also in good agreement with data from Hotta and Mizuguchi (1980, 1986).

The degree to which the closed-form solutions represent random wave transformation is directly attributed to the ability of the regular wave model (8) to predict breaking of individual waves. It is stressed that favorable results have been obtained without altering the original calibration of the regular wave model. Because the effect of beach slope and wave steepness on wave height decay appears to be well represented in the regular wave model (see Dally et al., 1985), the ability of the random wave models to predict the effect of these parameters on the behavior of the pdf is significantly enhanced. This also holds true for the behavior of statistically representative waves calculated using solution #1 as pursued in Dally (1988). The closed-form nature of the solutions intrinsically identifies the dimensionless parameters governing the problem, and allows the predicted response to them to be more easily examined. For example, intercomparison of Figures 2a, b and c clearly shows the effect of beach slope, while 4a and b display the effects of mean wave steepness, with all other parameters held constant. Although in solution #2 numerical quadrature is required to determine the marginal pdf, (28) and (42) are in closed form, and could be utilized as a starting point for stochastic treatment of other surf zone problems.

Numerical studies reported in Dally and Dean (1986) and Dally (1987) indicate that comparisons of the model to field data are improved when the formulation includes 1) non-linear effects in wave shoaling, and 2) the effects of the fluctuating mean water level and oscillatory current associated with surf beat. However, a closed-form solution that includes these effects has thus far been elusive.

References

- Battjes, J. A. and Janssen, J. P. F. M., 1978, "Energy Loss and Set-up Due to Breaking of Random Waves," Proc. 16th Conf. Coastal Eng., ASCE, Vol. 1, 569-587.
- Collins, J. I., 1970, "Probabilities of Breaking Wave Characteristics," Proc. 12th Conf. Coast. Eng., ASCE, Vol. 1, 399-412.
- Dally, W. R., 1987, "Wave Transformation in the Surf Zone," Ph.D. dissertation, Coast. and Ocean. Eng. Dept., U. of Florida (available through University Microfilms, Ann Arbor, Michigan).
- Dally, W.R., 1988, "Random Breaking Waves: A Closed-Form Solution for Planar Beaches," submitted to Coastal Eng.
- Dally, W. R. and Dean, R. G., 1986, "Transformation of Random Waves on Surf Beat," Proc. 20th Conf. Coast. Eng., ASCE, Vol. 1, 109-123.
- Dally, W. R., Dean, R. G., and Dalrymple, R. A., 1985, "Wave Height Variation Across Beaches of Arbitrary Profile", J. Geophys. Res., Vol. 90, No. C6, 11,917-11,927.
- Ebersole, B. A. and Hughes, S. A., 1987, "Duck 85 Photopole Experiment," U.S. Army Corps Engrs., Misc. Pap. CERC-87-18.
- Goda, Y., 1975, "Irregular Wave Deformation in the Surf Zone," Coast. Eng. in Japan, Vol. 18, 13-26.
- Horikawa, K. and Kuo, C. T., 1966, "A Study of Wave Transformation Inside Surf Zone," Proc. 10th Conf. Coastal Eng., ASCE, Vol. 1, 217-233.
- Hotta, S. and Mizuguchi, M., 1980, "A Field Study of Waves in the Surf Zone," Cosstal Engr. Japan, JSCE, Vol. 23, 79-89.

- Hotta, S. and Mizuguchi, M., 1986, "Wave Statistics in the Surf Zone," Abstracts 20th Conf. Coastal Eng., ASCE, 342-343.
- Hunt, J. N., 1979, "Direct Solution of Wave Dispersion Equation," J. Wtrwy., Port, Coast and Ocean Div., ASCE, Vol. 105, No. WW4, 457-459.
- Komar, P. D. and Gaughan, M. K., 1972, "Airy Wave Theory and Breaker Height Prediction," Proc. 13th Conf. Coastal Engr., ASCE, 405-418.
- Kuo, C. T. and Kuo, S. T., 1975, "Effect of Wave Breaking on Statistical Distribution of Wave Heights," Proc. Civil Eng. in the Oceans/3, ASCE, Vol. 2, 1211-1231.
- Longuet-Higgins, M. S., 1983, "On the Joint Distribution of Wave Periods and Amplitudes in a Random Wave Field," Proc. Roy. Soc. Lond., A389, 241-258.
- Mase, H. and Iwagaki, M., 1982, "Wave Height Distributions and Wave Grouping in Surf Zone", Proc. 18th Conf. Coast. Eng., ASCE, Vol. 1, 58-76.
- Moore, B. D., 1982, "Beach Profile Evolution in Response to Changes in Water Level and Wave Height," Master's thesis, Dept. Civil Engr., Univ. of Delaware, Newark.
- Sallenger, A. H. and Holman, R. A., 1985, "Wave Energy Saturation on a Natural Beach of Variable Slope," J. Geophys. Res., Vol. 90, No. C6, 11939-11944.
- Singamsetti, S. R. and Wind, H. G., 1980, "Characteristics of Shoaling and Breaking Periodic Waves Normally Incident to Plane Beaches of Constant Slope," Report M1371, Foegepast Onderzock Waterstaat, The Netherlands.
- Thornton, E. B. and Guza, R. T., July 1983, "Transformation of Wave Height Distribution," J. of Geophys. Res., Vol. 88, No. C10, 5925-5938.
- Thornton, E. B., Wu, C.-S. and Guza, 1984, "Breaking Wave Design Criteria," Proc. 19th Conf. Coastal Eng., ASCE, 31-41.
- Weggel, J. R., 1972, "Maximum Breaker Height," J. of Wtrwys, Hrbrs, Coast. Eng. Div., ASCE, Vol. 98, No. WW4, 529-548.

CHAPTER 61

DESIGN WAVES AND THEIR PROBABILITY DENSITY FUNCTIONS

by

J Rossouw

Abstract

Design wave heights were estimated from measured data using a virtually continuous data set consisting of 8 years of waverider data. Evidence is given which shows that waveriders tend to malfunction during storms. Special care was taken to select independent and identically distributed samples from the data before fitting a number of probability distributions to the selected wave heights. Bootstrap techniques were used to select the models that give the best fit to the data as well as to determine the confidence bands for the predicted design wave heights. It is shown that once the model for the long term distribution of wave height is chosen, relatively narrow confidence bands can be obtained for the most probable value of up to the 100 year return period wave if maximum use is made of the available data. Uncertainty about the selection of the model and the representativeness of the measurements however reduces the usefulness of these confidence bands. A plea is also made in the paper to stop using the concept of a wave with a certain recurrence interval but rather to specify a wave with a given risk of being exceeded within the design life of the structure.

1. The Data Set

Data obtained from the four sites shown in Figure 1 were used to compile a data set which gave a 90 per cent coverage over an 8 year period. These four sites from Cape Town in the West to Port Elizabeth in the East showed remarkable similarity in simultaneously recorded wave heights over distances as much as 700 km apart. An example of simultaneously recorded wave heights at stations 2 and 3 is shown in Figure 2. Similar examples were also shown in Rossouw et al (1982). The reason for the similarity in wave height over such large areas is due to the large size of the weather systems responsible for the higher wave events. A typical example of such a weather system is shown in Figure 3. Large spatial

Senior Lecturer, Dept of Civil Engineering, University of Stellenbosch, Republic of South Africa

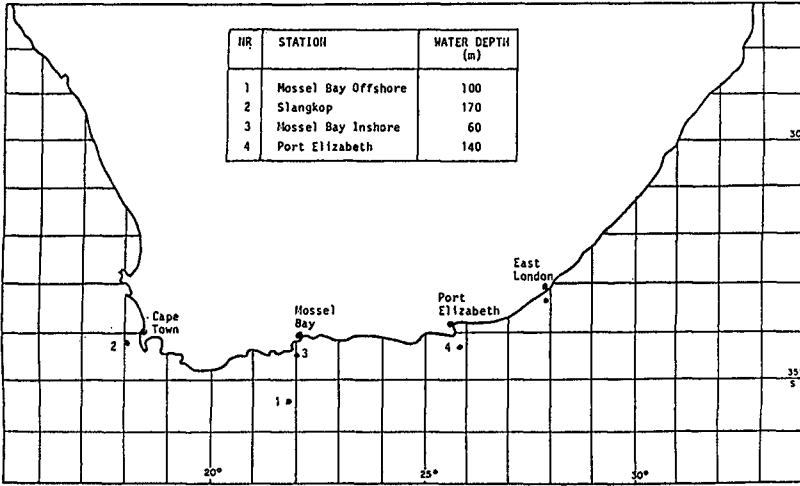


FIGURE 1: RECORDING SITES

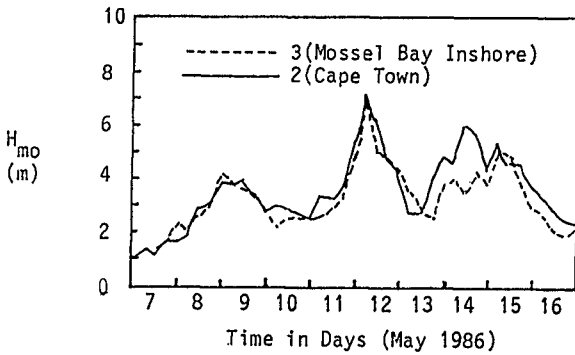


FIGURE 2: COMPARISON IN H_{mo} BETWEEN CAPE TOWN AND MOSSEL BAY

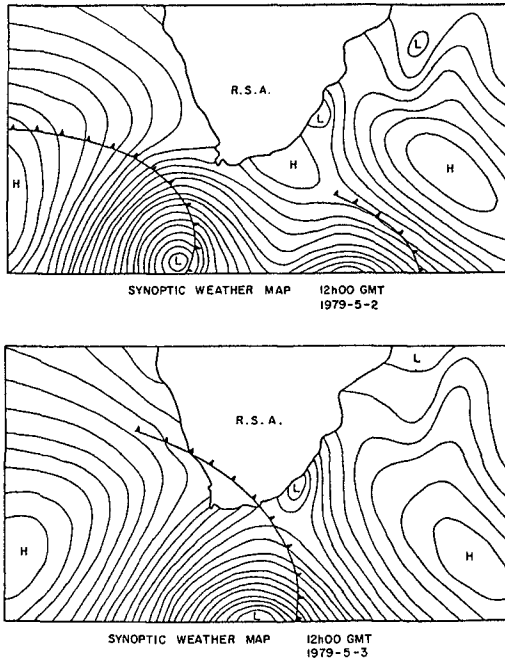


FIGURE 3: PASSAGE OF A COLD FRONT CAUSING HIGH WAVES ALONG THE RSA SOUTHERN COAST (ROSSOUW (1982))

variation in wave heights is not to be expected within such a weather system. These weather systems regularly move from West to East past the South African south coast and generates high waves at the four recording sites shown in Figure 1.

The data set was compiled by using the measurements at site 1 as basis and by filling gaps in this data set with data from stations 2, 3 and 4 in that order of preference. In this process it was noted that the waverider has a tendency to malfunction during the peak of the storms. Examples of this is shown in Figure 4. After filling the gaps a careful study was made of the weather maps during the periods where no records were available from any of the four stations, to ensure that no major storms were omitted from the data set.

2. Sampling from the data set

The basic data set consisted of 10 537 values of H_{mo} recorded at 6 hourly intervals. To make the maximum use of this data set it is important to obtain the maximum number of samples from the data set which will be independant and identically distributed.

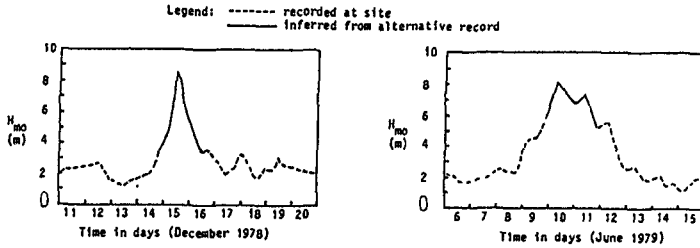


FIGURE 4: TWO EXAMPLES WHERE WAYERIDER MALFUNCTIONED DURING PEAK OF STORM

2.1 Independence of the data

To test for independence between the recorded H_{mo} values, the serie-correlation coefficient were calculated using a lag of 6h, 12h, 18h, etc. The results are summarized in the Table 1 below:

TABLE 1: SERIE-CORRELATION COEFFICIENT AS FUNCTION OF LAG

LAG (HRS)	6	12	18	24	30	36	42	48	54	60	90	120
CORR COEFF	0,85	,71	,58	,46	,35	,27	,21	,16	,13	,093	,026	,008

The 6 hourly H_{mo} values are highly correlated with a serie-correlation coefficient of 0,85. The serie-correlation coefficient gradually reduces with increasing lag and only becomes smaller than 0,1 with a lag of 60 hours. To ensure that independent values of H_{mo} are selected it will therefore be necessary to ensure that not more than one sample is taken in each 60 hour period. When studying the recorded H_{mo} values, difficulty was experienced in selecting an independent event for each 60 hour period. This is illustrated in Figure 5 where the wave heights recorded during the passage of a series of cold fronts at roughly 5 day intervals are shown.

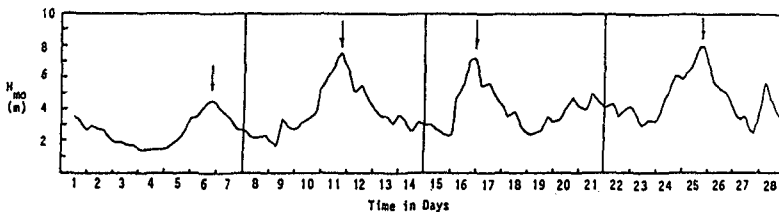


FIGURE 5: SELECTION OF MAXIMUM H_{mo} PER WEEK

It was therefore decided to rather base the selection of independent H_{mo} values on an event basis. The maximum H_{mo} recorded in each week of the recording period was therefore selected as a basis for the fitting of probability distributions and care was taken to ensure that the same event did not feature in successive weeks.

2.2 Identical distribution of the data

In an effort to obtain identically distributed samples, the months which shows similarity in recorded height were grouped together. In the Table 2 below the mean and standard deviation of the maximum weekly H_{mo} values are given.

TABLE 2: MEAN AND STANDARD DEVIATION OF MAX WEEKLY H_{mo} PER MONTH

	MAY	JUNE	JULY	AUG	SEPT	OCT	NOV	DEC	JAN	FEBR	MARCH	APRIL	YEAR
NUMBER OF WEEKS	31	28	29	30	31	28	29	31	32	29	30	31	359
MEAN	4,726	4,864	4,897	4,920	5,087	4,629	4,003	4,019	3,919	3,745	4,090	4,158	4,418
STANDARD DEVIATION	1,630	1,237	0,898	0,995	1,210	1,191	0,825	1,171	0,787	1,031	1,132	0,913	1,198

The mean values for the winter months May to September are fairly constant around 4,9 m whereas the mean for the summer months November to April are also nearly constant around 4,0 m. The standard deviations show no clear pattern with high values in the months where extreme storms occurred (i e May) and low values in the months that were free of such storms (i e January). For the purposes of selecting identically distributed data, the stormy months May to September were grouped together. The 149 weekly maximum values of H_{mo} obtained during these months were therefore used to represent the best estimate of independent and identically distributed samples.

2.3 Influence of sampling method on the predicted design wave heights

The influence of the sampling method on the predicted design wave heights were studied by calculating the most probable value of the 10 and 100 year wave according to the Extreme 1 distribution using the method of moments to fit the data. The sampling method used varied from using all 6 hour records for all months (10 537 records) to only using the maximum H_{mo} recorded in each year (8 records). The results are summarized below:

TABLE 3: EXTREME 1 DISTRIBUTION - COMPARISON OF SAMPLING METHODS

3.1 DATA FROM ALL MONTHS

Sampling method	N	H ₁₀	H ₁₀₀
All data	10 357	9,80	11,63
Max H _{mo} per week	359	9,73	11,88
Max H _{mo} per month	96	9,52	11,68
Max H _{mo} per year	8	9,53	11,88

3.2 DATA FROM STORMY MONTHS

Sampling method	N	H ₁₀	H ₁₀₀
All data	4 463	9,92	11,91
Max H _{mo} per week	149	9,50	11,72
Max H _{mo} per month	40	9,29	11,46
Max H _{mo} per year	8	9,53	11,88

As can be seen from the above table, the predicted design waves are very insensitive to the method of sampling with the most probable 10 year H_{mo} varying from 9,3 m tot 9,9 m and the 100 year H_{mo} from 11,3 m to 11,9 m. Neither the dependence of the data when using all the data, nor the non-identical distribution of the data when the calmer summer months are included, seem to seriously influence the result.

According to Wallis (1988) correlation between data should not alter the expected values but will influence the uncertainty of the estimates as measured by the confidence limits or r m s errors. In the example above however it should be considered fortuitous that such similarity in results were obtained when varying the number of samples from 8 to 10 537.

The fact that inclusion of the data from the calmer summer months in the data set did not seriously influence the result is not surprising due to the small difference in wave height between the summer and winter and the fact that the winter storms will dominate in the total data set.

3. Model selection

The procedure that is most often followed for selecting an appropriate model for the long term distribution of wave height is to fit the data to a number of these models and to select the model which fits the data best according to some goodness of fit criteria. This procedure have led many engineers and researchers to develop a preference for a particular model. In an effort to obtain a better fit of the model to the data, the number of parameters used in the model are often also increased.

The method of model selection described above has been severely criticized by a number of researchers such as Wallis (1988) and Linhart and Zucchini (1986). Authors such as Wallis (1988) have found that if they generate data according to a particular distribution and then use the above procedure of model selection, they frequently select a different distribution than the one used for the generation of the data. He illustrates for instance that by using 4 of the most popular models for the long term distribution of flood intensity and generate data according to one of these distributions, the correct distribution will be chosen less than 50 per cent of the time if 100 data points are used.

An approach to improve model selection is suggested by Linhart and Zucchini (1986). They propose the use of bootstrap sampling [Efron (1982)] whereby the models are not only fitted to the original data set but also to data obtained from resampling the original data set. Here it is important to have independent and identically distributed samples. The process of model selection proposed by them are as follows:

- (i) Select a number of likely models (Weibul, Extreme I, Log-normal, etc).
- (ii) Select a goodness of fit criteria - say Kolmogoroff discrepancy.
- (iii) Select a random sample of size n (with replacement) from the original observations to obtain a bootstrap sample.
- (iv) Calculate the parameters of the models selected in (i) above using the method of maximum likelihood.
- (v) Calculate the maximum discrepancy for each distribution.
- (vi) Repeat steps (iii) to (v) a large number of times (say 100) and keep track of the discrepancies.
- (vii) The model which gives the lowest average discrepancy over the 100 repetitions is chosen as the most appropriate.

This bootstrap sampling technique was applied to the 149 weekly maximum H_{mo} values recorded during the stormy months. Six probability distributions were considered i e the Gamma, Normal, Log-normal, Exponential, Weibul, and Extreme I distributions. The Kolmogoroff discrepancy was used as goodness of fit criteria and the method of maximum likelihood for parameter estimation. The results are summarized in the Table below showing the percentage of the time that the various models were selected, the average discrepancy for each model and the most probable value of the 100 year wave (H_{100}) for each model

TABLE 4: BOOTSTRAP SELECTION OF MODELS

Model	% Selected	Ave discrepancy	H_{100} (m)
Log-normal	54	0,066	10,7
Gamma	28	0,071	9,9
Extreme I	12	0,074	12,3
Normal	6	0,096	8,9

The result of this bootstrap method clearly illustrates the dilemma we face in model selection. The goodness of fit criteria chosen indicate that the first three models listed above all fit the bulk of the data reasonably well. The upper tail of these models do however differ significantly which result in large differences when these distribution are extrapolated to obtain design values. Emphasis on the upper tail of the distribution can be incorporated in the goodness of fit criteria but a sound statistical criteria whereby the degree of emphasis could be decided, is not available.

4. Confidence limits

Two types of uncertainties pertaining to the prediction of the extreme values of significant wave height lend themselves to statistical analysis i e:

- (i) If the long term distribution of wave height is perfectly known such as would be the case if we had an infinitely long and perfect wave record, there is still uncertainty about the largest wave that will occur within the next N years.
- (ii) If we are sure about the model that describes the long term distribution of wave heights, but we have to estimate the parameters of this distribution from a limited wave record, we are uncertain about the values of these parameters.

Other uncertainties which cannot so readily be addressed in statistical terms include:

- (iii) Decisions about the most appropriate model to describe the long term distribution of wave height.
- (iv) Whether the data recorded over a number of years can be considered representative of the long term distribution of the wave height.

Case (i)

This case can best be illustrated by means of an example. Let us assume that we have an infinitely long wave record and the maximum H_{mo} recorded during each year of the record follows an Extreme I distribution as follows:

$$H_{mo}(p) = 8,09 - 0,85 \ln(-\ln p) \dots\dots\dots (1)$$

where $p = 1 - \frac{1}{T}$ with T the return period in years.

The most probable 100 year wave, i e the wave that will occur on average once in a 100 years, is then given for

$$p = 1 - \frac{1}{100} = 0,99 \text{ by}$$

$$H_{mo}(0,99) = H_{mo_{100 \text{ years}}} = 12,0 \text{ m}$$

If the infinitely long record is broken into 100 year intervals, the highest H_{mo} in each 100 years will obviously not be the same but follow a distribution as shown in Figure 6.

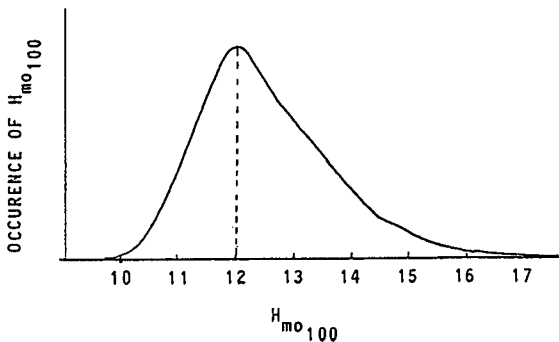


FIGURE 6: DISTRIBUTION OF $H_{mo_{100 \text{ years}}}$

The general expression relating the wave height with a given risk (r) of being exceeded during T years to probability (P) is given by

$$p_T^r = (1-r)^{1/T} \dots\dots\dots (2)$$

If a designer therefore is designing a structure with a design life of say 30 years and he is only willing to take a 10 per cent risk of that wave height being exceeded during the 30 years, he must in our example substitute

$$p_T^r = (1 - 0,1)^{1/30} = 0,9965 \text{ in equation 1 to obtain:}$$

$$(H_{mo}^0)^{0.1} = 8,09 - 0,85 \ln(-\ln ,9965) = 12,9 \text{ m}$$

The reason for labouring this well known concept even to a learned audience such as the attendees of an ICCE, is that the author has found great confusion amongst engineers and designers with respect to concepts such as a wave with a given recurrence interval and its confidence levels. The risk stated above has nothing to do with the confidence bands that are most often quoted. The confidence bands refer to the accuracy with which the wave with a given return period can be estimated if an infinitely long record is not available. With a wave record of only a few years duration there will be considerable uncertainty about the values of 12,0 m and 12,9 m obtained for H_{100} years and $(H_{mo}^0)^{0.1}$ in the example above. This uncertainty is reflected by the confidence bands.

At this point I would also like to make a plea that the concept of a wave with a given return period be scrapped in all specifications for design. I cannot see any sense in specifying that a structure should be designed for a "100 year wave" if the life of the structure will only be 30 years. Even more ridiculous is the specification that an operation that will last for one month should be designed for a "10 year wave". It makes a lot more sense to specify a wave height with a given risk of being exceeded within the 30 year life of the structure or within the one month of the operation. Let us therefore always specify H_h^r when h is the design life of the structure or the duration of an operation and r is the risk of exceeding H during the period h. In this way the designer and his client will know exactly where they stand and not be lulled into a false sense of security in the case where they have for example designed a structure with a 30 year life for the so-called "100 year wave", without realizing that they face a 26% risk of seeing the design wave within the life of the structure.

Case (ii)

The most commonly quoted confidence bands are those where a model for the long term distribution of wave height is assumed and the accuracy with which the parameters of the distribution can be estimated based on a limited record length, is assessed. The accuracy of the estimate of a wave height with a given probability of exceedance is then mainly a function of the record length. The confidence bands narrow with increasing record length and in the case of an infinitely long record length reduces to zero in which case the problem reduces to Case (i) above.

Confidence bands for a number of the more popular distributions have been established either theoretically or by Monte Carlo simulation. Zucchini and Adamson (1984) have also shown that bootstrap sampling techniques can be successfully employed to estimate confidence bands once an appropriate model for the long term distribution of the appropriate variable (waves in our case) have been selected. Efron (1987) further expanded on this method.

For the purpose of establishing confidence bands it is important to use independent and identically distributed samples. For the data used in this paper such samples could include the maximum H_{m0} recorded per year (8 samples), the maximum H_{m0} recorded in each stormy month (40 samples) or the maximum H_{m0} recorded in each week during the stormy months (149 samples). Assuming that these samples belong to an Extreme I distribution, the confidence with which the most probable value of the 100 year H_{m0} , or $(H_{m0})_{100}^{0.83}$, could be estimated was calculated using the bootstrap technique. The results are summarized in Table 5.

It is interesting to note that if the parent distribution is assumed known, and if maximum use is made of the 8 years of available data, the confidence bands for the most probable value of the 100 year H_{m0} becomes relatively narrow i.e. the value at 95% confidence is only 12% higher than the most probable value.

Cases (iii) and (iv)

In the general case where both the distribution and its parameters must be estimated from a limited data base, strict statistical treatment becomes impossible. The large number of distributions that have been proposed for the long term distribution of wave height and the different goodness of fit criteria that can be used in selecting the best fit model, makes it impossible to assess the certainty whereby a given model can be selected. This has been clearly illustrated earlier. If we add to these the uncertainties pertaining to the

representativeness of the samples, the problem becomes even more complicated. Doubts about the representativeness of the sample stems from such factors as the loss of records during storms, long term variations in wave climate, extreme events occurring that belong to a different parent distribution and did not form part of the sample, etc. Most of these uncertainties can be of the same order of magnitude or larger than those associated with the accuracies with which the parameters of a distribution can be estimated for a few years of data.

TABLE 5: 95% CONFIDENCE BANDS AS FUNCTION OF SAMPLING METHOD

Sampling Method	Number of samples	Probability associated with (H_{mo})	$\frac{(H_{mo})_{100}^{0.63} [95\%]}{(\hat{H}_{mo})_{100}^{0.63}}$
Max per year	8	1 - 1/100 = 0,99	1,35
Max per month in stormy months	40	1 - 1/500 = 0,998	1,20
Max per week in stormy months	149	1 - 1/2166 = 0,9995	1,12

5. Summary and Conclusions

1. There is a tendency for waveriders to malfunction near the peak of severe storms. Care should be taken with every data set to ensure that major storms are not truncated or even totally omitted.
2. The general practice of obtaining design wave heights by fitting distributions to data recorded at 3 hr to 6 hr intervals without regard for the independence of the records still seem to be the best approach to use, especially with short data sets. Correlation between the data will however influence the uncertainty of the estimates as measured by confidence limits or rms errors.
3. The selection of an appropriate model for the long term distribution of wave height still remains the most uncertain part in the process of design wave height determination. Bootstrap techniques can be of some help in this process.

4. It should be remembered that the confidence bands associated with extreme events that can be treated statistically only forms part of the overall uncertainty. In all cases the true confidence bands will be wider.
5. It is recommended that the concept of a wave with a given return period be replaced by a wave with a given risk (r) of being exceeded within the design life (h) of a structure (H_T^r). It should be realized that this wave height is only a most probable value and has an associated confidence interval which can be rather wide and is impossible to accurately assess in typical cases of h and r with the short history of wave recording.

6. Acknowledgements

The support of the Division of Earth, Marine and Atmospheric Sciences and Technology of the South African Council for Scientific and Industrial Research in supplying the data and helping with some of the analyses is gratefully acknowledged.

References

- Efron B (1982): The jackknife, the bootstrap and other resampling plans. CBMS-NSF regional conference series in applied mathematics (Philadelphia).
- Efron B (1987): Better bootstrap confidence intervals. Journal of the American Statistical Association. Vol 82, No 397. p 171 - 200.
- Linhart, H and Zucchini, W (1986): Model selection, John Wiley, N.Y.
- Rossouw J, Coetzee L W and Visser C J (1982): A South African Wave Climate Study, Proc 18th Coastal Engineering Conference, Cape Town, ASCE, Vol 1.
- Wallis J R (1988): Catastrophes, computing, and containment: Living with our restless habitat. IBM Research Report. RC 13406 (60023).

CHAPTER 62

REALIZABLE WAVE PARAMETERS IN A LABORATORY FLUME

E.R. Funke¹, E.P.D. Mansard¹ and G. Dai²

ABSTRACT

In order to establish a sound basis for the methodology deployed for the generation of realistic waves under laboratory conditions, a comparison is presented between numerical and physical realizations derived from the Random Phase and the Random Complex Spectrum method for wave synthesis. The comparisons are made in terms of 12 critical wave parameters, including three wave grouping parameters. The results indicate that, for the physical realizations of the limited conditions tested, the two methods give compatible results which fall within the expected band of variability. All physical waves undergo some evolutionary change during propagation which affects predominantly the spectral characteristics. For physical waves produced by the Random Phase method, this change increases the variability of some wave parameters. A sample analysis of one case, applying second order wave and wave generation theory to a numerical simulation, suggests that certain differences between numerical and physical simulations can be explained by non-linear wave theory.

INTRODUCTION

For the laboratory evaluation of designs for coastal and offshore structures, it is common practice to simulate wave trains which satisfy a given variance spectral density. This simulation can be achieved through a variety of synthesis techniques. Among these are two commonly used Fourier techniques which have been referred to as the Random Phase method (RPH) and the Random Complex Spectrum (RCS) method (Mansard & Funke, 1986). The RPH method is a spectrally deterministic technique whereas the RCS method is spectrally non-deterministic.

¹ Hydraulics Laboratory, National Research Council,
Ottawa, Ont., Canada, K1A 0R6

² Guest Scientist from the Nanjing Hydraulic Research Institute,
Nanjing, China

Both the RPH and the RCS methods are based on the inverse Fourier transform of a given target spectral density. In the case of the RPH method, the square root of the given spectral density (i.e. the amplitude spectrum) is paired with a randomly selected phase spectrum. From this a complex spectrum is produced which is then inverse Fourier transformed to produce a time series of the synthesized wave train. Different random selections of the phase spectrum will produce different time series. If any one of these time series is spectrum analyzed, the spectral density so produced will be smooth and match the target spectrum.

In contrast, the Random Complex Spectrum method creates a situation in which the specified distribution of energy in the frequency domain is preserved only within the bounds of probability. It consists of generating a Gaussian distributed white noise complex spectrum which is then filtered by multiplication with the desired amplitude spectrum. The complex product is then inverse Fourier transformed. Individual time series realizations from this synthesis will produce spectra which are not smooth because of the variability of spectral estimates. Only the average of a large number of sample spectra will match the target spectrum.

Each of the above two methods have their own proponents who justify their use in physical models. However, some controversy has arisen around the question of validity of the RPH method (Tucker et al. 1984, Elgar et al 1985, and Medina & Aguilar, 1985). The essence of the criticism is the claim that the RPH method produces insufficient variability of wave parameters and therefore does not represent nature correctly. One wave parameter of concern is wave grouping.

Perhaps the most important comment which can be made at this point, is that the differences are only noticeable for relatively short wave-record lengths. As the length of a synthesized, non-repetitive time series approaches infinity, the two methods are absolutely identical. Evidently, in practice, one cannot make simulations infinitely long. Any meaningful simulation must be carried out over a finite duration of time and that is where one finds the source of the present problem.

The second point which must enter into the consideration is the question of how well numerical simulations represent the conditions which actually prevail in wave flumes for physical model studies. Although, for modern wave generation systems, the numerical synthesis of a wave record forms the input to the control system of the wave machine, the wave train measured in the flume at different locations, may not carry the same statistical characteristics of its progenitor. Linear wave generation has its own way of affecting a simulation. As long as physical model studies are an essential part of our research and design engineering repertoire, this question is relevant.

Mansard and Funke (1986) carried out a numerical study to evaluate the differences in simulations caused by these two

techniques. By varying the random numbers used in the synthesis, 200 different realizations of a 200 second long time series were simulated numerically from a given target spectrum with a peak frequency of 0.55 Hz. At a scale of 1 in 36, this record length corresponds to a full scale sample duration of 20 minutes, which is a typical record length for full scale wave measurements. The resulting series contained approximately 110 waves and were subjected to several frequency and time domain analyses. Twelve different parameters were computed and then assembled into independent wave parameter lists for subsequent statistical analysis.

The results of the study showed that the differences between the RPH method and the RCS method, in terms of the selected parameters, are small, even for these relatively short wave records. This conclusion was based on a statistical analysis of average, standard deviation as well as maxima and minima of the twelve parameters, computed for 200 realizations of each case.

When waves are produced in a laboratory flume for simulation purposes, it is common practice to adjust the wave generator stroke gain until the waves produced have the specified significant wave height; a condition generally specified by the client. However, waves synthesized by the RCS method must be expected to exhibit variability of variance from record to record, and as a result the significant wave height will also show variability. By adjusting the wave machine stroke gain, one does intervene in the natural process. For the study by Mansard and Funke (1986), each record was rescaled so as to fix the variance of each wave record to that specified in accordance with laboratory practice. On the other hand, in the study presented here, the simulations with the RCS method are performed in two ways, once with rescaling and once without rescaling.

The 1986 study was restricted to only 12 wave parameters which were considered important at that time. This investigation, however, looked at a total of 27 wave parameters, 12 of which are included in this publication. The remainder are to be published in a separate report later. The study presented here complements the 1986 study and, furthermore, adds insight into the question of physical realizability.

EXPERIMENTAL SET-UP

The experimental set-up is shown in Figure 1. Experiments were carried out in a flume of dimensions 1.2 x 1.2 x 67 m. Waves were generated in a depth of 0.7 m and were monitored at a distance of 8.7 m and 25.3 m from the paddle. An effective dissipation of the incident energy was ensured by a mildly sloping permeable gravel beach (1:25 slope) designed to minimize the reflection of long wave components. Previous evaluation of a beach of this type indicated that its average reflection coefficient can be expected to be below 5% for the frequency band from 0.3 Hz to 1.3 Hz.

The wave generator was operated in the piston mode. Much care was used in its calibration to ensure that the wave paddle excursions corresponded to the theoretical values. All wave generation was carried out with the application of linear wave generation theory.

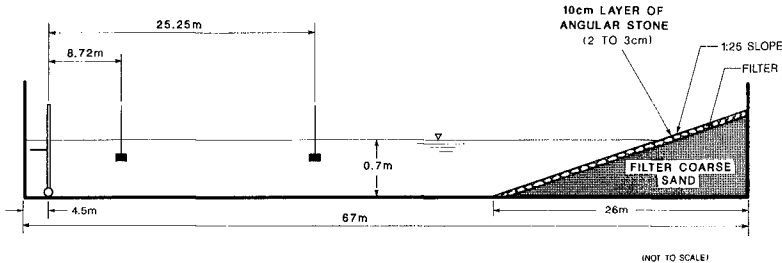


FIGURE 1

SKETCH OF THE EXPERIMENTAL SET-UP

Repeatability tests were carried out on several specimen wave records. The following table gives repeatability values for four different parameters.

TABLE I

Repeatability Results over 22 Tests at $x = 8.7$ m		
	% AVERAGE ABSOLUTE DIFFERENCE	% MAXIMUM DIFFERENCE
H_{m0}	0.64	1.3
$H_{1/3}$	1.00	2.6
H_{max}	1.48	3.1
GF	0.83	3.1

TEST CONDITIONS

The investigation described here was limited to a JONSWAP target spectral density with a peak frequency $f_p = 0.55$ Hz, a peak enhancement factor $\gamma = 3.3$, and a significant wave height $H_{m0} = 0.15$ m.

From the target spectral density, a total of 600 time series were generated using both the RPH and the RCS methods of wave synthesis, i.e.

- 200 time series using the Random Phase method,
- 200 time series using the Random Complex Spectrum method, and
- 200 time series using the Random Complex Spectrum method, with the record variance rescaled to the target value of the variance.

Measurements for physical model tests were initiated after the wave trains had stabilized in the tank. This involved generally a waiting period of 3 minutes after wave generation commenced. Following each test, the tank was allowed to

settle before a new test was started. The measurement duration was fixed to be identical to the recycling period of the synthesized wave trains.

ANALYSIS

The measured water surface elevations for each of the 600 tests were subjected to several conventional and non-conventional analyses. Spectral density analysis was used to demonstrate that the target spectra were achieved with adequate fidelity. Figure 2 gives eight samples of these, two pairs for the RPH and two for the RCS methods. The spectra shown correspond to measurements taken at 8.7 m and 25.3 m.

Twenty-seven different spectral and time domain wave parameters were computed. Of these twelve are presented here. These are:

- f_p the peak frequency as determined from the frequency at which the spectral density is a maximum,
- f_{pD} the peak frequency as determined by the Delft method (IAHR List of Sea State Parameters), :

$$f_{pD} = \frac{\int_{f_1}^{f_2} f \cdot S_{\eta}(f) df}{\int_{f_1}^{f_2} S_{\eta}(f) \cdot df}$$

where f_1 is the first and f_2 is the last crossing of a threshold that is 80% of the spectral peak value.

- $H_{1/3,d}$ the significant wave height by zero down-crossing analysis,

$H_{max}/H_{1/3}$ the ratio of the maximum and the significant wave height as computed from zero down-crossing analysis,

- $\bar{s}_{z,d}$ the average steepness of all waves as computed from zero down-crossing analysis. This is given as:

$$\bar{s}_{z,d} = (1/N) \text{SUM}[H_i/L_i] \text{ for } i=1,N$$

where H_i and L_i are the i th down-crossing wave height and wave period respectively.

- \bar{s}_c' the average crest front steepness as computed from zero down-crossing analysis (Kjeldsen & Myrhaug 1979). This is defined as:

$$\bar{s}_c' = (1/N) \text{SUM}[a_{c,i}/L'_i]$$

where $a_{c,i}$ and L'_i are the i th wave crest and wave crest front length respectively.

- $\bar{\mu}_H$ the average horizontal asymmetry as computed by Kjeldsen & Myrhaug (1979),

$$\bar{\mu}_H = (1/N) \text{SUM}[a_{c,i}/H_i] \text{ for } i=1,N$$

where $a_{c,i}$ and H_i are the i th wave crest and wave height respectively.

- $\bar{\mu}_v$ the average vertical asymmetry. This parameter differs from that given by Kjeldsen & Myrhaug (1979) and is based on a definition suggested by Goda (personal communication), i.e.

$$\bar{\mu}_v = (1/N) \text{SUM}[L_i'/(L_i'+L_i'')] \text{ for } i=1,N$$

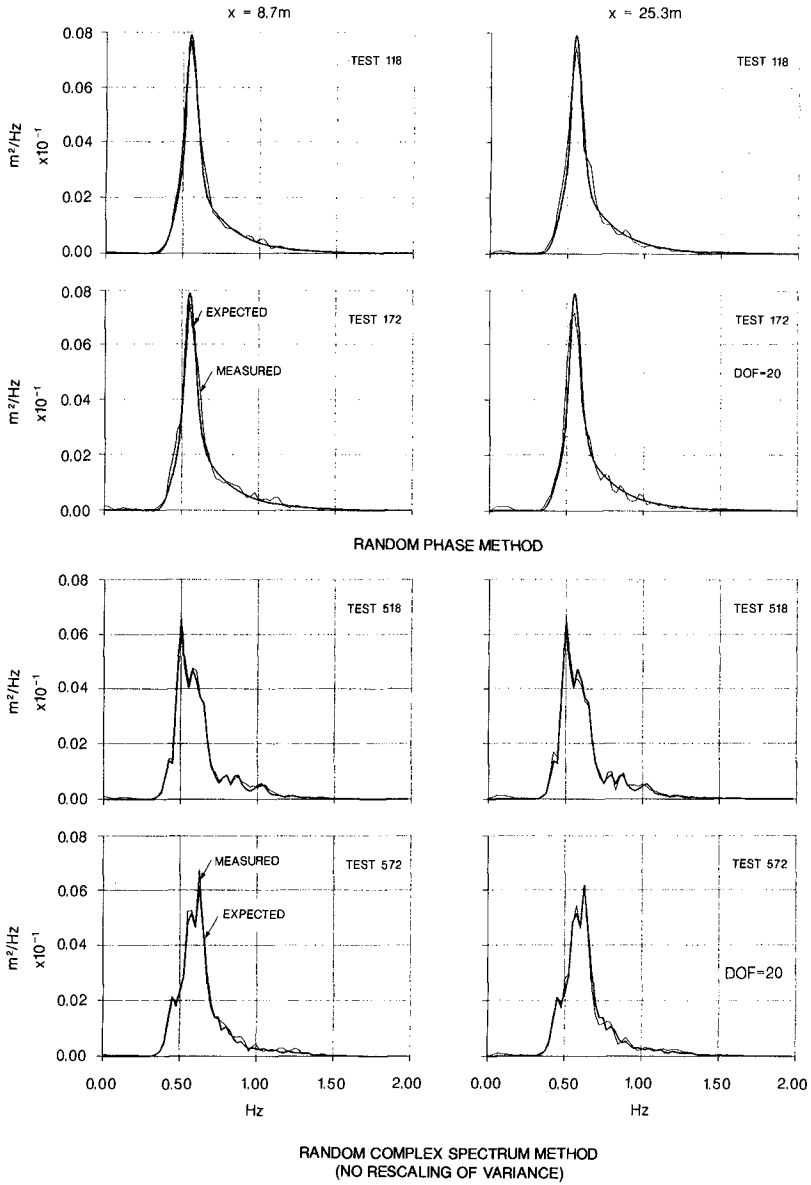


FIGURE 2
REALIZATIONS OF SPECTRAL DENSITIES IN A LABORATORY FLUME
($H_{m0}=0.15\text{m}$ $f_p=0.55\text{Hz}$ $\gamma=3.3$)

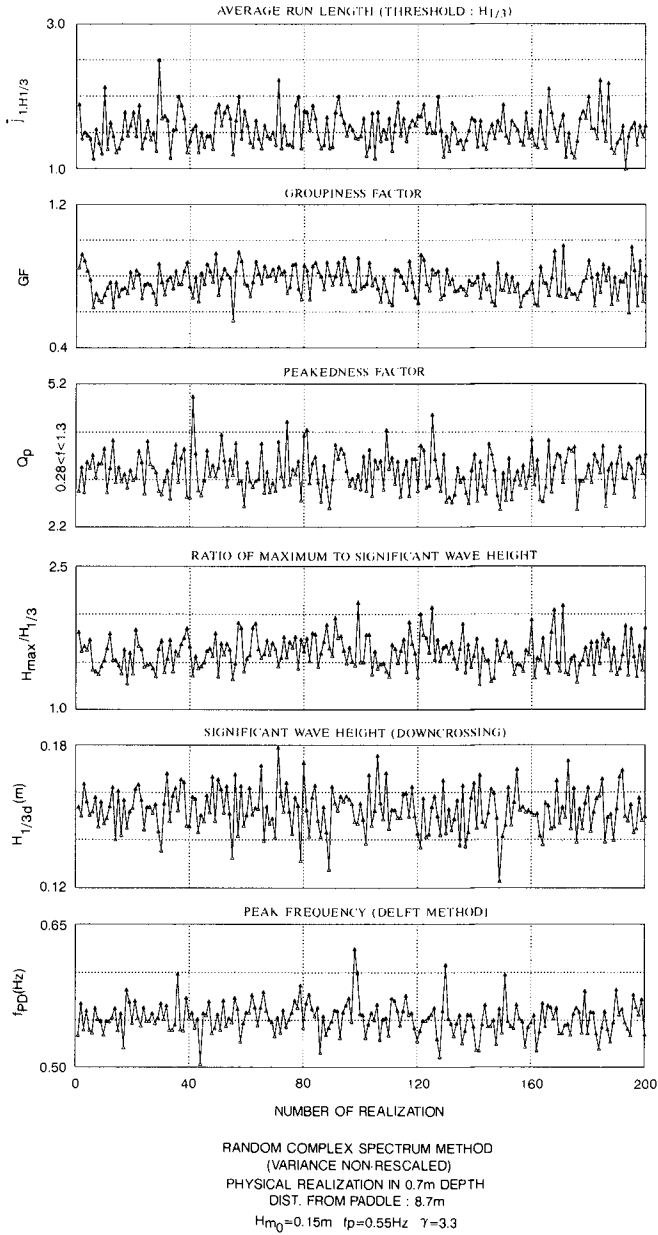


FIGURE 3
 STATISTICAL VARIABILITY OF WAVE PARAMETERS

where L_i' and L_i'' are the i th crest front and crest rear wave lengths respectively. However, as Kjeldsen has pointed out (personal communication), this parameter can be expected to assume the value 0.5 under normal laboratory conditions and in the absence of wind and current.

Q_p the Goda peakedness factor (Goda, 1985). This is given as:

$$Q_p = (2/m_0^2) \int_{f_2}^{f_1} f \cdot S_{\eta}^2(f) \cdot df$$

where $f_1 = 0.28$ and $f_2 = 1.38$ Hz.

GF the SIWEH groupiness factor (Funke & Mansard, 1979). This is given as:

$$GF = \sqrt{m_{0,E} / m_0}$$

where $m_{0,E}$ is the zeroth moment of the groupiness spectrum.

$\bar{J}_{1,H}$ the average run length of waves greater than the average wave height \bar{H}_0 , as computed from zero down-crossing analysis (Goda, 1976), and

$\bar{J}_{1,H_{1/3}}$ the average run length of waves greater than the significant wave height $H_{1/3,d}$, as computed from zero down-crossing analysis (Goda, 1976).

The chosen wave parameter values from each wave record were assembled in ordered lists, some of which are illustrated graphically as time series in Figure 3 for the case of a physical realization of a non-rescaled, RCS method synthesized waves as measured 8.7 m from the wave board.

The lists of wave parameters were then subjected to statistical analysis to yield the average, the standard deviation, the maximum and the minimum values.

RESULTS

In order to facilitate comparison, the results of the analysis are presented in graphical form in Figures 4a, 4b and 4c. These are given in terms of the mean, the extrema, as well as the mean + and - one standard deviation. For each parameter the results are placed in three separate groups, i.e.

- results from the RPH method of synthesis,
- results from the RCS method of synthesis but rescaled to force the target variance on each wave record, and
- results from the RCS method of synthesis but without rescaling.

Then, for each group, results are again shown separately for:

- numerical synthesis only,
- a physical realization of the numerical synthesis as measured at 8.7 m from the wave board, and
- a physical realization of the numerical synthesis as measured at 25.3 m from the wave board.

DISCUSSION OF RESULTS

The main conclusions of the study are as follows:

- As could be expected the numerical realizations of the RPH method have no variability for the parameter f_p , and very little variability for f_{pd} and Q_p . In the case of the last two parameters, the small amount of variability must be attributed to computational noise.
- When a wave record synthesized by the RPH method is converted to a physical wave in a wave flume, then the variability of the f_p , f_{pd} and Q_p parameters increases, but will not equal the variability achieved by the RCS method.

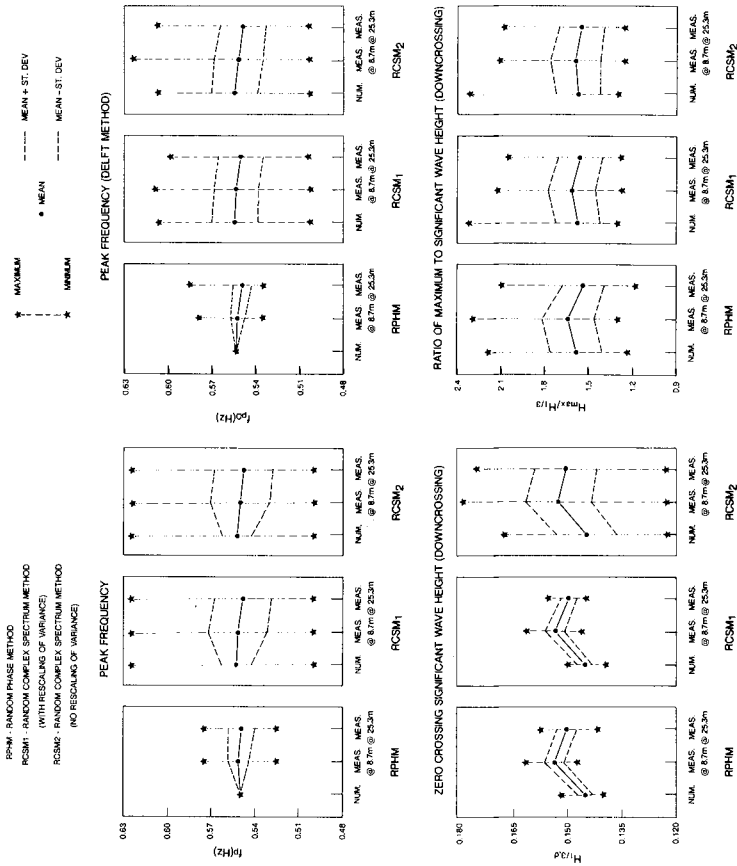


FIGURE 4a. STATISTICAL VARIABILITY OF WAVE PARAMETERS

- The mean value and the variability of the parameter $H_{1/3,d}$, as derived by the RPH and the rescaled RCS methods, are almost identical.
- As could be expected, the variability of $H_{1/3,d}$ is significantly larger for the non-scaled RCS than for the rescaled RCS method.
- The following parameters exhibit little differences between the RPH and the RCS method:
 - o $H_{max}/H_{1/3}$ the ratio of the maximum and the significant wave height,
 - o μ_H the average horizontal asymmetry,
 - o μ_V the average vertical asymmetry,
 - o GF the SIWEH groupiness factor,

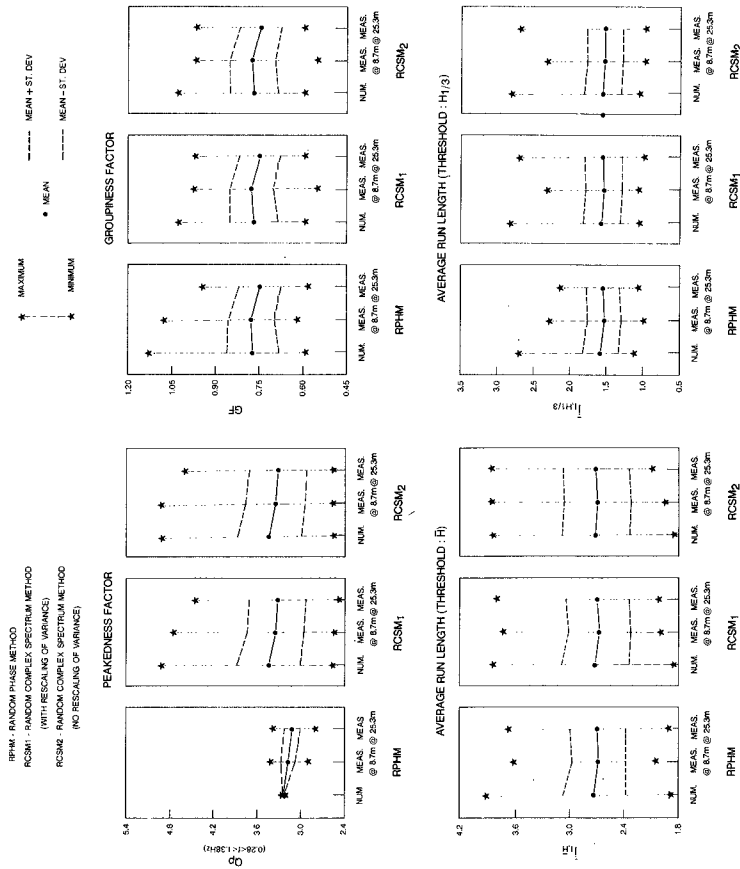


FIGURE 4D. STATISTICAL VARIABILITY OF WAVE PARAMETERS

- $\bar{J}_{1,\bar{H}}$ the run length of waves higher than the average wave height, and
- $\bar{J}_{1,H_{1/3}}$ the run length of waves higher than the significant wave height.

This favourable comparison with regard to wave grouping diminishes one of the concerns expressed by Tucker et al. (1984).

- the conversion of a numerical simulation into a physical realization has a remarkable impact on several parameters whose definition depend on the wave crest. From this it can be concluded that, for the conditions which prevailed for the test under study, the crest

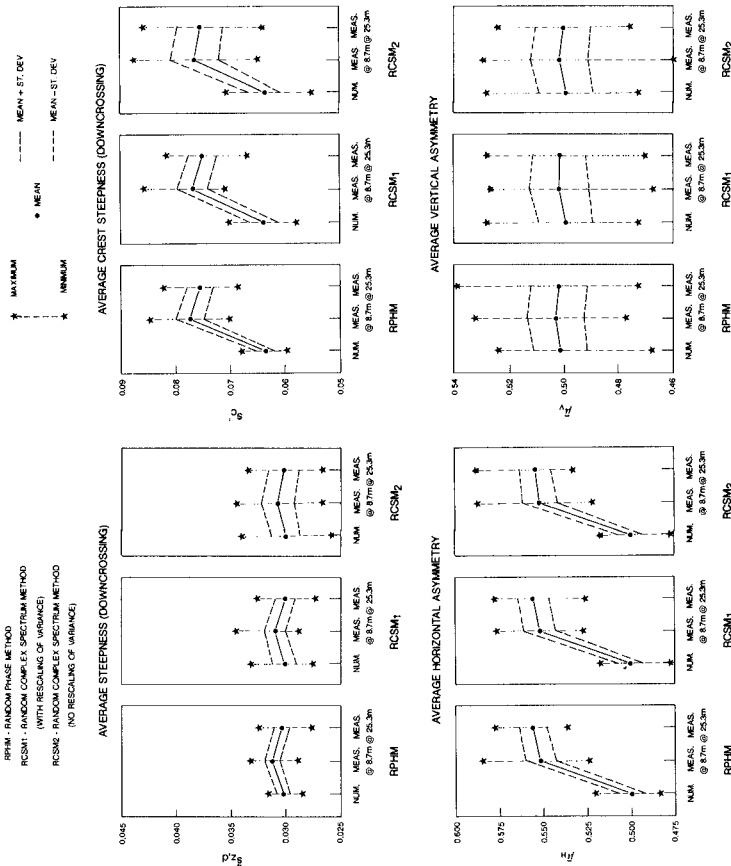


FIGURE 4c. STATISTICAL VARIABILITY OF WAVE PARAMETERS

heights in physical simulations are greater than those obtained by numerical simulations. These parameters are:

- $H_{1/3,d}$ the significant wave height by zero crossing analysis,
 - s'_c the crest front steepness, and
 - $\overline{\mu}_H$ the average horizontal asymmetry.
- There is no significant difference in the average vertical asymmetry $\overline{\mu}_v$ between numerical and physical simulations in the absence of wind and currents. In other words, the physical waves are, on the average, symmetrical.
 - In general, the differences between the RPH and the RCS methods are small for physical simulation. In fact, it can be seen that there is almost as large a difference between two records selected at random from one method than there is between records selected from the two different methods.
 - There is no apparent relationship between the wave run length parameter and the SIWEH groupiness factor. Both evidently measure different aspects of the wave grouping phenomenon. This is apparent from Figure 3.

To further investigate the differences between numerical and physical simulations, an attempt was made to reconstruct one wave train through the application of second order effects. As stated above, the conversion of numerical simulations to physical realizations was undertaken by means of linear wave generation theory. By applying second order wave and wave generation theory to one of the numerical simulations, it was possible to calculate the second order wave components which were naturally locked to the wave and those which were inadvertently produced because of the first order approximation. These were predicted for the one case at the two probe positions (Barthel et al 1983, Sand & Mansard, 1986).

A comparison is made in Figure 5 between this second order reconstruction and the corresponding wave trains measured. From this it is apparent that most of the differences between numerical and physical simulations are predictable. This result also suggests that numerical simulations for wave conditions in the coastal zone should be carried out with the inclusion of second order effects.

REFERENCES

BARTHEL, V., E.P.D. MANSARD, S.E. SAND and F.C. VIS, "Group Bounded Long Waves in Physical Models". Ocean Engineering, vol 10, no 4. 1983.

ELGAR, S., R.T. GUZA and R.J. SEYMOUR, "Wave Group Statistics from Numerical Simulations of a Random Sea", Applied Ocean Research, vol 7, no 2, 1985.

	$\bar{s}_{z,d}$	\bar{s}_c	\bar{P}_H
MEASURED	.03	.09	.56
SYNTHESIZED (1st-ORDER)	.03	.06	.50
SYNTHESIZED (2nd-ORDER)	.03	.08	.54

	$\bar{s}_{z,d}$	\bar{s}_c	\bar{P}_H
MEASURED	.03	.08	.56
SYNTHESIZED (1st-ORDER)	.03	.07	.50
SYNTHESIZED (2nd-ORDER)	.03	.08	.54

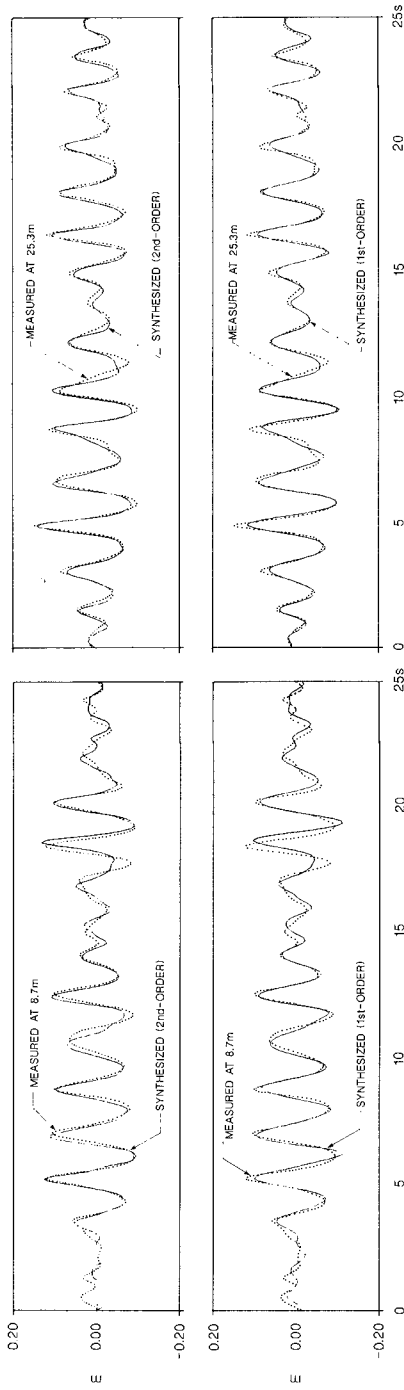


FIGURE 5
COMPARISON BETWEEN MEASURED AND SYNTHESIZED WAVE PROFILES

FUNKE, E.R. and E.P.D. MANSARD, "On the Synthesis of Realistic Sea States in a Laboratory Flume", NRCC Hydraulics Laboratory Report LTR-HY-66, Aug. 1979.

Goda, Y., "On Wave Groups", BOSS Conference, Trondheim, 1976.

GODA, Y., "Random Seas and Design of Maritime Structures", Book, University of Tokyo Press, 1985.

IAHR, "List of Sea State Parameters", Joint Publication by the IAHR Section on Maritime Hydraulics and PIANC, Supplement to Bulletin no 52, General Secretariat of PIANC, Brussels, Belgium, 1986.

KJELDSSEN, S.P. and D. MYRHAUG, "Formation of Wave Groups and Distributions of Parameters for Wave Asymmetry", VHL Report no STF 60 A79044, River and Harbour Laboratory, Trondheim, Norway, 1979.

MANSARD, E.P.D. and E.R. FUNKE, "On the Statistical Variability of Wave Parameters", National Research Council Canada, Hydraulics Laboratory Technical Report TR-HY-015, NRC no 26604, September 1986.

MEDINA, J.R., J. AGUILAR, "Comments on Numerical Simulation of a Random Sea: A Common Error and its Effect upon Wave Group Statistics", Letters to the Editor, Applied Ocean Research, vol. 7, no 2, 1985.

SAND, S.E. and E.P.D. MANSARD, "Description and Reproduction of Higher Harmonic Waves", National Research Council Canada, Hydraulics Laboratory Technical Report TR-HY-012, NRC no 25339, January 1986.

TUCKER, M.J., P.G. CHALLENGER and D.J.T. CARTER, "Numerical Simulation of a Random Sea: A Common Error and its Effect Upon Wave Group Statistics", Applied Ocean Research, vol. 6, no 2, 1984, pp. 118-122

CHAPTER 63

Spectral Wave Attenuation by Bottom Friction: Experiments

Ole Secher Madsen¹ and Moises Michel Rosengaus²

ABSTRACT

This paper presents a summary of carefully conducted laboratory experiments on sediment response and resulting wave attenuation for waves, periodic as well as simulating a wave spectrum, propagating over an 18-m-long bottom section covered by a 10-cm-thick layer of 0.2-mm-diameter quartz sand. The results for wave-generated bedform geometry as well as the equivalent Nikuradse roughness are obtained. The results show that the sediment response to the agitation of a wave spectrum may be approximately described by the sediment response to an equivalent periodic wave having the same root-mean-square near-bottom orbital velocity and excursion amplitude as the spectral wave. This equivalent wave, defined by the near-bottom characteristics of the spectral wave, is identical to that derived by Madsen et al. (1988) in the context of dissipation within the wave boundary layer. Although limited by the range of experimental conditions achieved in this study, the results obtained here and in the companion paper suggest a predictive methodology for the evaluation of spectral wave attenuation from knowledge of sediment and wave characteristics.

INTRODUCTION

As waves propagate into waters of finite depth the waves respond to the presence of the bottom, e.g., through shoaling, depth refraction, and energy dissipation, while the bottom, consisting of movable sediment, responds to the presence of waves by exhibiting bedforms. In the present context of wave attenuation, the wave-sediment interaction is of crucial importance since the bottom bedforms and sediment transport caused by the wave motion itself, in turn, determine the bottom roughness and hence the rate of energy dissipation within the bottom boundary layer.

In a companion paper (Madsen et al., 1988) an approximate theory for the turbulent boundary layer flow over a rough bottom and the associated dissipation of energy has been

1 Professor of Civil Engineering, R. M. Parsons Laboratory, MIT, Cambridge, MA 02139, USA

2 Hydraulics Specialist, Instituto Mexicano de Tecnologia del Agua, Jiuetpec, Morelos, Mexico (formerly Graduate student, R. M. Parsons Laboratory)

developed for a wave motion specified by its directional frequency spectrum. While overcoming some of the problems of currently available theories for the evaluation of spectral dissipation by bottom friction, the theory by Madsen et al. (1988) assumes the equivalent Nikuradse roughness of the bottom, k_b , to be known a priori. From the preceding discussion of the response of a movable bed to the agitation by waves it is evident that the equivalent bottom roughness of a movable bed is a function of wave-sediment interaction, i.e., it is a dependent variable.

Based on the limited data of Carstens et al. (1969) and Stefanick's (1979) comprehensive review of experimental data on the geometry of wave-generated bedforms Grant and Madsen (1982) proposed a predictive expression for k_b in terms of sediment and wave characteristics. A major shortcoming of the Grant-Madsen relationship is that it, as others, e.g., Lofquist (1986), Vongvisessomjai (1987) is derived from experimental data obtained exclusively for monochromatic waves. To apply any of the existing relationships for movable bed roughness, in conjunction with a theory for spectral dissipation, to predict spectral wave attenuation by bottom friction therefore requires the determination of the characteristics of a periodic wave which is equivalent to the spectral wave in the context of wave-sediment interaction. To demonstrate that such an equivalent periodic wave does exist and to determine its characteristics are the objectives of the experimental study summarized in this paper.

The philosophy behind the experimental methodology and procedures used in the present study is to measure the attenuation of water waves (periodic as well as simulated spectral waves) propagating over a long section of movable bed and from the measured attenuation of each incident wave component backfigure the appropriate value of the wave friction factor for each incident wave component using the theoretical model for spectral wave attenuation developed by Madsen et al. (1988). From knowledge of the wave friction factor and the incident wave condition, which according to Madsen et al. (1988) is represented by a periodic wave having the same root-mean-square near-bottom orbital velocity and excursion amplitude as the simulated wave spectrum, the Grant and Madsen (1986) relationship between periodic wave characteristics, equivalent bottom roughness, and wave friction factor is used--in reverse--to back out a value of the equivalent bottom roughness, k_b . The geometry of bottom bedforms generated by the waves, whose attenuation was determined, is also determined and related to the wave and sediment characteristics as well as to the measured values of the equivalent bottom roughness, k_b , in order to arrive at a predictive relationship for the equivalent bottom roughness of a movable bed valid for spectral waves.

EXPERIMENTAL SET-UP

Laboratory experiments were performed in a 0.75-m-wide, 0.90-m-deep, 30-m-long wave flume in the R. M. Parsons Laboratory. This wave flume is equipped with a programmable piston-type wave maker and has a 1-on-10 sloping ab-

sorber beach, which in the present experiment was covered by 7.5-cm-thick horsehair mats to further decrease reflections. At the wave maker a trapezoidal wooden ramp provided a smooth transition to a level 10 cm above the flume bottom. The region between the ramp--approximately 3 m from the wave maker--to the start of the absorber beach--approximately 19 m from the wave maker--was covered by a 10-cm-thick layer of very uniform 0.2-mm-diameter Ottawa quartz sand.

The wave maker was programmed to simulate the generation of incident periodic waves, wave groups consisting of two frequency components, and wave spectra. Two different spectral simulation methods were used: one simulating the spectrum as equally spaced frequency components, the other representing the spectrum by different frequency components of equal energy. Although of no fundamental importance to the study it is mentioned for completeness that the spectral shape simulated in our experiments was that of a Neuman spectrum. In the majority of the experiments the water depth above the movable bed test section was 0.60 m.

In order to mobilize the bed material it was necessary to generate waves of large amplitudes and wave lengths. Our standard wave condition corresponded to a 6-cm-amplitude, 2.65-sec-period wave for which $h/L = 0.1$ in the 0.6-m-deep section. Wave group experiments were conducted with frequencies centered around the 2.65-sec-period while this period was taken as the peak period in spectral simulations. Due to limited wave-making capability it was only possible to generate multi-component wave conditions with an energy content equal to half of that of the standard periodic wave. The incident and reflected wave components were determined from surface profile measurements obtained from two three-gauge arrays (Goda and Suzuki, 1976) located 3 m and 18 m from the wave maker.

Bottom bedform geometry was determined photographically by taking pictures of 1-m sections of the bed profile at four stations along the test section. These pictures, including horizontal and vertical scales, were then projected onto a digitizing tablet and analyzed. Using a vertically mounted laser to trace the bottom profile at different distances from the flume sidewalls it was shown that the trace along the sidewalls accurately represented the bedform geometry.

EXPERIMENTAL PROCEDURE

Given the philosophy behind the experiments as outlined in the Introduction the procedure to be followed is in principle quite simple. From the analysis of Madsen et al. (1988) we may write the energy conservation principle for each wave component when only bottom dissipation is considered

$$c_{gn}\rho g a_n \left[\frac{\partial a_n}{\partial x} \right]_{bf} = -E_{d,n} = -\frac{1}{4}\rho f_{wr} u_{br} u_{bn}^2 \quad (1)$$

where, for a finite number of wave frequency components

$$u_{br} = \sqrt{\sum_n u_{bn}^2}$$

$$A_{br} = \sqrt{\sum_n (u_{bn}/\omega_n)^2} = u_{br}/\omega_r \quad (2)$$

defines the representative periodic wave, and

$$u_{bn} = \frac{a_n \omega_n}{\sinh k_n h} \quad (3)$$

Thus, for a single wave component--whether it is alone or one of two or more--we have from Eqs. (1) through (3)

$$\left[\frac{\partial a_n}{\partial x} \right]_{bf} = -f_{wr} \frac{u_{br}}{4g c_{gn}} \left[\frac{\omega_n}{\sinh k_n h} \right]^2 a_n \quad (4)$$

In principle the experimental determination of a_n at two stations, Δx apart, suffices to determine a value of f_{wr} from Eq. (4). In practice, however, life is unfortunately not that simple.

First of all the experimental determination of Δa_n involves the "small" difference between two "large" quantities. As an example we may take the standard periodic wave ($a_n = 6$ cm, $T_n = 2\pi/\omega_n = 2.65$ sec, $h = 0.60$ m) and a friction factor of $f_{wr} = 0.2$ to obtain a change in amplitude of $\Delta a \approx 7$ mm over the 15-m-long test section. While this value of Δa is well above the accuracy with which the individual amplitudes is determined experimentally--estimated to be of the order 0.5 mm--it should be recalled that component amplitudes of the order 1 to 2 cm are used in spectral simulations. Thus, we are in some cases attempting to measure differences of the order a few mm, i.e., approaching the magnitude of uncertainty of each measurement used to determine the difference. For this reason alone it is essential that the experiments be conducted with great thoroughness and repeated several times in order to minimize the effect of experimental errors.

However, other effects in addition to those directly related to measurement accuracy play a role in these experiments. Owing to the requirement of long waves of substantial amplitude--to set the bottom sediment in motion--it can be expected that nonlinear effects come into play. To illustrate this, assume the change of amplitude, Δa_n , to have been determined experimentally over a distance Δx . Formally, we may then write

$$\frac{\partial a_n}{\partial x} \approx \frac{\Delta a_n}{\Delta x} = m = m_{nl} + m_{sw} + \left[\frac{\partial a_n}{\partial x} \right]_{bf} \quad (5)$$

in which m_{nl} denotes amplitude changes associated with nonlinearity, m_{sw} the changes associated with dissipation along the side walls, and $(\partial a_n / \partial x)_{bf}$ is the quantity expressing the contribution of bottom friction, i.e., the quantity we are looking for. A priori we cannot neglect the unwanted contributions, m_{nl} and m_{sw} , in particular when the overall requirement of accuracy is kept in mind.

To evaluate the magnitude of the terms $m_{nl} + m_{sw}$ in Eq. (5) preliminary experiments were conducted for conditions corresponding to a flat bed. The measured amplitude change in these preliminary experiments (denoted by subscript p)

$$\left[\frac{\Delta a_n}{\Delta x} \right]_p = m_p \simeq m_{nl} + m_{sw} + m_{fb} \quad (6)$$

were taken to represent nonlinear and sidewall effects also in the movable bed runs. The bottom friction effect, m_{fb} in Eq. (6), was calculated theoretically using the sediment grain size as the bottom roughness.

For experiments with simple periodic waves the nonlinear effects were eliminated by correcting the wave maker motion as suggested by Madsen (1971). For all other experiments a series of about five preliminary runs were performed to determine the nonlinear and sidewall contributions using Eq. (6). Following the preliminary runs the wave condition was maintained in the flume for sufficiently long time to ensure the bedforms on the bottom to be fully developed (in some cases this took several hours). Several wave measurements were then performed corresponding to fully developed bed conditions with bottom bedform geometry determined between individual wave measurements (to ensure that the bed indeed was fully developed). Combining the preliminary and the fully developed wave measurements, as outlined above, produced experimental results for the isolated effect of wave attenuation caused by bottom friction, which in turn were used in Eq. (5) to obtain friction factors.

SUMMARY OF RESULTS

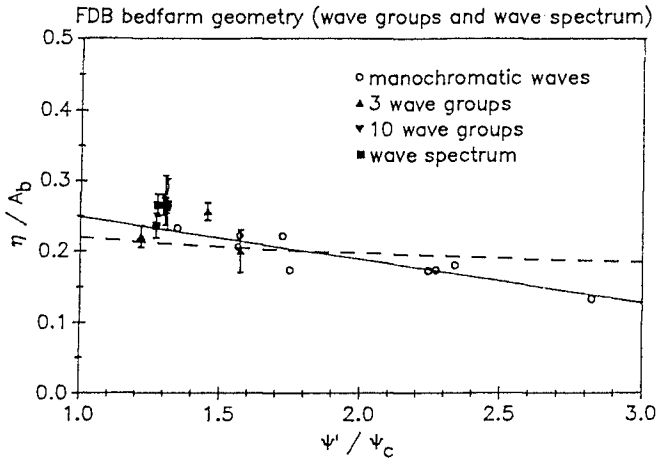
Since the present results are preliminary in nature due to the limited range of experimental parameters covered, only a summary of the conclusions most significant to application will be presented here. Further details may be obtained from Rosengaus (1987) and in subsequent publications. By comparison of bedform geometry generated by simple periodic and multi-component (spectral) waves it is found that the representative wave defined by Eq. (2) may be used to describe the response of a movable bed to wave agitation.

This conclusion is supported by the results presented in Figure 1a and b which shows measured ripple height, η , normalized by the excursion amplitude of the representative wave, defined by Eq. (2), and ripple steepness (η/λ), respectively, as functions of the sediment mobility parameter ψ'/ψ_c where

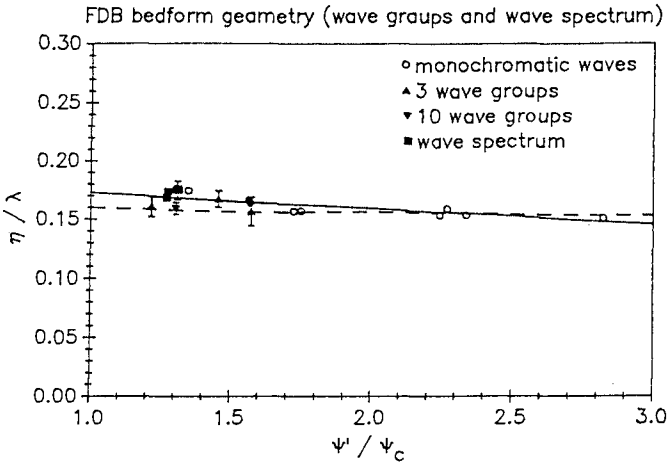
$$\psi' = \frac{\tau_b'}{(s-1)\rho g d} \quad (7)$$

is the Shields parameter based on grain size roughness evaluated for the representative wave and ψ_c is the critical value for initiation of sediment motion (see Madsen and Grant, 1976, for details).

For comparison the empirical relationships derived by Stefanick (1979) and used by Grant and Madsen (1982) are



a: Fully developed bedform height for non-monochromatic waves



b: Fully developed bedform steepness for non-monochromatic waves

Figure 1: Comparison of Bedform Geometry.

shown as dashed lines while new relationships derived from this investigation

$$\frac{\eta}{A_{br}} = 0.31 - 0.06(\psi'/\psi_c)$$

$$\frac{\eta}{\lambda} = 0.19 - 0.014(\psi'/\psi_c) \quad (8)$$

are shown as solid lines. As is evident from the results presented in figures 1a and b the agreement between bedform geometry generated by monochromatic and multi-component waves (groups and spectra) is excellent, but tested only within a range of (ψ'/ψ_c) slightly above unity. Use of Eqs. (8) should therefore be limited to values of (ψ'/ψ_c) less than about 3 or, in the terminology of Grant and Madsen (1982), for conditions corresponding to the "equilibrium range." The relatively small difference between the present results for ripple geometry and the predictive relationships by Grant and Madsen (1982) tentatively suggests the use of their relationship for conditions beyond the equilibrium range.

A slightly modified version of the Grant and Madsen (1982) relationship for the equivalent bottom roughness of a movable bed, k_b , as a function of bedform geometry can be used also for multi-component (spectral) waves when these are represented by the periodic wave defined by Eq. (2), i.e.

$$\frac{k_b}{A_{br}} = K \frac{\eta}{A_{br}} \frac{\eta}{\lambda} \quad (9)$$

is found to apply within the equilibrium range with the constant K, originally given as 28 by Grant and Madsen (1982), being replaced by K = 20, when using their empirical relationships for ripple geometry, and by K = 23, when the relationships given by Eq. (8) are used.

Table 1
Spectral Wave Friction Factors

<u>Frequency</u> (rad/sec)	<u>Amplitude</u> (cm)	<u>Near-bottom</u> <u>velocity</u> (cm/sec)	<u>Friction factor</u>
1.634	1.63	6.22	0.199
2.136	1.65	6.04	0.140
2.388	1.49	5.31	0.231
2.702	1.27	4.36	0.142
2.953	1.26	4.18	0.040
3.393	1.30	3.99	0.222
3.958	1.35	3.68	0.267
6.346	1.13	1.19	0.159

In support of this conclusion results from an "equal component amplitude" spectral simulation experiment are presented in Table 1. With a single exception the friction factors obtained for the different frequency components are

remarkably similar (mean value of 0.194 and coefficient of variation 25% when the single exception is excluded). A weighted average of the friction factors listed in Table 1 which preserves total measured energy dissipation (weighting factor u_{br}^2) gives a value of 0.192 (0.176 if the single exception is not excluded). Corresponding to this wave condition the representative wave, defined by Eq. (2), is characterized by

$$u_{br} = 13.06 \text{ cm/s}, \quad a_{br} = 5.86 \text{ cm}, \quad T_r = 2\pi/\omega_r = 2.23 \text{ sec}$$

and use of the Grant and Madsen (1982) empirical relationships for bedform geometry with $K = 20$ in Eq. (9) gives a value of $k_b/A_{br} = 0.68$. Similarly, use of Eq. (8) with $K = 23$ in Eq. (9) results in a value of $k_b/A_{br} = 0.94$. It is important to note here that when the information on relative bottom roughness is used to predict the representative value of the friction factor this must be done using the generalized friction factor relationship given by Grant and Madsen (1982, Figure 3) since this relationship was used (in reverse) when establishing Eq. (9) from experimental values of the friction factor. Thus, with these values of relative roughness use of Figure 3 in Grant and Madsen (1982) yields predicted values of the friction factor of 0.18 and 0.21, respectively, in excellent agreement with the experimentally obtained values. Again, this conclusion is limited by the range of experimental parameters covered, i.e., within the "equilibrium range" of bottom bedforms. Tentatively, however, one may adopt the Grant and Madsen (1982) formulation, with the modification of the form drag term, $K = 20$ in Eq. (9), as indicated by the present results for conditions beyond the equilibrium range.

SUMMARY AND CONCLUSIONS

The results of carefully conducted experiments have been used to show that a representative periodic wave defined by Eq. (2) as the wave having the same root-mean-square near-bottom orbital velocity and excursion amplitude as a wave motion specified by its frequency spectrum may be used in conjunction with empirically derived relationships for movable bed roughness, to predict the equivalent bottom roughness, k_b , from knowledge of wave and sediment characteristics. With knowledge of k_b for a movable bed, the theory developed in the companion paper (Madsen et al., 1988) may be used to predict the spectral wave attenuation due to bottom friction.

It is, however, emphasized that the above conclusion should be regarded as preliminary until further experiments, covering a wider range of experimental parameters, can support its general validity. Thus, the present experiments were limited to one single sand size and the wave conditions were such that only bottom bedforms within the equilibrium range (as defined by Grant and Madsen, 1982) were generated. Presently the experimental investigation is being continued and extended to a finer sand (0.1-mm diameter) with an improved wave generation capability (larger waves). Both of these modifications and extensions

should contribute to the removal of the limitations of the present results.

ACKNOWLEDGMENTS

The research presented here was supported by the U.S. Department of Commerce National Atmospheric and Oceanic Administration's Office of Sea Grant under Grant NA86AA-D-SG089 and by the Office of Naval Research under Grant N00014-86-K0325. The expert typing skills of Read Schusky are also acknowledged.

REFERENCES

- Carstens, M. R., F. M. Nielson, H. D. Altinbilek. 1969. Bedforms generated in the laboratory under oscillatory flow: Analytical and experimental study. U.S. Army Corps of Engineers, CERC, Tech. Memo No. 28.
- Goda, Y., Y Suzuki. 1976. Estimation of incident and reflected waves in random wave experiments. Proc. 15th Coastal Engineering Conf., ASCE 1:828-845.
- Grant, W. D., O. S. Madsen. 1982. Movable bed roughness in oscillatory flow. J. Geophys. Res. 87(C1):469-481.
- Grant, W. D., O. S. Madsen. 1986. The continental-shelf bottom boundary layer. Ann. Rev. Fluid Mech. 18:265-305.
- Lofquist, K. E. B. 1986. Drag on naturally rippled beds under oscillatory flows. U.S. Army Corps of Engineers, CERC, Misc. Paper CERC-86-13.
- Madsen, O. S. 1971. On the generation of long waves. J. Geophys. Res. 76(36):8672-8683.
- Madsen, O. S., W. D. Grant. 1976. Quantitative description of sediment transport by waves. Proc. 15th Coastal Engineering Conf., ASCE 2:1093-1112.
- Madsen, O. S., Y.-K. Poon, and H. C. Graber. 1988. Spectral wave attenuation by bottom friction: Theory. Proc. 21st Coastal Engineering Conf., ASCE.
- Rosengaus, M. M. 1987. Experimental study on wave-generated bedforms and resulting wave attenuation. Sc.D. Thesis, Dept. of Civil Engineering, Mass. Inst. of Technology.
- Stefanick, T. A. 1979. A realistic model of wave attenuation due to bottom friction. S.M. thesis, Dept. of Civil Engineering, Mass. Inst. of Technology.
- Vongvisessomjai, S. 1987. Wave friction factors on sand ripples. ASCE Specialty Conference, Coastal Sediments '87 1:393-408.

CHAPTER 64

A Barotropic 3D-Model for the Study of Currents around the Atlantic Coast of the Iberian Peninsula.

I. Rodriguez. Programa de Clima Maritimo. Madrid. Spain
J. Kröhn. GKSS Forschungszentrum Geesthacht, FRG
J.O. Backhaus. Institut für Meereskunde, University of Hamburg, FRG.

Abstract

We intend to present a brief description of the fundamentals of a barotropic version of the 3D numerical model of the Institut für Meereskunde-Hamburg altogether with some results concerning the application of the model to the simulation of tidal currents in the Spanish Atlantic waters.

1 Introduction

In 1984 the Climate Marine Program (PCM) of the Spanish Directorate of Ports and Coasts decided to get involved into the modelling of sea currents induced by tides and winds at the waters surrounding the Iberian Peninsula and the Canary Islands.

The main motivation was the scarcity of data of this kind all along the Spanish coastline, as well as the need for numerical tools as a help in the study of local coastal problems.

We also consider its use as a support for navigation and fishery activities and data banking assimilation. P.C.M. established this year an agreement of technical assistance with two German institutions: the G.K.S.S.-Forschungszentrum at Geesthacht and the Institut für Meereskunde in Hamburg (IFM).

The purpose of this agreement was the implementation of a barotropic version of the 3D model developed by the IFM in the area of interest for PCM.

The strategy contemplated two stages.

The first one accomplished the implementation of a large scale barotropic model for tidal and wind induced dynamics.

A winter episode has been simulated. And charts of tidal and wind induced currents have been produced. This model will also provide consistent boundary conditions for smaller scale regional models.

PCM in a second stage will apply the model to smaller scale areas incorporating new features of the original version such as the baroclinic pressure gradient.

2 Model Description

The barotropic three dimensional numerical model is

based on a two-time level semi-implicit scheme.

Momentum equations in S-E and W-E directions as well as the continuity equation have been vertically integrated for each of the horizontal layers in which the water column is divided.

For the layer of thickness "h" the equations are:

- Momentum balance

$$\frac{\partial U}{\partial t} - fV + gh \frac{\partial \tau}{\partial x} = X + \Delta \left[A_v \frac{\partial}{\partial z} \left(\frac{U}{h} \right) \right]$$

$$\frac{\partial V}{\partial t} + fU + gh \frac{\partial \tau}{\partial y} = Y + \Delta \left[A_v \frac{\partial}{\partial z} \left(\frac{V}{h} \right) \right]$$

- Mass balance

$$0 = \frac{\partial U}{\partial x} + \frac{\partial V}{\partial y} + \Delta W \Leftrightarrow \frac{\partial \tau}{\partial t} = - \left(\frac{\partial U}{\partial x} + \frac{\partial V}{\partial y} \right)$$

U, V - Horizontal components of transport for the layer

\bar{U}, \bar{V} - Horizontal components of transport for the whole water column. (Vertically Integrated)

ΔW - Vertical velocity difference between top and bottom of the layer

τ - Free surface elevation.

f - Coriolis parameter.

g - Acceleration of gravity

A_v - Vertical eddy viscosity coefficient.

The most important terms involved in the equations have been explicitly pointed out:

- Local Inertia terms
- Coriolis force
- External horizontal pressure gradient
- Vertical diffusion terms expressed through the eddy viscosity analogy.

Additional terms like those of horizontal diffusion and advection are indicated by the letters X, Y.

The main features of the numerics can be summarized as follows (Backhaus 1983, 1985):

a) In order to avoid instabilities arising from a forward-in-time approximation of the Coriolis terms a second order approximation has been used for those terms. This introduces a coupling of spatial derivatives of the free surface elevation in both momentum equations through a rotation operator.

By doing this additional boundary conditions need to be defined when computing cross derivatives of the free surface elevation in the vicinity of solid boundaries.

b) Advective and horizontal diffusion terms are solved explicitly. Advective terms are updated in a Lagrangian way by means of a vector - upstream scheme.

c) A semiimplicit treatment of the free surface elevation has been used in all terms involving this variable.

This allows the scheme to get free of the stringent limitation for the time-step given by the Courant-Friedrichs-Lewy stability criterion, as would be the case if the external gravity waves were approximated in an explicit way ($\Delta t < \Delta L / \sqrt{2gh}$).

d) The model considers the horizontal eddy viscosity coefficient as time and space dependent.

An implicit additional system has been introduced for the vertical diffusion terms.

This has been done because once that grid size and layer thickness have been fixed, the stability criterion for an explicit approximation of those terms would represent an artificial upper limit for the vertical eddy viscosity coefficient ($A_v < \Delta z^2 / (2\Delta t)$).

As a consequence, unrealistic description of the flux could take place when a high rate of vertical momentum transfer is required, as would be the case when severe wind forcing is being simulated.

e) A semi-implicit formulation for the quadratic bottom stress is introduced for the sake of numerical stability.

f) Spatial derivatives are centered in time (Crank-Nicholson approach) which leads to a scheme essentially neutral with regard to damping of amplitudes.

The sequence of advancing one time-step proceeds in this way:

First, the horizontal elliptic system for the free surface is obtained by replacing the momentum divergence terms in the vertically integrated equation of continuity (vertical diffusion terms cancel out).

The system is solved by means of an iterative procedure (successive over-relaxation algorithm).

Once that the free surface elevation at the new time level is known, an interim solution for transports can be computed from the pressure gradient terms and all other terms explicitly treated.

Finally, the vertical implicit system involving layer

transport for each water column is established. The equation system is solved by means of a gaussian algorithm.

Boundary conditions are introduced into the model via the coefficients of the free surface elevation system.

Open boundary tidal constants for several harmonics are obtained from the global oceanic model of Schwiderski (1° size).

3 Details of the Model

The horizontal grid used for the model is of the type Arakawa-C. It has the pressure points and transport points half a grid size apart. (Fig. 1)

The horizontal grid size is 12' in latitude and 20' in longitude which means an approximate medium length for the area of about 25 Km.

The real topography for the area has been considered, after an smoothing process up to a depth of 5 Km. (Fig. 2)

The water column has been divided into six vertical layers.

The layer boundaries are: 30, 100, 200, 600, 1500, 5000 meters. The bottom layer thickness accommodates to the sea bottom.

The time step is 20 minutes which gives a CFL factor of about 13.

The performance of the model on an IBM 3090-150 computer is 1 day simulation equivalent to 3.5 CPU minutes.

4 Results

Verifications runs have been carried out with single tidal harmonic components: M2 and S2.

After obtaining stationarity the results of amplitude and phase were compared with the observed ones for points placed along the coast and in the deep sea zone (tidal gauges).

The model behaves very well, producing results very close to the observed ones as it is shown in the graphics included. (Fig. 3)

In order to attain the stationarity of the fortnight spring-neap cycle the model was run for several months with those two tidal harmonics.

A medium factor of about two has been obtained when comparing the tidal ranges of spring to neap tides. (Fig. 4)

At first glance, from the huge ranges obtained high velocities could be expected in the area. This is only true in

the near shore of Bay of Biscay, for as the main part of the domain is deep sea the velocities in the surface layer for the spring hypothesis are less than 0.2 Knots. (Fig. 5)

The graphic output for this spring-neap tidal analysis has been made by drawing the tidal ellipses for several points in the area. (Fig. 3)

The tidal ellipses represent the curve described by the extremity of the velocity vector of each point along a tidal cycle referred to an arbitrary zero time (Highwater at Cadiz)

As, in the Bay of Biscay the velocities are much greater than in the rest of the domain the tidal ellipses in this zone have been removed for the sake of clarity. (Fig. 7, 8)

An interesting feature of the tidal ellipses pattern is the change of sense of rotation from clockwise in the shelf of the Bay of Biscay to anticlockwise in the rest of the area. (Fig. 6)

Other intering points to be mentioned are the two distorted north-south oriented tidal ellipses along the iberian coastline which coincide with two topographic bumps in this zone; and the distorted shapes of tidal ellipses polarized in N-E direction in the area of Madeira and Canary Islands.

This last point requires further explanation, but it seems coincident with the observed pattern in the Canary Islands. (Fig. 6)

There is no observed change of sense of rotation for the ellipses along the water column. The huge thickness (3.5Km) of the bottom layer can overshadow this feature. The most noticeable effect of friction is on the Bay of Biscay shelf where it causes the transition to more open ellipses. (Fig. 6, 7, 8)

5 Conclusions

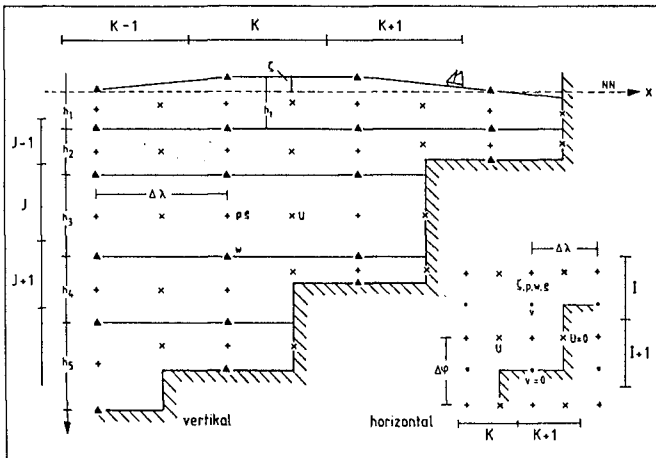
- . Fine scale barotropic 3-dim. model set up and verified
- . Sea - level variation within 5 - 10% of observed values.
- . Not expected large variation of tidal ellipses (shape sense of rotation and alignment with topography)
 - Madeira/Canary Is.: currents almost linearly polarized.
 - Bay of Biscay: change from anti-clockwise to clockwise rotation
 - Off Iberian peninsula: topographic bumps induced rectilinear distortion of ellipses
 - Bay of Biscay shelf: friction caused transition to more open ellipses
- . Model output:

- Simulation of a winter episode involving the five most significant partial tides (M2, S2, N2, O1, K1) and actual wind stress. The latter obtained from six-hourly surface pressure field from the ECMWF.
 - Production of Tidal Atlas for water levels and currents
 - Boundary values for finer scale regional models (e.g. fisheries, pollution, ...)
- . Develop regional barotropic models
 - . Develop large scale/regional baroclinic models

6 References

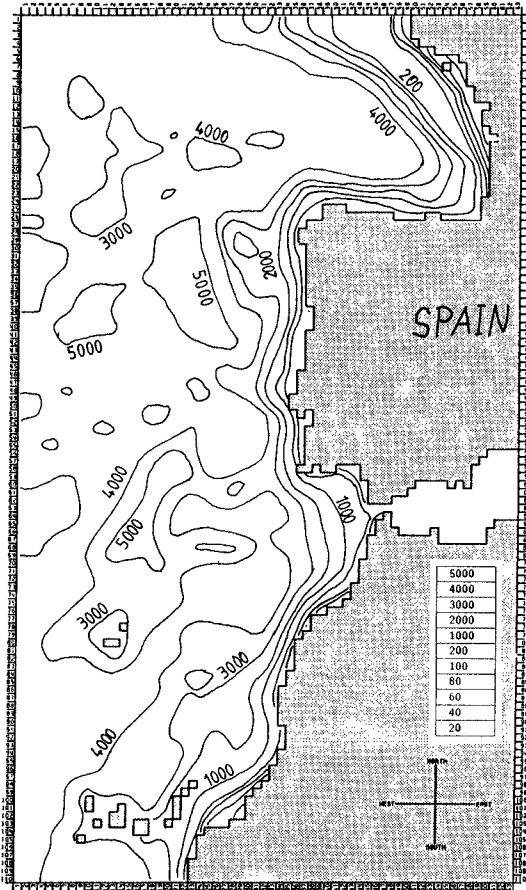
A three dimensional model for the simulation of shelf sea dynamics. Prof. Jan O. Backhaus, Institut für Meereskunde, University of Hamburg.

Fig.1.-

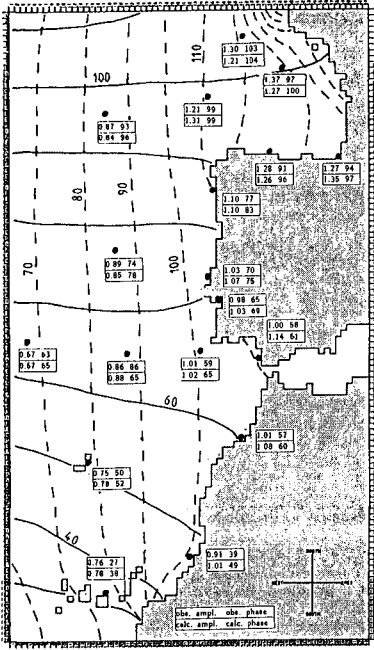


Horizontal and vertical computational grid. U, V - momentum components (east, north), w - velocity component (positive up), p - (internal) pressure, ρ - density, ζ - surface elevation, h_i - layer thickness, NN - mean sea level

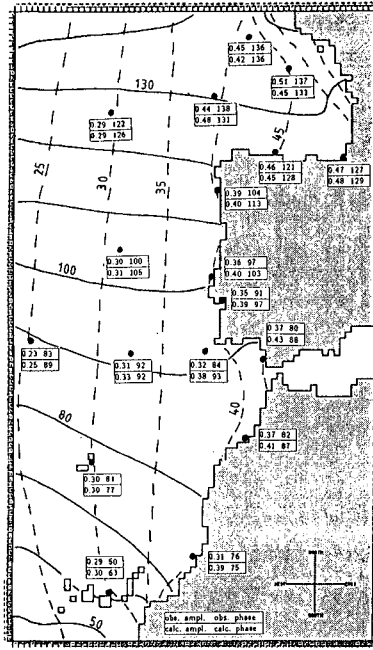
Fig.2.-



Topography of model area (meters)



M₂ tide: amplitude (cm) and tidal phase (degrees), referred to moon's transit at Greenwich. Boxes: comparison of observed and computed values (see explanation at bottom of figure)



S₂ tide: amplitude (cm) and tidal phase (degrees), referred to moon's transit at Greenwich. Boxes: comparison of observed and computed values (see explanation at bottom of figure)

Fig. 3.-

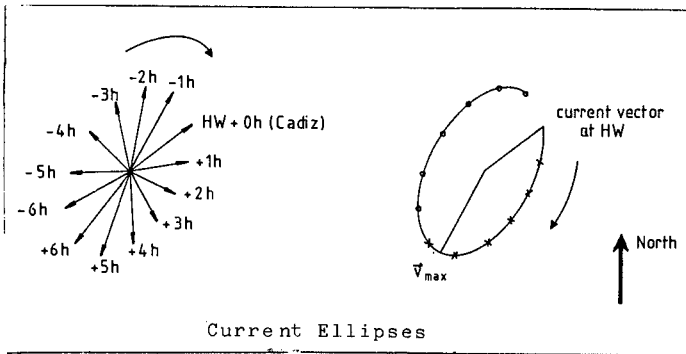
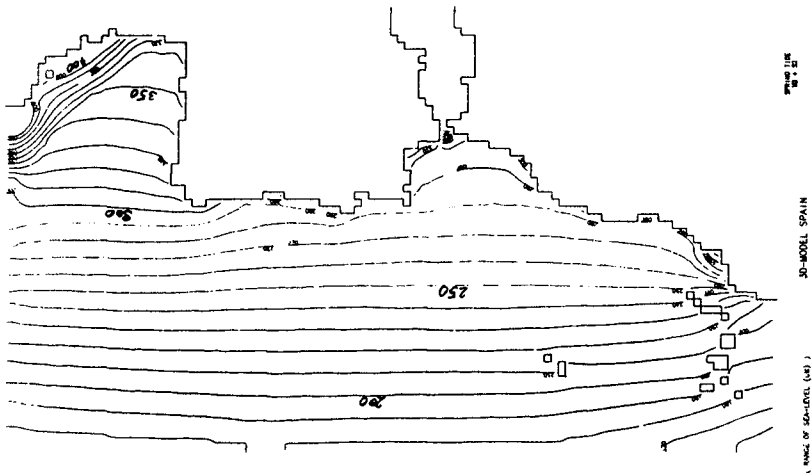
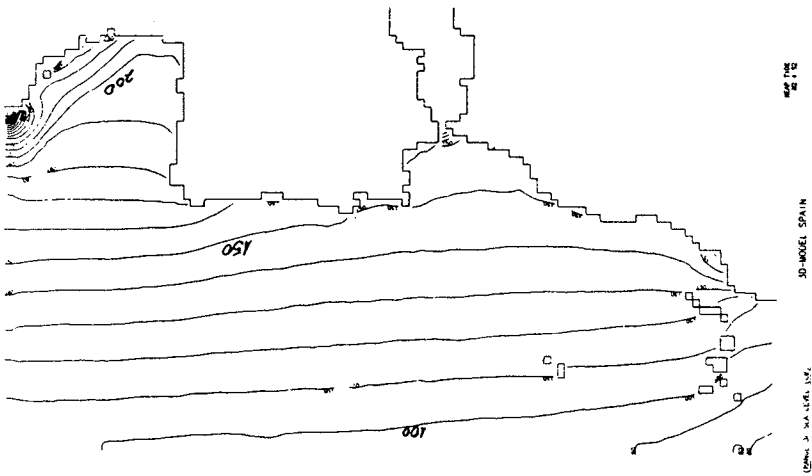


Fig. 4.-

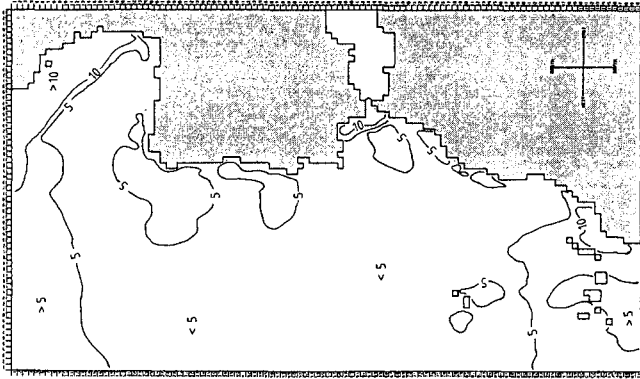


Spring Tide. Range of sea level (cm)



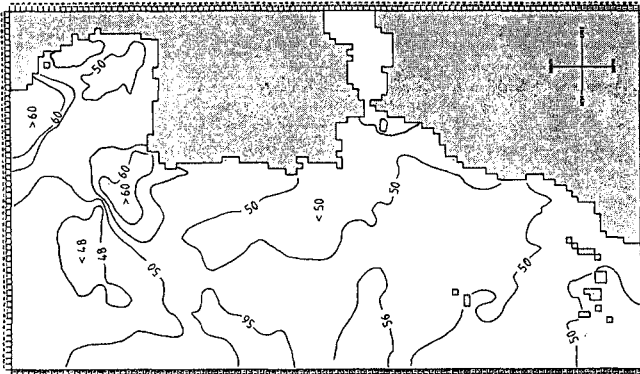
Neap Tide. Range of sea level (cm)

Fig. 5.-



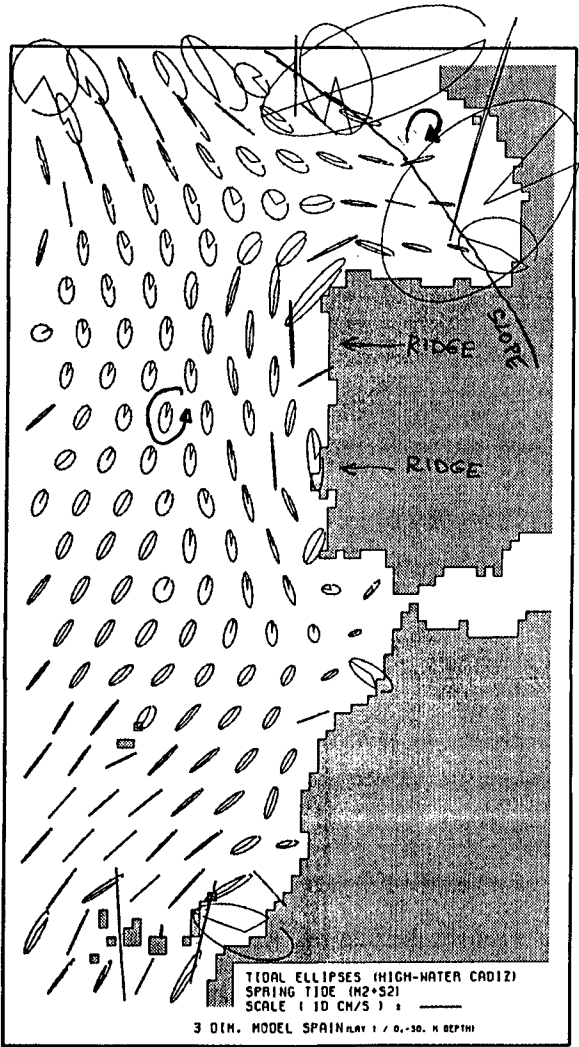
Spring tide ($M_2 + S_2$); Maximum currents (cm/s)

CURRENTS



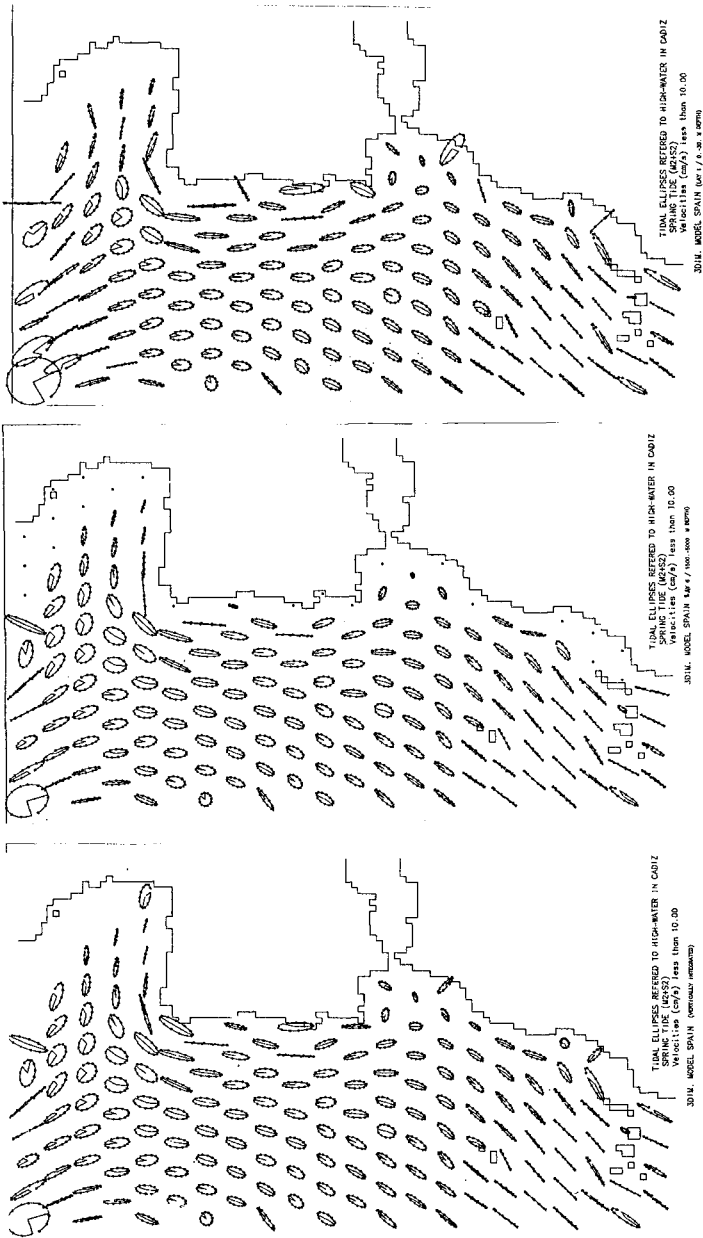
Ratio of maximum neap and maximum spring currents (in percent)

Fig. 6.-



Spring tide: current ellipses (referred to high - water at Cadiz) surface layer

Fig. 7.- SPRING TIDE

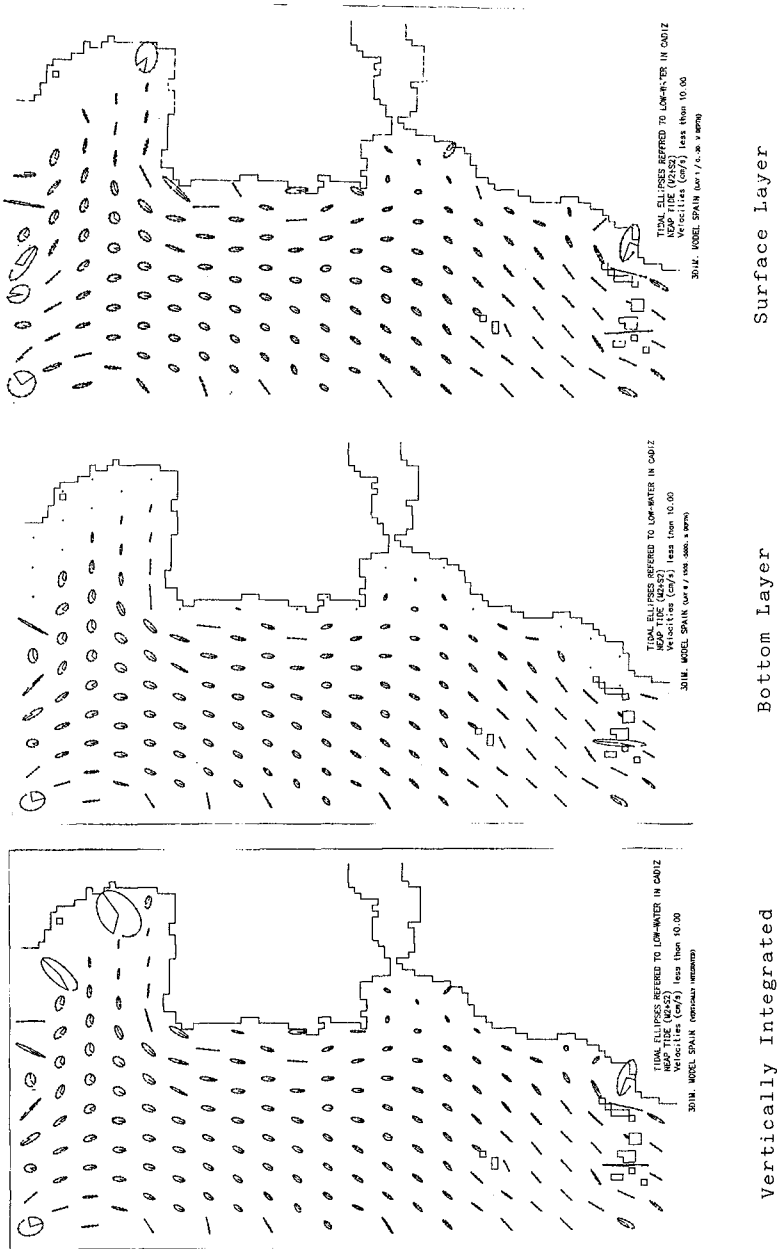


Surface Layer

Bottom Layer

Vertically Integrated

Fig. 8.-- NEAP TIDE



CHAPTER 65

Kinematics of Breaking Waves in Coastal Regions

William J. Easson¹, Matthew W.P. Griffiths² and Clive A. Greated³

Waves breaking on various slopes in a wave flume are examined. Plunging and spilling breakers are considered. The parametric results show the consistency of the measurement and the independence of scale. A method is given for predicting the maximum breaking height for a wave of known period in a known depth. The velocity is measured to the crest of the wave and comparisons with numerical and analytical solutions demonstrate the shortcomings of many of the established methods of predicting wave kinematics.

Introduction

Breaking waves are of significant importance in the design and understanding of many aspects of Coastal Engineering such as breakwaters, bed movement and inshore construction. Yet the kinematics of these waves are not fully understood despite considerable advanced theoretical and numerical work (e.g. New et. al., 1985). Mathematical models are limited in several ways at present. For example, although deep and shallow waves may be modelled it has not been possible to include changes in bed topography such as linear slopes. Also, the flow field becomes complex when the plunging jet of a breaker hits the forward face making the spilling or surging breakers difficult to model.

Experimentally, the measurement of kinematics is complicated by the two-phase situation which exists above the still water level precluding the use of many standard velocity probes. For this reason mathematical models have usually been inadequately compared with surface profiles.

Due to the difficulty of obtaining breaking wave kinematics, designers have tended to rely on the tried and tested industry standards such as Stokes and Cnoidal theory or Dean's stream function. Recently, higher-order versions of Dean have been available, applicable to larger waves (Chaplin, 1980). All of these assume two dimensional, regular non-breaking waves and necessarily provide limited

-
1. Lecturer, Department of Mechanical Engineering, University of Edinburgh, The King's Buildings, Mayfield Road, Edinburgh EH9 3JL, UK
 2. Postgraduate student, Fluid Dynamics Unit, Department of Physics, University of Edinburgh.
 3. Director, Fluid Dynamics Unit, Department of Physics, University of Edinburgh.

descriptions.

Furthermore none of the above methods can give a reliable limiting wave height and the question of whether the 'design wave' might be breaking is dependent on data gathered from elsewhere on height over depth ratios (Griffiths et al, 1987). For this reason several companies have commissioned site-specific studies at the Edinburgh

Fluid Dynamics Unit to discover if the design wave was a breaker and if so what its kinematics were (Birkinshaw et. al., 1988).

This paper will look at spilling and plunging breakers on beds of various slopes in terms of their parameterisation and internal kinematics. A method of using these results will then be proposed.

Experimental method

Regular waves are generated in a narrow tank by a computer-controlled absorbing wavemaker. The wavemaker is in 'deep' water (0.9 m) and the waves are run up a slope of variable degree. For gentle slopes and flat beds an initial steep slope is used (fig. 1).

The velocity measuring technique is Laser Doppler Anemometry. The non-intrusive system records the frequency of variation of light scattering intensity as minute seeding particles pass through the crossing volume of two laser beams. The application of this technique to breakers may be found in Easson & Greated (1984). The method of signal analysis allows measurements up to the crest of the breaking wave which is not common in most systems but will be shown to be of great importance.

Wavelength, height, and velocity were measured using still photography and a video-camera. (figs. 2, 3).

Results

(a) Parametric

The wave parameters measured were deep water height (H_0), breaking height (H_b), breaking depth (d_b), maximum crest elevation (H_{1b}) and trough depression (H_{2b}) wavelength at breaking (L_b) and velocity at breaking (C_b) (see fig. 4). The breaking point is when the crest first becomes vertical. For ease of presentation and application of the results the deep water steepness ($S_0 = H_0/l_0$) has been used as the reference axis. This has been shown to be useful and valid over the range $0.015 < S_0 < 0.115$ in a previous publication (Griffiths et al, 1987), as would be expected since Froude scaling applies here. Furthermore no correction factors are required in applying these results to full scale waves.

The range of slopes considered is 1:15, 1:30, 1:50 and flat bed. Most of the waves produced spilling breakers but the longest waves on the 1:30 slope (small S_0) and most of the waves on the 1:15 slope became plunging breakers.

The first plot (fig. 5) shows the depth at which the waves broke. All length scales have been non-dimensionalised by the deep water wavelength so $d_b' = d_b/gT^2$. This shows that the depth of breaking is independent of slope or period and is purely a function of deep water steepness.

The limits are as expected with the graph passing through zero (no height, no breaking) and tending towards the deep water breaking limit ($S_0 \approx 0.14$) as the breaking depth increases. Figure 6 shows the breaking wave height which is also independent of slope or period and tend towards a deepwater limit of 0.022 at $S_0 = 0.142$. This has been compared with the regular criteria of $H_b' = 0.027$ and the irregular limit of $H_0' = 0.020$. (Ochi and Tsai, 1983).

It is possible, using figs 5 and 6, to read off the breaking wave height given the design parameters of depth and period. For example, a 12.5s wave in a depth of 25 m (typical North Sea) gives $d' = d/gT^2 = 0.016$. From fig. 5, $S_0 = 6.0$ which from fig. 6 gives $H' = 0.011$. Therefore the breaking wave limit height is $H_b = gT^2 \times H' = 16.8$ m. If hindcasting has predicted a height greater than this then the wave will be breaking.

Designers have often used the criterion $H_b/d_b > 0.78$ to determine whether a wave is breaking. This is derived from shallow water solitary wave theory (Munk, 1949) and should not be used for intermediate depths. Figure 7 shows H_b/d_b against S_0 for our results. Previously (Griffiths et al, 1987) the 1:30 results were shown to match the results of other investigators on this slope; they also extended the range to deeper water. Weggel (1982) proposed an empirical upper limit based on the 1:30 slope results. Several significant points may be drawn from this figure. Firstly, the flat bed results tend to the solitary wave limit at small S_0 and the Weggel line is overly conservative. Secondly, the H/d ratio is slope dependent - a fact which is not apparent from figures 5 and 6. Finally, the Weggel line cannot be applied to slopes greater than 1:30 as the plunging breakers here exceed the H_b/d_b ratio predicted.

Svendsen and Buhr Hansen (1976) plot wavelength over depth at breaking as a function of deep water steepness. The results here (fig. 8) confirm the slope of Svendsen's empirical mean value line and extend the range of results towards the deep water limit.

(b) Kinematic results

Velocities were measured under the crest of the wave at a range of elevations from the bed to the crest peak at the instant of breaking. Figure 9 shows the velocity variation from bed to crest of five wave frequencies breaking at a particular depth (185 mm) on a 1:50 slope. The most important general characteristic is the large increase in velocity in the crest where the graph steepens considerably. Thus although the near bed velocities are as expected the crest velocities differ considerably from non-breaking waves. The curvature of the graph is greatest for the short waves which have lower velocities below SWL. The group of points to the right of the graph are the five celerities associated with the frequencies studied, plotted at the maximum elevation of the crest. In each case the velocity curve tends towards the celerity at crest indicating that this is the maximum velocity (although it may only pertain to a very small fraction of the crest volume) and that the condition $v = c$ does indeed represent a useful criterion for wave breaking.

Figure 10 shows the velocity under the crest of a 1 Hz wave breaking at 185 mm depth for different slopes. There is no significant difference between the 1:50 and 1:30 results but higher velocities were measurable for the 1:15 slope due to the larger volume of water

travelling at velocities around c in the plunging jet. (c.f. figures 2 & 3). The plunging breaker was also slightly higher than the others.

Finally, the quality of these results has enabled a direct comparison with some of the established theories. This is only possible when crest values can be obtained. The lack of crest values invalidates the comparisons made by previous investigators as this is where the major differences between breakers and non-breakers arise. Figure 11 shows the velocity variation with elevation for one particular wave but the trends are typical over the full range of conditions investigated. The comparisons are with Linear, Stokes V and Deans V and IX. (We are grateful to Professor J. Chaplin for the comparison with Deans IX (Chaplin, 1980)). The measured velocities tend towards the indicated celerity/height point and the best fit curve has been drawn. The Stokes V has also been indicated by a full curve. Interestingly, the linear theory gives a better fit than Stokes in the crest. The two Deans solutions are better approximations with the ninth giving a significant improvement in the crest. However, even this falls 20% short of the maximum expected velocity. Note that all the theories tend to over-predict the velocity below SWL.

Conclusions

By testing a range of frequencies, Froude scaling has been shown to apply to breaking waves. The parametric results have shown good agreement with those of other experimenters and have usefully extended the range of measurements. A method has been presented for the evaluation of limiting wave heights in the design of offshore structures using graphical procedures. The H/d ratio for breaking is slope dependent but is only significantly so for shallow/plunging breakers. Throughout the range measured the velocity in the crest tends to a maximum equal to the celerity at the highest point of the wave. The established theories tend to underestimate the crest velocity and overestimate the velocities below SWL.

It is important to remember, in the application of these results, that the two-dimensional, regular wave assumption has been made, as is the present industry practice. A project is currently under way, at Edinburgh University, using the instantaneous full-field anemometry technique known as Particle Image Velocimetry (PIV) (Gray & Greated, 1988) to measure the velocities under irregular breaking waves.

Acknowledgements

Mr. Griffiths is a postgraduate student in receipt of a CASE studentship with B.P International. The authors would particularly like to acknowledge the help and access to industrial procedures afforded by B.P. This project is part of the managed Fluid Loading Programme of MTD Ltd. We are also grateful for the encouragement and interest shown by various members of that organisation.

REFERENCES

1. Birkinshaw, M., W.J. Eason, C.A. Greated, and R.M. Webb, "Breaking wave design - a case history," Proc. Inst. Civil Engineers, part 2, vol. 85, pp. 415-433 1988.

2. Chaplin, J.R., "Developments in stream function wave theory," *Coastal Engineering*, vol. 3, pp. 179-205, 1980.
3. Easson, W.J. and C.A. Greated, "Breaking wave forces and velocity fields," *Coastal Engineering* vol. 8, pp. 273-241, Elsevier, Amsterdam, 1984.
4. Gray, C. and C.A. Greated, "The application of particle image velocimetry to the study of water waves," *Lasers and Optics in Engineering*, Elsevier Applied Science. In Press
5. Griffiths, M.W.P., W.J. Easson, and C.A. Greated, "Large wave loading on structures - a reappraisal," *Integrity of Offshore Structures - 3*, pp. 77-94, Elsevier, London, 1987.
6. Munk, W.H., "The solitary wave theory and its application to surf problems," *Annals of the New York Academy of Science*, vol. 51, pp. 376-462, 1949.
7. New, A.L., P. McIver, and B.H. Peregrine, "Computations of overturning waves," *J.F.M.*, vol. 150, pp. 233-251, 1985.
8. Ochi, M.K., and C.H. Tsai, "Prediction of occurrence of breaking waves in deep water," *J. Physical Oceanography*, vol. 13, pp. 2008-2019, 1983.
9. Svendsen, I.A. and J. Buhr Hansen, "Deformation up to breaking of periodic waves on a beach," *Proc. Coastal Engineering*, pp. 477-496, 1976.
10. Weggel, J.R., "Maximum breaker height for design," *Coastal Engineering*, vol. 6, pp. 551-568,

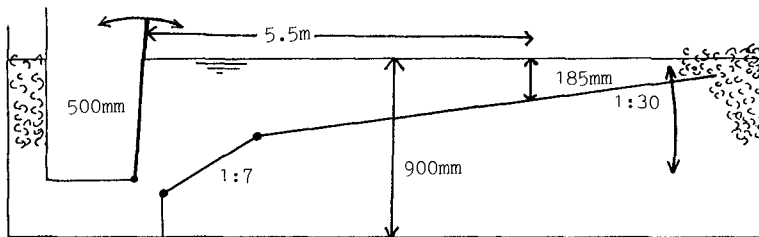


Fig. 1 - Typical beach dimensions

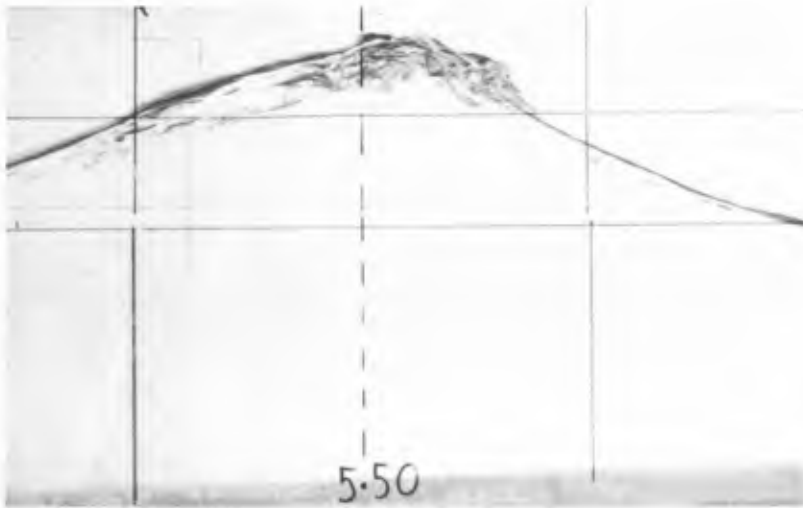


Fig. 2 - Depth induced spilling



Fig. 3 - Depth induced plunging

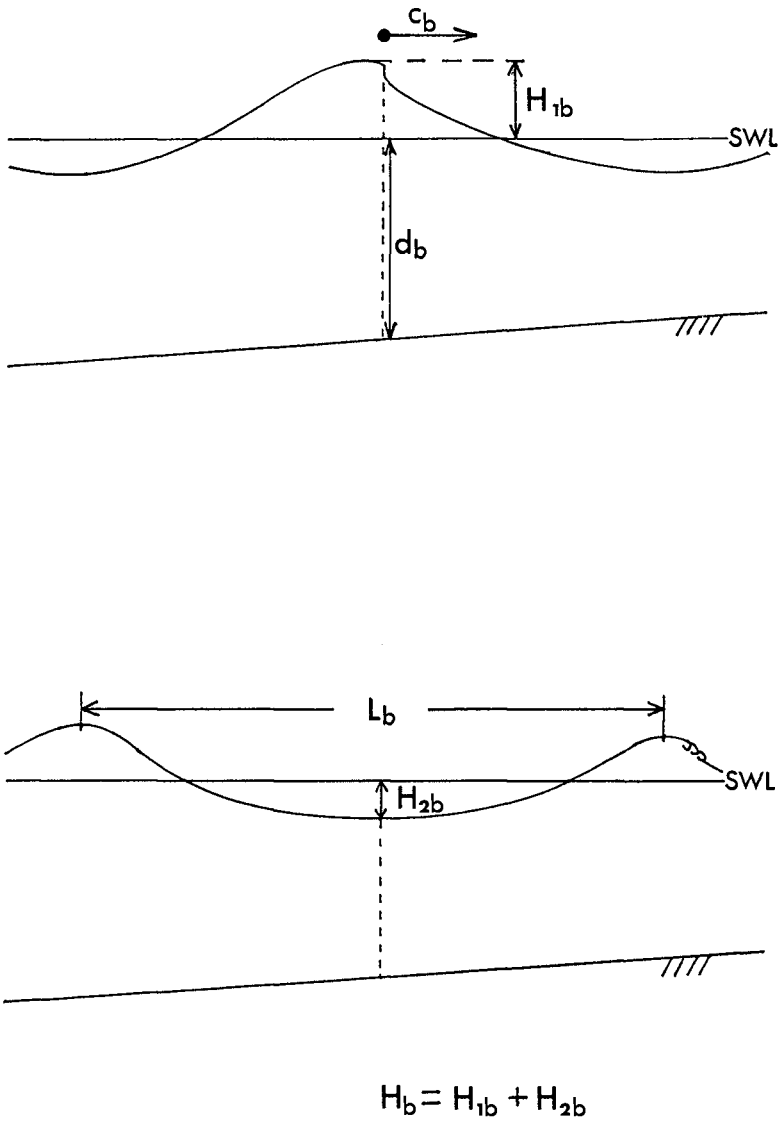


Fig. 4 - Definition of parameters at measuring point

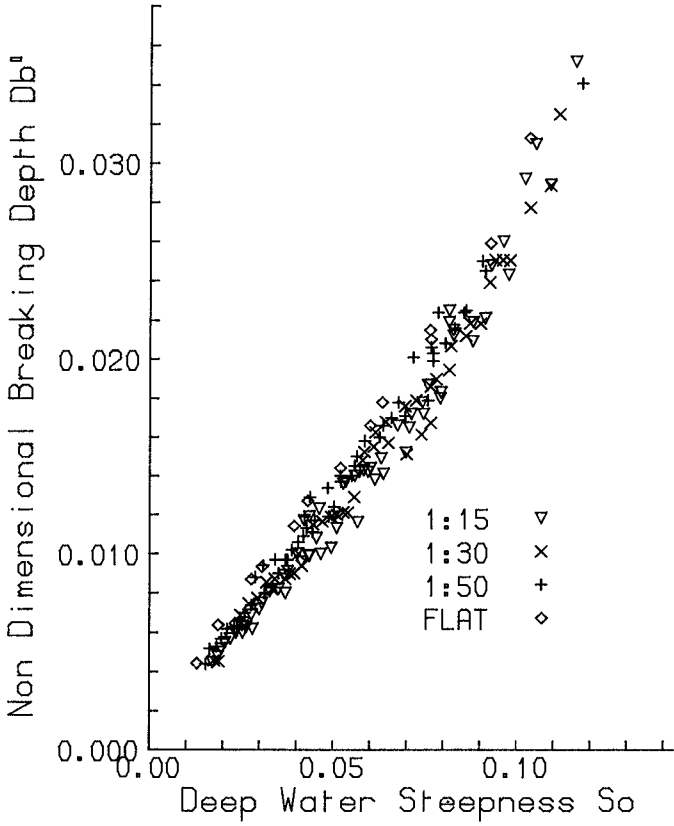


Fig. 5 -

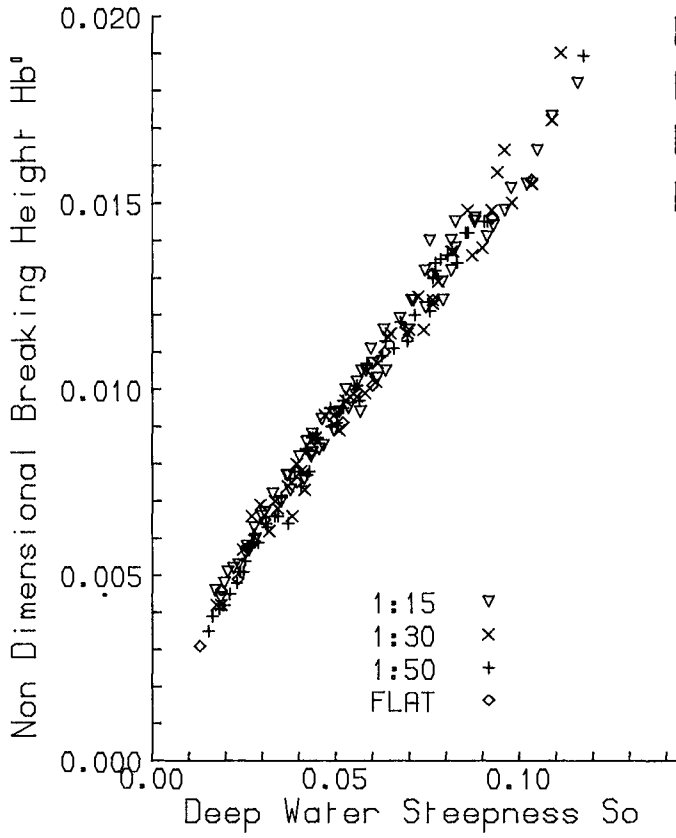


Fig. 6 -

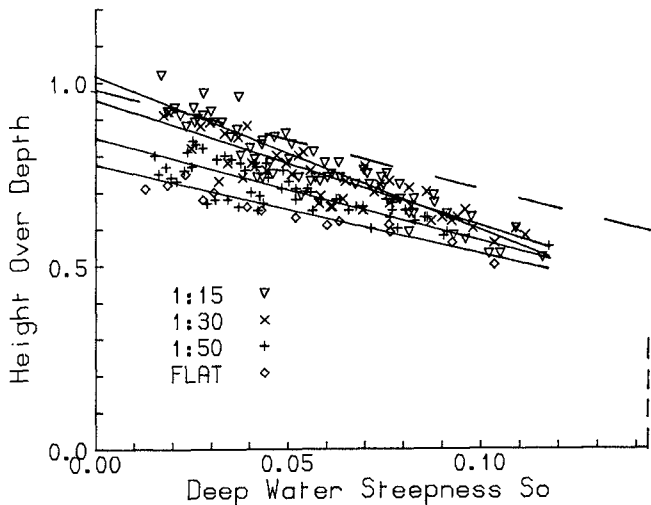


Fig. 7 - H/d at breaking. The four solid lines are best fits to the results from each slope (steepness increases with greater H/d). The dashed line is Weggel's empirical line.

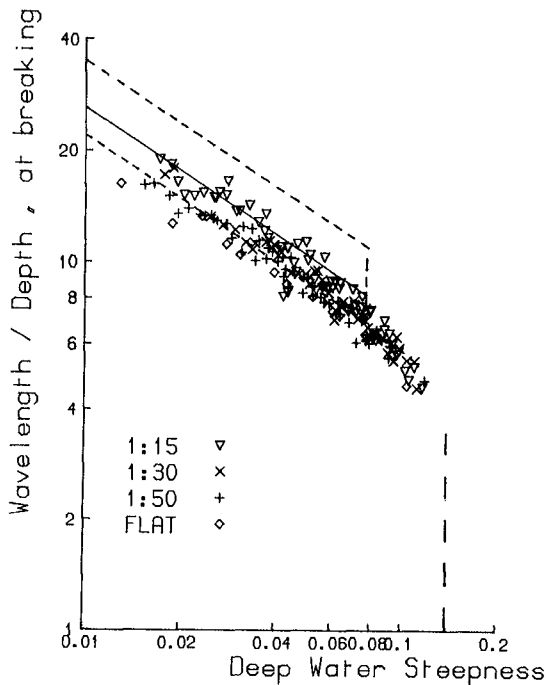


Fig. 8 - Comparison with Svendsen (boxed area indicates extent of Svendsen's scatter)

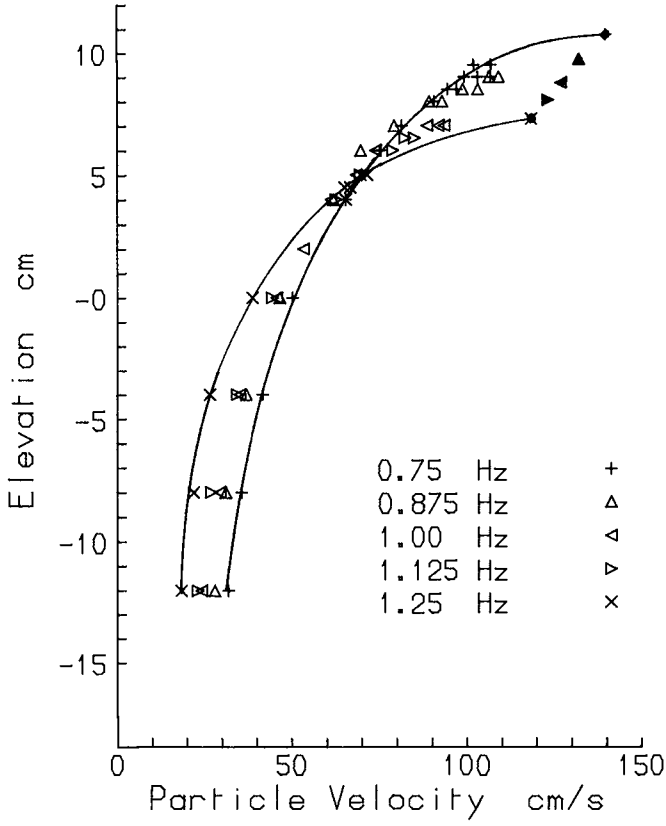


Fig. 9 - Particle velocity v. elevation. Dependence on frequency (1.50 slope)

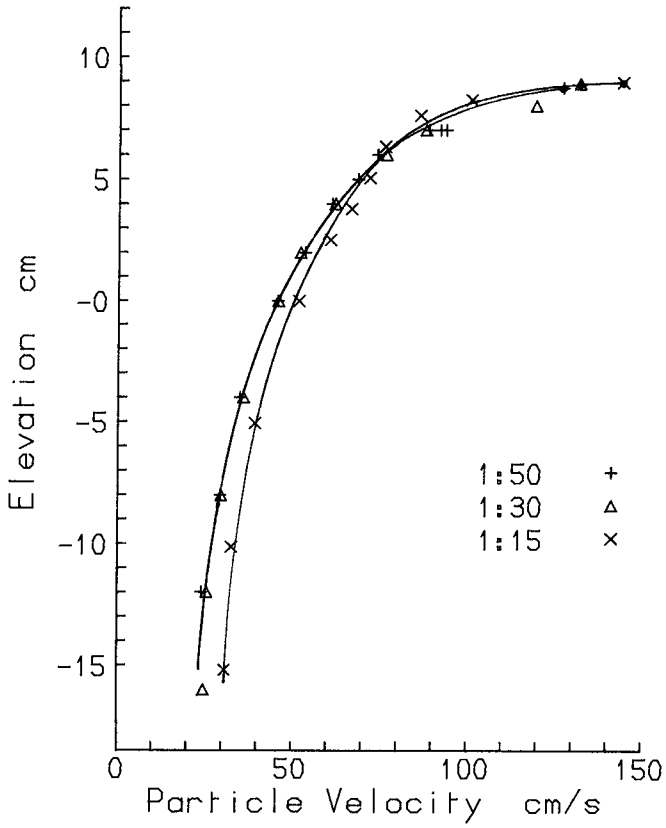


Fig. 10 - Particle velocity v. elevation. Dependence on slope.
(1 Hz wave.)

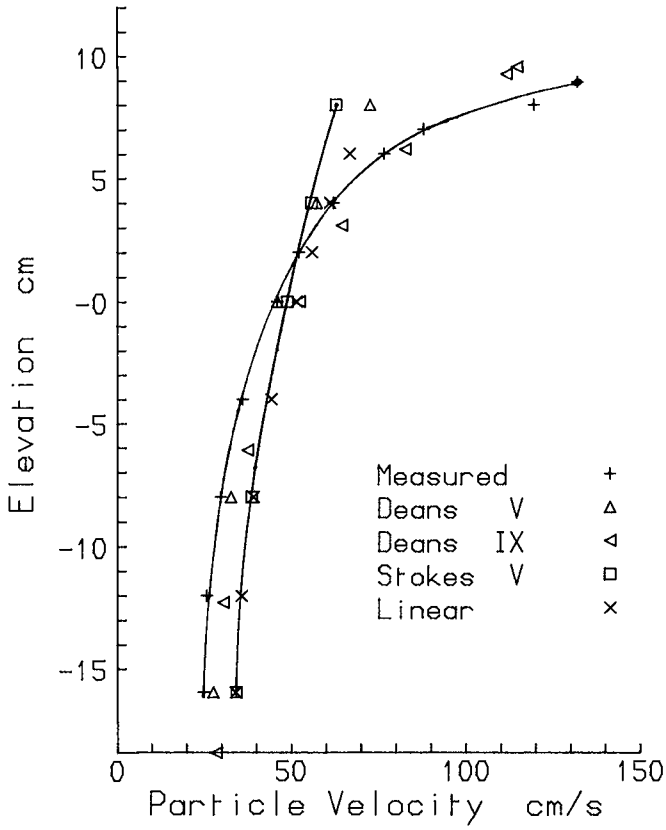


Fig. 11 - Particle velocity v. elevation. Comparison with theory (1 Hz, 1.30 slope.)

CHAPTER 66

WAVE GROUP ANALYSIS BY THE HILBERT TRANSFORM

Robert T. Hudspeth, M.ASCE*
Josep R. Medina, M.ASCE**

ABSTRACT

A methodology based on linear theory is presented for analyzing wave groups from a random sea representation in the complex plane. A wave height function $[H(t)]$, a local frequency function, $[\Omega(t)]$, and an orbital velocity function $[V(t)]$ are defined from the Hilbert transform of the sea surface elevation. Envelopes computed by the Hilbert transform are compared with the SIWEH. A three axes representation of the mean lengths of runs of waves is employed to compare the lengths of runs computed by the discrete wave method with runs computed by the Hilbert transform method.

INTRODUCTION

The presence of groups of waves in random seas and the corresponding variability of setback along the coast can produce low frequency resonances in the coastal zone (see Battjes (1988) and Bowers (1988)). Tucker (1950) noted that long waves nearshore were caused by wave groups. Since Goda (1970) demonstrated that random ocean waves have a natural tendency to form groups of waves that are larger for more peaked spectra, a variety of observations and theories of wave groups for engineering applications have been developed.

Engineering Interest

Hsu and Blenkarn (1970) pointed out that slow drift oscillation of vessels and mooring forces are related to the sequence of waves in random seas. Ewing (1973) noted that ships can capsize or be damaged by severe motions caused by high wave groups. Johnson et al. (1978) and Bruun (1985) described how wave groups can have a significant affect on the stability and behavior of rubble mound structures.

Barthel et al. (1983) observed that wave groups generate second order long waves in wave flumes when random wave generators are used. Medina and Hudspeth (1987) showed that wave grouping characteristics are strongly related to the statistical variability of the sea state parameters and,

*Professor, Department of Civil Engineering, Oregon State University.

**Profesor Titular, Department of Transportation, E.T.S.I. Caminos, Univ. Politécnic de Valencia, Spain.

therefore, the uncertainty of wave climates estimated from records can be influenced by wave groupiness. Burchart (1979) and Longuet-Higgins (1984) introduced the concept that wave grouping characteristics in random seas is a significant design element that should be taken into consideration in the design of coastal and ocean structures.

Theories

Although Rice (1954) provided a compact theory for an analysis of the envelopes in random signals and Tucker (1950) demonstrated the importance of the groups of high waves in the generation of coastal long waves and harbor resonance, Goda (1970) was the first to give a simple methodology for analyzing the presence of wave groups in random seas. Goda (1970) introduced the length of runs of waves to measure wave groups and defined a spectral peakedness parameter, Q_p , which indicated that larger wave groups are associated with higher values of Q_p . The basic Goda methodology has been the most widely used to analyze wave groups from real ocean records.

Nolte and Hsu (1972) and Ewing (1973) proposed to analyze wave groups by an envelope function. Funke and Mansard (1979) introduced the Smoothed Instantaneous Wave Energy History (SIWEH) method and an associated Groupiness Factor, GF, to characterize wave groups. Kimura (1980) proposed a Markov chain model to predict the probability density function (pdf) of the length of runs. Goda (1983) found that observations of long-travelled swell waves in the Pacific Ocean agreed quite well with the Kimura theory. Battjes and Vledder (1984) also observed that wave groups in the North Sea were in agreement with the Kimura predictions.

Longuet-Higgins (1984) employed the envelope theory of Rice to demonstrate the similarities between the formulas given by Kimura (1980) for discrete waves and those given by Rice (1954) for envelopes. Medina and Hudspeth (1987) demonstrated the similarity between the SIWEH method and the square of the envelope. They also found that the Goda peakedness parameter, Q_p , and a new parameter, Q_e , provided a relationship between the variability in the variance of the time series and the spectrum of the envelope.

Linear Assumption

Rye (1982) provided a lengthy review of the methodologies and observation of wave groups in random seas and concluded that all of the significant characteristics of wave groups in records of sea surface elevation could be obtained from the variance spectrum. The linear hypothesis of wave groups was also supported by the results of Elgar et al. (1984, 1985) for water depths greater than 10 meters. These observations and those provided by Battjes and Vledder (1984) justify the assumption that the linear hypothesis can correctly analyze wave groups from one-dimensional records in deep water.

If we assume that wave groups in random seas may be analyzed by an ergodic Gaussian stochastic model, then the corresponding variance spectrum contains all of the information required. Medina and Hudspeth (1987) proposed to analyze random waves in the complex plane by using the Hilbert transform to describe the orbital movement of points in the sea surface. They introduced a wave height function, $H(t)$, a local frequency function, $\Omega(t)$, an orbital velocity function, $V(t)$, and other functions to describe random waves in the complex plane. Here we examine the stochastic proper-

ties of some of these functions and introduce some new techniques to characterize wave groups from real ocean records.

WAVE ENVELOPE ANALYSES

Assuming that the vertical displacement of a point in the sea surface, $\eta(t)$, is a realization of an ergodic Gaussian process defined by its one-sided variance spectrum, $S_\eta(f)$, it may be approximated by

$$\eta(t) = \sum_{m=1}^M R_m \cos(2\pi f_m t + \theta_m) \quad (1)$$

where M = the total number of discrete Fourier components; R_m and f_m = the amplitude and frequency of the "mth" wave component, respectively; and θ_m = a random phase angle uniformly distributed in the interval $U[0, 2\pi]$. Tuah and Hudspeth (1982) and Medina et al. (1985) used the following relationship between the amplitude and the variance spectrum:

$$R_m^2 = C_m S_\eta(f_m) \Delta f_m = -2 \ln(U_m) S_\eta(f_m) \Delta f_m; \quad m = 1, 2, \dots, M \quad (2)$$

where U_m = a random variable uniformly distributed in the interval $U[0, 1]$; C_m = a chi-squared random variable with two degrees of freedom; and Δf_m = a discrete frequency interval in the variance spectrum.

Bendat and Piersol (1986) define the Hilbert transform of $\eta(t)$ as

$$\hat{\eta}(t) = \sum_{m=1}^M R_m \sin(2\pi f_m t + \theta_m) = \sum_{m=1}^M R_m \cos\left(2\pi f_m t + \theta_m - \frac{\pi}{2}\right) \quad (3)$$

and an analytic signal or complex-valued function as

$$AF(t) = \eta(t) + j\hat{\eta}(t) = A(t) \exp[j(\theta(t) + \phi)] \quad (4)$$

where $j = \sqrt{-1}$; $\eta(t)$ = a real signal; $\hat{\eta}(t)$ = its Hilbert transform; $A(t)$ = the amplitude of the envelope; and $[\theta(t) + \phi]$ = a phase angle. The Hilbert transform may be implemented exactly in the frequency domain when $\eta(t)$ is periodic (FFT simulations) and may be implemented approximately in the time domain using the optimum Hilbert filters given by McClellan et al. (1979).

A schematic representation of a wave record in the complex plane is illustrated in Fig. 1 where $\eta(t)$ and $\hat{\eta}(t)$ are the vertical and horizontal displacements, respectively, of a point in the sea surface. A wave analysis in the complex plane provides definitions of instantaneous functions of variables which control the process and which have physical interpretations. The instantaneous functions of wave height [$H(t)$], frequency [$\Omega(t)$], and orbital velocity [$V(t)$], may be defined as follows:

$$H(t) = 2A(t) = 2[\eta^2(t) + \hat{\eta}^2(t)]^{1/2} \quad (5)$$

$$\Omega(t) = \frac{1}{2\pi} \frac{d}{dt} \{\text{ARCTAN} [\hat{\eta}(t)/\eta(t)]\} \quad (6)$$

$$V(t) = 2\pi A(t) \Omega(t) = \pi H(t) \Omega(t) \quad (7)$$

Note that these functions are constant values for regular waves.

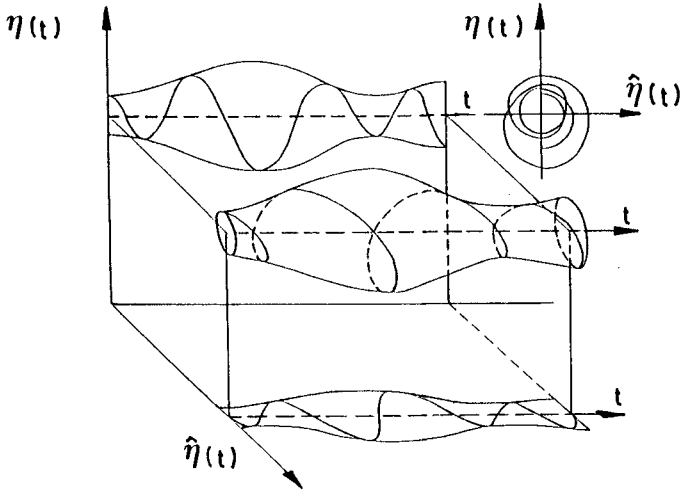


Fig. 1. Representation of the Orbital Movement of a Point in the Sea Surface.

WAVE HEIGHT FUNCTION

It is of interest to compare the envelopes computed by the Hilbert transform method with the SIWEH method.

Funke and Mansard (1979) introduced the Smoothed Instantaneous Wave Energy History (SIWEH) method to estimate the low frequency component of $\eta^2(t)$ in their analyses of the slow oscillations of floating structures. The objective of the SIWEH filters was to isolate the low frequency components of $\eta^2(t)$. Medina and Hudspeth (1987) demonstrated that the squared-wave height function, $H^2(t) = 4A^2(t)$, is the target function which exactly isolates the low frequency components of $\eta^2(t)$ and can be interpreted as eight times the instantaneous variance function.

For linear random waves, $\eta(t)$ and $\hat{\eta}(t)$ are independent (see Pinkster, 1984); $A^2(t)$ and $H^2(t)$ are chi-squared distributed with two degrees of freedom; and, therefore, $A(t)$ and $H(t)$ are Rayleigh distributed with the following properties:

$$\sigma[H^2(t)] = E[H^2(t)] = 8 m_0 \tag{8}$$

$$E[H(t)] = \sqrt{2\pi m_0} \tag{9}$$

$$\sigma[H(t)] = \sqrt{(8 - 2\pi) m_0} \tag{10}$$

where $\sigma(\cdot)$ = variance; $E(\cdot)$ = expectation operator; and

$$m_0 = \int_0^\infty S_\eta(f) df = \sigma^2[\eta(t)] \tag{11}$$

From Rice (1954), Nolte and Hsu (1972), Bendat and Piersol (1986), and Medina and Gudspeth (1987), the spectra of $H(t)$ and $H^2(t)$ are approximately given by

$$S_H(f) \doteq (8 - 2\pi) m_0 \Gamma_\eta(f) ; S_{H^2}(f) \doteq (64 m_0^2) \Gamma_\eta(f) \quad (12a,b)$$

$$\Gamma_\eta(f) = \frac{2}{m_0} \int_0^\infty S_\eta(f+x) S_\eta(x) dx \quad (13)$$

where S_H = the variance spectrum of $H(t)$; and $S_{H^2}(f)$ = the variance spectrum of $H^2(t)$; and $\Gamma_\eta(f)$ = the spectral density function (unit variance).

An exact instantaneous variance function, $H^2(t)/8$, can be determined for long periodic random realizations by implementing the Hilbert transform in the frequency domain. In the time domain, an approximate temporal Hilbert filter given by McClellan et al. (1979) with 95 points (Pierce, 1985) can be used. The output, using this approximate temporal filter, will be noted by $H_p^2(t)/8$.

The Hilbert filter method is an alternative to the SIWEH method introduced by Funke and Mansard (1979) and also to the LVTS method proposed by Thompson and Seelig (1984). Figures 2 and 3 compare these methods for relatively broad and narrow spectra, respectively. Figure 2 compares the exact FFT [$H^2(t)/8$] and the approximate temporal [$H_p^2(t)/8$] with the SIWEH(t) for an NSA-FFT simulation of a relatively broad-banded JONSWAP spectrum ($\gamma = 1$, $f_p = 0.1$ Hz). Figure 3 compares the same functions for a relatively narrow-banded JONSWAP spectrum ($\gamma = 10.0$ and $f_p = 0.1$ Hz).

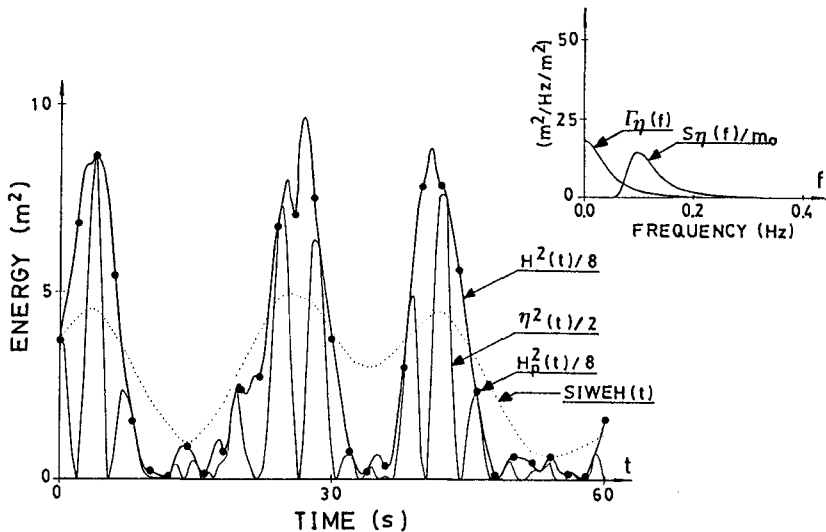


Fig. 2. Comparison between the SIWEH, the Exact FFT Hilbert Transform [$H^2(t)/8$], the Approximate Temporal Filter [$H_p^2(t)/8$], and $\eta^2(t)$ for JONSWAP ($\gamma = 1.0$, $f_p = 0.1$ Hz).

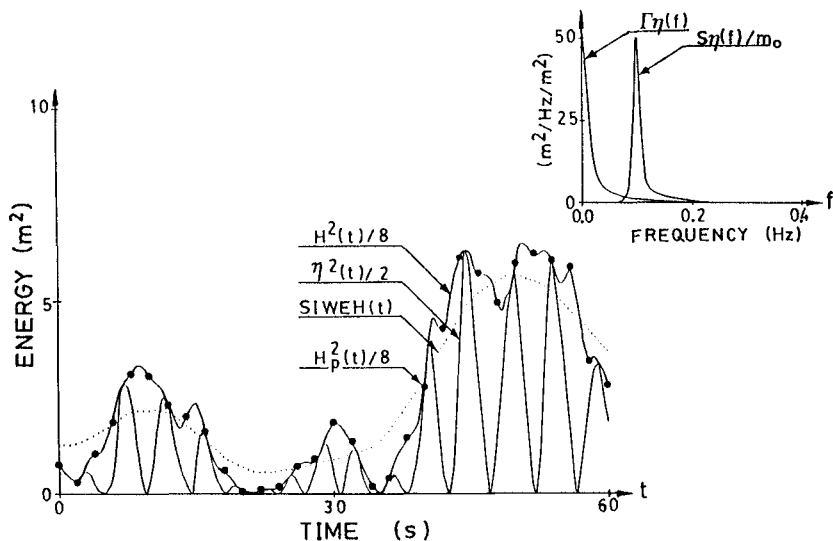


Fig. 3. Comparison between the SIWEH, the Exact FFT Hilbert Transform $[H^2(t)/8]$, the Approximate Temporal Filter $[H_p^2(t)/8]$, and $\eta^2(t)$ for JONSWAP ($\gamma = 10$, $f_p = 0.1$ Hz).

Figure 2 demonstrates that $H_p^2(t)/8$ is an excellent approximation to $H^2(t)/8$ while SIWEH(t) is a relatively poor estimator of $H^2(t)/8$. However, real records are not free of noise and it is necessary to examine the sensitivity of these methods to external noise. If we define an error function $\epsilon(t)$ as

$$\epsilon(t) = \left[\left\{ \begin{matrix} H_p^2(t)/8 \\ SIWEH(t) \end{matrix} \right\} - H^2(t)/8 \right] / m_0 \quad (14)$$

then the magnitude measured by the standard deviation $[\sigma(\epsilon)]$ and the correlation coefficient $[r_{\epsilon H}]$ between $\epsilon(t)$ and $H^2(t)/8$ can be used as parameters to indicate the goodness-of-fit of each method.

Figure 4 compares the mean values of $\sigma(\epsilon)$ and $r_{\epsilon H}$ from 40 realizations using NSA simulations and the JONSWAP spectra with 10% (variance) of white noise. The average standard deviation $[\bar{\sigma}(\epsilon)]$ is less than 2% for the temporal Hilbert filter $H_p^2(t)/8$ with no noise, but rises to 45% when 10% of spectral variance is noise. The SIWEH(t) method using a Bartlett window smoothes the envelope giving larger negative average correlation coefficients $r_{\epsilon H}$ for lower values of the peak enhancement factor γ (i.e., wider spectra).

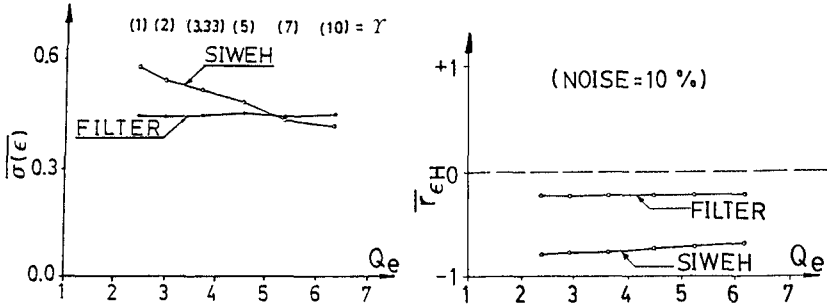


Fig. 4. Comparison between Temporal Hilbert Filter and SIWEH for 40 NSA Simulations of JONSWAP Spectra with Noise (10% Variance).

Figure 5 compares the mean and standard deviations of the SIWEH Groupiness Factor, GF, with the peakedness parameter, Q_e , for 40 NSA realizations without noise and with 10% noise. The Groupiness Factor, GF, is defined as the relative standard deviation of the estimated variance function to the variance of the process. The theoretical lines denoted by $GF_0 \pm \sigma$ correspond to sample spectra of $H^2(t)$ that are, approximately, chi-squared distributed with two degrees of freedom. For NSA simulations, this theoretical approximation tends to underestimate the coefficient of variation of GF_0 . The Groupiness Factor, GF, increases with Q_e indicating that there is less smoothing of $H^2(t)/8$ with increasing values of γ .

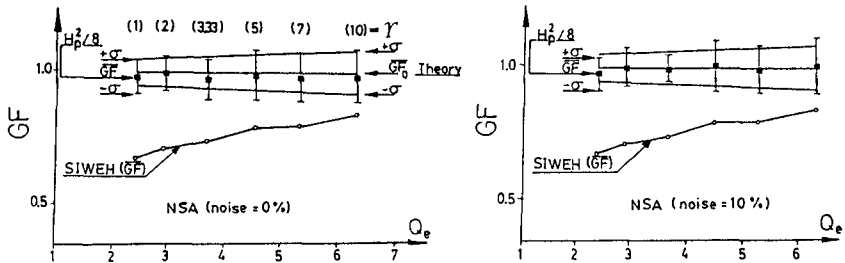


Fig. 5. Comparison of Groupiness Factor Computed by Temporal Hilbert Filter and SIWEH for 40 NSA Simulations of JONSWAP Spectra.

Therefore, the SIWEH Groupiness Factor is a parameter that reflects the low pass filter characteristics used and the narrowness of the spectrum.

Figure 6 shows the wave height function estimated for a hurricane wave record from Wave Project 11 using the temporal Hilbert filter proposed by McGlellan et al. (1979) with $k = 95$. The values between the discrete times of the widely sampled envelope time series ($\Delta T = 3.2$ seconds) have been interpolated using an FFT numerical technique. As was noted by Medina and Hudspeth (1987), the wave height function contains

sufficient low frequency information from wave records using a minimum amount of data because the larger sampling interval ΔT has a high enough Nyquist frequency to retain the important information from the square wave height spectrum, $S_{H_2}(f)$.

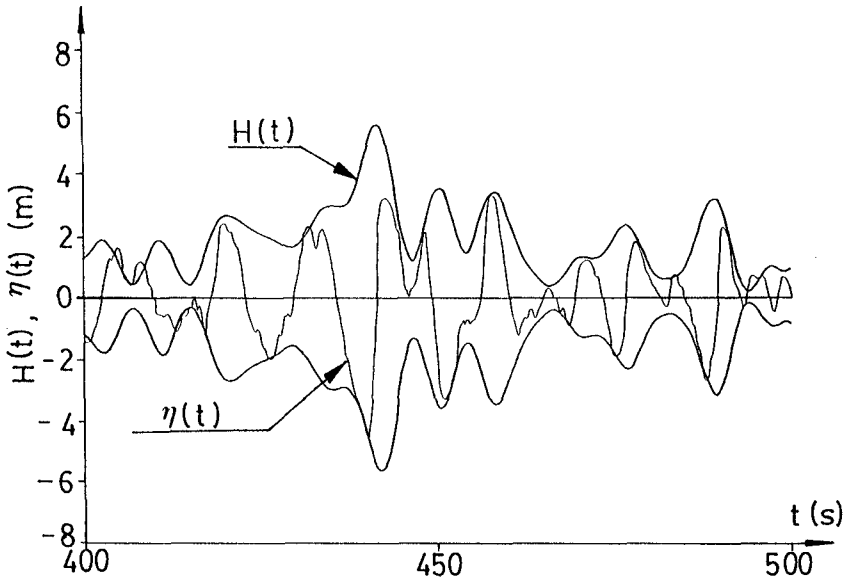


Fig. 6. Wave Height Function for a Wave Project II Wave Record Sampled at $\Delta T = 3.2$ sec and Numerically Interpolated via FFT ($\eta(t)$ sampled at $\Delta t = 0.2$ sec).

LOCAL FREQUENCY FUNCTION

The local frequency function defined by Eq. (6) represents the instantaneous frequency of the orbital movement of a point in the sea surface.

The variable Ω is non-Gaussian, has a large kurtosis, and is centered about the mean frequency $f_{01} = m_1/m_0$. However, if the values of Ω corresponding to increasing levels of H are selected, the standard deviation of Ω decreases. These preliminary results from the analysis of numerically simulated waves indicate an inverse relation between the variance of Ω , $\sigma^2(\Omega)$, and the wave height function, $H(t)$. On the other hand, the observed mean frequency, $\bar{\Omega}$ is approximately $f_{01} = m_1/m_0$, and independent of the H level selected.

Longuet-Higgins (1975) extended the work of Rice (1954) to estimate the joint distribution between wave heights and wave periods assuming a narrow-banded process. This theoretical derivation used approximations for the derivative of the phase angle which are directly related to $\Omega(t)$. Considering the definition of $H(t)$ and $\Omega(t)$ in relation to the complex

envelope given by Longuet-Higgins (1975), the fluctuation of the orbital velocity, $v(t)$, may be defined as

$$v(t) = \pi H(t) [\Omega(t) - f_{01}] \quad (15)$$

For a narrow-banded process, the equations given by Rice (1954) and Longuet-Higgins (1975) can be transformed to estimate the joint probability density function of (H, v) according to

$$p(H, v) = \frac{H}{4m_0} \exp\left[-\frac{H^2}{8m_0}\right] \frac{1}{\sqrt{2\pi} \sigma_v} \exp\left[-\frac{v^2(t)}{2\sigma_v^2}\right] \quad (16)$$

where the variance of $v(t)$ is

$$\sigma_v^2 = (2\pi)^2 \nu^2 f_{01}^2 m_0 \quad (17)$$

where $\nu^2 = (m_2 m_0 / m_1^2 - 1)$, and the simplest stochastic model to describe jointly $[H(t), v(t)]$ is a stochastic process of two independent variables that are Rayleigh and Gaussian distributed, respectively.

The stochastic properties of $H(t)$ are described approximately by the spectra given by Eqs. (12) and (13) and by the exact Rayleigh distribution for the variable H . On the other hand, the stochastic properties of $v(t)$ can be defined independently of $H(t)$ by a Gaussian process with a variance approximated from Eq. (17).

The spectral density function of $v(t)$ for broad-banded spectra has been analyzed from DSA-FFT numerical simulations by comparing it with the spectra of $V(t)$ and $H(t)$ where

$$V(t) = \pi H(t) f_{01} + v(t) = V_0(t) + v(t) \quad (18)$$

where $V_0(t) = \pi H(t) f_{01}$ is the narrow-band approximation and $v(t)$ is a fluctuating orbital velocity.

$H(t), v(t)$, and spectral parameters have been calculated from a set of 40 DSA-FFT simulations of JONSWAP spectra with $\gamma = 1$ and $\gamma = 10$ ($f_p = 0.1$ Hz). The results obtained from these simulations indicate the following:

- The fluctuating orbital velocity, $v(t)$, is independent of the wave height function, $H(t)$.
- The variance of $v(t)$ [σ_v^2] is correctly given by Eq. (17) for narrow and wide spectra. However, if $v(t)$ is numerically calculated from a time series of the water surface elevation sampled with time interval Δt , the variance decreases when Δt increases ($\Delta\sigma_v^2 < 8\%$ if $\Delta t < 1/10 f_p$ and $\gamma < 10$).
- The spectrum of $v(t)$ has a positive maximum at zero frequency and is affected (as noted previously) by the Fourier transform of the temporal window Δt in numerical calculation of $v(n\Delta t)$. Sample $S_v(f)$ are approximately chi-squared distributed about the mean value with two degrees-of-freedom.

Figure 7 illustrates the mean spectra of $v(t)$ calculated numerically from a set of 40 DSA-FFT simulations of JONSWAP spectra ($\gamma = 1$ and 10, $f_p = 0.1$ Hz, $f_{max} = 4 f_p$, and $\Delta t = 0.5$ sec).

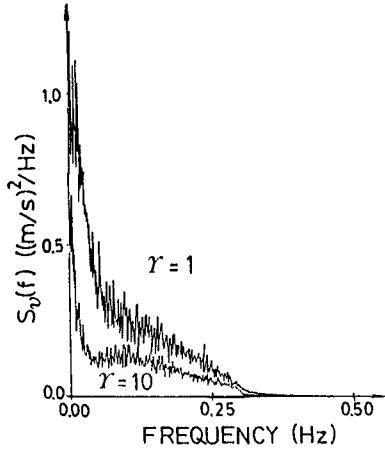


Fig. 7. Mean Spectrum of Fluctuating Orbital Velocity from 40 DSA-FFT Simulations of JONSWAP Spectra, $f_p = 0.1$ Hz and $\Delta t = 0.5$ sec ($\gamma = 1$ and 10).

Given the variance spectrum of the process, $S_v(f)$, a realization of $H(t)$ can be obtained using Eqs. (9), (12a) and (13). Using Eqs. (17) and (18) and spectra estimated in Fig. 7, it is possible to generate Gaussian time series of $v(t)$ independently from $H(t)$. The local frequency function can then be approximated by

$$\Omega(t) = f_{01} + \frac{v(t)}{\pi H(t)} \tag{19}$$

The first term of Eq. (19) represents the narrow-banded approximation and the second term represents the fluctuating component induced by spectral wideness. Note that the contribution from the second term decreases with increasing $H(t)$.

RUNS OF WAVES: THREE AXES REPRESENTATION

Assuming that successive upcrossings of $H(t)$ at a threshold level h are uncorrelated, Longuet-Higgins (1984) estimated the pdf of the length of runs based on the envelope to be given by the following:

$$p(2\ell_h) = \frac{1}{(2\bar{\ell}_h)} \exp \left[-\frac{2\ell_h}{2\bar{\ell}_h} \right] \tag{20}$$

$$p(1\ell_h) = \frac{1}{(1\bar{\ell}_h)} \exp \left[-\frac{1\ell_h}{1\bar{\ell}_h} \right] \tag{21}$$

$$\begin{pmatrix} 2 \\ 1 \end{pmatrix} \bar{\ell}_h = \exp \left[\frac{h^2}{8m_0} \right] \quad (22)$$

in which ${}_1\bar{\ell}_h$ and ${}_2\bar{\ell}_h$ = the length of run of high waves and total run of waves, respectively; $p(\cdot)$ = the probability density function, and h = threshold level. Run lengths calculated from both a succession of discrete waves and from the envelope could follow the exponential model because of the similarities found between the formulas given by Kimura (1980) for discrete waves and by Rice (1954) and by Longuet-Higgins (1984) for the envelope.

Three Axes Representation

Equations (20) and (21) demonstrate that the pdf of the length of runs of waves are controlled by the mean length of run at different levels. Therefore, the representation of these mean lengths of run of waves will characterize the statistical structure of wave groups. Longuet-Higgins (1984) gave the following estimation of the average length of run of high waves:

$${}_1\bar{\ell}_h = \frac{1/\delta}{\sqrt{4\pi} (h/\sqrt{8m_0})} \quad (23)$$

in which $\delta^2 = 1 - (m_1^2/m_0m_2) = \nu^2/(1+\nu^2)$. Equations (23) and (22) can be rewritten as

$$({}_1\bar{\ell}_h) = \exp[\alpha_0] / \left(\frac{h}{\sqrt{8m_0}} \right)^{\beta_0} \quad (24)$$

$$\begin{pmatrix} 2 \\ 1 \end{pmatrix} \bar{\ell}_h = \exp \left[\left(\frac{h}{\sqrt{8m_0}} \right)^{\beta_1} \exp(\alpha_1) \right] \quad (25)$$

where Eq. (24) is equivalent to Eq. (23) if $\beta_0 = 1$ and $\alpha_0 = -1/2 \ln(4\pi \delta^2)$ and Eq. (25) is equivalent to Eq. (22) if $\alpha_1 = 0$ and $\beta_1 = 2$.

Introducing the following change of variables:

$$u = \ln \left(\frac{h}{\sqrt{8m_0}} \right) ; \quad v = \ln({}_1\bar{\ell}_h) ; \quad w = \ln \left[\ln \left(\frac{{}_2\bar{\ell}_h}{{}_1\bar{\ell}_h} \right) \right] \quad (26a,b,c)$$

Equations (24) and (25) can be transformed into the following equations for straight lines:

$$w = \alpha_1 + \beta_1 u ; \quad v = \alpha_0 - \beta_0 u \quad (27a,b)$$

If the exponential approximation is valid, this permits a graphic representation in three axes of pairs of values $({}_1\bar{\ell}_h, {}_2\bar{\ell}_h)$ that should fit on

straight lines with $\alpha_1 = 0$, $\beta_1 = 2$, $\beta_0 = 1$ and α_0 depends on the spectral shape.

Figure 8 illustrates a three-axes representation of the mean length of waves observed from envelopes of 40 DSA-FFT simulations of JONSWAP spectra ($\gamma = 10$, $f_p = 0.1$ Hz, $f_{max} = 4 f_p$) sampled at intervals of $\Delta T = 0.5$ sec), and $\Delta T = T_{01}$. Also runs of discrete waves in the same simulations and observations of Goda (1983) of long-traveled swell waves are represented.

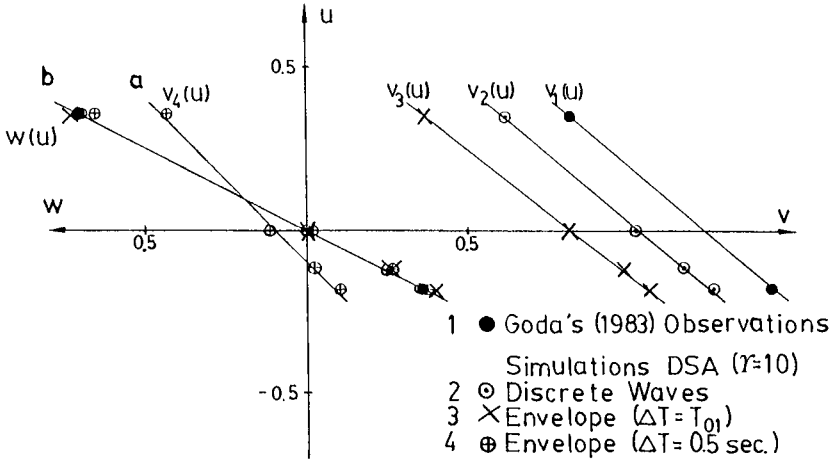


Fig. 8. Three-Axes Representation of Mean Length of Runs Estimated by Discrete Waves and by Envelope (40 DSA Simulations of JONSWAP Spectrum $\gamma = 10$, $f_p = 0.1$ Hz).

The exponential approximation agrees quite well (lines 'a', and 'b') using the envelope sampled at small time intervals. Although line 'b' seems quite robust (related to the Rayleigh distribution), line 'a' depends on the sampling time interval of the envelope; showing larger length of runs for a larger ΔT .

Figure 9 shows the mean length of runs obtained from simulations ($\gamma = 1$ and 10) and from analysis of discrete waves. The square of the wave height function, $H^2(t)$, has been filtered with a rectangular window of length T_{01} . The agreement depends on γ and demonstrates that the analysis of length of runs of waves using the envelope is far different from that using discrete waves. Neither sampling nor filtering $H(t)$ permit a comparison of these results.

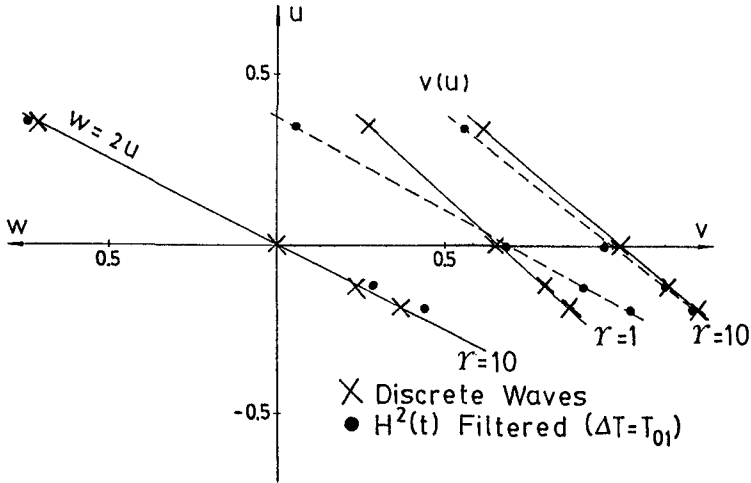


Fig. 9. Three-Axes Representation of Mean Length of Runs Estimated by Discrete Waves and by Temporal Hilbert Filter with a Rectangular Window $\Delta T = 1/f_{01}$ for JONSWAP Simulations ($\gamma = 1$ and 10 , $f_p = 0.1$ Hz).

CONCLUSIONS

Based on a linear assumption, and supported by observations of different authors in non-shallow waters, the analysis of waves in the complex plane leads to definitions of a wave height and a frequency which represent the instantaneous values of these variables for random seas. Efficient Hilbert filters in the time domain make it possible to define with reasonable precision the waves in the complex plane and to compare the results with other analyses.

The use of temporal Hilbert filters to estimate $H^2(t)/8$ is the best method to define the instantaneous variance function of a record. The isolation of the low frequency components of $\eta^2(t)$ by this methodology is better than the SIWEH and other empirical methods. The Groupiness Factor, GF, is not an efficient way to characterize wave grouping characteristics because of the amount of smoothing that is introduced in relatively broad-banded spectra.

The local frequency function $\Omega(t)$ can be defined on the basis of a mean value $f_{01} = m_1/m_0$ and a fluctuating component that is inversely proportional to the wave height function, $H(t)$.

A three-axes representation of mean length of runs of waves shows that neither sampling nor filtering $H(t)$ makes it possible to compare directly the results from analyzing a sequence of discrete waves with an analysis from the continuous wave height function.

ACKNOWLEDGEMENTS

We gratefully acknowledge the financial support provided by the U.S.-Spain Joint Committee for Scientific and Technological Cooperation under Grant CCA8510095 and by the Office of Naval Research under the University Research Initiative (URI) Contract No. N00014-86-K-0687.

REFERENCES

- Barthel, V., Mansard, E.P.D., Sand, S.E., and Vis, F.C. (1983): "Group Bounded Long Waves in Physical Models," Ocean Engineering, Vol. 70, No. 4, pp. 261-294.
- Battjes, J.A. (1988): "Surf-Zone Dynamics," Ann. Rev. Fluid Mechanics, Vol. 20, pp. 257-293.
- Battjes, J.A., and Vledder, V. (1984): "Verification of Kimura's Theory for Wave Group Statistics," Proceedings, 19th ICCE, 1984, Houston, TX, pp. 642-648
- Bendat, J.S., and Piersol, A.G. (1986): Random Data. Analysis and Measurement Procedures, (2nd Ed.), John Wiley, pp. 484-516.
- Bowers, E.C. (1988): "Wave Grouping and Harbour Design," Proceedings of the Institution of Civil Engineers, Part 2, June 1988, Vol. 85, pp. 237-258.
- Bruun, P. (ed.), (1985): Design and Construction of Mounds for Breakwaters and Coastal Protection, Elsevier Science Publ., Amsterdam, 1985.
- Burchart, H.F. (1979): "The Effect of Wave Grouping on On-Shore Structures," Coastal Engineering, No. 2, pp. 189-199.
- Elgar, S., Guza, R.T., and Seymour, R.J. (1984): "Groups of Waves in Shallow Water," Journal of Geophysical Research, Vol. 89, No. C3, pp. 3623-3634.
- Elgar, W., Guza, R.T., and Seymour, R.J. (1985): "Wave Group Statistics from Numerical Simulations of a Random Sea," Applied Ocean Research, Vol. 7, No. 2, pp. 93-96.
- Ewing, J.A. (1973): "Mean Length of Runs of High Waves," Journal of Geophysical Research, Vol. 78, No. 12, pp. 1933-1936.
- Funke, E.R., and Mansard, E.P.D. (1979): "Synthesis of Realistic Sea States in a Laboratory Flume," National Research Council of Canada, HLR Report LTR-HY-66.
- Goda, Y. (1970): "Numerical Experiments on Wave Statistics with Spectral Simulation," Report of the Port and Harbour Research Institute, Vol. 9, No. 3, 1970.
- Goda, Y. (1983): "Analysis of Wave Grouping and Spectra of Long-Traveled Swell," Report of the Port and Harbour Research Institute, Vol. 22, No. 1, 1983.
- Hsu, F.H., and Blenkarn, K.A. (1970): "Analysis of Peak Mooring Forces Caused by Slow Vessel Drift Oscillations in Random Seas," Proceedings, OTC Conference, Houston, TX, 1970, Paper No. 1159.

Johnson, R.R., Mansard, E.P.D., and Ploeg, J. (1978): "Effects of Wave Grouping on Breakwater Stability," Proceedings, 16th ICCE, 1978, Hamburg, Germany, pp. 2228-2243.

Kimura, A., (1980): "Statistical Properties of Random Wave Groups," Proceedings, 17th ICCE, 1980, Sydney, Australia, pp. 2955-2973.

Longuet-Higgins, M.S. (1975): "On the Joint Distributions of the Periods and Amplitudes of Sea Waves," Journal of Geophysical Research, Vol. 80, No. 18, pp.2688-2694.

Longuet-Higgins, M.S. (1984): "Statistical Properties of Wave Groups in a Random Sea State," Phil. Trans. Royal Soc. London, A312, pp. 219-250.

McClellan, J.H., Parks, T.W., and Rabiner, L.R. (1979): "FIR Linear Phase Filter Design Program," in Programs for Digital Signal Processing, IEEE Press, John Wiley, NY, pp. 5.1.1-5.1.6.

Medina, J.R., Aguilar, J., and Diez, J.J. (1985): "Distortions Associated with Random Sea Simulators," Journal of Waterway, Port, Coastal, and Ocean Engineering, ASCE, Vol. 111, No. 4, pp. 603-628.

Medina, J.R., and Hudspeth, R.T. (1987): "Sea States Defined by Wave Height/Period Functions," Proceedings, IAHR Seminar on Wave Analysis and Generation in Laboratory Basins, 22nd IAHR Congress, September 1-3, 1987, Lausanne, Switzerland, pp. 249-259.

Nolte, K.G., and Hsu, F.H. (1972): "Statistics of Ocean Wave Groups," Proceedings, OTC Conference, Houston, TX, 1972, OTC Paper No. 1688.

Pierce, R.D. (1985): "Extreme Value Estimates for Arbitrary Bandwidth Gaussian Processes Using the Analytical Envelope," Ocean Engineering, Vol. 12, No. 6, pp. 493-529.

Pinkster, J.A. (1984): "Numerical Modeling of Directional Seas," Proceedings, Symp. on Description and Modeling of Directional Seas, Tech. Univ. of Denmark, June 18-20, Copenhagen, Denmark, Paper No. C-1, 1984.

Rice, S.O. (1954): "Mathematical Analysis of Random Noise," Bell System Technical Journal, Vol. 23, 1944, and Vol. 24, 1945. (Reprinted in Selected Papers on Noise and Stochastic Processes, N. Wax, Ed., Dover Publications, Inc., New York, NY, 1954, pp. 123-244.)

Rye, H. (1982): Ocean Wave Groups, Dept. Marine Technology, Norwegian Institute of Technology, Report UR-82-18, 1982.

Thompson, E.F., and Seelig, W.N. (1984): "High Wave Grouping in Shallow Water," Journal of Waterway, Port, Coastal and Ocean Engineering, ASCE, Vol. 110, No. 2, pp. 139-157.

Tuah, H., and Hudspeth, R.T. (1982): "Comparisons of Numerical Random Sea Simulations," Journal of Waterway, Port, Coastal, and Ocean Engineering Division, ASCE, Vol. 108, No. WW4, p. 569-584.

Tucker, M.J. (1950): "Surf Beats: Sea Waves of 1 to 5 min. Period," Proceedings of the Royal Society, A, Vol. 202, pp. 565-573.

CHAPTER 67

On the Methodology of Selecting Design Wave Height

Yoshimi Goda*, M. ASCE

ABSTRACT

A statistically-rational method of extreme wave data analysis is presented. A combination of the Fisher-Tippett type I and the four Weibull distributions is proposed as the candidates of distribution functions. The least square method is used for data fitting. The best plotting position formula for each function is determined by the Monte Carlo method with 10,000 simulations per sample size.

Confidence intervals of estimated extreme wave heights for given return periods are evaluated by simulations and expressed in the form of empirical formulas, for both the cases when the true distribution is known and unknown. An example of extreme wave data analysis is given.

1. INTRODUCTION

Design waves must be decided upon by the responsible engineer in charge of a maritime project. He looks for various data source on storm waves and asks statisticians to make extreme wave analysis. Based on the statistical estimate of wave height for a certain return period, he makes a final decision. The statistical procedure for this purpose is rather confused at present, however, with several different methods being employed in various occasions. Some procedure is not recommendable from the statistical point of view, and some other is quite complicated to use. There is a need for a clear and sound statistical method for extreme wave data analysis.

Another problem in extreme data analysis is the lack of information on the statistical uncertainty or confidence interval of estimated extreme value for a given return period (hereinafter called "return value" for the sake of simplicity). For the Fisher-Tippett type I distribution (abbreviated as FT-I), a formula is given in Gumbel's book (1958, Sec. 6.2.3). Lawless (1974) also gave integral form-

* Professor, Yokohama National University, Department of Civil Engineering, 156 Tokiwadai, Hodogaya-ku, Yokohama, Japan 240.

ulas for the FT-1 distribution for the case when the parameters are estimated by the maximum likelihood method. Both formulas are applicable for the annual maximum series data but inapplicable for the partial-duration series data. For the Weibull distribution, there is practically no formula available for the confidence interval of return values. The problem of confidence interval when the true distribution is unknown has only been mentioned by Petruaskas and Aagaard (1970), but they did not give any formula for its estimation.

The present paper tries to give a clear view of the practical procedure of extreme wave data analysis, which is statistically sound and easily applicable. The confidence interval of return values will also be estimated for several distribution functions used in the analysis. Detailed descriptions can be found in Goda (1988) in Japanese.

2. CLASSIFICATION OF EXTREME WAVE STATISTICS

Total Sample Method versus Peak Value Method

Two different methods are currently employed to prepare extreme statistics of storm waves. The first one may be called the total sample method which employs the all wave data recorded at a regular interval of a few hours. The second one may be called the peak value method which picks up the peak wave heights of individual storms and thus composes a set of extreme wave data.

The total sample method was proposed by Draper (1966), when wave observation projects at various countries were at their initial stages and the accumulation of wave data was short in terms of the time span of observation. This method is applicable even when the observation is a few years long and it is easy to use. However, the method violates the condition of statistical independence between individual data, because the regularly recorded wave heights are mutually correlated; the correlation coefficient remains over 0.3 to 0.5 with the time lag of 24 hours (see a review by Goda 1979). Therefore, use of the total sample method should be refrained in the present days when longer wave data by observations and/or hindcasting are available.

The total sample method also has an ambiguity in the selection of unit time in assessing return wave heights. One may take the recording interval of a few hours, but he may use one day as the unit time instead. Depending on the unit time, the return wave heights vary. Medina and Aguilar (1986) have proposed to employ the mean period between successive storms in their attempt to compromise the total sample method with the statistical condition of independent data.

Annual Maximum Series versus Partial-Duration Series

The data set for the peak value method can be either the annual maximum series or the partial-duration series. The latter refers to the series of peak storm wave heights in

the order of appearance. The annual maximum series data is clear in definition and easy to deal with. Most of wave data, however, cover rather short time spans, say less than 40 years by hindcasting and 10 years by instrumental observations. Therefore, the partial-duration series is the usual data source for extreme wave analysis.

In the analysis of partial-duration series data, the mean number of storm waves per year is an important parameter. It is called here as the **mean rate** and denoted with λ . The annual maximum series data can be treated as the case with $\lambda = 1$, although the meaning is slightly different. In practice of extreme wave analysis, the data above a certain threshold height are usually adopted to constitute the data set. Such data is called the **censored data** in contrast with the **uncensored data** which is composed of all storm wave data. The ratio of the number of adopted data N to the whole number of storm data N_T is hereby called the **censoring parameter** and denoted by ν : i.e., $\nu = N/N_T$. Burcharth (1988) calls the method utilizing the censored partial duration series data as the Peak-over-threshold method.

Methods of Data Fitting to Distribution Functions

There are four methods for fitting a set of extreme wave data to some distribution function. They are the graphical method, the method of moments, the least square method, and the maximum likelihood method. The graphical method is susceptible to subjective judgment and not recommended except for initial analysis. The moment method requires fewer calculation than the least square method, but cannot deal with the censored data. The maximum likelihood method is theoretically rigorous and favored by many statisticians, but the calculation is cumbersome even though the present computers can handle it with ease.

The least square method is a sophistication of the graphical method, but it has been neglected by most of statisticians except for a few such as Blom (1963) by reasons unknown. It is simple and clear in the calculation process, and therefore it is adopted in the present paper for extreme wave data analysis.

3. DISTRIBUTION FUNCTIONS AND PLOTTING POSITION FORMULAS

Candidates of Distribution Functions

In the extreme data analysis of various environmental phenomena such as rainfall, flood discharge, strong wind, and storm waves, selection of distribution functions to be fitted to the data is always a problem. No theoretical justification is provided for the selection except that the FT-I should be applicable if the basic population to define the maximum of a group of data belongs to the exponential distribution. In some occasion, a particular distribution such as the FT-I or the log-normal is assumed as applicable to the data set even without any theoretical support. In many occasions, however, several candidate functions are tested and the best fitting distribution is adopted.

Petruaskas and Aagaard (1970) have proposed to choose among a set of the FT-I and the seven Weibull distributions with the shape parameter fixed at certain values. As will be seen later, the capability of the extreme data analysis to recognize the parent distribution among several candidates is rather low when the sample size is less than 100 or so. Therefore, it is better to restrict the number of candidate distributions. The present paper proposes the following set of five functions:

FT-I distribution:

$$F(x) = \exp\{-\exp[-(x-B)/A]\} \quad (1)$$

Weibull distribution:

$$F(x) = 1 - \exp\{-(x-B)/A\}^k \quad (2)$$

$$: k = 0.75, 1.0, 1.4, \text{ and } 2.0$$

The distribution function $F(x)$ represents the probability of nonexceedance of the variate x , and A , B , and k are called the location, scale, and shape parameters, respectively. It is often useful in the extreme statistics to introduce the reduced variate y which is defined by

$$y = (x-B)/A \quad (3)$$

The log-normal distribution is not adopted here, because its characteristics are quite similar with those of the Weibull distribution with $k = 2.0$ and it requires the calculation of the error function, which is not easy to make with a pocket calculator.

Selection of Plotting Position Formulas

A drawback of the least square method for extreme data analysis is the necessity of choosing a right plotting position formula for each distribution function. Figure 1 is an example of the histograms of the ordered extreme data and its nonexceedance probability. The parent distribution is the FT-I ($A = 1.0$ and $B = 0$), and 100 samples with 10 data each are randomly drawn from the population. In each sample, the largest data $x_{(1)}$ are sorted out and its histogram is shown in the right. The nonexceedance probability F_1 corresponding to $x_{(1)}$ is shown in the top as a histogram.

The probability to be assigned to each ordered extreme data, which depends upon the ordered number and the total data number only, is called the plotting position. Cunnane (1978) has made a critical review of this problem and denounced the recommendation by Gumbel (1958) of the Weibull formula, which is expressed as

$$\hat{F}_m = 1 - m/(N + 1) \quad (4)$$

where m is the descending ordered number from the largest.

A plotting position formula should be so selected to

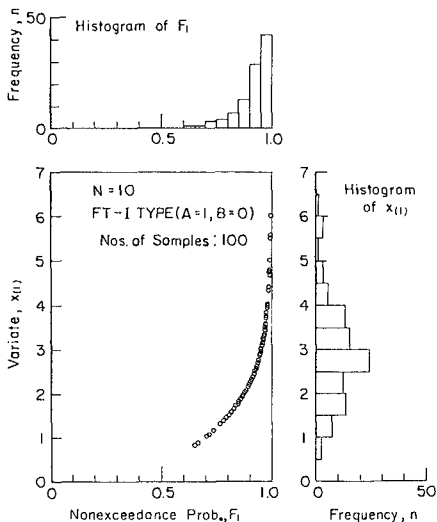


Fig. 1 Distribution of the largest data in a sample from FT-1.

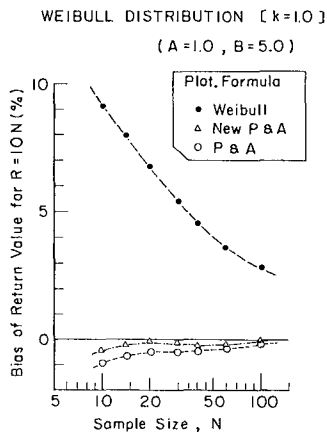


Fig. 2 Mean bias of return values due to plotting formulas in Weibull distrib. ($k=1.0$).

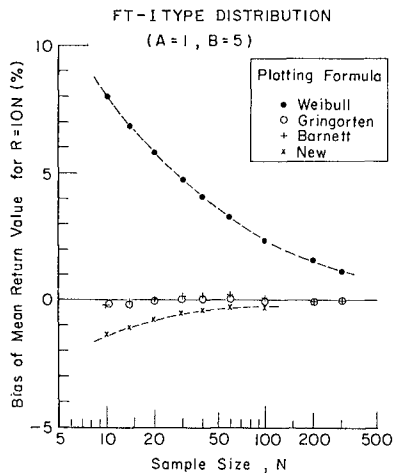


Fig. 3 Mean bias of return values due to plotting formulas in FT-1 distribution.

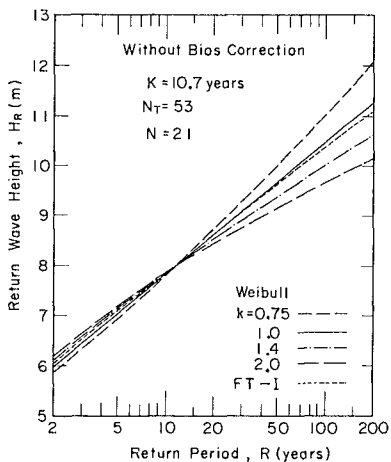


Fig. 4 Example of return wave height estimation with various distribution functions.

yield no bias on the mean and the least root-mean-square error of the return values. The first choice would be the use of the probability corresponding to the expected value of the ordered variate, or $F\{E\{x_{(m)}\}\}$. Gringorten (1961) has derived the following formula for the FT-I distribution:

$$\text{FT-I: } \hat{F}_m = 1 - (m - 0.44)/(N_T + 0.12) \quad (5)$$

$$: m = 1, 2, \dots, N$$

in which N_T is the number of whole extreme data including those below a threshold value. Use of N_T instead of N (number of adopted data) is to enhance the possibility of recognizing the parent distribution for the case of censored data, after the suggestion by Muir and El-Shaarawi (1986). For the Weibull distribution, Petruaskas and Aagaard (1970) have presented the following formula:

$$\text{Weibull: } \hat{F}_m = 1 - (m - \alpha)/(N_T + \beta) \quad (6)$$

where

$$\alpha = 0.30 + 0.18/k, \quad \beta = 0.21 + 0.32/k \quad (7)$$

Figure 2 shows the bias of return values caused by use of various plotting position formulas for the case of FT-I distribution. The sample size is varied from 10 to 300, and 10,000 uncensored samples are simulated by the Monte Carlo method at each sample size. The bias is defined here as $100 \times (\hat{x}_R/x_R - 1)$, where \hat{x}_R and x_R refer to the estimated and true return values, respectively. The return values are evaluated at the return period being 10N.

It is clear in Fig. 2 that the Weibull formula yields conspicuous positive bias, indicating a tendency of over-estimation. The formula by Barnett (1975) though not presented here gives practically no bias just as same as Gringorten's formula. The formula denoted as "New" has the expression same as Eq. 6 but with the constants $\alpha = 0.51$ and $\beta = 0.18$. This formula has been derived as to yield the best fitting to $F\{E\{x_m\}\}$, but it yields slightly negative bias. Figure 2 clearly indicates the Gringorten formula to be used for the FT-I distribution. Poor performance of the Weibull formula has also been reported by Carter and Challenor (1983) with a small scale Monte Carlo simulation, in which they compared the effectiveness of various methods of extreme data analysis.

Figure 3 shows a similar comparison of plotting position formulas for the Weibull distribution with $k = 1.0$. The Weibull formula again exhibits large positive bias. The formula by Petruaskas and Aagaard (denoted as "P & A") shows a tendency to yield slightly negative bias. A modification is made here by changing the constants as

$$\alpha = 0.20 + 0.27/\sqrt{k}, \quad \beta = 0.20 + 0.23/\sqrt{k} \quad (8)$$

The new formula is denoted as "New P & A" in Fig. 3. This plotting formula is used in this paper hereinafter.

For the log-normal distribution, the appropriate plotting position formula is that by Blom (1958) in the form of Eq. 6 with $\alpha = 3/8$ and $\beta = 1/4$. Use of the Weibull formula yields positive bias as demonstrated in a simulation study by Earle and Baer (1982). The amount of bias reported by them has been confirmed in the author's simulation (Goda, 1988); use of the Blom formula for the same condition has yielded no bias.

4. DATA FITTING AND CALCULATION OF RETURN VALUES

For a given set of extreme wave data, the first step of data processing is to rearrange the data in the descending order from the largest to the smallest. Then the nonexceedance probability \hat{F}_m is assigned to each data by Eqs. 5, 6, and 8 by assuming the FT-I and the four Weibull distributions as the candidate functions. For each \hat{F}_m , the following reduced variate $y_{(m)}$ is then calculated:

$$\text{FT-I:} \quad y_{(m)} = -\ln[-\ln \hat{F}_m] \quad (9)$$

$$\text{Weibull:} \quad y_{(m)} = [-\ln(1 - \hat{F}_m)]^{1/k} \quad (10)$$

Because there should exist a linear relation between the ordered variate $x_{(m)}$ and its reduced variate $y_{(m)}$, the following equation is assumed and solved by the least square method to yield the estimates \hat{A} and \hat{B} of the scale and location parameters:

$$x_{(m)} = \hat{A} y_{(m)} + \hat{B} \quad (11)$$

Table 1 is an example of the above procedures applied for an extreme data of typhoon waves measured at the depth of 50 m at a location facing the Pacific. The measurement has been continued for more than 15 years, and the portion of successful recording covering $K = 10.74$ years is used in the analysis. There were 53 typhoon waves during this effective observation period of 10.74 years, and thus $N = 53$ and $\lambda = 4.93$ per year. The wave heights exceeding 4.0 m have been chosen for the analysis, and there were 21 such data; i.e., $N = 21$ and $\nu = 0.396$.

The nonexceedance probabilities \hat{F}_m listed in Table 1 are all above 0.61, because the total number of typhoon waves $N_T = 53$ is used in evaluating \hat{F}_m by Eqs. 5 and 6. Even if the threshold height is changed to 4.5 m and the number of data is reduced to $N = 18$, the probability \hat{F}_m remains at the same value so long as N_T is the same.

The return value or the expected extreme wave height for a given return period R is then calculated by the following equation with the estimated parameters \hat{A} and \hat{B} :

$$x_R = \hat{A} y_R + \hat{B} \quad (12)$$

where

$$\left. \begin{aligned} y_R &= -\ln[-\ln(1 - 1/(\lambda R))] && : \text{FT-I} \\ y_R &= [\ln(\lambda R)]^{1/k} && : \text{Weibull} \end{aligned} \right\} \quad (13)$$

Table 1. Example of Extreme Wave Data Fitting to Several Distribution Functions [units in meters]
 - N = 21, N_T = 53, K = 10.7 years -

m	x _m	FT-I		Weibull (0.75)		Weibull (1.0)		Weibull (1.4)		Weibull (2.0)	
		\hat{F}_m	y _m	\hat{F}_m	y _m	\hat{F}_m	y _m	\hat{F}_m	y _m	\hat{F}_m	y _m
1	8.36	0.9895	4.55	0.9909	7.88	0.9901	4.61	0.9893	2.95	0.9886	2.12
2	7.02	0.9706	3.51	0.9722	5.48	0.9714	3.55	0.9706	2.46	0.9699	1.87
3	6.94	0.9518	3.01	0.9535	4.46	0.9527	3.05	0.9518	2.21	0.9511	1.74
4	6.85	0.9330	2.67	0.9348	3.82	0.9339	2.72	0.9331	2.04	0.9324	1.64
5	6.74	0.9142	2.41	0.9161	3.35	0.9152	2.47	0.9144	1.90	0.9136	1.57
6	6.20	0.8953	2.20	0.8974	3.00	0.8965	2.27	0.8957	1.79	0.8945	1.50
7	5.92	0.8765	2.03	0.8787	2.71	0.8778	2.10	0.8769	1.70	0.8762	1.45
8	5.68	0.8577	1.87	0.8599	2.46	0.8591	1.96	0.8582	1.61	0.8574	1.40
9	5.57	0.8389	1.74	0.8412	2.26	0.8404	1.84	0.8395	1.54	0.8387	1.35
10	5.42	0.8200	1.62	0.8225	2.08	0.8216	1.72	0.8207	1.47	0.8199	1.31
11	5.34	0.8012	1.51	0.8038	1.92	0.8029	1.62	0.8020	1.41	0.8012	1.27
12	5.10	0.7824	1.41	0.7851	1.78	0.7842	1.53	0.7833	1.35	0.7825	1.24
13	5.09	0.7636	1.31	0.7664	1.65	0.7655	1.45	0.7646	1.30	0.7637	1.20
14	4.95	0.7447	1.22	0.7477	1.53	0.7468	1.37	0.7458	1.25	0.7450	1.17
15	4.81	0.7259	1.14	0.7290	1.43	0.7281	1.30	0.7271	1.21	0.7262	1.14
16	4.77	0.7071	1.06	0.7103	1.33	0.7093	1.24	0.7084	1.16	0.7075	1.11
17	4.63	0.6883	0.99	0.6916	1.24	0.6906	1.17	0.6896	1.12	0.6888	1.08
18	4.61	0.6694	0.91	0.6729	1.16	0.6719	1.11	0.6709	1.08	0.6700	1.05
19	4.41	0.6506	0.84	0.6542	1.08	0.6532	1.06	0.6522	1.04	0.6513	1.03
20	4.34	0.6318	0.78	0.6355	1.01	0.6345	1.01	0.6335	1.00	0.6325	1.00
21	4.11	0.6130	0.71	0.6168	0.95	0.6158	0.96	0.6147	0.97	0.6138	0.98
$\bar{x} = 5.565$		A = 1.091		A = 0.614		A = 1.147		A = 2.084		A = 3.560	
$\sigma_x = 1.101$		B = 3.617		B = 4.029		B = 3.374		B = 2.334		B = 0.786	
		r = 0.9842		r = 0.9621		r = 0.9790		r = 0.9878		r = 0.9910	

Figure 4 exhibits the result of estimating the return wave heights for the data of Table 1. Depending on the distribution functions fitted to the data, the return wave heights vary and the difference increases as the estimate is made to longer return periods.

There is no absolute criterion to choose a particular function among several candidates fitted to an extreme data. For practical purposes, the correlation coefficient r between the ordered variate x_(m) and its reduced variate y_(m) can serve as the basis of selection. In the example of Table 1, the Weibull distribution with k = 2.0 indicates the highest correlation with r = 0.9910 and is chosen as the distribution best fitted to the data.

5. STANDARD DEVIATION OF RETURN VALUE WHEN THE TRUE DISTRIBUTION IS KNOWN

A set of extreme wave data being analyzed is regarded as a sample drawn from an unknown population of storm waves. Another set of extreme waves to be obtained in the coming several tens of years will form a sample different from the present sample, even if no long-term climatic change exists. The two sets of extreme data will surely yield different distribution functions and the return wave heights will eventually be different.

Figure 5 shows some results on the statistical variability of return values. A population with the FT-I distribution (A = 1 and B = 5) is assumed, and Monte Carlo simula-

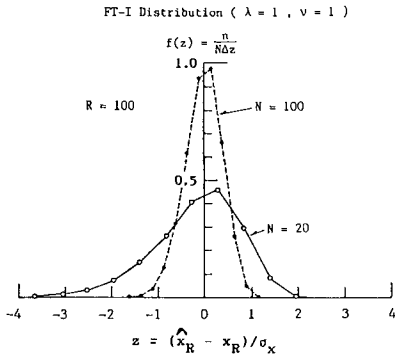


Fig. 5 Distribution of estimated return values in dimensionless form.

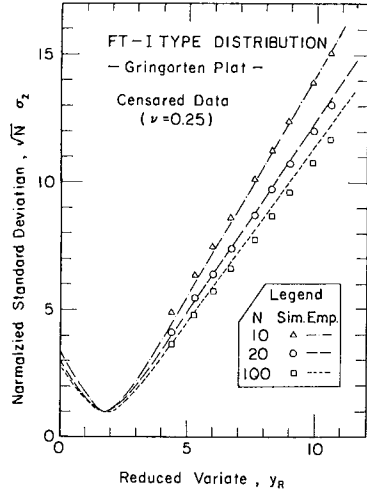


Fig. 6 Example of standard deviation of return values in censored samples from FT-I.

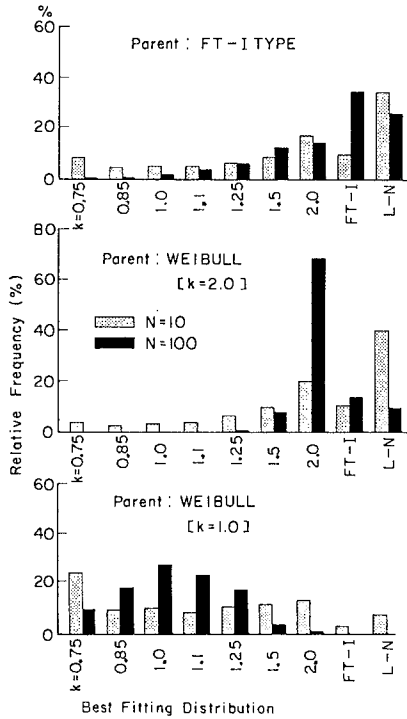


Fig. 7 Relative frequencies of best-fitted distributions for random samples.

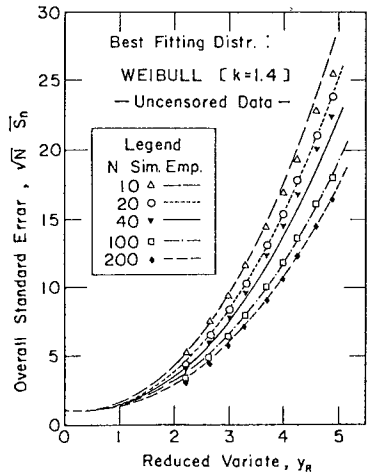


Fig. 8 Example of standard error of return values when the true distribution is unknown.

tions are carried out to yield 10,000 uncensored samples each for the sample size $N = N_T = 20$ and 100. By fitting the FT-I function to each sample, the return value at the return period $R = 100$ is estimated. The difference between the estimated and true return value is normalized with the standard deviation of each sample σ_x . Figure 5 presents the histograms of this normalized deviation in the form of probability density. As seen clearly, the deviation may exceed $2\sigma_x$ in case of the sample with $N = 20$ and $1\sigma_x$ for $N = 100$.

Monte Carlo simulations have been carried out for various combinations of the distribution functions, the sample size, and the censoring parameter, in order to obtain sufficient data on the statistical variability of the return values. For each combination, the standard deviation of the dimensionless variate $z = (\hat{x}_R - x_R) / \sigma_x$ has been evaluated. Figure 6 is an example of the standard deviation σ_z multiplied by \sqrt{N} in order to reduce the influence of the sample size on data presentation. The data are those of censored ones ($v = 0.25$) sampled from the FT-I distribution.

Empirical formulations of the standard deviations of the return values have been tried by referring to the formula cited by Gumbel (1958) as in the following form:

$$\sigma_z = [1.0 + a (y_R - c + \epsilon \ln v)^2]^{1/2} / \sqrt{N} \quad (14)$$

where

$$a = a_1 \exp[a_2 N^{-1.3} + \kappa (-\ln v)^{1/2}] \quad (15)$$

The coefficients in the above equations are assigned the values listed in Table 2. The dashed and dotted curves in Fig. 6 represent the empirical predictions of the standard deviations of the return values.

Table 2. Coefficients of Empirical Formulas for Standard Deviation of Return Values When the True Distribution Is Known

Distribution	a_1	a_2	κ	c	ϵ
FT-I	0.84	9.0	0.93	0.0	1.33
Weibull (k=0.75)	1.65	11.4	-0.63	0.0	1.15
Weibull (k=1.0)	1.92	11.4	0.00	0.3	0.90
Weibull (k=1.4)	2.05	11.4	0.69	0.4	0.72
Weibull (k=2.0)	2.24	11.4	1.34	0.5	0.54

Once the dimensionless deviation σ_z is evaluated, the standard deviation of the return value can be approximately estimated as $\sigma(\hat{x}_R) = \sigma_z \sigma_x$. The confidence interval of the return value is then constructed with $\sigma(\hat{x}_R)$.

6. PROBLEM OF FINDING TRUE DISTRIBUTION

The capability of finding out the true distribution from a random sample of extreme data has been tested with Monte Carlo simulations. Figure 7 demonstrates some results. A parent distribution is assumed, and 10,000 uncensored random samples with the size 10 and 100 were prepared. For

each sample, a group of nine candidate distributions were applied and the best fitting one was selected by the criterion of the largest correlation coefficient between $x_{(m)}$ and $y_{(m)}$. The ordinates in Fig. 7 shows the relative frequency of the best-fitted function, while the abscissa stands for the distribution functions: $k = 0.75$ to 2.0 denote the Weibull distributions and "L-N" stands for the log-normal distribution. The set of Weibull distributions is same as that used by Petruaskas and Aagaard (1970).

It is clear in Fig. 7 that a small sample has only a small chance of selecting the parent distribution as the best-fitting one. Even at the sample size $N = 100$, samples from the FT-I distribution can be mistaken as those belonging to the log-normal distribution. Such competitive power of the log-normal against the FT-I and the Weibull distributions is one reason for the rejection of the former from the candidates of the distributions functions in the present proposal of extreme data analysis.

The low capability of a statistical data analysis in recognizing the true distribution function is due to the statistical variability of random samples. The standard deviation of an uncensored sample with the size 40 from the Weibull distribution ($k = 1.0$), for example, can be less than 0.5 times or more than 1.7 times the population value. A sample with a small deviation tends to be better fitted by the distribution with narrower spreading, and vice versa. Use of the statistical method other than the least square method may slightly enhance the capability of recognizing the true distribution, but the amount of enhancement will be small.

7. BIAS CORRECTION TO RETURN VALUE WHEN THE TRUE DISTRIBUTION IS UNKNOWN

Fitting of an extreme data to a distribution other than the true one causes a certain bias to the estimated return values, even though the right plotting position formula is employed. For example, if a sample from the Weibull with $k = 1.0$ is judged to be best fitted to the Weibull with $k = 0.75$, the return values will be overestimated because of the latter's characteristic of having a longer tail.

An attempt for the correction of this kind of bias is made in this paper, by assuming the five candidate distributions have the equal probability of existence in the nature. Another series of Monte Carlo simulations have been made with 2,000 to 10,000 samples for each combination of the parent distribution, sample size, and censoring parameter. Each sample is analyzed with the procedure described in this paper, and the return values are estimated and compared with the true values. The difference is normalized as $z = (\hat{x}_R - x_R) / \sigma_x$ and its ensemble mean is calculated for each distribution function which is best fitted to samples taken from various parent distribution functions. The ensemble mean of the dimensionless difference \bar{z}_n is thought to represent the bias due to not-knowing true distribution and is empirically formulated as in the following:

Table 3. Example of the Estimation of Return Wave Heights with Bias Correction and Their Standard Errors

Return Period (years)	FT-I		Weibull(0.75)		Weibull(1.0)		Weibull(1.4)		Weibull(2.0)	
	H _R (m)	σ (H) (m)	H _R (m)	σ (H) (m)	H _R (m)	σ (H) (m)	H _R (m)	σ (H) (m)	H _R (m)	σ (H) (m)
2.0	6.2	0.4	5.9	0.3	6.0	0.4	6.2	0.5	6.4	0.5
5.0	7.3	0.7	6.8	0.5	7.1	0.6	7.3	0.7	7.6	0.8
10.0	8.1	0.9	7.6	0.7	7.9	0.8	8.1	0.9	8.4	1.0
20.0	8.9	1.2	8.3	1.0	8.8	1.1	8.9	1.2	9.3	1.3
50.0	10.0	1.6	9.4	1.4	9.9	1.5	10.0	1.5	10.4	1.7
100.0	10.8	1.9	10.1	1.6	10.7	1.8	10.6	1.9	11.2	2.1

$$\bar{Z}_n = \begin{cases} A_c (y_R + \alpha \ln \nu)^p & : y_R > -\alpha \ln \nu \\ 0 & : y_R \leq -\alpha \ln \nu \end{cases} \quad (16)$$

The coefficients A_c and α and the exponent p are assigned the following values depending on the distribution functions and the censoring parameter:

FT-I :

$$\left. \begin{aligned} \nu &= 1.0 ; \\ A_c &= \begin{cases} 0.046 - 0.40[\log_{10}(60/N)]^3 & : N < 60 \\ 0.046 \exp\{-2.5[\log_{10}(N/60)]^2\} & : N \geq 60 \end{cases} \\ \alpha &= 0.9, \quad p = 1.0 \end{aligned} \right\} \quad (17)$$

$$\left. \begin{aligned} \nu &= 0.5 \text{ \& \ } 0.25 ; \\ A_c &= 0.01 - 0.044[\log_{10}(N/300)]^4 \\ \alpha &= 0.9, \quad p = 1.0 \end{aligned} \right\} \quad (18)$$

Weibull (k = 0.75) :

$$\left. \begin{aligned} A_c &= \begin{cases} 0.030 \exp\{-0.6[\log_{10}(N/4)]^2\} & : \nu = 1.0 \\ 0.025 \exp\{-0.7[\log_{10}(N/15)]^2\} & : \nu = 0.5 \text{ \& \ } 0.25 \end{cases} \\ \alpha &= 2.7, \quad p = 1.6 \end{aligned} \right\} \quad (19)$$

Weibull (k = 1.0) :

$$\left. \begin{aligned} A_c &= \begin{cases} -0.028 N^{-0.25} & : \nu = 1.0 \\ -0.0022 - 0.0006[\log_{10}(N/50)]^2 & : \nu = 0.5 \text{ \& \ } 0.25 \end{cases} \\ \alpha &= 1.0, \quad p = 2.1 \end{aligned} \right\} \quad (20)$$

Weibull (k = 1.4) :

$$\left. \begin{aligned} A_c &= \begin{cases} -0.40 N^{-0.8} & : \nu = 1.0 \\ -0.10 N^{-0.4} & : \nu = 0.5 \text{ \& \ } 0.25 \end{cases} \\ \alpha &= 0.5, \quad p = 2.7 \end{aligned} \right\} \quad (21)$$

Weibull (k = 2.0) :

$$\left. \begin{aligned} A_c &= \begin{cases} -0.50 N^{-0.7} & : \nu = 1.0 \\ -0.64 N^{-0.6} & : \nu = 0.5 \text{ \& \ } 0.25 \end{cases} \\ \alpha &= 0.35, \quad p = 3.4 \end{aligned} \right\} \quad (22)$$

The bias correction can be made by using \bar{Z}_n as

$$(x_R)_{cor} = \hat{x}_R - \bar{Z}_n \sigma_x \quad (23)$$

Table 3 lists the return wave heights with bias correction for the data of Table 1. The bias correction by the

above formula may have been excessive, being judged from the fact that the Weibull distribution with $k = 2.0$ predicts the largest return heights after bias correction. This is due to the assumption of the equal probability of the five distribution employed. A responsible engineer may adjust the amount of bias correction in his selection of design waves.

8. STANDARD ERROR OF RETURN VALUE WHEN THE TRUE DISTRIBUTION IS UNKNOWN

When the true distribution is unknown, the standard error of the estimated return value differs from the standard deviation formulated as in the form of Eq. 14. By using the simulation data for the above bias correction, empirical formulation has been made for the standard error of return value with bias correction. The standard error is defined as $\bar{S}_n = \sigma [(\hat{x}_R - x_R)/\sigma_x]$ and is formulated as

$$\bar{S}_n = \{1.0 + A_s |y_R + \alpha \ln v|^p\} / \sqrt{N} \quad (24)$$

The coefficient A_s is expressed as below,

$$A_s = b_1 + b_2 [\log_{10} (N/N_c)]^2 \quad (25)$$

and the coefficients α , b_1 , b_2 , and N_c and the exponent p are assigned the values as in Table 4: α is common with Eqs. 16 to 22. An example of the comparison between the simulation data and empirical formula is shown in Fig. 8.

Table 4. Coefficients of Empirical Formulas of Standard Error of Return Values when the True Distribution Is Unknown

Distribution	ν	b_1	b_2	N_c	p	ϵ
FT-I	1.0	0.24	0.36	80	1.6	0.9
	0.5, 0.25	0.46	0.14	50	1.6	0.9
Weibull (k=0.75)	1.0	0.57	0.18	20	1.2	2.7
	0.5, 0.25	0.41	0.22	20	1.2	2.7
Weibull (k=1.0)	1.0	0.55	0.15	15	1.7	1.0
	0.5, 0.25	0.38	0.17	20	1.7	1.0
Weibull (k=1.4)	1.0	0.37	0.08	1000	2.3	0.5
	0.5, 0.25	0.46	0.09	20	2.3	0.5
Weibull (k=2.0)	1.0	0.30	0.36	80	3.2	0.35
	0.5, 0.25	0.56	0.20	100	3.2	0.35

The absolute magnitude of the standard error can be estimated as $\sigma(\hat{x}_R) = \bar{S}_n \sigma_x$. The columns of $\sigma(H)$ in Table 3 list the estimated standard errors of return wave heights for the extreme wave data listed in Table 1. By taking the one-sigma or two-sigma criterion, one can easily construct the confidence interval of the return wave heights.

9. PROBLEM OF MULTI-POPULATIONS

Any statistical data analysis must satisfy the condition of homogeneity: i.e., all the data under analysis should belong to the same population. Extreme waves are generated by hurricanes, monsoons, frontal systems, and others. Strictly speaking, these meteorological disturb-

ances create different populations of storm waves and they should be analyzed separately. Resio (1978), for example, demonstrated the necessity of separate analysis of extreme waves off Cleveland in Lake Erie. Carter and Challenor (1981) also discussed the effect of seasonal variations of wind speeds and wave heights on the estimation of their return values.

Separation of extreme waves according to their generating sources is feasible and the extreme data analysis can be made for each type of storm waves. For each population data, the best distribution function is fitted and the return wave height is estimated separately. To estimate the overall return value, the method by Carter and Challenor (1981) can be modified as follows. First, the distribution function for the partial-duration series data is converted to that corresponding to annual maximum series data by assuming the Poisson distribution. Then, the overall distribution function is evaluated as the product of all the individual distribution functions. Thus,

$$\begin{aligned} F(x) &= \prod_{j=1}^n \exp\{-\lambda_j [1 - F_j(x)]\} \\ &= \exp\left\{-\sum_{j=1}^n \lambda_j [1 - F_j(x)]\right\} \end{aligned} \quad (26)$$

where n denotes the number of populations, and λ_j and F_j are the mean rate and the best-fitted distribution function of the j -th population, respectively. The overall distribution function thus evaluated represents the nonexceedance probability of annual maximum wave height. The return wave height for the return period R is numerically evaluated as the height corresponding to the probability of $F = 1 - 1/R$.

10. CONCLUDING REMARKS

The present paper is essentially an extension of the work by Petruaskas and Aagaard (1970). The plotting position formulas have been examined and modified. The number of candidate distribution functions is reduced from eight to five, in recognition of low capability of the extreme data analysis in separating the true distribution from other candidates. The magnitude of errors owing to not-knowing the true distribution is estimated in terms of both the bias and the standard deviation. Empirical formulations are presented to estimate the amounts of bias and standard error of return wave heights.

It should be emphasized that any estimation of return value is accompanied by the statistical variability due to sampling error. In other words, an extreme wave data under analysis is but a sample taken from an unknown population of storm waves. Depending on the characteristics of a particular sample relative to those of population, the result of extreme data analysis might be an overestimate or an underestimate compared with the population value,

which remains unknown. A responsible engineer should take this uncertainty into account when he has to make selection of design waves. The formula of standard error presented as Eq. 24 would serve as a guide to measure the magnitude of uncertainty.

The uncertainty of return wave height can only be reduced through the increase of the time span of wave observation or wave hindcasting. Sampling of many storms as much as possible within a given time span is also helpful in reducing the amount of standard error of return wave height. In this sense, further continuous efforts of instrumental wave observations of longer duration should be encouraged.

REFERENCES

- Barnett, V. (1975): Probability plotting methods and order statistics, Applied Statistics, 24(1), pp.95-108.
- Blom, G. (1958): Statistical Estimates and Transformed Beta-Variables, John Wiley & Sons, New York, Chap.12.
- Blom, G. (1962): Nearly best estimates of location and scale parameters, Contributions to Order Statistics (ed. by A.E. Sharman and B. G. Greenberg, John Wiley & Sons, New York, pp.34-46.
- Burcharth, H.F. (1988): Draft Report of Sub-group B "Uncertainty related to environmental data and estimated extreme events," PIANC PTC II Working Group 12 on Analysis of Rubble Mound Breakwaters.
- Carter, D.J.T. and Challenor, P.G. (1981): Estimating return values of environmental parameters, Quart. J. R. Met. Soc., 107, pp.259-266.
- Carter, D.J.T. and Challenor, P.G. (1983): Methods of fitting the Fisher-Tippett type I extreme value distribution, Ocean Engng., 10(3), pp.191-199.
- Cunnane, C. (1978): Unbiased plotting positions - a review, J. Hydrology, 37, pp.205-222.
- Draper, L. (1966): The analysis and presentation of wave data - a plea for uniformity, Proc. 10th ICCE, pp.1-11.
- Earle, M.D. and Baer, L. (1982): Effects of uncertainties on extreme wave heights, J. Wat., Port, Coast, and Ocn. Div., Proc. ASCE, 108(WW4), pp.456-478.
- Goda, Y. (1979): A review on statistical interpretation of wave data, Rept. Port & Harb. Res. Inst., 18(1), pp.5-32.
- Goda, Y. (1988): Numerical investigations on plotting formulas and confidence intervals of return values in extreme statistics, Rept. Port & Harb. Res. Inst., 27(1), pp.31-92. (in Japanese.)
- Gringorten, I.I. (1963): A plotting rule for extreme probability paper, J. Geophys. Res., 68(3), pp.813-814.
- Gumbel, E.J. (1958): Statistics of Extremes, Columbia Univ. Press, New York.
- Lawless, J.F. (1974): Approximation to confidence intervals for parameters in the extreme value and Weibull distributions, Biometrika, 61(1), pp.123-129.
- Medina, J.R. and Aguilar, J. (1986): Discussion to "Wave statistical uncertainties and design of breakwater" by B. Le Mehaute and S. Wang (Sept. 1985), J. Wat., Port, Coast, & Ocn. Div., ASCE, 112, pp.609-612.
- Muir, L.R. and El-Shaarawi, A.H. (1986): On the calculation of extreme wave heights: a review, Ocean Engng., 13(1), pp.93-118.
- Petruaskas, C. and Aagaard, P.M. (1970): Extrapolation of of historical storm data for estimating design wave heights, Prepr. 2nd Offshore Tech. Conf., OTC1190.
- Resio, D.T. (1978): Some aspects of extreme wave prediction related to climatic variations, Prepr. 10th Offshore Tech. Conf., OTC3278.

CHAPTER 68

UNSTEADY FLOW AROUND A VERTICAL CIRCULAR CYLINDER IN A WAVE

Kenjiro Hayashi*
and
Toshiyuki Shigemura**

ABSTRACT

The unsteady characteristics of flow around a vertical circular cylinder in a typical wave, under which the lift force acting on it is very stable and has a frequency which is twice that of the incident wave, have been investigated experimentally. The relationship between the fluctuating flow velocities near the boundary layer separation points and the lift force acting on a sectional part of the cylinder has been understood quantitatively. To clarify the region where the appearance of stable lift force occurs, the long time records of lift forces acting on vertical cylinders in waves are also performed.

1. INTRODUCTION

In order to develop the study of wave forces acting on the offshore structures, it is important to understand the flow around a vertical circular cylinder in waves. The principal phenomenon of this flow is characterized by the formation of vortices which are shed from the surface of a cylinder. However, it is not understood so well as those in steady flow. This may be due to the complexity of flow round a vertical cylinder in waves, because the incident fluid motion varies along the axis of vertical cylinder with possessing a vertical velocity component. A lot of experimental works remain to be made in these area.

When the wave depth parameter d/L (d =depth of mean water level, L =wave length) is small, shallow water wave, the variation of incident flow with depth is small and the amplitude of vertical velocity component is small compare with that of horizontal velocity component. Therefore, the flow around a vertical cylinder is nearly two dimensional and quite similar to those in harmonically oscillating two dimensional flow, plane oscillatory flow. On the other hand, when the wave depth parameter d/L is large, deep water wave, the flow around a vertical cylinder is three dimensional

* Assistant Professor, Dept. of Civil Engineering, National Defense Academy, 1-10-20 Hashirimizu Yokosuka, 239 Japan.

** Professor, Dept. of Civil Engineering, National Defense Academy, M. ASCE.

because the variation of incident flow along the axis of cylinder is large and the amplitude of vertical velocity component is nearly equal to that of horizontal velocity component.

Many studies have been made to understand the process of vortex shedding from a cylinder in these oscillating flow, plane oscillatory flow and wave, since the original work of Keulegan and Carpenter(1958). They observed the vortex formation round a submerged horizontal cylinder placed in harmonically oscillating flow produces in the node of standing waves and found a close relationship between the vortex-shedding frequency and a Keulegan-Carpenter number defined as $KC=U_m.T/D$ in which U_m is the maximum horizontal water particle velocity during a wave period T and D is a diameter of cylinder.

The relationship between the vortex-shedding patterns and KC number has been obtained by the visualization studies of the flow round a cylinder in waves and in plane oscillatory flow, see for example Bidde(1971) and Bearman(1979). Williamson(1985) made simultaneous force measurement and visualization round a cylinder in plane oscillatory flow by oscillating a cylinder in still water and obtained the detailed description of vortex shedding and the relation of the vortex motions to the lift force profiles in each regime of KC number corresponding to each of vortex shedding pattern.

In order to understand quantitatively the characteristics of flow round a cylinder in these oscillatory flow, the measurements of flow velocities round a cylinder and surface wave pressure on the circumference of a cylinder in waves have been made by Isaacson and Maull(1976), Iwagaki and Ishida(1976), Hayashi and Takenouchi(1980, 1985), Bearman et al.(1985) and Grass et al.(1987).

Hayashi and Takenouchi(1980,1985) measured the horizontal velocity around a vertical cylinder in a wave and the surface wave pressure on the circumference of it by using a Laser-Doppler anemometer and a pressure transducer. These measurements were made in a special flow condition under which the total lift force acting on the cylinder is very stable for a long time with having a frequency which is twice that of incident wave and major portion of vortex shedding and formation take place periodically on mainly one side of the cylinder. The vortex shedding pattern observed was quite similar to those generally observed in waves and in plane oscillatory flow in the approximate range of KC between 7 to 15. The characteristics of time variation and the phase average distributions of both the horizontal flow velocities and the surface wave pressures have been obtained.

Grass et al.(1987) also measured the velocity around a cylinder in waves and in plane oscillatory flow. They find the presence of vortex induced velocity enhancement effect occurring in the flow field round a cylinder both in plain oscillatory flow and in surface waves in the approximate

range of KC between 9 to 12. This velocity enhancement effect is also identified in the results of Hayashi and Takenouchi(1980,1985).

The study described herein is an extension of our study described above, Hayashi and Takenouchi(1979, 1985), clarifying the relationship between the flow around a vertical circular in waves and the forces acting on it. The scope of present study is to investigate the relationship between the flow near the boundary layer separation points and the lift force acting on a sectional part of the cylinder in a wave. The flow near a separation point of boundary layer has an important aspect of vortex shedding phenomenon. However, detail experimental information is scarce in the case of oscillatory flow. In order to clarify the region where the appearance of stable lift force occurs, the long time records of lift forces acting on the vertical circular cylinders in waves were also performed.

2. EXPERIMENTS

2.1 Measurement of Flow Velocity and Surface Wave Pressure

The detailed description of the experimental arrangement used in these measurements has been given previously in our study, Hayashi and Takenouchi(1980,1985). The experiments were carried out in the 39.6m long flume of the Department of Civil Engineering at the National Defense Academy. This flume is 0.6m wide and is equipped with a ballistic-pendulum type wave generator. A long beach with a slope of 1:6.7 is installed at the other end of flume to absorb the wave energy.

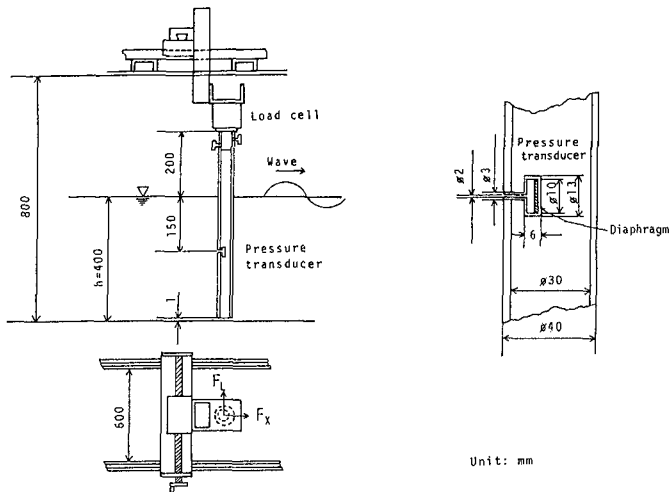


Fig.1 General arrangement of test cylinder

The general arrangement of a test cylinder made of acrylic plastic tube is shown in Fig.1. It was mounted in the flume at a section 24.6m from the paddle of wave generator and 7m from the toe of long beach. For the measurement of the total inline force F_x and total lift force F_y acting on a test cylinder, the upper end of the test cylinder was attached to a load cell(Three Component Strain Gauge Type Load Cell, LMC-3501-1 Nissho Ltd.) which was mounted on a two-dimensional traversing device straddling on the wave flume.

For the measurement of the fluctuating surface wave pressure P on the circumference of the test cylinder at the level of 19cm below the still water level, a diaphragm type pressure transducer(PM10-01, ST Institute Co.) was attached to a pressure tapping placed on a surface of the test cylinder. The test cylinder was attached to the load cell, so arranged that it can be rotated around its axis to bring the pressure tapping to any desired orientation.

The measurements of fluctuating horizontal water particle velocity U , the velocity component in the direction of wave propagation, at the points along a diameter through the cylinder parallel to the wave crest were made by using a laser doppler anemometer(LDA) of a 15mw He-Ne type(Kanomax 27-0900 ser.) and a hot wire anemometer. These velocity measurements were made at the level of 16cm below the still water level. The general view of optical system of LDA working in a forward scatter dual beam mode is shown in Fig.2. In order to eliminate an ambiguity of flow direction when flow reverses under wave motion, the frequency sifter was used in this LDA system.

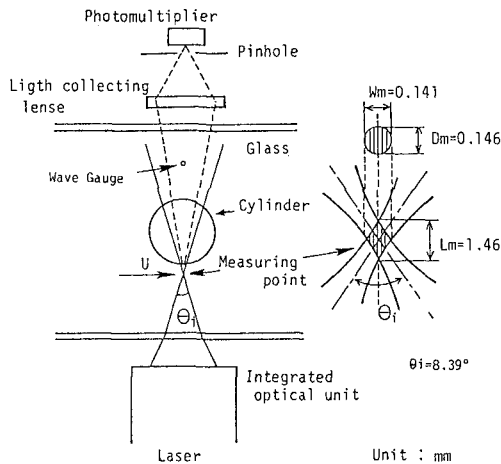


Fig.2 Optical system of laser doppler anemometer

These measurements described above were made in a regular wave; wave period $T=1.6$ sec., wave height $H=10$ cm, wave length $L=2.9$ m, and still water depth $d=40$ cm, which is the same used in our previous work, Hayashi and Takenouchi(1980,1985). The

wave depth parameter d/L is about 0.138. The KC numbers at water surface and at the bottom of flume are 12.5 and 8.2 respectively, i.e. the variation of incident flow with depth is small. The KC number and the Reynolds number at the level of 15cm below the still water level are about 10 and 7700 respectively. The flow pattern around the test cylinder near the level of the measuring points U and P, about 16cm below the still water level, was observed by using a video recorder camera. Aluminum powder was spread in water.

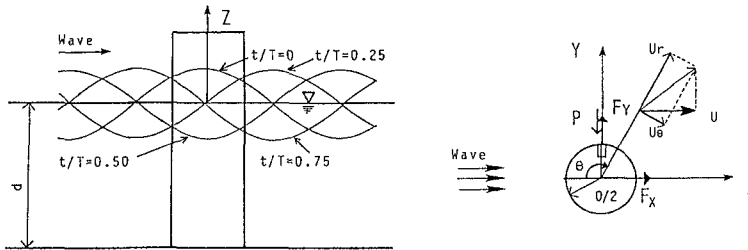


Fig.3 Coordinate system

The coordinate system is shown in Fig.3. The measurement of surface wave pressure P was made at 19cm below the still water level and at 24 angular positions θ by rotating the cylinder at 15 degrees interval around its center axis. The signal of the pressure transducer at each angular point θ was recorded on the magnetic tape recorder simultaneously with the signals of wave gauge and the load cell for a total of about 5 wave periods. Using these data, it is possible to obtain the phase average surface wave pressure distribution circumference of the test cylinder and the phase average sectional inline and transverse forces over 5 wave periods for several wave phase t/T .

The measurements of velocity U were made at the level of 16.5cm below the still water level and at $X=0$ cm by varying Y from -7cm to 8cm. Instead of traversing the measuring points of velocity, the test cylinder was moved in the direction of Y coordinate. The signals from velocity meters were also recorded on the magnetic tape recorder with the signals from the wave gauge, the load cell and the pressure transducer for the total of 5 wave cycles and subsequently analyzed by a signal analyzer. Using this recording method, it is possible to obtain the relationship between the fluctuating velocity U and both the surface pressure P and wave forces F_x and F_y .

2.2 Long Time Measurement of Lift Forces

The long time measurements of lift forces were carried out by using a same facility described above. Two circular cylinders made of acrylic plastic tubes were mounted on a load cell as shown in Fig.1. They were 3cm and 4cm in diameter and 60cm in length. In order to eliminate the end effect, the clearance between the lower end of test cylinders and the bottom of wave flume was kept less than

1mm. Test runs were made at wave period T ranging from 0.8sec. to 2.2sec. At each wave period approximately 4 to 10 wave heights H were generated. The still water depth d was kept at 40cm. The approximate range of rms.KC number and rms.Re number were from 1 to 24 and 200 and 2200. The natural frequency of the test cylinders in still water were 12Hz for $D=3\text{cm}$ and 10Hz for $D=4\text{cm}$ respectively. The analog signals from the load cell and the wave gage were recorded on a magnetic tape recorder over a time interval about 800 wave periods.

3. RESULTS AND DISCUSSION

The record of the time variation of the total lift force F_y obtained from the experiment of flow velocity and wave pressure is shown in Fig.4. As shown in this figure, the time variation of F_y is very stable for a long time.

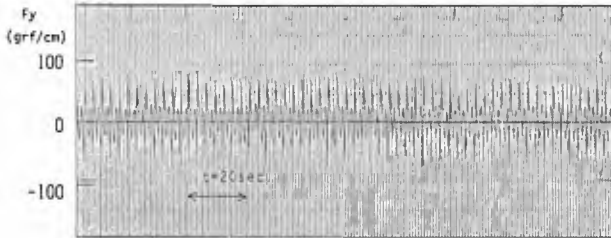


Fig.4 Long time variation of amplitude of lift force

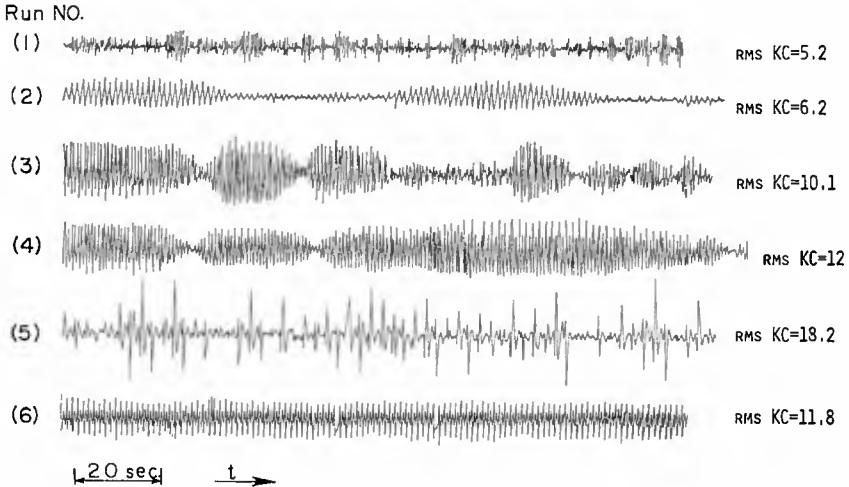


Fig.5 Time variation of lift forces for several rms.kC

The time history of lift force acting on a vertical cylinder in waves has generally irregular characteristics of intermittency and modulation of its amplitude as shown in Fig.5, which is reproduced from a reference, Hayashi and Takenouchi(1979). These irregular characteristics may be due to the sensitivity of lift force to the stream turbulence and poor spanwise correlation of vortex shedding along a cylinder's axis. However, we can recognize the appearance of stable lift force as shown in Fig.4 in this figure, for the case of $\text{rms.KC}=11.8$.

In the case of plane oscillatory flow, it is recognized that the stable lift force appears in the range of KC approximately between 7 to 16 and in this range of KC, the vortex shedding is very stable with taking place on only one side of cylinder, see for example Maull and Milliner(1978), Ikeda and Yamamoto(1981), Williamson(1985) and Grass et al. (1987). The region of stable lift force in waves may be also represented in KC numbers which are related to the case of plane oscillatory flow. However, we should note that there are important differences between the unsteady natures of flow in waves and those in plane oscillatory flow as described previously in introduction.

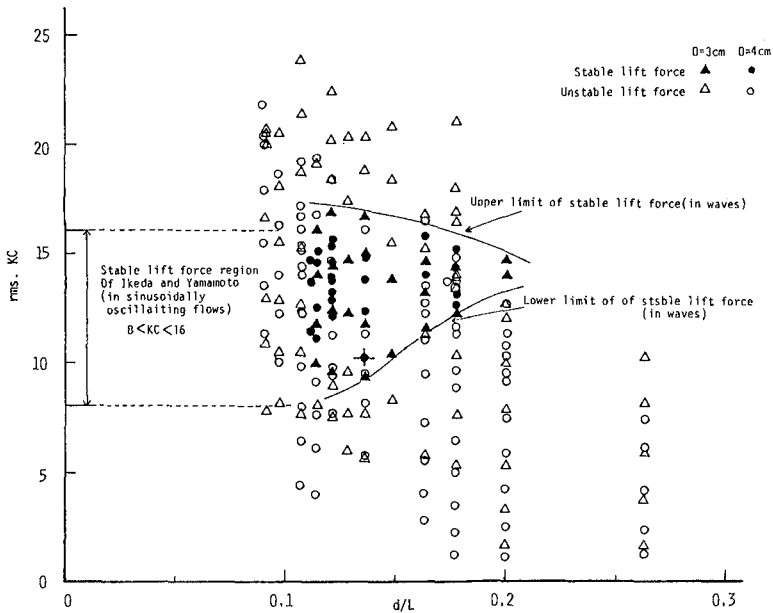


Fig.6 Region of stable lift forces plotted against d/L and rms.KC

The relationship between the configuration of time history of lift forces, which were obtained in the present experiments, and both rms.KC and d/L is shown in Fig.6. In this figure, the black symbols show the appearance of stable lift force. The region of stable lift force for the case of

plane oscillatory flow obtained by Ikeda and Yamamoto(1981) are also shown in this figure. The quantity of present data is not sufficient to define exactly the region of stable lift force acting on a vertical cylinder in waves. This figure shows that the stable lift force occurs in the range of rms.KC between about 9 to 16, for the range of d/L between about 0.1 to 0.2. For the high value of d/L > 0.2, the stable lift force does not appear. This may be due to the fact that the vortex shedding is poorly correlated along the axis of the test cylinder, because the variation of incident flow along the cylinder axis increases with the increase of d/L. For the low value of d/L < 0.1, the stable lift force also does not appear. This may be due to the increased influence of wave nonlinearity.

While farther dependence of the stable lift forces in waves on Reynolds number is possible as mentioned by Maull and Milliner(1978) and Ikeda and Yamamoto(1981), such dependence is not clear in the present data.

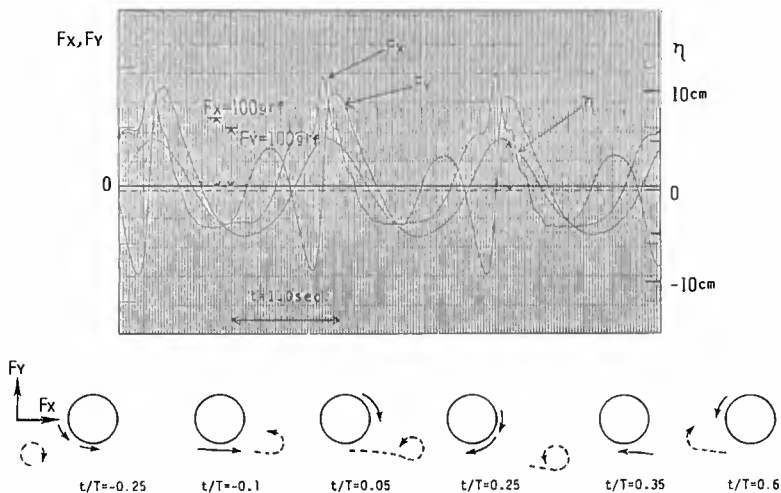


Fig.7 Time variations of lift force F_y , inline force F_x , and free surface elevation η with vortex shedding patterns

In the present experiment of flow velocity U and surface wave pressure P , the time variation of lift force F_y is very stable for a long time as shown in Fig.6. The relationship between this F_y , and inline force F_x and water surface elevation θ with time are shown in Fig.7. The frequency of F_y is two times as much as those of F_x and η .

The process of vortex shedding in a period of incident wave is also shown in Fig.7. These sketches of vortex shedding patterns were estimated from the observation of flow near the level of velocity measurement U and surface wave pressure P , which were made by using a video camera in the present work, and the velocity distributions around a

vertical cylinder in waves which were obtained for several wave phases in our previous study by the author(1980,1985). The major portion of vortex shedding and its activity, which occur during each half cycle, take place periodically on only one side of the cylinder, negative side of Y coordinate. These are quite similar to those generally observed in plane oscillatory flow in the range of KC between about 7 to 13, which has been described in detail by Williamson(1985) and Grass et al.(1987).

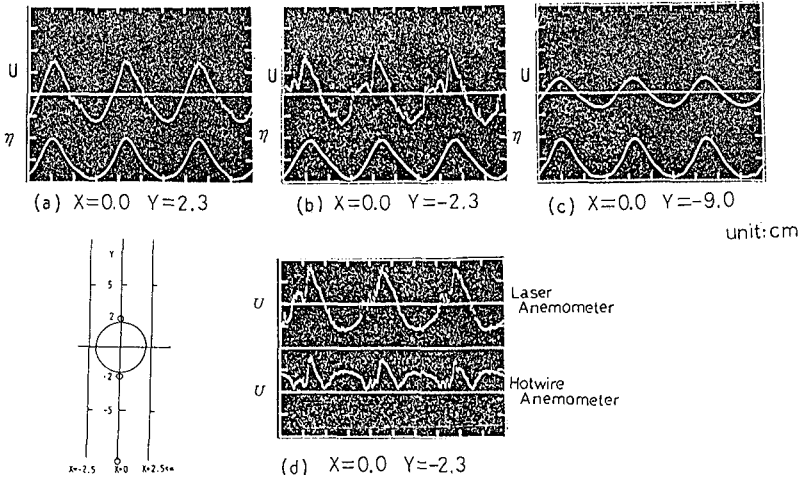


Fig.8 Out put signals of velocities U and water surface elevation η

Time variations of horizontal water particle velocity U at various Y points of $X=0\text{cm}$, which were obtained by using the LDA, are demonstrated in Fig.8 (a),(b) and (c) respectively. To show the phase of incident wave, the time variation of water surface elevation η measured by the wave gauge mounted just beside the test cylinder as shown in Fig.1 is also demonstrated in these figure. The time variation of U demonstrated in Fig.8(c) shows that of incident wave, because the measuring point of U at $Y=-9\text{cm}$ is enough far from the test cylinder so that the existence of cylinder is negligible. We can recognize remarkably that the fluctuation of U at $Y=-2.3\text{cm}$ is large compared to that of U at $Y=2.3\text{cm}$. This is due to the fact that the major portion of vortex shedding and its activity take place on only one side of the cylinder, $Y<0$, as shown in Fig.7. In order to show the accuracy of the LDA measurement for the fluctuating velocity U , a comparison of velocity signals from the simultaneous measurement using the LDA and the hot wire anemometer which were placed at nearly same position at $X=0\text{cm}$ and $Y=-2.3\text{cm}$ is demonstrated in Fig.8(d). We can recognize that they almost agree except for very small velocity.

Figure 9 shows the relationship between the phase variations of pressures P at $\theta=90^\circ$ and $\theta=-90^\circ$, the

velocities U at $X=0\text{cm}$, $Y=-2.2\text{cm}$ and -2.2cm , the lift force F_y and free surface elevation η . The velocity U at $Y=2.2\text{cm}$ and the pressure P at $\theta=90^\circ$, and the velocity U at $Y=-2.2\text{cm}$ and the pressure P at $\theta=-90^\circ$ were measured simultaneously respectively. Although a little is known about boundary layer separation from the test cylinder in the present work, the points of $\theta=90^\circ$ and $\theta=-90^\circ$ seem to be near the separation point of it. The influences of the appearance of asymmetric vortex shedding on both phase variations of velocities U and pressures P are clearly recognized.

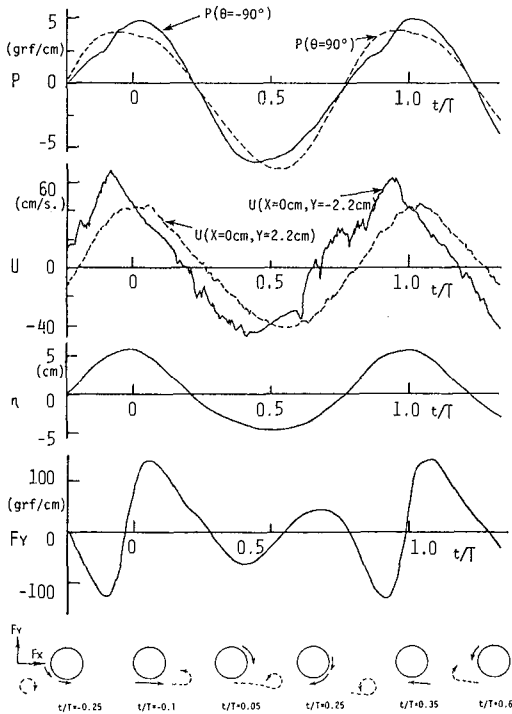


Fig.9 Phase variations of wave pressures P , velocities U and lift force F_y

Figure 10 shows the details of phase variation of the velocities U at the points of $X=0\text{cm}$, $Y=2.2\text{cm}$ and $Y=-2.2\text{cm}$, and the free surface elevation η . These records cover 5 cycles of the incident wave period and identify the origin of cycle. In order to investigate the influence of both the presence of the test cylinder and the vortex sheddings on the velocities U at these points, theoretical curves calculated from Stokes third order wave theory and linear diffraction wave theory are plotted in this figure. The measured velocities U at $Y=2.2\text{cm}$ is predicted quite well by

linear diffraction wave theory, but the velocity U at $Y=-2.2\text{cm}$ deviates markedly from the diffraction theory. We can

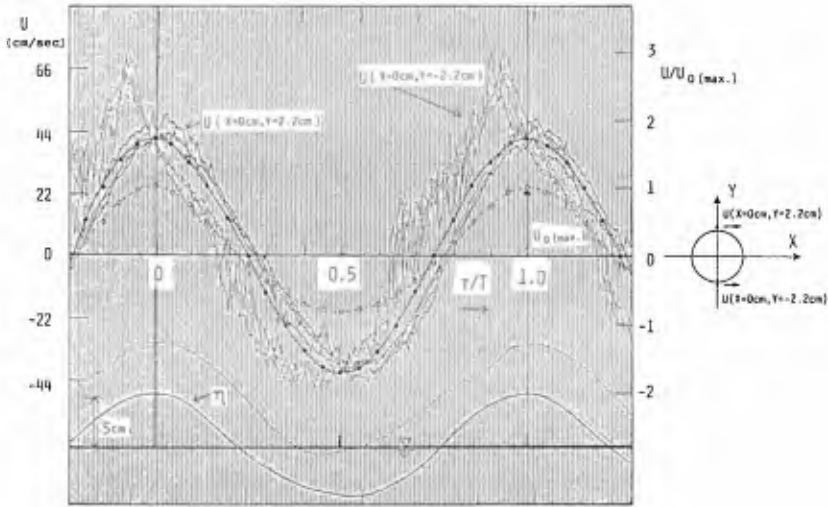


Fig.10 Details of phase variations of velocity U at $X=0\text{cm}$, $Y=-2.2\text{cm}$ and $Y=2.2\text{cm}$
 (—●— Linear diffraction wave theory)
 (- - - ○ - - - Stokes third order wave theory)

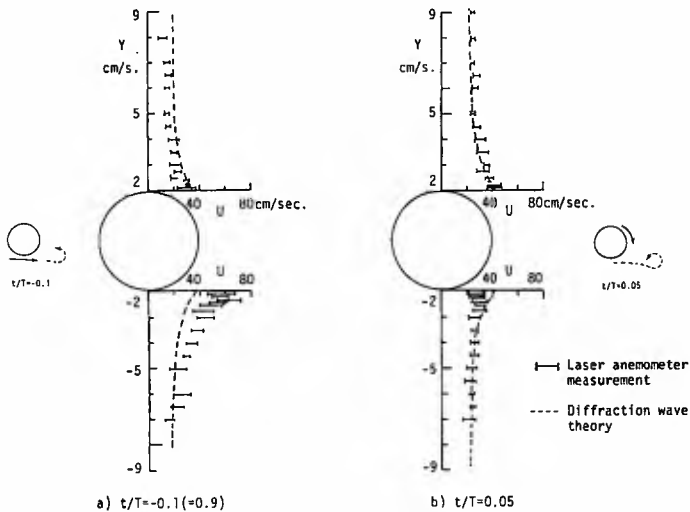


Fig.11 Distributions of wave velocities U around test cylinder at $X=0\text{cm}$ for $t/T=-0.1$ and $t/T=0.05$

recognize that the phase of U at $Y=-2.2\text{cm}$ proceeds faster than that of these wave theories. These may be due to the fact that the major portions of vortex shedding and its activity take place on the negative side of Y coordinate as described in Fig.7.

The distribution of measured horizontal velocity U at $X=0\text{cm}$ plotted at $t/T=-0.1(=0.9)$ and $t/T=0.05$ are shown in Fig.11 (a) and (b). In order to show the influence of the vortex shedding which appears mainly in the negative side of Y coordinate, see Fig.7, the theoretical curve of Linear diffraction wave theory is also plotted in these figures respectively. At $t/T=-0.1$, the crest of wave is approaching to the test cylinder and the peak value of F_y acts in the direction of negative Y coordinate as shown in Fig.7. In this case, the incident flow is passing from left to right with increasing the horizontal velocity U . The measured velocity U exceeds the value of Linear diffraction wave theory in the range of $-5\text{cm}<Y<-2\text{cm}$. This phenomenon, which is called the velocity enhancement by Grass et al.(1987), may be due to the existence of vortices which are shed and formed in the negative side of X coordinate during a last half wave cycle and then converted back over the negative side of Y coordinate. On the other hand, the measured velocity U near the test cylinder in the positive side of Y decreases as compared with the theoretical value. This phenomenon may be due to the existence of a counterclockwise circulation round the test cylinder. At $t/T=0.05$, the crest of wave has just passed through the cylinder and the incident flow is passing from left to right with decreasing the horizontal velocity. At this phase, the peak value of F_y appears in the direction of positive Y coordinate. The measured velocity U decreases in the range of $-3\text{cm}<Y<-2\text{cm}$ and increases just near the cylinder in the part of positive Y coordinate as compared with theoretical value. This phenomenon may be due to the existence of a clockwise circulation round the cylinder, which have been induced by the vortex sheddings from the surface of the test cylinder around $\theta=-90^\circ$.

In order to obtain a quantitative relationship between the flow around the cylinder and the lift force acting on it, following analysis was carried out. The lift force ΔF_{yc} acting on a vertical cylinder in waves may be estimated by Eq.(1), which is an approximation of Laggally's theorem and is equal to the Kuta and Jukovsky theorem as explained by Sawamoto et al.(1980).

$$\Delta F_{yc} = -\rho \Gamma U_0 \quad (1)$$

where ρ is fluid density, Γ is the total circulation around a cylinder induced by vortex sheddings, and U_0 is the incident horizontal velocity (=free stream velocity). If we suppose that the circulation Γ is evaluated by Eq.(2),

$$\Gamma = (U_1 - U_2) \cdot \pi \cdot D / 2 \quad (2)$$

the lift force ΔF_{yc} can be re-written as follow,

$$\Delta F_{yc} = -\rho \cdot (U_1 - U_2) \cdot \pi \cdot D \cdot U_0 / 2 \quad (3)$$

where U_1 and U_2 are the velocities at diametrically opposite surface points on the central cross-section of a cylinder.

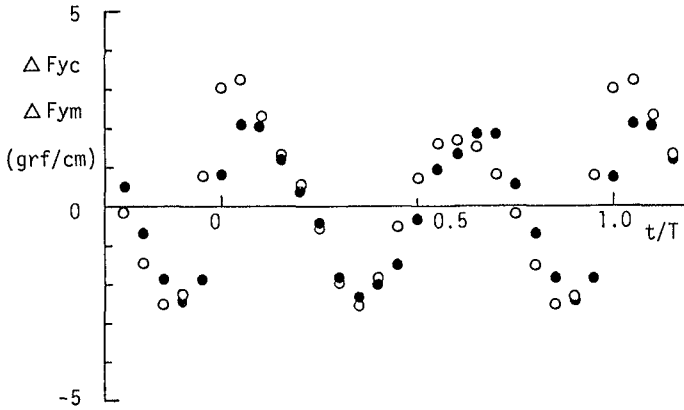


Fig.12 Phase variations of lift forces
(● ΔF_{yc} , ○ ΔF_{ym})

Figure 12 shows the phase variation of ΔF_{yc} which was calculated by substituting the measured velocities u at $X=0\text{cm}$, $Y=-2.2\text{cm}$ and $Y=2.2\text{cm}$ into Eq.(3). The phase variation of the measurement lift force ΔF_{ym} , which is computed by integrating the measured surface pressure distribution around a test cylinder for several wave phases t/T , is also plotted in this figure. It is quite interesting that the calculation value of ΔF_{yc} evaluates quite well the phase variation of the measured lift force ΔF_{ym} in spite of very rough assumption is used in the calculation of ΔF_{yc} .

4. CONCLUSIONS

In this study, the unsteady characteristics of flow around a vertical cylinder in a wave have been obtained quantitatively by measuring the flow velocities U and the surface wave pressure P . The influence of the asymmetric vortex sheddings, which were obtained by a visualization of flow around the cylinder using video camera, to the velocities U and the surface wave pressures P have been obtained. The relationship between the flow velocities U near the boundary layer separation points on the cylinder surface and the lift force acting on a sectional part of it have been studied quantitatively by using a Kuta and Jukovsky theorem.

The dependence of a stable lift forces in waves on rms.KC number and wave depth parameter d/L is confirmed. However, farther depends of it on Reynolds number is not clear in the range of Reynolds number used in the present experiment.

ACKNOWLEDGMENT

We gratefully acknowledge the several valuable advises given by professor J.R. Chaplin(of The City University in London).

REFERENCES

- Bearman, P.W. and Graham, J.M.R. and Singh, S., 1979, Forces on Cylinders in Harmonically Oscillatory Flow, in Mechanics of Wave Induced Forces on Cylinders(ed. T.L. Shaw).
- Bearman, P.W., Chaplin, J.R., Graham, J.M.R., Kostense, J.K., Hall, P.F., and Klopman, G., 1985, The loading on a cylinder in post-critical flow beneath periodic and random waves., Proc., 4th. Int. Conf. on the Behaviors of Offshore Structures, Delft, pp. 213-225.
- Bidde, D.B., 1971, Laboratory study of lift forces on circular piles, Journal of the Waterways, Harbors and Coastal Engineering Division, ASCE., Vol. 97, No. WW4, pp. 595-614.
- Grass, A.J., Simons R.R. and Cavanagh, N.J., 1987, Vortex-induced velocity enhancement in the wave-flow field around cylinders, Proceedings of the 6th. International Offshore Mechanics and Arctic Engineering Symposium - Volume 1I, pp. 155-164.
- Hayashi, K. and Takenouchi, T., 1979, The fundamental study of flow field around a vertical cylindrical pile subjected to waves, Proceedings, 20th. Japanese Conference on Coastal Engineering, Japan Society of Civil Engineers, pp. 406-410 (In Japanese).
- Hayashi, K. and Takenouchi, T., 1985, Characteristics of flow around a vertical circular cylinder in a wave, Coastal Engineering in Japan, Vol.28, pp. 207-222.
- Ikeda, S. and Yamamoto, Y., Lift forces on cylinders in oscillatory flows, Report of Dept. of Foundation Engineering and Construction Engineering, Saitama University, Vol.10, pp. 1-15.
- Iwagaki, Y. and Ishida, H., 1976, Flow separation, wake vortices and pressure distribution around a circular cylinder under oscillatory flows, Proc. 15th Coastal Engineering Conference, Honolulu, pp. 2341-2356.
- Isaacson, M. de St. Q. and Maull, D.J., 1976, Transverse forces on vertical cylinder in waves, Journal of the Waterways, Harbor and Coastal Engineering Division, ASCE., Vol.102, WW1, pp.49-60.
- Keulegan, G.H. and Carpenter, L.H., 1958, Forces on cylinders and plates in an oscillating fluid, Journal of Research of the National Bureau of Standards, Vol. 60,

No.5, pp. 423-440.

Maul, D.J. and Milliner, M.G., 1978, Sinusoidal flow past a circular cylinder, Coastal Engineering, Vol.2, pp. 149-168.

Sawamoto, M., Kikuchi, K., Ohba, M. and Kashiwai, J., 1980, Force on a circular cylinder in an oscillatory flow, Coastal Engineering in Japan, Vol.23, pp. 147-158.

Williamson, C.H.K., 1985, Sinusoidal flow relatives to circular cylinders, Journal of Fluid Mechanics, Vol.155, pp. 141-174.

CHAPTER 69

A Steady-State Wave Model for Coastal Applications

Dr. Donald T. Resio*

A steady-state spectral model is presented. This model produces a solution equivalent to a full time-stepping spectral model, but at much reduced computational times. Comparisons shown here demonstrate that the spectral model provides a good representation of shallow-water wave propagation phenomena and that wind effects can significantly influence near-coast wave conditions.

Introduction

Over the last twenty years a wide range of numerical models have been developed to assist coastal engineers, planners, and scientists in the estimation of near coastal wave conditions. Early models were based on monochromatic wave theory and ray tracing methods. Subsequently, models have developed along two lines, monochromatic and spectral. The major distinction between the two approaches pertains to the degree of randomness assumed in the physical system. If waves are primarily deterministic, variations in the phase function must be considered and nonlinear behavior of the type discussed by Yuen and Lake (1975) or Berkhoff (1976) can result. On the other hand, if waves are considered to be a random superposition of essentially linear components, nonlinear behavior must be treated as independent of phase. Nonlinearities of this kind relate to wave-wave interactions of the type discussed by Hasselmann (1962) and result in energy fluxes among the linear components which can become very important in shallow water (Resio, 1987, 1988). Also, as will be discussed later, diffusive energy fluxes due to spatial variations in energy can also be treated independent of consideration of the phase function.

In deep water, spectral models have gained a clear advantage in terms of being able to represent important aspects of wave generation, propagation and decay. In near coastal environments, some persist in using linear, monochromatic models (refraction diagrams, shoaling coefficients, monochromatic diagrams, etc.), however most

*President, Offshore & Coastal Technologies, Inc. (OCTI),
911 Clay Street, Vicksburg, MS 39180, U.S.A.

serious applications have now moved on to either spectral models or nonlinear models of combined refraction-diffraction of the type described by Berkhoff (1976) and Ebersole et al. (1986). Unfortunately, both of these classes of models require considerable computer resources for their execution. The purpose of this paper is to introduce a variation of spectral modeling which is much more efficient in terms of computer time and storage requirements than previous methods. The accuracy of this model and its potential application in various situations is then discussed.

Theoretical Considerations

Overview

Although all of the equations used below can be generalized to include the effects of currents, for simplicity and in order to express these equations in terms of energy densities rather than action densities, it is assumed here that currents are negligible. In this case in the absence of energy sources and sinks, we have

$$(1) \quad F(\underline{k}) = \text{constant}$$

along a wave range where \underline{k} is the wave number vector and $F(\underline{k})$ is the energy density at that point. Or, if energy sources and/or sinks are significant we have, along a ray \underline{s} ,

$$(2) \quad \frac{\partial F(\underline{k})}{\partial \underline{s}} = \sum S'_i(\underline{k}) \frac{\partial \underline{s}}{\partial t}$$

where S' represents a single source/sink term and t is time. In conventional spectral models, a spatial grid such as seen in Figure 1 is laid out. At each point in such a grid, an equation equivalent to (2) is solved

$$(3) \quad \frac{\partial E(f, \theta^x, y, t)}{\partial t} = \frac{\partial c c_g E(f, \theta^x, y, t)}{\partial x} c_{gx} + \\ \frac{2 c c_g E(f, \theta^x, y, t)}{\partial y} c_{gy} + \\ \sum S_i(f, \theta, x, y, t)$$

where $E(f, \theta^x, y, t)$ is the conventional spectral energy density in frequency-direction space, c is the phase velocity and c_g the group velocity, respectively, of waves with frequency f , x and y are orthogonal spatial axis, subscripts "x" and "y" denote component values in those directions, and $S_i(f, \theta)$ represents the effects of the i^{th} source term. The five-dimensional nature of (3) readily infers one of the major problems associated with its computer solution. The dependence of energy densities and sources on x, y, t have been explicitly written in equation (3) in order to point out this problem. In subsequent usage, dependencies on space and time will be assumed but not written; thus, $E(f, \theta, x, y, t)$ will now only be written as $E(f, \theta)$. At each point in the grid, equation (3) must be solved for each frequency-direction component over each

time stop. A "typical" number of frequencies and directions is about 300. If we use as an example a grid covering 10 miles by 10 miles with a spatial resolution of 1/4 mile, equation (3) must be solved about 80 million times in a simulation in order to achieve steady-state conditions (i.e., in order to perform the appropriate wave transformation).

Some groups have attempted to use a different approach to solve the problem of predicting near coastal wave spectra (Abernethy, et al., 1977). As seen in Figure 1, wave rays can be "backtracked" out from a point of interest. It is then possible to calculate equation (3) at each point along each of the rays shown there, provided that the form of the source terms in (3) are such that the spectral components can be considered as uncoupled. Unfortunately, the wind source term, wave-wave interactions and wave breaking are not treated adequately in this context. In all existing wave models, the net energy input into frequency components above the spectral peak becomes quite coupled by the normalization methods used to achieve a particular equilibrium range behavior. Also, the net source to the forward face due to wave-wave interactions and the redistribution of energy on the rear face depends on the local spectral shape. Similarly wave breaking depends on the total energy in the spectrum. Since information of this kind is not calculated, the source term treatment in such a model must necessarily be somewhat arbitrary and imprecise. Thus, if we seek an accurate solution to (3), we are left with the need to perform our calculations over an entire grid, rather than along rays passing irregularly through it. In this way all complete spectral information is available at each grid point and all source terms can be reasonably estimated.

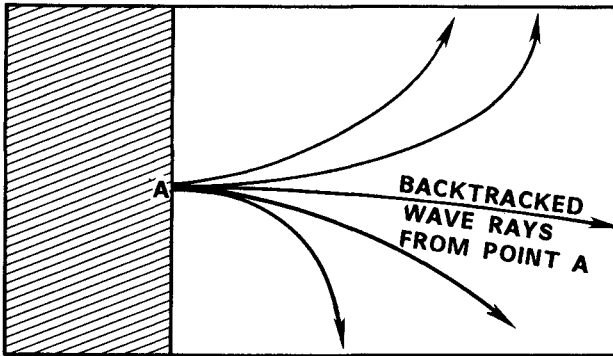


Figure 1. Example of wave rays converging on Point A at the coast.

Let us assume that we are not interested in energy propagating away from a coast. Even if such waves exist they will not affect the incoming waves very much since the peak frequencies in incoming spectra will almost always be very different from the outgoing spectra. In this context,

all of the source terms and propagation effects can be seen to reside essentially within a half-plane. This is the key to recognizing a much more efficient solution method for steady state wave transformations.

The coastal wave transformation process can be regarded as one involving internal mechanisms (primarily wave-wave interactions and wave breaking) and external mechanism (primarily wind forcing and possibly some bottom interactions). For a given spectrum at the seaward boundary, if winds are relatively constant over the time span required for the waves to propagate across the grid (typically only 15 minutes to 1 hour for near-coast simulations), a simplified solution to (3) may be employed with essentially no loss of accuracy. In this context let us proceed to a solution of the transformations of the wave transformations from the first column to the second. An adequate solution for this problem can, by induction, be extended to the remainder of the grid.

Propagation

Since (3) is an inhomogeneous partial differential equation, solution techniques usually solve the homogeneous part first (essentially wave propagation) and then solves the inhomogeneous part (the effects of source terms). In order to avoid time consuming calculations, some simplifications are in order. If a ray passing from column 1 to column 2 does not pass through a caustic, Snell's law may be used to specify the angle and height variation from one depth to another

$$(4) \quad \theta_2 = \sin^{-1}(\theta_1 c_2 / c_1)$$

where subscripts "1" and "2" refer to the column locations. For waves which pass through a caustic, an approximate solution is used.

$$(5) \quad \theta_2 = 2 \tan^{-1}(\tan(\theta_1) \exp(-\frac{\partial c}{\partial h} \frac{\partial h}{\partial s} \Delta s / 2c_g))$$

where h is the local water depth and Δs is the distance along s from a point in column 1 to a point in column 2. Regardless of whether or not the wave ray passes through a caustic, it is assumed that $F(k)$ remains constant as it should for a conservative system. In terms of the frequency-direction form for spectral energy densities used in equation (3) this means that

$$(6) \quad cc_g E(f, \theta) = \text{constant}$$

which provides sufficient information for closure of the propagation problem. A modeling system based on this approach can be used to construct ray segments "piecewise" from column to column.

Divergence-Convergence Effects

Equation (6) is the typical form for wave propagation found in most spectral models today. Its validity as seen

here follows from the ray-based concept of wave propagation. However, if we examine the situation in Figure 2 as an example of a potential problem, we see waves propagating along the trough of a bathymetric feature. The wave ray traveling straight down the trough will not move to either side since the slope orthogonal to the ray path is zero. Whereas this may actually be true for the infinitesimal-width ray exactly in the center, it is not true for any rays displayed any distance whatsoever to either side. If, for example, all the energy in a spectrum were concentrated in that energy band propagating down the trough, the usual solution method would indicate that there would not be no change in wave height down the trough. It can be shown that, in general, the ray-based solution method does not represent divergence-convergence of wave rays over a grid cell. Thus, for a more accurate solution as may be warranted in sensitive applications, a divergence-convergence term is explicitly added to the solution method here. The form of this term is

$$(7) \quad \frac{\partial E(f, \theta)}{\partial t} = \nabla \cdot \Gamma_n$$

where Γ is the net flux of energy across a row boundary of the grid.

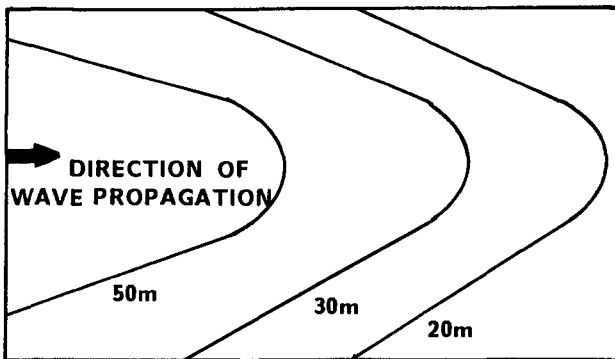


Figure 2. Example bathymetry for waves propagating over a crest.

Consideration of Diffraction in a Spectral Model

A detailed treatment of diffraction within the steady-state spectral model introduced here is considerably beyond the scope of this paper; however, a brief description of the general methodology will be given. First, one must recognize that since spectra are assumed to have random phases, phase relationships for a diffracted wave are only fixed between that wave and the individual component which created it. Thus, one cannot convert directly from a solution to the Fresnel Integrals and presume that the amplitude functions represent freely propagating waves. Instead, it is necessary to treat any phase-dependent

amplitude interaction in the context of a bound wave, bound to the spectral component which created it. However, it appears, as will be shown later, that phase-dependent solution techniques may only be required in situations with very steep energy cutoffs and very narrow spectral widths.

If we ignore phase effects, diffraction resembles a diffusion process. Any variation in wave amplitude along a wave creates results in a spatial redistribution and redirection of the wave energy. The following is used to represent the effects of diffraction in areas not affected by steep surface-piercing structures.

$$(8) \quad E_j(f, \theta_i)^{n+1} = \sum_{\kappa=-1}^{+1} \sum_{\lambda=-2}^{+2} \epsilon_{\kappa\lambda} E_{j+\kappa}(f, \theta_{i+\lambda})$$

where the subscript j refers to a grid row, i references an angle band, and $\epsilon_{\kappa\lambda}$ is a matrix of normalized multipliers.

Source/Sink Integration

The source terms employed in this model are similar to those discussed in Resio (1987, 1988). There are four source terms in the model:

1. wind inputs;
2. energy fluxes due to wave-wave interactions;
3. wave breaking; and
4. bottom interaction effects.

For all tests of source terms, bottom friction and other bottom interaction effects will be assumed to be negligible compared to nonlinear energy fluxes.

Tests of Steady-State Spectral Model

Tests of Propagation Only

A simple case to demonstrate that the spectral representation of refraction and shoaling used here is consistent with theoretical monochromatic results can be found in the propagation of waves with different periods and propagation directions across a slope with parallel depth contours. For this case, the monochromatic waves were approximated by a spectrum with energy in an angular band of one degree centered on the specified approach angle with a frequency band of 0.01 hertz. As seen in Table 1, the computed results show very good agreement with theoretical predictions.

Table 1
Wave Height Comparison

Angles (o)	Depths (ft.)							
	50		20		10		5	
	a	b	a	b	a	b	a	b
0	.96	.96	.92	.92	.98	.99	1.11	1.11
10	.96	.96	.92	.92	.98	.98	1.11	1.10
	9.70	9.70	8.00	7.80	5.70	5.90	4.60	4.30
20	.96	.95	.91	.91	.97	.96	1.09	1.08
	19.30	19.40	15.50	15.40	11.60	11.70	8.30	8.60
30	.95	.95	.89	.89	.94	.94	1.05	1.05
	29.20	29.00	22.90	22.90	17.20	17.20	12.60	12.50
40	.95	.95	.86	.86	.90	.90	.99	.99
	38.40	38.50	29.80	29.90	22.30	22.40	16.00	16.20
50	.94	.94	.82	.82	.84	.84	.92	.92
	48.10	47.90	36.70	36.50	26.90	27.00	19.50	19.40
60	.92	.92	.76	.76	.75	.75	.82	.82
	57.30	57.10	42.40	42.30	30.90	30.80	21.80	22.10
70	.87	.87	.65	.65	.63	.63	.68	.68
	65.70	65.60	47.00	46.80	33.80	33.80	24.10	24.00
80	.73	.73	.48	.48	.45	.46	.49	.49
	72.80	72.60	49.80	49.90	35.50	35.60	25.20	25.30

NOTE: a = theoretical result
b = model result

To test this model in a situation in which linear models are expected to be inaccurate, the model was run for the elliptical shoal, monochromatic test case described in Vincent and Briggs (1988), which is patterned after that of Berkhoff et al. (1982). The bathymetry for this case is shown in Figure 3. Figure 4 shows a comparison of the waves predicted by this model to those measured in the laboratory. Also shown in that figure are the modeled results of a finite difference solution to the "mild slope" equation (Ebersole et al., 1986). As seen there, the spectral model can reproduce the monochromatic, even for this nonlinear case, results quite well.

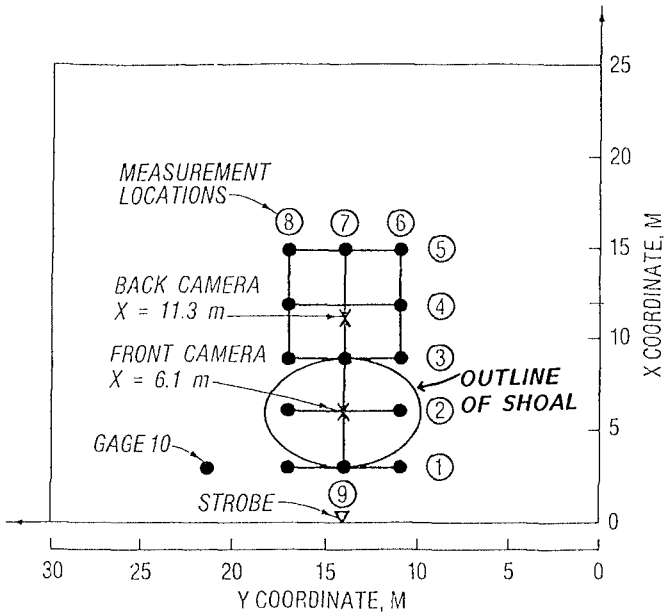


Figure 3. Laboratory set-up for waves over an elliptical shoal (from: Vincent and Briggs, 1988).

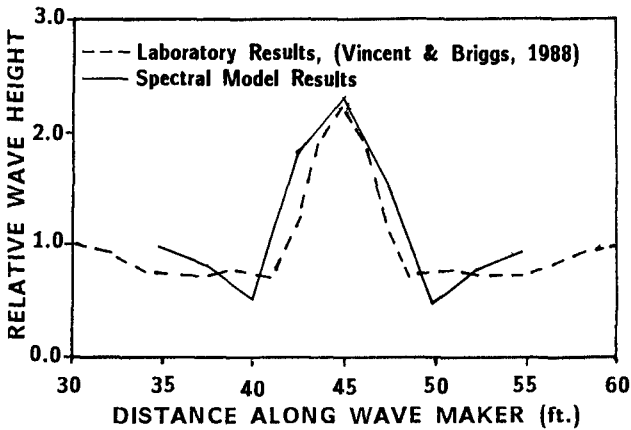


Figure 4. Comparisons of results from spectral model to laboratory measurements for monochromatic case.

Our next test drops the artificial constraint of monochromatic waves and examines model behavior for more realistic cases with reasonable wave spectra. Vincent and Briggs (1988) set up a series of laboratory tests on

bathymetry shown in Figure 3 in the directional wave basin located at the U.S. Army Engineer Coastal Engineering Research Center. The input spectrum tested here is shown in Figures 5 and 6. Waves were measured along a cross-section located about 17 feet behind the crest of the shoal as seen in Figure 3. Figure 7 gives a comparison of the steady-state spectral model's performance compared to the measured waves, along with the "equivalent" monochromatic solution (i.e. the solution obtained by treating these wave spectra as equivalent monochromatic waves). Clearly, the influence of spectral shape cannot be neglected. In fact, for waves typical of moderate storm conditions, the monochromatic approximation overpredicts wave heights by about 120%. Even for the case of a spectrum typical of swell, the monochromatic predictions are too high by about 100%. In neither of these test cases were waves observed to be undergoing wave breaking over the shoal; thus, the results shown in Figure 7 should be a fair examination of propagation effects only for realistic wave spectra.

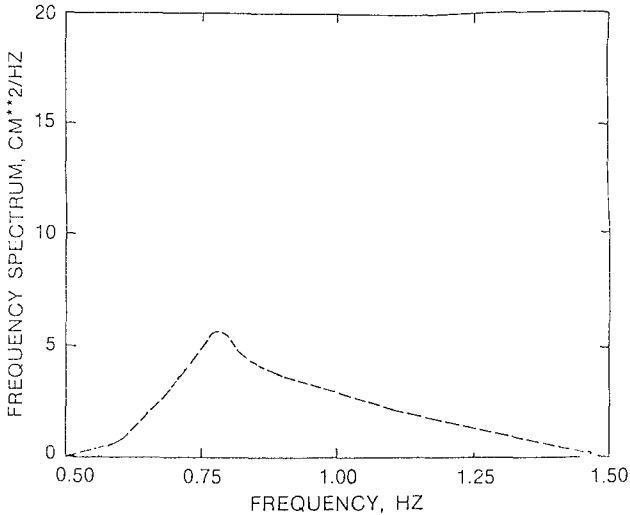


Figure 5. Input frequency spectrum for test case.

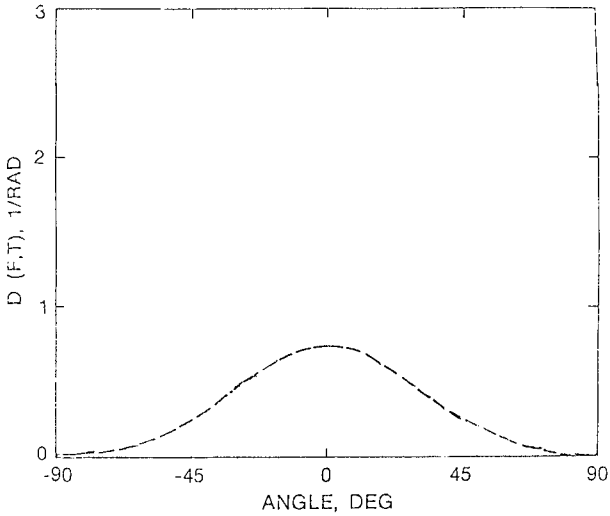


Figure 6. Angular distribution of energy for test case.

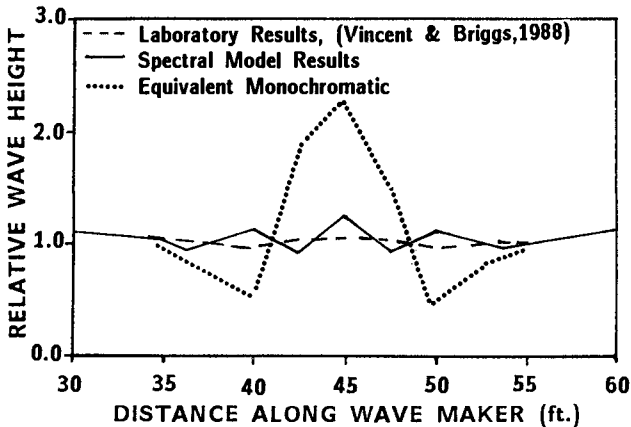


Figure 7. Comparison of results from spectral model to laboratory measurements for broad directional spectrum. Equivalent monochromatic results shown for reference.

Tests of Propagation and Source Terms Together

As some final test cases, let us consider first a situation with a 40-knot wind blowing perpendicular to the coast over a planar shelf with constant slopes of 1/10 and 1/100. The boundary deep-water spectrum is specified to have a JONSWAP shape ($\delta = 3.3$, $f_m = 0.10$ hz, $\alpha = 0.013$, $\sigma_a = 0.07$, $\sigma_b = 0.09$) with a $\cos^{2\theta}$ angular distribution of energy. Table 2 shows the behavior of wave height as a function of distance from shore for the case with the wind source term included and for the case with the wind source neglected.

Next, let us consider a 40-knot wind blowing at an angle of 50° relative to the coast compared to the zero-wind case. Table 3 shows these results. Differences such as seen in Tables 2 and 3 could be very critical on sensitive projects.

Table 2

Comparison of Predicted Wave Heights (Metres) for 40-Knot Wind Blowing Straight Toward Coast and No Wind

Depth	Slope = 1/10		Slope = 1/100	
	No Wind	40-Knot Wind	No Wind	40-Knot Wind
90	6.11	6.11	5.84	5.97
80	6.06	6.07	5.60	5.82
70	5.99	6.01	5.38	5.68
60	5.90	5.94	5.18	5.54
50	5.79	5.83	4.97	5.39
40	5.64	5.69	4.75	5.22
30	5.47	5.53	4.52	5.01
20	5.32	5.38	4.27	4.75
10	5.33	5.35	3.82	4.07

Table 3

Comparison of Predicted Wave Angles (Degrees) for 40-Knot Wind Blowing at 50° Angle to Coast and No Wind

Depth	Slope = 1/10		Slope = 1/100	
	No Wind	40-Knot Wind	No Wind	40-Knot Wind
90	0	0.3	0	0.5
80	0	1.2	0	6.4
70	0	2.5	0	10.3
60	0	3.0	0	15.4
50	0	3.3	0	17.5
40	0	3.1	0	18.2
30	0	2.2	0	16.8
20	0	1.5	0	14.9
10	0	0.9	0	6.3

Conclusions

A steady-state spectral model has been briefly described here. This model has a run time typically over 100 times faster than time-step solutions to comparable problems. Tests of this model support the following conclusions relative to shallow-water wave modeling:

1. The model described here, even neglecting phase-dependent behavior, can produce reasonable simulations of a wide range of wave conditions, both monochromatic and spectral, even in conditions which significant nonlinear behavior is expected;
2. Equivalent monochromatic methods cannot produce accurate results for realistic wave spectra; and
3. Simulations of areas on the scale of 5 miles or more should consider wind effects on nearshore waves; otherwise, the simulated results can deviate significantly from conditions expected under the action of winds.

Appendix.--References

- Abernethy, C.L., Snell, R.J., and Stuert, K.B. (1977). "Computation of the refraction of wave spectra. Programme listings and user's notes." Report No. IT 131, Hydraulics Research Station, Wallingford, England.
- Berkhoff, J.C.W. (1976). "Mathematical models for simple harmonic linear water waves, wave diffraction and refraction." Publication No. 1963, Delft Hydraulics Laboratory, Delft, The Netherlands.
- Berkhoff, J.C.W., Booy, N., and Radder, A.C. (1982). "Verification of numerical wave propagation models for simple harmonic linear water waves." Coast. Eng., 6, 255-279.
- Ebersole, B.A., Cialone, M.A., and Prater, M.D. (1986). "Regional coastal processes numerical modeling system. Report 1: RCPWAVE-- A linear wave propagation model for engineering use." Tech. Report No. CERC-86-4, Dept. of the Army, Waterways Experiment Station, Vicksburg, MS.
- Hasselmann, K. (1962). "On the non-linear energy transfer in a gravity-wave spectrum--General theory." J. Fluid Mech., 12(1), 481-500.
- Resio, D.T. (1987). "Shallow-water waves. I: Theory." J. Wtrway., Port, Coast., Oc. Eng., 113(3), 264-281.
- Resio, D.T. (1988). "Shallow-water waves. II: Data comparisons." J. Wtrway., Port, Coast. Oc. Eng., 114(1), 50-65.
- Vincent, C.L., and Briggs, M.J. (1988). "Refraction - diffraction of irregular waves over a mound." Submitted to J. Wtrway., Port, Coast., and Oc. Eng.
- Yuen, H.C., and Lake, B.M. (1975). Phys. Fluids., 18, 956.

CHAPTER 70

COMPARISONS OF NUMERICAL RANDOM WAVE SIMULATORS

by Josep R. Medina¹, M.ASCE, and
Carlos R. Sánchez-Carratalá²

ABSTRACT

A review of unidimensional numerical random sea simulators is provided, centering the attention on the measurement of distortions introduced by the different simulation techniques. Simulators by wave superposition are analyzed, with the conclusion being that they generate significant distortions on the realizations when the number of simulated points are larger than two times the number of wave components. Composed simulators are proposed for the purpose of generating long non-periodic realizations using FFT algorithms.

In order to qualify simulators, a justification, based on physical properties of random waves, is given to use m_0 , m_1 , Q_e and m_2 as the best spectral parameters to characterize processes. Mean values and variabilities of wave heights and periods are controlled by these parameters. A new robust technique is developed to estimate the parameters of an AR(p) model corresponding to a given target spectrum, $S_\eta(f)$. MA(q) and ARMA(p,q) approximations are studied. The source of pseudo-random numbers to generate the input white noise has a critical impact on the statistical properties of the output.

INTRODUCTION

Numerical random sea simulation techniques of stochastic processes defined by a continuous variance spectrum are used to solve numerous coastal and ocean problems. Numerical descriptions in time of the sea surface is a basic input of a variety of design methods in maritime engineering (Goda, 1985). On the other hand, given the increasing quality of the servo-control mechanisms for wave generation in laboratory, numerically synthesized records are also the input of most modern wave generators for physical modelling (see Funke and Mansard, 1987). Therefore, the numerical and physical experiments

¹Profesor Titular, Dept. Transportation, ETSI Caminos, Univ. Politécnicá de Valencia, SPAIN

²Research Asst., Dept. Transportation, ETSI Caminos, Univ. Politécnicá de Valencia, SPAIN

are the two main areas of application of numerical random wave simulators.

From the earlier papers of Borgman (1969) and Goda (1970), which showed engineering applications of linear simulators, a variety of random wave simulation approaches have been used in different numerical experiments. Hudspeth (1974) utilized a nonlinear simulator to predict wave forces on piles. Goda (1977) studied the statistical variability of ocean waves by analyzing the results given by a linear directional simulator. Hudspeth and Chen (1979) used linear and nonlinear unidirectional random wave simulators for the dynamic analysis of multilegged pile-supported ocean structures. Goda (1981) employed a linear directional simulator to study the directional resolution of different estimation techniques of directional spectrum. Goda (1983) and Elgar et al. (1984, 1985) used linear simulators to compare sea wave group characteristics of synthesized records with field measurements.

On the other hand, Funke and Mansard (1987) described a number of wave generation techniques in physical modelling, pointing out conceptual differences among wave generators and also the distance between numerical and physical simulations. However, most modern laboratory wave generators use numerically simulated waves as input of the servo-control element. Therefore, a first level of distortions is associated with the simulation technique itself and can be analyzed testing the corresponding numerical simulators.

Tuah and Hudspeth (1982) compared linear and nonlinear NSA and DSA FFT simulations; the result was that NSA synthesized records showed better statistical characteristics. Medina et al. (1985) gave a systematic contrast of linear simulators by wave superposition, pointing out the distortions induced by each simulator. Miles and Funke (1987) analyzed the limitations of the available numerical simulation techniques, which may be overshadowed in physical experiments, as a previous step to the installation of a multi-mode segmented wave generator at the NRC Hydraulics Laboratory.

This paper analyzes the different linear simulation techniques based on wave superposition, and also analyzes ARMA models to synthesize records by filtering white noise in the time domain. General criteria for qualifying simulators are given to rationalize the selection of a simulator for a given application. Finally, new AR simulators of low order and composed synthesizers are introduced with efficient methods to generate non-periodic realizations via FFT algorithms.

NUMERICAL SIMULATORS

Borgman (1969) pointed out the two main methods of generating realizations corresponding to an ergodic Gaussian process defined by its variance spectrum, $S_{\eta}(f)$.

The wave superposition method generates realizations by addition of sinusoidal functions with amplitudes and frequencies in accordance with $S_{\eta}(f)$ and random phases. The filtering of white noise produces realizations by passing a white noise through a linear filter, the transfer function of which is on a par with $S_{\eta}(f)$. The extension of the unidimensional simulation to 2D can be easily implemented by using wave superposition. However, said extension requires the design of new filters to propagate the simulations in the space by using white noise filtering (see Samii and Vandiver (1984)). Miles and Funke (1987) have studied the extension of the 2D simulation techniques to the 3D.

* Wave Superposition *

The linear simulators by wave superposition describe the vertical displacement of the sea surface by addition of sinusoidal waves:

$$\eta(n\Delta t) = z_n = \sum_{m=1}^M R_m \cos(2\pi f_m n\Delta t + \theta_m); \quad 0 < f_m < 1/(2\Delta t) \quad (1)$$

in which $\eta(n\Delta t)$ is a random time series of the ensemble corresponding to the stochastic process, discretized at time intervals Δt ; M is the number of wave components, R_m and f_m are the amplitudes and frequencies calculated from the wave spectrum of the process as

$$R_m^2/2 = S_{\eta}(f_m)\Delta f_m; \quad 0 < f_m < 1/(2\Delta t) \quad (2)$$

where Δf_m is the frequency interval related to the frequency component f_m ; and $S_{\eta}(f_m)$ is the variance spectrum characterizing the ergodic Gaussian stochastic process to be simulated. The real spectrum of the realization generated with Eq.1 is

$$S_{\eta}(f) = \sum_{m=1}^M (R_m^2/2)\delta(f-f_m); \quad 0 < f_m < 1/(2\Delta t) \quad (3)$$

in which $\delta(f)$ is the Dirac's Delta function.

Medina et al. (1985) analyzed a five step method for creating simulators by wave superposition; each step generates distortions on the results in the following manner: first, the target continuous variance spectrum, $S_{\eta}(f)$, needs a cut-off frequency lower than the folding frequency imposed by the aliasing phenomenon ($f_{max} < 1/(2\Delta t)$). Second, the linear assumption permits one to divide the target spectrum in M band spectra. Third, each band spectrum is substituted by a regular wave component with a frequency in the frequency band and an amplitude related (deterministically or non-deterministically) to the variance of the band spectrum. Fourth, a pseudo-random number generator will provide the random basis of the Monte Carlo experiment. Finally, efficient numerical algorithms can reduce the computational time which indirectly affects the quality of the simulator. According to Medina et al. (1985) simulations should be non-periodic, non-deterministic and should fit reasonably the spectral characteristics of the target spectrum. A general plan to qualify simulators,

given below, allows one to select the appropriate simulators from the large number of methods available.

* Filtering of White Noise *

The second general method to synthesize random realizations corresponding to an ergodic Gaussian stochastic process is the filtering of white noise through a linear filter. The general method is to define an ARMA filter, the transfer function of which corresponds to the target spectrum, $S_\eta(f)$. The autoregressive-moving average model (ARMA) is described by

$$\eta(n\Delta t) = z_n = -\sum_{k=1}^p a_k z_{n-k} + w_n + \sum_{m=1}^q b_m w_{n-m} \quad (4)$$

in which z_n is the time series generated, w_n is the white noise time series with variance σ_w^2 , a_k are the p autoregressive parameters, and b_m are the q moving-average parameters. The model described by Eq.4 is referred to as ARMA(p, q). From Box and Jenkins (1976), the spectrum of the realizations synthesized by the Eq.4 is

$$S_\eta(f) = 2\sigma_w^2 \Delta t |H(f)|^2 = 2\sigma_w^2 \Delta t \frac{|1 + \sum_{m=1}^q b_m \exp(-jm\Delta t 2\pi f)|^2}{|1 + \sum_{k=1}^p a_k \exp(-jk\Delta t 2\pi f)|^2}; \quad (5)$$

; $0 < f < 1/(2\Delta t)$

in which $H(f)$ is the frequency response function of the linear filter, Δt is the discretization time interval, σ_w^2 is the variance of the white noise input, and $S_\eta(f)$ is the target spectrum.

Taking into consideration that simulators by wave superposition tend to generate periodic or deterministic realizations of long duration, the filtering of white noise avoids these problems. Unfortunately, the calculation of the ARMA parameters to fit the target spectrum and the source of white noise are elements which can also produce large distortions on the results.

CRITERIA TO QUALIFY SIMULATORS

The selection of a numerical simulator (or the corresponding physical generator) to carry out a numerical (or physical) experiment depends on the available criteria to qualify the simulators. To establish a general plan for qualifying simulation techniques is essential for selecting appropriate simulators for specific problems.

A realization of a process defined by a continuous variance spectrum can not be periodic. As a result, harmonic simulators should be avoided, including those long simulations based on FFT algorithms. On the other hand, according to Medina et al. (1985), a sinusoidal function can be considered a deterministic autoregressive process AR(2) with two parameters and, therefore, the time series given by Eq.1 only have $2M$ non-deterministic points. Consequently, the length of simulations by wave superposition should be limited to $2M$ points. Finally, the simulated process should have spectral characteristics which are similar to the target process. A number of opinions and parameters have been given and it is not

clear what the best parameters are for characterizing target spectra.

* Suitable Spectral Characteristics *

What are the most appropriate spectral parameters to characterize variance spectra?. This question has not as yet been answered and the solution probably depends on the engineering application in which the spectral description is used. However, some properties of random signals can be taken into consideration to give a reasonable answer.

If $\eta(t)$ is the sea surface elevation with the spectrum $S_{\eta}(f)$, the spectral moments are defined as

$$m_n = \int_{f_{\min}}^{f_{\max}} f^n S_{\eta}(f) df \tag{6}$$

and therefore, the variance of the vertical displacement of the sea surface, $\eta(t)$, is $\sigma_{\eta}^2 = m_0$; the variance of the vertical velocity, $\dot{\eta}(t) = d\eta(t)/dt$, is $\sigma_{\dot{\eta}}^2 = (2\pi)^2 m_2$; the variance of the vertical acceleration, $\ddot{\eta}(t) = d^2\eta(t)/dt^2$, is $\sigma_{\ddot{\eta}}^2 = (2\pi)^4 m_4$; the mean period of the orbital movement of sea surface is $T_{03} = m_0/m_1$; the mean zero-up-crossing period is $T_{02} = (m_0/m_2)^{0.5}$; and the mean crest-to-trough period is $T_{24} = (m_2/m_4)^{0.5}$. Other mean periods can be defined although no easy physical interpretation can be given.

According to Blackman and Tukey (1959) the variability of the variance of the process depends on the spectral peakedness. Using the dimensionless spectral peakedness parameter Q_e , given by Medina and Hudspeth (1987)

$$\frac{\sigma(z_{rms})}{E(z_{rms})} = \left(\frac{Q_e/8}{N\Delta t/T_{01}} \right)^{1/2} \tag{7}$$

in which

$$Q_e = (2m_1/m_0^3) \int_{f_{\min}}^{f_{\max}} S_{\eta}^3(f) df \tag{8}$$

Therefore, the spectral moments are not the only parameters necessary for defining the stochastic properties of the simulations. As noted by Medina and Hudspeth (1987), the dimensionless spectral peakedness parameter Q_e is not only related to the variability of the variance, but also to the wave grouping characteristics. A general order of parameters can be suggested for the most common applications:

- 1.- The most important parameter is the total variance of the process, $\sigma_{\eta}^2 = m_0$. This parameter controls the magnitude of wave heights, which have a major impact on most engineering applications.
- 2.- Fixed $\sigma_{\eta}^2 = m_0$, the first moment, m_1 , determines the mean period of the orbital movement of the sea surface, $T_{01} = m_0/m_1$. The mean wave periods are probably the second most important variable for maritime engineering applications.
- 3.- Having characterized the mean values of wave heights and periods by m_0 and m_1 , the third most important parameter should control the variability of variance.

The dimensionless spectral peakedness parameter Q_e , shown in Eq.8, can characterize the variability of variance. This variability is also related to wave groupiness, variability of significant wave height, and other basic sea state parameters.

- 4.- The fourth most important parameter can be the second spectral moment, m_2 , because the variability of periods tends to be dependent on the parameter $\nu = (m_0 m_2 / m_1^2 - 1)^{1/2}$ given by Longuet-Higgins (1975). Hudspeth and Medina (1988) give stochastic properties of the instantaneous frequency as function of ν .

SIMULATION BY WAVE SUPERPOSITION

Using the criterion of non-periodic realizations, the Goda's (1970) and Borgman's (1969) simulators could be considered more suitable than the harmonic DSA and NSA simulators given by Tuah and Hudspeth (1982). However, the criterion of non-deterministic realizations would only permit one to use those non-harmonic simulators for short realizations (2M points), while DSA and NSA simulators can generate large non-deterministic realizations with the same computational time. The non-periodic realizations obtained from non-harmonic simulators by wave superposition progressively distort the stochastic properties when the number of simulated points increase by more than 2M.

The periodicity of DSA and NSA FFT simulations can be avoided by modulating the simulations by a basic frequency, f_0 , non-harmonic of $\Delta f = 1/(N\Delta t)$. However, the envelopes of these simulators are periodic $N\Delta t$, a fact which is also an undesirable characteristic. By composing non-harmonic FFT simulators it is possible to get non-periodic realizations with non-periodic envelopes of an indefinite length.

Goda (1977, 1981), and Miles and Funke (1987) present different aspects of the extension of simulators by wave superposition to 3D. As noted by Goda (1977) and Medina et al. (1985), the addition of many waves with the same frequency and random phases in directional simulation generates random unidimensional realizations given by Eq.1, but the amplitudes are non-deterministic, and can be modelled by

$$R_m^2/2 = (C_m/2) S_{\eta}(f_m) \Delta f_m = -\ln(U_m) S_{\eta}(f_m) \Delta f_m; \quad (9)$$

$$; m=1, 2, \dots, M$$

instead of the deterministic relation given by Eq.2. U_m and C_m are random variables uniformly and chi-squared distributed with two degrees of freedom. The Eqs.2 and 9 correspond to the relation between DSA and NSA simulators described by Tuah and Hudspeth (1982). The simulators, based on Eq.9 instead of Eq.2, are also named "random Fourier coefficient" (RFC) methods to differentiate them from the "random phase" methods (RP) used by Miles and Funke (1987). DSA (RP) simulators via FFT can be modified to generate non-harmonic simulations. Considering ocean spectra are zero for low frequencies, one can select a

basis frequency , f_0 , non-harmonic of $\Delta f=1/(N\Delta t)$ and then

$$\begin{aligned} \eta(n\Delta t) &= z_n = \sum_{m=1}^M R_m \cos(2\pi(f_0+f_m)n\Delta t + \theta_m) = \\ &= \sum_{m=1}^M R_m (\cos(2\pi f_0)z'_n - \sin(2\pi f_0)\hat{z}'_n) \end{aligned} \quad (10)$$

in which

$$z'_n = \sum_{m=1}^M R_m \cos(2\pi f_m n\Delta t + \theta_m) \quad (11)$$

and \hat{z}'_n is the Hilbert transform of z'_n . The time series simulated by Eq.10, z_n , have longer periods than $N\Delta t$. For instance, if $f_0=(5+1/7)\Delta f$, the period of the realizations given by Eq.10 is $7N\Delta t$; however, the realizations would have envelopes with a period of $N\Delta t$. The composition of simulators enlarges the period of time series and envelopes. By taking several non-harmonic frequencies f_0 and composing simulators, it is possible to generate, via FFT, almost non-periodic realizations with non-periodic envelopes.

The simulators by wave superposition fit the spectral characteristics well. Periodicity and deterministic behaviour can be studied by analyzing the variability of the variance of long simulations. Fig.1 shows the representation of the C.V. of z_{rms} calculated from forty realizations using DSA and NSA simulators and the method

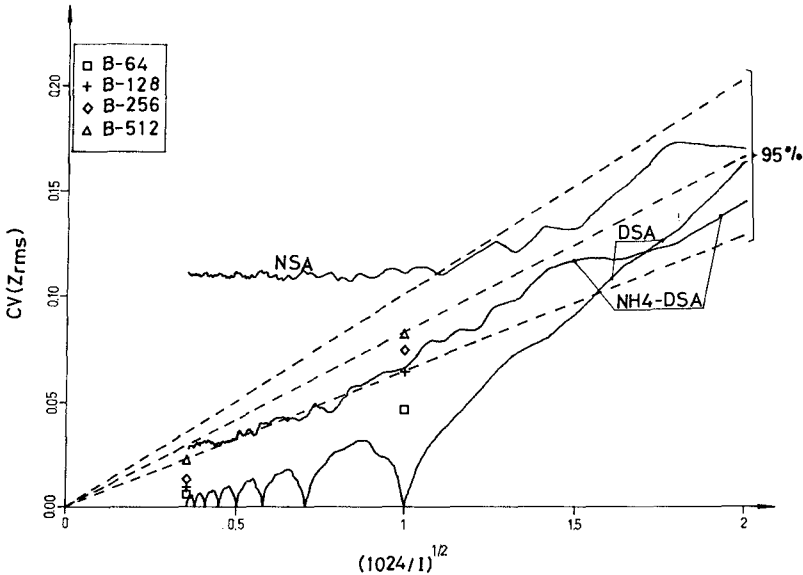


Fig.1: Coefficient of Variation of z_{rms} in long simulations. The graph shows the mean values from 40 DSA and NSA simulations of JONSWAP ($N=1024$, $\Delta t=0.5$ s, $\gamma=1$, $f_0=0.0635$ Hz, $f_{max}=1/(2\Delta t)$), compared with results of Borgman's simulator with different number of wave components and composed non-harmonic FFT simulator with 4 components. "I" is the number of points of the simulation.

proposed by Borgman (1969) with different number of components. DSA simulations have unrealistic low variabilities when N approximates to $1/(\Delta f \Delta t)$ while NSA simulators have variabilities as predicted by linear theory, up to the full period of simulation. Borgman's simulator only gives reasonable variabilities if the number of components is large in comparison with the number of points in the simulations analyzed ($M > N/2$).

FILTERING WHITE NOISE

The filtering of white noise generated by Eq.4 can theoretically produce indefinitely non-periodic and non-deterministic realizations with a prescribed variance function, by only taking the appropriate ARMA parameters to fit the target spectrum according to Eq.5. However, these simulators have two critical points: the source of white noise and the method to determine the ARMA parameters.

The spectrum of the output of the linear filter given by Eq.4 is the square of the absolute value of the frequency response function, $|H(f)|^2$, multiplied by the spectrum of the input (white noise). Unfortunately, the spectrum of random time series generated by computer can depart from the perfect white shape, even though the time series passes the usual tests of randomness. Hull and Dobell (1962) pointed out the extreme difficulty in justifying the random behaviour of numerically synthesized white noise time series. Additionally, these simulators require a precise and robust enough methodology to determine the ARMA parameters to fit the target spectrum.

AR(p)

If only the autoregressive parameters in Eq.4 are considered, the process is then described by

$$\eta(n\Delta t) = z_n = - \sum_{k=1}^p a_k z_{n-k} + w_n \quad (12)$$

and the spectrum of the output is related to the set of parameters by

$$S_\eta(f) = \frac{2\sigma_w^2 \Delta t}{\left| 1 + \sum_{k=1}^p a_k \exp(-jk\Delta t 2\pi f) \right|^2}; \quad 0 < f < 1/(2\Delta t) \quad (13)$$

in which a_k are the p autoregressive parameters. Holm and Hovem (1979) presented a method for describing sea states by an AR filter with 15 to 30 parameters, while Houmb and Overvik (1981) proposed the inclusion of a fixed MA parameter to a basic AR(34) model.

Spanos and Hansen (1981), Spanos (1983), and Spanos and Mignolet (1986) have analyzed different methods to calculate the AR parameters corresponding to a known spectrum. The equations of Yule-Walker can be derived from Eq.12 which leads to the corresponding Toeplitz matrix equation system. For JONSWAP or PM spectra, the solution of this system gives a spectrum with correct spectral

moments but sharp fluctuations about the mean value (good m_0 , m_1 and m_2 but bad Q_e). Increasing the number of parameters, p , the Toeplitz matrix becomes gradually ill conditioned and the solution is unstable. As noted by Spanos and Mignolet (1986) a stable finite AR representation exists and admits an inverse MA representation if and only if

$$\int_0^{f_d} \log(S_\eta(f))df > -\infty; f_d = 1/(2\Delta t) \tag{14}$$

where f_d is the folding frequency. This relation is not satisfied by the PM spectrum and although Spanos (1983) proposed a sophisticated method to improve the solution by approximated spectral shapes, Spanos and Mignolet (1986) concluded that it "is not permissible to determine a

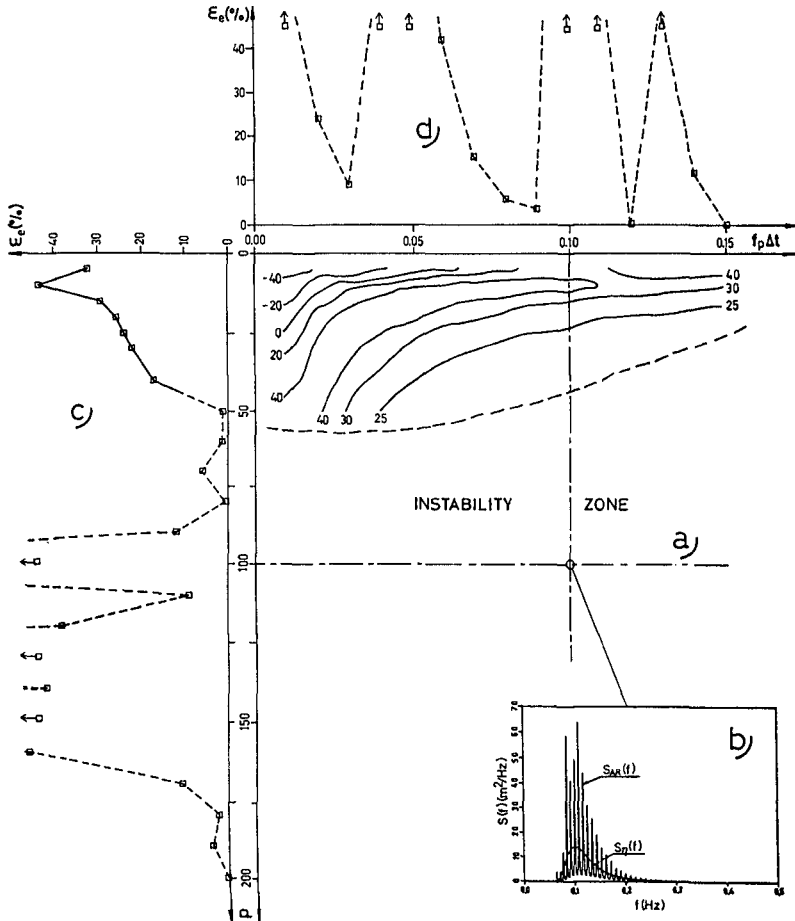


Fig.2: Classic AR approximation: a) Map of errors E_e ; b) Typical target and AR spectra; c) Values of E_e with $\Delta t f_p = 0.1$; and d) Values of E_e with $p = 100$. The target spectrum is JONSWAP ($N = 1024$, $\gamma = 1$, $f_p = 0.1$ Hz, $f_{max} = 1/(2\Delta t)$)

reliable AR representation of the PM spectrum in a straight forward manner"; and they consequently proposed ARMA models for simulations of ocean spectra.

From Eq.14 it is easy to infer that the instability of the AR model is generated by the frequencies with low energy. A simple method for eliminating the zeros in $S_\eta(f)$ is to add a very low level of white noise to the process which is to be simulated. The addition of a white noise with a variance of 0.1% to 0.3% of the total variance can solve the instability problem and generate an admissible level of distortions in simulations because larger noise intensities are always present in Nature and Laboratories for most common ocean engineering applications. The consideration of a very low level of white noise on the target spectrum (whose variance is detracted first from the spectrum) before the calculations of AR parameters using Yule-Walker equations will be referred to as the proposed new robust method.

Fig.2-a shows the map of relative errors of the peakedness parameter Q_e , which is sensitive to fluctuations around the target spectrum. The map of relative errors of Q_e , ξ_e , shows a region of instability in which small differences in parameters or variables of simulation can critically change the simulator. The relative error ξ_e is defined as

$$\xi_e = (\hat{Q}_e - Q_e) / Q_e \quad (15)$$

in which \hat{Q}_e is the spectral peakedness parameter corresponding to the fitted AR approximation. Although the errors of the target spectral moments are low, these simulators show very large errors of Q_e . Fig.2-b shows a typical AR spectrum, as compared to the target spectrum.

On the other hand, Fig.3-a shows the map of errors of ξ_e for the proposed new robust method, adding a white noise of variance 0.25% m_0 to the target spectrum. The new AR approximations are stable and much better for higher order p . The new errors of spectral moments m_1 and m_2 are less than 1%, if $f_p \Delta t > 0.1$, and show a monotonic decreasing behaviour with p and $f_p \Delta t$. Therefore, the proposed new method to determine AR approximations can be considered superior to the classic method, and it is applicable to a variety of ocean spectra.

MA(q)

Taking only the moving average parameters in Eq.4, the MA(q) model is described by

$$\eta(n\Delta t) = z_n = w_n + \sum_{m=1}^q b_m w_{n-m} \quad (16)$$

The spectrum of the output is then

$$S_\eta(f) = 2\sigma_w^2 \Delta t \left| 1 + \sum_{m=1}^q b_m \exp(-jm\Delta t 2\pi f) \right|^2; \quad 0 < f < (1/2\Delta t) \quad (17)$$

in which b_m are the q moving average parameters. Kimura and Kimura (1987) have presented a method to

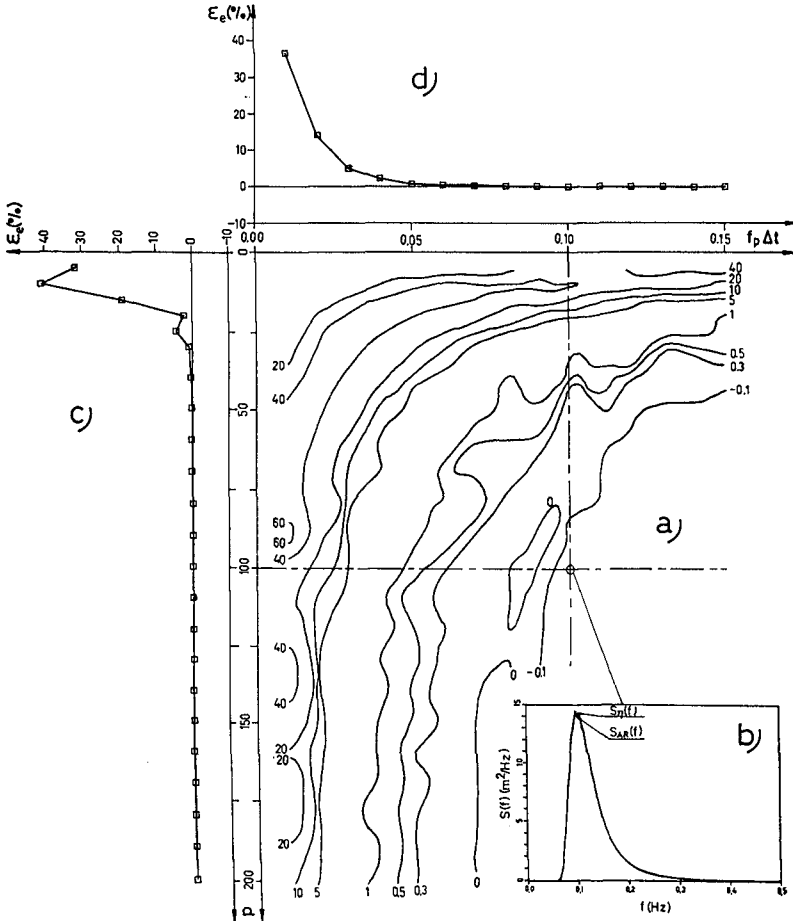


Fig.3: New robust AR approximation with 0.25% of white noise: a) Map of errors E_e ; b) Typical target and AR spectra; c) Values of E_e with $\Delta t f_p = 0.1$; and d) Values of E_e with $p = 100$. The target spectrum is JONSWAP ($N = 1024$, $\gamma = 1$, $f_p = 0.1$ Hz, $f_{max} = 1/(2\Delta t)$)

determine the parameters of a $MA(q)$ approximation for a given target spectrum, $S_\eta(f)$. The method basically consists of the calculating of the parameters of an $AR(q)$ approximation to $S_\eta(f)$ and then the calculating of the $MA(q)$ parameters by

$$\sum_{m=0}^i a_{i-m} b_m = \delta_i; \quad i = 0, 1, \dots, q \tag{18}$$

in which δ_i is the discrete Dirac's Delta function, and $a_0 = b_0 = 1$ using Eq.16 for the $MA(q)$ model. The proposed method by Kimura and Kimura (1987) is equivalent to the solving of the equations of Yule-Walker and to the determining of the MA parameters, using Eq.18. The parameters of the $AR(q)$ model corresponding to $S_\eta(f)$ are

the same as the parameters of the MA(q) model fitted to $1/S_\eta(f)$, which is the inverse filter of the MA(q) model fitted to $S_\eta(f)$. Eq.18 reflects the relations between the parameters of these two inverse MA filters.

Obviously, the quality of the MA(q) approximation proposed by Kimura and Kimura (1987) depends on the AR(q) model taken as basis. The proposed new method to estimate robust AR parameters given in the previous section is also useful for getting better MA(q) approximations. Fig.4 shows a typical evolution of errors generated by the MA(q) model based on a robust AR(q) estimation with 0.25% of white noise. The relative error of Q_e , ϵ_e , is compared with the corresponding relative errors of m_1 , ϵ_1 , and m_2 , ϵ_2 , as well as with the relative error of Q_e for the AR(q) model taken as basis.

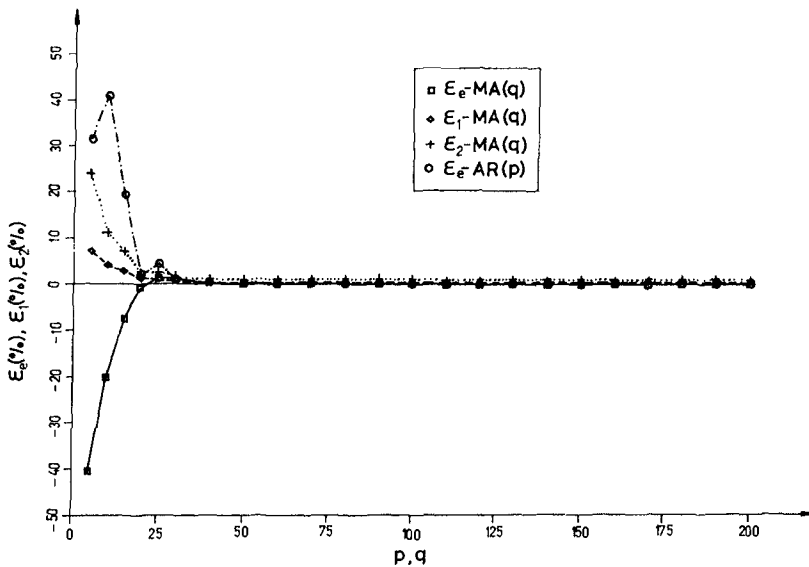


Fig.4: Errors ϵ_e , ϵ_1 , ϵ_2 of MA approximation based on the new robust AR model with 0.25% of white noise. The values are compared with the ϵ_e of the AR model. The target spectrum is JONSWAP ($N=1024$, $\Delta t=1.0$ s, $\gamma=1$, $f_p=0.1$ Hz, $f_{max}=1/(2\Delta t)$)

ARMA(p, q)

Spanos and Mignolet (1986) have proposed two alternative procedures to obtain the unknown coefficients a_k and b_m in Eq.5 to fit the target spectrum, $S_\eta(f)$. The methods are based on the work of Samarasinghe et al. (1985) and Graupe et al. (1975).

*** Auto/Cross-Correlation Matching (ACM) ***

This method is based on a first representation of the process by an AR filter, followed by the equalization of the autocovariance of the output and the cross-covariance of input-output.

* Power Order Matching (POM) *

This technique is based on the equalizing of the z powers of the transfer functions of the ARMA and AR model, which is used as the basis. It can be shown that this method is equivalent to matching the cross-covariance of input-output of the AR and ARMA approximations for $i=0$ to $p+q$.

* Evaluation of ACM-POM *

The quality of these simulators depends on the AR approximation used as basis. Spanos and Mignolet (1986) show good ARMA approximations ACM(7,7) and POM (8,8); but those results were based on special satisfactory AR(100) model which used a Taylor expansion approximation of the PM spectrum. The models proposed by Spanos and Mignolet (1986) are only valid for a specific spectrum and for simulation characteristics (Δt , p , and q). Changes in Δt , p , and q can produce unsatisfactory results.

Using the proposed new robust technique to estimate the AR(m) approximation, the ACM and POM methods have been applied to a JONSWAP spectrum ($\gamma=1$, $f_p=0.1$ Hz, $f_p \Delta t=0.1$). The results for $p=q$ show local good approximations that can not be generalized for different target spectra. Larger orders of filtering do not generate better filters.

CONCLUSIONS

After analyzing and contrasting different unidimensional numerical random sea simulations, the following conclusions can be stated:

- 1.- The stochastic properties of simulations by wave superposition are distorted when the number of points of the simulations are larger than two times the number of wave components.
- 2.- Composing modulated DSA simulators, efficient non-harmonic realizations via FFT can be generated.
- 3.- The spectral parameters m_0 , m_1 , Q_e , and m_2 have been analyzed, justifying this rational sequencing of parameters to characterize the appropriate spectral shapes. They are related to mean value and variability of wave heights and periods.
- 4.- A new robust method for determining the AR(p) model for a given target spectrum is given. The method is based on the addition of a very low level of white noise to the target spectrum and then the solving of the Yule-Walker equations.
- 5.- The MA(q) and ARMA(p,q) approximations to the basic AR(m) model have been analyzed. The MA(q) are competitive.
- 6.- Simulators by filtering white noise are quite sensitive to the spectral characteristics of the method used for generating the white noise time series.

ACKNOWLEDGMENTS

We gratefully acknowledge the financial support provided by the Dirección General de Puertos y Costas

(Ministerio de Obras Públicas y Urbanismo) and also by the U.S.-Spain Joint Committee for Scientific and Technological Cooperation, under Grant GGA8510095.

REFERENCES

- Blackman, R.B. and Tukey, J.W. (1959): "The Measurement of Power Spectra," Dover Publications, Inc., New York, pp. 19-20.
- Borgman, L.E. (1969): "Ocean Wave Simulation for Engineering Design," Journal of the Waterways and Harbors Division, ASGE, Vol. 95, No. WW4, Proc. Paper 6925, Nov., 1969, pp. 557-583.
- Box, E.P. and Jenkins, G.M. (1976): "Time Series Analysis: Forecasting and Control," 2nd Ed., Holden-Day, Inc., San Francisco, Calif., 1976.
- Elgar, S. Guza, R.T., and Seymour, R.J. (1984): "Groups of Waves in Shallow Water," Journal of Geophysical Research, Vol. 89, No. C3, pp. 3623-3634.
- Elgar, S., Guza, R.T., and Seymour, R.J. (1985): "Wave Group Statistics from Numerical Simulations of a Random Sea," Applied Ocean Research, Vol. 7, No. 2, pp. 93-96.
- Funke, E.R. and Mansard, E.P.D. (1987): "A Rationale for the Use of the Deterministic Approach to Laboratory Wave Generation," IAHR Seminar on Wave Analysis and Generation in Laboratory Basins, 22nd IAHR Congress, Sept. 1-4, 1987, Lausanne, pp. 153-195.
- Goda, Y. (1970): "Numerical Experiments on Wave Statistics with Spectral Simulation," Report of the Port and Harbour Research Institute, Vol. 9, No. 3, Yokosuka, Japan, Sept., 1970, pp. 3-57.
- Goda, Y. (1977): "Numerical Experiments on Statistical Variability of Ocean Waves," Report of the Port and Harbour Research Institute, Vol. 16, No. 2, Yokosuka, Japan, June, 1977, pp. 3-26.
- Goda, Y. (1981): "Wave Simulation for the Examination of Directional Resolution," presented at the Sept., 1981, ASGE & ECORE International Symposium Directional Wave Spectra Applications '81, held at Berkeley, Calif.
- Goda, Y. (1983) "Analysis of Wave Grouping and Spectra of Long-travelled Swell," Report of the Port and Harbour Research Institute, Vol. 22, No. 1, Yokosuka, Japan, Mar., 1983, pp. 3-41.
- Goda, Y. (1985): "Random Seas and Design of Maritime Structures," University of Tokyo Press, 1985.
- Graupe, D., Krause, D.J., Moore, J.B. (1975): "Identification of Autoregressive Moving-Average Parameters of Time series," IEEE Transactions in Automatic Control, Vol. AG-20, Feb., 1975, pp.104-107.
- Holm, S., and Hovem, J.M. (1979): "Estimation of Scalar Ocean Wave Spectra by the Maximum Entropy Method," IEEE Journal of Oceanic Engineering, Vol. OE-4, No. 3, July, 1979, pp. 76-83.
- Houmb, O.G., and Overvik, T. (1981): "Some Applications of Maximum Entropy Spectral Estimation to Ocean Waves and Linear Systems Response in Waves," Applied Ocean

- Research, Vol. 3, No. 4, pp. 154-162.
- Hudspeth, R.T. (1974): "Wave Force Predictions from Nonlinear Random Sea Simulations," Offshore Technology Conference, Dallas, Texas, 1974, pp. 471-485.
- Hudspeth, R.T., and Chen, M.C. (1979): "Digital Simulation of Nonlinear Random Waves," Journal of the Waterway, Port, Coastal and Ocean Division, ASCE, Vol. 105, No. WW1, Proc. Paper 14376, Feb., 1979, pp. 67-85.
- Hudspeth, R.T., and Medina, J.R. (1988): "Wave Groups from Analyses of Wave Height Functions," 21st ICCE, Torremolinos, June 20-25, 1988.
- Hull, T.E., and Dobell, A.R. (1962): "Random Number Generators," Society of Industrial Applied Mathematics Review, Vol. 4, No. 3, July, 1962, pp. 230-254.
- Kimura, A., and Kimura, T. (1987): "Low Price Random Signal Processor with High Efficiency Numerical Filters," IAHR Seminar on Wave Analysis and Generation, Sept. 1-4, 1987, Lausanne, Switzerland, pp. 435-445.
- Medina, J.R., Aguilar, J., and Diez, J.J. (1985): "Distortions Associated with Random Sea Simulators," Journal of Waterway, Port, Coastal, and Ocean Engineering, ASCE, Vol. 111, No. 4, pp. 603-628.
- Medina, J.R., and Hudspeth, R.T. (1987): "Sea States Defined by Wave Height and Period Functions," IAHR Seminar on Wave Analysis and Generation in Laboratory Basins, XXII IAHR Congress, Lausanne, Switzerland, Sept. 1-3, 1987, pp. 249-259.
- Miles, M.D. and Funke, E.R., (1987): "A Comparison of Methods for Synthesis of Directional Seas," Proc. of the 6th International Offshore Mechanics and Arctic Engrg. Conditions, ASME, pp. 247-255.
- Samaras, E.F., Shinozuka, M., and Tsurii, A. (1985): "ARMA Representation of Random Vector Processes," Journal of Engineering Mechanics, ASCE, Vol. 111, No. 3, Mar., 1985, pp. 449-461.
- Samii, K., and Vandiver, J.K. (1984): "A Numerically Efficient Technique for the Simulation of Random Wave Forces on Offshore Structures," 16th OTC, Houston, TX, Paper No. OTC-4811, pp. 301-308.
- Spanos, P-T.D., and Hansen, J.E. (1981): "Linear Prediction Theory for Digital Simulation of Sea Waves," Journal of Energy Resources Technology, ASME, Vol. 103, Sept., 1981, pp. 243-249.
- Spanos, P-T.D. (1983): "ARMA Algorithms for Ocean Wave Modeling," Journal of Energy Resources Technology, ASME, Vol. 105, Sept., 1983, pp. 300-309.
- Spanos, P-T.D., and Mignolet, M.C. (1986): "Z-Transform Modelling of P-M Wave Spectrum," Journal of Engineering Mechanics, Vol. 112, No. 8, August, 1986, pp. 745-759.
- Tuah, H., and Hudspeth, R.T., (1982): "Comparisons of Numerical Random Sea Simulations," Journal of the Waterway, Port, Coastal and Ocean Division, ASCE, Vol. 108, No. WW4, Proc. Paper 17488, Nov., 1982, pp. 569-584.

CHAPTER 71

STORM STATISTICS IN THE NORTH SEA

By

B.A. Salih¹, R. Burrows² and R.G. Tickell³

1.0 INTRODUCTION

Effective planning of offshore activities requires statistical information detailing storm occurrences and durations (defined as exceedences of an H_s threshold). This information is often referred to as persistence.

The frequency of storm events and the probability associated with a number of successive sea states being above (or below) a given threshold level is often required by engineers to estimate the potential work period and down-time as well as to incorporate the lead and lag times needed to stop and restart interrupted operations due to severe weather conditions.

However, until recently, a lack of sufficiently long data bases has precluded any meaningful investigation of this nature. Unrepresentative or misleading results can follow from data records that were measured over only a limited number of years. Furthermore, significant distortions may be introduced if the data record is not continuous as data gaps interrupt the persistence pattern.

As more recorded data have become available, concerted efforts have been made on this topic; most notably by Houmb and Vik who developed a probabilistic model describing the statistics of storm (and calm) durations and frequencies at varying levels of sea state intensity.

The present study investigates the adequacy of the semi-empirical procedure proposed by Houmb and Vik and also discusses the development of two new modelling techniques. The performance of these models are examined against wave data measured at the BP Forties field in the North Sea. A number of new statistical descriptors relating to the profile and intensity of storms have also been developed.

It is recognised that wave period (T_z) and directional information must ultimately be incorporated in a storm climate model. However, this is beyond the scope of the present discussion.

1 Engineer, Dobbie & Partners, 17 Lansdowne Road, Croydon, CR9 3UN, England.

2, 3 Senior Lecturers, Department of Civil Engineering, University of Liverpool, Liverpool, L69 3BX. England

1.1 DEFINITIONS

In the work reported here, the definition of storm events as proposed by Houmb & Vik (1976) is adopted:

A storm is defined as a period of time during which the significant wave height, H_s , exceeds a threshold α (see Figure 1). The onset of a storm condition at α is marked by an upcrossing of the level $H_s = \alpha$. Measures of storm (D_s), calm (D_c) and storm inter-arrival (D) durations are also indicated.

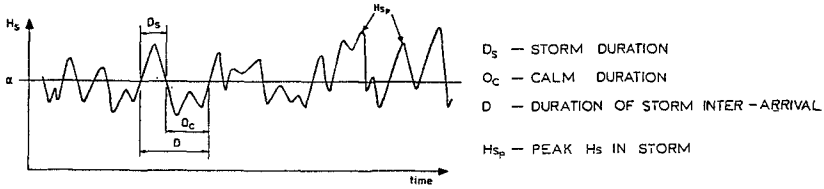


Figure 1: Definition of storm occurrences and durations.

1.2 DATA

The data used in this study have been measured at the BP Forties Field located in the North Sea.

The original data bank contained measurements extending over the period from June 1974 to December 1981. Measurements of significant wave height based on 20 minute recordings of sea surface elevation were made using Wave Staff and Wave Rider Buoy instruments. Unfortunately, the data is not continuous. In some cases measurements are missing over periods of up to several months. Owing to the importance of a continuous data set for the assessment of storm statistics, the data was subjected to a rigorous treatment and various steps were followed to compensate for data gaps (see Salih, 1987). As a result, it was possible to extract 5 years of almost continuous data covering the period from January 1977 to December 1981.

1.3 RESULTS AND DISCUSSION

1.3.1 Houmb and Vik Model

Initially attention is focused on the semi-empirical procedure proposed by Houmb and Vik (1977) and later developed by Pastene-Beytia (1976) and Dale (1979). The analysis of threshold crossings yields that the storm frequency at a given threshold is expressed as:

$$f_s(\alpha) = \frac{C(\alpha - A)^{C-1}}{B^C \sqrt{2\pi}} \sigma_{\dot{H}_s|\alpha} \exp\left[-\left(\frac{\alpha - A}{B}\right)^C\right] \dots\dots\dots(1.1)$$

Where $\sigma_{\dot{H}_s|\alpha}$ is the standard deviation of the first time derivative of the H_s time trace at the sea state level α , and A, B and C are the pa-

rameters of the Weibull distribution approximating $p(H_s)$.

The expression is derived utilising the main assumptions that:

a) The marginal distribution of H_s can be approximated by a 3-parameter Weibull pdf. The validity of this has been demonstrated by many studies in the field of Long-Term wave statistics (see Burrows et al, 1986). The analysis of the Forties data supports the Weibull distribution as an accurate description the probability 'mass' and the extreme tail of the H_s distribution.

Nevertheless, the Weibull distribution is often noted for its poor representation of the lower values of H_s . Thus the use of alternative distributions such as the Log-Normal, as proposed by Ochi (1978), and the NMI modified Log-Normal, proposed by the National Maritime Institute (and now British Maritime Technology) (see Fang et al, 1982) has also been assessed against observations. Statistical goodness-of-fit tests, however, has established the Weibull distribution as a superior descriptor of the observed $p(H_s)$ (see Salih, 1987).

b) The second important assumption in the procedure is that the distribution of $\hat{H}_s|H_s$ can be represented by a mean-zero Gaussian distribution with a variance, $\sigma^2_{\hat{H}_s|H_s}$ that linearly varies with level α .

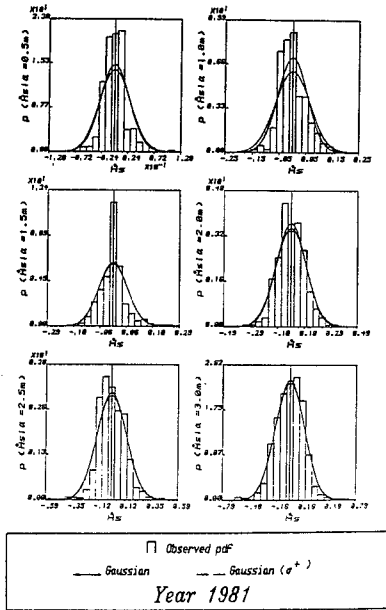
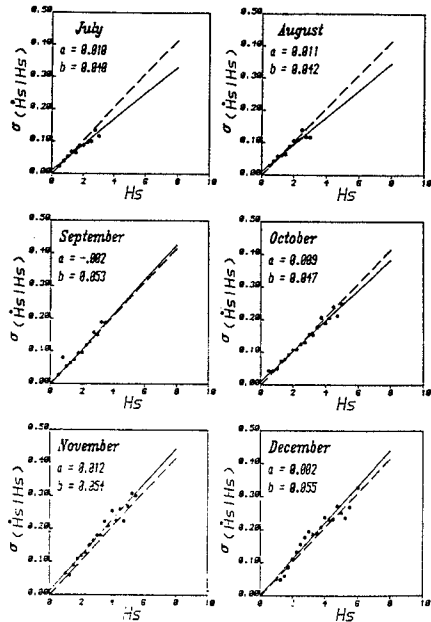


Figure 2:
Probability density
functions of H_s with
Gaussian pdf superimposed.
 Year 1981



— Weighted Least Square Regression Line — 5 Years
 Dots Denote Observations

Figure 3:
Variation of standard
deviation of $H_s|H_s$
with H_s thresholds.

Figure 2 and Figure 3 point to the acceptability of both these assumptions. Houmb & Vik noted no seasonal variation in the $\sigma_{Hs|\alpha}$ versus α relationship. An alternative procedure for storm modelling proposed by Graham (1983) implies that there is no seasonal variation in the relationship between $\sigma_{Hs|Q(Hs)}$ and $Q(Hs)=1-P(Hs)$.

The results of this study, however, indicate the existence of a systematic seasonal variation in the relationship in question. It can be noted from Figure 3 that the summer and winter months' linear relationships fall on either sides of the average 'yearly' $\sigma_{Hs|\alpha}$ versus α relationship.

This systematic variation has been taken as a justification to parameterise the linear relationship (in the form of $\sigma_{Hs|\alpha} = \kappa \alpha$) in terms of Hs statistics. As the main input to the storm model are the Weibull fit parameters, the slope of the straight line, κ , has been regressed against A, B and C and the following least square relationship has been found to provide reasonably accurate estimates:

$$\kappa = 0.0476 A^{0.201} B^{0.116} C^{0.185} \dots\dots\dots(1.2)$$

The expression of Equation 1.2 has been used to predict frequencies of storm events at varying levels of sea states and have been found to compare favourably with observations as can be seen from Figure 4. The different curves arise from the use of the Weibull and NMI modified Log-Normal distributions for $p(Hs)$ and the average 'yearly' estimates of $\sigma_{Hs|Hs}$.

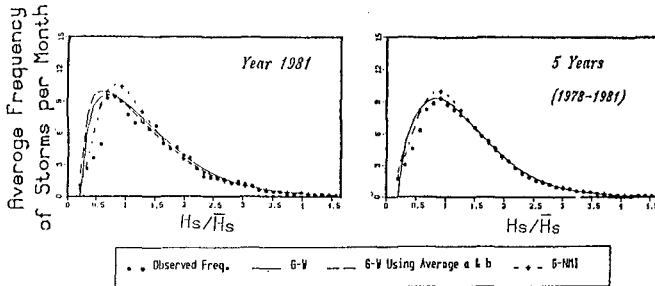


Figure 4: Average frequency of storm occurrences with prediction from Houmb & Vik model.

The average duration of storms, $\bar{D}_S(\alpha)$, can be obtained from Equation 1.1 as

$$\bar{D}_S(\alpha) = \frac{\text{Total time } (Hs > \alpha)}{\text{Total number of storms}} = \frac{1-P(Hs)}{f_S(\alpha)}$$

$$\bar{D}_S(\alpha) = \frac{B^C \sqrt{2\pi}}{C(\alpha - A)^{C-1} \sigma_{Hs|\alpha}} \dots\dots\dots(1.3)$$

The average durations of calms, defined as non-exceedence of the α level, and the average inter-arrival of storms (and calms) can be expressed as:

$$\bar{D}_c(\alpha) = \frac{F(\alpha)}{f_c(\alpha)} = \frac{1.0}{f_c(\alpha)} - \bar{D}_s(\alpha) \dots\dots\dots(1.4)$$

Hence the average duration of storm inter-arrivals at level α becomes:

$$\bar{D}_i(\alpha) = \bar{D}_s(\alpha) + \bar{D}_c(\alpha) = \frac{1.0}{f(\alpha)} \dots\dots\dots(1.5)$$

Average durations evaluated from Equation 1.3 to Equation 1.5 are compared with observations in Figure 5; again the modelling procedure closely approximates the observed behaviour. The noted discrepancy between long durations, in part at least, arises from sampling problems and also in how to deal with long sequences which extend beyond the seasonal date windows (ie storms in February, say, terminating in March or starting in January).

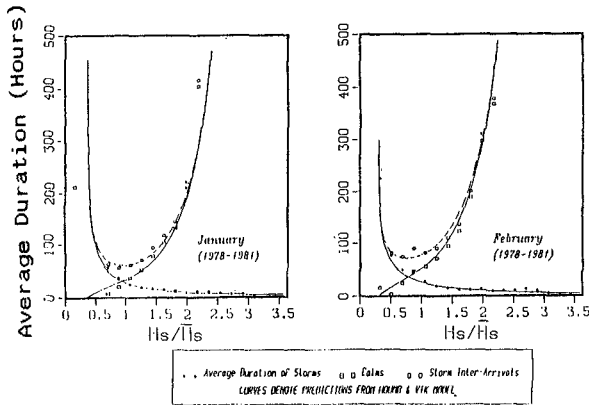


Figure 5: Average Durations of storms, calms and storm inter-arrivals with predictions from Houmb & Vik model.

1.3.1.1 Distribution of Durations

The use of a basic Poisson model for the description of storm events has been argued by Houmb & Vik. The suitability of this model requires that: (a) the arrival rate of storms is stationary, (b) the probability of storm occurrences in a short interval of time is proportional to the length of the interval and (c) the probability of multiple storm events in a short period of time is insignificant compared to a single event.

If the storm events are described by a Poisson model, then distribution of storm durations is exponential. Whilst some of the theoretical

justification for the adoption of exponential model for storm durations follows from a Poisson assumption for storm events, as indicated by Houmb and Vik, the underlying assumptions are not fully satisfied in practice. Houmb & Vik, however, found little empirical evidence to support this and instead proposed the use of the more general 2-parameter Weibull distribution. Dale (1979) reports, nevertheless, that the distribution of storm durations at Seven Stones' light vessel off the South West coast of England become exponentially distributed at higher threshold levels of sea state.

Figure 6 points to the general acceptability of the Weibull model and also confirms Dale's observation that the distributions, towards the higher thresholds, become exponential. This is perhaps an indication that the assumptions inherent in the Poisson model become more valid at these thresholds.

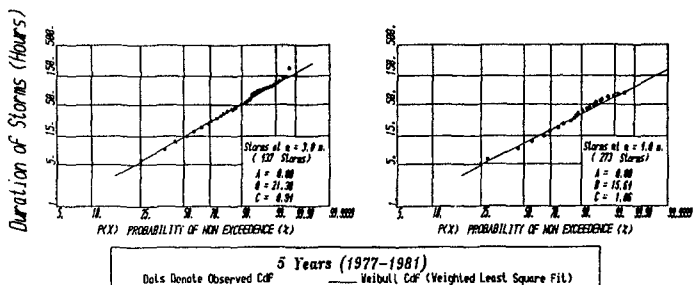


Figure 6: Distribution of storm durations with 2 parameter Weibull model superimposed.

1.3.2 Gaussian Transformation Model

It was anticipated that the technique of transforming a general set of correlated random variables into the Gaussian form would enable the utilisation of the wealth of theory available for Gaussian processes.

The time series of $H_s, H_s(t)$, modelled by a Weibull distribution can be transformed into a mean-zero Gaussian process, $X(t)$, of unit variance by applying the approximate formulae for Gaussian transformation given by Abramowitz & Stegun (1964),

$$X(t) = f - \frac{C_0 + C_1 f + C_2 f^2}{1 + d_1 f + d_2 f^2 + d_3 f^3} + \text{error} \dots\dots\dots(1.6)$$

where $|\text{error}| < 0.00045$, and

$$f = \sqrt{\ln\left(\frac{1}{Q(H_s(t))}\right)} \dots\dots\dots(1.7)$$

$Q(H_s(t))$ is the exceedence probability of $H_s(t)$ ($\int_{H_s(t)}^{\infty} p(H_s) dH_s$).

The basis of this procedure is illustrated diagrammatically in Figure 7. The original process, $H_s(t)$, and its Gaussian transform peak jointly

and crossings of the level $H_s = \alpha$ corresponds to crossings of $X = \beta$ in the transformed domain.

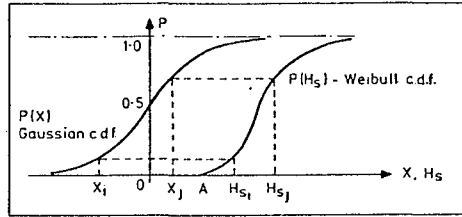


Figure 7: Gaussian transformation of random variables using distribution functions.

The Gaussian transform of $H_s(t)$ is characterised by a wide band power spectrum. Estimates of the spectral band width parameter, ϵ , derived from duration statistics, are found to be approximately 0.950 for summer months and 0.965 for winter months.

Various storm characteristics can be expressed in terms of the standard deviation of X , which is unity by virtue of Equation 1.6, and that of the first time derivative of X , \dot{X} , using results of the classical mathematics associated with stationary Gaussian processes. The frequency of storm occurrences is equivalent to the frequency of up-crossings of the level β ,

$$N^+(\beta) = \frac{1}{2\pi} \frac{\sigma_{\dot{X}}}{\sigma_X} \exp\left[-0.5 \left(\frac{\beta}{\sigma_X}\right)^2\right] \dots\dots\dots(1.8)$$

The frequency of up-crossing by $H_s(t)$ of the sea state threshold level of α can be obtained as

$$N^+(\beta) = N^+(\alpha) \dots\dots\dots(1.9)$$

The average durations can be deduced by the same arguments followed to obtain Equation 1.3 through Equation 1.5

In order to justify the application of the theory of stationary Gaussian processes, the problem of non-stationarity has been avoided herein by considering monthly periods. This implies that the statistics for monthly periods are assumed stationary from year to year.

The predictions of average storm, calms and inter-arrival duration arising from the use of this technique are found to compare favourably with the observed behaviour as can be noted from Figure 8. The predictions are also presented in Table 1 alongside estimates obtained from the Houmb and Vik procedure. It is apparent the transformation technique provides, on the whole, the more accurate predictions.

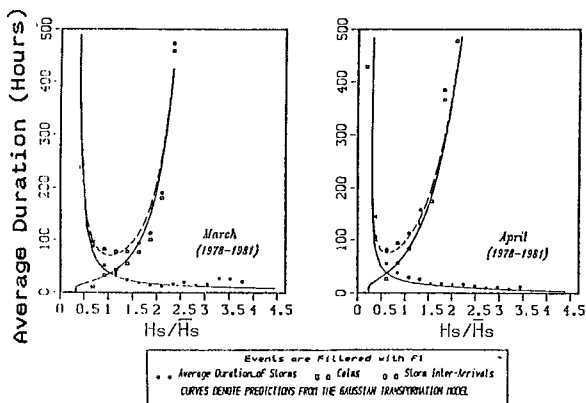


Figure 8: Average Durations of storms, calms and storm inter-arrivals with predictions from Gaussian transformation model.

α/\bar{H}_s	Observed	Houmb & Vik	Gaussian Transf.	Markov Weibull	Markov log-Norm.
0.5	271.5	106.4	153.3	69.9	134.2
1.0	30.8	24.7	29.2	21.9	22.7
1.5	17.5	12.4	16.9	14.2	13.0
2.0	10.4	7.8	12.3	10.3	9.7

January

α/\bar{H}_s	Observed	Houmb & Vik	Gaussian Transf.	Markov Weibull	Markov log-Norm.
0.5	153.3	105.4	108.6	57.2	123.2
1.0	41.9	30.1	36.0	26.0	28.3
1.5	23.9	14.8	21.4	16.4	17.1
2.0	9.8	9.0	15.3	9.0	13.0

October

Table 1. Average duration of storms and inter-arrivals with predictions from Houmb & Vik, Gaussian Transformation and Markov models

The main advantage of the transformation technique is that additional statistical descriptors of 'storm shape' can be established from theory. In particular, the distribution of peak amplitudes of a wide-banded Gaussian process can be used to predict the distribution of peak H_s attained within the duration of a storm. This aspect is to be discussed in a later section.

Furthermore, the technique enables more complex measures of storm statistics to be developed; the theory relating to Gaussian processes can be utilised to establish probability distribution of storm duration. Price and Bishop (1974) derive a distribution for exceedence duration by following a method originally proposed by Rice (1944,1945) However, the resulting expression is inherently complex and requires the evaluation of various higher order spectral moments. In the absence of a long stationary data base, such spectral moments cannot be reliably determined and in subsequence this aspect has not been pursued in the present study.

1.3.3 Markov Chain Model

The use of the first order Markov chain theory to model the time series of Hs requires that only successive sea states, Hs_i and Hs_{i+1}, are statistically correlated. In reality, however, sea states several time steps apart may exhibit appreciable statistical correlation. Thus, at first the validity of the Markov theory, defined to the first order, may be suspect.

Nevertheless, it has been established from the study of the Homb & Vik procedure that $\sigma_{Hs|Hs}$ increases with the threshold level of Hs. Hence, lesser correlation between successive larger sea states can be anticipated since the linear correlation coefficient is inversely related to the variance. Therefore, the acceptability of the Markov model, at least at these higher levels of Hs, is likely to be enhanced.

The Markov model used in the context of storm modelling requires the identification of two states of the process Hs(t), namely that of exceedence and non exceedence of the level α . The transition probabilities (see Kimura, 1980 and Longuet-Higgins, 1984) associated with these two states can be represented as:

$$p_+ = \int_{\alpha}^{\infty} \int_{\alpha}^{\infty} p(Hs_{i+1}, Hs_i) dHs_i dHs_{i+1} / \int_{\alpha}^{\infty} \int_{\alpha}^{\infty} p(Hs_i, Hs_{i+1}) dHs_i dHs_{i+1}$$

$$p_- = \int_0^{\alpha} \int_0^{\alpha} p(Hs_{i+1}, Hs_i) dHs_i dHs_{i+1} / \int_0^{\alpha} \int_0^{\alpha} p(Hs_i, Hs_{i+1}) dHs_i dHs_{i+1} \dots (1.10)$$

Where $p(Hs_i, Hs_{i+1})$ represents the joint probability density function of successive sea states.

It can be shown that the probability of J_s sea states consecutively exceeding the level α is given by:

$$p(J_s) = p_+^{J_s-1} (1-p_+) \dots \dots \dots (1.11)$$

and it follows that the mean number of sea states exceeding α is:

$$J_s = \sum_1^{\infty} J_s \times p(J_s) = \frac{1}{(1-p_+)} \dots \dots \dots (1.12)$$

Similarly, the distribution of storm inter-arrivals can be formulated as:

$$p(J_i) = (1 - p_+)(1 - p_-)(p_+^{J_i-1} - p_-^{J_i-1}) / (p_+ - p_-) \dots\dots\dots(1.13)$$

and the mean number of sea states between storm inter-arrivals follows as:

$$J_i = \sum_2^{\infty} J_i x p(J_i) = \frac{1}{1-p_+} + \frac{1}{1-p_-} \dots\dots\dots(1.14)$$

The only problem remains to choose a suitable probability distribution to model $p(H_{s_i}, H_{s_{i+1}})$: An obvious choice may be the bi-variate Weibull distribution originally developed by Rice (1944, 1945) and Ulhebeck (1943) and applied more recently by Kimura (1981) to model the joint probability distribution of individual wave heights and periods, $p(H, T_z)$. However, it has been found that the conditional statistics of the observed $p(H_{s_i}, H_{s_{i+1}})$ is characteristically different from that inherent in bi-variate Weibull function (see Salih, 1986).

The use of the bi-variate Log-Normal probability distribution, used by Ochi (1987) to model the long-term joint distribution of H_s and average zero crossing periods has also been investigated; more accurate representation of the conditional probabilities is obtained than with bi-variate Weibull model. It must be noted, however, that this choice does not affect the relative merits of either the Log-Normal or Weibull functions to describe the marginal distribution of H_s , $p(H_s)$.

Using both of these bi-variate distributions, the average durations of storms are predicted from the Markov model and the results are presented in Table 1. Also included in this table are the corresponding estimates for the Houmb & Vik and the Gaussian transformation procedures to enable the direct comparison of the various models.

It is apparent that the Markov model consistently underestimates the average durations at the lower thresholds. This arises mainly from the fact that successive sea states are strongly correlated at these levels and thus the assumptions inherent in the Markov model are more severely violated. In line with this reasoning, the predictions become in closer agreement with observed averages towards the higher sea state levels. The accuracy of the Markov model can be of the same order, and occasionally marginally better, as that noted for the Houmb and Vik procedure.

This property renders the Markov model particularly useful for engineering applications where the synthesis of storm statistics at these higher thresholds can be of particular importance.

Furthermore, the Markov model enables the modelling of the distribution of storm durations without the need to invoke any extra assumptions. Figure 9 shows that the Markov predictions are in close agreement with the observed distributions for storms at higher thresholds.

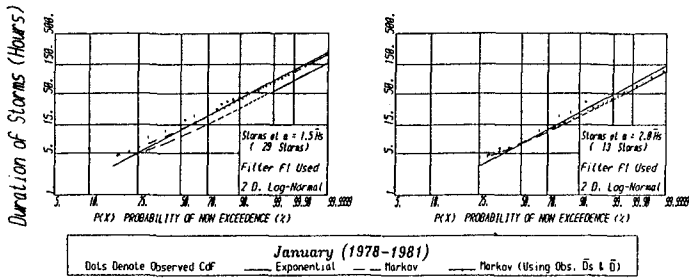


Figure 9: Distribution of storm durations with predictions from Markov model.

1.4 STORM SHAPE DESCRIPTORS

The storm models discussed do not provide information regarding profiles and energy contents of the storm events. A variety of statistics can be utilised for describing the storm intensity or severity at given threshold level of sea state. A complete description of the probability distribution of H_s within the duration of the storm would be an ultimate solution. However, this is expected to be rather complex and difficult to test empirically. An alternative approach, that is of lesser complexity, would be to specify certain statistics that characterise the storm profile and from which the severity of the storm can be inferred.

It is considered that useful insight may be obtained by investigating the distributions of the peak H_s attained in a storm, (H_{s_p}), the mean H_s within the storm events, (\bar{H}_{s_g}), or the distribution of the root mean square H_s , ($\sqrt{\bar{H}_{s_g}^2}$). The latter statistic may be taken as a measure of mean sea state energy per unit time.

Figure 10 plots the probability distribution of peak H_s attained within the duration of a storm normalised by the threshold level α .

The predictions arising from the Gaussian transformation model are super-imposed on Figure 10.a. These are based on the expression for distribution of amplitudes in a wide-banded Gaussian process. The results are found to follow the observed behaviour quite reasonably. However, the match is far from exact and the discrepancy arises from certain assumptions associated with the theoretical model (principally that the theory relates to the description of all 'local' maxima whilst only storm 'global' peaks are of significance to this application).

The 2-parameter Weibull distribution has been found to accurately model the upper half of the distribution of H_{s_p} as can be noted from Figure 10.b.

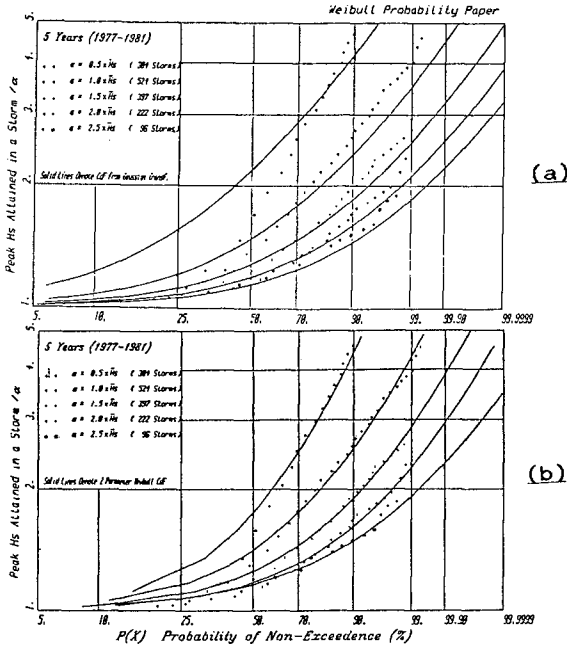


Figure 10: Distribution of peak Hs within a storm.
(a) with predictions from the Gaussian transformation model
(b) with predictions from 2 parameter Weibull model

Figure 11 shows that the average Hs within the duration of a storm can be modelled accurately by a 2-parameter Weibull distribution. The use of other empirical distributions has also been assessed and established that the shifted exponential and Gamma distributions prove generally acceptable for this purpose.

The distribution of root mean square Hs within the storms can be used to provide information relating to the energy content of the storms. Using expressions from the linear wave theory it follows that:

Energy per unit surface area is proportional to $E[Hs^2]$

The results presented in Figure 12 point to the suitability of the 2-parameter Weibull model.

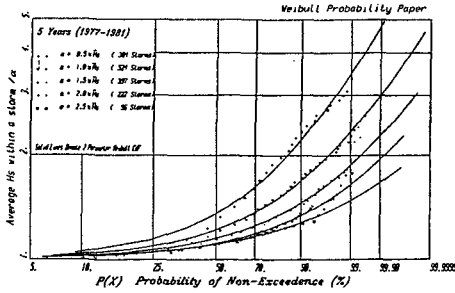


Figure 11: Distribution of average H_s within a storm.

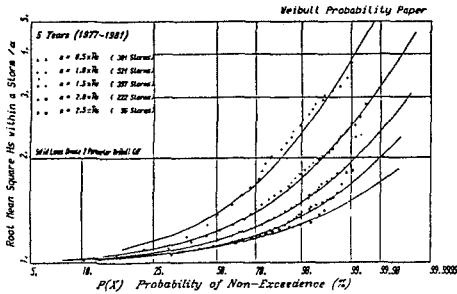


Figure 12: Distribution of root mean square H_s within a storm.

1.5 CONCLUSIONS

It is concluded, as judged from the Forties data, that the Gaussian transformation technique provides more accurate predictions of average durations of events than the other two models considered in this study. Furthermore, the potential of utilising the wealth of theory relating to Gaussian processes makes the technique a viable and indeed a superior alternative to the more traditional procedure proposed by Houmb and Vik.

The distribution of maxima of a wide band Gaussian process has been used to predict the distribution of storm peaks and the results of the present study point to the general validity of the resulting distribution particularly towards higher sea state thresholds.

However, further testing and calibration of the transformation model requires access to longer data bases that can be used, for example, to reliably extract the various, higher order, spectral parameters required for the definition of the distribution of durations.

The Markov model proves a useful tool in characterising the storm statistics at higher thresholds of sea states where both the average durations and the distribution of durations are reasonably well represented. It is important to note that the specification of the distribution of durations is an integral part of the Markov approach.

Similar studies are now required on data sets from differing locations and degrees of exposure in order to assess the site specific element of the storm models discussed herein.

1.6 ACKNOWLEDGMENTS

The wave data used in this study was supplied by BP and MAREX UK and the writers are most grateful for this support. The overall study was financed by the Marine Technology Programme of SERC and by Shell (UK). Funds to present the paper were made available by Dobbie and Partners.

REFERENCES

1. Abramowitz, M. and Stegun, I.A., - "Handbook of Mathematical Functions", Applied Maths. Series 55, National Bureau of Standard, 1964.
2. Burrows, R. and Salih B.A., - "Statistical Modelling of Long-Term Wave Climates", Proceedings of the 20th Coastal Engineering Conference, Vol I, pp. 42-56, 1986.
3. Dale, J., - "Non-Stationary Statistics of Storms", M.Eng. Thesis, Department of Civil Engineering, University of Liverpool, 1979.
4. Fang, Z.S. and Hogben, N., - "Analysis and Prediction of Long-Term Probability Distributions of Wave Heights and Periods", National Maritime Institute (NMI), R 146, 1982.
5. Graham, C., - "Parameterisation and Prediction of Waveheight and Wind Speed Persistence Statistics for Oil Industry and Planning Purposes", Coastal Engineering, Vol 6, pp. 303-329, 1982.
6. Houmb, O.G., - "On the Duration of Storms in the North Sea", 1st International Conference, P.O.A.C., Trondheim, August 1971.
7. Houmb, O.G. & Vik, I., - "On the Duration of Sea State", Division of Port and Ocean Engineering, Norwegian Institute of Technology, Trondheim, 1977.
8. Kimura, A., - "Joint Distribution of the Wave Heights and Periods of Random Sea Waves", Coastal Engineering in Japan, Vol 24, 1981.
9. Longuet-Higgins, M.S., - "Statistical Properties of Wave Groups in a Random Sea State", Philosophical Transactions of the Royal Society of London, Vol 312 A 1512, pp. 219-250, 1984.
10. Ochi, M.K., - "On Long-Term Statistics for Ocean and Coastal Waves", Proceedings of the 16th Coastal Engineering Conference, Vol I, pp. 59-75, 1978.
11. Pastene-Beytia, J.E., - "The Short and Long-Term Statistics of a Random Sea", M.Eng. Thesis, Department of Civil Engineering, University of Liverpool - 1976.

12. Price, W.G. and Bishop, R.E.D., - "Probabilistic Theory of Ship Dynamics", Chapman and Hall - 1974.
13. Rice, S.O., - "The Mathematical Analysis of Random Noise", Bell System Technology Journal, Vol 23 pp. 282-332 and 24 pp. 46-156, 1944 and 1945.
14. Salih, B.A., - "Long-Term Wave Statistics" - Internal Report, Department of Civil Engineering, University of Liverpool, 1986.
15. Salih, B.A., - "Persistence Characteristics of Sea State", Internal Report, Department of Civil Engineering, University of Liverpool, 1987.
16. Uhlenbeck, G.E., - "Theory of Random Processes", M.I.T. Radiation Laboratory Report, No. 454, 1943.

CHAPTER 72

STATUS OF U.S.A. OCEAN ENERGY RECOVERY ACTIVITIES

Young C. Kim¹ Lloyd Lewis² Michael E. McCormick³ Larry S. Slotta⁴

Abstract

The state of the art of ocean energy recovery activity in the United States is described. The technologies discussed in the paper include extraction of wave, tidal, ocean thermal and ocean current energy. This status report is intended to provide a description of the various ocean energy technologies and an assessment of potential benefits that might be expected and potential problems that might be encountered.

Ocean Wave Energy Conversion

The present efforts in wave energy conversion in the United States are those at the Department of Energy (DOE), academic institutions and small specialized companies. Of the many types of wave energy extraction (McCormick, 1981), four are now under study and development in the U.S. These are the pneumatic wave energy converter, the contouring raft system, the tandem flap and two types of wave pump devices.

As illustrated in Figure 1, the pneumatic wave energy conversion system (PWECS) incorporates a wave-excited oscillating water column and a pneumatic turbine. The air above the water column is alternately compressed and expanded resulting in an alternating pressure difference across the turbine. A one-meter PWECS was tested in the second deployment of the KAIMEI in the Sea of Japan in 1985 (JAMSTEC, 1987). This effort was partially funded by DOE through the International Energy Agency. Improvements in capture chamber geometry and turbine performance are presently under study (McCormick, 1978; Richards and Weiskopf, 1987) at the U.S. Naval Academy. Efforts are also underway to improve the coupling of the counter-rotating rotors and incorporate a ring-generator into the design (Focas, 1981).

1. Professor of Civil Engineering, California State University, Los Angeles, California 90032
2. Program Manager, Wind/Ocean Technologies Division, U.S. Department of Energy, Washington, D.C. 20585
3. Professor and Director, Ocean Engineering, U.S. Naval Academy, Annapolis, Maryland 21402
4. President, Slotta Engineering Associates, Inc., Corvallis, Oregon 97339

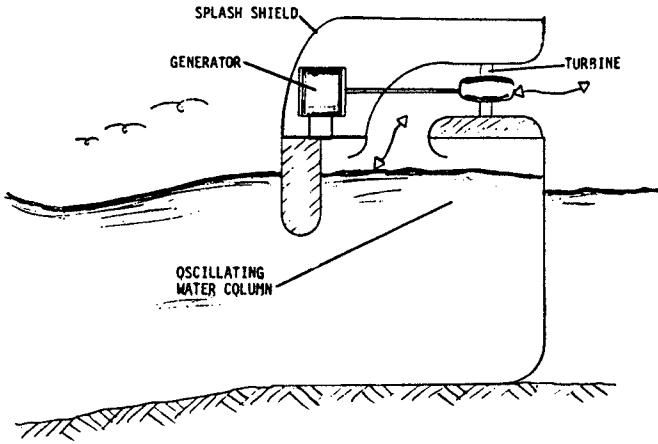


Figure 1. Schematic of a U.S. Naval Academy Pneumatic Wave Energy Conversion System

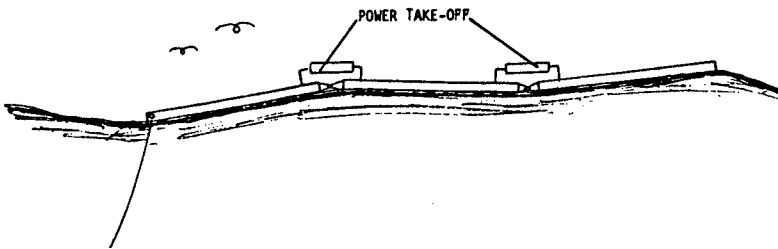


Figure 2. Sketch of a Sea Energy Corporation Contouring Raft Wave Energy Converter

The contouring-raft system is under development by the Sea Energy Corp. (Hagerman, 1987). The configuration is similar to that in Figure 2. Sea Energy is planning a test of a prototype 500 kw "one-raft" system utilizing a yoke attached to a mooring point and working through a hydraulic power system. Model testing of a 1:25 scale system is being performed for regular and random waves.

The Q Corporation (Division of Van Dresser Corporation), with partial DOE support, has developed the tandem flap wave energy converter illustrated in Figure 3 (Scher, 1985). Because of its ability to capture both incident and a portion of the transmitted wave energy (due to reflection from the second flap), it is significantly more efficient than a single flap device. A 10 kw version of the tandem flap design was tested in Lake Michigan in 1987 with uncertain results due to power takeoff and other component failures. Q Corp. plans further system modifications and both tank and field tests in the future (Q Corporation, 1985; Wilke, 1985).

Two point-absorber systems for wave energy extraction have been developed in the United States. Figure 4 illustrates the principal components of the DELBUOY system developed by ISTI-Deleware Inc. (Hicks, 1988; Pless, 1982). The system comprises a light weight, shallow draft cylindrical buoy driving a submerged, single-acting positive displacement pump tethered to the seafloor. The motions of the buoy open the pump for the pressure stroke with energy stored in the natural rubber return springs used to refill the system. Clean seawater is drawn into the pump through prefilters to remove particulate matter. The flow of pressurized seawater from the pump is rectified using check valves with pressure surges damped by hydraulic accumulation. The pump output is then passed through the reverse osmosis filter with approximately 80% of the flow returning to the sea and 20% as freshwater pumped to the shore through low pressure plastic pipelines. Full scale system tests were performed at the University of Puerto Rico in 1980-1985 and to date eight full-scale prototype have been built and tested. Future designs are expected to produce up to 12,000 gallons per day of freshwater.

A second point-absorber system is the Wave Energy Module (WEM) illustrated in Figure 5 developed by U.S. Wave Energy, Inc. (Hopke, 1985). The WEM consists of two parallel discs connected with hydraulic piston pumps. One disc is buoyant and rides on the ocean surface while the other (reaction plate) is suspended at a depth where motion due to waves is small. Hydraulic fluid is transferred from the piston pumps to a high-pressure accumulator and is then fed to a hydraulic motor connected to a generator. A 1:40 scale model was tested at Worcester Polytechnic Institute and University of Massachusetts in the 1970s. In 1979 1:10 scale model tests were performed on Lake Champlain. Future plans include a full scale prototype test in the North Atlantic by the Newfoundland Oceans Research and Development Corporation.

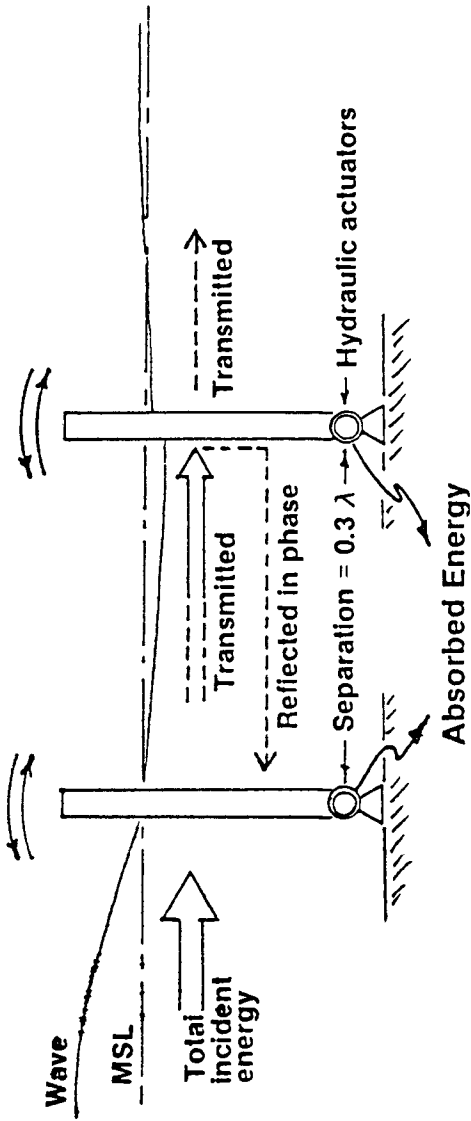


Figure 3. Schematic of Q Corporation Tandem Flap Wave Energy Conversion Device

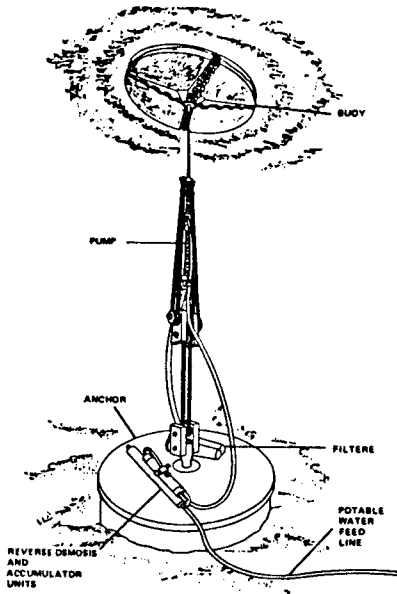


Figure 4. Schematic Diagram of the DELBUOY System

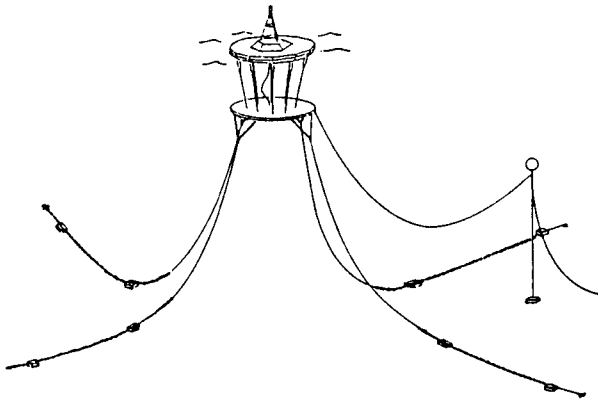


Figure 5. Schematic Diagram of U.S. Wave Energy Inc. Wave Energy Module

Tidal Energy Conversion

Plans for a large scale electrical powerplant using the tides were proposed as early as 1919 for the Passamaquoddy Bay in Maine and the Cobscook basins of the Bay of Fundy. Tidal power studies for DOE (Wayne, 1977; Main, 1980) focused on the development of sites in Passamaquoddy Bay in Maine and Cook Inlet in Alaska. From a life-cycle cost point of view, the Passamaquoddy project is attractive. The Half Moon Cove tidal project site is illustrated in Figure 6. The design is for a single pool, single effect extraction cycle. The tidal basin is initially filled by opening gates during a flood tide. At high tide, the gates are closed and some three hours later generation of energy begins. The average output would be 10.6 MW for 5 1/2 hours. Application for a preliminary Federal Energy Regulatory Commission permit was filed in 1987 for this project.

Ocean Thermal Energy Conversion

The potential areas of OTEC deployment in the vicinity of the U.S. include: Hawaii, Gulf of Mexico, and territories and possessions in the Caribbean and Pacific. The magnitude of the OTEC resource in these areas has been estimated to be 10^5 MW. The most suitable sites for early OTEC landbased deployment are steep sloped islands where the cold deep water is found close to shore. A temperature difference of about 20°C can be exploited to run a heat engine that produces electrical power. One principle employed for OTEC is the Rankine closed cycle illustrated in Figure 7. A working fluid such as ammonia boils at tropical sea surface temperatures (i.e., 26°C) in an evaporator and this ammonia vapor in turn drives a gas turbine which runs a generator. The vapor is then condensed to a liquid by cold seawater (i.e., 6°C) pumped from 800-1000 m ocean depths, and the cycle is repeated. In 1979 a small, floating OTEC plant known as Mini-OTEC (Figure 8) was deployed off the Island of Hawaii by Lockheed in conjunction with the State of Hawaii and Dillingham Corporation. Mini-OTEC produced about 50 kw (gross). Sea Solar Power Corporation has developed a 100 MW floating plant closed cycle OTEC concept (Sea Solar Power, 1987) as illustrated in Figure 9. With a depth and length of 63 and 120 m respectively, the semi-submersible spar design would weigh about 25,000 metric tons and support a 1,200 m long 8.5 m diameter cold water pipe. It would use Freon-22 as a working fluid. The net-power output and auxiliary power requirements would be met by four 34 MW turbogenerator sets. In a cost-shared effort by Ocean Thermal Corporation, DOE and the State of Hawaii, a 40 MW pilot plant was designed in two phases. This plant is illustrated schematically in Figure 10 (OTC, 1984). The status of these projects is uncertain because of current low oil prices and the projected high initial capital cost for the OTEC plants.

Another OTEC power cycle currently under investigation by DOE is the open or Claude cycle as illustrated in Figure 11. In this concept, seawater itself can be considered the working fluid. After initial



Figure 6. Location Drawing of Half moon Cove Tidal Project

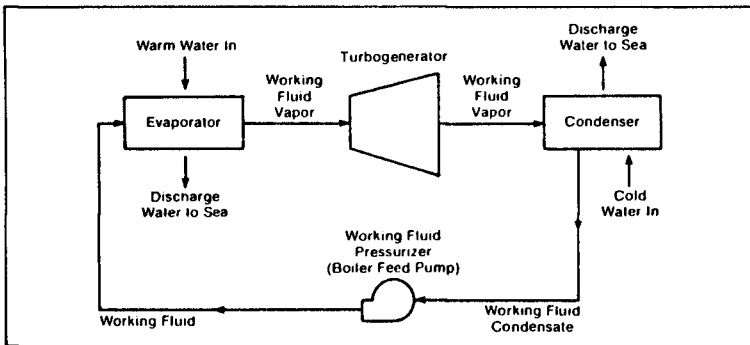


Figure 7. Schematic of a Closed-Cycle OTEC System

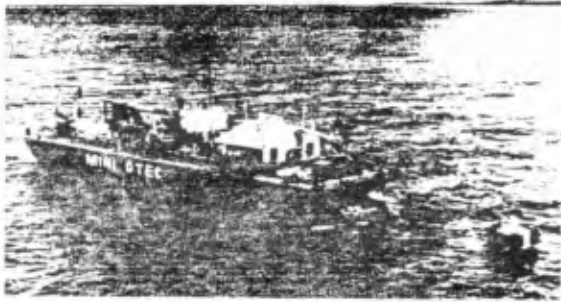


Figure 8. Mini-OTEC Producing Electricity off the Coast of Hawaii

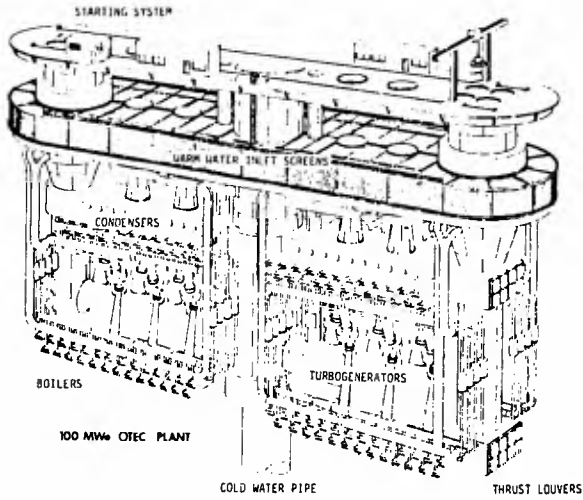


Figure 9. Sea Solar Power Inc. OTEC Concept

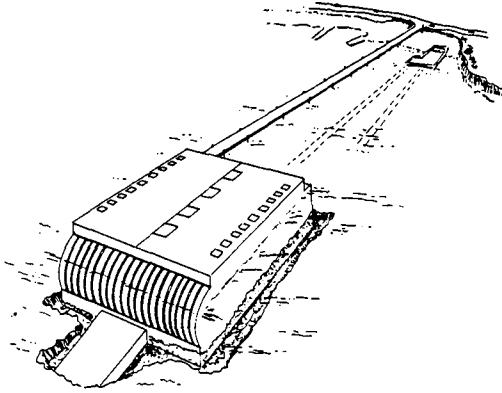


Figure 10. Ocean Thermal Corporation 40 MW OTEC Power Plant at Kahe Point, Hawaii

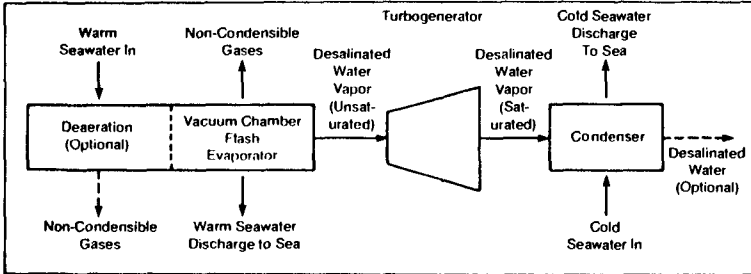


Figure 11. Schematic of an Open-Cycle (Claude-Cycle) OTEC System

deaeration to extract noncondensable gases, warm seawater is flash evaporated in a vacuum chamber. Desalinated water vapor drives a steam turbine which in turn drives a generator. The water vapor is then either condensed in a direct contact condenser and discharged to the sea, or condensed with a surface condenser producing desalinated water as a byproduct. The latter feature is particularly attractive in arid tropical islands. A 165 kw open cycle OTEC experiment is planned to be conducted through a cost-shared project between DOE and the Pacific International Center for High Technology Research at the Natural Energy Laboratory of Hawaii, Kailua-Kona, Hawaii (Lewis, 1987). After a series of open cycle component evaluations (presently underway), an apparatus will be constructed and used to validate system performance predictions, identify technical issues and obtain data scalable to future commercial size plants. These experiments will be supported by an upgraded seawater supply system recently installed at the site (Lewis, 1988). This system included the installation of a 1.0 m diameter cold-water pipe capable of delivering 840 l/s (410 l/s to the OTEC facility, 430 l/s to State mariculture projects). The pipe represented the largest diameter, longest (2,060 m) pipe tranversing the steepest slopes ever spanned.

Ocean Current Energy Conversion

In waters adjacent to the United States, the significant ocean current resource is limited to the Florida Current and the Gulf Stream off the southeast coasts. Estimates of extractable energy from these sources vary from 10,000 to 25,000 MW. Two axial flow rotary current energy systems have been developed by U.S. companies. Aerovironment, Inc. with DOE support, developed a ducted hydraulic turbine called Coriolis for applications to the Florida Current (Figure 12). Rim suspended two stage counter rotating catenary rotors were designed to feed energy to rim-mounted generators. Completed research included hydraulic performance evaluation of the rotors, Analyses of anchoring and mooring configurations, and system economic studies (Lissaman, 1979).

A similar device was developed by the UEK Corporation and is illustrated in Figure 13 (Vauthier, 1984). Energy in a flowing stream is converted to mechanical energy by a two-stage turbine. A radial outflow stage is followed by an axial flow stage. The inlet flow is through a venturi-shaped 3.7 m diameter shroud which concentrates the flow energy. The entire mechanism is tethered by cables so as to be held in the current stream, or suspended below a support platform. The device has been tested in Chesapeake Bay by towing it behind a tugboat. The New York State Power Authority has purchased one unit for evaluation.



Figure 12. The Aerovironment, Inc. Coriolis Ocean Turbine

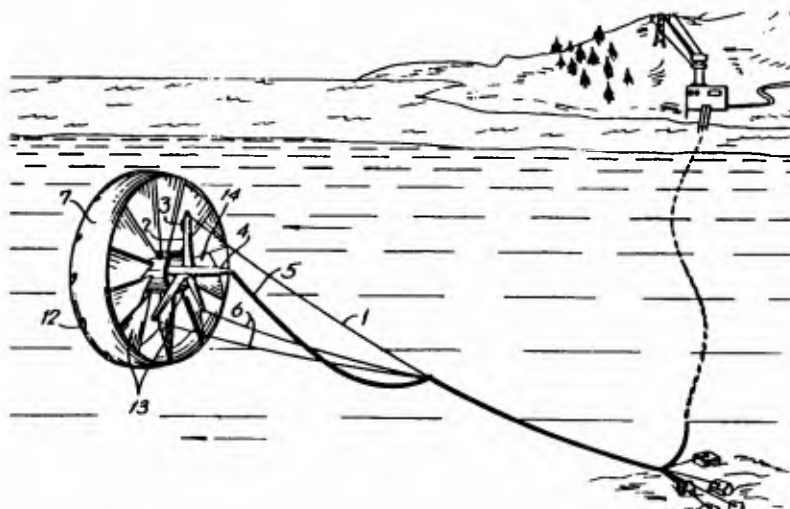


Figure 13. The UEK Corporation Underwater Kite

Conclusions

There is an abundant resource for ocean energy development in waters adjacent the United States and its territories. There is a high potential for extraction of energy in these waters from ocean waves, ocean thermal gradients, tides and ocean currents at selected sites. However, the existence of these resources does not imply immediately usable energy, since any device built to operate in these environments must be competitive with conventional land-based energy producing systems. Nevertheless, at some remote sites where conventional generation of power is relatively expensive, it is possible that an ocean energy source would provide economic power in the near future.

References

- Focas, D., "Straflo Turbines for Tidal Applications," Proceedings of the 2nd International Symposium on Waves and Tidal Energy, Cambridge, England, 1981.
- Hagerman, G.M. and Gordon, C.K., "Conceptual Design of a Prototype 500 KW Contouring Raft Wave Energy Conversion Device," Proceedings of the Renewable Energy Technology Symposium and International Exposition, Anaheim, California, 1987.
- Hicks, D.C., Pless, C.M. and Mitcheson, G.R., "DELBUOY Wave Powered Seawater Desalination System," Proceedings of the Marine Technology Society Oceans' 88, Baltimore, Maryland, 1988.
- Hopke, H.H. and Grant, A.D., "The Wave Energy Module," Proceedings of the 4th International Conference on Energy for Rural and Island Communities, Inverness, Scotland, 1985.
- JAMSTEC, "Open Sea Trials," International Energy Agency Report on Development of Wave Power by Japan Marine Science and Technology Center, Yokosuka, Japan, Vol. 4, 1987.
- Lewis, J.F., Trimble, L. and Bowers, J., "Open Cycle OTEC Seawater Experiments in Hawaii," Proceedings of the Marine Technology Society Oceans' 87, Halifax, Nova Scotia, 1987.
- Lewis, L.F., Van Ryzin, J. and Vega, L., "Steep Slope Seawater Supply Pipeline," Proceedings of the 21st International Conference on Coastal Engineering, American Society of Civil Engineers, Malaga, Spain, 1988.
- Lissaman, P., Radkey, R.L., Thompson, D.I. and Mouton, W.J., "An Evaluation of Hydroelastic and Dynamic Behavior of Key Components of the Ocean Turbine System," Report ET 20518/1, Aerovironment Corp. for U.S. Department of Energy, Washington, D.C., 1979.

- Main, C.T., "Half Moon Cove Tidal Project Feasibility Project," Chas. T. Main, Inc., Boston, Massachusetts for U.S. Department of Energy (Report FC07-801D12089), Washington, D.C., 1980.
- McCormick, M.E., "A Conceptual Design of a Counter Rotating Wave Energy Conversion Turbine," U.S. Naval Academy (Report EW-19-78), Annapolis, Maryland, 1978.
- McCormick, M.E., Ocean Wave Energy Conversion, Wiley Interscience, New York, New York, 1981.
- OTC "40 MW OTEC Power Plant, Final Technical Report," Ocean Thermal Corporation, New York, New York for the U.S. Department of Energy (Report DE-AC02-78ET-20480), Washington, D.C., 1984.
- Pless, C.M., "Seawater Powered Desalination," Proceedings of the Offshore Mechanics/Deepsea Systems Symposium, American Society of Mechanical Engineers, Fairfield, New Jersey, 1982.
- Q Corporation, "The Experimental and Theoretical Evaluation of an Engineering Model of the Tandem Flap Wave Energy Conversion Device," Q Corporation, Troy, Michigan, 1985.
- Richards, D. and Weiskoff, F.B., "Studies and Testing of the McCormick Pneumatic Wave Energy Turbine with Some Comments on PWECS," Proceedings of the Symposium on the Utilization of Ocean Waves, American Society of Civil Engineers, La Jolla, California, 1987.
- Sea Solar Power, "Ocean Thermal Energy Conversion, An Option for Puerto Rico, Review of Sea Solar Power, Inc. Proposal," Southern States Energy Board, Atlanta, Georgia, 1987.
- Scher, R.M., "A Study of Flap Type Wave Absorbing Devices," Q Corporation, Troy, Michigan and University of Michigan, Ann Arbor, Michigan, 1985.
- Vauthier, P. and Dement, D.K., "Ocean Current Electric Generation, the Underwater Electric Kite," Proceedings of the 5th World Hydrogen Energy Conference, Toronto, Canada, 1984.
- Wayne, W.W., "Tidal Power Study for U.S. Energy Research and Development Administration," Stone and Webster Engineering Corporation, Boston, Massachusetts, 1977.
- Wilke, R.O., "The Tandem Flap Wave Energy Conversion Device Great Lakes Experimental Test Program," Q Corporation, Troy, Michigan for Solar Energy Research Institute (Report ZX-6-06000-1), Golden, Colorado, 1985.

CHAPTER 73

LONG WAVES IN A SPANISH HARBOUR

Jose C. Santás López (*)
Gregorio Gómez Pina (**)

ABSTRACT

Short and Long Wave data recorded in Bilbao Harbour (Spain) have been analyzed in order to study water movements at the inner basins under storms conditions . Some of the trends obtained in prototype have been correlated with model test (regular long wave and irregular short waves) .

This harbour has been chosen for this research on the one hand because of the availability of the physical model and on the other hand because of the means provided by the Bilbao Port Authority

1.- INTRODUCTION

For a long time, there has been a great concern to know the behaviour of harbour basins with regard to long waves. These long waves can induce resonant effects in water bodies, and consequently, in moored ships. As a result, moored ship operations become much less efficient.

After the well known Longuet-Higgins' article, in 1964 (Longuet-Higgins, 1964), the amplitude of the long waves associated to wave grouping (β), was calculated. The expression for this magnitude was the following :

$$\beta = - 3 . g . a^2 / 2 . \omega^2 . h^2$$

Where : a = short wave amplitude ; $\omega = 2\pi/T$; T = wave period ;
h = water depth.

The wave set-down period (T_{SD}) corresponds to the wave grouping, being the former a function of the wave grouping grade and the wave peak period (T_{P}). The experimental evaluation of T_{SD} can be done in different ways : based in the number of waves in a group (Sand, 1982 a), from the SIWEH spectrum (Funke & Mansard, 1980), and also, as a mean value of the up-zero crossing period, obtained from the SIWEH spectrum T_{Z} (SIWEH) (Iwagaki, 1986).

This set-down wave is feeded by a second order mechanism from the short wave, in different ways (Bowers, 1977). In a harbour, this long wave will be as a bounded long wave (BLW), as a free long wave produced by the energetic imbalance at the harbour entrance, due to water

(*) Head of the Oceanog. Eng. Div. , CEPYC-CEDEX , Madrid .

(**) Head of the Exper. Harbour Div. , CEPYC-CEDEX , Madrid .

Antonio López st., 81 . 28026-Madrid . Spain

depth differences (FLW) , and as caused by wave breaking phenomena on a beach , located near a harbour , such as surf-beats and edge waves.

The resulting long wave can be in resonance with the different harbour basins if T_{B} is close to the natural period of the basins, giving rise to resonant amplifications.

The BLW has been widely studied and its parameters have been correlated with waves characteristics outside the harbour, for both unidirectional and directional waves, having a kind of energy spreading D_0 for the latter (Sand,1982 a, and 1982 b). An application of the BLW parameters was carried out for Sines Harbour by Vis et al, 1985.

This piece of work shows the results obtained in Bilbao Harbour where the BLW, FLW, and resonant amplifications were simultaneously detected under severe storm conditions. Regular long wave model tests were carried out to characterize harbour resonant responses. Also, irregular wave model tests were performed to compare trends in the prototype and model, in regard to long wave energy transfer outside and inside harbour basins.

2.- FIELD DATA ANALYSIS

Waves outside the harbour were recorded in a Datawell Waverider , located at a water depth of $h=50$ m (Fig.1). The signal transmitted by the buoy is collected at a station where it is recorded every 1 ó 3 hours, depending on whether there is an "alarm signal" or not (wave conditions such as $H_m > 4$ m., and $T_m > 16$ seg). The recording equipment consists of a HP-86 computer. The 5,000 data of each record are stored on a hard disk ($\Delta t = 0.5$ seg), transferred later to a moveable disk, and sent to the CEPYC, in Madrid. Sampling characteristics were chosen after studying the stationary and representative conditions of the calculated statistical and spectral

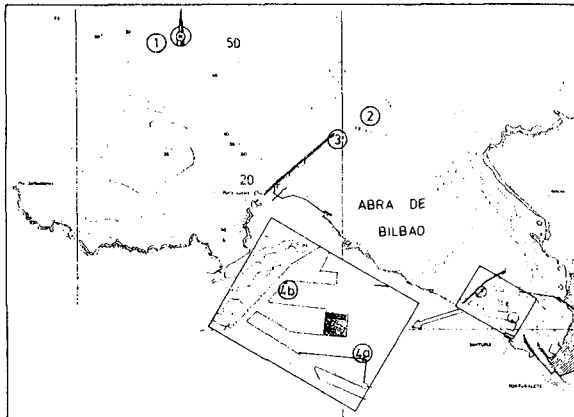


Fig 1: Position of measurement systems : Outside Waverider (1) ; "Morro" Waverider (2) ; Meteorological Station (3) and Pressure Sensors (4a & 4b) .

parameters (A. Fernandez , 1988). A deefp description of this system is shown in Martinez , Santás and Sanz , 1988 .

Long waves were registered by a pressure sensor, manufactured at the CEPYC, consisting of a differential thin film strain gauge, located in a watertight chamber, filled with silicone oil. The outer connexion was made by two openings in the sensor. One of these openings was feeded by a hydraulic filter to remove the tide long wave. The filter characteristics are : 6 dB high pass, crossing frequency $1/(6hr)$. The high frequency removing is done by the hydrodynamic attenuation of the water column in the sensor, installed at a water depth of 6 meters.

The information supplied by this pressure wave sensor was digitalized ($\Delta t = 2.5$ seg), using series of 4096 points, and recorded on other HP-86 system, transferred to a moveabl disk system later, and sent to the CEPYC, in Madrid.

The data analysis carried out later , based on the above mentioned information, is summed up bellow :

A) Waverider :

- Standard statistical parameter calculations
- Spectral calculations : FFT previous filtering ($T < 4$ seg, and $T > 25$ seg), and later smoothing (18 freedom degrees). The resulting time series will be called "*Outside Short Wave*" (OSW), and its corresponding spectrum $S(OSW)$.

- SIWEH calculations : long wave time series and spectrum , statistical analysis of typical values, estimation of T_w and grouping factor GF (Funke & Mansard, 1980). The SIWEH long wave will be called "*Outside Long Wave*" (OLW), and its corresponding spectrum $S(OLW)$.

B) Inner Wave gauge

- Surface wave recomposition, in amplitudes and phases, for the 10 min. $> T > 10$ sec. band, using the hydrodynamic wave attenuation factor K, given as :

$$K = \cosh (k.h) / \cosh (k.b)$$

where h = instantaneous water depth ; k = wave number ; b = distance from the bottom.

A frequency filter transference function was used to correct FFT data. Short and long wave band differentiation were defined in the following way :

Long wave : $1/(10 \text{ min}) < f < 0.04 \text{ Hz}$ (ILW)

Short wave : $1/(35 \text{ seg}) < f < 0.1 \text{ Hz}$ (ISW)

Typical statistical parameter calculations, for both time series, called "*Inside Long Wave*" (ILW), and "*Inside Short Wave*" (ISW) were made

Spectrum calculations for both time series with a previous Bingham smoothing, and a later Bartlett smoothing . The number of freedom degrees for ISW and ILW were 30 and 18, respectively.

2.1.- PROTOTYPE WAVE DATA STORAGE

Wave data storage began in March, 1986. The long wave pressure gauge was initially placed in position 4a (Figure 1), changing this position to 4b, in March 87, where it is still placed.

It was considered interesting to analyze the data only where long wave height was higher than 10 cms. The storms analyzed corresponded to the following days :

Position 4a : a) March 24-27, 1986
 Position 4b : b) April 20-21, 1987; c) September 4-5, 1987 ;
 d) January 22-26, 1988; e) January 30-February 12, 1988; f) March 16-17, 1988.

Figure 2 shows the time series for $H(z,s)$, corresponding to the Waverider (OSW), the inside short wave (ISW), and the inside long wave (ILW) for the stage a).

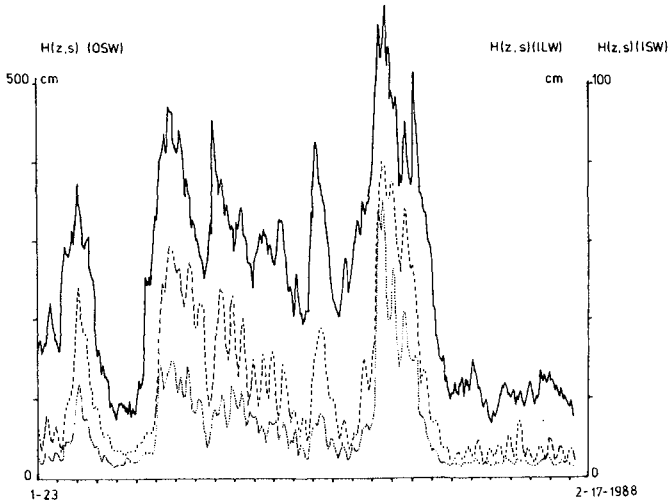


Fig. 2 : Wave Time Series $H(z,s)$: (——) Outside Short Wave (OSW), (----) Inside Short Wave (ISW), (.....) Inside Long Wave (ILW) . Data from 1.23.1988 to 2.17.1988 .

3.- RESULTS OBTAINED FROM PROTOTYPE MEASUREMENTS

First of all the short wave data OSW and ISW were correlated and compared. Two interesting aspects were found :

-The correlation between significant wave heights $H(z,s)$ inside (ISW), and outside (OSW) was in the range of 8 and 13% (fig. 3a), depending on the wave period.

- The significant and mean wave periods $T(z,s)$, and $T(z)$ have a small increment, between 7% and 9%. This fact is also found for the peak period T_p (Fig. 3b).

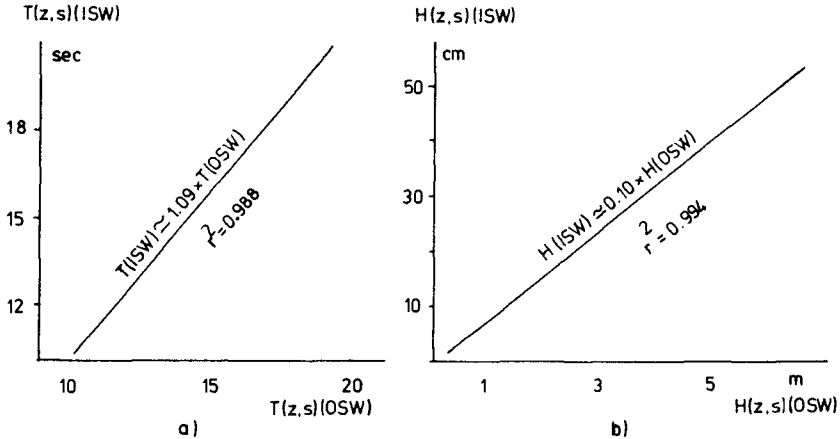


Fig. 3 : Comparison of Statistical Results between ISW and OSW
 3a) : $T(z,s)$; 3b) : $H(z,s)$.

As it will be explained later, similar trends appear in the physical model. Moreover, the values obtained for wave agitation coefficient inside the harbour, from both mathematical and physical models, appear to be within the above mentioned range for $H(z,s)$.

In regard to the long wave measured (ILW) inside the harbour and the short wave outside it (OSW), the main findings are as follows :

- The correlation between $H(z,s)$, (OSW), and (ILW) depends very much on the measurement area, which is indicative of some resonant mechanism. For location 4a (Fig.1) this correlation was found to be

$$H(z,s) (ILW) = 1.586 \cdot 10^{-3} \cdot [(H.T) (OSW) / h]$$

This kind of correlation fits better than the quadratic one used in Sand's, with data obtained from the stage a). However, for position b), which is more favorable for resonant effects due to its basin location, the correlation was found to be (with $r^2 = 0.8050$) :

$$H(z,s) (ILW) = 0,0732 + 4,841 \cdot 10^{-5} \cdot [(H.T)^2 (z,s) (OSW)] / h$$

Whereas for a best fit of (H,T) , the following formula is obtained ($r^2 = 0.72$) :

$$H(z,s) (ILW) = - 0.1177 + 6,319 \cdot 10^{-3} \cdot [(H.T) (z,s) (OSW)] / h$$

This last expression shows a degree of five times better for position 4a than for 4b (Fig. 4a and 4b). This explains a resonant effect for the long wave energy.

The unexpected fact that the quadratic expression for (H,T) is not clearly accomplished, could be explained by considering an

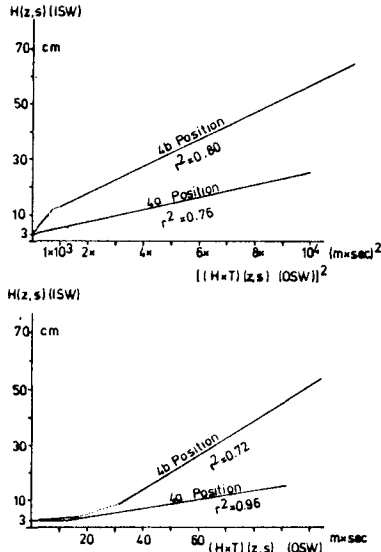


Fig. 4.- Correlation between $H(z,s)$ (ILW) and the Product $(H * T(z,s) (OSW))^2$: 4a) Lineal Fitting. 4b) Quadratic Fitting

amplification of the set-down proportional to H , instead to H^2 , in the inner harbour area. This amplification is due to an attenuation of the amplification factor caused by flow separation at the harbour entrance (Bowers, 1977).

The results calculated from the ILW, OLV, and SIWEH waves, obtained from the outside wave record, have also been correlated.

It was expected to obtain characteristic values of the number of waves in a group $(Df/f(p))$, taking into account the grouping factor GF. These values would allow to evaluate the transfer function G_{nm} between the short waves and the long set-down wave. However, the authors were not able to find a good correlation between the parameters GF and $(Df/f(p))$

The comparison between the values of $T(z)$ (SIWEH) or $T(z)$ (OLW) with $T(z)$ (OSW) has not given a high level of correlation. There seems to be a tendency to show increasing values towards the storm peak, and then decreasing slowly. The correlation between $T(z)$ (OLW) and Tz (OSW) was found to be somehow better in the following way :

$$Tz(\text{SIWEH}) = 6.6 \cdot T(z,s) (\text{OSW}) ; R^2 = 0.42$$

This expression is close to the value of the parameter $fp/Df = 5$, as found in Sedivy (Sand, 1982 a).

However, a certain value was systematically found for Tc (SIWEH) covering the range of 40-70 seg, coincident with the second spectral peak interval.

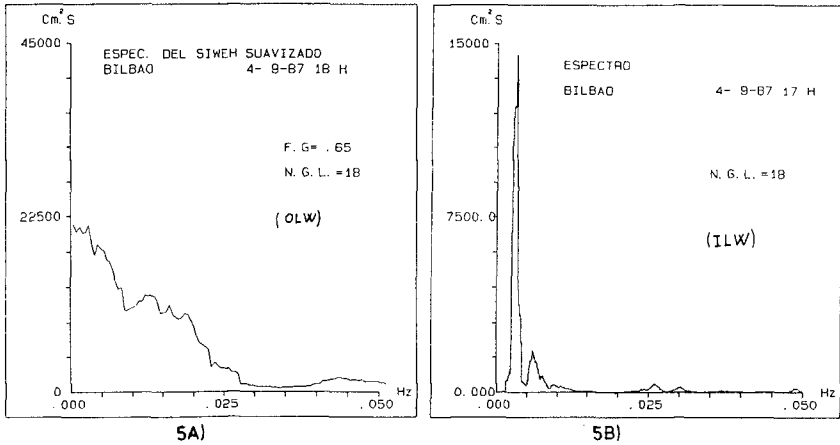


Fig.5.- Energy Spectra : A) SIWEH for the Outside waves (OLW)
B) Inside Long Wave (ILW).

When the SIWEH was smoothed by using a nine bands moveable rectangular window, the first spectral peak showed within the 250-350 sec. range, with other peaks within the ranges of 100-150 sec, and 40-50 sec. These results might indicate the existence of a main grouping period for the set-down, around the 40-50 secs, together with higher groupings, related to the subharmonics, being the latter responsible for the most important energy peaks in the SIWEH. Thus, the set-down should be understood as a wave family which is able to cause harbour resonance for some characteristic periods.

The ILW spectra show a well determined structure, with the maximum spectral peak in between 280 and 366 secs, and other peaks which only appear under storm conditions, around 40 and 180 seconds, respectively (fig.5a)

4.- MODEL TESTS

Different model tests were carried out for Bilbao Harbour (with regular and irregular waves, and also with moored ships). Some aspects of interest, related to the above mentioned long wave analysis performed in prototype, are presented hereafter. An undistorted scale 1:150 was used.

4.1.- REGULAR LONG WAVE MODEL TESTS

The purpose of these tests was to obtain a broad and detailed information of the resonant behaviour of the different harbour basins. The wave period range tested was from $30 \text{ s.} < T < 300 \text{ s.}$

4.1.2.- METHODOLOGY

The two main basins were filled with fluorescent cork spheres in order to observe the general way of oscillation of the two basins, for each exciting wave period. Maximum horizontal and transversal peak to peak water displacements, near the berthing places, were measured in detail, for the outer and inner harbour basins. Also, the existence of vortexes was remarked. Additionally, surface water displacements were measured in other points of interest alongside the berthing places. A very detailed information on the behaviour of the two basins was elaborated, remarking the bollard numbers at which characteristic water displacements were observed.

It should be remarked that, although wave periods were calibrated, wave heights were estimated visually. Therefore, the measurements of water surface displacements should not be understood quantitatively, since long waves could not be defined exactly by any known characteristic parameter such as the Ursell parameter.

4.1.3.- ANALYSIS OF RESULTS

The results were analyzed in two ways :

A) Representing in a plan view of the harbour (Fig.6A) the observed displacements in front of their corresponding bollards (crossing bars), together with the interpolated displacements in the bollards where no measurements were taken (white bars). Even though the spatial amplitude displacement distribution is sinusoidal, a linear distribution was adopted for comparative purposes. (Figs. 6b and c). The theoretical positions of nodes (χ_0 : main; χ_1 : first; χ_2 : second) were also indicated in the aforementioned figures, for each exciting wave period, using the simplifcative formulations for rectangular basins.

In regard to the use of the above mentioned simplifcative assumptions for rectangular basins, the following conclusions were drawn, after analyzing the behaviour of the two basins in the present physical model:

- The inclination of the quay called "Muelle Adosado", located at the end of the outer basin, induces a reflection of the standing wave, which makes the inclined basin behave in a different way than a rectangular one. Two interesting aspects should be pointed out :

- The antinode does not clearly appear in the vertical wall, at the basin end, due to the existence of horizontal water displacements in the direction of the inclined quay, caused by the above mentioned reflective effect of the standing wave.

- The section reduction at the change of alignment, in the inner main basin, causes an increment of the horizontal velocities of the standing wave. This effect is increased by the relative closeness of the first oscillating node.

B) Representing the maximum horizontal displacements (peak to peak) against the exciting wave periods (within the range of 30-300 secs), for the two main harbour basins.

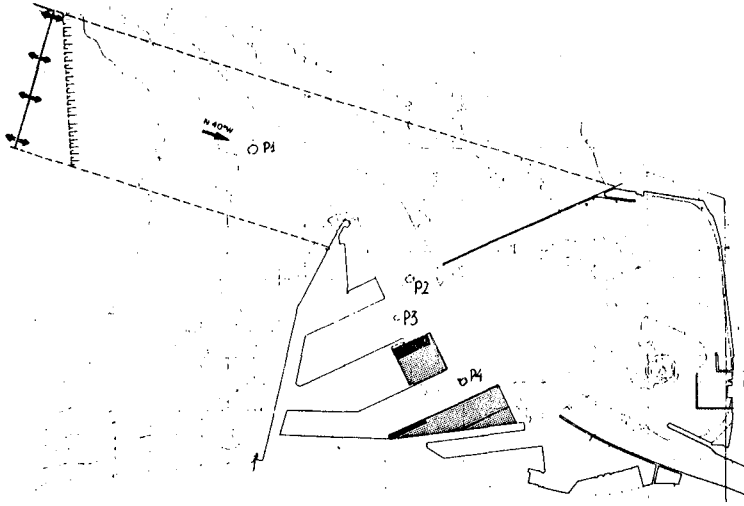


Fig. 6.- Physical Model : a) General Lay-out.

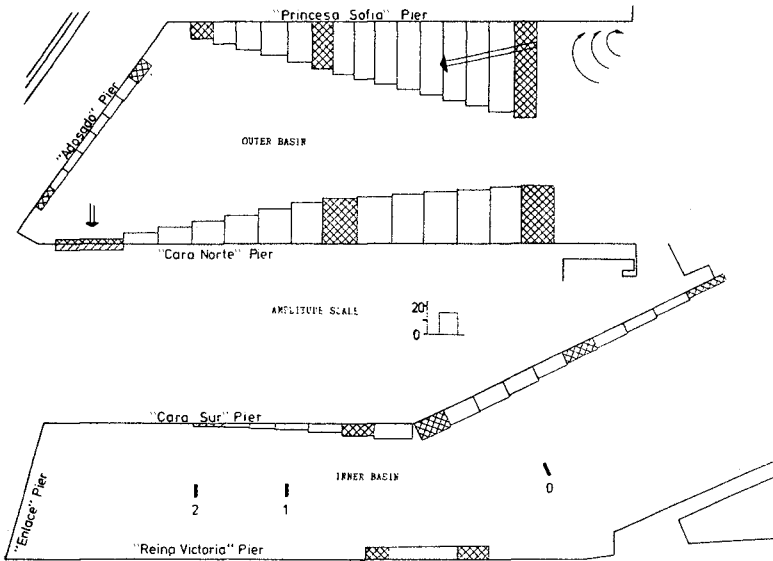


Fig. 6.b&c- Example of Horizontal Water Displacements Parallel to Quays : b) Outer Basin ($T = 250$ s.), c) Inner Basin ($T = 200$ s.)
 [XXXXXX] Measured Data, [] Interpolated, [/////] Perp. displacement towards the berthing, \oplus Drifting, \odot Vortex, [] Theoretical node position.

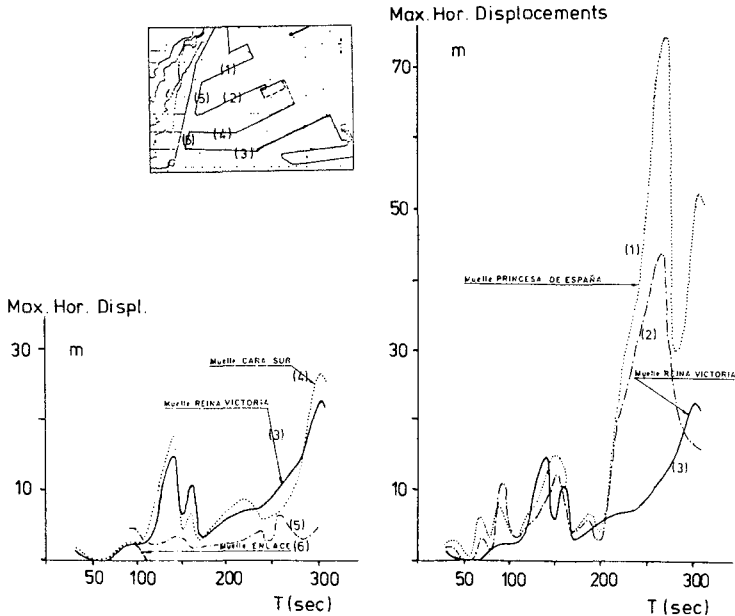


Fig.7.- Results of the Physical Model with Regular Waves :
Max. Horizontal Displacements at the Two Basins against the
Exciting Wave Periods.

4.1.4.- MODEL TEST CONCLUSIONS

After analyzing the figures shown in A), the following conclusions were obtained, related to the behaviour of the two harbour basins.

Outer Harbour Basin (Fig.6b)

It can be seen, from the figures, that the oscillatory displacement amplitude distribution looks like one corresponding to a standing or quasi-standing wave, with maximum displacements located near the node.

The "theoretical" resonant period of the basin was found in the range of 200-235 seg., depending on the oscillating length adopted (from the center of the Adosado Quay, or from the end). This range could be extended because of the longer wave standing trajectories caused by the reflection in the inclined pier at the bottom of the basin.

The above mentioned long wave reflective phenomenon was also shown in the model tests, by the transversal displacements experimented in the Cara Norte Quay, specially in bollard 5 (see bollard plan).

Another point to be remarked is the higher displacements found at the Princesa de España Quay with respect to its opposite one (Cara

Morte). Horizontal displacements up to 75 meters were measured at the Princesa de España Quay (bollard 3, near the entrance). Also, a drift displacement of 45 m. was observed in that bollard.

Inner Harbour Basin (Fig.6c)

The movements observed at the inner basin are significantly smaller than those found at the outer basin, and they are also distributed more uniformly.

The largest displacements are found at the change of alignment in the inner basin. The reasons for this could be as follows :

- The oscillation node is close to this area.
- This change of alignment is coincident with a reduction of the transversal section of this basin, which causes an acceleration of the confined mass of water.
- The antinode appears to be located at the end of the basin, which does not occur at the outer basin.

After analyzing the figures explained in B) (Fig.7), the following conclusions are drawn :

The Princesa de España Quay seems to be very sensitive to small wave period increments. For instance, for the range of $T = 200-260$ secs., the horizontal water displacement shifts from a value of 6 m., to the maximum one of 75 m., and then decreases down to 30 m., for the range of $T = 260-280$ secs, increasing again up to a new maximum (52.5 m.), for $T = 280-300$ secs., showing a decreasing trend after it.

The outer basin shows two distinctive peaks for its longitudinal oscillation, for the two parallel quays (Princesa de España and Cara Norte). The first peak is located near $T = 150$ secs., and the second peak around $T = 240-260$ secs. This second peak induces the largest water displacement (about five times more).

The outer and inner basins show similar trends in longitudinal oscillations (two distinctive peaks), although they both differ considerably in the oscillation amplitudes, as it was already explained.

The position of the main oscillating node seems to be a significant parameter for the way in which longitudinal water oscillations occur at the two parallel piers. The more symmetrical location of the main node at the inner basin, due to the lower inclination of the quay at the end, makes the two parallel piers (Cara Sur and Reina Victoria) oscillate in a very similar way.

The transversal water movements of the two basins are very small compared to the longitudinal ones.

4.2.- IRREGULAR WAVE MODEL TESTS

After analyzing wave spectra at different harbour areas (Fig.6a), energy transfer was found from the main peak period ($T_p = 17$ secs.) towards much higher periods in the range of 103-310 secs. The fact

that the maximum basin amplifications in the regular wave model tests are found around wave peak periods of 150 and 260 secs, could establish the existence of some kind of resonant effect, around these periods, when irregular waves are used in the model.

It should be remarked that the spectral analysis carried out in the model was based on 512 points, which only allow to know the range of wave energy transference, without clearly distinguishing the peak periods for the long wave. At the present, a more detailed wave spectral analysis (4096 points) is being performed at the CEPYC (Iribarren et al) to distinguish the spectral peaks much better.

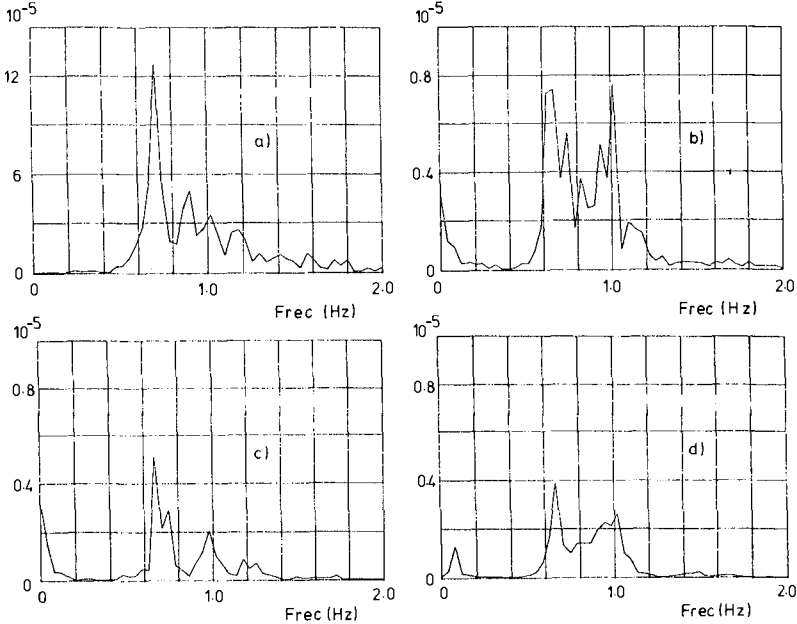


Fig. 8.- Example of Wave Energy Spectra Obtained in the Physical Model:
 a) Outside Waves (P_1); b) Same for Santurce Entrance (P_2); c) Outer Basin Entrance (P_3); d) Inner Basin Entrance (P_4). (Points shown in Fig.6A; max. freq. 2 Hz).

5.- DISCUSSION

The set-down amplitude has been parametrized by Sand (1982) by means of the transfer function $G_{nm}(D\theta).h$. For the case of deep or shallow water, the following asymptotic expressions for unidirectional waves ($D\theta = 0$) were found, function of the P parameter ($P = \text{SQR}(h/g)/T_p$):

$$\begin{aligned}
 P < .15 \text{ ---- } G_{nm}(D\theta=0).h &= (3/8.\pi^2) . P^{-2} . (1/(1+Df/fp)) \\
 P > 3 \text{ ---- } " &.h = 2 . \pi^2 . P^2 . (Df/fp) . (2+(Df/fp))
 \end{aligned}$$

For the case of directional waves ($D\theta \neq 0$), the solutions were presented in a graphic way.

The considered depth h corresponds to the measurement point of the incident waves. However, this transference function grows when decreasing water depth, in the following way :

$$G_{rim} (D\theta = 0) \cdot h \propto (1 / k^2 \cdot h^3)$$

This implies that set-down will grow with water depth decrease. Thus, an increase in the mean water level will be expected in the recordings. Comparisons between the results obtained from the waverider and those from the Bilbao Port in this zone showed that such a variation could not be detected as far as the entrance of the inner basin, located at 18 m. water depth. Furthermore, the results from the physical model testes seemed to confirm this fact, the peak not appearing in the range of 40-60 secs., up to this point.

The above mentioned findings made possible to estimate the wave set-down amplitude for a water depth of 22 m, considered as a mean value for the outer zone.

As for directional waves, a mean value of $D\theta = 27^\circ$ was obtained, for a directional buoy (wavescan), located outside the harbour ($h \approx 300$ m.), during December-87 (Arribas and Morón, 1988). A value of $D\theta = 20^\circ$ was adopted, corresponding to the tabulated results showed below. The number of waves in a group may be of 5, as considered by Sand, whose value is in the order of the data (item 3). The wave peak periods, under storm conditions, are within the range of 12 and 20 secs., and the P parameter results : $.075 < P < .125$, which corresponds to shallow water conditions.

In order to evaluate the set-down amplitude, $A_s = A_m$ was taken which is equivalent to consider two wave amplitudes very close in frequency, and thus creating a wave energy train equivalent to the original one, having H_m as a significant wave height. Under these conditions, the values obtained for β/H_m^2 were as follows :

	$\beta = (G_{rim} (D\theta=0) \cdot h) * H_m^2 / 16 h$				
<u>Dθ</u>	<u>TP=12</u>	<u>TP=15</u>	<u>TP=18</u>	<u>TP=20</u>	
0	.0068	.0106	.0153	.0189	
20	.0018	.0020	.0022	.0023	
P =	.124	.0998	.083	.075	

When these values are referred to real values measured in prototype, the results are as follows :

<u>Date</u>		<u>O.S.W.</u>		<u>β</u>		<u>I.L.W.</u>	
<u>Day / Time</u>	<u>Hs</u>	<u>TP</u>	<u>Dθ=0</u>	<u>Dθ=20</u>	<u>Hs(ILW)</u>	<u>Position</u>	
4.9.87 14	2.57	15.0	.07	.013	.016	4b	
10.2.88 11	5.81	14.4	.36	.068	.72	4b	
25.3.86 3	6.5	15.0	.44	.080	.12	4a	

For small wave heights, $H_m(OSW) < 1.5$ m., in position 4a, wave heights in the range of 0.02 were detected almost continuously, probably corresponding to the case of a free wave generated by the change in water depth at the harbour entrance. Taking this fact into account, the measured wave heights ILW obtained in position 4b are higher than the calculated set-down, and they must correspond to resonant amplifications induced by the set-down. Wave spectra obtained from the physical model show similar tendencies.

If wave spectra at the entrance of Basins 1 and 2 are compared to the wave spectrum considered as "exciter" (Figs. 6a and 8), the peak corresponding to the long wave appears in the range of 50-250 secs., growing towards the end of the basins.

Therefore, it seems possible to confirm the hypothesis that the set-down is amplified by resonant oscillations, although not in its principal mode, but in the subharmonic ones whose periods are close to the natural periods of the basins studied. That is way the peak period of waves at the end of the basins grows simultaneously with the decrease of the total energy, acting the set-down, because of its second order characteristics, as an energy transfer.

6.- CONCLUSIONS

1) The mechanism of set-down comes out as a wave packet whose frequency distribution corresponds approximately with that adopted by the SIWEH spectrum outside the harbour, being able to generate resonancies according to its frequency band.

2) Set-down generates an energy transfer from the usual wave frequencies towards lower frequencies, producing an increase of the peak period, altogether with a general decrease of the total energy. In the present case, a decrease around 7-9% for T_c , coincident with a decrease for H_m of 90-92%. has been detected

3) Calculations of statistical parameters carried out from the SIWEH have only permitted to obtain an imprecise idea of the number of waves in a group, as well as of the main set-down period, from the $T(z,s)$ and T_c parameters, respectively.

4) SIWEH spectrum shows approximately the existence of several waves, corresponding with the set-down subharmonics. Furthermore, SIWEH spectra peaks coincide with bands of accused energy detected for Long Wave spectra analyzed at the end of the basins, thus being the probable origin of resonances depending on the natural periods of the basins.

5) The resonant modes detected in the physical model, using regular waves, show in a semiquantitative way, the existence of amplitudes of a certain importance, for the horizontal water displacements in the outer harbour basin whereas the inner basin is less susceptible to resonances.

6) The model tests with regular waves have allowed to study the behaviour of the outer and inner harbour basins, analyzing the response of those basins with respect to a large range of wave exciting periods. In the neighbourhood of the natural modes of oscillation, the amplification grows rapidly and resonant effects may appear, even with energies not being exactly in the natural frequency of oscillation. The non strictly regular geometry of the basins fosters the lack of a well determined frequency of oscillation but a relatively narrow frequency band where resonant effects could be developed under severe storm conditions.

7.- ACKNOWLEDGEMENTS

The authors are indebted to Mr.J. Lozano and Mr.J.R. Iribarren for their help during the analysis of the results of the model tests with irregular waves. Mr.M. Seillan and Mr.R. Amarilla, Argentinian scholarship holders at the CEPYC, collaborated in the studies related to regular waves, and Ph.Dr.Mr. A. Fernández, Miss.C.Benito and Mr.F. Muñoz made an important collaboration in the field data analysis. The authors greatly appreciate the cooperation as well as the means provided by the Bilbao Port Authority .

REFERENCES

- Arribas Perea M.A. and A.Marón Loureiro ,1988 ; "Metodología para el análisis de Información de Boyas Oceano-meteorológicas " , D.G.P.C. , M.O.P.U. , Internal communication .
- Bowers , E.C. , 1977 ; "Harbour resonance due to set-down beneath wave groups" ; J. Fluids Mech. 79 , part 1 , 71-92 .
- CEPYC-CEDEX , 1984 ; Techn. Study : "Estudio Oceanográfico del Puerto Autónomo de Bilbao" , M.O.P.U.
- Fernández , A. , C. Benito Guinea and A. Navarro Sanz , 1988 : "Estudio de la variación de parámetros de oleaje en función de la toma de datos" , 6th. Nat. Asamb. of Goedesy and Geophysics ; I.G.N. ; M.O.P.U.
- Funke , E.R. and Mansard , E.P.D. , 1980 ; "On the syntesis of realistic sea states" , Proc . of Coast. Eng. Conf. A.S.C.E. , 2974 - 2991
- Iribarren ,J. and C.Benito ; 1988 ; Personal comunication ; CEDEX - CEPYC .
- Iwagaki Y. and H. Mase , 1986;"Wave group analysis of natural wind waves based on modulation instability theory"; Coast. Eng. 10 (1986) , 341-354 .
- Longuet-Higgins , M.S. and R.W.Stewards , 1964 ; Deep Sea Research , 11 ,529-542 .
- Martinez , M. J.C.Santças and L.Sanz , 1988 ; "Spanish network for measurement and recording of waves" , Int. Conf. on Coast. Eng. , p.n^or. P-50.
- Sand Stig E.,1982 ;"Long waves problems in Laboratory models",J.Waterw. Port. Coast. and Oc. Div ; A.S.C.E. ; 108 , WW4 , 492-503 .
- Sand Stig E.,1982 ;"Long Waves in directional seas",Coast. Eng. , 8 , 195 - 208 .
- Vis F.C. , A. Mol , M.M. Rita and C.Deelen , 1985 ; "Long waves and harbours design" , Proc. of Int. Conf. on Hyd. and Num. Modelling of Ports and Harbours ; J-1;249-255 .

SUBJECT INDEX

Page number refers to first page of paper.

- Accretion, 2738
Aeration, 166
Air chambers, 2326
Alaska, 2574, 2818
Altimeters, 1508
Analysis, 2952
Approximation methods, 2144, 2927
Armor units, 644, 2063, 2075, 2102,
2116, 2129, 2284, 2299, 2355, 2370,
2385, 2416, 2418, 2445, 2479
Armored units, 2144
Armour units, 1983
Australia, 2626
- Barrier islands, 2681
Bars, riverine, 1167
Bathymetry, 2655
Bayesian analysis, 62
Beach erosion, 1, 121, 322, 1197,
1253, 1330, 1411, 1426, 1437, 1482,
1493, 1508, 1558, 1721, 1818, 1857,
1882, 1911, 1937, 1983, 2028, 2090,
2738, 2791, 2840, 2855, 2896,
153501543
Beach nourishment, 1323, 1411,
1482, 1558, 1882, 1922, 2806, 2825,
153501543
Beaches, 32, 77, 136, 151, 219, 292,
539, 553, 705, 807, 1182, 1238,
1295, 1338, 1396, 1618, 1631, 1676,
1736, 1763, 1959, 2116, 2784, 2867
Bed load movement, 1774, 1803
Bed ripples, 1748, 1868
Bed roughness, 492, 1842, 2692
Bedforms, 849, 1868, 2692
Belgium, 2855
Berms, 1997, 2284, 2416, 2818
Berths, 2966
Blocks, 2159, 2479
Boundary conditions, 181, 393, 624,
2561
Boundary element method, 624
Boundary layer, 234, 743, 914, 1129,
1280, 1603
Boundary layer flow, 492
Brazil, 261
Breaking waves, 234, 292, 350, 377,
393, 419, 478, 539, 578, 632, 682,
871, 1020, 1035, 1058, 1113, 1167,
1212, 1238, 1368, 1646, 1721, 2174,
2272, 2340, 2504
Breakwaters, 47, 121, 166, 246, 281,
624, 782, 1073, 1573, 1997, 2013,
2028, 2075, 2129, 2229, 2272, 2326,
2355, 2430, 2469, 2479, 2489, 2504,
2840, 2882
Buoys, 2923
- Caissons, 2469, 2489
Calibration, 2013
California, 2129, 2455
Caribbean, 1618
Case reports, 756, 1265
Channels, waterways, 2896, 2911
Cnoidal waves, 219, 553, 588
Coastal engineering, 1, 204, 350, 363,
463, 858, 871, 884, 929, 941, 999,
1011, 1045, 1058, 1152, 1323, 1411,
1437, 1452, 1631, 1788, 1842, 1882,
1911, 1922, 2144, 2589, 2603, 2626,
2641, 2666, 2818, 2855, 2952
Coastal environment, 2574, 2615
Coastal management, 1, 2090, 2738,
2896
Coastal morphology, 1, 322, 1084,
1295, 1330, 1618, 1689, 1736, 1788,
1818, 1857, 2825
Coastal processes, 32, 181, 743, 1084,
1152, 1227, 1253, 1265, 1323, 1330,
1338, 1382, 1396, 1426, 1437, 1452,
1544, 1603, 1618, 1631, 1646, 1661,
1676, 1704, 1774, 1803, 1922, 1937,
1952, 1974, 2655, 2772, 2784, 2825,
2867
Coastal structures, 1, 166, 281, 655,
756, 782, 1020, 1310, 1482, 1573,
2043, 2053, 2090, 2174, 2189, 2299,
2370, 2385, 2400, 2455, 2504, 2681,
2791, 2840
Coastal zone, 2028
Coefficients, 47
Comparative studies, 644, 2681
Composite materials, 1588
Computation, 292, 1974
Computer aided drafting (CAD), 463
Computer applications, 463
Computer models, 2991
Computerized design, 463
Concrete blocks, 2043, 2053, 2144,
2174, 2370, 2400
Concrete construction, 2102, 2385,
2418
Conical bodies, 2257
Construction, 2416, 2723, 2753, 2791
Cost minimization, 2416
Currents, 77, 136, 363, 971, 1035,

Volume 1 – 1- 998

Volume 2 – 999-1980

Volume 3 – 1981-2998

- 1140, 1212, 1368
 Curtain walls, 2430
 Cylinders, 914, 2201, 2216

 Damage assessment, 2818
 Damage prevention, 1558
 Damping, 2952
 Data collection, 2753
 Deformation, 393
 Deltas, 1323
 Design, 655, 782, 1280, 1997, 2043,
 2063, 2159, 2174, 2299, 2326, 2385,
 2416, 2489, 2666, 2723, 2753, 2979
 Design criteria, 756, 1020, 1197,
 1411, 2129, 2284, 2504
 Design data, 770
 Design events, 756
 Design waves, 822, 899, 2504
 Differential equations, 2603
 Diffusion coefficient, 166
 Dikes, 335, 1897, 2174, 2340
 Discharge, 1573, 2521
 Displacement, 1464
 Distribution functions, 899
 Docks, 2313
 Dolos, 2075, 2129, 2355, 2385, 2418,
 2445
 Dunes, 1197, 1426, 1588, 1721, 1857,
 2090
 Dye studies, 2626
 Dynamic analysis, 2469
 Dynamic response, 1763, 2189, 2469,
 2923

 Ecology, 2574, 2615
 Economic factors, 1558
 Eddie viscosity, 492
 Eddies, 234, 1646
 Eddy viscosity, 408, 478, 505, 1661
 Effluents, 2521
 Energy absorption, 2313, 2966
 Energy conversion, 2489
 Energy dissipation, 292, 363, 408,
 492, 578, 1045, 1113, 1833, 2326
 Energy losses, 1842, 2216
 Energy transfer, 999
 Entrainment, 2550
 Environmental factors, 1238
 Environmental impacts, 1330, 2574
 Equations of motion, 419
 Equilibrium, 1045
 Equilibrium profile, 1396, 1618
 Erosion, 1197, 1368, 1897, 2299
 Erosion control, 1588
 Estimating, 2445
 Estimation, 62

 Estuaries, 1212, 1573, 1788, 2655,
 2692, 2707, 2784
 Eutrophication, 2615
 Experience, 2455
 Experimental data, 270, 153501543

 Failures, 1897, 2053, 2063
 Failures, investigations, 2818, 2923
 Fenders, 2966
 Field investigations, 524, 539, 1522,
 1618, 1833, 2430, 2626
 Field tests, 47, 136, 1588, 1763
 Finite difference method, 1129
 Finite element method, 32, 2313,
 2445
 Finite elements, 2561
 Fishing, 2927
 Floating breakwaters, 2189
 Flood control, 2855
 Flood forecasting, 1197
 Florida, 2772
 Flow characteristics, 2201
 Flow patterns, 505
 Flow visualization, 234
 Fluid dynamics, 718
 Fluid-structure interaction, 17
 Flumes, 448, 612, 770, 835, 871, 1140,
 1763, 1803
 Flushing, 2626
 Forecasting, 566, 602, 667
 Fourier transform, 246, 307
 France, 2707
 Frequency analysis, 2272
 Friction, 505, 849, 1073
 Friction factor, 363, 492, 2013

 Geomorphology, 2681
 Grain size, 1952, 1959
 Grain size analysis, 1129
 Grains, 718
 Gravel, 2116
 Gravity foundations, 2469
 Gravity waves, 512, 667, 2201
 Grid systems, 2655
 Groins, structures, 2882

 Harbor engineering, 463, 782, 984,
 1997, 2896
 Harbors, 32, 47, 270, 463, 1227, 2242,
 2784, 2818, 2882, 2911, 2979
 Head loss, 270
 Hurricanes, 1098
 Hydraulic design, 2400
 Hydraulic models, 770, 2242, 2840,
 2979
 Hydraulic performance, 795

- Hydraulics, 2589, 2666
 Hydrodynamics, 463, 505, 1058,
 1382, 1974, 2189, 2479, 2655
 Hydrostatics, 682

 Ice loads, 2400
 In situ tests, 2355
 Inlets, waterways, 433, 2681
 Innovation, 2326
 Intake structures, 2723
 Islands, 322, 2738

 Japan, 2028, 2063, 2791
 Jetties, 1911, 2896

 Kinematics, 377, 448, 871

 Laboratory tests, 91, 612, 632, 795,
 835, 849, 1646, 1748, 1763, 1842,
 1897, 1983, 1997, 2430
 Lakes, 2840
 Land fill, 2806, 2855
 Linear functions, 884
 Littoral current, 408, 1182
 Littoral currents, 77, 234, 393, 705,
 1113, 1238, 1396, 1689, 1736, 1959,
 1974, 2521, 2603
 Littoral drift, 1152, 1182, 1238, 1253,
 1330, 1382, 1396, 1437, 1452, 1603,
 1676, 1818, 1937, 1959, 1974, 2772,
 2825
 Loading, 2257
 Long waves, 91, 219, 270, 984

 Marinas, 2626
 Markov process, 956
 Mathematical models, 246, 281, 566,
 1129, 1603, 1689, 1897
 Mats, 2400
 Measuring instruments, 77
 Mediterranean Sea, 566
 Methodology, 884, 899, 1857
 Mineralogy, 1338
 Mixing, 2521
 Model accuracy, 566
 Model studies, 2692
 Model tests, 644, 770, 984, 1265,
 2075, 2257, 2923
 Model verification, 433
 Modeling, 121, 261, 335, 718, 956,
 1952, 2418, 2589
 Models, 270, 492, 698, 743, 795, 807,
 822, 1098, 1212, 1253, 1676, 1736,
 1818, 1833
 Monitoring, 2806
 Monte Carlo method, 899

 Mooring, 2189, 2923, 2952, 2979
 Movable bed models, 1227, 1544

 Nearshore circulation, 106, 393, 408,
 578, 1058, 1113, 1452, 1522, 1704,
 2561, 2603, 2626, 2655
 Netherlands, 2825
 New Jersey, 2806, 2867
 Nonlinear differential equations, 732
 Nonlinear response, 1803
 North Sea, 322, 956, 1788
 Norway, 1997
 Numerical analysis, 743
 Numerical calculations, 307, 624,
 2430, 2589
 Numerical models, 350, 393, 433,
 463, 512, 578, 588, 602, 858, 929,
 941, 1113, 1167, 1265, 1295, 1426,
 1437, 1911, 1937, 2013, 2159, 2189,
 2445, 2561, 2655, 2666, 2707
 Nutrient loading, 2615

 Ocean disposal, 2521
 Ocean engineering, 2927
 Ocean environments, 2536
 Ocean thermal energy conversion,
 971
 Ocean waves, 204, 335, 602, 655,
 1464
 Oceanography, 602
 Offshore engineering, 2536
 Offshore pipeline, 2641
 Offshore platforms, 62, 261, 956,
 2257, 2313
 Offshore structures, 914, 1280, 2257
 Oil spills, 2574
 Oregon, 1338
 Oscillations, 151, 270, 2952, 2966
 Oscillatory flow, 718, 743, 1140
 Outfall sewers, 2615
 Outwash, 1922
 Overtopping, 335, 770, 795, 1983

 Perturbation theory, 705
 Physical properties, 941
 Phytoplankton, 2615
 Piers, 1310
 Pile tests, 1368
 Piles, 1310, 2229
 Plastic pipes, 2641
 Plates, 2272
 Plunging flow, 632, 682
 Polyethylene, 2641
 Polymers, 1588
 Pore pressure, 1011
 Pore pressure measurement, 2242

- Pore water pressure, 1842
 Porous materials, 1073
 Ports, 756, 1997, 2882, 2911
 Potential flow, 17
 Predictions, 644, 698, 871, 1098,
 1167, 1253, 1396, 1426, 1508, 1676,
 1803, 1857, 2201, 2536, 2692
 Pressure distribution, 682, 2504
 Probabilistic methods, 2063
 Probabilistic models, 1352
 Probability density functions, 524,
 807, 822
 Probability distribution, 655, 822
 Probability theory, 1011, 2053
 Profiles, 1482, 1493, 1631, 1676,
 1882, 2806, 153501543
 Project evaluation, 2806
 Prototype tests, 718, 1265, 1721, 2355
 Pump intakes, 2723
 Pumped storage, 1897

 Quality assurance, 2102
 Quantitative analysis, 2772

 Radar, 667
 Random waves, 91, 770, 807, 835,
 941, 1736, 1748, 1763, 1911, 2257
 Recreational facilities, 1558, 2840,
 2867
 Reefs, 335
 Regeneration, 1437
 Rehabilitation, 2855
 Reliability, 2063
 Reliability analysis, 2053
 Remote sensing, 667
 Repairing, 2075
 Research needs, 1
 Resonance, 270
 Restoration, 1411
 Return flow, 448
 Revetments, 281, 782, 795, 2043,
 2116, 2159, 2174, 2340
 Reviews, 377, 2784
 Reynolds number, 2979
 Reynolds stress, 478
 Rip current, 408
 Rip currents, 32, 1603
 Risk analysis, 2574
 Rivers, 1573
 Rock properties, 2299
 Rock structures, 2116
 Roughness coefficient, 644
 Rubble-mound breakwaters, 770,
 2053, 2063, 2102, 2116, 2144, 2242,
 2284, 2385, 2416, 2418, 2455, 2818

 Sand, 718, 1588, 1882
 Sand transport, 1152, 1182, 1212,
 1238, 1280, 1295, 1338, 1382, 1721,
 1748, 1868, 1897, 2772
 Sand waves, 1748
 Sandbars, 2882
 Scale effect, 153501543
 Scale models, 2159, 2911
 Scattering, 2216
 Scour, 1310, 1368
 Scouring, 1280
 Sea floor, 1035, 1352, 1464, 1748,
 1868, 2927
 Sea flow, 1842
 Sea level, 2825, 2867
 Sea state, 322, 655, 667, 956, 2340
 Sea walls, 281, 335, 782, 795, 1493,
 1882, 1983, 2090, 2455, 2882
 Sea water, 2641, 2723
 Sediment, 849
 Sediment concentration, 1661, 2738
 Sediment control, 2723
 Sediment deposits, 1573
 Sediment transport, 234, 1084, 1140,
 1152, 1167, 1182, 1227, 1280, 1338,
 1368, 1382, 1396, 1452, 1493, 1508,
 1522, 1544, 1676, 1689, 1704, 1721,
 1736, 1774, 1803, 1818, 1868, 1882,
 1911, 1952, 1959, 2707, 2772
 Sediment yield, 2867
 Selection, 2966
 Sensitivity analysis, 1959
 Service life, 2102
 Settlement analysis, 2927
 Sewage treatment plants, 2753
 Shallow water, 612, 807, 929, 1020,
 1035, 1310
 Shaoling, 632
 Shear stress, 77, 1084, 1140, 2550
 Ship motion, 2911, 2952, 2966
 Ships, 2979
 Shoaling, 106, 419, 588, 807, 1035,
 1212
 Shock, 2340
 Shore protection, 644, 1482, 1493,
 1788, 2028, 2090, 2370, 2455, 2840,
 2882
 Shoreline changes, 539, 1253, 1265,
 1295, 1426, 1544, 1937, 2791, 2825,
 2867
 Simulation, 91, 835, 858, 899, 941,
 2299, 2911
 Simulation models, 106, 505, 1857,
 2201, 2923
 Siphons, 2753
 Skewness, 1508

- Slope stability, 2116, 2400
 Slopes, 281, 419, 2641
 Soil analysis, 1352
 Soil layers, 1352
 Soil liquefaction, 1352
 Soil mechanics, 1011
 Soil stabilization, 1588
 Soil stresses, 1352
 Solitary wave, 219, 624, 1073, 2479
 Sonar, 1508
 Spain, 204, 858, 984, 1323, 1330, 1411, 2784, 2896
 Spectral analysis, 524, 2536
 Stability, 1997, 2028, 2053, 2075, 2174, 2284, 2299, 2370, 2489
 Stability criteria, 2043
 Stabilization, 2791
 Standing waves, 151
 State-of-the-art reviews, 971, 2043
 Statistical analysis, 91, 756, 835, 1011, 1522, 2028, 2536
 Statistical data, 655, 956
 Statistics, 106
 Steady flow, 1140
 Steady state models, 929
 Stochastic processes, 292, 941, 2536
 Stoke's law, 17
 Storm surges, 999, 1493
 Storms, 566, 756, 956, 984, 1197, 1426, 1464, 1482, 1508, 1544, 1558
 Stratified flow, 2550, 2561
 Stress, 2418, 2692
 Structural behavior, 2075, 2355
 Structural design, 2129
 Structural failures, 2445
 Structural response, 2385, 2445
 Structural strength, 2102
 Submarine pipelines, 1464
 Surf beat, 1058, 1167
 Surf zone, 77, 151, 292, 377, 408, 419, 478, 539, 578, 612, 632, 705, 807, 999, 1058, 1167, 1182, 1295, 1382, 1646, 1661, 1704, 1774, 1833, 1959, 153501543
 Surface waves, 246, 512
 Suspended load, 1897
 Suspended sediments, 1129, 1452, 1603, 1646, 1661, 1704, 1842, 2707

 Taiwan, 1152, 2370, 2882
 Technology assessment, 971
 Theories, 181, 307, 588, 1073
 Thermal pollution, 2521
 Thermal power plants, 2521
 Three-dimensional analysis, 1689, 2284

 Three-dimensional flow, 705
 Three-dimensional models, 667, 858, 2574
 Tidal bores, 2589
 Tidal currents, 433, 858, 1227, 1508, 2536, 2666, 2707
 Tidal flats, 1788
 Tidal marshes, 2666
 Tidal power plants, 971
 Tidal waters, 2681, 2692, 2896
 Tides, 512, 2867
 Time series analysis, 350
 Topography, 1937, 2603, 2738
 Tracers, 1338, 1774
 Trends, 1
 Turbulence, 478, 743, 2550
 Turbulent boundary layer, 1661
 Turbulent diffusion, 1661, 1704, 2589
 Turbulent flow, 1646
 Two-dimensional models, 350, 505, 2991

 Uncertainty analysis, 1045
 Undertow, 705, 1833
 Undertown, 478
 Underwater structures, 2753
 United Kingdom, 1922
 Unsteady flow, 624, 914
 Uplift pressure, 2313

 Velocity distribution, 1661
 Velocity profile, 682, 743, 1368
 Vertical cylinders, 17
 Vortex shedding, 1310
 Vortices, 914, 2927

 Waste heat, 2521
 Wastewater treatment, 2753
 Water depth, 307, 419, 2469, 2911, 2979
 Water flow, 2013, 2589
 Water level, 999
 Water levels, 539
 Water pollution, 2615
 Water purification, 166
 Water supply systems, 2641
 Water tunnels, 718, 1084
 Water waves, 246, 433, 448, 682, 705, 732, 743, 1129, 1508, 1842, 2216
 Wave action, 166, 281, 782, 1113, 1464, 1482, 1631, 1803, 1868, 1911, 2189, 2242, 2284, 2340, 2370, 2400, 2469, 2603
 Wave attenuation, 363, 478, 492, 849
 Wave climatology, 204, 261, 2806, 1535 1543

- Wave crest, 17, 307, 871, 1020
- Wave defraction, 393, 2189
- Wave diffraction, 17, 47, 121, 433, 732, 929, 2216
- Wave dispersion, 578, 612
- Wave energy, 62, 106, 261, 292, 971, 1721, 1833, 2272, 2326, 2489, 2991
- Wave equations, 181
- Wave forces, 77, 914, 1084, 1140, 1227, 1280, 1295, 1310, 2144, 2201, 2257, 2313, 2355, 2418, 2430, 2445, 2479, 2504, 2784, 2911, 2966
- Wave generation, 91, 448, 612, 667, 698, 835, 941, 1098, 1544, 2991
- Wave groups, 204, 884, 984
- Wave height, 106, 136, 151, 307, 363, 419, 524, 553, 588, 667, 732, 807, 822, 871, 884, 899, 956, 1182, 1197, 1983, 2229, 2469, 2504
- Wave measurement, 47, 62, 136, 204, 322, 377, 524, 588, 667, 1152, 2229, 2355, 2991
- Wave pressure, 2159, 2340, 2489
- Wave propagation, 32, 62, 181, 350, 363, 377, 419, 512, 553, 929, 999, 1073, 2229
- Wave propatation, 246, 433
- Wave reflection, 47, 136, 219, 393, 553, 782, 1073, 1493, 1763, 1983, 2013, 2216, 2272, 2489
- Wave refraction, 121, 393, 433, 588, 732
- Wave runup, 17, 151, 219, 553, 644, 655, 795, 1167, 1763, 1857, 1922, 1983, 2013, 2053, 2129, 2370
- Wave spectra, 47, 62, 91, 261, 350, 492, 602, 612, 849, 929, 999, 1011, 1045, 2229
- Wave tanks, 632, 1482, 1588, 1952, 2550
- Wave velocity, 151, 377, 448, 524
- Waves, 2991
- Weirs, 335
- West Germany, 1788
- Wetlands, 2666
- Wind direction, 602
- Wind forces, 77, 261, 433, 632, 698, 929, 2550
- Wind velocity, 1098
- Wind waves, 512, 566, 602, 698, 1011, 1045, 1098, 2550

AUTHOR INDEX

Page number refers to first page of paper.

- Acinas, Juan R., 698
Aguilar Herrando, José, 1323, 2896
Aguilar, Jose, 1974
Ahrens, John P., 795
Alejo, M., 2479
Allsop, N. W. H., 281, 782
Aminti, Pierluigi, 770
Andersen, Ole Holst, 1603
Anglin, C. D., 2418, 2840
Anglin, C. David, 2385
Arcilla, A. S., 350
Arcilla, A. S., 463, 1382
Arenillas Parra, Miguel, 1330
Armanini, Aronne, 1129
Asano, Toshiyuki, 743
Auerbach, M. H., 1588
Awaya, Yoichi, 234
- Backhaus, J. O., 858
Baird, W. F., 2418
Baird, William F., 2385, 2416
Bakker, W. T., 718, 2825
Banno, Masato, 1868
Barnett, Michael R., 1493
Basco, David R., 682, 2589
Beil, N. J., 1482
Bendykowska, Genowefa, 612
Berenguer, José Ma, 1411
Bertolotti, Andrea, 2666
Bertotti, Luciana, 566
Bezuijen, A., 2159
Bijker, E. W., 1368
Bijker, Eco W., 2090
Blázquez, Rafael, 1352
Bodge, Kevin R., 1396
Boon, John D., 1508, 1618
Borden, G. W., 1588
Bowen, A. J., 1452, 1522
Bowen, Anthony J., 136
Bryden, I. G., 1020
Burcharth, H. F., 2284
Bürger, W., 2242
Burrows, R., 956
Byres, Ronald, 2189
- Campello Chorro, José L., 1323
Castel, David, 1676
Cavaleri, Luigi, 566
Chang, Jo Y. -H., 1464
Chang, S. G., 2370
Christodoulou, George C., 2561
Claassens, H., 2075
Clemens, Karen E., 1338
- Cooker, Mark, 624
Cortés Gimeno, Rafael, 1330
Costa, F. Vasco, 2966
Crowley, J. B., 181
- Daemrich, Karl-Friedrich, 322
Dai, G., 835
Dai, Guanying, 2469
Dally, William R., 807
Dalrymple, Robert A., 246, 2216
Davidson, D. D., 2416
Davis, Gregory A., 539
de Bruyn, C. A., 1368
De Luis, Jose E., 566
de Reus, J. H., 433
De Rouck, J., 2102
de Souza, Maria Helena Severo, 261
de Vriend, H. J., 1689
de Vroeg, J. H., 2825
Dean, Robert G., 807, 1558
Deb, Manas Kumar, 553
Dedeyne, R., 2102
Deguchi, Ichiro, 335, 1573
Deigaard, Rolf, 1603
del Río, J. G., 2615
Dette, H. H., 1721
Dette, Hans-Henning, 292
Dibajnia, Mohammad, 578
Dieckmann, Reinhard, 2681
Díez González, J. Javier, 1323, 1330
Diez Gonzalez, Jose Javier, 2784
Díez González, Jose Javier, 2896
Díez, J. J., 2615
Diez, Jose Javier, 1974
Dingemans, Maarten W., 32
Dodd, N., 732
Doering, J. C., 1452
Douglas, Barry, 2229
Douglass, S. L., 2806
Douglass, Scott L., 632, 2867
Drouin, Alain, 2272
- Easson, W. J., 1020
Easson, William J., 871
Economou, George D., 2561
Edge, B. L., 1588
Edge, Billy, 2416
Edge, Billy L., 2723
Egozcue, J. J., 350
Eisenberg, Y., 2753
Endo, Taiji, 2053, 2063, 2144
Enríquez, Javier, 1411
Escobar Paredes, Victor A., 2896

- Esteban Chapapria, Vicent J. de, 1323, 1330
 Fasano, R. A., 2753
 Feldmeth, C. Robert, 2666
 Fenaish, T. A., 1426
 Fisher, J. S., 1426, 1857
 Flick, Reinhard E., 2666
 Foda, Mostafa A., 1464
 Franco, Leopoldo, 770
 Fredsøe, Jørgen, 1603
 Frigaard, Peter, 2284
 Fritsch, D., 2707
 Führböter, Alfred, 2174
 Funke, E. R., 91, 106, 835

 Gadd, Peter E., 644, 2400
 Gao, Ming, 2469
 Gingerich, Kathryn J., 1182
 Girard, R. K., 106
 Goda, Yoshimi, 899
 Godo, Hitomi, 743
 Gofas, Th. C., 2753
 Goldsztejn, Eduardo, 2979
 Graber, Hans C., 492
 Grass, Anthony J., 363
 Gravens, Mark B., 1265
 Greated, C. A., 1020
 Greated, Clive A., 871
 Green, Malcolm O., 1508, 1618
 Griffiths, Matthew W. P., 871
 Grüne, Joachim, 2340
 Guarga, Rafael, 2979

 Haines, J. W., 1522
 Hallermeir, Robert J., 1197
 Hands, Edward B., 1911
 Hanson, Hans, 1265
 Hardy, Thomas A., 588
 Hashimoto, Noriaki, 62
 Hatheway, Darryl J., 2772
 Hattori, Masataro, 2144
 Hayashi, Kenjiro, 2923
 Hayashi, Kenjiro, 914
 Hedegaard, Ida Brøker, 1603
 Heimbaugh, Martha S., 795
 Herbich, John B., 2229
 Hettiarachchi, S. S. L., 782
 Hindes, F. S., 2753
 Hirayama, Ken-ichi, 1035
 Holthuijsen, L. H., 602
 Horikawa, Kiyoshi, 478, 1748, 2201
 Hosoi, Yoshihiko, 166
 Hotta, Shintaro, 151
 Hou, Ho-Shong, 1152
 Howell, Gary L., 2355

 Hsu, Tai-Wen, 121, 1631
 Huang, Jianwei, 1227
 Hudspeth, Robert T., 884
 Huntley, David A., 136
 Hwang, Sheng-Yeh, 2603

 Ifuku, Makoto, 1661
 Igarashi, Tatsuyuki, 1646
 Ikeno, Masaaki, 2326
 Imberger, J., 2626
 Inagaki, Keiji, 2144
 Instanes, Arne, 1997
 Isaacson, Michael, 2189
 Ismail, N. M., 2521
 Isobe, Masahiko, 393, 524
 Ito, Masahiro, 1544
 Iwagaki, Yuichi, 743
 Iwata, Koichiro, 2326

 Jamieson, Wayne W., 2257
 Jensen, Ole Juul, 756

 Kaczmarek, L., 1011
 Kakinuma, Tadao, 1661
 Katoh, Kazumasa, 1253
 Katsui, Hidehiro, 1280
 Kawata, Yoshiaki, 1310
 Kendall, Thomas R., 2129
 Kim, Young C., 971
 Kimura, Akira, 419, 655
 Kinose, Koichi, 1212
 Kjeldsen, Søren Peter, 667
 Klinting, P., 756
 Kobayashi, Nobuhisa, 1167
 Kobune, Koji, 62
 Komar, Paul D., 1238, 1338
 Kondo, Kosuke, 47, 2430
 Kostense, Jan K., 32
 Kraus, Nicholas C., 588, 1182, 1265, 1295
 Kriebel, David L., 17
 Krogstad, Harald Elias, 667
 Kröhn, J., 858
 Kubo, Masayoshi, 2952
 Kubota, Susumu, 151
 Kuo, Shih-Duenn, 2882
 Kyriacou, Andreas, 363

 Lai, C. P., 2313
 Langerak, A., 2692
 Larson, Magnus, 1295
 Latham, John-Paul, 2299
 Laustrup, C., 2159
 Law, Andrian W. -K., 1464
 Lee, Jiin-Jen, 2313
 Leendertse, Jan J., 2574, 2692

- Lee-Young, J. S., 1140
 Leidersdorf, Craig B., 2400
 Lewis, Lloyd, 971
 Lewis, Lloyd F., 2641
 Lin, Ming-Chung, 2603
 Lin, S. C., 2370
 Lionello, Piero, 566
 List, Jeffrey H., 1508
 Liu, Paul C., 1045
 Liu, Philip L. -F., 1911
 Liu, Shiao-Kung, 2574
 Lo, Jen-Men, 999
 Lorenz, Rene S., 705
 Losada, M. A., 1073, 2479
- McCormick, Michael E., 971
 McDougal, William G., 2400, 2445
 McGill, Preston G., 2445
 Machemehl, Jerry L., 644
 MacIntosh, K. J., 2840
 McMillen, Richard I., 2536
 Madsen, Ole Secher, 492, 849
 Madsen, P. A., 505
 Maeno, Yoshi-Hiko, 1842
 Magoon, Orville T., 2416, 2455
 Manikian, Victor, 644
 Mansard, E. P. D., 106, 835
 Mansard, Etienne P. D., 2257, 2385
 Marón, Adolfo, 204
 Martin, Paul A., 2216
 Martinez, F. M., 270
 Martínez, Felipe M., 1352
 Martínez Martínez, Jesus, 2738
 Massel, S. R., 1011
 Mather, D., 1020
 Matsumi, Yoshiharu, 2927
 Matsunaga, Nobuhiro, 234, 2550
 Medina, Josep R., 884, 941
 Medina, R., 1073, 2479
 Melby, Jeffrey A., 2445
 Miles, M. D., 91
 Mizuguchi, Masaru, 151
 Mizumura, Kazumasa, 2053, 2063
 Mogridge, Geoffrey R., 2257
 Möller, J. P., 1882
 Monso, J. L., 350
 Monsó, J. L., 463
 Moutzouris, C. I., 1959
 Murakami, Hitoshi, 166
 Murakami, Y., 1937
- Nadaoka, Kazuo, 1646
 Naeæss, Steinar, 1997
 Nairn, Robert B., 1818
 Nath, John H., 448
 Naverac, V. S., 270
- Negro Valdecantos, Vicente, 1437
 Nicholls, Robert, 1922
 Nielsen, Peter, 539, 1952
 Noguchi, Yuuji, 2144
- Ochi, Michel K., 2536
 Oelerich, Johannes, 292
 Ohishi, H., 1937
 Ohnaka, Susumu, 393
 Ohshimo, Tetsunori, 47, 2430
 Okamoto, Shunsaku, 2952
 Okayasu, Akio, 478
 Okushima, Shuji, 1212
 Olsen, Richard Bjarne, 667
 Osterthun, Manuela, 2681
 Ou, Shan-Hwei, 121, 1631
 Ouellet, Yvon, 2272
 Oumeraci, H., 2242
 Overton, M. F., 1426, 1857
 Ozaki, Akira, 408
- Papanicolaou, Panos, 377
 Park, San-Kil, 335
 Partenscky, H. W., 2242
 Partensckv. Hans Werner, 2681
 Partenscky, Hans-Werner, 2504
 Peregrine, D. H., 732
 Peregrine, Howell, 624
 Pilarczyk, K. W., 2043, 2116
 Pina, Gregorio Gómez, 984
 Poole, Alan B., 2299
 Poon, Ying-Keung, 492
 Pope, Joan L., 2455
 Pous, J., 1382
 Powell, K. A., 1763
 Pruszkak, Zbigniew, 1774
 Puntigliano, Fernando, 2979
- Quecedo Gutierrez, Manuel, 1437
- Radder, A. C., 433
 Raichlen, Fredric, 377
 Ramsden, Jerald D., 448
 Rauw, Charles I., 2416
 Readshaw, J. S., 106
 Ren, Rushu, 153501543
 Resio, Donald T., 929
 Rhodes, Perry E., 1197
 Ribberink, J. S., 1689
 Ribeiro, Carlos Eduardo Parente,
 261
 Rodriguez, I., 858
 Roelvink, J. A., 1736
 Rosati, Julie Dean, 1182
 Rosengaus, Moises Michel, 849
 Rossouw, J., 822

- Rubio, J., 1073
 Rugbjerg, M., 505
 Ruol, Piero, 1129
 Ryan, P. J., 2521
- Saeki, Hiroshi, 408, 1035
 Sakai, Shigeki, 1035
 Sakuramoto, H., 2791
 Salih, B. A., 956
 Sánchez-Carratala, Carlos R., 941
 Santás López, Jose C., 984
 Sasaki, Mikio, 408
 Sato, Shinji, 1748
 Sawaragi, Toru, 335, 1573
 Sayao, Otavio J., 1818
 Schade, Daniel, 322
 Schäffer, Hemming A., 1058
 Schlueter, Roger S., 2723
 Scholtz, D. J. P., 2075
 Schwab, David J., 2991
 Schwartz, R. A., 2626
 Scott, R. Douglas, 2385
 Scott, R. D., 2418
 Seikmoto, Tsunehiro, 47
 Sekimoto, Tsunehiro, 2430
 Seo, Seung Nam, 2216
 Serra Peris, Jose, 2784
 Seyama, Akira, 419, 2927
 Seymour, Richard J., 1676
 Sheng, Y. Peter, 2655
 Shibayama, Tomoya, 478
 Shigemura, Toshiyuki, 914, 2923
 Shimoda, Naokatsu, 2326, 2952
 Shiraishi, Naofumi, 2053, 2063
 Siefert, Winfried, 1788
 Sierra, J. P., 350, 463
 Simoen, R., 2855
 Simons, Richard R., 363
 Skyner, D., 732
 Sleath, J. F. A., 1140
 Sloan, Robert L., 2455
 Slotta, Larry S., 971
 Smallman, J. V., 281
 Smit, E. S. P., 2825
 Snook, M. W. G., 1020
 Sobey, Rodney J., 307
 Soler, E., 2615
 Sorensen, R. M., 1482, 2806
 Sorensen, Robert M., 2867
 Sparboom, Uwe, 2174
 Stephens, R. V., 281
 Stiassnie, M., 732
 Stive, Marcel J. F., 1736
 Strzelecki, Michael S., 1167
 Suh, Kyung Duck, 246
 Sumiya, M., 2791
- Sunamura, Tsuguo, 1295
 Svendsen, Ib A., 705, 1058
 Swart, D. H., 181, 1882
 Synolakis, Costas Emmanuel, 219, 553
- Taerwe, L., 2102
 Takahashi, Shigeo, 2489
 Takehara, Kosei, 234
 Takezawa, Mitsuo, 151
 Tallent, James R., 1833
 Tanaka, Hitoshi, 1803
 Tatavarti, Rao V. S. N., 136
 Tedesco, Joseph W., 2445
 Teisson, Ch., 2707
 Thompson, Alex C., 2013
 Thornton, E. B., 77
 Tickell, R. G., 956
 Tolman, Hendrik L., 512
 Tørum, Alf, 1997
 Toue, Takao, 1280
 Toyoshima, Osamu, 1983
 Treadwell, Donald, 2416
 Treadwell, Donald D., 2455
 Tsuchiya, Yoshito, 1310, 1544, 1833, 1868, 2589
 Tsuru, Masahito, 1212
 Tsuzuki, Susumu, 2201
 Tu, S. W., 2521
 Turcke, D. J., 2418
 Turcke, David J., 2385
 Twu, S. W., 2370
 Tzang, Shiao-Yih, 121
- Uda, T., 2791
 Uda, Takaaki, 2028
 Uda, T., 1937
 Ueno, Seizo, 1646
 Uliczka, K., 1721
 Ura, Masaru, 2550
- Van Damme, L., 2102
 van de Graaff, Jan, 2090
 Van den Bosch, Peter, 32
 van der Meer, J. W., 2116
 van Kesteren, W. G. M., 718
 Van Ryzin, Joseph, 2641
 van Vledder, G. Ph., 602
 Van Wyk, A. C., 2911
 Vandenbossche, D., 2855
 Vega, Luis, 2641
 Verslype, H., 2855
 Vidal, C., 1073
 Vidoar, A., 1382
 Visser, Paul J., 1897
 Vogel, J. A., 433

- Vold, Svein, 1997
Vongvisessomjai, Suphat, 1084
- Walker, James R., 2666
Walton, Todd L., Jr., 1911
Wang, Hsiang, 1493
Wang, Liang, 153501543
Wang, P. F., 2655
Warren, I. R., 505
Watanabe, Akira, 393, 578, 2201
Watanabe, M., 1937
Watts, George M., 2818
Webber, Norman, 1922
Weckmann, Javier, 2818
Weggel, J. R., 2806
Weggel, J. Richard, 632, 2867
Werner, Gosta, 612
Whitford, D. J., 77
Wiegel, R. L., 2521
- Wiegel, Robert L., 1
Wouters, J., 2159
Wright, L. Don, 1508
Wu, T. S., 2655
Wurjanto, Andojo, 1167
- Yamaguchi, Masataka, 1113
Yamamoto, Masato, 2053, 2063
Yamashita, Takao, 682, 1833, 2589
Yanagishima, Shin-ichi, 1253
Yang, Jihua, 2469
Yeend, John S., 2772
Yen, Kai, 153501543
Young, Ian R., 1098
Yu, Z. H., 718
- Zeidler, Ryszard B., 1704, 1774
Zwamborn, J. A., 2075, 2911
Zyserman, Julio A., 1603

CHAPTER 74

Dynamic Wave Setup

Jen-Men Lo, M. ASCE¹

Abstract

The wave setup for a given wave spectrum was re-evaluated with the radiation stress term including the low-frequency terms. This setup which is referred to here as "dynamic wave setup", was compared with the steady setup, which is generated by including only the non-periodic radiation stress terms.

The results of the study showed that the dynamic wave setup is greater than the steady wave setup, sometimes almost double its value. Therefore, the dynamic wave setup is important for engineering applications, particularly in the study of storm surges and coastal engineering problems.

Introduction

Longuet-Higgins and Stewart (1963) showed theoretically from their concept of radiation stress, and Bowen et al. (1968) verified it in the laboratory, that there is a water level setdown outside the surf zone followed by a water level setup within the surf zone because of the presence of the wave motion.

Longuet-Higgins and Stewart (1963) considered only the monochromatic waves, but Collins (1972), Battjes (1974), and Wu et al. (1978) re-evaluated wave setup by considering the radiation stress for a given spectrum.

The radiation stress derived for a wave spectrum should include the interaction between any wave component and itself as well as the interaction between any wave component and other wave components. However, the studies carried out by Collins (1972), Battjes (1974), and Wu et al. (1978) considered only the self-interaction terms.

Lo (1981) derived the radiation stress term for any given wave spectrum. In this derivation both non-periodic and long-period oscillation (low frequency) terms were included. The low-frequency terms were generated from the non-linear transfer of energy of the phase difference between different wave components.

The purpose of this study is to re-evaluate wave setup for a given wave spectrum with the radiation stress term including the low-frequency terms. This setup which is referred to here as "dynamic wave setup" was compared with the

¹ Research Scientist, Kuwait Institute for Scientific Research, Hydraulics and Coastal Engineering Group, P. O. Box 24885, 13109, Safat, Kuwait.

steady wave setup, which was generated by including only the non-periodic radiation stress terms.

Governing Equations for the Surf Beat Wave on a Sloping Bottom

The motion is considered irrotational and the fluid incompressible. Integrating the continuity and momentum equations from the bottom, $Z = -h$, to the free surface, $Z = \eta$ (water surface displacement), imposing the Leibnitz rule, and substituting the no-flow bottom boundary condition (BBC), the kinematic free surface boundary condition (KFSBC), and applying the time average over one incoming wave period one can obtain the governing equations for the sloping bottom surf beat wave. For convenience, only a uniform bottom slope will be considered.

Leibnitz Rule. The Leibnitz rule of differentiation will be used to obtain a derivative from within an integral. It is stated as follows

$$\int_{\alpha(x)}^{\beta(x)} \frac{\partial f(x,z)}{\partial x} dz = \frac{\partial}{\partial x} \int_{\alpha(x)}^{\beta(x)} f(x,z) dz - f(\beta,z) \frac{\partial \beta(x)}{\partial x} + f(\alpha,z) \frac{\partial \alpha(x)}{\partial x} \quad (1)$$

where $f(x, z)$ is any function; x is a variable of integration; z is a dummy variable of integration; α and β are limits of integration.

Boundary Conditions. At the bottom, $Z = -h$, a no-flow boundary condition exists. In vector form

$$\vec{V} \cdot \vec{n} = 0 \quad (2)$$

where

$$\vec{V} = u\vec{i} + v\vec{j} + w\vec{k} \quad (3)$$

$$\vec{n} = \frac{\left(\frac{\partial h}{\partial x} \vec{i} + \frac{\partial h}{\partial y} \vec{j} + \vec{k} \right)}{\sqrt{\left(\frac{\partial h}{\partial x} \right)^2 + \left(\frac{\partial h}{\partial y} \right)^2 + 1}} \quad (4)$$

(Unit vector normal to the bottom)

where $\vec{i}, \vec{j}, \vec{k}$ are unit vectors in the x, y, z directions; \vec{V} is the velocity vector and u, v, w are the x, y and z components of the velocity vector. BBC can be rewritten as

$$u \frac{\partial h}{\partial x} + v \frac{\partial h}{\partial y} + w = 0, \quad \text{at } z = -h(x,y)$$

At the free surface, the vertical velocity (w) must account for the changes in the instantaneous water surface (η)

$$w = \frac{D\eta}{Dt} = \frac{\partial\eta}{\partial t} + u \frac{\partial\eta}{\partial x} + v \frac{\partial\eta}{\partial y}, \quad \text{at } z = \eta \quad (5)$$

This is the KFSBC.

Continuity Equation. The general form of the continuity equation in three dimensions is

$$\frac{\partial\rho}{\partial t} + \frac{\partial\rho u}{\partial x} + \frac{\partial\rho v}{\partial y} + \frac{\partial\rho w}{\partial z} = 0 \quad (6)$$

Integrating each term with respect to depth between $Z = -h$ and $Z = \eta$, and imposing the Leibnitz Rule

$$\begin{aligned} \frac{\partial}{\partial t} \int_{-h}^{\eta} \rho dz - \rho_{\eta} \frac{\partial\eta}{\partial t} - \rho_{-h} \frac{\partial h}{\partial t} + \frac{\partial}{\partial x} \int_{-h}^{\eta} \rho u dz - (\rho u)_{\eta} \frac{\partial\eta}{\partial x} - (\rho u)_{-h} \frac{\partial h}{\partial x} + \\ \frac{\partial}{\partial y} \int_{-h}^{\eta} \rho v dz - (\rho v)_{\eta} \frac{\partial\eta}{\partial y} - (\rho v)_{-h} \frac{\partial h}{\partial y} + (\rho w)_{\eta} - (\rho w)_{-h} = 0 \end{aligned} \quad (7)$$

Invoking the boundary conditions BBC and KFSBC, the above equation simplifies to

$$\frac{\partial}{\partial t} \int_{-h}^{\eta} \rho dz - \rho_{-h} \frac{\partial h}{\partial t} + \frac{\partial}{\partial x} \int_{-h}^{\eta} \rho u dz + \frac{\partial}{\partial y} \int_{-h}^{\eta} \rho v dz = 0 \quad (8)$$

Considering the depth (relative to still water level) as constant in time, and the problem as two-dimensional (no dependency on the y - direction), the above equation becomes:

$$\frac{\partial}{\partial t} \int_{-h}^{\eta} \rho dz + \frac{\partial}{\partial x} \int_{-h}^{\eta} \rho u dz = 0 \quad (9)$$

Consider the horizontal water particle velocity as the superposition of two components,

$$u = u_I + u_s \quad (10)$$

where

u_I = the horizontal water particle velocity of the incoming wave

u_s = the horizontal water particle velocity of the surf beat wave which is uniform over depth since the water depth is relatively shallow in comparison to the surf beat wave length.

Thus, for a fluid of constant density ρ , the continuity equation becomes

$$\frac{\partial}{\partial t}(h + \eta) + \frac{\partial}{\partial x}u_s(h + \eta) + \frac{\partial}{\partial x} \int_{-h}^{\eta} u_I dz = 0 \quad (11)$$

The time averages are defined

$$\bar{F} = \frac{1}{T} \int_0^T F dt \quad (12)$$

then

$$F_s = \bar{F}_s = \frac{1}{T} \int_0^T F_s dt$$

where T is the incoming wave period, and F_s represents a general surf beat variable. Time averaging the continuity equation, we obtain

$$\frac{\partial \bar{\eta}}{\partial t} + \frac{\partial}{\partial x}u_s(h + \bar{\eta}) + \overline{\left(\frac{\partial}{\partial x} \int_{-h}^{\eta} u_I dz\right)} = 0 \quad (13)$$

where $\bar{\eta} = \eta_s$ is the water surface displacement of the surf beat wave. The time-averaged water surface displacement of the incoming wave, $\bar{\eta}_I$, is zero.

Following the definitions of Phillips (1966) for the total flux

$$M_x = \overline{\int_{-h}^{\eta} \rho u_I dz} \quad (14)$$

and for the mean transport velocity

$$u_I = \frac{M_x}{\rho(h + \eta)} \quad (15)$$

The continuity equation can be written as

$$\frac{\partial \eta_s}{\partial t} + \frac{\partial}{\partial x}(u_s + u_I)(h + \eta_s) + \frac{\partial}{\partial x}(\overline{u_I \eta_I})_{z=0} = 0 \quad (16)$$

where

$$\frac{\partial}{\partial x}(u_s + u_I)\eta_s \ll \frac{\partial \eta_s}{\partial t}$$

The final result is then

$$\frac{\partial \eta_s}{\partial t} + \frac{\partial}{\partial x} (u_s + u_I)h + \frac{\partial}{\partial x} (\overline{u_I \eta_I})_{z=0} = 0 \quad (17)$$

Equation of Motion. Without considering the shear stresses, the general form of the equations of motion are:

x Direction.

$$\frac{\partial u}{\partial t} + \frac{\partial u^2}{\partial x} + \frac{\partial uv}{\partial y} + \frac{\partial uw}{\partial z} = \frac{1}{\rho} \frac{\partial P}{\partial x} \quad (18)$$

z Direction.

$$\frac{\partial w}{\partial t} + \frac{\partial uw}{\partial x} + \frac{\partial vw}{\partial y} + \frac{\partial w^2}{\partial z} = -\frac{1}{\rho} \frac{\partial P}{\partial z} - g \quad (19)$$

where p = pressure, and g = gravitational constant.

Following the same procedure as outlined before the final equation of motion for the case of two dimensional sloping bottom surf beat wave becomes

$$\frac{\partial (u_s + \overline{u_I})h}{\partial t} = -gh \frac{\partial \eta_s}{\partial x} - \frac{1}{\rho} \frac{\partial S_{xx}}{\partial x} - \frac{\partial}{\partial t} (\overline{u_I \eta_I})_{z=0} \quad (20)$$

where

$$S_{xx} = \rho \int_{-h}^0 (\overline{u_I^2 - w_I^2} dz) + \frac{1}{2} \rho g \overline{\eta^2} \quad (21)$$

It should be noted that the sloping bottom surf beat wave problem is governed by equation of motion (Eq. 20), and the continuity equation (Eq. 17).

Irregular Wave Conditions

The irregular sequence of linear waves can be represented as an infinite sum of simple harmonic waves

$$\eta(x, t) = \sum_n a_n \cos(k_n x - \sigma_n t + \epsilon_n) \quad (22)$$

where

$$a_n = \sqrt{2\rho_\eta(\sigma)\Delta\sigma}$$

$P_\eta(\sigma)$ = the energy density spectrum of the irregular sea, varying with wave angular frequency σ , and

ϵ_n = the phase angle (radians) for the n th wave component.

When small amplitude wave theory is used to estimate the flow regime in a wave system from the surface profile, the linear relationship between the surface profile and the velocity potential results in

$$\phi(x, z, t) = - \sum_n \frac{a_n g}{\sigma_n} \frac{\cosh k_n (h+z)}{\cosh k_n h} \sin(k_n x - \sigma_n t + \epsilon_n); \quad (23)$$

the dispersion relationship is given by

$$\sigma_n^2 = g k_n \tanh k_n h \quad (24)$$

also the horizontal and vertical water particle velocity components are given by

$$u(x, z, t) = \sum_n \frac{a_n k_n g}{\sigma_n} \frac{\cosh k_n (h+z)}{\cosh k_n h} \cos(k_n x - \sigma_n t + \epsilon_n) \quad (25)$$

and

$$w(x, z, t) = \sum_n \frac{a_n k_n g}{\sigma_n} \frac{\sinh k_n (h+z)}{\cosh k_n h} \sin(k_n x - \sigma_n t + \epsilon_n) \quad (26)$$

After some algebraic manipulation the following equations result:

$$\eta^2 = \sum_{n=1}^N a_n^2 \cos^2 \theta_n + \sum_{m=1}^{N-1} \sum_{n=m+1}^N a_m a_n [\cos(\theta_m - \theta_n) + \cos(\theta_m + \theta_n)], \quad (27)$$

$$u^2 = \sum_{n=1}^N A_n^2 \cos^2 \theta_n + \sum_{m=1}^{N-1} \sum_{n=m+1}^N A_m A_n [\cos(\theta_m - \theta_n) + \cos(\theta_m + \theta_n)], \quad (28)$$

$$w^2 = \sum_{n=1}^N B_n^2 \sin^2 \theta_n + \sum_{m=1}^{N-1} \sum_{n=m+1}^N B_m B_n [\cos(\theta_m - \theta_n) + \cos(\theta_m + \theta_n)] \quad (29)$$

where N is the total number of the wave components, and

$$\theta_n = k_n x - \sigma_n t + \epsilon_n$$

$$A_n = -a_n \sigma_n \frac{\cosh k_n(h+z)}{\sinh k_n h}$$

$$B_n = -a_n \sigma_n \frac{\sinh k_n(h+z)}{\sinh k_n h}$$

The sum of the phases are not considered for the surf beat wave problem, because they are in the high frequency region. Then

$$\begin{aligned} S_{xx} &= \frac{\rho}{z} \sum_{n=1}^N \frac{a_n^2 \sigma_n^2}{\sinh^2 k_n h} h + \frac{1}{4} \rho g \sum_{n=1}^N a_n^2 \\ &+ \rho \sum_{m=1}^{N-1} \sum_{n=m+1}^N \frac{a_m a_n \sigma_m \sigma_n \sinh(k_m - k_n)h}{(k_m - k_n) \sinh k_n h \sinh k_m h} \cos(\theta_m - \theta_n) \\ &+ \frac{\rho g}{z} \sum_{m=1}^{N-1} \sum_{n=m+1}^N a_m a_n \cos(\theta_m - \theta_n) \end{aligned} \tag{30}$$

and

$$\overline{(u_I \eta_I)}_{z=0} = \frac{1}{2} \sum_{m=1}^N \sum_{n=1}^N a_m a_n \sigma_n \frac{\cosh k_n h}{\sinh k_n h} \cos(\theta_m - \theta_n) \tag{31}$$

Method of Solutions

The governing equations are

1. Equation of Motion

$$\frac{\partial q}{\partial t} = -gh \frac{\partial \eta_s}{\partial x} - \frac{1}{\rho} \frac{\partial S_{xx}}{\partial x} - \frac{\partial}{\partial t} \overline{(u_I \eta_I)}_{z=0} \tag{32}$$

2. Continuity Equation

$$\frac{\partial \eta_s}{\partial t} + \frac{\partial q}{\partial x} = - \frac{\partial}{\partial x} \overline{(u_I \eta_I)}_{z=0} \tag{33}$$

where

$$q = (u_s + u_l)h$$

The complete mathematical solution of these equations is complicated. However, these equations can be solved numerically by applying finite difference techniques to the method of characteristics. This procedure accounts for bottom slope (wave reflection) and the transient nature of the problem.

Due to the depth variations and associated changes in the slopes of the characteristic lines, the characteristic lines in the x - t plane form a curved network and the results require interpolation to give values on a regular rectangular grid system. This problem can be resolved through the introduction of the following dimensionless variables, which will transform the curved characteristics to straight lines:

$$\begin{aligned}
 1. \quad Y &= \frac{\sqrt{x}}{x_2} \\
 2. \quad t' &= \frac{t}{T} \\
 3. \quad Z &= \frac{\eta_s C_2 \sqrt{Y}}{U^2 T} \\
 4. \quad Q &= \frac{q}{U^2 T \sqrt{Y}} \\
 5. \quad r &= 1 - \sqrt{\frac{h_1}{h_2}} \\
 6. \quad F_1 &= \frac{1}{u^2} \left[\frac{1}{\rho} \frac{\partial S_{xx}}{\partial x} + \frac{\partial}{\partial t} (u_l \eta_l)_{z=0} \right] \\
 7. \quad F_2 &= - \frac{C_2}{u^2} \left[\frac{\partial}{\partial x} (u_l \eta_l)_{z=0} \right]
 \end{aligned} \tag{34}$$

where

$$T = (x_2 - x_1) / \bar{C}$$

$$\bar{C} = (C_1 + C_2) / z$$

$$C_1 = \sqrt{g h_1} = \sqrt{g m x_1}$$

$$C_2 = \sqrt{g h_2} = \sqrt{g m x_2}$$

$$U = 0.22815 \text{ gm } h_{b(max)}$$

x_1 is the distance from shore ($x = 0$) to the wall boundary; x_2 is the distance from shore to the offshore boundary, and m is the beach slope.

By using the above transformations, the equation of motion and continuity equation are rewritten in the form

$$\frac{\partial Q}{\partial t'} + \gamma \left[\frac{\partial z}{\partial Y} - \frac{z}{2Y} \right] = - \frac{F_1}{\sqrt{Y}} \quad (35)$$

$$\frac{\partial z}{\partial t'} + \gamma \left[\frac{\partial Q}{\partial Y} - \frac{Q}{2Y} \right] = - \frac{F_2}{\sqrt{Y}} \quad (36)$$

The sum of these equations gives

$$\frac{d(Q+z)}{dt'} = \frac{\gamma}{2Y} [z-Q] - \frac{F_1}{\sqrt{Y}} - F_2 \sqrt{Y} \quad \text{for } \gamma = \frac{dY}{dt'} \quad (37)$$

and the difference of these equations gives

$$\frac{d(Q-z)}{dt'} = \frac{\gamma}{2Y} [z+Q] - \frac{F_1}{\sqrt{Y}} + F_2 \sqrt{Y} \quad \text{for } \gamma = - \frac{dY}{dt'} \quad (38)$$

A path in the Y, t' plane having a constant slope $\pm\gamma$ is the characteristic line and the values of $Q \pm Z$ along such lines are in accordance with equations 37 and 38. These equations are solved by finite different methods.

1. *Boundary Condition.* At the shore, where the water depth equals zero, this is a singular point. For convenience, a wall will be assumed for the calculations, i.e., the no-flow boundary condition at the wall is $q = 0$. In deep water, the forcing function of the surf beat wave is very small. Therefore, the boundary condition at offshore is a radiative condition; the surf beat wave will propagate offshore and no surf beat wave will enter the system under consideration from offshore.
2. *Initial Condition.* The sloping bottom surf beat problem is a transient problem. The transient nature is due to the increase in the surf beat wave height during propagation toward shore under the action of the forcing function, S_{xx} . At time zero, no wave occurs on the water surface, then later an incoming wave group propagates from infinity to shore with a surf beat wave force at the speed of the incoming wave velocity due to the forcing function induced by the incoming wave.
3. *Changing Breaking Zone.* A spilling wave breaking was assumed in this model, the incoming wave breaking height and local depth are related by

$$a_b = kh$$

The value of k is constant. In this study, the constant k will be taken as 0.39 and the wave height in the surf zone will depend only on the water depth. For an irregular wave field, the location of wave breaking will vary with the water depth. Therefore, the wave breaking process occurs in an area instead of at only one location as the regular wave breaking process.

Comparison of the Steady Wave Setup with the Surf Beat Wave Simulation Model

A given deep water wave spectra and the surf beat wave simulation model is applied to compare the difference between the surf beat wave and the steady wave setup. Figure 1 shows the assumed deep water wave spectra. The width of the energy frequency band ϵ defined by Rice (1945) is equal to 0.16. The incoming wave periods range from 8 to 12 seconds, and ten wave components with equal frequency increment are selected from the given spectrum. The significant wave height is 4.76 ft. In the simulation model, the bottom slope is 0.02, the offshore boundary water depth is 80 ft and the shore boundary water depth is 1.2 ft. The time step is 1.383 s.

**SPECTRUM NO. 2
SIGNIFICANT WAVE HEIGHT = 4.76 FEET
WAVE PERIODS FROM 8 TO 12 SECONDS
WIDTH OF THE FREQUENCY BAND = 0.16**

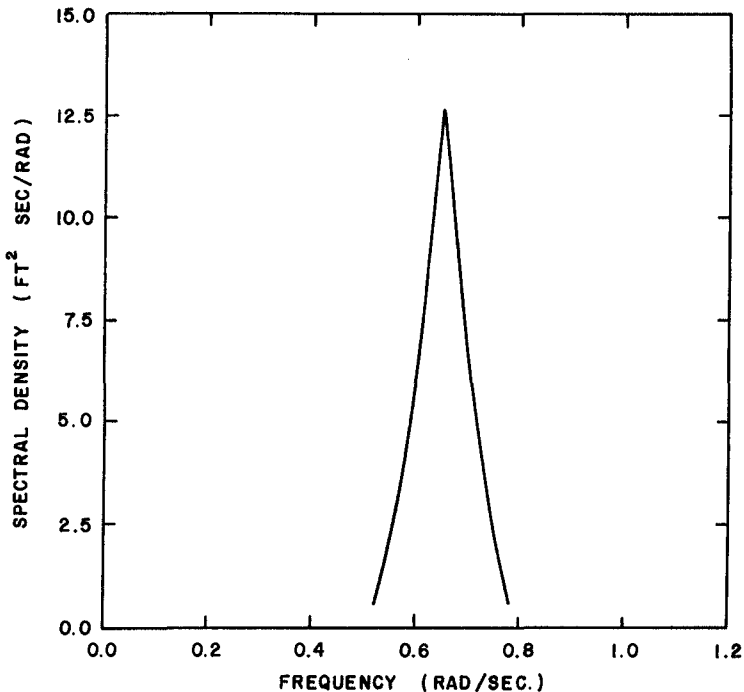


Figure 1. Deep water incoming wave spectrum for the study of the correlation between the surf beat and the wave envelope.

Figure 2 presents the comparisons of the steady wave setup with the surf beat wave on the shore boundary, where the steady wave setup is calculated from

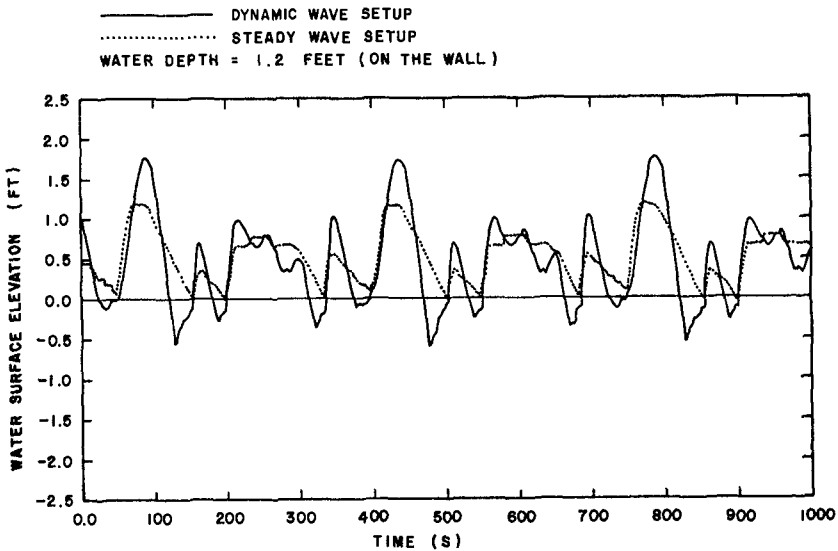


Figure 2. Comparison of the steady wave setup with the dynamic wave setup (simulated by using the wave spectrum in Figure 1).

$$\bar{\eta} = -\frac{K^2 h_b}{16} - \frac{\frac{3}{8} K^2}{1 + \frac{3}{8} K^2} (h_1 - h_b) \quad (39)$$

and h_1 is the water depth at the shore boundary, h_b is the wave breaking depth, K is a constant (here it is 0.78). It is clear that the steady setup and the surf beat wave are almost in phase; however, the crest of the surf beat wave is higher than the steady wave setup height. This setup due to the existence of the surf beat wave is referred to as the "dynamic wave setup", because it includes the contribution from both the non-periodic and low frequency radiation stress terms, and the steady wave setup is generated by including only the non-periodic radiation stress terms.

Conclusions

The results of the study showed that the dynamic wave setup is greater than the steady wave setup, sometimes almost double its value. This is due to the existence of the surf beat wave. Therefore, the dynamic wave setup is important for engineering applications, particularly in the study of storm surges and coastal engineering problems.

References

- Battjes, J. A. 1974. Computation of set-up, longshore currents run-up and overtopping due to wind-generated waves. Communications of Hydraulics Department of Civil Engineering, Delft University of Technology, (Holland), Report No. 74-2.
- Collins, J. I. 1972. Prediction of shallow-water spectra. *Journal of Geophysical Research*, **77**(11):2693-2707.
- Collins, J. I. 1972. Longshore currents and wave statistics in the surf zone, U. S. Government Report.
- Lo, Jen-Men. 1981. Surf beat : numerical and theoretical analyses. Ph.D. dissertation, Department of Civil Engineering, University of Delaware, Newark, Delaware, USA.
- Longuet-Higgins, M. S. and R. W. Stewart. 1963. A note on wave set-up. *Journal of Marine Research*, **21**:4-10.
- Rice, S. O. 1945. The mathematical analysis of random noise. *Bell System Technical Journal*, **24**:46-156.
- Wu, F. H. Y., M. A. Tayfun and J. I. Collins. 1978. Singular and spectral wave set-up models. Tetra Tech Report, TC 3205-02, California, USA.

CHAPTER 75

Pore pressure induced by wind waves in sand bed

S.R. Massel * and L. Kaczmarek **

Abstract

The two projects (LUBIATOWO 79 and LUBIATOWO 86) were aimed at study pore pressure behaviour in natural sand bed in the coastal zone of the Baltic sea under the action of storm waves. During both projects, the wave induced pore pressures at the various levels in the sea bed were measured. The collected data were used to verify the applicability of the various theoretical approaches. In the conclusion, the range of the application of the particular analytical method is given.

1. Introduction

The problem of wave induced pressures and stresses in natural sea beds is important with regard to the design of foundations for various ocean and nearshore structures, such as gravity type breakwaters, offshore oil storage tanks and drilling rigs. The subject is also important when one considers the floatation of buried pipelines and the burial of rubble mounds by waves.

The wave-induced flow in a porous bed experiences a flow resistance and transmits forces, seepage forces, to the soil skeleton. From a hydrodynamic point of view the flow induced by waves in a porous bed is of interest since energy dissipation, i.e., wave attenuation, is associated with this flow. Early papers (Putnam, 1949; Reid and Kajiura, 1957; Liu, 1973; Moshagen and Tørum, 1975) have focused on a permeable sea bed with a fixed rigid grain skeleton. Moshagen and Tørum (1975) considered the wave-induced flow in a porous medium under the assumption of a compressible pore fluid but an incompressible soil. They found that the inclusion of pore fluid compressibility in the analysis of wave-induced pore pressures in a porous soil significantly altered the vertical seepage forces acting on the soil.

Yamamoto et al. (1978) have developed a quasi-static model of a poro-elastic sea bed using the equations developed by Biot (1941). They obtained solutions which, when best fit to laboratory data of pore pressure, showed reasonable

* Professor, Director of Institute of Hydroengineering, 80-288 Gdańsk, Poland.

** Research Assistant, Institute of Hydroengineering, 80-288 Gdańsk, Poland

for both magnitude and phase. Mei and Foda (1980) have shown that the boundary layer approximation well known in fluid dynamics, greatly facilitates the solution of Biot's equations for a variety of boundary conditions.

However, besides the numerous theoretical solutions, the published laboratory and field data are very scarce. Dunlap et al. (1978), Bennett and Faris (1979), and Cross et al. (1979) have presented the results of the experiments on the pore pressure generation in the sediments of Mississippi and coastal zone of Pacific. However, they are mainly related to the long-term changes. The relation of the observed pressure to the surface oscillations was not considered. The major objective of the present study is to describe the field measurement projects, i.e. LUBIATOWO 79 and LUBIATOWO 86 which were aimed at studying pore pressure behaviour in natural sand bed in the coastal zone of the Baltic Sea. The pore pressure measuring system is described and experimental results are compared with results of various analytical approaches.

2. Field experiments

2.1. Scope of the work

The field experiments were carried out at the Coastal Research Station in Lubiatowo (Poland) in the Southern Baltic (water depth $h \approx 6 \div 7$ m).

A set of over one hundred records were taken for various wave conditions at one profile. Simultaneous measurements of the sea surface oscillations, water pressures at two points in the water layer and pore pressures at four points in the soil layer were carried out (Fig. 2.1).

2.2. Porous layer characteristics

According to the geological information in the vicinity of the point of measurements, the thickness of the rather uniform sand is equal to ~ 6.5 m. The soil is of fine-grained type ($D_{10} = 0.135 \cdot 10^{-3}$ m, $D_{20} = 0.135 \cdot 10^{-3}$ m, $D_{60} = 0.150 \cdot 10^{-3}$ m, $D_{90} = 0.180 \cdot 10^{-3}$ m). Because the uniformity coefficient is less than 6 and the contents of the fraction $\leq 0.074 \cdot 10^{-3}$ m is less than 5%, the fine-grained sand can be classified as a poorly graded and fairly clean.

The density of soil or the porosity was not measured "in situ". Thus, only some estimation can be made. For very dense packing the porosity is about 26%, while for very loose it is about 47%. The large forces which were needed to push the pore pressure gauge indicated a rather dense packing of the sand at the measuring profile. Therefore, the porosity of sand is likely to be in the range 30 \div 40%.

Moreover, the experimental data on the permeability of the bed material were lacking. Thus, we adopted an empirical formulae to estimate the permeability from the grain-size distribution characteristics. The conclusion from these estimates is that the permeability coefficient is in the range of $10^{-5} \div 10^{-4}$ m/s.

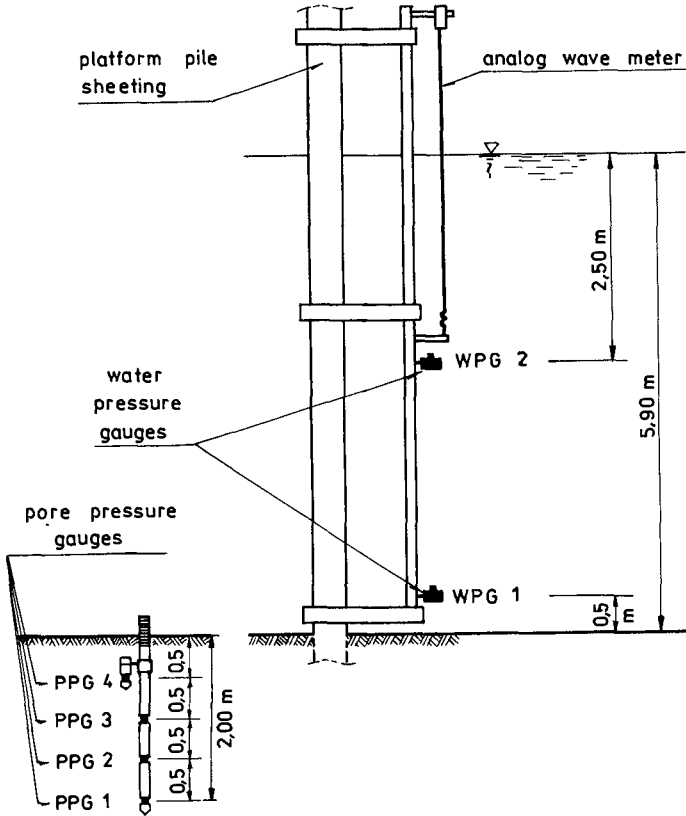


Fig. 2.1. Measurement gauges lay-out

2.3 Instrumentation and measurements

All sensors were arranged in one profile and the measurement signals were transferred by cables to the Station building on shore. Due to access convenience, the gauges were attached to a framework fixed to the sheet-pile section of the platform.

The data were recorded in the real time in digital form. The system of transmission and acquisition of data consists of the modules of PCM transmitter and receiver, Camac system, microcomputer BIZON 580, PC computer and analog and digital recorder. The technical description of the instrumentation and transmission modules can be found elsewhere (Massel and Moshagen, 1980, Kaczmarek, 1987) and it will not be repeated here.

3. Statistical and spectral analysis of data

The surface waves observed in the coastal zone are the waves caused by the wind and then propagating under the restoring force of gravity. Under the assumption of the narrow-band spectrum and uniform distribution of the random phase, the surface ordinates a Gaussian distribution (Phillips, 1977). Such assumptions is expected to be realistic for small amplitude waves, specially in the deep water. However, the statistical analysis of the collected records indicates that the wave motion can be treated as nearly Gaussian process. Therefore:

$$p(\zeta) = p_n(\zeta) \left\{ 1 + \frac{\gamma_1}{3!} H_3 \left(\frac{\zeta}{\sigma_\zeta} \right) + \frac{\gamma_2}{4!} H_4 \left(\frac{\zeta}{\sigma_\zeta} \right) + \dots \right\} \quad (3.1)$$

where $p_n(\zeta)$ - Gaussian distribution, γ_1 - skewness, γ_2 - kurtosis, and $H(\cdot)$ - Hermitte polynomial. In fact γ_1 and γ_2 are both small values for the surface waves and the pore pressure. This is clearly demonstrated in Fig. 3.1. in

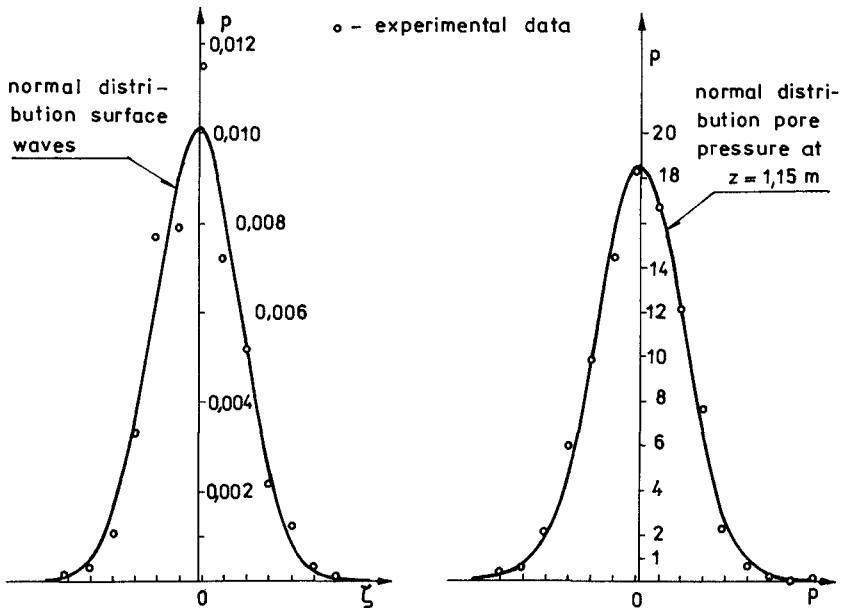


Fig. 3.1. Probability density distribution for surface waves and pore pressure.

which the corresponding probability density distributions are compared.

For the farther analysis we assume additionally that the system: surface waves - pore pressure is the linear system. Hence:

$$S_p(\omega) = |H(\omega)|^2 \cdot S_\zeta(\omega) \tag{3.2}$$

in which:

- $S_\zeta(\omega)$ - spectral density for the surface elevation,
- $S_p(\omega)$ - spectral density for the pore pressure, and
- $H(\omega)$ - transfer function.

As the empirical spectral density functions are known, the transfer function can be easily obtained. In the Figs. 3.2 and 3.3, the function $H_{p\zeta}(\omega)$ for the pore-pressure gauges at two points: $z = -1.0$ m (one meter below the bottom surface) and $z = -1.5$ m (one and half meter below the bottom surface). As should be expected, the function $H_{p\zeta}(\omega)$ is the decreasing function of the frequency. It should be noted, that during the measurements, the spectral peak frequency for the surface waves was in the interval of $0.80 \leq \omega_p \leq 1.50$ [rd/s], while the mean wave heights (\bar{H}) were of order $(0.50 \div 1.5$ m).

The calculations of the coherence function $\hat{\delta}_{p\zeta}^2$ (not shown here) indicate that the high values of the $\hat{\delta}_{p\zeta}^2$ function are related to the frequency band:

$$(0.6 \div 0.7) \leq \frac{\omega}{\omega_p} \leq (1.8 \div 2.) \tag{3.3}$$

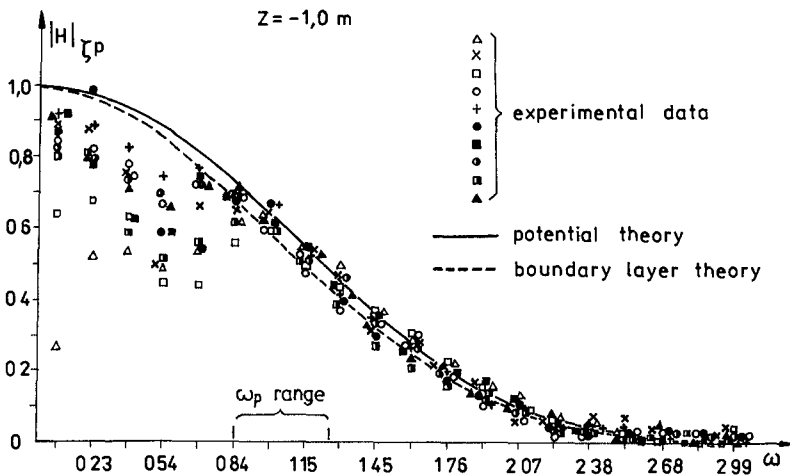


Fig. 3.2. Transfer function $H_{p\zeta}(\omega)$ for pressure gauge at $z = -1.0$ m

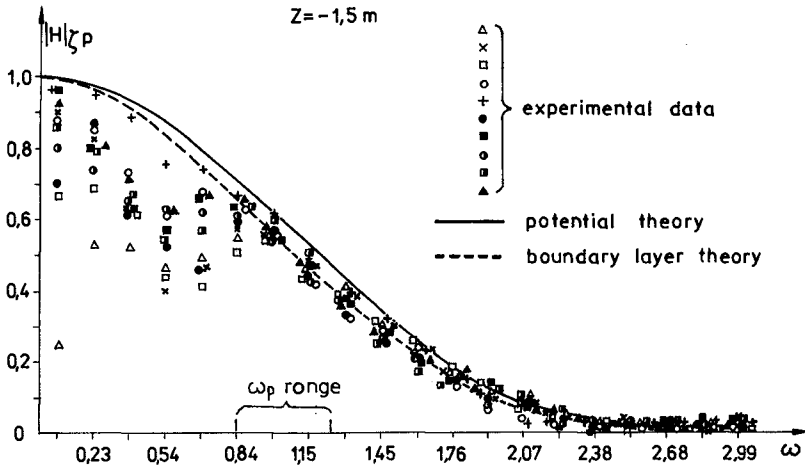


Fig. 3.3. Transfer function $H_{pz}(\omega)$ for pressure gauge at $z = -1.5$ m

Outside that band the value of the coherence function is very small. Thus, the usefulness of the theoretical linear model for the pore-pressure decaying is restricted to the frequency band given above.

4. Validity of the potential theory approach

In order to simplify the analysis we assume that the regular long-crested wave with a frequency ω is propagating on the constant water depth. A homogeneous isotropic sediment is considered which has a constant thickness ($h_n - h$) on a rigid and impermeable bed rock h - water depth, h_n - depth of nonpermeable bed/.

The x axis is taken on the sea surface and the positive direction of the z axis is vertically upward.

We assume, that the soil skeleton obeys Hooke's law, i.e. the soil has linear, reversible isotropic, nonretarded mechanical properties. The exact solution for the pore-water pressure, the displacements, and the effective stresses in such elastic bed induced by water waves is based on the consolidation theory developed by Biot (1941). Since a complete description of the solution is given in the original paper, as well as in many text books (e.g. Verruijt, 1969), it will not be repeated here.

The general solution simplifies considerably in the special case, when $G/E'_w \rightarrow 0$, in which G - shear modulus of soil, i.e.

$$G = \frac{E_s}{2(1+\nu)} \quad (4.1)$$

where E - Young's modulus and ν - Poisson ratio.

The apparent bulk modulus of pore-water containing a some amount of air (E'_w) is related to the true bulk modulus of elasticity of water ($E_w = 2.3 \cdot 10^9$ N/m²) by the relation:

$$\frac{1}{E'_w} = \frac{1}{E_w} - \frac{1-S_r}{P_o} \quad (4.2)$$

where S_r - the degree of saturation and P_o is the absolute pore-water pressure.

The condition $G/E'_w \rightarrow 0$ corresponds to the soil completely saturated with pore-water which does not contain gas. Since the value of G for the fine sand as in LUBIATOWO experiments is about $10^7 \div 10^8$ N/m², the stiffness ratio, G/E'_w becomes:

$$G/E'_w \approx 10^{-2} \div 10^{-1} \quad (4.3)$$

The general solution of the boundary value problem under the condition $G/E'_w \rightarrow 0$ yields (Yamamoto et al., 1978; Massel, 1981):

$$\nabla^2 p = 0 \quad (4.4)$$

and

$$p \approx \cosh k(z+h_n), \quad (4.5)$$

in which k - wave number related to the frequency ω by the classical dispersion relation.

The result (4.4) is the same as that obtained by Massel (1976) (see also Putnam, 1949, Reid and Kajiura, 1957) who assumed that the soil is rigid and water is incompressible (the potential solution). The pressure attenuation for this case is small and independent of the permeability of the soil. From the theory given in Massel' (1976) paper, the following transfer function can be deduced:

$$H_{p\zeta}(\omega) = \frac{\cosh k(z+h_n)}{\cosh k(h_n-h) \cdot \cosh kh} \quad (4.6)$$

when the pore-pressure is expressed in the water column. The solution (4.6) is shown in the Figs. 3.3 and 3.4 by the solid lines. They confirm the general agreement between theory and experiment; especially in the frequency band, in which the coherence function $\hat{f}^2 \geq 0.75$. Out of this range, for the low frequencies, the experimental transfer function is smaller than the theoretical one. Reason for such behaviour is not quite clear.

5. Others theoretical solutions

The solution of Biot's equations for the various boundary conditions is greatly facilitated by the boundary layer approximation introduced by Mei and Foda (1980).

In this approximation, two regions with different physical mechanisms are distinguished. In the interior of the soil the water and solid skeleton velocities are assumed to be of the same order. On the other hand, near the bottom surface, the drainage is much easier and relative fluid velocity is higher. The solution of the problem consists of the solution of the typical elasto-static problem and the boundary layer correction being appreciable only within this layer.

The results of the calculation, according Mei and Foda (1980) approximation, are shown in Figs. 3.3. and 3.4. by the dotted lines. The agreement with the experimental data is quite good.

It should be noted that the calculations using the full Yamamoto et al. (1978) solution for true G/E'_w value were carried out. The results of calculations are in complete agreement with those of the boundary layer approximation; therefore they are not shown in Figs. 3.3 and 3.4.

6. Conclusions

In recent years the understanding of the interaction of the wave motion and the porous sea and the ability to predict the pore-pressure has increased considerably. A lot of the theoretical solutions were obtained. They include the effects of the stiffness of porous medium and the bulk modulus of water elasticity on the pore pressure attenuation, displacements and stresses in the porous media. However, the field data are not numerous. In the paper, the two field experiments were reported. The pore pressure attenuation was measured at a few levels in the porous media under the wind waves action. The collected data were processed and the statistical and spectral characteristics were found. The comparison of the experimental data with the various theoretical solutions demonstrates that the boundary layer approximation and the full Yamamoto et al. (1978) solutions properly reflects the observed physical mechanisms. The potential theory only slightly overpredicts the experimental values. However, it should be noted that this conclusion is true for the soil conditions similar to that in LUBIATOWO experiments (fine-grained sand).

7. References

- Bennett, R.H., and Faris, J.R. (1979). "Ambient and dynamic pore pressure in fine-grained submarine sediments: Mississippi Delta". Appl. Ocean Res., 1(3).
- Biot, M.A. (1941). "General theory of three-dimensional consolidation". Jour. Appl. Phys., 12, 155-164.

- Cross, R.H. et al. (1979). "Attenuation of wave-induced pore pressure in sand". Proc. Speciality Conf. Civil Eng. in Oceans. San Francisco.
- Dunlap, W.A. et al. (1978). "Pore pressure measurements in underconsolidated sediments. Offshore Techn. Conf., No 3168.
- Kaczmarek, L. (1987) "Wind wave induced pore pressure in a natural sea-bed". Tech. Rep. CPER9.5/51, 28 pp.
- Liu, P.L.F., (1973) "Damping of water waves over porous bed". Proc. ASCE, Jour. Hydr. Div., 99, 2263-2271.
- Massel, S.R. (1976) "Gravity waves propagated over permeable bottom. Proc. ASCE, Jour. Waterways, Herb. and Coastal Eng., 101/WW1/, 49-57.
- Massel, S.R. (1981) "Hydrodynamics in ocean engineering". PWN Warszawa, 150 pp. in Polish .
- Massel, S.R., and Moshagen, H. (1980). Wind wave induced pore pressures in a natural sea bed". Measurements at Lubiatowo Coastal Research Station". Techn. Rep., River and Harbour Lab., Trondheim - Institute of Hydro-engineering, Gdańsk, 34 pp.
- Mei, C.C., and Foda, M.A. (1980) "Boundary layer theory of waves in a poro-elastic sea bed". Proc. Inter. Symp. on Soil under Cyclic and Transient Loading, Swansea, 609-618.
- Moshagen, H., and Tørum, A. (1975) "Wave induced pressures in permeable seabeds". Proc. ASCE, Jour. Waterways, Harb. and Coastal Eng., Div., 101, 49-58.
- Phillips, O.M. (1977). "The dynamics of the upper ocean". Camb. Univ. Press, 336 pp.
- Putnam, J.A. (1949) "Loss of wave energy due to percolation in a permeable sea bottom". Trans. Am. Geoph. Un., 30, 349-356.
- Reid, R.O., and Kajiura, K. (1957). "On the damping of gravity waves over a permeable sea bed". Trans. Am. Geoph. Un., 38, 662-666.
- Yamamoto, T., Koning, H.L. Sellmeijer, H., and Van Jijum, E., (1978). "On the response of a poro-elastic bed to water waves . Jour. Fluid Mech., 193-206.
- Verruit, A. (1969). "Elastic storage of aquifers". In "Flow through porous media" ed. R.J.M. De Wiest . Academic Press.

CHAPTER 76

PROBABILITY OF WAVE BREAKING IN THREE-DIMENSIONAL SEAS.

D. Mather, M.W.G. Snook, C.A. Greated, *
W.J. Easson,** and I.G. Bryden. ***

Introduction

Current guidance notes for the design of offshore or coastal structures to withstand breaking waves are based on the behaviour of long-crested, monochromatic waves. It has been acknowledged for some time that although useful for first approximations and in some cases conservative load estimation, the adoption of long-crested wave theories and design principles for a short-crested sea environment may be inappropriate.

Halliwell & Machen (1981) have shown that in shallow water, isolated breaking waves under short-crested conditions can occur with greater elevations and hence potentially greater destructive power than existing design codes predict. Similarly work by Easson & Greated (1984) has highlighted deficiencies in wave theories to predict particle velocities and accelerations within waves by direct non-contact measurement of these properties, the implications being that such theories may significantly underestimate the total wave loading encountered under breaking waves. These observations call into question our ability to predict accurately and so design to withstand wave breaking effects in short-crested environments.

This paper reviews some of the present approaches to the prediction of wave breaking or whitecapping occurrences and compares data

* Department of Physics, University of Edinburgh, The King's Buildings, Mayfield Road. EDINBURGH. EH9 3JZ. Scotland.

** Department of Mechanical Engineering, University of Edinburgh, Mayfield Road, EDINBURGH. Scotland.

*** Department of Offshore Engineering, Heriot-Watt University, Riccarton, EDINBURGH. Scotland.

collected offshore with simulations conducted in wave basin facilities in Edinburgh, which illustrate that wave breaking can occur at wave steepnesses significantly below those which are commonly assumed to represent the onset of breaking implying that design procedures must recognise and allow for this.

Survey of Reported Studies

Several authors have investigated the statistical properties of wave breaking by the visual observation of sea or model sea conditions to characterise properties of breaking or whitecapping wave crests.

Holthuijsen & Herbers (1986) observed the occurrence of whitecaps at a wave recording buoy in open sea conditions off the Dutch coast, the situation being such as to effectively represent a deep sea environment. Concurrent with the wave data, a visual identification time history technique for identifying the occurrence of whitecaps at the buoy permitted their correlation with wave elevation. By this method, each wave crest between zero-downcrossings could be individually distinguished as a whitecap or an undisturbed, plain wave. Their work compared the marginal and joint probability distributions of a number of wave characteristics (height, period, steepness, etc.) for both wave types together with a brief look into breaking occurrences within wave groups and as a function of wind speed. Unfortunately, although directional measurements were made at the site by the buoy, the nature of the resulting wave spectra were not presented.

Certain of the present authors recently pursued a similar series of investigations under model conditions using a video time logging technique (Mather et.al. 1988) to identify the occurrence of whitecaps on the resulting time history and other wave crest instabilities which were judged to be breaking waves. Under these idealised conditions - free of the effects of wind input, non-stationary wave conditions and currents - it was shown that no single geometric property of directionally spread waves recorded by a conventional omni-directional probe, could be used to distinguish breaking from plain waves.

These appear to be the only experiments reported which visually identify the breaking of waves and correlate them to elevation time histories in a three-dimensional environment, that is to say other than in a wave flume.

Papers by Kjeldsen & Myrhaug (1980) and Kjeldsen et.al. (1981) have established a number of wave geometry properties determined from single point measurements which are useful first descriptions of individual waves. In addition to the conventional definition of Wave Steepness (see Appendix), they also define Crest Front and Rear Steepnesses, Horizontal and Vertical Crest Assymetries. They established the advantages to be gained from using an analysis based on the Zero-Downcrossings rather than Crest or Zero-Upcrossing Period, from the standpoint of physically representative parameters and visual interpretation. They justify their opinion that the joint probability density function of Crest Front Steepness and Wave Height (evaluated between zero-downcrossings i.e. Crest to Preceding Trough) provides the most relevant characteristic for the useful forecasting of breaking waves (at high values of each property) but no guidance is given as to the quantitative regression line useful for this purpose.

Snyder and Kennedy (1983) investigated the probability of occurrence of whitecapping over an area at a fixed instant of time as distinct from other authors who considered temporal characteristics at discrete points. They argue the virtues of a variety of plausible wave and sea-surface characteristics which may potentially influence the occurrence of wave breaking. They assume that a single property may be adopted to form the basis of their theory and suggest on heuristic grounds that this must be a scalar quantity and exhibit relative maximum values only at wave crests. This leads to the identification of wave elevation, vertical surface acceleration and surface curvature as candidate properties. The use of elevation as an identifier is readily dismissed since breaking can be observed over a range of wave heights, just as some of the largest waves do not necessarily break. The argument used to dismiss the adoption of surface curvature is that of the practical difficulties to be encountered in quantitative description, analytical treatment and especially its measurement. Such problems of description and analysis stages are not insurmountable as work by Longuet-Higgins (1962) and Glazman (1985) demonstrates, whilst those of measurement do not seem to have been addressed in recent years in the context of water waves, despite the advances in topographic and remote-sensing methods.

X-Band microwave backscatter experiments by Kwoh & Lake (1984) operating with wavelengths of approximately 3cm, reported that backscattering events occurred in discrete bursts which were highly correlated with wave breaking events, contributions to these signals coming from the "background waveform" (the dominant source) and parasitic capillaries. Experimenting with a scanning laser-slope gauge they point out that scattering begins slightly before breaking under relatively smooth surface conditions, whereas conventional microwave backscatter detection relies on Bragg-Wave size surface roughness and that at peak response time the only high frequency feature in their tests are small radii wave crests implying that this small scale curvature may be a causal property of wave breaking. Srokosz (1988) however has pointed out that turbulence behind a breaking wave also leads to locally high curvatures and thus cannot reliably be applied as a characteristic, prerequisite to breaking.

The remaining identifier, that of vertical component surface acceleration, has so far seemed to yield the most promising identification results both in experiments (Snyder et.al. 1986) and theoretically [Longuet-Higgins 1969, Ochi & Tsai 1983, Srokosz 1984, Tung & Huang 1987, Huang et.al. 1986).

Huang et.al. (1986) developed an analytical description of whitecap coverage using the acceleration threshold criterion applied to probabilistic expressions of wave crest amplitude. As with other theories, they apply the restriction that wave breaking only occurs at wave crests in their model and so do not generalise the total coverage to include the effect of entrained foaming water which can be distinguished visually. The model is based on the Wallops spectrum (Huang et.al. 1981), containing the influence of the wind frictional velocity u_* , but the method could easily be applied to the more widely adopted Pierson-Moskowitz or JONSWAP system. In the work of Snyder et.al. the probabilistic description was obtained without adopting the (empirical) u_* and so is to be preferred as an analytic predictive tool although the empirical relationship in the Huang & Long model is probably no less valid and indeed may be preferred for its relative simplicity.

The work of Ochi & Tsai (1983) was one of the earliest to develop a probabilistic function for wave breaking occurrences, basing their efforts on the need to establish a more reliable statistical relationship between wave height and wave period, of those waves which would break. Their Figure 3 illustrates the difficulty in applying a single numerical relationship between these properties either as an average or an upper limiting criteria.

Model Simulation of Sea States

The Fluid Dynamics Unit at Edinburgh University has obtained wave data in the form of elevation plus two subsurface particle velocity components from a Southern North Sea platform site.

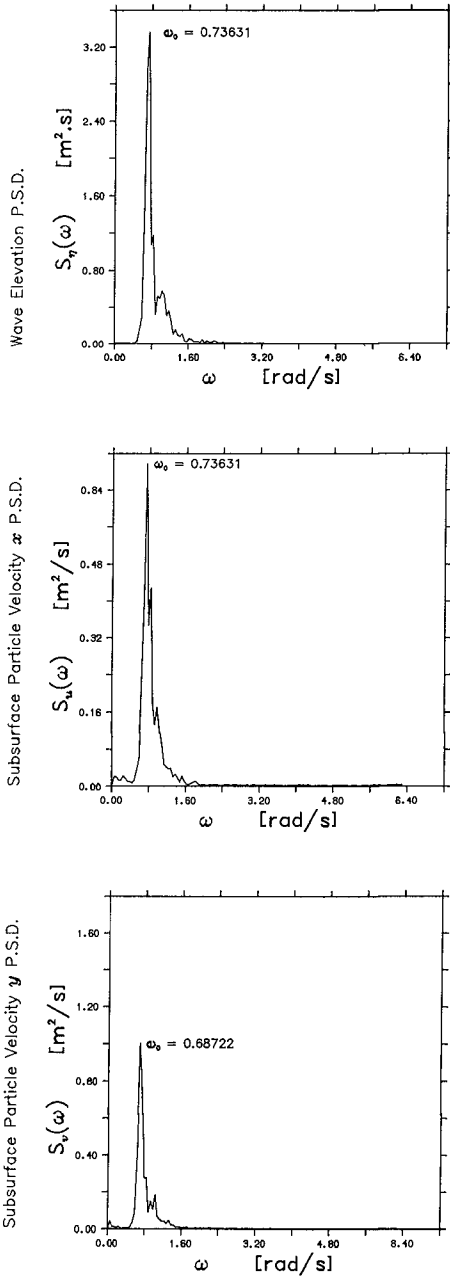
To extract the requisite spectral information from these records, the "Extended" Maximum Likelihood Method, due to Isobe et.al. (1984) was implemented. Sample resulting omni-directional point spectra of wave elevation and particle velocities together with the directionally spread variation of elevation spectra are shown in Figure 1. The growth in the spectral peak and its spread to lower frequencies as the storm developed was clearly visible when comparing successive sample spectra.

To investigate the probabilistic properties of wave breaking in the sea states computed from the site data, wave basin reproduction of these results was undertaken in the Edinburgh University Wide Wave Basin. This facility is described elsewhere [Salter, 1981] but briefly occupies a working area of 23m x 5m with 1.2m depth and with eighty, 0.3m width wavemakers occupying one long side. The wave generation system currently implemented is the "mixed frequency snake" summation of wavefronts permitting specification of the reproduced seas' RMS amplitude and discrete spectral form together with a discrete comb type directional spreading function.

The task of evaluating the directional wave spectrum in the wave basin poses the same problems of the same task at full size. In our experiments, the same analysis technique (the EMLM) was used as for determining the site directional spectrum, except that rather than elevation / velocity component combinations of data being analysed, it was decided to construct and use an array of conventional fixed wave probes. Seven probes were used and arranged as two regular, common-axis Mercedes-Benz style stars each of differing arm radius. This arrangement is more valuable in situations where the principal wave direction is unknown rather than for our application in a wave basin of known direction but the experience gained will, we feel, be of value when more fully assessing the analysis procedure at a later date.

Based upon visual inspection of the site spectra, we chose to attempt our simulations with the peak enhanced JONSWAP spectral form combined with the Cosine-power directional spreading function over a restricted range of angular values considered appropriate for modelling purposes ($\pm 45^\circ$) and beyond which the site data fell off to less than three percent of the peak value. The success of the simulations hinges on finding suitable parameters of the existing formulations, to match in a least squares way, the model form to the site results (Figures 2,3).

For the purposes of simulation this approach is not ideal, and the



British Gas / HGB Offshore Data
 η, u, v Frequency Spectra ... Data Set #9

FIGURE 1

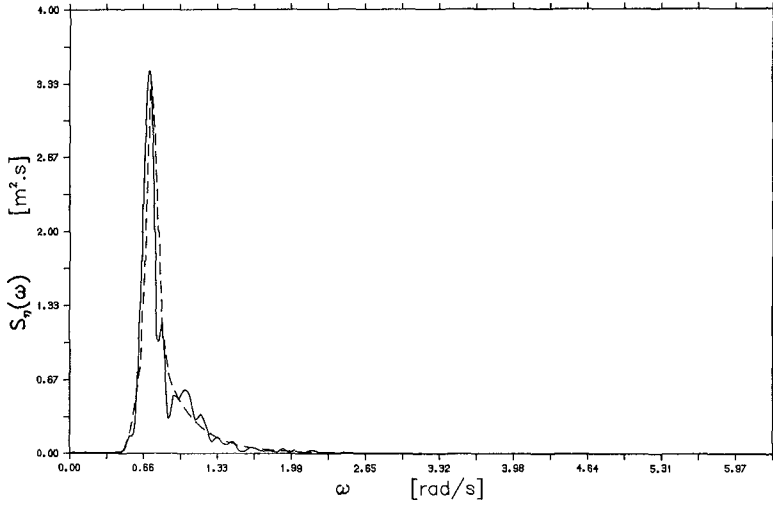


FIGURE 2

Wave Elevation Parameterised Spectra

British Gas / HGB Data Set #9

Site Data Full Line

Parameterised JONSWAP ($\gamma = 3.75$) Dashed

Peak Frequency $\omega_p = 0.73631$ rad/s

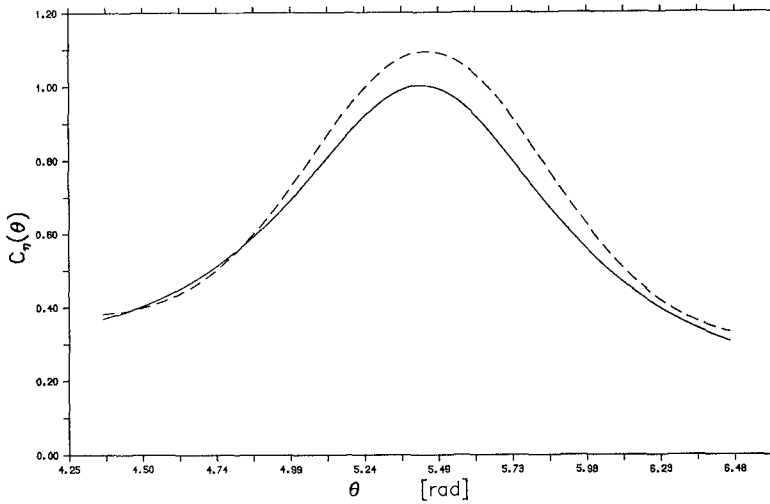


FIGURE 3

Wave Elevation Parameterised Spectral Spreading

method proposed by Bryden & Greated (1984) in which white noise is passed through a digital filter offers realistic advantages. The filter used for wavemaker control can be formed to directly match the measured spectral output of the site data and so overcome the effects of mis-match between the real data and parameterised form. In so doing the greater influence of high-frequency components on wave breaking effects can be more reliably investigated below the upper limits of frequency reproduction possible with flexible-fronted wavemakers. The parameterised spectral forms invariably concentrate their modelling accuracy at the spectral peak and over the average rate of decay beyond that, without accounting for subtle variations which may occur - and were readily distinguishable in the spectra we evaluated throughout the storm - in the tail of the spectrum. This method is implemented in the Heriot-Watt University wave basin facility, but unfortunately this task was committed to other work at the scheduled time for testing. The Edinburgh Wide Wave Tank was however available and although not geared to White Noise Filtering wave generation, the reproduction of the parameterised spectra was well within its' capabilities.

The JONSWAP spectral form may represent a developing and developed sea-state by virtue of the peak enhancement factor (γ). In order to match the parameterisation to the measured spectra, the following justifications were adopted.....

- Peak frequencies will be the same $\omega_{0J} = \omega_0$
- Range of frequencies must match $\omega_{maxJ} = \omega_{max}$
- Total power in the spectrum must match $\int S_J(\omega)d\omega = \int S(\omega)d\omega$
- Peak spectral energies must be the same $S_J(\omega_0) = S(\omega_0)$

The parameterised spreading function was based solely on the measured spreading at the peak frequency (ω_0) and was not evaluated as a function of frequency so reducing the amount of computation necessary,

Least squares fitting of each parameterisation (frequency and direction) was adopted to optimise the spreading parameter (s) about the principal direction and for matching the third and fourth of the above frequency spectra constraints.

The original scope of the experimentation was to investigate the probability of wave breaking at an early stage of storm development (swell conditions) and then at the height of the same storm for which data was available, together with the effect of introducing or ignoring any directionality. As our experiments progressed it became clear that the record selected to represent the swell condition was not going to yield any significant breaking wave results as the physical size of the model sea was too small for reliable visual breaker identification in addition to the more implicit reason that wave breaking is generally to be associated with local rather than distant sea state generation. The number of breaking waves which did occur - even in an extended length test - were so few that there was too low a level of confidence in the results to yield an adequate statistic. As a consequence of the tests were re-defined to examine the effect on the breaking wave statistic of an increase in the energy content of the evaluated spectral form at the peak of the storm.

Four situations were reproduced from the parameterisations of available offshore wave spectral data. The first reproduced the omni-directional spectrum in a uni-directional (monochromatic) form, as is common practise, whilst the second introduced spreading according to the Cosine-power function suitably scaled to maintain the constant total power of the spectrum. The third and fourth tests used the same spectral form, peak frequency and frequency range but with an increase in the area under the spectral curve corresponding to a rise in the RMS waveheight of 40% based on a Rayleigh distribution. The technique adopted for identifying the geometric properties of the individual breaking waves is described elsewhere [Mather et.al. (1988)] and briefly, relates the time locations of visually identified breaking waves (from a video replay), to the wave record obtained from the reference wave probe. In this way each breaking crest is "flagged" to allow further investigation of whatever geometric or temporal property may be of interest (e.g. steepness, crest asymmetry, etc.)

Test Results

Probability density function histograms of geometry properties for each of the lower energy sea-states are shown in Figures 4,5, overlaying in each case the probability density histograms of breaking waves and all waves (plain and breaking). The properties illustrated were chosen from consideration of the results of Kjeldsen et.al. (1981), which were those most promising readily computed geometric characteristics likely to distinguish breaking from non-breaking waves. Review of our results led us to conclude that for each of the properties evaluated, breaking waves could occur over their whole range of realisable values.

In many instances the low number of samples of breaking waves lead to seemingly spurious results detached from the main body of the probability distribution, for example in all instances of elevation. Also clear is that the highest waveheight, longest periods, highest elevations or greatest steepnesses that do occur do not always break. This characteristic is particularly unsettling in each case of wave steepness, where the steepest identified breaking waves only exist up to about 75% of the values attained by plain waves. This may be a consequence of the fact that a visually identified breaker has to possess some whitecap which may have formed some relatively long time (at model scales) before passing the wave elevation probe. As a result the elevation will have diminished and the corresponding steepness reduced. Plain waves may on the other hand retain their form all the way up to breaking and inspection of the scales for each wave steepness shows that no waves occurred above values of between 0.055, 0.060 in each seastate of differing average wave height and director spreading. The values obtained for wave steepness on an individual wave basin were all significantly below the maximum value limited by breaking proposed by Hallam et.al. (1978) of 0.142. Small numbers of plain (i.e. non-breaking) waves did approach this value but with so many waves, this number became sufficiently insignificant as not to be apparent on the histograms.

The same problem is encountered when plotting the joint probability distribution (contour plots, Figures 6,7) in that as a wave breaks, its elevation and thus waveheight is reduced so that identified individual wave breaking occurrences on these figures are shifted away from their values at the point of breaking to that noted in each case,

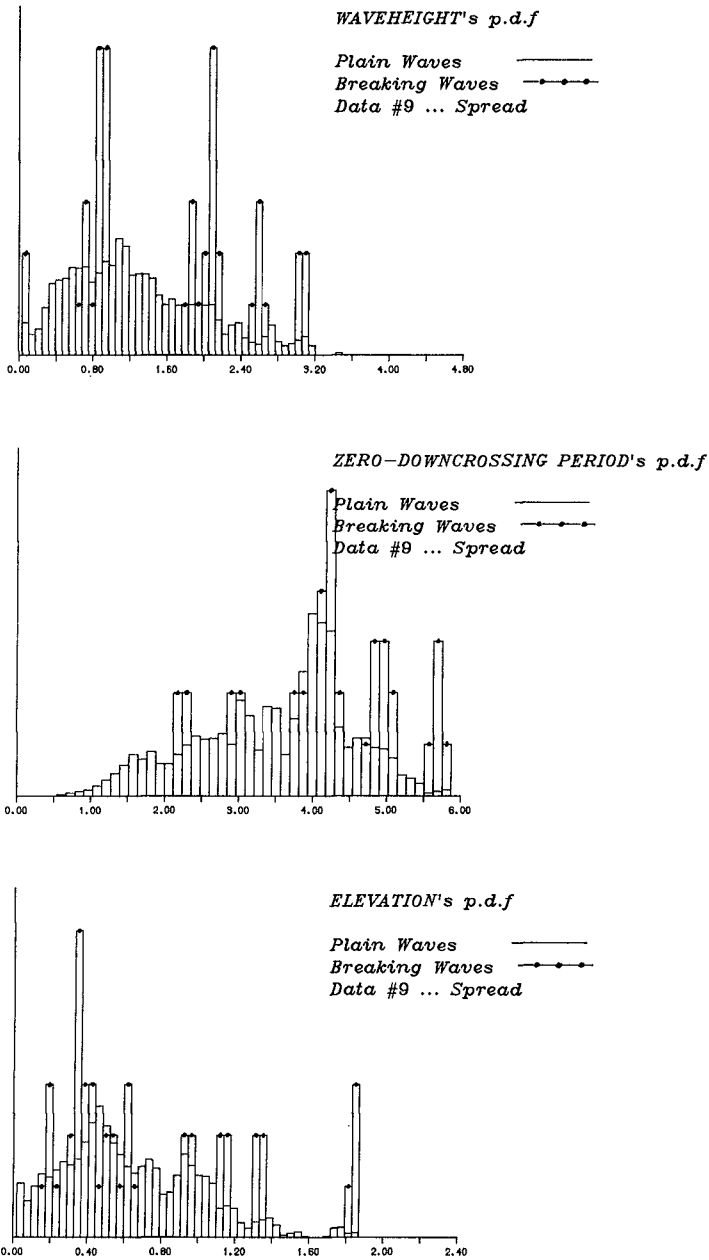


FIGURE 4 abc

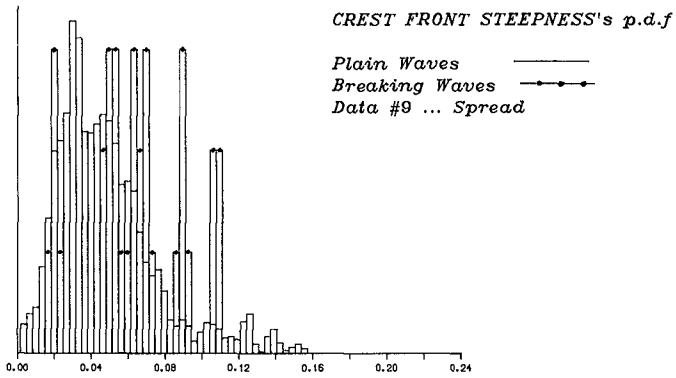
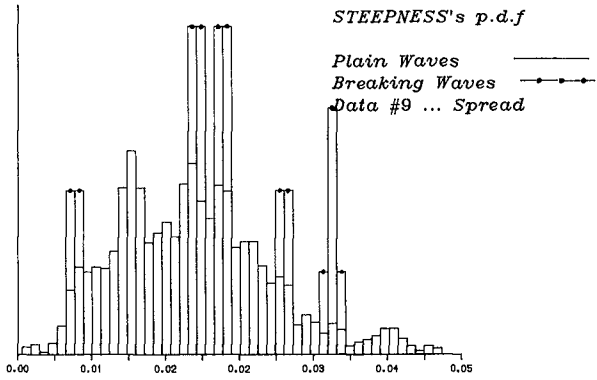


FIGURE 4 de

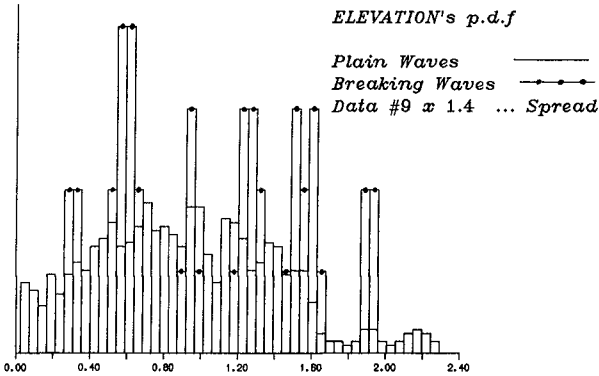
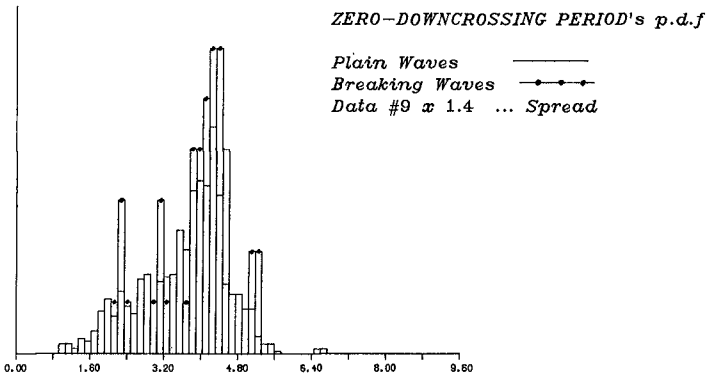
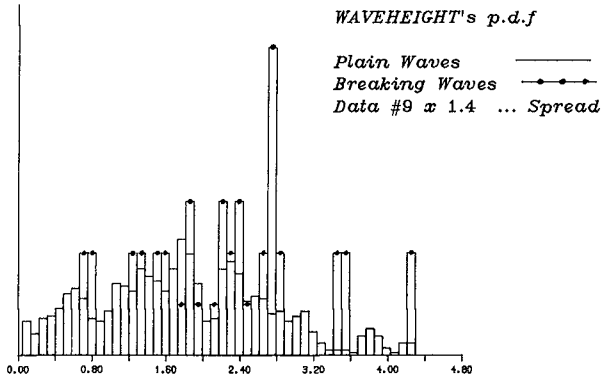


FIGURE 5 abc

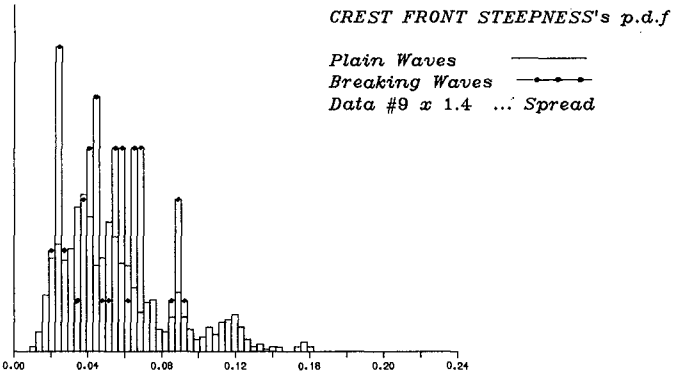
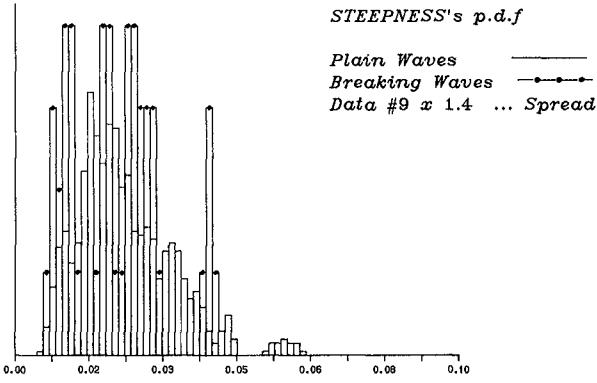


FIGURE 5 de

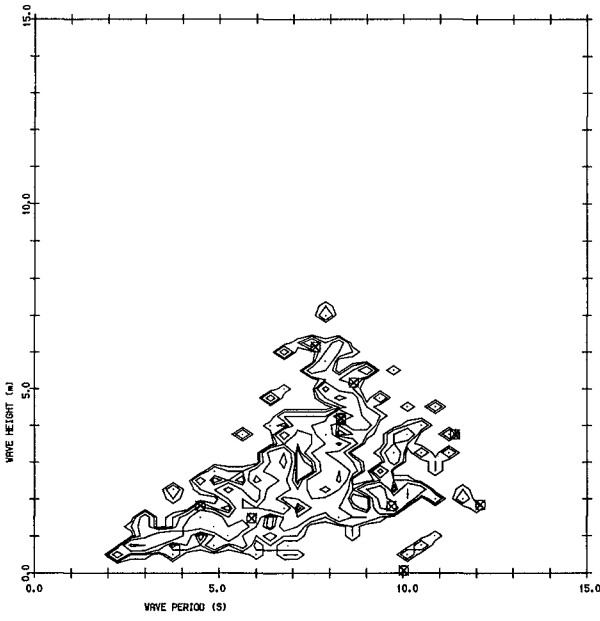


FIGURE 6

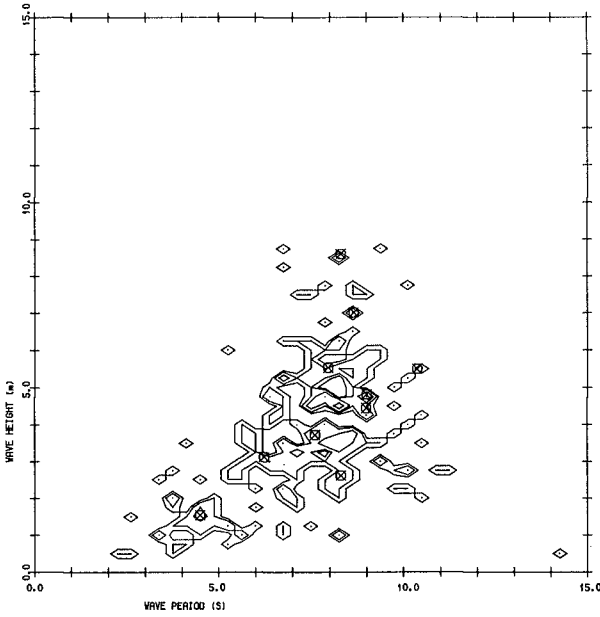


FIGURE 7

these being the values observed at the elevation probe.

Two interesting points of note arise when comparing the monochromatic and directionally spread plots in each case of RMS waveheight. The introduction of a directional spread eliminates the occurrences of outlying, extreme value combinations of waveheight and period over the observed test periods though this observation cannot necessarily be assumed to be true when considering extreme value occurrences. This appears to be accompanied in each case by a drift of values towards the regression line equivalent to the maximum wave steepness.

Conclusions

These tests lend support to earlier work by Holthuijsen & Herbers (1986) and Mather et.al. (1988) that in directional seas there seems to be no obvious relationship between the occurrence of visually identifiable breaking events and any of the geometrically defined wave characteristics in current use. Future work in this field at the University of Edinburgh is to concentrate on attempts to relate the probability of wave breaking to sea-state spectral characteristics and simulations of directionally spread sea surfaces.

Acknowledgement

The authors wish to acknowledge British Maritime Technology Ltd. for financial support under the CASE scheme for Mr. Mather and are grateful to British Gas plc for access to the offshore site data. Many thanks also to Professor Stephen Salter and Mr. David Skyner at the University of Edinburgh and Dr. Meric Srokosz at the Institute of Oceanographic Science, Wormley for assistance during different stages of the preparation of this paper.

References

- Bryden, I.G. & Greated, C.A.
Generation of Three-Dimensional Random Waves,
J. Phys. D. Appl. Phys., Vol.17 (1984) Pp.2351-2366.
- Eason W.J. & Greated, C.A.
Breaking Wave Forces and Velocity Fields
Coastal Engineering, Vol.8 (1984) Pp.233-241.
- Glazman, R.E.
Statistical Characterisation of Sea Surface Geometry for a Wave
Slope Field Discontinuous in the Mean Square.
J. Geophysical Res., Vol.91 (1986) Pp.6629-6641
- Hallam, M.G. Heaf, N.J. & Wootton, L.R.
Dynamics of Marine Structures.
Report UR8, CIRIA Underwater Engineering Group (1978).
- Halliwell, A.R. & Machen, P.C.
Short-Crested Breaking Waves in Water of Limited Depth
Proc. Instn. of Civil Engrs. Vol.71 Part 2, Sept. (1981)
Pp.663-674.
- Holthuijsen, L.H. & Herbers, T.H.C.
Statistics of Breaking Waves Observed as Whitecaps in the Open Sea
J. Phys. Oceanography, Vol.16, Feb. (1986) Pp.290-297.
- Huang, N.E., Long, S.R., Tung, C.C., Yuen, Y. & Bliven, L.F.
A Unified Two-Parameter Wave Spectral Model for a General Sea State
J. Fluid Mechanics, Vol.112 (1981) Pp.203-224.

- Huang, N.E., Bliven, L.F., Long, S.R., & Tung, C.C.
An Analytic Model for Oceanic Whitecap Coverage
J. Phys. Oceanography, Vol.16 (1986) Pp.1597-1604
- Isobe, M., Kondo, K. & Horikawa, K.
Extension of MLM for Estimating Directional Wave Spectrum
Proc. Symp or Description and Modelling of Directional Seas
June (1984), Denmark.
- Kjeldsen S.P. & Myrhaug, D.
Wave-Wave Interaction, Current-Wave Interactions and Resulting
Extreme
Waves and Breaking Waves.
Proc. 17th Conf. Coastal Engineering, Sydney (1980).
- Kjeldsen, S.P., Lystad, M. & Myrhaug D.
Forecast of Breaking Waves on the Norwegian Continental Shelf
Project Report - Ships in Rough Seas (1981) N.H.L.
- Longuet-Higgins, M.S.
The Statistical Geometry of Random Surfaces
Hydrodyn. Instab. Proc. Symp. Appl. Math. (1962) Pp.105-143.
- Longuet-Higgins, M.S.
On Wave Breaking and the Equilibrium Spectra of Wind-Generated
Waves
Proc. Roy. Soc. A., Vol.310, (1969) Pp.151-159.
- Mather, D., Bryden, I.G. & Greated, C.A.
Analysis of Visual and Time Series Data from Breaking Wave Fields
Proc. Conf. Offshore Mechanics and Arctic Engineering, Feb. (1988),
Houston.
- Ochi, M.K. & Tsai, C.H.
Prediction of Occurrence of Breaking Waves in Deep Water
J. Phys. Oceanography, Vol. 13 Nov. (1983) Pp.2008-2019.
- Salter, S.H.
Absorbing Wave-Makers and Wide Tanks
Proc. Conf. on Directional Wave Spectra Applications, (1981) New
York.
- Snyder, R.L. & Kennedy, R.M.
The Formation of Whitecaps by a Threshold Mechanism: Part I
J. Phys. Oceanography, Vol.13, Aug. (1983) Pp.1482-1492
- Srokosz, M.A.
On the Probability of Wave Breaking in Deep Water
J. Phys. Oceanography, Vol.16, Feb. (1986) Pp.382-385
- Srokosz, M.A.
Private Communication (1988).
- Tung, C.C. & Huang, N.E.
The Effect of Wave Breaking on the Wave Energy Spectrum
J. Phys. Oceanography, Vol.17, Aug. (1987) Pp.1156-1162.

CHAPTER 77

A NEW PARAMETER FOR WAVE BREAKING WITH OPPOSING CURRENT ON SLOPING SEA BED

Shigeki Sakai*
Ken-ichi Hirayama**
Hiroshi Saeki***

INTRODUCTION

Opposing currents affect the wave breaking processes. The condition of wave breaking caused by opposing currents in deep water is described by the ratio of the wave celerity to the velocity of the opposing current (Yu(1952)). For the wave breaking caused by the opposing currents in shallow water on a flat bed, the equation given by Miche(1951) for the breaking criteria without current remains available (Iwagaki et al.(1980)). However, it is the breaking of shoaling wave in the presence of opposing current on a uniform slope, which is of concern in this paper.

Sakai et al.(1981) showed that the wave breaking affected by opposing currents on a sloping sea bed is characterized by a normalized unit width discharge q^* , as well as an incident wave steepness H_o/L_o and a slope of sea bed S , where q^* is defined as $q^* = q/g^2 T^3$; q : a unit width discharge, g : the gravitational acceleration, T : a wave period. They proposed diagrams for the breaker height and the breaking depth as a function of these three parameters. The breaker index curves in their diagrams show the relationships between the breaker height (or the breaking depth) and q^* for waves with particular values of H_o/L_o and S , and it is much more convenient to give a general expression for the breaker indices for arbitrary conditions of q^* , H_o/L_o and S .

The purpose of this study is to formulate the effects of these parameters on wave breaking, based on the results of systematic experiments performed by the authors, and to derive an empirical and simplified expression for the breaker height and depth in the presence of opposing currents.

* Dept. of Civil Eng., Univ. of Delaware, Newark, DE 19716, USA
(presently, Dept. of Civil Eng., Iwate Univ., 4-3-5 Ueda, Morioka, 020 Japan)

** Dept. of Civil Eng., Iwate Univ., 4-3-5 Ueda, Morioka, 020 Japan

*** Dept. of Civil Eng., Hokkaido Univ., Kita-13, Nishi-8, Sapporo, 060 Japan

The original idea is to choose the ratios of the breaker height (or depth) with opposing currents to the breaker height (or depth) without currents, and to search for an individual functional relationship between the ratios and each parameter (q^* , H_0/L_0 and S). Then, with the help of statistical approaches, these relationships are reorganized into a more simple relationship between the ratios and a new parameter.

EXPERIMENTS

Experiments were conducted by using two wave channels, one of which is 26m long, 1m deep and 0.36m wide; the other is 24m long, 0.8m deep and 0.36m wide. These have the same systems of wave generation and of water circulation. The slopes of the bottom were 1/50, 1/30 and 1/15.

Data acquisition of wave profiles was started when the first wave was generated, and the wave height was measured using five wave profiles from the sixth to the tenth, in order to avoid the reflecting waves. An incident wave height and length were calculated with the linear theory for wave with uniform current. The breakpoint was defined as a point which has the highest wave height. Experimental conditions of the unit width discharge, the wave period and the incident wave height are shown in table 1, and the ranges of the normalized unit width discharge and the incident wave steepness on each sea bed slope are given in Appendix A.

Table 1 Experimental conditions

unit width discharge	q : 0.0 ~ 790.0 ($\text{cm}^3/\text{s}/\text{cm}$)
wave period	T : 0.83 ~ 2.40 (s)
incident wave height	H_0 : 1.1 ~ 24.0 (cm)

NEW PARAMETER

In the present study, the breaker height (or depth) in the presence of the opposing current is examined, as compare to the breaker height (or depth) in the absence of the current. In this approach, the breaker height (or depth) in the absence of the current is expected to be described as a function of the incident wave steepness and the sea bed slope. The results of the present experiments without currents give the relationships between the breaker height (or depth) and the incident wave steepness for each sea bed slope, as shown in Appendix B-1 and B-2. In stead of scattering of data, the average lines were obtained for each cases. In the following discussion these average lines will be used to estimate the breaker height (or depth) without current. In these figures, the breaker index curves proposed by Goda(1970) are also illustrated. The present results are consistent with Goda's curves.

The influence of opposing currents appears in the change of breaking depth more significantly than in that of breaker height, and the normalized unit width discharge q^* explains the effects of opposing currents on wave transformation(Sakai and Saeki(1984)). The first step is to examine the relationship between R_h and q^* , where R_h is the ratio of breaking depth with and without opposing currents. Figure 1 shows the relationships between R_h and q^* for given H_0/L_0 on the slope

1/30. Rh depends on q* linearly, and then the relationship is expressed by the regression line for each condition of Ho/Lo. Since the slopes of regression lines (SRL)h depend on Ho/Lo, the relationship between (SRL)h and Ho/Lo is examined. Figure 2 shows that (SRL)h is inversely proportional to Ho/Lo on a logarithmic scale in cases where Ho/Lo < 0.05. (SRL)h also depends on the slope of sea bed. As shown in Figure 3, (SRL)h is proportional to the slope of sea bed S on a logarithmic scale. Then, the slope of regression line (SRL)h is described as follows:

$$(SRL)h \propto (H_0/L_0)^{-a} \cdot S^b = ((H_0/L_0) \cdot S^{-c})^{-a} \quad (1)$$

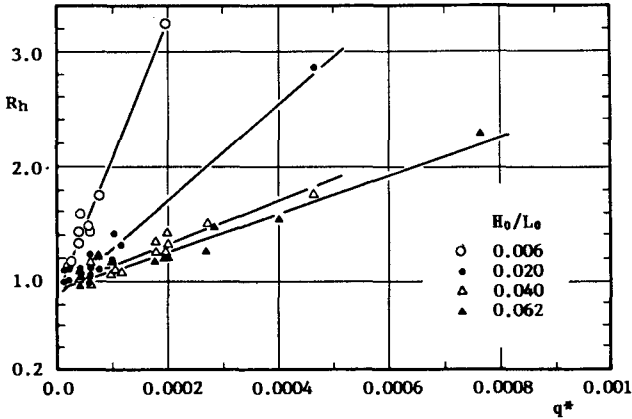


Figure 1 Relationship between Rh and q* (S=1/30)

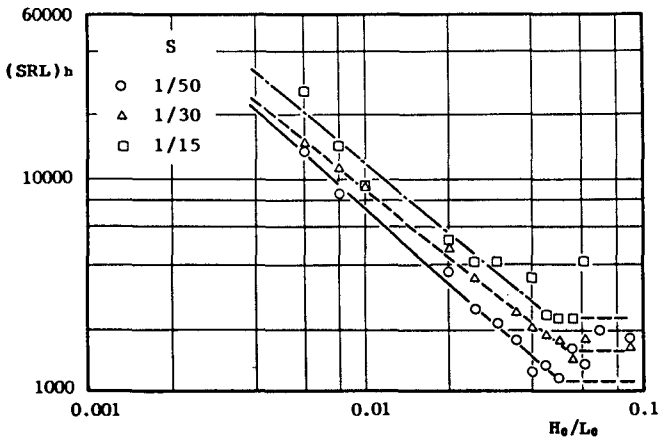


Figure 2 Effect of Ho/Lo on (SRL)h

To explain the combined effects of H_o/L_o and S on $(SRL)_h$, the optimum value of c was found to be between 0.11 and 0.76. Figure 4 shows the relationship between $(SRL)_h$ and the combined parameter of H_o/L_o and S , with $c=0.41$, which gives the highest coefficient of correlation. Using the slope of regression line in this figure, $(SRL)_h$ can be formulated as a function of H_o/L_o and S .

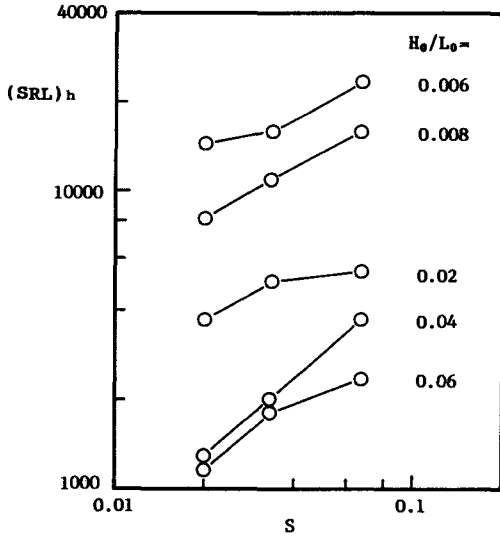


Figure 3 Effect of S on $(SRL)_h$

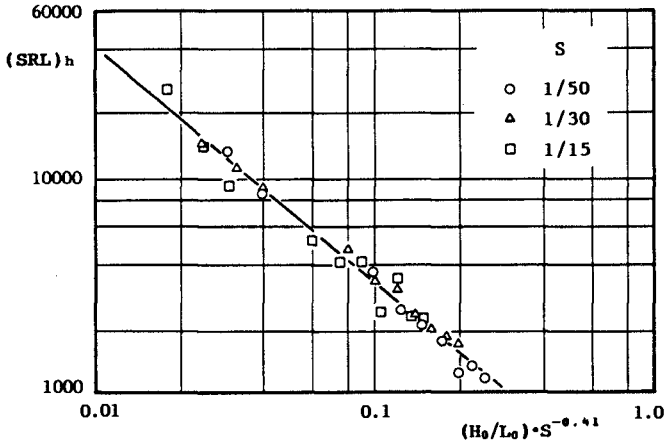


Figure 4 Combined effect of H_o/L_o and S on $(SRL)_h$, with $c=0.41$

The relationships between RH and q^* are illustrated in Figure 5, where RH means the ratio of breaker height with and without opposing currents. The slope of regression line (SRL)H was examined as to be related to H_0/L_0 and S. A similar relationship was also obtained as follows:

$$(SRL)_H \propto (H_0/L_0)^{-a'} \cdot S^{b'} = ((H_0/L_0) \cdot S^{-c'})^{-a'} \quad (2)$$

The optimum value of c' is between 0.14 and 0.65. Figure 6 gives (SRL)H expressed by the combined parameter of H_0/L_0 and S, with $c'=0.37$.

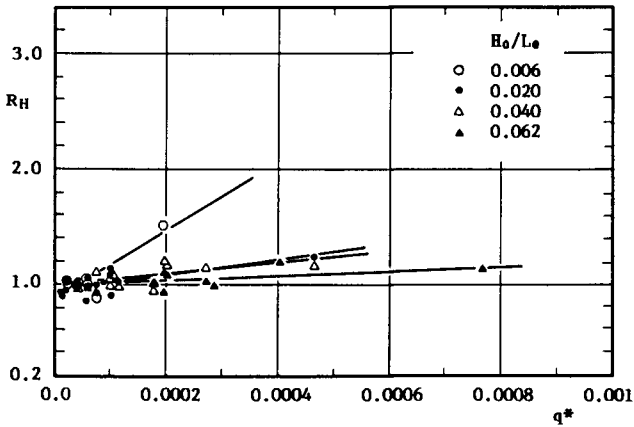


Figure 5 Relationship between RH and q^* ($S=1/30$)

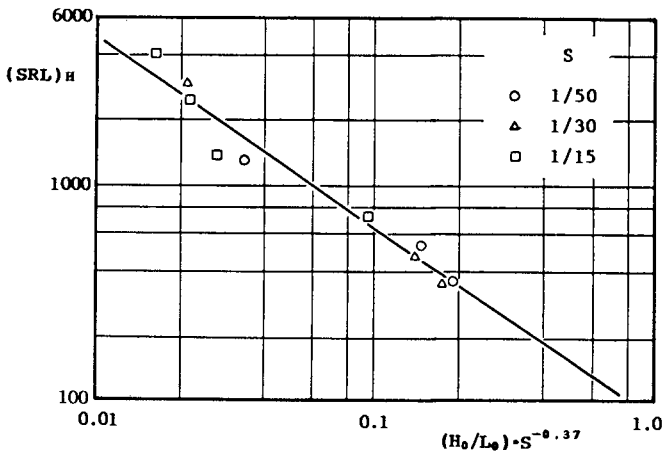


Figure 6 Combined effect of H_0/L_0 and S on (SRL)H, with $c'=0.37$

For a given H_0/L_0 and S , both R_h and R_H are proportional to q^* on a normal scale (see Figures 1 and 5). If the product of q^* and $(SRL)h$ (or $(SRL)H$) is chosen as a parameter, the relationship between R_h (or R_H) and this parameter will be described by a single line. Since the range of optimum value of c overlaps with that of c' , and it will be more convenient to define a single parameter, a new parameter was defined for both R_h and R_H , as follows:

$$\epsilon = \begin{cases} \frac{q^*}{H_0/L_0} \sqrt[4]{S} & H_0/L_0 \leq 0.05 \\ \frac{q^*}{0.05} \sqrt[4]{S} & H_0/L_0 > 0.05 \end{cases} \quad (3)$$

For waves with H_0/L_0 larger than 0.05, H_0/L_0 is assumed to be 0.05, since Figure 2 shows that $(SRL)h$ is not inversely proportional to H_0/L_0 for such cases.

Using the proposed parameter, all data were rearranged into a relationship between the ratios and ϵ . Both ratios (R_h and R_H) depend on ϵ linearly as shown in Figure 7, and ϵ explains the combined effects of q^* , H_0/L_0 and S on the wave breaking on a uniform slope, fairly well. Consequently, from the regression lines in this figure, R_h and R_H are formulated as follows:

$$R_h = \begin{cases} 0.93 + 170\epsilon & \epsilon \geq 0.0004 \\ 1.0 & \epsilon < 0.0004 \end{cases} \quad (4)$$

$$R_H = \begin{cases} 0.96 + 30\epsilon & \epsilon \geq 0.0013 \\ 1.0 & \epsilon < 0.0013 \end{cases} \quad (5)$$

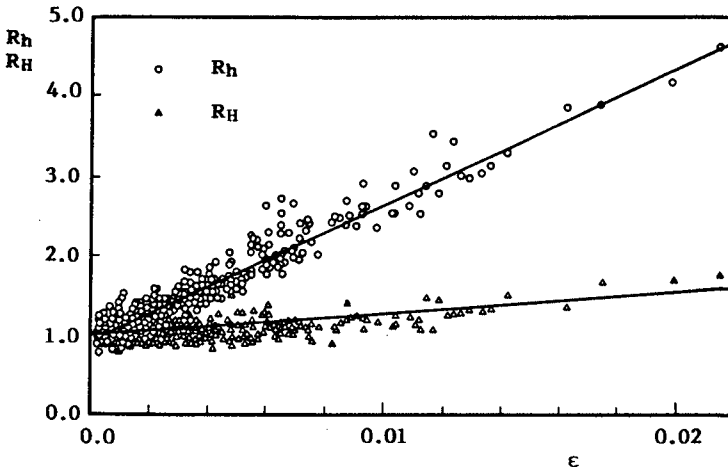


Figure 7 Expressions for R_h and R_H by ϵ

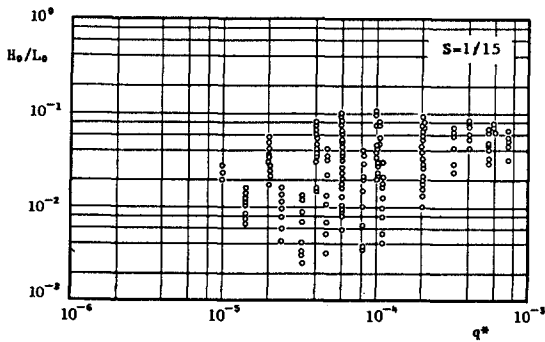
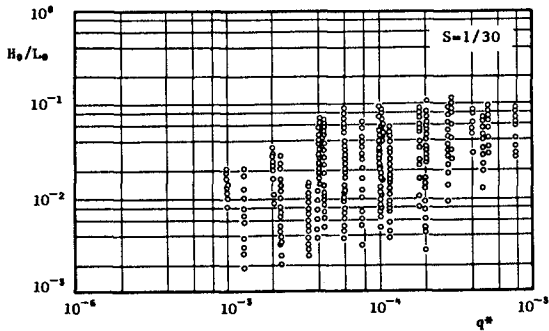
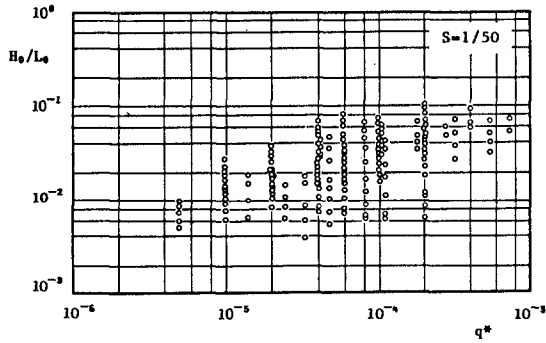
CONCLUSIONS

In the present study, the influences of opposing current on wave breaking were formulated as functions of a new parameter ϵ , which accounts for the combined effects of the unit width discharge, the incident wave steepness and the sea bed slope. These formulations give the ratios of the breaker height(or depth) with and without opposing currents. Several results have been reported for wave breaking without currents. For example, Goda(1970) proposed diagrams for the relationships between the ratio of the breaker height to the incident wave height and the incident wave steepness. For the breaking depth or the maximum breaker height in a given depth, Weggel(1972) described the ratio of water depth to wave height at breakpoint as a function of breaker height, incident wave length and sea bed slope. Goda(1975) also gave another expression derived from his diagrams. These formulations and diagrams have been widely used to predict the breaker height and depth without currents. The present formulations gives the breaker height(or depth) with opposing currents, by using the breaker height(or depth) without current predicted by the previous studies.

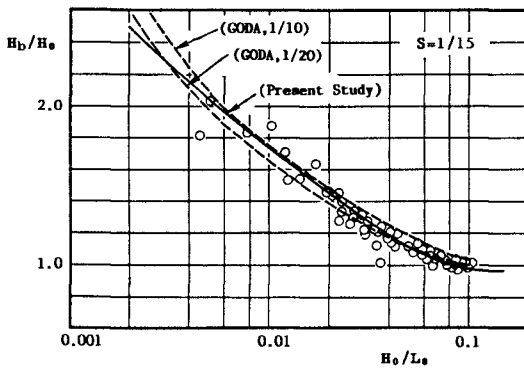
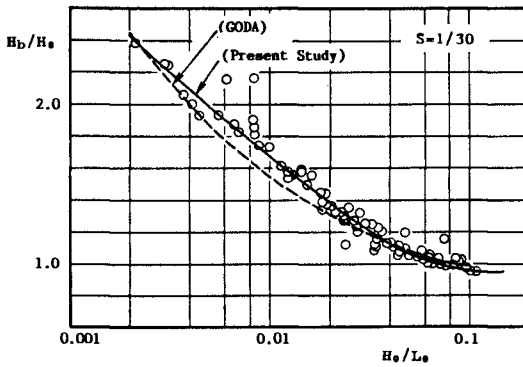
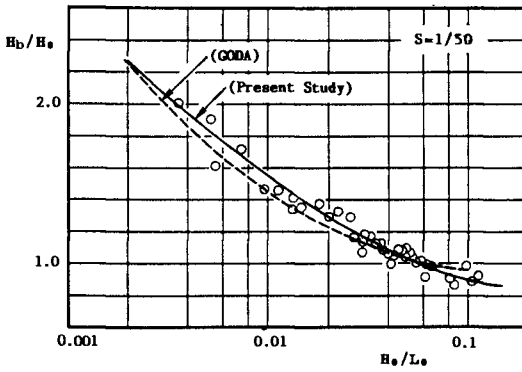
REFERENCES

- Goda,Y.(1970), "A Synthesis of Breaker Indices", Transactions of the Japanese Society of Civil Engineers, JSCE, Vol.2, Pt.2.
- Goda,Y.(1975), "Irregular wave deformation in the surf zone", Coastal Engineering in Japan, JSCE, Vol.18, 13-26
- Iwagaki,Y. et al.(1980), "Fundamental Study on Breaking of Waves due to Currents"(in Japanese), Proc. of 27th Japanese Conference on Coastal Engineering, JSCE, 30-34
- Miche,M.(1951), "Le Pouvoir Reflechissant des ouvrages Maritimes, Exposes a l'action de la Houle", Annales Ponts et Chaussees, 12 Annee, 285-319
- Sakai,S. et al.(1981), "Effects of Opposing Current on Wave Breaking on Slope"(in Japanese), Proc. 29th Japanese Conference on Coastal Engineering. JSCE, 138-143.
- Sakai,S. and H. Saeki(1984), "Effects of Opposing Currents on Wave Transformation on Sloping Sea Bed", Proc. of 19th Coastal Engineering Conference, ASCE, 1132-1148
- Weggel,J.R.(1972), "Maximum Breaker Height", Journal of the Waterways, Harbors and Coastal Engineering Division, ASCE, Vol.98, WW4, 529-548
- Yu, Y.Y.(1952), "Breaking of Waves by Opposing Current", Transaction of AGU, AGU, Vol.33, No.1, 39-41

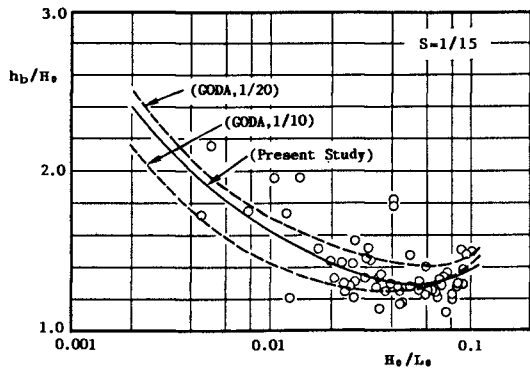
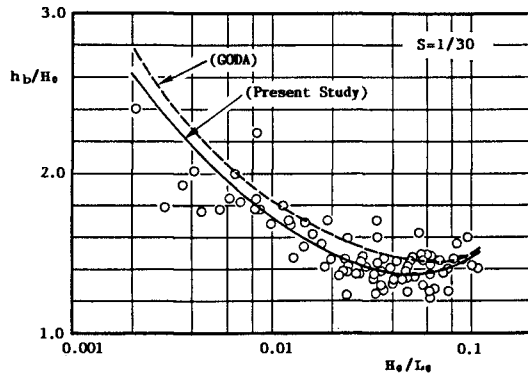
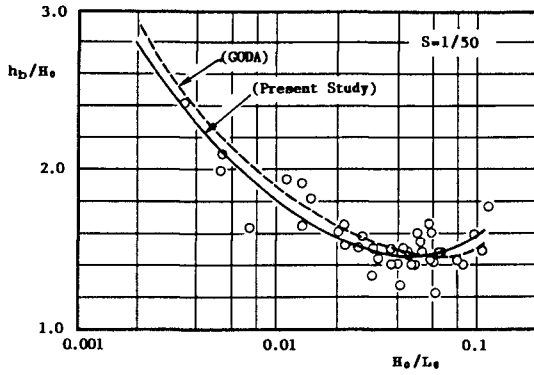
Appendix A Ranges of normalized unit width discharge and incident wave steepness



Appendix B-1 Breaker height without current



Appendix B-2 Breaking depth without current



CHAPTER 78

WHAT IS THE SLOPE OF EQUILIBRIUM RANGE IN THE FREQUENCY SPECTRUM OF WIND WAVES?¹

Paul C. Liu²

Abstract An effort to empirically assess the slope of the equilibrium range in a wind-wave frequency spectrum with a large number of data recorded in the Great Lakes did not serve to clarify the uncertainty between a -4 or a -5 frequency exponent representation. The uncertainty is further compounded by indications that the slope is not necessarily unique, it tends to vary with wave momentum. For sufficiently well-developed wind waves the exponent appears to cluster between -3 and -4. For practical applications the f^{-4} equilibrium range is perhaps an effective approximation. What the correct slope is for the equilibrium range, or even whether or not a unique slope exists, remains elusive and has yet to be satisfactorily substantiated.

Introduction

The slope of the equilibrium range on the high frequency side of a wind-wave frequency spectrum has been subjected to continued uncertainty over the last 35 years. In the decade of 1950s, there were three separate spectral representations with slopes of -6, -7, and -5 for the high frequency side of the spectrum developed respectively by Neumann (1953), Darbyshire (1955), and Roll and Fischer (1956). Phillips (1958) resolved these differences by inferring that a range of frequencies on the high frequency side of the spectrum will be dynamically saturated between energy input and dissipation processes, independent of wind stress, and proportional to the -5th power of frequency based on dimensional considerations. Oceanographers and coastal engineers have adhered to this f^{-5} equilibrium range concept since then, as many observations appeared to substantiate it. Recent observations, however, show evidence that the frequency spectrum is actually proportional to f^{-4} on the high frequency side rather than the widely used f^{-5} . Phillips (1985) re-examined the processes of energy input from wind stress, wave breaking and wave-wave interactions and revised his earlier concept by concluding

1 GLERL Contribution NO. 629.

2 Oceanographer, NOAA/Great Lakes Environmental Research Laboratory, 2205 Commonwealth Blvd., Ann Arbor, Michigan 48105

theoretically that the frequency spectrum $S(f)$ is in fact proportional to $g u_* f^{-4}$, where u_* is the wind friction velocity, as Toba (1973) and others have found empirically. While the ocean-wave community has gradually accepted this new concept (e.g., Battjes et al., 1987), there are still measurements showing f^{-5} to be a good representation. So what is the slope of equilibrium range in the frequency spectrum of wind waves? In this paper this question is explored, using a large number of measured wind-wave spectra in the Great Lakes to make a detailed examination of the equilibrium range slope of a wave spectrum.

Data

Eight NOAA Data Buoy Center (NDBC) buoys are deployed in the Great Lakes (Figure 1) during the ice-free period of the year, providing measurements of air and surface water temperature, wind speed and direction at 5 m above the water surface, and surface wave frequency spectra. The data used here were recorded by the NDBC buoys during 1981-1986. The wave spectra were calculated with 24 degree of freedom and a 0.4 Hz high frequency cutoff, from 20 minutes of hourly accelerometer measurements. A detailed description of the NDBC buoy measurement system is given in Hamilton (1986). A comparison of wave measurements obtained from a NDBC buoy and a Waverider buoy is presented in Schwab and Liu (1985).

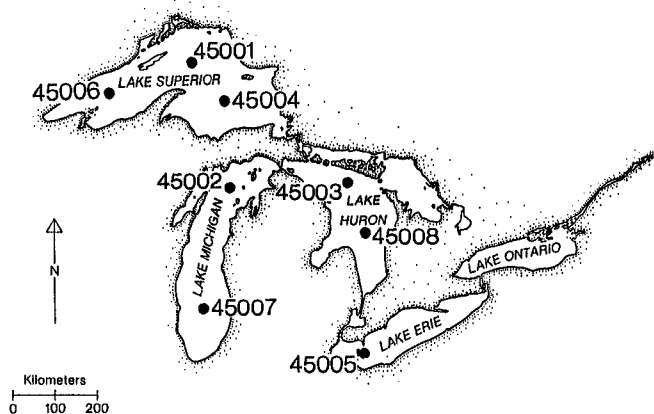


Figure 1. Location map of the eight NDBC buoys in the Great Lakes.

With the wind speed and the air and water temperatures given from the measurements, the wind friction velocity u_* used in this study was readily obtained using the formula for overwater roughness length by Charnock (1955) with the formulation of stability length by Businger et al. (1971), assuming a constant neutral drag coefficient of $1.6 \times$

10^{-3} . This method is basically similar to various other methods of estimating u_w as shown in Liu and Schwab (1987).

Results and Discussions

An episode of well-defined wave growth was examined first. The episode was recorded from the Northern Lake Michigan Buoy 45002 on November 23, 1984. As shown on the left hand side of Figure 2, the wind was blowing steadily from the southwest direction with wind speeds increasing continuously from 7 ms^{-1} to over 15 ms^{-1} . Because of the relatively calm conditions prior to the episode, the wave field developed steadily with significant wave height growing from less than 1 m to 4.5 m over a 19-hour interval. The wave spectra recorded during the episode are plotted on the right hand side of Figure 2. The pure wave growth is exhibited by the continuous shifting of the front faces at the low frequency side of the spectra toward lower frequencies. The high frequency side of the spectra bands together to signify the equilibrium range. To see the slope of the equilibrium range we draw a f^{-5} line and a f^{-4} line along the banded part of the spectra. It is clear that either of the two straight lines could be considered good representation of the equilibrium range. Thus we are not able to visually delineate precisely which one provides a better representation.

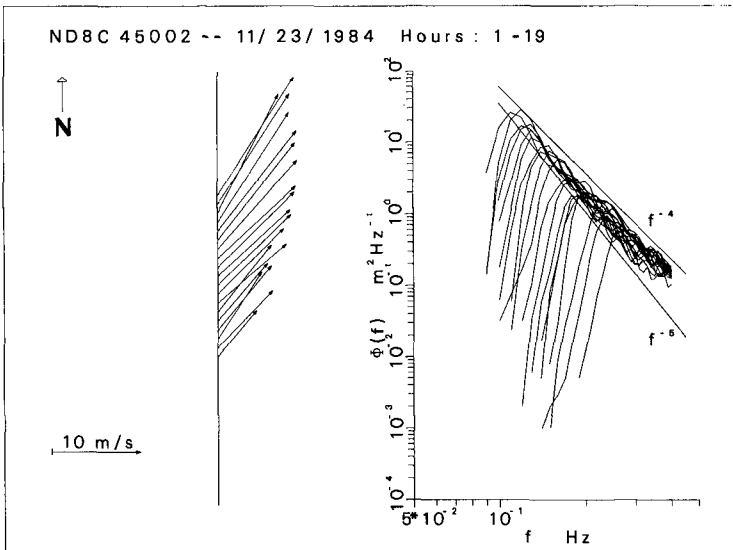


Figure 2. Wind vectors and wave spectra plots of a growing wave episode in Northern Lake Michigan.

Normalizations

Several normalization schemes for studying spectral representation are available in the literature. One, proposed by Toba (1973) simply normalizes the spectral density $\Phi(f)$ by the peak energy density $\Phi(f_p)$ and the frequency f by the peak energy frequency f_p . A scheme adopted in Liu (1971) and others uses the same frequency normalization, but nondimensionalizes the spectral density by a factor of $f_p E^{-1}$ where E is the total energy integrated from the spectrum. Another scheme normalizes the spectral parameters with wind friction velocity u_* and acceleration of gravity g to yield normalized density and frequency as $\Phi(f)g^2u_*^{-5}$ and fu_*g^{-1} respectively. Phillips (1985) and several other authors have used this u_* normalization. An application of these three normalizations to the November 23, 1984 episode is shown in Figure 3. In the graphs the -4 as well as -5 slope lines are also drawn for comparison. Again, as in the case of the dimensional spectral plots, it is difficult to distinguish the best representation for the equilibrium range.

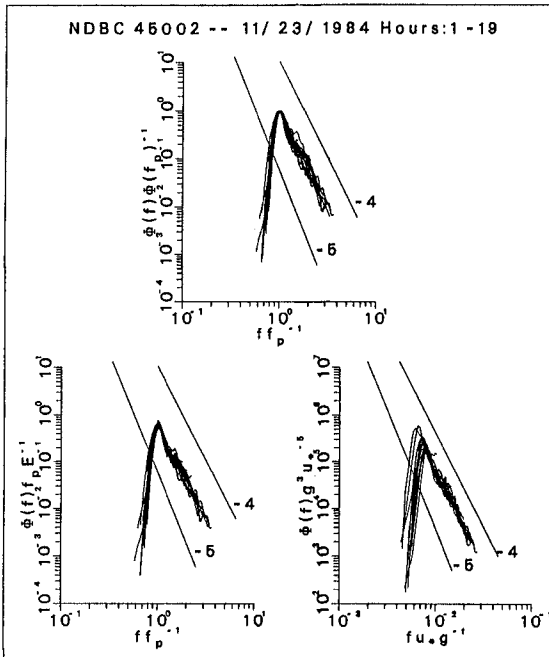


Figure 3. An application of three different normalizations to the growing wave episode spectra; -4 and -5 slope lines are included for comparison.

A frequency spectrum with f^{-5} equilibrium range is generally represented by

$$\Phi(f) = \beta(2\pi)^{-4}g^2f^{-5} \tag{1}$$

on the high frequency side. If (1) is valid then the normalized spectral density $\Phi(f)(2\pi)^4f^5g^{-2}$ should be independent of frequency and approaching the value β at the high frequency side. Similarly a frequency spectrum with f^{-4} equilibrium range can be represented by

$$\Phi(f) = \alpha(2\pi)^{-3}gu_*f^{-4} \tag{2}$$

In order for (2) to be the correct representation, the parameter $\Phi(f)(2\pi)^3f^4(gu_*)^{-1}$ should also be independent of frequency and approaching the value α at the high frequency side.

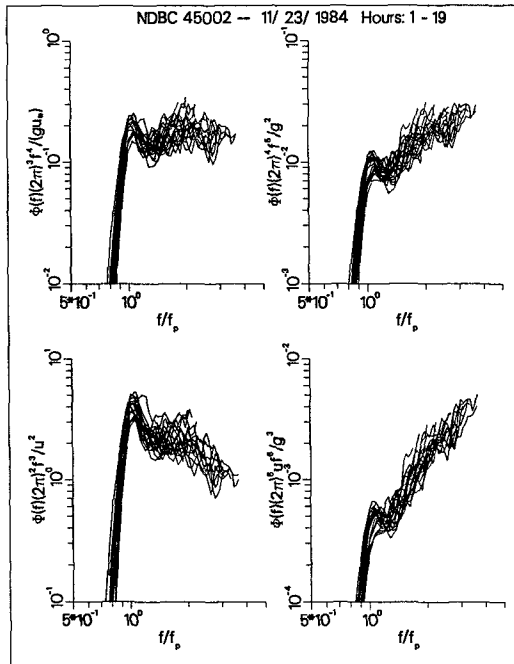


Figure 4. Normalizing the growing wave episode spectra with frequency exponents of 3, 4, 5, and 6 respectively shown clockwise from the lower left.

Rather than confining the exponent to merely -4 or -5, the formulations (1) and (2) can be generalized to allow any exponent i by

$$\Phi(f) = \alpha_i(2\pi)^{-i+1}g^{i-3}u_*^{5-i}f^{-i} \tag{3}$$

and then expect the normalized parameter $\Phi(f)(2\pi)^{i-1}g^{-i+3}u_*^{-5+if^i}$ to be constant and independent of frequency at the high frequency side if a given i is the valid exponent. Figure 4 shows the normalizations deduced from (3) for the same November 23, 1984 episode for $i = 3, 4, 5,$ and 6 . The results are now clearly distinctive. Only the bundle of f^{-4} normalizations shows a reasonably constant trend at the high frequency side. Thus this episode of wave growth spectra emerged to support the f^{-4} formulation.

Yet another normalization scheme is given in Donelan *et al.* (1985), which averages the high frequency side of the spectral density between $1.5f_p$ and $3f_p$ and uses it to normalize the whole spectrum. This scheme avoids the use of u_* , but the results are essentially the same as those in Figure 4.

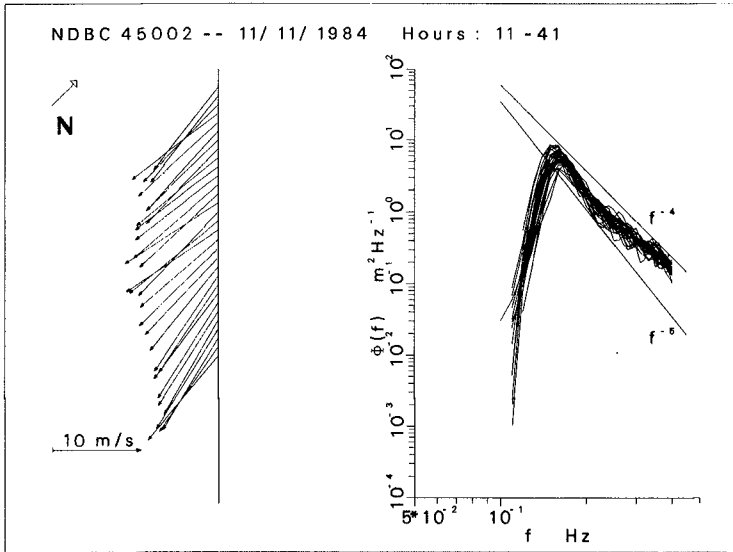


Figure 5. Wind vectors and wave spectra plots of a well-developed wave episode in Northern Lake Michigan.

An Episode of Well-Developed Waves

If all the field measurement could provide results that are similar to Figure 4, then the results would lead to evident conclusions. Expecting to show the universality of the f^{-4} equilibrium range sustained in Figure 4, another episode measured from the same Northern Lake Michigan buoy only 12 days earlier was selected. This was an episode of well-developed waves with winds blowing from the north at virtually constant wind speeds of 12 ms^{-1} over 30 hours. This wind field generated significant wave heights of 2 m to 2.8 m during the episode. As shown in Figure 5 all the spectra were banded together over all frequency components as expected for a fully-developed wave field. The same normalization deduced from (3) that led to Figure 4

is applied to this episode and presented in Figure 6. These results are also distinctive. The constant trend of the normalization at the high frequency side is displayed, however, by the f^{-3} normalization rather than the f^{-4} .

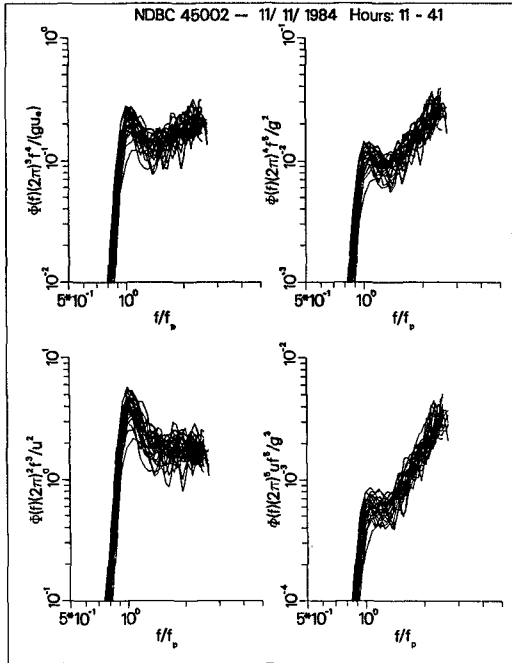


Figure 6. Normalizing the well-developed wave episode spectra with frequency exponents of 3, 4, 5, and 6 respectively shown clockwise from the lower left.

These two episodes as presented in Figures 4 and 6 are not typical. Rather these were ideal cases selected from a large amount of available data to provide definitive and consistent results. The results presented in Figures 4 and 6 are, however, clearly inconsistent.

An immediate question arises: Is this inconsistency due to instrumentation? This seems not to be the case, since both episodes were recorded by the same NDBC buoy 45002 during a time period the gauge was known to be working properly - and 45002 is one of the earliest and most persistently operating gauge in the Great Lakes. It is conceivable that the slope of equilibrium range in the wave spectra is not unique, and that the growing and well-developed waves may render different slopes.

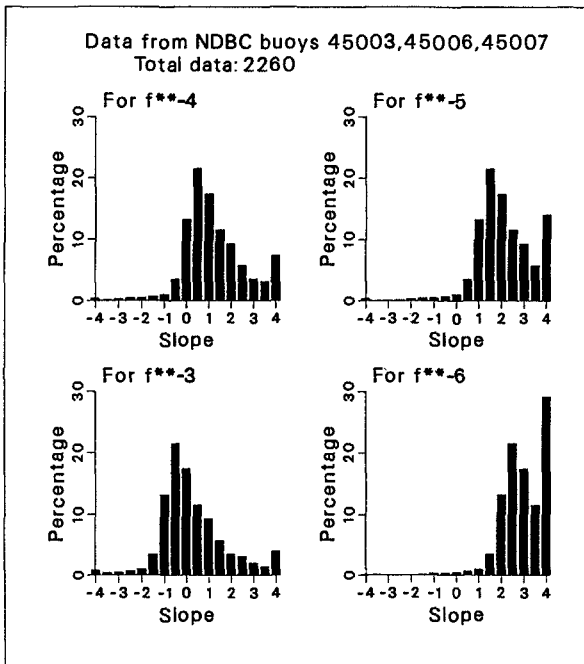


Figure 7. Percentage distributions of fitted slopes at the high frequency side of normalized wave spectra with frequency exponents of 3, 4, 5, and 6.

Examining Large Data Set

To further explore the "non-unique" nature of the equilibrium range slope in the wind wave spectra, many more data of selected episodes had to be examined. To do this systematically we arbitrarily combined 40 days of data that had been measured during October and November of 1984 from each of the three buoys 45003, 45006, and 45007 yielding a sample data set covering a variety of field measurement conditions. Spectra with peak-energy frequency higher than 0.25 hz were eliminated, to ensure the data were mainly well-developed or sustained growth waves. It is not practical to present graphs similar to Figures 4 and 6 for over 2200 items of data, but the same normalizations given in Figures 4 and 6 were applied to the data set and subsequently a linear regression line was fitted to each normalized spectrum between the frequency range of $1.5f_p$ and $3f_p$. A valid f^{-1} representation would render mostly "near zero" slopes to signify a constant trend over the normalized equilibrium range. Figure 7 presents the percentage distributions of these slopes, analogous to the four graphs given in Figures 4 and 6. Note that even though the four figures in Figure 7 were obtained from four separate normalizations, they were in fact the same distribution sliding over

different slope abscissa. In general, both f^{-3} and f^{-4} normalizations provide the most near zero slopes. This is consistent with the different results obtained in Figures 4 and 6, and it appears that the equilibrium range slope may very well not be unique.

To this point, in the normalization with f^{-1} , the equilibrium range frequency exponent i has been set to be 3, 4, 5, or 6. Alternatively, this requirement can be relaxed by simply fitting a linear regression line between the $1.5f_p$ and $3f_p$ range to the original wave spectra. The slope of the fitted line which may or may not be an integer, denoted by the exponent n as in f^{-n} , thus represents the actual measured equilibrium range slope of the spectra. The resulting percentage distribution of these exponents obtained from applying this approach to the combined data set is shown in Figure 8. Again, there is no single prevalent exponent, but the larger percentages lie between exponents 3.5 and 5.5.

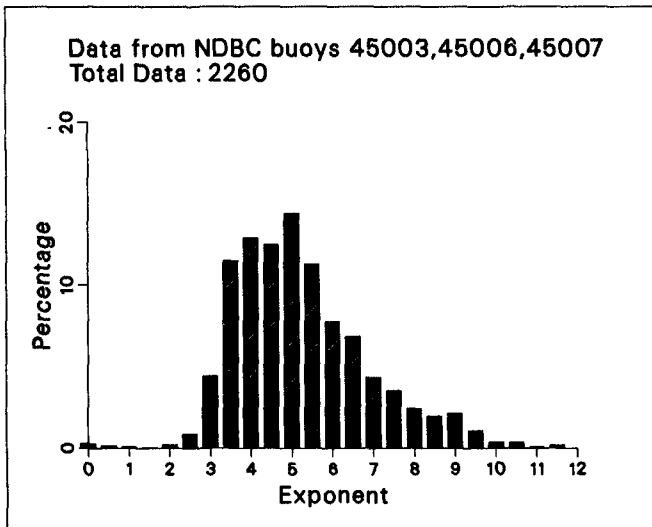


Figure 8. Percentage distribution of the exponents n obtained by fitting the high frequency side of the original wave spectra with a logarithmic line of the form f^{-n} .

All of these results are consistent in that they lack clear indications of the existence of a unique equilibrium range slope. The inconsistent results shown in Figures 4 and 6 can now be readily justified as being characteristic of the non-uniqueness of the equilibrium range slope.

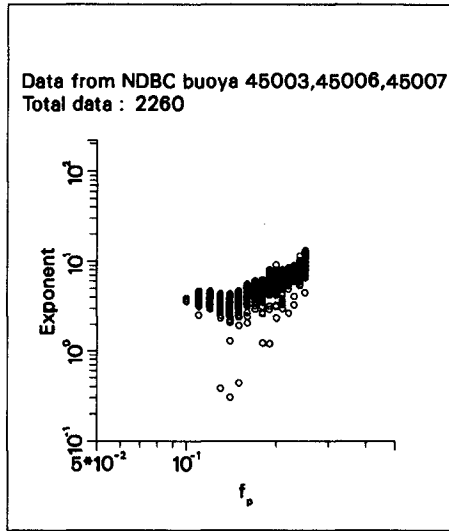


Figure 9. Correlating frequency exponents n of the equilibrium range, as in f^{-n} , with peak-energy frequency f_p .

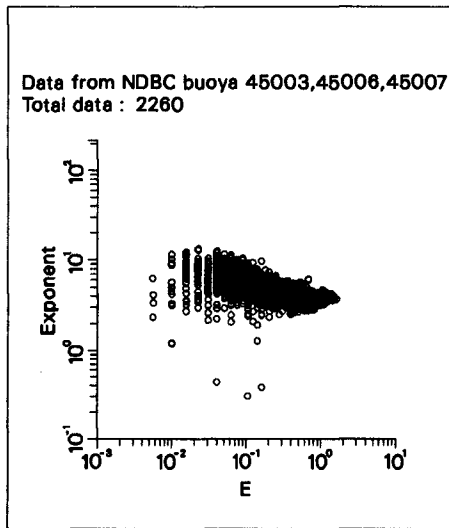


Figure 10. Correlating frequency exponents n of the equilibrium range, as in f^{-n} , with total energy E .

Correlating the Equilibrium Range Frequency Exponent

Having been generally established that the frequency exponent of equilibrium range is not unique in this extensive data set, it is of interest to examine briefly the variability of the exponent. Meaningful correlations are lacking between the exponent and commonly used nondimensional parameters; however, the exponent tends to correlate well with dimensional parameters. Figures 9, 10, and 11 show respectively the exponent's correlation with peak-energy frequency, total spectral energy, and wave momentum. Basically the figures show that the exponent, at early wave growth stage, exhibits a decreasing trend versus decreasing peak-energy frequency, increasing wave energy, and consequently, increasing wave momentum. At the stage of well-developed or fully-developed waves the exponent appears to be unchanging and eventually settled between the absolute values of 3 and 4.

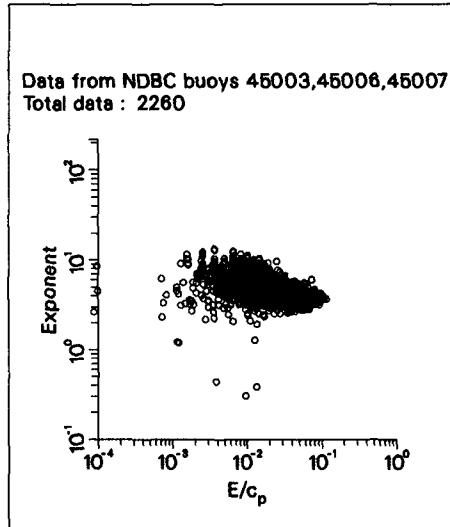


Figure 11. Correlating frequency exponents n of the equilibrium range, as in f^{-n} , with wave momentum E/c_p .

The non-uniqueness of the equilibrium range slope have been recognized by other investigators previously. Spectral representations with non-predetermined frequency exponent have been proposed for the high frequency side of the spectrum. Huang *et al.* (1981) deduced that the exponent was a function of the significant wave slope. Barenblatt and Leykin (1981) showed that the exponent relates to $g/(f_p u_*^2)$. The present analyses, however, do not seem to support either of these earlier results.

Concluding Remarks

This study was originally expected to simply delineate the applicability of f^{-4} or f^{-5} representation for the equilibrium range of the wind wave spectra. Examining over 2200 well-developed storm wave spectra recorded in the Great Lakes has not resolved the uncertainty. There are well documented cases for f^{-4} , f^{-5} , f^{-3} , and others, but the data seem not to converge and lead to a unique frequency exponent. As most of the exponents lie in the -3.5 and -5.5 range and between -3 and -4 for the fully developed cases, a representation of f^{-4} is perhaps a useful approximation for practical applications. What the correct slope is for the equilibrium range, or even whether or not a unique slope emerges, remains elusive and has yet to be satisfactorily substantiated.

REFERENCES

- Barenblatt, G. I. and I. A. Leykin, 1981: On the self-similar spectra of wind waves in the high frequency range. *Izvestiya, Atmospheric and Oceanic Physics Acad. Sci. USSR (English Translation)*, 17, 35-41.
- Battjes, J. A., T. J. Zitman, and L. H. Holthuijsen, 1987: A reanalysis of the spectra observed in JONSWAP. *J. Phys. Oceanogr.*, 17, 1288-1295.
- Businger, J. A., J. C. Wyngaard, Y. Izumi and E. F. Bradley, 1971: Flux-profile measurements in the atmospheric surface layer. *J. Atmos. Sci.*, 28, 181-189.
- Charnock, H., 1955: Wind stress on a water surface. *Quart. J. Roy. Meteorol. Soc.*, 81, 639-640.
- Darbyshire, J., 1955: An investigation of storm waves in the North Atlantic Ocean. *Proc. Roy. Soc.*, A230, 560-569.
- Donelan, M. A., J. Hamilton and W. H. Hui, 1985: Directional spectra of wind-generated waves. *Phil. Trans. R. Soc. Lond.*, A 315, 509-562.
- Hamilton, G. D., 1986: National Data Buoy Center programs. *Bull. Am. Meteorol. Soc.*, 67, 411-415.
- Huang, N. E., S. R. Long, C. C. Tung, Y. Yuan, and L. F. Bliven, 1981: A unified two-parameter wave spectral model for a general sea state. *J. Fluid Mech.*, 112, 203-224.
- Liu, P. C., 1971: Normalized and equilibrium spectra of wind waves in Lake Michigan. *J. Phys. Oceanogr.*, 1, 249-257.
- Liu, P. C. and D. J. Schwab, 1987: A comparison of methods for estimating u_w from given u_z and air-sea temperature differences. *J. Geophys. Res.*, 92C, 6488-6494.

- Neumann, G., 1953: On ocean wave spectra and a new method for forecasting wind generated sea. *Tech. Memo. 43*, U. S. Beach Erosion Board, 42p.
- Phillips, O. M., 1958: The equilibrium range in the spectrum of wind-generated ocean waves. *J. Fluid Mech.*, 4, 426-434.
- Phillips, O. M., 1985: Spectral and statistical properties of the equilibrium range in wind-generated waves. *J. Fluid Mech.*, 156, 505-531.
- Roll, H. U. and G. Fischer, 1956: Eine kritische Bemerkung zum Neumann Spektrum des Seeganges. *Deuts. Hydrogr. Z.*, 9, 9-14.
- Schwab, D. J. and P. C. Liu, 1985: Intercomparison of wave measurements obtained from a NOMAD buoy and from a Waverider buoy in Lake Erie. *Proceedings Oceans 85*, MTS and IEEE Ocean Engineering Society, 1131-1137.
- Toba, Y., 1973: Local balance in the air-sea boundary processes. III. On the spectrum of wind waves. *J. Oceanogr. Soc. Japan*, 29, 209-220.

CHAPTER 79

SURF BEAT GENERATION ON A MILD-SLOPE BEACH

Hemming A. Schäffer¹ and Ib A. Svendsen²

ABSTRACT: Two dimensional generation of surf beats by incident wave groups is examined theoretically. An inhomogeneous wave equation describes the amplitude of the surf beat wave. The forcing function is the modulation of the radiation stress. The short waves are amplitude modulated both outside and inside the surf zone causing the long wave generation to continue right to the shore line. Resonant generation as shallow water is approached is included. The analytical solution is evaluated numerically and shows a highly complicated amplitude variation of the surf beat depending on the parameters of the problem.

1. INTRODUCTION

Field observations show that on mild slope beaches a significant amount of wave energy occurs at frequencies far below the peak frequency of the incoming sea waves. The existence of such long waves were first reported by Munk (1949) who also speculated that the components with period around 2 minutes were caused by variation in height of the surf and he coined the name "surf beats." Also Tucker (1950) found long waves of 1-5 minute period with a height that increase linearly with the height of the short period sea, and a time lag corresponding approximately to the time it would take for a wave group to reach the breaker zone or beach and for a long wave generated there to be reflected back to the observation point. Longuet-Higgins and Stewart (1962,64) suggested that while the short waves are destroyed by breaking, the set-down wave generated by and following the wave groups outside the surf zone as a forced wave is reflected at the beach and propagates seaward as a free wave.

Since the first recording, numerous observations have shown that the energy of surf beat can actually be very substantial and in some cases even exceed that of the high frequency wind waves (Wright et al., 1982) and the amplitudes at the shoreline can be comparable to that of wind waves (Guza & Thornton, 1982,85).

Although no final proof has been established, it seems widely accepted today that the surf beats are generated by mechanisms in the nearshore region and that they are associated with modulations of the amplitude of the short-period incoming waves. However, several possible ways in which energy can be transferred from the high

¹Visiting Scholar, Dept. of Civil Engineering, Univ. of Delaware, Newark, DE 19716 (present address Inst. Hydrodyn. & Hydr. Eng., DTH, Denmark).

²Professor, Dept. of Civil Engineering, Univ. of Delaware, Newark, DE 19716 (mailing address for this paper).

frequency wind waves to the surf beats have been considered with more or less decisive results. It is likely that several possible mechanisms can be active either separately or at the same time. Closely related to the question of generation is the nature of the long wave motion in the nearshore region. In particular, it has been discussed extensively whether the nearshore long wave motion is dominated by forced or free waves; by progressive or standing waves, and whether it consists of crossshore directed (essentially two-dimensional) waves or trapped edge waves, which are three dimensional reflection-refraction wave patterns.

The present work assumes that the surf beat can exist as a two-dimensional motion. It is inspired by the work of Symonds et al. (1982) who investigated a mechanism for generating two dimensional surf beat that had not been considered previously. That mechanism is based on the fact that waves initially of different height will break at different distances from the shore line and (more important) have a different height at breaking. The surf beats are generated by the variation which this breaking pattern causes in the total radiation stress in the region between the extreme seaward and shoreward positions of the breakpoint. The varying breakpoint generates a shoreward moving long wave with the frequency of the wave groups, and since the forcing takes place only in the breaker region the long wave is a free wave through the rest of the surf zone. At the shoreline this wave is fully reflected so that a standing long wave is formed in the surf. Outside the surf zone the reflected wave continues seaward as a progressive wave.

In the model of Symonds et al., the groupiness of the waves is totally destroyed at the breaking point which is why there is no surf beat generation in the actual surf zone. A saturation model with a constant wave height to water depth ratio is used for the waves in the surf zone.

In the work presented in the following, we allow the wave groups to be maintained all the way to the shoreline. Measurements as well as experiments with the surf zone model developed by Svendsen (1984) indicates that if there is a variation in wave height at the breaker point the waves will remain different through the surf zone. For simplicity, we model this by introducing a breaker height variation at a fixed breaking point. This will represent the other extreme relative to the situation studied by Symonds et al. Observations show that the true picture probably represents a combination of the two: a varying breakpoint with some groupiness left in the surf zone. A somewhat similar problem was studied by Foda & Mei (1981) using a multiple scale expansion and different assumptions about the relative magnitude of the wave components involved. Our result contains a resonant interaction which was also included in the analysis by Freilich & Guza (1984) although under different assumptions about the magnitude of the bottom slope.

2. DESCRIPTION OF MODEL CONDITIONS

Since the phenomena associated with wave groups are quite complicated it may be useful to give a more detailed description of the situation which is created mathematically in the following.

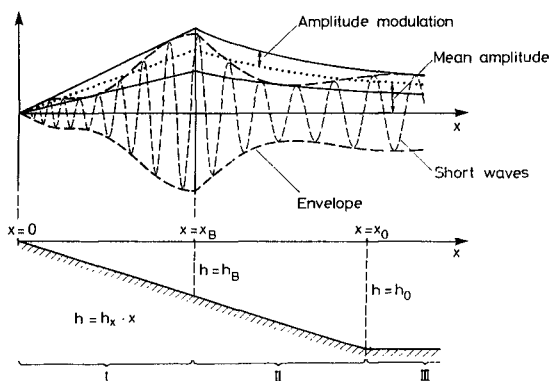


Fig. 1: Sketch of bottom topography and short wave variation considered.

Region III

The situation is depicted in Fig. 1. We consider a region of constant depth which could be a continental shelf, say, (region III in the figure). In the present study we simplify by letting the groupiness of the waves be caused by two regular incoming wave trains with slightly different wave number $k_0(1+\epsilon)$ and $k_0(1-\epsilon)$ the second with a much smaller amplitude than the first. This implies that the surf beat wave becomes a simple wave of constant period which allows us to seek analytical solutions to the problem. The basic equations used, however, can also be applied to the general case of a time varying wave height as in a train of irregular Stokes waves, but this would require a numerical solution.

In region III we assume a quasi-uniform state. The modulation of the waves causes a variation in radiation stress which generates a set down wave, and we assume that the length of the wave height modulation is much larger than the depth so that the set down wave is a long wave. This set down wave and its propagation into the shore region was neglected by Symonds et al. (1982).

Present in region III is also an outgoing long wave which represents the results of the transformations and reflections taking place in the nearshore region. The amplitude and phase of that wave is one of the unknowns of the problem.

Region III is primarily introduced to be able to establish well defined and reasonably simple seaward boundary conditions for the problem.

Region II

In region II the depth is decreasing sufficiently gently that we can assume local solutions for short and long wave components. Thus the short wave will be shoaling towards the breaking point x_B . During this process, however, the balance between the variation in radiation stress and set down wave is constantly changing which causes the forced set down wave to grow. As the short waves approach breaking their group velocity approaches that of the forced wave creating a state of almost resonance. We describe this dynamical process (in contrast to the equilibrium situation in region III) by a WKB approximation.

For most values of the governing parameters we find that in spite of the resonant interaction the energy transferred from the short wave

to the forced wave is relatively small, and we therefore omit in the present paper to take the effect of this energy flux into account in the development of the short waves. There is no principle difficulty though in extending the formulation to include this effect as well.

At the transition point x_0 between region III and II the solutions for the two regions are matched by requiring continuity in mass and momentum flux for the long wave solution. These conditions cause a partial reflection at x_0 of the set down waves, whereas it is assumed that no such reflection occurs for the short waves (either because of sufficiently deep water or because the transition between horizontal and sloping bottom actually takes place sufficiently smoothly to allow the short waves to adjust).

Region I

At x_B the short waves are assumed to break. Since there is a temporal variation in the height of the waves reaching this point, we have a time-varying breaker height at x_B . The dissipation of energy in the surf zone is proportional to H^3 and therefore, although the wave height variation will decrease shorewards, those waves that are highest at the (fixed) breakpoint will always remain the highest, etc. Thus this mechanism implies that the groupiness of waves remains present all the way to the shoreline. It also implies that the generation process responsible for the modification of the forced long wave continues through the surf zone.

Again we have chosen to use the simplest possible description of the processes involved. Thus a saturation model based on $a=\gamma h$, where h is the water depth, is used to describe the wave height variation in the surf zone of the short waves. Essentially the specification of wave height as a fraction of depth replaces solution of the energy equation for the short waves. Since the short wave height varies as the groups propagate shorewards, this means that the parameter γ is $\gamma(x,t)$.

The matching at x_B again requires continuity in the mass and momentum flux for the long wave motion. The abrupt shift in the rate of change of the radiation stress represents a source of difference at the two sides of the matching point.

At the shoreline the long wave is fully reflected and radiated seaward as a free wave. The background for this assumption is discussed below and involves some aspects that, although known from other areas of wave dynamics, do not seem to have been applied before to analyze the behavior of surf beats near the shoreline.

3. THE GOVERNING EQUATIONS

The governing equations for the surf beat are derived from the depth integrated and time averaged equations for waves and currents (see e.g. Phillips, 1977; Mei, 1983). In those equations the set-up/set-down will then correspond to the long wave surf beat and the time-varying current will represent the particle motion in that long wave. Since the equations are derived under the assumption that the current velocity is uniform over depth, their use implies that we assume the surf beat is everywhere a long wave (as already indicated). On the other hand, the equations contain all relevant non-linear terms in the current discharge and set-up (including the momentum flux due to the mass flux Q_S in the waves). Thus the description of the long wave component of the wave motion is actually equivalent to that given by the nonlinear shallow water equations.

The total water particle velocity u is split into

$$u = u_w + U \quad (3.1)$$

where U is the velocity in the current, u_w that of the oscillatory motion so that $\bar{u}_w = 0$ below wave trough level ($\bar{\quad}$ meaning average over a wave period).

The relevant equations are then the continuity equation

$$\frac{\partial b}{\partial t} + \frac{\partial \bar{Q}}{\partial x} = 0 \quad (3.2)$$

where b is the elevation of the mean water surface and

$$\bar{Q} = Q_c + Q_s \quad ; \quad Q_s = \overline{\int_{-h_0}^{\eta} u_w dx} \quad ; \quad Q_c = \int_{-h_0}^c U dz \quad (3.3)$$

η is the total surface elevation measured from a horizontal reference level. The equation of shore-normal (x) momentum is

$$\frac{\partial \bar{Q}}{\partial t} + \frac{\partial}{\partial x} \left[\frac{\bar{Q}^2}{h} + \frac{1}{\rho} S_{xx} \right] + gh \frac{\partial b}{\partial x} + \frac{\bar{\tau}_b}{\rho} = 0 \quad (3.4)$$

in which h is the local depth (including the long wave surface elevation), S_{xx} is the shore wave radiation stress and $\bar{\tau}_b$ the mean bottom shear stress (which we will neglect here).

Since we are particularly interested in the surface elevation b of the long waves we first eliminate \bar{Q} from the linear terms of (3.2) and (3.4) by cross differentiation. This yields

$$\frac{\partial^2 b}{\partial t^2} - \frac{\partial}{\partial x} \left[gh \frac{\partial b}{\partial x} \right] - \frac{\partial}{\partial x} \left[\frac{\bar{Q}^2}{h} + \frac{1}{\rho} S_{xx} \right] = 0 \quad (3.5)$$

It is assumed that the total motion of any point consists of a quasisteady regular wave on which we superimpose a small perturbation (the amplitude modulation) that varies in time. Thus all wave averaged quantities have the form

$$f(x, t) = f_0(x) + f_1(x, t) \quad (3.6)$$

In particular the depth h is

$$h(x, t) = h_0(x) + b_0(x) + b_1(x, t) \quad (3.7)$$

By assuming that there is a steady state basic solution of wave height variation it can be inferred that for this solution there is no net mass flux. Hence by continuity $Q_0 = 0$ and

$$\bar{Q}(x, t) = Q_1(x, t) \quad (3.8)$$

When these assumptions are substituted into (3.5) we get the following equation for b_1

$$\frac{\partial^2 b_1}{\partial t^2} - \frac{\partial}{\partial x} \left[g(h_0 + b_0) \frac{\partial b_1}{\partial x} + gb_1 \frac{\partial b_0}{\partial x} \right] - \frac{\partial^2 S_{xx,1}}{\partial x^2} = 0 \quad (3.9)$$

where $S_{xx,1}$ represents the variation in S_{xx} due to the wave height modulation for the short waves (vide (3.6)).

Finally, realizing that at most points $b_0 \ll h_0$ we neglect terms proportional to $b_0 b_1$ so that the governing equation for the surf beat amplitude b_1 becomes

$$\frac{\partial^2 b_1}{\partial t^2} - \frac{\partial}{\partial x} \left(gh_0 \frac{\partial b_1}{\partial x} \right) - \frac{1}{\rho} \frac{\partial^2 S_{xx,1}}{\partial x^2} \quad (3.10)$$

This is a wave equation with a forcing term which represents the effect the wave height modulation has on the slowly varying surf beat. It is the same equation that was used by Symonds et al. (1982) but only in the region of the breaker point variation. Chu & Mei (1970) and Mei & Benmoussa (1984) derive the same equation for 3D by a multiple scale expansion of slowly varying Stokes waves.

Following Mei & Benmoussa (1984) we let the short wave motion be composed of two waves with almost the same wave numbers

$$\begin{aligned} \eta_1 &= \frac{1}{2} a_1 \exp \left[i \int k_1 dx + \omega_1 t \right] + * \\ \eta_2 &= \frac{1}{2} \delta a_1 \exp \left[i \int k_2 dx + \omega_2 t \right] + * \end{aligned} \quad (3.11)$$

where * means complex conjugate.

In region III we have k_1 and k_2 constant and we define k_0 and ϵ so that

$$k_1 = k_0(1+\epsilon) \quad ; \quad k_2 = k_0(1-\epsilon) \quad \text{for } x > x_0 \quad (3.12)$$

The equivalent change in wave frequencies are given by the dispersion relation. We have

$$\omega_g = \frac{1}{2} (\omega_1 - \omega_2) \approx \frac{\partial \omega}{\partial k} \cdot \epsilon k_0 = c_{g0} \epsilon k_0 = \frac{c_{g0}}{c_0} \epsilon \omega_0 \quad \text{for } x > x_0 \quad (3.13)$$

where c_{g0} is the group velocity in region III for the wave with wave number k_0 and frequency ω_0 and $c_0 = \omega_0/k_0$. Equation (3.13) also defines ω_0 as approximately $(\omega_1 + \omega_2)/2$.

The total short wave motion $\eta = \eta_1 + \eta_2$ can then be written

$$\eta = \frac{1}{2} A \exp \left\{ i \left[\int k_0 dx + \omega_0 t \right] \right\} + * \quad (3.14)$$

where A is a complex amplitude. With

$$\Omega_0 = \frac{c_{g0}}{c_0} \omega_0 \quad , \quad K_0 = k_0 \cdot \frac{c_{g0}}{c_g} \quad (3.15)$$

we get

$$A = a_1 \left[\exp \left\{ i \epsilon \left[\int K_0 dx + \Omega_0 t \right] \right\} + \delta \exp \left\{ -i \epsilon \left[\int K_0 dx + \Omega_0 t \right] \right\} \right] \quad (3.16)$$

or

$$\left. \begin{aligned} A &= a_1 \left[e^{i\theta} + \delta e^{-i\theta} \right] \\ \text{where } \theta &= \epsilon \left[\int K_0 dx + \Omega_0 t \right] \end{aligned} \right\} \quad (3.17)$$

The radiation stress S_{xx} for the short waves is then given by

$$\frac{1}{\rho} S_{xx} = \frac{g|A|^2}{2} \left[\frac{2c_g}{c} - \frac{1}{2} \right] \quad (3.18)$$

If we therefore write S_{xx} according to (3.6) we see that

$$\frac{1}{\rho} S_{xx,0} = \frac{g}{2} a_1^2 (1+\delta^2) \left[\frac{2c_g}{c} - \frac{1}{2} \right] \quad (3.19)$$

$$\frac{1}{\rho} S_{xx,1} = g a_1^2 \delta \left[\frac{2c_g}{c_0} - \frac{1}{2} \right] \exp(2i\theta) \quad (3.20)$$

Inside the surf zone the more general expression applies:

$$\frac{1}{\rho} S_{xx} = g|A|^2 P \quad (3.21)$$

In the present context, however, we will, for simplicity, allow P to be approximated by $(2c_g/c_0 - 1/2)$ since this only changes the results quantitatively not qualitatively.

The variation of b_1 and $S_{xx,1}$ is described by

$$b_1 = b_a \exp(2i\epsilon\Omega_0 t) \quad (3.22)$$

$$S_{xx,1} = S_a \exp(2i\epsilon\Omega_0 t) \quad (3.23)$$

so that

$$S_a = a_1^2 \delta \rho g \left[\frac{2c_g}{c_0} - \frac{1}{2} \right] \exp\left(2i\epsilon \int K_0 dx\right) \quad (3.24)$$

which substituted into (3.10) yields

$$\frac{\partial}{\partial x} \left[h_0 \frac{\partial b_a}{\partial x} \right] + 4\epsilon^2 \frac{\Omega_0^2}{g} b_a = -\frac{1}{\rho g} \frac{\partial^2 S_a}{\partial x^2} \quad (3.25)$$

This is the equation we solve.

Variation of Carrier Wave Amplitude

The two wave components a_1 and $a_1\delta$ which together form the carrier wave will show a variation that in region II corresponds to a simple shoaling under conservation of energy flux. Thus in region II we have

$$a_1 = \left(\frac{c_g \infty}{c_g} \right)^{1/2} a_\infty \quad ; \quad a_\infty = a_1(h=\infty) \quad (3.26)$$

In the surf zone (region I) the wave heights actually ought to be determined by one of the surf zone models developed in recent years as e.g. Svendsen (1984). This implies solving the energy and momentum equations using realistic descriptions for the relevant wave properties such as radiation stress, energy flux, and energy dissipation. If we assume that the wave height modulation in the wave groups is moderate, the breaker type will be virtually the same for all waves. Except perhaps for violently plunging waves (for which we know very little) this means that if two waves initially have different heights at the breaker point, the highest will remain so throughout the surf zone. Essentially this further implies that some groupiness is conserved also beyond the breaker point. How much of the original wave height modulation that actually is maintained will depend on how the variation in wave height influences the position of

the breaker point, an effect we, as mentioned earlier, have neglected here by using a fixed breaking point.

The above mentioned groupiness would result also from the wave model by Svendsen (or other wave models based on solving the energy equation). For simplicity, however, we choose a simpler representation of this physical feature by using a modified saturation model. In the surf zone we let

$$|A| = \gamma h \quad (3.27)$$

where $\gamma^2 = \gamma_0^2 + \gamma_1^2 e^{2i\theta}$. Particularly for $|A|^2$ we get

$$\begin{aligned} |A|^2 &= |A_0|^2 + |A_1|^2 \\ &= \left(\gamma_0^2 + |\gamma_1|^2 \left(e^{2i\theta} + * \right) / 2 \right) h^2 \end{aligned} \quad (3.28)$$

The values of γ_0 and γ_1 are then according to the saturation hypothesis determined by the breaker heights of the waves. Since before breaking we have

$$|A|^2 = (a_{\infty}^2(1+\delta^2) + a_{\infty}^2\delta(e^{2i\theta} + *)) \frac{c_{g\infty}}{c_g} \quad (3.29)$$

we get

$$\gamma_0^2 = \frac{a_{\infty}^2(1+\delta^2)}{c_{gB}^2 h_B^2} c_{g\infty} \quad (3.30)$$

and

$$\gamma_1^2 = \frac{2a_{\infty}^2\delta}{c_{gB}^2 h_B^2} c_{g\infty} \quad (3.31)$$

where index ∞ refers to deep water, index B to the values at the breaking point.

4. MATCHING AND BOUNDARY CONDITIONS

To obtain a solution over the three regions described in Section 2, we need a boundary condition at the outer end of region III, matching conditions between II and III and between I and II, and a boundary condition at the shore line. Since (3.25) is a second order equation a total 2x3 conditions are required to establish the solutions in the three regions.

Seaward Radiation Condition

The seaward boundary condition is a radiation condition stating that there are no free waves propagating towards the shore, only the bounded (and known) set down wave.

Matching Conditions

At x_0 and x_B the propagation conditions change, which causes changes in the constants of the general solution. We ensure continuity at those points by requiring that

$$\begin{bmatrix} b_a \end{bmatrix}_{x_0^-}^{x_0^+} = 0 \quad ; \quad \begin{bmatrix} b_a \end{bmatrix}_{x_B^-}^{x_B^+} = 0 \quad (4.1a,b)$$

This corresponds to assuming continuity in mass flux across x_0 and x_B . Similarly, continuity in momentum flux can be obtained by applying (3.4) on the two sides of each matching point in combination with (4.1a,b). This yields

$$\left[\frac{\partial b_a}{\partial x} \right]_{x_0^-}^{x_0^+} = - \frac{1}{\rho g h(x_0)} \left[\frac{\partial S_a}{\partial x} \right]_{x_0^-}^{x_0^+} \quad (4.2a)$$

$$\left[\frac{\partial b_a}{\partial x} \right]_{x_B^-}^{x_B^+} = - \frac{1}{\rho g h_B} \left[\frac{\partial S_a}{\partial x} \right]_{x_B^-}^{x_B^+} \quad (4.2b)$$

These relations indicate that db_a/dx will show a discontinuity at the two matching points, of which the one at x_B is by far the most significant.

Boundary Condition at the Shore Line

The model assumes that the short waves are entirely destroyed by breaking. No similar mechanism, however, is available for the long forced wave which will approach the shore line with a finite amount of energy. The wave must therefore be fully reflected there.

It is worth noticing that near the shoreline we actually stress the assumptions underlying the solution, which are that the bottom slope is gentle (i.e., $\Lambda = h_x L/h$ remains small) and the amplitude to depth ratio γ_s is small. As $h \rightarrow 0$, however, wave length of the long wave will go to zero as $h^{1/2}$. Hence the slope parameter Λ will grow as $h^{-1/2}$ for a constant h_x . Similarly, the amplitude to depth ratio of the long wave does not remain small.

The growth of Λ and γ_s near the shoreline indicates that the motion is more appropriately described by the nonlinear shallow water equations. However, the basic equations (3.2) & (3.4), and therefore also (3.5), remain valid even under those conditions since no assumptions as to the magnitude of Λ or γ_s have been invoked at the derivation of those equations. As mentioned previously, (3.2) and (3.4) correspond to this approximation, so that, close to the shore those two equations represent the appropriate description. Further away from the shore the NLSW-equations can then be matched to the linear solution as e.g. the wave equation (see Carrier, 1966).

In the present case (3.10) is a linearized form of (3.5) since some approximations have been introduced to get from (3.5) to (3.10). Therefore (3.10) does not represent a proper approximation as $h \rightarrow 0$.

This also applies to the WKB approximation used to transform (3.10) to (3.25), since that approximation also requires $\Lambda \ll 0(1)$ corresponding to small changes in depth over a wave length. It does of course also require $\gamma_s \ll 1$.

For the time being we have chosen to disregard the problem and simply assume that the linearized equation (3.22) applies to the shoreline. The requirement of full reflection then corresponds to requiring that close to the shoreline the wave motion is a purely standing wave with zero net energy flux. Since this approach is in agreement with the actual physical situation it only means that the description is not accurate near the shoreline. At some distance this solution should be the same as if a more correct matching with the NLSW approximation had actually been made.

5. SOLUTION FOR THE SURF BEAT AMPLITUDE

The complete solution to the homogeneous version of (3.25) can be expressed in terms of two linearly independent Hankel functions representing two waves propagating shoreward and seaward respectively. The complete solution to the inhomogeneous equation (3.25) can then be found by the method of variation of parameters. In region I and II we get ($i = 1, 2$) the complex solution

$$b_{a,i} = \left[H_0^{(1)}(a\sqrt{x}) \left[-C_i^{(1)} + \int^x H_0^{(2)}(a\sqrt{x}) \frac{d^2 S_a}{dx^2} dx \right] - H_0^{(2)}(a\sqrt{x}) \left[C_i^{(2)} + \int^x H_0^{(1)}(a\sqrt{x}) \frac{d^2 S_a}{dx^2} dx \right] \right] \frac{i\pi}{2\rho g h_x} \quad (5.1)$$

where $a = 4\omega g / \sqrt{g h_x}$. In region III the solution is

$$b_{a,3} = C_3 e^{i2\omega g x / \sqrt{g h_0}} + b_{a,0} \quad (5.2)$$

where $b_{a,0}$ is the incoming, forced set-down wave, for which we have

$$b_{a,0} = -\frac{1}{\rho} \frac{S_a}{g h_0 - c_{g0}^2} \quad (5.3)$$

The five constants $C_{1,2}^{(1)}$, $C_{1,2}^{(2)}$ and C_3 are then determined by the four matching conditions and by the boundary condition at the shoreline.

The latter requires that the amplitude of the two wave components are the same and hence yields directly

$$C_1^{(1)} = C_1^{(2)} \quad (5.4)$$

The four other constants are found numerically by solution of the flow complex equations resulting from applying the matching equations. The details are left out here.

6. NUMERICAL RESULTS

After determining the equations for the integration constants in (5.1) (5.2) and (5.3) numerical results have been calculated by evaluating the $\partial^2 S_a / \partial x^2$ term by numerical differentiation and similarly the integrals by numerical quadrature.

The problem under study has a substantial number of independent parameters. Clearly the bottom slope h_x is a parameter, but since the bottom steepness that the waves actually "feel" depends on the waterdepth to wavelength ratio the relevant measure of the bottom slope can be shown from the solution to be $\Lambda = h_x L/h$ where L is the local wave length defined as cT . Λ is assumed to be small in order to allow the waves to adjust to the local depth as assumed in the basic equations. In the solution Λ occurs in connection with the matching process at h_0 and h_B which leads to the two parameters

$$\Lambda_0 = \frac{h_x L_0}{h_0} \quad \& \quad \Lambda_B = \frac{h_x L_B}{h_B} \quad (6.1)$$

The value of Λ_B is actually determined by the assumed breaker index γ .

Other (small) parameters are the ratio of group wave number to carrier wave number

$$\epsilon = (k_1 - k_2) / 2k_0 \quad (6.2)$$

and the steepness of the carrier wave system

$$\epsilon_s = a_m \omega_0^2/g \tag{6.3}$$

The small parameter

$$\delta = a_2/a_1 \tag{6.4}$$

describes the weakness of the amplitude modulation causing the wave groups. Hence the problem is characterized by a total of five (small) parameters. In addition the dimensionless carrier wave frequency $\omega_0^2 h/g$ is of course important for the carrier wave description and particularly the value of $\omega_0^2 h_0/g$ connects the scale of the bottom geometry (h_0) to the length scale of the waves (g/ω_0^2).

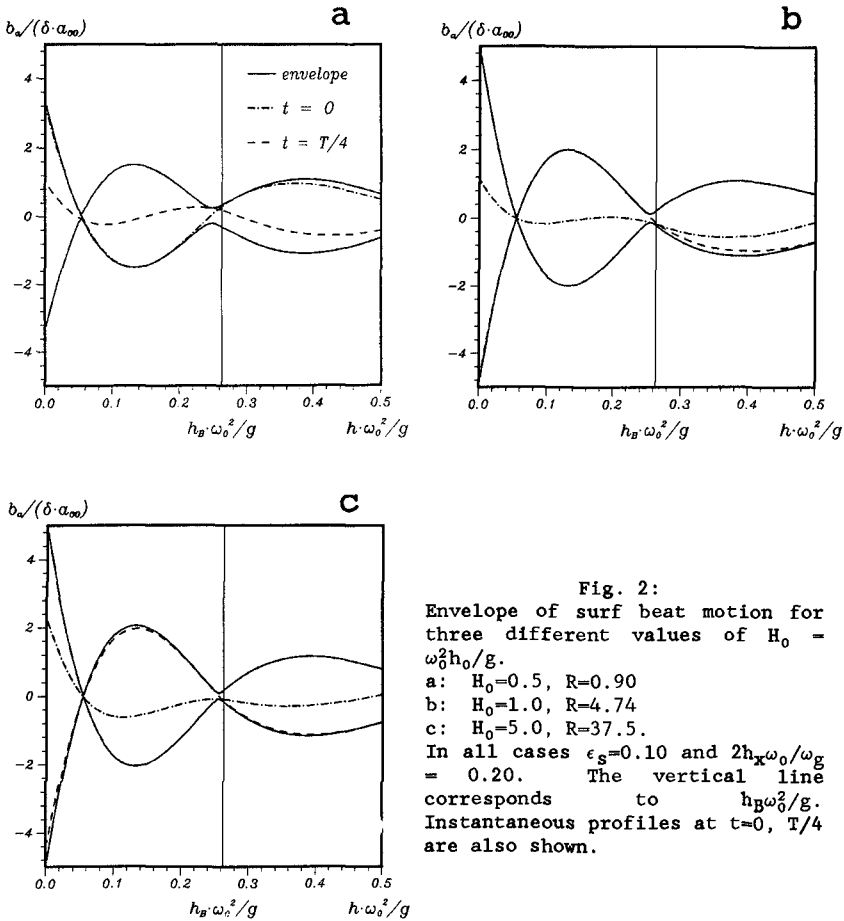


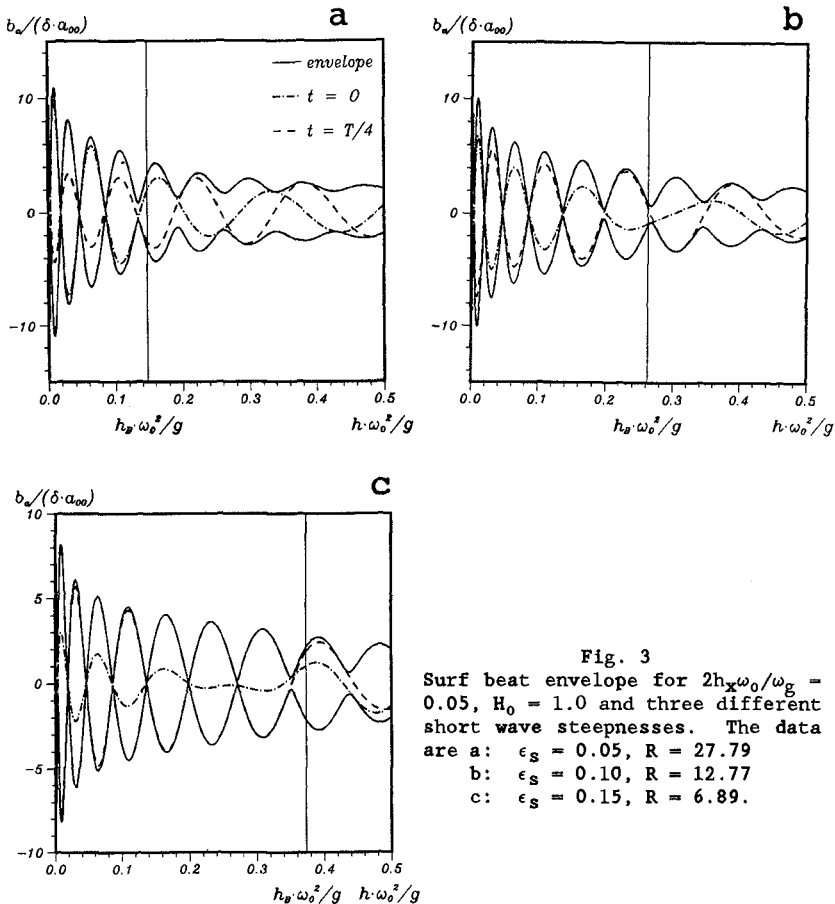
Fig. 2:
Envelope of surf beat motion for three different values of $H_0 = \omega_0^2 h_0/g$.
a: $H_0=0.5, R=0.90$
b: $H_0=1.0, R=4.74$
c: $H_0=5.0, R=37.5$.
In all cases $\epsilon_s=0.10$ and $2h_x \omega_0/\omega_g = 0.20$. The vertical line corresponds to $h_B \omega_0^2/g$. Instantaneous profiles at $t=0, T/4$ are also shown.

Fig. 2 shows the variation of the solution for the envelope b_a for a selection of parameter values. The three parts a, b & c corresponds to three different values of the parameter $H_0 = \omega_0^2 h_0/g$ (0.5, 1.0 and 5.0). In all three cases all other parameters have been kept

unchanged so that the three figures indicate the effect of increasing the depth h_0 in front of the slope (see Fig. 1) relative to the wave length of the carrier wave system.

Since it is difficult to compare the wave patterns as a whole we have chosen here to focus on the ratio between the amplitude of the wave propagating seawards in the constant region depth over the amplitude of the incoming set-down wave in the same region. This "reflection coefficient" R is a measure of how much the original set-down wave is amplified by energy transferred from the short wave system.

The variation of R we see in Fig. 2 is mainly due to the fact that the amplitude of the free (reflected) wave varies as $h_0^{-3/2}$ whereas the set-down wave decreases as h_0^{-1} as h_0 increases. Notice that for $H_0 = 1.0$ and 5.0 the figure does not show the whole slope region.



In Fig. 3 the total slope length has been kept constant and the position of the breaker point varied. The reflection coefficients of up to 28 show a significant amplification of the set down wave. On

the other hand, the value of R is biggest for the most narrow surf zone.

From those observations one might arrive at the conclusion that the surf beat generation primarily takes place on the slope seaward of the breaker point. This idea might be further supported by the fact that in the surf zone the minimum envelope amplitudes are very small as if the amplitude of the outgoing, reflected wave were nearly the same as the shoreward moving surf beat. (Clearly this becomes a better and better approximation the closer we get to the beach, as should be expected.)

To check this conjecture Fig. 4 shows numerical experiments with the same general data as in Fig. 3b (which is repeated in Fig. 4a for comparison). In Fig. 4b, however, we have artificially suppressed the surf beat generation inside the surf zone by letting the right hand side of (3.25) be zero in region I. Thus the long wave in the surf zone is now a standing free wave. We see there is a substantial reduction in the height of the surf beat generated as measured by the reflection coefficient, which drops from 12.77 to 8.58.

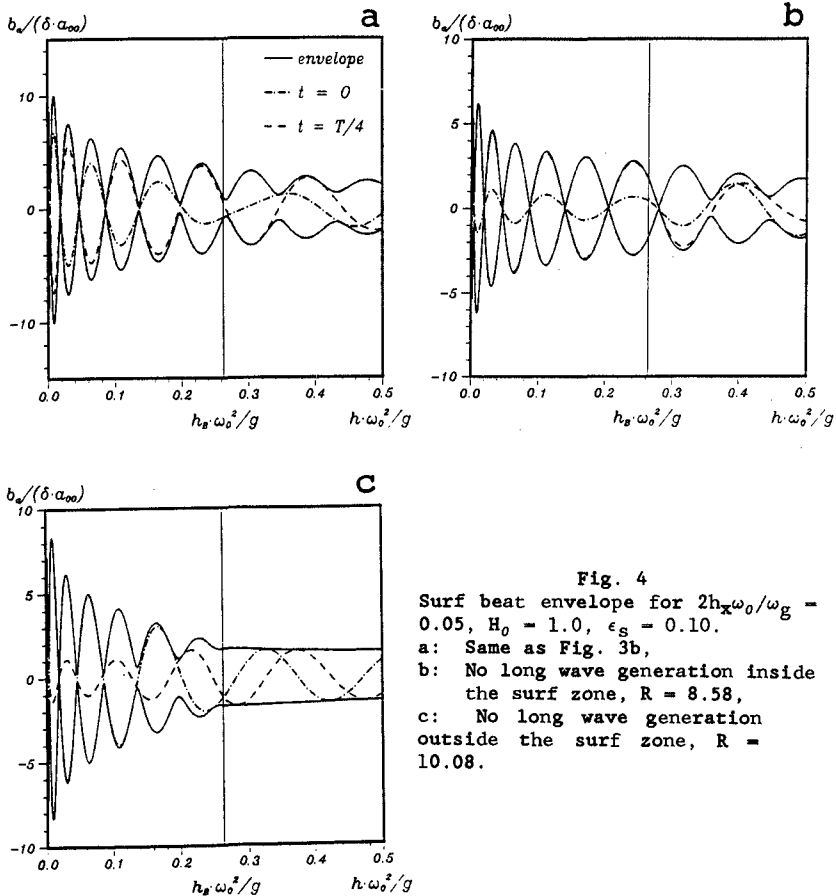


Fig. 4
Surf beat envelope for $2h_s \omega_0 / \omega_g = 0.05$, $H_0 = 1.0$, $\epsilon_S = 0.10$.
a: Same as Fig. 3b,
b: No long wave generation inside the surf zone, $R = 8.58$,
c: No long wave generation outside the surf zone, $R = 10.08$.

Similarly Fig. 4c shows a numerical experiment in which there is no long wave generation at all until in the surf zone. There the long wave motion outside the breaker point is a purely progressive wave moving seaward after having been reflected from the shoreline. This seaward oriented wave is now 10.8 times the set-down wave we would have had in the constant-depth region III had the generation been normal. In Fig. 5a-c the same type of experiment has been repeated for the same wave period and slope width but with the breaker point moved seaward by a change in carrier wave steepness. The picture is seen generally to be the same.

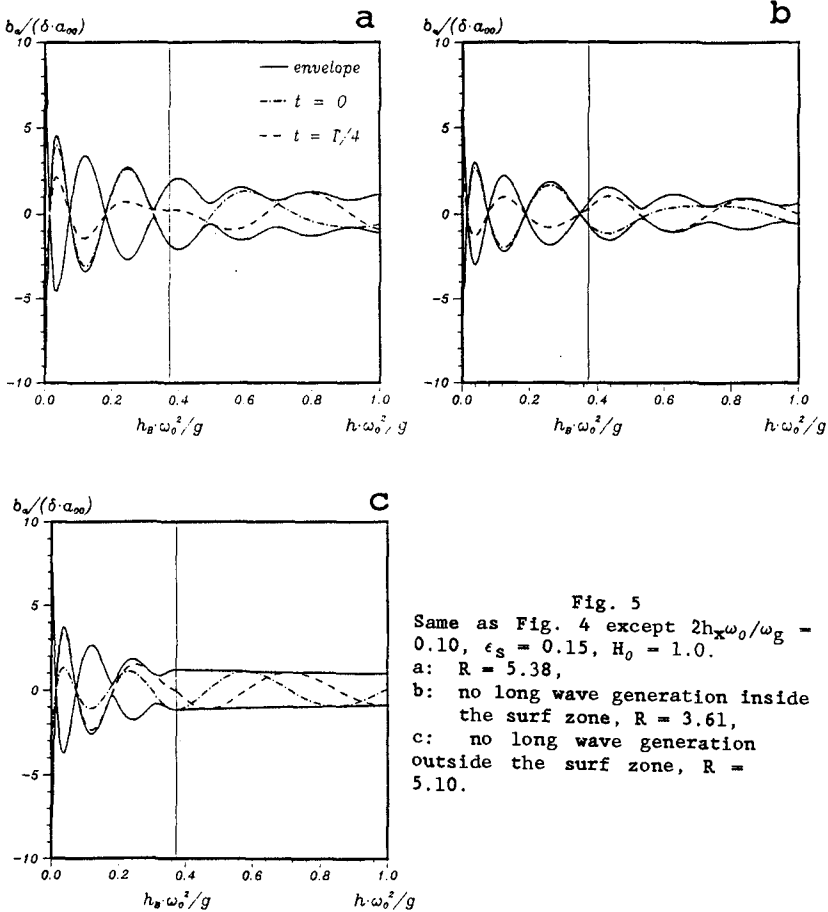


Fig. 5
 Same as Fig. 4 except $2h_x\omega_0/\omega_g = 0.10$, $\epsilon_s = 0.15$, $H_0 = 1.0$.
 a: $R = 5.38$,
 b: no long wave generation inside the surf zone, $R = 3.61$,
 c: no long wave generation outside the surf zone, $R = 5.10$.

As mentioned in section 2, as the waves move to shallower water the wave number of the wave groups approaches the wave number of the free wave solution to (3.25) and hence the generation process assumes the character of a resonant transfer of energy from the short waves to the shoreward moving long wave. This aspect of the process is equivalent to the resonant interaction first pointed out for water waves by Mei & Unluata (1972). Only here we meet a somewhat more complicated form where the wave number of the driving force instead of being constant

is slowly drifting towards the resonant wave number as the waves move shoreward. Although we have not yet studied the details of this situation it is undoubtedly the resonant nature of the process which is responsible for the large amplification indicated by the enormous reflection coefficients. On the other hand, since the nearly resonant interaction only takes place over a finite distance the amplitude of the surf beat of course remains finite.

7. ACKNOWLEDGMENTS

This research was carried out on a contract with the Danish Engineering Science Research Council. Ivar C. Jonsson is acknowledged for useful comments on this presentation.

8. REFERENCES

- Carrier, G.F. (1966). "Gravity Waves on Water of Variable Depth," J. Fluid Mech., 24, 4, 641-659.
- Ghu, V.H. & C.C. Mei (1970). "On Slowly Varying Stokes Waves," J. Fluid Mech., 41, 873.
- Foda, M.A. & C.C. Mei (1981). "Nonlinear Excitation of Long-Trapped Waves by a Group of Short Swells," J. Fluid Mech., 111, 319-345.
- Freilich, M.H. & R.T. Cuza (1984). "Nonlinear Effects on Shoaling Surface Gravity Waves," Phil. Trans. Roy. Soc., 311, 1-41.
- Cuza, R.T. & E.B. Thornton (1985). "Observations of Surf Beat," J. Geophys. Res., 90, C2, 3161-3172.
- Cuza, R.T. & E.B. Thornton (1982). "Swash Oscillations on a Natural Beach," J. Geophys. Res., 87, C1, 483-491.
- Longuet-Higgins, M.S. & R.W. Stewart (1964). "Radiation Stresses in Water Waves: A Physical Discussion with Applications," Deep Sea Research, 11, 529-562.
- Longuet-Higgins, M.S. & R.W. Stewart (1962). "Radiation Stress and Mass Transport in Gravity Waves, with Application to Surf Beats," J. Fluid Mech., 13, 481-504.
- Mei, C.C. (1983). The Applied Dynamics of Ocean Surface Waves, John Wiley & Sons, N.Y.
- Mei, C.C. & C. Benmoussa (1984). "Long Waves Reduced by Short-Wave Groups Over an Uneven Bottom," J. Fluid Mech., 139, 219-235.
- Mei, C.C. & U. Unluata (1972). "Harmonic Generation in Shallow Water Waves," in Waves on Beaches, R.E. Meyer ed., Academic Press, N.Y.
- Munk, W.H. (1949). "Surf Beats," Trans. Am. Geophys. Union, 30, 849-854.
- Phillips, O.M. (1977). The Dynamics of the Upper Ocean, Cambridge Univ. Press.
- Svendsen, I.A. (1984). "Wave Height and Set-up in a Surf Zone," Coastal Eng., 8, 303-329.
- Symonds, C., D.A. Huntley & A.J. Bowen (1982). "Two Dimensional Surf Beat: Long Wave Generation by a Time-Varying Breakpoint," J. Geophys. Res., 87, C1, 492-498.
- Tucker, M.J. (1950). "Surf Beats: Sea Waves of 1 to 5 Min Period," Proc. Roy. Soc. Lond., A202, 565-573.
- Wright, L.D., R.T. Cuza & A.D. Short (1982). "Surf Zone Dynamics on a High Energy Dissipative Beach," Mar. Geol., 45, 41-62.

CHAPTER 80

Solitary Wave Transmission through Porous Breakwaters

by

C. Vidal*, M. A. Losada*, R. Medina* and J. Rubio*

Abstract

A semi-empirical theory is formulated to predict wave reflection and transmission at a porous breakwater of rectangular cross section for normally incident solitary waves. The solution is based on the linearized form of the governing equations and on equivalent linearization of the friction loss in the porous structure.

Experimental results of transmission coefficients are presented for a large range of incident wave amplitudes, with several gravel sizes, water depths and breakwater geometries.

Experimental and theoretical results are compared and evaluated; the comparison shows satisfactory agreement for the transmission coefficient.

* Universidad de Cantabria. Spain.

Introduction

When a wave or surge reaches a rubble mound breakwater, it will be partly or totally reflected, depending on the permeability of the structure. Part of the flow may penetrate the porous barrier, and consequently the reflection is only partial. The incident wave energy is, in this way, split into reflected and transmitted. Reflection features determine the accessibility of the harbor trough its influence on the wave energy at the entrance, while transmission characteristics assess the effectiveness of the breakwater in protecting the harbor from the energy of incident waves.

An extensive literature has been reported to model the reflection-transmission features of a porous structure. The main approximations made in the literature are: the incident wave is harmonic and normal to the structure, the breakwater is a homogeneous isotropic medium governed by Darcy or Forchheimer type flow, the structure is of rectangular cross section. Sollit and Cross 1972, presented a summary of analytical approaches up to 1972. Madsen 1974 simplified the analysis presenting a linear long-wave model by assuming a Forchheimer type of flow and a linearized coefficient of friction. An extension of his model including trapezoidal cross section was given by Madsen and White, 1976. A statistical approach for random waves passing a perforated and porous breakwater was given by Massel and Mei, 1977. A generalization of Sollit and Cross work for multilayered structure with arbitrary cross section was presented by Sulisz, 1985. Damping of the incident and reflected waves due to bottom friction was considered in the long wave transmission through porous breakwater approach given by Scarlatos and Singh, 1987.

The long wave assumption made by several authors accounts for severe wave condition for most breakwaters. The governing equations for long waves in shallow water are the Boussinesq equations with the solitary wave as a typical solution. Theoretically, solitary waves have the advantage that, although non-linear, they can be described with two parameters: the wave height and the depth: experimentally they propagate with constant shape in constant depth and generally they can be separated from reflected waves. The objective of this study is to develop a semi-empirical model to the leading order for the motion of an incident solitary wave, the reflected wave and transmitted wave resulting from the presence of a normal rectangular cross section porous breakwater. This model will be checked with experimental tests. We assume first, that following ratios are small:

$$ak \ll 1 \quad kh \ll 1 \quad kb \ll 1 \quad O(b) \leq O(h)$$

in which a =wave amplitude, k =wave number, h =depth and b =breakwater width.

Following the procedure used by Mei, Liu and Ippen, 1974 for periodic long waves impinging on slotted or perforated breakwater and also used by Mei, 1983 for solitary waves climbing onto a shelf, three separate regions can be distinguished, within each of which different physical processes are dominant. In the evolution region, which is many wave lengths away from the breakwater, dispersion and nonlinearity are important and Boussinesq equations must be used. In the intermediate region roughly one wave length away from the breakwater, nonlinearity and dispersion are of second order in wave slope. In the neighborhood of the breakwater, where the typical distance is b , the loss friction effects are important but the apparent inertia due to local acceleration is not.

Theoretical formulation

Within the intermediate region, one-dimensional linearized equations are sufficient to the leading order:

$$\eta_x + h u_x = 0 \quad (1)$$

$$u_x + g \eta_x = 0 \quad (2)$$

the governing equations for the motion inside the porous rubble-mound are

$$n \eta_x + h u_x = 0 \quad (3)$$

$$(1/n) u_x + g \eta_x + (C_1 \mu / \rho d^n) u + (C_2 / d n^2) u^2 = 0 \quad (4)$$

where C_1 and C_2 account for the laminar and turbulent friction loss respectively and n is the porosity of the structure. The effect of friction loss is localized within $O(h)$ or $O(b)$ and can be represented as a boundary condition:

$$\eta_a - \eta_b = \frac{C_1 \mu}{d^n n g f} b u_b + \frac{C_2}{d g n^2} b u_b^2 \quad (5)$$

where subscripts $()_a$, $()_b$ indicate upstream and downstream respectively, and the apparent inertia (local acceleration) has been ignored in accordance with $kb \ll 1$.

As in the theory for perforated breakwater and for the scattering of a solitary wave at a sudden depth change and equivalent linear condition

$$\eta_a - \eta_b = c_a u_b \quad (6)$$

such that the total square error

$$e = \frac{C_1 \mu}{d^2 n g \rho} b u_b + \frac{C_2}{d g n^2} b u_b^2 - c_b u_b \quad (7)$$

is minimized over the wave period

$$\bar{e} = \int_{-\infty}^{\infty} e^2 dt$$

the minimum occurs when $\delta \bar{e} / \delta c_b = 0$. The optimum value of c_b is:

$$c_b = \frac{C_1 \mu}{d^2 n g \rho} b + \frac{C_2 b}{d g n^2} \frac{\bar{u}_b^2}{u_b^2} \quad (9)$$

we assume the incident wave is given by the solitary wave

$$\eta_1 = a_1 \operatorname{sech}^2 \lambda_1 (x - ct)$$

in which

$$\lambda_1 = (3 a_1 / 4 h^3)^{1/2}$$

$$c = (g h)^{1/2} (1 + a_1 / 2 h) \approx (g h)^{1/2}$$

Experimentally it has been observed that the transmitted and the reflected waves are similar in shape (sech^2 profiles) but not solitary waves, that is:

$$\eta_a = a_1 \operatorname{sech}^2 \lambda_1 (x - ct) + a_1 R \operatorname{sech}^2 \lambda_1 (x+ct) \quad (13)$$

$$\eta_b = a_1 T \operatorname{sech}^2 \lambda_1 (x - ct + \theta) \quad (14)$$

where R, T represent the reflection and transmission coefficients and θ is a phase shift. To the leading order, this phase shift is negligible when $kb \ll 1$. The corresponding horizontal velocities are:

$$u_a = (g a_1 / c) \left[\operatorname{sech}^2 \lambda_1 (x - ct) - R \operatorname{sech}^2 \lambda_1 (x+ct) \right] \quad (15)$$

$$u_b = (g a_1 T / c) \operatorname{sech}^2 \lambda_1 (x - ct) \quad (16)$$

We remark that the experimental assessment of constant λ_1 , can also be deduced from no phase shift and Eq. 1 in order to continuity to be satisfied for all t .

With these velocities, the coefficient c_w is:

$$c_w = \frac{C_1 \mu}{d^n n g \beta} b + \frac{C_2 b}{d n^n} \frac{a_1 T}{c} \quad (17)$$

Substituting Eq (13), (14), (16) into the boundary condition Eq (6), we obtain

$$1 + R = T \left(1 + \frac{c_w g}{c} \right) \quad (18)$$

Condition Eq 1 implies for the continuity of mass flux

$$1 - R = T \quad (19)$$

Combining Eq (18) with Eq (19), we obtain

$$T = \left[1 + \frac{c_w g}{2 c} \right]^{-1} \quad (20)$$

$$R = \left[\frac{c_w g}{2 c} \right] \left[1 + \frac{c_w g}{2 c} \right]^{-1} \quad (21)$$

the structure of Eq 20 also appears in the scattering of sinusoidal waves by perforated breakwater, in the scattering of solitary waves at a sudden depth change or in the scattering of sinusoidal waves by a porous breakwater.

Experimental Tests.

The tests were carried out in the 68 m long, 2 m wide, and 2 m deep wave channel of the water sciences Department of the University of Cantabria. In a length of 20 m, the flume has glass walls to allow visual observations. The incident solitary waves were generated with the procedure sketched by Goring, 1978. With this procedure, roughly one wave length away from the paddle the volume of water pushed by the paddle resembles a solitary wave.

As the solitary wave propagates on the horizontal smooth concrete bottom the frequency dispersion balances the non-linear effects and the waves remain stable without appreciable change. Only side wall and bottom friction cause a decrease of the wave amplitude. The measured profiles of the damped waves at the model test (47 m away from the paddle) are closely represented by the theoretical profile of Boussinesq, 1871. The agreement of both profiles is better on the upper 3/4 (Fig. 1).

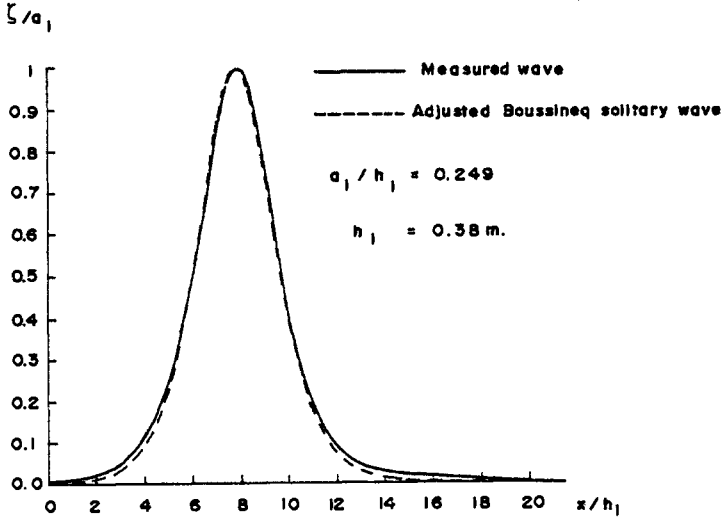


Fig. 1.- Recorded solitary wave and adjusted Boussinesq

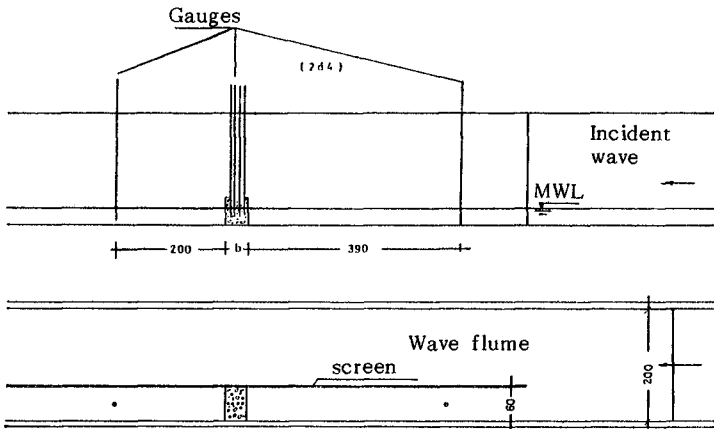


Fig. 2.- Experimental arrangement

TABLE I
TEST PARAMETERS AND EXPERIMENTAL RESULTS

*D ₅₀	*h	*b	*a ₁	T
1.43	30.0	20.0	1.92	0.45
1.43	30.0	20.0	4.28	0.38
1.43	30.0	20.0	7.91	0.31
1.43	30.0	40.0	1.97	0.34
1.43	30.0	40.0	4.41	0.29
1.43	30.0	40.0	7.97	0.21
1.43	24.6	40.0	1.91	0.30
1.43	24.6	40.0	4.29	0.24
1.43	24.6	40.0	7.64	0.19
2.43	30.2	20.0	1.87	0.57
2.43	30.2	20.0	4.27	0.45
2.43	30.2	20.0	7.07	0.38
2.43	30.2	20.0	9.39	0.34
2.43	25.8	20.0	1.90	0.55
2.43	25.8	20.0	4.40	0.43
2.43	25.8	20.0	7.05	0.34
2.43	25.8	20.0	9.49	0.32
2.43	25.8	20.0	11.46	0.29
2.43	31.7	40.0	1.95	0.50
2.43	31.7	40.0	4.63	0.34
2.43	31.7	40.0	7.64	0.28
2.43	31.7	40.0	10.21	0.25
2.43	24.9	40.0	2.19	0.33
2.43	24.9	40.0	4.74	0.29
2.43	24.9	40.0	7.65	0.23
2.43	24.9	40.0	10.31	0.21
2.43	24.9	40.0	12.37	0.19
3.15	30.1	40.0	2.01	0.46
3.15	30.1	40.0	4.38	0.34
3.15	30.1	40.0	7.22	0.28
3.15	30.1	40.0	9.65	0.25
3.15	25.0	40.0	1.84	0.43
3.15	25.0	40.0	4.23	0.33
3.15	25.0	40.0	6.87	0.26
3.15	25.0	40.0	9.02	0.25
3.15	25.0	40.0	10.78	0.21
3.15	30.1	20.0	1.99	0.57
3.15	30.1	20.0	4.53	0.46
3.15	30.1	20.0	7.38	0.39
3.15	30.1	20.0	9.96	0.37
3.15	25.1	20.0	1.86	0.56
3.15	25.1	20.0	4.36	0.46
3.15	25.1	20.0	6.83	0.38
3.15	25.1	20.0	9.30	0.35
3.15	25.1	20.0	11.18	0.34

* centimetres

The permeable structures tested had rectangular form and their characteristics are shown in table I. The tests were carried out with gravel of D₅₀=1.43, 2.43 cm and small cubic blocks of 3.15 cm side length. The measured porosities were n=0.44 for gravel and n=0.42 for cubes. The structures were 20 to 40 cm wide and water depth varied from 25 to 30 cm.

A wide range of incident wave amplitudes were tested so that the parameter a₁/h₀ range was 0.05 < a₁/h₀ < 0.5. Note that this last parameter (a₁/h₀=0.5) violates the small wave amplitude hypothesis.

The experimental arrangement is shown in figure 2. As the flume width was excessive for the test requirements it was divided longitudinally by a screen so that the model covered a width of only 60 cm. Within this new narrow channel all the measuring equipment was placed

as shown in figure 2. Upstream and downstream the model, two gauges were placed in order to measure the incident and the transmitted wave. Inside the permeable structure the pressure and water level were measured at several points depending on the structure width. A complete documentation of the experimental program is presented by Medina, 1988.

The experimental results of transmission coefficients for the different models are presented in table I. The transmission coefficient decreases when the structure width increases, the incident wave amplitude increases and the gravel size decreases. The influence of the water depth on the transmission coefficient is less important, and the transmitted wave amplitude decreases when the water depth decreases. Though the cubic block size is much larger than the gravel size, the transmission coefficient is slightly larger due to the lower porosity.

Comparison of theory and experiment.

For the experimental coefficients C_1 , C_2 , (Eq.17) we take the expressions given by Muskat, 1946, also used by Englund, 1953 and Madsen, 1974.

$$C_1 = \alpha (1-n)^2 / n$$

$$C_2 = \beta (1-n) / n$$

where $\alpha = 1092$, $\beta = 0.81$

The comparison of experimental transmission coefficient, T , and predicted transmission coefficient, T_t , for all the data given in table I is presented in fig. 3. The line $T_t=T$ is also drawn. As is evident from the comparison in fig. 3, the difference is small and the predicted transmission gives a reasonable representation of experimental data. Note that the experiments correspond to values of the parameter $0.05 < a_1/h < 0.5$ thus the agreement is good even for not too small wave amplitude ratio.

The influence on the transmission coefficient due to the grain size, incident wave amplitude, water depth and breakwater width is represented in figures 4-5 in which theoretical (lines) and measured (symbols) coefficients are drawn.

Figure 4 shows the influence of the breakwater width on the transmission; the transmission decreases when the width increases. Figure 5 shows the influence of the incident wave amplitude; the transmission decreases when the a_1/h ratio increases, we can also observe the agreement between predicted and measured coefficients for a wide range of the ratio a_1/h ($0.05 < a_1/h < 0.5$).

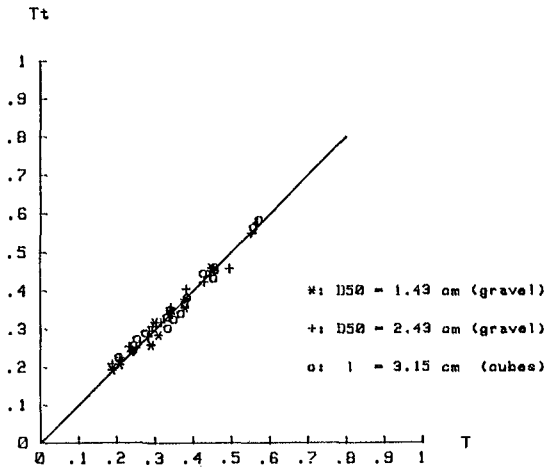


Fig. 3

Experimental versus Theoretical transmission

Summary and Conclusions

Based on a semi-empirical formulation, a simple solution for the reflection and transmission coefficients for a given incident solitary wave has been derived. This solution was based on the leading order of the governing equations and a linearized form of the friction loss in the porous structure. The linearization procedure was a slight modification of the Lorentz condition for sinusoidal waves. The coefficients depend on the geometry of the structure the incident wave amplitude, the water depth and on the properties of the porous medium (porosity and grain diameter).

Experimental results of transmission coefficients have been reported for a wide range of the involved parameters. These results have been compared with the predicted values showing a satisfactory agreement for the transmission coefficient.

Acknowledgments

This study was sponsored partially by the Dirección General de Puertos y Costas and the Comisión Asesora Científica y Técnica.

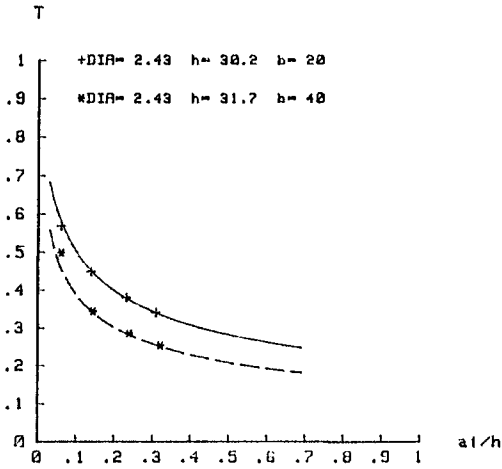


Fig. 4.- Influence of breakwater width on the transmission

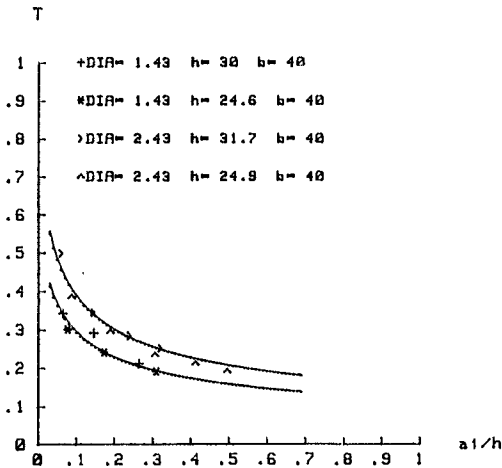


Fig. 5.- Influence of incident wave amplitude on the transmission

LIST OF REFERENCES.

- Boussinesq, M.J. 1871; "Théorie de l'intumescence liquide appelée onde solitaire ou de translation se propageant dans un canal rectangulaire", C.R. Aca. Sci. 72:755.
- Engelund, F. (1953); "On the laminar and turbulent flows of ground water through homogeneous sand", Trans. Danish Acad. Tech. Sci. 3(3).
- Goring, D.G. (1978); "Tsunamis- the propagation of long waves onto a shelf", Rep N. KH-R-38, W.M. Keck Laboratory of hydraulics and water Resources, California Institute of Technology.
- Madsen, O.S. 1974; "Wave transmission through porous structures", ASCE, J.W. Harbors Coastal Eng. Div., 100 (WW3):169-188.
- Madsen, O.S. and White, S.M. 1976; "Energy dissipation on a rough slope", ASCE, J.W. Harbors Coastal Eng. Div., 102 (WW1):31-48.
- Massel, S.R. and Mei, C.C. 1977; "Transmission of random wind waves through perforated or porous breakwater", Coastal Eng., 1:63-78.
- Medina, R. 1988; "Sobre la transformación de ondas solitarias. Propagación en un escalón y en medio poroso", Tesis doctoral, Departamento de Ciencias y Técnicas del Agua y del Medio Ambiente, Univ. de Cantabria.
- Mei, C.C. Liu, P.L.F. Ippen, A.T. (1974); "Quadratic head loss and scattering of long waves", J. Waterway Harbors Coastal Eng. Div. Proc. ASCE 100, 217-239.
- Mei C.C. (1983) "The applied dynamics of Ocean surface waves", J. Wiley and sons Inc. N.Y.
- Muskat, M. (1946); "The flow of homogeneous fluids through porous media", J.W. Edwards, Inc. Ann Arbor, Michigan.
- Scarlato, P.D. and Singh, V.P. 1987; "Long wave through porous breakwaters", Coastal Eng. 11:141-157.
- Sollit, C.K; Cross, R.H. (1972); "Wave transmission through permeable breakwater", Proc. XIII Coastal eng. Cong. ASCE, Vancouver, B.C. Canadá.
- Sulisz, W.(1985); "Wave reflection and transmission at permeable breakwaters of arbitrary cross-section", Coastal Engineering, 9:pp 371-386.

CHAPTER 81

TIME-DEPENDENT WAVE SHEAR STRESS

By Suphat Vongvisessomjai¹, M.ASCE

ABSTRACT

A knowledge of bed shear stress induced by waves is required to understand dynamic processes of nearshore morphologies as a results of sediment transport. However, the information on the stress is still incomplete due to lack of measured data. The study analyzes the unsteady horizontally averaged shear stresses measured over mobile beds in a water tunnel. It is found from the analysis that the presence of the third and fifth harmonics in the shear stress is in good agreement with the measured concentration of suspended sediments.

INTRODUCTION

Magnitude and phase of bed shear stress induced by waves over mobile bed depend on characteristics of waves and wave induced ripples on the bed. The magnitude of bed shear stress can be computed from known wave friction factor over mobile bed, Grant and Madsen (1982) and Vongvisessomjai (1987). Lofquist (1986) provided experimental results of the time-dependent drags on naturally rippled sand beds tested in a water tunnel which were obtained from the measured difference between pressure gradients in the test section split longitudinally into two channels, one containing the sand bed and the other having a smooth metallic bottom. Two sands were used, with diameters 0.55 and 0.18 mm. The bottom stress, including skin friction and profile drag components was found to be a fairly complicated function of the phase and not proportional to the square of the simultaneous sinusoidal velocity far above the bed. Average values of the bottom stress and coefficient of energy dissipation were both typically an order to magnitude greater than for a flat surface roughened with fixed grains. The wave friction factors on mobile beds f_{ws} , computed from the coefficient of energy dissipation \bar{f}_1 of Lofquist (1986) with the conversion $f_{ws} = (3\pi/4) \bar{f}_1$, were found to have the same order of magnitudes as those obtained by Vongvisessomjai (1987).

The time-dependent wave shear stresses obtained by Lofquist (1986) are analyzed and quantified for the phases, and the obtained friction factors together with the earlier results are used to develop a new expression.

¹ Professor, Division of Water Resources Engrg., Asian Inst. of Tech., P.O. Box 2754, Bangkok 10501, Thailand.

METHODOLOGY

The velocity field over the self-formed 2 dimensional ripple of $h = \eta \cos(2\pi x/\lambda)$ can be expressed as a sum of the fundamental component ($n = 0$) and its higher harmonics ($n = 1, 2, 3...$) caused by the presences of eddies or turbulences generated from the interaction of the fundamental component and the ripples as

$$u(x,z,t) = \sum_n \epsilon^n u_n(x,z,t) \dots\dots\dots(1)$$

where $\epsilon =$ a small parameter.

The corresponding shear stresses along the ripple bed can be expressed as

$$\tau_o(x,t) = \sum_n \epsilon^n \tau_{on}(x,t) \dots\dots\dots(2)$$

where subscript o denotes the bed, $z = 0$.

These velocity field, shear stresses and eddies will cause sediment suspension in the form

$$c(x,z,t) = \bar{c}(x,z) + \sum_n \epsilon^n c_n(x,z,t) \dots\dots\dots(3)$$

These unsteady two dimensional velocity, the unsteady shear stress along the ripple and the suspended sediment concentration are too complicated to be measured and quantified. Only some measurements are presently available for horizontally averaged values of the above parameters which can be expressed respectively as

$$\bar{u}(z,t) = \frac{1}{\lambda} \int_0^\lambda u(x,z,t) dx = \sum_n \epsilon^n \bar{u}_n(z,t) \dots\dots\dots(4)$$

$$\bar{\tau}_o(t) = \frac{1}{\lambda} \int_0^\lambda \tau_o(x,t) dx = \sum_n \epsilon^n \bar{\tau}_{on}(t) \dots\dots\dots(5)$$

$$\bar{c}(z,t) = \bar{c}(z) + \sum_n \epsilon^n \bar{c}_n(z,t) \dots\dots\dots(6)$$

The following analysis is based on the approach of Lofquist (1986) in analyzing his experimental results. The freestream velocity of flow above the bed and beyond its effects is

$$u_\alpha = \left(\frac{2\pi a}{T} \right) \sin \left(\frac{2\pi t}{T} \right) = U \sin \theta \dots\dots\dots(7)$$

where t is the time T is the period and $2a$ is the orbital diameter of the water motion. Equation (7) defines the maximum velocity, U , and the phase, θ . The bed surface profile, assumed two dimensional and periodic with length λ , has elevation $h(x,\theta)$, where x is the horizontal coordinate. The average bottom stress is then defined by

$$\bar{\tau}_o(\theta) = \frac{1}{\lambda} \int_0^\lambda \left[\tau_h + (p_h - p_\alpha) \frac{\partial h}{\partial x} \right] dx \dots\dots\dots(8)$$

where τ_{t_1} is the local tangential stress on the bed, and $(P_h - P_a)$ is the difference between pressures at the bed surface and at any fixed elevation beyond the influence of the bed. Separate integrals for the two terms in the integrand would resolve $\tau_o(\theta)$ into components expressing the effects of tangential and normal stresses, the latter being a form drag. However, such a separation is generally impossible. A stress coefficient has been made dimensionless for bottom stress by dividing by ρU^2 , rather than by $\rho u_o^2(\theta)$, in order to keep it proportional to the bottom stress throughout the cycle where ρ is the density of water,

$$f(\theta) = \frac{2 \bar{\tau}_o(\theta)}{\rho U^2} = f_s(\theta) + f_n(\theta) \dots\dots\dots(9)$$

The dimensionless local tangential stress over the smooth boundary for laminar flow is

$$f_s(\theta) = \beta_4 \sin(\theta + \pi/4) \text{ where } \beta_4 = \sqrt{\frac{\nu}{a^2\omega}} \dots\dots\dots(10)$$

and the dimensionless normal stress is

$$f_n(\theta) = \beta_1 \bar{D}(\theta) \text{ where } \beta_1 = \frac{2H}{\rho LU^2} \dots\dots\dots(11)$$

in which $\omega = 2\pi/T$; H = height of pressure taps from bed; and L = distance between pressure taps.

The measured differential pressure $\bar{D}(\theta)$ is found to be the summation of the fundamental harmonic $D_1(\theta)$ and its higher odd harmonics as

$$\bar{D}(\theta) = D_1(\theta) + D_3(\theta) + D_5(\theta) + \dots \dots\dots(12)$$

It was found from the experiments that there existed a shift of the mean level of ripple bed from the initial bed of \bar{h} , a correction of $2\bar{h}/a = \beta_3$ is made to Eq. 9 as

$$f(\theta) = \beta_1 \bar{D}(\theta) - \beta_3 \cos \theta + \beta_4 \sin(\theta + \pi/4) \dots\dots\dots(13)$$

ANALYSIS AND RESULTS

Expressions of friction factor on fixed bed are first summarized for comparison with the obtained friction factor on mobile beds from this analysis. The friction factor can then be used to compute the magnitude of the maximum bed shear stress. The analysis of the phase of the shear stress is finally made.

Friction Factor of Fixed Bed.— Jonsson (1966) defined the wave friction factor $f_w = 2 \bar{\tau}_{om}/(\rho U^2)$ where subscript m denotes the maximum value and expressed it in terms of the relative smoothness of the bed $k_* = a/k_s$ as

$$\frac{1}{4\sqrt{f_w}} + \log \frac{1}{4\sqrt{f_w}} = -0.08 + \log k_* \dots\dots\dots(14)$$

The above expression was later confirmed by two additional sets of tests in a water tunnel by Jonsson and Carlsen (1976).

Kamphuis (1975) reanalyzed the measured values of the friction factors obtained by Riedel, Kamphuis and Brebner (1972) and proposed an expression for the friction factor also in terms of k_* as

$$\frac{1}{4\sqrt{f_w}} + \log \frac{1}{4\sqrt{f_w}} = -0.35 + \frac{4}{3} \log k_* \dots\dots\dots(15)$$

Grant and Madsen (1979) derived an expression of friction factor for combined waves and currents in fully rough turbulent flow. A relationship between f_w and k_* could be obtained for the limiting condition of a pure wave motion as

$$f_w = 0.08/[Ker^2 2(\zeta_c)^{1/2} + Kei^2 2(\zeta_o)^{1/2}] \text{ for } k_* > 1 \dots\dots\dots(16)$$

and $f_w = 0.23$ for $k_* < 1$; in which the dimensionless roughness length $\zeta_o = k_s/(30\ell)$; the characteristic length $\ell = 0.4 u_*/\omega$; the shear velocity $u_* = \sqrt{f_w} 2U$; Ker and Kei = Kelvin functions of zero order.

Vongvisessomjai's (1984) expression of wave friction factor

$$f_w = 0.287 k_*^{-2/3} \dots\dots\dots(17)$$

Friction Factor of Mobile Bed.- Grant and Madsen (1982) presented a model to predict the roughness in unsteady oscillatory flows over mobile beds using data of Carstens et al. (1969). The total roughness was the sum of the form drag component and the sediment transport component:

$$\frac{1}{k_*} = 2B \frac{\eta}{a} \frac{\eta}{\lambda} + 160(s+K) \frac{D}{a} \left[\left(\frac{\psi}{\psi_c} \right)^{1/2} - 0.7 \right]^2 \dots\dots\dots(18)$$

in which $K = 1/2$ for spherical sand; $\psi =$ Shields parameters; and $\psi_c =$ critical value of Shields parameter for initiation motion. Based on the law-of-the-wall, the expression of friction factor of the fixed bed, Eq. 16, was adopted for that of the mobile bed using k_* of Eq. 18.

Profiles of mean and unsteady concentration were derived by Vongvisessomjai (1986) from the mass conservation equation using the diffusion coefficient profile adapted from the eddy viscosity profile of Vongvisessomjai (1984) taking into account changes of the friction factor and boundary layer thickness in the presence of suspension. The theoretical profiles were expressed explicitly as functions of the friction factor, velocity and shear stress profile parameters, and the settling velocity of the sediment relative to the fluid velocity. The tabulated data available and the new experimental data of the mean concentration were used to fit the theoretical profile. The ratio of the friction factor f_{ws}/f_w obtained was then correlated to the densimetric sediment Froude number $Fd_* = U^2/[(s-1)gD]$ and the relative bed smoothness $a_* = a/D$ as

$$\frac{f_{ws}}{f_w} = 0.866 Fd_*^{-0.50} a_*^{0.17} \text{ for fine sand}$$

or

$$f_{ws} = 0.185 Fd_*^{-0.50} a_*^{0.17} \quad \text{for } f_w \dot{=} 0.214 \dots\dots\dots(19)$$

Vongvisessomjai (1987) based on his friction factors obtained from suspended sediment profile data and those of Carstens et al. (1969) expressed f_{ws} as function of Fd_* , a_* and $D_* = (s-1)gD^3/\nu^2$.

$$f_{ws} = 0.049 Fd_*^{-0.44} a_*^{0.21} D_*^{0.22} \dots\dots\dots(20)$$

The data used for the present analysis are from Carstens et al. (1969), Lofquist (1986) and Vongvisessomjai (1986). Table 1 summarizes the sources and characteristics of the data. Note that Vongvisessomjai (1986) used various concentration profile data, $D = 0.14$ mm from Nakato et al. (1977) and Kennedy and Locher (1972), $D = 0.18$ mm from Hom-ma et al. (1965) and $D = 0.21$ mm for his own data.

TABLE 1.—Sources and Characteristics of Data of Wave Friction Factor

Source (1)	T (s) (2)	a (cm) (3)	D (mm) (4)	$k_* = a/(4\eta)$ (5)	f_{ws} (6)	Symbol (7)
Carstens	3.55	8-31	0.19	1.2-15	0.077-0.20	⊙
	3.55	8-45	0.30	1.0-23	0.070-0.38	⊖
	3.55	10-42	0.59	1.0- 8	0.193-0.54	○
Lofquist	4-15	14-55	0.18	1.3-3.2	0.099-0.22	⊞
	2-11	17-52	0.55	0.8-1.6	0.128-0.42	□
Author						
a) Author	2.00	9.55	0.21	1.77	0.083	▲
	1.00	3.18		1.14	0.132	
	1.00	6.37		1.59	0.059	
b) Nakato	1.00	9.55		1.59	0.053	
	2.40	10.20	0.14	1.41	0.137	▽
	1.80	7.50		1.56	0.107	
c) Kennedy	1.20	5.10		1.42	0.079	
	1.00	4.82	0.14	2.19	0.085	▽
d) Hom-ma	1.30	5.29	0.18	1.51	0.087	▲
	1.60	5.27		1.41	0.125	
	1.60	7.10		1.73	0.080	
	1.60	9.12		2.05	0.071	
	1.72	6.75		1.63	0.104	
	1.72	9.25		2.02	0.086	

The friction factors of the mobile beds will first be compared with those expression for fixed beds, Eqs. 14-17. This depends on how to define the roughness of the bed, k_s , or the relative smoothness of the bed, $k_* = a/k_s$:

- i) Madsen and Grant (1976) used $k_s = D$ and $k_* = a/D$;
- ii) Kamphuis (1975) used $k_s = 2D$ and $k_* = a/(2D)$;
- iii) Horikawa and Watanabe (1967) used $k_s = 4\eta$ and $k_* = a/(4\eta)$;
- iv) Swart (1976) used $k_s = 25\eta(\eta/\lambda)$; and
- v) Grant and Madsen (1982) used $k_s = 28\eta(\eta/\lambda)$.

Note that $k_s = 25\eta(\eta/\lambda) \doteq 4\eta$ when $\eta/\lambda = 1/6$ for growing ripple or equilibrium ripple.

Figs. 1a) and 1b) show the comparison plots of friction factors of the mobile beds with those expression for fixed beds, Eqs. 14-17, using the relative smoothness of the bed a) $k_* = a/[25\eta(\eta/\lambda)]$ and b) $k_* = a/D$ respectively. It can be seen in Fig. 1a) that the four expressions of friction factors for fixed beds have about the same magnitudes but mostly overestimate the measured values when assuming b) $k_* = a_* = a/D$.

The new expression of f_{ws} when data of Lofquist (1986) with the conversion $f_{ws} = (3\pi/4) \bar{F}_1$ are added to data of Carstens et al. (1969) and Vongvisessomjai (1986) is

$$f_{ws} = 0.043 Fd_*^{-0.31} a_*^{0.16} D_*^{0.21} \dots\dots\dots(21)$$

From the above f_{ws} , the Shields parameter which is important to describe the sediment transport can be determined as

$$\psi = \frac{1}{2} f_{ws} Fd_* = 0.022 Fd_*^{0.69} a_*^{0.16} D_*^{0.21} \dots\dots\dots(22)$$

Since the above friction factor of the mobile bed f_{ws} depends on three dimensionless parameters (D_* , Fd_* and a_*) its dependence on these three parameters as well as $\psi = Fd_*/a_*^{1/2}$ and D_* or the diameter of the sediment D are shown in Fig. 2. The 3 diameters of fine, medium and coarse sands of Carstens et al. (1969) are used as the representatives in Fig. 2a) while in Fig. 2b) the 6 and 3 densimetric Froude numbers (Fd_*) respectively of the coarse sand and the fine sand of Lofquist (1986) are used as the representatives. Also included in Fig. 2b) are the 9 curves obtained by Lofquist (1986) with the conversion $f_{ws} = (3\pi/4) \bar{F}_1$ which show how his curves are smoothed to the present expression, Eq. 21. The additional plot of f_{ws} versus a_* of Carstens et al. (1969) and Vongvisessomjai (1986) has been presented in Fig. 1b).

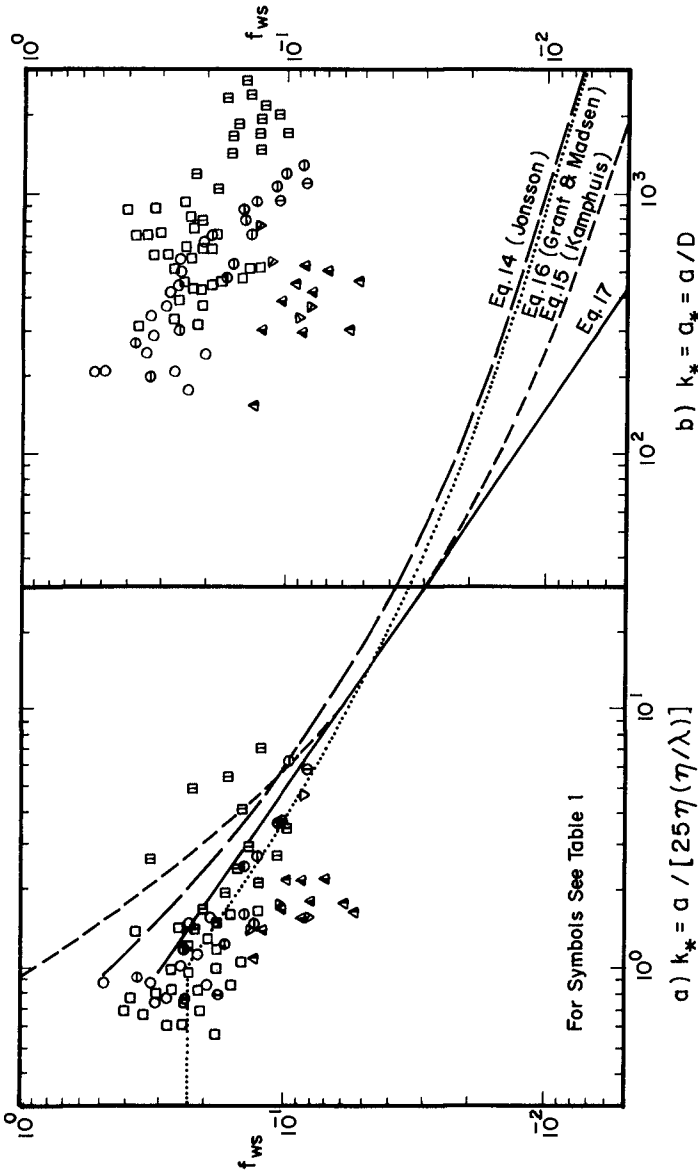


Fig. 1.— Comparison of Measured Friction Factors on Mobile Beds with Expressions of Friction Factors on Fixed Beds

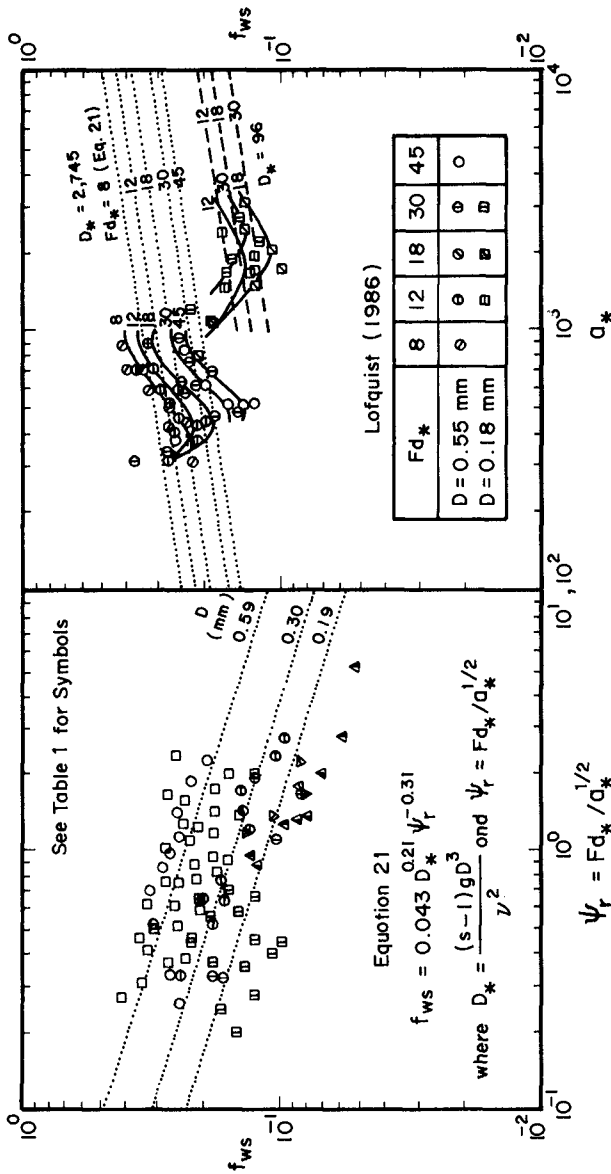


FIG.2 - Comparison of Measured Friction Factors on Mobile Beds with Equation 21

Phase of Bed Shear Stress.—Lofquist (1986) presented graphically the phase variations of dimensionless shear stress $f(\theta)$ of Eq. 13 for all experimental results for coarse sand and fine sand. Lofquist kindly provided all parameters used in plotting the graphs to the author for further quantification of the contributions by the fundamental harmonic and its higher harmonics. Tables 2 and 3 summarize results of coarse and fine sand experiments respectively. It can be seen from the tables that values of $-\beta_3$ (correction due to the presence of ripples on bed) and β_2 (tangential stress over smooth boundary) are small compared with $\beta_1 \bar{D}(\theta)$ (normal stress).

The dimensionless normal stresses $\beta_1 \bar{D}(\theta)$ of Eq. 13 for Run Nos. C28, C13 and C01 are plotted in Fig. 3. Run No. C28 is an example of high contributions of the third and the fifth harmonics where $D_{3m}/D_{1m} = 1.1733$ and $D_{5m}/D_{1m} = 0.5352$; Run No. C13 is an example of high $D_{3m}/D_{1m} = 0.5421$ and low $D_{5m}/D_{1m} = 0.0746$ while Run No. C01 is an example of low $D_{3m}/D_{1m} = 0.0581$ and high $D_{5m}/D_{1m} = 0.2503$ where subscript m denotes the maximum value. It can be seen from these three examples that the resultant normal stresses have two peaks in half a cycle $\theta = \pi$ which imply that they have four peaks in a cycle $\theta = 2\pi$. The measured suspended sediment concentration by Homma et al. (1965) and Nakato et al (1977) also exhibited four peaks in a cycle which could be quantified by the theory proposed by Vongvisessomjai (1986).

The densimetric sediment Froude number Fd_* , the relative bed smoothness a_* and the densimetric sediment Froude-Reynolds number D_* which have been used in correlating with f_{ws} are then used in correlating with D_{3m}/D_{1m} and D_{5m}/D_{1m} listed in Tables 2 and 3. The results obtained are

$$\frac{D_{3m}}{D_{1m}} = 2,670 Fd_*^{1.50} a_*^{-1.68} D_*^{-0.44} \dots\dots\dots(23)$$

$$\frac{D_{5m}}{D_{1m}} = 1.49 Fd_*^{0.60} a_*^{-0.64} D_*^{0.003} \dots\dots\dots(24)$$

The wave friction factor $f_{ws} = 2 \tau_{Qm}/(\rho U^2)$ is the maximum of the dimensionless shear stress $f(\theta)$ which is mainly contributed by $D_1(\theta)$, $D_3(\theta)$ and $D_5(\theta)$. Using results of f_{ws} and $\beta_1 D_{1m}$ listed in Tables 2 and 3 for coarse sand and fine sand respectively, a relationship is found

$$f_{ws} = 1.13 (\beta_1 D_{1m}) \dots\dots\dots(25)$$

The fundamental harmonic of the normal stress is the main contribution to the resultant stress, only 13 percent is contributed by higher harmonics and other factors.

The obtained results from this study could be used to further advance on the analytical descriptions of time-dependent sediment transport and suspension.

TABLE 2.--Results of Coarse Sand Experiments ($D_* = 2,745$)

Run	f_{ws}	$\beta_1 D_{1m}$	D_{3m}/D_{1m}	D_{5m}/D_{1m}	$\beta_1 \times 100$	$-\beta_3 \times 100$	$\beta_4 \times 100$	Fd_*	a_*
(1)	(2)	(3)	(4)	(5)	(6)	(7)	(8)	(9)	(10)
C01	0.2853	0.2354	0.0581	0.2503	1.472	5.079	0.768	8.21	435
C02	0.2177	0.1794	0.3750	0.1058	1.245	5.079	0.642	18.50	435
C03	0.2483	0.2006	0.1271	0.2545	1.261	5.079	0.710	12.31	435
C04	0.2467	0.2080	0.1069	0.1399	1.354	4.761	0.686	12.35	464
C05	0.2580	0.1934	0.1680	0.1773	1.222	5.540	0.741	12.34	399
C06	0.2106	0.1940	0.2233	0.1713	1.233	5.917	0.766	12.14	374
C07	0.2641	0.2230	0.0514	0.1473	1.223	4.385	0.659	12.36	504
C10	0.2182	0.2292	0.2037	0.1638	1.121	1.475	0.924	8.19	316
C11	0.2691	0.2342	0.3945	0.1482	1.029	2.224	0.835	12.30	316
C12	0.2832	0.2421	0.5674	0.0730	1.367	2.961	0.755	18.35	316
C13	0.2773	0.2598	0.5421	0.0746	1.430	3.698	0.755	18.33	316
C15	0.2552	0.2144	0.0504	0.0950	1.242	0	0.615	12.31	580
C16	0.2891	0.2445	0.0245	0.1412	1.262	0.100	0.616	12.29	580
C17	0.3150	0.2660	0.0580	0.1371	1.323	0.194	0.680	8.25	580
C18	0.2825	0.2330	0.0627	0.1527	1.053	0.294	0.556	18.47	580
C19	0.2396	0.2068	0.5845	0.3035	1.728	0.388	0.491	30.46	580
C22	0.3477	0.2930	0.0861	0.1382	1.388	0	0.621	8.24	697
C23	0.3513	0.2962	0.0708	0.0903	1.449	0	0.733	12.37	697
C24	0.3141	0.2721	0.0224	0.1390	1.428	0	0.507	18.51	697
C25	0.1871	0.1766	0.2487	0.1985	1.580	0	0.507	30.79	697
C26	0.1845	0.1687	0.2672	0.1956	1.244	0	0.643	18.39	465
C27	0.1812	0.1672	0.5655	0.2200	1.053	0.779	0.544	30.70	472
C28	0.1628	0.1586	1.1733	0.5352	1.223	1.403	0.466	46.07	526
C33	0.1779	0.1555	0.2338	0.1995	0.839	0	0.639	18.22	443
C34	0.1977	0.1708	0.1251	0.1341	0.691	0	0.706	12.22	443
C35	0.2356	0.2038	0.0512	0.0921	0.800	0	0.779	8.25	443
C36	0.1496	0.1286	0.5233	0.3463	0.669	0	0.536	30.43	486
C38	0.2113	0.1806	0.2613	0.2012	0.873	0	0.643	17.73	443
C39	0.1911	0.1676	0.3520	0.2608	0.872	0	0.643	17.74	443
C40	0.2085	0.1802	0.3206	0.2077	0.874	0	0.643	17.75	443
C41	0.2160	0.1833	0.2173	0.1020	1.393	0	0.574	18.00	551
C42	0.2361	0.2035	0.4150	0.2355	1.231	0	0.496	30.68	566
C43	0.1986	0.1749	0.8459	0.8166	1.137	0	0.430	45.92	617
C44	0.2196	0.1948	0.1923	0.0167	0.902	0	0.591	18.42	515
C45	0.2771	0.2420	0.0823	0.1599	1.251	0	0.659	12.20	508
C46	0.2773	0.2364	0.0448	0.0267	1.357	0	0.734	8.16	501
C47	0.2146	0.1828	0.3230	0.1022	0.995	0	0.476	30.58	617
C48	0.2467	0.2122	0.3066	0.1553	0.995	0	0.467	30.72	639
C49	0.1835	0.1678	0.4950	0.5842	1.950	0	1.402	45.87	704
C50	0.2526	0.2152	0.0570	0.1200	0.961	0	0.553	18.42	588
C51	0.3169	0.2701	0.0100	0.1379	1.136	0	0.616	12.23	580
C52	0.3454	0.2908	0.0397	0.1237	1.543	0	0.682	8.17	580
C53	0.3091	0.2596	0.0518	0.1134	1.215	0	0.562	12.33	697
C54	0.3951	0.3331	0.0807	0.1250	1.602	0	0.622	8.19	697
C55	0.2828	0.2358	0.0264	0.1538	0.977	0	0.505	18.39	704
C56	0.2290	0.1958	0.2367	0.0769	1.411	0	0.428	30.68	762
C57	0.2375	0.2005	0.2489	0.2170	1.194	0.086	0.368	45.88	842
C58	0.3296	0.2759	0.1000	0.1287	1.239	0	0.503	12.30	871
C59	0.4154	0.3497	0.0592	0.0998	1.918	0	0.557	8.17	871
C60	0.3294	0.2763	0.0641	0.1150	1.628	0	0.453	18.40	878

TABLE 2 (Continued)

Run	f_{ws}	$\beta_1 D_{1m}$	D_{3m}/D_{1m}	D_{5m}/D_{1m}	$\beta_1 \times 100$	$-\beta_3 \times 100$	$\beta_4 \times 100$	Fd_*	a_*
(1)	(2)	(3)	(4)	(5)	(6)	(7)	(8)	(9)	(10)
C61	0.2476	0.2096	0.0667	0.1745	1.572	0	0.384	30.77	943
C62	0.2120	0.1846	0.1307	0.1911	1.131	0.086	0.719	12.33	424
C63	0.2707	0.2375	0.1637	0.0720	1.456	0.137	0.797	8.19	424
C64	0.1831	0.1732	0.3277	0.0641	0.932	0.253	0.646	18.37	432
C65	0.1864	0.1726	0.5544	0.2273	1.002	0.423	0.548	30.58	464
C66	0.1421	0.1281	0.8019	0.2827	1.192	0.615	0.466	45.71	526
C67	0.2740	0.2562	0.2360	0.0392	1.374	0.210	0.840	12.28	312
C68	0.2241	0.3261	0.1760	0.1457	1.458	0.361	0.930	8.19	312
C69	0.2573	0.2396	0.6632	0.2377	1.260	0.661	0.757	18.47	319
C70	0.2745	0.2571	1.1181	0.4229	1.571	1.101	0.637	30.71	343
C71	0.2585	0.2409	1.5154	0.3462	2.004	1.636	0.542	45.76	385
C72	0.2429	0.2235	0.5336	0.1846	1.644	0.353	0.748	18.63	319
C73	0.2179	0.1859	0.1235	0.1336	0.679	-0.661	0.504	18.56	704
C74	0.1819	0.1655	0.3227	0.1392	0.890	0.149	0.640	18.42	439
C75	0.1751	0.1579	0.2335	0.2849	0.888	0.282	0.622	18.46	464
C76	0.1642	0.1693	0.3863	0.1459	0.849	0.492	0.672	18.35	399
C77	0.1845	0.1876	0.4784	0.1768	0.889	0.694	0.690	18.45	377
C78	0.1767	0.1557	0.2041	0.2302	0.889	0.646	0.599	18.45	501

TABLE 3.—Results of Fine Sand Experiments ($D_* = 96$)

Run	f_{ws}	$\beta_1 D_{1m}$	D_{3m}/D_{1m}	D_{5m}/D_{1m}	$\beta_1 \times 100$	$-\beta_3 \times 100$	$\beta_4 \times 100$	Fd_*	a_*
(1)	(2)	(3)	(4)	(5)	(6)	(7)	(8)	(9)	(10)
F01	0.1256	0.1086	0.2098	0.0283	1.043	0.386	0.801	18.40	1496
F02	0.1298	0.1094	0.3092	0.1130	1.025	0.423	0.750	18.42	1707
F03	0.1301	0.1138	0.0591	0.0794	1.251	0.715	0.841	12.26	1663
F04	0.1503	0.1286	0.0630	0.0513	1.396	0.927	0.940	8.17	1629
F05	0.1237	0.1042	0.1334	0.2653	1.037	1.302	0.750	18.41	1707
F06	0.1593	0.1308	0.1570	0.1538	1.326	1.838	0.623	30.61	1862
F07	0.1098	0.0933	0.1581	0.1351	1.420	0.087	0.686	18.38	2040
F08	0.1279	0.1075	0.0852	0.0653	0.864	0.150	0.782	12.19	1929
F10	0.1263	0.1056	0.2013	0.0440	1.588	0.270	0.583	30.71	2184
F11	0.1397	0.1194	0.0201	0.0655	1.059	0.041	0.626	18.28	2461
F12	0.1708	0.1441	0.0460	0.0535	0.885	0.070	0.705	12.22	2372
F13	0.1498	0.1294	0.1016	0.0498	1.613	0.124	0.528	30.39	2682
F14	0.1275	0.1184	0.0674	0.0814	1.051	0.171	0.801	18.41	1496
F15	0.1673	0.1434	0.0795	0.0568	1.271	0.301	0.903	12.27	1441
F16	0.1682	0.1389	0.0954	0.1768	1.900	0.522	0.674	30.60	1641
F17	0.1887	0.1674	0.1729	0.1813	0.903	0.123	0.941	18.34	1086
F18	0.1826	0.1672	0.1445	0.1317	0.013	0.211	1.057	12.26	1053
F20	0.2106	0.1989	0.2421	0.4439	1.084	0.084	1.098	18.35	799
F21	0.2233	0.2036	0.0346	0.1108	1.260	0.143	1.231	12.27	776
F23	0.1390	0.1149	0.1626	0.0322	0.903	0.025	0.559	18.42	3070
F28A	0.1199	0.1119	0.1579	0.0023	2.084	0	0.748	18.59	1707
B	0.1378	0.1179	0.1158	0.0196	2.084	0	0.748	18.59	1707
C	0.1053	0.0916	0.1795	0.0636	2.084	0	0.748	18.59	1707
D	0.0092	0.0792	0.2755	0.0656	1.041	0	0.748	18.59	1707

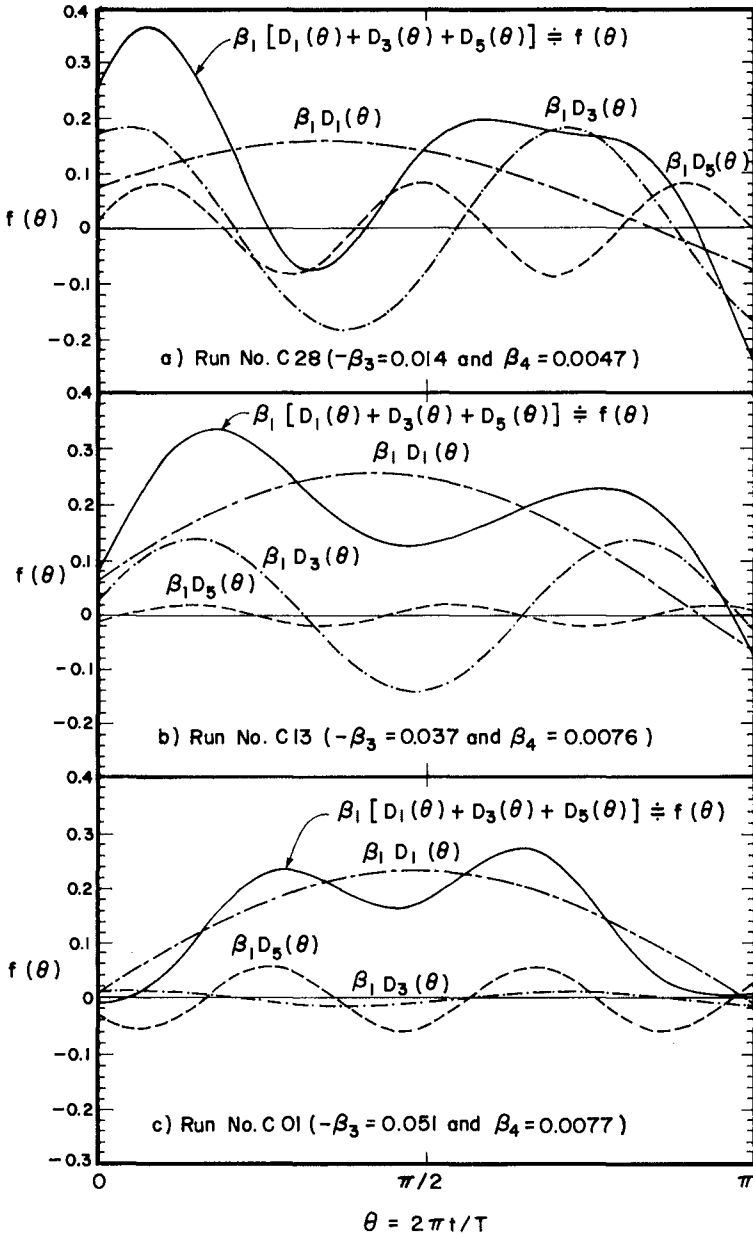


FIG. 3. - Phase of Bed Shear Stress, Eq. 13

CONCLUSIONS

The following conclusions can be drawn from this study:

(a) The wave friction factors on mobile beds were slightly smaller than those computed from expressions of friction factors for fixed beds with the use of ripple geometry as bed roughness [$k_s = 25\eta(r/\lambda)$] but they were one order of magnitude greater than the computed values with the use of sand grain as bed roughness ($k_s = 2D$).

(b) The wave friction factor on mobile beds f_{ws} was then correlated with the densimetric sediment Froude number Fd_* , the relative bed smoothness a_* and the densimetric sediment Froude-Reynolds number D_* (Eq. 21).

(c) The measured phases of the bed shear stresses over mobile beds of sands indicated the presence of eddies generated on the ripple bed which conformed to the measured profiles of suspended sediment concentration.

(d) The relative magnitudes of the third and the fifth harmonics over the fundamental harmonic were also correlated with Fd_* , a_* and D_* (Eqs. 23 and 24).

ACKNOWLEDGEMENTS

The author would like to express his sincere thanks to Mr. Karl E.B. Lofquist, U.S. Department of Commerce-National Bureau of Standards, in providing data for the analysis of the phase of shear stress.

REFERENCES

- CARSTENS, M.R., NIELSON, R.M., and ALTINBILEK, H.D., "Bed forms generated in the laboratory under an oscillatory flow: analytical and experimental study," Technical Memo, No. 28, US Army Corps of Engineers, Coastal Engineering Research Center, 1969.
- GRANT, W.D. and MADSEN, O.S., "Combined wave and current interaction with a rough bottom," Journal of Geophysical Research, Vol. 84, No. C4, 1979, pp. 1797-1808.
- GRANT, W.D. and MADSEN, O.S., "Movable bed roughness in unsteady oscillatory flow," Journal of Geophysical Research, Vol. 87, No. C1, 1982.
- HOM-MA, M. HORIKAWA, K., and KAJIMA, R., "Study on suspended sediment due to wave action," Coastal Engineering in Japan, Vol. 8, 1965, pp. 85-103.
- HORIKAWA, K., and WATANABE, A., "Study on sand movement due to wave action," Coastal Engineering in Japan, Vol. 10, 1967, pp. 39-57.
- JONSSON, I.G., "Wave boundary layers and friction factors," Proceedings of the Tenth International Conference on Coastal Engineering, Vol. 1, 1966, pp. 127-148.

- JONSSON, I.G., and CARLSEN, N.A., "Experimental and theoretical investigations in an oscillatory turbulent boundary layer," Journal of Hydraulic Research, Vol. 14, No. 1, 1976, pp. 45-60.
- KAMPHUIS, J.W., "Friction factor under oscillatory waves," Journal of the Waterways, Harbors and Coastal Engineering Division, ASCE, Vol. 101, No. WW2, 1975, pp. 135-144.
- KENNEDY, J.F. and LOCHER, F.A., "Sediment suspension by water waves," Waves on Beaches and Resulting Sediment Transport, R.E. Meyer, Ed., Academic Press, New York, NY, 1972, pp. 249-295.
- LOFQUIST, K.E.B., "Drage on naturally rippled beds under oscillatory flows," Miscellaneous Paper CERC-86-13, US Army Corps of Engineers, Coastal Engineering Research Center, 1986.
- MADSEN, O.S. and GRANT, W.D., "Sediment transport in the coastal environment", Report No. 209, Ralph M. Parsons Lab. for Water Resources and Hydrodynamics, Massachusetts Inst. of Tech., 1976.
- NAKATO, T., LOCHER, F.A., GLOVER, J.R. and KENNEDY, J.F., "Wave entrainment of sediment from rippled beds," Journal of the Waterways, Harbours and Coastal Engineering Division, ASCE, No. WW1, Vol. 103, 1977, pp. 83-100.
- RIEDEL, H.P., KAMPHUIS, J.W., and BREBNER, A., "Measurement of bed shear stresses under waves," Proceedings of the Thirteenth International Conference on Coastal Engineering, Vol. 1, 1972, pp. 587-603.
- SWART, D.H., "Predictive equations regarding coastal transports," Proceedings of the Fifteenth International Conference on Coastal Engineering, Vol. 2, 1976, pp. 1113-1132.
- VONGVISESSOMJAI, S., "Oscillatory boundary layer and eddy viscosity," Journal of Hydraulic Engrg., ASCE, Vol. 110, No., 4, 1984.
- VONGVISESSOMJAI, S., "Profile of suspended sediment due to wave action," Journal of Waterways, Port Coastal and Ocean Engrg., ASCE, Vol. 112, No. 1, 1986.
- VONGVISESSOMJAI, S. "Wave friction factor on sand ripples". Proc. Specialty Conf. on Advances in Understanding of Coastal Sediment Processes, Vol. 1, 1987, pp. 393-408.

CHAPTER 82

A PARAMETRIC HURRICANE WAVE PREDICTION MODEL

Ian R. Young*

ABSTRACT

A spectral wave model based on a numerical solution of the Radiative Transfer Equation is used to create a synthetic data base on wave conditions within hurricanes. The results indicate that both the velocity of forward movement and maximum wind velocity within the storm play an important role in determining both the magnitude of the waves generated and also the spatial distribution of these waves. An equivalent fetch for hurricane wave generation which is a function of these two parameters is proposed. This concept, together with the standard JONSWAP fetch limited growth relationships, provide a simple means for estimating wave conditions within hurricanes.

INTRODUCTION

Hurricane generated waves play a significant role in the design of almost all coastal and offshore structures in tropical and semi-tropical regions. Despite their obvious importance, the complex processes active in their generation are only beginning to be understood. The physics of the generation process within hurricanes is complicated by the rapidly turning winds which generate cross-seas. The non-linear interactions within such seas have only recently been investigated (Young et al., 1987). Progress has also been hindered by the lack of reliable field data. Buoy measurements represent only point data in the two-dimensional spatial wave field and only recently have provided directional information. More promising are remote sensing techniques such as Synthetic Aperture Radar (SAR) and Radar Altimeters (ALT) which have provided data from a limited number of hurricanes (King and Shemdin, 1978; Gonzalez et al., 1982; McLeish and Ross, 1983; Beal et al., 1986; Holt and Gonzalez, 1986). Although such instruments represent a significant advance, the small number of hurricanes for which data exists cover only a very limited range of storm parameters.

Recent advances in the physics of numerical wave prediction models (Komen et al., 1984; Hasselmann, S. et al., 1985) have enabled the development of operational hurricane prediction models which yield results consistent with the increasing field data base (Young, 1987c). Due to the complexity of these models they are, however, computationally expensive.

* Lecturer, Dept. Civil Engineering, University College, Australian Defence Force Academy, Northcott Drive, Canberra, ACT, 2600, Australia.

In order to develop an extensive synthetic data base, the model of Young (1987c) has been run for a wide range of hurricane parameters. The data from these numerical experiments will be used to clarify the wave generation process within hurricanes and to develop a simple parametric model suitable for wave prediction in deep water.

MODEL DESCRIPTION

The model used for the numerical experiments is called ADFA1 (Young, 1987c). It is a Second Generation (SWAMP, 1985) spectral wave model based on a numerical solution of the Radiative Transfer Equation (Hasselmann, 1960). Details of the model have been presented elsewhere (Young, 1987a,c). In particular, the model has a simple but very flexible treatment of the nonlinear source term which is of particular importance under the rapidly turning winds of hurricanes (SWAMP, 1985). An extensive comparison with field data under tropical cyclone conditions off the north-west coast of Australia has been presented by Young (1987b,c). These results clearly validate model performance under such conditions.

The model was used to generate a synthetic data base covering a wide range of hurricane parameters. The three wind field parameters varied were: velocity of forward movement, V_{fm} ; maximum wind velocity in storm, V_{max} and radius to maximum winds, R . To cover the three-dimensional parameter space completely would involve a prohibitively large number of runs. It is reasonable to assume that R is simply a scaling parameter and hence for the majority of the experiments was held constant. A total of 43 experiments were conducted, the parameters being shown in Table 1.

Successful numerical modelling of hurricanes represents a conflict of scales. A grid of large geophysical extent is required to ensure all significant atmospheric forcing occurs within the grid and to predict the arrival of remotely generated swell. In order to resolve the eye structure and the associated strong winds, however, a relatively fine grid is required. To accommodate these constraints at acceptable computational expense, ADFA1 uses a system of nested grids.

A course grid with a spatial extent of 750km \times 1050km with a resolution of 30km and a computational time step of 30mins was used to provide boundary conditions to a nested finer grid of extent 360km \times 330km with a 15km resolution and time step of 15mins. Runs were commenced with the hurricane near the southern boundary of the course grid where it was held stationary for a period of two days to enable sea conditions to build up from an initially calm state. The storm was then moved off in a northerly direction at its velocity of forward movement. All results presented are from the finer grid whose south-west corner was located 300km east of the course grid western boundary and 650km north of its southern boundary. In all cases sea conditions had reached steady state by the time the hurricane entered the finer grid.

The hurricane wind field model used for the atmospheric forcing was a slightly modified form of that proposed by Graham and Hudson (1960). The original model had the region of maximum winds in the right rear quadrant whereas the modified form adopted here positions this region in the right forward quadrant, 70° from the direction of forward movement. This modification is consistent with observations from the NOAA hurricane program and has also been adopted in other modelling

applications (SWAMP, 1985). In reality, the wind field is almost certainly more complex than the simple model used, with considerable variability between storms. In view of the accuracy with which hurricane parameters can be estimated in practice, however, there is little point in attempting a more sophisticated approach.

HURRICANE WAVE GENERATION

The advent of remote sensing techniques and particularly the Synthetic Aperture Radar (SAR) has provided considerable insight into the directional properties of hurricane generated waves. SAR data from a number of hurricanes (King and Shemdin, 1987; Gonzalez et al., 1982; McLeish and Ross, 1983; Beal et al., 1986; Holt and Gonzalez, 1986) consistently shows swell ahead of hurricanes radiating out in a fan shaped pattern from the centre of the storm. The hurricanes investigated by these experiments have all had slow to moderate velocities of forward movement ($V_{fm} = 2.5 - 5ms^{-1}$). King and Shemdin (1978) have, however, speculated that V_{fm} would have a critical role in determining these trends. Figs. 1 show contour plots of directional wave spectra at various points relative to the centre of the hurricane. Plots are presented for a storm with $V_{max} = 40ms^{-1}$ and values of $V_{fm} = 2.5$ and $12.5ms^{-1}$. Each of the contour plots has been normalized such that the spectral peak has a value of one; contours being drawn at 0.9, 0.5, 0.1 and 0.01. The maximum frequency shown on the polar grid is 0.25 Hz. In each of the spectra a relatively high frequency peak with a broad directional distribution centred about the local wind direction can be seen (ie. locally generated wind-sea). In addition, many of the spectra also exhibit a lower frequency swell peak. For the slower moving storm (Fig. 1a), examination of the spectra ahead of the storm centre clearly show swell radiating out from a region to the right of the storm centre in a similar fashion to that reported in the SAR data. Tracing this swell back along wave rays at the appropriate group velocity reveals that it was generated in the intense wind region to the right of the storm. This swell ($f = 0.08Hz$) has a group velocity of $9.8ms^{-1}$ and as such propagates ahead of the storm ($C_g > V_{fm}$). The more rapidly moving storm (Fig. 1b) has a velocity of forward movement, $V_{fm} = 12.5ms^{-1} > C_g$ and consequently no swell is evident ahead of the storm.

This result confirms the speculation of King and Shemdin (1978) as to the importance of V_{fm} in determining the wave field. V_{max} also plays an important role since it can be expected that the peak frequency of the dominant waves will decrease with increasing V_{max} (ie. C_g increases with increasing V_{max}). For a given V_{max} , if V_{fm} is relatively slow, the dominant waves will "outrun" the storm and appear as swell ahead of the storm. Conversely, if V_{fm} is relatively fast, the waves will be left behind the storm and no swell will be present ahead of the storm.

The maximum significant wave height within the hurricane, $H_s(max)$ as a function of both V_{max} and V_{fm} is shown in Fig. 2. For a given value of V_{max} , $H_s(max)$ gradually increases as a function of V_{fm} until a peak is reached, after which the wave height rapidly decreases. The V_{fm} at which this peak occurs increases with V_{max} . The reason for this behaviour is evident in Fig. 3 which shows the group velocity of the spectral peak frequency of the maximum waves in the storm as a function of both V_{fm} and V_{max} . Maximum wave conditions occur when the waves have a group velocity slightly greater than V_{fm} . Bretschneider (1957) proposed that maximum wave conditions would occur when $V_{fm} = C_g(max)$. Under such

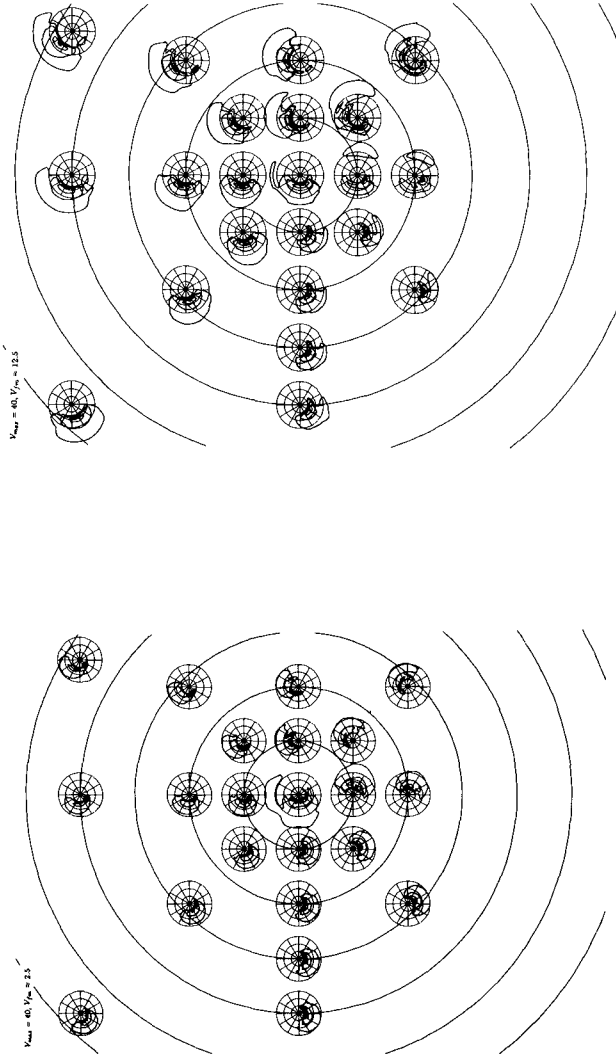


Fig. 1. Contour plots of directional wave spectra at various points within hurricanes with $V_{max} = 40ms^{-1}$ and $V_{fm} = 2.5ms^{-1}$ and $12.5ms^{-1}$. Circular lines are drawn at distance R, 2R, 3R etc. from the storm centre. Note, a southern hemisphere storm is shown.

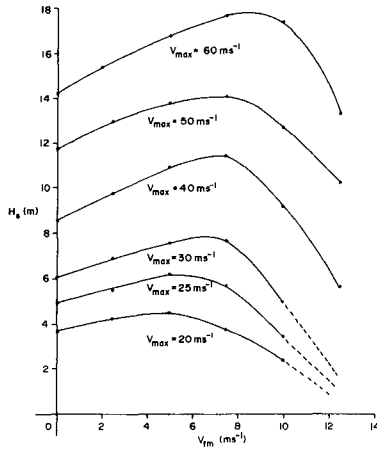


Fig. 2. Maximum significant wave height in a hurricane, $H_s(max)$ as a function of V_{fm} and V_{max} .

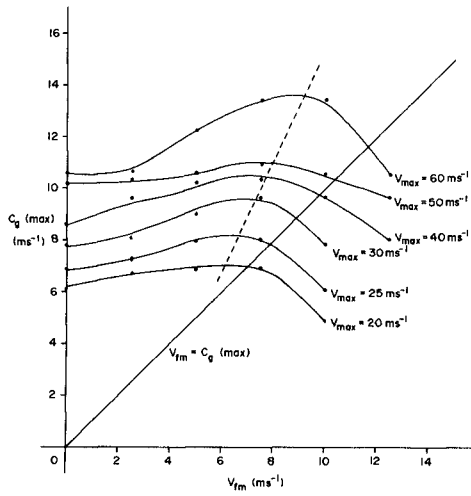


Fig. 3. Group velocity of the maximum waves in a hurricane, $C_g(max)$ as a function of V_{fm} and V_{max} .

a condition waves would move forward with the hurricane and experience an extended fetch. Due to the effect of nonlinear wave-wave interactions, however, there is a continual migration of the spectral peak to lower frequencies (Hasselmann et al., 1973). Consequently, there will be a tendency for the dominant waves to continually move to lower frequencies and "outrun" the storm (King and Shemdin, 1978). Only under fully arisen sea conditions when the peak frequency reaches the Pierson-Moskowitz value (Pierson and Moskowitz, 1958) does the spectral peak migration stop (Komen et al., 1984). As such conditions seldom, if ever, occur in hurricanes, the waves which will dominate are those which remain in the high wind regions for the maximum time.

EQUIVALENT FETCH

Bretschneider (1957) has used the concept of an equivalent fetch within a hurricane to apply fetch limited wave growth relationships to these situations. As already shown, the equivalent fetch must be a function of both V_{max} and V_{fm} .

The JONSWAP (Hasselmann et al., 1973) fetch limited growth relationship is

$$\frac{gH_s}{U_{10}^2} = 0.0016 \left(\frac{gF}{U_{10}^2} \right)^{0.5} \quad (1)$$

where U_{10} is the 10m wind velocity and F the fetch length. Replacing U_{10} by V_{max} , which is an appropriate wind scaling parameter for hurricane conditions, Eq. 1 can be written as

$$\frac{gH_s(max)}{V_{max}^2} = 0.0016 \left(\frac{gF}{V_{max}^2} \right)^{0.5} \quad (2)$$

Applying Eq. 2 to the present data and solving for F , yields the equivalent fetch values shown in Table 1. Initially, only the results for the storms with $R = 30km$ will be considered. The fetch dependence on R , however, will be investigated later. A polynomial approximation to the results yields:

$$F_{30} = aV_{max}^2 + bV_{max}V_{fm} + cV_{fm}^2 + dV_{max} + eV_{fm} + f \quad (3)$$

where $a = -6.525 \times 10^1$, $b = 4.518 \times 10^2$, $c = -3.669 \times 10^3$, $d = 6.570 \times 10^3$, $e = 2.021 \times 10^4$, $f = 2.394 \times 10^4$; V_{max} , V_{fm} both have units of $[ms^{-1}]$ and F_{30} is the equivalent fetch for $R = 30km$ (units of [m]). Eq. 3 is presented in graphical form in Fig. 4. It is clear from this figure that for a given V_{max} , there is a value of V_{fm} which will give the maximum equivalent fetch and hence maximum wave conditions. As V_{max} increases, the value of V_{fm} which produces the maximum equivalent fetch also increases. This occurs since higher values of V_{max} will generate waves with high group velocities and hence a more rapidly moving storm is required to maximize the equivalent fetch.

This rather simple model can also be applied to determine the spectral peak frequency of the maximum waves in the storm, $f_m(max)$. Reformulating the JONSWAP result gives

$$\frac{g}{2\pi f_m(max)V_{max}} = 0.045 \left(\frac{gF}{V_{max}^2} \right)^{0.33} \quad (4)$$

Fig. 5 shows a comparison between the values of $f_m(max)$ generated by the wave model and shown in Table 1 with those calculated from Eq. 4 using the values of

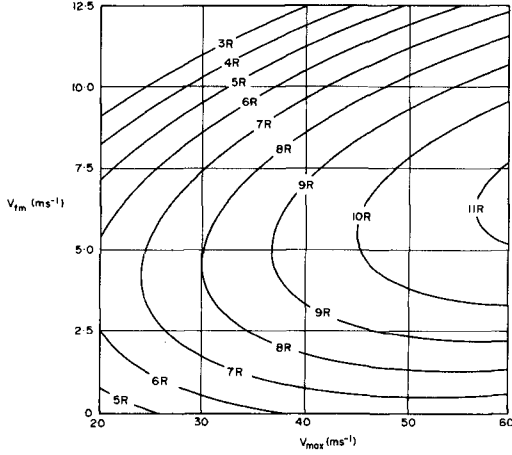


Fig. 4. Contour plot of the equivalent fetch (expressed in terms of R, which equals 30km) as a function of V_{fm} and V_{max} .

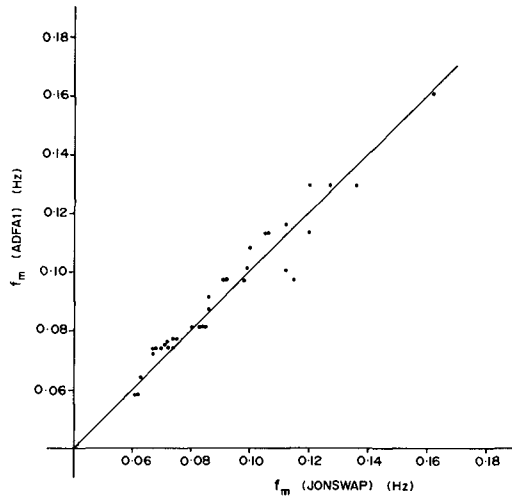


Fig. 5. Peak spectral frequency within the hurricane predicted by the spectral wave model, $f_m(max)$ (ADFA1) versus that predicted by the equivalent fetch assumption, $f_m(max)$ (JONSWAP).

Run No.	V_{fm} (ms^{-1})	V_{max} (ms^{-1})	R (km)	$H_s(max)$ (m)	F	$f_m(max)$ (Hz)
1	0.0	20	30	3.7	4.4R	0.129
2	0.0	25	30	5.1	5.3R	0.113
3	0.0	30	30	6.1	5.3R	0.101
4	0.0	40	30	8.6	5.9R	0.091
5	0.0	50	30	11.8	7.1R	0.077
6	0.0	60	30	14.3	7.3R	0.074
7	2.5	20	30	4.2	5.6R	0.116
8	2.5	25	30	5.5	6.2R	0.108
9	2.5	30	30	6.9	6.8R	0.097
10	2.5	40	30	9.7	7.5R	0.081
11	2.5	50	30	13.0	8.6R	0.075
12	2.5	60	30	15.4	8.4R	0.074
13	5.0	15	30	3.0	5.1R	0.129
14	5.0	20	30	4.5	6.5R	0.113
15	5.0	25	30	6.2	7.9R	0.097
16	5.0	30	30	7.5	8.0R	0.087
17	5.0	40	30	10.9	9.5R	0.077
18	5.0	50	30	13.8	9.7R	0.074
19	5.0	60	30	16.8	10.0R	0.064
20	7.5	20	30	3.7	4.4R	0.113
21	7.5	25	30	5.7	6.6R	0.097
22	7.5	30	30	7.7	8.4R	0.081
23	7.5	40	30	11.4	10.4R	0.076
24	7.5	50	30	14.1	10.2R	0.072
25	7.5	60	30	17.7	11.1R	0.058
26	10.0	20	30	2.4	1.8R	0.160
27	10.0	25	30	3.4	2.4R	0.129
28	10.0	30	30	5.0	3.6R	0.100
29	10.0	40	30	9.1	6.6R	0.081
30	10.0	50	30	12.7	8.2R	0.074
31	10.0	60	30	17.4	10.8R	0.058
32	12.5	40	30	5.6	2.5R	0.097
33	12.5	50	30	10.2	5.3R	0.081
34	12.5	60	30	13.3	6.3R	0.074
35	5.0	40	15	9.3	13.8R	0.081
36	5.0	40	45	11.8	7.4R	0.074
37	5.0	40	60	12.2	5.9R	0.074
38	5.0	25	15	5.2	11.1R	0.110
39	5.0	25	45	6.4	5.6R	0.097
40	5.0	25	60	6.6	4.5R	0.097
41	5.0	60	15	14.5	14.9R	0.074
42	5.0	60	45	17.1	6.9R	0.064
43	5.0	60	60	18.2	5.9R	0.058

Table 1. The synthetic hurricane data base

F from Table 1. The agreement between the two is very good. This is particularly so when it is considered that estimates of f_m from spectral models such as ADFA1 are not particularly robust due to the discrete frequency resolution of such models.

RADIAL DEPENDENCE

As indicated earlier, it was assumed that the radius to maximum wind, R , was a scaling factor. Runs 35 to 43 were included to investigate this influence. Comparing the equivalent fetch values calculated from these runs, and presented in Table 1, with the values for the equivalent runs with $R = 30\text{km}$ shows that the scaling relationship is not linear. (ie. Doubling the radius to maximum winds does not double the equivalent fetch.) Fig. 6 shows the equivalent fetch as a function of radius to maximum winds. In order to collapse the data onto one curve, values have been normalized in terms of the equivalent results for a radius to maximum winds of 30km. (ie. the $R = 30\text{km}$ run with the same values of V_{fm} and V_{max}). These results can be approximated quite well by the relationship

$$F/F_{30} = 0.75 \log_{10} R / (30 \times 10^3) + 1 \quad (5)$$

where F is the equivalent fetch for a hurricane with a radius to maximum winds, R (units of [m]) and F_{30} is the equivalent fetch for the hurricane with the same values of V_{fm} and V_{max} but with a radius to maximum winds of 30km. In practice, F_{30} can be calculated from Eq. 3.

Eq. 5 provides a means of determining F and hence $H_s(max)$ for any value R . Since F is directly related to H_s for given V_{fm} and V_{max} , it would appear to be a far more appropriate spatial scale parameter than R .

PARAMETRIC MODEL

Applying the results in the previous sections, it is possible to develop a relatively simple yet flexible parametric model for hurricane wave prediction in deep water. Given V_{fm} , V_{max} and R , an effective radius R' can be defined from Eq.5

$$R' = 22.5 \times 10^3 \log_{10} R - 70.8 \times 10^3 \quad (6)$$

where both R and R' have units of metres. Using R' , V_{fm} and V_{max} the equivalent fetch, F is determined from Eq.3

$$F/R' = aV_{max}^2 + bV_{max}V_{fm} + cV_{fm}^2 + dV_{max} + eV_{fm} + f \quad (7)$$

where $a = -2.175 \times 10^{-3}$, $b = 1.506 \times 10^{-2}$, $c = -1.223 \times 10^{-1}$, $d = 2.190 \times 10^{-1}$, $e = 6.737 \times 10^{-1}$ and $f = 7.980 \times 10^{-1}$. Again, all values are in standard S.I. units. The maximum significant wave height and associated spectral peak frequency can be determined from the modified JONSWAP relationships, Eqs. 2 and 4.

SPATIAL DISTRIBUTION

The model presented in the previous section provides a means for determining the maximum significant wave height and its associated spectral peak frequency but no insight into the spatial distribution of these quantities within the storm. As with $H_s(max)$, the spatial distribution of significant wave heights is also a function of both V_{fm} and V_{max} . Hence it is not possible to present simply one spatial distribution diagram in a manner similar to that of Bretschneider (1957). Due

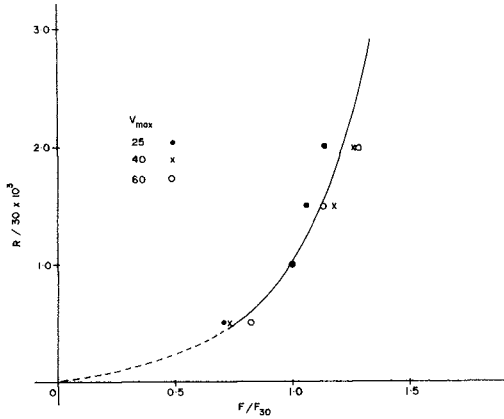


Fig. 6. Dependence of the equivalent fetch, F , on the radius to maximum winds, R . Values are presented in terms of the equivalent fetch for a hurricane with $R=30\text{km}$. The solid line is Eq. 5.

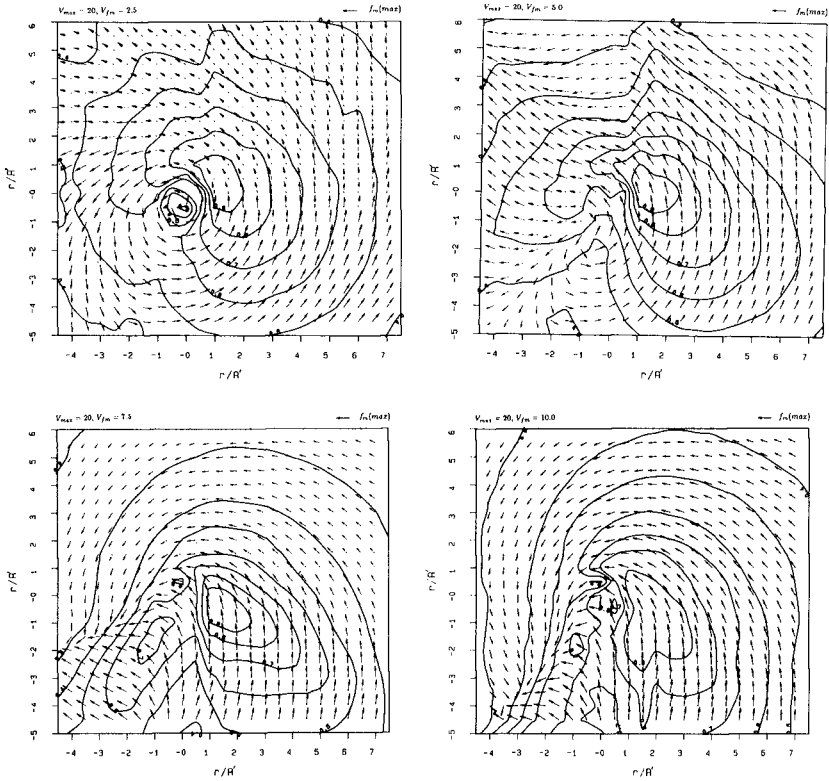


Fig. 7(i). Contour plot of $H_s/H_s(max)$ for hurricanes with $V_{max} = 20\text{ms}^{-1}$. Vectors indicate mean direction of wave propagation. Vector lengths are directly proportional to $T_m = 1/f_m$. Scale is shown at top right.

to space limitations, the spatial distributions for all the runs cannot be presented here. Due to the importance of such results for design purposes, however, as many as is practical appear in Figs. 7. A more complete set of such figures has been presented by Young (1988). Figs. 7 show contours of significant wave height; the values being normalized such that $H_s(max)$ has a value of one. Spatial distances have also been presented in a nondimensional form in terms of r/R' , where r is the distance from the storm centre and R' the effective radius to maximum winds, as defined by Eq. 6. Superimposed on the plots are vectors; the direction being the mean wave direction obtained by integrating the directional spectrum and the length being proportional to the wave period of the spectral peak ($T_m = 1/f_m$).

A number of consistent trends are clear in the spatial distributions as a function of V_{fm} and V_{max} . Typical distributions are characterized by a crescent shaped region to the right of the storm as reported by numerous other authors. This region occurs since the wind velocity is a maximum here and also because the wind direction is approximately parallel with the storm track. Hence, waves generated in this region move forward with the hurricane and maximize the time for which they experience strong winds. The actual position of the crescent shaped region varies with V_{fm} . For slowly moving storms the region is in the right front quadrant. As V_{fm} increases and the hurricane "outruns" the waves it generates, the region moves into the right rear quadrant. The mean wave direction also varies with V_{fm} . As mentioned earlier, for slowly moving storms, swell radiating out from the storm centre dominates the wave field ahead of the storm. As V_{fm} increases, the storm "outruns" the swell and the waves ahead of the storm are entirely locally generated and in the local wind direction. A similar situation occurs in the left rear quadrant. Waves generated ahead of, but close to the storm centre, will be moving to the left. For a slowly moving storm these waves will have had sufficient time to propagate out of the region by the time the storm centre passes over the area. Therefore, waves in the left rear quadrant of slowly moving storms are largely locally generated. For rapidly moving storms, however, waves generated directly ahead of the storm have not had sufficient time to propagate away from the region before the storm moves forward. As a result, conditions in the left rear quadrant are extremely confused with swell moving to the left and locally generated waves moving to the lower right. This is consistent with the SAR data of King and Shemdin (1987) which shows swell in this quadrant propagating in opposition to the wind for Hurricane Gloria which had $V_{fm} = 8.3ms^{-1}$.

The rate of decrease in H_s with distance from the centre of the hurricane varies with V_{max} . This occurs since the relationship between wind speed and wave height is not linear. The result being that there is a more gradual decline in relative wave height with distance from the storm centre for the more intense storms.

Although presented in terms of the non-dimensional spatial scale, r/R' , Figs. 7 all correspond to a value of $R = R' = 30km$. The validity of scaling spatial distributions in terms of R' and hence using these diagrams for other values of R was tested using Runs 35-43 which have a variety of values of R . Due to space limitations, results are not presented here but can be found in Young (1988). These results show that, not only the equivalent fetch, F but also the spatial distribution can be scaled in terms of R' .

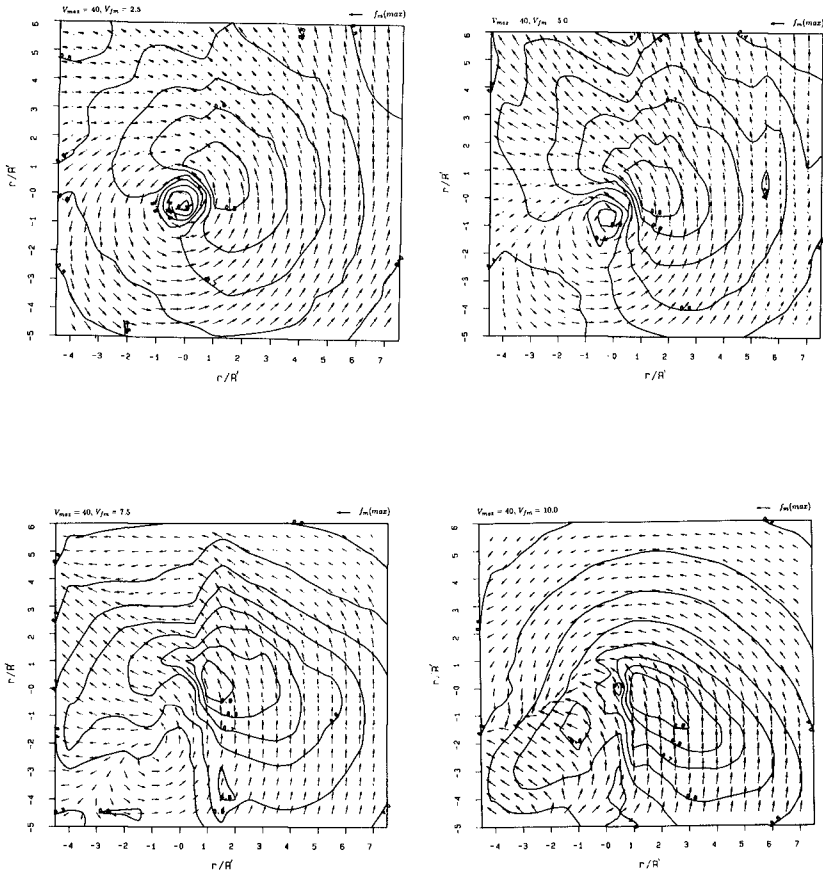


Fig. 7(ii). Contour plot of $H_s/H_s(max)$ for hurricanes with $V_{max} = 40ms^{-1}$. Vectors indicate mean direction of wave propagation. Vector lengths are directly proportional to $T_m = 1/f_m$. Scale is shown at top right.

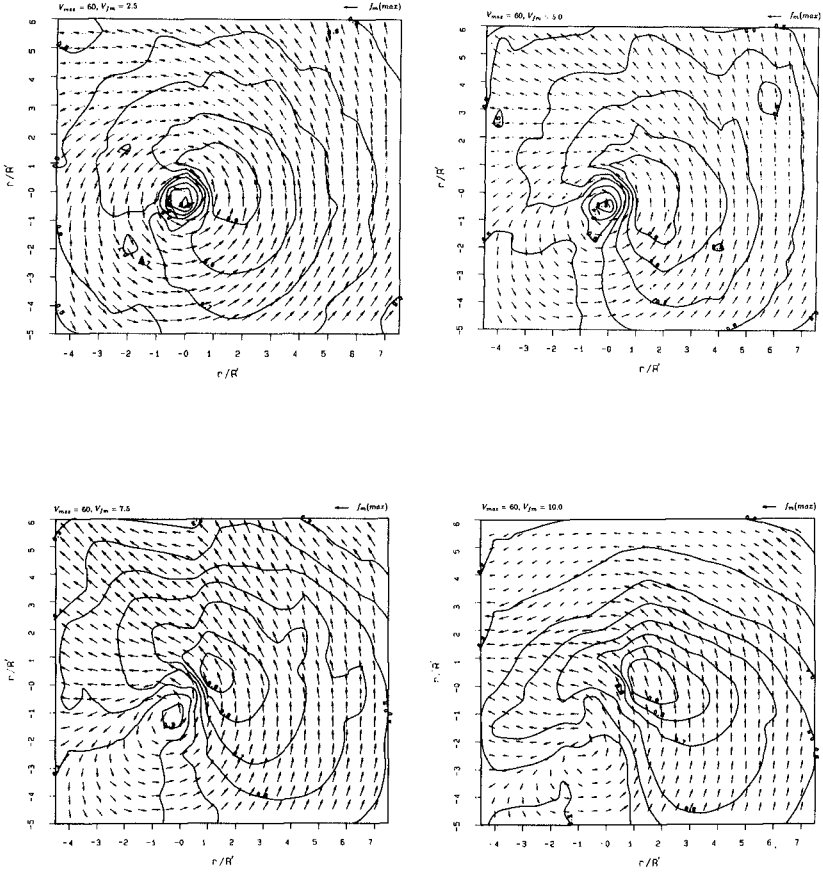


Fig. 7(iii). Contour plot of $H_s/H_2(max)$ for hurricanes with $V_{max} = 60ms^{-1}$. Vectors indicate mean direction of wave propagation. Vector lengths are directly proportional to $T_m = 1/f_m$. Scale is shown at top right.

CONCLUSIONS

An extensive set of numerical experiments have been conducted to determine the influence of the hurricane wind field parameters V_{fm} , V_{max} and R in determining the wave field. V_{fm} and V_{max} play a dual role in determining the maximum significant wave height within the storm, $H_s(max)$, the spatial distribution of waves and the directional properties. This is explained using the concept of an equivalent fetch. For slowly moving storms, waves generated in the intense wind regions to the right of the storm have group velocities greater than V_{fm} , propagate ahead of the storm and experience only a relatively short equivalent fetch. The opposite situation occurs for rapidly moving storms with the waves being left behind the storm. For an optimum combination of V_{fm} and V_{max} waves spend maximum time in the intense wind region, have the maximum equivalent fetch and consequently produce the greatest values of $H_s(max)$. The third parameter, R , acts as a nonlinear spatial scaling parameter.

Based on the concept of the equivalent fetch and the standard JONSWAP fetch limited growth relationships, a simple parametric model has been developed for the maximum significant wave height within the storm, $H_s(max)$ and its associated spectral peak frequency, $f_m(max)$. The spatial distribution of H_s and f_m can be found in terms of the maximum values using a series of field plots expressed in terms of the nondimensional distance parameter r/R' .

The model has a significant advantage over other simple parametric models (Bretschneider, 1957; Ross, 1976) in that it recognizes the important role played by both V_{fm} and V_{max} in determining the spatial distribution of wave parameters within a hurricane. Obviously the model is limited to deep water conditions and cases where the hurricane wind field parameters are relatively constant. For more involved cases the added expense of a full spectral wave model is required.

ACKNOWLEDGEMENTS

The author wishes to thank the management of Woodside Offshore Petroleum Pty. Ltd. and the North West Shelf Joint Venture Participants for making available the tropical cyclone data presented in the paper. The participants in the LNG phase of the project are Woodside Petroleum Pty. Ltd., BHP Petroleum Pty. Ltd., BP Developments Australia Ltd., California Asiatic Oil Company, Japan Australia LNG (MIMI) and Shell Development (Aust.) Pty. Ltd.

REFERENCES

- Beal, R., C., Gerling, T. W., Irvine, D. E., Monaldo, F., M. and Tilley, D., G., 1986, "Spatial Variations of Ocean Wave Directional Spectra from the SEASAT Synthetic Aperture Radar", *Jnl. Geoph. Res.*, 91, C2, pp2433-2449.
- Bretschneider, C., L., 1957, "Hurricane Design Wave Practices", *ASCE, Jnl. Waterways and Harbors*, 83, WW2, No. 1238.
- Gonzalez, F., I., Thompson, T., W., Brown, W., E. and Weissman, D., E., 1982, "SEASAT Wind and Wave Observations of Northeast Pacific Hurricane Iva, August 13, 1978", *Jnl. Geoph. Res.*, 87, C5, pp3431-3438.
- Graham, H. E. and Hudson, G. N., 1960, "Surface Winds Near the Centre of Hurricanes (and Other Cyclones)", *National Hurricane Research Project, Rep. No. 39*,

U.S. Dept. of Commerce, Washington, D.C.

Hasselmann, K., 1960, "Grundgleichungen der Seegangsvorhersage", Schiffstechnik, 7, pp191-195.

Hasselmann, K., et al., 1973, "Measurements of Wind Wave Growth and Swell Decay during the Joint North Sea Wave Project", Herausgegeben vom Deutsch. Hydrograph. Institut, Reihe A, No. 12, 95pp.

Hasselmann, S., Hasselmann, K., Allender, J.H. and Barnett, T.P., 1985, "Computations and Parameterizations of the Nonlinear Energy Transfer in a Gravity-Wave Spectrum. Part II: Parameterizations of the Nonlinear Energy Transfer for Applications in Wave Models", Jnl. Physical Oceanography, 15, pp1378-1391.

King, D.B. and Shemdin, O.H., 1978, "Radar Observations of Hurricane Wave Directions", 16th Int. Conf. on Coastal Eng., Hamburg, pp209-226.

Komen, G.J., Hasselmann, S. and Hasselmann, K., 1984, "On the Existence of a Fully Developed Wind-Sea Spectrum", Jnl. Physical Oceanography, 14, pp1271-1285.

McLeish, W. and Ross, D.B., 1983, "Imaging Radar Observations of Directional Properties of Ocean Waves", Jnl. Geoph. Res., 88, C7, pp4407-4419.

Pierson, W.J. and Moskowitz, L., 1964, "A Proposed Spectral Form for Fully Developed Wind Seas Based on the Similarity Theory of S.A. Kitaigorodskii", Jnl. Geoph. Res., 69, pp5181-5190.

Ross, D., 1976, "A Simplified Model for Forecasting Hurricane Generated Waves", Bull. Amer. Met. Soc., January. Presented at Conference on Atmospheric and Oceanic Waves, Seattle, Washington, March 29-April 2.

SWAMP Group, 1985, "The Sea Wave Modeling Project (SWAMP): Principal Results and Conclusions", Plenum Press, 256pp.

Young, I.R., 1987a, "A General Purpose Spectral Wave Prediction Model", Dept. Civil Eng., Aust. Defence Force Academy, Res. Rep. No. 16.

Young, I.R., 1987b, "Validation of the Spectral Wave Model ADFA1", Dept. Civil Eng., Aust. Defence Force Academy, Res. Rep. No. 17.

Young, I.R., 1987c, "A Shallow Water Spectral Wave Model", To appear Jnl. Geoph. Res.

Young, I.R., 1988, "A Parametric Model for Tropical Cyclone Waves", Dept. Civil Eng., Aust. Defence Force Academy, Res. Rep. No. 28.

Young, I.R., Hasselmann, S. and Hasselmann, K., 1987, "Computations of the Response of a Wave Spectrum to a Sudden Change in Wind Direction", Jnl. Physical Oceanography, 17, 9, pp1317-1338.

CHAPTER 83

A NUMERICAL MODEL OF NEARSHORE CURRENTS DUE TO IRREGULAR WAVES

Masataka Yamaguchi*

ABSTRACT

This paper presents a numerical model of nearshore currents due to irregular waves. The radiation stress is estimated by a current-depth refraction model for irregular waves, in which the energy dissipation due to wave breaking is modeled through the use of a saturated frequency spectrum in shallow water. The model is in reasonable agreement with measured wave height, mean water level variation and observed nearshore current patterns. Next, the model is applied to the computation of wave transformation and nearshore currents on a uniformly sloping beach and on model topographies with complicated contour lines. Comparison with the results based on a regular wave model shows that wave irregularity has a smoothing effect on cross-shore distributions of wave height, mean water level variation and longshore currents, but that it does not have much effect on nearshore current patterns.

1. INTRODUCTION

In most nearshore current models, a regular wave theory including finite amplitude wave theory (Yamaguchi, 1986) has been used for the calculation of wave transformation in shoaling water and in the surf zone, and the resulting radiation stress which is a driving force of nearshore currents. Since ocean waves are irregular waves approximated by the superposition of many component waves with different frequency and direction, a nearshore current model taking into account the effect of wave irregularity is needed for better understanding and description of coastal phenomena. Nevertheless, it seems that there are no numerical models of nearshore currents due to irregular waves applicable to an arbitrary bottom topography, although analytical models of longshore currents by Collins(1972), Battjes(1972) and Thornton & Guza (1986) and a numerical model of longshore

* Prof., Dept. of Ocean Eng., Ehime Univ., Bunkyocho 3, Matsuyama 790, Ehime Pref., Japan

currents by Hubertz (1984), are available. Therefore, the aim of this study is to present a numerical model of near-shore currents due to irregular waves, in which wave transformation is computed by a current-depth refraction model, and to establish its applicability by comparison with the results of experiments and observations of wave transformation and nearshore currents. Then, based on the numerical computations, the effect of wave irregularity on them and the characteristics of nearshore currents on two-dimensional model topographies are discussed.

2. MODEL DESCRIPTION

(1) Wave transformation model

The wave transformation model is to solve the conservation equation of wave action spectral density ($w = E(k_x, k_y) / \sigma_m$) and the equations for wave number components (k_x, k_y) simultaneously, where $E(k_x, k_y)$ is the wave number spectrum and σ_m the relative angular frequency. The former is written as

$$\frac{\partial w}{\partial t} + \frac{dx}{dt} \frac{\partial w}{\partial x} + \frac{dy}{dt} \frac{\partial w}{\partial y} + \frac{dk_x}{dt} \frac{\partial w}{\partial k_x} + \frac{dk_y}{dt} \frac{\partial w}{\partial k_y} = 0 \quad (1)$$

and the latter is

$$\begin{aligned} \frac{\partial k_x}{\partial t} + (C_g \cos \theta + U) \frac{\partial k_x}{\partial x} + (C_g \sin \theta + V) \frac{\partial k_x}{\partial y} \\ = -\frac{gk^3 \operatorname{sech}^2 kD}{2\sigma_m} \frac{\partial D}{\partial x} - k_x \frac{\partial U}{\partial x} - k_y \frac{\partial V}{\partial x} \\ \frac{\partial k_y}{\partial t} + (C_g \cos \theta + U) \frac{\partial k_y}{\partial x} + (C_g \sin \theta + V) \frac{\partial k_y}{\partial y} \\ = -\frac{gk^3 \operatorname{sech}^2 kD}{2\sigma_m} \frac{\partial D}{\partial y} - k_x \frac{\partial U}{\partial y} - k_y \frac{\partial V}{\partial y} \end{aligned} \quad (2)$$

where C_g is the group velocity of the component wave, θ the wave direction, k the wave number, $D (= h + \eta)$ the total water depth including the mean water level variation η , h the still water depth and (U, V) are the wave-induced nearshore current components.

These equations mean that the wave action spectral density in a nondissipative system is conserved along the characteristics defined by

$$\frac{dx}{dt} = C_g \cos \theta + U, \quad \frac{dy}{dt} = C_g \sin \theta + V \quad (3)$$

where the wave number components are computed from

$$\begin{aligned} \frac{dk_x}{dt} &= -\frac{gk^3 \operatorname{sech}^2 kD}{2\sigma_m} \frac{\partial D}{\partial x} - k_x \frac{\partial U}{\partial x} - k_y \frac{\partial V}{\partial x} \\ \frac{dk_y}{dt} &= -\frac{gk^3 \operatorname{sech}^2 kD}{2\sigma_m} \frac{\partial D}{\partial y} - k_x \frac{\partial U}{\partial y} - k_y \frac{\partial V}{\partial y} \end{aligned} \quad (4)$$

Thus, the conservation of the wave action spectral density expressed in frequency-direction space is written as

$$w(f, \theta) = (C_g + U \cos \theta + V \sin \theta) E(f, \theta) / (2\pi k \sigma_m) = \text{const} \quad (5)$$

and is rewritten in the following equation

$$E_2(f_2, \theta_2) = \left\{ \frac{(C_{\sigma 1} + U_1 \cos \theta_1 + V_1 \sin \theta_1) / (k_1 \sigma_{m1})}{(C_{\sigma 2} + U_2 \cos \theta_2 + V_2 \sin \theta_2) / (k_2 \sigma_{m2})} \right\} E_1(f_1, \theta_1) \quad (6)$$

where f is the absolute frequency, $E(f, \theta)$ is the directional spectrum and subscripts '1' and '2' denote the variables at different positions. This is the basic relationship used to compute the transformation of directional spectra. The model can estimate the effects of not only depth-refraction and wave shoaling, but also current refraction.

The energy dissipation due to wave breaking is modeled through the use of a saturated frequency spectrum proposed by Kitaigorodskii et al. (1975)

$$E_{\infty}(f) = \alpha g^2 (2\pi)^{-4} f^{-3} \phi(\omega_h) \quad (7)$$

$$\phi(\omega_h) = \alpha^{-1} (1 + 2\omega_h^2 x / \sinh 2\omega_h^2 x)^{-1}, \quad \omega_h^2 = \sigma_m^2 D / g, \quad x = gk / \sigma_m^2$$

where α is the equilibrium constant at the high frequency tail and g the acceleration of gravity. Assuming the invariability of angular distribution in directional spectra associated with wave breaking, directional spectra including the effect of depth-controlled wave breaking are re-evaluated by

$$E_{new}(f, \theta) = E_{old}(f, \theta) E_{\infty}(f) / E_{old}(f) \quad (8)$$

where directional spectra with subscripts 'new' and 'old' mean directional spectra before and after the inclusion of the wave breaking effect respectively.

The radiation stress components (S_{xx} , S_{xy} , S_{yy}) and wave statistics are obtained by the numerical integration of directional spectra with respect to wave direction and frequency using

$$\begin{aligned} S_{xx} &= \int_0^{\infty} \int_0^{2\pi} \rho g \{n \cos^2 \theta + (n-1/2)\} E(f, \theta) d\theta df \\ S_{xy} = S_{yx} &= \int_0^{\infty} \int_0^{2\pi} \rho g n \cos \theta \sin \theta E(f, \theta) d\theta df \\ S_{yy} &= \int_0^{\infty} \int_0^{2\pi} \rho g \{n \sin^2 \theta + (n-1/2)\} E(f, \theta) d\theta df \end{aligned} \quad (9)$$

and

$$\begin{aligned} E(f) &= \int_0^{2\pi} E(f, \theta) d\theta, \quad m_0 = \int_0^{\infty} E(f) df, \quad m_1 = \int_0^{\infty} f E(f) df, \quad m_2 = \int_0^{\infty} f^2 E(f) df \\ H_{1/3} &= 4.00 \sqrt{m_0}, \quad T_{1/3} = 1.20 \sqrt{m_0 / m_2}, \quad H_{rms} = 2.83 \sqrt{m_0}, \quad T_{m01} = m_0 / m_1 \end{aligned} \quad (10)$$

$$\bar{\theta} = \tan^{-1} \left\{ \int_0^{\infty} \int_0^{2\pi} E(f, \theta) \cos \theta d\theta df / \int_0^{\infty} \int_0^{2\pi} E(f, \theta) \sin \theta d\theta df \right\}$$

where $n = C_g / C$, C is the wave celerity of the component wave, ρ the density of fluid, m_n the spectral moment, $E(f)$ the frequency spectrum, $H_{1/3}$ the significant wave height, $T_{1/3}$ the significant wave period, H_{rms} the root mean square wave height, T_{m01} the mean wave period and $\bar{\theta}$ the mean wave direction.

The input directional spectrum at the offshore boundary is given by the Bretschneider-Mitsuyasu-type frequency spec-

tral model with $\cos^{2S}(\theta/2)$ type angular distribution function

$$E(f, \theta) = E(f) \cdot D(f, \theta)$$

$$E(f) = 0.257 (H_{1/3})_0^2 (T_{1/3})_0 (T_{1/3})_0 f^{-5} \exp[-1.03 ((T_{1/3})_0 f)^4] \phi(\omega_h) \tag{11}$$

$$D(f, \theta) = \frac{2^{2s-1} \Gamma^2(s+1)}{\pi \Gamma(2s+1)} \cos^{2s} \left(\frac{\theta - \theta_0}{2} \right)$$

where S is the energy concentration factor, θ_0 the principal wave direction, Γ the Gamma function, and subscript '0' indicates the wave conditions in deep water. The input frequency spectrum is modified by the introduction of the shallow water effect. Consequently, significant wave height and wave period in deep water $((H_{1/3})_0, (T_{1/3})_0)$ are different from those at the offshore boundary of the computation region located in shallow water $((H_{1/3})_M, (T_{1/3})_M)$. In most cases, it is not $(H_{1/3})_0$ and $(T_{1/3})_0$ but $(H_{1/3})_M$ and $(T_{1/3})_M$ that are prescribed beforehand in the computation. The values of $(H_{1/3})_0$ and $(T_{1/3})_0$ to be given as input conditions are determined in a trial and error manner so that $(H_{1/3})_M$ and $(T_{1/3})_M$ computed from Eq.(11) agree approximately with the prescribed $(H_{1/3})_M$ and $(T_{1/3})_M$.

Numerical computation is conducted making use of a piecewise ray method as shown in Fig. 1. The method is to trace a wave ray backward only by one time step and to interpolate wave action spectral density at the tip point of the ray. The wave ray is followed by solving Eq. (3) and Eq. (4) with the Runge-Kutta method. In the ray computation, both input wave direction and current direction have to be reversed. The interpolation is executed in two steps. First, the Lagrange interpolation formula with third order accuracy is applied to the wave action spectral densities at the grid points surrounding the ray point in order to estimate the wave action spectral densities for the prescribed input directions, putting the wave direction at the ray point between them. It is given as

$$\omega_{i+r, j+s} = \sum_{i=i-1}^{i+2} \sum_{j=j-1}^{j+2} \left(\prod_{k=i}^{k=i-1} \frac{x - x_k}{x_i - x_k} \right) \left(\prod_{k=j}^{k=j-1} \frac{y - y_k}{y_j - y_k} \right) \omega_{ij} \tag{12}$$

$$r = (x - [x]) / \Delta x, \quad s = (y - [y]) / \Delta y$$

Second, the wave action spectral density for wave direction at the ray point is obtained by applying a linear interpolation on wave direction to the action densities estimated above.

$$w(f, \theta_m) = w(f, \theta) = w(f, \theta_k) + |w(f, \theta_{k+1}) - w(f, \theta_k)| \cdot \left(\frac{\theta - \theta_k}{\theta_{k+1} - \theta_k} \right) \tag{13}$$

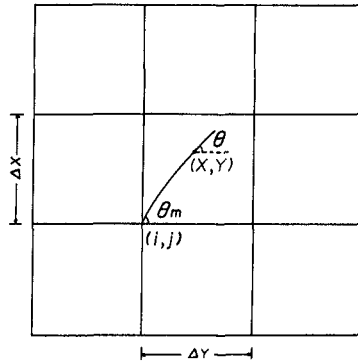


Fig. 1 Computation of direction of propagation.

(2) Nearshore current model

The equations used in the computation of nearshore currents are vertically-integrated continuity and momentum equations and they are expressed as

$$\begin{aligned} \frac{\partial \rho D}{\partial t} + \frac{\partial M_x}{\partial x} + \frac{\partial M_y}{\partial y} &= 0 \\ \frac{\partial M_x}{\partial t} + \frac{\partial}{\partial x}(UM_x) + \frac{\partial}{\partial y}(UM_y) &= -\rho g D \frac{\partial \eta}{\partial x} + \frac{\partial}{\partial x}(\bar{L}D \frac{\partial U}{\partial x}) + \frac{\partial}{\partial y}(\bar{L}D \frac{\partial U}{\partial y}) \\ &\quad - \left(\frac{\partial S_{xx}}{\partial x} + \frac{\partial S_{xy}}{\partial y} + \tau_{bx} \right) \\ \frac{\partial M_y}{\partial t} + \frac{\partial}{\partial x}(VM_x) + \frac{\partial}{\partial y}(VM_y) &= -\rho g D \frac{\partial \eta}{\partial y} + \frac{\partial}{\partial x}(\bar{L}D \frac{\partial V}{\partial x}) + \frac{\partial}{\partial y}(\bar{L}D \frac{\partial V}{\partial y}) \\ &\quad - \left(\frac{\partial S_{yx}}{\partial x} + \frac{\partial S_{yy}}{\partial y} + \tau_{by} \right) \end{aligned} \tag{14}$$

where $M_x = \rho DU$ and $M_y = \rho DV$.

The Longuet-Higgins expression (1970) is used as the lateral mixing term

$$\bar{L} = N_c \rho l_x \sqrt{gD} \tag{15}$$

where l_x is the distance measured from the real shoreline and $N_c (=0.01)$ the constant. The bottom friction components (τ_{bx}, τ_{by}) are obtained with Nishimura's expression (1983) for regular waves, which approximates the usual quadratic formula with high accuracy

$$\begin{aligned} \tau_{bx} &= \rho c_f \left\{ \left(w + \frac{\bar{u}^2}{w} \cos^2 \theta \right) U + \frac{\bar{u}^2}{w} \sin \theta \cos \theta V \right\} \\ \tau_{by} &= \rho c_f \left\{ \frac{\bar{u}^2}{w} \sin \theta \cos \theta U + \left(w + \frac{\bar{u}^2}{w} \sin^2 \theta \right) V \right\} \\ w &= \left(\sqrt{U^2 + V^2 + \bar{u}^2 + 2W\bar{u}} + \sqrt{U^2 + V^2 + \bar{u}^2 - 2W\bar{u}} \right) / 2 \\ W &= U \cos \theta + V \sin \theta, \quad \bar{u} = 2u_{max} / \pi, \quad u_{max} = \pi H / T \sinh kd \end{aligned} \tag{16}$$

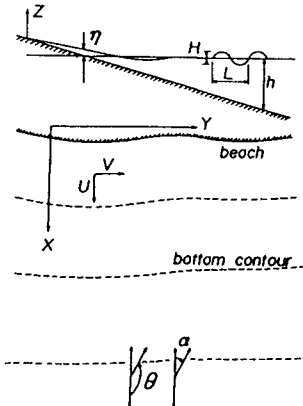


Fig. 2 Coordinate system used in nearshore current model.

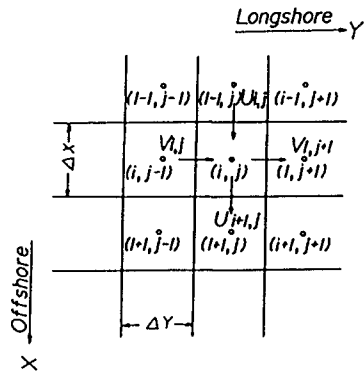


Fig. 3 Configurations of variables in finite difference model.

because their expressions in the case of irregular waves are not known by the author at least, where $c_f (=0.01)$ is the friction factor. The wave-induced velocity is estimated approximately by the small amplitude wave theory using H_{rms} , T_{m01} and $\bar{\theta}$ computed from the wave transformation model.

A finite difference method is used to solve the governing equations of nearshore currents. Fig. 2 is the coordinate system. The x and y axes are taken in the offshore direction, and in the longshore direction respectively and the z axis is taken vertically upward. Finite difference approximation is made by the forward difference in time and by the central difference in space under the configuration of variables shown in Fig. 3. Zero initial condition, fixed offshore and moving onshore boundary conditions, and periodic longshore boundary conditions are imposed respectively.

(3) Flow of computation

The computer program starts by determining the spatial distribution of wave characteristics under the given input conditions of offshore waves and bottom topography, and then nearshore current computation is made using the radiation stress components obtained from the wave transformation model.

A steady state solution is accomplished for 1000 to 2400 iterations of alternating computations of wave transformation and nearshore currents. In this case, computation of wave characteristics is executed every 18 iterations of nearshore current computation in order to save computer processing time. A schematic diagram of computation flow is shown in Fig. 4.

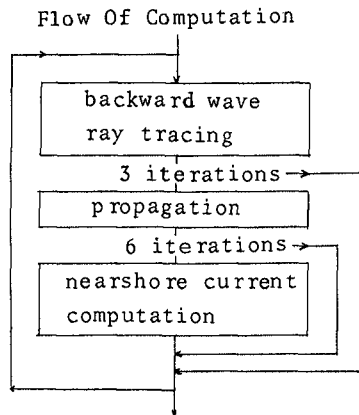


Fig. 4 Schematic diagram of computation flow.

Table 1 describes numerical conditions used in the computations of this study. Numbers of frequency segments and directional segments are 14 and 19 respectively.

3. EXPERIMENTAL AND OBSERVATIONAL VERIFICATIONS OF THE MODEL

(1) Comparison with experiments

A preliminary test in a smaller computational region was tried in order to tune the wave transformation model. Fig. 5 is a comparison between the computations and the experiments on wave height variation with normal incidence of waves on a uniformly sloping beach conducted by Battes and Janssen (1978). In order to approximate long-crested incident waves generated in the experiment, the value of 800 is used for

Table 1 Conditions used in the computations.

Model topography	Num. of grid MxN	Grid dist. (m)	$(H_{1/3})_0$ (m)	$(T_{1/3})_0$ (s)	$(H_{1/3})_M$ (m)	$(T_{1/3})_M$ (s)	α_M ($^\circ$)	S	Num. of iterations
S. B.	24x8	1	0.304	2.15	0.204	1.74	0	800	1000
S. B.	45x8	1	0.304	2.15	0.204	1.74	0	800	2400
S. B.	45x8	1	0.221	2.25	0.147	1.81	0	800	2400
S. B.	23x8	12.5	1.30	4.20	1.00	3.54	30	20	1000
S. B.	23x8	12.5	1.30	4.20	1.00	3.54	30	800	1000
SY. C.	27x20	5	1.41	4.28	1.00	3.51	0	20	1000
ASY. C.	27x20	5	1.41	4.28	1.00	3.51	30	20	1000
SY. V.	27x20	20	2.06	3.95	2.00	3.66	0	20	1200
SY. V.	24x35	20	2.06	3.95	2.00	3.66	30	20	1200
C. B.	24x73	20	2.18	3.95	2.00	3.56	-20	20	1080
Sonu	19x26	5	0.586	5.00	0.300	3.77	0	40	1000

S. B.: straight beach, SY. C.: symmetrical concave topography, ASY. C.: asymmetrical concave topography, SY. V.: symmetrical convex shoreline, C. B. : arbitrarily curved bay, Sonu : bottom topography in Sonu's observation

the energy concentration factor in the directional spectral model and the direction data is taken to range from $162^\circ - 198^\circ$. The computation in the surf zone results in slightly greater value than the experiment. Thus, a correction to the saturated frequency spectrum in shallow water being used for the estimation of energy dissipation due to wave breaking is introduced to improve the correspondence with the experiment. The correction factor is determined as

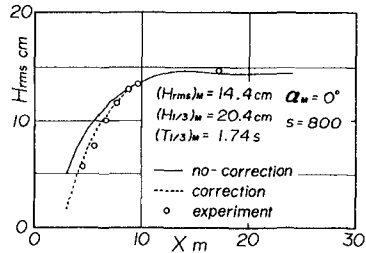


Fig. 5 Tuning of wave transformation model.

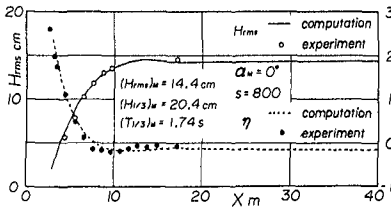


Fig. 6 Comparison of computed and measured wave heights and mean water level variations on a uniformly sloping beach.

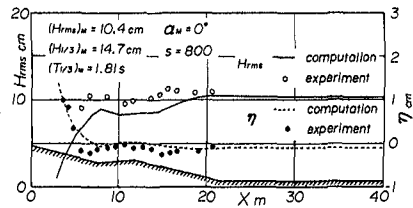


Fig. 7 Comparison of computed and measured wave heights and mean water level variations on a uniformly sloping beach with long-shore bar.

$$\beta = \begin{cases} -0.0471 \log^2 \left(\frac{H_{rms}}{D} \right) - 0.206 \log \left(\frac{H_{rms}}{D} \right) \\ -0.875; \left(\frac{H_{rms}}{D} \right) > 0.484 \\ 1; \left(\frac{H_{rms}}{D} \right) \leq 0.484 \end{cases} \quad (17)$$

Cross-shore distributions of wave height and mean water level variation computed in a larger computational region for the same case are re-compared with the experiment in Fig. 6. As a matter of course, the computation of wave height variation is in good agreement with the experiment. Consequently, the computation of mean water level variation also shows good correspondence with the experiment.

Fig. 7 is another comparison between the computation and the experiment by Battjes and Janssen on a uniformly sloping beach with a longshore bar. The agreement of wave height variation is not always satisfactory compared to that of wave set-up and set-down, because energy dissipation due to wave breaking is not well-formulated in the present model.

(2) Comparison with observation

Fig. 8 illustrates the observed nearshore current patterns by Sonu (1972) and the corresponding results computed by the present model. The model reproduces well the qualitative features of the complicated nearshore current patterns found in the observation, such as the onshore currents on both sides of the region and the rip currents in the central part. But, in a quantitative sense, outflow from the rip channel in the computation seems to be a little stronger than that in the observation.

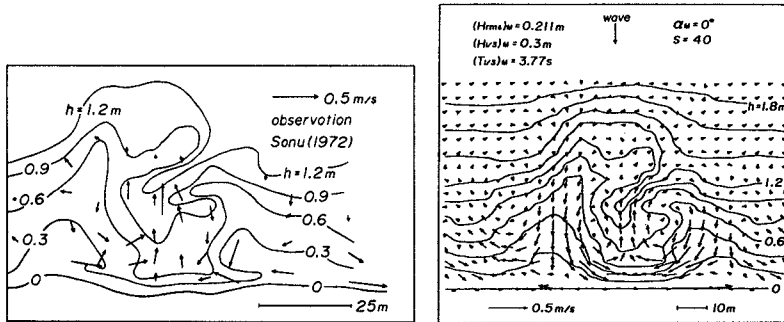


Fig. 8 Nearshore current patterns observed by Sonu(1972) and the corresponding results computed by the present model.

4. COMPUTATIONAL RESULTS AND CONSIDERATIONS

(1) Computations on model topographies

The model is applied to the nearshore current computations on a uniformly sloping beach and on model topographies with two-dimensional variation of bottom contour. The computations are compared with those based on regular wave

theory (Yamaguchi et al. 1983 and 1985) and the effect of wave irregularity on wave transformation and nearshore currents is discussed.

(2) Uniformly sloping beach

The cross-shore distributions of wave height, wave direction, mean water level variation and longshore current profile on a plain beach with a slope of 0.016 are drawn in Fig. 9. In the case of irregular waves, the computations using energy concentration factor $S = 20$ or 800 or neglecting the wave-current interaction are carried out. The effect of wave-current interaction is weak in this case and the effect of the energy concentration factor appears distinctly in longshore current velocity. Compared to the case of regular waves, the variations of wave height and wave direction in the surf zone and in shoaling water is slower. As a result, offshore variations of the resulting radiation stress, wave set-up and set-down and longshore current velocity have a similar tendency, and the magnitudes of mean water level variation and longshore current velocities become smaller.

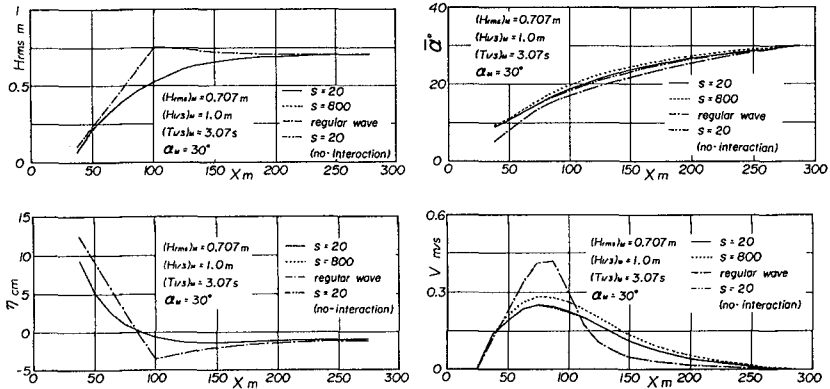


Fig. 9 Cross-shore distributions of wave height, wave direction, mean water level variation and longshore currents on a uniformly sloping beach.

(3) Bottom topography with a concave contour line

The bottom topography model proposed by Noda (1974) is first chosen for the computation of nearshore currents on a two-dimensional topography and it is expressed as

$$h(x, y) = ix [1 + A_0 \exp\{-3(x/20)^{1/2}\} \sin^{10}\{(\pi/\lambda)(y - x \tan \epsilon)\}] \quad (18)$$

where i is a mean beach slope of 0.025, λ the longshore beach length of 80 m, A_0 the maximum amplitude of the bottom undulation of 20 m and ϵ the skewness of the bottom undulation of 0° or 30° . The model topographies with $\epsilon = 0^\circ$ and with $\epsilon = 30^\circ$ are referred to as symmetrical concave topography and asymmetrical concave topography respectively.

Fig. 10 show the nearshore current patterns with normal

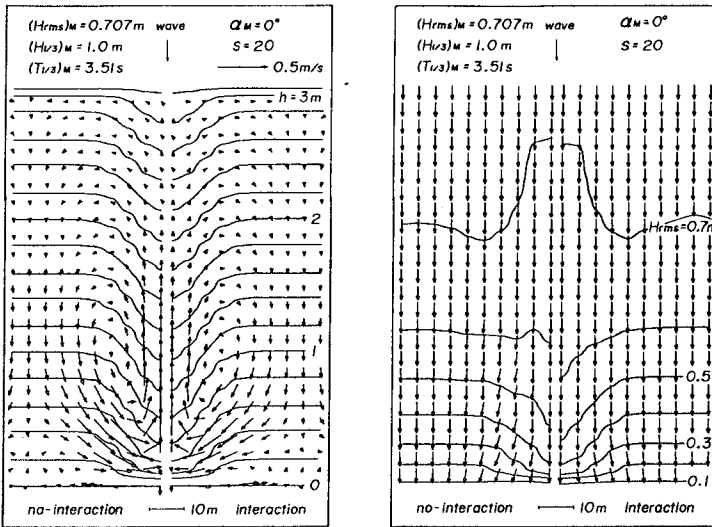


Fig. 10 Effect of wave-current interaction on nearshore currents, wave height and wave direction on a symmetrical concave topography.

incidence of waves on the symmetrical concave topography. The case neglecting wave-current interaction is on the left hand side and the normal case is on the right hand side. We can see the formation of a pair of seaward nearshore current cells and a pair of weak and flat cells near the shoreline, and the neglect of wave-current interaction increases cross-shore current velocity such as in the case of regular waves.

Fig. 11 illustrates the current patterns with oblique incidence of waves on the asymmetrical concave topography. Meandering longshore currents are predominant, but a small and flat circulation cell in the region with concave contour line near the shore is also found.

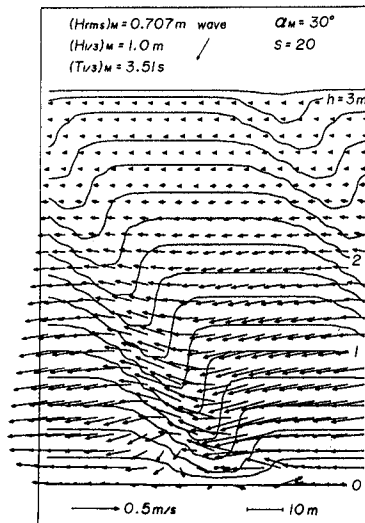


Fig. 11 Nearshore current patterns on asymmetrical concave topography.

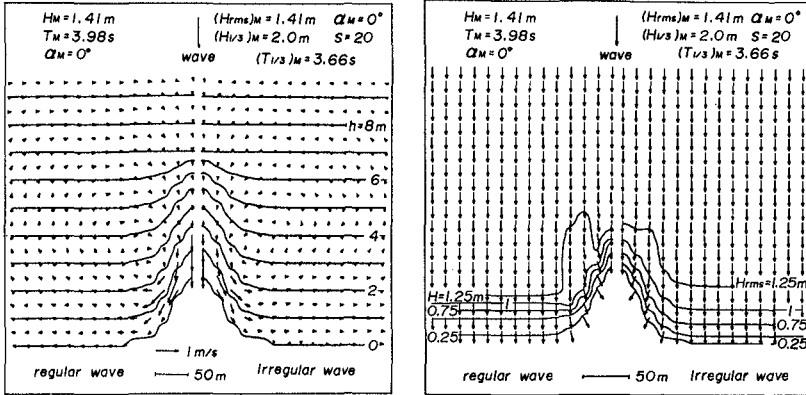


Fig. 12 Effect of wave irregularity on nearshore currents, wave height and wave direction on a model topography with convex shoreline.

(4) Bottom topography with a convex shoreline

Fig. 12 show the spatial distributions of wave height and wave direction, and the corresponding nearshore current patterns on a two-dimensional model topography with convex shoreline. On the left hand side of each figure, the results based on a regular wave theory are given as well. In the computations, root mean wave height and peak period of frequency spectrum and principal wave direction are used as input conditions. In each case, a pair of nearshore current cells with rotational direction contrary to the case of symmetrical concave topography mentioned above are formed and on the center line of the computational region, the onshore current is accelerated toward the shoreline and the current direction turns to be tangential to the contour line. Current patterns in both cases are very similar to each other, but current velocity in the case of irregular waves is smaller by about 30 %.

Fig. 13 is the current pattern in the case of obliquely incident waves. Predominant longshore currents develop along the contour line and a weak counterclockwise circulation cell appears near the shoreline in the upwave region.

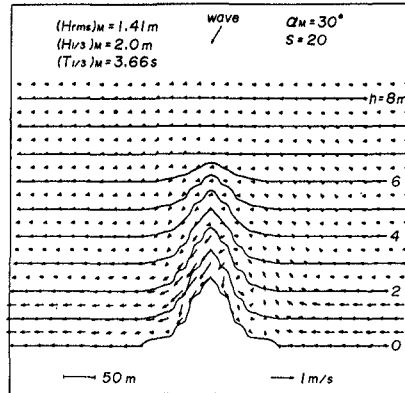


Fig. 13 Nearshore current patterns on a model topography with convex shoreline.

(5) Bottom topography with an arbitrarily curved shoreline

Nearshore current patterns on a curved bay computed by regular and irregular wave models are shown in Fig. 14. Both these figures demonstrate the predominant longshore currents in the outer region and a clockwise nearshore circulation cell in the inner region. This cell exists irrespective of incident wave direction. But, a weak offshore circulation cell found in the case of regular waves disappears in the case of irregular wave case.

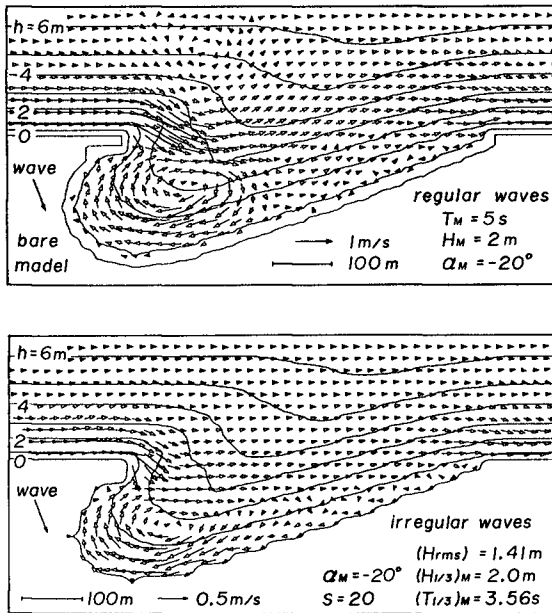


Fig. 14 Spatial distribution of nearshore current patterns on a curved bay computed by the numerical models with regular and irregular wave theories.

5. CONCLUSIONS

A numerical model of nearshore currents induced by irregular waves was proposed and its validity was supported by reasonable correspondence with experimental and observational results. Moreover, the effect of wave irregularity was considered, based on numerical computations. Comparison with the results based on a regular wave model shows that wave irregularity has a smoothing effect on cross-shore distribution of wave height, mean water level variation and longshore currents, but that it does not have much effect on nearshore current patterns.

6. ACKNOWLEDGMENTS

Thanks are due to Messrs. K. Hosono and H. Kawahara, former graduate course students of Ocean Engineering, Ehime University, for their valuable help during the study. A part of this study was accomplished with the support of the Science Research Fund of the Ministry of Education, for which the author expresses his appreciation.

REFERENCES

- Battjes, J.A. (1972): Set-up due to irregular waves, Proc. of 13th ICCE, Vol. III, pp. 1993 - 2004.
- Battjes, J.A. and J.P.F.M. Janssen (1978): Energy loss and set-up due to breaking of random waves, Proc. of 16th ICCE, Vol. I, pp.569 - 589.
- Collins, J.I. (1972): Longshore currents and wave statistics in the surf zone, Rep. No. TC-149-2, Tetra Tech. Inc.
- Hubertz, J.M. (1984): Modeling of nearshore driven currents, Proc. of 19th ICCE, Vol. III, pp. 2208 - 2219.
- Kitaigorodskii, S.A. et al. (1975): On Phillips' equilibrium range in the spectra of wind generated gravity waves, Jour. Phys. Oceanogr., Vol. 5, pp. 410 - 420.
- Longuet-Higgins, M.S. (1970): Longshore currents generated by obliquely incident sea waves Part 2, Jour. Geophys. Res., Vol. 75, No. 33, pp. 6778 - 6801.
- Nishimura, H. (1982): Numerical simulation of nearshore circulation, Proc. of 29th Conf. on Coastal Eng. in Japan, pp. 333 - 337 (in Japanese).
- Noda, E. (1974): Wave-induced nearshore circulation, Jour. Geophys. Res., Vol. 79, No. 27, pp. 4097 - 4106.
- Sonu, C.J. (1972): Field observation of nearshore circulation and meandering currents, Jour. Geophys. Res., Vol. 77, No. 8, pp. 3232 - 3246.
- Thornton, E.B. and R.T. Guza (1986): Surf zone longshore currents and random waves: Field data and models, Jour. Geophys. Res., Vol. 16, pp. 1165 - 1179.
- Yamaguchi, M. et al. (1983): A numerical solution of near-shore currents taking account of wave-induced mass flux, Proc. of 30th Conf. on Coastal Eng. in Japan, pp. 480 - 484 (in Japanese).
- Yamaguchi, M. et al. (1985): A numerical model of nearshore currents applicable to coastal area with an arbitrarily curved shoreline, Proc. of 32nd Conf. on Coastal Eng. in Japan, pp. 248 - 252 (in Japanese).

Yamaguchi, M. (1986): A numerical model of nearshore currents based on a finite amplitude wave theory, Proc. of 20th ICCE, Vol. 1, pp. 849 - 863.



Vicedo Lugo

PART II

COASTAL PROCESSES

Vicedo Lugo



CHAPTER 84

NON-UNIFORM SUSPENDED SEDIMENTS UNDER WAVES

Aronne Armanini (*)

Piero Ruol (**)

Abstract

An original mathematical formulation for suspended sediments in a two-dimensional wave boundary layer is presented. The model accounts for non-immediate adaptation of sediments to the hydrodynamic conditions, and allows to include the effect of sorting of the different diameters considered.

The mathematical model is numerically solved through a finite difference scheme.

It is suitable that results compare favourably with experimental data by Staub et alii.

1) Introduction

While in the last decade a number of mathematical formulations regarding the velocity distribution in a wave boundary layer have been proposed (including numerical and analytical solutions [Kesteren and Bakker, 1984] [Kajiura, 1968]), less effort has been devoted to the problem of predicting the sediment distribution [Justesen and Fredsoe, 1985] [Bakker, 1974]. In particular for aspects concerning bed-boundary conditions and non-uniformity of material.

In the present paper an original formulation of the bed-boundary condition in a two-dimensional wave boundary layer, accounting for non uniform material, is proposed. The problem has been solved through a mathematical model, in which the fluid flow and the sediment concentration equations are solved numerically.

(*) Professor of Hydraulics, Dept. of Eng., University of Trent, Mesiano di Povo, Trento, Italy.

(**) Ph.D. Candidate, Inst. Maritime Constr., University of Padua, Via Ognissanti, 39 Padova, Italy.

2) Equations of motion

The fluid flow equations are usually solved aside from the sediment presence by means of momentum equation. For a two-dimensional turbulent boundary layer the general equation appears:

$$\frac{\partial u}{\partial t} + u \frac{\partial u}{\partial x} + v \frac{\partial u}{\partial y} = - \frac{1}{\rho} \frac{\partial p}{\partial x} - \frac{\partial}{\partial x} \overline{u'u'} - \frac{\partial}{\partial y} \overline{v'u'} \quad 1)$$

For a wave boundary layer advection terms, as well as the horizontal diffusion term are neglected; moreover the pressure term is substituted by the inertial term external to the boundary layer; as a consequence, eq.1) reads:

$$\frac{\partial(u-U_0)}{\partial t} = \frac{\partial}{\partial y} \left(\epsilon \frac{\partial u}{\partial y} \right) \quad 2)$$

where the turbulent diffusion coefficient:

$$-\epsilon = \frac{\overline{u'v'}}{\partial u / \partial y} \quad 3)$$

has been introduced.

Upon introduction of the defect velocity $u_d = u - U_0$, eq.2) becomes:

$$\frac{\partial u_d}{\partial t} = \frac{\partial}{\partial y} \left(\epsilon \frac{\partial u_d}{\partial y} \right) \quad 4)$$

To solve eq. 4), a turbulent closure hypothesis and adequate bed boundary conditions must be assigned. The following expressions are assumed for the turbulent diffusion coefficient:

$$\epsilon = l^2 \frac{\partial u}{\partial y} \quad 5)$$

where l is a turbulent mixing length, function of the boundary layer thickness δ , for which the following Escudier formulation [Lauder and Spalding, 1972] is assumed:

$$l = 0.41 y \quad \text{for} \quad y \leq 0.22 \delta \quad 6a)$$

$$l = 0.09 \delta \quad \text{for} \quad y > 0.22 \delta \quad 6b)$$

The bed boundary conditions are imposed according to the universal law of the wall:

$$\frac{u}{u_*} = \frac{1}{K} \ln(y^+ E) \quad \text{for } y^+ = \frac{u_* y}{\nu} \geq 11.6 \quad 7a)$$

$$\frac{u}{u_*} = y^+ \quad \text{for } y^+ < 11.6 \quad 7b)$$

the latter being referred to the presence of a viscous sublayer next to the wall, and E being a roughness parameter (E=9 for hydraulically smooth walls).

Eq. 4), 5), and 6) are solved numerically through a Preissman finite difference-scheme [Lyn and Goodwin, 1987]. The first points of the integration mesh were chosen according to either eq. 7a) or 7b). Eq.7b), being a non-linear equation, solving for u^* requires an iterative procedure based on Newton-Raphson scheme.

The mathematical model warrants sufficient generality to be applied both under simple waves and under superimposed waves and current conditions; however, only the first case is dealt with in this paper.

The results of the mathematical model have been compared with some experimental data obtained by Jonsson and Carlsen [1976] in an oscillating tunnel. Comparison between measured and predicted velocities for different phase angles are reported in Fig. 1

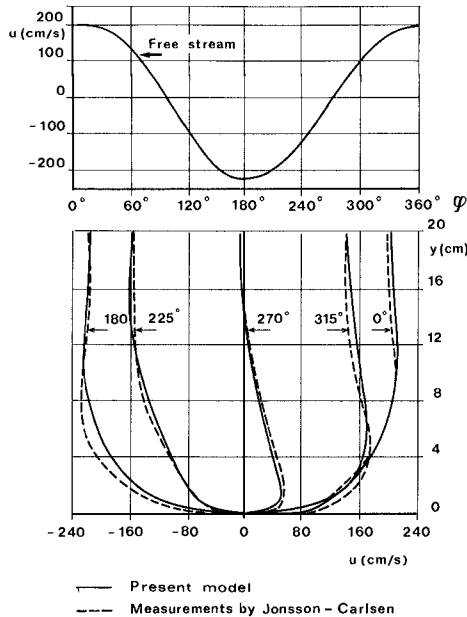


Fig.1. Velocities in the free stream and comparison between measured and predicted ones as a function of height for different phase angles.

3) Equations of sediment transport

3.1) Uniform grain-size hypothesis

The general suspended sediment transport equation in a two-dimensional turbulent boundary layer is written as:

$$\frac{\partial c}{\partial t} + \frac{\partial(u c)}{\partial x} + \frac{\partial(v-w) c}{\partial y} = - \frac{\partial \overline{u'c'}}{\partial x} - \frac{\partial \overline{v'c'}}{\partial y} \quad 8)$$

in which w is the fall velocity and c the volume concentration of sediments.

The vertical component of velocity, the horizontal diffusion term and the advection term have been neglected, as usual.

The turbulent diffusion coefficient ϵ_s for the solid phase was introduced in the form:

$$- \epsilon_s = \frac{\overline{v'c'}}{\partial c / \partial y} \quad 9)$$

and was assumed equal to that of the momentum (eq. 3 - 6); therefore eq 8) becomes:

$$\frac{\partial c}{\partial t} = \frac{\partial}{\partial y} (w c + \epsilon \frac{\partial c}{\partial y}) \quad 10)$$

The boundary conditions generally considered to define the proper boundary value problem are: zero concentration far from the bed, and bottom concentration (at a reference level $y=a$), as a function of the grain properties and of the flow conditions (i.e. θ Shields parameter); The latter appears:

$$c(a) = c_b = f(\theta) \quad \text{being} \quad \theta = \frac{u_*^2}{(S-1)g D} \quad 11)$$

A more appropriate bed-boundary condition, accounting for non-instantaneous adaptation of sediment concentration to the flow conditions, has already been proposed by the authors [Armanini and Ruol, 1987]. The net flux, at the reference level $y=a$ is, in fact:

$$D = -(w c + \epsilon \frac{\partial c}{\partial y})_a \quad 12)$$

The first term represents the downward flux and the second one the upward flux (pick-up rate). It is reasonable to assume [Di Silvio and Armanini 1982, 1985] that the first term (deposition) depends on the upstream boundary condition, while the second term (erosion) depends on the flow conditions and is the same as for local equilibrium condition.

Under this assumption the erosion flux (pick-up rate) is

just equal to $(-w c_b)$ where c_b is the bottom concentration in a channel flow with the same Shields parameter. In this way the bottom boundary condition becomes:

$$D = -w [c(a) - c_b] \tag{13}$$

According to the methodology considered for the solution of the motion equations, eq. 10) is solved numerically through the Preissman finite difference scheme [Lyn and Goodwin, 1987].

In fig.2) the vertical distribution of the concentration under the two bottom boundary conditions is shown. It does appear that the hypothesis of immediate adaptation of the bottom concentration to the equilibrium condition (eq.11), produces a positive gradient of the concentration next to the bed, which is somewhat devoid of physical content, whenever the friction velocity falls under the critical Shields threshold value; this phenomenon does not appear with the suggested boundary condition (eq.13).

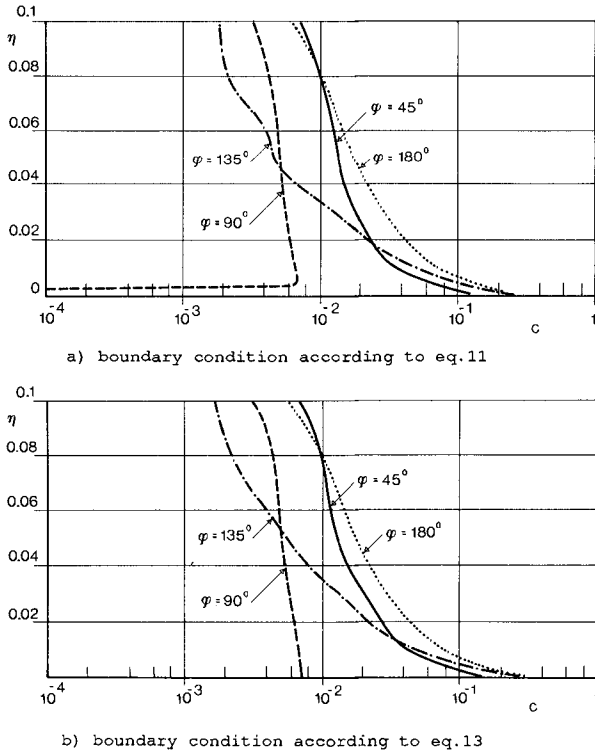


Fig.2 Comparison between the two different bed-boundary conditions in determining the concentration c as a function of dimensionless height $\eta = (y-z)/(H-z)$ for mean grain size $D_{50} = 0.19\text{mm}$.

In Fig.3 the variation of dimensionless concentration during a wave period is compared with the experimental results of Staub et alii [1984]. In the same figure the simulation carried out by Justesen and Fredsøe [1985] is also reported: the present model seems to yield a better agreement with the experimental data.

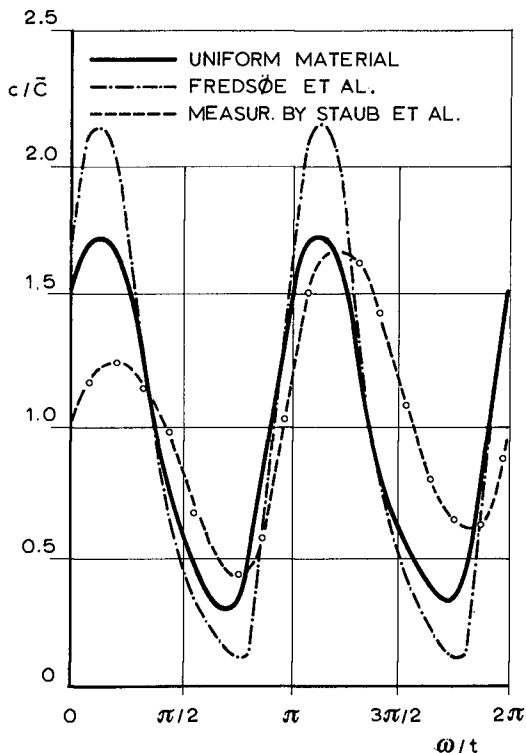


Fig.3 Comparison between measured and predicted variation of dimensionless concentration during one wave period at 1.8cm above the bottom.
($D_{50} = 0.19\text{mm}$; $u_{\text{max}} = 1.28\text{m/s}$; $T = 9.1\text{s}$)

3.2) Non uniform grain size hypothesis

In many cases the mean diameter alone is not able to represent correctly the concentration distribution and the sediment transport. In fig. 4) the mean concentration integrated over the boundary layer thickness and along the period is reported.

From the figure it does appear that, at least in a certain range of diameters (0.12-0.17mm), at a small variation of particle diameter a strong variation of mean concentration is observed.

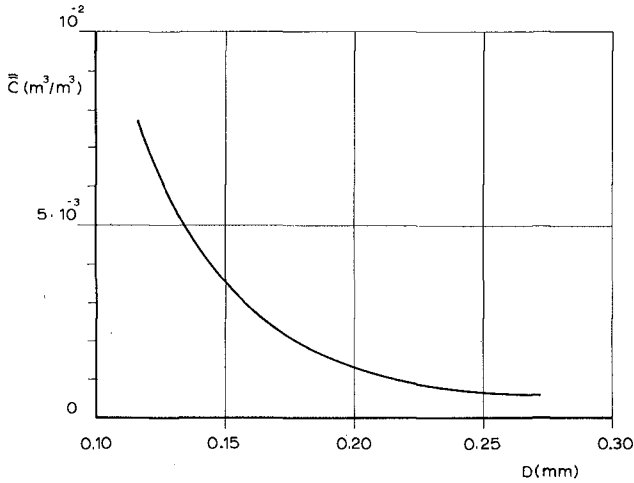


Fig.4 Average concentration (over depth and period) versus grain diameter in the case of uniform material model. ($u_{max} = 1.2m/s$; $T = 9.1s$)

In order to overcome these limitations it is then convenient to divide the grain size distribution curve into a discrete number of classes j [Ruol, 1988]. The continuity equation of suspended sediments for each class is then the same as for uniform material (eq.10):

$$\frac{\partial c_j}{\partial t} - w_j \frac{\partial c_j}{\partial y} = \frac{\partial}{\partial y} \left(\epsilon \frac{\partial c_j}{\partial y} \right) \tag{14}$$

On the other hand in assigning the bed- boundary conditions it is necessary to account for the mutual interactions among the various classes. The upward flux for each class can be assumed, as for uniform material, the same as in equilibrium condition, but multiplied by the actual concentration for the j -th class on the bed (β_j):

$$\beta_j w_j c_b(\theta_j) \tag{15}$$

the downward flux, instead, depends on the effective concentration near the bed. As a consequence, the net flux at the reference level a , becomes:

$$D_j = - w_j [c(a)_j - \beta_j c_b(\theta_j)] \tag{16}$$

Eq. 16), which represents the new bed-boundary condition, contains the new variable β_j ; one more equation is then necessary to solve the problem. This equation is given by the volume sediment balance in the active layer at the

bottom surface:

$$\frac{\partial}{\partial t} (\beta_j \Delta) = -D_j + \beta_j^* \sum_k D_k \tag{17}$$

in which Δ is the thickness of the bed layer instantaneously involved in the mixing process during the erosion-deposition process, that is, in the exchange process between the sediments of the bottom and of the stream.

It is easy to show that β_j^* equals β_j whenever sedimentation prevails over erosion, and the actual bed concentration above the exchange layer during erosion processes.

Finally it must be:

$$\sum_k \beta_k = 1 \tag{18}$$

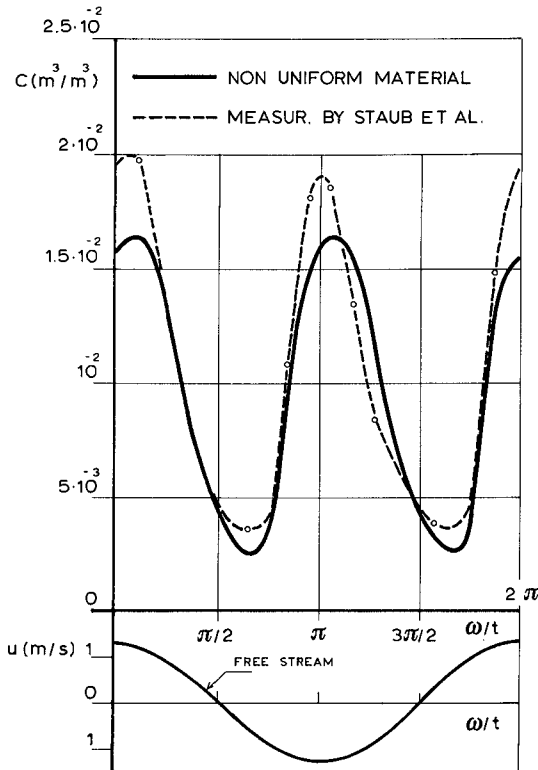


Fig.5 Velocities in the free stream ($u_{max} = 1.2\text{m/s}$; $T = 9.1\text{s}$) and comparison between measured and predicted variation of total concentration during one wave period at $y=1.2\text{cm}$ above the bottom. ($D_1=0.13\text{mm}$ {20%}; $D_2=0.20\text{mm}$ {80%})

In fig.5) the concentration obtained from computations accounting for two grain-size fraction are compared with experimental data by Staub et Al. [1983].

The differences between uniform and non uniform material models are much more pronounced as becomes more evident the non-uniformity of gradation curve. The results shown in the present paper are related to the experimental data by Staub et alii, where the gradation curve are almost uniform. Nevertheless the vertical distribution of concentration is more sensitive to the gradation of the material than the mean concentration.

In fig. 6) a comparison between the results obtained from the two-fraction and from the uniform material models are shown. The vertical distribution of the single diameter concentrations (D_1 , D_2), of the total concentration (D_1+D_2), and the vertical distribution of the corresponding uniform material (D_{50}) concentrations are plotted together.

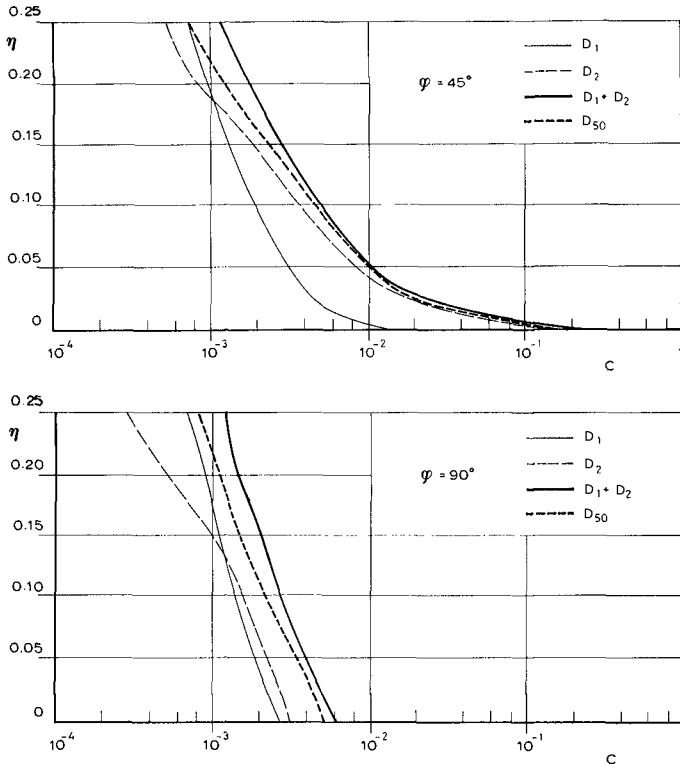


Fig.6a Vertical distribution of the concentration obtained from the two-fraction run ($D_1=0.13\text{mm}$ {20%}; $D_2=0.20\text{mm}$ {80%}) compared with the corresponding uniform material run ($D_{50}=0.19\text{mm}$) for different phase angles ($\varphi = 45^\circ, 90^\circ$).

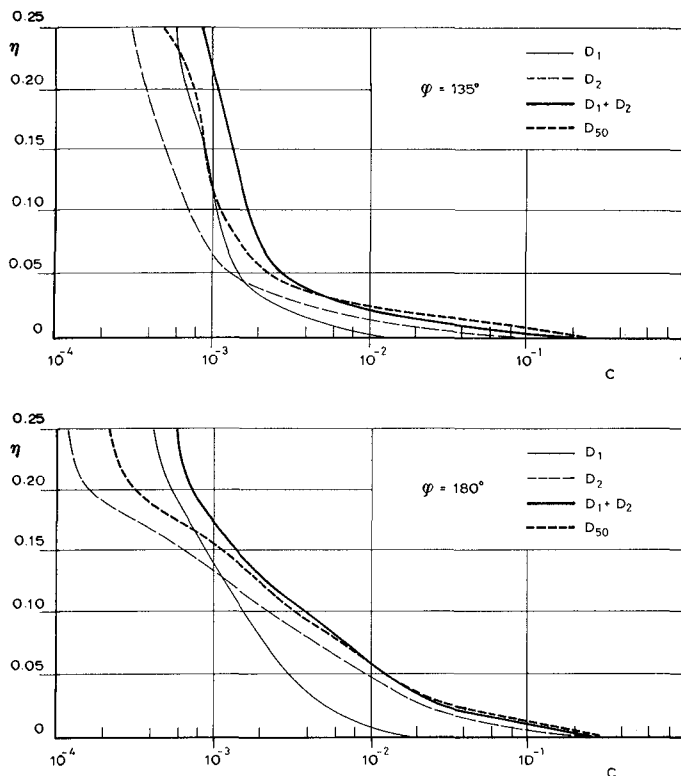


Fig. 6b Vertical distribution of the concentration obtained from the two-fraction run ($D_1=0.13\text{mm}$ {20%}; $D_2=0.20\text{mm}$ {80%}) compared with the corresponding uniform material run ($D_{50}=0.19\text{mm}$) for different phase angles ($\varphi=135^\circ, 180^\circ$).

4) Conclusions

A mathematical model of vertical distribution of concentration of suspended sediments in a two-dimensional wave boundary layer is presented. The model includes a bed boundary condition capable to account for non-immediate adaptation of concentration to hydrodynamic conditions. The model has been extended in order to describe the mutual interaction between different grain size classes in the case of non uniform grain size distribution.

It is opinion of the writers that the model will find a wider applicability if adapted to the sloping beach case by integration over the boundary layer thickness, (in a way already proposed by Armanini and Di Silvio [1982] [1988] for a channel flow). In this case in fact the model should be able to describe the sorting effect induced through the breaking zone.

5) References

- [1] Armanini A., Di Silvio G., 1982: "Sudden morphological modifications along a mountain river simulated by a mathematical model", APD-IAHR, Bandung.
- [2] Armanini A., Di Silvio G., 1985: "Transport of suspended sediments along channels with a trench" XXI Congr. I.A.H.R. vol.3 pp.527-532, Melbourne.
- [3] Armanini A., Di Silvio G., 1988: "A one-dimensional model for the transport of a sediment mixture in non-equilibrium condition" Journ. of Hydraulic Res. Vol.26, n.3 ,pp.275-291.
- [4] Armanini A., Ruol P., 1987: "Distribution of suspended sediments in a wave boundary layer" Euromech 215, S.Margherita Ligure pp.80-83.
- [5] Bakker W.T., 1974: "Sand concentration in an oscillatory flow". Proc. Coast. Eng. Conf. , ch.66.
- [6] Di Silvio G., Armanini A., 1981: "Influence of the upstream boundary conditions on the erosion-deposition process in open channels" XIX Congr. IAHR n.22 New Delhi.
- [7] Jonsson G., Carlsen N.A., 1976: "Experimental and theoretical investigation in an oscillatory turbulent boundary layer" Journ. Hydr. Res. 14, n.1 pp.45-59.
- [8] Justesen P., Fredsoe J., 1985: " Distribution of turbulence and suspended sediment in the wave boundary layer" Rep. 62, pp.61-67, Inst. Hydrodyn. and Hydr. Eng., Tech. Univ. Denmark.
- [9] Kajiura K., 1968: "A model of the bottom boundary layer in water waves". Bull. Earthquake Res. Inst., vol.46.
- [10] Kesteren W.G.M., Bakker W.T., 1984: "Near bottom velocities in waves with a current; analytical and numerical computations". Proc. Coast. Eng. Conf. ch.79, pp. 1161-1177.
- [11] Launder B., Spalding D.B. 1972: "Mathematical models of turbulence". Academic Press. London and New York. 169 p.
- [12] Lyn D., Goodwin P., 1987: "Stability of a general Preissman scheme". Journ. of Hydr. Eng., vol.113 n.1.
- [13] Ruol P. 1988: "How to represent bed materials in sediment transport models under waves" Proc. Conf. Trasp. sol. nei corsi d'acqua, Trento Italy, 9-10 jun.
- [14] Staub C., Svendsen A., Jonsson I., 1983: "Measurements of the instantaneous sediment suspension in oscillatory flow". Prog. Rep. 58, Inst. Hydrodyn. Tech. Univ. Denmark.
- [15] Staub C., Jonsson I., Svendsen A., 1984: "Variation of sediment suspension in oscillatory flow" Proc. Coast. Eng. Conf., ch.155 pp. 2310-2321.

CHAPTER 85

INITIAL MOTION IN COMBINED WAVE AND CURRENT FLOWS

J.S. Lee-Young* and J.F.A. Sleath**

Abstract

Measurements are presented of the conditions for the initial motion of sediment under combined steady and oscillatory flow. The measurements were made in a steady flow flume with an oscillating tray set into its bed. The direction of oscillation of the tray was at right angles to the axis of the steady flow flume. Four different grades of sand were tested.

It is found that the critical condition for the initiation of motion is reasonably represented by a critical value of the vector sum of the component shear stresses assuming no nonlinear interaction between the steady and oscillatory flows. The resultant bed shear stress was also calculated with the aid of several combined wave-current models. The results of these various approaches are compared with Shields curve.

Introduction

The conditions under which sediment first begins to move due to a flow of fluid are of great importance in many engineering problems. There have consequently been numerous studies of the initial motion condition in both pure steady flow and in pure oscillatory flow (see, for example, Sleath 1984). On the other hand, there have been surprisingly few investigations of the initial motion condition for combined steady and oscillatory flow. Hammond and Collins (1979) studied the case where the steady and oscillatory flows are collinear. More recently, Katori et al (1984) have made measurements of steady and oscillatory flows at right angles to each other. The aim of the present paper is to study the second of these two cases.

Experimental Layout

The experimental apparatus is shown schematically in Fig. 1. The sediment is contained in a tray set into the bed of the flume. The tray oscillates (see Sleath, 1976,

*Research student, Cambridge University Engineering Department, Trumpington Street, Cambridge CB2 1PZ England

**Lecturer, Cambridge University Engineering Department, Trumpington Street, Cambridge CB2 1PZ England

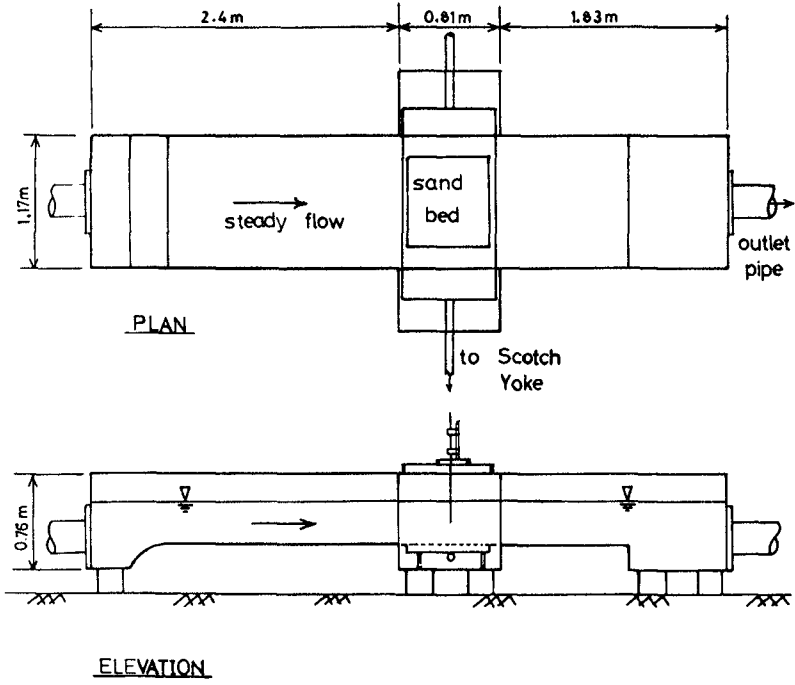


Fig. 1. Schematic drawing of the combined steady and oscillatory flow flume

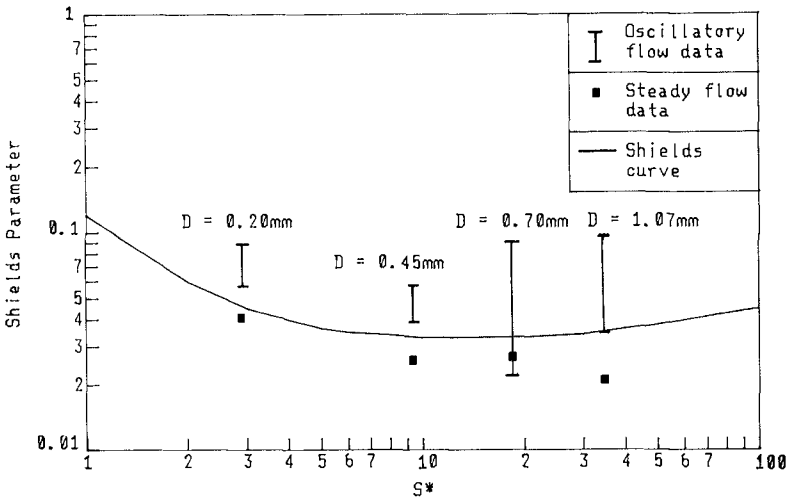


Fig. 2. Results of initial motion experiments under steady flow alone and oscillatory flow alone

for a description of the mechanism) with simple harmonic motion in a direction at right angles to the axis of the steady flow flume. The amplitude of oscillation can be varied from 0 to 0.19 m and the working period ranges from 0.5 secs up to about 6.0 secs.

The steady flow is provided by two re-circulating pumps. With the aid of a control valve on the inlet pipe the mean steady current can be varied from 0 to 0.4 m/s. The steady velocity was monitored throughout the tests at a point just upstream of the oscillating tray and at a height of 0.04 m above the bed. In addition, a number of vertical traverses were made which indicated that the velocity profile was logarithmic up to that height at this position.

Four different sands were used in the tests. Their median diameters were 0.20 mm, 0.45 mm, 0.70 mm and 1.07 mm.

The normal test procedure was as follows. At the start of the test the bed of sand was carefully levelled. The bed of sand was then caused to oscillate at a fixed period T and amplitude A_b . Finally, the steady flow velocity was gradually increased until threshold conditions were observed. The criterion adopted for initial motion was Kramer's (1935) weak motion regime.

The depth of water was held equal to 0.17 m for the finest sand and 0.12 m for the other sands.

Experimental Results

As well as performing initial motion experiments under combined flow conditions, initial motion under, (a), pure steady flow and, (b), pure oscillatory flow was also examined. The reason for this was two-fold. First it was necessary to check that the rig worked correctly and produced results, under these conditions, which were comparable with other published values, and secondly it was necessary to find the limits between which we could expect the combined flow results to lie.

The results of experiments under conditions (a) and (b) are shown in Fig. 2. The shear stresses under pure oscillatory flow were found assuming a quadratic drag law in which the wave friction factor was taken from Kamphuis (1975) friction factor curves. It is seen that the data lies close to the Shields curve. Following Madsen and Grant (1976) the Reynolds number has been replaced in Fig. 2 by

$$S_* = \frac{D}{4v} \sqrt{\frac{(\rho_s - \rho)}{\rho}} gD \quad (1)$$

where D is median grain diameter and ρ_s and ρ are, respectively, sediment and fluid density.

The raw results for the critical conditions under which sediment just begins to move in combined steady and oscilla-

tory flow are shown in Figs. 3 - 6. In these figures u_w is the amplitude of the velocity of the oscillating tray and u_c is the depth-averaged steady current just upstream of the test section. In order to guide the eye, curves of the form

$$\left(\frac{u_w}{u_{w0}}\right)^n + \left(\frac{u_c}{u_{c0}}\right)^n = 1 \quad (2)$$

have been drawn through the experimental points. In this equation u_{w0} and u_{c0} are the critical values of u_w when the steady current is zero and u_c when the oscillatory velocity is zero, respectively. Values of n between 2 and 4 appear to give the best agreement with the experimental results.

Inertia Effects

One problem with a study of sediment entrainment in an oscillatory tray apparatus is the inertia force acting on the grains of sediment. If we consider spherical particles of diameter D and dry density ρ_s there is an additional force (i.e. in addition to the forces which the particle would experience if it were on a stationary bed in an oscillating flow) equal to

$$(\rho_s - \rho) \frac{\pi D^3}{6} \frac{\partial u}{\partial t}$$

where u is the velocity of the tray.

For the finest sand used in these experiments the additional force due to inertia is negligible compared with the other forces acting on the grains. However, for the coarser sands this is not always the case, particularly at the lowest periods of oscillation. It would be possible to make a correction to the experimental results to allow for this additional force. However, this requires a knowledge of the phase relationships of the forces acting on the particle, the horizontal and vertical directions in which they act and, finally, some estimate of the shape of the grains. When the required correction is large this procedure is not very reliable. Consequently, in the comparison of different models outlined below only those experimental results for which the magnitude of the additional force is less than 30 % of the magnitude of the force which the grains would experience on a stationary bed have been retained. For the purposes of deciding which results to retain the force for a stationary bed has been taken as the vector sum of the forces calculated for oscillatory flow and steady flow separately. The same set of experimental results is used in each of the Figures 8 - 11.

Although the magnitude of the additional force in the retained experimental results may be as much as 30 % of the magnitude of the force for a stationary bed the actual error in the resultant force is generally much less than that.

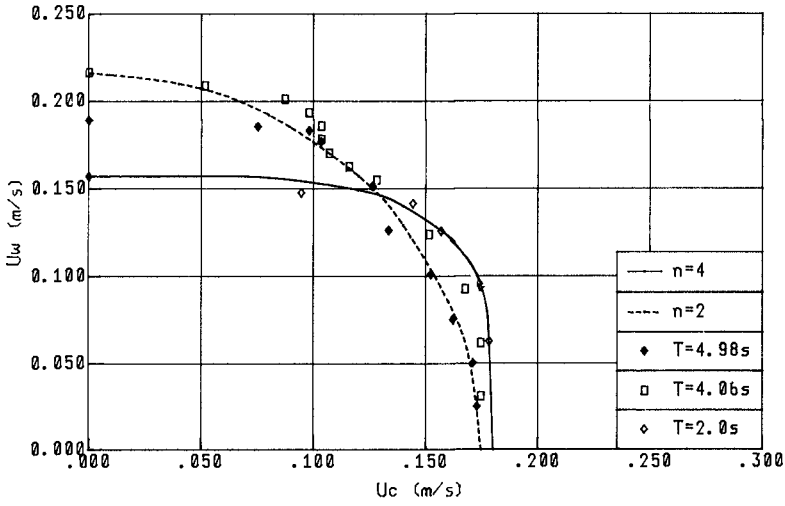


Fig. 3. Critical velocities for $D = 0.20$ mm

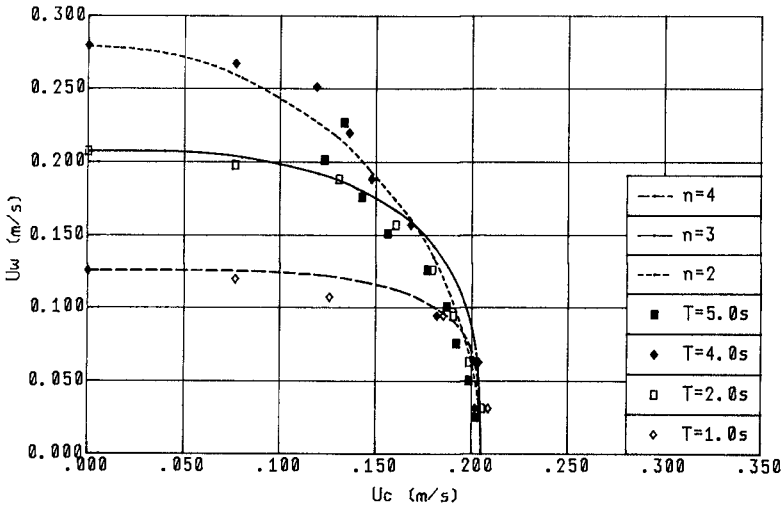
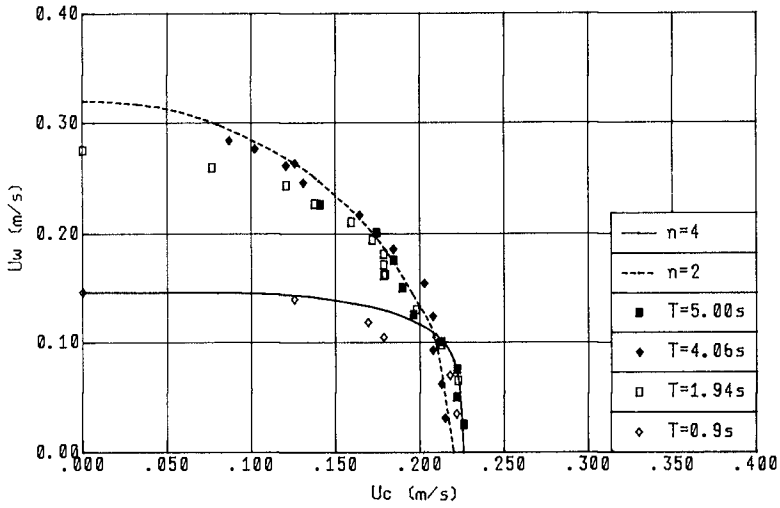
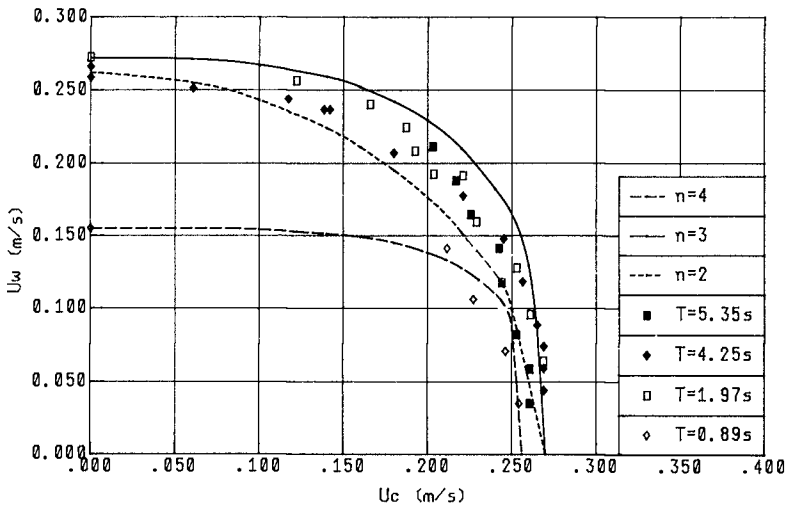


Fig. 4. Critical velocities for $D = 0.45$ mm

Fig. 5. Critical velocities for $D = 0.70$ mmFig. 6. Critical velocities for $D = 1.07$ mm

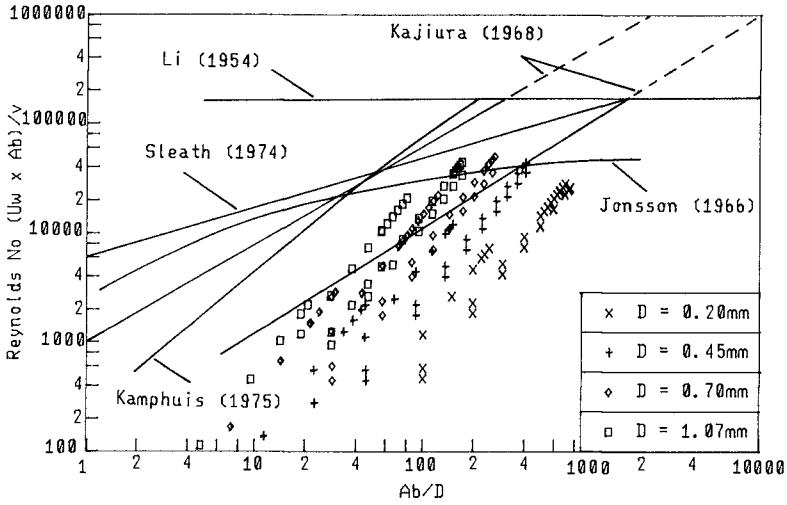


Fig. 7. The oscillatory flow parameters compared with various relationships for transition of an oscillatory flow boundary layer over a flat bed of sand

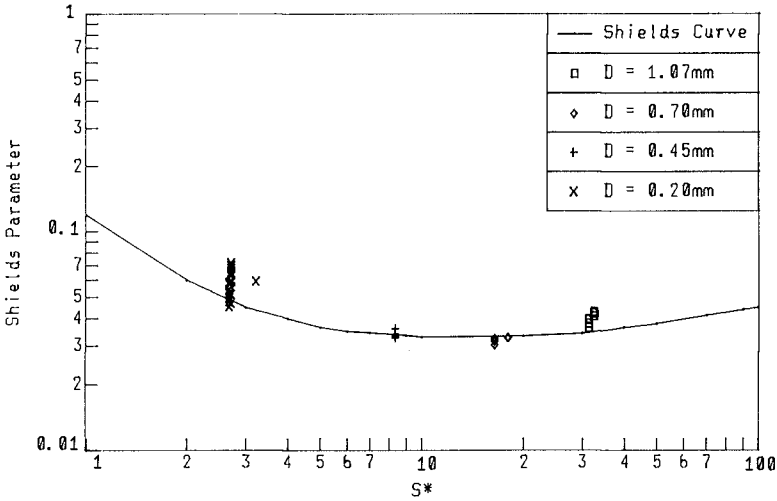


Fig. 8. Initial motion data assuming no non-linear interactions

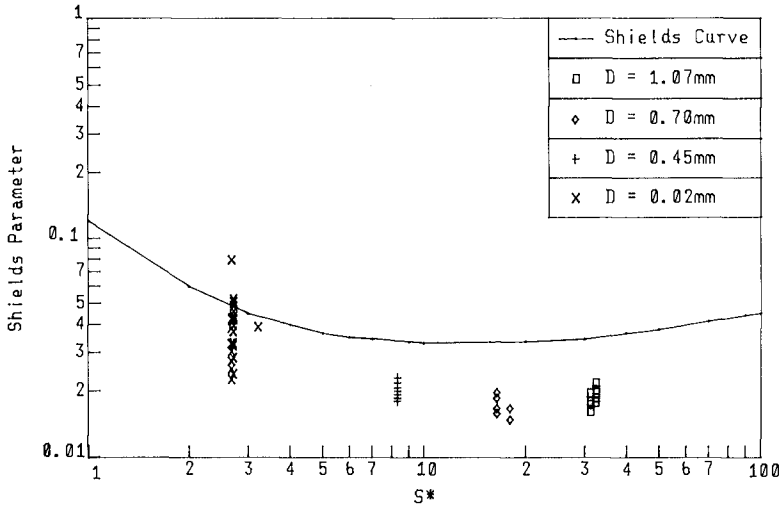


Fig. 9. Initial motion data as analysed by Bijker's (1967) model

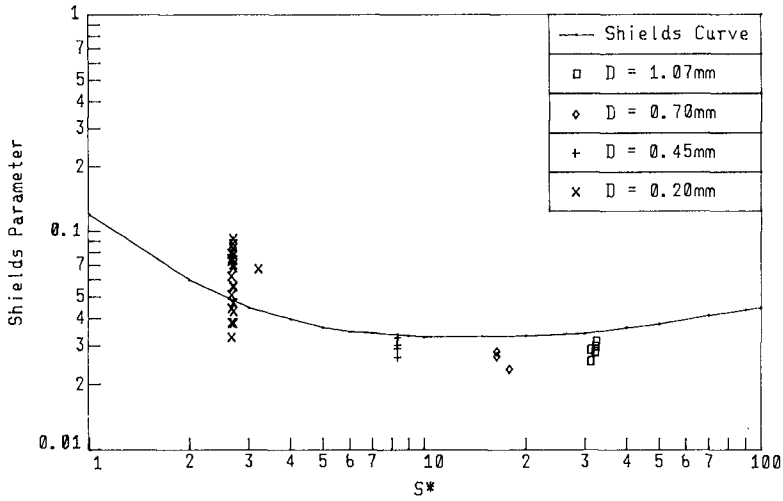


Fig. 10. Initial motion data as analysed by Grant and Madsen's (1979) model

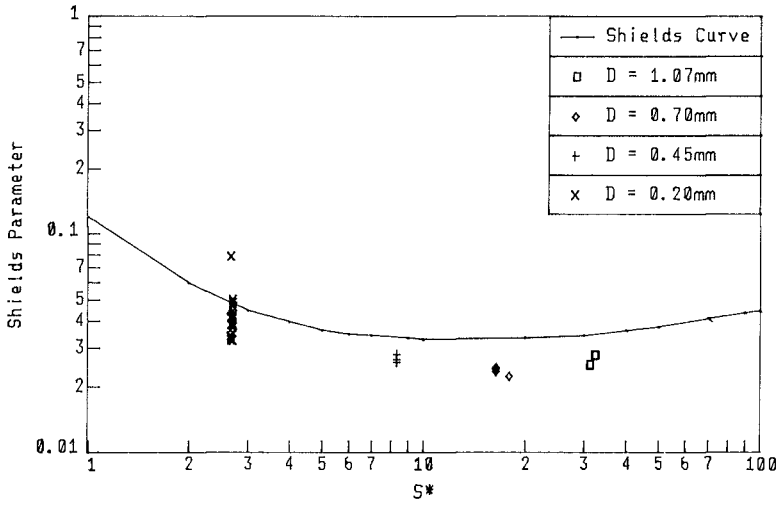


Fig. 11. Initial motion data as analysed by Christoffersen and Jonsson's (1985) model

This is because the additional force is in quadrature with the velocity of the tray and is consequently nearly 90° out of phase with the resultant force on the grains. Also, when the steady current is large this additional force is at a significant angle to the direction of the resultant force which further reduces the overall error. In order to test this conclusion, the comparisons shown in Figs. 8 - 11 were carried out both with a correction for the additional force and also without one. There appeared to be no significant difference between the two sets of results. Consequently, only the uncorrected results are shown in Figs. 8 - 11.

Comparison of Different Models for Combined Shear Stress

It is probably reasonable to assume as a first approximation that the initial motion condition corresponds to a critical value of the bed shear stress. To conform with usual practice we use the term shear stress to mean the horizontal force on the grains per unit area of bed. Lift forces are not entirely negligible but will be ignored for the moment. The problem is how to evaluate the shear stress in a combined flow.

The simplest assumption which we can make is that the resultant shear stress is the vector sum of the shear stress τ_w for the oscillatory flow assuming no effect of the steady current, and that for the steady flow τ_c , assuming no effect of the oscillation, i.e.

$$\tau = (\tau_w^2 + \tau_c^2)^{\frac{1}{2}} \quad (3)$$

We note, in passing, that shear stress proportional to velocity squared would lead to $n = 4$ in Eq. (2) whereas $n = 2$ would correspond to shear stress directly proportional to velocity.

Eq. (3) relies on the assumption that there is no non-linear interaction between the steady and oscillatory components of the flow. This assumption is more likely to be correct if the flow is laminar rather than turbulent. Fig. 7 shows how the critical values of $u_w A_b / \nu$ and A_b / D for the present experiments compare with the criteria for transition to turbulence proposed for oscillatory flow by various investigators. The fact that so many of the points lie below or only slightly above Kajiura's (1968) curve for the initiation of turbulence is an indication that turbulence generation by the oscillatory flow would have been negligible in most of the tests. On the other hand, the steady flow Reynolds numbers are well above the limit for transition in almost all cases. We conclude that the flow would have been turbulent in almost all of the tests but not strongly so in the immediate vicinity of the bed.

In view of this conclusion about turbulence, and consequently of the improbability of there being no non-linear interaction between the steady and oscillatory components of the flow, it is rather surprising to find in Fig. 8 that the

experimental values of Shields parameter calculated with the aid of Eq. (3) all lie close to Shields curve. In Eq. (3), τ_w was calculated from Kamphuis (1975) curves for friction factor and τ_c from the assumption of a logarithmic velocity profile up to the reference point just upstream of the oscillatory tray.

The other methods used to calculate the resultant shear stress are those proposed by Bijker (1967), Grant and Madsen (1979) and Christoffersen and Jonsson (1985). The corresponding Shields diagram plots of the experimental results are shown in Figs. 9, 10, 11. We see that the closest agreement between the experimental results and Shields curve is provided by the methods of Grant and Madsen and of Christoffersen and Jonsson with, perhaps, slightly less scatter using the latter method. Surprisingly, the scatter with all three of these methods is greater than that obtained from Eq. (3).

Conclusions

The results of this experimental study suggest that Shields curve may be used to predict initial motion of sediment in combined steady and oscillatory flow. A simple model, in which the resultant shear stress is calculated on; the assumption that there is no non-linear interaction between the steady and oscillatory flows, gave the closest agreement between Shields curve and the measurements but good agreement was also shown by the models of Grant and Madsen (1979) and Christoffersen and Jonsson (1985).

AppendixReferences

- Bijker E.W. 1966 The increase of bed shear in a current due to wave motion. Proc. 10th Conf. Coastal Engrg. Tokyo, pp.746-765
- Christoffersen J.B. and Jonsson I.G. 1985 Bed friction and dissipation in a combined current and wave motion. Ocean Engrg., 12, No.5, pp.387-423
- Grant W.D. and Madsen O.S. 1979 Combined wave and current interaction with a rough bottom. J. Geophys. Res., 84, C4, pp.1797-1808
- Hammond T.M. and Collins M.B. 1979 On the threshold of transport of sand-sized sediment under the combined influence of unidirectional and oscillatory flow. Sedimentology (1979), 26, pp.795-812
- Jonsson I.G. 1966 Wave boundary layers and driction factors. Proc. 10th Conf. Coastal Engrg. Tokyo, pp.127-148
- Kajiura K. 1968 A model of the bottom boundary layer in water waves. Bull. Earthquake Res. Inst. 46, pp.75-123
- Kamphuis J.W. 1975 Friction factors under oscillatory waves. Proc. ASCE J. Waterways Harbors Coastal Engrg. Div. 101 (WW2), pp.135-144
- Katori S., Sakakiyama T. and Watanabe A. 1984 Measurement of sand transport in a cross unidirectional-oscillatory flow tank. Coastal Engrg. in Japan, 27, pp.193-203
- Kramer H. 1935 Sound mixtures and sound movement in fluvial models. Transactions ASCE 100, Paper No. 1909, pp.798-878
- Li H. 1954 Stability of oscillatory laminar flow along a wall. BEB Tech. Memo 47
- Madsen O.S. and Grant W.D. 1976 Quantitative description of sediment transport by waves. Proc. 15th Conf. Coastal Engrg. II, pp.1093-1112
- Sleath J.F.A. 1974 Velocities above rough bed in oscillatory flow. J. Waterways Harbors and Coastal Engrg. Div. ASCE 100 (WW4), pp.287-304.
- Sleath J.F.A. 1976 On rolling-grain ripples. J. Hydraulic Research 14 (1), pp.69-81
- Sleath J.F.A. 1984 Sea Bed Mechanics. John Wiley & Sons, New York.

CHAPTER 86

Study of Shelf Waves vs Sand drift in NW coast of Taiwan

by
Ho-Shong Hou, Ph.D., P.E. Professor

- * Head, Transportation Engineering Dept., Institute of Transportation, MOC, Taipei, R.O.C.
- * Chief, Project office of Transportation Engineering Preliminary Planning, IOT, MOC, R.O.C.

ABSTRACT

For the planning and design of harbor and coastal Engineering, most important affected factors are waves and littoral drift.

This research deals with analysis of the measured waves and the budget of the beach material whether it is deposited or scoured in the North-western coast of Taiwan; and the relationship between wave energy and littoral transport rate. For processing this research the field Survey wave measurement, sand sampling, and echo sounding is necessitated. The objective of this research is to establish the model of waves and littoral transport budget. Therefore, the results of this research are planned to submit to the planning and design of harbor and coastal engineering works of the Taiwan west sandy coast.

The main contains of this research are consisted of

- (1) Analysis, observations and investigations of the field oceanographic data, winds, waves, coastal geomorphology and littoral drift of the North-western coast of Taiwan.
- (2) Analysis of the shelf waves from the actual measured wave records.
- (3) Research of the wave decaying process of the continental shelf waves.
- (4) Statistical research of the measured waves and establishment of the practical model of the relationship between the shelf wave energy and the littoral transport rate in the north-west coast of Taiwan.

- (5) Plotting time history of significant wave heights and significant wave periods in the Taiwan Strait.

1. Introduction

Based on the wave pattern, the geographical location and the disposition of rivers, the littoral drift moves predominantly from NE to SW direction in section I as shown in Fig. 1. Seven rivers of rapid stream bring tremendous amount of sediments from the high mountain to the nearshore of this section in typhoon season (i.e. from June to September). But for the winter monsoon season, i.e. from October to the next April, the waves induced by NE monsoons migrate littoral drift from north toward south.

Applying the energy approach for unidirectional steady flow derived by Bagnold (1963), the theoretical relationship between the littoral immersed weight transport rate and the alongshore breaking wave energy is found out. It reveals that the relationship is not strictly linear, i.e. the larger part of the alongshore breaking wave energy is supplied for transporting the sediment as the former increases. But for a coast having a steady oceanographical condition, the relationship could be considered as linear relation since the alongshore breaking wave energy is not varying very much.

By using the shelf wave records and the littoral drift quantity obtained from long-term echo-sounding map, the relationship between alongshore breaking wave energy and littoral immersed weight transport rate is found out.

2. Information of Oceanographical Data

For the movable-bed investigation of Lin-Kou Power Plant (Located in the NW coast of Taiwan), the following field investigation is undertaken.

1) Wind & Waves: The monsoon of this area starts from September to April of the next year, the prevailing wind direction is NE-ENE, and the wave direction of the nearshore is NNE, the maximum wave height of strong monsoon is 4M, while the wave period is 9.0 sec. The maximum significant wave height of hurricane attacking $H_{1/3} = 4.75M$, the corresponding period $T_{1/3} = 12$ sec.

2) River sediment discharge: The sediment which affects obviously on the Lin-Kou Power Plant is from the Tansui River, the river sediment transport rate is 6.095×10^6 MT/year.

3) Littoral transport: Based on the sounding data of Lin-Kou coastal area, including survey maps of 1971, 1975, 1977, 1978 and 1983; and the sand sampling data, it is recognized that sediment transport toward south.

a) Coastal morphology: The mean beach slope of nearshore zone is $1/66$, the sea-bed slope of depths from -15M to -20M is $1/300$, is flat, the profile near the intake structure is steeper than those of other profiles. Therefore, it is very clear that the effect of wave action is severe, the littoral transport is obvious as Fig. 2.2 shown.

b) Sediment particle: Based on the field measurement, the coastal area of this region spreads over the cobble stone, the distribution of sand particle after Sieve analysis is shown as Fig. 2. From the figure, the sediments of the breaking zone and inner shore zone of the power plant area $d_{50} = 0.3-0.4$ m/m, while contour of -5M to -10M , d_{50} is 0.2 m/m, therefore the sand particle of the upstream of the plant site is bigger than that of the downstream site, it is recognized that the littoral transport direction is from north to south, as shown in Fig. 2.3.

c) Littoral transport rate: Based on the echo sounding data, using mesh method to calculate the littoral transport rate of the deposit sand around the coastal area of the plant site. It is 37.5×10^4 M^3/year , and could be found out from Fig. 2.4.

d) Tide and tidal current: The tide is belong to semidiurnal tide. The mean high water level of the spring tide is 3.1M , while the mean lowwater level of the spring tide is -0.3M . Tidal current is measured about 0.75 m/sec or so.

3. Statistical Analysis of Self Waves

Waves in Taiwan Strait, i.e. self waves, are to be divided into three patterns, i.e., waves in winter monsoon, waves in hurricane and waves generated by convective wind in the summer. Statistical characteristics of significant waves extracted from the meteorological

and wave measuring records along the continental shelf for 4 years are shown in Fig. 3.1 (Tang, 1986).

Wave records obtained from cassette type wave meter are continuously measuring the whole year in the NW coast located in the nearshore area of Tou-Yuan Fig. 3.2, Fig. 3.3, Fig. 3.4, Show that relationship between wave period, wave height vs percent frequency in January (winter), in August (summer) and the whole year's record (all available data). While Fig. 3.5 shows that correlation between wave height and wave period in January and in September. Their range for wave height is from 20 cm to 4m, wave period is from 5 sec to 15 sec or more. The waves in the NW coast are slightly stronger than those of the mid-west coast of Taiwan.

4. The calculation of the alongshore breaking wave energy:

The wave is affected by the effects of shoaling, refraction, bottom friction and percolation. By neglecting the effects of bottom friction and percolation as wave is propagating toward the surf zone, there the breaking wave height is equal to

$$H = H_o K_r K_s \tag{4.1}$$

where K_r and K_s are refraction coefficient and shoaling coefficient respectively. The mathematical representation is as follows

$$K_r = (B_o/B)^{1/2} \tag{4.2}$$

$$K_s = (C_{go}/C_g)^{1/2} \tag{4.3}$$

where B is the separation of the wave rays and prefix "o" represents the characters of deep water. As the bottom slope is smaller than 1/10, then K_r and K_s could be calculated from the four equations derived by Chao, Y.Y. (1970) as follows

$$C^2 = \left(\frac{g}{k} \right) \tanh kh \tag{4.4}$$

$$\frac{d}{ds} = \frac{1}{c} \left(\sin\theta \frac{\partial c}{\partial x} - \cos\theta \frac{\partial c}{\partial y} \right) = - \frac{1}{c} \frac{dc}{dB} \tag{4.5}$$

$$H_o (C_g)_o B_o = H^2 \cdot C_g \cdot B = \text{constant} \tag{4.6}$$

$$\frac{d^2 B}{ds^2} - P^{(1)} \frac{dB}{ds} + P^{(2)} B = 0 \tag{4.7}$$

$$P^{(1)} = \frac{1}{c} \left(\cos\theta \frac{\partial c}{\partial x} + \sin\theta \frac{\partial c}{\partial y} \right) \tag{4.8}$$

$$P^{(2)} = \frac{1}{c} \left(\sin^2\theta \frac{\partial^2 c}{\partial x^2} - 2 \sin\theta \cos\theta \frac{\partial^2 c}{\partial x \partial y} + \cos^2\theta \frac{\partial^2 c}{\partial y^2} \right) \tag{4.9}$$

where D is water depth, θ is the angle between X axis and wave direction, S is the distance along wave ray and C is the phase velocity. Use

numerical method to get

$$D_{n+1} = D_0 + \left(\frac{\partial D}{\partial x}\right)_n dx + \left(\frac{\partial D}{\partial y}\right)_n dy + \frac{1}{2} \left(\frac{\partial^2 D}{\partial x^2}\right)_n dx^2 + \left(\frac{\partial^2 D}{\partial x \partial y}\right)_n dx dy + \frac{1}{2} \left(\frac{\partial^2 D}{\partial y^2}\right)_n dy^2 \quad (4.1)$$

$$P_{n+1} = [(4-2P_n^{(0)} \Delta s^2)/(2-P_n^{(0)} \Delta s^2)] B - [(2+P_n^{(0)} \Delta s^2)/(2-P_n^{(0)} \Delta s^2)] B_{n-1} \quad (4.11)$$

The subscript "n" represents the value of the nth calculation, as shown in Fig. 4.1. where X axis is taken parallel to the shoreline. Developing these numerical calculations to get "THE WAVE CHARACTER COMPUTING PROGRAM" (Hou, 1980), the wave characters such as K_r , K_s , H , C_g and θ could be found out at any water depth $h=D$. Since $\theta = \frac{\pi}{2} - \alpha$ as shown in Fig. 4.1. then

$$(P_{\ell})_b = \frac{1}{8} \rho g H_b^2 (c_g)_b \cos \theta_b \sin \theta_b \quad (4.12)$$

is the alongshore breaking wave energy. For the self wave energy it is obtained as $(P_{\ell})_b = 2.25 \times 10^{10} \text{ kgm}^2/\text{sec}^2/\text{m-yr}$.

5. Relationship between shelf waves and littoral drift in the NW coast of Taiwan.

From the echo sounding data, the littoral transport rate (I_{ℓ}) of the NW coast is calculated as $37.5 \times 10^4 \text{ m}^3/\text{yr}$.

I_{ℓ} and $(P_{\ell})_b$ are in units of cgs system.

But for the Taiwan Strait where the climate is so steady that the alongshore breaking wave energy fluctuate slightly, the relationship between I_{ℓ} and $(P_{\ell})_b$ could be expressed as

$$I_{\ell} = K(P_{\ell})_b \quad (5.1)$$

Where K is constant and is equal to 0.14 for the north western coast of Taiwan.

The NW coast has the relation of $I_{\ell} = 0.14 (P_{\ell})_b$. This equation could be applied for the coast of similar oceanographic conditions and beach characteristics to estimate the littoral transport rate. Therefore, the harbor planning and shore protection could be based on.

The relationship between I_{ℓ} and $(P_{\ell})_b$ is not exact linearly proportional to each other, this is proved by Eq(5.1) which is originally prepared by Komar and Inman (1970) there is a upper limit $K = 0.77$. Adding the data of the author, reanalyzing the total data by the least square method to get a regression line which is expressed as $I_{\ell} = 0.154 (P_{\ell})^{1.0695}$ as shown in Fig. 5.1.

Reference

- 1) Bagnold, R.A. (1963) "Mechanics of Marine Sedimentation" THE SEA, Interscience Publishers, New York, 3:507-528.
- 2) Bruun, Per (1966) Tidal Inlets and Littoral Drift, University of Florida.
- 3) Komar, P.D. and D.L. Inman (1970) "Longshore Sand Transport on Beaches", J. of Geophysical Research, Vol. 76, No.3.
- 4) Galvin, C.J., Jr. (1972) "Wave Breaking in Shallow Water", Waves on Beaches and Resulting Sediment Transport, edited by Meyer, R.E., 1972, Academic Press.
- 5) Taiwan Power Co. (1980) "The Research Report of Littoral Transport of Lin-Kou Power Plant".
- 6) H.S. Hou, C.P. Lee, G.H. Weng, T.J. Liaw (1980), "The Movable-Bed Model Investigation of North-East Sandy Coast of Taiwan". Research Rpt. of NTCMST. Keelung.
- 7) H.S. Hou, C.-P. Lee and L-H Lin (1980) "Relationship Between Alongshore Wave Energy and Littoral Drift in the Mid-West Coast at Taiwan, R.O.C." 17th ICCE. Sydney, Australia, Sept., 1980.
- 8) H.S. Hou, T.J. Liaw (1982), "The Movable-Bed Model Investigation of the 2nd Tansui Fishery Harbor Out-Breakwater Construction Stage". Research Rpt. of NTCMST., Keelung.
- 9) H.S. Hou (1982), "Researches of Harbor Site Investigation, Planning, and Design of Coastal Shipping System in Taiwan, R.O.C.", Special Report No.7 by Institute of Harbor and Marine Technology.
- 10) H.S. Hou (1983). "Planning and Design of coastal and Harbor Engineering", Special Report No.9 by Institute of Harbor and Marine Technology.
- 11) H.S. Hou, T.J. Liaw (1983), "Hydraulic Model Experiments Deal with Shoaling Problem of Littoral Transport for Improvement on the Intake and Outlet of Lin-Kou Power Plant", Special Report No. 12 by Institute of Harbor and Marine Technology.
- 12) H.S. Hou (1985) "Littoral Drift Model Investigation along the Taiwan Coast and Research of the Related Problems of Inlet Planning (II)," NTU-INA-Tech Rept. 216.

- 13) H.S. Hou (1986), "Case Study - Model Study of Lin Kou Power Plant"
Short Course, 20th ICCE, Dynamics of Sand Beaches. Nov. 8-9, 1986,
The Olympic Hotel, Taipei, R.O.C.
- 14) F.L.W. Tang (1986), "Wave Forecasting and Wave Statistics in Taiwan
Strait". Short Course, 20th ICCE, Dynamics of Sand Beaches. Nov.
8-9, 1986, The Olympic Hotel, Taipei, R.O.C.
- 15) H.S. Hou (1987) "Offshore Mechanics and Research of the Related
Problems of Port Planning (III)" NTU-INA Tech Rept. 248.

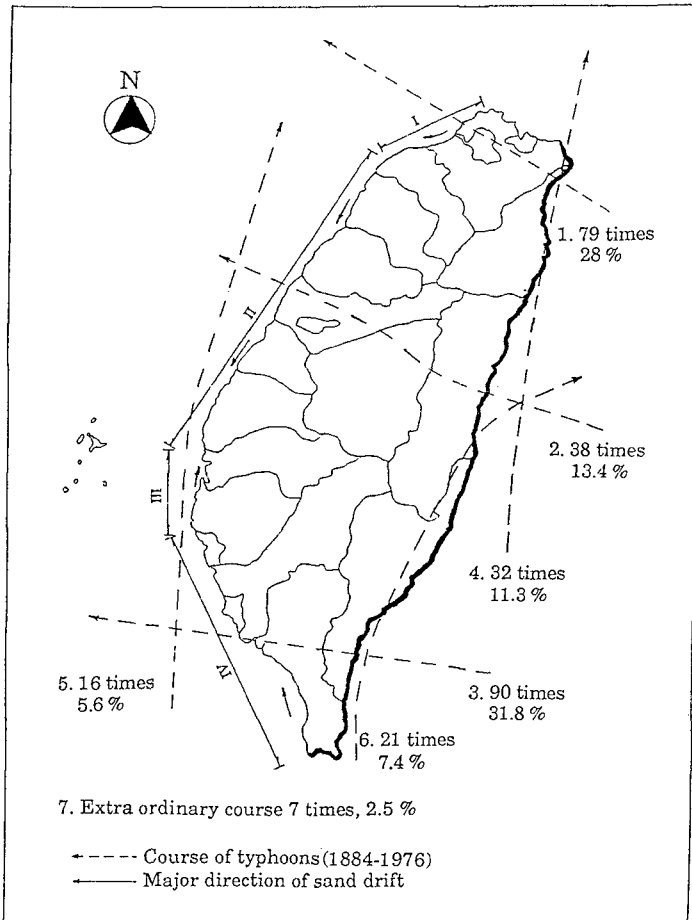


Fig.1 The sketch of the prevailing direction of littoral drift at Taiwan sandy coast

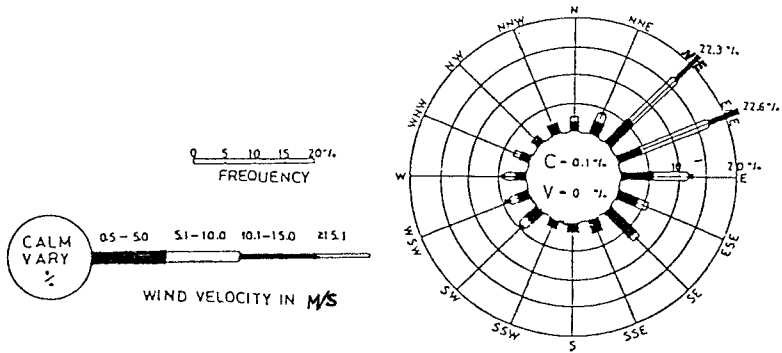


Fig.2.1 Wind Rose of the NW coast

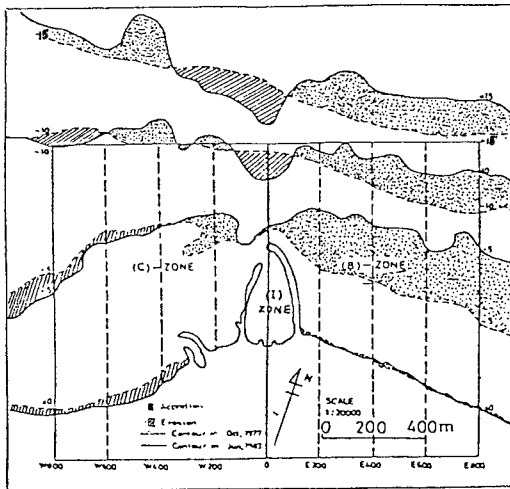


Fig 2.2 Accretion and Erosion of the Profile near the Linkou

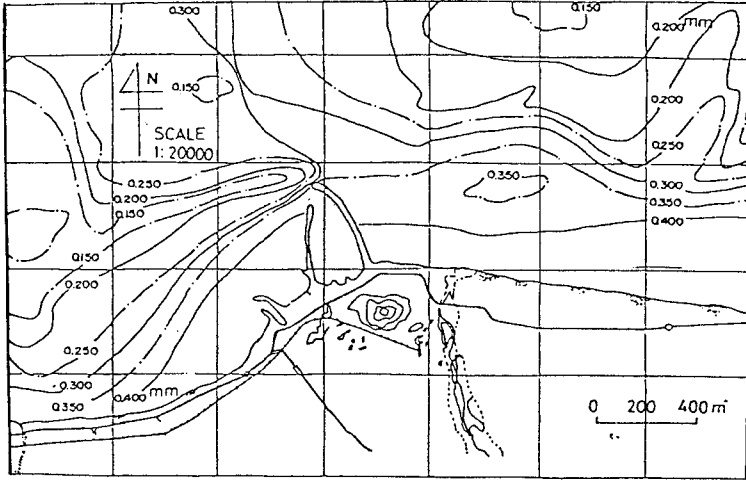


Fig.2.3 Sediment Particle d_{50} Distribution in the Nearshore Area of Linkou (mm)

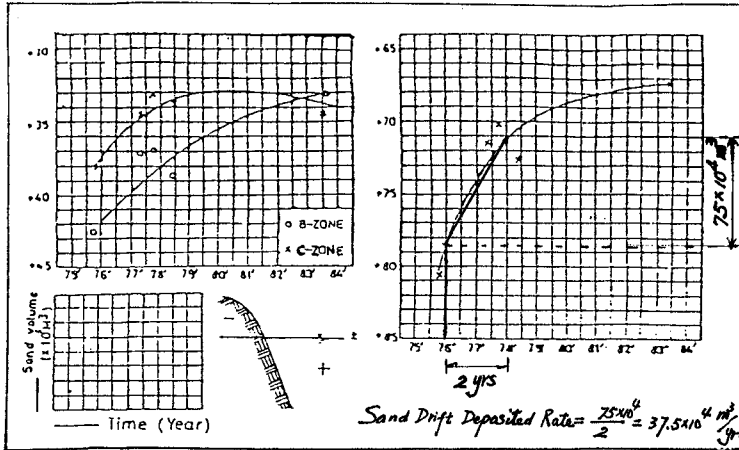


Fig.2.4 Sand Volume Change of Surveyed Zones B, C & B+C

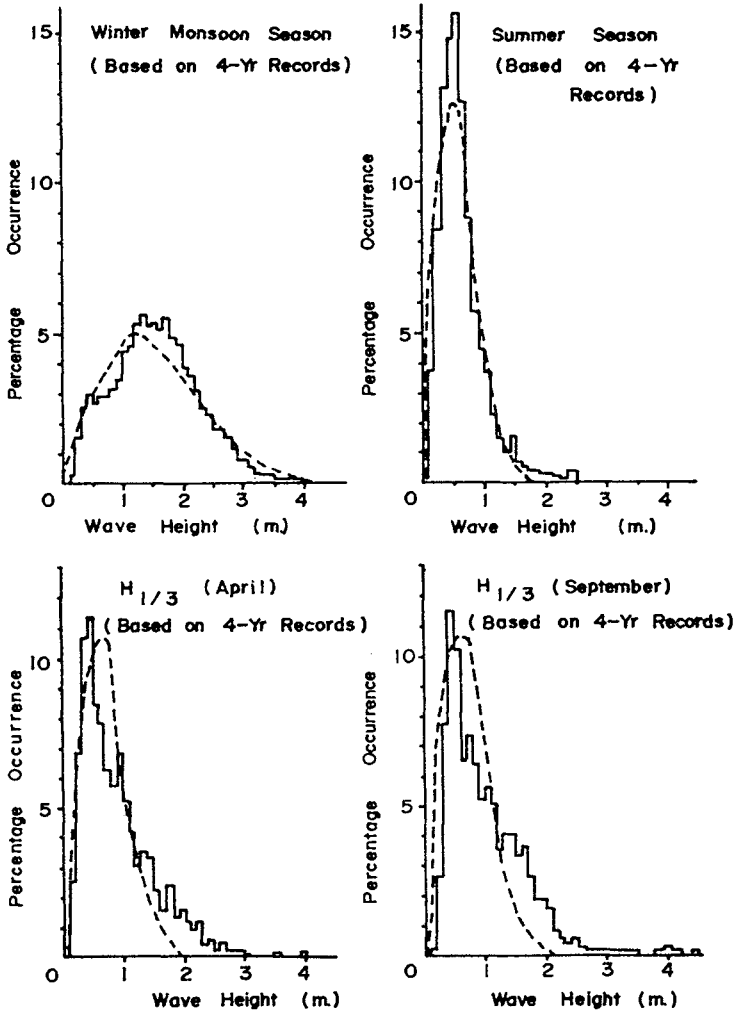


Fig.3.1 Distribution of Significant wave height (Self Waves)

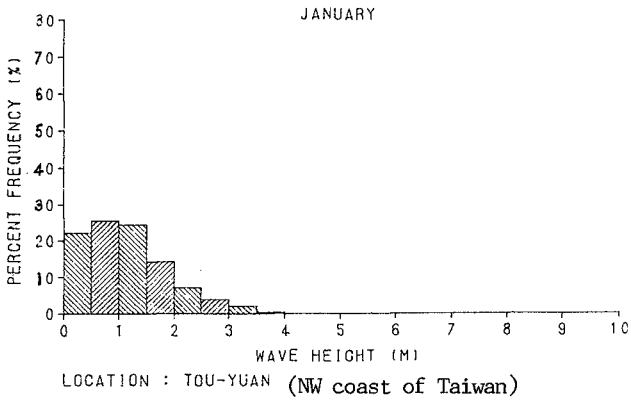
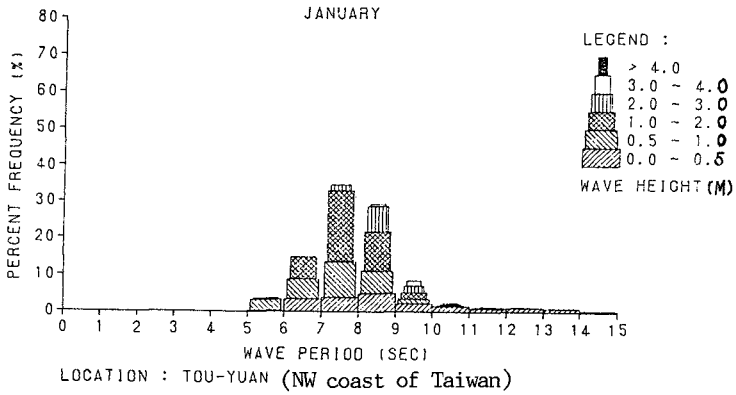


Fig.3.2. Relation of Wave period, Wave height vs Percent Frequency in NW coast of Taiwan (Winter)

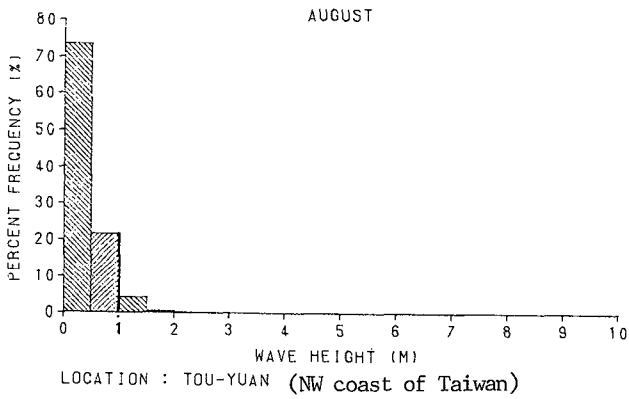
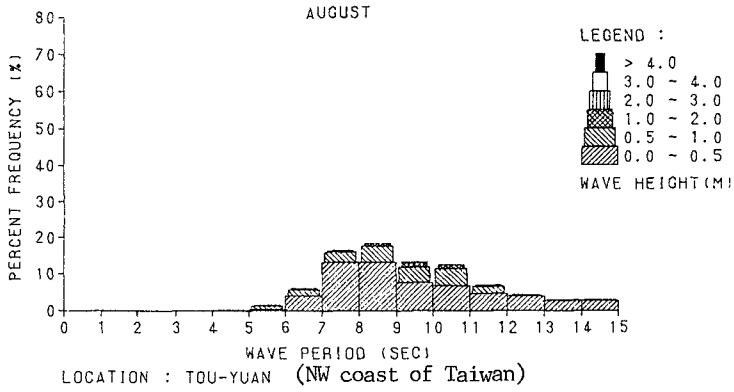


Fig.3.3 Relation of Wave period, wave height vs percent frequency in NW coast of Taiwan (Summer)

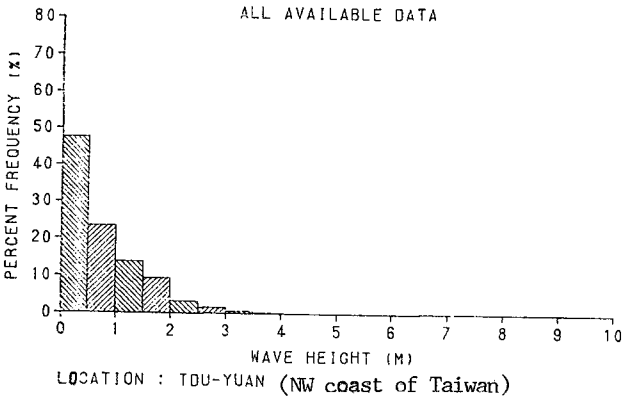
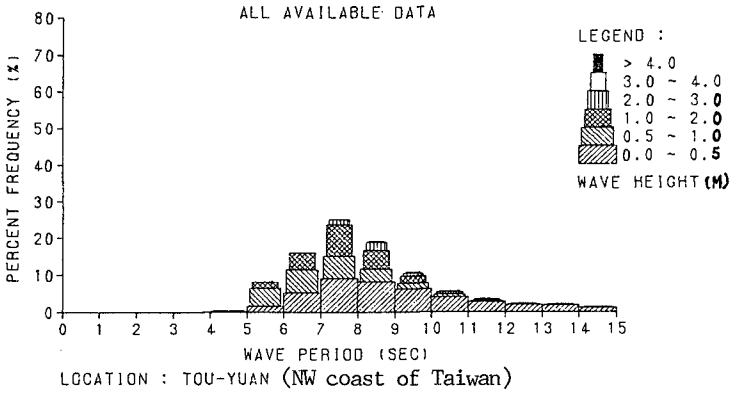


Fig.3.4 Relation of wave period, wave height vs percent frequency in NW coast of Taiwan (the whole year)

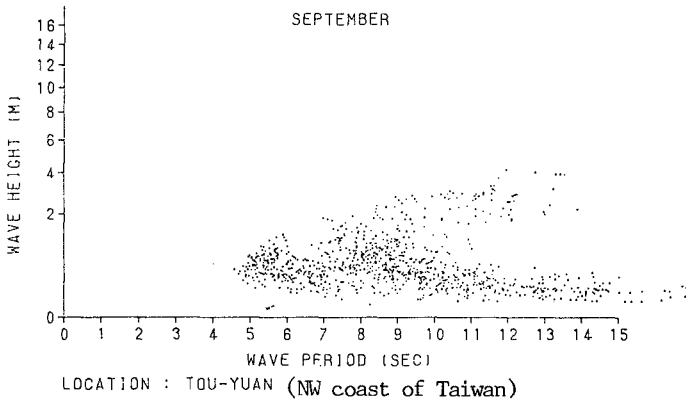
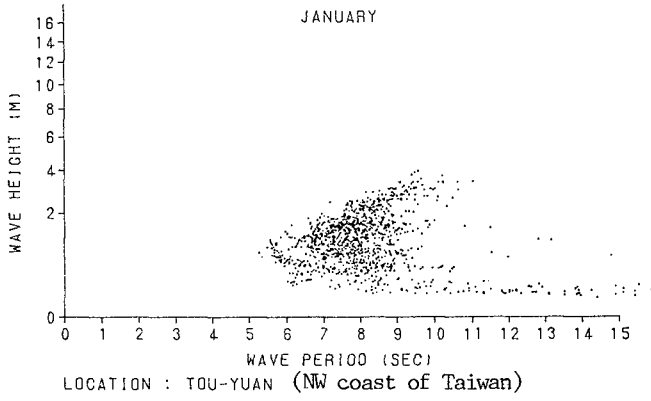


Fig.3.5 Correlation between wave height and wave period in NW coast of Taiwan.

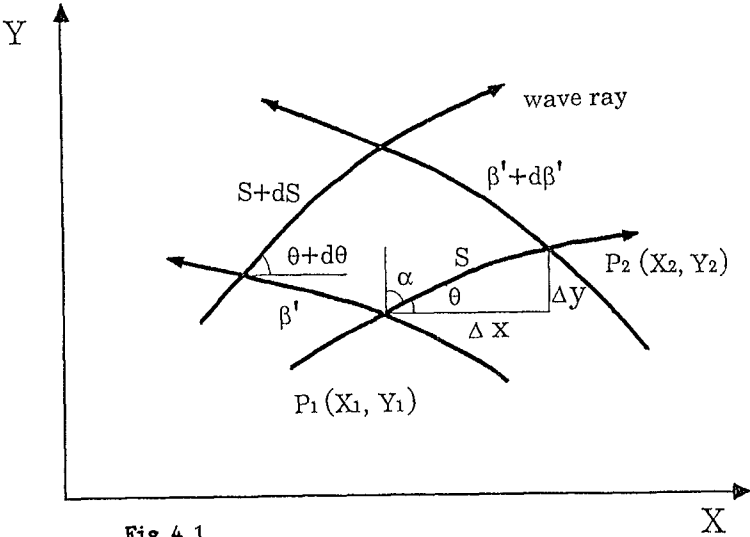


Fig. 4.1

The diagram of the wave refraction

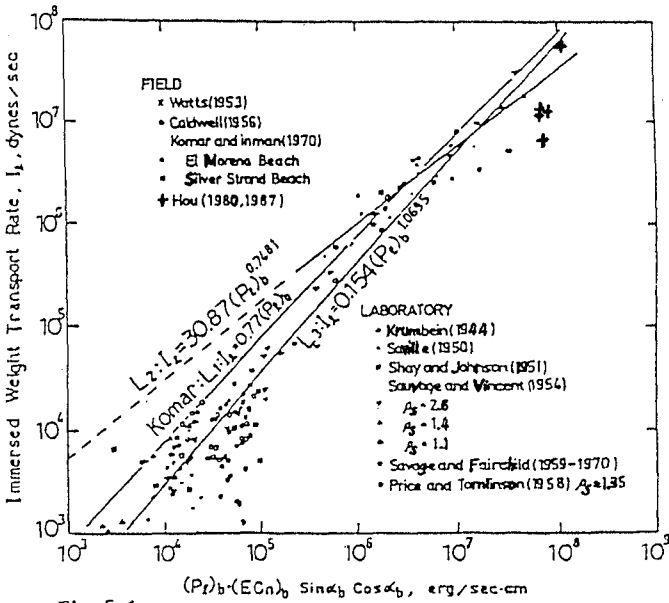


Fig. 5.1

The relationship of the alongshore breaking wave energy and the immersed weight transport rate

CHAPTER 87

SWASH OSCILLATION AND RESULTING SEDIMENT MOVEMENT

by Nobuhisa Kobayashi¹, Michael S. Strzelecki² and Andojo Wurjanto³

ABSTRACT: A numerical model for predicting the swash oscillation on a beach is described and compared with field data on wave setup and swash statistics on a moderately steep beach with a nearshore bar.

INTRODUCTION

The swash zone on a beach forms the boundary zone between the surf zone and backshore. Wave run-up is the upper limit of wave uprush and determines the landward boundary of the area affected by wave action. Few studies have been performed for the hydrodynamics and resulting sediment movement in the swash zone probably because existing hydrodynamic models such as those proposed by Battjes and Stive (1985) and Svendsen et al. (1987) do not account for the variations of hydrodynamic quantities over a wave period which are essential in the swash zone. A quantitative understanding of sediment transport in the swash zone is required for better establishing the landward boundary condition for existing cross-shore sediment transport models such as that proposed by Stive (1986) and De Vriend and Stive (1987). Furthermore, the temporal variation of the horizontal fluid velocity is normally required even in the surf zone to predict the instantaneous sediment transport rate from which the net transport rate can be computed.

In this paper, the numerical model of Kobayashi et al. (1987) developed for predicting the waterline oscillation on the rough impermeable slope of a coastal structure is slightly modified and applied to predict the swash oscillation on a natural beach. Kobayashi and Greenwald (1986,1988) showed that the numerical model could predict the measured temporal variations of hydrodynamic quantities on a 1:3 gravel slope with an impermeable base. Moreover, Kobayashi and Watson (1987) showed that the numerical model could also be applied to coastal structures with smooth slopes by adjusting the friction factor associated with the slope roughness. Kobayashi and Wurjanto (1988) extended the numerical model to predict wave overtopping over coastal structures. These applications of the numerical model to coastal structures were limited to uniform slopes of 1:5 or steeper as well as composite slopes. On the other hand, Kobayashi et al. (1988) modified the numerical model slightly to predict the wave transformation in the surf and swash zones on gentle slopes as well as the wave reflection and swash oscillation on

¹Assoc. Prof., Dept. of Civil Engrg., Univ. of Delaware, Newark, DE 19716.

²Civil Engineer, Planning Div., U.S. Army Corps of Engineers, Baltimore District, P.O. Box 1715, Baltimore, MD 21203.

³Crad. Student, Dept. of Civil Engrg., Univ. of Delaware, Newark, DE 19716.

relatively steep beaches. The slight modification was related to the effect of the wave-induced current on the seaward boundary condition used in the numerical model, which influenced the computed mean water level on gentle slopes. The modified numerical model was compared with small-scale test data for monochromatic waves spilling on gentle slopes. The comparison included the comprehensive test results for a 1:40 smooth slope presented by Stive (1980) and Stive and Wind (1982) as well as the undertow measurement for a 1:34.25 smooth slope performed by Hansen and Svendsen (1984). The numerical model was shown to be capable of predicting the development of the wave profile asymmetry about the vertical axis from the symmetric cnoidal wave profile outside the breakpoint to the sawtooth profile in the inner surf zone. The computed shoreline oscillation on the gentle slope showed the dominance of the setup over the swash in accordance with the empirical formulas proposed by Battjes (1974). As a whole, the numerical model was in good agreement with the gentle slope data except that the numerical model based on the finite-amplitude shallow-water equations predicts the depth-averaged velocity only and can not predict shoaling without wave breaking over the horizontal distance which is large relative to the wavelength. In order to take the seaward boundary location far seaward of the breakpoint, the numerical model would need to be matched with a numerical model based on the Boussinesq equations for a sloping bottom (Peregrine, 1967) such as the time domain model of Abbott et al. (1984) and the frequency domain model of Freilich and Guza (1984). In addition, Kobayashi et al. (1988) compared the modified numerical model with the wave reflection and swash excursion measurements for monochromatic waves plunging and surging on a 1:8.14 slope described by Guza and Bowen (1976) and Guza et al. (1984). The agreement between the model and the data was only qualitative probably because the wave reflection data was obtained on the basis of linear standing wave theory and the visual measurements of swash excursion on the relatively steep slope were difficult to define quantitatively. Kobayashi et al. (1988) also conducted small-scale tests for monochromatic and transient grouped waves on a 1:8 slope with and without an idealized nearshore bar at the toe of the 1:8 slope. The numerical model was shown to be capable of predicting the measured shoreline oscillations fairly well.

In the following, the numerical model used by Kobayashi et al. (1988) is described concisely and compared with the field data on swash oscillations on a moderately steep beach with a nearshore bar given by Holman and Sallenger (1985). As a first attempt, incident random waves are approximated by monochromatic waves, although any incident wave train in the time domain could be specified as input at the seaward boundary of the numerical model. This monochromatic approximation may be reasonable for the swash oscillation in the incident frequency band but excludes the swash oscillation in the infragravity frequency band which was not negligible for the field data. The sediment transport mechanics in the swash zone on a natural beach are discussed only briefly at the end of this paper.

ONE-DIMENSIONAL UNSTEADY NUMERICAL FLOW MODEL

Under the assumptions of alongshore uniformity and normally incident waves, the finite-amplitude shallow-water equations for an impermeable beach of arbitrary geometry are expressed as (Kobayashi et al., 1988)

$$\frac{\partial h'}{\partial t'} + \frac{\partial}{\partial x'} (h'u') = 0 \quad (1)$$

$$\frac{\partial}{\partial t'} (h'u') + \frac{\partial}{\partial x'} (h'u') = -gh' \frac{\partial \eta'}{\partial x'} - \frac{1}{2} f' |u'|u' \quad (2)$$

where t' =time; x' =horizontal coordinate taken to be positive in the landward direction with $x'=0$ at the seaward boundary of the numerical model; h' =instantaneous water depth; u' =instantaneous depth-averaged horizontal velocity; g =gravitational acceleration; η' =instantaneous free surface elevation above the still water level (SWL); and f' =bottom friction factor which is assumed constant. The prime indicates the dimensional variables which are normalized in the following. The vertical coordinate z' is taken to be positive upward with $z'=0$ at SWL. The arbitrary beach geometry is specified by d_t' =water depth below SWL at $x'=0$ and θ' =local angle of the bed varying with respect to $x' \geq 0$. Denoting the reference wave height and period by H_r' and T_r' , respectively, which are assumed to be given, the following dimensionless variables are introduced:

$$t = \frac{t'}{T_r'} \quad ; \quad x = \frac{x'}{T_r' \sqrt{gH_r'}} \quad ; \quad u = \frac{u'}{\sqrt{gH_r'}} \quad (3)$$

$$z = \frac{z'}{H_r'} \quad ; \quad h = \frac{h'}{H_r'} \quad ; \quad \eta = \frac{\eta'}{H_r'} \quad ; \quad d_t = \frac{d_t'}{H_r'} \quad (4)$$

$$\sigma = T_r' \sqrt{\frac{g}{H_r'}} \quad ; \quad \theta = \sigma \tan \theta' \quad ; \quad f = \frac{1}{2} \sigma f' \quad (5)$$

In terms of the normalized coordinate system, the bed is located at

$$z = \int_0^x \theta dx - d_t \quad ; \quad \text{for } x \geq 0 \quad (6)$$

Substitution of Eqs. 3-5 into Eqs. 1 and 2 yields

$$\frac{\partial h}{\partial t} + \frac{\partial m}{\partial x} = 0 \quad (7)$$

$$\frac{\partial m}{\partial t} + \frac{\partial}{\partial x} \left(m h + \frac{1}{2} h \right) = -\theta h - f |u|u \quad (8)$$

in which $m=uh$ is the normalized volume flux per unit width.

Eqs. 7 and 8 expressed in the conservation-law form of the mass and momentum equations except for the two terms on the right hand side of Eq. 8 are solved in the time domain using the explicit dissipative Lax-Wendroff finite difference method based on a finite-difference grid of constant space size Δx and constant time step Δt as explained by Kobayashi et al. (1987). The initial time $t=0$ for the computation marching forward in time is taken to be the time when the incident wave train specified as input arrives at the seaward boundary, $x=0$, and no wave action is present in the computation domain $x \geq 0$. The landward boundary on the beach is located at the moving shoreline where the water depth is essentially zero. For the computation, the shoreline is defined as the location where h equals an infinitesimal value δ . The shoreline oscillation is computed using the predictor-corrector-smoothing procedure explained by Kobayashi et al. (1987). The seaward boundary at $x=0$ is taken to be located seaward of the breakpoint where the flow at $x=0$ can be assumed to be subcritical and satisfy the condition $u < \sqrt{h}$. Expressing Eqs. 7 and 8 in the

characteristic forms, the equation for the characteristics, $\beta = (-u + 2\sqrt{h})$, advancing seaward at $x=0$ is given by Kobayashi et al. (1987)

$$\frac{\partial \beta}{\partial t} + (u - \sqrt{h}) \frac{\partial \beta}{\partial x} = \theta + \frac{f|u|u}{h} \quad ; \quad \text{along } \frac{dx}{dt} = u - \sqrt{h} \quad (9)$$

Eq. 9 is discretized using a simple first-order finite difference to obtain the value of $\beta = (-u + 2\sqrt{h})$ (Kobayashi et al., 1987). In addition, the total water depth at the seaward boundary is expressed in the form

$$h = d_t + \eta_i(t) + \eta_r(t) \quad ; \quad \text{at } x = 0 \quad (10)$$

in which η_i and η_r are the free surface variations with respect to t at $x=0$ normalized by the reference wave height H_r' . The incident wave train seaward of the breakpoint is specified by prescribing the variation of η_i with respect to $t \geq 0$. The term $\eta_r(t)$ in Eq. 10 accounts for the difference between the actual value $\eta = (\eta_i + \eta_r)$ at $x=0$ and the prescribed value η_i . For reflective slopes such as coastal structures, $\eta_r(t)$ may be regarded as the normalized free surface variation associated with the reflected wave train at $x=0$ (Kobayashi et al., 1987). For dissipative beaches, incident wave reflection may be negligible but $\eta_r(t)$ accounts for the secondary effects excluded from the prescribed variation of $\eta_i(t)$. Kobayashi et al. (1988) used the following approximate expression of $\eta_r(t)$ in terms of the value of β at $x=0$ computed using Eq. 9:

$$\eta_r(t) \approx \frac{1}{2} \sqrt{d_t} \beta(t) - d_t - C_t \quad ; \quad \text{at } x = 0 \quad (11)$$

$$\text{with } C_t = -\frac{1}{2} \sqrt{d_t} \bar{u}_t \quad (12)$$

where \bar{u}_t = value of the time-averaged horizontal velocity \bar{u} at $x=0$. Substitution of Eq. 11 into Eq. 10 yields the value of h at $x=0$ for given $\eta_i(t)$ and estimated C_t . The value of u at $x=0$ is then obtained from $u = (2\sqrt{h} - \beta)$ at $x=0$. The nonlinear correction term C_t associated with the time-averaged velocity \bar{u}_t was not included in the numerical model developed for coastal structures by Kobayashi et al. (1987). This term was shown by Kobayashi et al. (1988) to improve the prediction of wave set-down and setup on a gentle slope.

The time-averaged mass and momentum equations corresponding to Eqs. 7 and 8 can be expressed as

$$\bar{m} = \bar{h}u = 0 \quad (13)$$

$$\frac{d}{dx} \left[\bar{h}u^2 + \frac{1}{2} \overline{(\eta - \bar{\eta})^2} \right] = -\bar{h} \frac{d\bar{\eta}}{dx} - f \overline{|u|u} \quad (14)$$

where the overbar denotes time averaging and $\bar{\eta}$ is the vertical difference between the mean and still water levels. Use is made of the condition of no flux into the assumed impermeable beach to derive Eq. 13. The left hand side of Eq. 14 is the normalized gradient of the cross-shore radiation stress (e.g., Svendsen et al., 1987) under the assumptions of vertical uniformity and hydrostatic pressure. In this paper, the computed temporal variations of h and u at given location are used to compute the cross-shore variations of $\bar{\eta}$ and \bar{u} without using Eqs. 13 and 14. Rearranging Eq. 13, the time-averaged horizontal velocity \bar{u} can be expressed as

$$\bar{u} = - \overline{(\eta - \bar{\eta})(u - \bar{u})} (\bar{h})^{-1} \quad (15)$$

For gentle slopes with little wave reflection, $(\eta - \bar{\eta})$ and $(u - \bar{u})$ are expected to be in phase, resulting in $\bar{u} < 0$ from Eq. 15. The computed seaward velocity \bar{u} was found to be smaller than the undertow measured below the wave trough since the numerical model does not account for the vertical variation of the time-averaged horizontal velocity (Kobayashi et al., 1988). An approximate value of \bar{u}_t may be found using Eq. 15 with the assumption of incident monochromatic linear long wave at the seaward boundary where the wave height and period are given by H' and T' , respectively. Under this assumption, $(\eta - \bar{\eta}) \approx (K_S/2) \cos(2\pi t)$, $(u - \bar{u}) \approx (\eta - \bar{\eta})/\sqrt{d_t}$ and $\bar{h} \approx d_t$ at $x=0$, where $K_S = H'/H'_t$ and $T' = T'_t$ is assumed. For gentle slopes with little wave reflection, \bar{u}_t and C_t may hence be approximated by

$$\bar{u}_t \approx -K_S^2(8d_t^{3/2})^{-1}; \quad C_t \approx K_S^2(16d_t)^{-1} \quad (16)$$

It should be mentioned that Kobayashi et al. (1988) used $K_S=1$ since the reference wave height H'_t was taken to be the wave height H' at the seaward boundary. For steep slopes with significant wave reflection for which η_t is on the order of unity, it might be more reasonable to assume that $\bar{u}_t \approx 0$ and $C_t \approx 0$, but the effect of C_t on η_t in Eq. 11 is generally very small. For the previous comparisons made for coastal structures by Kobayashi et al. (1987), $d_t \geq 3$ and $K_S=1$, so that $C_t \leq 0.02$. For gentle slopes, it is necessary to choose a smaller value of d_t so that the seaward boundary is not located too far seaward of the breakpoint (Kobayashi et al., 1988).

COMPARISON WITH SWASH OSCILLATIONS MEASURED ON A BEACH

The numerical model is compared with the wave setup and swash statistics on a moderately steep beach given by Holman and Sallenger (1985). The field data were collected over a 3-week period in October, 1982 at the Army Corps of Engineers Field Research Facility located at Duck, North Carolina. Fig. 1 shows the beach profile on October 26, 1982 which was given as an example profile in their paper.

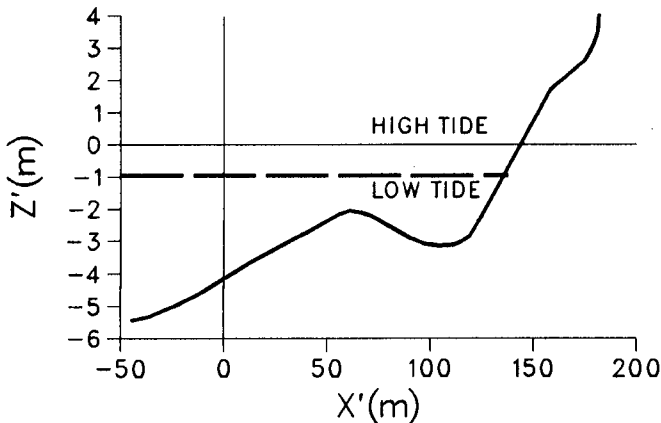


Fig. 1. Beach Profile with High and Low Tides

The slope angle θ'_f of the steep foreshore composed of coarse sand (mean size of 1-2 mm) varied between 5° and 9° (Sallenger et al., 1985). The position and height of the single bar shown in Fig. 1

varied in response to storm events, while the bar morphology varied from linear to crescentic. The incident wave data were collected from a wave-rider buoy in approximately 20-m depth. The significant wave height and peak period based on the measured spectra were given by Holman and Sallenger (1985) and are used herein as the reference wave height H'_f and period T'_f used for the normalization in Eqs. 3-5. During the experiment, $H'_f = 0.4-4.0\text{m}$ and $T'_f = 6-16\text{s}$. No information on wave direction was given in their paper. The tide data was provided by a tide gauge located outside the surf zone for all but the largest storm. The measured tidal range was -0.35m to 1.10m relative to the datum. The swash oscillation data were collected by using longshore-looking time-lapse photography together with large markers. A frame was shot every second for a total run length of 35 min. Sixty-one films were digitized, most at two longshore locations 100 and 150 m from the camera, but some films with apparent longshore variability were digitized more intensively. The digitized time series of the shoreline oscillation for each run were transformed to the vertical component from which the mean and the standard deviation σ_s were calculated. The tidal elevation was subtracted from the calculated mean to find the setup, whereas the significant swash height was taken as $4\sigma_s$. The total runup was defined as the sum of the setup and $2\sigma_s$. The setup and swash statistics were calculated for a total of 154 time series. Holman and Sallenger (1985) normalized the setup, swash height and total runup by the significant wave height H'_f and plotted the normalized setup, swash height and total runup as a function of the surf similarity parameter defined as

$$\xi = \frac{\sigma \tan\theta'_f}{\sqrt{2\pi}} = T'_f \left(\frac{g}{2\pi H'_f} \right)^{1/2} \tan\theta'_f \quad (17)$$

where σ is defined in Eq. 5 and the foreshore slope $\tan\theta'_f$ ranged from 0.09 to 0.16 for the range of $\theta'_f = 5^\circ-9^\circ$ indicated by Sallenger et al. (1985). In order to reduce the scatter of the plotted data points, the data were split into three sections corresponding to low, mid and high tides. The cutoff tidal elevations were arbitrarily taken as 0.25 and 0.70 m of the measured tidal range of -0.35 to 1.10 m. The mid and high tide data were similar, while the low tide data showed some influence of the single bar depicted in Fig. 1. As a result, the mid tide data is excluded from the following comparison.

The one-dimensional numerical model is based on the assumption of alongshore uniformity and normally incident waves. The field data may have satisfied these assumptions approximately near the shoreline when the bar morphology was linear and edge waves were absent. Sallenger and Holman (1987) analyzed the measured cross-shore flow during a storm in October, 1982. Prior to the storm, the bar was reasonably linear and shore parallel. The bar became increasingly crescentic when the wave heights were decreasing following the storm. The measured infragravity band spectra had characteristics consistent with either high-mode edge waves or standing (leaky) waves. As a result, the basic assumptions may not have been satisfied always, but the numerical model may still be applied to predict the trend of the scattered data points plotted by Holman and Sallenger (1985) since the assumptions of alongshore uniformity and normally incident waves must have been satisfied for some of the plotted data points. For the following computation, the beach profile shown in Fig. 1 is used as a typical profile neglecting the beach profile changes. The representative tidal elevations relative to the datum for the high and low tide data are simply taken as 0.90m and -0.05m , respectively. The vertical coordinate z' with $z'=0$ at SWL shown in Fig. 1 is that

assumed for the high tide. The seaward boundary of the numerical model located at $x'=0$ in Fig. 1 is taken to be sufficiently seaward of the bar so that the normalized incident wave profile $\eta_1(t)$ at $x'=0$ may be specified as input using an appropriate wave theory for an essentially horizontal seabed. The water depth below SWL at $x'=0$ in Fig. 1 is $d_t=4.15\text{m}$ for the high tide and $d_t=3.20\text{m}$ for the low tide. As a first attempt, the incident random waves measured in approximately 20-m depth are assumed to be represented by the monochromatic wave whose height and period are the significant wave height H'_T and the spectral peak period T'_T used by Holman and Sallenger (1985) to plot their data. Table 1 shows five different cases selected for the subsequent computation to represent the range of the wave conditions associated with the field data except that cases with larger wave heights are excluded to avoid wave breaking seaward of the selected seaward boundary location. The surf similarity parameter ξ

TABLE 1. Five Different Wave Conditions Used for Computation

Case	$H'_T(\text{m})$	$T'_T(\text{s})$	σ	ξ
1	2.0	7	15.5	0.73
2	0.9	7	23.1	1.09
3	1.6	12	29.7	1.40
4	0.8	11	38.5	1.82
5	0.8	14	49.0	2.31

is defined in Eq. 17 where the foreshore slope $\tan\theta'_f=0.118$ at the still water shoreline for the beach profile shown in Fig. 1. The range of ξ for the selected cases corresponds to that for the field data. For each case, a shoaling analysis is performed to find the wave height H' at $x'=0$ where the water depth d_t below SWL is taken as 4.15 m for the high tide and 3.20 m for the low tide. In this paper, the shoaling analysis and the specification of the normalized incident wave profile $\eta_1(t)$ for $t \geq 0$ are made using cnoidal wave theory for $U_r \geq 26$ and Stokes second-order wave theory for $U_r < 26$ in which U_r = Ursell parameter at $x'=0$ defined below (Svendsen and Brink-Kjaer, 1972). Table 2 summarizes the estimated monochromatic wave characteristics at

TABLE 2. Wave Characteristics at Seaward Boundary for High and Low Tides

Case	d_t	K_s	L	U_r	r
H1	2.08	1.03	11.1	61	0.02
H2	4.61	1.07	10.1	24	0.02
H3	2.59	1.58	21.5	283	0.05
H4	5.19	1.35	17.4	79	0.11
H5	5.19	1.58	23.0	161	0.17
L1	1.60	1.16	14.0	141	0.02
L2	3.56	1.10	12.2	46	0.02
L3	2.00	1.93	27.6	734	0.04
L4	4.00	1.56	21.0	171	0.07
L5	4.00	1.85	27.9	359	0.10

the seaward boundary of the numerical model for the five cases listed in Table 1, where the capital letters H and L indicate the high and

low tides, respectively. In Table 2, $d_t = d'_t/H'_t$ and K_s , L and U_r are defined as

$$K_s = \frac{H'}{H'_t} \quad ; \quad L = \frac{L'}{d'_t} \quad ; \quad U_r = \frac{H'(L')}{(d'_t)} = \frac{K_s L}{d'_t} \quad (18)$$

where L' =wavelength at $x'=0$. The assumption of finite-amplitude shallow-water waves in the computation domain $x' \geq 0$ may be appropriate since $L \gg 1$ and $U_r \gg 1$. Table 2 also lists the computed reflection coefficient r for each case. The value of r is estimated as the height of the computed periodic variation of $\eta_r(t)$ divided by K_s , as will be explained later, where the period and height of the periodic variation of $\eta_i(t)$ are equal to unity and K_s , respectively. The computed reflection coefficient r increases with the increase of the surf similarity parameter ξ . This trend is similar to that for coastal structures (Kobayashi and Watson, 1987). However, the value of r in Table 2 with the corresponding value of ξ in Table 1 is smaller than that based on the empirical formula, $r=(0.1\xi) \leq 1$, for smooth plane slopes proposed by Battjes (1974) even if $H'=K_s H'_t$ is used instead of H'_t in Eq. 17 to reduce the value of ξ for each case.

For the subsequent computation, use is made of approximately 400 nodes in the computation domain $x' \geq 0$ in Fig. 1 with the dimensional space size $\Delta x' = 0.46\text{m}$ between the two adjacent nodes. Correspondingly, the dimensionless space size of the finite difference grid is in the range of $\Delta x = 0.0097 - 0.022$ for the ten cases listed in Table 2. The number of time steps over one normalized wave period of unity is taken as $(\Delta t)^{-1} = 4000$ except that $(\Delta t)^{-1} = 5000$ is used for Case L2 due to numerical instability. The computational shoreline is defined by $h = \delta = 0.002$ since the increase of this value from $\delta = 0.001$ used for smooth steep slopes (Kobayashi and Watson, 1987) tends to improve the numerical stability in the vicinity of the computational shoreline. The measured shoreline oscillation is defined by the physical water depth $h' = \delta'_t$ in which $\delta'_t \approx 0.5$ cm for the photography technique used by Holman and Sallenger (1985) and $\delta'_t = 3.0$ cm for the dual-resistance wire sensor used by Guza and Thornton (1982) whose data are also included in the following comparison. For $H'_t = 0.8 - 2.0$ m as shown in Table 1, $\delta_r = (\delta'_t/H'_t) > \delta = 0.002$. The numerical damping coefficients for reducing high frequency numerical oscillations at the rear of breaking wave crests are taken as two for gentle slopes (Kobayashi and DeSilva, 1987; Kobayashi et al., 1988). The bottom friction factor f' is tentatively assumed to be $f' = 0.05$ on the basis of the limited calibration made by Kobayashi and Watson (1987) for small-scale smooth slopes without beach sand, neglecting the scale effects and the effects of moving sediment particles on f' (Kobayashi and Seo, 1985). The previous sensitivity analyses performed by Kobayashi et al. (1987) indicated that the computed results should not be very sensitive to the value of f' .

The computed results for the ten cases listed in Table 2 are given in the thesis of Strzelecki (1988). The computed results for Case H3 are presented as an example in the following. Fig. 2 shows the periodic cnoidal wave profile $\eta_i(t)$ specified at $x=0$ and the temporal variation of $\eta_r(t)$ computed using Eq. 11 with Eq. 16. The normalized wave period is unity. The detailed variation of $\eta_r(t)$ is shown in Fig. 3. The depression of η_r during the transition period $0 \leq t \leq 5$ appears to be related to the depression of the mean water level under large waves (Longuet-Higgins and Stewart, 1962) since the incident wave train initially propagates into the region of no wave action. The temporal variation of $\eta_r(t)$ for $t \geq 10$ consists of steady and oscillatory components. The steady component is the wave set-down

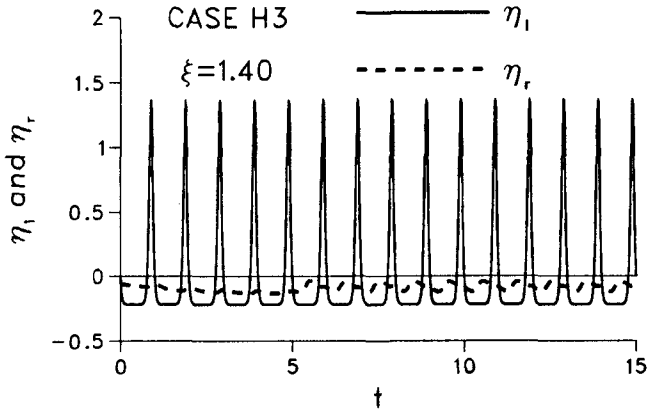


Fig. 2. Specified $\eta_i(t)$ and Computed $\eta_r(t)$ at Seaward Boundary

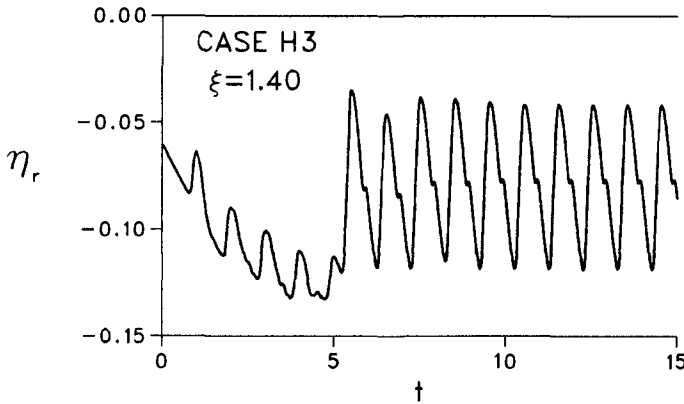


Fig. 3. Detailed Variation of $\eta_r(t)$ at Seaward Boundary

$\overline{\eta_r} = \overline{\eta_r}$ at $x=0$ since $\overline{\eta_i} = 0$ for the assumed cnoidal wave profile. The oscillatory component is associated with the reflected wave. The reflection coefficient r listed in Table 2 is taken as the height of this oscillatory component divided by the height of $\eta_i(t)$, that is, K_s . Fig. 4 shows the computed shoreline oscillations corresponding to the water depth $\delta'_i = 0.5$ and 3cm plotted in the form of the normalized vertical elevation Z_r as a function of t . During wave downrush, the shoreline location is sensitive to the water depth δ'_i used to define its location since a thin layer of water remains on the relatively steep foreshore during wave downrush (Kobayashi et al., 1988). After the initial transient oscillation, the temporal variation of Z_r for $t \geq 6$ is composed of steady and oscillatory components. The steady component is the normalized setup on the foreshore denoted by $\overline{Z_r}$, while the oscillatory component is the normalized swash about the setup level. The maximum and minimum values of $Z_r(t)$ after the establishment of periodicity are denoted by R and R_d in which R and R_d are the run-up and run-down normalized by the reference wave height H'_i , respectively. The value of $(R - R_d)$ is the

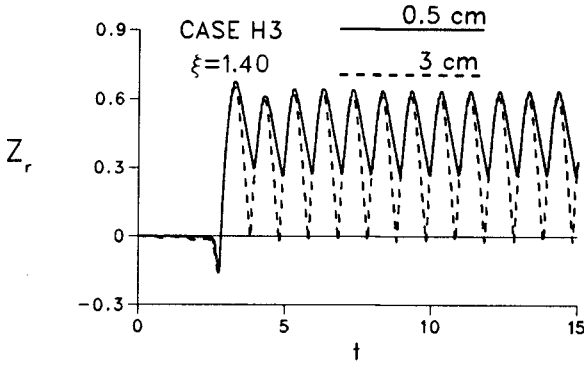


Fig. 4. Shoreline Oscillations for $\delta_z = 0.5$ and 3 cm

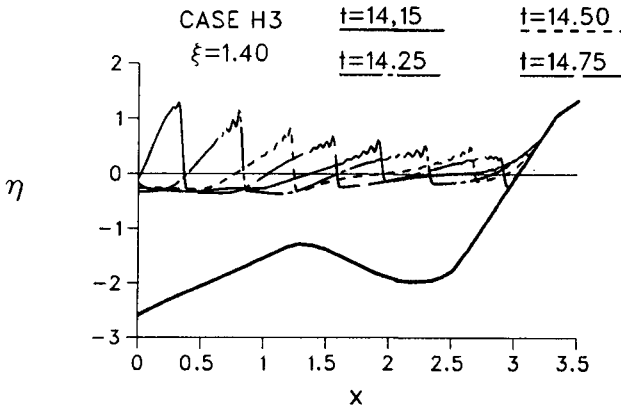


Fig. 5. Free Surface Variations During One Wave Period

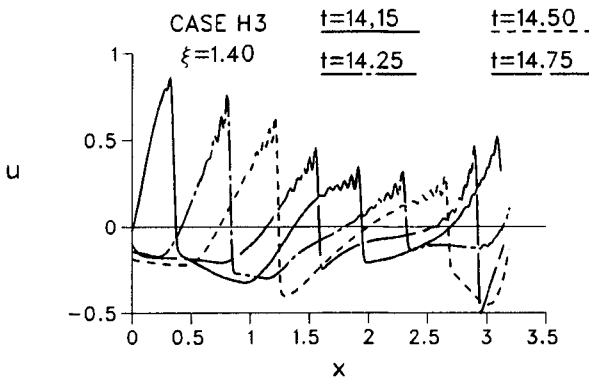


Fig. 6. Horizontal Velocity Variations During One Wave Period

normalized swash height. The computed values of \bar{Z}_r , R and R_d for given δ'_r are obtained using the computed variation of $Z_r(t)$ during $t_p \leq t \leq (t_p+1)$. For Case H3, $t_p=14$ is used since the periodicity is definitely established before $t=14$. $t_p=14$ is also found to be adequate for the other cases except for Cases L1 and L2 for which $t_p=24$ is used to ensure the definite periodicity. Figs. 5 and 6 show the computed cross-shore variations of η and u at $t=14$, 14.25, 14.5, 14.75 and 15, respectively. The normalized beach profile given by Eq. 6 is also shown in Fig. 5. The computed variations of η and u at $t=14$ and 15 are identical. The effects of the bar on the variations of η and u landward of the bar are apparent in Figs. 5 and 6. Figs. 7 and 8 show the computed cross-shore variations of the time-averaged free surface elevation $\bar{\eta}$ above SWL and the time-averaged horizontal velocity \bar{u} , respectively, where the time averaging is performed for

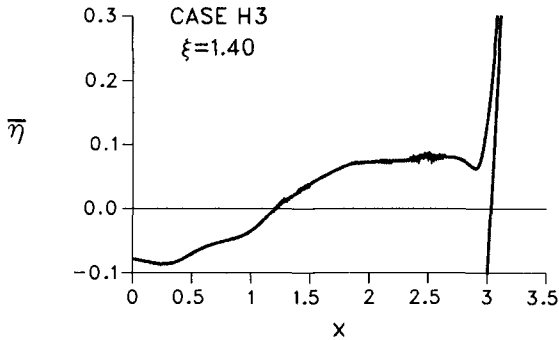


Fig. 7. Cross-Shore Variation of Mean Water Level

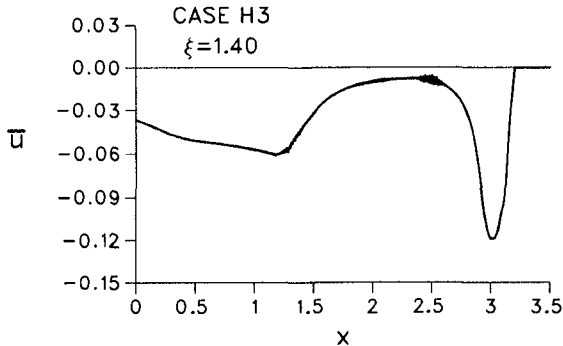


Fig. 8. Cross-Shore Variation of Mean Horizontal Velocity

$t_p \leq t \leq (t_p+1)$. The effects of the bar on the setup and mean velocity landward of the bar are apparent in these figures. Fig. 7 indicates that the mean water level on the steep foreshore will be affected by the large swash oscillation. Fig. 8 suggests that the bar may modify the cross-shore variation of the undertow noticeably, although u is not the same as the undertow (Kobayashi et al., 1988).

The values of \bar{Z}_r , R and $(R-R_d)$ for $\delta'_r=0.5$ and 3 cm computed for each of the ten cases in Table 2 are plotted in Fig. 9 as a function of the surf similarity parameters ξ for the high and low tides. The data points in Fig. 9 are read from the figures given in Holman and Sallenger (1985) where \bar{Z}_r , R and $(R-R_d)$ are assumed to be the same as the nondimensional setup, total runup and significant swash height

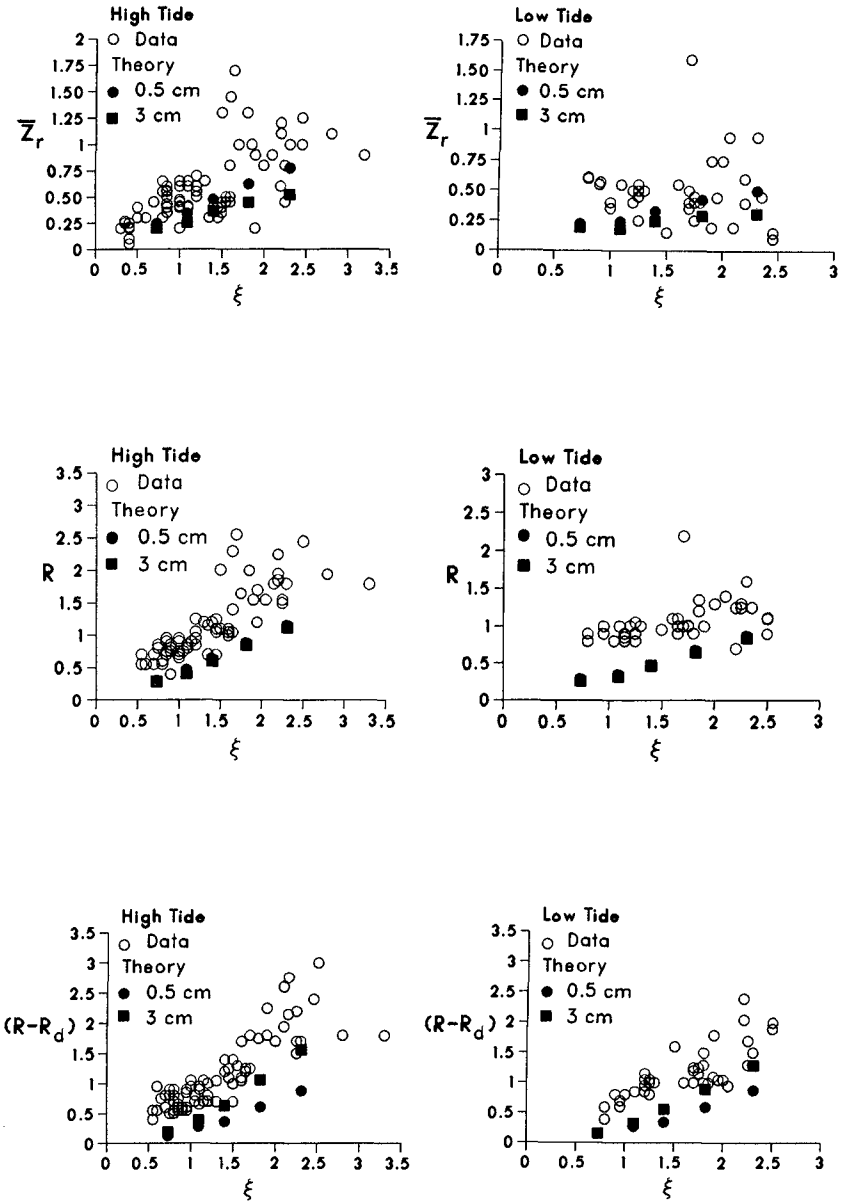


Fig. 9. Comparisons of Measured and Computed Setup, Run-up and Swash Height for High and Low Tides

calculated from the mean and standard deviation of the measured time series of the shoreline location with $\delta'_t \approx 0.5$ cm on the foreshore slope of approximately 0.1. The data points for the high tide included those measured by Guza and Thornton (1982) on a beach slope of approximately 0.023 using a wire sensor with $\delta'_t=3$ cm. These data points were in the region of $\xi < 1$. The differences between these two data sets were discussed by Guza et al. (1984). The computed results for $\delta'_t=0.5$ and 3 cm suggest that the two measuring techniques will yield large differences in $(R-R_d)$ and \bar{Z}_r for $\xi \geq 2$. Intercalibration of the two techniques on a low-slope beach indicated that the film technique registered a slightly higher mean and a 35% larger standard deviation than the wire sensor. The intercalibration results are consistent with the computed results for \bar{Z}_r but opposite to the computed results for $(R-R_d)$. Considering the subjective interpretation of run-down of the films especially for large values of ξ , it appears to be difficult to specify an appropriate value of δ'_t for the film technique unlike the wire sensor with a specific value of δ'_t . The effects of permeability neglected in the numerical model may not be negligible on the foreshore slope composed of coarse sand (Packwood, 1983). However, the permeability effects should reduce the computed values of R and $(R-R_d)$. The underestimation of R and $(R-R_d)$ by the numerical model is expected to be caused mainly by the monochromatic wave approximation which may be reasonable only for the swash oscillation in the incident frequency band. The computed values of $(R-R_d)$ with $\delta'_t=3$ cm for the high and low tides are plotted on Fig. 10(a) of Holman and Sallenger (1985) which

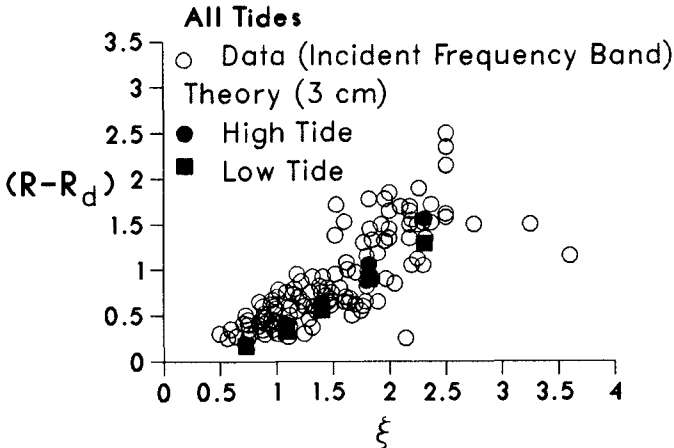


Fig. 10. Comparison with Swash Height in Incident Frequency Band

showed the nondimensional significant swash height in the incident frequency band (frequency ≥ 0.05 Hz) for all tides. The computed points with $\delta'_t=3$ cm follow the trend of the scattered data points well as shown in Fig. 10. However, the computed points with $\delta'_t=0.5$ cm, which are not shown in Fig. 10, are less than those shown in Fig. 10. Figs. 9 and 10 imply that the monochromatic approximation without regard to the swash oscillation in the infragravity frequency band will underestimate the swash height and run-up even on the moderately steep foreshore. Extension of the numerical model to random waves is

definitely required, although wave group statistics in shallow water are not well known (Elgar et al., 1984).

SEDIMENT TRANSPORT IN SWASH ZONE

Kobayashi (1988) assembled and synthesized recent publications which might contribute to the improvement of our quantitative capabilities for predicting shoreline changes due to the cross-shore sediment transport in the surf and swash zones on beaches. The comparisons shown above suggest that an accurate prediction of the swash oscillation including the effects of random waves and actual beach profiles is essential for predicting the resulting sediment movement in the swash zone. It should be stated that purely empirical models for beach and dune erosion might work reasonably well for highly erosive storm events if storm surge is more important than swash. Nevertheless, an improved understanding of the hydrodynamics and resulting sediment movement in the swash zone is required for better establishing the landward boundary condition for such an erosion model as well as for predicting accretion and berm building. Even for laboratory data with monochromatic waves, it appears to be difficult to explain the detailed processes of berm building. Kobayashi and DeSilva (1987) applied a Lagrangian sediment transport model to predict the movement of individual bedload particles in the swash zone under monochromatic wave action. The Lagrangian model, which did not include the correction term C_t in Eq. 11, was found to explain observed erosion and bar formation of an initially uniform sand slope but could not predict observed accretion and berm building. The major reason appeared to be the large water velocity during the wave downrush predicted by the numerical model which neglected the permeability effects.

ACKNOWLEDGEMENT

This work is a result of research sponsored by NOAA Office of Sea Grant, Department of Commerce, under Grant No. NA85AA-D-SG033 (Project No. R/OE-3). The U.S. Government is authorized to produce and distribute reprints for government purposes notwithstanding any copyright notation that may appear herein.

REFERENCES

- Abbott, M.B., McCowan, A.D. and Warren, I.R. (1984). "Accuracy of short-wave numerical models." J. Hydraulic Engrg., ASCE, 110(10), 1287-1301.
- Battjes, J.A. (1974). "Surf similarity." Proc. 14th Coast. Engrg. Conf., ASCE, 466-480.
- Battjes, J.A. and Stive, M.J.F. (1985). "Calibration and verification of a dissipation model for random breaking waves." J. Geophys. Res., 90(C5), 9159-9167.
- Elgar, S., Guza, R.T. and Seymour, R.J. (1984). "Groups of waves in shallow water." J. Geophys. Res., 87(C3), 3623-3634.
- Freilich, M.H. and Guza, R.T. (1984). "Nonlinear effects on shoaling surface gravity waves." Philos. Trans. R. Soc. London, Ser. A, 311, 1-41.
- De Vriend, H.J. and Stive, M.J.F. (1987). "Quasi-3D modelling of nearshore currents." Coast. Engrg., 11, 565-601.
- Guza, R.T. and Bowen, A.J. (1976). "Resonant interactions for waves breaking on a beach." Proc. 15th Coast. Engrg. Conf., ASCE, 560-579.
- Guza, R.T. and Thornton, E.B. (1982). "Swash oscillations on a natural beach." J. Geophys. Res., 87(C1), 483-491.

- Cuza, R.T., Thornton, E.B. and Holman, R.A. (1984). "Swash on steep and shallow beaches." Proc. 19th Coast. Engrg. Conf., ASCE, 708-723.
- Hansen, J.B. and Svendsen, I.A. (1984). "A theoretical and experimental study of undertow." Proc. 19th Coast. Engrg. Conf., ASCE, 2246-2262.
- Holman, R.A. and Sallenger, A.H. (1985). "Setup and swash on a natural beach." J. Geophys. Res., 90(C1), 945-953.
- Kobayashi, N. and Seo, S.N. (1985). "Fluid and sediment interaction on a plane bed." J. Hydraulic Engrg., ASCE, 111(6), 903-921.
- Kobayashi, N. and Greenwald, J.H. (1986). "Prediction of wave runup and riprap stability." Proc. 20th Coast. Engrg. Conf., ASCE, 1958-1971.
- Kobayashi, N., Otta, A.K. and Roy, I. (1987). "Wave reflection and runup on rough slopes." J. Wtrway, Port Coast. and Oc. Engrg., ASCE, 113(3), 282-298.
- Kobayashi, N. and Watson, K.D. (1987). "Wave reflection and runup on smooth slopes." Proc. Coast. Hydrodynamics, ASCE, 548-563.
- Kobayashi, N. and DeSilva, C.S. (1987). "Motion of sediment particles in swash zone." Proc. Coast. Hydrodynamics, ASCE, 715-730.
- Kobayashi, N. and Greenwald, J.H. (1988). "Waterline oscillation and riprap movement." J. Wtrway, Port Coast. and Oc. Engrg., ASCE, 114(3), 281-296.
- Kobayashi, N. (1988). "Review of wave transformation and cross-shore sediment transport processes in surf zones." J. Coast. Res., 4(3), (in press).
- Kobayashi, N. and Wurjanto, A. (1988). "Wave overtopping on coastal structures." J. Wtrway, Port Coast. and Oc. Engrg., ASCE (in press).
- Kobayashi, N., DeSilva, C.S. and Watson, K.D. (1988). "Wave transformation and swash oscillation on gentle and steep slopes." J. Geophys. Res., (submitted).
- Longuet-Higgins, M.S. and Stewart, R.W. (1982). "Radiation stress and mass transport in gravity waves, with application to 'surf beats'." J. Fluid Mech., 13, 481-504.
- Packwood, A.R. (1983). "The influence of beach porosity on wave uprush and backwash." Coast. Engrg., 7, 29-40.
- Peregrine, D.H. (1967). "Long waves on a beach." J. Fluid Mech., 27, 815-827.
- Sallenger, A.H., Holman, R.A. and Birkemeier, W.A. (1985). "Storm-induced response of a nearshore-bar system." Marine Geology, 64, 237-257.
- Sallenger, A.H. and Holman, R.A. (1987). "Infragravity waves over a natural barred profile." J. Geophys. Res., 92(C9), 9531-9540.
- Stive, M.J.F. (1980). "Velocity and pressure field of spilling breakers." Proc. 17th Coast. Engrg. Conf., ASCE, 547-566.
- Stive, M.J.F. and Wind, H.C. (1982). "A study of radiation stress and set-up in the nearshore region." Coast. Engrg., 6, 1-25.
- Stive, M.J.R. (1986). "A model for cross-shore sediment transport." Proc. 20th Coast. Engrg. Conf., ASCE, 1550-1564.
- Strzelecki, M.S. (1988). "Wave setup and swash on a beach and wave transmission over a nearshore bar." Will be presented to the University of Delaware in partial fulfillment of the requirements for the Master's degree in Civil Engineering.
- Svendsen, I.A. and Brink-Kjaer, O. (1972). "Shoaling of cnoidal waves." Proc. 13th Coast. Engrg. Conf., ASCE, 365-383.
- Svendsen, I.A., Schäffer, H.A. and Hansen, J.B. (1987). "The interaction between the undertow and the boundary layer flow on a beach." J. Geophys. Res., 92(C11), 11845-11856.

CHAPTER 88

TOWARD AN IMPROVED EMPIRICAL FORMULA FOR LONGSHORE SAND TRANSPORT

Nicholas C. Kraus¹, M. ASCE, Kathryn J. Gingerich²,
and Julie Dean Rosati³, AM. ASCE

ABSTRACT

This paper presents results of two field experiments performed using portable traps to obtain point measurements of the longshore sand transport rate in the surf zone. The magnitude of the transport rate per unit width of surf zone is found to depend on the product of the local wave height and mean longshore current speed, but correlation is much improved by including two correction terms, one accounting for local wave energy dissipation and the other for the fluctuation in the longshore current. The field transport rates are also found to be compatible with laboratory rates obtained under combined unidirectional and oscillatory flow. Total transport rates previously reported for this experiment program are revised with recently determined sand trapping efficiencies.

INTRODUCTION

More than 30 years ago, it was empirically established that the longshore transport of sand on beaches is related to the height and direction of the incident breaking waves (Watts, 1953; Caldwell, 1956). Considerable effort has been made since then to improve empirical predictive capabilities for engineering applications. To a great extent, however, the present field data base rests on the tracer experiments of Komar and Inman (1970) and Kraus et al. (1983), and similar techniques which average over long time intervals and wide spatial extent. Such field programs have been directed mainly toward measuring the total longshore sand transport rate in the surf zone, and variability in the data is high.

Point measurements of local longshore sand transport rates are needed to determine dependencies of the rate on wave type and form, turbulence, current velocity, water depth, grain size, and beach morphology. This paper describes results of two field data collection projects performed by the Coastal Engineering Research Center (CERC), U.S. Army Engineer Waterways Experiment Station, which were aimed at

(1) Senior Research Scientist, (2) Research Physical Scientist, and (3) Hydraulic Engineer, Coastal Engineering Research Center, U.S. Army Engineer Waterways Experiment Station, P.O. Box 631, Vicksburg, MS 39180-0631.

measuring the local longshore sand transport rate by means of portable traps. This method is labor intensive but direct, and the determined rates, as averages over minutes, are compatible with modern engineering methodologies aimed at predicting sand transport and beach evolution. Main emphasis is placed on point measurements of the longshore sand transport rate per unit width of surf zone, with some results summarized for the vertical distribution of transport rates and total surf zone transport rates. Complete descriptions of the experiments and listings of the data are given in CERC technical reports (Kraus, Rosati, and Gingerich, 1989; Kraus, Gingerich, and Rosati, in prep.).

METHODOLOGY

Site

Results pertain to two field data collection projects performed in September 1985 and September 1986 at CERC's Field Research Facility (FRF). The FRF is located along the Outer Banks of North Carolina just north of the village of Duck. The data collection projects were named DUCK85 (Mason, Birkemeier, and Howd, 1987) and SUPERDUCK, respectively. A location map and site description are given by Kraus and Dean (1987). The experiments were conducted on a sandy beach at the north end of the FRF property line, approximately 1000 m from the FRF research pier. Most experiment runs were carried out in the south longshore feeder current of a moderate-sized rip current that frequently appears about 50 m north of the property line. Operation in this area provided unidirectional and quasi-steady longshore currents. In spite of the presence of the rip, the bottom contours where the traps were placed were predominantly plane and parallel. During DUCK85, the steeply sloping foreshore was composed mainly of gravel, whereas a sand substrate characterized the surf zone. Median grain size in the surf zone during both experiments was approximately 0.17 mm.

Equipment and Field Procedure

The longshore sand transport rate was measured with portable traps called streamer traps. The traps used in 1985 are described in Kraus (1987) and Kraus and Dean (1987). Hydraulic efficiency tests performed in a uniform flow flume led to redesign of the streamer nozzle that was then used during SUPERDUCK (Rosati, 1988; Rosati and Kraus, 1988). Figure 1 shows a trap used at SUPERDUCK. The nozzle is made of 1/16-inch stainless steel and is 15 cm long, 2.5 cm high, and 2.5 cm wide. A streamer consisting of 0.107-mm polyester filter cloth approximately 2 m long is attached to the nozzle. The streamer collects sand flowing into it while allowing water to pass through. Streamer nozzles are mounted vertically on stainless steel racks and located forward of the rack by curved steel bars to be upstream of the influence of the rack.

Sand trapping efficiencies of both types of streamer nozzles were determined by Rosati (1988) and used to revise DUCK85 results reported by Kraus and Dean (1987). Table 1 gives values of sand trapping efficiencies determined for both nozzle types. "On-Bed" sand trapping efficiencies were determined for nozzles resting on the bottom in a uniform flow tank with mid-flow speeds in the range of 60 to 66 cm sec⁻¹. This range of flow speeds produced a flat bed condition as found in the surf zone at DUCK85 and SUPERDUCK. "Off-Bed" efficiencies were determined for nozzles located above the bottom in mid-flow speeds ranging from 22 to 76 cm sec⁻¹.

The longshore current velocity was measured with one or two 2-component, 13-cm diameter ball, Marsh-McBirney electromagnetic flow meters mounted on tripods. The meters were connected to a super-minicomputer data logger on shore which gave a graphic display of the record and allowed data analysis upon completion of a run. Wave height and period were measured by the photopole method which has been described by Ebersole (1987) and Ebersole and Hughes (1987). The procedure involved filming the water surface elevation at poles placed at approximately 6-m intervals across the surf zone using as many as eight 16-mm synchronized movie cameras.



Figure 1. Streamer trap used at SUPERDUCK.

Table 1. Sand trapping efficiency factors for streamer nozzles in uniform flow (after Rosati, 1988).

<u>Nozzle Type</u>	<u>On-Bed^a</u>	<u>Off-Bed^b</u>
DUCK85 (15×9 cm)	0.13 ± 0.03 ^c	0.92 ± 0.05
SUPERDUCK (15×2.5×2.5 cm)	0.68 ± 0.31 ^d	1.02 ± 0.03

a) Nozzle resting on bed; collects bedload and suspended load.

b) Nozzle positioned above bed; collects suspended load only.

c) Maximum deviation about the mean value as determined by the 95% confidence limit.

d) Error estimate based on limited number of points.

At DUCK85 a spatial sampling method (SSM) was used, in which traps were simultaneously deployed across the surf zone to measure the cross-shore distribution of the longshore sand transport rate. Trapping intervals were 10 min. Measured waves and currents from the trapping periods were analyzed in corresponding time segments to give estimates of the local forcing functions. The SSM results are described in Kraus and Dean (1987); however, magnitudes of transport rates reported there are incorrect because of a miscalculation in the original analysis and adjustment of measured quantities by the trapping efficiencies given in Table 1. Revised results of the SSM runs are presented here.

Longshore sand transport rate data collection at SUPERDUCK emphasized a temporal sampling method (TSM) in which traps were interchanged from 3 to 14 times at the same location. Trapping intervals typically were 6 min. Waves and currents were also measured as described above. Data from photopoles located immediately seaward and shoreward of the trap location were analyzed to define the average wave height at the trap and to obtain the cross-shore gradient of wave height at the trap. Typically, traps were centered between photopoles.

Mean water surface elevations were obtained from both the photopole record and a tide gage located on the FRF research pier. The beach profile was surveyed in the immediate vicinity of the experiments at least once a day from a survey station mounted on the pier.

Analysis Technique

The wave and current data were subjected to standard statistical and time series analysis. Sand collected in the streamers was weighed at the beach in a drip-free state that has been shown to be closely correlated with the dry weight of a sample (Kraus and Nakashima, 1986). Samples from selected runs of each experiment day were retained for grain size analysis and drying to determine the empirical coefficient relating drip-free and dry sand weight. Example results of vertical and cross-shore distributions of grain size were described by Kraus and Dean (1987) for the DUCK85 experiments. The median grain size of the trapped sand did not significantly vary with elevation in the water column or across the surf zone.

The streamer trap gives a direct measure of the flux f of sand at each nozzle in units of weight of sand per unit width normal to the transport direction per unit elevation per unit time. Measured fluxes for each streamer were adjusted by dividing by the average trapping efficiencies given in Table 1, and fluxes in areas between nozzles were obtained by interpolation. Integration of the flux through the water column gives the transport rate density i , which can be expressed as the immersed weight transport rate per unit width:

$$i = \int_{-h}^{\eta} f \, dz, \quad [i] = \frac{N}{m * \text{sec}} \quad (1)$$

in which η is the mean water surface elevation, z is the elevation measured from the still-water level, and h is the water depth at the trap. The measured transport rate density, which is obtained as a dry weight of trapped sand, was expressed as a standard immersed weight rate.

For the SSM, transport rate densities were integrated across the surf zone by use of the trapezoid rule to give the total immersed weight longshore sand transport rate I :

$$I = \int_0^{X_b} i \, dx, \quad [I] = \frac{N}{\text{sec}} \quad (2)$$

in which x is the cross-shore distance with origin at the mean water line, and X_b is the width of the surf zone. The location of the break point was determined from photopole data as the location of the maximum root mean square (rms) wave height; this quantity is known to within ± 3 m. If a trap was located outside the surf zone, the seaward limit of integration was extended to that point. Longshore transport immediately outside the breaker zone was found to be very small.

Calculated transport rates were correlated with simple combinations of measured mean wave height H and longshore current speed V , as discussed below, to obtain empirical predictive relations. Most theoretical and empirical expressions for the longshore sand transport rate density i based on either wave energy dissipation or bottom shear stress reduce to a simple dependence on the product HV . The present data set of local sand transport, wave, and current measurements allows detailed examination of the relationship between transport rate and forcing parameters.

RESULTS

Table 2 provides a summary of the range of wave, current, and sand transport conditions comprising the presently analyzed data set. Wave heights and periods given for DUCK85 pertain to breaking waves over a nominal measurement interval of 12 min, and values of the transport rate and current pertain to a 10-min interval. Wave quantities and current speeds for SUPERDUCK represent average values at the traps for a transport collection interval of 6 to 8 min.

Table 2. Range of wave, current, and transport rate conditions.

	H_s^a (m)	H_{rms} (m)	V (m sec ⁻¹)	T^b (sec)	i^c (kg m ⁻¹ min ⁻¹)	i^d (N m ⁻¹ sec ⁻¹)
<u>DUCK85</u>						
Maximum	1.19	0.86	0.33	10.3	8.88	0.89
Minimum	0.83	0.57	0.08	8.9	0.21	0.02
<u>SUPERDUCK</u>						
Maximum	1.05	0.73	0.58	10.1	14.30	1.43
Minimum	0.53	0.42	0.09	6.1	0.44	0.04

a) Significant wave height; b) Average wave period.

c) Dry mass longshore sand transport rate density.

d) Immersed weight longshore sand transport rate density.

Transport Rate Density

Discussion in this section will center on 39 values of the transport rate density obtained in six TSM runs performed during SUPERDUCK. Rms wave height is used in the present analysis, unless otherwise specified, because correlations were always slightly higher with rms wave height than with significant wave height.

Standard formulas for i derived from either a bottom shear stress approach (e.g., Komar, 1971) or a wave energetics approach (e.g., Inman and Bagnold, 1963) reduce to a leading dependence on the product of wave height and longshore current speed if linear shallow water wave theory is employed. Thus, as a first step, measured transport rate densities were plotted with respect to the quantity $\rho g H V$, in which ρ is the density of seawater, and g is the acceleration due to gravity. The result is shown in Figure 2, in which the straight line is a best fit from linear regression analysis. Values of the determined regression equation coefficients and the correlation coefficient squared (r^2) are listed in Table 3. Figure 2 shows that the measured transport rate densities are fairly well described by a purely linear function of HV . However, scatter is relatively great, and the trend in the data suggests a power law dependence on HV .

Qualitative observations made during DUCK85 indicated that the trapped amount of sand depended on the intensity of water agitation occurring at or immediately seaward of a trap. For example, the transport rate appeared to increase in turbulent white water as compared to calmer green water for traps located at approximately the same depth. The white, agitated water was produced by waves breaking at the trap or convected to the trap by waves breaking immediately seaward. The local gradient of the wave height dH/dx was identified

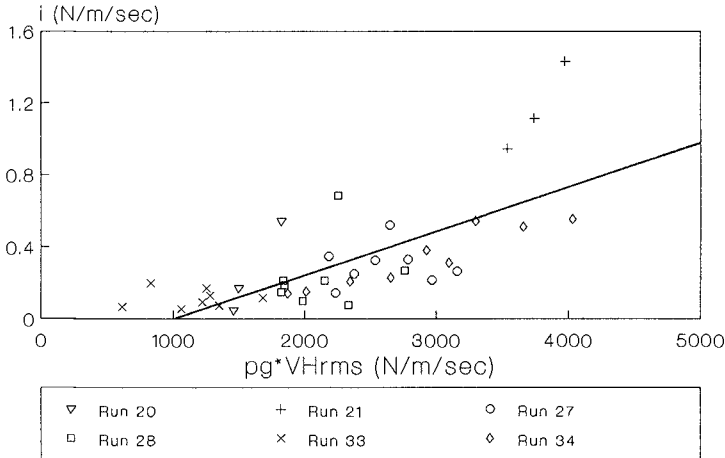


Figure 2. Longshore sand transport rate density versus HV .

Table 3. Summary of regression results for the equation

$$i = k [\rho g HV (1 + \alpha dH/dx + \beta S_v/V) + \text{const.}]$$

Expression	$k \cdot 10^4$	α	β	const. ($N m^{-1} sec^{-1}$)	r^2
$H_g V$	1.8	0	0	$-1.2 \cdot 10^3$.45
$H_{rms} V$	2.5	0	0	$-9.9 \cdot 10^2$.51
$H_{rms} V(1 + \alpha dH/dx)$	2.0	20	0	$-7.7 \cdot 10^2$.66
$H_{rms} V(1 + \alpha dH/dx + \beta S_v/V)$	1.5	20	1.8	$-2.4 \cdot 10^3$.77

as a readily evaluated measure of water agitation, and the SUPERDUCK TSM experiments were configured to provide this quantity. The gradient of the wave height was calculated from the nearest two poles (i.e., over a 6-m interval). This quantity was usually negative, indicating a decrease in wave height as the waves moved toward shore. However, in some cases the gradient was positive, indicating that broken waves were reforming.

The gradient of wave height was introduced as a correction to the quantity HV in the form of $HV(1 + \alpha dH/dx)$ in which the value of the empirical coefficient α was determined by iteration to provide the best linear least squares fit. The resultant plot and regression line are given in Figure 3. Visual agreement and the correlation coefficient are considerably improved over Figure 2, which involved only the product HV .

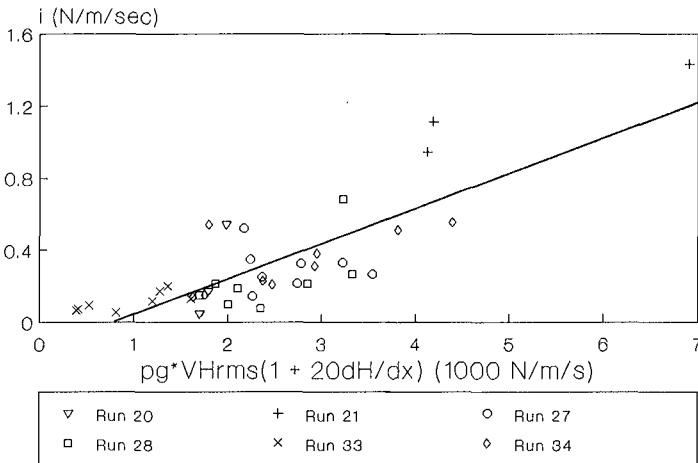


Figure 3. Longshore sand transport rate density versus $HV(1 + \alpha dH/dx)$.

The longshore current speed used in the above analysis is the average of a time-varying flow. The sand transport rate should depend on the range of current speed as well as the average. As a measure of the range, the coefficient of variation of the current speed S_v/V was chosen, in which S_v is the standard deviation of the speed during the averaging interval. The coefficient of variation was conceptualized as providing a correction to the leading term HV , and the quantity $HV(1 + \alpha dH/dx + \beta S_v/V)$ was used for regression. The result is shown in Figure 4, and associated values of determined coefficients are given in Table 3. Grouping of the data points about the regression line is improved over previous plots, and the apparent necessity of using a nonlinear or power law function of HV , as was suggested by Figure 2, is eliminated.

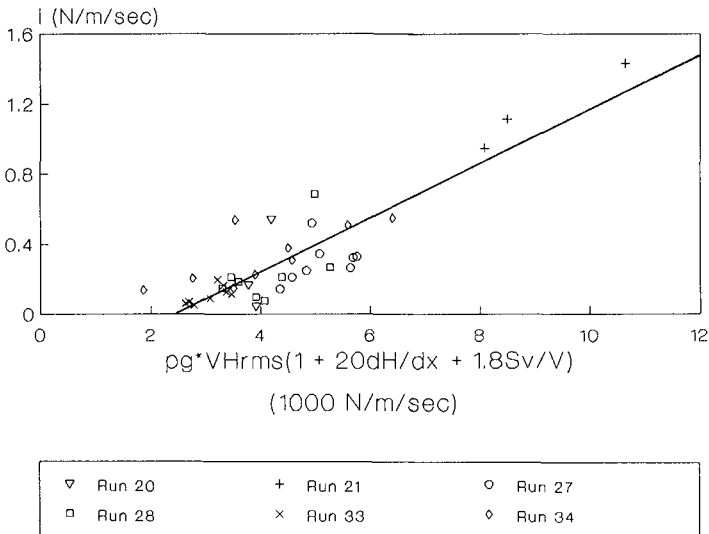


Figure 4. Longshore sand transport rate density versus $HV(1 + \alpha dH/dx + \beta S_v/V)$.

The correlation lines in Figs. 2, 3, and 4 all intercept the positive x-axis. The value of the intercept is partially an artifact of the use of a straight-line regression analysis. However, the intercept may be interpreted as an effective cutoff for transport of significance in engineering applications, since transport rates lying below this value evidently have a much weaker dependence on the quantity HV than the plotted measured values.

Stepwise correlation analysis indicated that there was no relation between the quantities H , dH/dx , V , and S_v . In a situation where the longshore current is produced by obliquely incident waves, the magnitude of the current speed is proportional to the square root of the wave height. In the present case, V and H were not related because the experiments were performed in or near the feeder current of a rip current. Caution should be taken in general use of the correct-

ion term proportional to α , as most TSM measurements were performed on a plateau with a very mild slope. Values of dH/dx ranged from 0.035 to 0.032 and values of S_v/V ranged from 0.02 to 0.37. The present empirical formulation is expected to lead to erroneous results if the value of either of the correction terms exceeds unity.

Comparison with Laboratory Data

Katori, Sakakiyama, and Watanabe (1984) measured the sand transport rate produced in a unique cross-flow tank in which a unidirectional current and an oscillatory current were made to intersect at right angles. Experiments were performed for pure unidirectional flow and for combined unidirectional and uniform flow; here, only the latter measurements are considered. The cross-flow tank replicated surf zone flow conditions, except that turbulence generated from the surface by breaking waves was absent. Uniform flow speeds achieved in the tank reached values in the range of longshore current speeds encountered at SUPERDUCK. However, sand ripples typically appeared in the test section of the tank, evidently because of the absence of turbulence from breaking waves, whereas ripples were not observed in the surf zone during SUPERDUCK. Transport rate densities obtained by Katori et al. were compared with rates obtained at SUPERDUCK to examine magnitudes and trends.

Katori et al. (1984) expressed measured transport rates in nondimensional form as:

$$\Phi = \frac{q}{w_o d} \quad (3)$$

in which q is the bulk transport rate density (units of $m^3 m^{-1} sec^{-1}$), w_o is the sand fall speed, and d is the median grain diameter. Three uniform quartz sands of median diameter 0.2, 0.4, and 0.7 mm were used. Measured transport rates were found to be closely correlated to a quantity called the "dimensionless flow power," introduced by Watanabe (1982). The dimensionless flow power is defined as:

$$\theta = \frac{(\tau_m - \tau_c) V}{\rho (sgd)^{1.5}} \quad (4)$$

in which τ_m is the maximum shear stress at the bottom produced by the combined flow, τ_c is the shear stress for inception of sand movement, V is the magnitude of the steady current, $s = \rho_s/\rho - 1$, and ρ_s is the density of quartz. Katori et al. (1984) obtained the result $\Phi = 1.8 \theta^{1.5}$ for transport rates ranging over two orders of magnitude for their complete data set. They argued that the power 1.5 may have been artificially high because of limitations in experiment conditions. One characteristic viewed as a limitation was the unsteadiness of the unidirectional current in the combined flow tests, a condition that actually mimics the longshore current in the field.

In the present study, quantities analogous to Φ and Θ were calculated for the SUPERDUCK data. The shear stress was taken as $\tau_m = 1/2 \rho f_w (U_m^2 + V^2)$, in which f_w is the friction factor introduced by Jonsson (1967), and U_m is the amplitude of the wave orbital velocity at the bottom, which was calculated by shallow water linear wave theory using measured water depth and rms wave height. The critical shear stress in Eq. 4 was assumed to be zero for the field measurements. Katori et al. (1984) had used a combined wave and current friction factor to calculate shear stress.

Nondimensionalized SUPERDUCK transport rates are plotted in Figure 5 together with the data of Katori et al. (1984). The total set of measured transport rates and flow powers spans more than three orders of magnitude. The best-fit power law for the 56 points was

$$\Phi = 0.85 \Theta^{1.1} \quad (5)$$

with $r^2 = 0.90$. The approximate agreement in trends in the laboratory and field data is surprising because transport in the laboratory was dominated by ripple processes, whereas field transport occurred over a flat bed under highly turbulent flow conditions. This result is encouraging and supports the validity of energetics-based transport concepts. Regression on the 39 SUPERDUCK data points gave $\Phi = 1.14 \Theta^{0.95}$, with $r^2 = 0.54$. This r^2 -value is essentially the same as found for the simple $i \propto HV$ analysis given in Table 3 and is not as good as the agreement produced by introducing corrections for the gradient in wave height and variability in the current (cf. Figure 4). Thus, introduction of the friction factor through Eq. 4 did not provide an improvement over the simple empirical transport relation using only HV . (For completeness, the 15 laboratory points used here were described by $\Phi = 1.10 \Theta^{1.3}$, with $r^2 = 0.91$.)

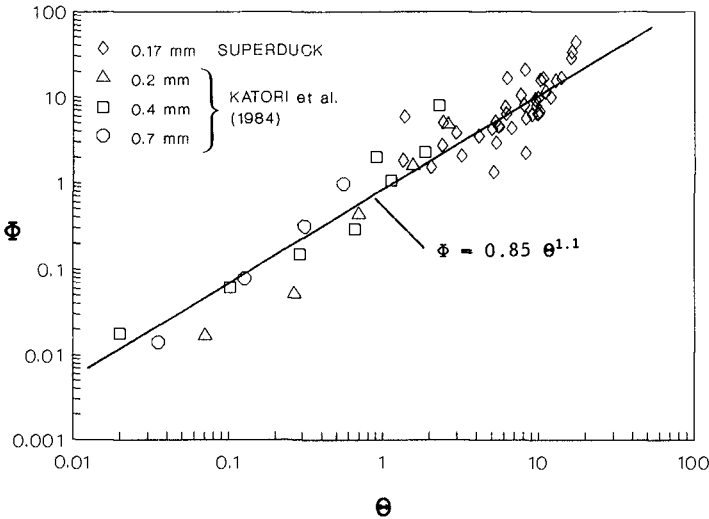


Figure 5. Dimensionless transport rate versus flow power.

Lateral Distribution of the Transport Rate

Figure 6 shows an example of cross-shore transport rate distributions obtained during a 10-min SSM experiment at DUCK85. The lengths of the histograms represent the magnitude of the longshore flux of sand measured at the specified location and elevation. Similar figures have been given by Kraus and Dean (1987); however, the values in Figure 6 have been revised. The flux decreases sharply with increase in elevation, independent of location in the surf zone. This regular decrease in flux was found in all experiments. On the basis of these observations, Kraus and Dean (1987) proposed an expression for the transport rate density of the form:

$$i(x, z) = i_0(x) * p(h, z) \quad (6)$$

in which i_0 is a "magnitude function" for the transport rate, assumed to depend on local wave, current, water depth, and beach conditions, z is elevation above the bed, and p is a "shape function," assumed to have a universal form for the surf zone as:

$$p = e^{-\lambda(z/h)} \quad (7)$$

The average value of λ obtained from the DUCK85 data was 3.6 with a standard deviation of 0.86 for 55 trap deployments, whereas for the SUPERDUCK data the average λ was 2.8 with a standard deviation of 0.82 for 44 deployments.

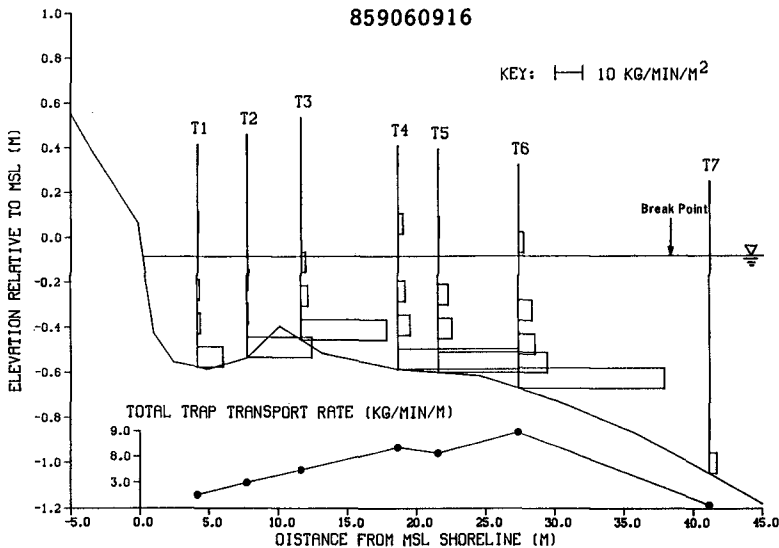


Figure 6. Example of vertical distributions of the longshore sand flux across the surf zone.

These revised values of λ indicate that sand movement at and close to the bed formed the major portion of the transport. This reverses the conclusion of Kraus and Dean (1987) and supports the idea that "bedload" transport predominates over suspended load (Komar, 1978) for the range of wave and current conditions and grain size encountered in these experiments.

The following expression was obtained for the magnitude function in Eq. 6 on the basis of the SUPERDUCK TSM data:

$$i_o = k_o [\rho g HV (1 + \alpha_o dH/dx + \beta_o S_v/V) + \text{const.}] \quad (8)$$

where the subscript "o" denotes values determined for $z = 0$ in Eq. 6. This equation had $r^2 = 0.74$, and values of the empirical coefficients were: $k_o = 9.4 \cdot 10^{-4}$; $\text{const.} = -3.0 \cdot 10^3 \text{ N m}^{-1} \text{ sec}^{-1}$; $\alpha_o = 20$; and $\beta_o = 1.8$.

Total Transport Rate

Total longshore sand transport rates measured during DUCK85 were found to be well correlated with a quantity $R = VX_b H_b$ called the discharge parameter (Kraus and Dean, 1987). Since the product $X_b H_b$ is proportional to the cross-sectional water area of the surf zone, R is proportional to the average discharge of water moving alongshore. Figure 7 shows total transport rates plotted as a function of R for eight DUCK85 runs. The surf zone width was typically 30-40 m, and 6 or 7 traps were used. Figure 7 contains one additional data point than an analogous figure given by Kraus and Dean (1987).

Assuming that a linear dependence exists between I and R , the following regression equation plotted as the straight line in Figure 7 is obtained with $r^2 = 0.76$:

$$I = 2.7 (R - R_c) \quad (9)$$

in which the intercept $R_c = 3.9 \text{ m}^3 \text{ sec}^{-1}$ is interpreted as a threshold value for significant longshore sand movement. In Eq. 9, I is expressed in N sec^{-1} and R in $\text{m}^3 \text{ sec}^{-1}$.

The longshore current which generated the transport rates plotted in Figure 7 and described by Eq. 9 was not directly related to oblique wave incidence, but was associated with the circulation of a rip current cell. Therefore, predictions from Eq. 9 cannot be directly compared to the CERC formula (Shore Protection Manual, 1984) for the total longshore sediment transport rate. Inman and Bagnold (1963) have given a predictive equation for I based on wave-energetics concepts that was shown by Komar and Inman (1970) to be compatible with the CERC formula. The Inman and Bagnold equation is:

$$I = K' (EC_g)_b \frac{V}{U_m} \quad (10)$$

in which $(EC_g)_b$ is the wave energy flux at breaking (evaluated for rms wave height), V is the average longshore current speed and U_m is the maximum wave orbital velocity under breaking waves. The value of the empirical coefficient $K' = 0.28$ determined by Komar and Inman (1970) is consistent with the value of the empirical coefficient commonly used in the CERC formula.

If shallow water linear wave approximations are used, the functional form of Eq. 10 reduces to $H_b^2 V$, which is essentially equivalent to the discharge parameter R if the surf zone bottom can be approximated by a plane sloping surface. Thus the basic functional forms of Eqs. 9 and 10 are similar, except for the incorporation of an effective threshold in Eq. 9.

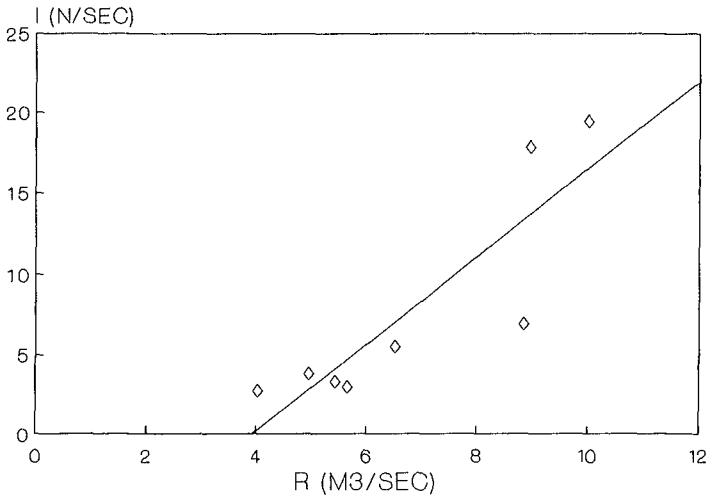


Figure 7. Total immersed weight longshore sand transport rate versus discharge parameter.

CONCLUDING DISCUSSION

These direct measurements of the longshore sand transport rate per unit width of surf zone confirm the functional form of previously derived theoretical models of transport which have a leading dependence on the product of wave height and longshore current speed. The results also indicate that considerably improved correlation between the transport rate and local waves and currents can be obtained by including corrections due to turbulence introduced by breaking waves and the variation in the longshore current speed. [Recently, Roelvink and Stive (personal communication, 1988) have derived a theoretical expression for the transport rate density that includes an explicit contribution from breaking wave-induced turbulence.] The next stage of analysis will include more data from the SUPERDUCK field project and other experiments, and an investigation of higher-order moments of the wave orbital velocity and longshore current.

In experiments involving use of portable traps, the bottom streamer nozzle, which collects both bedload and suspended load near the bottom, contained the major portion of the total transport at the trap. The vertical profile of the transport rate density decreased rapidly with elevation from the bed, and both the estimated transport rate density at the bottom and profile shape could be reasonably approximated by simple functions.

Field sand transport rates showed surprising compatibility with laboratory transport rates generated under intersecting uniform and oscillatory flows, despite the fact that the bed surfaces were quite different (flat in the field and rippled in the laboratory). The nondimensionalized transport rates were reasonably well described by an energetics-based predictive relation which reduces to the functional form of HV. Incorporation of a friction coefficient did not improve correlation above an empirical HV-predictive form; however, the range in wave period, which would change the friction factor, was limited in the field experiments.

The trend in total surf zone sand transport rate as displayed in Figure 7 is supportive of the energetics theory of Inman and Bagnold (1963). It also suggests that a simple empirical transport rate formula for the total transport rate expressed in the basic functional form H_b^2V or H_bX_bV may apply equally as well as more sophisticated formulas based on quantities such as wave energy flux and wave orbital velocity.

ACKNOWLEDGEMENTS

Space does not permit us to properly acknowledge all the individuals who resolutely labored to collect the field data. They are acknowledged in the data reports. We would like to thank Mr. Sadakazu Katori, Coastal Consultants, Inc., Tokyo, Japan, for providing his laboratory data. The experiments described and the resulting data presented herein, unless otherwise noted, were obtained under the work unit "Surf Zone Sediment Transport Processes" of the Shore Protection and Restoration Program of the United States Army Corps of Engineers by the Coastal Engineering Research Center at the Waterways Experiment Station. Permission was granted by the Chief of Engineers to publish this information.

REFERENCES

- Caldwell, J. M. 1956. "Wave Action and Sand Movement near Anaheim Bay, California," Tech. Memo. No. 68, Beach Erosion Board, U.S. Army Corps of Engrs., 21 pp.
- Ebersole, B. A. 1987. "Measurements and Prediction of Wave Height Decay in the Surf Zone," Proc. Coastal Hydrodynamics, R. A. Dalrymple, ed., Am. Soc. Civil Engrs., pp. 1-16.
- Ebersole, B. A. and Hughes, S. A. 1987. "DUCK85 Photopole Experiment," Misc. Pap. CERC 87-18, U.S. Army Engr. Waterways Expt. Station, Coastal Engrg. Res. Center, Vicksburg, Miss., 62 pp.
- Inman, D. L. and Bagnold, R. A. 1963. "Littoral Processes," In: The Sea, M. N. Hill, ed., Interscience, New York, pp. 529-533.
- Jonsson, I. G. 1967. "Wave Boundary Layer and Friction Factors," Proc. 10th Coastal Engrg. Conf., Am. Soc. Civil Engrs., pp. 127-148.

- Katori, S., Sakakiyama, T., and Watanabe, A. 1984. "Measurement of Sand Transport in a Cross Unidirectional-Oscillatory Flow Tank," Coastal Engrg. in Japan, 27, pp. 193-203.
- Komar, P. D. 1971. "The Mechanics of Sand Transport on Beaches," J. Geophys. Res., 76(3), pp. 713-721.
- Komar, P. D. 1978. "Relative Quantities of Suspension Versus Bed-Load Transport on Beaches," J. Sed. Petrol., 48(3), pp. 921-932.
- Komar, P. D., and Inman, D. L. 1970. "Longshore Sand Transport on Beaches," J. Geophys. Res., 75(30), pp. 5914-5927.
- Kraus, N. C. 1987. "Application of Portable Traps for Obtaining Point Measurements of Sediment Transport Rates in the Surf Zone," J. Coastal Res., 3(2), pp. 139-152.
- Kraus, N. C. and Dean J. L. 1987. "Longshore Sediment Transport Rate Distribution Measured by Trap," Proc. Coastal Sediments '87, N. C. Kraus, ed., Am. Soc. Civil Engrs., pp. 881-896.
- Kraus, N. C. and Nakashima, L. 1986. "Field Method for Determining Rapidly the Dry Weight of Wet Sand Samples," J. Sed. Petrol., 56(4), pp. 550-551.
- Kraus, N. C., Isobe, I., Igarashi, H., Sasaki, T. O., and Horikawa, K. 1983. "Field Experiments on Longshore Sand Transport in the Surf Zone," Proc. 18th Coastal Engrg. Conf., Am Soc. Civil Engrs., pp. 969-988.
- Kraus, N. C., Rosati, J. D., and Gingerich, K. J. 1989. "DUCK85 Surf Zone Sand Transport Data Report," Tech. Rep., U.S. Army Engr. Waterways Expt. Station, Coastal Engrg. Res. Center, Vicksburg, Miss.
- Kraus, N. C., Gingerich, K. J., and Rosati, J. D. in prep. "SUPERDUCK Surf Zone Sand Transport Data Report," Tech. Rep., U.S. Army Engr. Waterways Expt. Station, Coastal Engrg. Res. Center, Vicksburg, Miss.
- Mason, C., Birkemeier, W. A., and Howd, P. A. 1987. "An Overview of DUCK85, A Nearshore Processes Experiment," Proc. Coastal Sediments '87, N. C. Kraus, ed., Am. Soc. Civil Engrs., 818-833.
- Rosati, J. D. 1988. "Calibration of a Portable Sediment Trap for Use in the Nearshore," unpub. M.S. Thesis, Dept. of Civil Engrg., Mississippi State Univ., Starkville, Miss.
- Rosati, J. D. and Kraus, N. C. 1988. "Hydraulic Calibration of the Streamer Trap," J. Hydraulic Engrg., 114(12), in press.
- Shore Protection Manual. 1984. 4th ed., 2 Vols. U.S. Army Engr. Waterways Expt. Station, Coastal Engrg. Res. Center, U.S. Govt. Printing Office, Washington, DC.
- Watanabe, A. 1982. "Numerical Models of Nearshore Currents and Beach Deformation," Coastal Engrg. in Japan, 25, pp. 147-161.
- Watts, G. M. 1953. "A Study of Sand Movement at South Lake Worth Inlet, Florida," Tech. Memo. No. 42, Beach Erosion Board, U.S. Army Corps of Engrs., 24 pp.

CHAPTER 89

GENERIC TREATMENT OF DUNE EROSION FOR 100-YEAR EVENT

by
Robert J. Hallermeier*
and
Perry E. Rhodes#
Member ASCE

Abstract

Quantitative procedures provide the eroded dune geometries expected during an extreme storm on U.S. Atlantic and Gulf coasts. A criterion for either dune face retreat or dune removal is based on measured erosion cross sections in many cases where the pre-storm dune proved to be a durable barrier to wave effects. After that decision, the eroded profile is constructed using specified planar segments cut into or across the existing dune. This empirical treatment appears appropriately detailed for assessing hazards due to the 100-year event considered within the U.S. National Flood Insurance Program, and an example assessment is outlined. Additional discussion addresses other site-specific factors possibly affecting dune erosion, along with another potential application for this simplified methodology.

INTRODUCTION

The Federal Emergency Management Agency develops a Flood Insurance Study (FIS) for each community participating in the U.S. National Flood Insurance Program (NFIP). The focus of an FIS is expected effects in the flood having a one-percent chance of being equalled or exceeded in any year. This "base flood" is equivalent to the 100-year event for a given site, expected to recur once each 100 years on the average. Open-coast communities are subject to particularly extreme hazards due to storm surge and wave action from large water bodies. Coastal areas of special flood hazard in 100-year events are designated as V zones, having the potential for inundation by water flows with significant velocity. Within a V zone, floodwater depth is sufficient to permit a wave height of at least 3 feet (0.9 meters).

*Senior Coastal Scientist, Dewberry & Davis

#Senior Coastal Engineer and Associate, Dewberry & Davis,
8401 Arlington Boulevard, Fairfax, Virginia 22031 USA

Proper delineation of V zones requires quantitative determination of wave effects associated with the base flood, including coastal erosion.

Coastal sand dunes usually extend above local 100-year flood elevations, but such apparent barriers to flooding may not prove durable in view of the massive erosion associated with extreme storms. Several levels of dune effectiveness as a flooding barrier need to be distinguished, as outlined in a schematic manner by Figure 1. These four cases correspond to the eroded dune providing:

- a. a reliable barrier to flood effects from the sea;
- b. a nearly complete barrier, with some overtopping;
- c. a partial barrier, with some wave transmission; or
- d. an ineffective barrier, as relatively deep water and high waves reach past the initial dune site.

Sound analysis of potential flood hazards thus requires an objective estimate of dune geometry during the base flood.

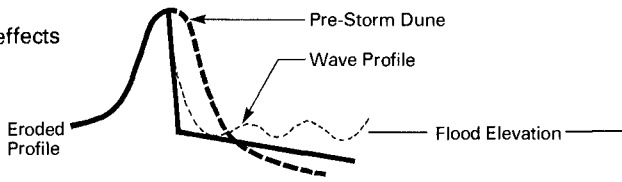
Treatment of expected erosion must be consistent with other NFIP methodologies. First, it should be recognized that the base flood represents a statistical measure rather than the actual effects arising in some particular coastal storm. Second, erosion assessment must conform to the standard FIS transect viewpoint: representative shore-normal profiles are considered. Third, the 100-year still-water flood level (SWFL) has a known elevation on a given coastal transect, evaluated prior to treating additional wave effects expected to occur in the base flood. Fourth, eroded dune geometry must be determined by a uniform but perhaps highly simplified method, appropriately reflecting basic physical principles, as in FIS procedures for treating wave dimensions (National Academy of Sciences, 1977).

This paper outlines objective procedures specifying coastal dune erosion expected to accompany the base flood. These estimates of eroded dune geometry are meant for application at exposed U.S. sites along the Atlantic Ocean and Gulf of Mexico. The present erosion treatment has a broad empirical basis and appears appropriate in the context of other NFIP methodologies for wave effects in extreme events.

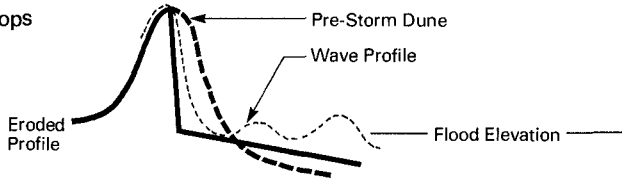
DUNEFACE RETREAT AND DUNE REMOVAL

The Federal Emergency Management Agency (1986) assessed usual procedures and developed several recommendations to correct weaknesses in FIS identification of coastal high-hazard areas, or V zones. Recognizing the transient and sensitive nature of coastal sand dunes, it was recommended that the entire primary frontal dune be designated a V zone. Since NFIP regulations prohibit alteration of sand dunes in V zones, this serves to protect natural dunes. Substantial construction standards and adequate insurance rates now automatically apply in this area exposed to high hazards, by means of an NFIP rule effective October 1, 1988 (Federal Emergency Management Agency, 1988).

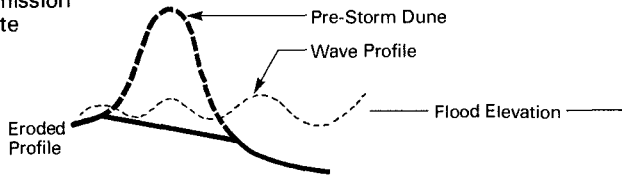
A. Effective barrier remains to storm effects



B. Wave runup overtops dune remnant



C. Some wave transmission past initial dune site



D. Inland penetration of appreciable wave action past initial dune site

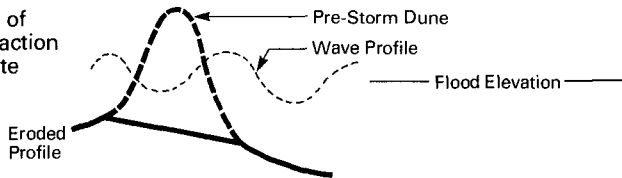


Figure 1. Schematic illustration of possible levels of flood protection provided by eroded frontal dunes

Another recommendation was for full consideration of storm-induced erosion in determining effects of the base flood. Coastal erosion can be crucial to the inland extent of V zones, but FIS treatments of erosion had been rather variable, with occasional underestimation of wave penetration associated with the base flood. The required erosion methodology would be capable of taking objective account of the range in expected effectiveness of existing dune barriers.

Figure 2 provides examples of sizable coastal erosion in the distinct categories of duneface retreat and dune removal. These instances relate to Gulf coast landfalls of Hurricane Eloise in 1975 and Hurricane Frederic in 1979, with profile changes documented by the Florida Department of Natural Resources (1987). In one case, the sizable dune remained intact as a barrier to coastal flooding, whereas the other dune was completely eradicated by storm-induced erosion. Methodology appropriate for NFIP application must provide the eroded profile geometry corresponding to each case.

Available computation models treating dune erosion were reviewed and found to have unproven capability for the entire range of effects possible in U.S. base floods. Two well documented but fundamentally different models, those by Kriebel and Dean (1985) and by Vellinga (1986), address only sand transport directed seaward, and thus can treat only cases of duneface retreat. Another important consideration is the marked variability of actual dune erosion in severe storms and the more sizable scatter to be expected in computed erosion amounts. For closely-spaced profiles along a coastal reach exposed to nearly constant storm forces, measured erosion cross section might have a median value of $2X$ and a range from X to $3X$, but computed erosion would likely vary from 0 to $4X$.

Simplified procedures specifying expected erosion geometry appear appropriate in view of the limited capabilities of available computation models and the NFIP need to treat an idealized 100-year event. Such procedures for immediate FIS application have been developed using documented erosion in extreme storms along the U.S. Atlantic and Gulf coasts. The first necessary element in this erosion treatment is a criterion to decide whether duneface retreat or dune removal would be associated with the 100-year event at a site.

EXPECTED DUNEFACE RETREAT IN 100-YEAR EVENT

The central analysis in this methodology development defined the sand reservoir above SWFL required for a dune to remain intact during specific storms. Published data were reviewed to accumulate 38 separate cases of duneface retreat, where pre- and post-storm profiles confirm that all eroded sand was transported seaward. In each case, the existing dune at a site provided a durable and effectively unlimited barrier during the particular storm. The data define a relationship between erosion cross sections and

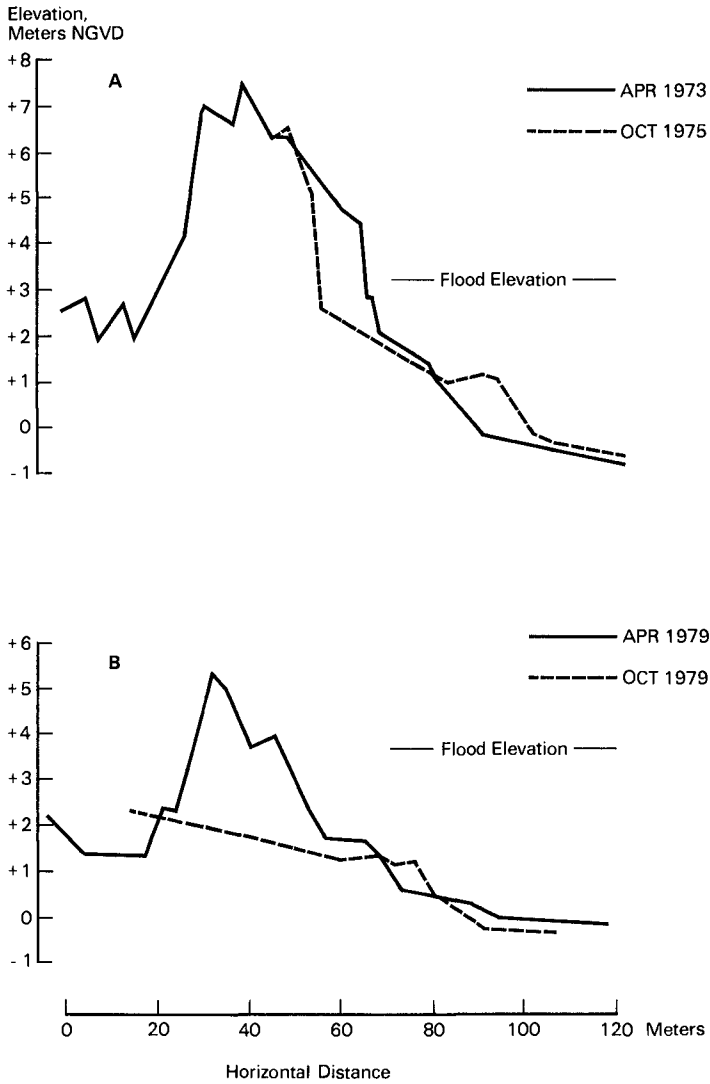


Figure 2. Examples of duneface retreat and dune removal, as documented by Florida Department of Natural Resources (1987). Effects are: A - September 1975 Hurricane Eloise, Profile R-15, Walton County, Florida; B -September 1979 Hurricane Frederic, Profile B-13, Baldwin County, Alabama.

storm intensities, as measured by recurrence interval for SWFL at specific sites, and thus indicate expected erosion in duneface retreat for the 100-year event (Hallermeier, Rhodes, and Buckley, 1988).

These 38 cases include hurricane and extratropical storm impacts in 11 states, with particularly good representation of sites in Florida, North Carolina, New Jersey, and New York. The data base was restricted to the U.S. Atlantic and Gulf coasts, to ensure that flooding is definitely related to storm effects (rather than tsunamis, for example). The exception to these geographical limits is inclusion of five events documented for the Dutch North Sea coast (Vellinga, 1986), to provide better coverage of duneface retreat in extreme extratropical storms, for which U.S. examples are scarce. In addition, to address effects relating to extreme storms rather than seasonal cycles, the data set was limited to events where SWFL has a recurrence interval of two years or longer. The exception (Birke-meier, 1979) is a December 1977 extratropical storm at sites where a more extreme event had occurred two months earlier, likely ensuring a generally meaningful response to the later storm.

About half these cases have changes recorded on multiple profiles, where median erosion is taken to summarize storm effects. Erosion is measured above the open-coast flood elevation, since such elevated change leads to failure of the initial dune barrier. The database includes median cross-sectional erosion from 5 to 105 m² for coastal floods with recurrence intervals of 1.25 to 300 years. Relatively common events have much better representation than truly extreme events, but data are rather uniformly distributed when considered using the logarithm of recurrence interval. The number of cases appears sufficient to be considered large for the purposes of statistical analysis.

Over the wide ranges represented, the trend in these field data is definite, yielding this relationship for median erosion in duneface retreat:

$$\text{Erosion [m}^2\text{]} = 8 (\text{Recurrence Interval [yr]})^{0.4} \quad (1)$$

Figure 3 presents residual differences between the measured erosion area and that given by the relationship in separate cases, along with an empirical error band for results. For the generic 100-year event, results indicate that expected duneface retreat will amount to (50 ± 15)m² above local SWFL at U.S. Atlantic or Gulf sites. The uncertainty in this estimate refers to median erosion, not the actual erosion variability along the coast in a specific storm.

Figure 3 reveals little pattern among residual differences, showing this relationship has no distinct empirical defect. Relatively large underestimates of erosion appear somewhat more common than large overestimates, so that the expected duneface erosion has not been summarized as too extreme. However, few U.S. frontal dunes are massive enough to permit the indicated erosion for the 100-year event. This

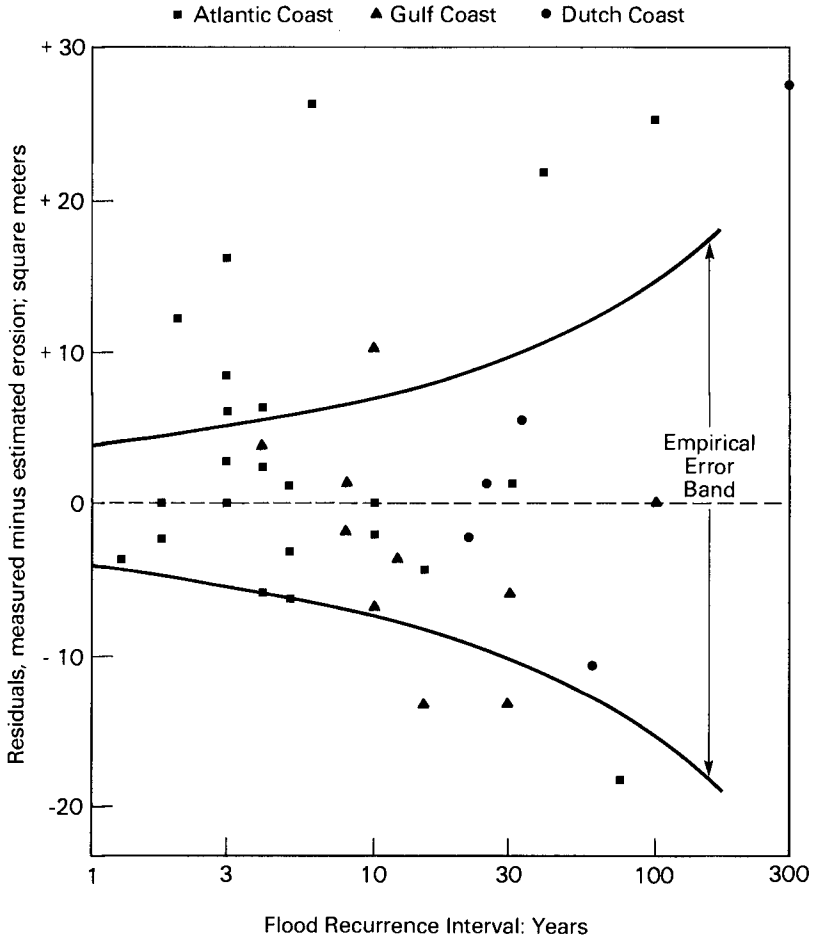


Figure 3. Residuals between measured erosion cross section and that from equation 1, for 38 cases of duneface retreat.

finding is certainly not surprising, since overwash is recognized to be a crucial process on barrier islands.

ERODED GEOMETRIES

The preceding results are expressed as a definite rule for FIS application in treating base flood effects (Federal Emergency Management Agency, 1988). For erosion to be limited to duneface retreat, an initial cross section of at least 50 m² is required above 100-year SWFL and seaward of the dune crest. With lesser cross sections, the existing dune will be considered to be completely eroded in analyzing effects of the base flood. An exception to this cross-sectional requirement may be granted at a specific site where authoritative historical documentation demonstrates that sand dunes have withstood storm surge and wave action approximating that expected for the base flood.

There is no intermediate erosion geometry between duneface retreat and dune removal. The basic reasoning is that when duneface retreat would proceed past the dune crest to the steep landward face, the dune remnant becomes susceptible to rapid and complete removal. This erosion treatment appears fundamentally consistent with the experienced field judgment expressed in original guidelines for identifying V zones (U.S. Army Engineer District, Galveston, 1975): "Unless historical data indicate that sand dunes in the area have repeatedly withstood wave attack during storms, they should not be considered as effective surge and wave barriers." New procedures permit definitive and objective analysis for the extent of sizable wave action in the base flood.

Figure 4 outlines the entire treatment of sand dune erosion appropriate in an FIS. Figure 4a indicates the Frontal Dune Reservoir examined in deciding between duneface retreat or dune removal for the base flood. Figure 4b demonstrates the geometric construction giving the retreated dune profile. Figure 4c shows the eroded profile appropriate in cases where the pre-storm dune is completely removed.

In regard to the Frontal Dune Reservoir of Figure 4a, consideration is restricted to sand located above 100-year SWFL and seaward of the steep rear slope. The vertical line as the landward boundary to the frontal dune reservoir seems a proper simplification, given that a steep escarpment occurs in duneface retreat and that sand in the rear dune wedge has some resistance to removal. The indicated reservoir is a straightforward measure for primary dunes with a prominent ridge or with a mound configuration but a marked rear slope. For some complicated dune profiles, judgment may be required to identify the dune segment expected to be fully effective in resisting removal.

The geometry for duneface retreat in Figure 4b represents a simplification of the erosion computation model developed by Delft Hydraulics Laboratory (Vellinga, 1986). Besides a

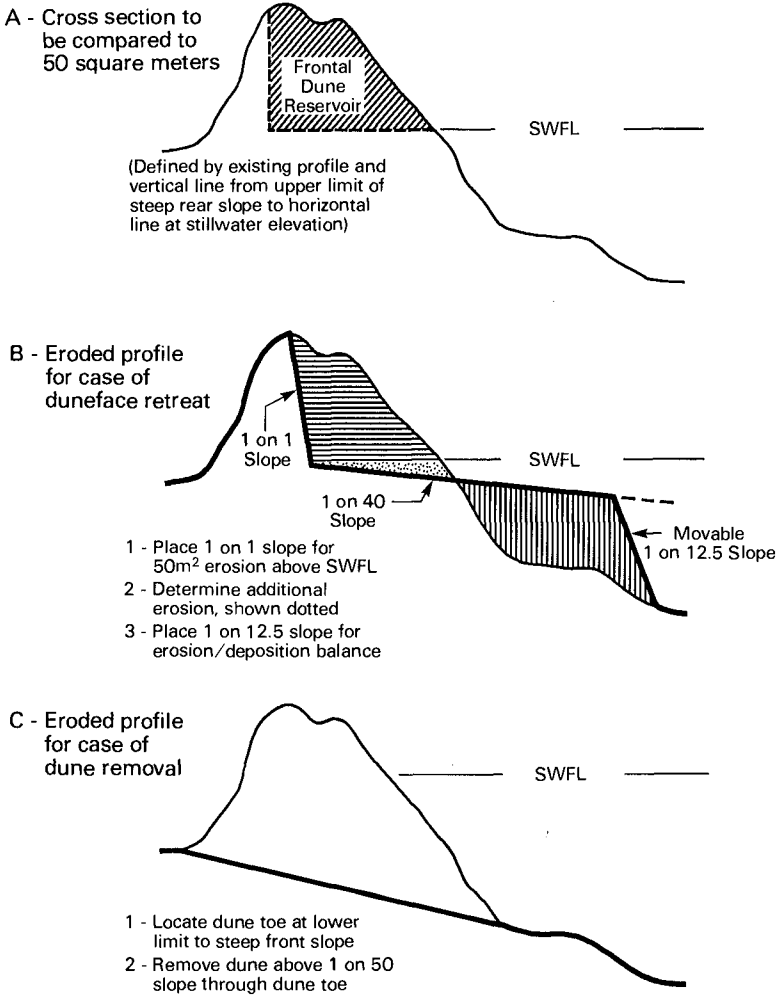


Figure 4. Treatment of sand dune erosion in 100-year event for a coastal Flood Insurance Study.

rectilinear rather than a curvilinear eroded profile, the present treatment specifies erosion above 100-year SWFL to be 50 m^2 , as expected in a generic 100-year event on the U.S. Atlantic or Gulf coasts. The constructed profile provides a balance between erosion and deposition, by adjustable seaward extent of the 1 on 40 slope segment between the 1 on 1 duneface escarpment and the 1 on 12.5 terminus to sand deposition. This eroded geometry is spliced onto unaffected landward and seaward segments of the existing profile, to give a complete transect suitable for assessing potential overwash of the dune remnant in the base flood.

Where the frontal dune reservoir is less than 50 m^2 , dune removal is effected as in Figure 4c. This procedure erases the major vertical projection of the primary frontal dune from a given transect, yielding a gentle seaward-dipping ramp for storm waves and flood waters. That ramp begins at the dune toe, defined as the seaward point on the steep duneface, with the 1 on 50 slope taken as an appropriate inclination in view of the extensive 1 on 40 slope occurring in duneface retreat with a steep landward barrier. This erosion treatment shows distinct agreement with post-storm profiles for Gulf coast cases of frontal dune removal in the 1957 Hurricane Audrey, 1965 Hurricane Betsy, 1979 Hurricane Frederic, and 1985 Hurricane Kate. There is no attempt to balance dune erosion by sand deposition elsewhere, since current knowledge of overwash processes is inadequate to address that redistribution (Birkemeier, et al., 1987).

There are major differences between eroded profiles in the two distinct categories. Duneface retreat occurs almost entirely above SWFL, but a cut at much lower elevation can take place during dune removal. For a sizable dune not meeting the stated cross-sectional criterion, erosion quantity might amount to three times that expected for duneface retreat in the 100-year event. However, potential alternatives in estimated erosion geometry for marginal dune cross sections may have diminished effects on FIS hazard assessment due to the rule that the primary frontal dune is entirely a V zone. Exceptions will occur where landward elevations in dune removal control V-zone extent.

Figure 4 procedures are intended for immediate FIS usage in treating the base flood at typical sandy sites on the U.S. Atlantic or Gulf coasts. This erosion methodology is efficient and objective, with a broad empirical basis in recorded storm effects on these coasts. Erosion estimates should be finalized with full consideration of documented historical storm effects at the particular study site.

EXAMPLE OF FIS APPLICATION

This example treats dune erosion expected to be associated with the 100-year event for a coastal site in Massachusetts. As shown in Figure 5, the shore topography is divided into two reaches, each represented by a typical

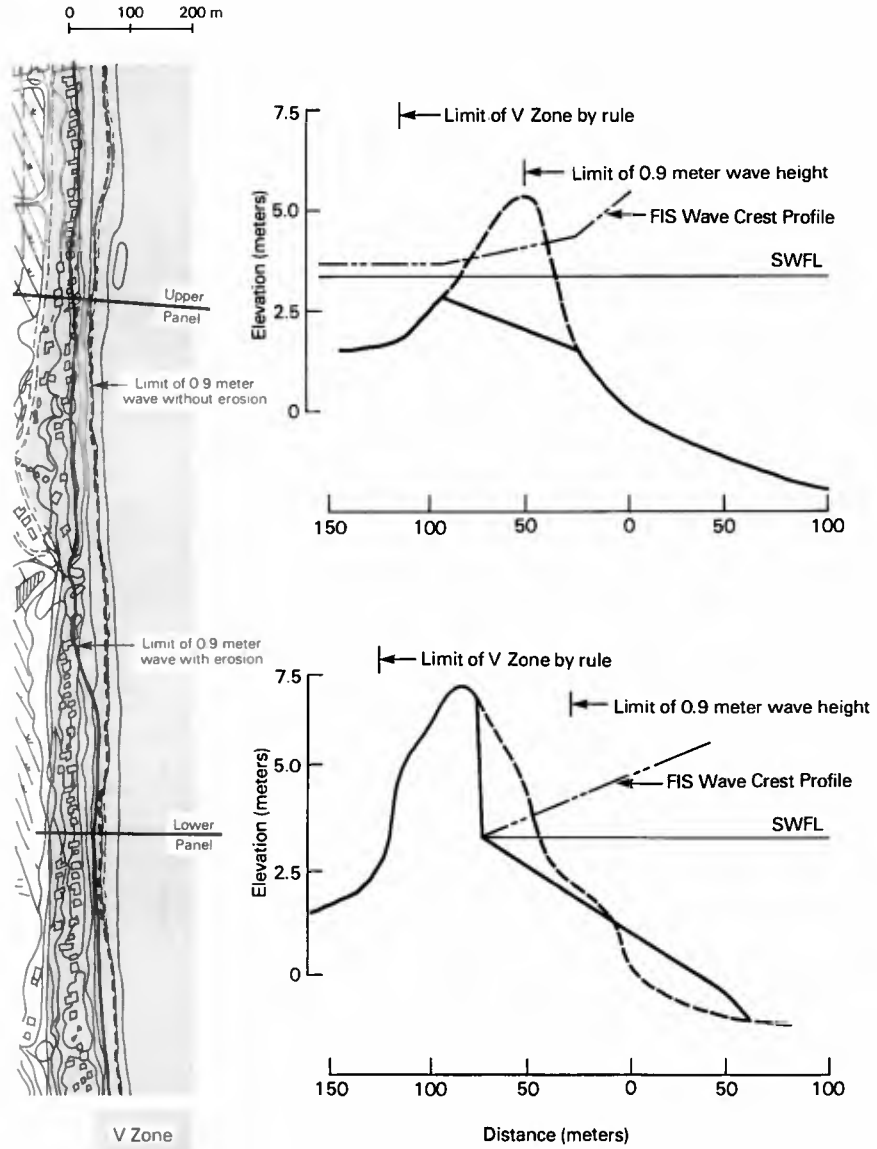


Figure 5 - Coastal topography (at left) and two representative transects in example of dune erosion treatments and FIS V Zone determination.

transect profile. On the upper transect, the Frontal Dune Reservoir is less than 50 m² so that the dune removal procedure is employed. The resultant profile is entirely submerged by the 100-year SWFL, permitting propagation of a 3-foot-high wave about to the initial dune crest. The inland limit to 3-foot wave height is generally dependent on the width of the dune, the location of the dune toe, and the SWFL.

The entire dune will be designated as V zone by NFIP rule, although the high-hazard zone according to wave height would not be so extensive in this example. For cases where the eroded profile allows the propagation of 3-foot-high waves past the pre-storm dune, the rule will have no effect since the V zone identified by wave height analysis will extend further inland. In either case of dune removal, expected erosion certainly can make the entire frontal dune an area of high hazard in the 100-year event, regardless of the wave height criterion.

The Frontal Dune Reservoir exceeds 50 m² for the other transect of Figure 5 and the duneface retreat procedure is applied. The resultant profile allows 3-foot-high waves to approximately the face of the pre-storm dune. This is slightly landward of the limit to 3-foot-high waves if no erosion is presumed. As with all cases of duneface retreat, the rule defining the primary frontal dune as V zone will fundamentally control the hazard zonation.

The V zone for FIS purposes is indicated on the topography shown in Figure 5. The limits of 3-foot wave heights with and without the erosion treatment are also delineated. This example demonstrates that dune erosion allows increased wave penetration, more so with dune removal than with duneface retreat. However, the main consequence of erosion treatment in an FIS will usually be in the determination of flood elevations including wave effects. The extent of the V zone is often controlled by the new NFIP rule, except for narrow dunes with low elevations landward.

FURTHER DISCUSSION

This erosion methodology offers maximum simplification along with the absolutely necessary distinctions for the intended application. Flood elevation and dune cross-sectional area are the predominant factors in the present schematization of expected erosion. Other site and storm characteristics are thought to affect dune erosion in a particular event, but the lack of definitive parametrizations for effects of ignored variables precludes quantitative considerations as a supplement to the present generic procedures.

One potentially important factor is the storm surge duration, since massive dune erosion must require appreciable time to occur. Also, storm intensity has been characterized by recurrence interval of local flood elevation, but erosion is actually caused by associated waves impacting

the dune. A fundamental obstruction to more detailed erosion treatment in the present application is that the base flood is simply a water elevation recurring at a definite frequency; this 100-year event cannot be specified as a certain storm surge and wave sequence. The present erosion methodology has a broad empirical basis, reflecting expected effects in various storms and thus approximating a generic event.

Another notable set of site-specific factors includes dune characteristics such as sand size, consolidation, and vegetation. Those variables must figure in dune resistance to erosion, but general quantitative guidance is not available. The present treatment is based on effects at a variety of sites, and can be expected to be usually applicable to sand dunes established by natural processes. Another presumption is that detailed dune geometry can be summarized by cross-sectional area; any independent effect of dune height can be considered in terms of wave runup and overtopping after erosion assessment is completed.

The Dutch computation model incorporates strong dependences of erosion cross section on both sand size and dune height (van de Graaff, 1986). Effects of those dependences can be compensatory only if higher dunes are naturally associated with coarser sands, which seems unlikely. Thus, the most significant factor ignored in the present treatment appears to be detailed dune characteristics, since storm intensity has been at least partially considered by means of the flood recurrence interval. Still, the relationship in Equation 1 accounts for a majority of the variance in the present data base, demonstrating the usefulness of a simplified erosion treatment. Considering the natural irregularity in erosion amounts, there appears to be little room for improvement by detailed consideration of causative and response variables.

The only site characteristics treated in the Figure 4 procedure are the 100-year SWFL and some aspects of existing shore profile. However, exceptionally wide sand beaches have been documented to limit the extent of dune erosion or wave damages during extreme storms, and such sheltering effects should be taken into account. For duneface retreat, a stable inner surf zone is provided by slope of 1 on 40, and comparable existing shore slope must limit dune erosion by effecting gradual dissipation of storm waves. That shore situation must complicate eroded profile construction with the specified duneface erosion and sand balance, but a simple and consistent adjustment of procedure might limit retreat to the point defined by 1 on 40 slope from usual sea level up to 100-year SWFL. Note that the existing profile considered should be that for the season when extreme storms are expected at the site.

The present erosion procedures are intended for sandy open-coast sites where the basic transect viewpoint is adequate. This excludes application in three-dimensional regions such

as an inlet vicinity, or near coastal structures influencing water level, waves and erosion. Even focusing on relatively ideal sites, it appears that only rather generalized erosion treatment might have a direct empirical basis since data are scarce. Present simplifications presume that erosion is mainly independent of site-specific details: existing conditions may reflect some long-term equilibrium, so that a generic response to the 100-year event can be anticipated.

OTHER APPLICATIONS

Without additional investigation, present results cannot be applied with confidence beyond the geographic limits of the data base. This guidance could be useful for quantitative erosion analyses where a simplified viewpoint suffices. Away from the 100-year recurrence interval addressed here, erosion geometries would require empirical modification: bed slopes steeper than 1 on 40 or 50 will be appropriate in dissipating smaller waves of more common storms. However, the erosion climatology of equation 1 has a broad basis and is conducive to other direct applications, for example, in designing artificial sand dunes as storm protection.

Considering a dune project with a 50-year design life, there is 50% risk of a 73-year event as the extreme, according to the binomial distribution usually employed (U.S. Interagency Advisory Committee on Water Data, 1982). That event entails erosion of a frontal dune reservoir of 44.5 m² according to equation 1. Likely storm events between dune maintenance operations determine the needed increase of the sand reservoir over that required to withstand the design storm. With a 10-year interval chosen between dune replenishments, notable expected storms (50% risk) have recurrence intervals of 14.9 and 6.1 years, presuming a berm provides protection against storms less severe than a 5-year event. Those two storms could yield additional upper-dune erosion totaling 40 m², nearly doubling advisable cross section.

Natural recovery or dune growth by aeolian processes would lessen requirements for placed sand. However, computations refer to erosion expected with established dunes, and should be increased for a safe upper bound to effects with loose sand. It seems clear that such estimates could assist in optimization of interrelated design choices: berm and dune geometries; maintenance interval and project lifetime; etc.

CONCLUDING COMMENTS

Geometries provided for duneface retreat and dune removal are recommendations for appropriate erosion treatments rather than official FIS procedures. Present results are certainly liable to improvement based on advances in detailed erosion modeling and particularly in knowledge of

dune removal processes. Fundamental simplifications here currently seem necessary and appropriate in view of the marked variability of storm-induced erosion quantities, limitations apparent in published erosion treatments, and the basic idealization in FIS consideration of base flood effects along representative transects. Given present knowledge of dune erosion processes in extreme storms, only a simple treatment of coastal erosion can be expected to provide sufficiently generic estimates for a 100-year event.

REFERENCES

- Birkemeier, W. A. (1979). "Effects of the 19 December 1977 Coastal Storm on Beaches in North Carolina and New Jersey," Shore and Beach (January), pp. 7-15.
- Birkemeier, W. A., Kraus, N. C., Sheffner, N. W., and Knowles, S. C. (1987). "Feasibility Study of Quantitative Erosion Models for Use by the Federal Emergency Management Agency in the Prediction of Coastal Flooding," Technical Report CERC-87-8, Waterways Experiment Station, Corps of Engineers, Vicksburg, Mississippi, 102 pp.
- Dewberry & Davis (1988). "Basis of Dune Erosion Treatment for Coastal Flood Insurance Studies," report to Federal Emergency Management Agency, Washington, D.C., 95 pp.
- van de Graaff, J. (1986). "Probabilistic Design of Dunes; An Example from the Netherlands," Coastal Engineering, Vol. 9, pp. 479-500.
- Federal Emergency Management Agency (1986). "Assessment of Current Procedures for the Identification of Coastal High Hazard Areas (V Zones)," Washington, D.C., 133 pp.
- Federal Emergency Management Agency (1988). "National Flood Insurance Program; Flood Plain Management Standards; Final Rule," Federal Register, Vol. 53, pp. 16269-16280.
- Florida Department of Natural Resources, Division of Beaches and Shores (1987). "Data Bank on Storm Changes in Sequential Coastal Profiles," magnetic tape, Tallahassee, Florida.
- Hallermeier, R. J., Rhodes, P. E., and Buckley, M. (1988). "Jeopardy of Frontal Dune Removal in Extreme Coastal Storms," paper submitted for publication in Science.
- Kriebel, D. L., and Dean, R. G. (1985). "Numerical Simulation of Time-Dependent Beach and Dune Erosion," Coastal Engineering, Vol. 9, pp. 221-245.
- National Academy of Sciences (1977). "Methodology for Calculating Wave Action Effects Associated with Storm Surges," Washington, D.C., 29 pp.
- U.S. Army Engineer District, Galveston (1975). "Guidelines for Identifying Coastal High Hazard Zones," Galveston, Texas, 87 pp.
- U.S. Interagency Advisory Committee on Water Data (1982). "Guidelines for Determining Flood Flow Frequency," Bulletin #17B of the Hydrology Subcommittee, U.S. Department of the Interior, Geological Survey, Reston, Virginia, 183 pp.
- Vellinga, P. (1986). "Beach and Dune Erosion During Storm Surges," Delft Hydraulics Communication No. 372, Delft, The Netherlands, 169 pp.

Calculation of On-offshore Sand Movement and Wave Deformation on Two-dimensional Wave-current Coexistent System

Koichi Kinose* ,Shuji Okushima* and Masahito Tsuru**

Abstract

In this paper, we proposed a method of calculation to predict quantitatively the on-offshore sand movement and the wave deformation on a wave-current coexistent system by assuming a river mouth. And the calculated results were compared with the experimental data obtained for the coexistent system in a two-dimensional wave tank. The distribution of wave height on the breaker zone was analyzed by use of BORE MODEL. It was required for the calculation of the sand transport rate. The model was established on the assumption that the value of energy loss in a breaking wave was equivalent to that of bore. The wave height distribution on the offshore side of breaking point was presumed employing the third order approximate solution of Stokian wave on the coexistent system. The breaking point was obtained by use of Miche's criteria equation. The local sand transport rate could be calculated by use of POWER MODEL. The predominant direction of sand drift was recognized using relations for judgement which were derived from the experimental results. The transformation of sea bottom and river one was estimated on the basis of the calculated distributions of the wave height and the sand transport rate. The results obtained by this analytical method agreed well with the experimental results.

I. Introduction

In order to perform studies about closure of river mouth by sand drift, it is necessary to have a deep understanding of wave deformation and sand movements on a wave-current coexistent system where waves and the steady flow interact. Inman and Bowen¹⁾, Abou-Seida²⁾ and Tanaka et al.³⁾ have made experiments on

* National Research Institute of Agricultural Engineering
2-1-2, Kannondai, Tsukuba-shi, Ibaraki, 305 Japan.

** Department of Civil Engineering, Science University of Tokyo

sand transport rates and shapes of ripples under wave-current coexistent system. Watanabe⁴⁾ proposed a bed load formula applicable to coexistent system on the basis of a power model. Jonsson⁵⁾ and Sakai et al.⁶⁾ have calculated wave shoaling on coexistent system. In the present work, we will try as the initial step to construct a model simulating the on-offshore sand movement, the wave deformation due to wave and steady flow, and the two-dimensional bottom transformation. For this analysis, we considered the wave-current coexisting system by assuming a river mouth as shown in Fig.1. In addition, the results will be compared with the experimental data measured in a wave tank.

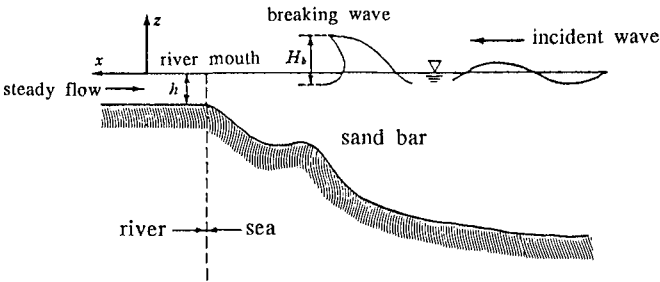


Fig.1 Wave-current coexistent system assumed to be river mouth.

II. Distribution of on-offshore sand transport rate

The sand transport rate on the wave-current coexistent system will be discussed in this chapter for the estimation of sea and river mouth bottom transformation.

2.1 Bed load formula

The local transport rate of bed load at a given point could be estimated by use of the power model proposed by Watanabe⁴⁾. The transport rate per unit width, q_{net} , can be obtained as the sum of the component q_w caused by wave motion and the component q_f caused by steady flow.

$$\begin{aligned}
 q_f &= A_f \frac{\tau - \tau_c}{\rho g} U_f \\
 q_w &= A_w \frac{\tau - \tau_c}{\rho g} U_w
 \end{aligned}
 \tag{1}$$

where A_w and A_f are non-dimensional constants, respectively, which are to be determined from laboratory or field data, τ is the maximum bed shear stress, τ_c is the critical shear stress, ρ is the fluid density, and g is the acceleration of gravity. U_f is the velocity of the steady flow and U_w is the bottom velocity amplitude of

orbital motion induced by wave. The critical shear stress can be obtained from the critical Shields parameter ψ_c ⁴.

$$\begin{aligned}\psi_c &= 0.11 \text{ for } d/\delta_L < 1/6.5 \quad (\text{fine sand}) \\ \psi_c &= 0.06 \text{ for } d/\delta_L > 1/4.0 \quad (\text{coarse sand}) \quad (2) \\ \psi_c &= \frac{\tau_c}{\rho s g d}, \quad \delta_L = \sqrt{\frac{\nu T}{\pi}}\end{aligned}$$

where d is the median diameter of the sand, s is the specific gravity of immersed sand, δ_L is the thickness parameter of the boundary layer, ν is the kinematic viscosity of the fluid, and T is the wave period. When the diameter is intermediate between fine sand and coarse sand, the value of ψ_c is determined by interpolation. The value of q_w and q_f given by equation(1) are the net transport rate. On the assumption of a rough bottom, the value of τ can be obtained from the friction law proposed by Tanaka and Shuto⁵) for the coexistent system. The friction law is shown in the Appendix.

Based on the above discussion, the local net transport rate, q_{net} , is given by

$$q_{net} = q_f + q_w \quad (3)$$

2.2 Expression of velocity field

By analogy with the analysis of phenomena in the vicinity of river mouth, the direction of the steady flow is considered to be offshore. Assuming that waves progress up a steady flow, the bottom velocity amplitude of orbital motion induced by the wave can be indicated from a small amplitude wave theory.

$$U_w = \frac{\pi H/L(L/T + U_f)}{\sinh kh} \quad (4)$$

where H is the wave height, h is the water depth, and L , k are the wave length and the wave number, respectively. The values of L and k are given by the following equations.

$$\begin{aligned}C &= \frac{L}{T} + U_f = \left(\frac{g L}{2\pi} \tanh kh \right)^{1/2} \\ k &= \frac{2\pi}{L}\end{aligned} \quad (5)$$

where C is the relative wave celerity to the steady flow. If the velocity of the steady flow exceeds a critical value, the wave does not progress up the steady flow. Its critical velocity U_{fc} can be obtained by

$$U_{fc} = \frac{C_0}{4} \tanh kh \quad (6)$$

where C_0 is the wave celerity at the deep water free from the effect of the steady flow. When $U_f > U_{fc}$, it is assumed that only the steady flow acts as the driving force of sand drift.

On the other hand, the vertically averaged velocity, U_f , is used for the calculation of the sand drift component, q_f . That is,

$$U_f = \frac{q_c}{h} \quad (7)$$

where q_c is the discharge per unit width.

2.3 Judgment of predominant direction of sand drift

The direction of the sand drift, q_f , is offshore, because the flow direction is considered to be offshore like that in the river mouth. But the predominant direction of q_w does not necessarily coincide with the direction of wave progress. Sunamura⁶⁾ has indicated that the direction of sand drift might change under the condition where equation(8) is satisfied.

$$\Phi = \gamma U_{r0} \quad (8)$$

where γ is an empirical constant, Φ is Hallermeier's parameter, and U_{r0} is Ursell parameter. They are expressed as follows by the long wave assumption, respectively.

$$\Phi = \frac{H^2}{s d h} \quad , \quad U_{r0} = \frac{g T^2 H}{h^2} \quad (9)$$

However, equation(8) is found from an experimental study of an uniformly sloping movable bed in a non-coexistent system where only wave acts. Sunamura has concluded that γ was equal to 0.13 on the surf zone in his experiments.

Taking the effect of the steady flow into consideration, equations(8) and (9) must be modified for the analysis of the wave-current coexistent system. The Ursell parameter on the coexistent system is shown as the following equation by applying the long wave assumption to the wave celerity, C , in the equation(5).

$$U_r = U_{r0} \left(1 - \frac{1}{2} \frac{H}{h} \frac{U_f}{U_w} \right)^2 \quad (10)$$

The relative intensity U_f/U_w in the above equation, which indicates a relative intensity ratio of the steady flow to the wave, was introduced for the judgment of the predominant direction of the sand drift, q_w . Using these parameters the judgment can be done as the follows. The zone of sand movement by wave and steady flow is divided into two regions; *pre-breaking* and *post-breaking region*.

In the post-breaking region, the values of Φ and U_r are calculated by use of equations(9) and (10), respectively, and a point, x_h , where the relation of Φ and U_r satisfies equation(11), is searched.

$$\Phi = \gamma U_r \quad (11)$$

Here, the value of U_f/U_w at point x_h is supposed to be β .

The direction of sand drift, q_w , induced by wave motion can be recognized using relations in equation(12).

$$\begin{aligned} \text{if } \beta > 0.15 & \quad \text{then offshore for all over the surf zone} \\ \text{if } \beta \leq 0.15 \text{ and } U_f/U_w > \beta & \quad \text{then offshore at a given point.} \\ \text{if } \beta \leq 0.15 \text{ and } U_f/U_w \leq \beta & \quad \text{then onshore at a given point.} \end{aligned} \quad (12)$$

In the pre-breaking region, we employ the relations shown in equation(13) .

$$\begin{aligned} \text{if } U_f/U_w > 0.15 & \quad \text{then offshore at a given point.} \\ \text{if } U_f/U_w \leq 0.15 & \quad \text{then onshore at a given point.} \end{aligned} \quad (13)$$

The critical value (0.15) of β could be given from the results of our previous experimental study⁷⁾.

III. Wave deformation of incoming waves on coexistent system

The wave height variation due to changes of depth and velocity of the steady flow will be considered. The zone of wave deformation is also divided into two regions; *pre-breaking* and *post-breaking region*.

3.1 Wave shoaling and breaking criterion

In the pre-breaking region, we employ the equation given by Sakai, Saeki and Ozaki⁸⁾ to calculate the wave deformation. This equation is the third order approximate solution of Stokian wave on the wave-current coexistent system. It is introduced on the basis of a wave energy flux conservation. The solution is shown in the Appendix.

Miche's criterion can be valid for a breaking criterion of regular waves on the coexistent system, as being pointed out by Iwagaki⁹⁾ and Sakai¹⁰⁾.

$$\left(\frac{H}{L}\right)_b = \alpha \tanh(kh)_b \quad (14)$$

where subscript b indicates the quantities of the breaking point. The value of α is equal to 0.142 in the case of only wave action. But in the wave-current coexistent system, its value is inclined to decrease according to the increase of the velocity. The breaking point can be calculated by using the ratio of water depth to wave length obtained from the wave height calculation mentioned above.

3.2 Wave height distribution in post-breaking region

In order to obtain the wave height distribution in the post-breaking region, it was assumed that breaking wave has the same process as that of the energy dissipation in bores. The energy loss per unit width of bore is given by

$$\Delta E' = \frac{1}{4} \rho g (h_2 - h_1)^3 \sqrt{\frac{g(h_1 + h_2)}{2h_1h_2}} \quad (15)$$

where h_1 and h_2 are the water depths before and after bore, respectively. The energy loss¹¹⁾ per unit length can be represented by the following equation(16) on the basis of the long wave assumption.

$$h^2 = h_1 \cdot h_2$$

$$\Delta E = \frac{\Delta E'}{L} = \frac{\Delta E'}{CT} = \frac{B}{4} \frac{\rho g H^2}{T} \left(\frac{H}{h} \right) \quad (16)$$

where B is

$$B = \frac{(h_2 - h_1)^3}{H^3} \quad (17)$$

where H is the wave height at a given point in the surf zone.

The wave energy flux taking the mean energy level as a reference on the wave-current coexistent system was given by Jonsson¹²⁾. That is,

$$E = \frac{1}{8} \rho g H^2 (C_g - U_f) \left(1 - \frac{U_f}{C} \right) \quad (18)$$

where C and C_g are the relative wave celerity and the relative wave group celerity to the steady flow, respectively. They can be obtained by use of equation(5). In a shallow water, this equation becomes,

$$E = \frac{1}{8} \rho g H^2 \left(\sqrt{gh} - U_f \right) \left(1 - \frac{U_f}{\sqrt{gh}} \right) \quad (19)$$

Based on the assumptions discussed above, the wave height after breaking is able to be given by the energy flux conservation equation.

$$\frac{dE}{dx} + \Delta E = 0 \quad (20)$$

The x-axis is taken as pointing onshore direction. In order to calculate the wave height distribution in the surf zone for an arbitrary bottom configuration, we performed a numerical solution using equations(16) and (19). In the breaking waves, a turbulent kinetic energy is produced in the surface roller. In addition, turbulence is also induced by the systematic eddy near the breaking point. Consequently, the value of B in equation(16) depends on the location of the surf zone. However, the value on the wave-current coexistent system could not be known in detail. Therefore, the following equations, which were given for a non-coexistent system by Mase¹³⁾, had to be used.

i) In cases that $m > 1/20$

$$0.9 < h/h_b \leq 1.0 : B = 1$$

$$0.6 < h/h_b \leq 0.9 : B = 13 - \frac{40}{3} \frac{h}{h_b} \quad (21)$$

ii) In cases that $m < 1/20$

$$\begin{aligned} 0.6 < h/h_b < 1.0 & : B = 11 - 10 \frac{h}{h_b} \\ h/h_b \leq 0.6 & : B = 5 \end{aligned} \quad (22)$$

where h_b is the breaking water depth and m is the beach slope.

IV. Prediction of bottom profile transformation

The continuity equation for the bottom material is indicated as follows.

$$\frac{\partial z_b}{\partial t} = - \frac{\partial h}{\partial t} = - \frac{\partial q_{net}}{\partial x} \quad (23)$$

where z_b is the bottom level taking the still water level as a reference, and t is the elapsed time from the beginning of the wave-current action. In the practical numerical analysis, the following equation⁴⁾ was employed to restrain the appearances of radical irregular bottom profiles and steep gradients of the bottom more than the angle of repose of the immersed sand. These phenomena may not occur in real beaches.

$$\frac{\partial z_b}{\partial t} = - \frac{\partial}{\partial x} \left(q_{net} - \epsilon_s |q_{net}| \frac{\partial z_b}{\partial x} \right) \quad (24)$$

where ϵ_s is the positive constant. In addition, we used a finite difference method in which staggered mesh scheme is applied to equation(24). The stability of the calculus is indicated by

$$\Delta t \leq \frac{1}{2} \frac{\Delta x^2}{\epsilon_s |q_{max}|} \quad (25)$$

where q_{max} is the maximum value of q_{net} .

V. Comparison between experimental and calculated results

The comparison between the experimental and the calculated results will be discussed in this chapter. Assuming a river mouth as shown in Fig.2, the experiments on the wave-current coexistent system were carried out under the conditions as listed in Table 1. The experimental apparatus consisted of a piston-type wave maker and a pump for the generation of the steady flow in a wave tank(30m long, 1.0m high, and 0.6m wide).

5.1 Method of experiment

A model was formed out of the sand listed in Table 1. It was composed of two parts; the river mouth(4m long, flat) and the sloping beach(12m long, 1/20). The wave height and the change of bottom profile induced by wave and steady flow were measured with spaces of 1cm by use of wave gauge and sand-level-meter which were loaded on the observation truck.

Table 1 Condition of experiments.

Case	(1) q _c (cm ² /s)	(2) H ₀ (cm)	(3) T(s)	(4) h(cm)	(5) (cm/s)	(6) Fr	(7) d ₅₀ (mm)	(8) s	C _s
A	197.2	6.49	2.2	4.38	45.02	0.69	0.37	1.72	2.96
B	138.2	6.49	2.2	4.86	28.43	0.41	0.37	1.72	2.96
C	35.8	4.68	2.2	6.96	5.13	0.062	0.28	1.44	2.57
D	133.6	17.51	1.6	8.25	16.20	0.18	0.28	1.44	11.86

- (1): discharge per unit width
- (2): wave height
- (3): wave period
- (4): depth of river mouth
- (5): velocity at river mouth
- (6): Froude number
- (7): median diameter of sand
- (8): specific gravity of immersed sand

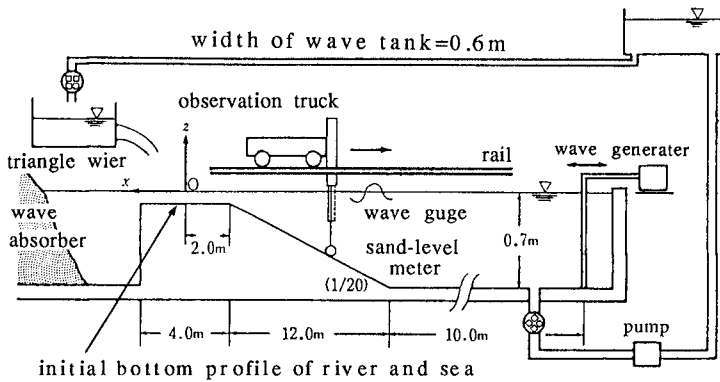


Fig.2 Schematic drawing of experimental apparatus for wave-current coexistent system.

The net transport rate of sand drift was calculated from the profile change at 20-minute intervals by use of the difference equation of equation(23). In Table 1, the waves which caused an accretion of the beach were worked for Cases of A, B and C, and in the Case of D the wave produced an erosion of the beach. In addition, the classification of the wave-type for two-dimensional laboratory beach transformation in terms of a parameter, C_s, was used here. It was proposed by Sunamura and Horikawa¹⁴⁾.

$$\frac{H_0}{L_0} = C_s \cdot m^{-0.27} \cdot \left(\frac{d}{L_0}\right)^{0.67} \tag{26}$$

where H_0 is the deep water wave height and L_0 is the deep water wave length. If $C_s < 4$, the beach is accreted, while if $C_s > 8$, the beach is eroded.

5.2 Wave height distribution

Figs.3(a) through (d) show the comparison between the experimental and calculated results of the wave height distribution. In determining the breaking height on the wave-current coexistent system for the numerical calculation, the value of α in equation(14) was taken as 0.132. The bottom profiles at the time of wave height measurement are also shown in the figures. These bottom profiles are used for the calculation of the wave height. Figs.3(a) through (c) and (d) correspond to cases of plunging breaker and spilling breaker, respectively. The calculated results for the wave height near the breaking point in the case of spilling breaker have a tendency to give smaller values than the experimental results as shown in Fig.3(d). But good agreements are found between the experimental and calculated results in the cases of plunging breaker. From the above results, it may be concluded that the wave height calculation model succeeds fairly well in predicting the experimental results.

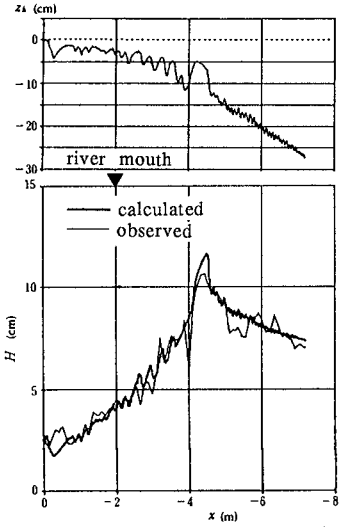
5.3 Distribution of sand transport rate

Figs.4(a) through (d) show the comparison between the experimental and calculated distributions of the sand transport rate. Here, in order to match with the wave height calculation, the bed velocity amplitude U_w in the pre-breaking region was calculated by use of the third order approximate solution of Stokian wave. In the post-breaking region, U_w is obtained using the linear long wave theory.

The procedures of the calculation for the transport rate, q_{net} , will be illustrated in the following;

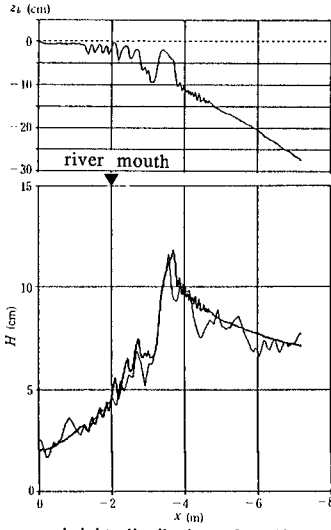
- 1) The local transport rate at a given point is calculated by use of equations(1) through (7) under the assumption of $A_f = |A_w| = 1$.
- 2) The predominant direction of transport rate, q_w , at a given point is judged with equations(9) through (13). If the direction is offshore, A_w is equal to 1, while if the direction is onshore, A_w is equal to -1.
- 3) Comparing the peak value of the calculated distribution of transport rate with that of observed distribution and finding the both peak values to be equal each other, then the $A_f (= |A_w|)$ is required one.
- 4) The final value of the transport rate at the each point is obtained multiplying the value of the transport rate given in procedure 1) by $A_f (= |A_w|)$ gotten above.

(a) Case A
bottom profile formed by action of wave
and steady flow for 60 minutes.



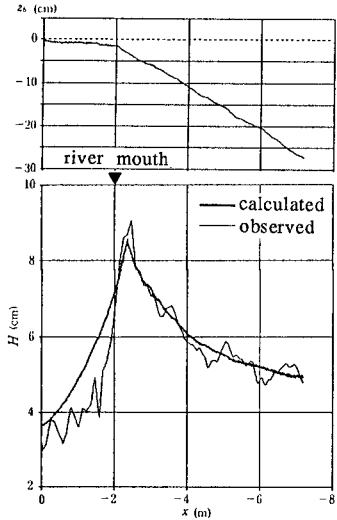
wave height distribution after 60 minutes.

(b) Case B
bottom profile formed by action of wave
and steady flow for 40 minutes.



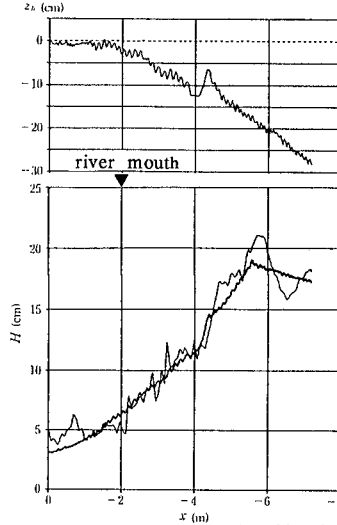
wave height distribution after 40 minutes.

(c) Case C
bottom profile just before action of wave
and steady.



wave height distribution after 1 minutes.

(d) Case D
bottom profile formed by action of wave
and steady flow for 20 minutes.



wave height distribution after 20 minutes.

Fig.3 Comparison between calculated and experimental results of wave height.

In determining the direction of sand drift at the each point, the value of γ in equation(11) is taken as 0.32 for the numerical calculation. In the calculations, the both values of A_f and $|A_w|$ are taken to be equal for all over the surf zone. The values obtained from the experiments are shown in Fig.5.

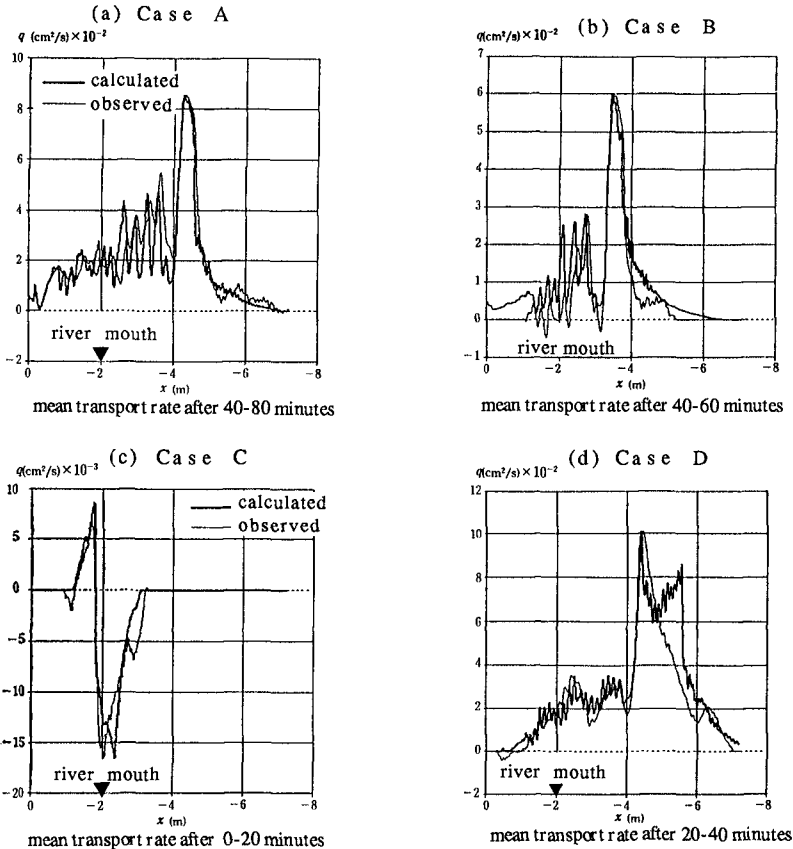


Fig.4 Comparison between calculated results and experimental results of distributions of on-offshore transport rate.

5.4 Beach profile transformation

Fig.6 shows an example of the calculated bottom profile, and it is compared with the experimental data in Case of C. The profile was formed under the action of wave and current for 20 minutes, and the initial profile which was observed just before beginning of wave-current action is shown in Fig.3(c). Using the calculated distributions of the wave height and the sand transport rate, the prediction of bottom transformation was done at intervals of 1cm

from the difference equation of equation(24) under the conditions of $\epsilon_s=2.0$ and $\Delta t=10\text{sec}$. The value of A_f or A_w for the sand transport rate calculation was obtained from the experimental results as shown in Fig.5. In average, the profile calculated by use of this model agrees well with that obtained from the experiment.

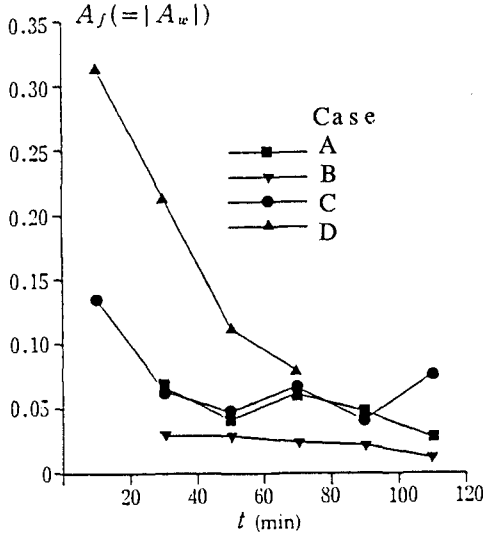
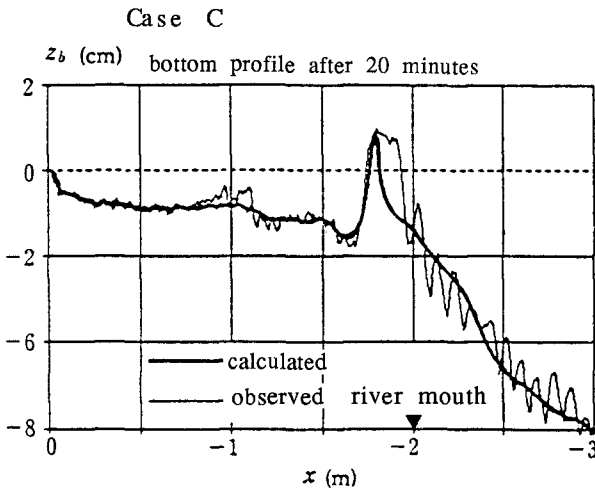


Fig.5 Change of value $A_f (= |A_w|)$ with elapsed time.



initial profile of bottom is shown in Fig.3(c)

Fig.6 An example of calculation for beach transformation due to wave and current.

VI. Conclusion

The conclusions in this study are indicated as follows;

- 1) The local transport rate of sand drift in the both regions of pre-breaking and post-breaking could be estimated with the application of the bed load formula proposed by Watanabe.
- 2) The predominant direction of sand drift could be recognized using the judgment equation which was derived from our previous study.
- 3) The distribution of wave height on the post-breaking region could be analyzed by use of a bore model. And the distribution in the pre-breaking region could be obtained from the third order approximate solution of Stokian wave on the coexistent system.
- 4) The prediction of the bottom transformation in the two-dimensional coexistent system could be done by use of the equation of continuity of the sand transport rate.
- 5) The results obtained by this analytical model agreed well the experimental results of laboratory. That is, the model developed in this paper is capable of describing aspects of two-dimensional sand movement, wave deformation and beach transformation on a wave-current coexistent system.

Appendix

(1) The friction law for the wave-current coexistent system

The next equations indicate the friction law given by Tanaka and Shuto⁵⁾ on the assumption of rough bottom.

(i) Friction coefficient

$$f_{cw} = 2B \left(\frac{\bar{u}_c}{\hat{u}_w} \right)^2 + 4BC \frac{\bar{u}_c}{\hat{u}_w} \cos \alpha + 2C^2$$

$$B = \frac{\kappa}{\ln(h/z_0) - 1}$$

$$C = \begin{cases} \frac{\kappa}{\pi} \left\{ 0.25 + 0.101 \left(\ln \frac{\sigma z_0}{\hat{u}_w} - \frac{1}{2} \ln f_{cw} + 0.24 \right)^2 \right\}^{-1/2}, & \frac{\hat{u}_w}{\sigma z_0} \geq 50 \\ 0.738 f_{cw}^{-1/4} \left(\frac{\hat{u}_w}{\sigma z_0} \right)^{-0.408}, & 50 \geq \frac{\hat{u}_w}{\sigma z_0} \geq 10 \end{cases}$$

where f_{cw} is the friction coefficient, z_0 is the roughness length, \bar{u}_c is the velocity averaged over the section of steady flow, \hat{u}_w is the bottom velocity amplitude of orbital motion induced by wave and σ is the angular frequency.

(ii) Maximum Shear stress on the coexistent system

$$\tau = \frac{1}{2} \rho f_{cw} \hat{u}_w^2$$

where τ is the maximum shear stress acting to the bottom.

2) *The third order approximate solution of Stokian wave on the wave-current coexistent system.*

The next equations indicate the third order approximate solution of Stokian wave given by Sakai, Saeki and Ozaki⁸⁾.

(i) Velocity potential

$$\Phi = Ux + \frac{C-U}{k} \{ (\lambda A_{11} + \lambda^3 A_{13}) \times \cosh k(h+z) \sin\theta + \lambda^2 A_2 \cosh 2k(h+z) \sin 2\theta + \lambda^3 A_3 \cosh 3k(h+z) \sin 3\theta \}$$

$$\zeta = \frac{1}{k} (\lambda f_1 \cos\theta + \lambda^2 f_2 \cos 2\theta + \lambda^3 f_3 \cos 3\theta)$$

$$B = B_0 + \lambda B_1 + \lambda^2 B_2 + \lambda^3 B_3$$

$$C = C_0 + \lambda C_1 + \lambda^2 C_2 + \lambda^3 C_3$$

$$k = 2\pi/L, \lambda = ka, \theta = k(x - Ct)$$

$$\begin{aligned} A_{11} &= \frac{1}{\sinh\beta} & , & & f_2 &= \frac{1}{4} \frac{\cosh\beta}{\sinh^3\beta} (\cosh 2\beta + 2) \\ A_{13} &= -\frac{\cosh^2\beta}{8\sinh^5\beta} (5\cosh^2\beta + 1) & , & & f_3 &= \frac{3}{64} \frac{8\cosh^6\beta + 1}{\sinh^6\beta} \\ A_2 &= \frac{3}{8} \frac{1}{\sinh^4\beta} & , & & B &= \frac{U^2}{2} + \frac{a^2 g}{2} k \frac{1}{\sinh 2\beta} \\ A_3 &= \frac{1}{64} \frac{11 - 2\cosh 2\beta}{\sinh^7\beta} & , & & (C-U)^2 &= \frac{g}{k} \tanh\beta \left(1 + \frac{\lambda^2 \cosh 4\beta + 8}{8 \sinh^4\beta} \right) \\ f_1 &= 1 & , & & \pi \frac{H}{L} &= \left(\lambda + \frac{3}{64} \lambda^3 \frac{8\cosh^6\beta + 1}{\sinh^6\beta} \right) \end{aligned}$$

$$\beta = kh$$

where Φ is the velocity potential, ζ is the surface level variation, L is the wave length and H is the wave height.

(ii) Energy flux

$$W = \rho \frac{C}{k} \{ U(C-U) Q_1 + (C-U)^2 Q_2 \}$$

$$Q_1 = \lambda^2 \frac{1}{\sinh^2\beta} \left[\frac{1}{2} \sinh\beta \cosh\beta + \frac{\lambda^2}{32} \frac{\cosh\beta}{\sinh^5\beta} \{ -4\cosh^6\beta + 20\cosh^4\beta - 16\cosh^2\beta + 9 \} \right]$$

$$\begin{aligned} Q_2 &= \lambda^2 \frac{1}{\sinh^2\beta} \left[\frac{1}{4} (\sinh\beta \cosh\beta + \beta) + \frac{\lambda^2}{8} \left\{ \frac{1}{8\sinh^6\beta} (\sinh\beta \cosh\beta + \beta) \right. \right. \\ &\quad \times (-20\cosh^6\beta + 16\cosh^4\beta + 4\cosh^2\beta + 9) + \frac{\cosh\beta}{4\sinh^3\beta} \\ &\quad \left. \left. \times (16\cosh^4\beta + 2\cosh^2\beta + 9) \right\} \right] \end{aligned}$$

where W is the energy flux, U is the velocity of steady flow and C is the relative wave celerity.

References

- (1) Inman, D. L. and A. J. Bowen: Flume experiments on sand transport by waves and Currents, Proc. 8th Conf. on Coastal Engng., pp.137-150, 1963.
- (2) Abou-Seida, M. M: Sediment transport by waves and current, Tech. Rep. No.HEL-2-7, Univ. of California, Berkley, 1964.
- (3) Tanaka, H., H. Ozasa and A. Ogasawara: Experiments on sand movement by waves and current, Rep. Port & Harbor Res. Inst., Vol.12, No.4, 1973 (in Japanese).
- (4) Watanabe, A., K. Maruyama, T. Shimuzu and T. Sakakiyama: Numerical prediction model of three-dimensional beach deformation around coastal structures, Proc. of Japanese Conf. on Coastal Engng., pp.406-410, 1984(in Japanese).
- (5) Tanaka, H. and N. Shuto: Friction coefficient for a wave-current coexistent system, Coastal Engng. in Japan. Vol.24, pp.105-128, 1981.
- (6) Sunamura, T: Prediction of on-offshore sediment transport rate in the surf zone including swash zone, Proc. of Japanese Conf. of Coastal Engng., pp.316-320, 1984(in Japanese).
- (7) Kinose, K. and S. Okushima: Sand transport near sand bar on two-dimensional wave current coexistent system, Proc of '87 Annual Meeting of Japan Society of Irrigation, drainage and Reclamation Engng., pp.68-69, 1987(in Japanese).
- (8) Sakai, S. and A. Ozaki: Effect of Current on wave Shoaling, Proc. of 29th Japanese Conf. on Coastal Engng., pp.70-74, 1982(in Japanese)
- (9) Iwagaki, Y, T. Asano, T. Yamanaka and F. Nagai: Fundamental study on breaking of waves due to currents, Proc. of 27th Japanese Conf. on Coastal Engng., pp.30-34, 1980(in Japanese).
- (10) Sakai, S., K. Ota, H. Oba, T. Kuribayashi and H. Saeki: Shoaling of irregular waves affected by opposing current, Proc. of Japanese Conf. on Coastal Engng., pp.224-228, 1985(in Japanese).
- (11) Mase, H., A. Matsumoto and Y. Iwagaki: Calculation of random wave transformation in shallow water, Proc. of JSCE, No.375 /II-6, pp.221-230, 1986(in Japanese).
- (12) Jonsson, I.G and J.D. Wang: Interaction between wave and current, Proc. of 12th Conf. on Coastal Engng., pp.489-507, 1970.
- (13) Mase H. and Y. Iwagaki: Wave height distributions and wave grouping in surf zone, Proc. of 18th Conf. on Coastal Engng., pp.58-69, 1982.
- (14) Sunamura, T. and K. Horikawa: Two-dimensional beach transformation due to waves, Proc. of 14th Conf. on Coastal Engng., pp.920-938, 1974.

CHAPTER 91

MOVABLE-BED EXPERIMENTS OF SHANTOU HARBOR

Huang Jianwei*

ABSTRACT

The paper, based on the macroscopic analysis of the sediment movement, deals with the movable-bed model experiments of the coast under the combined action of the wave and tidal current. By these experiments we mainly desire to solve the problem of the way how to regulate the outer sandbar, including the rational trend of the guide dike, its length and the expected siltation amount in the navigation channel.

1. INTRODUCTION

Shantou Harbor is an important commercial port in the north-east of Guandong Province and lies at the estuary which is the junction of two rivers, i.e. Rongjiang and Hanjiang.

As the result of the sediments transported from the upstream, i.e. Rongjiang and Hanjiang, the tide and wave actions in the seaboard region as well as the influence of coastal reclamation, the sediment deposits in the harbor basin in the inner navigation channel of Shantou Harbor have grown up. Especially, the development of the sandbar in the outer navigation channel not only affects the navigable depth of the passage of Shantou Harbor, but will obstructs the further expansion of the deep-water berth of the harbor as well.

The navigation channel outside of Shantou Harbor was dredged three times respectively in 1977, 1979 and 1980. However, the dredged channels were still silted up to the original states between six and nine months after dredging them. The obstruction of the further development of Shantou Harbor by the outer sandbar and the severe silting conditions after dredging of the outer navigation channel have attracted much attention of the production and construction departments concerned as well as scientific research institutions.

*Senior Engineer, Nanjing Hydraulic Research Institute, China

2. PROBLEMS ENCOUNTERED IN THE DESIGN OF COASTAL MOVABLE-BED MODEL UNDER THE COMBINED ACTION OF WAVE AND TIDE

2.1 About in-shore and off-shore models

French scholar C. Migniot, after summing up the experiences of movable-bed model for the investigation of the French coast, pointed out that with our gradual understanding of sediment transport process, the laws governing these natural phenomena have been found to be more and more complicated and the similarity of all conditions to the prototype can hardly be obtained in the same model for sediment study. Therefore, making selections from reproduction phenomena are required and the model scales specially used for the selected experiment type would be adopted. Portugal scholar Castanho, Canadian scholar J.W. Kamphuis and Chinese scholar Chen Zixia have made some specialized discussions in this respect. Especially Kamphuis explicitly divides a coastal movable-bed model into two kinds, i.e. inshore model and offshore model. Either of these two kinds of model, however, lays respective emphasis on its reproduction. They have different condition of similarity and different sediment transport scale and scale of scouring and silting time.

Basing upon the findings in our experiments as well as our specific purpose of experiment and specific district, we use the movable-bed model for regulation of the outer sandbar --- the offshore model, and movable-bed model for sand catching effect by sediment retention dike --- inshore model.

2.2 About rate of distortion of the coastal movable-bed model under combined action of wave and tide

In the experiments on the movable-bed model for sandbar regulation, it is necessary to stimulate the combined action of two dynamic effects by the wave and tide at the same time. A distorted model should also be made, because both the similarity requirements of the sediment under the combined action of the wave and tide and the problems of the experimental equipment and sand material should almost be considered.

According to the few examples that can be found for the time being the rate of distortion of coastal movable-bed models under the combined action of wave and tide is from 3 to 8.

It may be seen from the description above-mentioned that, if the wave diffraction is not selected as the key conjunction in the model reproduction and proper material taken as the model sand to satisfy the starting similarity and the falling similarity of the sediment movement, some model distortion should be allowable.

3. MOVABLE-BED MODEL TESTS FOR THE SANDBAR REGULATION

3.1 Analyses of evolution and grain size of the sediment

The sandbar in the navigation channel outside of Shantou Harbor was dredged four times respectively in September of 1977, July of 1979, October of 1980 and September of 1981. The cross sections of the excavated channel after silting are shown in Fig.1.

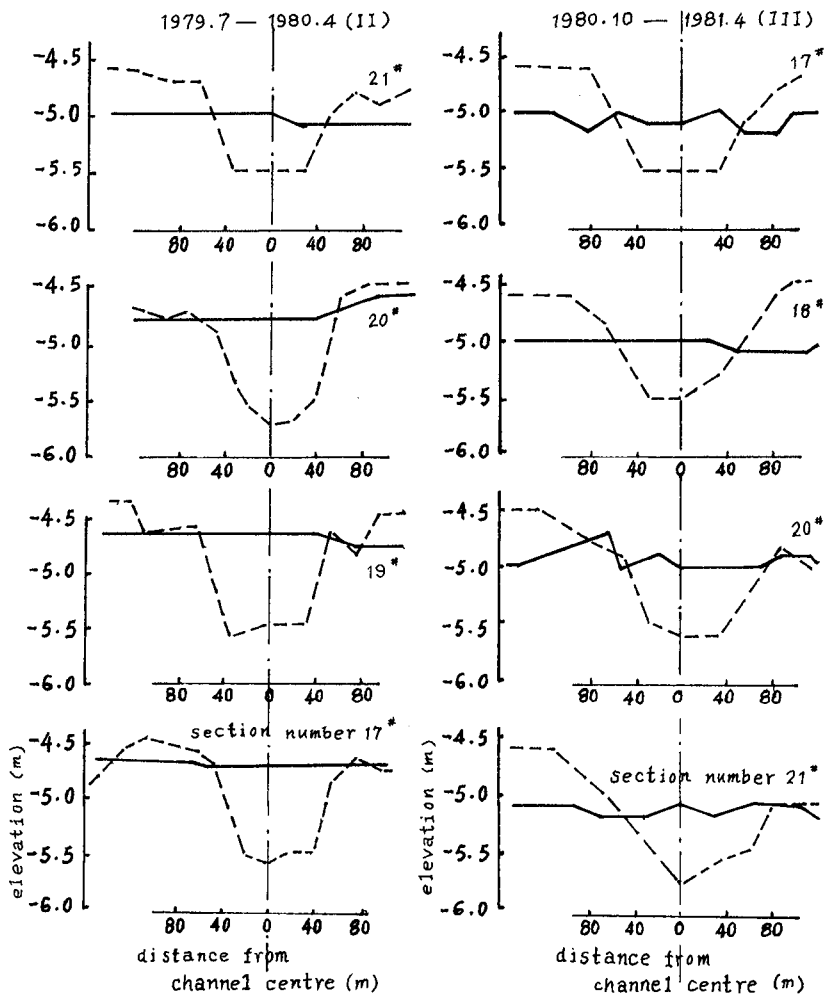


Fig.1 Variations in cross sections of the outer navigation channel after the first and second time's excavating

It can be seen from Fig.1, after the excavating of the first three times, from 1977 to 1981, the excavated channel was silted up respectively within 8, 9 and 6 months, the range of which being 150m wide on east and west side of the channel. There existed no evident navigation channel at all. The mean water depth after silting-up basically restored to be natural water depth of the year before 1977. While silting-up the navigation after dredging, the scouring action on either side of the channel occurred and the scouring range was wider and wider one after another.

In order to make a further inquiry into the condition of the siltation after channel excavating, we made analysis of the grain sizes of four silt samples on the vertical line taking in one year after the second time dredging, in the navigation channel within the sandbar. Its results are shown in Fig.2.

From the figures, we know the deposited silt in the channel basically have the grains of 0.1mm fine sand, amounting about to 75-80% of the total. Besides, 20-25% or so is silty clay of 0.009mm grain diameter. The former coincides with the size grades of the sediments of the beach face nearby (see Fig.2) and the latter is the size grades of suspension load in the river.

It can be seen from above analyses for the evolution and grain sizes, the main cause of the siltation of navigation channel is the restoration of the natural balance for the reason that the sea-bottom sediments of the shoal on the east of the channel, under the eastward wave action, was in the form of transportation on the bed load as well as of semi-suspended load.

3.2 Design of the movable-bed model

Similarity of the bottom load movement contains the starting similarity, the similarity of scouring and silting, sediment transport similarity, the time similarity of scouring and silting and location similarity of silting. For starting similarity, we have

$$\lambda_v = \lambda_{u_0} = \lambda_{v_k} \quad (1)$$

The starting similarity under the current action may use Dou Guoren's formula written in the form

$$\lambda_{v_k} = \lambda_\phi \lambda_\gamma^{1/2} \lambda_d^{1/2} \quad (2)$$

in which

$$\lambda_\phi = \frac{[\ln 11 \frac{H}{\Delta} (1 + 0.19 \frac{\gamma}{\gamma_s - \gamma} \frac{\epsilon_\kappa + gh\delta}{gd^2})^{1/2}]_p}{[\ln 11 \frac{H}{\Delta} (1 + 0.19 \frac{\gamma}{\gamma_s - \gamma} \frac{\epsilon_\kappa + gh\delta}{gd^2})^{1/2}]_m} \quad (3)$$

For computing the bottom sediment discharge under tidal current action, Dou Guoren's formula may be used:

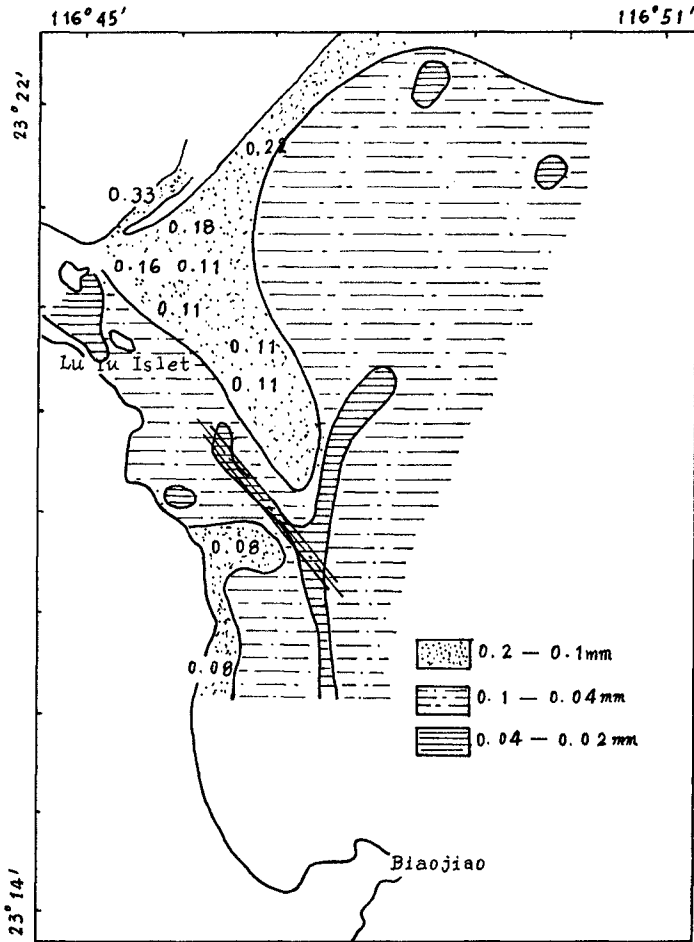


Fig.2 Distribution of bottom sediment at outer sandbar

$$q_{sb} = \frac{K_o}{C_o^2} \frac{\gamma_s \gamma}{\gamma_s - \gamma} (v - v_k) \frac{v^3}{g\omega} \quad (4)$$

While the bottom sediment discharge under the action of wave, Lua Zhaosen's formula may be used:

$$q_{sb} = \frac{2.4 K_2 \gamma \gamma_s}{C_o^2 (\gamma_s - \gamma)} (u - u_k) \frac{u^4}{g\omega} \frac{T}{L} \quad (5)$$

in which u is the mean orbital vibration velocity of particle in oscillating wave.

At present, a satisfactory research result on the bed load transport under the combined action of wave and tide has not been achieved. We have made some model verification and comparison tests for many formulas of bed load transportation and realized that Dou Guoren's and Luo Zhaosen's formulas are consistent with the measured results.

From equations (4) and (5) we get sediment transport scale:

$$\lambda_{qsb} = \frac{\lambda_{\gamma_s}}{\lambda_{\gamma_s} - \gamma} \frac{\lambda_v^4}{\lambda_{Co}^2 \lambda_\omega} \quad (6)$$

the time scale of scouring and silting: $\lambda_t = \frac{\lambda_{\gamma_o} \lambda_H \lambda_L}{\lambda_{qsb}} \quad (7)$

and the settling velocity scale: $\lambda_\omega = \frac{\lambda_v \lambda_H}{\lambda_L} \quad (8)$

The determined values of various scales are shown in Table 1.

3.3 Selection of the model material

We have made some preparative tests under the actions of wave and tidal current in the end, the saw-dust medium-size of grain diameter $D_{50} = 0.4$ mm, was selected as the model material in the test.

The evolution analysis and the movement limit of bed load under wave action indicated that the sediment movement in the sandbar area was rather active, being in a state of surface layer movement and complete movement, while in the area beyond -8m, its water depths and topography were basically in stable condition, its sediment movement being in a state of surface layer movement and more and more weaker as it moves offshore. As stated above, if the wave height and wave period are regulated to a proper value, it would be easy to realize the similarity of the sediment movement regime in the above-mentioned area.

Table 1 : Scale for movable-bed model

Name of scale	Symbol	Computed value	Adopted value
Horizontal scale	λ_1		500
Vertical scale	λ_h		80
Current velocity scale	λ_v	8.944	8.944
Wave height scale	λ_H	80	80
Wave length scale	λ_L	80	80
Wave period scale	λ_T	8.944	8.944
Bottom orbit velocity scale	λ_{u_o}	8.944	8.944
Mass-transport scale	λ_v	8.944	8.944
Starting velocity scale	λ_{v_k}	8.944	8.944
Chezy coefficient scale	λ_c	2.50	2.10
Settling velocity scale	λ_ω	1.43	1.01
Grain diameter scale	λ_d		0.275
Dry density scale	λ_{γ_o}		2.55
Sediment discharge scale	λ_{qsb}	150	87
Scouring and silting time scale	λ_t	667	1168

Basing on the relation between the navigation channel water depth after dredging and the silting speed, it indicates that the mean water depth in the dredged channel less than 5 months after dredging could restore to its original water level. Three hours after the beginning of the experiment the longitudinal profile of the excavated channel in the model has a better coincidence in silting regime with that of the prototype. Thus obtaining the actual model scale of scouring and silting time $\lambda_{t2} = 1168$.

3.4 The experiments of regulation schemes

Though the comparison and selection of various options, the movable-bed model experiments finally gives the proper trend and length of the guide dike and the expected siltation in the dredged channel. Its results are shown in Fig.3 and Table 2.

The test results indicate: The option of constructing a 5.2km sediment retention dike attaching 2.75km submerged dike is rather adaptable.

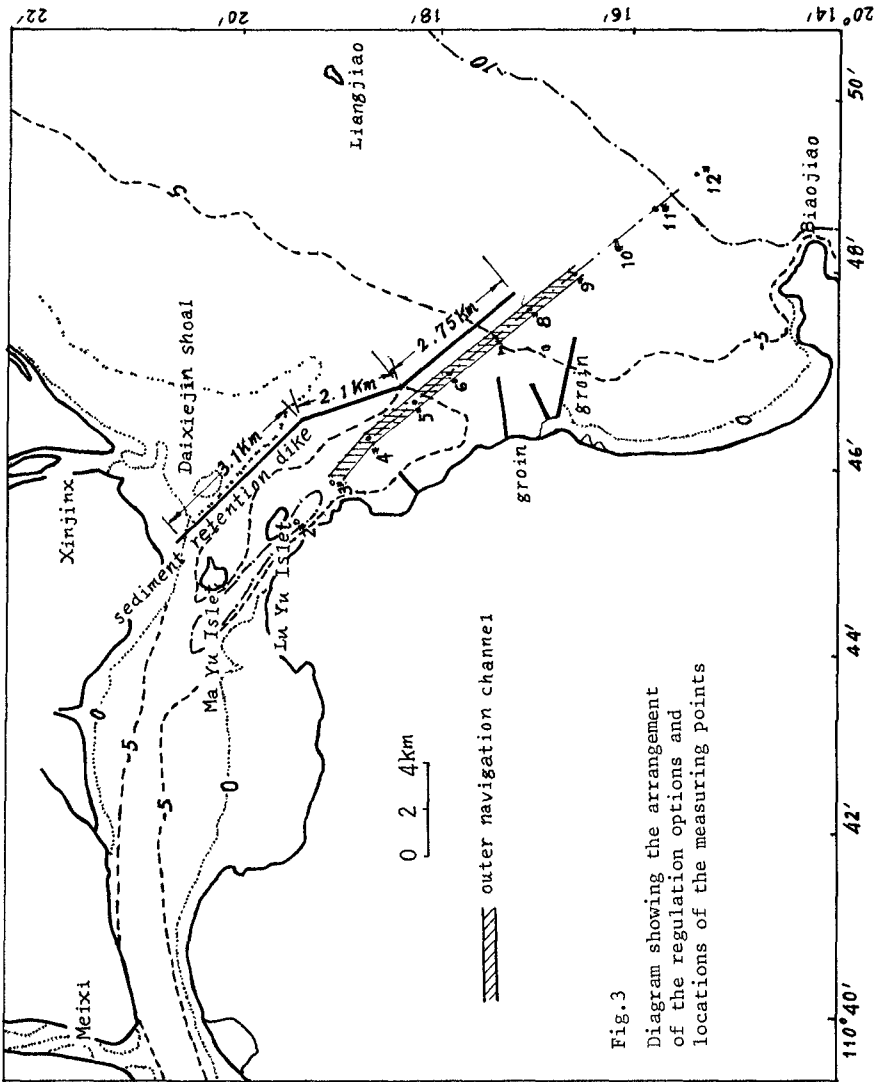


Fig. 3
Diagram showing the arrangement
of the regulation options and
locations of the measuring points

Table 2 : Comparison of the options

Options	Silting quantity in the channel at initial stage ($\times 10^4 \text{ m}^3/\text{year}$)	Silting trend in the channel in further	Resistance to typhoon's silting	Scouring at the dike head
1. To excavate the navigation channel	160	a little reduction	not possessing	
2. To excavate the navigation channel +5.2km sediment retention dike	70	a little reduction	not possessing	greater transverse current and scouring
3. To excavate the navigation channel +5.2km sediment retention dike+2.75km submerged dike	50 - 55	decreased year by year	possessing	basically has no dike head transverse current and scouring
4 To excavate the navigation channel +5.2km sediment retention dike+2.75km submerged dike + two southwest groins	50	decreased year by year	possessing	basically has no dike head transverse current and scouring
5. To excavate the navigation channel +5.2km sediment retention dike+2.75km overflow dike	35 - 40	decreased year by year	possessing	basically has no dike head transverse current and scouring

4. CONCLUSIONS

1. The paper discusses the theory and practice of the coastal movable-bed model tests under the combined action of the tide and wave for the regulation of the outer sandbar at Shantou Harbor on the test results. Our research shows that two kinds of the coastal movable-bed model should be devised according to the experimental purposes and the practice. That is off-shore model and in-shore model; the movable-bed model for the regulation of the outer sandbar at Shantou Harbor belongs to the off-shore model.
2. Our research also indicates that, if we do not select the diffraction phenomenon as the key conjunction in the model reproduction and select fit material as the model sand, which meet the falling similarity of the sediment movement, some model distortion would be allowable.
3. The key point of the determination of the scale of scouring and silting time in the coastal movable-bed model experiment lies in the selection of a better sediment transport formula and sediment transport scale.
4. The macroscopic analysis of the sediment movement in the current of outside and inside of Shantou Harbor indicates Shantou Bay is a type of estuary with the tide action as a dominant factor. The sediment deposit of the outer sandbar mainly comes from Xinjinxi and Wai Sha river and transported from northeast to southwest under the action of the tide and wave. Generally speaking, there is small quantity of sediment deposit in the whole seas and fundamentally in the state of dynamic equilibrium. The main reason of the siltation in the navigation channel is the bed load in the sea bottom transport on the spot and in semi-suspension condition to cause the restoration of natural balance of the sediment and then the siltation of the excavated navigation channel.
5. By way of the fixed-bed model tests under tidal current action as well as the movable-bed model tests under the combined action of the tide and wave, we have made some comparison tests for different option for the outer sandbar regulation. The test results indicate: A 5.2km sediment retention dike attaching a 2.75km submerged dike is rather adaptable, possessing the effects of restricting the water way to scour the sand as well as the retention of the sediment.

5. REFERENCES

- Bijker, E.W. Some considerations about scales for coastal models with movable bed. Delft Hydraulics Laboratory, Publ. No.50, 1967.
- Chen Zixia et al. Model test on the sedimentation accumulation at Island Terminal. Proc. of the First International Symposium on River Sedimentation, Beijing, 1980
- Dou Guoren. Law of all-sand model similarity and its designing examples. Water Conservancy & Transportation Science Information, March, 1977.
- Huang Jianwei et al. The model experimental report on the regulation of the sandbar outside of Old Harbor District of Shantou Harbor. Nanjing Hydraulic Research Institute, 1986.

- Huang Jianwei et al. The sediment transporting regularities of the sandbar outside of Shantou Harbor and a preliminary analysis of its regulatory prospect. Nanjing Hydraulic Research Institute, 1986.
- Kamphuis, J.W. Practical scaling of coastal models. Proc. 14th International Conference on Coastal Engineering, Copenhagen, 1974, Vol.III, Chapter 121.
- Lou Zhaosen and Xin Wenjie. Research report on the conditions of the harbor construction at Shuidong Bay and the practicability of the Navigation Channel Development at the Sandbar. Nanjing Hydraulic Research Institute, June, 1987.
- Mignot, C. Représentation des transports et des dépôts de sédiments dans les modèles réduits maritimes, 1972.
- You Fanghu et al. A finding and research report on the sediment silting in the Navigation Channel through the Sandbar outside of Shantou Harbor. Institute of Oceanography of the Chinese Academy of Sciences, 1981.

CHAPTER 92

ENVIRONMENTAL CONTROLS ON LITTORAL SAND TRANSPORT

Paul D. Komar¹

ABSTRACT

Quantities of sand transported along beaches are generally related to the "longshore component of wave power", P_L , through the proportionality $I_s = KP_L$ where I_s is the immersed-weight sand transport rate and K is a dimensionless proportionality factor. A more-generally applicable relationship is that of Bagnold, $I_s = K'(ECn)_b \bar{v}_L / u_m$ where $(ECn)_b$ is the energy flux or total power of the breaking waves, \bar{v}_L is the longshore current, u_m is the mean orbital velocity under the waves, and K' is another dimensionless coefficient. It is apparent that sediment transport rates on beaches should depend on environmental factors such as the grain diameter or settling velocity, and possibly on factors such as the beach slope or wave steepness. However, examinations of such dependencies for K and K' within the field data are hampered by problems with large random scatter within any one data set, and by systematic differences between separate studies which have employed diverse measurement techniques. Examinations of the field data for K and K' variations indicate that meaningful dependencies on sediment grain diameters and other factors cannot be established with confidence in the sand-size range. Limited data available from gravel beaches support the expected decreases in K and K' with increasing grain sizes. These data are too few in numbers to establish firm trends, but do suggest that future investigations to establish dependencies on environmental factors would be most profitably undertaken on gravel beaches. The measurements collected in recent years from sand beaches suggest revisions in average K and K' coefficients to be used in transport evaluations, but such revisions must be coordinated such that $K/K' = 2.7$ so as to maintain agreement with the longshore current data:

INTRODUCTION

It has been 35 years since George Watts collected the first field measurements of sand transport rates along beaches which permitted correlations with the causative wave conditions (Watts, 1953). Since that time, a number of studies have contributed to our data base, investigations which have obtained measurements from beaches in lakes, bays, and along ocean shores. The list of published field studies now includes 16 beach locations, yielding data for various types of correlations between sand transport rates, the wave conditions, and longshore current magnitudes. Given the considerable amount of accumulated data from a variety of beach locations, the question arises as to whether we can now detect environmental controls on the resulting sediment transport rates, that is, factors beyond the direct dependence on the wave power and

¹College of Oceanography, Oregon State University, Oceanography Admin. Bldg. 104, Corvallis, OR 97331-5503

angle of wave breaking. Various dependencies have been suggested including a simple correlation with the beach sediment grain size (or alternately the grain settling velocity), the beach slope, or more complex combinations of various environmental parameters. The objective of this study is to reexamine those suggested correlations to determine whether improved predictions of longshore sediment transport rates are possible if we include considerations of such environmental factors. This examination of environmental factors necessitates a compilation and general review of the existing data, which will be undertaken in the first section of this paper. The second half of the paper will then be devoted to examining possible dependencies on the various environmental factors. This examination will be limited to field data, even though many of the proposed correlations with environmental parameters are based on measurements from laboratory wave basins. The laboratory data are not included here due to the well-known uncertainties in the scaling of the laboratory sand-transport measurements, and because the ultimate goal is to establish predictive relationships for prototype beaches.

FIELD DATA AND EMPIRICAL CORRELATIONS

The initial motivation for studying the longshore transport of beach sediments came in response to adverse impacts due to jetty construction which interrupts this transport. It is not surprising then that the first quantitative investigation of this process, the study by Watts (1953), made use of sand blockage by jetties, specifically those at South Lake Worth Inlet, Florida. This approach has continued to be employed by various investigations, including the studies of Caldwell (1956), Bruno and Gable (1976), Bruno et al. (1980, 1981), and most recently those by Dean et al. (1982) and Dean et al. (1987). The locations of these various studies are given in Table 1 together with relevant environmental parameters. There are obvious problems associated with the use of jetties or breakwaters to measure longshore sediment transport rates, the foremost being the local effects of the structures on waves and currents, and the long-term nature of the measurements. In some cases it takes a month or longer for sufficient quantities of sand to accumulate in order to make the volume determinations meaningful, an interval during which waves and currents are continuously changing.

Beginning in the 1960's, sand tracers came into use to determine "instantaneous" littoral transport rates that could be related to relatively constant conditions of waves and currents. There are three potential approaches in the use of tracers to measure sand transport rates; (1) the spatial-integration method, (2) the time-integration method, and (3) the dilution method. These approaches have been reviewed by Komar (in press). Investigations that have employed this technique for determining correlations between sand transport rates and the wave conditions include Komar and Inman (1970), Knoth and Nummedal (1977), Inman et al. (1980), Duane and James (1980) and Kraus et al. (1982); Table 1 gives the locations of these several studies.

The data listed in Table 1 are not of uniformly high quality, so there is a temptation to eliminate some. Most obvious in this respect are the early measurements of Watts (1953) and Caldwell (1956), which involved long-term averaging of the sand transport determinations, and had basic weaknesses in their measurements of the wave conditions. Rather than a whole-scale casting out of certain data sets at the start, all will be retained in the analyses undertaken here. In that way we can focus on potential errors and systematic differences between the various studies and measurement techniques, an approach that will be important in discerning whether there are environmental controls on longshore sediment transport rates.

TABLE 1: Field Data for Longshore Sediment Transport Rates

Source	Location	D ₅₀ (mm)	# of points	K	K'
Watts (1953a) ¹	Ft. Lake Worth Inlet, Fla.	0.40	4	0.89(.73-1.03)	
Caldwell (1956)	Anaheim, Calif.	0.40	6	0.63(.16-1.65)	
Moore & Cole (1960)	Cape Thompson, Alaska	1.0	1	0.18	0.18
Komar and Inman (1970)	El Moreno, Mexico Silver Strand, Calif.	0.60	8	0.82(.48-1.15)	0.35(.22-.53)
		0.18	4	0.77(.52-.92)	0.22(.06-.36)
Lee (1975)	Lake Michigan	?	8	0.42(.24-0.72)	
Knoth & Nummedal (1977)	Bull Island, S.C.	0.18	5	0.62(.23-1.0)	
Inman, et al. (1980)	Torrey Pines, Calif.	0.20	2	0.69(.26-1.34)	
Duane & James (1980)	Pt. Mugu, Calif.	0.15	1	0.81	
Bruno, et al. (1981) ²	Channel Islands Harbor, Calif.	0.2	7	0.87(.42-1.5)	
Kraus, et al. (1982)	Ajigaura, Japan Shimokita Hirono Oarai	0.25	3		0.19(.16-.22)
		0.18	2		0.32(.28-.36)
		0.59	2		0.091(.08-.10)
		0.29	4		0.18(.16-.19)
Dean, et al. (1982)	Santa Babara, Calif.	0.22	7	1.15(.32-1.63)	
Dean et al. (1987)	Rudee Inlet, Va.	0.3	3	1.00(.84-1.09)	

¹Only the monthly-averaged data of Watts (1953a) are used in the analysis.

²Includes only the data where the wave statistics are based on measurements by gauges, not those based on LEO visual observations.

Data from the studies listed in Table 1 are plotted in Figure 1 as the transport rate versus

$$P_L = (ECn)_b \sin \alpha_b \cos \alpha_b \quad (1)$$

where $(ECn)_b$ is the wave energy flux or power evaluated at the breaker zone, and α_b is the wave breaker angle. P_L is often referred to as the "longshore component of wave energy flux or power." Longuet-Higgins (1972, p. 210) has taken exception of this terminology, but P_L has continued to be employed in littoral sand transport evaluations, although now it is sometimes written as $C_b S_{xy}$ where $S_{xy} = En \sin \alpha \cos \alpha$ is the longshore-directed component of the radiation stress.

The sand-transport rate can be expressed either as the volume transport rate, Q_s , or as an immersed-weight transport rate, I_s , defined as

$$I_s = (\rho_s - \rho) g a' Q_s \quad (2)$$

where ρ_s and ρ are respectively the sand and water densities, and a' is a pore-space factor such that $a'Q_s$ is the volume of solid sand alone, eliminating pore spaces

included in the Q_s volume transport rate (a' is usually taken as 0.6). One advantage of using I_s is that this immersed-weight transport rate accounts for the density of the sediment grains. Also important is that I_s and P_{λ} have the same units, so that the relationship

$$I_s = KP_{\lambda} \quad (3)$$

is homogeneous, that is, the K proportionality coefficient is dimensionless. In that Inman and Bagnold (1963) were the first to employ a littoral sand transport relationship having the form of equation (3), I will refer to this correlation as the "Inman equation."

The available field data are plotted in Figure 1, and it can be seen that the measurements are reasonably consistent with the direct proportionality given by equation (3). The solid line yields the proportionality coefficient $K = 0.77$, a value obtained by Komar and Inman (1970). The dashed line for $K = 0.57$ will be discussed later. By using $K = 0.77$ and taking ρ_s as the density of quartz sediments, one obtains the derivative relationship

$$Q_s = 6.8 P_{\lambda} \quad (4)$$

where Q_s has units m^3/day and P_{λ} is Watts/meter. Equation (4) applies only to quartz-density sands, and the value of the proportionality coefficient depends on the units employed; for example, the coefficient becomes 1.5×10^4 if Q_s is yds^3/yr and P_{λ} is $\text{ft-lbs}/\text{sec-ft}$. These latter units correspond to the comparable formula presented in the *Shore Protection Manual* (CERC, 1984), but the value obtained here for the proportionality coefficient is almost exactly twice that given in SPM. The reason for this difference is that in the SPM formula, the calculation of the wave energy and P are based on the significant wave height, $H_{1/3}$, whereas in the present analyses wave energies are based on the root-mean-square wave height, H_{rms} , the height which corresponds to the correct assessment of the wave energy as evaluated from complete spectra. In that $H_{1/3}/H_{\text{rms}} \approx 1.42$ (Longuet-Higgins, 1952), the calculated wave energies and powers would differ by a factor $(1.42)^2 \approx 2$. From this it is apparent that the SPM formula is equivalent to equation (3) and the results obtained earlier by Komar and Inman (1970). Of particular importance, this points out the need for recognizing that in using these relationships, one must be aware of whether they are based on significant wave heights or rms wave conditions.

Comparisons between the longshore sand transport rate and P_{λ} as undertaken above are empirical with little thought given to the physical processes. Early workers such as Grant (1943) stressed that sand transport in the nearshore results from the combined effects of waves and currents, the waves placing sand in motion and the longshore currents producing a net sand advection. Such a model was given a mathematical framework by Bagnold (1963), and applied specifically to the evaluation of sediment transport on beaches by Inman and Bagnold (1963). Their analysis yielded the "Bagnold equation",

$$I_s = K'(ECn)_b \frac{\bar{v}_{\lambda}}{u_m} \quad (5)$$

where \bar{v}_{λ} is the mean longshore-current velocity, in practice measured at the mid-surf position, and u_m is the maximum horizontal orbital velocity of the waves evaluated at the breaker zone. K' is a dimensionless coefficient which again must be

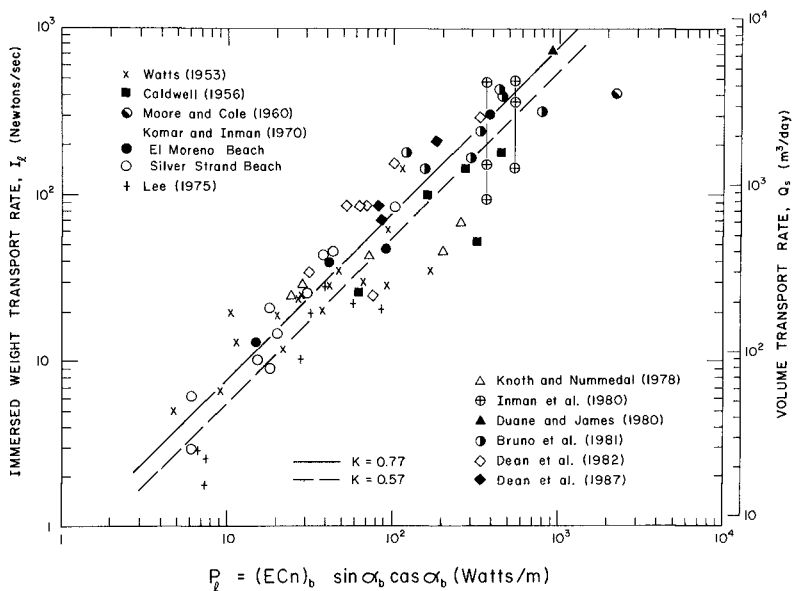


Fig. 1: Test of the Inman relationship, equation (3), for the longshore sand transport rate with the field data listed in Table 1.

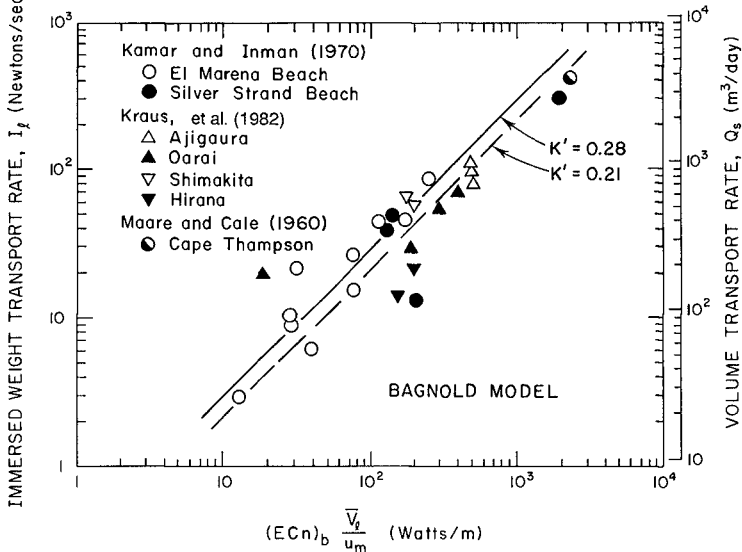


Fig. 2: Test of the Bagnold relationship, equation (5), for the longshore sand transport rate.

based on sediment-transport measurements.

Komar and Inman (1970) utilized their data on sand transport rates to make the first test of equation (5), employing direct measurements of longshore currents as well as wave parameters. Their data are shown in Figure 2, yielding $K' = 0.28$ when considered alone. Kraus et al. (1982) subsequently obtained measurements from several beaches in Japan, and the addition of their data suggests a reduction of the coefficient to $K' = 0.21$, the dashed line in Figure 2.

Komar and Inman (1970) found that their sand-transport data agreed with both equations (3) and (5), even though those relationships were seemingly based on different models. However, it was demonstrated that a simultaneous solution of these two equations yields

$$\bar{v}_L = (K/K')u_m \sin\alpha_b \cos\alpha_b \quad (6a)$$

or

$$\bar{v}_L = 2.7 u_m \sin\alpha_b \cos\alpha_b \quad (6b)$$

if one takes $K/K' = 0.77/0.28 = 2.7$ from the sand-transport correlations. This relationship, based initially on sand-transport considerations, was found to agree closely with available measurements of longshore currents, and is similar in form to the relationship derived theoretically by Longuet-Higgins (1970) based on radiation stress evaluations. Substituting $u_m \propto \sqrt{gh_b} \propto \sqrt{gH_b/\gamma}$, equation (6b) can also be expressed as

$$\bar{v}_L = 1.17 \sqrt{gH_b} \sin\alpha_b \cos\alpha_b \quad (6c)$$

A comparison between this form of the relationship and available field and laboratory data sets for longshore currents again demonstrates that agreement is excellent (Komar, 1979; Komar and Oltman-Shay, in press).

One significance of this connection between the two relationships for the sand transport through the longshore-current equation is that the Bagnold relationship, equation (5), derived on the basis of considerations of processes of sand transport, should be viewed as more fundamental than the Inman equation which empirically correlates the sand transport with P_L . Equation (3) or other correlations with P_L should be applied only on beaches where one can be certain that the longshore current is produced solely by an oblique wave approach and hence given by equation (6). If the nearshore currents are affected by tides, cell circulation with rip currents, or by local winds, then the more basic equation (5) must be used with direct measurements of \bar{v}_L . This is confirmed by the sand-transport measurements of Kraus et al. (1982) at Oarai Beach. At that site the data were obtained in the sheltered region of a breakwater where the longshore current results from the combined effects of obliquely-incident waves and a longshore variation in wave heights. Under such conditions an evaluation of the sand transport from P_L alone would be erroneous. This is especially illustrated by one measurement series where the direction of the longshore current and sediment transport was opposite to that expected from oblique-wave incidence. Even when the longshore currents and sand transport are produced entirely from waves breaking obliquely to the beach, the use of the Bagnold model, equation (5), may still be preferable to correlations with P_L in that it is usually easier and more accurate to measure \bar{v}_L than to measure breaker angles. Coastal engineering evaluations of sand-transport rates on beaches should be based more often on equation (5) than on the P_L wave-power approach.

The connection between equations (3) and (5) for sand transport evaluations via equation (6) for the longshore current also places constraints on the respective K and K' coefficients since we must have $K/K' = 2.7$ for agreement with the longshore current data. In that longshore currents can be measured more accurately than sand transport rates, the 2.7 value is better established than the individual values of K and K'. It also requires that if we reduce K' from 0.28, as first established by Komar and Inman (1970), to $K' = 0.21$ given by Kraus et al. (1982), then we must also reduce the proportionality between I_s and P_λ to $K = 0.57$. This value yields the dashed line in Figure 1 and, given the large scatter of the data, the result is still a reasonable fit.

VARIATIONS IN THE K AND K' COEFFICIENTS

Considerable scatter is seen in Figures 1 and 2, and this is reflected in the K and K' proportionality coefficients in equations (3) and (5) for the individual data sets. These coefficients are compiled in Table 1 as averages and total ranges. The average K-values for the data sets are as high as 1.15 from Dean et al. (1982), and a low of 0.18 for the single measurement of Moore and Cole (1960). The question arises as to whether these variations in K and K' reflect environmental conditions such as sediment grain sizes, or whether they result from random scatter and systematic differences in procedures between the several studies.

Dependencies on Grain Sizes and Settling Velocities

The first investigation to use field data to examine possible environmental controls on the K coefficient of equation (3) was the study of Komar and Inman (1970). That study included two beaches of contrasting grain sizes (0.60 versus 0.18 mm), and the near equality of the average K coefficients (0.82 versus 0.77) from those two sites was taken as an indication of a lack of dependence on sediment diameter, at least within the limited range of sand sizes. This was further explored by Komar (1978) utilizing the then available field and laboratory data; it was again concluded that no relationship could be established between K and the beach sand-grain diameter or settling velocity.

With the inclusion of additional measurements, later investigators have reached the opposite conclusion; i.e., that the field measurements of transport rates do reveal a dependence on the grain size of the beach sediment (Bruno, et al., 1980, 1981; Dean et al., 1982; Dean et al., 1987). Figure 3 (left) is the plot of K versus the median grain diameter D_{50} from Dean et al. (1987), the plot and curve being the same as that

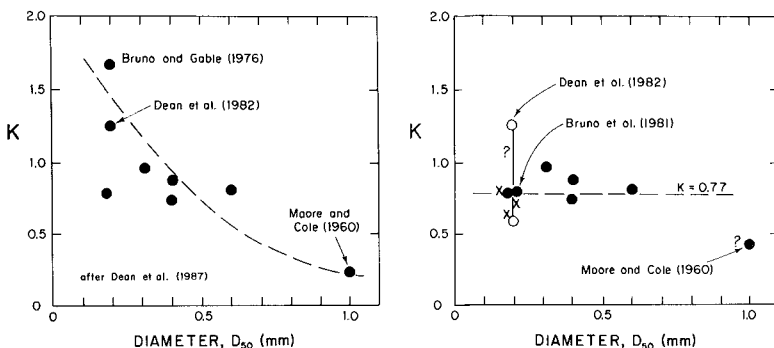


Fig. 3: K of eq. (3) versus the median grain diameter of the beach sand: (left) as analyzed by Dean et al. (1987), and (right) as re-analyzed here.

originally given in Bruno et al. (1981) excepting for the addition to two data points. The trend of decreasing K with increasing D_{50} is seen to be determined mainly by the K values obtained in the studies of Bruno and Gable (1976), Dean et al. (1982) and by Moore and Cole (1960). Unfortunately, the values from those three studies are either uncertain or clearly erroneous. The $K = 1.61$ plotted value from Bruno and Gable (1976) for the Channel Islands Harbor, California, was based on wave measurements collected by the Littoral Environment Observations (LEO) program. Bruno et al. (1980, 1981) later demonstrated the inadequacy of those visual data, and revised the coefficient downward to $K = 0.87$ on the basis of more reliable measurements from wave gauges. Unfortunately, the 1.61 value was mistakenly retained in their comparison with D_{50} , and this was perpetuated by Dean et al. (1987) in the plot of Figure 3 (left). The revised $K = 0.87$ coefficient was based on an assumed value of $a' = 0.65$ for the pore-space factor; other studies have assumed $a' = 0.6$, and if this value is employed, the coefficient is further reduced to $K = 0.80$, effectively the same as the 0.77 value proposed earlier by Komar and Inman (1970). This reduced K value is that plotted in the revised graph in Figure 3 (right).

Also uncertain is the $K = 1.23$ average coefficient obtained by Dean et al. (1982, 1987) at Santa Barbara, California, as part of the Nearshore Sediment Transport Study. Waves were measured by two S_{xy} gauges located offshore in approximately 9 m depth. It was found in the analysis that the west gauge yielded S_{xy} values which are approximately a factor 2 larger than those based on the east gauge. In their correlations with the sand-transport measurements, Dean et al. used the results from the east gauge. Had they instead used the west gauge, the $P_{\chi} = C_b S_{xy}$ wave powers would have been approximately 2 times larger and the resulting proportionality coefficient with the sand-transport data would have been reduced to $K \approx 1.23/2 = 0.61$. This potential reduction is illustrated in Figure 3 (right), but it is not actually possible to determine which value, 1.23 or 0.61, should be employed in the correlation with D_{50} . It is clear, however, that too much weight should not be given to the average K value determined from the Santa Barbara data.

The single measurement of Moore and Cole (1960) is particularly important in the Dean et al. (1987) correlation between K and sediment grain size, Figure 3 (left), since it was derived from a coarse-sand beach where $D_{50} = 1$ mm. Unfortunately, this K -value from Moore and Cole is particularly questionable. The sand transport rate was determined from beach accretion within a breached area, so there is some uncertainty whether the total transport was measured. More important, the wave parameters were estimated visually. The velocity of the longshore current was measured, so it is possible to test the data of Moore and Cole against the Bagnold model of equation (5) to determine a K' coefficient. This yields $K' = 0.18$ which is effectively the same as the 0.21 value based on the combined data of Komar and Inman (1970) and Kraus et al. (1982). The Moore and Cole data point is seen in Figure 2 to agree with the trend established by the other measurements. This suggests that the mean breaker angle (25°) determined visually by Moore and Cole is too large, and this in turn makes P too large and hence K too small. Longshore currents generally can be measured more accurately than breaker angles, and this probably accounts for their data being more consistent with the Bagnold model of equation (5) than with the wave-power relationship of equation (3). This conclusion is further supported by comparisons of their data with equation (6) for the mean longshore-current velocity; their reported significant-wave breaker height [5.5 ft = 1.7 m ($rms-H_b = 1.2$ m)]

and angle $[\alpha_b = 25^\circ]$ yield a predicted longshore current $\bar{v}_L = 1.8$ m/sec from equation (6c), whereas the measured current was only 0.64 m/sec. Working in the opposite direction, assuming the measured breaker height and longshore current are correct, then the breaker angle according to equation (6c) would have been approximately $\alpha_b = 9.5^\circ$. This angle reduces the corresponding P of equation (1), and the K coefficient of the Inman equation is accordingly increased to 0.43. This value is plotted in Figure 3 (right), and even though higher than the value used by Bruno et al. (1981) and Dean et al. (1987), it still possibly suggests a decrease in K with increasing D_{50} . However, given the uncertainties of the visual wave and current measurements of Moore and Cole, and that the measurement of sand accretion may not have accounted for the total transport, too much reliance should not be based on the resulting K value being lower than those found in other studies.

A similar analysis has been undertaken for K' in the Bagnold equation (5), and the results are given in Figure 4. It is apparent that there is no acceptable dependence of K' on D_{50} . The measurement of Moore and Cole (1960) fits within the data scatter rather than suggesting a decrease in K' at large D_{50} .

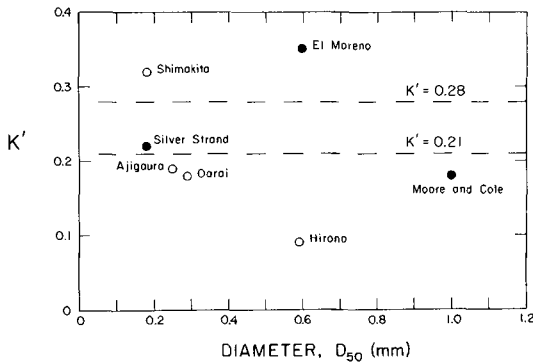


Fig. 4: K' of eq. (5) versus the median grain diameter of the beach sand. The data include those of Komar and Inman (1970), Kraus et al. (1982) and Moore and Cole (1960) [Table 1].

Grain-settling velocities of the beach sediments depend primarily on their sizes. As expected, attempts at correlations between K or K' and settling velocities are no better than found above for the median diameters.

It is expected that both K and K' should decrease as the sand size or settling velocity increase. The absence of such trends undoubtedly results from the considerable scatter in the field measurements, scatter that results from both random and systematic errors. The several studies that provide data for sand transport rates on beaches contrast markedly in their techniques, involving both tracer experiments and blockage by jetties. It should come as no surprise that there are systematic differences in the results and that it would be difficult to establish dependencies on environmental factors such as D_{50} . Another problem is that essentially all of the data used above come from beaches with D_{50} between 0.15 and 0.60 mm, the one exception being the uncertain measurement of Moore and Cole (1960) at $D_{50} = 1$ mm.

If dependencies between K and D_{50} are to be established from field data, it will probably require that the measurements come from gravel beaches. Only with such a considerable increase in D_{50} might we find sufficiently large changes in K and K' that they will not be masked by systematic differences in measurement techniques. This is indicated by the study of Hattori and Suzuki (1979) on a gravel beach in Japan where $D_{50} \approx 2$ cm. Using tracer gravels, they measured longshore movements of 2 to 3 m/day under normal sea conditions, but as much as 400 m/day during storms. They found a good correlation between the mean advection rates of the gravel particles and P . If it is assumed that the movement has a thickness of one clast diameter, then their correlation is equivalent to $I_s \approx 0.2P$. Robert Nicholls (pers. comm.) has provided me with K values for their experiments on shingle beaches in England which involved the use of aluminum pebbles as tracers; Nicholls and Webber (1987) discuss the experiments with respect to sorting patterns of the pebbles according to their sizes and shapes. Three measurement series yield $K = 0.011, 0.012$ and 0.043 on two beaches where $D_{50} \approx 4$ cm. These limited results from gravel beaches do demonstrate the expected decrease in K from its value for sandy beaches. The results indicate that additional studies on gravel beaches could yield trends of K and K' versus D_{50} . However, it is also apparent that such analyses of coarse-sediment transport should include considerations of threshold criteria, modifying equations (3) and (5) to account for limits on particle movement.

Dependence on Beach Slope

There is a strong relationship between the beach slope and sediment grain size, so it might be anticipated that attempts to correlate K and K' with the beach slope would fare no better than the above correlations with diameters. There is an additional problem in that several of the studies do not report average beach slopes, so a smaller quantity of data is available to test such a correlation.

No correlation could be found between K and the beach slope within the sand-size range. The correlation between K' and beach slope is shown in Figure 5. Based on their data, Kraus et al. (1982) suggested that K' decreases with increasing beach slope. It is seen in the graph that such a trend is indicated by the low $K' = 0.09$ value obtained at Hirono beach, based on two individual sand-transport measurements (Table 1). However, the $K' = 0.36$ value for El Moreno Beach in the study of Komar and Inman (1970) diverges markedly from that trend. Therefore, it is too early to establish any

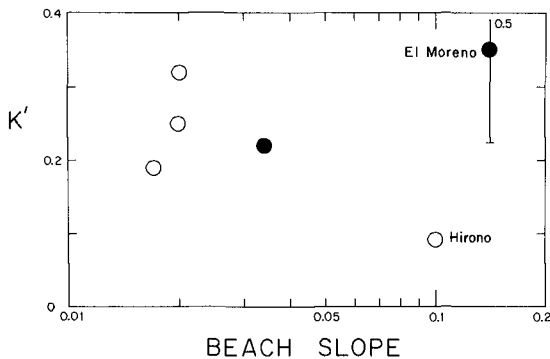


Fig. 5: K' of eq. (5) versus the beach slope. The data include those of Komar and Inman (1970) and Kraus et al. (1982) [Table 1].

dependence of K or K' on the beach slope for sand beaches. I have not yet attempted to extend the correlations to gravel beaches as undertaken above for mean grain diameters.

It of interest that the magnitude of the longshore current, as given by equation (6), does not depend on the beach slope. The *Shore Protection Manual* (CERC, 1984) and Galvin (1987) have proposed longshore-current relationships which contain a direct dependence on the beach slope, but these have been shown to yield serious errors when adequately tested with the available data (Komar, 1979; Komar and Oltman-Shay, in press). The implication to the longshore sediment transport is that any dependence on the beach slope will have to enter primarily through changes in concentrations of suspended sediments or thicknesses of the moving bedload carpet.

Dependencies on Wave Steepness and Other Wave Parameters

Laboratory studies such as that by Özhan (1982) have found a strong correlation between K and the wave steepness; the dependence was explained in terms of the control of the wave steepness on the breaker type (plunging, etc.). It is difficult to utilize field data to test such a relationship. The studies that evaluated sand transport rates by blockage at jetties involve very long time spans during which wave steepnesses and other wave parameters continuously change. Such correlations with field data will necessarily have to be limited to investigations where sand tracers were employed since these involve shorter intervals of time. Accordingly, I have tested the correlation between K and the deep-water wave steepness with the measurements of Komar and Inman (1970); the results, Figure 6, do not establish any reasonable trend.

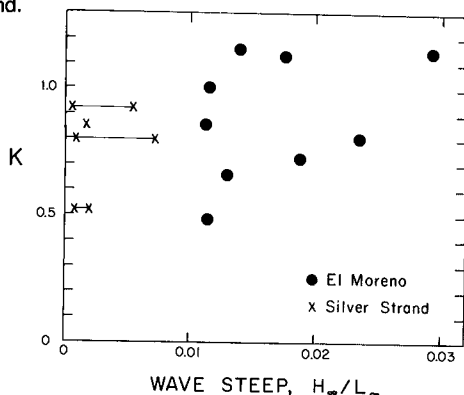


Fig. 6: K of eq. (3) versus the deep-water wave steepness. The data are those of Komar and Inman (1970) [Table 1].

Bailard (1984) has undertaken a detailed analysis of the bedload and suspension components of the transport. His analysis predicts that the coefficient in equation (3) is given by $K = 0.05 + 2.6\sin^2\alpha_D + 0.007u_m/w_s$, where w_s is the settling velocity of the beach sand. Bailard found good agreement by combining field and laboratory data. However, the inclusion of the field data involved mean values for each beach, ignoring the considerable variations in breaker angles (α_D) and in orbital velocities (u_m) which depend on the wave-breaker heights. I have tested this proposed relationship for K with the individual measurements contained within the data set of Komar and

Inman (1970), and could find no agreement.

Dependencies on Combined Wave and Beach Parameters

Some success has been achieved in analyzing surf-zone processes in terms of the Iribarren number, $\xi = m/(H_{\infty}/L_{\infty})^{1/2}$, which combines the beach slope m with the wave steepness. Any test of dependencies of K and K' on ξ requires data from different beaches having a significant range of beach slopes, but where the sand-transport determinations involved only short time periods so that H_{∞}/L_{∞} is nearly constant. The data of Table 1 are inadequate to meet these requirements. However, we already have established that K and K' do not depend on the beach slope for sandy beaches, although such a correlation will likely be found once the analysis is extended to gravel beaches and provides a larger range of slopes. Analyses with individual data sets show no dependence on H_{∞}/L_{∞} . Given these two findings, we can conclude that the present data cannot be used to establish variations of K and K' with the Iribarren number.

The heuristic model of Dean (1973) presents rational analyses of cross-shore and longshore transports of sediments. According to this model, the K coefficient in the Inman relationship, equation (3), is dependent on the wave-breaker height (H_b), breaker angle, grain settling velocity and beach slope (m) according to

$$K \propto m \sqrt{H_b} \cos \alpha_b / C_f w_s$$

where C_f is a drag coefficient. The principal new parameter introduced here that has not been tested is the proposed dependence on H_b . This again must be examined with data from short-term sand-tracer experiments so that breaker heights are relatively constant. Accordingly, I again used the data of Komar and Inman (1970); no trend was apparent between either K or K' and H_b .

Through a multi-stage analysis, Kamphuis et al. (1986) derived the empirical correlation $K \propto m H_b / D_{50}$ for the coefficient in the Inman relationship. The dependencies on the beach slope m and D_{50} would tend to be offsetting due to their positive correlation. Based on the empirical relationship $m = 1.8(H_b/D_{50})^{-0.5}$ established in their analyses, Kamphuis et al. further concluded that $K \propto (H_b/D_{50})^{0.5}$. Since we have been unable to find individual correlations between K and D_{50} , m or H_b , it can be concluded that this combined dependence proposed by Kamphuis et al. is not supported by the field data from sandy beaches.

SUMMARY OF CONCLUSIONS

The large quantity of field data available from a number of studies, Table 1, now makes it possible to re-examine the values of the K and K' proportionality coefficients respectively in equations (3) and (5). The connection between the two sand-transport relationships through the longshore current, equation (6), requires that $K/K' = 2.7$. The data of Komar and Inman (1970) yielded $K' = 0.28$ for the Bagnold equation, but subsequent measurements by Kraus et al. (1982) from several beaches suggest that the coefficient be reduced to $K' = 0.21$. This requires that K in the Inman equation (3) be reduced from 0.77 to 0.57; given the appreciable scatter of the data, Figure 1, such a modification in the mean value for K is acceptable.

Of particular interest to this study has been whether, by using the combined field data in Table 1, we can discern environmental controls on variations in K and K' . A

number of such dependencies have been proposed in the literature. Here we initially explored direct correlations with environmental parameters such as beach-sand grain sizes, beach slopes and breaker heights, rather than using dimensionless combinations which would obscure the dependencies. Several studies have suggested that K decreases with increasing D_{50} , the median diameter of the beach sand. However, the analyses here lead to the conclusion that those previous correlations resulted from an erroneous K value for the Bruno and Gable (1976) data, and the likelihood that the K value employed for the Moore and Cole (1960) data was too large. The revised diagram of K versus D_{50} (Fig. 3 - right) provides little confidence for any dependence within the range of sand sizes. However, the limited data from gravel beaches do support the expected decrease in K with increasing D_{50} , but the measurements are too limited to establish a reasonable correlation. The results were similarly negative in attempts to correlate K and K' with beach slopes, wave-breaker heights, and finally with combinations of parameters such as the wave steepness and the Iribarren number.

It is apparent that K and K' should depend on basic environmental parameters such as sediment grain sizes. Therefore, the absence of such trends must result from the quality of the data. This should come as no surprise in view of the various techniques that have been used to measure sand transport rates on beaches and to collect the data on waves and currents. This has introduced appreciable systematic differences in the results from the several studies, along with considerable random uncertainties within individual data sets. Given the considerable difficulties in collecting data on waves, currents and sediment transport in nearshore field studies, and the general uncertainty in the scaling of laboratory results, it is hard to envision how this situation can be rectified.

ACKNOWLEDGEMENTS

I would like to thank Robert Nicholls for providing me with his unpublished data for gravel transport on beaches. This paper is a result of research sponsored by the Oregon State University Sea Grant Program, supported by NOAA Office of Sea Grant, Department of Commerce, under grant number NA85AA-D-SG0095.

REFERENCES

- Bagnold, R.A. (1963) Mechanics of marine sedimentation: In *The Sea*, M.N. Hill (Editor), Wiley-Interscience, New York, p. 507-582.
- Bailard, J.A. (1984) A simplified model for longshore sediment transport: Proc. 19th Coastal Engr. Conf., p. 1454-1470.
- Bailard, J.A. and D.L. Inman (1981) An energetics bedload model for a plane sloping beach: local transport: Jour. Geophysical Res., v. 86, p. 2035-2043.
- Bruno, R.O. and C.G. Gable (1976) Longshore transport at a total littoral barrier: Proc. 15th Coastal Engr. Conf., ASCE, p. 1203-1222.
- Bruno, R.O., R.G. Dean and C.G. Gable (1980) Littoral transport evaluations at a detached breakwater: Proc. 17th Coastal Engr. Conf., ASCE, p. 1453-1475.
- Bruno, R.O., R.G. Dean, C.G. Gable, and T.L. Walton (1981) Longshore sand transport study at Channel Island Harbor, California: U.S. Army Corps of Engrs., Coastal Engr. Res. Center., Tech. Paper No. 81-2, 48 pp.
- Caldwell, J. (1956) Wave action and sand movement near Anaheim Bay, California: U.S. Army Corps of Engrs., Beach Erosion Board, Tech. Memo. No. 68, 21 pp.
- CERC (1984) Shore Protection Manual: U.S. Army Corps of Engr., Coastal Engr. Res. Center, U.S. Govt. Printing Office, Washington, D.C.
- Dean, R.G. (1973) Heuristic models of sand trans in the surf zone: Proc. 1st

- Australian Conf. on Coastal Engr., Engineering Dynamics in the Surf Zone, Sydney, p. 208-214.
- Dean, R.G., E.P. Berek, C.G. Gable, and R.J. Seymour (1982) Longshore transport determined by an efficient trap: Proc. 18th Coastal Engr. Conf., ASCE, p. 954-968.
- Dean, R.G., E.P. Berek, K.R. Bodge, and C.G. Gable (1987) NSTS measurements of total longshore transport: Coastal Sediments '87, ASCE, p. 652-667.
- Duane, D.B. and W.R. James (1980) Littoral transport in the surf zone elucidated by an Eulerian sediment tracer experiment: Jour. Sedimentary Petrology, v. 50, p. 929-942.
- Galvin, C.J. (1987) The continuity equation for longshore current velocity with breaker angle adjusted for a wave-current interaction: Coastal Engr., v. 11, p. 115-129.
- Grant, U.S. (1943) Waves as a transporting agent: Amer. Jour. Sci., v. 241, p. 117-123.
- Hattori, M. and T. Suzuki (1979) Field experiment on beach gravel transport: Proc. 16th Coastal Engr. Conf., ASCE, p. 1688-1704.
- Inman, D.L. and R.A. Bagnold (1963) Littoral processes: In *The Sea*, M.N. Hill (Editor), Wiley-Interscience, New York, p. 529-553.
- Inman, D.L., J.A. Zampol, T.E. White, D.M. Hanes, B.W. Waldorf, and K.A. Kastens (1980) Field measurements of sand motion in the surf zone: Proc. 17th Coastal Engr. Conf., ASCE, p. 1215-1234.
- Kamphuis, J.W., M.H. Davies, R.B. Nairn, and O.J. Sayao (1986) Calculation of littoral sand transport rate: Coastal Engineering, v. 10, p. 1-21.
- Knoth, J.S. and D. Nummedal (1977) Longshore sediment transport using fluorescent tracer: Coastal Sediments '77, ASCE, p. 383-398.
- Komar, P.D. (1978) The relative significance of suspension versus bed-load on beaches: Jour. Sedimentary Petrology, v. 48, p. 921-932.
- Komar, P.D. (1979) Beach-slope dependence of longshore currents: Jour. Waterway, Port, Coastal and Ocean Div., ASCE, v. 105, WW4, p. 460-464.
- Komar, P.D. (in press) Littoral sediment transport: In *Handbook of Coastal and Ocean Engineering*, J.B. Herbich (Editor), Gulf Publishing Co.
- Komar, P.D. and D.L. Inman (1970) Longshore sand transport on beaches: Jour. Geophysical Res., v. 75, n. 30, p. 5514-5527.
- Komar, P.D., and J. Oltman-Shay (in press) Nearshore currents: In *Handbook of Coastal and Ocean Engineering*, J.B. Herbich (Editor), Gulf Publishing Co.
- Kraus, N.C., M. Isobe, H. Igarashi, T.O. Sasaki, and K. Horikawa (1982) Field experiments on longshore transport in the surf zone: Proc. 18th Coastal Engr. Conf., ASCE, p. 969-988.
- Lee, K.K. (1975) Longshore currents and sediment transport in west shore of Lake Michigan: Water Resources Res., v. 11, p. 1029-1032.
- Longuet-Higgins, M.S. (1952) On the statistical distribution of the height of sea waves: Jour. Marine Res., v. 11, p. 245-266.
- Longuet-Higgins, M.S. (1970) Longshore currents generated by obliquely incident waves: Jour. Geophysical Research, v. 75, p. 6778-6789 and 6790-6801.
- Longuet-Higgins, M.S. (1972) Recent progress in the study of longshore currents: In *Waves on Beaches*, R.E. Meyer (editor), Academic Press, N.Y., p. 203-248.
- Moore, G.W. and J.Y. Cole (1960) Coastal processes in the vicinity of Cape Thompson, Alaska: In *Geologic Investigations in Support of Project Chariot in the Vicinity of Cape Thompson, Northwestern Alaska - Preliminary Report*, Kachadoorian et al. (editors), U.S. Geological Survey Trace Elements Investigation Report 753, p. 41-55.
- Nicholls, R.J., and N.B. Webber (1987) Aluminum pebble tracer experiments on Hurst Castel Spit: Coastal Sediments '87, ASCE, p. 1563-1577.

- Özhan, E. (1982) Laboratory study of breaker type effect on longshore sand transport: *In* Mechanics of Sediment Transport, B.M. Sumer and A. Müller (editors), Proc. Euromech 156, A.A. Balkema, Rotterdam, p. 265-274.
- Watts, G.M. (1953) A study of sand movement at South Lake Worth Inlet, Florida: U.S. Army Corps of Engrs., Beach Erosion Board, Tech. Memo. No. 42., 24 pp.

CHAPTER 93

Predictive model for daily changes of shoreline

Kazumasa Katoh¹ and Shin-ichi Yanagishima²

Abstract

Beach profiles have been being measured every day on sandy beach at the Hazaki Oceanographical Research Facility, facing to the Pacific Ocean. Based on the data obtained during the period from March 12, 1986 to September 11, the relation between the daily changes of shoreline position and energy flux of incident waves is analyzed. A tentative predictive model of the short-term shoreline changes is proposed. A combination of this model and the one-line theory is examined.

1. Introduction

A shoreline changes due to the longshore sand transport in a long-term. A practical numerical simulation model, the one-line theory can predict the long-term shoreline changes. The shoreline also changes due to the cross-shore sand transport in a short-term. There is, however, no reliable method to calculate the short-term ones during and after a storm, mainly because of lack of information on the actual changes of shoreline.

The authors have measured the beach profile every day for 184 days. Based on the data obtained, the relation between the short-term shoreline changes and the energy flux of incident waves are examined. Furthermore, a black box model for predicting the short-term changes are developed.

2. Field observation (on beach profile)

The site of field observation is a entirelyly natural sandy beach. It is facing to the full wave energy of the Pacific Ocean (see Figure 1). A foreshore slope is mild, about 1/50, and the mean diameter of sediments on a beach is 0.18mm. According to eleven aerial photographs taken

1) Chief of Littoral Drift Lab., 2) Member of Littoral Drift Lab., Port & Harbour Research Institute, Ministry of Transport, 3-1-1, Nagase, Yokosuka, Japan.

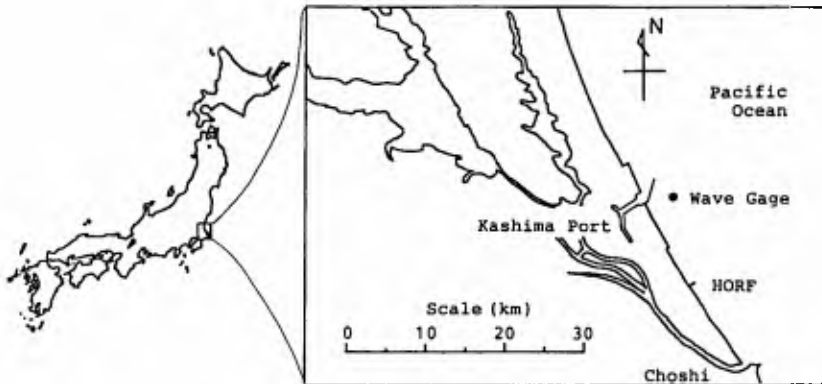


Figure 1 Site of field observation



Photo. 1 Hazaki Oceanographical Research Facility

during a period from 1947 to 1984, the location of shoreline has been stable since 1979. On this beach, Port and Harbour Research Institute, Ministry of Transport, has constructed the Hazaki Oceanographical Research Facility (HORF) in 1986 for carrying out field observation in the surf zone even under sever sea conditions. The research pier is a 427 meters long concrete structure supported by 0.8 meter diameter concrete-filled steel piles in a single line, at 15 meters interval. The pier deck is 2.5 meters wide and 7 meters above L.W.L.(Photo. 1).

Beach profiles of 500 meters from the tip of pier to the backshore were measured with an interval of 5 meters once a day during 184 days from March 12 to September 11, 1986. The sea bottom profile was surveyed with a sounding lead

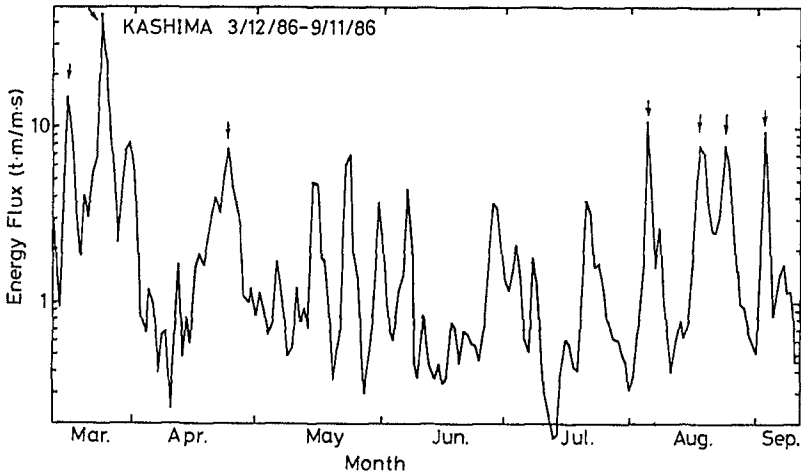


Figure 2 Changes of daily mean wave energy flux

Table 1

Representative high waves

from the pier deck. The land survey of the backshore and foreshore was done by using a transit and surveyor's staff.

The offshore waves have been measured near Kashima Port (see Figure 1) during twenty minutes of every two hours at the depth of 22 meters below the datum line. The daily mean energy flux has been calculated with the significant wave data of every two hours.

Month :Day	Energy Flux (tm/ms)	Maximum waves	
		H _{1/3} (m)	T _{1/3} (s)
3:16	15.4	4.04	9.3
3:24	45.9	6.76	10.7
4:24	7.8	3.06	10.1
8: 5	11.0	4.12	9.1
8:18	8.0	3.12	11.9
8:24	8.2	3.10	9.2
9: 3	9.6	3.35	10.9

Figure 2 shows the daily mean energy flux of incident waves during the period from May 12 to September 11, 1986. The energy flux was small in the months from May to July, while it was large in the other months. Storms larger than 3.0 meters in the significant wave height occurred seven times on days denoted by arrows in Figure 2. The daily mean energy flux, the maximum significant wave height and period on the storm day are listed in Table 1. The tide level is being observed every hour in Kashima Port. Figure 3 shows the distribution of frequency of tide level.

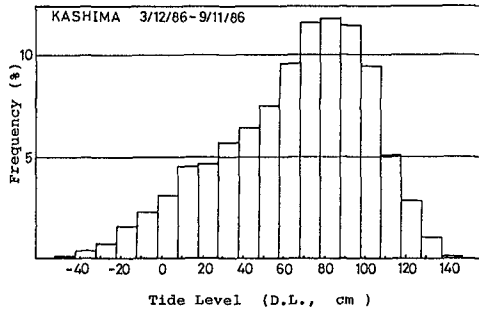


Figure 3 Frequency of tide level

3. Daily changes of shoreline position

3.1 Outline of profile changes

Figure 4 shows the mean profile during observation relative to the datum line. The on-offshore reference coordinate is inherent in HORF. Beach slope above the datum line is nearly constant, $1/50$. Sunken places of 15 meters interval in offshore side of reference point 150m are the local scour around the piers.

The dotted points in Figure 4 are the standard deviation of profiles at every measuring point from the mean profile. The standard deviations of sea bottom levels have a general tendency to increase in the offshore direction. However, it has the minimum value at the reference point 25m, where the mean level is +0.28 meter above the datum line. Then, the level at the minimum value point is not apt to change.

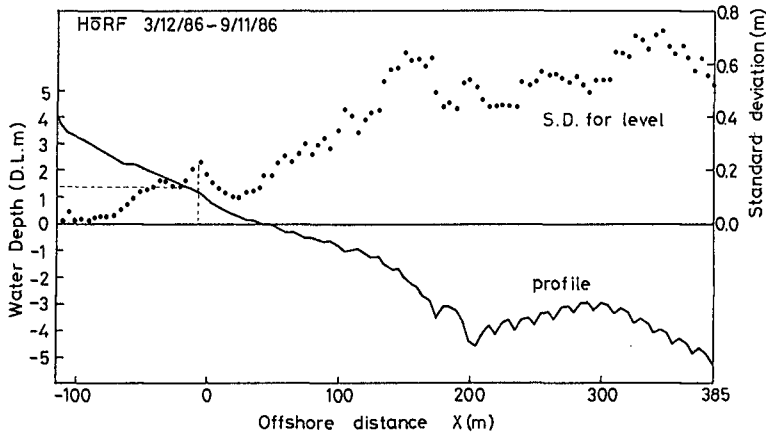


Figure 4 Mean profile and standard deviation of profiles

According to the authors' visual observation on the beach and from the pier deck, the shallow water area and the beach was nearly plane.

3.2 Feature of shoreline changes

The changes of foreshore profile was maximum at the mean level of +1.4 meters above the datum line, as seen in Figure 4. This level is corresponding to the maximum water level during observation. In this paper, the shoreline position is defined at an intersection of beach profile and a level of +1.4 meters above the datum line. The shoreline positions was calculated by interpolating the beach profile data of 5 meters interval.

Figure 5 shows the daily on-offshore changes of shoreline position. The shoreline was in onshore-side in the high energy flux months of March, April and August, while it was in the offshore-side during the low energy flux period from May to July. Then, a whole trend of shoreline changes are

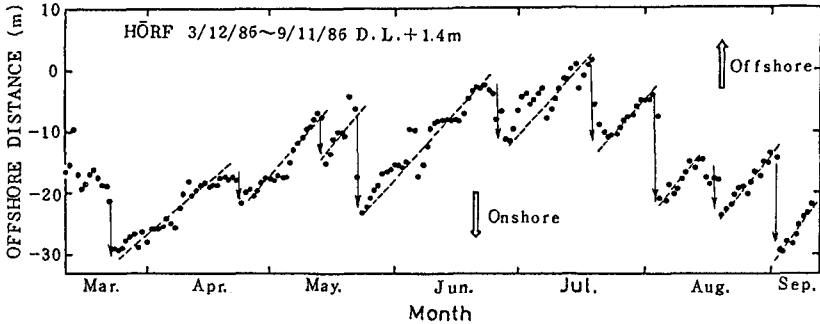


Figure 5 On-offshore changes of shoreline position

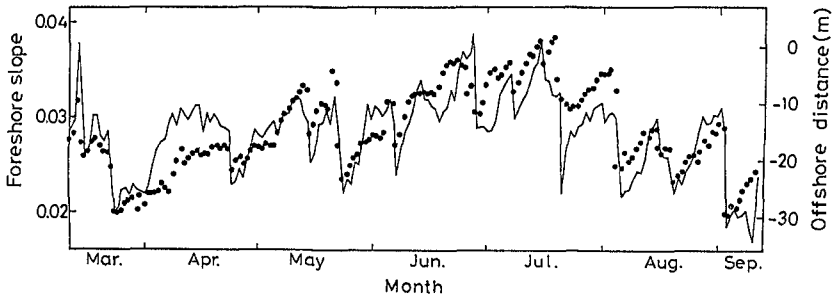


Figure 6 Changes of foreshore beach slope

roughly corresponding to the changes of incident energy flux.

The shoreline positions shifted in the offshore direction, independent of wave energy flux, in the accretionary process. Nine broken lines in Figure 5 approximate the accretionary process. The broken lines are nearly parallel each others, which means that the shoreline advanced with almost constant speed. The inclinations of the broken lines give the value of 0.68 meter/day for the speed of progression in average. On the other hand, the shoreline rapidly recessed in one or two days in erosional process as shown by arrows in Figure 5. The rapid recession have occurred even in the low energy flux months such as May, June, and July.

The solid line in Figure 6 shows the changes of mean foreshore slope calculated by the least square method with the data from the reference point -20m to +25m. The shoreline position are also plotted in this figure. The changes of the slope and the shoreline position have a same tendency, although there is a some discrepancy between them. The foreshore slope suddenly became to be mild when the shoreline rapidly recessed in the erosional process.

4. Relation between shoreline position and energy flux

Sunamura(1984) proposed the following semi-empirical relation among the foreshore beach slope ($\tan\beta_f$), sediment grain size (d), and the waves:

$$\tan\beta_f = 0.12[H_B/(g^{1/2}Td^{1/2})]^{-1/2}, \quad (1)$$

where H_B is the wave breaker height and T is wave period. The wave breaker height in Eq.(1) can be eliminated by using a following relation (Sunamura and Horikawa,1974),

$$H_B/H = (\tan\beta)^{0.2}(H/L)^{-0.25}, \quad (2)$$

where $\tan\beta$ is mean bottom slope, H and L are offshore wave height and wave length, respectively. Then, we will have Eq.(3) instead of Eq.(1),

$$\tan\beta_f = 0.19d^{1/4}(\tan\beta)^{-0.1}(L^{1/3}/H)^{3/8}. \quad (3)$$

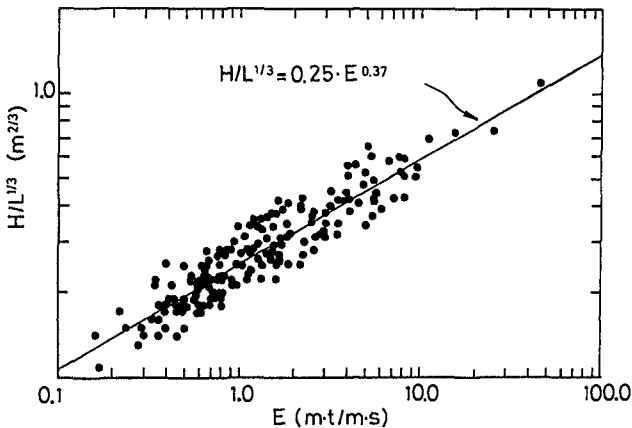


Figure 7 Relation between $H/L^{1/3}$ and energy flux

Figure 7 shows the relation between $H/L^{1/3}$ and the daily mean energy flux during the observation. The wave length was calculated by the small amplitude wave theory with the daily mean significant wave period. The height was reversely calculated based on the daily mean energy flux and mean wave period. As seen in Figure 7, there is a strong relation between them, a solid line in the figure, which is expressed as

$$H/L^{1/3} = 0.25E^{0.37}, \quad (4)$$

where E is the daily mean energy flux. By substituting Eq.(4) into Eq.(3), we have

$$E = [0.32d^{0.25}(\tan\beta)^{-0.1}]^{7.19}(\tan\beta_f)^{-7.19}. \quad (5)$$

Next, a simple relation between the foreshore slope and the shoreline position will be introduced. Let the

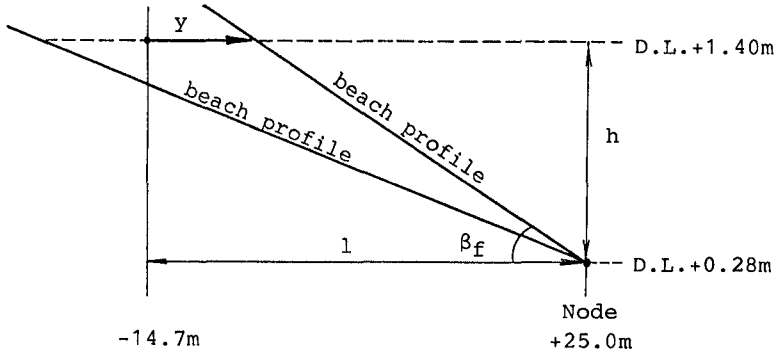


Figure 8 Relation between foreshore slope and shoreline position

reference point 25m be a node since the standard deviation of level changes at this point was minimum as seen in Figure 4. The mean level of reference point 25m is +0.28 meter above the datum line. Figure 8 illustrates the relation between the foreshore slope and the shoreline position. A symbol l is the horizontal distance from the node to the time averaged shoreline position, 39.7 meters. A symbol h is the vertical distance from the node to the level of shoreline, 1.12 meters. A symbol y is the location of shoreline, taking the origin at the mean shoreline position and being positive in the offshore direction. From this concept figure, the foreshore slope is represented by

$$\tan\beta_f = h/(l-y). \quad (6)$$

By substituting Eq.(6) into Eq.(5), and by introducing the actual values of $d=0.18\text{mm}$ and $\tan\beta=1/60$ in the study site, and by normalizing the daily mean energy flux with the mean value of energy flux during the observation, 2.48tm/ms , we have

$$\hat{E} = 4.19 \times 10^{-10} [(l-y)/h]^{7.19}, \quad (7)$$

where \hat{E} is the dimensionless energy flux.

Figure 9 shows a plot of the dimensionless wave energy flux (\hat{E}) versus the shoreline position (y) for 184 cases (days). Essentially speaking, the cross-shore component of energy flux must be considered. The measurement of wave direction, however, is not being done in Kashima Port. Then, the absolute energy flux are utilized without any further calculation. This approximation will introduce a little error of less than 3% when an angle of wave incidence to beach is less than ± 10 degrees. The curved line in Figure 9 is Eq.(7) with the slightly modified constant of 7.15×10^{-10} and an exponential index of 6.0, which can be approximated on the figure by a straight broken line as

$$y = -16.0 \log \hat{E} + 1.63, \quad (8)$$

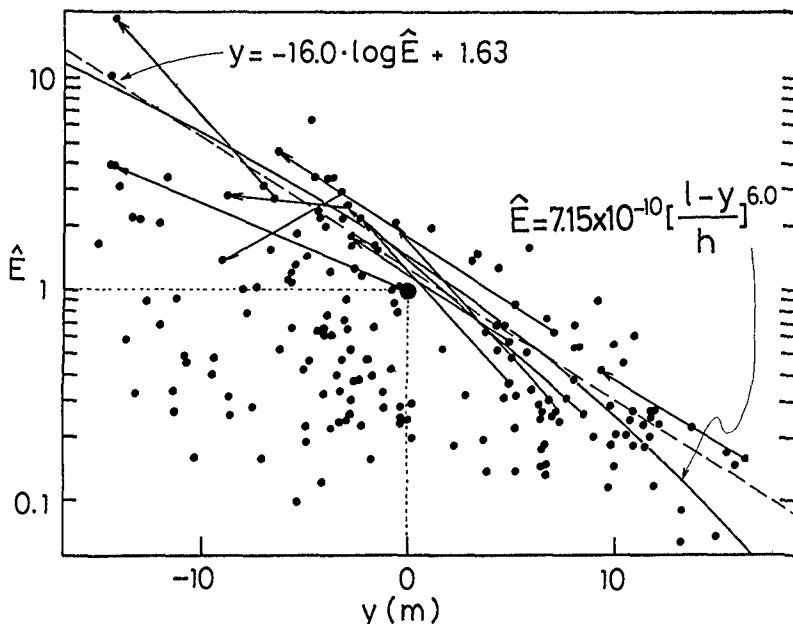


Figure 9 Relation between energy flux and shoreline position

where log is a common logarithm and a unit of y is in meter.

In Figure 9, the rapid recessions more than 5 meters in a day are connected with arrows. The direction of arrows are the same as those of shoreline changes, that is leftward in the figure. It is recognized that the arrows lie parallel near the straight broken line of Eq.(8). According to Figure 9, the shoreline position rapidly recesses by the lower energy flux when the more it is being advanced.

On the other hand, almost all data in the accretionary processes are plotted in the lower side of the broken line in Figure 9.

Furthermore, a relation between the averaged shoreline position ($y=0$) and the mean energy flux (\hat{E}) is just near the broken line, a larger closed circle. This situation is interesting and will be discussed later.

5. Tentative predictive model for daily shoreline changes

The shoreline advances with the constant speed in the accretionary process, while it rapidly recesses in one or two days in the erosional process. Then, without taking into account the time lag of shoreline changes behind the external force, the authors have developed an empirical predictive model for the daily shoreline changes as follow.

The shoreline position and the dimensionless energy flux on the i -th day are denoted by y_i and \hat{E}_i , respectively.

[Step 1] By assuming the accretionary process, the shoreline position on next day can be predicted by a following equation:

$$y_{i+1} = y_i + 0.68 \quad (\text{meter}). \quad (9)$$

[Step 2] The assumption in Step 1 must be confirmed by plotting the data of (y_{i+1}, \hat{E}_{i+1}) in Figure 9. If it will be plotted in the lower side of the broken line, that is,

$$y_{i+1} < -16.0 \log \hat{E}_{i+1} + 1.63 \quad (\text{meter}) \quad (10)$$

y_{i+1} predicted by Eq.(9) is decided to be the shoreline position.

[Step 3] If it will be in the upper side of the broken line, it will be in the erosional process. Then, the shoreline position rapidly recesses along the broken line. A new position of y_{i+1} depends on \hat{E}_{i+1} according to the following equation:

$$y_{i+1} = -16.0 \log \hat{E}_{i+1} + 1.63 \quad (\text{meter}). \quad (11)$$

The above procedure from Eq.(9) to (11) is expressed in one equation as

$$y_{i+1} = \min[y_i + 0.68, -16.0 \log \hat{E}_{i+1} + 1.63], \quad (12)$$

where the symbol $\min[a,b]$ gives the smaller of a or b .

Figure 10(a) shows the relations between the dimensionless energy flux and the shoreline position during the

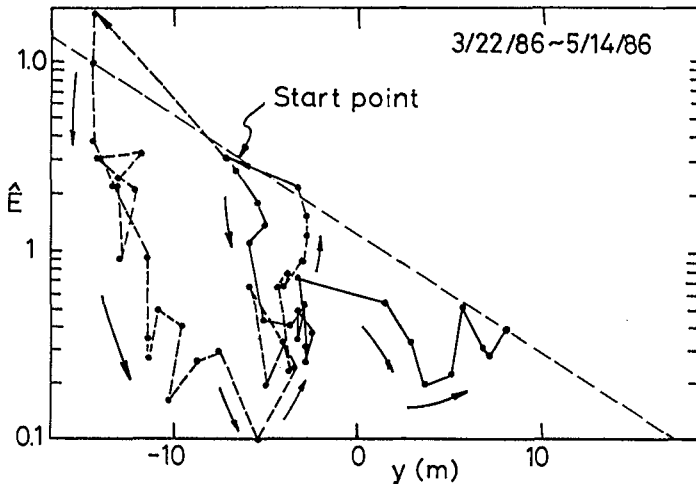


Figure 10(a) Relation between \hat{E} and y (March 22 to May 14)

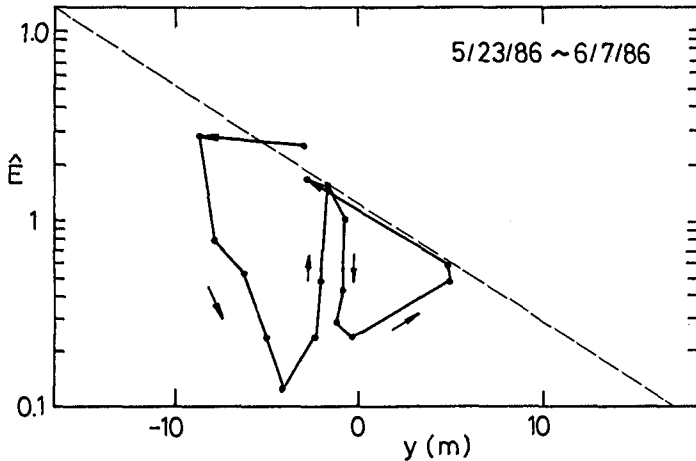


Figure 10(b) Relation between \hat{E} and y (May 23 to June 7)

period from March 12 to May 14, 1986. Broken lines connect the time series data for the first half period and solid lines for second one. A broken straight line in this figure is corresponding to Eq.(8). At first, a rapid recession occurred along Eq.(8) when the value of energy flux was large. After that, the shoreline position gradually advanced with a decrease of wave energy flux up to be $y=-5\text{m}$. In turn, the wave energy flux became to be large, which eventually made the relation between the energy flux and the shoreline position to be on the broken line of Eq.(8). On that day, another rapid recession occurred again along the broken line. Next day, the shoreline position started to advance again under the lower energy flux.

Figure 10(a) shows the time series data during the period from May 22 to June 7, 1986, in the same manner as Figure 10(a). A rapid recession occurred also in this case at first. Subsequently, the shoreline position gradually advanced. During the accretionary process, there was temporary increase of wave energy flux, just reaching to the broken line. The rapid recession, however, did not occur. The shoreline position continued to advance, because the relation between the wave energy flux and the shoreline position on the next day was in the lower side of the broken line. On the last day, the wave energy flux became to be beyond the broken line and another rapid recession occurred along the broken line.

By using Eq.(12), the shoreline position have been successively predicted with the time series data of wave energy flux (see Figure 2). A result of prediction is shown with solid lines in Figure 11 by comparing with the dotted data of actual shoreline position. In calculation, an initial condition is the measured position of shoreline on May 12. As seen in Figure 11, the predicted shoreline

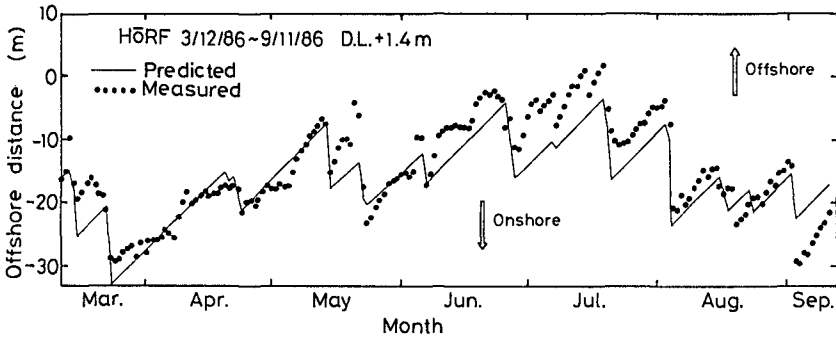


Figure 11 Comparison of changes of shoreline position predicted and those observed

position almost agree with the measured ones.

6. Possibility of combination of the present model and the one-line theory

For practical purpose of predicting the short-term shoreline changes, the present model must be combined with the one-line theory. For this purpose, any mutual contradiction between both models are not basically allowed. Concerning to this problem, the following four items are pointed out:

(a) Both models treat the mechanism of sand transport and the other phenomena in the surf zone in a black box. Therefore, both modeling accuracies of phenomena are almost the same each other.

(b) The external force in the present model is the cross-shore component of energy flux. That in the one-line theory is the longshore one. Therefore, there is no physical contradiction between the models.

(c) The time series data of energy flux are utilized in the present model, while the time averaged energy flux during a objective period is usually utilized in the one-line theory. Fundamentally speaking, the time series data have to be utilized also in the one-line theory. However, it will take much computer processing time for calculating the wave deformation. Usage of averaged energy flux in the one-line theory is only for convenience.

(d) The one-line theory can predict the long-term shoreline changes by inputting the mean energy flux. As shown in Figure 9, the relation between the time averaged energy flux ($E=1$) and the averaged position of shoreline ($y=0$) is just near the broken line, along which the rapid recession of shoreline position occurs. In short, the shoreline position predicted by the one-line theory with the averaged energy flux practically satisfies the relation

of Eq.(8). Therefore, the shoreline position predicted by both models agree at the basic point.

The above consideration shows that there will be no problem in combining them into a new model. The combined model will be able to predict not only the long-term shoreline changes but also the short-term one. The present model, however, is the empirical one, and has the following incomplete points which must be studied further:

- (1) The definition of shoreline position with the level of +1.4 meters above the datum line is not general.
- (2) The effect of changes of sea bottom topography such as bars and troughs on shoreline changes is unknown.
- (3) The changes of tide level is not taken into account in the present model.
- (4) The mechanism of shoreline changes in the short-term has not been known.

7. Conclusions

The conclusions obtained in this study are as follows:

- (a) The shoreline advanced with the constant speed of 0.68 meters/day in the accretionary process.
- (b) In the erosional process, the shoreline rapidly recesses in one or two days. The rapid recession of shoreline depends not only on large energy flux of waves but also on the position of shoreline. In other words, the shoreline recesses by the lower energy flux when the shoreline has advanced, while it advances by the higher energy flux when it has recessed.
- (c) The empirical criterion of an occurrence of rapid shoreline recession is obtained.
- (d) Based on the results of data analyses, the authors have proposed a tentative predictive model of the short-term shoreline changes. This model can predict the shoreline position in order with the time series data of wave energy flux.
- (e) The present model can be combined with the one-line theory without any contradictions.

References

- (1) Sunamura, T. and K. Horikawa (1974): Two-dimensional beach transformation due to waves, Proc. of 14th ICCE, pp.920-938.
- (2) Sunamura, T. (1984): Quantitative predictions of beach-face slopes, Geol. Soc. Am. Bull., Vol.95, pp.242-245.

CHAPTER 94

PROTOTYPE APPLIGATIONS OF A GENERALIZED SHORELINE CHANGE NUMERICAL MODEL

by

Hans Hanson¹, Mark B. Gravens², and Nicholas C. Kraus³, M.ASCE.

ABSTRACT

Three case studies are described in which long-term shoreline response was simulated using a numerical model. One project was along Kachemak Bay, Alaska and involved evaluation of design alternatives that included a detached breakwater, beach fill, and a revetment. The second project was on the north New Jersey coast and characterized by a long seawall and numerous groins. The third project was a model test of shoreline change behind three detached breakwaters Lake Erie. The shoreline response model used, called GENESIS, is demonstrated to have applicability to a wide range of commonly encountered shore protection situations.

INTRODUCTION

Numerical simulation models provide a powerful and unique capability for engineering studies of complex shoreline change occurring under realistic field conditions. Before the development of the modeling system GENESIS, each application of a numerical shoreline response model required extensive modification of an existing model and special refinements for the particular study. To allow application to an arbitrary prototype situation, considerable time was spent on devising a flexible and general internal structure of GENESIS. Through a simple interface, the user can simulate the effects on the shoreline of groins, jetties, detached breakwaters, seawalls, and beach fills. Almost arbitrary numbers, locations, and combinations of such structures can be represented, and user-specified operations can be introduced almost arbitrarily in space and time. The model is economical to run and, therefore, simulations can be performed for wide spatial extents and long time intervals. This paper presents results of applications of GENESIS to three prototype situations. The case studies demonstrate that GENESIS is capable of simulating long-term shoreline change in the field and assisting in the refinement of engineering analysis of shore protection alternatives involving beach fill and various types of structures.

(1) Associate Professor, Dept. of Water Resources Engineering, Lund University, Box 118, S-22100 Lund, Sweden; (2) Hydraulic Engineer; and (3) Senior Research Scientist, Coastal Engineering Research Center (CERC), U.S. Army Engineer Waterways Experiment Station, P.O. Box 631, Vicksburg, MS 39180-0631 USA.

GENESIS

GENESIS allows simulation of shoreline change occurring over a period of months to years as caused primarily by the action of breaking waves. The project horizontal length scale typically varies from one up to tens of kilometers. The model is generalized in the sense that it can be used to simulate shoreline change under a wide variety of user specified beach and coastal structure configurations. In addition, the input wave conditions can be entered either (a) from an arbitrary depth as a single value specified by the user and involving a simplified wave refraction calculation, assuming parallel bottom contours, or (b) through interaction with a more rigorous wave refraction model RCPWAVE (Ebersole et al. 1985) allowing specification of an irregular bottom bathymetry (Figure 1).

GENESIS is based on the one-line (shoreline contour) theory of beach change (Pelnard-Considère, 1956). The same concept has been used in a number of previous studies (e.g., Price et al. 1973, Perlin 1979, LeMéhauté and Soldate 1980). In particular, Kraus et al. (1985), Kraus et al. (1988), and Hanson and Kraus (1986a) present applications of the model employed as an engineering tool for making shoreline change forecasts for a real beach. Based upon the results of these studies, recommendations for remedial measures were given.

BASIC EQUATIONS

As an extensive description of GENESIS, discussing basic assumptions, limitations, and governing equations is given in Hanson (1987), only a short review will be presented here.

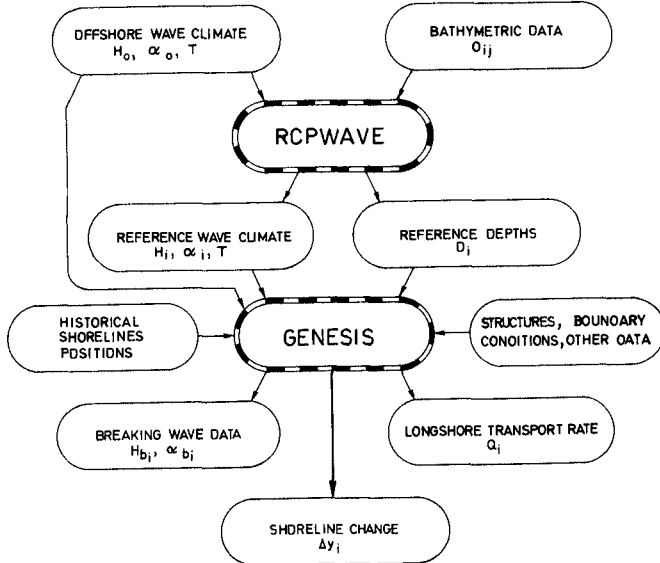


Figure 1. Relation between the wave model RCPWAVE and the shoreline change model GENESIS.

Mass conservation

Following the assumption that the bottom profile moves in parallel to itself to the depth of closure, conservation of sand for an infinitely small length, dx , of shoreline can be formulated as:

$$\frac{\partial y}{\partial t} + \frac{1}{D_B + D_C} \frac{\partial Q}{\partial x} = 0 \quad (1)$$

where y is the shoreline position (m), x is the longshore coordinate (m), t is the time (s), D_B is the average berm height above the mean water level (m), D_C is the depth of closure (m), and Q is the longshore sand transport rate (m^3/s). In order to solve Eq. (1), expressions for the two quantities D_C and Q must be formulated. The berm height, D_B , is taken from the measured or assumed profile.

Depth of closure

For applications involving bypassing of sand at structures, knowledge of the depth to which sand is actively transported alongshore is required. Studies of beach change taking place over a long period of time (years) indicate that the profile varies to the depth of closure, D_C , associated with the wave climate over this long time period. Various values have been suggested for this depth (e.g. Willis and Price, 1975; Kraus and Harikai, 1983; Hands, 1983). These are all of the same order as the formulation of Hallermeier (1983), giving the annual depth of closure as slightly more than twice the extreme annual significant wave height. In the light of these formulations, and keeping the potential errors involved in determining these relations in mind, GENESIS uses a simple relation:

$$D_C = 2 H_{mas} \quad (2)$$

where H_{mas} is the maximum annual significant wave height (m) for the existing site. The value of H_{mas} for a given site must be specified by the user operating GENESIS. Alternatively, measured profiles can be compared and a closure depth estimated. H_{mas} would then be back-calculated by Eq. (2). It is also assumed that the dry portion of the beach profile, from the shoreline to the berm crest, moves with the wet part of the profile while maintaining its shape.

Longshore sand transport

Kraus et al. (1981) and Kraus and Harikai (1983) showed that the simulation of shoreline evolution, especially in the diffraction shadow zone near structures, is greatly promoted by taking the longshore gradient of breaking wave heights into account. For this reason, in GENESIS, the longshore sand transport volume rate, Q , is calculated as:

$$Q = (H^2 C_g)_b (a_1 \sin 2\alpha_{bs} - a_2 \cos \alpha_{bs} \frac{\partial H}{\partial x})_b \quad (3)$$

where C_g is the wave group velocity (m/s), α_{bs} is the angle of wave crests to the shoreline, the subscript b denotes the breaking condition, and the non-dimensional parameters a_1 and a_2 are given by:

$$a_1 = \frac{K_1}{16 (\rho_s/\rho - 1) (1 - p) 1.416^{5/2}} \quad (4)$$

$$a_2 = \frac{K_2}{8 (\rho_s/\rho - 1) (1 - p) \tan\beta 1.416^{5/2}} \quad (5)$$

where K_1 and K_2 are calibration parameters, ρ_s and ρ are the densities of the sediment (quartz sand) and water (kg/m^3), p is the sediment porosity, and $\tan\beta$ is the average bottom slope. The factor 1.416 is used to convert from significant to RMS wave height. The first term in Eq. (3) expresses the longshore transport rate due to obliquely incident waves and is commonly known as the CERC-formula (SPM 1984). The second term, introduced by Ozasa and Brampton (1980), accounts for the longshore sand transport rate caused by the longshore variation in breaking wave height and is especially important in the diffraction zones near structures where the longshore wave height gradient often is strong (Kraus 1983).

HOMER SPIT SIMULATION

Homer Spit, a narrow peninsula southeast of the City of Homer, is between 90 and 450 m wide and extends approximately 7 km into Kachemak Bay in southcentral Alaska (Figure 2). At the tip of the spit are a small-boat harbor and a city dock that is used for year-round shipping. Apart from its commercial importance Homer Spit is also a cultural and social asset, being the only recreational beach in this part of Alaska.

A two-lane road leads from Homer to these developments following the southwestern shores of the peninsula (Figure 3). Since its construction in 1927, the inshore half of the roadway has experienced maintenance problems. Severe storms causing high water levels in combination with intense wave action have overtopped and washed out stretches of the roadway. Various means, including the installation of groins, revetments, and bulkheads have been attempted to control the erosion at the

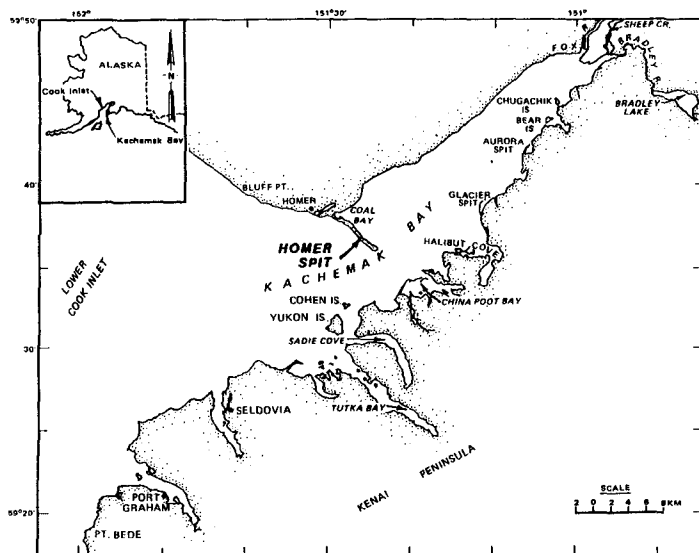


Figure 2. Location map for the study area at Homer Spit.

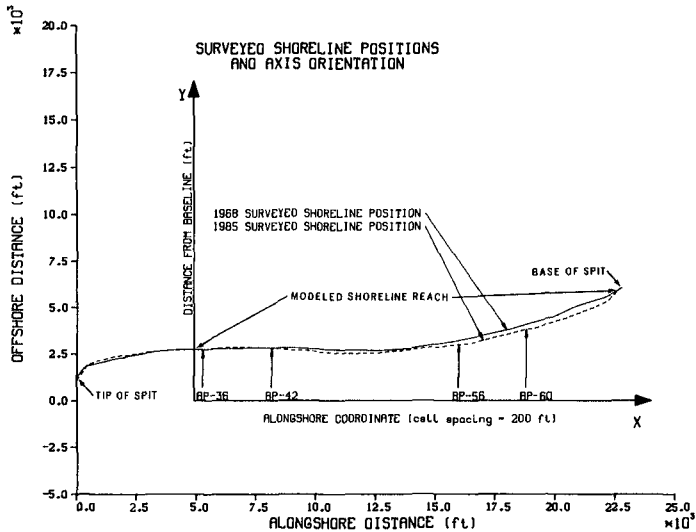


Figure 3. Map of Homer Spit, Alaska showing the extent of the calculation area.

southwestern beach facing outer Kachemak Bay and to mitigate damages to the roadway during extreme storm events. Results of these efforts have not been satisfactory.

The analyses performed by the Coastal Engineering Research Center (CERC) for the Alaska District of the Corps of Engineers (Smith et al. 1985, Chu et al. 1987) included: wind data analysis, deep-water wave hindcast, wave transformation modeling from deep to shallow water, tidal circulation analysis, geological history and sediment sample analysis, beach profile analysis, and longshore sediment transport estimate. By means of wave transformation modeling, a representative 1-year time-varying series of nearshore wave height, period, and direction specified at a 6-hr interval for each of the 79 model calculation grid cells was established.

Modeling Conditions

The input wave data set was prepared at 6-hr intervals, and the longshore sediment transport rates and associated shoreline change were also calculated with a simulated 6-hr time-step. Due to the large tidal range and the significant differences in the average sediment grain size at low, mean, and high tidal levels, the standard version of CENESIS was modified. For compatibility with the shoreline change model, the tide level was simulated at successive time-steps in a cyclical fashion through four representative stages: mean tide, mean high, mean, and mean low. This procedure, in effect, results in a semi-diurnal representation of the tidal cycle. The tides at Homer Spit are indeed semi-diurnal but do have a pronounced diurnal inequality. However, simulation of the tides in the stated manner is consistent with the accuracy of the shoreline change model. Representative grain sizes associated with the respective tidal stage were as determined from the sediment sample analyses: mean low tide, 0.25 mm; mean tide level, 10.23 mm; and mean high tide, 8.13 mm.

The inclusion of tidal changes necessitated input of the average water depth (controlling wave refraction and diffraction) and berm height (affecting the continuity relation) at the various tidal levels. Consistent with the one-line theory of shoreline change, only one contour line was modeled (shoreline at mean tide elevation), but the longshore sediment transport rate (Eq. 3) and corresponding shoreline change (Eq. 1) were calculated at three tide levels based on the particular physical properties (transport parameter K_1 and berm height) estimated for each elevation of the profile.

The longshore grid spacing in GENESIS was set to 200 ft (61 m). This spacing was considered sufficient for evaluating alternative plans but still allowed economical computer execution times. The grid was extended beyond the project area on both sides to obtain termination points that would provide appropriate boundary conditions. Two shoreline surveys of Homer Spit were judged to be adequate for use in the shoreline modeling calibration: October 1968 and August 1985. From inspection of the survey data, two nearly stationary sections of the shoreline were identified. Therefore, a fixed-beach boundary condition, in which the boundary shoreline position is constrained not to move, was implemented at each location. This condition allows sediment to move across the boundary from each side.

Model Calibration

The calibration procedure for GENESIS is to determine the transport parameters K_1 and K_2 of Eqs. (4) and (5) by reproducing measured shoreline change that occurred at the target site between two surveys (here, the 1968 and 1985 surveys). The simulation of shoreline change for this 17-year period was accomplished with the initial shoreline position given by the 1968 measured shoreline. The calibration constants K_1 and K_2 were systematically varied in successive runs of the model, and comparisons were made between the calculated and the measured shorelines of 1985. In addition to visual comparisons of plots, a measure of the calibration error, denoted as Yerr, was calculated to obtain an objective fitting criterion:

$$Yerr = \sum_{i=1}^N \frac{|Y_{calc85} - Y_{meas85}|}{|Y_{meas68} - Y_{meas85}|} \quad (6)$$

where Y_{calc85} = calculated shoreline position 1985; Y_{meas85} = measured shoreline position 1985; Y_{meas68} = measured shoreline position 1968; N = total number of calculation cells; and i = cell number.

As Yerr approaches zero, the accuracy of the calibration increases. Although Yerr was used as a numerical indicator of the relative accuracy of the calibration runs (on the order of 100 runs), the final judgement was based on inspection of plots of the full two-dimensional features of the shoreline planform. The model run chosen as the best fit is shown in Figure 4, giving the values of the calibration constants K_1 (mean low tide, 0.77; mean tide, 0.50; mean high tide, 0.55) and K_2 (0.15). The measured and calculated shorelines agree well.

If sufficient shoreline survey and wave data are available, the calibrated model is run to simulate observed shoreline change in a time interval not spanned by the calibration to verify that the calibration constants are independent of the time interval. Because of a severe earthquake in 1964, only the two previously mentioned shoreline surveys

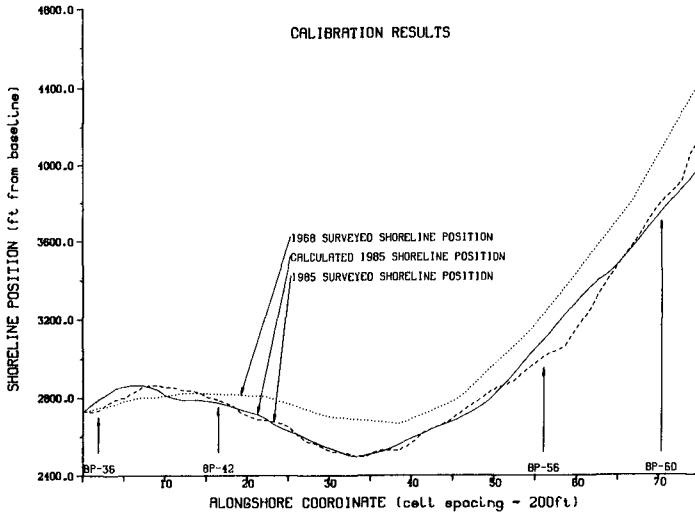


Figure 4. Results of shoreline change model calibration for Homer Spit.

were found suitable. Hence, verification could not be performed, thereby necessitating scrutiny of the sensitivity of the calibrated model to quantify variations in predicted results. A full description of this procedure is given in Chu et al. (1987).

Evaluation of Alternative Plans

Five design alternatives for erosion control (some alternatives including several variations) were analyzed using GENESIS. The alternatives simulated were: a. without-project, b. revetment extension, c. revetment extension with beach fill, d. beach fill, and e. offshore breakwater. A total of 19 alternative erosion control measures were modeled and studied. One best alternative from each of the general design options was selected for a comparative study (see Figure 5). Three of the alternatives shown (1A, 2A, and 5F) indicated considerable erosion and were not recommended for implementation. The remaining two alternatives were (3C) the extension of the existing revetment 610 m towards the tip of the spit combined with a beach fill (30 m added berm width and 610 m alongshore) and (4C) a major beach fill (23 m added berm width and 2,320 m alongshore).

It was difficult to determine which of these two alternatives would best solve the erosion problems at Homer Spit in that the extent of the specified beach fill will ultimately determine the shoreline position. However, model results clearly indicated that nourishment of the existing beach could control coastal erosion problems at Homer Spit. Revetment extension is required to protect the roadway during periods of high tide and storms. A structural approach without beach nourishment may resolve a local problem, but the area of erosion will migrate further down-drift.

Thus, as a conclusion, beach fill, along with extended revetment was considered as the most effective means for erosion control and storm damage reduction at the project area.

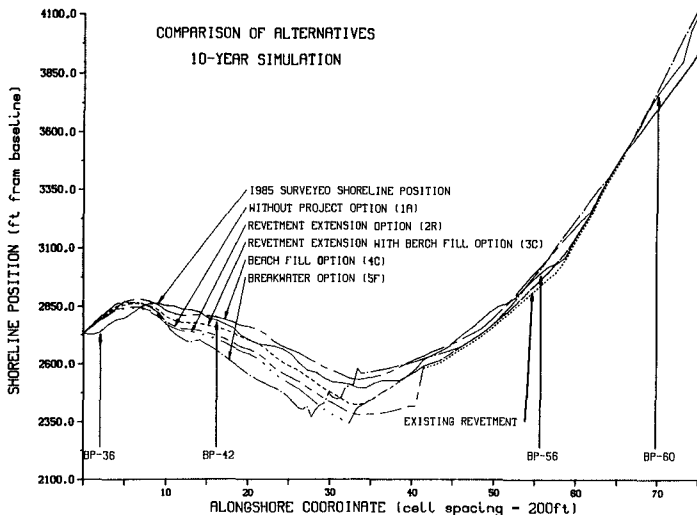


Figure 5. Ten-year simulations of alternative plans for Homer Spit.

SANDY HOOK SIMULATION

This study area constitutes 30 km of the New Jersey barrier island chain from Sandy Hook to Shark River (Figure 6). The coast has been suffering from severe erosion for a century. As an attempt to restore the beach and to secure the integrity of the shore protection structures, a shore protection plan was prepared by the New York District of the Corps of Engineers. The scope of the CERC study was to interpret data and to provide a predictive shoreline change model to assist in the implementation of this plan.

The northern part of the study area consists of Sandy Hook, one of the most famous and most investigated spits in the world. The spit, extending about 16 km into the New York Bight, was originally formed by sand eroding from the adjacent 30 km of the barrier island shores. Ever since the erosion became an increasing problem in the late 19th century, especially from Sea Bright to Monmouth Beach, an increasing portion of the beach has been protected with seawalls, revetments, and groins. Partially as a result of blocking off this sediment supply, sediment transport to the north decreased, causing erosion at the southern part of Sandy Hook, called the "critical zone". This critical zone was of particular interest for the present study as GENESIS was calibrated for this area.

Modeling Conditions

A large portion of the beach south of Sandy Hook is protected by an almost continuous rubblemound seawall and numerous groins. The seawall was modeled according to the principles discussed in Hanson and Kraus (1986b). This seawall constraint is imposed at the same level of approximation as the assumptions used to derive the shoreline change model. Thus, wave reflection, scouring, and flanking are not simulated. The lengths and locations of 91 operating groins were taken from aerial photographs and maps. Very short groins and non-functioning groin remnants were not included. The longshore transport of sand around the

end of a groin is called bypassing, and the transport of sand over and through a groin is called transmission. In this study, there were no data sets available to estimate groin bypassing or transmission. Since the groins in the modeled area are mainly built of heavy, grouted stone, the transmission was set to zero. It is recognized that a limited amount of overtopping does occur during high tide and high wave conditions, but specification of that effect is not possible at the present time. Sand

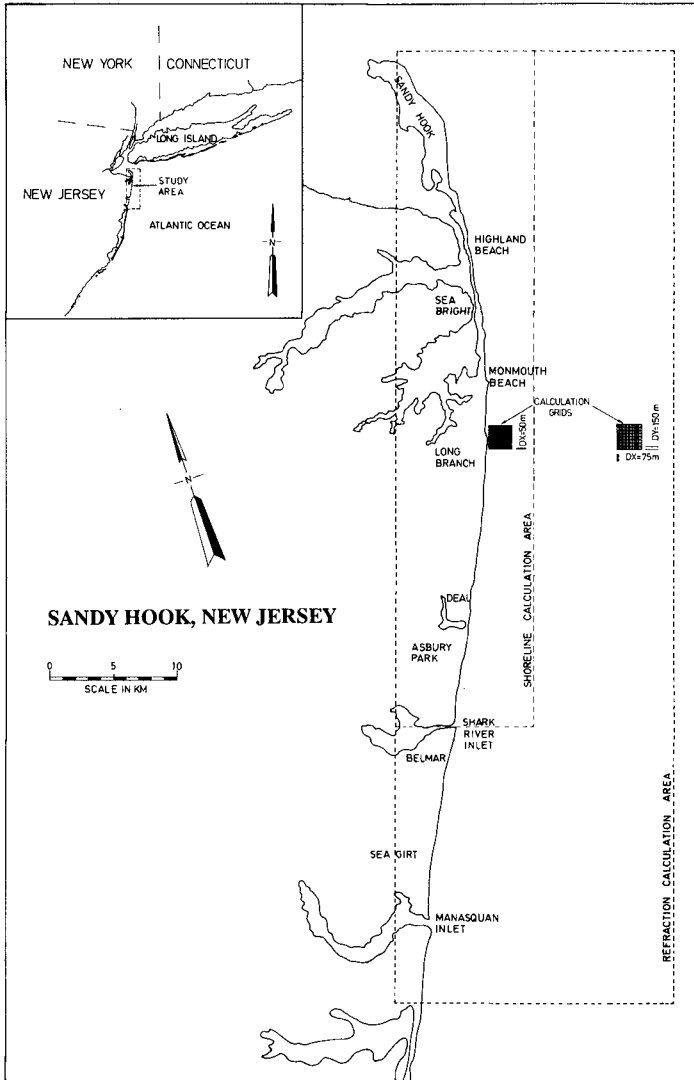


Figure 6. Location map for the study area, showing the extent of the calculation areas and grids for north New Jersey. (Modified from Kraus et al. 1988).

bypassing was calculated according to algorithms incorporated in GENESIS (Hanson 1987).

As no long-term wave measurements were available for the study area, the Wave Information Study (WIS) technique (Jensen, 1983) was used to generate a 20-year hindcast time series of wave height, period and direction at 18 m depth. To keep the data files to a reasonable size, three representative years were selected from the 20-year time series. Wave transformation along the shoreline from the nominal 18 m depth up to breaking was calculated using the wave model RCPWAVE.

Model Calibration

Due to extensive and unrecorded shore protection activities, it was not possible to calibrate and verify the model for the project coast south of Sandy Hook. Instead, the southern part of Sandy Hook, exhibiting beach erosion and with very little human intervention, was used. The dates of major beach fills were known and could be avoided. The calibration was made for an 11-year period, using shoreline surveys taken in 1971 and 1982. An objective fitting criterion, analogous to Eq. (6), was used to obtain $K_1 = 0.4$ and $K_2 = 0.1$. Using these values for K_1 and K_2 , the model was verified from 1932 to 1953. As shown in Figure 7, agreement between the measured and calculated shorelines was very good.

As seen from the basic Eq. (1), the shoreline change in time, $\partial y/\partial t$, is proportional to the longshore gradient of the longshore sand transport rate, $\partial Q/\partial x$, and not to Q itself. Thus, in principle, it would be possible to calibrate and verify the model and still have a significant error in the magnitude of the longshore transport rate. Therefore, it was decided to calculate the annual longshore sand transport from Shark River to Sandy Hook and to compare these figures with previous studies. The result from the calculation is shown in Figure 8. The numbers along the shore give the average annual longshore transport rates in thousands of cubic meters for the three years of wave data. The results agree qualitatively with previous studies: the transport being to the north and somewhat increasing with distance moved northward. Quantitatively, however, the rates are less than those reported in previous

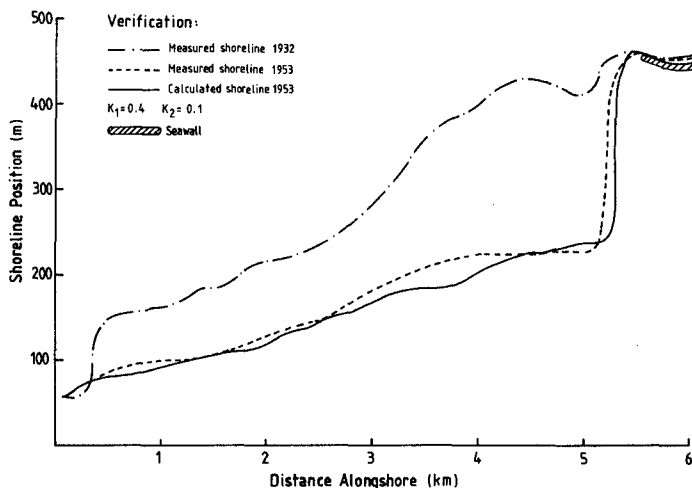


Figure 7. Result of model verification for Sandy Hook, New Jersey.

studies. Therefore, a reanalysis of the wave data, explicitly taking wave sheltering from Long Island into account, is presently being performed.

LAKEVIEW PARK SIMULATIONS

In 1977, three rubble-mound detached breakwaters were constructed at Lakeview Park, Lorain, Ohio, located on Lake Erie. These were the first breakwaters in the United States intended specifically to protect and stabilize a bathing beach (Pope and Rowen, 1983), in this case created by a beach fill (Figure 9). The purpose of the fill was to protect the park and serve as a recreational beach at the same time. In addition to the breakwaters, the beach fill was held in place by one groin on each side.

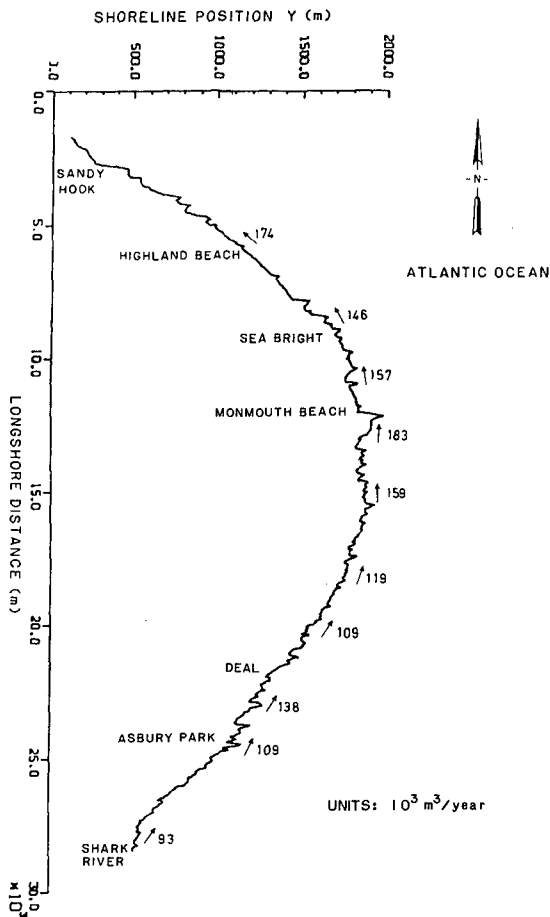


Figure 8. Calculated sand transport rates for northern New Jersey coast. (Modified from Kraus et al. 1988)

Modeling Conditions

The shoreline position and bottom contours were monitored by the Corps of Engineers, both before and after the fill, providing excellent data for a numerical model simulation. The wave data immediately available was limited, however, including only representative wave heights and periods from five different directions and their percentage distribution in time. Little information existed on the actual wave climate (height, period, and direction) between shoreline surveys. A wave time series, prepared at 6-hr intervals to be used in the model calibration/verification procedure, was synthesized for application of GENESIS. All necessary shoreline and structure configuration data were taken from survey charts on a 25-ft (7.6 m) interval. The total distance between the two groins was 1,200 ft (366 m).

Using this limited amount of data, the shoreline change was simulated for the first 24 days after the fill was completed. As the wave input was established on limited information it is likely that, for a short-term simulation as the one made here, the actual mean wave climate could deviate significantly from the representative values.

Model Calibration

Starting with the initial fill shoreline of 1 October 1977, a series of simulations were carried out to reproduce the measured shoreline position of 24 October 1977 (Figure 10). In addition to varying the calibration parameters K_1 and K_2 between the respective simulations, it was found necessary to assume that the average deepwater wave direction deviated 20 deg to the east from the representative values given by the input wave data. This calibration procedure gave values of $K_1 = 0.3$ and $K_2 = 0.3$.

A comparison between the measured and calculated shorelines of 24 October shows that the agreement, from a qualitative standpoint, is good. The model produces three well-developed salients (emerging tombolos) at

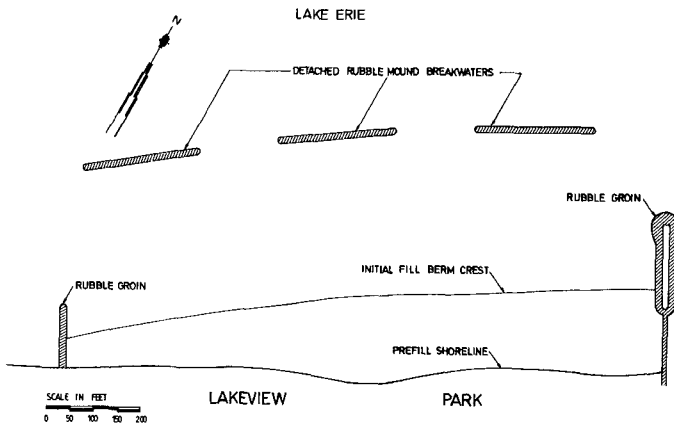


Figure 9. Shoreline and structure configuration at Lakeview Park, Lorain, Ohio.

the proper locations. However, the left-most calculated salient is somewhat too large whereas the other two are too small. An explanation for these discrepancies could be the simplified description of the bathymetry in the area. Due to the limited available wave data, it was decided not to use the wave model RCPWAVE. Instead, all wave calculations were made within GENESIS, assuming bottom contours were parallel to the calculated representative offshore contour line.

In a beach fill project of this type, the volumetric changes can be as informative as the shape of the shoreline. In terms of this volumetric change, the computational results were successful: the measured gain was 59,000 ft³ (1,670 m³) and the calculated gain was 53,000 ft³ (1,500 m³). Thus, the model accounted for 90 per cent of the volumetric change.

Evaluation

Being a small and well documented area, Lakeview Park serves well as a test case for a simulation model. Extensive monitoring of the bathymetry was not balanced with a similar wave documentation. The success of a model application is, to a large extent, limited by the degree to which the true wave climate can be reproduced. However, the lack of reliable wave data at the same time makes the area representative of most coastal projects. The site was therefore considered as an interesting and realistic test of GENESIS. Under the circumstances, and considering the limited effort spent on calibrating the model, the results were very encouraging.

In order to make more accurate predictions of shoreline evolution at the site, the following improvements would have to be made. The wave refraction pattern should be analyzed using the wave model RCPWAVE and the true bottom topography (this was not possible at the time). The breakwaters may also be overtopped, implying that wave transmission will contribute to mould the beach plan form. In addition, wave transmission through the detached breakwaters is believed to have a significant influence on shoreline change and should be represented.

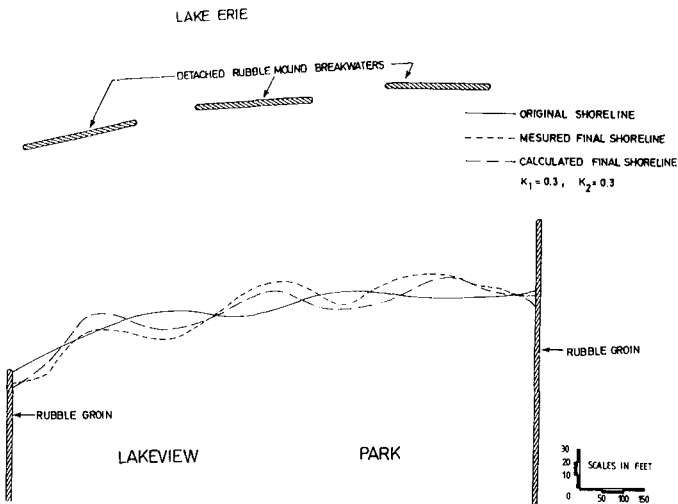


Figure 10. Measured and calculated shorelines at Lakeview Park.

SUMMARY

A numerical modeling system called GENESIS was developed to simulate the interaction between waves, longshore sediment transport, coastal structures, and other engineering activities in the nearshore area. The purpose of the model is to simulate shoreline change on a regional scale and in a long-term perspective ranging from a few months to several years. As opposed to previous models, GENESIS is generalized in the sense that it can be easily applied to almost any open coast and simulate the effects of almost arbitrary numbers, locations, and combinations of groins, jetties, breakwaters, seawalls, and beachfills. The capabilities of GENESIS were demonstrated through three prototype applications: Homer Spit, Alaska; Sea Bright, New Jersey; and Lorain, Ohio.

The calculated examples show that GENESIS is easily applied to quite complex prototype conditions and that the model is capable of simulating long-term shoreline change along coasts controlled by structures as well as open-coast natural beaches.

ACKNOWLEDGEMENTS

This study was partially supported by the work unit "Surf Zone Sediment Transport Processes," under the Shore Protection and Restoration Program of the U.S. Army Corps of Engineers, Waterways Experiment Station, Coastal Engineering Research Center. MC and NCK appreciate the permission granted by the Chief of Engineers to publish this information. The work by HH was carried out under contract No. DAJA45-85-C-0032 through the U.S. Army Research, Development and Standardization Group. This support is gratefully acknowledged.

REFERENCES

- Chu, Y., Gravens, M.B., Smith, J.M., Corman, L.T., and Chen, H.S. 1987. "Beach Erosion Control Study, Homer Spit, Alaska," Miscel. Paper CERC-87-15, US Army Engr. Waterways Expt. Station, Coastal Engg. Res. Center, Vicksburg, MS.
- Ebersole, B., Cialone, M.A., and Prater, M.D. 1985. "RCPWAVE - A Linear Wave Propagation Model for Engineering Use," Technical Report CERC-86-4. US Army Engr. Waterways Expt. Station, Coastal Engg. Res. Center, Vicksburg, MS, 160 pp.
- Hallermeier, R.J. 1983. "Sand Transport Limits in Coastal Structure Design," Proc. of Coastal Structures '83, Am. Soc. of Civil Engrs., pp. 703-716.
- Hands, E.B. 1983. "Erosion of the Great Lakes Due to Changes in the Water Level," In: Komar, P.D. ed., CRC Handbook of Coastal Processes and Erosion, CRC Press, Boca Raton, Fla., pp. 167-190.
- Hanson, H. 1987. "GENESIS - A Generalized Shoreline Change Numerical Model for Engineering Use," Report No. 1007, Dept. of Water Resources Engg., Univ. of Lund, Sweden.
- Hanson, H. and Kraus, N.C. 1986a. "Forecast of Shoreline Change Behind Multiple Coastal Structures," Coastal Engineering in Japan, Vol. 29, pp. 195-213.
- Hanson, H. and Kraus, N.C. 1986b. "Seawall Boundary Condition in Numerical Models of Shoreline Change," Tech. Rep. CERC-86-3, US Army Engr. Waterways Expt. Station, Coastal Engg. Res. Center, Vicksburg, MS, 59 pp.

- Jensen, R.E. 1983. "Methodology for the Calculation of a Shallow Water Wave Climate," Wave Information Study Report, No. 8, US Army Engr. Waterways Expt. Station, Coastal Engg. Res. Center, Vicksburg, MS.
- Kraus, N.C. 1981. "One-Line Development and Simulation for Oarai Beach," NERC Report No. 13, Cooperative Research of Surf Zone Dynamics, Part 3, Beaches Near Breakwaters and Rocky Coasts, Nearshore Environment Research Center, pp. 155-192.
- Kraus, N.C. 1983. "Applications of a Shoreline Prediction Model," Proc. of Coastal Structures '83, Am. Soc. Civil Engrs., pp. 632-645.
- Kraus, N.C. and Harikai, S. 1983. "Numerical Model of the Shoreline Change at Oarai Beach," Coastal Engg., Vol. 7, No. 1, pp. 1-28.
- Kraus, N.C., Hanson, H., and Harikai, S. 1985. "Shoreline Change at Oarai Beach - Past, Present and Future," Proc. 19th Coastal Engg. Conf. Am. Soc. Civil Engrs., pp. 2107-2123.
- Kraus, N.C., Hanson, H., Scheffner, N.W., Chou, L.W., Cialone, M.A., Smith, J.M., and Hardy, T.A. 1988. "Coastal Processes at Sea Bright to Ocean Township, New Jersey," Miscell. Paper CERC-00, US Army Engr. Waterways Expt. Station, Coastal Engg. Res. Center, Vicksburg, MS.
- LeMéhauté, B. and Soldate, M. 1980. "A Numerical Model for Predicting Shoreline Changes," Miscell. Rep. 80-6, US Army Engr. Waterways Expt. Station, Coastal Engg. Res. Center, Vicksburg, MS, 72 pp.
- Ozasa, H. and Brampton, A.H. 1980. "Mathematical Modeling of Beaches Backed by Seawalls," Coastal Engg., Vol. 4, No. 1, pp. 47-64.
- Pelnard-Considère, R. 1956. "Essai de Theorie de l'Evolution des Forms de Rivage en Plage de Sable et de Galets," 4th Journees de l'Hydraulique, Les Energies de la Mer, Question III, Rapport No. 1, pp. 289-298.
- Perlin, M. 1979. "Predicting Beach Planforms in the Lee of a Breakwater," Proc. Coastal Structures '79, Am. Soc. Civil Engrs., pp. 792-808.
- Pope, J. and Rowen, D.D. 1983. "Breakwaters for Beach Protection at Lorain, OH," Proc. Coastal Structures '83, Am. Soc. Civil Engrs., pp. 753-768.
- Price, W.A., Tomlinson, D.W., and Willis, D.H. 1973. "Predicting Changes in the Plan Shape of Beaches," Proc. 13th Coastal Engg. Conf., Am. Soc. of Civil Engrs., pp. 1321-1329.
- Smith, O.P., Smith, J.M., Cialone, M.A., Pope, J., and Walton, T.L. 1985. "Engineering Analysis of Beach Erosion at Homer Spit, Alaska," Miscell. Paper CERC-85-13, US Army Engr. Waterways Expt. Station, Coastal Engg. Res. Center, Vicksburg, MS.
- SPM. 1984. "Shore Protection Manual," 4th ed., 2 vols., US Army Engr. Waterways Expt. Station, Coastal Engg. Res. Center, US Govt. Printing Office, Washington, DC.
- Willis, D.H. and Price, W.A. 1975. "Trends in the Application of Research to Solve Coastal Engineering Problems," In: Hails, J. and Carr, A. (eds.), Nearshore Sediment Dynamics and Sedimentation, Wiley, N.Y., pp 111-121.

CHAPTER 95

Inception of Sand Motion around a Large Obstacle

by

Hidehiro Katsui* , Takao Toue**

ABSTRACT

To select a material for the top layer of the scour protection in the vicinity of a large-scale offshore structure, it is required to know when the material starts to move as a result of waves and currents. But, inception of the motion of sand particles in a region, where diffraction wave superimposes on incident wave and the water particles depict a resulting orbit of ellipse, differs from that calculated by formulae established in the two dimensional wave field.

This paper reveals the discrepancy in calculation when the conventional formulae were used and the data obtained by model experiment. It makes reference, also, to a possible method for a more accurate evaluation of the inception of motion.

1. Introduction

This paper describes the basic study of the local inception of motion of the sand particles which should provide important information in the design of the scour protection for large scale offshore structures.

Scour prevention work has a long history and has progressed rapidly in couple of decades as result of the demands and encouragement from the field of oil production in the North Sea and similar in the world. Before any further discussion of the subject, let us focus on the involved in the rip-rap type of protection as it has a popular practical application and the results of a study of this particular

* Senior Research Engineer, Technical Research Center, Taisei Corporation, 344-1 Nasemachi, Totsukaku, Yokohama, 245, Japan

** Research Engineer, ditto(present: Student of Post Graduate Course at University of Florida, U.S.A.)

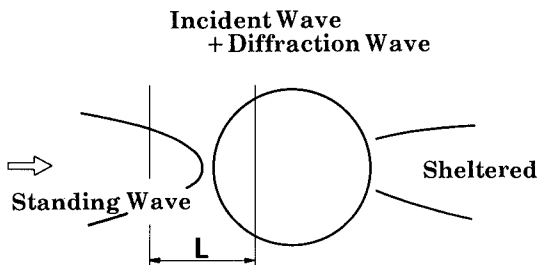
type can be applied to a wide range of other types.

In the design of a scour protection, generally the first to be investigated are the external environmental forces which cause the bottom sand or material of the protection, usually made of coarse shingles, to move. Then the design features of the protection such as, area, resistance, thickness, durability etc. are to be decided on.

For river structures and jacket members, which are subjected to a steady flow or are small in size compared to the wave length, a considerable amount of expertise concerning the mechanism of local scour and the protection work involved has been collected up to now. However, for a large scale offshore structure, where the diameter of which reaches an order of a wave length or KC number in question is smaller than 0.5, sufficient expertise is not available concerning the protection work nor even the external forces.

Lets confine the problem to the condition of regular waves for the sake of simplicity. The wave field around a large scale structure can be divided roughly into three sections as shown in Fig.1. Firstly, in the front area where the standing wave is dominant, knowledge of the breakwater can be applied to the scouring phenomenon, what Irie(1984) has contributed for example. Secondly, in the sheltered area, there are no problems except for sand deposition. Thirdly, a considerably wide area is covered by the field where the diffraction wave is superimposed on the incident wave. Here on the bottom, the water particle depicts the orbit of ellipse as is shown later in Section 5(see Fig.14). The pure incident wave which is a single plane wave exists only in remote area away from the structure.

The question now remains whether the force which puts the particles in motion at this area is the same as that under the plane wave where the oscillatory flow is just in a single direction. To put the question more concretely, "Is the bottom shear stress the same as predicted by the conventional formulae established in the field of pure sinusoidal wave motion in one direction under two dimensional boundary layers? "



Plane Wave

Fig.1 Wave field around a structure

As it is difficult to measure bottom shear directly in the diffraction wave field, so it is difficult to calculate the three dimensional boundary layer equation. Thus the research has begun where a series of model experiments are conducted to see what really happens around a large scale structure under waves. This paper presents a comparison from the observation of the movement of sand particles under plane waves and their movement under diffraction waves.

2. Experiment

The sand movement was investigated where the water depth was constant and the bottom was flat without any ripples. These conditions are plausible for the purpose of looking into the very early stage on particle motion on the top layer of scour protection, which is normally designed and executed flat.

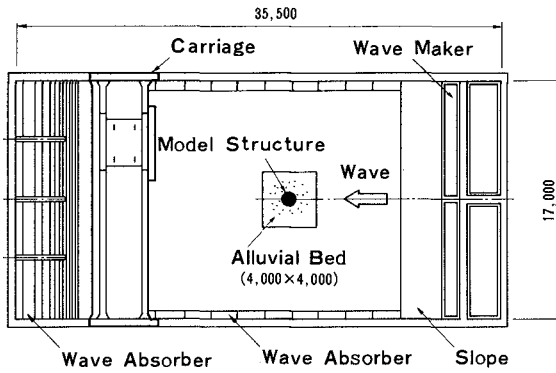


Fig.2 Experimental facility

Table 1 Conditions of experiment

Sand	Grain Size	$D_{50} = 0.58 \text{ mm}$	
Bathymetry	Water Depth	$h = 30 \text{ cm}$	
Waves	Period	$T = 0.8, 1.0, 1.5, 2.0 \text{ s}$	
	Height	$H = 6.0 \sim 9.0 \text{ cm}$	
	Direction	$\theta = 0^\circ, 45^\circ$	
Structures	Shape and Size	Circular $\phi = 117 \text{ cm}$	Square $D = 117 \text{ cm}$
	Height	I : Upright	II : Submerged
	Sketch		
		I (Upright)	II (Submerged)

The experiment was carried out in a wave basin $35\text{m} \times 17\text{m}$ (see Fig.2) with the water depth kept a 30cm. The model offshore structures, measuring 117cm, were installed on a sand bed $4\text{m} \times 4\text{m} \times 1\text{cm}$. The grain size of the sand was chosen as large as $D_{50} = 0.58\text{ mm}$ with quite a uniform distribution, with the shingle material to be used in the scour protection in mind, and also giving the sand function as a tracer.

Gravity type oil production platforms being kept in mind, the shapes of the structure were made basically circular, and square to investigate the effect of flow separation at the corner of the square type. A submerged type, as a model of a submerged storage tank, was also investigated .

The water depth and the structure size were scaled down to the 1/66 model from the prototype planned somewhere offshore east of China. The waves were chosen so that the threshold of the inception of motion could be well resolved by observation. The wave condition together with the types of structures are listed in Table 1.

The movement of the sand was observed by a periscope and video camera. The periscope, a simple combination of a plastic pipe, 80 mm in diameter, with a plate of glass at the bottom, was put into the water to a depth of 10 cm to enable the observation of the movement of the bottom sand without the view being disturbed by the up and down movement of the water surface. Fig.3 shows how the observation device was set up. The observation points around a structure were so disposed by 10 cm pitch mostly to cover the region of 1 diameter cylinder by half of it as is displayed in Fig.4. There were a total of 268 observation points.

The observation procedure was as follows; As soon as the wave field became stationary, a computer control in the carriage mounting the observation device started to repeat a stop and go motion to follow the pre-programed paths of the observation points. Observation for one location took only half a minute and the total time took about three hours, during which it was found that the bottom remained almost flat even where the movement of the sand was greatest.

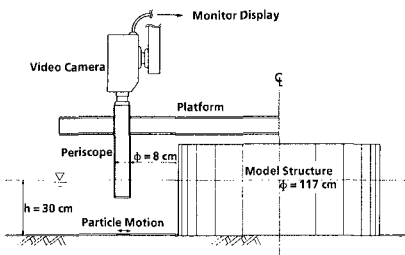


Fig.3 Observation device

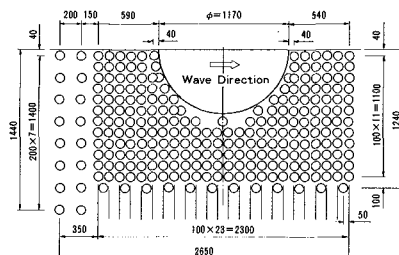


Fig.4 Observation points

3. Theoretical back ground

3.1 Inception of motion of particles under plane wave field

There have been already extensive research contributions in the area of prediction of inception of motion of particles under plane wave field. They are categorized into three approaches which follows;

(1) Critical velocity u_c is evaluated from Eq.(1), originally presented to give critical water depth, with the aid of linear (or nonlinear) wave theory.

$$(H/H_0)^{-1} (\sinh 2nh/L)(H_0/L_0) = \alpha(L_0/D)^n, \quad (1)$$

where H and L are wave height and wave length respectively at water depth h , suffix 0 indicates those parameters in the deep sea and D is diameter of sand particles. α and n are constants summarized in a table presented by Noda(1981), which vary with the condition of the boundary layer originally given by, Ishihara·Sawaragi(1960), Sato·Tanaka(1962) Horikawa·Watanabe(1966).

(2) The more direct method of obtaining critical velocity is to use Eq.(2).

$$u_c = \beta \cdot \Delta^{\gamma} \cdot D^{50^{\delta}} \cdot T^{\epsilon}, \quad (2)$$

where Δ is specific gravity of sand particle in water and T is wave period. $\beta, \gamma, \delta, \epsilon$ are constants given by many researchers such as Bagnold(1946), Goddet(1960), Komar·Miller(1974). The merit of this formula is that it reflects the direct results of the experiments, but the demerit is that those constants vary with the different experiments.

(3) The third approach to calculating the threshold of the movement of sand particles is to use Eq.(3) and Eq.(4).

$$u_* / u_{b0} = \sqrt{f_w / 2} = F_1(a_b / k_s, T), \quad (3)$$

$$u_* c = F_2(u_* D^{50} / \nu), \quad (4)$$

where, u_* , $u_* c$ is the shear velocity and critical shear velocity respectively, f_w is the friction factor. u_{b0} is the velocity amplitude outside the bottom boundary layer, a_b is the amplitude of the excursion of water particles on the bottom, k_s is the bottom roughness and ν is the kinematic viscosity. The function form F_1 is given by Kajiura(1965), Jonsson(1966), Horikawa·Watanabe(1966), while F_2 is given by Shield's curve for steady flow as an approximation, or by Madsen·Grant(1976) in the oscillatory flow condition.

Eq.(3) gives shear velocity based on the consideration of the

boundary layer, while Eq.(4) gives critical shear velocity, which is an experimental parameter. However, it is not certain at present whether these parameters can be applicable under the diffraction wave field where water particle motion is more complicated than with uni-directional oscillation.

3.2 Boundary layer equation under diffraction wave field

So far, the boundary layer equation of the oscillatory flow has been treated on the x-z plane, with x coordinate taken in the direction of the horizontal motion of the water particle induced by single directional wave (plane wave) motion and z in the vertical direction in which the boundary layer develops.

Here, to investigate the bottom shear caused by the multi-directional flow on the bottom where the path is elliptical, the boundary layer should be modeled in the x-y-z region, of which the x-y plane is taken on the bottom. In this respect, Tanaka-Shuto(1981), Fredsøe(1984) developed the models.

Tanaka(1981) treated the flow inside the boundary layer as a wave-current coexistent system. Let $u = (u_x, u_y)$: the combined velocity inside the boundary layer on the x-y plane, p: water pressure, $\tau = (\tau_x, \tau_y)$: bottom shear stress, ρ : density of water, t : time, then,

$$\partial u / \partial t = -(1/\rho) \nabla p + \partial(\tau/\rho) / \partial z \quad . \quad (5)$$

It is assumed that the shear stress can be estimated by the velocity of the oscillatory component u_w by

$$\tau / \rho = K_z (\partial u_w / \partial z) \quad , \quad (6)$$

where K_z is given by

$$K_z = \kappa u_w^* z \quad . \quad (7)$$

u_w^* is the shear velocity under the wave-current coexistent system. With the boundary condition at outside edge of the boundary layer, Tanaka derived Bessel's equation and thus obtained the solution for the bottom shear in the wave-current coexistent system.

However, the attempt by the authors to apply his theory to the field where the orbital motion of water is elliptical (without current) failed to bear anything new in evaluating bottom shear. The reason for this was because, with the assumptions of Eqs.(6) and (7), the solution of the bottom shear stress τ_b depicts a complete similar Lissajous figure(ellipse) as the velocity u_b at the outside of the boundary layer, with a constant phase lag. This means there was no change in the maximum shear as is predicted by the two dimensional treatment.

Fredsøe(1984) has started with the same basic equations as Eqs.(5),(6),(7), and has derived the more direct equation to obtain shear stress but with the more simple assumption that the orbital motion is circle and the phase lag between a flow outside the boundary layer and that inside the layer is negligibly small, which is not always the case. His conclusion is that the shear stress with the circle orbit increases by 10-15% more than with the simple oscillatory flow. However, the assumption that the phase lag can be neglected is rather difficult to accept.

4. Experimental result

4.1 Verification for method of experiment

There are some uncertainties when it comes to defining sand particle movement, which has caused some deviations in the data obtained by various researches so far. There was a fear that the presence of the periscope disturbed the bottom flow. To judge whether the observation was correctly carried out and to compare the criteria of movement defined by the authors with that of established results, the verification experiment was carried out for the plane wave.

Fig.5 shows the result. The symbols in the figure show the rank of movement. The curves are also drawn using Eq.(1) to Eq.(4) for the sake of comparison. Dashed lines represent the initial movement obtained by Isihara·Sawaragi and Jonnson+Shields. The solid lines indicate the severe movement shown by Horikawa·Watanabe and Sato-Tanaka. The lines of Komar-Miller and Goddet fall firmly on these solid lines. The result of the experiment is in good agreement with the calculation lines, except for the small deviations. This means that the observation method was correct.

4.2 Inception of sand motion around a large structure

In Fig.6 shows the result of the observation on the movement of sand

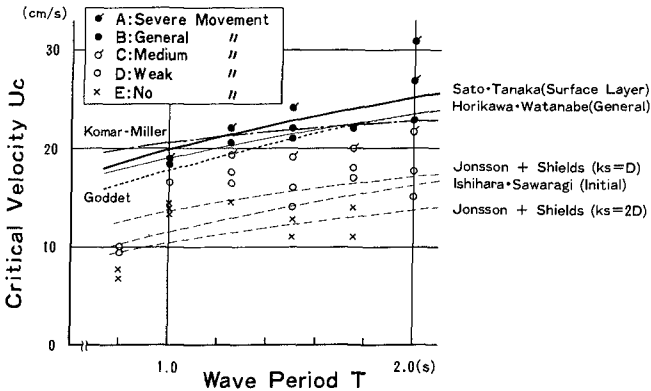


Fig.5 Critical velocity under plane waves

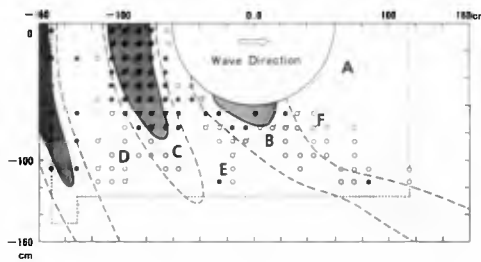


Fig.6 Particle movement(Circular-I, $T=1.0s$, $H=8.0cm$)

particles around a large scale circular cylinder. The observation area is enclosed by dotted lines and is somewhat rectangular in shape. The symbols have the same meanings as in Fig.5, while, for simplicity no symbols inside the observation area indicate no movement. The curves in Fig.6 are drawn by the method explained in Section 3.1. First, the bottom velocity field around a cylinder was calculated using potential wave theory, then it was compared with the threshold data obtained from the experiment for verification under plane waves explained in Section 4.1(see Fig.5). The data read from Fig.5 as follows; $u_c = 0.15$ m/s for the initial movement for $T=1.0-2.0s$, $u_c=0.175, 0.205, 0.225$ m/s for the general movement for $T= 1.0, 1.5, 2.0s$ respectively. The light gray zones, enclosed by dashed lines, are for the initial movement, while dark zones, enclosed by solid lines, are for the severe movement. No color indicates no movement theoretically.

The general impression of the comparison of the state of movement between the experiment and the calculation is that they agree quite well. As for the initial movement, the sheltered area noted by character A in the figure agrees well, while in B and C where the particles were expected to move, they actually didn't move, and in D, E and F where no motion was expected some movement in fact occurred. As for the general movement, the agreement is fairly good.

The pattern of the sand movement in front of the cylinder ("front" here means the area facing the direct wave attack, and "lee" means the sheltered area, the opposite side of the front area), generally corresponds to that of the diffraction wave height. Severe movement occurred at the node, no movement or weak movement occurred at the antinode.

To summarize, even in the region of diffractive wave, the front side of the cylinder where the long crested standing wave was dominant, hence wave motion was rather two dimensional, as well as in the sheltered lee side where only small amplitude diffraction waves with their long crests penetrated, inception of motion agreed well with the conventional motion criteria. In other regions, such as to the side of the front of the cylinder where the orbit of the bottom water particles was circle or ellipse, the conventional formulae for inception were no longer valid, in the strict sense.

When the wave height decreases by only 1 cm, the pattern of the movement exhibits quite a significant change, as is shown in Fig.7. In this case, the calculations predict the general trend of movement well, but, the agreement does not reach the same extent as in the previous case. Especially to the side of the front area, the agreement becomes less. The prediction of the weak movement in this region by conventional formulae becomes more difficult than in the case of single plane waves.

The change of the wave period also changes the pattern of the movement. Fig.8 and Fig.9 show the case of $T=1.5s$ and $2.0s$ respectively. The same comment as the above is drawn about the agreement. The longer the wave period, the more lee side the severe

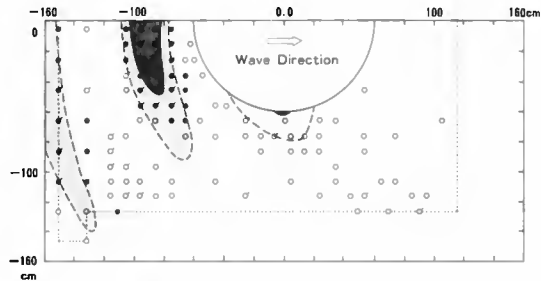


Fig.7 Particle movement(Circular-I, $T=1.0s$, $H=7.0cm$)



Fig.8 Particle movement(Circular-I, $T=1.5s$, $H=6.0cm$)

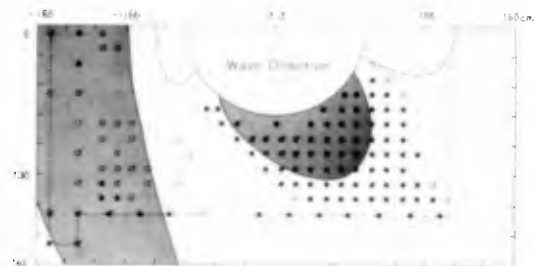


Fig.9 Particle movement(Circular-I, $T=2.0s$, $H=8.0cm$)

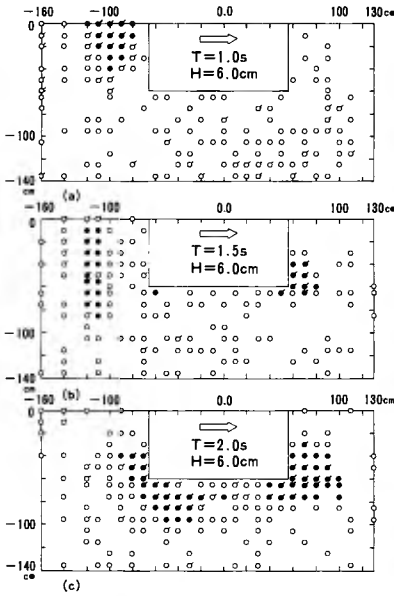


Fig.10 Particle movement (Square-I, $\theta=0^\circ$)

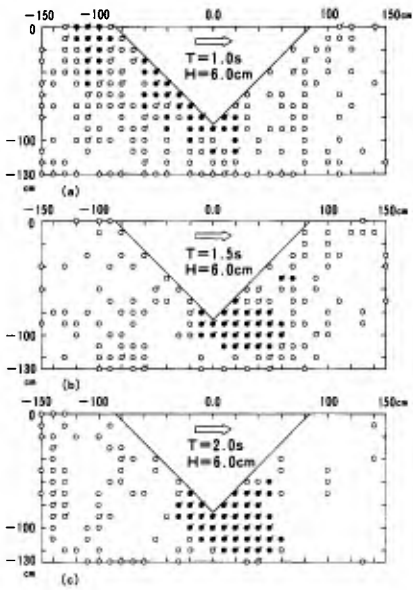


Fig.11 Particle movement (Square-I, $\theta=45^\circ$)

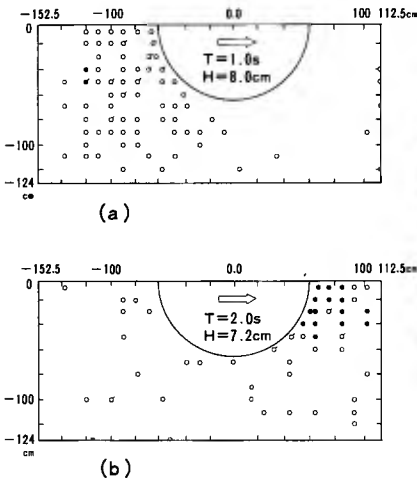
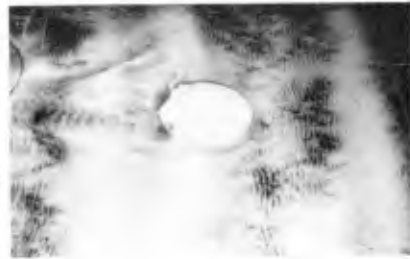


Fig.12 Particle movement (Circular -II)



Photograph 1 Wave breaking on the top of a submerged cylinder (Circular -II)

movement area shifted. The agreement of the calculation and the experimental result is generally good. However, again, the disagreement to the side of the front region is not negligibly small.

Fig.10 and Fig.11 show the cases of the square cylinder, in which wave directions are $\theta = 0^\circ$ and 45° respectively. Square cylinders generally give a similar pattern of movement to that of the circular one. Again, the longer the period, at the side of the region further back the more severe the movement becomes. A characteristic of the square type is the accelerated motion at the corners. This trend is emphasized when the corner locates where the water velocity becomes most accelerated as in the case where $\theta = 45^\circ$, shown in Fig.11.

The movement patterns of shown so far are generally similar to the scour patterns obtained in the model experiment done by the authors(Toue ·Katsui 1985), as well as in one conducted by Rance (1980).

There is less impact at the bottom of a submerged structure as shown in Fig.12(a). However, it sometimes helps wave breaking at the top of the body, hence the particles in the lee side are easy to move even in the sheltered area(see Fig.12(b)). Photograph-1 shows how a wave breaks on the top of a submerged circular cylinder.

4.3 Ripple formation around a structure

The bottom configuration was also measured with the thicker layer(depth:30cm) of finer sand($D_{50}=0.15$ mm), which was easier to move. Photograph-2 and Fig.13 show two examples of the results, which give a general view of the scour pattern around a circular type cylinder and a square type cylinder respectively. The pattern of erosion and deposition in the front area corresponded to that of severe motion. Erosion occurred to the side at the front and in the lee side.

Laboratory experiment on the morphology of the bottom, however, has its limitations. Whenever the data, such as the scour hole depth or scouring area, are translated to the case of the prototype or to the design procedure, special care should be taken with the scale effect. But, the pattern of the ripple formation around a structure is quite typical in the region to the side of the front where diffraction waves dominate as can be clearly seen in Photograph-3. This fact may give some clues in understanding the mechanism of bottom shear or presumable special flow.

5. Possible approaches to understanding the phenomena

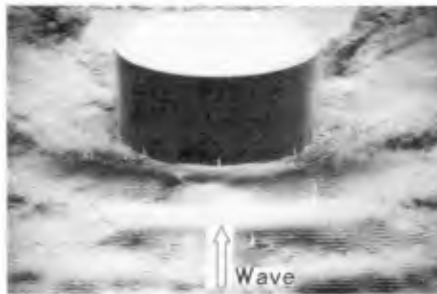
It was confirmed that the inception of sand particle motion in the region where waves from different directions are superimposed on each other differs from what is calculated by conventional two dimensional formulae. This phenomenon could be considered inherent, too, in front



Fig.13 Bird's eye view of measured bottom change
(Square-I, $\theta=0^\circ$, $T=1.0\text{s}$, $H=10.0\text{cm}$, $t=120\text{min}$)



Photograph 2 Bottom change around a cylinder
(Circular-I, $T=1.0\text{s}$, $H=11.0\text{cm}$, $t=120\text{min}$)



Photograph 3 Ripple pattern to the side of the front of a cylinder

of a breakwater when waves come obliquely to the normal direction of the breakwater and thus making a short crested standing wave field.

The phenomenon should be fully understood for the proper design of the scour protection around a structure. The reasonings can be accounted for in several possible ways; the measurement error, the nonlinearity of the bottom velocity (the velocity was estimated by linear wave theory), the special transformation of the bottom shear caused by the the elliptical orbital motion of the water particles or the induced flow around a structure.

As for the first possibility, there might have been, to some extent, wave reflection from the other end of the wave basin, inhomogeneity of the incident wave and the ambiguous judgement of sand movement despite the efforts to avoid them. The use of the linear wave theory to obtain the bottom velocity proved not to influence the accuracy. However, most of the above suspicions are cleared up with the verification test for the plane wave field already stated at Section 3.1.

Secondly, it would be natural to consider that the development of the boundary layer is influenced by the elliptical orbital motion of the water particles. Fig.14 shows the elliptical Lissarjous figure of the velocity vector, which is typical in the region to the side of the front of the cylinder. Even though the attempt by the authors failed to introduce theoretically the special development of the boundary layer there, the bottom shear, hypothetically, may be distorted both in amplitude and in phase lag from those in the two dimensional flow field, as Fredsøe(1984) partially has introduced the bottom shear where the orbital motion was circle.

The third possibility is the formation of the flow. In the experiment, the flow was also observed using dye from the point of view of directional flow not quantity of flow. There was a steady flow from the side of the cylinder to its lee side with a magnitude of a few cm's per second. It can be understood to a certain degree with the help of Fig.15, which shows a flow pattern of mass transport velocity around a circular cylinder inside the boundary layer. The figure was calculated after Mei(1983). But, in front of the cylinder, the flow

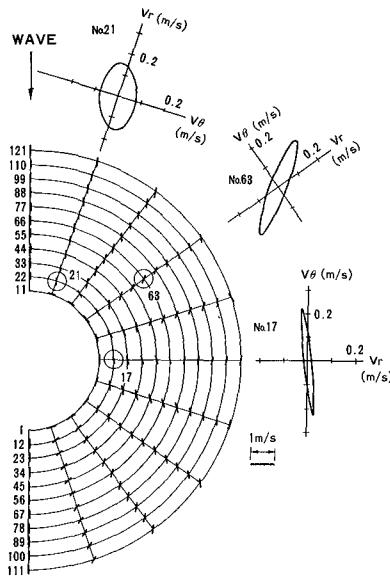


Fig. 14 Lissajous figures of bottom velocity vector around a cylinder(Circular -I)

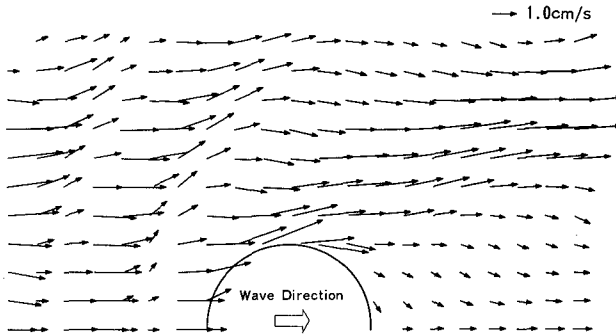


Fig.15 Mass transport velocity around a circular cylinder
(Circular -I, $T=1.0\text{cm}$, $H=10\text{cm}$)

was observed to be in the offshore direction (against the direction of the wave incidence), with a magnitude of the same or a little stronger than that of the side flow. Thus in the area to the side of the front of the cylinder there was a kind of dead space with respect to the steady flow, in which the dye stayed for a considerably long time creating a circulation with the concentration of the dye color being faded at this particular place. Fig.15 cannot account for this kind of flow pattern. This fact indicates that there should be some other mechanism which creates the flow around the structure, something which may be caused by the gradient of radiation stress as is the case in the surf zone.

6. Conclusion

The basic, or preliminary, study of the inception of sand particle motion around a structure using the model experiment was carried out, as well as a simple application of the formulae established in plane wave motion. Through this study, it was confirmed that at the area where the wave motion is more two dimensional, areas like front area or sheltered area, the conventional formulae are applicable, but in the area where the wave field is more complex that the orbital motion of water particles depict circular or elliptical path, there are discrepancies between such formulae and the experimental results.

The reasons of the discrepancies can be ascribed to two kinds of phenomena. One possibility is the flow induced by mass transport inside the boundary layer and/or by a flow which is presumably caused by the gradient of radiation stress around a structure. The second reason could be that the boundary layer, hypothetically, may develop in a more complex manner such as with some distortion in three dimensional space in the area where water particle figures the elliptical Lissajous.

Further research is required both on the theoretical treatment and to obtain a more precise measurement data concerning the flow in the region where multi-directional waves are superimposed themselves.

Acknowledgement

The authors wish to express their appreciation to Professor Jørgen Fredsøe, Technical University of Denmark, for his courtesy of giving significant suggestions.

Reference

- 1) Bagnold, R.A. (1946): Motion of waves in shallow water; Interaction between waves and sand bottoms, Proc. Roy. Soc. London Ser. A, Vol. 187, pp. 1-18
- 2) Goddet, J. (1960): The initial stage of the transport of materials under wave action, La Houille Blanche, Paris, France, No. 2, pp. 122-146
- 3) Fredsøe, J. (1984): The turbulent wave boundary layer along a vertical wall, Prog. Rep. 61, Inst. Hydrodyn. and Hydraulic Eng. Tech. Univ. Denmark, Sept. pp. 23-33
- 4) Horikawa, K. and A. Watanabe (1966): A consideration of the movement of the sand under wave action, Proc. 13th Japanese Conf. on Coastal Eng., pp. 126-134 (in Japanese)
- 5) Irie, I., K. Nadaoka, T. Kondo and K. Terasaki (1984): Two dimensional sea bed scour in front of breakwaters by standing waves, Report of Port and Harbour Research Institute, Vol. 23, No. 1, pp. 3-52
- 6) Ishihara, T. and T. Sawaragi (1960): Critical velocity for sand drift; Critical water depth and transport-rate, Proc. 7th Japanese Conf. on Coastal Eng., pp. 47-58 (in Japanese)
- 7) Jonsson, I.G. (1966): Wave boundary layers and friction factors, Proc. 10th International Conf. on Coastal Eng., Vol. I, pp. 127-148.
- 8) Kajitara, K. (1965): On the bottom friction in an oscillatory current, Bull. Earthq. Res. Inst. Vol. 42, No. 1, pp. 147-173
- 9) Komar, P.D. and M.C. Miller (1974): Sediment threshold under oscillatory waves, Proc. 14th International Conf. on Coastal Eng., Vol. II, pp. 756-775
- 10) Madsen, O.S. and W.D. Grant (1976): Sediment transport in the coastal environment, Ralph M. Parsons Lab. for Water Resource and Hydrodynamics, M.I.T. No. 209
- 11) Mei, C.C. (1983): The applied dynamics of ocean surface waves, John Wiley & Sons, New York, pp. 419-434
- 12) Noda, H. and Hashimoto (1981): Sand drift and shore protection facilities, Gihodo Press, p. 36. (in Japanese)
- 13) Rance, P.J. (1980): The potential for scour around large object; Scour protection Techniques around offshore structure, The Society of Underwater Technology, One-day seminar, pp. 41-54
- 14) Sato, S. and N. Tanaka (1962): Sand motion on the horizontal bottom under waves, Proc. 9th Japanese Conf. on Coastal Eng., pp. 95-100 (in Japanese)
- 15) Tanaka, H. and N. Shuto (1981): Friction coefficient for wave-current coexistent system, Coastal Engineering in Japan, Vol. 24, pp. 105-128
- 16) Toue, T. and H. Katsui (1985): On a scour around a large circular cylinder, Proc. 32nd Japanese Conf. on Coastal Eng., pp. 425-429 (in Japanese)

CHAPTER 96

BEACH PROFILE CHANGE: MORPHOLOGY, TRANSPORT RATE, AND NUMERICAL SIMULATION

Magnus Larson¹, Nicholas C. Kraus², M.ASCE, and Tsuguo Sunamura³

ABSTRACT

An empirically based engineering numerical model is presented for simulating beach profile change in the surf zone produced by wave-induced cross-shore sand transport. The model simulates the dynamics of macroscale profile change, such as the growth and movement of berms and breakpoint bars. Model development was founded on two data sets from large wave tank experiments consisting of 42 cases with different incident wave conditions, median grain size, and initial beach shape. Model predictions are tested with field data, and reasonable agreement is found.

INTRODUCTION

Techniques to predict shore-normal evolution of the profile to changes in incident waves and water level are needed for design, maintenance, and evaluation of beach stabilization and shore protection projects. Time scales involved range from days for storm-induced beach and dune erosion to months for adjustment of beach fill to equilibrium. This paper presents a practical empirically based numerical model of beach profile change developed for engineering design which simulates the formation and movement of bars and berms. The model is applicable to describing profile change resulting from cross-shore sand transport produced by varying water level and short-period breaking waves in the range of approximately 3-20 sec.

The numerical model was developed through extensive investigation of beach profile change obtained in large wave tanks (LWTs) under controlled conditions, in order to understand the fundamental processes of macroscale profile change and cross-shore sand transport. Quantitative relationships were derived from the LWT data set to identify the important parameters of profile change and to establish cause and effect relationships between the incident waves and profile response.

(1) Assistant Professor, Department of Water Resources Engineering, Institute of Science and Technology, University of Lund, Box 118, S-221 00 Lund, Sweden.

(2) Senior Research Scientist, Coastal Engineering Research Center (CERC), U.S. Army Engineer Waterways Experiment Station, P.O. Box 631, Vicksburg, MS 39180-0631, USA.

(3) Professor, Institute of Geoscience, University of Tsukuba, Ibaraki 305, Japan.

The numerical model was then tested by reproducing LWT measurements and, when satisfactory agreement was obtained, it was applied to predict measured profile change in the field produced under time varying waves and water level. This paper summarizes and integrates results presented in more detail in four publications by the authors (Larson 1988, Larson and Kraus 1988a,b,c).

PROCEDURE

Field data sets useful for developing models of beach profile change are lacking because of the required high resolution measurement in time and space of the profile and the waves and water level that produced the change. Due to the great spatial and temporal variability of waves and the three-dimensional character of nearshore bathymetry, it is also difficult to extract cause and effect relationships between waves and profile change resulting solely from the wave-induced, cross-shore component of sand transport. However, any engineering simulation model must ultimately be tested with field data prior to actual application.

The most fruitful approach for empirical investigation of beach profile change appears to be use of data obtained with LWTs. Such facilities enable controlled reproduction of near-prototype conditions of beach slope, wave height and period, turbulence induced by wave breaking, and resultant sand transport and beach change. The problem of scaling encountered with small laboratory tanks is eliminated, and the required high resolution measurement of the profile can also be attained. Recently, two extensive independent data sets on beach profile change have become available from experiments performed using LWT and monochromatic waves. These experiments involved combinations of waves, water levels, beach slopes, and sand sizes that exist in the field, but with the advantages of true two-dimensionality, control of the external (wave) force, and an optimized measurement schedule. These data sets were selected for use in the present investigation and intensively analyzed.

One data set was obtained in experiments performed by the U.S. Army Corps of Engineers (CE) in the years 1956-1957 (Saville 1957) and 1962, recently compiled by Kraus and Larson (1988a). In the CE experiments 18 cases have been documented of which most were started from a plane slope of 1/15. The wave parameters ranged from periods between 3.75 and 16.0 sec and generated wave heights between 0.55 and 1.68 m in the horizontal section of the tank. The water depth in the horizontal section was in the range of 3.5-4.6 m in the different cases, and two grain sizes were employed with median diameters of 0.22 and 0.40 mm.

The second data set derives from experiments performed at the Central Research Institute of Electric Power Industry (CRIEPI) in Japan (Kajima et al. 1983a, 1983b). The CRIEPI experiments followed the pattern of the CE experiments. Quartz sand of median grain sizes 0.27 and 0.47 mm was employed in 24 cases of which 17 cases involved initial uniform beach slopes of 1/10, 1/20, 3/100, or 1/50. The cross-shore distribution of wave height was also measured between profile surveys.

RESULTS

Quantification of Morphologic Features

Profile morphologic features of interest are formations created by wave action, directly or indirectly, during time scales of several tens of the wave period. These features, particularly bars and berms, were defined with respect to the initial profile, which provided an unambiguous characterization for relating profile response to wave and beach properties.

The equilibrium profile is the shape achieved by a beach exposed to waves of constant characteristics for a long duration. In the equilibrium state sand particles may move, but there is no net transport along the profile. Despite the stochastic character of microscale fluid and sediment motion, as well as small variations in applied forces moving the sand, macroscale changes of physical and derived quantities from the experiments approached an apparent equilibrium value in a remarkably smooth manner.

If the profile is not in equilibrium with the waves passing over it, net transport of material occurs. It is of considerable scientific and engineering significance to predict whether a beach will erode or accrete, i.e., form a bar or a berm under given wave and beach conditions. In the present study, a new criterion was developed based on the deepwater wave steepness H_0/L_0 and the dimensionless fall speed parameter H_0/wT using only LWT data (H_0 =deepwater wave height; L_0 =deepwater wavelength; w =sand fall speed; T =wave period). Fig. 1 is a plot of the prototype-scale data together with the developed empirical criterion to distinguish bar/berm profiles. The criterion is

$$\frac{H_0}{L_0} = 0.00070 \left(\frac{H_0}{wT} \right)^3 \tag{1}$$

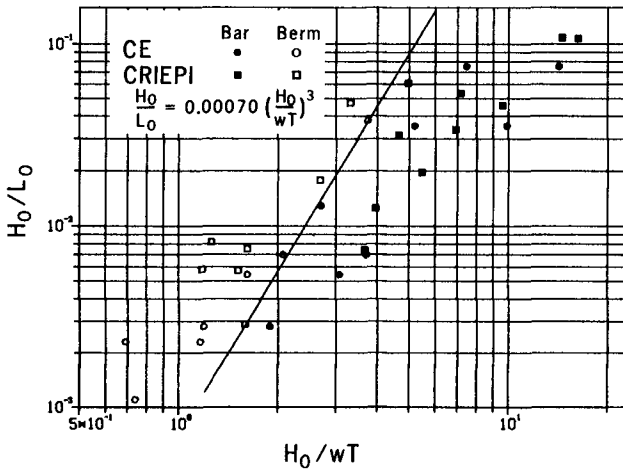


Fig. 1 Criterion for distinguishing bar and berm profiles.

Extensive correlation and regression analyses were conducted to investigate relations between geometric properties of the different profile morphologic features and wave and beach characteristics. The primary parameters used were: H_o , L_o , T , w , breaking wave height H_b , water depth h , median grain size D , and beach slope $\tan\beta$. Also, non-dimensional quantities were formed, both for deepwater and breaking conditions, such as H/L , H/wT , $\tan\beta/\sqrt{H/L}$, D/H , and D/L , in which L is the local wavelength. These quantities were related to geometric properties of the profile, presented in selected examples next.

Under steady waves and constant or slowly varying water level, the evolution of bars and berms was found to be regular, exhibiting clear growth and equilibrium properties that were readily described by simple regression expressions. The dimensionless fall speed H_o/wT emerged as an important parameter in predicting both profile response and geometric properties of various morphologic features. The strong relationship between wave and sand characteristics and morphologic features reinforced the possibility of quantitatively predicting the evolution of macroscale features of the profile in an empirical formulation.

As a bar moves offshore it simultaneously increases in volume to approach an equilibrium size. Fig. 2 shows evolution of bar volume for the main breakpoint bar for the CE experiments. Correlation analysis involving wave and beach profile parameters showed that equilibrium bar volume V_{eq} was most closely related to wave height and sand fall speed (or grain size). A larger wave height implied a larger bar volume, and a higher fall speed (or larger grain size) produced a smaller bar volume. A regression relationship was derived relating the non-dimensional equilibrium bar volume to the quantities H_o/wT and H_o/L_o according to

$$\frac{V_{eq}}{L_o^2} = 0.028 \left(\frac{H_o}{wT}\right)^{1.32} \left(\frac{H_o}{L_o}\right)^{1.05} \quad (2)$$

Eq. 2 explained 70% of the variation in the data. Larson and Kraus (1988a) present a number of alternative relationships in which other geometric properties of the profile are related to wave and beach parameters.

As a bar moved offshore, its height increased so that the depth to the crest h_c remained approximately constant during a run. Depth at the bar crest at equilibrium was closely related to breaking wave height and insensitive to wave period and sand parameters:

$$h_c = 0.66 H_b \quad (3)$$

Speed of bar movement was calculated using both the bar crest and center of mass as reference points. Fig. 3 displays the speed of bar migration for the CE cases using the mass center as reference. Positive speeds indicate bar movement directed offshore. The main trend was similar for all cases, exhibiting a high initial speed of bar migration and then slowing as the profile approached equilibrium shape. The negative speeds occurring during Case 911 were produced by a water level variation imposed to simulate a tide, which caused the bar to move onshore during phases of increased water level.

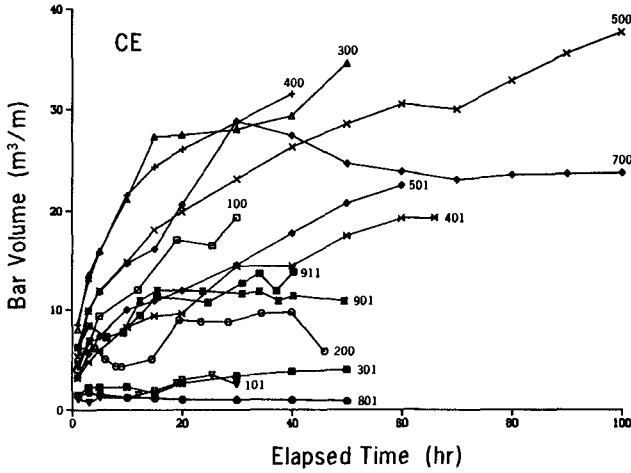


Fig. 2 Growth of bar volume with elapsed time for the CE data.

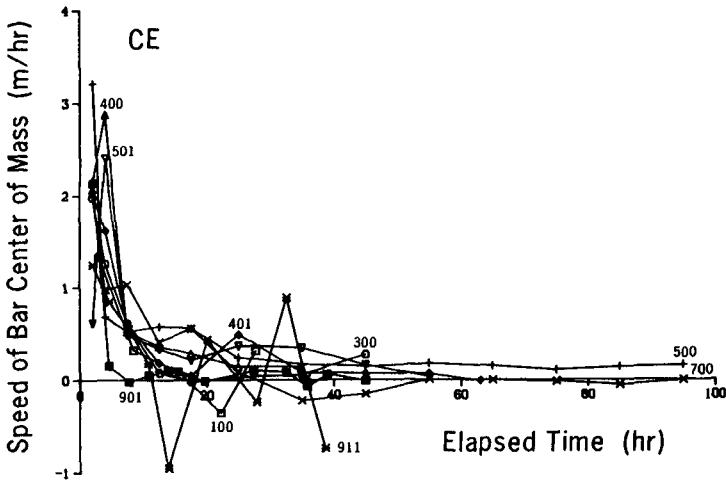


Fig. 3 Speed of bar center of mass (CE data).

Values of bar slopes formed in the LWTs under monochromatic waves are typically greater than those observed in the field. The difference between wave tank and field results is attributed to the action of random waves and varying water level, which would widen the breaker zone and smooth profile features in the field. Another factor is that steady wave conditions usually are not of sufficient duration in the field for the profile to reach equilibrium form.

Net Cross-Shore Sand Transport Rate

The main objectives of the analysis of the cross-shore transport rate were to: (1) demonstrate that the net transport rate produced by breaking waves is reliably predicted if described in a macroscale framework, and (2) develop empirically based formulas for the net transport rate in terms of wave and beach parameters.

The average net cross-shore transport rate was obtained by integrating the equation of mass conservation between two beach profiles in time. Fig. 4 shows calculated distributions of the net cross-shore sand transport rate associated with one CE case. Transport directed offshore has a positive sign, and the coordinate system originates at the initial still-water shoreline. Decay of the transport rate with time is clear from Fig. 4, and the maximum rate calculated from the final two surveys is more than one order of magnitude smaller than the maximum from the first two surveys. The peak in the transport rate distribution translated seaward with the break point, and thus the bar moved seaward.

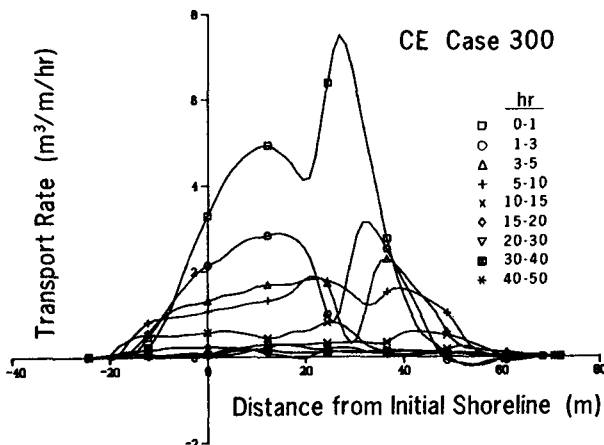


Fig. 4 Calculated distributions of net cross-shore sand transport rate for one CE case.

Four regions with specific sand transport relationships were defined in analogy with zonations of nearshore wave dynamics (for example, Svendsen et al. 1979; Basco and Yamashita 1987), as shown in Fig. 5. One region extends from the seaward limit of significant profile change to the break point, called the pre-breaking region (Zone I). In this region the transport rate is influenced by transport in the zone of wave breaking through the sand flux at its shoreward boundary, but the governing transport processes on either side of the boundary are different. Zone II corresponds to the breaker transition region and is located between the break point and the plunge point. From the location of the plunge point to the point of wave reformation one specific region, Zone III, is defined where the waves are fully broken and gradually decay (inner region in hydrodynamic terms). In this region the energy dissipation of the waves due to breaking becomes fully developed. Transport conditions in the swash zone differ from

those prevalent in the surf zone, making it logical to define a fourth transport region, Zone IV.

The net transport rate in the zone of broken waves, where the most active transport is expected to occur, showed good correlation with the wave energy dissipation per unit water volume (Dean 1977). The net transport rate in the pre-breaking zone and in the breaker transition zone decayed exponentially with distance offshore both for erosional and accretionary cases. The exponential decay coefficient was related to the grain size and the breaking wave height (see Eq. 5). On the foreshore the net transport rate showed an approximately linear behavior, decreasing in the shoreward direction from the end of the surf zone.

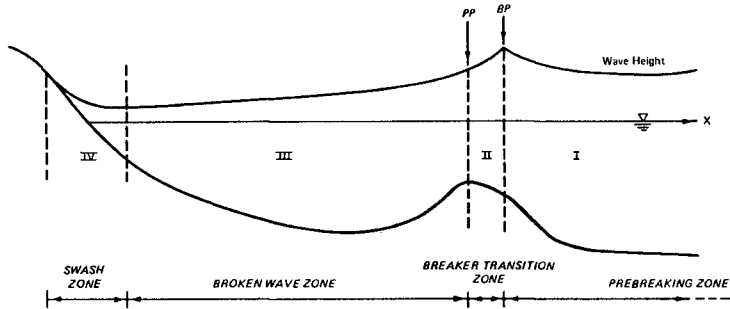


Fig. 5 Four principal zones of cross-shore sand transport.

Distributions of the net cross-shore transport rate calculated from measured profile change over intervals on the order of hours displayed regular and smooth properties, despite the random character of the grain-by-grain movement that actually took place. Consequently, it appears possible to estimate the net cross-shore sand transport rate with sufficient reliability to predict the development of main morphologic features of the beach profile.

Numerical Model of Beach Profile Change

A deterministic numerical model was developed to predict beach profile change resulting from cross-shore sand transport (Larson and Kraus 1988c), focusing on the main morphologic features of bars and berms. Many of the assumptions and relationships used in development of the model are founded on observations made from the LWT data. Changes in the beach profile are assumed to be produced by breaking waves; therefore, the cross-shore transport rate is determined from the local wave, water level, and beach profile properties, and the equation describing conservation of beach material is solved to compute profile change as a function of time.

The wave height distribution across-shore is calculated by applying small-amplitude wave theory to the point of breaking, and then the breaker decay model of Dally et al. (1985) is used to provide the wave height in regions of breaking waves. The profile is divided into specific regions (Zones I-IV) according to the wave characteristics at the given time step for specification of transport properties. The distribution of the cross-shore transport rate is then calculated from semi-empirical relationships applicable to the four regions. At the

shoreward end of the profile the runup limit constitutes a boundary with no transport across it, whereas the seaward boundary is determined by the depth at which no significant sand transport occurs. Once the distribution of the transport rate is known, profile change is calculated from the mass conservation equation. This procedure is performed with the incident wave conditions and water level pertaining to the given time step.

The direction of the net cross-shore transport rate is determined in the model by Eq. 1, whereas the magnitude is a function of the transport rate in zones of fully broken waves. The waves are considered to be fully broken in the model from the plunge point to the end of the surf zone or to the point where wave reformation occurs. The location of the plunge point is determined from the location of the break point and the breaking wave height. Seaward from the plunge point an exponential decay of the transport rate with distance is applied with different decay coefficients shoreward and seaward of the break point. The transport rate in Zone I is written

$$q = q_b e^{-\lambda x} \quad (4)$$

where x = cross-shore coordinate originating at the break point; q_b = transport rate at the break point; and λ = spatial decay coefficient.

The spatial decay coefficient λ is determined from an empirical relationship given by the LWT data according to

$$\lambda = 10.3 \left(\frac{D}{H_b} \right)^{0.47} \quad (5)$$

The transport rate in Zone II is also described by an exponential decay but with a smaller value of the decay coefficient, 0.2λ .

A transport relationship similar to that used by Kriebel and Dean (1985) is applied in a region of fully broken waves (Zone III) with a term added to account for the effect of local slope. A steeper slope is expected to increase the transport rate down the slope. The transport relationship is

$$q = \begin{cases} K \left(D - D_{eq} + \frac{\epsilon}{K} \frac{dh}{dx} \right) & D > D_{eq} - \frac{\epsilon}{K} \frac{dh}{dx} \\ 0 & D < D_{eq} - \frac{\epsilon}{K} \frac{dh}{dx} \end{cases} \quad (6)$$

where q = net cross-shore LWT transport rate; K = empirical coefficient; D = wave energy dissipation per unit volume; D_{eq} = equilibrium energy dissipation per unit volume; and ϵ = empirical coefficient for the slope-dependent term.

The transport rate distribution in Zone IV is specified as a linear decrease from the end of the surf zone to the runup limit. Avalanching is initiated in the model if the local slope exceeds 28 deg at any point on the grid, and the process continues until an angle of 18 deg is reached. Larson (1988) describes the procedure for redistributing

the sand in the model to simulate avalanching, and the limiting slopes are based on the LWT data analysis.

The numerical model was applied to simulate beach profile evolution for nine erosional cases from the LWT experiments. Values of model parameters were varied to minimize the sum of squares of the difference of measured and calculated depths for all profile surveys for a given case. After some experimentation, the empirical coefficient in the slope term in Eq. 6 was set as $\epsilon = 0.001 \text{ m}^2/\text{sec}$, leaving K and D_{eq} free to be varied in the calibration procedure. In calibration simulations, optimal values of D_{eq} were found to be on the order of 75% of those predicted by the design curve of Moore (1982), who used an energy dissipation approach with no slope dependence.

Seven cases from the LWT data were used for the calibration, and two independent cases were used to verify the generality of the optimal parameter values. Fig. 6 compares the calibration result for one of the CRIEPI cases, showing the profile evolution predicted by the model and the measured final profile. Also, the measured wave heights at the end of the run are shown together with the calculated wave height distribution. Values of K obtained in individual calibrations showed no strong dependence on wave and sand parameters. Qualitatively, K tended to decrease with increasing grain size and to increase with decreasing wave period. For predictive use, a single optimal value of K was determined by minimization of the total sum of squares for all profiles surveyed for the studied cases. A minimum occurred at $K = 1.6 \cdot 10^{-6} \text{ m}^4/N$, and this value was used in the verification.

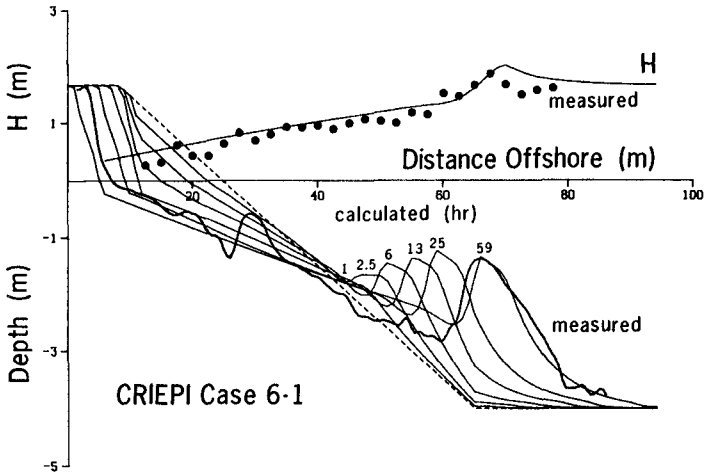


Fig. 6 Example of model calibration.

Fig. 7 displays the simulation result for one CE verification case. The volume of the main breakpoint bar, and the amount of erosion on the foreshore are well predicted. However, the crest of the bar is located somewhat too seaward, whereas the trough is not sufficiently deep. Details of the inshore features are not reproduced in the numerical model because secondary breaking was not allowed to operate, as reproduction of the main breakpoint bar was the primary goal of the

calibration. Larson (1988) describes model tests performed to reproduce multiple bars.

Field Test

The numerical model was used to simulate beach profile change measured at the CERC's Field Research Facility (FRF) at Duck, North Carolina. This test represents a generalization of the model from monochromatic to random waves, the latter approximated by statistically representative waves allowed to vary in time together with the water level. Howd and Birkemeier (1987) compiled four years of profile change data taken at the FRF along two pairs of transects surveyed biweekly to approximately 10-m depth and more frequently surveyed during storms. Statistically representative wave height and period were available at 6-hr intervals at a depth of 18 m, and water levels at 1-hr intervals.

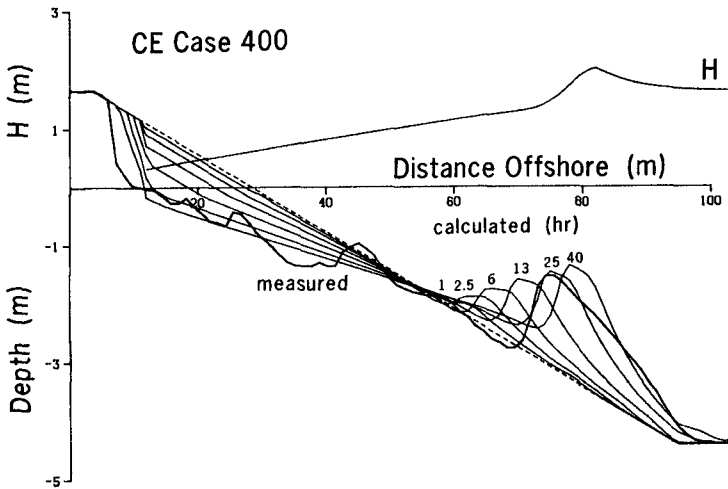


Fig. 7 Example of model verification.

Five 3- to 12-day long, primarily erosional storm events, as indicated by significant seaward bar movement, were selected for simulation. Events were chosen which showed a minimum influence from longshore transport as determined by comparison of evolution of the neighboring profile. Four events were used for calibration of the model and one for verification. A median grain size of 2.0 mm was used on the foreshore and a grain size 0.15 mm further seaward to simulate the bimodal character of the beach sediment.

At first, calibration parameters determined from the LWT comparisons were used in trial model runs. However, time rate of change of simulated profile development proved too rapid and bar development too pronounced, necessitating recalibration of the transport coefficient for the four storm events. The transport coefficient found applicable to the field profile change had a smaller value than that pertaining to the LWT calibrations (field average: $0.7 \cdot 10^{-6} \text{ m}^4/\text{N}$). Because of the fixed shoreline position at the FRF, which makes the foreshore act as a seawall to some extent, it is not clear whether the field-determined

value of K has general applicability. Some decrease was expected since K qualitatively showed a weak inverse dependence on wave period in the LWT experiments, and the wave periods in the field were somewhat longer than in the laboratory experiments. Values of other empirical transport-related parameters in the model were the same as determined in the LWT calibration. Fig. 8a displays the wave height, wave period, and water level variation during one event, and Fig. 8b shows a typical calibration result, including the measured initial and final profile and the simulated final profile. Movement of the bar was fairly well predicted by the model, although the amount of material moved was underestimated, and the trough was not sufficiently pronounced.

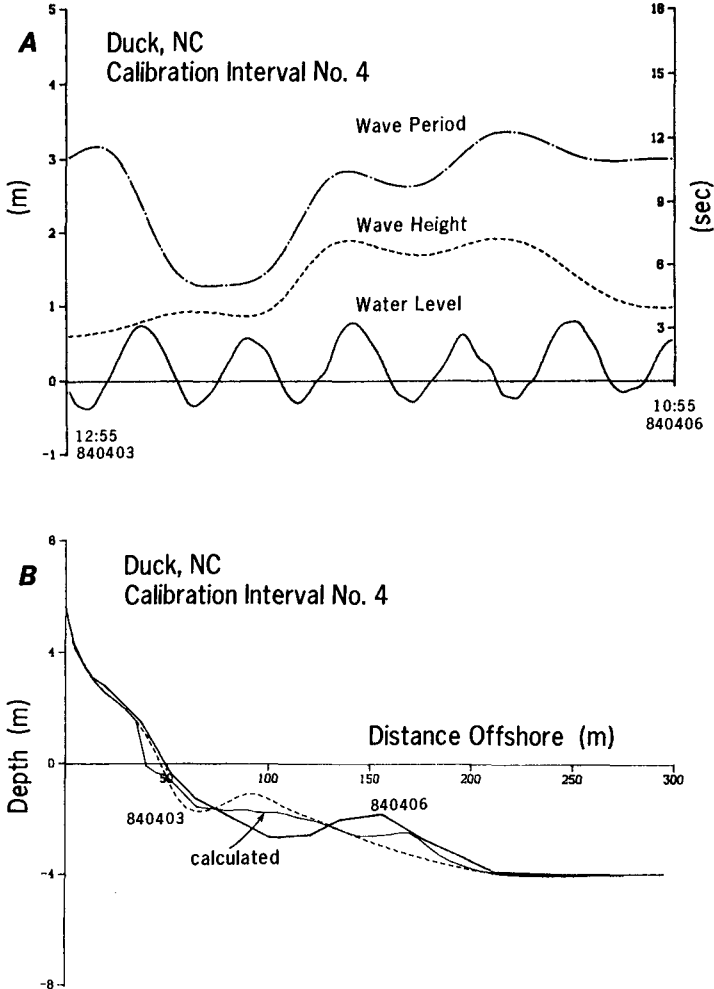


Figure 8. Calibration of numerical model against field data from Duck for one event. Variation with time of: (a) H, T, and water level; and (b) profile simulation result.

The field-calibrated model was used to simulate profile change that took place during another storm event to verify generality of the prediction. The wave and water level input are shown in Fig. 9a and the simulation result in Fig. 9b. The model reproduced main changes in the beach profile that occurred during the storm, with both bars moving offshore. Movement of the inner bar was overestimated, whereas the outer bar was located correctly but had a smaller volume than measured. In Fig. 9b the difference in measured beach volume was $45 \text{ m}^3/\text{m}$ (a loss in beach volume, constituting 25% of the total absolute volume moved across the profile). This difference is attributed mainly to differentials in longshore sand transport.

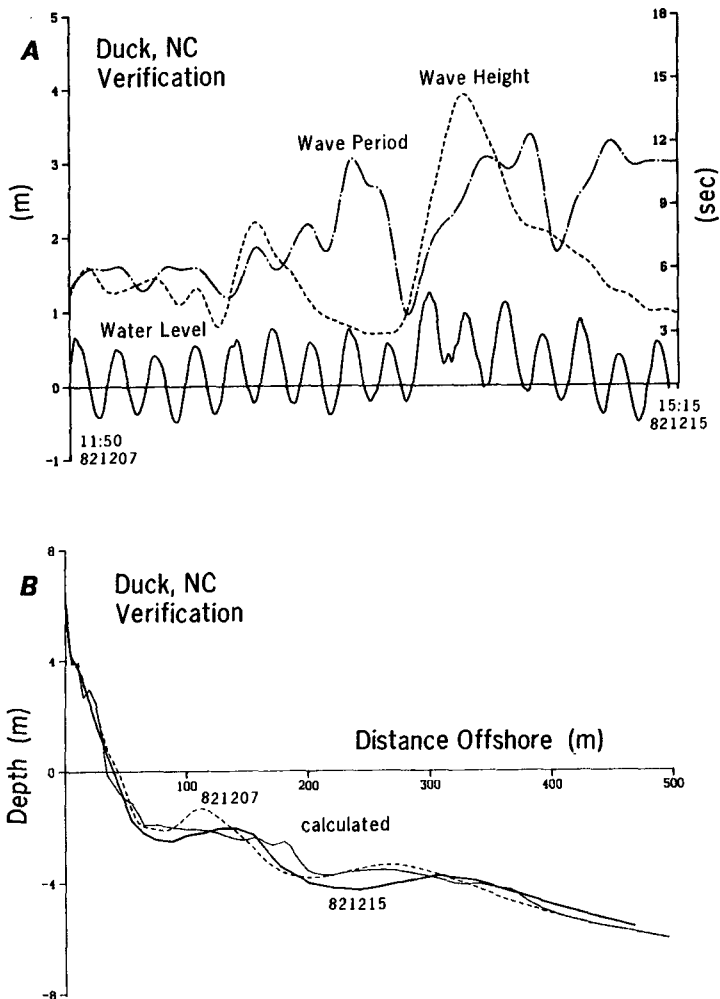


Figure 9. Verification of numerical model against field data from Duck for one event. Variation with time of: (a) H, T, and water level; and, (b) profile simulation result.

The importance of using varying forcing conditions in field simulations is illustrated in Figs. 10a, b, which show the verification condition calculated with (a) no change in water level and varying measured waves, and (b) average waves and no water level variation, respectively. The two calculated bars appearing in Fig. 10a correspond to the two peaks in the wave height time history. The bar shown in Fig. 10b was generated under five days of constant waves and water level, and is also unrealistic. The simulated results with constant forcing conditions shown in Figs. 10a, b are considerably inferior to the result obtained with varying waves and water level (Fig. 9).

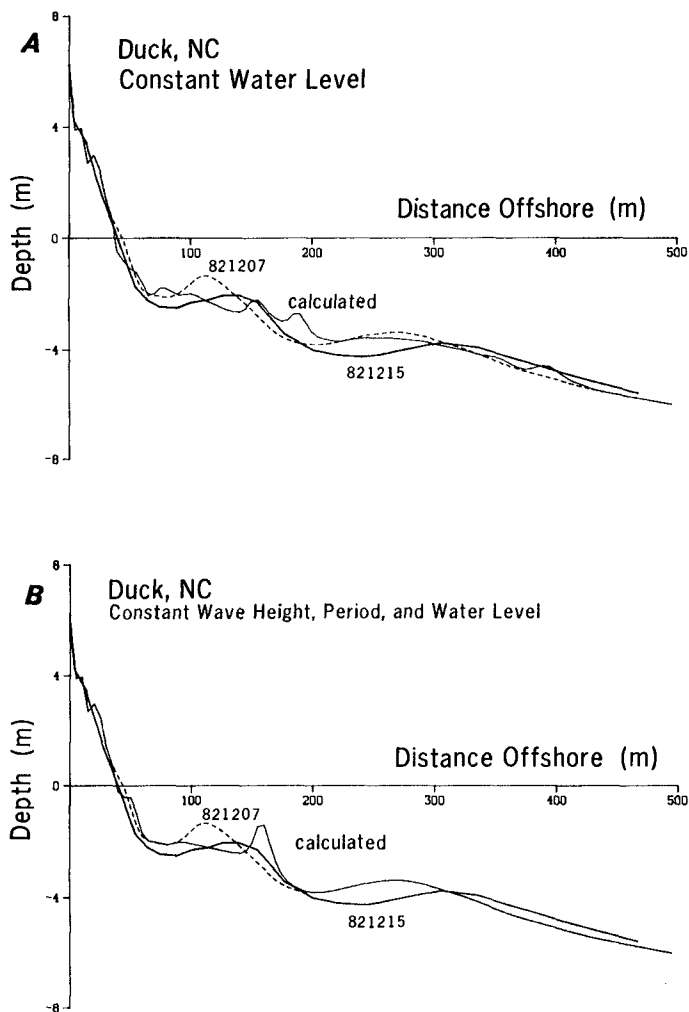


Fig. 10 Model prediction and field measurement: (a) omitting water level variation; and (b) omitting variation in H, T, and water level.

CONCLUDING DISCUSSION

A large data set comprised of 42 cases from two independent prototype-scale tank experiments was used to develop an empirical model of net cross-shore sand transport and beach profile change. The model reproduced bar formation and growth in the tank experiments, which involved monochromatic waves, and it performed well in a severe test to reproduce measured bar movement in the field over five separate simulations, each encompassing events of 3- to 12-day duration. The field comparisons were severe as all profile change, wave, and water level data were used directly as measured, and only one model parameter was adjusted in calibration.

Although not shown here, the model was subjected to extensive sensitivity analysis with input conditions and model parameters varied beyond the range of values available in the data set (Larson 1988, Larson and Kraus 1988c). Reasonable trends in predictions were always found. In addition, the model was run for several thousands of time steps; the calculated profile always reached a physically reasonable shape at earlier times and did not change in subsequent thousands of time steps. Thus the model is very stable and can be expected to reproduce the correct temporal rate of profile change.

Breaking waves are the sole driving force causing sand transport in the model in its present state. However, since the model operates in a general way using a transport rate combined with the material conservation equation, in principle other sand transporting mechanisms could be incorporated if their transport rate relations are available. These mechanisms could include wave reflection from the beach or from seawalls, and transport induced by long-period wave motion. The model is economical to run and has performed well in test applications to simulate month-long adjustment of beach fill involving storm and recovery wave and water level conditions (Kraus and Larson 1988b).

ACKNOWLEDGEMENTS

This study was partially supported by the work unit "Surf Zone Sediment Transport Processes," under the Shore Protection and Restoration Program of the U.S. Army Corps of Engineers, CERC, Waterways Experiment Station. NCK appreciates the permission granted by the Chief of Engineers to publish this information. The work by ML was carried out under contract No. DAJA45-86-C-0046 through the U.S. Army Research, Development and Standardization Group - UK.

REFERENCES

- Basco, D. R., and Yamashita, T. 1987. "Toward a Simple Model of the Wave Breaking Transition Region in Surf Zones," Proc. 20th Coastal Engng. Conf., Am. Soc. Civil Engrs., pp 955-970.
- Dally, W. R., Dean, R. C., and Dalrymple, R. A. 1985. "A Model for Breaker Decay on Beaches," Proc. 19th Coastal Engng. Conf., Am. Soc. Civil Engrs., pp 82-98.
- Dean, R. C. 1977. "Equilibrium Beach Profiles: U.S. Atlantic and Gulf Coasts," Dept. of Civil Engng., Ocean Engng. Rep. No. 12, Univ. of Del., Newark, DE.
- Howd, P. A., and Birkemeier, W. A. 1987. "Beach and Nearshore Survey Data: 1981-1984 CERC Field Research Facility," Tech. Rep. CERC-87-9, Coastal Engng. Res. Center, U.S. Army Eng. Waterways Experiment Station, Vicksburg, MS.

- Kajima, R., Shimizu, T., Maruyama, K., and Saito, S. 1983a. "Experiments of Beach Profile Change with a Large Wave Flume," Proc. 18th Coastal Engrg. Conf., Am. Soc. of Civil Engrs., pp 1385-1404.
- Kajima, R., Saito, S., Shimizu, T., Maruyama, K., Hasegawa, H., and Sakakiyama, T. 1983b. "Sand Transport Experiments Performed by Using a Large Water Wave Tank," Data Rep. No. 4-1, Central Res. Inst. for Electric Power Industry, Civil Engrg. Div. (in Japanese)
- Kraus, N. C., and Larson, M. 1988a. "Beach Profile Change Measured in the Tank for Large Waves, 1956-1957 and 1962," Tech. Rep. CERC-88-6, Coastal Engrg. Res. Center, U.S. Army Eng. Waterways Experiment Station, Vicksburg, MS.
- Kraus, N. C., and Larson, M. 1988b. "Prediction of Initial Profile Adjustment of Nourished Beaches to Wave Action," Proc. Beach Preserv. Techn. '88, Florida Shore and Beach Preserv. Assoc., in press.
- Kriebel, D. L., and Dean, R. G. 1985. "Numerical Simulation of Time-Dependent Beach and Dune Erosion," Coastal Engrg., Vol 9, pp 221-245.
- Larson, M. 1988. "Quantification of Beach Profile Change," Rep. No. 1008, Dep. of Water Resources Engrg., Inst. of Science and Technology, Univ. of Lund, Lund, Sweden.
- Larson, M., and Kraus, N. C. 1988a. "Beach Profile Change, 1: Morphology," submitted for publication.
- Larson, M., and Kraus, N. C. 1988b. "Beach Profile Change, 2: Net Cross-Shore Sand Transport Rate," submitted for publication.
- Larson, M., and Kraus, N. C. 1988c. "Beach Profile Change, 3: Numerical Model," submitted for publication.
- Moore, B. D., 1982. "Beach Profile Evolution in Response to Changes in Water Level and Wave Height," Unpubl. M.S. Thesis, Univ. of Del., Newark, DE.
- Saville, T. 1957. "Scale Effects in Two Dimensional Beach Studies," Trans. from the 7th General Meeting of the Intern. Assoc. of Hydraulic Res., Vol 1, pp (A3)1-10.
- Svendsen, I. A., Madsen, P. A., and Buhr Hansen, J. 1979. "Wave Characteristics in the Surf Zone," Proc. 14th Coastal Engrg. Conf., Am. Soc. of Civil Engrs., pp 520-539.

CHAPTER 97

LOCAL SCOUR AROUND CYLINDRICAL PILES DUE TO WAVES AND CURRENTS COMBINED

by

Yoshiaki KAWATA* M.ASCE and Yoshito TSUCHIYA** M.ASCE

ABSTRACT

Local scour depth around a pile due to waves only is small, but under waves and weak currents combined it became large. If the flow velocity increases, the maximum scour depth increases and may approach to that by running water. In the processes of the scouring, Kármán vortex play an important role in deciding characteristics of a scour hole. In the case of the horseshoe vortex predominant, the maximum scour depth is found at the upstream end of a pile, but in the coupled field of waves and currents, the initial scouring position is a little apart from a pile in the offshore side and make an angle of about 45 degree in the shoreward direction. This depends on a vortex shedding from a pile. By using light weight aggregate, the effect of ripples on local scour depth is made clear.

1. INTRODUCTION

In recent year, we have a lot of various coastal structures in the shallow water, such as artificial reclaimed islands, access bridges, breakwaters and piers for fishing and field observation. When these structures are designed, many factors for desirable construction must be taken account. One of them is local scour around cylindrical piles of pier type structures.

Some studies on local scour due to waves have been made in hydraulic experiments and in field observations, as reviewed by Herbich et al.(1984). Local scour depth due to waves is not so large in comparison with that due to uni-directional flow. As to the experimental results obtained by Herbich et al. and through our preliminary tests, conditions of waves and weak currents combined makes scour depth large in comparison with that only by waves. The conditions can be usually seen in the nearshore zone in which several currents such as longshore currents, rip currents and undertow coexist with waves. The scouring mechanism is not so clear, therefore, it is very difficult to predict the scour depth and area around a cylindrical pile in the nearshore environment.

* Assoc. Prof., Disaster Prevention Research Institute,
Kyoto University, Goka-sho, Uji, Kyoto 611, Japan

** Prof.,DPRI, Kyoto University

Studies on local scour due to currents only have been made by Shen et al.(1969), Raudkive et al.(1983) and other many investigators in river engineering. The works show that the horseshoe vortex is a dominant factor to determine the characteristics of local scour around a pile in uni-directional flow. Moreover, two types of scour may be identified as follows: (1) Clear water scour where sediment is removed from the scour hole and not replenished by the approach flow; and (2) Live-bed scour where sediment is continuously supplied into the scour hole by the approach flow. Their experiments also suggested that the scour depth increases with increase in mean water velocity in the clear water regime and reaches a maximum at a velocity approximately equal to the threshold velocity with which bed sediment is no longer removable from the hole. With live-bed scour, an equilibrium is attained when the rate of sediment transport into the scour hole by the approach flow is equal to the rate of sediment removed from the hole. The equilibrium scour depth in the live-bed scour regime is usually smaller than the maximum scour depth in the clear water scour regime. These characteristics are not clear yet under the condition of waves and currents combined. Moreover, the enlargement of the scour hole with time have not studied in detail, so that the limitation of the data keeps the physical modelling of scouring incomplete.

The objectives of this investigation are to examine processes of local scour around a cylindrical pile due to waves and currents combined in the regimes of clear water scour and live-bed scour and to make clear the effect of ripples on the characteristics of scouring.

2. EXPERIMENTS ON LOCAL SCOUR

2.1 Experimental apparatus and methods

Hydraulic experiments on local scour around a cylindrical pile were carried out in a recirculating wave flume at the Ujigawa Hydraulics Laboratory, Disaster Prevention Research Institute, Kyoto University. The experimental apparatus is shown in Fig.1. The flume used was 40m long , 50cm wide and 65cm deep with a piston type wave generator at the end. This is a double-deck type flume in which rate of mass transport in waves in the upper deck can return in the offshore

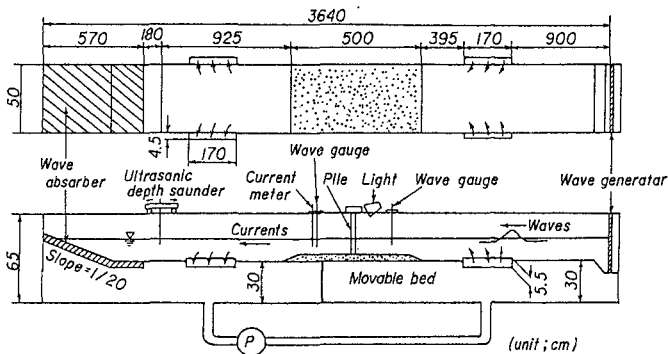


Fig. 1 Experimental apparatus and wave flume.

direction in the lower one. Pump system equipped in the flume can generate recirculating currents. We set a cylindrical pile in the midst of the movable bed of 5m long. Two kinds of sediment were used, i.e., one is very fine sand with a mean diameter of 0.11mm and its density of 2.65gr/cm^3 , and another is light weight aggregate whose diameter and density are 0.85mm and 1.81gr/cm^3 respectively. Under the usual experimental wave condition, ripples are not formed on the movable bed of the light weight aggregate. Two capacitance type wave gauges and an electro-magnetic current meter were used.

All experiments were run at a depth of 10cm on the movable bed and with a constant wave period of 1.4s. The wave heights were changed 0 to 6cm systematically and the mean flow velocities were 13.4, 12.1, 6.71, 0 and -12.0cm/s , in which sign minus means reverse flow. Cylindrical piles of diameter 1.6, 2.0, 2.4, and 3cm were used. The depth of the local scour was measured continuously with a hundred plastic optical fibers of diameter 0.5mm and a high speed VTR as shown in Fig.2. The number of the lights which pass through the optical fibers is equal to the depth of the local scour in real time. We measured the local scour depth both at the offshore and onshore sides of a pile. When ripples were formed on the movable bed, their heights and lengths were measured with a ultra-sonic depth sounder.

2.2. SCOUR PROCESSES

At first, the scour processes due to waves in our experiments are as follows: The local scour did not occur when the wave height was smaller than about 2cm in every piles used. As the wave height increases, scour holes were formed in the clear water scour regime. The scour due to Karman vortexes was observed at the bed nearly 2cm away from a pile and at an angle of nearly 45 degrees in the direction of wave propagation. We observed sediment suspension due to formation of the vortexes which were formed along the surface of the pile, and after that shed behind it. The vortex moved upward and downward in accompany with wave motion. The sediment movement is not so active at first and thus the scour depth is very shallow. The scour depth at the onshore side was generally larger than that at the

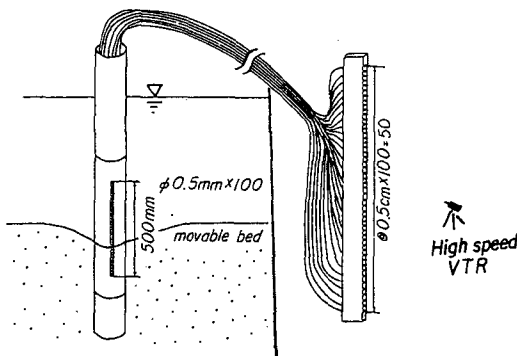


Fig. 2 Schematic diagram of a test pile with one hundred optical fibers and a high speed VTR.

offshore side because shoreward flow due to mass transport may strengthen a vorticity at the onshore side.

When the wave height was more than about 4cm, ripples were formed all over the surface of the movable bed. The depth of live-bed scour was nearly equivalent to the ripple height and the ripple length was usually of the same order of a pile diameter. Therefore, it was very difficult to estimate the scour depth. In this case, the sediment concentration near the bed generated by the vortex was very dense, but the scour depth is not so large.

Secondly, the scour processes due to currents are briefly explained. When the mean flow velocity was 6.71cm/s, local scour did not occur. When it was 13.4cm/s, scouring hole whose plan shape looked like a horseshoe was dug quickly. At the lee side of the pile, a slight accretion of sediment was recognized. When flow velocity was -12.0cm/s(reverse flow), the scour processes, of course, were very similar to the cases in which flow velocity was 13.4cm/s.

In the coupled field of waves and currents ($u=6.71$ cm/s), much sediment was easily swirled up with the vortices generated behind a pile (onshore side), and the initial scouring position is slightly apart from a pile in the onshore side and make an angle of 45 degrees in the onshore direction as shown in Fig.3. This depends on the vortex shedding from a pile. The size and the depth of the hole were much larger than those due to waves only. As time went by, the scouring also occurred at the offshore side. After this stage, sediment which was swirled up at the offshore side of the pile was carried away due to currents, but some suspended sediment inside a scour hole can not be carried out with currents. Therefore, the former leads to net loss of sediment from the hole. This is a typical process of local scour enlargement at the offshore side of the pile. At the onshore side, the process of scouring is similar to that at the offshore side. However, some sediment which was flew up over the hole at the onshore side deposited on the edge of the scour hole at the onshore side. Behind the holes (onshore side), small ripples were formed.

In an equilibrium stage of live-bed scour, the shape of the scour hole was semicircular at the offshore side, and trapezoidal at the onshore side. When the wave height becomes larger than that at the beginning of ripple formation, it was very difficult to distinguish

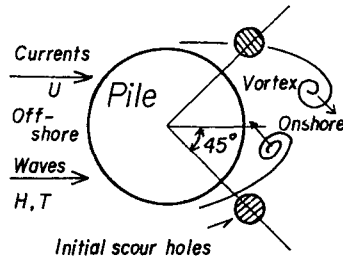


Fig. 3 Vortex shedding with a vertical axis and location of initial scouring.

between the trough of the ripple and the scour hole. The scouring processes in $u=13.4\text{cm/s}$ resembled those in the cases of $u=6.71\text{cm/s}$, but the horizontal scales and the depth of the scour holes were much larger than the latter case. In the first stage, the vortex which looks like a horseshoe one contributes to local scour as well as the scouring process due to currents only. After this stage, the scouring advanced as same as that in the case of $u=6.71\text{cm/s}$. In some experiments, small ripples were formed at the onshore side of the scour hole. When wave height was larger, ripples were formed all over the bed. With the reverse flow ($u=-12.0\text{cm/s}$), the scour processes were very similar to the cases of those at the velocity of 13.4cm/s . The shape of the scour hole in the former case, of course, was almost opposite to that in the latter case.

3. CHARACTERISTICS OF LOCAL SCOUR

Characteristics of local scour around a pile due to waves and currents combined are very different from those due to currents only. Using the data obtained in our experiments, we analyzed them with traditional method of dimensionless expressions.

3.1 Bottom topography of scour hole

Figure 4 shows the bottom topography of the scour hole given under the condition of wave period of 1.4s , wave height of 3.0cm , pile diameter of 3.0cm and current velocity of 13.4cm/s in the live-bed scour regime. At the offshore side of the pile, a hole like a reverse-circular corn is formed, and the offshore slope of the hole is an angle of 43 degrees and very uniform. This value is a little smaller than the angle of repose of the sand. At the onshore side, however, the plan shape of the scour hole looks like a trapezoid, and a narrow and flat zone of accretion is formed behind the pile (in the onshore side). In this area the shedding vortexes are being developed and bottom sediment are easily flown up. Mild bottom slope continues from this area to onshore side and at further onshore area, deposition of some sediment makes the bed flat and on the surface, small ripples are

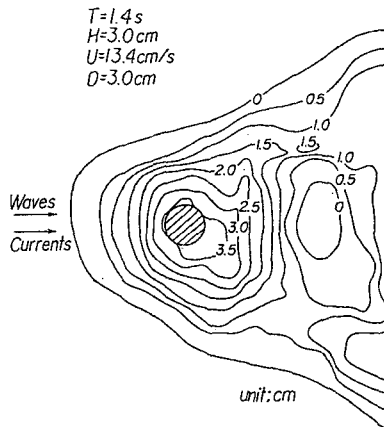


Fig. 4 Bottom topography of a typical scour hole.

generated. The lateral width of the scour hole increases shorewards with the distance from the pile. These characteristics depend on moving trajectories of the vortices which shed from the pile and moves to onshore at an angle of 45 degrees in the onshore direction.

Figure 5 is a cross section of the scour hole along the longitudinal axis of the flume. The experimental conditions are as same as in the case of those in Fig. 4. At the offshore side of the pile, the angle of the bed slope is about 45 degrees. At the onshore side, the slope close to the pile is gentle, and with increase of the distance from the pile, it becomes steeper and approaches to 45 degrees. Fig. 6 shows a cross section of the scour hole along the transverse direction. The mean bed slopes both on the right and left sides of the pile make an angle of about 45 degrees to the horizontal bed and their shapes are nearly symmetric. It is found from our experiments that the bed slope of the scour hole is nearly equal to an angle of repose (it is about 45 degrees), but along the lines which make an angle of about 45 degrees in the shoreward direction as already shown in Fig.3, the slope is a little small due to active movement of sediment by vortices.

3.2 Time development of scouring

Figure 6 illustrates some examples of the time development of scour depth z with time t in the case of a 3cm diameter pile with the parameter of wave height. The data may be each composed of three straight-line segments on a semilog graph paper. The first segment is associated with the slow scouring by the shedding vortices. The middle segment describes the development of the scour hole as the vortices move away from the pile and grow in strength. The last segment indicates an equilibrium stage. The development of scour in clear water scour is essentially as same as that in live-bed scour.

In the case of scour due to waves only, accretion of sediment is found at the offshore side of the pile. In the case of scour due to waves and currents at the velocity of 6.71cm/s, local scouring around a pile is so small that the effect of currents on local scour is very weak. This is due to a small amount of suspended sediment which is picked up by small waves. At a flow velocity of 13.4cm/s, local scour advanced much more in comparison with the other cases. This means that under the waves and currents combined, the local scour depth around a pile chiefly depends on the flow velocity.

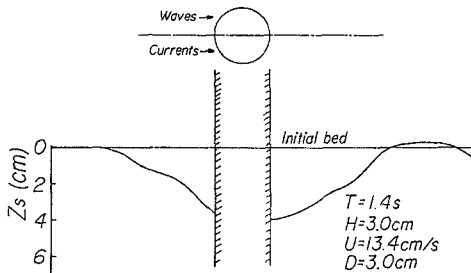


Fig. 5 Cross section of a scour hole in the longitudinal direction of the flume.

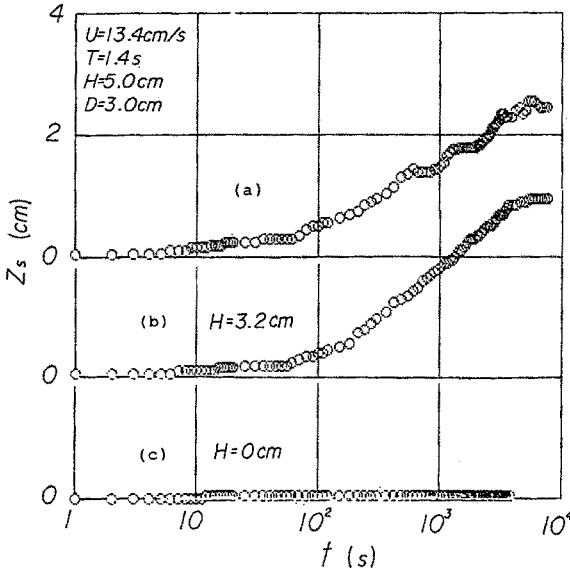
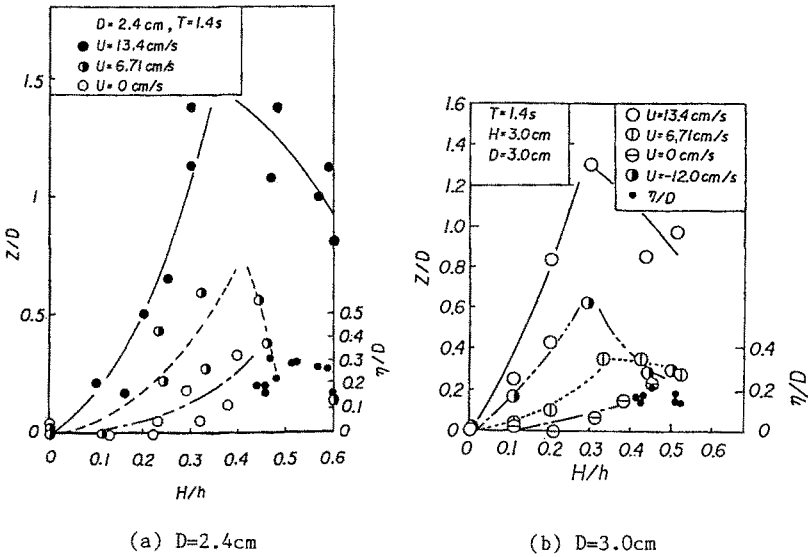


Fig. 6 Some examples of time development of clear water scour.



(a) $D=2.4\text{ cm}$

(b) $D=3.0\text{ cm}$

Fig. 7 Maximum scour depth and ripple height vs. wave height.

3.3 Equilibrium maximum scour depth

Figure 7 shows the relationship between the dimensionless maximum scour depth and the dimensionless wave height in the cases of a pile diameter of 2.4 and 3.0cm respectively. Measuring point of the maximum scour depth is onshore side of a pile. In this figure, the dimensionless height of ripples which are formed in the dimensionless wave height of more than about 0.3 to 0.4 is also shown with small circles. With our experiments, the maximum scour depth is the largest under the conditions of the limit of beginning of ripple formation, i.e., the initial stage of live-bed scour regime. In clear water scour, the scour depth increases with increase of H/h . When H/h is more than about 0.3 (In live-bed scour regime in which movable bed is covered with ripples.), the maximum scour depth is as large as or slightly larger than the height of ripples except for the case of $u=13.4\text{cm/s}$. Our experiments shows that the length of ripples are larger than a diameter of a pile. Therefore, it is difficult to take away the local depression corresponding to trough of ripples from local scour depth. In the case of $u=13.4\text{cm/s}$, the scour process quickly advances due to large flow velocity, and thus the outflow rate of sediment transport from the scour hole is larger than those in other cases. Therefore, the maximum scour depth becomes large.

In Fig.8, the relationship between dimensionless radii of scour hole both in the onshore and offshore directions. The line in this figure indicates empirical relationship corresponding to each flow velocity. From Fig.8, the dimensionless radius of scour hole in the onshore direction is generally greater than that in the offshore direction. As the flow velocity increases, the horizontal size of the scour hole becomes large, as shown in Fig.4 and also the asymmetry of the plan shape of the scour hole in the longitudinal direction advances. This phenomenon can be explained with the characteristics of a vortex around a pile. The vortex which firstly sheds at the offshore side of the pile in a half cycle of wave period, moves to the onshore

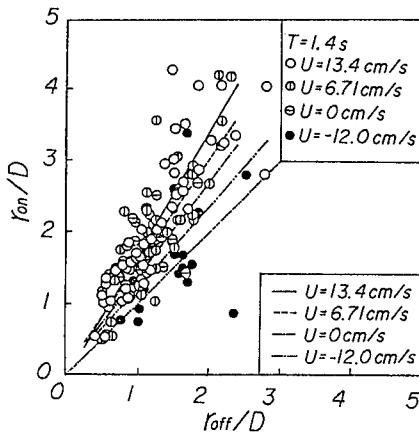


Fig. 8 Relationships between onshore and offshore radii of a scour hole.

side with growth in the next half cycle. Therefore, pick up rate of sediment at the onshore side of a pile is larger than that in the offshore side. In the case of waves only as shown in Fig.7, the onshore radius of a scour hole is also larger than the offshore one, though the scour hole is smaller than that under waves and currents combined. In the case of reverse flow at a velocity of -12.0cm/s , the data are much scattered in comparison with other cases. Experimental observation shows that difference between shoreward water particle velocity and seaward one under wave motion (nonlinear waves) contributes to this small asymmetry of the scour hole.

Figure 9 reveals the relationship between the dimensionless mean radius of the scour hole and the dimensionless wave height with the value of flow velocity as a parameter. The mean radius is defined as a half of the sum of the onshore and offshore radii of the scour hole. In this figure, the dimensionless ripple length is also shown. From the figure, it is found that the radius of the scour hole increases with increase of the wave height and the flow velocity. When wave height becomes larger and ripples are formed, the ripple length is as large as the mean diameter of a scour hole, and changes of ripple length with H/h is approximately equal to those in a scour hole. Therefore, in any case, the ripple length is larger than a diameter of a pile. Under these conditions, it is very difficult to estimate quantitatively a real scour depth. Taking scales of ripple length and a pile diameter in the field into account, their relationship is quite different from the experimental one, even if a ripple length depends on sediment diameter and an amplitude of water particle velocity. When it is necessary to predict a local scour depth around a pile in the field, the effect of ripples on local scouring process in the experiment should be made clear.

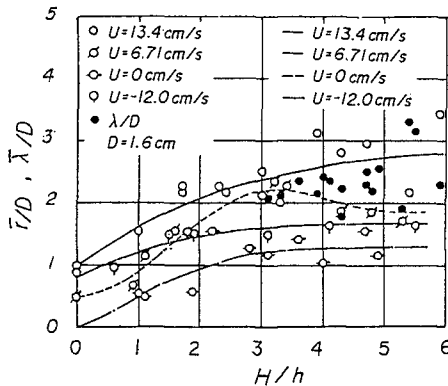


Fig. 9 Radius of scour hole and ripple length vs. wave height.

4. EFFECT OF RIPPLES ON LOCAL SCOUR

In our experiment with sand, ripples are always formed in live-bed scour regime. In order to obtain real local scour depth, it is necessary to exclude the contribution of ripple height. In the field, the pile diameter of a pier-type coastal structure is usually larger than a length of ripples which are appeared on the sea bottom, so that a local scour depth is larger than a ripple height. Therefore, there is a scale effect in the experimental data. In this chapter, we discuss the effect of ripples on local scour with the experimental data in no-ripple and live-bed scour regime which is obtained by using light weight aggregate.

Figure 10 shows the relationship between dimensionless local scour depth and dimensionless wave height at a velocity of 13.4cm/s in no-ripple regime. The critical dimensionless wave height between clear water scour and live-bed scour is around 0.35. After over this value, the scour depth also increases and rapidly decreases in the range of more than 0.42. In this figure it is not recognized the effect of wave period on local scour depth.

Figure 11 also shows the local scour depth in the two cases of no-ripple and ripple regime. In ripple regime, the data(open circle) are scattered within the area which is get between two dotted curves. The changes of local scour depth with wave height is similar to those of ripple height. Therefore, the scattering of the data might be not due to experimental error but due to existence of ripples. If the crest of ripples coincides with the location of a pile, local scour depth nominally becomes small. On the contrary, the trough comes, it increases. On the basis of our experiment, the effect of ripples on local scour is appeared due to following two mechanisms:

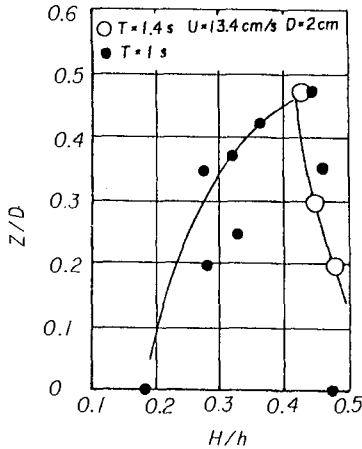


Fig. 10 Maximum scour depth vs. wave height in no-ripple regime.

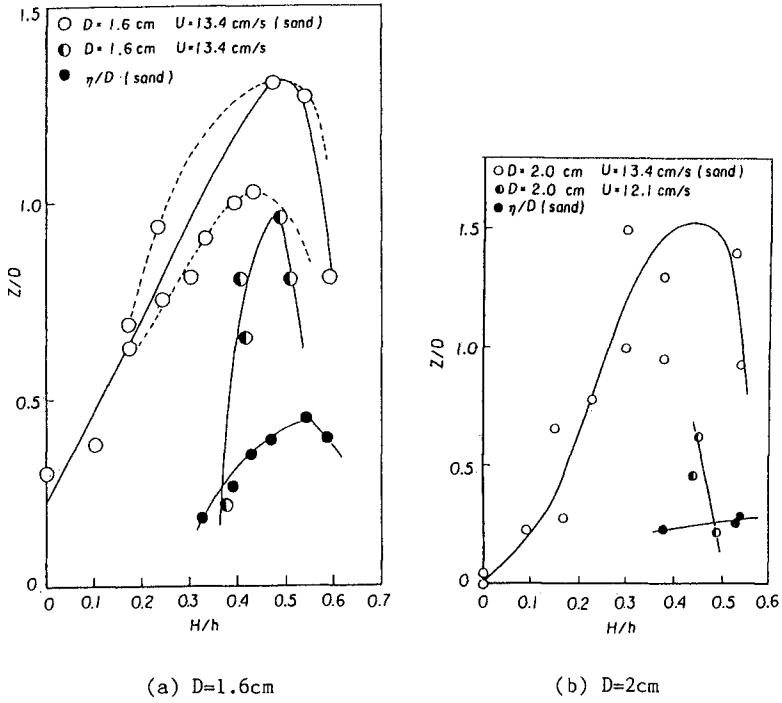


Fig. 11 Comparison of maximum scour depth in ripple and no-ripple regime.

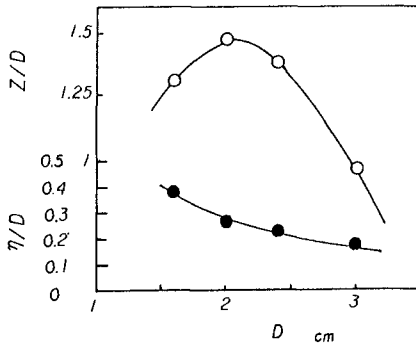


Fig. 12 Changes of scour depth and ripple height with a pile diameter.

- (1) When ripples are generated on the bottom, the inflow rate of sediment transport into the scour hole reduces in comparison with that on a plane bed, because ripples spend certain energy of waves and currents.
- (2) Suspended sediment cloud over ripples is easily spread out in the downstream area, therefore, transported sediment can not always be trapped with the scour hole.

From Fig.11, it is found that the dimensionless maximum local scour depth increases with increase of a pile diameter in ripple regime, but in no-ripple regime, this tendency become opposite. Moreover, the formation and characteristics of shedding vortexes are much affected with a pile diameter. Figure 12 show the changes of maximum scour depth and ripple height with a pile diameter.

5. MODELING OF LOCAL SCOUR

The most successive expression to explain mechanism of local scour around a cylindrical pile by running water was given by Shen et al.(1969) who introduced the concept of circulation. According to the conservation law of circulation, changes of bed shear stress in horse-shoe vortex region were obtained with development of scouring. This model have been modified by many researchers and some formulae are proposed to estimate the maximum scour depth under clear water scour. The horseshoe vortex with a almost horizontal axis is continuously generated along the sides of a pier.

Under wave motion, however, the horseshoe vortex is not clearly formed around a pile and the scour depth is not so large in comparison with that by running water. In the research field of wave forces, effects of a vortex formed with a vertical axis on lift force have been investigated. Through our experimental observation, Kármán vortex is a dominant factor to decide mechanism of local scour around a pile. Bottom sediment is easily picked up by the vortex and scoring process advances. Our physical model of local scour due to waves and currents combined introduces the effects of the vortex on sediment transport from scour hole by us(1987). Numerical simulation can roughly estimate the maximum scour depth. However, our model introduces many assumptions to predict the maximum scour depth due to incomplete knowledges about circulation of karman vortex and the formula of rate of sediment transport in the coupled field of waves and currents. We will reserve it for another occasion.

6. CONCLUSIONS

We investigated experimentally the characteristics of local scour around a cylindrical pile due to waves and currents combined, and made clear the effect of ripples in both clear water scour and live-bed scour regimes.

The main conclusions in our study can be summerized as follows:

1. Local scour depth around a pile due to waves only is small, but under waves and currents combined it became larger. If the flow velocity increases, the maximum scour depth increases and may come up to that in the steady flow. In the processes of the scouring, a vor-

tex with a vertical axis (Karman vortex) is dominant to decide characteristics of a scour hole. In the case of the horseshoe vortex in the steady flow, the maximum scour depth is found at upstream end of a pile, but in the coupled field of waves and currents, the initial scouring position is a little apart from a pile in the offshore side and make an angle of about 45 degree in the shoreward direction. This depends on a vortex shedding from a pile. It is found that the equilibrium scour depth around a pile in clear water scour is generally larger than that in live-bed scour.

2. By using light weight aggregate, the effect of ripples on local scour depth is made clear. In no-ripple regime, the scour depth suddenly decreases over a critical wave height due to increase of inflow rate of sediment transport. On the contrary, in ripple regime, suspended sediment cloud is not always trapped by a scour hole, so that its depth remains to be a certain value. The scattering of the data about scour hole depth might depend on the existence of crest and trough of ripples.

REFERENCES

- Herbich, J.B., R.E. Schiller, R.K. Watanabe and W.A. Dunlap(1984). Sea Floor Scour, Design Guidelines for Ocean-Founded Structures, Ocean Engineering, Marcel Dekker, Inc., pp.145-201.
- Raudkive, A.J., and R. Ettema(1983). Clear-water scour at cylindrical piers, Journal of the Hydraulic Engineering, Proceeding of ASCE, Vol.109, No.HY3, pp.338-350.
- Shen, H.W., V.R. Schnider and S. Karaki(1969). Local scour around bridge piers, Journal of the Hydraulics Division, Proceedings of ASCE, Vol.95, No.HY6, pp.1919-1940.
- Tsuchiya, Y., Y. Kawata and M. Nishikori(1987). Local scour around a cylindrical pile due to waves and currents combined, Proc. 34th Japanese Conf. on Coastal Eng., JSCE, pp. 402-406(in Japanese).

CHAPTER 98

STUDIES FOR VILLAJYOYOSA'S BEACH REGENERATION (SPAIN)

José L. Campello Chorro *
Vicent J. de Esteban Chaparria **
José Aguilar Herrando ***
J. Javier Díez González **

ABSTRACT

In the last two years a whole of studies was realized in order to determine precise solutions to the regeneration of Villajoyosa's beach, in the spanish mediterranean coast. Investigations were carried out to the surrounding coastal areas based in field investigations and laboratory analyses of the beaches materials.

INTRODUCTION

In the last years, the spanish mediterranean coast has been subjected to a great deal of tourists. This supposed an increase in the population seasonal and permanent, wich has been solved with a lot of urban development and an intensification in uses of all types, wich have produced, and will continue producing, negative results on the coast. In many cases, these are superior than some produced in portual works. In must cases, the human activity developed in the coastal area goes well beyond geomorphologic processes. Alicante province is one of the coastal area in wich this demand has been present because its special climatologic and landscape conditions.

SITUATION AND CHARACTERISTICS

Villajoyosa village is placed between Alicante and Benidorm (fig. 1), finding a position around Amadorio river's mouth. The existence of a locked delta with a certain disymmetry is checked in this mouth. This river, with a typical mediterranean regime, is today regulated by Amadorio dam, placed about four kilometers upstream from the mouth. Between this and the port, esentially fishing and sporting, takes place the Villajoyosa's

- - - - -
*Ingeniero Director Grupo de Ptos. Sur. ALICANTE (SPAIN).

**Prof. Dto. Ocean. e Ing. Costas. Un. Pol. MADRID (SPAIN).

*** Prof. Dto. Puertos. Univ. Pol. Valencia (Spain).

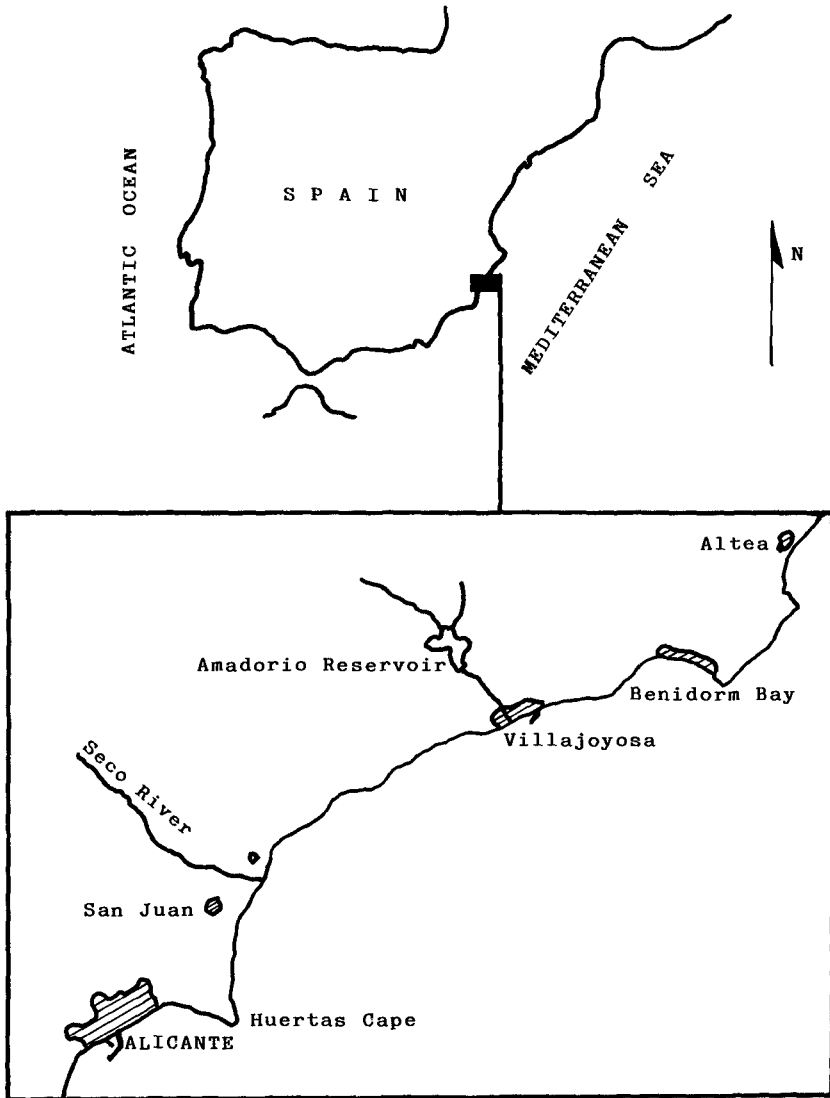


FIG. 1

beach integrated by hard grainsgravel, crashed stone and coble in most cases calcareous and ofitic. Its longitude is about 1400 m., and it was used to strand ships in old ages, according to a picture pated in the first years of the 19th Century, and wich is today found in the Naval Museum (Madrid), being used Alcocó Cala to search.

The line of this beach is not rectilinear, since, as well as its general curvature shaped like a big cave, the existence of reef and rocky outcrops have induced small hemitombol.

The beach has suffered a continuous erosion in the last years, getting important damages in several works which have been done recently, specially in a seaside promenade with which an important part of beach was occupied and in the way that merger the old maritime neighbourhood, in the old inner part of Villajoyosa with the port.

GEOMORPHOLOGIC FRAME

Separating Altea and Benidorm Bays we find Helada Mountain Range. It is a classic barrier of NE-SW direction formed in many cases by materials which belong to Cretaceous period, with a submerged extension appearing in the small Benidorm Island. In the South there are Quaternary sandy sediments, especially the beaches of "levante" and "poniente" of Benidorm. Further away the change to limestone along the length of the coast which is developed to the South. Around Villajoyosa there is a whole, with more than 500 m. in power, of flischoid type, composed by clayly marls, levels of clay loams, bio-sandy and fossiliferous limestones. All this are completed by a length of a rocky coast which gives way further away to the South to a low, backer coast, which have produced the presence of some deltas, such as Amadorio's, as we mentioned before, or gully Torre's one. Along the area there are small caves in which hard materials are found.

VILLAJOYOSA HARBOUR

The port was built in the place pointed in the mentioned picture of 1800. Villajoyosa harbour has been investigated because it can mean some disturbances to the surrounding area. The harbour was planned in 1917, June. Works, consisting in the breakwater construction starting at the Punta de L'Alcocó, began in 1923, March. After many paralysations and vicissitudes, works were not finished to 1940 referring to the basic part. Beach has been gradually eroded after the breakwater construction, going materials into the harbour. Therefore a counter-dike was constructed.

In 1944 was planned a breakwater extension, and another one in 1952. The first one was disapproved, but the second was carried out, finishing the works in 1963 : 183 m. of new breakwater was constructed. Several storms (1943, February and December, 1947, January, 1965, January) pushed to make maintenance works. In 1984, January was planned a new extension of the harbour (Fig. 2) still not approved. Therefore predictions show negative influences to the near shoreline.

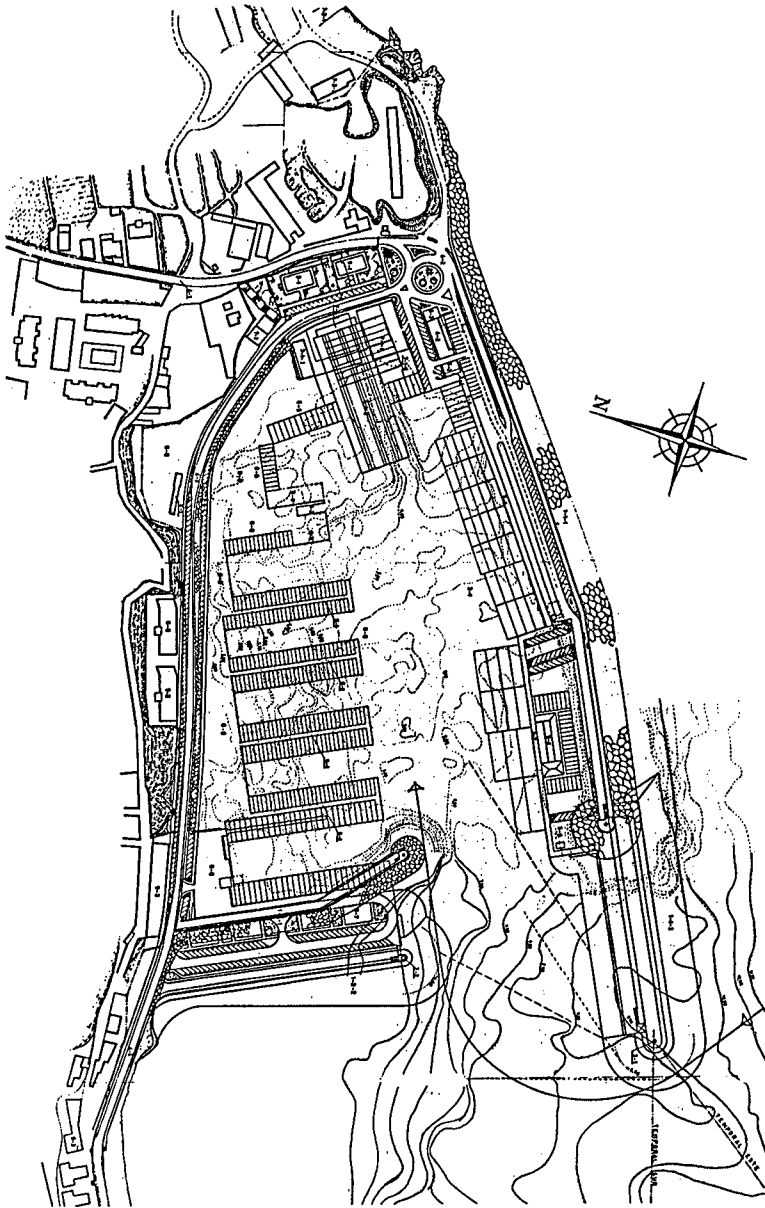


FIG. 2

STUDIES DONE AND CONCLUSIONS

With views to determine precise solutions to the regeneration of Villajoyosa's beach a whole of studies was realized referred to the determination of the coastal movement in our days, as well as in sedimentologic and batimetric analyses (Fig. 2, 3). On the other hand, we tried to study materials retained in Amadorio's Dam, but it was not possible get a quantification. It was investigated the influency in the beach erosion of the works realized that have been mentioned above. At last the possible sourcer of the precise materials to the beach regeneration were located, studying in this way the registered and enviromental impact in different means for the different alternatives.

Some of the studies developed were included in a general one of the Alicante coast. Studies show the independence of the coastal Villajoyosa area from near, especially with the north area. Works has investigated the clasification of the coastal zone in different "Morphodinamic coast units" of several orders, as a function considering littoral dynamics, materials and geomorphologic frame.

In this case all that shows the Benidorm Bay connected to the Altea one as a result of the granulometric and mineralogic analyses. Nevertheless Villajoyosa area shows very different mineralogic compositions in the beach materials. That clearly mean another "Morphodinamic coast unit". It was been possible to demonstrate have the materials of Villajoyosa's beach are inmerged with the contributions of Amadorio's River and also with streams which ran into this area which belongs to the second order "Morphodinamic coast unit" "Punta Plana Punta dels Banyets".

Coastal dynamic, with a clear tendency to the N-S, presents important partial components to the other direction, although they are inferior also the materials like autochtonous. Presence of high contents of anfibols and piroxen, and the longitudinal variation of the roundness grade in white quartz let confirm existence of real means of littoral transport towards the South around Amadorio's River mouth. However influence of its materials is losen quickly and this coastal area shows very clearly an important and general isolation as it has been studied widely considering different methods to determine littoral transport rates.

FRACCION RETENIDA TAMIZ ASTM N° 50			
TAMANO DE PARTICULA(mm): 0,30-0,42		RETENIDOS: 49,4	
FRACCION CARBONATADA : 97,1			
COMPOSICION MINERALOGICA EN % DE LA FRACCION NO CARBONATADA			
CUARZO BLANCO	63	TURMALINA	
CUARZO ROJO	9	EPIDOTA	
CUARZO AZUL		CIRCON	
CUARZO NEGRO		ANFIBOLES	8
MIXTOS CUARZO		PIROXENOS	1
MOSCOVITA		OXIDOS	3
BIOTITA		OPACOS	
		RESTOS BIOLOG.	17
MORFOLOGIA CUARZO BLANCO EN%		GRADO DE REDONDEO	
REDOND.	3	POCO ROD.	48
MUY ROD.	46	NO ROD.	3
		49	

FRACCION RETENIDA TAMIZ ASTM N° 80			
TAMANO DE PARTICULA(mm): 0,18-0,30		RETENIDOS: 19,2	
FRACCION CARBONATADA : 95,1			
COMPOSICION MINERALOGICA EN % DE LA FRACCION NO CARBONATADA			
CUARZO BLANCO	50	TURMALINA	
CUARZO ROJO	10	EPIDOTA	
CUARZO AZUL		CIRCON	
CUARZO NEGRO		ANFIBOLES	12
MIXTOS CUARZO		PIROXENOS	
MOSCOVITA		OXIDOS	4
BIOTITA		OPACOS	1
		MAGNETITA	*
REST. BIOLOG.	23	ILMENITA	*
MORFOLOGIA CUARZO BLANCO EN%		GRADO DE REDONDEO	
REDOND.	6	POCO ROD.	32
MUY ROD.	48	NO ROD.	14
		48	

FIG. 2 MINERALOGIC ANALYSES

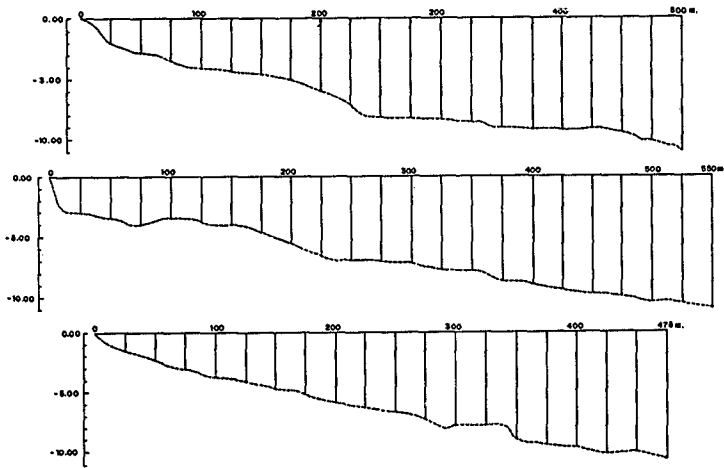


FIG. 3 VILLAJOSYA'S BEACH PROFILES

REFERENCES

- * ASENSIO AMOR, I. et al. (1973) : "Aspectos sedimentológicos del litoral de Alicante". Estudios Geológicos, Vol. XXIX, nº 3, pp. 253-264.
- * DIEZ GONZALEZ, J.J. (1982) : "Bases para una aproximación a la dinámica litoral del País Valenciano". R.O.P. (Madrid).
- * ESTEBAN CHAPAPRIA, V. (1987) : "Procesos litorales en las costas valencianas al Sur del Cabo de San Antonio". Tesis Doctoral. Univ. Politécnica de Valencia.
- * LLORCA BAUS, C. et al. (1985) : "La vila del mar i el mar de la Vila". Exmo. Ayto. de Villajoyosa.

CHAPTER 99

COASTAL PROCESSES IN GUARDAMAR BAY (SPAIN)

Vicent J. de Esteban Chapapría *
J. Javier Díez González *
Miguel Arenillas Parra **
Rafael Cortés Gimeno ***

ABSTRACT

The surrounding coastal area of the Segura's River mouth has registered in the last years many erosion problems. It is one of the biggest coastal conjunct in the spanish mediterranean coast. A whole of studies was carried out to determine littoral and coastal processes in this area.

INTRODUCTION

As regard to the complete characterization of the conjunct coastal-littoral existing in Guardamar Bay some studies were realized some years ago to determine actuals and subactuals littoral processes in this area of the spanish mediterranean coast in order to the resolution of determined problems created around the Segura's River mouth.

Recently general occupation of the coastal area has generated deep disfunctions in many of them. Since that coast has experimented a deep reevaluation due to tourism some works and actions have been got in general, which have not considered secondary effects that werw going to be done, producing erosive problems in a lot of coastal formations. Environmental degradation needs quick actions. However coastal arrangement requires exhaustive knowledge of coastal processes because its consideration lets have the reliability needed to undertake any action.

SITUATION. GEOMORPHOLOGIC

Guardamar Bay is placed in the great morphodynamic coastal unit which is between Santa Pola and Cervera Capes, in Alicante province. It constitute one of

*Depto. Ocean. e Ing. Costas. Univ. Pol. MADRID (Spain)

**Cát. Geol. Apl. Univ. Pol. MADRID (Spain)

***Cát. Geol. Apl. Univ. Pol. VALENCIA (Spain)

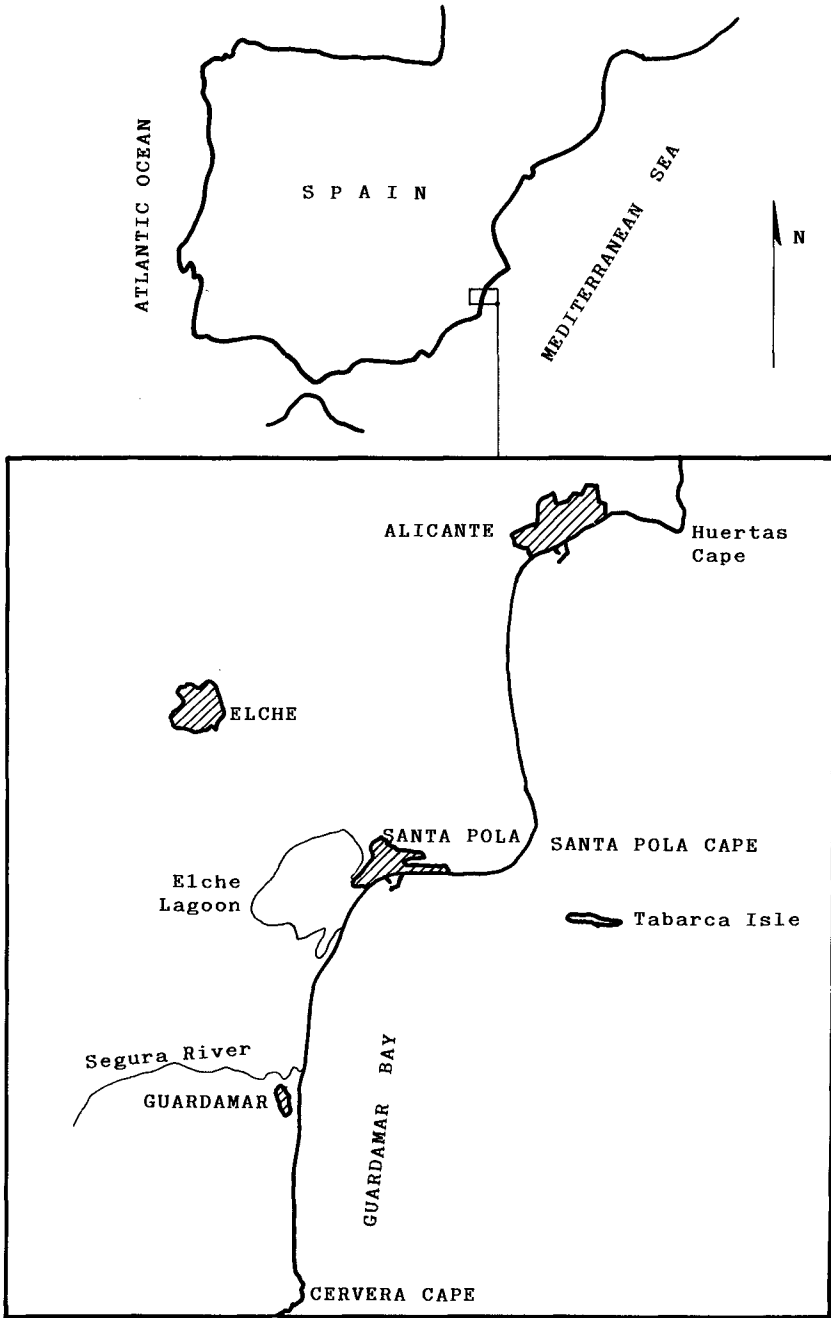


FIG. 1

the most relevant coastal formation in the Spanish Mediterranean (Fig. 1). Behind it a very wide saltwater lagoon place formed in Segura-Vinalopó depression known under the generic name of "Albufera de Elche" (Elche Lagoon). Uninterruptedly the sandy formation spread to Cervera Cape, orientated to the E. An important dune field expands in this stretch around Segura River mouth. Great dunes are used up along determined directions due to problems derived from its mobility there were reforestations in the beginning of the century. Segura River mouth was situated artificially to drain easily lowland areas. Recently two jetties were built for its channelization. Because building a shorter than the built at present time over the south side, mouth was filled of sediments. In spite of all problems have continued and even have increased, this has been necessary to raise it again.

Sandy formation starts in the south of Santa Pola harbour almost uninterrupted to the Cervera Cape, although with important singularity (Vinalopó and Segura Rivers, and its mentioned above channelization, Punta Pilas, etc.). It is referred to a coastal front oriented to the E. Beaches are named in different ways because of historic and situation seasons, although the formation is unique and with maintained characteristics. Along then a whole of traditional buildings used as second dwellings are placed longitudinally and they have supposed to be a problem for transversal sediment movement. This is especially grave near Cervera Cape because it makes up a completely built-up and degraded area with increasing erosive problems.

FIELD INVESTIGATIONS AND ANALYSES DONE

The above mentioned fact induced development of studies to the determination of the present littoral dynamic from the previous determination of the directional frequency, seasonal and annual wind wave regime and results about theoric determination of littoral transport from were also taken initially. This potential littoral transport was got also from directional, seasonal and annual points of view. Therefore it has been possible to establish the dynamic conditions of the sandy coastal front and to correlate them to other results, taking into consideration waves propagation phenomenon, especially referred to wave refraction. Also it was possible to study eolian deposits in the area: Fig. 2 shows rose diagram obtained by the classification of dunes in transverses and longitudinals. That allows study the wind regime. Also was studied sedimentology of beach materials and bathymetric campaigns were done in all the area, investigating coast line evolution from aerial photographs from different years. Fig. 3 and 4 show grain size analyses of beach material proceeding from north area (Fig. 3a) and south of the Segura River mouth (Fig. 3b). Mineralogic results (Fig. 4) are of sand strand of the second place mentioned above.

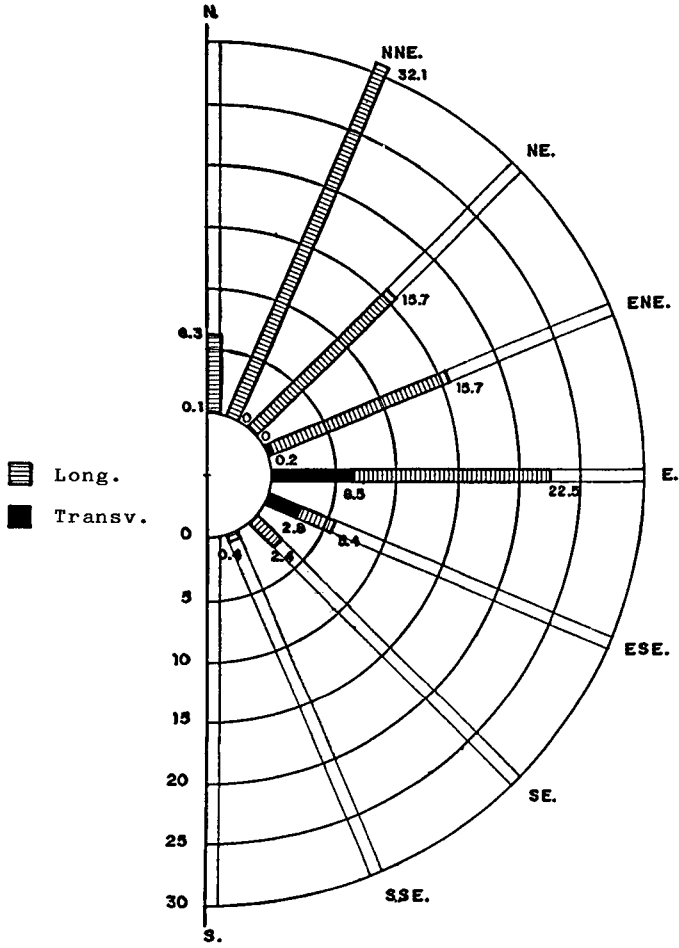


Fig. 2 Rose diagram of Guardamar dunes

GRAINSIZE ANALYSIS

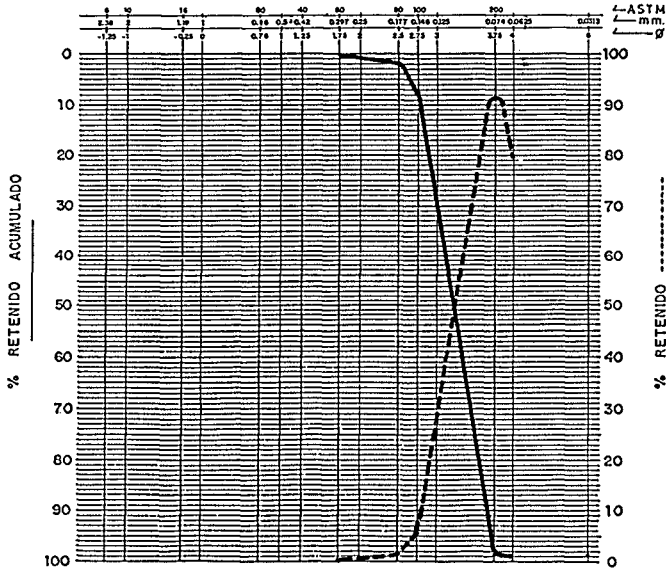


FIG. 3a

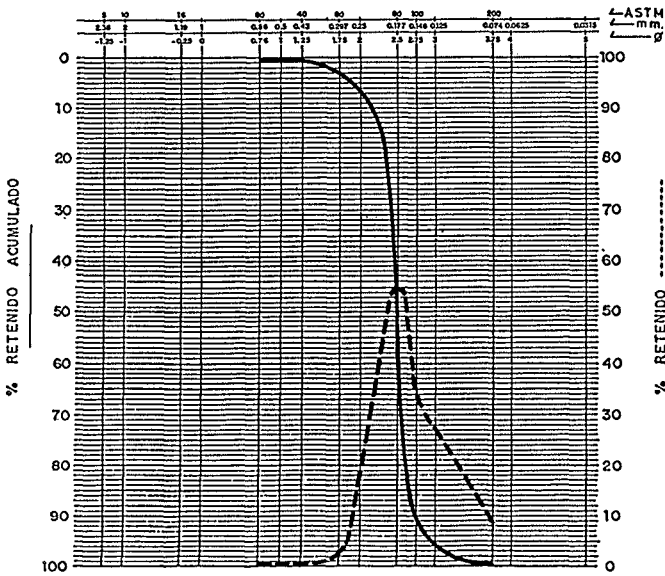


FIG. 3b

FRACCION RETENIDA TAMIZ ASTM N° 50			
TAMANO DE PARTICULA(mm): 0,30-0,42		%RETENIDO: 3,39	
FRACCION CARBONATADA : 57,6 %			
COMPOSICION MINERALOGICA EN % DE LA FRACCION NO CARBONATADA			
CUARZO BLANCO	85	TURMALINA	
CUARZO ROJO	8	EPIDOTA	
CUARZO AZUL	5	CIRCON	
CUARZO NEGRO	2	ANFIBOLES	
MIXTOS CUARZO		PIROXENOS	
MOSCOVITA		OXIDOS	
BIOTITA		OPACOS	
MORFOLOGIA CUARZO BLANCO EN%		GRADO DE REDONDEO	
REDOND. 6	POCO ROD. 31	52	
MUY ROD. 53	NO ROD. 10		

FRACCION RETENIDA TAMIZ ASTM N° 80			
TAMANO DE PARTICULA(mm): 0,18-0,30		%RETENIDO: 52,26	
FRACCION CARBONATADA : 53,4 %			
COMPOSICION MINERALOGICA EN % DE LA FRACCION NO CARBONATADA			
CUARZO BLANCO	84	TURMALINA	
CUARZO ROJO	10	EPIDOTA	
CUARZO AZUL	2	CIRCON	
CUARZO NEGRO	2	ANFIBOLES	*
MIXTOS CUARZO		PIROXENOS	
MOSCOVITA		OXIDOS	2
BIOTITA		OPACOS	
MORFOLOGIA CUARZO BLANCO EN%		GRADO DE REDONDEO	
REDOND. 11	POCO ROD. 40	48	
MUY ROD. 36	NO ROD. 13		

FRACCION RETENIDA TAMIZ ASTM N° 100			
TAMANO DE PARTICULA(mm): 0,15-0,18		%RETENIDO: 32,31	
FRACCION CARBONATADA : 55,8 %			
COMPOSICION MINERALOGICA EN % DE LA FRACCION NO CARBONATADA			
CUARZO BLANCO	82	TURMALINA	1
CUARZO ROJO	13	EPIDOTA	
CUARZO AZUL	2	CIRCON	
CUARZO NEGRO		ANFIBOLES	1
MIXTOS CUARZO		PIROXENOS	
MOSCOVITA		OXIDOS	1
BIOTITA		OPACOS	
MORFOLOGIA CUARZO BLANCO EN%		GRADO DE REDONDEO	
REDOND. 13	POCO ROD. 26	54	
MUY ROD. 49	NO ROD. 12		

FRACCION RETENIDA TAMIZ ASTM N° 200			
TAMANO DE PARTICULA(mm): 0,07-0,15		%RETENIDO: 11,95	
FRACCION CARBONATADA : 60 %			
COMPOSICION MINERALOGICA EN % DE LA FRACCION NO CARBONATADA			
CUARZO BLANCO	64	TURMALINA ANG.yR.	8
CUARZO ROJO	16	EPIDOTA	
CUARZO AZUL	5	CIRCON	
CUARZO NEGRO	3	ANFIBOLES	1
MIXTOS CUARZO		PIROXENOS	
MOSCOVITA		OXIDOS	3
BIOTITA		OPACOS	
MORFOLOGIA CUARZO BLANCO EN%		GRADO DE REDONDEO	
REDOND. 33	POCO ROD. 41	62	
MUY ROD. 23	NO ROD. 3		

FIG. 4 Mineralogic Analysis

WAVE REFRACTION AND LITTORAL TRANSPORT RATES

In order to understand the effect and influence of wave refraction it has been established six point along the area to determine results. Wave periods and heights of 6, 8 and 10 sec., and 2, 6 and 8 m. were fixed respectively. A computer program was applied to find incident waves in deep water from S, SE, E and NE, and determine refraction coefficients and wave angle of incidence. Fig. 5 shows results in central point of the area.

Littoral transport rates were after calculated utilizing CERC methods :

$$Q = \sum \left[p_v \times \left\{ 3.59 \times 10^6 \sum_n \left[(H_o \times K_r)^{5/2} p_{H_V} \sin 2\alpha_b \right] \right\} \right]$$

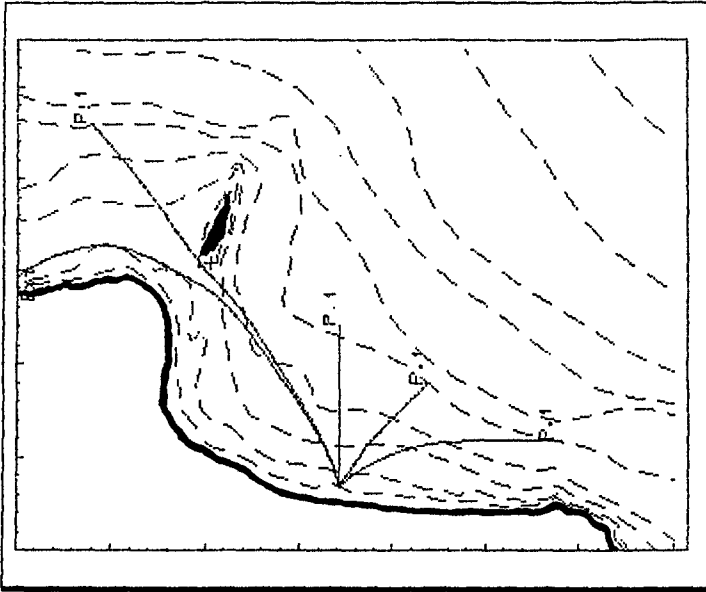


DIAGRAMA DE REFRACCION EN PLAYA DE GUARDAMAR
 T = 6 s P.I. = 49.96 m
 Dt = 6 s Dx = 700 m Dy = 540 m

Ortogonal	Punto	Coord. X (m)	Coord. Y (m)	Prof. (m)	Ang. con DX+ (DEG)
1	1	17070.0	3405.0	4.8	45.0
1	142	28773.0	5932.3	50.0	-7
2	1	17070.0	3405.0	4.9	58.0
2	87	21780.6	8945.6	50.0	45.3
3	1	17070.0	3405.0	4.8	66.0
3	100	17109.9	12074.7	50.0	90.8
4	1	17070.0	3405.0	4.8	99.0
4	274	3948.2	25006.1	50.0	130.5
5	1	17070.0	3405.0	4.8	99.5
5	300	44.7	14610.4	8.8	220.3

FIG. 5 Wave refraction diagram result

In addition, for the three southeast points referred

it has been considered littoral transport induced by wave generation in Guardamar Bay.

Waves from E,SE and S reach the shoreline. Logically refraction is bigger in waves from SE and S. Waves from NE have a different way as a function of its characteristics : biggest reach the north area across seasurface between Santa Pola Cape and Tabarca Isle, but do not reach southeast areas, except its extreme. It is due to the island. So there is a large stretch that it is not reached by waves from NE, these who would induce bigger littoral transport rates. Smaller waves reach the half north area across channel and in the south arrive waves from the Guardamar Bay. Estimated littoral transport rates are shown in Table 1.

---TABLE 1---

<u>POINT</u>	<u>Q₁</u>	<u>Q₂</u>	<u>Q(m³/y)</u>
1. PLAYA LISSA	-281.800	-	-281.800
2. PLAYA PINET	-35.300	-	-35.300
3. PLAYA PINET (*)	+168.900	-	+168.900
4. PLAYA PESQUERAS	+442.400	-	+442.400
5. PLAYA GUARDAMAR	+221.400	+29.500	+250.900
6. PLAYA LA MATA	+199.000	+35.400	+234.400
7. CABO CERVERA	+209.000	+35.000	+244.000

(*) Were considered two orientations of the shoreline
Sign + indicates direction to the south.

REFERENCES

- * AGUILAR HERRANDO, J. (1984) : "Naturaleza y distribución de las corrientes producidas por la rotura del oleaje". Tesis Doctoral. Universidad Politécnica de Valencia. Spain.
- * DIEZ GONZALEZ, J.J. (1982) : "Bases para una aproximación a la dinámica litoral del País Valenciano". R.O.P. Madrid. Spain.
- * DIEZ GONZALEZ, J.J. et al. (1982) : "Shore management in Santa Pola Bay (Alicante, Spain)". Proc. of Congress Int. Assoc. of Eng. Geol. New Delhi.
- * ESTEBAN CHAPAPRIA, V. (1987) : "Procesos litorales en las costas valencianas al Sur del Cabo de San Antonio". Tesis Doctoral. Universidad Politécnica de Valencia. Spain.

CHAPTER 100

TRACERS OF SAND MOVEMENT ON THE OREGON COAST

KAREN E. CLEMENS¹ AND PAUL D. KOMAR²

ABSTRACT

The study of sand mineralogy and grain rounding can help answer many questions of immediate concern to coastal engineers or to broader issues of beach preservation. The heavy-mineral contents of sands, together with statistical techniques such as factor analysis, can be used to delineate sediment sources, trace transport paths, and map out patterns of mixing during sediment dispersal. Variations in the degree of grain rounding can similarly be used to trace sand movements, or to obtain additional information concerning the history of the sediment particles.

The techniques of studying sand mineralogies and grain rounding, and the types of problems they can address, are illustrated by research on the Oregon coast. Heavy mineral compositions of Oregon beach sands are the products of mixing contributions from four sources; the Columbia River on the north, the smaller rivers draining the Coast Range, the Umpqua River on the southern Oregon coast, and the Klamath Mountains of southern Oregon and northern California. Numerous headlands now prevent the longshore transport and mixing of sands from these multiple sources. The beach-sand compositions instead reflect along-coast mixing during Pleistocene lowered sea levels when blockage by headlands was absent. At that time there was a net littoral sand transport to the north, evident from the dispersal of Klamath-derived sands. With a rise in sea level and accompanying migrations of the beaches, headlands eventually interrupted the along-coast mixing of nearshore sands. Therefore, the north to south variation in compositions of beach sands is in part a relict pattern inherited from mixing during lowered sea levels. This has been modified during the past several thousand years by some additions of sand to the beaches from sea-cliff erosion and from rivers. However, studies of sediment mineralogy and grain rounding indicate that sands derived from most rivers draining the Coast Range are presently trapped in estuaries and so are not significant sources of beach sand. The Columbia River now supplies sand to Oregon beaches only to the first headland, Tillamook Head. At that headland there is a marked change in mineralogy and grain rounding with angular, recently supplied Columbia River sand to the north and rounded relict sand to the south.

¹Greenhorn & O'Mara, Maryland Trade Center, 7500 Greenway Center Dr.,
Suite 700, Greenbelt, MD 20770

²College of Oceanography, Oregon State University, Corvallis, OR 97331

INTRODUCTION

The mineral compositions of sands and properties of individual particles such as their degrees of rounding can be utilized to trace movements of sediments in the coastal zone. This was illustrated many years ago by the pioneering studies of Parker Trask who investigated the movement of beach sand along the southern California coast (Trask, 1952). Trask was able to demonstrate that the sand filling the harbor at Santa Barbara comes from a distance of more than 160 km up the coast. He concluded this by using the heavy mineral augite as a tracer, a mineral whose source is ancient volcanic rocks near Morro Bay to the north of Santa Barbara. This mineral, together with the lighter quartz and feldspar, moves to the south along the beaches as littoral drift, until it is trapped by the Santa Barbara breakwater.

This simple example from the work of Trask illustrates the potential of applications in the use of the mineralogy of sediments to determine their sources and transport paths. In this example there was a clear application to an engineering problem – shoaling in the Santa Barbara boat basin. However, such techniques can be used to examine a range of questions concerning sources and losses of beach sands: Will dam construction on a river cut off a major source of beach sand?; Are river sands able to pass through estuaries to reach ocean beaches?; Is erosion of cliffs backing the beach a major source of nearshore sands?; Is the sand on the beach able to pass around headlands? Answers to such questions are often important to the proper design of coastal engineering structures, and to the preservation of beaches.

It is unfortunate that coastal engineers seldom draw upon this type of information. Considerable advances have been made in the techniques of studying sand mineralogies and grain rounding since the study of Trask (1952). These advances now permit more refined analyses and interpretations. A general objective of this paper is to illustrate the types of studies that can be undertaken, utilizing examples from the Oregon coast. These examples include the findings of studies which have attempted to determine the sources of beach sands on the central-Oregon coast, and examinations of the exchange of sand between estuaries and adjacent beaches. The Oregon coast is ideal to illustrate the types of investigations that can be undertaken in that all of the questions cited above are relevant to an understanding of beach-sand sources and transport paths.

TECHNIQUES OF STUDY

Heavy minerals such as augite contained within sands are distinguished from the light minerals, principally quartz and feldspars, by their contrasting densities. Laboratory techniques to separate the light and heavy minerals have in the past employed the heavy liquids bromoform (density 2.88 g/cm³), tetrabromoethane (2.95) and methylene iodine (3.30). These heavy liquids are highly toxic, and so considerable care must be taken in the mineral separations. Fortunately, the use of the much safer sodium polytungstate (3.00) has recently been introduced (Callahan, 1987). Identification of the individual heavy minerals is accomplished with a microscope using standard petrographic techniques. The heavy-mineral separates are mounted on slides in a liquid such as Canada Balsam which has a known index of refraction, and usually some 100 to 300 non-opaque heavy minerals are identified and counted. This yields the percentages of the various non-opaque heavy minerals.

Variations in the degree of grain rounding can also be used to trace sand movements, or to obtain additional information concerning the history of the sand. Roundness is a measure of the sharpness of the grain's corners and edges, and is

distinguished from sphericity which is a measure of the degree to which the grain deviates from a sphere. When grains are transported, collisions abrade their sharp edges so that the average degree of rounding progressively increases. In the case of sand-size grains, it has been shown that transport in rivers causes very little abrasion and rounding, and would produce minimal changes over typical river lengths (Kuenen, 1959). On the other hand, the long-term action of surf on beaches can eventually lead to grain rounding. It is difficult to evaluate the time periods required for rounding sand grains on beaches, but most investigators qualitatively assess it as involving thousands of years.

A major problem in studies of grain rounding has been in its quantification. Powers (1953) and Shepard and Young (1961) provide standardized series of grain images ranging in degrees of roundness. Comparisons between grains of the sample and these images allows one to place them in one of six categories ranging from "very angular" to "well rounded", or to assign corresponding numbers 1 through 6. However, this approach is subjective and can be viewed as only semi-quantitative. We have been able to use this approach in studies of Oregon coast sands due to the significant differences in angularity between the fresh river sands and the beach sands which have suffered appreciable abrasion. A more quantitative and reproduceable approach has been introduced by Schwartz and Shane (1969) and Ehrlich and Weinberg (1970) which involves Fourier analyses of the digitized outlines of the grains. The lower harmonics in such analyses relate to the overall shape of the grain, being more of a measure of the grain's sphericity, while the higher harmonics in part reflect the grain's degree of rounding. Studies such as that by Mazzullo et al. (1984) demonstrate that analyzing grain shapes by this approach can yield information on sand sources and transport paths. Techniques have been devised which automatically digitize grain outlines viewed under a microscope, with subsequent derivations of the harmonics of the Fourier analyses. This is necessary in that when the application is to trace sand movements, measurements are required on hundreds of grains in any given sample.

OREGON-COAST MINERAL STUDIES

The Oregon coast provides an ideal location to illustrate the usefulness of studies of sand mineralogy and grain rounding to obtain a better understanding of sources and transport paths of coastal sands. There are multiple sources having reasonably distinctive mineralogies which supply sands to the nearshore. The rivers contain angular sand grains which are progressively rounded during transport on beaches. It will be seen that combined studies of mineralogy and grain rounding indicate that Oregon beach sands have had a long and complex history. Contrasts in mineralogies and grain rounding between beach and river sands have also permitted detailed examinations of transport paths within Oregon estuaries.

Coastal Morphology and Potential Sand Sources

Much of the Oregon coast consists of a series of large rocky headlands which separate and isolate stretches of beaches. The headlands are composed of highly resistant volcanic rocks, while the beaches exist in areas backed by more easily eroded sedimentary rocks. This segments the coast into a series of pocket beaches where the lengths of the stretches of beach vary from about 5 to 100 km depending on the spacings of the volcanic rocks which form headlands. The northern half of the Oregon coast is shown in Figure 1, which illustrates this interplay of headlands and pocket beaches. The headlands extend well offshore from the beaches, and generally have considerable along-coast lengths. This implies that they prevent or severely limit any bypassing of beach sands. As will be seen, this view is supported by studies

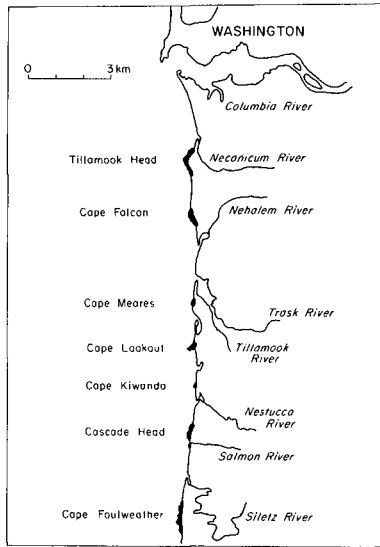


Fig. 1: The northern coast of Oregon, showing the interplay between headlands and beaches.

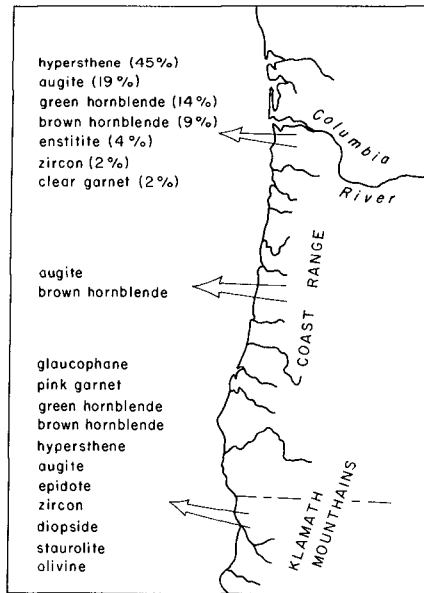


Fig. 2: Schematic of the principal sources of heavy minerals used to trace sand movements on the Oregon coast.

of beach-sand compositions and grain rounding. Therefore, the headlands act to isolate the individual beaches. Portions of the beaches form sand spits behind which are found bays and estuaries of the rivers that drain the Coast Range. Other portions of the beach are backed by sea cliffs eroded into Tertiary mudstones and siltstones, or into Pleistocene sand deposits that are part of uplifted marine terraces. These terrace deposits are raised beach and dune sands, so their erosion can be a significant source of sand to the modern beaches.

The Columbia River is potentially the largest source of sand to the nearshore. Its drainage basin is very large and contains many different types of rocks. A result of this is that sand supplied to the coast by the Columbia contains a wide variety of heavy minerals with hypersthene, augite and hornblende being the most abundant (Fig. 2). It is known that sand derived from the Columbia has resulted in beach accretion on the Oregon coast south to Tillamook Head (Fig. 1). However, at present most of the sand derived from the Columbia is transported northward along the Washington coast.

A number of rivers of various sizes reach the Oregon coast from the nearby Coast Range (Fig. 1), and these are another potential source of beach sands. This range of low mountains (450-m average elevation) contains volcanic rocks which yield augite, the mineral that together with a small amount of brown hornblende dominate river-sand compositions (Fig. 2). South of Cape Blanco the Coast Range gives way to the older but higher Klamath Mountains. The Klamaths contain complexly folded metamorphic rocks and intrusions of serpentized ultrabasic and granitic rocks; these yield a wide spectrum of heavy minerals (Fig. 2), with glaucophane, pink garnet and other metamorphic minerals being tracers unique to this source.

Compositional Variations of Oregon Beach Sands

There have been a number of studies of the mineralogies of Oregon beach sands, largely induced by the economic potential of concentrated deposits of the opaque minerals (Kulm et al., 1968; Scheidegger et al., 1971; Komar and Wang, 1984). These studies demonstrated that Oregon beach sands have had multiple sources. Of particular interest is that metamorphic minerals such as pink garnet, which clearly originated in the Klamath Mountains, are traceable northward along nearly the full length of the Oregon coast. The southward dispersal of sand derived from the Columbia River was less apparent in the results of those studies, and it was uncertain how much sand has been derived from rivers that drain the Coast Range. There appeared to be along-coast variations in the relative mixtures of sands derived from these potential sources, but this had not been clearly delineated by the early investigations. In addition, an important question involved whether the rocky headlands are effective in blocking along-coast sand movements. Does the finding of Klamath Mountain sands in the beaches along nearly the entire Oregon coast imply that there is bypassing in spite of the large sizes of most of the headlands?

In order to answer such questions, we undertook a detailed study of the mineralogy and grain rounding of Oregon beach sands (Clemens, 1987; Clemens and Komar, 1988). Sand samples were collected from 26 beaches extending from immediately south of the Columbia River to Cape Blanco on the south-Oregon coast. Sand samples were also obtained from rivers and sea cliffs that are potential sources of beach sand. In total 18 different minerals were identified in microscopic analyses of the samples, but the major constituents are augite, hornblende, hypersthene and garnet. The percentages of those four major heavy minerals are plotted in Figure 3, revealing how they vary with along-coast distance south of the Columbia River. The

most noticeable variation is in the percent of augite, which dominates beach-sand compositions between Tillamook Head, the first headland south of the Columbia River, and Cape Foulweather midway through the study area. These augite-rich beach sands appear to reflect contributions by the Coast Range volcanics directly landward from this stretch of coast. North of Tillamook Head the percentage of augite abruptly drops as the beach is richer in hornblende and hypersthene, minerals that are clearly derived from the Columbia River. The content of garnet in the beach sands systematically increases toward the south (Fig. 3), an expected distribution in view of its source in the Klamath Mountains of southern Oregon. Of interest is that garnet is found in beach sands all the way north to Tillamook Head, some 500 km north of its source.

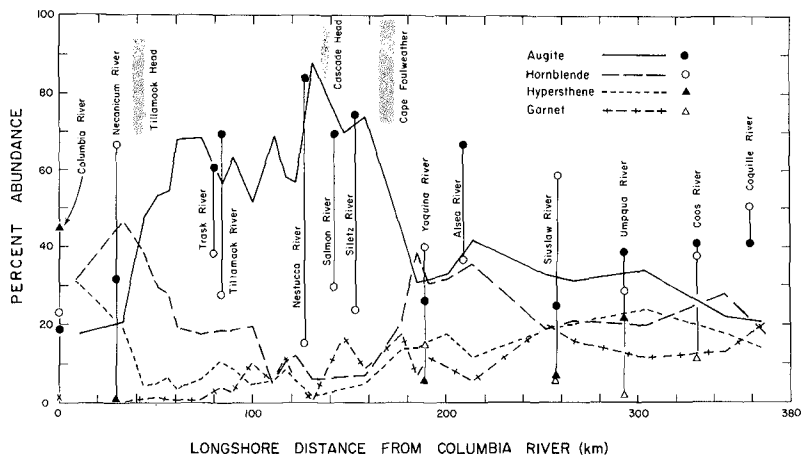


Fig. 3: Along-coast variations in abundances of the principal heavy minerals found in Oregon beach and river sands. [from Clemens and Komar (1988)]

The along-coast distributions of individual minerals, Figure 3, has already permitted tentative interpretations of sources and dispersal routes of beach sands on the Oregon coast. We have identified minerals that are suggestive of various sources and have qualitatively assessed their relative contributions along the length of the coast. The abrupt compositional changes at Tillamook Head and Cape Foulweather indicate that at least those headlands are effective in blocking longshore sand movements on the beaches.

Factor analysis is in general a more powerful approach to interpreting mineral assemblages than relying on individual minerals. Factor analysis examines natural groupings of minerals found within the assemblages contained in the series of individual samples (Imbrie and van Andel, 1964). The technique searches for end-member vectors or factors which can be summed in varying proportions to yield the mineralogies of the samples. Such an analysis (Q-mode factor analysis) was undertaken on the heavy-mineral percentages found in the Oregon beach-sand samples (Clemens and Komar, 1988). Three dominant factors were derived which account for 89% of the compositional variations in the samples. The mineral compositions of these end-member factors are given in Figure 4, and their

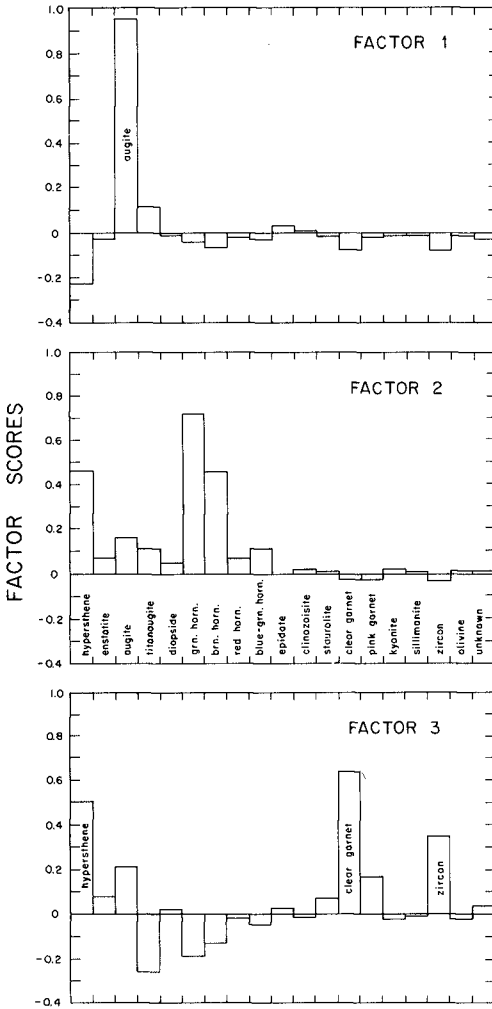


Fig. 4: Compositions of the factors obtained in factor analyses of the heavy mineral compositions of Oregon beach-sand samples. [from Clemens and Komar (1988)]

along-coast variations are graphed in Figure 5. Factor 1 consists almost entirely of augite, and it is seen that this factor dominates the beach-sand compositions between Tillamook Head and Cape Foulweather. In this case, since there is a source consisting of essentially one mineral, the results from the factor analysis correspond closely with our analysis based on individual minerals (Fig. 3). Factor 2 is rich in hypersthene and green and brown hornblende (Fig. 4). This factor has a bimodal distribution along the coast (Fig. 5). Its main loading, approaching 1, occurs on the beach north of Tillamook Head and is clearly associated with the Columbia River which is rich in those minerals. The more southerly increase in Factor 2, extending from 190 km south of the Columbia to the end of our sample range at 365 km south, is most likely contributed by the Umpqua River. Sand derived from that river has a high content of both hypersthene and hornblende, as well as augite, and with its large drainage basin the Umpqua could have been a major source of beach sand (more so than the other rivers draining the Coast Range). Therefore, Factor 2 appears to be associated with two major sources that are similar in compositions, the Columbia and Umpqua Rivers. This interpretation is verified if the river-sand samples are included in the factor analysis together with the beach samples. The Columbia River is then identified as 100% Factor 2, and the Umpqua River sand is found to consist of nearly equal portions of Factors 1 and 2.

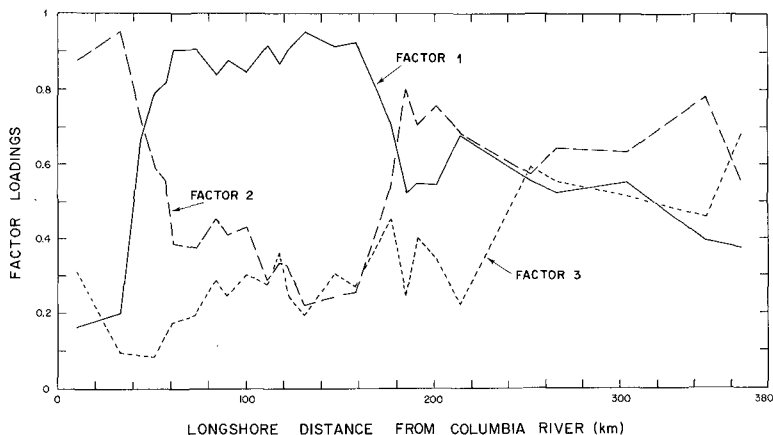


Fig. 5: Along-coast loadings of the three factors (fig. 4) obtained in the analyses of the beach-sand compositions. [from Clemens and Komar (1988)]

Factor 3 is rich in garnet and zircon (Fig. 4), and also includes the metamorphic minerals staurolite and epidote. This composition, together with its northward, along-coast decrease (Fig. 5), clearly points to a source in the Klamath Mountains. This interpretation is the same as in Figure 3 which was based on garnet alone, but is more firmly established here by a complete assemblage of metamorphic minerals.

It is apparent that more information about sand sources and dispersal paths can be obtained from factor analyses than from distributions of individual minerals. Considerable interpretation is still required, but the end-member factors can generally be traced back to specific sources. These sources may not necessarily be individual rivers, but instead could be rock terrains. This is the case on the Oregon coast where it is better to think in terms of the sources being the metamorphic rocks

of the Klamaths, the augite-rich volcanics of the Coast Range, and the hypersthene and hornblende-rich rocks of the Cascade Mountains. We have seen that the Umpqua River combines two of these terrain sources.

The switch from Factor 1 (Columbia River sand) to Factor 2 (Coast Range) is seen in Figure 5 to be abrupt at Tillamook Head, more so than the change in augite alone (Fig. 3). This further substantiates the ability of Tillamook Head to block longshore movements of beach sands. While determining the heavy-mineral compositions of the samples, differences in grain rounding were also noted in the sands on opposite sides of Tillamook Head. North of this headland the heavy-mineral grains are highly angular and many delicate crystals are present, while to the south they are noticeably more rounded. This change was further established by using the photo-comparison roundness scale of Shepard and Young (1961). Roundness was evaluated for about 50 grains of each mineral in a sample, yielding a distribution of roundness values for a mineral. Such analyses were primarily performed on augite, but some evaluations were also made for hypersthene, hornblende and quartz. The results are shown in Figure 6 for samples from the Columbia River, and from the beaches to the south of the Columbia but on opposite sides of Tillamook Head. A significant change in rounding is seen to occur at Tillamook Head, the beach sands to its north being more angular than to the south. Augite in the beach north of Tillamook Head appears to retain the same degree of high angularity as sand in the Columbia River. This, together with the fragile nature of some of the mineral crystals in the beach sands, indicate active contributions from the Columbia. The rounder grains on the beaches south of Tillamook Head suggest a much longer residence time for those sands in the nearshore.

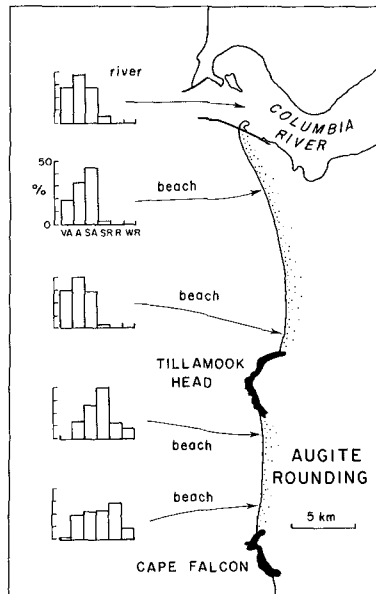


Fig. 6: Histograms of grain rounding for augite in river and beach sands: VA - very angular; A - angular; SA - subangular; SR - subrounded; R - rounded; WR - well rounded.

The only other headland which demonstrates a marked compositional change in beach-sand mineralogies on its north and south sides is Cape Foulweather (Figs. 3 and 5). This change can be attributed to differences in materials derived primarily from sea-cliff erosion. North of Cape Foulweather most of the cliff erosion has been in alluvium derived from the Coast Range and therefore is rich in augite (like the rivers draining the Coast Range). Pleistocene marine terraces are more important south of Cape Foulweather, and these terraces contain uplifted beach and dune sands. These old deposits contain a full spectrum of minerals from the various sources including the Columbia River and the Klamath Mountain metamorphics.

It might mistakenly be concluded from our results that Tillamook Head and Cape Foulweather are the only headlands that are effective in blocking movements of sand on the modern beaches. However, blockage by those headlands is made apparent by differences in sand sources on their opposite sides. If the sand sources to the north and south are much the same and the long-term history of the sands do not differ, then there will be no compositional or textural differences. Tillamook Head and Cape Foulweather are not unusually large, nor do they extend to deeper water than most of the other headlands. Therefore, it is probable that the other headlands are also effective barriers to longshore sand movements, even though this could not be established directly by our analyses of beach sands.

The results of our investigations of Oregon beach-sand mineralogies and grain rounding have confirmed that the compositions are derived from the mixing of sands from multiple sources. All beaches, excepting those south of the Columbia River to Tillamook Head, contain significant quantities of metamorphic minerals derived from the Klamath Mountains of southern Oregon and northern California. This indicates a northward transport of sand along the coast, but this transport cannot occur now due to the presence of headlands. Instead, it must have taken place during Pleistocene lower stands of sea level when headlands did not interrupt such sand movements. With a rise in sea level at the end of the ice ages and accompanying migrations of the beaches, the formerly continuous beach became segmented and isolated between headlands. Therefore, much of the along-coast variation in beach-sand mineralogies on the Oregon coast is relict, preserving the longshore patterns established thousands of years ago when sea levels were lower. The beach-sand compositions have been altered somewhat during the last few thousand years following their isolation between headlands. Most noteworthy has been the growth of the beach north of Tillamook Head due to large sand contributions by the Columbia River. However, elsewhere the additions must have been comparatively small since the volumes have not been sufficiently large to obscure the relict pattern established thousands of years ago. This implies that modern-day inputs of sand to most Oregon beaches from sea cliff erosion and from rivers draining the Coast Range are relatively small.

Exchanges of Sand Between Beaches and Estuaries

A primary reason for the small contributions of sands to beaches from rivers draining the Coast Range is that most of these rivers are separated from the ocean by estuaries. To varying degrees, these estuaries trap the river sands. This has been established by Kulm and Byrne (1966) and Byrne and Kulm (1967) in Yaquina Bay, by Scheidegger and Phipps (1976) in Grays Harbor, Washington, and by Peterson et al. (1982, 1984) in several other Oregon-coast estuaries.

In their investigations of Yaquina Bay, the estuary of the Yaquina River, Kulm and Byrne (1966) were able to establish the three realms of deposition diagramed in

Figure 7; a marine realm which extends approximately 2.5 km into the bay from the ocean inlet, a fluvial realm in the upper reaches of the bay, and a broad "mixed" realm which is a zone where the two sand sources mix in varying proportions. These were delineated on the basis of sediment grain sizes, compositions, and particle rounding. The compositional distinctions included not only differences in heavy minerals found in the marine versus fluvial sands, but also in the mineralogy of the feldspars and the distribution of "yellow grains". Yellow grains are diagnostic of marine sands where they constitute about 10% of the light-mineral fraction; they consist primarily of weathered feldspars and chert, and are derived from erosion of terrace sands in the sea cliffs. Because they are distinctive and easily recognized, yellow grains can serve as a simple tracer of marine-sand movements into Yaquina Bay (Fig. 8). Heavy minerals such as staurolite and kyanite, found in the beach sands but not in the Yaquina River, were also used by Kulm and Byrne as tracers of marine-sand movement into Yaquina Bay.

Peterson et al. (1982) has demonstrated a similar pattern of mixing of marine and fluvial sands in Alsea Bay. However, the use of factor analysis of heavy-mineral assemblages, together with quantitative measurements of grain rounding, permitted a more detailed mapping of the transport paths of sands in this estuary. Based on the abundances of 15 non-opaque heavy-mineral varieties in surface sand samples, two factors were obtained in a factor analysis which account for 95% of the sample variance. One factor consisted almost exclusively of augite, and this end member represents contributions by the Alsea River. In contrast, the marine-related factor was composed of a number of minerals including hypersthene, hornblende and garnet. The weightings assigned to these two factors for each sand sample in Alsea Bay represented the respective contributions by the river versus the marine beach. Peterson et al. also noted that the augite and hornblende grains of fluvial origin are angular, while those of marine origin are rounded. This provided another means to evaluate sources and trace sand movements in Alsea Bay. The delineation of sand mixing in Alsea Bay by the two methods, factor analysis of heavy-mineral compositions and grain rounding, yielded essentially the same results. The general patterns are similar to those found by Kulm and Byrne (1966) in Yaquina Bay (Fig. 7), with marine sand dominating near the mouth, a broad zone of marine-fluvial mixing, and pure riverine sands occurring only in the upper reaches of the estuary. However, more details of the mixing patterns were established in Alsea Bay, the tidal channels clearly serving as conduits of sand transport throughout the central estuary with an interfingering of sands from the two sources. Repeated sampling in different seasons revealed that down-channel transport of fluvial sands occurs during winter periods of high river discharge, while beach-sand intrusions under tidal currents occur during the summer months of low river discharges.

Similar analyses have been conducted in other Northwest estuaries: Grays Harbor, Washington (Scheidegger and Phipps, 1976), the Sixes River estuary, Oregon (Boggs and Jones, 1976), Tillamook Bay, Siletz Bay, and the estuaries of the Siluslaw and Salmon Rivers (Peterson et al., 1984). Although these investigations demonstrated that most Northwest estuaries act as traps for both fluvial and marine sands, it is more difficult to establish whether some river sand is able to pass through an estuary to become a source of beach sand. Small rivers such as the Sixes River studied by Boggs and Jones (1976), have essentially no estuary, and during winter floods the riverine sands are flushed out onto the neighboring beaches. However, since the rivers are small, the volumes of sand contributed to the beach are small. More uncertain is whether the larger rivers, such as the Yaquina and Alsea,

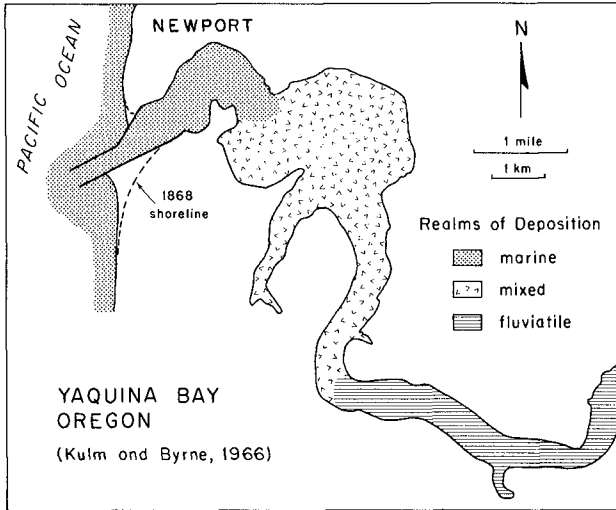


Fig. 7: Realms of sand deposition in Yaquina Bay. [after Kulm and Byrne (1966)]

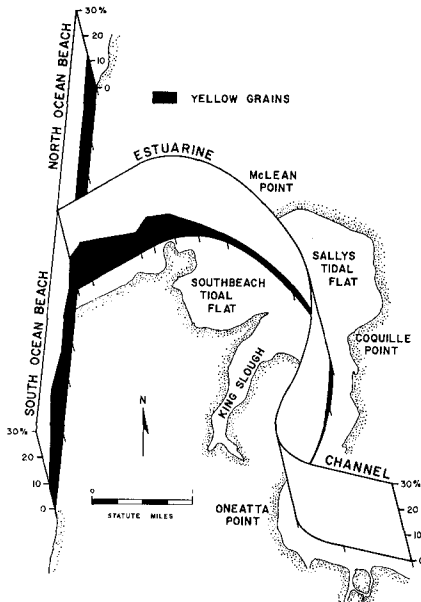


Fig. 8: Distribution of "yellow grains" in Yaquina Bay, used as a tracer of marine-sand movements into the estuary. [from Kulm and Byrne (1966)]

supply sands to Oregon beaches. Heavy minerals transported by these rivers are abundant on the adjacent beaches, and this correspondence might suggest that some river sands do pass through the estuaries. However, it is possible that most of the beach sand derived from rivers draining the Coast Range is relict, and reached the beaches during lower stands of sea levels when drowned-river estuaries were not present. It is likely that the degree of grain rounding will be the key to determining whether the Coast Range sands found on the modern beaches are relict or represent recent additions. Clemens and Komar (1988) analyzed the rounding of augite in beach samples from Neskowin near the Nestucca River, again using the photographic chart of Shepard and Young (1961). We found something of a bimodal distribution in the sand angularity, and suggested that the more angular mode might represent recent contributions by the Nestucca River while the mode of higher grain rounding represents relict augite in the beach sand. The Nestucca River has a reasonably small estuary so it could be expected that some riverine sand does reach the ocean beach. The results from this one location suggest that a comprehensive study of grain rounding of Oregon beach sands would help answer questions concerning which rivers are presently supplying sands to the nearshore. However, it is also apparent that using the photo roundness scale of Shepard and Young would be inadequate in this application, and that the more quantitative approach of using Fourier shape analyses would be required.

SUMMARY OF CONCLUSIONS

Studies of the mineralogies and grain rounding of sands on the Oregon coast have helped answer many questions relevant to the preservation of beaches and have led to an increased understanding of estuarine sedimentation. Differences in beach-sand mineralogies and grain rounding on opposite sides of headlands confirm that they are effective in blocking longshore sand movements and therefore isolate the beaches. The mineralogy studies have further established that most beaches contain relict sands, transported alongshore from various sources during lowered sea levels when headlands did not exist, and then onshore with the rising sea at the end of the last glacial period. This origin explains the observed patterns of along-coast variations in beach-sand mineralogies. Our research has established that sea-cliff erosion is a source of sands to some beaches, although the quantities generally are not so large as to have completely diluted and masked the relict sands on the beaches. Studies of estuarine sedimentation show that the river-drowned estuaries are sinks of both river and beach sands; additional research is required to establish whether measureable quantities of riverine sands are able to bypass these estuaries to reach the ocean beaches.

These Oregon-coast studies have been used in this review to illustrate the types of applications and questions that can be addressed using techniques of mineral compositions and textures to trace sand movements. Such studies could be used by engineers working in other coastal areas to assist in the proper design of structures and to help in the preservation of our coastlines.

ACKNOWLEDGEMENTS

We would like to thank L. D. Kulm for his helpful comments in reviewing this paper. This paper is a result of research sponsored by the Oregon State University Sea Grant Program, supported by NOAA Office of Sea Grant, Department of Commerce, under grant number NA85AA-D-SG0095.

REFERENCES

- BOGGS, S., and JONES, C.A. (1976) Seasonal reversal of flood-tide dominated sediment transport in a small Oregon estuary: *Geol. Soc. Amer. Bull.*, v. 87, p. 419-426.
- BYRNE, J. V., and KULM, L. D. (1967) Natural indicators of estuarine sediment movement: *Jour. Waterways and Harbors Div., Proc. Amer. Soc. Civil Engrs.*, v. 93, no. WW2, p. 181-194.
- CALLAHAN, J. (1987) A nontoxic heavy liquid and cheaper filters for separation of mineral grains: *Jour. Sedimentary Petrology*, v. 57, p. 765-766.
- CLEMENS, K. E. (1987) Along-coast variations of Oregon beach-sand compositions produced by the mixing of sediments from multiple sources under a transgressing sea: Unpubl. Master's Thesis, Oregon State Univ., Corvallis, 75 p.
- CLEMENS, K. E., and KOMAR, P. D. (1988) Oregon beach-sand compositions produced by the mixing of sediments under a transgressing sea: *Jour. Sedimentary Petrology*, v. 58, p. 519-529.
- EHRlich, R., and WEINBERG, B. (1970) An exact method for characterization of grain shape: *Jour. Sedimentary Petrology*, v. 40, p. 205-212.
- IMBRIE, J., and VAN ANDEL, T.J. H. (1964) Vector analysis of heavy mineral data: *Geol. Soc. America Bull.*, v. 75, p. 1131-1156.
- KOMAR, P. D., and WANG, C. (1984) Processes of selective grain transport and the formation of placers on beaches: *Jour. of Geology*, v. 92, p. 637-655.
- KUENEN, Ph. H. (1959) Experimental abrasion 3. Fluvial action on sand: *Amer. Jour. Science*, v. 172-190.
- KULM, L. D., and BYRNE, J. V. (1966) Sedimentary response to hydrography in an Oregon estuary: *Marine Geology*, v. 4, p. 85-118.
- KULM, L. D., SCHEIDEGGER, K. F., BYRNE, J. V., and SPIGAI, J. J. (1968) A preliminary investigation of the heavy mineral suites of the coast rivers and beaches of Oregon and northern California: *The Ore Bin*, v. 30, p. 165-180.
- MAZZULLO, J., EHRlich, R., and HEMMING, M.A. (1984) Provenance and areal distribution of Late Pleistocene and Holocene quartz sand on the southern New England continental shelf: *Jour. Sedimentary Petrology*, v. 54, p. 1335-1348.
- PETERSON, C., SCHEIDEGGER, K. F., and KOMAR, P. D. (1982) Sand-dispersal patterns in an active-margin estuary of the northwestern United States as indicated by sand composition, texture and bedforms: *Marine Geology*, v. 50, p. 77-96.
- PETERSON, C., SCHEIDEGGER, K. F., KOMAR, P. D., and NIEM, W. (1984) Sediment composition and hydrography in six high-gradient estuaries of the northwestern United States: *Jour. Sedimentary Petrology*, v. 54, p. 86-97.
- POWERS, M.C. (1953) A new roundness scale for sedimentary particles: *Jour. Sedimentary Petrology*, v. 23, p. 117-119.
- SCHEIDEGGER, K. F., KULM, L. D., and RUNGE, E. J. (1971) Sediment sources and dispersal patterns on Oregon continental shelf sands: *Jour. Sedimentary Petrology*, v. 41, p. 1112-1120.
- SCHEIDEGGER, K. F., and PHIPPS, J. P. (1976) Dispersal patterns of sand in Grays Harbour estuary, Washington: *Jour. Sedimentary Petrology*, v. 46, p. 163-166.
- SCHWARTZ, H.P., and SHANE, K.C. (1969) Measurements of particle shape by Fourier analysis: *Sedimentology*, v. 13, p. 179-212.
- SHEPARD, F.P., and YOUNG, R. (1961) Distinguishing between beach and dune sands: *Jour. Sedimentary Petrology*, v. 31, p. 196-214.
- TRASK, P. D. (1952) Sources of beach sand at Santa Barbara, California, as indicated by mineral grain studies: *Beach Erosion Board Tech. Memo. No. 26*, U.S. Army Corps of Engrs., 24 p.

CHAPTER 101

PROBABILISTIC ANALYSIS OF SEAFLOOR LIQUEFACTION

Rafael Blázquez *
Felipe M. Martínez **

To investigate the reliability of a sandy soil layer in an ocean wave environment a liquefaction model is used in conjunction with a first order reliability method. Thus, sensitivity indices of the soil-water system with respect to the uncertain strength and input variables are computed, and the relative importance of the various factors defining the problem can be determined. The relationship of this approach with more conventional design methods (deterministic models, risk models) is discussed along with the range of applicability of the different safety measurements.

INTRODUCTION

When ocean waves propagate over a cohesionless oceanfloor, hydrodynamic pressures are continuously being generated at a rate which depends mainly on the permeability of the material. Sandy soils with low permeability coefficients are unable to dissipate the excess pore pressures, which eventually may become equal to the total stresses acting on the soil element. The result is the complete loss of all intergranular effective stress and bearing capacity of the material, a cyclic instability phenomenon known as liquefaction of the sand.

In this paper the liquefaction behavior of seafloor soils is evaluated by means of an analytical model-proposed earlier in the literature-which takes into account the physics of the phenomenon. Based on that model the following steps are taken:

- a) Carry out a parametric study to rank the relative importance of the factors governing liquefaction processes (deterministic approach).

* Research Engineer and Physicist, PhD; Head of the Section of Stochastic Analysis, CEPYC (Madrid-SPAIN), Formerly Visiting Lecturer, Civil Engineering Department, Department, University of California (Berkeley, USA).

* Director Centro de Estudios de Puertos y Costas, (CEPYC)-CEDEX. Antonio López, 81, 28026 Madrid, SPAIN

- b) Incorporate uncertainties in input/output variables into a fully probabilistic analysis of the problem.
- c) Use reliability techniques to compute sensitivity factors and critical values of the random variables.
- d) Compare the above methodology with classical risk methods.

DETERMINISTIC APPROACH

For the purposes of this study, a simplified pore pressure analysis of the liquefaction phenomenon, first described by Layas (1982) and Rahman and Jaber (1986), has been chosen. In this model harmonic linear waves are used, with fixed periods, T , and wave lengths, L , related by the formula:

$$T = \sqrt{\frac{2\pi L}{g \tanh(kd)}} \quad (1)$$

where $k = \frac{2\pi}{L}$ is the wave number and d is the water depth.

Two cases are considered:

- a) Undrained model (infinite layer)
- b) Drained model (finite layer)

Undrained model

If the permeability of the soil is zero, the pore pressure, u_g , generated at the sand layer (semi-infinite half space) at depth z is derived, according to the following algorithm.

1. Assume a linear pore pressure generation curve, $u_g(t)$:

$$\frac{u_g}{\sigma'_{v0}} \approx \frac{N}{N_1} = \frac{t}{t_1} \quad (2)$$

(σ'_{v0} =initial effective stress; N_1 =no. of cycles to liquefaction)

2. Assume a liquefaction cyclic strength curve, $\tau_1(N_1)$, of fatigue type:

$$\frac{\tau_1}{\sigma'_{vc} D_r} = a N_1^{-b} \quad (3)$$

(a, b =constants; D_r =relative density)

3. Compute the hydrodynamic pressure on the sea bed by linear wave theory:

$$p_0(x,t) = \frac{\gamma_w H}{2 \cosh(kd)} \cos(kx - \omega t) \quad (4)$$

(k =wave number; ω =wave frequency; d =water depth)

4. Compute the wave-induced shear stresses in the soil by elasticity theory:

$$\tau(x, z, t) = \frac{\gamma_w H K z}{2c \cosh(Kd)} e^{-Kz} \cos(Kx - \omega t - \psi) \quad (5)$$

5. Evaluate the liquefaction time at depth z , t_1 , from the conditions at the onset of liquefaction (equations 2, 3 and 4) written for $z = z_0$, $N = N_1$, and $t = t_1$ =

$$t_0 = T \cdot N_0 = T \cdot \left[\frac{\gamma' 2a \cdot D_r \cdot c \cosh(Kd)}{\gamma_w H K} \right]^{\frac{1}{b}} e^{Kz_0/b} \quad (6)$$

Then, substituting in eq. (2), yields:

$$u_g = \frac{\gamma' z t}{t_0} \quad (7)$$

where γ' is the buoyant unit weight of the soil.

Notice that the amplitude of the harmonic expressions 4 and 5 is independent of x , meaning that at the same depth the induced stresses at different horizontal positions have the same maximum values. Therefore neglecting the differences in phase, only one-dimensional responses need to be considered (Seed and Rahman, 1978).

Drained model

For a permeable stratum the equation governing the pore pressure response of the soil, u , becomes:

$$c_v \frac{\partial^2 u}{\partial z^2} = \frac{\partial u}{\partial t} - \frac{\partial u_g}{\partial t} \quad (8)$$

where c_v is the consolidation coefficient of the sand.

Equation 8 quantifies the balance of the simultaneous generation and dissipation of pore pressures that continuously occurs inside the soil layer. By inserting in eq. 8 the corresponding value of the generation rate term:

$$\frac{\partial u_g}{\partial t} = C z e^{-Kz} \frac{\gamma'}{T} = \left(\frac{\gamma_w \pi}{\gamma' a D_r} \right)^{\frac{1}{b}} \left(\frac{H/L}{\cosh\left(\frac{z\pi d}{L}\right)} \right)^{\frac{1}{b}} z e^{-Kz} \frac{\gamma'}{T} \quad (9)$$

and solving for the appropriate boundary and initial conditions, namely (Fig. 1):

$$\text{B.C. } \left\{ \begin{array}{l} \text{previous top} \longrightarrow [u(z, t)]_{z=0} = 0 \end{array} \right. \quad (10-1)$$

$$\left\{ \begin{array}{l} \text{impervious bottom} \longrightarrow \left[\frac{\partial u}{\partial z}(z, t) \right]_{z=D} = 0 \end{array} \right. \quad (10-2)$$

$$\text{I.C. } \longrightarrow [u(z, t)]_{t=0} = 0 \quad (10-3)$$

the following expression for the excess pore-pressure curves is found:

$$u(z, t) = \frac{C}{c_v} \frac{\gamma'}{T} \left\{ w(z) + v(z, t) \right\} \quad (11)$$

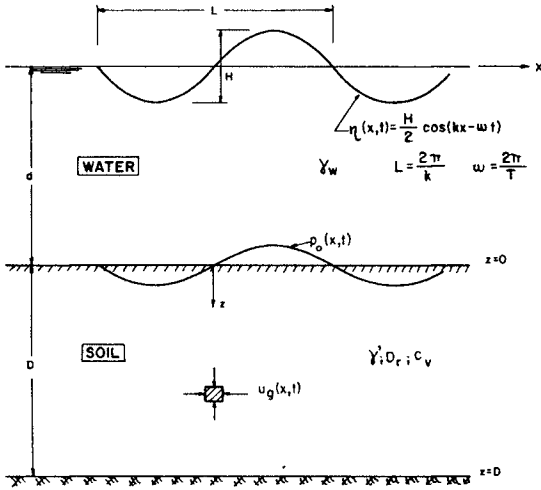


Fig.1. Scheme of the problem.

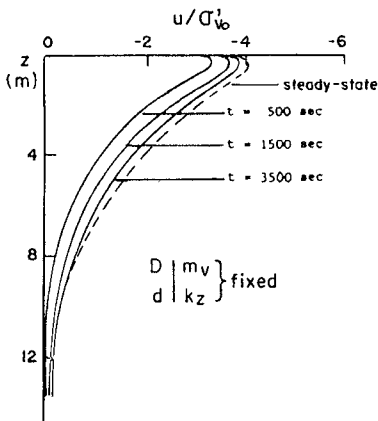


Fig.2. Dynamic isochrones at different stages of the storm. Drained layer (after Layas, 1982)

in which:
$$w(z) = \left(\frac{2}{z^3} - \frac{z}{z^2}\right) e^{z^2} + \left(\frac{D}{z} - \frac{1}{z^2}\right) e^{\frac{zD}{z} - \frac{2}{z^3}} \quad (12-1)$$

and
$$v(z,t) = -\frac{2}{D} \sum_{n=0}^{\infty} \left\{ h(\alpha_n, D, z) \right\} e^{-c_v \alpha_n^2 t} \sin(\alpha_n z) \quad (12-2)$$

are, respectively, the steady-state and transient components of the dynamic pore pressure curves.

In the above expressions,

$$\alpha_n = \frac{2n+1}{2} \frac{\pi}{D} \quad (13-1)$$

is a geometrical value, whereas

$$z = -\frac{K}{b} \quad (13-2)$$

is a parameter related to the input storm as well as the mechanical properties of the soil. Obviously, as $t \rightarrow \infty$ the term $v(z,t)$ vanishes, and the limiting (steady-state) isochrone becomes fixed in shape:

$$u(z) = \frac{C \gamma'}{c_v T} w(z) \quad (14)$$

Figure 2 exemplifies this behavior for different times of evolution of a given storm at a liquefiable site.

Factor of safety. Parametric study

The model described in the previous section defines the factor of safety against liquefaction at a given time and depth within the layer as:

$$(SF)_d = \frac{u}{\sigma'_v} \quad (15)$$

For the particular case of impervious soil, $u = u_g$, and the safety factor becomes:

$$(SF)_u = \frac{u_g}{\sigma'_v} = \frac{t}{t_1} \quad (16)$$

Where t_1 is a known parameter (eq.6). In both cases the onset of liquefaction (safety factor=1) is defined as the state in which the pore pressure generated by the ocean waves equals the initial effective pressure at some point in the deposit (soil resistance).

Since the parameter SF constitutes a global index of the safety of the deposit against liquefaction under various drainage conditions, its sensitivity to the variables involved is of practical importance.

To investigate further this point a classical parametric study has been carried out on a digital

computer. Table I shows the mean values assumed for all variables (reference state), whereas the corresponding ranges of variation and their effects on $(SF)_u$ and $(SF)_d$ are represented, side by side, on Figures 3 to 11 for a storm of 10 minutes duration. From a comparative analysis of these figures it can be concluded that:

- a) The safety factor increases with the wave length and all soil parameters but b (when H and/or b increases the safety factor decreases).
- b) Wave height and consolidation coefficient affect significantly the liquefaction behavior of the soil.
- c) The liquefaction resistance of drained deposits is roughly one order of magnitude (ten times) greater than that of undrained ones.
- d) Monotonic variations of the geometrical parameters (d, D) lead to non-monotonic trends for the safety factor. For this reason these parameters are assumed fixed hereafter.

PROBABILISTIC APPROACH

Basic Concepts

In order to evaluate realistically the liquefaction potential of the stratum of sand, the method employed should take into account the probabilistic nature of the problem. Uncertainties in the dynamic behavior of the soil and/or in its geotechnical parameters are important and cannot be neglected. Furthermore, very often the input load is defined statistically, and so the wave parameters are random in nature.

Again, according to the time span used in the study, two types of models are considered:

- a) Reliability models (short term conditions)
- b) Risk models (long term conditions)

Reliability model

In this case the wave parameters are those associated to storm conditions at the sea, which in turn depend on the location of the site relative to the zone of wave generation. Then, for a given storm (fixed time), a reliability technique is used to compute the probability of liquefaction of the deposit for the assumed sea states.

A mean-centered, first-order, second-moment reliability technique (FOSM model) has been proposed recently by Layas (1982), but no quantitative results were reported. In this paper a first-order marginal distribution method (Madsen

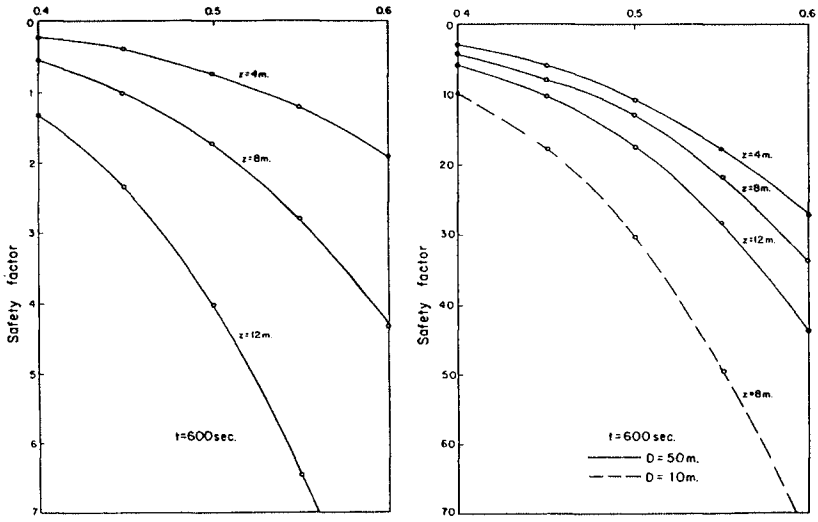


Fig.3. Parametric study.

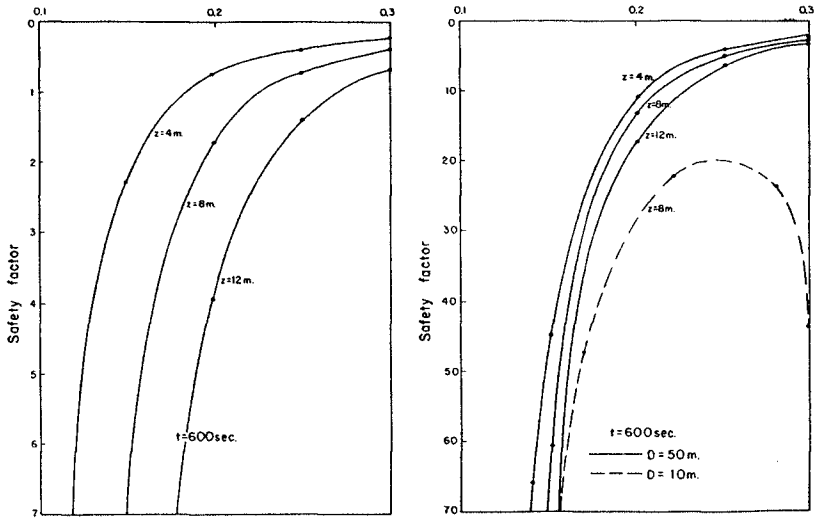


Fig.4. Parametric study (cont.)

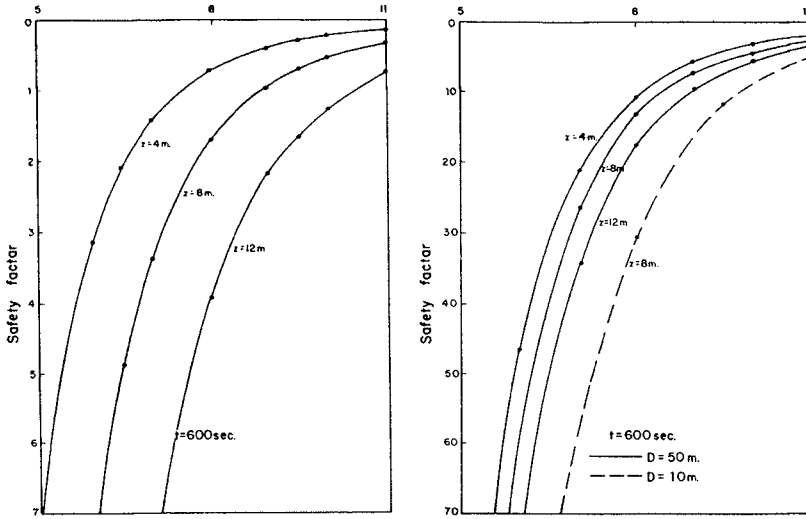


Fig.5. Parametric study (cont.)

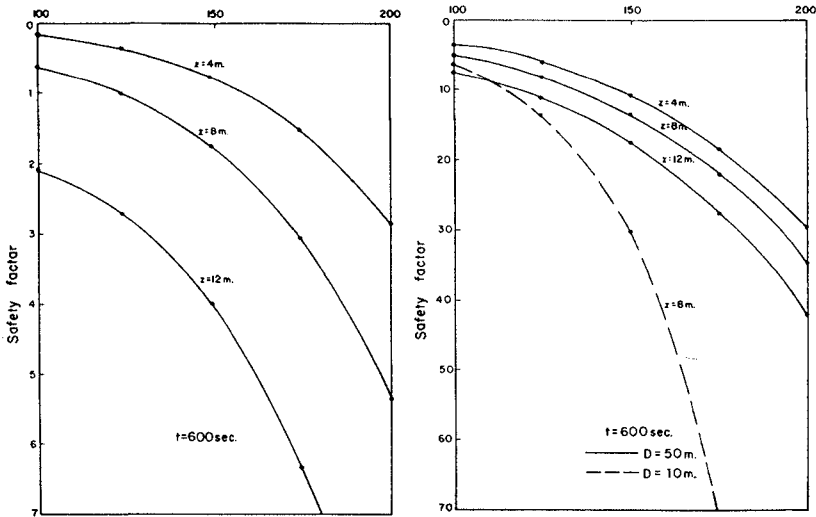


Fig.6. Parametric study (cont.)

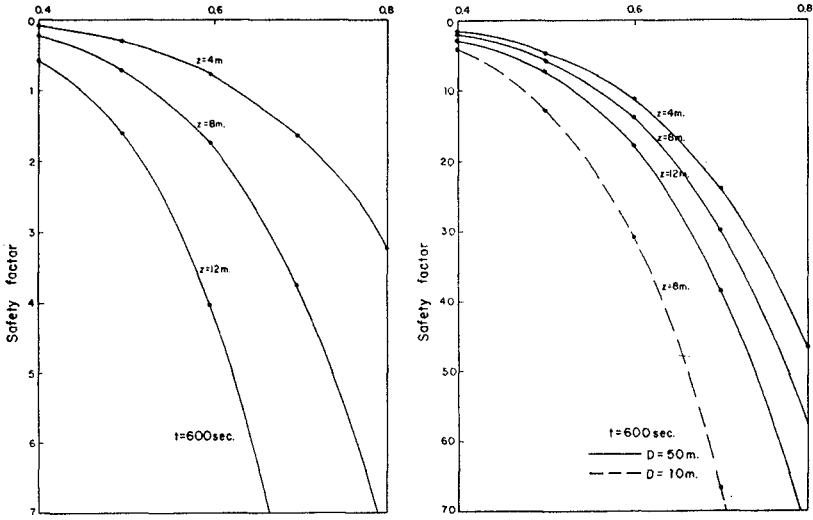


Fig.7. Parametric study (cont.)

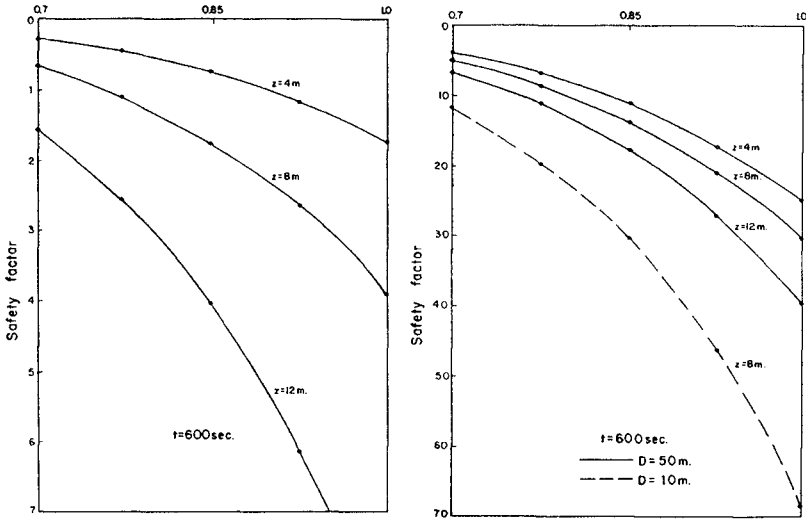
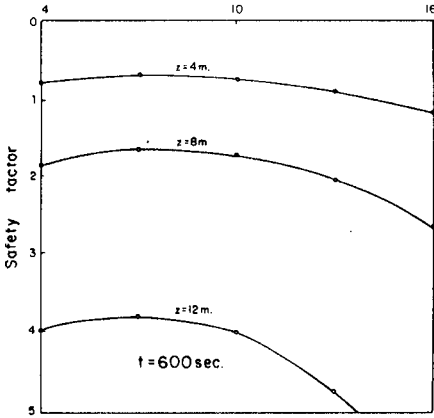


Fig.8. Parametric study (cont.)

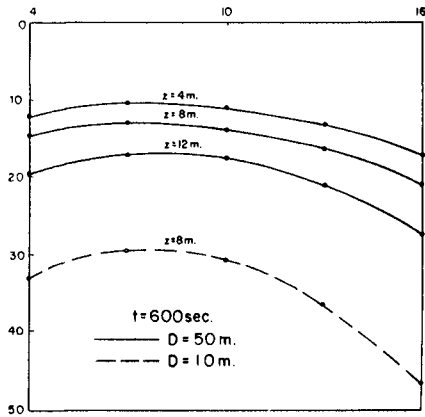


d

Fig.9 Parametric study (cont.)

d

Fig.9 Parametric study (cont.)



Thickness of soil layer, D (m.)

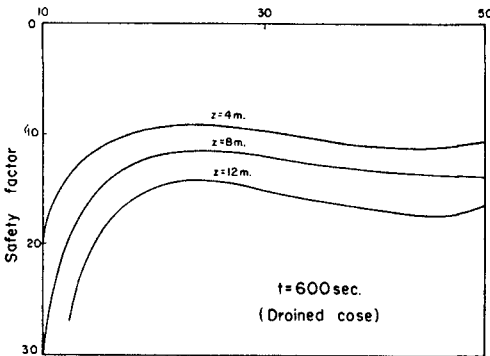


Fig. 10. Parametric study (cont.)

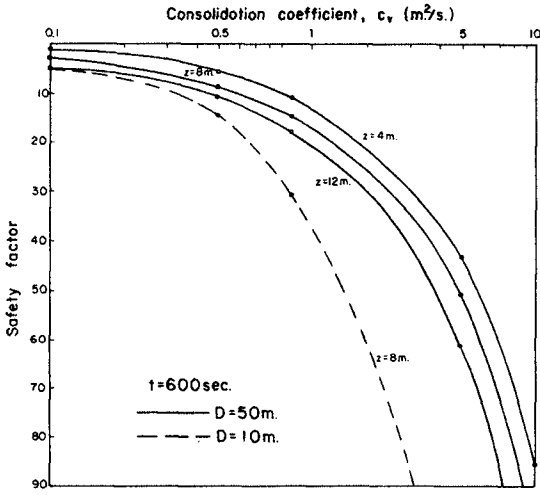


Fig. 11. Parametric study (cont.)

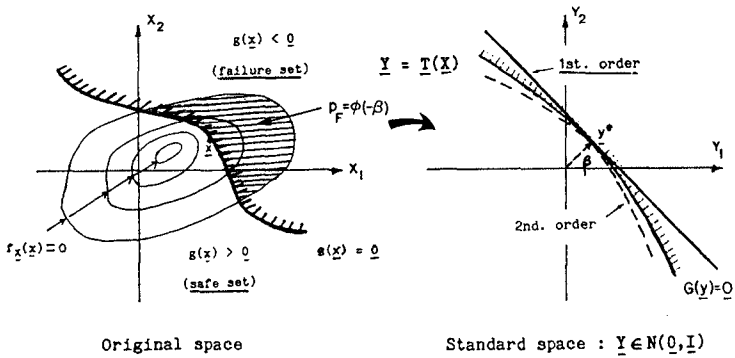


Fig.12. Reliability analysis. Computational procedure.

et al, 1986; Blázquez and Der Kiureghian, 1987) has been applied to compute the liquefaction susceptibility of the layer (unimodal system). Within this contest, the value of the actual short term probability of failure, p_1 , is computed as:

$$p_e = \int_{g(\underline{x}) < 0} f_{\underline{x}}(\underline{x}) d\underline{x} \quad (17)$$

in which $g(\underline{x})=0$ is the limit state function of the layer in the liquefaction mode of failure and $f_{\underline{x}}(\underline{x})$ denotes the pdf of the set of joint random variables, \underline{x} , describing the state fo the layer. Figure 12 depicts schematically the way to proceed in order to compute p_1 for a specific case, namely $\underline{x}=(x_1, x_2)$. Details on the computation procedure may become quite involved and are given elsewhere (Der Kiureghian and Liu, 1986).

For the liquefaction problem, the limit-state functions are formulated as follows:

Undrained case

$$\{g_{\underline{x}}(\underline{x})=0\} \equiv \{u_g - \sigma'_v = 0\} \equiv \left\{ \gamma' z \left[1 - \frac{t}{T} \left(\frac{\gamma' 2a D_r \cosh(Kd)}{\gamma_w H K} \right)^{-\frac{1}{b}} e^{-\frac{Kz}{b}} \right] = 0 \right\} \quad (18-1)$$

Drained case

$$\{g_{\underline{x}}(\underline{x})=0\} \equiv \{u - \sigma'_v = 0\} \equiv \left\{ \gamma' \left(z - \frac{C}{c_v T} [w(z) + v(z,t)] \right) = 0 \right\} \quad (18-2)$$

where z, t are parameters and the other symbols stand for random variables. The statistical distribution and first two moments of these variables is given in Table II. Only first order reliability analysis is considered in the present work.

Figure 13 illustrates the results of such an analysis. The probability of liquefaction of either a drained or undrained stratum at a given time and location is computed for a fixed geometry of the problem, specified in terms of water depth and thickness of the layer. A sample calculation (point P; Fig 13) is shown below:

Sample Calculation (point P)

Variables	x_i^*	γ_i	Parameters
H	9.61	0.737	t = 600 sec. z = 6 m. D = 50 m. d = 4 m.
L	164	-0.301	
D_r	0.50	-0.398	
γ'	0.75	-0.338	β (First order) = 1.71 p_1 (First order) = 0.0438
a	0.47	-0.298	
b	0.20	0.058	
c_v	1.34	-0.023	

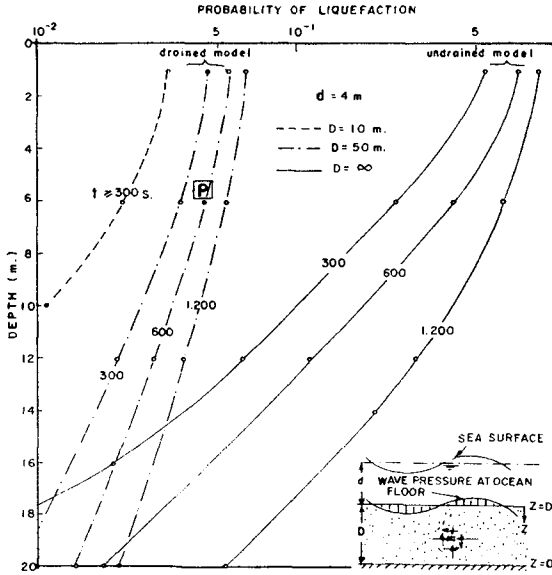


Fig.13. Probability of liquefaction. First-order reliability analysis.

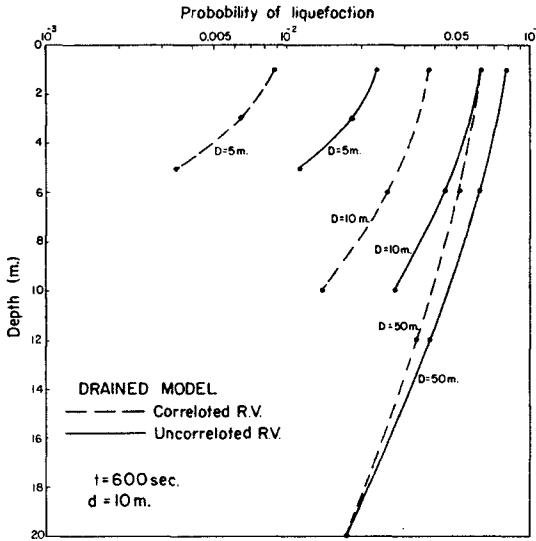


Fig.14. Effects of correlation and layer depth on the probability of liquefaction.

This calculation indicates that, for drained soils, the liquefaction behavior of the soil is mostly influenced (γ_i high) by the wave height and drainage conditions and, to a less degree and with opposite sign, by the relative density of the sand. The same conclusions apply to undrained deposits which, other conditions being equal, are roughly one order of magnitude unsafer than drained ones.

The combined effects of correlations among random variables and layer depth have also been investigated and are displayed graphically in Figure 14. A quick inspection of this figure reveals the probability of liquefaction becomes higher as the degree of correlation decreases and/or the length of the drainage path increases. Also, as could be expected, deep-sea deposits are less susceptible to liquefaction than surficial seabeds. This effect is more dramatic for thin permeable layers (Figure 15).

Risk model

In this case the joint distribution function of the set X of random variables (eq. 17) is no longer employed. Wave input and liquefaction response random variables are split up, and the annual (long term) probability of liquefaction of a given soil layer is written as:

$$(p_e)_{D_r} = \int_0^H (p_l | H, D_r) f_H(H) dH \quad (19)$$

Where $(p_l | H, D_r)$ = the probability of liquefaction at the site for specified values of the significant wave height and the relative density of the soil, and $f_H(H)$ = the density function of the sea state H . The last function is independent of the geomechanical properties of the site and can be derived from the long-term statistics of the severity of the sea, a topic that has been thoroughly discussed in the literature (Ochi, 1982). On the contrary, the conditional local probability of liquefaction for a given wave climate at the site, $(p_l | H, D_r)$, is not well known yet and depends solely on the uncertainties in the liquefaction model.

As an example, Figure 16 shows the risk of liquefaction at a depth of 1 m for loose and dense sand deposits located at two well different sites in the Spanish shoreline, namely Bilbao (Biscay Gulf) and Alicante (Mediterranean Sea). The dramatic effect of the wave climate in the expected liquefaction behavior of the soil is self-evident.

Conclusions

Application of probabilistic techniques to the liquefaction analysis of sandy soil layers in an ocean

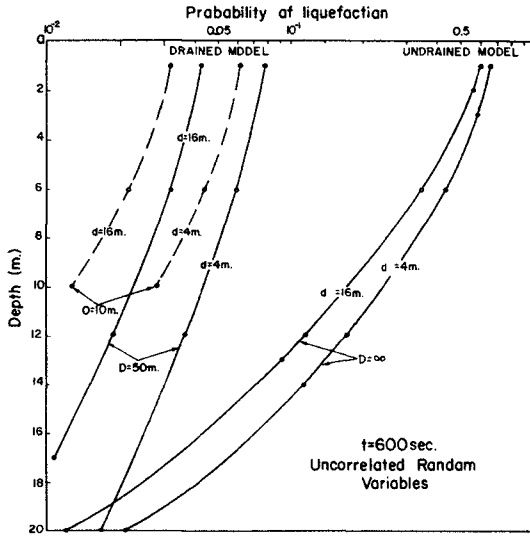


Fig. 15. Effect of water depth on the probability of liquefaction.

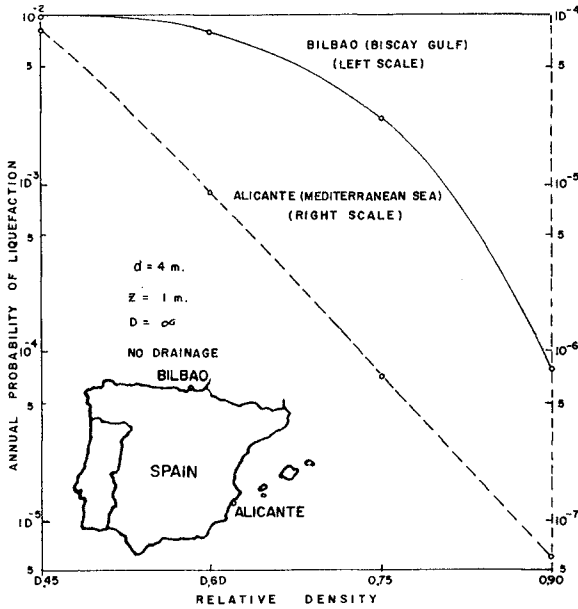


Fig.16. Risk of liquefaction at two sites on the Spanish coast.

wave environment is reviewed. The following conclusions can be drawn:

- * Seafloor liquefaction failure is mostly influenced by drainage conditions, and to a less degree by wave height and relative density of the sand.
- * Drained soil deposits are roughly one order of magnitude safer than undrained ones.
- * Uncorrelated models of liquefaction reliability are overconservative, especially for thin soil layers.
- * The probability of liquefaction increases with the thickness of the layer (\Rightarrow slower rate of consolidation) and shallow water depth (\Rightarrow less confinement).
- * Risk liquefaction models-in which wave action and liquefaction resistance are uncoupled-can be easily derived from reliability models for long-term wave conditions.

REFERENCES

- Blázquez, A. and A. Der Kiureghian (1987), "Seismic Reliability of Retaining Walls", Fifth ICASP, Vancouver, Canada, Vol 2, pp. 1149-156.
- Der Kiureghian, a. and P.L. Liu (1986), "Structural Reliability under Incomplete Probability Information", Journal Engineering Mechanics, ASCE, 112:1, pp. 85-104.
- Layas, F.M. (1982), "Response and Stability of Ocean Floor Soils under Random Waves", PhD thesis, North Carolina State University, Raleigh, N.C., USA.
- Madsen, H.O, S. Krenk and N.C. Lind. (1986), "Methods of Structural Safety", Prentice-Hall, Englewood Cliffs, N.J., USA.
- Ochi M.K. (1982), "Stochastic Analysis and Probabilistic Prediction of Random Seas", Advances in Hydroscience, Vol. 13, pp. 218-375.
- Rahman, M.S. and W.Y. Jaber (1986), "A Simplified Drained Analysis for Wave-Induced Liquefaction in Ocean Floor Sands", Soils and Foundations, Vol. 26, Nov. 3, pp. 37-68, Sept.
- Seed, H.B. and Rahman, M.S. (1978), "Wave-induced pore pressure in relation to ocean floor stability of cohesionless soils", Marine Geotechnology, Vol. 3, No.2, pp. 123-150

CHAPTER 102

EROSION AROUND A PILE DUE TO CURRENT AND BREAKING WAVES

E.W. Bijker¹, M. ASCE, and C.A. de Bruyn²

ABSTRACT

Tests have been performed on a vertical pile subject to current only and to a combination of current with normal waves and current with breaking waves. The scour around the pile produced by current only is decreased by normal short waves superimposed upon that current and increased when breaking waves are superimposed upon the current. After analysis of the velocity profiles in the undisturbed area upstream of the pile and next to the pile, the following explanation is found for this phenomenon. When normal short waves are superimposed upon a current, the bottom shear stress of the combination of current with waves is increased more in the undisturbed area than next to the pile in the scour area. This results in a decrease of the scour around the pile. Due to the large values of the orbital velocity under breaking waves this effect is reversed for the combination of a current with breaking and relatively long waves. This results in an increase of the scour around the pile.

1. INTRODUCTION

Around piles of jack-up platforms along the Dutch coast in a zone where breaking waves occur occasionally, scour depths have been observed which are significantly more than the normally occurring 1.0 to 1.5 times the pile diameter. Normally the scour around a structure due to a combination of waves with current is less than the scour as a result of current only (Bijker, 1986). In order to try to find an explanation for the unexpected deep scour with a combination of current and breaking waves, tests have been performed in a flume and in a basin of the Laboratory of Fluid Mechanics of the Delft University of Technology. Since there are no bracings between the legs of a jack-up platform and the distance between the legs is large as compared with their diameter, one single pile is studied.

2. TESTS

2.1 General

Three test-series have been performed, with an as much as possible constant mean current velocity, $v = 0.40$ m/s, a water depth, $h = 0.285$ m, and a mean grain size diameter $D_{50} = 0.2$ mm.

Tests of series I have been performed in a flume of 0.8 m width and with a pile diameter $\phi = 0.048$ m.

¹ Professor of Coastal Engineering and ² Graduate Student, Faculty of Civil Engineering, Delft University of Technology, Stevinweg 1, 2628 CN Delft, The Netherlands.

Tests of series II have been performed in a wave basin with the wave direction perpendicular to the current direction. The pile diameter was again 0.048 m.

Tests of series III have also been performed in the wave basin, but with a pile diameter $\phi = 0.09$ m.

2.2 Specific conditions

All series have been performed with three conditions, viz.:

- A. Only current, no waves. The water depth varied between 0.283 and 0.296 m and the current velocity between 0.391 and 0.461 m/s.
- B. Current with normal short waves. Current velocity and water depth were as much as possible equal to that for current only. The wave height varied between 0.034 and 0.108 m and the period between 0.97 and 1.23 s.
- C. Current with breaking waves. Current velocity and water depth were again almost equal to those for conditions A and B. The height of the breaking waves varied between 0.190 and 0.214 m with periods between 2.83 and 3.11 s.

In all tests rather uniform sand with a mean grain size $D = 0.2$ mm was used.

All tests are summarized in Table 1. Velocity profiles have been measured in most tests by means of an electromagnetic current meter (made available by Delft Hydraulics) in the undisturbed area upstream of the pile and next to the pile at a distance of 0.02 m from the wall of the pile. The bed form has been measured with a profile-follower.

The tests of series I have been performed in a flume of 25 m length with a width of 0.8 m which at the inflow side was equipped with a generator for regular waves. The sand bed had a thickness of about 0.1 m. The pile was placed at a distance of 10 m downstream of the inflow of the flume. It is assumed that at this place the flow will be completely adjusted. A sketch of the flume is given in Figure 1. From comparison with the tests in the basin it is concluded that the current pattern around the pile is somewhat influenced by the limited width of the flume. The influence is, however, so small that the tests will still demonstrate the differences between the various conditions.

During the tests of this series I the direction of propagation of the waves has been in the flow direction.

The tests of series II and III have been performed in a wave basin which is shown in Figure 2. The current was guided towards the test section by two training walls. In the tests of series II and III the wave direction has been perpendicular to the current direction and the -regular- waves were guided from the wave generator by training walls to the test section. At the end of these training walls the waves will diffract. The influence of this diffraction is, however, negligible at the location of the pile. Opposite to the wave generator a wave damping slope has been installed.

Since the distance between the location of the pile and the upstream side of the actual test section is rather short, sand has been applied on the slope upstream of the test section. This sand has avoided excessive scour of the 0.2 m thick sand layer at the upstream side of the test section and by the roughness it assisted in establishing the equilibrium velocity profile. Measurements of the velocity profile near the pile have indicated that this goal has been reached.

In Figure 3 typical examples of normal short waves and relatively long breaking waves are given. The orbital velocities at the bottom corresponding to short and breaking waves are given in Figure 4. Figure 5 shows the various measuring lines in the wave basin along which depths are measured. The values of the maximum scour are indicated

Table 1

Date	Uz cm/s	Uz norm. cm/s	F' cm	F'' cm	U _B cm/s	H cm	CZ cm	M cm	T s	T ₅₀ cm/s	AD cm	T ₅₀ cm/s	S _B cm/s	S _E cm/s
I A	V 4.43 N 6.56	3.85 5.69	5.92 21.12	3.7	46.1 49.5	29.5 35.6	6.48					1.88 4.88	4.86 9.78	4.34
I B	18-11 V 4.42 N 5.41	3.87 4.73	5.48 18.56	2.4	45.7 58.2	28.3 35.6	5.88	2.48	1.23	7.46	1.46 1.19	2.33 5.32	5.34 18.73	6.32
26-11	V 4.43 N 4.93	3.87 4.31	5.91 7.56	4.5	45.8 49.9	38.3 35.7	6.38	6.48	1.23	13.28	2.68 11.48	3.84 5.93	7.41 11.89	11.84
I C	V 2.65 N 3.81	2.41 2.75	1.88 1.23	5.8	43.8 45.8	29.6 35.9	7.88	19.28	3.11	53.88	26.28 23.65	9.58 22.46	12.34 28.84	36.75
II A	V 4.17 N 4.91	4.15 4.79	7.59 19.88	3.8	48.2 37.4	29.6 34.4	6.55					1.69 2.89	2.66 3.49	2.24
II B	21-1 V 3.15 N 5.81	3.34 5.31	2.77 23.68	2.2	37.7 35.4	27.3 32.9	5.88	6.38	1.16	13.78	2.58 1.76	3.84 3.82	5.68 4.14	5.95
19/23-1	V 3.45 N 3.21	3.76 3.48	4.77 4.21	3.4	36.7 36.8	27.8 38.6	3.88	18.75	1.16	23.88	4.25 3.12	5.72 5.17	8.75 7.43	12.81
II C	26-1 V 1.77 N 4.32	1.54 3.75	8.81 4.89	2.8	46.1 49.4	27.4 32.6	7.88	19.28	2.83	54.88	24.78 17.76	15.58 17.85	15.24 21.35	35.83
28/29-1	V 2.95 N 5.37	2.63 4.79	8.71 15.35	2.5	44.9 44.5	29.8 33.7	8.18	21.48	2.83	49.88	26.78 15.62	14.55 19.47	14.89 19.47	37.78
III A	V 3.89 N 5.82	3.88 5.14	6.57 28.99	4.8	39.1 35.6	28.3 37.8	8.15					1.69 2.42	2.48 2.45	1.88
III B	12-5 V 4.27 N 4.68	4.39 4.75	9.55 12.59	2.8	38.9 41.8	28.2 35.1	8.88	9.28	8.97	16.33	2.47 1.51	3.69 4.15	6.93 6.66	8.48
14/15-5	V 3.68 N 5.44	3.62 5.48	4.13 25.15	3.4	39.8 39.3	28.3 37.2	8.95	9.28	1.16	19.35	3.55 2.16	4.87 4.11	8.43 6.39	12.88
III C	14/15-5 V 6.52 N 5.16	2.23 5.43	8.38 19.24	2.8	45.4 49.6	31.8 39.7	11.88	15.28	1.88	37.18	11.18 8.67	12.32 11.43	14.22 17.32	36.92
13-5	V 1.77 N 4.35	1.81 4.44	8.85 7.92	3.2	38.2 44.7	28.5 37.9	8.48	21.88	2.81	58.88	26.28 17.28	13.94 15.72	12.93 17.78	31.34

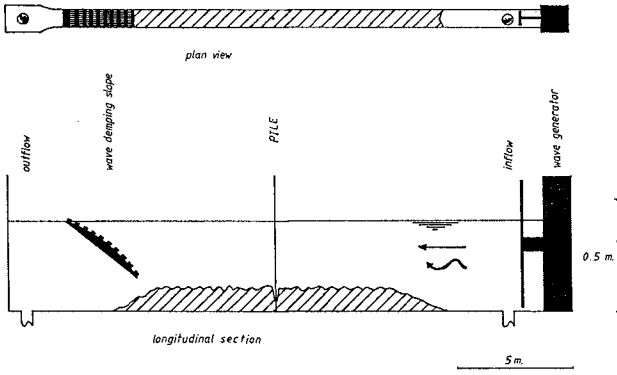


Figure 1
Flume

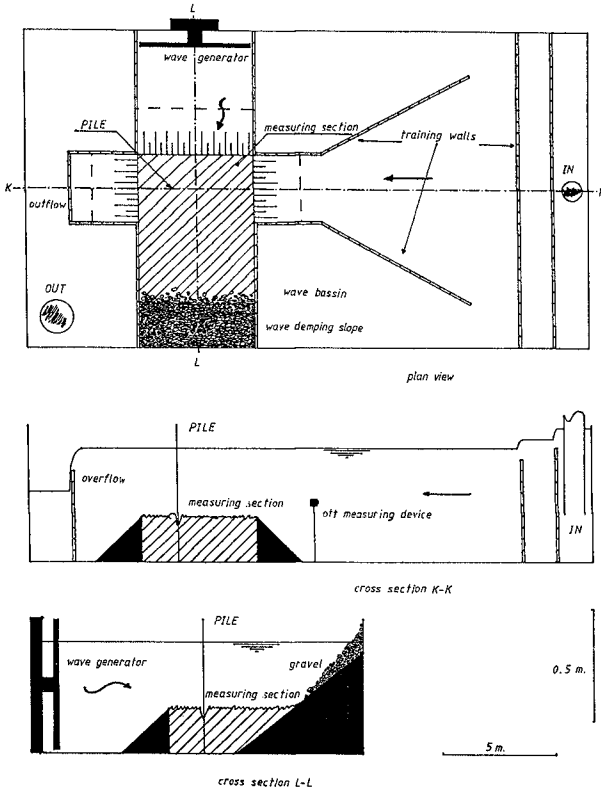


Figure 2
Wave basin

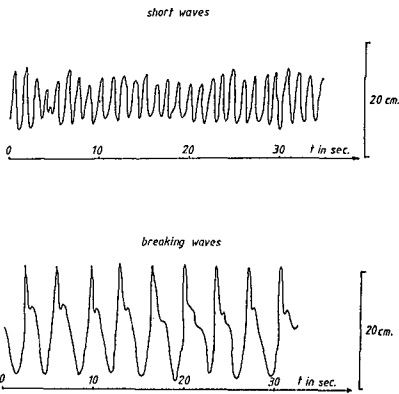


Figure 3
Typical wave profiles

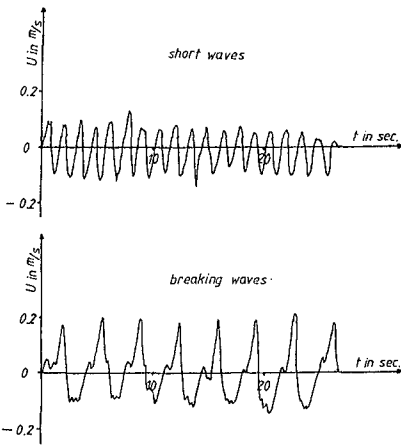


Figure 4
Typical orbital velocity profiles

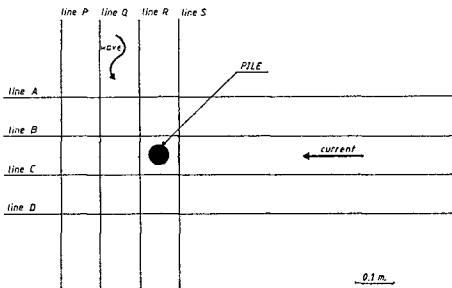


Figure 5
Measuring lines

in Table 1 with the line indication and an asterisk (so deepest point in line C is indicated by C*).

3. TEST RESULTS

3.1 Principles

The principle reason for any scour development around a structure is the difference in transport capacity upstream of the structure and around it. The possible relative increase -or decrease- of suspended load with respect to bed load in the scour area will result in extra -or less- erosion than would result from the change of the value of the total transport (Leeuwestein et al., 1985, and Bijker, 1986). Since, however, in this case the length of the scour area is rather limited, this effect can probably be neglected and the change of the bed load transport, dS_b/dx , will be the determining parameter.

Although in principle a method for the computation of the transport and subsequent scour development around a structure is available (Leeuwestein and Wind, 1984), it was not considered feasible to apply this method here since the transport module in this procedure is not yet fully developed. Also a more general computation of transports upstream and around the structure is not considered for the following reasons.

- a. The development of the velocity distribution should be measured very detailed and the actual scour computation would require extensive transport computations.
- b. The current around the pile is accelerating and the effect of an accelerating current on the transport is not yet fully understood.

The main goal in this research is, therefore, to explain the difference in scour development under the various conditions and to define the main parameters which determine this development.

3.2 Scour data

In order to give an impression about the order of magnitude of the transport, the quantities as measured in the wave basin and as calculated for the undisturbed conditions are given in Table 2.

Table 2: Measured and calculated transports

Condition	Measured S_{tot} in m^3/h	Calculated S_{tot} in m^3/h
A	0.05 - 0.10	0.05
B	0.10 - 0.20	0.19
C	0.50 - 1.00	0.54

The transport is calculated by the method suggested by Bijker for the combination of waves and current (Bijker, 1971).

In the ultimate (equilibrium) situation of the scour development the transport upstream of the pile and around the pile must be equal. Since, however, the flow lines around the pile are closer together than upstream of the pile, the transport per unit of width around the pile will be, also in the equilibrium situation, somewhat bigger than in front of the pile in the undisturbed area. The bottom shear stress around the pile must be, therefore, also in the equilibrium situation, bigger than in the undisturbed area.

In the Figures 6 through 8 some typical profiles along line B are shown. Since these profiles resulted from momentary surveys, the maximum scour depths are not necessarily equal to those given in Table 1.

4. DISCUSSION

4.1 Bottom shear stresses

The final scour around a structure will depend, as demonstrated in Chapter 4, on the ratio between the transport upstream of the structure and around it. It is difficult to calculate this transport, but at any rate it will be a function of the bottom shear stress. Therefore, these bottom shear stress values will be compared. As it is not well possible to measure these bottom shear stresses directly, they will be determined from the velocity profiles.

In the Figures 9 through 11 the velocity profiles for the undisturbed flow are given. The bottom shear stress can be calculated from the velocity profile under the assumption that it is that of a completely developed boundary layer. Such a profile can be described according to Prandtl (1926) and von Karman (1930) by

$$v(z) = \frac{v_*}{\kappa} \ln \frac{z}{z_0} ,$$

with $v_* = \sqrt{\tau/\rho}$ = shear stress velocity, z = height above the bottom, z_0 = height above the bottom, where $v(z)$ is theoretically zero and κ is the constant of von Karman, equal to 0.4.

Since it is difficult to determine exactly the height of a measuring point above a rippled sand bed, the formula is written as

$$v(z) = \frac{v_*}{\kappa} \ln \frac{z' + \Delta z}{z_0' + \Delta z} ,$$

in which z' is the height above the assumed bottom and Δz is the difference between the assumed and real bottom.

With a least square procedure the value of Δz is chosen in such a way that the difference between the actual profile and the logarithmic profile is minimal. In this way the most reliable value of v_* can be determined.

4.2 Combination of waves and current

The above described method cannot be used in case of a combination of waves and current because the bottom shear stress is determined by the actual velocity, which in this case is fluctuating in magnitude and direction through the orbital motion. This velocity differs from the velocity component in the main flow direction which is measured by the electromagnetic current meter (Bijker, 1968, 1971). The resultant bottom shear stress can be written as: (Bijker, 1986)

$$\tau_{cw} = \tau_c + \frac{1}{2} \tau_w ,$$

in which $\tau_w = \frac{1}{2} f_w \rho \hat{u}_b^2$, with f_w = bed friction coefficient according to Jonsson (1966). Swart (1976) has written this factor as

$$f_w = \exp \left[-5.977 + 5.21 (a_b/r) - 0.194 \right] ,$$

with a_b = amplitude of the orbital motion at the bottom and r = bottom roughness.

This formula holds for $a_b/r > 1.47$. For $a_b/r < 1.47$, f_w remains constant and equal to 0.32.

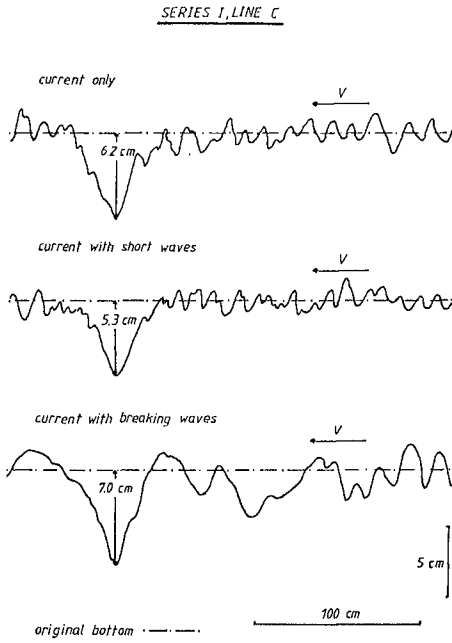


Figure 6
Typical scour profile

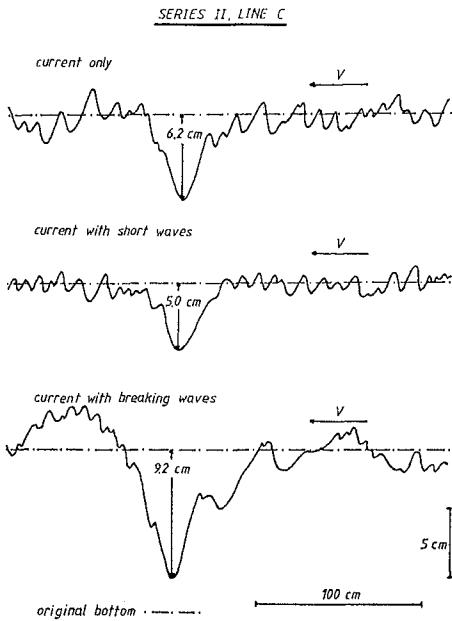


Figure 7
Typical scour profile

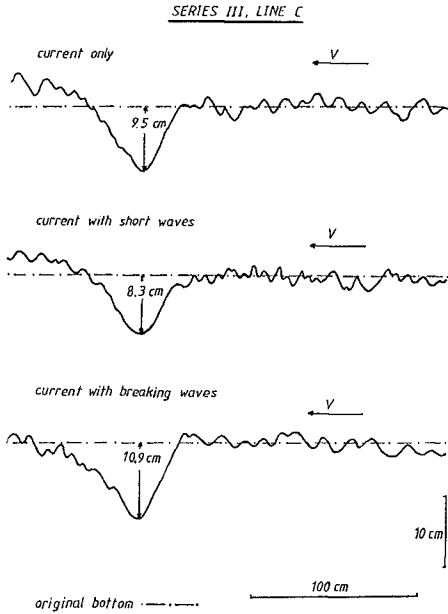


Figure 8
Typical scour profile

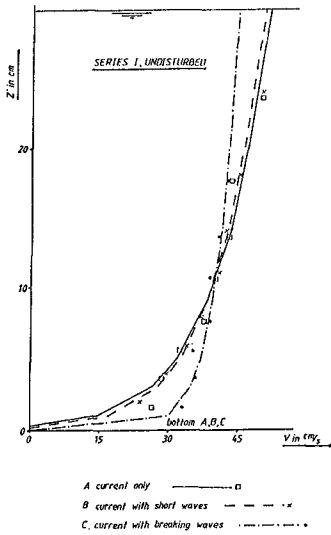


Figure 9

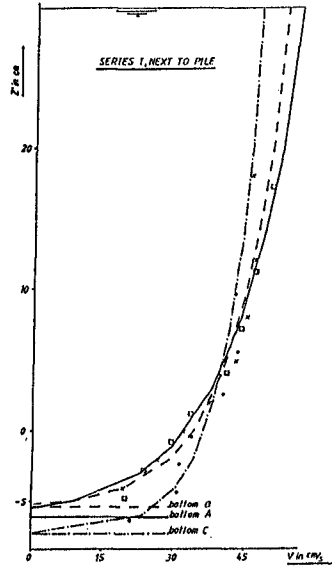


Figure 12

Typical velocity profiles

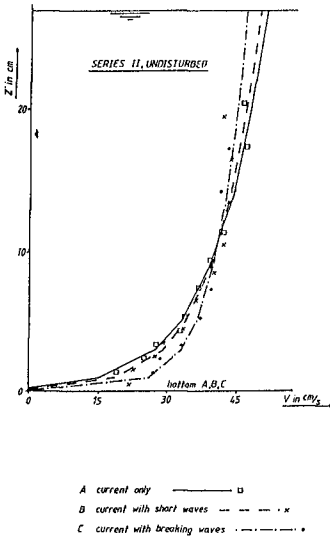


Figure 10

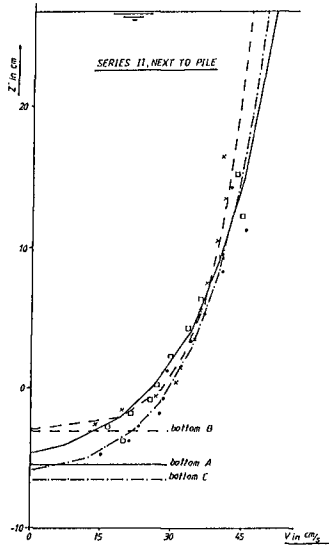


Figure 13

Typical velocity profiles

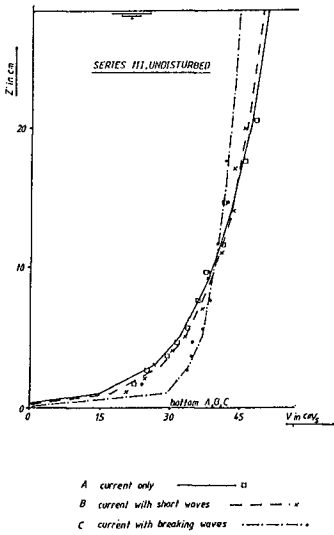


Figure 11

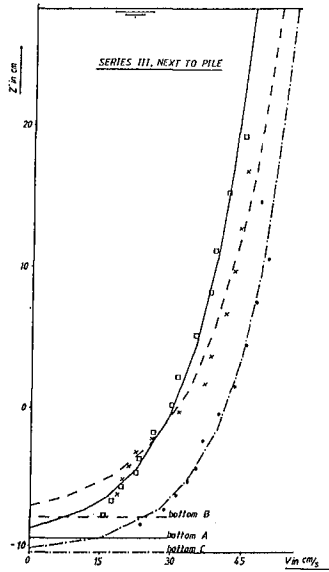


Figure 14

Typical velocity profiles

The values of f_w as function of a_b/r are shown in Figure 15. The value of r can be determined from the velocity profile with current only as $33 z_0$ and is given as r' in Table 1. The value can also be estimated from the ripple size and is given in Table 1 as r'' . The agreement is acceptable, but since the determination of the bottom roughness through the velocity profile is physically the most justified, this value is used as reference. In the flume the average of the calculated values is 0.05 m and in the basin 0.07 m.

4.3 Velocity profiles for the current

The velocity profiles of Figures 9 through 11 are all normalized to a mean velocity of 0.4 m/s. The profiles for current only and for the combination of waves and current are almost equal. There is some steepening of the profile for the combination of waves and current which is most likely the result of the greater value of the turbulent mixing coefficient in the case of a combination of waves and current (Van de Graaff, 1988). This is even more so in the case of breaking waves with much higher orbital velocities. The velocity profiles next to the pile above the scour hole (Figures 12 through 14), which are also normalized to the undisturbed velocity of 0.40 m/s, show the same tendency. However, in series III with the larger pile diameter of 0.09 m, the velocities measured next to the pile are relatively larger than for the smaller pile diameter of 0.048 m in series I and II. The reason is that the velocities are always measured at equal distances (0.02 m) from the pile wall. For the large pile the velocities are measured, therefore, relatively closer to the pile and so they are higher.

4.4 Velocity profiles for orbital motion

The orbital velocities are calculated by the first order linear wave theory and the results are shown, together with the measured values, in Figures 16 and 17 for series II and III with waves and current perpendicular to each other. The measurements next to the pile show an orbital velocity which is approximately 20% less than the calculated value due to the shadow working of the pile. For breaking waves the difference between calculated and measured values is greater.

4.5 Shear stress

From the velocity profiles in the scour hole next to the pile a much higher value is calculated for the apparent bottom roughness. This is caused by the increased turbulence as a result of the deceleration of the current in the scour hole. Therefore, the bottom shear stress is increased. The bottom shear stress of the waves is, however, not increased since this shear stress has already the maximum value due to the low value of a_b/r . This results in a relatively smaller increase of the value of $\tau_{cw} = \tau_c + \frac{1}{2} \tau_w$ in the scour area for the situation with waves and current than for the situation with current only. This leads to a lower value of the equilibrium depth of the scour hole in the case of waves and current than for current only.

In the case of the combination of current with breaking waves, the value of the orbital excursion at the bottom is so high that the maximum value of f_w is not reached. In this case the value of f_w in the scour hole is, therefore, greater than for the undisturbed area. This increase of f_w is just as the increase of τ_c the result of the increased apparent bottom roughness in the scour hole. This results in a relatively higher value of τ_{cw} in the scour hole for the combination of breaking waves and current than for current only.

The various values of the ratio between the bottom shear stress in the scour hole (τ_{cw}/N) and in the undisturbed area (τ_{cw}/V) are shown in Figure 18.

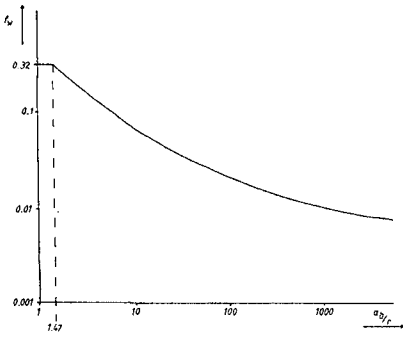
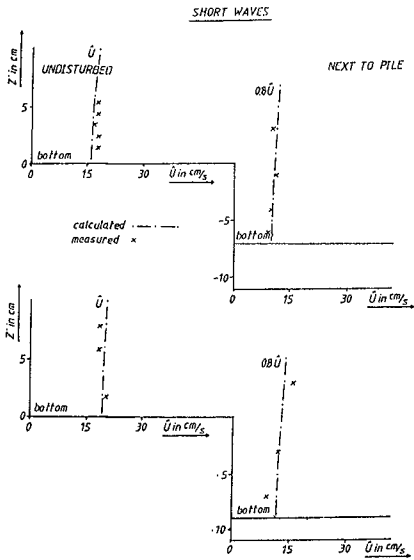


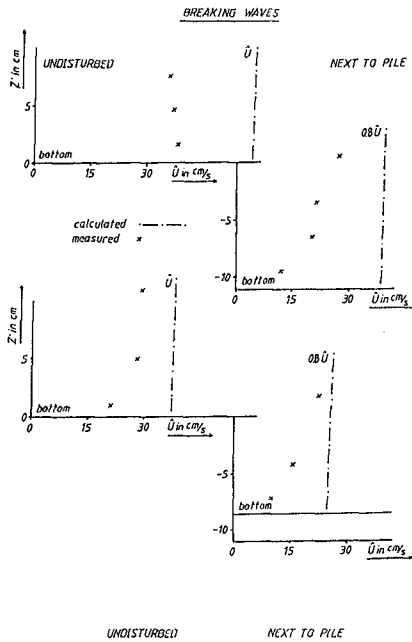
Figure 15
Relation f_w versus ab/r



Series II

Figure 16
Typical orbital velocity profiles

Series III



Series II

Figure 17

Typical orbital velocity profiles

Series III

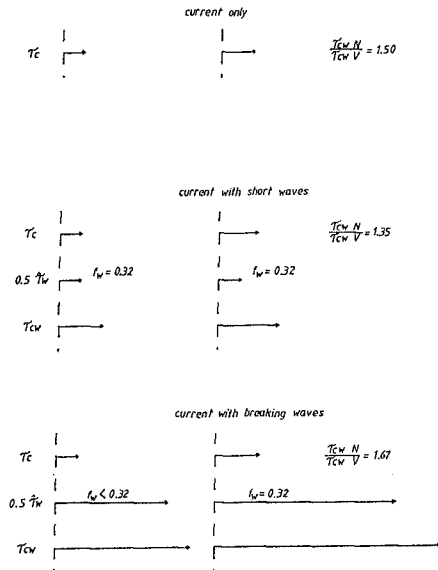


Figure 18

Comparison of bottom shear stresses

The equilibrium depths of the scour hole have been explained by the effect of the apparent bottom roughness in the scour hole on the bottom shear stress for the situation with current only and for the situation with a combination of current with breaking and non-breaking waves. When the equilibrium depth is not yet reached, the scour is simply the result of the increased velocities around the pile. Only the extent to which the equilibrium scour develops will differ for the various circumstances.

4.6 Comparison with prototype situations

This research has been started because of the observed strong scour around the piles of a jack-up platform placed in -sometimes- breaking waves. The difference between the prototype situation and these tests is caused by the difference in bottom roughness. In front of the pile, in the undisturbed flow, the roughness in the prototype is probably not more than 2 to 3 times the roughness in the model. However, in the scour hole, around the pile, the roughness depends on the depth of the scour hole which is a function of the pile diameter. This diameter will be in the prototype 10 or 20 times that in the tests and the relative increase of the bottom roughness in the scour hole will be, therefore, more in the prototype than in the model. This results in a greater increase of f_w in prototype conditions with breaking waves than in the model. This leads to a greater value of the equilibrium scour depth. In prototype conditions indeed scour depths of 1 to 3 times the pile diameter have been found.

4.7 Conclusions

Normally waves will not increase, but even decrease the scour around a structure as compared with that by current only. The depth of this scour is in the order of 1.5 times the pile diameter. In the case of breaking waves this value can be, however, considerably higher. This may necessitate protective measures where otherwise the scour could be accepted.

5. REFERENCES

- Bijker, E.W., 1967. Some considerations about scales for coastal models with movable bed. Delft Hydraulics Laboratory, Publ. No.50.
- Bijker, E.W., 1971. Littoral drift as function of waves and current. Proc. A.S.C.E., Journ. of Waterw., Harbors and Coastal Eng. Div., WW4, November 1971.
- Bijker, E.W., 1986. Scour around structures. Proc. on the 20th Intern. Conf. on Coastal Engineering, Taipei, Taiwan, 1986, Vol.II, pp.1754-1768.
- Graaff, van de J., 1988. Sediment concentration due to wave action (in preparation).
- Karman, von Th., 1930. Mechanical similarity and turbulence. Proc. of the 3rd Intern. Congress of Applied Mechanics, Stockholm, Sweden, 1930, pp.85-92.
- Leeuwestein, W. and H.G. Wind, 1984. The computation of bed shear in a numerical model. Proc. of the 19th Intern. Conf. on Coastal Engineering, Houston, Texas, 1984, Vol.II, pp.1685-1702.
- Leeuwestein, W., E.W. Bijker, E.B. Peerbolte and H.G. Wind, 1985. The natural self-burial of submarine pipelines. Proc. of the 4th Intern. Conf. on Behaviour of Offshore Structures (BOSS'85), Delft, The Netherlands, 1985, pp.717-728.
- Prandtl, L., 1926. On fully developed turbulence, Zürich, Switzerland, 1926, pp.72-74.
- Swart, D.H., 1974. Offshore sediment transport and equilibrium beach profiles, Delft Hydraulics Laboratory, Publ. No.131.

CHAPTER 103

IMPROVED LONGSHORE SAND TRANSPORT EVALUATION

A.S.- Arcilla, Professor*
A. Vidoar, Research Ass.*
J. Pous, Research Ass.*

Abstract

In this paper an improved bulk formulation for the longshore sediment transport rate is presented. It is based on a simplified hydrodynamic analysis of surf zone flow and supplemented by an exhaustive dimensional analysis. The proposed model includes the effect of the surf zone dynamic state (e.g. variation of longshore sand transport, ll , with breaker type) and it is now being used in the one- and two-line shoreline evolution models developed by the Maritime Engineering Laboratory in Barcelona.

1. Introduction

The interest of engineers in estimating longshore sand transport comes from the need to study coastal evolution in order to solve existing coastal problems.

General longshore sand transport models have been developed in recent years, all of them using stringent simplifying hypotheses, due to the poor present understanding of the physics of the problem. These models are usually based on extensive data measurement campaigns without providing the level of accuracy their cost would suggest.

Because of these drawbacks in the research stage, most of the models are still under development (analyses of basic hypotheses, comparison with other data sets, etc.). In this context, the bulk formulations, basically because of their simplicity, have been the most extensively calibrated and used for coastal engineering analyses.

2. Background

In nearly all approaches to longshore sand transport evaluation, no matter whether they are energetics based (Komar and Inman, 1970)(Bailard, 1981) or shear-stress based (Bijker, 1971)(Swart, 1976), the influence of the surf-zone dynamic state (e.g. breaker type) on the ll model or formulation is seldom considered. This influence is slight-

*Maritime Engineering Laboratory
Catalonia University of Technology in Barcelona, SPAIN.

ly better understood for surf zone hydrodynamics, which are the driving factor for the sediment transport. As it was proposed in earlier works (S.-Arcilla et al., 1986) the mean rate of wave energy dissipation per unit area, D (across-shore integrated value) can be related to the Iribarren parameter (Iribarren, 1949) (Battjes, 1974):

$$I_r = \frac{m}{(H_b/L_o)^{1/2}} \quad (2.1)$$

where:

m : bottom slope (average for the surf-zone).

H_b : breaker wave height.

L_o : deep water wave length.

This relationship can be derived from bore theory, energetic balance and dimensional analysis, and has been tested with an extensive data set, including field and laboratory measurements.

Similarly, and due to the relationship between the driving term for longshore currents and D (established from the alongshore momentum balance equation) the longshore current velocity, V_l , was also shown to be related to the surf zone dynamic state, via Iribarren's parameter (S.-Arcilla et al. 1986)

Both fits showed a bell-shaped trend for the relationship between the non-dimensional D and V_l and I_r , relating thus the breaker type with the amount of dissipated energy and the value of the longshore current. As an intermediate result of the research, the bottom friction coefficient, C_f , was also shown to be a function of the Iribarren parameter. The remaining step of this research is to analyse the influence of the surf zone dynamic state on the longshore transport rate, starting from the relationships obtained for D and V_l . This point is developed in the following sections.

3. Predictive Formulation

3.1. General

The sediment transport rate expressed in units of submerged weight per unit time, shall be denoted by I . This variable, as said before, has been evaluated in various ways during the last decades. One of the most physically-based approaches consists in assuming I to be proportional to a stirring term times a transporting term. This approach is shown in (Bagnold, 1966) (Bijker, 1968) and (Soulsby, 1986). The significant differences in the details illustrate the difficulties and uncertainties associated to this problem. In this paper, the alongshore component of I , across-shore integrated, is expressed by:

$$I_l = K_l V_l l_b (Z_b - Z_{bcr}) \quad (3.1)$$

in which:

I_l : alongshore component of the sediment transport rate, expressed in Newtons/second and corresponding to the sub-

merged weight of sediment passing through a section (active profile) of the surf zone per unit time.

K1: dimensionless proportionality parameter.

V1: across-shore averaged longshore current velocity.

lb: some measure of the width of the surf zone (e.g. horizontal distance from breaker- to shore-line).

τ_b : bottom shear stress.

In equation (3.1) the transporting term is (V1.lb) and the stirring term is ($\tau_b - \tau_{bcr}$). This last term includes a threshold condition in the form of a critical value, τ_{bcr} , for the bottom shear stress. This means that for $\tau_b \leq \tau_{bcr}$, there is no Il. For $\tau_b > \tau_{bcr}$ the sediment transport rate is given by (3.1). The transporting term requires a longshore current and, thus, a non-zero value of D (mean rate of wave energy dissipation per unit time) to act. The stirring term, on the other hand, is associated to τ_b and depends on the dynamics of the wave/current boundary-layer.

The transporting term associated to V1, will be mainly due to the incident energy flux, Efi, because these incident waves (Hbi) will generate a significant dissipation, D, and, thus, V1 associated to the breaking process. The reflected waves (Hr), in an across-shore integrated sense, will generate smaller D and V1.

The stirring term, on the other hand, will be due to both wave trains (incident and reflected) because both of them generate a boundary layer and, thus, contribute to τ_b . In other words, the reflected waves will increase the roughness felt by the current and τ_b is, therefore, estimated based on a total wave-height, H_T :

$$H_T = H_{bi} + \beta H_r \quad (3.2)$$

in which $\beta = \beta(Ir)$ is a parameter between 0 and 1. We can now consider the effect of increased reflection (due, e.g., to some new structure built in the surf zone) on the across-shore integrated sediment transport rate, Il. Increased reflection means that H_T increases from which both τ_b and the stirring term increase. On the other hand, for a given incident energy flux (Efi) and width of the surf zone (lb), increased reflection (Efr) implies a smaller D, according to the equation (S.-Arcilla et al., 1986):

$$E_{fi} = E_{fr} + D lb \quad (3.3)$$

Therefore, the effect of increased reflection is to reduce D and V1 and, consequently, the transporting term. The global effect on Il, product of a stirring term that increases and a transporting term that decreases, is not easy to estimate a priori and must be obtained from the Il formulation.

3.2. Il Formulation

This formulation requires, according to equation (3.1), estimates for both V1 and τ_b . They will be derived from simplified hydrodynamic arguments. On the other hand, K1 and τ_{bcr} will be empirically calculated, by comparing this model with an alternative formulation derived from dimensional a-

analysis.

i) V1 ESTIMATION

The alongshore component of the vertically integrated momentum conservation law reads for stationary conditions (e.g. (Mei, 1983)):

$$\frac{\partial S'_{xy}}{\partial x} + \frac{\partial S''_{xy}}{\partial x} + \tau_{yb} = 0 \quad (3.6)$$

in which:

S'_{xy} : excess momentum flux tensor due to wave motion.

S''_{xy} : excess momentum flux tensor due to turbulent motion.

τ_{yb} : bottom shear-stress (y-component).

We can now evaluate the wave thrust in terms of D (Longuet-Higgins, 1970):

$$\frac{\partial S'_{xy}}{\partial x} = D \frac{\sin \alpha b}{Cb} \quad (3.5)$$

and D can be written (including reflection effects) as (S.-Arcilla et al., 1986):

$$D = \rho_w g \frac{Hb i^2}{T} \frac{\sqrt{2\pi}}{8} \gamma^{1/2} I_r \cos \alpha b (1 - Kr^2) \quad (3.6)$$

The bottom shear stress is usually expressed by the following linearised equation (obtained assuming small $V1$ and αb):

$$\tau_{yb} = \rho_w C_f U_{orb} V1 \quad (3.7)$$

Substituting all these equations into (3.4), we can obtain (after neglecting turbulent mixing):

$$V1 = F(I_r) m (gHbi)^{1/2} \sin 2\alpha b \quad (3.8)$$

in which $F(I_r)$ is a function of Iribarren's parameter.

ii) τ_b ESTIMATION

The τ_b estimation is based on the eddy-viscosity concept which allows us to write:

$$\tau_b = \rho_w A_H \frac{\partial U_c}{\partial z} \quad (3.9)$$

in which:

ρ_w : mass density of sea-water

A_H : eddy viscosity coefficient

U_c : characteristic velocity in the boundary layer

z : vertical coordinate, positive upwards

The eddy viscosity coefficient, A_H , is estimated using the model proposed in (Battjes, 1975).

$$A_H = M \cdot h_{Turb} \cdot U_{Turb} \quad (3.10)$$

in which M is a parameter of order $O(1)$ and h_{Turb} and U_{Turb} are respectively, the length and velocity scales of the turbulent motion. By writing $U_{Turb} = (D/\rho_w)^{1/3}$ it is easy to obtain:

$$U_{Turb} = f_1(Ir) U_{orb} \quad (3.11)$$

with U_{orb} being the wave orbital velocity and $f_1(Ir)$ a function of Iribarren's parameter.

The vertical velocity gradient is expressed by:

$$\frac{\partial U_c}{\partial z} \approx \frac{U_{orb}}{z_0} \quad (3.12)$$

in which z_0 is the thickness of the boundary layer and U_c has been approximated by U_{orb} because the wave boundary layer is expected to be much thinner than that of the current and, thus, more relevant for the calculation of Z_b . If we express z_0 by (e.g. (Nielsen, 1986))

$$z_0 = (A_H \cdot T)^{1/2} \quad (3.13)$$

and substitute all previous equations into (3.9) it is easy to obtain:

$$Z_b = \rho_w f(Ir) G(\theta) U_{orb} \quad (3.14)$$

with θ the mobility parameter.

iii) 11 FORMULATION

Substituting (3.8) and (3.14) into (3.1) we get:

$$11 = \rho_w \hat{F}(Ir) (gHbi)^{3/2} Hbi \sin 2\alpha b(\hat{G}(\theta) - \hat{G}(\theta_{cr})) \quad (3.15)$$

The obtained formulation, apart from including a threshold level for incipient motion, presents an explicit variation of the transport rate with the breaker type or, more generally, with the surf zone (S.Z.) dynamic state (via Ir). This allows to consider (albeit in an across-shore integrated manner and somewhat simplistically) the effect of increased reflection or other changes in the S.Z. dynamic state on the transport rate.

The functions $F(Ir)$ and $G(\theta)$ will be calibrated in section 5, making use of some of the results obtained from the dimensional analysis presented in section 4.

4. Dimensional Analysis

4.1. General

The general expression of the dimensional formula for longshore sand transport (in a longshore uniform coast with a plane shore) following (Kamphuis et al., 1986) can be written as:

$$I_1 = f(\mu, \rho_w, g, \rho_s, D, \psi, F(D), x_c, y_c, h_b, H_b, T, \alpha_b) \quad (4.1)$$

where: μ (dynamic viscosity), ρ_w (water density) and g (gravity acceleration) are the fluid parameters; ρ_s (sediment density), D (characteristic grain diameter), ψ (grain shape factor) and $F(D)$ (granulometric distribution function) are the sediment parameters; x_c (across-shore characteristic scale) and h_b (water depth at breaking point) are the domain parameters; H_b (breaking wave height), T (wave period) and α_b (angle of wave incidence at breaker line) are the wave parameters.

Stationary conditions are assumed (time is not included) and only wave parameters are included since currents are considered to be wave induced. Other variables usually related to longshore transport conditions (e.g., wave orbital velocity, u_{orb} , or the sediment fall velocity, w), turn out to be, in this context, not-independent parameters and will, thus, appear only by exchange. Shape and granulometric distribution factors are not included (in general) in the data set used for calibration, and they will not be further considered.

For the development of the dimensional analysis four sets of repeaters have been employed: $\rho_w, g, H_b, \rho_w, h_b, T, \rho_s, g, D, \rho_w, g, H_b, T$. The main conclusion of these analyses was that the first set provided a better fit while giving the more physically meaningful parameters. This set was, therefore, chosen for the development of the model and is the only one here presented. Applying the Π theorem, and noticing that 8 non-dimensional parameters are expected to appear (13 independent variables, 2 or which are neglected and three of which are taken as repeaters, i.e. associated to the measurement system), the following expressions are obtained:

$$\Pi_{I1} = \frac{I_1}{\rho_w g H_b^2 (g H_b)^{1/2}} \quad (4.2)$$

$$\Pi_{II} = \emptyset \left(\frac{\mu}{\rho_w H_b (g H_b)^{1/2}}, \frac{\rho_s - \rho_w}{\rho_w}, \frac{\rho_w H_b}{\rho_s D}, \frac{x_c}{H_b}, \frac{y_c}{H_b}, \frac{h_b}{H_b}, \frac{g^{1/2} T}{H_b^{1/2}}, \alpha_b \right) \quad (4.3)$$

Combining these expressions Π_{I1} can be approximately written as:

$$\Pi_{I1} = \emptyset (Re, Ir, Id, \theta, m) \sin 2\alpha_b \quad (4.4)$$

in which

Re: Reynolds number (ratio between inertial and viscous forces).

θ : Mobility or shields Number (ratio between disturbing and resisting forces).

I_D : Dean number (ratio between fall velocity and a characteristic wave velocity)(Dean, 1973)(Dalrymple, 1976).

and assuming that the relationship between the angle of wave incidence (α b) and the longshore sand transport is (Komar and Inman, 1970)(Longuet-Higgins, 1972):

$$I_l \propto \sin 2\alpha b \quad (4.5)$$

The expression for the θ function has been thoroughly calibrated with the following field and laboratory data:

- field data : (Watts, 1953)(Komar, 1969)(Kana, 1977)(Kana, 1980)(Inman et al., 1980)(Gable, 1981)(Bruno et al., 1981)(Kraus et al., 1982).

- laboratory data:(Kamphuis et al., 1978)(Vitale, 1981)(Saiyao and Kamphuis, 1983).

The calibration has been based mainly on field values due to scale effects. Exhaustive analyses have been performed in order to select the most adequate data from each set, deleting those data not fulfilling the imposed quality checks. The breaking depth, h_b , was obtained via Goda's criterion when not measured. Curve adjustment and fitting was obtained both visually and by a least-squares technique.

4.2. Relationships among parameters

4.2.1. Iribarren parameter/Dean number

Both parameters refer to onshore/offshore transport and beach profile variations. It is easy to show, from physical arguments, that a relationship as the one shown in figure 4.1 (corresponding to field data) must exist between the two parameters, defined by (2.1) and $I_D = H/wT$.

The proposed relation can be derived from the influence of grain size, D_{50} , on both bottom slope, m and fall velocity, w . This results in a somewhat equivalent use of the two parameters for across-shore-integrated analyses (e.g. I_l). As a consequence, only I_r will be employed in what follows.

4.2.2. Reynolds number/Mobility number

Both parameters refer to the stage of flow development and, thus, to the stage of transport. They are related for initiation of motion conditions (Shields threshold curve). By combining their expressions, they can also be related for actual transport conditions:

$$Re = \theta^{2/3} f(k)$$

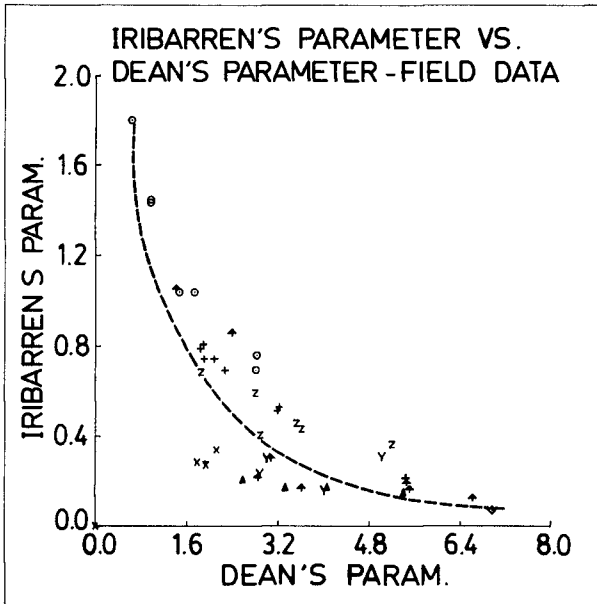


Figure 4.1: Iribarren parameter versus Dean's number (field data).

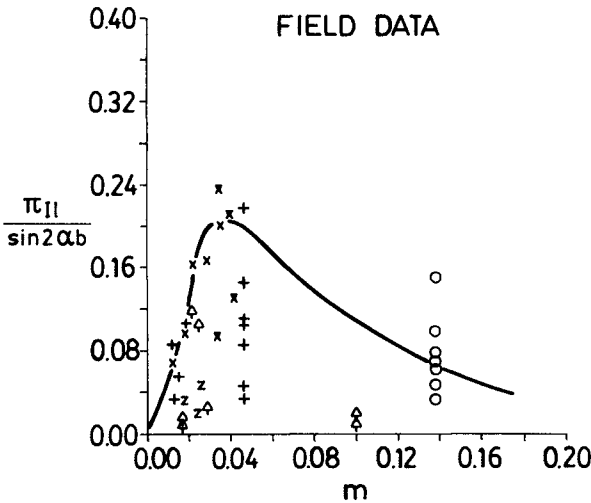


Figure 4.2: $\frac{\pi_{II}}{\sin 2\alpha b}$ versus m (beach slope) and the corresponding least-squares fit.

where k is a parameter depending on fluid and sediment characteristics. This relationship suggests the use of just one of the two parameters in this type of analysis. Only θ will be, thus, used in the subsequent development.

4.2.3. Bottom slope/Mobility number

A simple plot of these two variables provides an acceptable relationship for both field and laboratory data. These results are similar to those obtained by Kamphuis et al., 1982 and 1986) and suggest to discontinue the explicit use of m in equations such as (4.4). The influence of m on I_1 is, therefore, included via I_r .

4.2.4. Other relationships

Various other relationships among these parameters can be easily obtained. Since they are not required for the development of the I_1 formulation they will not be here included. Due care should be exercised when employing these relations due to the spurious effects inherent to this type of analysis.

4.3. I_1 formulation

The dimensional analysis formulation for I_1 is obtained by substituting the relationships derived in sections 4.2.1, 4.2.2 and 4.2.3 into equation (4.4):

$$I_1 = \sin 2\alpha b \cdot \emptyset(I_r, \theta) \quad (4.7)$$

This simplified expression is functionally identical to the one derived in section 3 (see equation 3.15).

The variation of I_1 with m , obtained by performing a least-squares fit to measured I_1 field data, turned out to be of the form (figure 4.2):

$$I_1 \propto m^{1/2} \cdot 10^{-8} m \quad (4.8)$$

The relationship $\Pi_{I_1} \propto m^{1/2}$ was also proposed by (Bruun et al., 1986) and (Deigaard et al., 1986). The $10^{-8} m$ factor included here provides not only a better fit but also a bell shaped variation with breaker type coherent with the corresponding laws of evolution obtained for D and V_1 (see section 2).

To derive the form of the \emptyset function let us consider the variation of Π_{I_1} with I_r . According to section 3, I_1 can be written as a stirring term times a transporting term. The first one can be shown to be proportional to D divided by some characteristic velocity while the second is mainly dependent on V_1 (see equation 3.1). Since both D and V_1 have been shown to vary in a bell-shaped manner with I_r , this same behaviour should be expected for Π_{I_1} . When plotting Π_{I_1} versus I_r (figure 4.3) a bell-shaped trend is in fact found. The mobility number θ appears to act as a parameter of the obtained family of curves, controlling the scale of the process. This type of variation with I_r is fully cohe-

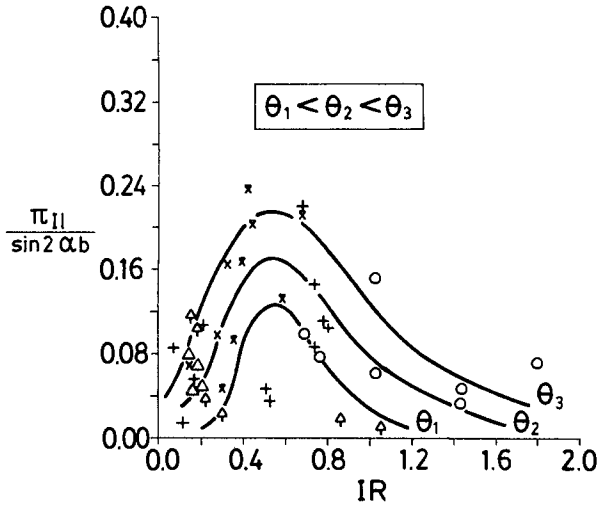


Figure 4.3: πI_l versus Iribarren parameter (Ir) with θ (mobility number) as family parameter.

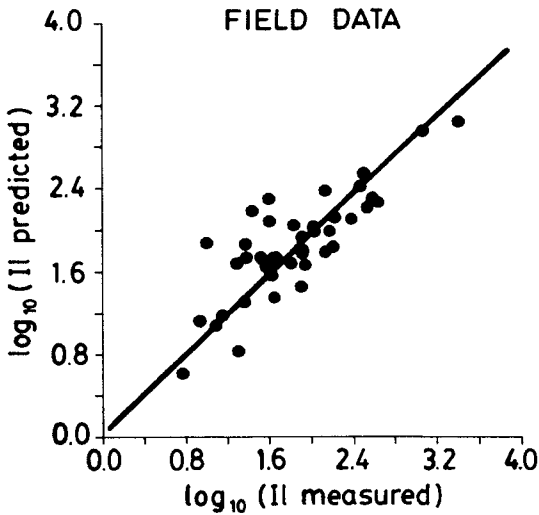


Figure 5.1: I_l predicted versus I_l measured (field Values).

rent with the variation of $\overline{I_1}$ with m given by equation (4.8) and it shall be further exploited in section 5.

5. Calibration of the Model

The variation of I_1 with m in equation (3.15) must be via the $F(Ir)$ function. Using the variation of $\overline{I_1}$ with m obtained in the previous section we may then write:

$$\hat{F}(Ir) = A Ir^{1/2} 10^{-8} Ir \quad (5.1)$$

This is the simplest possible function varying with m as prescribed by the dimensional analysis and possessing a bell-shaped behaviour with the breaker type.

Likewise, the simplest possible function of θ including this parameter as a scale factor is:

$$\hat{G}(\theta) = \left(\frac{\rho_s - \rho_w}{\rho_w} \right) \theta^c \quad (5.2)$$

in which the first term has been included to express I_1 as a function of $(\rho_s - \rho_w)$ instead of (ρ_w) .

The resulting final equation for I_1 is obtained by substituting (5.1) and (5.2) into (3.15):

$$I_1 = (\rho_s - \rho_w) A Ir^{1/2} 10^{-8.00} Ir^{3/2} Hbi^{5/2} \sin 2\alpha b. (\theta^c - \theta_{cr}^c) \quad (5.3)$$

By performing a least squares fit to measured I_1 values (field data only) it is easy to obtain:

$$\begin{aligned} A &= 4.8 \times 10^{-3} \\ c &= 0.44 \\ \theta_{cr} &= 12.77 \end{aligned}$$

in which the factor 10^{-3} in A can be obtained from dimensional analysis considerations. The quality of the obtained fit was not very sensitive to the precise θ_{cr} value, probably indicating that threshold conditions cannot be accurately established with the available data base.

To illustrate the structure of this formulation it is compared in Table I with three other well known models for I_1 . This comparison is by no means exhaustive since many other significant I_1 models have not been included (e.g. (Dean, 1973)(Watanabe et al., 1988)). Its main purpose is to give a feeling of the functional structure obtained with various formulations. A quantitative measure of the corresponding goodness of fit appears in Table II. The agreement obtained with the proposed formulation is shown in figure 5.1. It should be, however, mentioned that the number of free parameters for the fit of the proposed model is higher

I1 model	PARAMETER DEPENDENCY						
	Hb	T	m	D ₅₀	K _R (via I _r)	αb	P _s
CERC, 1970	Hb ^{2.5}	-	-	-	-	sin2αb	-
Kamphuis et al. 1986	Hb ^{3.5}	-	m ¹	D ₅₀ ⁻¹	-	sin2αb	P _s - P _w
Kraus et al. 1986	Hb ^{2.5}	-	m ⁻¹	-	-	sin2αb	P _s - P _w
Arcilla et al. 1986	Hb ^{2.69}	T ^{1/2}	m ^{1/2}	D ₅₀ ^{-0.44}	10 ^{-0.201r(1-K_R)^{7/6}}	sin2αb	(P _s -P _w)(P _s /P _w) ^{0.66}

Table 1: Parameter dependency of various I1 models compared to the formulation proposed in this paper.

I1 model	S _{RSE}
CERC, 1970	0.6058
Kamphuis et al. 1986	0.3679
Kraus et al. 1988	3.7216
Arcilla et al. 1988	0.3308

Table II: Fit obtained with various I1 formulations using the following measure (standard error) of the scatter:

$$S_{RSE} = \sqrt{\frac{1}{N-1} \left[\sum (\log_{10}(I1) \text{ predicted} - \log_{10}(I1) \text{ measured})^2 \right]^{1/2}}$$

than for other formulations. This could be associated to the obtained reduction in dispersion. It should also be pointed out that the high scatter obtained for (Kraus et al., 1988) model is probably due to the fact that apparently there were some misprints in the coefficients reported in the original paper and used here for the fit (Kraus personal communication).

6. Conclusions

1. A bell-shaped variation with I_r (and thus, with the breaker type) has been obtained from physical arguments and field data for the following variables: D (mean rate of wave energy dissipation per unit area), V_l (mean longshore current velocity) and I₁ (mean alongshore sand

transport rate).

2. A reasonable correlation has been found between the following pairs of dimensionless parameters:

- Iribarren's and Dean's parameters
- Reynolds and mobility parameters
- Beach slope and mobility parameter

This means that these parameters can be used somewhat equivalently in the context of across-shore integrated transport evaluation. It should also be remarked that this conclusion is limited to the employed data base and could also be affected by some spurious effects, always present when dealing with dimensionless parameters obtained from dimensional analysis. Because of this the predictive formulation proposed has been directly calibrated from equations (4.8) and (5.3), therefore avoiding the use of repeated variables in the two axes of the fitting diagram. The correlation among dimensionless parameters can illustrate the dangers of using models exclusively based on dimensional analysis.

3. The proposed I1 formulation calculates this variable as a transporting term (proportional to $V1$) times a stirring term (proportional to τb). The main advantages of this model are:

- It allows using different formulations for any of the two terms involved.
- It explicitly shows the variation of I1 with I_r and θ parameters and, in general, with the surf-zone dynamic state. In particular, this model includes the effect of varying reflection on I1.
- It provides a slightly better fit to the employed data base than other available formulations.

The proposed model represents, thus, an attempt to provide a more precise and physically based I1 formulation. This conclusion must be, however, interpreted in the context of the limitations (in quantity and quality) associated to the available I1 field data.

7. References

- Bailard, J.A. (1984) "A simplified model for longshore sediment transport". Proc. Int. Conf. Coastal Eng. 1984.
- Bijker, E.W. (1968) "Litoral drift as a function of waves and current". Delft Hyd. Lab. Pub. n° 58.
- Dean, R.G. (1973) "Heuristic models of sand transport in the surf zone". Proc. Conf. on Eng. Dyn. in the Surf Zone, Sidney, Australia, p. 208-214.
- Kamphuis, J.W. and Readshaw, J.S. (1978) "A model study of alongshore sediment transport rate". Int. Conf. on Coastal Eng. ASCE.

- Kamphuis, J.W., Davies, M.H., Nairn, R.B. and Sayao, O.J. (1986) "Calculation of littoral sand transport rate". Coastal Eng., 10, 1-21.
- Komar, P. and Inman, D.L. (1970) "Longshore sand transport on beaches", Journal Geophys. Res., Vol. 75 n^o 30 pp.5914-5927.
- Kraus, N.C., Hanson, H. and Larson, M. (1988) "Threshold for longshore sand transport and application to a shoreline change simulation model". IAHR. Symp. on Math. Modelling of Sediment Transport in the Coastal Zone.
- S.- Arcilla, A., Vidaor, A. and Monsó, J.L. (1986) "Influence of breaker type in surf zone dynamics". Proc. Int. Conf. Coastal Eng. 1986.
- Sayao, O.S. and Kamphuis, J.W. (1983) "Littoral sand transport rate: Model tests 1977-1982" CE, Res. Rep. 79, Civil Eng. Dep., Queen's Univ., Kingston, Canada.
- Soulsby, R.L. (1988) "The structure of suspended sediment transport formulae for unidirectional and wave-plus-current flows". IAHR Symp. on Math. Modelling of Sediment transport in the Coastal Zone.
- Vitale, P (1981) "Movable bed laboratory experiments comparing radiation stresses and Energy Flux factor as predictors of longshore transport rate", res. n^o 81-4, C.E.R.C.

CHAPTER 104

LONGSHORE CURRENT AND TRANSPORT ACROSS NON-SINGULAR EQUILIBRIUM BEACH PROFILES

Kevin R. Bodge¹ (Associate Member, ASCE)

ABSTRACT

The longshore current and longshore sediment transport distributions are described across an equilibrium beach profile comprised of an intersecting planar foreshore and a concave-up profile. Such a profile shape avoids the singularity associated with the infinite-slope at the shoreline described by traditional equilibrium profile forms and allows prediction of beach processes at and above the shoreline. The mathematical expressions which describe the distributions are simplified and can be more readily applied relative to expressions previously presented in the literature. The findings are in general agreement with similar previous analytic studies and indicate that the current and transport maxima are generally located at about the intersection of the planar and concave-up portions of the profile.

INTRODUCTION

Recent analytical solutions and data indicate that the longshore current and transport distributions across non-planar beaches can be markedly different than that predicted for planar beaches (see Sawaragi and Deguchi, 1978; Berek and Dean, 1982; Sternberg et al., 1984, Bodge and Dean, 1987; Fulford, 1987; Kraus, Rosati and Gingerich, 1988; Bodge, in press; among others). Since few natural beaches are planar in profile, the solution of the longshore current and transport distributions across non-planar beaches is relevant to improved understanding and modelling of littoral processes for physically realistic beach profiles.

BACKGROUND

Bruun (1954) and Dean (1977) have suggested that equilibrium beach profiles are described by the form

$$h = a x^{2/3} \quad (1)$$

¹Senior Engineer, Olsen Associates, Inc., 4438 Herschel Street, Jacksonville, FL 32210.

where h =depth, x =distance offshore, and a is a dimensional coefficient. A disadvantage of the concave-up profile described by this equation is the infinite beach slope at the shoreline ($x=0$) which leads to (i) a singularity in the description of the longshore current and transport at the shoreline, and (ii) no description of the swash zone. In contrast, most equilibrium profiles in nature are characterized by a relatively planar beachface which extends from the berm to just below the shoreline.

McDougal and Hudspeth (1984) analytically considered the wave-induced set-up and longshore current and transport across beach profiles described by a planar foreshore and an $ax^{2/3}$ -type profile seaward of the foreshore. These authors considered both "stress" and "energetics" longshore transport models after Komar (1977) and Bagnold (1963), respectively.

In the present study, the set-up, longshore current and longshore transport across such a combined planar-foreshore/concave-up profile is analytically described using (1) the longshore current solutions described by Longuet-Higgins (1970) and in part by McDougal and Hudspeth (1984), respectively, across the planar and concave-up portions of the profile; (2) a simplistic assumption that the local wave height is proportional to the local set-up water depth, and (3) a distributed longshore transport model described by Bodge and Dean (1987).

THE NON-SINGULAR EQUILIBRIUM BEACH PROFILE

Consider a beach profile such as shown in Figure 1 with x -axis directed offshore and origin $x=0$ at the still water shoreline. The profile is composed of two mathematically described segments: (1) a planar foreshore of slope m_f , and (2) a concave-up profile of the form $h=ax^{2/3}$, where h is the still-water depth and a is a shape parameter. The profiles intersect at the "match-point" $x=x_m$. The usual origin of the concave-up profile (i.e., at depth $h=0$) is displaced seaward of the x -axis origin by the distance δ . Specifically,

$$h = \begin{cases} m_f x & x < x_m \\ a(x-\delta)^{2/3} & x \geq x_m \end{cases} \quad (1)$$

Requiring that the bottom depths and slopes are identical at the match-point x_m yields

$$x_m = \frac{4}{9} \frac{a^3}{m_f^3} \quad (2)$$

and

$$\delta = \frac{x_m}{3} \quad (3)$$

That is, the location of the match-point can be simply

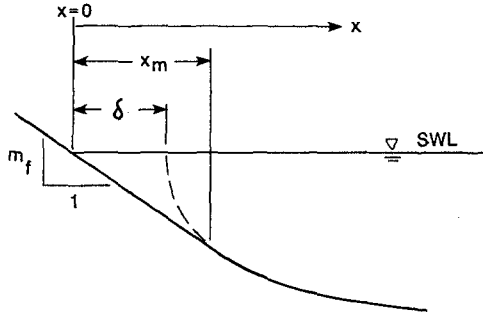


Figure 1: The non-singular equilibrium beach profile.

described by the foreshore slope and the shape factor of the concave-up part of the profile.

WAVE-INDUCED SET-UP

The variation in mean water surface associated with change in onshore radiation stress, or wave-induced set-up $\bar{\eta}$, has been shown to be equal to

$$\bar{\eta} = \begin{cases} v(h_b - h) - \frac{\kappa^2}{16} h_b & x \leq x_b \\ \frac{-H^2 k}{8 \sinh 2kh} & x \geq x_b \end{cases} \quad (4)$$

after Longuet-Higgins and Stewart (1964), and Dean and Dalrymple (1984), among others, where h_b and x_b are the still-water depth and location of the wave breakpoint, respectively, H is the local wave height, and k is the wavenumber. Shoreward of the breakpoint, the wave height H is assumed proportional to the total water depth d , where

$$\kappa = H/d \quad (5)$$

and

$$v = \frac{3\kappa^2}{8 + 3\kappa^2} \quad (6)$$

Across the planar foreshore part of the profile, the slope of the set-up water surface is uniform and equal to $-v m_f$. The point of intersection of the set-up water surface and the foreshore, x_s , is

$$x_s = \frac{(v - \kappa^2/16) h_b}{(v - 1) m_f} \quad (7)$$

This location corresponds to the "set-up still water line", or more precisely, the mean water line in the influence of static wave set-up.

The total water depth d across the profile is

$$d = h + \bar{\eta} \quad (8)$$

Combining Eqs. (1), (4), and (8), the total water depth across the non-singular equilibrium profile is

$$d = \begin{cases} (1-\nu) m_f x + (\nu - \frac{\kappa^2}{16}) h_b & x_s \leq x \leq x_m \\ (1-\nu) a (x-\delta)^{2/3} + (\nu - \frac{\kappa^2}{16}) h_b & x \geq x_m \end{cases} \quad (9)$$

For purposes of notation, observe that the set-up water surface slope across the planar foreshore part of the profile is

$$s_f = (1-\nu) m_f \quad (10)$$

McDougal and Hudspeth (1981, 1984) showed that the total water depth across the concave-up $h=ax^{2/3}$ profile can be well-approximated by the form

$$d = \tilde{a} x^{1/2} \quad (11)$$

This expression models the set-up water surface well except as x approaches 0 (since d does not go to zero as $x \rightarrow 0$). However, the poorer fit near $x=0$ is essentially inconsequential in the present case if the exact form of the set-up water surface is used across the planar foreshore part of the profile; i.e., in the region $x=0$. Accordingly, the following expressions are adopted for the total water depth:

$$d = \begin{cases} s_f x + (\nu - \frac{\kappa^2}{16}) h_b & x_s \leq x \leq x_m \\ \hat{a} (x-\delta)^{1/2} & x \geq x_m \end{cases} \quad (12)$$

Requiring continuity of total water depth and water surface slope at the matchpoint x_m yields

$$\hat{a} = s_f \sqrt{2(x_m - x_s)} \quad (13a)$$

$$\delta = \frac{1}{2} (x_m + x_s) \quad (13b)$$

Non-dimensionalizing all length scales by the distance to the breakpoint x_b yields

$$D = \begin{cases} s_f X + (\nu - \frac{\kappa^2}{16}) s_b & X_s \leq X \leq X_m \\ \hat{A} (X - \hat{\Delta})^{1/2} & X \geq X_m \end{cases} \quad (14)$$

$$\hat{A} = s_f \sqrt{2(X_m - X_s)} \quad (15a)$$

$$\hat{\Delta} = \frac{1}{2} (X_m + X_s) \quad (15b)$$

where upper-case denotes non-dimensional terms such as

$$X = x / x_b \quad (16)$$

and where the term s_b has been introduced as

$$s_b = h_b / x_b \quad (17)$$

LONGSHORE CURRENT

In dimensional form, wave-induced longshore current can be described through the depth- and time-averaged equation of motion in the alongshore direction (Bowen, 1969; Longuet-Higgins 1970),

$$-\frac{\partial}{\partial x} S_{xy} + \tau_{by} + \frac{\partial}{\partial x} (\mu_e d \frac{\partial v}{\partial x}) = 0 \quad (18)$$

where S_{xy} is the onshore-directed flux of the alongshore component of momentum, τ_{by} is the alongshore component of bottom stress, v is the depth- and time-averaged longshore current, and μ_e is the turbulent eddy viscosity. Following the classical approximations of Longuet-Higgins (1970) and others,

$$\tau_{by} = -\frac{\kappa}{\pi} C_f \rho \sqrt{gd} v \quad (19)$$

where C_f is an empirically determined friction factor of order 0.01. The turbulent viscosity is assumed to vary linearly with distance offshore

$$\mu_e = N \rho x \sqrt{gd} \quad (20)$$

where N is a numerical constant.

Non-dimensionalizing all length-scales by the breaker distance x_b and velocity by the classical Longuet-Higgins solution of longshore current at the breaker line with no mixing, i.e.,

$$v_o = \frac{5}{16} \frac{\kappa \pi}{C_f} \sin \theta_b \sqrt{gd_b} s_b \quad (21)$$

where θ is the wave angle and the "b" subscript refers to breaking conditions, the alongshore equation of motion (Eq. 18) becomes

$$\frac{N \pi}{\kappa C_f} \frac{\partial}{\partial X} (XD^{3/2} \frac{\partial V}{\partial X}) - D^{1/2} V = -D^{3/2} \frac{\partial D}{\partial X} \frac{1}{s_b^2} \quad (22)$$

where upper-case denotes non-dimensional terms once again such as

$$V = v/v_o \quad \text{and} \quad X = x/x_b \quad (23)$$

To determine the longshore current, Eq. (22) must be solved across each of three regions across the non-singular equilibrium profile: (i) the planar foreshore, (ii) the concave-up segment landward of the breakpoint, and (iii) the concave-up segment seaward of the breakpoint. Both the magnitude and gradient of the velocity must be matched between each region. McDougal and Hudspeth (1984) demonstrated these solutions but the resultant expressions are somewhat cumbersome and tedious to apply.

In the present study, Eq. (22) is solved for the longshore current across each of the three regions; both the magnitude and gradient are matched at the planar/concave-up matchpoint x_m but only the magnitude is matched at the breakpoint x_b . The resulting discontinuity in the velocity gradient at the breakpoint is small for the physically-typical case where x_m is small compared to x_b (i.e., where the toe of the foreshore is located close to shore relative to the breakpoint).

Incorporating the non-dimensional expressions for total water depth D (Eq. 19) to Eq. (22), and solving for velocity subject to the above-described matching conditions, the non-dimensional longshore current is given by

$$V = \begin{cases} A_1 (X-X_s)^{P_1} + \left(\frac{s_f}{s_b}\right)^2 \frac{1}{i - \frac{s_f}{2P}} (X-X_s) & X_s < X < X_m \\ C_1 \left[\frac{\cosh(\lambda \tilde{X}^{1/4})}{\lambda \tilde{X}^{1/2}} - \frac{\sinh(\lambda \tilde{X}^{1/4})}{\lambda^2 \tilde{X}^{3/4}} \right] + \frac{\hat{A}^2}{2s_b^2} & X_m < X < 1 \\ C_2 \left[\frac{1}{\tilde{X}^{1/2}} + \frac{1}{\lambda \tilde{X}^{3/4}} \right] \exp(-\lambda \tilde{X}^{1/4}) & X > 1 \end{cases} \quad (24)$$

where

$$P_1 = -\frac{3}{4} + \left(\frac{9}{16} + \frac{1}{P}\right)^{1/2} \quad (25)$$

$$P = \frac{N \pi s_f}{\kappa C_f} ; \quad P \neq 2/5 \quad (26)$$

$$\lambda = 4/\sqrt{P_2} \quad (27)$$

$$P_2 = \frac{N \pi \hat{A}}{C_f} = P \sqrt{2(X_m - X_s)} \quad (28)$$

$$\tilde{X} = (X - \hat{\Delta}) \quad (29)$$

The coefficients are given by

$$A_1 = (X_m - X_s)^{-P_1} \left[C_1 \phi - \alpha (X_m - X_s) + \frac{\hat{A}^2}{2s_b^2} \right] \quad (30)$$

$$C_1 = -\frac{\hat{A}^2}{2s_b^2} \left(3Q + \lambda Q^2 + \frac{3}{\lambda} \right) \exp(-\lambda Q) \quad (31)$$

$$C_2 = \frac{\hat{A}^2}{2s_b^2} \left[-\frac{3Q}{\lambda} \cosh \lambda Q + (Q^2 + \frac{3}{\lambda^2}) \sinh \lambda Q \right] \quad (32)$$

and where

$$\alpha = \left(\frac{s_f}{s_b}\right)^2 \frac{1}{1 - \frac{5}{2}P} ; \quad P \neq 2/5 \quad (33)$$

$$\Phi = \frac{1}{\lambda R^2} \cosh \lambda R - \frac{1}{\lambda^2 R^3} \sinh \lambda R \quad (34)$$

$$R = (X_m - \hat{\Delta})^{1/4} \quad (35)$$

$$Q = (1 - \hat{\Delta})^{1/4} \quad (36)$$

Application of Eqs. (24) through (36) can be cumbersome. However, each of the terms in Eq. (24) which describe the longshore current can be expressed solely as a function of the non-dimensional matchpoint location X_m and the mixing parameter P . Recall that X_m is simply described by

$$X_m = x_m / x_b \quad (37)$$

where

$$x_m = \frac{4}{9} \left(\frac{a}{m_f}\right)^3 \quad (38)$$

and

$$x_b = \left(\frac{H_b}{\kappa a}\right)^{3/2} + \frac{4}{27} \left(\frac{a}{m_f}\right)^3 \quad (39)$$

Hence, the non-dimensional longshore current profile can be readily calculated from the (i) breaking wave height H_b , (ii) breaker index κ , (iii) concave-up beach shape parameter a (commonly denoted by "A" in the literature), (iv) foreshore slope m_f , and (v) selection of a mixing parameter P , where $P \neq 0.4$.

Figures 2 through 9 depict each of the terms necessary to evaluate the longshore current distribution from Eq. (24) for a breaker index $\kappa = 0.8$, for various chosen values of the mixing parameter P and for calculated values of the non-dimensional planar-foreshore/concave-up matchpoint location X_m .

Figure 10 illustrates the non-dimensional longshore current across the non-singular equilibrium beach profile for various locations of the profile matchpoint X_m . Note that the current maxima approximately corresponds to the location of the profile matchpoint.

Figure 11 illustrates longshore current distributions observed across beaches with non-singular equilibrium shaped profiles -- compared to the distributions predicted for each case by Eq. (24) for several values of the mixing parameter. The first five cases represent

dye observations from a moveable-bed laboratory model for five different breaking/surf conditions; the last case is from current meter data collected at Duck, N.C., (Bodge and Dean, 1987). The agreement is fairly good, although the longshore current distributions observed in the laboratory appear displaced landward by about 2/10'ths of a surf zone width relative to the predicted distributions.

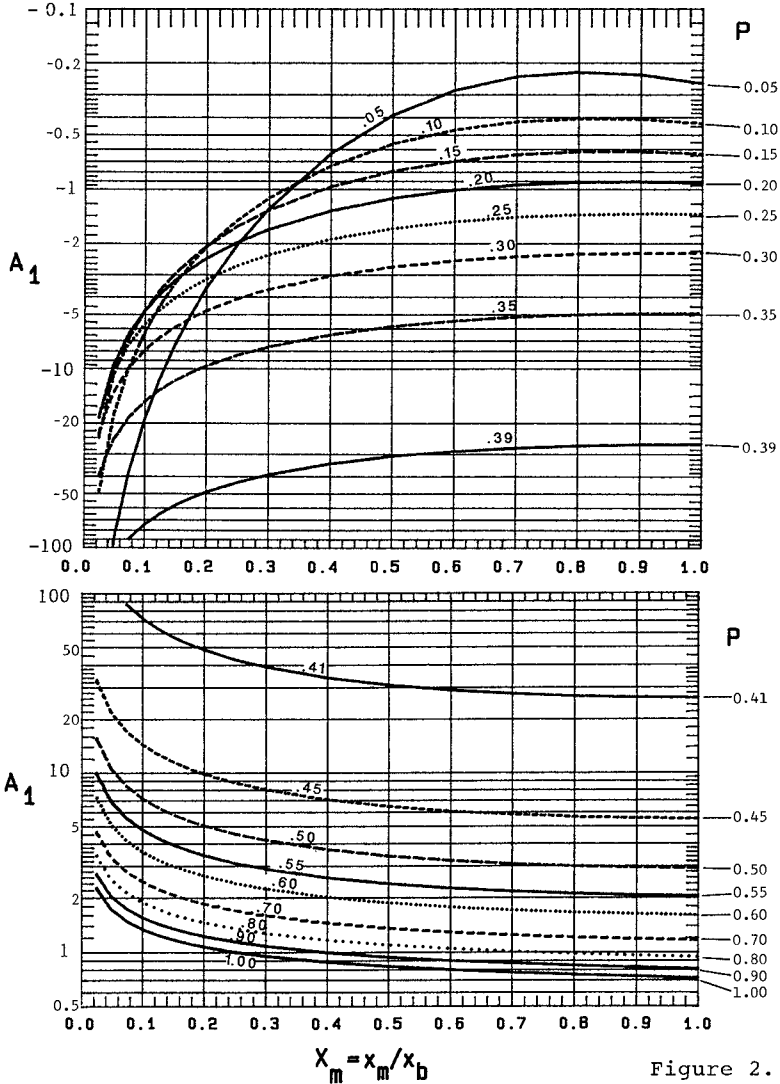


Figure 2.

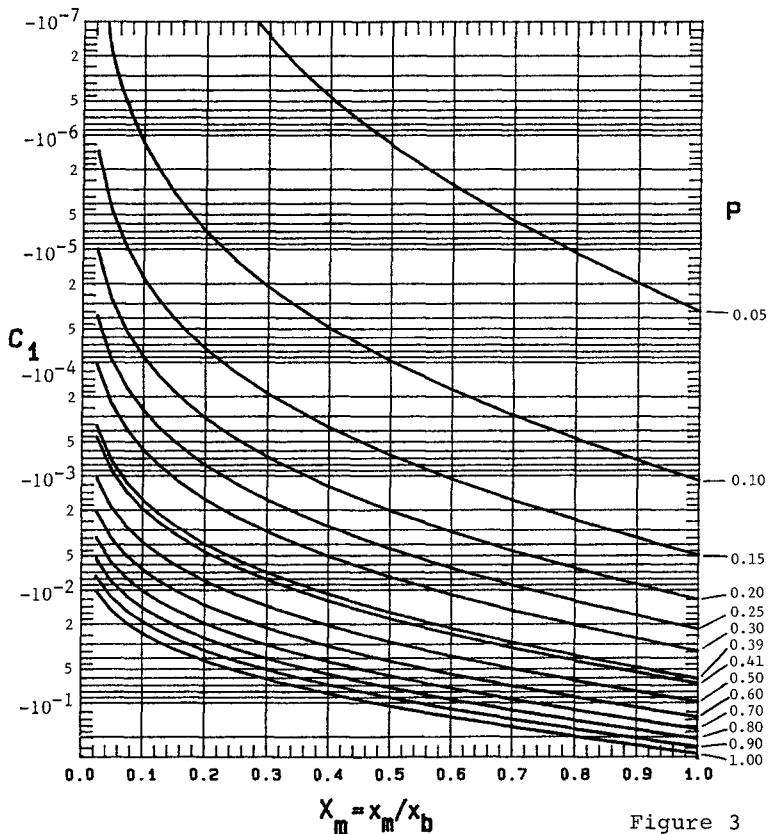


Figure 3

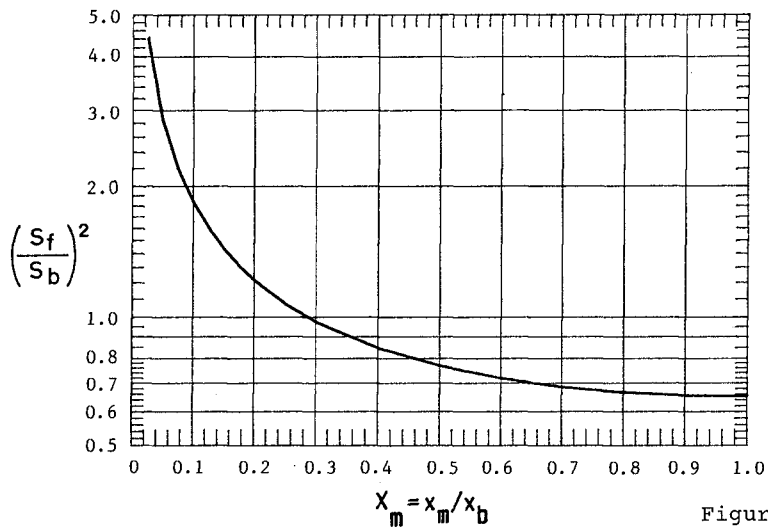


Figure 4

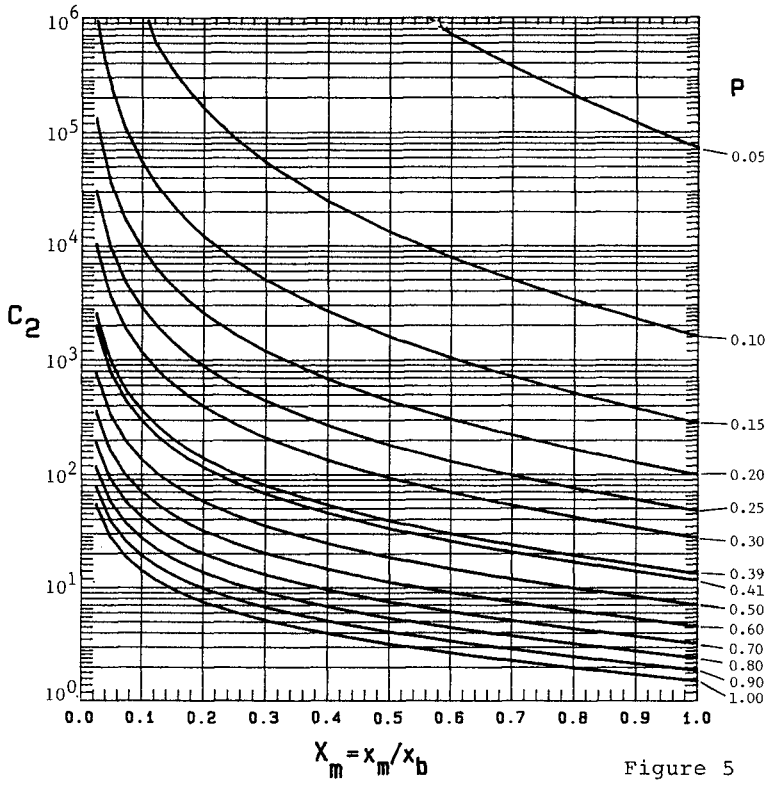


Figure 5

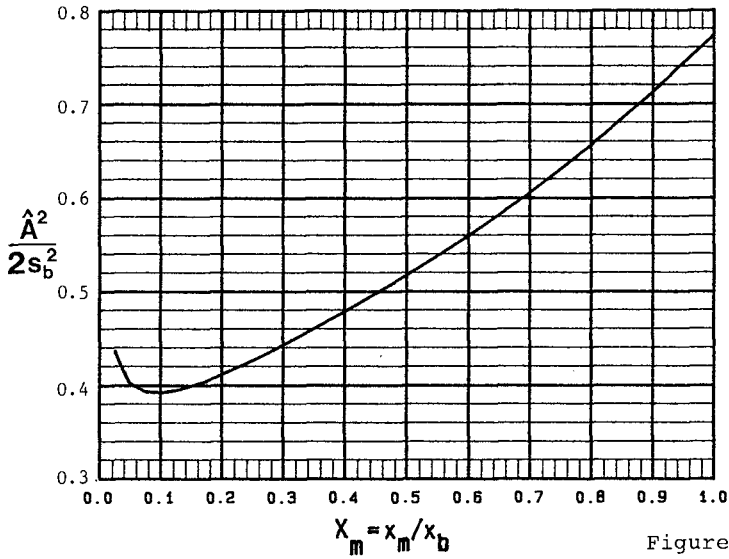


Figure 6

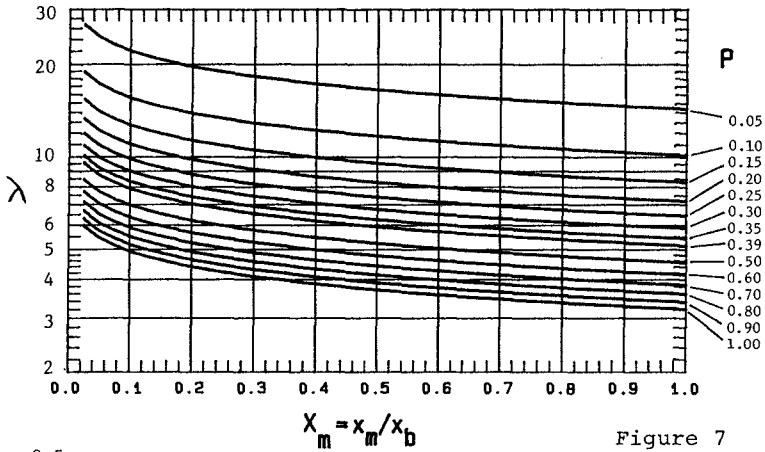


Figure 7

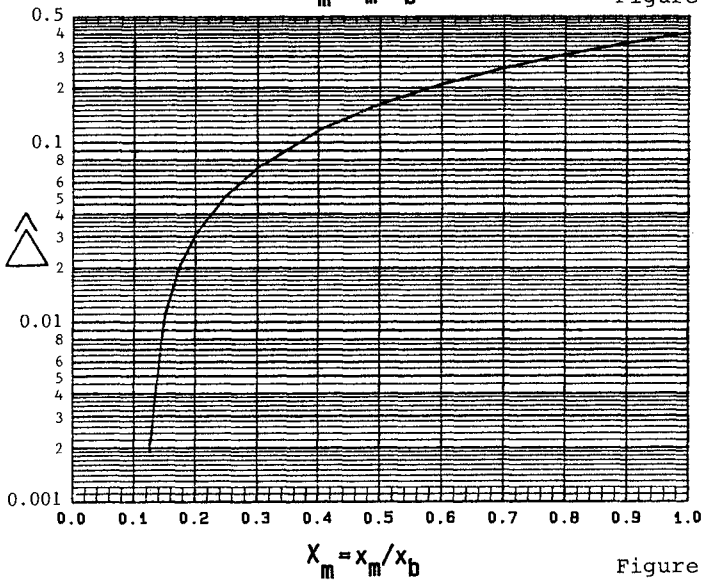


Figure 8

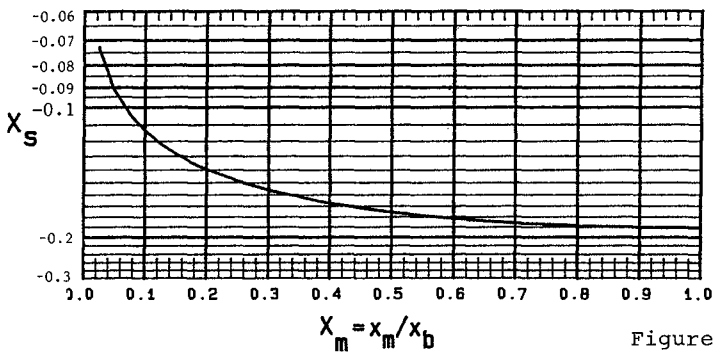


Figure 9

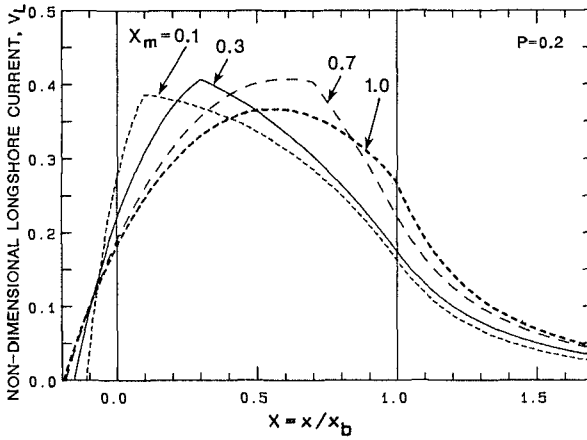


Figure 10: Longshore current predicted across a non-singular equilibrium profile for various profile matchpoints.

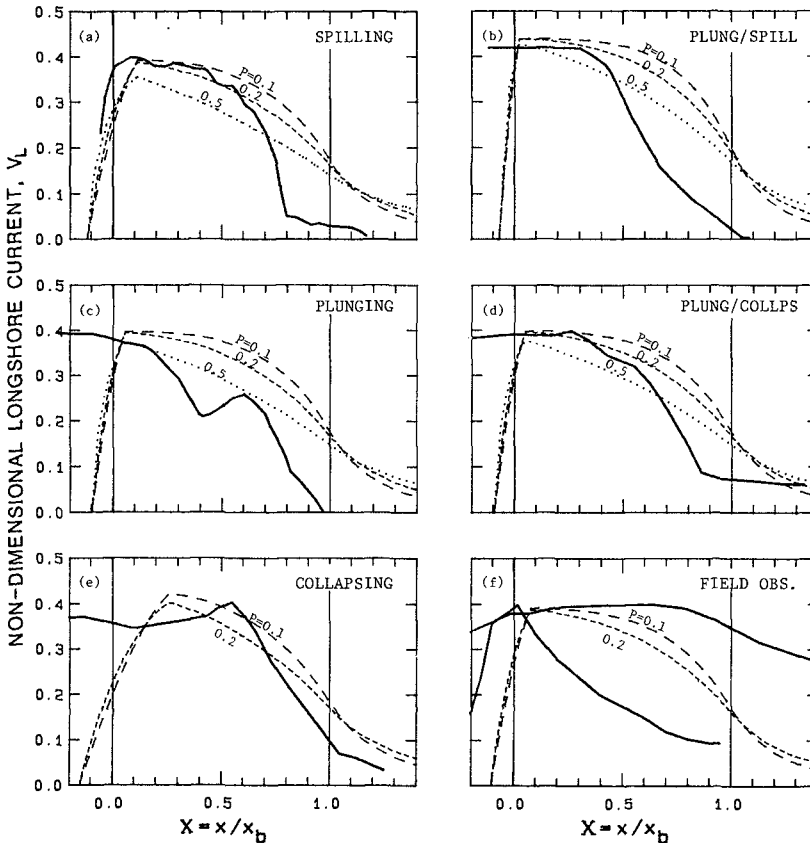


Figure 11: Observed (bold) and predicted (dashed) longshore current distribution across non-planar beaches.

LONGSHORE SEDIMENT TRANSPORT

Bodge and Dean (1987) presented a distributed longshore transport model based upon results of short-term impoundment of longshore sediment transport across rapidly-deployed, low-profile groins in the field and laboratory environments. Their expression suggests that sediment is mobilized in proportion to the rate of local wave energy dissipation per unit surf zone volume and is transported alongshore by local longshore current; viz.,

$$q_{\ell}(x) = k_{\ell} \frac{1}{h} \frac{\partial}{\partial x} (e c_g) v \quad (40)$$

where $q_{\ell}(x)$ is the local longshore sediment transport rate per unit offshore distance, k_{ℓ} is a dimensional coefficient of proportionality, and ec_g is the local wave energy flux.

Again assuming that local wave height is proportional to the local water depth, and non-dimensionalizing lengths by the breaker distance and velocities by the planar-beach no-mixing longshore current at the breakpoint, Eq. (40) becomes

$$Q_{\ell} = D^{1/2} s_b^{-3/2} v \frac{dD}{dX} \quad (41)$$

where Q_{ℓ} is the local (not total) longshore transport rate per unit distance offshore normalized by the local rate at the breakpoint; i.e.,

$$Q_{\ell} = q_{\ell} / q_{\ell b} \quad (42)$$

where

$$q_{\ell b} = k_{\ell} \frac{5}{16} \rho g^{3/2} \kappa^2 d_b^{1/2} v_o s_b \quad (43)$$

Equation (41) can be evaluated to yield the longshore sediment transport distribution across the surf zone (landward to the location of the set-up still water line x_g) via Eq. (24) for the longshore current and Eq. (14) for the total water depth. Figure 12 illustrates the transport distributions for various locations of the profile matchpoint X_m . Note that the maxima closely corresponds to the location of the profile matchpoint.

Figure 13 compares the longshore transport distributions across a non-singular equilibrium profile as predicted by the "energetics" model (Bagnold, 1963), the "stress" model (Komar, 1977), and the present model (Bodge and Dean, 1987).

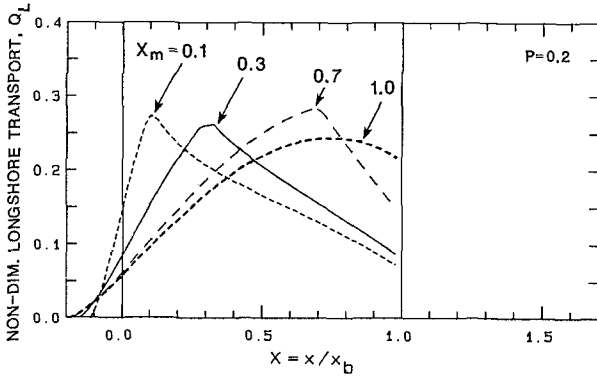


Figure 12: Longshore transport across a non-singular equilibrium profile for various profile matchpoint locations.

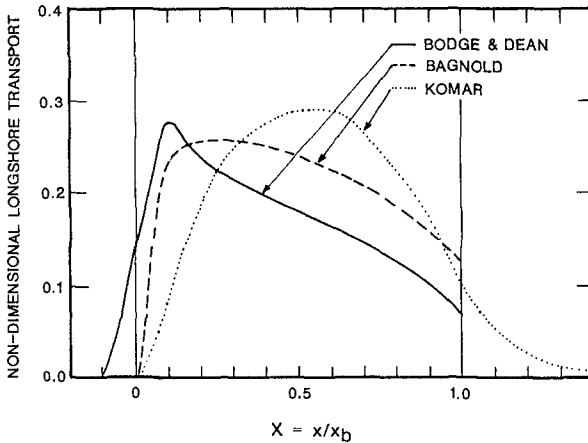


Figure 13: Comparison of longshore transport distribution models evaluated for a non-singular equilibrium profile with matchpoint $X_m=0.1$ and mixing parameter $P=0.1$.

SUMMARY AND CONCLUSIONS

The non-singular equilibrium beach profile consists of a planar foreshore "matched" to a concave-up profile across the surf zone. The longshore current and sediment transport distributions across such a profile can be readily developed through knowledge of the foreshore slope, concave-up profile shape parameter, breaker height, and selection of a Longuet-Higgins type mixing parameter. The current and transport maxima are predicted at or about the location of the planar-foreshore/concave-up profile matchpoint. Since this point is typically located fairly close to shore relative to the breakpoint, this suggests that the peak current and transport are more closely located to shore than to the

breakpoint. This result agrees with similar solutions for non-planar beaches, such as McDougal and Hudspeth (1981, 1984), but is in contrast to classical predictions for planar beaches -- where current and transport is predicted as maximum at the outer half of the surf zone and vanishing at the shoreline. Moreover, the results for the non-planar beach, as in the present study, agree more closely with recent field and laboratory observations.

REFERENCES

- Bagnold, R.A., 1963. Beach and Nearshore Processes Part I: Mechanics of Marine Sedimentation. In: M.N. Hill (ed.), The Sea: Ideas and Observations, Vol. 3. New York: Interscience, 507-528.
- Berek, E.P. and R.G. Dean, 1982. Field Investigation of Longshore Transport Distribution. Proc., 18th Int. Conf. on Coastal Eng., ASCE, 1620-1639.
- Bodge, K.B., in press. A Literature Review of the Distribution of Longshore Sediment Transport Across the Surf Zone. J. Coastal Research.
- Bodge, K.B. and R.G. Dean, 1987. Short-Term Impoundment of Longshore Transport. Proc., Coastal Sediments '87, ASCE, 468-483.
- Bowen, A.J. The Generation of Longshore Currents on a Plane Beach. J. Marine Research, 27, 206-215.
- Bruun, P., 1954. Coast Erosion and Development of Beach Profiles. Beach Erosion Board, Tech. Memo. No. 44, Washington, DC.
- Dean, R.G., 1977. Equilibrium Beach Profiles: U.S. Atlantic and Gulf Coasts. Ocean Eng. Rpt. No. 12, Dept. of Civil Eng., Univ. of Delaware, Newark, DE; 45 pp.
- Fulford, E.T., 1987. Distribution of Sediment Transport Across the Surf Zone. Proc., Coastal Sediments '87, ASCE, 452-467.
- Komar, P.D., 1977. Beach Sand Transport: Distribution and Total Drift. J. Waterway, Port, Coastal and Ocean Eng., ASCE, 103, WW2, 225-239.
- Kraus, N.C., Rosati, J.D. and K.J. Gingerich, 1988. Longshore Sediment Transport in the Surf Zone. Proc., 21st Conf. on Coastal Eng., ASCE.
- Longuet-Higgins, M.S., 1970. Longshore Currents Generated by Obliquely Incident Sea Waves, 1 and 2. J. Geophysical Research, 75(33), 6778-6801.
- McDougal, W.G. and R.T. Hudspeth, 1981. Wave Induced Setup/Set-down and Longshore Current; Non-Planar Beaches: Sediment Transport. Oceans, IEEE, 834-846.
- McDougal, W.G. and R.T. Hudspeth, 1984. Longshore Sediment Transport on Dean Beach Profiles. Proc., 19th Int. Conf. on Coastal Eng., ASCE, 1488-1506.
- Sawaragi, T. and I. Deguchi, 1978. Distribution of Sand Transport Rate Across a Surf Zone. Proc., 16th Int. Conf. on Coastal Eng., ASCE, 1596-1613.
- Sternberg, R.W., N.C. Shi and J.P. Downing, 1984. Field Investigations of Suspended Sediment Transport in the Nearshore Zone. Proc., 19th Int. Conf. on Coastal Eng., ASCE, 1782-1798.

CHAPTER 105

DESIGN OF POCKET BEACHES. THE SPANISH CASE

José Ma Berenguer *
Javier Enríquez **

Pocket beach is a usual method to restore an eroded or regressive coast without natural sand supply. Nowadays, there are more than 40 of these beaches on the Spanish coasts and a lot of them all over the world.

This paper deals with the design parameters of pocket beaches, based on the analysis of data collected from 24 existing beaches on the Mediterranean coast of Spain. Fourteen of these beaches have been studied in detail; nine of them located on the Alboran Sea and the other five on the coast of Cataluña. Data from 40 additional beaches have also been considered.

Different parameters such as structural design, location of breakwaters, beach planform, beach profile, wave conditions at the site and sedimentary conditions have been analyzed. A mathematical model has been used for the study of the shoreline equilibrium planform.

Practical coastal criteria design considerations have been drawn from the observed behaviour of the aforementioned beaches.

1.- INTRODUCTION

The term "pocket beach" is going to be used for all those beaches which have been artificially created using constructions that limit them laterally, and also in certain cases frontally, either totally or partially. By definition, the term suggests that the dimensions are limited and generally reduced.

* Civil Engineer, Deputy Director of the Harbour Division at the "Centro de Estudios de Puertos y Costas"(CEDEX)

Antonio López, 81, 28026 Madrid, SPAIN

** Civil Engineer, Head of the Coastal Defence Division at the "Centro de Estudios de Puertos y Costas"(CEDEX)

This work is concerned with those pocket beaches protected by works parallel to the coast. Beaches which are bounded by groynes that are straight and perpendicular to the coast are thus excluded. On the other hand, constructions that are of the detached breakwater kind, L-shaped or T-shaped or curved groynes and platform islands are those which will be studied.

The main purpose of these constructions is to obtain a stable and safe beach. Pocket beaches undoubtedly have their advantages and drawbacks. Each and every coastal problem has its own specific characteristics, (purpose, wave climate, environment, etc.), and this makes the indiscriminate use of theoretical plans and the extrapolation of practical solutions unadvisable even if they have been successful in other cases.

The methods that have been developed in coastal engineering for the control of sedimentary processes which are of an erosive nature, are basically three.

1. To protect the coast with works that prevent or limit the direct action of the waves on sedimentary deposits.
2. To reduce or alter the rate of littoral transport.
3. To supply new sediment to the beaches in order to replace the losses or to increase size.

The pocket beaches are a compendium of all these systems and as such can act in any of these three capacities. Their projection parallel to the coast reduces the average energy that reaches the shoreline. The differential way in which this effect is brought about, causes a considerable change in the littoral transport of sand. Finally the reduced dimensions of the physiographical micro-unity created make it possible to gain stable and economical beach by artificial nourishment or natural trapping of new sand.

In recent years, the increase of pocket beaches has been remarkable. In Mediterranean countries where tidal effects are insignificant, especially in Spain, Italy, France and Israel, this system of beach regeneration has been widely used because of its rapid results and its economical nature. Japan also has a lot of experience in this kind of work.

In Spain, there are over 40 beaches of this kind. They are usually situated on stretches of coastline where there is a lot of tourism and in which there is also a fairly rapid erosional process as a consequence of either causes exogenous to coastal use (dams, wells), or endogenous causes (marinas, coastal works, dredging, etc.).

2.- PREVIOUS RESEARCH

The influence of detached breakwaters on the coast and the formation of tombolos has been studied by several researchers. Sawaragi (1957), using movable-bed model, analyzed the variation induced on the longshore current by this kind of coastal structures. Shinohara and Tsubaki (1966) developed a new physical model for the analysis of the role of detached breakwaters in the formation of tombolos. Toyoshima (1974) carried out a statistical survey of 308 detached breakwaters constructed in Japan, looking for a series of relationships between the lengths of the works, their distance from the coast and the accumulations caused in the sheltered area.

The planform of tombolos in the lee of breakwaters has been studied by Perlin (1979) through the use of a numerical model. One of the conclusions points to the considerable influence that the parameter L_0 (wave length) has in the shape of the resulting tombolo. Noble (1978) carried out an analysis of the behaviour of diverse coastal protection structures and their effects on the beaches, reaching the conclusion that an off-shore breakwater has virtually no influence on the coast when its distance from the coast is over six times its length. Berenguer (1986) presents graphs which are similar to Toyoshima's; these are drawn up from different artificial beaches on the Spanish Mediterranean Coast.

The study of the planform of the beaches formed behind offshore structures, whether these be natural or artificial has been the subject of considerable Coastal Engineering work. Sauvage (1954) was one of the first authors to analyze the equilibrium of these coastal formations, showing that the shape of the planform was markedly elliptical. Yasso (1965) checked, by analyzing real cases, of adjustment of the planforms of the beaches to logarithmic spirals of equation $r = e^{\theta \cot \alpha}$, where r is the radius from the pole of the spiral, θ is the horizontal angle from the origin and angle α is the constant angle of the radii to the tangents of the curve.

Silvester et al. (1970), (1972), using prototype data, concludes that the beach planforms between headlands consist of three distinct zones:

- an arc behind the headland which is located upstream in the direction of littoral transport.
- a stretch which is logarithmic spiral in shape.
- a straight stretch which extends downstream towards the next headland.

Applying these conclusions, Silvester and Ho (1972) have used the logarithmic spiral for the stabilization of artificial reclamations through the concept of headland control.

Garau (1973), using observations* made at various beaches of the Spanish Mediterranean Coast, defines the planforms of the diffraction beaches through their sediment filling and emptying processes. His most important conclusions are that the maximum emptying curve would be a logarithmic spiral whose centre is in the diffraction pole and that the characteristic angle of the family of spirals depends basically on the friction angle of the sand in the trough of water, and which can be generalized for a value of $\alpha = 60^\circ$.

Rea and Komar (1975) developed a numerical model of evolution of spiral beaches behind a rocky headland. Font, Sanabria and Silva (1976) include the effects of the gradient at the height of the breaking wave and the associated current. The longitudinal current is estimated as a consequence of the obliqueness of the incident wave and of the set-up gradient caused by this. Dean (1978) presents a method for calculating the equilibrium shape of pocket beaches. In this method the bathymetry is considered stable when the wave front is tangent everywhere to the local bottom contours. The calculation is carried out for relatively narrow openings with normal and oblique waves. For high wave-periods the planform obtained is markedly semi-circular.

Another of the aspects dealt with in the question of beaches situated in diffraction zones, is the hydrodynamic conditions required in the sheltered area for the systems to be equilibrium in the face of a specific wave condition. This question has caused different authors to try and clarify the processes associated with the propagation of waves in the diffraction zone (currents, set-up, etc.). The works of O'Rourke and Le Blond (1972), and Gourlay (1974) (1976), are to be found in this section. The presence of longshore currents in the sheltered zone when the beach is stable, phenomenon confirmed in tests by Gourlay, contrasts with the assumptions made by other authors with regard to the stability situation on a protected beach.

Walton (1977), after analyzing the planform of spiral beaches, concludes that their position is at all points perpendicular to the energy vector of the incident waves. Rosen and Vajda (1982) deduce that the stability of a tombolo is achieved when the bathymetric lines are such that the diffracted waves have a component of movement quantity opposite to the gradient of average level induced by the radiation stress.

3.- METHODOLOGY

The basis of the present study is the experience achieved in cases where constructions are already present on the Spanish Coast. This is why a detailed study of formal and sedimentological characteristics of 14 "pocket beaches" on the Mediterranean Coast have been carried

out. Nine of these beaches are to be found in a limited marine area, which is the Alborán Sea, that reaches the coast of the province of Málaga. The other five are in Catalonia: two in the province of Gerona and three in Tarragona. In addition to these beaches, some geometrical parametres of another ten beaches are analyzed, all of these also on the Mediterranean Coast.

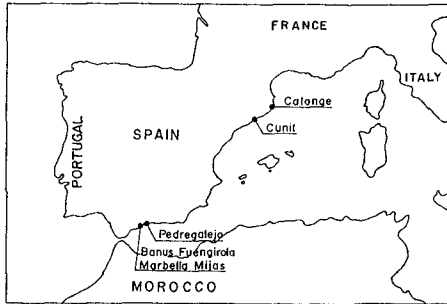


Fig. 1.- Site Location.

4.- DATA COLLECTION

Table 1 shows the main information collected from each of the beaches studied. In 10 of these, the information has been obtained through special field studies whereas in the rest, the data has been got from plans and aerial photography.

The information includes the following aspects:

- Geometrical characteristics: The measurements have been carried out using topographical techniques. The criterion used for the determining of distances between points of contact between water and land has been to adjusted to situations of mean sea level.
- Bathymetry: The survey has been extended to the inside of the cell, the gap and the outer area in front of the gap. The depth of the bottom within each cell has been determined at base, with at least 5 profiles.
- Slope: The slope measurements refer to those carried out at different points throughout the length of the beach face.
- Granulometric distribution: On 12 beaches, sediment samples have been collected on both the subaerial and submerged parts of the beach. These samples have been dried, weighed and sifted by the ASTM series.

The parameters used for defining the characteristics of pocket beaches are set out in fig. 2.

5.- WAVE CLIMATE

Tidal and wave conditions on the Spanish Mediterranean Coast are fairly uniform. The maximum range of astronomical tides varies between 0.30 m. (Catalonia) and 0.85 m. (Málaga). Wave energy in the whole area is moderate. The significant height of the one year return period storm, is in Málaga about 3.0 metres, and slightly higher in Catalonia. For calculation purposes, the characteristic value of the parameter "wave length", L , has been estimated from data obtained by wave buoys located in these two areas. The average of the zero-crossing significant period, $T_{z,s}$, of all the wave records in which $H_S \geq 1.0$ m. during a complete year, has been calculated:

Catalonia: $H_S \geq 1.0$ m. (percentage of exceedence: 8'9%)
 $T_{z,s} = 8.62$ sec.

Málaga: $H_S \geq 1.0$ m. (percentage of exceedence: 3'8%)
 $T_{z,s} = 7.37$ sec.

6.- RESULTS AND DISCUSSIONS

6.1.- Beach planform

From the analysis of the principle geometrical parameters, it is found that the planform of pocket beaches follows a pattern which is very similar in all the cases examined. In fig. 3, values of A_0 and A_1 have been drawn for each beach. It can be observed how the points obtained generally adjust to the following straight line:

$$A_0 = 2 A_1 \quad (1)$$

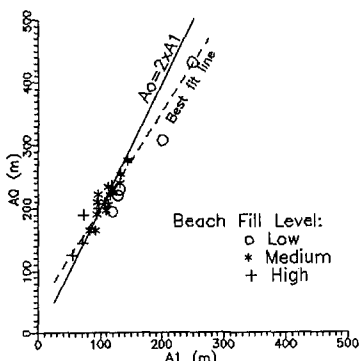


Figure 3.- Relation between A_0 and A_1

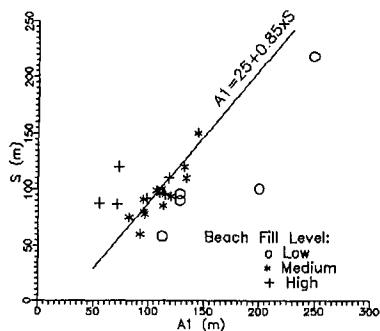


Figure 4.- Relation between A_1 and S

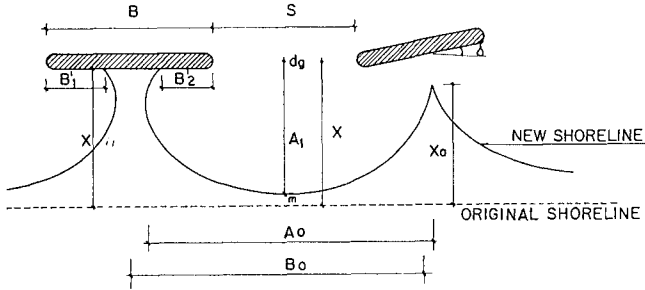


Figure 2.- Definition of pocket beach parameters.

Beach	X(m)	S(m)	A1(m)	A0(m)	Dg(m)	B0(m)	Dm(mm)
BANUS 1	150	90	128	230	3.40	247	0.29
BANUS 2	150	94	120	224	-	250	-
BANUS 3	156	95	115	220	4.10	222	0.84
BANUS 4	144	91	95	210	-	190	-
DON PEPE	108	78	96	222	-	192	-
MARBELLA-1	130	110	134	254	-	260	-
MARBELLA-2	-	99	107	210	2.70	-	0.25
MARBELLA-3	-	75	82	165	2.80	-	0.25
MARBELLA-4	160	150	144	276	-	-	-
MARBELLA-5	-	88	55	125	1.50	-	0.25
MARBELLA-6	-	87	71	145	2.50	-	0.25
MARBELLA-7	-	120	73	190	-	-	-
FUENGIROLA	120	60	92	165	2.10	210	0.31
MIJAS	108	120	132	240	-	-	-
PEDREGALEJO-1	110	80	95	190	3.50	220	1.86
PEDREGALEJO-2	122	92	98	200	3.70	225	1.12
PEDREGALEJO-3	124	110	118	235	3.50	268	1.86
PEDREGALEJO-4	148	58	112	195	3.50	202	1.86
CUNIT 1	120	96	110	196	-	230	-
CUNIT 2	150	96	128	220	2.70	249	0.15
CUNIT 3	210	101	200	308	3.50	313	0.14
CUNIT 4	270	218	248	430	3.55	520	0.13
CALONGE-1	125	85	113	205	5.70	247	1.89
CALONGE-2	128	100	112	234	6.40	255	1.42

Table 1.- Summary of Basic Data.

The points that correspond to beaches with a high or low fill level move away from this general tendency. It should be observed in fig. 3 that the best fit line does not correspond exactly to the relationship mentioned. However, with a view to facilitating engineering design and to take into consideration the beach fill level, this relationship has been taken as the line of approximate adjustment.

In addition, an analysis of the planform has been carried out using a computer program that brings about the optimum adjustment of a logarithmic spiral to a given shoreline, in accordance with Yasso's method. Previous studies that have taken place at the CEPYC (J.M. Berenguer (1981), J. Almenar (1983), J. Enríquez (1984)) showed how, considering the two halves of the cell separately, the planform of these stretches adjusted reasonably well to the logarithmic spirals with a pole at the head of the detached breakwaters, that in each case caused diffraction, and characteristic angles (α) of around 60° - 65° . Taking the pocket beach as a whole, the optimum adjustment is obtained using the logarithmic spiral, whose characteristic angle (α) is situated between 80° and 90° , the pole of the curve being close to the average point of the gap. With a view to design, a theoretical central circumference at the centre point of the gap adjusts very closely to the aforementioned beach line. When there is a low-fill level the beach line will lag behind with respect to the circumference mentioned, and when this level of filling is high, the shore line will stand out with respect to this theoretical curve.

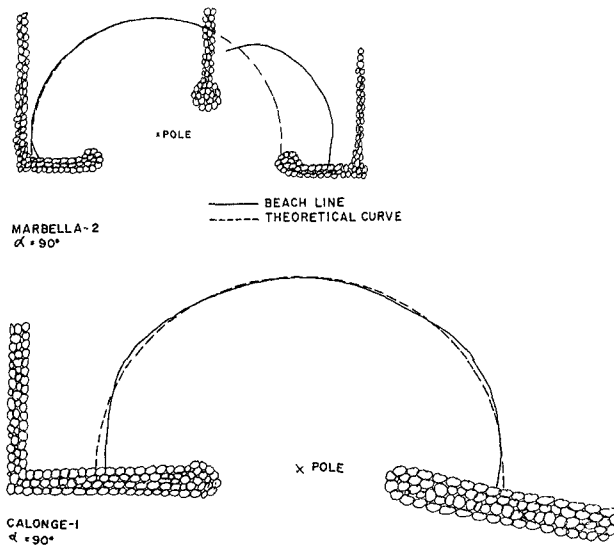


Figure 5.- Examples of adjust of beach planform.

The determining of the radius of the theoretical circumference that defines the shoreline of the cell in each case, can be found by using fig. 4. This figure represents the relationship between the opening of the gap (S) and the distance from the shore (A₁). A good adjustment of these points is obtained with line of equation.

$$A_1 = 25 + 0.85xS \quad (2)$$

The points corresponding to cells with a high or low level of filling deviate considerably from this straight line.

Another interesting result obtained in the analysis is the one shown in fig. 6. The product (XB₀) represents the surface area of water in the lee of the new works, while A₁² is proportional to the surface of water that will remain after the filling of the cell with sand, given that this surface area is assumed to be a semicircle with an area (π A₁²/2). The relationship obtained is that expressed by the equation

$$XB_0 = 2.5A_1^2 \quad (3)$$

Using this relationship as a basis, the maximum surface area (S_p) of beach that could be stable can be obtained

$$S_p = XB_0 - (\pi A_1^2 / 2) \quad (4)$$

Thus: $S_p = 0.37 X.B_0 \quad (5)$

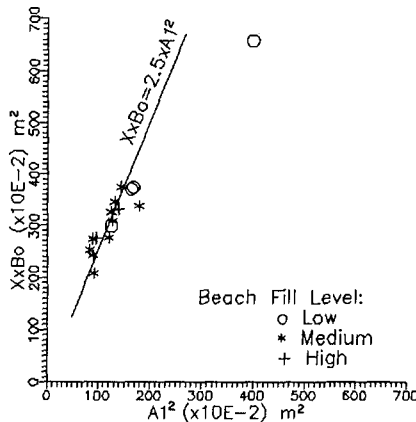


Figure 6.- Relation between A₁² and XxB₀

6.2.- Beach profiles.

The general bottom configuration of a pocket beach presents a characteristic that makes it different from the typical pattern of an open beach. The groynes or breakwaters that make up the pocket beach, act as wave filters to a greater or lesser extent. At any point on the beach, the range of variation of the wave height is considerably reduced and as a consequence, so is its wave steepness. The direction of the wave as it propagates towards the shallower zones of the beach becomes more independent with respect to the deep-water direction, when the breakwater gap is narrower. Restrictions of both energy and direction, cause marked differences to the profiles of the submerged beach as regards its position along the shoreline, but with great annual stability.

In most of the theoretical studies carried out up to the present on pocket beaches, the simplification of assuming a symmetry of actions and responses along a central axis, has been adopted.

This hypothesis is only borne out in two cases:

- a) When the directional distribution of the wave energy is more or less constant in time and has an incidence near to the normal direction of the gap.
- b) When the relationship between the width of the gap (S) and length of wave (L) is small enough, in such a way that the action of the filter caused by the breakwaters through diffraction is considerable.

In all other cases, the assymetry shows itself clearly in the form of the profiles of the different zones of the beach, and also, but in a less clear way, in the planform of the shoreline.

The homologous profiles have been compared by grouping homogeneous beaches together according to their climatic and sedimentary characteristics. The most significant conclusions obtained in this analysis are summarized in the following line (see fig. 7).

- Within one single beach the diverse profiles take on characteristic forms in accordance with their position.
- In the areas exposed to greater wave energy, (profile num. 3, central), the profiles take on a parabolic shape similar to that of an open beach without bar.
- The end profiles (num. 1 and num. 5) of the cells present two clearly differentiated zones. The upper part of the profile where the residual energy of the wave after diffraction, is capable of moving the sediment by drag and suspension, and the lower part with a gentle slope, where the wave acts dragging

the material along the bottom. A marked step is produced as a transition of the two, and its slope depends on the angle of internal friction of the sediment and its height from the depth of the gap. The lower limit of the highest zone is a function of the height of the residual wave of the most severe storms that reach the cell every year.

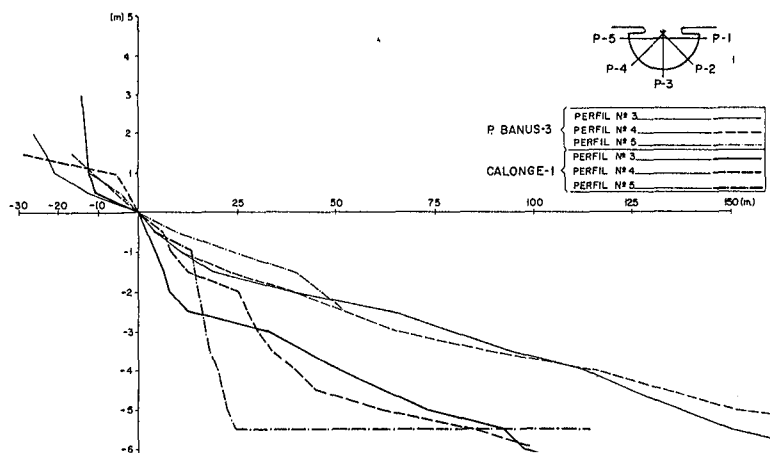


Figure 7. Beach profiles from two selected pocket beaches

Within one cell the transition between the central profile and the ends (profiles num. 2 and num. 4) takes place gradually and in accordance with the spatial variation of the resulting energy from the process of double diffraction. The progressive reduction of wave height as the sheltering increases, implies a change in the steepness of the wave, and with this a different response on the beach profile.

6.3.- Sediment-size distribution

This analysis has been carried out on 12 beaches from which over 25 samples were taken from each.

With a view to design, it is considered essential to carry out a survey of two relationships: the distribution of the average grain-size according to depth and the relationship between the average grain-size and the slope of the bottom.

In fig. 8 the relationship between the relative diameter (D_i/D_m) and the relative depth (d_i/d_g) of the samples corresponding to profiles num. 2, 3 and 4 of three beaches is represented. D_i is the mean size of each sample, D_m is the average of the mean size of all the samples in the cell, d_i is the depth where the sample is collected and d_g is the depth at the centre of the gap.

As can be observed, in beaches with fine and medium sand, (Cunit-4 and Banús-1) the dispersion of the relative diameter becomes progressively smaller with the relative depth. In beaches with coarse sand, (Calonge-2) a considerable discontinuity is caused, together with a greater dispersion in the samples situated near the shore.

As regards the relationship between the slope of the bottom at a point (m) and the size of the sediment (D_5) at this very point, fig. 9 shows a general increase of (D_{50}) as (m) increases. All the samples taken on the 12 beaches have been included in this figure. The high dispersion in the results does not make it possible to draw exact conclusions from this analysis. It is possible that the reduced wave energy that reaches the inside of the cells contributes to the irregular size distribution observed in the sediment that makes up this kind of beach.

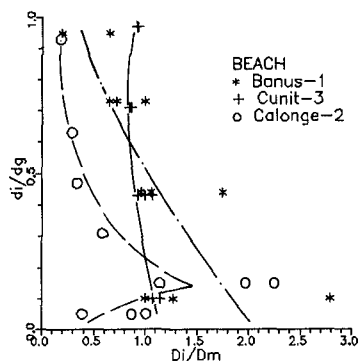


Figure 8.— Relation between D_i/D_m and d_i/d_g

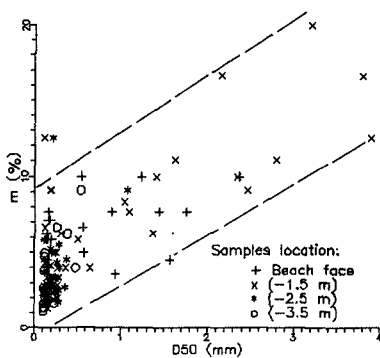


Figure 9.— Relation between D_{50} and m

6.4.— Other factors

In addition to the relationship between the various pocket beach parameters previously studied, others have been sought that help to define relationships between them that are useful in designing. In particular, an attempt has been made to relate the surface of the gap (Sd_g) and the dimensions of the resulting beach ($A_1^2 D_m$). As a consequence of the relationship that exists between the mean size of the sediment (D_m) and the general slope of the submerged beach, this parameter can be adopted as a measure of the volume of water contained in the cell.

The results are presented in fig. 10, in which it can be seen just as expected that the greater the gap surface, the larger the cell. For values of (Sd_g) situated at the interval $1.5 \cdot 10^2 < Sd_g < 5 \cdot 10^2$ the fitting to a straight line such as that shown is reasonably good, this being a very useful tool for the evaluation of the balance between the different parameters, both geometrical and granulometrical, that define a pocket beach. Below a value of $1.5 \cdot 10^2$, it is logical that the adjustment line undergoes inflection and shows a tendency towards the origin of coordinates as the size of the cell becomes smaller. For the adjustment of the upper zone of the graph it will be necessary to rely on additional data in the future, that will make it possible to increase it for values of (Sd_g) above $5 \cdot 10^2$.

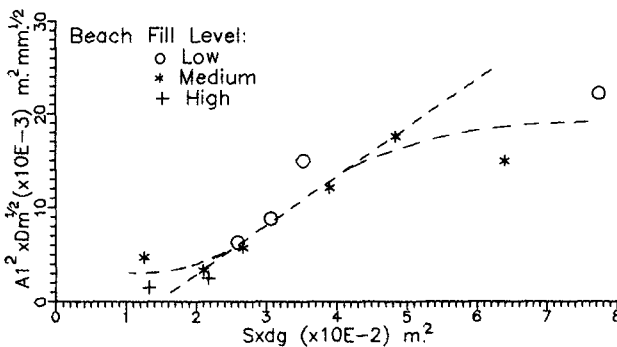


Figure 10.- Relation between $Sxdg$ and $A1^2 Dm^{1/2}$

7.- CONCLUSIONS

A rigorous analysis of a high percentage of pocket beaches on the Spanish Mediterranean Coast has been carried out. A total of 24 of these beaches have been studied from geometry, bathymetry, and granulometric characteristics of sediment perspectives.

The limited amount of wave energy that reaches the inside of the cell, causes specific areas of the beach to show profiles that are hardly shaped by the waves, with slopes close to the natural slope of the sediment. This phenomenon is clearly visible at the end profiles of virtually all the cells that have been studied, where swift changes in the profile occur as a result of the lack of there being sufficient energy to form normal beach profiles.

Another consequence of the low and irregular exposure to the wave energy that occurs on these beaches is the great irregularity observed in the granulometric distribution of the sediments that it is made up of.

It has been demonstrated that the planform of the shoreline can be predicted with sufficient accuracy, by means of different kinds of theoretical curves. In beaches where the variables S , A_1 and L are within the range of those analyzed ($1 \leq S/L \leq 5$ and $1.5 \leq A_1/L \leq 5$, being L the wave length at the gap) it has been possible to get a good adjustment using arcs of circumference whose centre is in the middle of the gap of the cell. The radius of the theoretical circumference that defines the shoreline can be estimated by the equation that relates the parameter (S) (to be defined in the design) with (A_1).

Knowing the characteristics of the sand that is going to form the new beach, fig. 10 provides a quick method of assuring that the diverse design parameters established adjust to a balanced relationship between them.

It should be observed that given the similarity of characteristics (wave climate, dimensions, sand size, etc), of most of the beaches analyzed in this survey, the range of validity of application of the partial conclusions is, to a certain extent, limited. Its application to other markedly different types must take place with caution and by engineering experience.

REFERENCES

- Berenguer, J.M., (1986) "Características de los diques exentos en España", Curso de Ingeniería de Costas, CEPYC.
- Dean, R.G., (1978) "Diffraction Calculation of Shoreline Planforms", Proc 15th Conf.Coastal Eng. 2, 1903-1917.
- Font, J.B., P. Sanabria and A.Silva, (1974) "Geometria des Playas Protegidas en Equilibrio", Proc., VI Congreso Latino Americano de Hidráulica, p. C3-1 to C3-12, July.
- Garau Sacrista, C (1973), "El rozamiento y la estabilidad de las playas", Revista de Obras Públicas Num. 3099 y 3100, Julio, Agosto.
- Gourlay, M.R. (1974), "Wave Set-up and Wave Generated Currents in the Lee of a Breakwater or Headland". Proc. 14th Conf. on Coastal Eng.
- Gourlay, M.R. (1976), "Non Uniform Alongshore Currents" 15th Conference on Coastal Engineering. ch. 40, pp. 701-720.
- Noble, R.M. (1978), "Coastal Structures' Effects on Shorelines" Proc. 16 Conf. on Coastal Eng. Vol. III, ch. 125, pp. 2069-2085.

- O'Rourke, J.G. and P.H. LeBlond, (1972) "Longshore Currents in a Semi-Circular Bay", J.Geophy. Res. Vol. 77, p. 444-452.
- Perlin, M., (1979), "Predicting Beach Planforms in the Lee of Breakwater" Symp. on Coastal Structures 79, ASCE, vol. 2, pp. 792-808.
- Rea, C.C. and Kohar, P.D., (1975) "Computer Simulation Models of a Hooked Beach Shoreline Configuration" Jour. Sed. Petrology vol. 45, no 4, p. 866-872.
- Rosen D.S. and Vajda. M., (1982) "Sedimentological Influences of Detached Breakwaters". Proc. Conference on Coastal Engineering. ASCE.
- Sauvage de St. Marc M.G., and Vincent, M.G., (1954), "Transport littoral, formation de fleches et de tombolo", Proc. of 5th Conf. on Coastal Eng.
- Sawaragi, T., (1957), "Effects of Shore Structures on Coastal Sand Drift (Report No. 1), "4th Conf. on Coastal Engineering in Japan.
- Shinohara, K. and Tsubaki, T., (1966), "Model Study on the Change of Shoreline of Sandy Beach by the Offshore Breakwater", Proc. 10th Conf. on Coastal Engineering, pp. 550-563.
- Silvester, R., (1970), "Growth of Crenulate-Shaped Bays to Equilibrium", Journal of the Waterway and Harbours Division, May 1970, WW2, pp. 275-287.
- Silvester, R. and HO, S.K., (1972), "Use of Crenulate Shaped Bays to Stabilize Coasts", Proc. 13th Conf. on Coastal Eng., Vol w, pp. 1347-1366.
- Toyoshima. O. (1974), "Design of a Detached Breakwater System". Proc. Conference on Coastal Engineering. ASCE.
- Toyoshima. O. (1976), "Changes of Sea Bed Due to Detached Breakwaters". Proc. Conference on Coastal Engineering. ASCE.
- Toyoshima. O., (1982), "Variation of Foreshore Due to Detached Breakwaters". Proc. Conference on Coastal Engineering. ASCE.
- Walton, T.L. (1977), "Equilibrium Shores and Coastal Design", Proc., ASCE Speciality Conference on Coastal Structures, p. 1-16, Nov.
- Yasso, W.E. (1965), "Plan Geometry of headland bay beaches" Jour. Geology: v. 73, p. 702-714

CHAPTER 106

DUNE EROSION AND SEDIMENT PROFILE DUE TO WAVE UPRUSH

T. A. Fenaish*
M. F. Overton, Assoc. M. ASCE**
J. S. Fiaher, M. ASCE***

Introduction

Shorelines are continually adjusting in response to the changing hydraulic and meteorological conditions. Storms that generate large waves and surge conditions can alter the nearshore topography and relocate the beach shoreline, often with substantial amounts of beach and dune erosion. Such storms pose a major threat to coastal developments for which the economic impact can be significant. The ability to predict the rate of erosion and, consequently the shoreline change, is important in making decisions regarding the planning and managing of the coastal regions.

In general, the available methods for the prediction of beach and dune erosion are based on the assumption of post-storm equilibrium profile. In this approach it is assumed that, for a given set of wave and surge conditions, the entire beach reaches a steady-state, and that the volume of sand released from the dune is equal to the volume of sand required to establish this profile. Existing methods that are based on this concept include those developed by Edelman (1968, 1972), Vellinga (1982, 1983, 1986), Kriebel and Dean (1984), Sargent and Birkemeier (1985), and Kobayashi (1987). The reliance of these methods on the assumption of steady-state condition limits their application to extreme events generated by severe storms. Generally, storms do not have sufficient duration or intensity, such that the beach profile attains equilibrium during the storm.

A numerical model has been developed to predict beach adjustment due to dune erosion during a single storm event. In this model, the estimation of the shoreline change is based on the mechanics of sediment-

* Research Assistant, Dept. of Civil Engineering, North Carolina State University, Raleigh, NC.

** Associate Professor, Dept. of Civil Engineering, NCSU

*** Professor, Dept. of Civil Engineering, NCSU.

swash interaction at the dune face, Overton, et al. (1988). This approach estimates the magnitude of dune erosion and beach adjustment associated with each swash, with no dependency on an equilibrium beach profile. Therefore, for a given storm condition, the total change in the beach profile is determined by a series of swash attacks. This technique has the advantage of considering small events in which post-storm equilibrium conditions can not be reached, as well as extreme events. In the numerical scheme presented herein, attention is restricted to the prediction of dune erosion and subsequent beach adjustment due to a single swash.

Methodology

The dune erosion and sediment profile model consists of three distinct components - the hydrodynamics of a bore impacting a vertical barrier, the volume of sand eroded from the dune due to that impact, and the redistribution of that volume of sand on the beach face during the subsidence of the bore. The first two components have been discussed elsewhere in the literature and will be discussed herein only briefly. Attention is focused on the development of the third component of the model - the adjustment of the beach face due to the erosion event.

The wave uprush is idealized as a bore propagating over a sloping beach. Input data include the depth of the bore at the seaward edge, the slope of the beach, the location of the dune relative to the mean water level, and the sediment characteristics. The bore motion on the beach is described using a two-dimensional hydrodynamic model. This model solves the momentum and continuity equations using a finite-difference technique. The finite-difference mesh is placed at right angles to the beach face in order to simplify computations. The model determines the bore height and velocity as it travels up the sloping beach, impacts with, and retreats from the onshore barrier (dune). The solution algorithm of the velocity and pressure fields are based on a modified SOLA-SURF code, Hirt et al. (1975). Modifications include those which incorporate the sloping beach and the moving boundary of the borefront. The hydrodynamics of the bore model are verified using a simplified analytical solution for the horizontal bed case, as well as a series of laboratory experiments for the sloping bed case.

The volume of sand released from the dune by the impacting bore is computed in terms of a force parameter which in turn is a function of the flow characteristics at the dune face. This functional relationship is derived from laboratory tests designed to isolate a single bore and determine its erosive power, Overton, et al. (1988). This relationship has been modified for use in the hydrodynamic model, Overton, et al. (1987).

The amount of sand extracted from the dune is redistributed in front of the dune by the retreating bore. The resulting sediment profile is computed as a function of the backwash flow parameters and the sediment characteristics. The third component of the model which predicts the deposition pattern in the dune vicinity is based upon both theoretical considerations as well as laboratory results. Because of the nature of the flow pattern at the wall and the importance of turbulence in the mechanics of sediment transport, laboratory experiments were conducted for the development, calibration and independent verification of the model.

Experimental Study

Wave Flume:

The experiments were performed in the Civil Engineering wave flume at North Carolina State University. The glass walled flume, is 15.0 m long, 0.6 m wide, and 0.9 m deep. Young (1986), in his investigation of dune erosion due to wave uprush, modified the flume to isolate a single bore. The flume was divided by a sheet of plywood into two portions. The lower portion was used as a reservoir, and the upper portion as the main channel with plywood surface bottom as shown in Figure 1. A head tank, equipped with back and front rotating gates, was installed inside the flume. The head tank was 1.8 m long, 0.6 m wide, and 0.6 m deep. The front gate was equipped with a cantilever weight and springs allowing a sudden release of the gate and, consequently, the water in the head tank. The water released from the head tank formed a

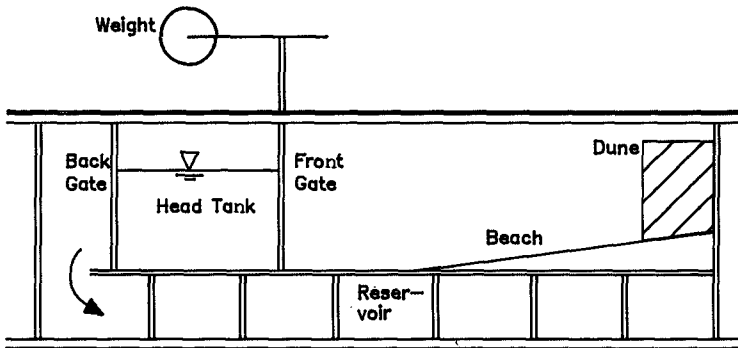


Figure 1. Schematic Diagram of Experimental Setup.

bore propagating on the sloping beach. As the bore impacted with the upstream boundary and retreated, the

back gate was opened, using a release spring, allowing the backwash to flow back to the reservoir and thus preventing reflection. A plywood beach, 2.4 m long, was installed at an angle of three degrees to the horizontal bottom of the channel and 1.2 m in front of the head tank. A vertical barrier of plywood was erected at the end of the sloping beach to serve as the dune boundary.

Dune Model:

The sand dune model was constructed in a box inside the flume. The box extended the full width of the flume and had a fixed back board and removable front. The sand used to build the dune had a mean grain size, d_{50} , of 0.68 mm and a grain size distribution as shown in Figure 2. The oven dried sand was then rained into the

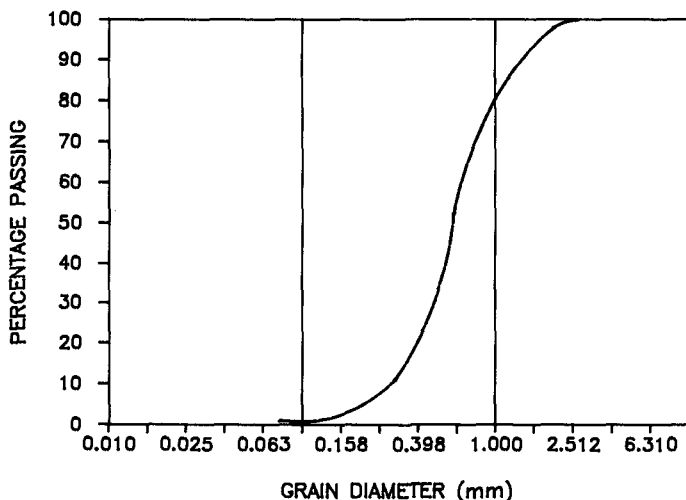


Figure 2. Grain Size Distribution Curve.

box from a constant head of 0.3 m so that a uniform degree of compaction was attained. The sand was rained in using a shallow plastic tray containing two rows of 8 mm diameter holes, three holes in each row. After the sand set in place, 7.5 l of water were poured at the top of the dune at a slow, constant rate. The dune was then allowed to drain for 30 min through holes provided in the front board. The amount of water and the drainage time were determined such that a sufficient strength was developed in the dune to maintain a vertical face when the front was removed. After removing the front of the box the first 6 cm of the dune front were scraped away to eliminate any cracks or instabilities caused by the sand leaning on the front board.

A video cassette recording system equipped with time display and single frame advancement was used to record the impact of the bore with the upstream boundary in all tests. A transparent plastic sheet containing a scale, used to depict the initial dune and beach profiles before each run, was mounted on the glass side of the flume, covering the dune area and extending in front of the dune about 100 cm. In addition, a 35 mm camera was utilized to record the dune and beach profiles immediately before and after each test.

Experimental Procedure:

The dune was constructed at the upstream boundary of the flume and the entire sloping beach was covered with a uniform layer of sand. The sand layer was 4.0 cm thick and had the same characteristics as that of the dune. Two sets of tests, at initial head tank elevations of 23 cm, and 26 cm, were conducted. Each set of tests had three repeats at the same head tank water level. In addition to the video tape, still photos of the initial dune and beach profile before each test, and the eroded dune profile and deposition pattern after the completion of each test were also taken. One photo was taken normal to the front of the dune to record the uniformity of the eroded profile across the width of the dune.

The volume of sand eroded from the dune, and the deposition pattern in the dune vicinity were computed from still photos. The negatives of the still photos were mounted on slides and then projected on a screen so that the eroded dune profile and deposition pattern could be traced on a sheet of paper. The eroded area of the dune and the sedimentation curve were then determined utilizing a Summagraphics Model 1201 digitizer board and Sigmascan computer software.

Sediment Profile in the Dune Vicinity

Generally, the eroded volume of dune sediment deposited on the beach is a function of the retreating bore flow variables and sediment characteristics. In order to determine the backwash flow variables that best represent the sediment profile, it is important to analyze: (1) the laboratory results of the deposition pattern and (2) the flow behavior as described by the verified numerical scheme. Based on visual observations of several flume tests, the volume of sand eroded is agitated and kept in suspension by the highly turbulent flow. As the bore begins to retreat, the flow becomes more stable and most of the sediment load is observed to quickly settle with the exception of the smaller size particles. In other words, the deposition pattern is mostly controlled by the flow parameters of the less turbulent backwash and not the flow field at the time of impact. Laboratory results also show that the sediment profile extended approximately 25 cm in front of the dune. A significant volume of the sediment load,

consisting mainly of large to medium size particulae, is deposited in the first 10 to 15 cm.

The numerical hydrodynamic results reflect qualitatively what was seen in the laboratory. During the period of impact of the bore with the dune, the flow field (velocity and depth) is highly unstable, Figurea 3 and 4. The depth increasea rapidly while the velocity

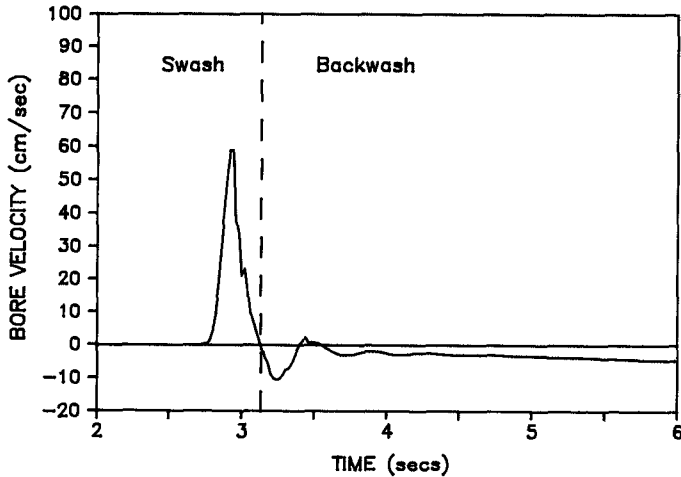


Figure 3. Bore Velocity Averaged over Depth at 6 cm from the Dune Face, Initial Depth of 26 cm.

goea to zero. As the backwash process begins, the depth begins to decrease and the velocity reversea direction. Both velocity and depth then stabilize changing almost linearly with time. The flow field in the 25 cm in front of the dune varies predictably with distance from the dune. The maximum depths and velocities are reduced and there is a shift in time for the maximum but the general shape of the curves ia the aame aa that in Figures 3 and 4.

Baaed on the above analysi, the sediment profile in front of the dune ia computed in terms of the backwaah flow height and velocity in the 25 cm adjacent to the dune face and the aediment properties. The flow height is defined aa the average height in this regime. The water height is obtained by computing the water height in each time increment and then averaging over the time period that the bore is in contact with the dune and propagating down slope. The flow velocity ia defined as the depth averaged velocity in the aame 25 cm in front of the dune and over the aame period of time.

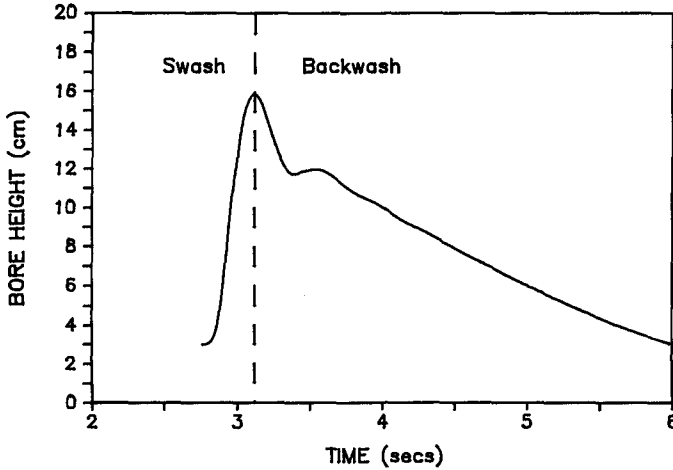


Figure 4. Bore Height at 3 cm from the Dune Face, Initial Depth of 26 cm.

The sediment characteristics utilized in this algorithm are the specific weight, the grain size distribution, and the fall velocity. The sand used in this model has a specific weight of 2.65, and grain size distribution as shown in Figure 2. The fall velocity of the sand particles is computed using the following equation, Henderson (1966)

$$W_s = C [(SS - 1)gd_s]^{1/2} \quad (1)$$

and,

$$C = \left[\frac{2}{3} + \frac{36 n^2}{gd_s^3 (SS-1)} \right]^{1/2} - \left[\frac{36 n^2}{gd_s^3 (SS-1)} \right]^{1/2} \quad (2)$$

where n is the kinematic viscosity of the fluid, d_s is the grain size diameter, and SS is the specific gravity of the sediment.

Having determined the retreating flow height and velocity, and sediment properties, the sedimentation profile in the dune vicinity is computed as outlined below.

(1) The grain size distribution curve is subdivided into representative intervals. The sediment volume ratio (V_k) and the average grain size diameter (d_g) for each interval are determined.

(2) The fall velocity (W_s) of each grain size is computed using Eq. 1. The settling time (t_s) of each particle is then calculated as the ratio of the average backwash height, and its fall velocity (W_s). The maximum distance (X_s) travelled by each grain size is computed in terms of its settling time (t_s) and the average backwash velocity.

(3) In order to determine the depth of deposition (Y_s) for a given grain size (d_s), it is assumed that its corresponding volume of sand (V_s) is uniformly distributed over the area of deposition. The depth of deposition is then computed as the ratio of the volume of sand eroded over the deposition area. The area over which a given grain size may be distributed is estimated based on the study of the mechanism of sediment transport and laboratory visual observations. In general, the smaller the particle size, the longer a particle will stay in suspension. Therefore for a given sand sample which has a wide range of particle sizes, the small sand particles at the lower end of the curve have a relatively longer settling time than those at its upper end. Thus, based on the settling time of each grain size, most of the small grains do not settle in the immediate vicinity of the dune as do those of large grain sizes. In order to determine the deposition area of the small particles, the point where they begin to settle should be estimated first. This is done by arbitrarily dividing the grain size distribution curve into three zones: lower, middle, and upper. The lower and upper grain zones consist of the relatively small and large grain sizes, $d_s < 0.5$ and $d_s > 1.0$, respectively, while the middle zone consists of the rest of the sand particles, $0.5 < d_s < 1.0$. In order to prevent the smaller size particles ($d_s < 0.5$) from settling too soon, it is required that the deposition area for the lower zone material begins at a distance in front of the dune equal to the travel distance of the smallest particle in the upper zone. The deposition depth (Y_s) is computed as the ratio (V_s/X_d).

(4) Finally the individual deposition patterns of each distribution interval are superimposed to yield the total sedimentation profile due to a single wave wash in front of the dune.

Results

Applying the above methodology as the third component of the erosion and sediment profile model, the redistribution of sediment in front of the dune after the retreat of a single swash event can be computed numerically. Two tests at different head tank levels were conducted in the laboratory. The first of these, with a head tank level of 26 cm, was used to qualitatively study the process and to aid in the development of the model. The numerical versus the experimental results are shown in Figure 5. Note that

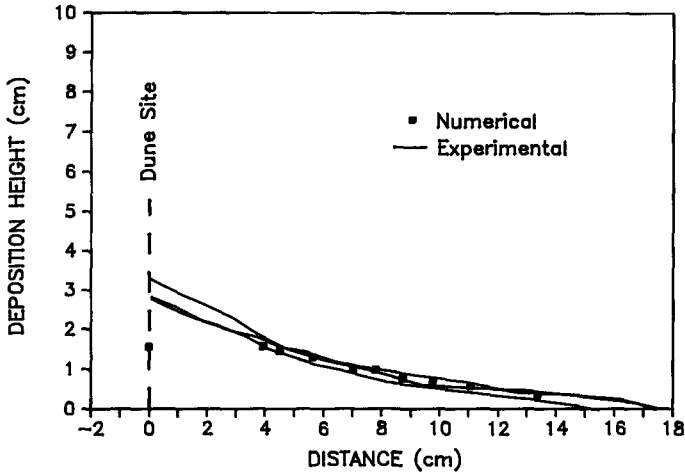


Figure 5. Comparison of Numerical and Three Replicate Experimental Sediment Profiles, Head Tank Level, 26 cm.

the high degree of correlation between the numerical and the experimental results is because the data were used to calibrate the model. In order to further test the ability of the model to reproduce deposition patterns, an independent set of data at 23 cm initial head tank elevation was used. The numerical model was run with head tank elevation set at 23 cm with no additional adjustments to the model. Figure 6 shows comparison of numerical and experimental beach profiles obtained. The model closely predicts the experimental results though with a slight over estimation of the depth of deposition along the beach face. Based on the limited number of cases investigated to date, it is shown that this approach is a viable alternative to use in the prediction of beach and dune erosion due to a storm event.

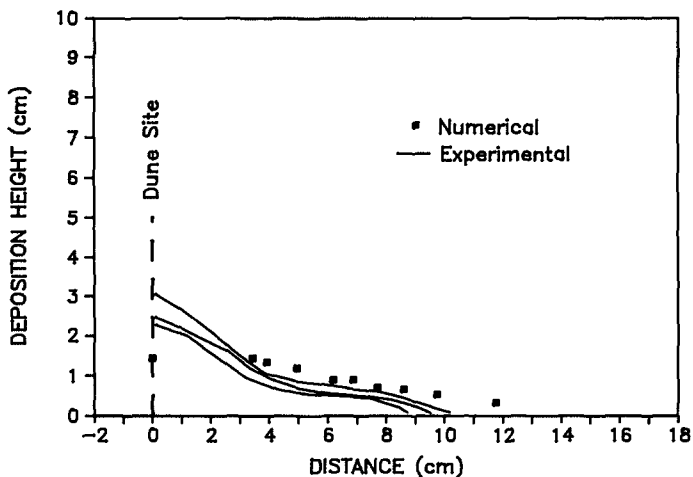


Figure 6. Comparison of Numerical and Three Replicate Experimental Sediment Profiles, Head Tank Level, 23 cm.

References

- Edelman, T., "Dune Erosion and Storm Conditions," Proceedings of the 11th Conference on Coastal Engineering, London, England, Vol. 1, Sept. 1968, pp. 719-722.
- Edelman, T., "Dune Erosion During Storm conditions," Proceedings of the 13th Conference on Coastal Engineering, Vancouver, Vol. 2, July 1972, pp. 1305-1311.
- Henderson, F.M., "Open Channel Flow," McMillan Co., New York, New York, 1966.
- Hirt, C.W., Nichols, B.D., and Romero, N.C., "SOLA - A Numerical Solution Algorithm for Transient Fluid Flows," Los Alamos Scientific Laboratory Report LA-5852, 1975.
- Kobayashi, N., "An Analytical Solution for Dune Erosion by Storms," Journal of Waterway, Port, Coastal, and Ocean Engineering, ASCE, Vol. 113, No. 4, July 1987.

- Kriebel, D.L., and Dean, R.G., "Beach and Dune Response to Severe Storms," Proceedings of the 19th Conference on Coastal Engineering, Houston, Texas, Vol. 2, Sept. 1984, pp. 1584-1599.
- Overton, M.F., Fisher, J.S., and Fenaish, T. "Numerical Analysis of Swash Forces on Dunes," Proceedings Coastal Sediments'87, ASCE, 1987, pp. 632-641.
- Overton, M.F., Fisher, J.S., and Young, M.A., "Laboratory Investigation of Dune Erosion," ASCE J. Waterway, Port, Coastal, and Ocean Engineering, May, 1988, pp. 367-373.
- Sargent, F.E., and Birkemeier W.A., "Application of the Dutch Method for Estimating Storm-Induced Erosion," Final Report, Storm Erosion Studies Work Unit 31467, U S Army Engineering Waterways Experiment Station, 1985.
- Vellinga, P., "Beach and Dune Erosion During Storm Surges," Ph.D. Thesis, Delft Technical University, 1986.
- Vellinga, P., "Predictive Computational Model for Beach and Dune Erosion During Storm Surges," Coastal Structures, 1983, pp. 806-819.
- Vellinga, P., "Beach and Dune Erosion During Storm Surges," Coastal Engineering, Vol. 6, No. 4, 1982.
- Young, M.A., "Modeling of Storm-Induced Dune Erosion Due to Wave Uprush" M.S. Thesis, Department of Civil Engineering, North Carolina State University, 1986.

CHAPTER 107

Barcelona's littoral regeneration looking forward to the Olimpic Games. Numerical model

Vicente Negro Valdecantos *

Manuel Quecedo Gutierrez **

* Civil Engineer. Research Assistant. University of Madrid. Spain.

** Civil Engineer. M. Sc.

1.- ABSTRACT

The modern technique of Coastal Engineering has enabled the succesful modification of the environment, the recuperation and the stabilization of those sandy areas which due to human action, were in a process of regression and erosion. This work developes a mathematical and numerical model to adjust and analyze the variations between the dissipative profiles and the reflectives ones. The research also emphasizes the enveloping profile to calculate the stable behaviour of the beach.

2.- INTRODUCTION

After several series of observations to get data about bathymetry topography, location of sand, the littoral process, sea, swell, tides, the longitudinal and onshore-offshore current, the authors analyzed the conditions of the progressive erosion of our shoreline during the last decades. Considering these series of initial conditioners, the design criteria were developed in a mathematical and numerical model divided in the following chapters:

- a) Variations between the dissipative and reflective profiles.
- b) Incipient motion on a granular bed in water waves.
- c) The depth at breaking and the signigicant wave height.
- d) Beach profiles.
- e) Numerical model to adjust. Enveloping profile in

$$x/x_{\text{máx}} \quad d/d_{\text{max}}$$

3.- VARIATIONS BETWEEN THE DISSIPATIVE AND REFLECTIVE PROFILES

Equilibrium profiles have been studied extensively through the history of coastal engineering. For many years it has been held that the steepness H_0/L_0 , the ratio of the deep water waves of the wave height and wave length divided the bar and berm profiles; the dimensionless fall velocity H_0/T_w , the erosion parameter Q/H_{0d} , the grain size D_{50} , the depth d , and the relations between the steepness and the fall velocity separate the dissipative and the reflective profile.

The numerical model calculates the beach profile shape depending of wave climate and the variations with H_0 , L_0 , γ_s , γ_w , D_{50} data.

In Table 1, the authors include the initial variables and the design criteria.

5.- THE DEPTH AT BREAKING AND THE SIGNIFICANT WAVE HEIGHT

A large number of factors influence the shape of beach profiles in nature. The series of observations to get data about bathymetry are considered the design criteria to establish the refraction, diffraction and the breakpoint.

The depth at breaking and the relationship with the significant wave height, type of breaker, broken wave and the accreting, transition and eroding beaches correspond with the occurrence of surging, plunging and spilling breakers respectively.

The authors analyze the different criteria and adjust several ones to compute the break point and the type of breaker.

In table 2, they include the variables and the design criteria. Numerical model uses the following formulae:

- Munk
- Weggel
- Gumbak
- Goda

TABLE 2. MODEL OF WAVE BREAKING

-	Boussinesq	(1881)	$H/d = 0,73$
-	McGowan	(1881)	$H/d = 0,781$
-	Michell	(1893)	$H/L = 0,127$
-	Gwyther	(1900)	$H/d = 0,83$
-	Miche	(1944)	$H/d = 2 H/L/\text{arcth}(7,04 H/L)$
-	Davies	(1951)	$H/d = 0,83$
-	Packham	(1952)	$H/d = 1,03$
-	Yamada	(1957)	$H/d = 0,828$
-	Laitone	(1962)	$H/d = 0,7273$
-	Lenau	(1966)	$H/d = 0,827$
-	Horikawa-Kuo	(1966)	Grafico
-	Kishi-Saeki	(1966)	$H/d = 5,618 m^{0,40}$
-	Camfield-Street	(1967)	$H/d = 0,75 + 25 m - 111 m^2 + 3.870 m^3$ $0 \leq m \leq 0,045$
-	Galvin	(1969)	$\frac{H}{d} = \frac{1}{B - \tau iK}$ $B = 1,40 - 6,85$ $\tau = 4 - 9,25 i$ $0 \leq K \leq 2 ; K \approx 1$
-	Collins	(1969)	$H/d = 0,72 + 5,60 m$
-	Bryar-Smith	(1970)	$H/d = 0,86$
-	Grimshaw	(1971)	$H/d = 1,21$
-	Strel Koff	(1971)	$H/d = 0,85$

Weggel	(1972)	$\frac{H}{d} = \frac{b}{1 + a/\sqrt{gT^3}}$ $b = \frac{1,56}{1 + e^{-19,5i}}$ $a = 43,70 (1 - e^{-19i})$
Goda	(1975)	$K_s H_0; D/L_0 \geq 0,20$ $H_{1/3}$ $m \ln (B_0 H_0 + B, d), B_{\max} H_0, K_s H_0$
Gumbak	(1977)	$\frac{H}{d} = 0,80; \quad Ir < 0,20$ $\frac{H}{d} = 0,87 \quad Ir > 0,63; \quad 0,20 \leq Ir \leq 0,66$ $\frac{H}{d} = 1,20; \quad 0,66 \leq Ir \leq 2,20$
Ostendorf-Madsen	(1979)	$H/d = 0,829$
Ostendorf-Madsen	(1979)	$H/d = (0,80 + 5m)^2 \quad H/L / \operatorname{argth} (7,14 H/L)$ $m < 0,10$ $H/d = 0,13^2 \quad H/L / \operatorname{argth} (7,14 H/L)$ $m > 0,10$

6.- BEACH PROFILES

To find a connection between the depth, the wave height and length, the grain diameter, the dimensionless fall velocity and to evaluate the response of the beach, the bar or berm profiles the researches have been studied the problem through the history of the Coastal Engineering. The lineal relation, the adjustment of storm profiles by cubic parabolas, the location of the inflection point and the shoreline process of regression are the problems to analyze and resolve.

In table 3, the authors include the state of art and they develop a mathematical and numerical model to determine the variations between bar and berm profiles. Considering the initial data:

- Beach shape
- Motion initiation by oscillatory flow
- Break point
- Beach profile

The numerical model evaluate in 600 points in x and depth the value of each profile, the risk of failure depending of the grain size and wave climate, and the enveloping profile of the stable beach.

The mathematical curve adjusts the stable beach, the validity of each one (Bruun, Larras, ...) and with the initial data the defensive barrier that we need is created an artificial beach. We shall emphasize the enveloping profiles in dimensionless parameters:

$$x/x_{\text{máx}}$$

$$d/d_{\text{máx}}$$

TABLE 3. BEACH PROFILES

- Bruun (1954, 1956, 1978, 1986) $x = L_0 \sqrt{2\pi y} \left(2 \left(\frac{2\pi y}{L_0} \right) + \frac{1}{3} \left(\frac{2\pi y}{L_0} \right)^2 + \dots \right)$
 - $y < L_0/8 \quad y^{3/2} = px$
 - $y^{5/4} = px$
 - $y^{3/2} = px$

- Keulegan y Krumbein (1949) $y = px^{4/7}$

- Inmann y Bagnold (1963) $y = px$

- Larras $\frac{y}{L_0} = k \left(\frac{x}{L_0} \right)^m$
 - $k = f(H_0, L_0, D, \xi, \xi_0)$
 - $m = g(H_0, L_0, \xi, \xi_0)$

- Sitarz (1969) $x = ay^2 + x_0$
 - $a = f(D, H_0, \xi, \xi_0)$
 - $x_0 = g(A_1, H_0, D, \xi, \xi_0)$

A_1	43,50 Berm
	66 Bar
	75 Nature

- Dean (1973)

$$y = A_D x^{2/3}$$

$$A_D = \frac{24}{5} \frac{f(D)}{f g \sqrt{g} \gamma_b^2}^{2/3}$$

f(D) = Energy wave regime

 $\gamma_b = H/d$ breaker point

- Vellinga (1982,19854)

$$y \frac{7,60}{H_{0s}} = 0,47 (7,6/H_{0s})^{1,28} x$$

$$x (W_f/0,0268)^{0,56} x + 18 \frac{1}{2} - 2,00$$

$$y = 0,70 \left(\frac{H_0}{L_0}\right)^{0,17} w_f^{0,44} x^{0,78}$$

 $H_0 = 7,6$ m

T = 12 sg

 $D_{50} = 0,225$ mm

- Sunamura (1980, 1984)

$$y = 0,75 \left(\frac{D}{H}\right)^{0,25} \left(\frac{L}{H}\right)^{0,15} x$$

- Horikawa (1980, 1984)

$$y = 0,21237 H^{-0,50} D^{-0,25} T^{-0,50} x$$

- Sayao (1982)

$$y = 0,082 x^{0,633} D_{50} = 0,225 \text{ mm}$$

- Hattori y Kawamata (1982)

$$y = p x^{2/3}$$

$$\frac{H_0}{L_0} \text{tg } B \frac{w_f}{gT} = k$$

Beach profile shape

TABLE 1. Dissipative and reflective profile

-	Jonson (1952)	$0,025 < \frac{H_o}{L_o} < 0,030$	
-	Saville (1957)	$0,025 \approx \frac{H_o}{L_o}$	
-	Iwagaki-Noda (1962)	$\frac{H_o}{L_o}, \frac{H_o}{D_{50}}$	
-	Sitarz (1963)		< 0,60 Berm
		$\frac{H}{T (g (s - 1) D)^{1/2}}$	
			> 0,60 Bar
-	Nayak (1970)	$\frac{H_o}{L_o}, \frac{H_o}{D_{50}}, \frac{\gamma_s}{\gamma_w}$	
-	Dean (1973)		< 0,85 Berm
		$\frac{H_o}{T_w}$	
			> 0,85 Bar
			> T/2 Bar
		tf	
			< T/2 Berm
		$\frac{H_o}{L_o} > 1,70 \frac{\tau_{wf}}{gT}$	Bar

- Van Hijum (1974) $\frac{H_o}{L_o} > 2,50 \frac{D_{90}}{H_o}$ Bar
 $< 0,54$ Berm
 $\frac{H_o}{T_w D_{50}}$
 $> 0,54$ Bar
- Sunamura y Horikawa (1974) $\frac{H_o}{L_o} > 4 \text{ tg } \alpha^{-0,27} \left(\frac{D}{L_o}\right)^{0,67}$ Bar
- Dalrymple y Tompson (1976) $\frac{Q}{H_o d_i}$ erosion parameter
- Hattori y Kawamata (1980) $< 0,50$ Berm.
 $\frac{H_o}{L_o} \text{ tg } B$
 $\frac{w}{gT}$
 $> 0,50$ Bar.
- Gourlay (1980) $< 1,55$ Berm
 $\frac{H_o}{T_w}$
 $> 1,55$ Bar

Marine sand, D_{50} 0,20 a 0,30 mm.

$< 0,40$ Berm

$$\frac{H_0}{T_w}$$

$> 0,40$ Bar

$D_{50} \approx 2 \text{ mm.}$

Wang (1981)

$$I_w = \frac{H_b^{\frac{1}{2}}}{g^{\frac{1}{2}} T \text{tg}\alpha}$$

$I_w \downarrow$ Berm

$I_w \uparrow$ Bar

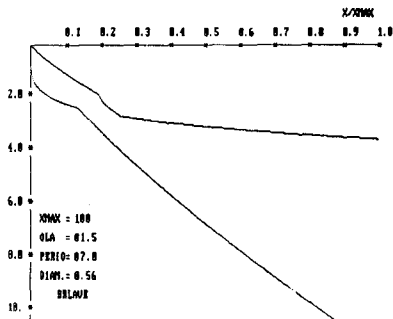
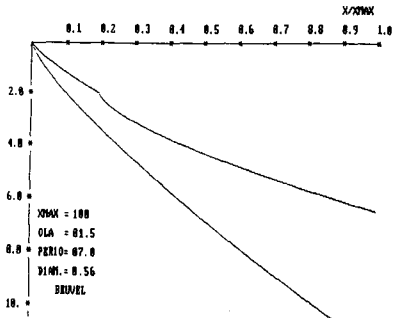
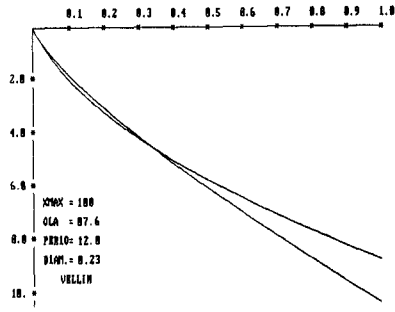
4.- INCIPIENT MOTION ON A GRANULAR BED IN WATER WAVES

Motion initiation on a granular bed by oscillatory flow is of great importance to coastal engineers, it is a necessary condition for bed erosion and to determine the changes onshore-offshore in beaches, to establish the failure and to use in different beach profiles.

The numerical model adjusts three formulae in this case:

- Swart $u = 4,58 D_{50}^{0,38} T^{0,043}$
- Hallermeier $u = \left(8 \left(\frac{\gamma_s}{\gamma_w} - 1 \right) g D_{50} \right)^{\frac{1}{2}}$
- Vellinga $\log \left(\frac{1}{w} \right) = 0,476 (\log D)^2 + 2,18 \log D + 3,190$

- Readshaw (1982) $y = 0,112 x^{0,98} \quad D_{50} = 0,56 \text{ mm}$
- Bailard (1981) $y = p x^{\frac{1}{2}}$
 $y = p x^{2/7}$
- Sayao (1982) $y = A x^n \quad n > 1, D_{50} > 0,60 \text{ mm}$
 $n < 1, D_{50} < 0,60 \text{ mm}$
- Garau (1974-1984) $m_o = 0,075 + 0,035 L_n D_{50}$
 $m_s = 0,025 + 0,010 L_n D_{50}$
 $m_p = 0,0223 + 0,005 L_n D_{50}$
 $t_g = m = 0,138 + 0,056 L_n D_{50}$
- Garau-Friedman
(stable beachline) $m_{sa} = (0,0255 + 0,010 L_n D_{50}) \frac{1}{K_a^{1,11}}$
 $m_{oa} = (0,075 + 0,035 L_n D_{50}) \frac{1}{K_a^{1,22}}$



7.- SUMMARY AND CONCLUSIONS

The modern Technique of Coastal Engineering has enabled the successful modifications of the environment and the recuperation and stabilization of those sandy areas which due to human action were in a process of regression and erosion.

The research has developed the mathematical adjustment of curves to the storm profile and the berm profile according to Bruun, Vellinga, Larras, Sitarz ... and the behaviour of the beaches of Barcelona in which both human action (growing, construction, harbour works...) and maritime actions (sea movements) have produced a remarkable backward movement and regression.

The numerical model is able to analyze the variations between the dissipative profiles and the reflective ones, and to make the enveloping profile in

$$x/x_{\max}$$

$$d/d_{\max}$$

Which will enable us to adjust a stable profile to the beach.

The behaviour of the beaches of Barcelona may consider as fossil ones, near the breaker zone and with D_{50} between $0,16 \text{ mm} \leq D_{50} \leq 2 \text{ mm}$.

The numerical model was developed in the University of Madrid and the results were analyzed by experimental data for the beach profile tests in the Spanish Center of Investigation (CEDEX, CEPYC. Madrid).

8.- ACKNOWLEDGEMENTS

This research was supported by the Madrid University the author wish to thank Professor Suarez Bores and Mr. Victoriano Fernández. Both of them provided valuable comments.

The author is grateful for the efforts of Mr. Quecedo, civil Engineer and M.Sc. He was dedicated to programme the numerical model.

CHAPTER 108

Wave-Induced Flow And Nearshore Suspended Sediment

J.C. Doering* and A.J. Bowen

1. INTRODUCTION

It has been realized for nearly one hundred years that the transport of sediment is related to the characteristics of a wave, in particular its shape. Cornish (1898) noticed that the shoreward velocity associated with a wave crest was more effective at moving coarse sediment than was the seaward velocity associated with the wave trough. Cornish's observation was consistent with the theory of Stokes (1847), which predicts the onshore velocity associated with the wave crest is stronger and of shorter duration than the offshore velocity associated with the wave trough. This horizontal asymmetry of the cross-shore flow, which is a reflection of the wave shape, is known as velocity skewness. It has been suggested that "the existence of the beach depends on small departures from symmetry in the velocity field balancing the tendency for gravity to move material offshore" (Bowen, 1980). Although the concept of velocity skewness has been incorporated into detailed predictors of sediment transport (Bowen, 1980; Bailard and Inman, 1981) it is only one of many facets that needs to be understood in order to make the accurate prediction of sediment transport realizable. A comprehension of sediment transport is hampered by both an incomplete knowledge of the hydrodynamics and a lack of instrumentation to directly measure instantaneous sediment concentration and the accurate prediction of sediment transport is probably the most enigmatic problem in coastal engineering.

Occasionally, suspended sediment concentration has been inferred from *in situ* pumps and hand-held tubes, but these methods lack the temporal and spatial resolution necessary to elucidate the details of the interaction between the wave-induced flow and the sediment. Recently, a miniature optical backscatter sensor (MOBS), which provides a time series of suspended sediment concentration at a "point", was developed by Downing *et al.* (1981). During a recent field experiment a vertical array of 5 of these optical backscatter sensors and a collocated flow meter was deployed close to the sea bed. These collocated measurements provide a unique opportunity to investigate the response of near-bed suspended sediment concentration to the wave-induced flow.

Department of Oceanography, Dalhousie University, Halifax, Nova Scotia B3H 4J1 Canada

* Presently at Hydraulics Lab., National Water Research Institute, P.O. Box 5050, Burlington, ON L7R 4A6

2. FIELD MEASUREMENTS

Data were collected at Pte. Sapin, New Brunswick, as part of the Canadian Coastal Sediment Study. This field experiment was conducted during October–November, 1983. Data from a Marsh–McBirney flow meter, measuring the horizontal components of the flow, and a colocated miniature optical backscatter sensor (MOBS) were used to examine the temporal response of suspended sediment to the wave-induced flow field. The MOBS and flow meter were located at 0.02 m and 0.12 m above the sea bed, respectively. Note that only the lowest MOBS sensor data is used in this paper; a description of the data from all five sensors can be found in Hanes and Huntley (1986).

Data for this paper is confined to a run collected on the 20th of October (run FM). The significant wave height for run FM was 0.20 m. The instrument array was located well seawards of wave breaking in about 1.1 meters of water. Figures 1a and 1b show the first twelve minutes of cross-shore velocity (u) and near-bed sediment concentration (c) for the 20th of October at Pte. Sapin, respectively. Since the alongshore velocity is much smaller than the cross-shore velocity ($\frac{\langle v^2 \rangle}{\langle u^2 \rangle} \sim 0.06$), the alongshore component of the flow is neglected from this analysis and discussion. It is obvious from figure 1 that the concentration of near-bed suspended sediment responds to both the individual waves and the wave groupiness. The response of the concentration to the flow associated with the passage of each wave is intriguing because the concentration seems to respond strongly and rapidly to the onshore flow associated with a wave crest, but very weakly to the offshore flow associated with a wave trough. A close inspection of figure 1a suggests that the cross-shore flow is strongly skewed; in particular, the onshore velocities are considerably stronger and of shorter duration than the offshore velocities (this can be readily seen with respect to the horizontal line denoting the mean flow). The suggestion from figure 1 is the stronger onshore flows associated with the skewed wave crests exceed the threshold velocity for the mobilization and subsequent suspension of sediment, while the weaker offshore flows associated with the “flattish” wave troughs do not. In addition, this suggestion implies that there should be a net onshore transport of sediment by the wind-waves at this height because the onshore flow will advect a high concentration of sediment shoreward whereas the offshore flow will advect a low concentration seaward. The cross-shore transport of suspended sediment at this height is given by the product $u \cdot c$, and is shown in figure 1c. The shoreward transport of suspended sediment associated with a wave crest is clearly larger than the seaward transport associated with a wave trough, as anticipated. For Bagnold-type models of sediment transport the instantaneous cross-shore sediment transport varies with the velocity moment $u^3|u|$, which is shown in figure 1e. However, $u^3|u|$ is in general very strongly correlated with u^3 , the dimensional skewness of the flow (figures 1e and 1d, respectively). For the present case $r^2 = .93$. Thus, the transport of suspended sediment is intimately related to the skewness of the flow; the covariance of $u \cdot c$ and u^3 is readily apparent from figure 1.

Particularly interesting is the way the transport tracks u^3 even though the effect of a critical stress (threshold velocity) has not been included, nor has any representation of the settling characteristics of the sediment. Obviously both effects need to be included in a realistic model, the critical stress for suspension must

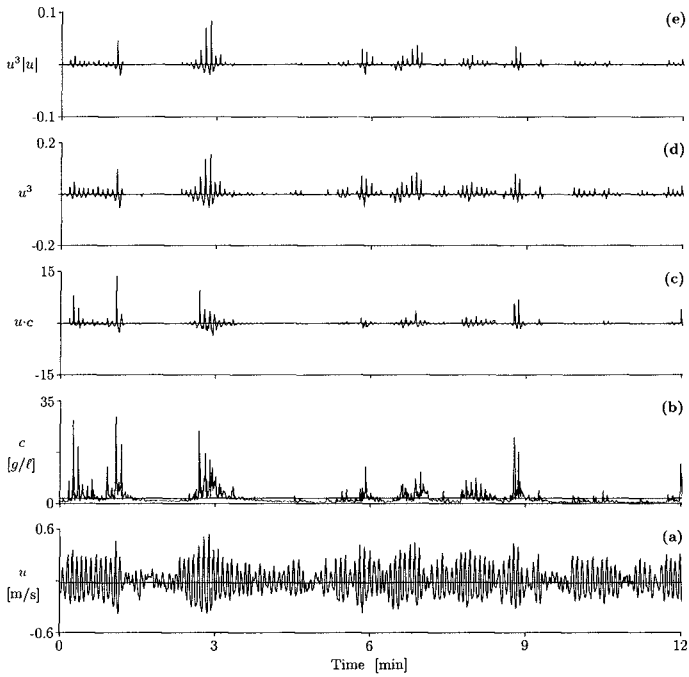


Figure 1 Time series of cross-shore velocity (a), near-bed sediment concentration (b), instantaneous suspended load transport (c), and two moments of the cross-shore velocity field, u^3 (d) and $u^3|u|$ (e) for the first twelve minutes of run FM at Pte. Sapin. A positive velocity denotes an onshore flow. The horizontal line through each record denotes the mean.

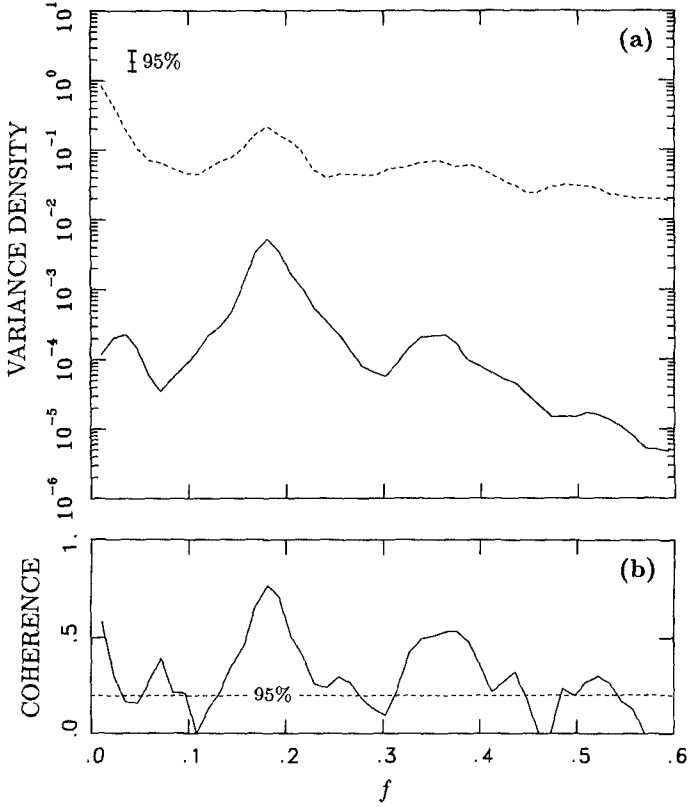


Figure 2 (a) Spectra of cross-shore velocity (—) and MOBS (- -) for run FM at Pte. Sapin. Error bars show the 95% confidence limits. (b) Coherence between the spectra in (a). The 95% confidence limit for zero coherence is given by - - -. There are 100 degrees of freedom and $\delta f = 0.0121$ Hz.

become a critical parameter at large grain sizes, the settling velocity at small sizes (the parameter af/w where a is the wave amplitude and w the grain settling velocity seems to be the appropriate non-dimensional parameter).

3. ANALYSIS

Figure 2 shows the cross-spectral analysis between the collocated flow and sediment concentration measurements. The "power" spectrum of the cross-shore flow shows a well-defined peak at 0.18 Hz ($T_p = 5.5$ s). A relatively well-defined first harmonic peak ($f = 0.36$ Hz) is also evident. The shape of the roll-off between 0.4–0.6 Hz is somewhat suggestive of a second harmonic "peak". The skewness observed in the time series of cross-shore flow (figure 1a) suggests that the primary and these harmonics are phase-coupled. This of course cannot be determined from a "power" spectral analysis (a bispectral analysis is discussed later). An infragravity wave peak at $f = 0.036$ Hz ($T \sim 28$ s) is also observed in the spectrum of the cross-shore flow.

If the response of the concentration to the offshore flow were comparable to that of the onshore flow, then the period of the concentration response would be twice that of the cross-shore flow. On the other hand, if the concentration responded more strongly to either the onshore flow or the offshore flow, then the period of the concentration response would be expected to be the same as that of the cross-shore flow. The "power" spectrum of the concentration time series shows that the peak period of the response is the same as the cross-shore flow. This observation is consistent with the suggestion that the concentration responds primarily to the flow associated with the wave crest. Finally, figure 2b indicates that except for the "valleys" in the "power" spectrum of the cross-shore flow, which separate the infragravity, primary, first harmonic, and second harmonic frequency bands, the concentration and cross-shore flow are significantly coherent.

Figure 3 shows the real and imaginary parts of the bispectrum of the cross-shore flow. The definition and properties of the bispectrum can be found in Elgar and Guza (1985), Doering and Bowen (1986), and many others. In a few words though, the bispectrum is used to identify triad(s) (*i.e.*, three phase-coupled frequencies) and to determine the relative contribution of a triad to the total skewness and asymmetry (a measure of the lack of vertical, as opposed to horizontal, symmetry) of the waves in a record. The peak centered at (0.18 Hz, 0.18 Hz) denotes phase-coupling between primary and first harmonic frequencies, and is suggestive of a self-self sum interaction between primary wavetrains. The smaller peak located at (0.36 Hz, 0.18 Hz) indicates phase-coupling between first, primary, and second harmonic frequencies. These two peaks clearly indicate that harmonic wavetrains are phase-coupled to the primary. The wind-wave skewness (S_{ww}) arising from these two interactions is relatively large, $S_{ww} = 0.676$. This confirms that the cross-shore flow is strongly skewed. However, the wind-wave asymmetry (A_{ww}) arising from these two interactions is relatively small, $A_{ww} = -0.159$; that is, the waves are almost vertically symmetric. The depression located at (0.16 Hz, 0.02 Hz) indicates that negative skewness arises from phase-coupling between primary wavetrains and long waves. The infragravity wave skewness and asymmetry arising from this interaction are -0.176 and 0.017, respectively; hence, the biphasic of this interaction

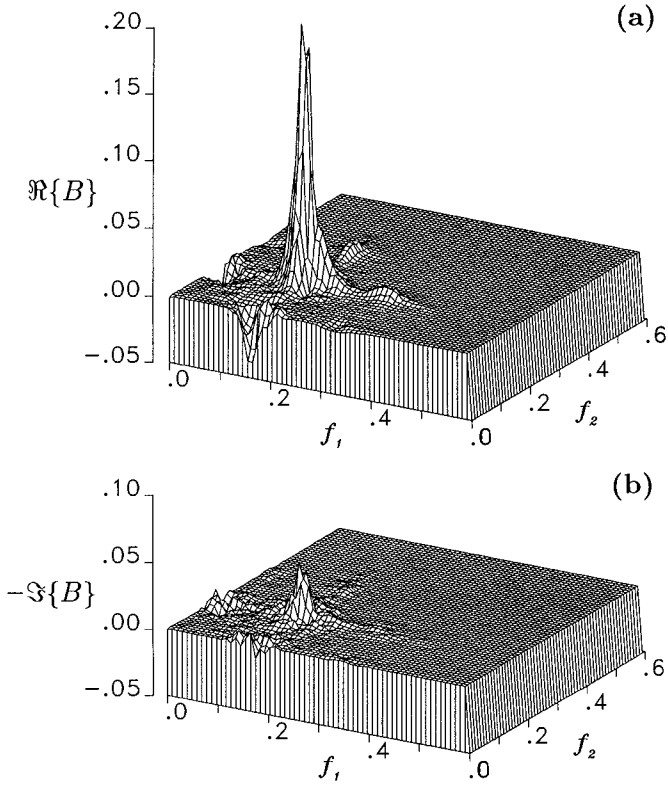


Figure 3 Real (a) and imaginary (b) parts of the bispectrum of cross-shore velocity for run FM at Pte. Sapin. $\delta f = 0.0098$ Hz.

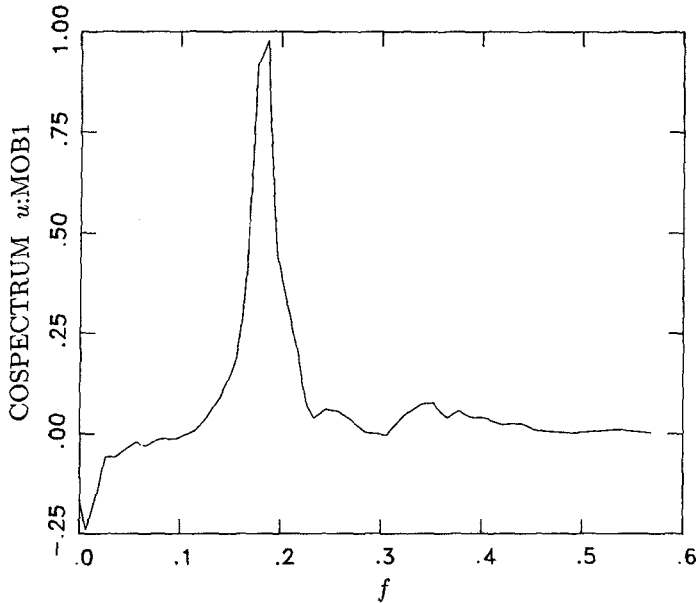


Figure 4 Cospectrum between cross-shore velocity and the MOBS for run FM at Pte. Sapin. The units of the cospectrum are $(g/\ell)(m/s)Hz^{-1}$. There are 58 degrees of freedom and $\delta f = 0.0098$ Hz.

($= \tan^{-1}\{A/S\}$) is -174° . The negative skewness and biphasic of $\sim -180^\circ$ that are observed for this interaction are consistent with the classical concept of a bound wave (Longuet-Higgins and Stewart, 1962, 1964); that is, an interaction between two primary wavetrains forms a wave group, which forces a second-order bound wave at the difference frequency that is 180° out of phase with the envelope of the wave group (§2.2–2.3). For a Bagnold-type model of transport skewnesses that are opposite in sign imply transport in opposite directions. For the present data where a positive velocity denotes an onshore flow, positive skewness implies an onshore transport and negative skewness, an offshore transport.

To determine the net transport in the cross-shore direction at some height above the sea bed, the cospectrum of the cross-shore flow and concentration c at that height is formed, *i.e.*, $\langle u \cdot c \rangle$. Figure 4, reproduced from Huntley and Hanes (1987), shows the cospectrum between the MOBS sensor and the cross-shore velocity. The most striking feature is the large positive or onshore flux of sediment by the primary waves. The indication here is the strong onshore flow associated with the passage of a skewed wave crest leads not only to the mobilization and suspension of sediment, but also to an onshore transport. This implies that the bulk of the sediment at this height (of ~ 2 cm above the sea bed) settled before the offshore flow associated

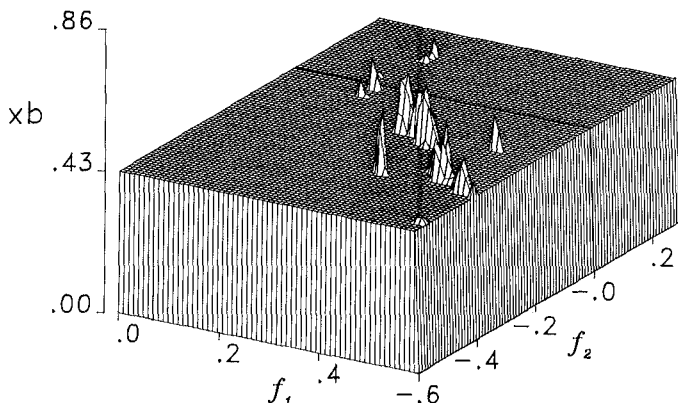


Figure 5 Cross-bispectrum between cross-shore velocity and the MOBS signal for run FM at Pte. Sapin. There are 32 degrees of freedom and $\delta f = 0.0098$ Hz.

with the wave trough could transport it back, *i.e.*, the net flux of sediment was onshore, which is consistent with figure 1 where a much higher concentration was observed during the onshore flow. The offshore transport of sediment by infragravity waves is probably due to the offshore skewed flow associated with the bound long wave forced by a wave group (Longuet-Higgins and Stewart, 1962; Wells, 1967); the general tendency for stronger offshore flow to occur when the waves are large, provides a perturbation which tends to move sediment seaward (Shi and Larsen, 1984). This cospectrum does not necessarily imply that the beach was locally accreting, as neither the transport by the alongshore current nor the mean flow have been considered.

The evidence presented so far is consistent with the idea that the wind-waves result in an onshore transport of sediment because the flow associated with them is skewed onshore (*i.e.*, the strong onshore velocities exceed the threshold velocity required to mobilize, suspend, and transport the sediment, whereas the offshore velocities generally do not), while the interaction of the infragravity waves with the sediment suspended by the wind-waves leads to an offshore transport of sediment because the flow associated with these long waves is skewed offshore. In other words, the suggestion is the response of concentration should be phase-coupled to the wave-induced flow. One can test this idea using the cross-bispectrum.

Figure 5 shows the unique part of the cross-bicoherence spectrum between velocity and concentration. The peaks shown are above the 95% significance level for zero cross-bicoherence. The convention adopted is that $u(f_1) \pm u(f_2) \rightarrow c(f_3)$, where $u(f_1)$, $u(f_2)$, and $c(f_3)$ denote frequencies in the velocity and concentration series, respectively, and $f_1 + f_2 = f_3$. This convention assumes that coupling between the spectral components of the wave-induced flow are phase-coupled to

the variation in concentration. The broad peak centered at (0.36 Hz, -0.18 Hz) indicates that first harmonic and primary frequencies in velocity are phase-coupled to $0.36 + (-0.18) = 0.18$ Hz, or the primary in concentration. The peak at (0.54 Hz, -0.36 Hz) indicates that phase-coupling between second and first harmonic frequencies in velocity are also coupled to fluctuations at the primary frequency in concentration. Collectively, these two peaks indicate that phase-coupling between the primary and its harmonics in velocity, which result in a strongly skewed flow (figure 3a), are coupled to primary fluctuations in concentration. The small peak at (0.19 Hz, -0.03 Hz) indicates that primary and long waves in velocity are also coupled to primary fluctuations in concentration; this peak suggests the interaction of long waves with the sediment suspended by the wind-waves.

4. DISCUSSION

The observations in the preceding section suggest that the response of concentration is strongly coupled to the wave-induced flow; for this grain size range the complexities of the critical stress for suspension and the fallout of sediment play a minor role and might be adequately modelled in a relatively simple way. The interesting part is that the sedimentary response depends critically on the instantaneous velocity, clearly reflecting the pattern of both the individual waves and the wave groups.

Historically, the predictors used to model nearshore sediment transport, assume that the total rate of sediment transport can be empirically related to simple, time-averaged characteristics of the incident wave field, *e.g.* breaker height, angle of incidence with respect to shore-normal, and the depth of water at the location of breaking. More detailed predictors assume that the sediment is suspended by the waves and then transported by the superposition of a mean flow. Most bulk predictors of sediment transport do not explicitly incorporate any of the effects of velocity skewness, wave groups, settling velocity, or a critical velocity. In light of this and the many other sweeping assumptions that are implicit in these models, it is not surprising that they are not accurate predictors of sediment transport (Fleming *et al.*, 1986; Baird *et al.*, 1986).

If the skewness of the flow is linked to the mobilization, suspension, and transport of sediment as suggested by the observations in this paper, then the implication is the cross-shore variation of skewness should lead to convergences and divergences of sediment. For example, if the flow is skewed onshore through the shoaling region, reaches a maximum seaward of wave breaking, and then becomes skewed offshore in the surf zone due to a dominance of infragravity wave skewness, then this implies a convergence of sediment and thus the formation of a breakpoint bar. This idea for bar formation is consistent with the skewness observations on a barred beach by Greenwood and Sherman (1984), who observed that velocity skewness tended to be positive on the lakeward side of a bar and negative on the landward side of a bar. However, whether or not a bar actually forms and where it forms will also depend on the spatial variation of the mean flow; that is, it is the skewness of the total flow (*i.e.*, including the mean) that must be considered, not just the skewness of the oscillatory component. Bowen (1980) has suggested that an onshore skewed flow is required to balance the downslope component of

gravity; therefore, the bar would be expected to form seaward of the location of zero skewness. However, the bar could form closer to the location of zero skewness if the downslope component of gravity is partly balanced by an onshore mean flow in the bottom boundary layer (Longuet-Higgins, 1953).

The role of the wave skewness in the longshore direction is probably much less important due to the existence of strong longshore currents in the mean flow. However, the role of wave groups in mobilising the sediment may well be important and it is far from clear that this groupiness is well parameterised by a mean quantity such as incident wave energy.

5. CONCLUSIONS

Colocated measurements of near-bed suspended sediment concentration and velocity were used to investigate the variation of sediment concentration with respect to the wave-induced flow. The data clearly showed that sediment responds to both the individual waves and to wave groups. The response of sediment concentration to the individual waves within a wave group is particularly interesting because the concentration responds strongly to the onshore flow associated with wave crests, but very weakly to the offshore flow associated with a wave trough. These field measurements clearly show the behavior of sediment concentration and sediment transport depends on some high power of the velocity with very little time lag. They suggest that the traditional assumption that bulk transport is simply related to basic characteristics of the incident waves, such as peak period, breaker height, and angle of breaking, is tenuous.

The cospectrum of cross-shore velocity-concentration, which was used to examine the wave-induced transport of suspended sediment by the cross-shore velocity, showed that there was a strong onshore transport of sediment due to wind-wave frequencies and a weaker offshore transport due to infragravity waves. The onshore transport observed at the primary frequency suggests that the strong onshore flow associated with the passage of each skewed wave crest leads not only to the mobilization and suspension of sediment, but also to an onshore transport of the sediment. Moreover, the implication is the bulk of the sediment suspended by the passage of a wave crest (at this height of ~ 2 cm above the sea bed) settles before the offshore flow associated with the following wave trough can transport it back seaward; the net transport of suspended sediment at this height is strongly shoreward. The offshore transport by infragravity waves is apparently due to the offshore skewed flow associated with the bound long wave forced by a wave group (Longuet-Higgins and Stewart, 1962, 1964).

Shi and Larsen (1984) suggested that the offshore transport of fine silt and sand on the continental shelf might be due to the offshore flow associated with the long wave forced by a wave group. The cospectrum observation tends to confirm this suggestion. Moreover, this cospectrum observation underlines the sedimentary importance of infragravity wave energy in the nearshore, and again undermines the traditional assumption that the transport of sediment is strictly a wind-wave related phenomenon.

All the observations shown in this paper collectively suggest that sediment dynamics is fundamentally related to the time variability of the velocity field. The

sediment is not simply stirred up by the waves and moved by the mean flow. The important parameters include the mean value of the high movements of the flow field such as skewness, as theoretically suggested. In light of this relation between sediment transport and velocity skewness, it was suggested that the cross-shore variation of skewness should lead to convergences and divergences of sediment. For example, if the flow is skewed onshore in the shoaling region due to a dominance of wind-wave skewness and offshore in the surf zone due to a dominance of infragravity wave skewness, then this leads to the possibility of a convergence of sediment and the formation of a break point bar. However, a complete model for transport should also include: the contribution to moments from the mean flow; the downslope component of gravity, *i.e.*, a beach slope dependence; higher order velocity moments such as those that appear in Bagnold-based models for bed and suspended load transport; a threshold velocity for the initiation of transport and a representation of the settling behavior of the grains.

REFERENCES

- Baird, W. F., J. S. Readshaw, and O. J. Sayao, 1986. Nearshore sediment transport predictions Stanhope, Lane, Prince Edward Island, National Research Council Canada, C²S² report 21.
- Bailard, J. A. and D. L. Inman, 1981. An energetics bedload model for a plane sloping beach: Local transport, *J. Geophys. Res.*, **86**, 2035-2043.
- Bowen, A. J., 1980. Simple models of nearshore sedimentation; beach profiles and longshore bars, in *The Coastline of Canada*, S. B. McCann, editor, Geological Survey of Canada, Paper 80-10, 1-11.
- Cornish, V., 1898. On sea beaches and sand banks, *Geol.*, **2**, 628-674.
- Doering, J. C. and A. J. Bowen, 1986. Shoaling surface gravity waves: A bispectral analysis, *Proc. of the 20th Conf. on Coastal Eng.*, ASCE, 150-162.
- Downing, J. P., R. W. Sternberg, and C. R. B. Lister, 1981. New instrumentation for the investigation of sediment suspension processes in shallow marine environments, *Mar. Geol.*, **42**, 14-34.
- Elgar, S. L. and R. T. Guza, 1985. Observations of bispectra of shoaling surface gravity waves, *J. Fluid Mech.*, **161**, 425-448.
- Fleming, C. A., B. M. Pinchin, and R. B. Nairn, 1986. Evaluation of coastal sediment transport estimation techniques, National Research Council Canada, C²S² report 19.
- Greenwood, B. and D. J. Sherman, 1984. Wave, currents, sediment flux, and morphological response in a barred nearshore system, *Mar. Geol.*, **60**, 31-61.
- Hanes, D. M. and D. A. Huntley, 1986. Continuous measurements of suspended sand concentration in a wave dominated nearshore environment, *Cont. Shelf Res.*, **6**, 585-596.
- Huntley, D. A. and D. M. Hanes, 1987. Direct measurements of suspended sediment transport, *Proc. of Coastal Sediments 87*, ASCE, 723-737.

- Longuet-Higgins, M. S., 1953. Mass transport in water waves, *Proc. Roy. Soc.*, **A245**, 535-581.
- Longuet-Higgins, M. S. and R. W. Stewart, 1962. Radiation stress and mass transport in gravity waves, with application to "surf beats", *J. Fluid Mech.*, **13**, 481-504.
- Longuet-Higgins, M. S. and R. W. Stewart, 1964. Radiation stresses in water waves; a physical discussion with applications, *Deep-Sea Res.*, **11**, 529-562.
- Shi, N. C. and L. H. Larsen, 1984. Reverse sediment transport induced by amplitude-modulated waves, *Mar. Geol.*, **54**, 181-200.
- Stokes, G. G., 1847. On the theory of oscillatory waves, *Trans. Cambridge Philos. Soc.*, **8**, 441-455.
- Wells, D. R., 1967. Beach equilibrium and second-order wave theory, *J. Geophys. Res.*, **72**, 497-504.

CHAPTER 109

WAVE-INDUCED BREAKOUT OF HALF-BURIED MARINE PIPES

Mostafa A. Foda¹
Adrian W-K Law²
Jo Y-H Chang²

ABSTRACT

An experimental study is conducted in order to identify the major physical processes leading to the breakout of half-buried submarine pipelines from the seafloor under ocean wave action. Both the hydrodynamic loading on the exposed surface of the pipe, as well as the resulting displacement history of the pipe, were recorded and analyzed in order to identify the critical pipe-soil-wave conditions for the detachment of the pipe from the seabed. The paper also examines the balance of the pipe under the combined lift and drag loading from the water wave. An experimental breakout force-time power law is obtained and compared to available theoretical breakout models.

1. INTRODUCTION

During severe storm or hurricane conditions, wave-induced loading on submarine pipelines can be large enough to detach some of the placed pipes from the sea floor, causing them to move or float to great distances with the ocean currents. Numerous reports of this type of failure to submarine pipes are documented in the literature (e.g. Blumberg 1964, Grace 1978, Christian *et al.* 1974, Nataraja and Gill 1983). With the repeated storm-induced failures of marine pipes, the cost of maintaining their operational integrity can be quite high (e.g. Gerwick 1986). The needed improvement of the cost-effectiveness of the present design and maintenance practice for marine pipelines can clearly be established by gaining more insight into the various processes that constitute the failure mechanism.

This paper aims at studying the mechanical stability of the pipe-soil system under wave action. In particular, we focus on the conditions that lead to pipeline detachment or 'breakout' from the sea floor under hydrodynamic wave loading. We attempt to do that by simulating the breakout process in the laboratory, and further identifying the critical wave-soil-pipe conditions for pipeline breakout. The experimental study is conducted for the configuration of partially buried pipe in a sandy bed under shallow water wave forcing. Partial burial is a commonly observed configuration of submarine pipelines on the sea floor. This may differ from the initial set-up of the pipeline, which may simply be through the direct laying of the pipe on top of the seabed if the water depth is large, or the full or the partial burial of the pipe if the water depth is small. Subsequent interaction between the pipe and the soil will most likely change such initial setting. A marine pipe would then enter into cycles of partial exposure and reburial under the usually variable wave climate conditions. For example, the pipeline may be totally buried initially, but becomes partially

¹Associate Professor, Department of Civil Engineering, University of California, Berkeley, California 94720.

²Graduate Student, Department of Civil Engineering, University of California, Berkeley, California 94720.

exposed due to the erosion of the cover soil by waves. The opposite process of self-burial of the pipe may occur instead due to the erosion of soil particles from underneath the fully-exposed pipe, resulting in the gradual sagging of the pipe into the seabed (e.g. Leeuwestein *et al.* 1985, Hulsbergen 1984, Mao 1986). Another process that results in a partial-burial situation occurs when the pipe is initially laid in an open trench in the seabed. After placing the pipe, local waves and currents at the site will work the spoils back to the artificially-dug trench, leading to a partial-burial configuration.

The first part of this study will focus on the hydrodynamic loading of water waves on partially-buried pipes. This will be done by measuring, in the wave flume, the wave-induced pressure over the exposed surface of the pipe. Then, by integrating the pressure distribution we calculate the resulting forces; drag and lift, and moments on the pipe. Most of the previous studies on wave forcing on submarine pipes were concerned with unburied pipes, with or without close proximity to the seabed (e.g. Sarpakaya 1976, Verley *et al.* 1987). Ismail *et al.* (1986) reviewed the very limited data available on wave loading on partially-buried pipes and stressed the need for detailed measurements of both the hydrodynamic forces as well as the seepage-flow loading on partially-buried marine pipes. In the present study, the measured wave forces will be correlated with wave parameters in order to obtain nondimensional force coefficients for both the drag and lift forces. The widely used Morison Equation will be used to curve-fit the measured drag force on the exposed surface of the pipe, and best-fit coefficients of drag C_D and added mass C_M will be obtained for the range of Keulegan-Carpenter numbers of our experimental set-up. A nondimensional lift-force coefficient C_L will be obtained following a similar procedure.

Then, the study will concentrate on the response of the pipe-sand system to the applied wave forcing. In particular, we examine how will the pipe react to the applied forcing, and how does the detachment process take place. Earlier body breakout studies were concerned with the detachment process under constant applied lift force (e.g. Liu 1969, Muga 1969, DeHart and Ursell 1967). A complete detachment was observed to take place only after the lift force has been applied for a certain period of time, normally called 'the breakout time'. The process is usually very slow in the beginning, concluded by a rather sharp release at the breakout time. It was concluded that this almost yield-type release is related to the strong coupling between the body and the saturated bed. Foda (1982, 1983) developed a theory that describes the quasistatic detachment of a large semiburied object from a poroelastic bed. In the theory, this initial resistance to body movement is attributed to the development of negative pore-pressure, or 'mud-suction' at the body-soil interface, which gives rise to a certain seabed holding strength against body breakout. The nature of this mud-suction resistance can be illustrated by considering the behavior at the body-soil interface. Initially, as the body moves upward in response to the applied lift force, some pore water will have to be moved, or sucked, upward in order to fill in the resulting gap between the body and the soil. Such movement of pore water requires pore-pressure gradient in order to push the flow through the pores against viscous resistance stresses (Darcy's law), giving rise to the negative pore-pressure at the body-soil gap. The yield-type release will occur late into the lift-off process, when the body-soil gap is wide enough to allow ambient water from above the bed to flow laterally into the gap through its periphery. The resistance to such lateral flow into the gap is far less than that for the upward pumping of pore water into the gap, and at this stage there is virtually no resistance to the further expansion of the body-soil gap, and hence the quick release. The analysis resulted in a general breakout time-force power law of the form:

$$F_b = C t_b^{-n} \quad ; \quad n = 1.5 \quad (1)$$

where t_b is the breakout time, F_b is the breakout force, or the applied lift force in excess of the submerged weight of the body, and C is a material constant that depends on the permeability, stiffness and porosity of the saturated bed, as well as the size of the body (Foda 1983). However, the above law is limited to the conditions of the boundary-layer

theory of Mei and Foda (1981), which requires that the pipe diameter D is much larger than the seabed boundary-layer thickness δ which is roughly proportional to $\sqrt{k/\mu\omega}$ where k is the soil permeability, μ is water viscosity, and ω is wave frequency. Mei *et al.* (1985) developed another breakout law for bodies on a porous but rigid bed that has the same form as (1), but with a different material constant C and power n ($n = 1$). This law would be more applicable to pipes with a small enough diameter.

Foda (1985) extended his theory to the present case of a half-buried marine pipe under the oscillatory loading of water waves. The hydrodynamic loading on the pipe is calculated assuming a potential flow above the seabed. Furthermore, it was assumed that the pipe diameter D is much smaller than both the wave length L and the water depth h , so that wave scattering by the pipe was ignored. Only the vertical equilibrium of the pipeline was considered under the wave-induced lifting force, which is composed in this case of an average lift force plus an oscillatory component. The analysis has shown that for typical physical parameters, the wave period $T \approx 10$ sec is usually much shorter than the quasistatic breakout time t_b , and hence one expects that the oscillatory wave-induced force component will not influence, to leading order, the breakout process of the pipe.

The possibility of resonating the system by the oscillatory force was also examined. The obtained response function of the pipe-seabed system was shown to exhibit a weak nonlinearity of the order $\epsilon = T/t_b \ll 1$. This should lead to the slow generation of higher harmonics and hence raises the possibility of resonating the system when one of the generated harmonics approaches the system's natural frequency. However, the analysis has shown that the natural frequency of a 'typical' pipe-soil system would be much higher than water wave frequency, so that a long chain of generated higher harmonics would be needed in order to approach the resonance condition.

The present experimental study examines many of the features of the above mentioned breakout models, along with the associated assumptions and limitations. This includes investigating the nature of the pipe breakout (quasistatic or resonant), the relative role of pore-pressure vs. soil effective stresses in holding the pipe in place, and the ultimate mode of failure for the supporting soil at breakout.

2. EXPERIMENTAL SETUP

The experimental work was conducted in the 8 ft (W) \times 5 ft (H) \times 180 ft (L) wave flume at the Richmond Field Station of the University of California at Berkeley. The relatively large cross-sectional area of the flume allowed the building of a reasonable-size sand basin inside the flume to model the seabed. A layout of the experimental setup is shown in Figure 1a. The flume is fitted at one end with a mechanical flap-type wave maker that generates monochromatic water waves, with a range of possible wave amplitudes and frequencies. At the other end of the flume, a 20° sloping beach with four layers of horse-hair mats is built to absorb the incoming wave energy. The test section is built about 50 ft from the wave maker where there is a side-viewing glass window in the flume's concrete wall. As shown in Figure 1, the test section is made of a rectangular sand basin 2 ft high, 8 ft wide and 4.5 ft long. Two 20°-plywood ramps are fitted at both ends of the basin in order to provide smooth transitions for the water wave as it passes over the test section. The sand used in the experiments was a well sorted medium-size sand of $D_{50} = 0.3$ mm. The basin was filled with the sand, manually compacted in the dry, then an 8" PVC pipe was placed across the flume, half-buried in the sand bed. The length of the pipe was cut slightly shorter than the width of the flume (8 ft) to prevent friction between the pipe and the flume's concrete walls. The pipe would then be connected to the various sensors of the experiment, feeding into a data-acquisition system whose details are discussed in the following section. Then, the flume would be filled with water to a total depth of 4 ft (2 ft of water above the sand bed).

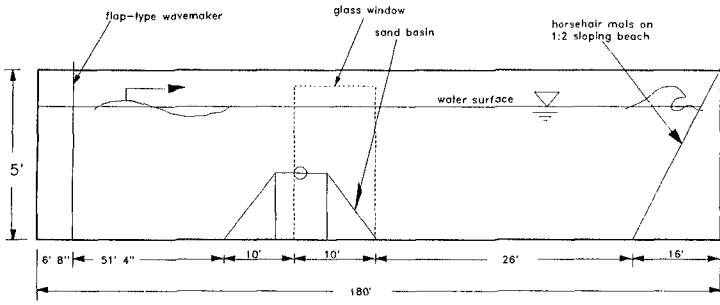


Figure 1a: A sketch of the flume dimensions

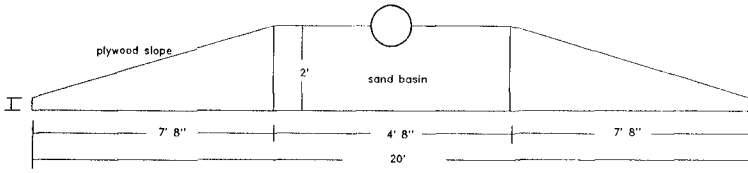


Figure 1b: The sand basin dimensions

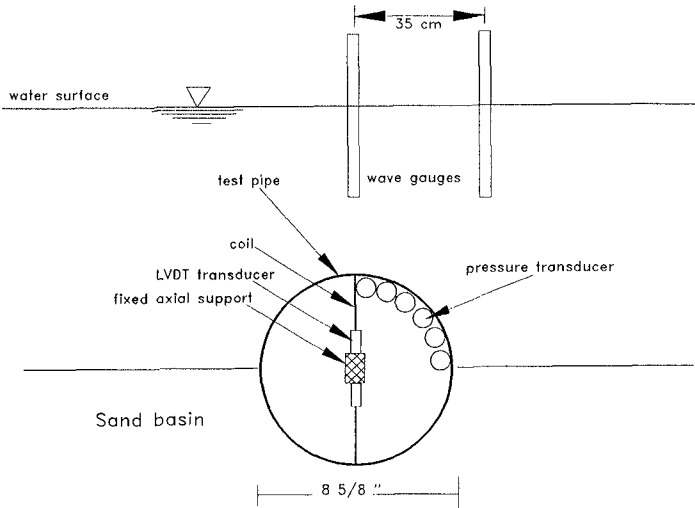


Figure 2: Experimental Setup

A typical experimental run would start by turning on the motor of the wave maker to generate a monochromatic wave of pre-set wave height and frequency (typically, 6" and 3 sec, respectively), and continuously recording the measurement data on water pressure around the pipe, pore pressure measurements, wave profile above and near the pipe, and the displacement history of the pipe, until failure, or detachment, of the pipe from the sand bed occurs (or until termination of the run if breakout does not occur). In many runs, the whole test section would be videotaped to record the visible behavior of the pipe-soil system throughout the experiment.

3. DATA-ACQUISITION SYSTEM:

In order to measure the wave-induced hydrodynamic loading on the pipe a total of six pressure transducers (Data Instrument Model AB High Performance 0-6 psi) was used to measure pressure distribution over one quarter of the exposed pipe surface (Figure 2). The pipe would simply be rotated 90° to measure water pressure over the other quarter surface. The pressure transducers were placed inside the 8"-pipe at the midlength section. The transducers were connected to the outside of the pipe through an array of small holes 15-degrees apart drilled through one quarter of the pipe's wall. Small plastic tubings (1/8" inner diameter, 4" long) were used to connect these holes to the diaphragm-type pressure transducers. The output signals from the transducers were then amplified by accurate strain gauge conditioners (Daytronic 9178A), enhancing the resolution to about $1 N/m^2$. Although this accuracy is over the manufacturer recommended limit (0.25% of full range), calibration of the transducers showed a repeatable linear curve with constant slope, indicating that the extrapolation of accuracy is valid.

The measurement of pore-pressure, or mud-suction stress, along the pipe-soil interface was made following the same procedure by rotating the pipe so that the measurement holes would be on the buried half of the pipe surface.

As for the movement of the pipe, two Linear Variable Differential Transformers, LVDT, were used to measure both the vertical and the horizontal components of the pipe's displacement. Since the pipe was totally immersed into water, a hermitically-sealed type was selected (Schaevitz 500HPA). The selected LVDT has a measurement range of about one inch and an accuracy of 1/4000 of an inch using an analog transducer amplifier (ATA101) from the same company. The magnetic coils of the two LVDTs were mounted on an aluminum frame that runs through the center of the pipe, with its ends fixed on the side walls of the wave flume (Figure 2). One coil is mounted in a vertical orientation, while the other is mounted horizontally, normal to the axis of the pipe. The metallic center rods of the LVDTs were then placed through, but not touching, their respective magnetic coils and attached to the the pipe's interior wall. In this arrangement, both the vertical and the horizontal displacement of the pipe can be measured by detecting the relative motion between the coil and the center rod of each LVDT, without restraining the free motion of the pipe under wave loading.

The wave profile is measured by using two double-wire wave gauges which relate changes in resistance and hence voltage of the partially-immersed wires with changes in water level. The accuracy of the recorded water level was about 0.3 mm with careful calibration. One wave gauge was located directly above the pipe and the other was about 35 cm downwave towards the dissipative beach. The gauges were isolated electronically to avoid possible interference and together they measured the wave profile at the test section and also the amount of reflection from the beach. They are excited and their signals amplified by strain gauge conditioners (Daytronic 9178A) similar to those used for the pressure transducers.

The data-processing unit was an IBM PC/AT equipped with two data acquisition cards (IBM Data Adapter and Datatranslation Data Board DT2801). This provides for 12 channels

with 12-bit accuracy. A program is written in C-language to allow the start or termination of the recording of any signal at any time during the experiment independently or synchronically with other signals. In addition, during the recording, the program can still report values of any desired signal. These features add more flexibility on memory storage and early detection of errors.

4. THE BREAKOUT EXPERIMENT:

In all of the conducted experiments, the observed behavior was very similar, consisting primarily of two distinct phases. First, there is the build-up phase, which covers more than 90% of the duration of the experiment. Then, there is the short phase of actual pipe-breakout from the sand bed. During the build-up phase, there is hardly any discernible movement of the half-buried pipe. The only visible movement was that of some of the sand grains on the surface of the sand bed, which quickly resulted in the establishment of a regular ripple pattern on both sides of the pipe. However, in the near proximity of the pipe (about one pipe diameter distance on either side), no motion of sand grains was visible and the sand surface there remained flat throughout this phase. In other words, one can say that in our set-up soil erosion did not play any role in the ensuing behavior of the pipe-sand system.

The duration of this build-up phase ranged from about half an hour to a little less than 5 minutes. During this phase, the pipe was clearly subjected to the hydrodynamic lift and drag due to the passing of water waves above it. Flow separation was observed to take place in all the experiments. Separation was made visible by injecting liquid dye near the exposed surface of the pipe. The dye would quickly encounter and make visible one or more of the shedded vortices from the surface of the pipe. Such viscous separation would result in an asymmetric distribution of pressure around the pipe, and hence a net loading on it. Another cause for pressure asymmetry is the added-mass effect associated with the unsteadiness of the flow. Furthermore, there is the lift-force component associated with the Bernoulli's effect, where the increase in velocity at the summit of the pipe is accompanied by a decrease in pressure, i.e. a lift. The details of the measured hydrodynamic loading on the pipe will be given in the following Section.

By examining the displacement record of the pipe during this initial build-up phase, we observe that the response of the pipe to these applied hydrodynamic loadings is in the form of a very small oscillatory motion, with a very slow net movement in the upward direction. Figure 3 shows the vertical displacement history of the pipe center during a typical run. In this Figure, the amplitude of the pipe oscillation is about .008 inch, and the average rate of rise of the pipe during this build-up phase is of the order of .10 inch/minute, which can hardly be detected by the naked eye. Superimposed on this gradual rise, there was an even slower rotational movement of the pipe around its longitudinal axis. This suggests that the pipe is actually rolling out of the sand bed, as opposed to being uniformly lifted off from the bed. With the wave coming from left-to-right the observed net rotation was always anticlockwise. In other words, the combined rise and roll motion of the pipe did have an effective pivot point (point of zero net displacement) which was always at the wave-maker side from the pipe center. The rotational displacement was measured by placing markers at equal distances on the pipe wall and visually recording the difference between the reading at the two pipe-soil contact lines. This would typically reach a maximum value, at pipe breakout, of about 10-15 degrees.

It is important to note that throughout this phase where the pipe is slowly building up towards the ultimate breakout, the soil mass surrounding the pipe remained intact, with no sign of any soil failure, such as soil sliding, erosion or soil liquefaction. Finally, near the end of this build-up phase, the pulsating motion of the pipe becomes easier to detect by the naked eye, and this signals the start of the very short second phase of pipe breakout.

As seen in Figure 3, the very slow, almost unnoticeable rise of the pipe during this long build-up phase is followed by the rather sudden and violent release of the pipe from the sand bed in the breakout phase. The release is so sudden that it is relatively easy to identify a specific time when that happens, and we may term that the 'breakout time'. From Figure 3 we see that approaching the breakout time there is no significant increase in the amplitude of the oscillatory motion, and that the breakout is essentially associated with the increase in the net rise component of the motion. This should quite reasonably exclude resonance as the possible mechanism for such a breakout. Instead, it is a quasistatic process through which the pipe gradually detaches itself from the sand bed, against the so-called 'mud-suction' resistance force. The eventual breakout occurs due to the dissipation of this mud-suction force at breakout time. The details of the breakout mechanism will be discussed later in this paper. But first, we discuss the hydrodynamic loading that forces such breakout.

5. HYDRODYNAMIC LOADING:

Figure 4 shows the distribution of dynamic water pressure on the exposed half-surface of the pipe during one wave cycle (wave period of 2.9 seconds and wave height of 6"). This is obtained by combining two 1/4-surface data, under identical wave profiles. For any point on the exposed pipe surface, it is seen that pressure is nearly in-phase with the wave profile, i.e., the maximum and minimum pressure occur almost under the crest and trough of the wave, respectively. From the Figure, it is seen also that under either the crest or the trough, the pressure distribution has a minimum near the summit of the pipe (near points 6 and 7), where the kinetic energy is a maximum due to the pipe-induced contraction of the flow, (the Bernoulli's effect). This will clearly result in a net lift force on the pipe. Aside from that, there is some asymmetry in crest and trough pressure distribution around the summit point. This may be attributed to flow separation effect. A more pronounced asymmetric distribution of pressure is however due to the added-mass effect and is evident in the Figure near the wave's nodal points (time = 1.0 s and 2.0 s), where flow acceleration is maximum. This asymmetry and the resulting loading on the pipe are due to the pipe-induced deceleration of a certain amount of fluid mass in the pipe's vicinity.

By integrating the measured pressure distribution over the pipe surface, the wave-induced drag and lift can be found. Figure (5) shows sample results for the measured drag force on the half-buried pipe. The Figure also shows the least-square fitting of the data in the form of a Morison Equation:

$$F_D = \frac{1}{2} C_D \rho(D/2) u|u| + C_M \rho(\pi D^2/2) \frac{du}{dt} \quad (2)$$

where $u(t)$ is the unsteady ambient water velocity near the pipe, D is the pipe diameter, ρ is the water density, C_D is the drag coefficient, C_M is the added-mass coefficient. The ambient water velocity was estimated using Dean's stream-function calculation. First, the stream-function was tuned to reproduce the measured water surface elevation $\eta(t)$, and then the corresponding bottom water velocity was calculated. Figure 6 shows a sample of the calculated bottom velocity for a measured $\eta(t)$. Over many selected wave cycles, the best-fit values for the drag coefficient ranged between -0.188 to +0.861, while the added-mass coefficient ranged from 1.51-2.08. From potential theory, assuming no flow-separation, the added-mass coefficient (which should be the same for either a half or a full cylinder) is predicted to have a value of 2 (Lamb 1932). For real fluids, the values of C_M and C_D would depend on the Keulegan-Carpenter Number $U_0 T/D$, where U_0 is the amplitude of the velocity oscillation, T is the wave period, as well as on Reynolds Number $U_0 D/\nu$, where ν is the kinematic viscosity (e.g. see Sarpakaya 1976 for full cylinders near flat bed). In our experiments, the Keulegan-Carpenter Number was around the value of 6, and the Reynolds Number was in the order of $(0.8 - 1.0) \times 10^6$.

PIPE DISPLACEMENT HISTORY

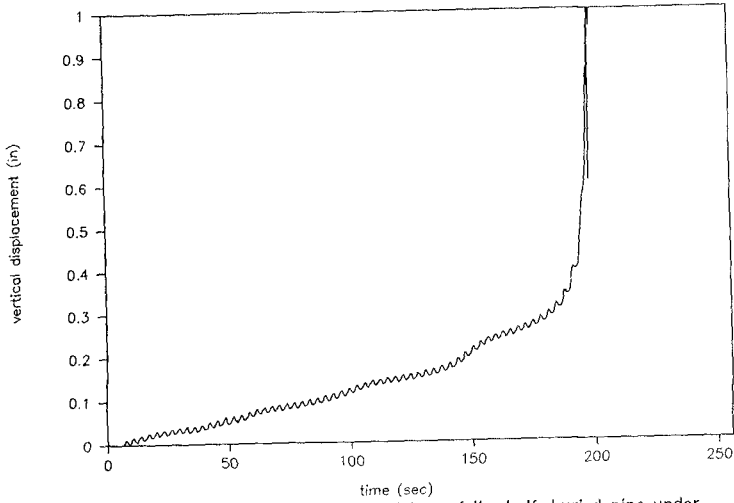


Figure 3: Vertical displacement history of the half-buried pipe under 6"-2.9sec water wave

PRESSURE DISTRIBUTION

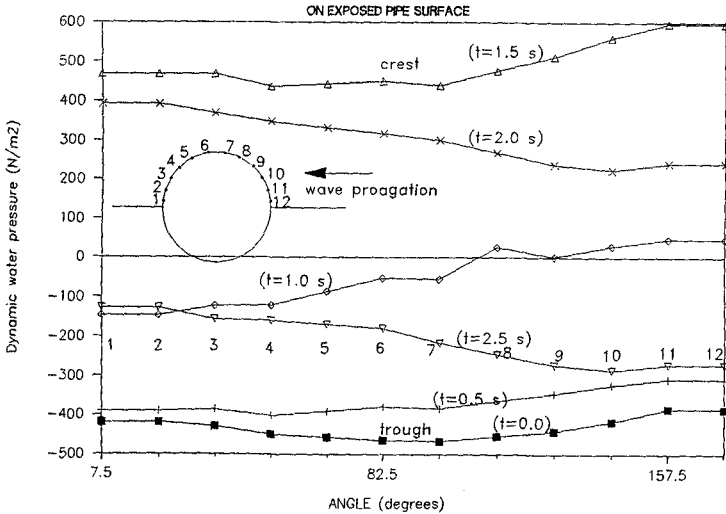


Figure 4: Measured water pressure on the exposed half-surface of the pipe over one full wave cycle (wave height 6", wave period 2.9 sec).

HYDRODYNAMIC DRAG ON THE HALF-PIPE

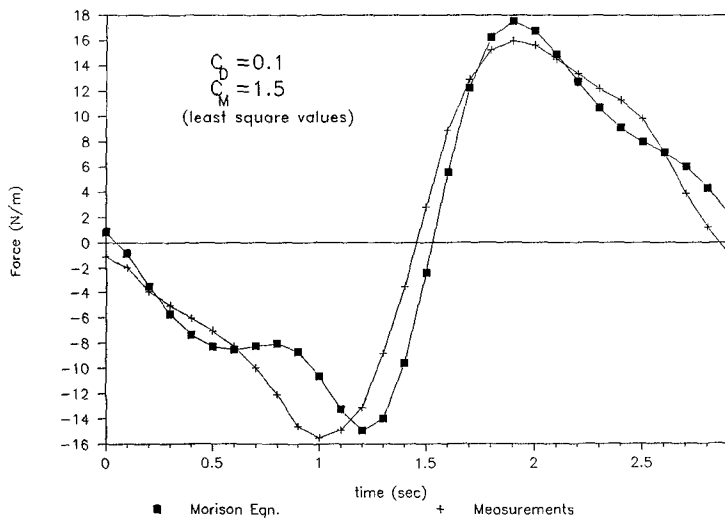


Figure 5: Curve fitting the measured drag force on the half-surface of the pipe with Morison Equation.

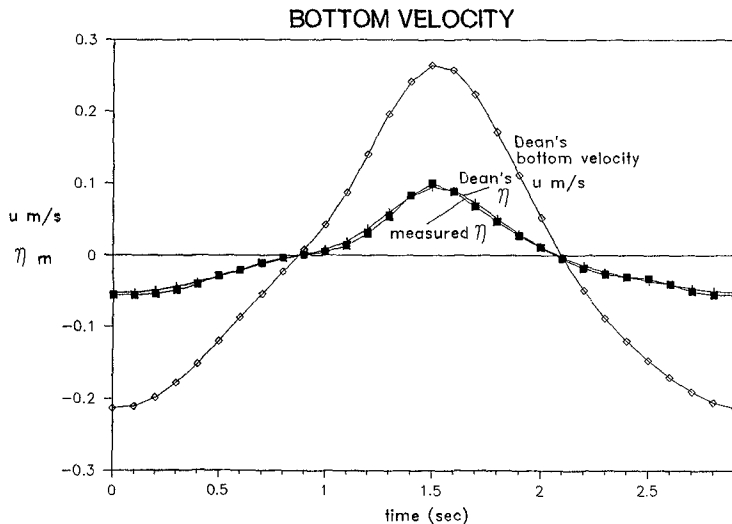


Figure 6: Comparison between measured vs. predicted water wave profile, and the resulting bottom velocity u using Dean's stream function.

As for the lift force F_L , we used the following expression to curve-fit the data

$$F_L = \frac{1}{2} C_L \rho D u^2 \quad (3)$$

where C_L is the nondimensional lift coefficient. The best-fit value for C_L , averaged over many wave cycles, was found to be 2.556, which is close to the theoretical value of 2.66 from potential flow theory (e.g. Milne-Thomson 1967).

Figure 7 shows sample results for the measured resultant hydrodynamic force on the pipe during one wave cycle. Notice that the resultant pressure force is passing, by definition, through the center of the pipe. With the wave propagating from right-to-left, the resultant force is rotating in an anticlockwise sense with a non-constant angular velocity, as is seen from the variation of the force angle θ with time. Clearly, the average angular velocity of the resultant force is equal to the wave frequency ω , but as seen from $\theta(t)$, the resultant force tends to slow down (below ω) when the force is near vertical, upward or downward, with a fast transition (above ω) between them. Notice also that the wave average drag and lift forces are much smaller than the respective amplitudes of the oscillatory forces. The wave-average lift is always directed upward, and its magnitude is found to be very close to the potential theory calculation, i.e., by wave-averaging (3) with $C_L = 2.66$. However, the far smaller net drag is observed to fluctuate in magnitude and even in direction; sometimes in the wave direction (Fig 7a) and sometimes opposite to the wave direction (Fig 7b).

6. THE BREAKOUT MECHANISM:

If the wave-averaged lift force exceeds the buoyant weight of the pipe, then the pipe will try to move upward in response. This will initiate two types of resistance forces along the pipe-sand interface, both acting to keep the pipe in place. One is the shear stress between the pipe and the sand grains, and the other is the negative pressure in the pore water below. That negative pore-pressure would be developed as some pore water will be forced to move upward along with the upward-moving pipe. For typical, low-permeability soils, the developed negative pore-pressure can be quite appreciable even for a very slight initial motion of the pipe. For example, a 1-m diameter pipe with an initial motion of only one hundredth of an inch above a fine-sand bed (permeability $k = 10^{-12} \text{ m}^2$) will produce, according to Darcy's law, a negative pore-pressure impact force of the order of 10^5 N-s/m . On the other hand, the value of the sand shear stress has an upper limit given by the relatively low Coulomb sliding shear for this unconfined, near-surface sand around the pipe.

The rate of vertical movement of the pipe will depend on the rate of water penetration into the developing gap between the pipe and the soil below. This water penetration can come from two possible sources: (a) the seepage flow of water into the gap across the soil surface, and this depends on the soil properties, especially its permeability and stiffness, and (b) the ambient water flow above the seabed through the gap periphery, which according to the lubrication theory is proportional to the gap thickness to the third power. In the initial stages of lift-off, the gap thickness is very small and thus its expansion will be essentially due to the penetration of pore water through the soil matrix. Since the pore water flow through the soil is typically very slow (governed by soil permeability), the pipe lift-off velocity during this stage will be very small (see Fig 3). With time, the gap thickness becomes large enough so that the lateral flux of ambient water through the gap periphery gains dominance over the pore water flux. As a result, the resistance to further gap expansion becomes much smaller than the pull-up force (e.g. lubrication theory), and hence the quick release at breakout time.

This is the basis of the theoretical breakout model of Foda (1985). In reality, however, there are a number of other factors that may be contributing to the breakout process, but are

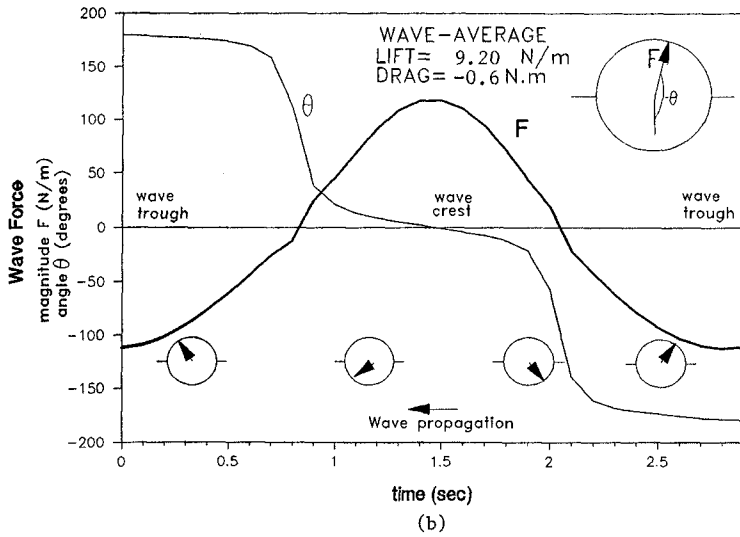
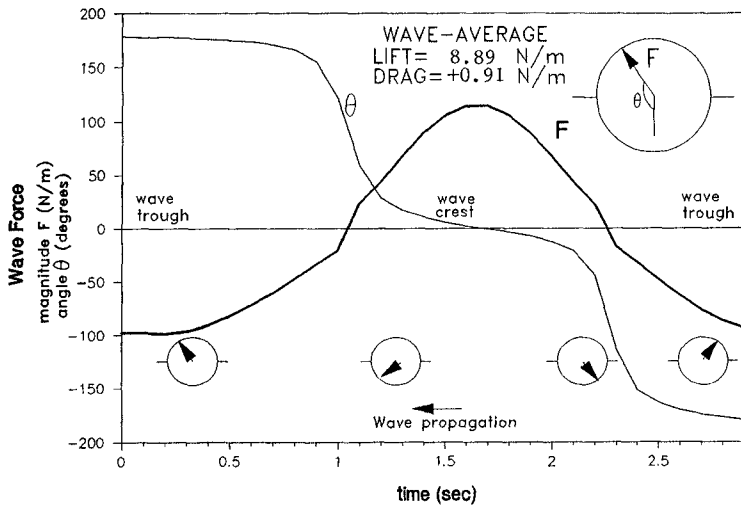


Figure 7: The variation of the total wave force magnitude and direction over two selected wave cycles.

not considered in this idealized model of Foda. For example, there is the question of the role of wave-induced drag force during the breakout process. In the above discussion, we focused on the response due to the applied lift force, which if acting alone on the pipe would result in a uniform lift-off of the pipe away from the underlying soil. However, in reality, the pipe is responding to the combination of lift and drag forcings. Furthermore, the model assumes that the pipe resistance against breakout is entirely provided by the negative pore-pressure or mud-suction stress at the pipe buried surface. In general, however, there will be some direct contact between the pipe surface and the sand solid skeleton, and hence there is the combination of pore pressure and effective (solid) soil stress that will be acting there, and it is of interest to compare the relative magnitudes of the solid vs. pore-fluid stresses that are actually acting on the buried pipe surface.

By integrating the pressure over either the upper, exposed surface l_e , or the lower, buried surface l_b , we get the corresponding fluid loadings on the pipe as follows:

$$(F_L, F_D)_{h,p} = \int_{l_e, l_b} p(\theta, t) (\sin \theta, \cos \theta) d\theta \tag{5}^\dagger$$

where F_{Lh}, F_{Dh} are the hydrodynamic lift and drag forces, and F_{Lp}, F_{Dp} are the pore-water lift and drag forces, respectively. It is further seen from Figure 4 that the pipe displacement is very small so that we may invoke the static balance equations in both the horizontal and vertical directions:

$$F_{Dh}(t) = -[F_{Dp}(t) + F_{Ds}(t)] \tag{6a}$$

$$F_{Lh}(t) = -[W + F_{Lp}(t) + F_{Ls}(t)] \tag{6b}$$

where F_{Ls} and F_{Ds} are the remaining soil lift and drag forces on the pipe due to the direct contact between the pipe and the soil's solid skeleton, and W is the submerged weight per unit length of the pipe.

A Fast Fourier Transform (FFT) is performed on Equations 6a,b in order to separate out the balances at the wave-averaged or zeroth-harmonic mode from the first and higher harmonic balances. The results for the fluid loadings are shown in Figures 8a,b. The discrete Fourier transform is defined as:

$$\overline{F}(m, \Delta\omega) = \frac{T_0}{N} \sum_{n=0}^{N-1} F(n, \Delta t) e^{-i2\pi mn/N}; \quad m=0,1,\dots,N/2 \tag{7}$$

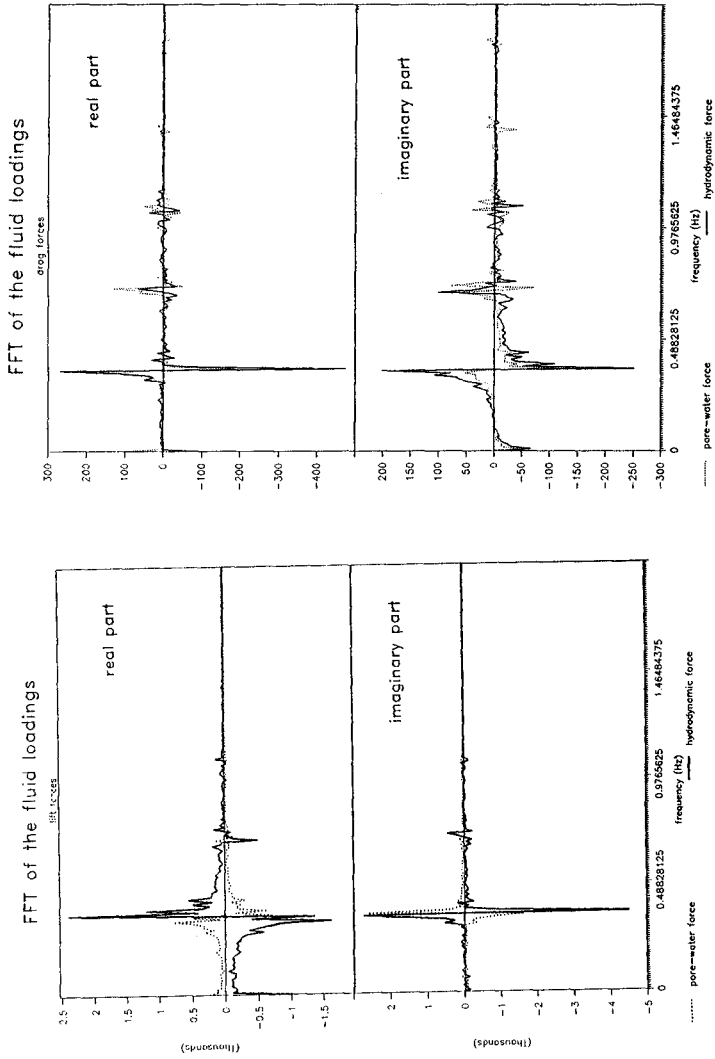
where the overbar denotes the Fourier transform, Δt is the sampling time increment which is taken here to be equal to 0.1 sec, N is the total number of data points, $T_0=N\Delta t$ is the duration of sampling, taken equal to 102.4 sec, and the incremental frequency $\Delta\omega=2\pi/T_0$. The results in Figures 8a,b correspond to the initial period (i.e. the first 102.4 s) of a selected breakout experiment with the same conditions as those for Figure 4.

Let us first examine the zeroth-harmonic ($m=0$) vertical response, which requires from (6b) that,

$$\overline{F}_{Lh}(0) / T_0 = - [W + (\overline{F}_{Lp}(0) + \overline{F}_{Ls}(0)) / T_0] \tag{8}$$

By accurately measuring the dry weight of the pipe and subtracting the water buoyancy we obtained a value of $W = 7.796 \text{ N/m}$. Furthermore, as seen from Figure 8a, we find that the

[†]Equation (4) is missing due to an error in numbering the equations.



(a) (b)
Figure 8: The Fast Fourier Transform of the hydrodynamic (solid lines) and pore-water (dotted lines) loadings on the half-buried pipe; (a) lift forces, (b) drag forces.

wave averaged hydrodynamic lift $-\overline{F}_{Lh}(0)/T_a$ is equal to $1021.8/102.4 = 9.98 \text{ N/m}$, while the wave-averaged pore-water suction force $F_{Lp}(0)/T_a$ is equal to $230.8/102.4 = 2.25 \text{ N/m}$, which virtually satisfies the vertical balance in (8) with negligible contribution from the soil effective stress forcing on the pipe; a mere -0.066 N/m according to (8). Turning to the zeroth-harmonic horizontal balance (see Figure 8b), we find a steady-state hydrodynamic drag on the pipe of a magnitude of 0.73 N/m , in the direction of wave propagation. We also find that the steady-state pore-water reaction force is equal to 0.817 N/m acting in the opposite direction. Again, there is an almost complete balance between the hydrodynamic and pore-water forces, with only a small contribution from the soil effective-stress loading, equal to the difference 0.087 N/m . It is curious, however, to note that these small soil loadings in both the horizontal and vertical directions are acting in the same direction as the the forcing hydrodynamic loadings. A partial explanation of this observation will be offered shortly.

We turn next to examine the balance of forces at the primary first harmonic, @ the wavemaker frequency $1/T = 0.345 \text{ Hz}$; $T = 2.9 \text{ sec}$. First, from Figure 8a we see that there is a 180° phase-shift between the hydrodynamic and pore-water vertical loadings almost throughout the frequency spectrum. But, we also see that the pore-water vertical force balances out only a proportion α of the forcing hydrodynamic loading, i.e.

$$\overline{F}_{Lp} = -\alpha \overline{F}_{Lh} \quad (9)$$

Except for a few very low frequencies near $m=0$ (giving higher values for α), the value of α is found to be relatively constant around $\alpha = 0.55$. That is to say that roughly 55% of the total soil reaction force to the unsteady hydrodynamic lift on the pipe is taken up by the pore-pressure. The remaining 45% of the soil reaction has to come from the soil-effective stress loading on the pipe. This contrasts drastically with the above-mentioned steady-state ($m=0$) results, where there is negligible effective stress contribution to the balance of forces.

The role of effective stresses is even more prominent in the horizontal forces balance. From Figure 8b it is seen that the unsteady ($m \neq 0$) hydrodynamic and pore-water drag forces on the pipe are in fact in-phase. This means that the pore-water unsteady drag is reinforcing, not balancing, the hydrodynamic unsteady drag. Therefore, it is the role of the soil solid skeleton to provide the effective stress loading necessary to balance the combined fluid drag force (hydrodynamic + pore-water). On the other hand, it should be noted that even this combined fluid drag on the pipe is an order of magnitude smaller than the hydrodynamic lift, as can be seen by comparing the ordinate scales in Figures 8a vs. 8b. Furthermore, we note that the drag-induced effective stress is not additive to the lift-induced effective stress, since they are almost 90° out-of-phase. This is evident from Figures 8a,b where we have two almost real lift spectra, and two almost imaginary drag spectra. It is also a consequence of the dominance of the added-mass drag component, as discussed before and as evident in Figure 5.

From the above, we may conclude that the pipe is in constant contact with the underlying soil, and the resulting effective stress loading on the pipe is, in part, balancing a proportion (~45%) of the wave lift force, and in part balancing the total fluid drag on the pipe. The elastic pipe displacement should be in-phase with the effective-stress loading, and thus should follow the same pattern as that of the force F in Figure 7, with a resulting anticlockwise orbital path of the pipe center over one wave cycle.

Superimposed on this oscillatory motion, there is the zeroth-harmonic response due to wave-averaged lift and drag forces. As predicted by Foda (1985), this response is entirely in the form of a mud-suction force or negative pore-pressure along the pipe-soil interface. The resulting motion is a gradual lift-off of the pipe as shown in Figure 3. The much smaller steady-state drag force is causing a slight antisymmetry in the mud-suction stresses and hence a very small deviation from the uniform lift-off condition. In other words, the

slow pipe motion will have both a net vertical upward component as well as a much smaller horizontal component in the same direction as the fluid drag, i.e. in the direction of wave propagation.

Next, we briefly discuss some of the possible dynamic interaction between the first and zeroth harmonic responses (e.g. Foda 1985). In particular, we heuristically discuss one specific possibility, namely, the role of the first-harmonic drag force on the net, or zeroth-harmonic pipe motion. First, we note that due to the oscillatory fluid drag, the pipe will be bouncing back-and-forth against the sides of the soil circular interface. The problem can be modelled as a simple elastic bouncing of a body off an elastic surface with an oblique impact angle. Therefore, as the pipe impacts on this nonvertical soil surface it will clearly bounce back from the surface acquiring a small additional vertical velocity in the upward direction. This is because the elastic strains in the soil due to this horizontal pipe impact will include vertical compressional strains along the circular soil interface. This small upward bounce, or roll-out, due to wave drag would clearly occur regardless of the direction of the drag. Therefore, there should be a net, or a wave-averaged (zeroth-harmonic) upward motion, as well as an upward effective-stress force on the pipe due to such mechanism. An indication of such upward effective-stress force was observed above when considering the balance of forces according to Equation (8). However, the obtained magnitude of this force, from the analysis that follows Equation (8), is seen to be negligibly small so that, at least in our case, such roll-out mode of motion is deemed to be of little significance to the total breakout process.

Finally, Figure 9 shows the experimentally obtained data on the breakout force-time relation. The breakout force F_b is defined here as the net uplift force acting on the pipe, which is given by

$$F_b = \bar{F}_{Lh}(0)/T_0 - W \quad (10)$$

and the breakout time t_b is determined from the recorded displacement histories (similar to Figure 4) when the slope of the curve reaches 90% of vertical. The best-fit power law that runs through the experimental data was obtained using a least-square routine, and is given in SI-units by

$$t_b = A F_b^{-0.93} ; A = 1477 \quad (11)$$

The exponent is very close to Mei *et al.* (1985) power law for breakout of flat-bottomed bodies from a porous rigid bed. Their law is given by

$$t_b = \tau(\mu L^{7/3} k^{-2/3}) F_b^{-1} \quad (12)$$

where μ is the water viscosity, k is the soil permeability, L is contact width of the two-dimensional body, and τ is a nondimensional coefficient that ranges between 0.4-0.62 depending on the assumed slip boundary condition at the bed surface. Using conformal mapping, the above analytical relation was extended to our configuration of a half-buried pipe and the details are given in Law *et al.* (1988). The result is a modification in the value of τ from that for flat-bottomed bodies. For example, for a no-slip boundary condition at the bed surface, we get

$$\tau = 1.9 \quad (13)$$

The increase in the value of τ , and hence the breakout time t_b , is due to the nonuniform shape of the resulting gap between the pipe and the bed, with the smallest gap thickness being at the gap periphery. This will clearly reduce the lateral flux of ambient water through the gap periphery, as compared to the case of a flat-bottomed body, and hence delay the breakout time.

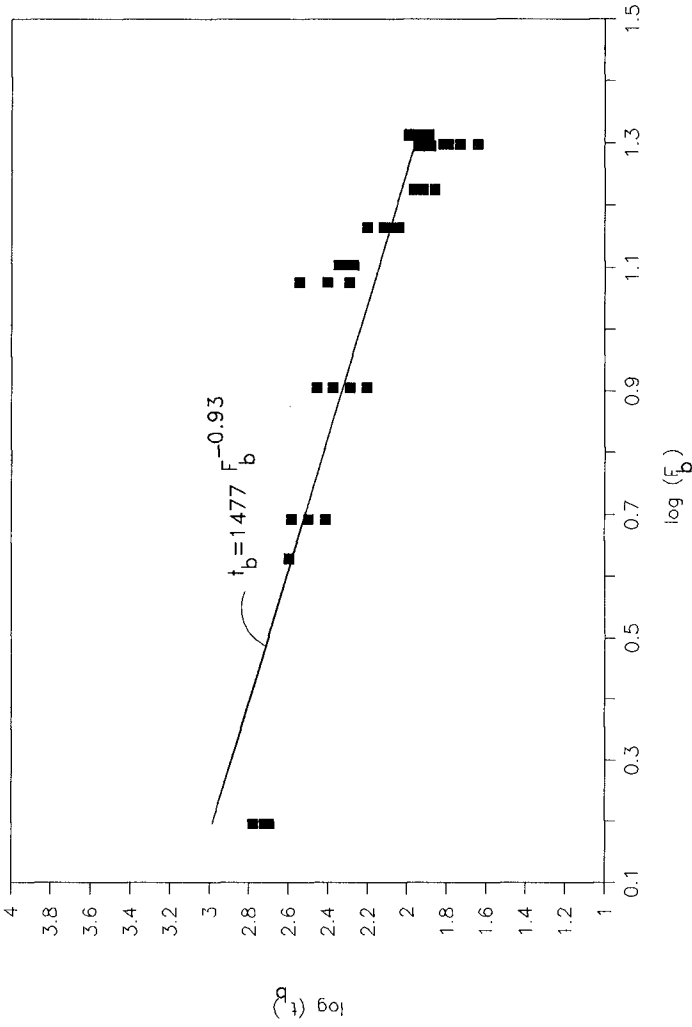


Figure 9: The experimentally-obtained breakout force-time relation

Now, recasting the constant coefficient A in (11) to be of the form of the material constant of the law in (12), where $\mu = 10^{-3} \text{ kg/m-s}$, $k = 0.32 \times 10^{-10} \text{ m}^2$ (measured using a constant head permeometer), $L = \pi D/2$, and $D = 0.2191 \text{ m}$, we find that the corresponding value of the free parameter τ is equal to

$$\tau_{\text{exp}} = 1.78 \quad (14)$$

which is very close to the theoretical value in (13).

ACKNOWLEDGMENTS

This research was sponsored by NOAA, National Sea Grant College Program, Department of Commerce, under grant number NA85AA-D-SG140, project number R/OE-2, through the California Sea Grant College Program.

REFERENCES

- Blumberg, R., "Hurricane winds, waves and currents test, marine pipeline design," Pipeline Industry, June-Nov. 1964.
- Christian, J.T., Taylor, P.K., Yen, J.K. and Erali, D.R., "Large diameter underwater pipeline for nuclear power plant designed against soil liquefaction," Offshore Technology Conference Proc., 2, 597-602, 1974.
- DeHart, R.S. and Ursell, C.R., Southwest Research Institute Report on Contract N-ONR-336300, 1967.
- Foda, M.A. "On the extrication of large objects from the ocean bottom, the breakout phenomenon," J. Fluid Mechanics, 117, 211-231, 1982.
- Foda, M.A. "Breakout theory for offshore structures seated on seabed," Proc. Specialty Conf. Geotech. Practice In Offshore Engineering, 288-299, Austin-TX, ASCE 1983.
- Foda, M.A. "Pipeline breakout from seafloor under wave action," Applied Ocean Research, Vol 7(2), 79-84, 1985.
- Gerwick, B.C.Jr. "Construction of Offshore Structures," New York: Wiley, 1986.
- Grace, R.A. "Marine Outfall Systems: Planning, Design and Construction," New Jersey: Prentice-Hall 1978.
- Husbergen, C.J. "Stimulated self-burial of submarine pipelines," OTC-2967, Houston-TX, May 1984.
- Ismail, N.M., Wallace, N.R. and Nielsen, R., " Wave forces on partially buried submarine pipelines," OTC-5285, 27-36, Houston-TX, May 1986.
- Law, A. and Foda, M.A., "Breakout of half-buried pipe from a rigid porous bed," Technical Report HEL- (in-press), University of California, Berkeley, 1988.
- Leeuwestein, N., Bijker, E.W., Peerbolte, E.B. and Wind, H.G., "The natural self-burial of submarine pipelines," BOSS'85, Delft July 1985, Amsterdam: Elsevier, Dev. Mar. Technol., Vol.2, Paper C18, 717-728, 1985.

Liu, C.L., "Ocean sediment holding strength against body breakout," U.S. Naval Civil Eng. Lab., Port Hueneme-CA, Tech. Rep. R635, 1969.

Mao, Y., "The interaction of a pipeline with an erodible bed," Institute of Hydrodynamics and Hydraulic Engineering, Technical University of Denmark, Research Series Paper No. 39, 1986.

Mei, C.C., Yeung, R.W. and Liu, K.P., "Lifting of a large body from a porous seabed," J. Fluid Mechanics, 152, 203-215, 1985.

Mei, C.C. and Foda, M.A., "Wave-induced response in a fluid-filled poro-elastic solid with a free surface - A boundary-layer theory," Geophy. J. R. Astro. Soc., 66, 597-637, 1981.

Milne-Thomson, M.N. "Theoretical Hydrodynamics," 5th ed., New York:MacMillan.

Muga, B.J., "Ocean bottom breakout forces, including field test data and the development of an analytical method, Tech. Rep. R591, U.S. Naval Civil Eng. Lab., Port Hueneme-CA., 1969.

Nataraja, M.S., Gill, H.S., "Ocean wave-induced liquefaction, J. Geotech. Eng., 109(4), 573-590, 1983.

Sarpakaya, T., "Forces on cylinders near a plane boundary in a sinusoidally oscillating fluid," Trans. ASME J. Fluid Eng., 98, 499-505, 1976.

Verley, R.L. and Reed, K., "Prediction of hydrodynamic forces on seabed pipelines," OTC-5503, 171-180, Houston-TX, April 1987.

CHAPTER 110

Perched Beach Profile Response to Wave Action

R. M. Sorensen* F. ASCE
N. J. Beil**

Abstract

Wave tank experiments were conducted to investigate the response of a perched beach profile to storm wave attack. Irregular waves having a JONSWAP spectrum were used for all of the test runs. Beach profile erosion was measured initially for a 1:20 slope nourished profile without a toe structure in place. This established base test profiles for comparison with subsequent erosion profiles with a toe structure or sill in place. The subsequent tests with a sill were conducted with the sill placed at a range of depths along the nourished profile slope.

Each of the test conditions was subjected to erosive wave attack for 42 hours with periodic interruptions for measurement of resulting beach profiles. Test results are presented and interpreted to evaluate the effect of the sill structure on beach profile response and the effectiveness of the structure in retaining the beach. Scaling of the results to prototype conditions is also discussed.

Introduction

A common solution to beach erosion problems is to periodically nourish the beach by the placement of sand fill. Often a structure is constructed to compliment nourishment - the structure increasing the stability of the fill to storm wave attack and/or deficiencies in longshore sediment transport. Common types of beach stabilization structures include groins and offshore breakwaters. The perched beach concept is a variation on the use of offshore breakwaters for stabilizing nourished beaches and protecting shore facilities.

A low submerged sill is constructed offshore and parallel to shore. Sand fill is placed landward of the sill, creating the perched beach (see Figure 1). The toe structure retains the perched beach, greatly reducing the

* Professor, Department of Civil Engineering, Lehigh University, Bethlehem, PA 18015

** Senior Project Engineer, Kidde Consultants Inc., Baltimore, MD 21204

volume of sand required to nourish the beach. The sill also triggers breaking of the larger waves thereby providing a measure of protection to the shore even if the fill were not in place.

Most commonly, the sill structure would be constructed of a homogeneous mound of stones. A preceding study (Givler and Sorensen, 1986 and Sorensen, 1987) investigated stability requirements for a submerged homogeneous stone sill structure. This investigation is concerned with the response of a nourished perched beach profile to storm wave attack. It involves two-dimensional wave tank experiments using irregular waves and a sand beach with and without a sill structure in place. Additional information on several aspects of this study are given in Beil and Sorensen (1988).

Research Facility

The experiments were conducted in a 32.7 m long, 0.91 m wide, 0.91 m high wave tank with a programmable spectral wave generator. The wave generator has an absorption capability, i.e. reflected waves are sensed at the generator paddle and subtracted from the primary wave being generated. This capability allows for long term generator operation without the buildup of troublesome reflected waves.

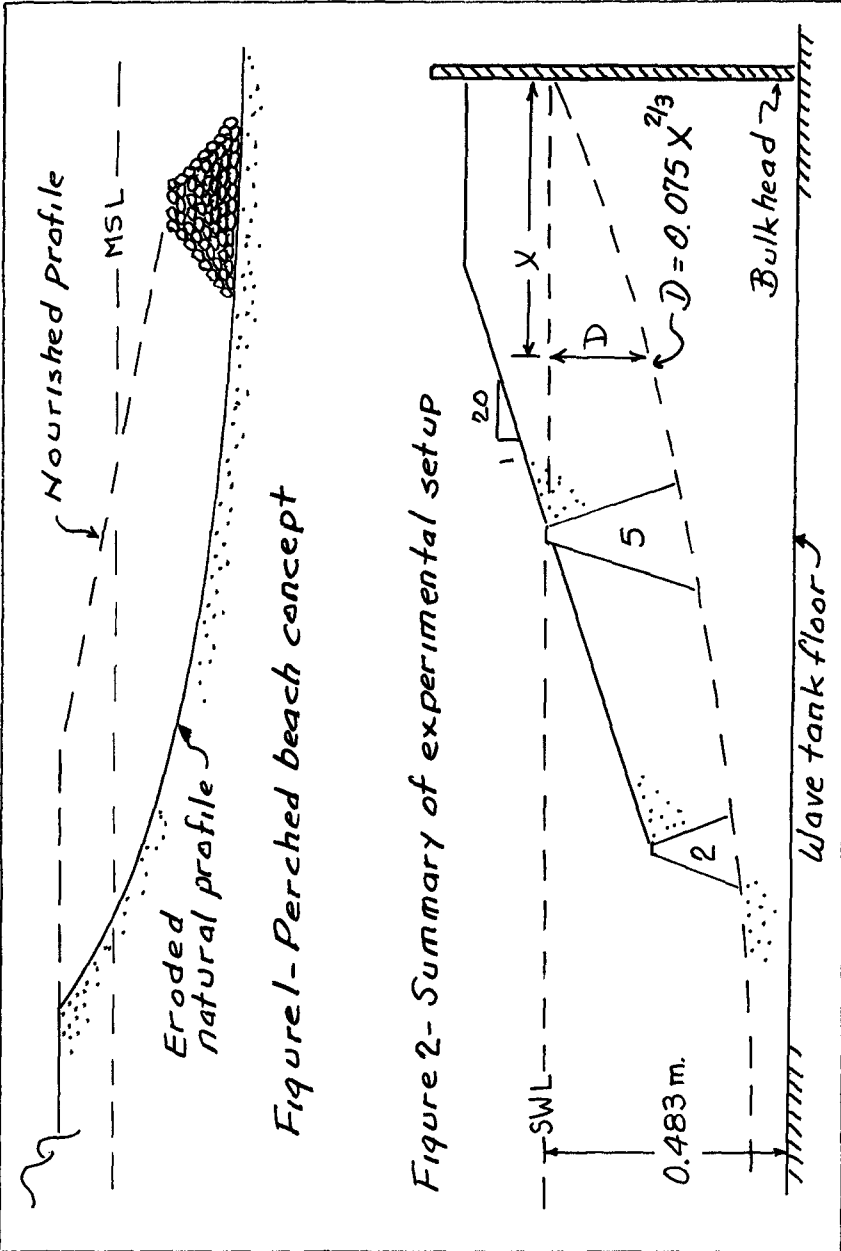
A parallel-wire resistance wave gage was installed 8.23 m from the wave generator and seaward of the toe of the sand beach. Output from the wave gage was recorded in analog form on chart paper and in digital form (0.12 hz) on a portable PC.

Beach profiles were measured along the tank centerline by a point gage mounted on a carriage that moved along the wave tank rails. Gage readings were made at 0.03 m horizontal intervals along the active portion of the beach profile.

The beach was made of a fine, uniformly graded sand having a median diameter of 0.145 mm and a corresponding median diameter fall velocity (V_f) of 0.018 m/s (calculated for 20 degrees C, S.G. = 2.65).

Experimental Set-up and Procedure

The experimental set-up is summarized schematically in Figure 2. All tests were run with a tank water depth of 0.483 m. A bulkhead was installed at a distance of 24.7 m from the wave generator. The sand beach was placed in front of the bulkhead with a berm crest elevation of 0.57 m above the tank floor and extending 2.44 seaward from the bulkhead. The nourished beach face extended sea-



ward from the berm at a 1:20 slope for all of the tests with and without the sill structure. The 1:20 slope was selected based on a review of recent beach nourishment projects in the U.S. (Hobson, 1981).

The same wave conditions were used for all of the tests. They were JONSWAP spectrum waves with a significant height (H_s) of 0.09 m and a peak period (T_p) of 1.6 sec measured at the toe of the beach slope. These waves yield a fall time parameter ($H_s/V_f T_p$) equal to 3.1. Kriebel et al. (1986) show that waves having a fall time parameter in excess of 2.0 to 2.5 should produce an erosive or storm type beach profile. This was confirmed by the resulting beach profile behavior.

Five test cases were investigated (Figure 2). The first consisted of a 1:20 nourished profile without a toe structure. The remaining four cases (2 through 5) were perched beach conditions with a sill located at various depths below the SWL and along the 1:20 beach face slope. The four sill crest depths were 1.0, 0.5, 0.25 and 0 times the incident significant wave height (i.e. 0.091, 0.046, 0.023, and 0 meters below SWL). For the four perched beach conditions, the beach profile seaward of the sill was a typical natural profile (Dean, 1977) as shown in Figure 2.

The sill structure was constructed of plywood with a crest width of 7.62 cm and 1:1.5 front and rear slopes. The seaward slope of the sill was covered with a plastic artificial turf material to reduce wave agitation in front of the sill.

Waves were run for a total of 42 hours for each of the five test cases. After the first six hours of waves the generator was stopped and the beach profile was measured. The profile was measured again at 12 hours, 18 hours, 24 hours, and 42 hours. At the 42 hour time period profile change was still occurring for each test case but the beach had approximately reached an equilibrium condition.

Experimental Results

The experimental data for the five test cases consists of beach profiles for the 0, 6, 12, 18, 24, and 42 hours of wave attack for the selected storm wave condition. Those portions of the measured profiles that are of primary interest are shown in Figures 3A to 3E. The profile for the first case (without a structure) is truncated at the seaward extreme of profile erosion. The profiles for the other cases are truncated a short distance seaward of the structure. These give sufficient scale in the figures to see what changes occurred from the

structure to the beach face, the area of greatest interest. The regions seaward of the point of truncation just show successive accumulations of sand tapering seaward.

Table 1 is a tabulation of horizontal retreat distances for the point on the beach profile at the still water line. The distances are measured from the original filled profile position before the start of wave attack and are for the given time intervals. Note that initially (0 - 6 hrs) the retreat is the least for the nonperched profile and increases as the structure crest moves up the profile to the SWL. Also note that the total retreat after 42 hours follows the same pattern, primarily owing to the large early retreat rates. However, after the initial 6 hour period, the retreat rate is reversed for the four perched cases with the retreat rate being minimum from hour 6 to hour 42 for the case with the structure crest at the SWL. It appears that, after the initial adjustment (which could be allowed for in the initial fill placement) location of the sill crest at the still water line results in the least recession of the beach face. Particularly in comparison to the nonperched profile, there is a significant reduction of later retreat with a sill installed near the SWL.

Figure 4 shows the initial fill profile, the 42-hour nonperched profile and the 42-hour perched profile with the sill crest at the SWL. Comparison of these profiles largely summarizes the effect of the sill structure on the resulting beach response and demonstrates the greatly reduced volume of fill required for the perched beach. A larger net volume of sand is transported further seaward for the nonperched condition.

Figure 5 is a summary of the 42 hour profiles landward of the sill structure for each of the four perched beach test cases. The beach face had a consistent slope of 1:5. There was a platform fronting the beach face that had a less consistent slope (but one that did not change with a noticeable trend) of about 1:50. As discussed above, the distance from the sill to the beach face progressively decreased for decreasing submergence of the sill crest as did the depth to the break between the beach face slope and the platform slope.

Scale Effects

The storm wave characteristics employed in these tests were limited largely by the wave amplitude generating capability of the wave generator. This in turn largely dictated the spectral peak period employed so that the resulting wave steepness was similar to typical prototype storm waves. An indication of the scaled prototype conditions represented by these tests can be obtained from

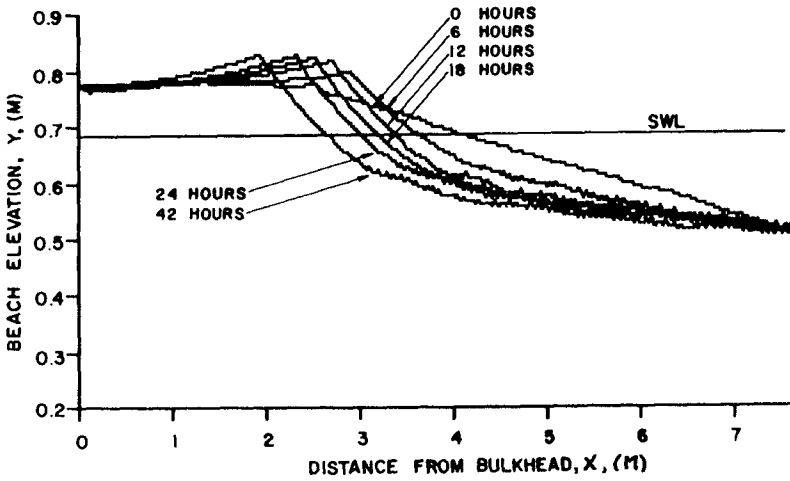


Figure 3A - Nourished beach, no structure.

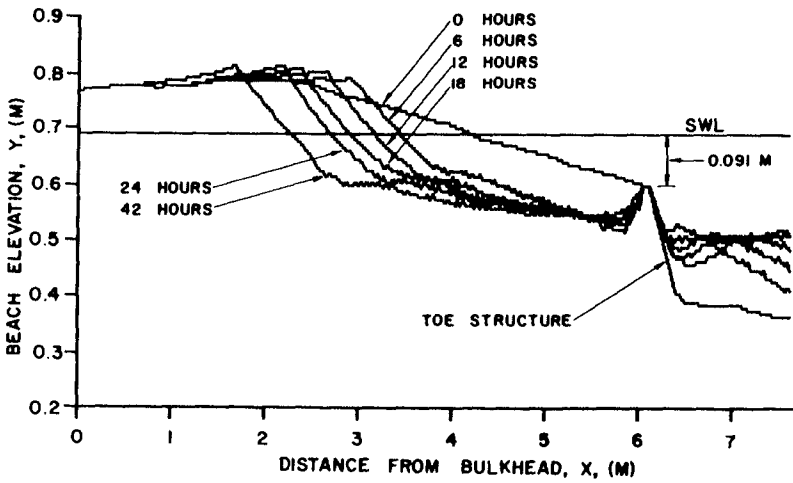


Figure 3B - Perched beach, structure crest depth 0.091 meters.

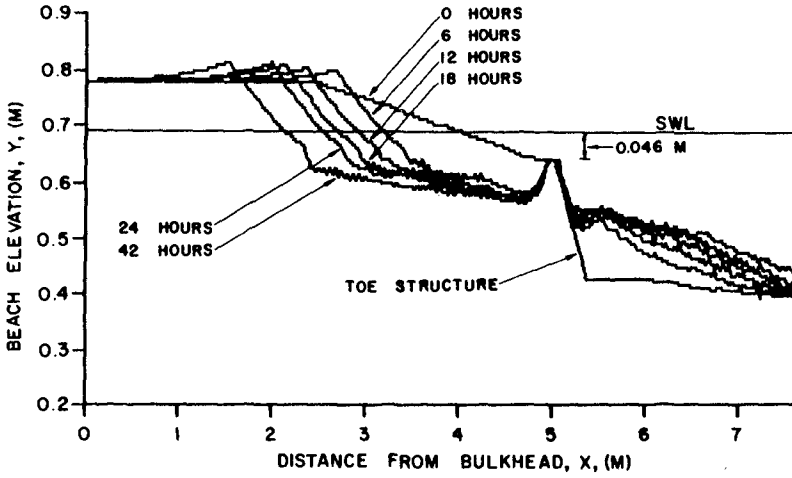


Figure 3C - Perched beach, structure crest depth 0.046 meters.

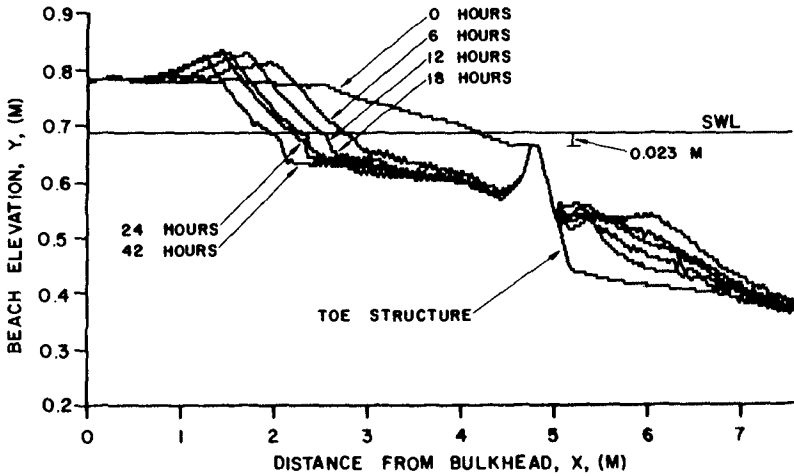


Figure 3D - Perched beach, structure crest depth 0.023 meters.

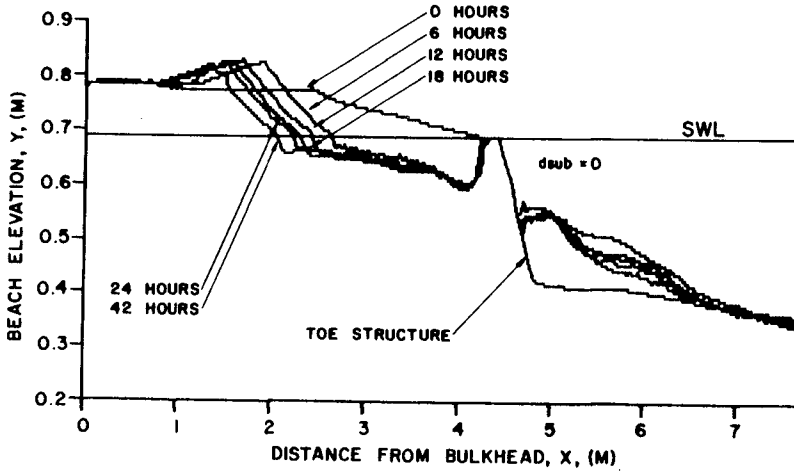


Figure 3E - Perched beach, structure crest depth 0.0 meters.

Test	$\frac{d_{sub}}{H_s}$	0-6 hrs	6-12 hrs	12-18 hrs	18-24 hrs	24-42 hrs	Total
1	-	.498	.234	.186	.198	.480	1.596
2	1.0	.786	.264	.270	.216	.552	2.088
3	0.5	.816	.258	.222	.162	.552	2.010
4	0.25	1.428	.246	.216	.072	.336	2.298
5	0	1.662	.216	.120	.066	.168	2.232

Table 1 - Retreat of SWL point (meters) for time intervals shown.

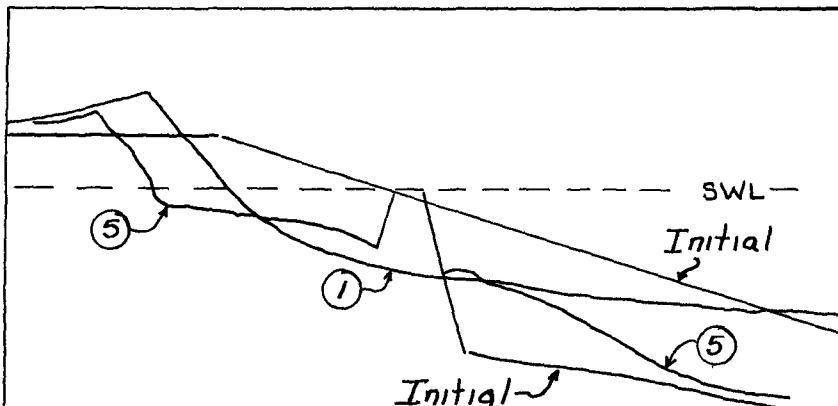
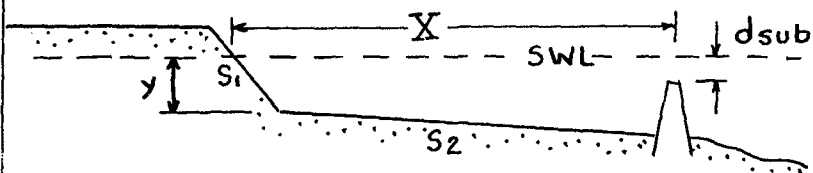


Figure 4 - Initial and 42 hour profiles for Cases 1 and 5



Test	$d_{sub}(m)$	S_1	S_2	$X(m)$	$Y(m)$
2	0.091	0.19	0.015	3.79	0.09
3	0.046	0.19	0.023	3.06	0.06
4	0.023	0.20	0.014	2.78	0.045
5	0.0	0.19	0.023	2.47	0.015

Figure 5- 42 hour profile geometries, for Cases 2 through 5

the recent work of Kriebel et al. (1986). They showed that erosive beach profiles can be scaled using Froude similarity (equal model and prototype Froude Numbers) and equal fall time parameters in model and prototype. With these two criteria, the model profile can be scaled up to prototype dimensions without distortion of profile geometry.

Assuming a prototype median sand diameter of 0.45 mm ($V_f = 0.065$ m/s) which is typical for beaches on the north shore in New Jersey and the model fall time parameter value of 3.1, along with Froude similarity requirements, yields an equivalent prototype significant wave height of 1.2 meters and a spectral peak period of 5.8 seconds (i.e. length ratio = 13.04, time ratio = 3.61). These values are somewhat low for typical storm wave conditions on the New Jersey shore which would be more in the order of 7 seconds period and 2 meters or more in height. Higher and longer waves than those used in the experiments would likely have resulted in a somewhat flatter beach face slope and more sand loss, in turn resulting in a greater distance between the sill and the beach face.

Discussion and Conclusion

The experiments presented herein are for only one wave condition and thus do not provide the range of data needed for the design of a perched beach under various conditions. However, the results suggest that a perched beach with the sill crest near the still water level can be an effective concept for beach nourishment under appropriate conditions - for example, where there is a steep offshore slope or a narrow shelf width. Significantly less fill volume is required with a sill in place and offshore losses should be reduced. So, a perched beach may be cost effective for many locations. Additional data, covering a much wider range of conditions, are needed.

References

- Beil, N. J. and R. M. Sorensen (1988) "An Investigation of Perched Beach Profile Response to Wave Action" H. R. Imbt Hydraulics Lab Report 115-88, Lehigh University, Bethlehem, PA.
- Dean, R. G. (1977) "Equilibrium Beach Profiles, U.S. Atlantic and Gulf Coasts", Ocean Engineering and Technical Report No. 12, University of Delaware, Newark, DE.
- Givler, L. D. and R. M. Sorensen (1986) "An Investigation of the Stability of Submerged Homogeneous Rubble-mound Structures Under Wave Attack", H. R. Imbt Hydraulics Lab Report 110-86, Lehigh University, Bethlehem, PA.

Hobson, R. D. (1981) "Beach Nourishment Techniques" Report 3 - Typical U.S. Beach Nourishment Projects Using Offshore Sand Deposits, U.S. Army Coastal Engineering Research Center, Ft. Belvoir, VA.

Kreibel, D. L., W. R. Dally and R. G. Dean (1986) "Undistorted Froude Model for Surf Zone Sediment Transport" Proceedings, 20th International Conference on Coastal Engineering, Taipei, pp. 1296-1310.

Sorensen, R. M. (1987) "Evaluation of Perched Beach Concept for Shore Stabilization" Proceedings, Coastal & Port Engineering in Developing Countries, Beijing, pp. 318-326.

CHAPTER 111

EFFECTS OF A VERTICAL SEAWALL ON PROFILE RESPONSE

Michael R. Barnett¹, A. M., ASCE, and Hsiang Wang²

ABSTRACT

An attempt is made to determine beach profile response due to the presence of a vertical seawall placed in various cross-shore positions, and to examine the differences between natural beaches and seawall-backed beaches in response to normally incident wave attack. The investigation was mainly restricted to two-dimensional profile response under erosive wave conditions, with beach recovery response monitored to a limited extent. Spatial and temporal profile response was investigated by examining time-series profile configuration, volumetric changes, sediment transport patterns, and quasi-equilibrium profile configuration. Additionally, dominant profile features such as the break point and reflection bars (as well as scour at the toe of the seawall-backed profiles) were observed and quantified.

INTRODUCTION

An emerging concern by coastal communities and engineers is the effect of seawall placement along beach-dune systems. Since seawalls are most likely to be placed along eroding coastlines, any added erosional pressure due to the presence of the structure is deemed serious.

Important questions raised by interrupting a natural system with a seawall are

- 1) will the presence of the seawall accelerate the erosion process of the beach fronting it;
- 2) what effect does cross-shore placement of the seawall have on profile response;
- 3) what is the resulting profile configuration under erosive wave conditions;
- 4) will profile recovery be impeded by the structure.

¹Coastal Engineering Specialist, Florida Sea Grant Extension Program, 336 Weil Hall, University of Florida, Gainesville, Florida 32611 USA

²Professor, Coastal & Oceanographic Engineering Department, 336 Weil Hall, University of Florida, Gainesville, Florida 32611 USA

These concerns regarding construction and placement of a seawall necessitate that quantitative and qualitative relationships and trends be investigated. The focus of this study was to examine a fundamental aspect of a seawall-beach system by assessing the influence of a vertical seawall on beach profile response through laboratory experimentation.

Numerous field and laboratory investigations documenting seawall-beach interaction exist, but very few tests have focused on structural influence on profile response. Kraus (1987) provides a detailed literature review of over 70 laboratory, field, theoretical, and conceptual studies; due to space limitations here, the reader is referred to this thorough treatment for a more detailed background on the subject.

OBJECTIVES AND SCOPE

The main objectives of this investigation were to determine beach profile response due to the presence of seawalls, and to examine the differences between natural beaches and beaches fronting seawalls in response to normally incident wave attack. Seawall location was varied throughout the experiments, with each location subjected to the same wave conditions as the "no-seawall" tests. The present investigation differs from previous investigations in that the initial profile shape of $Ax^{2/3}$ has not been examined in detail with a seawall placed along the profile.

The experiments involved monitoring temporal and spatial changes of beach forms on natural and seawalled beaches under various wave conditions and seawall positions. The results were analyzed toward an understanding of:

- 1) characteristic profiles;
- 2) volumetric changes;
- 3) patterns and mechanisms of sediment movement; and
- 4) equilibrium profile configurations.

Profile features of special interest include break point bar formation and the presence of reflection bars. For seawall-backed beaches, the scour trough at the structure toe, the eroded and accreted volumes, and the rates of erosion and recovery were also examined.

DESIGN OF THE EXPERIMENTS

Selection of the initial profile geometry for all tests is based on an empirical relationship proposed by Dean (1977); the same criterion was employed by Kriebel et al. (1986) for tests without a seawall. To simulate natural conditions, similarity criteria are established on the assumption that the energy dissipation per unit volume along a beach profile is uniform, and that the wave properties can be properly scaled by Froude criteria.

Beach Profile Geometry. Each of the model tests conducted in the present study was molded to an initial profile of $Ax^{2/3}$; this profile geometry was determined by Dean (1977). Dean postulated that if the energy dissipation per unit volume in the surf zone is uniform and is a function of sand grain size, D , only, then the following relationship exists:

$$\frac{1}{h} \frac{\partial F}{\partial x} = \zeta_*(D) \quad (1)$$

where F is the energy flux per unit width, h is the water depth, x is a shore-normal coordinate, and $\zeta_*(D)$ is a constant depending on D only. By applying linear wave theory assumptions and shallow water approximations, the following relationship is derived:

$$h(x) = \left\{ \left[\frac{\zeta_*(D)}{\frac{24}{5} \rho g^{1/2} \kappa^2} \right]^{2/3} \right\} x^{2/3} \quad (2)$$

The quantity enclosed by { } is defined as $A(D)$, leaving

$$h(x) = A(D)x^{2/3} \quad (3)$$

This profile shape was examined by Dean and compared to over 500 natural beach profiles along the U.S. Atlantic and Gulf coasts. All initial profiles in the present study utilized the geometry represented by (3).

Similarity Criteria. In order for the laboratory model to faithfully represent prototype conditions, similarity criteria should be established and observed. Constructing a moveable bed model requires the horizontal scale, vertical scale, and grain size and specific gravity of the bed material to be specified.

To maintain proper similarity between model and prototype requires the geometry conditions, flow conditions, and sediment transport processes to be similar. By utilizing an undistorted model with sediment identical to the prototype, the transport process can be approximately simulated if

- 1) the Froude criterion is fulfilled for the flow field;
- 2) the sediment fall velocity scale ratio behaves as the square root of the length scale; and
- 3) the sediment is large enough to ensure a turbulent boundary layer and to ensure that the properties of the granular material are maintained.

Empirical Orthogonal Functions. By utilizing empirical orthogonal functions (eigenfunctions) to represent a series of beach profiles, all the profile data in that series may be represented in a compact form by showing spatial and temporal variations of dominant profile features. Profile variations are taken from an elevation, h , measured a distance, x , from a baseline over time intervals of variable spacing. Profile elevation at a given time may be represented by h_{xt} , where x represents an index for the spatial profile coordinate and t represents the temporal index.

The empirical eigenfunction analysis seeks to represent h_{xt} in terms of a linear expansion of the product sum of the spatial and temporal eigenvectors in the form

$$h_{xt} = \sum_{n=1}^N w_n c_{nt} e_{nx} \quad (4)$$

where w_n is the weighting coefficient for each of the N eigenvectors, c_{nt} is the temporal eigenvector, and e_{nx} is the spatial eigenvector.

The data set input into such a form results in a set of empirical eigenfunctions which best fit the data in a least-squares sense. The first set of eigenvectors, for the mode $n = 1$, represents the largest percentage of the total variance of the data set, or the dominant mode of the transport process in this case, while successively higher modes represent successively higher order perturbations. This method has been applied to beach profile field data by Winant et al. (1975), Aubrey (1979), and Kriebel et al. (1986).

As each eigenvector exhibits the property of orthogonality, individual eigenfunctions represent a certain percentage of the variance of the mean square of the data; therefore, each solution is unique in that it is not correlated to any other solution, allowing for an explanation of the variance from the input data set (Kriebel et al., 1986). Hence, large numbers of variables may be expressed by those few empirical functions which describe the major percentage of the mean square value of the data.

APPARATUS, PROCEDURE, AND CONDITIONS

System Components

Wave tank. The laboratory tests were conducted in the "air-sea" tank at the University of Florida Coastal Engineering Laboratory. The usable portion of the tank is 37 m long, 1.2 m high, and partitioned by a 1.9 m high concrete block wall into two sections of equal width, each approximately 0.87 m wide. The section of the tank in which the laboratory tests were conducted has one wall constructed of glass panels to permit visual observation of profile changes. The beach was constructed with the toe 18 m from the wave generator and with an approximate profile length of 17 m. The tank dimensions, along with the location of the profile in the tank, are shown in Figure 1.

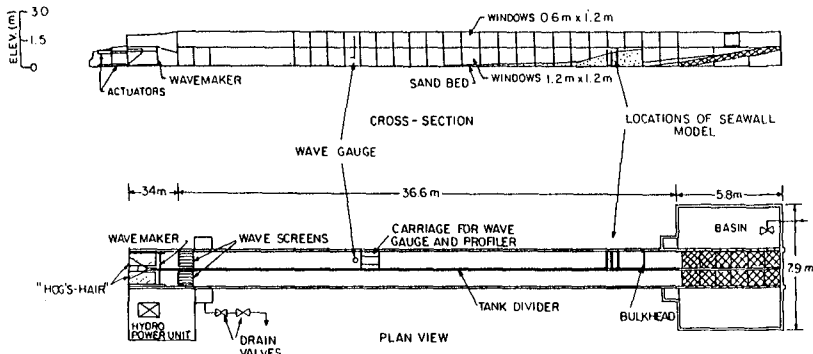


Figure 1. Schematic of Test Facility.

Sediment. The bed material used in the model tests was a fine quartz sand with a median grain diameter of 0.15 mm as determined by sieve analysis of samples obtained at four locations along an eroded equilibrium profile; a settling tube analysis was also performed. Two independent tests were performed on each sample, and the median fall velocity was determined to be 1.77 cm/sec.

Seawall model. The model seawall was constructed of 13 mm plywood 0.85 m wide and 0.88 m high coated with fiberglass resin to protect against both warping and abrasion. All experiments which were conducted with a seawall had the model installed vertically and flush with the tank bottom.

Instrumentation. Data acquisition was accomplished by utilizing a capacitance-type wave gauge and a Mark-V Electronic Profile Indicator (capacitance-sensing bottom profiler) mounted on a motorized cart which ran along parallel rails located above the test section.

Procedure

Initial Conditions. In each test, the sand bed was initially molded to an $Ax^{2/3}$ profile shape, with an A value of $0.075 \text{ m}^{1/3}$ and a beach face slope of 1/5 from the point of tangency to an elevation above the expected runup limit (Kriebel, Dally, and Dean, 1986). At this elevation, a 30 cm wide berm was constructed, the landward extent of which served as a control point for all profiles. The wave tank tests conducted by Saville (1957) were selected as the prototype tests; based on calculation of the sediment fall velocities, Kriebel et al. (1986) found the prototype to model time scale to be 3.09, and the length ratio to be 9.6. These values were also adopted for the present study. Once the profile was graded, the tank was filled with fresh water and the sand bed was allowed to soak for 10 to 12 hours. Before beginning a test, monochromatic waves were run against the initial profile for one to two minutes to allow for further bed consolidation; the initial profiles were then recorded by moving the profiler along the entire bed.

Data Acquisition. Each experiment was run a sufficient duration to reach a quasi-equilibrium condition (that is, no appreciable changes in profile configuration over time). Wave data were collected intermittently, and profile data were acquired as a time series to monitor profile evolution.

Further Profile Data Conditioning. Two independent profiles were taken at approximately one-third the cross-tank distance from each of the flume walls at each time interval in an attempt to reduce the error introduced by cross-tank variations. Such variations were also noted by Kriebel et al. (1986); possible causes are: wall boundary layer producing wave refraction, uneven bed compaction, and reflected wave interaction with incident waves.

A short series of experiments was conducted to test the profile recovery characteristics of a seawall-protected beach versus a "natural" (unprotected) beach. To accomplish this, the profiles were first subjected to erosive wave conditions accompanied by a storm surge; after eroding the profile for a fixed length of time, the water level was reduced, and lower steepness waves were produced.

Test Conditions

Figure 2 illustrates the seawall locations, water depths, and initial profile geometry used in the present investigation. Table I lists pertinent test parameters such as water depth, wave height, wave period, and seawall location. The letter designations for each Test Classification listed (A, B, C, and D) refer to tests with identical input wave conditions and water depths. Tests 1-13 were performed under erosive wave conditions, both with and without a 10 cm model scale storm surge (0.96 m full scale). This value was chosen to prevent overtopping of the seawall and, for the natural beach test cases, to prevent overtopping of the berm. Tests 14 and 15 were conducted to determine the rate and extent of profile recovery on one natural and one seawall-backed beach, respectively.

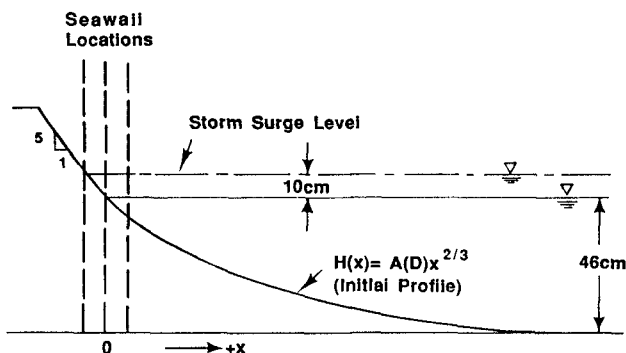


Figure 2. Schematic of Test Conditions.

Table I. Pertinent Test Parameters.

Test Number and Classification	Period (sec)	Water depth (cm)	Wave height (cm)	Seawall location, (m from 46 cm SWL)
1 A	1.81	46	11.75	N/A
2 A	1.81	46	11.75	-0.3
3 A	1.81	46	11.75	0.0
4 A	1.81	46	11.75	+0.3
5 B	1.30	46	8.80	N/A
6 B	1.30	46	8.80	-0.3
7 B	1.30	46	8.80	0.0
8 B	1.30	46	8.80	+0.3
9 C	1.81	56	11.75	N/A
10 C	1.81	56	11.75	N/A
11 C	1.81	56	11.75	-0.3
12 C	1.81	56	11.75	0.0
13 C	1.81	56	11.75	+0.3
14 D	1.81	46	4.00	N/A
15 D	1.81	46	4.00	-0.3

RESULTS AND DISCUSSION

Composite Profiles

Wave data were obtained periodically between profile data-taking intervals; wave height records were acquired by sampling with the capacitance gauge immediately seaward of the profile toe. Reflection envelopes were obtained by moving the gauge horizontally in the direction of wave propagation at a fixed rate of speed.

For tests with a 46 cm water depth, profile configurations both with and without seawalls were remarkably similar in overall planform. With the exception of local effects due to the presence of the seawall, the main bar-trough features existed for all profiles. The presence of the seawall on the profile shifted the location of the break point bar and also created a scour trough at the toe of the structure. For an elevated water level (10 cm storm surge), on the other hand, the profiles backed by a vertical wall were markedly dissimilar in final planform to those profiles without a seawall. This is apparently due to the artificially reduced surf zone width and increased wave reflection created by the wall. Reflection bars were more evident for the walled profiles than the "natural" beach profiles for the storm surge conditions; reflection coefficients were higher for the seawall-backed profiles.

Test Classification A experiments exhibited a similar trend in the formation and migration of the break point bar. Breaking waves rapidly formed a small break point bar formation at a distance of 4.3 m to 5.3 m from the baseline (intersection of 46 cm SWL with the initial profile). Bar migration in all tests in this category ($H = 11.75$ cm, $T = 1.81$ s) was observed to be offshore, with the break point location becoming fairly well-stabilized between 3.23 hours and 4.2 hours model time, as seen in Figures 3 and 4; once this occurred, bar width decreased and bar height increased. Sediment transport seaward of the break point bar then became predominantly offshore, forming a large trough 3.1 m to 3.5 m in length, with an offshore bar at the profile toe.

Test Classification B experiments also exhibited a consistent unidirectional mode of offshore sediment transport. Break point location ranged from 1.7 m (Test 7, seawall at SWL) to 2.8 m ("natural" beach) from the baseline.

Laboratory experiments conducted to simulate a 10 cm storm surge with the same wave conditions as Tests 1 through 4 displayed rapid bar formation. Bar migration for the "natural beach" tests was observed to progress offshore, with bar location stabilizing at 3.5 m from the baseline (see Figure 5). Test 10 was conducted as both a confirmation of the repeatability of the test program (Test 9) and as a means to establish initial conditions for the "natural" recovery test (Test 14).

Classification C experiments which investigated the effects of varying seawall location (Tests 11 through 13) established break point bar formation within the first 0.5 hours of testing. Bar migration for all tests was minimal due to the "fixed" shoreline created by the wall; as shown by figure 6, this, coupled with a comparatively high reflection

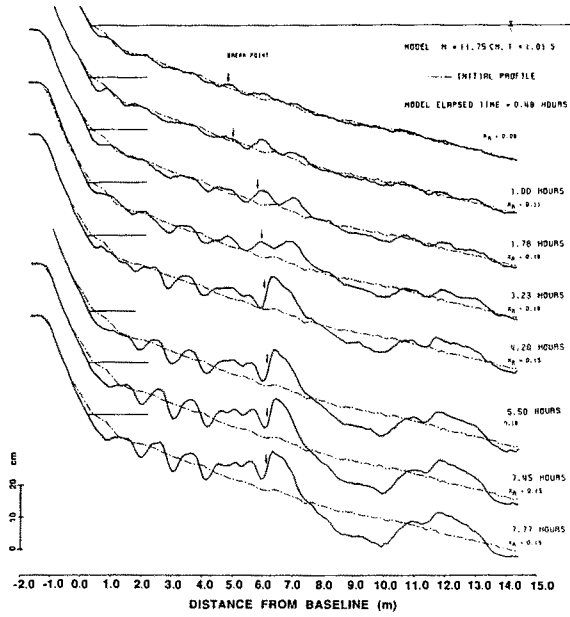


Figure 3. Time-series Profile Evolution, Test 1.

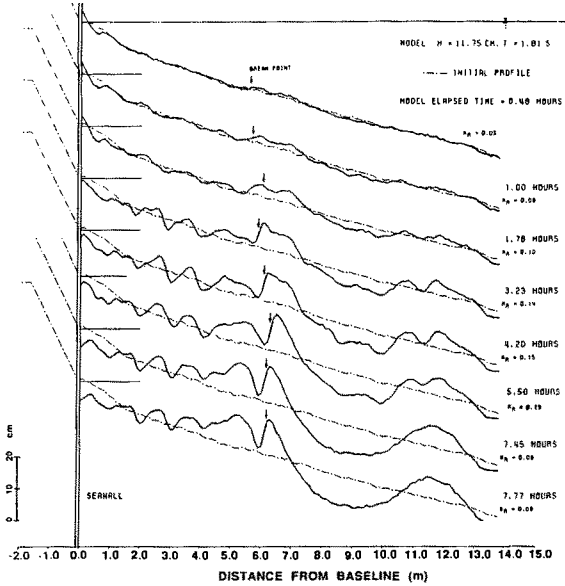


Figure 4. Time-series Profile Evolution, Test 3.

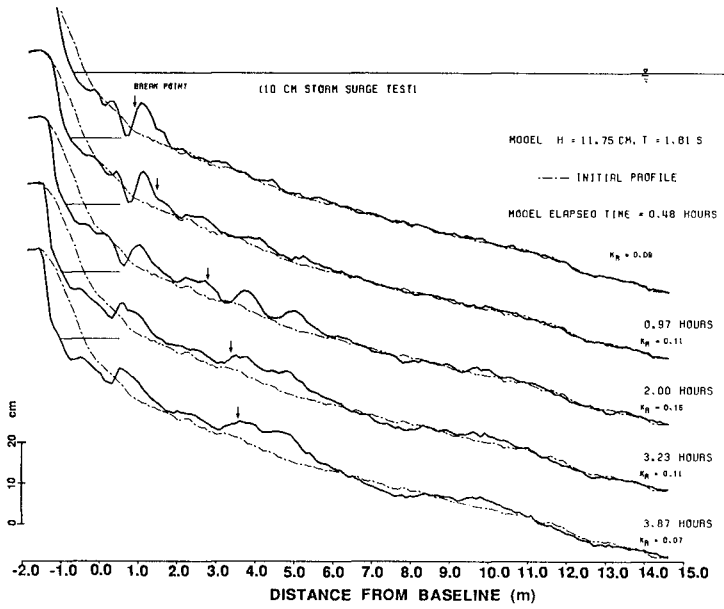


Figure 5. Time-series Profile Evolution, Test 9.

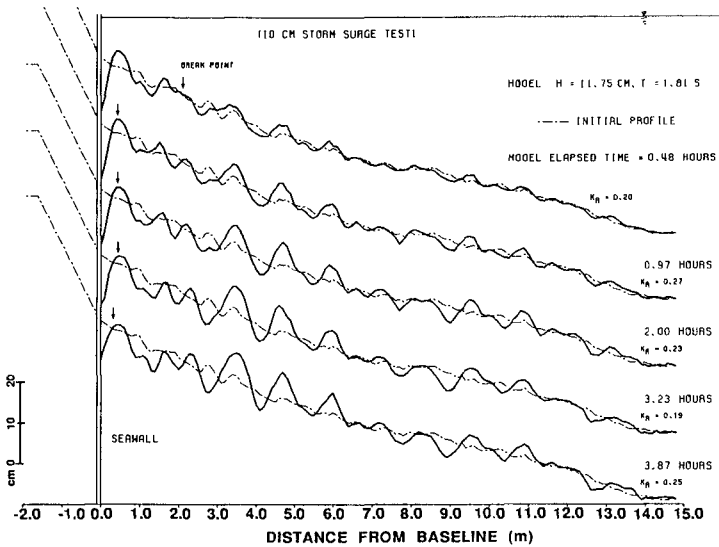


Figure 6. Time-series Profile Evolution, Test 12.
(Same wave parameters as Test 9).

coefficient, led to bar formation in proximity to the structure (0.5 m to 1.0 m). All tests displayed a partial recovery of the toe scour volume after a maximum scour condition at roughly 2.0 hours elapsed model time. This recovered volume was transferred from the break point bar crest to the scour trough. Bedform undulations seaward of the break point showed continuous growth throughout the test, with a dominant bar spacing of 1.2 m to 1.3 m, or approximately one-quarter the incident wavelength. Smaller bar formations randomly spaced along the profile acted to disrupt the dominant reflection bar spacing.

The recovery tests (Test Classification D), which were conducted by reducing the water level to 46 cm at the termination of Tests 10 and 11 for the "natural" and seawalled beaches, respectively, showed an apparent isolation of the seaward half of the profile from any significant bar migration (caused by the reduced water level and wave height). Break point bar location in Test 14 shifted onshore approximately 1.1 m due to water level reduction.

Volumetric Profile Changes

Volume Changes over Profile Length. Break point bar formations within each test classification displayed nearly identical maximum volumes, despite the fact that bar location was dependent on seawall position. For Test Classification A, bar volumes ranged from 110 cm³/cm (seawall located -0.3 m (shoreward) of 46 cm SWL) to 123 cm³/cm for the natural profile. Test Classification B bar volumes ranged from 60 cm³/cm (natural profile) to 74 cm³/cm (seawall +0.3 m). Maximum bar volumes for Test Classification C varied between 62 cm³/cm (seawall + 0.3 m) and 70 cm³/cm (natural profile).

Comparison of Denial Volume to Eroded Toe Volume. The volume change obtained with a natural profile subjected to erosive wave conditions was compared to the additional volume eroded in front of a seawalled beach; regions of interest are shown schematically in Figure 7. The final eroded profiles of the natural beach cases were selected as the baseline profiles for this study; final eroded profiles for the seawalled beaches were then used to calculate volume change. This procedure was performed for tests 1 through 13; the results appear in Figure 8. A linear regression analysis yielded a least-squares fit with a slope of 0.616. The additional volume eroded at the seawall toe was less than the volume denied to the profile upon placement of the seawall on the beach. Only one case (Test 6) exhibited a larger toe scour volume than the volume denied the profile (results plotted in Figure 8 are for final volumes only).

Empirical Eigenfunction Analysis

Standard Analysis. A standard eigenfunction analysis was performed on the laboratory data; as with the results obtained by Winant et al. (1975), the mean beach function was found to represent over 99 percent of the mean square value of the data. Laboratory test results also showed similarity to the second and third eigenfunction data obtained at Clearwater Beach, Florida by Kriebel et al. (1986).

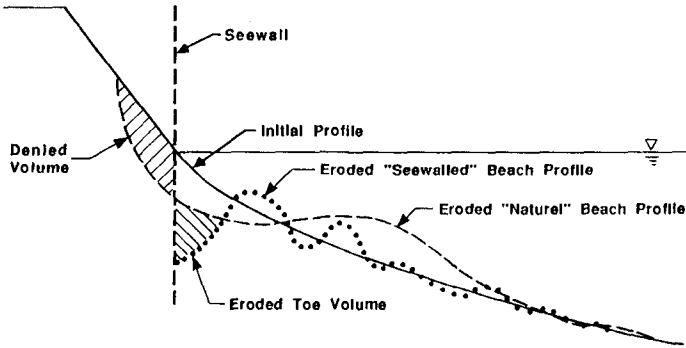


Figure 7. Schematic of Profile Features of Interest.

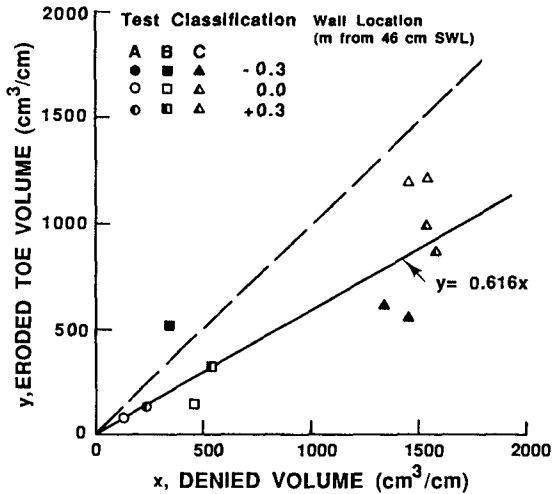


Figure 8. Denied Volume versus Eroded Toe Volume.

Modified Eigenfunction Analysis. Based on further interpretation of the remaining data, the influence of the initial profile on the mean profile configuration (first eigenfunction) was found to be highly dominant. Since the field studies cited previously dealt with spatial and temporal changes over long periods of time, no true "initial" profile existed in these investigations. Hence, a modified eigenfunction analysis was undertaken in which the method of analysis was unchanged, but the input data set was reformatted such that the initial profile acted as a baseline configuration. All profiles within a test set were subtracted from the initial profile, and the eigenfunction analysis performed on this modified data; typical results are illustrated in Figures 9 and 10. Additionally, the temporal

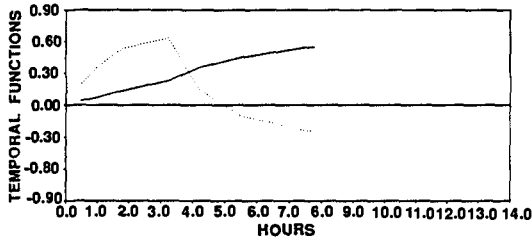
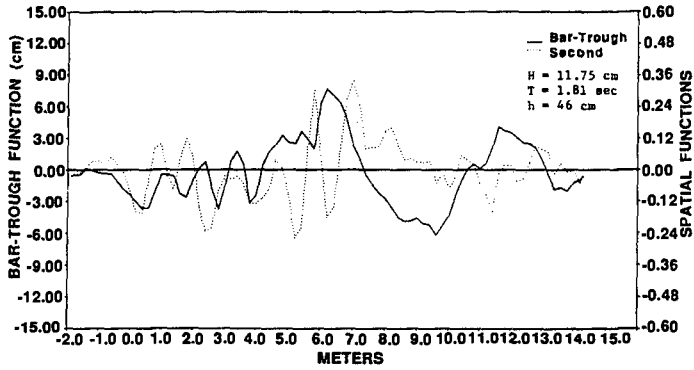


Figure 9. Modified Eigenfunction Analysis, Test 1.

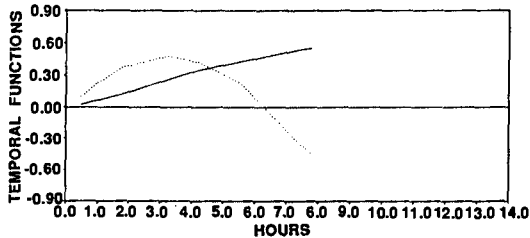
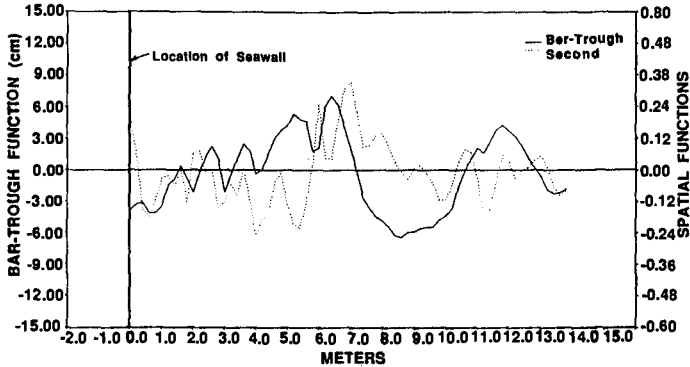


Figure 10. Modified Eigenfunction Analysis, Test 3.

functions were unified such that all values originated as positive, with an erosion from the modified mean profile assigned a negative spatial value, and an accretion a positive spatial value.

The first three eigenfunctions represent over 97.5 percent of the variance from the mean in all test cases. The first eigenfunction, referred to as the "bar-trough" function, explains 79.88 to 95.91 percent of the variance from the mean square value of the data. The second eigenfunction represents 60.0 to 86.8 percent of the variation from the first eigenfunction, with 6.2 to 29.0 percent of the variance explained by the third eigenfunction. Due to the complex behavior exhibited by the third eigenfunction, only the first and second eigenfunctions were analyzed.

The first eigenfunction appears to represent a "bar-trough" behavior along the profile length. The solid line for the spatial function (shown in Figures 9 and 10) displays the location and magnitude of the bar and trough features present in each profile as a weighted average of the input data; by coupling the first temporal function with the first spatial function in each plot, the time rate of change of the profile features could be interpreted.

Tests 1 through 3 showed maxima on either side of the break point bar crest which dominated the first 3.23 hours of the test, then diminished in effect with further profile evolution. By comparing these features with Figures 3 and 4, the dual-crested bar was observed to initially steepen, then become subdominant upon emergence of single-peaked, highly skewed break point bars. The maxima which appear shoreward of the break point correspond to the skewness of the berm erosion or toe scour trough and bar feature (depending on whether a seawall was located on the profile).

For the storm surge tests, the seawalled profiles revealed numerous reflection bars. The main incongruity between the storm surge and normal water level tests with erosive wave conditions was the behavior of the second temporal function. A rapid decrease from an initial peak value was noted in all storm surge tests, which corresponds to a temporal decrease in the scour trough skewness. The no-seawall tests showed a peak spatial function value at the shoreward dune erosion limit, which corresponded to the temporal steepening of the dune face.

The recovery tests displayed extremely "noisy" second spatial functions due to the presence of well-established reflection bars which exhibited minimal spatial change over the seaward half of the profile (owing primarily to a decreased wave height); numerous maxima and minima over the shoreward portions of the profile were also revealed. Temporal changes differed greatly between the two test cases, with the seawalled profile demonstrating a more stable trend of the skewness of the surf zone bar formations in the latter 4.0 hours of testing than that exhibited by the no-wall case. The seawalled profile did not exhibit a relative minimum value of the bar skewness in the vicinity of the break point bar; however, both profiles exhibited a distinct break point bar-trough feature (due primarily to the reduction in water level) which caused the bed to scour shoreward of the break point.

SUMMARY AND CONCLUSIONS

Summary of Investigation. Due to the recent attention being focused on the effects of seawall placement on eroding coastlines, there exists a need to examine the resulting profile configuration along with the erosion or recovery rates to ascertain whether the presence of the structure is detrimental to the beach-dune system. A laboratory test series was developed which examined the cross-shore effects of seawall placement on profile response. Erosive wave conditions comprised the majority of the experiments; a limited study of beach recovery characteristics was also undertaken. A substantial set of laboratory data was obtained, and the results have been presented in a comparative sense to further emphasize the structure effects. The complete data set and analysis are presented in Barnett (1987).

Important Findings. The test results were examined by time-series profile evolution, volume change over profile length, and empirical eigenfunction analysis. For all cases tested, profile configurations with and without a seawall were remarkably similar in overall planform; this suggests that the major transport process is not significantly influenced by the presence of the seawall.

Under erosive wave conditions, the dominant spatial feature is a bar-trough system, with the bar forming in proximity to the wave breaking point and the trough occurring near the still water shoreline. The presence of the seawall accentuates the trough into a scour hole instead of spanning over the swash zone, as is the case with a natural beach. However, while local scour was noted to be severe in many of the seawalled profiles, the volume of sand retained upland of the structure (which would otherwise be eroded under identical wave conditions without a seawall) was found experimentally to be approximately 60% greater than the additional volume eroded at the toe of the structure.

Wave reflection, often considered to be a major adverse influence on scour in front of a seawall, did not appear to play a significant role. Reflection bars of varying quantity and spacing did occur, but were usually secondary features of a predominantly bar-trough system. Water depth, on the other hand, appeared to be a dominant factor affecting erosion for all cases tested, with higher water levels causing a significant increase in erosion. For the seawalled cases, the break point bar was in proximity to the wall; the natural profiles displayed a more seaward bar location. This affected the recovery process when the water level returned to normal.

The empirical eigenfunction analysis is a useful tool for examining profile evolution. By conducting a modified eigenfunction analysis, the spatial and temporal behavior of the profile evolution process was more readily facilitated. The primary bar-trough system and the secondary reflection bar system were clearly revealed in spatial plots for all erosive test cases. The primary system accounted for more than 80 percent of the variation from the initial profile. A relatively smooth spatial function coupled with a slowly-varying temporal function revealed the stable nature and steady evolution of the bar-trough system.

The "noisy" behavior exhibited by the second spatial function of the recovery tests showed the recovery process to be more unstable. The primary recovery process was the removal of the break point bar and the redistribution of sand both onshore and offshore. The more prominent primary spatial function in the seawalled case revealed a more efficient recovery.

The seawalled beach exhibited a more substantial recovery volume in the vicinity of the structure toe than that observed for the natural profile, which showed only a small berm growth. This is not sufficient evidence to construe that placement of a seawall on an eroded beach will promote recovery; rather, the recovery process appears possible on a seawalled beach provided the water level and wave conditions are capable of transporting sediment to the scour trough created under erosive conditions. Further recovery tests should be conducted to confirm this assumption.

REFERENCES

- Aubrey, D.G., "Seasonal Patterns of Onshore/Offshore Sediment Movement," Journal of Geophysical Research, AGU, Vol. 84, No. C10, October, 1979, pp. 6347-6354.
- Barnett, M.R., "Laboratory Study of the Effects of a Vertical Seawall on Beach Profile Response," UFL/COEL-87/005, University of Florida, Coastal & Oceanographic Engineering Department, Gainesville, FL, May, 1987.
- Dean, R.G., "Equilibrium Beach Profiles: U.S. Atlantic and Gulf Coasts," Ocean Engineering Report 12, Department of Civil Engineering, University of Delaware, Newark, DE, 1977.
- Dean, R.G., "Physical Modelling of Littoral Processes," In: R.A. Dalrymple, Physical Modelling in Coastal Engineering, Univ. of Delaware, Newark, DE, 1985, pp. 119-139.
- Kraus, N.C., "The Effects of Seawalls on the Beach: A Literature Review," Coastal Sediments '87, ASCE, Vol. 1, 1987, pp. 945-960.
- Kriebel, D.L., Dally, W.R., and Dean, R.G., "Beach Profile Response Following Severe Erosion Events," UFL/COEL-86/016, Coastal & Oceanographic Engineering Department, University of Florida, Gainesville, FL, December, 1986.
- Saville, T., "Scale Effects in Two-Dimensional Beach Studies," Proceedings of the Seventh General Meeting of the International Association of Hydraulic Research, LNEC, Lisbon, Portugal, Vol. II, 1957, pp. A3.1-A3.8.
- Winant, C.D., Inman, D.L., and Nordstrom, C.E., "Description of Seasonal Beach Changes Using Empirical Eigenfunctions," Journal of Geophysical Research, AGU, Vol. 80, No. 15, May, 1975, pp. 1979-1984.

CHAPTER 112

BED RESPONSE TO FAIRWEATHER AND STORM FLOW ON THE SHOREFACE

Malcolm O. Green¹, John D. Boon², Jeffrey H. List²
and L. Don Wright²

Abstract

Bailard's (1981) model of combined-flow, total-load sediment transport was used to calculate sediment flux at 8-m depth on a wave-dominated shoreface during fairweather and during a storm. Waves were skewed onshore during fairweather, however it was the reversing tidal current that controlled predicted transport direction. Transport direction during the early phase of the storm was also controlled by the mean flow, this time a wind-driven jet-like flow with an offshore component. As the storm progressed, waves became more organized and highly skewed, and by the end of the storm, predicted sediment transport was turned onshore by the shoreward-skewed waves against the mean flow. Measurements of changes in relative bed elevation at the 8-m depth site were used to verify the transport predictions. A total of 6 cm of accretion occurred over 4.5 days of low-energy flow. It was found that predicted onshore transport was strongly correlated with erosion at the 8-m depth site, and predicted offshore transport was strongly correlated with accretion. Five cm of scour occurred during the initial phase of the storm, followed by 15 cm of rapid accretion. Onset of accretion was coincident with the organization of surface waves into long-period swell, and the maximum accretion rate was coincident with the most highly-skewed waves.

¹Department of Earth Sciences, University of Cambridge, Downing Street, Cambridge, CB2 3EQ, United Kingdom.

²Virginia Institute of Marine Science, School of Marine Science, College of William and Mary, Gloucester Point, VA 23062, U.S.A.

Introduction

Direct measurement of sediment transport by combined wave and current flow has not kept pace with measurement of the velocity fields that drive transport. Consequently, although the properties of the velocity field that are theoretically germane to sediment transport are generally recognized, and in some cases well understood, models that link bed response to flow properties remain largely untested.

Properties of the combined flow relevant to sediment transport include, in one form or another, the mean, variance, and skewness. The mean flow advects sediment suspended in the water column; the variance is a measure of the kinetic energy available for entraining sediment from the bed; and velocity skewness translates into net transport of that component of the sediment load that fluctuates with the instantaneous velocity. Rigorous extensions of Bagnold's (1963) unidirectional transport model by Bowen (1980) and Bailard (1981) have given specific form to the relevant flow properties and subsequently stimulated much research. Bailard (1981) gave the following equation for total-load (sum of bedload and suspended load) time-averaged sediment transport:

$$\begin{aligned} \langle i_t \rangle = & (\rho C_f c_b / \tan \phi) [\langle U_t^3 \rangle + (\tan \beta / \tan \phi) \langle |U_t|^3 \hat{i} \rangle] \\ & + (\rho C_f c_s / w) [\langle |U_t|^3 U_t \rangle + (-s \tan \beta / w) \langle |U_t|^5 \hat{i} \rangle] \dots (1) \end{aligned}$$

where U_t is the instantaneous velocity, β is the local bed slope, ϕ is the coefficient of internal friction of the bed, w is the sediment settling velocity, ρ is the fluid density, C_f is a drag coefficient, c_b and c_s are the suspended-load and bedload efficiencies respectively, and $\langle i_t \rangle$ is an immersed-weight transport rate (units of weight per time per unit width, i.e. mass/time³). The angle brackets denote time-averaging, and boldface characters indicate vector quantities. \hat{i} is the unit vector in the cross-slope direction, positive downslope, and for the purposes of the following analysis, the unit vector \hat{i} also corresponds to the shore-normal direction (positive offshore).

The two terms in equation (1) that involve time-averages of odd or signed powers of the instantaneous velocity, i.e. $\langle U_t^3 \rangle$ in the bedload term and $\langle |U_t|^3 U_t \rangle$ in the suspended-load term, reflect the skewness of the velocity distribution and denote the bedload and suspended-load fluxes that are driven by and parallel to the instantaneous velocity. Both terms are identically zero for a symmetrical, zero-mean velocity distribution. The

two terms that involve time-averages of powers of absolute values of the instantaneous velocity, i.e. $\langle |U_t|^3 \rangle$ in the bedload term and $\langle |U_t|^5 \rangle$ in the suspended-load term, reflect the flow energy and are considered to govern the bedload and suspended-load fluxes that fall downhill under the influence of gravity. Unlike the former terms, both of these terms are non-zero for a symmetrical, zero-mean velocity distribution.

Guza and Thornton (1985) decomposed the total velocity into mean ($\bar{}$) and oscillatory ($\tilde{}$) components:

$$U_t = (\tilde{u} + \bar{u})\hat{i} + (\tilde{v} + \bar{v})\hat{j} \dots\dots\dots(2)$$

where \hat{j} is the unit vector in the alongslope direction, and showed how each component theoretically contributes to each of the terms in the transport equation. The terms involving velocities in equation (1) are frequently referred to as "velocity moments" although this is technically inaccurate, firstly because they are not dimensionless, and secondly, and more importantly, because they are not computed from a zero-mean velocity distribution. The mean flow skews the velocity distribution and adds kinetic energy; the mean flow cannot be presumed a priori to be subordinate, in terms of sediment transport, to the oscillating component of the total velocity.

The objective of this paper is to test the theoretical links between the properties of the velocity distribution and sediment transport as expressed in equation (1). The data set, obtained from 8-m depth on a wave-dominated, microtidal shoreface, consists of simultaneous measurements of near-bed velocities and changes in relative bed elevation at a single point. Sediment flux thus was not measured directly, however the record of local sedimentation is useful for the stated objective if it is viewed as the product, and therefore the close analog, of sediment transport.

Observed velocity distributions are described, and the contributions made by the mean flow and oscillating flow to each of the velocity "moments" in the transport equation are compared. Equation (1) is used to calculate sediment transport, and the transport predictions are tested by seeking purely qualitative correlations between terms in the transport equation and observed changes in relative bed elevation.

Methods

Observations were made over a period of 8 days from 6 to 14 September, 1985, at 8-m depth on the shoreface that fronts the barrier-island coast at Duck, North Carolina, on the U.S. Atlantic coast (Figure 1). The experiment was one

component of a larger nearshore processes experiment, DUCK85, which was conducted at the U.S. Army Corps of Engineers' Field Research Facility; details of the DUCK85 experiment can be found in Mason et al. (1987).

Currents were measured at 20 cm above the bed with a 4.0-cm diameter Marsh-McBirney electromagnetic current meter supported on a bottom-mounted tripod and controlled by a Sea-Data Model 635-9RS logger. Currents were sampled at 1 s intervals for 2048 s every 2 hours. Relative bed elevation was measured using a Datasonics Model ASA-920 digital sonar altimeter (DSA) mounted 4 m from the main tripod on a platform supported by pipes driven 50 cm into the seabed. The DSA is a high-resolution (0.15 cm) sonar device that converts reflected travel time of a high-frequency (1 MHz) acoustic pulse into a digital number that is proportional to the distance between the transducer and the seabed. Green and Boon (1988) described the calibration of the unit, its zero stability, and its performance over a rippled bed and when suspended sediment concentration is high, and concluded that the altimeter performed reliably and predictably in the field. The DSA was polled every 8 s by the Sea-Data logger, for a total of 256 observations per 2048-s burst.

Green (1987), drawing from bathymetric and side-scan sonar data, demonstrated that the Duck shoreface exhibits scant longshore variability, and is well represented by a simple two-dimensional concave-upwards profile. If it is assumed that sediment transport along the straight and parallel contours of the Duck shoreface is uniform, then it is the cross-shore component of the instantaneous velocity that controls erosion and sedimentation seaward of the surfzone. Thus, the longshore component of velocity can be neglected; for the purposes of the following analysis it is assumed that $U_t = (\bar{u} + \bar{u}')\hat{i}$, and all sediment fluxes are thus cross-shore fluxes.

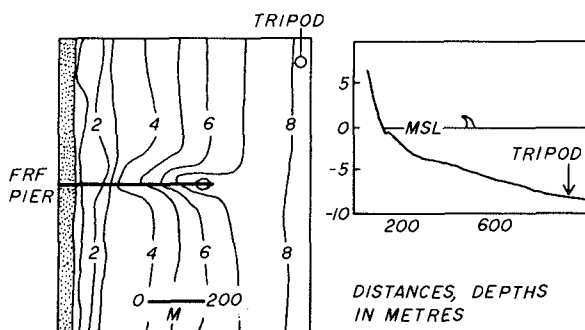


Figure 1. Experiments were conducted at 8-m depth seaward of the surfzone. The Field Research Facility (FRF) is situated in the southern Mid-Atlantic Bight, between Cape Hatteras to the south and Chesapeake Bay to the north. Bathymetry based on surveys by personnel of the FRF.

Predicted Sediment Transport

During the first 4.5 days of the deployment, waves were low (<60 cm) and long (10 s) and the wind light (<6 m/s) and directed offshore. A shift of the wind to the northeast (onshore) at 0700 hours on September 11 signalled the end of fairweather conditions; for the next 3.5 days, the wind blew from the northeast at speeds generally in excess of 10 m/s. See Wright et al. (1986) for a detailed description of the evolution of the storm.

Prior to the storm, the burst standard deviation of the cross-shore component of velocity measured at $z = 20$ cm averaged 10 cm/s (Figure 2), and most of the variance was due to surface gravity waves: infragravity band (0.01 to 0.05 Hz) energy in the velocity record was two orders of magnitude smaller than energy in the incident band (0.05 to 0.5 Hz). The burst-averaged cross-shore current attained maximum speeds of -5 cm/s, and the sign of \bar{u} reversed at approximately the semi-diurnal frequency (Figure 2), indicating a strong contribution by the astronomical tide.

Current energy in the incident and infragravity bands increased through the storm at approximately equal rates. The burst standard deviation of the cross-shore velocity reached a peak of nearly 40 cm/s 2.2 days after the windshift (Figure 2), at which time the significant wave height was 2.10 m and individual maxima in the cross-shore velocity exceeded 150 cm/s. The mean flow during the storm resembled a jet-like coastal flow, (Wright et al., 1986), setting alongshore to the south at an average of 33 cm/s and offshore at a maximum of 10 cm/s.

Those terms in equation (1) that denote sediment flux parallel to the instantaneous velocity are governed themselves by both the mean and skewness of the velocity distribution. Shown in Figure 3 are observed values of

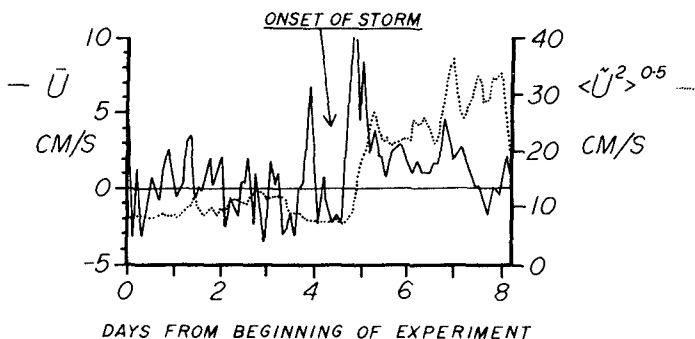


Figure 2. Burst mean cross-shore current speed (\bar{u}) and burst standard deviation of the cross-shore component of velocity ($\langle \tilde{u}^2 \rangle^{0.5}$), both measured at $z = 20$ cm, 8-m depth. The onset of the northeaster storm is indicated.

$\langle \tilde{u}^3 \rangle$, which reflects the wave-orbital velocity asymmetry only since the mean flow is removed; and $\langle U_t^3 \rangle$, which reflects the asymmetry of the total flow. The averaging period corresponds to the burst duration. Observed values of $\langle u^3 \rangle$ were negative throughout the fairweather period, which indicates a higher than Gaussian occurrence of large negative (i.e. onshore) velocities and which is consistent with the expectation from theory of relatively long (10 s) waves in relatively shallow water (~10 m) being skewed in the direction of propagation. In contrast, during the early stages of the storm there was no consistent sign to the wave skewness, which reflects the stage of developing wind-waves at that time with surface waves driven locally before the strong northeast wind. Approximately 1.3 days after the onset of the storm, $\langle \tilde{u}^3 \rangle$ again became consistently negative, and thereafter increased in magnitude. Towards the end of the experiment, 3.5 days from the onset of the storm, $\langle \tilde{u}^3 \rangle$ attained its largest negative value, reflecting the marked asymmetry of the organized long-period and large-amplitude swell that was the legacy of the storm.

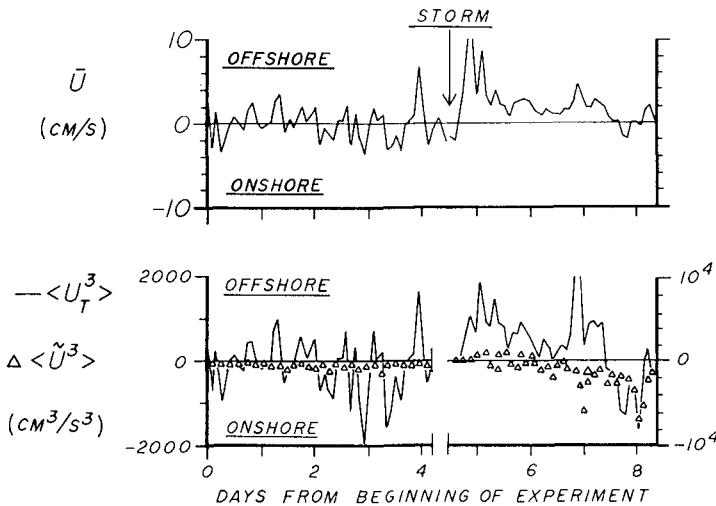


Figure 3. Wave-orbital velocity skewness, $\langle \tilde{u}^3 \rangle$, and total velocity skewness, $\langle U_t^3 \rangle$, measured at the 8-m depth site, $z = 20$ cm. Horizontal axis is time in days from the beginning of the experiment; note the break of scale at 4.5 days which corresponds to the onset of the storm. The vertical scale on the left refers to the fairweather period, and the vertical scale on the right to the storm period. Also shown is the mean cross-shore current speed flow at $z = 20$ cm.

The oscillatory velocities, however, did not usually make the major contribution to the skewness of the total flow. Except at the end of the storm, when wave-orbital velocities were most highly skewed, the sign of the total-flow skewness (i.e. $\langle U_t^3 \rangle$) was the same as the sign of the mean cross-shore flow, regardless of the wave asymmetry (Figure 3). Thus, the skewness of the observed velocity distributions was controlled by the tidal mean flow during fairweather, by the wind-driven mean flow for much of the storm, and by the oscillatory component of the total flow only towards the end of the storm. The higher-order signed velocity moment that appears in the suspended-flux term (i.e. $\langle |U_t|^3 U_t \rangle$) behaved in essentially the same fashion as the lower-order moment, and need not be examined further here.

In contrast, the mean flow was less important to those velocity terms that reflect the kinetic energy of the flow and that govern the downhill sediment flux. The third-order zero-mean term, $\langle |\tilde{u}|^3 \rangle$, averaged $1.56 \langle \tilde{u}^2 \rangle^{3/2}$ and $1.59 \langle u^2 \rangle^{3/2}$ over the fairweather and storm periods respectively, where the theoretical value is $1.20 \langle \tilde{u}^2 \rangle^{3/2}$ assuming a monochromatic sea and $1.60 \langle \tilde{u}^2 \rangle^{3/2}$ assuming a linear random sea (Guza and Thornton, 1985). The fifth-order zero-mean term, $\langle |\tilde{u}|^5 \rangle$, averaged $5.76 \langle \tilde{u}^2 \rangle^{5/2}$ and $6.26 \langle u^2 \rangle^{5/2}$ over the same periods, where the theoretical value is $1.92 \langle \tilde{u}^2 \rangle^{5/2}$ and $6.38 \langle \tilde{u}^2 \rangle^{5/2}$ assuming monochromatic and linear random seas respectively. Over the fairweather period, the mean flow increased the value of the third-order zero-mean term by 8% on average (i.e. $\langle |U_t|^3 \rangle / \langle |\tilde{u}|^3 \rangle = 1.08$) and the fifth-order zero-mean term by 13% on average. During the storm, 10% and 19% on average were added to the third- and fifth-order zero-mean terms respectively by the mean flow.

Sediment flux at the 8-m depth site was predicted from the velocity data using equation (1) and averaging over the burst length (34 minutes). The predicted burst-averaged bedload flux, suspended-load flux, and total-load flux are shown in Figure 4 for both the fairweather and storm periods. All fluxes are cross-shore components and the following constants were assumed: $C_f = 0.003$ (Sternberg, 1972), adjusted to apply to the velocity at $z = 20\text{cm}$; $\epsilon_b = 0.21$, $\epsilon_s = 0.025$ (Baillard, 1981); $w = 1.5\text{ cm/s}$ (determined in the laboratory); $\tan \phi = 0.63$ (Guza and Thornton, 1985); and $\tan \beta = 0.0055$ (measured).

During the fairweather period, the bedload and suspended-load components of the predicted total load were approximately equal in magnitude, while during the storm, suspended load accounted for approximately three-quarters

of the predicted total load (Figure 4). Since the factor $\rho C_f c_b / \tan \phi$ is three orders of magnitude greater than the factor $\rho C_f c_b \tan \beta / \tan^2 \phi$, for the gravity component of the bedload flux to be comparable in magnitude to the velocity-driven component, the total velocity must be both energetic ($\langle |U_t|^3 \rangle$ large) and nearly symmetrical about zero ($\langle U_t^3 \rangle$ small), which was generally never the case in either fairweather or storm conditions. Similarly, $\rho C_f c_s / w$ is four orders of magnitude greater than $\rho C_f c_s^2 \tan \beta / w^2$, and thus the gravity component of the suspended-load flux was subordinate to the velocity-driven component. Thus, during fairweather, since the mean flow controlled the total-flow skewness and the sediment flux was predominantly driven by the instantaneous velocity, the cross-shore components of the predicted bedload and suspended-load fluxes reversed sign in phase with the mean (tidal) flow (Figure 4). During the early stage of the storm, when the total-flow skewness was controlled by the wind-driven mean flow, predicted net sediment flux was directed offshore, and during the later stage of the storm, when the total-flow skewness was controlled by the wave asymmetry, predicted sediment flux was directed onshore (Figure 4).

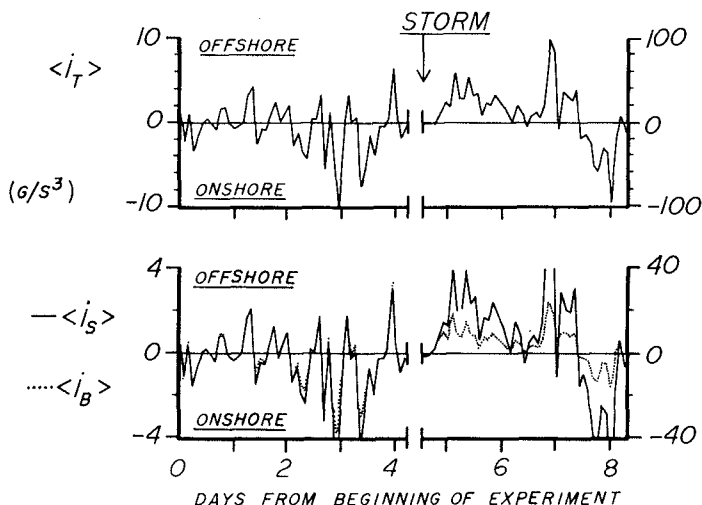


Figure 4. Predicted cross-shore total-load, suspended-load and bedload sediment flux at the 8-m depth site. The horizontal axis is time in days from the beginning of the experiment; note the break of scale at 4.5 days which corresponds to the onset of the storm. The vertical scale on the left refers to the fairweather period, and the vertical scale on the right to the storm period.

Observed Bed Response to Fairweather and Storm Flow

Fairweather

The DSA record was burst-averaged after all wild points in the data were removed. Generally, during low-energy conditions, the DSA signal was quite flat, however, when spikes did occur, they were easily recognized and removed. Green and Boon (1988) provide a discussion of the editing procedure, and show actual time-series of instantaneous relative bed elevation.

In a series of laboratory tests, Green and Boon (1988) also demonstrated that the sonic beamwidth was finite, and that positioning the instrument at a height above the bed greater than eight times the height of the wave ripples guaranteed that only the tops of the wave ripples were sensed. Since bedforms at the 8-m depth site were symmetrical wave ripples 3 cm high by 15 cm long, and the DSA was located approximately 50 cm above the bed, the DSA record should therefore not be confounded by the local topography.

The burst-averaged relative bed elevation over the fairweather segment of the experiment, expressed as cm below the fixed elevation of the transducer, is shown in Figure 5. Over the 4.5 days of low-energy preceding the storm, a total decrease in relative bed elevation of nearly 6 cm was recorded. Assuming the absolute elevation of the DSA is fixed, three points substantiate the conclusion that the observed change in relative bed elevation represents accretion at the 8-m depth site: divers observed no local bed disturbances induced by the instrument; migrating wave ripples (3 cm high by 15 cm long) could not have caused the observed signal; and the zero drift of the DSA was negligible (Green and Boon, 1988).

Green (1987) applied a combined-flow boundary-layer model to the fairweather velocity data and showed that the combined-flow skin friction at 8-m depth exceeded that necessary to initiate sediment transport for almost the entire fairweather period. Green also modelled the sediment-flux divergence associated with the competent fairweather combined wave and current flow, and showed that the cross-shore distribution of sediment sinks and sources on the shoreface associated with onshore transport differed fundamentally from that associated with offshore transport. At 8-m depth, erosion was predicted to occur under net onshore transport during fairweather, and accretion was predicted to occur under net offshore transport. Thus, if the observed change in relative bed elevation during times of predicted onshore transport differs consistently from that observed during times of predicted offshore transport, then this would be at least qualitative verification of the transport predictions provided by equation (1).

Inspection of the DSA record in Figure 5 reveals a connection between predicted transport direction and

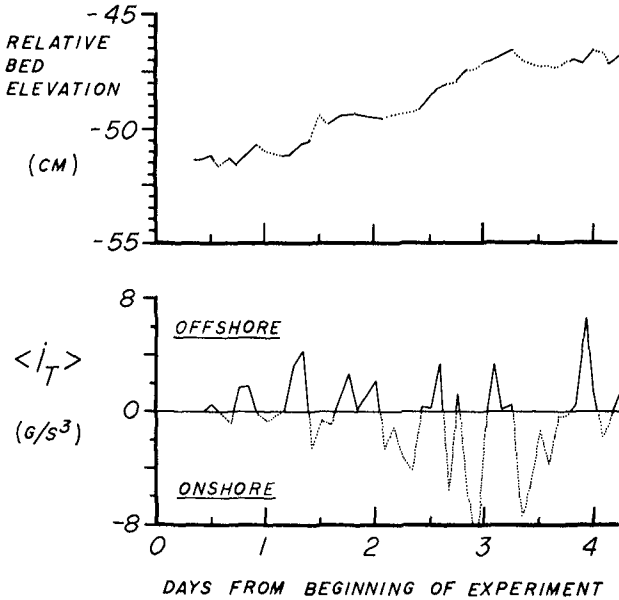


Figure 5. Burst-averaged relative bed elevation, expressed as cm below the fixed elevation of the DSA transducer, and predicted total-load sediment flux at 8-m depth during the fairweather period. Both records are marked with a solid line when the predicted transport was offshore and with a dotted line when the predicted transport was onshore.

	PREDICTED TRANSPORT DIRECTION	
	Offshore	Onshore
	-----	-----
	+0.00388	-0.00218
	+0.00221	-0.00267
$\frac{dz}{dt}$	+0.00083	+0.00094
(cm/min)	+0.00017	+0.00154
	+0.00375	-0.00065
	+0.00204	-0.00267
	+0.00171	-0.00592
	+0.00317	
	-----	-----

Table 1. Observed time-rate-of-change of relative bed elevation at 8-m depth during fairweather, calculated over consecutive bursts in which predicted transport direction (onshore or offshore) remained constant.

observed bed response at the 8-m depth site: times of predicted offshore transport (the solid line in the lower panel) correspond to times of relatively rapid accretion (the solid line in the upper panel), and times of predicted onshore transport (dotted line in lower panel) correspond to erosion or relatively slower accretion (dotted line in upper panel), with only a couple of exceptions. There were seven separate periods when the predicted total sediment flux was onshore over consecutive bursts and eight separate periods when the predicted total sediment flux was offshore over consecutive bursts. The change in burst-averaged relative bed elevation over each of these periods was calculated and these values are shown in Table 1, grouped by predicted transport direction. The observed rates of change in relative bed elevation (Table 1 and Figure 5) confirm the link between predictions and observations: there is a strong correlation between predicted offshore transport and observed accretion, and between predicted onshore transport and observed erosion at the 8-m depth site. Equation (1) is therefore a useful predictor, at least qualitatively, of the bed response to competent fairweather flow at this 8-m depth site. A more quantitative verification, comparing observed and predicted sedimentation rates, for example, would require a detailed analysis of the sediment-flux divergence associated with the competent flow.

The correlation between mean flow, which was driving transport direction at 8-m depth, and bed response highlights a fundamental difficulty with equation (1). Although the vertical variation of the mean flow in a combined-flow boundary layer is known theoretically (e.g. Grant and Madsen, 1979), it is not at all clear at which elevation the mean flow must be measured for use in the transport model. This problem precludes any further analysis of transport rates here, even though transport directions predicted on the basis of the velocity measured at $z = 20$ cm appear justified. Green (1987) circumvented this difficulty by using a traction model of transport, in which the combined-flow bed shear stress drives the sediment flux. The importance of the mean flow also emphasizes a potential deficiency of the electromagnetic current meter, which is presently in widespread use. Although Bowen and Doering (1984) found that the measurement of pure-wave skewness using electromagnetic current meters was rather more consistent than expected, and indeed the skewness measurements reported herein appear to be sensible, recent detailed laboratory tests by Aubrey and Trowbridge (1985) have shown that it may be difficult to obtain accurate estimates of the mean flow using these instruments.

Storm

The DSA data obtained during the storm were significantly noisier than the fairweather data; high concentrations of suspended sediment in the line-of-sight of the transducer caused premature echoes and signal scattering that occasionally resulted in complete loss of

echo detection (Green and Boon, 1988). Even after removal of the primary spikes, significant noise remained in the record, which may have biased the estimates of burst-averaged relative bed elevation. Therefore, only gross trends can be examined with confidence. The major features of the storm record were: a negligible change in bed level in response to the initial impulse of the wind; -5 cm of bed scour during the mid-phase of the storm; and -15 cm of rapid accretion during the waning phase of the event (Figure 6).

A significant feature of the storm record is the change from erosion to rapid accretion of the bed that occurred approximately two days after the onset of the storm. This corresponded to a sudden increase in the magnitude of the predicted total-load transport (Figure 6), however there was no fundamental change in the sedimentation rate corresponding to the predicted change in transport direction shortly afterwards. The initiation of accretion was also roughly coincident with the beginning of the period of wave organization following the initial phase of the storm, as reflected by the wave skewness (Figure 6); furthermore, as the wave-orbital velocities became increasingly skewed, the accretion rate increased, culminating in a maximum in both towards the end of the experiment.

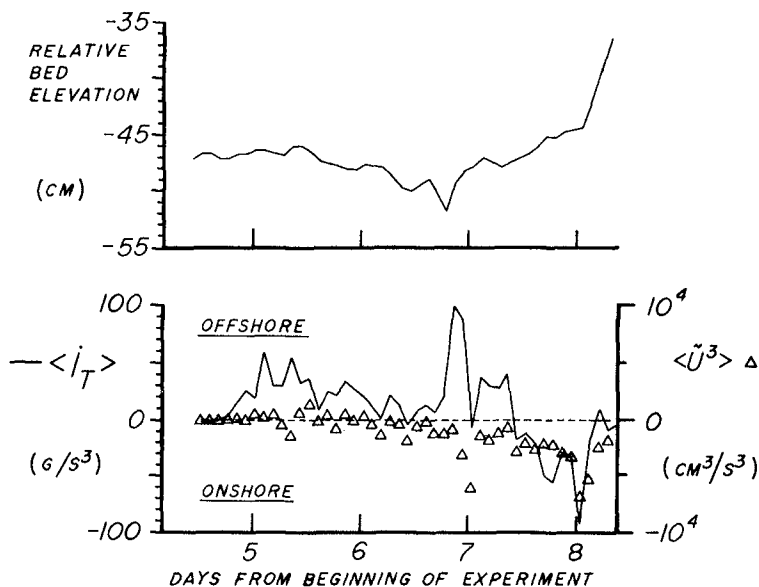


Figure 6. Burst-averaged relative bed elevation, expressed as cm below the fixed elevation of the transducer, predicted total-load sediment flux, and wave-orbital velocity skewness at 8-m depth during the storm.

Storm sedimentation thus differed fundamentally from fairweather sedimentation, and equation (1) failed as an indicator of bed response under the storm conditions. This test, however, does not necessarily constitute invalidation of the transport model; it may be that there is a complex relationship between sedimentation (measured by the sonar altimeter) and sediment transport (predicted by equation 1) during high-energy conditions. For example, it appeared that the bed responds primarily to the oscillatory component of the combined flow. Another possibility is that the measured accretion reflects the migration of a large-scale bedform under the sensor; Wright et al. (1986) argued that the rapidity of the accretion was suggestive of a pulse-like migration of a sediment front or large-scale bedform over the installation site, and showed side-scan sonar imagery to support that hypothesis.

Conclusions

During fairweather at the 8-m depth site, the predicted cross-shore burst-averaged bedload and suspended-load fluxes were approximately equal in magnitude and, since the near-bed velocity was both highly skewed and not very energetic, the predicted downslope flux of sediment under the influence of gravity was relatively insignificant. The mean flow dominated the asymmetry of the observed velocity distributions, indicating that transport direction was controlled by the tidal mean flow rather than by the wave-orbital velocity asymmetry.

There was a strong correlation between observed sedimentation rates at 8-m depth during low-energy conditions and net burst-averaged sediment transport predicted by Ballard's (1981) combined-flow transport model. This correlation constitutes qualitative verification of the transport predictions. Since it was the mean flow at 20 cm above the bed that dominated the significant terms in the transport equation, fundamental difficulties in the transport equation and potential instrument deficiencies cannot be ignored.

Predicted net transport during the storm was directed offshore under the dominant control of the wind-driven mean flow, except towards the end of the storm when predicted net transport was turned onshore by highly-skewed wave-orbital velocities. Unlike fairweather transport, suspended load constituted more than 75% of the total load during the more energetic storm flow. There appeared to be a correlation between the skewness of the oscillatory component of the total flow and sedimentation during the storm, even though the mean flow again dominated predicted net transport. While not invalidating the transport predictions, since the exact relationship between sedimentation and sediment transport is unknown, the oscillatory flow may control storm sedimentation, at least during certain phases of the storm.

Acknowledgements

This study was supported by the Virginia Institute of Marine Science and the National Science Foundation, Grant No. OCE-8610635. We thank Bob Gammisch for expert assistance in the field, and Captain Durand Ward of the R/V Captain John Smith. Thanks are also due to Curt Mason and Bill Birkemeier of the U.S. Army Corps of Engineers' Field Research Facility. Contribution No. 1459 from the Virginia Institute of Marine Science.

References

- Aubrey, D.G. and Trowbridge, J.H., 1985. Kinematic and dynamic estimates from electromagnetic current meter data. *J. Geophys. Res.*, 90: 9137-9146.
- Bagnold, R.A., 1963. Mechanics of marine sedimentation. In: M.N. Hill (Editor), *The Sea*, Vol. 3. Wiley-Interscience, New York, pp. 507-528.
- Bailard, J.A., 1981. An energetics total load sediment transport model for a plane sloping beach. *J. Geophys. Res.*, 86: 10,938-10,954.
- Bowen, A.J., 1980. Simple models of nearshore sedimentation; beach profiles and longshore bars. In: S.B. McCann (Editor), *The Coastline of Canada*. Paper 80-10, *Geol. Surv. of Canada*. p. 1-11.
- Bowen, A.J. and Doering, J.C., 1984. Nearshore sediment transport: estimates from detailed measurements of the nearshore velocity field. *Proc. 19th Int. Coastal Eng. Conf.*, Houston, A.S.C.E., pp. 1703-1714.
- Grant, W.D. and Madsen, O.S., 1979. Combined wave and current interaction with a rough bottom. *J. Geophys. Res.*, 84: 1779-1808
- Green, M.O., 1987. Low-energy bedload transport by combined wave and current flow on a southern Mid-Atlantic Bight shoreface. Unpublished Ph.D. Dissertation, College of William and Mary, Williamsburg, Virginia, 160 pp.
- Green, M.O. and Boon, J.D., 1988. Response characteristics of a short-range, high-resolution, digital sonar altimeter. *Mar. Geol.*, in press.
- Guza, R.T. and Thornton, E.B., 1985. Velocity moments in nearshore. *Proc. A.S.C.E., J. Waterway, Port, Coastal and Ocean Eng.*, 111: 235-256.
- Mason, C., Birkemeier, W.A. and Howd, P.A., 1987. Overview of DUCK85 nearshore processes experiment. *Coastal Sediments '87*, New Orleans, pp. 818-833.
- Sternberg, R.W., 1972. Predicting initial motion and bedload transport of sediment particles in the shallow-marine environment. In: D.J.P. Swift, D.B. Duane and O.H. Pilkey (Editors), *Shelf Sediment Transport: Process and Pattern*. Dowden, Hutchinson and Ross, Stroudsburg, Pennsylvania, pp. 6-82.
- Wright, L.D., Boon, J.D., III, Green, M.O. and List, J.H., 1986. Response of the mid shoreface of the southern mid-Atlantic Bight to a "northeaster". *Geo-Marine Letters*, 6: 153-160.

CHAPTER 113

Phase-Locking of Modes in the Nearshore: Field Evidence

J. W. Haines*

A. J. Bowen*

Field investigations have shown that infragravity frequencies may dominate nearshore fluid motions (Bowen and Huntley, 1984). Theoretical studies have suggested that the modal structure of the infragravity field, including the degree of modal coupling, is important in generating complicated beach morphologies (Holman and Bowen, 1982) but previous analyses of field data have not provided a description of the infragravity field which is sufficiently detailed to assess the importance of these ideas.

In this paper we present a statistical method which, when applied to data from any large sensor array, provides the desired description of the infragravity field. The method is applied to data from the NSTS (Nearshore Sediment Transport Study) experiment. The variance of the observed velocity field is described by a set of free wave modes. The results indicate that a complicated infragravity field composed of both edge waves and leaky modes is present. The modes modelled are also found to be significantly coupled over a range of modal pairs and frequencies.

Introduction

Results from the analysis of extensive sets of field data have convincingly demonstrated the importance of infragravity motions in the nearshore (Bowen and Huntley, 1984). Observations show that these lower frequency motions may dominate the velocity and elevation fields at the shoreline and across the inner surfzone (Guza and Thornton, 1982). Numerical and analytical models have suggested that these infragravity waves may be important agents of morphologic evolution and may significantly modify the incident wind-wave field. Evaluation of such models requires knowledge of the detailed structure of the infragravity wave field in natural systems.

Bowen and Inman (1971) and Guza and Inman (1975) considered simple models of phase-locked edge waves progressing in opposite directions alongshore. The second-order mean drift velocity and the alongshore variations in shoreline run-up due to these standing edge waves were shown to produce zones of convergence leading to the formation of shoreline cusps and crescentic bars. More complicated infragravity wave fields were modelled by Holman and Bowen (1982). They described the mean drift due to coupled modes of variable mode number and direction of propagation. The resulting time-averaged velocity field varied both across and along the beach, providing a mechanism for the generation of complicated topography varying alongshore on a variety of scales.

These theoretical studies suggest that the coupling or phase-locking of infragravity modes is necessary for the generation of three-dimensional topography. Field evidence for the existence of coupled modes is scarce. Holman and Bowen (1984) showed that standing edge waves were present on a beach bounded by reflective headlands. More complete descriptions of the infragravity field, utilizing large sensor arrays, have failed to address the possible coupling of modes. In this paper we shall describe a new method of describing a large data set in terms of prescribed modes (Haines, et al., in prep.). The method returns

* Department of Oceanography, Dalhousie University, Halifax, NS B3H 4J1 Canada

the time-averaged modal amplitudes, the degree of modal coupling and the relative phase between modes. The resulting detailed picture of the infragravity wave field should provide constraints for physical models of infragravity wave generation, interaction and decay.

Theory and Background

A variety of motions in the nearshore zone are driven by the flux of momentum due to wind-generated waves incident on the beach. The response to this forcing is spread across a broad band of frequencies. The higher frequencies, harmonics of the incident waves and turbulence at the boundaries may stir up and transport the underlying sediment. Larger scale spatially coherent responses to the forcing are predominantly confined to the infragravity frequencies; i.e. those frequencies below the incident wave band. Theoretical investigations have identified a number of possible infragravity responses to various types of forcing.

Both forced and free responses may occur in the nearshore. A broad-banded (in frequency and direction) incident wave field will result in a similarly complicated forcing function. Modification of the incident field due to shoaling and breaking may significantly alter the forcing (Symonds *et al.*, 1982). We are concerned here with the free wave response of the system as described by the linearised shallow-water equations of motion. These solutions include both trapped modes confined to the nearshore and leaky modes which may propagate into and out of the region.

The trapped modes, or edge waves, are a discrete set of modes described by the eigen-solutions of the shallow-water equations (Eckart, 1951). For a planar beach with slope $\tan \beta$ the velocity potential and dispersion relation are given by

$$\Phi_n = \Re \{ g\sigma^{-1} e^{-l_n x} L_n(2l_n x) \alpha_n e^{i(l_n y + \sigma t)} \} \tag{1}$$

and

$$\sigma^2 = gl_n(2n + 1) \tan \beta. \tag{2}$$

In the above equations

- Φ is the velocity potential,
- σ is the radial frequency,
- l_n is the wave number,
- n is the mode number,
- L_n is the Laguerre polynomial of order n ,
- α_n is the complex modal amplitude,

(x, y) are the offshore/alongshore coordinates and \Re denotes the real part.

These shallow-water solutions are valid for low modes where $(2n + 1) \tan \beta \ll 1$ and are appropriate for the modes and beach slope to be discussed further (Guza and Davis, 1974).

The leaky modes, including incident and reflected waves, form a continuum of modes in (σ, k) space. The velocity potential and deepwater dispersion relation are given approximately by

$$\begin{aligned} \Phi_i &= \Re \{ g\sigma^{-1} (J_0(x), iY_0(x)) \alpha_i e^{i(l y + \sigma t)} \}, \\ \Phi_r &= \Re \{ g\sigma^{-1} (J_0(x), -iY_0(x)) \alpha_r e^{i(l y + \sigma t)} \}, \end{aligned} \tag{3}$$

and

$$\sigma^2 = g|K| \tanh |K|h, \tag{4}$$

where J_0, Y_0 are the zeroth order Bessel functions, subscripts (i,r) denote incident and reflected waves, h is the water depth, and K is the vector wavenumber. These solutions are valid when $\sin \delta \tan \beta$ is small, where δ is the angle of incidence (Guza and Bowen, 1975).

The higher mode edge waves and the leaky modes are quite similar in structure. This, along with the large number of possible modes, complicates observational studies seeking to identify modes. An array capable of separating motions due to many similar modes would be prohibitively large. In addition the modes are likely to be coupled. The modes may arise from a common forcing, or from coherent forcing functions, and the total response must satisfy external boundary conditions. Thus it is likely that the modes are coherent or phase-locked, i.e. $\langle \alpha_n \alpha_m^* \rangle \neq 0$ (where * denotes the complex conjugate and $\langle \rangle$ denotes time averaging).

The modal structure of the infragravity field and the degree of modal coupling are important parameters in models of generation of beach morphology (Holman and Bowen, 1982). A detailed description of the modal response to forcing will also contribute to improved understanding of the dynamics of the nearshore. The large number of possible modes and the potential for coupled modes requires special treatment of observations made in the nearshore. We shall describe and apply a method which utilizes observations from a variety of sensor types and locations, and which explicitly considers modal coupling. Additionally the method may be used to address the relationship between the estimated modal response and observed forcing variables.

Previous investigators have shown that the bulk of observed infragravity energy may be described by free wave modes. Oltman-Shay and Guza (1987) applied maximum-likelihood 2-D spectral estimators to data collected on California beaches during the NSTS study. The method employed utilized only a single observed variable from sensors located along a shore parallel line. Additionally the method assumes the modes are random in phase. The results of the analysis showed that much of the observed energy fell along edge wave modal dispersion lines. The modal structure of the field, as suggested by this method, varied dramatically depending on the variable type (alongshore or cross-shore velocity) subjected to the analysis. This is consistent with the observation that higher modes (and leaky modes) have a relatively large cross-shore velocity component.

Huntley (1988) examined the same data using a qualitative method to assess the importance of modal coupling. He found strong evidence that, over the period of the observations, modes present were coupled. This coupling was associated with alongshore inhomogeneity in the observed velocity field. No quantitative assessment of the modal coupling or relative phases between modes was possible.

We shall present a method which allows simultaneous incorporation of a variety of variables from any sensor location. The method also explicitly estimates the coupling and relative phases of the modes modelled. We shall briefly discuss how measured indices of the forcing might be included to yield estimates of the gain between the forcing and the modal response as modelled.

The Method of Analysis

The observations will be modelled as the resultant of a linear superposition of modes at a single frequency, σ_0 . The observations from the i^{th} sensor, $\theta_i(t)$, are given by

$$\theta_i(t) = \alpha_j(t) f(\phi_{ij}(x, y) \exp i(\ell_j y_i + \sigma_0 t)) + \epsilon_i(t) \quad (5)$$

where i denotes the i^{th} sensor and j the j^{th} mode and $j_{max} < i_{max}$. $\epsilon_i(t)$ is the error term at the i^{th} sensor which may contain unmodelled spatially coherent motions. The function $f()$ depends on the sensor location and the variable type. The model is complex and $\theta_i(t)$ may be thought of as the complex demodulate of the observed series at σ_0 .

The model equation may be written in vector form as

$$\underline{\theta} = \mathbf{E}\underline{\alpha} + \underline{\epsilon} \quad (6)$$

where \mathbf{E} is the matrix of modal coefficients and $E_{i,j}$ defines the j^{th} mode at the i^{th} sensor. The cross-spectral matrix of observations, $\langle \underline{\theta} \underline{\theta}'^* \rangle$, (where $'$ is the transpose) at frequency σ_0 is given in terms of the cross-spectral matrix of modal amplitudes by

$$\langle \underline{\theta} \underline{\theta}'^* \rangle = \mathbf{E} \langle \underline{\alpha} \underline{\alpha}'^* \rangle \mathbf{E}' + \text{errors.} \tag{7}$$

It has been shown (Haines *et al.*, in prep.) that the least squares estimate of $\langle \underline{\alpha} \underline{\alpha}'^* \rangle$ is given by

$$\langle \widehat{\underline{\alpha} \underline{\alpha}'^*} \rangle = (\mathbf{E}'^* \mathbf{E})^{-1} \mathbf{E}'^* \langle \underline{\theta} \underline{\theta}'^* \rangle \mathbf{E} (\mathbf{E}'^* \mathbf{E})^{-1}. \tag{8}$$

The quantity minimised is the squared error between the predicted and observed series, summed over the entire cross-spectral matrix. This formulation guarantees that the predicted cross-spectral matrix and the cross-spectral matrix of modal amplitudes are physically realizable and so may be interpreted as cross-spectral matrices. This provides estimates of modal power, coherences and relative phases. As the solution is a linear transformation of the cross-spectral matrix of observations, significance levels follow from standard formulae.

The method may be simply understood by solving (6) in the time domain. The least squares solution gives

$$\hat{\mathbf{a}} = (\mathbf{E}'^* \mathbf{E})^{-1} \mathbf{E}'^* \underline{\theta}. \tag{9}$$

Squaring and averaging, or forming $\langle \hat{\mathbf{a}} \hat{\mathbf{a}}'^* \rangle$, returns (8). Similarly from (9) we may define a cross-spectral matrix of residuals given by

$$\begin{aligned} \langle \underline{\epsilon} \underline{\epsilon}'^* \rangle &= \langle \underline{\theta} \underline{\theta}'^* \rangle + \mathbf{E} (\mathbf{E}'^* \mathbf{E})^{-1} \mathbf{E}'^* \langle \underline{\theta} \underline{\theta}'^* \rangle \mathbf{E} (\mathbf{E}'^* \mathbf{E})^{-1} \mathbf{E}'^* \\ &\quad - \mathbf{E} (\mathbf{E}'^* \mathbf{E})^{-1} \mathbf{E}'^* \langle \underline{\theta} \underline{\theta}'^* \rangle - \langle \underline{\theta} \underline{\theta}'^* \rangle \mathbf{E} (\mathbf{E}'^* \mathbf{E})^{-1} \mathbf{E}'^*. \end{aligned} \tag{10}$$

This matrix is also physically realizable. Decomposition of the cross-spectral matrix of residuals will indicate whether spatially coherent motions remain which are not adequately described by the model fitted.

In practice the sensor array may be incapable of resolving the wide range of modes possible. The model must be limited to those modes which are well resolved. The degree to which modes modelled are resolved is indicated by the condition of the matrix $(\mathbf{E}'^* \mathbf{E})$, where the condition is the ratio of the smallest to largest eigenvalues of the matrix. This provides a useful tool for array design as the matrix may be formed, for given topography and frequency, prior to collecting data. The resolution of the array will vary with frequency as the modal shapes vary and frequency dependent models may be necessary. As a general rule of thumb the condition of the model matrix should exceed the estimated noise to signal ratio of the array.

The incorporation of a variety of sensors may necessitate weighting of the model. This will prevent single energetic observations from dominating the fit. The most straightforward approach is to weight the model by the standard deviation of the observations.

The modelling may also be extended to include forcing variables. In such a case the observed forcing time series are included as observation series and simply passed through the fitting step. The forcing series, $F(t)$, are modelled as

$$F_i(t) = E_{i,j} \alpha_n(t) + 0, \tag{11}$$

where $E_{i,j} = 1$ when $j = n$ and 0 otherwise. The result is that $F_i = \alpha_n$, and the final fitted cross-spectral matrix includes terms of the form $\langle F_i \alpha_m^* \rangle$.

Application

The method of analysis described has been applied to a single data run from the NSTS experiment. Measurements were made at Torrey Pines beach, San Diego in November of 1978. Torrey Pines is a 3 km long beach with slope approximately .02 below MSL. The incident wave field is directionally restricted by offshore islands and for the November 21 run examined 17 two-component Marsh-McBirney flowmeters were deployed. The data were sampled at 64 Hz , low-pass filtered and reduced to 2 Hz . The cross-spectral estimates have a bandwidth of $.00049\text{ Hz}$ giving 10 degrees of freedom. The incident wave field was characterised by a peak frequency of $.067\text{ Hz}$ and a significant wave height of $.86\text{ m}$ (Guza and Thornton, 1985). The cross-spectral matrix is modelled as described and the results averaged across frequency to increase the degrees of freedom. This allows us to model the variation in modal shapes with frequency rather than averaging prior to fitting.

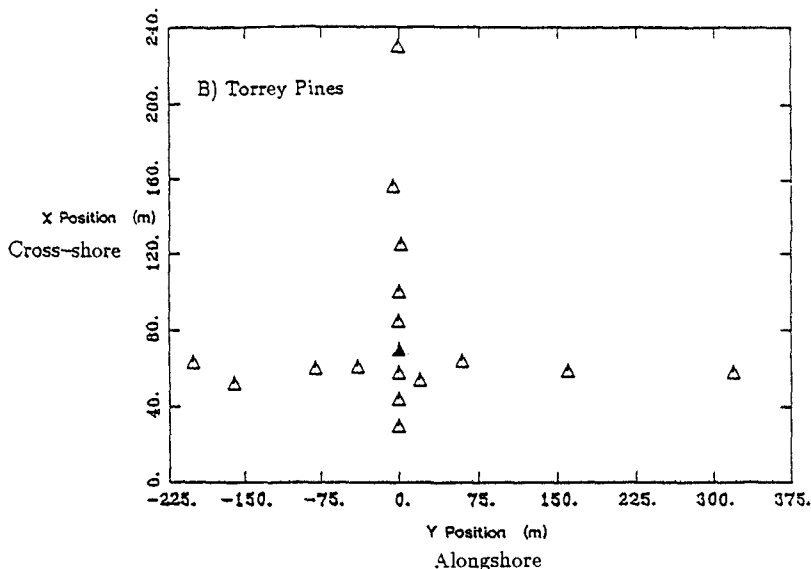


Figure 1. Configuration of flowmeters used in analysis. Symbols indicate position of Marsh-McBirney electromagnetic flowmeters. Shoreline is lower horizontal axis.

The array configuration is shown in Figure 1. The studies previously discussed (Oltman Shay and Guza, 1987, Huntley, 1988) used only the alongshore transect and treated the two velocity components separately. We simultaneously model all the available data. This is particularly helpful in avoiding the spectral gaps caused when an offshore position sees a node in a measured variable. Given the large number of modes possible, some care was taken in choosing a model, as the results of Oltman-Shay and Guza (1987) suggested a wide range of modes were present during the study. However, it is necessary to fit a restricted number of modes which will be representative of the entire field. After a number of trials we chose to fit edge wave modes 0,1,2,4 and 7 (progressive in either direction) and an incident and reflected pair. We chose to fit the same model across all frequencies in order to identify the frequency dependence of the modal field. At any particular frequency simpler models

are as efficient at describing the data - but the complete model is superior across the entire frequency range.

The success of the model in describing the observations is shown in Figure 2. Across most of the range the bulk of the variance and the spectral peaks are well described. The more energetic alongshore velocities are better described than the cross-shore velocities, though the residual variance for the two sensor types is comparable. At low frequencies the model fails to describe the motions present. It is clear that no simple edge wave model will fit these motions. Eigenvector analysis of the cross-spectral matrix of residuals shows that the bulk of the unexplained variance is spatially coherent. This indicates that coherent motions incompatible with edge/leaky wave models are present.

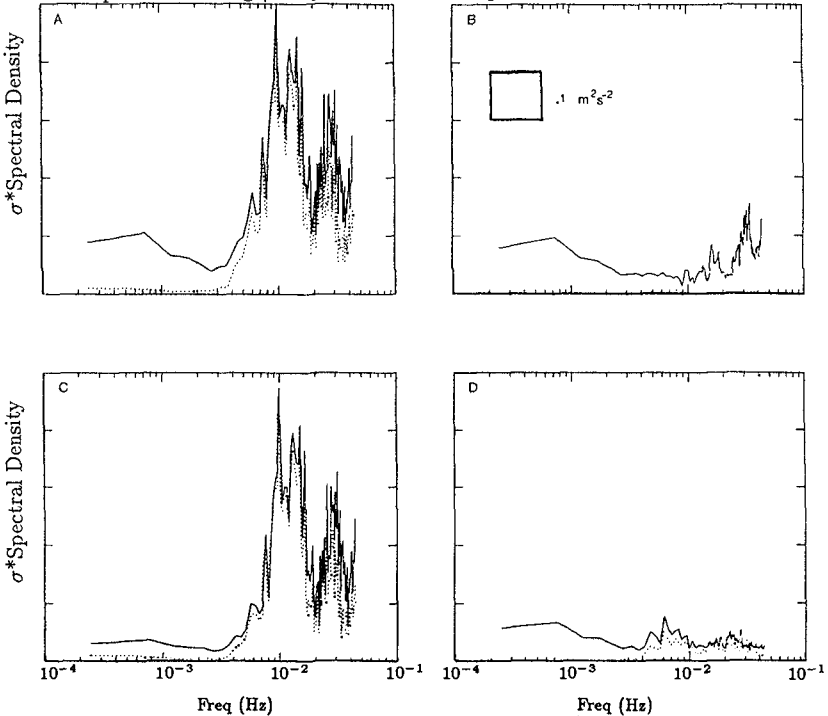


Figure 2. Integrated variance measured (—) and predicted (- -). Variance is integrated across a) the total array, c) the cross-shore velocity sensors and d) the alongshore velocity sensors. Panel b) shows the total residual variance.

As a rough but independent check of the results Figure 3 shows the predicted shoreline run-up for the model fitted. Measured run-up (Guza and Thornton, 1985) is also shown. The predicted run-up has been calculated by assuming that a standing wave of twice the reflected wave amplitude is seen at the shoreline in addition to the edge waves. Given the limitations of this model and the significant residual energy the agreement is encouraging. Figure 4 shows the predicted run-up for a number of alongshore positions. The substantial variation shows that the degree of modal coupling found is important. It also points out the dangers of assuming spatial homogeneity and the advantages of having shoreline data to verify and constrain modelling techniques.

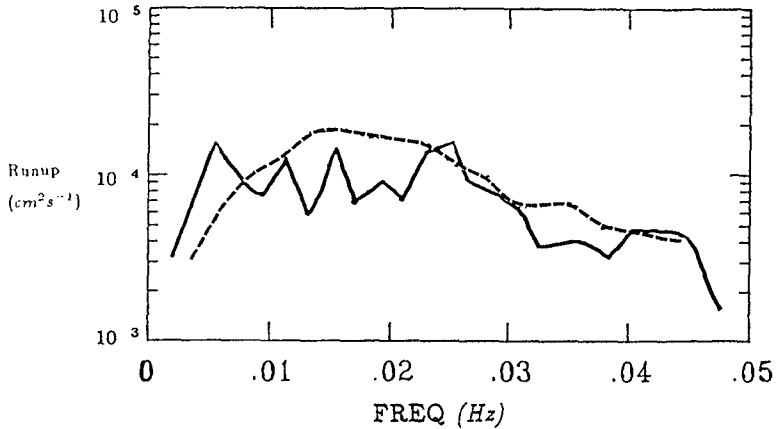


Figure 3. Measured (—) and predicted (---) shoreline run-up spectra at Torrey Pines.

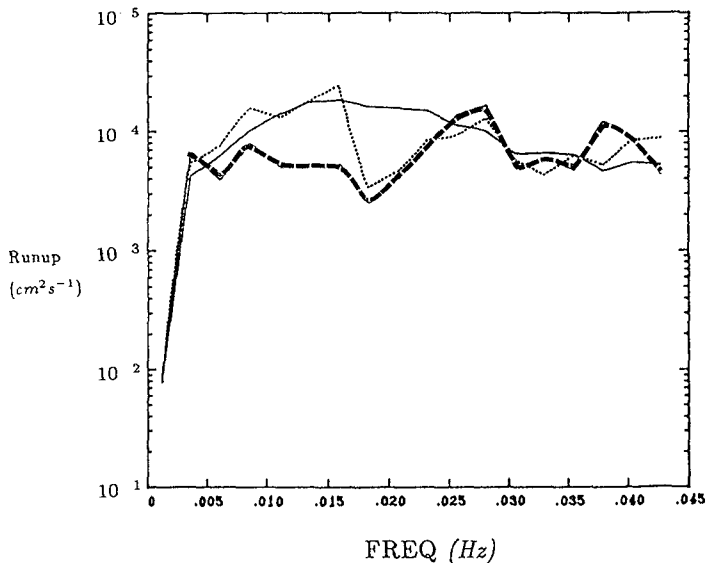


Figure 4. Predicted run-up spectra at Torrey Pines at $y = 0$ (—), $y = 250$ (· · ·) and $y = 500$ (---).

The predicted run-up spectra clearly suggest that the wave field is inhomogeneous. This has important implications for sediment transport and beach profile modelling. In particular it validates the modelling assumptions of Holman and Bowen (1982) that phase-locked modes are important.

The estimated modal amplitude spectra are shown in Figure 5. All modes show negligible amplitude at the lowest frequency. With the possible exception of mode zero, all modes

show enhanced modal amplitudes around $.015Hz$. Modes higher than mode zero show a second peak between $.025$ and $.030Hz$. There is a tendency for northward progressive waves (dotted lines) to be slightly larger, the greatest differences appearing in the neighbourhood of the spectral peaks. Above $.025Hz$ mode zero is forced to small amplitudes as it decays inshore of the array. In general the modal amplitude spectra indicate:

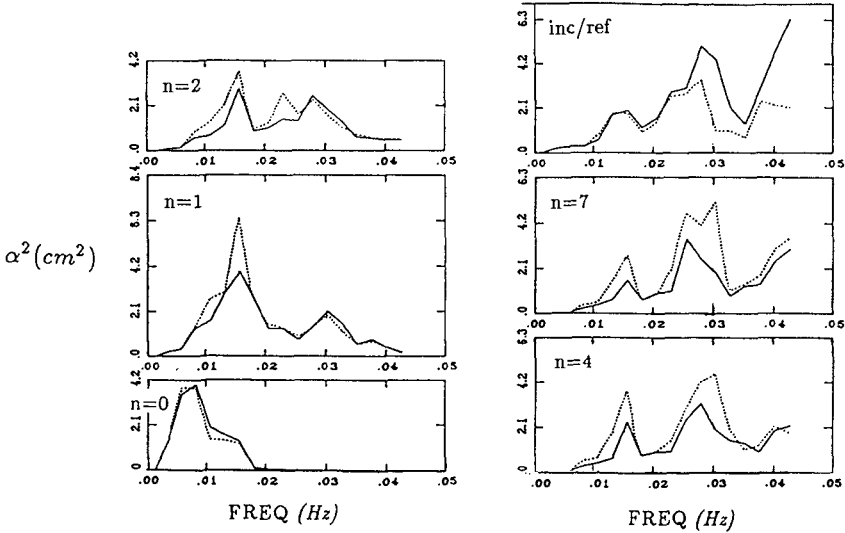


Figure 5. Shoreline amplitude spectra for modes fitted. Mode numbers are indicated in upper left hand corner of spectral plots. Solid (dashed) lines indicate positive (negative) alongshore progression for edge waves and the incident (reflected) wave in the upper right hand panel.

- 1) A wide range of modes, including high modes and leaky waves are present.
- 2) The two directions of edge wave propagation show roughly equivalent amplitudes, with a slight enhancement of the northward propagating waves.
- 3) There are two distinct peaks in the amplitude spectra. The peaks are present for all modes higher than zero. This frequency structure is also seen in the incident and reflected waves.
- 4) Modes higher than two show evidence of increasing amplitude above $.035Hz$.
- 5) The higher frequency peak, $\sim .025 - .030Hz$, is dominated by higher modes with amplitude increasing with mode number.
- 6) The incident wave amplitude increases sharply at the upper frequency limit, and the incident wave is uniformly larger than the reflected wave.

Figures 6 and 7 show the gain and phase for the mode zero and incident and reflected wave pairs. Significantly non-zero gain is equivalent to significantly non-zero modal coupling. The mode zero pair shows significant coupling over a wide range of frequencies, although primarily outside the energetic region of the amplitude spectra. Phase shows no obvious σ^2 dependence which would indicate the presence of an alongshore reflector. The incident/reflected pair also shows significant coupling with the gain less than 1 and generally decreasing with frequency. This frequency dependence of the reflection coefficient has been

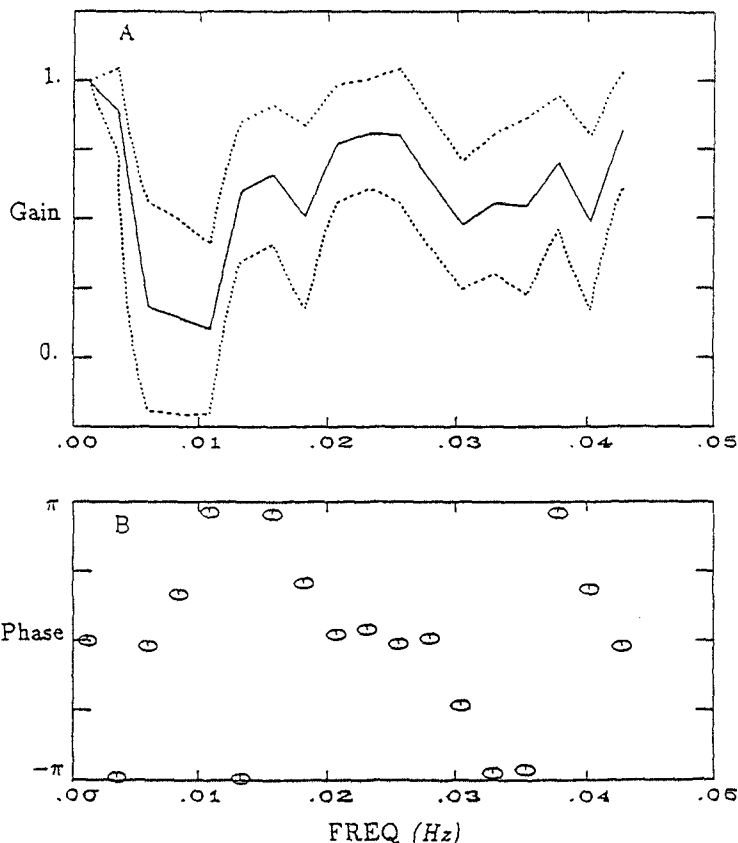


Figure 6. Gain, a), and phase, b), between oppositely progressing mode zero edge waves. Dashed lines on gain plot are upper and lower 95% confidence levels (Jenkins and Watts, 1968).

suggested by a number of authors (Elgar, 1985). The pronounced, quasi-linear trend to the phase is unexplained. Because the incident and reflected waves are largely nondispersive at these frequencies, a linear phase shift may suggest that the cross-shore origin is misplaced, i.e. reflection is occurring away from the shoreline. Determination of this reflection point would require a physical model for the process being described. Phase differences may also be attributable to nonlinearities in run-up or the effects of a porous beach face. These introduce what are presumably higher order modifications to the modelled waves.

Significant squared coherences are shown in Table 1 for all modal combinations at selected frequencies. The occurrence of significant coherences is substantially greater than that expected for a system composed of noise. Apart from a slight tendency for higher modes to be coupled to the incident wave, there appear to be no particular pairs which exhibit consistently high coupling. Significant coupling also seems unrelated to modal amplitude

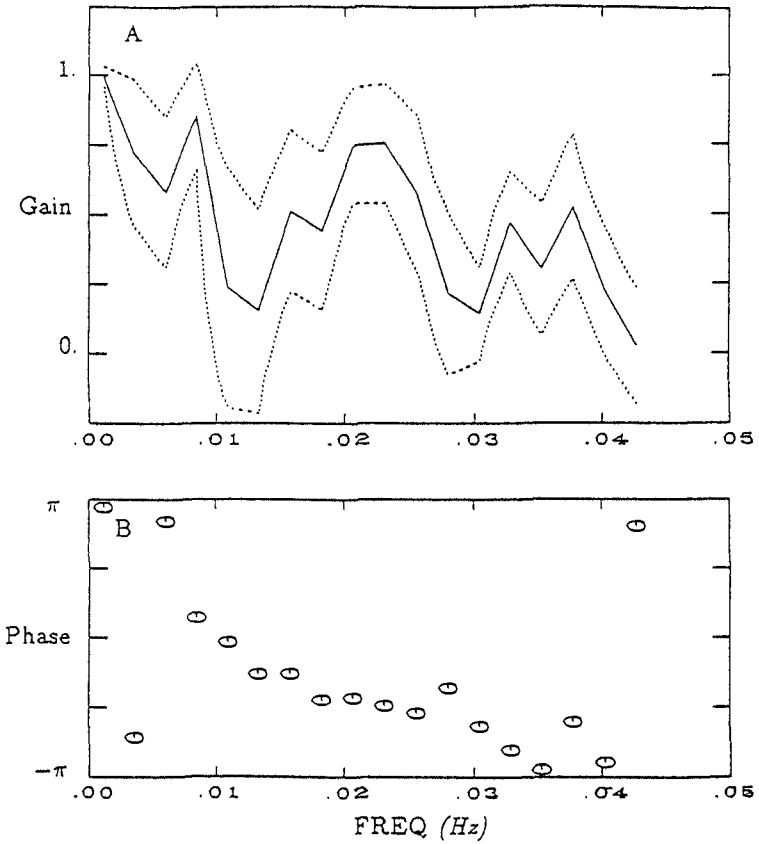


Figure 7. Gain, a), and phase, b), between incident and reflected waves. Dashed lines on gain plot are upper and lower 95% confidence intervals (Jenkins and Watts, 1968).

or frequency.

Conclusions: We have presented and applied a method of extracting modal information from observed dynamic variables. The method uses all available data and explicitly considers phase-locking of modes. The method may be extended to include forcing variables.

The data set examined comprised an unusually large sensor array. Even so it is not possible to consider all the modes which might be expected to be present. The results of the

Table 1
Modal Coupling - Torrey Pines

	0 ⁺	0 ⁻	1 ⁺	1 ⁻	2 ⁺	2 ⁻	4 ⁺	4 ⁻	7 ⁺	7 ⁻	I	R
0 ⁺	-	-	.65	.14	.32	.26	-	.27	-	.21	.20	.20
0 ⁻		-	.18	.69	.30	.36	.27	-	.19	-	-	-
1 ⁺			-	.38	.87	.29	.55	-	.33	-	-	-
1 ⁻				-	.28	.88	-	.58	-	.36	-	-
2 ⁺					-	.12	.87	-	.67	-	.13	-
2 ⁻						-	-	.88	-	.69	-	-
4 ⁺	$\sigma = .0061Hz$						-	-	.94	.25	.24	-
4 ⁻								-	.25	.95	.23	.21
7 ⁺									-	.47	.31	.19
7 ⁻										-	.31	.26
I											-	.38
R												-
	0 ⁺	0 ⁻	1 ⁺	1 ⁻	2 ⁺	2 ⁻	4 ⁺	4 ⁻	7 ⁺	7 ⁻	I	R
0 ⁺	-	.43	-	-	-	-	-	-	-	-	-	-
0 ⁻		-	-	-	-	-	-	-	-	-	-	-
1 ⁺			-	.18	.45	-	-	-	.19	-	.14	.20
1 ⁻				-	-	.40	-	-	-	-	-	-
2 ⁺					-	-	.45	.25	-	.27	-	-
2 ⁻						-	-	.73	-	.49	-	.12
4 ⁺	$\sigma = .0134Hz$						-	-	.77	-	-	.13
4 ⁻								-	-	.93	.36	.32
7 ⁺									-	.22	.32	.38
7 ⁻										-	.47	.44
I											-	-
R												-
	0 ⁺	0 ⁻	1 ⁺	1 ⁻	2 ⁺	2 ⁻	4 ⁺	4 ⁻	7 ⁺	7 ⁻	I	R
0 ⁺	-	.64	-	-	-	.14	-	.19	.26	.49	.76	.76
0 ⁻		-	-	-	-	-	.25	-	.49	.25	.75	.76
1 ⁺			-	-	-	-	-	-	-	-	-	-
1 ⁻				-	-	-	-	-	-	-	-	-
2 ⁺					-	-	.37	-	-	-	-	-
2 ⁻						-	-	.47	-	.14	-	-
4 ⁺	$\sigma = .0208Hz$						-	-	.74	.12	.19	.19
4 ⁻								-	-	.74	.19	.16
7 ⁺									-	.13	.49	.39
7 ⁻										-	.46	.48
I											-	.63
R												-

Table 1 The coherence squared between modes. Significant values of coherence squared (Jenkins and Watts, 1968) are shown for all modal pairs. +/- indicates a wave progressing northward/southward.

Table 1 - continued
 Modal Coupling - Torrey Pines

	0 ⁺	0 ⁻	1 ⁺	1 ⁻	2 ⁺	2 ⁻	4 ⁺	4 ⁻	7 ⁺	7 ⁻	I	R
0 ⁺	-	.49	-	.13	-	.14	.19	.40	-	.14	.45	.16
0 ⁻		-	.13	-	-	-	.24	.36	-	-	.38	.20
1 ⁺			-	-	-	-	-	.17	-	-	-	-
1 ⁻				-	-	-	-	-	-	-	-	-
2 ⁺					-	-	.19	-	.12	.26	-	-
2 ⁻						-	-	-	.13	-	-	-
4 ⁺	$\sigma = .0281Hz$						-	.12	.30	.13	.25	-
4 ⁻								-	.15	.39	-	.25
7 ⁺									-	.55	-	-
7 ⁻										-	.13	.18
I											-	-
R												-
	0 ⁺	0 ⁻	1 ⁺	1 ⁻	2 ⁺	2 ⁻	4 ⁺	4 ⁻	7 ⁺	7 ⁻	I	R
0 ⁺	-	.28	.83	.38	.12	-	-	-	-	-	-	-
0 ⁻		-	.30	.77	-	.15	-	.13	-	-	.15	-
1 ⁺			-	.43	-	-	-	-	-	-	-	-
1 ⁻				-	-	-	-	-	-	-	-	-
2 ⁺					-	-	-	-	-	-	-	-
2 ⁻						-	-	-	-	-	-	-
4 ⁺	$\sigma = .0354Hz$						-	-	-	.13	.25	.20
4 ⁻								-	-	-	.27	-
7 ⁺									-	.38	.19	-
7 ⁻										-	.14	-
I											-	.18
R												-
	0 ⁺	0 ⁻	1 ⁺	1 ⁻	2 ⁺	2 ⁻	4 ⁺	4 ⁻	7 ⁺	7 ⁻	I	R
0 ⁺	-	.67	.92	.55	-	-	-	-	.21	.32	.53	.22
0 ⁻		-	.80	.90	-	-	.15	-	.24	.14	.57	.18
1 ⁺			-	.45	.12	-	-	-	.73	.37	.52	.25
1 ⁻				-	-	-	.12	-	.25	.17	.69	.14
2 ⁺					-	-	-	-	-	-	-	-
2 ⁻						-	-	.14	-	-	-	-
4 ⁺	$\sigma = .0427Hz$						-	.14	.23	-	-	-
4 ⁻								-	-	-	-	-
7 ⁺									-	-	.15	-
7 ⁻										-	.30	-
I											-	-
R												-

Table 1 The coherence squared between modes. Significant values of coherence squared (Jenkins and Watts, 1968) are shown for all modal pairs. +/- indicates a wave progressing northward/southward.

fit suggest a variety of modes are present and that significant phase-locking occurs. This has important implications for sediment transport, beach morphology and the modelling of edge wave dynamics.

References

- Bowen, A.J., and D.L. Inman, Edge waves and crescentic bars, *J. Geophys. Res.*, 76, 862-8671, 1971.
- Bowen, A.J., and D.A. Huntley, Waves, long waves and nearshore morphology, *Marine Geology*, 60, 1-13, 1984.
- Eckart, C., Surface waves in water of variable depth. Wave report, SIO Ref. 51-12, Scripps Inst. Oceanogr., La Jolla, CA, 99pp, 1951.
- Elgar, S., Shoaling surface gravity waves, Ph.D. thesis, Scripps Inst. Oceanogr., La Jolla, CA 123 pp., 1985.
- Guza, R.T., and R.E. Davis, Excitation of edge waves by waves incident on a beach, *J. Geophys. Res.*, 79, 1285-1292, 1974.
- Guza, R.T., and A.J. Bowen, Finite amplitude edge waves, *J. Mar. Res.*, 34, 269-293, 1976.
- Guza, R.T., and Inman, D.L., Edge waves and beach cusps, *J. Geophys. Res.*, 80, 2997-3012.
- Guza, R.T., and E.B. Thornton, Observations of surf beat, *J. Geophys. Res.*, 80, 2997-3172, 1985.
- Haines, J.W., K.R. Thompson, and D. Wiens, Fitting dynamical modes to data. (in prep.)
- Holman, R.A., and A.J. Bowen, Bars, bumps and holes: models for the generation of complex beach topography, *J. Geophys. Res.*, 87, 457-468, 1982.
- Holman, R.A., and A.J. Bowen, Longshore structure of infragravity wave motions, *J. Geophys. Res.*, 89, 6446-6452, 1984.
- Huntley, D.A., Evidence for phase-coupling between edge wave modes, (in prep.)
- Jenkins, G.M., and D.G. Watts, Spectral analysis and its applications, Holden-Day, Oakland, CA, 525 pp., 1968
- Oltman-Shay, J., and R.T. Guza, Infragravity edge wave observations on two California beaches, *J. Phys. Oceanogr.*, 17, 644-663, 1987.
- Symonds, G., D.A. Huntley and A.J. Bowen, Two-dimensional surf beat, long wave generation by a time-varying breakpoint, *J. Geophys. Res.*, 87, 492-498, 1982.

CHAPTER 114

BEACH PROFILE CHANGE UNDER VARYING WAVE CLIMATES

Yen Kai⁽¹⁾ Ren Rushu⁽²⁾ Wang Liang⁽³⁾

Abstract

In the present paper results of experimental study of two-dimensional transformation of sandy beach under varying wave climates are presented. The varying wave climates were composed of different systems of regular waves exerted one after another on the model beach. Through experiments it was found that sandy beach transformation within surf zone could be expressed by the changes of characteristic point A and characteristic slope $\tan \beta$, and that although the expression for beach erosion-accretion criteria is dimensionless, similitude scale effects should still be taken into consideration.

I. Introduction

Beach erosion-accretion process changes with wave climates. A new beach profile is always developed from the profile created by preceding wave climate. However, previous experimental studies on beach profile change were usually carried out by assuming an initial straight beach slope i_0 , which is not in conformity with the natural situation. To avoid this a series of tests on beach transformation were conducted using varying wave climates, i.e. different systems of regular waves one after another. Part of experimental results has been published⁽³⁾, in which the conception of characteristic point A and characteristic slope $\tan \beta$ was introduced and a beach erosion-accretion criterion was proposed. In the present paper some new experimental results and advancement in the authors' research works will be given.

II. Experimental Investigation

From 1980 to 1987, experiments were performed in a wave basin, 23.8m long, 8.7 m wide and 0.58 m deep. The model stretch is separated lengthwise into six wave flumes, each 17 m long, 0.48 m wide. Ordinary quartz sand of different sizes were used and four different initial beach slopes 1/5, 1/10, 1/15 and 1/20 were moulded in wave flumes. The ground water level in the model was controlled so as to maintain its original still water level in the wave basin.

(1) Professor and Hon. President, (2) Associate Professor, (3) Research Assistant, Hohai University, Nanjing, China

Three kinds of waves climates were used:

1st kind: A train of regular waves with constant wave height H_0 and wave period T acting intermittently on model beach in varying durations. Through experiments the relations between initial, intermediate and equilibrium profiles can be observed. The wave climates used in 1st kind are shown in Table 1.

Table 1 Experimental conditions of 1st kind wave climates

Sand size d_{50} Flume No. case	$d_{50} = 0.30^{mm}$				$d_{50} = 0.69^{mm}$		H_0 (cm)	T (sec)	No. of tests & dura- tions(hr)	
	No.1	No.2	No.3	No.4	No.5	No.6				
A-1	1/5	1/10	1/15	1/20		1/10	6.8	1.25	1×8	
A-2	1/5	1/10	1/15	1/20		1/10	6.8	1.25	2×4	
A-3	1/5	1/10	1/15	1/20		1/10	6.8	1.25	4×2	
A-4	1/5	1/10	1/15	1/20		1/10	6.8	1.25	8×1	
A-5	1/5	1/10	1/15	1/20		1/10	6-8	1.25	16×0.5	
A-6	1/5	1/10	1/20		1/20	1/10	1/5	6.8	1.25	2
A-7	1/5	1/10	1/20		1/20	1/10	1/5	6.8	1.25	54
B-1	1/5	1/10	1/15	1/20		1/20	1/10	5.1	1.25	1×8
B-2	1/5	1/10	1/15	1/20		1/10	1/5	5.1	1.25	2×4
B-3	1/5	1/10	1/15	1/20		1/10	1/5	5.1	1.25	4×2
B-4	1/5	1/10	1/15	1/20		1/10	1/5	5.1	1.25	2
C-1	1/5	1/10	1/15	1/20		1/10	1/5	5.1	1.25	8
C-2	1/5	1/10	1/15	1/20		1/10	1/5	6.8	1.00	2×4
C-3	1/5	1/10	1/15	1/20		1/10	1/5	6.8	1.00	4×2
C-4	1/5	1/10	1/15	1/20		1/10	1/5	6.8	1.00	8×1
C-5	1/5	1/10	1/15	1/20		1/10	1/5	6.8	1.00	16×0.5
C-6	1/5	1/10	1/20		1/20	1/10	1/5	6.8	1.00	2
C-7	1/5	1/10	1/20		1/20	1/10	1/5	6.8	1.00	22
C-8	1/5	1/10	1/20		1/20	1/10	1/5	6.8	1.00	136

2nd kind: Wave climates consisting of constant regular waves and different systems of regular waves with varying wave height H_0 and wave period T . Through experimental studies of the actions of constant waves and different systems of waves on straight as well as on transformed beaches, the transformation relations for different beach configuration in surf zone can be observed. The wave climates used in 2nd kind are shown in Table 2. In Table 2(a), E-K are constant wave cases. The experiments were continued until the beach profile reaches the state of equilibrium or quasi-equilibrium. In Table 2(b), groups A and BC were performed using wave cases F, H, I, J, K, arranged in the order and for the duration shown.

Table 2 Experimental conditions of 2nd kind wave climates
(a) Constant regular waves

Wave Case	E	F	G	H	I	J	K
H_0 (cm)	6.80	2.96	2.32	4.96	4.28	7.00	9.42
T (sec)	1.25	2.20	2.70	1.42	1.80	1.24	0.87
Test Duration (hr)	21.0	60.0	32.5	24.0	28.0	27.0	35.0
Flume Number	1	2	3	4	5	6	
Initial Slope i_0	1/5	1/10	1/20	1/20	1/10	1/5	
d_{50} (mm)	0.30	0.30	0.30	0.69	0.39	0.69	

(b) Systems of regular waves

Wave Group	A					BC				
Case Order	K	J	I	F	H	F	I	J	K	H
Test Duration (hr)	34.5	3.0	5.0	8.0	13.0	34.5	10.5	13.0	12.5	13.0

3rd kind: Wave climates consisting of constant regular waves and different systems of regular waves with constant wave height H_0 and varying wave period T, varying H_0 and constant T as well as varying H_0 and T (Table 3). Through experiments under this kind of wave climates, we can get some more knowledge of two-dimensional transformation of sandy beach under varying wave climates.

III. Erosion-Accretion Parameters and Beach Types within Surf Zone

1. Erosion-accretion parameters

Through experiments mentioned above, it can be noted that in the course of beach transformation under a certain wave action there is a point on the beach profile, located near the wave breaking point, undergoing very little change as shown in Figure 1 and Figure 2. The same point also existed in T. Sawaragi's model test (1980)⁽⁶⁾. We defined this point as the characteristic point A. Make use of its relative stable position, point A can be taken as a coordinate origin on the beach profile to facilitate the study of beach transformation processes. Slope $\tan\beta$ formed by connecting the characteristic point and shoreline point may be defined as the characteristic slope. Characteristics slope $\tan\beta$ changes simultaneously with advance and recession of the shoreline in the course of beach transformation, i.e. in the course of beach erosion $\tan\beta$ tends to become gentle with the recession of shoreline, conversely, in the course of beach accretion $\tan\beta$ tends to become steep with advance of shoreline. In the state of erosion-accretion equilibrium the characteristic slope will almost remain unchanged and may be denoted by $\tan\beta_c$. So by comparing the characteristic slopes before and after a certain series of wave action, we can judge whether the shoreline is advancing or receding and define the types of beach erosion-accretion accordingly. For this reason point A and $\tan\beta$ may be chosen as two important parameters to account for beach transformation within surf zone. Figure 3 shows that when a certain wave action is continued,

Table 3 Experimental conditions of 3rd kind wave climates

Flume Number	1	2	3	4	5	6	H_0 (cm)	T (sec)	Test Duration (hr)
Initial slope i_0	1/5	1/10	1/20	1/20	1/10	1/5			
d_{50} (mm)	0.40	0.40	0.40	0.54	0.39	0.40			
Wave Group	Case Order								
T	T ₃						5.85	1.2	30
	T ₉						6.93	1.2	23
	T ₁₉						8.90	1.2	30
	T ₁₄						7.96	1.2	16.6
H	H ₄						6.92	0.98	13.3
	H ₃₅						7.31	1.70	14.3
	H ₂₅						7.42	1.53	16.3
	H ₁₃						6.92	1.34	16.6
H_0/L_0	$H_0/L_0 - 22$						5.34	1.74	16.9
	$H_0/L_0 - 34$						6.31	1.84	16.2
	$H_0/L_0 - 38$						3.66	1.34	15.5
	$H_0/L_0 - 7$						3.61	1.48	17.8
S_y	$S_y - 16$						2.71	2.63	15.8
	$S_y - 12$						3.91	1.77	20.4
	$S_y - 30$						8.16	1.54	15.9
	$S_y - 15$						10.60	0.98	15.8
	$S_y - 4$						6.92	0.98	17.5
	$S_y - 17$						3.44	1.90	20.4
B - 17							3.44	1.90	20.2

the characteristic slope gradually reduces its developing speed and finally attains a state of equilibrium or quasi-equilibrium, which can be denoted by $\tan\beta_c$.

2. Beach types within surf zone

Beach erosion-accretion within surf zone has great influence on the stability of shoreline. According to whether the shoreline is advancing or receding and the beach is under erosion or accretion within surf zone, the beach profile within surf zone could be classified into three types as shown in Figure 2:

Type I: The shoreline recedes and surf zone is under erosion.

Type II: The beach profile and shoreline have reached quasi-equilibrium state.

Type III: The shoreline advances and surf zone is under accretion. When the wave action is continued, the beach profile would always transform from type I or type III into type II as shown in Figure 3.

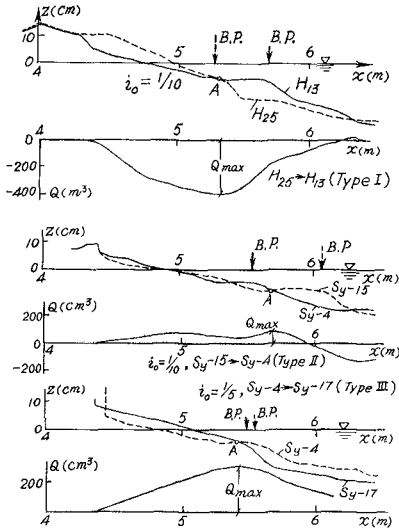


Fig.2 Beach types within surf zone and distribution of net on-offshore sediment transport load

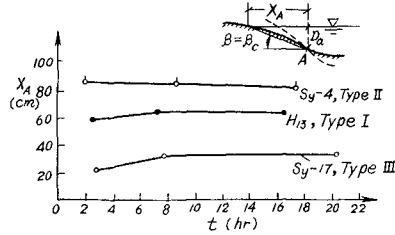


Fig.1 Distance x_A between characteristic point A and equilibrium shoreline point versus time t

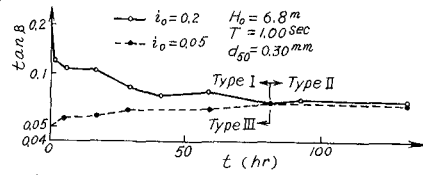


Fig.3 Characteristic slopes $\tan\beta$ change with advance and retreat of the shoreline in the course of beach transformation and tend to attain equilibrium

IV. Beach Criterion Number

1. Model scales

The authors' experimental data are compared with Sunamura and Hori-kawa's criterion (1974)⁽⁸⁾ as shown in Figure 4. The data points from 205m long large wave tank (R. Kashima et al, 1982)⁽²⁾ are also shown in the figure. It shows that for Sunamura's small wave tank, the beach erosion-accretion criterion number $K=4 - 8$, but for the large wave tank $K=18$, and from the author's experiments the criterion number for the two different grain sizes are different. Although the expression for beach erosion-accretion criteria has been made dimensionless, yet the wave and grain size effects have not been eliminated. Obviously such criteria can not be used in practice.

Since beach erosion-accretion transformation is principally produced in the surf zone, a normal similarity of wave is also required in the model in order to satisfy the dynamic similarity of wave action within the surf zone, i.e. the following relations should be satisfied:

$$\left. \begin{aligned} \lambda_H &= \lambda_L = \lambda_D \\ \lambda_T &= \lambda_D^{0.5} \end{aligned} \right\} \quad (1)$$

When prototype sand is used the beach model is a distorted model, so the following relations also should be satisfied:

$$\lambda_d = \lambda_w = 1 \quad (2)$$

$$\lambda_l = \lambda_D^\alpha \quad (3)$$

where $\lambda_H, \lambda_L, \lambda_T, \lambda_D$ represent the scale of wave height, wave length, wave period and water depth respectively, λ_l is the horizontal scale: λ_d and λ_w are the scale of sand grain size and settling veloci-

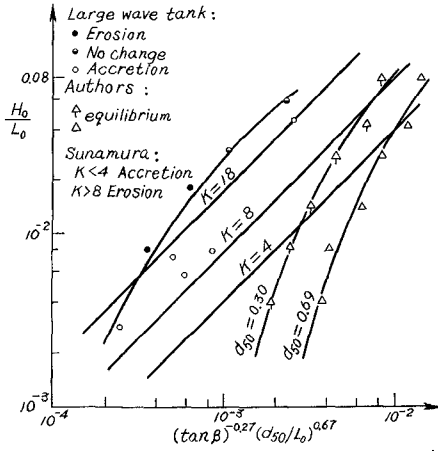


Fig. 4 Examination of similarity of T. Sunamura's erosion-accretion criterion.

ty respectively. In order that the criterion number K obtained in model may be used in practice, the scale of number K must equal one in any situation, i.e.:

$$\lambda_K = 1 \tag{4}$$

If the relations in equation (1) and (3) are substituted into Sunamura's criterion, and adopt $\alpha = 1.5$, Sunamura's criterion can be rewritten as:

$$\lambda_K = \left(\frac{\lambda_H}{\lambda_d} \right)^{0.67} \left(\frac{\lambda_D}{\lambda_l} \right)^{0.27} = \frac{\lambda_H^{0.535}}{\lambda_d^{0.67}} \tag{5}$$

It is obvious that, the above equation is not simultaneously in accord with the prerequisites indicated in equation (2) and (4). If $\lambda_d = 1$, then $\lambda_K \neq 1$, λ_K is directly proportional to $\lambda_H^{0.535}$, i.e. criterion number K will be increased with increase in wave force; while if $\lambda_H = 1$, λ_K is inversely proportional to $\lambda_d^{0.67}$, i.e. the criterion number K will be increased with decrease in sand size. So that, Sunamura's criterion for large wave tank, small wave tank and different sand grain sizes exhibited non-identity as shown in Figure 4.

The criterion expression of CERC (1975)⁽⁹⁾, $K = H_0/\omega T$, was verified. The scale of the criterion can be written as

$$\lambda_K = \lambda_H^{1/2} / \lambda_\omega \tag{6}$$

when $\lambda_\omega = 1$, then $\lambda_K = \lambda_H^{1/2}$. Obviously, in CERC's criterion λ_K is a value affected by wave height or wave length, the value K increases with the wave height or wave length, so the criterion of CERC is rather limited for use.

2. Beach erosion-accretion criterion

A beach erosion-accretion criterion was presented in 1986 by authors, which is:

$$\frac{H_0}{L_0} = K \left(\frac{\omega}{gT} \right)^{1.3} \left(\frac{U_c}{\omega} \right)^{0.4} (\tan\beta)^{-1.5}, \quad K = C f_w^{0.2} \quad (7)$$

In this formula several points are worthy to mention. First, the conception "characteristic slope" $\tan\beta$ is introduced instead of initial straight slope i_0 , to make the criterion applicable to any stage of beach evolution and irregular beach profile under varying wave climates.

Second, the critical velocity for incipient movement of the sediment U_c is introduced which is an important factor in determining the net sediment transport on the beach under wave actions. Moreover, the ratio of bottom frictional velocity of wave motion to settling velocity U_* / ω indicates the direction of net sediment transport on the beach (T. Sawaragi, 1982)⁽⁶⁾ and reflects what kind of sediment movement is dominant between suspended load and bed load. The tendency of beach to attain equilibrium state is shown by the value of U_* to approach $\sqrt{2 f_w} U_c$. Thus, on an equilibrium beach $\sqrt{2 f_w} U_c / \omega$ could be used instead of U_* / ω , where f_w is the frictional coefficient.

Third, the criterion formula satisfies the scale relations. After analysing over 100 data sets of the authors' as well as other researchers' experiments the following results were obtained: A beach will be in the state of quasi-equilibrium when $0.32 \leq K \leq 0.83$, with average value $K=0.5$, in erosion state when $K > 0.83$; and in accretion state when $K < 0.32$. The data extent is: $H_0=2.32 \sim 176^{cm}$, $T=0.87 \sim 12^{sec}$, $D_{50} = 0.2 \sim 6.1^{mm}$ ⁽³⁾.

V. Characteristic Point and Equilibrium Characteristic Slope

1. Characteristic point A

In the paper of 1986⁽³⁾, it has been indicated that on model beach composed of a certain kind of sand under the action of different systems of waves run in succession, a new characteristic point will be produced when one wave system is changed into another, whatever the previous beach transformation process may be. The position of point A (relative to the equilibrium shoreline) created by a certain wave case on any beach profile (irregular beach profile or simple straight beach) is generally the same. That is to say, the relative position of point A is closely related to wave parameters and sediment properties only and is almost irrespective of the previous processes of evolution of beach transformation.

Based on the above analysis a statistical formula for calculating water depth D_a at point A was obtained:

$$D_a / L_0 = 0.52 (H_0 / L_0)^{0.96} (U_c / \omega)^{0.33} \quad (8)$$

the data extent is: $H_0=2.32 \sim 176^{cm}$, $T=0.87 \sim 12^{sec}$, $d_{50}=0.2 \sim 6.1^{mm}$.

For any type of beach profile, the point A corresponds also to the point where the net sediment transport rate or net sediment load reached a limiting value as shown in Figure 2.

Using net on-offshore sand transport formula of Watanabe (1981)^(2,7), $\phi = 3(\psi - 0.12)\psi^{0.5}$, taking its limiting value, and then considering the correction for the effects of beach slope and sand size, another formula for calculating water-depth D_a at point A is obtained:

$$\frac{D_a}{L_0} = 0.192 \left(\frac{\rho_s - \rho}{\rho} \right)^{-0.8} \left(\frac{U_c^2}{g d_{50}} \right)^{3/15} \left(\frac{H_0}{L_0} \right)^{0.8} \quad (9)$$

where ϕ is the non-dimensional transport rate and ψ is the Shields parameter. If the wave parameters H_0 and L_0 as well as beach sand size d_{50} (cm) are known, the value of D_a can be calculated.

Formula (9) is compared with formula (8) by 56 experimental data obtained from large and small wave flumes. The relative error for formula (9) is 0.28 and for formula (8) is 0.43. It is clear that formula (8) is simpler than formula (9), but the latter seems to be more accurate and rational in theory.

2. Equilibrium characteristic slope

Equilibrium characteristic slope $\tan\beta_c$ can be calculated from formula (7) using average value $K=0.5$.

It is interesting to note that in the course of beach transformation under varying wave climates, although the initial and intermediate beach profile or characteristic slope $\tan\beta$ are not the same, yet when a certain wave action is continued, the beach always tends to transform into the same equilibrium or quasi-equilibrium characteristic slope as shown by the black data points of group $S_y - 12$, $S_y - 15$, $S_y - 4$ and $S_y - 17$ in Figure 5.

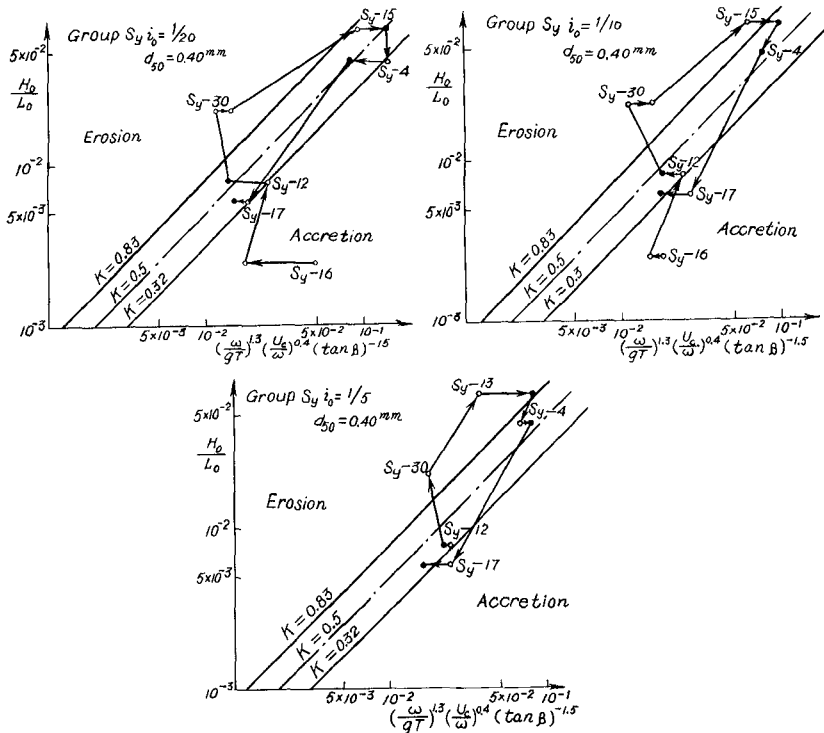


Fig. 5 H_0/L_0 versus $(\omega/gT)^{1.3} (U_c/\omega)^{0.4} / (\tan\beta)^{1.5}$ for wave climates of group S_y

Conclusion

1. Based on the shoreline recession-advance and beach erosion-accretion, the beach profile within surf zone could be classified into three types.
2. Two-dimensional beach transformation under varying wave climates could be expressed by the changes of characteristic point A and characteristic slope $\tan\beta$. Point A and slope $\tan\beta$ are closely related to wave characteristics and sediment properties only and could be obtained from formulæ (7) and (9).
3. Although the expression for beach erosion-accretion criteria is dimensionless, similitude scale effects should still be taken into consideration. Without similarity consideration the criterion may not be available for use.

References

1. Hallermeier, R. J., (1978) "Use for a calculated limit depth to beach erosion", Proc. of the 16th coastal Engineering Conf., pp.1493 - 1512.
2. Kashima, R., Shimizu, T., Maruyam, K., and Saito, S., (1982) "Experimental study of on-offshore sediment transport in a large wave tank", Proc. 29th Japanese Conf. Coastal Eng. pp. 125-129.(in Japanese).
3. Ren Rushu and Wang Liang, (1986) "Investigation on two-dimensional transformation of sand beach under wave action", Proc. of 3rd International Symposium on River Sedimentation, pp.378 - 387.
4. Saville, T., (1975) "Scale effects in two-dimensional beach study", Proc. 7th IAHR, pp. A3-1-A3-10.
5. Sawaragi, T. and Deguchi, I., (1980) "On-offshore sediment transport rate in the surf zone", Proc. of the 17th Coastal Engineering Conf., pp 1195 - 1214.
6. Sawaragi, T., (1982) Sediment transport and beach erosion, Morikita Publishing Company, Tokyo. (in Japanese).
7. Shimizu, T., Saito, S., Maruyam, K., Kashima, R., et al, (1985) "Experimental study of on-offshore sediment load distribution model in a large wave tank", Proc. 32th Japanese Conf. Coastal Eng. pp 311 - 314
8. Sunamura, T., Horikawa, K., (1974) "Two-dimensional beach transformation due to waves", Proc. of the 14th coastal Eng. Conf., pp 920-938.
9. U. S. army CERC, (1975) Shore Protection Manual, Vol I, pp 4-81-4-83.
10. Van Hijum, E., (1974) "Equilibrium profiles of coarse material under wave attack". Proc. of the 14th coastal Eng. Conf. pp.939 - 957.
11. Xu Xiao, (1981) Two-dimensional transformation of Sandy beach and on-offshore sediment transport, Master Thesis, East China Technical University of Water Resources, Nanjing, China, (in Chinese).

CHAPTER 115

REPRODUCTION MODELS OF BEACH CHANGE BY STORM WAVES

Masahiro Ito¹ and Yoshito Tsuchiya²

ABSTRACT

This paper presents a technique to reproduce, by a two-dimensional moveable-bed model, beach change due to the time-dependent storm waves which are generated by the passage of an atmospheric depression. In the model test, scaling conditions for sand grain-size, vertical and horizontal lengths, and wave height and period characteristics were established by applying the authors' scale-model relationship which was reported; and wave duration time also was decided. A method of employing regular waves in the model to represent irregular waves in the field is proposed. From the results, it was shown that the model can reproduce well the beach change in the field using the regular waves having the mean wave properties in the irregular waves.

1. INTRODUCTION

Coastal disasters, such as a beach erosion and seawall collapse which are caused by rapid sediment transport that occurs during storm conditions, continue to be frequently reported. One very important method used to approximate the coastal disaster, in hopes of preventing it, is the movable-bed model which can very closely approximate the beach change processes under the conditions of time-varying waves. However, because the scale-model relationship was not properly, we could not extrapolate the quantitative results which were obtained by the moveable-bed scale model test to the actual prototype, and therefore the results were applied qualitatively. It is necessary to establish the scale-model relationship and the experimental technique for the moveable-bed model test which is applicable for short-term beach change by unsteady time-dependent waves, as occur in the field.

As an example of a moveable-bed model investigation, Vellinga (1982) tried to reproduce, by a two-dimensional model, erosion of a coastal sand dune on the Dutch coast, the Netherlands due to wave action during an extreme storm surge. In the model test, vertical and

1 Associate Professor, Department of Civil Engineering, Meijo University
Tempaku-ku, Nagoya 468 Japan

2 Professor, Disaster Prevention Research Institute, Kyoto University
Kyoto, 611 Japan

horizontal scales were distorted, and the model sediment grain-size was determined by a new parameter which was composed of both the dimensionless sediment-settling parameter proposed by Dean (1973) and the vertical scale. Also, Hughes (1983) examined the application of Dean's dimensionless parameter, Froude's time scale of vertical scale, and the distorted model between the vertical and horizontal scales. The relationship which Hughes proposed was verified by results which reproduced the coastal dune erosion in the Florida Panhandle, USA caused by the 1975 Hurricane Eloise, using two-dimensional model test and regular waves. Tsuchiya et al. (1985) considered experimentally how to efficiently control beach erosion due to the T-type groin and the artificial headland works at Shirarahama, Wakayama, Japan using a three-dimensional movable-bed model and regular waves. The model test condition was established using the modified author's scale-model relationship for length and grain-size scales, Froude's scale for time scale, and an undistorted scale for vertical and horizontal scales.

In these previous experimental studies, the reproduction of filed beach profiles by model test are not only defined quantitatively, but also in how to determine set the optimum regular waves for the model. Therefore, as the first step, the approach due to regular waves is hoped strongly rather than use of the time-dependent irregular waves as are found in the field, due to the lack of an adequate irregular wave scaling relationship.

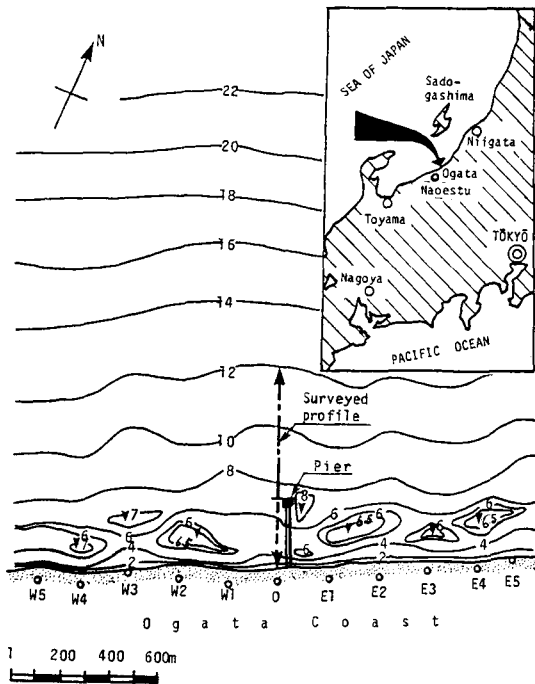


Figure 1 Bottom topography of Ogata coast and study site.

2. CONDITIONS IN STUDY SITE

(1) Coastal morphology

The Ogata coast facing the Sea of Japan is about 100km southwest from Niigata-city, Japan and has a considerably straight shoreline as shown in Figure 1. The sediment grain-size of this coast becomes gradually fine in the offshore direction, and its medium grain-size diameter, d_{50} , is 1.5 to 0.2mm. The beach profiles ranging from shoreline to about 300m offshore had been surveyed at one week intervals using a rod along an observation pier known as the Ogata Wave Observatory of the Disaster Prevention Research Institute, Kyoto University. The beach profile farther than 300m offshore, that is, deeper than a water depth of 8m, had been surveyed occasionally by using an ultrasonic sounding instrument. The sea bottom farther than 300m offshore has an average slope of 1/100. A longshore exist bar within the zone from the shore to about 300m offshore, beyond this 300m offshore distance the seabed contours remain fairly straight and parallel to the shoreline. Therefore, the topography of this coast may be considered almost two-dimensional in the on-offshore direction.

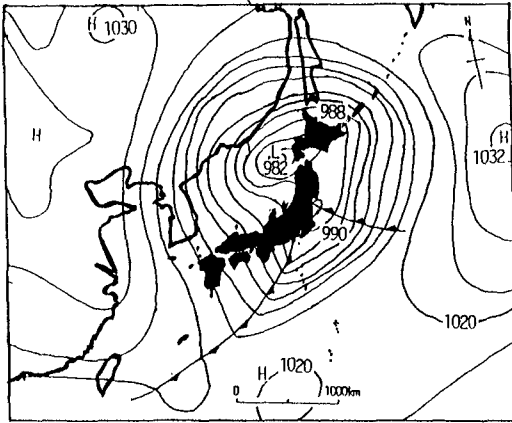
(2) Wave climate

Wave conditions in this area are usually observed at the offshore end of the observation pier in a depth of 6m, and Naoetsu Port Office, about 10km distance from the Ogata, in a depth of about 21m.

The Naoetsu Port Office continues to perform daily wave observations. From March 14-18, 1981 a large-scale lower atmospheric depression passed through the Sea of Japan, off the Ogata coast. Figure 2 shows the weather chart on the 15th when the Ogata coast wave attack was most severe. In Figure 3, time histories for significant wave height and period during the 15th to the 17th at the observation pier are shown using heavy solid and broken lines, respectively, while those at Naoetsu harbor are shown using thin solid and broken lines, respectively. As shown in this figure, the wave period records observed at the two positions agree well with each other. Whereas, records of wave height at the two positions do not completely agree with each other. This discrepancy of wave height higher than 4m is attributed to the generation of wave breaking because the measurement station of observation pier is relatively shallow. However, there was a good agreement for waves smaller than 4m height. Because the time history of waves observed at the two positions agreed well with each other, we choose to use the wave records which were observed in Naoetsu instead of Ogata. Figure 4 shows the time history of the maximum wave height, H_{max} , the significant wave height, $H_{1/3}$, and the mean wave height, H_{mean} , for 1 hour, which were calculated using the wave records observed at Naoetsu during the storm from the 10th to the 18th. During this period, the dominant incident waves at the Ogata coast attacked at nearly normal incidence to the shore, so that the coastal condition could be considered two-dimensionally.

3. SCALE-MODEL RELATIONSHIP USED

The scale-model relationship was used to design the model such that the Ogata coast beach change processes, due to storm waves, could be reproduced. The scale-model relationship, which is indicated as the similitude zone in Figure 5, had been earlier defined by the authors (1984) by considering experimentally the similarity between the



15 March 1981

Figure 2 Weather chart of the storm at maximum intensity attacked to the Ogata coast on 15 March 1981.

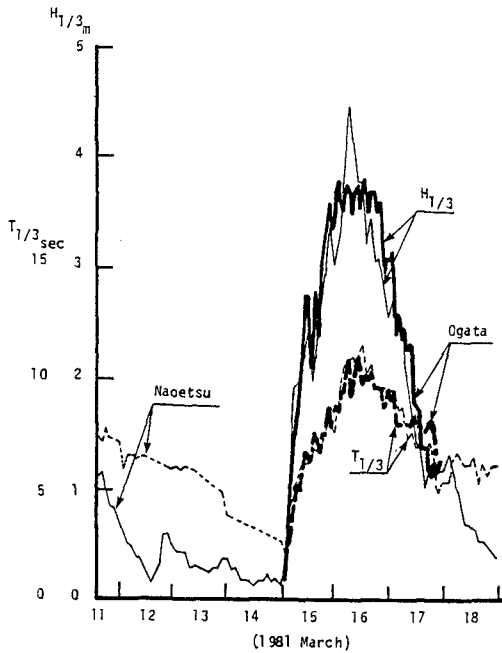


Figure 3 Time history of the significant wave height and period for 1 hour observation averaging at the tip of Ogata's pier and in Naoetsu harbour during 15 March 1981 to 17.

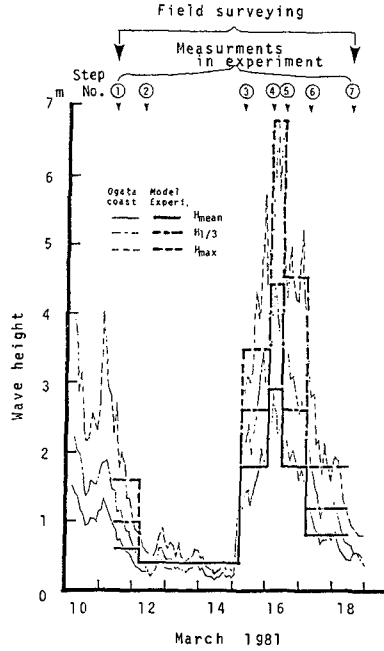


Figure 4 Variation of wave height during storm and experimental waves used.

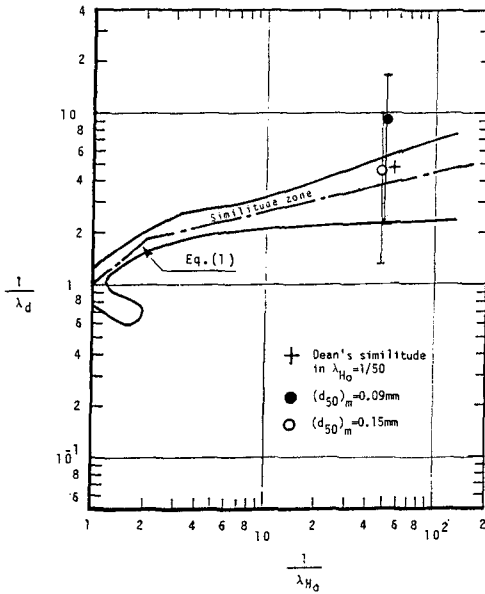


Figure 5 Scale-model relationship and experimental conditions set up in model.

large-scale beach profile and medium to small-scale ones under equilibrium conditions. Also, the wave duration time scale used in the model test was determined by using the authors (1986). This time scale was introduced from experimental results which were derived under conditions established according to the authors' scale-model relationship. These scale-model relationships are summarized as follows:

(1) The vertical and horizontal length scales of the beach profile are taken as the same (i. e., undistorted or geometric similarity).

(2) Wave characteristics such as wave height and period are determined by the Froude law.

(3) The beach sediment used in the model should be the sand or silica-sand which has the same specific gravity as the sea-bottom sediment of the prototype.

(4) The grain-size scale $\lambda_d = (d)_m / (d)_p$ between the grain-size of model sand, $(d)_m$, and prototype, $(d)_p$, is determined by the relationship indicated by the dot-dashed line in Figure 5. This relationship is given by

$$\frac{1}{\lambda_d} = 1.7^a \left(\frac{1}{\lambda_l}\right)^b \tag{1}$$

where $a=1$, $b=0.87$ for the range of experimental scale $1 \geq \lambda_l \geq 1/2.2$; $a=0$, $b=0.2$ for $\lambda_l < 1/2.2$, and λ_l is the scale of length $(1/n)$, that is, experimental scale.

(5) Time scale, λ_t , is given by

$$\frac{1}{1.6} \sqrt{\lambda_l} \leq \lambda_t \leq \frac{1}{0.65} \sqrt{\lambda_l} \tag{2}$$

Then we use the time scale which is indicated the average tendency of Eq. (2), given as

$$\lambda_t = \sqrt{\lambda_l} = 1/\sqrt{n} \tag{3}$$

This relationship is none other than the Froude's time scale.

4. MODEL TEST CONDITION

The experimental scale of the model was set at $1/50$, and the sand-grain size scale was then determined by Eq. (1) to be $\lambda_d = (d)_m / (d)_p = 1/3.7$. The median grain-size of on-offshore direction in the Ogata coast ranges from $(d_{50})_p = 1.5 \sim 0.2 \text{ mm}$, therefore, according to Eq. (1), the model sand grain-size should range from $(d_{50})_m = 0.41 \sim 0.05 \text{ mm}$. Especially, the sediment grain-size, where the beach profile at the Ogata coast changes remarkably, is $(d_{50})_p = 0.4 \text{ mm}$, therefore, two kinds of silica-sands were used, $(d_{50})_m = 0.09$ and 0.15 mm , which have a uniform grain-size distribution. The sorting coefficient of these silica sands are 1.32, and the specific gravity in the air is 2.71. The grain-size scale between the two kinds of silica-sands and the field sediment are shown in Figure 5. The value of sediment grain-size in the field are scattered, so that their representative values and scattering ranges are shown in this figure. This figure shows the silica-sand, $(d_{50})_m = 0.15 \text{ mm}$ (open circle) sufficiently satisfies the scale-model relationship, however the $(d_{50})_m = 0.09 \text{ mm}$ silica-sand is shifted slightly upward from the scale-model relationship. The time dependency of

the wave height and period during the storm were considered by separating the storm term into some time intervals which wave height and period were evaluated, furthermore, three classification methods were employed for comparison purpose, mean significant and maximum, as shown in Figure 4. In the model test the three types of waves were then scaled down to $1/50$ by the Froude law and regular waves employed. Therefore, wave height, period, and wave duration time were each taken as a variable in the model. Figure 6 shows that the mean tidal level in Naoetsu during the storm, 11th to 18th, varies from -2cm to 45cm . From this figure, it is clear that the passing of the lower depression generated a significant storm surge. Therefore, it is assumed that this tidal change influenced the Ogata coast as well. If the variation of tidal level is scaled down to $1/50$, the range of variation in the model becomes 0.94cm . Then, water level in the model test, that is the water depth of wave flume was held a constant. The model test conditions which were set by thus modeling technique, were arranged in Table 1.

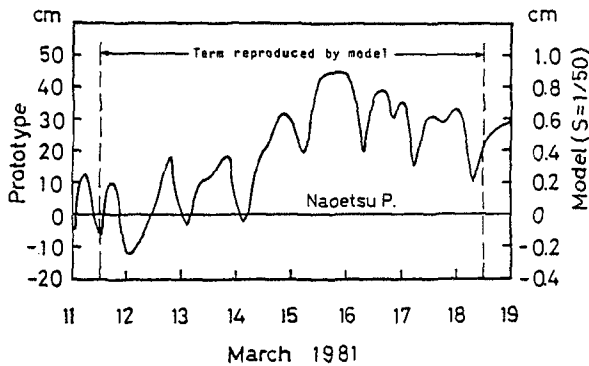


Figure 6 Variation of tidal level and storm surge in Naoetsu.

Table 1 Experimental conditions to reproduce beach processes of Ogata coast.

Run No.	Grain size d_{50} mm	Wave characteristics	Step No.							
			①	② -1	-2	-3	③	④	⑤	⑥
			$t=2h33m$	3h	6h	9h37m	3h32m	1h16m	2h33m	4h14m
2	0.15	H(cm)	1.2	0.8	0.8	0.8	3.5	5.8	3.5	1.6
		Hmean T (s)	0.71	0.71	0.71	0.71	0.71	1.13	1.13	0.71
4	0.09	H_s/L_0	0.0211	0.0141	0.0141	0.0141	0.0525	0.0335	0.0222	0.0283
		H(cm)	2.0	0.8	0.8	0.8	5.2	8.8	5.2	2.4
1	0.15	$H_{1/3}$	1.06	0.92	0.92	0.92	0.92	1.6	1.6	0.92
		T (S)	1.06	0.92	0.92	0.92	0.92	1.6	1.6	0.92
5	0.09	H_0/L_0	0.0125	0.0079	0.0079	0.0079	0.0511	0.0234	0.0139	0.0235
		H(cm)	3.6	0.8	0.8	0.8	7.0	13.6	9.0	3.6
3	0.15	Hmax	1.06	0.92	0.92	0.92	0.92	1.7	1.98	1.13
		T (s)	1.06	0.92	0.92	0.92	0.92	1.7	1.98	1.13
6	0.09	H_0/L_0	0.0257	0.0079	0.0079	0.0079	0.068	0.0309	0.0142	0.0222
		H(cm)	3.6	0.8	0.8	0.8	7.0	13.6	9.0	3.6

5. REPRODUCTION BY MODEL TEST

Movable-bed model tests were carried out in a medium-sized wave flume of dimensions 28m long, 0.5m wide and 1m deep, with a flap-type regular wave generator. An initial model beach profile was formed in the on-offshore direction corresponding to a 900m offshore distance in the prototype. This initial profile corresponds to the location indicated by the survey profile line in Figure 1, taken on the 11th just prior to the storm. Wave properties are varied according to Step Nos. ①~⑦ in Table 1, while the wave duration intervals are specified by the Froude's time scale for the step like functions shown in Figure 4. The changes in beach profile were also measured at the times indicated in Step Nos. ①~⑦ in Table 1. We classified the measured beach profile data into the following three groups, and discussed each from the standpoint of the reproduction of field beach profile.

(1) Beach profile

Figure 7 shows the beach changes in the model due to regular waves. The beach profiles that changed more significantly than those in the step are only shown in this figure. In this figure, the initial beach profile marked by ① (Step No. ①), and final beach profile by ⑦ are shown overlapping their corresponding field beach profile. From this figure, it is found that sand dunes (reflection bars) form on the onshore and offshore sides of the longshore bar when the significant and maximum waves were employed. The influence of the partial standing waves is considered to contribute to bar formation.

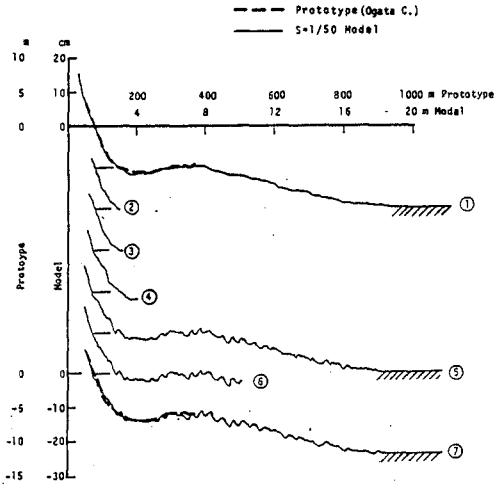
The initial and final Ogata coast beach profiles, 11th and 18th, were used to examine and compare the reproductive capability of the based on variations in sediment grain-size and wave height classification, where the solid and dash-dotted lines represent grain-sizes of 0.09mm and 0.15mm, respectively as shown in Figure 8. From this figure, it is shown that the reproduction of the beach profile is best when using regular waves which correspond to the mean waves of the observation records, that the reproduction capability significantly decays as the order of the wave exceeds the significant. However, the sediment grain-size was found to produce little effect on model reproduction as compare to wave scaling.

(2) Shoreline change

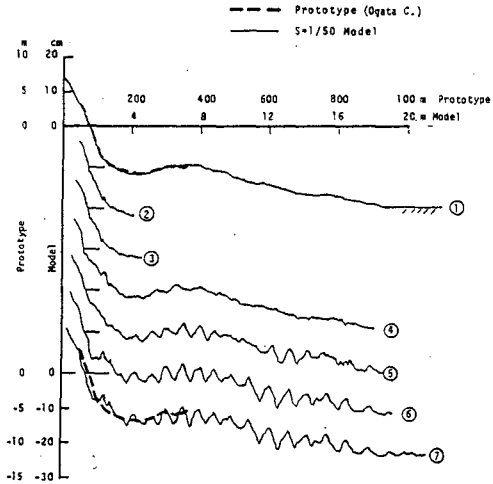
The temporal changes in the shoreline of the model tests from the initial state on the 11th by the mean, significant and maximum waves are arranged in Figure 9, such that the profiles corresponding to the two of sediment grain-sizes are distinguishable. In this figure, the results are shown only for Step No. ⑦ (final experimental data), along with the corresponding range of experimental error. Also, a field shoreline measurement taken on the 18th is shown along with the tidal variation corresponding to that day. From the comparison of the shoreline change by the model tests with the field, it is found that, when mean waves are used in the experiment, the reproduction is much better than profile reproduction using the significant and maximum waves.

(3) Sand volume change

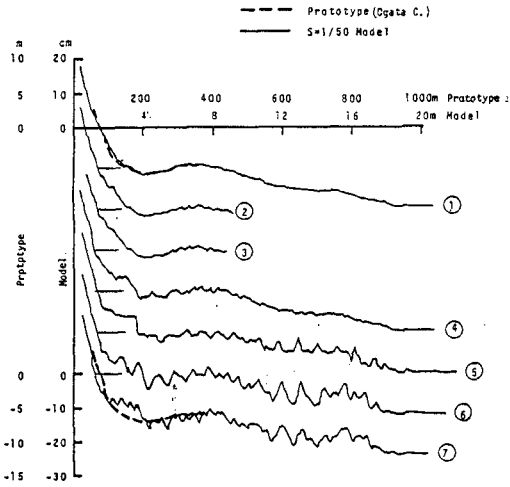
We examine the reproduction in term of the sand volume change which can be calculate from the beach profile change. The sand volume change per 1m width in the field was calculated over a 260m



7 (a) mean wave height, H_{mean} , Run No. 2



7 (b) significant wave height, $H_{1/3}$, Run No. 1



7 (c) maximum wave height, H_{max} , Run No. 3
 Figure 7 Reproduction of beach change processes in the model due to the regular waves.

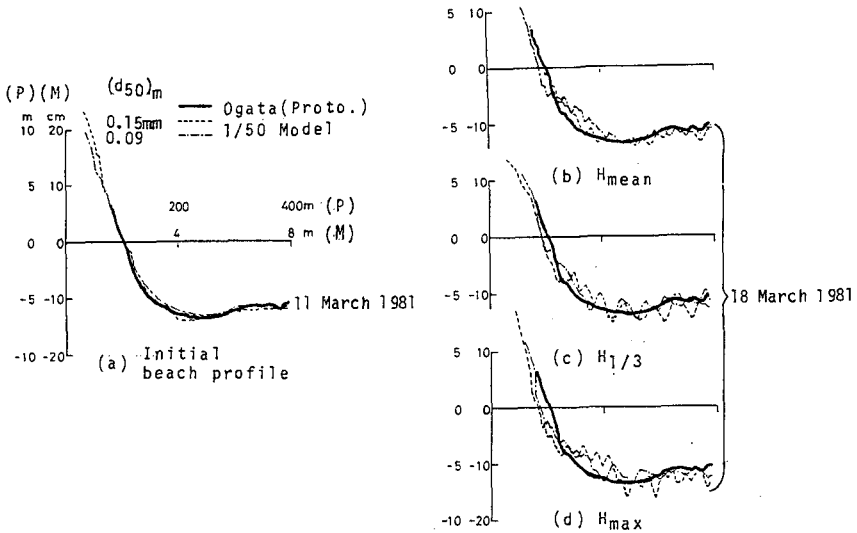


Figure 8 Comparison between the Ogata coast beach profile on the 11th and initial beach profiles, and between the Ogata coast on the 18th and model beach profiles reproduced by three kinds of waves.

range included the shoreline, for the period between the 11th and the 18th. By calculating the sand volume change of the model in the same manner and taking the scale into consideration, a comparison is made between the model and the field as shown in Figure 10. In this figure the differences in both sediment grain-sizes and wave properties are distinguished. As is seen in the comparison, the model test results which were used the mean and the significant waves reproduce the field very well, however, field reproduction is very poor for both sediment grain-sizes when employing the maximum waves.

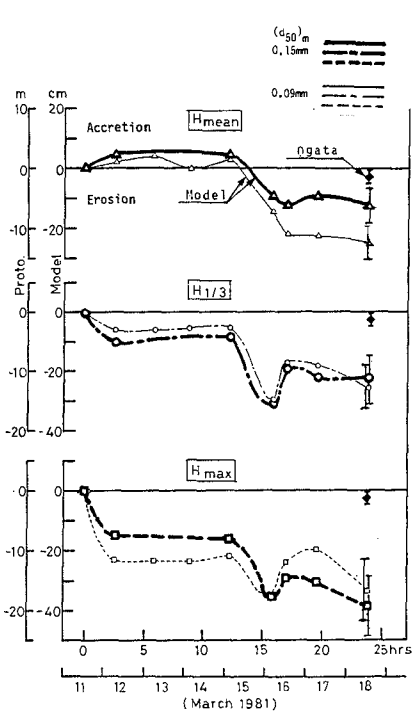


Figure 9 Reproduction of shoreline change.

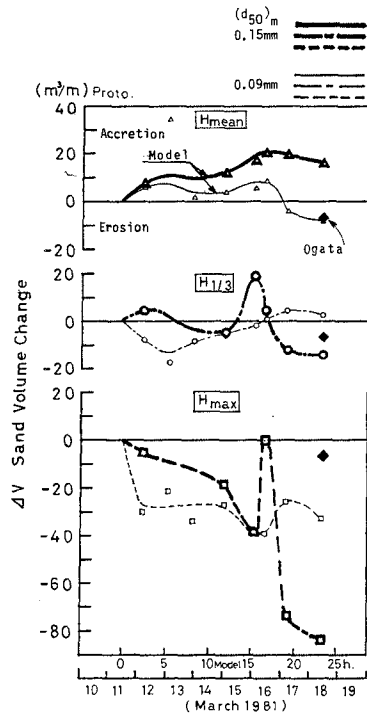


Figure 10 Reproduction of sand volume change.

6. DISCUSSION

Some scale-model relationships of beach change processes have reported till now, as reviewed by Hallermeier (1985). This model test study was performed applying the author's scale-model relationship which was described in the sections 3. (1)~3. (5). Therefore, quoting the scale-model relationship which is possible to compare to the author's one, we discuss about the relation between them. Especially, the fall time parameter which is introduced from the criterion separating on-offshore transport by Dean (1973) is frequently quoted in the study on the similitude of beach change, so that we examine the correspondence between the authors' and Dean's scale-model relationship.

Dean (1973) studied experimentally the onshore or offshore direction of sediment motion, and reported that the normal and storm beach profiles can be classified by:

$$\frac{H_0}{L_0} > 1.7 \frac{\pi w}{g T} \quad \text{offshore (storm profile)} \quad (4. a)$$

$$\frac{H_0}{L_0} < 1.7 \frac{\pi w}{g T} \quad \text{onshore (normal profile)}$$

or

$$\frac{H_0}{w T} = c \quad (4. b)$$

where H_0 is the wave height in deep water, L_0 the wave length in deep water, g the gravity acceleration, w the settling velocity of sediment, T the wave period, and c the constant. Eq. (4. b) is described as the fall time parameter. Letting the notation $\lambda_{parameter}$ represent the ratio of the model to the prototype and using Froude similitude between the wave period and the length, the scale-model relationship of Eq. (4. b) is finally written as follows:

$$\lambda_w = \lambda_l^{1/2} \quad (5)$$

Because the experimental scale of the model tests is $\lambda_l = 1/50$, the required settling velocity rate of model and prototype sediments by Eq. (5) becomes

$$\frac{(w)_m}{(w)_p} = \frac{1}{7.1} \quad (6)$$

As mentioned above, the sea-bed sediment grain-size at Ogata coast varies from $(d_{50})_p = 0.2\text{mm}$ to 1.5mm in on-offshore direction and its typical grain-size is $(d_{50})_p = 0.4\text{mm}$. By using the relationship between the sediment grain-size and the settling velocity, that is, Eq. (6), the sediment grain-size to be used in model becomes $(d_{50})_m = 0.06 \sim 0.14\text{mm}$ and the typical size is $(d_{50})_m = 0.086\text{mm}$. Thus when $(d_{50})_p = 0.4\text{mm}$, the grain-size scale by Dean's parameter becomes $\lambda_d = (d)_m / (d)_p \cong 1/4.7$, while author's similitude is $\lambda_d = 1/3.7$. The comparison between authors' similitude (dotted dash line) and Dean's grain-size scale is shown by the cross symbol "+" in Figure 5. From this comparison, it is interesting to note Dean's grain-size scale is slightly shifted from the authors, that is, the grain-size of the model obtained by Dean's grain-size scale relationship becomes slightly finer than the authors.

Therefore, one of the two kinds of sediments which were used in this model test approximately agrees with the grain-size scale by the authors and Dean.

Table 2 Synthetic evaluation of the model reproduced processes of Ogata coast.

Run No.	Wave characteristics	Beach profile	Shoreline change	Sand volume
2 4	Mean wave H_{mean}	○	○	△
1 5	Significant wave $H_{1/3}$	△	△	○
3 6	Maximum wave H_{max}	◆	◆	◆

○ : "very good" reproduction △ : "good" reproduction ◆ : "bad" reproduction

7. SUMMARY AND CONCLUSION

In this model study the Ogata coast beach profile changes were modeled according to the methods described in sections 3. (1), 3. (3), and 3. (4) for the initial beach profile, wave characteristics, sediment material, and its grain-size, respectively. The model waves were varied according to the measured Ogata coast storm wave intensity, and the wave duration time of regular waves in the model test were scaled down using Eq. (3). Wave characteristics were determined by the method described by 3. (2). Beach change processes due to time-dependent storm waves were found to be reproduced by using model waves corresponding to a one hour mean wave representation of field observations.

The two different sediment grain-sizes used in model test did not have a clear effect upon the reproduction.

The degree of reproduction due to regular waves corresponding to H_{mean} , $H_{1/3}$ and H_{max} with regard to the beach profile, the shoreline change, and the sand volume change are summarized in Table 2. From this table, it is found that, when the beach profile was reproduced very well, the reproduction of shoreline change and sand volume change were also.

It is concluded that reproduction in the model tests is "very good" when the regular waves corresponded to the mean wave in the field was used; "good", when using significant waves; and "bad" when using maximum waves.

The sediment grain-size of model which was determined by the authors' scale-model relationship was nearly equal to the value derived by Dean's relationship where the typical sediment grain-size in the Ogata coast was $(d)_p=0.4\text{mm}$. It should be noted that sediment grain-size of model, determined by Deans' scale-model relationship, changes depending on the settling velocity of sediment of field (prototype).

8. REFERENCES

- 1) DEAN, R. G. (1973) Heuristic models of sand transport in the surf zone, Proc. Eng. Dyn. in Surfzone, Institution of Engineers, Australia, pp. 208-214.
- 2) HUGHES, S. A. (1983) Movable-bed modeling law for coastal dune erosion, Jour. Water Port Coast. and Ocean Eng., ASCE, pp. 164-179.
- 3) HALLERMEIER, R. J. (1985) Unified modeling guidance based on a sedimentation parameter for beach changes, Coastal Engineering, Vol. 1, No. 1, pp. 27-70.
- 4) ITO, M. and TSUCHIYA, Y. (1984) Scale-model relationship of beach profile, Proc., 19th ICCE, ASCE, pp. 1386-1402.
- 5) ITO, M. and TSUCHIYA, Y. (1986) Time scale for modeling beach change, Proc., 20th ICCE, ASCE, pp. 1196-1209.
- 6) TSUCHIYA, Y., KAWATA, Y. and SILVESTER, R. (1985) Beach processes of Sirarahama and its preservation(2), Disaster Prevention Research Institute Annuals, Kyoto Univ., Vol. 28, B-2, pp. 565-590 (in Japanese).
- 7) VELLINGA, P. (1982) Beach and dune erosion during storm surges, Coastal Engineering, Vol. 6, No. 4, pp. 361-387.

CHAPTER 116

REALISTIC ECONOMIC BENEFITS FROM BEACH NOURISHMENT

Robert G. Dean*, M., ASCE

ABSTRACT

A method is presented and illustrated with examples to establish appropriate storm damage reduction and recreational benefits from beach nourishment projects. Unlike previous methods, benefits to project adjacent areas are recognized due to sand transport out of the project area and deposition on adjacent beaches. Assuming homogeneity along the shoreline, the character of storm damage reduction and recreational benefit relationships are such that sand transported from a project area and deposited on adjacent beaches always results in an increase rather than a reduction in benefits. A central element in calculating storm damage reduction benefits is the establishment of a proportional damage curve for upland structures as a function of beach width and storm return period. To illustrate the method, limiting cases are presented in which (A) all sediment remains within the area placed, and (B) all sediment spreads out immediately over a long segment of shoreline. Using Monte Carlo simulation to represent the random character of the storms, the method is applied to 15 realistic cases with varying project lengths, representative wave heights, added beach widths and interest rates. The present worth storm damage reduction and recreational benefits are calculated to demonstrate the effects of the various parameters. It is found that for short project lengths and relatively large wave heights, the benefits from project adjacent areas exceed those in the project area where the sand is placed. Although no littoral control structures, such as jetties are included in the present application, the method could be extended readily to include their effects.

INTRODUCTION

Policies and methodologies should evolve continuously to remain consistent with modern understanding of coastal processes and the true equities of those residing along the shoreline. Several changes have occurred in the last few decades that argue for an examination and modifications of present economic analysis procedures relating to beach

*Graduate Research Professor, Coastal and Oceanographic Engineering Department, University of Florida, Gainesville, FL 32611.

nourishment: (1) It is now clear that on a long, uninterrupted shoreline, good quality sand placed in a beach nourishment project will eventually be transported out of the region placed, but will remain within the active nearshore system, (2) Sand transported from a project area and deposited on project adjacent areas provides not only continuing damage reduction and recreational benefits, but provides enhanced benefits, and (3) With increasing concern over the use of "hard structures" as a means of shoreline control, beach nourishment will play an increasing future role.

This paper considers the economic consequences of sand eroded from a beach nourishment project area and deposited on project adjacent areas. Realistic damage reduction relationships and recreational benefits for a widened beach are utilized to demonstrate that this evolution process actually results in a net increase in project benefits. Benefits from simple limiting cases are examined in which (1) the sand remains in the area placed, and (2) the sand spreads out immediately. A direct procedure is presented to account for total present worth project benefits. The procedure utilizes Monte Carlo simulation to faithfully represent the probability of storm occurrences.

Although the methodology presented here is not applicable to shorelines which include features which would cause longshore sediment transport interruptions, the concepts could be extended readily for such cases.

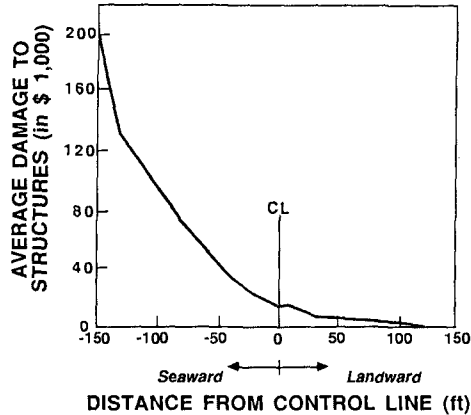
CONCEPTS

There are two simple concepts which are critical to the methodology presented here:

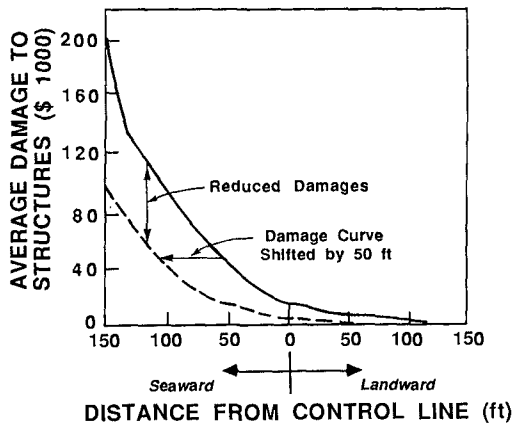
- (1) Good quality sand placed in a beach nourishment project will be eroded from the area placed but will remain indefinitely in the active nearshore region, and
- (2) The greatest storm damage and recreational benefits are generally realized for the initially narrower beaches.

The first concept will be considered as valid without much discussion. Although "good quality sand" is a matter of degree, here it refers to sand that is greater than 0.14 mm or so in diameter and that is coarser than or as coarse as the material originally present on the beach. For those nourishment materials in which the above is not the case, this paper refers to that sand fraction which is compatible. Monitoring results from a number of beach nourishment projects have demonstrated the first concept, for example at Port Canaveral, FL (Dean, 1988) and Captiva Island, FL (Tackney and Associates, 1983).

The second concept is illustrated by Figure 1a which represents a survey (by Shows, 1978) of the structural damage caused by Hurricane Eloise (1975) in Bay County, FL as a function of proximity of the structures relative to a jurisdictional control line which is generally parallel to



- a) Damage to Structures in Relation to their Location with Control Line (Resulting from Study of 540 Structures in Bay County after Hurricane Eloise, by Shows, 1978).



- b) Damage Reduction Due to Beach Nourishment Advancing the Profile Fifty Feet Seaward.

Figure 1. Structural Damages Due to Hurricane Eloise (1975) and Example of Reduced Damages by Beach Nourishment Advancing the Shoreline Seaward by Fifty Feet.

the shoreline. Of particular significance in Figure 1a is the steeply sloped portion of the damage curve near its seaward end and the relatively mild slope near its landward end. It is instructive to consider the effect of a beach nourishment project which displaces the beach seaward by a certain amount such as 50 ft as shown in Figure 1b. It is seen that due to the slope characteristics discussed above, the greatest damage reductions occur for those structures

which initially have very little beach in front of them. Figure 2 presents the damage reduction per structure associated with an additional one foot of beach width. For the narrower initial beach widths, the reduction is approximately \$3,000 per structure whereas for greater initial beach widths, the damage reduction per structure is less than \$500. In summary, the damage reduction benefits are greater for beaches which are initially much narrower.

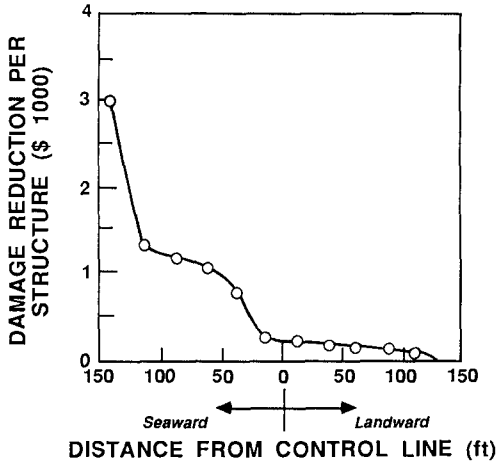
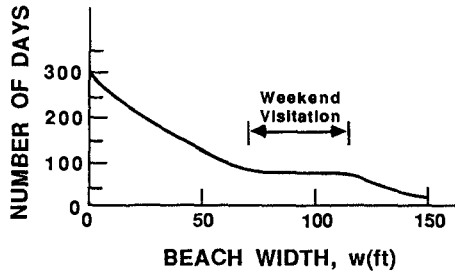


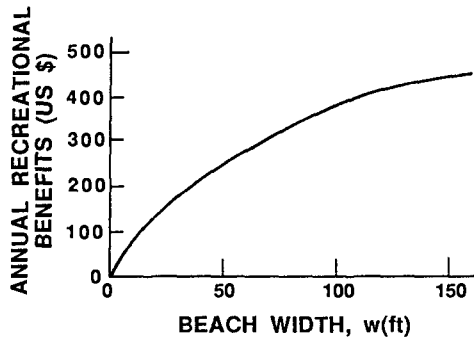
Figure 2. Damage Reduction Per Structure Resulting from a One Foot Wide Additional Beach, as a Function of Structure Location Relative to Control Line. Based on Hurricane Eloise Data.

The same concepts demonstrated above for damage reduction benefits apply for recreational benefits. Figure 3 presents the hypothetical usage and associated recreational benefits for beaches of varying widths. The number of people using the beach will increase with beach width; however, the rate of increase decreases for the greater widths. The results in Figure 3b are based on a visitation value of \$6.00 per visitor per day and a plan area visitation requirement of 200 square feet. The annual recreational benefits associated with an additional foot of beach width versus initial beach width, based on Figure 3, are presented in Figure 4. As before, it is seen that the greatest benefits occur for the initially narrower beaches.

Referring to Figure 5, the significance of greater benefits for initially narrower beaches is that as a beach nourishment project evolves with the beach fronting the project area narrowing and the project adjacent beaches widening, benefits are lost in the initially wider project area. This loss of benefits is small compared to the gain of relatively large benefits in the initially narrow project adjacent areas. Assuming that the value of the upland structures protected by the project and the initial beach



a) Number of Days Per Year that Full Beach Width is Used.



b) Annual Recreational Benefits vs Beach Width Per Foot of Beach Length.

Figure 3. Hypothetical Usage and Recreational Benefits of Sandy Beaches.

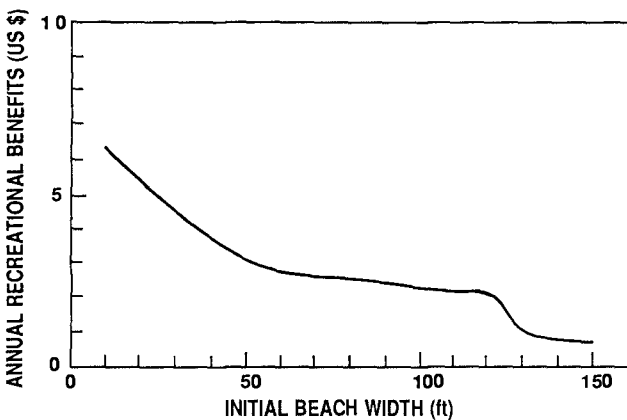


Figure 4. Annual Recreational Benefits Per Additional Foot of Beach Width as a Function of Initial Beach Width, Per Foot of Beach Length. Developed from Figure 3b.

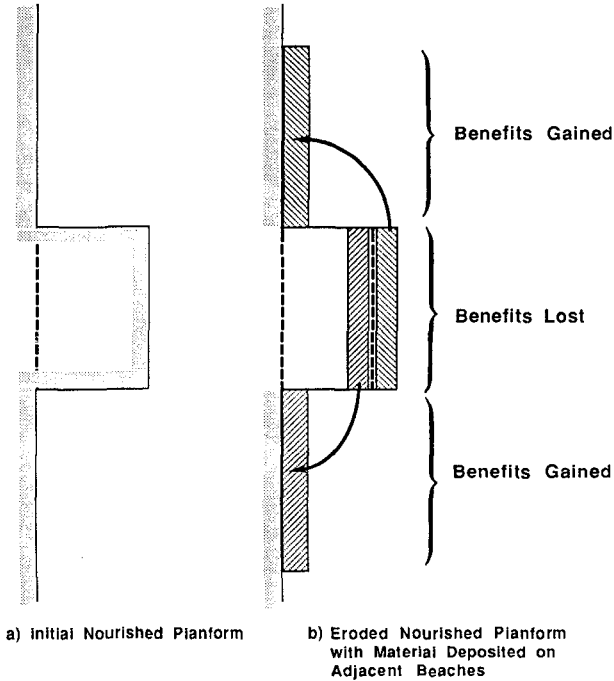


Figure 5. Schematic of Erosion of Nourished Area and Deposition in Project Adjacent Areas.

widths in project adjacent areas are uniform along the beach, there is always a net gain in storm reduction benefits as a result of project evolution. Similarly with respect to recreational benefits, assuming that the need for and access to recreational beaches are uniform, etc., the net effect of project evolution is a gain in recreational benefits.

METHODOLOGY

The methodology will be described and illustrated for idealized cases of no project evolution and rapid project evolution and general cases of benefits due to project evolution over realistic time frames.

Shoreline Evolution Model

The shoreline evolution model adopted here will be that due to Pelnard-Consideré for an initially rectangular planform as presented in Figure 6. The factor G is the so-called "longshore diffusivity" and for small angles of wave incidence is

$$G = \frac{K H_b^{5/2} \sqrt{g/\kappa}}{8(s-1)(1-p)(h_* + B)}$$

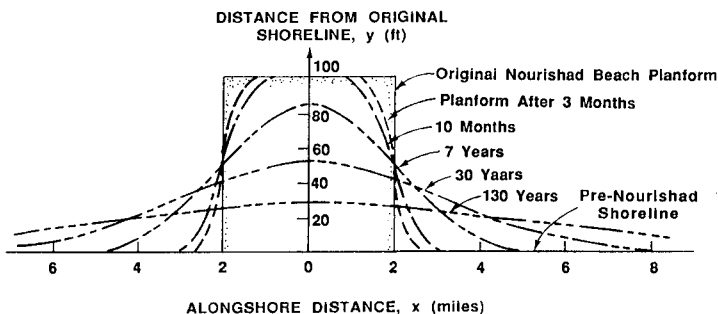


Figure 6. Example Solution of Evolution of Initially Rectangular Beach Planform. Pelnard Considered Method. Wave Height, $H_b = 2.0$ ft, Initial Nourished Beach Width = 100 ft, Fill Length, $l = 4$ miles, $t = \text{time}$.

in which K is the sediment transport factor usually taken as 0.77, H_b is the representative breaking wave height, g is gravity, κ is the spilling breaker ratio (on the order of 0.8), s is the ratio of sediment specific gravity to that of the water in which transport is occurring, p is the in situ porosity and $(h_s + B)$ is the vertical extent of beach profile response.

Storm Damage Reduction Benefits

Development of storm damage reduction benefits commences with the establishment of the relationship of a proportional storm damage factor, D , as a function of beach width fronting the structure, w , and storm return period, T_R . Figure 7 presents one example of such a relationship which has been used in the state of Florida Beach Management Plan. Development of this relationship is by no means trivial and should be based on an analysis of the expected damage to a range of representative structures as well as calibration with available storm results if such data are available. The proportional storm damage factor, D , depends on the foundation and structural and elevation characteristics of the buildings as well as the beach morphology, and presence and integrity of coastal protection structures, etc.

With the availability of $D(w, T_R)$ it is possible to predict the present worth damage reduction benefits $PWDRB(N)$ during N years by the following equation

$$PWDRB(N) =$$

$$\sum_{n=1}^N \frac{1}{(1+I)^n} \int_{\text{Project Area}} V(x, n) [D(w(x, n), T_R(n)) - D(w_0, T_R(n))] dx$$

$$+ \sum_{n=1}^N \frac{1}{(1+I)^n} \int_{\text{Project Adjacent Areas}} V(x, n) [D(w(x, n), T_R(n)) - D(w_0, T_R(n))] dx \quad (1)$$

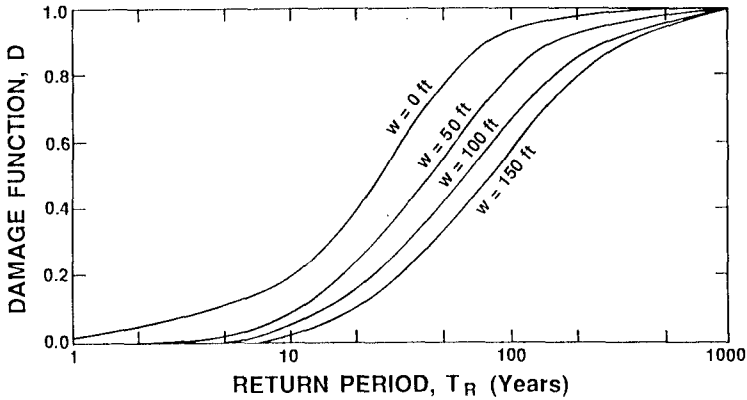


Figure 7. Hypothetical Proportional Storm Damage, D, as a Function of Storm Return Period, T_R , and Beach Width, w .

in which I is the interest rate and $V(x, n)$ represents the structure value at a location, x , at a time n years into the future. $T_R(n)$ is the storm return period n years into the future. The two integrals differ only in their respective intervals of integration and are written separately here to illustrate the contributions from the two areas.

Eq. (1) accomplishes the objective of providing methodology for quantifying storm damage reduction. However, it is instructive to develop concepts further. Referring to Figure 7 which presents the proportional storm damage factor, D , the expected damage by a single storm $D(w)$ as a function of beach width, w , is

$$\bar{D}(w) = \int_0^1 D(w, T_R) p(D) dD \tag{2}$$

in which p is the probability density function and is related to the cumulative probability distribution P by

$$p(D) = \frac{dP}{dD} \tag{3}$$

and noting that

$$T_R = \frac{1}{P} \tag{4}$$

Eq. (2) simplifies to

$$\bar{D}(w) = \int_0^1 D(w, T_R) \frac{dP}{dD} dD = \int_0^1 D(w, T_R) dP \tag{5}$$

Figure 8 presents \bar{D} as a function of beach width as developed from Eq. (5). It is noted that this distribution is qualitatively similar to damages experienced in Hurricane Eloise (Figure 1) which was approximately a 70 year storm.

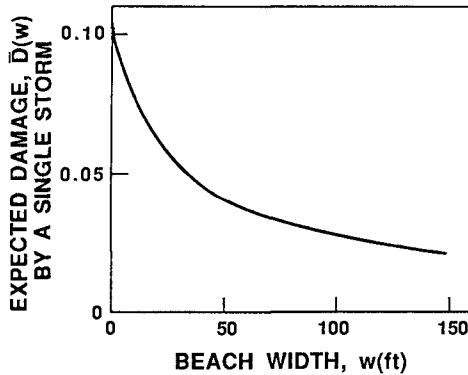


Figure 8. Expected Damage $\bar{D}(w)$ Due to a Single Storm as a Function of Beach Width, w .

Assuming that the value of the upland structures remain constant with time and that damaged structures are rebuilt to the same standards (both considerable assumptions), the present worth damage factor, PWDF(w) as a function of beach width for N years into the future is

$$PWDF(w, N) = \sum_{n=1}^N \frac{1}{(1+I)^n} \bar{D}(w) = \frac{1}{I} \left[1 - \frac{1}{(1+I)^N} \right] \bar{D}(w) \quad (6)$$

and again, I is the interest. The bracketed factor in Eq. (6) approaches unity with large N . Table I presents values of $PWDF(w, \infty)$ for several beach widths interest rates. It is noted that the present worth damage factor can range as high as 1.31 for the case of zero beach width and an interest rate of 8%.

TABLE I

PRESENT WORTH DAMAGE FUNCTION, $PWDF(w, \infty)$
VERSUS BEACH WIDTH, w , FOR ALL FUTURE DAMAGE

Interest Rate	Present Worth Damage Function, $PWDF(w, \infty)$ For Beach Width, w			
	0 ft	50 ft	100 ft	150 ft
6%	1.75	0.67	0.47	0.35
8%	1.31	0.50	0.35	0.26
12%	0.88	0.33	0.23	0.18

Idealized Cases

In contrasting project benefits realized within the project area to those outside the project area, it is instructive to consider two simple cases:

Case (A). All sediment remains within the area placed, and

Case (B). The sediment placed spreads out immediately over a long segment of shoreline.

Case (A).

The expected storm damage reduction benefits due to a single storm are

$$(SDRB)_A = [\bar{D}(w_0 + \Delta w) - \bar{D}(w_0)] \ell \tag{7}$$

Case (B).

Denoting the (long) distance over which the sediment has been distributed as ℓ' and the associated additional width as $\Delta w'$, we have

$$(SDRB)_B = - \left(\frac{\partial \bar{D}}{\partial w} \right)_{w_0} \Delta w' \ell' \tag{8}$$

and since sediment is conserved $\Delta w \ell = \Delta w' \ell'$,

$$(SDRB)_B = - \left(\frac{\partial \bar{D}}{\partial w} \right)_{w_0} \Delta w \ell \tag{9}$$

The ratio, R_{SD} , of storm damage reduction benefits for the case of sand spreading out immediately to the case in which sand remains where placed is

$$R_{SD} = \frac{- \left(\frac{\partial \bar{D}}{\partial w} \right)_{w_0} \Delta w}{[\bar{D}(w_0 + \Delta w) - \bar{D}(w_0)]} \tag{10}$$

It is noted that the ratio R_{SD} is always greater than unity. As shown in Figure 9, the interpretation is simple with the numerator representing the tangent of the damage curve at w_0 and the denominator the secant slope between w_0 and $w_0 + \Delta w$. Due to the character of the curve, the ratio will always exceed unity. Figure 10 presents the ratio R_{SD} vs w_0 for several values of Δw .

The same general discussion presented above applies to recreational benefits relationships. The ratio of benefits R_{RB} for a project that spreads out immediately to one that remains in place is

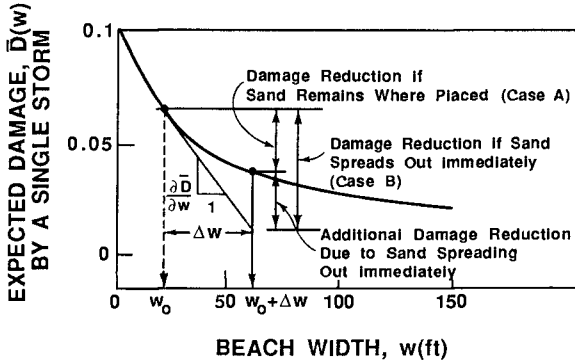


Figure 9. Interpretation of Damage Reduction Benefits if Sand Remains Where Placed (Case A) and if Sand Spreads Out Immediately (Case B).

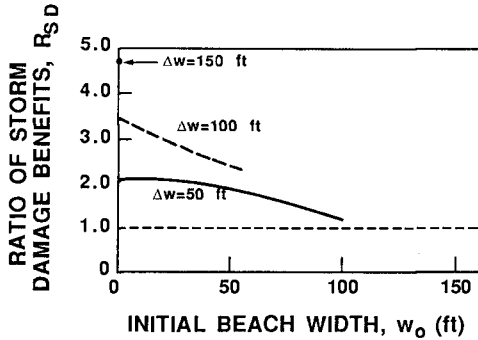


Figure 10. Ratio of Storm Damage Benefits, R_{SD} , vs Initial Beach Width, w_0 , and Additional Beach Width, Δw . R_{SD} is Ratio of Storm Damage Benefits for Sand Which Spreads Out Immediately to Those for Which Sand Remains Where Placed.

$$R_{RB} = \frac{\left(\frac{\partial R}{\partial w}\right)_{w_0} \Delta w}{[R(w_0 + \Delta w) - R(w_0)]} \quad (11)$$

and this ratio will always exceed unity by the same argument as for the damage reduction benefits. For the recreational benefits shown in Figure 3, values of the ratio, R_{RB} , are presented in Figure 11.

RESULTS

Prior to presenting results for the general case, in which the beach planform evolves with time, it is worthwhile to consider the variables which will tend to favor Case A (sand remains in place) or Case B (sand spreads out immediately). Case A conditions would tend to dominate for:

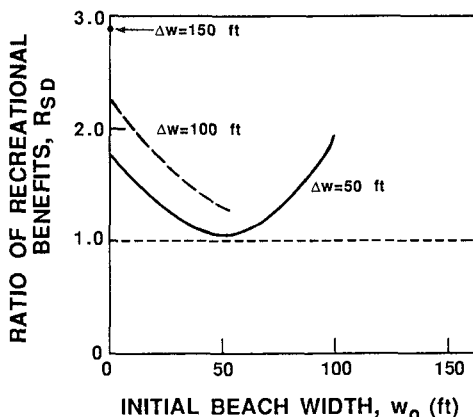


Figure 11. Ratio of Recreational Benefits, RRB , vs Initial Beach Width, w_0 , and Additional Beach Width, Δw . RRB is Ratio of Recreational Benefits for Sand Which Spreads Out Immediately to Those for Which Sand Remains Where Placed.

- Large Beach Fill Lengths, l
- Low Wave Height, H_b
- Small Transport Coefficient, K
- Small Additional Beach Widths, Δw
- High Interest Rates, I

and vice versa for Case B.

The methodology described in the previous section was incorporated into a computer program which was "exercised" for the variable values shown in Table II. Results will be presented in two different forms.

Figure 12 presents variations of storm damage and recreational benefits with time for Run 5. The relatively large wave height and short beach fill associated with Figure 12 favors Case B conditions and it is seen that the dominant benefits occur within the adjacent project areas. It is also of interest to note that the benefits in the project adjacent areas lag those in the project area due to the time required for sediment transport to these adjacent areas. The longer project lengths and smaller wave heights would favor Case A conditions and the benefits inside the project area would dominate and commence quite early.

Table II summarizes results for all 15 runs conducted.

SUMMARY AND CONCLUSIONS

The methodology and results presented herein support the following statements.

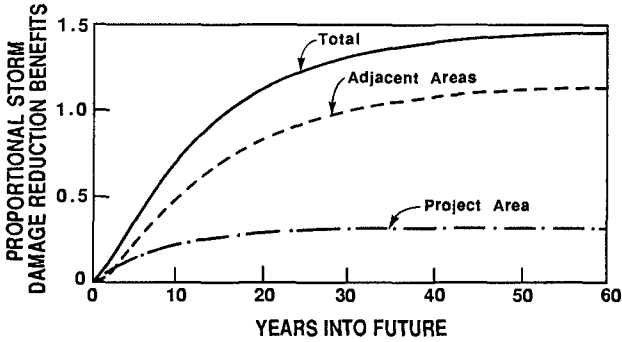
Wider beaches seaward of structures perform as effective energy dissipators during storm conditions and, where

TABLE II. PRESENT WORTH STORM DAMAGE AND RECREATIONAL BENEFITS FOR VARIOUS WAVE AND PROJECT CONDITIONS

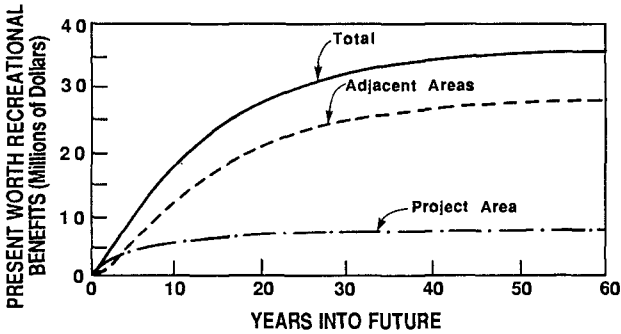
Run	Characteristics				Storm Damage Reduction*			Recreational Benefits**			
	Project Length, l , (miles)	Wave Height H_b (ft)	Initial Beach Width w_0 (ft)	Added Beach Width Aw (ft)	Interest Rate I	In Project Area	In Project Adjacent Area	Total	In Project Area	In Project Adjacent Area	Total
1	1.0	1.0	0	100	0.08	0.368	1.037	1.405	4.4	12.7	17.1
2	1.0	2.0	0	100	0.08	0.176	1.434	1.610	2.1	17.8	19.9
3	1.0	4.0	0	100	0.08	0.072	1.561	1.633	0.9	19.7	20.6
4	2.0	1.0	0	100	0.08	0.592	0.532	1.124	15.4	13.0	28.4
5	2.0	2.0	0	100	0.08	0.323	1.136	1.459	7.6	27.9	35.5
6	2.0	4.0	0	100	0.08	0.148	1.470	1.618	3.6	36.7	40.3
7	4.0	1.0	0	100	0.08	1.009	0.084	1.093	55.9	4.2	60.1
8	4.0	2.0	0	100	0.08	0.525	0.672	1.197	26.6	32.7	59.3
9	4.0	4.0	0	100	0.08	0.280	1.234	1.514	13.0	60.7	73.7
10	2.0	2.0	0	150	0.08	0.388	.679	2.067	10.1	38.5	48.6
11	2.0	2.0	50	100	0.08	0.066	0.178	0.244	4.9	14.5	19.4
12	2.0	2.0	100	150	0.08	0.057	0.144	0.201	7.4	21.7	29.1
13	2.0	2.0	0	100	0.12	0.240	0.697	0.937	5.7	17.0	22.7
14	2.0	2.0	0	100	0.04	0.506	2.413	2.919	11.7	60.0	71.7
15	16.0	2.0	0	100	0.08	1.733	0.002	1.735	392.4	0.5	392.9

*Relative to immediately adjacent upland property values within project area

**Expressed in millions of dollars



a) Proportional Present Worth Storm Damage Reduction Benefit Components vs. Years into Future.



b) Present Worth Recreational Benefits vs. Years into Future.

Figure 12. Present Worth Storm Damage Reduction and Recreational Benefits. $H_b = 2.0$ ft, $l = 2.0$ miles, $w_0 = 0.0$, $\Delta w = 100.0$ ft., Interest Rate = 8%, Run No. 5.

the demand exists, also provide recreational benefits. These benefits can be enhanced through increasing beach widths by nourishment projects.

Beach nourishment projects conducted with good quality sand will evolve with erosion occurring within the project area and deposition in the project adjacent areas. Good quality sand will remain within the active nearshore region and provide continuing storm damage reduction and recreational benefits.

A simple method is presented for quantifying the benefits in and adjacent to beach nourishment project areas. Considering limiting cases in which (a) all sand stays within the area placed, or (b) all sand placed spreads out

rapidly demonstrates that the potential benefits are greater for the latter. Example calculations for realistic cases demonstrate that the benefits for project adjacent areas can be substantial relative to those in project areas. The relative benefits in project adjacent areas increase with: short project length, large wave height, large sediment transport coefficient, low interest rate, and large additional beach width.

Accounting methodologies for benefits of beach nourishment projects should be representative of modern understanding of sediment transport processes and the equities of those residing along the shoreline and thus should recognize the benefits from sand transported from the project area and deposited in project adjacent areas.

Although the method presented here applies to the case of projects placed on long uninterrupted shorelines, similar procedures could be applied to situations where littoral controls exist, such as jetties at a channel entrance.

ACKNOWLEDGEMENTS

The work leading to this paper was carried out under funding by the Office of Sea Grant and by the Division of Beaches and Shores of the Florida Department of Natural Resources. This support is gratefully acknowledged.

REFERENCES

- Dean, R.G. (1988) "Sediment Interaction at Modified Coastal Inlets: Processes and Policies", in Hydrodynamics and Sediment Dynamics of Tidal Inlets, D. Aubrey, Editor, Woods Hole Oceanographic Institution, Woods Hole, Mass. (In Press).
- Pelnard Considere, R. (1956) "Essai de Theorie de l'Evolution des Formes de Rivage en Plages de Sable et de Galets", 4th Journees de l'Hydraulique, Les Energies de la Mer, Question III, Rapport No. 1.
- Shows, E.W. (1978) "Florida's Coastal Setback Line - An Effort to Regulate Beachfront Development", Vol. 4, Nos. 1/2, Coastal Zone Management Journal, p. 151-164.
- Tackney and Associates (1983) "Physical Monitoring Captiva Beach Restoration Project", Final Report, August.

CHAPTER 117

Effects of structure on deposition of discharged sediment around rivermouth

by

Ichiro Deguchi* and Toru Sawaragi**

ABSTRACT

The influence of coastal structures on a discharged flow and a depositional pattern of discharged sediment from a river are investigated experimentally. It is found that a pair of offshore detached breakwaters, as well as a pair of jetties, had a little influence on them. The offshore detached breakwater has also a function to prevent rivermouth from filling up with depositional sediment by waves. A numerical procedure for the prediction of depositional pattern of discharged sediment is developed based on the experimental results. The proposed numerical procedure is shown to reproduce depositional patterns around a rivermouth without structures and a jetty-protected rivermouth satisfactorily. However, the flow pattern around the offshore detached breakwater-protected rivermouth can not be reproduced.

INTRODUCTION

Until now, jetties have been widely used to protect a rivermouth from blockage. This is because a jetty possesses an effective function to trap sediment transported in the longshore direction. However, this function of jetty produces an abrupt discontinuity of sediment transport and consequently brings erosion of a coast around a rivermouth. The decrease of discharged sediment due to constructions of dams and improvements of river channels accelerate the erosion.

Therefore, to deal with rivermouthes by constructing coastal structures successfully, it is required that such structures have functions not only to prevent the rivermouth from blockage but also not to bring an extreme discontinuity of sediment transport in the longshore direction. It is also desired that the discharged sediment from the rivermouth should be fed back effectively to the beach around the rivermouth.

*Assocl. Prof., Dept. of Civil Engineering, Osaka University

**Prof., Dept. of Civil Engineering, Osaka University
Yamada-oka, Suita-city, Osaka 565, Japan

The authors have been conducting a series of investigations to establish the optimum design method for rivermouth treatments. This study is a part of the investigations in which the effects of jetties and offshore detached breakwaters, which will be one alternative of jetties, on the behavior of discharged sediment from the river are discussed based on the experimental results. A numerical model for predicting the depositional pattern of discharged sediment is also proposed and the applicability of the model is verified through experiments.

EXPERIMENTS ON THE DEPOSITIONAL PATTERN OF DISCHARGED SEDIMENT

The effects of jetties and offshore detached breakwaters on the discharged flow from the river and depositional patterns of discharged sediment were first investigated by conducting three-dimensional experiments in a wave basin of 5m wide, 15m long and 0.6m deep. A sketch of the wave basin and the model river constructed in it is shown in Fig.1 together with the coordinate system and symbols used in the following descriptions.

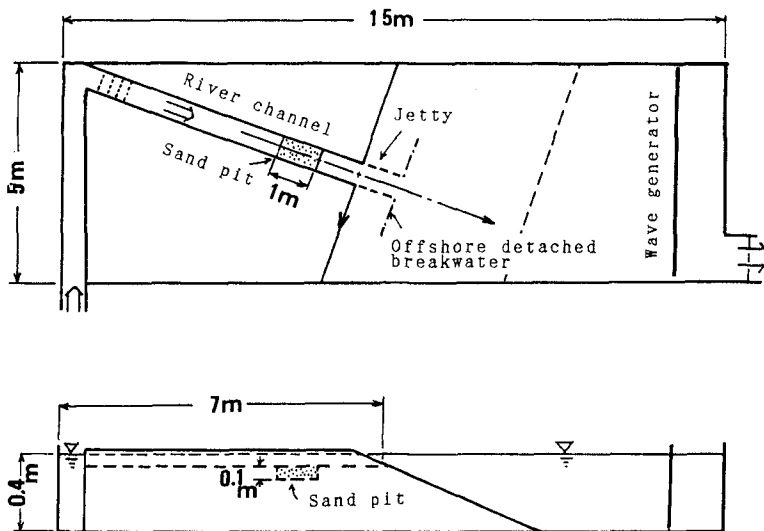


Fig.1 Sketch of wave basin and model rivermouth

A width of the model river channel, B , was 0.5m and a depth at the rivermouth, h_0 , defined at $X=0$ in the figure was 6.5cm. A river discharge, Q_r , in the experiment was kept constant to be 11700cm³/sec and a mean discharged velocity at the rivermouth, U_0 , was 45-47cm/sec.

Two kinds of sand of mean grain size $d_{50} = 0.15\text{mm}$ (fine sand) and 0.35mm (median sand) were used as a bed material of the river and were discharged from a pit by feeding sand into the pit so that a volume of sand in the pit became almost constant. A depth and a length of the pit was 10cm and 1.0m . Fine sand was easily brought into suspension by currents and median sand was mainly transported as bed load.

Jetties and offshore detached breakwaters of different length, the dimensions of which are given in Table 1, were used. The locations of these structure are illustrated in Fig.1.

Table 1 Dimension of structure

Structure		Length:Ls(m)	Ls/B	Ls/Lo
Jetties	I	0.5	1.0	0.5
	II	1.0	2.0	1.0
Offshore detached breakwater	I	0.8	1.6	0.8
	II	1.2	2.4	1.2

Lo:the wave length in deep water

A mean water depth of the wave basin was 30cm and a bottom slopes of the river channel and beach were $1/100$ and $1/10$, respectively.

After measuring velocities and surface displacements around the rivermouth on a fixed bed, sand was discharged. Depositional patterns were measured after 2 hr's sediment discharge with a resistance type bottom profiler. The velocity was measured with a 2-component electromagnetic current meter in the middle layer and capacitance type wave gauges were utilized to measure surface displacements. Trajectories of tracers thrown into the river and around the rivermouth were also recorded by a video-camera to analyze flow patterns.

A deformation of depositional pattern caused by waves was measured by generating waves obliquely to the shore line for one hour. A height and a period of incident waves were 4cm and 0.8sec and an angle of wave incidence was 20° .

The effects of jetties and offshore detached breakwaters on the discharged flow and depositional patterns of discharged sediment were investigated based on the experimental result.

Figure 2 shows the effects of coastal structures on the velocity, U , of the discharged flow and the mean water level, E , along the center line of the river channel ($Y=0$).

The discharged velocity and the mean water level measured in the jetty-protected rivermouth shown by open circles do indicate almost the same values as the results obtained in the case where there was no coastal structure which are illustrated by closed circles.

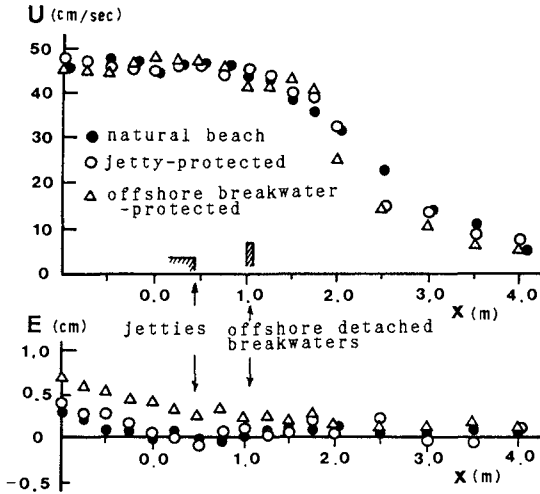


Fig. 2 Effects of coastal structures on the discharged velocity and mean water level

When the offshore detached breakwaters were constructed, the rise of mean water level behind them became conspicuous when compared with other two cases shown in the figure. However, the corresponding difference in the discharged velocity in that region can not be found. Although the discharged velocity decreases a little in the region of $2m < X < 3.5m$ ($4 < X/B < 7$), it recovers to the same velocity as other two cases.

Figure 3 shows examples of discharged flow patterns. Figures (a) is the case of natural rivermouth without structures. Figures (b) and (c) correspond to the cases of jetty-protected rivermouth and offshore detached breakwater-protected rivermouth.

In the case of natural rivermouth, the discharged flow did not spread in the longshore direction and an entrainment of surrounding water can be seen in the wide region.

In the case of jetty-protected rivermouth, the entrainment of surrounding water took place no sooner than the discharge flowed out of the jetties. Of course, strong divergence can not be found.

On the other hands, at the rivermouth where the offshore detached breakwaters were constructed, the remarkable entrainment took place within a narrow region near the shoreline and the discharged flow diverged outwards behind the breakwaters. However, in the offshore of the breakwater, a small volume of surrounding water was again entrained and the discharged flow did not diverged significantly.

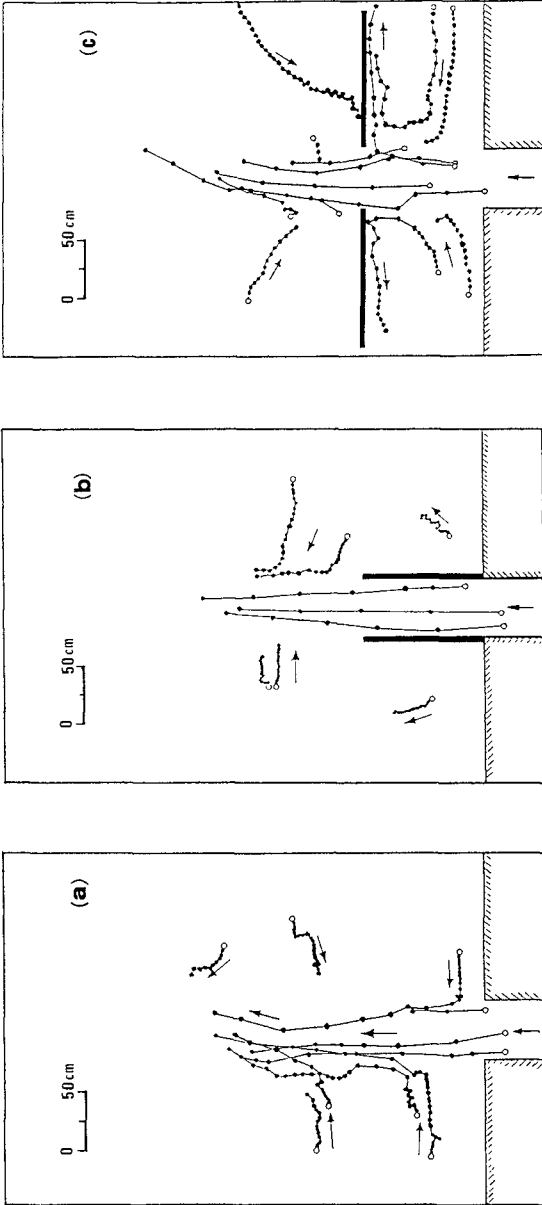


Fig.3 Flow patterns around rivermouth

Figures 4 to 6 illustrate the depositional pattern of discharged sediment (Fig. (a)) and the deformation of depositional pattern due to waves (Fig. (b)). The bed material of these cases was median sand which was mainly transported as bed load by the discharged flow and wave action. Fine solid lines in Fig. (a) indicate contours of the change of water depth took place within 2 hrs and those in Fig. (b) give contours of deposited sand after 1 hr wave generation.

Fig. 4 is the case of natural rivermouth and Figs. 5 and 6 are the results of jetty-protected and offshore detached breakwater-protected rivermouth. When we compare Fig. (a) of these figures, the following facts can be found out:

- 1) The maximum deposition takes place at about $X=1.5m(X/B=3)$ regardless of the existence of the coastal structures and this point corresponds to the place where the decrease of discharged flow began in Fig. 2.
- 2) Discharged sediment did not spread in the longshore direction. These results agree with those obtained by Butakov (1971), Suga et al. (1986) and so on. However, behind the breakwater which is shown in Fig. 6, a small portion of discharged sediment was trapped. These depositional patterns correspond well to the flow patterns shown in the former figures.

As mentioned before, fine sand was easily brought into suspension by currents and waves and the direction of net cross-shore sediment transport by waves was in the offshore. On the other hand, median sand was transported as bed load by currents and waves and the direction of net cross-shore sediment transport by waves was in the onshore.

When compared Fig. (a) with Fig. (b) of Fig. 4, it is found that the depositional pattern of discharged sediment was flattened by wave action and a part of deposited sediment was transported in the longshore direction in the breaker zone around the rivermouth. The same deformation as this was observed around the rivermouth protected by short jetties.

Any longshore movement can not be seen around rivermouth protected by long jetties shown in Fig. 5 because the length of the jetty was longer than the breaker zone. Further, a significant part of deposited sediment was transported in the onshore direction and redeposited between the jetties. As the results, the sectional area of discharged flow decreased.

Around the rivermouth protected by the offshore detached breakwaters given in Fig. 6, the depositional pattern was also flattened by waves and a small portion of the deposited sand in the offshore of the breakwater was carried through the gap of the breakwaters and redeposited behind the breakwater. However, the sectional area of the discharged flow was not reduced by these sand movements.

In the cases of fine sand, decrease of sectional area by wave action did not take place even in the case where the long jetties were constructed.

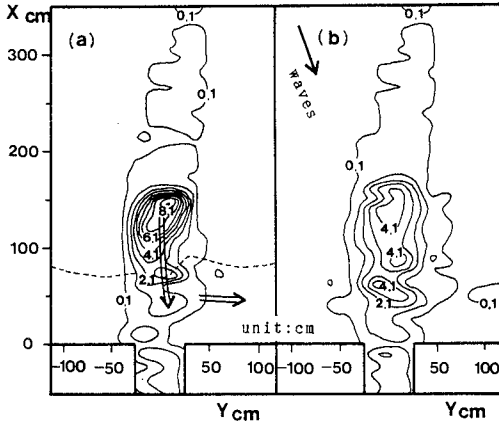


Fig.4
Depositional pattern of
discharged sediment
(without structure)

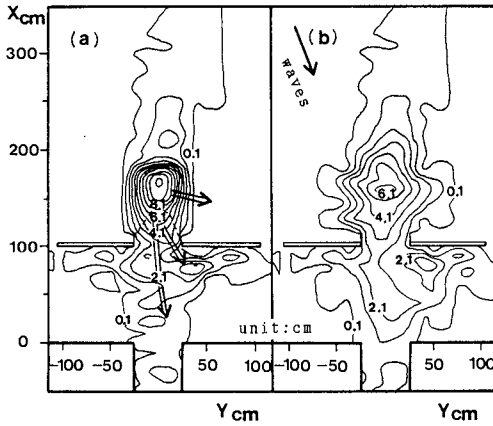


Fig.5
Depositional pattern of
discharged sediment
(with jetties)

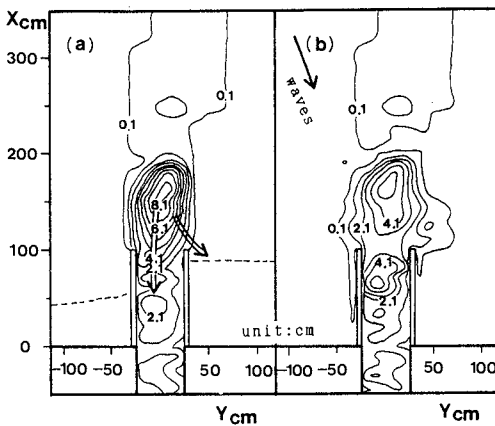


Fig.6
Depositional pattern of
discharged sediment
(with offshore detached
breakwaters)

From these results, we can conclude that coastal structures used in the experiments do not affect the river discharge significantly. Depositional patterns of discharged sediment are also not deeply influenced by the structures. However, when the grain size of discharged sediment is coarse enough so that it is transported in the onshore by waves, a special consideration has to be paid in the planning of rivermouth treatments. Further, the offshore detached breakwater is shown to be an alternative of the jetty.

NUMERICAL PROCEDURE FOR PREDICTION OF DEPOSITIONAL PATTERNS OF DISCHARGED SEDIMENT

Generally, the change of water depth is expressed by the following equation in the coordinate system given in Fig.7:

$$\frac{\partial h}{\partial t} = \frac{1}{1-\lambda} \left(-\frac{\partial}{\partial x} [U_s \bar{C} dz + \frac{\partial}{\partial y} [V_s \bar{C} dz + \Delta Q_s] \right) \quad (1)$$

where λ is the void ratio of sediment, \bar{C} is the concentration of sediment, (U_s, V_s) are the sediment migration speed in x- and y-direction and ΔQ_s is the vertical sediment flux.

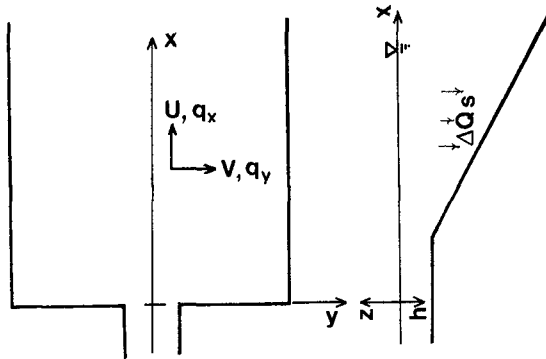


Fig.7 Coordinate system

Based on Eq.(1), some numerical procedures for the prediction of topographic change in the coast have already been proposed and practical simulations in the fields were carried out. The authors also proposed a numerical model for predicting topographic changes around the rivermouth (Sawaragi et al.(1985)). However, in the model, the contribution of discharged sediment from the river was not taken into account.

In this study, we constructed a numerical model for predicting depositional patterns of discharged sediment from the river in the coastal region. The numerical model consists of three parts as shown Fig.8.

First of all, the flow fields around the rivermouth was calculated based on vertically and temporally averaged mass and momentum conservation equations. Then, the horizontal flux and the vertical flux of sediment are estimated and

finally, the change of water depth around the rivermouth is calculated from Eq.(1).

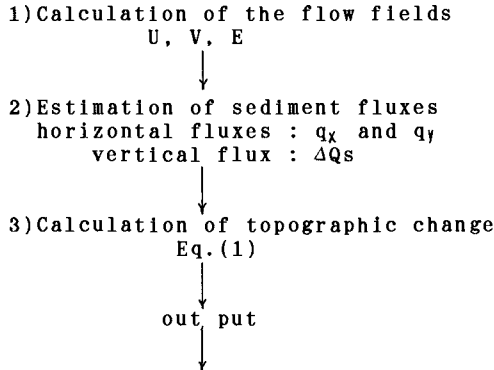


Fig.8 Flow of the numerical model

1) Calculation of the flow fields

Fundamental equations for the calculation of flow fields are

$$\frac{\partial E}{\partial t} + \frac{\partial}{\partial x} U(h+E) + \frac{\partial}{\partial y} V(h+E) = 0 \quad (2)$$

$$\frac{\partial U}{\partial t} + U \frac{\partial U}{\partial x} + V \frac{\partial U}{\partial y} = -g \frac{\partial E}{\partial x} - \frac{T_x}{\rho(h+E)} + L' \nabla^2 U \quad (3)$$

$$\frac{\partial V}{\partial t} + U \frac{\partial V}{\partial x} + V \frac{\partial V}{\partial y} = -g \frac{\partial E}{\partial y} - \frac{T_y}{\rho(h+E)} + L' \nabla^2 V \quad (4)$$

where U and V are the vertically averaged cross-shore and longshore velocities of discharged flow, E is the surface displacement from the still water, T_x and T_y are the time averaged bottom shear stresses in the x - (cross-shore) and y - (longshore) direction and L' is the horizontal mixing coefficients. In the present numerical model, following expressions for (T_x, T_y) and L' are used:

$$(T_x, T_y) = \rho f_w F_c(U, V) / 2, \quad F_c^2 = (U^2 + V^2) \quad (5)$$

$$f_w = (2g/100) / \{18 \log(12R/k_s)\}^2$$

$$L' = 0.01(h+E) \sqrt{g(h+E)} / \tan \theta \quad (6)$$

where R is the hydraulic radius, k_s is the equivalent roughness height and $\tan \theta$ is the bottom slope.

These equations are transformed into finite difference equations at homogeneous grid points and solved by so-called ADI method. A homogeneous grid system of a distance $\Delta S = 20\text{cm}$ was used and a time increment Δt was 0.15sec .

A boundary condition for the discharge of the river was given as a surface elevation, E_0 , at the upstream end of the river channel. By preliminary calculations, E_0 was determined to be 0.8cm to give the discharge of 11.7 l/sec at the rivermouth whose depth was about 6.5cm .

2) Horizontal and vertical flux of sediment

When the sediment concentration is in equilibrium, a formula of sediment transport rate in a steady state can be applied to the horizontal sediment flux, i.e., the 1st(=q_x) and 2nd(=q_y) terms in the right hand side of Eq.(1). In this study, the authors apply the following Rijn's formula (Rijn(1985)) to estimate the horizontal sediment flux:

$$\begin{aligned} \vec{q} &= (q_x, q_y) = \vec{q}_b + \vec{q}_s \\ \vec{q}_b &= C_b \delta_b \vec{U}_{sb}, \quad \vec{q}_s = F d C_a \vec{U}_{ss} \end{aligned} \quad (7)$$

In these equations, C_b and C_a are the sediment concentration in the bed load layer and the reference level, δ_b is the thickness of bed load layer, U_b and U_s are the migration speeds of sand in the bed load layer and suspended load layer and F is the vertical distribution function of the concentration of suspended sediment. These are given by the following equations:

$$\begin{aligned} C_b &= 0.18 C_0 T / D_* \quad (C_0 = 0.65), \quad C_a = 0.015 (d_{50} / z_a) (T^{1.5} / D_*^{0.3}) \\ |\vec{U}_{sb}| &= 1.5 T^{0.6} \{ (\rho_s / \rho - 1) g d_{50} \}^{0.5}, \quad \vec{U}_{ss} = \vec{U} \\ \delta_b &= 0.3 d_{50} D_*^{0.7} T^{0.5}, \\ F &= \{ (z_a / d)^{z'} - (z_a / d)^{1.2} \} / (1 - z_a / d)^{z'} (1.2 - z') \end{aligned}$$

in which, $T = (u_*^2 - u_*'^2) / u_*'^2$, $u_*'^2 = g / C_z^2 (U^2 + V^2)$, $C_z = 18 \log(12R / K_s)$, $d = h + E$, $D_* = d_{50} \{ (\rho_s / \rho - 1) g / \gamma^2 \}^{1/3}$, $z' = W_f / \beta K u_* + 2.5 (W_f / u_*)^{0.8} (C_a / C_0)$, and $\beta = 1 + 2 (W_f / u_*)^2$.

W_f and K in the above expressions are the settling velocity of sand and Karman's constant and z_a is the height of the referent level of suspended sediment. In the calculation, z_a is assumed to be 0.01*d. u_{*}' is the critical shear velocity for the sand movement. The authors apply u_{*}' on the horizontal bottom proposed by Iwagaki(1956). The effect of bottom slope on u_{*}' is taken into account as the influence of the gravity at the critical stage of the sand movement.

In the Rijn's expression, the suspended load was formulated by giving the bed load as a boundary condition. Therefore, to reproduce depositional patterns observed in the experiments numerically, a special technique was used which will be mentioned afterward.

On the other hands, various expressions for the vertical flux ΔQ_s in Eq.(1) have been proposed (for example, Sawaragi et al.(1985), Hosokawa et al.(1986)). In this study, ΔQ_s was defined as the volume of settling sediment which entered the calculation region from the upstream boundary of the river channel and was determined from the convection diffusion equation:

$$\Delta Q_s = +\bar{C} W_f \quad (8)$$

$$\frac{\partial \bar{C}}{\partial t} + U \frac{\partial \bar{C}}{\partial x} + V \frac{\partial \bar{C}}{\partial y} = \frac{\partial}{\partial x} (K_{sx} \frac{\partial \bar{C}}{\partial x}) + \frac{\partial \bar{C}}{\partial y} (K_{sy} \frac{\partial \bar{C}}{\partial y}) + \frac{1}{d} (K_{sz} \frac{\partial \bar{C}}{\partial z} + W_f \bar{C})_{z=h} \quad (9)$$

where K_{sx} and K_{sy} are the diffusion coefficient of suspended sediment and are estimated by the following expression (Murray(1968)):

$$K_{sx} = K_{sy} = 0.15 Fc d \quad (10)$$

Eq.(9) is solved numerically at the same grid points as the calculation of flow fields to determine the vertical flux of Eq.(8) with the boundary condition at $X = X_{start}$ as

$$C = Cor = \frac{1}{d} \int q_x dz \quad (11)$$

3) Calculation of the change of water depth

Change of water depth, that is, the depositional patterns of discharged sediment from the rivermouth was calculated from Eq.(1).

The topographic change took place within a unit time Δt is expressed by the sum of those caused by vertical flux Δh_v and horizontal flux Δh_h as follows:

$$\frac{\Delta h}{\Delta t} = \frac{1}{\Delta t} (\Delta h_v + \Delta h_h) , \quad \frac{\Delta h_v}{\Delta t} = \frac{1}{1-\lambda} \Delta Q_s ,$$

$$\frac{\Delta h_h}{\Delta t} = \frac{1}{1-\lambda} \left(\frac{\partial q_y}{\partial x} + \frac{\partial q_x}{\partial y} \right) \quad (12)$$

The change of water depth caused by ΔQ_s is easily estimated provided that ΔQ_s is given. However, it is required a special treatment to reproduce depositional pattern brought about by the horizontal flux in the experiments. Because in the experiments, sediment was discharged from the sand pit to the river channel of the fixed bed where there is no source of suspended sediment.

Therefore, in the calculation of the change of water depth, the following procedure was employed:

For the simplicity, consider the phenomena in one-dimension and let Δx and Δt be the space and time increments as shown in Fig.9.

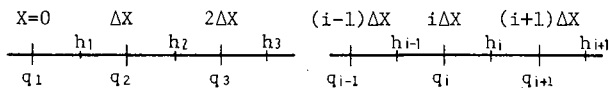


Fig.9 Discretization scheme for the calculation of topographic change due to the horizontal sediment flux

Then, during $t=0-\Delta t$, only q_1 at $x=0$ takes place. During time $t=\Delta t-2\Delta t$, q_1 and q_2 occur at $x=0$ and Δx . During $t=(n-1)\Delta t-n\Delta t$, sediment movement takes place in the region $x < (n-1)\Delta x$. At this time, the change of water depth Δh_i at $x=i\Delta x$, can be expressed by

$$\Delta h_i = \{(n-i+1)q_i - (n-i)q_{i+1}\} (\Delta t / \Delta X) / (1-\lambda) \quad (13)$$

In the calculation of Δh we used this procedure in both x - and y -direction.

APPLICABILITY OF THE NUMERICAL MODEL

Figure 10 illustrates calculated and measured flow patterns in the case where there was no coastal structures. Calculated results is shown by the velocity vectors and measured result is illustrated as the trajectories of floats.

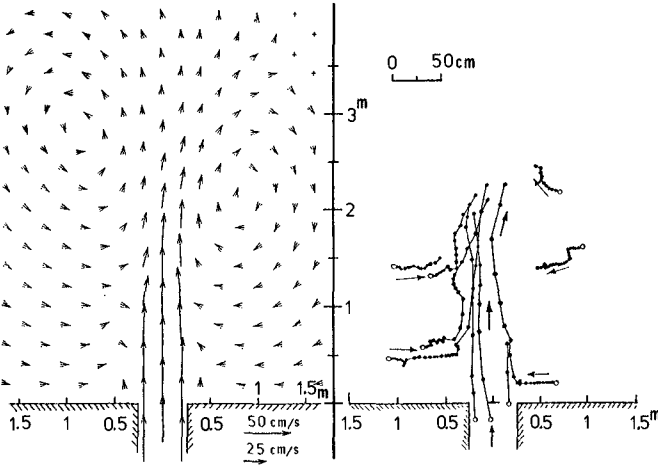


Fig.10 Calculated and measured flow pattern around river-mouth without structure

Figure 11 shows the comparison of measured and calculated discharge velocity U and mean surface displacement E along the center line of the river channel.

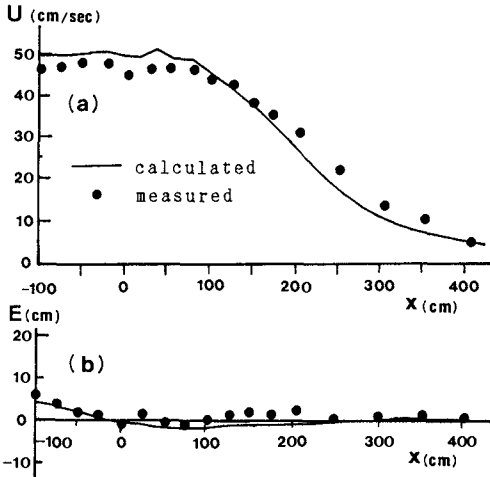


Fig.11 Comparison between calculated and measured discharged velocity and mean water level along a center line of the river channel

These results show that the present numerical procedure for predicting flow field is adequate.

Figure 12 illustrates the comparison of measured and calculated depositional profiles along the center line of the river channel. Fig.(a) is the case of fine sand and (b) is the case of median sand.

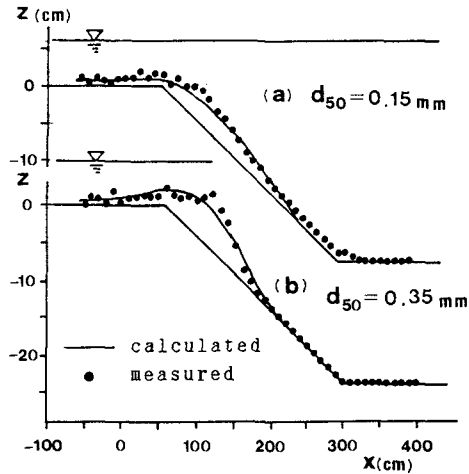


Fig.12 Comparison between calculated and measured depositional profile along a center line of the river channel

From the figure, it can be seen that the depositional profiles of discharged sediment can be predicted by the present model accurately regardless of the grain size of discharged sediment.

Figures 13(a) illustrates the depositional pattern of discharged sediment in the case of fine sand without structure which corresponds to Fig.12(a). Figure 13(b) shows the predicted depositional pattern. When compared with these figures, it is judged that depositional pattern can also be predicted fairly well by the present model.

In Figs.(c) and (d), changes of water depth caused by vertical sediment flux ΔQ_s , bed load and suspended load are shown separately.

Although the effects of ΔQ_s extended till $X > 3m$, the amount of the topographic change is small. Change of water depth caused by bed load did not expand beyond $X = 2.0m$ which coincides with the critical depth where the bottom shear stress exceeded the critical shear of the sediment movement shown by the arrow in the figure. On the other hands, deposition due to suspended load extended far beyond this critical depth.

The same degree of agreements can be seen between measured and predicted depositional patterns in the cases of jetty-protected rivermouth. However, when the offshore detached breakwaters were constructed, discharged flow pattern in the experiments can not be reproduced by the present model. Therefore, there is some room for further improvements of the model.

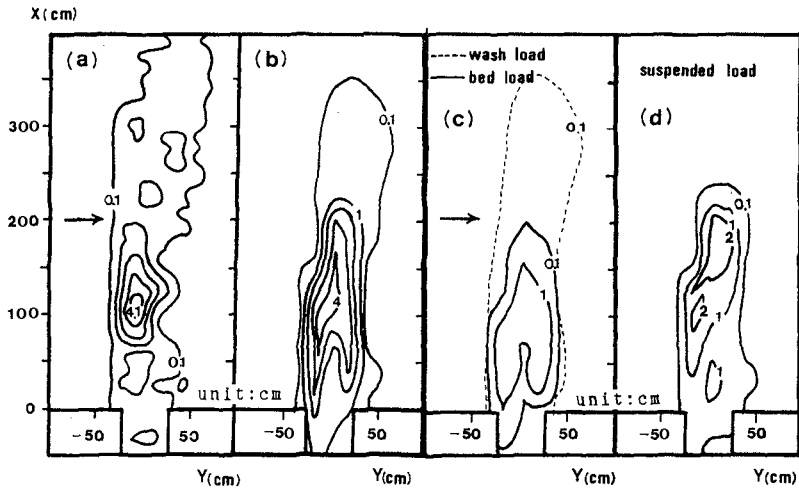


Fig.13 Depositional pattern of discharged sediment in the case of fine sand

CONCLUSIONS

The effects of coastal structures on the discharged flow and depositional patterns of discharged sediment from the river were investigated through experiments. A pair of offshore detached breakwaters is shown to be one alternative of a pair of jetties which have been commonly constructed as a countermeasure against a blockage of rivermouth.

A numerical procedure is also developed for predicting the depositional patterns of discharged sediment. The depositional patterns measured around the rivermouth without structures and around the jetty-protected rivermouth can be reproduced by the numerical procedure precisely. However, the flow pattern measured around rivermouth protected by the offshore detached breakwater can not be reproduced exactly.

REFERENCES

- Butakov, A.N. (1971) : Study of development and deformation of mouth bar, Proc. 14th Conf. on IAHR, Paris, pp.95-102.
- Hosokawa, Y., N.Tanaka, M.Kudaka and K.Sato (1986) : Method for forecasting quantity of sedimentation in trenches and its application in the field, Proc. 33rd Japanese Conf. on Coastal Engineering, pp.312-316 (in Japanese).
- Iwagaki, Y. (1956) : Basic study on the critical shear stress for sand movement in the open channels, Proc. JSCE, Vol. 41, (in Japanese).
- Murray, S.P. (1968) : Simulation of horizontal turbulent diffusion of particle under waves, Proc. 10th ICCE, pp. 446-466.
- Rijin, L.C. (1985) : Sediment transport, Delft Hydraulic Labo. Publication No.334.
- Sawaragi, T., J.S.Lee and I.Deguchi (1985) : A new model for a prediction of beach deformation around a rivermouth, Proc. Int'l. Sympo. Ocean Space Utilization '85, Vol.2, pp.229-236.
- Suga, K., T.Ishikawa, K.Nadaoka and H.Tanaka (1987) : Formation of sand terrace in front of a river mouth and its decline, Technical Note in Proc. of the Japan Society of Civil Engineers, No.381/II-7, pp.227-230 (in Japanese).

CHAPTER 118

DUNE STABILIZATION WITH A SAND/GEL COMPOSITE SYSTEM

M. H. Auerbach*, G. W. Borden*, and B. L. Edge, ASCE-M**

ABSTRACT

The effectiveness of a novel sand/gel composite system for the temporary stabilization of coastal dunes was demonstrated in wavetank and field testing. The composite consists of 97% beach sand and water, with a few percent of a biodegradable aqueous polymeric gel made from non-toxic ingredients. The gel binds the sand into a firm but resilient composite that is natural in appearance and resists erosion from waves and tides. The composite is applied by pneumatic gun to the front face of a dune to a few feet below the berm level for toe protection.

This paper describes the initial development and performance of the composite system in wavetank tests at the Oregon State University Wave Research Facility and field trials at Anastasia State Park, St. Augustine, Florida; Chuck's Steak House, Melbourne Beach, Florida; and Ocean Dunes Condominiums, Fort Fisher, North Carolina.

INTRODUCTION

Storm and tidal erosion threatens thousands of miles of shoreline and associated coastal property in the US and throughout the world. Current stabilization methods include permanent armoring, such as concrete seawalls, rock revetments, groins and jetties, and temporary measures such as sand-filled bags and replenishment with dredged sand. Several states in the US have prohibited hard erosion control structures. The cost-effectiveness and environmental consequences of these approaches remain uncertain.

The Chemical Division of Pfizer Inc. has produced water-soluble polysaccharide thickeners and gelants for numerous applications in the oilfield and other industries

* Assistant Director and Director, respectively, Specialty Chemicals R & D, Pfizer Central Research, Eastern Point Road, Groton, CT 06340

** President, Cubit Engineering division of Kimley-Horn, 207 East Bay Street, Charleston, SC 29401

for over ten years. The adaptation of this technology for coastal erosion control was investigated.

EXPERIMENTAL PROGRAM

Laboratory Testing

A wide range of gel/sand compositions was evaluated in the laboratory using a water impact test device. Successful compositions, based on a weight loss/hour limit under continual water impact, had unconfined compression strength values of 3000 - 30,000 lb/ft².

Environmental Exposure

The leading composition candidates were prepared in a small cement mixer, cast in 1 ft³ wooden pans and anchored in the sand at a 45° angle on the eastern bank of the mouth of the Thames River in Groton, Connecticut. Although not subject to appreciable wave impact at this Long Island Sound location, the pans were totally submerged twice a day at high tide. Successful compositions endured intact for over seven months with only minor gouges from driftwood impacts, until the pans were uprooted in a storm.

Emplacement Testing

Pilot sand drum tests showed that ungelled polymer solution sprayed onto the sand surface did not penetrate significantly. Shank-injected ungelled polymer solution did not permeate the sand but left gel-filled voids. Large batch mixing of sand with ungelled polymer solution in a cement mixer and shoveling onto a dune was not possible because of rapid polymer gelation kinetics. Accordingly, the pneumatic gun approach, where sand and polymer gel component solutions are comixed with large amounts of air and sprayed onto the dune, was attempted.

Gun Trials

Five trials were conducted from 1985-87 with commercial gunite equipment at sand feed rates of 120-200 lb/min (1.6-2.7 ft³/min composite) to test various spray nozzle designs, equipment configurations, and component combinations. Numerous beach pans were sprayed full and evaluated for pregel slump and drying rate. Several of these composite panels were placed on the Groton beach for confirmation of environmental endurance. These panels also remained intact without erosion for the several month exposure period.

OSU WAVETANK TRIALS

To evaluate the full-scale strength and erosion resistance of the composites under controlled conditions, tests were conducted at Oregon State University's Wave Research Facility in May, 1986. The 12-ft wide x 18-ft

deep x 350-ft long tank has a computer-controlled hydraulically-driven wave generator.

Dune Preparation

A 1:1.2 sloping berm was prepared with movable concrete slabs covered with sand in the bottom of the tank. The berm was seasoned with gentle waves and three 8-ft dunes were constructed about 20 feet apart with a 1:1 sloping surface at the end of the tank with local sand. A thin non-woven geotextile was placed over the front surface of each dune to keep the sand base from blowing away during spraying and from washing out if the composite should crack during wave testing. The composites were emplaced with a pneumatic gun onto this filter fabric at a rate of 2.0-2.7 ft³/min.

Each composite was about 2-ft thick at the bottom, 1-ft thick at the top, and 7 feet high (Figure 1). Different compositions and feed configurations were used for each dune. As the weather in Corvallis in May was cool and damp, a wooden frame and plastic tent were erected over the dune end of the wavetank and kerosene heaters were placed inside to speed composite drying. Colored horizontal stripes were painted on the composite surfaces to measure runup, and a swash gauge was built in the tank to measure wave velocity.

Wave Testing

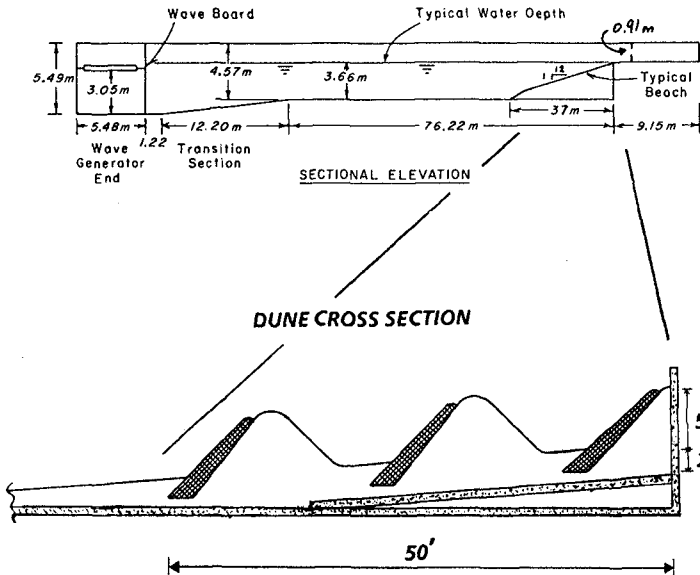


Figure 1. OREGON STATE UNIVERSITY WAVE RESEARCH FACILITY

The tank was filled with water to the base of the front dune. Monochromatic and Bretschneider spectrum random waves were generated with 7-11 ft/sec velocity, 1-11 second period, and 2-5 foot height (Figure 2). Conditions were controllable to allow berm sand to erode away from the dune face or accrete against it. They were chosen so that sand and gravel were thrown against the composite for lengthy periods to exacerbate erosion. The water level was adjusted so that the bores ran up to the top of the composite without constantly overtopping the dunes. In many cases, the waves broke just in front of the dune so that the swash generated was almost entirely dissipated on the dune itself. These conditions simulated average US East Coast annual storms, and likely represented a more severe 2-3 year event.

One dune was tested each day. Each dune was exposed to wave impacts for 4-6.5 hours. Aside from minor sloughing of a crusty skin from one of the composites and loss of a chunk from another because of a gunning defect, there was no appreciable erosion of the composites during testing (Figure 3).

At the end of the first dune test, a 1-ft hole was dug in the center of the composite with a shovel and wave

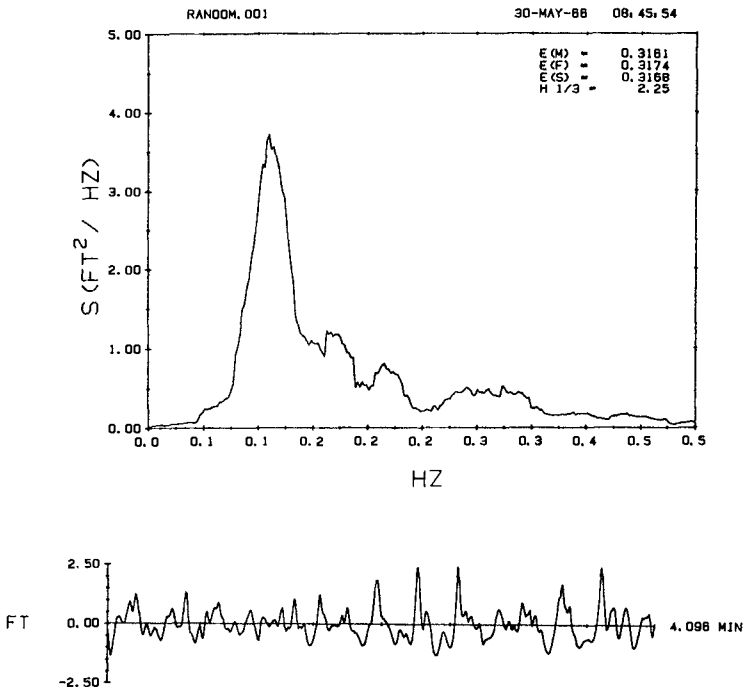


Figure 2. OSU BRETSCHNEIDER WAVE SPECTRUM

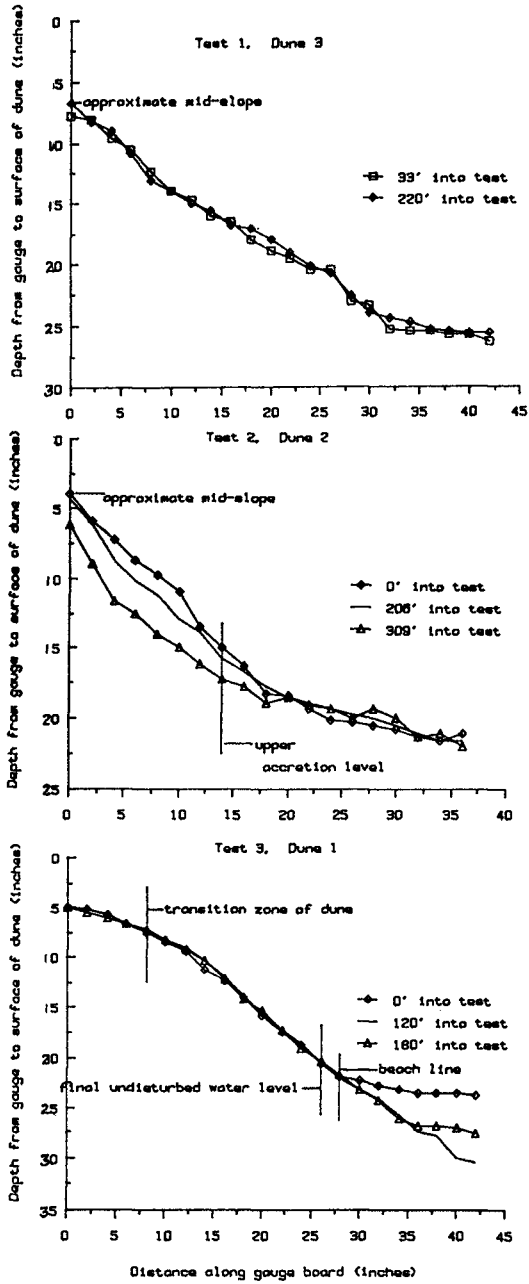


Figure 3. OSU Wavetank Tests
Surface Profiles of Test Dunes
Measured 2-ft from Right Side of Dune

uprush pumped water into the hole. With the exposed geotextile intact, no sand was lost from the dune base and the composite hole was not widened by additional wave impacts. After wave tests on the second dune were completed, a hole was dug in the composite and the geotextile was cut open. Additional waves for a half hour created a 2-ft diameter cavity in the dune base underneath without breaking the composite.

After each day's testing was completed, the intact dune was removed from the tank with a clamshell and the berm repaired for the next test. After all three composites were tested and removed, a fourth dune was built in the tank with untreated sand as a control. Full amplitude 8-second waves (~ 3-ft height) obliterated 80% of this dune within seven minutes, leaving a vertical escarpment.

SHORELINE FIELD TRIALS

Three field tests of the sand/gel composite system have been initiated to date. These are summarized in Table 1 and described below.

Florida Field Trial I - Anastasia

Permitting: Permission was granted by the Florida Department of Natural Resources, Division of Recreation and Parks, in November, 1986, for a field test at the south end of Anastasia State Recreation Area in St. Augustine.

As the east coast of Florida is a prime nesting area for endangered marine turtles, the US Department of Interior Fish and Wildlife Service was also consulted about the test. No turtle nests had been observed at the south end of the park in several years, so no turtle monitoring was required. The USDI FWS also advised that the Anastasia Island beach mouse (Peromyscus polionotus phasma) was not listed as an endangered species but was a candidate for listing. P. p. phasma, a subspecies of the common beach mouse and closely related to the Santa Rosa Island, Perdido Key, Choctawhatchee, and Alabama beach mice, lives among vegetation behind the dune face (USDI FWS, 1986) and would not be affected by the test.

Emplacement: The composite was designed to extend several feet below the berm to provide toe protection and prevent it from being undercut during a storm that might lower beach elevation by several feet. A trench 3 feet deep was excavated in front of 90 feet of eroded dune just south of the beach access ramp. The dune surface was dressed to a 1:1 slope to the bottom of the trench and geotextile was unrolled along the dune face. Beach-compatible sand was imported from a local pit to build a 200-ft control dune south of the test section (sieve analyses in Table 2). The 90-ft test dune was gunned with composite in two configurations (Figure 4) using beach sand from the toe trench. After spraying was completed, a heated tent was erected over the composite to expedite

Table 1: SAND/GEL COMPOSITE FIELD TRIALS

Site	Anastasia State Park	Chuck's Steak House	Ocean Dunes Condos
Location	St. Augustine, FL	Melbourne Beach, FL	Fort Fisher, NC
Empl. Date	December 1986	April 1988	May 1988
Elevation			
Crest	+ 12.0 NGVD*	+ 17.0 NGVD	+ 17.0 NGVD
Toe	+ 5.0 NGVD	+ 8.0 NGVD	+ 8.0 NGVD
Height	7 feet	9 feet	9 feet
Length	90 feet	170 feet	100 ft
Slope	1:1	1:1	1:1
Thickness			
Crest	12 inches	15 inches	16"
Toe	24 inches	18 inches	22"
Ft ³ /lin-ft	15.0	18.0	20.5
Spray Rate	1.8-2.4 ft ³ /min	1.7-4.5 ft ³ /min	2.6-5.4 ft ³ /min
Profile Monitoring (Number Profiles - Total Feet)			
N Control	5 - 75	5 - 180	4 - 300
Composite	6 - 90	5 - 170	6 - 200
S Control	5 - 75	6 - 250	8 - 700
Other Monitoring	Storms	Storms	Storms
	Vegetation	Vegetation	Vegetation
	Sea Turtles	Waves/Tides	

* National Geodetic Vertical Datum

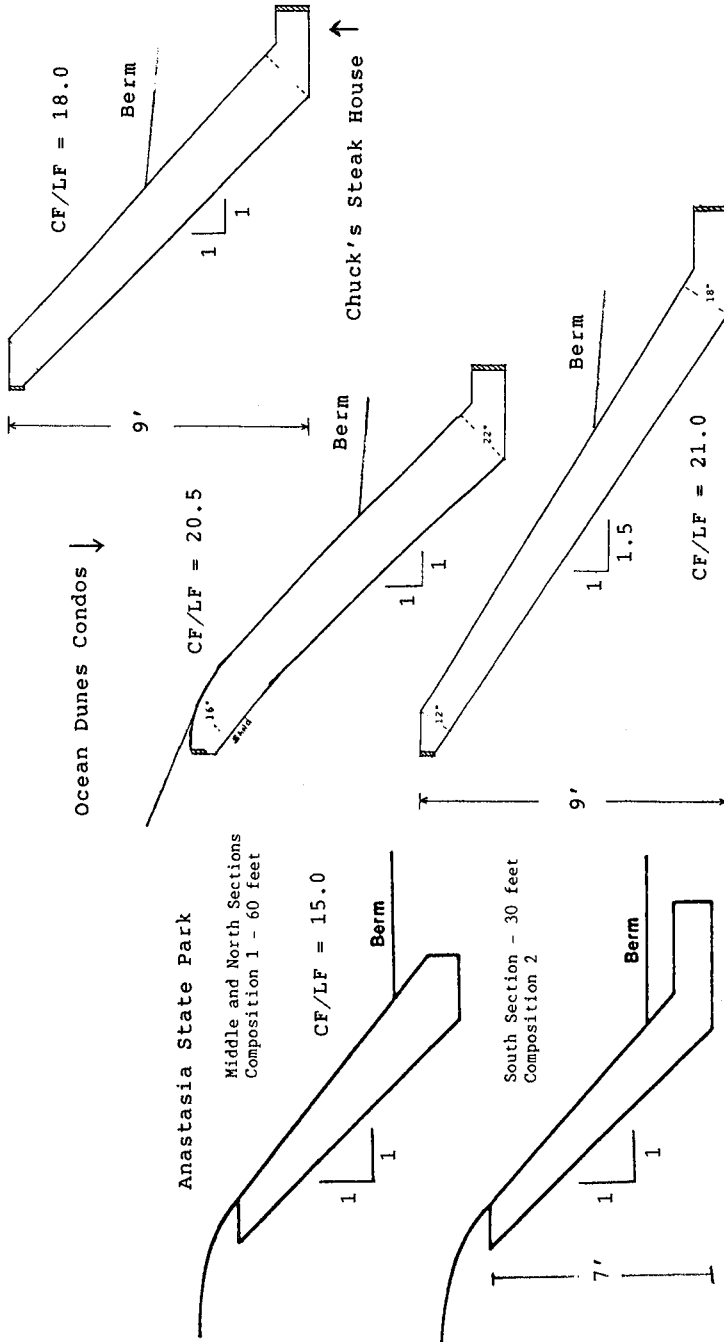


Figure 4. Sand/Gel Composite Cross-Sections

drying, a precaution taken because of the cool, damp weather and possibility of storms in northeast Florida in December. The tent was removed after a week of drying and the side flanks were covered with sand and the berm in front of the composite was replaced.

Table 2: Anastasia Sand Analyses

Sand	% H ₂ O	% Retained on - Mesh					Pass 200
		40	60	80	100	200	
Beach	9.4	0.0	5.0	61.6	24.4	8.8	0.24
Imported	9.6	0.0	5.5	53.6	29.6	11.0	0.30

Monitoring: The test area was videotaped before, during, and after the emplacement. Survey monuments were installed atop the test and control dunes and 16 profile measurements were made from the dune top to mean sea level at monthly intervals at the positions shown in Figure 5. Analysis of the data from the first 15 months of profile measurements indicate there was no significant difference in sand erosion or accretion rate in front of the composite vs. in front of the adjacent control dunes (Table 3).

Storm Exposure: A major northeaster hit the test area on January 5, 1987, two weeks after the emplacement was completed. The storm surge was not recorded at the Mayport tide gauge 60 miles north, but wave uprush was observed running up to the top of the composite by Park Rangers. This was confirmed by a storm hindcast performed by the Institute for Storm Research, Houston, TX. Beach elevation was lowered 1.5-2 feet and 2-5 foot escarpments were created in the adjacent control dunes, while the composite remained intact. No other storms have impacted the composite. The escarpments on both sides have since filled in with accreted sand. Selected dune profiles are shown in Figure 6.

Vegetation: In April, 1987, 600 sea oat seedlings (*Uniola paniculata*) were planted above and alongside the composite by children volunteers from the St. Johns County 4-H Club with guidance from the US Department of Agriculture Soil Conservation Service. The plants were watered several times by the St. Augustine Beach Volunteer Fire Department. The seedlings atop the composite were trampled later by park patrons (see below), while those on the adjacent control dunes with less traffic are lush and vigorous. Voluntary railroad vine (beach morningglory, *Ipomoea pes-caprae*) from behind the dune have grown over the top of the composite down to the berm, with new roots penetrating the composite in several places. New plants also appeared in the rebuilt control dunes and in the berm in front of the composite. Ghost crab burrows were occasionally seen in the base of the composite.

Foot Traffic/Vandalism: The only noticeable damage to the composite has been the result of frequent foot traffic and occasional vandalism by park patrons. Some shovel

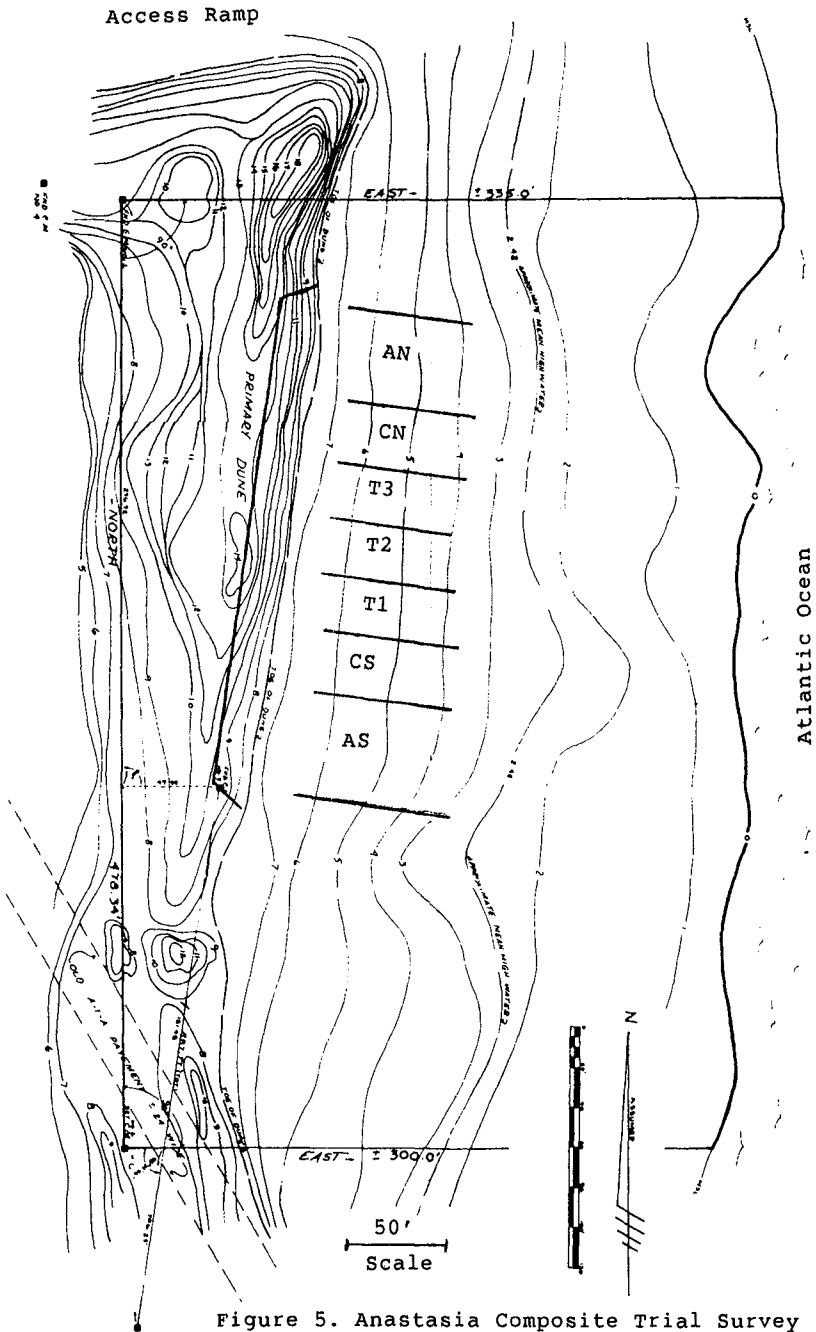


Figure 5. Anastasia Composite Trial Survey

Table 3: Anastasia Trial Beach Profile Analysis

<u>LEGEND</u>		Section (Total 240 ft)		Period (Total 466 days)	
AS:	South Adjacent Dune	-	45 ft	1:	12/29/86 - 1/8/87; 10 days
CS:	South Control Dune	-	30 ft	2:	1/8/87 - 2/23/87; 46 days
T1:	South Test Section	-	30 ft	3:	2/23/87 - 3/25/87; 30 days
T2:	Middle Test Section	-	30 ft	4:	3/25/87 - 6/1/87; 68 days
T3:	North Test Section	-	30 ft	5:	6/1/87 - 6/29/87; 28 days
CN:	North Control Dune	-	30 ft	6:	6/29/87 - 8/3/87; 35 days
AN:	North Adjacent Dune	-	45 ft	7:	8/3/87 - 8/25/87; 22 days
				8:	8/25/87 - 9/16/87; 22 days
				9:	9/16/87 - 10/26/87; 40 days
				10:	10/26/87 - 12/1/87; 36 days
				11:	12/1/87 - 1/27/88; 57 days
				12:	1/27/88 - 3/1/88; 34 days
				13:	3/1/88 - 4/8/88; 38 days

RESULTS

Sec/ Per	Unit Volume Change Cu-Yd/Lin-ft (+: accretion; -: erosion)										
	AS	CS	T1	T2	T3	CN	AN	Avg/Ft	Cum Av	Tot Cu-Yd	Cum Cu-Yd
1	-4.4	-4.9	-5.0	-4.7	-4.8	-4.3	-3.4	-4.42	-4.42	-1060	-1060
2	1.5	1.6	1.8	1.9	2.1	1.7	1.5	1.69	-2.73	405	-656
3	-2.1	-2.2	-2.2	-2.5	-2.8	-2.9	-2.6	-2.45	-5.18	-589	-1244
4	6.1	6.1	6.1	6.8	7.3	7.2	7.0	6.63	1.45	1592	348
5	6.8	6.9	7.3	7.0	6.4	6.0	5.7	6.56	8.01	1575	1923
6	-2.6	-2.2	-2.0	-1.5	-1.0	-0.4	1.0	-1.18	6.84	-283	1640
7	0.6	0.8	1.5	1.0	1.7	3.0	2.7	1.61	8.45	387	2027
8	0.3	-0.1	-1.3	-2.3	-2.9	-3.6	-4.5	-2.06	6.38	-495	1532
9	-3.1	-3.8	-4.0	-3.5	-3.7	-3.3	-2.7	-3.36	3.03	-805	727
10	-8.4	-8.2	-8.1	-8.4	-8.3	-8.7	-9.1	-8.48	-5.45	-2034	-1307
11	3.7	3.9	3.8	1.4	1.7	2.2	4.3	3.12	-2.33	748	-559
12	4.3	3.7	2.9	3.5	4.1	4.9	3.6	3.88	1.55	931	372
13	3.5	1.7	1.2	2.1	1.5	0.6	-0.4	1.47	3.02	352	724
Total	6.4	3.3	1.9	0.8	1.5	2.3	3.0	3.02			

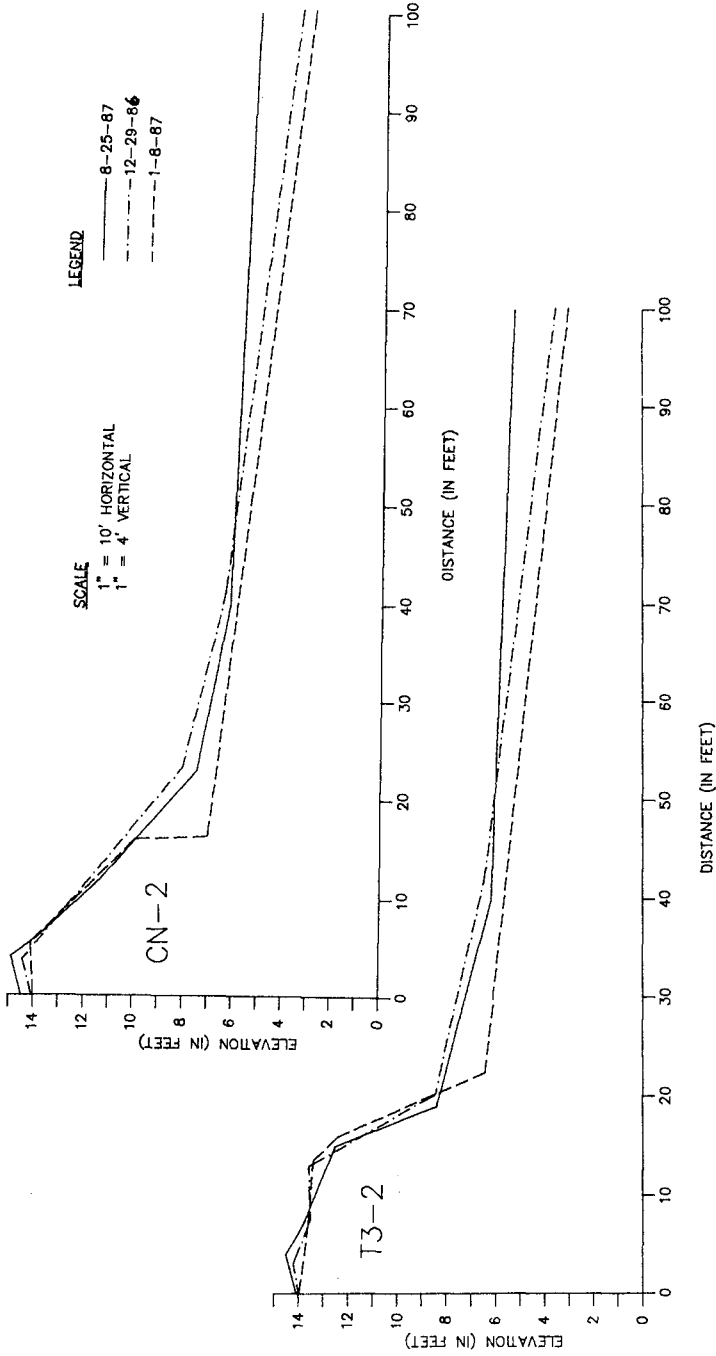


Figure 6. Anastasia Trial Dune Profiles

cuts and graffiti were gouged in the face of the test material and several distinct sets of toeholds were dug in the middle of the composite by climbers. The north control dune was also worn down by heavy foot traffic. The south third of the test section, which was prepared with a somewhat different gel composition, appeared to have softened in the heavy summer 1987 rains, and was broken through to the geotextile by repeated foot traffic.

The damage was repaired in September, 1987, and again in June, 1988. The toeholds and gouges were patched with small batches of fresh composite hand-mixed in a bucket. The patches have remained intact in the composite surface.

Florida Field Trial II - Chuck's

Because of a lack of turtle nesting at Anastasia, a site was chosen for a field trial adjacent to Chuck's Steak House, a restaurant in south Brevard County. This is located in the densest loggerhead and green turtle nesting area of the Western Hemisphere, with plentiful historical data on nesting activity (Ehrhart, 1986a, 1986b, 1987).

Permitting: Permits were applied for and received from the Brevard County Office of Natural Resources Management; the Florida Department of Environmental Regulation; the Florida Department of Natural Resources, Division of Beaches and Shores; and the US Army Corps of Engineers. Comprehensive site surveys, work plans, environmental impact statements, and dune profile, vegetation, and turtle nesting monitoring plans were required for permit approval.

Emplacement: The composite was emplaced in April, 1988, along 170 feet of dune surface in a similar manner to that used at Anastasia. Further details are given in Table 1 and Figure 4. The composite was allowed to air dry for one week and then berm sand was restored such that half of the composite's height was below the berm elevation at + 12.5 ft NGVD.

Monitoring: The emplacement operation was videotaped and dune profile survey markers were set. Arrangements for daily monitoring of marine turtle activity from May - October were made with the Department of Biological Sciences of the University of Central Florida, Orlando. Sea oats and railroad vine seedlings were planted in May, 1988, in the sand above the composite and in the north and south control dunes adjacent to the composite flanks.

Foot Traffic/Vandalism: This site is on private property much more isolated than Anastasia. Accordingly, there is very little beach traffic most of the time. From April to October, however, the restaurant hosts very popular beach parties every Sunday afternoon which draw hundreds of people. A few gouges appeared in the composite in May, 1988; further damage has been prevented by posting a guard during the parties. The damage was repaired with patch composite material in June, 1988.

North Carolina Trial - Ocean Dunes

Because of the lack of significant storm exposure at Anastasia, a site adjacent to the Ocean Dunes Condominiums, Fort Fisher, was chosen for a field trial. This area has endured several severe winter storms that caused property damage in the last few years. A permit for a test was obtained under the North Carolina Coastal Area Management Act from the Department of Natural Resources and Community Development.

Composite was emplaced along 200 feet of eroding dune in two configurations (Figure 4) in May, 1988. The composite was air-dried for one week and the berm was replaced as at Chuck's Steak House. Dune profile monitoring along 1200 feet of beach was initiated to measure longshore sand transport effects. As this is a private development, no significant damage from foot traffic has been observed.

CONCLUSIONS

The sand/gel composite system has been shown to be resistant to erosive forces, natural in appearance and compatible with beach vegetation. As intended, it appears to be resilient and environmentally compatible. Monitoring of the three field trials will continue for several years.

This technology is intended to stabilize threatened dunes against typical tides and storms long enough to allow natural vegetation to take hold, perhaps 3-5 years. In time, the composite should slowly disintegrate back to sand and water. Individual pieces of composite material, if broken free in a severe storm or hurricane, should break up in the surf and not accumulate on the beach. This novel system will hopefully provide a cost-effective, environmentally acceptable alternative to current approaches for coastal protection.

ACKNOWLEDGEMENTS

We gratefully appreciate the support and assistance of the following key people in carrying out this program: Merrill Lozanov and Dr. Irving Goldman, Pfizer Central Research; Sheldon Brandes, Pfizer Chemical Division; C. W. Hartsfield, Florida Department of Natural Resources, Division of Recreation and Parks; Ralph Clark and Neal Rogers, Florida Department of Natural Resources, Division of Beaches and Shores; Ross Witham and Alan Huff, Florida Department of Natural Resources, Division of Marine Resources; John Roche and Doug Carter, Florida Park Service; Derek Busby, Brevard County Office of Natural Resources Management; Earl Possardt, US Department of Interior, Fish and Wildlife Service; Calvin Hubbard, Don Hamer, and Keith Salvo, US Department of Agriculture, Soil Conservation Service; Cynthia Goodman, St. Johns County Extension Service; Henry Beeker, North Carolina Department of Natural Resources and Community Development; Dr. Charles Sollitt, Department of Civil Engineering, Oregon State University; Dr. Llewel-

lyn Ehrhart, Department of Biological Sciences, University of Central Florida; Dr. Richard Seymour, Scripps Institution of Oceanography, University of California at San Diego; and Dr. John Fisher, Department of Civil Engineering, North Carolina State University.

APPENDIX - REFERENCES

1. L. M. Ehrhart and B. E. Witherington, "Human and Natural Causes of Marine Turtle Nest and Hatchling Mortality and Their Relationship to Hatchling Production on an Important Florida Nesting Beach," Florida Game and Fresh Water Fish Commission Project GFC-84-018, 12 June 1986.
2. L. M. Ehrhart and B. E. Witherington, "Studies of the Ecology of Indian River Marine Turtle Populations and Marine Turtle Nesting Beach Productivity in South Brevard County, Florida," 1986 Progress Report to Bureau of Marine Research, Florida DNR Contract C3848, 15 December 1986.
3. L. M. Ehrhart and P. W. Raymond, "Loggerhead and Green Turtle Nesting Densities in South Brevard County, Florida, 1981-84," in W. N. Witzell, ed., Ecology of East Florida Sea Turtles, NOAA Tech. Rep. NMFS 53, USDC, 1987.
4. US Department of Interior, Fish and Wildlife Service, "Beach Mouse Recovery Plan," Atlanta, GA (1986)

CHAPTER 119

Littoral Drift Model for Natural Environments

Rolf Deigaard ¹⁾, Jørgen Fredsøe ²⁾, Ida Brøker Hedegaard ¹⁾
Julio A. Zyserman ²⁾ and Ole Holst Andersen ¹⁾

ABSTRACT

The littoral drift model developed at DHI and ISVA, see Deigaard et al. (1986b) has been extended to include the effects of the irregularity of the waves, of a coastal current and a wind acting on the surf zone. Further, a mathematical model to simulate the near-shore current pattern along a barred coast with rip channels has been developed.

The influence on the littoral drift of the irregularity of waves, wind, coastal current, and rip channels is discussed. It is concluded that irregularity of waves and presence of rip channels must be considered while coastal current and wind action are of minor importance.

INTRODUCTION

The modelling of longshore sediment transport has been improved significantly during the last decade. From formulae based on 'longshore energy flux' originating from the incoming waves, a more detailed formulation of the problem is now appearing. However, it is common to most of the approaches that the description still relies on regular incoming waves which meet a coast with a constant slope, and with quasi-uniform longshore conditions.

The purpose of this paper is to discuss the influence on the littoral drift of the natural variability of waves and coastal profiles. Besides analysis is carried out of the effect on the littoral drift of a coastal current and a wind blowing over the surf zone.

The starting point of the present analysis is the littoral drift model, developed at DHI and ISVA, and described by Deigaard et al. (1986b). It is a mathematical model which consists of two main elements.

-
- 1) Danish Hydraulic Institute (DHI), Agern Allé 5, DK-2970, Hørsholm, Denmark.
 - 2) Institute of Hydrodynamics and Hydraulic Eng. (ISVA), Technical University of Denmark, DK-2800 Lyngby, Denmark.

- A hydrodynamic module describing the wave height and direction in the coastal zone and the wave generated littoral current.
- A sediment transport module which calculates the local sediment transport rate as a function of the local hydraulic parameters. The sediment transport rate is integrated over the coastal profile.

The processes involved in wave transformation are refraction, shoaling and breaking. The associated variation in radiation stresses is used to calculate the shore normal component causing a wave set-up and the shear component of the radiation stress, S_{xy} . The shear component is driving the littoral current, \bar{v} it is constant outside the breaker line where no energy dissipation occurs. The littoral current is calculated from the balance between bed shear stress τ_b , cross-shore momentum exchange and the gradient in shear radiation stress:

$$\tau_b - \frac{d}{dx} (\rho E D \frac{dV}{dx}) = - \frac{dS_{xy}}{dx} \quad (1)$$

where x is the cross-shore coordinate, ρ is the density of water, E the momentum exchange coefficient, D the water depth, and V is the depth averaged littoral drift velocity.

The local sediment transport is calculated by the model described by Fredsøe (1984), Fredsøe et al. (1985), and Deigaard et al. (1986a). The bed load and suspended load transport is calculated separately. The suspended load is normally dominant in the surf zone; it is described by the vertical turbulent diffusion equation:

$$\frac{\partial c}{\partial t} = \frac{\partial}{\partial z} (\epsilon_s \frac{\partial c}{\partial z}) + w \frac{\partial c}{\partial z} \quad (2)$$

where z is the vertical coordinate, c the sediment concentration, t is time, ϵ_s turbulent diffusion coefficient, and w is the settling velocity. ϵ_s is calculated by taking the turbulent wave-current boundary layer as well as the turbulence generated by breaking or broken waves into account. The boundary conditions for Eq. (2) are zero flux of sediment through the water surface and a time-varying near-bed concentration calculated by the model of Engelund and Fredsøe (1976).

Fig. 1 gives an example of model results showing the profile of the littoral current and the littoral sediment transport rate across a coastal profile with one longshore bar.

The above described model has a number of limitations, the most important being:

- . the incoming waves are unidirectional and regular
- . the conditions along the coast are uniform
- . only driving forces from the waves are included.

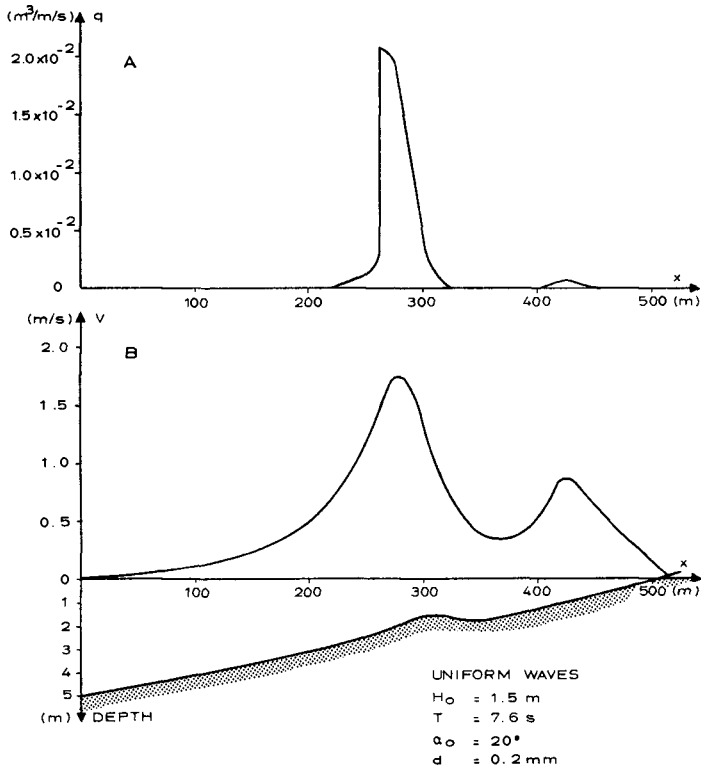


Fig. 1. Example of model results.
 A: Littoral Sediment Transport Rates.
 B: Profile of Littoral Current and Coastal Profile.

In the following it is described, how the model has been modified to overcome these limitations, and the effect of the various mechanisms treated is discussed.

IRREGULAR WAVES

The effect of irregular waves versus regular monochromatic waves has been included in the modelling of the long-shore current as well as of the sediment transport rate.

The longshore current velocity profile driven by irregular waves with directional spreading was analysed in detail by Battjes (1974) and the present model conforms with his results. The present model describes the irregular wave situation as a series of regular wave trains each characterised by its height H_i , period T_i , direction α_i and frequency of occurrence, ϕ_i . Each of the regular wave trains is then tracked across the coastal profile, which makes it possible to use the empirical non-linear wave height transformation inside the breaker line of this wave train and to take the integrated wave set-up caused by the combined wave trains into account. The directional spreading of the waves can be modelled by prescribing the distribution of wave directions for a series of wave trains, or by reducing the driving shear radiation stress of the wave trains according to the directional distribution of the wave energy. The results used here are based on the latter method using the cosine spreading function (Mitsuyasu et al. (1975):

$$H(\theta) = \frac{2^{2s-1}}{\pi} \frac{\Gamma^2(s+1)}{\Gamma(2s+1)} \cos^{2s}((\theta - \theta_0)/2), \quad (3)$$

where θ is the direction relative to the main direction θ_0 .

The reduction of the shear force component of the radiation stress for this distribution is shown in Fig. 2. The effect of irregular waves is illustrated in Fig. 3, showing a longshore velocity profile generated by regular waves, by unidirectional waves with a Rayleigh distribution of the incoming waves, and by waves with a directional spreading characterised by Eq. (3) with $s = 20$ and $s = 3$, and regular height of the incoming waves.

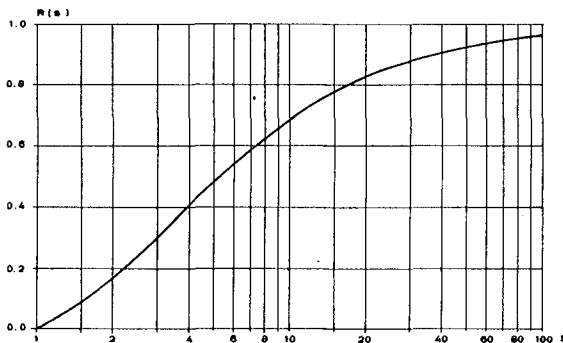


Fig. 2. The Reduction of the Longshore Shear Component of the Radiation Stress due to Directional Spreading.

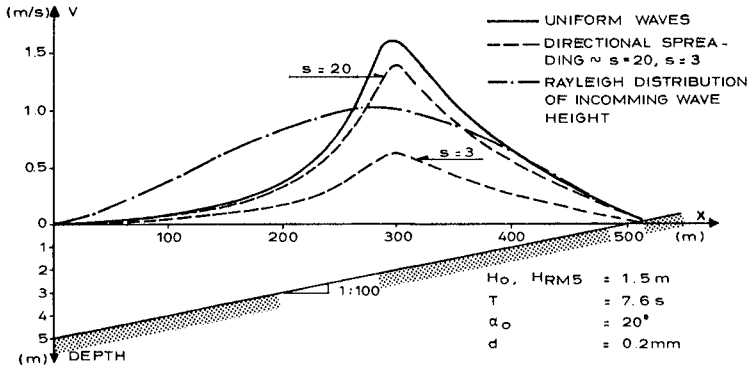


Fig. 3. Longshore Velocity Profiles.

The sediment transport rate is strongly influenced by the irregularity of the waves. The two most important effects are: A) The near bed orbital motion is irregular, which has to be taken into account when calculating the suspended sediment concentrations. B) In the surf zone only a fraction of the waves at a given point will be breaking/broken as there will be a fraction of the smaller waves which are breaking further inshore. The two effects are treated independently.

The irregular wave orbital motion has been analysed by using a time series of waves derived from a Pierson-Moskowitz spectrum. The nearbed wave orbital motion is calculated by a transfer function according to linear wave theory. The time series of the wave orbital velocity has been used in the model of Fredsøe et al. (1985) to calculate variation in time of the suspended sediment concentration and the sediment transport rate. The response of the mean current velocity profile to the irregular wave condition has not been analysed in detail, and two extreme situations have therefore been considered: 'full response' and 'no response'. By 'full response' it has been assumed that the mean current velocity profile outside the wave boundary layer adjusts immediately to the instantaneous wave conditions. In the case of 'no response' it has been assumed that the outer velocity and eddy viscosity profiles are determined from the mean bed shear stress integrated over the entire simulation period, and the outer velocity profile is thus kept constant.

Fig. 4 shows an example of a time series of water surface elevation and the suspended sediment transport rate.

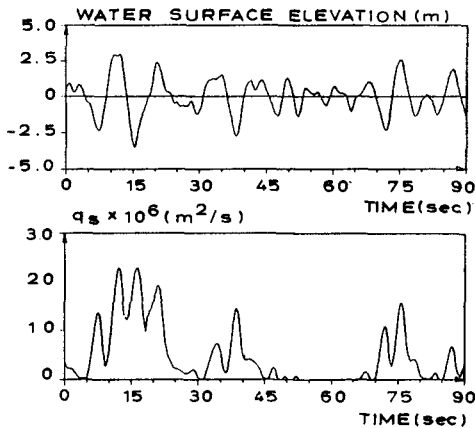


Fig. 4. Time Series of Surface Elevation, and Suspended Sediment Transport Rate, q_s , calculated for the following Parameters:
 $H_{rms} = 3.5$ m, $T_s = 10$ s, $D = 10$ m, $V = 0.1$ m/s,
 $d = 0.22$ mm. 'Full Response'.

The purpose of these sediment transport calculations has been to determine the wave parameters which are best able to describe the time-averaged sediment transport under irregular waves.

In order to determine these wave parameters a series of numerical tests have been carried out. For all the tests, V was taken as $0.1U_{b,rms}$ of the corresponding series, where $U_{b,rms}$ is the root-mean-square of the orbital velocity amplitudes.

The value of q_s determined for each test was compared to that determined for a regular wave of height H and period T . From the analysis of the 16 combinations of H and T used for the sinusoidal motion it turns out that the best representation of the mean suspended sediment transport due to irregular waves over the whole range of values of $U_{b,rms}$ studied is given by the regular waves having $H = H_{rms}$ and $T = T_s$, as shown by Fig. 5.

Fig. 5 also illustrates the influence of changing the eddy viscosity profile outside the wave boundary layer from 'full response' to 'no response'. In general, the difference is of order 10% or less.

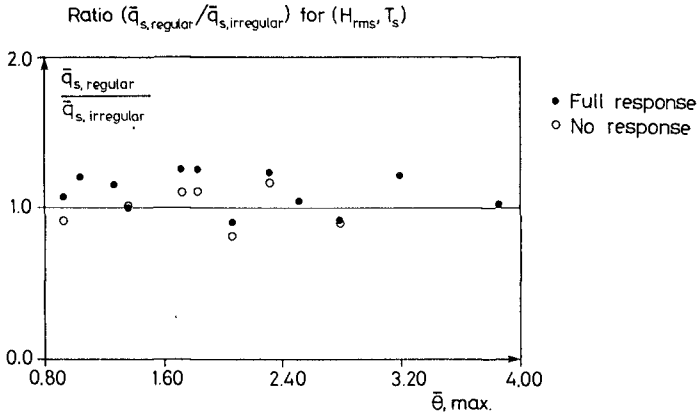


Fig. 5. Comparison between the Mean Suspended Sediment Transport due to Regular and Irregular Waves, and Illustration of the Influence of Current Response.

In the surf zone only a fraction of the waves is breaking due to the irregularity. The effect of breaking and broken waves is modelled according to Deigaard et al. (1986a) by describing the production, vertical spreading and decay of turbulence generated by the passage of the front of a spilling breaker or a broken wave. The input parameters, wave height H_b and period T_b , to this model are modified to reflect the conditions in the surf zone with irregular waves. First the wave period is increased to actual period of wave breaking, i.e. the non-broken waves are neglected, cf. Fig. 6.

$$T_b = \frac{\sum T_i \phi_i}{\sum \phi_{bi}} \quad (4)$$

where subscript 'bi' indicates that only breaking/broken waves are considered.

The representative wave height is determined from the energy dissipation, using a bore to characterise the dissipation in the passing wave fronts. The dissipation is thus proportional to the cube of wave height, giving:

$$H_b^3 = \frac{\sum H_{bi}^3 \phi_{bi}}{\sum \phi_{bi}} \quad (5)$$

This wave height and period is thus used in each location to characterise the production of turbulence by passing breaking or broken waves.

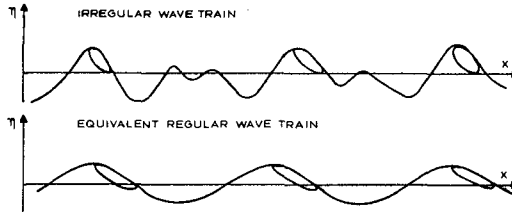


Fig. 6. Illustration of an Irregular Wave Train and the Equivalent Regular One.

Fig. 7 shows examples of the distribution of the transport in the coastal profile, calculated from regular and irregular waves. The main effect of including irregular waves is a much more smooth distribution of the transport and a reduction of the total transport by a factor of 0.3 in this particular case. The directional spreading of the waves $s = 20$ and $s = 3$ causes a reduction of the sediment transport in regular unidirectional waves by a factor 0.7 and 0.1, respectively.

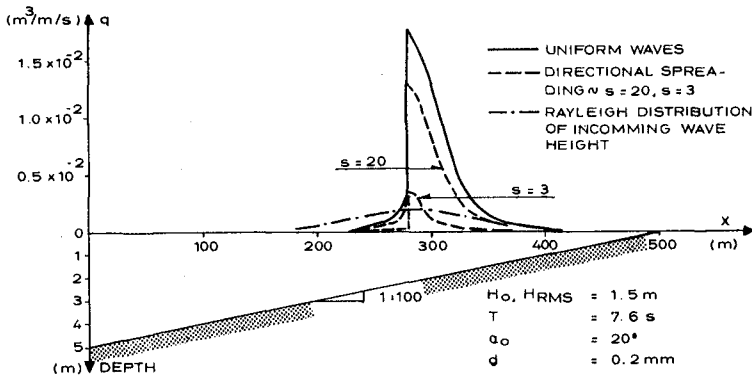


Fig. 7. Distributions of the Longshore Sediment Transport across a Plane Coast.

A comparison has been made between the calculated longshore sediment transport and the backfilling of a 1.600 m long trench (volume: 200.000 m^3) dredged through a three-bar coastal profile at the Danish North Sea Coast, cf. Mangor et al. (1984). The backfilling during a storm in the spring of 1982 is considered with measured wave heights up to $H_s = 4.75 \text{ m}$. At this period the trench, width 90 m,

depth 10 m, was only dredged at the outer bar. The total backfilling of the trench in this period was measured to be 90.000 m^3 (solid) grain volume. Fig. 8 shows the distribution of the backfilling and the calculated distribution of the longshore transport on the outer bar during the storm. The wave heights have been assumed to follow the Rayleigh distribution. The calculations have been made for two directional spreadings, s , of which the smallest one is the most likely on that specific location.

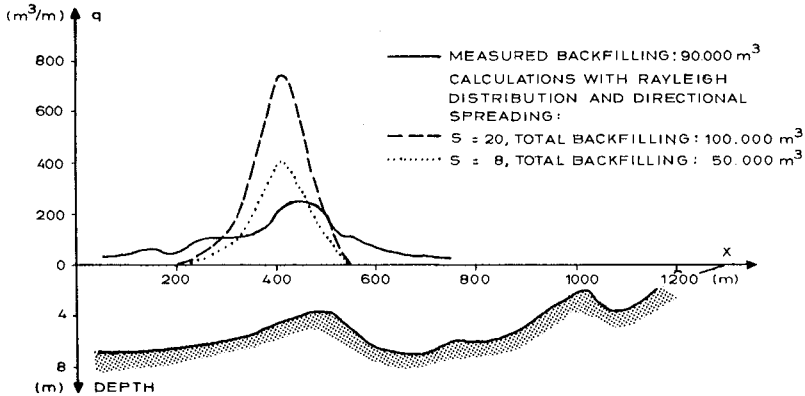


Fig. 8. Comparison between Measured Backfilling, cf. Mangor et al. (1984), and Calculated Backfilling.

WIND-DRIVEN AND COASTAL CURRENTS

In addition to radiation stress gradients, wind and coastal current can contribute to the forces driving the longshore current. The effect of wind shear stress and a coast parallel current has been included in the model. The wind shear stress is expressed through a friction factor (given the value: $f_w = 0.005$) and the wind speed, U_{10} at 10 m elevation:

$$\tau_w = \frac{\rho_a}{2} f_w U_{10}^2 \quad (6)$$

ρ_a is the density of air. τ_w is resolved into a shore normal and a shore parallel component according to the angle α_w between the wind direction and the shore normal direction. The shore normal component is included in the calculation of set-up and the shore parallel component is added to the driving forces of the littoral current.

The coastal current is assumed to be driven by a shore parallel gradient of the water surface, I , and the contribution to the driving force for the littoral current is ρgDI , where D is the local water depth.

The resulting equation for the littoral current thus becomes:

$$\tau_b - \frac{d}{dx} (\rho ED \frac{dV}{dx}) = - \frac{dS_{xy}}{dx} + \tau_w \sin \alpha_w + \rho gDI \quad (7)$$

The effect of wind and current has been analysed for the basic conditions: $H = 1.5$ m, $T = 7.6$ s, $d = 0.2$ mm, and a coastal slope of 1:100. Three wave directions are considered: $\alpha = 10^\circ$, 20° , and 45° . Three wind speeds have been considered $U_{10} = 5$ m/s, 10 m/s and 20 m/s, the wind is assumed to be parallel to the direction of wave propagation at deep water. Three coastal current velocities, measured at 5 m water depth, are analysed: $V = -0.25$ m/s, 0.25 m/s, and 0.50 m/s.

The results are summarised in Fig. 9, showing the transport, normalised by the situation without wind or coastal current plotted against the total driving force normalised by the driving force due to waves alone. The driving force due to wind or water surface slope has been integrated over the area between the breaker line and the coastline, while the driving force due to the waves is the shear radiation stress, S_{xy} at the breaker line. The driving forces due to waves, wind and water slope can easily be calculated, and generalised plots similar to Fig. 9 can then be used to estimate the relative importance of the different contributions. The difference between the effect of wind and current, revealed in Fig. 9, is due to the difference in distribution across the coastal profile; wind shear stress is constant while current-induced bed shear stress decreases with decreasing depth. For the same integrated force the coastal current will thus give a larger contribution near the breaker line where the sediment concentration and transport are highest.

RIP CURRENT

Along natural coasts bars, interrupted by rip channels, often show up as a result of a complex current and sediment transport pattern.

Rip currents can be generated as follows: The incoming waves break on the foreslope of the bar. When the waves pass the crest of the bar and enter the deeper waters of the trough, they cease breaking and are reformed as non-breaking waves, and shoaled and refracted once again until breaking occurs again on the inner beach.

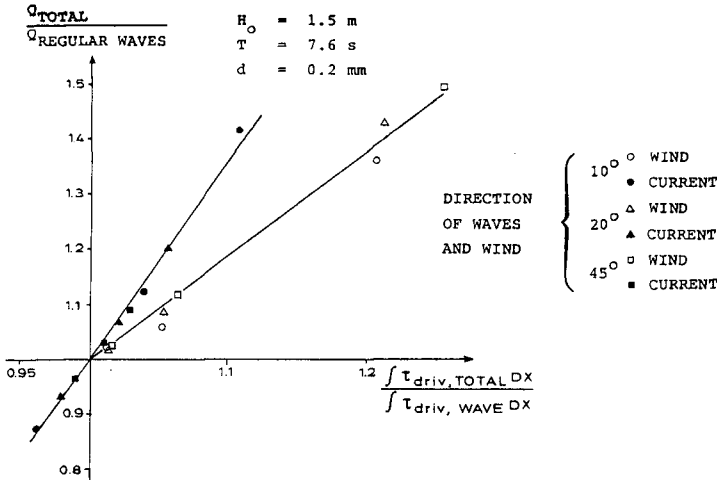


Fig. 9. The Sediment Transport including the Effect of Wind or Current normalised by the Transport due to Waves only versus the Total Driving Forces Normalised by Driving Forces due to Waves only.

The process of wave-breaking dissipates energy, producing a gradient in the components of the radiation stress tensor S . At the holes, the greater depths will cause that the waves are not breaking, but will instead continue propagation towards the shoreline. As a result of this, the wave set-up produced by the cross-shore component of the radiation stress S_{xx} will be small at the holes, and greater behind the bar.

This results in a net pressure gradient accelerating the water at the trough towards the holes. Afterwards this mass of water flows through the holes in the seaward direction in the form of rip-currents. The amount of water carried by the rips is compensated by the water transported over the crest of the bar. Under these conditions, a flow will exist at the trough behind the bar even for waves having an angle of incidence normal to the shoreline.

A mathematical model of flow in this situation has been developed. The model solves a simplified version of the equations describing the conservation of mass and momentum for time- and depth-averaged steady flow, see Zyserman and Fredsøe (1988).

Fig. 10 shows the flow field obtained using this model when the bar length was $L = 180 \text{ m}$, the width of the holes was $Y_b = 50 \text{ m}$, and the coastal profile was as shown on Fig.

10. The parameters of the incoming (uniform, unidirectional) waves were as follows: $H_0 = 1.2$ m, $T = 7.5$ s, $\alpha_0 = 45^\circ$. For comparison the corresponding longshore current velocity profile for a uniform coast is shown.

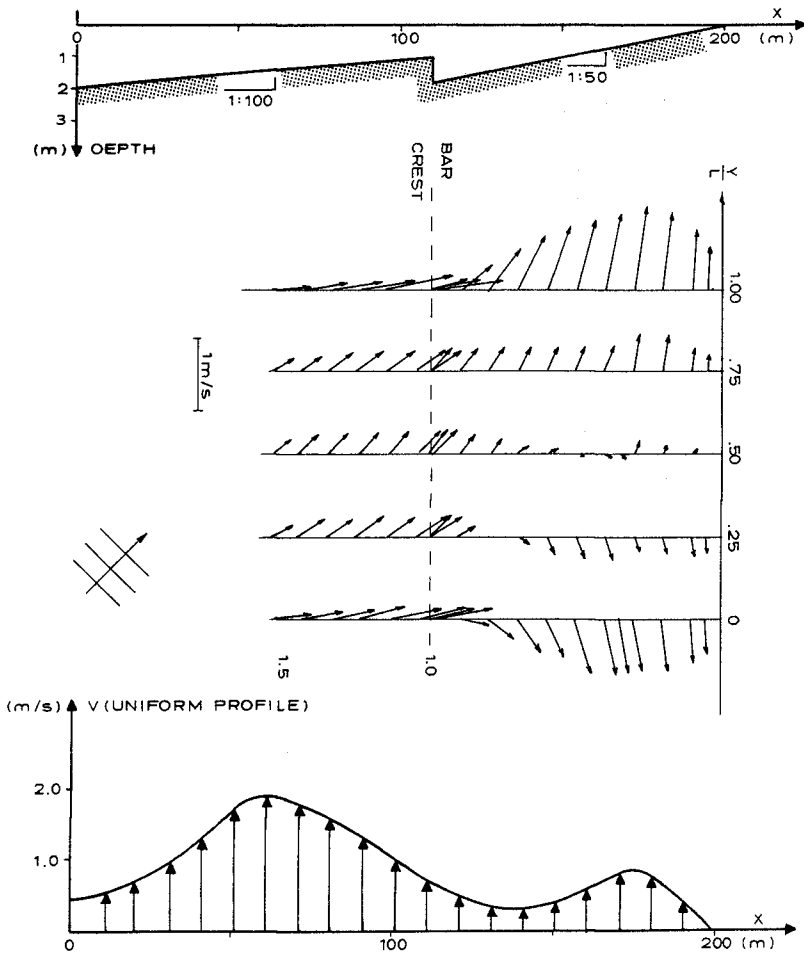


Fig. 10. Wave-Generated Currents on a Barred Coast with and without Rip Channels.

The following conclusions can be extracted from the results obtained for the wave-induced flow: a) The maximum velocity of the current on the bar is greatly reduced. The main cause for this is the cross-shore flow over the bar. The water carried in from offshore must continuously be accelerated up to the longshore velocity, which drains a considerable amount of longshore momentum. b) The flow reverses at some locations in the trough due to the pressure gradient which is opposite to the forcing term provided by the gradient of the shear component of the radiation stress tensor, S_{xy} . c) The velocity of the flow in the trough behind the bar crest becomes important, especially close to the holes.

Calculated current fields have been combined with the sediment transport model to describe the cross-shore variation of the longshore transport q_s as well as the total longshore transport Q_s for several transversal sections along the bar.

Due to the variability of the longshore current profile along the bar, the total transport varies from one section to another. In order to compare the sediment transport with that corresponding to the uniform situation, the average value of Q_s along the bar was calculated.

Fig. 11 shows the relation between the average longshore sediment transport when rip-currents are present \bar{Q}_s and the transport for the uniform situation Q_0 as a function of the ratio between Y_b and L , where Y_b has been kept constant equal to 50 m. In these examples the characteristics of the shore and of the waves were chosen as for the situation, shown in Fig. 10.

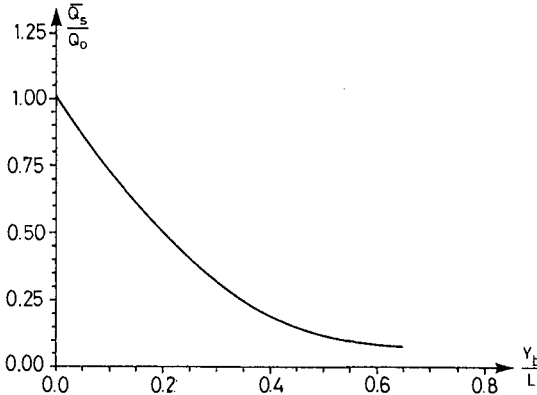


Fig. 11. Influence of Rip Currents on the Longshore Transport of Sediment. Coastal Profile and Wave conditions as Fig. 10.

It can be seen that the longshore sediment transport decreases for decreasing distance between rips, i.e. for shorter bars. This fact is easily explained by the reduction in the magnitude of the longshore current velocity when L decreases, due to an increased influence of the rip-currents.

CONCLUSION

A detailed description of littoral drift has been applied on a natural environment. It can be concluded that such a detailed model is rather sensitive to even small changes in the hydrodynamic description.

The following can be concluded from the test examples carried out with the extended littoral drift model including irregular waves, Fig. 7, coastal current and wind, Fig. 9, and the calculation of sediment transport along a barred coast with rip channels, Fig. 11:

- . Both the irregularity of the waves and the presence of rip channels strongly reduce the total littoral drift compared to monochromatic waves and uniform conditions.
- . The modifications of the littoral drift due to coastal current and wind action are less important.

The analysis rises a more general conclusion concerning the subject - modelling of littoral drift: Bearing in mind that all parameters in the models represent a physical phenomenon it must be concluded that the calculated littoral drift varies considerably by changing these parameters inside realistic ranges. The above means that modelling the littoral drift demands more information about the conditions (waves, coastal profiles etc.) than up till now has been established as basis for an investigation of littoral drift.

REFERENCES

- Battjes, J.A. (1974) Computation of Set-up, Longshore Currents, Run up and Overtopping due to Wind-Generated Waves. Delft Technische Hogeschool.
- Deigaard, R., Fredsøe, J. and Hedegaard, I.B. (1986a) Suspended sediment in the surf zone. *Journal of the Waterway, Port, Coastal and Ocean Engineering*, ASCE, Vol. 112, No. 1, pp. 115-128.
- Deigaard, R., Fredsøe, J. and Hedegaard, I.B. (1986b) Mathematical model for littoral drift. *Journal of the Waterway, Port, Coastal and Ocean Engineering*, ASCE, Vol. 112, No. 3, pp. 351-369.
- Engelund, F. and Fredsøe, J. (1976) A sediment transport model for straight alluvial channels, *Nordic Hydrology*, 7, pp. 293-306.
- Fredsøe, J. (1984) The turbulent boundary layer in combined wave-current motion. *Journal of Hydraulic Engineering*, ASCE, Vol. 110, No. HY8, pp. 1103-1120.
- Fredsøe, J., Andersen, O.H. and Silberg, S. (1985) Distribution of suspended sediment in large waves. *Journal of the Waterway, Port, Coastal and Ocean Engineering*, ASCE, Vol. 111, No. 6, pp. 1041-1059.
- Mangor, K., Sørensen, T. and Navntoft, E. (1984) Shore approach at the Danish North Sea Coast, monitoring of sedimentation in a dredged trench. *Proc. Coastal Engineering Conference*, pp. 1818-1829.
- Mitsuyasu, H., Tasau, F., Suhara, T., Mizuno, S., Ohkusu, M., Honda, T. and Rikiishi, K. (1975) Observations of the directional spectrum of ocean waves using a clover leaf buoy. *Journ. Phys. Oceanography*, Vol. 5, pp. 750-760.
- Zyserman, J. and Fredsøe, J. (1988) The effect of rip-currents on the longshore sediment transport. *Second International Symposium on Wave Research and Coastal Engineering*, Hannover, F.R. of Germany.

CHAPTER 120

CARIBBEAN BEACH-FACE SLOPES AND BEACH EQUILIBRIUM PROFILES

John D. Boon* and Malcolm O. Green**

ABSTRACT

Field measurements performed on two Caribbean islands revealed that two-dimensional nearshore bottom morphology is well represented by Dean's (1977) model of the beach equilibrium profile, $h = A x^m$, where h is depth below mean water level at a distance x offshore and A is a scale factor. For the curvature, m , we obtained an average value of approximately $m = 1/2$ through least squares curve fitting of observed profile data, yielding a more concave and therefore steeper profile inshore than $m = 2/3$, the average previously reported by Dean for quartz sand beaches in the United States. Furthermore, an objective measure of beach steepness was found to be $A^{1/m}$, a quantity which utilizes both of Dean's parameters and which may serve as a surrogate for the beach-face slope, $\tan \beta$, on highly concave beaches. Reasonable correlations were found between $A^{1/m}$ and the environmental parameter, H_b^2/gDT^2 , where H_b is breaker height, D is sediment grain size, T is wave period and g is gravitational acceleration. Improved prediction of Caribbean beach slopes and beach equilibrium profiles is an important practical result.

INTRODUCTION

Beaches on the islands bordering the Caribbean Sea differ in at least two respects from beaches in temperate zones: (1) they consist mainly of skeletal calcium carbonate sands of marine origin rather than quartz and feldspar-rich detrital sands, (2) much of the time they experience fairweather waves of relatively low energy and steepness produced either locally by trade winds or received as swell from distant storms (Wilson, 1969; Wilson et al., 1973; Terwindt et al., 1984). Mean tidal range is also minimal (less than 20 cm) within the eastern Caribbean basin (Kjervfve, 1981) around which most of the Caribbean islands are located.

As a result of coastal processes dependent on these factors, Caribbean island beaches typically have a steep, concave-upward profile and lack an offshore bar and bar-related surf zone. Morphodynamically, they exemplify the reflective beach state (Wright and Short, 1984; Wright et al., 1985) wherein incident waves are strongly reflected and thus are conducive to nearshore standing wave motions at subharmonic frequencies. Exceptions do exist. Dissipative surf zones with offshore

* Virginia Institute of Marine Science, Gloucester Point, VA 23062 USA

** Department of Earth Sciences, University of Cambridge,
Cambridge CB3 0EZ United Kingdom

bars and plunging breakers are occasionally seen and certain beaches contain an abundance of black sands rich in ferromagnesian minerals rather than pure calcium carbonate. Pocket beaches lying between rocky headlands are more common than long, straight beaches, however, and the former may have steeper slopes due in part to the absence of strong longshore currents (Bailard, 1981).

Our research interests throughout this study have focused on the question of predictability among various elements of Caribbean beach morphology and the extent to which this knowledge may prove useful in beach construction or restoration projects. Among these elements, none has appeared more promising than the quantitative description of the two-dimensional form of beach profiles in approximate equilibrium with existing environmental parameters including wave height and period, and sediment grain size.

DESCRIPTION OF THE STUDY ENVIRONMENT

Ten carbonate beaches were selected for study on the island of Sint Maarten/St. Martin (Netherlands Antilles/ French West Indies) located in the extreme northeast corner of the Caribbean Sea at the top of the Lesser Antillean arc system (Figure 1). Additional beaches were surveyed on the island of Curacao (Netherlands Antilles) located at the

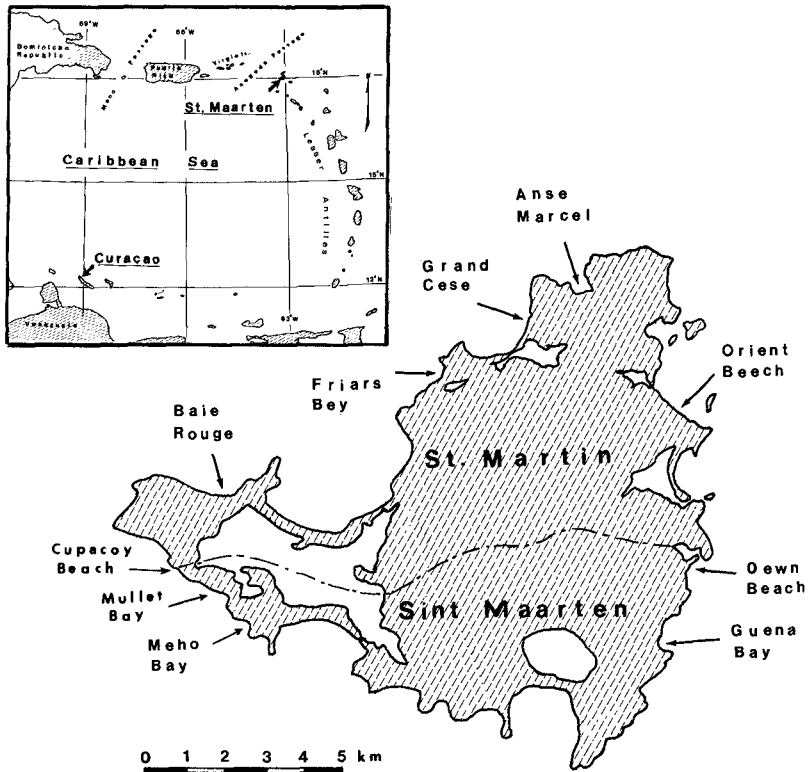


Figure 1. Location of Study Area and Beaches Surveyed.

southern margin of the Caribbean Sea near Venezuela. Due to the extremely narrow shelf (150 to 200 meters wide) surrounding almost the entire coast of Curacao, only one of its beaches possessed a fully covered, natural sand bottom (Playa Abao) suitable for the purposes of this study. Sint Maarten/St. Martin lies at the western boundary of an elongate, raised shoal platform known as the Anguilla Bank, a feature approximately outlined by the 100-meter depth contour, beyond which depths in excess of 500 m are quickly reached.

Beaches along the southwest side of Sint Maarten are fully exposed to deep water waves (100-meter depth contour less than 2 kilometers from shore). Wave energy reaching this coast consists mostly of ocean swell from the Caribbean Sea, or the Atlantic via the Anegada Passage, mixed with only intermittent local wind waves due to ample protection from dominant northeast and easterly trade winds (Netherlands Antilles Meteorological Service, 1981).

The eastern side of the island is bordered by an extensive shallow platform wherein the 30-meter depth contour lies approximately 5 kilometers from shore. The coastline here is generally rocky or fronted by reefs. Numerous pocket beaches are found along the east coast behind reef platforms. Beaches on the north side of St. Martin are characterized by relatively low energy conditions since this side fronts the narrow and sheltered Anguilla Channel between Sint Maarten and the neighboring island of Anguilla. Deep water waves in this region have a mean height of approximately 1.5 - 2.0 meters; about half of all waves have a period of 6 seconds or less and about one-third have a period of between 6 and 9 seconds (U.S. Naval Weather Service Command, 1974).

Curacao differs from Sint Maarten/St. Martin in having little or no shelf. A submerged terrace about 60 meters deep occurs a short distance offshore, in some places only 125 meters from the shoreline. Consequently, very few natural beaches are able to retain sand cover and most consist of coral rubble at the foreshore and step. The only exceptions are found among a few small pocket beaches located at the heads of narrow limestone cliff re-entrants prevalent at the northwest corner of the island, the largest example of which is Playa Abao. Curacao lies within the trade wind belt at a latitude where the dominant winds are from the east. Deep water wave height averages about 1 meter with more than half of all waves having periods of 6 seconds or less (U.S. Naval Weather Service Command, 1974). Swell waves with periods of 9 seconds or more are rare.

DATA COLLECTION METHODS

Beach profiles from the backshore to the wave step were measured with an automatic level and metric surveyor's rod. The nearshore profile from the approximate still water line (depth zero) to an offshore distance of approximately 120 meters was surveyed by divers who carried the profile out to depths of 4 to 6 m where the sand cover on the offshore bottom typically begins to thin. At one beach (Playa Abao) the entire profile was surveyed using rod and level measurements. At all other beaches, depths were measured by divers using an electronic depth gauge. The depth sensing device consisted of a Sonometrics model SP91 pressure sensor (accurate to approximately ± 4 cm) mounted in a clear plastic tube containing batteries, amplifier circuitry and a digital voltmeter displaying the depth in centimeters. Wave filtering was done by visually averaging the readout over several wave periods.

Distances to marks on the bottom were measured using a 50-meter fiberglass tape and depths were recorded at each mark. Taped (slant) distances were later corrected to horizontal distances in a surveying program written for a portable computer. Divers also collected bottom samples in small plastic vials and recorded the sample numbers and depth-distances on an underwater slate together with descriptions and measures of bedforms. Sediment samples were later introduced into a rapid sand analyzer to determine size characteristics based on the formulation of Gibbs et al. (1971). The graphic mean size and Inclusive Graphic Standard Deviation of Folk and Ward (1957) were used to represent sediment size in this study.

Bulk density determinations were made using selected carbonate sand samples which revealed an average density of approximately 2.65 g/cm^3 , the density of quartz. Although pure crystals of calcite and aragonite have a greater density than quartz, most of the carbonate sands examined consisted of porous coral fragments and broken plates of calcareous algae (Halimeda sp.), sediments similar to those described by Folk and Robles (1964).

Following each beach survey, a sample of breaking wave heights (H_b) and breaker periods (T) were recorded using the metric survey rod and a stop watch. Mean breaker period and root-mean-square breaker height were then calculated for each site. Water temperature was also recorded and found to be nearly constant at 28.5°C .

BEACH EQUILIBRIUM MODEL

Among the processes that drive the cross-shore exchange of sediment between the beach and the nearshore region are: asymmetric waves, rips, combined wave and steady current flow, downwelling and upwelling, gravity flows and "groupy" waves (Wright, 1987). The temporal and spatial expression of the nearshore seabed morphology is influenced simultaneously and at different times by at least all of these processes. Dean (1977) argued that the details of the individual processes could be neglected and the offshore profile of equilibrium modelled in terms of very simple propositions regarding "destructive" or sediment-mobilizing forces that mold the bed profile. Dean showed that the time-integrated, two-dimensional equilibrium profile over an unspecified distance seaward could be modelled by the power equation

$$h = A x^m \quad (1)$$

in which h is the depth below still water level expressed as a function of x , the distance seaward from the shoreline. "A" is a scale parameter numerically equal to the depth at a unit distance from shore whereas "m" is a parameter representing the degree of profile concavity ($m < 1$), convexity ($m > 1$) or a plane profile ($m = 1$). The theoretical values obtained for the parameters in equation (1) vary according to the way in which the destructive forces are expressed: assuming uniform energy dissipation per unit volume in the surf zone gives $m = 2/3$, whereas $m = 2/5$ results from assuming either uniform alongshore shear stress or uniform energy dissipation per unit surface area in the surf zone.

Bowen (1980), using an energetics model of suspended sediment transport based on symmetric wave orbital motion and a "perturbation" or drift velocity in the nearshore zone, also obtained an expression for the equilibrium beach profile similar to equation (1) with an $m = 2/3$ exponent. However, by including a higher harmonic term to simulate

asymmetrical wave orbital motion, Bowen obtained a new approximation of $h \approx g(5.7w_s/\sigma^2)^{2/5}$ where w is the grain settling velocity of the beach sediment and $\sigma = 2\pi/T$ is the wave radian frequency. This equation, which is valid for both the surf and nearshore zones, yields an $m = 2/5$ exponent and implies that the parameter A should be a function of the wave period in addition to sediment grain size or settling velocity.

Based on least squares fitting of equation (1) to some 502 profiles measured from the shoreline to approximately 365 meters offshore (3 to 5-meter depths) along the U.S. East and Gulf coasts, Dean (1977) adopted a mean value of $m = 2/3$ to be used as a functional constant although m for individual profiles ranged from about 0.2 to 1.2 in value. Justification for selecting $m = 2/3$ was based in part on the apparent Gaussian distribution and observed central tendency of the 502 m -values reported by Dean and partly for the convenience of examining variations in A with m held fixed. The latter variation was attributed to a functional relationship between A and the grain diameter, D (Moore, 1982; Dean, 1983) or to the equivalent settling velocity, w , of the bed sediment. Dean (1987) recently noted a close fitting of available A and w data from detrital (quartz) sand beaches by an empirical equation given as $A = 0.067 w^{0.44}$, where A has units of meters^{1/3}, (since m was fixed at $2/3$) and w is in cm/s.

The use of particle settling velocity rather than particle size would appear to be more in keeping with governing fluid dynamic processes but this assumes that w has been determined with the necessary adjustment for the in-situ water temperature, a correction that may show considerable variation from one beach (or season) to the next. Particle settling in the Stokes (viscous) range increases by more than 50 percent as water temperature increases from 5 °C to 20 °C, extremes not at all uncommon in the temperate zone. Water temperatures are, of course, higher and less variable in tropical regions (nominally 25 °C to 30 °C); Hydraulic-equivalent grain sizes should be larger there when compared with grains of the same physical size in colder, temperate regions. Meaningful grain settling velocity data should therefore be based upon stated field (not laboratory) water temperature, a practice not commonly evident at present in the literature.

Dean's theoretical arguments leading to the general expression for the equilibrium profile (equation (1) with $m = 2/3$) are strictly applicable to dissipative surf zones although the profiles used by Dean to verify the model and support the choice for m extend well beyond the surf zone into the nearshore region. Since Dean's field examples mainly represent beaches with dissipative surf zones, other surf-zone types may contain exceptions to the $m = 2/3$ "rule", and, if so, it is of interest to know under what conditions they may occur. The singular dependence of the A parameter on either particle size or sediment settling velocity may also require further examination; one intuitively expects the A parameter to be a function of wave characteristics as well as beach sediment properties.

The Equilibrium Profile on some Caribbean Beaches

The fitting of equation (1) to the observed profile data obtained at our study sites was, in general, quite successful. In a typical example from Mullet Bay, shown in Figure 2, the fitted profile is designated as FP3458 in which the parameters determined by least squares methods are $A = 0.34$ and $m = 0.58$. In Figure 3 (Baie Rouge), the fitted profile is FP6550 ($A = 0.65$, $m = 0.50$).

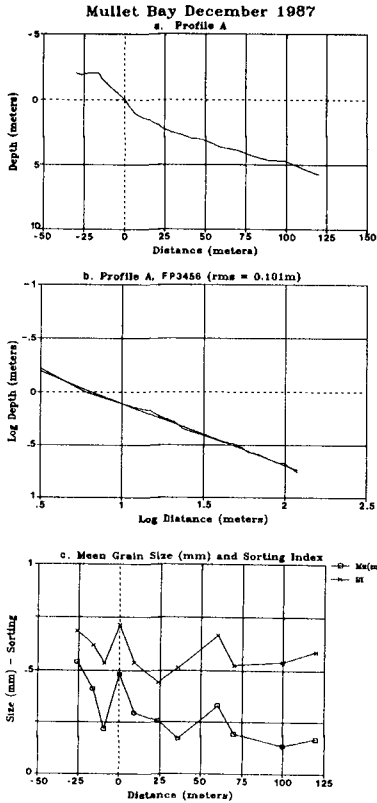


Fig. 2 Beach Profile Data, Mullet Bay

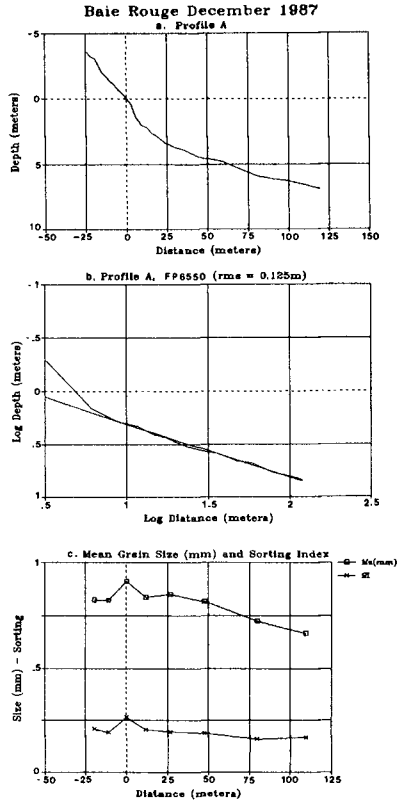


Fig. 3 Beach Profile Data, Baie Rouge

Only one measured beach profile, that of Guana Bay (Figure 4) on Sint Maarten, failed to achieve a reasonable fit. The reason for the deviant shape is presently unclear but the Guana Bay beach differed from all others in being fully dissipative and habitually displaying a wide surf zone with large, plunging breakers approximately 50 meters offshore; the profile, however, steepens markedly beyond this point and thereafter resembles the shape that other profiles have closer to shore. Guana Bay lies between headlands on the windward side of the island and is the only windward beach not protected by an offshore reef.

Table 1 contains the fitted values of the parameters A and m together with root mean square deviations of the observed profile points from the least squares line of best fit. It is noted that the mean value of m for the eleven fitted profiles (two profiles, A and B, were measured at Maho Beach) is approximately 0.55 with a standard deviation of ± 0.10 . The present sample of Caribbean beach profiles is perhaps too small to warrant a definitive statement on the exact distribution of m-values for this population. However, if the assumption of normality is made, one can infer (using the Student's t statistic at the 0.995 level of confidence, one-tailed test) that the population mean is less than 0.67, the m-mean reported by Dean (1977).

Table 1. Summary of Parametric Values for Surveyed Beaches on Curacao, Sint Maarten, Netherlands Antilles and St. Martin, French West Indies.

BEACH	m	A	$\tan \beta$	$A^{1/m}$	fit rms	D1	D2	H_b	T
Playa Abao	0.544	0.356	0.08	0.150	0.069	0.25	0.13	20.0	5.0
Maho(A)	0.502	0.431	0.12	0.187	0.071	..no data	..no data		
Maho(B)	0.470	0.487	0.13	0.216	0.080	0.40	0.31	32.5	9.0
Mullet Bay	0.580	0.338	0.11	0.154	0.101	0.41	0.21	44.2	9.8
Cupecoy Beach	0.637	0.301	0.14	0.152	0.130	0.53	0.35	51.8	10.1
Baie Rouge	0.498	0.650	0.13	0.421	0.125	0.85	0.78	39.2	12.2
Friars Bay	0.512	0.416	0.19	0.180	0.098	0.25	0.13	12.0	10.0
Grand Case	0.432	0.506	0.15	0.207	0.229	0.50	0.27	10.0	9.5
Anse Marcel	0.479	0.395	0.16	0.144	0.139	0.25	0.15	13.0	10.0
Orient Bay	0.773	0.135	0.09	0.075	0.212	0.22	0.47	32.4	7.3
Dawn Beach	0.610	0.246	0.16	0.100	0.297	0.29	0.35	49.2	7.3
AVERAGE	0.549								
STD.DEV.	0.097								

m, A: Least squares parameters for fitted model profile, $h = A x^m$.
 $\tan \beta$: Beach-face slope
 fit rms: Root-mean-square deviation from model profile in meters.
 D1: Beach-face mean sand size in mm.
 D2: Nearshore mean sand size in mm.
 H_b : Breaker height (rms) in cm.
 T: Breaker period in sec.

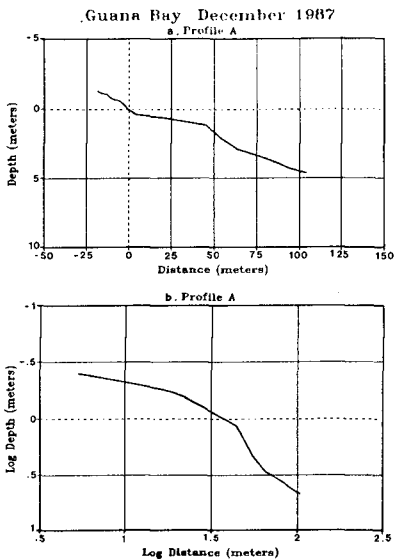


Fig. 4 Beach Profile Data, Guana Bay

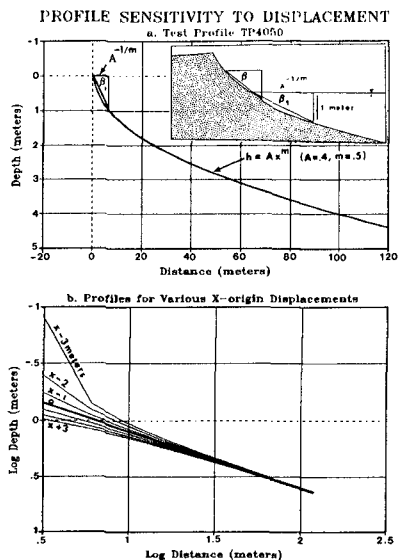


Fig. 5 Simulated Profiles with x-origin Displacements from shoreline zero

Profile Sensitivity to Measurement Error

Field profiles modelled by equation (1) require the precise location of the h, x reference or "zero" point. The vertical reference is taken to be the mean water level averaged over the diurnal tidal period and the horizontal reference is found as the intersection of mean water level at the shoreline. Due to the extremely small variation in tidal range (including "weather" tides) at the study locations, we considered that the major error in defining the profile reference would be the error associated with the elimination of gravity wave motion. Consequently, we found the point of sea level intersection on the beach foreshore by visual estimation, choosing a point just above the lower limit of the swash zone. Since depths below mean water level were obtained with a pressure gauge, we assumed these measures to be independent of horizontal distance. To test the sensitivity of the measured profiles to possible errors in reference location, a typical beach profile was simulated using representative model parameters ($A = 0.4$ and $m = 0.5$) to produce a test profile (Figure 5a). Following its construction, the test profile was re-measured (numerically) after each one of a series of fixed x -origin displacements landward and seaward of the reference point. The erroneous profiles, shown in Figure 5b, suggest that measures of real profiles will be most affected by x -origin measurement error occurring in the first 10 meters of the profile but that little change will be noted seaward of that point. Fitting of model profiles in the range $x = 10$ to 100 meters on log-log linear plots will be only slightly affected by a horizontal error of nearly 3 meters in x -origin location.

Beach Slope based on the Equilibrium Profile

The parameter A is a potentially useful representation of beach slope or steepness in the nearshore zone since, from equation (1), it is simply the depth at a unit distance from the shoreline. The parameter A in equation (1), however, has units of length^{1-m} . It is therefore impossible to compare A values in the same units when m is allowed to vary, as we believe it must in some situations. Basically, this problem arises due to a lack of unique spatial scale. One could, for example, make the variable x in equation (1) dimensionless by dividing it by the distance out to wave base (depth at which waves initiate bottom sediment motion) but this distance clearly varies as a function of the local wave regime. To achieve standardization, we propose to make horizontal distances nondimensional using x_1 , the distance seaward to a depth (h_1) of one meter, roughly the order of the usual depth at the surf zone limit. At this depth, equation (1) yields a "scaling" distance of $x_1 = A^{-1/m}$ and a new, dimensionless representation of beach slope is obtained as

$$\tan \beta_1 = h_1/x_1 = A^{1/m} \quad (2)$$

in which both of the fitted curve parameters, A and m , are utilized. The slope angle, β_1 , is given a subscript to distinguish it from β , the angle of the beach-face slope with which it overlaps (Fig. 5a). The former angle approaches 90° as m approaches 0 (vertical wall) and approaches 45° when $m \gg 1$ (highly convex profile). Therefore, assuming that a two-dimensional beach profile can be represented adequately by equation (1), we conclude that equation (2) is an objective means of expressing the beach slope and is probably intermediate between what is termed beach-face slope (tangent extending from about mid-foreshore to about the low tide mark) and various linear approximations of $\tan \beta$ taken across the nearshore region (e.g., Bowen, 1980, Fig. 1.1). For the steep, reflective-type profiles under discussion here, we consider

that equation (2) may provide a close approximation to the beach-face slope, $\tan \beta$, as discussed in the next section.

RESULTS AND DISCUSSION

Nearshore beach slopes, calculated as $A^{1/m}$, are presented in Table 1 along with the corresponding values of beach-face slope, $\tan \beta$, obtained from leveling data on the beach-face of the eleven beach profiles of the present study. In several instances the two measures of slope are quite similar but, overall, it is clear that $A^{1/m}$ is more variable, showing greater range of slope values than $\tan \beta$.

Values of the dimensionless parameter $H_b/g^{0.5}D^{0.5}T$ were determined for comparison with beach slope, where H_b is breaker height, D is beach sediment grain size, T is breaker period and g is the acceleration due to gravity. Sunamura (1984) has shown that beach-face slope ($\tan \beta$) may be quantitatively predicted using

$$\tan \beta = [0.013/(H_b^2/gDT^2)] + 0.15 \quad (3)$$

which was determined from existing laboratory data, or

$$\tan \beta = 0.12/(H_b/g^{0.5}D^{0.5}T)^{0.5} \quad (4)$$

which was based on field data. Table 2 contains data from the present field experiment in which two sets of $H_b/g^{0.5}D^{0.5}T$ values were determined, one using the mean sand grain diameter from the beach-face and one using the mean grain diameter from the nearshore zone. Samples taken near the wave step were excluded as they usually contained very coarse material of limited extent (e.g., Figure 2c). Plots showing the four combinations of data ($\tan \beta$ versus $A^{1/m}$, beach-face versus nearshore sand size) are shown in Figure 6 with the curve for equation (4).

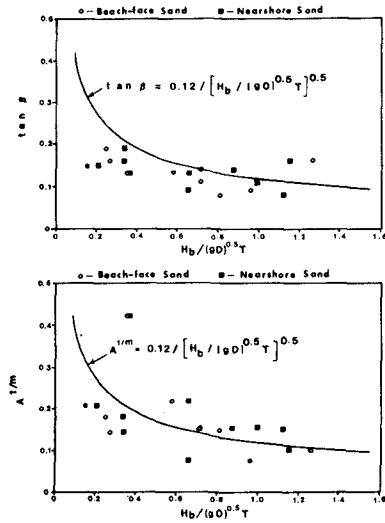


Fig. 6 Beach slope measured as $\tan \beta$ and $A^{1/m}$ plotted against the dimensionless parameter $H_b/(gD)^{0.5}T$

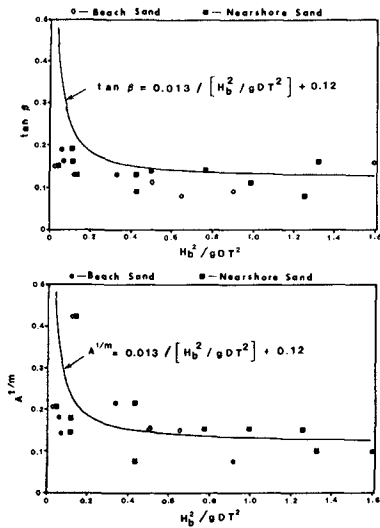


Fig. 7 Beach slope measured as $\tan \beta$ and $A^{1/m}$ plotted against the dimensionless parameter H_b^2/gDT^2

Table 2. Comparison of Beach Slope with functions of $H_b/g^{0.5}D^{0.5}T$

f1(D1)	f1(D2)	f2(D1)	f2(D2)	tan β	$A^{1/m}$	Beach
0.150	0.204	0.023	0.042	0.15	0.207	Grand Case
0.242	0.336	0.059	0.113	0.19	0.180	Friars Bay
0.262	0.339	0.069	0.115	0.16	0.144	Anse Marcel
0.352	0.367	0.124	0.135	0.13	0.421	Baie Rouge
0.577	0.655	0.332	0.429	0.13	0.216	Maho(B)
0.711	0.994	0.506	0.988	0.11	0.154	Mullet Bay
0.711	0.875	0.506	0.766	0.14	0.152	Cupecoy Beach
0.808	1.120	0.652	1.254	0.08	0.150	Playa Abao
0.955	0.654	0.913	0.428	0.09	0.075	Orient Beach
1.264	1.150	1.597	1.322	0.16	0.100	Dawn Beach

D1: Beach-face mean sand size in cm.

D2: Nearshore mean sand size in cm.

$$f1(D1) = H_b/g^{0.5}D1^{0.5}T \quad f2(D1) = (H_b/g^{0.5}D1^{0.5}T)^2$$

$$f1(D2) = H_b/g^{0.5}D2^{0.5}T \quad f2(D2) = (H_b/g^{0.5}D2^{0.5}T)^2$$

In Figure 6, tan β shows little, if any, systematic variation with $H_b/g^{0.5}D^{0.5}T$. The beach slope calculated as $A^{1/m}$ does show the expected variation with the independent variable, allowing for scatter in the data similar to that seen in Sunamura's graphs (Sunamura, 1984, Figures 1 and 2). Although Sunamura attributed some of the scatter to inaccuracies in the measure of tan β , he pointed to 1) spatial and temporal change in D and 2) temporal changes in H_b and T as the leading sources of error. As expected, less error was associated with laboratory as opposed to field data plots.

The quantity $H_b/g^{0.5}D^{0.5}T$ is in part an index for wave steepness since the numerator contains wave height and the denominator furnishes a length based on joint wave-sediment properties. A similar quantity can be derived as a ratio of wave and sediment-related forces expressed as unit mass accelerations. Taking the numerator as H_b/T^2 and the denominator as gD/S where $S = \delta H_b$ is the suspension distance of sand particles above the bottom and $\delta \approx 1$ (Dean, 1973), this ratio is simply the steepness index squared or H_b^2/gDT^2 . Values of the latter appear in Table 2 and in Figure 7 using averages of beach-face and nearshore sand samples, respectively, for the mean grain size, D. This figure shows tan β and $A^{1/m}$ plotted against H_b^2/gDT^2 with Sunamura's (1984) laboratory data curve, equation (3), superimposed in slightly modified form (constant reduction in slope of 0.03) to obtain the apparent best fit to our data. Again, the best dependent or predicted variable appears to be $A^{1/m}$ rather than tan β and the corresponding curve of best fit is

$$A^{1/m} = [0.013/(H_b^2/gDT^2)] + 0.12 \quad (5)$$

There is no overly compelling reason to select plots based on beach-face rather than nearshore sediment samples (Figures 6 - 7) as better predictors of beach slope. At first glance it is noted that nearshore sediments are generally finer (e.g., Mullet Bay, Figure 2C) and so produce slightly larger values of H_b^2/gDT^2 . This is not always the case, however. Certain beaches on the windward side of Sint Maarten (Orient Bay and Dawn Beach) contained coarse sands that appear to be

rather than beach-face sand sizes would appear to rank them too low on the scale of H_b^2/gDT^2 . Since beach-face sediment is affected more by the ambient wave regime and less by local variations among nearshore (and offshore) sediment sources, it is considered best to use for determinations of D in equation (5).

CONCLUSIONS

Practical applications for the above results are immediately obvious. Beach construction or restoration projects in low-energy, carbonate environments of the type described require an estimate of fill type (grain size) and amount necessary to achieve a desired two-dimensional profile over existing bottom. An equilibrium beach profile can be readily determined through use of equation (1) and the necessary estimates for the parameters A and m . Given a suitable estimate for the parameter m , the parameter A is readily calculated from the beach slope, $\tan \beta_1 = A^{1/m}$, predicted by equation (5). Pending further investigation, an appropriate average estimate for carbonate beaches on Caribbean islands appears to be $m = 0.55$.

It has been shown that $A^{1/m}$ provides a useful and objective estimate of beach slope on Caribbean island carbonate beaches (equation 5). The sudden inflection in the left side of the curve in Figure 7 implies that a small change in wave height or steepness in this region will be accompanied by a large change in beach slope. Beaches composed of very coarse sand will be particularly susceptible to such change. This is consistent with reports we have obtained from hotel owners on the western side of Sint Maarten that sudden and often severe subaerial erosion typically occurs in winter when Atlantic storm waves reach this side of the island.

In a definitional sense, $A^{1/m}$ is not equivalent to the mostly subaerial beach-face slope ($\tan \beta$) but is an indicator of the subaqueous nearshore slope ($\tan \beta_1$) as shown in Figure 5a. Nevertheless, on the steep, highly concave and barless beaches studied here, there appears to be ample justification to use $A^{1/m}$ in place of $\tan \beta$ in predictor equations for beach-face slope of the type presented here. Since the parameters A and m are determined by least squares fitting of the observed nearshore profile over most of its length (excluding perhaps the first 6 meters from shore), the measure of $A^{1/m}$ is not only objective but its precision can be judged by goodness-of-fit criteria.

Also, we seem to have observed near agreement between our field results and Sunamura's empirical curve for laboratory results, equation (3). Equation (3) has the same form as equation (5) but differs from it by a constant denoting a small offset in the dependent variable, $\tan \beta_1 = A^{1/m}$; With this minor adjustment, Sunamura's curve appears to fit our data reasonably well when using the squared term, H_b^2/gDT^2 , as the independent variable. Given the potential use for equation 5 in field applications, it is worth noting that equation 3 is based on a very large collection of laboratory data which fit this curve quite well. Additional data from the field are needed to verify the relationship.

ACKNOWLEDGEMENTS

The authors gratefully acknowledge the assistance given by Grabowsky & Poort International N.V. of Curacao and Sint Maarten in aid of this project. We thank Lauro J. Calliari for his contribution to the field data collection effort and laboratory analyses. Contribution No. 1447

of the Virginia Institute of Marine Science and School of Marine Science, College of William and Mary, Gloucester Point, VA 23062.

REFERENCES CITED

- Bailard, J.A., 1981. An energetics total load sediment transport model for a plane sloping beach. *J. Geophys. Res.*, 86:10938-10954.
- Bowen, A.J., 1980. Simple models of nearshore sedimentation; beach profiles and longshore bars. In: S.B. McCann (Ed.), *The coastline of Canada*, Geol. Survey of Canada, paper 80-10, pp. 1-11.
- Dean, R.G., 1973. Heuristic models of sand transport in the surf zone. In: *Engineering Dynamics of the Coastal Zone*, First Austr. Conf. on Coastal Engineering, Sydney, Australia, pp. 208-214.
- Dean, R.G., 1977. Equilibrium beach profiles: U.S. Atlantic and Gulf Coasts. *Ocean Engineering Tech. Rpt. No. 12*, Dept. Civil Engineering and College of Marine Studies, Univ. of Delaware.
- Dean, R.G., 1983. Principles of beach nourishment. In: P.D. Komar (Ed.), *CRC Handbook of Coastal Processes and Erosion*, CRC Series in Marine Science, chapter 11, pp. 217-231.
- Dean, R.G., 1987. Coastal sediment processes: Toward Engineering Proceedings, Vol. I, ASCE Coastal Sediments '87, May 2-14, 1987, New Orleans, La.
- Folk, R.L. and W.C. Ward, 1957. Brazos River bar: A study in the significance of grain size parameters. *J. Sed. Pet.*, 27:3-26.
- Folk, R.L. and R. Robles, 1964. Carbonate sands of Isla Perez, Alacran Reef Complex, Yucatan. *J. of Geol.*, 72: 255-292.
- Gibbs, R.J., Matthews, M.D. and Link, D.A., 1971. The relationship between sphere size and settling velocity. *J. Sed. Pet.*, 41:7-18.
- Kjerfve, B., 1981. Tides of the Caribbean Sea. *J. of Geophys. Res.*, 86:4243-4247.
- Moore, B.D., 1982. Beach profile evolution in response to changes in water level and wave height. M.S. Thesis, Univ. of Delaware, Dept. of Civil Engineering, 92p.
- Netherlands Antilles Meteorological Service, 1981. Hurricanes and tropical storms of the Netherlands Antilles. Curacao, N.A.
- Sunamura, T., 1984. Quantitative predictions of beach-face slopes. *Geol. Soc. Am. Bull.*, 95:242-245.
- Terwindt, J.H.J, C.H. Hulsbergen and L.H.M. Kohsiek, 1984. Structures in deposits from beach recovery, after erosion by swell waves around the southwestern coast of Aruba (Netherlands Antilles). *Mar. Geol.*, 60:283-311.
- U.S. Naval Weather Service Command, 1974. Summary of Synoptic Meteorological Observations, Caribbean and Nearby Island Coastal Marine Areas, Vol. 5, N.T.I.S., Springfield, VA.

- Wilson, W.S., 1969. Field measurement of swell off the island of Aruba. Tech. Rpt. 56, Chesapeake Bay Institute, The Johns Hopkins University, 64 p.
- Wilson, W.S., D.G. Wilson and J.A. Michael, 1973. Analysis of swell near the island of Aruba. *J. Geophys. Res.*, 78:7834-7844.
- Wright, L.D., A.D. Short and M.O. Green, 1985. Short-term changes in the morphodynamic states of beaches and surf zones: An empirical predictive model. *Mar. Geol.*, 62:339-364.
- Wright, L.D., 1987. Shelf-surfzone coupling: Diabathic shoreface transport. Keynote Address, Proceedings, Vol. I, ASCE Coastal Sediments '87, May 12-14, 1987, New Orleans, La.
- Wright, L.D. and Short, A.D., 1984. Morphodynamic variability of surf zones and beaches. *Mar. Geol.*, 56:93-118.

CHAPTER 121

BEACH PROFILE CHARACTERISTICS DUE TO THE INCLINED WAVES

Tai-Wen Hsu * and Shan-Hwei Ou **

ABSTRACT

The result of a theoretical approach shows that the beach profile characteristics is governed by a modified Iribarren number which includes the effects among the factors of initial beach slope, wave angle and wave steepness. A series of experiments are conducted in a three-dimensional movable bed model on the conditions of two different initial beach slopes, two incident wave angles as well as several erosive wave steepnesses. The relative importance of each factor involved in the parameter is discussed. It is shown that the modified Iribarren number is effective in the analysis of beach profile characteristics under the action of inclined waves. The empirical relationships between beach profile changes and the modified Iribarren number are proposed on the basis of experimental results.

1. INTRODUCTION

A knowledge about the characteristics of beach profiles under the action of waves is of great importance to a number of coastal engineering problems. Various factors such as the

* Graduate Student, Dept. of Hydraulics & Ocean Engineering, National Cheng Kung University, Tainan, Taiwan 70101, Republic of China.

** Professor, Ph.D., Dept. of Hydraulics & Ocean Engineering, National Cheng Kung University, Tainan, Taiwan 70101, Republic of China.

wave steepness, nearshore current, beach slope and bottom sediment are involved in the beach profile changes. Clarification of these individual factors and evaluation of their mutual interaction are quite important to the determination of the beach profile characteristics. Although much efforts have been devoted to obtain the empirical relationships between the beach profile changes and the different pertinent variables involved in the beach process, a definite solution has not yet been provided because of the complicated nature of the sediment transport in the surf zone.

Previous experimental studies were commonly performed in a two-dimensional wave flume, in which incident waves were normal to the shoreline. In the natural beach, however, the incoming wave often possesses a breaking angle to the shoreline. There are few data on the beach profile changes caused by the inclined breaking waves. Brater and Ponce-Campos (1976) performed a movable bed test in a wave basin with incoming waves oblique to the shoreline, but only the parameter of sand bluff recession was analyzed in his experiments.

The data of the beach profiles compiled in this paper are all belong to the erosive type. As shown in Fig.1, the

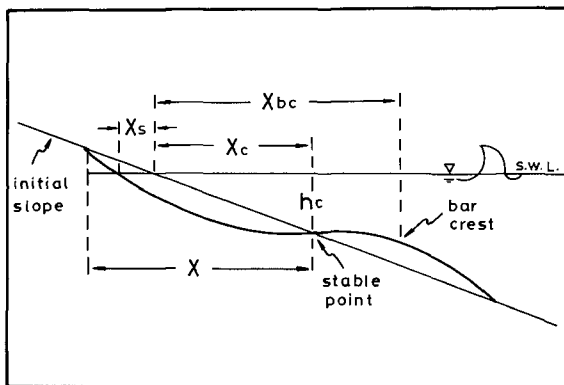


Fig.1 Definitions of beach profile characteristics

items of beach profile characteristics discussed in the present study include the erosion length X , the distance of the stable point X_c , the distance of bar crest X_{bc} and the water depth at the stable point h_c . A modified Iribarren number, $\xi_o^{1/6} \cos \alpha_b$, is proposed based on the concept of wave energy flux to correlate the beach profile changes with the inclined breaking waves, where $\xi_o = \tan \beta / (H_o/L_o)^{1/2}$ is the Iribarren number, $\tan \beta$ is the initial beach slope, H_o and L_o are the wave height and the wave length at deep water respectively, and α_b is the angle of breaking wave. The relative importance of each factor involved in this parameter is discussed. According to the experimental results, the empirical relationships between the beach profile changes and the modified Iribarren number were obtained by applying linear regression analysis.

2. THEORETICAL CONSIDERATION

A non-dimensional length L^* is selected to represent the characteristics of beach profile changes. The functional relationship of L^* associated with the non-dimensional sediment transport rate is expressed as

$$L^* = f_1(Q_s^*) \tag{1}$$

where Q_s^* is a dimensionless sediment transport rate.

Based on the concept of Bagnold (1963), littoral sand transports are responsible to the wave energy flux. A linear correlation is given by

$$Q_s = k_1 I \tag{2}$$

where Q_s is the volume transport rate, I is the wave energy flux evaluated at the surf zone, and k_1 is a dimensional proportionality coefficient.

As drawn in Fig.2, the wave energy flux F between two wave crests can be written as

$$F = E_b C_{gb} \Delta l \cos \alpha_b \tag{3}$$

where E_b is wave energy per unit width, C_{gb} is the group velocity of waves, subscript b represents relative quantities in the breaking point, Δl is the width between two wave crests. The wave energy flux to a unit shoreline length becomes

$$I = E_b C_{gb} \cos \alpha_b \tag{4}$$

Substitution of Eq.(4) into Eq.(2) gives

$$Q_s = k_1 E_b C_{gb} \cos \alpha_b \tag{5}$$

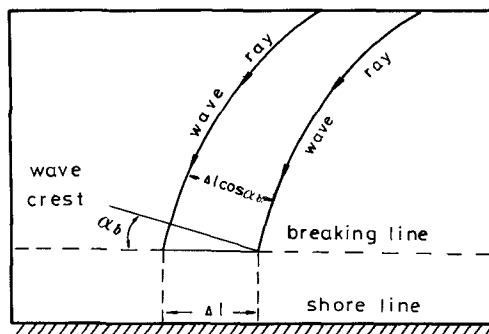


Fig.2 Sketch of the wave energy transmitted on shoreline

From the linear long wave theory, E_b and C_{gb} are evaluated by the following equations, respectively :

$$E_b = 1/8 \rho g H_b^2 \quad (6)$$

$$C_{gb} = \sqrt{gd_b} \quad (7)$$

in which ρ is the fluid density, g is the acceleration of gravity, H_b the breaking wave height, d_b the breaking water depth. The dimensionless sediment transport rate is formulated in the form of

$$Qs^* = \frac{Qs}{\rho g u_b d_b^2} = \frac{k_1^* E_b C_{gb} \cos \alpha_b}{\rho g u_b d_b^2} \quad (8)$$

where $k_1^* = \gamma' k_1$, is a dimensionless coefficient, γ' is the submerged weight of the sand, u_b is the amplitude of the velocity at the bed in surf zone. For linear wave theory, u_b can be written as

$$u_b = \frac{\pi H_b}{T \sinh \frac{2\pi d_b}{L_b}} \quad (9)$$

where T is the wave period, L_b is the wave length in the surf zone. In the shallow water area, $\sinh \frac{2\pi d_b}{L_b}$ can be expressed as

$$\sinh \frac{2\pi d_b}{L_b} = \frac{2\pi d_b}{L_b} \tag{10}$$

and

$$L_b = \sqrt{gd_b} T \tag{11}$$

Insertion of Eqs.(10) and (11) into Eq.(9) yields

$$u_b = \frac{H_b}{2} \left(\frac{\sqrt{g}}{d_b} \right) \tag{12}$$

Combination of Eqs.(6),(7),(8) and (12) leads to

$$Qs^* = k_2 (H_b/d_b) \cos \alpha_b \tag{13}$$

where k_2 is a constant. The ratio of wave height and water depth at breaking point was found to be related to the Iribarren number(Battjes,1974). Based on available experimental data, Sunamura (1980) proposed the relationship

$$\frac{H_b}{d_b} = 1.1 \xi_o^{1/6} \tag{14}$$

According to Eqs.(13) and (14), the transport rate can be rewritten as

$$Qs^* = k_3 \xi_o^{1/6} \cos \alpha_b \tag{15}$$

where k_3 is a constant. By comparing Eqs.(1) and (15), we have

$$L^* = f_2 (\xi_o^{1/6} \cos \alpha_b) \tag{16}$$

It is convenient to assume that the Eq.(16) has the functional form of

$$L^* = a_1 (\xi_o^{1/6} \cos \alpha_b)^{b_1} = a_1 \xi_o^{b_1/6} (\cos \alpha_b)^{b_1} \tag{17}$$

where a_1 , b_1 and b_2 are coefficients to be determined by experimental results. It is interesting to note that the physical parameters governing the beach profile changes include the wave steepness H_o/L_o at deep water, the initial beach slope $\tan \beta$ and the angle of breaking wave.

If the incoming waves are normal to the shoreline, Eq.(17) can be simplified as

$$L^* = a_1 \xi_o^{b_2} \tag{18}$$

It has been recognized that the dynamics of the breaking waves in the surf zone is relevant to the Iribarren number (Battjes, 1974; Wang and Yang, 1980). Eq.(18) makes it plausible that ξ_0 is also of great importance for beach profile characteristics under the action of normal incident waves. The phase-difference τ/T defined by Kemp(1960) is found to be an important parameter to the beach profile changes (Sunamura and Horikawa, 1974), where τ denotes the time for a wave to travel from its breaking point to the uprush limit. An empirical relationship derived by Hsu, Lee and Ou(1986) showed that the parameter τ/T is related to Iribarren number. The usefulness of Iribarren number for the analysis of beach profile changes due to normal incident waves was also confirmed in their studies.

3. EXPERIMENT AND PROCEDURE

The experiments were performed in a three dimensional wave basin of 16m long, 12m wide and 0.7m deep. The testing arrangements for both normal and inclined incident waves are shown in Fig.3 and Fig.4, respectively. The test section of movable bed model were placed with a uniform slope by using fine coal with median diameter of 0.15mm and specific gravity of 2.07.

Two different initial beach slopes (1/16 and 1/25), two wave angles(0° and 30°) as well as several erosive wave steepnesses were selected for the model tests. All experimental conditions are summarized in Table 1. The angles of breaking waves were calculated by the method proposed by Wang and Le Mehaute (1980).

Battjes(1974) clarified the types of breakers on the basis of the classification of Galvin(1968) as follows:

$\xi_0 > 3.3$: surging breaker

$3.3 > \xi_0 > 0.5$: plunging breaker

$\xi_0 < 0.5$: spilling breaker

The experimental data of $\tan\beta = 1/25$ falling in the domain of 0.161 ~ 0.328 belong to spilling breaker while values of $\tan\beta = 1/16$ ranging from 0.256 to 0.580 correspond to transition between spilling breaker and plunging breaker.

Waves of constant characteristics were generated by a flat type wave maker. Wave characteristics were measured by capacity type wave gauges and a recorder unit. Beach profiles were measured by an electric platform at a half hour time interval along the beach. Normally, it will take three hours for the profile to reach equilibrium condition for normal incident waves. In order to examine the relations between beach profile characteristics and inclined wave behavior inside the surf zone, it is assumed inclined waves will take the same time for reaching the equilibrium conditions.

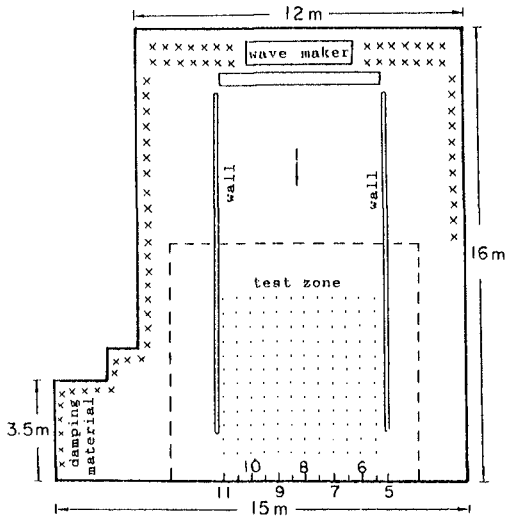


Fig.3 Arrangements of wave basin for normal incident waves

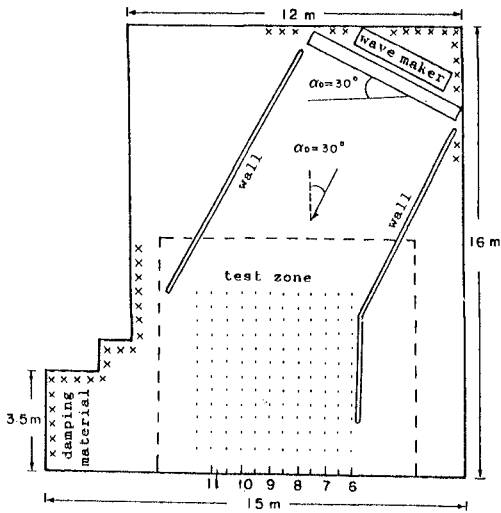


Fig.4 Arrangements of wave basin for inclined incident waves

Table 1 Wave conditions

$\tan\beta$	α_0 (deg)	T (sec)	H_0 (cm)	H_0/L_0	α_b (deg)
$\frac{1}{16}$	0°	1.0~1.2	2.84~9.63	0.0182~ 0.0493	0°
$\frac{1}{25}$	0°	1.0~1.2	2.32~8.28	0.0149~ 0.0619	0°
$\frac{1}{16}$	30°	1.0~1.2	2.61~10.17	0.0116~ 0.0597	6.8~12.6

Only three successive profiles in the middle part of the movable bed were taken for the analysis of beach profile characteristics because of the boundary effects on the test zone. Only the first type of erosive beach profile (Sunamura and Horikawa, 1974) was analyzed in the present study. Fig. 5 shows four typical examples of beach profile variation of four successive sections for the cases of different wave steepnesses.

4. RESULTS AND DISCUSSION

Erosion Length

The erosion length, X , is defined as the distance from stable point to the maximum upper erosion point as shown in Fig. 1. The understanding of erosion length in sandy beach is essential for shore protection practices. Experiments (Chang, 1982) indicate that the erosion length depends on the location of the breaking point and its value is larger than 0.8 times the distance between the breaking point and the origin point of still water level.

Fig. 6 illustrates the relationship between the dimensionless erosion length X/L_0 and the wave steepness H_0/L_0 . The data of $\tan\beta = 1/30$ plotted here were compiled from Cheng (1974). His experiment were conducted in a two dimensional wave flume. Four lines drawn in this figure were obtained by a linear regression analysis for different initial beach slopes and angles of incident waves. The value of X/L_0 increases remarkably as H_0/L_0 increases. The data of the inclined incident waves show the same tendency for the cases

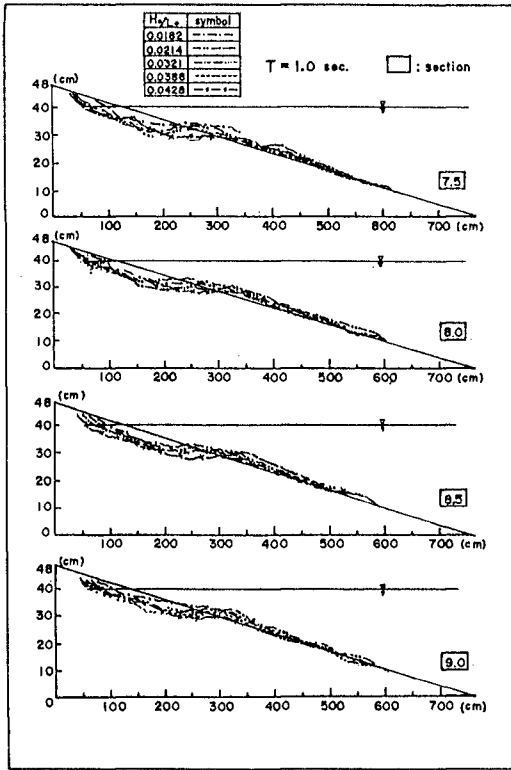


Fig.5 Typical variation of beach profiles for different wave steepnesses ($\tan\beta = 1/16$)

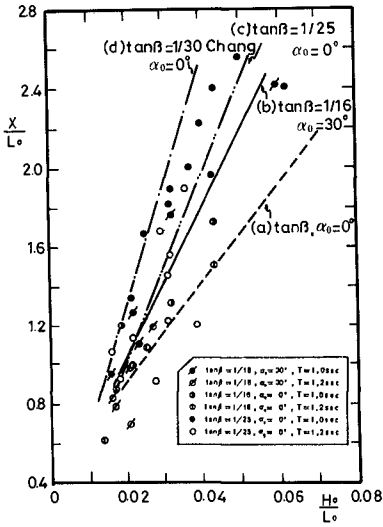


Fig. 6 Relationship between X/L_0 and H_0/L_0

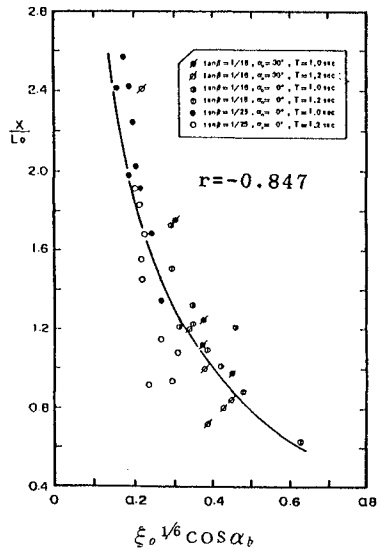


Fig. 7 Relationship between X/L_0 and $\xi_0^{1/6} \cos \alpha_b$

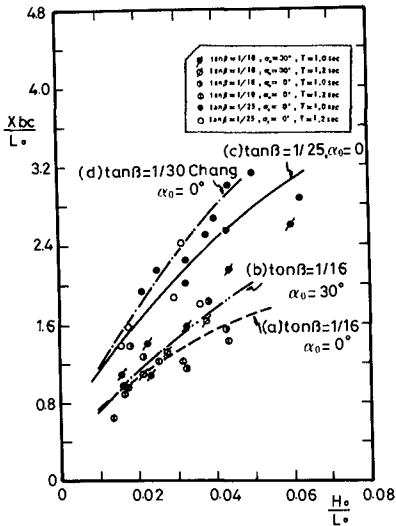


Fig. 8 Relationship between X_{bc}/L_0 and H_0/L_0

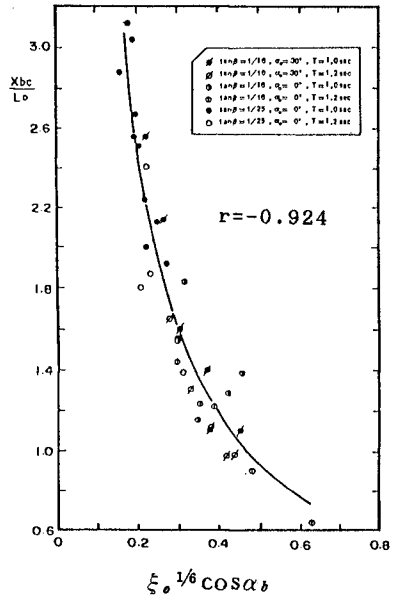


Fig. 9 Relationship between X_{bc}/L_0 and $\xi_0^{1/6} \cos \alpha_b$

of normal waves. In addition, it is seen that the erosion length increases with milder initial beach slope for normal incident waves. In this case, the effect of initial beach slope on erosion length for larger wave steepnesses is obviously found. For the same initial beach slope, the inclined waves produce greater erosion length than the normal waves. This may be due to the local variation of longshore sediment caused by the inclined waves.

The empirical relationship between the dimensionless erosion length X/L_o and the modified Iribarren number $\xi_o^{1/6} \cos \alpha_b$ as developed from theoretical consideration above is shown in Fig.7. By using linear regression method, the best fit line is given by

$$X/L_o = 0.443 \xi_o^{-0.92} \cos \alpha_b^{-5.54} \quad (r = -0.847) \quad (19)$$

where r is the correlation coefficient. The points with larger values of $\xi_o^{1/6} \cos \alpha_b$ give broadly scattering in Fig.7. This is interpreted as a smaller wave steepness H_o/L_o has larger value of $\xi_o^{1/6} \cos \alpha_b$ for constant beach slope and angle of incoming waves. Under this condition, the beach profile tends to become accretion type as pointed out by Johnson(1949).

The Distance of Bar Crest

The sediment eroded from foreshore is deposited offshore as a longshore bar. The distance of the bar crest X_{bc} is defined as the distance between the bar crest and the origin point of still water level as shown in Fig.1. Laboratory studies were conducted by Horikawa, Sunamura and Kito(1973) to investigate the situation of bar crest response to various wave characteristics. An empirical relationship was proposed on the basis of available experimental data:

$$X_{bc} / L_o = B(H_o/L_o) \quad (20)$$

where $B = -67.4 + 20.5 \log(t/T)$, is a dimensionless time factor, and t is the time for model test. Hughes and Chiu(1981) performed an experiment in a wave flume. A parameter $H_o/\omega T$ was proposed to analyze the location of bar crest due to severe storms, where ω is the fall velocity of a sediment particle. Experimental results by Chang(1974) indicated the location of bar crest is related to the wave breaking point. His experiments also showed a bar crest is formed outside the wave breaking point and its maximum distance is within 1.6 times the distances between the wave breaking point and the original point of still water level.

Fig.8 gives plots of X_{bc}/L_o versus H_o/L_o for the cases of different initial beach slopes and wave directions. Each curve in the figure is obtained by fitting exponential function for different initial beach slopes and angles of incident waves. The experimental data show that the ratio of

X_{bc}/Lo increases with an increase of H_o/Lo . By comparing curves (a) and (b), it is found that values of inclined waves seemed to be slightly greater than normal waves. Furthermore, it is shown that the initial beach slope has significant effect on the location of bar crest for normal incident waves.

Fig.9 depicts the relationship between X_{bc}/Lo and $\xi_o^{1/6} \cos \alpha_b$. The value X_{bc}/Lo decreases with the increase of $\xi_o^{1/6} \cos \alpha_b$. It is noted that the modified Iribarren number is shown to be highly effective in representing the data by linear regression method. The result is expressed as

$$X_{bc}/Lo = 0.458 \xi_o^{-1.03} \cos \alpha_b^{-6.20} \quad (21)$$

Depth and Location of Stable Point

Available experimental and field data of beach profiles indicate that there exists usually a stable point on beach profiles near the breaker zone. At the stable point, sediment of a given size will be in oscillating equilibrium and without net movement. Raman and Earattupuzha(1972) found out a relationship between location of stable point and wave characteristics on the basis of experimental results. Hallermeier(1978) used a sediment entrainment parameter to calculate the water depth of the stable point. Kubo and Tomaki(1981) analyzed the water depth of the stable point from field data.

Fig.10 gives plots of the water depth of the stable point h_c against wave height H_o in deep water. The straight lines in the figure is the linear regression results. The experimental data show that the water depth of the stable point is proportional to the wave height at deep water. From lines (a) and (b), the inclined waves appear to have larger values than normal waves for the same initial beach slopes. The water depth of the stable point increases as the initial beach slope becomes smaller from 1/16 to 1/25. The line obtained by Hallermeier(1978) plotted in the figure shows the similar trend to the case of normal waves for $\tan \beta = 1/25$.

Fig.11 is the relationship between dimensionless water depth of stable point h_c/Lo and the modified Iribarren number $\xi_o^{1/6} \cos \alpha_b$. Although the experimental data scatter broadly over a wide range of $\xi_o^{1/6} \cos \alpha_b$, it is found that a higher value $\xi_o^{1/6} \cos \alpha_b$ leads to a reduction in the value of h_c/Lo . The result of linear regression gives

$$h_c/Lo = 0.011 \xi_o^{-1.41} \cos \alpha_b^{-8.43} \quad (r=-0.702) \quad (22)$$

The correlation coefficient is not good for the reason of random data base.

Fig.12 is a plot of non-dimensional location of the stable point X_c/Lo and the wave steepness H_o/Lo . The effect of the initial beach profile on the location of stable point

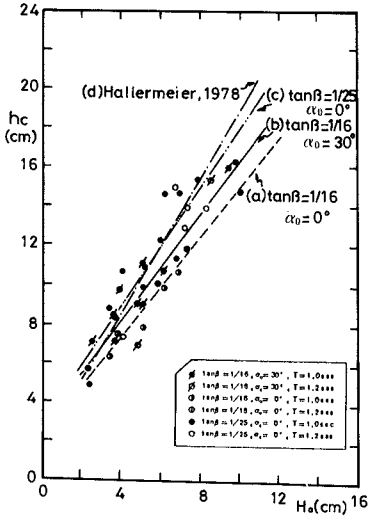


Fig. 10 Relationship between h_c and H_o

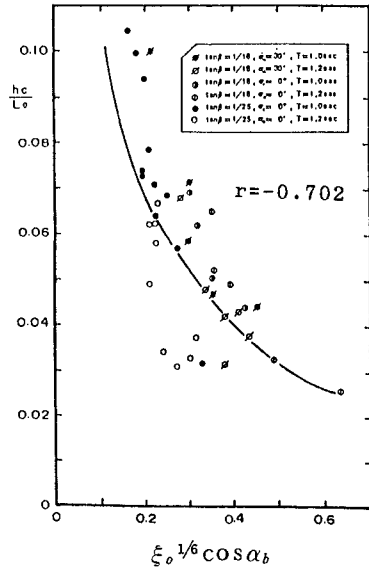


Fig. 11 Relationship between h_c/L_o and $\xi_o^{1/6} \cos \alpha_b$

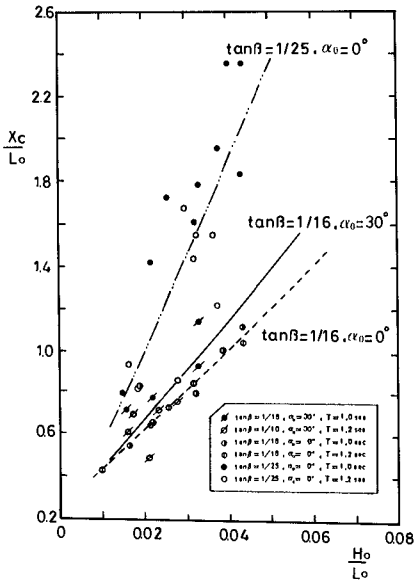


Fig. 12 Relationship between X_c/L_o and H_o/L_o

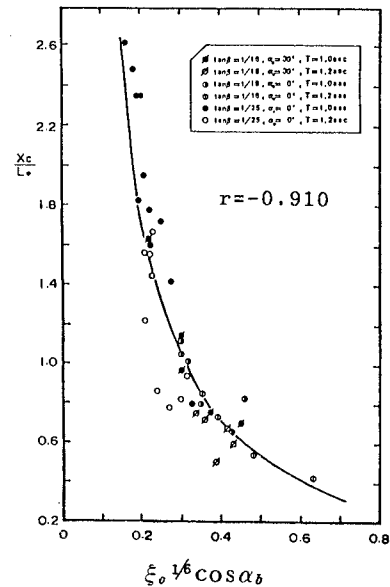


Fig. 13 Relationship between X_c/L_o and $\xi_o^{1/6} \cos \alpha_b$

for normal waves is obviously found. The inclined waves have larger value than normal waves for $\tan\beta = 1/16$. Fig.13 is a plot of non-dimensional location of the stable point X_c/L_0 versus the modified Iribarren number $\xi_0^{1/6} \cos\alpha_b$. The value of X_c/L_0 decreases as the value of $\xi_0^{1/6} \cos\alpha_b$ increases. The best fit line in this figure can be expressed as

$$X_c/L_0 = 0.211\xi_0^{-1.29} \cos\alpha_b^{-7.74} \quad (r=-0.910) \quad (23)$$

A higher correlation coefficient reveals that the location of the stable point can be adequately described in terms of the modified Iribarren number. According Eq.(23), X_c/L_0 tends to decrease as α_b increases. This is due to the fact that longshore current is generated by obliquely incident waves and its corresponding longshore sediment transport is dominated in the surf zone.

5. CONCLUSIONS

A theoretical development based on wave energy approach found that the beach profile is governed by a modified Iribarren number. This parameter covers the effects among the factors of the initial beach slope, wave angle and wave steepness. A laboratory movable bed tests were undertaken in the wave basin to find out the relationship between beach profile characteristics and the modified Iribarren number. The analysis of experimental data confirms the usefulness of this parameter in expressing the beach profile changes under the action of inclined waves.

REFERENCES

1. Bagnold, R.A. : Mechanics of marine sedimentation , in The Sea , edited by M.N. Hill, 3, Interscience Publ., 507- 528, 1963.
2. Battjes, J.A. : Surf similarity, Proc. 14th International Conf. on Coastal Eng., Copenhagen, 466-480, 1974.
3. Brater, E.F. and D. Ponce-Campos: Laboratory investigation of shore erosion , Proc. 15th Intern. Conf. on Coastal Eng., Hawaii, 1493-1511, 1976.
4. Chang, R.H. : An experimental study on equilibrium beach profile, M.S. thesis, National Cheng Kung Univ., Tainan, Taiwan, 1974.
5. Cheng, W.C.: Beach profile characteristics under wave action, M.S. thesis, National Cheng Kung Univ., Tainan, Taiwan, 1982.
6. Galvin, C.J.J.: Breaker type classification on three laboratory beaches, J. Geophys. Res., 89, 3651-3659, 1968.
7. Hallermeier, R.J. : Uses for a calculated limit depth to beach erosion, Proc. 16th Intern. Conf. on Coastal Eng., Hamburg, 1493-1512, 1978.

8. Horikawa, K., T. Sunamura and Kito H. : A study on beach transformation due to waves, Proc. 20th Conf. on Coastal Eng. in Japan, 357-363, 1973.
9. Hsu, T. W., Y. K. Lee and S.H. Ou : Beach profile characteristics under the action of normal incident waves, J. of Harbor Technology, 2, 139-154, 1986.
10. Hughes, S.A. and T.Y. Chiu : Beach and dune erosion during severe storms, Coastal and Oceanographic Engineering Dept., Univ. of Florida, 200p., 1981.
11. Johnson, J.W. : Scale effects in hydraulic models involving wave motion, Trans. of Amer. Geophys. Union, 30, 517-525, 1949.
12. Kemp, P.H. : The relationship between wave action and beach profile characteristics, Proc. 7th Intern. Conf. on Coastal Eng., The Hague, 262-277, 1960.
13. Kubo, M. and S. Temaki : On the stable point in sandy beach profile, Proc. 28th Conf. on Coastal Eng. in Japan., 247-250, 1981.
14. Raman H. and J.J. Earattupuzha : Equilibrium conditions in beach wave interaction, Proc. 13th Intern. Conf. on Coastal Eng., Vancouver, 1237-1257, 1972.
15. Sunamura, T. : A laboratory study of offshore transport of sediment and a model for eroding beaches, Proc. 17th Intern. Conf. on Coastal Eng., Sydney, 1051-1070, 1980.
16. Sunamura, T. and K. Horikawa : Two-dimensional beach transformation due to waves, Proc. 14th Intern. Conf. on Coastal Eng., Copenhagen, 920-938, 1974.
17. Wang, H. and W.-C. Yang : A similarity model in the surf zone, Proc. 17th Intern. Conf. on Coastal Eng., Sydney, 529-546, 1980.
18. Wang, J.D. and B. Le Mehaute : Breaking wave characteristics on a plane beach, Coastal Eng., 4(2), 137-149, 1980.

CHAPTER 122

Sediment Suspension due to Large Scale Eddies in the Surf Zone

by

Kazuo NADAOKA, Seizo UENO and Tatsuyuki IGARASHI

Dept. Civil Eng., Tokyo Institute of Technology
O-okayama 2-12-1, Meguro-ku, Tokyo 152, JAPAN

ABSTRACT

Laboratory experiments using a fiber-optic LDV system and a small pressure transducer have been made to reveal detailed characteristics of the velocity field in the surf zone and its relationship to the sediment suspension with special reference to the three-dimensional large scale eddies referred to as "obliquely descending eddies", the existence of which was recently revealed by Nadaoka (1986). A conditional sampling technique has been used to find that the obliquely descending eddies bring highly intermittent intensive turbulence to the bottom with the large onshoreward momentum at the upper layer of the water and thus essentially characterize the turbulent flow field in the surf zone. Visual observation and concentration measurements, especially a coherence analysis of two data sets of concentration close to the bottom, have shown that the sediment suspension is mostly governed by such large scale eddies in a wide extent of the surf zone; i.e., the eddies hit the bottom and then lift up the sediment into suspension, yielding the spot-like sediment cloud in accordance with the three-dimensional eddy structure.

1. Introduction

The effect of wave breaking is one of the most significant factors for the coastal sedimentary process. In this respect, Miller (1976), Shibayama and Horikawa (1985), and others have discussed sand suspension by the action of the large scale vortices generated immediately after the wave plunging (Fig. 1). The generation of such vortices, which

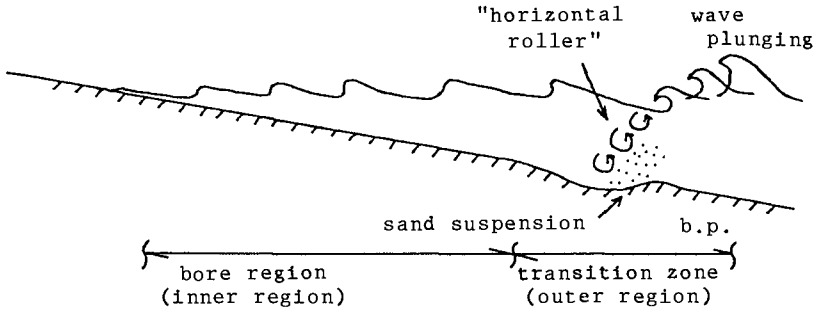


Fig. 1 "Horizontal rollers" and sediment suspension. (Miller 1976, Shibayama & Horikawa 1986, etc.)

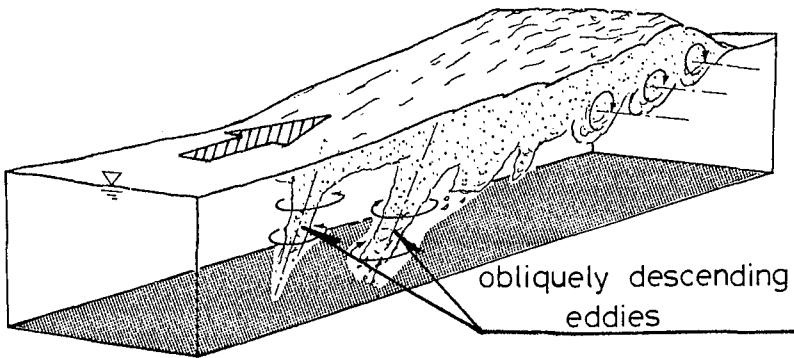


Fig.2 Schematic representation of the large scale eddy structure under breaking waves. (Nadaoka 1986)

are called "horizontal rollers", is a local phenomenon in the sense that it is limited in space within the transition zone or outer zone. In another word, they don't affect sediment suspension in the inner region or bore region.

For spilling breaker condition, on the other hand, Deigaard et al.(1986) have discussed the effect of the turbulence originated from breaking water surface on the vertical diffusion of the bottom sediment, by using the transport equation for turbulent kinetic energy. However, the real physical process of the sediment suspension under spilling breaker as well as turbulent bore has been not yet well understood, mainly because of our limited knowledge of the turbulent velocity field structure within the surf zone.

Recently, Nadaoka(1986) has found the inherent eddy structure of the breaking waves in a wide extent of the surf zone. That is, around the wave crest, dominant eddies have nearly two-dimensional flow structure the axis of which is parallel to the crest line, while behind the wave crest, the

flow structure changes quickly into that of obliquely downward stretched eddies with strong three-dimensionality which is referred to as "obliquely descending eddies" (Fig.2). Therefore, it is worth to pay our attention to these obliquely descending eddies, because they may act as possible agitator of the bottom sediment in the surf zone.

The main purpose of the present study is to clarify the detailed characteristics of the turbulent velocity field in the surf zone and its relationship to the sediment suspension with special reference to the "obliquely descending eddies" under the turbulent bore.

2. Experimental Equipments and Procedure

The wave channel used for the experiments was 0.6 m deep, 0.4 m wide and 20 m long, equipped with a flap-type wave generator. The experiments were made both for a fixed bed and a movable bed. In the former case, a wooden slope of 1 on 20 was installed at one end of the channel and in the latter ground coal of 0.21mm in median diameter and of 1.45 in its specific weight was placed with the depth of 15cm on the slope, as shown in Fig.3. The use of the ground coal for the bed material was to suppress the generation of the ripples under the wave action as much as possible, because in the natural surf zone condition the ripples is hardly developed.

The experiment was carried out under the condition of wave period $T=1.27s$, equivalent offshore wave height $H_0^*=15.5$ cm, offshore wave steepness $H_0^*/L_0=0.061$. Regular waves generated by the wave maker produced a spilling-type breaker, the depth and wave height of which, h_b and H_b , were 16.7 cm and 14.7 cm, respectively. It should be noted that, under the spilling breaker condition, there exists no horizontal roller.

Horizontal and vertical velocity components, u and w , were measured with a two-component fiber-optic laser-Doppler velocimeter of back-scattered fringe mode (FLV, Hino et al., 1984). The water surface fluctuation η was measured with a

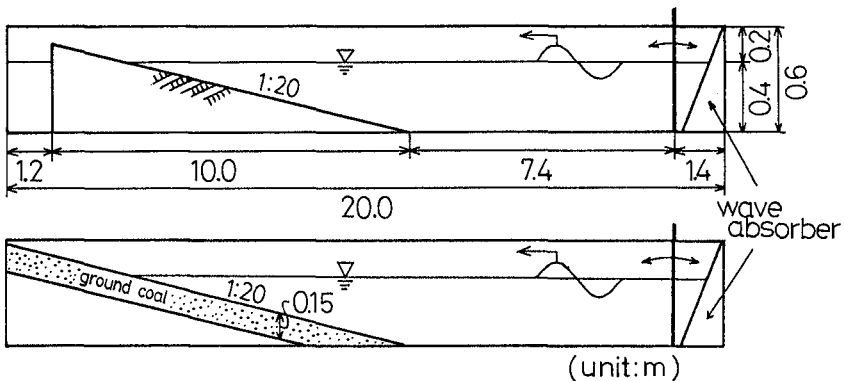


Fig.3 Experimental equipment.

capacitance-type wave gauge at right above the velocity measuring point which was located at $h/h_b = 0.67$ (h is the still water depth). At the measuring section, breaking waves were confirmed to be well developed into so-called "turbulent bore". A small pressure transducer of 1 cm in diameter, 3 mm in thickness and 1 kHz in its frequency response was used for the measurement of bottom pressure fluctuation at the measuring section. The concentration of the suspended bottom sediment for the movable bed experiment was measured by a light-attenuation-type sensor, the position of which was manipulated to be kept at nearly the same height above the bottom through the movable bed experiment.

3. Characteristics of Velocity Field Associated with Oblique Eddies

3.1 Intermittent structure of bottom turbulence and pressure fluctuation

Figure 4 shows the phase-averaged distribution of the turbulence intensity u' and w' at the several heights z above the bottom. The origin of the horizontal axis corresponds to the phase of the zero-up crossing point of the water surface profile. The values indicated were calculated by averaging about 200 records of the high-frequency velocity component data which is obtained through a moving-average filter with a averaging time of 0.1 s. We can see in this figure that the dependence of the turbulence intensity on the phase variation as a whole is not so distinct, though the turbulence intensity at $z = 6.7$ cm slightly increases around the phase of wave crest. Especially, the turbulence intensity close to the bottom is almost uniform except the region around the phase of the wave crest, where the intensity becomes larger probably corresponding to the increase of the orbital velocity.

Figure 5, on the other hand, is a typical example showing the raw data of the water surface fluctuation η immediately above the velocity measuring point, the bottom pressure fluctuation p , and the velocity fluctuation u and w close to the bottom ($z=0.7$ cm). In this figure, the bottom turbulence occurs not uniformly, but appears in a quite intermittent manner with the bottom pressure disturbances at the instants indicated by the arrows. Further, we should note that such an intermittent occurrence of the bottom turbulence can be found not under the wave crest, but around the phase of the zero-down crossing point. This means that these intermittent turbulence is not caused by the bottom shear stress due to orbital wave motion.

3.2 Conditional sampling analysis of velocity field associated with the oblique eddies

Comparison between Figs. 4 and 5 leads us to the idea that the intermittent characteristics of the bottom turbulence may be lost through the averaging process by the usual phase-averaged method because of the random occurrence of the intensive bottom turbulence, as shown in Fig. 5.

Considering the occurrence of such a highly intermittent

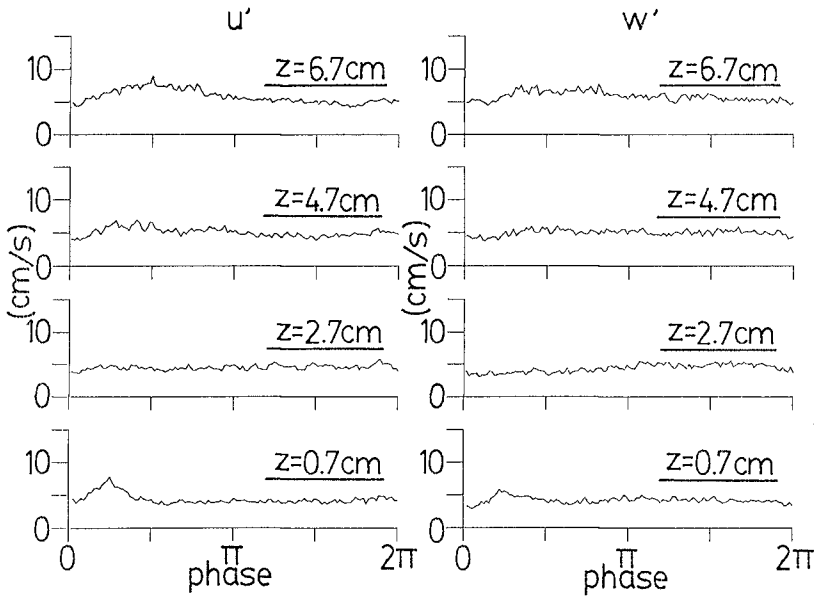


Fig. 4 Distributions of phase-averaged turbulence intensity u' and w' .

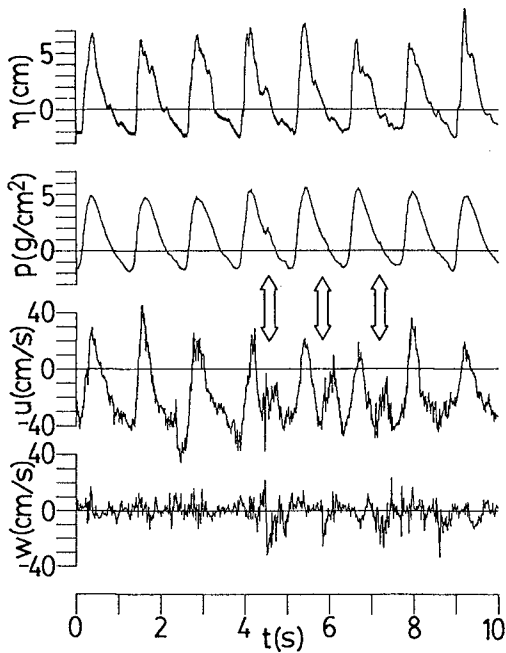


Fig. 5 An example of time series of η , p , u and w .

bottom turbulence behind the wave crest, we can expect that these disturbance is caused by the action of the obliquely descending eddies mentioned first. The results of the visual observation of the eddy evolution seemed to support this expectation. To confirm this point more quantitatively, we have investigated the flow structure related to the intermittent bottom disturbances by applying a conditional sampling technique.

In Fig. 5, we can find also that the pressure disturbance occurs not so frequently as compared with the velocity disturbances. Its possible explanation is that the pressure disturbance occurs only at the instant when the pressure gage is directly hit by an obliquely descending eddy. Considering this characteristics of the pressure record, we can utilize it as a trigger signal for the conditional sampling to detect distinctively the velocity data corresponding to the intermittent bottom turbulence. Namely, by inspecting whether the magnitude of the pressure disturbance exceed the prescribed threshold level or not, we can classify each individual wave record separated by the zero-up crossing method into conditionally sampled or rejected records. The scanning of the pressure disturbance for the conditional sampling was done within the phase interval $[\pi/2, 3\pi/2]$ of each individual wave record, because the apparent pressure fluctuation calculated by the moving-average method may emerge in the phase intervals $[0, \pi/2]$ and $[3\pi/2, 2\pi]$ through the effects of the water surface fluctuation around the wave crest and of the higher harmonics due to the wave nonlinearity (Fig.6). The number of the wave records obtained through this conditional sampling is about 50, 1/10 of the total wave records.

Figure 7 represents the phase-averaged distribution of the turbulence intensity u' and w' , where the solid and broken lines correspond to the conditionally sampled and rejected data, respectively. We can clearly see in this figure that the turbulence intensity of the sampled data at the most upper measuring point attains relatively large value around the wave crest and this intensive turbulence propagates obliquely downward as indicated by the arrows, while the turbulence intensity of the rejected data exhibits no appreciable dependence on the phase variation. This means that the obliquely descending eddies bring intensive turbulence to the bottom behind the wave crest.

Figure 8 shows another result of the conditional sampling analysis where the phase-averaged distributions of the mean velocity, $\langle u \rangle$ and $\langle w \rangle$, of the conditionally sampled and non-conditioned data are represented by the full and broken lines, respectively. In this figure, we can recognize that, in the large turbulence regions, both the onshoreward and the downward mean velocities are enhanced in the sampled records. This fact is directly related with the increase of the downward transport of the onshoreward momentum as described in what follows.

The left and right figures in Fig. 9 represent the phase-averaged distributions of the momentum transport for the sampled and rejected records, respectively. The solid lines indicate the phase-averaged product of the horizontal and the vertical velocity fluctuation, $\langle (u-\bar{u}) \cdot (w-\bar{w}) \rangle$, where the over bar means an operator to take a time average. Comparing

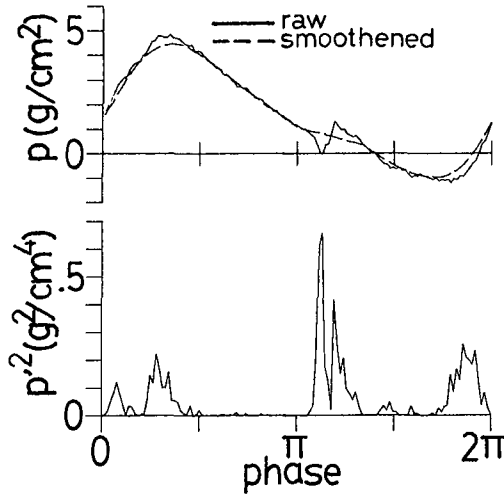


Fig. 6 Raw and smoothed data of p . p' is the difference between these two data.

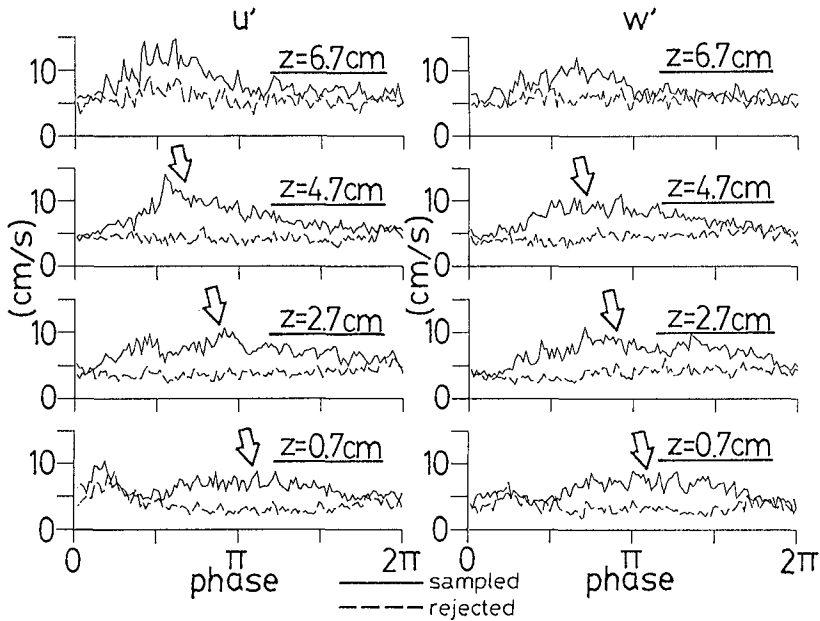


Fig. 7 Phase-averaged distributions of the turbulence intensity u' and w' for conditionally sampled and rejected records.

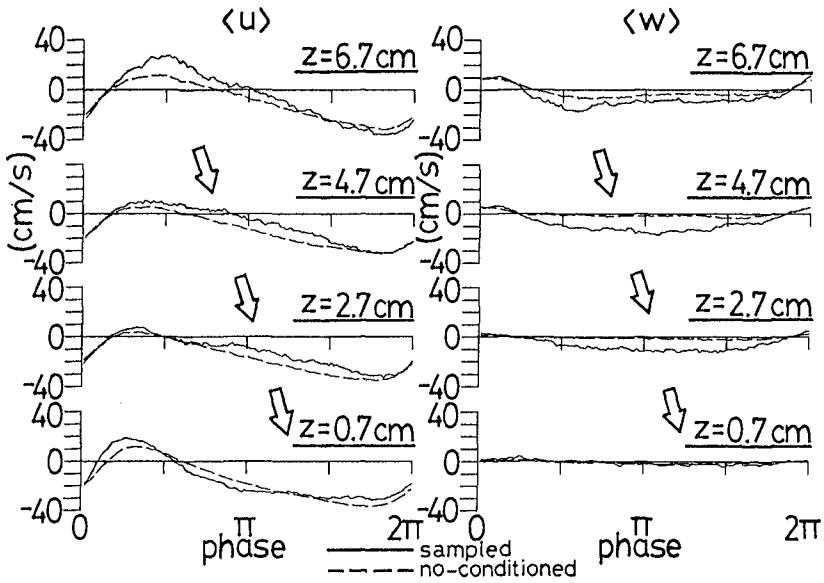


Fig. 8 Distributions of phase-averaged velocity $\langle u \rangle$ and $\langle w \rangle$ for conditionally sampled and no-conditioned records.

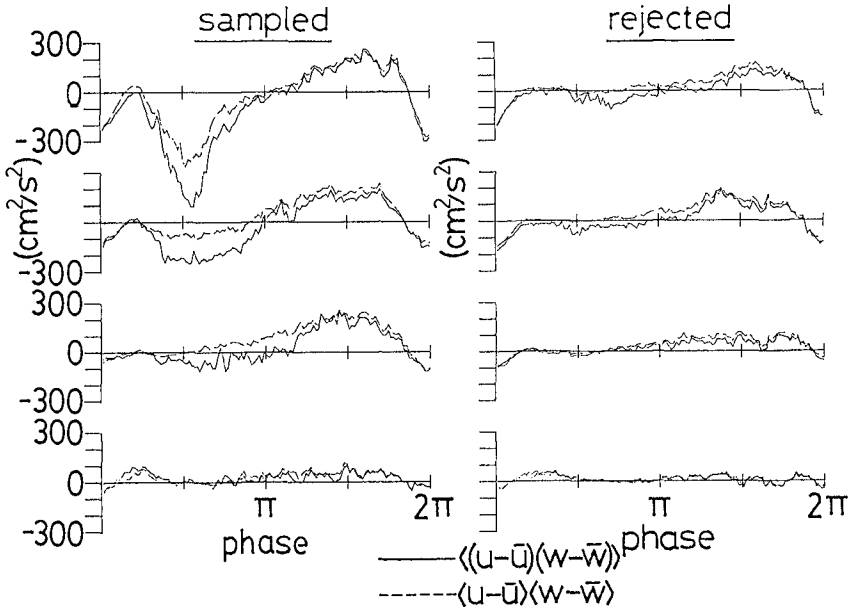


Fig. 9 Distributions of phase-averaged momentum flux for conditionally sampled and rejected records.

the left and the right figures, we can clearly see that the momentum transport of the sampled records considerably increases as a whole.

The broken lines, on the other hand, represent the product of the phase-averaged horizontal and vertical velocity fluctuation, $\langle u-\bar{u} \rangle \cdot \langle w-\bar{w} \rangle$. The difference between the solid and broken lines corresponds to the turbulent momentum transport. The fact that the difference becomes large in the highly turbulent regions means that the production of an appreciable magnitude of the Reynolds stress accompanies the evolution of the oblique eddies.

In summary, all of these results are consistent with the following conceptual model based on the obliquely descending eddies. That is, the eddies transport the intensive turbulence obliquely downward with the large onshoreward momentum at the upper layer of the water, and then brings the highly intermittent turbulent velocity and pressure fluctuation to the bottom.

Considering these results obtained through the fixed-bed experiments, we can easily expect that this eddy action to the bottom plane causes sediment suspension in a wide extent of the surf zone. To obtain more definite results on the relationship between the eddy action and resultant sediment suspension, we have made movable-bed experiments, as described as follows.

4. Relation between the Obliquely Descending Eddies and the Sediment Suspension

4.1 On-offshore distribution of the mean sediment concentration close to the bed

The on-offshore distributions of the time-averaged concentration \bar{c} both at $z=0.5\text{cm}$ located within the bedload layer and at $z=1.0\text{cm}$ just above the layer are shown in the bottom of Fig. 10. The values indicated were based on the data measured during the time interval of about 70s from the instant when the wave set-up was established until the time when the sediment ripples were generated. The initial bottom surface configuration was smoothed for each run.

The upper figure, on the other hand, shows the distribution of the bottom turbulence intensity w' and of the amplitude of orbital velocity u normalized by the linear long wave speed at the breaking point. These values of w' and u are those measured at $z=0.7\text{cm}$ in the fixed-bed experiments. Unlike for the values of the turbulence intensity indicated in Figs. 4 and 7, the averaging time for the numerical filtering of the raw data is the time of the incident wave period, because the vertical component of the near-bottom velocity contains negligibly small magnitude of the orbital velocity as compared with the turbulence. Hence w' -values so obtained include almost all contribution of the oblique eddy motion.

Comparing the shape of these distributions each other, we can recognize that the sediment concentration level \bar{c} in the bed load layer correlates well to u_m , while \bar{c} above the layer varies in accordance with the bottom turbulence inten-

sity w' . This result suggests the close relationship between the sediment suspension and the action of the oblique eddies.

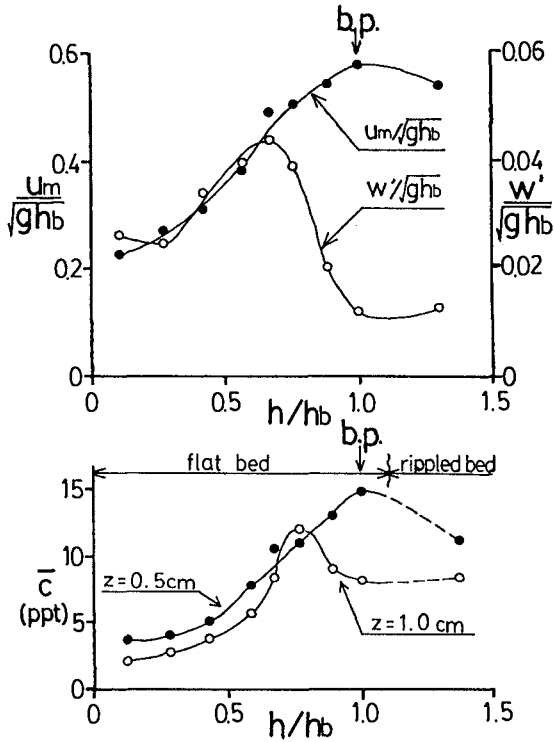


Fig. 10 Spatial distributions of mean concentration \bar{c} at $z=0.5$ and 1.0 cm and those of bottom turbulence intensity w' and amplitude of orbital velocity u_m .

4.2 Visualization of the eddy evolution and the resultant occurrence of sediment suspension

To confirm this relationship from a visual aspect, we have taken some photos from a side wall of the wave channel.

Photo 1 and Figure 11 are examples showing a sequence of pictures and their tracings around the velocity measuring section taken successively by a motor-driven 35 mm camera. The vertical rod shown in the photos is the stem of the sensor to measure the sediment concentration. The instants taking the photos are indicated by the arrows denoted by the alphabets of A to H in Fig. 12, where both the water surface elevation η and the bottom sediment concentration c at $z = 1.0$ cm at the velocity measuring section are represented. The records shown in Fig. 12 were those obtained immediately after the starting of the wave generator; thus the first

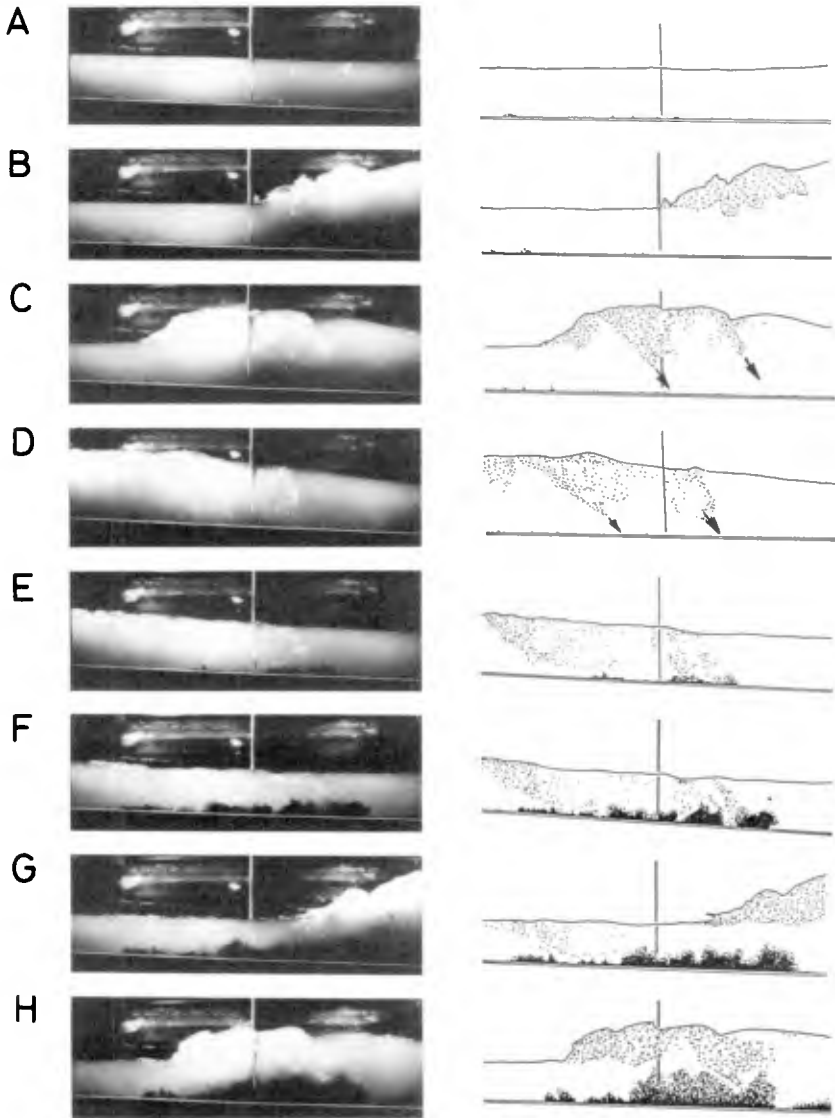


Photo 1 Development of obliquely descending eddies and sediment suspension.

Fig.11 Tracing of Photo 1.

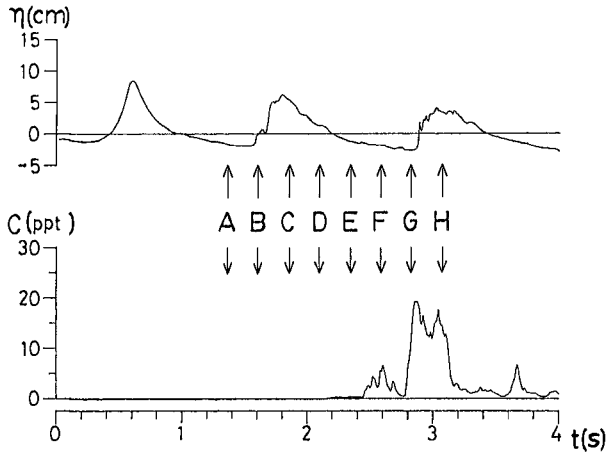


Fig.12 The instants taking the photos and the time histories of η and c .

wave indicated in the figure is a non-breaking wave. The figure indicates that the sediment concentration increases not under the first non-breaking wave, but around the phase of the trough of the second breaking wave.

The brighter regions of the photos indicate the air bubbles involved in the eddies, which are sketched in [Fig.11](#) by the speckles. The dark regions close to the bottom in E to H, on the other hand, indicate the suspended sediment cloud. From these photos and figures, we can describe the process of the eddy development and associated sediment suspension as follows.

- (A)..... No appreciable sediment suspension can be found, though there exists the sediment movement due to sheet-flow.
- (B)..... The horizontal eddies grow to appear in front of the bore crest.
- (C)..... The eddies develop into the obliquely descending eddies behind the wave crest. The sediment suspension, however, cannot be found yet at this stage.
- (D)..... The oblique eddies stretch toward the bottom as indicated by the arrows.
- (E)..... Immediately after the instant when the eddies hit the bottom surface, the sediment suspension appears in the vicinity of the bottom.
- (F)..... A large amount of the sediment is lifted up into suspension by the eddy action, increasing the concentration value as shown in [Fig. 12](#).
- (G)..... The sediment clouds migrate offshore with the backwash of the bore. And then they are convected upward by the heaving orbital motion preceding to the passage of the wave crest.
- (H)..... The subsequent oblique eddies evolve toward the bottom.

4.3 3-D structure of suspended sediment cloud in the surf zone

The dependence of the sand suspension on the oblique eddies mentioned above may be confirmed more quantitatively by investigating the spatial structure of the suspended sand cloud; i.e., if the oblique eddies lift up the bottom sediment into suspension, the resultant sediment cloud will show the strong three-dimensionality with the horizontal scale comparable to that of the diameter of the eddies. So to investigate the spatial structure of the sediment cloud close to the bottom, we have measured simultaneously the sediment concentration c_1 and c_2 by the two probes aligning several distances apart in the direction perpendicular to the plane of the orbital wave motion.

Figure 13 shows the time histories of the water surface elevation η as well as c_1 and c_2 both outside and inside the surf zone. The values of c_1 and c_2 in this figure are those measured by the probes manipulated to keep their heights at 1.5cm above the bottom and separated with 4cm each other in the horizontal cross-channel direction.

The values of c_1 and c_2 outside the surf zone well correlate to each other and exhibit strong dependance on the phase variation with the two marked peaks within the one

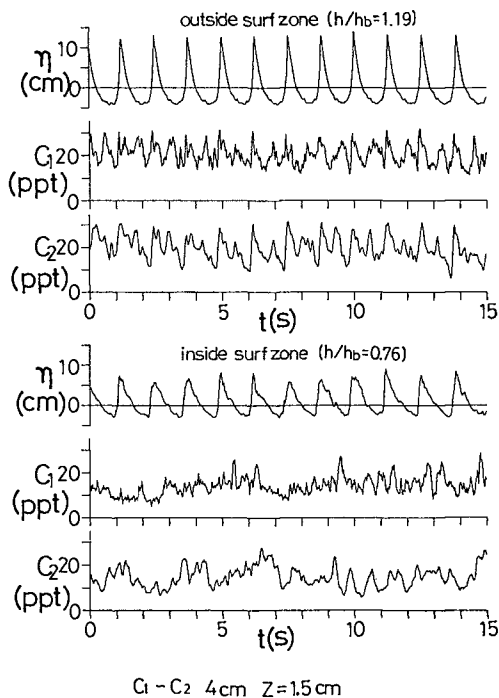


Fig. 13 An example of the time histories of η as well as c_1 and c_2 both outside and inside the surf zone.

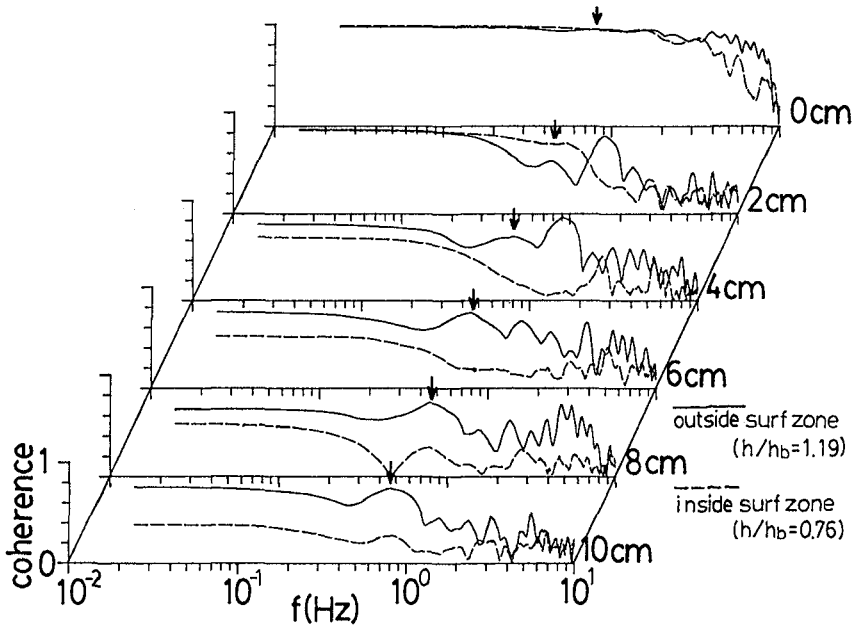


Fig.14 Coherence between bottom concentration records for several probe spacings.

wave period, though the high frequency component is slightly lost in c_2 record as compared with c_1 , because the frequency response of the probe for c_2 is lower than that for c_1 . The concentration variation inside the surf zone, on the contrary, shows no definite phase-dependance, and the correlation between these two records is rather poor. These facts suggest that the sediment suspension within the surf zone is mostly governed by the turbulence, especially by the obliquely descending eddies, generated with the wave breaking, though, in the outside of the surf zone, the wave fluid motion is a unique action to the sediment suspension, which is nearly two-dimensional phenomenon.

Then to investigate the correlation structure between c_1 and c_2 more quantitatively, we have calculated the coherence between c_1 and c_2 . The results are shown in Fig.14, where the coherence values with the horizontal axis of frequency f . The data used are those measured for the initially smoothed bed during the time interval of about 80 s from the instant when the wave set-up was established to the time when the sediment ripples were generated.

The coherence outside the surf zone denoted by full lines retain high values even for the large probe spacings, demonstrating two-dimensionality of sediment suspension outside the surf zone. On the contrary, the coherence within the surf zone represented by broken lines decreases rapidly

with the probe spacings. The decrease is most noticeable in the frequency range from 0.8 to 5 Hz which is corresponding to the period of the incident waves and its higher harmonics and is comparable to the frequency of the eddy occurrence. This means that the sediment suspension inside the surf zone occurs in a quite spot-like manner and is consistent again with the proposed model of sediment suspension by the oblique eddies.

5. Conclusions

The results and conclusions obtained in the present study can be summarized as follows.

1) "Obliquely descending eddies" bring highly intermittent turbulence to the bottom with the large onshoreward momentum and thus essentially characterize the turbulent flow field in the surf zone.

2) The eddies hit the bottom and then lift up the sediment into suspension, yielding the spot-like sediment cloud in accordance with the 3-dimensional eddy structure.

Acknowledgment

This study was financially supported by a grant in aid for scientific research, No.61460165, Ministry of Education, Science and Culture, Japanese Government.

References

- Deigaard, R., Fredsoe, J. and Hedegaard, I.B.(1986): Suspended sediment in the surf zone, *Jour. of Waterway, Port, Coastal and Ocean Engineering, ASCE*, Vol.112, No.1, pp.115-127.
- Hino, M., Sawamoto, M., Yamashita, T., Hironaga, M. and Muramoto, T.(1984): Prototype 2-dimensional LDV adopting optical fibers, Laser-Doppler Velocimetry and Hot-Wire/Film Anemometry, Association for the Study of Flow Measurement.
- Miller, R.L.(1976): Role of vortices in surf zone prediction: sedimentation and wave forces, *Beach and Nearshore Sedimentation, Soc. Econ. Paleontol. Mineralog., Spec. Publ. No. 23*, pp.92-114.
- Nadaoka, K.(1986): A fundamental study on shoaling and velocity field structure of water waves in the nearshore zone, *Doctoral Dissertation, Tokyo Inst. of Tech. (reproduced in Tech. Rept. of Dept. Civil Eng., Tokyo Inst. of Tech. No.36, pp. 33~125, 1986.)*
- Shibayama, T. and Horikawa S.(1985): Sediment transport due to breaking waves, *Proc. of 20th Int. Conf. on Coastal Eng., ASCE*, pp.1509-1522.

CHAPTER 123

Suspended Sediment Concentration in the Surf Zone

Makoto Ifuku¹⁾ and Tadao Kakinuma²⁾

Abstract

The water particle velocity, the pressure fluctuation and suspended sediment concentration near the bottom were measured in the surf zone. Data were obtained on the mean sediment concentration, phase lag between onshore velocity and suspended sediment concentration. The near-bottom velocity distributions under finite amplitude waves were calculated on the basis of the turbulent boundary layer theory by using time-independent/dependent eddy viscosities and Prandtl mixing length theory. The concentrations at reference level were estimated from the Kalkanis' theory using the velocity value at the top of a sand particle and the distributions of suspended sediment concentration were calculated on the basis of the turbulent diffusion theory by using time-independent/dependent diffusion coefficients. The computed mean values of the suspended sediment concentration agree with those observed by Noda, the authors and Nielsen and those measured by Deigaard et al.. The computed phase lag agrees well with observed by the authors.

1. Introduction

In order to investigate the sediment transport phenomena in the surf zone, it is necessary to study the sediment suspension mechanism due to waves. Many investigators have been concerned with sediment suspension. Early studies, such as those of Fairchild(1959), Homma and Horikawa(1962) and Noda(1967) were made with siphons, pumped sampler and suspended sampler. With these types of sampler it is difficult to obtain accurate records of concentration variation. For these most recent studies, such as those of Homma et al.(1965), Sleath(1982), Brennimeyer(1974) and Wright et al.(1982) the records of concentration variation were obtained in laboratory and on site. Sleath(1982) measured the variation of sediment concentration at a fixed point above

1) Associate Professor, Department of Ocean Engineering, Ehime University, Matsuyama, Japan

2) Professor, Department of Ocean Engineering, Ehime University, Matsuyama, Japan

a ripple crest in oscillatory flow. He showed that stronger peaks in the concentration records are observed at phases where the velocity at the upper edge of the boundary layer reverses, while weaker peaks are found at phases where the velocity is approximately maximum. He expressed the characteristics of the boundary layer in oscillatory flow in terms of the vortex near the ripple and elucidated the mechanism of sediment suspension. However, in the discussion of initial motion of sediment, accurate knowledge of the near-bottom water particle velocity in the turbulent boundary layer is important in order to evaluate drag, lift, inertia and body forces acting on sediment.

The present paper deals with the details of near-bottom water particle velocity and suspended sediment concentration on the basis of field data. Meanwhile, numerical analysis has also been performed on the basis of the turbulent boundary layer theory and diffusion theory to elucidate theoretically the observed and experimental suspended sediment concentrations.

2. Field observation and data analysis

2.1 Sites and method of observations

The field observations were conducted at Baishinji coast near Matsuyama city in Ehime Prefecture, Japan, over the periods from 15 December 1982 to 19 March 1983 and from 21 December 1983 to 19 March 1984. The observation points were located 120 and 100 m off the coastal breakwater and the mean water depths at these points were 2.0 and 1.7 m (Fig. 1). The mean beach slope around both the points were approximately 0.01.

The field instrumentation system used was composed of 3 sets of two-component electromagnetic flow meters MODEL551(MARSH McBIRNEY), a pressure transducer MODEL 205-2 (Setra Systems) and a turbidimeter MODEL MA-101 RD(Hokuto Riken).

Station I

The instruments were mounted on a frame and fixed on the bottom using 8 concrete blocks.

The levels of electromagnetic flow meter were 0.07, 0.65 and 0.98 m above the bottom and the horizontal velocities were measured. The levels of the turbidimeter and the pressure transducer were 0.04 and 0.72 m above the bottom respectively.

Station II

An electromagnetic flow meter was set at the level of 0.3 m above the bottom and the cross-shore and vertical components of water particle velocity were measured. The other two were set at the levels of 0.45 and 0.70 m to measure the cross-shore and longshore components. The levels of the turbidimeter and the pressure transducer were 0.34 and 0.49 m

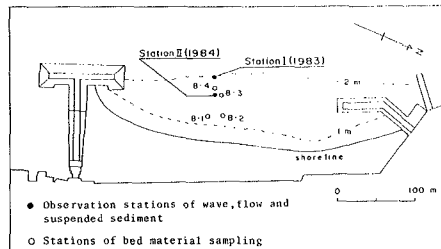


Fig.1 Observation stations of wave, flow, suspended sediment and bed material.

above the bottom respectively.

The turbidimeter was an optical type and composed of six light sources and a receiver. Data obtained were transmitted to a shore station, where they were recorded on a data logger XR-30(TEAC).

2.2 Data analyses

Records of velocity, pressure fluctuation and turbidity (suspended sediment concentration) were digitized for a interval of 0.2 s at every 15 min. The zero-up-crossing method was employed to calculate the velocity and pressure fluctuation of the significant wave. First, spectral analyses were performed to obtain the power spectrum, cross spectrum, physical spectrum of velocity and suspended sediment concentration as well as directional spectrum.

2.3 Significant wave and bed material

During the 1983 observation the significant wave height and period were 0.41-0.53 m and 4.4-4.7 s, while in 1984 they were 0.33-0.79 m and 4.4-5.3 s. The frequency of breaker occurrence is defined as the ratio of the number of breakers to the number of waves in each data set. In both years, most of breakers visually were of the spilling type. Sampling of bed material performed in November 1983 at B-1 and 2 and in January 1984 at B-3 and 4. Bed material around the observed sites consisted entirely of sand with a median diameter of 0.18 mm.

3. Results of data analysis

3.1 Power spectrum of suspended sediment concentration

The great majority of power is in the low frequency range (0.016 Hz - 0.025 Hz), although a weaker peak appears at the peak frequency of wind waves (approximately 0.25 Hz). The power of suspended sediment concentration falls off as: $f^{-0.5}$ - f^{-1} (f : frequency) and f^{-3} - $f^{-3.5}$ in the low and high frequency ranges, regardless of the frequency of breaker occurrence, while the profiles of cross-shore velocity and pressure fluctuation depend on the frequency of breaker occurrence. Fig. 2 shows the power spectrum of the suspended sediment concentration and cross-shore velocity; (a) and (b) are in the case of the low and high frequency of breaker occurrence respectively.

3.2 Suspended sediment concentration and near-bottom cross-shore velocity

Fig.3 shows the physical spectrum of cross-shore velocity observed 0.07 m above the bottom together with the time series of suspended sediment concentration observed at 0.04 m above the bottom. The uppermost figure is for the lower frequency band, 0.02-0.078 Hz; next is for 0.098-0.156 Hz; third is for the peak frequency band of wind waves, 0.176-0.234 Hz and the fourth is for 0.391-0.449 Hz. The lowest figure shows the time series of suspended sediment concentration. Energy density of the physical spectrum in the lower frequency band is approximately one-fifth as large as that in the peak frequency band. The

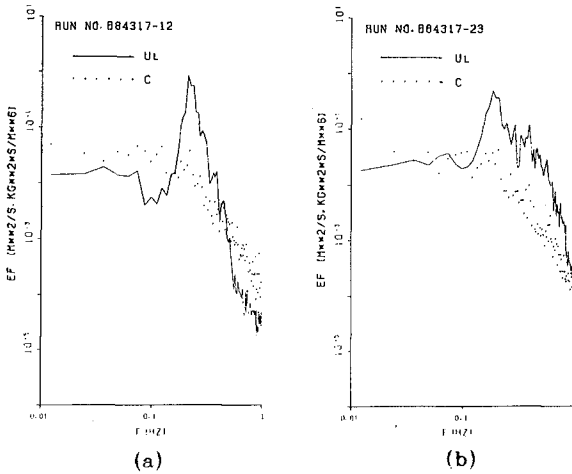


Fig.2 Power spectra of suspended sediment concentration and cross-shore velocity, where the frequencies of breaker occurrence are (a) 14 % and (b) 20 %.

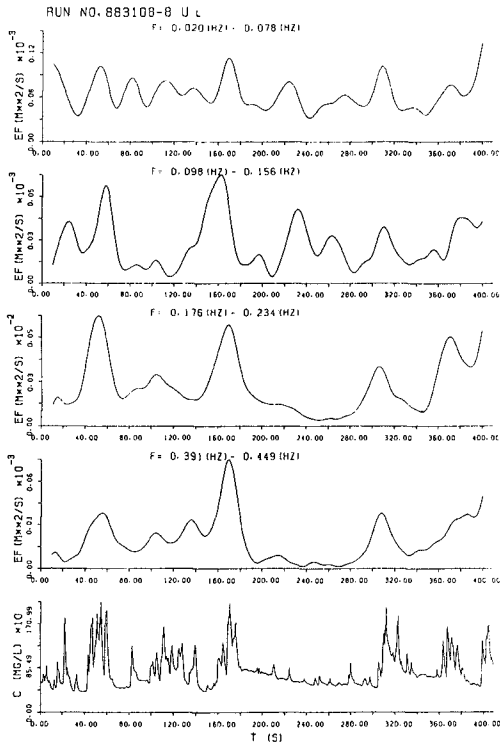


Fig.3 Physical spectra of cross-shore velocity at the level of 0.07 m and time series of suspended sediment concentration at 0.04 m above the bottom.

suspended sediment concentration is quite high when energy densities in the peak and quarter frequency bands of wind waves are high. Thus the fact that higher values of suspended sediment concentration occur at a 40-60 s time interval seems to be related to lower and peak frequency components of cross-shore velocity. The above discussion is very interesting in comparison with the results of Brenninkmeyer(1974) and Wright et al.(1982), who suggested that suspended sediment concentration is related to swells or long period waves and surf beat on the basis of power spectrum analyses of wave, cross-shore velocity and suspended sediment concentration observed in the surf zone.

3.3 Phase lag between cross-shore velocity and suspended sediment concentration

Fig.4 shows the histogram of phase lag between a peak of cross-shore velocity and that of suspended sediment concentration during a wave cycle. The histograms were obtained through the analyses of 107 and 120 waves in (a) and (b) where the frequencies of breaker occurrence are 13 % and 19 % respectively. The maximum values in the histogram appear at the phases $\pi/2$, 1.3π in (a) and $\pi/2$, 1.1π in (b).

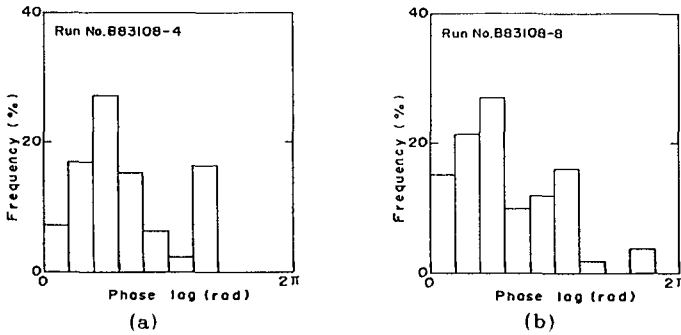


Fig.4 Histograms of phase lag between onshore velocity and suspended sediment concentration, where the frequencies of breaker occurrence are (a) 13 % and (b) 19 %.

4. Numerical analysis

4.1 Basic equations

(a) Water particle velocity in the turbulent boundary layer

The x - axis is taken along a horizontal bottom and z - axis vertically upwards. The velocity components in the x - and z - directions are denoted by u and w .

The equation of motion for a two-dimensional turbulent boundary layer is given as follows:

$$\frac{\partial u}{\partial t} + u \frac{\partial u}{\partial x} + w \frac{\partial u}{\partial z} = -\frac{1}{\rho_f} \frac{\partial p}{\partial x} + \frac{1}{\rho_f} \frac{\partial \tau}{\partial z} \tag{1}$$

in which t is the time, p is the pressure, ρ_f is the density of fluid, and τ is the shear stress. If the mean flow is parallel to the

bed, Eq.(1) is reduced to

$$\frac{\partial u}{\partial t} = -\frac{1}{\rho_f} \frac{\partial p}{\partial x} + \frac{1}{\rho_f} \frac{\partial \tau}{\partial z} \quad (2)$$

The pressure gradient just outside the boundary layer is given by

$$-\frac{1}{\rho_f} \frac{\partial p}{\partial x} = \frac{\partial u_b}{\partial t} \quad (3)$$

in which u_b is the horizontal velocity at the upper edge of the boundary layer.

If the above expression also holds in the boundary layer, Eq.(2) becomes

$$\frac{\partial(u - u_b)}{\partial t} = \frac{1}{\rho_f} \frac{\partial \tau}{\partial z} \quad (4)$$

(b) Concentration

The one-dimensional turbulent diffusion equation for sediment concentration is given as follows:

$$\frac{\partial C}{\partial t} + w \frac{\partial C}{\partial z} = \frac{\partial}{\partial z} \left(K_z \frac{\partial C}{\partial z} \right) + w_0 \frac{\partial C}{\partial z} \quad (5)$$

in which C is the sediment concentration, K_z is the turbulent diffusion coefficient, and w_0 is the settling velocity of sediment.

4.2 Initial and boundary conditions

Eqs.(4) and (5) were solved numerically using a finite difference method with Crank-Nicholson implicit scheme. The initial and boundary conditions for Eq.(4) are

$$\begin{aligned} u(z, 0) &= 0 \\ u(z_0, t) &= 0 \\ u(\delta_b, t) &= u_b(t) \end{aligned} \quad (6)$$

in which z_0 is the roughness length and δ_b is the thickness of the turbulent boundary layer. Initial and boundary conditions for Eq.(5) are

$$\begin{aligned} C(z, 0) &= 0 \\ C(\delta_B, t) &= C_0(t) \\ K_z \frac{\partial C}{\partial z} + w_0 C &= 0, \quad z = h \end{aligned} \quad (7)$$

in which δ_B is the thickness of the bed-layer, $C_0(t)$ is the sediment concentration in the bed-layer, and h is the water depth.

4.3 Evaluations of parameters

The vertical distance from the bottom to the water surface is divided by 101 points. The vertical distance from the bottom to the level of three grain diameters is divided into the interval of one-half a grain diameter, and above the level the intervals are determined so as to form a geometric progression. The computational time-step is

determined as $T / 96$ (T : the wave period).

(a) Velocity in the boundary layer

The eddy viscosities are assumed to be

$$Nz(z) = \alpha \kappa \sqrt{f} u_{bm} z \quad (8-1)$$

$$Nz(z, t) = \alpha \kappa \sqrt{f} |u_b(t)| z \quad (8-2)$$

where α is the constant of proportionality, κ is the Karman constant, f is the bottom friction factor and u_b is the maximum velocity at the upper edge of the boundary layer. Bottom friction factor is calculated from the empirical expression given by Kakinuma and Ifuku(1985):

$$\begin{aligned} f &= 1.95\theta^{-0.87} & 2 \leq \theta \leq 40 \\ f &= 0.39\theta^{-0.42} & 40 \leq \theta \leq 190 \end{aligned} \quad (9)$$

where $\theta = \rho_f u_{bm}^3 / (\rho_s - \rho_f) g d_{50}$, ρ_s is the density of sediment ($\rho_s = n\rho_f + (1-n)\rho_s'$, n is the porosity, ρ_s' is the density of dry sediment), g is the acceleration gravity, and d_{50} is the median diameter of sediment.

The roughness length, according to Bakker-van Doorn(1978), is

$$z_0 = \eta / 33 \quad (10)$$

where η is the ripple height, which is estimated from Nielsen's empirical relationship(1981):

$$\eta = 21 a_m \theta^{-1.85} \quad (11)$$

where a_m is the half stroke of water particle at the bottom.

Noda(1969) evaluated the thickness of turbulent boundary layer as

$$\delta_b = 25\delta \quad (12)$$

where $\delta = \sqrt{\nu T / 2\pi}$ (ν : the kinematic viscosity). At each point, until the difference of normalized velocity between the times of mT (m : integer) and $(m+1)T$ becomes less than 10^{-5} , calculation is continued.

(b) Concentration

The sediment concentration in the bed-layer, according to Kalkanis(1965), is

$$C_0 = 2P\rho_s d \cdot V / 3 \int_{z_0}^{\delta_b} u dz \quad (13)$$

where d is the particle size of sediment, V is the speed of sediment propagation and P is the pick-up rate:

$$P = \frac{1}{\sqrt{2\pi}} \int_{B_* \Psi^{-1} / \eta_0}^{\infty} \exp(-z^2/2) dz \quad (14)$$

where $B_* = 4/3 C_L \eta_0$, C_L is the lift coefficient, $1/\eta_0$ is an empirical constant, and $\Psi' = (\rho_s - \rho_f) g d / \rho_f u_0^2$ (u_0 : the local water particle velocity). It is difficult to estimate the speed of sediment propagation in Eq.(13). In the present analysis it is set to be equal to the cross-sectional mean velocity of water particles in the bed-layer.

The turbulent diffusion coefficients are assumed to be

$$K_z = \beta \alpha \sqrt{\bar{f}} u_{bm} z \quad (15-1)$$

$$K_z = \beta \alpha \sqrt{\bar{f}} |u_b(t)| z \quad (15-2)$$

$$K_z = \gamma (l_T u^2 + l_L w^2) / q \quad (15-3)$$

where β, γ are the constant of proportionality, l_T and l_L are the characteristic length ($l_L = \alpha l_T$; α : the constant of proportionality), and $q = (u^2 + w^2)^{1/2}$.

The settling velocity of sediment is calculated by

$$w_0 = \sqrt{\frac{4}{3} \frac{d}{C_D} \frac{\rho_s - \rho_f}{\rho_f} g} \quad (16)$$

where C_D is the drag coefficient. In the case of Reynolds number, $Re = w_0 d / \nu$ being less than 5, the drag coefficient can be estimated (1968) by

$$C_D = \frac{24}{Re} + 4.5 \quad (17)$$

At each point until the difference of normalized concentration between the times of mT and $(m+1)T$ is less than 10^{-5} , calculation is continued. In the present study, the fluids are sea water for Noda's, the authors' and Nielsen's observed results and fresh water for the results obtained by Deigaard et al. The water temperatures are assumed to be 10°C for the authors' results and 20°C for the others' results. The sediment is sand and density and porosity have been taken at 2.65 g/cm^3 and 0.3 respectively. Sand grain sizes are $0.30, 0.18, 0.12-0.22$ and 0.12 mm for Noda's, the authors', Nielsen's and Deigaard et al. results, respectively. The characteristic length, l_T , is assumed to be the distance from the bottom.

5. Numerical results

Parametric analysis is performed by using the observed data obtained by Noda, the authors and Nielsen and measured data by Deigaard et al. The significant waves obtained through field observations by Nada, authors and Nielsen and laboratory measurement by Deigaard et al., are in the range that Stokes wave theory of second order, third order and cnoidal wave theory and Stokes wave third order are valid (1977), respectively. Einstein and El-Samni (1949) reported that the lift coefficient has a constant value 0.178 on the basis of measurement of the pressure difference. It was assumed here that the lift coefficient is 0.2 and $1/\eta$ is 1.5 after Kalkanis and w_0 has been taken to be the value at the top of the sand particle and the thickness of the bed-layer is twice sand particle.

5.1 Velocity in the turbulent boundary layer

The velocity profiles at various phases during a cycle of wave motion in the turbulent boundary layer are shown in Fig. 5. The maximum value of the water particle velocity at phase 6 is approximately 1.03 times as

large as that at the upper edge of boundary layer. In the case that the shear stress is evaluated by using time-dependent eddy viscosity or Prandtl mixing length theory the over-shooting is more significant than the case that the shear stress is evaluated by using time-independent eddy viscosity at phases 6.25, 6.375, 6.5 and 6.875 and the levels which arise the over-shooting are lower at above-mentioned phases where the water particle velocities are negative. In the cases that the shear stress is evaluated by using time-dependent eddy viscosity and Prandtl mixing length theory, both profiles show the similar trend.

Fig.6 shows the temporal variation of water particle velocity at the sand particle level. The velocity profiles are asymmetric and the phase of the maximum velocity is ahead of that at the upper edge of boundary layer by approximately $\pi/12$.

5.2 Concentration

(a) Variation of sediment concentration in the bed-layer

Fig.7 shows the variation of the sediment concentration in the bed-layer depending on the instantaneous value of $1/\psi'$. The concentration in the bed-layer is calculated on the assumption that the thickness of the bed-layer is equal to twice the grain diameter in Eq.(13). For larger value of $1/\psi'$ in the range of present analysis, the concentration in the bed-layer is asymptotic to about 0.3. This tendency is similar to the result obtained by Deigaard et al.(1986).

(b) Temporal variation of sediment concentration at several heights

Fig.8 shows the temporal variation of suspended sediment concentration; in (a)-(f) are in the cases that the relative heights are 1.67×10^{-4} , 1.44×10^{-3} , 2.44×10^{-3} , 1.22×10^{-2} , 1.93×10^{-2} and 2.41×10^{-2} respectively. With being off from the bottom, suspended sediment concentration decreases and the peak of suspended sediment concentration leads gradually. At $z/h=1.93 \times 10^{-2}$, is the height at which suspended sediment concentrations are observed, the peak of suspended sediment concentration appears at phase 6.25 approximately. It is the phase where the cross-shore velocity at the upper edge reverses approximately.

(c) Temporal variation of sediment concentration and phase lag between cross-shore velocity and sediment concentration

Fig.9 shows the computed temporal variations of suspended sediment concentration at 0.04 m from the bottom in comparison with the histogram of phase lag between maximum value of observed onshore velocity and maximum value of suspended sediment concentration during a wave cycle. Peaks in the histogram are found at $\pi/2$ and 1.3π in (a) and $\pi/2$ and 1.1π in (b)-corresponding to peaks in the computed temporal variation of suspended sediment concentration. The temporal variation, calculated by using time-independent turbulent diffusion coefficient, has its peaks at the above-mentioned phases; but the value of both peaks is approximately the same, and the computed temporal variation disagrees with the histogram of phase lag. The temporal variations which are computed by using time-dependent turbulent diffusion coefficient has its peaks at the above-mentioned phases and the agreement between that computed and observed is good. It is, however, worth noting that the computed temporal variation which is computed by using Eq.(15-3) could

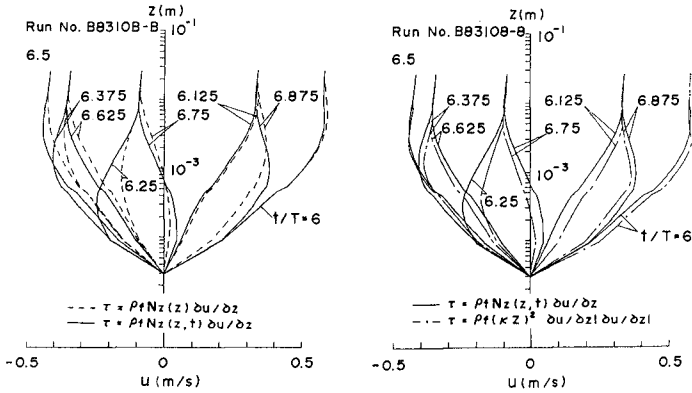


Fig.5 Velocity distributions in the turbulent boundary layer.

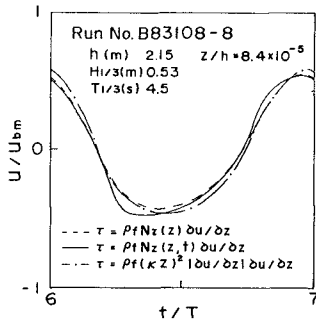


Fig.6 Temporal variations of water particle velocity at the sand particle level.

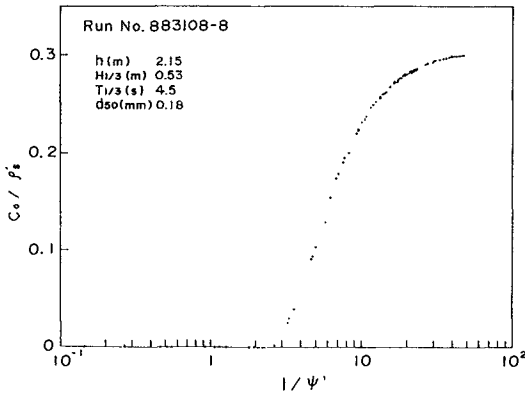


Fig.7 Relationship between the concentration in the bed-layer and $1/\psi'$.

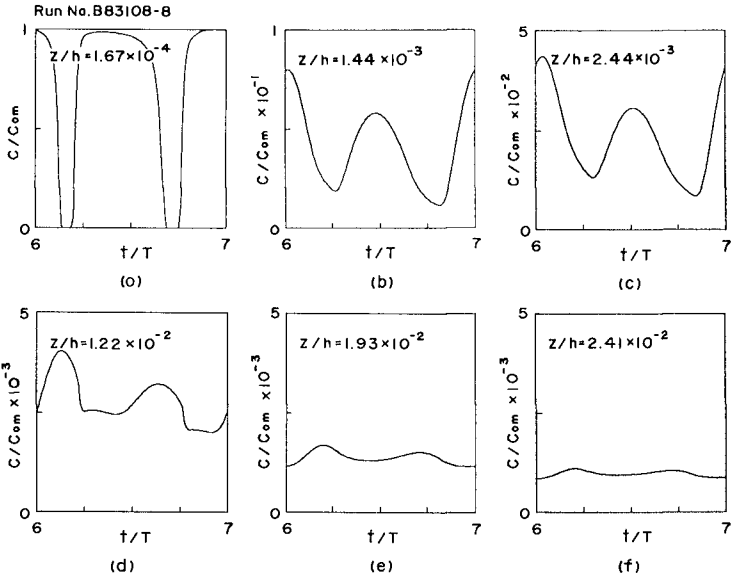


Fig.8 Temporal variations of suspended sediment concentration.

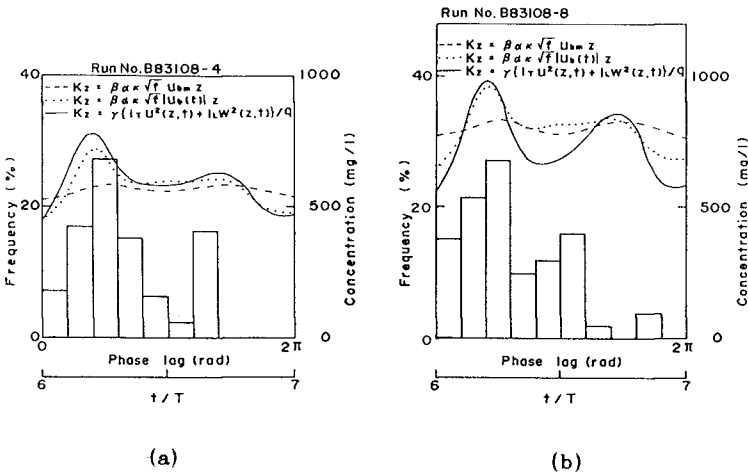


Fig.9 Computed temporal variations of suspended sediment and histogram of phase lag between maximum onshore velocity and maximum concentration observed in a wave cycle, where the frequencies of breaker occurrence are (a) 13% and (b) 19%.

elucidate the histogram of phase lag better than one computed by using Eq.(15-2).

(d) Vertical distributions of sediment concentration

Fig.10 shows the distributions of the computed suspended sediment concentration averaged over a wave cycle in comparison with those observed. The broken, solid and dotted lines are in the case that the shear stresses are evaluated by using Eq.(8-2) and the turbulent diffusion coefficients are evaluated by using Eqs.(15-1),(15-2) and (15-3) respectively. In the present analysis the constant of proportionality, α , in Eq.(8-2) is set to be equal to 0.1. The steepening of the profiles occurs at lower level above the bottom. However, the computed distributions that the turbulent diffusion coefficients are evaluated by using Eqs.(15-1) and (15-2) could not elucidate the suspended sediment concentration at higher levels above the bottom. It is,however,worth noting that the distribution of suspended sediment concentration calculated by using Eq.(15-3) could elucidate the concentration at the level farther from the bottom.

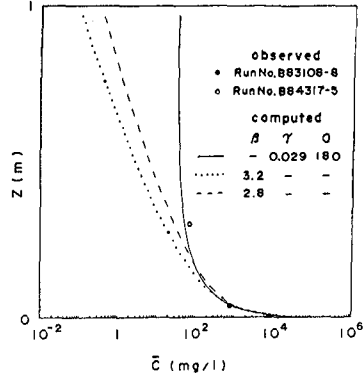


Fig.10 Distributions of mean suspended sediment concentration.

Fig.11 shows the distributions of the computed mean suspended sediment concentration in comparison with those observed; (a) and (b) are in the case of non-breaking wave by Noda and plunging breaker by Nielsen. The solid and dot-dash lines are in the case that the shear stresses are evaluated by using time-dependent eddy viscosity and Eq.(8-2) and the turbulent diffusion coefficient is evaluated by using Eq.(15-3) respectively. In the present analysis the constant of proportionality, α , in Eq.(8-2) is set to be equal to 0.1. Though exhibiting appreciable discrepancy, the computed distributions agree well with those observed.

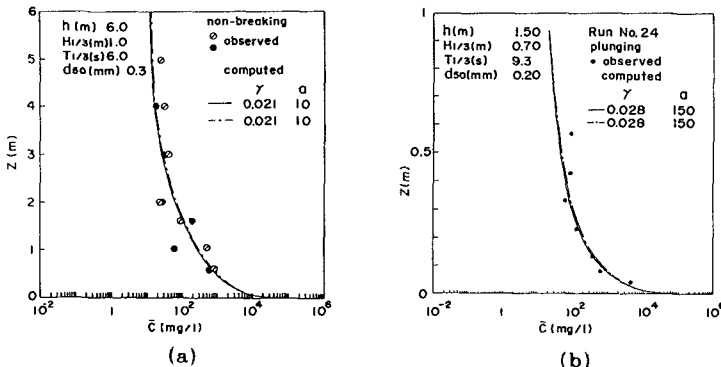


Fig.11 Distributions of mean suspended sediment concentration; (a) Noda's data, (b) Nielsen's data.

5.3 Relationship between γ , a and characteristics of wave and bed material

Fig.12 shows the relationship between the constant of proportionality γ in Eq.(15-3) and the ratio of significant wave height to the median diameter $H_{1/3}/d_{50}$. With increasing $H_{1/3}/d_{50}$, the constant of proportionality, γ , decreases. For the same value of $H_{1/3}/d_{50}$, the constant of proportionality, γ , is largest for the plunging breaker.

Fig.13 shows the relation between the constant of proportionality, a , in Eq.(15-3) and the ratio of significant wave height to the mean water depth, the constant of proportionality, a , increases.

5.3 Turbulent diffusion coefficient

Fig.14 shows the distributions of the nondimensional turbulent diffusion coefficient which could elucidate the observed distributions of suspended sediment concentration; (a) and (b) are in the case of non-breaking wave by Noda and plunging breaker by Nielsen respectively. In this figure solid lines represent the instantaneous values of turbulent diffusion coefficient and the broken line represents the value averaged over a wave cycle. The symbols represent the value computed by Eq.(18) on the basis of the distributions of mean suspended sediment concentration. The nondimensional turbulent diffusion coefficient averaged over a wave cycle is proportional to z/h from the bottom to the level that the relative height is approximately 0.1 and proportional to $(z/h)^2$ at levels farther from the bottom.

$$\bar{K}_z = -w_0 \bar{C} / (\partial \bar{C} / \partial z) \quad (18)$$

where \bar{C} is the time-averaged sediment concentration.

6. Conclusions

Velocity, pressure fluctuation and suspended sediment concentration were measured near the bottom in the surf zone. The results were discussed in comparison with the calculated velocity distribution in the turbulent boundary layer and suspended sediment concentration. The following conclusions have been obtained through the present study.

(1) The histogram of phase lag between maximum concentration and maximum onshore velocity during a wave cycle exhibit peaks at phases $\pi/2$ and 1.1π or 1.3π .

(2) Good agreement between the observed results and the computed results is obtained concerning the phase lag between concentration and water particle velocity and mean value of suspended sediment concentration.

(3) The turbulent diffusion coefficient averaged over a wave cycle is proportional to z/h near the bottom and proportional to $(z/h)^2$ near the water surface.

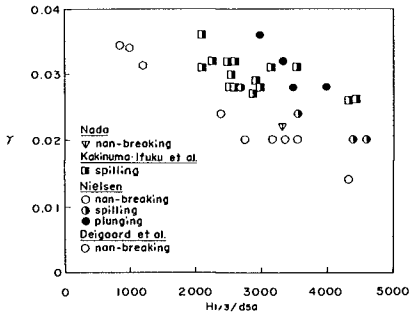


Fig.12 Proportional constant, γ as a function of $H_{1/3}/d_{50}$.

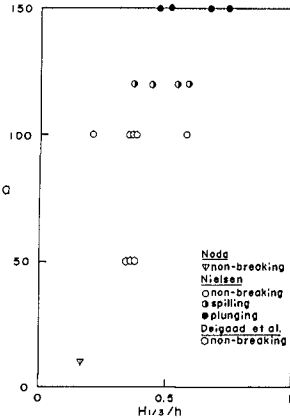


Fig.13 Proportional constant, α as a function of $H_{1/3}/h$.

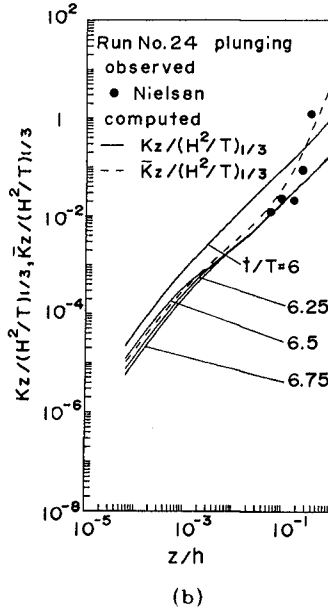
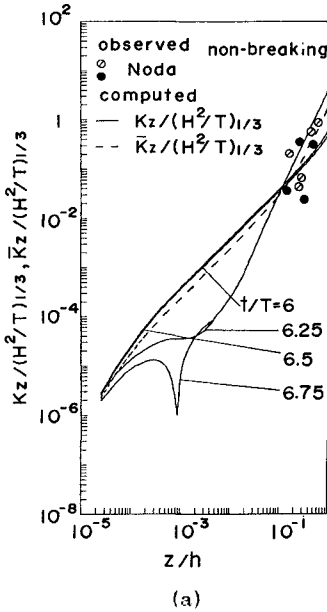


Fig.14 Nondimensional turbulent diffusion coefficient as a function of relative height.

References

- 1) Bakker, W.T. and Th. van Doorn(1978): Near bottom velocities in waves with a current, Proc. 16th Coastal Eng. Conf., pp.1394-1413.
- 2) Brenninkmeyer, B.M.(1974): Mode and period of sand transport in the surf zone, Proc. 14th Coastal Eng. Conf., pp.812-827.
- 3) Deigaard, R., J.Fredsoe and I.B. Hedegaard(1986): Suspended sediment in the surf zone, J. Waterway, Port, Coastal and Ocean Eng., ASCE, pp.115-128.
- 4) Einstein, H.A. and El-Samni El. S.A.(1949): Hydrodynamic forces on a rough wall, Rev. Mod. Phys., pp.520-524.
- 5) Fairchild, J.C.(1959): Suspended sediment sampling in oscillatory wave action, Beach Erosion Board, Tech. Memo 115p..
- 6) Homma, M. and K. Horikawa(1962): Suspended sediment due to wave action, Proc. 8th Coastal Eng. Conf., pp.168-193.
- 7) Homma, M., K. Horikawa and R. Kajima(1965): A study on suspended sediment due to wave action, Coastal Eng. Japan, Vol.8, pp.85-103.
- 8) Kakinuma, T. and M. Ifuku(1985): Bottom friction factor on beaches, Proc. 32nd Japanese Conf. Coastal Eng., pp.234-237.(in Japanese)
- 9) Kalkanis, G.(1965): Transportation of bed material due to wave action, U.S.Army, Coastal Res.Center, Tech. Memo 2, pp.1-114.
- 10) Kestin, J.(1968): Boundary Layer Theory, 6th ed. McGraw Hill, p.108.
- 11) Nielsen, P.(1981): Dynamics and geometry of wave generated ripples, J.G.R., Vol.86, No.C7, pp.6467-6472.
- 12) Noda, H.(1967): Sediment suspension by waves, Proc. 14th Japanese Conf. Coastal Eng., pp.306-314.(in Japanese)
- 13) Noda, H.(1969): Development of turbulent boundary layer by waves, Proc. 16th Japanese Conf. Coastal Eng., pp.23-27.(in Japanese)
- 14) Sleath, J.F.A.(1982): The suspension of sand by waves, J. Hydraul. Res., Vol.19, pp.439-452.
- 15) U.S.Army Coastal Eng. Res. Center(1977): Shore Protection Manual, Vol.2, p.35.
- 16) Wright, L.D., R.T.Guza and A.D. Short(1982): Dynamics of high energy dissipative surf zone, Marine Geology, Vol.45, pp.41-61.

CHAPTER 124

VALIDATION OF CROSS-SHORE TRANSPORT FORMULATIONS

Richard J. Seymour, M.ASCE¹ and David Castel²

ABSTRACT

Seymour and King (1982) evaluated eight models for predicting cross-shore transport using beach profile data from the Torrey Pines experiment of the Nearshore Sediment Transport Study (NSTS). None of the models showed useful skill in predicting the sense, or direction, of transport. Three more data sets were acquired under NSTS and have been used in the present work to re-evaluate the original four models as well as another six not previously tested. The three new data sets include two nominally plane West Coast beaches and a barred beach on the Atlantic coast, each under a variety of wave conditions. Six of the models evaluated claimed a capability to predict the sense of the cross-shore transport, two predicted the beach slope as a result of cross-shore movement, and two gave detail predictions of changes to the beach profile position and shape.

The performance of the six models predicting direction of transport ranged from a skill factor of 0.49 (less than chance) to only 0.68. Five of the models required large changes to their calibration factor (usually based upon laboratory data) in order to have approximately the same skill in predicting erosion or accretion. One of the slope models was validated and the other gave no useful results. One of the two generalized models gave interesting results in predicting the time history of profile changes on the plane beaches for which it was developed. The other general model was not evaluated because it exhibited the lowest skill in predicting direction of transport.

INTRODUCTION

Following the first field experiment in the Nearshore Sediment Transport Study at Torrey Pines Beach, CA (see Seymour, 1983 for a review of the NSTS program) Seymour and King (1982) attempted to use the observed beach changes to evaluate the predictive capability of a number of formulations related to cross-shore transport. Of the twelve models reviewed, eight were found capable of making predictions of the transport knowing incident wave height and period - and in some cases the sand size and beach slope as well. The model performance was evaluated by determining the squared correlation coefficient between the beach face volume response and the forcing function prescribed by the model. The best of these, Dean (1973), based upon a dimensionless ratio that has come to be known as the Dean Number, and a modification by Hattori and Kawamata (1980) in which beach slope is added to the Dean Number, explained only about a third of the variance in the volume of the beach face. The other models ranged down to about 2% of the variance explained. This disappointing performance may have been due in part to the characteristics of the data set employed to test the models. A thorough analysis of this is given in Seymour (1988a), which concludes that the Torrey Pines data set was noisy, lacked significant erosional events, and was unlikely to provide general insights into cross-shore transport mechanisms.

¹ Head, Ocean Engineering Research Group

² Senior Engineer, Ocean Engineering Research Group, Scripps Institution of Oceanography, University of California San Diego, La Jolla, CA 92093

NSTS produced three other beach profile data sets which did not suffer from the problems seen with Torrey Pines. These sets, which included data on waves and tides as well as characteristic sand sizes, were published in Seymour (1986). The three locations were Leadbetter Beach at Santa Barbara, CA (29 day series), Scripps Beach at La Jolla, CA (25 day series) and Virginia Beach, VA (23 days with a one day gap in the profiles). Santa Barbara and Scripps are typically without bars except for breaker bars which form immediately following major erosive events. Virginia Beach typically has a within-surf-zone bar that moves rapidly in response to changing wave conditions. These three data sets provided an attractive opportunity to reevaluate the cross-shore models and to include some others that had not been treated in the earlier work.

SELECTION OF MODELS

Of the eight models evaluated in Seymour and King (1982), four were in a form which would allow the prediction of a threshold point - that is, the incident wave condition above which erosion would be predicted and below which accretion would be expected, for a given beach condition. These four were Dean (1973), Hattori and Kawamata (1980) and two models contained in Short (1978). Two other threshold-type models were added for this study, Quick and Har (1985) and Sunamura and Horikawa (1974). With the exception of Quick and Har, these models were formulated to give only the direction of cross-shore transport. The formulations for the six threshold models are shown in Table I.

Two other models were added that attempted to describe the beach slope. Dalrymple and Thompson (1976), using laboratory data, established a linear relationship between the slope at mean sea level and the Dean Number. Dean (1977) established empirically an exponential shape for beach profiles, independent of wave or sediment characteristics, which takes the form

$$Y = AX^m$$

where Y = water depth and X = offshore distance

Both of these models lent themselves to testing with the present data.

Finally, two models were added that claimed to predict the time history of changes to the beach profile caused by cross-shore transport. These were Quick and Har, mentioned above, and Swart (1976). The Quick and Har model establishes an equilibrium profile based upon the Dean Number in which the major readjustment is a rotation of the profile. The model of Swart is an empirically-based, numerical formulation which allows for both rotation and translation of the beach face. A description of these models is contained in Seymour (1988b).

EVALUATING THRESHOLD MODELS

To evaluate these models, time histories were prepared of the daily sediment loss or gain for each site based upon changes in the profiles. In each case, the changes were interpreted as being caused entirely by cross-shore transport. The rationale for this interpretation and an assessment of its validity for each site is provided in Seymour (1988a). The variability is shown in Figure 1. This quantitative record could then be converted to a binary form of time series in which only the sign of the change is preserved. The six models provide just such a binary (erode/accrete) prediction and this was compared to the measured result. The skill of the predictor is represented by two numbers: the percentages of correct predictions for accretion and for erosion. It was interesting to note that the original four models used in the Torrey Pines study all exhibited an almost complete one-sidedness with these data - that is, they tended to predict either all erosion or all accretion. They had nearly perfect skill in one direction and almost zero skill in the other. This characteristic is illustrated in Figure 2, which shows the as-formulated predictions of Dean's model. The two models added for this study had approximately equal skill (as formulated) in predicting erosion or accretion - but these skill factors were less than 0.5 and therefore not as effective as random chance predictions. The thresholds for all of the models were adjusted until they had a nearly equal skill in predicting either erosion or accretion. The results are shown in Table II.

Table I			
RESULTS OF THRESHOLD PREDICTION STUDIES			
Dean (1973)	$(2R)\frac{H}{wT}$	<	1 ONSHORE
		>	1 OFFSHORE
Short (1979) Height model	H	<	120 cm ONSHORE
		>	120 cm OFFSHORE
Short (1979) Power model	$\left[\frac{\rho g^2}{16\sigma}\right]H^2T$	<	30 Kw/m ONSHORE
		>	30 Kw/m OFFSHORE
Hattori and Kawamata (1980)	$2\frac{H\beta}{wT}$	<	0.5 ONSHORE
		>	0.5 OFFSHORE
Quick and Har (1985)	$\left[\frac{H}{wT}\right]_{INITIAL}$	>	$\left[\frac{H}{wT}\right]_{FINAL}$ ONSHORE
		<	$\left[\frac{H}{wT}\right]_{FINAL}$ OFFSHORE
Sunamura and Horikawa (1974)	$\frac{1.845}{g^{0.33}}H\frac{\beta^{0.27}}{(Td)^{0.67}}$	<	4 ONSHORE
		>	8 OFFSHORE

where:

R = arbitrary constant
H = deep water significant wave height
w = sediment fall speed
T = period of spectral peak
g = gravitational constant
 β = beach slope
 ρ = fluid density
d = diameter of sand grains

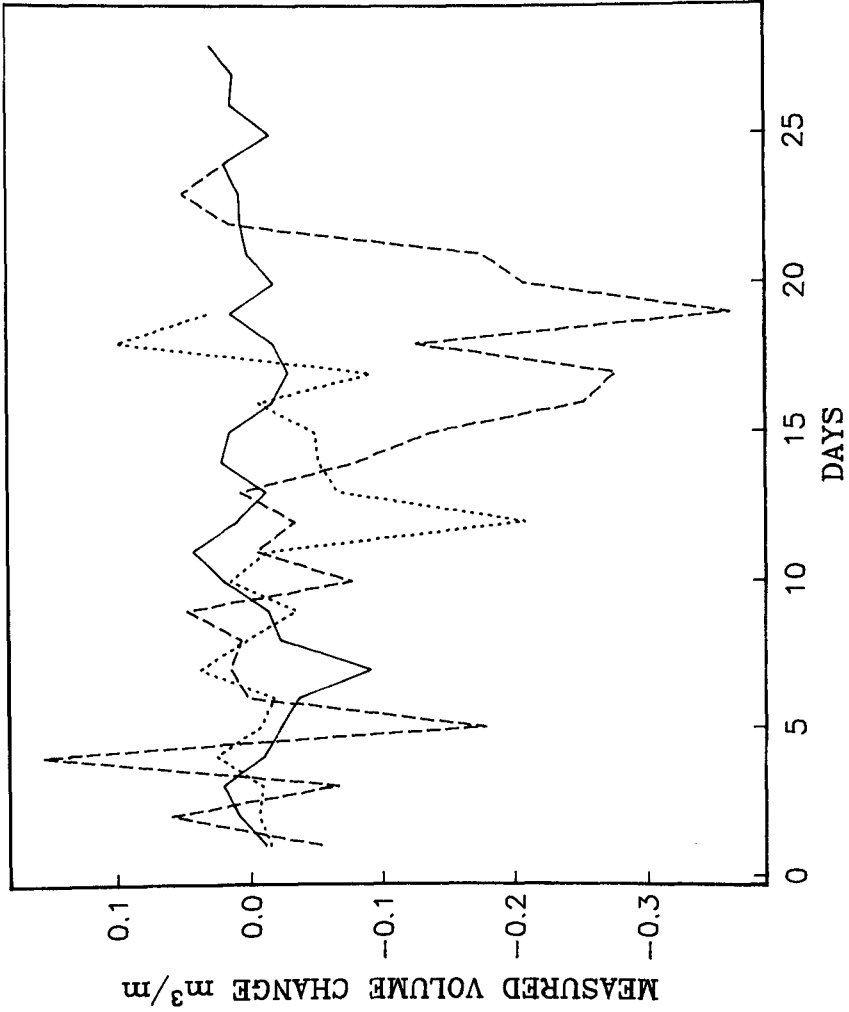


FIGURE 1

Time histories of the observed daily volume changes in the three data sets. (—) Scripps Beach, (-----) Santa Barbara, (.....) Virginia Beach.

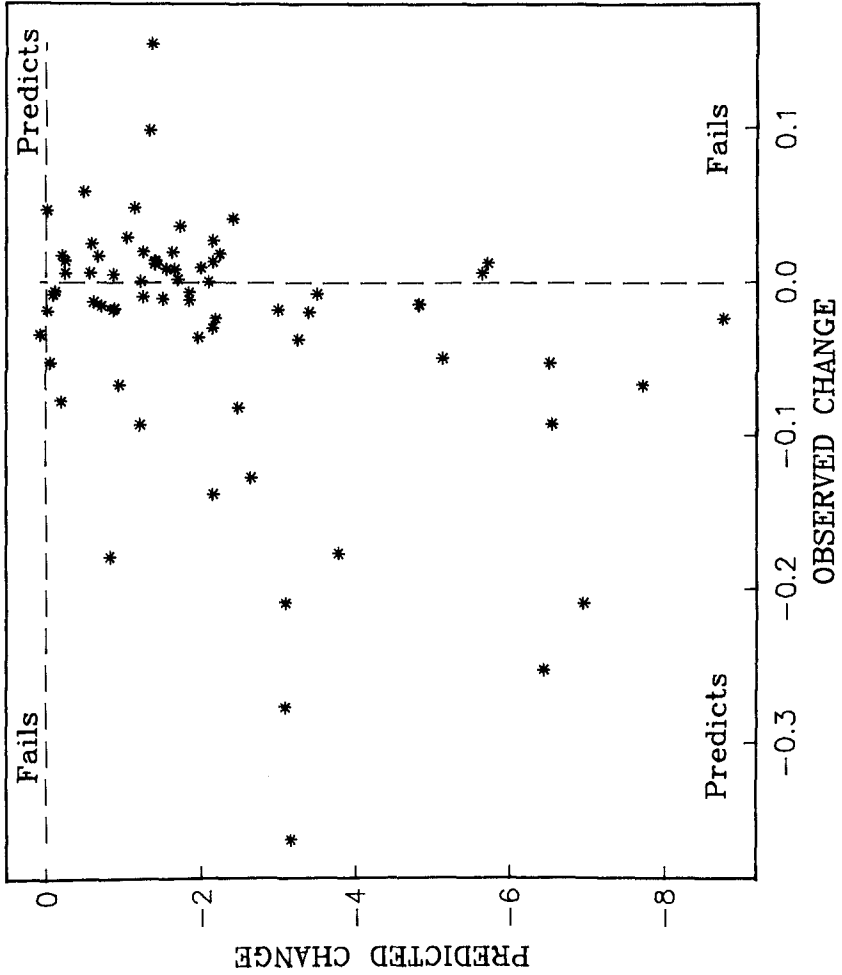


FIGURE 2

Comparisons of predictions of erosion or accretion using the model of Dean (1973) with observations. All three data sets are included.

TABLE II
RESULTS OF THRESHOLD PREDICTION STUDIES

Model	formulated threshold	adjusted threshold	skill factor
Dean	1.0	2.62	0.62
Short (height)	120	66	0.65
Short (power)	300	43	0.63
Hattori & Kawamata	0.5	0.064	0.68
Quick & Har	1.0	1.01	0.49
Sunamura & Horikawa	9-18	13.2	0.60

Inspection of Table II shows that the predictive capability of the best of these models is quite limited, with wrong estimates expected about one-third of the time. The worst of the models succeeds less often than chance alone. Therefore, they should be used with caution. Although the differences in predictive capability between models are barely significant, it is of interest to note two things. First, Short's model considering only wave height does as well as the more complex model of Dean that includes period and sediment size (indirectly, through fall speed). Second, the alteration to the Dean Number by Hattori and Kawamata in adding the beach slope causes some increase in predictive capability, adding credence to the generally-accepted idea that this parameter is a first order factor in cross-shore transport.

EVALUATING SLOPE PREDICTION MODELS

Two models that attempt to describe the general slope or shape of the beach were evaluated against this data base. The first, by Dalrymple and Thompson (1976), gives a graphical relationship between the beach slope at mean sea level and the Dean Number. The validity of this relationship was tested by calculating slopes for each profile and plotting them against the corresponding Dean Number. The results are shown in Figure 3. Inspection of this plot shows that the proportionality found under monochromatic laboratory waves is not seen in the field. There appears to be no discernible effect of Dean Number on beach slope for these data.

The second relationship tested was the exponential profile contained in Dean (1977) and described above. Best fit values for the coefficient A and the exponent m were plotted for each profile. A smoothed histogram of the distributions of these parameters are shown in Figure 4. Dean gave a typical value of 0.67 for the exponent, m , based upon Atlantic and Gulf Coast data. Figure 4 shows good agreement for these data as well. The value of the coefficient, A , is site-specific, varying from 0.065 to 0.13 and increasing with increasing sediment size, as predicted by Dean (1977). All three sites in this data set are well characterized by the $X^{0.67}$ model.

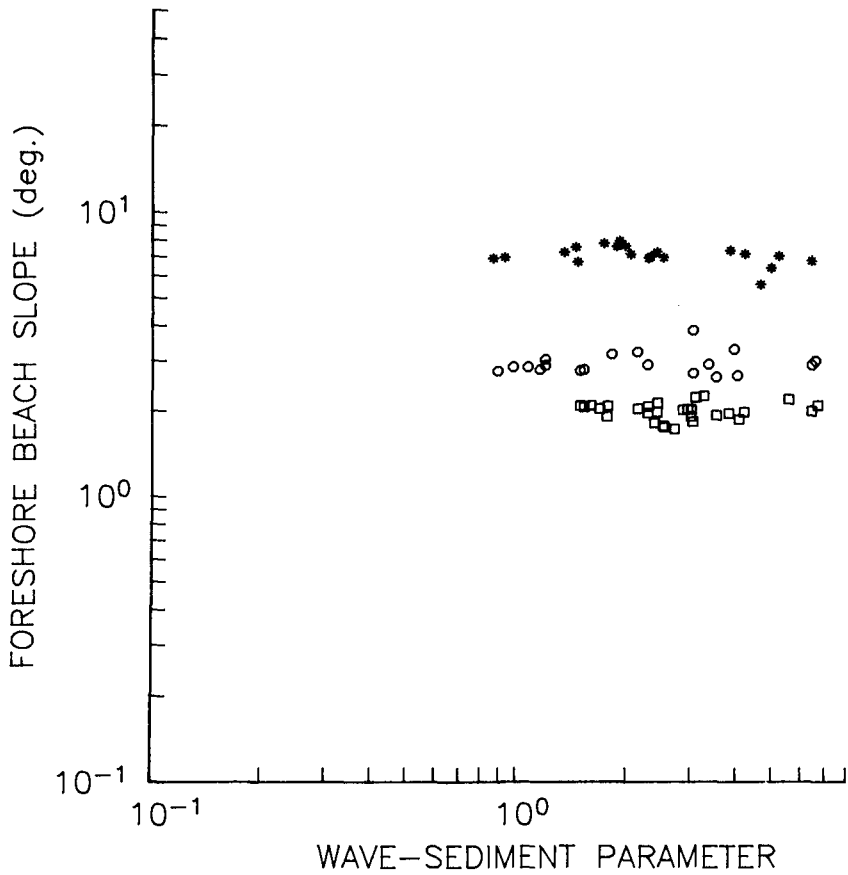


FIGURE 3

Beach slope compared to Dean Number (Wave Sediment Parameter) as described in Dalrymple and Thompson (1976). \square Scripps Beach, \circ Santa Barbara, and $*$ Virginia Beach.

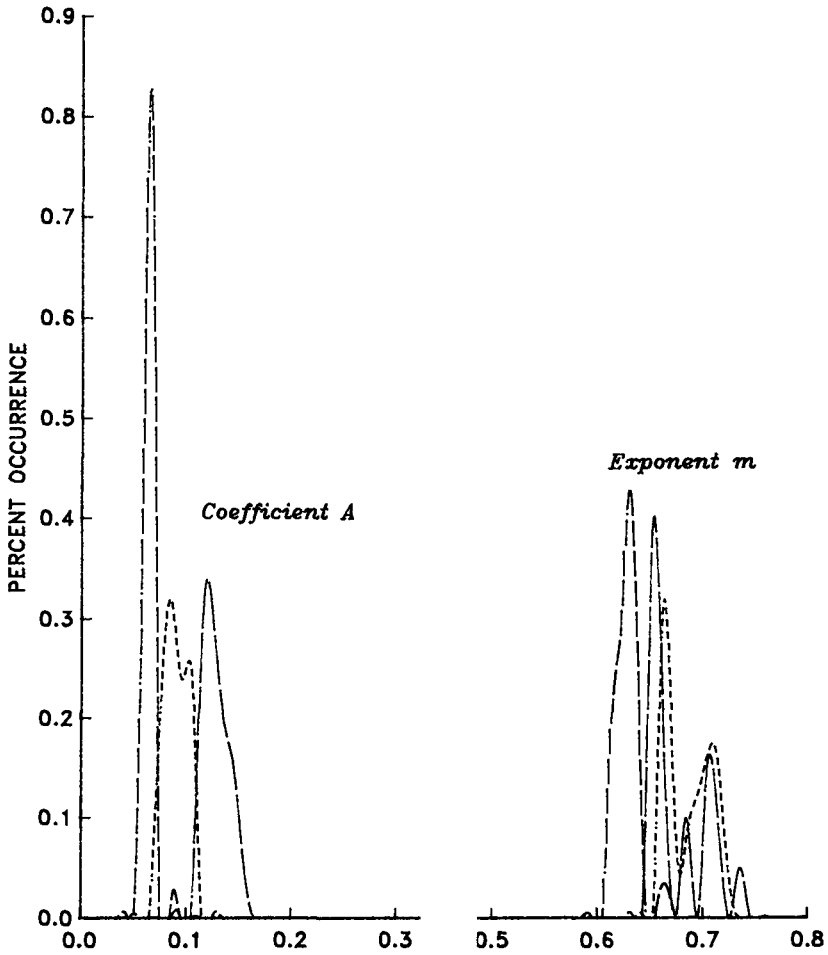


FIGURE 4

Smoothed histograms of the occurrences of the coefficients and exponents in the power law for beach contours from Dean (1977) in the form $Y = AX^m$. [Data from Santa Barbara has the shortest dash length, Scripps Beach has intermediate dash length and Virginia Beach has the largest dashes.]

EVALUATING PROFILE CHANGE MODELS

The model of Quick and Har (1985) was used in the threshold evaluations, where it showed the least skill of any of those tested. This formulation, based as most others on monochromatic laboratory moveable bed experiments, assumes that the beach slope will rapidly adjust to a new slope (based upon the model of Dalrymple and Thompson) as Dean Number changes, and that this slope will then follow the Dean exponential form into deeper water. Therefore, according to this model, beach response to cross-shore forcing is dominated by slope adjustment. It is interesting to compare this with the results of the analysis by empirical orthogonal eigenfunctions of the change in profiles in this data set contained in Seymour (1988a). This study shows that 97% of the variance about the mean profile at Santa Barbara was caused by horizontal motion of the profile without change of slope or shape. Only in the Scripps Beach set was there any substantial effect of slope change (coupled with a change in concavity) but the hinge point was well above mean sea level, rather than below as predicted by Quick and Har. Given the poor performance in predicting direction and its dependence on the Dalrymple and Thompson model, the decision was made not to undertake the substantial task of programming this model for varying tidal elevations and no further evaluations of it were performed.

Swain and Houston (1983, 1984) and Swain (1984) had shown that the model of Swart (1976) exhibited some skill in modeling the major erosional event at Santa Barbara. The Swart model has a number of relatively complex geometric constraints on the profile and its rate of change that depend, in general, on how far it differs from some equilibrium profile (which is never achieved, in practice.) Seymour (1988b) contains a description of the major attributes of this model, which allows for changing sea level through tides.

The Swart model was evaluated by setting the initial profile, inputting wave height, period and tide height changes, and allowing it to proceed without further correction through the entire data set for each site. The results for each case are shown in Figures 5 through 7. The model shows interesting skill in predicting the Scripps Beach and Santa Barbara sets, which are of the unbarred type for which the model was formulated. The Virginia Beach set, which is dominated by bar movement rather than beach face excursion, is not modeled satisfactorily by the Swart model. The model was used without adjustment of any of the parameters. It is clear from Figure 6, the Santa Barbara simulation, that the model moves much faster than nature and that significant improvement in predictive skill could have been achieved by some alterations to the time constants.

DISCUSSION AND CONCLUSIONS

This study has resulted in an objective analysis of a number of cross-shore transport models which, collectively, probably represent close to the present state of the art. The list of models evaluated was not exhaustive, but served to illustrate that the understanding of, and the corresponding ability to make useful predictions of, cross-shore transport lags well behind that of longshore transport.

The poor performance, or outright failure, of models based upon laboratory moveable bed experiments with monochromatic waves in predicting cross-shore transport in the field has been emphatically demonstrated by these findings. Taken in its entirety, this evidence suggests that there are very substantial differences in the response of sandy beaches to monochromatic and natural waves and that empirical relationships established in the laboratory with monochromatic waves are unlikely to produce useful predictive tools for real beach profile changes.

Further, the significant differences between the Virginia Beach response (which has been verified through the findings at Duck, NC - see, for example, Mason et al., 1984) and the West Coast beaches illustrates that a simple characterization of the sediment on the beach by a single grain diameter will not be enough to allow effective predictions. It is clear that the dominant sediment transport mechanisms are quite dissimilar for the two beach types. A realistic model for cross-shore transport, involving the necessary physics, appears to be well beyond the present state of the art.

Scripps Beach 10/08/80 - 11/04/80

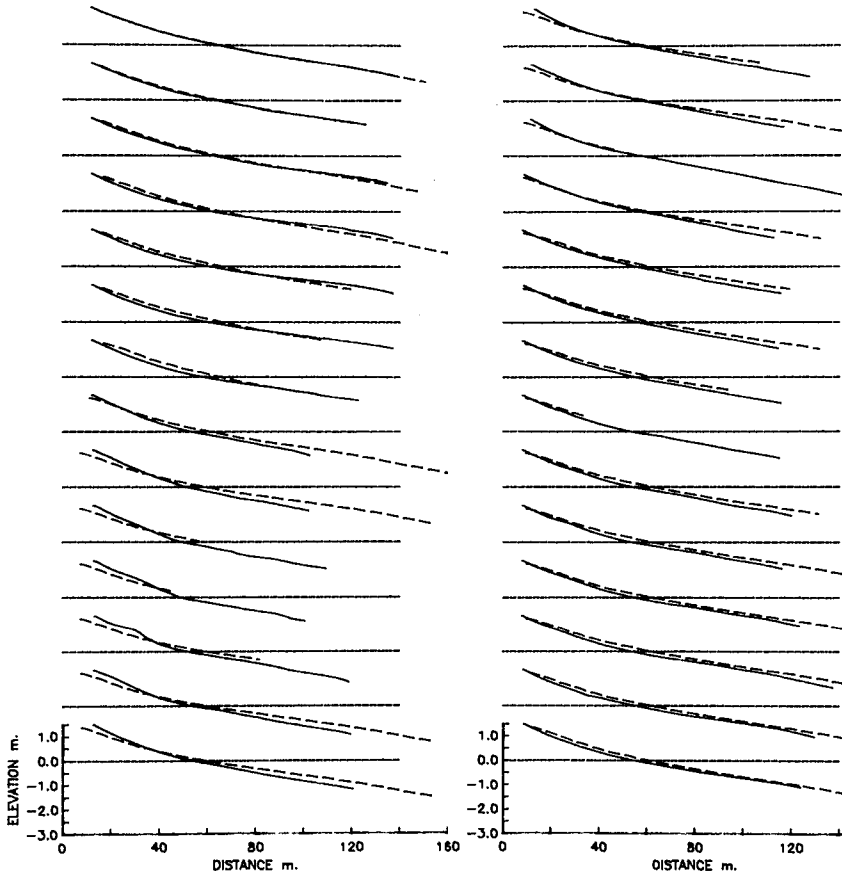


FIGURE 5

Comparison of observed beach profiles at Scripps Beach with the predictions using the model of Swart (1976). (-----) indicates predictions. Sequence starts at upper left and proceeds downward in each column. Horizontal lines are mean sea level.

Santa Barbara 2/1/80 - 2/25/80

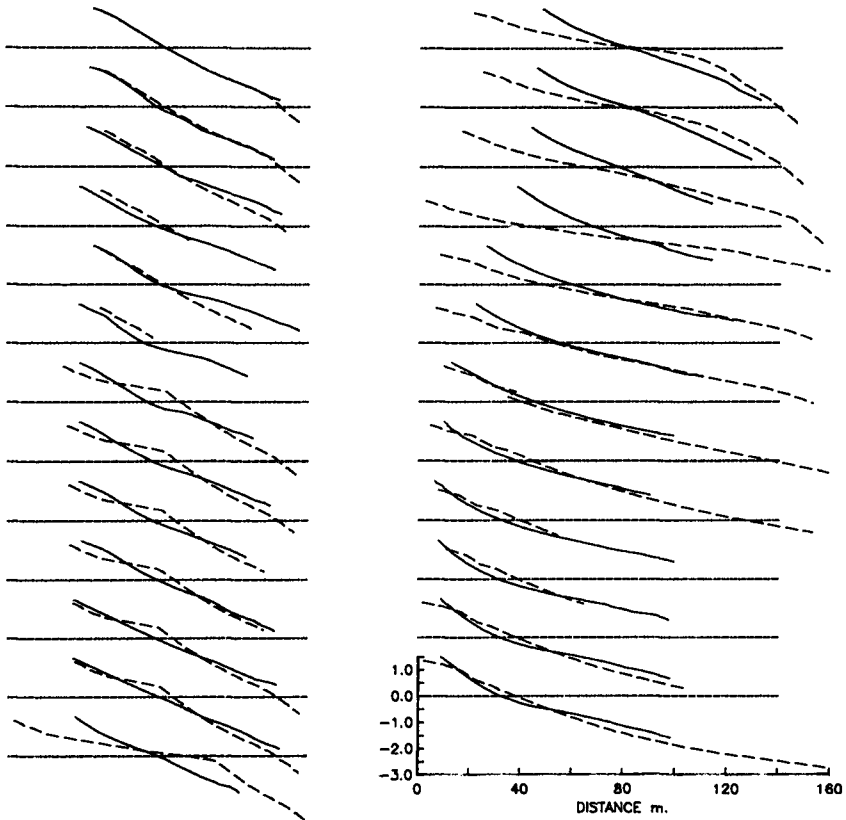


FIGURE 6

Comparisons of observed beach profiles at Santa Barbara with predictions from the model of Swart (1976).

Virginia Beach 10/1/80 - 10/20/80

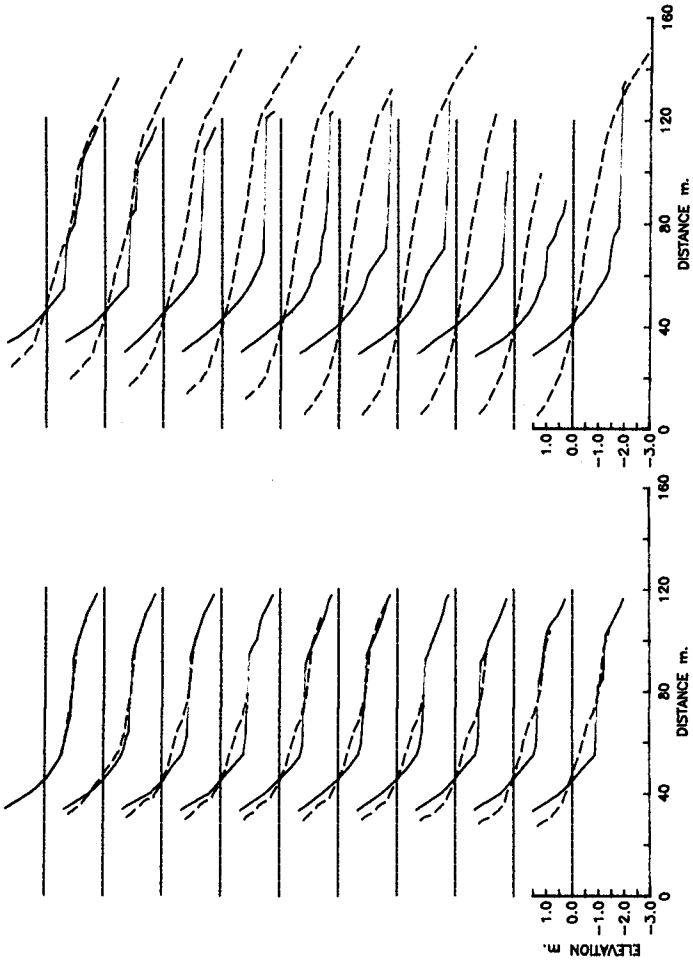


FIGURE 7

Comparisons of observed beach profiles at Virginia Beach with predictions from the model of Swart (1976).

REFERENCES

- Dalrymple, R. A. and W. W. Thompson, 1976. Study of equilibrium beach profiles, *Proceedings*, Fifteenth Coastal Engineering Conference, July 11-18, Honolulu, HI, ASCE, New York: 1277-1296.
- Dean, R. G., 1973. Heuristic models of sand transport in the surf zone, *Proceedings*, Conference on Engineering Dynamics in the Surf Zone, Sydney, Australia, 7 pp.
- _____, 1977. Equilibrium beach profiles: U. S. Atlantic and Gulf Coasts, Ocean Engineering Report No. 12, Department of Civil Engineering, University of Delaware, Newark, Delaware.
- Hattori, M. and R. Kawamata, 1980. Onshore-offshore transport and beach profile change, *Proceedings*, Seventeenth Coastal Engineering Conference, March 23-28, Sydney, Australia, ASCE, New York: 1175-1194.
- Mason, C., A.H. Sallenger, R.A. Holman and W.A. Birkemeier, 1984. DUCK82 - a coastal storm processes experiment. *Proceedings*, Nineteenth Coastal Engineering Conference, Houston, TX, September 3-7, ASCE, New York: 1913-1928.
- Quick, M. C. and B. C. Har, 1985. Criteria for onshore-offshore sediment movement on beaches, *Proceedings*, Canadian Coastal Conference, St. John's, Newfoundland: 257-269.
- Seymour, R. J., 1983. The nearshore sediment transport study. *J. Waterway, Port, Coastal and Ocean Div.*, Proc. ASCE, 109 (1): 79-85.
- _____, 1986. Results of cross-shore transport experiments, *J. Waterway, Port, Coastal, and Ocean Engineering*, ASCE, 112 (1): 168-173.
- _____, 1988a. Cross-shore transport. In: *Nearshore Sediment Transport*, R. J. Seymour, ed. Plenum Press, New York, in press.
- _____, 1988b. Modeling cross-shore transport. In: *Nearshore Sediment Transport*, R. J. Seymour, ed. Plenum Press, New York, in press.
- Seymour, R. J. and D. B. King Jr., 1982. Field comparisons of cross-shore transport models, *J. Waterway, Port, Coastal and Ocean Division*, *Proceedings*, ASCE, 108 (WW2): 163-179.
- Short, A. D., 1978. Wave power and beach stages: a global model, *Proceedings*, Sixteenth Coastal Engineering Conference, August 27-September 3, Hamburg, Germany, ASCE, New York, 2: 1145-1163.
- Sunamura, T. and K. Horikawa, 1974. Two-dimensional beach transformation due to waves, *Proceedings*, Fourteenth Coastal Engineering Conference, June 24-28, Copenhagen, Denmark, ASCE, N.Y.: 920-938.
- Swain, A., 1984. Additional results of a numerical model for beach profile development. *Proceedings* of the Annual Conference, CSCE, Halifax, Nova Scotia, Canada, May.
- Swain, A. and R. J. Houston, 1983. A numerical model for beach profile development. Sixth Canadian Hydrotechnical Conference, CSCE, Ottawa, Canada, June, 2: 77.
- _____, 1984. Discussion to the Proceeding Paper 17749 by Richard J. Seymour, The Nearshore Sediment Transport Study, *J. Waterway, Port, Coastal and Ocean Engineering*, ASCE, February, 110 (1): 130-133.
- Swart, D. H., 1976. Predictive equations regarding coastal transports, *Proceedings*, Fifteenth Coastal Engineering Conference, July 11-17, Honolulu, HI, ASCE, N.Y.: 1113-1132.

CHAPTER 125

A QUASI-3D MATHEMATICAL MODEL OF COASTAL MORPHOLOGY

H.J. de Vriend^{*)} and J.S. Ribberink^{*)}

ABSTRACT

A semi-analytical model of 3D nearshore currents and sediment transport is presented. It describes the tidal motion, the waves, the surfzone currents and the sediment transport in complex coastal areas. The results of a first application, to a well-documented case at the Dutch coast, indicate the potential and the shortcomings of the model. The latter are analysed and suggestions for improvement are given.

INTRODUCTION

Mathematical models are increasingly important as a tool to predict the water and sediment motion in coastal areas. Still, most of these models consider only part of the sediment transport. Roughly speaking, they describe either the "longshore" or the "cross-shore" transport. More carefully formulated, they consider either the transport along with the time- and depth-averaged current, or the transport due to waves and vertical circulations (undertow) in a more or less cross-shore profile. In complex situations, this distinction makes little sense and neither transport component can be disregarded. In these situations, the 3D time-dependent flow field and the attending sediment motion have to be described (cf. De Vriend, 1986).

In view of the wide range of time scales involved, from some seconds for the wind waves through to half a day for the tide, fully-3D time-dependent simulations are hardly feasible for practical applications. Therefore, simplified models have to be used, taking due account of the relevant phenomena.

De Vriend and Stive (1987) propose a semi-analytical model of 3D nearshore currents, based on hydrostaticity and similarity hypotheses for the velocity components and the eddy viscosity. This so-called DVS-model, in a slightly modified form, is combined here with a sediment transport model based on the Bagnold-Bailard concept (Bailard, 1981), to yield a quasi-3D coastal transport model.

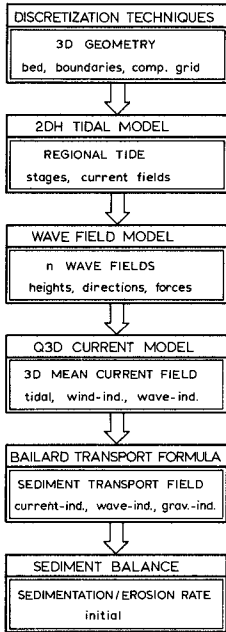
After a brief description of this model, a first practical application, with both "longshore" and "cross-shore" transport mechanisms at work, is described and discussed. It concerns the rapid formation of large sand bank systems on the former ebb-tidal deltas of the estuaries closed off by the Deltaworks (Kohsiek, 1988). The results are compared with field data, and the model formulation is reconsidered.

GENERAL OUTLINE OF THE MODEL

The model consists of the following basic elements (see Figure 1).

- A regional tidal model, giving the tidal stages and the boundary conditions for the flow model in the area of interest. The velocity field

^{*)} Senior researcher, DELFT HYDRAULICS, P.O. Box 152, 8300 AD EMMELOORD, The Netherlands



from this model can be used in the wave model, in order to have a rough indication of the effects of current refraction.

- A wave field model, describing the propagation and dissipation of wind waves in the area of interest.
- A quasi-3D current model, describing the wave orbital motion and the mean flow due to tide and wave action.
- A Bailard-type sediment transport formula, describing the near-bed transport due to waves (stirring, asymmetry transport) and currents ("convective" transport).
- The sediment balance equation, yielding the sedimentation/erosion rate under the given conditions.

These elements are put in line, as indicated in Figure 1, without any feedback mechanisms. This means that detailed current refraction, for instance, is disregarded, and that the dynamic interaction between the water and sediment motion and the bed topography changes are left out of consideration.

Figure 1 Aggregate flow chart of the quasi-3D morphological model

CURRENT MODEL

Primary and secondary flow

Key elements in the quasi-3D current model (De Vriend and Stive, 1987) are similarity approximations for the eddy viscosity, ν_t , and the wave-averaged velocity, \bar{U} :

$$\nu_t(x, y, z; t) = \bar{\nu}_t(x, y; t) \phi(\zeta) \quad (1)$$

$$\bar{U}(x, y, z; t) = \bar{U}(x, z; t) f_p(\zeta) + \sum_k \bar{U}_k(x, z; t) f_k(\zeta) \quad (2)$$

in which: x, y = horizontal co-ordinates,
 z = vertical co-ordinate,
 t = time,
 $\zeta = \frac{z - z_b}{h}$ = boundary-fitted vertical coordinate,
 z_b = bottom level,
 h = water depth, and
 $\bar{\cdot}$ = depth-average.

The first product in the RHS of (2) is called the "primary flow velocity". The vertical distribution function $f_p(\zeta)$ is chosen the same as in uniform shear flow under the same conditions (turbulence, waves, bed roughness, etc.). Hence the primary flow accounts for the (as yet unknown) depth-averaged velocity as if it concerned uniform shear flow.

The remaining part of the wave-mean velocity is called "secondary flow velocity", although this name is disputable. It is supposed to consist of a number of constituents, for each of which vertical similarity is assumed. In the present version of the model the secondary flow concerns

wave-induced undertow and boundary layer streaming, but there is no reason why it should be restricted to these phenomena.

In addition to the wave-mean velocity, there is an oscillatory velocity associated with the waves. For the time being, these velocities are simply added together, although in reality they are interacting (Davies et al., 1988; Klopman and De Vriend, 1988).

Depth-averaged current model

The depth-averaged mean velocity, \vec{U} , is computed with a horizontally two-dimensional shallow water model, including the effects of wind, tide and short waves. The latter exert their influence through the forcing, the bottom shear stress relationship and the mass balance (mass flux compensation). The wave influence on the horizontal eddy viscosity (Wind and Vreugdenhil, 1986; Yoo and O'Connor, 1988) is left out of consideration, as the model is meant for rather large-scale problems (model extension \gg surf zone width) with irregular waves.

The system of differential equations solved by the model can be written as

$$\frac{D\vec{U}}{Dt} = -g \vec{\nabla}(z_s) - \frac{\vec{\tau}_b}{\rho h} + \frac{\vec{F}_w}{\rho h} + \nu_h \vec{\nabla} \cdot \vec{\nabla}(\vec{U}) \quad (3)$$

$$\frac{\partial z_s}{\partial t} + \vec{\nabla} \cdot (h\vec{U}) + \vec{\nabla} \cdot \left(\frac{\vec{M}}{\rho}\right) = 0 \quad (4)$$

in which: g = acceleration due to gravity,
 z_s = level of the mean water surface,
 ρ = mass density of the fluid,
 $\vec{\tau}_b$ = bottom shear stress,
 \vec{F}_w = external driving force (wind, waves),
 ν_h = horizontal eddy viscosity, and
 \vec{M} = wave-induced mass flux.

Note that this system differs from the one in the DVS-model, in that the mass flux compensation is treated as a part of the primary flow, rather than as a secondary flow constituent. Thus the mass flux compensation can take place through a horizontal circulation or a circulation in the vertical plane, depending on the geometrical situation. Besides, it is continuous in the horizontal plane, now, so that the attending bed shear stresses and sediment transports are more smoothly distributed in space.

The wave-induced forces and mass fluxes can be derived explicitly from the wave model, as they depend on wave field properties only. The following formulations are used in the DVS-model

$$\vec{F}_w = \frac{D}{\omega} \vec{k}_w \quad (5)$$

$$\vec{M} = (1 + 7 \tilde{Q}_b \frac{h}{\lambda}) \frac{E}{\omega} \vec{k}_w \quad (6)$$

in which: D = energy dissipation rate per unit area,
 E = energy density of the wave field,
 ω = angular frequency of the waves,
 \vec{k}_w = wave number, as a vector in the direction of the wave energy flux,
 \tilde{Q}_b = fraction of the waves that is breaking ($0 \leq \tilde{Q}_b \leq 1$), and
 λ = wave length.

The bottom shear stress consists of two parts, due to the primary and the secondary flow, respectively. In the DVS-model, the secondary shear stress is supposed to be negligible in the depth-averaged flow computation. The primary shear stress depends on the current velocity and on the waves, so it cannot be computed on the basis of wave data only. In order to close the mathematical system (3) through (6), this shear stress has to be expressed in terms of the depth-averaged velocity.

In the present version of the depth-averaged current model, Bijker's (1966) shear stress enhancement formula is used, in the approximative form

$$\frac{\vec{\tau}_b}{\rho} = C_f \vec{U} |\vec{U}| \left[0.75 + 0.45 \left(\xi \frac{\hat{U}_{orb}}{|\vec{U}|} \right)^{1.13} \right] \geq C_f \vec{U} |\vec{U}| \quad (7)$$

in which: C_f = bottom friction factor for current only,

$$\xi = (f_w)^{\frac{1}{2}} (2C_f)^{-\frac{1}{2}},$$

f_w = Jonsson's (1966) friction factor for waves, and

\hat{U}_{orb} = amplitude of the near-bottom orbital velocity.

Following Visser's (1986) suggestion, the factor ξ is taken identically equal to 1. The orbital velocity in this expression is calculated as if it concerned regular and linear waves, with the mean amplitude and the peak period of the actual random wave field.

The shear stress relationship is closely connected with the turbulence model (vertical eddy viscosity, bottom boundary condition), and hence with the description of the primary velocity profile. In this respect, relationship (7) is not consistent with the original DVS-model (cf. Ribberink and De Vriend, 1988). Since the bed shear stress is the only aspect of the primary flow that is used in the sediment transport model, this inconsistency is not expected to have serious consequences for the model.

Primary flow profile

Consistently with the similarity assumption for the primary flow, the vertical profile function $f_p(\zeta)$ is solved from the horizontal momentum equation for uniform shear flow, rewritten to

$$\frac{\partial}{\partial \zeta} \left(\epsilon \frac{\partial f}{\partial \zeta} \right) = C_\tau \quad \text{with} \quad C_\tau \hat{=} \frac{|\vec{\tau}_{bp}| h}{\rho \bar{v}_c |\vec{U}|} \quad (8)$$

in which $\vec{\tau}_{bp}$ denotes the primary bottom shear stress.

With the parabolic/constant eddy viscosity distribution of the DVS-model and a prescribed level of zero-intersection of the (logarithmic) profile near the bottom, this leads to

$$f_p(\zeta) = \begin{cases} -\frac{3}{1+3 \ln(2F'\zeta_0)} \{ \ln \zeta - \ln(F'\zeta_0) \} & \text{for } F\zeta_0 \leq \zeta \leq \frac{1}{2} \\ \frac{3}{1+3 \ln(2F'\zeta_0)} \{ -2\zeta^2 + 4\zeta - \frac{3}{2} - \ln(2F'\zeta_0) \} & \text{for } \frac{1}{2} \leq \zeta \leq 1 \end{cases} \quad (9)$$

in which: ζ_0 = the level of zero-intersection for currents alone,

F' = amplification factor for the wave influence on the level of zero-intersection, and

$F\zeta_0$ = lowest level at which the logarithmic velocity profile holds good.

In the DVS-model, the amplification factor F' and F are formulated as proposed by Nielsen (1985). It is also possible, however, to choose a formulation that corresponds with (7):

$$F' = \exp \left[\kappa C_F^{-\frac{1}{2}} (1 - X_p^{-\frac{1}{2}}) \right] \quad (10)$$

in which κ denotes Von Karman's constant and X_p is defined by

$$X_p = \min \left\{ 1, 0.75 + 0.45 \left(\frac{\hat{U}_{orb}}{|\bar{U}|} \right) \right\} \quad (11)$$

Once F' is known, F follows from the same relationship as in Nielsen's model, viz.

$$F' = F \exp \left[\frac{1}{F} - 1 \right] \quad \text{and hence } F \approx eF' - 1 \quad (12)$$

in which e denotes the neperian.

Secondary flow

So far, the model has been elaborated for secondary flow due to wave breaking and for the residual streaming in the oscillatory boundary layer at the bottom.

Exploratory computations (De Vriend and Stive, 1987; Stive and De Vriend, 1987) indicate that the latter component is of minor importance to the short-term residual sediment transport. Therefore, only the breaking-induced secondary flow will be considered. The DVS-model uses the effective surface shear stress

$$\bar{\tau}_t = \left(\frac{1}{2} + 7 \frac{h}{\lambda} \right) \frac{D}{\omega} \bar{k}_w \quad (13)$$

to drive this part of the current, assuming $\bar{\tau}_t$ to act at the wave trough level, $\tau = \tau_t$. The corresponding secondary velocity can be written as

$$\bar{U}_1 = \bar{U}_{1,1} f_{s1}(\tau) + \bar{U}_{1,2} f_{s2}(\tau) \quad (14)$$

$$\text{with: } \bar{U}_{1,1} = \frac{\bar{\tau}_t h}{\rho \bar{v}_t \tau_t} \quad \text{and} \quad \bar{U}_{1,2} = \frac{\bar{\tau}_{bs} h}{\rho \bar{v}_t \tau_t} \quad (15)$$

Here $\bar{\tau}_{bs}$ denotes the secondary part of the bottom shear stress, directed along the vertical plane through the wave rays and as yet unknown in magnitude. The vertical distribution functions are those given by De Vriend and Stive (1987), which means that $f_{s1}(\tau)$ represents the velocity profile due to a surface shear stress and $f_{s2}(\tau)$ closely resembles the normal shear flow profile.

The magnitude of $\bar{\tau}_{bs}$ follows from the requirement that the depth-averaged secondary flow velocity must be zero. Hence

$$|\bar{\tau}_{bs}| = - \frac{\overline{f_{s1}} |\bar{\tau}_t|}{\overline{f_{s2}}} = - \left(\frac{1}{2} + 7 \frac{h}{\lambda} \right) \frac{\overline{f_{s1}} D}{\overline{f_{s2}} \omega} |\bar{k}_w| \quad (16)$$

$$\text{in which: } \overline{f_{s1}} = \frac{25}{144} \quad (17)$$

$$\overline{f_{s2}} = -\frac{25}{144} - \frac{5}{48} \tau_t \{-1 + 2 \ln(2F' \tau_o)\} \quad (18)$$

Note that the secondary flow is not the same as the flow due to the surface stress τ_t . The latter obviously has an f_{s1} -type profile. As $\overline{f_{s1}}$ is non-zero, however, the present framework of definitions, which forms the basis of the quasi-3D model, makes it necessary to split this flow into a primary and a secondary part, as shown in Figure 2. The secondary part is given by (14) sqq., the primary part is included in the primary flow model, with a minor inconsistency because $f_p(\zeta)$ and $f_{s2}(\zeta)$ are not exactly identical.

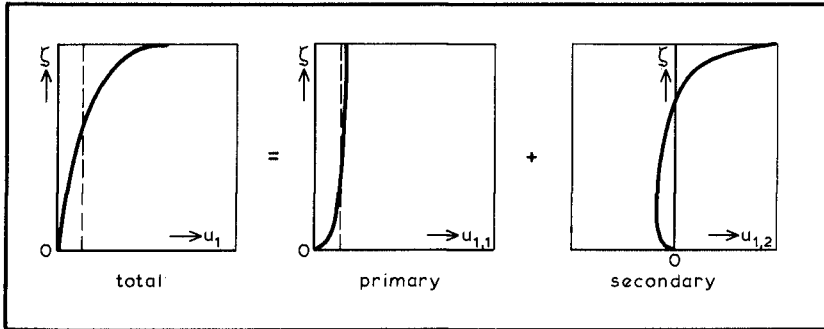


Figure 2 Splitting of the flow due to a surface shear stress

This primary flow contribution is driven by part of the wave-induced force \overline{F}_w in (3). This means that there is no guarantee for this contribution to be actually present. Depending on the geometrical situation, the relevant force field can just as well generate a water level set-up, or a current in a different direction, or any combination of these. Hence the interpretation of 3D currents due to breaking waves as a superposition of a longshore current with the primary profile and a cross-shore current (undertow) with the secondary profile (Svendsen and Lorenz, 1988) is only valid for very specific situations. In more general cases, a wide range of vectorial combinations of primary and secondary flow components can be found, and the notions "longshore" and "cross-shore" make no sense for such currents.

SEDIMENT TRANSPORT MODEL

Basic concept

A sediment transport model for coastal areas should include what uses to be called "longshore" and "cross-shore" transport components. In view of the discussion in the previous section, this should rather be "convective" and "wave-asymmetry" transport components.

Most of the usual coastal transport models pertain to the convective transport, with the wave-mean current as a transporting agent and wave action as one of the stirring mechanisms.

Such models are expected to fail in the complex situations considered herein.

On the other hand, the mechanisms underlying what is summarized by the term "wave-asymmetry" transport, such as vortex shedding at rippled beds

(Nielsen, 1988) and sheet-flow over a plane bed (Bakker and Van Kesteren, 1988), are far from being fully understood, let alone that well-established models would be available.

A pragmatic way-out is to adopt a sediment transport formula that is claimed to describe the instantaneous transport rate, and formally integrate the result over the waves. This approach was followed by e.g. Madsen and Grant (1976) and Bailard (1981). The latter adopted Bagnold's (1966) energetics approach and worked it out for colinear waves and currents. Although this model concept is still subject to doubt and will not apply to every possible set of conditions (cf. De Waal, 1987; Nielsen, 1988), it has yielded quite acceptable results in large-scale laboratory tests (Roelvink and Stive, 1988) and in practical applications (Stive, 1986). Therefore, it is incorporated in the present morphological model system, at least for the time being.

The transport formulae forming the Bailard-model, generalized to any vectorial combination of waves and currents, can be written as

$$\vec{q}_{bed} = A_{bc} \langle |\vec{U}_t|^2 \vec{U}_t \rangle - A_{bs} \langle |\vec{U}_t|^3 \rangle \vec{v}(z_b) \quad (19)$$

$$\vec{q}_{sus} = A_{sc} \langle |\vec{U}_t|^3 \vec{U}_t \rangle - A_{ss} \langle |\vec{U}_t|^5 \rangle \vec{v}(z_b) \quad (20)$$

in which: \vec{q}_{bed} = bed load transport rate,
 \vec{q}_{sus} = suspended-load transport rate,
 \vec{U}_t = equivalent instantaneous near-bed velocity,
 $A_{..}$ = factors depending on the sediment properties, etc., and
 $\langle .. \rangle$ = wave-average of the argument.

Note that this model includes both bed load and suspended-load transport. Besides, the down-slope gravitational transport component is taken into account in the bed load part. The bottom slope term in the suspended-load part represents the effect of convection by the slope-induced vertical velocity component.

Instantaneous near-bed velocity

The equivalent near-bed velocity, \vec{U}_t , in (19) and (20) remains to be specified. Following Bailard (1981), it consists of a mean and an oscillatory component. So, in a generalized form, this reads

$$\vec{U}_t = \vec{U}_o + \vec{U}_w \quad (21)$$

The definition of the mean flow part, \vec{U}_o , is not obvious, in view of the steep velocity gradients near the bottom. Bagnold's (1966) model was derived for steady uniform flow with a depth-invariant velocity and the usual quadratic friction law. Taking the bottom shear stress as determinative for the transport, the equivalent velocity can be expressed by

$$U_o = \left(\frac{\tau_b}{\rho C_f} \right)^{\frac{1}{2}} \quad (22)$$

or, in a generalized form for more complex steady flows,

$$\vec{U}_o = \frac{\vec{\tau}_b}{\rho C_f^{\frac{1}{2}} |\vec{U}_*|} \quad \text{with} \quad |\vec{U}_*| = \left(\frac{|\vec{\tau}_b|}{\rho} \right)^{\frac{1}{2}} \quad (23)$$

The oscillatory component of the equivalent near-bed velocity, \vec{U}_w , is filled in with the near-bed orbital velocity of waves in an inviscid fluid, as if there were no current and no bottom boundary layer. This is consistent with Bailard's (1981) approach.

Since wave-asymmetry is an important agent in wave-induced sediment transport, linear wave theory is not sufficient here. Instead, the orbital velocity is described with Rienecker and Fenton's (1981) Fourier-approximation technique for non-linear waves. Although the underlying theory is formally restricted to steady progressive waves on a horizontal bottom, the technique is applied throughout the wave field. Rienecker and Fenton showed this to be allowable for non-breaking waves, but the applicability to breaking waves is disputable. By lack of a good ready-to-use alternative, however, this point is ignored for the time being.

Elaboration of the time-mean transport

The formal algebraic elaboration of the generalized Bailard-formula, i.e. substitution of (21) into (19) and (20) and averaging over the wave period, becomes fairly complicated (cf. Guza and Thornton, 1985). Therefore, it was decided to evaluate the transport numerically in every point of the computational grid and at every time step of the computation. This turned out not to lead to prohibitive computer expenses.

VOORDELTA: A FIRST APPLICATION

Situation

The closure, as part of the Deltaworks, of several estuaries in the South-west of The Netherlands has started off a spectacular morphological evolution of the former ebb-tidal deltas (see, for instance, Kohsiek, 1988). After the in- and outgoing tide had been blocked, the dynamic equilibrium between the cross-shore actions of waves and currents was disturbed and the waves started pushing the seaward edges of the deltas onshore.

Within a decade, huge sand bank systems were formed in front of the barriers (Figure 3; also see: Van der Spek, 1987; Van den Berg, 1987), which raised questions about their future development and their impact on the coastal defence system, the local ecosystem, the possibilities of economical use, etcetera. Therefore, the Ministry of Public Works (Rijkswaterstaat) and DELFT HYDRAULICS are executing extensive studies in this area.

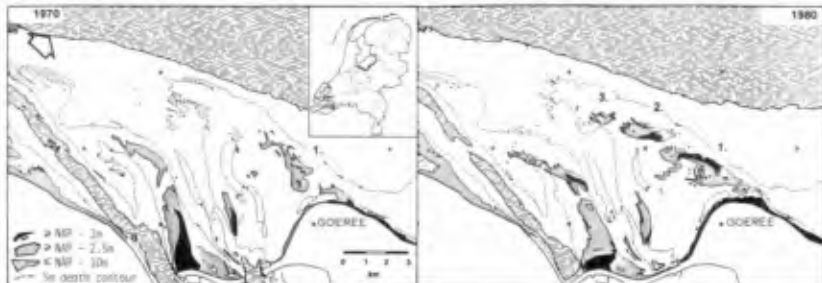


Figure 3 Deformation of the ebb-tidal delta in the mouth of the Grevelingen estuary, after closure of the Brouwersdam (from: Van der Spek, 1987)

As far as morphology is concerned, these studies are aiming at a better understanding and a hindcast of the observed phenomena, and at the prediction of future morphological developments.

As a part of these studies, a first practical application of the present model system was to hindcast and predict the morphological evolution of the ebb-tidal delta in front of the Brouwersdam, in the former mouth of the Grevelingen estuary (Figure 3).

Results of previous studies in the area

A preliminary hindcast study with a numerical model of coastal profile evolution (Stive, 1986; see Figure 4) indicated that the onshore transport due to wave asymmetry must be an important agent in the formation of the sand banks, with the offshore transport due to undertow and gravitational effects as a principal counteracting agent.

Further study of bathymetric and sedimentological data, and an extensive hindcast study with the coastal profile model (Steetzel and Stive, 1986) made clear, that the morphological processes in the later stages of development are essentially 3D, with an interaction between tidal and wave-induced currents. The following phenomena were expected to be important:

- "vertical" tide, with flooding and drying of sand banks and, correspondingly, time-varying wave penetration into the area behind the banks,
- tidal currents,
- wave-induced undertow,
- sediment stirring by waves, and
- wave-asymmetry transport.

A quasi-3D sediment transport model was set up in order to see how the combination of these phenomena works out, and as a tool in overall hindcast and forecast studies, for the Grevelingen delta as well as the adjacent Haringvliet and Eastern Scheldt deltas.

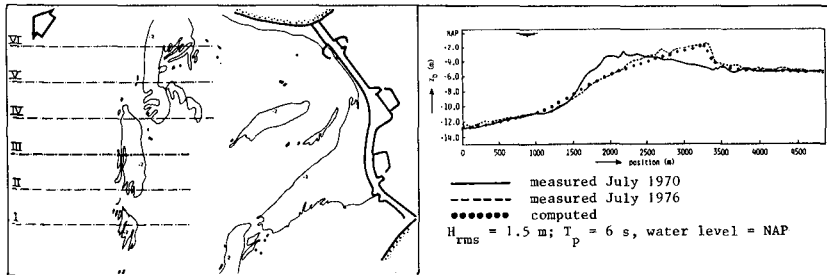
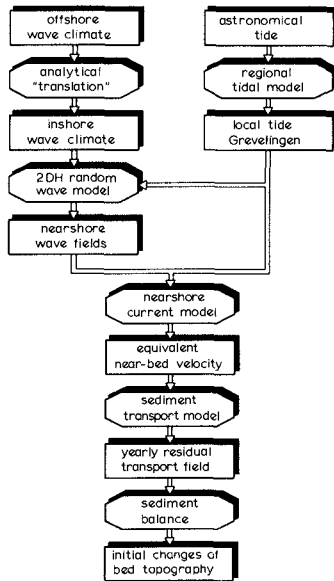


Figure 4 Results of hindcast with cross-shore profile model (from: Stive, 1986)

Set-up of the quasi-3D model for the Grevelingen delta

The composition of the quasi-3D model for the Grevelingen-area is outlined in Figure 5. The principal constituents are

- the regional tidal model RANDELTA-II (Langerak et al., 1978), based on the WAQUA-code and developed and validated to support the Deltaworks; this model is used to generate the tidal stages and a rough estimate of the current field to be put into the wave computations, and the tidal boundary conditions for the detailed current model,
- a series of wave models, one for each incoming wave direction, based on the HISWA-code (Holthuysen and Booij, 1986; Dingemans, 1987), which takes randomness of wave height and direction into account,
- a depth-integrated detailed current model for combined tidal and wave-induced currents, based on the curvilinear version of the WAQUA-code (Willemse et al., 1985), extended with wave effects as described in the foregoing (also see: De Vriend and Van Banning, 1988),



- the semi-analytical bottom shear stress model, including 3D flow effects, as described in the foregoing,
- the generalized Bailard transport formula, and
- a sediment balance module, yielding the initial rate of sedimentation and erosion for a given transport field.

Feedback mechanisms (wave-current interaction, topography-hydrodynamics interaction) are not included, for technical as well as economical reasons. This implies that the model results remain to be interpreted in terms of longer-term morphological evolutions.

The model constituents work on different types of grids and cover different areas, having the area of interest in common. This implies that a number of interfaces is needed to transform model results from one grid to another.

Figure 5 Flow chart Grevelingen model

The constituents, together with their interfaces and pre- and postprocessing facilities were brought together into an envelope system taking care of data management, job control, etcetera (cf. Boer et al., 1984). This made it possible to handle the large number of runs needed to represent the net effects of natural variability.

Schematization

Morphological changes, as a longer-term process, reflect the net effects of tide and wave climate, including their natural short-term variability. The model should therefore take this variability into account.

Since the system is multi-dimensional, complicated, and non-linear, spectral approaches and linear systems theory are likely to fail. Also a representative combination of tidal and wave conditions, yielding after e.g. one year the same morphological changes as the natural conditions, is hard to find, if it exists, at all. Therefore, a pragmatic schematization procedure was followed here (Van Banning and De Vriend, 1987; Steijn, 1988).

Key elements in this procedure are the selection of a morphologically equivalent tidal cycle and the schematization of the wave climate. The criterion for the tidal cycle selection is that the yearly transport rate, according to a given transport formula (in this case: Van Rijn's (1986) formula) should be the same for the repeated equivalent cycle and for the actual astronomical tide. In principle, this can yield a different equivalent cycle in every point of the model area. Therefore, a limited number of representative points was chosen, and the cycle with the best overall fit was selected.

The wave climate was schematized in three steps, viz.

- three representative wave directions (approximately NW, W and SW) were chosen on the basis of the available wave data,
- for each directional class, a representative wave height was chosen,
- each directional class, and the situation without waves, were attributed a certain weight, such that the weighed model results can be expected to represent the yearly transports and sedimentation/erosion rates.

Two criteria were used to determine these weights for the convective transport. The "longshore power" criterion (SPM, 1984) was used to account for the convective transport in the surf zone. The second criterion concerns the correct representation of the "stirring parameter", defined as the ratio between the primary bottom shear stress with and without waves. If this criterion is satisfied, the model is supposed to reproduce the convective transport outside the surfzone.

As the wave-asymmetry transport varies with a much higher power of the wave height than the convective transport, different weight factors were applied for this transport component. The criterion was a correct reproduction of the transport according to the Bailard formula without mean currents.

Like in the tidal schematization, full agreement can only be required in a small number of representative points.

Validation

A compound model like this is usually validated by checking the results of its principal constituents individually, and those of the model as a whole, against measured data, general observations, logical expectations, etcetera.

The available tidal data (water levels, current velocities) from the Grevelingen area were sufficient to check the detailed current model in situations without significant waves (Van der Spek and Steijn, 1988). Wave-driven current data, however, were not available in an identifiable form, so that earlier field and laboratory verifications (De Vriend and Van Banning, 1988) had to be relied upon.

Wave data from the area of interest are hardly available, but the wave model concept has been verified in the adjacent Haringvliet area (Holt-huijsen et al., 1988).

Sediment transport data are lacking, too, but the available sedimentological data (Van der Spek, 1987; Van den Berg, 1987) give some insight into the net displacement of sediment. Besides, the successful hindcast with the coastal profile model (Stive, 1986) gives confidence in the Bailard-formula.

In order to check the model as a whole, the morphological evolution of the area between the closure of the dam (1971) and 1984 was hindcasted and compared with bathymetric and sedimentological data. The outcome of this comparison will be discussed in the next sections.

ANALYSIS OF HINDCAST RESULTS

Results of the 2DH model version

In order to have a reference and a back-up for the quasi-3D model, a parallel run was made with a two-dimensional horizontal (2DH) version of the model, in which no secondary bottom shear stress was incorporated in the transport model. The results, shown in Figure 6, look rather satisfactory. Although the sediment transport rate is somewhat too high all over the area, the general picture from Figure 3 is represented: the bars tend to move onshore and towards the tip of the northern island, and a second array of bars tends to form half-way the first one and the dam. Besides, though not visible in the plots, the aggradation of the area behind the outer bars is reproduced.

Results of the quasi-3D model version

The results of the full quasi-3D model, including the secondary shear stress in the transport model, are shown in Figure 7. Even though the quasi-3D model takes more of the physical phenomena (viz. undertow) into

account than the 2DH model, its results are far worse: the bars are even moving seawards now!

This unexpected result needs further analysis. If the present case allows for a 2DH approach, the additional effects introduced by the quasi-3D model must be unimportant and should therefore do no harm. The present results show otherwise, which suggests that the quasi-3D model still contains a major inconsistency.

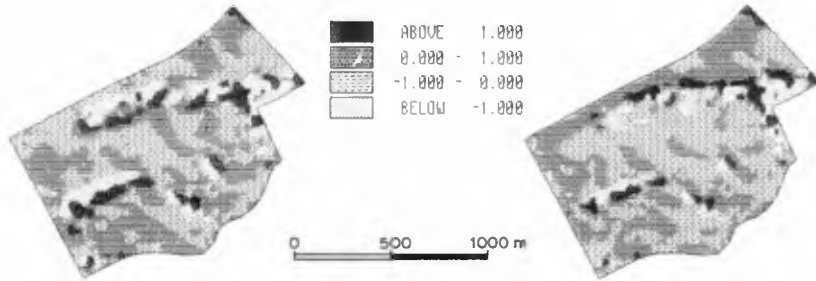


Figure 6 Sedimentation/erosion rate (2DH model version)

Figure 7 Sedimentation/erosion rate (quasi-3D model version)

Analysis and discussion

As was stated before, the hindcast studies with the cross-shore profile model indicated that the onshore wave-asymmetry transport should be the principal bank generating agent here, with the transport due to undertow and downslope gravitational effects as a counteracting agent. When introducing a net current across the bank, however, the undertow turned out to be easily dominated (Steetzel and Stive, 1986). According to the results of the 2DH detailed current model, such across-bank currents are present, indeed.

- The (NE-going) flood current is trapped between the coastline and the outer bank array and gives rise to a strong offshore current across the banks. The (SW-going) ebb current, however, more or less follows the alignment of the bank array, which is partly dry by that time. Hence the residual tidal current on the banks is directed offshore.
- Especially for waves from NW and W, the banks act more or less as an underwater bar, attached to Goeree at the one end and ending in the open sea at the other. This situation, which is very similar to the wave tank experiment reported by Dingemans et al. (1986), gives rise to a wave-induced horizontal circulation that is directed onshore on the top of the banks and directed towards the open-sea end in the channel behind them.

The velocities due to either of these currents dominate the undertow velocity. This suggests the bank formation to be due not only to wave-asymmetry transport, but also to the wave-induced horizontal circulation, with the residual tidal current as the principal counteracting agent. Besides, if the net effect is neatly reproduced by a cross-shore profile model containing much weaker currents only, the effects of the two currents must be almost balancing. This means that a relatively weak disturbance of this balance, e.g. by introducing 3D-effects in an inconsistent manner, can have strong effects.

Since the only difference between the 2DH and quasi-3D versions of the model lies in the secondary bottom shear stress, the quasi-3D model must be inconsistent in its incorporation of this stress. Upon closer inspec-

tion, the trouble must be caused by disregarding τ_{bs}^+ in the depth-averaged flow equations (3). This can be illustrated by considering the strongly simplified one-dimensional momentum equation

$$0 = -g \frac{\partial z}{\partial x} - \frac{\tau_{bx}}{\rho h} + \frac{F_{wx}}{\rho h} \quad (24)$$

in which the x-axis is directed onshore, perpendicular to the bank crest. Depending on the geometrical situation, the wave-induced force F_{wx} will contribute to sustaining a current or a set-up of the water level. In the Grevelingen area, with the wide channel behind the banks, only little set-up will build up. In that case, equation (24) reduces to

$$\tau_{bx} = F_{wx} \quad (25)$$

If the secondary shear stress is disregarded, like in the present model,

$$\tau_{bpx} = F_{wx} \quad (25)$$

In the sediment transport model, however, τ_{bs} is added to τ_{bp} , so

$$\tau_{bx} = \tau_{bpx} + \tau_{bsx} = F_{wx} + \tau_{bsx} \quad (26)$$

Since, according to (16), τ_{bsx} is negative (directed offshore; also see Figure 2), the onshore convective transport is systematically underestimated. This explains why the quasi-3D model predicts an offshore movement of the banks. It also explains why the 2DH-model works well in this particular situation with little set-up: the correct value of τ_{bx} is F_{wx} , and hence τ_{bpx} ! Although the 2DH model suffices for the Grevelingen area, this will not be so for all practical situations: set-up and undertow are not always negligible. Therefore, the inconsistency in the quasi-3D model has to be removed. The remedy is simple and straightforward: include τ_{bs}^+ in the depth-averaged current model.

CONCLUSIONS

A quasi-3D model of the yearly residual sediment transport and bed topography changes in complex coastal areas was applied to a practical situation, where previous studies had indicated that 3D effects (undertow) should be important.

In this particular case, however, a depth-integrated version of the model, without 3D effects, turned out to give a good hindcast of the observed morphological evolutions, in spite of remaining doubts about the transport model.

A comparison with the much worse results of the quasi-3D model provided the possibility to trace a major inconsistency in the latter: the secondary bottom shear stress should not be disregarded in the depth-averaged current model, if it is taken into account in the sediment transport model. Once this inconsistency has been removed, the model can be a useful tool for the analysis of morphological processes in complex coastal areas.

ACKNOWLEDGEMENT

The development of a pilot version of the model, as well as its application to the Grevelingen area, were performed by order of the Ministry of

Transport and Public Works (Rijkswaterstaat), by a joint project-team of this organization and DELFT HYDRAULICS. The authors are members of this team.

REFERENCES

- Bagnold, R.A., 1966. An approach to the sediment transport problem from general physics. USGS Prof. Paper, 422-1.
- Bailard, J.A., 1981. An energetics total load sediment transport model for a plane sloping beach. *J. Geoph. Res.*, **86**, C11, p. 10938-10954.
- Bakker, W.T. and Van Kesteren, W.G.M., 1986. The dynamics of oscillating sheetflow. Proc. 20th ICCE, Taipei, p. 940-954.
- Bijker, E.W., 1966. The increase of bed shear in a current due to wave action. Proc. 10th ICCE, Tokyo, p. 746-765.
- Boer, S., de Vriend, H.J. and Wind, H.G., 1984. A mathematical model for the simulation of morphological processes in the coastal area. Proc. 19th ICCE, Houston, p. 1437-1453.
- Davies, A.G., Soulsby, R.L. and King, H.L., 1988. A numerical model of the combined wave and current bottom boundary layer. *J. Geoph. Res.*, **93**, no. C1, p. 491-508.
- De Vriend, H.J., 1986. 2DH computations of transient sea bed evolutions. Proc. 20th ICCE, Taipei, p. 1698-1712.
- De Vriend, H.J. and Stive, M.J.F., 1987. Quasi-3D modelling of nearshore currents. *Coastal Engineering*, **11**, no. 5/6, p. 565-601.
- De Vriend, H.J. and Van Banning, 1988. Depth-averaged tidal and wave-induced current modelling for application in the Voordelta area of the Dutch coast. DELFT HYDRAULICS, Rept. H526-3 (in preparation).
- De Waal, J.C.M., 1987. Investigation on Bailard's transport formula, applied to cross-shore transport. Delft University of Technology, Dept. of Civil Engrg., M.Sc. thesis (in dutch).
- Dingemans, M.W., 1987. HISWA verification in the directional wave basin. DELFT HYDRAULICS, Rept. H228-1.
- Dingemans, M.W., Stive, M.J.F., Bosma, J., de Vriend, H.J., Vogel, J.A., 1986. Directional nearshore wave propagation and induced currents. Proc. 20th ICCE, Taipei, p. 1092-1106.
- Guza, R.T. and Thornton, E.B., 1985. Velocity moments in the nearshore. *J. Waterway, Port, Coastal and Ocean Engrg.*, **111**, no. 2, p. 235-256.
- Holthuijsen, L.B. and Booij, N., 1986. A grid model for shallow water waves. Proc. 20th ICCE, Taipei, p. 261-270.
- Holthuijsen, L.B., Booij, N. and Herbers, T.H.C., A prediction model for stationary short-crested waves in shallow water with ambient currents. To be published in *Coastal Engineering*.
- Jonsson, I.G., 1966. Wave boundary layers and friction factors. Proc. 10th ICCE, Tokyo, p. 127-148.
- Klopman, G. and De Vriend, H.J., 1988. Modelling of velocity profiles due to waves and currents in the coastal zone. Proc. 21st ICCE, Malaga.
- Kohsiek, L., 1987. Reworking of former ebb-tidal deltas into large long-shore bars following the artificial closure of tidal inlets in the southwest of The Netherlands. In: P.L. de Boer et al. (eds.) "Tide-influenced sedimentary environments and facies". Reidel Publ. Comp., Dordrecht.
- Langerak, A., de Ras, M.A.M. and Leendertse, J.J., 1978. Adjustment and verification of the Randdelta II model. Proc. 16th ICCE, Hamburg, p. 1049-1070.
- Madsen, O.S. and Grant, W.D., 1976. Sediment transport in the coastal environment. Mass. Inst. Techn., R.M. Parsons Lab., Rept. no. 209.
- Nielsen, P., 1985. A short manual of coastal bottom boundary layers and sediment transport. Public Works Dept. N.S. Wales, Coastal Engrg. Branch, Rept. TM 85/1.

- Nielsen, P., 1988. Three simple models of wave sediment transport. Coastal Engineering, 12, no. 1, p. 43-62.
- Ribberink, J.S. and De Vriend, H.J., 1988. Sediment transport formulations for waves and currents in the Voordelta area of the Dutch coast. DELFT HYDRAULICS, H526-2 (in preparation).
- Rienecker, M.M. and Fenton, J.D., 1981. A Fourier approximation method for steady waves. J. Fluid Mech., 104, p. 119-137.
- Roelvink, J.A. and Stive, M.J.F., 1988. Large scale tests of cross-shore sediment transport on the upper shoreface. Proc. IAHR-Symp. Sed. Transp. Coastal Zone, Copenhagen, p. 137-147.
- Shore Protection Manual, 1984. US Army Corps of Engineers, Waterways Exp. Station, Vicksburg.
- Stetzel, H.J. and Stive, M.J.F., 1986. Cross-shore transport study Voordelta. Delft Hydraulics Laboratory, Report H239 (in dutch).
- Steyn, R.C., 1988. Schematization of the natural conditions in multi-dimensional numerical models of coastal morphology. DELFT HYDRAULICS, Rept. H526-1 (in preparation).
- Stive, M.J.F., 1986. A model for cross-shore sediment transport. Proc. 20th ICCE, Taipei, p. 1551-1564.
- Stive, M.J.F. and De Vriend, H.J., 1987. Quasi-3D nearshore current modelling: wave-induced secondary current. Proc. ASCE Spec. Conf. "Coastal Hydrodynamics", Delaware p. 356-370.
- Svendsen, I.A. and Lorenz, R.S., 1988. Three dimensional flow profiles on littoral beaches. Proc. 21st ICCE, Malaga.
- Van Banning, G.K.F.M., de Vriend, H.J. and Boer, S., 1987. Schematization and validation of 2DH mathematical models in coastal morphology. Proc. "Coastal Sediments '87" Conf., New Orleans, p. 600-615.
- Van den Berg, J.H., 1987. Note on the isallobath map Voordelta 1975-1984. Rijkswaterstaat, Directorate Zeeland, Rept. ZL 87.0020 (in dutch).
- Van der Spek, A.J.F., 1987. Description of the development of the outer deltas of Haringvliet and Grevelingen. Rijkswaterstaat, Dept. Tidal Waters, Rept. GWA0-87-015 (in dutch).
- Van der Spek, A.J.F. and Steijn, R.C., 1988. Confrontation of mathematical model results and measured data for the Grevelingen outer delta. Rijkswaterstaat, Dept. Tidal Waters, Rept. GWA0-88.1320 (in prep.).
- Van Rijn, L.C., 1986. Three-dimensional modelling of suspended sediment transport for currents and waves. DELFT HYDRAULICS, Rept. H461/Q250/Q422.
- Visser, P.J., 1986. Wave basin experiments on bottom friction due to current and waves. Proc. 20th ICCE, Taipei, p. 807-821.
- Willemse, J.B.T.M., Stelling, G.S. and Verboom, G.K., 1986. Solving the shallow water equations with an orthogonal coordinate transformation. Int. Symp. Comp. Fluid Dyn., Tokyo (also: DELFT HYDRAULICS Comm. 356).
- Wind, H.G. and Vreugdenhil, C.B., 1986. Rip-current generation near structures. J. Fluid Mech., 171, p. 459-476.
- Yoo, D. and O'Connor, B.A., 1988. Turbulence transport modelling of wave-induced currents. Proc. Int. Conf. Comp. Mod. Ocean Engrg., Venice, p. 151-158 (Balkema, Rotterdam, 1988).

VERTICAL VARIABILITY OF COASTAL SEDIMENT TRANSPORT

Ryszard B. Zeidler*

ABSTRACT

The semiempirical theory of turbulent diffusion may be used as a mathematical tool for description of suspended sediment mechanics. The Author's solutions, with their exponential vertical profiles of sediment concentration, are presented in various ranges of time, space, and external factors. The inherent concept of eddy diffusivity K is shown to be ambiguous and incoherent. Therefore it is purposeless to investigate thoroughly the vertical profiles and other details of K . Accordingly, the Author makes use of his own and alien laboratory and field findings to propose such estimates of K under regular waves and currents which are not continuous functions of the vertical coordinate but instead are locally averaged over depth layers. These estimates become more complex in real coastal zones due to the randomness of waves and currents, wave breaking, three-dimensionality and nonstationarity of nearbed turbulence, a variety of interactions, and other sources of sediment dispersion. Hence gross estimates of averaged K seem even more appropriate; some formulae are put forward. The vertical profiles of sediment concentration are presented herein along with examples of sediment transport rates measured in nearshore zones.

1. SUSPENDED SEDIMENT IN TERMS OF DIFFUSION THEORIES

1.1. Analytical Solutions

The concentration of suspended sediment, C , in an unsteady two-dimensional flow with velocity u_0 may be described by the equation of turbulent diffusion

$$\frac{\partial C}{\partial t} + u_0(x, y) \frac{\partial C}{\partial x} = K_{01}(y) \frac{\partial^2 C}{\partial x^2} + \frac{\partial}{\partial y} (K_{02}(y) \frac{\partial C}{\partial y}) + w_s \frac{\partial C}{\partial y} \dots \quad (1)$$

in which

* Professor, Polish Academy of Sciences' Institute of Hydro-Engineering (IBW PAN), 7 Kościarska, 80-953 Gdańsk

K_{01}, K_{02} = eddy diffusivities
 w_s = settling velocity
 t = time.

The system of coordinates is shown in Fig. 1 where the initial and boundary conditions are outlined for the two problems distinguished, *A* and *B*.

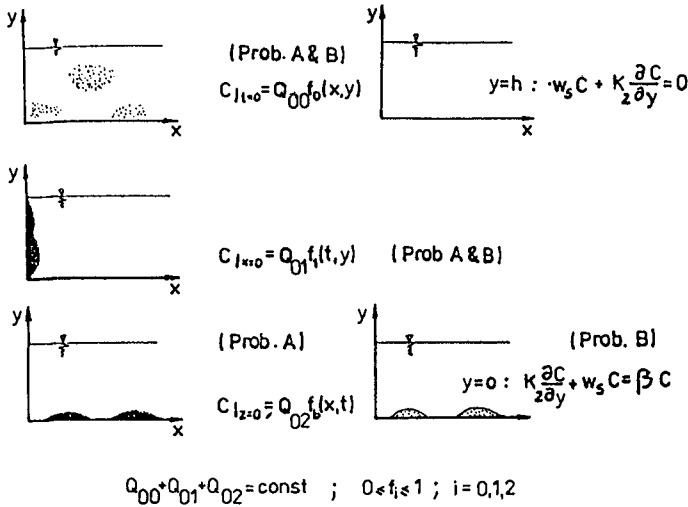


Fig. 1 Initial and Boundary Conditions

Eq. 1 in dimensionless form reads

$$\frac{\partial C^*}{\partial t^*} + 2au^*(x^*, y^*) \frac{\partial C^*}{\partial x^*} = \alpha_1^*(y^*) \frac{\partial^2 C^*}{\partial x^{*2}} + \alpha_2^*(y^*) \frac{\partial^2 C^*}{\partial y^{*2}} + (2b + \alpha_2^*(y^*)) \frac{\partial C^*}{\partial y^*} \quad (2)$$

in which

$$\begin{aligned} u_0 &= U u^*(x, y); & 0 \leq u^*(x, y) &\leq 1 \\ K_{01} &= K_1 \alpha_1^*(y); & 0 \leq \alpha_1^*(y) &\leq 1 \\ K_{02} &= K_{02} \alpha_2^*(y); & 0 \leq \alpha_2^*(y) &\leq 1 \\ a &= \frac{U \cdot h}{2\sqrt{K_1 \cdot K_2}}; & b &= \frac{w_s h}{2K_2}; & C^* &= \frac{C}{Q_{02}}; \\ x^* &= \sqrt{\frac{K_2}{K_1}} \frac{x}{h}; & y^* &= \frac{y}{h}; & t^* &= \frac{K_2}{h^2} t \end{aligned}$$

The asterisks will be neglected henceforth.

Eq. 2 has been solved for the so-called problem A_0 , with constant coefficients, and subsequently envelopes have been found for other versions of the problems A and B (Nguyen and Zeidler, 1982). The solution was obtained as polynomial series, by methods of integral transforms. It assumes the form

$$C(x, y, t) = C_1(x, y) + C_2(x, y, t) + Q_0 [C_3(y, t) + C_4(x, y, t)] + Q_1 [C_5(x, y) - C_6(x, y, t)] \quad (3)$$

in which each of the six terms $C_1 \dots C_6$ is linked to specific initial and boundary conditions, and $Q_0 = Q_{00}/Q_{02}$, $Q_1 = Q_{01}/Q_{02}$.

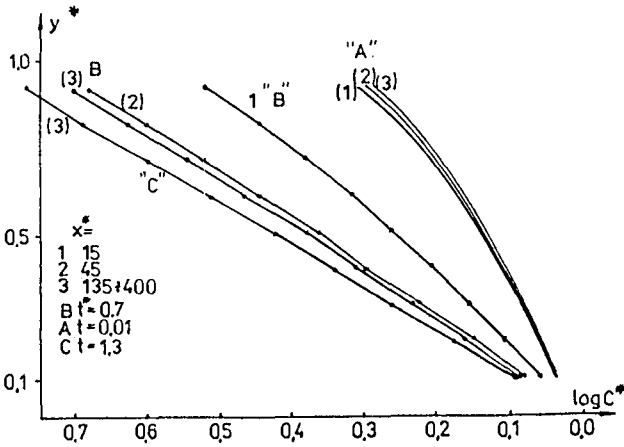


Fig. 2 Examples of Numerical Solutions to Problem A_0

The numerical results depicted in Fig. 2 make it easy to analyse Eq. 3. In the tested intervals of dimensionless $15 \leq x^* \leq 400$, $0.01 \leq t^* \leq 1.3$ one may see that the initial convex-up C -profiles, for $t^* = 0.1$, gradually transform into linear (in the semilog plot), for the longest time $t^* = 1.3$. Hence the concentration profiles in stabilized conditions (long $x \rightarrow X$ and $t \rightarrow T$) of the problem A_0 are exponential, as emphasized in Fig. 3a. Analysis of solutions to the other problems A and B (Nguyen and Zeidler, 1982) shows that they are contained within certain limits C^- and C^+ , as presented in Fig. 3b.

1.2. Experimental Evidence

It is appropriate to verify how Eq. 3 agrees with laboratory and field data. The vertical profiles of C have been checked as to their character, numerical values of the exponent b , and temporal variation. Longitudinal variation, $C(x)$, has been

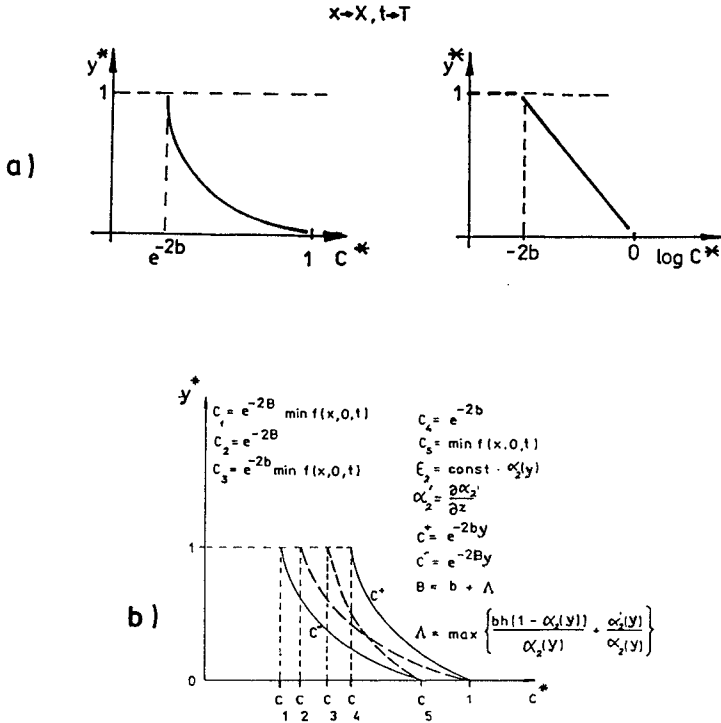


Fig. 3 Equilibrium Solutions to Problem A_0 (top) and to Problem A (bottom)

investigated, along with the effect of sand mixtures and other features. Several alien and three Polish sets of data, each embodying extensive series of C , have been employed, and many additional can be found in bibliographical sources. Some typical examples are presented below.

The numerous data utilized confirm the theoretical exponential vertical profile $C(y)$, with the following important modification. In the semilogarithmic plot, such as the one in Fig. 3a (right), the straight line is almost always replaced by two or three straight lines, in two or three layers: near-bed, central, and near-surface. The two lower layers are pronounced i.a. in the sets measured by Taggart et al (1972), who however adhered to the power-type profile, with corrections proposed

by A. T. Ippen. Fig. 4 shows that the exponential representation is much more natural if only the layered structure is accepted.

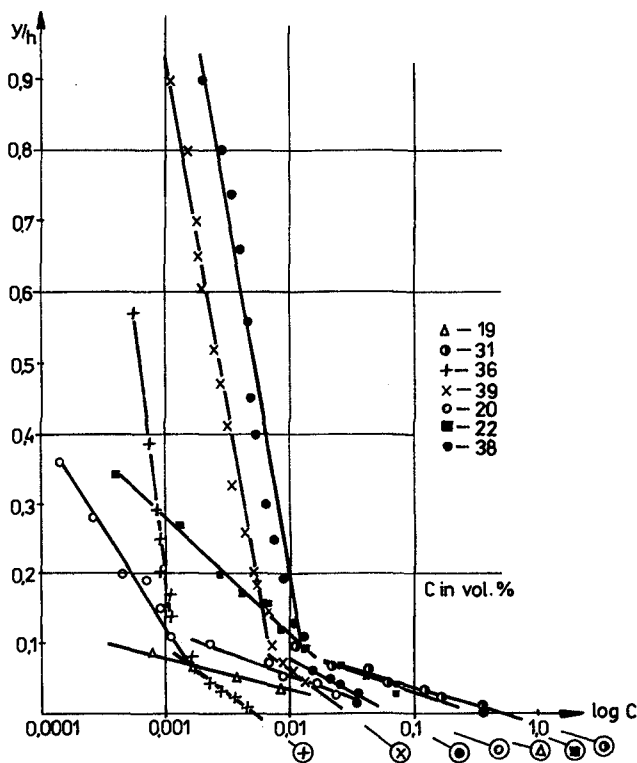


Fig. 4 Sediment Concentration Measured by Taggart et al (1972) in Runs 19...38

The theoretical exponent b agrees well with the experimental data if one assumes $b \approx 5 \frac{w_*}{u_*}$ near bed or $b \approx 2.5 \frac{w_*}{u_*}$ in the central layer; in which u_* = shear velocity. These figures are substantiated in Ch. 2.

One may postulate a few causes of the layered configuration of $C(z)$, such as sediment grading and the associated vertical variability of the von Karman constant.

However, the most important argument is due to the eddy diffusivity $K_y(y) \equiv K_{O_2}(y)$. It may be inferred that details of the variation of $K_y(y)$ are not essential and that a certain layer-averaged \bar{K}_y is sufficient to describe the basic features of $C(y)$, cf. Fig. 5. Further comments are provided in Ch. 2.

Numerous experimental data show that the layered exponential C -profiles are characteristic not only for flows but also under waves, cf. Skafel and Krishnappan

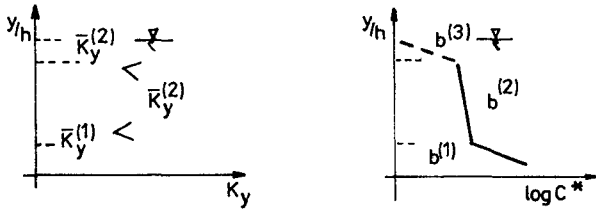


Fig. 5 Correspondence of Exponent b and Layer-Averaged \bar{K}_y

(1984), Antsyferov and Kosyan (1986) and many others. Some of the Author's results are presented in Ch. 3. It is also worth noting that such C -profiles are generated by different turbulence mechanisms, i.e. nearbed shear and friction, wave oscillations, wave breaking etc. Hence one may conclude that gross estimates of K , or its equivalents, provide better representation of complex coastal phenomena than detailed fields $K(y)$. These estimates are discussed in Ch. 3. The following arguments in Sec. 2.1 prove how ambiguous the detailed $K(\dots)$ could be.

2. EDDY DIFFUSIVITY IN THE COASTAL ZONE

2.1. Concept of Eddy Viscosity

The Reynolds equations read

$$\rho \frac{du}{dt} = \rho F - \text{grad } p + \mu \Delta u + \text{div } \Pi \tag{4}$$

in which

$u = iu_x + ju_y + ku_z =$ velocity

$F =$ external mass forces

$p, \rho =$ pressure and density, respectively

$\mu =$ dynamic coefficient of molecular viscosity,

while the Reynolds tensor Π is

$$\Pi = \begin{bmatrix} -\overline{\rho u_x'^2} - \overline{\rho u_x' u_y'} - \overline{\rho u_x' u_z'} \\ -\overline{\rho u_x' u_y'} - \overline{\rho u_y'^2} - \overline{\rho u_y' u_z'} \\ -\overline{\rho u_x' u_z'} - \overline{\rho u_y' u_z'} - \overline{\rho u_z'^2} \end{bmatrix} \tag{5}$$

One may distinguish diffusion theories, in which Π is coupled with the mean strain rate tensor S , and "differential" models, with expanded equations for Π . Let us dwell on the diffusion theory, and consider a few cases

1. Scalar eddy viscosity, homogeneous constitutive equation

$$\Pi_{ij} = \mu_T S_{ij} \quad (6)$$

The following defects are inherent

- (a) For $S_{ij} \rightarrow 0$ (and $u \neq 0$) one obtains $\Pi_{ij} \rightarrow 0$, which does not explain the occurrence of Π_{ij} in isotropic turbulence
- (b) Each component of Π_{ij} depends on one component of S_{ij} , in disagreement with observations, e.g. spatial structure of turbulence in 1-D flows
- (c) Traces of both sides in Eq. 6 disagree, i.e. $\text{tr}\Pi = -2\rho k < 0$

$$\text{tr}(\mu_T S) = \begin{cases} \mu_T \text{div}u = 0 & \text{for } \rho = \text{const} \\ \mu_T \text{div}u = -\frac{\mu_T}{\rho} \frac{d\rho}{dt} > < & \text{for } \rho \neq \text{const} \end{cases} \quad (7)$$

- (d) By definition, Π_{ii} is not greater than zero, while it can be positive by Eq. 6.

2. Eddy viscosity is a 2-nd rank tensor; homogeneous constitutive equation

$$\Pi_{ij} = \mu_{Tik} S_{jk} \quad (8)$$

or

$$\Pi_{xx} = \mu_{Txx} S_{xx} + \mu_{Txy} S_{xy} + \mu_{Txz} S_{xz}; \quad \Pi_{xy} = \mu_{Txx} S_{yx} + \mu_{Txy} S_{yy} + \mu_{Txx} S_{yz} \dots \text{etc.}$$

The following defects surface:

- (a) cf. (a) under (1)
- (b) $\text{tr} \Pi$ should be < 0 (see (c) under (1)) while from Eq. 8 one has $\text{tr} \Pi = \mu_{Tij} S_{ij} \gtrless 0$
- (c) For 1-D flow one obtains $\Pi_{zz} = \Pi_{zy} = \Pi_{yz} = 0$, in contradiction with experiments
- (d) Π components in Eq. 8 are asymmetric, in contrast to Eq. 5
- (e) cf. (d) under (1)

3. Eddy viscosity is a 2-nd rank tensor; inhomogeneous & composite constitutive equation

$$\Pi_{ij} = -2\rho\alpha_{ijk} + \frac{1}{2}(\mu_{Tii} S_{ij} + \mu_{Tjt} S_{it}) \quad (9)$$

in which

$$\alpha_{ij} \begin{cases} = 0 & \text{for } i \neq j \\ \neq 0 & \text{for } i = j \end{cases}$$

The following defects persist

- (a) incomplete set of constitutive variables
- (b) LHS & RHS traces of Eq. 9 are not necessarily equal

- (c) diagonal Π_{ii} can be positive in Eq. 9
- (d) cf. (b) under (1)
- (e) α must satisfy $\alpha_{ij} = \alpha E_{ij}$; otherwise α_{ij} is not a tensor
- (f) a new quantity, k , turbulence energy enters and must be found, so that the defects of the "differential models" are taken over.

More assumptions can be proposed, such as a 4-th rank tensor for μ_T and inhomogeneous constitutive equations etc. (Sawicki, 1988). Some corrections of the above schemes are likely but, for all possible versions, it must be concluded that the concept of eddy viscosity, and its theoretical implementation are, by and large, incoherent and vulnerable.

In addition, one must remember that eddy viscosity is not identical with eddy diffusivity

$$K = \beta \mu_T, \quad \text{with} \quad \beta \neq 1 \tag{10}$$

Hence, although the concepts of eddy viscosity and eddy diffusivity are widely used, it is better to apply them with caution, and restrict oneself to gross estimates.

2.2. Formulae for K; the Coastal Zone

Our primary finding in Ch. 1 may be summarized in the following dimensional triad

$$C \sim \exp(-2b\frac{y}{h}); \quad b = \frac{w_* h}{2K_y}; \quad \text{const } K_y \text{ in } 2 \cdots 3 \text{ layers} \tag{11}$$

One may make use of Prandtl's suggestion

$$K = \text{const } B(U_{\max} - U_{\min}) \tag{12}$$

in which

B = width of mixing zone

U_{\max}, U_{\min} = maximum and minimum velocity in the mixing zone, respectively.

One may also endeavour

$$K_y = \text{const } u_* \times h \tag{13}$$

in which u_* = shear velocity.

For open-channel flow Elder gave $\text{const} \equiv 0.23$, which in our case would yield

$$2b = 4.35 \frac{w_*}{u_*} \tag{14}$$

The search for a functional form of K can be more elaborate (Yaglom, 1976). Assume $\beta = 1$ and

$$K_{ij} = \begin{cases} \mu/\rho k_{ij} \left(\frac{\rho u_* y}{\mu} \right) & \text{for } y_+ = \frac{\rho y u_*}{\mu} > 0 \\ \kappa_{ij} u_* y & \text{for } y_+ \gg 1 \end{cases} \quad (15)$$

in which

$$\kappa_{yy} \equiv \kappa_1 = \frac{\kappa}{Pr_t} \rightarrow 0.45 \dots 0.48$$

$\kappa, Pr_t =$ von Karman and Prandtl coefficient, respectively

$k_{ij} =$ dimensionless quantity.

On the other hand, the classical arguments of linear shear stress profile and logarithmic velocity profile lead to the parabolic K ;

$$K_y = \kappa u_* y (1 - y/h) \quad (16)$$

Equations 15 and 16 may be compromised:

$$K_y = \begin{cases} 0.9 \kappa u_* h (1 - \frac{y}{h}) \\ \kappa u_* y (1 - \frac{y}{h}) \\ \kappa_* u_* y \end{cases} \quad \text{for } y = \begin{cases} 0.85 \dots 1.0h \\ 0.15 \dots 0.85h \\ 0 \dots 0.15h \end{cases} \quad (17)$$

Fig. 6 shows the above K_y together with respective values of $2b$ averaged in the three layers. The experimental data reviewed in this study, yielding $\frac{2\bar{b}}{w_s/u_*}$ about 10 near bed and 5 in the central layer (see Ch. 1) agree well with the analysis outlined in Fig. 6

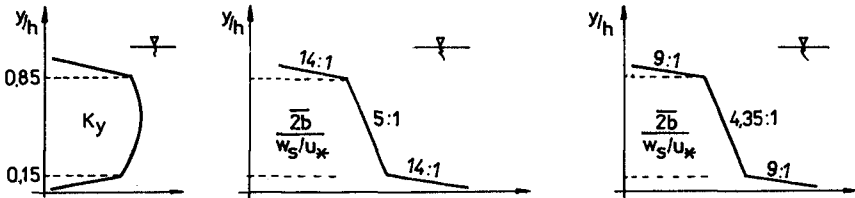


Fig. 6 Theoretically Postulated Values of b

Now examine the most common situations in the coastal zone. For waves (tilde), currents (overbar), long waves (Λ) and turbulence (prime) one has

$$u = \bar{u} + \hat{u} + \tilde{u} + u' \quad (18.1)$$

$$C = \bar{C} + \hat{C} + \tilde{C} + C' \quad (18.2)$$

Substituted into the diffusion equation

$$\frac{\partial C}{\partial t} + \frac{\partial u_i C}{\partial x_i} + w_s \frac{\partial C}{\partial y} + Q_c = 0 \tag{19}$$

with the source term Q_c , the components of Eq. 18 produce

$$\left(\frac{\partial}{\partial x_i}\right) \overline{u C} = \overline{u C} + \overline{\hat{u} \hat{C}} + \overline{\tilde{u} \tilde{C}} + \overline{u' C'}$$
(20)

the cross-terms being uncorrelated.

One usually assumes

$$\overline{\tilde{u} \tilde{C}} = -\tilde{K} \frac{\partial \tilde{C}}{\partial y}; \quad \overline{u' C'} = K \frac{\partial C}{\partial y} \tag{21}$$

Stive and Wind (1985) neglected $\overline{u' C'} \ll \tilde{u} \tilde{C}$, which might be unjustified, as the available data shows.

Various formulae have been proposed for \tilde{K} and K , e.g. Homma and Horikawa (1962) (1965), Kennedy and Locher (1972), Skafel and Krishnappan (1984), Antsyferov and Kosyan (1986). A certain insight into the possible structure of \tilde{K} , K ... is provided by the Author's data on coastal dispersion (Sec. 2.3).

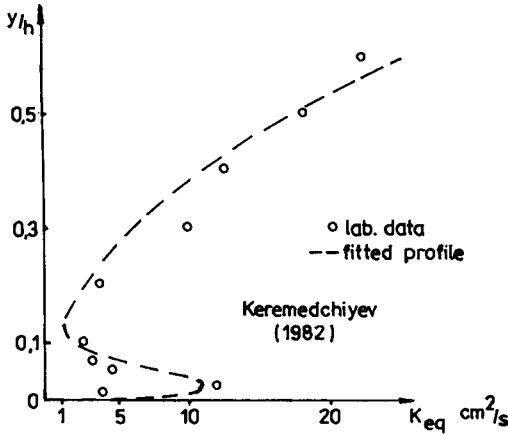


Fig. 7 Eddy Diffusivity Measured in Laboratory

It appears that the fluxes $\rho \overline{\tilde{u} \tilde{C}}$ and $\rho \overline{u' C'}$, i.e. \tilde{K} and K , respectively, are diversified over depth, which is signalled in Fig. 7, with the dominance of K , due to bottom turbulence, in the nearbed layer and \tilde{K} , due to wave-induced mixing in the central layer.

2.3. Laboratory and Field Investigations of Eddy Diffusivity

The Author carried out two extensive studies on the dispersion of passive matter. One of them has dealt with regular waves, in a laboratory flume, and the other was conducted in the field where random waves and turbulence dominated the dispersion.

In the wave flume, naturally buoyant particles were ejected at selected segments of bed ripples, and their movements were tracked with a high-speed camera. By this means the following Lagrangian properties of the nearbed layer could be obtained in various wave phases:

$$\overline{Y}(\tau) = \int_{t_0}^{t_0+\tau} \overline{V(x, t)} dt; \quad (22.1)$$

$$Y'(\tau) = Y(\tau) - \overline{Y}(\tau) = \int_{t_0}^{t_0+\tau} V'(x, t) dt \quad (22.2)$$

$$\begin{aligned} D_{ij}(\tau) = \overline{Y'_i(\tau)Y'_j(\tau)} &= \int_{t_0}^{t_0+\tau} \int_{t_0}^{t_0+\tau} \overline{V'_i(x_1 t_1) V'_j(x_1 t_2)} dt_1 dt_2 = \\ &= \int_{t_0}^{t_0+\tau} \int_{t_0}^{t_0+\tau} B_{ij}(t_1, t_2) dt_1 dt_2 \end{aligned} \quad (22.3)$$

Since the study is described elsewhere (Zeidler, 1972), we shall not dwell on the theory and some secondary aspects reported, such as spectra, but merely confine ourselves to the most relevant findings on the tensors of displacements Y and velocities V , that is D_{ij} and B_{ij} , respectively. The examples given in Fig. 8 depict the complexity of dispersion, even in these seemingly simple regular wave conditions. The vertical profiles of dispersion vary considerably over wave period (Fig. 8a), while the average dispersion after longer times (Fig. 8b) displays certain features of homogeneous turbulence. The Lagrangian velocity tensor B_{ij} also depends on a wave phase (Fig. 8c).

The field studies embodied simultaneous measurements of waves, water velocities and sediment concentration, the latter with a radioisotopic probe, in a vertical profile with smoothly moving instrumentation. The emission noise of the radioactivity source, Am-241, was filtered out, and all signals were processed to obtain correlational and spectral characteristics. The following results can be singled out for the frequency range $0.2 \lesssim f \lesssim 2 \text{ cps}$, which may be attributed to random surface waves.

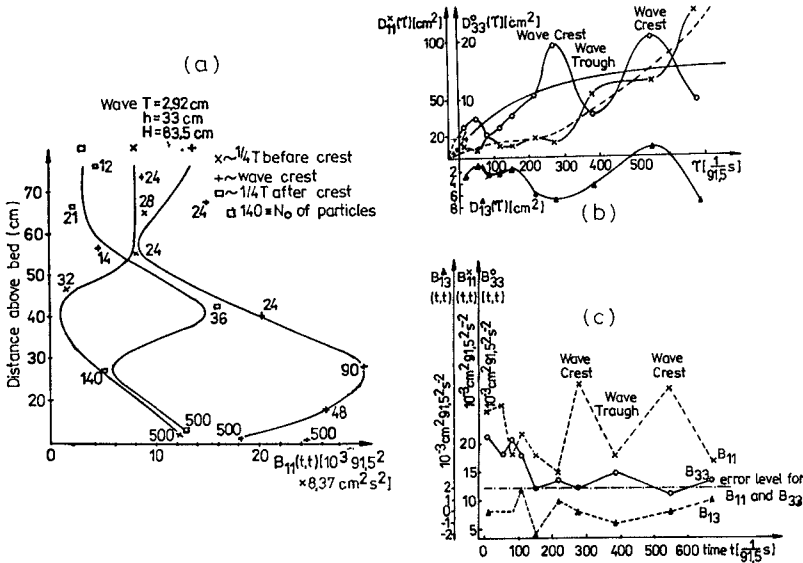


Fig. 8 Lagrangian Velocity Correlation Moments B_{ij} Across Depth (a) and in Time Domain (c) and Displacement Correlation Moments D_{ij} (b)

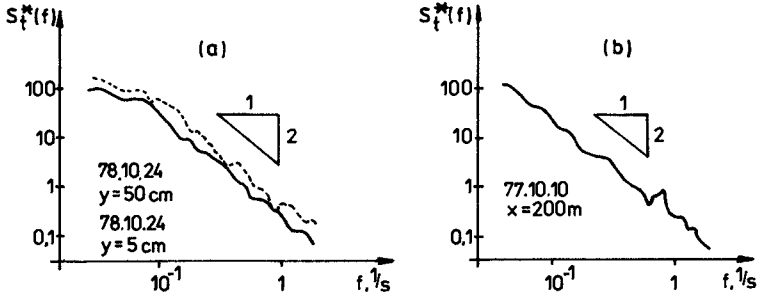


Fig. 9 Shear-Dominated Spectra of Sediment Concentration (a) and Fluorescent Dye (b) Measured in Field

Fluctuations of cross-shore water velocity, $u' \equiv u'_x$ are correlated best with surface waves, while fluctuations of the longshore velocity, $v' \equiv u'_y$, can be linked to shear flow. Fluctuations of sediment concentration measured have been found roughly analogous to concentration fluctuations of fluorescent tracers, which is illustrated in Fig. 9 showing spectra for the two kinds of passive coastal matter, i.e. suspended sediment (left) and a neutrally-buoyant tracer (right). Hence, fluo-

recent tracer studies may be utilized in sedimentation problems. It appears that in the situations covered, with random waves recorded in twenty-odd cycles, C' series were controlled strongly by bed shear near bottom and were dominated by waves at the free surface. The correlations $\overline{C'v'}$ are of important order of magnitude (Fig. 10). More research is however needed on both sediment concentration and turbulence. Inter alia, wave breaking still remains poorly explored as a very important source of turbulence.

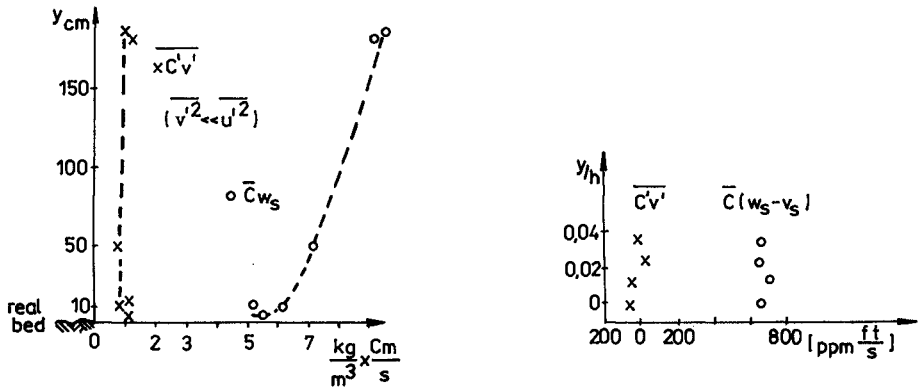


Fig. 10 Correlations $\overline{C'v'}$ for Random Waves (left) and Regular Waves (right, after Kennedy & Locher, 1972)

The Author also conducted other field studies, in particular a very extensive year-long coastal expedition in Senegal. Since they incorporate some other aspects as well, they are discussed in the next chapter.

3. SCHEMATIZATION OF SUSPENDED LOAD PROFILES

3.1. Gross Estimates of K

Chapter 1 and 2 show that vertical profiles of sediment concentration can be described in three layers, for which the exponents $2b$ in $C \sim C_0 \exp(-2by/h)$ can be postulated in various forms, depending on dispersion-controlling mechanisms.

A considerable bulk of data has been collected, which makes possible validation of the concept and formulae put forward. The data includes many alien sources, such as those mentioned above, e.g. some more recent by Skafel and Krishnappan (1984) Antsyferov and Kosyan (1986), and the Author's own data for the Baltic Sea, the Black Sea and particularly those from the coastal project off St. Louis, Senegal in 1980...81 (Zeidler, 1982 and Skaja & Zeidler, 1982). The results of the latter embody 98 vertical profiles of sediments concentration, ranging from instantaneous to averaged long-term ones, such as those exemplified in Fig. 11.

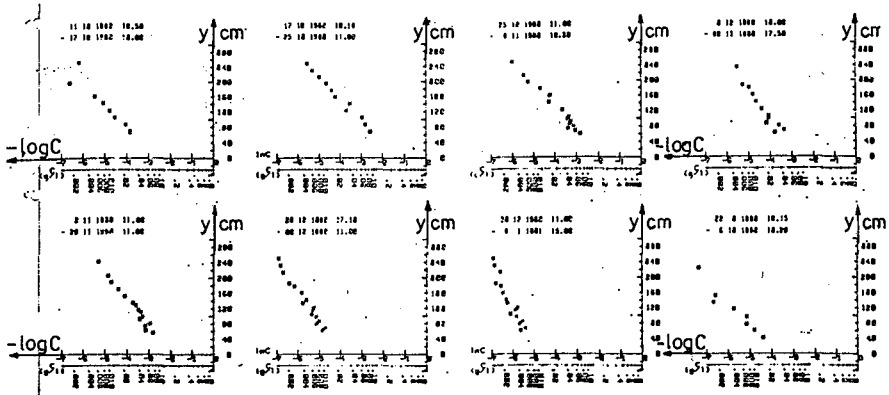


Fig. 11 Examples of Author's Concentration Profiles off St. Louis, Senegal

The available concentration profiles are exponential, so that their slopes can be identified with $2b = w_s h / 2\tilde{K}_y$. The following tentative conclusions may be drawn from the regression analysis attempted for $2b$.

1. In wave-dominated areas of motion, with $\tilde{K} \gg K$ one has

$$2b \approx 4w_s \frac{hT}{H^2}; \quad \sigma_{2b} \approx 1 - \frac{w_s T h}{H^2} \quad (R^2 \approx 0.7) \quad (23.1)$$

2. In wind wave-induced dispersion

$$\langle \tilde{K} \rangle \approx 2 \dots \tilde{K}_{\text{significant}} \quad (\tilde{R} \approx 0.6) \quad (23.2)$$

3. In bed shear-controlled areas (within surf zone), with $K \gg \tilde{K}$, one may postulate

$$2b \approx 40 \frac{w_b}{u_*} + \dots + O(h/l) \quad (R^2 \approx 0.6) \quad (23.3)$$

Other dispersion mechanisms can be dealt with similarly.

Extensive studies under CMEA programmes, in particular Lubiato'74, Lubiato'76, Kamchiya'77, Kamchiya'79, and other measurements in the two coastal research stations (Polish Lubiato and Bulgarian Kamchiya, or Shorpilovtsy) have shown that the layered structure of exponential concentration profiles persists everywhere in the coastal zone, both inshore and offshore. The profiles may be further schematized by attributing, to the nearbed and central layer, distinctly different slopes of the exponential branches (which are straight lines in the semilog

plot, cf. Fig. 3a). The slope is relatively mild in the offshore zone, becomes very steep in the breaking zone (where the two layers practically merge), and is again milder (particularly in the nearbed layer) in the inshore zone.

3.2. Examples of Cross-Shore Distributions of Suspended Sediment

In engineering computations, it is equally important to know both b and Q_{02}

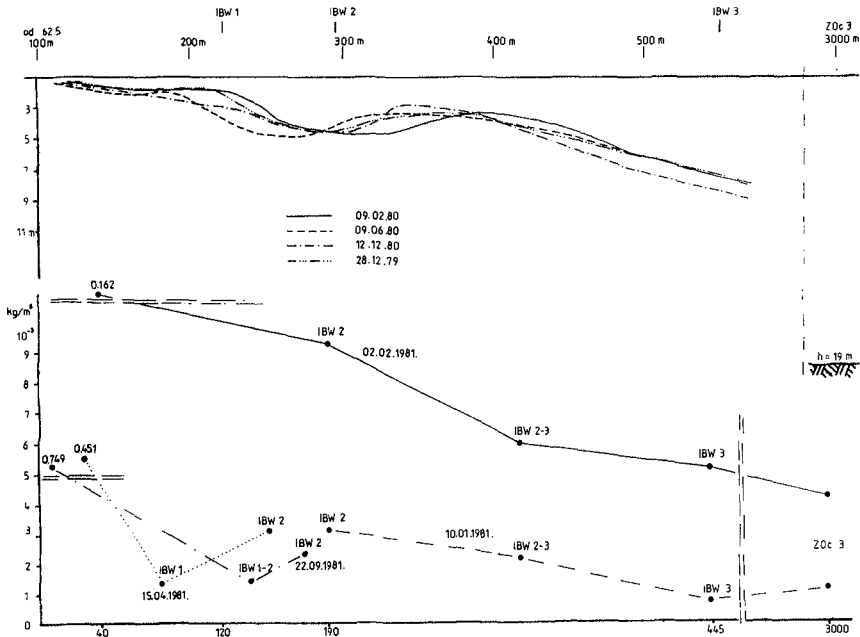


Fig. 12 Examples of Author's Cross-Shore Profiles of Suspended Mass (bottom) and Bed Topography (top) off St. Louis, Senegal

in the exponential profile $C = Q_{02} \exp(-2by/h)$. While b shows how much of the water depth is laden with sediment (or its practically important quantities), it is Q_{02} which determines the absolute magnitude of saturation with sediment. Vertical profiles of sediment concentration, such as those depicted in Fig. 11 not only provide figures for the exponent b but also yield estimates for Q_{02} and the suspended load. The data collected under the programmes mentioned in this paper gives insight into absolute magnitudes and notably the cross-shore distribution of suspended load, the latter being found through obvious integration of the concentration profile over the entire depth of water, with proper account for the layered structure of the C -profile.

Illustrated in Fig. 12 are some examples for the situations encountered off St. Louis, Senegal. It is interesting to note high figures in the zone of ultimate breaking and in the swash zone, where permanent turbidity was recorded, on most occasions, due to considerable turbulence. Although some correlations between Q_{02} and the coastal climate have already been formulated, a lot of work remains to be done before reliable estimates of b and Q_{02} will have been available for all possible coastal situations.

CLOSING REMARKS

The theoretical findings presented in this paper, supported by vast experimental evidence, point to the exponential profile as simple and well substantiated representation of the vertical distribution of suspended sediment concentration. The exponent has been correlated with external factors but more efforts are required for better quantitative description of coastal sediment fields in absolute physical terms. - A concise summary is provided in Abstract.

ACKNOWLEDGEMENTS

This study has been sponsored under the Polish Academy of Sciences' programme CPBP 02.12.2, which is gratefully acknowledged.

REFERENCES

1. Antsyferov S. M., Kosyan R. D., (1986), *Suspended Sediment in the Upper Shelf* (in Russian), Nauka, Moscow, 224p.
2. Homma M., Horikawa K., (1962), *A laboratory study on suspended sediment due to wave action*, Proceed. X Conf. IAHR, London, Vol. 1, 213-221.
3. Homma M., Horikawa K., Kajima R., (1965), *A study of suspended sediment due to wave action*, Coastal Eng. in Japan, Vol. 8, 85-103.
4. Kennedy J. F., Locher F. A., (1972), *Sediment suspension by water waves*, in *Waves on Beaches*, Acad. Press, 249-295.
5. Keremedchiyev S. D., (1982), *Morphologic analysis of equilibrium profile and wave parameters in laboratory conditions*, (in Bulgarian), Okeanologia (Sofia), No 9, 54-63.
6. Nguyen V. G. and Zeidler R., (1982), *Turbulent Diffusion of Suspended Sediment in Open-Channel Flow*, PRACE IBW PAN, Gdańsk, 160p.
7. Sawicki J. M., (1988), *Analysis of spatial models of turbulence*, Archiwum Hydrotechniki (in press).

8. Skafel M. G., Krishnappan B. G., (1984), *Suspended sediment distribution in wave field*, Journal Waterway ... Ocean Engineering, Vol. 110, No. 2, 215-230.
9. Skaja M., Zeidler R. B., (1982), *Longshore sediment transport rate*, 18th Intern. Conf. Coastal Eng. Abstracts, ASCE.
10. Stive M. J. F., Wind H. G., (1986), *Cross-shore mean flow in the surf zone*, Coastal Engineering Vol. 10, No. 4, 325-340.
11. Taggart W. C., Yermoli C. A., Montes S., Ippen A. T., (1972), *Effects of sediment size and gradation on concentration profiles in turbulent flow*, Rep. No. 152, Parsons Lab., Mass. Inst. Techn., 153p.
12. Yaglom A. M., (1976), *Semi-empirical equations of turbulent diffusion in boundary layers*, Fluid Dynamics Transactions, Vol. 7, p. I, IPPT PAN Warsaw, 99-144.
13. Zeidler R. B., (1972), *Nearbed turbulence under waves* (in Polish), Archiwum Hydrotechniki, Vol. XVIII, No. 2, 147-166.
14. Zeidler R. B., (1982), *Yearly measurements off St. Louis, Senegal*, 18th Intern. Conf. Coastal Eng. Abstracts, ASCE.
15. Zeidler R. B., (1987a), *Suspended sediment transport and beach profile evolution*, Discussion, Journal Waterway ... Ocean Eng., ASCE, Vol. 113, no. 1, 89-95.
16. Zeidler R. B., (1987b), *Concentration and transport rate of suspended sediment in marine and fluvial environments*, Euromech 215, Univ. Genoa, Ext. Abstr., 96-100.

CHAPTER 127

ABOUT THE INFLUENCE OF EROSION VOLUME ON CROSS-SHORE SEDIMENT MOVEMENT AT PROTOTYPE SCALE

by K. Uliczka¹⁾ and H. H. Dette²⁾

ABSTRACT

In order to estimate erosion of sand beaches attacked by storm surges, experiments at prototype scale are necessary, since small scale models do not reproduce physical processes in the surf zone.

The present study describes the influence of erosion volume on cross-shore sediment movement during the development of beach profile.

The discussion includes parameters which affect the erosion volume and the accuracy of assessment.

INTRODUCTION

Breaking waves of major storms cause a three-phase flow consisting of sediment, fluid and air in a complex three-dimensional pattern. In order to avoid unknown scaling effects the sediment motion under such conditions requires experimental investigations at full scale.

A set of such experiments was carried out in the "BIG WAVE CHANNEL" (GWK) - length: 324 m, depth: 7 m, width: 5 m - in Hannover. The aspects of the study described below relate to the influence of instantaneous erosion volumes on suspended sediment content from commencement of wave action to the equilibrium of beach profile.

These studies are a continuation of the series from which the analysis of sediment transport volumes was presented at 20th ICCE in Taipei.

The sediment transport calculated from suspended sediment measurements amounted to about 30 % of that given by profile surveys, Fig. 1. In the following the influence of erosion volume on the suspended sediment at a fixed location in the surf zone is discussed.

EXPERIMENTAL CONDITIONS

Repeated test series were carried out on a beach profile with foreshore. Fig. 2 shows the initial test profile. The dune had a 1 to 4 seaward slope from 2 m above still water level (SWL) to 1 m below SWL, followed by a 1 to 20 slope down to channel floor, i. e., it represented the conditions during a storm tide.

1) Assistant Scientist, Dipl.-Ing. 2) Chief Engineer, Dr.-Ing.
Leichtweiss-Institute, Division of Hydromechanics and Coastal Engineering, Techn. University of Braunschweig, Fed. Rep. of Germany

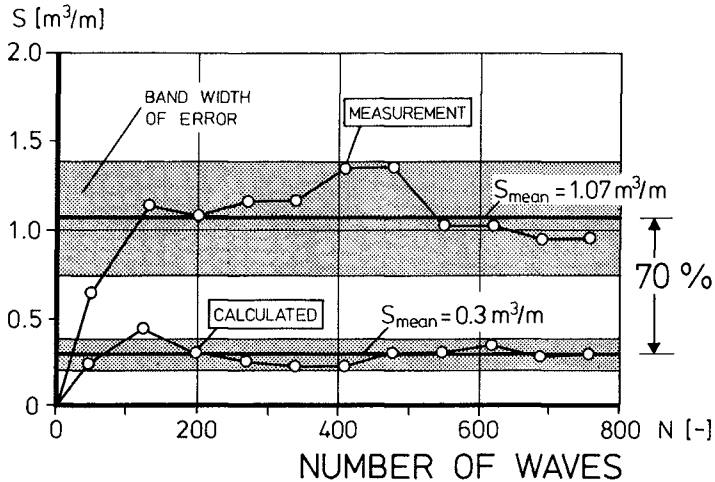


Fig. 1: Comparison of sediment transport between the calculated transport and that computed from profile changes during development phase of beach profile (Dette/Uliczka, 1986)

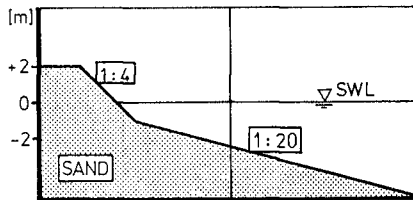


Fig. 2: Initial beach profile

The wave parameters selected were as follows:

1. Monochromatic waves: $H_{rms} = 1.5$ m, $T = 6$ s, $d = 5.0$ m
 $H_0/L_0 = 0.04$, $\xi_0 = 0.29$
2. Irregular waves (theoretical JONSWAP-spectrum):
 $H_{1/3} = 1.4$ m, $T_p = 6$ s, $d = 4.0$ m, $\gamma = 3.3$, $\alpha = 0.0081$,
 $\sigma_a = 0.07$, $\sigma_b = 0.09$

where ξ_0 is the similarity parameter and γ , α , σ_a and σ_b are parameters of the JONSWAP-spectrum, H is the wave height, T period, L wave length, d water depth. Subscript $_0$ refers to deep water values.

The measuring station for initial wave height was at $x = 150$ m and $x = 185$ m, respectively.

The sand used for the test series had the following parameters:

- $D_{50} = 330 \mu\text{m}$, $\sigma_g = 1.47$, $w = 0.0477 \text{ m/s}$
- $D_{50} = 220 \mu\text{m}$, $\sigma_g = 1.48$, $w = 0.0284 \text{ m/s}$

where σ_g is the geometric standard deviation and w the mean fall velocity of g_{sand} at 18°C .

The measurements were carried out in test increments:

- with monochromatic waves the generator was stopped after about 80 waves when the initial wave form became significantly effected by reflection,
- with irregular waves after about 9 minutes, equal to two repetition intervals of the generated wave spectrum.

Before restarting the waves the profile was surveyed and the sediment concentration samples analysed. Restarting followed after the water surface had calmed.

The vertical distribution of suspended sediment concentration in the breaker zone was obtained by the suction method. The results of sediment concentration and wave height are time-averaged data for about 80 monochromatic waves (8 minutes) and about 9 minutes for irregular waves (about 90 waves).

The horizontal distance of the measuring stations for suspended sediment from the initial dune face was $x = 26 \text{ m}$ ($D_{50} = 330 \mu\text{m}$, monochromatic waves), and $x = 22 \text{ m}$ ($D_{50} = 220 \mu\text{m}$, location B, irregular waves), Fig. 3. The difference in x of 4 m has to be noted, when comparing data.

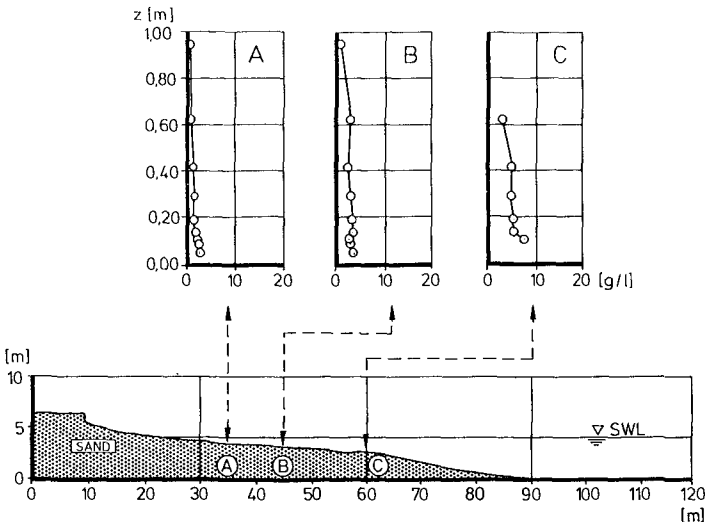


Fig. 3: Suspended sediment distribution over the equilibrium profile due to irregular waves ($D_{50} = 220 \mu\text{m}$)

At equilibrium conditions the sediment in suspension was measured at the station A, B and C, identical in Fig. 4. The measuring points for suspended sediment were vertically spaced as follows: 0.02 m, 0.02 m, 0.025 m, 0.025m, 0.05 m, 0.1 m, 0.125 m, 0.2 m, 0.325 m. On the average the lowest measuring point was 0.06 m above the bed but this varied with the movements of the bed and at times the lowest point was even buried.

Thus, the suspension was measured in the lower about 1 m thick layer.

SUSPENSION DISTRIBUTION ACROSS THE SURF ZONE AT EQUILIBRIUM CONOITIONS

The suspension distribution over the equilibrium profile due to monochromatic waves ($D_{50} = 330 \mu\text{m}$) was presented at the 20th ICCE. The sediment concentration distributions over the equilibrium profile of $D_{50} = 220 \mu\text{m}$ sand after about 2,000 irregular waves are plotted in Fig. 3.

The arithmetic mean of the 33 % highest waves, evaluated for the test increment at equilibrium conditions, yielded at the pongs A, B and C:

$$A: H_{1/3} = 0.9 \text{ m}, \quad B: H_{1/3} = 1.1 \text{ m}, \quad C: H_{1/3} = 1.4 \text{ m}$$

The water depths were:

$$d_A = 0.9 \text{ m}, \quad d_B = 1.3 \text{ m}, \quad d_C = 1.7 \text{ m}$$

The water temperature was about 20°C . The breaker zone extended from about $x = 65 \text{ m}$ to nearly $x = 30 \text{ m}$.

In order to give a description of wave conditions during the suspension measurements at equilibrium state a statistical expression for the breaker location was used. The waves were grouped into those with break-points seaward, landward and near ($\pm 1 \text{ m}$) the measuring station. This information was obtained by analysis of video-tape and yielded the following values (% of waves at station):

	seaward	near	landward
A:	74 %	13 %	14 %
B:	65 %	16 %	19 %
C:	6 %	39 %	55 %

The high percentage of breaking waves near the point C is reflected in the high suspended sediment concentration, as well as in the wave height.

Table 1 gives the sediment concentration data associated with irregular waves.

CALCULATION OF WAVE ENERGY

In order to compare the beach development due to monochromatic and irregular waves, wave energy was calculated for each test series before the waves reached the beach profile using the so-called linear, AIRY or first order STOKES' wave theory.

DUNE WITH FORESHORE			
IRREGULAR WAVES		$H_{1/3} = 1.4 \text{ m}$ $T_p = 6 \text{ s}$	
Height above bottom	Sediment Concentration		
	\bar{c}	\bar{c}	\bar{c}
m	g/l	g/l	g/l
0.05	2.8	3.7	-
0.09	2.5	2.8	-
0.11	2.2	2.7	7.6
0.14	2.0	3.6	6.2
0.19	1.8	3.2	5.3
0.29	1.7	3.1	4.8
0.42	1.4	2.5	5.1
0.62	0.9	2.4	3.1
0.94	0.8	1.8	-
Location	A	B	C

Table 1: Sediment concentration data for irregular waves ($D_{50} = 220 \mu\text{m}$)

The average wave energy per unit surface area is

$$\bar{E} = \frac{1}{8} \cdot \rho \cdot g \cdot \frac{1}{N} \sum_{i=1}^N H_i^2 \tag{1}$$

The erosion and suspended sediment data for profile development are plotted against accumulated wave energy instead of time or number of waves, i. e., against $\bar{E} N$, where N is the number of waves. For irregular waves is $N = \Delta t/T$, i. e., the duration of the test increment divided by peak wave period.

The energy flux, $\bar{E} c_g$, and the shape of the erosion volume and suspended sediment volume curves will be discussed in the section dealing with estimates of accuracy.

CALCULATION OF SUSPENDED SEDIMENT VOLUME

The suspended sediment mass during the development phase of beach profile was calculated from the expression

$$SV = \int_0^z \bar{c} \cdot b \cdot dz \tag{2}$$

where b is the length of profile unit and $z = 1.0 \text{ m}$, approx. Fig. 4 shows the suspended sediment mass in this lower about 1 m thick layer for the two grain sizes plotted against wave energy input per unit surface area seaward of breakers. Each point on the graph represents time-averaged sediment concentration volume for test increment at the energy input since commencement of test.

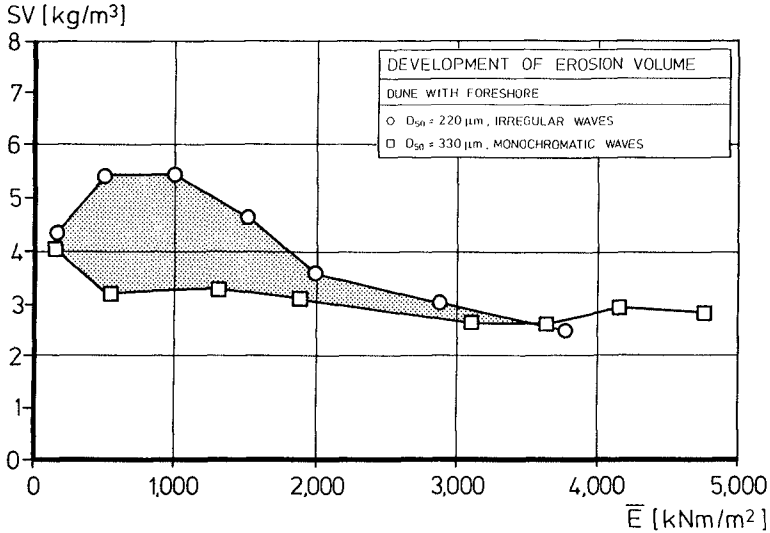


Fig. 4: Suspended sediment volume versus wave energy of monochromatic and irregular waves

The measured data on the suspended sediment volume yielded the following information:

- At the beginning of both test series the volumes coincided, but at about 1,000 kNm/m² the difference was about 40 %.
- When the equilibrium conditions of the profiles were approached suspended sediment volumes converged to about 2.5 kg/m³.
- The suspended sediment volume with monochromatic waves reached its maximum value in the first test increment whereas with irregular waves the suspension due to erosion reached its maximum after about five increments, Fig. 4.

It should be noted, that the accuracy of the sediment concentration measurements in the breaker zone was about $\pm 30\%$ related to the average (see Dette/Uliczka 1986).

Table 2 gives the data of suspended sediment volume due to monochromatic and irregular waves for the two grain sizes.

EROSION VOLUME AND SUSPENDED SEDIMENT VOLUME

The erosion volume was obtained by profile surveys after each test increment. The accuracy of profile measurements (± 0.01 m) in terms of erosion volumes is about $\pm 1\%$. The maximum erosion volume was about 15 m³ for monochromatic waves ($D_{50} = 330 \mu\text{m}$) and about 22 m³ per metre width for irregular waves ($D_{50} = 220 \mu\text{m}$).

DUNE WITH FORESHORE					
MONOCHROMATIC WAVES			IRREGULAR WAVES		
$D_{50} = 330 \mu\text{m}$			$D_{50} = 220 \mu\text{m}$		
Test Increment	\bar{E} kNm/m ²	SV kg/m	Test Increment	\bar{E} kNm/m ²	SV kg/m
1	137	4.1	1	170	4.4
3	547	3.2	3	509	5.4
7	1313	3.3	6	1019	5.5
10	1888	3.1	9	1528	4.6
15	3119	2.6	12	1994	3.6
17	3640	2.6	18	2886	3.0
19	4159	2.9	24	3781	2.5
21	4754	2.8			

Table 2: Data on suspended sediment volumes during development of beach profile under monochromatic and irregular waves (Test increments and energy input were continually summed, whereas the suspension data were time-average for each test increment)

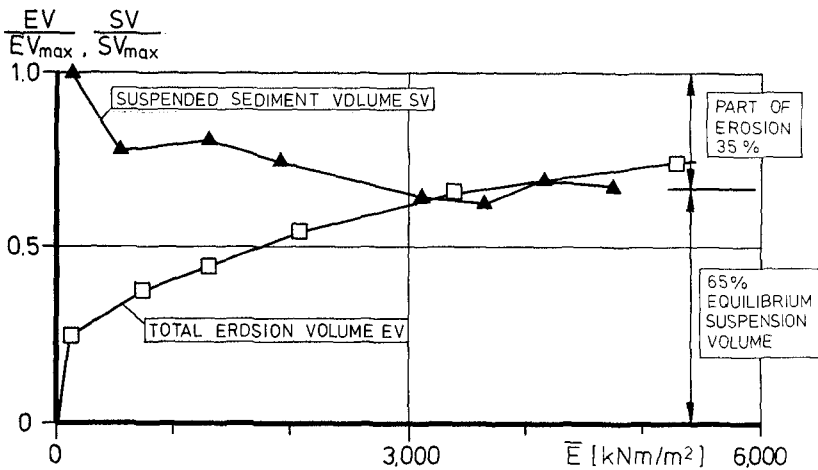


Fig. 5: Erosion volume and sediment in suspension volume as a function of wave energy input under monochromatic waves ($D_{50} = 330 \mu\text{m}$)

Erosion volume and suspended sediment volume were normalized with their maximum values. Fig. 5 and Fig. 6 show the erosion volume and suspended sediment volume as a function of wave energy under monochromatic waves ($D_{50} = 330 \mu\text{m}$) and irregular waves ($D_{50} = 220 \mu\text{m}$), respectively. The data on erosion volume are presented in Table 3.

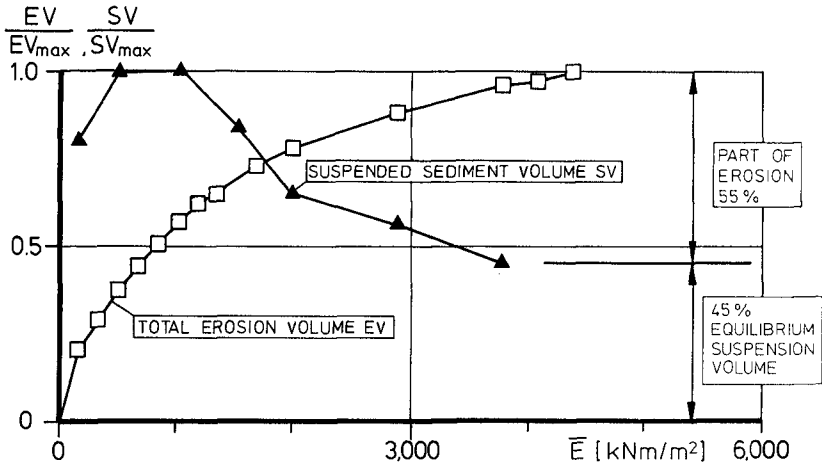


Fig. 6: Erosion volume and sediment in suspension volume as a function of wave energy input under irregular waves ($D_{50} = 220 \mu\text{m}$)

DUNE WITH FORESHORE					
MONOCHROMATIC WAVES			IRREGULAR WAVES		
$D_{50} = 330 \mu\text{m}$			$D_{50} = 220 \mu\text{m}$		
Test Increment	\bar{E} kJN/m ²	EV m ³ /m	Test Increment	\bar{E} kJN/m ²	EV m ³ /m
1	137	3.8	1	170	4.4
4	739	5.7	3	509	8.1
7	1313	6.8	5	849	11.0
11	2080	8.2	6	1019	12.3
16	3379	9.9	10	1697	15.7
23	5273	11.2	12	1994	16.8
27	6437	11.9	18	2886	19.0
29	7020	12.3	25	3930	20.7
39	9889	15.1	28	4378	21.6

Table 3: Data on erosion volume during the development of beach profile under monochromatic ($D_{50} = 330 \mu\text{m}$) and irregular waves ($D_{50} = 220 \mu\text{m}$) (Test D_{50} increments, energy input and erosion volume were continuously summed)

A smaller total erosion volume was generally associated with a smaller suspended sediment volume in the surf zone. This is a well known observation but some additional features immerge from the graphical presentation above:

- The erosion of the profile with sand $D_{50} = 220 \mu\text{m}$ started more intensively than that of coarser D_{50} sand at the same wave energy input
- After 3,000 kNm/m^2 about 90 % of the equilibrium erosion volume was reached for the finer sand, whereas for the coarser sand only 60 % erosion had occurred
- After 4,000 kNm/m^2 both suspended sand concentration profiles reached equilibrium conditions
- The effect on transport rate, described above, shows that the maximum suspension volume was reached with finer sand when about 40 % of erosion volume had been accomplished
- In terms of the equilibrium state, it is seen that 35 % and 55 %, respectively, of the maximum suspended sediment volume is transient sediment of the erosion process
- During the erosion process the suspended sediment volume at the measuring station reaches about twice the value at the equilibrium.

The 1.4 times higher suspended sediment volume of coarser sand ($65 \% / 45 \% = 1.4$) seems to be due to the higher energy density of monochromatic waves. Under irregular waves the sediment can settle out during periods of small waves of the wave spectrum. In order to find a direct relationship between suspended sediment volume and erosion volume the incremental data were analysed. The results are summarized in Table 4 and plotted in Fig. 7.

DUNE WITH FORESHORE			
MONOCHROMATIC WAVES $D_{50} = 330 \mu\text{m}$		IRREGULAR WAVES $D_{50} = 220 \mu\text{m}$	
EV m^3/m	SV kg/m	EV m^3/m	SV kg/m
3.8	4.1	(4.4)	(4.4)
1.4	3.2	1.8	5.4
1.6	3.3	1.3	5.4
0.7	3.1	0.5	3.6
0.6	2.6	0.4	3.0
0.7	2.9	0.3	2.5
0.7	2.8		

Table 4: Incremental data on erosion volume and suspended sediment volume under monochromatic and irregular waves

The volume in suspension and eroded for each point were determined for the same time. There appears to be a linear relationship between erosion volume and the volume in suspension.

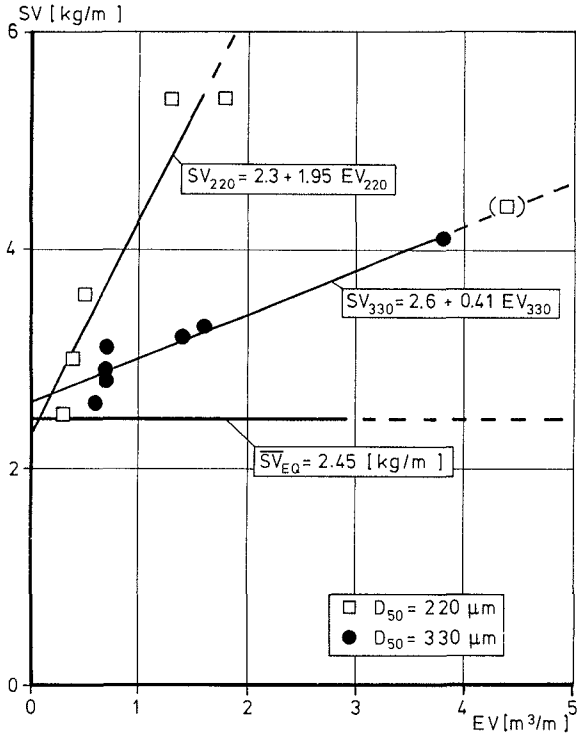


Fig. 7: Relationship between instantaneous suspended sediment volume and erosion volume for 330 μm -sand and monochromatic waves as well as 220 μm -sand and irregular waves

The suspended sediment volume at equilibrium state is about the same as presented in Fig. 4, i. e., about 2.5 kg/m after 4,000 kNm/m² energy input.

The slope of the Linear Regression Functions in Fig. 7 demonstrates the influence of grain size on suspended sediment concentration and erosion volume.

BEACH PARAMETER AND EROSION VOLUME

At first water level and wave conditions influence the erosion volume and the sediment movement as bed load and suspended sediment.

Below is a discussion of aspects of erosion as observed in full scale at the GWK.

A comparison of the growth of the erosion volumes, starting with different initial profiles, is shown in Fig. 8. The profiles were a 1 : 4 slope from channel floor to the top of dune (+ 2 m SWL) and that shown in Fig. 2, referred to as dune without and with foreshore.

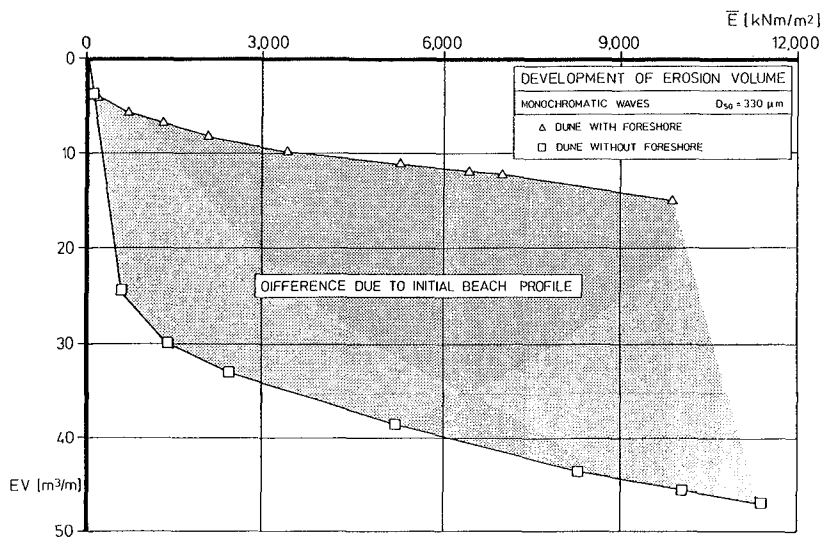


Fig. 8: Growth of erosion volume versus wave energy input for two different initial beach profiles

The erosion volume on the profile without foreshore is seen to be about three times that on the profile with foreshore. The 1 : 4 slope from channel bottom to the top of the dune lead to wave energy transformation directly in front of the dune face and therefore to large erosion volume as well as to extremely high suspended sediment concentration.

The influence of grain size on the erosion volume of a profile with dune and foreshore was determined by using two sediment sizes. A reduction of the mean diameter by about 30 % resulted in an increase of erosion volume by 100 % at energy input of 4,500 kNm/m², as shown in Fig. 9.

The comparison relates to the time, when the profile of the finer sand reached equilibrium. At the time only 70 % of the equilibrium volume of the coarser sand had been eroded.

Taking the total erosion volumes of both equilibrium profiles, after an energy input of 10,000 kNm/m², the difference was about 30 %. The energy input up to the equilibrium stage for the coarser sand was about twice that for the 220 μm-sand.

The foreshore slopes at both equilibrium profiles in the surf zone (330 μm and 220 μm sand) stabilised to about 1 : 20, whereas the slopes reported from nature for beaches with sand 220 μm are generally flatter.

DISCUSSION OF ACCURACY

The question of accuracy of the calculations and the data plots has been mentioned earlier.

If the erosion volume was plotted against the calculated energy input, both the data due to monochromatic and irregular waves should lead to

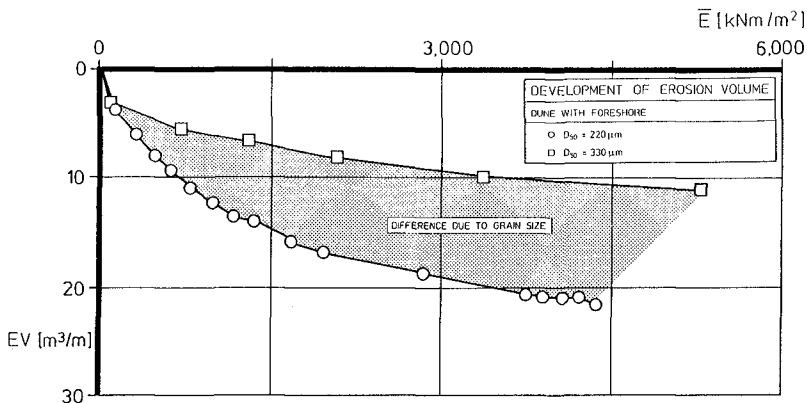


Fig. 9: Comparison of erosion volumes with different grain sizes

an identical function for equal initial profiles and the same grain size. Additional to the computation of average wave energy per unit surface area, energy flux was calculated at the measuring station in the wave channel, before breaking:

$$\bar{P} = \bar{E} n C \tag{3}$$

with

$$n = \frac{1}{2} \left[1 + \frac{4 \pi d/L}{\sinh(4 \pi d/L)} \right] \tag{4}$$

where d is the water depth, L the calculated mean wave length in the given depth of water, n is the relationship of wave group to wave phase velocity, and C is the mean wave propagation velocity in the given depth of water.

Fig. 10 shows the growth of the erosion volume of the profile with dune without foreshore under monochromatic and irregular waves using grain size $D_{50} = 330 \mu\text{m}$ versus wave energy, and Fig. 11 the growth of erosion volume from the same tests versus energy flux.

Plotted at the same scale, Fig. 10 and 11, the differences in terms of energy flux are a maximum with 5 % at monochromatic waves, whereas at irregular waves the curves coincide. This shows that the erosion volume and suspended sediment volume could be compared both on the basis of energy input or energy flux. Nevertheless, the discrepancy of erosion volumes due to monochromatic and irregular waves is at maximum more than 50 %.

The wave conditions (monochromatic or irregular waves) have a major influence on the process of beach erosion. The breaker form, breaker zone, rate of wave energy attenuation, velocity field etc. have a dominant influence on the sediment transport in the surf zone. As mentioned above, the higher energy density of monochro-

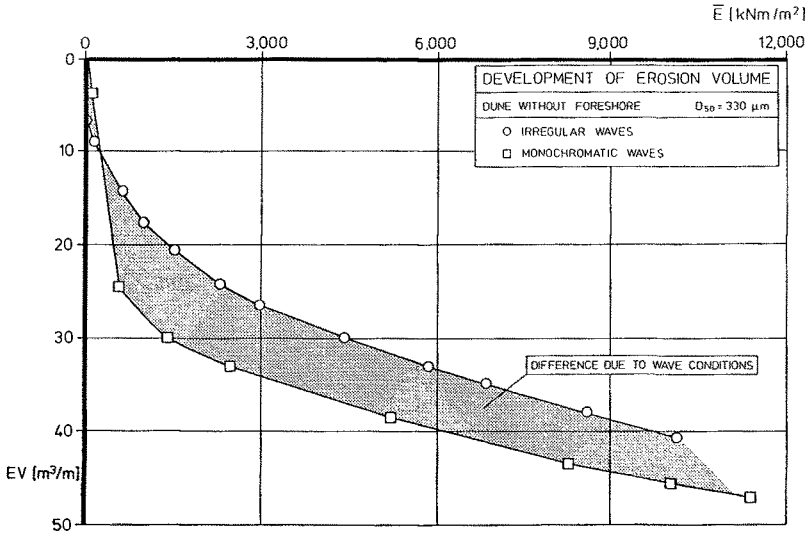


Fig. 10: Growth of erosion volume on the profile with dune without foreshore under monochromatic and irregular waves versus wave energy

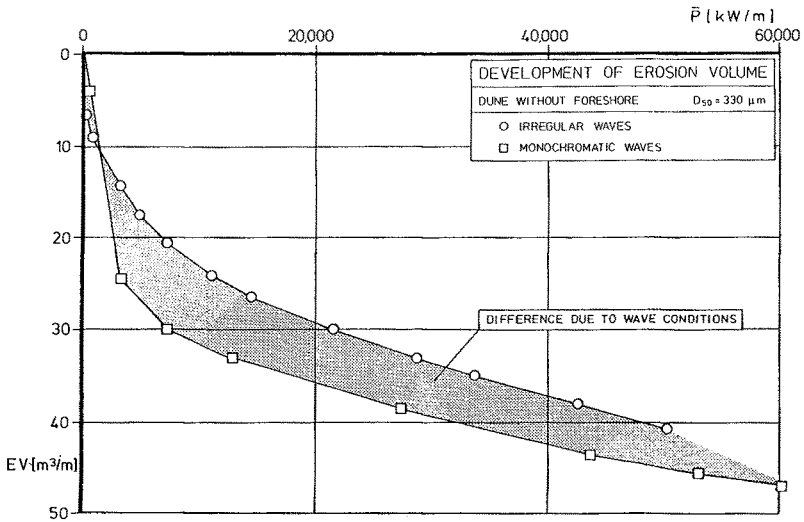


Fig. 11: Growth of erosion volume on the profile with dune without foreshore under monochromatic and irregular waves versus energy flux

matic waves at breaking leads to higher sediment transport, but under irregular waves the sediment can settle out during periods of smaller waves between groups of higher waves. The grouping as well as irregular waves leads to differences in turbulence intensity in the surf zone and hence to differences in the magnitude of the offshore sediment transport.

The computation of \bar{E} and \bar{P} by the extrem values of wave, trough and crest with zero down crossing method, does not describe these values correctly since the wave form is not accounted for. The method leads to an overestimating of the wave energy of irregular waves. The calculation of wave energy and energy flux from actual wave records or with higher order wave theories would improve the description.

CONCLUSIONS

Full scale test series, carried out in the BIG WAVE CHANNEL in Hannover, yielded information on the influence of erosion volume on cross-shore sediment movement in the surf zone and on the growth of erosion volumes for various initial conditions.

For comparison purpose the growth of erosion volume and suspended sediment volume were presented against the averaged wave energy input per unit surface area.

The suspended sediment volume (measured in the bottom 1 m thick layer) was related to the growth of erosion volume and was found to reach a constant value at the equilibrium conditions independent of grain size.

Initial beach profile and grain size used have a strong influence on the erosion process of a dune.

The accuracy of the results would be improved by inclusion of the detailed description of the wave form and the vortex intensity.

ACKNOWLEDGEMENT

The authors would like to acknowledge the sponsorship of the Deutsche Forschungsgemeinschaft (DFG = German Research Association) of the investigations described (Sonderforschungsbereich 205/TP A6). Additionally the authors like to express their sincere thanks to Prof. Dr.-Ing. A. J. Raudkivi, University of Auckland, for his generous support and his stimulating remarks during the preparation of this paper.

REFERENCES

- Detle, H. H., Uliczka, K., 1986: Velocity and sediment concentration fields across surf zones, Proc. 20th ICCE, Taipei, R.O.C.
- Detle, H. H., Uliczka, K., 1987: Prototype investigations on time-dependent dune recession and beach erosion, Proc. Coastal Sediment'87, New Orleans, U.S.A.
- Raudkivi, A. J., 1976: Loose boundary hydraulics, 2nd Edition, Pergamon Press, Oxford, GB.
- SPM Shore Protection Manual, Vol. I, U.S. Army, CERC, 1977

LIST OF SYMBOLS

b	m	width per unit beach profile
c	kg/m ³	time-averaged sediment concentration
C	m/s	wave propagation velocity
d	m	water depth
D	μm	grain size
D ₅₀	μm	mean grain size
\bar{E}	kNm/m ²	total wave energy per unit surface area
EV	m ³ /m	erosion volume per unit width of beach profile
g	m/s ²	gravitational acceleration
H _{rms}	m	root mean square wave height
H _o	m	deep water wave height
H _{1/3}	m	arithmetic mean value of 33% highest waves
L	m	wave length
L _o	m	deep water wave height
n	-	ratio of wave group and phase velocity
N	-	number of waves
\bar{P}	kW/m	energy flux
S	m ³ /m	total sediment transport
SV	kg/m	suspended sediment volume
T	s	wave period
T _p	s	peak period
w	m/s	fall velocity of D ₅₀
x	m	horizontal coordinate
z	m	vertical coordinate
α	-	Phillips-parameter for JONSWAP-spectrum
γ	-	shape parameter for JONSWAP-spectrum
ξ _o	-	similarity index
ρ	kg/m ³	water density
σ _a	-	shape parameter for JONSWAP-spectrum
σ _b	-	shape parameter for JONSWAP-spectrum
σ _g	-	geometric standart deviation for grain size

CHAPTER 128

Sediment Transport on Nearly-Prismatic Beaches

Marcel J.F. Stive* and J.A. Roelvink*

SUMMARY

Recent progress in the quantitative modelling of the undertow has stimulated the modelling of cross-shore sediment transport. More so than before it seems now possible to attempt the dynamic modelling of beach profile development. Also, integration of dynamic cross-shore sediment transport formulations in horizontally two-dimensional models for water motion and sediment transport has recently been suggested. This seems to be a first step of integrating depth-averaged 2DH-modelling with 2DV-profile-modelling. Here an overview is given of these developments and the understanding gained so far of the several current systems and the induced sediment transport and morphology that are found in the situation of random waves normally and obliquely incident on beaches which vary not or only slowly alongshore.

1. INTRODUCTION

Alongshore variations of bottom topography and/or the incident wave field (amplitude or phase) are the cause of mean nearshore currents in the form of circulation cells, nonuniform longshore currents or mixtures of these. Using the radiation stress concept many dynamics of these depth-averaged nearshore currents may be modelled (Bowen, 1969, and many others since; see Battjes, 1988, for a review).

In the case of no alongshore variations in topography and (obliquely) incident wave field the same concept yields a uniform longshore current. Here our interest is into this type of situation: viz. that of obliquely incident, horizontally uniform waves on beaches of which the alongshore variation of topography can be neglected for the horizontal current dynamics. It should be noted that in reality longshore periodicities in bottom topography and flow are generated without obvious externally imposed periodicities, particularly if the waves are of near-normal incidence (Sonu, 1972). However, we choose our longshore length scale such that these periodicities are averaged out. In this situation there are no distinct horizontal circulation cells with a depth-averaged nonzero flow, only a nearly-uniform longshore current.

In addition to this depth-averaged longshore current system we here consider the vertical circulation system resulting from the vertical imbalances of the mass and momentum fluxes, even though the depth-integrated flux balances are satisfied (cf. Stive and De Vriend, 1987, SDV furtheron). This vertical circulation system induces a near-bottom current field which in general significantly differs from the depth-averaged field.

* DELFT HYDRAULICS, P.O. Box 152, 8300 AD Emmeloord, The Netherlands

In the described case of oblique wave incidence we will find a vertically nonuniform (both in magnitude and direction) current field nearshore. In the upper half of the water column the mean velocity vector more or less follows the depth-integrated longshore current vector but close to the bottom the mean velocity vector is deviated towards the offshore due to the undertow (De Vriend and Stive, 1987, DVS furtheron and Svendsen and Lorenz, 1988). Obviously for the sediment transport the lower layers are the most relevant. Here, it is the sediment transport and eventually the resulting morphology that forms our main reason of interest in the watermotions.

In addition to these mean flow current systems the waves induce oscillatory currents in their propagation direction. Apart from their interaction with mean currents which may lead to net flows as well they may also be the cause of net sediment transport due to their asymmetrical features (cf. Bowen, 1980).

The purpose of this paper is to discuss some recent developments with respect to the understanding of the several current systems (section 2) and the induced sediment transport and morphology (section 3) that are found in the situation of random waves normally and obliquely incident on a nearly-prismatic beach.

2. CROSS-SHORE AND LONGSHORE WATERMOTIONS

2.1 Cross-shore flow due to normally incident waves

The first situation considered is that of a random wave field (with directionality and wave group effects neglected; see Section 5 Discussion) normally incident on a prismatic (i.e. alongshore homogeneous) coast of arbitrary cross-shore profile. In this situation we distinguish the following water motions which are both in cross-shore direction:

- a depth varying oscillatory flow, in phase with the random wave surface variations, and
- a depth varying mean flow, steady on the scale of many waves, which in the surfzone and below the wave trough level mainly consists of the undertow.

The oscillatory flow

For the present interest it appears furtheron that the importance of the oscillatory flow may be expressed by the following low order flow moments (cf. Bowen, 1980):

- the even moments $\langle |u|^3 \rangle$ and $\langle |u|^5 \rangle$, which are nonzero for symmetric velocities,
- the odd moments $\langle u|u|^2 \rangle$ and $\langle u|u|^3 \rangle$, which are zero for symmetric velocities.

The even moments are relatively easy to evaluate. Unlike the odd moments they do not depend on the wave asymmetry features. The theoretical estimate by Guza and Thornton (1985) for a random, linear sea (Gaussian model) gives satisfactory results. However, also a bichromatic model yields satisfactory results (Roelvink and Stive, 1988b).

The odd moments are zero for a symmetric velocity field, but can be nonzero for nonlinear waves such as occur nearshore. Specifically, in the nonbreaking cnoidal type waves the shoreward velocities are stronger and of shorter duration than the offshore flows, leading to nonzero values for the odd moments. On the other hand it appears (Stive, 1986) that the breaking skewtype waves do not contribute to the odd moments, since these

waves are symmetrical around the vertical rather than the horizontal plane. An evaluation of the odd moments according to second order Stokes theory (Stive, 1986) gave a first quantitative estimate, but important improvements were obtained by introducing a more general nonlinear theory (Roelvink and Stive, 1988a,b).

The undertow

In the present case of steady (on the time-scale larger than that of the wave groups), vertically two-dimensional motion of normally incident wave groups the depth-integrated total mass and momentum equations yield a depth-mean zero flow and in essence a balance between the radiation stress and the steady wave set-up. However, locally (in the vertical) the mass and momentum fluxes need not be in balance. The potential role of this imbalance driving a seaward directed returnflow or undertow, compensating for the shoreward mass flux above trough level, was first pointed out by Dyhr-Nielsen and Sørensen (1970).

To compensate for the wave-induced non-zero mass flux above wave trough level the depth-averaged net flow below wave trough level is seaward. In the case of non-breaking waves the resulting mean flow profile appears to resemble the so-called conduction solution (Longuet-Higgins, 1953) quite well. This implies that the mean flow in the central fluid region is seaward, but near the bottom it is strongly influenced by the dynamics of the bottom boundary layer, such that a shoreward flow results. In the case of breaking waves, however, the mass flux above trough level is enhanced due to the presence of the surface roller which is one of the manifestations of the breaking process. The effects near the water surface are strong enough to dominate the flow even near the bottom such that an all seaward flow results with its maximum close to the bottom, known as "undertow".

The non-zero mass flux above wave trough level due to the waves alone is theoretically known for periodic waves of constant form relative to an irrotational wave motion below trough level. This theoretical estimate combined with the mass flux in the roller as estimated by Svendsen (1984) may be considered to give an acceptably accurate estimate of the total mass flux above trough level. If we adopt the approach of DVS (1987) for the general case of random breaking waves, characterized by -mutually not interacting- fractions of breaking and non-breaking waves, the total estimate for the total mass flux above wave trough level (m), becomes:

$$m = \left(1 + Q_b \frac{7kh}{2\pi}\right) \frac{E}{c}$$

where the second term represents the empirically derived roller contribution, in which Q_b is the breaking wave fraction.

A crude estimate of the near-bottom undertow may be derived from the above estimate of m by assuming depth uniformity of the flow below wave trough level. A more accurate description including the near-bottom details can be obtained by evaluating the accompanying horizontal momentum balance locally in the vertical, following the above mentioned suggestions of Dyhr-Nielsen and Sørensen (1970). Since 1980 several quantitative evaluations of their concept have been presented in the literature. Key papers in this context are Dally and Dean (1984), who present an internally consistent approach but neglect specific breaking wave effects, Stive and Wind (1986), who indicate the importance of the near-surface layer in breaking waves, and Svendsen et al. (1987), who present an approach for the realistic inclusion of the bottom boundary layer under breaking waves. These three contributions are integrated in a generalized approach by SDV (1987).

A recent finding is (Roelvink and Stive, 1988a,b) that in the region just after the point of initial breaking there is a spatial shift between the maximum gradient of the wave height and that of the undertow. They have found that this is due to the time needed to convert organized kinetic and potential energy into small-scale, dissipative turbulent motion. The underlying reason for this finding is that in the above described undertow model the wave breaking induced shear stress at trough level used to model the effects of the surface layer is proportional to the ratio of wave energy dissipation over wave phase speed (see SDV, 1987). This shear stress is very important in the driving of the undertow and it appears that the lag found in the predictions of the undertow gradients is due to the incorrect assumption that the dissipation source term used in the wave height prediction model is a measure of the actual dissipation. A better interpretation is that this source term is a measure of the actual production of turbulent energy. The actual dissipation may then be derived with the aid of a turbulence model. The correction to the undertow improves the prediction importantly.

2.2 Cross- and longshore flow due to obliquely incident waves

The second situation considered is that of a random wave field (with directionality and wave group effects still neglected) obliquely incident on a prismatic coast of arbitrary cross-shore profile. In this situation we distinguish the following water motions.

Watermotions which are zero when depth- and time-averaged but nonzero when considered on the timescale of the wave period or when considered locally in the vertical, viz.

- wavepath directed, depth varying oscillatory flow, in phase with the random wave surface variations, and
- depth varying mean flow, steady on the scale of many waves, compensating for the wavepath directed mass flux above wave trough level, which in the surfzone and below the wave trough level mainly consists of the undertow.

In addition to these watermotions there are nonzero, time- and depth-averaged watermotions alongshore, viz.:

- a wave-induced mean longshore current, and (potentially)
- a mean current due to an alongshore pressure gradient (e.g. due to the tide).

The wavepath directed oscillatory watermotions clearly will have components both along- and cross-shore. The evaluation of these watermotions may straightforwardly be derived taken account of the local wave angle with the parallel depth contours. Here we further concentrate on the description of the time-averaged, vertically varying current system.

The traditional depth-integrated, horizontal circulation approach obviously has a too narrow physical basis to describe the in essence three-dimensional current pattern. For this we need models which deal with the flow in three dimensions. Since the three-dimensionality is such that the variations in the horizontal directions are zero or only weak compared to that of the vertical direction, flow models using a profile technique can be useful. A first, practical formulation combining the typical cross-shore vertical flow variations with the weaker horizontal flow variations due to alongshore nonuniformities was given by DVS (1987). Their approach can be considered a natural step between 2D and fully 3D models and is therefore termed quasi-3D approach. Here we discuss this approach and some consequences for the even more simplified situation of alongshore uniformity.

In the terminology of DVS (1987) the nonzero depth-averaged time-mean watermotions are termed the primary flow. The locally (in the vertical) nonzero but depth-averaged zero time-mean watermotions, for instance the undertow, are called the secondary flows. As the terminology indicates this approach assumes in essence that the secondary flows are weak enough to assume that their effects on the derivation of the primary flow are negligible. Furthermore, they assume that the primary flow profile and related primary bottom shear stress are in a single vertical plane. These assumptions allow a full uncoupling between the primary and secondary flows. This approach seems a reasonable first step, but it should be mentioned that in general the uncoupling will not be permitted, especially if the secondary flows are not much smaller than the primary flows. Interactions will then result, such as for instance described by Van Kesteren and Bakker (1986), who find that a sophisticated boundary layer approach for the combination of waves and currents under an angle shows the generation of a secondary flow due to the interaction between primary flow and the oscillatory wave motion.

If the uncoupling between primary and secondary flow is accepted, following DVS (1987) the primary flow may be determined from the conventional depth- and time-averaged horizontal momentum balance equations, and the secondary flow due to e.g. the surface breaking of the wavefield may be determined from the local balances of mass and horizontal momentum in the plane with its orientation in the direction of wave energy flux propagation.

The result of the suggested modelling approach yields a vertically nonuniform (both in magnitude and direction) current field nearshore. In the upper half of the water column the mean velocity vector more or less follows the depth-integrated longshore current vector but close to the bottom the mean velocity vector is deviated towards the offshore due to the undertow. An example of the resulting (computed) vertically rotating mean velocity vector for Egmond beach is given in Figure 1. A preliminary check with nature on this phenomenon as given in DVS (1987) indicates that it resembles reality, but more definitive comparisons are awaited.

This section on the formulation of the watermotions is concluded with a finding, which has obvious implications for the modelling of both the depth- and time-mean currents and the sediment transport (also see De Vriend and Ribberink, 1988). The principle calculations of SDV (1987) indicate that the magnitude of the secondary bottom shear stress is some 10% to 20% of the magnitude of the primary shear stress. The implication of this for the resulting near-bottom shear stress orientation and closely related near-bottom flow orientation may be indicated with the following approximations.

In the considered situation of obliquely incident waves to a prismatic coast the primary shearstress direction is alongshore and of approximate magnitude (cf. Longuet-Higgins, 1970):

$$\tau_p(b) = \frac{D_{br}}{c} \sin\theta$$

where D_{br} is the breaking dissipation and c the wave phase speed (also see Figure 2 for notations). The secondary bottom shear stress is in the wave energy flux direction and of approximate magnitude (SDV, 1987):

$$\tau_s(b) \approx 0.15 \left(0.5 + 7 \frac{kh}{2\pi} \right) \frac{D_{br}}{c}$$

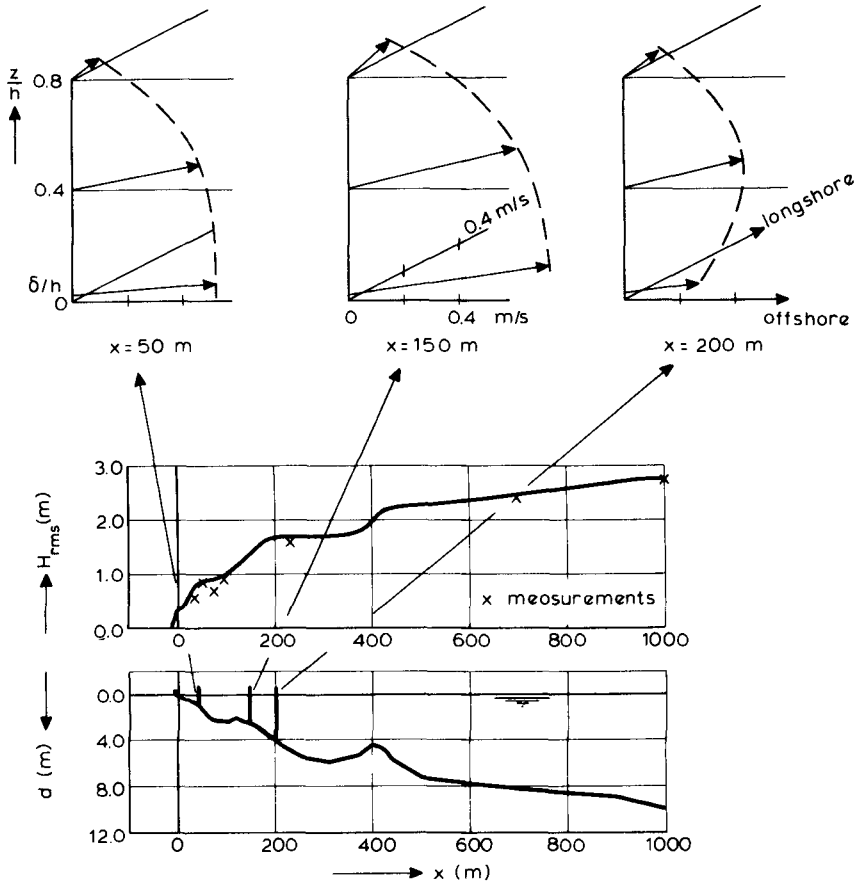


Figure 1 Model predictions of rotating mean velocity vector at Egmond beach (adapted from DVS, 1987)

The angle of the resulting velocity vector α may be derived from these approximations straightforwardly, taking into account the refraction of the wave field over the parallel bottom contours. As a result it appears that

$$\tan \alpha = \text{function} (kh, \theta_{inc})$$

which has been evaluated using Snell's law and the dispersion relationship with the result shown in Figure 2. It appears that the deviation towards the offshore direction of the resulting shearstress vector is stronger for the smaller angle of wave incidence. This is as expected since the longshore-current driving forces and resulting currents get weaker in this situation. This is in close correspondence with the field evidence gained and documented by Ingle (1966, pages 55-60), which is based on tracer experiments.

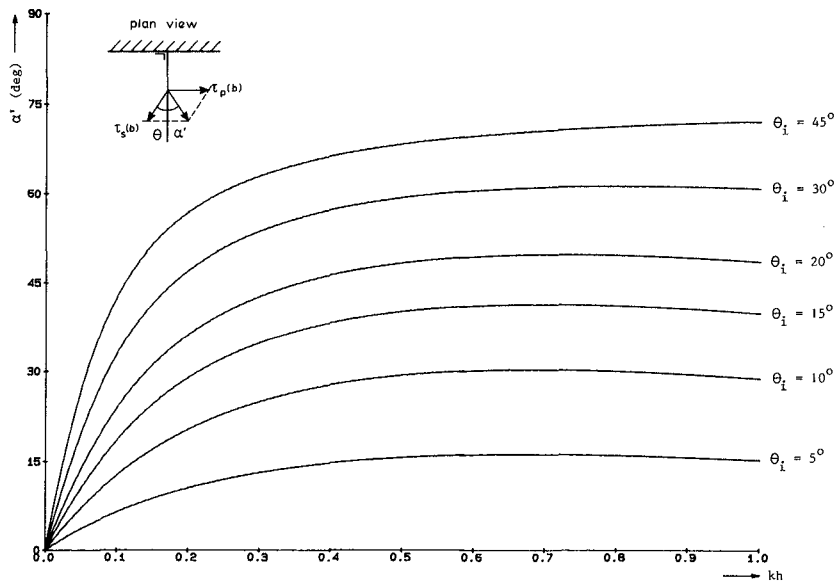


Figure 2 Increase of rotation towards the offshore direction of the resulting bottom shearstress for a decreasing angle of deep water wave incidence as a function of the relative waterdepth

3. SEDIMENT TRANSPORT AND CROSS-SHORE MORPHOLOGY

3.1 Instantaneous sediment transport formulation

Until quite recently nearshore sediment transport computations - in any rate those involving the alongshore horizontal dimension- were based on the concept of "waves or waves plus current stirr sediment up and the mean current transports the sediment". The existing formulations are usually based on an adapted uniform (river) flow formula, for instance the total bed and suspended load description after Bijker (1968) with a vertical sediment concentration description which is multiplied by the mean flow profile.

From the foregoing section it may be clear that the concept of "only the mean current transports" is considered insufficient: asymmetry-induced and wave-grouping induced effects can only be included in a formulation which is based on an instantaneous sediment transport description. The state-of-the-art in this respect is limited and with respect to accuracy not at the stage at which the above formulations are currently. It is considered essential though for the present problem. A reasonable first approximation seems to be the formulation of Bailard (1981), which is an extension of Bowen (1980) and Bailard and Inman (1981). In this formulation a distinction is made between bedload transport in a granular-fluid shear layer and suspended load transport in a layer of greater thickness, typically in the order of several centimeters. These transports are calculated as vertically integrated, but still instantaneous quantities.

Without going into the detail of the derivations and the formulations it may be schematically said that the instantaneous sediment transport is

assumed to respond in a quasi-steady manner to the time-varying flow on the one hand and to the downslope gravity force on the other hand, as follows:

$$q(t) = \text{const} \cdot u(t) |u(t)|^n + \text{const} |u(t)|^m \cdot \partial z_b / \partial x$$

with $n = 2,3$, $m = 3,5$ and $\partial z_b / \partial x$ is the local bed slope. Note that as expected for any suitable time-varying formulation the sediment transport rate, q , contains terms proportional to some power of the near-bottom, time-varying cross-shore flow, $u(t)$.

Field information of the last few years leads us to believe that the quasi-steady response assumption is valid for most natural beaches, but also in the laboratory it appears that under random waves the surf zone with sediments of 100 to 200 μm median grain diameter creates prevailing sheet flow conditions in the regions of significant sediment transport. Where the formulation fails is in the relatively protected areas in the trough behind breaker bars or somewhat more offshore, where one often may encounter rippled beds. For these regions a possible extension to the approach is to introduce non-steady response, for which it becomes important to include flow acceleration effects, resulting in terms with odd and even moments of the time-varying acceleration.

A further restriction to Bailards approach is the vertical integration that is performed, which assumes that the -known- vertical flow distribution is in a single plane. In the case of obliquely incident waves it was found in the foregoing that there is a vertical mean flow distribution which shows a rotation from alongshore in the upper water column towards the offshore in the lower part of the column. Clearly, a suitable formulation should also make inclusion of this effect possible. For the moment we must approximate the rotating velocity vector effect by choosing a representative near-bottom mean velocity, which in our case of obliquely incident waves will have both a cross-shore and an alongshore component.

So, for the time being it is suggested to rely on the above approach and we note that this involves basically the evaluation of the odd and even flow moments resulting from time-averaging of the above equation. The contributions to these moments for the purely cross-shore case are identified and analyzed in several publications each extending the foregoing ones (Bowen, 1980; Bailard, 1982; Stive, 1986; Roelvink and Stive, 1988a,b).

In the case of obliquely incident waves the near-bottom mean current will be composed of both the undertow and the primary flow, which then make an angle with the oscillatory current. Bailard's approach is also then quite straightforward. In the case of a small angle of wave incidence no major principle differences are expected in the cross-shore sediment transport distribution compared to the normally incident case. In general, the effect will be that of additional stirring for the cross-shore terms.

3.2 Cross-shore morphology of a nearly-prismatic beach

With the presented modelling approach for the near-bottom mean and oscillatory flow (section 2) and resulting sediment transport (section 3.1), which is applicable to a prismatic beach of arbitrary profile, we have available the constituents for a cross-shore sediment transport model with which profile deformations can be determined by applying the sediment balance equation.

The practical relevance of this schematized situation of a prismatic beach lies in applications dealing with the larger scale behaviour of an alongshore uniform coastal stretch which is not or only locally influenced by cross-shore structures. We assume then that on the larger -long-shore- scale the local circulation systems are averaged out and that the overall behaviour of the coastal stretch may well be described by assuming that the alongshore flows are negligible for normally incident waves or that they are uniform alongshore for obliquely incident waves. Our main interest is then into the development of the cross-shore profile, since it is only in the cross-shore direction that there are sediment transport gradients present resulting in bottom topography changes.

A small extension of this approach is for situations where there is a slow variation of an alongshore feature, such as the coastline direction. This variation is then assumed to be effective on a large timescale only, such that the local coupling of the weakly dynamic alongshore processes with the strongly dynamic cross-shore processes is the only (non-dynamic) interaction that needs to be accounted for. Some consequences of this approach are that locally the primary flow follows the parallel bottom contours, while the cross-shore primary flow is neglected. Examples are weakly curved coastal stretches or weakly curved coastal regions near estuary mouths.

Some first results based on this approach lead to interesting insights into the cross-shore profile development in case there are alongshore transport gradients present. An example is given in Figure 3, where the profile developments are compared for the case of no and a weak along-shore variation in the orientation of a coastal stretch. It appears that the existence of an alongshore gradient in the sediment transport influences bar formation and the mean profile slope in the surf zone.

4 DISCUSSION

An overview is given of the developments and understanding gained sofar of the current systems and the induced sediment transport and morphology that are found in the situation of random waves normally and obliquely incident on beaches which vary not or only slowly alongshore. For a similar overview in case the horizontal variations in alongshore and in cross-shore direction are equally important reference is made to De Vriend and Ribberink (1988) in these proceedings. Some of the aspects that need extra attention from the research point of view are indicated below.

the wave field

With respect to the natural representation of the wave field it should be noted that the aspect of randomness in the wave height decay has been included but sofar the effects of wave grouping and wave directionality have been disregarded. With regard to wave grouping effects reference is made to Roelvink and Stive (1988b), who present a first modelling approach. Their results indicate that outside the surfzone wave grouping reduces wave asymmetry effects, while the opposite is true inside the surfzone. With regard to wave directionality effects reference is made to Guza and Thornton (1986), but their results are not conclusive in this respect. Lastly, it should be mentioned that the approach sofar assumes uncoupling between breaking and nonbreaking waves, using the idea of applying the theory for the separate fractions.

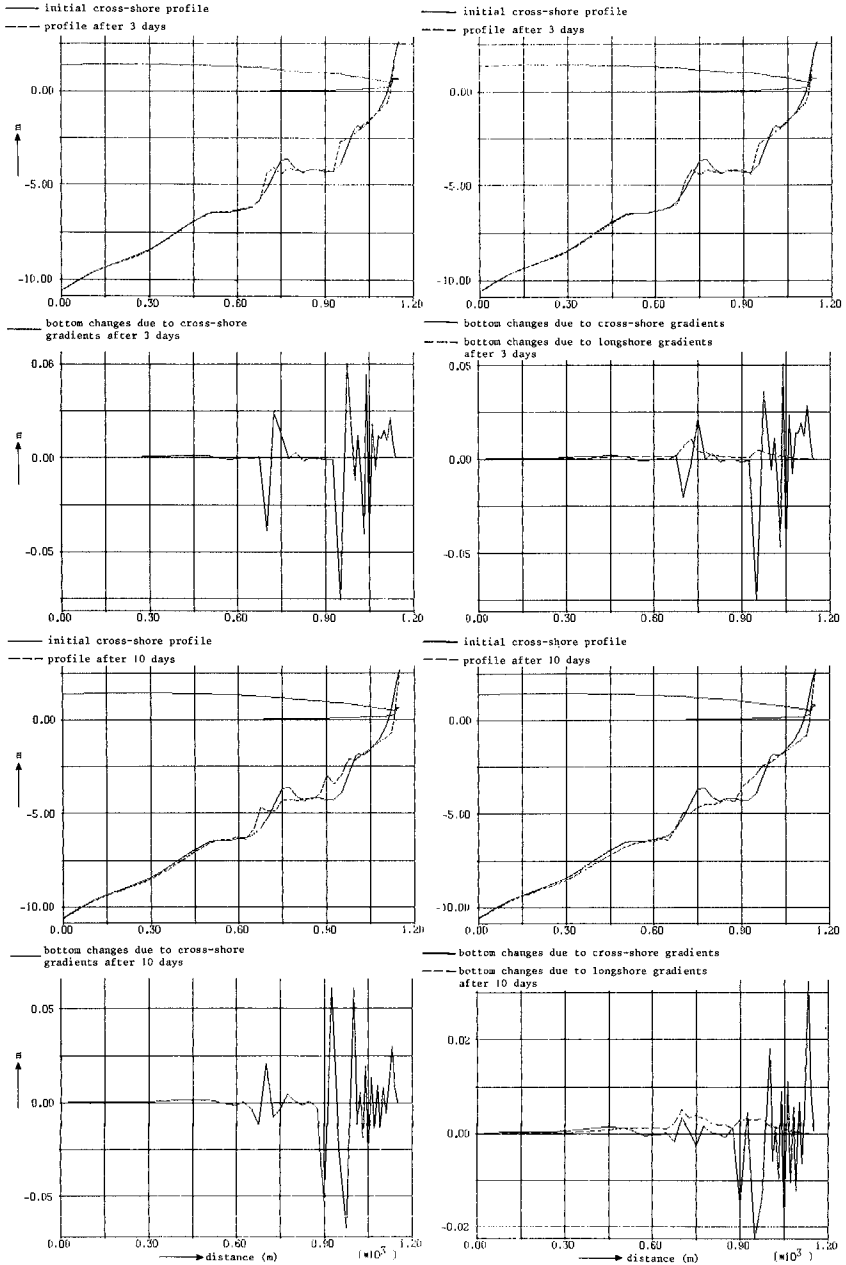


Figure 3 Cross-shore profile development and bottom changes per timestep ($\Delta t = 0.1$ days) in case of no (left) and a weak (right; radius of coastal curve of 2000 m) alongshore sediment transport variation (incident conditions $H_{rms} = 2$ m, $T_p = 8$ s, $\theta_{inc} = 10^\circ$)

mean flows

With respect to the cross-shore flows it is expected that the present modelling stage is satisfactory. Progress is needed with respect to the modelling of the combined longshore and cross-shore flows for obliquely incident waves. A first approach has been suggested with the quasi-3D formulation, but there are some important assumptions made. Of these the uncoupling between primary and secondary flow calculation should be mentioned here.

sediment transport

With respect to the sediment transport it is essential to have available an instantaneous transport description. An attractive first approach has been elaborated by Bailard (1981), but shortcomings are the quasi-steady response assumption and the depth-integrated approach.

morphology

With respect to the morphological evaluation it should be mentioned that even though the constituent formulations (for water and sediment motion) seem accurate this is not necessarily true when dealing with the morphological development. Progress with cross-shore morphodynamics has been made, but the predictive potential and the aspect of equilibrium profiles need further development. The addition of a longshore flow and sediment transport component needs further evaluation. Preliminary results indicate that longshore gradients can influence the mechanism of bar formation and the mean profile slope.

REFERENCES

- Bailard, J.A.**, 1981. An energetics total load sediment transport model for a plane sloping beach.
J. Geophysical Research, 86:10938-10954.
- Bailard, J.A.**, 1982. Modeling on-offshore sediment transport in the surf zone.
Proc. 18th Int. Conf. Coastal Eng., ASCE, pp. 1419-1438.
- Bailard, J.A. and Inman, D.L.**, 1981. An energetics bedload transport model for a plane sloping beach; local transport.
J. Geophysical Research, 86:2035-2043.
- Battjes, J.A.**, 1988. Surf-zone dynamics.
Annual Review Fluid Mechanics, 20:257-293.
- Bowen, A.J.**, 1969. Rip currents, Part 1: Theoretical investigations.
J. Geophysical Research, Vol. 74.
- Bowen, A.J.**, 1980. Simple models of nearshore sedimentation; beach profiles and longshore bars.
in: The coastline of Canada, ed. S.B.McCann, pp. 1-11.
Geological Survey of Canada, Ottawa.
- Bijker, E.W.**, 1968. Littoral drift as a function of waves and current.
Delft Hydraulics, Publication No. 58.
- Dally, W.R. and Dean, R.G.**, 1984. Suspended sediment transport and beach profile evolution.
J. Waterway, Port, Coastal and Ocean Eng., Vol. 110:15-33.
- De Vriend, H.J. and Ribberink, J.S.**, 1988. A quasi-3D mathematical model of coastal morphology.
Proc. 21st Int. Conf. Coastal Eng., ASCE, to appear.
- De Vriend, H.J. and Stive, M.J.F.**, 1987. Quasi-3D modelling of nearshore currents.
Coastal Engineering, 11:565-602.

- Dyhr-Nielsen, M. and Sørensen, T.**, 1970. Sand transport phenomena on coasts with bars.
Proc. 12th Int. Conf. Coastal Eng., ASCE, pp. 855-866.
- Guza, R.T. and Thornton, E.B.**, 1985. Velocity moments in nearshore.
J. Waterway, Port, Coastal and Ocean Eng., Vol. 111:235-256.
- Ingle, J.C.**, 1966. "The movement of beach sand".
Elsevier, Amsterdam; Developments in Sedimentology, 5, 221 p.
- Longuet-Higgins, M.S.**, 1953. Mass transport in water waves.
Philos. Transact. Roy. Soc., Ser. A, 245:535-581.
- Longuet-Higgins, M.S.**, 1970. Longshore currents generated by obliquely incident waves.
J. Geophysical Research, 75:6778-6801.
- Roelvink, J.A. and Stive, M.J.F.**, 1988a. Large scale tests of cross-shore sediment transport on the upper shoreface.
Symp. on Math. Mod. of Sed. Transp. in the Coastal Zone, Copenhagen, May 30-June 1.
- Roelvink, J.A. and Stive, M.J.F.**, 1988b. Bar generating cross-shore flow mechanisms on a beach.
J. Geophysical Research, to appear.
- Sonu, C.J.**, 1972. Field observations of nearshore circulation and meandering currents.
J. Geophysical Research, Vol. 77.
- Stive, M.J.F.**, 1986. A model for cross-shore sediment transport.
Proc. 20th Int. Conf. Coastal Eng., ASCE, pp. 1550-1564.
- Stive, M.J.F. and De Vriend, H.J.**, 1987. Quasi-3D nearshore current modelling: wave-induced secondary currents.
Coastal Hydrodynamics, Spec. Conf, ASCE, pp. 356-370.
- Stive, M.J.F. and Wind, H.G.**, 1986. Cross-shore mean flow in the surf zone.
Coastal Engineering, 10:325-340.
- Svendsen, I.A.**, 1984. Mass flux and undertow in a surf zone.
Coastal Engineering, 8:347-365.
- Svendsen, I.A. and Lorenz, R.S.**, 1988. Velocities in combined undertow and longshore currents.
Submitted to Coastal Engineering.
- Svendsen, I.A., Schaffer, H.A. and Hansen, J.B.**, 1987. The interaction between the undertow and the boundary layer flow on a beach.
J. Geophysical Research, 92:11845-11856.
- Thornton, E.B. and Guza, R.T.**, 1986. Surf zone longshore currents and random waves: field data and models.
J. Physical Oceanography, Vol. 16:1165-1178.
- Van Kesteren, W.G.M. and Bakker, W.T.**, 1984. Near-bottom velocities in waves with a current; analytical and numerical computations.
Proc. 19th Int. Conf. Coastal Eng., ASCE, pp. 1161-1177.

CHAPTER 129

Sand Ripple Geometry and Sand Transport Mechanism Due to Irregular Oscillatory Flows

Shinji Sato*

Kiyoshi Horikawa** F. ASCE

ABSTRACT

This paper describes characteristics of sand ripples and sand transport mechanism in regular and irregular oscillatory flows on the basis of detailed laboratory measurements. A set of empirical relations were proposed to evaluate the sand ripple geometry as well as the onset of the sheet flow transport. The applicability of the proposed relationships to the irregular wave conditions with prototype scales was confirmed with existing field data.

1. INTRODUCTION

In order to understand sediment transport due to waves, it is of great significance to elucidate the geometry of bed forms as well as the mechanism of sand movement. Although a number of laboratory investigations have been performed on the sand transport due to waves, most of them have been carried out only for the condition of monochromatic oscillatory flows. Laboratory experiments for the condition of irregular oscillatory flows are necessary for better understanding of sand movement under realistic conditions encountered on natural beaches.

The sand transport mechanism and bed form geometry under irregular waves were investigated through field measurements by Inman (1957), Dingle (1974) and Nielsen (1984). Detailed laboratory measurements of the net sand transport rate under irregular waves were recently carried out by Mimura et al. (1986) and Sato and Horikawa (1986). However, the influence of wave irregularity on sand movement mechanism should be further investigated since reliable data under well-controlled irregular waves are still insufficient.

The sand transport under sheet flow condition is frequently observed on

* Research Associate, Yokohama National University, 156 Tokiwadai, Hodogaya-ku, Yokohama 240, JAPAN

** Professor, Saitama University; Professor Emeritus, University of Tokyo

natural beaches where wave-induced velocities at the bottom exceed a critical value. The evaluation of the sand transport rate under sheet flow condition is of significance since the sand transport rate becomes extremely large. Since the reproduction of the sheet flow condition is difficult in laboratory wave flumes, most of the experimental investigations on sheet flow transport have been carried out by using oscillating beds or oscillatory flow tunnels. Manohar (1955) described characteristics of bed forms as well as the disappearance of ripples on the basis of experiments by using an oscillating bed. Komar and Miller (1975) expressed the condition for the ripple disappearance in terms of the Shields parameter and the Reynolds number of oscillatory flows. Horikawa et al.(1982) evaluated sand transport rates under sheet flow condition on the basis of the measurements of the velocity and the concentration of sand particles by using an oscillatory flow tunnel. Horikawa et al.(1982) also confirmed the applicability of the criteria for the onset of the sheet flow proposed by Manohar (1957) and Komar and Miller (1975). Further investigations on the sheet flow transport were conducted by Staub et al.(1984), Bakker and van Kesteren (1986) and Sawamoto and Yamashita (1987).

The objectives of the present study are to evaluate the geometry of sand ripples in irregular oscillatory flows and to discuss the effect of wave irregularity on sand transport mechanism. Characteristics of bed forms under irregular oscillatory flows are described for a wide range of conditions corresponding to the sand ripple regime and the sheet flow regime. Empirical relationships for the sand ripple geometry as well as the critical condition for the onset of the sheet flow are proposed which are applicable to the conditions with prototype scales.

2. FACILITIES AND PROCEDURES OF EXPERIMENTS

Experiments were performed in an oscillatory flow tunnel as shown in Fig. 1. The tunnel was equipped with a hydraulically-driven piston

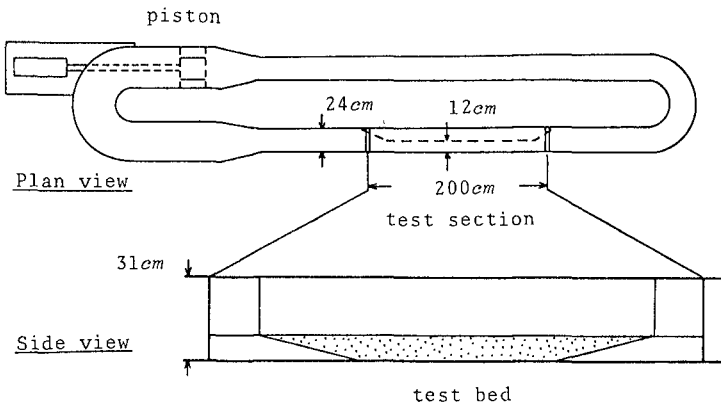


Fig. 1 Experimental facilities

controlled through an electric servo-system. The motion of the piston was controlled so as to reproduce the near-bottom water particle motion under regular and irregular waves based on the linear wave theory. Irregular oscillatory flows were simulated by assuming that the power spectrum of the irregular surface elevation was given by the Bretschneider-Mitsuyasu spectrum [Mitsuyasu (1970)]. The significant wave period was set to be in a range between 1s and 7s. Three kinds of irregular velocity histories were calculated for each wave period by assuming three different conditions for the depth to wavelength ratio h/L as illustrated in Fig. 2, in which the power spectrum density and the frequency are respectively nondimensionalized by the corresponding values at the peak of the power spectrum. Effects of the wave nonlinearity and the superimposed currents are not taken into consideration in the present study.

Two kinds of well-sorted sand were used as bed materials. The median diameters of the sands were 0.18mm and 0.56mm. The sand was filled in the test section to make initially flat test bed which was 160cm in length as shown in Fig. 3. A series of experiments (58 runs in total) were performed for the conditions of regular and irregular oscillatory flows. The width of the test section was reduced by half in some experimental runs in order to reproduce large-amplitude oscillatory

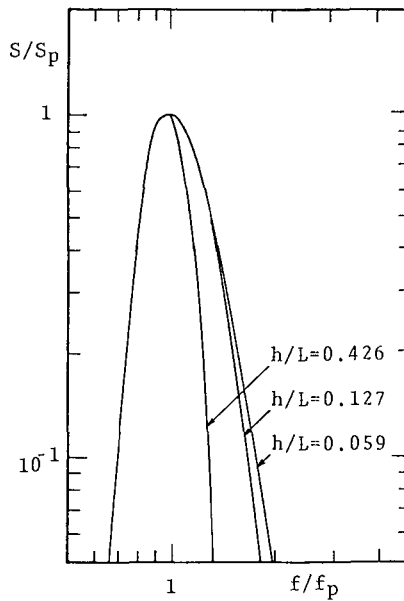


Fig. 2 Power spectra of velocity histories of irregular oscillatory flows

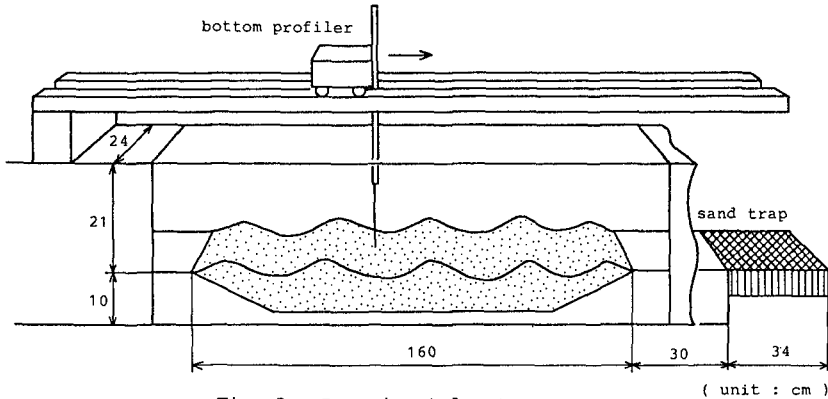


Fig. 3 Experimental set-up

(unit : cm)

flows.

Sand ripples were developed in 43 runs of the present experiments. Bottom profiles of the test bed were measured in detail by using a bottom profiler installed on the top of the tunnel. The wavelength and the wave height of the ripples were evaluated from the bottom profile measurements. In several runs of irregular oscillations, the ripple wave height was observed to vary in a range of 10% during the action of the oscillations. In such runs, ripple profiles were measured several times during the course of an experimental run. The ripple geometry was then determined as an average of these measurements. The development of bed forms and the type of sand movement for each run of the experiments were photographed through the side wall of the tunnel.

3. SAND RIPPLE GEOMETRY IN IRREGULAR OSCILLATORY FLOWS

In the analysis of several field investigations performed so far, the amplitudes of near-bottom velocity histories were calculated on the basis of the linear wave theory by using the significant wave height and period determined from the measured surface elevation. However, such evaluations sometimes induce considerable errors when the shape of the power spectrum density of near-bottom velocities is considerably different from that of the surface elevation. The great scatter of the published data in field investigations is considered to be partly attributed to the error in the evaluation of near-bottom velocities.

In order to understand the difference in the evaluation of near-bottom velocities, correlations were examined between the sand ripple geometry and hydraulic parameters evaluated in the following two methods. Figures 4 (a) and (b) show the relationship between λ/D and do/D for the condition of irregular oscillatory flows, in which λ is the ripple wavelength, do the diameter of the water particle displacement and D the sand grain diameter. The solid line indicates a regression relation for the ripple wavelength in regular oscillatory flows. The quantity do was

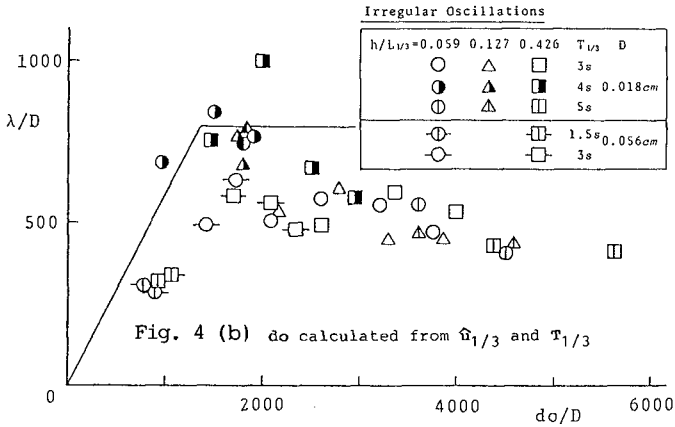
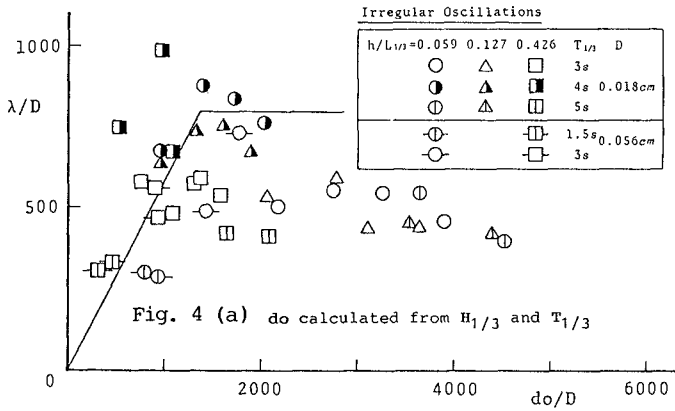


Fig. 4 Ripple wavelength in irregular oscillatory flows evaluated in Fig. 4(a) on the basis of the linear theory by

$$d_o = \frac{H_{1/3}}{\sinh kh} \tag{1}$$

where k denotes the wave number calculated by using the significant wave period. The evaluation of d_o was based on the following equation in Fig. 4(b):

$$d_o = \frac{\hat{u}_{1/3} T_{1/3}}{\pi} \tag{2}$$

in which $\hat{u}_{1/3}$ was the significant amplitude of velocity histories

evaluated by means of wave-by-wave analysis of the velocity history and $T_{1/3}$ was the corresponding significant wave period. The scatter of data in Fig. 4(b) appears smaller than that in Fig. 4(a). The above fact indicates that hydraulic parameters evaluated directly from near-bottom velocity histories are correlated better to the sand ripple geometry. It was also confirmed that the relationship between the ripple steepness and the Shields parameter Ψ was also correlated better when the Shields parameter was evaluated by using the significant amplitude of velocity histories. The hydraulic parameters for irregular oscillatory flows were therefore evaluated in the present study by using the significant amplitude of velocity histories.

The geometry of sand ripples was analyzed for a wide range of conditions by Brebner (1980), Nielsen (1981) and Sato et al.(1987). Sato et al. (1987) found that the sand ripple geometry was described for a wide range of conditions in terms of two hydraulic parameters, d_o/D and the following Shields parameter Ψ :

$$\Psi = \frac{1}{2} f_w \frac{\rho \hat{u}^2}{(\rho_s - \rho) g D} \tag{3}$$

where f_w is the friction factor, \hat{u} the velocity amplitude, ρ_s and ρ densities of sand and water and g the gravity acceleration.

Figures 5 and 6 respectively show the relationship between λ/d_o and $d_o/D\Psi^{1/2}$ and the relationship between η/λ and Ψ for the ripples observed

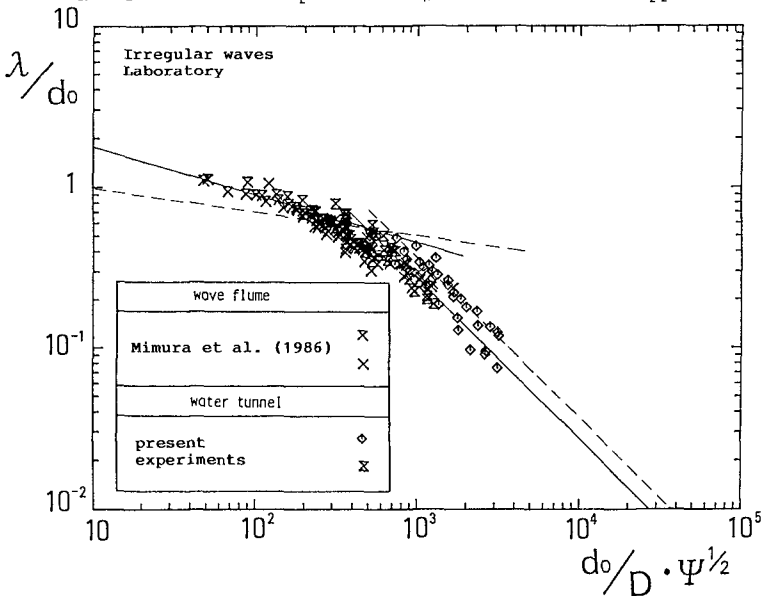


Fig. 5 Relationship between λ/d_o and $d_o/D\Psi^{1/2}$ for ripples in irregular oscillatory flows

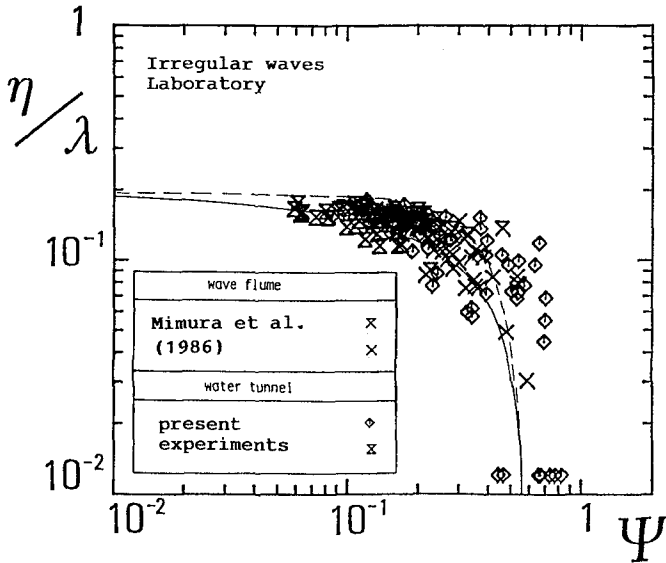


Fig. 6 Relationship between η/λ and Ψ for ripples in irregular oscillatory flows

in the present experiments, in which the solid lines represent the regression relations expressed by

$$\lambda/d_o = 3.55 (d_o/D \Psi^{1/2})^{-0.292} \quad \text{for } d_o/D \Psi^{1/2} < 480 \quad (4)$$

$$\lambda/d_o = 280 (d_o/D \Psi^{1/2})^{-1} \quad \text{for } d_o/D \Psi^{1/2} > 480 \quad (5)$$

$$\eta/\lambda = 0.191 (1 - \Psi/0.6) \quad (6)$$

and the broken lines represent the relations for the ripple geometry in regular oscillatory flows proposed by Sato et al.(1987). The wavelength of ripples in irregular oscillatory flows tends to become longer than that in regular oscillatory flows for the condition of small-amplitude oscillations, while ripples with shorter wavelength frequently developed in irregular oscillatory flows with large amplitude. The ripple steepness in irregular oscillatory flows tended to decrease considerably compared with that in regular oscillatory flows. The scatter of the data in the region of large Ψ seems to imply the need of further analysis on bed form characteristics in large-amplitude irregular oscillatory flows.

Figures 7 and 8 show the relationships for ripples on natural beaches. Although the scatter of the data is large compared with that of the data in laboratory measurements, it is verified that Eqs.(4), (5) and (6) also give good predictions of the geometry of sand ripples on natural beaches.

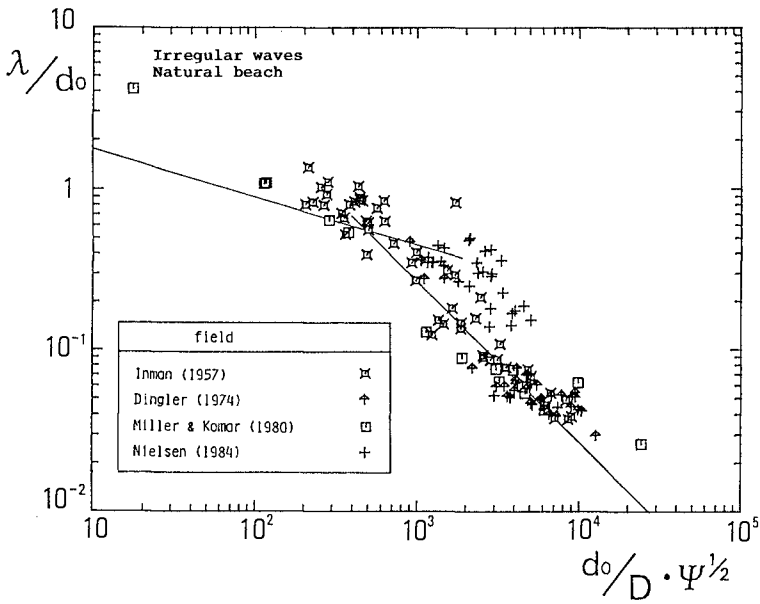


Fig. 7 Relationship between λ/d_0 and $d_0/D \Psi^{1/2}$ for ripples on natural beaches

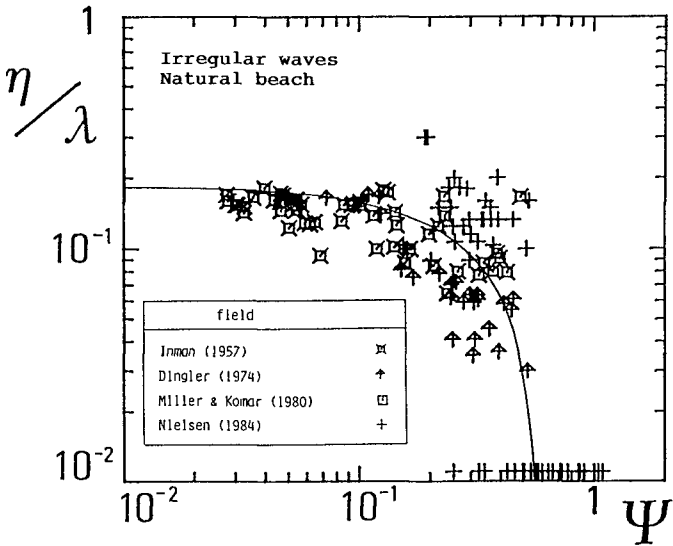


Fig. 8 Relationship between η/λ and Ψ for ripples on natural beaches

4. DISAPPEARANCE OF SAND RIPPLES

When the amplitude of oscillatory flows became large, sand ripples generally tended to disappear and sand particles began to be transported in the sheet flow. In regular oscillatory flows with large amplitudes, large-scale undulations, which were called dunes hereafter, were frequently generated as shown in Photo 1. The wavelength of the dunes was of the order of 1m. Flat bed then tended to develop with the further increase of the amplitude. The development of such dunes in regular oscillatory flows was also reported by Bosman (1981) and Sakakiyama et al. (1985). Characteristics of the dune geometry will not be further discussed in the present study since the length of the test bed in the present experiments was not considered to be enough to reproduce undisturbed dunes.

Photo 2 illustrates bed forms developed in a large-amplitude irregular oscillatory flow. Dunes were rarely generated under irregular oscillatory flows. On the other hand, small-scale two-dimensional ripples were generally observed in the transition region between the ripple and the non-ripple regime. The mechanism of the formation of these small-scale ripples was similar to the initial stage of ripple formation on a flat bed, that is, the geometry of these small two-dimensional ripples in large-amplitude irregular oscillatory flows were



Photo 1 Bed forms developed in a large-amplitude regular oscillatory flow

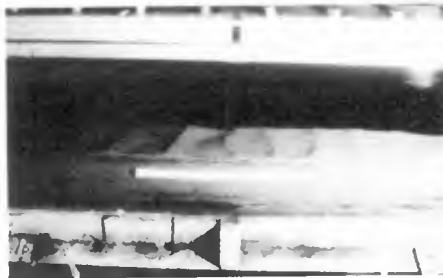


Photo 2 Bed forms developed in a large-amplitude irregular oscillatory flow

considered to be maintained by the iteration of conflicting actions of the ripple elimination due to large waves and the ripple formation due to relatively small waves.

Figure 9 shows the classification of bed forms under regular oscillatory flows. Open symbols indicate the presence of sand ripples and solid symbols indicate the disappearance of sand ripples. Data obtained by Bosman (1981) and Horikawa et al. (1982) were also plotted in the figure. Data were classified in the non-ripple regime when the ripple steepness was less than 0.05. Dunes were also classified in the non-ripple regime in the present study since sand particles on the duned bed were observed to be transported in sheet flow over the whole domain. The broken line in Fig. 9 represents the criterion for the onset of the sheet flow proposed by Komar and Miller (1975), in which ν is the kinematic viscosity of water. The relation proposed by Manohar (1955) was also examined for both regular and irregular oscillatory flows, which revealed that experimental data were not well classified by these criteria. The onset of sheet flow was therefore reanalyzed in the present study by using two parameters, do/D and Ψ , which were found to be essential parameters in describing the sand ripple geometry.

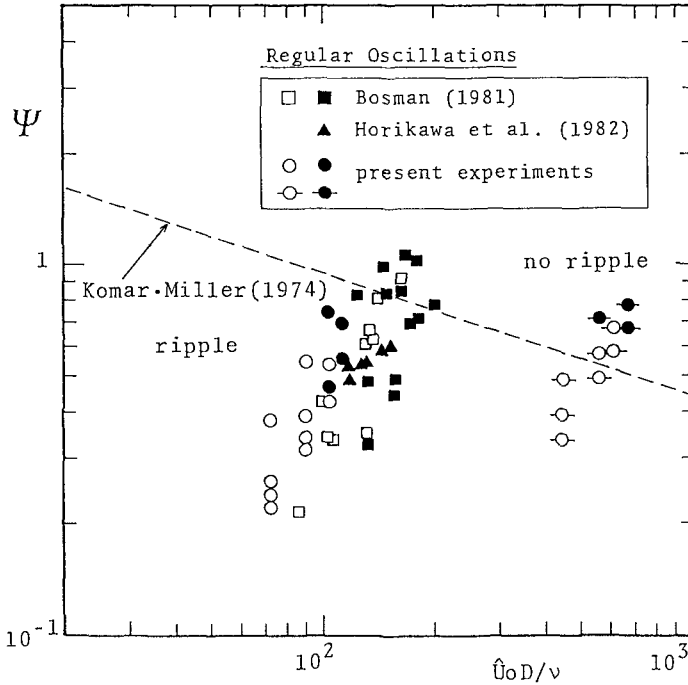


Fig. 9 Disappearance of ripples in regular oscillatory flows

Figure 10 shows the classification of bed forms under regular oscillatory flows in terms of do/D and Ψ . It is noticed that the disappearance of ripples was well described by the broken line in the figure which was expressed by

$$\Psi = 7.8 (do/D)^{-1/3} \quad (7)$$

Figure 11 shows the classification of bed forms under irregular oscillatory flows. Although the number of data was not sufficient, the critical condition for the disappearance of ripples in irregular oscillatory flows appeared to be described by Eq. (7).

Figure 12 shows the classification of bed forms on natural beaches. Values of do and Ψ were calculated on the basis of the linear theory by using the significant wave height and period of measured surface elevations. Although the scatter of the data is large, Eq. (7) appears to give an appropriate boundary between the ripple and the non-ripple regimes.

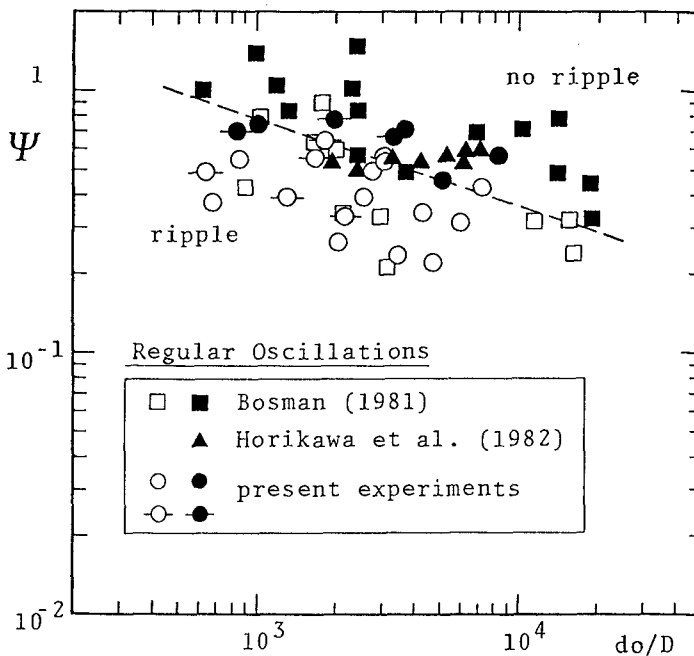


Fig. 10 Disappearance of ripples in regular oscillatory flows

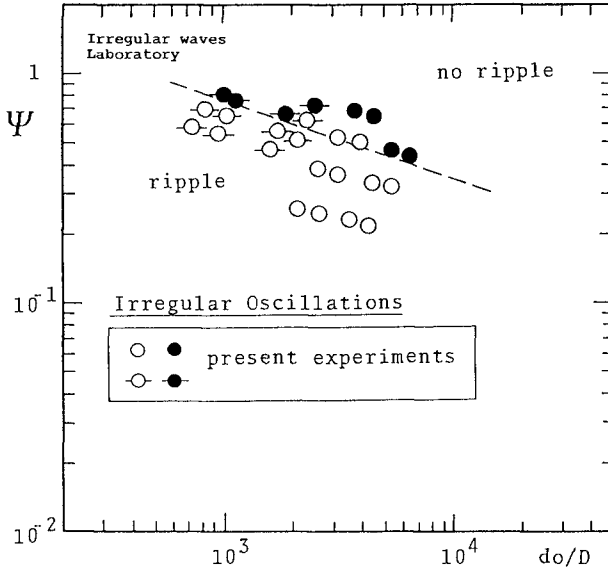


Fig. 11 Disappearance of ripples in irregular oscillatory flows

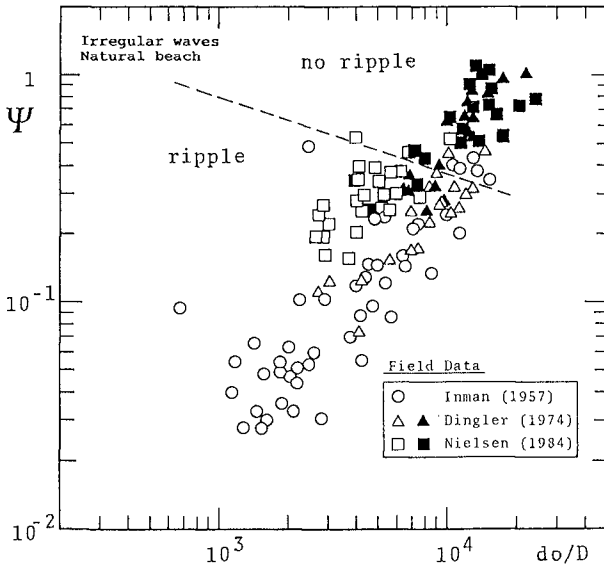


Fig. 12 Disappearance of ripples on natural beaches

Since the critical condition for the ripple disappearance was fairly described by Eq. (7), it is expected that the ripple steepness in large-amplitude oscillatory flows might be correlated better with a parameter $\Psi(d_o/D)^{1/3}$. Figure 13 shows the relationship between η/λ and $\Psi(d_o/D)^{1/3}$ for ripples in irregular oscillatory flows. The solid line represents a regression relation expressed by

$$\eta/\lambda = 0.170 (1 - (\Psi (d_o/D)^{1/3} / 7.8)^2) \tag{8}$$

Figure 14 shows the steepness of ripples on natural beaches. The correlation of data in Figs. 13 and 14 in the region of large Ψ is considerably improved compared with that in Figs. 6 and 8.

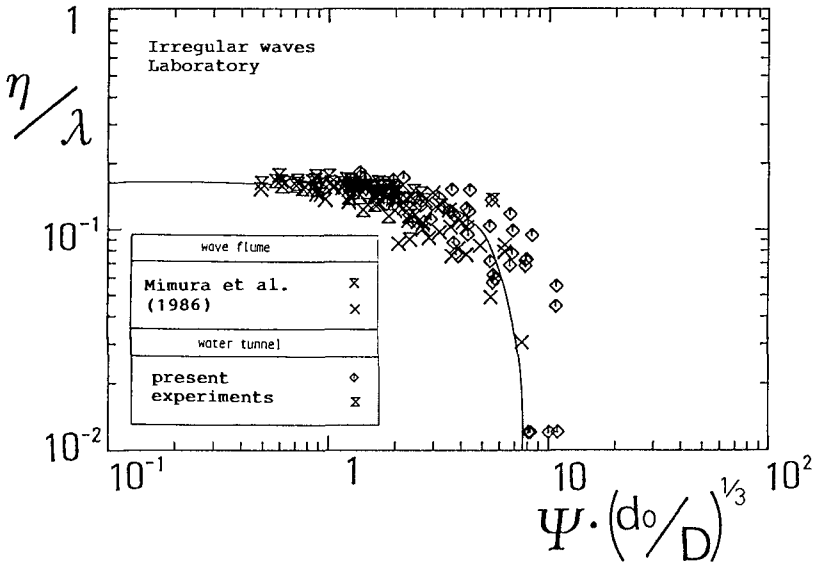


Fig. 13 Relationship between η/λ and $\Psi(d_o/D)^{1/3}$ for ripples in irregular oscillatory flows

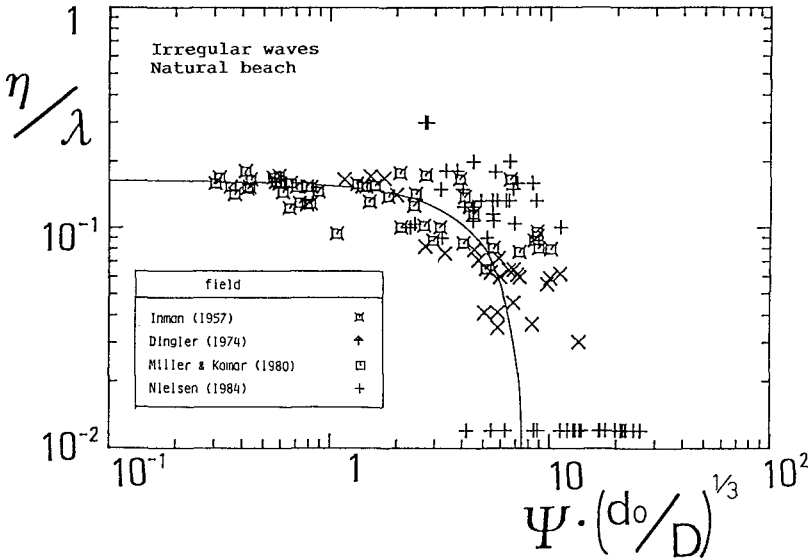


Fig. 14 Relationship between η/λ and $\Psi(d_0/D)^{1/3}$ for ripples on natural beaches

5. CONCLUDING REMARKS

Characteristics of the sand ripple geometry as well as the mechanism of sand movement in irregular oscillatory flows were investigated through a series of laboratory measurements. The sand ripple geometry and the critical condition for the disappearance of ripples were consistently expressed in terms of d_0/D and Ψ for both regular and irregular oscillatory flows. The applicability of the proposed relations to the condition with prototype scales was also confirmed with data on natural beaches.

REFERENCES

Bakker, W.T. and W.G.M. van Kesteren: The dynamics of sediment transport under oscillating sheetflow condition, Proc. 20th Conf. on Coastal Eng., pp.940-954, 1986.

Bosman, J.J.: Bed behavior and sand concentration under oscillatory water motion, Delft Hydraulics Lab., M1695-1, 49p., 1981.

Brebner, A: Sand bed-form length under oscillatory motion, Proc. 17th Conf. on Coastal Eng., pp.1340-1343, 1980.

Dingler, R.J.: Wave formed ripples in nearshore sands, Ph. D. Thesis, Univ. of California, 136p., 1974.

Horikawa, K., A. Watanabe and S. Katori: Sediment transport under sheet flow condition, Proc. 18th Conf. on Coastal Eng., pp.1335-1352, 1982.

Inman, D.L.: Wave generated ripples in nearshore sand, B.E.B. Tech. Memo., No. 100, 42p., 1957.

Komar, P.D. and M.C. Miller: The initiation of oscillatory ripple marks and the development of plane-bed at high shear stresses under waves, J. Sediment. Petrol., Vol. 45, No. 3, pp.697-703, 1975.

Manohar, M.: Mechanics of bottom sediment movement due to wave action, B.E.B. Tech. Memo., No. 75, 121p., 1955.

Mitsuyasu, H.: On the growth of spectrum of wind-generated waves (2), Proc. 17th Japanese Conf. on Coastal Eng., pp. 1-7, 1970(in Japanese).

Nielsen, A.F. and A.D. Gordon: Sediment responses to natural waves, Proc. 19th Conf. on Coastal Eng., pp.1799-1815, 1984.

Nielsen, P.: Dynamics and geometry of wave-generated ripples, J. Geophys. Res., Vol. 80, No. C7, pp.6467-6472, 1981.

Nielsen, P.: Field measurements of time-averaged suspended sediment concentrations under waves, Coastal Eng., Vol. 8, No.1, pp.51-72, 1984.

Sakakiyama, T., T. Shimizu, R. Kajima, S. Saito and K. Maruyama: Sand ripples generated by prototype waves in a large wave flume, Coastal Eng. in Japan, Vol. 28, pp. 147-160, 1985.

Sato, S., K. Mitani and A. Watanabe: Geometry of sand ripples and net sand transport rate due to regular and irregular oscillatory flows, Coastal Eng. in Japan, Vol. 30, No. 2, pp. 89-98, 1987.

Sato, S. and K. Horikawa: Laboratory study on sand transport due to asymmetric oscillatory flows, Proc. 20th Conf. on Coastal Eng., pp. 1481-1495, 1986.

Sawamoto, M. and T. Yamashita: Sediment transport in sheet flow regime, Coastal Sediments 87, pp. 415-423, 1987.

Staub, C., I.G. Jonsson and I.A. Svendsen: Variation of sediment suspension in oscillatory flow, Proc. 19th Conf. on Coastal Eng., pp. 1335-1352, 1984.

CHAPTER 130

The dynamic response of shingle beaches to random waves

K A Powell*

Abstract

An extensive laboratory investigation into the behaviour of shingle beaches has been undertaken using a large random wave flume. The study utilised a lightweight material scaled to reproduce the correct permeability of the beach, and the correct threshold and relative magnitude of the onshore/offshore movement. Results are presented describing both the wave reflection characteristics of the beach and the probabilistic distribution of wave run-up crests on the foreshore. Where possible the laboratory results are validated against field data.

1 Introduction

Although relatively scarce on a worldwide basis shingle, or gravel, beaches ($D_{50} = 10 - 60\text{mm}$) are a common feature around the UK coastline. However it is only in recent years that their considerable merits as coast protection structures have been fully recognised, and only over the last few years that this belated recognition has been transformed into a more widespread engineering application. This application is still restricted, however, not only by a paucity of information, regarding shingle beach processes under wave action, but also by a general lack of understanding as to how information which is currently available should be applied to a particular problem. In response to this situation an extensive series of model tests have been undertaken in the UK in recent years using both regular (Powell, 1986) and random waves. This paper summarises the procedures and results of the random wave investigation with particular emphasis on the wave reflection coefficients and wave run-up distributions.

2 Scaling Criteria for Model Beach Sediment

In order that a mobile bed physical model may accurately simulate natural beach processes it is necessary to ensure that the sediment used in the model is representative of that occurring in nature. For shingle beaches the model sediment should ideally satisfy three main criteria:

- a) The permeability of the shingle beach should be correctly reproduced.

Higher Scientific Officer

* Maritime Eng. Dept., Hydraulics Research Ltd,
Wallingford, OX10 8BA, UK

- b) The relative magnitudes of the onshore and offshore motion should be constant.
- c) The threshold of motion should be correctly scaled.

The first of these criteria basically governs the beach slope, the second determines whether the beach will erode or accrete under given wave conditions, and the third determines the wave velocity at which sediment motion will begin.

Yalin (1963) published a paper describing a method for modelling shingle beaches with the correct permeability and drag forces. For the permeability he stated that in an undistorted model the percolation slope must be identical to that of the prototype beach

$$\text{i.e. } \lambda_V^2 \lambda_K / \lambda_D = 1 \quad (1)$$

where λ is the model scale
 V is the flow velocity through the voids
 K is permeability, a function of the voids
 Reynolds number... $V D_{10} / \nu$
 D is sediment diameter
 and ν is kinematic viscosity

Assuming that the model is operated according to Froude's Law this equation can be re-written as

$$\lambda_D = \lambda K_p / K (Re_p / \lambda^{\frac{1}{2}} \lambda_D) \quad (2)$$

where the subscript p refers to prototype values. Provided that K_p , Re_p and the form of the function $K ()$ are known this equation can then be solved by successive approximation to define the particle size for the model sediment, for a given model scale.

The correct reproduction of the relative magnitudes of the onshore/offshore sediment motion requires the similitude of the dimensionless fall velocity parameter, $H_b/\omega T$, (see Shore Protection Manual, 1984).

$$\text{i.e. } \lambda H_b / \lambda_\omega \lambda_T = 1 \quad (3)$$

where H_b is the breaking wave height
 ω is the sediment fall velocity
 and T is the wave period

However the settling velocity for a sphere may be approximated by

$$\omega = (1.33 gD (\rho_s - \rho_f) / C_D \rho_f)^{\frac{1}{2}} \quad (4)$$

where ρ_s and ρ_f are specific gravities of the sediment and fluid respectively, and C_D is the drag coefficient for the settling particles (Rouse, 1950).

For a Froudian model therefore, assuming that the beach slope is correctly reproduced, equations 3 and 4 may be combined to yield an expression for the specific gravity of the model sediment:

$$\lambda \rho'_s = \lambda \lambda_{C_D} / \lambda_D \quad (5)$$

$$\text{where } \rho'_s = (\rho_s - \rho_f) / \rho_f \quad (6)$$

and λ_{C_D} is given as a non-linear function of the sediment particle Reynolds number by

$$\lambda_{C_D} = C_{D_p} / C_D (\text{Re}_p / \lambda^{\frac{1}{2}} \lambda_D) \quad (7)$$

Again, if C_{D_p} and Re_p are known, and λ_D has also been determined (i.e. equation 2), then equations 5, 6 and 7 can be solved for ρ_s , the specific gravity of the model sediment.

A second expression for the specific gravity of the model sediment is obtained through consideration of the threshold of motion of the sediment particles. For oscillating flow Komar and Miller (1973) proposed that for sediment sizes greater than 0.5mm, which is usually the case for shingle beach models, the threshold of movement would be defined by the expression,

$$U_m^2 / \rho_s' gD = 0.46 \pi. (d_o/D)^{0.25} \quad (8)$$

Where U_m is the peak value of the near bed orbital velocity at the threshold of motion and d_o is the near-bed orbital diameter. Re-working equation 8 and assuming a Froudian model yields the expression,

$$\lambda \rho'_s = \left(\frac{\lambda}{\lambda_D} \right)^{3/4} \quad (9)$$

It should be noted, however, that equation 7 was originally developed for predicting the threshold of movement of fully submerged gravel on a horizontal sea-bed subject to non-breaking waves. This is a very different situation to an emergent, sloping shingle beach subject to breaking waves, so the accuracy of the equation cannot be assured.

Generally equations 5 and 9 give conflicting requirements for the specific gravity of the model sediment, ρ_s , and one or other of the equations usually needs to be relaxed. This complication in the modelling of beach sediments is further compounded by the fact that there is only a very limited range of specific gravities amongst the readily available materials. Frequently, therefore, the selection of the model sediment is governed as much by availability as by theoretical considerations.

For the present study the scaling requirements have been plotted in graphical format in Figure 1. These may be satisfactorily met at a scale of 1:17 by the use of crushed anthracite (coal) which has a specific gravity of 1.39, and is readily available in a range of gradings. At the selected scale the specific gravity requirements for the model sediment, based on the threshold and direction of motion criteria are respectively 1.45 and 1.35, which are acceptably close to the value for anthracite.

3 Laboratory procedures and test programme

During the course of the study four different sizes, and two different gradings, of beach material (selected to cover the range of shingle sizes commonly found around the UK coast) were used to build the model beaches. The beaches themselves were always constructed at a 1:7 slope but up to 5 different depths of beach material were tested. Each beach was subjected to up to 29 wave spectra of the JONSWAP type covering the following range of conditions:

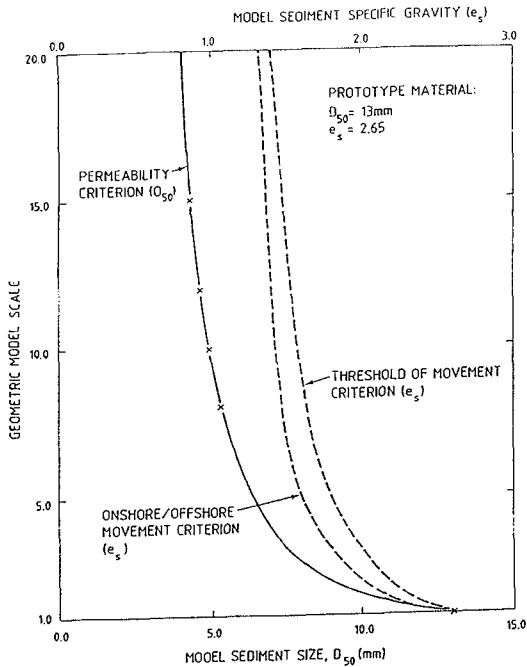


Fig 1 Sediment scaling criteria

$$0.05\text{m} < H_s < 0.175\text{m}$$

$$0.8\text{s} < T_z < 2.7\text{s}$$

$$0.005 < H_s/L_z < 0.06$$

The depth of water at the toe of the model was kept constant at 0.8m throughout the course of the study.

Amongst the measurements recorded during the investigation were the wave reflection coefficients for the model beaches and the wave run-up exceedance distributions on the beach face.

Wave reflections were recorded using 3 wave probes located at set positions along the centreline of the flume. The incident and reflected wave spectra were not directly measured but were calculated using an analysis program devised by Gilbert and Thompson (1978) and based on the method of Kajima (1969). The analysis method calculates values of K_r over a wide range of frequencies, but the procedure is only valid over a restricted band related to the probe spacing. For the current study, the use of three wave probes effectively provided three different probe spacings thus allowing a wide range of frequencies to be covered.

Because beaches are constantly adjusting their form in response to the incident wave conditions, it seems likely that the proportions of wave energy reflected or dissipated may also vary as the beach gradually evolves. To test this hypothesis three sets of measurements were made per experimental run, after allowing the beach an initial development period of $500 T_z$.

Attempts to record wave run-up distributions in laboratory beach models usually meet with two main problems.

- 1) The mobility of the beach - which tends to restrict the use of instrumentation on the beach face itself.
- 2) The presence of edge effects along the side walls of the flume - which can affect visual recordings taken at beach level.

To overcome these problems a simple method was developed for measuring wave run-up distributions along the centre line of the flume. This involved blacking out the half of the flume furthest from the observer whilst lighting the front half from above. The image of an illuminated marker board located outside the flume, and referenced to still water level, was then reflected into the flume and projected on to the centre line boundary, between the light and dark sections of the flume. The marker board was drawn up with twelve numbered bands in such a way that its image appeared correctly orientated. With a little practise an observer was able to record the total number, and hence proportion, of wave run-ups exceeding specified levels against the image of the marker board. Initial proving of the method demonstrated a high degree of repeatability, which appeared to be independent of the observers involved.

4 Wave Run-up distributions

Generally five wave run-up recordings, of $300T_z$ duration, were taken for each test, with each recording being separated by a $200 T_z$ interval. Prior to any measurements being taken the profile was allowed to evolve naturally for a period of $500T_z$. This was generally long enough for the major profile features to develop and subsequent analysis of the results showed no evidence of any duration dependent trends.

On completion of a test the records were processed to provide, firstly, the cumulative number of wave run-ups exceeding a specified level per record; and then, secondly, the combined exceedance probability of wave run-up, for those levels, for all five sets of data. The resulting probability distribution was then used in all subsequent analysis.

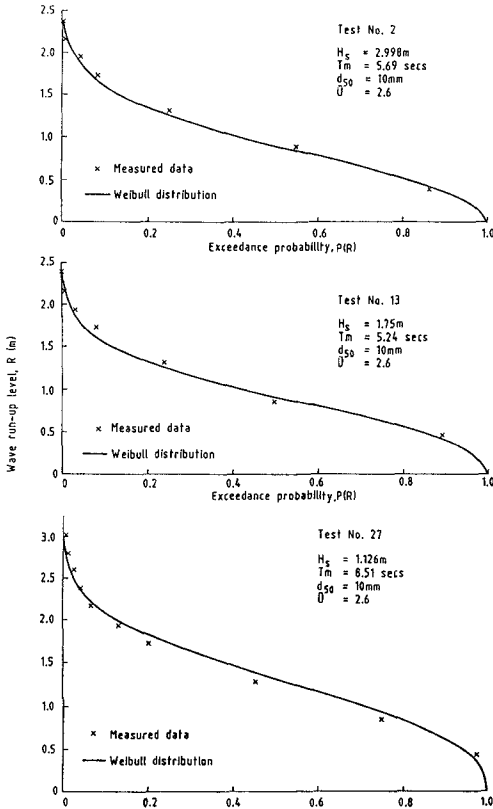


Fig 2 Typical wave run-up exceedance distributions

Typical wave run-up distributions recorded during the model tests are given in Figure 2. These measured distributions have been tested against theoretical Weibull and Rayleigh distributions of the form:

$$\text{Weibull : } P(R) = \exp(-B(R-C)^A) \quad (10)$$

$$\text{Rayleigh : } P(R) = A \exp\left(-\frac{BR^2}{2}\right) \quad (11)$$

where A and B are curve fitting coefficients
 C is a lower limiting value of R
 R is a specified level relative to still water level
 and P(R) is the probability of a wave run-up exceeding R

In this particular instance the lower limiting value C in the Weibull distribution has been taken as zero, and the run-up has therefore been measured relative to still water level rather than to an arbitrary mean water level which would necessarily include the component due to wave set-up.

Generally the differences between the two distributions are small when compared to the measured data. However the Weibull distribution usually returns slightly better correlation coefficients and hence provides a better fit to the data, particularly over the lower end of the range. The Weibull distribution was therefore taken as providing the best description of wave run-up on the model beaches. This is confirmed by Figure 2 where the theoretical Weibull distribution shows good agreement with the model data.

Detailed analysis of the results suggests that the Weibull coefficient B is a function of both wave height, H_s , and mean sea steepness, H_s/L_z . The precise form of the relationship is given in Figure 3 from which regression analysis yields:

$$B = 0.3 [H_s^{1.4} \exp(-30.0 H_s/L_z)]^{-1.6} \quad (12)$$

with a correlation coefficient, $r = 0.96$.

As may be seen, B is therefore proportional to H_s/L_z but inversely proportional to H_s . Thus for a constant value of A, increasing B (i.e. increasing sea steepness or decreasing wave height) reduces the probability of the wave run-up exceeding a specified level.

In contrast to coefficient B, the values of coefficient A appear to be largely independent of wave climate with a mean value of 2.2 and a standard deviation, $\sigma = 0.22$. Combining this mean value with equations 10 and 12 yields an expression for determining the probable distribution of wave run-ups on a shingle beach, relative to still water level,

$$\text{i.e. } P(R) = \exp(-BR^{2.2}) \quad (13)$$

where the value of B is given by equation 12.

Note that although equation 13 does not include any allowance for variations in beach sediment size, this was not found to be a serious handicap. Indeed throughout the test series no dependency between wave run-up and the beach material characteristics could be observed.

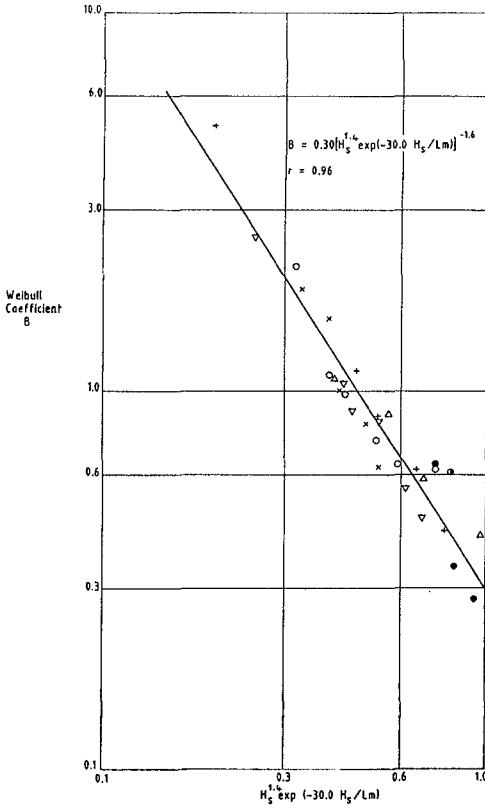


Fig 3 Weibull distribution - coefficient B

The applicability of equation 13 to the test results is confirmed by Figure 4. Here data gathered during field measurement exercises at Chesil Beach and Hurst Castle Spit (on the south coast of the UK) is compared with the predictions of equation 13 for values of $P(R) = 0.5$ and 0.02 . As can be seen the agreement between the predicted and measured values is good.

Observations made during the course of the test programme suggested that, even when fully developed, the beach crest would be overtopped by a small percentage of the wave run-ups. Analysis of the data, based on the assumption that it fitted a Weibull distributions, allowed this percentage to be estimated for each test condition. The resulting exceedance probabilities, calculated for a crest height formed after 3000 waves, suggest that generally less than 3% of the wave run-ups overtop the beach crest, with the mean probability of overtopping $P(R > h_c) = 0.015 \pm 0.011$. No systematic variations, based on wave conditions, are apparent within the results.

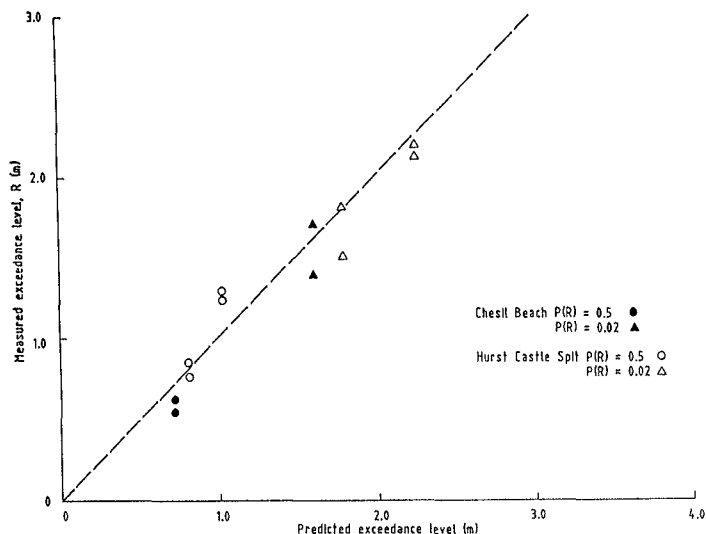


Fig 4 Comparison of measured and predicted run-up exceedance levels

5 Wave reflection coefficients

The effectiveness of a shingle beach in dissipating wave energy is an important measure of its usefulness as a coast protection structure. This is particularly true of beaches used as energy absorbing structures in enclosed waters (i.e. marina's etc) where high levels of reflected energy can have undesirable consequences for small vessels.

During the course of the present study an extensive series of measurements were made of wave reflection for a variety of wave and beach conditions. Generally three sets of reflection measurements were collected for each test, after first allowing a period of $500T_z$ for the main features of the beach to evolve. The reflection measurements were taken between 500-1000, 1500-2000 and 2500-3000 T_z from the commencement of the test. On-line analysis of the results produced details of the incident and reflected wave spectra together with values for the reflection coefficients, both for discrete frequency bands within the spectrum and for the wave spectrum as a whole.

Values of the characteristic reflection coefficient K_r (defined as $(S_r/S_i)^{1/2}$ where S_r and S_i are respectively the reflected and incident energy densities) calculated for each wave spectrum were found to be related to the incident spectral sea steepness, H_s/L_z . This relationship is depicted in Figure 5 for all K_r values obtained. The resulting trend shows that the proportion of wave energy reflected by a shingle beach is reasonably constant, at around 10%, for all values of sea steepness greater than 0.02 (i.e. breaking wave

conditions). For sea steepnesses less than 0.02 the effectiveness of the beach in dissipating wave energy reduces rapidly (i.e. higher levels of reflected energy). It is interesting to note that Figure 5 shows the material size, D_{50} , and the effective beach depth, D_R/D_{50} , (where D_B is the vertical depth of beach material) to be of little consequence to the overall K_R trend. This may suggest that wave energy is primarily dissipated in the processes of wave breaking, and overcoming frictional losses in flow over and within the surface layers of the beach. If this is so, flow within the body of the beach can be considered to add little to the overall dissipation of wave energy.

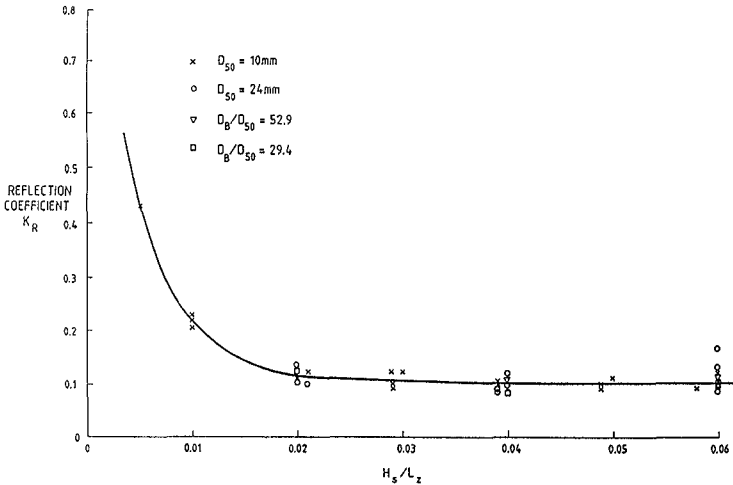


Fig 5 Wave reflection coefficients

6 Conclusions

The wave run-up and wave reflection characteristics of shingle beaches have been investigated using a scaled physical model in a random wave flume. The correct response of the model beach has been achieved through the accurate reproduction of both the beach permeability, and the threshold and direction of sediment motion. So far the conclusions arising from the study may be summarised as:

- 1) The probabilistic distribution of wave run-up crests on a shingle beach is most closely described by a Weibull distribution.
- 2) The probability of the run-up exceeding any given level on a shingle beach can be adequately determined from equations 12 and 13.
- 3) Using these equations the proportion of wave run-ups exceeding the wave-formed beach crest is found to be generally less than 2%, regardless of beach material size or the wave conditions.

- 4) The proportion of normally incident wave energy reflected by shingle beaches is nearly constant, at around 10%, regardless of the size, grading or active depth of the beach material.
- 5) For wave steepnesses greater than 0.02 the proportion of energy dissipated is also virtually independent of the incident wave conditions.

If should be noted that these results apply only to shingle beaches subject to normally incident wave action. Further research is underway to determine the effects of oblique wave attack on the wave run-up and reflection parameters.

7 Acknowledgements

This research was funded by the Ministry of Agriculture, Fisheries and Food under contract no. CSA 1034.

8 References

1. Coastal Engineering Research Centre. 1984. Shore Protection Manual. 2 Vols, 4th edition.
2. Gilbert G and Thompson D M. 1978. Reflections in random waves - the frequency response function method. HRS Report IT 137, Wallingford.
3. Kajima R. 1969. Estimation of an incident wave spectrum under the influence of reflection. Coastal Eng. in Japan, Vol. 12.
4. Powell K A. 1986. The hydraulic behaviour of shingle beaches under regular waves of normal incidence. PhD Thesis. University of Southampton.
5. Rouse H. 1950. Fundamental principles of flow, in Engineering Hydraulics, edited by H Rouse, Wiley, New York. pp. 1-135.
6. Yalin M S. 1963. A model shingle beach with permeability and drag forces reproduced. 10th Congress Int. Ass. Hyd. Research.

CHAPTER 131

ESTIMATES OF CROSS-SHORE BEDLOAD AND BED CHANGES

Zbigniew PRUSZAK¹ and Ryszard B. ZEIDLER²

ABSTRACT

Four series of tracer studies employing radioisotopic sand, tracked remotely from land, were carried out at the IBW PAN's coastal research station at Lubiatowo. Incipient motion of single grains with velocity v_{cr1} has agreed with Komar and Miller's (1974) formula, and has been 5...8 times smaller than v_{cr2} , the threshold velocity of water inducing bulk motion of sediment. The ratio of average nearbed water velocity, \bar{v} , to the effective speed of tracer sand, in the inshore zone, \bar{v}_s , is estimated about 100...1,000. The cross-shore sediment transport rates measured are ten times smaller than those predicted by Pruszek's (1987) energetics formula, the discrepancy being due to the real field phenomena of mixing and overburdening in a thick bed layer. Our wave flume and wave tank studies with movable bed point to the importance of initial slope in shore evolution. The laboratory findings on bed variability are extended by our 1987 field data obtained with an ultrasonic setup. Intensive cyclic depth changes are accompanied by varying transport rates computed from continuity equation.

1. INTRODUCTION

Sediment transport in the coastal zone, particularly in the bedload mode, still requires further analytical studies and experimental data. Field facilities of our Coastal Research Station at Lubiatowo and radiotracers were used to quantify sediment motion. An ultrasonic probe was devised and used at Kamchiya (or Shkorpilovtsy on the Bulgarian Black Sea) to measure short-term variability of bed topography. The latter provided a basis for cross-shore transport computations. The figures obtained are comparable with a theoretical prediction stemming from the

Polish Academy of Sciences' Institute of Hydro-Engineering, Sen. Res. Assoc.¹ and Professor², 80953 Gdańsk, IBW PAN

energetics approach, which was earlier verified in a wave flume with movable bed. The three sets of the studies, together with various estimates of sediment motion measures, are discussed hereafter.

2. FIELD MEASUREMENTS OF SEDIMENT MOVEMENT

2.1. Apparatus and Environment

Four series of measurements with radioactive tracers of bed movement were conducted in 1984, 1986 and 1987 at Lubiatowo. Each series lasted several days and embodied continuous monitoring of waves, currents, bed topography and sand transport.

The instrumentation setup at Lubiatowo was installed on a steel framework, referred to as a "Spider", 10x10 m in plan view, with a system of three carriages and trolleys which allowed for accurate tracking, with a scintillation probe, of the movement of radioactive tracers within the area of Spider. In all experiments the latter was placed in a shallow nearshore zone on a depth of up to 1.5 m some 50-60 m offshore; Fig. 1 depicts the layout of Spider and bed topography in 1986 and 1987.

Iridium glass beads with quite uniform diameters of 0.2 mm (1984), 0.15...0.2 mm (1986), 0.088...0.15 mm (1986) and 0.2...0.25 mm (1987), in the range of the mean diameter of the Lubiatowo sand, $D_{50} = 0.22$ mm, were used as radiotracers. The composition of the glass was roughly 48 % SiO_2 , 19 % Al_2O_3 , 17 % CaO , 6 % MgO , 5 % TiO_2 , 5 % K_2O and 0.25 % IrO_2 , which corresponded to the density of 2668 kg/m^{-3} . The radioisotope used, Ir-192, has the half-life period of 74.4 days. The principal radiation energy bands are 0.316 and 0.468 eV. Fifty-gram samples of radioactive sand were used in each experiment.

Waves were measured with a conductivity - type wire probe and a pressure transducer, water velocities with an electromagnetic current meter, and bed topography around Spider - manually by skin divers. The scintillation probe was moved and operated remotely from a land-based laboratory where all signals were collected and processed.

Wave parameters and water velocities measured in the

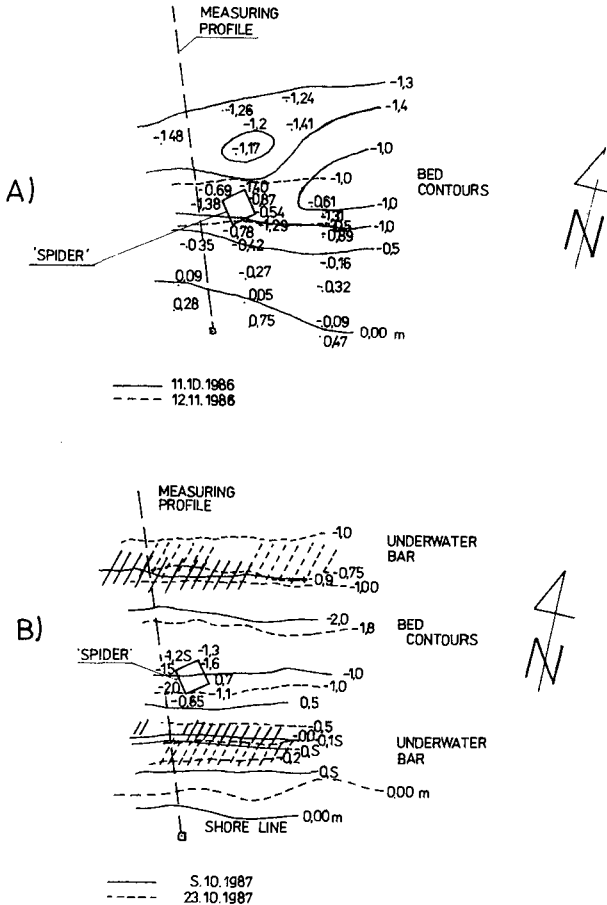


Fig.1 Bed Topography:(A) Lubiatowo '86; 11th Oct... 12th Nov '86
 (B) Lubiatowo '87; 5th Oct... 23d Oct '87

1986 and 1987 experiments are shown in Fig. 2 and Fig. 3, respectively. Wave crests were approximately parallel to the seaward side of Spider. In both series the prevailing longshore current was eastward.

2.2. Sediment Transport

Systematic tracking of the radiotracers within Spider has provided a background for the evaluation of various modes of sediment movement, cf. examples for 1986 and 1987 in Fig. 4, where the areas in different shades depict tracer activity, in pulses per second. Advection and dis-

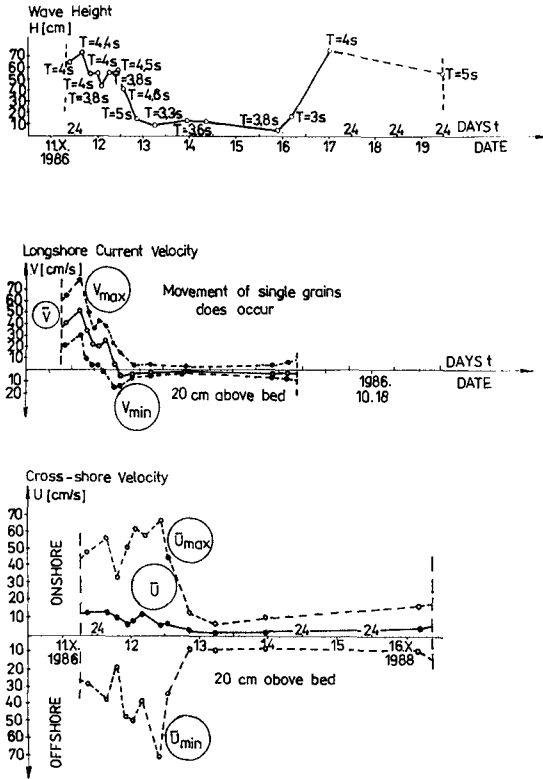


Fig. 2 Waves and Water Velocities in 1986

persion of the radiotracer provide estimates for incipient motion and bulk transport of sand.

Incipient motion has been linked to dispersion without any advection, i.e. any displacement of the centre of mass. Single grains with $D_{50} = 0.2 \text{ mm}$ begin to move under waves about $H \approx 15 \text{ cm}$ $T \approx 3.5 \dots 4 \text{ s}$, in water with the longshore and cross-shore velocity components of 5 and $8 \dots 10 \text{ cm s}^{-1}$, respectively (13th to 16th Oct '86). Similar results were obtained in 1984 and 1987. Hence the threshold velocity of water for grains with $D_{50} = 0.15 \dots 0.25 \text{ mm}$ can be given as $V_{cr1} = 8 \dots 10 \text{ cm/s}$. These findings roughly coincide with the field data by Davis (1980) who observed no movement of 1.4-mm grains for water velocities lower than 8 cm/s , along with the incipient motion for the range of $8 \dots 22 \text{ cm/s}$, the number of

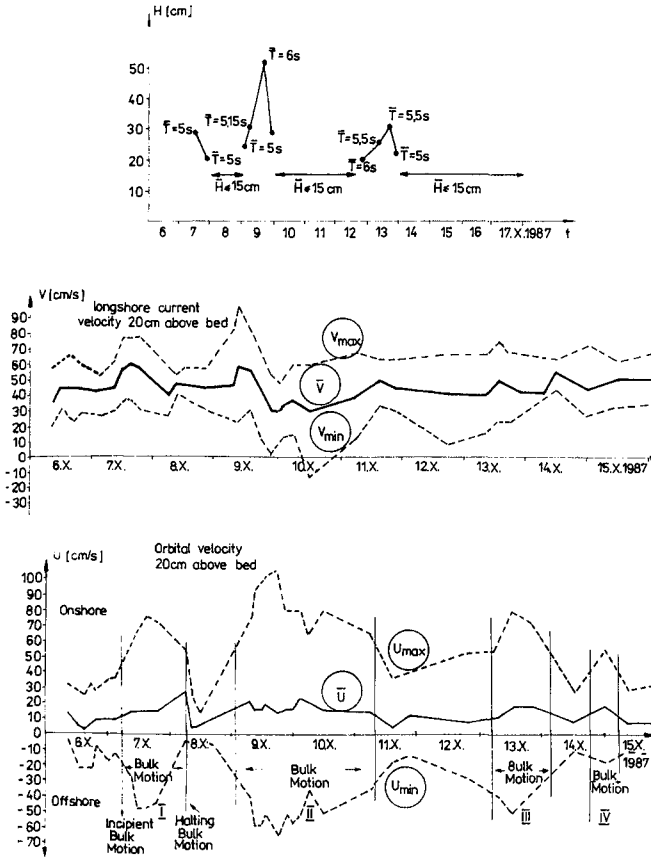


Fig. 3 Waves and Water Velocities in 1987

moving grains increasing with water velocity. Our estimates are also in line with the prediction by Komar and Miller (1974), which is worth noting as our waves were irregular.

Bulk transport, attributed to displacement of the centre of mass, has been observed for water velocities about 50...60 cm/s, cf. Figures 3 and 4. All studies of 1984, 1986 and 1987 point to the same critical velocity of water $V_{\text{cr}2} = 50...60\text{ cm/s}$ for sand grains with $D_{50} = 0.15...0.25\text{ mm}$.

The ratio of water velocity near bed to the effective sediment velocity i.e. the average velocity of the centre of mass is estimated about $10^3...10^4$. Some characteristic

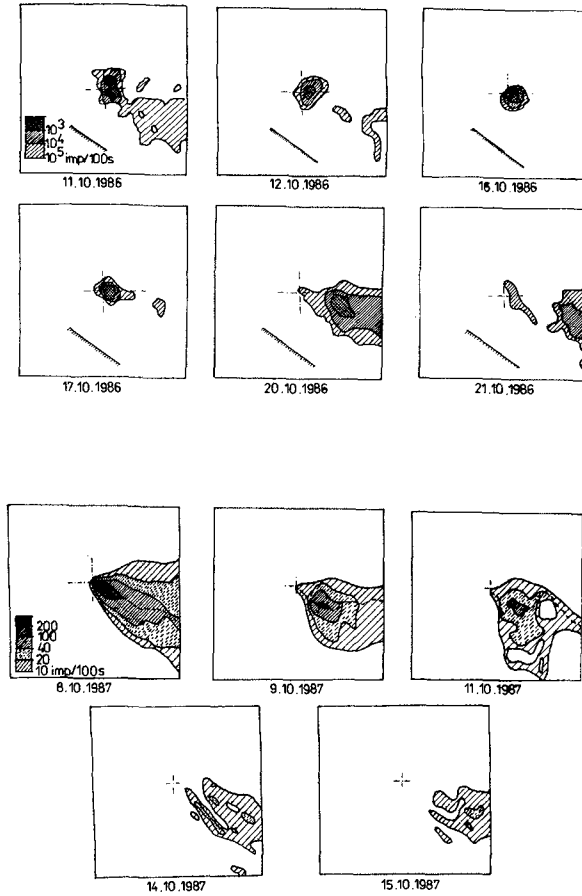


Fig.4 Plumes of Radioactive Sand Recorded within SPIOER

figures are given in Tab. 1.

Table 1.

Sand and Water Velocities

Year	D ₅₀ mm	V_{cr2} cm/s	V_s cm/hr	V/\bar{V}_s	Remarks
1984	0.2	60	12	10^4	1/curvilinear tracer trajectories
1986/1	0.15..0.25	50	12	10^3	2/bulk transport is depth-averaged
1986/2	0.088..0.15	20	8...9	10^3	
1987	0.2...0.25	55	10	$10^3..10^4$	

It should be remembered that our bulk transport is depth-averaged, so that the uppermost bed grains may move

faster even by one order of magnitude. If this is so then our estimates for V/\bar{V}_s are close to 10^2 obtained by Kato and Tanaka 1986. The velocity $\bar{V}_s = 75$ cm/hr given by Drapeau and Long (1984) for $D = 0.2...0.4$ mm might be higher due to persistent tidal flows.

The depth of penetration has been assessed by measuring the radioactivity in 2-cm layers cut of core samples. Six examples of the vertical distribution of moving sediment are shown in Fig. 5. Although the tracer was detected as deep as 15 cm below sea bed, this thick layer must not be identified with the bedload layer, as irregular restructuring of sea bed took place in various stages of the ex-

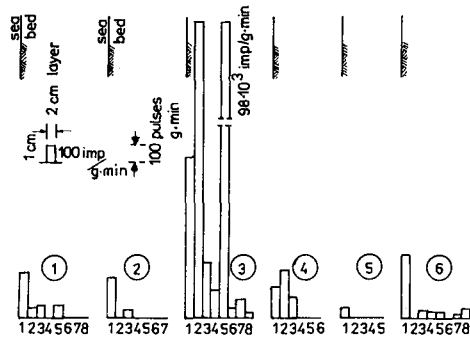


Fig. 5 Vertical Distributions of Radiotracers in 1987

periments. Generally, the vertical distribution varies from rectangular through parabolic (with a maximum at the sea bed) to Gaussian (with a maximum below bed), and seems to reflect a variety of sedimentation patterns encountered, from sheet flow through rapid overburdening to random mixing.

The absolute magnitude of the unit bedload rate at Lubiatowo was of the order of 2.5×10^{-3} kg/m·s, or 9 kg/m·hr. This value corresponds to the average effective thickness of bedload layer of 5 cm, $\bar{V}_s = 10...12$ cm/h, and to the concentration of sand increasing sharply to about 1700 kg m^{-3} (dry weight) a few grain diameters below the mud line. If \bar{V}_s is increased to 50 cm/hr due to the aforementioned reasons then the transport rate can be estimated as 40 kg/m·hr. It should be remembered that all experiments were conducted in fairly calm situations. Some other

estimates of. Drapeau and Long (1984), Lavelle et al. (1978) include higher figures, up to 60 kg/m hr, but pertain to more dynamic environments with stronger waves, currents and tides.

The critical bulk transport velocity V_{cr2} is about 5...6 times greater than the incipient motion velocity V_{cr1} . The regression analysis undertaken shows that V_{cr1} and small bedload rates are best correlated with H/T while V_{cr2} and higher bedload rates may be linked better to the mean velocity of water.

3. CROSS-SHORE SEDIMENT TRANSPORT

From among the numerous cross-shore bedload models available the one put forward by Pruszek (1987) has been taken for comparison against the field data presented above. The model is based on the assumption that the asymmetric oscillatory motion of water at seabed dominates the cross-shore bedload, and was originally tested against Pruszek's laboratory data. The formula proposed for the time - averaged cross-shore bedload rate reads

$$\langle q_b(x) \rangle = \sum_{i=1}^2 \alpha_i \frac{A_i [9fw \langle u^3 \rangle - \langle u \rangle V_{cr}]}{T_i g (\rho_s - \rho) (\tan \phi + \frac{u}{|u|} \tan \beta)} \quad 1$$

$$u_s = 0.25 \left(\frac{z}{D_{50}} + 4 \right) A_i \langle u(x) \rangle; \quad -4D_{50} \leq z \leq 2D_{50} \quad 2$$

in which

$$A_i = 1 - \frac{u_{cr}}{u_{cr} + T_i \int [u(x,t) - u_{cr}] dt} \quad 3$$

$\alpha_1 = 1$ for the wave crest phase $i=1$

$\alpha_2 = -1$ for the wave trough $i=2$

T_i = duration of the respective phase

ϕ = internal friction angle

β = bed slope angle

u_s = speed of sand grains

Obviously, the onshore transport is assumed in the crest phase, while offshore movement for wave trough.

The laboratory findings for the bedload measured in special traps are illustrated in Fig. 6. The experiments

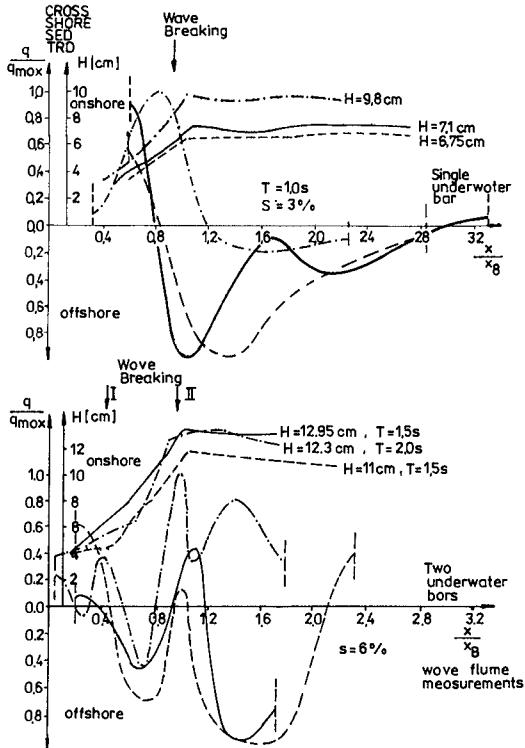


Fig. 6 Cross-Shore Transport Rate Measured in IBW PAN Wave Flume

were carried out in a 25-m long wave flume with movable bed (quartz sand with $D_{50} = 0.22\text{ mm}$). One or two bars were generated on initial bed slopes varying from 0 to 6%. Offshore transport prevailed seawards of the breaking point $x=x_b$. The clearcut transition to the landward transport behind the single bar $x < x_b$ is not confirmed on the profiles with two bars.

The values computed by Eq. 1 for the reported prototype situations at Lubiatowo are of the order of 1.0...0.5 $\text{kg/m}\cdot\text{s}$, hence about 10 times greater than those measured. Since Eq. 1 has been verified under laboratory conditions it must be inferred that the discrepancy is caused by different mechanics of sediment motion. Indeed, the figures given in Sec. 2 refer to bulk motion of the entire bedload layer, as judged from displacements of the radioactive plumes monitored whereas the computed quantities stem from

measurements in the wave flume in which either individual grains or at most thin laminae of sand were set in motion and tracked subsequently.

The disparity of prototype and laboratory is now being compromised through an elaborate analysis of the physical factors shaping the sediment transport in both environments, followed by inclusion of all relevant quantities into the eventual version of our bedload model.

4. SHORT-TERM BED VARIABILITY

4.1. Laboratory and Field Measurements

Extensive tests in the IBW PAN wave tank with movable bed have exposed the dominance of bed slope, and not the angle of wave incidence, among the important factors of shore evolution (cf. Fig. 7). Wave-generated currents have been found to give rise to the instability of some bed features. Under oblique waves the bars migrate with meandering littoral drift.

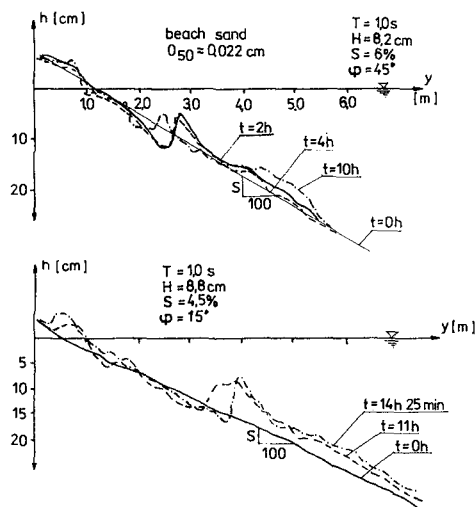


Fig. 7 Bed Profiles Generated in IBW PAN Wave Tank Experiments under Oblique Waves ($\varphi=15^\circ, 45^\circ$)

The type of shore profile is reached rather quickly but the ultimate equilibrium requires a fairly long duration of experiments (i.e. coastal processes). In other words, the bed reacts fast to changing wave climate but

adjusts slowly to the equilibrium profile. It is interesting to investigate this variability in the prototype.

Field studies on short-term variability of bed profiles were undertaken at Lubiatowo and Shkorpilovtsy. Special 210-kHz 20-W ultrasonic probes were arranged along the measuring profile to record bed changes. The absolute error is now 1 cm for 0.2...1 m elevation of the oscillators above bed. The advantages of the technique include ideal repeatability of depth measurements, small relative error, flexibility of measurements during storms, and nondestructibility. Further improvements (40-W power, 5° = beam in lieu of 20° etc.) are under way.

The tests at Lubiatowo were primarily technological. The measurements at Shkorpilovtsy were carried out from 23d to 27th October 1987. Waves with the parameters shown in Fig. 8 (top) were normal to shore. First breaking occurred on the sand bar (between probes 17 and 19), and was usually accompanied by collapsing at the shoreline.

Although preliminary, the following findings can be singled out:

- I/ bed changes are particularly intensive in the ultimate breaking zone
- II/ maximum hourly bed changes under the waves experienced were 10 cm, versus several centimetres over a few hours
- III/ bed changes are cyclic, and seem to oscillate about a certain long-term equilibrium profile
- IV/ the amplitude of bed changes decreases in the offshore direction; for the examples shown in Fig. 8 (bottom) the range of changes at station 21 has been about 20...25% of those encountered some 20 m from shoreline (station 5).

4.2. Sediment Transport Rate Estimates

The cross-shore sediment transport rate q_x may be computed from the continuity equation

$$\frac{\partial h}{\partial t} = \frac{1}{1-p} \left(\frac{\partial q_x}{\partial x} + \frac{\partial q_y}{\partial y} \right) \quad 4$$

in which p = porosity of bed sediment.

The bed changes have been measured, and the longshore transport q_y is neglected due to the normal wave

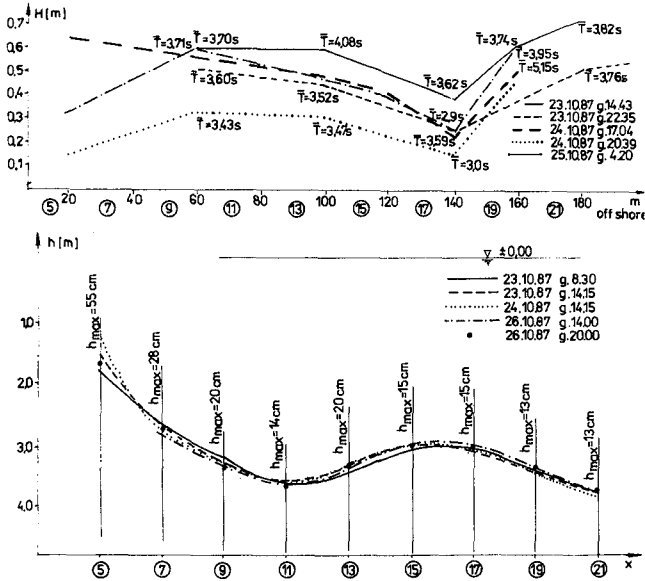


Fig.8 Examples of Waves (top) and Bed Topography (bottom) Measured at Shkorpilovtsy

incidence. Results of the computations are illustrated in Fig. 9.

The highest transport rates have been found for the area of breaking, in agreement with our wave flume experiments. The direction of cross-shore sediment transport varies with time, and seems to depend on the actual stage of shore evolution. Further studies, including those carried on at Shkorpilovtsy in 1988, are to shed more light on this important question of cross-shore evolution.

SUMMARY and CONCLUSIONS

Field studies with radioisotopic sand tracers were carried out at IBW PAN's coastal research station at Lubiatowo in 1984, 1986 and 1987. In the conditions outlined in Figures 1...4, two critical nearbed water velocities, v_{cr1} and v_{cr2} , have been found as respective estimates for incipient motion of single grains and bulk motion of sediment. The figures measured are 8...10 $cm\ s^{-1}$ and 50...60 $cm\ s^{-1}$, the first of them being in rough agreement with Komar and Miller's (1974) formula. The ratio of

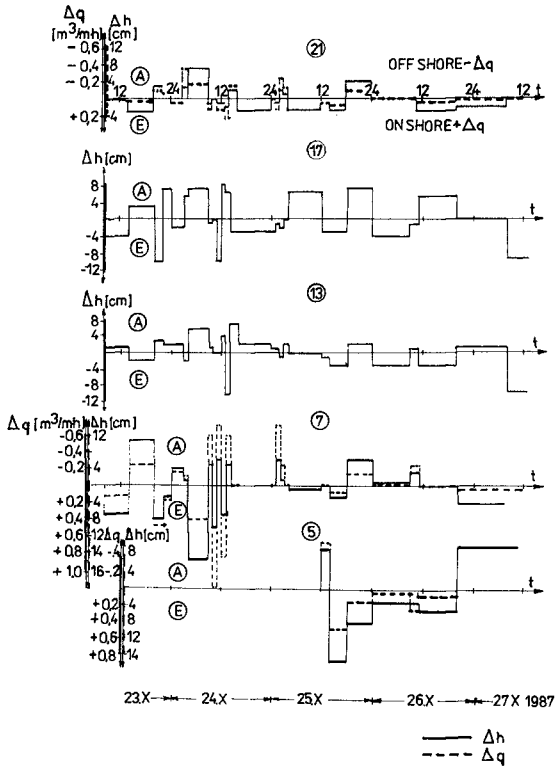


Fig. 9 Depth Increments Measured vs Sediment Transport Rates Computed

average nearbed water velocity \bar{V} , to the effective speed of tracer sand in the inshore zone \bar{V}_s , is estimated about 100...1,000, the figures in Tab.1 being divided by ten due to the noted curvilinearity of tracer trajectories. The order of magnitude of the speed \bar{V}_s itself is estimated as 1 m/hr.

The cross-shore transport rates measured, 0.01... 0.015 kg/m·s for the climate encountered, are ten times smaller than the figures computed by Pruszek's (1987) formula. The latter stems from the energetics approach, and has been calibrated against wave flume data for bedload in thin seabed laminae. The discrepancy is due to the real bulk motion of the entire bedload layer in the field, subject to the mixing and overburdening effects noted.

The reported wave flume and wave tank studies with movable bed point to the importance of initial bed slope in the evolution of shore profiles. Single-bar profiles

witness a clear-cut transition from the offshore transport seawards of the bar to the onshore transport on the opposite side, while for double-bar profiles the transitions are multiple.

The bed variability observed in the wave flume and wave tank was further explored in field studies employing special 210-kHz 20-W ultrasonic probes. The findings confirm intensive short-term bed changes in the ultimate breaker zone about 10 cm per one hour of a weak storm (cf. Fig. 8). Their amplitude decreases in the offshore direction. The short-term bed changes are cyclic, and seem to oscillate about a certain long-term equilibrium profile.

The first estimates of the cross-shore sediment transport rate obtained from the field measurements of bed changes agree with our wave flume experiments as to the occurrence of the highest rates about the breaking line. Further studies with our ultrasonic setup are expected to yield more precise data on cross-shore evolution and transport.

REFERENCES

- Davis A.G. (1980). Field observations of the threshold of sand motion in a transitional wave boundary layer. Coastal Engineering 4
- Drapeau G., Long B. (1984). Measurements of bedload transport in the nearshore zone using radioisotopic sand tracers, Proc. 19th Inter. Conf. Coastal Eng., ASCE, 1252-1264
- Katoh K., Tanaka N. (1986). Local movements of sand in the surf zone, Proc. 20th Intern. Conf. Coastal Eng., Pap. No 72, ASCE
- Komar P.D., Miller M.G. (1974). Sediment threshold under oscillatory waves. Proc. 14th Inter. Conf. Coastal Eng., ASCE
- Lavelle J.W. et al. (1978). Fair weather and storm sand transport on the Long Island, New York, inner shelf. Sedimentology, Vol. 25
- Pruszek Z. (1987). Some problems of mathematical modelling of total cross-shore sediment transport, Extended Abstracts, Euromech 215, S. Margherita Ligure (Genoa), September 15-19, 1987, Univ. Genoa

CHAPTER 132

Secular Change in Tidal Flat Heights

Winfried Siefert^{*)}

Introduction

The German North Sea Coast is relatively short (370 km); its shape is extremely irregular with estuaries, extended tidal flats, partly protected by sandy islands with deep tidal gullies between them (Fig. 1).

In order to gain more detailed information and sufficient knowledge about the variety and variations in this region, the German Coastal Engineering Board (KFKI, Kuratorium für Forschung im Küsteningenieurwesen) has initiated a high-level and extensive programme, "MORAN", "Morphological Alysis North-Sea-Coast". The purpose and the first ideas of the programme were presented by Siefert and Barthel (1981). Investigations are still under way.

It is of high interest whether the mean height of the tidal flats will rise, if the green house effect results in an acceleration of the mean sea level rise. In that case coastal protection in areas behind tidal flats will have to be changed completely, as then wave energy will no longer be dissipated in front of the coastline and will attack the dikes heavily.

So an analysis of the data of the tidal flat heights over more than 100 years and a comparison with the sea level rise seemed to be called for. This may give first indications to the future behaviour of the protective foreshore in times of faster rising water level.

^{*)} Prof. Dr.-Ing.; head, Hydrol. Res. Group, Hamburg Port Authority, Lentzkai, 2190 Cuxhaven, F.R. Germany

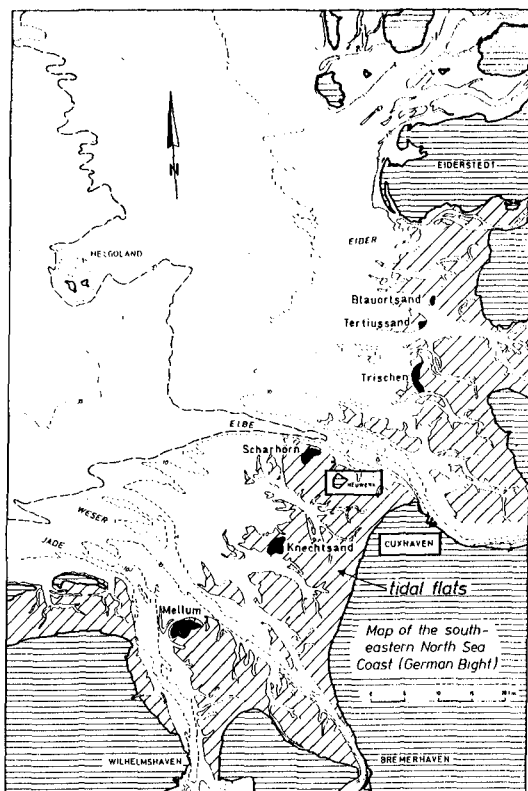


Fig. 1 Map of the German Bight with tidal flats

The stability of the wadden sea is of high interest also for other reasons: In the European tidal flats, more exactly in the channels of the tidal flats, fishing is carried out. Plaice and prawns are caught and mussels are farmed. The flats are particularly valuable as a nursery for important types of fish such as herring, plaice, sole, flounders, Kliesche and cod.

In addition the tidal flats are of great importance as a nature reserve and a health resort.

The Tidal Flats on the German North Sea Coast^{*)}

The south and part of the east coast of the North Sea are bounded by tidal flats. They stretch for a total length of

^{*)}Mainly based on Reineck (1978)

450 km along the Dutch, German and Danish coasts. The tidal flats of the southern North Sea measure 5 to 7 km on an average reaching a maximum of 10 to 15 km. They are intersected by rivers and numerous tidal channels.

The tides are semidiurnal. The average spring tide is approximately 2.6 m with a maximum of 4.1 m. Neap tide range is 1.8 m to 3.1 m. The tidal currents over the flats reach velocities of 30 to 50 cm/s, with a maximum (at storm surges) of 150 cm/s. In gullies the current velocities are about 100 cm/s and in large channels about 150 cm/s.

Waves are a very important factor. They come from various directions and with changing strength. The predominant wind direction is from the west. The wave movement over the tidal flats is the major factor influencing the distribution of sediments, and erosion and sedimentation.

Tidal currents and wave movement combine to transport large quantities of suspended load over the tidal flats. Measurements in the Neuwerk flat showed concentrations of suspension of 30 mg/l for a calm tide, and 300 mg/l was reached on a storm tide. If account is also taken of the shifting direction and volume with which the tide flows over the flats the transport of sediments during storm surges rises by two to three times above normal.

The water temperature of the body of water which inundates the flats fluctuates greatly and is related to fluctuations in air temperature. In the same way the salt content in the large marine bays also varies.

The present day tidal flats receive very little new sediment from outside. Most sediment changes take place within the flats in the form of redistribution, as will be shown later.

The origin of the sediments is predominantly re-worked glacial material. In addition there is a smaller proportion - especially pelitic fractions - brought down by rivers, but pelitic material can also come from older layers being eroded. The mud consists of clayey silt with a mixture of fine sand in varying proportions.

The sand on the tidal flats is fine with a mean diameter of about 0.1 mm. Subject to wave action, a fine-medium grained sand with a mean diameter of about 0.2 mm prevails on the beaches. The commonest mineral is quartz (80%), next in order come feldspat, mica and carbonate. Some 0.2-3.5% are heavy minerals like epidot, hornblende, garnet etc.



Fig. 2 Four comparisons of topographical maps

As well as the mineral component, the sediments include fecal pellets, mainly of mud. These are produced by snails, molluscs and worms. In addition the contents include foraminifera, ostracods, spines from sea urchins, peat debris and crushed shell. Gravel is mostly found in the channels, partly armouring the bed.

The lower edge of the Holocene lies at about NN-5m^{*}) in the vicinity of the present day embankments and at the seaward end of the flats about NN-15 to 20 m^{*}). This lower boundary fills deep channels in older layers. Some of these channels were already laid down in the Pleistocene period, and the outline of these old channels can still be traced as channels on the surface today.

The position of the larger channels changes only slowly - except when they suddenly break through sand bars or even barrier islands during storm surges. Small channels meander considerably (up to 100 m per year) and form bank cutting faces and point bars.

The Method of Analysis

Usually the changes in volume of material are evaluated by differential maps between two surveys. Fig. 2 gives an example for an area of 48 km² of tidal flat west of the island of Neuwerk (see Fig. 1) including one deep and some smaller channels. Parts with predominant erosion or sedimentation between 1965 and 1968, 1968 and 1972, 1972 and 1974, and also from 1965 to 1976 (from top to bottom on Fig. 2) can be identified. In addition to that one usually finds a graph containing the mean height over the continuous time, as given in Fig. 3. But analyses like these have to be studied carefully: Extrapolation is not reliable, the amount of redistribution of material within the area remains unknown, and so are the natural scattering and the artificial scattering due to the methods of levelling, echo sounding and data treatment as well.

That is why the MORAN project was started (Siefert, 1983 and 1987). The philosophy of the analysis is the comparison of a number of surveys (up to 16 within 35 years) with one another (giving a sum of up to 120 values) and to calculate the turnover height h_u and the net-balance height h_b as functions of wave climate and current energy during the time between the surveys. For that purpose the coastal area of 9.000 km² was divided into 9.000 units. Each of these were

^{*}) NN equals circa mean sea level

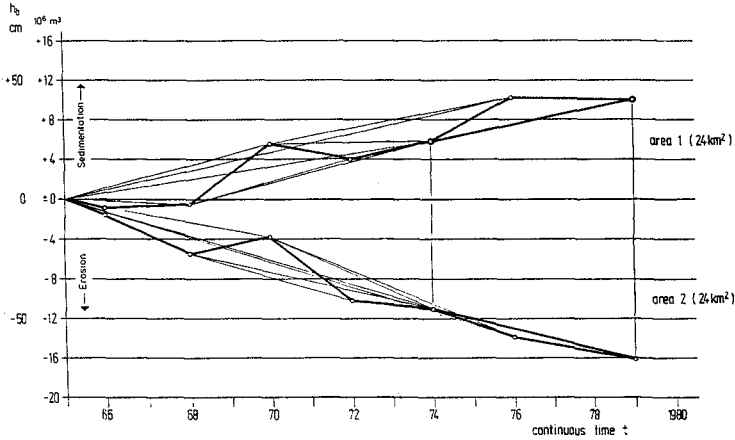


Fig. 3 Mean height changes (balance h_b) of two tidal flat areas from 1965 to 1979

subdivided into 100 small units of a size of 1 ha (Fig. 4). Each comparison of two surveys gives a table as in Fig. 5 for the small units and mean values for the 1 km²-unit respectively, whereby

balance = mean height change h_b in dm within time interval a in years,

turnover = mean topographical height change over all small units h_u in dm, either sedimentation or erosion, within the same time interval a .

Theoretical considerations (see Siefert, 1987) lead to the representation of the turnover height h_u over the time interval a by a saturation function such as

$$h_u = \bar{h}_u \cdot (1 - e^{-a/a_0})$$

as given in Fig. 6.

The morphological character of an area can thus be expressed by the two parameters \bar{h}_u and a_0 . The value \bar{h}_u/a_0 in cm/

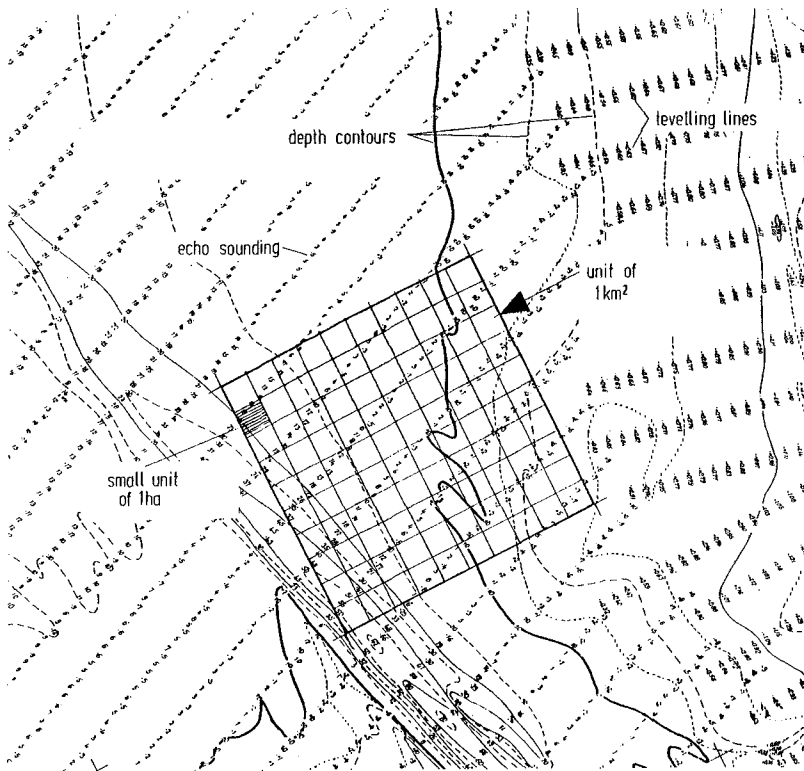


Fig. 4 Unit of 1 km² with subdivision; levelling and echo sounding data with depth contours

year represents the mean resedimentation rate; \bar{h}_U is the asymptotic turnover height that turns out as the result of long-term topographical comparisons (Siefert, 1983). As

$$h_b \leq h_U$$

by definition, the change of the mean topographical height has to be

$$h_b(a) \leq \bar{h}_U$$

and statistically reaches values of

$$h_b \approx (0.1 \text{ to } 0.4) \cdot \bar{h}_U$$

(Siefert, 1987). Moreover, theoretical considerations lead

		field 1				field 2							
		1	2	3	4	5	6	7	8	9	10		
1		0	1	-1	-2	-3	-3	-3	-3	-3	-2	$h_b = h_0$	
2		1	0	-1	-1	-2	-2	-2	-2	-2	-1		
3		4	0	-1	-2	-1	-1	-1	0	0	1		
4		-2	-3	0	3	1	0	0	1	0	0		
field 1	5	-3	-4	-2	-2	-1	0	1	1	2	2	field 2	
field 3	6	-5	-5	-4	-2	-2	-1	1	2	1	-1	field 4	
	7	-7	-2	0	-2	-5	-7	-6	-5	-5	-2		
	8	0	0	0	1	2	1	1	0	0	0		
	9	-1	-3	-3	-4	-4	-2	-1	-1	-1	-1		
	10	-2	-3	-4	-4	-4	-3	-2	-2	-2	-2		

1

top. change of small unit (ft/a)

		field 1	2	3	4	1km ² sum	mean
sedimentation	(dm)	10	8	3	6	27	0.27
erosion	(dm)	31	25	66	44	166	1.66
balance	(dm)	-21	-17	-63	-38	-139	$h_b = -1.39$
turnover points	(dm)	41	33	69	50	193	$h_0 = 1.93$
		25	25	25	25	100	

Fig. 5 Height difference in dm for each unit between two surveys within a time interval of "a" years (example)

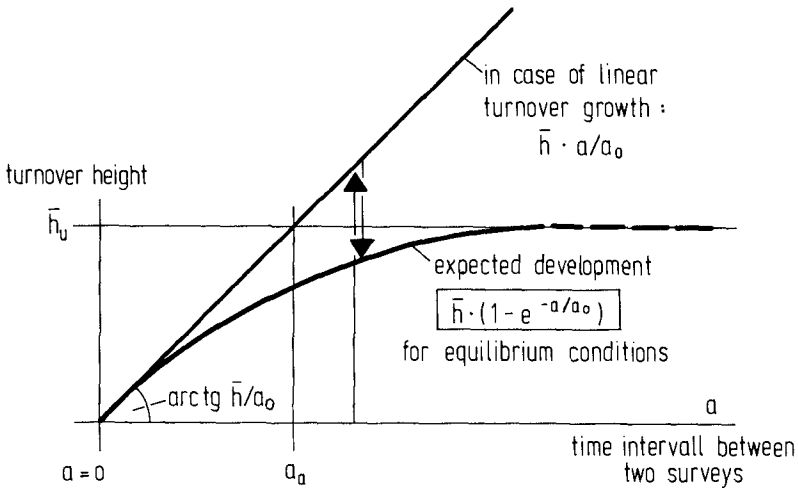


Fig. 6 Saturation function for h_0 over a

to the conclusion that the mean height of such a partial area remains constant over a period if the turnover height function can be proved to be horizontally asymptotic (Fig. 7).

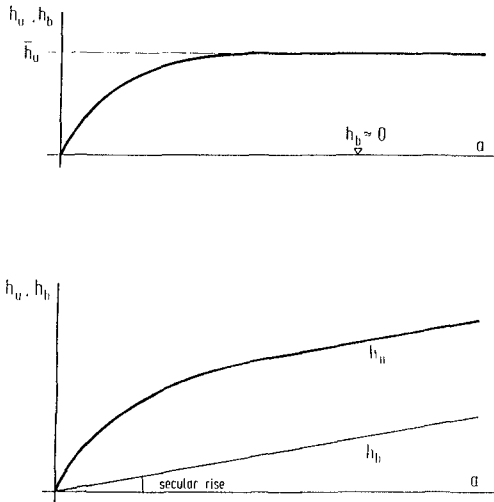


Fig. 7 Saturation function with horizontal asymptote presuming $h_b \approx 0$ for long a (top) and presuming secular rise of tidal flat height ($h_b \neq 0$ for long a) (bottom)

Results

In order to give an impression of the weakness of derivations from only a limited number of comparisons between topographical maps, Fig. 8 indicates 91 dots for turnover and balance heights out of 91 comparisons over $a = 1$ to 25 years. While the turnover heights can be described relatively precisely by a saturation function with a confidence interval of about $0.15 \cdot \bar{h}_u$, the individual balance heights vary between + 26 cm and - 24 cm. So one of the comparisons over $a = 5$ years gave a sedimentation height of 26 cm, another one gave an erosion depth of 17 cm, a third nearly zero. Of course, all of them are correct, but we have to keep in mind that each survey and therefore each comparison includes an element of chance.

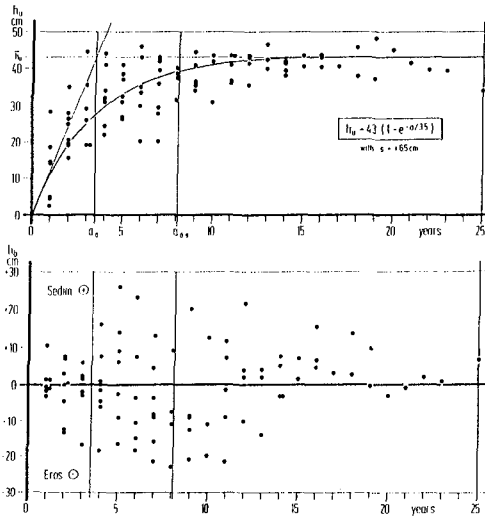


Fig. 8 Turnover and balance heights in a unit of 1 km^2 size for 91 topographical comparisons; time interval up to 25 years (Siefert, 1987)

Fig. 8 already indicates a horizontal asymptote over 25 years. Analyses show that especially in the higher parts of the tidal flats no secular change in height can be discerned within the last 35 years, though in the same period the mean high water level rose by about 15 cm, the mean storm surge level even more (example on Fig. 9).

Of particular interest is the evaluation of surveys of the tidal flat between Cuxhaven and Neuwerk from 1864 and 1913 (Fig. 1) and comparison with the actual situation. In this case reliable levellings across the tidal flat over a distance of about 10 km (Fig. 10) could be reconstructed by the original data set and be compared with modern data (Siefert and Lassen, 1987). The continuous development of the mean heights, including the sea level, is given in Fig. 11. It leads to the conclusion that there was a rise of tidal flat height until the 1950s, followed by an erosion period of 15 years and a slight sedimentation since. But taking into consideration that only two old surveys are being compared with 7 new levellings since 1954, it is worthwhile looking at the significance of the trends. That is possible

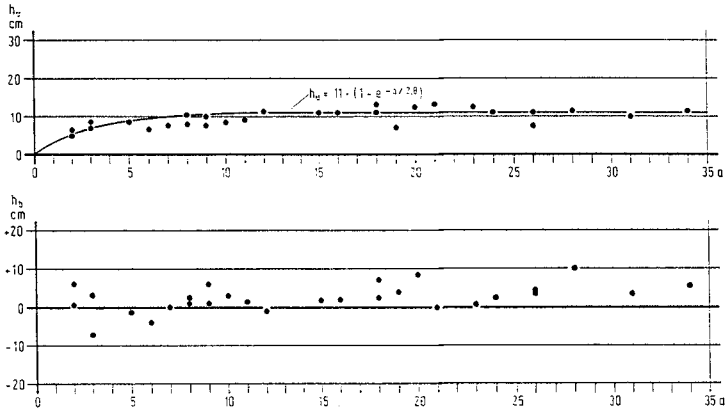


Fig. 9 Horizontal asymptote over 35 years indicates height stability without any long-term trend

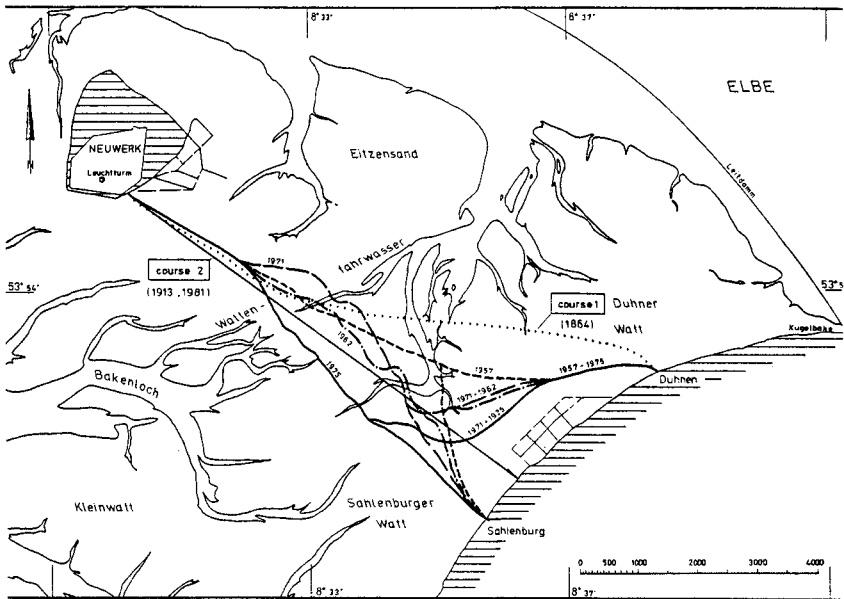


Fig. 10 Location of courses across the tidal flat from the mainland (Cuxhaven) to an island (Neuwerk)

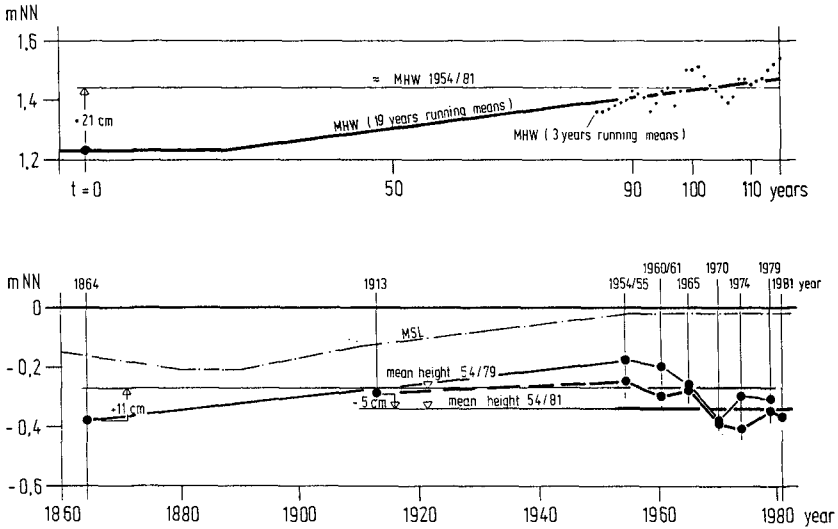


Fig. 11 Mean HW level (top), MSL and mean topographical height of the tidal flat courses of Fig. 10 from 1860 to 1980

by use of the morphological parameters on Fig. 12: The dependencies given by Siefert (1987) demanded \bar{h}_U in the middle of 20 and 45 cm and a_0 circa 4 years for wadden sea areas like these. The best-fit saturation function results in

$$h_U = 30 \cdot (1 - e^{-a/4})$$

with a confidence interval of ± 2.0 cm. So the resedimentation is at the small rate of

$$\bar{h}_U/a_0 = 7.5 \text{ cm/year}$$

and the horizontal asymptote can be proved over 120 years. So the "trends" of Fig. 11 are not at all significant; they belong to the natural scattering of yearly sedimentation-erosion-changes. It turns out that even within the last 120 years there was no rise of the mean height of the tidal flats, while the mean high water level rose by at least 20 cm and the mean storm surge level by twice that amount.

This result may be confirmed by another evaluation: The comparison of two topographical maps of an area of 4.500km² with a time interval of $a = 5$ years shows a mean "sedimen-

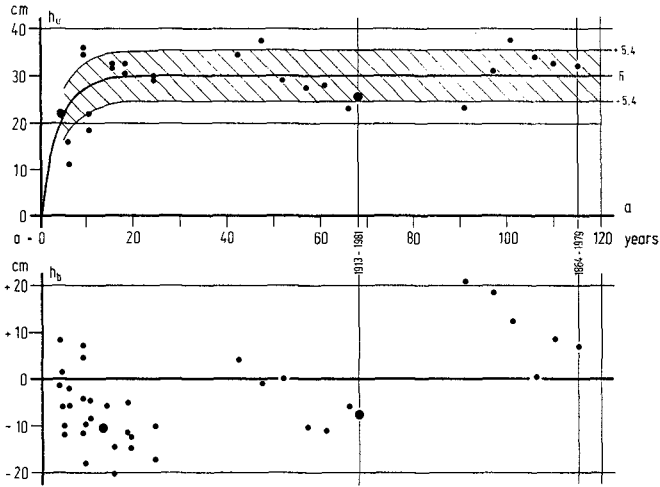


Fig. 12 Turnover (top) and balance heights for tidal flat routes of Fig. 10. The horizontal asymptote can be proved over 120 years (Siefert and Lassen, 1987)

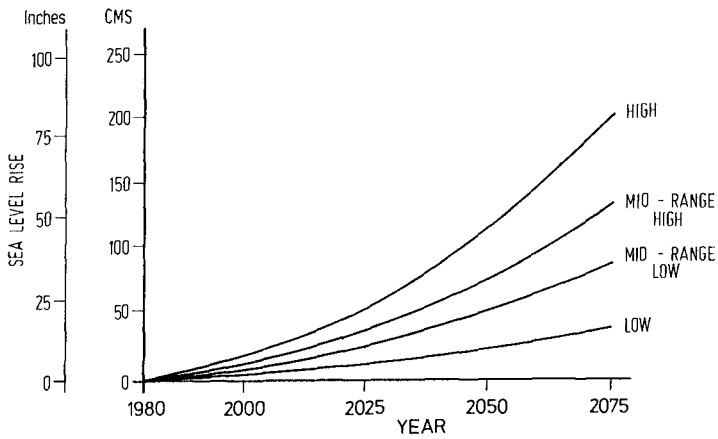


Fig. 13 Global sea level rise scenarios (Hoffman et al., 1983)

tation" of a mere 1 cm, while the turnover height is 70 cm. With a value

$$h_b / h_u = 0.014$$

this "trend" must be ignored. Any extrapolation is a matter of speculation.

Conclusions for Future Tidal Flat Development

The analysis of a large number of tidal flat units over 35 years, as well as the analysis of two courses across a tidal flat over the last 120 years, indicate that a significant height change parallel to the rising sea level has not taken place. If the future global sea level rise increases as presented in Fig. 13, the question is: Will the tidal flats rise in height with the same velocity and acceleration as the future mean sea level? If not, this poses serious problems for coastal protection work, as wave and current climates will change significantly. Moreover it is even possible that the mean tidal flat height may be reduced - due to increasing turbulence with rising water level, higher wave and current energy (see Fig. 14).

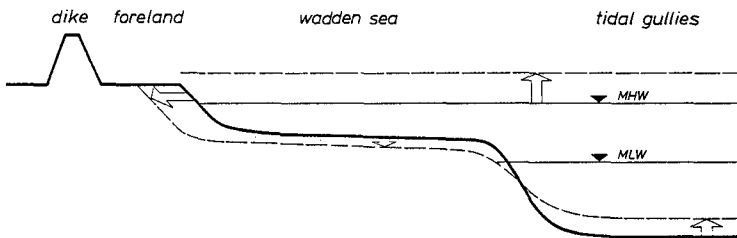


Fig. 14 Possible height development in the wadden sea due to rising sea level (Siefert and Lassen, 1987)

References

- HOFFMAN, J. Projecting Future Sea Level Rise. Gov.
KAYES, D. Printing Office, Washington D.C. 1983
TITUS, J.:
- REINECK, H.-E.: The Tidal Flats on the German North Sea
Coast. Die Küste, Vol. 32, 1978
- SIEFERT, W.: Morphologische Analysen für das Knecht-
sand-Gebiet. Die Küste, Vol. 38, 1983
- SIEFERT, W.: Umsatz- und Bilanzanalysen für das Kü-
stenvorfeld der Deutschen Bucht. Die Kü-
ste, Vol. 45, 1987
- SIEFERT, W. The German MORAN Project. Proc., 17th
BARTHEL, V.: ICCE, Sydney 1980, ASCE, New York 1981
- SIEFERT, W. Zum säkularen Verhalten der mittleren
LASSEN, H.: Watthöhen an ausgewählten Beispielen.
Die Küste, Vol. 45, 1987

CHAPTER 133

BED LOAD TRANSPORT DUE TO NON-LINEAR WAVE MOTION

by

Hitoshi TANAKA*

ABSTRACT

The bed load transport rate due to wave motion is measured in a wave flume. The modified stream function theory of the author (Tanaka (1988)) is applied to the formulation of the sediment transport rate in order to include the non-linearity. The proposed formula predicts well except near the surf zone where the effect of the acceleration plays an important role.

1. INTRODUCTION

Coastal sediment movement in the onshore-offshore direction has been studied by several researchers (e.g. Horikawa (1988)). Many of empirical formulas express the sand transport rate as a function of the bottom shear stress due to wave motion, which is usually estimated through the friction coefficient proposed by Jonsson (1966). His result is, in principle, only applicable to the linear wave motion. On the other hand, the non-linearity of wave motion has a considerable effect on the sediment transport in practice, especially in regard to both the direction and the rate of the net transport. Therefore, the non-linear effect of wave motion should be included in the formulation of sediment transport rate.

Up to present, however, no practical method had been available for estimation of the bottom shear stress due to non-linear wave motion, until the present author (Tanaka (1988)) made the effect of turbulence included in the stream function theory proposed by Dean (1965) for the non-linear wave motion. This modified stream function theory which enables to predict the bottom shear stress as well as the velocity profile is applied to the formulation of the bed load transport rate due to the non-linear wave motion.

The present study is restricted to the case of the

*Lecturer, Department of Civil Engineering, Tohoku University, Aoba, Sendai 980, Japan.

wave motion alone, although the author's modified stream function theory can be extensively applied to the wave-current combined motion.

2. EXPERIMENTAL PROCEDURE

In the present study, two series of experiments were carried out: bed load transports over a flat bed (Experiment A) and over a sloping beach (Experiment B). The experimental setups are shown in Figs.1 (a) and (b).

The series of Experiment A were carried out in a wave flume, 16m long, 30cm wide and 50cm deep. A part of the bottom was lowered at the middle of the flume, on which the sand of mean diameter of 0.2 mm or 0.51 mm was filled to form a layer 5cm thick and 1.5m long. The experiments were carried out for 15 different wave and sediment conditions. The experimental condition was so carefully chosen as for the sand to be transported as bed load in the onshore direction. Then, the sand transported from the test bed onto the shoreward fixed bed was collected to obtain the net transport rate. The surface of the fixed bed was roughened with the pasted sand of the same size in order to make the mobility of the sand grain uniform along the wave flume.

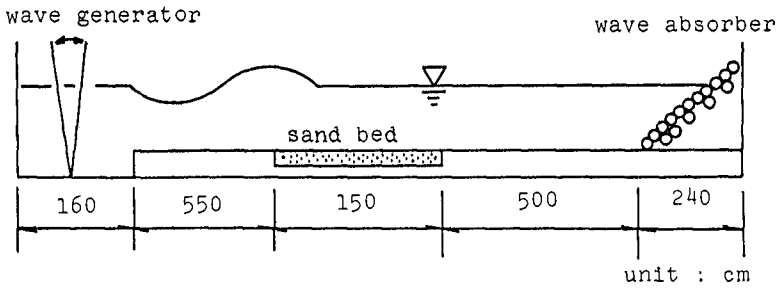
In the series of Experiment B, a beach of slope 1:20 was built with the sand of diameter 0.78 mm at the end of the wave flume. The beach was exposed to the wave action for 10 minutes. The change of the beach profile was measured and used to calculate the sand transport rate. The direct measurement of the sand transport rate was also carried out by use of a sand trap originated by Horikawa, Sunamura and Shibayama (1977). In this case, the wave period and equivalent deep water wave height were fixed as 1.52 sec and 11.8 cm, respectively.

3. BOTTOM SHEAR STRESS DUE TO NON-LINEAR WAVE MOTION

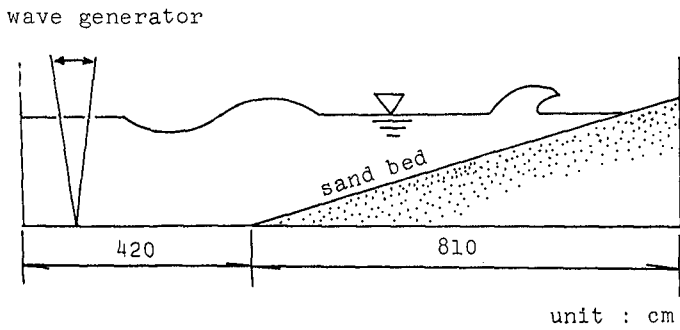
Although the modified stream function theory can be referred in the preceding paper (Tanaka (1988)), a brief description of the theory and examples of the calculated result will be given below.

Combining Dean's stream function theory (Dean (1965)) and the time-invariant eddy viscosity model (Tanaka and Shuto (1981)), the stream function can be given by the following expression (Tanaka (1988)).

$$\psi(x, z) = \frac{L}{\pi} z - \frac{u_*^2}{\kappa u_*^* c_w} z \left(\ln \left(\frac{z}{z_0} \right) - 1 \right) + \sum_{n=1}^N \sinh\{nk(z-z_0)\} \{X(n) \cos(nkx) + Y(n) \sin(nkx)\} \\ + \text{Real} \left[\sum_{n=1}^N \frac{ik\xi_n}{2c} \frac{H_1^{(0)}(\xi_n)}{H_0^{(0)}(\xi_{n0})} \{X(n) - iY(n)\} \exp(inkx) \right] \quad (1)$$



(a)



(b)

Fig.1 Experimental setup.

where x is the horizontal coordinate taken positive in the direction of wave propagation, z the vertical axis taken positive upwards with the origin at the bottom surface, L the wave length, T the wave period, u_c^* the friction velocity due to steady current, \hat{u}_{cw}^* the maximum shear velocity due to wave-current combined motion, κ the Karman constant (≈ 0.4), z_0 the roughness length ($\approx k_s/30$, k_s : Nikuradse's equivalent roughness), k the wave number ($= 2\pi/L$), $X(n)$ and $Y(n)$ the unknown coefficients, $i = \sqrt{-1}$, $\xi_n = 2e^{-\pi n/4\sqrt{ncz}}$, $\xi_{n0} = 2e^{-\pi n/4\sqrt{ncz_0}}$, $c = \sigma/(\kappa \hat{u}_{cw}^*)$, and σ the angular frequency. Real denotes the real part of the function in the square bracket. In the above expression, the wave-current combined motion is described in a coordinate system traveling with the wave speed.

The unknown coefficients, $X(n)$ and $Y(n)$, in this equation are determined so as to minimize the difference between the measured and predicted wave profiles and to uniform the Bernoulli constant. Another unknown value, \hat{u}_{cw}^* , is calculated through an iteration.

The bottom shear stress can be expressed in terms of the eddy viscosity and velocity gradient as follows.

$$\tau = -\rho \kappa u_{cw}^* z \left. \frac{\partial^2 \psi}{\partial z^2} \right|_{z=z_0} \quad (2)$$

An example of the calculation is shown in Figs. 2 and 3, for the case of the wave height, 8.6 cm, the wave period, 1.40 sec, and the water depth, 16.5 cm. The upper figure in Fig. 2 compares the measured wave profile (open circles) with the predicted (solid line). In the lower figure, the bottom shear stress estimated with the present theory (solid line) is shown with a prediction according to Jonsson's wave friction coefficient (line with black circles). Jonsson's friction coefficient gives only the maximum value but not the time-variation of the shear stress, the latter of which is obtained by the square of a sine function having its maximum value at the time of the wave crest, as is usually assumed.

The bottom shear stress predicted with the modified stream function theory reflects well the non-linear wave profile. The positive part of the shear stress has larger maximum value and shorter duration than the negative part. As long as the maximum value concerns, two theories give more or less similar results. However, the details are quite different, especially at the phase of the negative shear stress. This suggests that the difference between the two predictions becomes greater in the nearshore region, where waves become more sharp-crested and more asymmetric.

The vertical distribution of the estimated horizontal velocity (solid lines) is shown in Fig. 3. The prediction according to Dean's stream function theory (dotted lines) is also presented. Outside the boundary layer, the

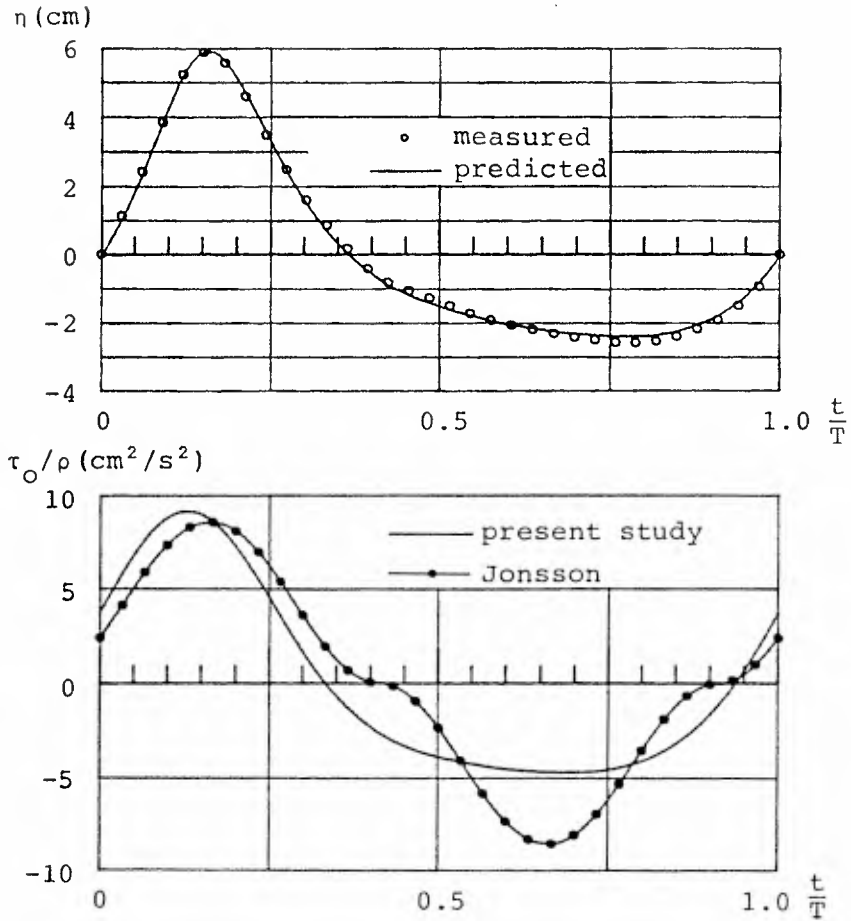


Fig.2 Time-variation of water surface level and bottom shear stress.

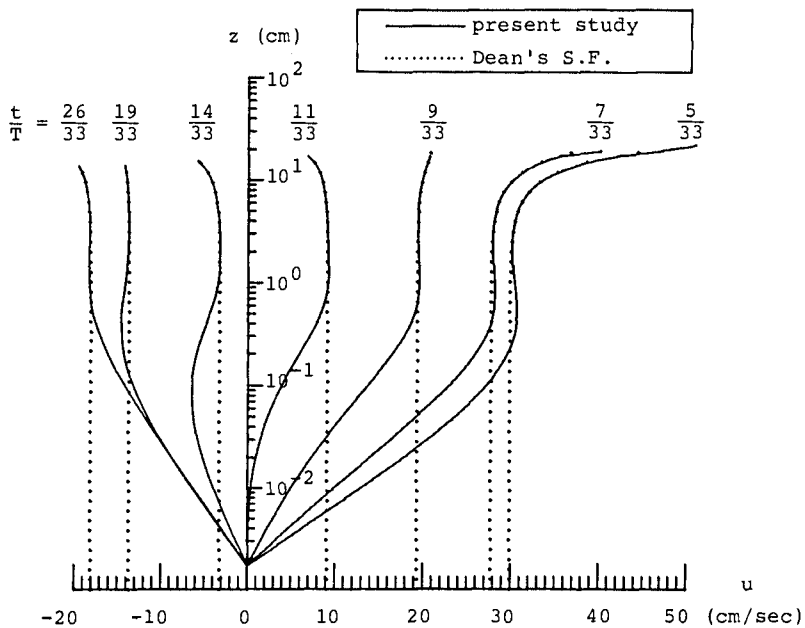


Fig.3 Vertical distribution of velocity profile.

difference between the two theories is very small. A distinct difference is found in the immediate vicinity of the bottom. This is of no wonder because Dean's method basing upon the potential theory can not satisfy the boundary condition there while the present author's theory can perfectly do.

Recent experimental measurements have revealed that Dean's stream function theory can be practically applicable to the estimation of the velocity field, except in the very vicinity of the bottom, near the surf zone over a sloping beach. Judging from this fact, it may be hopeful that the bottom shear stress obtained with the present theory can be used in the formulation of the sand transport rate not only on a flat bed but also on a sloping beach.

4. RESULTS AND DISCUSSIONS

4.1 Bedload transport over a flat bed

The instantaneous bedload transport rate is assumed to be expressed as a function of the instantaneous shear stress as follows, in an analogy to sediment movement due to steady current.

$$\frac{q_B(t)}{\sqrt{sgd^3}} = \alpha \text{sign}\{\tau^*(t)\} |\tau^*(t)|^m \{|\tau^*(t)| - \tau_{cr}^*\}^n \quad (3)$$

where q_B is the instantaneous bedload transport rate, s the immersed specific weight of sand, g the gravitational acceleration, d the diameter of sand particle, $\tau^*(t) = \tau(t)/(sgd)$, and τ_{cr}^* the critical Shields number. Values of α , m and n are to be determined from experiments. The time-variation of the bottom shear stress can be calculated with the modified stream function, Eq.(1). It should be noted again that we need the whole wave profile over one wave period for the calculation of the bottom shear stress.

On the basis of Eq.(3), the net transport rate over one wave period is given by,

$$\frac{\bar{q}_B}{\sqrt{sgd^3}} = \alpha F \quad (4)$$

where

$$F = \frac{1}{T} \int_0^T \text{sign}\{\tau^*(t)\} |\tau^*(t)|^m \{|\tau^*(t)| - \tau_{cr}^*\}^n dt \quad (5)$$

In the above equation, the integration should be restricted to the phase when the tractive force is greater than the critical shear stress.

The exponents, m and n , and the coefficient, α , in

Eqs.(3) and (4) will be determined so as to minimize the scattering of the experimental data.

The relationship between the measured net transport rate and the function F defined by Eq.(5) is examined for a various set of the exponents m and n. It is concluded that $m=0.5$ and $n=1.0$ are the best combination of the exponents. The result is shown in Fig.4, where the net transport rate depends linearly on the function, F, as expected in Eq.4, with the coefficient $\alpha = 3.5$.

In conclusion, the instantaneous transport rate of bed load can be given by

$$\frac{q_B(t)}{\sqrt{sgd^3}} = 3.5 \text{sign}\{\tau^*(t)\} |\tau^*(t)|^{0.5} \{|\tau^*(t)| - \tau_{cr}^*\} \quad (6)$$

or by the following expression which is convenient for comparison with the existing formulas for steady current.

$$\frac{q_B(t)}{u_*^3(t)d} = 3.5 \text{sign}\{\tau^*(t)\} \{|\tau^*(t)| - \tau_{cr}^*\} \quad (7)$$

where $u_*(t) = \sqrt{|\tau(t)|/\rho}$, and ρ is the density of the fluid.

In Fig.5, Eq.(7) is compared with the bed load formula for steady current in the alluvial channel. The dashed-and-dotted line is the result of the present study, Eq.(7). The solid line show the representative bed load formulas for the alluvial channel. The present study is close to the Sato et al. formula (1958) which is often called as the PWRI (Public Works Research Institute) formula and is widely used in Japan. Therefore, the present result will be smoothly continued to the sediment transport rate in steady current, as the excursion length of water particles becomes longer.

4.2 BEDLOAD TRANSPORT OVER A SLOPING BEACH

The bed load formula introduced in the preceding section is applied to a sloping beach case.

Beach profiles measured at $t=0$ min and $t=10$ min are shown in the upper figure of Fig.6. Since the beach profiles were not always two-dimensional but variable in the transversal direction, especially near the plunging point, values measured along three parallel longitudinal lines were averaged to determine the beach profile.

A sand bar developed near the plunging point, obviously nourished by the onshore sand transport from the seaward region. The sand transport rate is calculated from the measured beach profiles and is shown by the solid line in the lower figure. The direct measurements by use of a sand trap are also given by black circles, which show a good agreement with the solid line.

In order to apply Eq.(4) to the prediction of the bed-load transport rate on the slope, wave profiles were measured at the points where sand traps were installed.

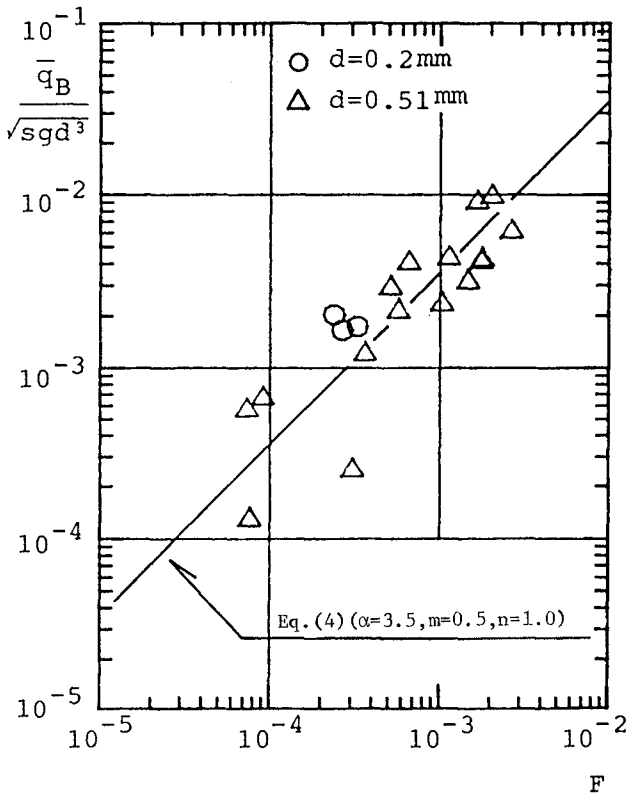


Fig.4 Bed load transport rate over a flat bed.

- (1) Sato et al. $n=0.015$
- (2) Sato et al. $n=0.025$
- (3) Ashida and Michiue $u_{*e}/u_* = 1.0$
- (4) Ashida and Michiue $u_{*e}/u_* = 0.5$
- (5) Einstein $u_{*e}/u_* = 1.0$
- (6) Einstein $u_{*e}/u_* = 0.5$
- (7) Kalinske
- (8) Brown

—•—present study

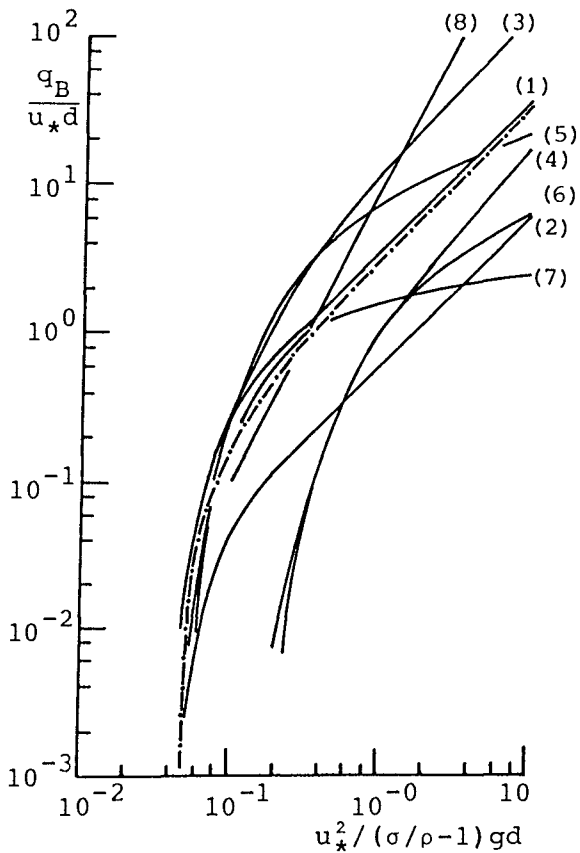


Fig.5 Comparison of bed load formulas.

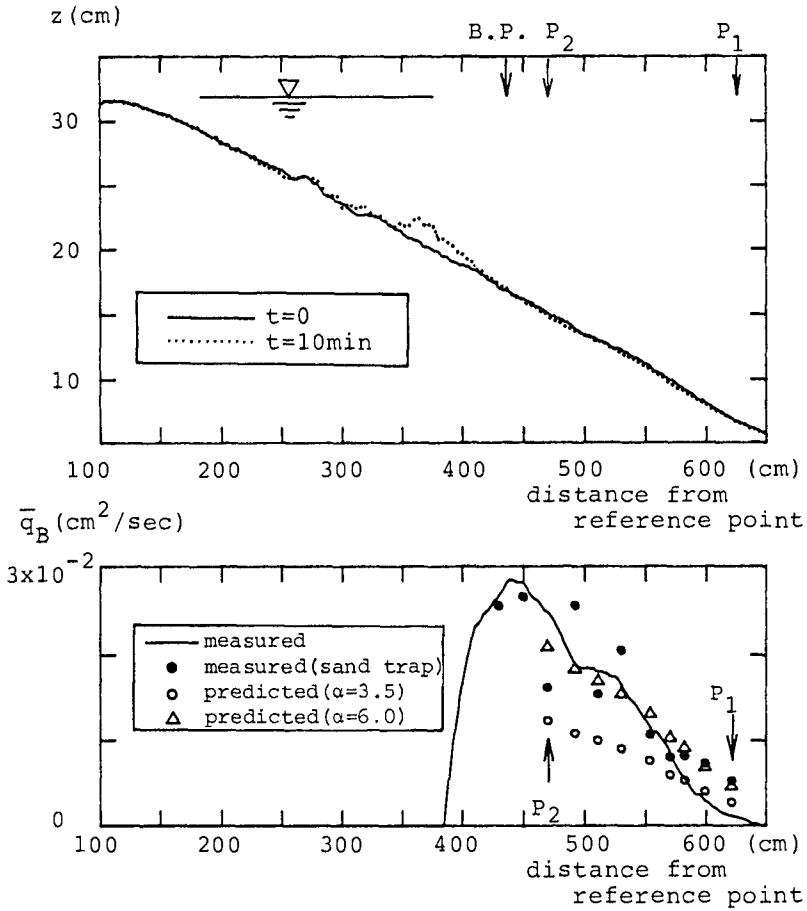


Fig.6 Change of beach profile and bed load transport rate.

Examples of the observed wave profile at P_1 and P_2 are shown in Figs.7 and 8, respectively. Open circles in the upper figures are the measured wave profiles, and solid lines the predictions. The predicted bottom shear stresses are shown in the lower figures.

At the point, P_1 , in the offshore region, the wave profile is nearly symmetrical with respect to the wave crest. The time-variation of the bottom shear stress is also symmetrical. The maximum value of the positive shear stress is slightly greater than that of the negative shear stress. At the point, P_2 , near the breaking point where asymmetry of the wave profile is remarkable as shown in Fig.8, the bottom shear stress, as a consequence, becomes quite asymmetrical with respect to the wave crest as well as with respect to the still water level.

The time-variation of the bottom shear stress thus obtained is substituted into Eq.(4) to predict the bed-load transport rate. The estimated values are shown by open circles in the lower figure of Fig.6.

At the measurement points in the offshore region, the measured sand transport rates show a good agreement with the predicted values. However, near the breaking point, the agreement becomes worse. If we substitute 6.0 into α , instead of 3.0, in Eq.(4), the agreement is considerably improved as shown by open triangles.

This result may suggest the importance of the acceleration in the sediment transport near the surf zone. The inertia force is usually neglected in the analysis of the motion of sand grains, compared with the drag force. Such a quasi-steady assumption can be only acceptable in the region far from the breaking point but not near the surf zone.

Therefore, it is concluded that the bed load formula established for the offshore condition needs modification to include the effect of the acceleration, if it will be extended to the more non-linear case. One possible way may be to express the coefficient α to reflect the effect of the acceleration.

5. CONCLUSION

In the previous studies on the sand movement due to wave motion, Jonsson's friction coefficient has been conveniently and widely used for the formulation of sand transport rate. This means that the non-linearity of wave motion was not adequately taken into consideration in those investigations. The present study, on the contrary, makes it possible to include the non-linear effect, by using the modified stream function theory of the author.

It is assumed that the instantaneous bed-load transport rate is expressed by Eq.(3) on the basis of the preceding studies on the sediment movement due to steady current. Exponents m and n in Eq.(3) are found to be 0.5 and 1.0, which ensure a smooth continuation from wave

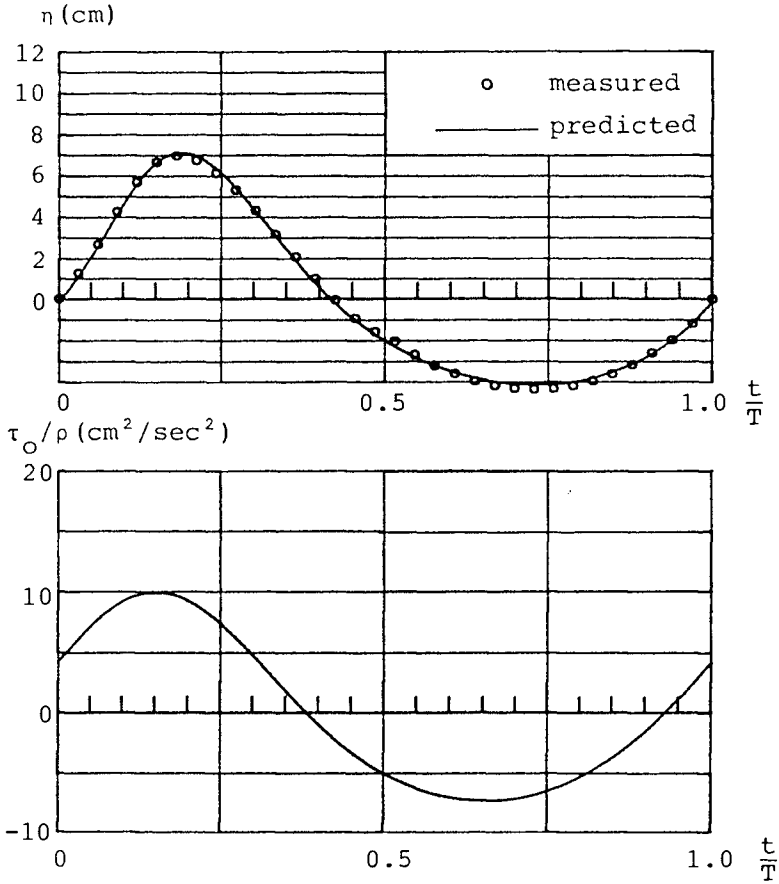


Fig.7 Time-variation of water surface level and bottom shear stress at measured point P_1 .

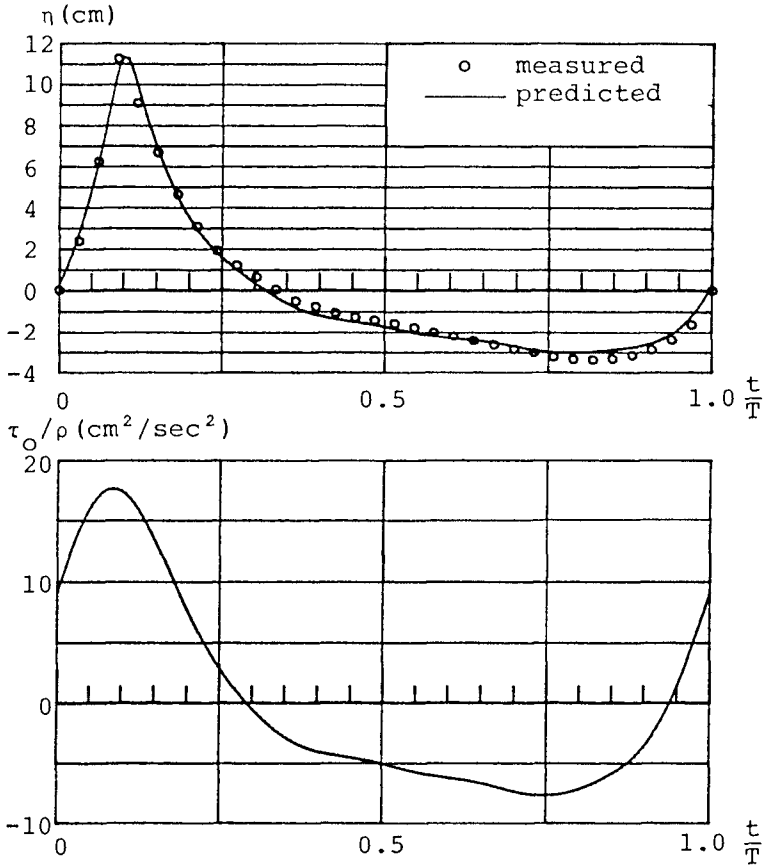


Fig.8 Time-variation of water surface level and bottom shear stress at measured point P_2 .

motion to steady flow as the excursion length of water particles becomes longer. The coefficient of proportionality α is determined as 3.0 in case of a flat bottom.

The measured sediment transport rate near the surf zone is remarkably greater than the predicted. This suggests that the quasi-steady assumption can no longer be applicable in this region.

ACKNOWLEDGEMENTS

The author wishes to express his grateful thanks to Professor Shuto, Tohoku University, for his helpful advice over the course of the study. A part of this study was financially supported by the Grant-in-Aid for Encouragement of Young Scientist of the Ministry of Education, Science and Culture, Japan.

REFERENCES

- Dean, R.G.(1965): Stream function representation of non-linear ocean waves, *J. Geophys. Res.*, Vol.70, No.18, pp.4561-4572.
- Horikawa, K., T. Sunamura and T. Shibayama(1977): Experimental study of two-dimensional shore transformation --- A method for measurement of sand transport rate in offshore region---, *Proc. 24th Japanese Conf. on Coastal Engng.*, pp.170-174 (in Japanese).
- Horikawa, K.(1988): *Nearshore Dynamics And coastal Process, Theory, Measurement, And Predictive Models*, pp.194-217, University of Tokyo Press.
- Jonsson, I.G.(1966): Wave boundary layer and friction factors, *Proc. 10th Conf. on Coastal Engng.*, pp.127-148.
- Sato, S., Kikkawa, H. and K. Ashida(1958): Study on the bed-load transportation, *J. Res. Pub. Works Res. Inst.*, No.98, pp.1-18 (in Japanese).
- Tanaka, H. and N. Shuto(1981): Friction coefficient for a wave-current coexisting system, *Coastal Engineering in Japan*, Vol.24, pp.105-128.
- Tanaka, H.(1988): Bottom boundary layer under non-linear wave motion, *Proc. ASCE, WW-Div* (in press).

CHAPTER 134

Physical Modelling of Beach Erosion and Littoral Drift

Otavio J. Sayao, M.ASCE¹ and Robert B. Nairn²

Abstract

A new procedure for physical modelling of beach sedimentary processes is presented. It is shown that the modelling requirements proposed by Dean (1985) are necessary but not sufficient for dynamic similarity. Quantification of scale effects due to slope and relative grain size scaling conditions enables extrapolation of the physical model results to prototype situations. Selected examples of the application of the proposed model design are also given.

1. Introduction

A model is dynamically similar to its prototype if all the dimensionless variables governing the model and prototype phenomena are identical. The dimensionless functional relationship of any mechanical quantity, particularly sediment transport, is given by,

$$\Pi_A = \varphi_A (x_1, x_2, \dots, x_n) \quad (1)$$

where Π_A is the dimensionless version of A (the mechanical quantity) and x_i are the dimensionless variables. For dynamic similarity between the model and prototype, the condition to be satisfied is:

$$(\Pi_A)_p = (\Pi_A)_m \quad (2)$$

where the subscript p refers to the prototype value of Π_A and the subscript m refers to the model value of Π_A .

In a conventional physical model of beach morphology with a rectangular co-ordinate system, the general model scale n is given by the vertical scale value n_z where n is defined as the ratio of the prototype value over the model value.

¹ F.J. Reinders and Associates Canada Limited, 201 County Court Blvd., Suite 500, Brampton, Ontario, L6W 4L2, Canada.

² Imperial College of Science and Technology, Dept. of Civil Engineering, London, SW7 2BU, England.

Thus, Equation 2 may be written as:

$$n\Pi_A = 1 \quad (3)$$

which is achieved if and only if,

$$(\alpha_i)_p = (\alpha_i)_m, \text{ or } n\alpha_i = 1 \quad (4)$$

is provided. If Equation 4 is satisfied then all α_i are identical in model and prototype and together with geometrical similarity, Π_A (the dimensionless version of a mechanical quantity of interest) is also identical in model and prototype.

2. Description of Littoral Processes

Sayao (1982) described sediment transport in the surf zone by the following dimensionless relationship:

$$\Pi_{Q_s} = \Phi(H_b/L_o, m_b, H_b/D, \rho_s/\rho) \quad (5)$$

where Π_{Q_s} is the dimensionless littoral transport rate, H_b/L_o is the breaking wave steepness, m_b is the beach profile slope which characterises energy dissipation in the surf zone, H_b/D is the relative grain size parameter, and ρ_s/ρ is the density ratio (sediment to water) which reflects the influence of the density of the grains.

An additional dimensionless variable, especially important in situations where cross-shore transport is dominant, is the dimensionless fall time parameter, F_b or F_o ,

$$F_b = \frac{H_b}{wT} \quad \text{or} \quad F_o = \frac{H_o}{wT} \quad (6)$$

where H_b is the breaker height, H_o is the deepwater wave height, T is the wave period and w is the fall velocity of the sand grains. According to Dean (1973), this parameter provides an indication of whether net onshore or offshore motion of sand will occur on a beach profile. A critical value of F_o is given in the Shore Protection Manual (US Army Corps of Engineers, 1977), for $F_o > 1$, recession of the shoreline will occur. The validity of this parameter in predicting the net cross-shore transport direction in situations where longshore transport is also appreciable can be confirmed by the laboratory data of Sayao (1982) and Readshaw (1979). Dean's fall time parameter is plotted versus deepwater wave steepness and the relative grain size parameter in Figures 1 and 2 for the results of these two three-dimensional model studies.

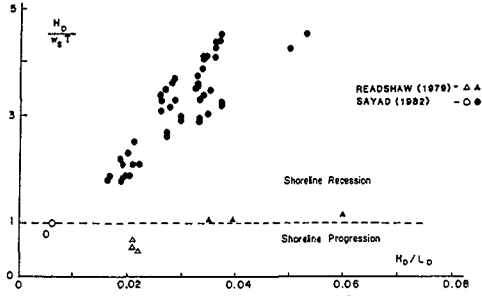


Figure 1. Dimensionless Fall Time vs. Wave Steepness

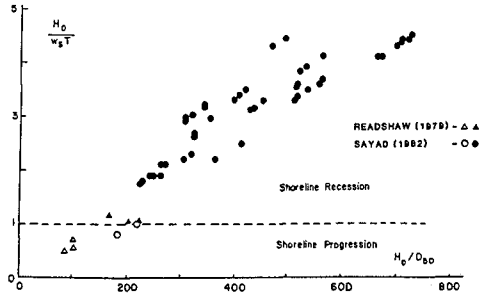


Figure 2. Dimensionless Fall Time vs. Relative Grain Size

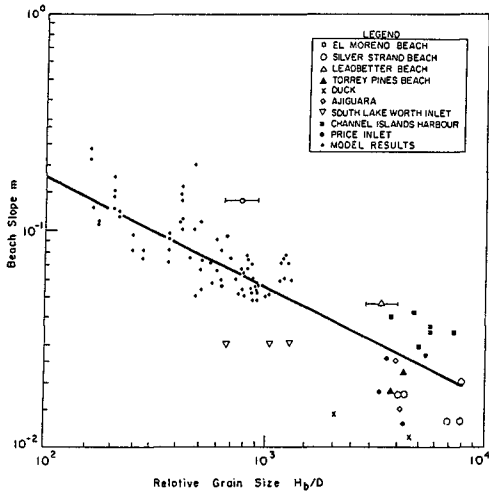


Figure 3. Beach Slope vs. Grain Size Relationship (from, Kamphuis et al., 1986)

3. Dynamic Similarity

Dynamic similarity is only achieved if all the prototype and model values of the dimensionless parameters on the right hand side of the following equation (Equation 5 extended to include the fall time parameter),

$$\Pi_{Q_S} = \varphi(H_b/L_o, m_b, H_b/D, \rho_s/\rho, F_o) \tag{7}$$

are equal, i.e. if their scales are:

$$n_{H_b/L_o} = 1; n_{m_b} = 1; n_{H_b/D} = 1, n_{\rho_s/\rho} = 1; n_{F_o} = 1.$$

Therefore, for physical model studies of surfzone processes (including cross-shore and alongshore sediment transport) in a given geometrically similar model, if the set of scaling conditions derived from Equation 7 are satisfied, then the dimensionless version of any mechanical quantity (e.g. Π_{Q_S} in Equation 7) is identical in model and prototype. The implications of each of these conditions are investigated.

- (i) A Wave Steepness Condition : $n_{H_b/L_o} = 1$.

The provision of this condition yields,

$$n_{H_b} = n_{L_o} \tag{8}$$

which results in a Froudian scale for the wave period as follows,

$$n_T = \sqrt{n} \tag{9}$$

This is a conventional scale for most physical models.

- (ii) A Beach Slope Condition : $n_{m_b} = 1$.

The representative beach slope is assumed to be,

$$m_b = d_b/\lambda_b \tag{10}$$

where the depth of breaking defines the offshore limit of the horizontal breaking distance λ_b , measured from the still water line. To satisfy this condition, the following equality must be achieved,

$$n_{d_b} = n_{\lambda_b} \tag{11}$$

This will only be possible in geometrically undistorted models with model grain size reduced geometrically as well, i.e.,

$$n = n_x = n_z = n_D \quad (12)$$

In an undistorted small scale hydraulic model all geometrical scales are the same. In a geometrically distorted model, the two horizontal scales n_x and n_y are identical but differ from the vertical scale n_z . The geometrical model distortion N may thus be defined as:

$$N = \frac{n_x}{n_z} = \frac{n_y}{n_z} \quad (13)$$

An empirical relationship for beach slope was given in Sayao (1982) as follows (see also Sayao et al, 1985),

$$m_b = 1.5 (H_b/D_{50})^{-\frac{1}{2}} \quad (14)$$

valid for medium and fine sands. Figure 3 shows a plot of beach profile slope versus the relative grain size parameter for the model data of Sayao (1982) and Readshaw (1979) and field data as compiled and analyzed by Davies (1984). Equation 14 shows good agreement with the trend of the data, albeit with large scatter. Sayao et al (1985) suggested that this relationship may be improved by introducing the wave steepness. However, comparison with available data did not improve scatter, indicating a need for the analysis of further field measurements where both wave characteristics and beach profiles are recorded simultaneously. Equation 14 can also be shown to fit the data of van Hijum and Pilarczyk (1982) for gravel beaches.

The relationship described by Equation 14 can be used to develop a scaling relation for the beach slope condition as follows,

$$n_{m_b} = (n_{H_b}/n_{D_{50}})^{-\frac{1}{2}} = (n_D/n)^{\frac{1}{2}} \quad (15)$$

If the model grain size is not reduced geometrically then

$$n_{m_b} = (n_D/n)^{\frac{1}{2}} = M_1 \quad (16)$$

where $M_1 \neq 1$ is the distortion due to the beach slope condition, which leads to a scale effect.

In an attempt to compensate for this distortion, Bijker (1967) suggested that for distorted models the geometric distortion should be equal to the ratio between the equilibrium beach slopes (which according to Dean, 1977 is a function of the grain diameter).

(iii) A Relative Grain Size Condition : $n_{Hb/D} = 1$.

The imposition of this condition yields

$$n_{Hb} = n_D \quad (17)$$

which will only be possible when the sand grain size is scaled down geometrically. In practice, this is only possible for shingle beaches or beaches with coarse sand grains. Thus, an imposed grain size distortion (M_2) may be present in beach models, when $M_2 \neq 1$, and the scale effect from this non-similarity is quantified as follows,

$$n_{Hb/D} = n/n_D = M_2 \quad (18)$$

(iv) A Density Ratio Condition : $n_{\rho s/\rho} = 1$.

To satisfy this condition the following must be provided.

$$n_{\rho_s} = n_{\rho} = 1 \quad (19)$$

In conventional physical models using water and sand this condition is fulfilled. Departure from this condition (for example, through the use of lightweight materials) leads to significant scale effects and dissimilarity between model and prototype morphological development in the surfzone (see Kamphuis, 1975).

(v) A Fall Velocity Condition : $n_{F0} = 1$.

The adherence to this condition leads to the Froudian scaling of fall velocity as derived from the following relationship,

$$n_{Hb} = n_w \cdot n_T \text{ or } n_w = \sqrt{n} \quad (20)$$

Based on the work of Dean (1973), fall velocity scaling has been suggested by many researchers (e.g. Dalrymple and Thompson, 1976; Kamphuis, 1982; Hallermeier, 1984; Ito and Tsuchiya, 1984; Dean, 1985; Kriebel et al, 1986 and Yalin et al, 1986).

Several scaling laws dealing with the distortion of the fall velocity condition

have also been presented in the literature (Valembois, 1961; LeMehaute, 1970; Vellinga, 1982 and 1986; Sayao and Guimaraes, 1984). For example, using the Vellinga (1982) scaling law:

$$N = n_x/n_z = (n_z/n_w^2)^\alpha \quad (21)$$

where by definition $N = n_x/n_z = n_y/n_z$ and the fall velocity scaling criterion, if satisfied, gives $n_x/n_z = 1$ for any value of the exponent α , i.e. no geometrical distortion. The value of the exponent α in Equation 21 varies between 0.25 (Vellinga, 1982 and 1986) and 0.50 (Valembois, 1961; LeMehaute, 1970; Sayao and Guimaraes, 1984).

4. Sediment Transport Scale and Time Scale for Littoral Processes

The dimensionless littoral transport rate (Π_{Q_s}) expression depends on the units of the sediment transport rate Q_s . Adopting Q_s as a volumetric rate (m^3/s), Sayao (1982) defined,

$$\Pi_{Q_s} = \frac{(1 - p) Q_s}{(\rho/\rho_s) H_b^2 (H_b/T)} \quad (22)$$

where p is the beach sand porosity. Assuming $n(1 - p) = 1$, the scale of dimensionless sediment transport in the littoral zone is,

$$n\Pi_{Q_s} = \frac{n\rho_s n_{Q_s} n_T}{n_\rho n_H^3} = \frac{n_{Q_s}}{n^{5/2}} \quad (23)$$

for Froudian models with sand as the model material.

The time scale for littoral processes (or morphological development) may be derived from Equation 23, using the definition of Q_s (in m^3/s) as,

$$n_{Q_s} = n_v/n_{t_s} \quad (24)$$

where n_v is the scale of volume of sand. Thus

$$n_{t_s} = n_v/n_{Q_s} = \frac{n_v}{n^{5/2} n\Pi_{Q_s}} \quad (25)$$

Equation 25 shows that the time scale is influenced by the scale of dimensionless transport rate and by the volumetric scale. There is a possibility that the former will be different from 1 and the latter to be different than n^3 depending on the model design (i.e. whether or not there are distortions due to deviation from the conditions (i) to (v) and whether or not there is geometrical distortion).

5. Proposed Moveable Bed Model Design

The design of a moveable bed model study is not a simple task. It requires a clear understanding of the potential scale effects, as well as a thorough interpretation of model results in order that solutions for the prototype engineering problem may be proposed. Also, prototype data must be available so that prototype parameters related to the coastal phenomena at the study site may be defined.

Further, it is necessary to define the physical model scales. It is proposed here that a geometrically undistorted model is used if at all possible. Otherwise, the scaling law of Equation 21 can be used to determine an appropriate geometrical distortion and model grain size.

With reference to the model grain size it is proposed that the fall velocity criterion is used in the moveable bed model study if possible. This is preferred over other scaling criteria (such as geometrically reduced model material) because:

(a) Dean's parameter would be the same in model and prototype. This means that both model and prototype beaches will be either eroding or accreting, and dynamic similarity of erosional and accretional processes is ensured.

(b) Scale effects resulting from the non-similarity of m and H_b/D are less detrimental and more easily quantifiable than the effects resulting from the non-similarity of F_o .

If fall velocity scaling cannot be used for model design due to other constraints, it is recommended that the moveable bed model should have F_o -values in the same region as the prototype ones, i.e., that for both model and prototype F_o -values are simultaneously above or below the critical value $F_o \sim 1$.

Finally, with respect to grain size, it is strongly recommended that the model value of H_b/D exceeds 300 to ensure that suspended load is able to occur at the model scale (see Nairn, 1985).

6. Quantification of Scale Effect

The modelling design criteria are summarised in Table 1. For the quantification of scale effect, a new procedure is presented for geometrically undistorted, fall velocity scaling models. In this case, distortions are due to non-similarity of beach profile slope and relative grain size. Thus using Equations 16 and 18, the combined scale effect M due to both contributing parameters is,

$$M = M_1 \cdot M_2 = (n_D/n)^{\frac{1}{2}} \cdot (n/n_D) = (n/n_D)^{\frac{1}{2}} \quad (26)$$

Also, $n_{\Pi Q_s}$ is not equal to unity but for these types of models,

$$n_{\Pi Q_s} = M = (n/n_D)^{\frac{1}{2}} \quad (27)$$

Hence, the rate of morphological development (or the littoral process time scale) may be quantified using Equations 25 and 27 as,

$$n_{t_s} = n/(n_D)^{\frac{1}{2}} \quad (28)$$

and the littoral transport rate scale becomes (using Equations 24, 27 and 28),

$$n_{Q_s} = n^2 \sqrt{n_D} \quad (29)$$

Both Equations 28 and 29 are valid for geometrically undistorted, fall velocity scaling models only. If other scaling criteria are used, the derivation of these equations would be different. The expressions apply to both alongshore and cross-shore sediment transport. However, caution is advised in applying the time scale expression (Equation 28) to cross-shore problems where either the model or prototype profiles are near a stable equilibrium form.

Table 1. Geometrically Undistorted Fall Velocity Scaling Model

Scale Condition	Similarity	Comment
(i) wave steepness	$n_H/L = 1$	Froudian model scale effect scale effect Sand in model Fall velocity scale is Froudian
(ii) beach slope	$n_m = M_1 (\neq 1)$	
(iii) relative grain size	$n_H/D = M_2 (\neq 1)$	
(iv) relative density	$n_{\rho_s/\rho} = 1$	
(v) Dean's parameter	$n_{F_o} = 1$	
time for littoral processes	$n_{t_s} = n/\sqrt{n_D}$	Equation 28
littoral transport rate	$n_{Q_s} = n^2 \sqrt{n_D}$	Equation 29

7. Applications of the Modelling Procedure

The recommended modelling procedure could be tested if a field data set were available. Unfortunately, due to the difficulties of determining sediment transport rates on beaches during storm events an ideal prototype data set is not presently available. However, the recommended procedure can be evaluated by (1) comparing pairs of flume test results at different scales (and thus regarded as model and prototype) and (2) the use of numerical models to compare profile development at different scales subject to the proposed modelling procedure.

Kriebel et al (1986) have used the fall velocity modelling procedure (originally

proposed by Dean, 1985) and compared small-scale flume results (model) with the large-flume experiments (prototype) of Saville (1957). For the Kriebel et al (1986) data, the time scale for littoral processes is calculated to be, $n_{ts} \sim 6$ and Figures 4 and 5 show profile comparisons according to Equation 28. The match of model and prototype profiles in these figures is fair, but so is the match shown in Kriebel et al (1986) based on a Froude time scale. Sediment transport in this example was predominantly directed offshore.

As an example of the sediment transport rate scale, experimental data presented by Mimura et al (1986) and shown in Figure 6, is used. In this case, using their coarse sand tests (Series B) as prototype and fine sand tests as model (Series A), $n \sim 2.1$ and $n_D = 4.2$ are found for two pairs of tests, the B8 and A9 tests on a $1/20$ initial profile, and the B2 and A3 tests on a $1/10$ initial profile. The calculated value for the sediment transport rate scale according to Equation 29 is $n_{Q_S} = 9.3$, and the experimental measurements of cross-shore sediment transport rate are in agreement with the proposed modelling procedure. (See Table 2). Also, beach profiles shown in Figure 6 are representative and show similar features. It should be noted that the tests of Mimura et al (1986) which have been investigated were characterised by onshore sediment transport.

Table 2. Cross-shore Transport Rate of Mimura et al (1986)

Initial Slope	Q_{Sp} ($m^3/hr.$)	Q_{Sm} (m^3/hr)	n_{Q_S}	comments
$1/20$	0.0113	0.001	11	compares well with Equation 29
$1/10$	0.01	0.001	10	

The recommended modelling procedure is also applicable to situations where alongshore sediment transport is predominant. Kamphuis et al (1986) have proposed an equation for alongshore transport rate as follows,

$$\Pi_{Q_S} = 0.002 (H_{bS}/D) (m/(H_{bS}/L_o))^{\frac{1}{2}} \tag{30}$$

Moreover, the applicability of this equation to both field results (from which its empiricity was derived) and model scale results was demonstrated by Sayao et al (1985). Equation 30 was shown to predict sediment transport rates around model circular sand islands at various scales and with different grain diameters based on the work of Nairn (1985), see Figure 7 reproduced from Sayao et al (1985). Since the variables in Equation 30 directly correspond to those of Equation 7, it follows that the time scale and sediment transport scale (Equations 28 and 29), based on the distortions of m and H_b/D respectively, will also apply to alongshore sediment transport models.

The cross-shore transport time scale was also investigated using the results of a numerical model for cross-shore sediment transport under random waves. The numerical model is based on a depth-integrated energetics approach as described by Nairn (1988). The modelling procedure is similar to that proposed by Stive (1986) based on the work of Bailard (1981). Profile change is determined from the net sediment transport rates calculated at points in a finite difference scheme

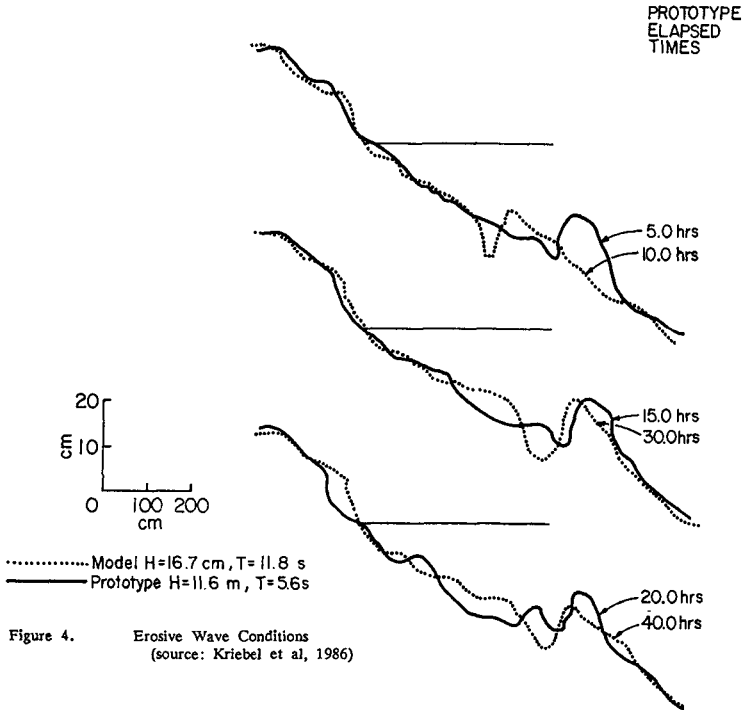


Figure 4. Erosive Wave Conditions
 (source: Kriebel et al, 1986)

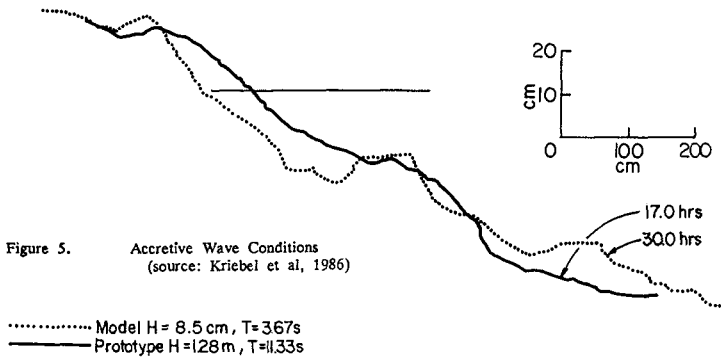
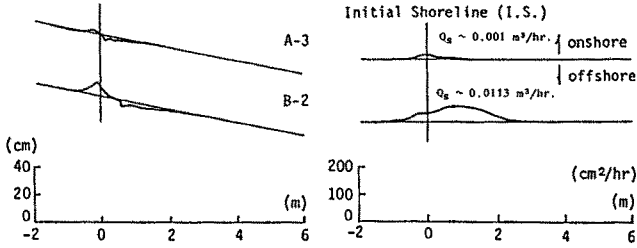
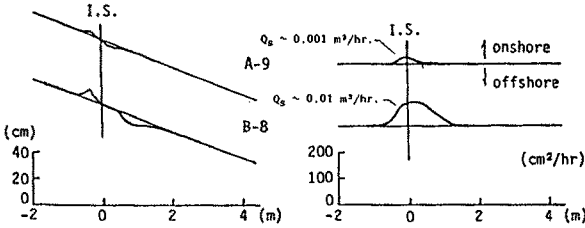


Figure 5. Accretive Wave Conditions
 (source: Kriebel et al, 1986)



Beach profiles and cross-shore sediment transport rate (initial slope=1/20, $d_{50}=0.75\text{mm}$)



Beach profiles and cross-shore sediment transport rate (initial slope=1/10, $d_{50}=0.75\text{mm}$)

Figure 6. Profiles and Cross-shore Transport (from, Mimura et al, 1986)

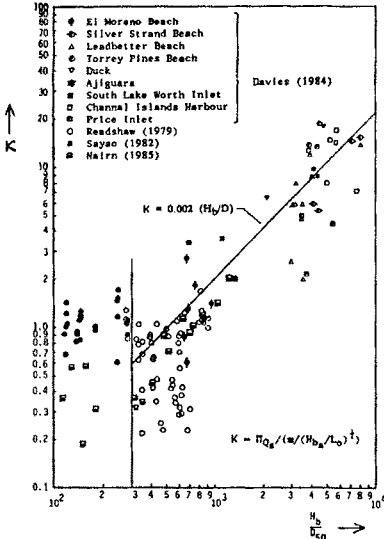


Figure 7. The Functional Dependency of Dimensionless Transport on H_b/D . (from, Sayao et al, 1985)

across the profile. The sediment transport rates are taken to be proportional to local flow characteristics (including both mean return flow and orbital velocities) which are calculated from a statistical representation of the wave height at any point on the profile. The model has been shown to successfully predict both small and large scale flume laboratory erosion tests. Two pairs of model and prototype tests have been investigated using the numerical model. The model was assumed to be a $1/10$ scale of a prototype which consisted of waves ($H = 1.23$ m, $T = 6.33$ s) incident on an initially plane $1/40$ profile with a sand grain size of 0.2 mm. This corresponds to a model test described by Stive (1986) with $H = 0.123$ m, $T = 2$ s and $D = 0.09$ mm. The results of two tests over different time periods are given in Table 3.

Table 3. Numerical Model Results.

PROTOTYPE RESULTS		MODEL RESULTS ($n = 1/10$)		
Prototype Period	Prototype Erosion Predicted (m^3/m)	Time Scales Used	Model Times	Predicted Prototype Erosion Volumes (m^3/m)
12 hrs.	15	$n_{t_s} = 6.7$	1.8 hrs	7.0
		$\sqrt{n} = 3.2$	3.8 hrs	12.2
180 hrs.	86	$n_{t_s} = 6.7$	27 hrs	49
		$\sqrt{n} = 3.2$	57 hrs	83

These results again demonstrate that the Froude time scale appears to be a better predictor of the offshore sediment transport time scale than that proposed by Equation 28.

8. Conclusions

The similarity of littoral processes including both cross-shore and alongshore sediment transport is due to 5 dimensionless parameters as follows (i) H_b/L_0 , (ii) m_b , (iii) H_b/D , (iv) ρ_s/ρ and (v) F_0 . In an ideal model the scales of each of these parameters should be equal to 1. However, this is generally not possible. The model design proposed is a geometrically undistorted Froude model with fall velocity scaling of the model sand. In this case scale effects are only due to

$$n_{m_b} \neq 1 \quad \text{and} \quad n_{H_b/D} \neq 1.$$

In the model proposed one can quantify the distortions due to the non-similarity of (ii) and (iii) by the following scales,

$$n_{t_s} = n/\sqrt{n_D} \quad (\text{Equation 28})$$

$$n_{Q_s} = n^2\sqrt{n_D} \quad (\text{Equation 29})$$

Comparisons to practical examples have successfully demonstrated the validity of these equations in situations of onshore transport in the cross-shore direction and for alongshore transport. The time scale for offshore sediment transport does however appear to be better represented by the Froude time scale than the scale proposed in Equation 28 above.

The conclusions noted above are based on comparisons to laboratory and numerical model results. Validation of the proposed model design and distortion expressions with a comprehensive field data set is still required pending the availability of an adequate data set.

9. References

- Bailard, J.A. (1981). An Energetics Total Load Sediment Transport Model for a Plane Sloping Beach. *J. of Geophys. Res.* (86), C11, pp. 10938-10954.
- Bijker, E.W. (1967). Some Considerations About Scales for Coastal Models with Moveable Bed. Delft Hydraulics Laboratory, Publication No. 50.
- Dalrymple, R.A. and Thompson, W.W. (1967). Study of Equilibrium Beach Profiles. *Proc. 15th Conf. on Coastal Eng. ASCE.* pp. 1277-1296.
- Davies, M.H. (1984). Littoral Transport Rate Prediction. M.Sc. Thesis. Queen's University, Kingston, Canada.
- Dean, R.G. (1973). Heuristic Models of Sand Transport in the Surfzone. *Proc. 1st Australian Conf. on Coastal Eng, Sydney,* pp. 208-214.
- Dean, R.G. (1977). Equilibrium Beach Profiles : U.S. Atlantic and Gulf Coasts. *Ocean Eng. Rept. No. 12. U. of Delaware, Newark,* 45pp.
- Dean, R.G. (1985). Physical Modelling of Littoral Processes. In "Physical Modelling in Coastal Engineering". R.A. Dalrymple, Ed., A.A. Balkema, Rotterdam, pp. 119-139.
- Hallermeier, R.J. (1984). Added Evidence on New Scale Law for Coastal Models. *Proc. 19th Conf. on Coastal Eng. ASCE.* pp. 1227-1243.
- Ito, M. and Tsuchiya, Y. (1984). Scale Model Relationship of Beach Profile. *Proc. 19th Conf. on Coastal Eng. ASCE.* pp. 1386-1402.
- Kamphuis, J.W. (1975). The Coastal Mobile Bed Model. *Civil Eng. Rept. No. 75. Queen's University, Kingston, Canada.*
- Kamphuis, J.W. (1982). Coastal Mobile Bed Modelling from a 1982 Perspective. *Civil Eng. Rept. No. 76. Queen's University, Kingston, Canada.*
- Kamphuis, J.W., Davies, M.H., Nairn, R.B. and Sayao, O.J. (1986). Calculation of Littoral Sand Transport Rate. *Coastal Eng. 10,* pp. 1-21.
- Kriebel, D.L., Dally, W.R. and Dean, R.G. (1986). Undistorted Froude Model for Surfzone Sediment Transport. *Proc. 20th Conf. on Coastal Eng. ASCE.* pp. 1296-1310.

- LeMehaute, B. (1970). Comparison of Fluvial and Coastal Similitude. Proc. 12th Conf. on Coastal Eng., ASCE, pp. 1077-1096.
- Mimura, N., Otsuka, Y. and Watanabe, A. (1986). Laboratory Study on Two-Dimensional Beach Transformation Due to Irregular Waves. Proc. 20th Conf. on Coastal Eng. ASCE. pp. 1393-1408.
- Nairn, R.B. (1985). Scale Series Approach to Coastal Mobile Bed Modelling. M.Sc. Thesis, Queen's U., Kingston, Canada.
- Nairn, R.B. (1988). Prediction of Wave Height and Mean Return Flow in Cross Shore Sediment Transport Modelling. Proc. IAHR Symposium on Mathematical Modelling of Sediment Transport in the Coastal Zone. Copenhagen, pp. 193-202.
- Readshaw, J.S. (1979). A Model Study of Alongshore Sediment Transport. M.Sc. Thesis, Queen's U., Kingston, Canada.
- Saville, T. (1957). Scale Effects in Two-Dimensional Beach Studies. Proc. 17th General Meeting of IAHR. Lisbon, Vol. 1, p. A3-1 to A3-10.
- Sayao, O.J. (1982). Beach Profiles and Littoral Sand Transport. Ph.D. Thesis. Queen's U., Kingston, Canada.
- Sayao, O.J. and Guimaraes, J.C. (1984). Experimental Verification of Similarity Criteria for Equilibrium Beach Profiles. Proc. 19th Conf. on Coastal Eng. ASCE. pp. 1342-1357.
- Sayao, O.J., Nairn, R.B. and Kamphuis, J.W. (1985). Dimensional Analysis of Littoral Transport. Proc. of the Canadian Coastal Conf., Newfoundland, pp. 241-255.
- Stive, M.J.F. (1986). A Model for Cross-Shore Sediment Transport. Proc. 20th Conf. on Coastal Eng. ASCE.
- U.S. Army Corps of Engineers (1977). Shore Protection Manual. Coastal Eng. Res. Centre. 3rd Ed., Washington.
- Valembois, J. (1961). Etude Sur Modele du Transport Littoral, Conditions de Similitude. Proc. 7th Conf. on Coastal Eng. ASCE. pp. 277-307.
- van Hijum, E. and Pilarczyk, K.W. (1982). Gravel Beaches. Delft Hydraulics Laboratory. Publication No. 274.
- Vellinga, P. (1982). Beach and Dune Erosion During Storm Surges. Coastal Eng. 6., pp. 361-387.
- Vellinga, P. (1986). Beach and Dune Erosion During Storm Surges. Ph.D. Thesis. Delft U. of Technology.
- Yalin, M.S., Sayao, O.J. and Lai, G.Y. (1986). Physical Modelling of Suspended Solids in Open Channels. Proc. of Euromech 192. W. Betcheler, Ed., A.A. Balkema, pp. 161-169.

CHAPTER 135

Field Calculations of Wave Energy Dissipation and Related Beach Profile

By

James R. Tallent 1
Takao Yamashita 2
Yoshito Tsuchiya 3

Introduction

The process by which wave energy dissipates across the surf zone and its affect on the bed profile is, of course, a topic of immediate concern and debate. Various concepts of the wave energy dissipation process have been modeled, however, additional research is needed before confidence can be placed in a particular calculation scheme. In addition to the problems associated with proper model derivation a method of application and result interpretation of actual surf zone field data must be devised and understood. This is, of course, prerequisite to any realistic use of a wave energy dissipation model in an engineering project. The following study was therefore conducted in order to examine the applicability of surf zone field data to wave energy dissipation models and to investigate the bed profile relationship.

Two wave energy dissipation models were selected for comparison in this study, the 'Undertow Model'(UM) which is based on the conservation of wave energy flux across the surf zone (3), and the 'Turbulent Bore Model'(TBM) which is based on hydraulic jump theory (2). Individual waves were identified in the wave record by employing the zero up-crossing method, and wave energy calculations were based on small amplitude wave theory, Svendsen's non-linearity parameter B_0 (4), and the 1/3 Significant Wave classification.

Wave elevation data which was collected before, during, and after the occurrence of a storm typical to the Ogata coast, ($H_{max}=5.5$ m.), was used for energy dissipation calculations. Lastly, an Ogata coast average cross-shore energy dissipation estimate was used in conjunction with Dean's Equilibrium Beach Profile Equation (2), to examine the stability of Ogata Coast, Japan.

- 1 Visiting Researcher, D.P.R.I., Kyoto University, Japan
- 2 Instructor, D.P.R.I., Kyoto University, Japan
- 3 Professor, D.P.R.I., Kyoto University, Japan

Field Measurements and Data Processing

Measurements necessary to calculate the wave energy dissipation rate were made by instruments mounted on D.P.R.I.'s T-shaped observation pier located at Ogata coast, Japan. This pier, shown in Figure 1b, is 255.6 meters in length normal to the shoreline, and 100 meters in length at the offshore T-section. A total of 14 wave gauges were positioned along the pier, as indicated in Figure 1a. In this figure, wave gauges are referred to as 'C' for capacitance type or as 'U' for ultrasonic type.

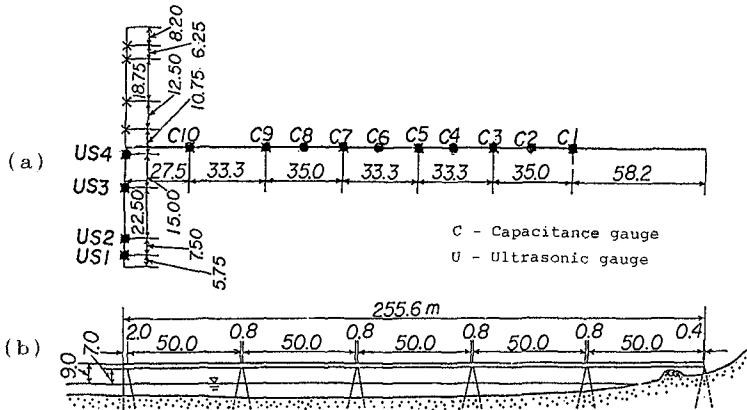


Figure 1. Ogata Coast T-shaped observation pier

Calibrations of wave gauges were continuously performed in order to determine and retain their accuracy. Wave elevation data was collected over a three day period, during which the coastal storm occurred. Wave data was stored on analogue data recorders. Digitalizing of records was accomplished by use of an A-D converter which operated at a sampling rate of 0.08 seconds. A high pass filter of 100 seconds and a low pass filter of 2.5 seconds were used to remove the long wave components and high frequency breaking wave fluctuations, respectively. Filter selection was based on record observation. The resulting wave data was then partitioned into 22 minute blocks and individual waves identified by the zero up-crossing method. Beach profile measurements were made by depth soundings conducted along D.P.R.I.'s T-shaped observation pier.

Theoretical Considerations

There are several ways by which the potential energy of irregular waves can be approximated. However, due to our data being limited to surf zone surface fluctuations,

where periodic wave theories are invalid, we choose to evaluate potential energy on the basis of individual wave elevation measurements, incorporating non-linearity through Svendsen's B_0 parameter, Equation 1. The B_0 variation with profile shape is described in Table 1 (1). Note that if B_0 equal 1/8 (0.125) the wave shape is of sinusoidal form and potential energy is evaluated by small amplitude wave theory.

$$B_0 = \frac{1}{T} \rho g \int \frac{\eta^2}{\rho g H^2} dt = \frac{\eta^2}{H^2} \quad (1)$$


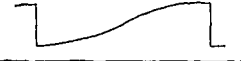


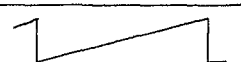
	Profiles	B_0
	Sinusoidal	0.125
	Cnoidal	< 0.125
	Parabolic	0.089
	Linear	0.083

Table 1. Nonlinearity parameter B_0 (after Basco, 1986)

Consequently, small amplitude wave theory estimates, Equation 2, and B_0 modified potential energy estimates, Equation 3, are employed for comparison in the energy dissipation calculations.

$$E_1 = \frac{1}{16} \rho g H^2 \quad (2)$$

$$E_2 = \frac{\rho g}{2T} \int_0^T \eta^2 dt = \frac{1}{2} \rho g H^2 B_0 \quad (3)$$

Where T is the wave period, ρ is the fluid density, g is the gravitational acceleration, η is the water surface elevation measured from the MWL, and H is the wave height.

The 'Undertow' model may be described as the conservation of wave energy flux across the surf zone. This relation may be expressed as:

$$\frac{\partial}{\partial x} (W_w + W_r) = D \quad (4)$$

where W_w and W_r represent the wave and residual (turbulent)

energy fluxes, respectively. The flux of externally opposing energy sources are represented by D . In summing the external and residual energy fluxes an expression is derived which allows us to calculate energy dissipation across the surf zone in terms of wave elevation alone, Equation 5.

$$\frac{\partial W_W}{\partial x} = D - \frac{\partial W_R}{\partial x} = -DISS \quad (5)$$

Furthermore, if we make the assumption that wave energy is traveling at group velocity C_g , the wave energy flux may be written as:

$$W_W = E C_g = E \sqrt{gh} \quad (6)$$

where E is the sum of both potential and kinetic energy and h is the water depth. By employing the small amplitude and B_0 modified wave energy estimates, along with Equations 2 and 3, and the 1/3 significant wave height classification, three energy flux relations are derived, Equations 7-9. These three relations will each be substituted into the dissipation relation of Equation 5, to examine computational variations.

$$W_A = \bar{E} z C_g = \bar{E} z \sqrt{gh} \quad (7)$$

$$W_B = (Ez)_{1/3} C_g = (Ez)_{1/3} \sqrt{gh} \quad (8)$$

$$W_C = (E1)_{1/3} C_g = (E1)_{1/3} \sqrt{gh} \quad (9)$$

The second method used to calculate the cross-shore energy dissipation rate was derived from hydraulic jump theory and is known as the 'Turbulent Bore Model' (TBM), Equation 10. This model is applicable only where the breaking wave propagates in a nearly constant form, such as that of a quasi-steady bore. Therefore, the cross-shore wave shape characteristics, described by B_0 , must be investigated in order determine the region of model applicability.

$$DISS = \frac{\rho g h (d_c - d_t)^3}{T \quad 4 d_t d_c} \quad (10)$$

where h is the mean water level, T is the wave period, d_c and d_t are the depth measurements from the crest and trough, respectively, and $DISS$ is the rate of change of wave energy per unit shoreward distance expressed in the units of tons/sec/meter, Figure 2.

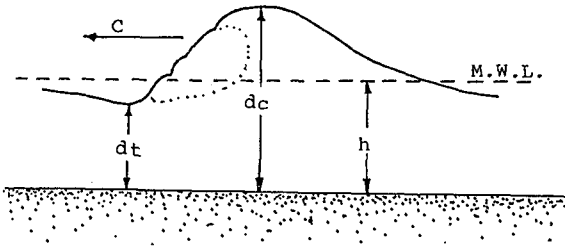


Figure 2. Turbulent Bore Model variables

The Ogata coast is best described as a high energy reflective type beach, while Dean's 'Equilibrium Profile Equation' was derived from typical low energy dissipative beaches, Equation 11. A comparison between the measured and the calculated profile will allow us to determine how unstable the profile is presently.

$$h = A x^{2/3} \tag{11}$$

where h is the water depth, A is a parameter describing fluid and sediment properties, and x is the offshore distance. Furthermore, if: the $2/3$ constant is replaced with the variable α , the spilling breaker assumption is adopted, Equation 12, and the energy dissipation relations described in Equations 5 and 6 are employed, an equation is derived which describes the cross-shore wave energy dissipation/beach profile relation, Equation 13.

$$H = \gamma h \tag{12}$$

$$DISS = \frac{5}{16} \alpha \rho g^{3/2} \gamma^2 h^{(3/2 - 1/\alpha)} A^{1/\alpha} \tag{13}$$

where γ is assumed to equal 0.8.

Results and Conclusions

All data collected before, during and after the coastal storm was divided into five time series, each representing a particular stage of the storm, and containing six hours of data. Data sets N15, N18, and N19 correspond to sea state conditions best described as initial storm (steep short period waves), fully developed storm (well defined long crested waves), and post storm (swell), respectively. In Figure 3, cross-shore energy fluxes are shown for the relations described in Equations 7-9, and for the three storm stages described above. Several conclusions may be

drawn from this figure, they include: 1) energy flux calculations based on the significant wave and small amplitude wave theory, are significantly larger and more scattered than results based on W_A or W_B , 2) the steep negative energy flux gradients seaward of wave gauge C8 indicates the region of rapid wave height decay, initial breaking, 3) shoreward of wave gauge C7 the energy flux gradients are slightly positive, especially for the fully developed storm, N18, possibly corresponding to wave rebuilding, and 4) from C3 shoreward large inflections in the energy flux gradient correspond to visual observations of incident and reflected wave interaction.

Because the W_B energy flux calculation, Figure 3, required the Bo parameter to be evaluated in terms of it's 1/3 significant value, it was necessary to investigate the Bo /wave-order relationship to clarify it's role. Therefore, in Figure 4, the variations in the Bo parameter with orders of increasing wave magnitude are presented at five surf zone locations.

The asterisk in the Figure 4 series indicates the locations of the 1/3 significant wave. To the left of the asterisk waves are of a greater order than the 1/3 significant and to the right the order is smaller. It is interesting to note that the wave shape parameter significantly fluctuates for wave orders less than the 1/3 significant, however, to the left of the asterisk the Bo parameter remains fairly constant. This observation indicates that the surf zone 1/3 significant Bo value may be used to approximate average surf zone energy characteristics.

As previously mentioned the TBM may be applied only where the breaking wave propagates in constant form, therefore, the Bo parameter must also be investigated in terms of it's cross-shore characteristics. In Figure 5 the cross-shore Bo variations are shown for the entire observation period, data blocks N15-N19, where an individual line within each data block represents a 22 minute Bo average.

In comparing each data block differences may be observed in the cross-shore Bo trends, however, between wave gauges C10 and C7 all data blocks show a similar Bo tendency. Therefore, within this zone of relatively constant Bo the TBM was applied and compared with dissipation results derived from the UM, Figure 6, where Diss-1 and Diss-2 represent TBM results based on 1/3 significant and individual wave measurements, respectively. The lower three curves are UM calculations based on the three previously defined energy flux relations.

Conclusions based on this figure include: 1) TBM calculations based on the significant wave component,

Diss-1, are approximately 2.0-2.5 times greater than calculations based on the UM, 2) TBM calculations based on individual wave measurements are of the same order of magnitude as UM calculations (approximately 0.01 tons/sec/mm) and 3) during the initial storm stages, N15-N16, maximum wave energy dissipation values are generated by the TBM, however, because maximum storm conditions were actually observed during the period corresponding to N17 we may conclude that the TBM is inapplicable for short period waves.

Finally, a comparison is made between the calculated, Equation 10, and measured beach profiles, Figure 7. Calculation assumptions include: 1) $Diss = 0.01 \text{ ton/sec/m}$, 2) $\gamma = 0.8$, and 3) $h = 5.6 \text{ m}$. Also, the parameters A and B were both varied in order to determine the best fit solution to the measured Ogata Coast profile.

In this study and several others, significant differences have been noted between dissipative ($\alpha = 2/3$ generated) and reflective type beach profiles, suggesting that Dean's equation may be valid only under certain undefined conditions and that additional parameters are needed to describe the reflective profile.

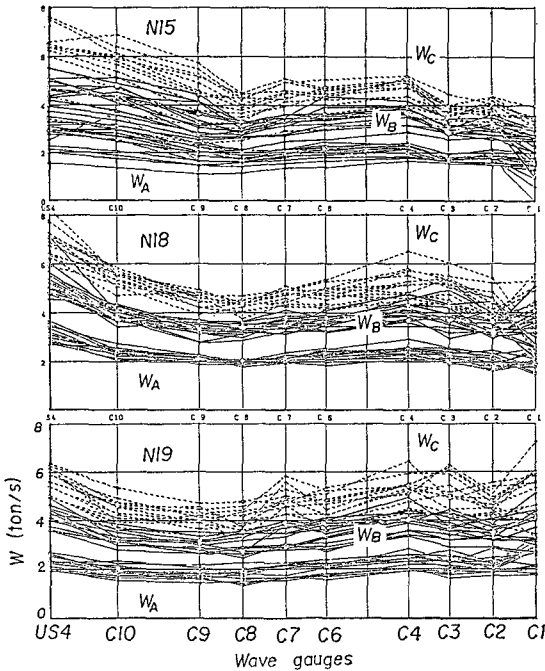


Figure 3. Cross-shore energy flux trends

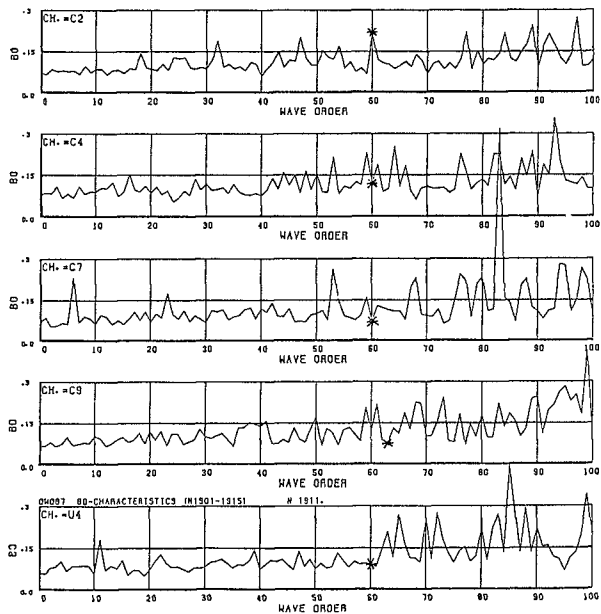


Figure 4. Ordered surf zone B_0 characteristics

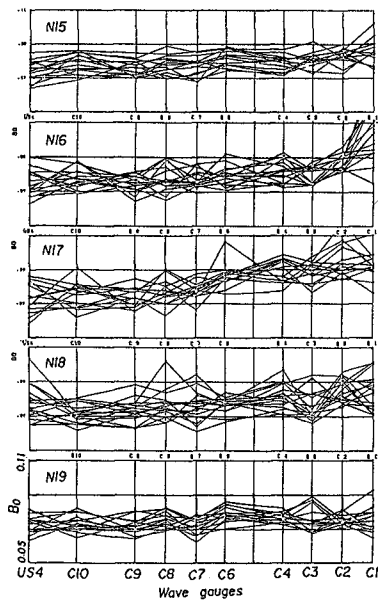


Figure 5. Cross-shore B_0 characteristics

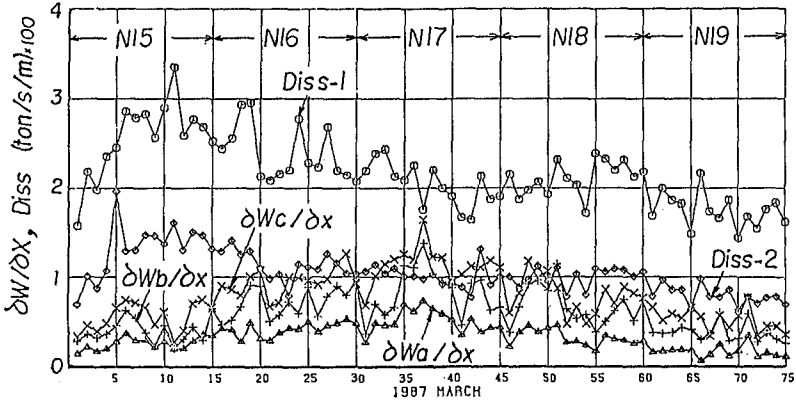


Figure 6. Wave energy dissipation comparison

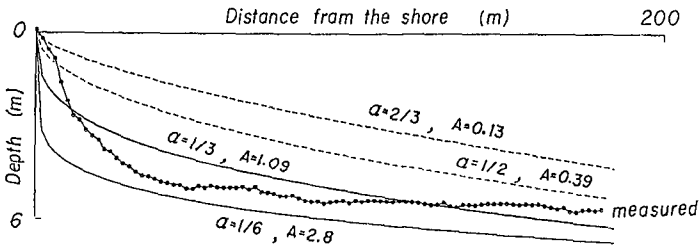


Figure 7. Comparison of measured and calculated profiles

References

- 1) Basco, D.R., Yamashita T.: Toward a Simple Model of the Wave Breaking Transition Region in the Surf Zones, Proc. 20th ICCE, pp. 955-970, 1986
- 2) Dean, R.G.: Equilibrium Beach Profiles: U.S. Atlantic and Gulf Coast, Ocean Engineering Report No. 12, Dept. Civil Engineering, University Delaware, 1977.
- 3) Svendsen I.A.: Mass Flux and Undertow in the Surf Zone, Coastal Engineering, Volume 8, Number 4, pp. 347-365, 1984
- 4) Svendsen I.A., Madsen, P.A., and Hansen, J.B.: Wave Characteristics in the Surf Zone, Proc. 16th ICCE, 1978

CHAPTER 136

Effects of Energy Loss near Bed Surface on Wave-Induced Pore Pressure in Sand Layer

Yoshi-Hiko MAENO, M.ASCE*

ABSTRACT

The effects of energy loss near the interface between the water and the sand bed on the wave-induced pore pressure are investigated by laboratory experiments. The interface between them includes the complicated factors: (1) roughness of seabed surface such as ripples; (2) boundary layer thickness in the sediment; (3) concentration of suspended sediments. These factors have been studied with respect to dimensionless parameters (e.g. Reynolds number, sediment Reynolds number, the ratio of orbital diameter to sand grain diameter, and Shields number), since many experimental formulas including these parameters have been proposed for predicting the geometry of roughness and the concentration of suspended sediments. The parameters described above are examined in relation to the damping characteristics of the wave-induced pore pressures. The transmissivity of pressure is constant until a critical value of the dimensionless parameters, and then decreases with increasing parameters. The critical values indicate the bed regime boundary of flat bed to ripple bed. Examinations of wave-induced pore pressure make it possible to predict the bed regime boundary.

INTRODUCTION

The energy losses near the interface between the water and the surface layer of the sand bed are investigated in the relation to the transmission of the wave pressures to the wave-induced pore pressures. The energy losses affect the wave-induced instability of the surface layer of the bed. Recently the wave-induced liquefaction has been studied and considered as the transient phenomena near the surface layer of the bed. On the other hand, Maeno & Hasegawa(1987c) indicated that the rapid attenuation of wave-induced pore pressures is observed in the surface layer of the bed, and that the attenuation of pore pressures in the surface layer differs from that in the sublayer. The attenuation characteristics depend on the energy losses. Since the wave-induced pore pressure relates the instability of the seabed, examinations of the energy losses are required for making clear the mechanism of wave-induced instabilities of the bed.

* Assistant Professor, Dept. of Civil Engng., Maizuru College of Technology, 234 Shiraya, Maizuru, Kyoto, 625 Japan.

The interface between the water and the bed includes the many complicated factors: e.g., (1) the roughness of seabed surface such as dunes and ripples; (2) the concentration of suspended sediments; (3) the boundary layer thickness in the sediments. Although the factors are related to each other and the other factors may exist, the selection of these factors is reasonable on the basis of the observation in laboratory experiments. The surface geometry of sand bed is not idealized flat but rippled under wave action. The roughness of bed surface causes the complicated stream regimen such as vortex. The sediments are suspended by the interaction between the severe oscillatory flow and the bed roughness.

Maeno & Hasegawa(1985a,b) had investigated the characteristics of wave-induced pore pressure in sand layer by wave tank experiments. They measured the wave-induced pore pressures, observing the bed forms of flat bed to ripple bed. The difference between the measured pore pressure and the predicted one can be explained by these factors of energy losses.

The geometry of the bed roughness and the concentration of suspended sediments have been investigated by many authors and the many empirical formulas have been proposed for the prediction of them. The intrinsic parameters also have been indicated. The empirical formulas for ripple geometry such as the wave length and the wave steepness have been proposed with reference to the Reynolds number, the Shields number and the orbital diameter. The empirical formulas for the concentration of suspended sediments also have been proposed with reference to the Shields number. This study examines the relationship between these parameters and the transmissivity of pore pressures.

INTRINSIC PARAMETERS OF ENERGY LOSSES

Tsuchiya & Banno(1987) indicated the three dimensionless parameters as the index of classification for criteria of ripple formation. Those are the Shields number, the sediment Reynolds number (or the sediment fluid number) and the ratio of the orbital diameter of water particle in the wave motion to the diameter of the sediment grain. The many formulas for the concentration of suspended sediments are related to the Shields number, and those for the geometry of bed roughness also are related to the Reynolds number, the Shields number and the ratio of orbital diameter to sediment grain diameter. Since no studies examine the bed roughness and the concentration of suspended sediments in relation to the transmissivity of the wave pressures to the wave-induced pore pressures, this study examined the relationship between the damping characteristics of wave-induced pore pressure and the following four parameters: (1) the ratio of orbital diameter of water particle; (2) the Shields number; (3) the Reynolds number; (4) the sediment Reynolds number.

First, the ratio of orbital diameter of water particle to the grain diameter of sediments is defined as follows:

$$d_0/D = H/\sinh(kh)D \quad (1)$$

where d_0 = the orbital diameter of the water particle in the wave motion; H = the wave height; k = the wave number($=2\pi/L$); h = the water depth and D = the grain diameter of sediments and regarded as the median diameter of sediment grain, d_{50} .

Secondly, the Shields number is defined as follows:

$$\psi = \frac{u^{*2}}{(\rho_s / \rho_w - 1)gd_{50}} \tag{2}$$

$$u^* = \sqrt{(fw/2)u_m} \tag{3}$$

$$u_m = \pi d_0/T \tag{4}$$

where u^* = the shear velocity; u_m = the maximum value of the horizontal velocity just outside the boundary layer; ρ_s and ρ_w are the densities of sand and water, respectively; g = the gravity acceleration; T = the period of the oscillatory flow; fw = the wave-current friction coefficient and Swart(1976) defined it as following form:

$$fw = 0.0025\exp[5.21(a/ks)-0.19] \quad \text{for } a/ks > 1.57 \tag{5}$$

$$fw = 0.3 \quad \text{for } a/ks < 1.57 \tag{6}$$

where a = the orbital amplitude of fluid just outside the boundary layer, $d_0/2$, and ks = the roughness length of the bed. Sleath(1984) suggested that the Engelund & Hansen(1967)'s formula of the roughness length of the bed is reasonable for many cases. Since Nabae sand is considerably uniform, the median grain diameter, d_{50} , substitutes for the grain size at the accumulation rate of 65 percents, d_{65} .

$$ks = 2d_{65} \tag{7}$$

Thirdly, the Reynolds number is defined as follows:

$$Re = u_m d_0 / \nu = \pi d_0^2 / (\nu T) \tag{8}$$

where ν = the kinematic viscosity of the fluid.

Finally, the sediment Reynolds number is defined as follows:

$$Re_D = u^*D / \nu \tag{9}$$

where D = the median grain size of sediment, d_{50} .

EXPERIMENTAL METHOD

Experiments were conducted on Nabae beach sand using the wave tank as shown in Figure 1, as well as our previous experiments (Maeno & Hasegawa; 1985a,b).

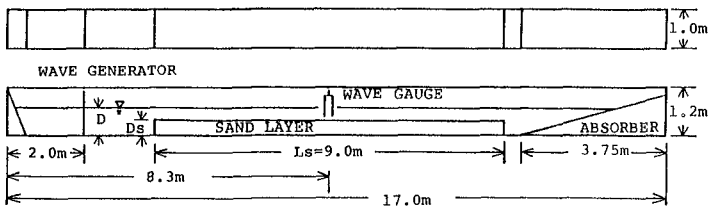


Figure 1. Experimental setup of the wave tank.

The wave tank generates the waves between the wave periods of 0.6s and 2.27s. The water depth is 0.41m over the sand bed. The length, the

width and the thickness of sand bed are 9.0m, 1.0m and 0.36m, respectively. The influences of bed size effects can be disregarded in the experiments. The physical properties of Nabae sand are given in Table 1. Table 2 tabulates the experimental conditions in addition to the published cases.

Table 1. - Properties of Nabae sand.

Specific gravity	2.70
Permeability	0.023 cm/s
Uniformity coefficient	1.53
Effective grain size	0.114 mm
Average grain size	0.160 mm

Table 2. - Experimental conditions.

Case	Length of bed (cm)	Dry density (t/m^3)	Water depth (cm)
(I)	250.0	1.61	41.0
(II)	166.0	1.54	41.0
(III)	99.5	1.67	41.0
(IV)	900.0	1.55	41.0
(V)	900.0	1.57	41.0
(VI)	900.0	1.62	41.0

The wave gauge is fixed just over the center of the bed. The pore pressures were measured at various vertical positions under the mud-line by four pressure transducers as shown in Figure 2, where the subscript z of P denotes the depth downward from the bed surface, and the x -axis is taken along the mud line of the sand bed.

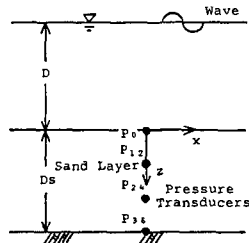


Figure 2. Definition of terms and set-up of pressure transducers.

The transmissivity of wave pressure is defined as the ratio of the measured pore pressure to the wave pressure predicted by Stokes' second order wave theory.

$$P_z = \frac{\rho g H}{2 \cosh(ND)} + \frac{3 \rho g N H^2 \tanh(ND)}{16 \sinh^2(ND)} \left[\frac{1}{\sinh^2(ND)} - \frac{1}{3} \right] - \frac{\rho g N H^2 \tanh(ND)}{16 \sinh^2(ND)} \quad (10)$$

EXPERIMENTAL RESULTS AND DISCUSSION

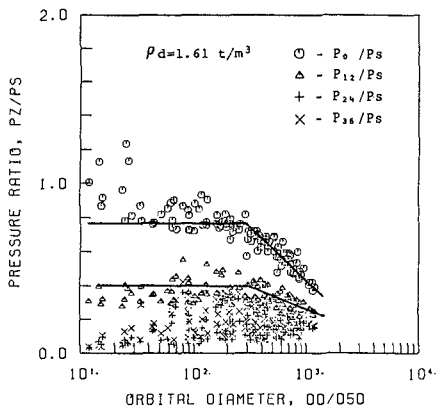
The relationships between the four dimensionless parameters pre-

viously described and the transmissivity of pressure in sand bed are investigated in order to study the effects of energy losses near the interface between the water and the sand bed on the damping characteristics of wave-induced pore pressures.

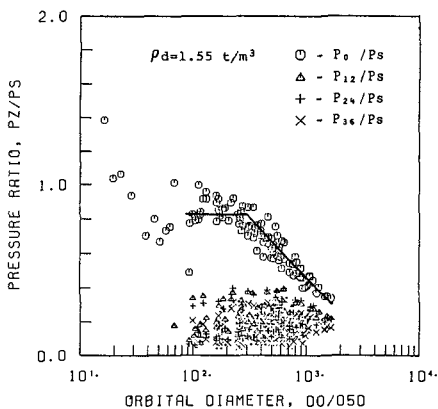
Relationship between Orbital Diameter and Transmissivity

Figures 3(a) and 3(b) show the relationship between the transmissivity of pressures and the ratio of the orbital diameter of water particle in the wave motion to the median grain size of sediment. The transmissivity of pressure keeps constant until a critical value, i.e., an orbital diameter of 300.0, and then decreases as the orbital diameter increases. This tendency is more clear in the wave pressure fluctuations at the bed surface and negligible in the deeper depth below mudline.

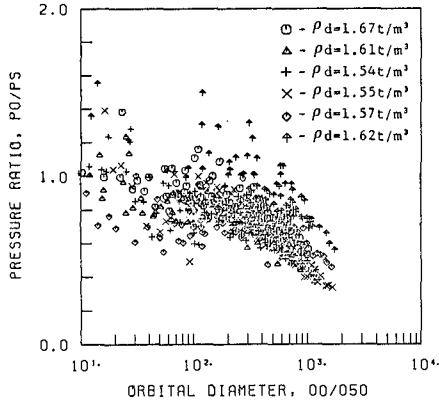
Figures 3(c) and 3(d) also show the relationship between the dimensionless orbital diameter and the transmissivities of pressure, P_0/P_s and P_{12}/P_s , for various sand bed conditions. The decreasing



(a) $\rho_d = 1.61 \text{ t/m}^3$



(b) $\rho_d = 1.55 \text{ t/m}^3$



(c) wave pressure for various bed conditions

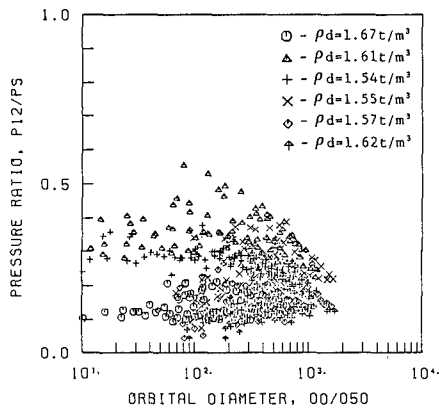
(d) pore pressure at $z=12\text{cm}$ for various bed conditions

Figure 3. Relationship between the orbital diameter of water particle and transmissivity

tendency of the dimensionless orbital diameter is more significant in the dense sand bed than in the loose sand bed. The critical value of the dimensionless orbital diameter is constant of 300, for various bed conditions.

Tsuchiya, Ueda and Oshimo(1984) showed that the dimensionless orbital diameter should be used for the index of the ripple formation for less than 1000. The experimental results are within this range of orbital diameter. The transmissivity of pressure shows rapid reduction near $d_0/D=1000$. Using the dimensionless orbital diameter many empirical formulas have been proposed for the ripple wave length (e.g., Kaneko & Honji,1979; Kaneko,1980). Sakakiyama et al.(1986) show that the ripple wave length increases with the orbital diameter until the ratio of ripple wave length to the orbital diameter reaches a limiting value of 2/3. Based on these backgrounds it is significant to examine

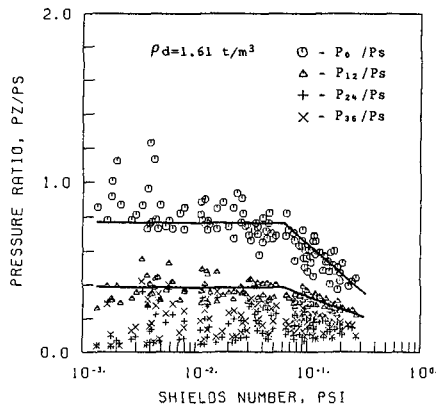
the transmissivity of pressure with reference to the orbital diameter.

Relationship between Shields Number and Transmissivity

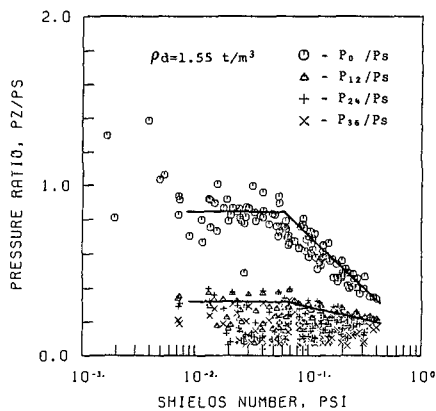
Figures 4(a) and 4(b) show the relationship between the transmissivity of pressures and the Shields number. The transmissivity also keeps constant until a critical Shields number of 0.06, and then decreases as the Shields number increases. This tendency is most predominant in the wave pressure fluctuation. The reduction of transmissivity with the Shields number becomes slower as the depth below the mudline increases. The transmissivity is constant with the Shields number for the deep depth below the mudline.

Figures 4(c) and 4(d) show the relationships between the transmissivities of pressures, P_0/P_s and P_{12}/P_s , and the Shields number for the various sand bed conditions. The critical value of the Shields number is almost 0.06 for all sand bed conditions.

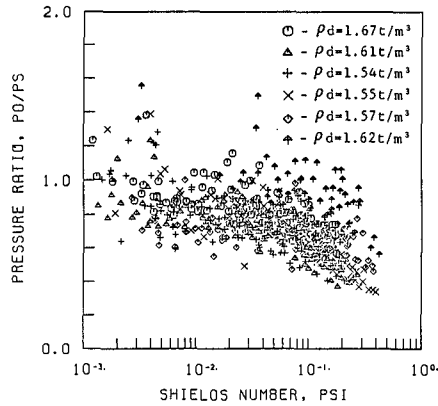
The Shields number is the key parameter in the empirical formulas of the ripple geometry such as the wave length and the wave steepness



(a) $\rho_d = 1.61 \text{ t/m}^3$



(b) $\rho_d = 1.55 \text{ t/m}^3$



(c) wave pressure for various bed conditions

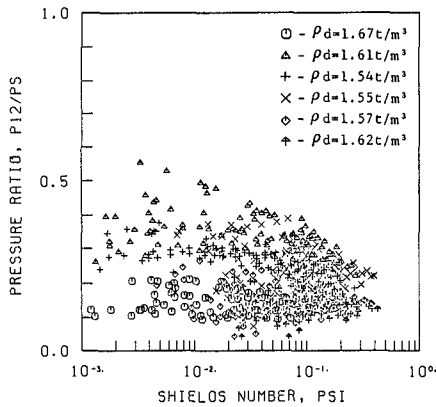
(d) pore pressure at $z=12\text{cm}$ for various bed conditions

Figure 4. Relationship between the Shields number and transmissivity

(e.g., Sakakiyama et al.,1986; Sato, Mitani and Watanabe,1988; Sato, Sugiura and Watanabe,1987). The empirical formulas for the concentration of suspended sediments near the bed surface have proposed in relation to the Shields number (e.g., Kawamata,1982). Kawamata(1982) showed that the concentration in a vortex layer on ripples depends on cubic the Shields number.

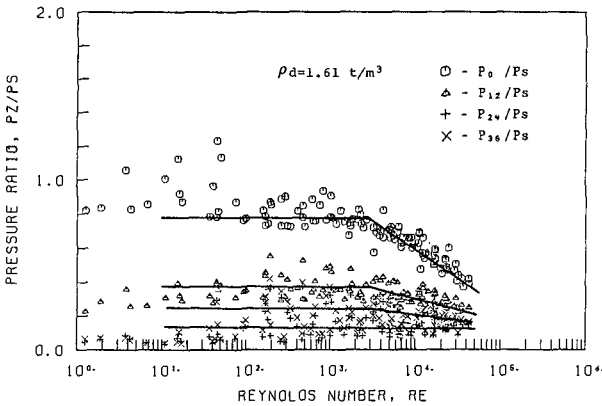
Therefore, examinations of the relationships between the transmissivities of pressures and the Shields number enable to obtain indirectly the relationships between the transmissivities and the ripple geometry and the concentration of suspended sediments. On the basis of the previous works, the wave length of ripple becomes small and the concentration of suspended sediments near the sand bed increases as the Shield number increases. Thus, the wave-induced pressures attenuates near the sand ripple, and the generation of wave pressures and

pore pressures are restricted. This inference is consistent with the experimental observation of the wave pressure propagation.

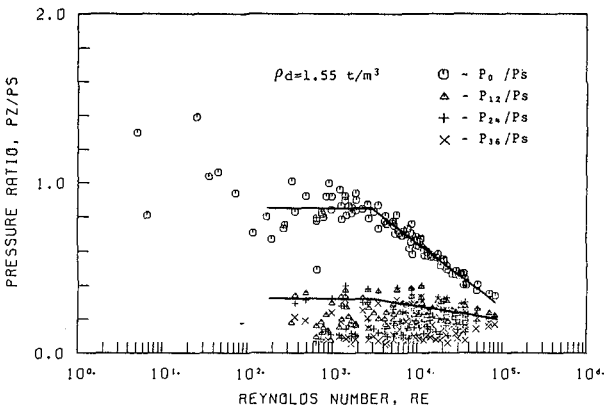
Relationship between Reynolds Number and Transmissivity

Figures 5(a) and 5(b) shows the relationship between the transmissivity of pressures and the Reynolds number. The transmissivity keeps constant until a critical Reynolds number of 3000.0, and then decreases as the Reynolds number increases. This tendency is most predominant in the wave pressure fluctuation. The reduction of transmissivity with the Reynolds number becomes slower as the depth below the mudline increases. The transmissivity of pore pressures is constant with the Reynolds number at the deep depth below the mudline.

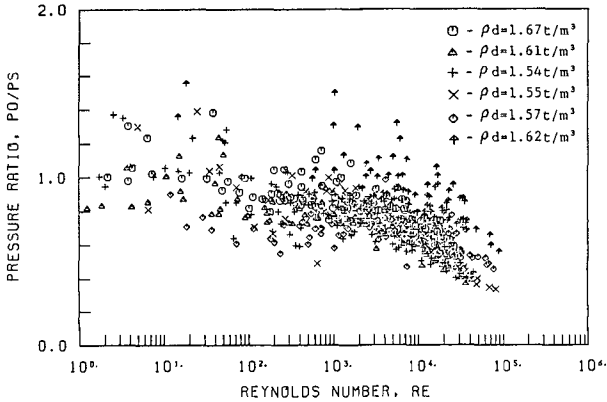
Figures 5(c) and 5(d) show the relationships between the transmissivities of pressures, P_0/P_s and P_{12}/P_s , and the Reynolds number for the various sand bed conditions. The critical value of the Reynolds number is almost 3000. for all sand bed conditions.



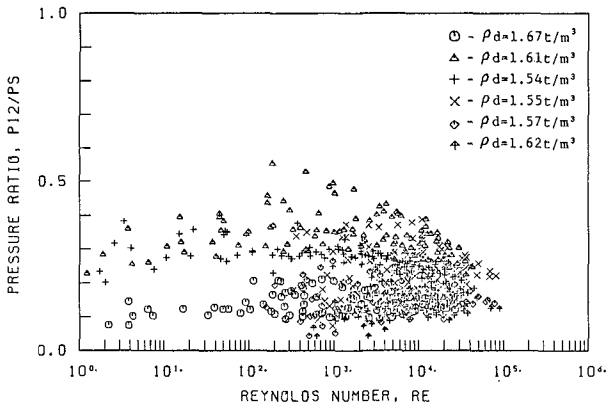
(a) $\rho_d = 1.61 \text{ t/m}^3$



(b) $\rho_d = 1.55 \text{ t/m}^3$



(c) wave pressure for various bed condition



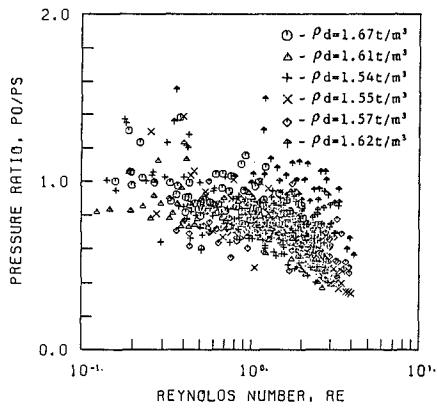
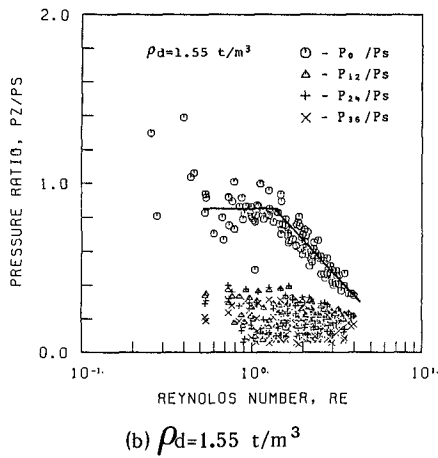
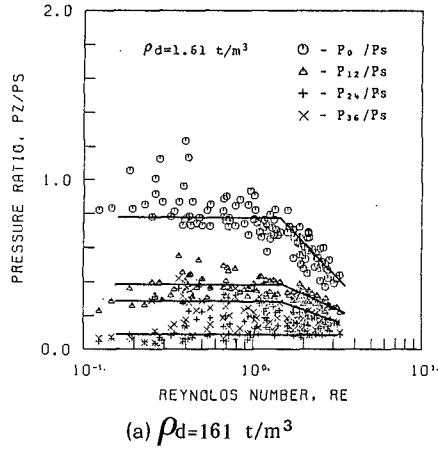
(d) pore pressure at z=12cm for various bed condition

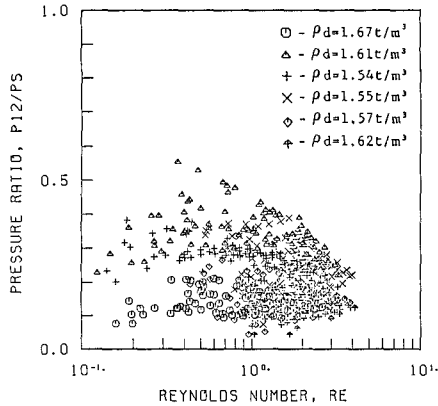
Figure 5. Relationship between the Reynolds number and transmissivity

Relationship between Sediment Reynolds Number and Transmissivity

Figures 6(a) and 6(b) show the relationship between the transmissivity of pore pressures and the sediment Reynolds number. The transmissivity also keeps constant until a critical sediment Reynolds number of 1.5, and then decreases as the sediment Reynolds number increases. The gradient of the reduction is most steepest at the sand bed surface, and becomes gentle as the depth of sand bed increases. The transmissivity of pressures is regarded as a constant value at the deep depth of sand bed.

Figures 6(c) and 6(d) show the relationship between the transmissivities of pressure, P_0/P_s and P_{12}/P_s , and the Reynolds number for the various sand bed conditions. The transmissivities of pressure start to reduce at the critical sediment Reynolds number of almost 1.5 for all sand bed conditions.





(d) pore pressure at $z=12\text{cm}$ for various bed conditions

Figure 6. Relationship between the sediment Reynolds number and transmissivity

The relationships between the transmissivities of pressures and the sediment Reynolds number are the same as those for the Reynolds number using the index of the orbital diameter of water particle instead of the median grain diameter. Since only a single sand is used in this experiments. The sediment Reynolds number should be examined, conducting additional experiments on the other sands that show any distributions of grain particle.

Sand Ripple Geometry and Transmissivity

All four parameters described above keep the transmissivities of pressures constant until a critical value of each parameter and linearly reduce them with increasing each parameter. This tendency is predominant in the dense sand bed and at the sand bed surface and becomes weaker as the depth of sand bed increases. This fact indicates that the damping characteristics of pressures change at a critical value of each parameter. Their critical values of each parameter are 1.5 for the sediment Reynolds number, 3000. for the Reynolds number, 0.06 for the Shields number and 300. for the dimensionless orbital diameter of water particle.

Riho, Watanabe and Horikawa (1981) proposed the following bed regime boundary of flat bed to rippled bed for both fine and coarse sands:

$$d_0'/d_m > 280 \text{ and } \psi > 0.1 \quad (11)$$

where d_0' = the orbital diameter of water particle in the finite amplitude wave action; d_m = the average grain diameter.

The critical values of both the dimensionless orbital diameter and the Shields number are in a good agreement with their bed regime boundary of flat bed to ripple bed. Since the ripple formation causes the complicated stream regimen such as vortex and increases the concentration of suspended sediments, the wave energy attenuates and decreases the rate of the wave pressure propagation into the sand bed. The damping characteristics of pressures are influenced by the energy losses near the interface between the water and the sand bed. Thus

examinations of the damping of pressures is a tool to investigate the complicated phenomena near the interface between the water and sand bed surface.

Recently, the criterion of ripple disappearance in the upper regime has been focused on and usually defined as the bed regime boundary of ripple bed to sheet flow. However, this study doesn't examine the other bed regime boundaries without flat bed to ripple bed in the relation to the damping characteristics of pressures in sand beds, since waves generated by wave tank is restricted in a narrow range of oscillatory flow velocity. If we conduct the laboratory experiment in water tunnel generating oscillatory flow and examine the damping characteristics of pore pressures in sand beds, we can obtain the bed regime boundary of ripple to sheet flow as well as that of flat to ripple. Since the wave pressure can easily propagate into the sand bed without damping based on the theoretical considerations, the transmissivity of pressures is inferred to change.

Therefore, the following bed regime boundaries can be determined by the damping characteristics of pore pressures: (a) no movement to flat bed; (b) flat bed to ripple bed; (c) ripple bed to sheet flow.

Boundary Layer in Sand Bed

Many types of instabilities of sand beds should be classified through their mechanisms. These mechanisms depend on their own bed conditions. For example, a bed condition is characterized by the composition and the constitution of sand beds, geotechnical properties of sediments, and so on. These bed conditions were discussed in our previous works (Maeno & Hasegawa, 1987b,c). The instability near the surface layer of sand beds is influenced by the effects of energy loss near the interface between the water and the sand bed. The interface between them includes the complicated factors as previously described. The boundary layer is assumed in the sediment, defining its thickness as the depth of the surface layer which depresses the wave-induced pore pressure. It is considered that the boundary layer has any contribution to cause the instabilities of sand beds such as the scour and the liquefaction.

In the boundary layer, the high erodibility may be caused, because its density is loosest; no solid skeleton in it is sufficiently composed; and it is considerably deformable. Thus, it is significant to investigate the correlation between the boundary layer thickness and the instability due to scour and erosion. The boundary layer is examined by laboratory experiments in a wave tank.

The elastic wave propagation theory predicts exponential attenuation of wave-induced pore pressures in a poro elastic media. This attenuation curve is valid for coarse sand beds (Yamamoto, 1977). However, the rapid attenuation curve is observed near the surface of fine sand beds (Maeno & Hasegawa, 1985b). Figure 7 shows the relationship between the damping ratio, P_z/P_0 , and the relative depth, z/D_s . This figure shows that the pore pressure is damped rapidly near the surface of a sand bed, and then is depressed slowly as the depth below the mudline increases.

The above experimental results indicate that there is a difference in mechanism of attenuation of pore pressure between near the surface and the inside of the sand bed. Since the surface layer of the sand bed is deformable; the soil skeleton in this layer is composed of the sand grains which are weakly combined with each other; wave-induced pore pressure easily squeezes out, and then attenuates greatly in the surface layer. The pore pressure, on the other hand, less attenuates

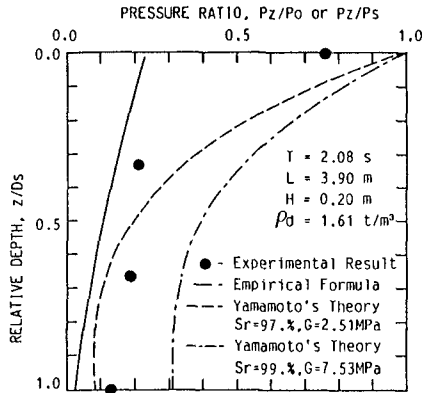


Figure 7. The relationship between the transmissivity of pressure and relative depth

in the sublayer below the surface layer, because the sublayer is relatively rigid and it is not easy for pore pressure to dissipate forward to bed surface. The above discussions suggest that the boundary layer may exist in the sand bed under wave loading. The boundary layer thickness should be predicted on the basis of laboratory experiments. Many difficulties, however, accompany these experiments. Those are the simultaneous measuring of pore pressures at various points, and the exact measuring near the surface of the bed. Since transducers disturb the flow of the pore fluid and the propagation of pressures in the beds, many miniature high quality transducers are required for these measurements. Overcoming these difficulties of laboratory experiments, the boundary layer thickness will be predicted experimentally. Moreover, the wave-induced instabilities near the surface layer will be classified based on these studies.

CONCLUSIONS

The following conclusions are obtained:

1. The energy losses near the interface between the sand bed and the water affect the wave-induced pore pressure in the surface layer of the sand bed. The effects of energy losses on the damping characteristics are examined in relation to the four dimensionless parameters: (1) the ratio of the orbital diameter of water particle to the sand grain diameter; (2) the Shields number; (3) the Reynolds number; (4) the sediment Reynolds number.
2. The transmissivity of pressure keeps constant until a critical value, and then decreases as all four dimensionless parameters increase. The rate of this reduction decreases as the depth below the mud line increases. The critical values are 300.0 for the orbital diameter, 0.06 for the Shields number, 3000.0 for the Reynolds number, and 1.5 for the sediment Reynolds number, respectively.
3. The critical values of both the dimensionless orbital diameter and the Shields number are in good agreement with Rihou et al.(1981)'s bed regime boundary of flat bed to ripple bed. The flat bed to ripple bed

boundary is determined by the damping characteristics of wave-induced pore pressures. Experimental results suggest that it is possible to determine the other bed regime boundaries by the proposed method that examines the relationship between the damping characteristics of wave pressures and the group of intrinsic dimensionless parameters.

REFERENCES

- Engelund, F.A., and Hansen, E., "A monograph on sediment transport in alluvial streams," Teknisk Forlag, Copenhagen, 1967.
- Kaneko, A., and Honji, H., "Double Structures of steady streaming in the oscillatory viscous flow over a wavy wall," *J. of Fluid Mechanics*, Vol.93, 1979, pp.727-736.
- Kaneko, A., "The wavelength of oscillation sand ripples," *Proc. of the 27th Japanese Conf. on Coastal Engrg., JSCE*, 1980, pp.207-210.
- Kawamata, R., "On suspended sediment transport model under waves on rippled bed," *Proc. of the 29th Japanese Conf. on Coastal Engrg.*, 1982, pp.218-222.
- Maeno, Y., and Hasegawa, T., "Characteristics of wave-induced pore water pressure in sand layer," *Proc. of International Symposium on Ocean Space Utilization*, 1985a, pp.475-484, Springer-Verlag.
- Maeno, Y., and Hasegawa, T., "Evaluation of wave-induced pore pressure in sand layer by wave steepness," *Coastal Engrg. in Japan*, JSCE, Vol.28, 1985b, pp.31-44.
- Maeno, Y., and Hasegawa, T., "Evaluation of wave-induced pore pressure in saturated sand bed," *Proc. of ASCE Specialty Conf. on Coastal Hydrodynamics*, Coastal Hydrodynamics, 1987a, 686-700.
- Maeno, Y., and Hasegawa, T., "In-situ measurements of wave-induced pore pressure for predicting properties of seabed deposits," *Coastal Engrg. in Japan*, JSCE, Vol.30, No.1, 1987b, pp.99-115.
- Maeno, Y., and Hasegawa, T., "Effects of energy loss near interface between water and bed on propagation of wave-induced pore pressures," *Proc. of Civil Engrg. in Ocean*, JSCE, Vol.3, 1987c, pp.101-106.
- Mei, C.C., and Foda, M.A., "Wave induced stresses around a pipe laid on a poro-elastic seabed," *Geotechnique*, Vol.31, 1981, pp.509-517.
- Riho, Y., Watanabe, A., and Horikawa, K., "Two-dimensional beach transformation and on-offshore sand transport," *Proc. of the 28th Japanese Conf. on Coastal Engrg., JSCE*, 1981, pp.217-221.
- Sakakiyama, T., Shimizu, T., Kajima, R., Saito, S., and Maruyama, K., "Sand ripples generated by prototype waves in a large wave flume," *Coastal Engrg. in Japan*, JSCE, Vol.28, 1986, pp.147-160.
- Sato, S., Sugiura, S., and Watanabe, A., "Sand transport mechanism and ripple disappearance in irregular oscillatory flows," *Proc. of the 34th Japanese Conf. on Coastal Engrg.*, 1987, pp.246-250.
- Sato, S., Mitani, K., and Watanabe, A., "Geometry of sand ripples and net sand transport rate due to regular and irregular oscillatory flows," *Coastal Engrg. in Japan*, JSCE, Vol.30, No.2, 1988, pp.89-98.
- Sleath, J.F.A., "Seabed Mechanics," John Wiley & Sons, New York, 1984, xx+335 pp.
- Swart, D.H., "Coastal sediment transport," *Computation of Longshore Transport*, Delft Hydraulics Laboratory Reports, R968, Part 1, 1976.
- Tsuchiya, Y., and Banno, M., "Seabed forms and their formation criteria," *Proc. of 34th Jap. Conf. on Coastal Engrg., JSCE*, 1987, pp.222-226.
- Tsuchiya, Y., Ueda, Y., and Oshimo, T., "A theory of threshold of sediment movement by wave action," *Proc. of the 31st Japanese Conf. on Coastal Engrg., JSCE*, 1984, pp.306-310.
- Yamamoto, T., "Wave induced instability in seabeds," *Proc. of ASCE Specialty Conf., Coastal Sediments '77*, 1977, pp.898-913.

CHAPTER 137

SIMULATION MODELING OF DUNE EROSION

M. F. Overton, Assoc. M. ASCE*

J. S. Fisher, M. ASCE**

Abstract

Using a combination of laboratory, field, and numerical techniques, we have developed a methodology for predicting the extent of dune erosion due to a given set of wave conditions and the beach and dune morphology. A basic assumption in this model is that the volume eroded from the dune is a function of the swash acting on the dune. Because the model is built on this premise, it is necessary to look at the mechanics of two ongoing processes in the storm environment. The first is the relationship between the swash characteristics and the volume of material eroded from the dune face. The second is the relationship between the time history of the swash characteristics at the dune face and the statistics of the storm event, the significant wave height and wave period.

Introduction

The process of dune erosion due to a storm event can be broken into five interacting components. Starting at the ocean side these are -- a statistical description of the storm, the individual wave, wave generated swash on the beach, the force on the dune face due to the swash and the volume eroded from the dune. Wrapped around these parameters is the fact that we are dealing with not a single event (a single wave and swash), but a series of wave and swash events generated during the storm period. However, in order to simplify the first cut description of the model and the process, we begin the discussion with our focus on an individual wave component and work from the dune face seaward.

* Associate Professor, Dept. of Civil Engineering, North Carolina State University, Raleigh, NC.

** Professor, Dept. of Civil Engineering, NCSU.

Methodology

The assumption that the volume eroded from the dune is a function of the swash acting on the dune is based on flume and field experiments. In a series of laboratory experiments, Overton, et al. (1988) showed that the volume eroded from a vertical planar dune during the action of a single swash is a function of the swash force. The swash force is defined as the product of the fluid density, the uprush velocity squared and the height of the uprush at the moment of impact. Applying this concept to the field, a set of experiments were designed to test this hypothesis for prototype scale dunes under natural swash conditions, Fisher, et al. (1987). At the Army Corps of Engineers Field Research Facility (FRF) at Duck, N. C., man-made dunes approximately one meter high and one meter wide were built on the beach and allowed to erode naturally during the rising tide. The experiments were conducted until either the dune was completely eroded (and/or overtopped) or the swash no longer hit the dune. While it is difficult to isolate the impact of a single swash on the amount of the dune eroded, it is apparent from the data that the total dune erosion during an event is linearly correlated with the summation of the swash force for each individual swash, Figure 1. This relationship seems to hold even when events are

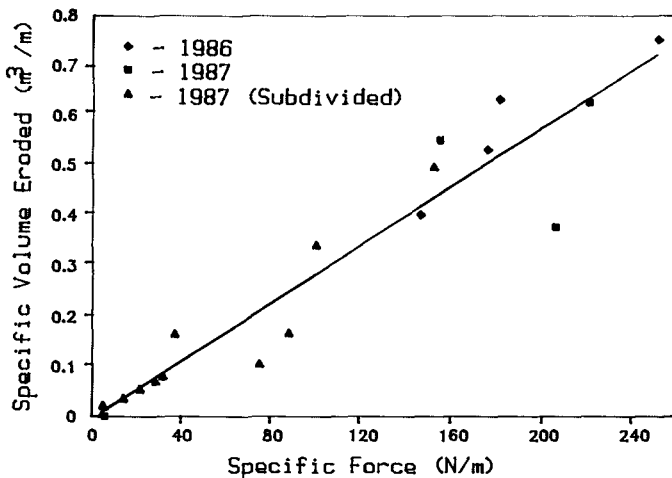


Figure 1. Specific force versus specific volume eroded from field experiments, Duck, N.C.

subdivided into smaller units of time. It is this concept, that a storm event can be represented by a single parameter (the sum of the force in each

individual swash) and thus the amount of dune eroded during that event can be predicted.

Given that we can reasonably predict the volume eroded at the dune face as a function of the swash force, how can we determine the force of any arbitrary swash as it hits the dune? The laboratory experiments investigated a limited range of bore sizes. To increase the flexibility of the model, a numerical model based on the two dimensional hydrodynamics of a bore propagating over a sloping planar beach and impacting with a vertical dune was developed. Variable parameters in the model are depth of the bore at the seaward boundary, distance to the dune from the mean water level and the slope of the beach. This enabled us to determine the velocity and depth of the bore during impact with the dune for a wide range of cases. Using these two parameters, the time history of the swash force on the dune face during impact is given in Figure 2. Note that the force varies rapidly with time, rising quickly

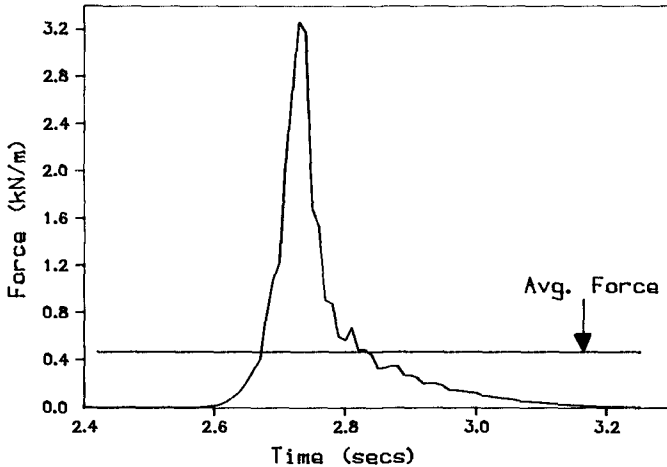


Figure 2. Swash force at the dune versus time - numerical results.

to its maximum and then decaying. In order to be compatible with the laboratory results for the prediction of the volume eroded, the average force during impact is used to represent the effect of a single swash, as discussed in Overton et al. (1987).

In order to reduce computation time in the simulation model, it is desirable to find a direct relationship between the input parameters in the hydrodynamic model and the output parameter, swash

force. Therefore, the relationship between the height of the bore, the distance to the dune, the alope of the beach, and the swash force was investigated. A limited range of parametric studies have been conducted to determine this relationship. First, the height of the bore was varied holding slope of the beach and distance to the dune constant. This relationship is nonlinear, as shown in Figure 3. Repeating this test for the same slope but for a greater distance (7 m compared to 3 m) to the dune yields similar results but with smaller magnitudes. The cut off at the low end of the curve (small bore heights) indicates that bores of this magnitude do not reach the dune with measurable force. Second, the impact of slope was investigated. Bore height versus swash force is plotted in Figure 4. For a

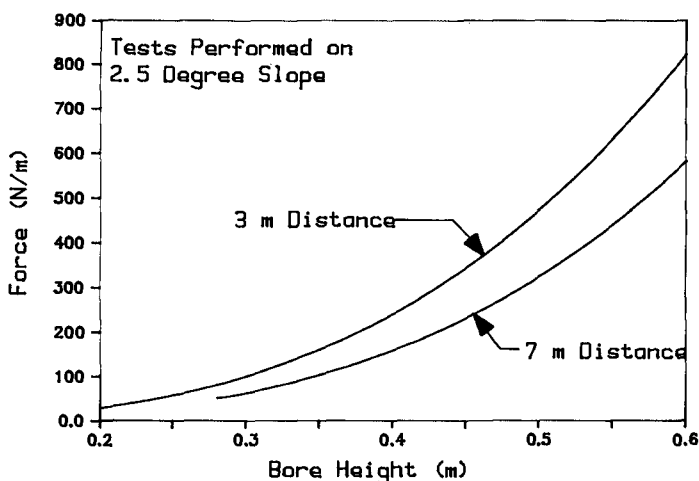


Figure 3. Swash force at the dune versus bore height, two distances - numerical results.

given distance to the dune, the steeper beach reflects more of the swash energy and the force at the dune is less for the same bore height when compared to that on a more shallow slope. Once a full set of these parametric curves has been generated for the range of applicable values, these relationships can be easily incorporated into the simulation model. This avoids having to run the hydrodynamic model each time a bore is generated on the beach.

How then are the bore characteristics (height and distance from the dune) generated from the wave information? Wave transformation from deep water to a point of breaking is well described using any number of

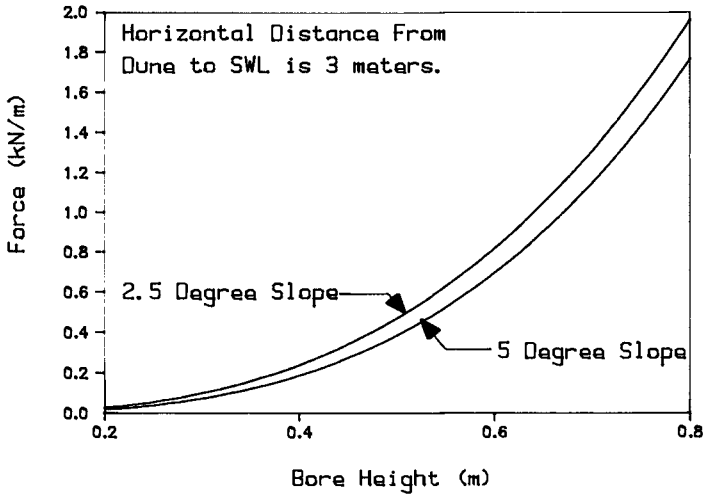


Figure 4. Swash force at the dune versus bore height, two slopes - numerical results.

accepted wave theories. It is the transformation of the breaking wave from a wave of propagation to a wave of translation in the surf zone which is not well understood but which is currently being studied by many investigators. Of particular interest for our application, is a recent set of laboratory experiments conducted by Papanicolaou and Raichlen (1987). Their primary interest was to focus on the breaking and subsequent landward propagation of solitary waves. One piece of information extracted from this set of experiments indicates that after breaking, the wave takes on a borelike form at a certain point on the beach. From this work, it is determined that the wave decays to about one half of its breaking height at the point in which it becomes borelike. The distance traveled from the breaking point is about 20 times the depth at breaking. Similar relationships were also shown to exist in an earlier paper by Svendsen et al., 1978. Therefore, given the height and depth at breaking, the height of the bore and the position along the beach can be determined.

What then are the deep water wave characteristics which represent the given storm event? A storm event can be specified in terms of its significant wave height, period and duration. At this point in the model development, we can no longer ignore the fact that a storm consists of a number of wave events which interact and alter the characteristics of a single swash. Going back through the model, how then do we account for the fact that there is a series of interacting wave components which characterize the storm environment and

not a set of isolated waves propagating without interference to impact with the dune.

Starting with the specification of the storm, we see that it is necessary to take the statistical representation of the storm and break this down into a representative set of individual waves, that is, a record of wave height versus time. Theoretically we can take each individual wave up to breaking, through the swash zone, up the beach as a bore and calculate the force of impact at the dune. However, because of swash-swash interactions in the surf zone, we know that each offshore wave does not generate a bore that propagates up the beach to impact with the dune. These interactions may be a function of the distance from mean water level to the dune, the dominant period and the distribution of wave periods in the offshore wave field, and the steepness of the beach as well as, perhaps, other factors. At this point this interaction, or the prediction of the swash period at the dune as a function of the offshore parameters and geometry, is not well understood. In order to better understand this phenomena for application to this model, we analyzed the 1986 and 1987 Duck data with respect to swash period. Data from eight individual field experiments were available for analysis. The offshore period, which was obtained from the offshore data which the FRF routinely collects, for these experiments ranged from about 6 seconds to 14 seconds. Defining the swash period as the

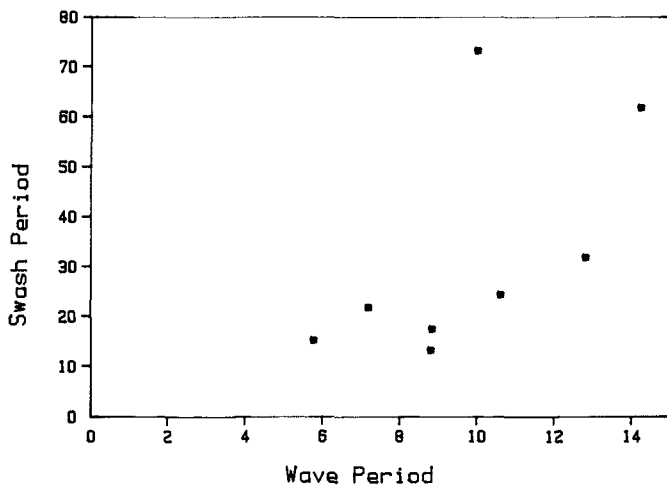


Figure 5. Offshore wave period versus swash period for field experiments at Duck, N.C.

duration of the experiment divided by the number of swash hits on the dune face during this period, the wave period can be plotted against the swash period for these eight experiments, Figure 5. There is no definitive correlation between these two periods as evidenced by the wide range of swash periods for a given wave period. A 10 second significant wave period produced awash periods from 10 to 70 seconds during different experiments. Attempting to determine whether distance from the dune was a dominating factor, the swash period versus horizontal distance from the dune is plotted in Figure 6. The different symbols correlate to different experiments. Four experiments were subdivided into smaller time increments and plotted as swash period versus distance for that subinterval. Distance from the dune changes during the experiment as the tide rises yielding a corresponding change in swash period. However, the offshore wave period is assumed to be constant for the entire experiment. Again, there is no definitive correlation between parameters, however, the trend of the data is intuitively correct. The awash period increases for greater distances to the dune and for the same offshore period.

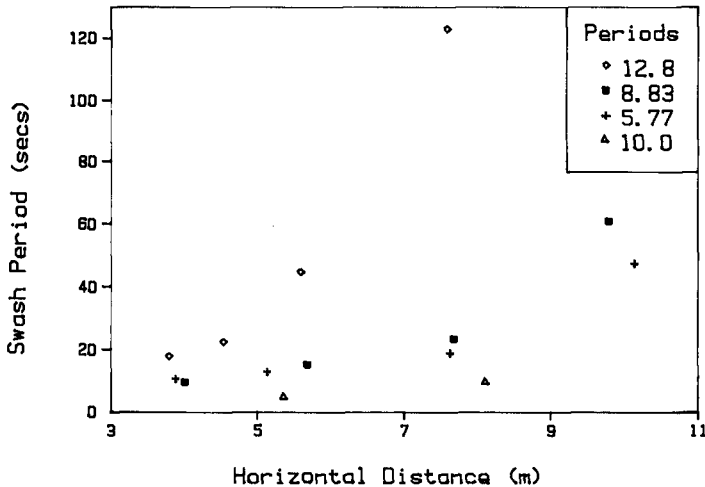


Figure 6. Swash period versus horizontal distance from the dune for four different offshore periods.

The question remains as to how to put the model together for multiple awashes. Starting at the ocean side, we will discuss how each component has been treated in this current version of the model.

Model Development

The assumed input information to the simulation model at the ocean boundary is the significant wave height, the wave period and the duration of the storm event. Using a Rayleigh distribution for the wave heights, we can generate a set of wave heights corresponding to a given significant wave height. The drawback to this approach is that it does not generate a wave time series for which a wave period for each individual wave can be determined. An alternative approach to adjust for this problem is to first use the significant wave height and period and an assumed spectral shape to form a wave spectra. The wave spectra can be represented by the summation of N number of individual wave components specified by a wave height and a wave period. While this technique may not produce a truly random data set, it does identify an individual wave height with a wave period. However, at this point in the model development, we have not tried this alternative approach.

Given a Rayleigh distribution of wave heights, each wave is propagated from deep water to the point of breaking using linear wave theory. The dominant wave period is used as the period of each individual wave. This yields a depth and height at breaking. From that the height of the bore and the position of the bore on the beach is determined from Papanicolaou et al. (1987). The hydrodynamic characteristics at the dune are determined from the results from the 2-D numerical model. At this point a swash force and the subsequent volume eroded for that individual wave is computed.

How are the second and subsequent waves treated? The timing of the generation of the bores and the correlating swash period are critical.

It is assumed that each deep water wave propagates without interference to breaking. From that point a bore is generated which propagates up the beach. In the development of the current methodology for dealing with the swash period, we tried two approaches and selected the one which produced the best results. Each approach is discussed below.

The first approach uses field results to calibrate the model in the following manner. One, a wave height fitting a Rayleigh distribution is generated from a random number generator and the specified significant wave height. Two, using results from the hydrodynamic model, check whether the bore hits the dune. If not, generate a new wave height and test again. If so, calculate swash force and advance in time an increment equal to the given swash period. For this approach, the swash period for the storm event must be known.

The second approach is let the algorithm determine the swash period. For example, for any given bore depth generated the swash may or may not reach the dune given a particular beach slope and the distance from the dune. Therefore, one alternative is to simply generate the set of bore depths and let the numerical model determine whether the bore reaches the dune. If not, advance in time a time step equal to the wave period without adding to the summation of the swash force term. If so, calculate the swash force, add to the summation series and advance in time. Obviously, using this approach there is no guarantee that the swash period of the model equals that of the field results.

Results

Four simulation tests were conducted using the 1987 Duck field data. Field data used as input in the simulation model were the offshore significant wave height and wave period, the slope of the beach, the distance from the dune to the mean water level, the change in mean water level due to the rising tide, the duration of the erosion event, and the swash period. Data from three experiments were used. Two experiments were simulated in their entirety while the third was divided into two sub-time periods and simulated as different events. Each set of test data was processed using both methods for dealing with the swash period. The results, erosion predicted versus erosion measured, are shown in Figure 7 using method one, in which swash

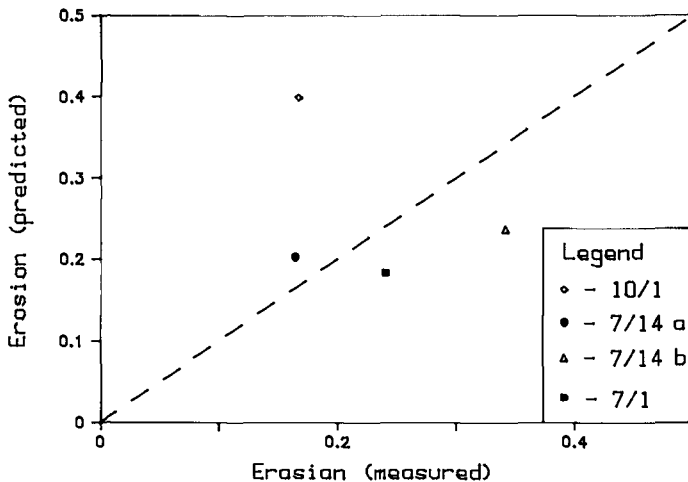


Figure 7. Predicted versus measured erosion.

period is taken as a known. As shown, three of the points are predicted fairly well, though with a tendency

to underestimate the erosion, while one point is over predicted by a factor of two. When comparing these results to those using method two, in which the swash period is determined by the algorithm, there is very good correlation between the predicted and measured for two of the points, 7/14a and 10/1. These are also the experiments which are best predicted in method one. Examining the output of this approach it is seen that the wash period as determined by the simulation algorithm closely approximates the measured swash from the field data. While it is not clear at this point why this correlation is occurring, it does point out that swash period is a significant factor in the simulation model.

Conclusions

The two key components to the simulation model are one, the relationship between the swash characteristics and the volume of dune eroded and two, the relationship between the statistics of the storm event and the time history of the swash characteristics at the dune face. While the simulation model presented herein has met with limited success and therefore has potential as a predictive tool for dune erosion, several components of the model must be refined. The most obvious of these is the swash period. While we have built a basis for predicting the magnitude of the swash force, we know little about the relationship between the timing of offshore waves and the timing of those waves which impact with the dune. Advances in the understanding of this phenomena will lead to an improved simulation model.

References

- Fisher, J. S., M. F. Overton and T. Chiaholm, "Field Measurements of Dune Erosion", 20th Coastal Engineering Conference, Taipei, Taiwan, November, 1986, pp. 1107-1115.
- Overton, M. F., J. S. Fisher and T. Fenaish, "Numerical Analysis of Swash Forces on Dunes", ASCE Coastal Sediments '87, New Orleans, Louisiana, May, 1987, pp. 632-641.
- Overton, M. F., J. S. Fisher and M. A. Young, "Laboratory Investigation of Dune Erosion", ASCE Journal of Waterway, Port, Coastal and Ocean Engineering, May, 1988, pp. 367-373.
- Papanicolaou, P. and F. Raichlen, "Wave Characteristics in the Surf Zone", ASCE, Conference on Coastal Hydrodynamics, Newark, Delaware, June 1987, pp. 765-780.

Svendsen, I. A., P. A. Madsen and J. B. Hansen, "Wave Characteristics in the Surf Zone", ASCE, 16th Coastal Engineering Conference, Germany, August, 1978, pp. 520-539.

CHAPTER 138

The Criterion of Ripple Formation by Wave Action

Yoshito Tsuchiya * and Masato Banno **

Abstract

In this paper, we emphasize that there must exist a common mechanism governing ripple formation in the case of both waves where the acceleration effect exists, and unidirectional flow, where the acceleration effect is usually ignored. Using a light sediment with an immersed specific gravity of about 0.8, which is nearly one-half that of natural sand, a series of ripple formation experiments were performed in order to determine the formation criterion. Using the experimental data, along with data collected by other researchers the ripple-formation criterion was investigated in terms of the ratio of water particle orbital diameter to sediment grain diameter as an acceleration parameter, on the so-called Shields diagram. Emphasis is placed on the importance of this ratio in the criterion of ripple formation in relation to that by unidirectional flow.

1. INTRODUCTION

Sand transport due to wave action or by combined wave & current action is one of the transport phenomena which takes place as prescribed by the laws governing sediment and fluid interaction. Many investigations on such a phenomenon have been actively carried out. One of the most salient futures pertaining to sediment transport by waves and by flowing water is the threshold of sediment movement. All the experimental data for the threshold of sediment movement can be plotted on a Shields diagram, but there exists an acceleration effect in wave motion. In relation to sediment transport, the relevant phenomena by waves and by flowing water must be identified and qualified in the mechanics of sediment transport.

The seabed sediment ripple is of great interest not only in understanding the formation phenomena, but also in establishing the mechanics of sediment transport by wave action. Many physical model experiments of beach change have been performed, but none have introduced seabed forms in their comparisons between model and prototype phenomena, as well as in their similitude. Physical model experiments should be carried by placing major emphasis on bed form similitude, which in turn results in a similitude of the governing physical phenomenon.

* Professor, Disaster Prevention Research Institute, Kyoto University, Uji, Kyoto 611. JAPAN.

** Civil Engineer, Division of Civil Engineering Design, Penta Oceans Construction Ltd., Tokyo 112. JAPAN.

When no bed form considerations are made severe scale effects may result in the comparison between model and prototype. It is therefore noted that, in physical model experiments seabed forms and their formation criteria are required in order to determine what seabed forms occur in the prototype.

Thus far, many attempts have been made to classify seabed forms, by Bagnold(1946), Manohar(1955), Komar & Miller(1975), Kaneko(1980) and Horikawa & Shibayama(1982), in terms of Shields number and other parameters such as sediment Reynolds number and the ratio of water particle orbital diameter to sediment grain diameter. As previously mentioned, the classification of bed forms by waves should be made in relation to that by unidirectional flow. It is however further mentioned that a common formation mechanism must exist between the sea and river beds, even though additional parameters may exist which specify a specific phenomenon. In 1975 Komar and Miller examined the seabed forms and their formation criteria in relation to those by unidirectional flow. In the criterion, experimental data of the sea bed forms were plotted on a Shields diagram where the sediment Reynolds number is defined using maximum water particle velocity. An empirical formula of the criterion from ripple to sheet flow condition was then proposed, however, no considerations were made on the acceleration effect due to wave motion on the criterion of ripple formation. Kaneko proposed a criterion of seabed forms in terms of the sediment mobility parameter and the ratio of boundary layer thickness to sediment grain diameter. In the criterion, seabed forms are classified into five such as no ripple, two-dimensional ripple, brick pattern, irregular ripple and sheet flow. Sunamura introduced the asymmetry of wave motion into the criterion of seabed forms and proposed a dimensionless sediment-wave parameter which was given from the threshold condition by Komar and Miller. Horikawa and Shibayama, on the other hand, proposed a criterion of sediment transport types using the Shields number and the ratio of sediment fall velocity to maximum water particle velocity, but not shear velocity. This criterion is not for seabed classification and its formation criterion, but the dimensionless parameters used are worthy of being considered in relation to the parameters employed by the other researchers.

In this paper, using a light sediment with an immersed specific gravity of about 0.8 which is nearly one-half that of natural sand, a series of ripple formation experiments were carried out in order to determine the formation criterion in the case of small sediment Reynolds number. Using the experimental data, along with data collected by other researchers the ripple formation criterion is investigated based on the ratio of water particle orbital diameter to sediment grain diameter on the so-called Shields diagram. This ratio expresses the effect of wave acceleration on sediment transport. Emphasis is placed on the importance of the ratio in the criteria of ripple formation in relation to that by unidirectional flow.

2. SAND TRANSPORT TYPES AND BED FORMS

In general, there are usually two states of sand transport which are only for convenience in their investigation. Recently, Shibayama and Horikawa(1982) proposed a classification of sand transport types in relation to the ripple formation. Four states are used to classify sediment transport, they are bed load, transition from bed load to suspended load, suspended load and sheet flow. Their classification is shown in Figure 1 where τ^* is the Shields number and u_0/w_0 the ratio of maximum water particle

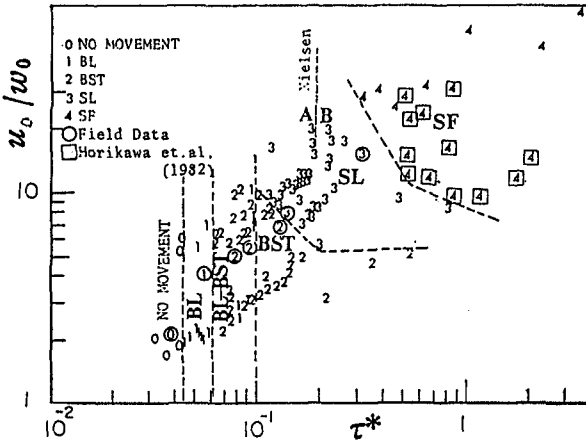


Figure 1. Classification of sand transport types by Shibayama & Horikawa

velocity at the sea bottom to fall velocity of the sand. These transport states are identified according to the resulting bed forms. In the case of no movement, sand does not apparently move by the wave action, but at the threshold condition a critical state is reached such that sediment movement is initiated. The transport state identified as flat bed describes a condition where sediment movement and transport exist yet the bed remains flat. In the state, sand moves mainly as bed load. At a certain state when the shearing stress acting on the sand bed becomes large, ripples appear. In this state, sand moves in suspension around the ripples, and this corresponds to suspended load in the classification of sand transport types by Shibayama and Horikawa. As the shearing stress becomes larger, a flat bed again results, and it is usually identified as sheet flow, first named by Bagnold(1946). The flat bed states occurring under conditions just after the movement threshold is reached and after ripple formation correspond to the lower and upper regimes of flow in the case of river bed mechanics.

3. THE CRITERIA FOR SEABED FORMS

The most important factors governing seabed formation are first considered by referring to both the previous investigations of seabed forms, their formation criteria and the threshold of sand movement. Secondly, using the main factors selected the criteria of seabed forms are proposed.

3.1 Classifications of Seabed Forms and Their Main Factors

As already mentioned, Komar & Miller(1975) classified seabed forms into three groups, no movement, ripple and sheet flow as shown in Figure 2 where u_0D/ν is the sand grain Reynolds number relative to the maximum water particle velocity at the bottom, not to the shear velocity. The sand transnsport phenomenon is well governed by the shearing stresses acting on the seabed, it is questionable as to why the sand grain Reynolds number u_0D/ν is used instead of u^*D/ν where u^* is the shear velocity.

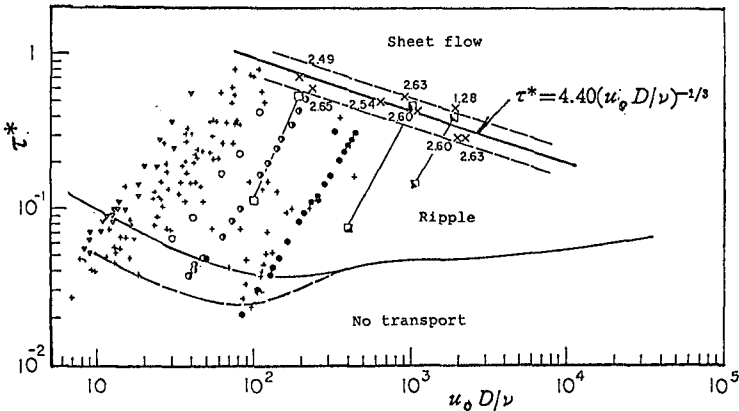


Figure 2. Classification of ripple formation by Komar & Miller(1975)

In Figure 2, it is clearly shown that the criterion for separation between no-movement and ripple is not well established, however, in the upper regime where sheet flow initiates, the criterion operates well, and results in an empirical formula in the form

$$\tau^* = 4.40(u_0D/\nu)^{-1/3} \tag{1}$$

In addition to the ripple to sheet flow classification scheme employed by Komar & Miller, Manohar(1955) considered the sand grain size effect in addition to the Shields number. Carsterns, Neilson & Altinbilek(1969) introduced the ratio of the water particle orbital diameter to the sand grain diameter into the criterion, however no graphical presentation was presented. In 1976, Dingler and Inman proposed an empirical criterion in the form

$$u_b^2/(\sigma/\rho-1)gD = 240 \quad (2)$$

In 1979, Nielsen proposed an empirical criterion in the form

$$\tau^* = 0.83 \quad (3)$$

And more recently Shibayama and Horikawa(1982) proposed the critical Shields number as 0.5 to 0.6., and 0.4 in the experiment by Shibayama(1984). The criteria proposed by Nielsen and Shibayama & Horikawa are independent of the sand grain Reynolds number. It is generally difficult to qualify the resistance law in the sheet flow. As stated by Komar and Miller(1975), the constitutive equation for two-phase flow by Bagnold(1956) is given by

$$\tau^* = C \tan \phi \quad (4)$$

where C is the static volume concentration being about 0.6 to 0.7 for natural sands and $\tan \phi$ is the coefficient of solid friction which varied from 0.375 to 0.75 in Bagnold's experiment. The critical Shields number therefore varies from 0.23 to 0.53. These values of the critical Shields number are close to those previously mentioned by Nielsen and Shibayama & Horikawa.

More recently, Kaneko(1980) classified seabed forms using two parameters, the sediment mobility parameter and the ratio of the sand grain diameter to the boundary layer thickness in Figure 3.

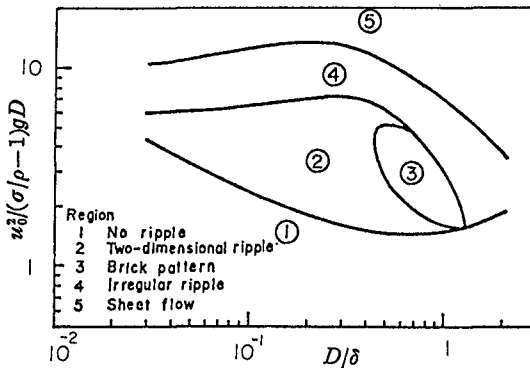


Figure 3. Classification of seabed forms by Kaneko(1980)

In this figure, the ratio is rewritten as

$$D/\delta = \sqrt{\pi D^2/\nu T} \quad (5)$$

where T is the wave period and ν the kinematic viscosity of water. The ratio, which is in the form of a Reynolds number, considers the effect of boundary shearing stress acting on

the seabed. He classified seabed forms into the following five stages, 1) no ripple, 2) two-dimensional ripple, 3) brick pattern, 4) irregular ripple and 5) sheet flow. The classification shows that a brick pattern forms under limited conditions defined by the two parameters, furthermore, the region over which the brick pattern forms is small relative to the regions occupied by the other four bed form classifications. In this classification, however, no consideration is made of the threshold of sand movement and the flat bed in the lower regime.

Furthermore, Sunamura(1981) introduced the asymmetry effect of the wave field on the bed forms using the Ursell parameter $U_r = HL^2/h^3$, where H is the wave height, L the wave length and h the water depth and a new parameter F , where

$$F = \frac{u_0^2}{(\sigma/\rho - 1)gD^{1/2}d_0^{3/2}} \quad (6)$$

where d_0 is the water particle orbital diameter. This parameter was introduced by Komar and Miller(1975) as a relation describing the threshold of sand movement. His classification is expressed as an empirical formula in the form

$$F = KU_r^{1/4} \quad (7)$$

where the coefficient K specifies seabed forms in the following five stages: 1) no movement, 2) flat bed, 3) ripple bed, 4) flattened-ripple bed and 5) sheet flow. The asymmetry of the wave field was shown to influence seabed formation, however, this effect will not be considered any further.

From the above considerations of seabed forms and their formation criteria, the expressions for the criteria from flat bed to ripple bed and ripple bed to sheet flow are not so clear, however, the dimensionless parameters for specifying the formation criteria are useful. River bed forms and their formation criteria are considered, and in this criteria the ratio of water depth to sand grain diameter is assumed to be very large, while ignored in the criterion for seabed forms. In the theory of the threshold of sand movement by Tsuchiya, Ueda and Oshimo(1984), as shown in Figure 4, the theoretical curves of the sand movement threshold are expressed by three parameters, the Shields number, sand grain Reynolds number or sediment-fluid number and the ratio of water particle orbital diameter to sand grain diameter. And in this paper, specified are four stages; they are no sand movement, flat bed, ripple and sheet flow, flat bed in the upper regime. Based on these considerations, the formation criterion of seabed can be expressed by

$$F_1(\tau^*, u^*D/\nu \text{ or } D_v^*, d_0/D) = 0 \quad (8)$$

where the ratio does not remarkably influence the threshold

of sand movement as shown in Figure 4, but as already mentioned by Tsuchiya (1987), the ratio effect is remarkable in the geometry of ripples when the ratio becomes greater than about 1000. Therefore an influence of the ratio on the criteria from flat bed to ripple and ripple bed to sheet

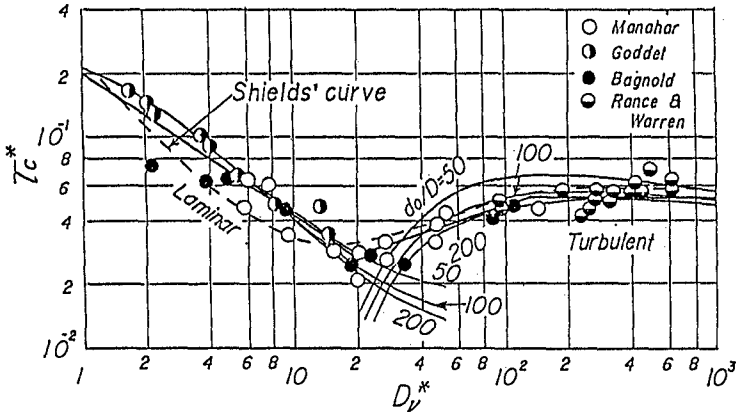


Figure 4. Criterion for the threshold of sand movement

flow may be expected to exist. It is well-known that the ratio expresses the acceleration effect in the wave motion. Physically, the seabed formation when the ratio becomes infinity may corresponds to that by unidirectional flow having an infinite value of the ratio of water depth to sand grain diameter. From this fact the flat beds in the lower and upper regimes may be defined as lower-flat bed and upper-flat bed, respectively.

The upper-flat bed corresponds to the so-called sheet flow. In these regimes, however, the essential difference between sea and river bed formation is the free surface effect which is described by the Froude number, and exists only in the river bed formation.

Additionally, dimensional analysis is used to describe the seabed forms and their formation criteria by Yalin(1964), Mogridge & Kamphuis(1973), Dingler & Inman(1976), and more recently Kaneko 1980) in the form

$$F_2\{u_0^2/(\sigma/\rho-1)gD, D^2/\nu T, d_0/D\} = 0 \tag{9}$$

Using expression (9) Kaneko derived Figure 3. Both expressions (8) and (9) are physically related to the shear velocity.

3.2 Experimental Data and Their Arrangement

Using a double-deck wave tank 38m long, 0.7m wide and 0.7m deep and a light sediment with an immersed specific gravity of about 0.8 and a diameter of 0.085cm, several experiments were carried out to determine seabed forms and

their formation criteria in the region of small sediment Reynolds number. Experimental data from this and other experiments are shown in Table 1 for the immersed specific gravities and diameters of the sediment used.

Table 1. The experimental data used

Researchers (Year published)	Immersed specific gravity ($\sigma/\rho-1$)	Grain diameter D in cm
Manohar(1955)	1.60	0.101
	1.65	0.028
Lofquist(1968)	1.65	0.055
	1.65	0.021
		0.018
		0.030
Carstens, Neilson & Altinbilek(1969)	1.62	0.059
	1.66	0.019
	1.65	0.020
Horikawa & Watanabe (1967)		
Sunamura(1981)	1.65	0.020
	1.65	0.070
	1.65	0.156
Tsuchiya & Banno (1988)	0.80	0.085

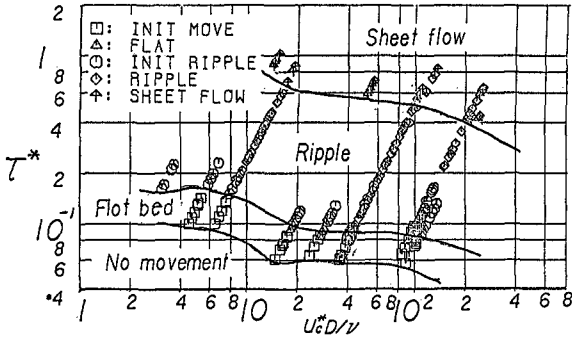
In the expression of the formation criterion by (8), the shear velocity, which results from the interaction between waves and sediment, should be carefully estimated. In this paper, formulas for the friction factor by Jonsson(1966) and Madsen & Grant(1980) were used. Practically, the friction factor can be expressed by Nielsen(1981) as

$$f_w = \exp \{5.12(5D/d_0)^{0.194} - 5.98\} \quad (10)$$

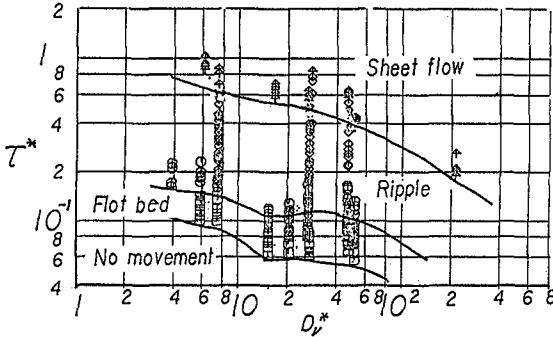
Using the experimental conditions of waves and the sediment properties shown in Table 1, the friction factor was calculated by (10) and Madsen & Grant' formula and then the shear velocity was obtained in relation to the maximum water particle velocity at the sea bed. Finally, all the dimensionless parameters in (8) were calculated.

Figure 5 shows an example of the changing stages of bed forms in relation to the Shields number and sediment grain Reynolds number or sediment-fluid number. In the figures, based on the bed forms specified by the researchers bed forms are shown with symbols which are initial movement, flat, initiation of ripple, ripple and sheet flow. All the experimental data were arranged in the sediment conditions as shown in the figure. From these figures, criteria for the four stages in seabed forms can be obtained. The criterion from no-movement to flat-bed in the lower regime is greatly due to the findings of observers, and as stated by Sleath (1984), the experimental data are very scattered.

However, the experimental data for the other criteria are not so scattered because observational findings of the criteria are generally obvious.



(a) In the case of sediment grain Reynolds number



(b) In the case of sediment-fluid number

Figure 5. Determination of the criteria from experimental data (1)

3.3 The Formation Criterion of Seabed Forms (1)

The formation criterion for seabed forms by (8) is shown in Figure 6 where only the Shields curve is shown for the threshold of sand movement. In the figure, the criteria from lower-flat bed to ripple bed and ripple bed to upper-flat bed, sheet flow are shown with the ratio of water particle orbital diameter to sand grain diameter. Using (10) Komar & Miller' empirical formula (1) can be transformed to

$$\tau^* = 3.22 f_w^{1/7} D_v^{*-3/7} \tag{11}$$

where in the estimation of the friction factor the value of d_0/D in (10) was evaluated as 3,400 by Carstens, Neilson & Altinbilek(1969) and 16,000 by Kennedy & Falcon(1965) for the criterion from ripple to sheet flow.

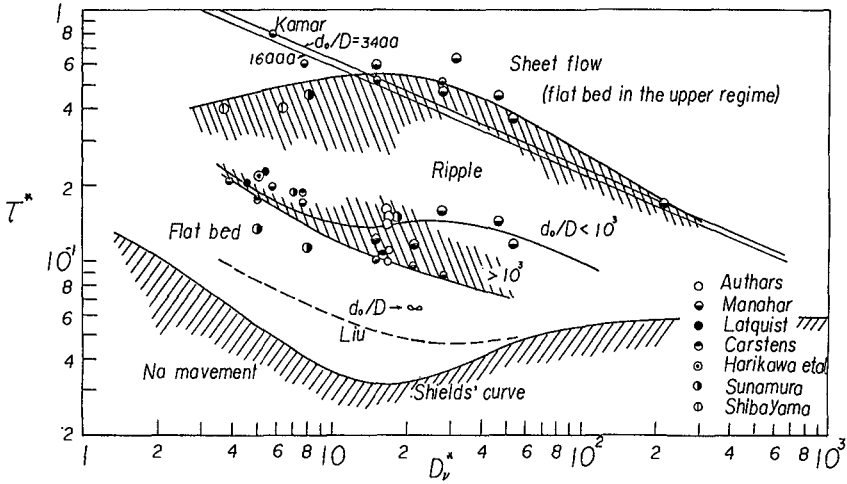


Figure 6. The formation criterion of seabed forms by (8)

In the formation criteria shown in Figure 6, no experimental data for the threshold of sand movement are shown due to the high degree of scatter. In Figure 1, the general trend of the experimental data are shown to be similar to the curves by Tsuchiya & Banno. It is noted that the criteria from lower-flat bed to ripple and from ripple to upper-flat bed can be described by the Shields number, the sediment grain Reynolds number or sediment-fluid number and the ratio of water particle orbital diameter. The experimental data is not enough to definitely specify the criteria, so that further experiments are needed especially for the regions where the sediment-fluid number are very small or greater than about 100, and for the case when light sediment is used in the wide range of d_0/D . However, it is noted from the figure that in the criterion from lower-flat bed to ripple the effect of the ratio of water particle orbital diameter to sand grain diameter clearly exists, that is, the values of the critical Shields number in the case of d_0/D values larger than 1,000 are plotted lower than those in the case of values smaller than 1,000. This tendency increases with the increase in the sediment-fluid number. And, the criterion changes with the sediment-fluid number. In the figure Liu's curve for the criterion from lower-flat bed to ripple by unidirectional flow is also shown. In this case, the value of d_0/D may be considered as infinity in relation to the criterion of ripple formation by waves. These tendencies show that the critical Shields number for larger sediment is smaller than that smaller sediment, that is, ripples formed in coarse sediment are generated by a smaller Shields number than that in fine sediment. Comparing Liu's curve for unidirectional flow with the curves for the criterion from lower-flat bed to ripple, the curve for the d_0/D values larger than 1,000 which are not so comparable to infinity may tend to approach Liu's

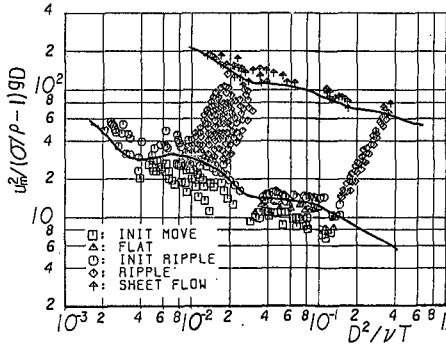
curve. The range of lower-flat bed becomes narrow with the increase of sediment-fluid number and may then vanish when the value becomes about 100, this tendency may be further supported by Liu's curve. In the region of smaller sediment-fluid number, the effect of the ratio d_0/D is not obvious and may disappear.

In the criterion from ripple to upper-flat bed, Komar & Miller's empirical formula (11) is shown in Figure 6. The average value of the critical Shields number may be very close to the values used by Shibayama & Horikawa (1982), but the Shields number changes with the sediment-fluid number. The curve shown in the figure by a solid line is very similar to Komar & Miller's, except for the region of small sediment-fluid number. In this criterion, the effect of the ratio of water particle orbital diameter to sand grain diameter disappears in the whole range of sediment-fluid number. The formation of sheet flow in the upper flat-bed is of course caused by high shear flow both in sediment transport by waves and unidirectional flow, however, it is recognized that in the upper-flat bed no interaction between the free surface and seabed forms by wave action exists, but pronounced interaction between the free water surface and river bed forms exists where the ratio of water depth to sediment grain diameter is most predominant. Therefore, the formation criterion of sheet flow by wave action can not be directly compared with that by unidirectional free surface flow.

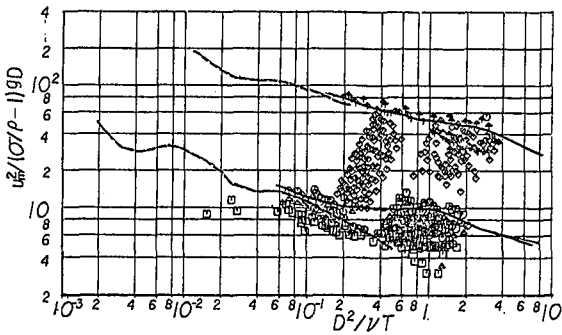
3.4 The Formation Criterion of Seabed Forms (2)

By use of (9) the formation criterion of seabed forms is considered. As already described, Kaneko (1980) proposed the criteria of seabed forms classifying them into his own five stages, as shown in Figure 3. Using the experimental data shown in Table 1 with the same dimensionless parameters as those by Kaneko, but classifying only four stages of seabed forms as used in the previous criterion, the formation criterion was examined.

Using Manohar's data shown in Table 1, all the dimensionless parameters in (9) were calculated and the results are shown in Figure 7 where (a) and (b) represent values of d_0/D smaller than 1,000 and larger than 1,000, respectively. It is obvious that the formation criterion of seabed forms can be made, but the effect of the ratio of water particle orbital diameter to sediment grain diameter is not so remarkable. In the region of large Reynolds number $D^2/\nu T$ in (a) and around the transition from lower-flat bed to ripple, larger values of d_0/D may result in larger values of the sediment mobility parameter. In the criterion from ripple to sheet flow, however, the influence of the ratio is hardly found. This may be supported by the result obtained by Figure 6.



(a) In the case where $d_0/D < 1,000$



(b) In the case where $d_0/D > 1,000$

Figure 7. Determination of the criteria from experimental data (2)

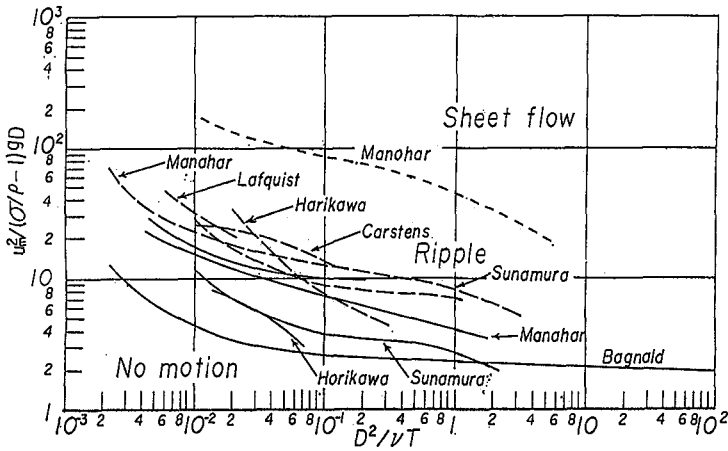


Figure 8. The formation criterion of seabed forms by (9)

In the figure, neglecting the effect of the ratio of water particle orbital diameter to sand grain diameter, the criteria are obtained separately by researchers in terms of the sediment mobility parameter $u_0^2/(\sigma/\rho-1)gD$ and the sediment Reynolds number $D^2/\nu T$. Figure 8 shows the criteria from no movement to flat bed, flat bed to ripple and ripple to upper-flat bed, respectively. On the threshold of sand movement, as already pointed out by Komar and Miller(1975), an effect of the ratio exists. And, by this expression the criteria from flat bed to ripple have a similar tendency in relation to the sediment Reynolds number, however, there is a large variation due to experimental conditions. This variation may be mainly due to the expression of the formation criteria, as well as experimental conditions.

It is recognized from this fact that the previous expression of the formation criterion of seabed forms is better than the latter one taking into account the mutual relation in the formation processes of bed forms by waves and unidirectional flows.

4. CONCLUSIONS

In the criterion of seabed forms, many investigations have been carried out in terms of the so-called Shields diagram and other dimensionless expressions derived by dimensional analysis. In this paper, using a light sediment some experiments were conducted, and using the experimental data, along with data collected by other researchers, the ripple formation criterion was studied as the formation criterion of seabed forms in relation to that by unidirectional flows. Further experiments are needed, but from the formation criteria of seabed forms the main conclusions are:

1) As shown in Figure 6, the formation criterion of seabed forms can be made on the Shields diagram by introducing the ratio of water particle orbital diameter to sand grain diameter which acts as an acceleration effect in the wave motion. When the ratio becomes infinity the critical Shields number for the criterion tends to the unidirectional one.

2) The criterion of sheet flow, upper-flat bed can be expressed both by the Shields number and sediment-fluid number. In this criterion, the ratio has little influence on the formation criterion.

Acknowledgement

We appreciate the help of Mr. James R. Tallent in the preparation of this manuscript. Part of this investigation was founded by a Grant-in-Aid for Scientific Research (No. 62420040) from the Ministry of Education, Science & Culture of Japan.

References

Bagnold, R.A. (1946): Motion of waves in shallow water,

- interaction between waves and sand bottoms, Proc. Roy. Soc. London, Series A, Vol. 187, pp. 1-15. Tech. Memo. No. 28, 16pp.
- Grant, W.D. & O.S. Madsen (1982): Movable bed roughness in unsteady oscillatory flow, Jour. Geophys. Res., Vol. 87, No. C1, pp. 469-481.
- Horikawa, K. & A. Watanabe (1967): A study on sand movement due to wave action, Coastal Engg. in Japan, Vol. 10, pp. 39-57.
- Inman, D.L. (1957): Wave-generated ripples in nearshore sands, CERC, US Army Corps of Enggr., Tech. Memo., No. 100, 14pp.
- Jonsson, I.G. (1966): Wave boundary layer and friction factor, Proc. 10th ICCE, ASCE, pp. 127-148.
- Kaneko, A. (1980): Wave length of ripples formed in oscillatory flow, Proc. 27th Japanese Conf. Coastal Engg., JSCE, pp. 207-210 (in Japanese).
- Kennedy, J.F. & M. Falcon (1965): Wave generated sediment ripples, MIT Hydrodynamics Lab., Rept. No. 86, 86pp.
- Komar, P.D. & M.C. Miller (1973): The threshold of sediment movement under oscillatory water waves, Jour. Sed. Pet., Vol. 43, No. 4, pp. 1101-1110.
- Komar, P.D. & M.C. Miller (1975): The initiation of oscillatory ripple marks and the development of plane-bed at high shear stresses under waves, Jour. Sed. Pet., Vol. 45, No. 3, pp. 697-703.
- Liu, H.K. (1957): Mechanics of sediment ripple formation, Proc. ASCE, Vol. 83, No. HY2, pp. 1-23.
- Lofquist, K.E.B. (1978): Sand ripple growth in an oscillatory flow water tunnel. CERC, US Army Corps of Enggr., TP78-5.
- Manohar, M. (1965): Mechanics of bottom sediment movement due to waves action, CERC, US Army Corps of Enggr., Techn. Memo. No. 75, 121pp.
- Mogridge, G.R. & J.W. Kamphuis (1973): Experiments on bed form generated by wave action, Proc. 13th ICCE, ASCE, pp. 1123-1142.
- Nielsen, P. (1981): Dynamics and geometry of wave-generated ripples, Jour. Geophys. Res., Vol. 86, No. C7, pp. 6467-6472.
- Sleath, J.F.A. (1978): Measurement of load in oscillatory flow, Jour. ASCE, No. WW4, pp. 291-307.
- Sunamura, T. (1981): Bedforms generated in a laboratory wave tank, Sci. Rept. Inst. Geoscience, Univ. Tsukuba, Sect. A, Vol. 2, pp. 31-43.
- Swart, D.H. (1976): Predictive equations regarding coastal transport, Proc. 15th ICCE, ASCE, pp. 1131-1139.
- Tschiya, Y., Y. Ueda & T. Oshimo (1984): A theory of the threshold of sediment movement by wave action, Proc. 31st Japanese Conf. Coastal Engg., JSCE, pp. 272-276 (in Japanese).
- Yalin, M.S. & R.C.H. Russell (1962): Similarity in sediment transport due to waves, Proc. 8th ICCE, ASCE, pp. 151-167.

CHAPTER 139

Extreme Erosion Event on an Artificial Beach

J P Möller* and D H Swart**

Abstract

At Oranjemund just north of the mouth of the Orange on the South-West African/ Namibian coastline the Consolidated Diamond Mines (Pty) Limited (CDM) is mining for diamonds in the inshore area. They use an artificially-built seawall of sand to keep the sea out of the paddocks which are being stripped and mined at bedrock level, which is well below sea level. The seawall runs parallel to the original shoreline at a distance of up to 350 m offshore. The beach profile is correspondingly very steep and under most conditions offshore sediment losses occur, which are compensated for by artificial nourishment. During February 1987 offshore losses of about 120 m³ per running metre of seawall were recorded from above the waterline. In this paper a data set is presented to serve as a basis for the calibration of on-offshore sediment models and some simulations are reported on.

1. Background

Diamonds have been mined on the west coast of South-West Africa/Namibia for more than 50 years (see Figure 1). As mining techniques have improved more and more diamonds have been taken out of what used to be the surf-zone area. CDM has perfected the technique of inshore mining by using seawalls or bunds constructed of sand (Figure 2). Details of the coastal engineering aspects of the mining technique have been given by Möller *et al* (1986). In essence the construction of a seawall of sand in the nearshore zone and its maintenance against wave attack amounts to a large-scale sand suppletion or beach management project. Figure 3 shows how a typical nearshore beach profile which has a nearly horizontal platform up to 400 m wide at 6 m below MSL has been modified by the construction of the seawall to a beachface with a nearly uniform slope of 1 in 25. At the top of this very steep beach profile sits the seawall proper with its foot at about 4 m above MSL and its crest - at about 10 m above MSL. The crest width of the wall

*Coastal Processes and Management Advice, EMA, CSIR, Box 320, Stellenbosch, Republic of South Africa.

**Programme Manager, Coastal Processes and Management Advice, EMA, CSIR, Box 320, Stellenbosch, Republic of South Africa.



FIG. 1 LOCALITY MAP



FIG. 2 AERIAL VIEW OF MINING AREA BEHIND SEAWALL

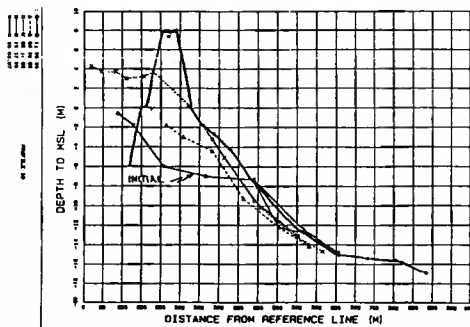


FIG. 3 BEACH AND NEARSHORE PROFILE DEVELOPMENT DUE TO SEAWALL CONSTRUCTION

varies between 17 and 25 m and the seaward slope is at the angle of repose or steeper. During extreme wave events classical dune erosion takes place and the seawall ("dune") has to be maintained on a round-the-clock basis by large earthmoving equipment. During periods when the earthmoving equipment can concentrate solely on beachwall building and maintenance it is possible to supply 16 000 m³ of sand to the seawall per day. The seawall is being extended northwards in the direction of the littoral drift by active dumping at a rate of approximately 800 m per year. To minimise maintenance costs the area behind the seawall is divided into paddocks which are, once mined out, left to be inundated by the sea again (see Figure 2). This means that only a localised area needs to be maintained. Nevertheless the length to be maintained is of the order of 800 m at times but could also be as short as 200 m if localised erosion problems are encountered. This means that the volume of artificial nourishment to the seawall can amount to between 20 and 80 m³/day per running metre of seawall. Under "normal" storm conditions this should be sufficient to counteract wave-induced erosion.

During a routine visit to Oranjemund on 24 and 25 February 1987 extreme wave conditions were observed. Four cross-sections were taken in front of the seawall during a 23-hour period to record the wave-induced erosion of the beach in front of the seawall and the seaward face of the seawall. This paper discusses the results obtained and relates them to available predicted techniques in literature.

2. Data

The data relevant to the particular storm is summarised here to serve as basis for use by researchers/engineers who want to verify onshore-offshore sediment models. The data can be subdivided into four types, namely, wave data, profile data, sand suppletion rates and grain size data.

2.1 Wave data

An offshore Waverider station at the site is situated in 106 m of water. The significant wave height with a 1 in 20 year return period, based on 8 years' worth of data at 6 hourly recording intervals is 4.5 m. Unfortunately it was out of commission during the event. Three other sources of wave data are available; (1) data from a Waverider situated to the south of the study area in the region from where the waves originate, (2) data on the format of that obtained by voluntary observing ships (VOS) gathered by lighter vessels operating in the area off Oranjemund and (3) visually observed wave heights at breaking by using the horizon as a reference.

Figure 4 shows the synoptic chart for 14h00 on the 22nd February 1987, which clearly shows the origin of the storm event.

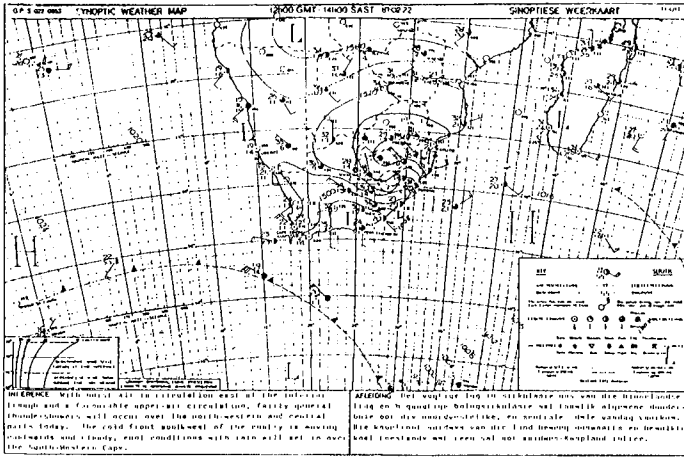


FIG. 4 SYNOPTIC CHART 14H00 : 22.02.1987

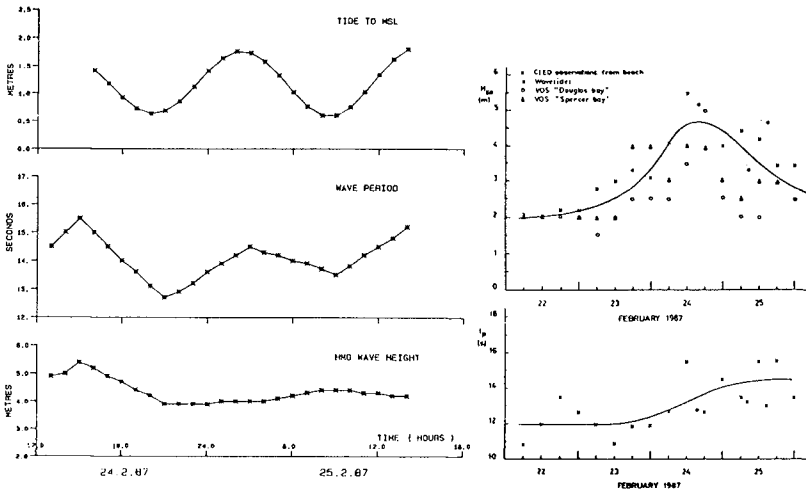


FIG. 5 WAVE DATA FROM VARIOUS SOURCES FOR FEBRUARY 1987 STORM AT ORANJEMUND

Waverider Waves in the area arrive predominantly from the south to southwesterly sectors. This is consistent with the main wave generating area which is situated in the so-called "Roaring Forties" to the southwest of South Africa. Studies have shown that wave heights attained during storm events at recording stations along the west coast are virtually the same but that a lag occurs as one moves up the coast, as is to be expected. The mean lag between Slangkop near Cape Town (see Figure 1 for location) and Oranjemund is about 24 hours. After applying the appropriate time lag the wave height variation at Oranjemund was found to be as shown in Figure 5. For reference the predicted tidal variation for this period is also shown on the figure.

Voluntary Observing Ships' data (VOS) By comparison with Waverider measurements for earlier storm events it has been found that VOS data in the area is extremely reliable. This is most probably due to the fact that two lighter vessels owned by the De Beers Marine group operate in the area on a regular basis. The mariners have a long experience of working in this particular area. The VOS data obtained from these lighters for the February storm are also shown in Figure 5.

Visually observed maximum wave breaker heights (CLEO) As part of a low-level monitoring programme (CLEO) along similar lines as the COPE programme in Queensland, Australia and the LEO programme in the USA, maximum wave heights are estimated by using the horizon as a frame of reference. Comparison to Waverider observations has shown that provided that the appropriate conversion is made to allow for refraction and shoaling between the Waverider and the breaker line and that a suitable factor is used to account for the correlation between the maximum wave in the spectrum and the significant wave height, reliable wave heights can be estimated by this technique. In the present case with a known crest level for the seawall and the extremely high maximum pre-breaker heights this technique was easy to apply (see Figure 6 for breaking wave fury observed from an elevation of MSL + 10 m). The exposed beachface below the seawall did not exceed a width of 20 m during the event. Therefore one was in close proximity to the breaker line. By taking shots to the extreme trough of the wave just before it broke as a virtually totally plunging wave as well as to the crest and to the horizon it was established that the maximum wave height at breaking was 8.5 m. Obviously the maximum height varied with time but during the late afternoon on 24 February, the maximum height varied between 7.5 m and 8.5 m. It would appear that these heights are far in excess of those values quoted earlier although the wave periods are roughly in line. The wave heights observed in this manner represents a maximum height over a 2-4 minute period. It is possible to use the relationship developed by Longuett-Higgins (1952) to transfer the observed wave heights to significant wave heights at breaking for 13 sec waves. On the basis of the synoptic chart on Figure 4 it is possible to calculate a combined shoaling/refraction coefficient of 1.1 between



FIG. 6 BREAKING WAVE FURY AS OBSERVED FROM SEAWALL (MSL + 10M)

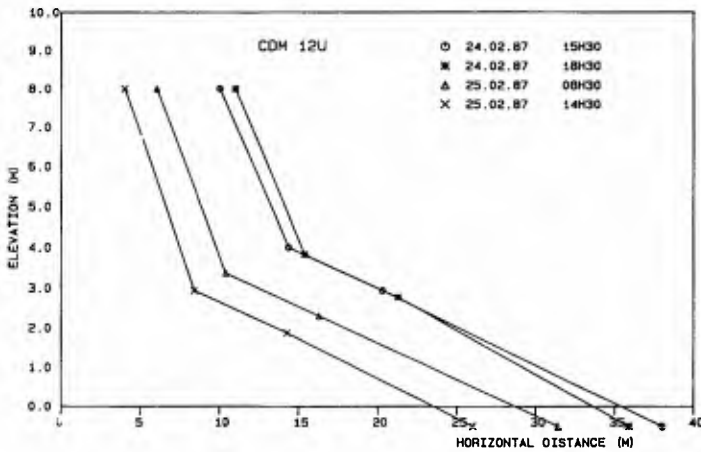


FIG. 7 BEACH FACE PROFILES MEASURED ON 24/25 FEBRUARY 1987

deep-sea and a water depth of 10 m. Therefore the wave height variation observed at the breaker line can be transferred to deep-sea significant wave heights. The results obtained in this manner are shown in Figure 5.

Summary It is clear that the data from the three sources show a similar trend, although there is some scatter, as is to be expected. The solid lines through the data represent the best estimate of the mean trend depicted in the data.

2.2 Profile data

As can be seen in Figure 3 the beach profiles are steep and the exposed beachface is at best fairly restricted. At 4 occasions during the 23-hour period a cross-section of the seawall and beachface was taken. This was done at extreme risk to the observers, because the beach face was only exposed for about two minutes at a time during which the staff-bearer had to go down a 6 m unconsolidated sand-slope onto the beach, taking off only metres ahead of the next onrushing wave. The four profiles are given in Figure 7. In the assessment of the profile changes observed due cognizance should be taken of the general morphological behaviour of this area.

The dominant wave direction in the area is approximately south-westerly which leads to a net northerly drift of sediment of about $1.4 \times 10^6 \text{ m}^3/\text{yr}$. The seawall acts as an obstruction and material is deposited on the beach south of the seawall. The fact that the seawall is maintained more than 200 m from the original waterline results in high sediment losses and extremely high sediment concentrations in the water. The suspended sediment is moved northwards and is deposited on the downdrift beach. This results in the unusual situation that the shoreline grows on both the updrift and downdrift ends of the seawall in the long term (see Figure 8).

During the event the seawall was perfectly straight. In addition, the area where the observations were done was more than a kilometre from the then northern extremity of the seawall. Waves broke parallel along a fairly long section of seawall. It can be concluded that the effect of longshore transport on the profile development can be neglected as a first approximation.

2.3 Sand nourishment

For the reasons outlined above, the nourishment rates along the seawall are fairly high, as can be seen on Figure 9, which contains monthly nourishment rates over a three year period. The volume of material given in this figure is the total volume needed for (1) so-called seawall building to advance the seawall to the north and (2) for maintenance purposes.

It was obvious that the seawall was steadily being eroded. Therefore although the general policy has been to

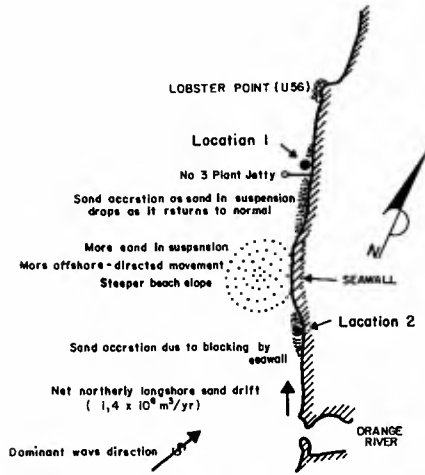


FIG. 8 SCHEMATIC REPRESENTATION OF NEARSHORE PROCESSES ADJACENT TO SEAWALL

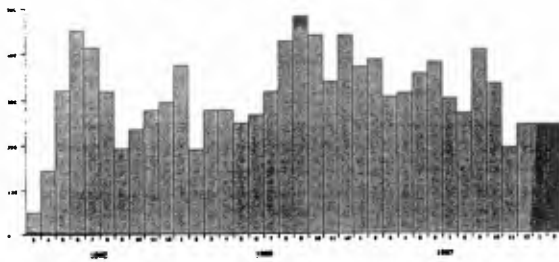


FIG. 9 INSHORE MINING PROJECT : MONTHLY FEEDING RATES

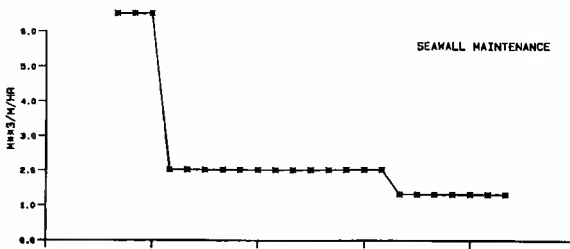


FIG. 10 SEAWALL MAINTENANCE DURING FEBRUARY 1987 STORM EVENT

work on a 24-hour a day basis with the effort being split between beachwall building and beachwall maintenance, all earth-moving equipment was diverted onto maintaining the paddock being stripped and mined at the time. The seaward face of this paddock is 500 m long. The material was being actively dumped on 400 m of sea wall along this paddock during the 24-hour period to try and curtail wave-induced erosion. A total of 1021 15 m³ truckloads of sand was dumped onto the sea wall and dozed into the water by bulldozer.

On the basis of the actual area renourished over time during the 24 hour period it was possible to construct Figure 10, which is the best estimate of seawall maintenance during the event, represented in cubic metres maintenance per metre of wall.

2.4 Grain size data

Available grain size data for the seawall area indicate that the median grain size is about 200 microns.

3. Comparison with predictive models

The data set described herein represents an extreme erosion event. It creates the opportunity to test onshore-offshore predictive models against such an extreme offshore sediment loss event. In this section two such comparisons are given, namely, with the D-profile concept of Swart (1974a, 1974b, 1976, 1986) and with the energetics approach of Nairn (1988). The full data set is available from the authors.

3.1 Profile concept of Swart

The empirical approach of Swart has been well documented. It uses of the concept that an equilibrium profile will eventually be formed if a given wave condition persists long enough. At any time during the transition from the initial conditions to the final (equilibrium) condition the quantity of onshore or offshore sediment transport taking place is proportional to the difference between the schematized profile at that time and the schematized equilibrium profile. In order to facilitate the profile schematization, the beach profile is broken into essentially three parts, namely, (1) that portion of the profile which is above (or landward of) the point of maximum uprush, the so-called **backshore**, (2) the area between the point of maximum uprush and the lower limit of the actively developing profile, which is characterized by very active sediment transport (mostly as suspended load) and by well-developed bars and other bedforms, the so-called developing profile or D-profile, and (3) the area below (or seawards of) the lower limit of the D-profile, where a transition basically takes place between the newly developing profile and the original profile. This last area is called the transition area and transport here usually takes place as bed load. Swart (1974a) compared his theoretically based framework with extensive model and

field data on profile development and presented empirical relationships for all parameters required to apply the technique in a predictive mode.

Over the past 14 years the technique has been extensively applied to a variety of coastal applications, with a large degree of success. Seymour (1988) concluded in a paper presented at this (ICCE) conference that the technique has the highest success rate of the onshore-offshore predictive models tested in his study.

Using the data described above a set of model input was prepared. Application of the model yielded satisfactory profile remoulding (Figure 11) and loss rates. Figures 12 and 13 which are highly compatible with the observed values, as deduced from the data presented earlier. Volumetric loss from above the water line is exceptionally close to the observed value, namely $130 \text{ m}^3/\text{m}$ as opposed to $123 \text{ m}^3/\text{m}$ over the 23 hour period. However, variations in the 0 m and +5 m contours are not as accurately predicted, specifically over the last 5 to 10 hours of the period. Nevertheless, the overall comparison is good and it can be concluded that this fairly simplistic method can give reliable results. A strong disadvantage of this technique is the fact that large-scale bedforms such as profile perturbations and breaker bars cannot be predicted.

3.2 Energetics Approach of Nairn

Bailard (1981) developed a model for the prediction of cross-shore sediment transport which utilised an energetics approach. Bailard assumed that instantaneous sediment transport is proportional to some power of the instantaneous orbital velocity at the bed. Stive (1987) used the same technique for random waves, and used the Stokes II wave theory to compute odd velocity moments needed as input for the model. Both bed load and suspended load are catered for, in three modes of transport, namely, asymmetric (onshore) transport, mean flow (offshore) transport and downslope (offshore) transport due to gravity. Nairn (1988) used the same techniques as Stive. As far as waves are concerned, the dissipation model for random breaking waves of Battjes and Janssen (1978) was used, whilst transfer of individual regular wave components in a probability density function was done according to the method of Dally (1987). Bottom changes were calculated using a Lax-Wendroff second-order scheme based on the flux of sediment across a finite difference section of the model (Nairn 1988). Rob Nairn graciously ran his model on the Oranjemund data set. The results obtained when applying the Nairn model are given in Figure 14. It shows that a very realistic profile readjustment took place, although reference to Figure 15 shows that the volumetric loss rates predicted by the model are too low by a factor of approximately two. This is not considered an insurmountable problem as the loss rates would be appreciably improved if the model could cater adequately for sediment removal from above the water line, which is obviously not a function of the mathematical technique used

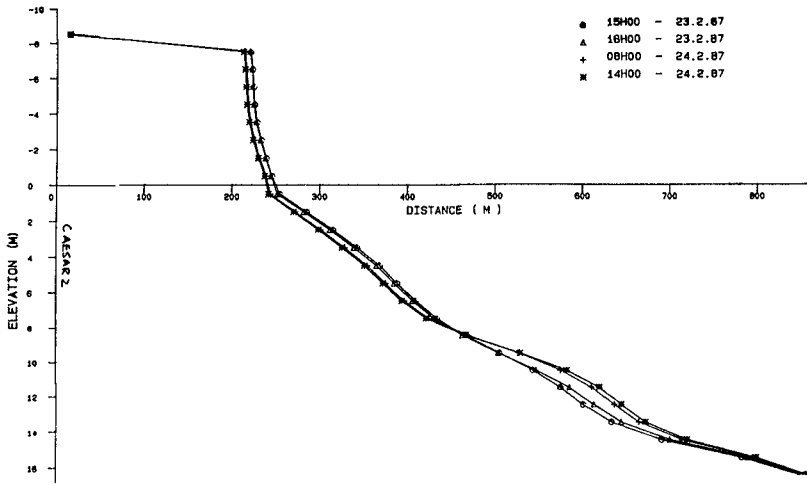


FIG. 11 MODEL PROFILE REMOULDING

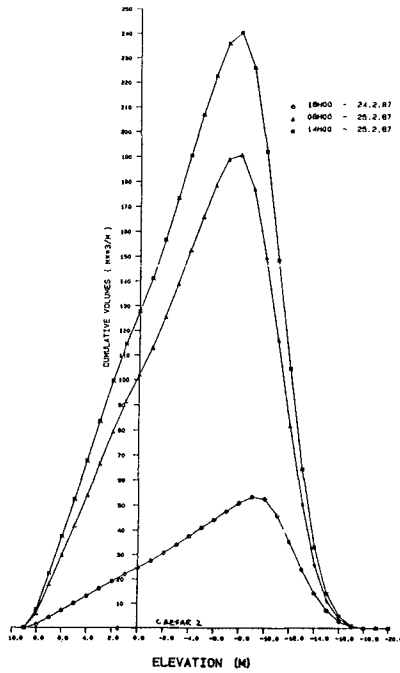


FIG. 12 MODEL EROSION RATES

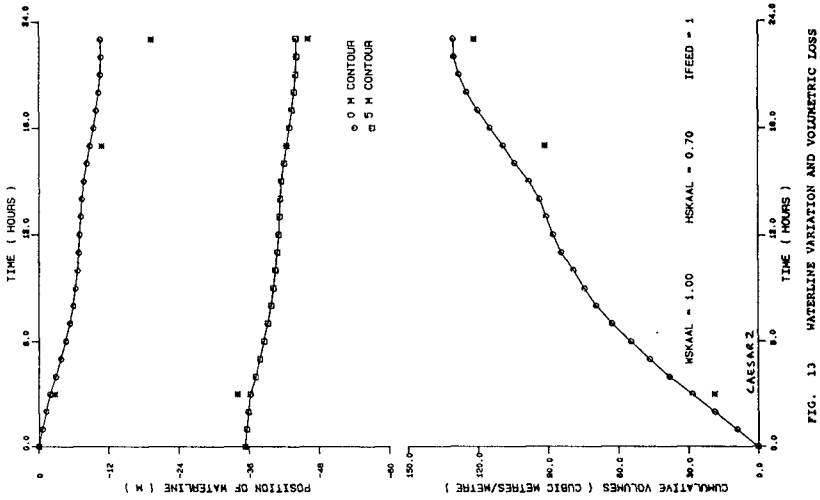


FIG. 13 WATERLINE VARIATION AND VOLUMETRIC LOSS

OUTPUT FILE IS SA7
WAVE HEIGHT DECAY,
SETUP AND EROSION
ON A BEACH

LEGEND

PREDICTED DATA
FOR TRANSFER OCEAN
--- 13 HRS. (25:02:07 14h30)
--- 10 HRS. (25:02:07 01h30)
Initial: 15h30 24:02:07

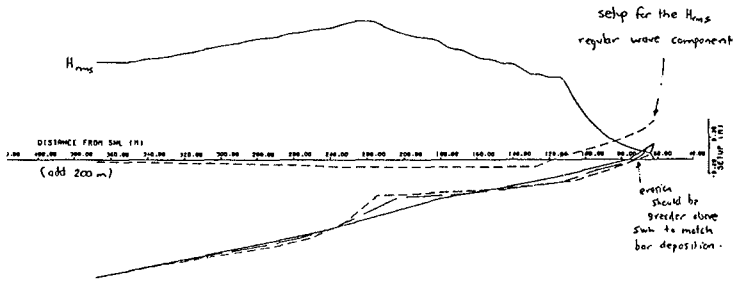


FIG. 14 MODEL PROFILE REMOULDING (NAIRN)

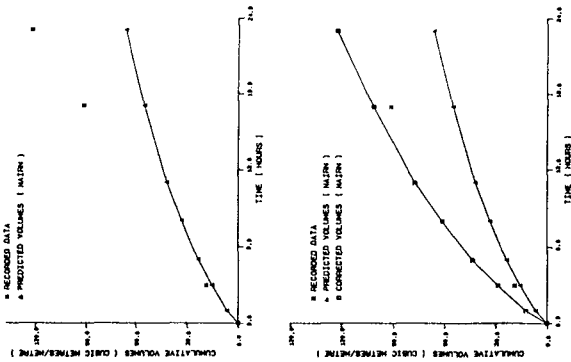


FIG. 15 RECORDED AND PREDICTED EROSION RATES

to calculate sediment movement seawards of the water line.

The results depicted in Figure 14 exhibit only a monotonic bar formation. It may be the result of the method in which bed profile changes are calculated presently which needs some pursuing.

Discussion of the results with Nairn lead to a quite plausible explanation for the discrepancy (Nairn, pers. comm.).

The band width of the input bivariate distribution of wave height and period does not have any significant effect on the predicted volumetric rates and can thus not explain the discrepancy. However, de Vriend (1987) suggests that in severe erosion conditions the suspended load exhibits a retardation in its response to a change in the transport capacity. Consequently, the sediment load at a point is partly determined by what has happened further upstream. This can lead to either underloading (actual transport < potential transport) or conversely, overloading (the so-called autosuspension condition). It is further stated that during the erosion of an unprotected dune a large overload of sediment is carried seawards by the undertow and the material is spread very quickly over a large area, which has a considerable influence on the dune erosion process.

The presently used theoretical development of the energetics sediment transport model only relates the sediment transport to the energetics of the flow. In lieu of the comments by de Vriend (1987) autosuspension will occur if

$$w < \bar{u}_s \tan \beta$$

where w is the fall velocity of the sand grains, \bar{u}_s is the mean flow velocity advecting the suspended load and $\tan \beta$ is the profile slope. It can be shown easily that autosuspension conditions could occur for many of the large waves in the spectrum during the storm event. Reasons for this include (1) the unnaturally steep slope of 1:20, even for a grain size of 0.5 mm (2) the wave exposure and potential for rapid return flows or undertow and (3) a steep dune face inducing avalanching which will trigger autosuspension. Moreover, autosuspension offers a plausible explanation of how so much material could be rapidly eroded and not show up as a pronounced bar deposit. Autosuspension can lead to self-maintaining turbidity currents which will carry and spread the sediment well outside the surfzone.

In conclusion, the Nairn approach yields a promising comparison with the observed profile changes, although the rate of change is at present still underpredicted.

4. Conclusions

- * A data set was presented which represents an extreme wave-induced erosion event, with a volumetric loss rate from above the water line of approximately $130 \text{ m}^3/\text{day}$. The data are available on request.
- * Computations with the semi-empirical D-profile approach of Swart (1986) and with the energetics model of Nairn (1988) show that it is possible to predict such extreme events and open some interesting avenues for more detailed research on the mechanism of extreme wave-induced sediment transport.

5. Acknowledgments

The logistic support of the Consolidated Diamond Mines (Pty) Ltd in compiling the data set is gratefully acknowledged. Thanks are also due to Rob Nairn of the Imperial College of Science and Technology who spent a substantial amount of time and effort to model this event with his technique.

6. References

- BAILLARD, J.A. (1981). An energetics bedload model for a plane sloping beach: Local transport. *Journal of Geophysical Research*. Vol. 86, No C3
- BATTJES, J.A. and JANSSEN, J. (1978). Energy loss and setup due to breaking of random waves. *Proc 17th International Conference on Coastal Engineering*
- DALLY, W.R. (1987). Wave transformation in the surf zone. Ph.D. Thesis, University of Florida
- de VRIEND, H.J. (1987). Two and three-dimensional modeling of coastal morphology. Recent developments at the Delft Hydraulics Laboratory. Report No 377
- LONGUETT-HIGGINS, M.S. (1952). On the statistical distribution of the heights of sea waves. *Journal of Marine Research*, Vol XI, 1952
- MÖLLER, J.P., OWEN, K.C. and SWART, D.H. (1986). Coastal engineering studies for inshore mining of diamonds at Oranjemund. *Proc. 20th International Conference on Coastal Engineering*. Taiwan
- NAIRN, R.B. (1988). Prediction of wave height and mean return flow in cross shore sediment transport modeling. *IAHR Symposium on Mathematical Modeling of Sediment Transport in the Coastal Zone*. Copenhagen
- SEYMOUR, R.J., CASTEL, D. (1988). Validation of cross-shore transport formulations. *Proc. 21st International Conference on Coastal Engineering*, Malaga

STIVE, M.J.F. (1987). A model for cross-shore sediment transport. Proc. 20th International Conference on Coastal Engineering, Taipei

SWART, D.H. (1974a). Offshore sediment transport and equilibrium beach profiles. Doctoral thesis, Technische Hogeschool, Delft

SWART, D.H. (1974b). A schematization of on-offshore transport. Proc. 14th International Conference on Coastal Engineering

SWART, D.H. (1976). Predictive equations regarding coastal transports. Proc. 15th International Conference on Coastal Engineering. Honolulu, Hawaii

SWART, D.H. (1986). Prediction of beach changes and equilibrium beach profiles. Lecture notes for short course on : Dynamics of Sand Beaches. Taipei, Taiwan

CHAPTER 140

A MODEL FOR BREACH GROWTH IN A DIKE-BURST

Paul J. Visser^{*}

ABSTRACT

A mathematical model for sand-dike breach erosion is presented. The heart of the model is a modified Bagnold (1963) energetics-based sand transport conception combined with a simplified Galappatti and Vreugdenhil (1985) pick up mechanism for the suspended load. The model has been tested to three laboratory experiments. The agreement between model predictions and experimental results is surprisingly good. Prototype calculations are presented for the 73 m high sand-dike of a proposed pumped-storage plant in the Netherlands.

1. INTRODUCTION

One of the possibilities for storage of energy is a water reservoir with a relatively high water level. In a flat country as The Netherlands a pumped-storage plant can be built by constructing an artificial basin surrounded by dikes. A proper location for the plant is along the coast against the Brouwersdam in the south-western part of The Netherlands. Recent feasibility studies conclude that the optimum dimensions of the reservoir are an area of about 15 km² and a water depth of about 70 m (resulting in a storage capacity of 20000 MWh and an electric power of 2000 MW). The ring-dike of the basin should be constructed with local sand ($D_{50} \approx 0.20$ mm).

Failure of the basin dike can result in a major disaster for the surroundings of the plant with losses of both human life and property. The possible consequences of an eventual dike-burst are important aspects for the determination of the acceptable failure probability of the basin. These consequences will depend on the behaviour of the flood wave, which in its turn will depend on the reservoir outflow hydrograph, particularly the maximum rate of outflow. The outflow hydrograph is governed largely by the growth of the breach with time.

The problem is comparable with that of earth-dam failures, for which the last 20 years a number of mathematical models has been developed, see Singh and Scarlatos (1988). These models, as also the model of Fujita and Tamura (1987) for the breaching of bursts in river

* Scientific Officer, Department of Civil Engineering, Delft University of Technology, P.O. Box 5048, 2600 GA Delft, The Netherlands.

dikes, assume bed load as the prevailing transport mechanism. But in case of failure of a high sand-dike suspended load transport will dominate. Since this results in a completely different breach erosion, these models cannot be applied here.

The aim of the investigation is a mathematical model which describes the growth of the breach and the discharge with time. The study was done for the NOVEM (Netherlands Company for Energy and Environment).

Starting point is a basin with an area of 15 km² and a water depth $H_w = 70$ m. It is assumed that the 73 m high ring-dike is

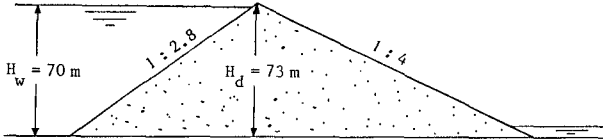


Fig. 1 Schematization of the cross-section of the high sand-dike

completely built up with sand ($D_{50} = 0.20$ mm), see Fig. 1. The inner and outer slopes are 1 : 2.8 and 1 : 4, respectively. All these quantities can also be varied. It is further assumed that the dike-burst starts with a small initial breach at the crest of the dike, for instance due to piping.

2. DESCRIPTION OF SAND TRANSPORT

A proper description of the pick up and transport of sediment is essential for the simulation of breaching processes. In the case of failure of the sand dike of a 70 m high reservoir, the outflow velocities will become very large (order of magnitude 20 m/s). None of the existing sediment transport formulae has been verified for these velocities. Hence, an energetics-based approach is applied in which the sand transport is expressed directly in the available power for it from the flow. Thus, a huge overestimation of the sand transport (as by some other formulae) is prevented.

The present approach is based on the energetics-based sediment transport conception of Bagnold (1963, 1966). The incorporation of the slope effect differs, however, from Bagnold's (1963) approach.

Bagnold expressed the sediment transport in the available energy ω per unit time and unit area of the bed surface:

$$\omega = \tau_b = C_f \rho u^3 \quad (1)$$

where τ_b is the bed shear stress, u is the depth-averaged current velocity, C_f is the drag coefficient for the bed (≈ 0.01) and ρ is the water density.

The Bagnold conception includes both bed load transport (capacity s_b) and suspended load transport (capacity s_s). Here the order of magnitude of the ratio s_b/s_s will be:

$$\frac{s_b}{s_s} \approx \frac{13}{\text{tg}\phi} \frac{W}{u} \approx \frac{13}{0.6} \frac{0.02}{20} \approx 0.02 \ll 1 \quad (2)$$

where ϕ is the internal angle of friction of the sediment in the bed load ($\phi \approx 32^\circ$ for sand) and W is the fall velocity of the sediment. So the bed load transport can be neglected with respect to the suspended load transport.

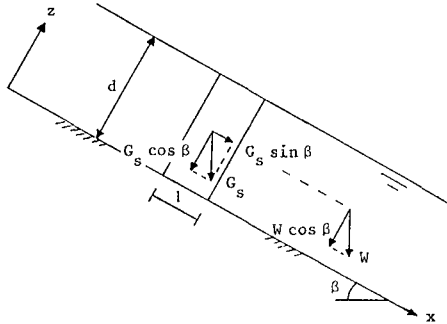


Fig. 2 Components $G_s \cos \beta$ and $W \cos \beta$ normal to the slope of G_s and W , respectively

Consider a column of water in the flow on a slope (with angle β) with an unit area of 1 m^2 (along the slope) and a height d equal to the water depth, see Fig. 2. If C_s is the immersed weight of the suspended material within this column and u_s is the average transport velocity of these solids, then the suspended load transport s_s , can be written as

$$s_s = C_s u_s \quad [\text{N/ms}] \quad (3)$$

The lifting work P (per unit time and unit width) by the turbulence which is required to keep the solids in suspension is

$$P = (C_s \cos \beta) (W \cos \beta) \quad (4)$$

This work is delivered by ω ; however, only a (small) part of ω is used for this:

$$P = e \omega \quad (5)$$

where e is the efficiency factor for the suspended load transport ($e = 0.01$ according to Bagnold, 1966).

Combining (1), (3), (4) and (5) yields

$$s_s = \frac{0.01 C_f \rho u_s u_s^3}{W \cos^2 \beta} \quad [\text{N/ms}] \quad (6)$$

The effect of the weight component $G_s \sin \beta$ is that the suspended sediment will push the fluid along s_s instead of vice versa. So $u_s > u$, but the difference will be small ($u_s \approx u$). Hence it is assumed that the contribution of $G_s \sin \beta$ to the lifting work P is negligible. This approach differs from that of Bagnold (1963) and Bailard (1981) who assumed contributions to P of $G_s \sin \beta u_s$ and $e C_s \sin \beta u_s$, respectively.

The weight of 1 m³ sand under water is: (1 - p) (ρ_s - ρ) g [N], in which p is the porosity, ρ_s is the sediment density and g is the acceleration of gravity. Now (6) can be written as:

$$s_s = \frac{0.01 C_f u^4}{(1 - p) \Delta g W \cos^2 \beta} \quad [m^2/s] \quad (7)$$

in which Δ = (ρ_s - ρ)/ρ. Equation (7) applies to the capacity of the suspended load transport. There remains the description of the process of pick up of sediment up to this capacity.

Fig. 3 shows schematically the two-dimensional situation of flow and sand transport on the outer or downstream slope in a stage which differs only slightly from the initial state (slope 1 : 4).

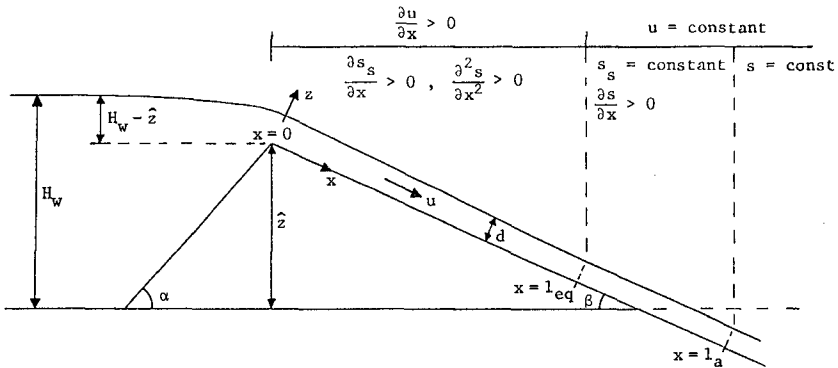


Fig. 3 Schematization of flow and sand transport on the downstream slope

The crest acts as a weir, the flow over it is critical. On the downstream slope, where the flow is super-critical, the current accelerates up to a distance $x = l_{eq}$ from the crest (x is the coordinate along the slope, $x = 0$ at the crest); there the current velocity reaches the equilibrium value for uniform flows

$$u_{eq} = \left(\frac{g d \sin \beta}{C_f} \right)^{1/2} \quad (8)$$

Upstream from the crest the sand transport is very small (in the experiments) or nothing at all (in practice, due to the revetment of the slope). The entrainment of sediment in suspension starts at the crest. For $x = l_a$ (= adaption length) the suspended load transport reaches its capacity; naturally l_a can be larger than L (= length of downstream slope), and always $l_a \geq l_{eq}$ due to the adaption process of the suspended load.

A description of the entrainment process for sediment in suspension is given by Galappatti and Vreugdenhil (1985). For small values of W/u_* as in the present situation, i.e. $W/u_* = W/(\sqrt{C_f} u) \approx 0.01$ (see (2), u_* is the bed shear velocity), their theory can simply be approximated as

$$s(x) = \frac{x}{l_a} s_s \quad \text{for} \quad 0 \leq x \leq l_a \quad (9)$$

where (with q is the outflow rate per unit width):

$$\ell_a = \frac{u d}{W \cos \beta} = \frac{q}{W \cos \beta} \tag{10}$$

3. MATHEMATICAL MODEL

3.1 Outflow rate

The maximum outflow rate Q_{max} will occur for large values of the water depth H_w in the reservoir, see Fig. 11. Then the flow in the breach is still critical, so the equation for the rate of outflow is:

$$Q = q b = m_o \frac{2}{3} \left(\frac{2}{3} g\right)^{1/2} b H^{3/2} \tag{11}$$

where m_o is the discharge coefficient (≈ 1.0), b is the average breach width and $H = H_w - \hat{z}$ (\hat{z} is the height of the breach top above the reservoir bottom, see Fig. 3).

3.2 Growth of breach in depth

The equation describing the erosion of the downstream slope is

$$\frac{\partial z_b}{\partial t} + \frac{\partial s}{\partial x} = 0 \tag{12}$$

where t is the time and $z_b = z_b(x, t)$ is the position of the sloping bottom in z -direction (z is the coordinate normal to the slope).

The suspended load capacity s increases for $0 < x < \ell_{eq}$ since u accelerates here. This means with (8) and (12)

$$\frac{\partial}{\partial x} \left| \frac{\partial z_b}{\partial x} \right| = \frac{\partial^2 s}{\partial x^2} > 0 \quad \text{for} \quad 0 < x < \ell_{eq} \tag{13}$$

i.e. the rate of erosion increases along the slope. Hence the downstream slope becomes steeper with increasing x and in time, see Fig. 4.

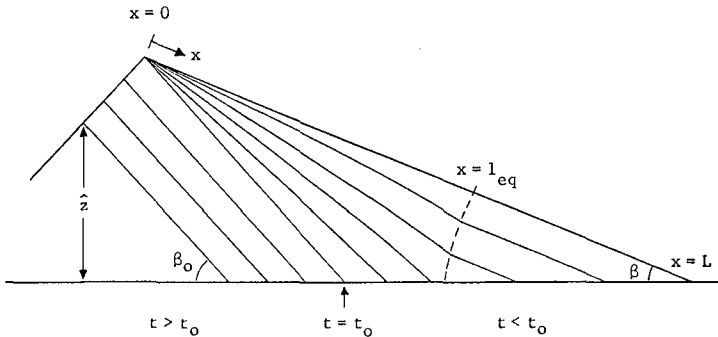


Fig. 4 Erosion of the downstream slope

If it is assumed that C_f and β are constant, then s is constant for $l_{eq} < x < l_a$ since u is constant here, see (7). This means that

$$\frac{\partial}{\partial x} \left| \frac{\partial z_b}{\partial t} \right| = 0 \quad \text{for} \quad l_{eq} < x < l_a \quad (14)$$

i.e. the rate of erosion is constant along this part of the slope, see Fig. 4.

Fig. 4 shows also the result of the above described development: the downstream slope becomes steeper and steeper. The steepness of the slope will not exceed, however, a certain limit $\tan \beta_o$. If this limit has been achieved on the entire slope (on $t = t_o$), then the erosion rate becomes also constant for $0 < x < l_{eq}$, see the straight lines in Fig. 4 for $t > t_o$. Thus, for $t \geq t_o$ the erosion of the downstream slope is completely determined by the erosion at $x = l_{eq}$, i.e. by the erosion at the toe of the slope ($x = L$):

$$-L \frac{dz_b}{dt} = s_L \quad \text{for} \quad t \geq t_o \quad (15)$$

where with (9):

$$s_L = \frac{L}{l_a} (s_s)_L \quad (16)$$

Substitution of $d = q/u$ into (8) gives for the current velocity at $x = L$:

$$u_L = \left(\frac{g q \sin \beta}{C_f} \right)^{1/3} \quad (17)$$

The relation between the fall $d\hat{z}$ of the breach top and the erosion dz_b of the downstream slope follows from a simple geometrical

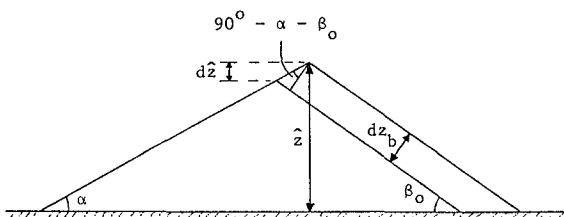


Fig. 5 Relation between $d\hat{z}$ and dz_b

consideration, see Fig. 5:

$$\frac{d\hat{z}}{dt} = \frac{\sin \alpha}{\sin (\alpha + \beta_o)} \frac{dz_b}{dt} \quad (18)$$

Substitution of (15), (16), (7), (10), (17), $\beta = \beta_o$ and (11), successively, into (18) gives:

$$\frac{d\hat{z}}{dt} = -k H^{1/2} = -k (H_w - z)^{1/2} \text{ for } t \geq t_0 \tag{19}$$

where $k = 0.0082 \frac{(g)^{1/2}}{\Delta (1-p)} \left(\frac{m_0}{C_f}\right)^{1/3} \frac{\sin \alpha (\sin \beta_0)^{4/3}}{\sin(\alpha + \beta_0) \cos \beta_0}$ (20)

3.3 Growth of breach width

Consider the small initial breach $A_0 B_0 C_0 D_0$ of Fig. 6 with an average width b_0 , a bottom width a_0 and a height h_0 . It is assumed that the angle of the side slopes is somewhat smaller than the angle of repose ϕ . The direction of the flow through the breach is perpendicular to the paper.

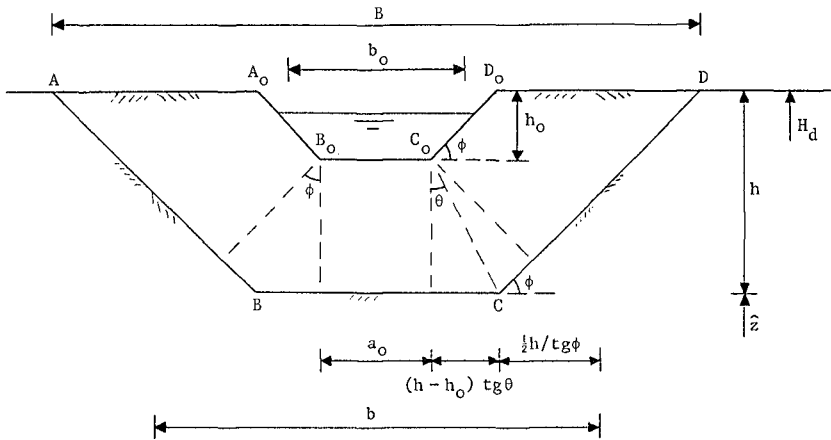


Fig. 6 Assumed growth of breach ABCD from initial $A_0 B_0 C_0 D_0$

The rate of erosion down below the side slopes is larger (due to larger current velocities) than higher on the slopes. This means that the slopes become steeper and steeper, until the situation gets unstable and the sides will slide into the channel. This is in accordance with the observations (which are described in chapter 4). Thus, it is assumed that the angle of the side slopes is constant and equal to ϕ . Hence, if the sand dike is homogeneous then the initial breach $A_0 B_0 C_0 D_0$ will develop into the breach ABCD with an average width b :

$$b = a_0 + 2 (h - h_0) \operatorname{tg} \theta + \frac{h}{\operatorname{tg} \phi} \tag{21}$$

and width B at the crest of the dike:

$$B = a_0 + 2 (h - h_0) \operatorname{tg} \theta + \frac{2h}{\operatorname{tg} \phi} \tag{22}$$

in which h is the breach depth and $0 < \theta < \phi$.

If $b_0 \ll b$ and $h_0 \ll h$, then (21) and (22) can be written as:

$$\frac{b}{h} = 2 \operatorname{tg} \theta + \frac{1}{\operatorname{tg} \phi} \quad (23)$$

$$\frac{B}{h} = 2 \operatorname{tg} \theta + \frac{2}{\operatorname{tg} \phi} \quad (24)$$

For sand: $\phi \approx 32^\circ$ Thus, with $0 < \theta < \phi$:

$$1.6 < \frac{b}{h} < 2.9 \quad (25)$$

$$3.2 < \frac{B}{h} < 4.4 \quad (26)$$

If the rate of erosion just left from the point C_0 equals to that just right from this point then $\theta = \phi/2$ and

$$\frac{b}{h} = 2.2 \text{ and } \frac{B}{h} = 3.8 \quad (27)$$

If the breach is schematized as shown in Fig. 7, then it

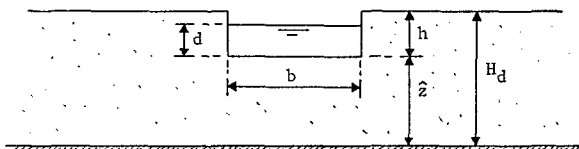


Fig. 7 Schematization of the breach

follows from the foregoing that the breach width b is simply related to the breach depth

$$b = r h = r (H_d - \hat{z}) \quad (28)$$

where r is a constant with a theoretical value of about 2.2 and H_d is the height of the dike.

The continuity equation for the total sediment transport S through the breach channel reads

$$\frac{\partial S}{\partial x} - \frac{\partial bh}{\partial t} = 0 \quad (29)$$

where (see Fig. 7):

$$S = s(b + 2d) \quad (30)$$

Substitution of (28) and (30) into (29) gives with $\partial h / \partial t = - \partial z_b / \partial t$ and the assumption that b and d are nearly constant along the slope:

$$\frac{b + 2d}{2b} \frac{\partial s}{\partial x} + \frac{\partial z_b}{\partial t} = 0 \quad (31)$$

i.e. (19) should be corrected to

$$\frac{d\hat{z}}{dt} = - \frac{b + 2d}{2b} k H^{\frac{1}{2}} = - f k H^{\frac{1}{2}} \quad (32)$$

Thus, $d\hat{z}/dt$ slows down with a factor f compared with the 2-dimensional situation. The factor f can be calculated for any \hat{z} from $d = q/u_L$, (11), (17) and (28).

3.4 Decrease of reservoir water depth

The decrease of the water depth in the reservoir follows simply from the equation describing continuity of mass:

$$A \frac{dH_w}{dt} = - Q \quad (33)$$

or with $H_w = H + \hat{z}$:

$$\frac{dH}{dt} + \frac{d\hat{z}}{dt} = - \frac{Q}{A} \quad (34)$$

The equations (32) and (34) form a system of coupled differential equations for H and \hat{z} .

4. EXPERIMENTS

Three experiments were performed for the verification of the model. Fig. 8 (lines for $t = 0$) shows the cross-section of the dike at

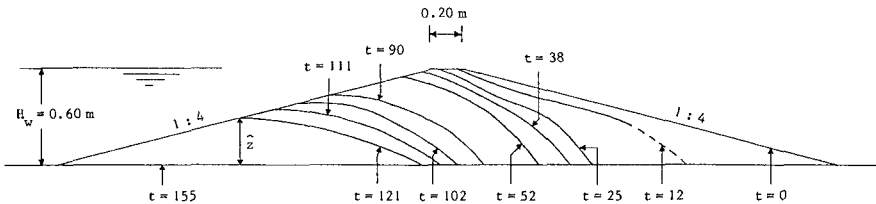


Fig. 8 Cross-section of the dike in the breach on different times t (in seconds) in Exp. 3

the start of each experiment, completely built up with sand: $D_{50} = 0.10$ mm in Exp.'s 1 and 3, $D_{50} = 0.20$ mm in Exp. 2. The upstream water depth was kept constant at 0.60 m, the downstream water depth at the start of the experiments was nil. The breach growth was video taped because of the very rapid process of breaching.

Exp. 1 was done in a large (wave) basin in which a 6 m long dike was constructed. The dike-burst started at $t = 0$ with the flow through a small initial channel in the crest of the dike. Fig. 9 shows the top width $B(t)$ of the breach as observed from the video tape.

Exp.'s 2 and 3 were performed in a flume with a width of 0.50 m. Exp. 3 is a two-dimensional experiment: the erosion of the dike took place over the total width of the flume. The observed development of the downstream slope (see Fig. 8) is in agreement with the reasoned one (see Fig. 4). The downstream slope in Exp. 3 became steeper until

$t = t_0 = 25$ s without any appreciable drop of the crest. Fig. 10 shows the observed top height $\hat{z}(t)$ in Exp. 3.

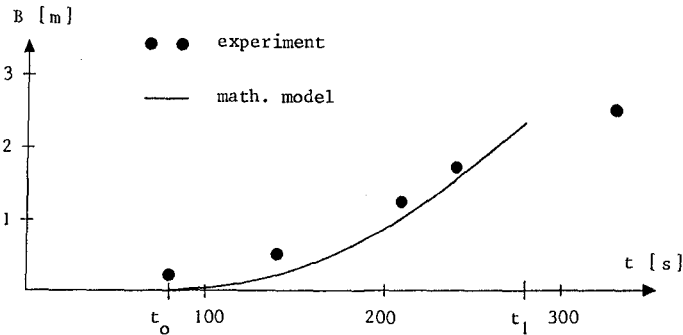


Fig. 9 Observed (Exp. 1) and theoretical top width $B(t)$ of the breach

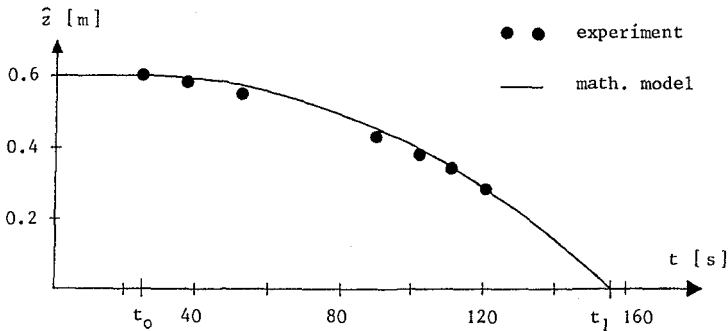


Fig. 10 Observed (Exp. 3) and theoretical top height $\hat{z}(t)$

5. VERIFICATION AND RESULTS

5.1 Comparison with experiments

The present breach erosion model has been verified to the data of the three experiments. In this paper only the testing for Exp.'s 1 and 3 is briefly described. As stated in chapter 3, the model can be applied after the steepening of the downstream slope, i.e. for $t > t_0$.

Fig. 10 shows the comparison of the computed and observed crest height $\hat{z}(t)$ of the dike in the breach. The calculation was done for $H_w = \text{constant} = 0.60$ m, $t_0 = 25$ s, $\alpha = 14^\circ$, $\beta_0 = \phi = 32^\circ$, $m = 1.2$, $\Delta = 1.65$, $p = 0.4$, $f = 1$ (2-dimensional) and $C_f = 0.06$. The rather large value of 0.06 for C_f was computed with (17) and $u = q/d$ using the observed water depths on the crest of the weir (for q) and on the downstream slope in an initial stage of Exp. 3. On $t = t_1 = 155$ s the dike in the flume was completely washed away.

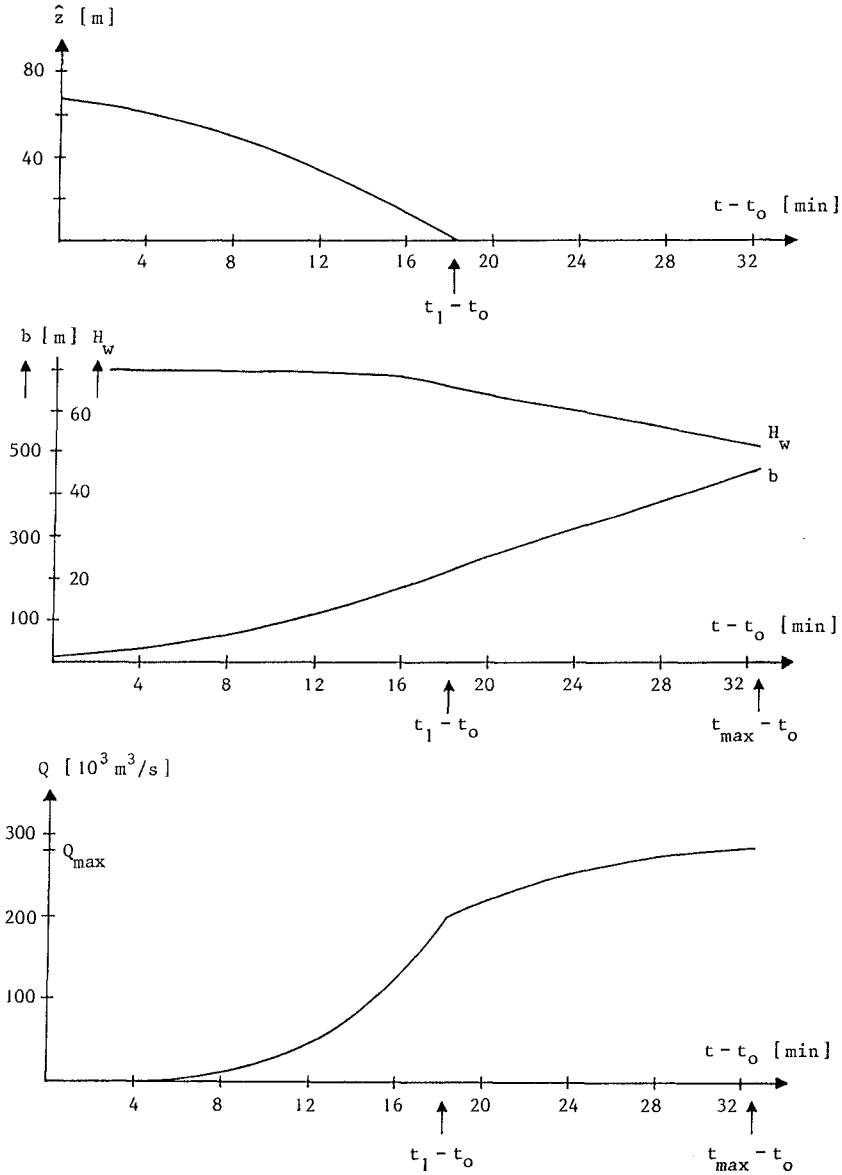


Fig. 11 Top height $\hat{z}(t)$, average breach width $b(t)$, reservoir water depth $H_w(t)$ and outflow rate $Q(t)$ as computed for the high sand-dike of Fig. 1.

The comparison of the computed and observed top width $B(t)$ of the breach in Exp. 1 is shown in Fig. 9. The calculation was done for $H_w = \text{constant} = 0.60 \text{ m}$, $t_o = 80 \text{ s}$, $\alpha = 14^\circ$, $\beta_o = \phi = 32^\circ$, $m_w = 1.2$, $\Delta = 1.65$, $p = 0.4$, $C_f = 0.06$ and $B/h = 3.8$.

It can be concluded from Fig.'s 9 and 10 that the agreement between model predictions and experimental data is very good.

5.2 Prototype calculations

Since the model is based on the process of entrainment of sand on a relatively steep slope, its validity is also limited to $t < t_1$.

In the present calculations the model was simply applied for $t_1 \leq t \leq t_o$ too (t_o is the time where Q is maximal), i.e. (28) for b with (19) for \hat{z} . For the rate of outflow, however, it was assumed that if $\hat{z} < 0$ then Q is determined by H_w (i.e. in (11) $h = H_w$) and the length of the circular weir upstream of w the scour hole and not influenced by the scour hole itself.

The results of the (numerical) computations for the sand-dike of the pumped-storage plant ($H_w = 70 \text{ m}$, $A = 15 \text{ km}^2$, $\alpha = 19.6^\circ$) with the basic values for the different parameters ($\beta_o = \phi = 32^\circ$, $m = 1.0$, $\Delta = 1.65$, $p = 0.4$, $r = 3$, $e = 0.01$ and $C_f = 0.015$) are shown in Fig. 11. The relatively large value of 0.015 for C_f was measured by the Dutch Public Works Department in the field during the final phase of a "sand-closure", i.e. in a situation with large current velocities.

The duration t_o can be estimated from the measured $t_o = 80 \text{ s}$ in Exp. 1 and the time-scale factor for the morphological process.

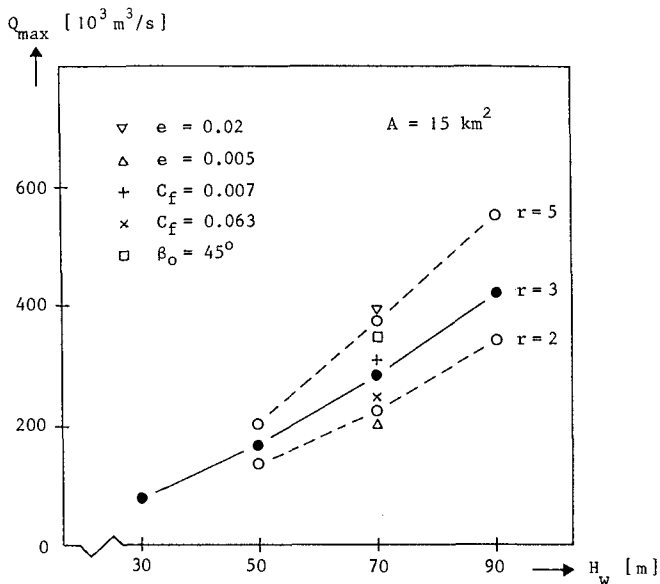


Fig. 12 Sensitivity of the computed Q_{max} for the different parameters

This gives $t_0 = 560 \text{ s} = 9.3 \text{ min.}$, see Visser, Ribberink and Kalkwijk (1986).

Thus, the model predicts for the outflow rate a maximum value:

$$Q_{\max} = 2.8 * 10^5 \text{ m}^3/\text{s} \quad \text{for} \quad t = t_{\max} = 2.5 * 10^3 \text{ s} = 42 \text{ min.}$$

Fig. 12 shows the sensitivity of the computed Q_{\max} for the different parameters, i.e. for the width/depth-ratio r of the breach, the efficiency factor e for the suspended load transport, the drag coefficient C_f for the bed, the critical slope angle β_0 and the reservoir water depth H_w . The model is especially sensitive for e and r .

6. DISCUSSION

The output of the study is a relatively simple model for the simulation of sand-dike breach erosion. The investigation was done for the feasibility study of a pumped-storage plant in the Netherlands. The model predicts for the 73 m high sand-dike of the water reservoir the following failure scenario in case a small initial gap springs up at the crest on $t = 0$:

- o $0 < t < t_0$: the slope angle β of the breach channel in the downstream slope will become larger,
- o $t = t_0 = 9 \text{ min.}$: β will reach a critical value β_0 , the flow rate will be still small and the erosion of the top will start (the duration t_0 is very sensitive to the initial conditions),
- o $t_0 < t < t_1$: erosion of the dike in the breach,
- o $t_0 = t_1 = 28 \text{ min.}$: the dike in the breach will be completely washed away, $Q_1 \approx 2.0 * 10^5 \text{ m}^3/\text{s}$,
- o $t_1 < t$: the breaching process will continue in both vertical and horizontal direction; for the outflow rate Q the increase of the breach width is of importance,
- o $t = t_{\max} = 42 \text{ min.}$: $Q_{\max} \approx 2.8 * 10^5 \text{ m}^3/\text{s}$.

The model is based on the erosion process of a relatively steep slope ($t_0 < t < t_1$) and was also tested as such to the results of three experiments. The agreement between model and experiments is surprisingly good.

For much lower dikes, as river or sea dikes, Q_{\max} will generally be much larger than Q_1 . It is clear that the modelling of the breach growth for $t > t_1$ should be improved before the model can be released for these dikes.

A sensitivity analysis indicates that the efficiency factor e for the suspended load transport and the width/depth-ratio r of the breach are the most sensitive parameters in the model; e is the most uncertain parameter. Measurements on the pick up and transport of sediment at high velocities ($\approx 10 \text{ m/s}$) should be done to reduce this uncertainty.

REFERENCES

- Bagnold, R.A., 1963. Mechanics of marine sedimentation. In *The Sea: Ideas and Observations*, vol. 3, Interscience, New York, pp. 507-522.
- Bagnold, R.A., 1966. An approach to the sediment transport problem from general physics. Geological Survey Professional Paper 422-I, U.S. Government Printing Office.
- Baillard, J.A., 1981. An energetics total load sediment transport model for a plane sloping beach. *Journ. Geophysical Res.*, vol. 86, pp. 10938-10954.
- Fujita, Y. and Tamura, T., 1987. Enlargement of breaches in flood levees on alluvial plains. *Natural Disaster Science*, vol. 9, pp. 37-60.
- Galappatti, R. and Vreugdenhil, G.B., 1985. A depth-integrated model for suspended sediment transport. *Journ. Hydraulic Res.*, vol. 23, pp. 359-377.
- Singh, V.P. and Scarlatos, P.D., 1988. Analysis of gradual earth-dam failure. *Journ. Hydraulic Eng.*, vol. 114, pp. 21-42.
- Visser, P.J., Ribberink, J.S. and Kalkwijk, J.P.Th., 1986. The development of the breach and rate of outflow in case of dike failures (in Dutch). Rep. 8-86, Hydraulic Eng. Group, Fac. of Civil Eng., Delft Univ. of Techn.

ACKNOWLEDGEMENT

The work upon which this paper is based was supported in part by the NOVEM B.V. (Dutch Company for Energy and Environment).

CHAPTER 141

SHORELINE AT JETTY DUE TO CYCLIC AND RANDOM WAVES

by

Todd L. Walton, Jr.¹, M. ASCE
Philip L-F. Liu², M. ASCE
Edward B. Hands³, M. ASCE

ABSTRACT

This paper examines the effects of random and deterministic cycling of wave direction on the updrift beach planform adjacent to a jetty. Results provided using a simplified numerical model cast in dimensionless form indicate the importance of the time series of wave direction in determining design jetty length for a given net sediment transport. Continuous cycling of wave direction leads to the expected analytical solution. Simplifications in the numerical model used restrict the applications to small wave angles, no diffraction, no reflection of waves off structure, no refraction, and no sand bypassing at jetty. The concept can be extended to more sophisticated numerical models.

INTRODUCTION

Coastal navigation structures such as jetties serve a number of practical purposes, two of which are: keeping the navigation channel open by prevention of sand transport into the channel, and providing a sand storage reservoir for bypassing to downdrift beaches (to prevent erosion due to the interruption of the natural longshore sand transport).

An important jetty design criteria is the determination of jetty length which is equivalent to

¹Research Hydraulic Engineer, Coastal Engineering Research Center, U.S. Army Engineer Waterways Experiment Station, Vicksburg, MS 39180-0631.

²Professor of Civil and Environmental Engineering and Associate Dean of Engineering College, Cornell University, Ithaca, NY 14853.

³Research Physical Scientist, Coastal Engineering Research Center, U.S. Army Engineer Waterways Experiment Station, Vicksburg, MS 39180-0631.

determination of the updrift fillet sand storage area necessary between dredging intervals. Under constant wave action (i.e. constant wave height, wave period, and wave breaker angle) simple design formula such as provided by the analytical solution of Pelnard-Considere (1956) can be used to provide an answer to this design question. Under more general conditions of changing wave climate, an analytical solution is not possible.

This paper examines the effects of changing wave climate (in particular wave direction deterministic cycling and random effects) on the updrift beach planform prior to the onset of natural bypassing around the jetty. Results of the type in this paper show the importance of the time history of wave climate on design jetty length for a given sand storage requirement. Simplifications in the numerical model used restrict the applications to: (1) small wave angles ($A_b < 15$ degrees), (2) no reversing wave climate, i.e. no diffraction effects, (3) no reflection of waves off structure, (4) no refraction, (5) no sand bypassing at jetty, and (6) no change in profile shape during shoreline advance. Each of these simplifications can be overcome by a more sophisticated numerical model than used in the present analysis.

MODEL

Two equations can be used to describe shoreline shape (e.g. Hanson and Kraus, 1980; Walton and Chiu, 1979). The first equation describes the continuity of sediment transport in the longshore direction:

$$(1/D) (\partial Q / \partial x) + \partial y / \partial t = 0 \quad (1)$$

where D = closure depth, Q = volumetric longshore sediment transport rate, and the coordinate system is shown in Fig. 1. The second governing equation relates the longshore sediment transport rate to wave and current parameters. The equation used in this note is that of the CERC type formulation (see CERC, 1984):

$$Q = K_c H_b^{5/2} \sin(2A_b) \quad (2)$$

where

$$K_c = [K g^{1/2}] / [16(s_s/s_f - 1)(1-a)] \quad (3)$$

with

$$A_b = A - \partial y / \partial x \quad (4)$$

where A = deep water wave angle; A_b = breaking wave angle; H_b = breaking wave height; K = a dimensionless constant (= 0.39 in CERC (1984)) relating the immersed weight sediment transport rate to the "longshore energy flux"; g = acceleration of gravity; s_s = specific gravity of sediment; s_f = specific gravity of fluid; and a = porosity of sediment (assumed = 0.6).

By assuming small wave angles and constant wave

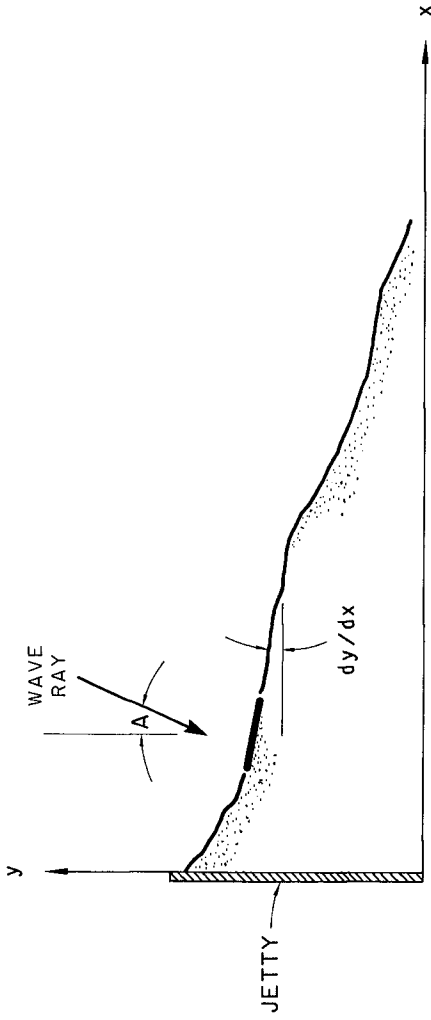


Fig. 1. - Shoreline Coordinate System

height along the beach the two equations can be reduced to the following form:

$$\partial y / \partial t = \epsilon (\partial^2 y / \partial x^2) \quad (5)$$

where

$$\epsilon = (2 K_c / D) H_b^{5/2} \quad (6)$$

with units of length²/time. This equation is a parabolic partial differential equation often referred to as the heat (or mass) diffusion equation.

This equation can be recast in dimensionless form by dividing the quantities x, y by $2(\epsilon t_s)^{1/2}$ where t_s is the desired solution time to obtain:

$$\frac{\partial \hat{y}}{\partial \hat{t}} = \frac{\partial^2 \hat{y}}{\partial \hat{x}^2} \quad (7)$$

where

$$\hat{t} = t / 4 t_s \quad (8a)$$

$$\hat{y} = ty / 2 (\epsilon t_s)^{1/2} \quad (8b)$$

$$\hat{x} = x / 2 (\epsilon t_s)^{1/2} \quad (8c)$$

Equation 7 can be solved for given initial conditions and boundary conditions and changing wave climate via an implicit numerical scheme known as the Crank-Nicholson method (see Burden and Faires, 1985) which ensures numerical stability. Initial conditions and boundary conditions for the jetty shoreline system remain the same in dimensional or dimensionless form and are given as:

$$\hat{y} = 0.0 \text{ at } \hat{t} = 0.0, \hat{x} \geq 0 \text{ (initial conditions)} \quad (9a)$$

$$\hat{y} = 0.0 \text{ at } \hat{x} = \infty, \hat{t} \geq 0 \text{ (b.c. far from jetty)} \quad (9b)$$

$$\partial \hat{y} / \partial \hat{x} = A \text{ at } \hat{x} = 0.0 \text{ (b.c. at semiinfinite jetty)} \quad (9c)$$

(or equivalently $A_b = 0.0$ at jetty)

The Crank-Nicholson scheme provides for stability under all conditions of time step Δt and distance step Δx . Numerical accuracy is provided via a sufficiently large number for the dimensionless quantity r where

$$r = \epsilon \Delta t / \Delta x^2 \quad (10)$$

In the present study the numerical model used $r = 1.0$ to provide acceptable accuracy (error 0.5 percent). In the case of constant wave conditions the model was verified by comparing the numerical model solution to the non-dimensional form of the analytical solution provided by Walton and Chiu (1979) as follows:

$$\tilde{y} = \hat{y} \sqrt{\pi} / A = \exp(-\hat{x}^2) - \hat{x} \sqrt{\pi} \operatorname{erfc}(\hat{x}) \quad (11)$$

RESULTS FOR DETERMINISTIC WAVE CYCLING

The following cases of deterministic wave cycling (where only wave direction is changing) were run on the model:

case 1a - 1 cycle, 10 - 0 square waveform
 case 2a - 2 cycles, 10 - 0 square waveform
 case 3a - 4 cycles, 10 - 0 square waveform
 case 4a - 8 cycles, 10 - 0 square waveform
 case 5a - 16 cycles, 10 - 0 square waveform
 case 6a - 80 cycles, 10 - 0 square waveform

A pictorial representation of the temporal wave direction change of cases 1a through 5a is shown in Fig. 2. Cases 1b-6b are similar only with reversed sequencing of wave direction (i.e. starting with $A = 0$ degrees at time $t = 0.0$). Time T represents a characteristic time period (the solution time), for example, a year if case 1a is used and there are two predominant wave directions lasting for 6 months each.

For each case the mean wave angle was $\bar{A} = 5$ degrees while the actual wave angle fluctuated about the mean from 0 to 10 degrees. Cases 1a,b and 3a,b are plotted on Fig. 3 in the non-dimensional format of Eq. 8 where the mean wave angle \bar{A} was used for the wave angle of Eq. 9. Note that the integrated shoreline change via this approach is the same in all cases, only the along-shore distribution of these changes differs between the different cases. Figure 3 also provides the analytical solution (Eq. 11) in the case of constant wave direction. Cases 6a and 6b have not been shown in Fig. 3 as they are essentially that of the analytical solution for the same average wave angle of $\bar{A} = 5$ degrees. Due to plotting resolution cases 2a,b; 4a,b; and 5a,b are not provided but can be interpolated between adjacent cases in Fig. 3. As would be expected for rapidly fluctuating direction around a mean wave direction, the numerical solution approaches the analytical solution with the same mean wave angle.

As an example of how such information might be used, consider a situation where dredging to initial conditions might occur each year (i.e. dimensional time period $T = 1$ year). If the wave climate is two seasonal (1 cycle) in the year with the wave angles shown as in case 1a (or 1b), an increase of jetty length on the order of 40 percent above that for constant wave conditions is necessary to prevent sand from spilling into the channel. Case 1b differs from case 1a only in phase (6 months for the example under consideration). The intent here is to show the importance of wave sequencing on the design considerations which often is overlooked.

Although the solution curves are non-dimensionalized, it must be recognized that different mean climate levels (i.e. different \bar{A}) will provide different sets of curves. This is shown in Fig. 4 where cases 1a and 1b (1 cycle) are shown along with cases 7a and 7b (1 cycle with wave direction shifting between 15 and 5 degrees, mean wave angle $\bar{A} = 10$ degrees). In case 7a it is noted that the increase in jetty length necessitated by the cyclic wave direction is only 20 percent above the non-dimensionalized analytical solution where $\bar{A} = 10$ degrees, but recall that the mean wave angle has doubled (10 versus 5 degrees) requiring the dimensional jetty length of the analytical solution to double.

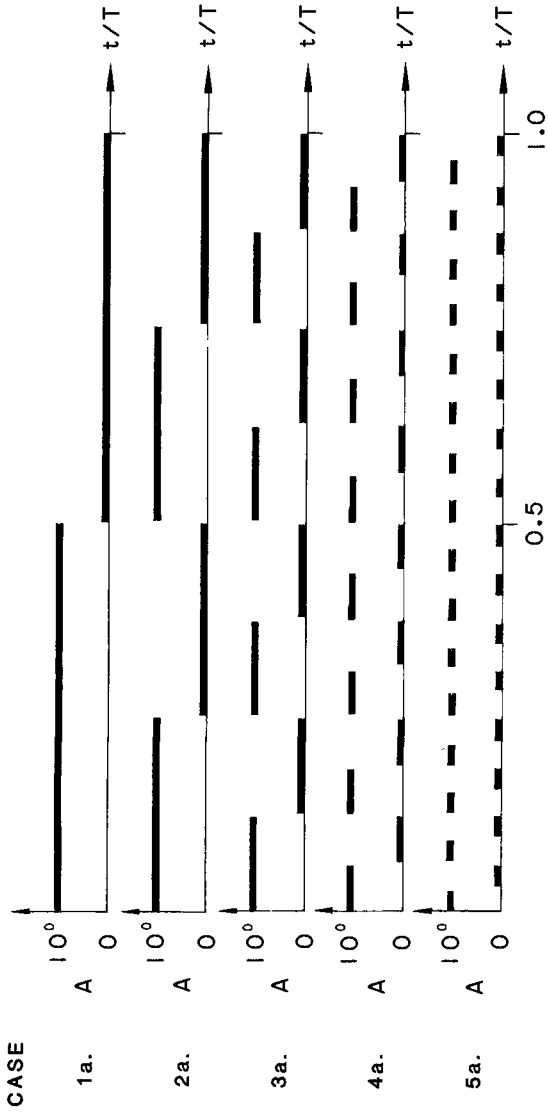


Fig. 2. - Temporal Representation of Cyclic Wave Direction

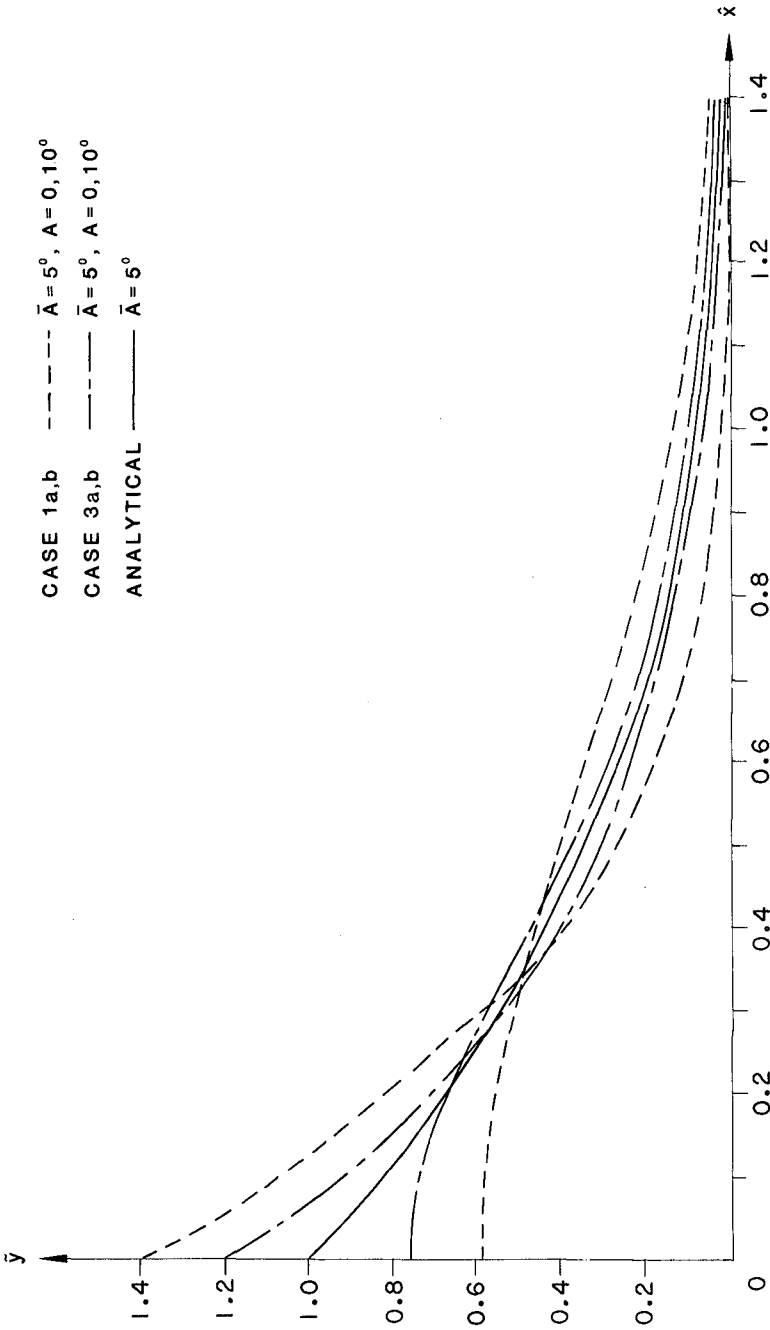


Fig. 3. - Results of Numerical Model for Cases 1a,b through 6a,b

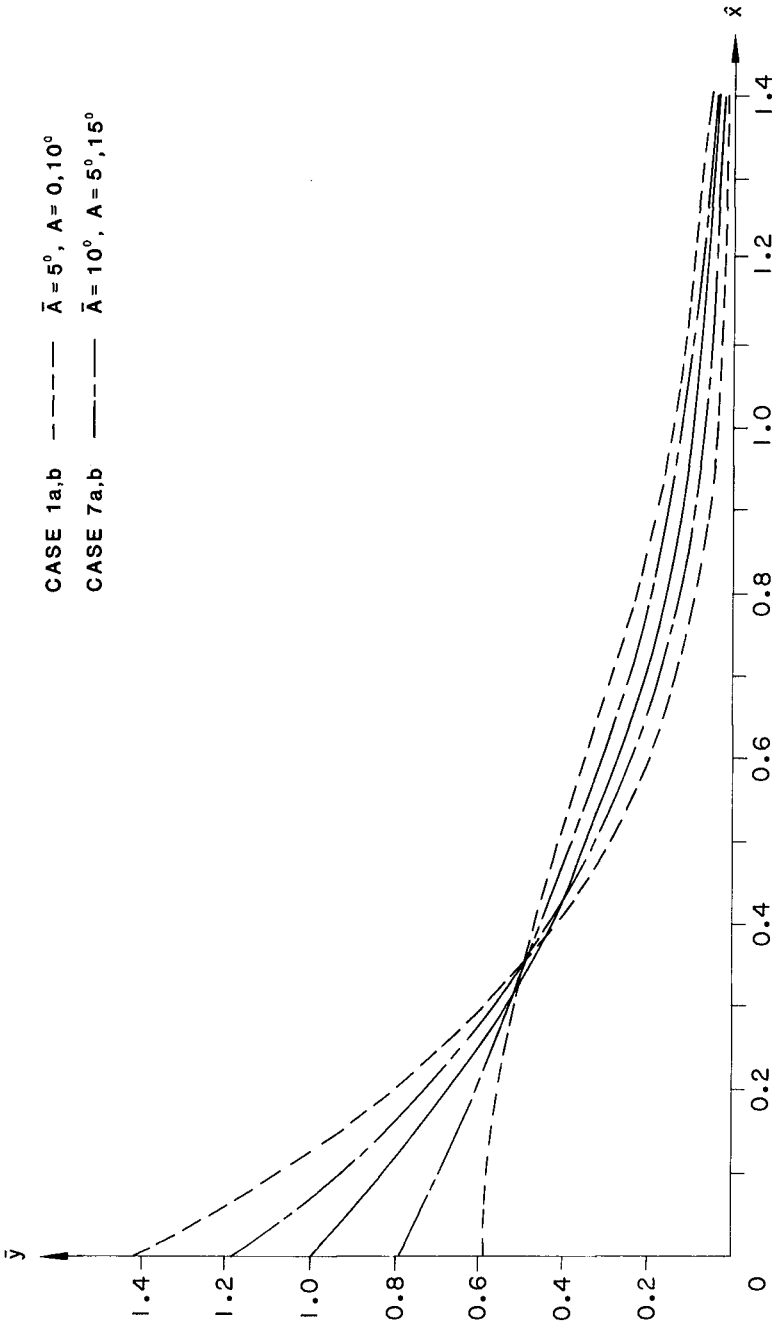


Fig. 4. Results of Numerical Model for Cases 1a,b versus 7a,b

RESULTS UNDER DIRECTIONAL UNCERTAINTY

LeMehaute and Wang (1983) have investigated the problem of shoreline response under random wave action via simulation of wave climate with known probability distribution. In the semi-infinite jetty and straight shoreline with constant wave condition case where the only random variable is wave direction, an expected shoreline shape as well as confidence intervals on shoreline shape can be obtained very simply. Such solutions are of value in evaluation of design parameters (such as jetty length) when wave climate uncertainty exists.

The expected shoreline shape in dimensionless form can be reexpressed as follows:

$$E[\hat{Y}] = (E[A] / \sqrt{\pi}) (\exp(-\hat{X}^2) - \hat{X} \sqrt{\pi} \operatorname{erfc}(\hat{X})) \quad (12)$$

where $E[\]$ represents the expected value and \hat{Y} is now replaced by the random variable \hat{Y} . The previous analytical solution, eq. 11, as provided in Fig. 3 can be used to find the expected shoreline by replacing A with $E[\]$ where A is also a random variable.

In the general case where wave direction is unknown to within $R = A_{\max} - A_{\min}$ degrees, the directional probability distribution function (PDF) can best be expressed as the uniform PDF where:

$$F(A) = (A - A_{\min}) / R \quad (13)$$

with $F(A)$ = probability that wave angle $< A$. For this particular PDF, the $A = A_u$ corresponding to an upper confidence limit with $1 - F(A_u)$ as the probability of exceedance (i.e. $\hat{Y} \leq \hat{Y}$) is $A_u = R F(A_u) + A_{\min}$. The $A = A_l$ corresponding to a lower confidence limit with probability $F(A_l)$ is $A_l = R F(A_l) + A_{\min}$. The lower and upper confidence interval shorelines can then be expressed by Eq. 11 and the Fig. 3 analytical shoreline using $A = A_u$ and $A = A_l$. Confidence limits for shorelines based on other PDF's can be found in a similar manner. The important point to note from this simplified analysis is that uncertainty in wave direction can lead to shoreline realizations having wide discrepancies from those projected based on expected wave conditions. In the case of a uniform PDF for wave direction as postulated, a 90 percent confidence interval shoreline can lead to a necessary increase of jetty length 80 percent above that required for the expected wave angle (for the given case of $A_{\min} = 0.0$).

CONCLUSIONS

A brief examination of the shoreline shape due to jetty construction under deterministic cyclic wave action and under uncertainty in wave direction has been provided for some simple hypothetical wave direction scenarios. Shorelines due to cyclic effects in wave direction show considerable deviation from solutions with the same mean wave direction. Time sequencing of

wave direction is thus seen to be of considerable importance in design studies. Uncertainty in wave direction also plays an important role in shoreline fluctuation and should be factored into design considerations. In realistic cases of design a more detailed model (i.e. Hansen and Kraus (1980)) might be used to optimize jetty length.

ACKNOWLEDGMENTS

The work presented herein was conducted under the Evaluation of Shore Protection Structures work unit of the Shore Protection and Restoration Program, Coastal Engineering area of Civil Works Research and Development being executed by the Coastal Engineering Research Center, U.S. Army Engineer Waterways Experiment Station, Vicksburg, MS. Permission was granted by the Chief of Engineers to publish this information.

APPENDIX 1. - REFERENCES

- Burden, R. L., and Faires, J. D., Numerical Analysis, PWS Publishing Company, Boston, MA, 1985.
- CERC, Shore Protection Manual, Coastal Engineering Research Center, U.S. Army Engineer Waterways Experiment Station, U.S. Government Printing Office, 1984.
- Hanson, H. and Kraus, N., "Numerical Model for Studying Shoreline Change in the Vicinity of Coastal Structures," Report No. 3040, Dept. of Water Resources Engineering, University of Lund, Lund, Sweden, 1980.
- LeMehaute B., Wang, J. D., and Liu, C. C., "Wave Data Discretization for Shoreline Processes," Journal of Waterway, Port, Coastal and Ocean Engineering, ASCE, Vol. 109, No. 1, 1983, pp. 63-78.
- Pelnard-Considerere, R., "Essai de Theorie de l'Evolution des Formes de Rivage en Plages de Sable et de Galets," 4th Journees de l'Hydraulique, Les Energies de la Mer, Question III, Rapport No. 1, 1956.
- Walton, T. L., Jr., and Chiu, T. Y., "A Review of Analytical Techniques to Solve the Sand Transport Equation and Some Simplified Solutions," Proc. of Coastal Structures 79 Conference, May 14-16, 1979, Alexandria, VA, American Society of Civil Engineers, New York, N.Y., 1979.

APPENDIX II. - NOTATION

The following symbols are used in the paper:

- a = porosity of sediment/sand,
(dimensionless);
- g = acceleration of gravity;
- s_f = specific gravity of seawater,
(dimensionless);
- s_s = specific gravity of sediment/sand,
(dimensionless);
- t = time;
- t_s = solution time;
- x = distance alongshore direction,
(x = 0.0 at jetty);
- \hat{x} = dimensionless distance alongshore
- y = distance to shoreline from baseline
in offshore direction;
- \hat{y} = dimensionless distance to shoreline
from baseline in an offshore
direction;
- A = offshore reference wave angle;
- A_D = breaking wave angle;
- A_{max} = maximum wave angle where
uncertainty exists;
- A_{min} = minimum wave angle where
uncertainty exists;
- A_l = wave angle corresponding to lower
confidence limit;
- A_u = wave angle corresponding to upper
confidence limit;
- D = water depth at offshore limit of
significant longshore sediment
transport;
- $E[]$ = expectation operator;
- $F()$ = probability of random variable ()
being less than or equal to value
given;
- K = dimensionless constant;
- K_C = dimensional constant,
(length/time);
- PDF = abbreviation for probability
distribution function;
- Q = volumetric sand/sediment transport
rate, (length/time);
- R = range of uncertainty in wave
direction;
- T = characteristic time of wave
direction cycling scenerio;
- \hat{Y} = random variable equivalent of \hat{y} ;
- ϵ = dimensionless "diffusion"
coefficient.

CHAPTER 142

CHARACTERISTICS OF SHINGLE BEACHES WITH REFERENCE TO CHRISTCHURCH BAY, S. ENGLAND

by Robert Nicholls* and Norman Webber⁺

ABSTRACT

The rapid recession of the shingle bank of Hurst Beach (up to 3.5m/yr) makes it an excellent natural laboratory for the study of the factors which influence the stability of shingle beaches. Studies have included: the significance of long period, high energy, swell waves - the classification and quantification of overwash processes - run-up and seepage characteristics - the effect of settlement of the underlying strata - and the implications for practices in shingle nourishment. The studies have revealed the distinctive character of shingle beaches as compared with the more fully researched sand beaches. More detailed research on shingle beaches is justified particularly in relation to (i) the run-up characteristics including its interaction with swash cusps and (ii) the influence of the subsidiary sand fraction on the beach characteristics.

INTRODUCTION

Pebble and cobble (henceforth called shingle) beaches, or at least beaches where the upper foreshore is predominantly shingle, are to be found in many parts of the world, but are nowhere of more coastal engineering significance than in Britain (Carr, 1983a). Whilst for recreational activities such beaches have less appeal than their sand counterparts, they are nonetheless one of the most efficient forms of coast protection.

In Southern and Eastern Britain, maintenance usually entails regular profile monitoring and, when needed, the construction of groynes and the recycling of shingle transported by littoral drift (e.g. Foxley & Shave, 1983). Projects involving shingle nourishment, usually from marine sources, are becoming increasingly favoured (e.g. Hayling Island, Hampshire and Seaford, Sussex).. This has raised important questions concerning the field characteristics of shingle beaches. The extensive literature on sand beaches is often misleading when applied to shingle beaches because of fac-

*Institute of Marine Studies, Plymouth Polytechnic, Drake Circus, Plymouth PL4 8AA, U.K.

+Department of Civil Engineering, The University, Southampton, SO9 5NH, U.K.

tors such as permeability (e.g. Muir-Wood, 1970).

The authors have over a number of years examined the processes operating on Hurst Beach, the shingle bank at the eastern end of Christchurch Bay between Saltgrass Lane and Hurst Castle (Fig. 1). Hurst Beach is being starved of littoral drift due to updrift coast protection works, comprising seawall and groynes at Milford-on-Sea and recently has experienced rapid recession of up to 3.5m/yr. (Nicholls & Webber, 1987a; 1987b). Thus, Hurst Beach makes an excellent natural laboratory where the processes which influence the stability of shingle beaches can be examined and quantified. Much of the work has been described in detail by Nicholls (1985). Some of the conclusions of pertinence to the stability of shingle beaches are summarised in this paper.

THE STUDY AREA

The beaches in the eastern half of Christchurch Bay (Fig. 1) are composed of shingle with a mean size in the range -2.5 to -5.5 phi (6 to 45mm) with subsidiary fine to coarse sand (125 to 1000 μ m) which mainly occurs on the foreshore. The form of the beach profiles on Hurst Beach are fairly typical of many of the shingle banks in southern Britain. The foreshore (average slope about 8°) is backed by a supratidal beach face (average slope about 11 to 13°) and a beach crest (Fig. 2). Landward of the crest the beach drops with a variable slope (typically 5 to 13°) to a saltmarsh. The crest height varies both temporally and spatially with a maximum elevation in the period 1980 to 1982 of 4.6m. O.D., 3.6m. above the highest predicted tide (O.D. approximates mean sea level). The net littoral drift is eastwards, but

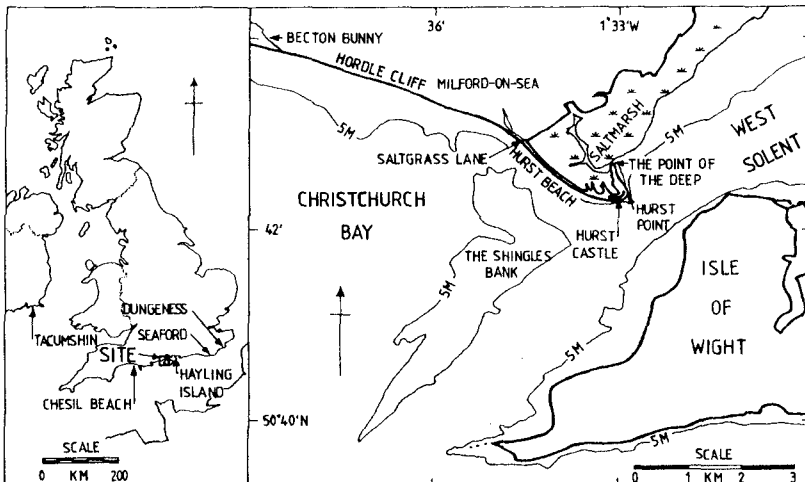


Fig. 1. Location Plan. Crown Copyright. Reproduced from Admiralty Chart 2219 with the permission of the Controller of Her Majesty's Stationery Office.

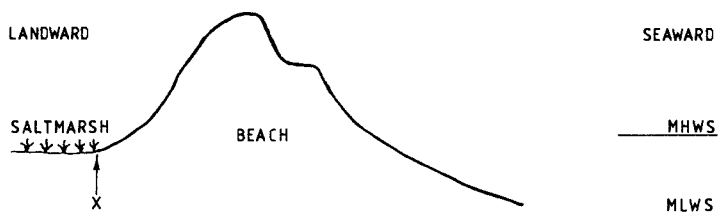


Fig. 2. A typical beach profile across Hurst Beach (vertical exaggeration X5)

with a sub-cell boundary (i.e. a minimum in the rate of net littoral drift) at Hordle Cliff, (Nicholls & Webber, 1987a).

The study area is exposed to waves generated in the Atlantic and the western English Channel. However, the Isle of Wight and the shallow shoal of the Shingles Bank, have a major effect on the energy and direction of waves impinging on the shoreline. In contrast to the British Isles generally, the tidal range is quite small, being 2.2m at springs. Storm surges can add up to 1m to water levels in this part of the English Channel. This means that, even during a neap tide, the highest predicted tide (HAT: 1.05m O.D.) may be exceeded. There are fast tidal currents off Hurst Castle in the narrow entrance to the West Solent, attaining a maximum of 2.3m/s. on mean spring tides.

LONG PERIOD WAVES

Long period, high energy swell waves originating in the Atlantic have caused significant overwashing of Hurst Beach on at least two occasions, 13 February 1979 and 2 January 1986. Both events coincided with a surge in the English Channel raising high water at Hurst Point to 1.4 and 1.0m. O.D., respectively. In February 1979, a high energy swell ($H_S = 7\text{m}$, $T_Z = 18\text{s}$) entered the English Channel from the Atlantic and caused considerable coastal damage, notably at Chesil Beach (Draper & Bownass, 1983). In Christchurch Bay the swell ($H_S < 2.5\text{m}$) caused significant overwashing of Hurst Beach and it appears that the recession of the landward margin (X in Fig. 2) was locally as much as 60m (Nicholls, 1985). In January 1986, swell waves again caused overwashing of both Chesil Beach (Dobbie & Partners, 1986) and Hurst Beach, although the damage was less severe. The energy spectrum from West Bexington (at the western end of Chesil Beach) at the height of the event shows energy present over a wide range of wave periods, with a main peak at 16 seconds and a secondary peak at 9 seconds, corresponding to locally generated waves. (Fig. 3). Two wave periods were also apparent in visual wave observations at Hurst Beach ($H_B = 2\text{m}$, $T = 9$ and 25s). The overwashing was evidently due to the longer waves. These two events are considered in more detail in subsequent sections.

Clearly, swell waves are an important factor when considering the stability of Hurst Beach. Indeed, when combined with a surge, they may, like Chesil Beach (Carr, 1983b) produce the greatest run-ups and this situation may apply generally wherever beaches are exposed to long fetches.

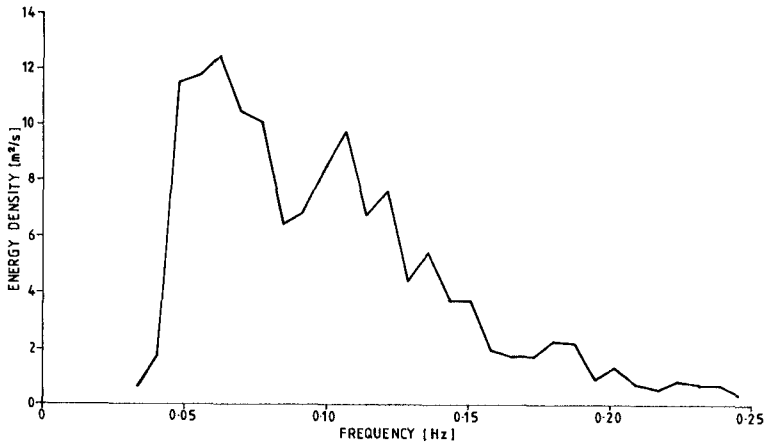


Fig. 3. The energy spectrum at West Bexington at 1030 GMT on 2 January 1986. (Measured by the Institute of Oceanographic Sciences).

OVERWASH PROCESSES

Overwash is defined as any swash that passes over the highest point of a barrier beach, which in the case of a shingle bank is the crest. Thus, overwashing causes sediment transport from the seaward to the landward side of the barrier. Overwash processes have received most attention on the sandy barrier islands of the East and Gulf Coasts of the USA (e.g. Leatherman, 1979; Oertel & Leatherman, 1985), but are also of importance on mixed sand and shingle barriers (Orford & Carter, 1982) and shingle banks. For instance the landward recession of Hurst Beach is caused by overwashing (Nicholls & Webber, 1987b) and a number of washover fans (the product of overwashing) can be seen on its landward margin. In Britain, such processes have often been described as 'overtopping' but it is best if this term is only used to describe processes which increase the height of the crest (cf Orford & Carter, 1982). Thus, overwashing may be seen as the 'failure' of a shingle bank.

On Hurst Beach two distinct forms of overwashing can be distinguished:

- (i) Crest-maintaining overwashing. The overwashing occurs without the height of the crest being reduced, e.g. Fig. 4 (small changes in the height of the crest of about 0.1m may occur);

- (ii) Throat-confined overwashing. The overwashing locally reduces the height of the crest to form what is usually termed a 'throat' or occupies a pre-existing topographic low. A washover fan is deposited on the landward side of the throat.

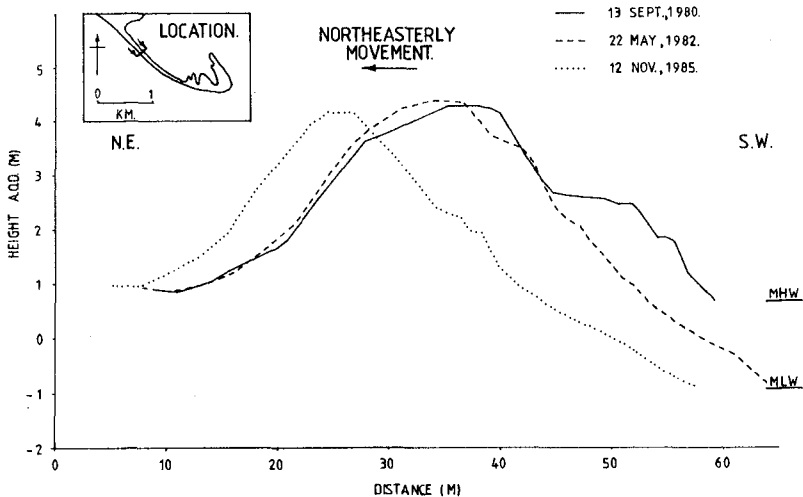


Fig. 4. Recession of a sample cross-section of Hurst Beach due to a series of crest-maintaining overwashing events (after Nicholls & Webber, 1987b).

Only the latter process has been described on sand barriers (e.g. Leatherman, 1979) or the mixed sand and shingle barriers of SE Ireland (Orford & Carter, 1982). The occurrence of crest-maintaining overwashing on shingle beaches is attributed largely to their high surface permeability. These two forms of overwashing may occur simultaneously at different locations (Fig. 5) and are clearly related: as the volume of wash passing over the crest increases so does the likelihood of the crest being reduced in height, causing a transition from crest-maintaining to throat-confined overwashing. The surface permeability must also be of significance in this transition. An extension of throat-confined overwashing to more widespread failures of the crest occurred on 23 November 1984, but individual throats were still present within the low sections of beach (see below).

On Hurst Beach, overwashing is most frequent at Saltgrass Lane, where the beach is most depleted. Throat-confined overwashing occurred on about 6 occasions per year between 1980 and 1982. More recently, shingle nourishment has reduced its occurrence. Elsewhere, overwashing occurred about twice a year between 1981 and 1987, although not all

the beach was affected in any one event. Overwashing usually occurs in response to storm waves combined with a surge, such that the tidal elevation approaches or exceeds the highest astronomical tide (1.05m O.D.). Two important exceptions are the overwashing of Hurst Beach by large swell waves, on 13 February 1979 and 2 January 1986, (see previously). Several large washover fans thought to have been deposited by throat-confined overwashing during the former event were still present on the back of Hurst Beach in May 1988.

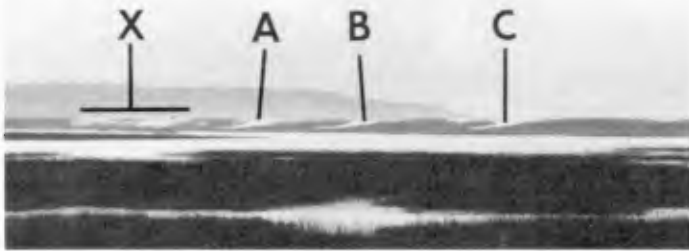


Fig. 5. Well-developed active regularly-spaced washover throats (A, B and C) on Hurst Beach on 2 January 1986. Crest-maintaining overwashing is occurring on the left of the picture (X).

Crest-maintaining overwashing is by far the more common process. Between 1980 and 1984, with the exception of three throats, all throat-confined overwashing occurred at Saltgrass Lane. However, on 23 November 1984, there was significant storm wave activity accompanied by a surge raising tidal levels to an estimated height of 1.6m O.D. The crest was reduced in height over a total distance of about 350m, comprising two lows containing 7 and 9 throats, respectively (Fig. 6).

Every throat formed in the period being considered was filled artificially in an attempt to reduce recession, usually using the washover deposits. Therefore, the long term evolution of the throats was not observed.

Crest-maintaining overwashing is a less efficient mechanism for net onshore sediment transport than throat-confined overwashing: the maximum measured volume of onshore transport over the crest during a single storm was $6\text{m}^3/\text{m}$ as compared to $150\text{m}^3/\text{m}$ due to throat-confined overwashing. An overwash budget for Hurst Beach is not available, but it is clear that infrequent throat-confined overwashing events could equal or exceed the net onshore transport caused by more numerous crest-maintaining overwash events.

Therefore it is worth considering if the prevention of overwashing should always be a principal aim in shingle beach management. Throat-confined overwashing is clearly unacceptable. In contrast, the shingle bank remains an effective barrier during crest-maintaining overwashing. Very few, if any, swashes reach the landward margin. The resulting landward movement of the bank is easily monitored, although as Fig. 4 illustrates, it can be quite rapid (3m/yr). The main benefit is the smaller volume of beach fill required. This approach may be useful as a short or medium term solution to problems at sites where some recession is permissible.

RUN-UP CHARACTERISTICS

Although no direct run-up measurements were made, the formation of washover throats on a beach with a uniform longshore section allows the position of a run-up maxima to be inferred. The run-up associated with these high energy events is of most interest in studies of coastal stability.

The spacings of the washover fans and overtop deposits formed on 23 November 1984 are shown in Fig. 6. In the case of the overtop deposits, the longshore peaks of run-up were indicated by a topographic maximum where vertical accretion had been most pronounced, rather than a topographic minimum as indicated by the throats (Fig. 6B). The sample comprises 27 measurements with a range between 10.3 and 45.7m. The distribution is approximately lognormal. The washover throats show two distinct modes at about 13 and 23m with a few larger spacings. The overtop deposit data is more scattered with the mode occurring at about 19m. The scatter is to be expected as the overtop deposits have a volume a tenth or less than the washover throats and as such will not 'record' the run-ups so clearly. Taking the dataset as a whole, there is a significant (sig. > 95%) decline in the spacings along Hurst Beach (Fig. 6C). The interpretation of this result is not clear. Not surprisingly, taking the scatter and this factor into account, autocorrelation showed no significant evidence of memory. However, when the results were compared with a Poisson distribution for longshore spacings of 10, 15 and 20m, the observed distribution was non-random in all cases (sig > 95%). Thus, the washover throats and overtop deposits show a preferred longshore spacing, but cannot be considered to be periodic.

On 2 January 1986 the throat-confined overwashing of Hurst Beach by the long period swell produced four small throats with a regular longshore spacing (mean = 37m, standard deviation = 2.69m) (Fig. 5). The adjacent crest-maintaining overwashing showed similar longshore spacing, although it was not possible to take direct measurements. This observation indicates that the run-up was exhibiting regularly-spaced maxima along the shore.

Thus two distinct overwash events of Hurst Beach have produced morphological evidence indicating non-randomly spaced longshore maxima of run-up. Orford & Carter (1984) have

described over 60 regularly-spaced washover throats on the mixed sand and shingle barrier of Tacumshin, S.E. Ireland. The modal spacing was about 40m and appeared to be controlled by high elevation beach cusps.

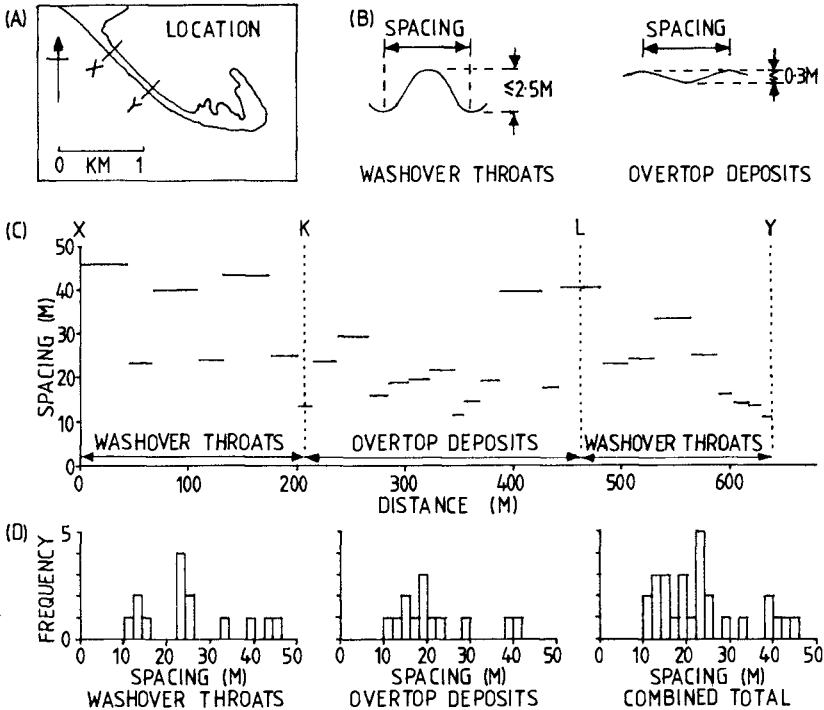


Fig. 6. The longshore spacing of the washover throats and overtop deposits formed on 23 November 1984. (A) Location Plan. (B) Definition sketches of spacing as measured on washover throats and overtop deposits. (C) The location of each longshore spacing between X and Y together with its magnitude. Spacings K and L are transitional between the two morphologies. (D) The numerical frequency distribution of the washover throats, the overtop deposits and their combined total.

Two distinct hypotheses may explain regularly-spaced run-up maxima:

- (i) longshore variation in the wave field e.g. phase-coupled edge waves;
- (ii) interaction of the run-up with pre-existing rhythmic three-dimensional beach morphology e.g. run-up amplification at swash cusps.

To some extent these two hypotheses are linked as it is generally considered that many three-dimensional beach

features are a product of edge waves e.g. swash cusps (Inman & Guza, 1982). However, it is important to distinguish between active longshore variation in the wave field and the influence of three-dimensional morphology which may modify the run-up a considerable period of time after the waves which produced it have ceased.

Large swash cusps with a similar mean spacing (36.6m), but a larger standard deviation (7.38m) than the washover throats are known to have been present on Hurst Beach prior to 2 January 1986. During the overwashing the beach face showed a rhythmic undulation which was in phase with the active throats. These are presumed to have been the subdued remnants of the pre-existing beach cusps. A similar mechanism may have occurred on 23 November 1984, although no evidence is available. By contrast, active edge wave control appears unlikely. The most easily excited edge wave and the one with the largest amplitude is a zero mode subharmonic edge wave (Inman & Guza, 1982). Such an edge wave would have produced longshore run-up maxima with a spacing of about 44 (23 November 1984) and 112m (2 January 1986), showing little agreement with the field data. Thus it is inferred that run-up amplification at swash cusps can be of significance on shingle beaches. Orford & Carter (1984) favoured an active edge wave control of the throat spacings they observed in Ireland. However, the wave conditions which produced the throats are poorly known and a similar mechanism to that inferred for the two events at Hurst Beach is quite plausible.

These results all illustrate our poor understanding of run-up on coarse-grained beaches and yet the maximum run-up is one of the most important parameters required in the design of shingle nourishment schemes. The occurrence of run-up maxima suggests that the results of two-dimensional flume model studies may be inappropriate for studies of maximum run-up. Even in the absence of the evidence presented, the formation of a single washover throat on a previously uniform length of beach leads to the same conclusion. Clearly, wave basin model studies combined with accurate field measurement of run-up characteristics on shingle beaches are required, (see Holman & Guza, 1984). These should include an analysis of the longshore structure of run-up and its interaction with three-dimensional topography. From the evidence presented, it is apparent that even with a uniform incident run-up, amplification of that run-up at swash cusps may occur and this process requires quantification. The common occurrence of swash cusps on shingle beaches may make this a significant factor. The run-up characteristics of long period high energy swell waves must also be considered.

SEEPAGE CHARACTERISTICS

Shingle beaches are highly permeable when compared to their sand equivalents. The piezometric and seepage characteristics of Hurst Beach were investigated along one cross-section using a line of standpipes (Fig. 7).

The constriction of the tidal flow between Hurst Point and the Isle of Wight causes a differential water level of up to 0.7m across Hurst Beach on the rising stage of equinoxial tides, i.e. higher water levels in Christchurch Bay than in the West Solent. This might be expected to produce landward seepage of seawater through the beach. However, this is not the case, and the water table shows its maximum amplitude at the landward margin (see Day 2 - Fig. 7). This apparently anomalous behaviour can be mainly attributed to the large permeability contrast, estimated to be of the order of 10^3 , between the relatively impermeable veneer of sand over the foreshore and the more permeable much less sandy washover deposits on the landward side. This example illustrates that while shingle beaches are highly permeable, the sedimentology, particularly the amount and location of sand, has a profound influence on the seepage characteristics of such beaches.

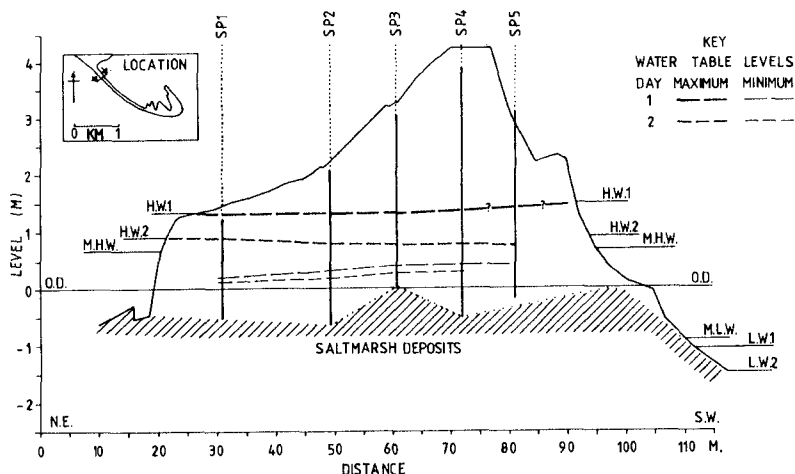


Fig. 7. Maximum and minimum water levels at five standpipes (SP1 to SP5) in Hurst Beach in response to an equinoxial tide and storm waves. (Day 1 - 8 March 1981) and an equinoxial tide and calm conditions (Day 2 - 5 April 1981). The elevation of high water for Day 1 in Christchurch Bay (on the south-west side) includes an estimate of wave set-up. The elevations of low water are estimated and only shown for guidance.

Landward seepage of seawater through the beach does occur, but only in association with wave activity. For instance on 8 March 1981, with breaking waves of up to 1.8m, the water table dipped landward throughout the tidal cycle (Fig. 7) with flows estimated to be in the range 0.3 to $1.7\text{m}^3/\text{h}/\text{m}$. The differing behaviour may be attributed to:

- (a) Offshore sediment movement of the sand veneer on the foreshore exposing more permeable sediments;

- (b) Increased differential water levels across the beach due to wave set-up, plus a contribution to the water table due to swash infiltration.

These effects are reinforced by high water levels produced by storm surges, because it appears that, in bulk terms, there is a vertical increase in the permeability of the beach.



Fig. 8. A seepage hollow formed on the landward side of Hurst Beach on 23 November 1984. Note the angle of repose slope. The man is 1.80m tall.

Between 1980 and 1986 the seepage of seawater through Hurst Beach was sufficient to cause local erosion of its landward margin on at least six occasions. This produces paired erosional seepage hollows and depositional fans (Fig. 8). Some of these occasions were significant storm surges but this was not always the case, wave height also being of importance. The elevation of some of the seepage hollows (up to 1.7m O.D.) demonstrates the high water levels which may be developed within the beach. These features display a wide range of morphology, some being similar, but on a smaller scale, to the so-called 'cans' of Chesil Beach (Carr & Blackley, 1974). The maximum volume of shingle eroded from a seepage hollow during a single storm was 10m^3 (or about $5\text{m}^3/\text{m}$). Once formed a seepage hollow may be active again producing an increase in size. However, the rapid recession of Hurst Beach leads to the regular infilling of the seepage hollows with washover deposits.

A feature of all the seepage hollows observed was an angle of repose slope (e.g. Fig. 8). Shingle is removed from the base of the hollow resulting in a slope failure migrating into the beach. Clearly if this process were to continue until the seepage hollow intersected the crest it would result in failure of the beach, creating a site for throat-confined overwashing. The size distribution of the seepage hollows suggests that this did not happen on Hurst

Beach during the period of observation. However, at Dungeness, Kent (Eddison, 1983) and in S.E. Ireland (Carter, Johnston & Orford, 1984) seepage erosion appears to aid overwashing. On a nourished shingle bank which will usually be designed to be static, the attritional losses caused by seepage erosion could ultimately have similar consequences. Thus, any beach profiling/monitoring should include any landward slope in addition to the seaward portion of the beach.

SETTLEMENT BENEATH BEACHES

As Hurst Beach moves northeastwards, due to overwashing, so it is moving across the Spartina saltmarsh which occurs in its lee. Saltmarsh deposits can often be seen on the foreshore but are rapidly eroded. The best such exposure known to the authors occurred between 1979 and 1980 when several hundred square metres of former saltmarsh surface was clearly exposed, including the dead and crushed Spartina stems and leaves (Fig. 9). The surface was horizontal as in the living saltmarsh, but levelling demonstrated that it was about 1.0m lower. After careful examination of a number of hypotheses it was concluded that the difference in elevation was due to the settlement of the saltmarsh deposits beneath the weight of the beach. The Spartina surface of the saltmarsh provides a useful datum for the direct measurement of such changes.

Cartographic evidence demonstrates that the settlement must have occurred in less than 10 years. The thickness of the deposits behind the beach exceeds 5m and includes an unknown thickness of highly compressible peat. The thickness of the beach sediments shows both temporal and spatial variation with a probable maximum of 4m at this site. A preliminary geotechnical analysis demonstrates that the settlement will not have reached completion in 10 years, although there is some uncertainty about long-term values.

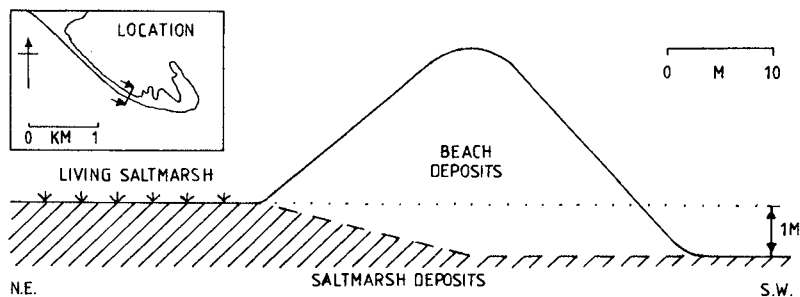


Fig. 9. A diagrammatic cross-section illustrating the settlement of the salt-marsh deposits which was visible across Hurst Beach between 1979 and 1980.

It is concluded that the geotechnical properties of the deposits beneath beaches may have significance when considering beach stability. This factor is independent of grain size and also applies to sand beaches (e.g. Dean, 1987). Rapid settlement will reduce the elevation of the overlying beach and thus on an eroding coastline will accentuate shoreline recession. In the static situation of nourishment, settlement must be considered when calculating volumes of beach fill. In effect, settlement provides a third potential loss of sediment in addition to offshore and longshore losses.

SHINGLE NOURISHMENT

In recent years, marine-dredged beach fill has become the dominant source for shingle nourishment in Britain on a tonnage basis. However, it normally contains considerable quantities of sand due to: (i) source and (ii) the method of delivery to the beach. Split bottom barges drop the dredged gravel as high on the foreshore as possible during the rising tide. On the falling tide the gravel is recovered and placed where required. This method inevitably mixes the sandy foreshore sediments with the beach fill which itself may contain finer material to assist pumping. Such mixtures of shingle and sand are rarely present on the supratidal portion of 'natural' shingle beaches, largely because they are eroded by waves. Thus, marine-dredged beach fill is usually unstable on the supratidal portion of a shingle beach. For instance, at Hurst Beach and Hayling Island marine-dredged beach fill was imported as described. During storms, offshore sediment movement occurred and vertical supratidal beach scarps, locally up to 2m high, developed. (Fig. 10). While subsequent onshore transport deposited shingle berms, the scarps persisted for months at both sites, migrating onshore during storms, before being removed artificially. At Hayling Island they reformed suggesting that they may persist for years without human interference.

Beach scarps up to 3m high are common features on some sandy beaches (Sherman & Nordstrom, 1985), but shingle will only support a vertical slope when sand fills the interstices, e.g. beach scarps up to 0.1m high have formed for short periods (hours) in the foreshore sediments of Hurst Beach. Thus, the scarps in the beach fill are an order of magnitude larger and much more persistent than any equivalent features on a natural shingle beach. Scarp formation was not observed, but clearly involves accentuated offshore sediment movement from the base. Once formed, the vertical scarp must cause wave reflection when active, accentuating offshore sediment transport in a similar manner to a sea-wall. This is not to say that the beach scarp is the primary cause of the erosion, it only being a response to the hydraulically unstable sediment distribution.

Therefore, it is best to use land-derived beach fill which usually contains little or no sand for shingle nourishment. However, the large scale of many recent and proposed nourishment schemes probably makes such sources inappropriate.

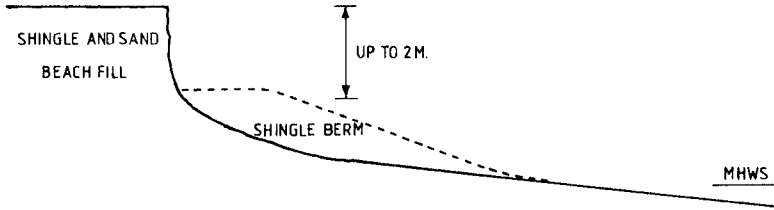


Fig. 10. A diagrammatic cross-section through a beach scarp on a nourished shingle beach.

Some improvements in marine delivery methods may be possible. If not, suitable allowance for beach scarping must be made during design. Assuming that the volume of beach fill is appropriate and longshore losses are small, in the long-term, scarping is not a problem; rather it should be seen as sorting of the beach fill. The shingle moved offshore is returned to the beach while the sand will remain on the foreshore and ultimately the beach will display a surface sorting similar to that seen on a 'natural' shingle beach.

CONCLUSIONS

Shingle beaches exhibit characteristics which are somewhat distinct from sand beaches. These include a far superior performance under wave action for equivalent volumes of beach material, so it is not surprising that shingle is becoming increasingly favoured as a nourishment material. However, field studies indicate a number of problems which require more research. Of particular importance is the observation that run-up shows longshore maxima. There is inadequate understanding of run-up on shingle beaches and its interaction with the swash cusps which are so often present. The role of the subsidiary sand component of the beach sediments is often ignored, but is of importance with regard to factors such as permeability and beach scarping. It is also important that existing shingle nourishment projects are monitored and studied.

ACKNOWLEDGEMENTS

The authors thank Dave Coats, Alan Carr, and Julian Orford for useful discussions, Laurie Draper, IOS for providing wave data, and Dobbie and Partners and their clients, Weymouth and Portland Borough Council and the Wessex Water Authority for permission to use unpublished work at Chesil Beach.

REFERENCES

- Carr, A.P. 1983a. Shingle beaches: aspects of their structure and stability. p 97-104. In Shoreline Protection. Thomas Telford Ltd., London.
- Carr, A.P. 1983b. Chesil Beach: Environmental, economic and sociological pressures. Geographical Journal. 149, 53-62.

- Carr, A.P. & Blackley, M.W.L. 1974. Ideas on the origin and development of Chesil Beach, Dorset. Proceedings of the Dorset Natural History and Archeological Society, 95, 9-17.
- Carter, R.W.G., Johnston, T.W. & Orford, J.D. 1984. Stream outlets through mixed sand and gravel coastal barriers: examples from southeast Ireland. Zeitschrift fur Geomorphologie, NF 28, 427-442.
- Dean, R.G. 1987. Coastal sediment processes: Toward engineering solutions. p 1-24. In: Proceedings of Coastal Sediments 87. ASCE, New York.
- Dobbie, C.H. & Partners. 1986. Chesil sea defence scheme: Report on flood event 2 January 1986. Unpublished.
- Draper, L. & Bowmass, T.M. 1983. Unusual waves on European coasts, February 1979. p 270-281. In: Proceedings of 18th Coastal Engineering Conference, ASCE, New York.
- Eddison, J. 1983. Flandrian barrier beaches off the coast of Sussex and southeast Kent. Quaternary Newsletter, 39, 25-29.
- Foxley, J.C. & Shave, K. 1983. Beach monitoring and shingle recharge. p 163-170. In: Shoreline Protection. Thomas Telford Ltd., London.
- Holman, R.A. & Guza, R.T. 1984. Measuring run-up on a natural beach. Coastal Engineering, 8, 129-140.
- Inman, D.L. & Guza, R.T. 1982. The origin of swash cusps on beaches. Marine Geology, 49, 133-148.
- Leatherman, S.P. (ed). 1979. Barrier Islands. Academic Press, New York.
- Muir-Wood, A.M. 1970. Characteristics of shingle beaches: the solution to some practical problems. p 1059-1076. In: Proceedings 12th Coastal Engineering Conference, ASCE, New York.
- Nicholls, R.J. 1985. The stability of the shingle beaches in the eastern half of Christchurch Bay. Ph.D. Thesis, Dept. of Civil Engineering, University of Southampton, 468 pp.
- Nicholls, R.J. & Webber, N.B. 1987a. Coastal erosion in the eastern half of Christchurch Bay. p 549-554. In: Culshaw, M.G. et al (eds) Planning and Engineering Geology. Geological Society, Engineering Geology Special Publication No. 4, London.
- Nicholls, R.J. & Webber, N.B. 1987b. The Past, Present and Future Evolution of Hurst Castle Spit, Hampshire. Progress in Oceanography, 18, 119-137.
- Oertel, G.F. & Leatherman, S.P. (eds). 1985. Barrier Islands. Special Issue. Marine Geology, 63.
- Orford, J.D. & Carter, R.W.G. 1982. Crestal overtop and washover sedimentation on a fringing sandy gravel barrier coast, Carnstone Point, S.E. Ireland. Journal of Sedimentary Petrology. 52, 265-278.
- Orford, J.D. & Carter, R.W.G. 1984. Mechanisms to account for the longshore spacing of overwash throats on a coarse clastic barrier in southeast Ireland. Marine Geology, 56, 207-226.
- Sherman, D.J. & Nordstrom, K.F. 1985. Beach scarps. Zeitschrift fur Geomorphologie. NF 29, 139-152.

CHAPTER 143

PREDICTION OF 3-D BEACH CHANGES ON THE FUJI COAST

OHISHI, H^{*}, T.UDA^{**}, Y.MURAKAMI^{***} AND
M.WATANABE^{***}

ABSTRACT

Beach changes around Tagonoura Port on the Fuji Coast were investigated by using the topographic survey data collected in the 15 years between 1968 and 1983. Temporal and spatial changes of the offshore distance from a reference point to certain contours were analyzed to elucidate the actual situation of topographic changes on the Fuji Coast, and the littoral transport rate on the downdrift coast of Tagonoura Port was found to be about $1.17 \times 10^5 \text{ m}^3/\text{yr}$ on the average between 1973 and 1983. It is concluded that a large amount of sediment eroded from the downdrift beach of Tagonoura Port is carried away toward a zone deeper than 20m. A numerical model predicting three-dimensional beach changes was also developed, taking account of both the vertical distribution of littoral transport and the effect of the wave-dissipating breakwaters.

1. INTRODUCTION

In recent years beach erosion has become severe along Japan's coasts. The Fuji Coast, surrounding Suruga Bay and formed by the fluvial sediment supply from the Fuji River, is one of these eroded coasts. Since the early 1960s sediment supply to this coast has decreased due to the influence of extensive excavation of the river bed, eroding the coast around the river mouth. Since 1959 the breakwater at Tagonoura Port has been constructed in the middle of the coast, and then the downdrift beach of the harbor was further eroded. As a countermeasure against beach erosion, wave-dissipating breakwaters, composed of concrete blocks parallel to the shoreline, have been constructed since 1973 on the downdrift coast of the harbor. The beach erosion on the Fuji Coast seems to be a typical example of beach erosion occurring along Japanese coasts from a caused point of view. For this reason, it is of primary importance to investigate the actual situation of the beach erosion and the effectiveness of the countermeasures along this coast in order to understand the beach erosion problems in Japan.

Along this coast, topographic surveys have been conducted once a year since 1968. This study aims to investigate beach changes around the harbor in the 15 years between 1968 and 1983 by using the topographic survey

* Head, Numazu Work Office, Chubu Regional Construction Bureau, Ministry of Construction, Shizuoka 410 Japan.

** Dr.Eng., Head, Coastal Eng. Div., Public Works Research Institute, Ministry of Construction, Ibaraki 305 Japan.

*** Numazu Work Office.

data. In order to analyze the field data, temporal and spatial changes of the offshore distances from a reference point to certain contours are studied. The validity of this method has been proved when applied to the analysis of beach profile changes on the Suruga Coast (Uda and Takeuchi, 1985) and Kochi Coast (Uda et al., 1986).

The temporal and spatial beach changes on the Fuji Coast are elucidated through this study, and the littoral transport rate on the downdrift coast of Tagonoura Port is evaluated. In particular, it is concluded that a large amount of sediment eroded from the downdrift beach of Tagonoura Port is carried away toward a zone deeper than 20m. The second aim of this study is to develop a numerical model which can predict three-dimensional beach changes. For this purpose, a model in which the vertical distribution of littoral transport is taken into account and the effect of the wave-dissipating breakwaters on the beach changes can be evaluated is developed.

II. METHOD OF INVESTIGATION

The Fuji Coast surrounds Suruga Bay facing the Pacific Ocean to the south (Fig.1). The water depth of Suruga Bay is so deep that the Fuji Coast has a steep slope as shown in Fig.1. At a location about 5.5km east of the mouth of the Fuji River lies Tagonoura Port, which was constructed in 1959. Topographic surveys have been conducted once a year since 1968 in the region between survey line No.0, adjacent to Numazu Port, and No.85, next to the mouth of the Fuji River. The survey line interval for the bottom sounding is 250m. In this study the bottom sounding data obtained over the 15 years between 1968 and 1983 are analyzed in order to investigate the beach changes on the Fuji Coast. For this purpose, temporal and spatial changes of the offshore distance from the reference point to certain contours between 2m above and 30m below the MSL are investigated.

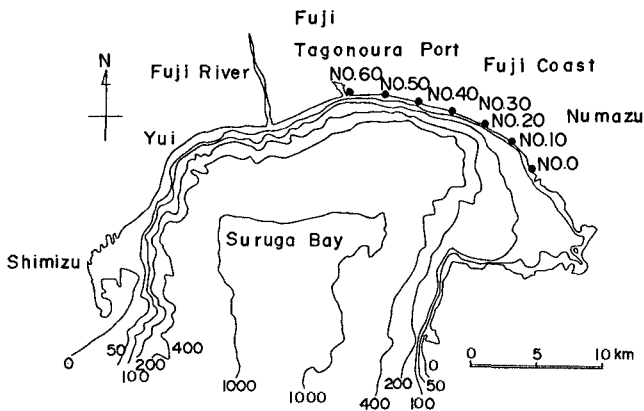


Fig.1 Location of the Fuji Coast

III. BEACH EROSION ON THE FUJI COAST

3.1 Spatial and temporal changes of shoreline configuration

First, the actual situation of the beach erosion on this coast will be studied focusing on shoreline changes before advancing the detailed analysis with respect to the movement of bottom contours in the shallow water zone. The changes in the shoreline configuration on the Fuji Coast are shown in Fig.2. The abscissa is taken for the number of the survey lines set along the coastline, in which No.0 and No.85 are located next to Numazu Port and the Fuji River, respectively. The locations of various facilities are denoted by the serial number in the figure. Since the interval of the survey lines represents 250m, the entire distance in Fig.2 includes 20.25km of shoreline. The ordinate expresses the change of shoreline positions measured in each year since 1968 until 1983 relative to the shoreline configuration in 1968.

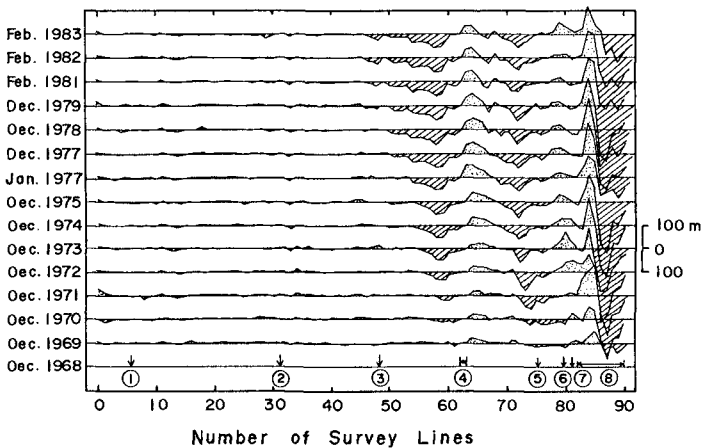


Fig.2 Temporal and spatial changes of the shoreline position on the Fuji Coast (1: Shinnakagawa Flood Way, 2: Showa No.2 Flood Way, 3: Showa Flood Way, 4: Tagonoura Port, 5: Nyudo Drainage channel, 6: Motofuji No.2 Drainage Channel, 7: Motofuji Drainage Channel, 8: Fuji River).

After the construction of the harbor breakwater in 1959, the east coast of the harbor has been gradually eroded. The eroded region extended from No.62 up to No.49, or 3.5km, until 1983. These features of the shoreline retreat in a region next to the harbor breakwater obstructing littoral transport show that the dominant direction of littoral drift on this coast is eastward. As the beach was eroded, wave-dissipating breakwaters, composed of the concrete blocks, have been constructed to counteract beach erosion, and at present, the whole coastline between Tagonoura Port and Showa Flood Way is covered by the concrete blocks. However, many concrete blocks have been scattered in this region due

to the scouring at the foot of the breakwaters and due to the wave action on the blocks(Kohno et al., 1986).

As is clearly understood in Fig.2, beach erosion was observed between Tagonoura Port and Showa Flood Way. Nevertheless, the shoreline configuration between Showa Flood Way and Numazu Port at No.0 has been of stable form during the same period. This implies that the eroded materials from the updrift coast were carried away in the offshore direction. This offshore movement of sand is important when studying the littoral drift on the Fuji Coast, so that this point will be discussed in detail in the later section. Furthermore, it is found from Fig.2 that beach erosion is also severe next to the mouth of the Fuji River. Just west of Tagonoura Port, where the shoreline has advanced in recent years in contrast with the shoreline retreat on the east coast, littoral sand has been lost partly by the offshore movement in front of the tip of the breakwater, and partly by the excavation of sand for use in the construction industry.

Figure 2 is useful to understand the spatial changes of the shoreline configuration, but in order to realize the time lag in shoreline changes existing between survey lines, it is favorable to take time as the independent variable. Therefore, the temporal changes of the shoreline positions between No.62 and No.45 located on the downdrift site of Tagonoura Port are shown in Fig.3. Time is taken as the abscissa and the ordinate is the change of the shoreline positions relative to the one measured in December, 1968 for the initial value. In addition, the sign(\square) in the figure expresses the time when the wave-dissipating breakwater was constructed at each survey line. The first one was built in 1973 at survey line No.58, and until 1978, 17 wave-dissipating breakwaters have been constructed along the shoreline. It should be noted that the construction time of the breakwaters corresponds to the shoreline retreat at each survey line fairly well, indicating that the construction site was extended eastward with the continuous shoreline retreat. Maximum shoreline retreat was observed at No.58 and it reaching about 50m in two years between 1971 and 1973. Thereafter the rate of the shoreline retreat became small by virtue of the wave-dissipating breakwater constructed in 1974. It is found that there exists a time lag in the initiation time of the shoreline retreat with the distance from No.62 next to Tagonoura Port. It was not until 1979 that the shoreline retreat began at No.48. In addition, it is understood that the rate of the shoreline change at the initial stage tends to decrease with the distance from the port, when compared with the shoreline changes observed at two survey lines located far from the port such as No.48 and in the vicinity of the port such as No.58.

3.2 Numerical simulation of change of shoreline configuration

Some features of the changes of the shoreline configuration observed on the coast just east of Tagonoura Port can be predicted by using the one-line model of

shoreline evolution as described in the following, if simple assumptions were made. First, it is assumed that the beach changes are caused only by the imbalance of littoral transport and do not depend on cross-shore sand transport. The definition sketch and the initial conditions are shown in Fig.4. Secondly, it is assumed that there exists a vertical wall totally obstructing littoral transport, like a jetty, at the righthand side of the region, and that the distance from the initial shoreline to the wave-dissipating breakwater of continuous type is equal to ℓ . Furthermore, the wave incidence is assumed to be from clockwise direction as shown in Fig.4. In the calculation, the diffraction effect of the jetty is neglected.

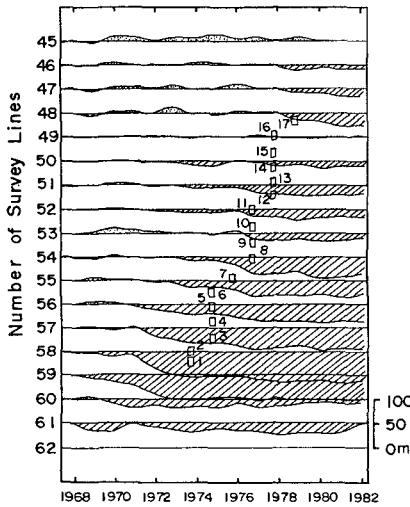


Fig. 3 Temporal changes of the shoreline positions in the region east of Tagonoura Port.

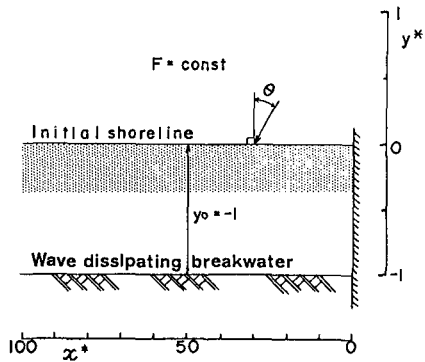


Fig. 4 Definition sketch of shoreline simulation model.

Fundamental equations of the one-line model of the shoreline evolution are expressed by Eqs. (1) and (2).

$$\frac{\partial q}{\partial x} + h \frac{\partial y}{\partial t} = 0 \tag{1}$$

$$q = F \left(- \frac{\partial y}{\partial x} + \tan \theta \right) \tag{2}$$

Where q : littoral transport rate, h : characteristic height of beach changes caused by littoral transport, x : longshore distance, t : time, F : coefficient depending upon the wave characteristics. In this study coefficient F and h are assumed to be constant in order to understand the essence of the phenomenon as easily as possible. Next, in order to simplify the analysis some dimensionless variables are introduced as follows:

$$y = \ell y^*, \quad x = \ell x^*, \quad t = \frac{\ell^2 H}{F} t^*, \quad \varphi = F \varphi^* \quad (3)$$

where ℓ is a characteristic length scale, and variables with the asterisk denote the dimensionless forms. Substituting these forms into Eqs. (1) and (2), then dimensionless forms of the equations are obtained.

$$\frac{\partial \varphi^*}{\partial x^*} + \frac{\partial y^*}{\partial t^*} = 0 \quad (4)$$

$$\varphi^* = - \frac{\partial y^*}{\partial x^*} + \tan \theta \quad (5)$$

In this calculation it is assumed that the shoreline does not retreat if the shoreline position coincides with the location of the wave-dissipating breakwater, and the breaker angle normal to the shoreline is equal to 10° . The results of the simulation of the shoreline evolution are expressed in Fig.5 showing the x^*-t^* diagram of the shoreline changes. The vertical axis and the abscissa are taken for the dimensionless longshore distance x^* and the dimensionless time t^* . The initial shoreline and the wave-dissipating breakwater are located at $y^*=0$ and $y^*=-1$, respectively, and the base line of y^* axis is moved upwards. It is found from Fig.5 that the beach downdrift of the jetty was rapidly eroded by the influence of the jetty, and that the time when the shoreline begins to retreat has a time lag with the longshore distance from the jetty. Furthermore, it is found that the duration required for the shoreline position to retreat to the location of the wave-dissipating breakwaters increases with the distance from the origin. These features obtained in the simulation are in good agreement with the field data shown in Fig.3, and it is concluded that the fundamental phenomenon of the shoreline changes caused by the obstruction of littoral transport can be understood through the present simple model.

3.3 Temporal and spatial changes of offshore distances

In the previous section, only the temporal and spatial changes of the shoreline configuration were discussed. In this section, temporal and spatial changes of the offshore distances from the reference point to some contours are studied in detail. First, the longshore distribution of the offshore distances from the reference points, which were determined along the foot of the coastal dike, to some contours selected at 5m intervals are shown in Fig.6. It can be clearly seen from Fig.6 that the bottom slope is steep between No.5 and No.25 because of the small intervals of the offshore distance to each contour, and that there exists a comparatively mild slope between No.25 and No.45. Beyond No.46, the contours have irregular shapes, expressing the irregular bottom topography.

Next, the changes of the offshore distance at some typical survey lines are investigated. For the typical survey lines, No.54 and No.58, located east of Tagonoura Port where the beach was eroded severely in recent years, are selected. Figure 7 shows the temporal change of the offshore distance from the reference point to some contours

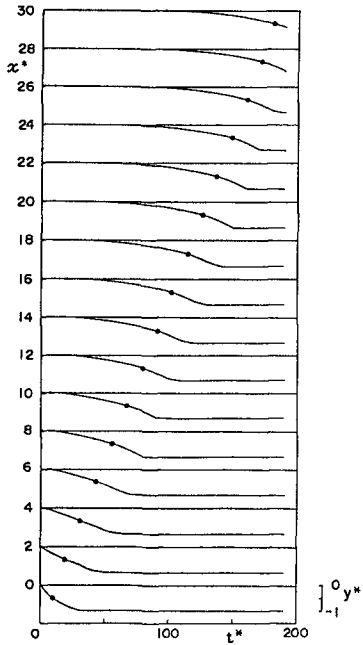


Fig. 5 x^*-t^* diagram of change of shoreline position.

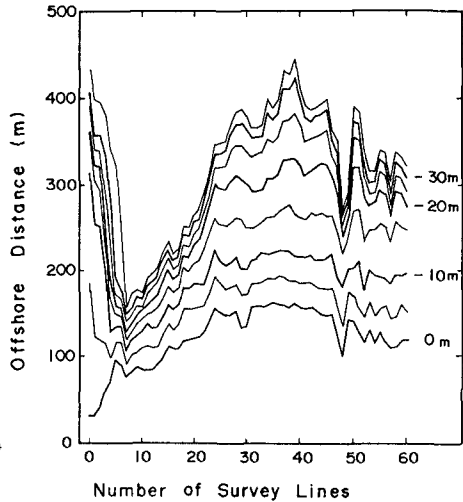


Fig. 6 Longshore distribution of offshore distance to some contours.

at No.54. The abscissa is the elapsed time, and the vertical axis is the offshore distance. The shoreline position began to retreat rapidly from Dec., 1975 and the contour lines between 2m above and 10m below the MSL retreated simultaneously with the shoreline change. This means that the beach profile in this region has changed its shape as a whole. By contrast, the change in offshore distance to contours deeper than 16m is small, except for the tendency of a gradual advance in the region deeper than 20m. This fact implies that part of sand eroded from the nearshore zone was carried away in the offshore direction, and therefore net loss of sand was caused on this beach, although the mechanism of the movement of sand is not known at present.

Similarly, the temporal changes of the offshore distance at survey line No.58, located 1km west of No.54 and 1km east of Tagonoura Port, are shown in Fig.8. It is found that the shoreline retreat at No.58 began faster than that at No.54 when Figs.7 and 8 are compared. Rapid retreat of the shoreline position began in 1971, 4 years earlier than that at No.54. The reason that the beach changes at No.58 were observed faster than the changes at No.54 is because of the proximity of survey line No.58 to the harbor structure obstructing littoral transport. The existence of the time lag in shoreline change shows that the beach erosion on this coast mainly depends upon the littoral transport. Further-

more, it is found from Fig.8 that the offshore distance defined between 2m above and 10m below the MSL gradually decreased, whereas the offshore distance to contours deeper than about 16m gradually increased, expressing the possibility of the offshore sand movement of part of the eroded sand.

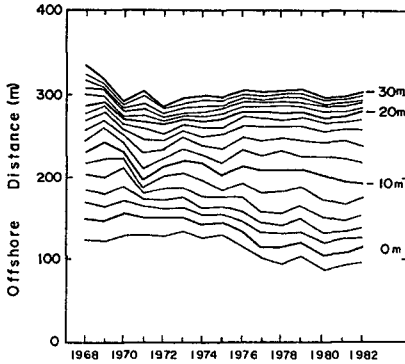


Fig.7 Temporal changes of offshore distance at survey line No.54.

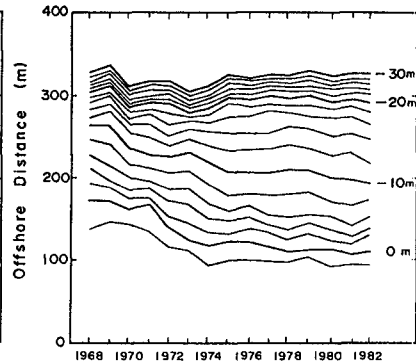


Fig.8 Temporal changes of offshore distance at survey line No.58.

Knowledge of the offshore movement of bed materials is of vital importance in order to formulate a plan to counteract beach erosion on this coast, because this movement results in the net loss of sand in the nearshore zone, and the beach will be eroded to a large extent in the long term. For the purpose, the cumulative value of the area surrounded by the contours and the abscissa in Fig.6 is calculated first, and then the change in the cumulative value (ΔS) with reference to the one measured in 1974 is obtained (Fig.9). For the calculation, 1983 bottom sounding data is selected, and the origin is set at No.60.

Cumulative area corresponding to the shoreline change shows the net loss in area in the longshore direction, and ΔS decreased about $5 \times 10^4 \text{ m}^2$ in 9 years up to No.0, adjacent to the breakwater of Numazu Port. Between No.60 and No.45, the rate of the decrease of ΔS is large, but thereafter it becomes small. In Fig.9, the changes in the area surrounded by the 5-m-interval contours are shown as well. It is found that ΔS corresponding to 5 and 10m deep contours undergoes a change similar to that corresponding to the shoreline. Namely, the absolute values of ΔS increase abruptly between No.60 and No.45, and they show a net loss in area at No.0. The losses of the areas attain about $7 \times 10^4 \text{ m}^2$.

On the contrary, the changes of the area surrounded by the 20, 25 and 30m deep contours contrast sharply with those measured in shallower zone. In the offshore zone ΔS increases with the distance from No.60, whereas ΔS in the shallow zone decreases. However, it should be noted that the eroded area in the shallow zone increased rapidly between No.60 and No.45, while the accreted area in the offshore

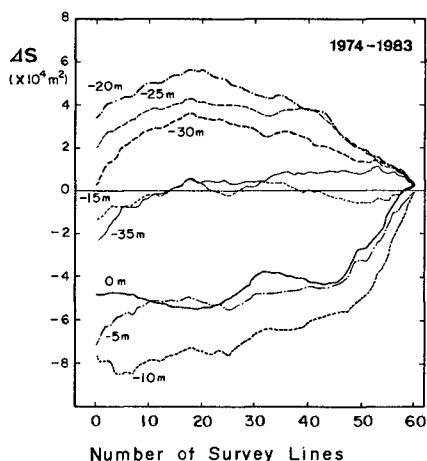


Fig.9 Longshore distribution of change of cumulative value of the area surrounded by offshore distance to some contours as shown in Fig.6.

zone tends to increase gradually from No.60 up to No.18. The increase rate of ΔS is especially large in the region where mild bottom slope was observed in the offshore zone as shown in Fig.6. These features indicate that a large amount of the sediment eroded on the downdrift beach of Tagounoura Port will be finally carried away toward the zone whose depth is between 20 through 30m. This kind of offshore sand movement along this coast was also confirmed through field investigations, using a radioactive tracer (Shuto et al., 1977). The results of the present study agree well with the findings of this field test.

3.4 Characteristic height of beach changes and littoral transport rate

On the east coast of Tagounoura Port, where beach erosion has been mainly due to the imbalance of littoral drift in recent years, temporal changes in the beach sections have been measured once a year so that the relationship between the changes in the sectional area and those of the shoreline position can be investigated. The calculation is carried out between No.61 and No.45, where beach changes caused by littoral transport are more dominant than those caused by cross-shore transport, judging by the movement of contours shallower than 10m which are very similar to each other, and the amount of sand carried in the offshore direction being comparatively small in this region, as shown in Fig.9. The characteristic height of beach changes caused by littoral transport can be determined empirically from the relationship between the change in the sectional area and that of the shoreline position. If the change in the sectional area (ΔA) can be expressed in terms of the change in shoreline position (Δy) for a linear relationship, then the regression coefficient becomes equal

to the characteristic height of beach changes caused by littoral transport (Uda et al., 1986). When the regression coefficient is calculated by using the data set, whose absolute values are small enough, the accuracy of the prediction in determining the regression coefficient will be lowered. Therefore, the profile data between No.52 and No.59 are used, where large beach changes are observed. In addition, the profile data at No.60 and No.61 are neglected, because these survey lines are located in the vicinity of the harbor structures, so that the local influences are considered to be predominant. The region of the calculation of the sectional area extends from the backshore to the 20m-deep location. As a result, the following relation stands between both variables with the correlation factor of 0.80.

$$\Delta A = 13.3 \cdot \Delta y + 150 \quad (6)$$

Where ΔA and Δy have the units of m^2 and m , respectively. The regression coefficient between ΔA and Δy is equal to the characteristic height of beach changes (h). Due to the relation in Eq.(6), h becomes 13.3m.

Next, littoral transport rate at a typical location east of Tagonoura Port will be evaluated based upon the field data of beach changes. The littoral transport rate can be evaluated on the basis of the continuity relation of sand volume by analyzing the temporal change of the total sand volume of the eroded beach located on the downdrift side of the coastal structure obstructing the continuous longshore movement of sand (Uda et al., 1986). First, the contour map on the downdrift coast of Tagonoura Port is shown in Fig.10.

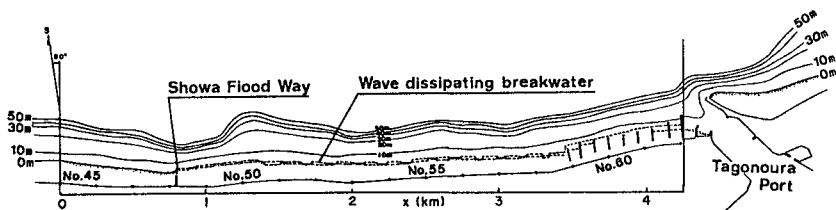


Fig.10 Contour map on the downdrift coast of Tagonoura Port and coordinate system for shoreline simulation.

There are 11 groins and 17 wave-dissipating breakwaters along the shoreline. In this map the region between No.45 and No.62 is selected for the calculation zone. It should be noted that at survey line No.45, far from the harbor, the littoral transport rate has kept constant to the dominant wave incidence on this coast, because at this site the shoreline configuration has not changed since 1968, as shown Fig.3. On the other hand, the littoral transport rate rounding the tip of the breakwater of Tagonoura Port is assumed to be negligibly small, because the water depth at the entrance channel to the harbor is sufficiently deep like as about 10m as shown in Fig.10. The total amount of littoral transport passing through No.45 is approximately equal to the volume change of sand in the test area between

No.45 and No.62. Strictly speaking, there may be a small amount of sand movement toward the offshore zone. If this is correct, such loss of sand should be added to the volume change to give the exact transport rate. However, in this study, it was impossible to measure this value reliably because of the relative low accuracy of the bottom sounding data in the far offshore zone, so that in the present study this is assumed to be negligible.

The change in the total sand volume in the eroded area can be approximately obtained from the change of the plane area in the eroded zone multiplied by the characteristic height of beach changes ($h=13.3m$). Because the characteristic height of beach changes is the vertical height of the rectangle whose sectional area and horizontal scale are equivalent to the measured sectional area and the change of the shoreline position, respectively. Therefore the multiplication of this vertical height by the change in the plane area in the eroded region results in the volume change. The result of this calculation is shown in Fig.11. The total volume of sand eroded has increased with time, although there is some scatter. The time derivative of the total sand volume approximately becomes equal to littoral transport rate at the downdrift end of the area examined as shown in Fig.10. The time derivative of the sand volume change becomes $Q=1.17 \times 10^5 m^3/yr$ between 1973 and 1983. This value is equal to the average littoral transport rate at No.45 in a period between 1973 and 1983.

IV. PREDICTIVE MODEL OF THREE DIMENSIONAL BEACH CHANGES

In this section a new one-line model of shoreline evolution is developed in order to predict three-dimensional beach changes with some improvements on the former model (Uda and Saito, 1987). In this model the vertical distribution of littoral transport is taken into account, and not only the change of the shoreline position but also the change of the offshore distance to certain contours are predictable by using this vertical distribution of littoral transport. The vertical distribution can be determined from the beach profile changes measured with time at a site, assuming that the beach slope is sufficiently small and the vertical distribution of beach changes during a short period is similar to that of littoral transport. For example, Figure 12 shows the results. To determine the distribution, the reference years selected are 1970 at No.58 and 1973 at No.54. Then, the changes in the offshore distance are divided by the change in the shoreline position to obtain the normalized distribution. There is scatter to some extent, but the vertical distribution of horizontal changes in the beach topography has a triangular shape, taking a maximum value at the MSL and decreasing monotonously above and below the MSL as shown in Fig.12. This distribution of littoral transport is approximately equal to the vertical distribution of littoral transport under the assumption that the vertical distribution of littoral transport does not vary so much, even if the beach profile changes are caused by the littoral transport over a short period.

In the calculation, the equation given by Savage was used for the littoral transport formula. The Savage coefficient is assumed to be 0.2. The littoral transport rate was vertically divided at each depth relative to the average of the normalized vertical distribution as shown in Fig.12 except above the MSL, where the maximum value was used to obtain the best fit with the measured beach changes.

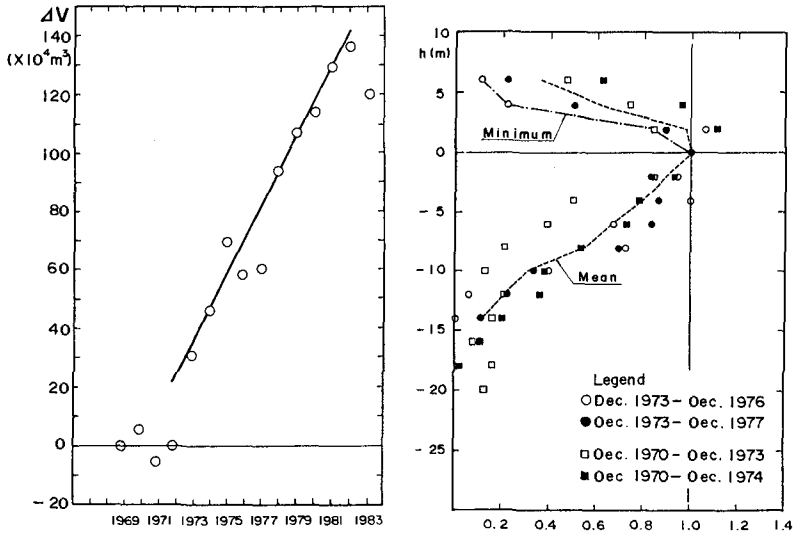


Fig.11 Temporal change of total eroded volume of sand on the downdrift coast of Tagonoura Port.

Fig.12 Vertical distribution of normalized horizontal distance in each depth.

On the Fuji Coast there are wave-dissipating breakwaters placed along the shoreline discontinuously as shown in Fig.10, and therefore a model of beach changes around the wave-dissipating breakwater is required as follows. First, in the simulation, the wave-dissipating breakwater is assumed to be of continuous type because the longshore distance in the opening is narrow compared with the longshore length of the wave-dissipating breakwater. Then the depth at the foot of the wave-dissipating breakwater is determined from the given beach profiles, because the location of the breakwater is already known. The wave-dissipating breakwaters, as shown in Fig.3, have been built since 1973, and therefore the total length of the wave-dissipating breakwater from No.62 was chosen so as to satisfy the actual situation of the construction. As is mentioned in Fig.10, between No.59 and No.62 there are groins but the coast between them is covered with the concrete blocks. Therefore the physical condition at this site can be assumed to be the same as at the wave-dissipating breakwater.

If a wave-dissipating breakwater is constructed along the coast, the beach behind the wave-dissipating breakwater is usually protected against beach erosion, and therefore littoral transport rate at this site will be reduced depending upon the location of the wave-dissipating breakwater. Here, the reduction of the littoral transport rate, named by the cutting ratio of littoral transport, is taken into account. The cutting ratio of littoral transport can be obtained, assuming that the littoral transport rate decreases with the ratio of the area above the depth of the tip of the breakwater with respect to the total area in the vertical distribution of littoral transport. The greater this point depth is, the more the littoral transport rate decreases. The beach changes are assumed to be observed only in the zone deeper than the point depth of the wave-dissipating breakwater, and the horizontal change of the beach topography is calculated from the vertical distribution of littoral transport.

For the initial condition, the bottom topography measured in 1970 was used, and the beach changes until 1983 are predicted. It is assumed that the incident wave height and period at the far offshore zone are equal to $H=0.85\text{m}$ and $T=9\text{sec}$, and the waves are incident from $\alpha=513^\circ\text{W}$ based upon the field observation conducted on the coast. Secondly, the longshore distributions of wave height and wave direction at a location of 10m deep along the coast are evaluated by wave refraction calculation using this incident wave. Furthermore, wave height and wave direction at the breaking point are calculated, assuming that the bottom contours in the shallow water zone are parallel at each location. Wave refraction calculation was performed repeatedly in a shallow water zone under the assumption that the incident wave at a location of 10m deep did not vary as much, even if beach changes occurred in the zone.

As the beach erosion proceeds, the bottom profile gradually tends to reach a stable profile, which is mainly determined by wave characteristics, bottom slope and grain sizes of the bed materials. In this study this stable profile is empirically determined. The beach profile at No.58 measured in 1982 may be selected for such a profile approximately, because the eroded beach section next to Tagonoura Port should approach the stable profile more rapidly. If the beach profile during the initiation time of the construction of the wave-dissipating breakwater has retreated compared with the stable beach profile, and if a part of the beach profile differed from the stable beach profile due to the difference of the bottom profile, their part of the retreated profile was used instead of the stable beach profile. After the beach profile reached to the stable form, it was assumed that the littoral transport rate is equal to the input data at the updrift end, and the same amount of sand can pass through the site with the stable profile.

The predicted changes of the offshore distance to some bottom contours after 4 and 8 years from the beginning are compared with the measured values in Figs.13 and 14. The

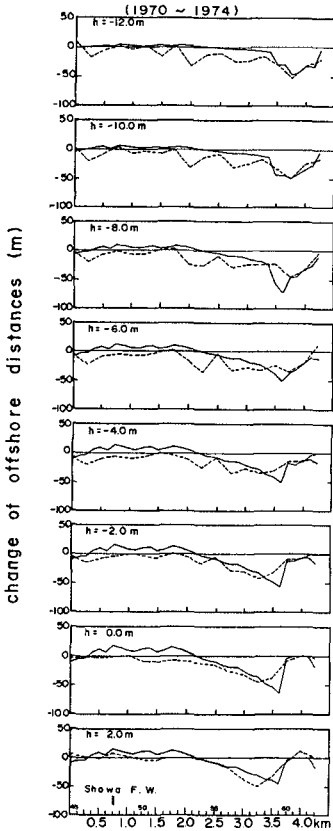


Fig.13 Comparison of measured and predicted changes of offshore distance after 4 years from the beginning.

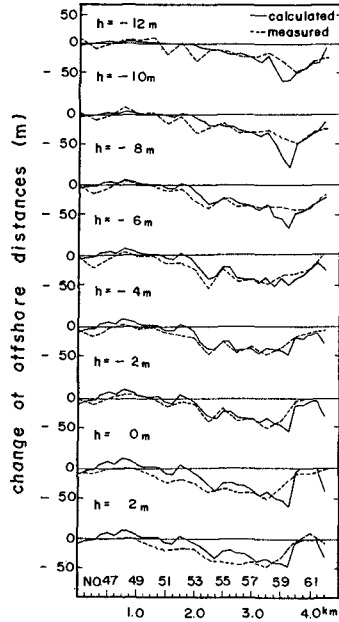


Fig.14 Comparison of measured and predicted changes of offshore distance after 8 years from the beginning.

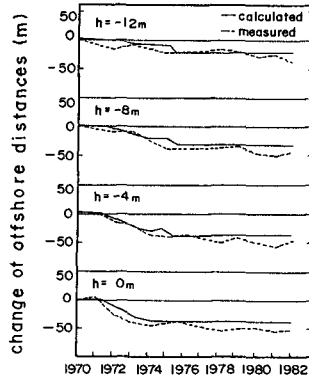


Fig.15 Comparison of temporal changes of measured and predicted offshore distances.

longshore distance along the coast is taken for the abscissa, and the changes in the offshore distances are compared. It is found that the predicted and measured changes of the

offshore distances to some contours agree well. It is difficult to understand the process of the temporal beach changes from Figs.13 and 14 alone, although they are useful in understanding the spatial beach changes. Therefore, temporal changes of the offshore distances to some contours are expressed in Fig.15, where survey line No.58 is selected as an example. It is concluded that the process of beach changes is well predicted from the point of view of temporal beach changes.

V. CONCLUSIONS

1) The littoral transport heading eastward was obstructed due to the construction of the breakwater of Tagonoura Port located in the middle of the Fuji Coast, and the downdrift coast of the harbor was severely eroded. The maximum retreat of the shoreline between 1968 and 1983 was about 60m at survey line No.58.

2) Beach erosion was severe between No.60 and No.45, and recently, retreat of the shoreline is tending to decrease. This is due to the decrease of the littoral transport itself on the coast and due to the effect of the construction of wave-dissipating breakwaters.

3) The littoral transport rate passing through No.45 located east of Tagonoura Port was found to be about $1.17 \times 10^5 \text{ m}^3/\text{yr}$ on an average between 1973 and 1983.

4) It is found that large part of the sediment eroded on the downdrift beach of Tagonoura Port is carried away toward the offshore zone, whose depth is between 20 through 30m.

5) A predictive model of three-dimensional beach changes was developed, in which the vertical distribution of littoral transport is taken into account and the effect of wave-dissipating breakwaters on beach changes can be evaluated. The predicted beach changes were in good agreement with observed ones.

REFERENCES

- Kohno, H., T.Uda and Y.Yabusaki (1986) : On the scattering of concrete armour units of detached breakwaters due to waves, Proc. 20th Coastal Eng. Conf., ASCE, pp.1972-1986.
- Shuto, N., J.Taguchi and T.Endo (1977) : On the movement of gravels on the Fuji Coast, Proc. 23th Japanese Conf. on Coastal Eng., pp.221-225. (in Japanese)
- Uda, T. and T.Takeuchi (1985) : An analysis of beach erosion on Suruga Coast, Coastal Eng. in Japan, Vol.28, pp.161-172.
- Uda, T., C.Agemori and N.Chujo (1986) : Beach changes caused by offshore dredging, Coastal Eng. in Japan, Vol. 29, pp. 215- 226.
- Uda, T. and H.Saito (1987) : Beach erosion on the Ogawarako Coast and prediction of shoreline evolution, Proc. Coastal Sediments '87, ASCE, pp.484-499.

CHAPTER 144

TOWARDS MODELLING COASTAL SEDIMENT TRANSPORT

By Peter Nielsen*

Abstract

Sediment transport data from the field and laboratory tests are used to gain insight into two fundamental questions. Firstly: What is the relative importance of coexisting waves and currents for the resulting sediment transport? Secondly: Is the influence of grain size as strong as traditional models predict, or is it as weak as the empirical CERC-formula indicates?

Wave tank data reveal that the oscillatory velocity will in most cases determine the direction as well as the magnitude of the shore normal sediment transport, and wave flume data on shore normal transport as well as field data on littoral drift show weaker grain size dependence than traditional sediment transport models predict. It is suggested that wave dominance as well as weak grain size dependence are manifestations of the fact that the dominant transport mechanisms are often more organised than the diffusion process on which many traditional models are based.

1. Introduction

The relative importance of waves, or more specifically the oscillatory velocity component $\tilde{u}(z,t)$, and steady currents $\bar{u}(z)$ has been the subject of considerable research and discussion. The conclusion of most of the theoretical work has been that the currents should be the most important with respect to the actual transport while u may well be the dominant factor in the entrainment process. Recent experimental work has shown however that the transport component resulting from the product of the oscillatory components of concentrations and velocities ($\tilde{u}\tilde{c}$) is often more important than $\bar{u}\bar{c}$. Examples of this evidence will be discussed below.

In this context it is of course important to acknowledge the fact that different types of steady currents will have different potential for transporting sediments depending on their strength close to the bed where the sediment concentrations are largest. For example, the steady boundary layer currents which are generated by the waves will generally be much stronger at the bed than currents which are driven by a uniform pressure gradient such as tidal currents or undertow, but they may not be apparent from measurements taken above the wave boundary layer.

*: Coast and Rivers Branch, Public Works Department, 140 Phillip Street, Sydney 2000, Australia.

Some insight into the problem of grain size dependance was gained by the study of Nielsen (1988) which tested three different models against wave flume data on shore normal transport. The first of these models is a diffusion model developed along the lines suggested by Nielsen et al (1978) and by Nielsen (1979). The second model is inspired by the "heuristic model" of Dean (1973) and the third is based on a simple "grab and dump" concept. The third model is much simpler than the two others, but it is also more reliable. More specifically, it shows a more realistic grain size dependence of the resulting transport than the two more traditional models. The traditional models tend to predict by far too strong decline of the sediment transport rate with increasing grain size.

Although the logical connection is not very direct it is interesting to note that a similar situation can be observed with respect to the total longshore transport or littoral drift. That is, existing traditional models like that of Deigaard et al (1987), which should be valid for a fairly common type of surf zones, predict a strong grain size dependence while the data, as presented in the Shore Protection Manual show no grain size dependence at all (see Figure 1).

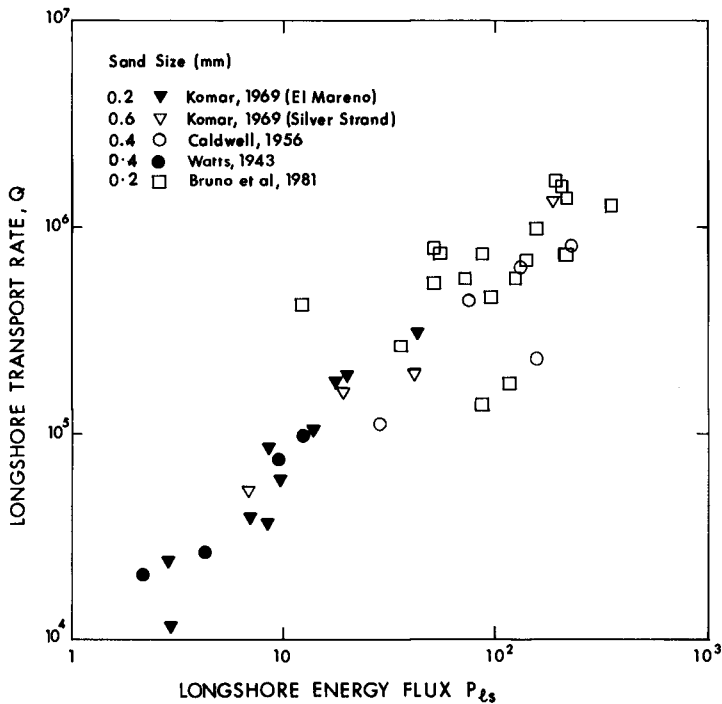


Figure 1: Littoral drift data as function of the longshore wave energy flux (from CERC 1984). The data shows no significant grain size dependence for the measured littoral drift.

To this which we may call "The C.E.R.C. formula paradox" one of the following explanations may apply:

- 1: The data is unreliable.
- 2: The processes modelled by Deigaard et al (1987) were not dominant in the surf zones where the measurements were made.

2. Relative Importance of u_c and u

Figure 2 is an illustration of the relative importance of waves ($\tilde{u}(z,t)$) and a superimposed steady current ($\bar{u}(z)$) for the sediment transport along a wave flume.

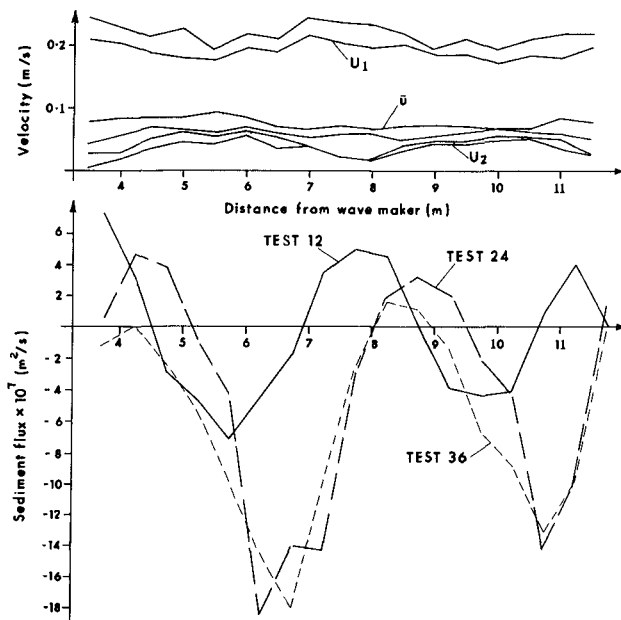


Figure 2: Wave flume sediment transport experiments by Schepers (1978). The hydrodynamic conditions (top) were similar in the three tests: $T=1.5$ s, and $D=0.30$ m. The envelopes of the velocity magnitudes u , U_1 , and U_2 are plotted as function of distance from the wave maker and were all measured 0.1m above the bed. The sediments had the following characteristics (d_s/w): Test 12: (0.125mm, 0.010m/s), Test 24: (0.250mm, 0.028 m/s), Test 36: (0.465mm, 0.050 m/s). The corresponding measured net sediment fluxes (bottom) show three important facts: (1) Even though the measured current $u(0.1)$ is always positive (shoreward), the sediment transport is predominantly negative. (2) The measured transport rates are of very similar magnitude despite the large difference in grain sizes. (3) The transport pattern for the coarser sand ($d_s/\Lambda > 0.004$) is shifted relative to that of the finest, probably because acceleration effects become more important relative to velocity magnitude with increasing grain size.

In the top part of the figure are shown the measured velocity components \bar{u} , U_1 and U_2 , where U_1 is the amplitude of the fundamental mode of the wave motion and U_2 is the amplitude of the second harmonic. The velocities were measured ten centimetres above the bed. The bottom part of the figure shows the corresponding, measured sediment transport rates. The experiments were carried out at the Delft University of Technology and have been described in more detail by van de Graaff and Tilmans (1980).

The first thing to note about the measured sediment transport rates is that although the steady current ten centimetres above the bed was at all points shoreward, the measured transport rates were predominantly offshore. Thus, the current velocity ten centimetres above the bed is no indicator for the direction of the resulting sediment transport.

For three dimensional situations there is also evidence that the waves are more dominant than one might have expected with respect to transport capacity. For example Davison (1987) has reported on tracer experiments where the centroid velocity as well as the larger axes of the "tracer ellipses" always tended to be in the wave direction rather than in the direction of the tidal currents. It is not clear from these experiments however if the transport is actually carried by u or by the steady wave induced boundary layer drift.

3. Sediment Transport in Pure Oscillatory Flow

In order to be able to model coastal sediment transport in general, it is important to understand how sand is transported in a purely oscillatory flow, i.e. a flow where $\bar{u} = 0$; but it can be difficult to generate such a flow in wave tanks because of wave induced mass transport. Most important in this context is the boundary layer drift under progressive waves which was described by Longuet-Higgins (1956).

However, in oscillating water tunnels, where the water motion is horizontally uniform this drift should not occur. Therefore, the oscillatory water tunnel (OWT) provides the best experimental facility for studying sediment transport in purely oscillatory flow.

Sato (1986) performed sediment transport experiments in an OWT which are of interest in this context. He found that with water velocities of the "Stokes-wave-type" i.e. with

$$u(t) = U_1 \cos \omega t + U_2 \cos 2\omega t \quad (1)$$

the resulting sediment transport was always "seaward" that is in the direction opposite to the largest instantaneous velocity.

This result is to some extent in conflict with the field observations of Doering and Bowen (1988) who found that the correlation between instantaneous velocities and concentrations was positive which means that the net sediment flux at the measuring point tended to be in the direction of the largest instantaneous velocities.

When the two authors found opposite results, it is most likely due to the fact that the bed forms were different in their experiments.

In Sato's tests the bed was covered by regular, sharp crested ripples while Doering and Bowen's field tests would have involved bed forms that were flatter and more rounded.

The trend found by Sato for sediment transport over sharp crested ripples is also apparent in the numerous wave flume tests of Vellinga (1975), Schepers (1978) and Tilmans (1979) which were analysed and modelled by Nielsen (1988). That is, those test show a clear tendency for the resulting transport to go in the direction opposite to that of the largest velocities. The reason for this is that the transport over sharp crested ripples is a two step process where the sand is not carried very far by the velocities which activate it. It is trapped behind the ripple crest and then later released to be transported in the opposite direction after the flow reversal.

While the results from Sato (1986) and those analysed by Nielsen (1988) show that velocity-moment-models like that of Bailard and Inman (1981) predict transport in the wrong direction over sharp crested ripples, such models might apply over more rounded bed forms.

4. Grain Size Dependence of Shore Normal Transport

Nielsen (1988) used three different approaches for modelling the Dutch flume experiments. The first was the traditional diffusion approach, the second was a heuristic entrainment and settling approach similar to that of Dean (1973) and the third was an ultra simplistic "grab and dump" model.

All of the models were quantified in terms of parameters from the steady concentration profiles only; that is, the reference concentration C_0 and the vertical length scale L_s defined by:

$$\bar{c}(z) = C_0 \exp[-z/L_s] \quad (2)$$

All of the three modelling approaches were reasonably successful and this shows the comforting fact that the immense complexity of the variation of $c(z,t)$ needs not be considered explicitly in order to obtain reasonable results. Only the time averaged concentration profile $\bar{c}(z)$ is needed, and fortunately experimental data on $\bar{c}(z)$ is abundantly available.

The model results can be summarised as follows:

Diffusion model:
$$Q = C_0 L_s U_1 S \left(\frac{U_{\max}}{U_{\min}} \right) F_d \left(\frac{L_s}{wT} \right)$$

Heuristic entrainment model:
$$Q = C_0 L_s U_1 S \left(\frac{U_{\max}}{U_{\min}} \right) F_c \left(\frac{L_s}{wT} \right)$$

Grab & Dump model:
$$Q = C_0 w A S \left(\frac{U_{\max}}{U_{\min}} \right)$$

Where U_1 is the velocity amplitude of the fundamental mode of the wave motion, U_{\max} and U_{\min} are the extreme shoreward and seaward velocities respectively, w is the sediment settling velocity, A is the water particle semi excursion and T is the wave period.

The skewness function $S(U_{\max}/U_{\min})$ was the same in all models and the two functions F_d and F_c of the time scale ratio L_s/wT are quantitatively similar.

From these formulae we can see how the resulting sediment flux Q depends on grain size with all other things being equal. Because C_0 and L_s are both decreasing functions of the grain size we see that the two first models predict a fairly strong decrease in Q for increasing grain size, while the "grab and dump" model predicts a more moderate grain size dependence. It turns out that the data basically confirm the weak grain size dependence predicted by the grab and dump model, see Figure 2 and Nielsen (1988) for more detail.

In essence the "grab and dump model" differs from the two more traditional models by assuming a more organised mode of transport. It basically assumes that the sand is moved in parcels. Inspection of the transport process for fairly coarse sand ($U_1/w < 10$) over rippled beds confirms that it does in fact have this kind of nature. For finer sand, the organised nature is not obvious, but the "grab and dump model" will still work (see Nielsen 1988).

The trapping mechanisms by which a vortex dominated flow can keep sand in suspension and transport it very effectively were described by Nielsen (1984). However, for fine sand ($U_1/w > 10$) the sand will on the average stay in suspension much longer than the life time of the vortices, and the success of the "grab and dump model" may thus be somewhat fortuitous for fine sand.

5. CONCLUSIONS

From the presently available data the following conclusions can be drawn about the relative importance of steady and oscillatory flow components with respect to sediment transport. For non breaking waves over horizontal beds the influence of, even fairly strong, currents is insignificant, see Figure 2.

Davison (1987) found that in an environment with tidal currents of similar though slightly smaller magnitude running perpendicular to the waves, the sediment transport inferred from radioactive tracers was always in the wave direction.

The role of the wave induced boundary layer drift over natural sand beds is however virtually unresolved. This is basically because these current themselves are not well known. The model of Longuet-Higgins (1956) is not known to be valid for turbulent boundary layers, and more recent "turbulent" models like that of Jacobs (1984) are not known to be valid for the relative roughness range which is typical for natural sand beds.

The transport due to purely (or almost purely) oscillatory flows over sharp crested bed forms goes in the direction opposite to that of the largest instantaneous velocities. This tendency may be reversed for rounded bed forms and flat beds so that velocity-movement-models like that of Bailard and Inman (1981) could apply to such situations.

Laboratory data on shore normal sediment transport (Figure 2) show a weaker grain size dependence than classical transport models would predict, and interestingly, the same is true for the littoral drift data shown in Figure 1. Judging from the results of Nielsen (1988) it might be inferred that the weak grain size dependence is due to the efficiency of highly organised transport modes which dominate the transport of coarser sediments.

It is not obvious that the implications from Nielsen (1988)'s study can be applied directly to the "CERC formula paradox" for littoral drift but it is possible that more organised (than diffusion) modes of transport tend to dominate for coarser sand and that such dominance leads to weak grain size dependence for littoral drift as well as for shore normal transport.

REFERENCES

- Bailard, J.A. and D.L. Inman (1981): An energetics bedload model for a plane, sloping beach : local transport. *Journal of Geophysical Research*, Vol 86, pp 2035-2043.
- C.E.R.C. (1984): *Shore Protection Manual. Fourth Edition, Vol.1.*
- Davison, A. (1987): A radioactive tracer study of sand-seagrass dynamics, in the nearshore region of Holdfast Bay, South Australia. Australian nuclear science and technology organisation. Lucas Heights Laboratories. ANSTO/C67.
- Dean, R.G., (1973): Heuristic model of sand transport in the surf zone. *Proc. First Australasian Conf. Coastal Eng., Sydney*, pp. 208-214.
- Deigaard, R., Fredsøe, J. and Hedegaard I.B., (1986): Mathematical model for littoral drift. *Journal of waterway, port, coastal and ocean engineering.* (A.S.C.E.), Vol. 112, No. 3, pp. 351-369.
- Doering, J.C. and A.J. Bowen (1988): Wave induced flow and nearshore suspended sediment. *Proc. 21st Int. Conf. on Coastal Engineering, Torremolinos.*
- Graaff, J. van de and Tilmans, W.M.K., (1980): Sand transport by waves. *Proc. 17th Int. Conf. Coastal Eng., Sydney*, pp. 1140-1157.
- Jacobs, S.J., (1984): Mass transport in a turbulent boundary layer under a progressive water wave. *Journal of Fluid Mechanics*, vol 146, pp 303-312.
- Longuet-Higgins, M.S., (1956): The mechanics of the boundary layer near the bottom in a progressive wave. *Proc. 6th Int. Conf. on Coastal Engineering, Florida*, pp 184-193.
- Nielsen, P., (1979): Some basic concepts of wave sediment transport. Series Paper 20, Institute of Hydrodynamics and Hydraulic Engineering (ISVA), Technical University of Denmark.
- Nielsen, P., (1984): On the motion of suspended sand particles. *Journal of Geophysical Research*, Vol 89, No C1, pp 616-626. *Erata: Vol 90, No C2, pp 3255-3256.*
- Nielsen, P., (1988): Three simple models of wave sediment transport. *Coastal Engineering Vol. 12*, pp.43-62.
- Nielsen, P., Svendsen, I.A. and Staub, C., (1978): Onshore-offshore sediment transport on a beach. *Proc. 16th Int. Conf. Coastal Eng., Hamburg*, pp. 1475-1492.
- Sato S. (1986): Oscillatory boundary layer flow and sand movement over ripples. Ph. D. Thesis, Dept. of Civil Engineering, University of Tokyo.
- Schepers, J.D., (1978): Zandtransport onder invloed van golven en een eenparig stroom bij variërende korrel diameter. Masters Thesis, Delft University of Technology.
- Tilmans, W., (1979): Zandtransport in de golf richting in relatief ondiep water. Masters Thesis, Delft University of Technology.
- Vellinga, P., (1975): Zandtransport door golven en de invloed van stoorgolven.

CHAPTER 145

LONGSHORE SEDIMENT TRANSPORT RATE vs. CROSS - SHORE DISTRIBUTION OF SEDIMENT GRAIN SIZES

C.I.Moutzouris (*)

ABSTRACT

Existing models for longshore sediment transport rate computations assume the sediment grain size and grain size-related parameters to be uniform in both the cross-shore and longshore directions. Field results from tideless beaches, which are briefly described in the paper, show that the latter change in both directions due to changing wave energy-levels. The sensitivity analysis described in the paper shows that both longshore current and transport rate computations are sensitive to the cross-shore changes in grain size. Finally, a modified linearity coefficient for the wave power equation is proposed based upon the cross-shore distributions of grain size as found in nature.

1. INTRODUCTION

It is now widely believed that sediment grain size is an important parameter in wave-induced sediment transport processes in the surf zone. As a result, attempts are increasingly being made to incorporate the grain size in models of longshore sediment transport rate computations. Some examples are as follows. Dean et al.(1983) plotted results from various previous studies and found that the linearity coefficient K of the empirical wave power equation increases with decreasing sediment size D . Theoretical predictions by Deigaard et al.(1986) indicate a similar decrease in K with increasing D . Detailed predictor models, such as the Bijker (1971) formula, have already incorporated the grain size and a number of other grain-related parameters.

In all existing models, however, grain size and grain size-related parameters are assumed to be uniform in both the cross- and longshore directions in the surf zone. Recent results from field measurements on tideless beaches along the Greek coast conducted by the team of the Civil Engineering Department, National Technical University of Athens, show clearly that grain size and grain size-related parameters

(*)National Technical University of Athens,Civil Engineering
Department,Patission 42,10682 Athens,Greece.

change in both directions, due to changing wave energy-levels. Changes are more predominant in the cross-shore direction. Maximum grain size is observed in zones of maximum energy, such as the breaker zone and zones of wave convergence. Changes are in most cases so drastic that selecting the values to be introduced into the models is a difficult task.

It therefore becomes clear that grain size and grain size-related parameters can no longer be considered to be uniform across the surf zone. Realistic models should not only introduce the influence of grain size but also the cross-shore changes.

In the present paper, a synopsis of the above-mentioned field results is presented and a sensitivity analysis of longshore sediment transport computations on the cross-shore changes of grain size is made. Finally, a modified linearity coefficient for the wave power equation is proposed, which is based on the cross-shore distribution of grain sizes, as found in nature.

2. CROSS-SHORE DISTRIBUTION OF GRAIN-RELATED PARAMETERS

Field measurements have been/are being made along various Greek beaches: Kokkino Limanaki, Marathonas, Linoperamata, Platanias, Plakias and Rio. Each beach has its own specific characteristics: Kokkino Limanaki is a small-scale pocket beach with a strongly arcuate coastline 310m long. It is exposed to medium wave energy from two dominant directions. Marathonas has a straight coastline and is exposed to medium wave energy from one direction only. Linoperamata is also a straight beach but receives high wave energy. Longshore transport occurs to the left and to the right. Platanias has a slightly arcuate coastline with medium to high wave energy. The equilibrium of the latter beach was recently disturbed by the construction of a small fishing harbour, which caused local erosion and accretion. Plakias is a large-scale pocket beach exposed to high wave energy. Finally, Rio is a shingle beach along a protruding headland which receives medium wave energy from both directions. Characteristics which are common include microtidal environments (maximum range: 25 to 30 cm) and locally generated sea states. Therefore, sediment distributions on the sea bed are almost exclusively wave-induced, which is considered to be highly advantageous.

Cross-shore distributions of grain size and grain size-related parameters are obtained from spot sediment samples collected with hand-operated grab samplers. Samples are limited to the upper 5cm of bed material so as to collect the sediment deposited during only the previous sea state. Samples are analysed in the laboratory. Grain sizes are computed by sieving according to the ASTM standards.

In the following paragraphs, a synoptical overview of the main results is presented. They concern wave-induced cross-shore distributions of grain size-related parameters, which reflect the hydrodynamic conditions prevailing across-shore.

A typical grain size distribution is shown in Fig.1, as found on the Marathonas beach. Noticeable differences in the

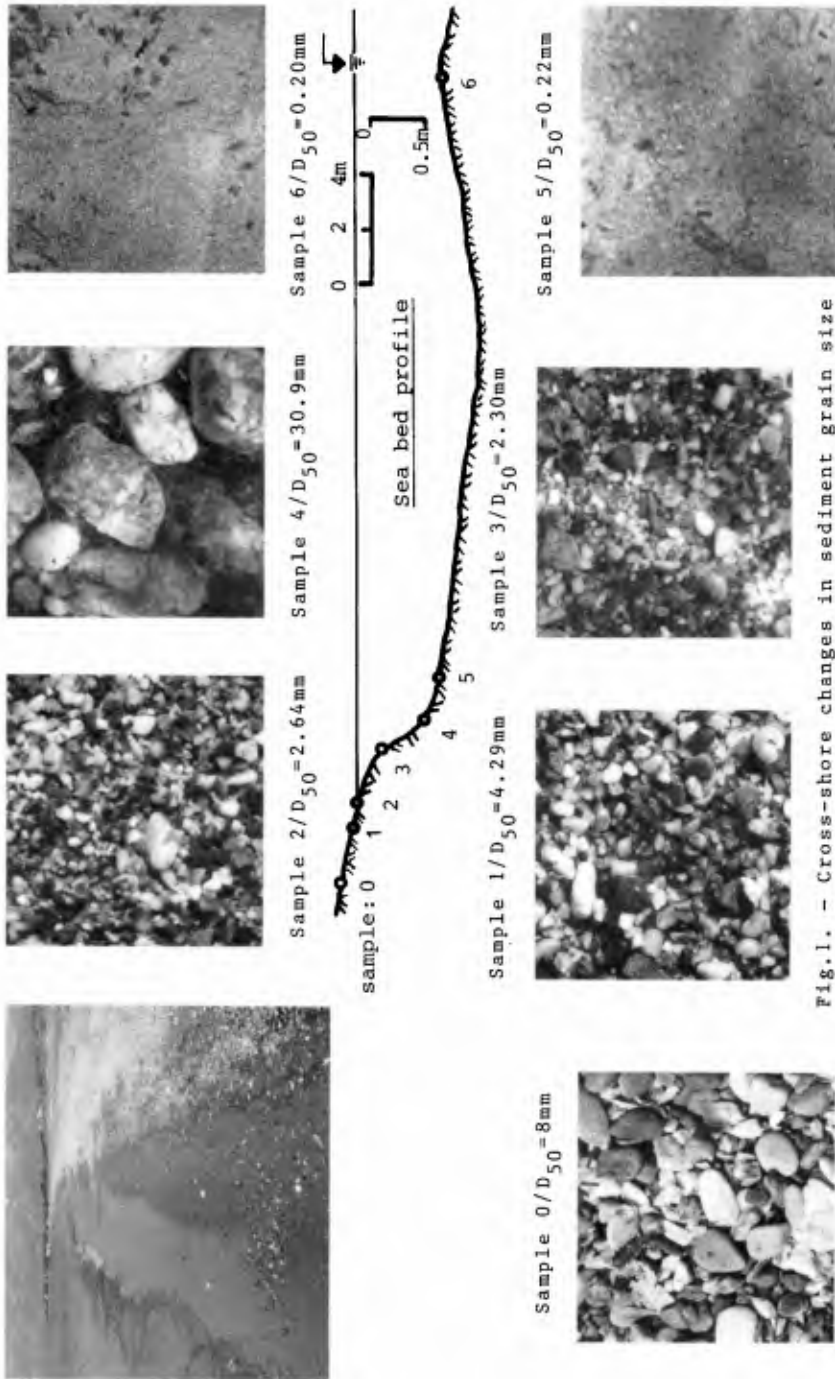


Fig. 1. - Cross-shore changes in sediment grain size (Marathona beach)

cross-shore sediment size distribution are observed throughout the beaches and under all wave conditions. A regular sediment sorting is detected in the cross-shore direction due to differing hydrodynamic loading. Grains are found to be coarser and worse sorted in zones of increased wave energy than in zones with lower energy levels, where grains are finer and better sorted.

Fig.2 shows a number of cross-shore distributions of statistical mean diameters for various types of beaches. D_{50} is the sediment grain diameter exceeded in size by 50% by weight in the sample population. M_z is the graphic mean diameter, as defined by Folk and Ward, 1957. The plunge step, where wave breaking occurs, is always found to be composed of the coarsest and worst sorted material, due to the increased action of breaking waves (Moutzouris and Kypraios, 1987). Grains are coarser and worse sorted at the toe of the step than at the crest. Therefore, the toe of the plunge step and the zone immediately seawards are composed of the coarsest material across the beach. From the plunge step shorewards, a regular decrease in grain size is observed. Sediment on the beach face is normally found to decrease in size and improve in sorting. Exceptions to this rule are due to the occasional presence of beach cusps, the terrigenous supply of coarser material, and the berm formation. In these cases, coarser material is found than normally. The offshore zone is covered with fine and rather well sorted material due to the decreased wave action.

Our field data indicate that all statistical diameters D_n (sediment grain diameter exceeded in size by 1-n% by weight) have a qualitatively similar distribution in the cross-shore direction as D_{50} (see Fig.3).

The settling velocity w of grains in water depends mainly upon the physical characteristics of the particles (such as the diameter, density, shape and roundness). Water temperature has a minor influence in beaches. As density is more or less constant across a beach, the most characteristic is grain size. It is, therefore, no wonder that the settling velocity of grains with median diameter D_{50} shows a qualitatively similar distribution across-shore as D_{50} (see Fig.3).

The porosity p is found to depend mainly upon the mode of flow. In the breaker zone, wave impacts on the bed cause compaction of the sediment and porosity decreases. At the beach face, water flow is mostly parallel to the sediment layer and porosity decreases. As a result, porosity is found to change across-shore. The maximum values observed were of the order of 0.40, which is the most common value of p in models (see Fig.3).

The distribution of the mean density ρ_s of the bed material across-shore is almost uniform (see Fig.3), which means that grain size and mean density do not appear to be inversely proportional to one another. Therefore, ρ_s is not influenced by the wave-energy changes across-shore.

3. SENSITIVITY OF LONGSHORE TRANSPORT RATES ON CROSS-SHORE CHANGES OF GRAIN-RELATED PARAMETERS

In the third part of the paper, the sensitivity of two

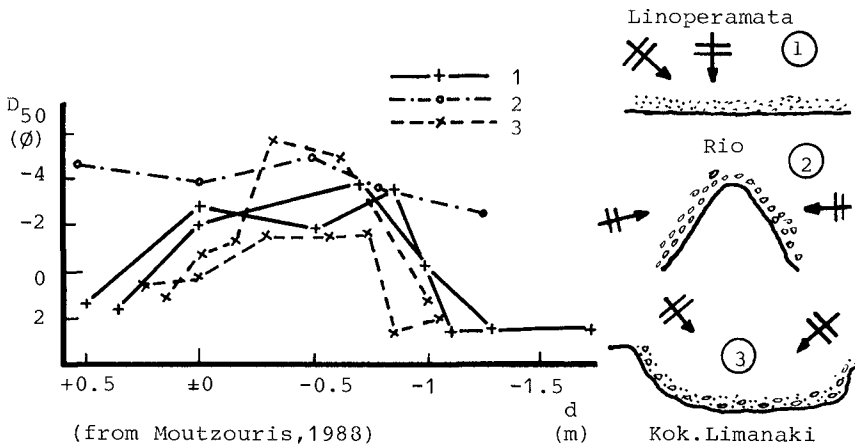
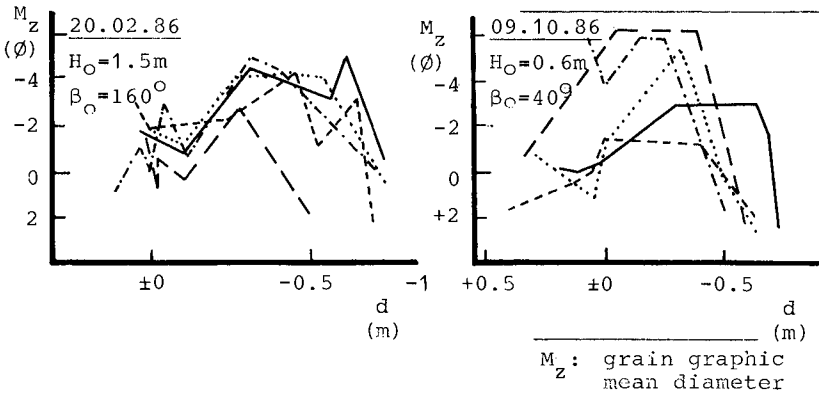
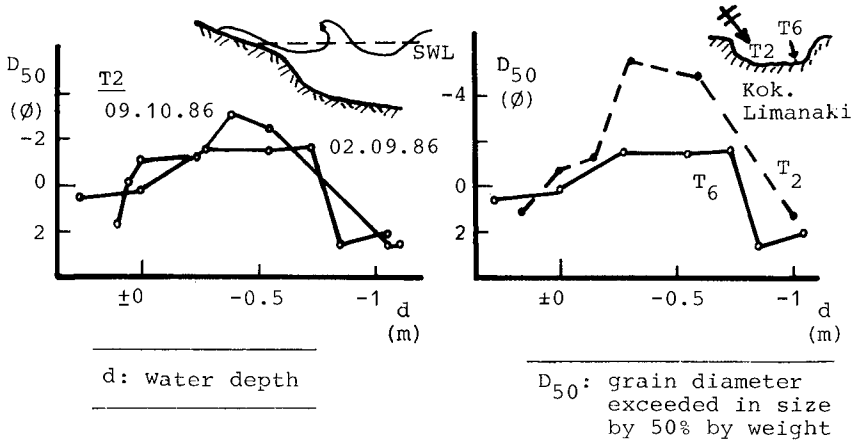


Fig.2.- Cross-shore distribution of characteristic statistical mean grain diameters

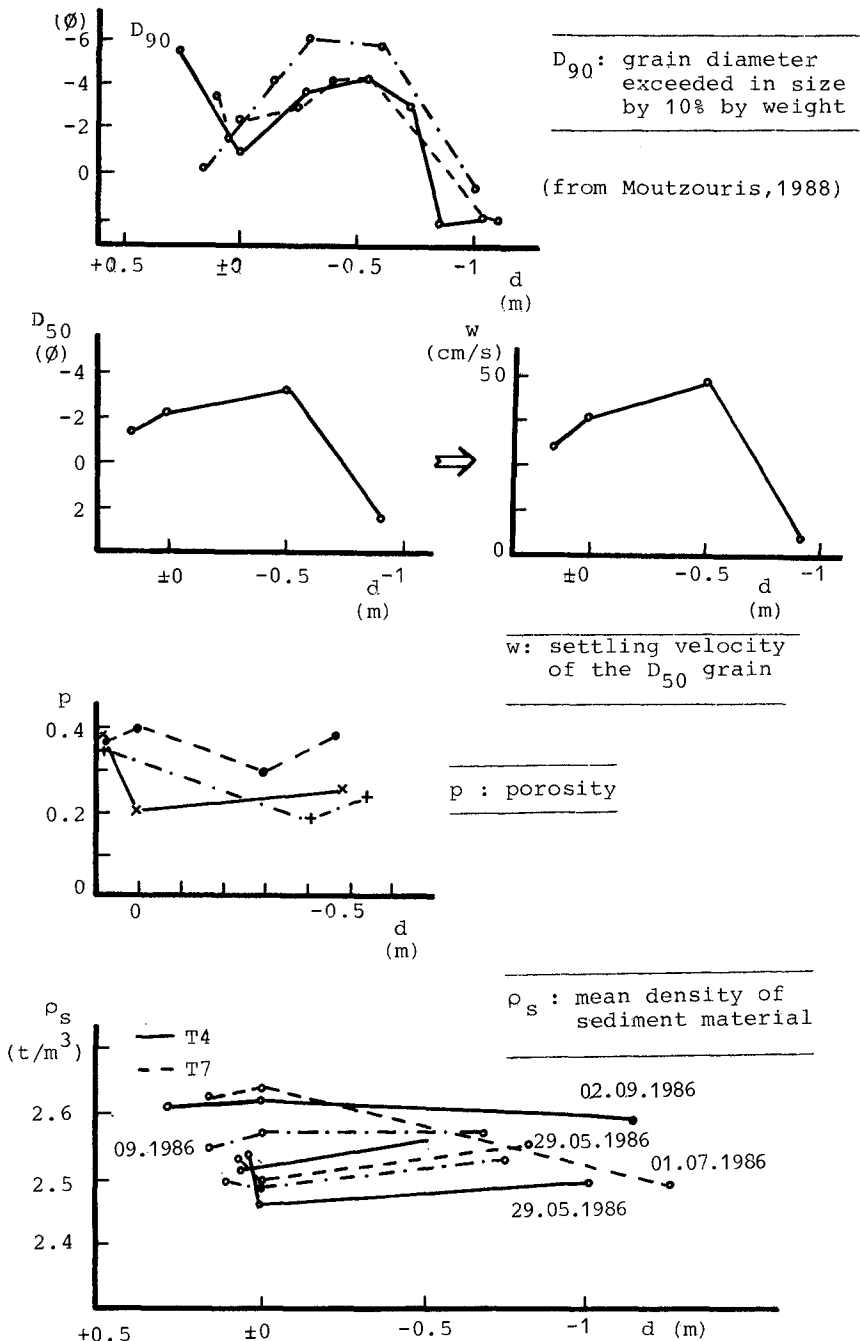


Fig.3.-Cross-shore distribution of various grain size-related parameters (Kok.Limanaki beach)

commonly used longshore sediment transport predictors on the cross-shore distribution of grain size and grain-related parameters is analysed. The predictors examined are the wave power equation and the Bijker formula.

The empirical wave power equation for the total longshore sediment transport rate S_t gives the spatially integrated immersed weight rate as a linear function of the total wave power available for transporting sediments. The best known and most widely used value of the non-dimensional linearity coefficient K is reported by Komar and Inman (1970) and is independent of the sediment characteristics. Their value was derived for sand size within the range of 0.18 and 0.6mm.

It has been increasingly argued recently that K could not be a constant but should depend upon some other parameters and most probably upon the sediment size. Dean et al (1983) plotted the values of K from various studies (Watts, Galdwell, Bruno and Gable, Komar and Inman, Johnson and Galvin, Moore and Cole, and Dean et al.) and found that K increases with decreasing sediment size D . Theoretical predictions by Deigaard et al. (1986) also indicate a decrease of K with increasing D . Komar (1988) does not seem to agree with such a dependency.

Fig.4 shows the cross-shore distribution of D_{50} , as found on one of our tideless beaches and the corresponding values of K , as computed from Dean et al (1983). x denotes the distance offshore, measured from the still water line. It can be seen that the longshore rate decreases by a factor of almost 3 if the largest diameter (0.75mm) is taken into account instead of the smallest one (0.37cm). The smallest diameter on the beach (0.37mm) gives almost 3 times higher transport rates than the largest diameter (0.75mm). It is therefore concluded that longshore transport rates computed with the wave power equation are very sensitive to the cross-shore changes in sediment grain size, if the linearity coefficient K is taken to be grain size-dependent. The Komar and Inman (1970) model would give a constant transport rate independent of the grain size distribution across-shore.

The Bijker formula computes the total longshore sediment rate as the sum of the bed and the suspended loads. Numerous grain size-related parameters are introduced in the formula.

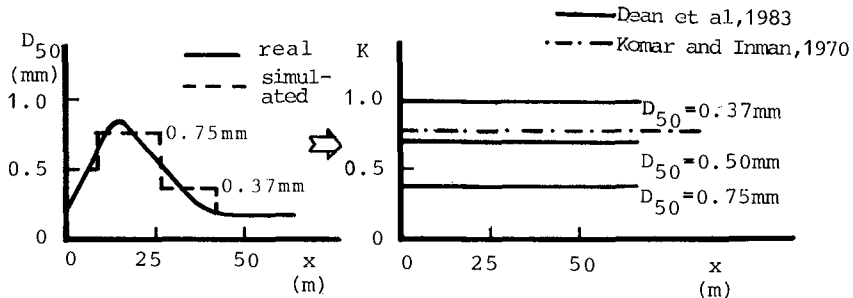


Fig.4. - Cross-shore distribution of the linearity coefficient

Among others are the D_{50} and D_{90} diameters, the Chezy roughness and wave friction coefficients (or factors), the grain settling velocity, the longshore current velocity, etc.

The sensitivity of the Bijker formula on the cross-shore distribution of grain size-related parameters is shown in Fig. 5, where S_t is the volumetric transport rate. These rates were computed with (a) a uniform grain size across the surf zone, as is common practice in transport rate computations, and (b) changing distributions, as found in the beaches of our field measurements. The results show that the Bijker formula is very sensitive to the cross-shore changes in size-related parameters. Of major influence upon the results is the sensitivity of the longshore current model introduced in the Bijker formula on the cross-shore changes in the grain size-related parameters. Fig. 6 shows the longshore current velocity according to the Longuet-Higgins (1970) and Komar (1975) models, as computed with grain size distributions observed in the field.

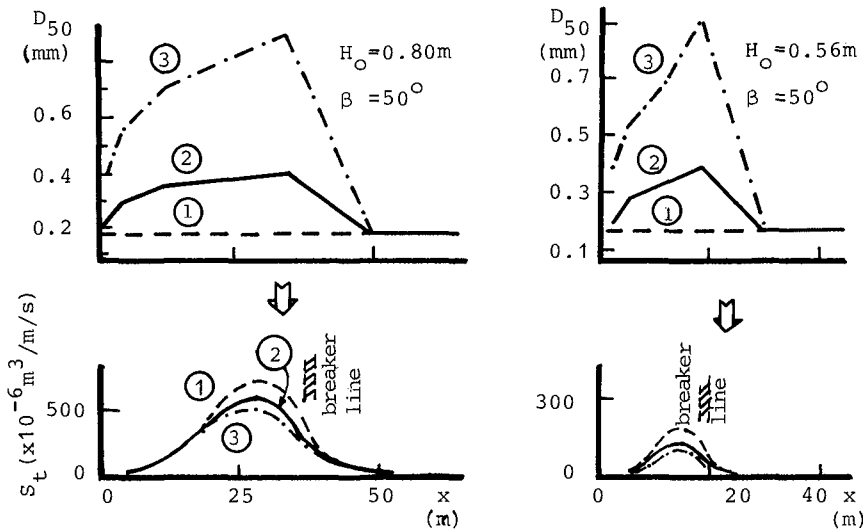


Fig. 5. - Sensitivity of the Bijker formula on the cross-shore changes in grain size-related parameters

It is finally concluded that neglecting the sediment size on a beach might be a first source of considerable errors in longshore transport rate computations. Assuming the grain size-related parameters to be uniform across-shore is a second source of equally important errors. The Bijker formula can take into account the cross-shore changes. The linearity coefficient of the wave power equation needs to be modified if the cross-shore changes are to be incorporated.

4. MODIFIED LINEARITY COEFFICIENT

In this part of the paper, a modified linearity coefficient K_m is proposed for use in the computations with the wave power equation. The modification seems necessary in view of

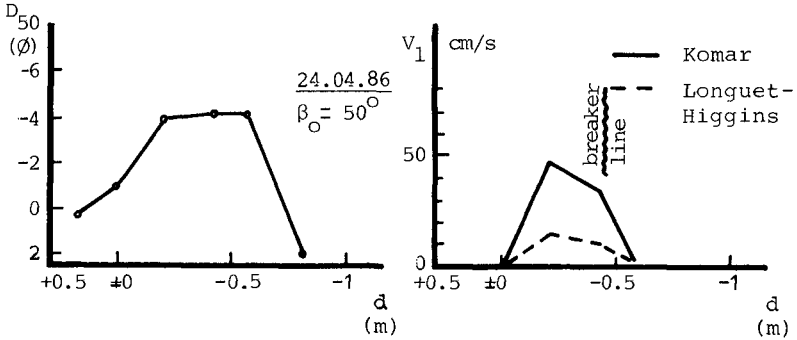


Fig.6.- Sensitivity of longshore current on the cross-shore changes in grain size

the results presented above.

The active zone of a beach is divided into a number of n successive sub-zones, with almost uniform grain size in each one. K_m is defined as the sum of the ponderated coefficients K , as proposed by Dean et al. (1983). In the general case of n sub-zones, the resulting $K_{m,n}$ is defined as:

$$K_{m,n} = \sum_{i=1}^n C_{n,i} K_{n,i}$$

with: $\sum_{i=1}^n C_{n,i} = 1$ and $C_{n,i} = \frac{l_{n,i}}{l_a}$

$l_{n,i}$ is the width of sub-zone i and l_a is the length of the active zone (see Fig.7).

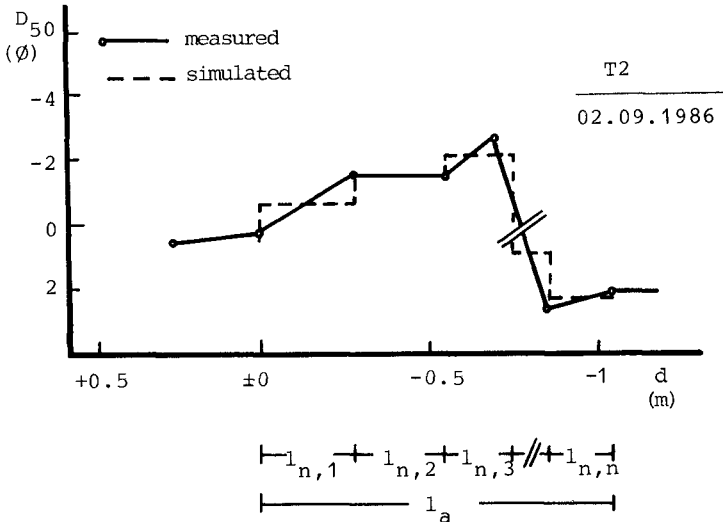


Fig.7.- Definition sketch

The coefficients $C_{n,i}$ can only be determined from field measurements. In the following paragraphs, data from our field measurements are presented for the cases of $n=3$ and $n=2$. In the case of $n=1$, the unique sub-zone has a width $l_{1,1}$ ($=l_a$) and $K_{m,1}$ coincides with the classical linearity coefficient, as defined by Komar and Inman and proposed by Dean et al. (1983).

In the case of $n=3$, the active zone is divided into the pre-breaker, breaker and after-breaker zones (see Fig.8) and $K_{m,3}$ is defined as:

$$K_{m,3} = C_{3,1} K_{3,1} + C_{3,2} K_{3,2} + C_{3,3} K_{3,3}$$

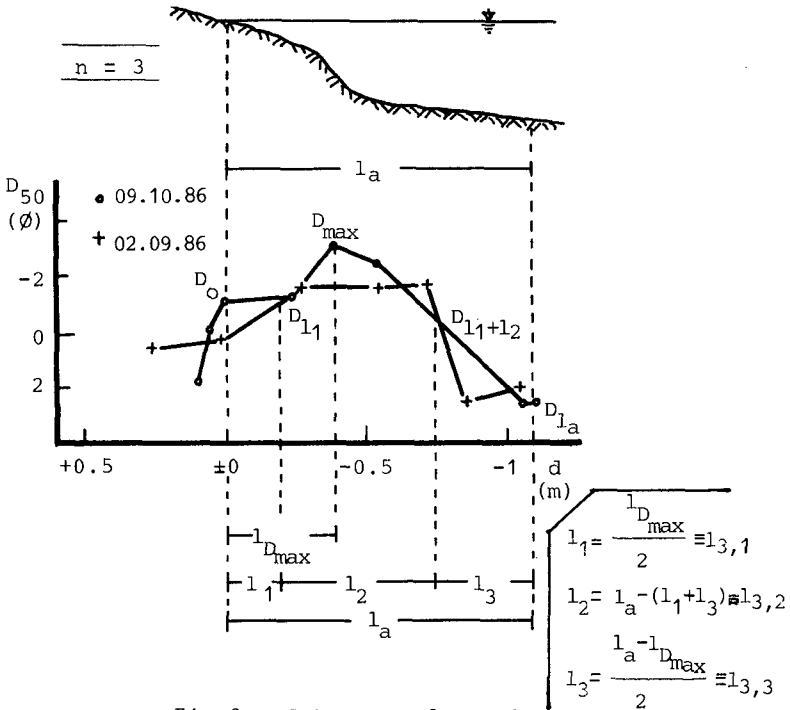


Fig.8.- Sub-zones for $n=3$

Data from our field measurements on the Kokkino Limanaki beach concerning coefficients $C_{3,1}$, $C_{3,2}$ and $C_{3,3}$ are plotted in Fig.9. It is found that:

$$C_{3,1} = 0.07 \quad \text{to} \quad 0.47 \quad \text{with} \quad \bar{C}_{3,1} = 0.21$$

$$C_{3,2} = 0.50 \quad (\text{by definition})$$

$$C_{3,3} = 0.16 \quad \text{to} \quad 0.38 \quad \text{with} \quad \bar{C}_{3,3} = 0.28$$

The following modified linearity coefficient could be proposed for the cases presented in Fig.9:

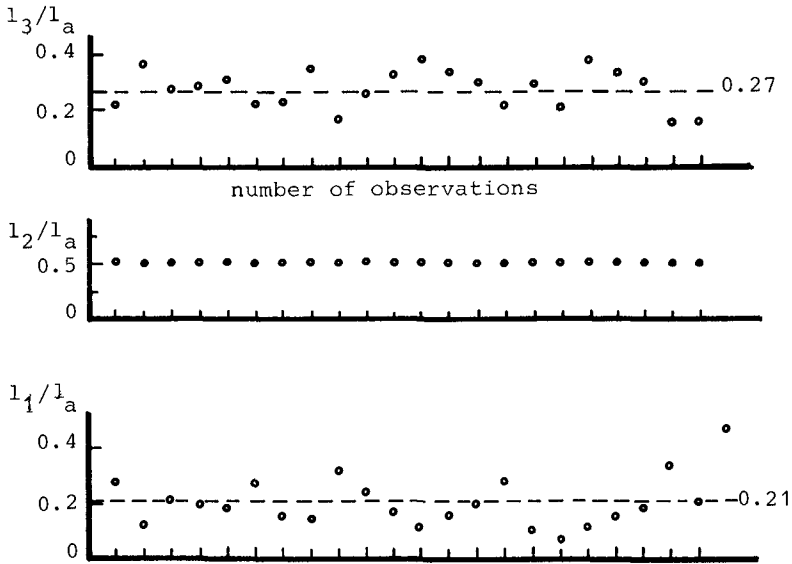


Fig.9. - Lengths of the sub-zones (n=3)
(Kokkino Limanaki beach)

$$K_{m,3} = 0.2K_{3,1} + 0.5K_{3,2} + 0.3K_{3,3}$$

$K_{3,1}$, $K_{3,2}$ and $K_{3,3}$ are linearity coefficients in sub-zones with almost uniform grain size. By adopting the results of Dean et al (1983), $K_{3,1}$, $K_{3,2}$ and $K_{3,3}$ are obtained as functions of the uniform grain size.

An estimation of $K_{m,3}$ is now made for the same beach considered above. The field measurements show the following range of values (see Fig.10):

$$\frac{D_{3,1}}{D_{3,2}} = 0.11 \quad \text{to} \quad 0.33 \quad \text{with} \quad \overline{\left(\frac{D_{3,1}}{D_{3,2}}\right)} = 0.23$$

$$\frac{D_{3,3}}{D_{3,2}} = 0.04 \quad \text{to} \quad 0.20 \quad \text{with} \quad \overline{\left(\frac{D_{3,3}}{D_{3,2}}\right)} = 0.10$$

It is repeated that these values reflect conditions, which prevailed along the beach during the period of field measurements. Therefore, it is necessary to examine the sensitivity of $K_{m,3}$ on the changes in $D_{3,i}$. Fig.11 shows the changes in $K_{m,3}$. It is found that $K_{m,3}$ decreases with increasing grain diameters and/or cross-shore size sorting. The value proposed by Komar and Inman, 1970, for the linearity coefficient is found to be rather higher than $K_{m,3}$. The values proposed by Dean et al, 1983, coincide with $K_{m,3}$ in the special case of $D_{3,1} = D_{3,2} = D_{3,3}$.

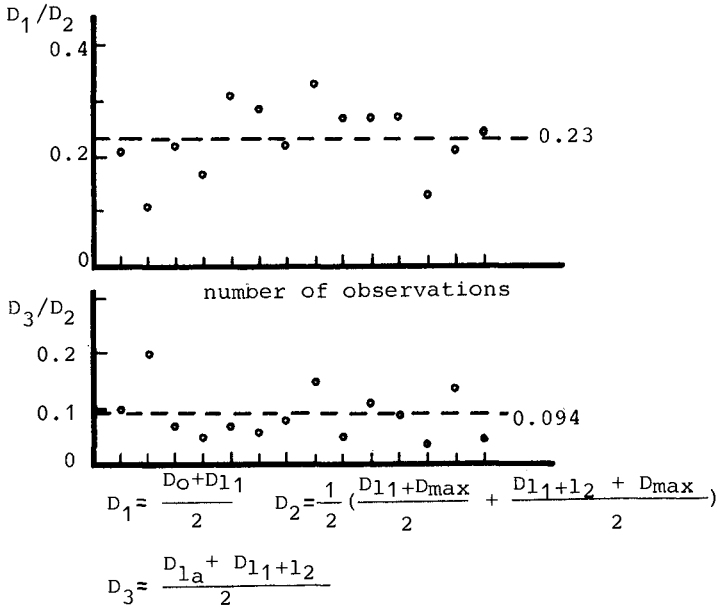


Fig.10. - Grain diameters in the sub-zones (n=3)

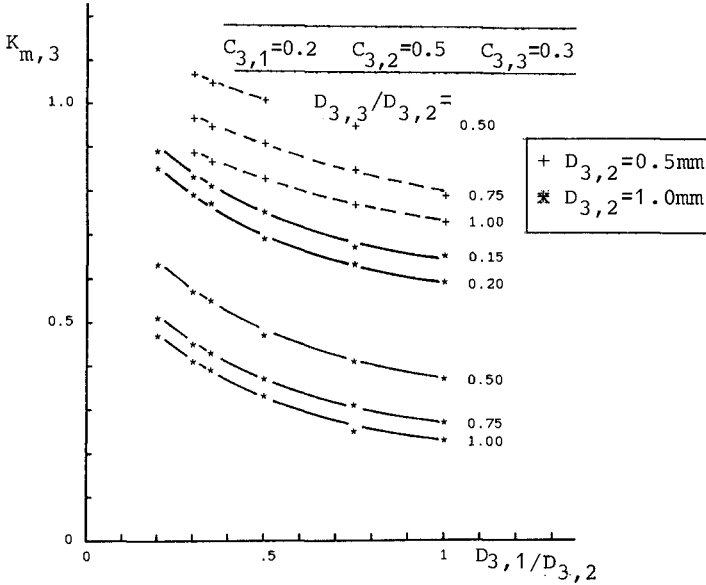


Fig.11. - Modified linearity coefficient (n=3)

In the case of $n=2$, it is proposed to divide the active zone into a pre-breaker zone and an after-breaker zone. The limit between the two zones is situated in the transition zone at the toe of the plunge step (see Fig.12). $K_{m,2}$ is now defined as:

$$K_{m,2} = C_{2,1} K_{2,1} + C_{2,2} K_{2,2}$$

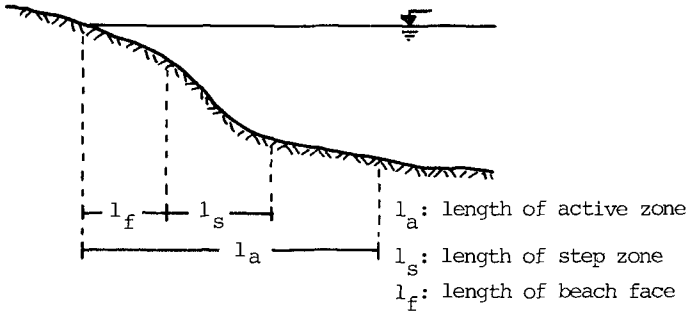


Fig.12. - Sub-zones for $n=2$

The after-breaker zone is comprised of the plunge step and the beach face with widths l_s and l_f , respectively. Data from the Kokkino Limanaki beach show that (see Fig.13):

$$\frac{l_s}{l_a} = 0.02 \text{ to } 0.14, \quad \frac{l_f}{l_a} = 0.04 \text{ to } 0.41$$

and

$$\frac{l_s + l_f}{l_a} = 0.08 \text{ to } 0.48$$

Therefore:

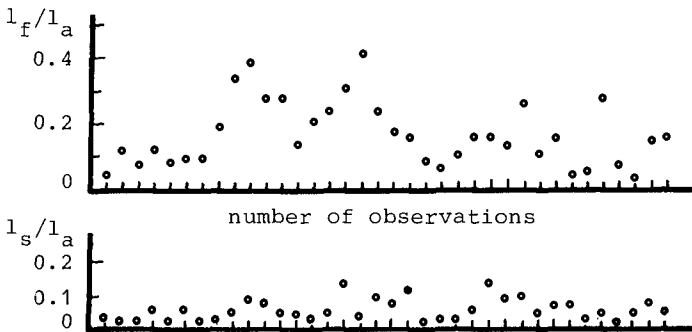


Fig.13. - Lengths of sub-zones ($n=2$)

$$C_{2,1} = 0.1 \text{ to } 0.5 \quad \text{and} \quad C_{2,2} = 0.9 \text{ to } 0.5$$

The sensitivity of $K_{m,2}$ on $D_{2,1}/D_{2,2} C_{2,1}$ and $C_{2,2}$ is examined in Fig.14.

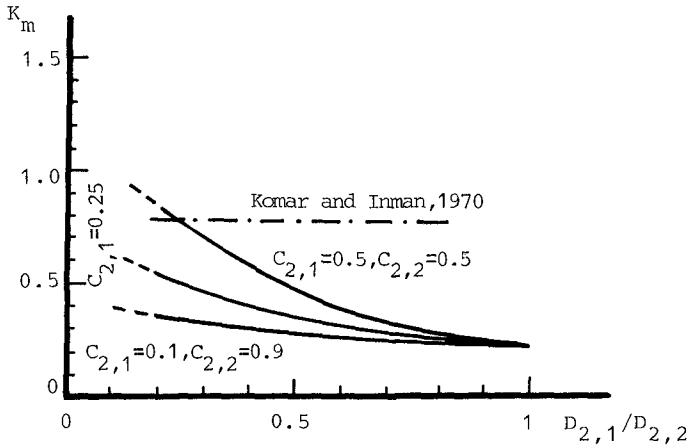


Fig.14. - Modified linearity coefficient ($n=2$)

5. DISCUSSION

The field results briefly presented in the paper are from tideless beaches with mixed sedimentary environments. Although beaches in most parts of the world are of this type, the research effort devoted to them has been too small compared to the extensive work carried out for beaches covered with fine sand. Special interest seems to have been given recently from researchers around the world (f.i. Komar, 1988, Moutzouris, 1988, Nicholls and Webber, 1988, van der Meer, 1988, etc) to beaches which are not exclusively sandy.

The results clearly show that the distribution of sediment grain size is non-uniform on the bed of natural beaches. Grain size and grain size-related parameters change considerably, especially in the cross-shore direction of beaches. The main reason for this is the changing wave-energy levels across-shore.

The cross-shore distributions are expected to be more uniform on tidal beaches due to the dispersion of sediment caused by tidal action. The degree of cross-shore grain uniformity on a beach is also dependent upon the range of sizes met on the beach. Sediment distribution is more uniform for beaches with narrow size ranges than for beaches with broad ranges.

Hydrodynamic conditions prevailing in the active zone of a beach is the main driving mechanism for longshore sediment

transport. Transport rates are also believed to depend upon the beach slope. Sediment size distribution found on a seabed immediately after a sea state reflects the hydrodynamic conditions during the sea state. Introducing the cross-shore distribution into a model for sediment transport computations is in a way equivalent to introducing the cross-shore hydrodynamic conditions and the beach slope because slopes are sediment size-dependent.

The sensitivity of longshore sediment transport models described in this paper is a consequence of the above statements. It is believed that no model can give realistic results for beaches with mixed sedimentary environments unless the cross-shore changes in grain size and grain size-related parameters are taken into account. Further research is necessary in relation to the latter considerations, as has been attempted in the present paper.

REFERENCES

- Bijker, E.W. (1971). Longshore transport computations. *Jour. Wat. Harb. Coast. Engin. Div., ASCE*, Vol. 97, WW4, pp. 687-701
- Dean, R.C., Berek, E.P., Cable, C.C., and Seymour, R.J. (1983). Longshore transport determined by an efficient trap. *Proc. 18th ICCE, Cape Town, Vol. II*, pp. 954-968
- Deigaard, R., Fradsøe, J. and Hedegaard, I.B. (1986). Mathematical model for littoral drift. *Jour. Wat. Port Coast and Ocean Engin.*, Vol. 112, No. 3, pp. 351-369
- Folk, R.L. and Ward, W.C. (1957). Brazos River Bar: A study of the significance of grain-size parameters. *Jour. Sedim. Petrol.*, Vol. 44, pp. 40-53
- Komar, P.D. and Inman, D.L. (1970). Longshore sand transport on beaches. *Jour. Ceoph. Res.*, Vol. 75, No. 30, pp. 5914-5927
- Komar, P.D. (1975). Longshore currents and sand transport on beaches. *Proc. Civ. Engin. in the Oceans Conf., ASCE*, pp. 333-354
- Komar, P.D. (1988). Environment controls on littoral sand transport. *Abstracts 21st ICCE, Torremolinos*, pp. 17-18
- Longuet-Higgins, M.S. (1970). Longshore currents generated by obliquely incident sea waves - Part I. *Jour. Ceoph. Res.*, Vol. 75, pp. 6778-6789
- Moutzouris, C.I. (1988). Wave-induced distribution of sediment size-related parameters on the nearshore sea bed. *Proc. Seminar on Coastal Data, Crenoble*, pp. 88-99
- Moutzouris, C.I. and Kypraios, N. (1987). Temporal and spatial grain size distribution of sediment in a tideless pocket beach. *Proc. Coastal Sediments '87, ASCE, N. Orleans, Vol. II*, pp. 1909-1924
- Nicholls, R. and Webber, N. (1988). Characteristics of shingle beaches with reference to Christchurch Bay, S. England. *Abstracts 21st ICCE*, pp. 498-499
- Van der Meer, J.W. (1988). Rock slopes and gravel beaches under wave attack. Ph.D. thesis, Delft University of Technology, Delft

CHAPTER 146

The theoretical temporal structure of the longshore currents

JOSE AGUILAR¹
JOSE JAVIER DIEZ²

1) INTRODUCTION

For a better Knowledge of the causes about the littoral solid transport is essential to experience advances in the littoral hydrodynamic. In this field the longshore currents are may be who play the most important role due to the intensity, the distribution and the relative duration of them, causing the movement of the solid particles due to the suspension of them and the friction in bottom.

The first theoretical formulation about the longshore currents were established by Bowen (1969), Longet-Higgins (1970) and Thornton (1970). Previously another works treated an approximation about the problem, obtaining a little precise results basing his works in simplest formulations, it shows in Sonu et al. (1966).

2) AN OBSERVATION ABOUT THE EXISTING SOLUTIONS.

The basic equations of motion are:

- The Conservation of mass equation
- The Conservation of energy equation
- The Conservation of momentum equation.

The conservation of energy equation is not used because two reasons:

1. It is a complex formulation
2. It utilize disipation mechanism that they are not simples and precises for his formulation.

With the proposit of obtain a simple expression about the phenomenon there are realized series of simplifications, where the most important are:

- a) Vertical and temporal averages in all the equations.
- b) Elimination of the "Y" variable considering the case like a quasi-orthogonal problem; in this way X is the independent variable.

-
- (1) - Prof. Titular de Puertos
Universidad Politécnic de Valencia.
 - (2) - Catedrático de Oceanografía e Ingeniería de Costas
Universidad Politécnic de Madrid.

- c) Utilization of Monochromatic waves.
This simplification together with the others represent waves like a curve $H(x)$.
- d) Utilization of ideal beach profiles, terms linealization and others.

Not all the models use the same simplifications, but the final results is always a distribution $V(x)$ (in some cases $V(x,y)$), that doesn't have in count the temporal nature of the phenomenon, eliminated by one of the simplifications before mentioned.

Battjes (1974) tried to improve this lack trough relations of the parallel velocity V with formulations of the radiation stress in truncated function of the Rayleigh distribution of the waves in a sea state.

3) A NEW ECUATION DEDUCTION.

The objetive is to establish a new ecuation were we will find the local longshore current velocity value $V(x,t)$, like a consequence of waves gived by the displacement of the sea surface, like a time serie.

In this way, the longshore current will be a variable in time, which structure is possible to study.

For it we have to revert to the classic basic equations of Navier-Stokes, and make a parallel deduction to them (Phillips 1966, Mei 1983) but without the temporal average.

In conclusion the most important Hypothesis are:

- 1) Admiting the "Shallow Water wave" simplification we have

$$U = \frac{C}{\delta} \zeta \quad (U_x, U_y) = U (-\cos\alpha, \sin\alpha)$$

$$Pz = pg (-z+h+\zeta)$$

$$C = \sqrt{g\delta} \quad \delta = h + d \quad (\text{Figure 1})$$

- 2) Accepting the Snell's Law :

$$\frac{C}{\sin \alpha} = \text{cte}$$

$$\frac{\partial \alpha}{\partial x} \approx \frac{\sin 2\alpha}{2 \delta} \quad \frac{\partial \delta}{\partial x} \quad \frac{\partial \alpha}{\partial y} = 0 \quad \frac{\partial \alpha}{\partial t} = 0$$

- 2) Admitting the hypothesis of "long crested waves" we have:

$$\frac{\partial \zeta}{\partial y} = -\operatorname{tg} \alpha \quad \frac{\partial \zeta}{\partial x} \approx -\sin \alpha \quad \frac{\partial \zeta}{\partial x}$$

- 3) For the internal stresses representation we can introduce it by the temporal adverage values:

$$\tau_{xy} \approx \rho \cdot \frac{gTH^2}{8\pi^2} \frac{\partial v}{\partial x}$$

Although the others hypothesis will guide us to a temporal equation, the inexistence of this equations take us to the mentioned expression. In this way we can interpret beginning with other previous models results, that the turbulent tensions have only a distribution effect on to the X axis; it has make that some works leaving aside this term presented models with anyone inclusion of this.

- 4) The Set-up will be the proposed by Bowen (1968)
 5) The section could be in any form $d = d(x)$ (Figure 1).
 6) The wave representation in breaking zone is in the following form (Figure 1):

$$\zeta_{X_i, Y_i, t} = \zeta_{X_o, Y_o, t} f_{fi} f_{ri}$$

... were

$\zeta_{X_i, Y_i, t}$ is the sea's displacement in (X_i, Y_i) point at instant t .

$\zeta_{X_o, Y_o, t-\Delta t}$ is the sea's displacement in a reference point (X_o, Y_o) .

Δt is the wave's time employed to go through the points (X_o, Y_o) and (X_i, Y_i)

$t \approx - \int_{X_o}^{X_i} \frac{dx}{C}$... in the hypothesis of "quasi-orthogonal" incidence

$f_{fi} = \frac{H_i}{H_o} = \sqrt{\frac{\sin 2\alpha_o}{\sin 2\alpha_i}}$ is the refraction factor at the point i

$f_{ri} = \begin{cases} 1 & \text{if } H_o f_{fi} \leq \sigma_b \\ \frac{1}{H_o f_{fi}} & \text{if } H_o f_{fi} > \sigma_b \end{cases}$ is a breaking form factor at the (X_i, Y_i) point

With it we are looking for a temporal series representation "Sea's displacement at (X_i, Y_i) point" in relation with the correspondent at (X_o, Y_o)

With all is possible formulate an ecuation of the type:

$$\frac{dV}{dt} \approx f \left(v, \frac{\partial V}{\partial x}, \frac{\partial^2 V}{\partial x^2}, x, t, z \right)$$

This equation is :

$$\begin{aligned} & \frac{\partial V}{\partial t} + \frac{\partial V}{\partial x} \left[-c \frac{z}{\delta} - \left(\frac{gTH^2}{8\pi^2\delta D} \left(\frac{\partial z}{\partial x} + \frac{\partial \delta}{\partial x} \right) + \frac{\partial}{\partial x} \left(\frac{gTH^2}{8\pi^2\delta} \right) \right) \right] + \\ & + \frac{\partial V}{\partial y} \left[2 \frac{cz}{\delta} \sin \alpha + 2V \right] + \frac{\partial^2 V}{\partial x^2} \left[-\frac{gTH^2}{8\pi^2\delta} \right] + \\ & + V \left[\frac{1}{D} \frac{\partial z}{\partial t} + \frac{\partial \delta}{\partial x} \left(\frac{cz^2}{D\delta} - \frac{cz}{2\delta^2} \right) + \frac{\partial z}{\partial x} \left(-\frac{c(D+z)}{D\delta} \right) \right] \\ & + v^2 \left[-\frac{\partial z}{\partial x} \frac{\sin \alpha}{D} \right] + \frac{1}{\rho D} \tau^B = \\ & = \frac{\partial z}{\partial x} \left[\frac{c^2 z}{D\delta^2} (2D+z) \sin \alpha + g \sin \alpha \right] + \frac{\partial z}{\partial t} \left[-\frac{c(D+z)}{D\delta} \sin \alpha \right] + \\ & + \frac{\partial \delta}{\partial x} \sin \alpha \left[-\frac{c^2 \delta^2 (D+z)}{D\delta^3} + \frac{g z^2}{\delta^2} + \frac{c^2 z^2}{2\delta^3} \right] + \frac{1}{\rho D} \tau^S \end{aligned}$$

$$D = \delta + z$$

$$\tau^B = \rho C_F \sqrt{\left(\frac{cz}{\delta}\right)^2 + \left(\frac{cz \sin \alpha}{\delta} + V\right)^2} \left(V + \frac{cz}{\delta} \sin \alpha\right) \dots \text{is the}$$

stress in the bed

$$\tau^S = \rho k W^2 \cos \theta \dots \text{or similar, is the stress due to}$$

$$k \begin{cases} 1.1 \cdot 10^{-6} & W \leq 7.2 \text{ m/s} \\ 1.1 \cdot 10^{-6} + 2.5 \cdot 10^{-6} \left(1 - \frac{7.2}{W}\right) & W > 7.2 \text{ m/s} \end{cases} \text{the wind action}$$

For the explicit form resolution we must utilize a small Δt . If we admit that the time discretization error is the same order of magnitude then the spatial discretization, beginning with the wave phases term we can obtain:

$$\frac{2\pi x}{L} + \frac{2\pi t}{T} \qquad \Delta x = C \Delta t$$

CONCLUSIONS

As a conclusion in accord with all before mentioned, we can conclude that we have basis for the study of the theoretical temporal structure of the longshore currents. This is based in anew deduction of the movement equation where we don't have to make a temporal averages in it development and let the incident wave comes from a unic time serie $\zeta(t)$ of the superficial sea displacement at (X_0, Y_0) point of reference in the contour, with discretization in Δt intervals.

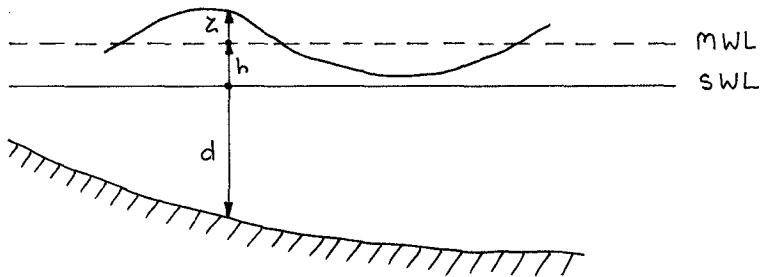


Figure 1: A section definition.

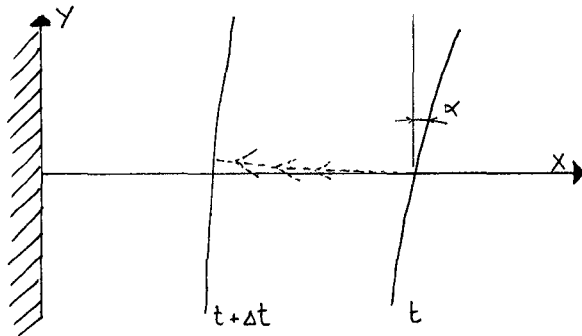


Figure 2: A Plant Definition.

REFERENCIAS

BATTJES, J.A. (1974). "Computation of Set-up, Longshore Currents, Run-up and Overtopping due to Wind-generated waves". Delft University

BOWEN, A. (1969). "The generation of Longshore Currents on a plane beach". J. of Marine Research Vol. 27, 2, pp. 206-215

LONGHUET-HIGGINS, M.S. (1970). "Longshore Current Generated by Obliquely incident Sea Waves. 2". J.of Geophysical Research. Vol. 75, n^o 33, pp. 6790-6801.

MEI C. (1983). "The Applied Dynamics of Ocean Surface Waves". John Wiley & Sons. N.Y.

PHILLIPS, O.M. (1966). "The Dynamics of the Upper Ocean". Cambridge University Press. London

SONU, C.; Mc. CLOY, J.M. y Mc. ARTHUR, D.S. (1966) "Longshore Currents and Nearshore Topographies" I.C.C.E., Chp. 32, pp. 325-349.

THORNTON, E.B. (1970). "Variation of Longshore Currents Across the Surf Zone". I.C.C.E., Chp. 18, pp. 291-308.

SUBJECT INDEX

Page number refers to first page of paper.

- Accretion, 2738
Aeration, 166
Air chambers, 2326
Alaska, 2574, 2818
Altimeters, 1508
Analysis, 2952
Approximation methods, 2144, 2927
Armor units, 644, 2063, 2075, 2102,
2116, 2129, 2284, 2299, 2355, 2370,
2385, 2416, 2418, 2445, 2479
Armored units, 2144
Armour units, 1983
Australia, 2626

Barrier islands, 2681
Bars, riverine, 1167
Bathymetry, 2655
Bayesian analysis, 62
Beach erosion, 1, 121, 322, 1197,
1253, 1330, 1411, 1426, 1437, 1482,
1493, 1508, 1558, 1721, 1818, 1857,
1882, 1911, 1937, 1983, 2028, 2090,
2738, 2791, 2840, 2855, 2896,
153501543
Beach nourishment, 1323, 1411,
1482, 1558, 1882, 1922, 2806, 2825,
153501543
Beaches, 32, 77, 136, 151, 219, 292,
539, 553, 705, 807, 1182, 1238,
1295, 1338, 1396, 1618, 1631, 1676,
1736, 1763, 1959, 2116, 2784, 2867
Bed load movement, 1774, 1803
Bed ripples, 1748, 1868
Bed roughness, 492, 1842, 2692
Bedforms, 849, 1868, 2692
Belgium, 2855
Berms, 1997, 2284, 2416, 2818
Berths, 2966
Blocks, 2159, 2479
Boundary conditions, 181, 393, 624,
2561
Boundary element method, 624
Boundary layer, 234, 743, 914, 1129,
1280, 1603
Boundary layer flow, 492
Brazil, 261
Breaking waves, 234, 292, 350, 377,
393, 419, 478, 539, 578, 632, 682,
871, 1020, 1035, 1058, 1113, 1167,
1212, 1238, 1368, 1646, 1721, 2174,
2272, 2340, 2504
Breakwaters, 47, 121, 166, 246, 281,
624, 782, 1073, 1573, 1997, 2013,
2028, 2075, 2129, 2229, 2272, 2326,
2355, 2430, 2469, 2479, 2489, 2504,
2840, 2882
Buoys, 2923

Caissons, 2469, 2489
Calibration, 2013
California, 2129, 2455
Caribbean, 1618
Case reports, 756, 1265
Channels, waterways, 2896, 2911
Cnoidal waves, 219, 553, 588
Coastal engineering, 1, 204, 350, 363,
463, 858, 871, 884, 929, 941, 999,
1011, 1045, 1058, 1152, 1323, 1411,
1437, 1452, 1631, 1788, 1842, 1882,
1911, 1922, 2144, 2589, 2603, 2626,
2641, 2666, 2818, 2855, 2952
Coastal environment, 2574, 2615
Coastal management, 1, 2090, 2738,
2896
Coastal morphology, 1, 322, 1084,
1295, 1330, 1618, 1689, 1736, 1788,
1818, 1857, 2825
Coastal processes, 32, 181, 743, 1084,
1152, 1227, 1253, 1265, 1323, 1330,
1338, 1382, 1396, 1426, 1437, 1452,
1544, 1603, 1618, 1631, 1646, 1661,
1676, 1704, 1774, 1803, 1922, 1937,
1952, 1974, 2655, 2772, 2784, 2825,
2867
Coastal structures, 1, 166, 281, 655,
756, 782, 1020, 1310, 1482, 1573,
2043, 2053, 2090, 2174, 2189, 2299,
2370, 2385, 2400, 2455, 2504, 2681,
2791, 2840
Coastal zone, 2028
Coefficients, 47
Comparative studies, 644, 2681
Composite materials, 1588
Computation, 292, 1974
Computer aided drafting (CAD), 463
Computer applications, 463
Computer models, 2991
Computerized design, 463
Concrete blocks, 2043, 2053, 2144,
2174, 2370, 2400
Concrete construction, 2102, 2385,
2418
Conical bodies, 2257
Construction, 2416, 2723, 2753, 2791
Cost minimization, 2416
Currents, 77, 136, 363, 971, 1035,

Volume 1 – 1- 998

Volume 2 – 999-1980

Volume 3 – 1981-2998

- 1140, 1212, 1368
 Curtain walls, 2430
 Cylinders, 914, 2201, 2216
 Damage assessment, 2818
 Damage prevention, 1558
 Damping, 2952
 Data collection, 2753
 Deformation, 393
 Deltas, 1323
 Design, 655, 782, 1280, 1997, 2043,
 2063, 2159, 2174, 2299, 2326, 2385,
 2416, 2489, 2666, 2723, 2753, 2979
 Design criteria, 756, 1020, 1197,
 1411, 2129, 2284, 2504
 Design data, 770
 Design events, 756
 Design waves, 822, 899, 2504
 Differential equations, 2603
 Diffusion coefficient, 166
 Dikes, 335, 1897, 2174, 2340
 Discharge, 1573, 2521
 Displacement, 1464
 Distribution functions, 899
 Docks, 2313
 Dolos, 2075, 2129, 2355, 2385, 2418,
 2445
 Dunes, 1197, 1426, 1588, 1721, 1857,
 2090
 Dye studies, 2626
 Dynamic analysis, 2469
 Dynamic response, 1763, 2189, 2469,
 2923
 Ecology, 2574, 2615
 Economic factors, 1558
 Eddie viscosity, 492
 Eddies, 234, 1646
 Eddy viscosity, 408, 478, 505, 1661
 Effluents, 2521
 Energy absorption, 2313, 2966
 Energy conversion, 2489
 Energy dissipation, 292, 363, 408,
 492, 578, 1045, 1113, 1833, 2326
 Energy losses, 1842, 2216
 Energy transfer, 999
 Entrainment, 2550
 Environmental factors, 1238
 Environmental impacts, 1330, 2574
 Equations of motion, 419
 Equilibrium, 1045
 Equilibrium profile, 1396, 1618
 Erosion, 1197, 1368, 1897, 2299
 Erosion control, 1588
 Estimating, 2445
 Estimation, 62
 Estuaries, 1212, 1573, 1788, 2655,
 2692, 2707, 2784
 Eutrophication, 2615
 Experience, 2455
 Experimental data, 270, 153501543
 Failures, 1897, 2053, 2063
 Failures, investigations, 2818, 2923
 Fenders, 2966
 Field investigations, 524, 539, 1522,
 1618, 1833, 2430, 2626
 Field tests, 47, 136, 1588, 1763
 Finite difference method, 1129
 Finite element method, 32, 2313,
 2445
 Finite elements, 2561
 Fishing, 2927
 Floating breakwaters, 2189
 Flood control, 2855
 Flood forecasting, 1197
 Florida, 2772
 Flow characteristics, 2201
 Flow patterns, 505
 Flow visualization, 234
 Fluid dynamics, 718
 Fluid-structure interaction, 17
 Flumes, 448, 612, 770, 835, 871, 1140,
 1763, 1803
 Flushing, 2626
 Forecasting, 566, 602, 667
 Fourier transform, 246, 307
 France, 2707
 Frequency analysis, 2272
 Friction, 505, 849, 1073
 Friction factor, 363, 492, 2013
 Geomorphology, 2681
 Grain size, 1952, 1959
 Grain size analysis, 1129
 Grains, 718
 Gravel, 2116
 Gravity foundations, 2469
 Gravity waves, 512, 667, 2201
 Grid systems, 2655
 Groins, structures, 2882
 Harbor engineering, 463, 782, 984,
 1997, 2896
 Harbors, 32, 47, 270, 463, 1227, 2242,
 2784, 2818, 2882, 2911, 2979
 Head loss, 270
 Hurricanes, 1098
 Hydraulic design, 2400
 Hydraulic models, 770, 2242, 2840,
 2979
 Hydraulic performance, 795

- Hydraulics, 2589, 2666
Hydrodynamics, 463, 505, 1058,
1382, 1974, 2189, 2479, 2655
Hydrostatics, 682
- Ice loads, 2400
In situ tests, 2355
Inlets, waterways, 433, 2681
Innovation, 2326
Intake structures, 2723
Islands, 322, 2738
- Japan, 2028, 2063, 2791
Jetties, 1911, 2896
- Kinematics, 377, 448, 871
- Laboratory tests, 91, 612, 632, 795,
835, 849, 1646, 1748, 1763, 1842,
1897, 1983, 1997, 2430
Lakes, 2840
Land fill, 2806, 2855
Linear functions, 884
Littoral current, 408, 1182
Littoral currents, 77, 234, 393, 705,
1113, 1238, 1396, 1689, 1736, 1959,
1974, 2521, 2603
Littoral drift, 1152, 1182, 1238, 1253,
1330, 1382, 1396, 1437, 1452, 1603,
1676, 1818, 1937, 1959, 1974, 2772,
2825
Loading, 2257
Long waves, 91, 219, 270, 984
- Marinas, 2626
Markov process, 956
Mathematical models, 246, 281, 566,
1129, 1603, 1689, 1897
Mats, 2400
Measuring instruments, 77
Mediterranean Sea, 566
Methodology, 884, 899, 1857
Mineralogy, 1338
Mixing, 2521
Model accuracy, 566
Model studies, 2692
Model tests, 644, 770, 984, 1265,
2075, 2257, 2923
Model verification, 433
Modeling, 121, 261, 335, 718, 956,
1952, 2418, 2589
Models, 270, 492, 698, 743, 795, 807,
822, 1098, 1212, 1253, 1676, 1736,
1818, 1833
Monitoring, 2806
Monte Carlo method, 899
- Mooring, 2189, 2923, 2952, 2979
Movable bed models, 1227, 1544
- Nearshore circulation, 106, 393, 408,
578, 1058, 1113, 1452, 1522, 1704,
2561, 2603, 2626, 2655
Netherlands, 2825
New Jersey, 2806, 2867
Nonlinear differential equations, 732
Nonlinear response, 1803
North Sea, 322, 956, 1788
Norway, 1997
Numerical analysis, 743
Numerical calculations, 307, 624,
2430, 2589
Numerical models, 350, 393, 433,
463, 512, 578, 588, 602, 858, 929,
941, 1113, 1167, 1265, 1295, 1426,
1437, 1911, 1937, 2013, 2159, 2189,
2445, 2561, 2655, 2666, 2707
Nutrient loading, 2615
- Ocean disposal, 2521
Ocean engineering, 2927
Ocean environments, 2536
Ocean thermal energy conversion,
971
Ocean waves, 204, 335, 602, 655,
1464
Oceanography, 602
Offshore engineering, 2536
Offshore pipeline, 2641
Offshore platforms, 62, 261, 956,
2257, 2313
Offshore structures, 914, 1280, 2257
Oil spills, 2574
Oregon, 1338
Oscillations, 151, 270, 2952, 2966
Oscillatory flow, 718, 743, 1140
Outfall sewers, 2615
Outwash, 1922
Overtopping, 335, 770, 795, 1983
- Perturbation theory, 705
Physical properties, 941
Phytoplankton, 2615
Piers, 1310
Pile tests, 1368
Piles, 1310, 2229
Plastic pipes, 2641
Plates, 2272
Plunging flow, 632, 682
Polyethylene, 2641
Polymers, 1588
Pore pressure, 1011
Pore pressure measurement, 2242

- Pore water pressure, 1842
- Porous materials, 1073
- Ports, 756, 1997, 2882, 2911
- Potential flow, 17
- Predictions, 644, 698, 871, 1098, 1167, 1253, 1396, 1426, 1508, 1676, 1803, 1857, 2201, 2536, 2692
- Pressure distribution, 682, 2504
- Probabilistic methods, 2063
- Probabilistic models, 1352
- Probability density functions, 524, 807, 822
- Probability distribution, 655, 822
- Probability theory, 1011, 2053
- Profiles, 1482, 1493, 1631, 1676, 1882, 2806, 153501543
- Project evaluation, 2806
- Prototype tests, 718, 1265, 1721, 2355
- Pump intakes, 2723
- Pumped storage, 1897

- Quality assurance, 2102
- Quantitative analysis, 2772

- Radar, 667
- Random waves, 91, 770, 807, 835, 941, 1736, 1748, 1763, 1911, 2257
- Recreational facilities, 1558, 2840, 2867
- Reefs, 335
- Regeneration, 1437
- Rehabilitation, 2855
- Reliability, 2063
- Reliability analysis, 2053
- Remote sensing, 667
- Repairing, 2075
- Research needs, 1
- Resonance, 270
- Restoration, 1411
- Return flow, 448
- Revetments, 281, 782, 795, 2043, 2116, 2159, 2174, 2340
- Reviews, 377, 2784
- Reynolds number, 2979
- Reynolds stress, 478
- Rip current, 408
- Rip currents, 32, 1603
- Risk analysis, 2574
- Rivers, 1573
- Rock properties, 2299
- Rock structures, 2116
- Roughness coefficient, 644
- Rubble-mound breakwaters, 770, 2053, 2063, 2102, 2116, 2144, 2242, 2284, 2385, 2416, 2418, 2455, 2818
- Sand, 718, 1588, 1882
- Sand transport, 1152, 1182, 1212, 1238, 1280, 1295, 1338, 1382, 1721, 1748, 1868, 1897, 2772
- Sand waves, 1748
- Sandbars, 2882
- Scale effect, 153501543
- Scale models, 2159, 2911
- Scattering, 2216
- Scour, 1310, 1368
- Scouring, 1280
- Sea floor, 1035, 1352, 1464, 1748, 1868, 2927
- Sea floor, 1842
- Sea level, 2825, 2867
- Sea state, 322, 655, 667, 956, 2340
- Sea walls, 281, 335, 782, 795, 1493, 1882, 1983, 2090, 2455, 2882
- Sea water, 2641, 2723
- Sediment, 849
- Sediment concentration, 1661, 2738
- Sediment control, 2723
- Sediment deposits, 1573
- Sediment transport, 234, 1084, 1140, 1152, 1167, 1182, 1227, 1280, 1338, 1368, 1382, 1396, 1452, 1493, 1508, 1522, 1544, 1676, 1689, 1704, 1721, 1736, 1774, 1803, 1818, 1868, 1882, 1911, 1952, 1959, 2707, 2772
- Sediment yield, 2867
- Selection, 2966
- Sensitivity analysis, 1959
- Service life, 2102
- Settlement analysis, 2927
- Sewage treatment plants, 2753
- Shallow water, 612, 807, 929, 1020, 1035, 1310
- Shaoling, 632
- Shear stress, 77, 1084, 1140, 2550
- Ship motion, 2911, 2952, 2966
- Ships, 2979
- Shoaling, 106, 419, 588, 807, 1035, 1212
- Shock, 2340
- Shore protection, 644, 1482, 1493, 1788, 2028, 2090, 2370, 2455, 2840, 2882
- Shoreline changes, 539, 1253, 1265, 1295, 1426, 1544, 1937, 2791, 2825, 2867
- Simulation, 91, 835, 858, 899, 941, 2299, 2911
- Simulation models, 106, 505, 1857, 2201, 2923
- Siphons, 2753
- Skewness, 1508

- Slope stability, 2116, 2400
Slopes, 281, 419, 2641
Soil analysis, 1352
Soil layers, 1352
Soil liquefaction, 1352
Soil mechanics, 1011
Soil stabilization, 1588
Soil stresses, 1352
Solitary wave, 219, 624, 1073, 2479
Sonar, 1508
Spain, 204, 858, 984, 1323, 1330,
1411, 2784, 2896
Spectral analysis, 524, 2536
Stability, 1997, 2028, 2053, 2075,
2174, 2284, 2299, 2370, 2489
Stability criteria, 2043
Stabilization, 2791
Standing waves, 151
State-of-the-art reviews, 971, 2043
Statistical analysis, 91, 756, 835,
1011, 1522, 2028, 2536
Statistical data, 655, 956
Statistics, 106
Steady flow, 1140
Steady state models, 929
Stochastic processes, 292, 941, 2536
Stoke's law, 17
Storm surges, 999, 1493
Storms, 566, 756, 956, 984, 1197,
1426, 1464, 1482, 1508, 1544, 1558
Stratified flow, 2550, 2561
Stress, 2418, 2692
Structural behavior, 2075, 2355
Structural design, 2129
Structural failures, 2445
Structural response, 2385, 2445
Structural strength, 2102
Submarine pipelines, 1464
Surf beat, 1058, 1167
Surf zone, 77, 151, 292, 377, 408, 419,
478, 539, 578, 612, 632, 705, 807,
999, 1058, 1167, 1182, 1295, 1382,
1646, 1661, 1704, 1774, 1833, 1959,
153501543
Surface waves, 246, 512
Suspended load, 1897
Suspended sediments, 1129, 1452,
1603, 1646, 1661, 1704, 1842, 2707

Taiwan, 1152, 2370, 2882
Technology assessment, 971
Theories, 181, 307, 588, 1073
Thermal pollution, 2521
Thermal power plants, 2521
Three-dimensional analysis, 1689,
2284

Three-dimensional flow, 705
Three-dimensional models, 667, 858,
2574
Tidal bores, 2589
Tidal currents, 433, 858, 1227, 1508,
2536, 2666, 2707
Tidal flats, 1788
Tidal marshes, 2666
Tidal power plants, 971
Tidal waters, 2681, 2692, 2896
Tides, 512, 2867
Time series analysis, 350
Topography, 1937, 2603, 2738
Tracers, 1338, 1774
Trends, 1
Turbulence, 478, 743, 2550
Turbulent boundary layer, 1661
Turbulent diffusion, 1661, 1704, 2589
Turbulent flow, 1646
Two-dimensional models, 350, 505,
2991

Uncertainty analysis, 1045
Undertow, 705, 1833
Undertown, 478
Underwater structures, 2753
United Kingdom, 1922
Unsteady flow, 624, 914
Uplift pressure, 2313

Velocity distribution, 1661
Velocity profile, 682, 743, 1368
Vertical cylinders, 17
Vortex shedding, 1310
Vortices, 914, 2927

Waste heat, 2521
Wastewater treatment, 2753
Water depth, 307, 419, 2469, 2911,
2979
Water flow, 2013, 2589
Water level, 999
Water levels, 539
Water pollution, 2615
Water purification, 166
Water supply systems, 2641
Water tunnels, 718, 1084
Water waves, 246, 433, 448, 682, 705,
732, 743, 1129, 1508, 1842, 2216
Wave action, 166, 281, 782, 1113,
1464, 1482, 1631, 1803, 1868, 1911,
2189, 2242, 2284, 2340, 2370, 2400,
2469, 2603
Wave attenuation, 363, 478, 492, 849
Wave climatology, 204, 261, 2806,
1535 1543

- Wave crest, 17, 307, 871, 1020
- Wave defraction, 393, 2189
- Wave diffraction, 17, 47, 121, 433, 732, 929, 2216
- Wave dispersion, 578, 612
- Wave energy, 62, 106, 261, 292, 971, 1721, 1833, 2272, 2326, 2489, 2991
- Wave equations, 181
- Wave forces, 77, 914, 1084, 1140, 1227, 1280, 1295, 1310, 2144, 2201, 2257, 2313, 2355, 2418, 2430, 2445, 2479, 2504, 2784, 2911, 2966
- Wave generation, 91, 448, 612, 667, 698, 835, 941, 1098, 1544, 2991
- Wave groups, 204, 884, 984
- Wave height, 106, 136, 151, 307, 363, 419, 524, 553, 588, 667, 732, 807, 822, 871, 884, 899, 956, 1182, 1197, 1983, 2229, 2469, 2504
- Wave measurement, 47, 62, 136, 204, 322, 377, 524, 588, 667, 1152, 2229, 2355, 2991
- Wave pressure, 2159, 2340, 2489
- Wave propagation, 32, 62, 181, 350, 363, 377, 419, 512, 553, 929, 999, 1073, 2229
- Wave propatation, 246, 433
- Wave reflection, 47, 136, 219, 393, 553, 782, 1073, 1493, 1763, 1983, 2013, 2216, 2272, 2489
- Wave refraction, 121, 393, 433, 588, 732
- Wave runup, 17, 151, 219, 553, 644, 655, 795, 1167, 1763, 1857, 1922, 1983, 2013, 2053, 2129, 2370
- Wave spectra, 47, 62, 91, 261, 350, 492, 602, 612, 849, 929, 999, 1011, 1045, 2229
- Wave tanks, 632, 1482, 1588, 1952, 2550
- Wave velocity, 151, 377, 448, 524
- Waves, 2991
- Weirs, 335
- West Germany, 1788
- Wetlands, 2666
- Wind direction, 602
- Wind forces, 77, 261, 433, 632, 698, 929, 2550
- Wind velocity, 1098
- Wind waves, 512, 566, 602, 698, 1011, 1045, 1098, 2550

AUTHOR INDEX

Page number refers to first page of paper.

- Acinas, Juan R., 698
Aguilar Herrando, José, 1323, 2896
Aguilar, Jose, 1974
Ahrens, John P., 795
Alejo, M., 2479
Allsop, N. W. H., 281, 782
Aminti, Pierluigi, 770
Andersen, Ole Holst, 1603
Anglin, C. D., 2418, 2840
Anglin, C. David, 2385
Arcilla, A. S., 350
Arcilla, A. S., 463, 1382
Arenillas Parra, Miguel, 1330
Armanini, Aronne, 1129
Asano, Toshiyuki, 743
Auerbach, M. H., 1588
Awaya, Yoichi, 234
- Backhaus, J. O., 858
Baird, W. F., 2418
Baird, William F., 2385, 2416
Bakker, W. T., 718, 2825
Banno, Masato, 1868
Barnett, Michael R., 1493
Basco, David R., 682, 2589
Beil, N. J., 1482
Bendykowska, Genowefa, 612
Berenguer, José Ma, 1411
Bertolotti, Andrea, 2666
Bertotti, Luciana, 566
Bezuijen, A., 2159
Bijker, E. W., 1368
Bijker, Eco W., 2090
Blázquez, Rafael, 1352
Bodge, Kevin R., 1396
Boon, John D., 1508, 1618
Borden, G. W., 1588
Bowen, A. J., 1452, 1522
Bowen, Anthony J., 136
Bryden, I. G., 1020
Burcharth, H. F., 2284
Bürger, W., 2242
Burrows, R., 956
Byres, Ronald, 2189
- Campello Chorro, José L., 1323
Castel, David, 1676
Cavaleri, Luigi, 566
Chang, Jo Y. -H., 1464
Chang, S. G., 2370
Christodoulou, George C., 2561
Claassens, H., 2075
Clemens, Karen E., 1338
- Cooker, Mark, 624
Cortés Gimeno, Rafael, 1330
Costa, F. Vasco, 2966
Crowley, J. B., 181
- Daemrich, Karl-Friedrich, 322
Dai, G., 835
Dai, Guanying, 2469
Dally, William R., 807
Dalrymple, Robert A., 246, 2216
Davidson, D. D., 2416
Davis, Gregory A., 539
de Bruyn, C. A., 1368
De Luis, Jose E., 566
de Reus, J. H., 433
De Rouck, J., 2102
de Souza, Maria Helena Severo, 261
de Vriend, H. J., 1689
de Vroeg, J. H., 2825
Dean, Robert G., 807, 1558
Deb, Manas Kumar, 553
Dedeyne, R., 2102
Deguchi, Ichiro, 335, 1573
Deigaard, Rolf, 1603
del Río, J. G., 2615
Dette, H. H., 1721
Dette, Hans-Henning, 292
Dibajnia, Mohammad, 578
Dieckmann, Reinhard, 2681
Diez González, J. Javier, 1323, 1330
Diez Gonzalez, Jose Javier, 2784
Diez González, Jose Javier, 2896
Díez, J. J., 2615
Diez, Jose Javier, 1974
Dingemans, Maarten W., 32
Dodd, N., 732
Doering, J. C., 1452
Douglas, Barry, 2229
Douglass, S. L., 2806
Douglass, Scott L., 632, 2867
Drouin, Alain, 2272
- Easson, W. J., 1020
Easson, William J., 871
Economou, George D., 2561
Edge, B. L., 1588
Edge, Billy, 2416
Edge, Billy L., 2723
Egozcue, J. J., 350
Eisenberg, Y., 2753
Endo, Taiji, 2053, 2063, 2144
Enriquez, Javier, 1411
Escobar Paredes, Víctor A., 2896

- Esteban Chapapria, Vicent J. de, 1323, 1330
 Fasano, R. A., 2753
 Feldmeth, C. Robert, 2666
 Fenaish, T. A., 1426
 Fisher, J. S., 1426, 1857
 Flick, Reinhard E., 2666
 Foda, Mostafa A., 1464
 Franco, Leopoldo, 770
 Fredsøe, Jørgen, 1603
 Frigaard, Peter, 2284
 Fritsch, D., 2707
 Führbøter, Alfred, 2174
 Funke, E. R., 91, 106, 835
 Gadd, Peter E., 644, 2400
 Gao, Ming, 2469
 Gingerich, Kathryn J., 1182
 Girard, R. K., 106
 Goda, Yoshimi, 899
 Godo, Hitomi, 743
 Gofas, Th. C., 2753
 Goldsztejn, Eduardo, 2979
 Graber, Hans C., 492
 Grass, Anthony J., 363
 Gravens, Mark B., 1265
 Greated, C. A., 1020
 Greated, Clive A., 871
 Green, Malcolm O., 1508, 1618
 Griffiths, Matthew W. P., 871
 Grüne, Joachim, 2340
 Guarga, Rafael, 2979
 Haines, J. W., 1522
 Hallermeir, Robert J., 1197
 Hands, Edward B., 1911
 Hanson, Hans, 1265
 Hardy, Thomas A., 588
 Hashimoto, Noriaki, 62
 Hatheway, Darryl J., 2772
 Hattori, Masataro, 2144
 Hayashi, Kenjiro, 2923
 Hayashi, Kenjiro, 914
 Hedegaard, Ida Brøker, 1603
 Heimbaugh, Martha S., 795
 Herbich, John B., 2229
 Hettiarachchi, S. S. L., 782
 Hindes, F. S., 2753
 Hirayama, Ken-ichi, 1035
 Holthuijsen, L. H., 602
 Horikawa, Kiyoshi, 478, 1748, 2201
 Hosoi, Yoshihiko, 166
 Hotta, Shintaro, 151
 Hou, Ho-Shong, 1152
 Howell, Gary L., 2355
 Hsu, Tai-Wen, 121, 1631
 Huang, Jianwei, 1227
 Hudspeth, Robert T., 884
 Huntley, David A., 136
 Hwang, Sheng-Yeh, 2603
 Ifuku, Makoto, 1661
 Igarashi, Tatsuyuki, 1646
 Ikeno, Masaaki, 2326
 Imberger, J., 2626
 Inagaki, Keiji, 2144
 Instanes, Arne, 1997
 Isaacson, Michael, 2189
 Ismail, N. M., 2521
 Isobe, Masahiko, 393, 524
 Ito, Masahiro, 1544
 Iwagaki, Yuichi, 743
 Iwata, Koichiro, 2326
 Jamieson, Wayne W., 2257
 Jensen, Ole Juul, 756
 Kaczmarek, L., 1011
 Kakinuma, Tadao, 1661
 Katoh, Kazumasa, 1253
 Katsui, Hidehiro, 1280
 Kawata, Yoshiaki, 1310
 Kendall, Thomas R., 2129
 Kim, Young C., 971
 Kimura, Akira, 419, 655
 Kinose, Koichi, 1212
 Kjeldsen, Søren Peter, 667
 Klinting, P., 756
 Kobayashi, Nobuhisa, 1167
 Kobune, Koji, 62
 Komar, Paul D., 1238, 1338
 Kondo, Kosuke, 47, 2430
 Kostense, Jan K., 32
 Kraus, Nicholas C., 588, 1182, 1265, 1295
 Kriebel, David L., 17
 Krogstad, Harald Elias, 667
 Kröhn, J., 858
 Kubo, Masayoshi, 2952
 Kubota, Susumu, 151
 Kuo, Shih-Duenn, 2882
 Kyriacou, Andreas, 363
 Lai, C. P., 2313
 Langerak, A., 2692
 Larson, Magnus, 1295
 Latham, John-Paul, 2299
 Laustrup, C., 2159
 Law, Andrian W. -K., 1464
 Lee, Jiin-Jen, 2313
 Leendertse, Jan J., 2574, 2692

- Lee-Young, J. S., 1140
 Leidersdorf, Craig B., 2400
 Lewis, Lloyd, 971
 Lewis, Lloyd F., 2641
 Lin, Ming-Chung, 2603
 Lin, S. C., 2370
 Lionello, Piero, 566
 List, Jeffrey H., 1508
 Liu, Paul C., 1045
 Liu, Philip L. -F., 1911
 Liu, Shiao-Kung, 2574
 Lo, Jen-Men, 999
 Lorenz, Rene S., 705
 Losada, M. A., 1073, 2479
- McCormick, Michael E., 971
 McDougal, William G., 2400, 2445
 McGill, Preston G., 2445
 Machemehl, Jerry L., 644
 MacIntosh, K. J., 2840
 McMillen, Richard I., 2536
 Madsen, Ole Secher, 492, 849
 Madsen, P. A., 505
 Maeno, Yoshi-Hiko, 1842
 Magoon, Orville T., 2416, 2455
 Manikian, Victor, 644
 Mansard, E. P. D., 106, 835
 Mansard, Etienne P. D., 2257, 2385
 Marón, Adolfo, 204
 Martin, Paul A., 2216
 Martinez, F. M., 270
 Martínez, Felipe M., 1352
 Martinez Martinez, Jesus, 2738
 Massel, S. R., 1011
 Mather, D., 1020
 Matsumi, Yoshiharu, 2927
 Matsunaga, Nobuhiro, 234, 2550
 Medina, Josep R., 884, 941
 Medina, R., 1073, 2479
 Melby, Jeffrey A., 2445
 Miles, M. D., 91
 Mizuguchi, Masaru, 151
 Mizumura, Kazumasa, 2053, 2063
 Mogridge, Geoffrey R., 2257
 Möller, J. P., 1882
 Monso, J. L., 350
 Monsó, J. L., 463
 Moutzouris, C. I., 1959
 Murakami, Hitoshi, 166
 Murakami, Y., 1937
- Nadaoka, Kazuo, 1646
 Naeæss, Steinar, 1997
 Nairn, Robert B., 1818
 Nath, John H., 448
 Naverac, V. S., 270
- Negro Valdecantos, Vicente, 1437
 Nicholls, Robert, 1922
 Nielsen, Peter, 539, 1952
 Noguchi, Yuuji, 2144
- Ochi, Michel K., 2536
 Oelerich, Johannes, 292
 Ohishi, H., 1937
 Ohnaka, Susumu, 393
 Ohshimo, Tetsunori, 47, 2430
 Okamoto, Shunsaku, 2952
 Okayasu, Akio, 478
 Okushima, Shuji, 1212
 Olsen, Richard Bjarne, 667
 Osterthun, Manuela, 2681
 Ou, Shan-Hwei, 121, 1631
 Ouellet, Yvon, 2272
 Oumeraci, H., 2242
 Overton, M. F., 1426, 1857
 Ozaki, Akira, 408
- Papanicolaou, Panos, 377
 Park, San-Kil, 335
 Partenscky, H. W., 2242
 Partensckv. Hans Werner, 2681
 Partenscky, Hans-Werner, 2504
 Peregrine, D. H., 732
 Peregrine, Howell, 624
 Pilarczyk, K. W., 2043, 2116
 Pina, Gregorio Gómez, 984
 Poole, Alan B., 2299
 Poon, Ying-Keung, 492
 Pope, Joan L., 2455
 Pous, J., 1382
 Powell, K. A., 1763
 Pruszk, Zbigniew, 1774
 Puntigliano, Fernando, 2979
- Quecedo Gutierrez, Manuel, 1437
- Radder, A. C., 433
 Raichlen, Fredric, 377
 Ramsden, Jerald D., 448
 Rauw, Charles I., 2416
 Readshaw, J. S., 106
 Ren, Rushu, 153501543
 Resio, Donald T., 929
 Rhodes, Perry E., 1197
 Ribberink, J. S., 1689
 Ribeiro, Carlos Eduardo Parente,
 261
 Rodriguez, I., 858
 Roelvink, J. A., 1736
 Rosati, Julie Dean, 1182
 Rosengaus, Moises Michel, 849
 Rossouw, J., 822

- Rubio, J., 1073
 Rugbjerg, M., 505
 Ruol, Piero, 1129
 Ryan, P. J., 2521

 Saeki, Hiroshi, 408, 1035
 Sakai, Shigeki, 1035
 Sakuramoto, H., 2791
 Salih, B. A., 956
 Sánchez-Carratala, Carlos R., 941
 Santás López, Jose C., 984
 Sasaki, Mikio, 408
 Sato, Shinji, 1748
 Sawaragi, Toru, 335, 1573
 Sayao, Otavio J., 1818
 Schade, Daniel, 322
 Schäffer, Hemming A., 1058
 Schlueter, Roger S., 2723
 Scholtz, D. J. P., 2075
 Schwab, David J., 2991
 Schwartz, R. A., 2626
 Scott, R. Douglas, 2385
 Scott, R. D., 2418
 Seikmoto, Tsunehiro, 47
 Sekimoto, Tsunehiro, 2430
 Seo, Seung Nam, 2216
 Serra Peris, Jose, 2784
 Seyama, Akira, 419, 2927
 Seymour, Richard J., 1676
 Sheng, Y. Peter, 2655
 Shibayama, Tomoya, 478
 Shigemura, Toshiyuki, 914, 2923
 Shimoda, Naokatsu, 2326, 2952
 Shiraishi, Naofumi, 2053, 2063
 Siefert, Winfried, 1788
 Sierra, J. P., 350, 463
 Simoen, R., 2855
 Simons, Richard R., 363
 Skyner, D., 732
 Sleath, J. F. A., 1140
 Sloan, Robert L., 2455
 Slotta, Larry S., 971
 Smallman, J. V., 281
 Smit, E. S. P., 2825
 Snook, M. W. G., 1020
 Sobey, Rodney J., 307
 Soler, E., 2615
 Sorensen, R. M., 1482, 2806
 Sorensen, Robert M., 2867
 Sparboom, Uwe, 2174
 Stephens, R. V., 281
 Stiassnie, M., 732
 Stive, Marcel J. F., 1736
 Strzelecki, Michael S., 1167
 Suh, Kyung Duck, 246
 Sumiya, M., 2791

 Sunamura, Tsuguo, 1295
 Svendsen, Ib A., 705, 1058
 Swart, D. H., 181, 1882
 Synolakis, Costas Emmanuel, 219, 553

 Taerwe, L., 2102
 Takahashi, Shigeo, 2489
 Takehara, Kosei, 234
 Takezawa, Mitsuo, 151
 Tallent, James R., 1833
 Tanaka, Hitoshi, 1803
 Tatavarti, Rao V. S. N., 136
 Tedesco, Joseph W., 2445
 Teisson, Ch., 2707
 Thompson, Alex C., 2013
 Thornton, E. B., 77
 Tickell, R. G., 956
 Tolman, Hendrik L., 512
 Tørum, Alf, 1997
 Toue, Takao, 1280
 Toyoshima, Osamu, 1983
 Treadwell, Donald, 2416
 Treadwell, Donald D., 2455
 Tsuchiya, Yoshito, 1310, 1544, 1833, 1868, 2589
 Tsuru, Masahito, 1212
 Tsuzuki, Susumu, 2201
 Tu, S. W., 2521
 Turcke, D. J., 2418
 Turcke, David J., 2385
 Twu, S. W., 2370
 Tzang, Shiao-Yih, 121

 Uda, T., 2791
 Uda, Takaaki, 2028
 Uda, T., 1937
 Ueno, Seizo, 1646
 Uliczka, K., 1721
 Ura, Masaru, 2550

 Van Damme, L., 2102
 van de Graaff, Jan, 2090
 Van den Bosch, Peter, 32
 van der Meer, J. W., 2116
 van Kesteren, W. G. M., 718
 Van Ryzin, Joseph, 2641
 van Vledder, G. Ph., 602
 Van Wyk, A. C., 2911
 Vandenbossche, D., 2855
 Vega, Luis, 2641
 Verslype, H., 2855
 Vidal, C., 1073
 Vidoar, A., 1382
 Visser, Paul J., 1897
 Vogel, J. A., 433

- Vold, Svein, 1997
Vongvisessomjai, Suphat, 1084
- Walker, James R., 2666
Walton, Todd L., Jr., 1911
Wang, Hsiang, 1493
Wang, Liang, 153501543
Wang, P. F., 2655
Warren, I. R., 505
Watanabe, Akira, 393, 578, 2201
Watanabe, M., 1937
Watts, George M., 2818
Webber, Norman, 1922
Weckmann, Javier, 2818
Weggel, J. R., 2806
Weggel, J. Richard, 632, 2867
Werner, Gosta, 612
Whitford, D. J., 77
Wiegel, R. L., 2521
- Wiegel, Robert L., 1
Wouters, J., 2159
Wright, L. Don, 1508
Wu, T. S., 2655
Wurjanto, Andojo, 1167
- Yamaguchi, Masataka, 1113
Yamamoto, Masato, 2053, 2063
Yamashita, Takao, 682, 1833, 2589
Yanagishima, Shin-ichi, 1253
Yang, Jihua, 2469
Yeend, John S., 2772
Yen, Kai, 153501543
Young, Ian R., 1098
Yu, Z. H., 718
- Zeidler, Ryszard B., 1704, 1774
Zwamborn, J. A., 2075, 2911
Zyserman, Julio A., 1603



Costa de Benalmadena—Malaga

PART III
COASTAL STRUCTURES

Playa D'Aro—Gerona, costa Brava



CHAPTER 147

GENTLE SLOPE SEAWALLS COVERED WITH ARMOUR UNITS

by
Osamu Toyoshima

ABSTRACT

Since the early 1960's, many seawalls against the beach erosion have been constructed in Japan, most of which were of vertical type. As a result, some of the seawalls even encouraged the beach erosion due to the reflected waves on the steep front of the seawalls. The author then proposed seawalls of new types with gentle front slope (1 to 3) covered with armour units in 1981, and over one hundred fieldworks have successfully been carried out.

In 1985, the author proposed reforming the existing vertical type seawalls into the gentler front slope (1 to 5 or 6) seawalls. The laboratory test on the gentle slope seawall was made, and some experimental fieldworks were carried out. At this time, these new type gentler slope seawalls are successful.

I. INTRODUCTION

On the 19th International Conference on Coastal Engineering, the author presented a paper titled "NEW TYPE BLOCKS FOR SEAWALL SLOPE PROTECTION" and proposed a gentle slope (1 to 3) seawall, covered with new type block named "Lotus-Uni" for measures against beach erosion. After the author's proposal, over one hundred works of the new type seawall have been carried out on various erosive sandy beaches in Japan, and most of these works have proved successful.

In 1985, the author proposed reforming the existing vertical type seawalls into the gentle slope (1 to 5 or 6) seawalls covered with Lotus-Uni. The reason for reforming is that, the existing vertical type seawalls have been disliked by inhabitants near the coast because of spray of seawater and environmental disruption.

II. THE EXPERIMENTAL WORKS OF THE GENTLE SLOPE SEAWALL

The first experimental works of the gentle slope (1 to 3) seawall was carried out on Muroran Coast, Hokkaido Prefecture, facing the Pacific Ocean, in 1982.

Dr.Eng., Professor, School of Marine Scie. & Tech., Tokai Univ. Orido 3-20-1, Shimizu, Shizuoka Pref. 424 Japan.

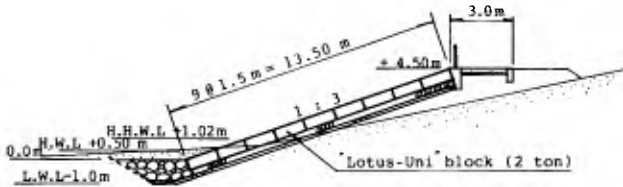


Fig. 1. Cross section of the new type seawall on Muroran Coast.

Fig. 1 shows the standard cross section of the new type gentle slope seawall covered with Lotus-Uni blocks. Nine blocks are arranged in each column, and no foundation nor shore protection works such as wave dissipation mounds were provided.



Photo 1. Experimental seawall immediately after the completion (1982).

As shown in Fig. 1, the lowest blocks of the slope were set on the height of the mean water level, and there existed very narrow foreshore in front of the seawall. Uprush water mass with sands and gravels runs up on to the slope. Under the block facing, there lie a 50cm thick layer of cobbles and a 10cm layer of gravels. Part of the uprush flows into the holes of and the spaces between the blocks as shown in Photo 1. Thus the flow rate of backrush decreases, and wave reflection diminishes, the erosive beach tunning accumulative.

A later view of the beach is given in Photo 2. The shoreline has advanced remarkably, and the sand beach has grown extensively. Most part of the seawall is buried under the accumulated sand, only one block row being visible. The experimental seawall successfully change the erosive beach into a stable beach.

The result of this experimental works supported the author's confidence that a seawall against beach erosion should have a rough and permeable facing, and its front slope should be gentle enough to diminish wave reflection.



Photo 2. A later view of the experimental seawall.

III. GENTLER - SLOPE SEAWALL

When a gentle slope seawall is constructed on a narrow foreshore, the toe will be under the water. A gentler slope will yield a deeper toe, which may cause higher wave runup. Hence the determination of crown height as well as slope gentleness becomes an important problem.

3.1 Laboratory tests on wave runup on gentle slope

In general, wave runup on a gentle slope is lower than that on a steep slope. Fig.2 shows diagrams of the wave runup height based on laboratory measurements by Saville (1958), where H_o is the offshore wave height and H_o/L_o the offshore wave steepness. The laboratory test was conducted using periodic waves on smooth impermeable slopes. The slope of the model seabed was 1/10.

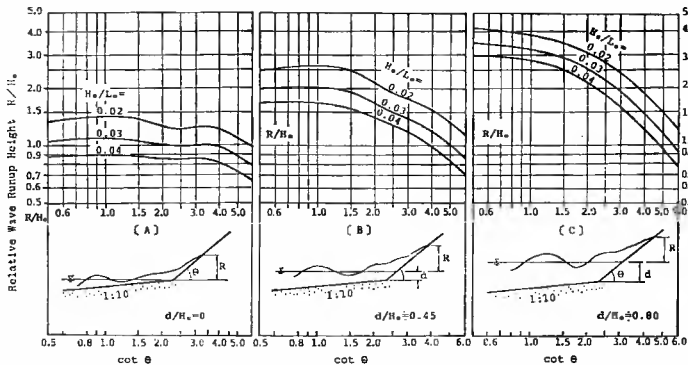


Fig.2 Wave runup height on smooth, impermeable slope faces on the seabed of 1/10 slope (Drawn after Saville, 1958).

The diagram [A] is for cases of the relative toe depth $d/H_o=0$, [B] for $d/H_o = 0.45$, and [C] for $d/H_o = 0.80$.

The relative wave runup height R/H_0 in [A] is comparatively small and varied little with the structure slope (1/cot), where as R/H_0 in [B] and [C] shows a considerable increase with the relative toe depth d/H_0 and with the slope. In the case of the structure slope of 1:5 or 1:6 (cot θ = 5 or 6), however, the runup height is considerably small and its variation with the toe depth is rather insignificant. then, the slope of 1:5 and 1:6 are very favorable to wave runup in comparison with the slope of 1:3 or 1:4. This is why the author regards gentler-slope seawalls as the optimum measure for shore protection.

Simultaneously with the proposal of the reforming the existing vertical type seawalls into the gentler-slope (1:5 or 1:6) seawalls, the author made some laboratory tests on the gentler-slope seawalls in the Tokai University.

The length of the two dimensions water tank was 52 m, water depth was 0.70m, slope of the model seabed was 1:20, all model slopes were made as smooth and impermeable, and regular waves were used.

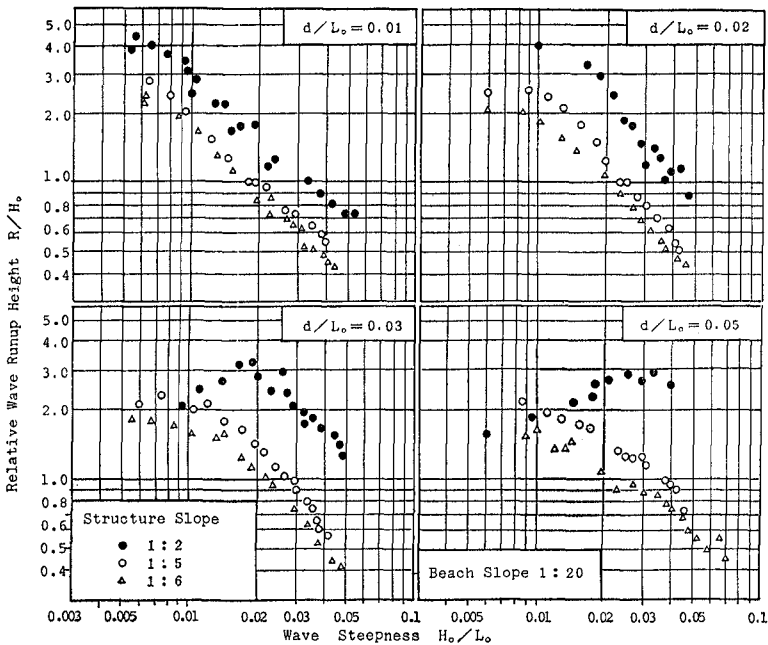


Fig.3 Wave runup height on smooth, impermeable slope faces on the seabed of 1:20 slope (by Toyoshima, 1985).

From the results of the laboratory test, as shown in Fig.3, it has become clear that,

- (1) the wave runup height on 1:5 and 1:6 slope are considerably small in comparison with 1:2 slope.
- (2) the depth at the toe of seawalls become deeper, gentler slope seawalls are advantageous on the runup heights, generally.

3.2 Experimental works of a reformed type seawall

A reformed type seawall with gentler slope, which toe was under the water, was experimentally constructed on Hongo Coast.

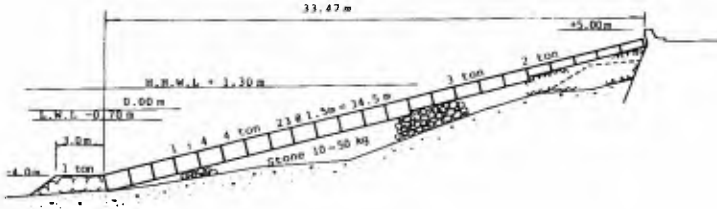
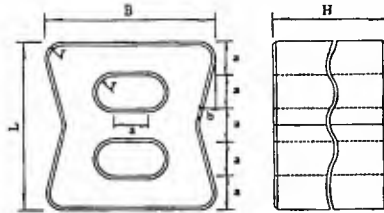


Fig.4 Reformed type experimental seawall on Hongo Coast.



Model	B	L	H	Weight
50 H			50 cm	2 ton
75 H	1.5 m	1.5 m	75 cm	3 ton
100 H			100 cm	4 ton

Fig.5 Lotus-Uni block specification.

Fig.4 shows the standard cross section of the experimental works of reformed type seawall with gentler slope (1:4) on Hongo Coast. Three models of Lotus-Uni block were used as facing blocks without any special foundations or rubble stone works.



Photo 3. A former view of Hongo Coast (1977).

Photo 3 shows a former view of Hongo Coast in 1977 after the construction of the old seawall. A little sand beach were remaining.



Photo 4. Before the experimental works on Hongo Coast.



Photo 5. The experimental seawall under construction.



Photo 6. The experimental seawall completed.

Sand beach remaining in Photo 3 disappears in Photo 4 which was taken before the experimental works. In winter stormy weather, considerable amount of splash overtopped the seawall in spite of armour units placed in its front. Photo 5 shows the experimental seawall under construction. The depth at the toe of the slope was about 4 m.

The works were completed in August, 1985, (Photo 6). Although this seawall has been attacked annually by severe winter waves, no collapse of the slopes or dispersion of the facing blocks has occurred up to now.

IV. GENTLER SLOPE SEAWALL ON KUROBE COAST

4.1 Construction of the experimental seawall

The first, real, reformed type, gentler (1:5) slope seawall, which toe was under the water, was experimentally constructed on Kurobe Coast, in fiscal 1986 and 1987.

The location of Kurobe Coast is shown in Fig.6, together with Muroran and Hongo Coasts. The Kurobe Coast is one of the most eroded coast in Japan. Fig.7 and Fig.8 show the location and area of the experimental seawall works in Kurobe Coast. The wave recorder located about 500 m offshore from the coast, and 5 km to the experimental works site. The water depth of the wave recorder site is 15 m, and the wave recorder is set at -14m depth.

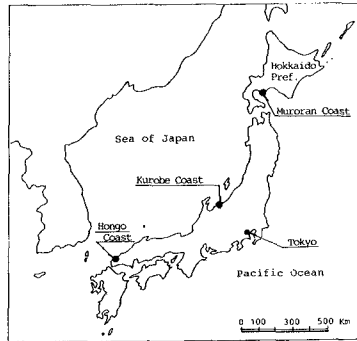


Fig.6 Location of Kurobe Coast and others.

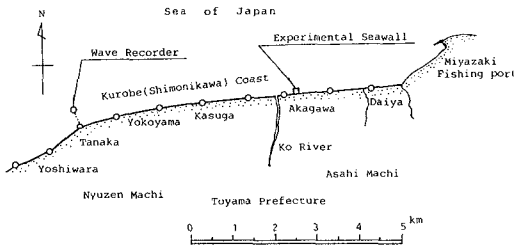


Fig.7 Location of the experimental seawall works.

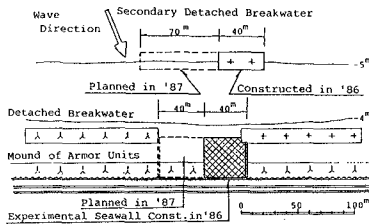


Fig.8 Areas of the experimental seawall works.

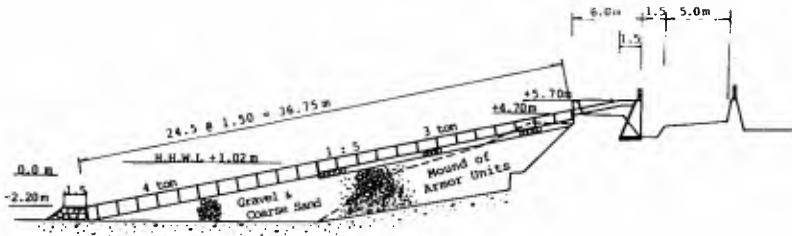


Fig. 9 Standard cross section of the experimental seawall.

In fiscal 1986, a part of the experimental seawall and the secondary detached breakwater were constructed. The predominant direction of severe winter waves is NNW. The cross section of the experimental seawall is shown in Fig. 9. The front slope is 1:5, and two models of Lotus-Uni, 4 ton and 3 ton, are used as the facing blocks without any special foundations. Removing the existing parapet wall, and reformation of the crown protection and retaining wall were carried out in fiscal 1987.

Photo 7 shows a latest view on the left-hand side of the experimental seawall construction site, and that is the same conditions before the experimental seawall works. There are vertical type seawalls, large mound of armour units for wave dissipation works and detached breakwaters. The weight of armour units for wave dissipation works and detached breakwaters are 8 ton and 20 ton respectively.



Photo 7. Left-hand side view of the experimental works.

First, as shown in Photo 8, the existing mound of armor units were removed. The existing seawalls are visible. Until the early 1960's, some narrow sandy beaches had been remaining in this area. However, immediately after the construction of this seawall, the beaches have vanished away. Then, large mound of armor units have been built, in order to protect the toe of seawalls from scouring and reduce the wave overtopping and splashing of sea water. However, these have been not enough to reduce the wave overtopping and splashing. And sometimes, the seawalls were damaged due to the leakage of the backfill sand.



Photo 8. First, mound of armour units were removed.



Photo 9. Filling of sand and gravel, which were diverted from the dredging of Miyazaki fishing port, located 4 km away from the site (cf. Fig.7).



Photo 10. Setting the Lotus-Uniblock on the rubble stone. The lowest block were set at -3.3 m water depth.

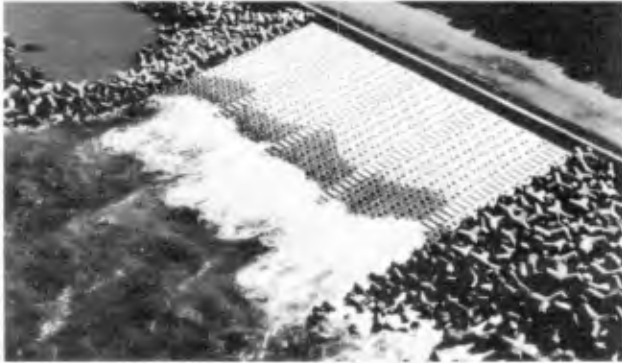


Photo 11. The works of the fiscal 1986 have completed in September 1986. The length of works is 40 m.

4.2 Observation of the wave runup on the seawall

After the completion of the experimental works, the first heavy wave struck the seawall in November 1986. On the 20th December 1986, pretty heavy waves attacked the Kurobe Coast, and overtopped the crown of the experimental seawall, as shown in Photo 12.



Photo 12. Heavy waves overtopped the crown of the experimental seawall, on the 20th December 1986.

The number of times of heavy wave attacks in the first winter season amounted to ten times. The wave runup heights on the experimental seawall were observed by eye measurement and video cameras in the field. Color lines were marked on the blocks for the observation of the wave runup height. These field observations have been done on each twenty minutes of the every 0'clock in the day time on stormy weather days.

Table 1 shows the data of the waves which were obtained from the wave recorder, and of the calculated relative runup heights on the experimental seawall based on the field observation.

Table 1. Data of the waves and the calculated relative runup height on the experimental seawall based on the field observation.

Date	Time	① Nos. of Runup	② Nos. of Waves	③ Runup Count In	④ H_o ($H_{1/10}$) m	⑤ T ($T_{1/10}$) s	⑥ L_o ($L_{1/10}$) m	⑦ Water Level +m	⑧ Water Depth dm	⑨ Runup Height Rm	⑩ H_o/L_o	⑪ d/L_o	⑫ R/H_o	
'86.11.26	10	120	245	25	2.28	7.4	85.4	0.38	3.58	3.09	0.027	0.042	1.36	
	11	125	233	23	2.16	7.5	87.8	0.37	3.57	3.12	0.025	0.041	1.44	
	12	127	231	23	2.12	7.8	94.9	0.36	3.56	2.97	0.022	0.038	1.40	
	13	117	213	21	2.58	8.9	123.6	0.32	3.52	2.99	0.021	0.028	1.16	
	14	108	223	22	2.25	8.6	115.4	0.31	3.51	3.49	0.020	0.030	1.55	
	15	109	210	21	2.25	9.2	132.0	0.27	3.47	2.75	0.017	0.026	1.22	
	11.27	12	96	178	18	1.70	9.9	152.9	0.22	3.42	4.92	0.011	0.022	2.89
		14	89	199	20	1.32	9.5	140.8	0.15	3.35	4.68	0.009	0.024	3.55
	12.15	10	145	213	21	2.18	7.2	80.9	0.25	3.45	2.79	0.027	0.043	1.28
		11	125	210	21	2.38	6.7	70.0	0.27	3.47	3.07	0.034	0.050	1.29
		12	131	218	22	2.73	6.9	74.3	0.30	3.50	3.48	0.037	0.047	1.27
		13	126	233	23	2.61	6.7	70.0	0.35	3.55	3.09	0.037	0.050	1.18
		14	126	233	23	2.45	6.5	65.9	0.38	3.58	3.02	0.037	0.054	1.23
		15	118	245	25	2.33	6.5	65.9	0.38	3.58	3.14	0.035	0.054	1.35
	12.20	10	80	178	18	3.34	9.9	152.9	0.26	3.46	5.14	0.022	0.023	1.54
11		92	159	16	3.66	9.2	132.0	0.26	3.46	5.29	0.028	0.026	1.44	
12		85	184	18	3.09	9.6	143.8	0.24	3.44	5.17	0.021	0.024	1.67	
13		95	164	16	3.45	10.2	162.3	0.23	3.43	5.12	0.021	0.021	1.48	
14		99	147	15	3.70	10.3	165.5	0.25	3.45	5.42	0.022	0.021	1.46	
15		89	144	14	3.22	10.3	165.5	0.28	3.48	4.93	0.019	0.021	1.53	
'87. 1.14	10	100	271	27	1.05	8.5	112.7	0.11	3.31	3.05	0.009	0.029	2.90	
	11	98	253	25	1.36	8.8	120.8	0.11	3.31	3.18	0.011	0.028	2.34	
	12	107	260	26	1.16	7.6	90.1	0.15	3.35	3.43	0.013	0.037	2.96	
	13	107	251	25	1.14	9.1	129.2	0.18	3.38	3.03	0.009	0.026	2.66	
	14	102	261	26	1.10	9.2	132.0	0.21	3.41	2.94	0.008	0.025	2.67	
	15	100	233	23	1.29	9.4	137.8	0.24	3.44	3.14	0.009	0.025	2.43	
	2. 4	10	88	161	16	3.33	10.5	172.0	0.12	3.32	5.36	0.019	0.019	1.61
		11	82	164	16	3.06	9.6	143.8	0.07	3.27	5.46	0.021	0.023	1.78
		12	87	171	17	2.73	9.3	134.9	0.03	3.23	5.32	0.020	0.024	1.95
		13	87	161	16	2.59	9.4	137.8	0.03	3.23	5.42	0.019	0.023	2.09
		14	91	173	17	2.25	9.3	134.9	0.04	3.24	5.81	0.017	0.024	2.58
		15	80	191	19	2.46	9.5	140.8	0.03	3.23	5.21	0.017	0.023	2.12
	2.26	10	89	217	22	2.68	8.3	107.5	0.13	3.33	4.35	0.025	0.031	1.62
		11	105	212	21	2.79	8.7	118.1	0.19	3.39	4.45	0.024	0.029	1.59
		12	93	243	24	2.40	9.0	126.4	0.23	3.43	4.45	0.019	0.027	1.85
13		89	244	24	2.36	7.9	97.4	0.28	3.48	4.26	0.024	0.036	1.80	
14		90	196	20	2.58	9.8	149.8	0.31	3.51	4.50	0.017	0.023	1.74	
15		89	199	20	3.00	10.7	178.6	0.32	3.52	4.73	0.017	0.020	1.58	
2.27	10	77	141	14	2.82	12.5	243.8	0.12	3.32	5.37	0.012	0.014	1.90	
	11	75	145	15	3.03	12.9	259.6	0.16	3.36	5.12	0.012	0.013	1.69	
	12	68	153	15	2.58	13.1	267.7	0.21	3.41	4.85	0.010	0.013	1.88	
	13	82	159	16	2.59	12.8	255.6	0.28	3.48	4.73	0.010	0.014	1.83	
	14	72	194	19	2.29	12.5	243.8	0.34	3.54	4.61	0.009	0.015	2.01	
	15	83	154	15	2.65	11.9	220.9	0.35	3.55	4.32	0.012	0.016	1.63	

Because of the great differences between number of recorded waves and observed runup waves to the experimental seawall, the author used the one-tenth highest wave and the same numbers of the highest wave runup, in the arrangement. For example, in the case of

the date the 20th December 1986,
time 14 o'clock

in the Table 1,

- (1) the number of the observed runup waves to the experimental seawall in twenty minutes is 99.
- (2) the number of the waves recorded in the wave recorder in twenty minutes is 147.
- (3) calculated number of the one-tenth highest wave is 15, and the same number of highest wave runup are adopted.
- (4) one-tenth highest wave height is 3.70 m.
- (5) one-tenth highest wave period is 10.3 s.
- (6) calculated offshore wave length L_0 is 165.5 m.
- (7) sea water level at that time is +0.25 m.
- (8) water depth at the toe of the seawall is 3.45 m.
- (9) the mean value of the highest 15 waves runup height, adopted in (3), measured from the sea water level is 5.42 m.
- (10) wave steepness H_0/L_0 (4)/(6) = $3.70/165.5 = 0.022$.
- (11) relative water depth d/L_0 (8)/(6) = $3.45/165.5 = 0.021$.
- (12) relative wave runup height R/H_0 (9)/(4) = 1.46

The wave runup height is

$$5.42 \text{ m} + 0.25 \text{ m} = + 5.67 \text{ m} \doteq + 5.70 \text{ m} \text{ (Crown height)}$$

Naturally, a number of runup waves overtopped the crown of the experimental seawalls, as shown in Photo 12.

4.3 Comparing the field observation data with laboratory test results

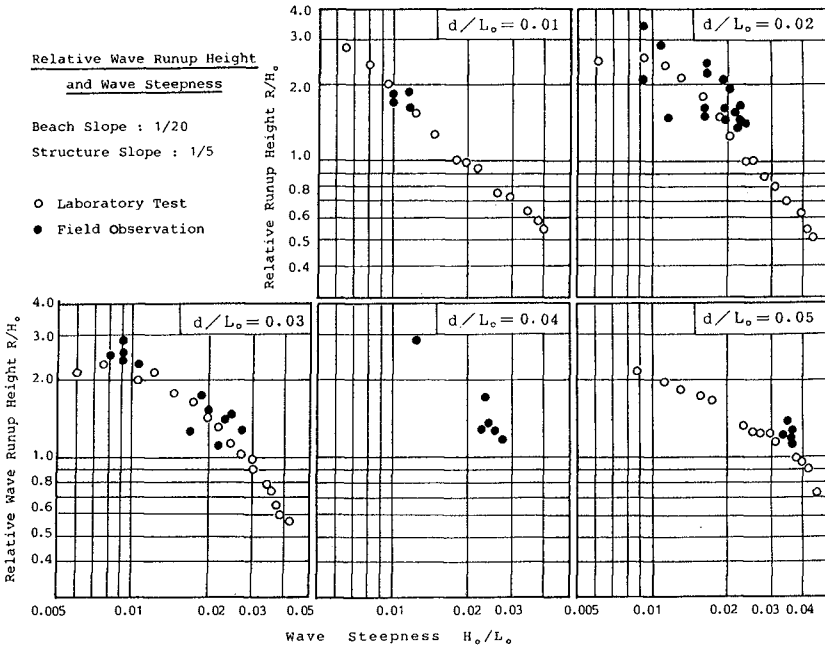


Fig.10. Comparison between the laboratory test and the field observation on the wave runup height on gentle slope seawalls.

The data of the field observation are plotted in Fig.10, together with the data of the laboratory test. Open circles are laboratory test and solid dots are field observation. At a glance, both of these data show a good agreement. The slope of the seawalls in the field are covered with armour units, but in the laboratory test all slope of model are smooth and impermeable. The waves in the laboratory test were regular waves. The wave recorder is 5 km away from the site of works, the runup waves are not the same waves as recorded by the wave recorder.

Although, there are many problems in these data and their calculation processes, the author considers that these results on the gentle slope 1:5 seawalls are very useful for designing of the shore protection in future.

4.4 The works of fiscal 1987 was completed



Photo 13. The works of fiscal 1987 was completed. The left half are of fiscal 1986.



Photo 14. Heavy waves attacked the Kurobe Coast, and some of them overtopped the experimental seawalls.

On 6th November 1987, heavy winter waves attacked the Kurobe Coast, and some of them overtopped the experimental seawalls. However, the spray of sea water on the gentle slope seawalls were excessively small in comparison

with that of existing vertical type seawalls with large mound of armour units.



Photo 15. The latest view of the experimental seawalls.

After the construction of the experimental works, one or two winter season are over, but there has not been any trouble, damage or collapse, on the body, slope, covering blocks, foot and toe of the experimental works. At this time, these new type gentler slope seawalls are successful.

V. CONCLUSION

Many of existing vertical type seawalls have lost their foreshore, and wave dissipation works are not effective enough to prevent the overtopping of the splash and sea water mass. On the basis of the successful results and experiences obtained through the experimental works, the author proposed to reform existing vertical type seawalls to gentler slope seawalls with armour unit facing.

In conclusion, in order to maintain better coastal environment, structures on an erosive coast are desired to satisfy the following conditions:

- (1) the wave reflection from the front slope should be minimized,
- (2) scouring at the structure toe should be prevented as well as erosion of the foreshore,
- (3) the whole structure should not collapse even if partial breakdown took place,
- (4) the crown of the structures should not be too high,
- (5) repairs and reinforcements should be easy, and
- (6) the structure should be rather simple and not too costly.

In this view, the gentler slope seawall with rough and permeable front slope is one of the most relevant countermeasures against the beach erosion.

REFERENCES

- Saville, T., Jr. (1958): Wave runup on composite slopes. Proc. 6th Coastal Eng. Conf.
- Toyoshima, O. (1984): New type blocks for seawall slope protection. Proc. 19th Coastal Eng. Conf.

CHAPTER 148

ON BERM BREAKWATERS

by
Alf Tørum¹, Steinar Næss²,
Arne Instanes³ and Svein Vold⁴

ABSTRACT

Two and three dimensional laboratory studies have been carried out on the stability of a berm breakwater concept. The study has to some extent been general and to some extent been connected to a project study of the stability of a berm breakwater for the fishing port of Årviksand, Norway.

INTRODUCTION

The main feature of a berm breakwater is that it has a rather thick cover layer of stones, relatively much smaller than on a conventional breakwater with one or two layers of cover blocks. The berm breakwater has been adopted several places as an economic solution when large cover blocks of natural stones are not available. It might also be an economical solution even when large cover blocks for a conventional breakwater are available.

The berm breakwater concept has become of interest in Norway in connection with plans for an extension of a breakwater at the Årviksand fishing port. Fig. 1 shows the layout of the harbour. The breakwater will be extended about 90 m into a maximum water depth of approxi-

¹ Head of Research/Professor. Norwegian Institute of Technology/ Norwegian Hydrotechnical Laboratory, 7034 Trondheim, Norway.

² Chief Engineer. Norwegian Coast Directorate. P.O. Box 8158 - Dep 0033 OSLO 1, Norway.

³ Research Engineer, Division of Structural Engineering, Norwegian Institute of Technology, 7034 Trondheim, Norway.

⁴ Research Engineer, Norwegian Hydrotechnical Laboratory, 7034 Trondheim, Norway.

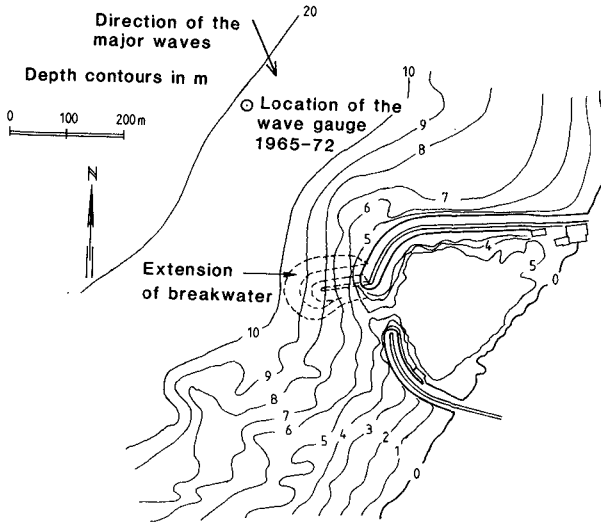


Fig. 1. Årviksand fishing port.

mately 13 m. The wave climate at the breakwater site has been evaluated from wave measurements during the time period 1965-1972 at 20 m water depth outside the harbour and from hindcast wave data in deep water from the time period 1955-1985 and refraction analysis. Based on the wave measurement and a Weibull distribution formulation the 50 and 100 year significant wave heights were estimated to be approximately 6.4 m and 7.2 m respectively. From the hindcast data and the refraction analysis the 100 year wave height was estimated to be approximately 6.2 m.

The differences in the estimated 100 year wave height reflects the uncertainty on the estimated wave climate which always is present at any harbour location on an open coast.

Based on a Weibull distribution fitting of the measured daily maxima, a simulation study has been performed based on a procedure described in [5]. The Weibull distribution which fits, by the method of moments, the data best has been used as the "parent" distribution. By a Monte-Carlo procedure daily maxima for seven-years of observation have been simulated one hundred times. Fig. 2 shows the probability density function for 50 year occurrence of significant wave height for water depth 20 m. The Weibull distribution parameter for the measured daily maxima were: Shape parameter 0.77, scaling parameter 0.660 m and location parameter 0.057 m. The shape

parameter is rather low for this location and explains partly the large scatter of the estimated 50 year significant wave height through the simulation study.

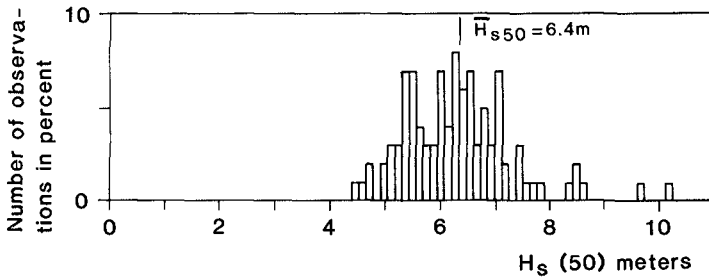


Fig. 2. Results of wave statistics simulation.

The uncertainty in the wave climate favours a breakwater design that is not too sensitive to the wave height with respect to stability. The berm breakwater is a concept that is of interest in this respect.

The stability results reported in this paper are partly from a student thesis work [1], to some extent related to Årvihsand harbour, partly from a general investigation of the stability of berm breakwaters and partly from a project study for Årvihsand harbour.

INTRODUCTORY TESTS ON THE STABILITY OF THE BERM BREAKWATER FOR ÅRVIHSAND HARBOUR

The existing north breakwater at Årvihsand is built as a conventional breakwater with one layer of cover blocks of natural stones. The average block weight on the outer most exposed part is 10 tons. Some introductory tests showed that if the breakwater was extended to a maximum water depth of 12 m, a breakwater with 10 tons cover blocks will be stable for a significant wave height of 4.5 - 5.0 m. The estimated necessary block weight for a conventional breakwater to stand wave heights of $H_s = 7.2$ m would be 25 - 30 tons. Flume tests were then carried out on a berm breakwater design as shown in Fig. 3. One test was also carried out for a design shown on Fig. 4.

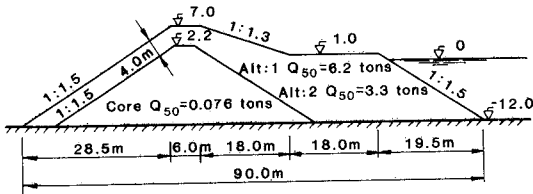


Fig. 3. Berm breakwater section - Introductory tests.

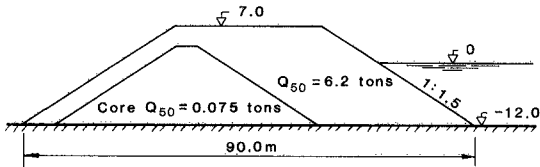


Fig. 4. Berm breakwater section - Introductory tests.

The model scale was 1:40. Two block weights in the berm were used: 1 average 3.3 tons, range 1 - 6 tons. 2 average 6.2 tons, range 1 - 14 tons.

Fig. 5 shows the flume with the breakwater model. The bottom configuration in front of the breakwater corresponded to the bottom configuration in front of the planned extension of the breakwater at Årviksand fishing port.

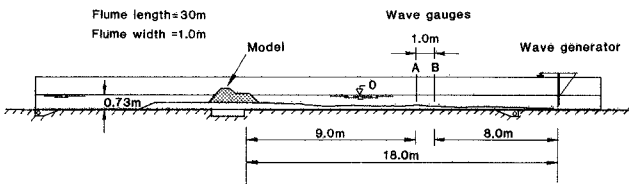


Fig. 5. Test flume.

During the tests two wave gauges were used. The water depth at wave gauge A corresponded to 20.8 m or approximately the water depth at the location of the wave gauge outside Årviksand in the time period 1965 - 1972.

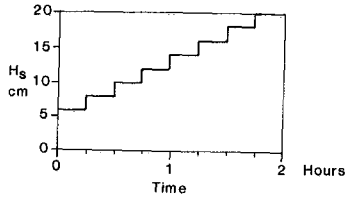


Fig. 6. H_s versus time.

The test programme used during the tests is shown in Fig. 6. The evolution with time of the significant wave height corresponds to a typical evolution during a heavy storm on the Norwegian coast. The wave spectrum was narrow with a peak period of 11.4 - 12 sec. The peak period was the same for all significant wave heights. The incoming and reflected waves were found by a procedure described by Goda and Suzuki [2]. It should be noted that for the highest significant waves the waves were non-Gaussian. For example were the skewness 0.78 and the kurtosis 3.82 for a significant wave height of 8.3 m. The highest waves would then break before they came to the breakwater.

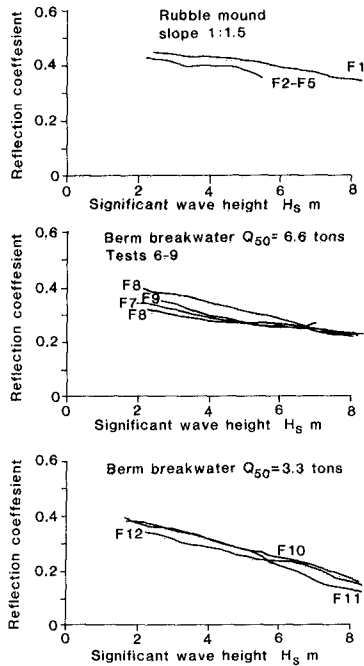
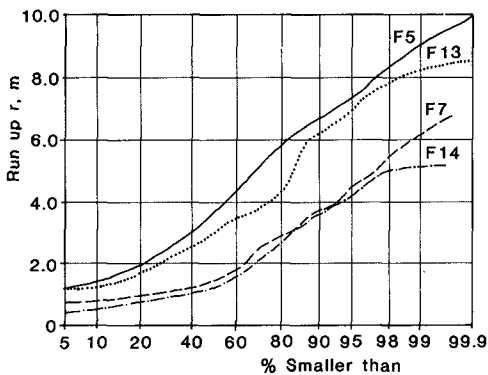


Fig. 7. Reflection coefficients.

The obtained reflection coefficients as a function of the significant wave height is shown in Fig. 7.

Run-up on the breakwater was also measured. Fig. 8 shows a run-up distribution. The run-up r is defined as the maximum run-up of each individual wave on the slope or within the breakwater.



————	$H_s = 5.3$ m	Rubble mound	10.3 tons	Test F5
.....	$H_s = 5.3$ m	Berm breakwater*	6.2 tons	Test F13
----	$H_s = 5.3$ m	Berm breakwater	6.2 tons	Test F7
-.-.-	$H_s = 5.3$ m	Berm breakwater	3.3 tons	Test F14

* "Full" berm, Fig. 4

Fig. 8. Run-up

The run-up on the berm breakwater is much less than on the conventional breakwater. It is also seen that the run-up on the "full" berm breakwater, Fig. 4, is not much less than on the conventional breakwater. Hence it is concluded that a low berm is very efficient from the run-up point of view.

Figs. 9 shows profiles after the tests for the maximum significant wave heights 8.60 m and 8.32 m respectively were completed.

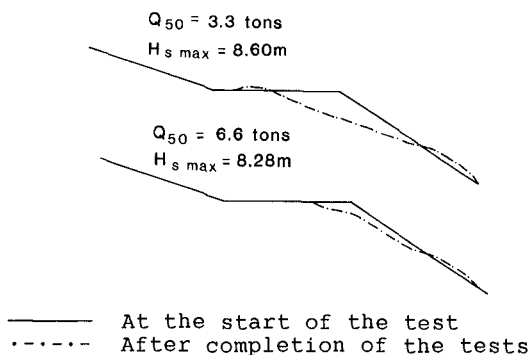


Fig. 9. Cross-section

The results of these introductory tests indicated that a berm breakwater could be built with an average block weight in the range 3.3 - 6.6 tons. The berm breakwater showed also less sensitivity to the variation in the significant wave height than the conventional breakwater. There was not a sudden collapse as normally is the case for a conventional breakwater. This is very useful for a location where there is a significant uncertainty on the wave climate. However, it was felt that there was a need for a more general flume study on the stability of the berm breakwater concept.

GENERAL TEST SERIES

The objective of these tests was to investigate more closely how the berm evolved with the wave height, wave spectrum and duration of the "storm". The general test series were conducted in the same flume as shown in Fig. 5 in scale 1:40. The tested cross-section is shown in Fig. 10. Two berm widths were tested: 30 and 45 cm (12 and 18 m).

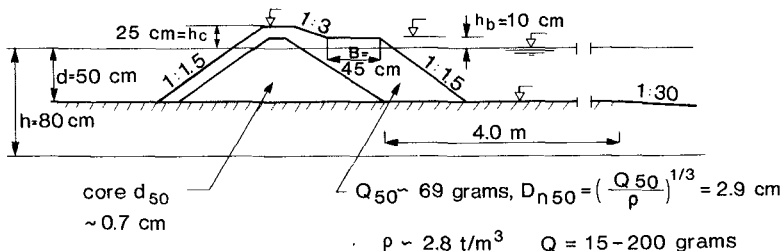


Fig. 10. Berm breakwater - General tests.

The "peak" period T_p corresponded to 12 and 16 sec. The spectrum corresponded to a JONSWAP spectrum. Two values of the peakedness parameter $\gamma = 1.0$ and $\gamma = 7.0$ were used. The wave height was varied in steps in different ways.

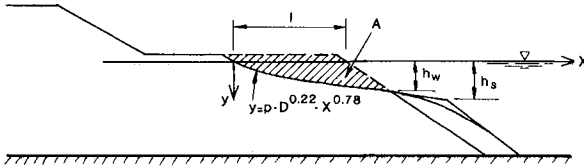


Fig. 11. Definitions.

The change of the berm is essential for the consideration of the stability of the breakwater. This change has been quantified by the number S introduced by van der Meer [3] as damage to a conventional breakwater. With reference to Fig. 11, S is defined as;

$$S = A / (D_{n50})^2$$

where:

A = cross sectional area removed from the berm

$$D_{n50} = \left[\frac{Q_{50}}{\rho_s} \right]^{1/3}$$

Q_{50} = 50 % of the stones has a weight larger than Q_{50}

ρ_s = specific density of the stone material

The recession of the berm, l , see Fig. 11, has been non-dimensionalized as

$$l / D_{n50}$$

If $l / D_{n50} > B / D_{n50}$, where B = berm width, unacceptable damage may occur.

In conventional breakwater design there is a consideration on static-stability. This means that the requirement is that the stones should not move at all. Sand and gravel beaches may on the other hand be dynamically stable. That is the individual grains may move heavily, but the profile does not in the long term sense change. This is also true for a berm breakwater. The profile is then dynamically stable. This means that the individual stones may move up and down the slope,

but the profile is stable in the long term sense. This applies especially to a two-dimensional profile, when the waves are coming normal to the breakwater. If the wave attack is oblique to the breakwater, stones can also move along the breakwater front. In this case the breakwater may not be dynamic stable.

The present program included basically two test series: One series, when the spectrum shape and peak period were varied, had a time evolution of the significant wave height, as shown in Fig. 12, corresponding to a typical evolution of an intense storm on the Norwegian open coast. In the other test series the duration of the tests for each variation of the wave height was much longer. The tests were carried out with no "repair" work on the breakwater after each wave height step had been completed. The program included one test, A, with a berm width of 30 cm (12 m). The remaining tests, B, were all for a berm width of 45 cm (18 m).

	Prototype		Model	
A	$T_p = 12$ sec	$\gamma = 1.0$	$T_p = 1.9$ sec	$\gamma = 1.0$
B 1-2	$T_p = 12$ sec	$\gamma = 1.0$	$T_p = 1.9$ sec	$\gamma = 1.0$
B 3	$T_p = 12$ sec	$\gamma = 7.0$	$T_p = 1.9$ sec	$\gamma = 7.0$
B 4	$T_p = 16$ sec	$\gamma = 1.0$	$T_p = 2.53$ sec	$\gamma = 1.0$
B 5	$T_p = 12$ sec	$\gamma = 1.0$	$T_p = 1.9$ sec	$\gamma = 1.0$

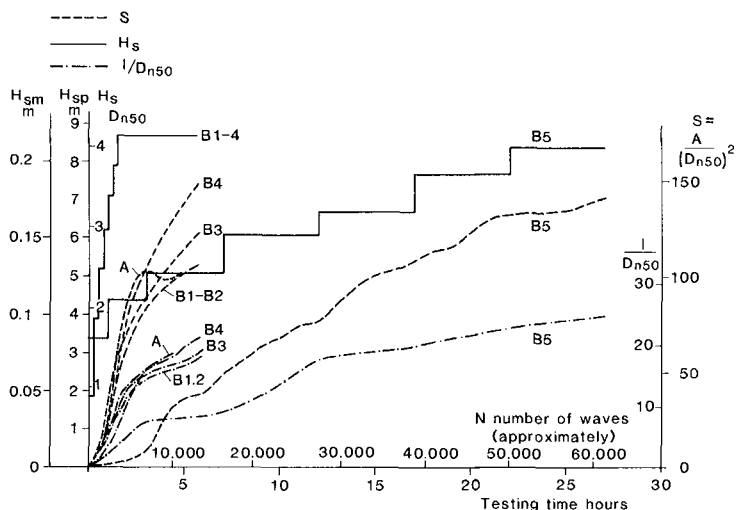


Fig. 12. General tests - Results.

The evolution with time and wave height of S and $1/Dn_{50}$ is also shown in Fig. 12.

It is seen that the value of S is depending on the peak period as well as on the width of the wave spectrum. It has also previously been found for example by Carstens et al. [4] that a narrow spectrum give a harder attack on a conventional rubble mound breakwater than a wide spectrum provided that the peak period is the same and provided that the significant wave height is the same. Van der Meer [3] found that the significant period was the average zero crossing period T_{02} . According to van der Meer [3] damage to a breakwater will be the same provided that the significant wave height is the same and the average zero upcrossing period is the same, irrespective of the spectrum shape.

However, on a conventional breakwater the damage is depending also on the Irribarren number

$$\xi = \text{tg}\alpha / (2\pi H_s / g T_{02}^2)$$

where α is the breakwater slope and $T_{02} = \sqrt{m_0/m_2}$, where m_n is the n th moment of the spectrum. A berm breakwater has not a well defined slope. However, the results presented in Fig. 12 indicate that the "damage" is depending on the peak period T_p .

In the Figs. 13 and 14 are shown typical evolution of the profiles for two test series. B2 is for the shorter duration tests and B5 is for the longer duration tests.

From Fig. 13 and Fig. 14 is seen that there seems to be a significant point located at a distance hw as shown in Fig. 11. The intersection between the profile and the original profile seems to be more or less at this point, irrespective of the scour of the slope.

Van der Meer [3] has investigated many of the parameters of importance for the evolution of the slope. He also gives an equation for the profile below the water line as indicated in Fig. 11. With the local origo given as the intersection between the still water line and the profile the profile is given by

$$y = p \cdot D^{0.22} \cdot x^{0.78} \quad (1)$$

It is not clearly stated by van der Meer which diameter, D , would be used, but it is assumed that it is the diameter Dn_{50} . The coefficient p is primarily a function of the wave steepness, $2\pi H_s / (gT_{02}^2)$. For the present test parameter values van der Meer's results give $p \approx 0.5$. With this value of p we have shown in Figs. 13 and 14 the profile as given by equation (1). For some reason there is an apparent difference between the profiles as obtained in the present study and the study by van der Meer [3]. Van der Meer carried out most of his tests in

relatively deeper water than used in the present study. However, van der Meer also carried out some tests with shallower water and states that there should not be any significant effects of the water depth, h , if $h/H_s > 2.2$, which is the case in the present study.

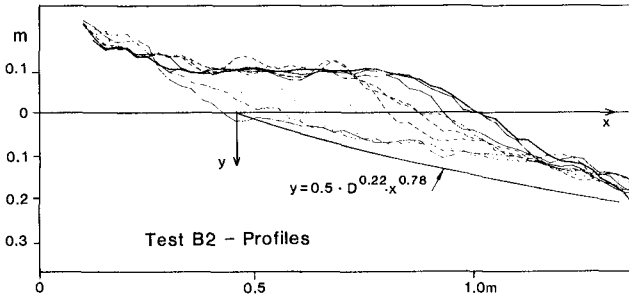


Fig. 13. Profile evolution.

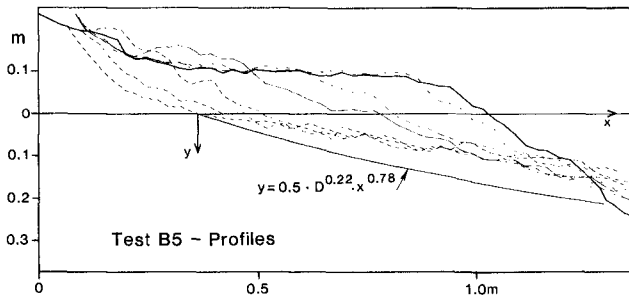


Fig. 14. Profile evolution.

There is obviously a time effect in the development of a dynamic stable profile. If we for example take the evolution with time of the wave height for the tests B1 - B4 (this evolution could be a typical evolution for the Norwegian coast) the value of l/Dn_{50} is equal to the berm width value $B/Dn_{50} = 15.5$ after approximately 6000 waves. The maximum significant wave height is then corresponding to $H_s/\Delta Dn_{50} \approx 4.0$, where $\Delta = \rho_s/\rho_w - 1$, ρ_w = specific density of the water.

For the long duration tests, B5, we have $l/Dn_{50} = 15.5$ after approximately 11 hours testing time or after approximately 25000 waves. The maximum significant wave height is then $H_s/\Delta Dn_{50} \approx 3.0$. This means that the design of the breakwater should be for $H_s/\Delta Dn_{50}$ somewhere between 3 and 4.

The tests with the 12 m wide berm (A-test) showed a berm

recession evolution about the same as for the tests with the wider berm (B-tests). However, due to the narrower berm, the core material finally became visible. This did not occur for any of the B-tests.

THREE-DIMENSIONAL STABILITY TESTS FOR THE BREAKWATER AT THE FISHING PORT OF ÅRVIKSAND

Based on the previous studies, the design shown in Fig. 15 was tested in a three-dimensional model of Årviksand fishing port. The model had a length scale of 1:60 and with a layout as shown in Fig. 1. The tests were run with high water + 3.0 m. The waves referred to were measured at a location corresponding to the location of the wave gauge during the field measurements in the time period 1965 - 1972. The peak period for the waves was $T_p = 14$ sec and the wave spectrum was approximately a JONSWAP spectrum with $\gamma = 7.0$. The time variation of the significant wave height was as shown in Fig. 16.

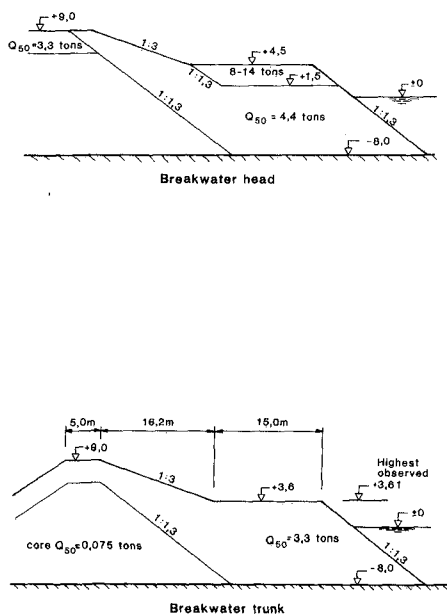


Fig. 15. Tested design for the Årviksand fishing port.

The first tests were carried out with a crest height + 9.0 m, or 6 m above the still water level.

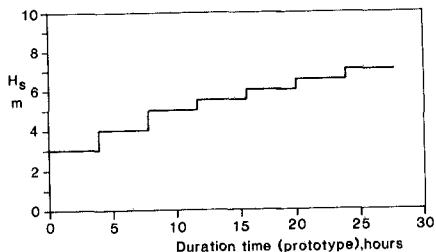


Fig. 16.

Fig. 17 shows the contours of the breakwater after 3.5 hours of testing time, or approximately 10,000 waves, with a maximum significant wave height of 7.0 m. It is seen that there is a damage on the back side of the breakwater due to overtopping at the middle part of the breakwater. The location of the damage is due to a concentration of the waves due to refraction towards the middle part of the breakwater.

The wave crest was then raised by 1.0 m to 10.0 m, or 7 m above the still water line. The breakwater was then tested for the same wave program, Fig. 16, as the previous design. Fig. 18 shows the contour map for the tested breakwater after 3.5 hours testing time. Although there were motions of stones up and down the breakwater slope as well as along the breakwater, mainly landwards, there was not any major damage to the breakwater. Some stones even moved over the breakwater crest.

Since storm duration is essential for consideration of the dynamic stability of the berm breakwater it is essential to consider statistically all the major storms the breakwater will encounter during its expected life time. The water level variation has also to be considered. The result of such a "fatigue" study is not included in this paper.

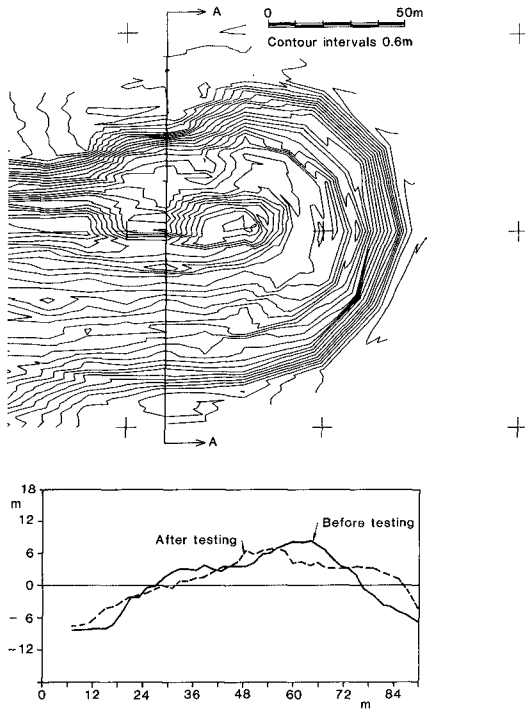


Fig. 17. Section A-A. Crest height + 9.0 m.

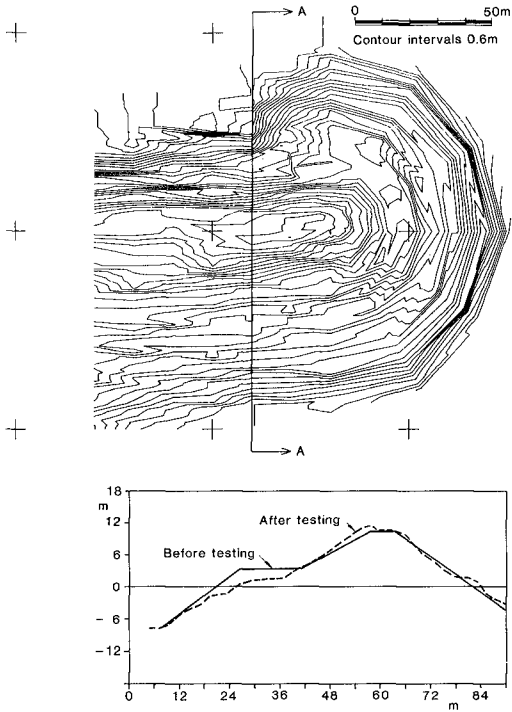


Fig. 18. Section A-A. Crest height + 10.0 m.

CONCLUSION

Based on the present study it is preliminary concluded that a berm breakwater should be designed for $H_s/\Delta D_{n50} = 3 - 4$, provided that the water depth ratio $h/H_s > 2.5$.

A berm breakwater should be subjected to a "fatigue" analysis. It is essential that a three-dimensional study is conducted on the stability of berm breakwaters.

ACKNOWLEDGEMENT

We appreciate the financial support to carry out this study from the Norwegian Coast Directorate and Selmer-Furuholmen Anlegg A/S.

REFERENCES

1. Instanes, A: Molostabilitet (Breakwater stability). M.Sc.-thesis, Norwegian Institute of Technology, December 1987 (In Norwegian).
2. Goda, Y. and Suzuki, Y: Estimations of incident and reflected waves in random wave experiments. Proceedings Coastal Engineering Conference, 1976, pp 828 - 845.
3. Van der Meer, J: Rock Slopes and Gravel Beaches under Wave Attack. Thesis Delft Technical University 26 April 1988.
4. Carstens, T, Trøtteberg, A. and Tørum, A: The stability of rubble mound breakwaters against irregular waves. Xth Conference on Coastal Engineering, Tokyo, 1966.
5. Environmental conditions on the Norwegian Continental Shelf. Barents Sea. Report - Phase 1 to ODAP. Norwegian Hydrotechnical Laboratory, Trondheim, 1 July 1988.

CHAPTER 149

NUMERICAL MODEL OF BREAKWATER WAVE FLOWS

Alex C Thompson*

ABSTRACT

A mathematical model of flow on a sloping breakwater face is described and results of calculations compared with some experimental results to show how the model can be calibrated. Flow above the surface of the slope is represented by the shallow water wave equations solved by a finite difference method. Flow within the breakwater is calculated by one of two methods. A solution of the linear seepage flow equations, again using finite differences or a simplified model of inflow can be used. Experimental results for runup and reflection coefficient are from tests performed at HRL Wallingford.

INTRODUCTION

The behaviour of waves on a breakwater particularly as far as they affect stability of the armour layer has been investigated extensively. Despite this the process is still poorly understood especially for slender concrete armour units, Burcharth 1987. Expensive physical model tests are undertaken for each new breakwater and the interpretation of these is uncertain. The writer has conducted experiments in simple flows to try and understand armour stability and scale effects Burcharth & Thompson 1983, 1984. If similar tests can be combined with a numerical model giving the velocities on a breakwater face the understanding of armour stability may be increased and the amount of physical model testing reduced. The calibration of the numerical model for a particular type of armour would be through simplified tests. This paper is concerned with a suitable numerical model for the task. One such model has been shown by Hibberd & Peregrine 1979 to give good results for a wave breaking and running up a shallow slope. This model is based on the shallow water wave equations so it calculates only the depth averaged velocity at any point on the slope. The detailed velocities in the breaking part of the wave may not be necessary to predict runup reflection and some measures of stability however. This seems to be confirmed by the work of Kobayashi 1986.

* RNC Greenwich UK

He has applied a model based on Hibberd & Peregrine's work to a steeper slope typical of a rock armoured breakwater with some success. Two main areas require investigation if the model is to be applied to slopes covered with concrete armour. Firstly it must be shown that the model works with a steeper slope (upto 1 on 1.5 say).

Secondly the effects of a porous armour layer and core must be accounted for. The assumption of an impermeable slope as used by Kobayashi may be reasonable for a rock armoured slope, it must be less valid for more porous armour such as those tested by Allsop 1983, Burcharth 1979 and Timco 1984. To separate the effects of core permeability and armour permeability and so make calibration of the numerical model easier physical model tests with an impermeable core have been performed. These are compared with calculations for an impermeable slope, a thin permeable layer and a permeable core.

MATHEMATICAL MODEL

The motion of the water on the breakwater face is described in this model by the one dimensional equations for nearly horizontal flow.

$$\frac{d(hu)}{dt} + \frac{d(uhu)}{dx} = \frac{-ghdn}{dx} - \frac{f/u}{2} \quad (1)$$

$$\frac{dh}{dt} + \frac{d(hu)}{dx} = 0 \quad (2)$$

Where h is the depth of water above the slope and u the mean velocity. Both are at a distance x from the toe of the slope and a time t after the start of motion. The water surface elevation above still water level is n ($n=h-D$). D is the still water depth and f the friction factor.

These equations are solved by writing them in finite difference form using the Lax Wendrof method. If equations (1) and (2) are combined and expressed in vector form this gives:

$$\frac{dU}{dt} + \frac{dF}{dx} + G = 0 \quad (3)$$

Where $U = \begin{Bmatrix} hu \\ h \end{Bmatrix}$ $F = \begin{Bmatrix} huu+gh/2 \\ hu \end{Bmatrix}$ $G = \begin{Bmatrix} ghtan\alpha+f/u \\ 0 \end{Bmatrix}$
 $\tan\alpha =$ tangent of slope angle.

A finite difference grid of constant space interval δx and time step δt is used. If the quantities at $x=j\delta x$ and time $t=n\delta t$ are given subscripts j and n then the finite difference equations are:

$$\begin{aligned}
 U(j,n+1) &= U(j,n) - \delta t / \delta x [F(j+1,n) - F(j-1,n)] / 2 + \delta x G(j,n) \\
 &+ (\delta t / \delta x)^2 [g(j,n) - g(j-1,n) - \delta x S(j,n)] / 2 \quad (4) \\
 g(j,n) &= [A(j+1,n) + A(j,n)] [F(j+1,n) - F(j,n) + \delta x (G(j+1,n) + G(j,n))] / 2
 \end{aligned}$$

$$A = \frac{dF}{dU} = \begin{Bmatrix} 2u & gh - uu \\ 1 & 0 \end{Bmatrix} \quad S = \frac{dG}{dt} = \begin{Bmatrix} -g \tan \alpha d(hu) / dx \\ 0 \end{Bmatrix}$$

Dissipation is introduced to damp the short waves which appear in the solution when a steep wave front is formed. This is applied after every time step using a dissipation constant AD with the value 0.1 in the equation:

$$U(j,n) = AD * U(j+1,n) + (1 - 2 * AD) * U(j,n) + AD * U(j-1,n) \quad (5)$$

The boundary conditions applied to produce a model of the flow on a slope were as follows. At the shore boundary the depth of flow becomes zero and the position of this point varies in the finite difference grid. Hibberd and Peregrine developed a comprehensive method of dealing with this condition which worked well on the thin runup layer formed on a smooth shallow slope. A simpler condition has been used here which is believed to be adequate for the steep rough slopes considered. Sufficient points are included in the calculation to cover the maximum runup. The depth h at each point is tested and if it is less than a minimum value h_m then h is set equal to h_m and the discharge hu is made zero. h_m is made 0.004 times the depth at the toe of the slope.

At the seaward end of the calculation both the water depth h and the discharge hu must be given as a function of time. The surface elevation of an incident wave n_i can be specified, as discussed below. The elevation of the reflected wave n_r can be found as in Kobayashi's work. These two quantities are added to give the total surface elevation at the toe of the slope. The discharge can then be found from the quantity β found in the backward characteristic equation. This quantity is defined as:

$$\beta = u - 2(gh)^{\frac{1}{2}} \quad (6)$$

The equation for β is:

$$d\beta + (u - c) \frac{d\beta}{dx} = g \tan \alpha \quad (7)$$

Where $c = (gD)^{\frac{1}{2}}$ is the wave speed.

The value of β can therefore be calculated at the seaward boundary from equation (7) at the start of a new time step. Using the definition of depth,

$$h = D + n_i + n_r$$

And from linear long wave theory,

$$u = (c/D)(n_i - n_r)$$

Putting these in equation (6) and using the binomial theorem to expand the square root gives:

$$n_r = (-c/g)(\beta/2 + c)$$

The incident wave n_i is taken as a sine wave for some calculations but in most cases a suitable profile is taken from Dean's stream function theory. A surface profile is chosen from Dean's tables according to the period and height of the wave selected and the surface co-ordinates stored in a data file.

Typical values of the time step etc used in the model can be given for the example of modelling waves on a 1:2 slope in a depth of 0.3m. This is the slope tested in a wave flume at HRL. The grid size δx in the x direction is 0.0075m and 150 points are used in the calculation. The time step δt is 0.00375s requiring 667 steps to calculate one period of a 2.5s wave, the longest period wave investigated.

Permeable Slope Model

The model described above is used to calculate wave action on an impermeable slope which forms the largest part of the work described here. It can also be linked to two models of flow in a permeable slope and a smaller number of calculations are made in this mode. The first model of a permeable slope assumes that flow takes place only in a thin layer just below the surface of the slope. This might approximate to the flow on a slope armoured with a very porous layer such as the experiments to be described. The water surface in this layer is assumed to rise at the same rate as the uprushing wave tip. If the thickness and porosity of the layer are specified the discharge into the layer from the water above the slope can be found. This discharge is taken to arise from a small number of points near the wave tip and to cause an equal velocity into the slope at each of these points. The water depth h and discharge hu at these tip points are then adjusted before the next time step of the Lax Wendrof computation is executed. The equations for this adjustment are:

$$h^1 = h - v\delta t \qquad hu^1 = hu(h^1/h) \qquad (9)$$

Where h^1 , hu^1 are the adjusted values of h , hu and v is the velocity into the slope. The downward velocity of water in the permeable layer is assumed to have a maximum value and outflow from the layer

is constant once this is reached. The wave tip can therefore leave the water surface in the layer behind and inflow only resumes when the wave tip rises above the water in the layer again. Typical parameters for this model for the HRL test case are: layer depth 0.042m (.07mxporosity0.6), number of tip points 5, maximum downward velocity 0.01m/s.

The second model of a permeable slope allows for a large region of any shape to underlie the slope. This has a constant permeability at present but the method can easily allow for variations in permeability, see Thompson 1986. The water motion in this permeable region is assumed to follow Darcy's law, implying a linearisation of the actual turbulent flow relationship between head gradient and velocity. The equation for the total head H at any point is then:

$$\frac{d(kdH)}{dx(dx)} + \frac{d(kdH)}{dy(dy)} = 0 \quad (10)$$

This equation is solved using a finite difference method as follows. The permeable region is covered by a grid with spacing Δx horizontally and Δy vertically. These spacings are equal and larger than the spacing δx in the grid for the Lax Wendrof solution. The finite difference version of equation (10) is the familiar five point formula solved by successive over-relaxation. This iterative method allows the solution for one time step to start from that for the previous step which will be quite close to the required solution. The same time step δt is used as for the Lax Wendrof solution of the flow above the slope. The free surface in the permeable region is moved using this time step and the boundary conditions on the slope taken from the next solution for water depth above the slope. Motion of the free surface is calculated by the formula:

$$\frac{dY}{dt} = - \left(\frac{dH}{dy} - \frac{dH}{dx} \tan\theta \right) \frac{k}{e} \quad (11)$$

where Y is the free surface elevation in the permeable region, H the total head, $\tan\theta$ is dY/dx , k is the permeability and e the porosity.

The total head H is put equal to Y on the free surface. The location of this in the grid changes as the surface moves and this is allowed for by taking the nearest grid point to the surface on each vertical grid line as the point where H is specified. In a similar way the surface of the slope is represented by the nearest points in the grid. The head H at these points is taken as the water depth above the slope plus the height of the point above the toe of the slope. Water depths are found from the solution for flow above the slope at grid points in the Lax Wendrof routine which coincide with the interior grid. The remaining boundaries of the permeable region are taken as zero flow boundaries and the gradient of H is set to zero at these points. For example this condition is

applied along a horizontal line level with the toe of the slope which is the bottom of the permeable zone in the present work. The seaward end of the free surface is forced to coincide with the tip of the wave on the slope.

The model of wave flow on the slope is linked with the interior flow model via the velocities into the slope. These are calculated from the head gradients at the slope surface found in the interior flow model. The discharge into the slope is calculated at each grid point on the slope in the permeable region this is then shared among the neighbouring grid points in the wave flow model and a velocity into the slope found for each of these. The velocities are then used to modify the wave flow solution as before from equation (10).

A typical application of the model is to the region shown in Fig 11. The permeable region under the slope has a maximum length of 1.17m and maximum height of 0.45m. This is covered by a grid of (40x16) points with spacing $\Delta x = \Delta y$ of 0.03m. The wave flow grid has spacing $\delta x = 0.0075m$ ($\Delta x/4$) and 150 points. A permeability k of 1.0m/s is used and a porosity e of 0.4.

PHYSICAL MODEL TESTS

The calculations are compared with results of tests performed at HRL Wallingford and described more fully in a companion paper at this conference, Stephens et al 1988. These tests are made on an impermeable slope of 1:2 with a water depth of 0.3m at the toe. Regular waves with period of 1.0, 1.5, 2.0 and 2.5s are generated in a long flume by a hydraulically actuated paddle and measurements made before reflections from the paddle build up. Incident and reflected wave heights are measured from two twin wire wave probes mounted offshore. A further 10 wave gauges are closely spaced above the slope and another gauge lies flat on the slope so that the wave motion can be followed in detail here. Video recordings of the wave on the slope are made for each test which can also be analysed to give details of the flow. Only the results on reflection coefficient will be discussed in this paper. Tests are made on a smooth slope and also on a slope covered with a single layer of SHED units 40mm deep.

CALCULATIONS MADE

The mathematical models described above are used to calculate the same situation as the physical model tests. That is regular waves are directed towards a plane slope of 1 on 2 in a water depth of 0.3m. The wave periods are 1.0, 1.5, 2.0 and 2.5s. A number of wave heights are produced at each period in the range .03 to .09m. The calculation produces values for the incident and reflected waveheight so that values of the reflection coefficient can be compared with the measured values. Also calculated are the runup of the waves on the slope and a stability number indicating the start of motion of rip rap or rock armour placed on the slope. The calculations are started with the water above the slope at rest and continued until the values of reflection coefficient etc repeat at

each wave. Usually 4 to 5 wave periods are sufficient with the short waves and 2 to 3 with the long waves. For the bulk of the computations the wave profiles chosen were Dean's 7A, 6A, 5A and 4A for the 1.0, 1.5, 2.0 and 2.5s waves respectively. The reflection coefficient etc are plotted against a surf similarity parameter or Iribaren number I_r defined as $T \tan \alpha / (2\pi H/g)^{1/2}$.

Impermeable Slope Model

Fig 1 shows the reflection coefficient measured and calculated for a rough slope. The measured results from the impermeable slope covered with a single layer of model SHED units are shown as crosses. It will be seen that these fall onto separate lines, one for each wave period. This may be because at a given wave period I_r increases as H decreases. Thus for fixed I_r longer wave periods have higher waves. The ratio of wave height to slope roughness will be less for the longer waves and this may explain the higher reflection at a given I_r for these waves. The different wave profiles at each period may be another cause of this effect. The computed results shown by the continuous lines are for a friction factor of 1.0 and of course only the model for water above the slope employed. This friction factor value gives a better agreement with the experimental results than the value of $f=0.3$ used by Kobayashi except for $T=2.5s$. Results with $f=0.3$ can be seen in Fig 3.

Fig 2 shows the reflection coefficient for a smooth slope. The measurements again appear as separate symbols and this time there is much less separation into different groups for each wave period. In this case, the reflection coefficient for $T=2.5s$ are slightly lower than for $t=2.0s$. The computed results use a friction factor $f=0.01$ and fit the experimental results quite well except for $T=1.0s$ when the reflection is too high. It may be that the breaking process is not modelled well enough here or that a higher friction factor is appropriate for $T=1.0s$. The present model uses a constant friction factor for simplicity.

Permeable layer model:

Fig 4 shows the results from the permeable layer model linked to the model for flow above the slope and used to calculate reflection coefficient. The effective depth of the layer is .024m calculated from a depth of .04m and porosity of .60 for the SHEDs in the physical model. A maximum downward velocity in the layer of .10m/s is assumed. The number of points affected by inflow at the wave tip is 20 which is found to be better than 5. The friction factor f is 0.3 the value which Kobayashi found suitable for a comparable surface roughness but which is too small to model the SHED layer if no inflow is allowed. With inflow included as here the calculated results agree quite closely with the experimental findings. In particular the separation into distinct lines for each wave period is reproduced. The results for $T=2.5s$ have been further enhanced by changing the wave profile from Dean's 4A to 7A as the wave height is reduced and I_r increases.

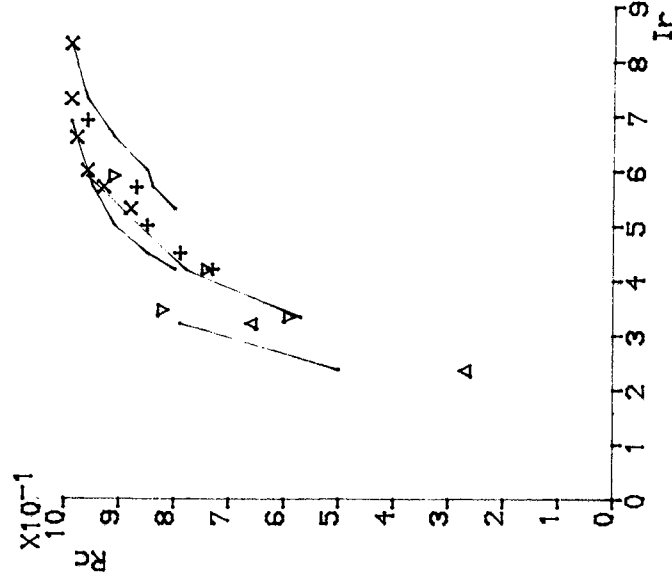


FIG 2 Reflection Coef. Smooth Slope.
 $\Delta, \nabla, +, \times$ measured $T=1, 1.5, 2, 2.5$ s
 --- calculated $f=0.01$ impermeable.

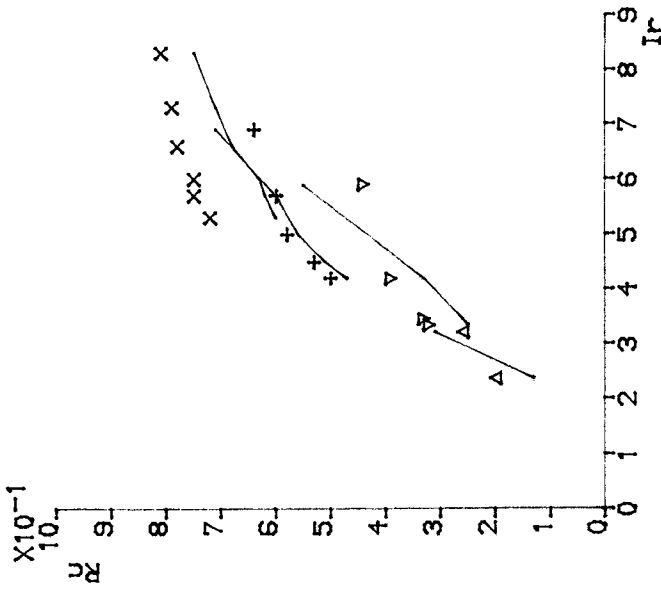


FIG 1 Reflection Coef. Rough Slope.
 $\Delta, \nabla, +, \times$ measured $T=1, 1.5, 2, 2.5$ s
 ---calculated $f=1.0$ impermeable.

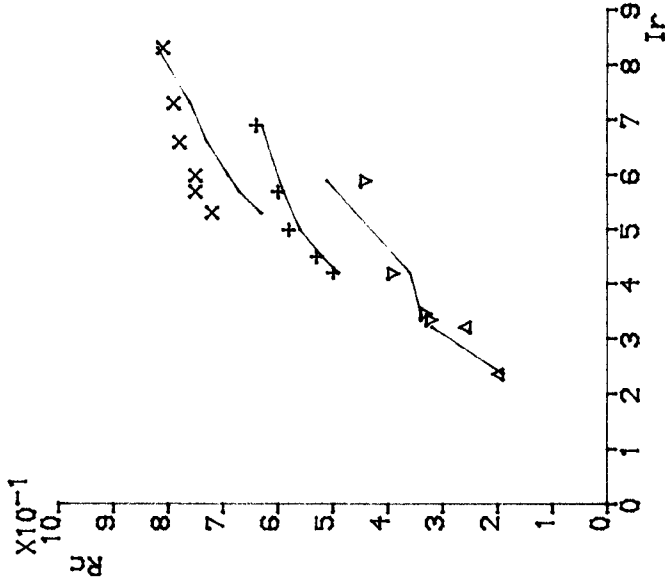


FIG 4 Reflection Coef. Rough Slope.
 Δ, ∇, \times measured $T=1, 1.5, 2, 2.5$ s
 -- calculated $f=0.3$ permeable layer.

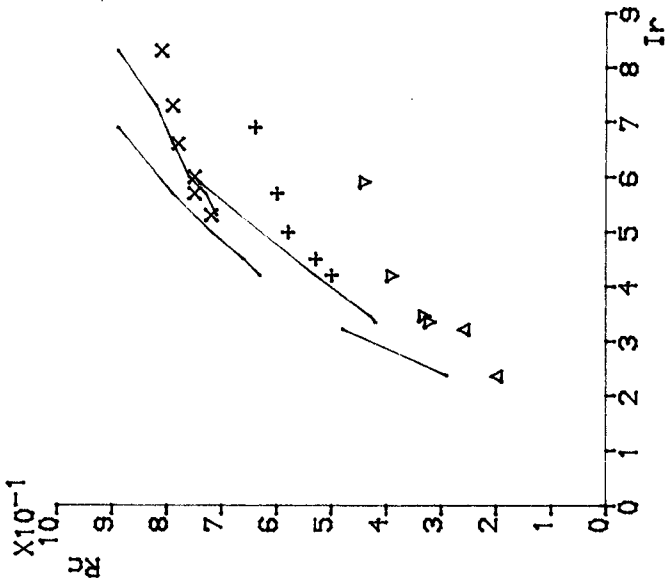


FIG 3 Reflection Coef. Rough Slope.
 Δ, ∇, \times measured $T=1, 1.5, 2, 2.5$ s
 -- calculated $f=0.3$ impermeable.

It is interesting that the wave profile assumed has a marked affect on many of the results of the computations. The run-up shows this especially as can be seen from Fig 5. Here the run-up divided by waveheight R/H is plotted against Irribaren number I_r . The full line shows results found with Dean's profiles and the crosses those with a sine profile. In both cases the impermeable slope model with $f=1.0$ was employed. Run-up/ H calculated with a sine profile is more strongly grouped by wave period and reaches a maximum at around $I_r=5$. With Dean's profiles however, results from all wave periods are closer to a single line and R/H continues to increase with I_r .

Fig 6 shows a comparison of calculated run-up with some experimental results from other sources. The higher solid line is based on work reported by Ahrens 1983 for smooth impermeable slopes. Starting from $I_r=0.4$ it shows the line $R/H=I_r$ up to $R/H=1.86$, the value predicted by Miche's law for sine waves on a slope of 1:2. This is then joined to points of increased R/H calculated from the crest height/wave height ratio for the wave profiles used at each wave period as in Ahrens 1983. The results calculated for an impermeable slope for $f=.01$ (x) fall close to this line. With $f=.3$ (+) calculated points fall below this but above the lower full line. This line is the experimental result quoted by Kobayashi 1986 from work by Ahrens on slopes covered with rip rap. The calculations with the permeable layer model (Δ) fall close to this line.

Fig 7 shows the calculated results for stability number N_s and some experimental results for rip rap. N_s is defined as $H/\Delta D$ where D the diameter of rock which is just stable is calculated using a similar model to that of Kobayashi with the same constants. The full line is the result of van der Meer & Pilarczyk for a slope of 1:2 and the lowest damage level. The calculated results with the permeable layer mode (x) and the impermeable slope model (+) both fall close to this line for I_r greater than 3.

Permeable Core Model:

Results from the permeable core model are more preliminary than those above and have yet to be compared with experimental data. For these first computations the permeable region is shown in Fig 11. All of this region is assumed to have a permeability of 1.0m/s and a porosity of 0.4. The permeability value follows from the linearisation of the true friction law used by Harlow 1980, $K=gd/kV_{av}$, with $k=1.0$, $d=.01m$, $V_{av}=0.1m/s$. Fig 8 shows the reflection coefficient calculated for 4 wave period/height combinations (+). The friction factor f is 0.3 as for the permeable layer model. The full line shows the reflection suggested by Seelig 1983 for breakwaters. This lies well below the results for an impermeable slope with only a single layer of armour units, for example Fig 4. The run-up found with a permeable core is given in Fig 9 (+). The full line is 0.5 times the smooth slope line from Fig 6 and lies just above calculated points. Stability numbers computed are given in Fig 10 (+). These lie well above the experimental value for an impermeable core shown as a full line. Finally Fig 11 shows a typical water surface profile above and

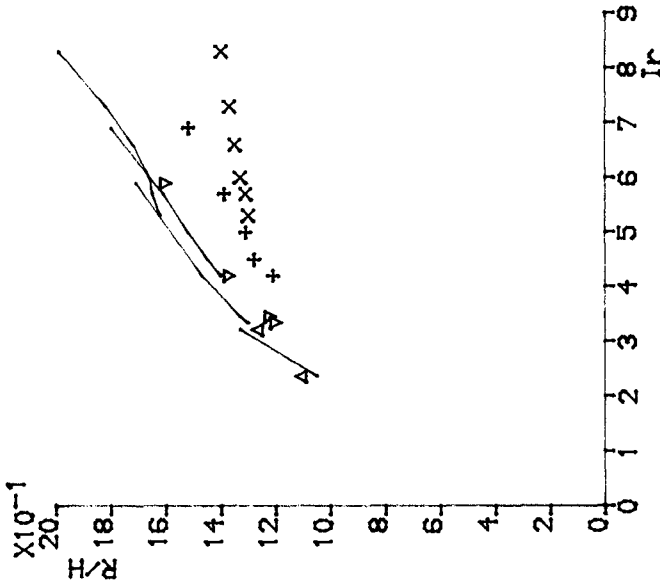


FIG 5 Runup/H Rough Slope.
 -- calculated Dean wave profiles
 Δ , ∇ , +, x calculated sine waves.

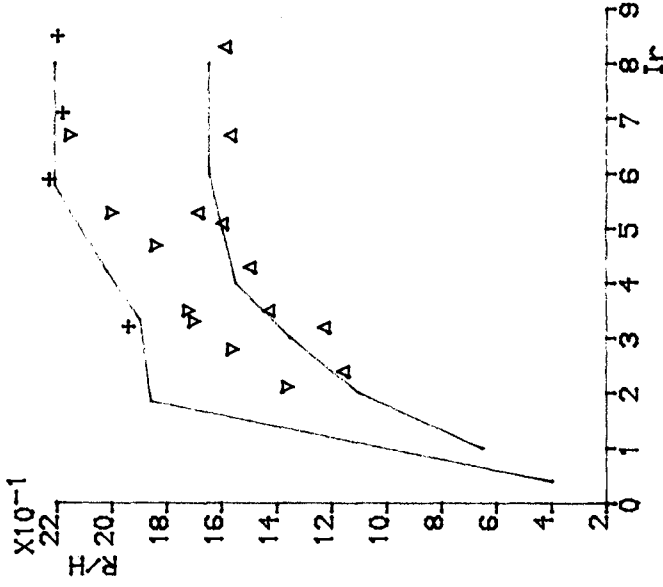


FIG 6 Runup/H.
 Δ permeable layer $f=0.3$, ∇ , + impermeable $f=0.3, 0.01$
 -- upper Ahrens, -- lower Kobayashi.

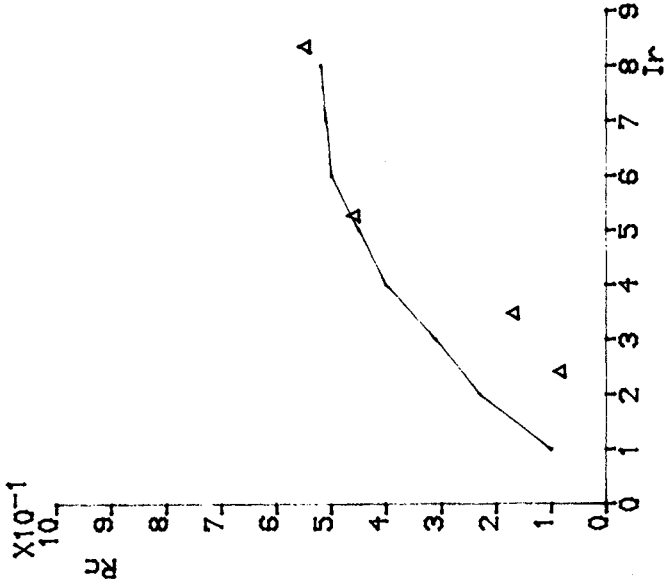


FIG 8 Reflection Coef. Permeable Core.
 Δ calculated, -- Seelig.

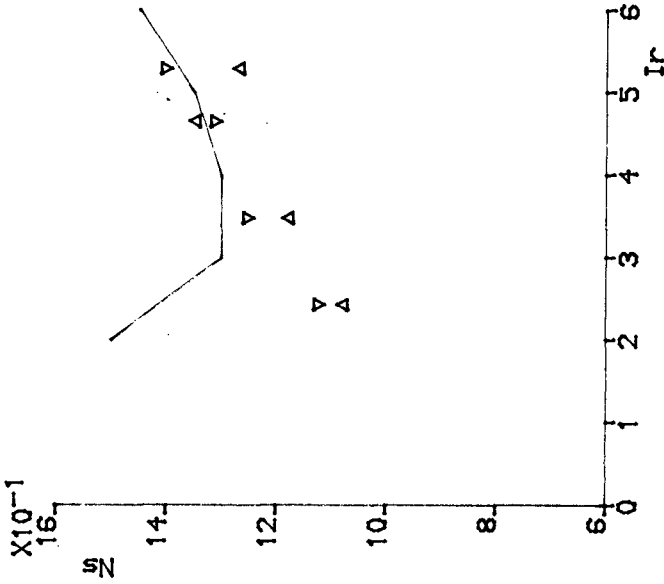


FIG 7 Stability Number.
 Δ , ∇ calculated $f=0.3$ permeable, impermeable.
 -- Piłarczyk.

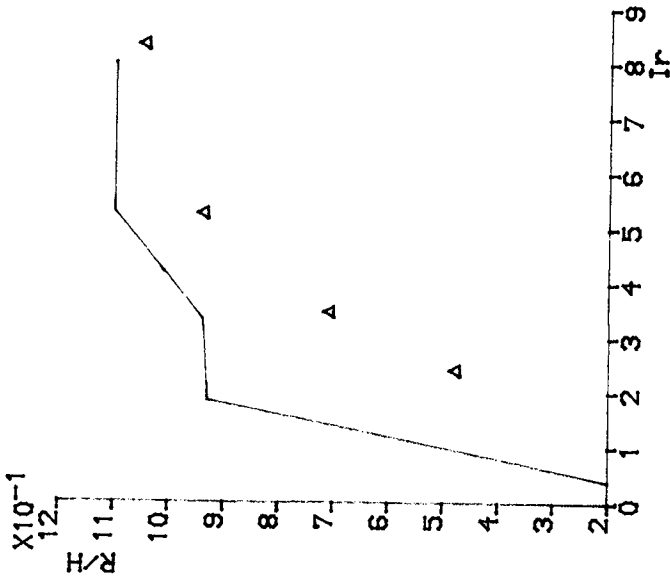


FIG 9 Runup/H Permeable Core.
 Δ calculated, -- Ahrens/2.

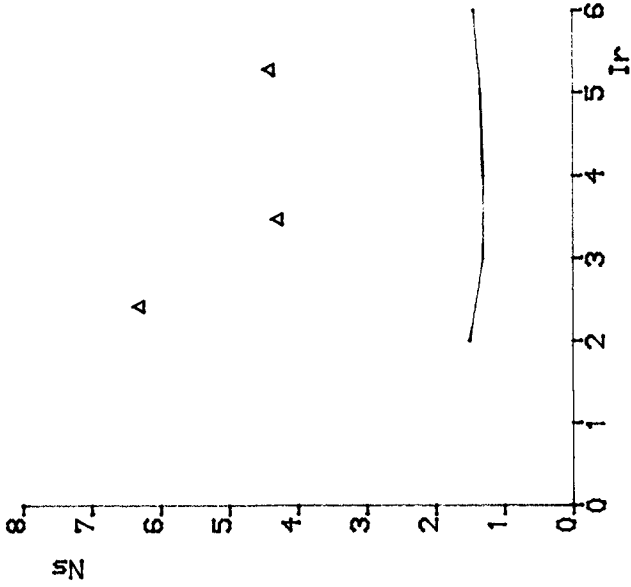


FIG 10 Stability Number Permeable Core.
 Δ calculated, -- Pilarczyk.

WAVE PERIOD 1.00 S
TIME AFTER START 1.00 S
WAVE HEIGHT 0.066 M
CORE PERMEABILITY 1.00 M/S

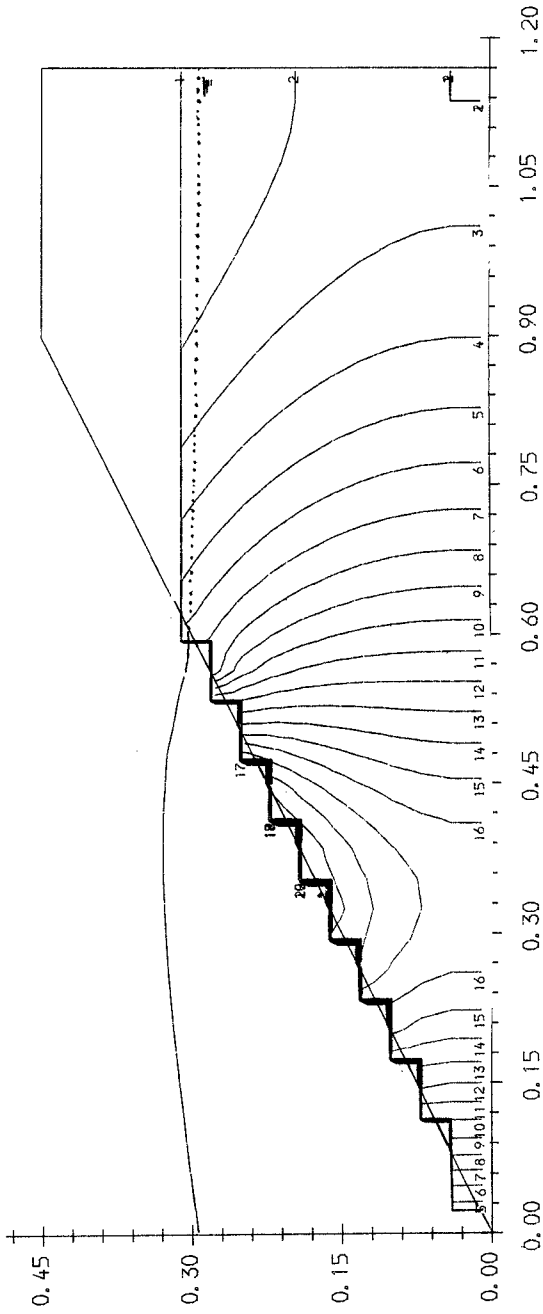


FIG 11 Head in core and on boundaries.

within the core and contours of Run-up/Waveheight R/H head within the core. Contour number 1 shows the location of the lowest head in the core and contour number 20 the highest head, the head values being the height of the water surface at these points.

CONCLUSIONS

The first model described above, based on the equations of nearly horizontal flow is able to calculate many of the important features of wave motion on a steep impermeable slope. It can be linked with the other models described which show promise in calculating the effects of permeable regions underlying the slope.

REFERENCES

AHRENS J P, "Wave run-up on idealised structures", Coastal structures '83, Washington 1983.

ALLSOP N W H & WILKINSON A R, "Hollow block breakwater armour units", Coastal structures '83, Washington 1983.

BURCHARTH H F, "The effect of wave grouping on onshore structures", Coastal Engineering, 2 (1979) 189-199.

BURCHARTH H F & THOMPSON A C, "Stability of armour units in oscillatory flow", Coastal structures '83, Washington 1983.

BURCHARTH H F, "Lessons from recent breakwater failures", World fed. of Eng, organisations, Vancouver 1987.

HARLOW E, "Large rubble mound breakwater failures", J. ASCE vol 106 WW2 1980.

HIBBERD S & PEREGRINE D, "Surf and run-up on a beach of a uniform bore", JFM vol 95 pt 2 1979.

KOBAYASHI N, ROY I & OTTA A K, "Numerical simulation of wave run-up and armour stability", OTC 5088, Houston 1986.

SEELIG W N, "Wave reflection from coastal structures", Coastal structures '83 Washington 1983.

STEPHENS R V, SMALLMAN J V & ALLSOP N W H, "Development and application of a mathematical model of wave action on steep slopes", 21st Coastal Eng. Conf., Torremolinos, 1988.

THOMPSON A C & BURCHARTH H F, "Stability of armour units in flow through a layer", 19th Coastal Eng. Conf., Houston 1984.

THOMPSON A C, "BASIC Hydrodynamics", Butterworths Scientific Ltd, 1986.

TIMCO G W, MANSARD E P D & PLOEG J, "Stability of breakwaters with variations in core permeability", 19th Coastal Eng. Conf., Houston, 1984.

CHAPTER 150

STATISTICAL ANALYSIS OF DETACHED BREAKWATERS IN JAPAN

Takaaki UDA*

ABSTRACT

Construction of detached breakwaters is one of the main countermeasures against beach erosion in Japan. The number of breakwaters has been rapidly increasing, with about 2500 constructed as of the end of 1981. This study aims at the investigation of the effect and stability of detached breakwaters along Japan's coasts on the basis of survey of 1552 breakwaters constructed by the Ministry of Construction. The existing conditions of the dimensions of the detached breakwaters are statistically analyzed; the optimal dimensions for sand deposition behind a breakwater are proposed, and the critical conditions for advance of the shoreline facing an opening of breakwaters are investigated. Furthermore, the relations between the scattering rate of concrete blocks and various conditions such as bottom slope, the depth at the breakwater, the offshore distance of the breakwater and the weight of the blocks are studied. It is concluded that, in order to prevent scattering, the weight of the blocks should be at least 1.5 times heavier than that calculated from the Hudson formula.

1. INTRODUCTION

The coastal zone has been highly utilized in Japan because of the shortage of plains in the Japanese archipelago. Every effort has been made to protect the coastline from erosion due to sea waves. In 1950's, full-scale coastal protective measures were initiated in Japan. In this period, coastal dikes were mainly constructed to prevent coastal disasters brought by storm surges. In the late 1950's, coastal dikes and revetments of the vertical wall type were introduced against beach erosion. Thereafter, groins were constructed, but there were several cases with less effect. In the 1960's, the field test of detached breakwaters was conducted for the first time to confirm their effectiveness. Since then, detached breakwaters have been constructed extensively to preserve or revive the sandy foreshore, as the damage to coastal dikes and revetments, triggered indirectly by the disappearance of the foreshore, increased. At present, construction of detached breakwaters is one of the main countermeasures against beach erosion, and many of them have been constructed along Japan's coasts to dissipate wave energy and prevent beach erosion. The number of detached breakwaters has been rapidly increasing with about 2500 constructed as of 1981. However, there are still many problems to be solved for construction of detached breakwaters. The planning method to ensure the effect and

* Dr.Eng., Head, Coastal Eng. Div., Public Works Res. Inst., Ministry of Construction, Ibaraki 305, Japan.

stability of detached breakwaters has not yet been established. This study, based upon survey of 1552 breakwaters built by the Ministry of Construction, aims at the investigation of the effect and stability of detached breakwaters (Seiji et al., 1987).

11. METHOD OF INVESTIGATION

The survey was conducted in order to study the existing situations of detached breakwaters in Japan. Questionnaires were distributed to the prefectural government offices and to the work offices of the Ministry of Construction to collect the information on each of the 1552 detached breakwaters constructed by the Ministry or by the prefectural governments as subsidiary works of the Ministry by the end of 1982.

The contents of the questionnaire are summarized in Table 1, in which the principal items are general matters, natural conditions, dimensions of the breakwater, kinds of concrete blocks, information on the scattering of the blocks and the effect of the breakwater. Although the details of the items are summarized in Table 1, there are some additional notes to be given. A serial number was attached to identify each breakwater. The difference between permeable and impermeable types was of interest, but all the breakwaters were of the permeable type. The water depth at the breakwater and the offshore distance to the breakwater

Table 1 Contents of the questionnaire.

Classification	Items
General Matters	name of the prefecture name of the coast number of the detached breakwater construction date
Design Conditions	design wave height design wave period tidal range bottom slope at the site water depth (reference: H.W.L.) offshore distance (reference: H.W.L.)
Dimensions of the Detached Breakwater	type (permeable or impermeable) placing (pellmell or uniform) crown height length elevation above the H.W.L. foundation
Kinds of Concrete Blocks	kind weight K_D value in the Hudson formula
Effect and Stability	subsidence of the blocks scattering of concrete blocks method of placing tombolo formation (yes or no) foundation (yes or no)

were measured above the H.W.L., whereas the crown height of the breakwater was measured above the standard mean sea level of Tokyo Bay.

In order to study the effect and stability of the detached breakwaters in general, the type of coasts was classified into five categories of A through E, as shown in Fig.1, based on the beach profile. The characteristic features of these coasts are as follows:

Type A: The coasts facing a bay or an inland sea, such as the Aomori Coast and the Toban Coast. The wave heights are low on these coasts compared with those on the coasts facing the open sea, and the critical depth for sand movement is small.

Type B: The coast with a fairly developed bar-trough topography, such as the Niigata Coast, the Ishikawa Coast and the Enshu Coast. The bottom slope in a region shallow enough for sand movement is mild, and the direction of mean incident waves is almost normal to the coastline.

Type C: The coast where the bottom slope in the shallow region is relatively steep without the formation of bar-trough topography, e.g., the Shimonikawa Coast and the Suruga Coast.

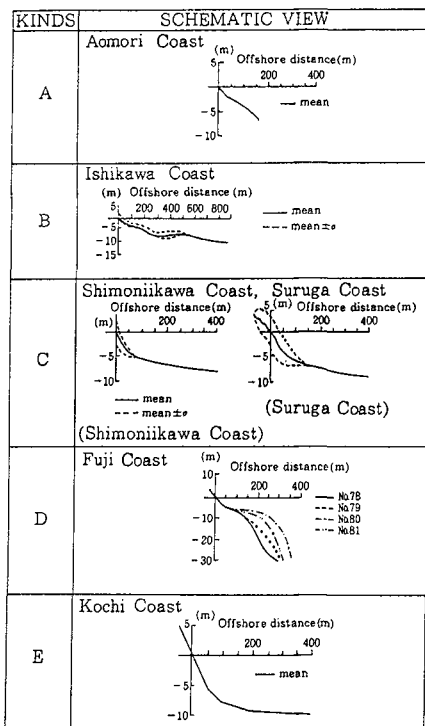


Fig.1 Type of the coasts classified into five categories of A through E.

Type D: The coast with an extremely steep slope of 1/3-1/10, e.g., the Fuji Coast in Suruga Bay.

Type E: The coast similar to Type C, but with a bar-trough topography sometimes observed in a far offshore zone, e.g., the Kochi Coast.

III. RESULTS OF SURVEY

3.1 Situations of detached breakwaters in Japan

The results of the survey about the dimensions of the detached breakwaters are shown in Figs.2 (a) to (h).

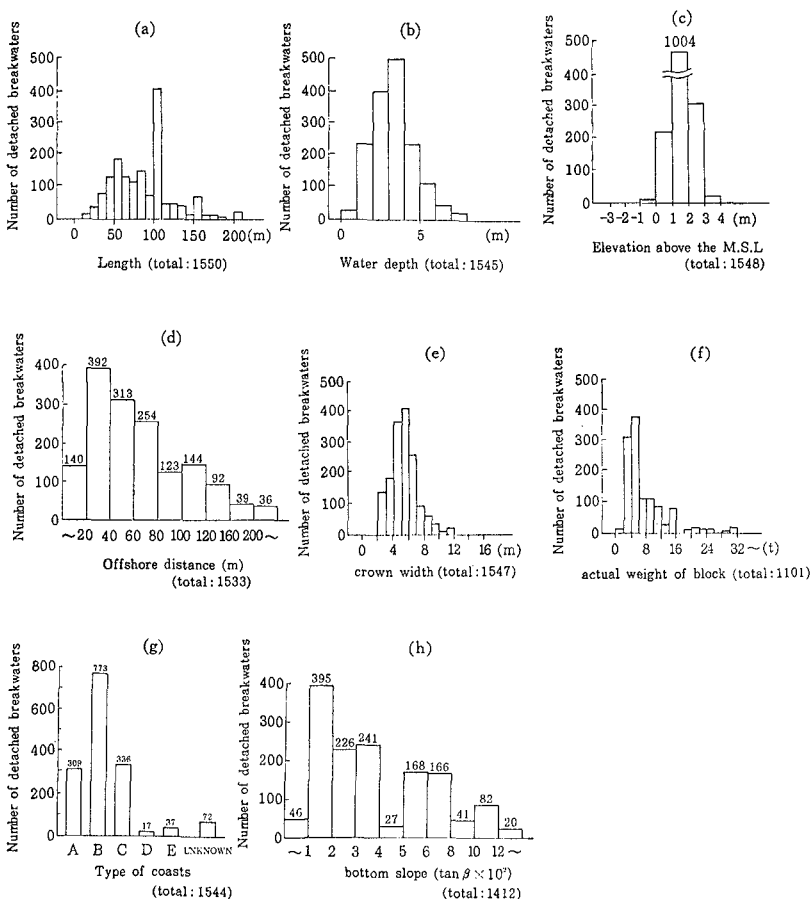


Fig.2 Frequency distribution of various dimensions of the detached breakwaters; (a) length, (b) water depth, (c) elevation above the M.S.L., (d) offshore distance, (e) crown height, (f) actual weight of block, (g) type of coasts and (h) bottom slope.

The maximum frequency of breakwater length, divided into 10m intervals, appears in the interval of 100-110m, amounting to 20%. The secondary peak is found in the interval of 50-60m. The maximum frequency of the water depths at the breakwaters is 3-4m, and it amounts to 30%. 90% of the breakwaters are located at a water depth less than 5m. The most frequent elevation of the breakwater above the M.S.L. is 1-2m and the frequency amounts to 65%. Regarding the distribution of the offshore distances, the number of breakwaters in each interval generally decreases with the increase in the offshore distance, except in the case less than 20m. The maximum number, 392, is included in the interval of 20-40m, amounting to almost 25%. The crown width varies between 2 and 12m, and the most frequent value is in the interval of 5-6m. The weight of the concrete blocks is mostly in the range from 2 to 6 tons, but there is an exceptional case of the Fuji Coast in Suruga Bay where 50-ton blocks were used (Kohno et al., 1986). Most breakwaters were built on the coasts of type B. All the data for type D, whose number is rather limited, belong to the Fuji Coast. The bottom slope ($\tan \beta$) at the breakwater was determined from the bottom topography before the construction of the breakwater, and its peak appears in the interval of 0.01-0.02. Few breakwaters were built on a coast with a slope milder than 0.01.

The sand deposition effect of the detached breakwaters was investigated statistically on the basis of tombolo formation. Figure 3 shows the percentage of tombolo formation. It is clearly seen that tombolos were formed in about 60% of all the cases. The frequency distribution of the maximum shoreline advance due to tombolo formation is shown in Fig.4. The shoreline advance ranges from 0 to 140m. The maximum frequency is found in the interval of 10-20m, and the cases with a shoreline advance of more than 100m is quite limited in number.

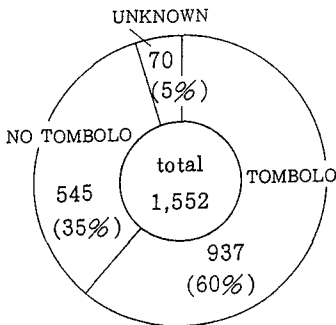


Fig.3 Percentage of tombolo formation.

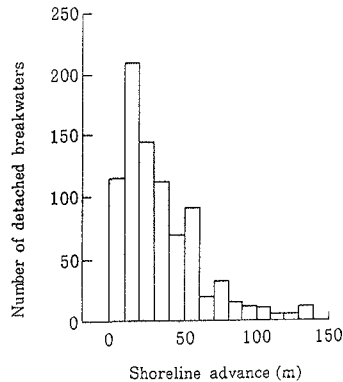


Fig.4 Frequency distribution of the maximum shoreline advance due to tombolo formation.

The number of the detached breakwaters with or without subsidence was investigated statistically as shown in Fig.5. It is found that the subsidence of the detached breakwater is observed in about half of the total number (1552). From this it is realized that the subsidence of the detached breakwater becomes an important problem regarding the stability of the breakwater. On the basis of 503 detached breakwaters whose subsided height is available, frequency distribution of the subsided height of detached breakwater is investigated as shown in Fig.6. The subsided height ranges between 0 and 2.8m. The most frequent subsided height of the breakwater is 1.0-1.2m, and the number amounts to 158.

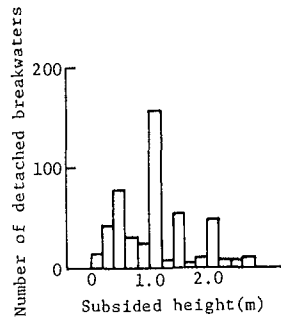
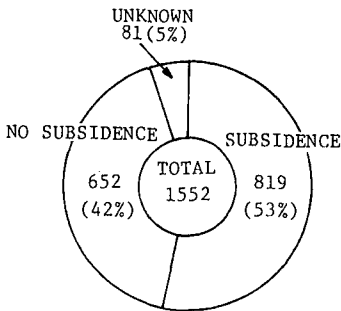


Fig.5 Percentage of the number of detached breakwater with or without subsidence of blocks.

Fig.6 Frequency distribution of the subsided height of detached breakwater.

Table 2 shows the percentage of the number of the subsided detached breakwater corresponding to the kinds of the bed materials. The ratio of the number of the subsided breakwater relative to the total number accounts for 64% (sand), 43% (gravels) and 10% (rock), respectively. The reason of the subsidence of the breakwater for the rocky bottom materials may be due to the fact that the interlocking of the concrete blocks near the top of the

Table 2 Percentage of the number of the subsided detached breakwater corresponding to kinds of the bed materials.

Subsidence Bottom materials	Subsidence			Total
	Exist	Nil	Unknown	
rock	(10%) 19	(73%) 141	(17%) 34	(100%) 194
gravel	(43%) 139	(56%) 183	(1%) 5	(100%) 327
sand	(64%) 678	(33%) 347	(3%) 42	(100%) 1067
silt	(100%) 1	(0%) 0	(0%) 0	(100%) 1
Total	(53%) 837	(42%) 671	(5%) 81	(100%) 1589

breakwater may be loosened by wave action. Comparing both foundations of sand and gravels, the ratio of the subsidence in the latter case is small. However, the ratio of the subsidence of the blocks is large enough in both cases, and it is necessary to take effective measures against subsidence if detached breakwater is constructed on the foundation of sand or gravels.

Percentage of the number of detached breakwater with or without scattering of blocks is shown in Fig.7 . Scattering of the blocks can be observed in 14% of the total. In addition, frequency distribution of the scattered distance of blocks is shown in Fig.8 in the case whose scattered distance is available. Scattered distance ranges between 0 and 13m, and the most frequent case of scattering distance is 4-5m .

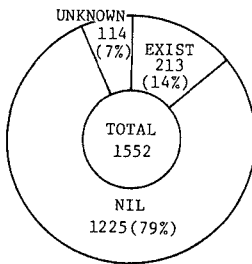


Fig.7 Percentage of the number of detached breakwater with or without scattering of blocks.

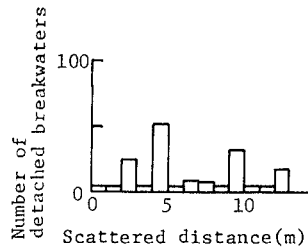


Fig.8 Frequency distribution of the scattered distance of the blocks.

3.2 Effect of detached breakwaters

The effects of detached breakwaters are mainly divided into two categories: the first is to cause the sand deposition behind the breakwater, and the second is to dissipate the incident wave. The former effect basically depends not only on the dimensions of the breakwater but on the rate of sand supply due to littoral drift. It is, however, difficult to study the influence of the littoral drift in general, because the conditions of sand supply differ to a large extent from place to place. Therefore, only the influence of the dimensions on sand deposition is discussed in this study.

The length l , the width of the opening l' , the offshore distance Y , and the water depth at the breakwater h' , are selected as the characteristic dimensions, as schematically shown in Fig.9. In order to indicate the effect of the detached breakwater on sand deposition behind the breakwater, an index T_a is introduced, which is defined by the ratio of the area of formed tombolo ($\approx 0.5 l_i \bar{B}_i$) to the area of the original sea surface behind the breakwater ($= l \cdot Y$). Figure 10 shows the relations between the index T_a and the nondimensional parameters showing the breakwater

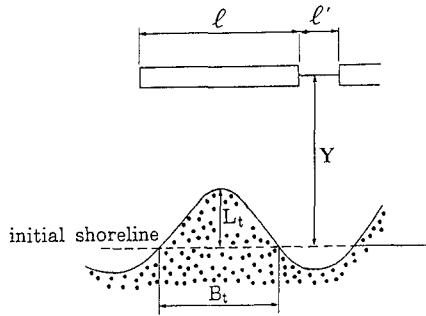


Fig.9 Characteristic dimensions of the detached breakwater (l : the breakwater length, l' : opening width, L_t : the tombolo length, B_t : the tombolo width, and Y : offshore distance.)

dimensions such as the ratios of the length to the offshore distance (l/Y) and of the relative water depth at the breakwater to the breaker depth (h'/h_b). The breaker depth was determined as follows. First, the data of the significant wave heights at each coast, measured in a typical year(1981), were ordered from the largest to the smallest. Secondly, the five largest data were selected and averaged to obtain a local reference wave height under relatively high wave conditions. This number of waves was selected since it seemed to be most significant in the discussion of stability and sand deposition under high wave conditions. Finally, the breaking depth was evaluated on the assumption that the ratio of the breaker height and the water depth at the breaking point is 0.78.

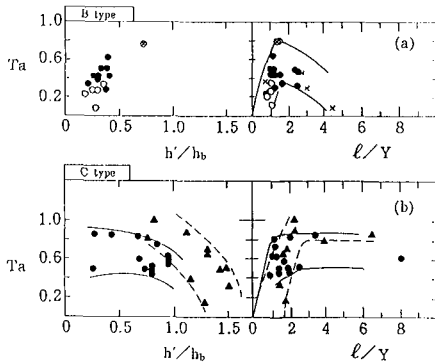


Fig.10 Relations among T_a , h'/h_b and l/Y . (The solid and open circles in (a) express the conditions of $l \approx 100m$ and $l \approx 150m$, respectively. The 'x' sign shows the other cases. The solid circles and triangles in (b) express the cases of the beach materials composed of sand and gravels, respectively.)

Figure 10 shows the relations among T_a , h'/h_b and l/Y on the coasts of type B (e.g., the Ishikawa Coast and the Niigata Coast) and type C (e.g., the Shimoniikawa Coast and the Suruga Coast), with additional classifications on the length of breakwaters and the kind of the beach materials. The solid and broken lines in the figure show the upper and lower limits of the data. The coasts of these two types were selected as typical coasts in Japan. Although the data were limited to the case of $h'/h_b < 1$ for the coasts of type B, T_a increase with h'/h_b under these conditions. The sand deposition effect due to the detached breakwaters improves with larger h'/h_b , and the relative scale of tombolo is larger when the location of the breakwater is closer to the breaking point. It was found that T_a takes the maximum value at $l/Y \approx 1.6$; that is, the relative area of the tombolo is maximized when $l \approx 1.6 Y$.

In the case of type C, the data are scattered compared with the data for type B. The value of T_a tends to decrease if $h'/h_b < 1$, which means that the relative area of tombolo decreases as the distance from the breaking point to the breakwater increases. As for the relation between T_a and l/Y , T_a appears to be maximum at $l/Y \approx 2.0$, and thereafter it remains constant in contrast with the decrease in the case of type B.

As described above, a tombolo is formed due to the sand deposition effect of detached breakwaters, if various conditions are satisfied. The formation of a tombolo behind the breakwater is normally considered to be a favorable effect. On the contrary, the retreat of the shoreline facing openings can be caused by the construction of the detached breakwaters. This sometimes causes serious problems such as wave overtopping over the revetment behind a detached breakwater and/or the scouring at the foot of the revetment, when the original foreshore is narrow. Figure 11 shows the relations between the change in the shoreline facing the openings and the dimensions of detached breakwaters on the basis of the field data. Three dimensionless parameters l'/l , l'/Y and l/Y were selected to indicate the breakwater dimensions, where l' , l and Y are the opening width, the breakwater length and the offshore distance, as illustrated in Fig.9. For the detached breakwaters built on the Japan's coasts, the ratios of the opening width to the length concentrate to certain values, so that the data are plotted separately for different l'/l values. In Figs.11 (a) to (c), the effect of each parameter is shown without regard to the other parameters. Let us consider the case of $l'/l \approx 0.3$ for example. In Figs.11 (b) and (c), l'/Y and l/Y are respectively taken in abscissa. Between these variable, the following relations hold:

$$l/Y = l/Y \cdot l'/l \approx 0.3 l'/Y \quad (1)$$

Consequently, Figs.11 (b) and (c) give the similar result. In the case of $l'/l \approx 0.3$, shoreline facing the openings of detached breakwaters always advance regardless of l'/Y . The tendency changes as l'/Y approaches to 2; that is, if the offshore distance of the breakwater approaches to one half

of the breakwater length.

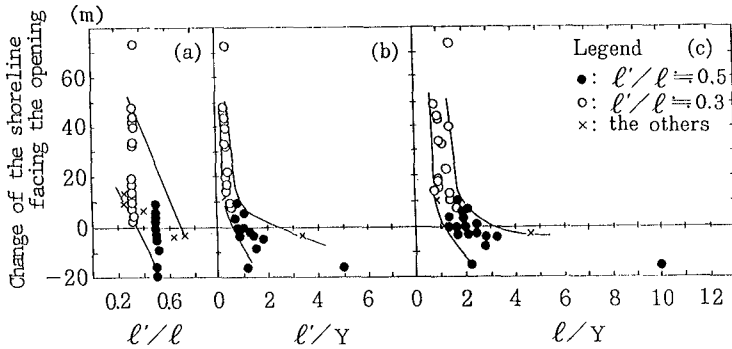


Fig.11 Relations between the change in the shoreline facing the openings and the nondimensional parameters indicating breakwater dimensions.

In the case of $l'/l \approx 0.5$, the possibility of the retreat of the shoreline facing the opening becomes high in contrast with the case of $l'/l \approx 0.3$. The critical condition for the shoreline advance may also be given by $l/Y \approx 2.0$. In other words, the shoreline retreats under the condition of breakwater length, if the offshore distance Y is less than $0.5l$. As described above, the shoreline facing the openings may retreat depending on the breakwater dimensions. This is due to the fact that the breakwater construction causes the increase in the wave height at a opening and, therefore, in the littoral drift from the opening toward the lee of the breakwater.

The second function of the detached breakwater is to dissipate the incident waves. This function can be discussed through the investigation of wave transmission coefficient. For the evaluation of the wave transmission coefficient K_T , the following formula has been proposed (Numata, 1975).

$$K_T = 1 / \{1 + 1.135(B_h/D)^{0.66} \cdot (H_i/L_i)^{0.5}\}^2 \tag{2}$$

where B_h is the mean width of the breakwater at the still water level, D is the height of a concrete block, H_i is the incident wave height and L_i is the incident wave length. Equation (2) holds only if the elevation of the crown of detached breakwater above the sea level is higher than the incident wave height.

The validity of the formula is examined by using the field data obtained through field investigations conducted on three coasts: namely, the Shimoniiikawa Coast, the Niigata Coast and the Enshu Coast. As shown in Fig.12, the average of the field data can be predicted fairly well by use of Eq.(2) if $H_i/L_i > 0.02$, whereas K_T is underestimated if the wave steepness is smaller than 0.02.

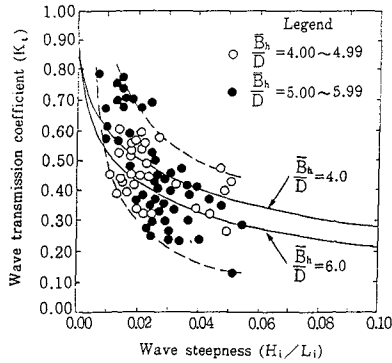


Fig.12 Comparison of the measured and predicted wave transmission coefficients.

3.3 Scattering of concrete blocks

Figure 13 shows the scattering rate, i.e., the ratio of the number of the breakwaters that suffered the scattering of concrete block to the total number of the breakwaters on the coasts of types A through E. The overall average scattering rates is 14.2%. The scattering rate of the coasts of type A is low compared with the others. This may be because the wave height is usually low in a bay and in an inland sea and consequently the wave forces acting on the concrete blocks and the changes in the beach topography caused by scouring around the blocks are small. On the other hand, the scattering rate for the coast of type D is as high as 52.9%. The scattering of concrete blocks on the coasts of this type was reported in the preceding paper (Kohno et al., 1986). Several reasons can be raised for this. First, on the Fuji Coast, incident waves tend to act on the concrete blocks without large attenuation, since the bottom slope is steep (1/3-1/10). The second reason is that strong wave actions cause the severe topographical changes around breakwaters.

The scattering rate of the concrete blocks is related to the various parameters characterizing breakwaters. Here,

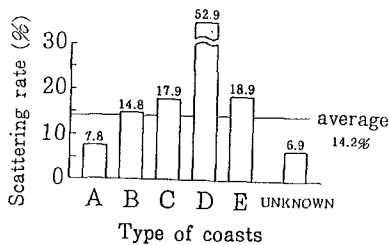


Fig.13 Scattering rate for the coasts of each type.

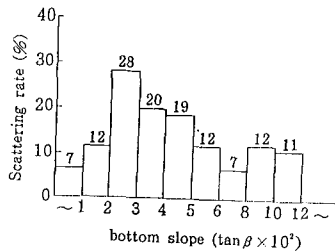


Fig.14 Scattering rate versus bottom slope.

three parameters are considered: the bottom slope, the water depth at the breakwater and the offshore distance. Figure 14 describes the relation between the scattering rate and bottom slope. The scattering rate has a maximum value of 28% for the bottom slope of 0.02-0.03, and it decreases for steeper beach slope, although it is expected that the steeper beach slope always causes the higher scattering rate. On mildly sloping coasts, the beach material is usually fine sand, and the bar-trough topography is easily formed. The instability associated with the subsidence of the blocks and the scouring around the blocks can be the main reason of serious scattering.

The scattering rate depending on the water depth is shown in Fig.15. The scattering rate tends to increase with the water depth, fluctuating in the range from 6 to 27%. This is due to the fact that the concrete blocks are scattered by the action of breaking waves. The breaking point gets closer to the location of the breakwater under storm wave conditions. The high scattering rate at the depth of 6-7m is doubtful, because only 41 breakwaters fall in this range as shown in Fig.2 (b). In this view, there might be a tendency that the scattering rate decreases as the water depth exceeds 5m.

Similarly, the scattering rate depending on offshore distance is plotted in Fig.16. The offshore distance less than 120m are divided into 20m intervals, while those greater than 120m are divided into 40m intervals. The scattering rate increases with the offshore distance up to 100m, and then tends to decrease. High scattering rates were measured at offshore distance between 80 and 120m possibly because the locations of the detached breakwaters are close to the breaking points.

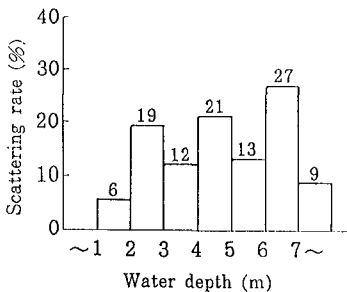


Fig.15 Scattering rate versus water depth.

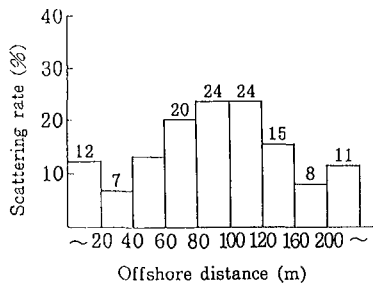


Fig.16 Scattering rate versus offshore distance.

The scattering rate was also investigated in relation with the weight of the concrete blocks. For this purpose, the ratio of the actual weight of the block to the weight calculated from the Hudson formula is introduced, where the design wave height is assumed to be equal to the water depth multiplied by 0.78, namely, the breaking wave height. The distribution of the number of the breakwaters that suffered

the scattering and the distribution of the scattering rate are shown in Figs.17(a) and (b). The largest number of the detached breakwaters appears in the interval where actual weight-calculated weight ratio is 1.1-1.2. A high scattering rate is observed when the actual weight is smaller than the calculated weight multiplied by 1.1, and the scattering rate tends to decrease as the ratio of the actual to the calculated weight increases. The extent of scattering was relatively small for majority of the breakwaters with concrete blocks heavier than 1.5 times the calculated weight. If the scattering rate is re-investigated excluding the cases with small extent of scattering, the scattering rate reduces to 3.1% as shown in Fig.17(b). Effective preventive measures against scattering is the use of the concrete blocks whose weight is at least 1.5 times as large as that calculated from the Hudson formula. A firm foundation such as a rock mound is also effective.

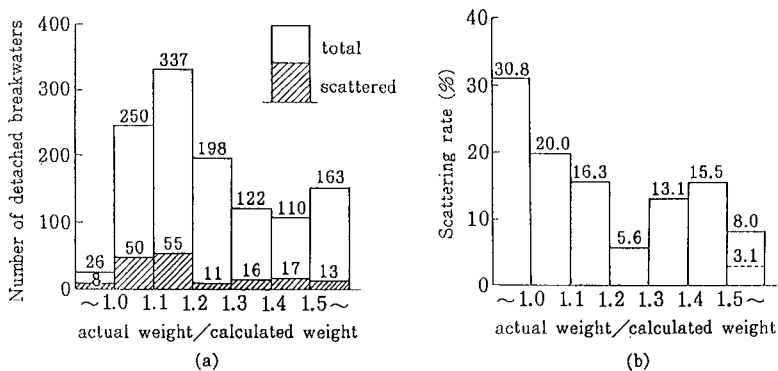


Fig.17 Number of scattered breakwaters and the scattering rate in relation with the weight of the concrete blocks.

Finally, the scattering rate of the concrete blocks is studied in relation with the kind of block placing, the foundation performance and the subsidence of the blocks. According to the preliminary investigation of the relation between the scattering rate and the kind of placing, the pellmell and uniform placings resulted in 19.5% and 11.0% scattering respectively. In studying the scattering of concrete blocks, it is important to consider the combined effects of the kind of placing and foundation performance as shown in Fig.18. The scattering rates in the cases of pellmell and uniform placings are almost the same if a foundation exists. Without foundations, however, the scattering rate in the case of pellmell placing becomes 18%, which is much larger than 8.5% in the case of uniform placing; the extent of scattering is greatly influenced by the kind of block placing. The influence of subsidence on the scattering of blocks is shown in Fig.19. The scattering rate for the breakwaters that subsided due to waves is 17.9%, which is nearly twice as large as the rate 9.4% for the breakwaters without subsidence.

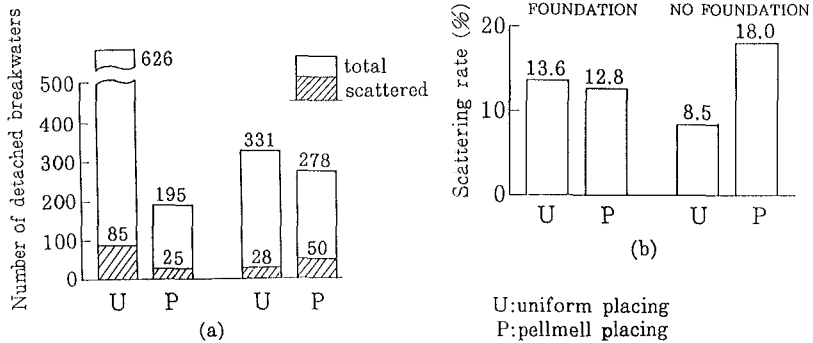


Fig.18 Combined effects of the kind of placing and the foundation performance on the scattering rate.

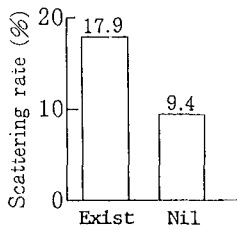


Fig.19 The scattering rate depending on the subsidence of concrete blocks.

IV. CONCLUSIONS

The dimensions of the detached breakwaters were statistically analyzed on the basis of the survey of 1552 breakwaters constructed by 1982. The main conclusions of this study are summarized as follows:

1) The optimal of a detached breakwater was evaluated for sand deposition behind the breakwater as well as the critical conditions for advance of the shoreline facing a breakwater opening.

2) The wave transmission coefficient to be used for prediction of the wave height distribution behind the breakwater can well be estimated by the formula given by Numata.

3) The scattering of concrete blocks was found in 13.7% of all the breakwaters surveyed.

4) The ratio of the number of the breakwaters that suffered scattering to the total number of the breakwaters on each coast takes the maximum value, when the bottom slope, the depth at the breakwater, and the offshore distance of the breakwater are equal to 0.02-0.03, 4-5m and 80-120m, respectively.

5) A high scattering rate appears when the actual weight of concrete blocks is smaller than 1.1 times the

weight calculated from the Hudson formula. The scattering rate reduces to 3.1% when concrete blocks heavier than 1.5 times the calculated weight are used.

6) The scattering rates of concrete blocks were 19.6% and 11.6% for the cases of pellmell and uniform placings. The scattering rate does not significantly depend on the kind of block placing, if a foundation is constructed. Otherwise, the scattering rate in the case of pellmell placing is more than twice as high as that in the case of the uniform placing. The extent of scattering is particularly influenced by the kinds of block placing in the case of detached breakwaters without foundation.

REFERENCES

- Kohno, H. , T.Uda and Y.Yabusaki (1986): On the scattering of concrete armor units of detached breakwaters due to waves, Proc. 20th Inter. Conf. on Coastal Eng., ASCE, pp.1972-1986.
- Numata, J. (1975) : Experimental study on wave dissipating effect of the breakwater composed by concrete armor units, Proc. 22nd Japan. Conf. on Coastal Eng., JSCE, pp.501-505.(in Japanese)
- Seiji, M. , T.Uda , and S.Tanaka (1987) : Statistical study on the effect and stability of detached breakwaters, Coastal Eng. in Japan, Vol.30, No.1, pp.131-141.

CHAPTER 151

Design aspects of block revetments

K.W. Pilarczyk*

1. Introduction

The increasing shortage and costs of natural materials in certain geographical areas has resulted in recent years, inter alia, in the rapid development of artificial (concrete) block revetments.

In general, two main types of revetments can be distinguished: permeable (stone pitching, placed relatively open block-mats) and (relatively-) impermeable (closed blocks, concrete slabs). Regarding the shape and/or placing technique a distinction can be made between: a) free (mostly rectangular-) blocks and b) interlocking blocks of different design (tongue-and-groove connection, ship-lap, cabling, blocks connected to geotextile by pins etc.).

In all these cases the type of sublayer (permeable/impermeable) and the grade of permeability of the toplayer are very important factors in the stability of these revetments. The design also needs to be made (executed) and maintained. Both aspects must therefore already be taken along within the stadium of designing.

At the moment there is a large variety of types of revetment-blocks and other defence systems (i.e. block-mats), see Fig. 1. Until recently no objective design-criteria were available for most types/systems of blocks. The choice (type and size) of the revetments built so far is only based on experience and on personal points of view, sometimes supported by small-scale model investigations.

In the light of new (stricter) rules regarding the safety of the Dutch dikes, as they have been drawn up by the Delta-Commission, the need for proper design-criteria for the revetments of dikes has evidently grown.

Because of the complexity of the problem no simply, generally valid mathematical model for the stability of the revetment are available yet. For restricted areas of application however, fairly reliable criteria (often supported by large-scale tests) have been developed in the Netherlands not only for the kind of revetment, but also for conditions of loads. This new approach is discussed in (Klein Breteler, 1988).

This paper presents a short state-of-the-art review of existing knowledge on the designing of different types of revetments and, where ever possible, the available stability criteria are mentioned. There is also given some comparison of the different types of revetments with their advantages and disadvantages and suggestions regarding their practical application.

2. Design requirements

In the design process of revetments, besides the specific functional requirements, the following technical aspects have to be taken under consideration:

*) Head Research & Development, Hydraulics and Geotechnics. Rijkswaterstaat, Road and Hydraulic Engineering Division, P.O. Box 5044, 2600 GA Delft, The Netherlands

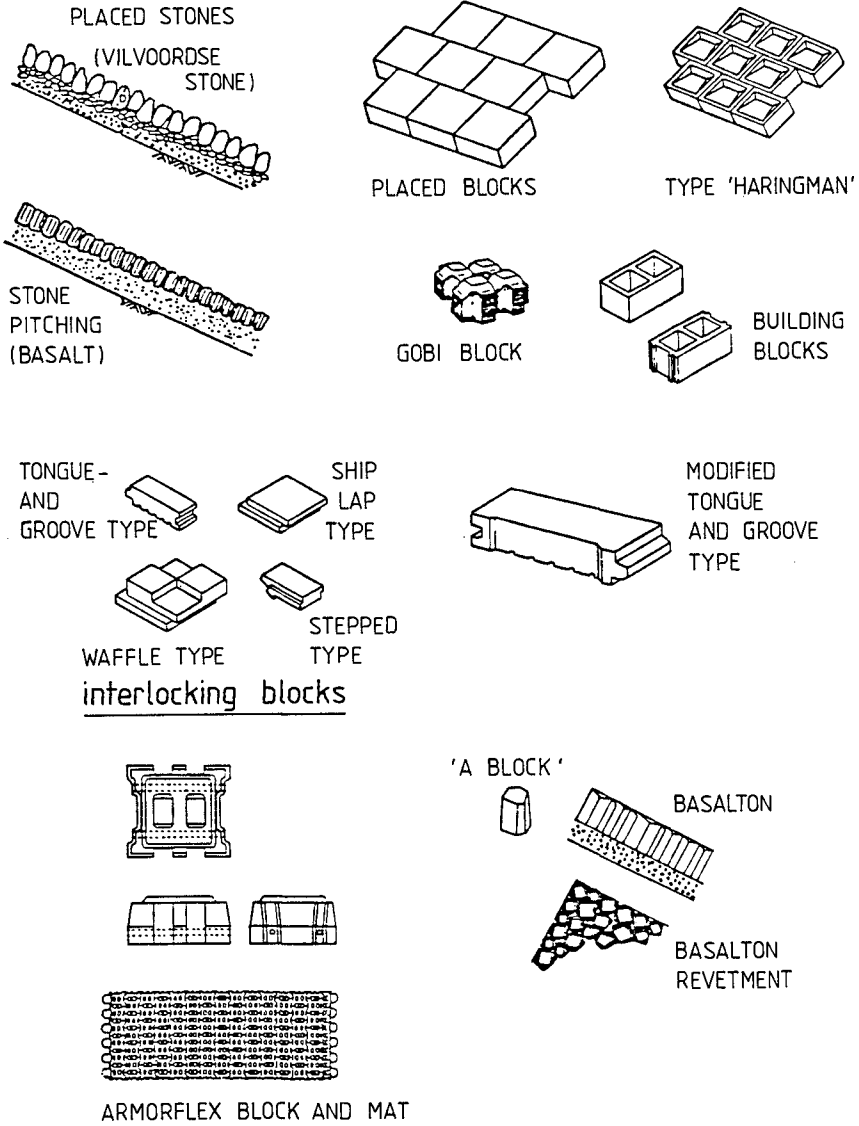


Figure 1. Examples of blocks tested on large scale

- stability (toplayer, sublayers, subsoil)
- flexibility
- durability (toplayer/concrete, geotextile, cables etc.)
- possibility of inspection of failure (monitoring of damage)
- low cost (construction/maintenance)

The best revetment is one which combines all these functions. Some of the aspects mentioned above will be discussed successively.

3. Stability criteria ("black-box" approach)

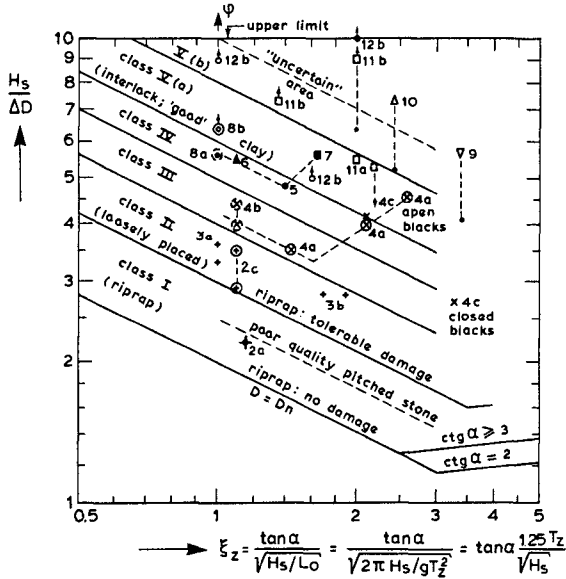
The total strength of a stable toplayer can be regarded as the sum of the contributions of different strength factors i.e. the static weight of the toplayer, the friction forces on the interface of adjoining elements, the jamming forces induced by sand or other granular materials in the voids/interspases between adjoining elements. The toplayer is unstable when the hydraulic loads exceed the stabilizing forces. Hydraulic loads are created by waves inducing time dependent pressures on the toplayer, that are transmitted to the sublayers causing pressure differences across the toplayer, that tend to lift blocks from the revetment. These pressure gradients cause also watermotions in the sublayers that endanger the internal stability of these granular layers or the stability of the interface between successive sublayers, causing a gradular deformation which may affect the stability of the toplayer. When the hydraulic loads (uplift pressures) exceed the stabilizing forces than the additional strength factors are mobilized to prevent damage to the toplayer i.e. inertia forces of the block and the water underneath, and pressure fall under the block to enable the inflow of water in the growing space between the moving element and the sublayers. For relatively smooth block revetments and for openings-percentage smaller than 10%, the drag forces are neglectable, and the (in-)stability of the block revetments is mainly influenced by the uplift forces. These uplift forces are directly dependent on the composition (hydraulic permeability) of the sublayers. That means also that the stability of the block revetments can not be treated separately from the sublayers and/or subsoils.

This last remark (conclusion) has very important practical consequences, namely:

- results from the small-scale model have limited value for practical application because these models are not able to reproduce the prototype sublayers and subsoils (the scaling rules are still not properly known); this explains also a large scatter in the results from the small-scale models,
- "black-box" approach (even based on a large-scale data) has limited value and should be applied with caution; in the black-box approach all the forces discussed above are integrated to one strength number - the changing of the composition of revetment (i.e. permeability of toplayer or sublayer) may strongly affect the total stability which is difficult to deduce from the black-box stability numbers,
- the problems mentioned above can be overbridged by applying the mathematical models as being recently developed in the Netherlands (Klein Breteler, 1988).

For the rough (first) approximation of the necessary dimensions of block revetments the following "black-box" model is being developed by Pilarczyk (1987) (PIANC, 1987) (see Fig. 2):

$$\frac{H_s}{\Delta D} = \psi \cdot \frac{\cos \alpha}{\sqrt{\xi_z}} \approx \psi \cdot \xi_z^{-0.5}$$



Note :

⊙ - no damage appeared

Δ¹⁰ - numbers refer to table

⊖ - possible replacement due to translation to irregular waves

D - block thickness
D = D_n for riprap

$$D_n = \left(\frac{M_{50\%}}{\rho_s} \right)^{1/3}$$

M_{50%} = average mass of stone

ρ_s = density of stone

H_s - significant wave height

T_z - average wave period

tan α - slope gradient; ctg α ≥ 2

ψ - strength coef. defined at ξ_z = 1

ξ_z - breaker similarity parameter

$$\frac{H_s}{\Delta D} = \psi \frac{\cos \alpha}{\sqrt{\xi_z}} \approx \frac{\psi}{\sqrt{\xi_z}} \quad (\text{assumed function})$$

ξ_z < 3 (breaking waves)

Figure 2. Classification of strength of block revetments

for $\xi_z < 3$ (breaking waves) and $\text{ctg}\alpha > 2$

$$\text{and } \xi_z = \frac{\tan\alpha}{\sqrt{H_s/L_0}} = \tan\alpha \frac{1.25 T_z}{\sqrt{H_s}} \text{ (breaker index)}$$

where: $H_s/\Delta D$ = strenght parameter, H_s = significant wave height, α = slope angle, T_z = average wave period, D = thickness of block, $\Delta = (\rho_s - \rho_w)/\rho_w$, relative density of block and ψ = stability factor. For riprap $D = D_{n50} = (W_{50}/\rho_s)^{1/3}$, ($W_{50} = 50\%$ by mass). For $\xi_z > 3$ the constant $H_s/\Delta D$ - value in $\xi_z = 3$ can be kept safely (N.B. for some types of block revetment the $H_s/\Delta D$ - values can increase a lot when ξ_z is large).

Note: The results of the recent large-scale tests (1987) indicated that the stability of the loosely placed blocks (cat. II), placed on the granular sublayer, can be approximated better by (Fig. 3):

$$\frac{H}{\Delta D} = \frac{\psi}{\xi_z} \quad (1 < \xi_z < 5 \text{ and } \text{ctg}\alpha > 2)$$

where: $\psi = 3.5$ - for less permeable (closed) blocks, and
 $\psi = 4.0$ - for relatively permeable blocks
 (open area 5 - 20%)

The open blocks have more reserve-stability than closed blocks; the $\psi = 5$ value can be applied as an upper-limit (tolerable movement of blocks).

In the case of frequent double-top storms it has to be advised to reduce the $H_s/\Delta D$ - values with 25% because of the long-term effect of loading.

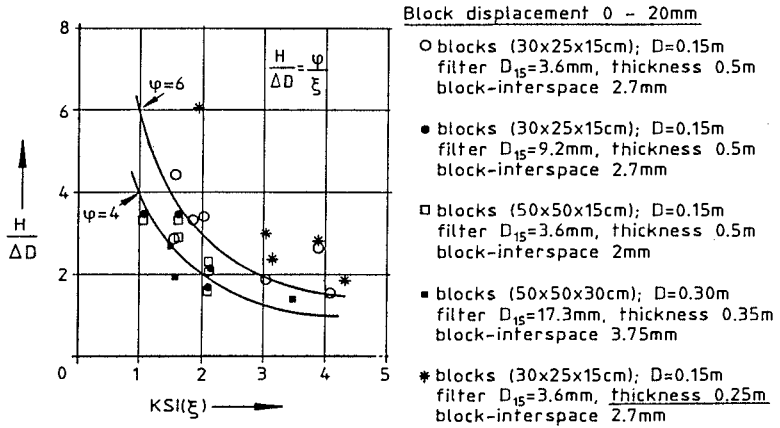
This model works rather well for riprap on relatively impermeable core (i.e. sand) and it also gives a good approximation for some block revetments. By using this model the strength of various types of block revetments can be directly compared to the strength of riprap revetments.

Stability factor (ψ) has been determined empirically. In view of the problems on the translation of the results of small-scale models into prototype, only the large-scale tests have been taken into account (Fig. 1). The results of this have been summarized below (ψ is defined at $\xi_z = 1$):

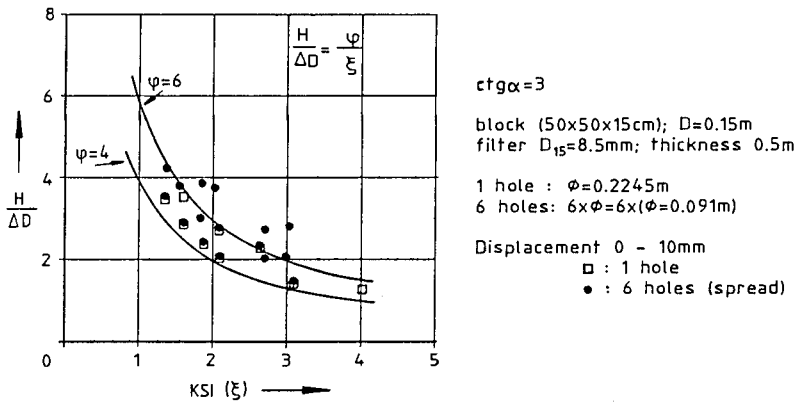
- I : $2 < \psi < 3$ riprap (2 layers) $N < 3000$ waves; $\psi = 2$ denotes "no-damage" and $\psi = 3$ denotes max. "tolerable damage"
- II : $3 < \psi < 4$ pitched stone, loose placed blocks, blocks connected by geotextile
- III: $4 < \psi < 5$ blocks interlocked by friction, grouted blocks connected by geotextile, cabled blocks
- IV : $5 < \psi < 6$ loose blocks directly on "good clay"
- V : $6 < \psi$ grouted (cabled-) blocks, mechanically interlocked blocks.

Remarks:

- 1 The upper and lower limits within a category are generally dependent on the quality of design and construction,
- 2 Filter requirements of the soil have to be met by the geotextile and/or granular sublayer,
- 3 Blocks placed directly on geotextile and well-compacted sand: max $H_s = 1.2$ m,
- 4 "Good-clay" = according to requirements given in the Guidelines (CUR/TAW, 1984) and smooth surface (no cavities),



a) Stability-function for closed-block revetments



b) Stability-function for open-block revetments

Figure 3. Stability-criteria for loosely placed blocks (1987).

- 5 Cat. V ($\psi \geq 6$) must be carefully designed and examined especially regarding the stability of sublayers (large scale check of design is recommended),
- 6 Because of practical reasons the block thickness less than 10 cm is not recommended (for cabled blockmats 8 cm).

4. Composition of construction

There is a large number of different types of toplayer, sublayer and subsoil and, it is obvious, that there are many possible combinations that can lead to a large number of possible constructions. This does not simplify the choice of a revetment. Some possible aspects and solutions that can play a part in the choice of the construction of the revetment are mentioned below.

- Stability of top-layers strongly depend on the sort/composition of sublayers and they must therefore be regarded as a whole. As an example, from the large-test results it appears that a block revetment on a sublayer of "good clay" provides more stability than one on a permeable sublayer.
- Instability (erosion) of sublayers and/or subsoil can lead to failure of a toplayer. The stability of top-layers and sublayers must therefore be designed steadily (with an equal opportunity of failure).
- A good tuning of the permeability of the toplayer and sublayers (including geotextiles) is an essential condition for an equal design. The permeability (k) of the different parts of the construction must increase from underneath to top: k , ground $<$ k , sublayer $<$ k , toplayer.

The strength of revetment increases with increasing the permeability of the toplayer and decreasing the permeability of the sublayer. Moreover, a thin permeable sublayer, reduces the uplift forces, but increases the internal gradients (the internal stability of the sublayers decreases).

- The granular filters are mostly expensive and difficult to realize (especially under water) within the filter-requirement limits. A substitutional solution is a geotextile (filter function) with a certain thickness of graded stone layer (with function to dump the internal hydraulic loads). A good and cheaper solution can also be realized by applying a thick layer of broadly graded waste products as minestone, slags, silix, etc. (well compacted).
- The use of blocks directly on sand-body (with geotextile in between) is restricted, at the present state of knowledge, to wave height of $H_s = 1.2$ m. The good compaction of sand is essential to avoid sliding or even liquefaction. For loads higher than $H_s = 1.2$ m a well graded layer of stone on a geotextile is recommendable (e.g. layer 0.2-0.3 m for $1.2 \text{ m} < H_s < 2.5 \text{ m}$).
- For placement of blocks directly on clay subsoil/sublayer, besides the requirement of right composition and homogeneity, the proper compaction and smooth surface (blocks placed as close as possible to the clay surface) are of primarily importance (CUR/TAW, 1984). In the case of "poor clay" (concerning composition and/or surface preparation) it should be recommended to protect the clay-surface by a multilayer (non-woven) geotextile and to use a lower value of ψ (i.e. $4 < \psi < 5$).
- The stability of (real) loose blocks is rather low ($\psi \approx 3$). The strenght of these blocks can be increase by introducing of the clenching forces between blocks, caused by friction and wash-in-material, or interlocking.
- The main advantage of applying block-mats and/or interlocked systems are:

- in general, higher stability of toplayer
 - mechanical placement (also from water side)
 - and the main disadvantages (or uncertainties):
 - durability/damage of binders (cables, pins, etc.)
 - less flexibility and inspection problems in respect to failure sub-layer
 - repair problems (especially under water)
 - connection of adjoining mats (especially under water)
- Many of these problems will be omitted if the sublayer is designed properly.

Although the grouting of these systems (i.e. grouting/ washing in by fine broken stones) decreases the flexibility, it can be helpful for some reasons.

- Disadvantages of non-grouted systems:
 - individual blocks can move (less stability of toplayer)
 - cables/pins loaded more frequently
 - abrasion of geotextile
 - erosion sublayer/subsoil can take place more easily
- Advantages of grouted (blinded) systems:
 - higher stability of toplayer (no movement of individual blocks)
 - if (at heavy attack) the mat will be lifted out, then there is less loading of cables/pins and interlocked-elements, and less abrasion of geotextile, because such mat will move as integral unit.
- Not every system can be grouted; if the interspaces between the blocks are too large, the grouting material will be easily washed out. In this respect the basalt-system (grouted but not cabled - see Fig. 1) has more advantages than other systems, because of the tapered vertical form and lack of cabling, the blocks can still follow a limited settlement, the settlement is immediately evident, and a washing out of grouting material is limited.
- Erosion or damage often starts at joints and transitions. Therefore, an important aspect of revetment construction, which requires special attention, are the joints and the transitions; joints onto other revetments materials, and transitions onto other revetment parts or other structures. If they are inevitable the discontinuities introduced should be minimized. This holds for differences in elastic and plastic behaviour and in the permeability of the sand tightness. Proper execution is essential in order to obtain satisfactory joints and transitions.

5. Conclusions

- Stability of block revetments strongly depend on the sort and composition of toplayers and sublayers and they must be regarded and treated as a whole.
- Because of scaling problems of sublayers the small-scale models are not suitable for investigation of stability problems of revetments.
- The value of "Black-Box" approach based on large scale tests is mainly limited only to the construction tested; the extrapolation to other compositions of construction involves many uncertainties.
- The "Black-Box" model as presented in this paper can be applied only for the rough (first) approximation of necessary dimensions of revetments.
- For detail design and/or more complicated cases the mathematical model as developed in the Netherlands (Klein Breteler, 1988) or large scale tests are recommended.
- Whatever calculation method and protective system is adapted, (local) experience and sound engineering judgement play on an important part in a proper design of protective structures.

The research on dike protection and other coastal defence systems is still going on in the Netherlands. Research is now being directed towards a better probabilistic description of the design, better understanding of the failure mechanisms, application of new or alternative materials, monitoring of damage, economical aspects of design and optimal choice of constructions applied incorporating future maintenance aspects.

6. References

- (1) CUR/TAW (1984). Guide to concrete dike revetments. Netherlands Centre for Research, Codes and Specification for Concrete (CUR) and Technical Advisory Committee on Water Defences (TAW), Report 119 (English version available).
- (2) BURGER, A.M., et al. (1988). Design method for block revetmen, 21st Internat. Conf. on Coastal Engineering, Torremolinos, Spain.
- (3) PIANC, PTC I, W.G.4 (1987). Guidelines for the design and construction of flexible revetments incorporated geotextiles for inland waterways.
- (4) PILARCZYK, K.W. (1987). Sea Defences: Dutch Guidelines on Dike Protection. Rijkswaterstaat, Road and Hydraulic Engineering Division, The Netherlands, Report WB-NO-87 110, April 1987.

No. Reference	Toplayer	Sublayer	Slope ctgr	$\frac{H_s}{\Delta D}$	ϵ_z	$\psi = \frac{H_s}{\Delta D}$ $\epsilon_z = 1$	Class	
1a M1983 1b WL Pub No. 332, 1984	Riprap - no damage "Tolerable" Riprap-damage	L L	Cr granular filter thick 2D50	2:6	full D = Dn	range 3.0	I ref.	
2a M2036 2b Sollitt 2c M2036 3a M1795 3b M1881-IX	Vilvoordse (pitched) Pitched stone, D=Dn Pitched basalt Placed blocks Placed blocks	L L L L L	brick rubble crushed stone brick rubble gravel gravel	3.5 2 3.5 4+berm 3	2.20 2.80R 2.9+3.5 3.3+3.6 2.8	1.15 1.3+2.6 1.10 1.0 1.7+1.9	2.5 3.0 3.5 3.5 4	II
4a C.E.R.C. (US) 4b C.E.R.C. 4c M1881-XII	Gobi blocks + geo- tex.(open blocks) Open/building blocks Placed blocks (closed)	L L L	fine gravel, 40% 2mm coarse sand sand 0,4 mm/ geotextile sand 0,2 mm/ geotextile	3.5 5 3	3.5R 4.0R 4.55R 4+4.4R 4.16R 2.70R	1.45 2.10 2.60 4.5* 2.10 3.30	4.0 4.5* 5.0*	III
5 M1900 6 M2036 7 M1910 8a M1795	Basalton (basalt) Placed blocks (haringman) Armorflex-blocks Placed blocks	L O L L	crushed stone (silex) minestone + thin l. gravel crushed stone/ good clay with rough surface	3 3.5 3 4	4.80 5.50 5.60 5.60	1.40 1.10 1.65 0.95	5.0 5.5 5.5 5.5	IV
8b M1795 9 C.E.R.C. 10 C.E.R.C. 11a Oregon (US) 11b M1910 12a 12b	Placed blocks Ship-lap blocks Tongue-and groove "modified" (6 mm relief slot) Armorflex-mats (grouted) Armorflex blocks (grouted) Placed blocks with interspaces (grouted) Basalton (grouted)	L I I C+G G C C	good clay crushed stone crushed stone sand 0,5 mm/ geotextile crushed stone/ gravel gravel crushed/stone/ silex	4 2 2 3 3 3 3 3	6.40 5.71R 7.3R 5.30R 5.50 7.3 9.0R 7.0R 5.0R 10.0R 15.0R	1.00 3.40 2.43 2.20 2.00 1.35 2.00 1+2.5 1.60 1.30 2.00	6.0** 6 a 7 7 a 8 7 a 8 8.0 8.0 10.0	V

Note: L = loose placed blocks, O=old; natural reinforcement/interlocking (i.e. sand, grass)
G = grouted (blinded/chocked by gravel, silex, slags, crushed stone)
C = cabled, I=interlocked blocks (artificial); R = tests with regular waves
*) Blocks/mats directly on compacted sand + geotextile only for $H_s < 1.5$ m
**) 'Good' clay: proper composition, compaction and smooth surface acc. to criteria

CHAPTER 152

RELIABILITY ANALYSIS OF RUBBLE-MOUND BREAKWATERS

Kazumasa Mizumura*
Masato Yamamoto**
Taiji Endo***
and
Naofumi Shiraishi****

To verify the effect of wave period on the motion of concrete blocks in rubble-mound breakwaters, simple physical models are employed and their motion is investigated by the numerical simulation. Finally, risk or reliability are calculated and the weight of concrete blocks for given physical condition is discussed by them.

Introduction

In Japan, many kinds of concrete blocks have been used to protect coastal structures. The weight of concrete blocks is computed by Hudson's formula for given design wave height, density of concrete blocks and breakwater slope. However, the weak points of Hudson's formula are described as follows:

1. It does not contain the effect of wave period;
2. It includes an uncertain parameter K_D ;
3. Incident wave height is not constant, but probabilistic; and
4. Reliability or risk are not considered with this formula. It says only safe or not.

Especially, the item 1 has been pointed out by field engineers for a long time. To study the above points, we introduce simple physical models to express the incipient motion of concrete blocks and analyze the motion for given parameters and physical conditions which are governed by appropriate probabilistic laws. Finally, the risk is defined by the ratio of the number of concrete blocks moved to the total number of trials.

Stability Analysis of Concrete Blocks

The incipient motions of concrete blocks in the rubble-mound breakwater which frequently occur are classified into three: They are sliding, rocking and lift-up. To analyze the sliding motion of a concrete block, the sliding force f_s

*Professor of Civil Engrg. Dept., Kanazawa Inst. of Tech., 7-1, Ogigaoka, Nonoichimachi, Ishikawa Pref., 921, Japan.
Assistant Manager, *Director and ****President, Nippon Tetrapods Co., Ltd., 2-7, Higashinakanukicho, Tsuchiura, Ibaraki Pref., 300, Japan.

and the resistance force f_R are expressed by referring Fig.1(a).

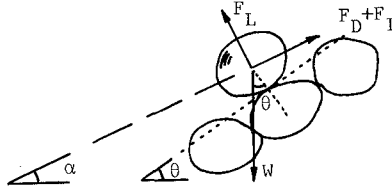


Figure 1(a). Motion of a Concrete Block

$$f_s = \epsilon_1[(F_D+F_I)\cos(\alpha-\theta)+F_L\sin(\theta-\alpha)] - \frac{\rho_s-\rho_w}{\rho_s} W \sin \theta \tag{1}$$

$$f_R = \left[\frac{\rho_s-\rho_w}{\rho_s} W \cos \theta - \epsilon_1 F_L \cos(\alpha-\theta) + \epsilon_1 (F_D+F_I) \sin(\theta-\alpha) \right] \mu \tag{2}$$

in which $F_D = \rho_w C_D (c_2 \ell^2) u |u| / 2$, (drag force); $F_I = \rho_w C_M (c_3 \ell^3) du/dt$, (inertia force); $F_L = \rho_w C_L (c_2 \ell^2) u^2 / 2$, (lift force); C_D = the drag coefficient; C_L = the lift coefficient; C_M = the virtual-mass coefficient; ρ_w = the water density; ρ_s = the density of a concrete block; θ = the repose angle of a concrete block; α = the angle of the breakwater slope makes with the horizontal; ℓ = a characteristic length of a concrete block; $c_1 \ell$ = the distance from the point of support of the center of gravity of the block; $c_2 \ell^2$ = the projected cross-sectional area of the block on a plane perpendicular to the direction of the velocity; $c_3 \ell^3$ = the volume of the block; μ = the friction coefficient; ϵ_1 = the sheltering coefficient for sliding motion; and W = the weight of the concrete block. The reason why the direction of the drag and the inertia forces on concrete blocks is upward along the slope is explained as follows: Since the force due to the interlocking effect among concrete blocks is not able to be easily computed, we assume that concrete blocks do not slide down against the interlocking effect. The dropping movement of concrete blocks is observed to be caused soon after the rocking, sliding or lift-up motions of concrete blocks by the experiments. Most of the movement of concrete blocks is produced by the rocking motion. In the rocking motion (Fig.(b)), the sliding and the resistance motion M_s

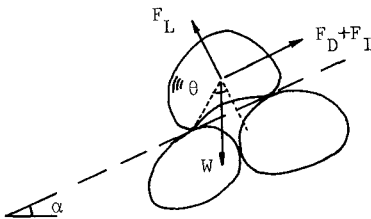


Figure 1(b). Motion of a Concrete Block

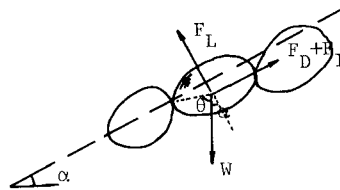


Figure 1(c). Motion of a Concrete Block

and M_R about the contact point of a concrete block for the condition of incipient motion are given (Walton et al. 1981) by,

$$M_R = \frac{\rho_s - \rho_w}{\rho_s} c_1 \ell W \sin\theta \cos\alpha \quad (3)$$

$$M_s = \varepsilon_2 [(F_D + F_L) c_1 \ell \cos\theta + F_L c_1 \ell \sin\theta] + \frac{\rho_s - \rho_w}{\rho_s} c_1 \ell W \cos\theta \sin\alpha \quad (4)$$

in which ε_2 = the sheltering coefficient for the rocking motion. In the lift-up motion, the lift force f_L and the normal component of the weight to the slope f_w are expressed as L (see Fig.1(c)):

$$f_L = \varepsilon_3 [(F_D + F_L) \sin(\alpha + \theta - \frac{\pi}{2}) + F_L \cos(\alpha + \theta - \frac{\pi}{2})] \quad (5)$$

$$f_w = \frac{\rho_s - \rho_w}{\rho_s} W \cos(\frac{\pi}{2} - \theta) \quad (6)$$

in which ε_3 = the sheltering coefficient for the lift-up motion.

Movability Condition of Concrete Blocks

It is not certain that the geometrical position of concrete blocks is similar to the proposed ones in the stability analysis. We define a word "movability" when concrete blocks are in the same condition as the proposed state in the stability analysis. To connect the movability condition with the stability analysis, the following assumptions are introduced:

1. The occurrence position of a concrete block which has the movability condition is uniformly distributed from the breakwater bottom to 90% of the significant wave height above the still water level along the breakwater face;
2. The number of the concrete blocks with the movability condition per one wave is k ; and
3. The movability condition of concrete blocks continues for n_i wave cycles for $i=1$ to k .

We consider that the process (2) and (3) are very analogous to service problems in the queueing theory. So the integers k and n_i for $i=1, 2, \dots, k$ are probabilistic variables and described by the Poisson process as follows:

$$p(k) = \frac{\exp(-\lambda) \lambda^k}{k!} \quad (7)$$

$$p(n_i) = \frac{\exp(-\lambda') \lambda'^{n_i}}{n_i!} \quad (8)$$

in which λ and λ' = parameters to govern the Poisson process.

Risk and Reliability

To calculate the risk or the reliability of the rubble-mound breakwater, let us define new variables R_s , R_r and R_ℓ as follows:

$$R_s = f_R - f_s \quad (9)$$

$$R_r = M_R - M_s \quad (10)$$

$$R_\ell = f_w - f_L \quad (11)$$

The variables on the right side in the above equations are derived in the stability analysis. The probability density functions $f(R_s)$, $f(R_r)$ and $f(R_\ell)$ are computed by the Monte Carlo method for given probabilistic variables. The failure probability or the risk of each concrete block is expressed by

$$P_s = \int_{-\infty}^0 f_s(R_s) dR_s \quad (12)$$

$$P_r = \int_{-\infty}^0 f_r(R_r) dR_r \quad (13)$$

$$P_\ell = \int_{-\infty}^0 f_\ell(R_\ell) dR_\ell \quad (14)$$

The reliability is shown as the difference of the risk from 1. Thus, if these three motions are assumed to be independent, the occurrence probability of motion for i -th block in the breakwater slope is given by

$$P_e(i) = P_s + P_r + P_\ell - P_s P_r - P_r P_\ell - P_\ell P_s + P_s P_r P_\ell \quad (15)$$

The whole failure probability of the rubble-mound breakwater P_w is obtained by computing the failure probability of union set for the failure probability of each block $P_e(i)$ as follows:

$$P_w = 1 - \prod_{i=1}^m [1 - P_e(i)] \quad (16)$$

in which m = the number of concrete blocks per unit width. Since the motions treated in the stability analysis are incipient, it is reasonable to assume that the motion of each block is independent in the above derivation.

Wave Conditions

The probability density functions of wave height and period are given by

$$P_{H/\bar{H}} = \frac{\pi}{2} \left(\frac{H}{\bar{H}} \right) \exp \left[-\frac{\pi}{4} \left(\frac{H}{\bar{H}} \right)^2 \right] \quad (17)$$

$$P_{T/\bar{T}} = 2.7 \left(\frac{T}{\bar{T}} \right)^3 \exp \left[-0.675 \left(\frac{T}{\bar{T}} \right)^4 \right] \quad (18)$$

in which \bar{H} = the mean wave height and \bar{T} = the mean wave

period. The cumulative distributions of the wave height and period are obtained by integrating Eqs.(17) and (18). The significant wave height and period are expressed by using the mean wave height and period, respectively.

$$H_{1/3} = 1.60 \bar{H} \quad (19)$$

$$T_{1/3} \approx 1.1 \bar{T} \quad (20)$$

In the sampling process, the waves satisfying the following condition are removed as the breaking waves before they reach the breakwater slope:

$$H/L \geq 0.142 \quad (21)$$

The condition the wave does not break on the breakwater slope is given by

$$\frac{H}{L} \leq \sqrt{\frac{2\alpha}{\pi}} \frac{\sin^2 \alpha}{\pi} \quad (22)$$

For the nonbreaking waves the shallow water theory gives the flow velocity and the acceleration

$$u = \sqrt{\frac{g}{h}} \frac{H}{2} \sin \sigma t \quad (23)$$

$$\frac{du}{dt} = \frac{g\pi H}{L} \cos \sigma t \quad (24)$$

in which H = the wave height; h = the water depth; $\sigma = 2\pi/T$; T = the wave period; and L = the wave length. The exerted force on a concrete block due to the wave breaking p_m is calculated by Goda's formula (Iwagaki & Sawaragi, 1979). The total force P_m exerted on the concrete block is given by

$$P_m = c_2 \ell^2 p_m \quad (25)$$

In this case it is assumed that the drag force F_D has a uniform distribution between 0 to P_m . In the stability analysis, the inertia force is neglected and the lift force F_L is transformed by

$$F_L = \frac{C_L}{C_D} F_D \quad (26)$$

For the broken waves, the velocity u' of the water mass at any location between the SWL and the point of maximum wave runup may be approximated by (Shore Protection Manual, 1977),

$$u' = \sqrt{gh_b} (1 - x_1/x_2) \quad (27)$$

and the wave height H' above the ground surface is written by

$$H' = h_c (1 - x_1/x_2) \quad (28)$$

in which $h_c \approx H_b/2$; h_b = the water depth at the breaking point; x_1 = distance from the still water line to the concrete block; and x_2 = distance from the still water line to the limit of wave runup. For the broken waves, the distance x_2 is suggested by

$$x_2 = 2 H_b \cot \alpha \quad (29)$$

For the nonbreaking waves, we substitute the above equations to get the velocity of the water mass and the wave height above the breakwater surface. But the limit of wave runup is obtained by (Gunbak et al. 1979),

$$\frac{R}{H} = \frac{0.8\xi}{1 + 0.5\xi} \quad (30)$$

in which $\xi = \tan \alpha / \sqrt{H/L}$, surf similarity parameter.

Other Conditions

Several parameters included in the formulation of the stability analysis are assumed to be probabilistic variables. The shape factors of the concrete block c_1 , c_2 and c_3 are supposed to be uniformly distributed between 0 and 4, 0.8 and 1.2, and 0.9 and 1.1, respectively. The value of the drag coefficient C_D , the lift coefficient C_L , and the virtual-mass coefficient C_M are also probabilistic. According to Christensen et al. (1982), in the case of a circular cylinder, these values are normal probability variables of which means and coefficients of variation are 0.60 and 0.24, 0.60 and 0.24, and 1.20 and 0.22, respectively. The friction coefficient of tetrapods μ behaves like the probability variable which is uniformly distributed from 0.5 to 0.6 (Takeda, 1981). The sheltering coefficients ε_1 , ε_2 and ε_3 are also considered as the probability variables. For the sliding, the rocking and the lift-up motions, they are assumed to be uniformly distributed from 0.8 to 1, 0.4 to 0.8, and 0 to 0.3, respectively. The repose angle of the concrete block is also the probability variable which is uniformly distributed from 56 to 63 degrees (Takeda, 1981).

Illustrative Examples

Fig. 2 compares the computed relative damage with the observed relative damage, introducing the queuing theory for different values of λ' and $\lambda = 1$. The value of λ' designates the average number of cycles for a concrete block to continue to have movability condition. From the same figure the value of $\lambda' = 0.3$ seems to be appropriate. In this study these values are used for the numerical calculations. Next, to apply our model to a designed rubble-mound breakwater, let us determine the weight of a concrete block by the following Hudson's formula:

$$W = \frac{\rho_s g H^3}{K_D \left(\frac{\rho_s}{\rho_w} - 1 \right)^3 \cot \alpha} \quad (31)$$

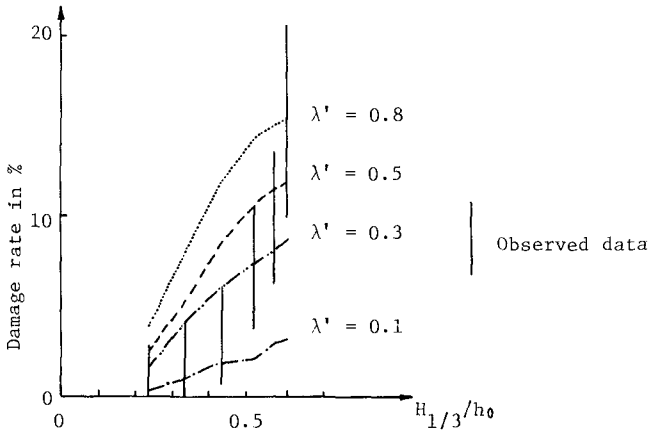


Figure 2. Comparison of Computed Relative Damage with Observed Relative Damage for Different Values of λ'

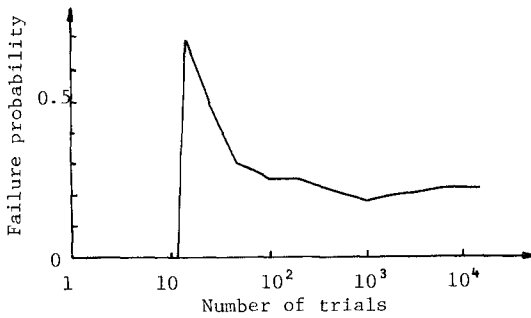


Figure 3. Effect of Number of Trials on Failure Probability

in which H = the design wave height and K_D = a parameter. The value of K_D is selected by the characteristics of a concrete block and the condition of wave breaking. For the values of $\rho_s/\rho_w = 2.23$, $\cot\alpha = 4/3$, $K_D = 8.3$ and $H = 4\text{m}$, the weight of a concrete block of 7.15 ton is computed by Eq. (31). Usually the weight of 8 ton is used by considering easiness of construction method and adding a safety factor. Our model can obtain the reliability or the risk for the arbitrary value of the weight of a concrete block. The weight of a concrete block to correspond to the required value of the reliability or the risk should be selected in the field. Fig.3 represents the effect of the trial number on the failure probability. The increase of the trial number the failure probability converges to a constant value. Fig.4 indicates the effect of the significant wave height on the failure probability. As expected, the fail-

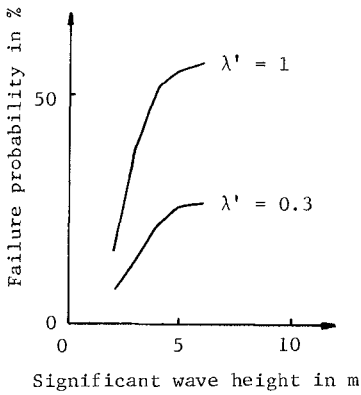


Figure 4. Effect of Significant Wave Height on Failure Probability

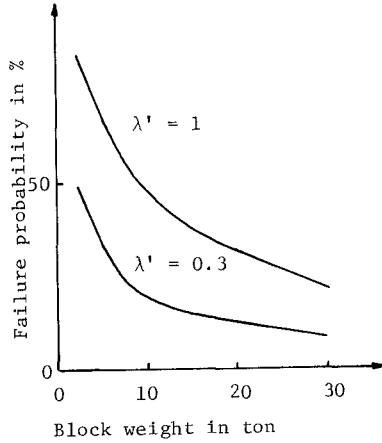


Figure 5. Effect of Concrete-block Weight on Failure Probability

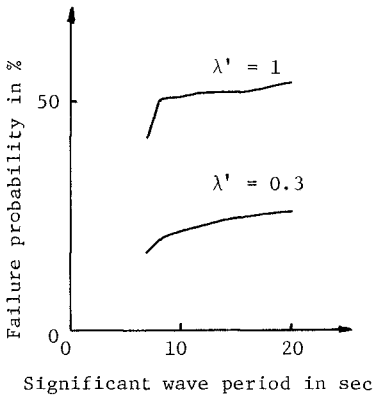


Figure 6. Effect of Significant Wave Period on Failure Probability

ure probability increases as the significant wave height becomes large. The rate of the increase becomes small after 5m. It is explained that some incident waves break before they reach the breakwater slope. Fig.5 shows the effect of the weight of concrete blocks on the failure probability. By increasing the weight of concrete blocks, the failure probability decreases. It corresponds to the increasing of the weight of concrete blocks in the field. Fig.6 represents the effect of the significant wave period on the failure probability. The influence of the wave period, which is not included in Hudson's formula, is found. Thus, the longer wave period has a high risk. Fig.7

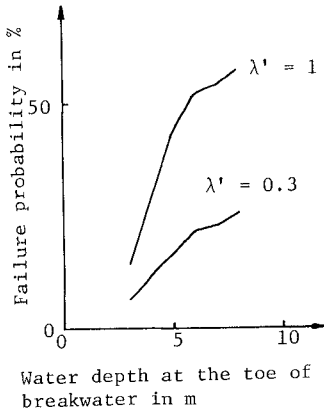


Figure 7. Effect of Water Depth at the Toe of Breakwater on Failure Probability

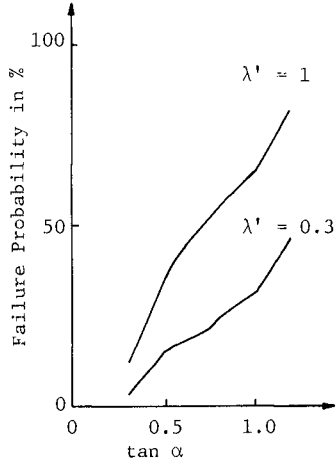


Figure 8. Effect of Breakwater Slope on Failure Probability

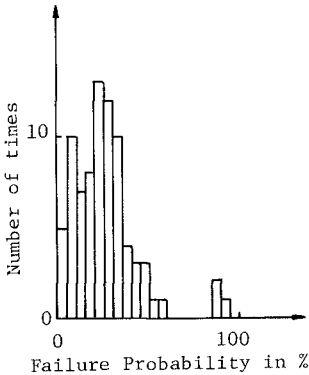


Figure 9. Failure Probability of Destroyed Rubble-mound Breakwaters

describes the effect of the water depth at the toe of the breakwater on the failure probability. Increase of the water depth gives high failure probability or risk. For the higher water level, more waves with larger wave height come on the breakwater slope. Fig.8 indicates the effect of the angle of the breakwater slope from the horizontal on the failure probability. The steep slope induces a high risk. Our model cannot consider the interlocking effect among blocks. Fig.9 shows the failure probability of destroyed rubble-mound breakwaters in Japan introducing the queuing theory when $\lambda = 1$ and $\lambda' = 0.3$. The failure probability using the weight of concrete blocks computed by Hudson's formula is between 10 % to 30 %. The destruction for the failure probability which is greater than 30 % is caused by unexpected design conditions. The destruction for the failure

probability which is less than 10 % is caused by phenomena except our model.

Concluding Remarks

Classifying the motion of concrete blocks into three kinds, the failure probability or the risk of the rubble-mound breakwater are obtained. The reliability is defined by the difference of the failure probability from 1. In a result, the influence of the wave period on the failure probability becomes remarkable. That is to say, attacking of waves with longer period induces high risk to the rubble-mound breakwater as expected. For the other design variables of rubble-mound breakwaters, the computed result is reasonable and does not contradict the field observation. The relative damage computed from the failure probability appropriately predicts the observed one. Since the motion of concrete blocks is concretely investigated, we can develop a new type of concrete blocks to increase the reliability of the rubble-mound breakwaters. Finally, it is found to be rational for us to discuss the failure probability, the risk, or the reliability than K_D value included in the Hudson's formula, when one designs the rubble-mound breakwaters.

Appendix 1.--References

- Christensen, P. T.(1982). Sstructural reliability theory and its applications. Springer-Verlag.
- Gunbak, A. R. and Bruun, P. M.(1979). "Wave mechanics principle on the design of rubble-mound breakwater." Proc. Port and Ocean Engrg. under Arctic Conditions, POAC 79, Nowegian Inst. of Tech., Trondheim, 1301-1318.
- Iwagaki, Y. and Sawaragi, T.(1979). Coastal engineering. Kyoritsu-Shuppan Co., Ltd., Tokyo (in Japanese).
- Takeda, H.(1981). "Stability analysis of concrete blocks." Summer Seminar on Hydraulic Engrg., Part B, JSCE, B.2.1-B.2.14 (in Japanese).
- Tanimoto, K., Haranaka, H. and Yamazaki, K.(1985). "Damage rate of concrete blocks to irregular waves." 32nd Japanese Conf. on Coastal Engrg., JSCE, 480-484 (in Japanese).
- United States Army Corps of Engineers, Coastal Engineering Research Center, Shore Protection Manual, Vol.2, United States Government Printing Office, Washington, D.C., 1977.*
- Walton, T. L. and Weggel, J. R.(1981). "Stability of rubble-mound breakwaters." J. WW Div., ASCE, 107(WW3), 195-201.

CHAPTER 153

Reliability Based Design of Rubble-Mound Breakwater

Masato Yamamoto*
Kazumasa Mizumura**
Taiji Endo***
and
Naofumi Shiraishi****

Abstract

The object of this present research is to study probabilistic design of armor blocks protecting composite breakwaters and to produce optimum design methodology for S-shaped breakwaters in terms of failure probability and construction cost. Failure probability in the vicinity of the still water level is greatest in the case of uniform sloped breakwaters. Therefore, S-shaped breakwaters of which the slope near the still water level is milder have a reduced risk of damage compared to uniform sloped ones. The optimum design index presents good economics and reliability in rubble-mound breakwater design.

Introduction

In recent years in Japan, as breakwaters have been constructed in deeper and deeper areas, armor block weights to protect caissons of composite breakwaters against wave action have also had to be increased. The block weights are generally determined using the Hudson formula with appropriate K_D values for each type of concrete block. However there are several problems in the usage of this formula in that, effects such as wave periods, probabilistic properties of wave heights and periods etc. can not be taken into account. Van Der Meer(1987) proposed formulae for calculation of stable armor units based on hydraulic model testing. These formulae can present the effects of wave periods. In addition he also produced probabilistic designs of rubble-mound breakwaters. When working group 12 of PIANC(1987) dealt with total reliability design for breakwaters including foundations, strength of armor units

*Research Engineer, Hydraulic Laboratory, Nippon Tetrapod Co., Ltd., 2-7, Higashi-Nakanuki, Tsuchiura, Ibaraki Pref., 300, Japan

**Prof. of Civil Engrg. Dept., Kanazawa Inst. of Tech., 7-1, Ogigaoka, Nonoichimachi, Ishikawa Pref., 921, Japan

***Director, Hydraulic Laboratory, Nippon Tetrapod Co., Ltd.

****President, Nippon Tetrapod Co., Ltd., Shinjuku Dai-Ichi Seimei Bldg., 2-7, Nishishinjukuku, Tokyo, 163, Japan

etc. and compared the results of levels I, II and III, the reliability theory for concrete blocks or armor stones was based on the formulae of Van Der Meer.

Mizumura et al (1988) proposed a theory for reliability design of rubble-mound breakwaters of level III. They calculated the incipient motion of an armor block using a simple physical model. According to them the stability of armor blocks depended on the wave periods.

In large wave areas the weight of blocks would have to exceed 100t in cases where the gradient of the protection is 1:4/3 or 1:1.5. In addition, in a case of a uniform sloped breakwater, the failure probability of concrete blocks would be greatest in the vicinity of the still water level obtained from the reliability analysis. As a result a complex sloped breakwater, a so called "S-shaped breakwater" should be utilized to increase stability. The failure probability of this S-shaped breakwater would be lower than that of a uniform sloped one. However, if an S-shaped breakwater were used, the cross-sectional area of armor blocks would become exceedingly large and the resulting construction cost extremely high. In this study, the authors introduce a simple index taking both the construction costs and failure probability of armor blocks of S-shaped breakwaters into consideration.

Method for Stability Analysis

In Japan, breakwaters like the one shown in Fig.1 are usually constructed.

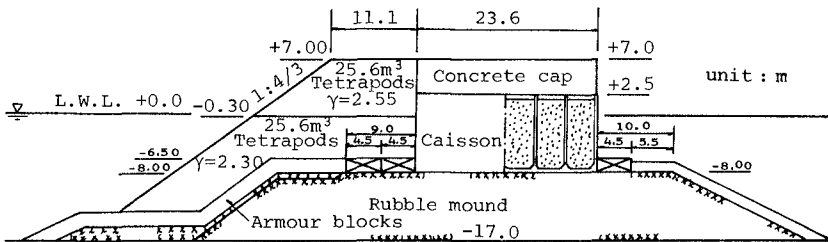


Fig.1 Typical Breakwater in Japan

In this type of breakwater, there are many possibilities for failure, as listed in Table 1.

Table 1 Risk Elements

- 1) Armor layer failure
 - *Movement of armor unit
- 2) Toe scouring and collapse
- 3) Caisson slide and overturning
- 4) Damage to structural elements
 - *Fatigue of materials
 - *Breakage of armor units
- 5) Material degradation due to chemical action
- 6) Others

However, it is too complicated to analyse all of the risk elements theoretically but in the case of composite break-

waters protected with armor blocks, as armor unit failure or caisson slide are the principal problems, the authors have focused on armor block motion as a first step to indicate reliability of design.

The movements of armor blocks under wave action are classified into three categories sliding, rocking and lifting-up as shown in Fig.2.

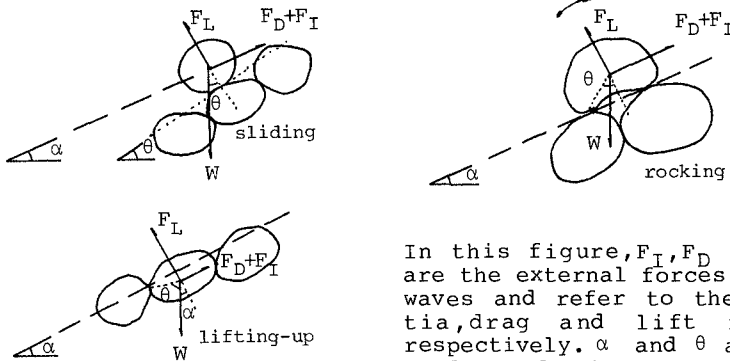


Fig.2 Motion of an Armor Unit

In this figure, F_I , F_D and F_L are the external forces due to waves and refer to the inertia, drag and lift forces respectively. α and θ are the angles of the armor block slope from the horizontal and the repose angle of blocks respectively. When a resistance

force (f_R) is smaller than these external forces (f_S), an armor unit moves as expressed below.

$$\begin{aligned} \text{Stable} \quad f_R - f_S &\geq 0 \\ \text{Unstable} \quad f_R - f_S &< 0 \end{aligned} \tag{1}$$

It is considered that the external forces acting on an armor unit are induced by two kinds of waves. One is waves breaking on the slope of the protection and the other is non-breaking waves. In the case of breaking waves, the wave force is calculated using Goda's formula (Goda 1985) while in the case of non-breaking waves, it is assumed according to the small amplitude wave theory up to the run-up wave height. Details of the theory were presented by Mizumura et al (1988).

Method for Reliability Analysis

Before mentioning risk analysis, the word "Movability" of an armor block has to be defined here. When the armor block concerned is located in the condition shown in Fig.2, the block is referred to as being in a state of movability. In other words, this armor block can not be interfered with by any block in its vicinity and resistance forces consist of only gravity and frictional forces.

The following assumptions are made to connect the movability condition with stability analysis.

- (1) The movable units distribute uniformly between the bottom and 90% of the significant wave height above the still water level along the breakwater slope.

(2) The number of armor blocks falling into a movability state is K.

(3) The movability state of an armor block continues for n_i sets of a combination of the wave height and period for i being 1 to K.

In accordance with these assumptions, processes (2) and (3) above can be simulated by a queueing theory. Integers K and n_i are probabilistic variables and the process can be described by the Poisson process and expressed as eqs. (2) and (3).

$$P(k) = \frac{\exp(-\lambda)\lambda^k}{k!} \quad (2)$$

$$P(n_i) = \frac{\exp(-\lambda')\lambda'^{n_i}}{n_i!} \quad (3)$$

where λ and λ' refer to the parameters to govern the Poisson process or its mean values.

The failure probability from each motion of an armor block can be expressed by the following equation using eq. (1).

$$P = \int_0^\infty \int_0^S f(r,s) dr ds \quad (4)$$

$$\text{where } f(r,s) = f_R - f_S \quad (5)$$

and $f(r,s)$ is the so-called risk function. P indicates the failure probability of any of the 3 motions as defined i.e. sliding, rocking or lifting-up.

Before the calculation of the failure probability, distribution of some coefficients, i.e. the drag coefficient, C_D , the virtual mass coefficient, C_I , the lifting-up coefficient, C_L and the repose angle of an armor unit etc. must be decided. These coefficients and any others that are necessary must also be treated as random variables in accordance with Mizumura et al (1988). Wave heights are assumed to be according to the Rayleigh distribution and in the case of wave periods, the square also belongs to the same distribution. The Monte Carlo method with sampling a pair of wave heights and periods from their distributions is applied to obtain the distribution of the reliability function with respect to each failure due to sliding, rocking and lifting-up.

The probability corresponding to sliding, rocking and lifting-up, referred to as P_S , P_R and P_L respectively, is calculated and the failure probability, of one armor block, $P_e(i)$, can be computed by the sum of each set, P_S , P_R and P_L as below,

$$P_e(i) = P_S + P_R + P_L - P_S P_R - P_R P_L - P_L P_S + P_S P_R P_L \quad (6)$$

if P_S , P_R and P_L are independent of each other. Therefore if the number of armor units per unit width of breakwater is written with m , the total failure probability P_w can be described as equation (7).

$$P_w = 1 - \prod_{i=1}^m (1 - P_e(i)) \quad (7)$$

The values of λ and λ' in eqs. (3) and (4) have to be determined. These values should be estimated using the results of the hydraulic model test performed by Tanimoto et al (1985). The trials can be made with various values of λ and λ' . Fig. 3 shows a comparison of the simulated failure probability with the result of the hydraulic model test.

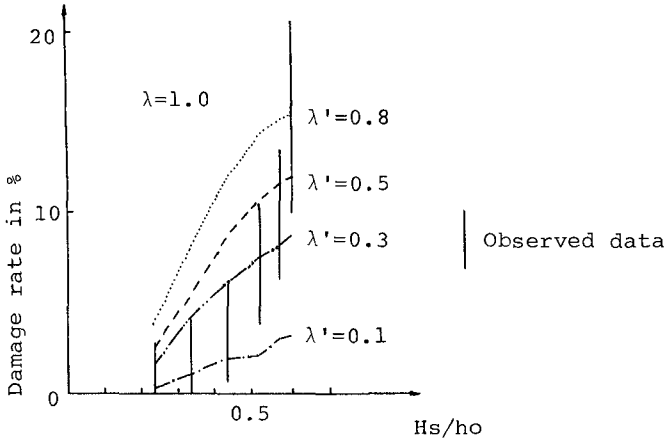


Fig.3 Comparison of Computed Relative Damage with Observed Relative Damage for Different λ' Values

From this figure, it can be seen that a λ value of 1.0 and of λ' 0.3 are appropriate and hereinafter, are used in the calculation.

Failure Probability of Uniform Sloped Breakwaters

Fig.4 shows a computed cross section of a breakwater.

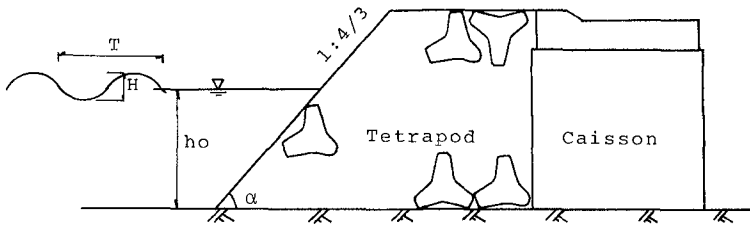


Fig.4 Sketch of Computed Cross Section of Uniform Sloped Breakwater

Tetrapods were selected as the armor blocks. The calculation conditions are summarized in Table 2.

Table 2 Calculation Conditions

$H_s = 4.0 \text{ m}$: $\tan \alpha = 0.75$
 $T_s = 10.0 \text{ sec}$: $W = 7.36 \text{ t}$
 $h_o = 6.0 \text{ m}$
 no wave overtopping

In this Table, W indicates the weight of a tetrapod obtained using the Hudson formula.

Fig.5 shows the spatial distribution of the total failure probability along the slope of the breakwater.

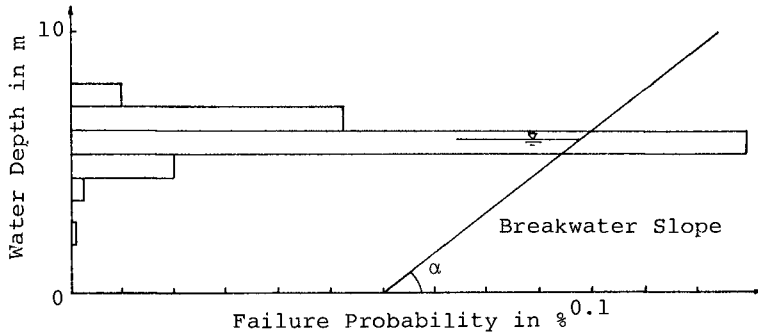


Fig.5 Spatial Distribution of Failure Probability

The risk became highest in the vicinity of the still water level as expected. This result agreed with results from hydraulic model tests and field observations conducted elsewhere except in cases of particular conditions. Therefore in any case of uniform sloped breakwaters, when armor blocks are located near the still water level, they are at more risk than in any other location.

Failure Probability of S-shaped Breakwaters

As mentioned above, the failure probability becomes a maximum near the still water level. Therefore if the failure probability in this vicinity decreased, the total risk would be reduced. An S-shaped breakwater such as the one shown in Fig.6 had to be utilized to decrease the risk of failure.

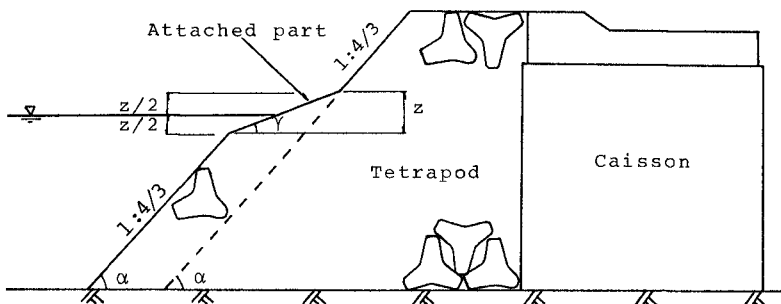


Fig.6 Sketch of S-shaped Breakwater

In this figure, γ is the angle of the attached part from the horizontal and z refers to the vertical length of the attached part.

Fig.7 shows an example of the spatial distribution of the failure probability along an S-type breakwater slope. In this calculation the values of γ and z were taken as 0.33 radians and 165cm respectively. The figure shows a failure probability significantly reduced compared with that shown in Fig.5. The beneficial effect of the S-shaped breakwater is evident.

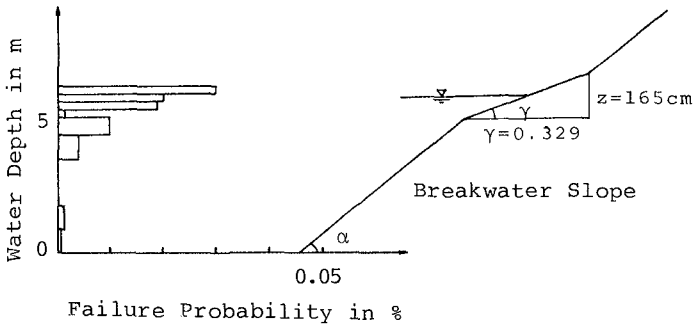


Fig.7 Spatial Distribution of Failure Probability

Fig.8 shows the failure probability of an S-shaped breakwater taking z as a parameter under the same calculation conditions as listed in Table 2.

Saville(1958) obtained run-up heights for composite sloped breakwaters, so in our calculation the run-up wave height was computed according to his method. In the range of small γ , the failure probability of small z was larger than that of large z . This meant that in the case where the gradient of the attached slope was milder, if the slope was longer, the risk would be reduced. When γ became larger, the failure probability of a small value of z e.g. 15cm became lower and where $z=165$ cm, it increased. Therefore in a range of large γ , it was seen that failure probabilities converge into one. Thus, the failure probability of an S-shaped breakwater varies in terms of z and γ and it becomes unclear how to decide the values of z and γ . In addition

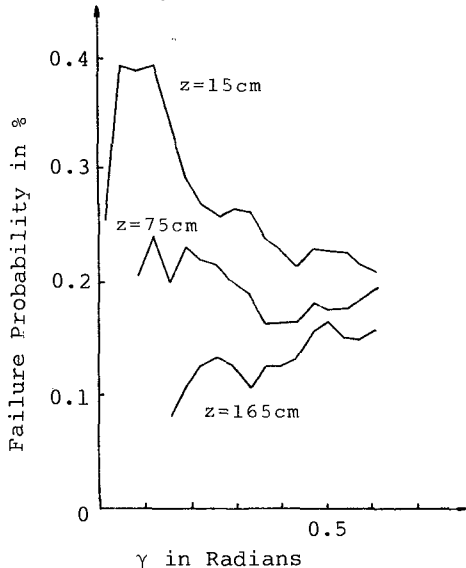


Fig.8 Failure Probability for S-type Breakwater

values of γ and z affect the area of the breakwater section and the construction cost is affected.

Optimum Design Index

An optimum design breakwater has to satisfy in terms of both reliability and economics. However the construction cost depends on the cross sectional area. From this view point, the authors employed an optimum design index, I , as expressed by the following equation under the simple assumptions that construction cost is proportional to cross sectional area.

$$I = \frac{1}{2} \left(\frac{P_f}{P_{f_0}} + \frac{A}{A_0} \right) \tag{9}$$

in which I is the optimum design index, P_f is the failure probability of an S-type breakwater, P_{f_0} indicates the same for a uniform sloped type, A shows the cross sectional area of the S-shaped breakwater and A_0 is the area of a uniform sloped one.

This index is very simple and implies that the weight of armor block stays the same. The index, however, is appropriate at this stage of design. The optimum design is made by employing γ and z values making I a minimum.

A cross sectional area is shown in Fig.9. The calculation conditions are the same as mentioned previously. The figure indicates the changes in the cross sectional area against γ with fixed z value. In the case where $z=165\text{cm}$, the cross sectional area is much larger than that in the case where $z=15\text{cm}$. So, the construction cost would be extreme for the greater value of z , while the failure probability shown in Fig.8 in the case where $z=165\text{cm}$ is lower than that of the smaller z value.

Fig.10 shows the optimum design index, I .

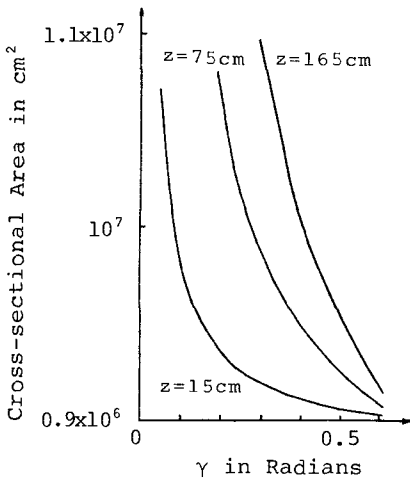


Fig.9 Cross-sectional Area for S-type Breakwater

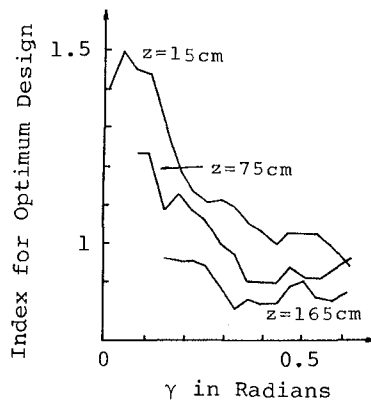


Fig.10 Index for Optimum Design

I is small for large z values. When z and γ become smaller, I becomes greater. This fact suggests that the attached part requires a gradient, i.e. the attached part is not always level. In the optimum S-shaped breakwater, the minimum value of I is 0.83 when γ is 0.33 and z is 165cm. P_f/P_{f0} and A/A_0 are calculated as 0.48 and 1.18 respectively. The spatial distribution of the failure probability of an S-type breakwater has already been shown in Fig.7. Thus, from the sample calculation, although construction of an S-type breakwater requires a mere 18% cost increase, the reliability becomes twice as good as that of a uniform sloped breakwater.

Fig.11 shows relationship between the significant wave height and γ , z, the failure probability and volume of protection part when the optimum design index, I, is a minimum in the case where the wave period and block weight are fixed at 10sec and 8t respectively.

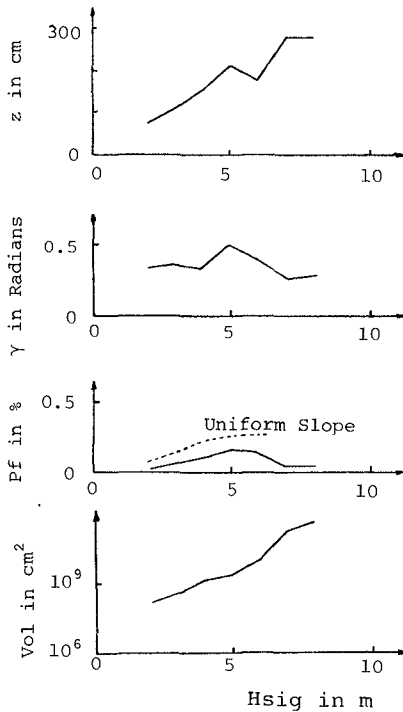


Fig.11 Relationship between H_{sig} and z, γ , P_f and Vol. when I is Minimum

In the graph of P_f , the broken line indicates the failure probability for a uniform sloped breakwater. If a uniform sloped breakwater is used, the risk of failure increases as indicated by the dotted line in terms of the incident wave height. In the case of an S-type breakwater, however, in a

range of wave height higher than 5m, the failure probability would be reduced by employing γ as less than 0.5 and z greater than 200cm. Thus, this figure proves useful for the optimum design of the S-shaped breakwaters when the design wave height changes.

Fig.12 indicates changes in the failure probability, γ , z and the volume of cross section when I is a minimum in terms of the wave period under the conditions where the wave height and weight of the armor block are fixed at 4m and 8t respectively. In the condition where T_{sig} is less than 10sec, the optimum design is made by employing γ of 0.3-0.5 radians (the gradient of the attached part is 1:1.8-1:3.2) and z being 110cm-130cm. In the case where T_{sig} is 10sec-20sec, I became a minimum by keeping γ as 0.5 (the gradient is 1:1.8) and z of 130cm. In this range of T_{sig} , the failure probability gradually increases and is less than that of the uniform sloped breakwater. Thus even though the wave period becomes longer, it is not necessary to enlarge the protection part to ensure the same reliability for an S-Shaped breakwater.

Fig.13 shows the influence of armor unit weight to the volume, the failure probability, γ and z under the condition where I is a minimum by holding the wave height and period constant as 4m and 10sec respectively.

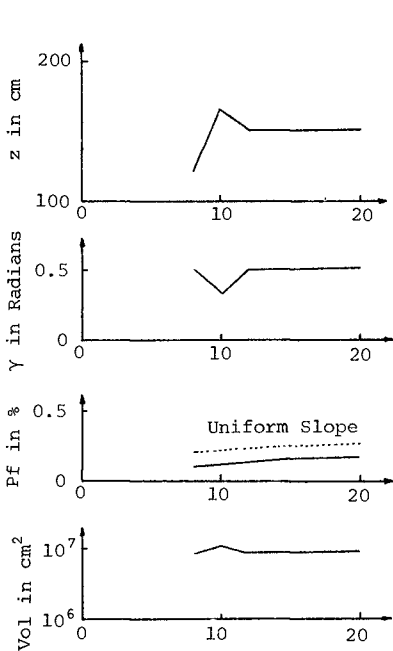


Fig.12 Relationship between T_{sig} and z, γ, P_f and $Vol.$ when I is Minimum

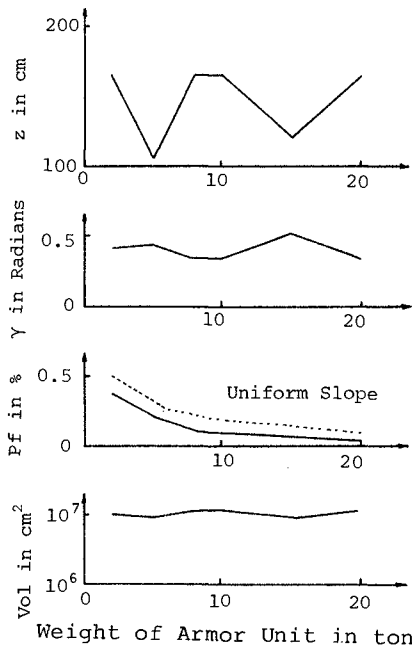


Fig.13 Relationship between Weight and z, γ, P_f and $Vol.$ when I is Minimum

As the weight of armor unit increases, the failure probabil-

ity decreases because the armor unit weight directly affects the resistance against the three kinds of block motion described previously. The volume of the protection part is almost constant when the armor unit weight becomes great. Therefore even if the weights of armor blocks increase, the construction cost does not become any higher.

As mentioned above in the optimum design, it is the wave height that most influences the construction cost and reliability compared with both the wave period and weight of armor block. Therefore if the design wave period is lengthened when designing an S-shaped breakwater, the cross sectional area need not be enlarged.

Conclusions

The following conclusions have been derived from this study.

1. The failure probability along the slope of the protection part was confirmed to be a maximum in the vicinity of the still water level in the case of a uniform sloped breakwater with armor blocks.

2. In the case of an S-type breakwater, the failure probability near the still water level became significantly lower than that of a uniform type. As a result the total risk is reduced significantly compared with that of a uniform sloped breakwater.

3. The optimum design index proposed in this study can describe both the reliability and economics of the S-shaped breakwaters. This index is most useful in producing optimum designs of breakwaters protected by armor blocks.

4. Simple calculations show that a small increase in construction expenditure results in greatly enhanced reliability.

5. The significant wave height has much more influence on construction cost than either the wave period or block weight when the optimum design index is a minimum.

References

Goda, Y., "Random Seas and Design of Maritime Structures", University of Tokyo press, pp.113-121, 1985

Mizumura, K., Yamamoto, M., Endo, T. and Shiraishi, N., "Reliability Analysis of Rubble-Mound Breakwaters", Proc. 21st International Conf. on Coastal Engrg., Malaga, Spain, 1988 (to be published)

PIANC PTC II Working Group 12, "Rubble Mound Breakwaters", Meeting Document, Le Havre, France, 1987

Saville, T., JR., "Wave Runup on Composite Slopes", Proc., 6th International Conf. on Coastal Engrg., 1958

Tanimoto, K., Haranaka, H. and Yamazaki, K. "Variation of Percent

Damage to Concrete Blocks due to Irregular Waves", Proc. 32nd Japanese Conf. on Coastal Engrg., JSCE, pp.480-484, 1985 (in Japanese)

Van Der Meer, J.W. "Stability of Cubes, Tetrapods and Accropode", Proc. Breakwaters'88 Conf., ICE, Eastbourne, UK, pp.59-68, 1988

CHAPTER 154

STABILITY AND STRUCTURAL BEHAVIOUR OF STRENGTH IMPROVED DOLOSSE

J A ZWAMBORN*, D J P SCHOLTZ** and H CLAASSENS***

ABSTRACT

Stability model tests and prototype breakage tests were done to provide data for the optimum design of dolos breakwater armouring.

Stability tests with irregular waves were done with dolosse with waist ratios of 0,33, 0,36, 0,38, 0,40 and 0,43 and breakwater slopes of 1:1,33, 1:1,5 and 1:2. All model dolosse had a mass of about 80 gr and were placed at a 'normal' density, $\rho = 1,00$. The results showed that regular waves with $H_{reg} = 1,1 H_{mo}$ must be used to get similar damage. Also, a significant reduction in stability is evident for dolosse with larger waist-to-height ratios and for the shorter period waves (Figures 4 and 5).

Some 50 9 t dolosse, without reinforcing and with different types of simple rail reinforcing, were tested for breakage behaviour, using a specially developed cushioning device to closely represent breakwater conditions. The results showed that unreinforced dolosse can withstand falls up to 1,5 m, without breakage and X or double-V rail reinforced units about double this height.

The results of these tests, together with specific model tests, were used to design an effective protection for the Table Bay main breakwater. The tests indicated the use of 25 t dolosse (minimum) but, because of the shallow waterdepth, the toe dolosse of the repair slope were reinforced (double-V rail reinforcing), stabilized by 75 mm steel chains, and bitumen grout will be placed to reduce their movements.

*Programme Manager: Maritime and Hydraulic Structures, CSIR, P O Box 320, Stellenbosch, 7600, South Africa.

**Research Engineer:" Maritime and Hydraulic Structures, CSIR, P O Box 320, Stellenbosch, 7600, South Africa.

***Deputy Harbour Engineer, SA Transport Services, P O Box 4245, Cape Town, 8000, South Africa.

INTRODUCTION

Procedures for the design of safe and economic dolos structures have been described by Zwamborn and Scholtz (1986). Three different design approaches were described, namely:

- (i) "No Movement" Design;
- (ii) "No Breakage" Design; (based on 'unbreakable' units)
- (iii) "Optimum" Design; using strength improved dolosse.

Low cost dolos strength improvement can be achieved by increasing the waist-to-height ratio, in other words, to make the dolosse thicker, and by using simple types of reinforcing, for example scrap rail reinforcing.

To assist with the design over 800 stability tests were done with regular and irregular waves, using model dolosse with five different waist ratios. Moreover, unreinforced 9 t dolosse and dolosse reinforced with three different types of rail reinforcing were used to check their structural behaviour under simulated 'near breakwater' loading conditions to acceptable degrees of movements for different types of dolosse.

These results, together with a series of site-specific stability tests, were used to design the major repair works for the Table Bay main breakwater at Cape Town, Republic of South Africa.

2. DOLOS STABILITY TESTS

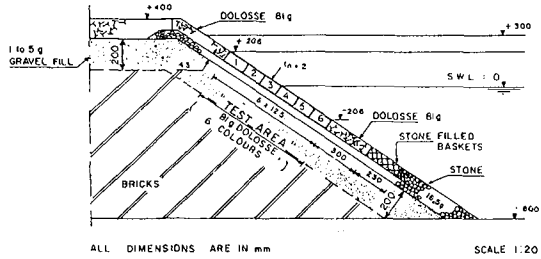
Stability tests on dolosse with different waist-to-height ratios ($r = 0,33, 0,38$ and $0,43$) reported by Scholtz et al (1982) showed a marked decrease in stability for the larger waist ratios, particularly for $r > 0,38$. Later tests by Burcharth et al (1986) indicated little influence of the waist-to-height ratio on dolos stability, particularly for the smaller damage values. To resolve this issue, a comprehensive test programme using irregular waves and 80 gr dolosse with waist-to-height ratios of $0,33, 0,36, 0,38, 0,40$ and $0,43$ has been carried out.

Test Facilities and Model Layout

The stability tests were carried out in a 127 m long by 3 m wide and 1,1 m deep test flume equipped with Seasim irregular wave generators, including an absorption system to reduce re-reflections. The flume was divided into three 0,75 m wide test channels leaving two narrow dummy channels on either side. Details of the test dolosse were as follows: $W = 78$ to 81 g, specific density 2,34 to 2,40 and $r = 0,33$ to $0,43$.

The standard 'mean' dolos packing density was used for all the tests, that is, $\emptyset = 1,00$ (number of dolosse per unit area, $N_n = \emptyset_n V^{-2/3}$, where V is the block volume and n the number of 'layers', Zwamborn and Van Niekerk, 1982) and 538

dolosse were placed on each of the $0,75 \times 0,75 \text{ m}^2$ test areas (Figure 1). The underlayers consisted of 16,5 g selected stone, that is W/5 g.



ALL DIMENSIONS ARE IN mm SCALE 1:20

FIG. 1: MODEL CROSS-SECTION

Test Wave Conditions

Wave Spectrum	T_p (s)	Target Wave heights, H_{m0} (mm)							
		31	50	69	90	112	129	155	163
Jonswap	1,25	31	50	69	90	112	129	155	163
	1,50	30	50	69	90	109	128	155	163
	1,75	30	51	72	93	113	134	152	163
PM	2,00	31	51	72	91	111	129	149	161
	1,75	31	52	72	92	113	130	146	161

Wave heights were measured 5,55, 5,80 and 6,20 m away from the model slope. Re-reflections of wave energy from the wave paddles was avoided by using the Seasim wave generators' absorption system. The incident and reflected wave spectra for the above test conditions were determined by the three-point method based on the least square technique reported by Monsard and Funke (1980).

Test Procedures and Damage Criteria

The model dolosse were placed at the prescribed packing density in one operation from the bottom upwards. The tests were carried out similar to the previous tests with regular waves, that is, each wave height interval (see test wave conditions) was tested for 60 min after which the damage was determined. All test series (up to 8 wave heights) were repeated between 3 and 8 times.

Damage was determined by recording displaced units (observations during the tests and using still photography) and rocking units (observations and single exposure cine camera technique). The following damage criteria were used:

- displacement (movement over at least a distance h)
- continuous rocking or full roll-over
- intermittent rocking (two-thirds of the test time)
- occasional rocking (one-third of time or less)

The test results have been presented relative to these criteria. 'Total' damage is defined as (a) + (b) + (c).

Test Programme

The following tests were carried out using up to 8 characteristic wave heights for each test series (test numbers):

Slope	Spectrum	T_p (s)	$r = 0,33$	$r = 0,36$	$r = 0,38$	$r = 0,40$	$r = 43$
1:1,5	JS	1,75	W_2 to 9	W_2 to 9	A_7 to 9	W_2 to 9	A_7 to 9
	JS	2,0	P_1 to 3	P_1 to 3		P_1 to 3	
	JS	1,5	P_4 to 6	P_4 to 6	A_4 to 6	P_4 to 6	A_4 to 6
	JS	1,25	P_7 to 9	P_7 to 9	A_1 to 3	P_7 to 9	A_1 to 3
	PM	1,75	PM_1 to 3	PM_1 to 3		PM_1 to 3	
1:2	JS	1,75	A_{13} to 15		A_{13} to 15		
1:1,33	JS	1,75	A_{10} to 12		A_{10} to 12		

Test Results

The mean results of the tests for different waist ratios at a slope of 1:1,5 are shown in Figure 2, together with the earlier test results for regular waves. A significant reduction in stability (wave height) for dolosse with larger waist ratios is evident from this figure. When rocking units are added to the displaced units, damage was found to increase by 100 per cent for $r = 0,33$, 80 per cent for $r = 0,36$ and 50 per cent for $r = 0,40$.

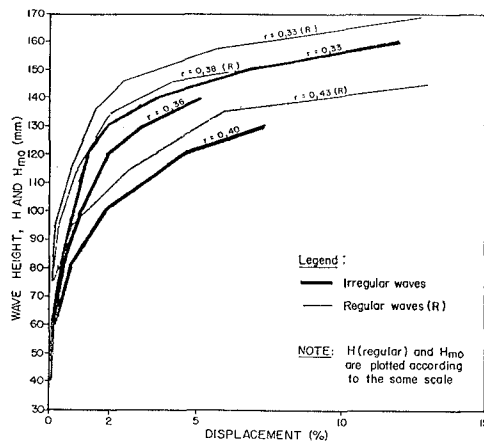


FIG. 2: EFFECT OF WAIST RATIO, REGULAR VERSUS IRREGULAR WAVES

It can also be derived from Figure 2 that regular waves of wave height $H_{reg} = 1,1H_{mo}$ cause the same damage as irregular waves with a characteristic wave height H_{mo} . Brorsen et al (1974) concluded from model tests on dolosse that similar damage is caused when $H \approx 0,8 H_s$ but after checking their results this was found to be incorrect; it should have been $H \approx 1,25 H_{mo}$ (the same error is carried through in Burcharth et al, 1986).

Most test were done with a Jonswap type of spectrum but comparative tests with a PM spectrum showed similar stability results for the various waist ratios.

A comparison of the effect of different breakwater slopes for $r = 0,33$ and $0,38$ is given in Figure 3. For dolosse with $r = 0,33$ and 2 per cent displacement, the H_{mo} values

are 116, 130 and 140 mm for slopes of 1:1,33, 1:1,5 and 1:2 respectively, thus somewhat increased stability for flatter slopes. In the case of $r = 0,38$, the differences in stability are seen to be much smaller.

Test results showed a significant reduction in stability for the shorter wave period (T_p) values, for instance, for $r = 0,33$ and Jonswap spectra with $T_p = 2,0$ and $1,25$ s resulted in 2 per cent displacement K_D values of 22 and 13 respectively. Similarly, for $r = 0,40$, K_D values of 12 and 6 were found.

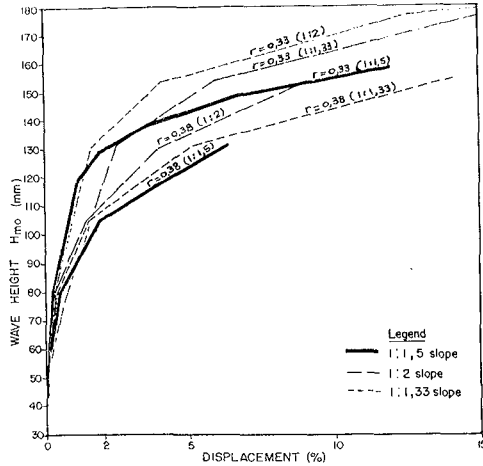


FIG. 3: EFFECT OF BREAKWATER SLOPE, IRREGULAR WAVES, $T_p = 1,75$ s

The overall test results are presented in Figures 4 and 5 which show the stability factors

$$K_D = \frac{\gamma_s H_{mo}^3}{W \Delta^3 \cot \alpha}$$

with H_{mo} = wave height;

$$\Delta = \frac{\gamma_s}{\gamma} - 1;$$

γ and γ_s = specific density of water and model dolosse

and α = breakwater slope angle;

versus the Iribarren number,

$$\zeta = \frac{\tan \alpha}{(H_{mo}/L_o)^{0,5}}$$

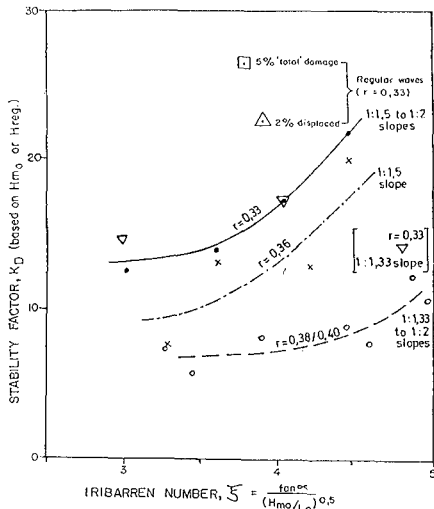


FIG. 4: STABILITY FACTORS FOR PRELIMINARY DESIGN - 2% DISPLACEMENT OR 5% 'TOTAL' DAMAGE

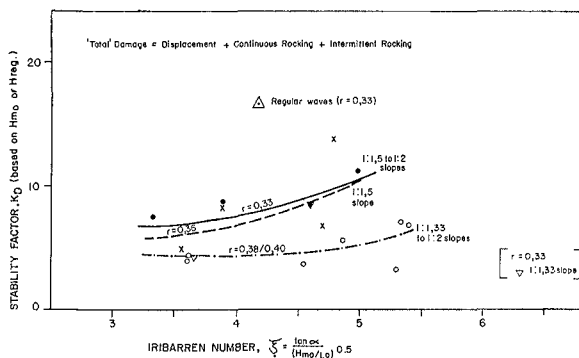


FIG. 5: STABILITY FACTORS FOR PRELIMINARY DESIGN -
2% 'TOTAL' DAMAGE

Figure 4 is based on 2 per cent displacement. This figure also represents the 5 per cent total damage quite well. Figure 5 is based on 2 per cent 'total' damage.

These figures display clearly the significant effects of the increased waist ratio's (reduced K_D values), and the wave period (low K_D values for shorter wave periods with minimum values for $2.5 < \bar{\gamma} < 3.5$). These figures also show the effect of irregular waves (H_{mo}) versus regular waves (H_{reg}) (Scholtz et al, 1983).

Figures 4 and 5 could be used for a first design, as a guide using Figure 4 (2% displacement or 5% total damage) for high quality strength reinforced dolos projects and Figure 5 (2% total damage) for lower quality and unreinforced dolos applications.

It should be mentioned here that the significant reduction in stability of the 'thicker' dolosse found in these tests contradicts the results reported by Burcharth et al (1986) which is *inter alia* thought due to different dolos packing densities and the small dolosse used by Burcharth (30 g), that is, possible scale effects.

3. STRUCTURAL TESTS ON DOLOSSE

To check on the structural strength of various types of simple reinforced dolosse, a series of breakage tests on 9 t dolosse were done at Cape Town.

Structural tests on dolosse were done elsewhere by dropping the units on a solid concrete base (drop test) or by letting a concrete ball hit the dolos (pendulum test). These test are effective in showing relative strengths, for instance, to show the effect of increased waist-to-height ratio's (Burcharth, 1981). However, the results of these tests cannot be used directly for the actual breakwater situation because the 'rigid'-base test is not representative for the breakwater armouring where a dolos, when moving, will drop on underlayer stone or on other dolosse that will move (yield) under the impact. A test procedure, closely representing the actual breakwater situation was therefore developed for the Cape Town tests.

Purpose of the Tests

The main purposes of the structural tests were:

- (a) to develop a test procedure, closely resembling the conditions in a breakwater armour, so that acceptable dolos movements can be defined better;
- (b) to determine the effectiveness of different types of simple reinforcement;
- (c) to determine the effect of repeated impact loading; and
- (d) to decide on the type of reinforcing of the 25 t dolosse for the Table Bay breakwater repair.

Test Dolosse

The test dolosse were 9 t with $h = 2,9$ m and $r = 0,30$. The concrete density was $2,4$ t/m³ and the design compressive strength was 40 MPa at 28 days. Test cubes showed strengths between 37 and 54 MPa while the equivalent cube strength based on cores, taken after 2 years (when the dolosse were tested) were found to be 23 per cent higher. The average tensile strength was found to be 1/15 of this value, that is, 4 MPa.

Unreinforced and dolosse reinforced with single rails, double-V rails and X-rails were tested (Figure 6). Scrap rails of 43 kg/m were used for the reinforcement, that is, 85, 115 and 168 kg/m³ respectively.

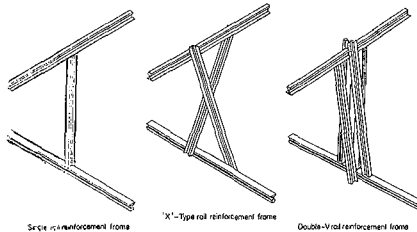


FIG. 6: TYPES OF RAIL REINFORCEMENT

Test Procedures

The basic swing test arrangement, (Zwamborn and Scholtz) was used for the tests. Various methods were tried to achieve a controlled yield and the best solution was found to be a set of three 250 mm long, 89 mm outside diameter and 4,05 mm thick pipes as an 'anvil' or 'cushioning' device (Figure 7).

The cushioning device was calibrated by comparing the deceleration of an impacting 9 t dolos in the swing test with that of a similar dolos which was dropped on 0,5 to 3 t breakwater underlayer stone and on other 9 t dolosse. The deceleration were measured with PCB Piezotronics shock accelerometers with a range of 500 g and a resolution of 0,01 g (Figure 8).

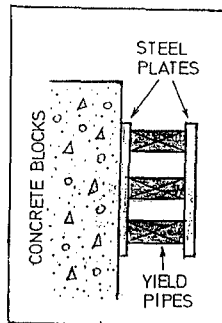


FIG. 7: CUSHIONING DEVICE

In this way, a test procedure was developed which closely represents the conditions in a breakwater situation where a dolos is lifted by the wave action and falls back onto the underlayer or on other dolosse (see also Zwamborn and Scholtz, 1986). Normally, the first fall height was 1,1 m which was increased in steps of 0,15 m to 1,7 m with unreinforced and 1,4 m with the reinforced units whereafter the step heights were increased to 0,3 m until the dolos broke or cracks occurred of at least 0,5 mm width or a fall height of 4,1 m was reached. Repeated impact tests were done using 80 and 64 per cent of the failure fall heights repeatedly, resulting in 90 and 80 per cent of the failure stresses.

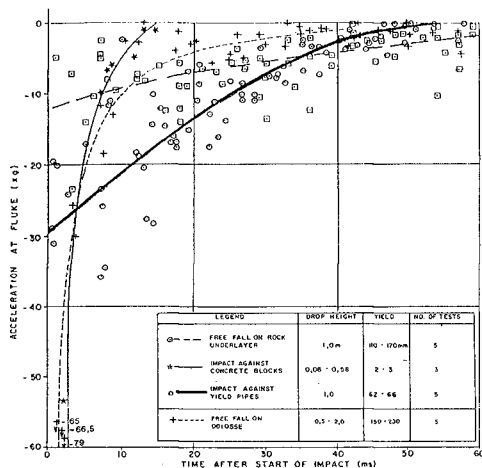


FIG. 8: CALIBRATION OF CUSHIONING DEVICE

Test Programme

The test programme included free-fall tests on rock (17 tests with 0,5, 1,0, 1,5 and 2,0 m fall heights) and free-fall tests on dolosse (5 tests with similar fall heights). Preliminary swing tests included tests against solid concrete blocks (3 tests, 10 to 15 t blocks) and tests using different pipe arrangements as cushioning device (21 tests).

The actual breakage tests included (a) head on swing tests, three dolosse each, unreinforced, single rail, X-rail and double-V rail; (b) side on swing tests, two dolosse each, as above; and (c) repeated impact, three unreinforced, one single rail, one X-rail and two double-V rail. A total of 51 9 t dolosse were used for the tests.

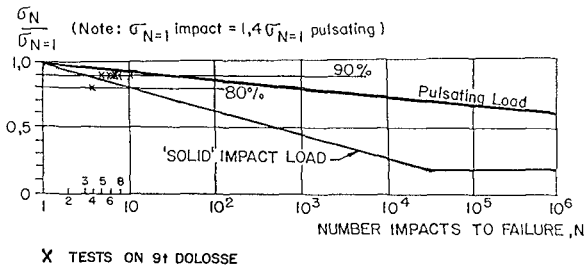
Test Results

Whereas unreinforced dolosse in a 'rigid' drop test break for fall heights of about 0,2 m, with a realistic yield, the critical fall heights were found to be well above 2 m. The failure fall heights found in the Table Bay tests compare very well with the Gioia Tauro tests (Grimaldi and Fontana, 1984).

With regard to the rail reinforcing, it is concluded from the test that:

- the single rail does not increase the dolos strength significantly, although breakage is retarded;
- the X-rail and double-V rail reinforcing increase the dolos strength by about 100 per cent (double fall height) and the dolosse were damaged but did not fail;
- since the double-V reinforcing requires about 50 per cent more steel, the X-rail reinforced dolos is the most cost/strength effective unit.

Also, since the critical drop heights for the 9 t Table Bay and the 30 t Gioia Tauro unreinforced and double-V reinforced dolosse are seen to be of the same order, it may be concluded that the reinforcing has the same degree of effectiveness independent of dolos size, provided the steel/concrete ratio (kg/m^3) is kept constant. With regard to repeated impact loading, the test results are shown in Figure 9 which is based on 200 kg dolos units (Burcharth, 1984).



(BURCHARTH 1984)

FIG. 9: REPEATED IMPACT LOADING

Burcharth's tests are based on a 'rigid' test layout and, as expected, the Table Bay results are seen to fall between the 'solid' impact load and pulsating load case, that is, in the breakwater situation, the dolosse will be able to withstand about twice the number of repeat loads (for example, 6 repeat loads at 90 per cent of the ultimate stress and 25 repeat loads at 80 per cent) compared with the 'rigid' case.

Application of Results

The test results can be used in the following way for the design of dolos armouring:

- single movements of unreinforced dolosse, with adjusted waist ratio (Scholtz et al, 1982) up to 1,5 m can be accepted;

- occasional rocking (less than one-third of the time) up to 0,5 m can be accepted for unreinforced dolosse;
- approximately double these values can be allowed when X or double-V reinforced units are used;
- intermittent (two-thirds of the time) and continuously rocking units will break in the case of unreinforced and crack in the case of reinforced units and must thus be accepted as eventual loss (included in 'total' damage).

4. TABLE BAY BREAKWATER REPAIRS

During the past two decades the seaward slope of the Table Bay harbour's main breakwater suffered appreciable damage, particularly during winter storms when the wave climate is more aggressive. Although repairs were carried out as required on an ad hoc basis, mostly by replacing missing or damaged armour units, it was suspected that the long-term effects of this maintenance work was not satisfactory.

Over the years the situation became progressively worse as the remains of broken armour units were left behind to form part of a conglomerate of various sizes of rock, rubble, gravel and sand. It became clear that the situation should be investigated in depth to ensure that the integrity of the breakwater was maintained and to curb the escalating maintenance cost. Because of the multitude of contributory factors it was concluded that the problem could best be investigated by modeling the existing situation. The complication of the accumulation of various types of debris extending for some distance seaward of the breakwater made any alterations to the existing shallow bed slopes at the breakwater almost impossible and certainly impractical.

Model Tests

It was decided to investigate different typical sections of the breakwater separately in a 3 m wide wave flume. At the selected scale of the model of 1/53, up to 160 m long breakwater sections could be studied in the flume. The 160 m long wave flume was equipped with an irregular wave generator capable of reproducing wave conditions up to and exceeding the 1 in 100 year design wave condition, that is $H_{mo} = 7,5$ m.

The finally adopted design consisted of a double layer of 25 t dolosse placed on the existing breakwater slope after partial clearing of the above-water part of the existing breakwater protection (see Figure 10). This solution which included a toe row of chained dolosse, showed a total damage (displacement > 0,5 m, dolos roll over and continuous rocking) of about 3% in the shallower part of the breakwater (- 3 m MSL) but about 20% for the deeper part (- 5 m MSL). For practical reasons, 25 t dolosse were used throughout but in the deeper section, the dolosse were all reinforced and two rows of toe dolosse were chained.

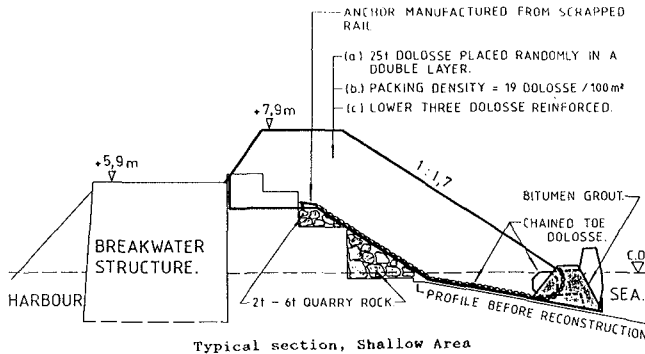


FIG. 10: TABLE BAY BREAKWATER REPAIR

Design Aspects

The dolos waist ratio was increased according to $r = 0,34 (25/20)^{1/6} \approx 0,36$ to strengthen the units.

Because of the hard nature of the sea bed it proved impractical to provide a proper toe berm for the breakwater slope and since this is a particularly vulnerable part of the breakwater, it was decided to introduce the following measures for the shallower part of the breakwater shown in Figure 10:

- rail reinforced dolosse were used for the lower three rows of the slope;
- to provide extra stability, the bottom row of reinforced dolosse were secured to the slope with chains;
- the practicality of using bitumen grout between the bottom rows would be investigated

Although the structural tests showed the X-type rail reinforcing to be most economical in terms of rail usage, the double-V type was used for the toe dolosse as the test results only became known during the construction period.

Manufacture of Dolosse

Concrete quality had to be very strictly supervised for the following reasons:

- the dolosse are expected to be subjected to higher than normal loads;
- due to practical constraints in the casting yard and to remain within the construction programme, dolosse were removed from the moulds after only 16 hours;
- to minimize the possibility of cracks which would allow the ingress of water to the rail reinforcing.

The concrete specified for the dolosse was a 40 MPa compressive strength mix with added pulverized fly ash and designed for maximum bending strength to counter the effects of early handling.

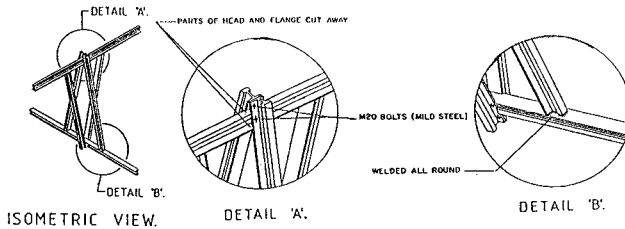


FIG. 11: RAIL REINFORCING (40 kg/m)

In most cases, 40 kg/m scrapped rails were used to manufacture the double-V type reinforcing frames (a few frames were made with 43 kg/m rails). Because of the number required (approximately 1500) the frames were built under workshop conditions using a combination of welding and bolting joints to facilitate the transport and on site assembly (see Figure 11).

Repair Work

Some of the factors that had to be taken into account in determining a placing pattern conforming to the design of the armour layer were:

- (a) Only short lengths of the breakwater could be left exposed during the clearing phase of the reconstruction.
- (b) As a result of the relative immobility of the rail mounted breakwater crane which operated from a movable section of track, provision had to be made for its protection against wave action during placing operations.
- (c) The reach limitations of the breakwater crane had to be taken into account.
- (d) The placing sequence of dolosse is important to ensure proper overlaying of the securing chains and proper interlocking between adjacent section of armour protection.

A typical placing pattern for one section, that is, one crane set-up position is depicted in Figure 12.

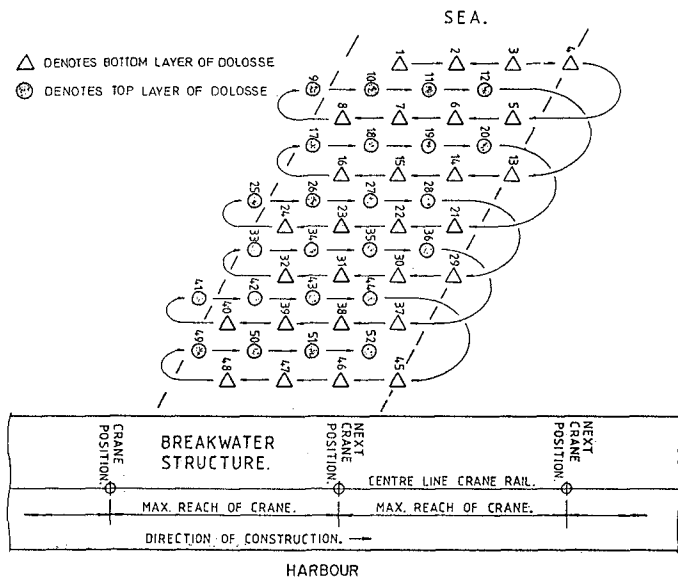


FIG. 12: DOLOSSE PLACING GRID

As the breakwater crane used for the reconstruction has built-in facilities for measuring angles and distance along the jib, the position of each dolos in the placing grid was translated to polar co-ordinates relative to each crane position. These polar co-ordinates were then used by the crane operator to locate the individual dolosse correctly. In practice it was found that after completing a section a visual inspection easily identified areas with obviously low packing densities, and additional units were placed where required. Generally the additional units amounted to approximately 4 per cent of the total number of units placed.

As a further precaution to reduce dolos movements in the vulnerable toe area bitumen grout will be placed between the bottom rows. Factors such as a suitable grout mix, placing temperature and practical considerations will be confirmed by full scale tests. During preliminary on site experimenting it was estimated that a volume placing density of around 5 m^3 per linear meter of breakwater should be sufficient to provide an acceptable degree of dolos to dolos binding.

Exact details such as underlayer profiles, dolos slope profiles and the placing position of each dolos was kept during construction for as-built record purposes. These records will be invaluable for future performance monitoring of the armour protection.

5. CONCLUSIONS

A comprehensive series of stability tests with irregular waves showed a significant reduction in dolos stability, particularly for waist-to-height ratios exceeding 0,36. This should be taken into account when the waist ratio of larger dolosse is increased to maintain sufficient strength.

The test results showed similar dolos stability for slopes between 1:1,33 and 1:2 for all dolos waist ratios except for $r = 0,33$ and a slope of 1:1,33 for which the stability is significantly less.

Wave period was also found to have a significant influence on dolos stability, that is, lower stability was found for smaller wave periods.

The inclusion of relatively simple rail reinforcement increases the dolos strength (fall height) by some 100 per cent and an optimum design of a dolos armour can be achieved by selectively using increased waist ratios and/or rail reinforcing in specific danger areas. The most cost effective rail reinforcement was found to be the X-type.

Detailed optimization studies were done for the repair of the Table Bay breakwater. Hydraulic model tests showed that a 25 t dolos armour would not be entirely stable in the toe area of the breakwater, which was situated only 3 to 5 m below water-level. By using a waist ratio of about 0,36, double-V rail reinforcement, anchor chains and bitumen grouting, a satisfactory practical solution was found for the essential and very difficult repair work for the Table Bay breakwater.

REFERENCES

- BROSEN, M, BURCHARTH, HF and LARSEN, T (1974). Stability of dolos slopes. Proc 14th ICCE, Copenhagen.
- BURCHARTH, HF (1981). Full-scale dynamic testing of dolosse to destruction. Coastal Engineering, Vol 4, No 3, Amsterdam.
- BURCHARTH, HF (1984). Fatigue in breakwater concrete armour units. Report Laboriet for Hydraulic of Havnebygning, Aalborg.
- BURCHARTH, HF and BREJNEGAARD-NIELSEN, T (1986). The influence of waist thickness of dolosse on the hydraulic stability of dolosse armour. Proc 20th ICCE, Taipei.
- GRIMALDI, F and FONTANA, F (1984). Redesign of main breakwater of Gioia Tauro (Italy). Proc Symp on maritime Structures in the Mediterranean Sea, Athens.

MONSARD, EPD and FUNKE, ER (1980). The measurement of incident and reflected waves in random wave experiments. Proc 15th ICCE, Hawaii.

SCHOLTZ, DJP, ZWAMBORN, JA and VAN NIEKERK, M (1982). Dolos stability, effect of block density and waist thickness. Proc 18th ICCE, Cape Town.

SCHOLTZ, DJP and ZWAMBORN, JA (1983). Effect of the waist thickness on stability of dolosse. CSIR Research Report 556, Stellenbosch.

ZWAMBORN, JA and VAN NIEKERK, M (1982). Additional model tests, dolos packing density and effect of relative block density. CSIR Research Report 554, Stellenbosch.

ZWAMBORN, JA and SCHOLTZ, DJP (1986). Dolos armour design considerations. Proc 20th ICCE, Taipei, Taiwan.

CHAPTER 155

SEAWALLS and SHORELINE PROTECTION

by:
Jan van de Graaff¹⁾
and
Eco W. Bijker²⁾

Abstract

All over the world shore-parallel constructions (seawalls; revetments; bulkheads) suffer from damage. It is argued that these constructions are in fact frequently built at places where they shouldn't.

1 Introduction

Coast managers are frequently faced with erosion of their sandy coasts. Valuable land is encroached by the sea. Owners of houses and hotels, bordering eroding coasts, often 'force' (sometimes by means of the politics) the coast manager 'to-do-something'. Not seldom it is then felt more important to do indeed 'something' than doing the right things.

Unfortunately, too often a seawall or a revetment is selected to overcome the direct erosion problems. However, just from the common coastal engineering practice it can be seen that seawalls or revetments do not solve the problems in the right way. Entirely destroyed seawalls can be observed along coasts all over the world. This destruction is by no means always due to the fact (that would be a legitimate reason) that the design conditions were surpassed during a single storm. No, the basic ideas behind the application of seawalls or revetments were in fact quite often wrong.

Demolished coastal constructions harm the prestige of 'coastal engineering' as a respectable profession and should be avoided as far as possible.

-
- 1) Senior scientific officer Delft University of Technology, the Netherlands.
 - 2) Professor Coastal Engineering Delft University of Technology, the Netherlands.

In this paper mainly the rôles of seawalls and revetments in the game of coastline erosion are discussed. Possible alternatives come hardly up for discussion.

2 Definitions and limitations of present discussion

Seawalls and revetments are shore-parallel constructions and are meant to protect the hinterland against flooding and/or erosion. They are situated against features like scarps, embankments, cliffs, dunes and promenades. The distinction between seawalls, revetments and also bulkheads is generally not quite clear. Throughout the present paper the term 'seawalls' will be used to indicate the type of constructions under consideration. (Shore-parallel constructions.)

Sandy beaches are mainly considered in the paper. So at least under 'usual' conditions a sandy beach, for instance for recreation use, is assumed to exist in front of the seawall.

Fig. 1 shows three typical cross-sections with a shore-parallel construction. Cases like case a) and b) are considered in the present paper (sandy beaches in front of the construction under usual conditions). Cases like case c) are not considered (no beach in front of the construction).

Case a) is typical for well-developed seaside resorts. On the benefit of a prosperous development often a clear distinction between 'sea' and 'land' is desired. A seawall can provide that.

Case b) is typical for important investments which are apparently at stake. The encroaching sea obviously causes erosion of the beaches and the dunes. With the shore-parallel construction the attack of the sea is thought to be beaten off.

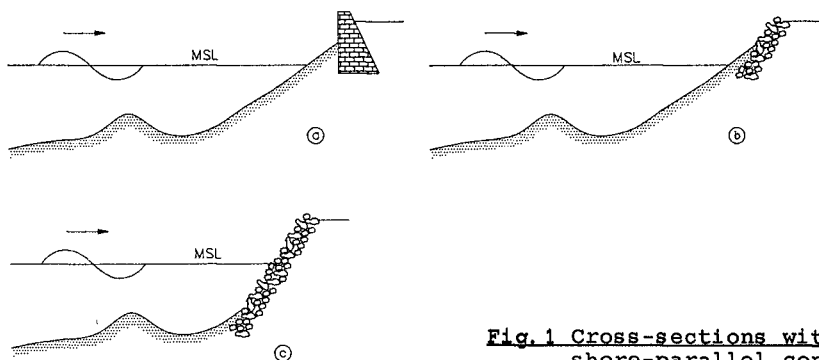


Fig. 1 Cross-sections with shore-parallel constructions

All over the world, however, damaged and even entirely demolished seawalls can be found. In many cases it is felt that in fact design errors are the main cause of the damage. Preventing of some of these errors in future is the main aim of the present paper.

3 Analysis of erosion problems

Seawalls are often built to overcome the felt 'problems' of our coasts. In principle two basic erosion problems with sandy coasts do exist, viz.:

- a) erosion/recession during a storm (surge) event
- b) gradual long term erosion

Fig. 2 shows in plan view a stretch of a coast at a certain moment in time (under 'usual' sea conditions). The 'problems' a) and b) can be clearly illustrated if the behaviour of cross-section A-A of Fig. 2 is considered as a function of a long time. For reasons of simplicity the behaviour of the position with respect to the reference line of the so-called dune-foot is considered to be representative for the behaviour of the entire cross-section (other characteristic profile features could also be selected). The dune-foot is the intersection point between the gentle beach slope and the steep slope of the dune front.

Fig. 3 shows three typical possibilities of the behaviour of a sandy coast.

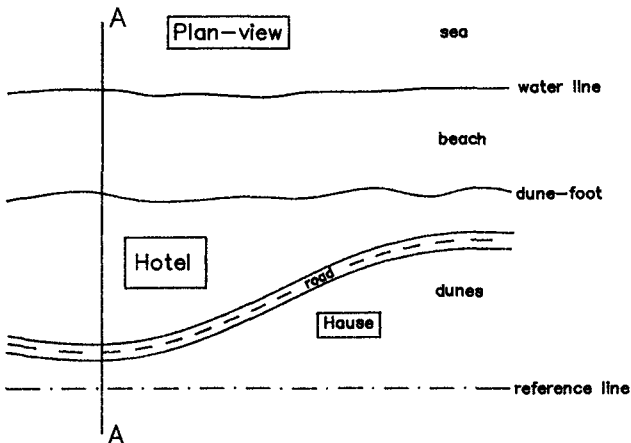


Fig. 2 Plan-view of coast

Fig. 3a represents an essentially stable coastline. However, storm (surge) events cause sudden recessions of the position of the dune-foot. Since the cross-section in consideration is, seen over a longer period, stable, a recovery of the dunes will take place in the years after the storm event. Depending on the seriousness of the storm event the magnitude of the recession can vary considerably. Fig. 3a represents in fact case a) indicated in this section.

Fig. 3b shows a gradually eroding coast (with surge events superimposed on that). The recovery after a surge is not entire. Fig. 3b represents case b).

[For the sake of completeness in Fig. 3c an accreting coast is shown (also with storm events). In the present discussions these cases are not considered since accreting coasts cause hardly 'problems' to the coast managers.]

4 Erosion/recession during a storm (surge) event

Erosion of the dunes and the upper part of the beaches can occur during a severe storm. The rate of recession during that event depends on the seriousness of the storm involved. During the storm not only the wave attack is greater than during usual conditions, but also the water level (surge level) increases to levels (far) higher than usual. Along coasts bordering oceans the increase in water level during the passage of a storm is often moderate; along coasts bordering funnel-shaped seas the increase of the water level may mount several meters.

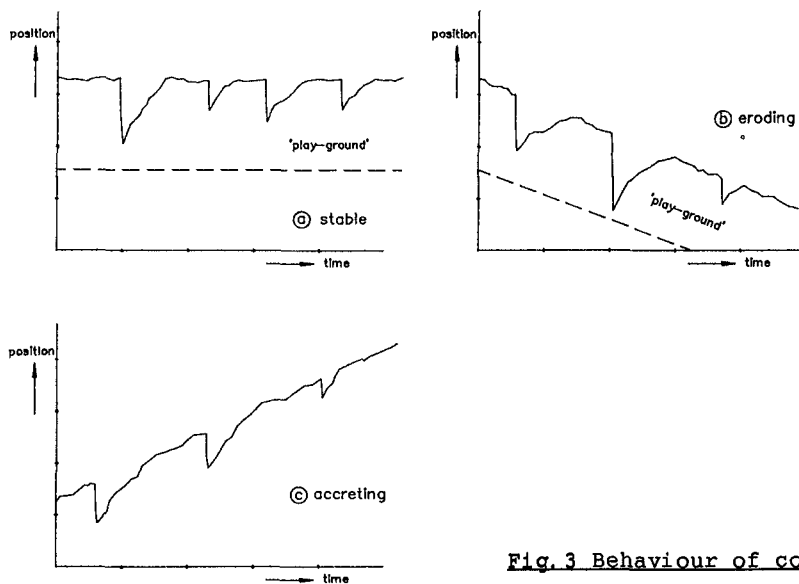


Fig. 3 Behaviour of coast

Fig. 4 shows schematically what happens during a severe surge. Material of the dunes is eroded and (mostly) settled again on the foreshore. Since the shape of the profile becomes less steep, the erosion process (the rate of erosion) slows down with time. After the surge a retreat distance RD can be observed.

Various methods are available at present to calculate the volume of dune erosion after the storm surge. [Kriebel and Dean (1985); Vellinga (1986).] These methods can be applied if the boundary conditions during the storm surge are known

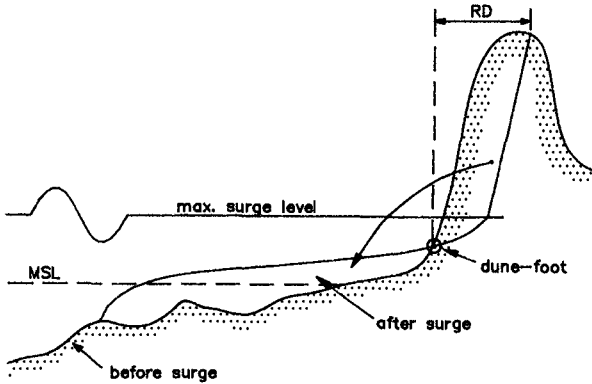


Fig. 4 Dune erosion process

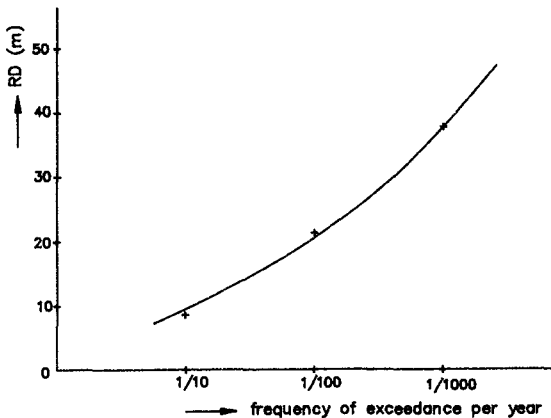


Fig. 5 RD as a function of frequency of exceedance

(wave height; wave period; maximum surge level; storm duration; particle size diameter; initial profile). Many of these boundary conditions have a highly stochastic nature. Nobody knows what the conditions will be next year. Based on long term observations and/or simulation calculations one is in fact only able to predict the probability of occurrence of a set of bad boundary conditions in a certain storm season or a certain year. With probabilistic methods [see e.g. Van de Graaff (1986)] one is eventually able to determine a figure like Fig. 5. Different retreat distances RD are expected depending on the frequency of exceedance.

In order to prevent superfluous damage the coast manager (or the 'society') has next to select an appropriate design frequency of exceedance (with a related design-RD distance). It should in fact be avoided that high investments in valuable goods like houses, hotels and roads are done in the selected design distance. From a coastal engineering point of view this seems quite logical. The sea needs a certain 'play-ground'. (In Figs. 3a and 3b arbitrary 'play-grounds' have been sketched.) Also from an economical point of view such a proceeding of a restriction policy can be simply justified. The everyday practice, however, is quite different. Partly due to a (sometimes pardonable) lack of insight in the 'tricks' of the sea, but also sometimes due to an almost blameworthy inability of the responsible authorities, too many valuable investments are done too close to the shoreline. A (apparently unexpected) rather severe storm surge may destroy consequently many buildings. After such an occasion the call for countermeasures will grow and it will be obvious that the construction of a seawall will come up as a possibility to avoid similar problems in future. It will be for sure that in this particular case a well-designed shore-parallel construction may indeed overcome the erosion problems due to a severe storm surge. A seawall can diminish the 'play-ground' of the sea. It should be stressed that a well-designed construction should be applied. E.g. Steetzel (1987) argues that if the erosion of the dunes is prevented due to the construction of a revetment against the dune front, severe erosion just in front of the revetment has to be expected. If the so-called 'denied' volume (= eroded volume from the dunes if the revetment was not there) is large, the depth increase in front of the construction may become quite considerable. Under Dutch design conditions, so far, erosion depths are expected of several meters below the initial beach profile. If the foundation depth of the construction is too small, stability problems for the entire construction may rise. In an essentially stable case, a recovery of the erosion pit will mostly follow soon after the storm [cf. Dean (1986)].

In conclusion it can be stated that in essential stable cases, where it is felt that the needed 'play-ground' of the sea should be restricted, a properly designed seawall might be applied.

5 Gradual long term erosion

Fig. 3b is characteristic in the case in consideration. The coast apparently recedes seen over a number of years. The yearly rate of recession depends of course on the particular situation, but is often up to some meters per year. [During real serious storm (surge) events the retreat might be up to some tens of meters per occasion (per day).]

A sneaking retreat of a built-up coastal area (with sometimes a storm surge event imposed on it), is extremely annoying to a coast manager. From time to time buildings have to be abandoned and often it can be almost precisely predicted when the next building is on its turn.

In cases like these too often the next (wrong) reasoning to build a seawall is followed:

- The coast (the built-up area) recedes.
- We have to stop this recession.
- Let us fix the dune front and the coast cannot recede further.
- Let us build a seawall to fix the dune front.

In the first years after the construction, unfortunately, all seems like a bed of roses. The erosion of the built-up area has been stopped indeed. The owners of the buildings are quite satisfied and the coast manager, happy with his great success, decides to build also a seawall along another eroding part of the coast which is under his control.

However, after the first happy years after the construction, a period with increasing problems starts. It will turn out that the erosion of the beaches in front of the seawall has continued or has even increased. The beaches in front of the seawall have lowered. The waves reach more easily and more frequently the seawall. The attack on the seawall increases. To prevent serious damage the seawall has to be reinforced or has to be 'protected'. In spite of these countermeasures the erosion of the beaches continues. After some time all the beaches have been disappeared. A situation like in Fig. 1c has been developed. There are, also under usual conditions, no beaches anymore for recreation purposes. The seawall has little by little changed in a seadike. In spite of these in fact dramatic developments, our coast manager remains often proud. The erosion by the sea has certainly been stopped. The encroachment of the sea of houses and roads has certainly ceased. That the beaches have been lost is a pity; it is all in the game. The costs of the regular reinforcements of the seawall are paid by the tax payers, so that does harm 'nobody'. At the end, after a number of years, only a few old persons know that in past nice sandy beaches did exist in this area.

What went wrong in fact?

The basic point is that it is a gradual erosion problem (cf. Fig. 3b). To overcome this type of problems, two methods are available in principle:

- 1) Feed from time to time artificially the amount of material which has apparently lost along the coastline (beach nourishment).
- 2) Try to interfere in the sediment transport process which causes the erosion. This interference should be such that the erosion stops in the area you like to save.

Method 1) is almost trivial. However, this method is increasingly attractive and can be applied almost always. The Dutch Manual on Artificial Beach Nourishment (1987) is recommended to consult if an actual beach nourishment scheme has to be designed.

Method 2) is more difficult to execute. First of all it should be established which sediment transports cause the erosion. If that has been established one has next to decide how to interfere actually.

Two main causes do exist for a gradual erosion of a part of a coast:

- a) Continuous offshore sediment transport from the upper parts of the beach profile (beach and dunes) to the deeper parts of the profile.
- b) Gradient in the longshore sediment transport.

Re a) Continuous offshore transport

Cross-shore directed sediment transports always take place in an actual cross-section of a beach profile. Depending on the wave conditions, water level and the shape of the initial profile, onshore or offshore transports take place through an arbitrary vertical cross-section. Seen over a relatively long period (from year to year for example) the shape of the beach profile often doesn't change so much (dynamic equilibrium). In a constant situation with respect to the boundary conditions (constant mean sea level and constant yearly wave climate), there is in usual cases no reason that a continuous offshore directed transport will be the reason for a gradual erosion of the coast. If a continuous offshore transport from the upper parts of the beach profile to the lower parts of the profile would occur, the beach profile would be flatter with time. Next it can be argued that the offshore transport rates will then slow down till an equilibrium has been reached. (The 'sea' had many centuries time to reach that!) Only if the supplied material to the deeper part of the profile is eroded again (e.g. by a gradient in the longshore transport in that region) a continuous cross-shore transport might be maintained. The real reason for the erosion of the coastline is then, however, not the offshore transport, but the mentioned gradient in the longshore transport on the deeper parts of the beach profile. The offshore sediment transport is only an intermediary mode of transport.

Only if the boundary conditions change with time, a more or less continuous offshore sediment transport might occur. This transport can be seen as 'necessary' in order to adjust

the shape of the beach profile so that it fits (again) with the 'new' boundary conditions. The global sea-level rise and an abrupt change in the wave climate are examples of changes in the boundary conditions. It will be clear that if these changes in the boundary conditions occur, a simple seawall cannot solve the induced erosion problem. Under usual conditions the seawall doesn't interfere in the underlying transport processes. (Only if the seawall is directly attacked, some interference might occur.) The erosion of the upper parts of the beach will continue. The seawall will be attacked more frequently and more intensively. If one likes to interfere actually in the (offshore) sediment transports one has to think of (submerged) detached offshore breakwaters. Such a construction might eventually effect (reduce) the wave action which approaches the coast and consequently might reduce the offshore sediment transports.

Re b) Gradient in the longshore sediment transport

In many cases a gradient in the longshore sediment transport is the main reason of the erosion problems of sandy coasts. Examples are the lee-side erosion near breakwaters or jetties and the erosion of convex coastlines.

Fig. 6 shows schematically the magnitude of the longshore sediment transport (e.g. in $m^3/year$) as a function of the position along an eroding coast. The increasing sediment transport with x is the reason of the erosion problems. The magnitude of the gradient dS/dx is a measure of the actual erosion problem. If one wants to stop the recession of the coast in stretch A-B in Fig. 6, one has to nourish volume V (see Fig. 6) along section A-B on a yearly basis or one has to 'change' in one way or another the sediment transports

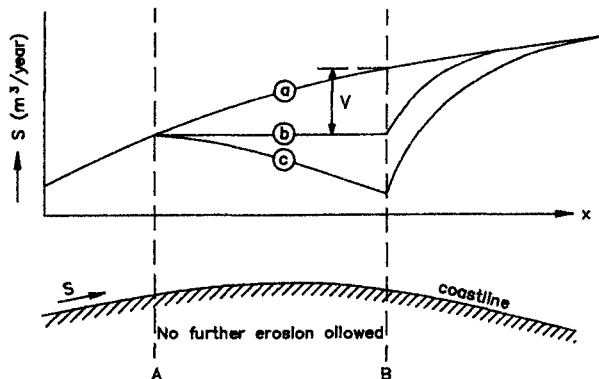


Fig. 6 Sediment transports along coast

along stretch A-B. Instead of a distribution of the sediment transports according to line a) in Fig. 6, a distribution according to line b) would in principle fulfil our requirements. The erosion in section A-B has stopped indeed ($dS/dx = 0$), but down stream of stretch A-B an increased erosion can be expected. (Increased dS/dx values in comparison with the initial situation.) To sketch a line like line b) is of course quite simple and is one thing, but how to acquire such a line in an actual case is another. It is for sure, however, that with a seawall by no means a situation like line b) can be reached. The basic problem was a gradient in the total longshore sediment transport and the longshore sediment transports take place (at least under usual conditions) on the foreshore and the shoreface. Since a seawall doesn't interfere in this type of sediment transport, no direct reducing effect can be expected. Only under storm conditions, when waves hit the shore-parallel construction directly, probably some reduction of the longshore sediment transports might be expected. In that case, however, it is also conceivable that, due to wave reflection, an increase of the longshore sediment transport will take place.

Since a shore-parallel construction near the dunes doesn't interfere generally in the sediment transports, the erosion continues; the shoreface, the foreshore and the beaches become deeper and at the end the attack of the sea on the seawall will intensify. Damage occurs; reinforcements of the seawall will be necessary. Nearly all seawalls built to restrict the further erosion at the lee-side of harbour breakwaters or jetties suffer from the stated problems.

As it has been indicated it is impossible to 'change' the sediment transport line a) in Fig. 6 to line b) with the help of a seawall. With the construction of groins or rows of (wooden) piles [perpendicular to the coast], or the construction of a (submerged) detached breakwater [parallel to the coast], the desired change from line a) to line b) is possible indeed. How to design these countermeasures actually, is a difficult coastal engineering problem, but from the 'physics' it can be understood at least that these constructions might help to overcome the erosion problem. (They interfere in the original sediment transports.) That a proper design of these countermeasures is indeed a difficult task can be illustrated with the help of Fig. 7. Case I line a) shows the same coastal erosion as Case II line c). The same gradients dS/dx occur, however, the magnitudes of the longshore sediment transport differ considerably. The lines b) and d) represent the ultimately desired sediment transport lines for Case I and Case II respectively. It is beyond doubt that the operation to achieve line b) from line a) calls for quite different countermeasures than to achieve line d) from line c). One has consequently to know quite precisely what the actual magnitudes of the sediment transports are, before a proper design of countermeasures can be made.

Changing the sediment transports along stretch A-B in fig. 6 from line a) to line b) is just necessary and sufficient to stop the erosion in that section. If line a) is changed in

line c) accreting of the section A-B can be expected. (That is in fact an 'over-kill' operation.) Accreting might be favourable to people living along section A-B. The erosion problems at the lee-side of section A-B will, however, consequently increase.

Since so many examples of the bad behaviour of seawalls are available, one might ask oneself whether seawalls will even worsen the erosion problems of the coasts they intend to protect. From the physics no sound support can be found for this idea. Seawalls do not interfere in the sediment transports, so consequently they will not increase the erosion problems. This hold at least till the time that some beaches are still present in front of the seawall under usual conditions. When all the beaches have disappeared (a case like Fig. 1c has been reached then), a quite different situation is reached. Increased as well as decreased sediment transports are conceivable depending on the actual conditions.

6 Conclusions

- Demolished seawalls harm the prestige of 'coastal engineering' as a respectable profession.
- The application of seawalls as a means to combat erosion of coasts should be restricted to a very limited number of cases.
- Only in essential stable cases where some reduction of the so-called 'play-ground' of the sea is required, a seawall would be an appropriate solution to achieve that goal.
- Along gradually eroding coasts, seawalls shouldn't be used to prevent further erosion. A seawall doesn't 'work' in these cases since a seawall doesn't interfere in the sediment transport processes.
- Generally seawalls don't 'destroy' beaches.

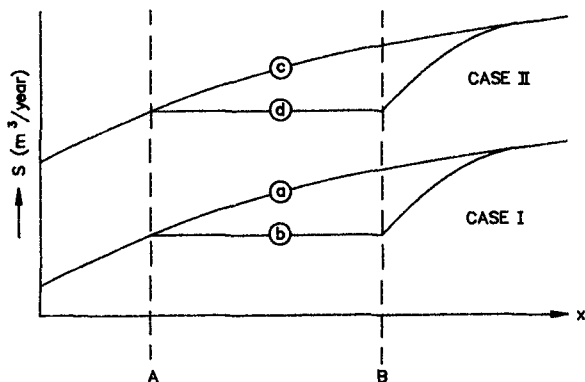


Fig. 7 Effect of magnitude of sediment transport

7 References

- Dean, R. G. (1986)
Coastal armoring: effects, principles and mitigation.
Proc. 20th Intern. Conf. on Coastal Engineering, Vol. III;
Chapter 135, Taipei.
- Graaff, J. van de (1986)
Probabilistic design of dunes; an example from the Netherlands.
Coastal Engineering, Vol. 9, pp. 479-500; Elsevier Science Publishers; Amsterdam.
- Kriebel, D. L. and R. G. Dean (1985)
Numerical simulation of time-dependent beach and dune erosion.
Coastal Engineering, Vol. 9, pp. 221-245; Elsevier Science Publishers; Amsterdam.
- Steetzel, H. J. (1987)
A model for beach and dune profile changes near dune revetments.
Proc. Coastal Sediments '87; Vol. I, pp. 87-97, New Orleans.
- Vellinga, P. (1986)
Beach and dune erosion during storm surges.
Ph. D. Thesis Delft University of Technology; also Delft Hydraulics Communications No. 372.
- Manual on Artificial Beach Nourishment (1987)
CUR/Rijkswaterstaat/Delft Hydraulics Report 130.
ISBN 90 212 6078 6, Gouda, the Netherlands.

CHAPTER 156

QUALITY AND DURABILITY OF CONCRETE ARMOUR UNITS

L. Van Damme *
L. Taerwe **
R. Dedeyne +
J. De Rouck ++

1. INTRODUCTION

The reliability of rubble mound breakwaters not only depends on the hydraulic stability but to a large extent on the strength of the armour units as well. In the debate on the shape of armour units, which turns out quite often to be merely academic in nature, generally too little attention is paid to the question of structural strength. On the occasion of the realization of the new outer harbour at Zeebrugge (Belgium) a serious effort has been made to arrive at a better understanding in the behaviour of concrete as construction material for armour units. This contribution gives an overview of the routine tests and of some particular investigations, carried out with respect to quality and durability of concrete armour units.

2. GENERAL CHARACTERISTICS OF THE ARMOUR UNITS

2.1. Types of armour units

In the Zeebrugge harbour extension works two types of armour units have been used : the Antifer cube (+60.000 units) and the HARO® (+13.000 units) (fig.1).

During the design of the main breakwaters the Antifer cube was chosen as armour unit. Consequently it has been used on the breakwaters protecting the LNG-terminal, which were built first.

-
- * Ministry of Public Works, Coastal Department,
Administratief Centrum, Vrijhavenstraat 3, 8400 Ostend,
Belgium
- ** Ghent State University, Laboratorium Magnel, Grote
Steenweg Noord 2, 9710 Ghent, Belgium
- + SECO S.V., Aarlenstraat 53, 1040 Brussels, Belgium
- ++ HAECON N.V. Consulting Engineers, Deinsesteenweg 110,
9810 Ghent, Belgium.
Ghent State University.

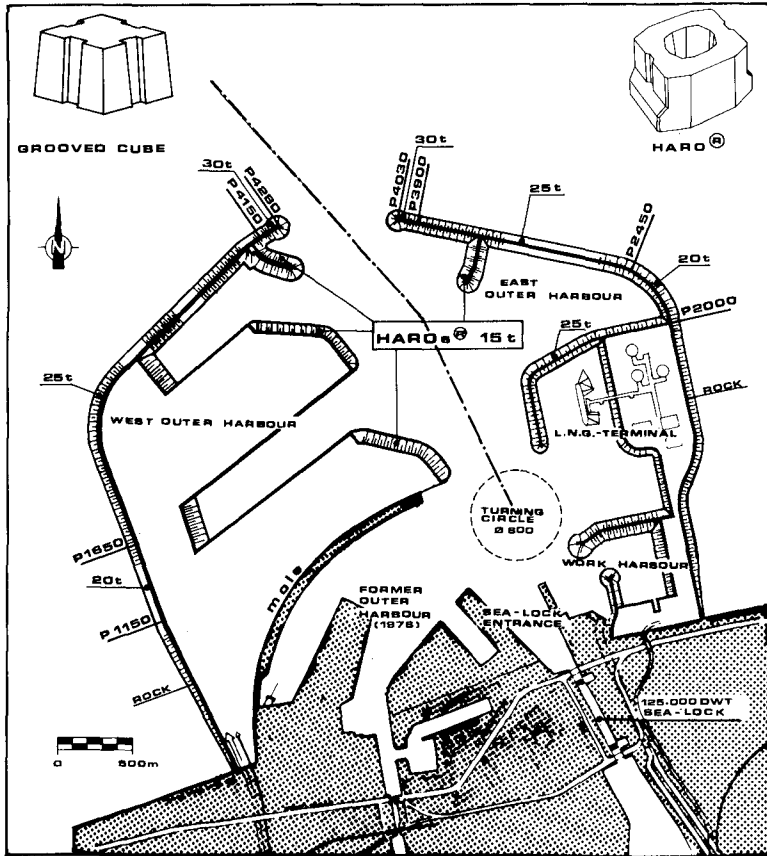


Figure 1 : Zeebrugge outer harbour, with indication of the types of armour unit

On the outer-harbour breakwaters, a slightly adapted grooved "cube" (the height is somewhat smaller than the bottom side) has been used. During the same optimization one has looked for concrete with higher density : a mean density of 2,47 t/m³ (1434 test results) has been achieved by adding lead slag. Depending on the location the weight of the units equals 20 or 25 tonnes. The main-breakwater heads have been armoured with 30t-grooved cubes.

Fig. 1 shows the areas, where the different units have been used.

During the design of the inner-harbour breakwaters the HARO[®] has been developed. The HARO[®] is a flat (height is less than the short side in plan view) concrete block with a large central opening. Both short sides are made wider at

the base, thus constituting an alternative type of block profile by weight. The corners of the block are asymmetrically tapered in plan. The general form of the block in plan is rectangular.

The criteria which have been taken into account during the development of the HARO[®] are :

- a high structural strength (given by its strong compact shape) ;
- hydraulic stability ($K_D > 15$) ;
- advantageous wave reflection and run-up characteristics ;
- simplicity of fabrication : no opening of the moulds and demolding in one single movement upwards ;
- simplicity in placement of the block on the breakwater slope ;
- economy : by using HAROs[®] the total volume of concrete needed in the armour layer decreases by more than 35% compared with grooved cubes. This has mainly been achieved by the reduced block weight ($K_D > 15$) and by the high porosity ($P = 52 \text{ à } 55\%$).

The inner-harbour breakwaters will be armoured with HAROs[®]. The specified characteristic density of the HARO[®], is $2,3 \text{ t/m}^3$.

More details on these types of armour units may be found in ref. (1) and (2).

2.2. Placement pattern

During the first construction phase (breakwaters surrounding the LNG terminal) the chosen placement pattern required very little re-positioning of the crane (fig. 2a). However hydraulic stability tests showed a rather high risk of jamming-up when tending towards the design conditions.

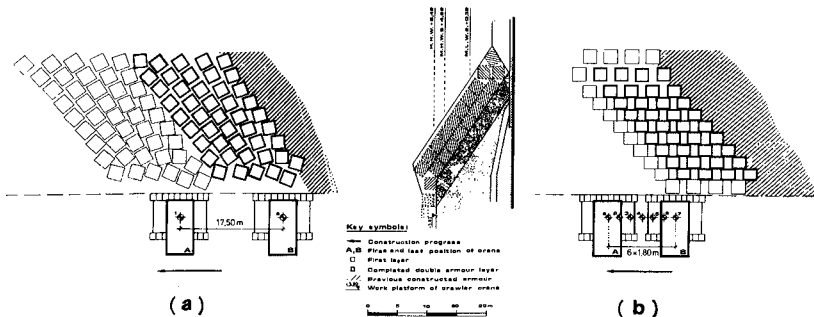


Figure 2 : Placement pattern of armour units.

A placement pattern to eliminate this phenomenon has been elaborated : Within the considered (upper or lower) layer each unit rests on the two adjacent blocks of the lower row. This placement pattern requires an almost continuous repositioning of the crane (fig. 2b). All units on the outer-harbour breakwaters and all HAROS® are placed according to this pattern.

2.3. Concrete composition

The concrete mix proportions to obtain a characteristic density of $2,3 \text{ t/m}^3$ are as follows :

- . cement LK30 300 kg/m^3
- . gravel (4/28) 1.300 kg/m^3
- . sand (0/5) 700 kg/m^3

This concrete composition holds for a mean water content of aggregates of ca. 2,5 %. To obtain a characteristic density of $2,4 \text{ t/m}^3$, as stipulated for the grooved cubes, lead slag is added at a rate of ca. 100 l/m^3 . The W/C ratio was lower than 0,4. A blast furnace cement (LK30), with no more than 15% Portland clinker, and low heat of hydration (200 kJ/kg at an age of 72 h) is used. The sand and gravel are marine aggregates with a sufficiently low chloride content and an acceptable shell content.

2.4. Concrete quality

A total of 2.313 compressive strength results are available over a period of 4 years. The test specimens are cubes with side length of 200 mm and cured under water until an age of 28 days. The following statistical characteristics were found :

mean	39.40	N/mm^2
standard deviation	4.59	N/mm^2
coefficient of variation	11.60	%
skewness	0.369	
curtosis	3.768	

On the basis of the values for skewness and curtosis, the normality hypothesis for the distribution function has to be rejected. This is due to the long term variation of the parameters which determine the strength characteristics of the concrete.

3. USE OF LEAD SLAG

3.1. Selection criteria

A higher density of concrete can be obtained by substituting heavy inert materials for part of the gravel. The selection of the most suitable aggregate requires the examination of several physical and mechanical concrete

properties, such as : density, compressive and tensile strength, segregation during mixing, plasticity, porosity, shrinkage, creep, capillar absorption, permeability, workability, optimal compaction, resistance against aggressive agents.

The following aggregates have been considered : natural rock, basalt, hematite, lead slag and iron. A cost comparison showed the lead slag mix to be the most economic (table 1).

Unit weight w_c of concrete (t/m^3)	Cost
Concrete :	
$w_c = 2,30$	1
Concrete with basalt ($w_b = 3,10 t/m^3$)	
$w_c = 2,41$	1,02
$w_c = 2,45$	1,12
$w_c = 2,51$	1,25
$w_c = 2,58$	1,39
Cyclops concrete with natural rock ($w_r = 2,65 t/m^3$)	
$w_c = 2,40$	1,10
Concrete with hematite ($w_h = 5 t/m^3$)	
$w_c = 2,40$	1,16
$w_c = 2,50$	1,34
$w_c = 2,65$	1,61
Concrete with lead slag ($w_l = 3,5 t/m^3$)	
$w_c = 2,42$	1,03
$w_c = 2,54$	1,07
$w_c = 2,65$	1,11
Concrete with iron cuttings ($w_i = 7,85 t/m^3$)	
$w_c = 2,40$	1,16
$w_c = 2,50$	1,35
$w_c = 2,65$	1,63

Table 1 : Cost comparison of high-density concrete

3.2. Tests on lead slag

Concrete containing lead has a very bad reputation, as expansion of lead in a humid environment may give rise to

splitting of concrete. However, lead slag as a residue from the lead production process has a negligible lead content.

A comprehensive analysis has been carried out in order to determine the behaviour of lead against cement and the behaviour of concrete containing lead slag against sea water.

The analysis has been conducted in the following way :

a) Mineral analysis of the slag

From slag samples, thin slices with a thickness of 30 to 40 microns have been taken. Examination of the slices showed the presence of various mineral components difficult to identify in an optical way. An analysis by electron microprobe was used to determine the composition of very small zones (1 micron). The components found are not likely to provoke serious damage for the intended utilization of the lead slag.

b) Reactivity of the slag with respect to cement

The reactivity of the slag with respect to cement has been analyzed by comparing the mechanical properties of two mortars realized with cement and two types of fine aggregates : an inert sand (quartz) and crushed slag. This part of the analysis revealed no significant difference of behaviour.

c) Simulation of sea-water attack

After three months of hardening in a humid chamber, mortar specimens were alternately immersed in and removed from sea-water. At an age of 4 1/2 months, mechanical resistance tests and microscopic examinations were carried out on specimens, subjected to sea-water attack and on reference specimens, one series being composed of normal sand and another series being composed of crushed slag.

The mechanical resistance showed higher values for both series exposed to sea-water. The corresponding results of sand and slag mortar were of the same magnitude (maximum deviation 8%). For both specimen types, no irregularities were noticed by microscopic examination, neither in the cement matrix nor at slag-cement or sand-cement interface.

d) Examination of core samples

At an age of about two years, core samples were taken from blocks on-site. The following characteristics were determined :

- density
- water absorption by immersion
- compressive strength.

The results of these tests correspond to values usually recorded for standard concrete and show no significant deviation from the reference values. The examination of ground-up slices taken from the cores showed that lead slag didn't instigate concrete disintegration.

The foregoing considerations show that the addition of lead slag, with a low lead content, to the concrete is not likely to alter the behaviour of this concrete over its design life.

4. THERMAL STRESSES

Different researchers have demonstrated the relationship between heat development due to hydration of cement and crack formation in young concrete. In order to verify the behaviour of concrete at early ages, a comprehensive investigation program was set up.

4.1. Temperature measurements in armour units

Two series of measurements on concrete blocks were carried out on the site, one in a winter period, the other during summertime.

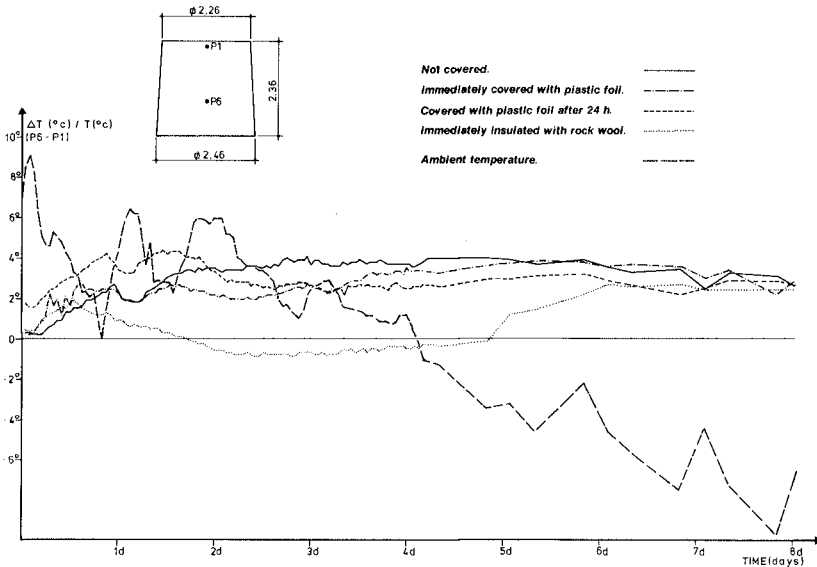


Figure 3 : Evolution of temperature difference between the core and the upper surface for 30 t cubes (winter time)

In the first test trial, four cubic blocks (30 t) were instrumented with 11 thermocouples. After removal of the mould, two blocks were covered with a plastic foil, one block was insulated with rock wool and one block was left unprotected. Fig. 3 shows the evolution of temperature difference between the core and the upper surface for these four 30t-cubes.

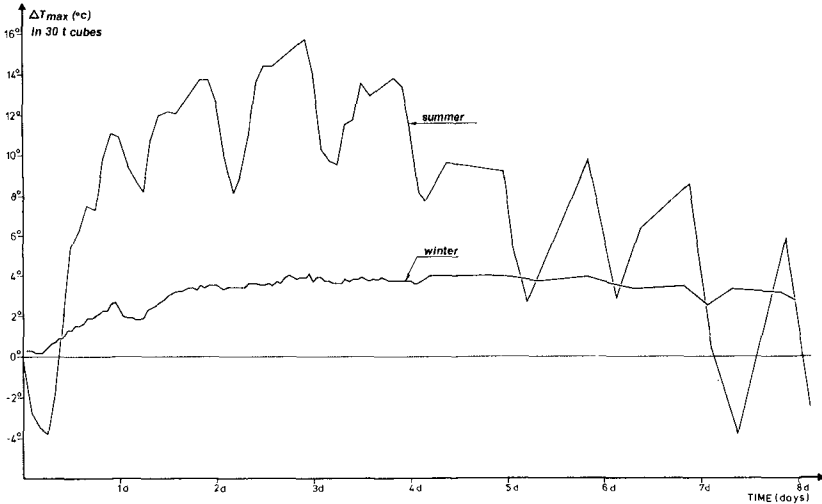


Figure 4 : Maximum measured temperature difference in the unprotected 30 t cubes

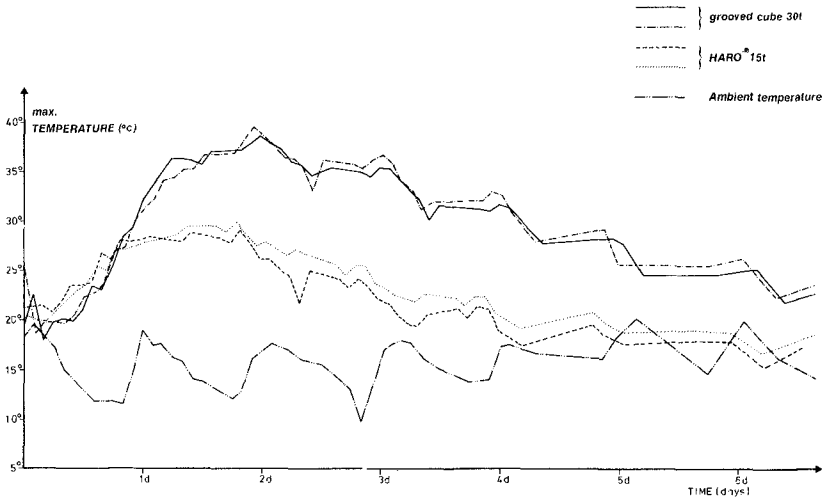


Figure 5 : Maximum temperature (measured in summer) for grooved cubes and HAROs®.

A second series of temperature measurements was carried out during a summer period on 2 cubic blocks (30t) and 2 HAROS[®] (15t). All blocks were left unprotected. Fig. 4 shows the maximum temperature difference between core and upper surface for the unprotected blocks i) in winter, ii) in summer. Fig. 5 also shows the maximum temperature, both in summertime, and for both grooved cube and the HARO[®]. Due to the central opening in the HARO[®] the temperature increase remains small.

4.2. Characteristics of cement and concrete

4.2.1. Properties of cement

The mechanical properties of cement type LK30 were determined on mortar prisms (40x40x160 mm). The compressive strength equals 17.4 N/mm² at 3 days, 28.8 N/mm² at 7 days and 41.8 N/mm² at 28 days.

Setting starts at 6h40 min. and ends at 9h20 min. (Vicat test).

A chemical analysis reveals the following composition :

calcium oxide	44,9 %	magnesium oxide	1,6 %
silicon oxide	30,1 %	loss on ignition	0 %
aluminium oxide	12,3 %	insoluble residue	1,5 %
ferric oxide	1,7 %	other components	0,2 %
sulphur trioxide	7,3 %		

The heat of hydration, determined by means of the conduction method, is found to be 53.7 kJ/kg at 24 h, 146.2 kJ/kg at 48 h and 198.4 kJ/kg at 72 h. It is clear that the heat of hydration of the cement used is rather low which is favourable in order to limit internal thermal stresses.

4.2.2. Mechanical properties of the hardening concrete

During the measuring trial, the compressive and the splitting tensile strength of cubes (side length 200 mm) is determined at several ages, both for on-site and laboratory cured specimens. The laboratory cured specimens are left in a humid chamber at 10°C and a relative humidity of at least 90%. Prisms for the determination of the secant modulus of elasticity are also cured in these environmental conditions.

The results for the concrete of the 30 ton cubes cast in summer are mentioned in table 2.

Age (days)	Curing	Compressive strength (N/mm ²)	Splitting tensile strength (N/mm ²)	Secant Modulus of Elasticity (N/mm ²)
1	site	2.63	0.19	4.300
	laboratory	2.64	0.18	-
2	site	-	0.99	31.000
	laboratory	-	1.08	-
3	site	18.0	1.59	36.200
	laboratory	23.2	1.93	-
7	site	-	1.98	35.400
	laboratory	-	2.87	-
28	site	32.0	2.76	42.500
	laboratory	40.8	3.24	-

Table 2 : Mechanical properties of the concrete used for the 30-ton cubes (summertime)

The results for the HAROs® also cast in summer are of the same order.

4.3. Thermal stresses in young concrete

The measured temperature and the secant modulus of elasticity, determined on the specimens were used to calculate the thermal stresses that develop in concrete blocks by means of a finite element program.

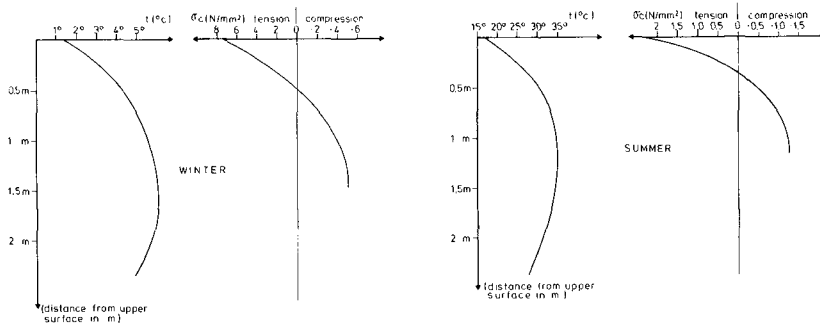


Figure 6 : Measured temperature distribution and calculated horizontal stress distribution along the vertical axis in 30 t cubes.

Fig. 6 gives the measured temperature distribution and calculated horizontal stress distribution along the vertical axis in a cubic block (30t).

The maximum tensile stress at the block's upper surface is obtained after 4 days in the winter and after 3 days in the summer.

It appears that the calculated tensile stresses due to hydration heat are comparable in magnitude with the tensile strength of the concrete at that time as shown in table 3. Consequently, cracks may arise at the block's surface.

	WINTER (4 days after casting)	SUMMER (3 days after casting)
calculated maximum tensile stress	0.75 N/mm ²	2.3 N/mm ²
tensile strength	0.4 N/mm ²	1.6 N/mm ²

Table 3 : Calculated maximum tensile stress versus available tensile strength of the young concrete

5. FROST RESISTANCE

After two severe winters, some blocks on the site showed a surface with exposed coarse aggregates due to the alternating action of freezing and thawing.

One could fear that with a repetition of that process the units could loose an important fraction of their weight or that an accelerated deterioration long before the presumed lifetime could take place and consequently cause stability problems.

In order to investigate the problem in detail, freezing and accelerated ageing tests were executed on specimens taken from the damaged blocks.

Frost resistance is related to the water-cement ratio and the air content of the concrete. Although the W/C ratio is below 0.40, the porosity at the surface, especially the upper surface, might be higher than in the core of the units. Tests on cores drilled near the surface showed water absorption ranging from 6 to more than 8 percent.

5.1. Freezing tests

A freezing test was executed on a large sample with a mass of 950 kg.

In the first stage the following environmental conditions were used :

- freezing chamber at -15°C
- laboratory conditions at 20°C
- salty water at 20°C .

A complete cycle has a duration of 24 hours. No breakage or deterioration of the blocks was observed after 3 cycles.

In the second stage, 15 cycles of two days each are performed. The first day at -15°C in the freezing chamber, the second day it is brought into salty water at 20°C . After the third cycle cracking of the block started and finally several branched cracks extending over the complete block were observed.

After the freezing test concrete quality was measured on cores drilled from the uncracked areas of the block. In comparison with reference values, a reduction of compressive and tensile strength is observed but the values are still acceptable taking into account the very severe conditions. The water absorption also decreased.

5.2. Accelerated ageing test

From several blocks, two cores are drilled. One as a reference specimen and the other one is used for the tests.

The test specimens are subjected to 12 ageing cycles over a total period of 24 hours, each consisting of consecutive periods of variations in temperature, ultraviolet and infrared radiation, artificial rain and freezing. After 12 cycles no breaking or deterioration was observed. Here too the concrete quality remains acceptable and the water absorption percentage is decreasing.

6. REMOVAL OF THE FORMWORK

Apart from thermal influences cracking may also occur while removing the formwork and as a result of drying-out of the surface.

About 16 hours after casting, demoulding takes place. To detach the mould from the young concrete, a hydraulic jack is used which pushes on a steel plate placed on top of the block. After the complete mould has slightly been lifted, it is further struck upwards in one single movement. During the whole operation, the mould is not opened.

Particularly attention is paid to avoid cracking of the young concrete, given its low resistance at the moment of

striking. The steel plate is therefore as large as possible in order to distribute the load.

Special attention was paid to the curing of the concrete. A heavy duty membrane compound was used in order to keep concrete surfaces permanently wet for the whole of the curing period. Nevertheless, where cracks were noticed they were treated with a synthetic resin.

7. ALKALI SILICA REACTION

Another possible cause of crack formation is internal damage of the concrete.

As the first blocks were placed almost 10 years ago, it was found useful to make a petrographic analysis of the concrete in order to investigate whether or not internal damage occurred due to the exposure to the marine environment. More particularly, alkali silica reaction (ASR) and ettringite formation are examined.

The ASR in concrete is a reaction which takes place in humid environment between aggregates (SiO_2 minerals) and the alkalis (Na, K) present in the cement in a humid atmosphere. The reaction results in a very expansive gel which causes the formation of cracks, which is accelerated when ettringite is formed in the cracks.

That aggregates that have been noticed for their sensitivity to alkalis belong to the granulometric fraction of sand and fine gravel. Some types of coarse aggregates also take an active part in the ASR e.g. flint stones, which generally have a white external layer. Also volcanic rock is known as a reacting aggregate.

The concrete, affected by ASR, is manufactured with a cement of the ordinary portland cement type.

As in many regions there is only a limited choice in aggregates and cement, this petrographic examination can provide useful information with respect to the durability of the concrete units.

8. RECOMMENDATIONS

The experience gained during the construction of the breakwaters at Zeebrugge has led to the development of the following proposals for obtaining high-quality concrete :

- A minimum cement content of 300 kg/m³.
- Use of low heat cement.
- A low water-cement ratio (<0.4).
- Good compaction of concrete, not only in the core of the unit but also close enough to the mould.
- Careful curing (use of curing compound).
- A rigid formwork, which is easy to remove.

- Removal of the formwork at an appropriate time depending on the setting-time of the cement and on the ambient temperature.
- Dense and impermeable aggregates approved for use by prior testing.
- Limitation of the initial temperature of fresh concrete.
- Insulation of the young concrete may be envisaged in order to limit the temperature gradient.

Although the application of these proposals in practice could be limited by local technical or economic constraints, it generally does not increase production costs.

In spite of the application of these guidelines and the extra care taken, about 1% of the concrete cubes placed in Zeebrugge present significant cracking. Although these cracks are not expected to cause stability problems, they are carefully followed.

No cracks are noticed in the HARO®-units.

9. ACKNOWLEDGMENT

The investigations on the quality and the durability of the concrete were supported by the N.V. De Vreese-Simon, supplier of marine aggregates, the Research Centre of the Belgian Cement Industry and the Magnel Laboratory for Reinforced Concrete.

10. REFERENCES

- (1) L.V. Van Damme, The main breakwaters of Zeebrugge, 18th International Conference on Coastal Engineering, Cape Town 1982.
- (2) J. De Rouck, F. Wens, L. Van Damme, J. Lemmers, Investigations into the merits of the HARO®-breakwater armour unit.
1987 Proceedings of Coastal & Port Engineering in Developing Countries. Volume I, p. 1055-1068, Beijing, China 1987.

Large verification tests on rock slope stability

J.W. van der Meer* and K.W. Pilarczyk**

ABSTRACT

A number of large scale tests on stability of rock slopes and gravel beaches is described and compared with small scale test results. The following topics are treated: the stability of a rock armour layer, the profile formation of a berm breakwater, the profile formation of gravel beaches, including ripple formation, and reflection and overtopping on rock slopes. The general conclusion is that scale effects could not be found.

INTRODUCTION

An extensive research program has been performed on static and dynamic stability of rubble mound revetments, breakwaters and gravel beaches. The first part was based on statically stable rubble mound breakwaters. Based on roughly 300 tests two new practical stability formulae were derived, including the wave period, storm duration, permeability of the structure and a clearly defined damage level.

The second part was concentrated on dynamic stability, i.e. the profile formation of rock slopes and gravel beaches under wave attack. About 150 tests were performed in this stage. The result was a computer program that can predict the profile for various wave conditions, including tides and storm surges.

All tests mentioned above were performed in small scale facilities with waves roughly between ten and twenty centimeters. It was stated at the beginning of the research program that the results derived in the small scale facilities should be verified on a larger scale in the Delta flume. These verification tests on scale effects are the subject of this paper.

For results on static stability one is referred to Van der Meer (1987a) and (1988a). Results on dynamic stability were presented by Van der Meer and Pilarczyk (1986) and Van der Meer (1987b). The complete research including set-up, analysis and data of tests was presented by Van der Meer (1988b).

MODEL FACILITY

The Delta flume has a length of 230 m, a width of 5 m and a depth of 7 m. The maximum significant wave height that can be generated is nearly two meters. The random wave generator was equipped with a system that measured and compensated for reflected waves from the structure. With this system standing waves and basin resonance were avoided.

* DELFT HYDRAULICS, P.O. Box 152, 8300 AD Emmeloord, The Netherlands
** RIJKSWATERSTAAT, P.O. Box 5044, 2600 GA Delft, The Netherlands

A surface profiler on a carriage was developed for the investigation. The profiler for the small scale facility was described in more detail by Van der Meer (1987a). The profiler of the Delta flume was constructed in the same way, but all length dimensions were increased by a factor 5.

RESEARCH TOPICS

Various aspects concerning rock slopes and gravel beaches were investigated in the Delta flume on a large scale. Static stability of rock slopes was investigated together in combination with run-up, run-down and reflection. A berm breakwater can be classified as initially dynamically stable and finally statically stable. A berm breakwater was tested with regard to profile formation and overtopping. Tests on dynamic stability of gravel beaches were divided into verification tests on profile formation and extrapolation tests with very small shingle.

STATIC STABILITY

The 300 tests on static stability of rock armour layers in the small scale facility resulted in two new practical stability formulae, given by:

$$H_s / \Delta D_{n50} * \sqrt{\epsilon_m} = 6.2 P^{0.18} (S/\sqrt{N})^{0.2} \quad (1)$$

for plunging waves ($\epsilon_m < \epsilon_m$ (transition)),

$$H_s / \Delta D_{n50} = 1.0 P^{-0.13} (S/\sqrt{N})^{0.2} \sqrt{\cot \alpha} \epsilon_m^P \quad (2)$$

for surging waves ($\epsilon_m > \epsilon_m$ (transition)), with:

$$\epsilon_m \text{ (transition)} = (6.2 P^{0.31} \sqrt{\tan \alpha})^{1/(P+0.5)} \quad (3)$$

where:

- H_s = significant wave height
- Δ = relative mass density = $\rho_a / \rho - 1$
- ρ_a = mass density of rock
- ρ = mass density of water
- D_{n50} = nominal diameter = $(W_{50} / \rho_a)^{1/3}$
- W_{50} = 50% value of the mass distribution curve
- ϵ_m = surf similarity parameter = $\tan \alpha / \sqrt{s_m}$
- α = slope angle
- s_m = wave steepness = $2\pi H_s / g T_m^2$
- T_m = mean wave period
- P = permeability coefficient of structure:
 - $P = 0.1$: impermeable core (lower limit)
 - $P = 0.4$: most multi-layer breakwaters
 - $P = 0.5$: permeable core
 - $P = 0.6$: homogeneous structure (upper limit)
- S = damage level = A / D_{n50}^2
 - $S = 2-3$: start of damage
 - $S = 5-8$: moderate damage
 - $S = 8-15$: filter layer visible (two layer system)
- A = erosion area of cross-section
- N = storm duration in number of waves

It was shown in the small scale tests that permeability of the structure had a large influence on stability. And especially the flow charac-

teristics in a small scale model might be due to scale effects. Therefore tests in the Delta flume were concentrated on two different structures: a structure with a permeable core ($P = 0.5$) and a structure with an impermeable core ($P = 0.1$).

Scale effects in small scale tests on armour stability were discussed by various researchers. The effect of the Reynolds number on stability was investigated by Dai and Kamel (1969), Thomsen et al. (1972), Broderick and Ahrens (1982), Jensen and Klinting (1983), Sørensen and Jensen (1985), Shimada et al. (1986) and Burcharth and Frigaard (1987). Although results are not throughout consistent, lowest values for which no scale effects will be present are often set at $Re = \sqrt{gH_s}D_{n50}/\nu = 1.10^4 - 4.10^4$, with ν = kinematic viscosity. The range of Reynolds numbers used in the small scale tests was about $4.10^4 - 8.10^4$. Thomsen et al. (1972) found no scale effects for $Re > 2.10^5$. Shimada et al. (1986) suggest a value of $Re > 4.10^5$. The results of Thomsen et al. and Shimada et al. were both obtained in large wave flumes with monochromatic wave attack.

Eleven tests of the small scale series were repeated in the Delta flume and were scaled up according to Froude's law by a linear factor of 6.25. The stones had an average mass of $W_{50} = 26.5$ kg, a nominal diameter of $D_{n50} = 0.214$ m, a mass density of $2,700$ kg/m³ and a grading of $D_{85}/D_{15} = 1.38$. The wave period was $T_m = 4.4$ s in all tests, the wave heights ranged from $0.7 - 1.2$ m. The slope angle was $1 : 3$. In total six test were performed on a permeable structure and five tests on an impermeable structure. The armour layer was rebuilt after each test which means that the data points in a wave height versus damage plot were independent.

The average of nine parallel profiles gives a clear picture of the structure and the damage. Figure 1 shows the profiles of the permeable structure and Figure 2 those of an impermeable structure, where the thin filter layer was placed on a concrete underlayer.

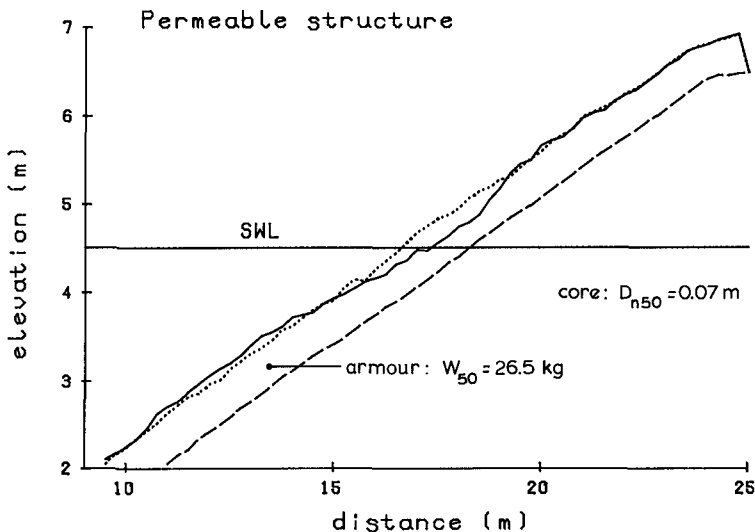


Figure 1 Cross-section with permeable structure in Delta flume

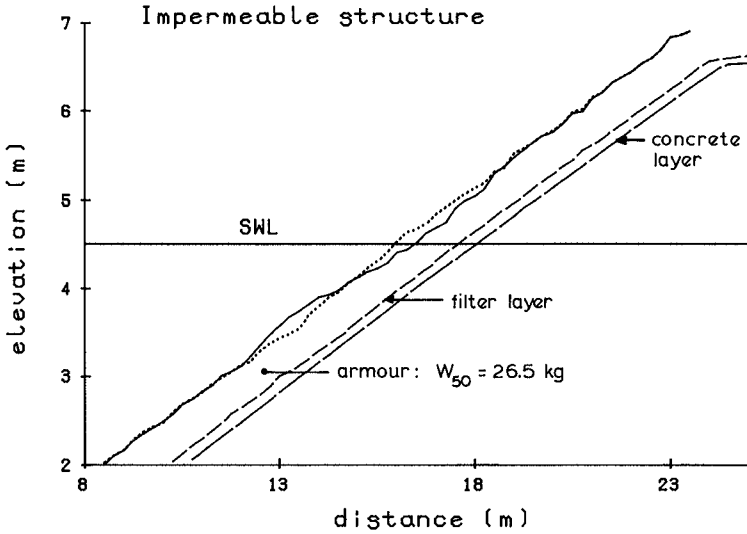


Figure 2 Cross-section with impermeable structure in Delta flume

Results of small and large scale tests can directly be compared in a dimensionless damage curve, where $H_s/\Delta D_{n50}$ is plotted versus the damage S . Figure 3 gives the results of the permeable core and Figure 4 the results of the impermeable core. Besides the different data points of the small and large scale tests, stability formula (1) was plotted in the figures (the curved line).

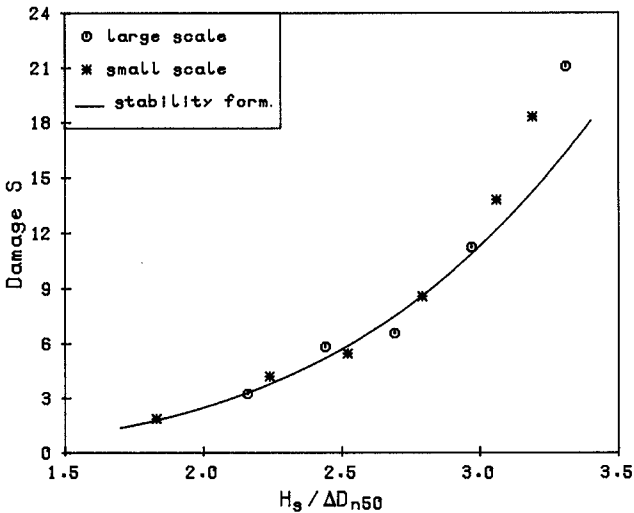


Figure 3 Results of permeable structure

From both Figures it can be concluded that the results of small and large scale tests are in close agreement. This confirms the validity of

stability formulae (1) and (2). The stability curve fits well with the data, although some difference is found in Figure 3 for extreme damage levels, $S > 12$ (filter exposed).

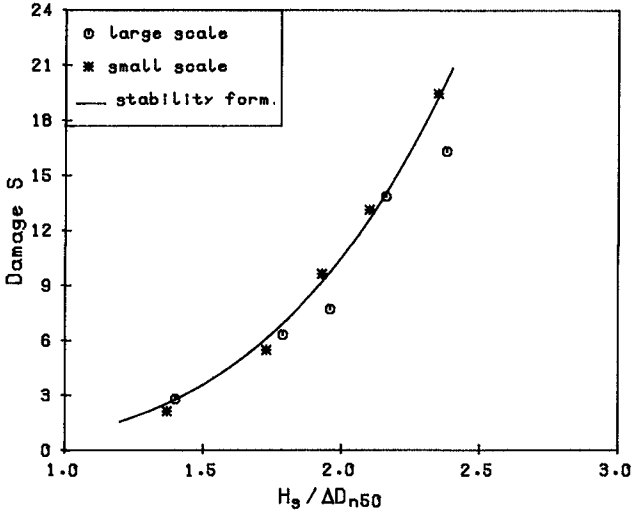


Figure 4 Results of impermeable structure

Comparison of reflection coefficients for small and large scale tests is shown in Figure 5 and coefficients are plotted versus the $H_s / \Delta D_{n50}$. The impermeable structure gives higher reflection coefficients in both cases than the permeable structure, where more energy is dissipated into the structure. The reflection for the impermeable structure is a little higher in the large scale tests. It is almost exactly the same for the permeable structure, the lower data points. In general the agreement is fair.

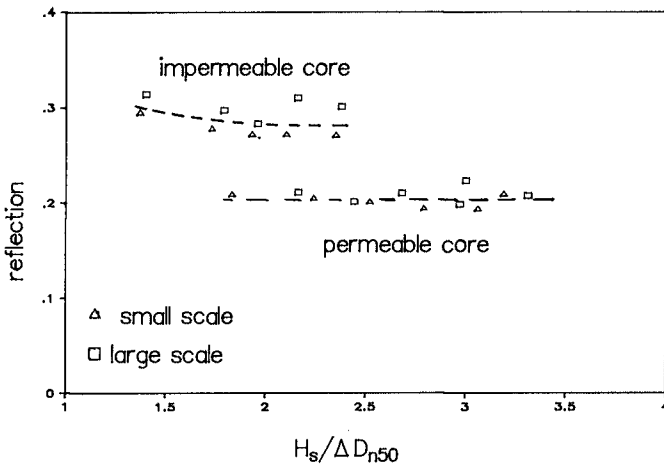


Figure 5 Reflection on rock slopes

The run-up was measured with a capacitance wire. Analysis showed, however, that the exceedance curves of the run-up gave a shift or nod about one meter above the still water level. Probably the wire was damaged at that point by a rolling stone. Therefore, run-up could not be compared with small scale tests.

The final conclusion of the large scale tests on static stability can be stated as follows: large scale model tests confirmed the validity of the small scale tests. The stability of an armour layer of rock was not influenced by the Reynolds number when Re was between $4 \cdot 10^4$ and $7 \cdot 10^5$. As these figures give the whole range of testing, the value of $Re = 4 \cdot 10^4$ can only be regarded as an upper boundary for which scale effects on rock armour stability might start.

BERM BREAKWATER

The design concept of the berm breakwater is clearly presented by Baird and Hall (1984). A berm breakwater is a structure that behaves dynamically stable under the first storms and is statically stable further on. The berm breakwater of St. George in Alaska was extensively tested (Delft Hydraulics (1985)). The actual design was performed in a three-dimensional basin on a scale of 1 : 35. Tests on scale effects were performed before the design stage started. One test was performed in a flume on a scale of 1 : 35 and repeated in the Delta flume on a scale of 1 : 7.

The berm breakwater consisted of 2 - 10 tons rock (0.046 - 0.233 kg in the small scale wave flume and 5.8 - 29.2 kg in the Delta flume). The depth limited wave height at the structure was about $H_S = 6$ m (0.17 and 0.86 m, respectively). The deep water wave height was up to 11 m (0.31 m and 1.57 m). The test consisted of 8 steps with various wave height - wave period combinations, including long swell with peak periods up to 25 s.

Figure 6 gives one of the profiles of the Delta flume test, together with the corresponding profile of the small scale test, but scaled up with a factor 5. The profiles of both tests are very similar. They show the same amount of erosion and subsidence (due to lack of filter layer) at the berm and at the rear of the crest due to overtopping. Even the depth of the scour hole is the same, although shape and length of the scour hole are different.

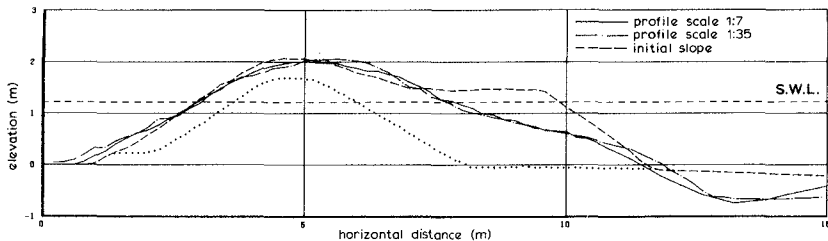


Figure 6 Profiles of berm breakwater in small and large wave flume measures on scale 1 : 7

The volume of erosion at the berm is given in Figure 7 versus the various steps of the test. The agreement between small and large scale test is very good up to step 5. In steps 6 to 8 the small scale test gives a little smaller amount of erosion.

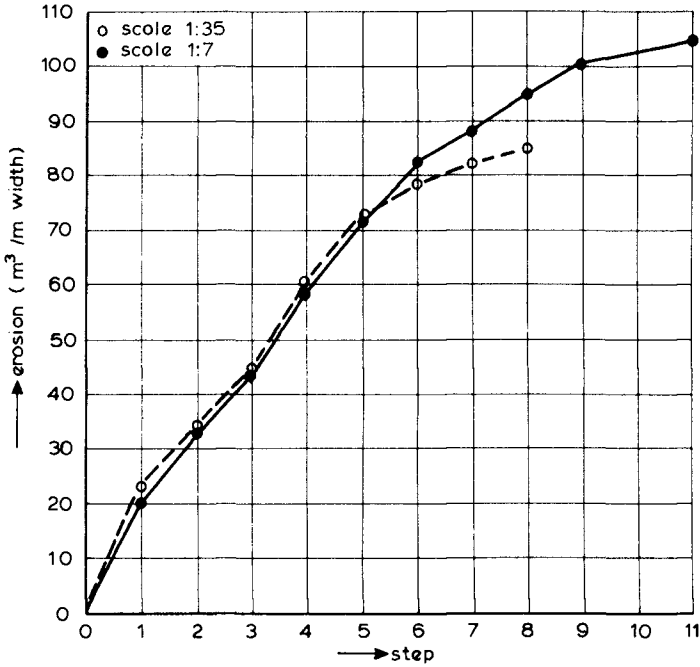


Figure 7 Erosion at berm developed during test

The comparison of overtopping in the berm breakwater tests (in prototype measures) is shown in Figure 8. The left plot shows the percentage of waves that reached the crest of the structure. The right plot gives the significant wave height behind the structure, generated by overtopping. The vertical axis gives the values of the Delta flume test and the horizontal axis the values of the small scale facility. The agreement of results is fair. Only the wave height behind the breakwater is consequently a little larger in the Delta flume.

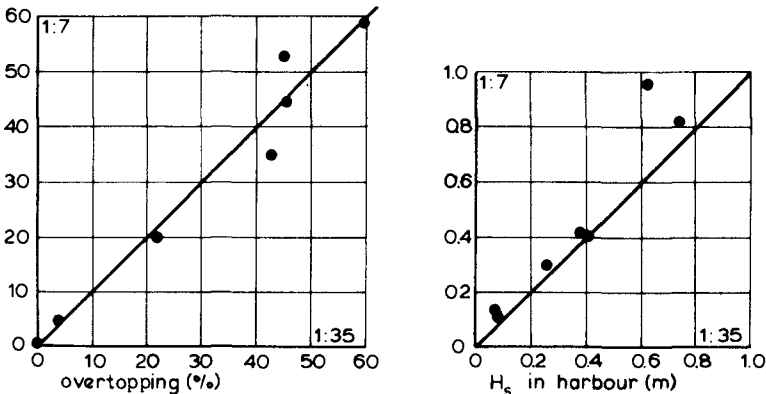


Figure 8 Results on overtopping

The complete analysis of the profiles, erosion and overtopping showed that no scale effects on stability were present in the small scale tests and it was proven that a scale of 1 : 35 for the three dimensional investigation would give reliable results.

DYNAMIC STABILITY

Dynamically stable structures are characterized by the forming of a profile under wave attack. In this case damage is not important, but the developed profile. Rock slopes can be classified as dynamically stable if the $H_S/\Delta D_{n50}$ value exceeds 3 - 4. Gravel or shingle beaches are described by $H_S/\Delta D_{n50}$ values in the order of 20 - 500.

Two topics were evaluated in the Delta flume. First the verification of some tests on gravel beaches, performed by Van Hijum and Pilarczyk (1982). Secondly the behaviour of very small shingle.

Two tests on gravel beaches were repeated on a 4.6 times larger scale. The small scale tests were presented by Van Hijum and Pilarczyk (1982 - tests 11 and 12). The diameter of the shingle was $D_{n50} = 0.0187$ m and the gradation $D_{85}/D_{15} = 1.64$. The initial slope was 1 : 5. The wave heights were respectively $H_S = 0.77$ and 1.00 m and the wave period was $T_m = 4.3$ s in both tests. This resulted in $H_S/\Delta D_{n50}$ values of respectively 26 and 33. The wave boundary conditions were not exactly the same in the small and large scale facility. Therefore it is very difficult to draw conclusions from a direct comparison of profiles. In stead of that the characteristic points of the profile, defined as dimensionless parameters by Van der Meer and Pilarczyk (1986), were compared.

Two of those dimensionless parameters are shown in Figures 9 and 10. The dimensionless crest height and step height (the point below the water level where the gentle upper slope changes into a steeper slope) are defined by respectively:

$$h_c/D_{n50} N^{0.15} \quad \text{and} \quad h_s/D_{n50} N^{0.07}$$

The vertical axis of Figures 9 and 10 is the combined wave height - wave period parameter $H_0 T_0$, defined by:

$$H_0 T_0 = H_S/\Delta D_{n50} * \sqrt{g/D_{n50}} T_m \quad (4)$$

where:

$H_0 = H_S/\Delta D_{n50}$ = dimensionless wave height parameter

$T_0 = \sqrt{g/D_{n50}} T_m$ = dimensionless wave period parameter related to D_{n50}

Figures 9 and 10 show all test results for an initial slope of 1:5 for a range of $H_0 T_0 = 100 - 4000$. The two tests in small and large wave facility have different symbols. The vertical difference in the Figures gives the difference in wave boundary conditions, the horizontal difference is important for comparison. Figure 9 shows a good agreement of test results and established relationship (the curve). Figure 10 shows that most of the large scale tests have a little smaller value for h_s . But within the variation of the results it is acceptable. From the analysis of all profile parameters it followed that no scale effects could be found.

Finally the discussion of the tests on very small shingle. The shingle had a mean diameter of 4 mm which is almost at the transition to sand.

Such small diameters are difficult to scale for small scale tests as scale effects will definitely be present. Light weight material might be a solution, but will probably give scale effects above the water level (where the crest is formed) resulting in a too steep crest. Only almost prototype tests can give reliable information. The wave heights ranged from $H_s = 0.7$ to 1.7 m and the wave periods from $T_m = 2.5 - 6$ s. This resulted in $H_s/\Delta D_{n50}$ values of $90 - 260$.

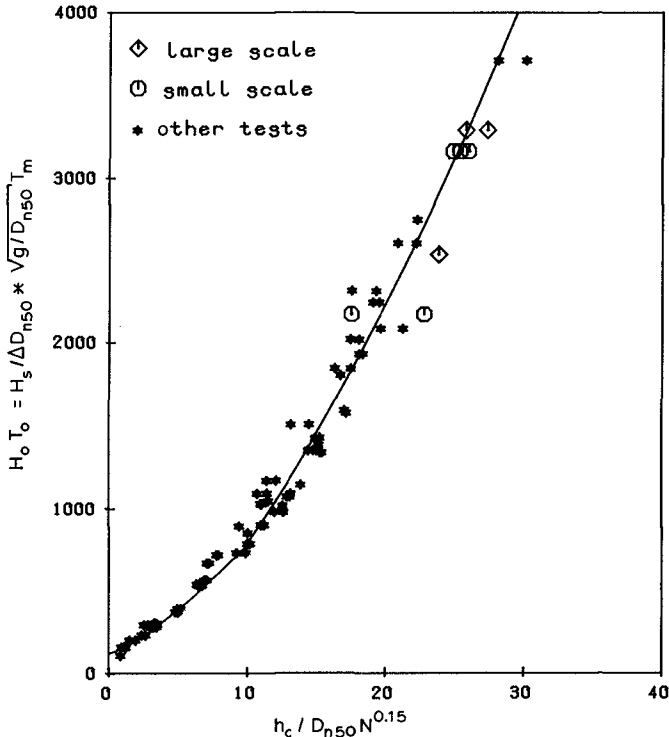


Figure 9 Evaluation of scale effects on crest height h_c

In total six tests were performed with this small shingle. The profiles were analyzed and used to develop a computer program which describes the profile formation of dynamically stable structures. Results were presented by Van der Meer (1986) and Van der Meer (1988b).

One phenomenon was never reported for shingle beach testing, although it is common for sand beaches. Namely the formation of ripples at the lower part of the slope, below the step. The authors are not aware of prototype measurements where ripple formation was reported. It will be difficult, however, to find ripples in prototype. First of all the sounding interval should be small enough to detect these ripples. Secondly, ripples are only formed for small shingle under high waves (storm conditions). They will be formed under the peak of the storm and probably with high water levels. The last part of the storm with lower water levels is able to flatten out the ripples formed before. And prototype profile measurements during the peak of the storm are rare.

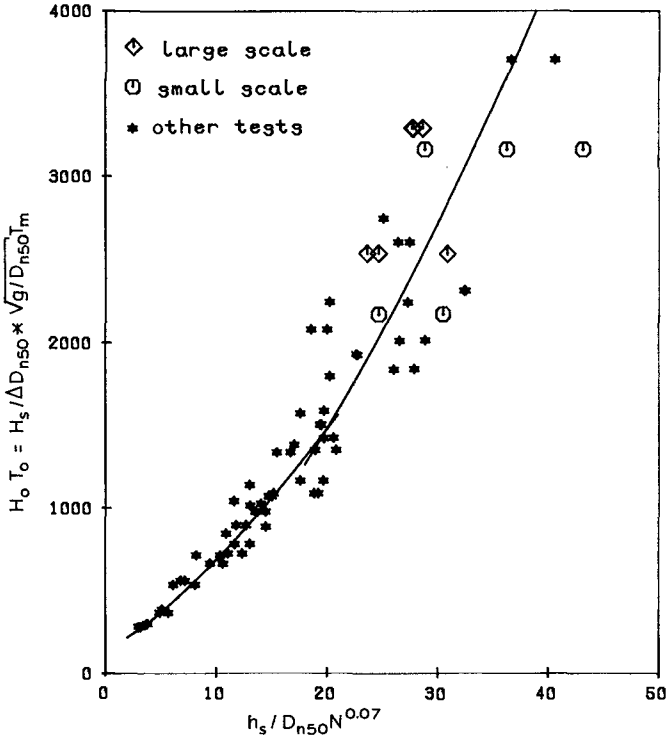


Figure 10 Evaluation of scale effects on step height h_s

The ripple phenomenon is very clearly shown in Figure 11 where 3 parallel profiles were plotted. The ripple height ranged between 10 and 40 centimeters and the ripple length ranged between 1 and 3 meters. As ripple formation has been studied for sand bottoms and slopes under wave attack and under flow conditions, it is interesting to compare the results for sand with very small shingle.

The best fit of the data was found with the results of Nielsen (1981). Nielsen defined the mobility number, ψ , which is a function of the water velocity at the bottom, u , calculated by linear wave theory:

$$\psi = u^2 / \Delta g D \tag{5}$$

Ripple crest height, η , and ripple crest length, λ , were related to the wave amplitude, $a = 0.5 H$. Nielsen gave the following relationships between crest height and length and the mobility number ψ .

ripple height:

$$\eta / a = 0.275 - 0.22 \sqrt{\psi} \tag{6}$$

ripple length:

$$\lambda / a = 2.2 - 0.345 \psi^{0.34} \tag{7}$$

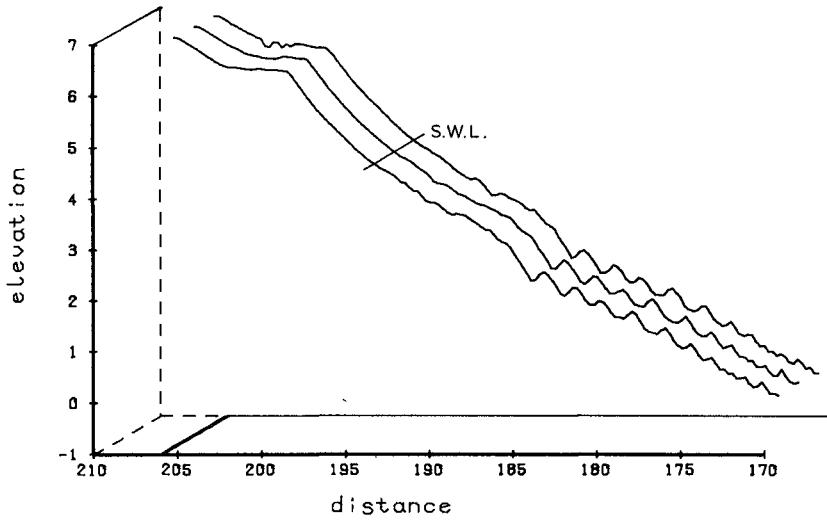


Figure 11 Ripple formation on 4 mm shingle

Equations 6 and 7 are shown in Figures 12 and 13 together with the results on shingle beaches. The general agreement is fair, although quite a lot of scatter is present. From the tests a boundary could be established for which ripple formation might start. This boundary is given by a $H_s/\Delta D_{n50}$ value in the order of 80 - 90 or a mobility number in the order of $\psi = 10$.

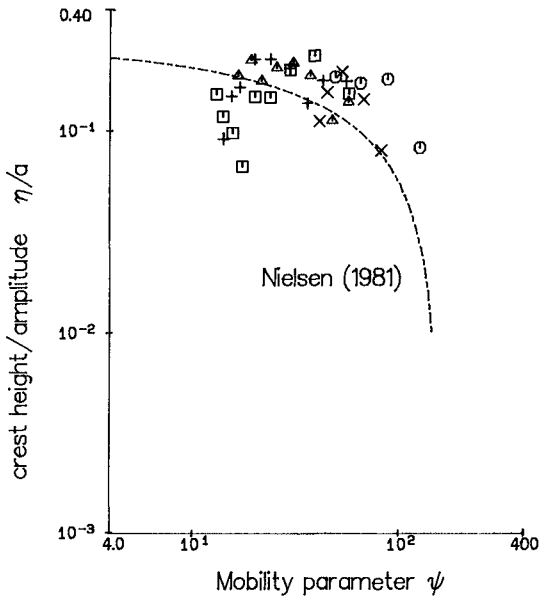


Figure 12 Ripple crest height of shingle versus mobility parameter ψ

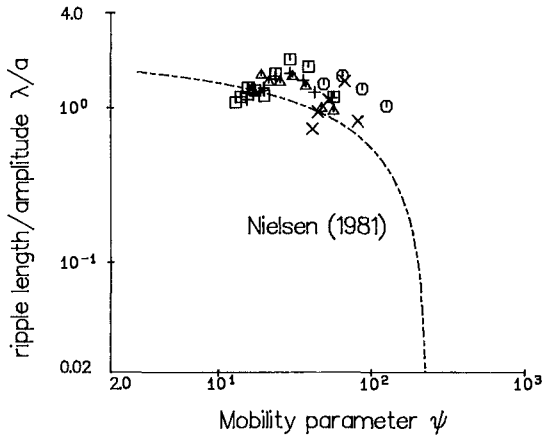


Figure 13 Ripple crest length of shingle beaches versus mobility parameter ψ

CONCLUSIONS

The conclusions derived from large scale testing of rock slopes and gravel beaches can be summarized as follows:

Small scale testing with wave heights higher than about 8 centimeters and for static stability with Reynolds numbers higher than 4.10^4 , did not show scale effects for:

- rock slope stability
- berm breakwater stability
- reflection and overtopping
- profile formation.

A Reynolds number of 4.10^4 does not mean that lower values are not possible. Lower values were simply not used in the tests.

Finally, ripple formation could be described by sand ripple theory and a boundary could be established where ripple formation might start.

REFERENCES

- Baird, W.F. and Hall, K.R., 1984. The design of breakwaters using quarried stones. Proc. of the 19th ICCE, Houston, USA, Ch. 173.
- Broderick, L.L. and Ahrens, J.P., 1982. Riprap stability scale effects. CERC, Technical Paper No. 82-3, USA.
- Burcharth, H.F. and Frigaard, P., 1987. On the stability of berm breakwater roundheads and trunk erosion in oblique waves. Seminar on unconventional rubble-mound breakwaters, Ottawa, Canada. Proc. published by ASCE, special issue of Journal of WPC and OE.
- Dai, Y.B. and Kamel, A.M., 1969. Scale effect tests for rubble-mound breakwaters. WES, Research Report H69-2, USA.
- Delft Hydraulics, 1985. St. George Harbor, Alaska. Two-dimensional tests on scale effects. Three-dimensional tests on breakwater stability. Report on model investigations, M2102.
- Jensen, O.J. and Klinting, P., 1983. Evaluation of scale effects in hydraulic models by analysis of laminar and turbulent flows. Coastal Eng., 7, pp. 319-329.

- Nielsen, P., 1981. Dynamics and geometry of wave-generated ripples. *Journal of Geophysical Research*, Vol. 86, No. C7, pp. 6467-6472.
- Shimada, A., Fujimoto, T., Saito, S., Sakakiyama, T. and Hirakuchi, H., 1986. Scale effects on stability and wave reflection regarding armor units. Proc. 20th ICCE, Taipei, Taiwan, Chapter 165.
- Sørensen, T. and Jensen, O.J., 1985. Reliability of hydraulic models of rubble-mound breakwaters as proven by prototype measurements. The Dock & Harbour Authority, March, pp. 155-157.
- Thomson, A.L., Wohlt, P.E. and Harrison, 1972. Riprap stability on earth embankments tested in large- and small-scale wave tanks. CERC, Technical Memorandum No. 37, USA.
- Van der Meer, J.W. and Pilarczyk, K.W., 1986. Dynamic stability of rock slopes and gravel beaches. Proc. 20th ICCE, Taipei, Taiwan, Ch. 125.
- Van der Meer, J.W., 1987a. Stability of armour layers - Design formulae. *Coastal Eng.*, 11, pp. 219-239.
- Van der Meer, J.W., 1987b. Application of computational model on berm breakwater design. Seminar on unconventional rubble-mound breakwaters, Ottawa, Canada. Proc. published by ASCE, special issue of *Journal of WPC and OE*.
- Van der Meer, J.W., 1988a. Deterministic design of breakwater armor layers. Proc. ASCE, *Journal of WPC and OE*, Vol. 114, No. 1.
- Van der Meer, J.W., 1988b. Rock slopes and gravel beaches under wave attack. Doctoral thesis, Delft University of Technology. Also published as Delft Hydraulics Communication No. 396.
- Van Hijum, E. and Pilarczyk, K.W., 1982. Equilibrium profiles and long-shore transport of coarse material under regular and irregular wave attack. Delft Hydraulics Publication No. 274.

CHAPTER 158

ANALYSIS OF 42-TON DOLOS MOTIONS AT CRESCENT CITY

Thomas R. Kendall, M. ASCE*

ABSTRACT

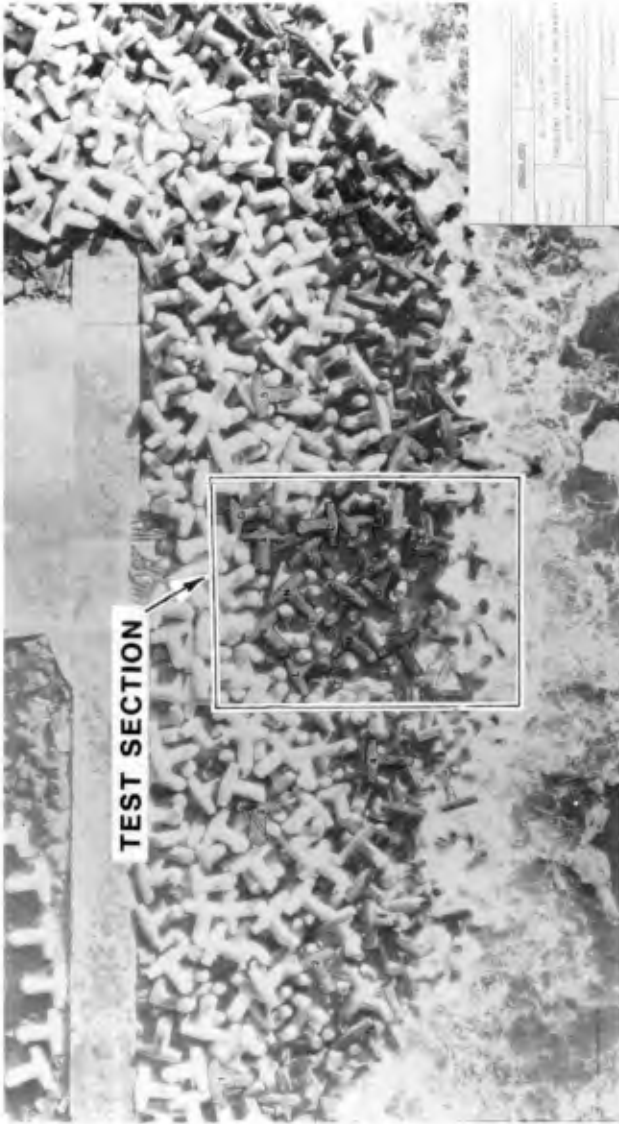
Photogrammetry has been applied to make precise measurements of post-construction displacements of 38.2-metric ton (42-ton) dolosse on the outer breakwater at Crescent City, California. Data from two storm seasons are currently available from this monitoring program which was initiated in November 1986 and which is expected to continue at least through the next three winters. Supplemented by conventional land surveys, wave measurements, aerial inspections, and side scan sonar underwater imagery, observations from the photogrammetric monitoring have led to several preliminary conclusions regarding regions of relatively large dolos movement, dolos nesting, the dependency on breakwater slope of uprush or drawdown dominated armor unit movement, and the relative importance of armor unit movement and boundary conditions in dolos breakage. This paper describes the methods used for, and results obtained from, this monitoring effort along with the application of these results to a Corps study (Howell, 1988) whose objective is to develop structural design criteria for the dolos concrete armor unit.

INTRODUCTION

The high incidence of breakage encountered in large concrete dolos armor units has led the Corps of Engineers to initiate a field data collection program aimed towards developing a structural design procedure for dolosse. The overall program being carried out includes field monitoring as well as physical modeling and numerical simulation of forces experienced by dolosse. The primary focus of this paper is on the results obtained to date from aerial photography and photogrammetric field monitoring of dolos displacements and breakage.

Field data have been collected from the outer breakwater at Crescent City, California (Figure 1), which was rehabilitated in 1986 by placing 680 steel

* Civil Engineer, U.S. Army Corps of Engineers, San Francisco District, 211 Main Street, San Francisco, CA 94105-1905



fiber-reinforced, 38.2-metric ton (42-ton) dolosse over an existing dolos section on the breakwater. The dolos section, which is approximately 100 meters in length, encompasses the seaward end of the trunk plus the bend to the breakwater's easterly dogleg extension. The section consists of a minimum of two dolos layers on a variable slope that averages between 4H:1V and 5H:1V and extends to toe depths ranging from 7.5 to 9 meters. Above the mean waterline, structure slopes are generally flatter than the average; below the waterline, the slopes are typically steeper. The bathymetry offshore of the structure is highly complex with numerous rock outcroppings.

The design wave height proposed by Hales (1985) for the rehabilitated section is a depth-limited breaking wave with a height of approximately 10.5 meters and a peak period of 15 seconds. Wave periods up to 20 seconds, however, are not uncommon and can occur with almost comparable height. The physical model study used to design the rehabilitation (Baumgartner, Carver, and Davidson; 1985) subjected the structure to depth-limited regular waves with a range of periods (up to 21 seconds) over a simulated extreme tidal cycle (maximum tide approximately 3 meters MLLW). Only during the highest tide and for the longest period waves were wave heights near 10.5 meters encountered. This condition occurred during one-twelfth of the design "hydrograph" used in the model.

As part of the 1986 rehabilitation, 17 of the new dolosse were instrumented with internal strain gages, including four with accelerometers, to measure dynamic and static structural response during placement and subsequent exposure to storm waves. These dolosse are arranged in a rectangular test section (14 in the top and three in the bottom layer) on the trunk of the breakwater. Data from the instrumented dolosse test section have been collected during the two winter storm seasons which have followed construction. Howell (1988) further discusses the features of, and data obtained from, these test section dolosse.

An important element of the field data collection program has been the assessment of dolos movement and overall structural stability, both within the test section and within the surrounding dolosse. To make this assessment, photogrammetric surveys of the breakwater's dolos section have been conducted approximately monthly over the two post-construction winter-storm seasons. While aerial photography and photogrammetry alone can only provide information about displacements, much can be inferred about dolos movements when these surveys are conducted repeatedly and supplemented by observations of dolos abrasion and breakage.

Unlike the highly unique and costly strain measurements, which were terminated after the second season, the relatively inexpensive photogrammetric monitoring, supplemented by conventional land surveys, wave measurements, aerial inspections, and side scan sonar underwater surveys, will continue to be conducted at least

through the next three winters.

The data obtained from these surveys are being used to answer the following specific questions:

1. What are the differences between the laboratory projected stability of the structure (i.e. the results of physical model studies conducted during the design of the rehabilitation project) and the observed field performance?
2. What are the full scale patterns of dolos response, i.e. the nesting and consolidation processes, dominant movement types, and regions, if any, of excessive movement or breakage?
3. Is breakage necessarily associated with armor unit movement and vice versa? and
4. What quantity of dolos breakage may compromise the breakwater's integrity?

In addition to answering these questions of interest to the field engineer, the photogrammetric monitoring allows the research engineer to visualize the bigger picture when interpreting results obtained from internal strain measurements within the test section. For example, changes in the static loading experienced by an instrumented dolos can often be traced to dolos settlement or to a shift in the boundary conditions evident in the photogrammetric record. The photogrammetric and breakage inspection records also allow comparisons to be made between the performance of test section dolosse and the remainder of the visual dolos field in an effort to assess how representative the test section results are. Additionally, information on dolos orientation collected from these surveys is being used to develop finite element models of the test dolosse, and, along with extensive post-construction data on the breakwater contours and surrounding bathymetry (2-foot contouring), to construct an "upgraded" physical model of the breakwater so that more refined comparisons between full scale and hydraulic model movements and loadings can be made.

PROCEDURES

Of critical importance to any photogrammetric monitoring program is the proper positioning and accurate surveying of the ground control targets which are used as the basis of scaling, levelling and coordinates of the photogrammetric stereo models. Additionally, targets must be clearly marked and identified on the objects to be monitored, in this case dolosse. As it is not practicable to maintain targets on all visible dolosse, only select dolosse (primarily those in the test section) have been targeted. By printing rectified aerial photography of the entire dolos field onto a transparent mylar base, overlays are made each month so that movements of non-targeted dolos can also be visualized (to the nearest 15 centimeters in plan). If, in the future, a more refined and three-

dimensional assessment of the movements of non-targeted dolos is deemed necessary, such an assessment can be made using the photography already taken by preparing photomaps outlining all visible dolosse using the same stereo model set up for the targeted dolosse. This photomapping approach was used to monitor dolosse movements on the jetties at Manasquan Inlet, New Jersey (Gebert and Clausner; 1984).

The twenty-six dolosse which have been marked in this monitoring project are shown in Figure 1. Eighteen of these are located in the instrumented section and eight are distributed uniformly throughout the remainder of the dolos field. Twenty two of these dolosse are located in the upper dolos layer and have been marked with three targets each which allows their movement to be described with six degrees of freedom. The remaining four, which are located in the lower dolos layer of the test section, have only one clearly visible surface each which has been targeted for monitoring.

All targets have been painted on the dolos surface with special anti-fouling paint to discourage marine growth from diminishing target visibility. Marine growth, however, has persisted on those dolosse nearest the waterline. To avoid excessive repainting of these relatively inaccessible targets, epoxy paints have recently been used. Three coats (epoxy primer, epoxy paint, and an epoxy polyurethane finish coat) have been applied to these targets for a total wet thickness of approximately 20 millimeters.

Each target is in the form of a cross, with legs approximately 8 centimeters in width by 45 centimeters in overall length. Each cross is also identified with its appropriate designation (e.g. A-1, A-2, etc.) which is visible in the photography, thereby providing positive identification as to which point is being measured.

Photography was initially taken with a 306.42-millimeter (12-inch) focal length mapping camera from an altitude of 366 meters (1200 feet) above sea level, resulting in a photo scale of 1:1200 (or 1 inch equals 100 feet). However, in order to provide more accuracy in the vertical dimension, a Wild 152.09-millimeter (6-inch) focal length precision mapping camera is now being used to take photography from an altitude of 183 meters (600 feet) above sea level, resulting in the same direct photo scale of 1:1200. While these lower altitude flights improve photogrammetric accuracy, they also make maintaining the same photo center from survey to survey quite difficult. As a result, the images produced from these lower altitude flights are not as suitable for visually tracking the gross movements of dolosse. Therefore, an additional high altitude flight is now made as part of each survey so that similar photo centers can be maintained from survey to survey and so that rectified and scaled photographic images which are produced from these each month at an enlarged scale of 1:120 on mylars are suitable for overlaying and movement detection.

A Cessna Tu-206 photo plane is the platform from which the aerial photography is taken. Black and White aerial film (Kodak Double-X Aerographic film #2405) is used. Two photographs, taken approximately 110 meters apart in a straight line pass which bisects the angle formed by the elbow of the breakwater, form the photogrammetric stereo model from which the dolos measurements are made. Additional photo passes are made, one to the left and one to the right of the designed flight line to offer additional stereomodels to choose from if shadows or overhanging dolos prevent 3-D viewing of any target.

A Qasco fully analytical (computer driven) stereoplotter is currently being used to form the stereomodels and make the individual measurements. Each measured set of tri-ordinates is recorded in a data file which is entered into a database and compared with previous measurements to detect position changes. For dolos which have not broken, results are then interpreted by converting individual target movements to dolos centroid translations along, and rotations about, each axis of the California State Plane Coordinate System. Local axes are defined on each dolos to facilitate the recording of dolos orientation.

Computer generated three-dimensional drawings are used to illustrate the dolos movements measured. Time-series graphics for each surveyed dolos are presented as "exploding diagrams" projecting from their respective dolos indicated on a base map (aerial photograph) of the dolos field (Figure 2). Multiple sheets are required to track all moving dolosse. A separate sequence is maintained for the photogrammetric surveys and the periodic land surveys which are conducted on targeted dolosse as a check on the photogrammetric results. The example sheet shown in Figure 2 has a graphic entry for the earlier two surveys (lower two rows) for all dolosse shown. However, between the second and third surveys, only dolos 'L' moved beyond the threshold used for precipitating an updated orientation graphic (15 centimeters movement on any target) and, therefore, the third (upper) survey row only shows an entry for dolos 'L'.

Periodic ground inspection and repainting of control survey and dolos targets is a requisite for a successful photogrammetric monitoring project, as is periodic ground surveying to compare the accuracy of the two methods.

Comparisons to date between tri-ordinates generated from simultaneous ground and photogrammetric surveys of 70 dolos targets show agreements between the two methods of approximately 3 centimeters (total three-dimensional vectorial displacement).

In addition to monitoring the movement of individual units in the dolos section, unit breakage is periodically inspected via helicopter. These aerial inspections of breakage are conducted over the entire dolos field at the time of each photogrammetric survey. Breakage is

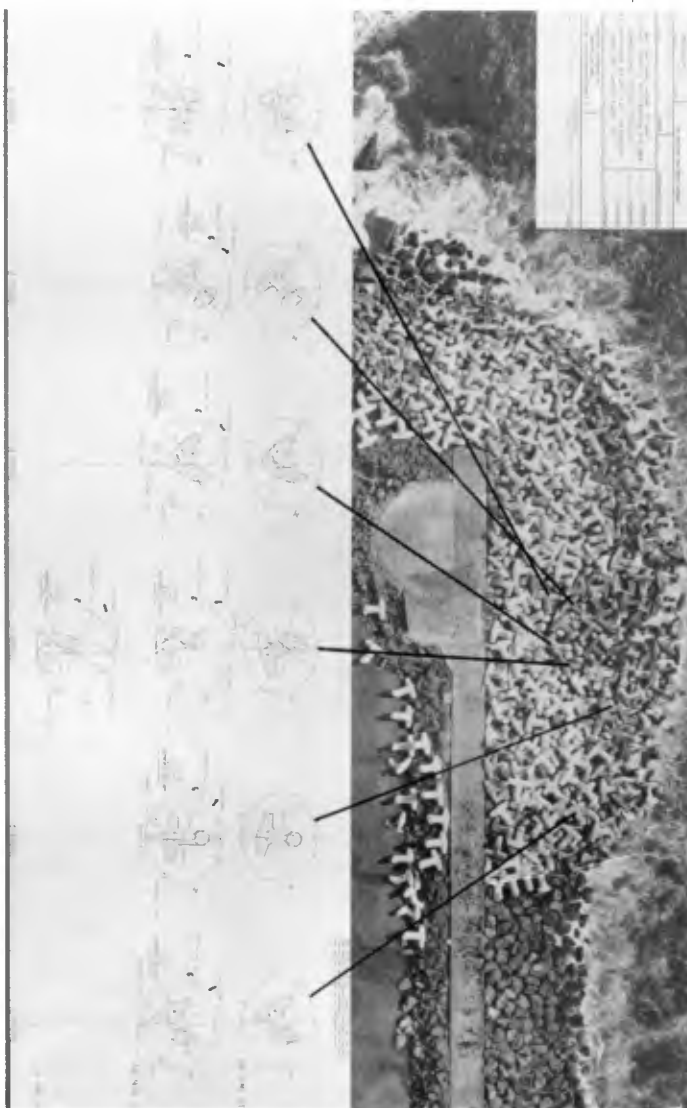


Figure 2 - "Exploding Diagrams" used to illustrate dolos displacement with time.

inventoried by recording all breaks on the most recent aerial photographic base sheet, which also serves as a breakage inspection map. In addition, multiple photographs (at least one of each break) are taken during the inspection and are indexed on the breakage inspection map.

Subsurface conditions are also monitored periodically via side scan sonar surveys. An EG&G Image Correcting Digital Sonar Model 260 is towed past the dolos area at least once before and after each winter storm season. Individual dolos breaks, structure slopes, and units displaced are not currently measurable in a repeatable, quantitative way with side scan sonar (Kucharski and Clausner; 1988), however, these surveys do allow for the detection of gross subsurface changes to the breakwater.

The Point St. George Buoy, which is located approximately ten kilometers offshore of Crescent City in approximately 60 meters of water, has provided a relatively continuous record of the local wave climate during the monitoring period. However, data collected from this buoy contained a nearly two-month long gap during the first winter season; during this period, the nearest continuously operating wave buoy was located offshore of Point Arena, which is approximately 240 kilometers to the south. While other wave gages and buoys were set up closer to the breakwater as part of the monitoring of the instrumented dolos test section, these only operated intermittently during the first season and the bulk of their second season data is yet to be reduced. Limited comparisons of the available nearshore wave data (12 meter water depth) and the Point St. George Buoy data collected during a period of typical long-period storm swells out of the west to southwest indicate strong similarities between the two records. Water levels near the breakwater are monitored using the tide station maintained at Crescent City Harbor.

OBSERVATIONS

Figure 3 relates the timing of all surveys conducted during the first two seasons to the wave power encountered. The dates of both land surveys and photogrammetric surveys are indicated on the figure. Offshore wave power as defined on the figure has been plotted (as opposed to wave energy) because of the importance of wave period to the stability of the highly porous dolos armor layers. The "reservoir effect" of the pores, as explained by Burcharth and Thompson (1983), makes dolosse more vulnerable to long-period waves.

The first winter season was relatively moderate and the second season was more severe. Based on the available wave and tidal records for the area, it is concluded that a small percentage of individual waves each season (more during the second) approached design magnitude. The design storm, however, was not experienced.

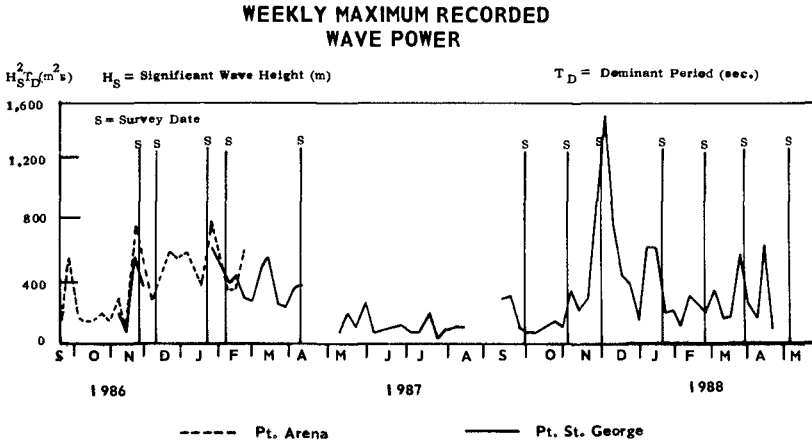


Figure 3 - Timing of dolos surveys relative to offshore wave power.

Movement

Dolos movement between the December 1986 and January 1987 surveys was the largest recorded to date; the subsequent storms of that first winter season and the more severe second winter season failed to produce substantial movement, even of those dolosse that had been previously mobile. This appears to indicate that the dolosse have consolidated and nested into a more stable matrix as a result of these earlier storms. The consolidating movement of the targeted dolosse produced by the series of storms that occurred in December 1986 and January 1987 is summarized in Table I.

TABLE I
CRESCENT CITY OUTER BREAKWATER
TARGETED DOLOSSE MOVEMENTS
FROM 10 DECEMBER 1986 TO 20 JANUARY 1987

	<u>AVERAGE</u>	<u>MAXIMUM</u>
TRANSLATION	27 cm	218 cm
(SETTLEMENT)*	(4 cm)	(29 cm)
ROTATION	6.1°-Z	34.5°-Z

* Settlement is a component of the total translation.

The movement of over 2 meters (almost half the unit dimension (15 feet, or 4.6 meters) of a 38.2-metric ton (42-ton) dolos) experienced during this period by dolos 'L' represents the largest recorded movement to date of all visible dolosse. Generally speaking, the upper layer dolosse experience larger movements than the more constrained lower layer dolosse; therefore, movement among the targeted dolos (85 percent of which are in the upper layer) is higher than the visible dolos field average.

Comparisons of rectified aerial photography showing the entire visible dolos field (including those dolosse visible in lower layers) indicate that most units to date have moved less than 15 centimeters, about 95 percent have moved less than 50 centimeters and about 99 percent have moved less than 120 centimeters. Of the one percent (or five of the approximately 500 visible dolosse) observed to have moved over 120 centimeters, three of these dolosse were broken dolosse, one was dolos 'L' which did not break but experienced the largest measured displacement, and one had disappeared beneath the waterline making it impossible to quantify the magnitude of its displacement. The broken dolosse which moved over 120 centimeters may have broken prior to experiencing the majority of the displacement evident between photographs.

To date, the dominant dolos movement has been upslope with slight settling plus rotation about the vertical or z-axis (yaw). Yaw was also the predominant dolos rotation observed by Gebert and Clausner (1984) at the Manasquan Inlet jetties. This type of rotation probably occurs more frequently because the upper layer dolosse are not constrained laterally as much as they are vertically; note that the settlement shown in Table I is a relatively small component of the total translation experienced.

Dolosse settlement at Crescent City was greatest during the early storms; more recent surveys show that detectable vertical motions are approximately balanced, i.e. an equal amount of elevating and settling occurs. This tends to support the notion that the dolosse have already consolidated and nested into a more stable matrix. Initial settling of the dolosse (and the associated tilting, wedging, and general constraining) corresponds to the observed test section trend of increased static loading through time for most all dolosse measured.

Jensen of the Danish Hydraulic Institute indicates that for structure slopes milder than 3.5H:1V, wave run-up dominates and the net armor unit movement is upslope; for steeper slopes, wave run-down dominates and the net armor unit movement is downslope (Sorensen and Jensen; 1986). Considering the structure slopes at Crescent City (typically flatter than 4H:1V in the zone of wave impact), the observed upslope movement of the dolosse is not surprising. Other recent full-scale monitoring of smaller dolosse on the East Coast and Great Lakes of the United States has documented downslope movements (wave run-down dominated) at structures with slopes ranging from 1.5H:1V to 3H:1V (Pope and Clark, 1983; Gebert and Clausner, 1984; Pope, 1988; Gebert, 1988). Full-scale observations of dolosse within the United States appear to support Jensen's conclusion that the critical slope which determines whether armor will move upslope with wave run-up or downslope with wave run-down is near 3.5H:1V.

At Crescent City, the greatest movement was recorded on the upper slope of the centrally located test section and in the vicinity of the waterline. Spatially averaged movements within the test section are quite comparable to those found

outside the test section, however, the region of high movement within the test section is generally located further upslope. Higher movement near the waterline is not surprising and has also been observed in dolosse at Cleveland Harbor (Pope and Clark; 1983). A possible explanation for the observed high movement on the upper slope of the test section is the existence of a slight contour dip or trough in the test section region of the breakwater, as well as the fact that many of the dolosse placed in this low spot, had initial boundary conditions that did not hinder sliding. It has also been suggested, based on the historic pattern of breakwater damage, that the test section may be located in an area where wave focusing occurs.

Breakage

Since placement two years ago, six broken dolosse have been detected. Five of the dolosse broke during the nesting storm sequence; one broke during the peak storms of the second season. Seven post-placement breaks are visible (one dolos broke in two places). Five of the breaks occurred at the dolos shank-fluke interface; two occurred mid-fluke. Breakage appears to be concentrated in the relatively mobile regions of the breakwater near the waterline. Breakage, however, did not occur within the equally mobile upper test section. All visible broken dolos pieces have remained stable, and breakage, thus far, appears to not have significantly compromised the breakwater's integrity.

An examination of the data collected by the instrumented dolosse indicates that these large dolosse can be loaded to near their structural capacity while simply resting in the dolos matrix under static loading conditions, leaving little residual strength for any dynamic loads. A variety of support conditions exist for the dolosse and some are clearly more detrimental than others. In one example, a dolos was placed in a cantilevered support condition after adjacent dolosse migrated approximately one meter upslope and vertically constrained its horizontal fluke. The dolos eventually broke. There is no indication of impact loading to the cantilevered portion of the dolos nor of any displacement of the constrained horizontal fluke, which leads to the conclusion that failure was caused primarily by poor boundary conditions accompanied by some wave-generated pulsating drag loads on the cantilevered portion of the dolos. Dolos movement, however, was ultimately responsible for the failure in that it caused the critical shift in boundary conditions supporting the dolos which ultimately failed. In another example, a dolos suffered a break across its horizontal fluke after enduring continuous impacts. The horizontal fluke of this dolos had been wedged between two adjacent vertical flukes which constrained the upslope movement and yaw of the dolos. During the first season's nesting storms, approximately one meter of upslope movement was experienced by these dolosse which were in contact. Minor residual movement occurred thereafter and the wedged horizontal fluke finally broke during the peak storms of the

second season.

These two examples of poor boundary conditions can be contrasted with the boundary conditions found in the dolos test section, where the placement of each dolos was coordinated by a field engineer who stood among the dolosse and radiod instructions to the crane operator. During placement, most test-section dolosse experienced a three-point landing. On the other hand, due to tong clearances, the different levels of experience of the crane operators used on the job, and the fact that a field engineer did not radio instructions to the crane operators during dolosse placement outside the test section, about 70 percent of the dolosse placed outside the test section experienced a two-point landing. These dolosse were then either wedged or clamped in by subsequently placed dolosse or were left to rock or tilt during nesting until wedged into a final support condition. This most likely resulted in boundary conditions which were more detrimental than those which resulted from the typical three-point landings experienced by dolosse in the test section.

These differences in boundary conditions may explain why dolosse have yet to break in the test section. While large movements occurred in the test section, these movements were of a much less detrimental nature and typically involved some sliding permitted by a dolos's exclusively vertical supports. Furthermore, these large movements occurred in a region relatively far from the waterline where dolosse are probably loaded less frequently.

While breakage has typically been associated with some amount of movement, either of the dolos which breaks or of adjacent units, it has not necessarily been associated with significant movement and vice versa. At the Manasquan Inlet jetties, Gebert and Clausner (1984) also observed that the largest displacements experienced were by dolosse which did not break. The dolosse at Manasquan Inlet weigh 14.6 metric tons (16 tons). For the even larger dolosse at Crescent City (which may have even less residual strength), it appears, thus far, that the extent to which movement causes a detrimental shift in boundary conditions is more important than the absolute magnitude of the movement itself.

Model and Field Performance Comparisons

To the extent that comparisons can be made between the observed performance of the breakwater physical model and the observed field performance of the structure itself, qualitative similarities between the two exist. Only very preliminary comparisons can be made for this two-year time period during which a small percentage of individual waves approached design height but the design storm, per se, was not encountered. Several differences also exist between model and prototype construction and reporting techniques.

The initial model used for designing the rehabilitation of the breakwater used fewer dolosse on a generally more uniform slope than the prototype and subjected the structure

to regular waves. In addition, the model only quantified dolos translations which exceeded the dolos unit length and rotations which were greater than 180 degrees, i.e. only those dolosse which had clearly moved out of their original location were recorded. Dolos breakage could not be modelled. By contrast, field monitoring thus far has recorded dolos translations which were all less than half the dolos unit length and rotations which were all less than 40 degrees; in addition, dolos breakage has been observed in the field. Furthermore, the model study basin could be drained to assess underwater displacements with much more clarity than the side scan sonar imagery collected in the field.

In spite of these differences, it does appear, thus far, that the use of trenching and buttressing (with stone) along the southern perimeter of the dolosse has produced a stable dolosse-stone transition in the field, similar to the model study finding. On the other hand, the northern dolosse-stone transition region, which proved to be a problem area in certain laboratory tests, has been an area where two above-water dolosse have broken and where side scan sonar records indicate some migration of the toe. Physical model testing of the breakwater is again being proposed so that various buttressing schemes, etc. may be tested for their effectiveness in stabilizing the northern dolosse-stone transition.

CONCLUSIONS

Photogrammetry has proven to be a reliable, safe, accurate, economical and repeatable method of monitoring the movement of dolos armor units on the outer breakwater at Crescent City. The photographs produced in this monitoring effort serve as a permanent record of high resolution images providing excellent visual documentation of dolos movement and breakage, even among non-targeted dolosse.

The principal observations made from the limited data available to date are summarized below:

The greatest movement of dolosse is on the upper slope of the centrally-located dolos test section and in the vicinity of the waterline. The movement on the upper slope is thought to result from the existence of a slight contour dip or trough in this region of the breakwater and because many of the dolosse placed there had initial boundary conditions that did not inhibit sliding.

Spatially averaged movement within the dolos test section is quite comparable to that found outside of the test section; however, the region of high movement within the test section is located further upslope.

The dominant dolos movement is upslope with slight settling plus rotation about the

vertical axis (yaw). Upslope movement is a consequence of the breakwater's mild slope which causes wave run-up forces to dominate.

Comparison of the interim results of the Crescent City monitoring program with the results of two other full-scale photogrammetric dolos monitoring programs conducted in the U.S. suggests that the critical slope which determines whether armor units will move upslope with wave run-up or downslope with wave run-down, is near 3.5H:1V.

Storms which occurred early during the first-post construction winter season have produced the largest dolos movements to date. Reduced movement during subsequent storms indicates that the dolosse have consolidated and nested into a more stable matrix.

Breakage, while typically associated with some amount of movement, has not necessarily been associated with significant movement and vice versa. For the large dolosse at Crescent City (which can have little residual strength), the extent to which movement causes a detrimental shift in boundary conditions appears more important than the absolute magnitude of the movement itself.

The photogrammetric monitoring of dolos movement will continue at Crescent City for at least the next three years. Results from the photogrammetric monitoring conducted during the first two post-construction winters are an integral part of the Corps intensive data collection effort which will be used to develop a structural design procedure for the dolos concrete armor unit.

ACKNOWLEDGMENTS

The work described in this paper has been conducted as part of the Crescent City Prototype Dolosse Study sponsored by the U.S. Army Corps of Engineers (USACE) San Francisco District. Funding for the fourth and fifth years of photogrammetric monitoring will be provided by the USACE Monitoring Completed Coastal Projects (MCCP) program. The author would like to acknowledge contributions of the following individuals to this effort: Bill Brick, Richard Lou, and Jim Wilkerson of USACE San Francisco District, the staff of Richard B. Davis Company, Ken Meme of Towill Inc., David Gilhousen of the National Data Buoy Center, Jeff Gebert of USACE Philadelphia District, Gary Howell, D.D. Davidson, and Jeff Melby of the Coastal Engineering Research Center, USACE Waterways Experiment Station, and Denise, my wife.

REFERENCES

Burcharth, H.F., and A. Thompson, 1983, "Stability of Armour Units in Oscillatory Flow," Proceedings of Coastal Structures '83, ASCE, New York, NY.

Baumgartner, R.C., R.D. Carver, and D.D. Davidson, 1985, Breakwater Rehabilitation Study, Crescent City Harbor, California, Technical Report CERC-85-8, U.S. Army Engineer Waterways Experiment Station, Vicksburg, MS.

Gebert, J.A., and J. Clausner, 1984, "Photogrammetric Monitoring of Dolos Stability, Manasquan Inlet, New Jersey," Coastal Engineering, 1984 Proceedings of the International Conference, ASCE, New York, NY.

Gebert, J.A., 1988, U.S. Army Engineer District, Philadelphia, PA, personal communication.

Hales, L.Z., 1985, Water Wave Refraction/Diffraction/Shoaling Investigation, Crescent City, California, Miscellaneous Paper CERC-85-3, U.S. Army Engineer Waterways Experiment Station, Vicksburg, MS.

Howell, G., 1988, "Measurement of Forces on Dolos Armor Units at Prototype Scale," Coastal Engineering, 1988 Proceedings of the International Conference, ASCE, New York, NY.

Kucharski, W., and J.E. Clausner, 1988, Underwater Inspection of Coastal Structures Using Commercially Available Sonars, Technical Report REMR-CO-108, U.S. Army Engineer Waterways Experiment Station, Vicksburg, MS.

Pope, J., and D.R. Clark, 1983, "Monitoring of a Dolos Armor Cover; Cleveland, OH," Proceedings of Coastal Structures '83, ASCE, New York, NY.

Pope, J., 1988, U.S. Army Engineer Waterways Experiment Station, Vicksburg, MS, personal communication.

Sorensen, T., and O.J. Jensen, 1986, "Experience Gained From Breakwater Failures," Developments in Breakwaters, Proceedings of the conference on Breakwaters '85, Thomas Telford Ltd, London.

CHAPTER 159

WAVE FORCE ON BREAKWATERS WITH CONCRETE BLOCK MOUND

Masataro Hattori¹, Keiji Inagaki²,
Yuuji Noguchi³, and Taiji Endo⁴

ABSTRACT

Analytical theory is derived for prediction of the wave force acting on a upright structure armored by concrete block mound of rectangular shape. The theoretical treatment starts from the linear long wave theory and the flow resistance in the mound is described by a linearized friction law. As a practical application of the theory, approximate method for the structure with sloping block mound is proposed. Experiments are conducted to verify the theory and approximate method.

1. INTRODUCTION

Mound-type structures consisting of rubble stones and concrete blocks have been attracted many attentions as an porous structure protecting effectively a harbor from the action of rough seas. In the past decades, analytical and experimental studies have been conducted to understand the reflection and transmission characteristics of the porous mound structure (Madsen and White, 1975; Massel and Mei, 1977). Excellent review of the previous studies up to 1972 is given by Sollitt and Cross (1975).

In addition, it has been well known among coastal engineers that mound-type structures backed by a caisson or vertical seawall reduce considerably wave forces acting on the backed-up structure as well as wave run-up and overtopping (Goda, 1985). In Japan, such the mound structures comprising randomly placed artificial concrete blocks are very common and have been constructed to reduce severe wave actions against the structures. Figure 1 shows an idealized typical cross-section of such a block mound breakwater of composite-type (or Japanese-type) (PIANC, 1988).

When the block mound is used for this purpose, it is especially important for coastal engineers to estimate the effectiveness of a given block mound on the wave force

1) Professor, Department of Civil Engineering, Chuo University, Bunkyo-ku, Tokyo 112. JAPAN

2) Associate Engineer, Yokkaichi City, Mie Prefecture 510.

3) Manager, R & D Section, Hydraulic Laboratory, Nippon Tetrapod Co., Ltd., Tsuchiura, Ibaraki Prefecture 300. JAPAN

4) Director, Hydraulic Laboratory, Nippon Tetrapod Co., Ltd., Tsuchiura, Ibaraki Prefecture 300. JAPAN.

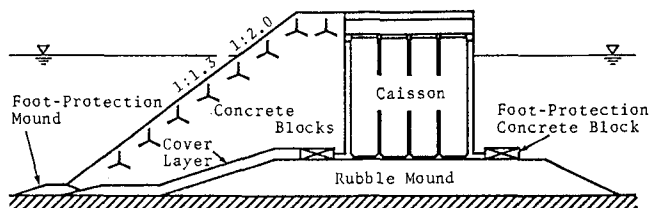


Fig. 1 Idealized typical section of a breakwater with concrete block mound.

reduction for a breakwater design. Incident wave energy is dissipated not only by wave breaking and frictional effect on the seaward slope of block mound, but also by resistance associated with oscillatory flows inside the mound. The interaction of incident waves with the block mound is a very intricate problem and relates various physical factors, such as wave properties, structural characteristics of the mound, and size and shape of concrete blocks.

Lack of adequate knowledge of these wave-structure interactions associated with the composite-type block mound breakwater has hindered from developing the analytical theory for predicting the wave force and reflection characteristics. As a result, laboratory model experiments have been recognized as one of possible and reliable approaches to the solution of such complicated problems. In Japan, more than 20 programs of laboratory experiments using regular and irregular waves have been made to deepen understanding on hydrodynamic behaviors of the composite-type structure with block mound, and to find a feasible standard design procedure for such structures. In spite of many intensive efforts, however, any empirical methods for predicting the wave force exerted on the backed-up structure have not been established yet with general confidence.

The principal aims of this study are as follows:

1. To develop an analytical theory for predicting the wave force acting on the caisson-type breakwater with rectangular block mound, and
2. To propose an approximate method for the estimate of wave force on the breakwater with sloping block mound.

An analytical solution for the present problem is derived under the following assumptions:

- (1) Long waves are normally incident on the breakwater.
- (2) The wave motion outside and inside the block mound can be described by linear long wave theory.
- (3) The block mound structure with a rectangular cross section is homogeneous and isotropic.
- (4) The flow resistance of the mound can be expressed by a linear relation in terms of the seepage velocity.

As Madsen and White discussed (1975), it is considered that wave conditions adopted in breakwater designs commonly falls in the long wave range of the spectrum. The linear long wave approximation, therefore, is used in the theoretical treatment.

An experimental program is carried out to confirm the validity of the theory and approximate method, and to determine empirical friction law.

2. THEORY

2.1 ANALYTICAL MODEL DERIVATION

The rectangular block mound with a width of l is located between $x = 0$ and $x = l$. The coordinate system is shown in Fig. 2. With the first and second assumptions, the governing equations for the wave motion outside the block mound ($x \leq 0$) are given as Eqs. (1) and (2).

$$(\partial \eta / \partial t) + h(\partial u / \partial x) = 0, \quad (1)$$

and

$$(\partial u / \partial t) + g(\partial \eta / \partial x) = 0, \quad (2)$$

in which η is the free surface elevation above the still water level, h is the constant water depth, u is the horizontal particle velocity, g is the gravitational acceleration, and t is the time.

Following to Kondo(1970) and Madsen and White(1975), the motion inside the block mound ($0 \leq x \leq l$) can be written as

$$(\partial \eta / \partial t) + (h/\epsilon)(\partial u / \partial t) = 0, \quad (3)$$

and

$$(S/\epsilon)(\partial u / \partial t) + g(\partial \eta / \partial x) + (f\omega/\epsilon)u = 0, \quad (4)$$

in which u is the seepage velocity, ϵ is the porosity of the mound, and ω is the angular frequency of the incident waves. The parameter S in the momentum equation (4) is given by Eq. (5) and represents effect of the unsteady fluid motion within the mound.

$$S = 1 + C_m(1 + \epsilon). \quad (5)$$

And f is the constant friction factor of the resistance law linearized using the Lorentz' Principle of equivalent work, and is written as

$$f\omega/\epsilon = \alpha + \beta|u|. \quad (6)$$

Two terms on the right hand of Eq. (6) represent laminar and turbulent flow resistance, respectively.

Since the governing equations are linear, we assume a periodic solution for the free surface elevation and horizontal particle velocity.

$$\eta(x,t) = \text{Real}[\zeta(x)e^{i\omega t}], \quad (7)$$

and

$$u(x,t) = \text{Real}[U(x)e^{i\omega t}], \quad (8)$$

in which $i = \sqrt{-1}$, and the amplitudes of η and u are functions of x only.

Outside the block mound, incident waves and partially reflected waves from the breakwater form a standing wave field. The flow inside the mound consists of two waves propagating in the positive and negative x -directions.

With the two matching conditions of the free surface elevation and particle velocity at the front surface of the block mound ($x=0$), and with the condition of no flow through the caisson ($x=l$), the final expressions for the wave motions both outside and inside the block mound are obtained as follows:

$$\text{For } x \leq 0 \text{ (outside the block mound):} \\ \eta(x,t) = (H_i/2)\{e^{-ik_0 x} + K_R e^{ik_0 x}\}e^{i\omega t}, \quad (9)$$

and

$$u(x,t) = U_i\{e^{-ik_0 x} - K_R e^{ik_0 x}\}e^{i\omega t} \quad (10)$$

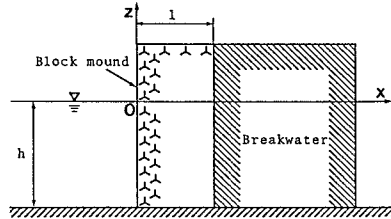


Fig. 2 Coordinate system.

For $0 \leq x \leq l$ (inside the mound):

$$\eta(x,t) = H_i \cosh\{ik(x-l)\} / \{ \cosh(ikl) + \tau \sinh(ikl) \} \times e^{i\omega t}, \tag{11}$$

and

$$u(x,t) = -2U_i \tau \sinh\{ik(x-l)\} / \{ \cosh(ikl) + \tau \sinh(ikl) \} \times e^{i\omega t}, \tag{12}$$

in which K_R is the reflection coefficient, as given by Eq. (13),

$$K_R = |H_r/H_i| = \{ |1 - \tau \tanh(ikl)| / |1 + \tau \tanh(ikl)| \}. \tag{13}$$

The wave number k_0 and horizontal velocity amplitude of incident waves U_i are given by the long wave theory as

$$k_0 = 2\pi/L_i = \omega/\sqrt{gh}, \tag{14}$$

and

$$U_i = (H_i/2) \sqrt{g/h}. \tag{15}$$

k is the complex wave number of waves inside the mound, and is given by

$$k = k_0(S - if)^{1/2}, \tag{16}$$

and τ is the parameter for simplifying the theoretical expression.

$$\tau = \epsilon(S - if)^{-1/2}. \tag{17}$$

H_i (real) and H_r (complex) are the incident and reflected wave heights outside the block mound.

Since the wave number k is complex, the theory indicates that waves propagating to the positive x -direction through the block mound is attenuated exponentially due to the frictional effect of the mound. Thus, we presume that the wave is perfectly reflected at the vertical front surface of caisson, and the wave force is calculated by a linear wave theory.

With the linear long wave assumption, the maximum horizontal wave force per unit width of the caisson, F_{Hm} , is written by Eq. (18), a function of the maximum surface elevation at the caisson, η_{ml} .

$$F_{Hm} = (\rho g/2) [2h \eta_{ml} + \eta_{ml}^2]. \tag{18}$$

By putting $x = l$ in Eq. (16), η_{ml} is written as

$$\eta_{ml} = \text{Real} \{ H_i / \{ \cosh(ikl) + \tau \sinh(ikl) \} \}. \tag{19}$$

2.2 DISCUSSIONS ON THE THEORETICAL RESULTS

Practical calculations are usually made with the known mound geometry and porosity as well as the incident wave condition. Parameter S given by Eq. (5), depends not only on the shape and size of blocks, but also on the unsteady flow characteristics inside the mound. Measurements of the added mass coefficient C_m in Eq. (5) are so difficult that it is necessary to assign an appropriate value to the parameter S before discussing the theoretical results. Madsen and White

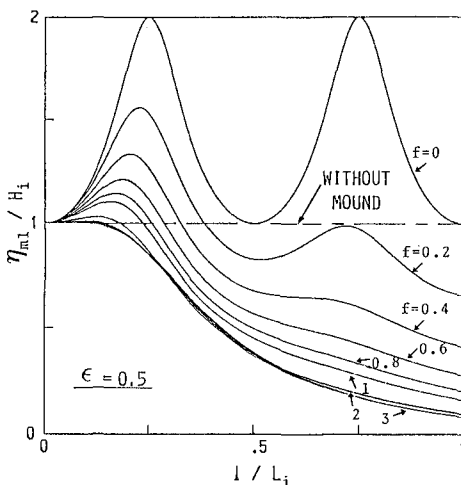


Fig. 3 Theoretical relation between η_{ml}/H_i and l/L_i .

(1975) discussed possible values of S and estimated to be $1 \leq S \leq 1.5$. They approximated it to be unity for practical circumstances. We shall, therefore, take $S = 1$.

The maximum wave force F_{Hm} is a function of η_{m1} only, so that dominant characteristics of the mound to the wave force reduction can be learned more clearly from the general behavior of the solution of Eq. (19) for η_{m1} , instead of Eq. (18) for F_{Hm} . An example of the numerical solution of Eq. (19) is presented in Fig. 3, showing the relative maximum surface elevation η_{m1}/H_i as a function of the relative mound width l/L_i for various values of the linearized friction factor f and for a mound porosity of $\epsilon = 0.5$. The broken line of $\eta_{m1}/H_i = 1$ corresponds to the perfect reflection at a vertical breakwater without block mound.

When $f = 0$, it refers to as a fictitious mound, in which only the net flow cross section is reduced to a half of that seaside of the mound. From Eqs. (11) and (19), the maximum surface elevation for $f=0$ is given as

$$(\eta_{m1}/H_i)_{f=0} = [\cos^2 k_0 l + \epsilon^2 \sin^2 k_0 l]^{-1/2} \quad (20)$$

Cyclic change of η_{m1}/H_i with respect to l/L_i indicates that standing waves with a node and antinode at the common boundary of outside and inside the block mound are formed in conditions of $l/L_i = 0.25$ and 0.50 . With the increase of the friction factor f , the cyclic change is attenuated, and η_{m1}/H_i tends to approach constant values with increase of the relative mound width,

when $f > 2$. According to Eqs. (6) and (12), increase in the friction factor may be a result either of decreasing the mound porosity or of increasing the incident wave height (Sollitt and Cross, 1972). From Fig. 3, therefore, a very interest process is found that when small waves are incident on the mound breakwater, the block mound gives rise to stronger wave force than without the mound. This results from the two following facts: (1) decrease in the net flow cross section, and (2) the resonance of the standing wave systems between outside and inside the block mound.

In a practical planning of coastal and harbor structures of block mound type, of a particular interest is the dependency of mound porosity on the wave force. Figure 4 is a numerical result showing the dependency of the mound porosity on the relative maximum free surface elevation η_{m1}/H_i for $l/L_i = 0.25$. Since actual range of the mound porosity is estimated to be 40 % to 60 %, it is noticed that the amplitude of standing waves at the caisson or the wave

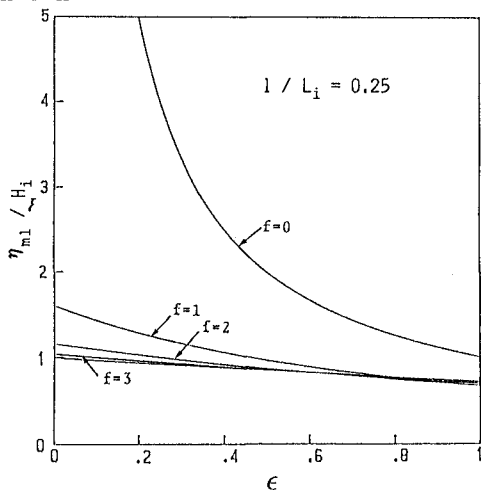


Fig. 4 Theoretical relation between η_{m1}/H_i and ϵ .

force does not depend noticeably on the mound porosity for practical circumstances, in which the friction factor becomes usually larger than 2.

In addition to the wave force reduction, another important function of the block mound is the damping of reflected waves from the breakwater. Figure 5 is an numerical example of the relationship between the reflection coefficient K_R and relative mound width l/L_i for $\epsilon = 0.5$. As the relative mound width increases, the reflection coefficient tends to approach to a constant value for the case when the friction factor is larger than 2. Reduction in the wave reflection by the block mound can not be expected, if the relative width is smaller than 0.1.

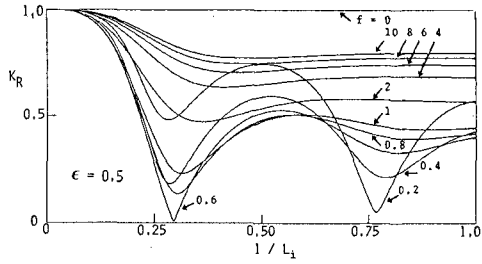


Fig. 5 Theoretical relation between K_R and l/L_i .

3. EXPERIMENTAL SETUP AND CONDITIONS

3.1 EXPERIMENTAL EQUIPMENT

Experiments were performed in a glass-walled wave flume of 1 m wide, 1 m deep and 50 m long. Figure 6 shows general arrangement of the experimental equipment. Waves were produced by a piston-type wave generator installed at one end of the wave flume. The wave flume was separated into two sections with a plywood bulkhead and equipped a steel beach of a slope of 1/50.

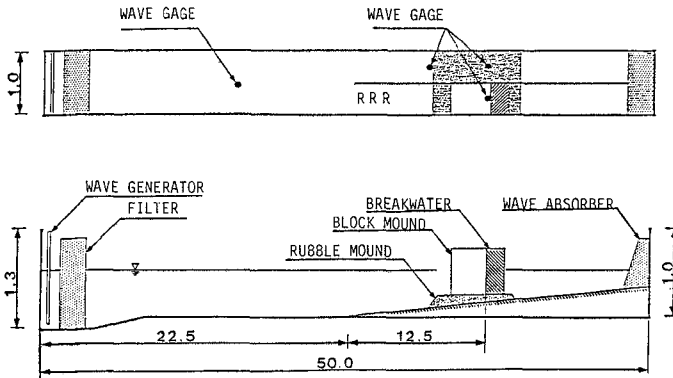


Fig. 6 General arrangement of experimental equipment. (Units:m)

In the test section with 0.50 m wide, model breakwaters comprising a steel rectangular parallelepiped as model caisson [0.466x0.20 m x 0.40 m, weight in air: 20 kg] and

rectangular or trapezoidal block mound was placed on a gravel mound of 5.0 cm high. The other section of the flume was used for measurements of incident waves as progressive waves at the breakwater location.

3.2 MODEL BLOCK MOUND

Rectangular model mounds with three different widths were comprised by model tetrapods of three different sizes, whose physical dimensions are described in Table 1. The block was contained in wire screen cribs, shaped as rectangular parallelepiped. In situ porosity was checked up by the total number of blocks used and volume of the crib.

Additional experiments were conducted to examine approximate method for predicting the wave force on the constructed with the same blocks used for the rectangular

Table 1 Dimensions of rectangular mounds(Tetrapods).

RELEVANT BLOCK SIZE*	B(cm)	5.0, 8.2, and 11.3
MOUND WIDTH	l(cm)	22.5, 30.0, and 45.0
HEIGHT	(cm)	40.0
IN SITU POROSITY	ε (%)	50.0

[*] The relevant block size is defined as $B = (abc)^{1/3}$, in which a, b, and c are long, intermediate and short sizes of a block]

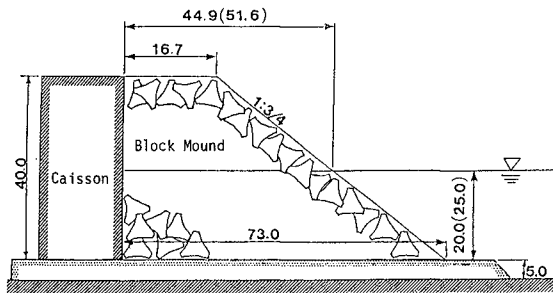


Fig. 7 Cross-section of sloping block mound(Units: cm).

mound. Figure 7 illustrates the dimensions of the trapezoidal block mound, constructed with the same blocks used for the rectangular model mound.

3.3 WAVE AND WAVE FORCE MEASUREMENT

Measurements of water free surface elevations at various locations, denoted in Fig. 6, were made using capacitance wave gages. In particular, simultaneous measurements of the free surface elevation at three offshore locations denoted by R in Fig. 6 were used for the computation of reflection coefficient of the breakwater. Resolution of incident and reflected waves was performed by means of the spectral component analysis with a simultaneous record of the free surface elevation at three adjacent locations of known relative distances (Goda, 1985).

Total horizontal wave forces acting on the model caisson were measured by using a specially designed force meter of cantilever-type, made of a steel square bar(40 mm×

70 mm × 1070 mm) (Hattori et al., 1979). The force meter was fixed on the backside of the caisson, and had a natural frequency of 13 Hz in a case when the caisson was placed in a water depth of 0.20 m. Outputs of the water surface elevation and wave force were recorded on a 7-channel analogue recorder. The data were digitized by an A-D converter at a sampling frequency of 100 Hz for extensive processing by computer.

Wave conditions are given in Table 2.

Table 2 Experimental conditions.

INCIDENT WAVE HEIGHT	H_i (cm)	1 to 17
PERIOD	T (s)	1.5 and 2.0
WATER DEPTH	h (cm)	20 and 25
BLOCK REYNOLDS NUMBER	$Re_B = BU_i/\nu$	$(1 \text{ to } 70) \times 10^3$

4. COMPARISONS OF THEORY AND EXPERIMENT

4.1 EMPIRICAL RELATIONSHIP FOR THE FRICTION FACTOR

The theoretical solutions indicate that the friction factor representing the hydraulic characteristics of the mound is a physically fundamental parameter for wave energy damping within the mound structures. Hence, the determination of the friction factor is a very important problem for the predictions of the wave force. To simplify the analytical treatment, the friction factor was assumed to be constant. In addition, the solutions were obtained by approximating the parameter S to be unity, because the added mass coefficient C_m of blocks could not be evaluated experimentally. It is, therefore, necessary to take into account of unsteady effect of the fluid motion in the determination of the friction factor.

In the previous studies, however, friction factor of rubble stones and concrete blocks were examined from experiments of steady and unidirectional flows in open channel or pipe (Shuto and Hashimoto, 1970; Sollitt and Cross, 1972). Based on some preliminary considerations and experiments, the friction factor was evaluated from measured maximum free surface elevation at the front of caisson breakwater, η_{m1} , with aids of Eqs. (11) and (16).

Since the friction factor is assumed to be independent of the time and space, we examine validity of the friction law of Eq. (6), in which the local seepage velocity u is replaced with the mean horizontal velocity inside the mound U_m , as given by Eq. (18).

$$U_m = (1/lT) \int_0^1 \int_t^{t+T} |u| dx dt = (8/3\pi l) \int_0^1 u_r dx, \tag{18}$$

in which u_r is the real part of the seepage velocity given by Eq. (12). Substituting Eq. (9) into Eq. (18), U_m for a special case of $f=0$ is written as Eq. (19).

$$U_m = (2\epsilon U_i/k_0 l) [\cos^2 k_0 l + \epsilon^2 \sin^2 k_0 l]^{-1/2} \cdot [1 - \cos k_0 l], \tag{19}$$

Figure 8 shows relationships of $f\omega/\epsilon$ and U_m , and indicates that the linear friction law similar to Eq. (6) is valid for the mean seepage velocity. According to Eqs. (18) and (19), the mean seepage velocity U_m is proportional to the velocity amplitude of incident waves U_i and the mound

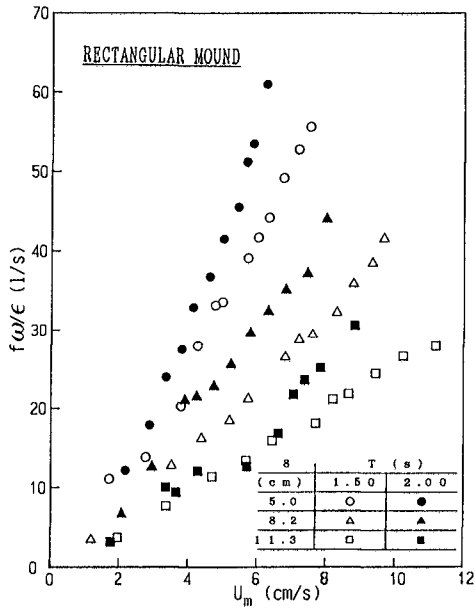


Fig. 8 Relationship between $f\omega/\epsilon$ and U_m .

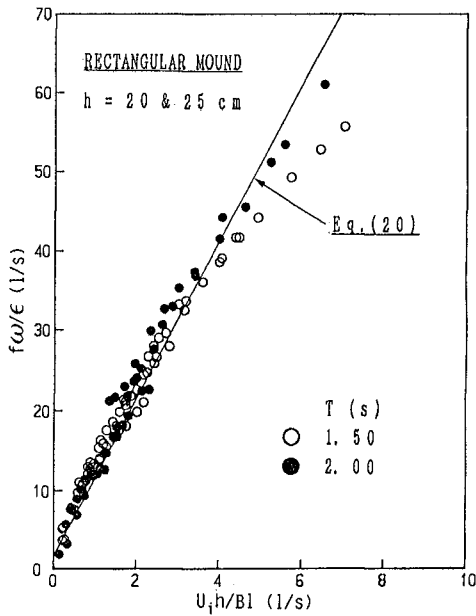


Fig. 9 Empirical friction law as a function of U_1 .
[$f\omega/\epsilon$ and $U_1h/B1$]

porosity ϵ , and is inversely proportional to the relative mound width l/L_i . Since U_m is generally a function of the friction factor, we can not explicitly calculate the friction factor from Eqs. (12) and (18) with a given incident wave condition and known mound properties.

From the standpoint of practical calculation of the friction factor, Fig. 9 is prepared for determining an empirical friction law as a function of the horizontal velocity amplitude of incident waves U_i , calculated from a linear wave theory. The best fitted line in Fig. 9 leads an empirical relationship for the friction factor of

$$f \omega / \epsilon = 2.0 + 10.4(U_i h / B l), \tag{20}$$

in which the factor $(h/B l)$ is introduced to describe the block mound characteristics.

4.2 REFLECTION COEFFICIENT

In order to examine applicability of the empirical relationship for the friction factor, experiments on the wave reflection were conducted. Figure 10 is an example of comparisons between the theoretical and experimental reflection coefficients K_R , with respect to the relative height of incident waves H_i/h for a relative mound width of $l/L_i = 0.206$. The friction factor is computed with the aid of Eq. (20). Although exhibiting some scatter of the data, the good agreement supports the determination of the friction factor adopted in this study, and validates the empirical equation (20).

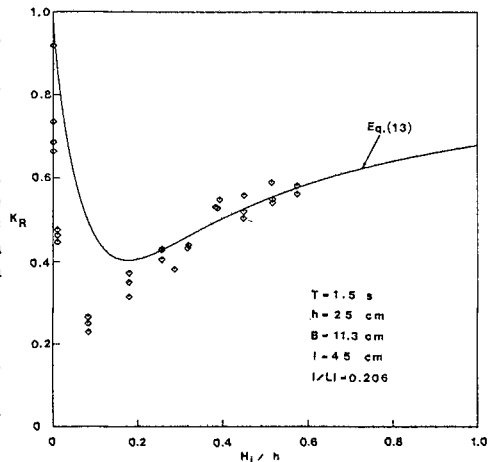


Fig. 10 Comparison between predicted and measured reflection coefficients.

4.3 MAXIMUM HORIZONTAL WAVE FORCE

As was mentioned previously, various factors influence on wave energy dissipation of the block mound. Hence, comparisons between experimental and predicted results of the maximum horizontal wave force on the upright caisson will be discussed by using the following dimensionless parameters, ϕ_m and K as given by Eqs. (21) and (22), which were derived from a dimensional analysis (Inagaki, Hattori, and Noguchi, 1986).

$$\phi_m = F_{mH} / \rho g H_i^2, \tag{21}$$

and

$$K = [(1 - \epsilon) / \epsilon]^{1/3} [(H_i l) / (h B)] \tanh k_0 h, \tag{22}$$

where ϕ_m is the relative maximum wave force per unit width of breakwater, and K is the parameter combining the characteristics of an incident wave and block mound. For examples, the term of $[(1 - \epsilon) / \epsilon]^{1/3} (l/B)$ on right hand of Eq. (22) represents the number of voids per unit width within

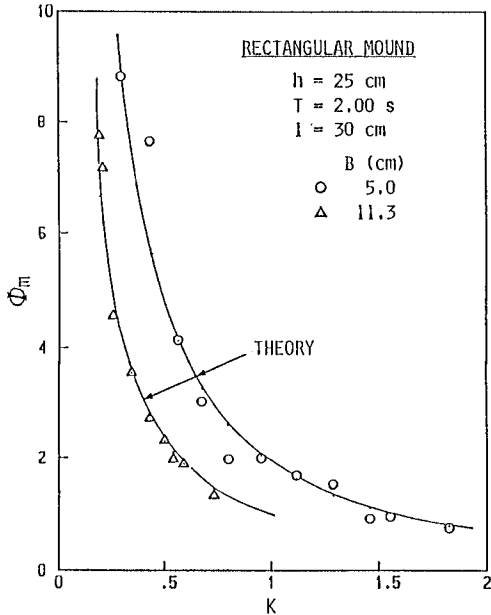


Fig. 11 Relationship between Φ_m and K .

the block mound. And $\tanh k_0 h$ is considered as a correction factor for the wave pressure distribution on the caisson.

Figure 11 is an experimental result on the relative maximum wave force Φ_m as a function of K . For comparison the predictions by the present theory are also shown. And Figure 12 shows a comparison between measured and predicted maximum horizontal wave force for all the experiments. The agreement between the theory and experiments is fairly good and confirms the general validity of the present theory for the rectangular block mound breakwater.

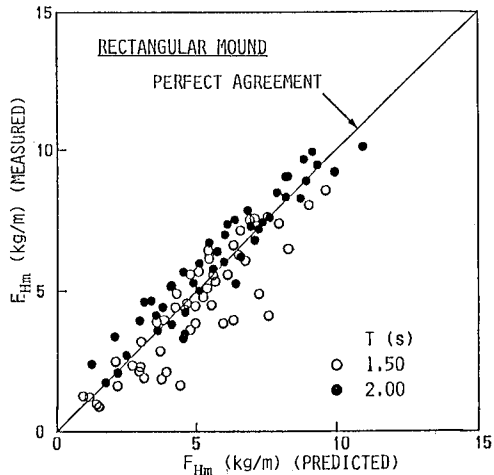


Fig. 12 Overall comparison between predicted and measured maximum wave forces.

5. APPROXIMATE METHOD FOR TRAPEZOIDAL BLOCK MOUND

5.1 PROPOSE OF APPROXIMATE METHOD

Wave motions at a block mound with steep front slope are very complicated and make the theoretical treatment more difficult than that for a rectangular block mound.

Sollitt and Cross (1972) proposed a concept of the equivalent rectangular breakwater which has the same submerged volume as that of the trapezoidal breakwater, and developed a semiempirical procedure for the prediction of reflection and transmission coefficients of permeable breakwater of trapezoidal shape. Hence, applicability of their approximate method to the present problem is examined

by a comparison of all the measured maximum wave forces with the predictions based on the equivalent rectangular mound concept by Sollitt and Cross. In the predictions, energy dissipation due to the wave breaking is evaluated by the same procedure as by Sollitt and Cross. Figure 13 shows an overall comparison between predicted and measured maximum wave forces. We can clearly recognize a systematic trend that the predictions always underestimate the wave force and the deviation between the prediction and experiment becomes larger with increasing the maximum wave force, corresponds to the increase of incident wave height.

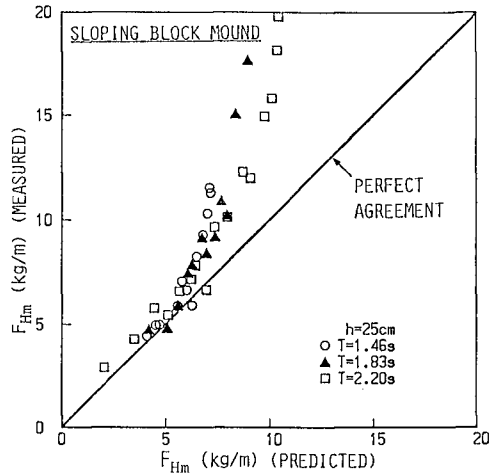


Fig. 13 Overall comparison between predicted and measured maximum wave forces.

According to experiments of trapezoidal block mounds, incident waves break and run-up on the sloping face of block mound. Water mass in the run-up wedge penetrates into the mound and flows through the upper portion of mound with narrower width than the submerged portion. As incident wave height increases, the water flow sometimes hit against the caisson and gives rise to additional wave force on the caisson. In addition, the water mass transport associated with the wave run-up on the sloping face rises the mean water level inside the mound above the still water level outside the mound. As a result, it spreads upwards the front surface area of caisson, to which wave forces are exerted.

Approximate method by Sollitt and Cross generally gives a wider mound width above the still water level than that of the actual mound. Thus, it does not reproduce reasonably well nonlinear effects of the wave motions observed both on the front slope and inside the block mound, and overestimates the energy dissipation due to flow resistance inside the mound. The experiments suggest that the following two effects of increasing the water depth around the block mound should be taken into account for the prediction of maximum wave force on a caisson backed by sloping block mound.

- (1) Vertical asymmetry of the free surface elevation around the still water level associated with incident waves, and
- (2) Wave set-up caused by the mass transport from the sloping face of the mound.

Consequently, we propose an approximate method that the sloping mound is replaced by an equivalent rectangular mound having the same width as that of the sloping mound at the mean water elevation including the wave set-up η_s and displacement of the mean water level from the still water level δ , as shown in Fig. 14. The mean water depth inside the block mound for determining the equivalent width of a sloping mound l_E is written as

$$h_E = h + \eta_s + \delta, \tag{23}$$

and

$$\delta = \eta_c - H_i/2, \tag{24}$$

in which η_c is the crest elevation above the mean water level outside the mound and calculated by Cnoidal wave theory of first order (Isobe, 1985).

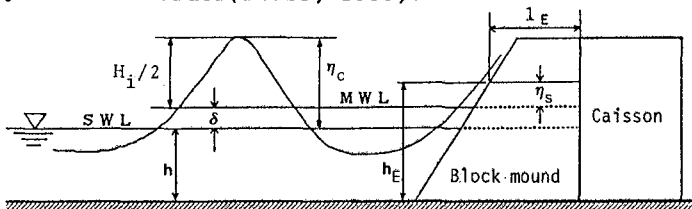


Fig. 14 Equivalent rectangular block mound.

5.2 WAVE SET-UP INSIDE BLOCK MOUND

Although many theoretical and experimental studies of the wave set-up on a natural beach have intensively been conducted, none of the published information has examined the wave set-up inside permeable structures. In order to examine the wave set-up inside the block mound, additional experiments both for the rectangular and sloping mound breakwaters were made. Deviation in the mean water level inside the mound from the still water level was evaluated from the time variation of free surface elevation measured at the front of the caisson.

Experimental results on the wave set-up inside the block mound are shown in Fig. 15, showing the relationship between the relative wave set-up η_s/H_i and the relative wave height H_i/h . Wave set-up inside the rectangular mound indicates a weak dependency on incident wave height. On the contrary, as seen in Fig. 15, that inside the sloping

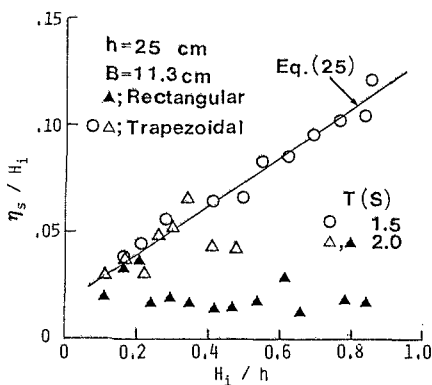


Fig. 15 Relation of η_s/H_i and H_i/h .

mound increases almost linearly with incident wave height, when $H_i/h > 0.1$. An empirical relationship between the wave set-up and incident wave height is obtained as

$$\eta_s/H_i = 0.02 + 0.11(H_i/h) \quad (25)$$

5.3 COMPARISONS BETWEEN PREDICTED AND MEASURED WAVE FORCE

Figure 16 shows an example of comparisons between predicted and measured maximum wave force, using the relationship between the nondimensional parameters, ϕ_m and K . From the fairly well agreements as seen in Fig. 16, it is concluded that the approximate procedure proposed here is applicable to the prediction of the wave force of a breakwater with sloping mound.

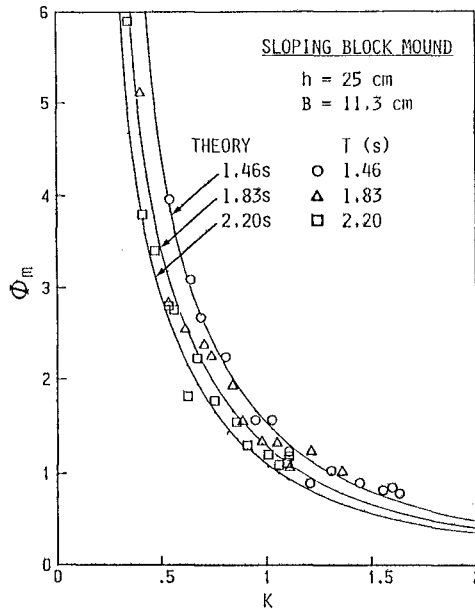


Fig. 16 Comparison between predicted and measured relative maximum wave forces ϕ_m .

To make both the analytical model and the approximate procedure generally applicable, the empirical equations for the friction law and for the wave set-up should be examined for various wave conditions and mound geometries.

6. CONCLUSIONS

In this paper, analytical theory are proposed for predicting the wave force acting on the upright caisson structure with a rectangular mound of concrete blocks of energy dissipation type. The theory is developed with approximation of the linear long wave. The wave damping

inside the block mound is treated by the equivalent linearization technique after the Lorentz's Principle of equivalent work, and empirical formula is used. The validity of the analytical theory is confirmed from comparisons with laboratory experiments.

For practical applications, approximate procedure is developed for the prediction of the wave force on the caisson armored with sloping block mound. The sloping block mound problem is solved by introducing an equivalent rectangular mound which has the same mound width as that of the sloping mound at the mean water elevation taking account of two nonlinear effects, the vertical asymmetry of incident wave profile at the sloping face and wave set-up inside the mound.

Although a number of assumptions have been introduced in the approximate procedure, the good agreement between predicted and measured maximum wave forces indicates that the procedure may be valuable for practical applications.

7. REFERENCES

- Goda, Y.(1985): Random Seas and Design of Maritime Structures, Univ. of Tokyo Press, 309 p.
- Hattori, M. et al.(1979): Experimental study on wave force against perforated breakwaters, Proc. of 26th Japanese Conf. on Coastal Eng., pp. 396-400 (in Japanese).
- Inagaki, K., M. Hattori, and Y. Noguchi(1986): Wave force reduction by armor block mound, Proc. of 33rd Japanese Conf. on Coastal Eng., JSCE, pp. 362-366 (in Japanese).
- Isobe, M.(1985): Calculation and application of first-order Cnoidal wave theory, Coastal Engineering, Vol.9, No.4, pp. 309-325.
- Kondo, H.(1970): An analytical approach to wave transmission through permeable structures, Coastal Engineering in Japan, JSCE, Vol. 13, pp. 31-42.
- Madsen, O. S. and S. M. White(1975): Reflection and transmission characteristics of porous rubble-mound breakwaters, Tech. Report No. 207, R.M. Parsons Lab., Dept. of Civil Eng., MIT.
- Massel, S.R. and C.C. Mei(1977):Transmission of random wind waves through perforated or porous breakwaters, Coastal Engineering, Vol. 1, pp. 63-78.
- PIANC(1988): Analysis of rubble mound breakwater, PTC Working Group 12, pp. 1-6.
- Shuto, N. and H. Hashimoto(1970): Hydraulic resistance of artificial concrete blocks, Coastal Engineering in Japan, Vol. 8, pp. 43-54.
- Sollitt, C.K. and R. H. Cross(1972): Wave reflection and transmission at permeable breakwaters, Tech. Report No. 147, R.M. Parsons Lab., Dept. of Civil Eng., MIT.

CHAPTER 160

BLOCK REVETMENT DESIGN WITH PHYS. AND NUM. MODELS

A. Bezuijen¹,
J. Wouters²,
C. Laustrup³,

Abstract

A combination of a physical model and numerical models has been used in the design of a block revetment for the Danish North Sea coast. The wave pressure loading on the revetment during design conditions was investigated in a physical scale model. The measured wave pressures were used as a boundary condition for the numerical models. Solutions for the flow equations through the coverlayer, filter layer and subsoil were then obtained in the numerical models, taking into account the influence of turbulence. With these solutions the stability of the coverlayer and subsoil was evaluated. The paper presents a description of the various models and information about the design of the revetment.

1. Introduction

Numerical models were developed within the scope of a research programme on block revetments in order to calculate the loading on a block revetment during wave attack, Hjortnaes-Pedersen et al (1987) and Bezuijen et al(1987). This research programme was commissioned by the Dutch Department of Public works (Rijkswaterstaat) and was performed by Delft Hydraulics in cooperation with Delft Geotechnics. The numerical models were used to calculate the pressure distribution in the filter layer and subsoil below a block revetment when the pressure distribution on the revetment due to wave attack is known. Both the wave pressures and the calculated pressures underneath the revetment determine the uplift pressures on the coverlayer of the revetment. These uplift pressures can be compared with the "strength" of the coverlayer. The wave pressures which were required as inputs for the numerical models were determined by means of physical model tests. Since only wave pressures on the slope had to be measured and the influence of wave impacts on the stability of a block revetment could be neglected, these pressures could be measured in a small scale model.

¹. Delft Geotechnics, Delft, The Netherlands

². Delft Hydraulics, Delft, The Netherlands

³. Kystinspektoratet, Lemvig, Denmark

The combination of a physical scale model and numerical models was used to evaluate the design of a dune toe protection which is now under construction in parts of the Danish North Sea coast. The design of the block revetment is presented in this paper and the physical model tests described. A brief description of the numerical models is given together with the results of the calculations for this revetment. Finally the modifications in the design, based on the results of the calculations, are discussed.

2. Block revetment used as dune protection

On some parts of the Danish North Sea coast erosion has been very large, on average 3 - 4 m a year. This has caused some dunes to disappear and others to become very weak. As a result the low areas behind the dunes are open to flooding. On these stretches of coast it is necessary to stop the erosion and to re-establish the flood protection. The measures being taken against the erosion are a combination of onshore and offshore beach nourishment and low detached breakwaters parallel and close to the shore line. The flood protection is being re-established by building artificial dunes protected by a concrete block revetment. Concrete blocks are being used because:

- a. They are cheap compared with other types of artificial coverlayers.
- b. Denmark has no quarries close to the North Sea coast.
- c. Concrete blocks look relatively attractive into the sandy coast environment.
- d. Constructional procedures are relatively easy and a high quality can be achieved.
- e. The concrete is very durable in a marine environment.

A sketch of the concrete block revetment is presented in Figure 1. Water level and wave conditions vary depending on the location. The conditions expected with a return period of 100 years, for the most exposed structure, are shown in Table 1.

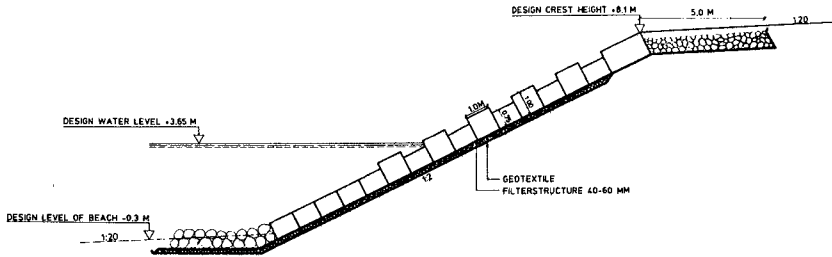


Figure 1: Original cross section for the design parameters given in Table 1

Waterlevel:	3.65 m above datum
Waves in a depth of 19 m	$H_s = 8.2$ m
	$T_p = 12$ s
Shore profile: slope	1:20 from -0.30 to -6.00 m below datum
	1:100 below -6.00 m below datum
Revetment slope	1:2 from - 0.30 to + 8.10 m above datum

Table 1: Design conditions

The design crest height at the various locations is taken as the sum of the high water level, the wind set-up and the maximum breaking wave height above still water level. For the conditions given in Table 1 the crest height will be 8.1 m. Since waves will run-up the slope to above the level of the block revetment, the first 5 m of the crest of the structure has been protected with rubble. The toe of the structure has been designed at such a level, that there will be no damage by scouring during the design storm.

The blocks are placed on a filter structure of 40 - 60 mm rubble between two layers of geotextile. The purpose of the upper layer is to prevent the rubble layer from being filled with sand from above. The blocks are 0.75 m high and weigh 3,000 kg. Some of the blocks are 1.0 m high in order to introduce slope roughness.

The following questions were raised when evaluating the design:

- Can block thickness be reduced?
- Is a 1:3 slope preferable to a slope of 1:2?
- What is the influence of revetment roughness on run-up produced by using blocks of different height?

3. Physical model

Small-scale model tests were carried out in a wave flume to obtain information about the wave pressure distribution on the slope. The wave flume has a depth of 0.8 m and is equipped with a system to compensate for wave reflections. The tests were carried out with irregular waves on slopes of 1:2 and 1:3. Since only the wave pressures on the slope had to be measured in a physical model test (to provide inputs for the numerical models) it was unnecessary to model the revetment itself. Only the geometry of the revetment and the foreshore were of interest in the physical model and these were modelled in concrete. The model layout is shown in Figure 2.

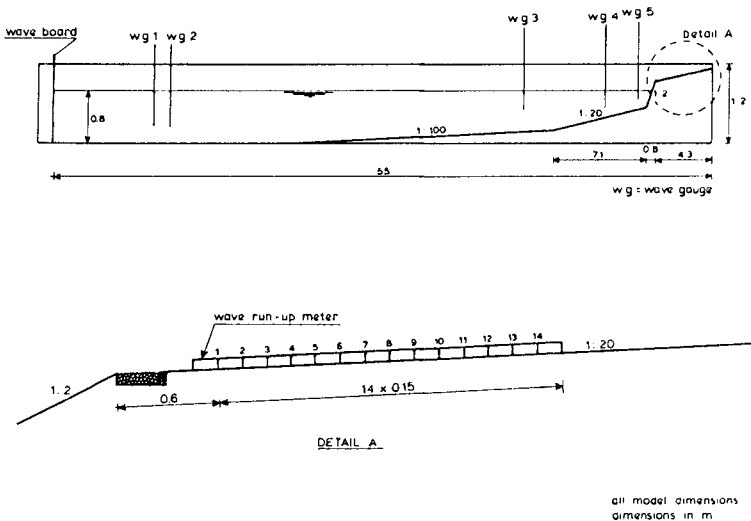


Figure 2: Model layout

Wave heights were measured on the profile with five wave gauges; run-up was measured with a wave run-up meter on the 1:20 slope, see Figure 2. The positions of the pressure gauges on the 1:2 slope are shown in Figure 3. Because wave impacts shorter than 0.2 s duration are not of importance to the stability of the revetment, the pressure signals could be filtered by a 6.25 Hz (in model 25 Hz) low pass filter. The low-pass filter is necessary to prevent interference with high frequencies. Most tests were run at a geometric scale of 1:16. The stability of the rubble on the crest was measured directly in the model tests and therefore this was modelled to the same geometric scale factor. The nearshore incident wave conditions for the model tests were calculated from the deep water conditions with the ENDEC computer program, Stive (1984).

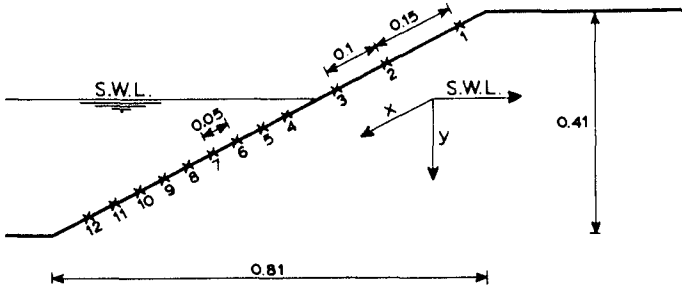


Figure 3: Location of wave pressure gauges on the 1:2 slope

The model tests indicated that the wave run-up on the 1:20 slope can be considerable and during the design conditions, Table 1, and with a crest height of 8.2 m in prototype, more than 10% of the waves passed the highest indicator of the wave run-up meter. This implies a wave run-up of over 43 m up the 1:20 slope. These run-up values led to an investigation of the run-up as a function of the crest height. The results are shown in Figure 4, for the design conditions given in Table 1.

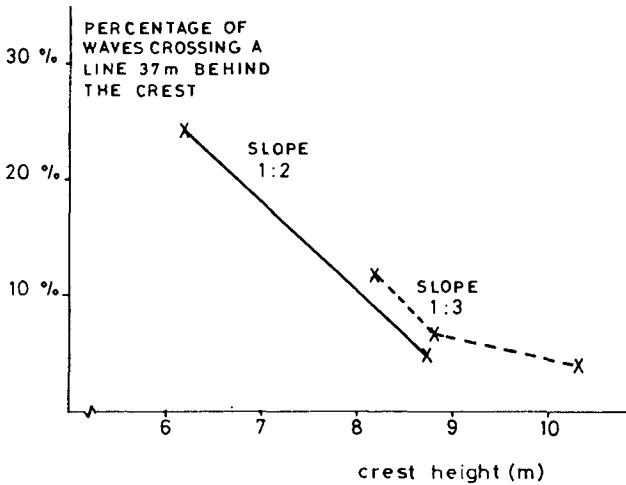


Figure 4: Percentage of waves crossing the 37 m line (see text) as a function of the crest height

On the 1:20 slope a line 37 m from the top of the revetment in prototype was chosen to indicate the extent of run-up, because information was available about the waves crossing this line also for the tests runned at different geometric scales.

More waves passed the 37 m line with the 1:3 slope than with the 1:2 slope, but the difference was small. It appeared that the increased roughness, obtained by using blocks of different height, would lead to a 10% reduction in the number of waves crossing the 37 m line during design conditions. During moderate storm conditions this reduction would be even higher. With a significant wave height of 3 m in deep water the reduction would be up to 25%.

The wave pressures measured in the physical model have been used in the numerical model. This topic is discussed in the following chapter.

4. Numerical models

In order to evaluate the stability of the revetment, it is essential to determine the uplift pressures on the blocks. These pressures are determined by the difference between the pore pressure in the filter layer under the blocks and the wave pressures on the blocks. If the mean uplift pressure on the block is larger than the pressure corresponding to the weight of the block plus the friction forces between adjacent blocks then a block can be lifted out of the revetment. The stability of the sand underneath the revetment is also important since no sliding may occur. These stability criteria cannot be investigated in a small scale model test because of the soil mechanical scale effects which occur in such a test. A large scale investigation is a possibility, but in this project it was decided to use a numerical approach to evaluate the stability criteria. The uplift pressures on the blocks and the stability of the blocks were calculated with the STEENZET/1 program, to calculate the pore pressure in the filter layer and the resulting block movement (see Section 4.1).

The pore pressure distribution in the subsoil was calculated with the STEENZET/2 finite element program which can be used to calculate the pressure distribution in both the filter layer and the subsoil, assuming no block movement (see Section 4.2). This pore pressure distribution was used in a stability calculation to evaluate the geotechnical stability against sliding. These numerical models are described briefly in the following sections.

4.1 STEENZET/1

The pressure distribution in the filter layer is determined by the flow through this layer and the flow through the joints around the blocks. The flow in the subsoil itself has no influence because of the low permeability of the sand compared to the permeability of the filter layer. Assuming a flow parallel to the slope in the filter layer, a flow perpendicular to the slope in the coverlayer and a coverlayer permeability which is concentrated in the "horizontal" joints, see Figure 5, the following formula can be derived for the potential in each joint:

$$\phi_i = \frac{1}{1 + 2 \frac{k b D}{k' l^2}} \left\{ \frac{k b D}{k' l^2} (\phi_{i-1} + \phi_{i+1}) + \phi_{t,i} \right\} \quad (1)$$

- Where: ϕ_i : the piezometric head in the filter layer (m)
 near joint i
 $\phi_{t,i}$: the piezometric head on the revetment (m)
 near joint i
 b : the thickness of the granular sublayer (m)
 D : the thickness of the blocks (m)
 l : the length of the blocks (m)
 k : the permeability of the filter layer (m/s)
 k' : the permeability of the cover layer (m/s)

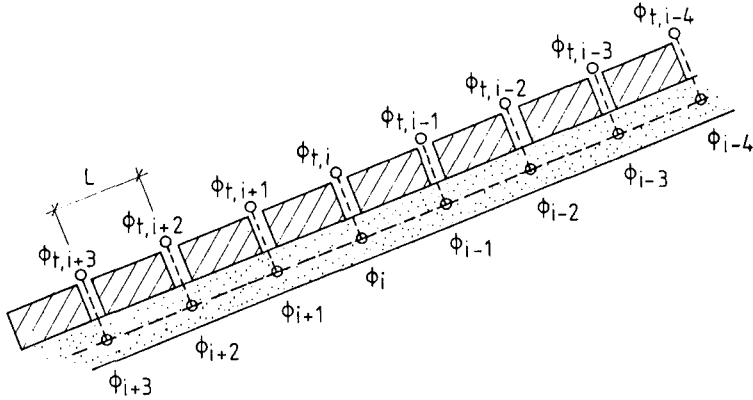


Figure 5: The STEENZET/1 finite difference scheme

At the phreatic surface the piezometric head in the filter layer is given by the position of the phreatic surface. At the lower end of the revetment the condition $\phi_{i+1} = \phi_{i-1}$ is assumed. If there is no phreatic surface, $\phi_{i-1} = \phi_{i+1}$ at the top of the revetment. The potential distribution in the filter layer can be solved numerically with Equation (1) for all joints if the different values of the piezometric head on the revetment ($\phi_{t,i}$) and the position of the phreatic surface are known. In the STEENZET/1 computer program this solution is obtained using an iterative scheme. Results of den Adel (1987) can be used to calculate the permeability of the filter layer. On the basis of permeability tests den Adel described the coefficients a and b in the Forchheimer relation ($i = av + bv^2$, with i the hydraulic gradient and v the filter velocity) as a function of the porosity and d_{15} of the granular material. The permeability of the cover-layer is determined by various flow resistances in and near the joints as described by Klein Breteler and Bezuijen (1988). Turbulence in the flow through the joints is included by adapting the permeability of the coverlayer to the calculated gradient during each iteration cycle. A linear flow condition is used in the filter layer.

The turbulent flow has therefore to be linearized. This linearisation is performed in such a way that the flow velocity calculated with the linear flow relation is the same as the flow velocity calculated using a turbulent permeability relation at a gradient equal to $\sin(\alpha)$, with α the slope angle.

The piezometric head on the revetment ($\phi_{t,i}$) is determined from measured wave pressures by linear interpolation of the results of the pressure gauges. The wave pressures measured in the small scale model can be transferred to prototype values by using Froude's law. The measured pressures can be scaled up using the geometric scale and the time scales using the square root of that scale. This means that the 50 Hz sampling frequency in the model tests, at a scale 1:16, corresponds to a 12.5 Hz sampling frequency in prototype.

The ϕ_i values were calculated for the various time steps using different values of $\phi_{t,i}$. The position of the phreatic surface is calculated for each time step by taking the still water level as a starting position and adapting the phreatic level to the nett flow of water in the filter layer. In this way the potential distribution can be calculated for each sampling of the wave pressures over a period of several waves. The results of this program have been compared with the results of large scale model tests and show good agreement (Bezuijen et al (1987)).

If the mean calculated uplift pressure on one block exceeds the pressure corresponding to the weight of the block and the friction forces, then a block will start to move. This movement can also be calculated in the program using a simple routine. The uplift pressure, multiplied by the block area, determines the uplift force. Subtracting the weight of the block and the friction force gives the nett force F_n , which causes block movement. The acceleration of the block can then be calculated using the well known relationship:

$$F_n = M_b \cdot a$$

Where: M_b : the mass of the block (kg)
 a : the acceleration of the block (m/s²)

Double integration of the acceleration giving the block movement.

The movement calculated in this way however is too large. In reality the block movement is less, because the moving block itself causes a pressure decrease in the filter layer. A routine that includes the influence of the moving block on the pressure distribution has been developed. This routine was not used in this project because, due to lack of experimental evidence, it was not certain that the results would always be on the safe side.

4.2 Results of STEENZET/1 calculations.

Calculations were made for slope angles of 1:2 and 1:3 and various coverlayer and sub layer permeabilities. The influence of the slope on the maximum uplift pressures appeared to be small. This means that a 1:2 slope is in fact the most economical. The results of a typical calculation are shown in the Figures 6 and 7. The black area shows the measured wave pressures and the grey area the uplift pressure, but only when larger than corresponding to the weight of the blocks. The vertical height of the area represents the pressure, in metres of water, at the location where the pressure was measured. Figure 6 shows the position of the wave front at maximum wave run down; there is hardly any water on the revetment and as a consequence the wave pressures are very small.

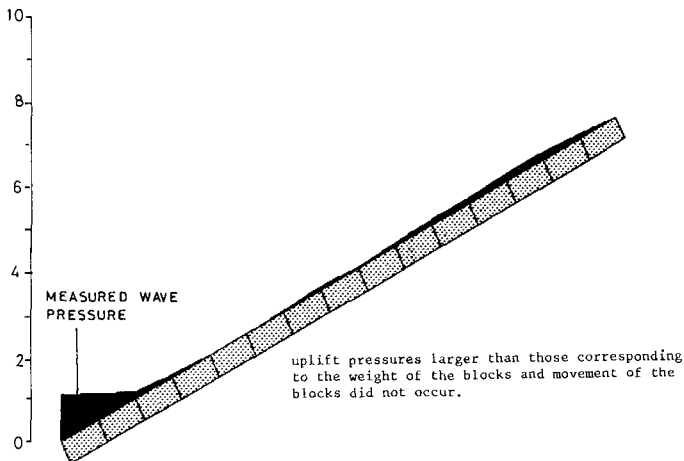


Figure 6: Wave pressure measured during wave run down.
Results of STEENZET/1 calculations

Figure 7 shows the pressure distribution just after wave impact. From these figures it is clear that, for the revetment being studied the highest uplift pressures can be expected just after wave impact, when two areas of high wave pressure occur on the revetment separated of an area of low pressures. The high wave pressures are transmitted through the filter layer, leading to high uplift pressures in the area with small wave pressures.

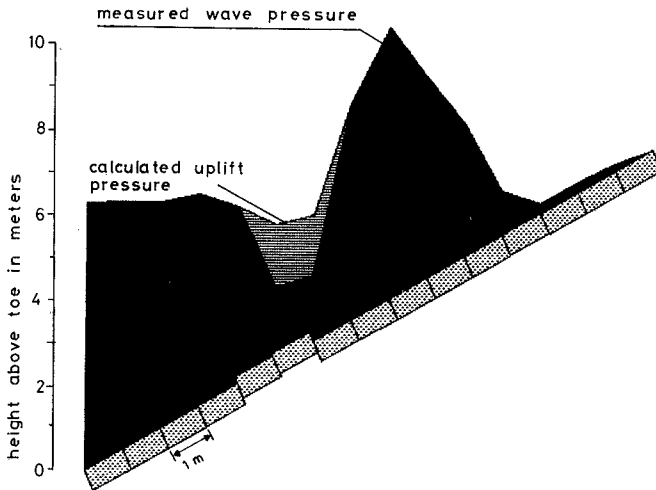


Figure 7: Wave pressure measured after wave impact. Uplift pressure when larger than corresponding to the weight of the blocks and calculated movement of the blocks. Results of STEENZET/1 calculations

Although during wave run down the filter layer is almost completely filled with water, the maximum wave run down does not appear to be a critical situation. The uplift pressure is never larger than the pressure that corresponds to the weight of the blocks. Due to the hydraulic gradient in the filter layer the pressure distribution in that layer is by no means hydrostatic, leading to small pore pressures and uplift pressures.

The permeabilities of coverlayer and filter layer had a distinct influence on the uplift pressures. The lowest uplift pressures were found for a minimum filter layer permeability and a maximum coverlayer permeability. The permeability of the coverlayer is determined by the permeability of the joints and is reduced due to the geotextile between the blocks and the filter layer. The design was therefore adapted and the geotextile removed. Without the geotextile some sand will be transported into the filter layer. However this sand will only reduce the filter layer permeability. Dutch experience has shown that this sand never causes trouble.

A design criterion had to be chosen for determining the block thickness. The criterion, no block shall ever move during design conditions, leads in fact to a very large block thickness and is too strict to be of practical use. The clamping forces between the blocks are completely neglected; however, due to these clamping forces, the strength of the revetment is increased significantly. Pulling tests have shown that sometimes forces more than 10 times the weight of a block are necessary to extract it from the revetment (Burger 1985). However the reliability of this extra strength decreases if calculations show that blocks immediately above and below can move at the same time. The following design criterion was therefore used; the revetment is considered to be stable if calculations with STEENZET/1 show that only one block moves and that the movement calculated is much smaller than the thickness of the block. In reality this will be a stable situation due to the clamping forces. Apply this criterion a block thickness of 0.5 m was found, assuming a filter material with d_{15} of 20 mm and an average joint width of 5 mm.

An unexpected result was the influence of the toe permeability on the calculated uplift pressures. This was simulated in the calculations by changing the permeability of the lowest joint in the revetment; Figure 8 shows this influence. The increased permeability leads to higher piezometric head in the lower end of the filter layer and, as a consequence higher uplift pressures.

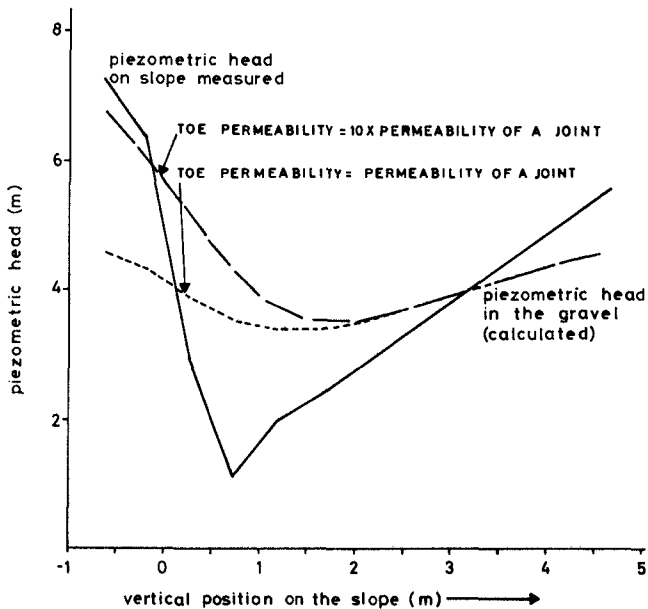


Figure 8: Influence of toe permeability on uplift pressures

4.3 STEENZET/2

The results of the STEENZET/1 calculations showed that a 1:2 slope would be more economical, because less concrete is needed. The calculation however omits the effects of sand body sliding. This kind of failure can occur locally when the grain stress in the sand is reduced by seepage. The pore pressure distribution in the subsoil due the wave attack was therefore calculated with the STEENZET/2 program.

STEENZET/2 is a 2-dimensional finite element program specially developed to calculate the pore pressure response under revetments due to wave attack. The model is based on what is referred to as the storage equation:

$$\nabla q = C \, d\phi/dt \quad (3)$$

Where: ϕ : the piezometric head (m)
 q : the specific discharge (m/s)
 $C = \rho g n \beta$ (1/m)
 ρ : the mass density of the fluid (kg/m³)
 g : acceleration due to gravity (m/s²)
 n : porosity ()
 β : compressibility (m²/KN)
 ∇ : d/dx, d/dy

With solutions of this equation it is possible to investigate the influence of the air content of the pore water on the results. The program can handle turbulent flow on the base of the Forchheimer relation and various materials can be considered. Measured wave pressures can be used as boundary conditions in the same way as in the STEENZET/1 program. A more extended description of this program is given by Hjortnaes-Pedersen et al(1987). The pore pressure distributions calculated with STEENZET/2, were used in a stability analysis as described by Bishop. This method is well known and is described in, for instance Terzaghi and Peck (1967).

4.4 Results of STEENZET/2 Calculations

Calculations were performed for the 1:2 slope and the block thickness indicated as stable by the STEENZET/1 calculations (0.5m). The element mesh used is shown in Figure 9. The model tests showed that a large amount of overtopping can be expected during design conditions and it was therefore assumed that, during these conditions, the sand body directly behind the revetment would be completely filled with water. Outward directed hydraulic gradients perpendicular to the slope, are most dangerous for revetment stability. The wave period which led to the highest uplift pressures in the STEENZET/1 calculations was used as a (time varying) boundary condition. Very little is known about the air content of the pore water and therefore calculations were run with different values of air content. Results are shown in Figures 10 and 11. In these figures lines of equal piezometric head are shown at the moment of maximum outward directed hydraulic gradient; the wave boundary condition is also shown at this particular moment.

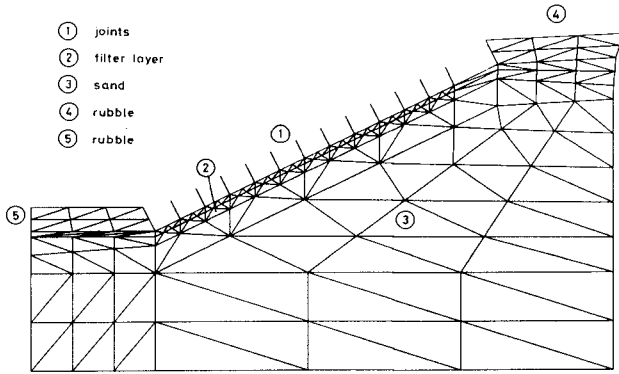


Figure 9: Finite element mesh used in STEENZET/2 calculations

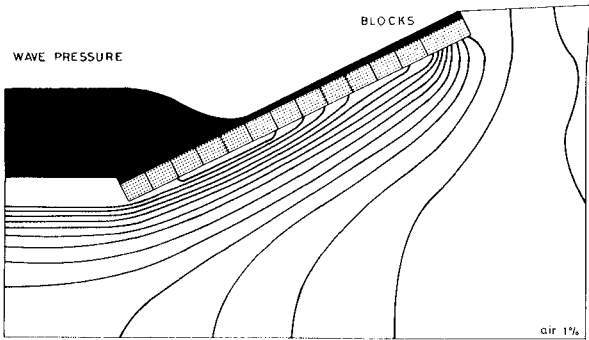


Figure 10: Measured wave pressures and calculated lines with equipotential. Results of STEENZET/2 calculations -assumed air content in the pore water: 1%

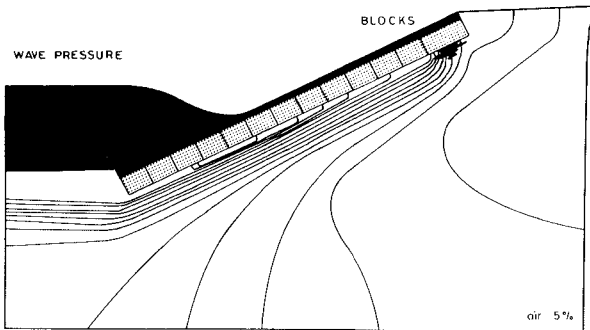


Figure 11: Measured wave pressures and calculated lines with equipotential. Results of STEENZET/2 calculations -assumed air content in the pore water: 5%

This wave condition was measured just after a period of rapid run down. Since Equation (3) is a transient equation, the boundary condition prior to this particular moment is also of importance. The figures clearly show the influence of the air content. The higher the air content, the higher the outward directed gradient. The stability calculations showed however that even with an assumed air content of 5%, the safety of the 1:2 slope against sliding is more than 1.5 with a friction angle of 35° for the sand, 40° for the gravel and schematizing the concrete blocks to a friction material with a friction angle of 25° . From these results it was concluded that the 1:2 slope will be stable against sliding during design conditions.

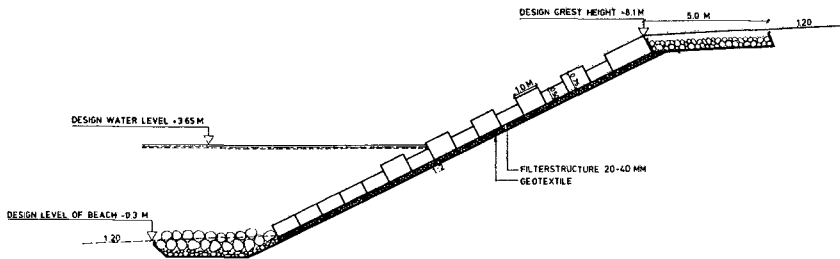


Figure 12: Adapted design based on model studies

5. Conclusions

The combination of physical and numerical models can be a valuable tool in the design of a placed block revetment. As a result of this study the following adaptations were made to the design:

- a heavier rubble is used for the crest protection.
- the geotextile between the blocks and the filter layer is removed.
- a filter layer of relatively small gravel (16-32 mm) is used.
- During the manufacturing process the surface of the blocks is made irregular so that the joints will be about 5 mm wide.
- The geotextile between the blocks and the filter layer is replaced by a filter of relatively small gravel in order to reduce the uplift pressures. This makes it possible to reduce the block thickness from 0.75 to 0.5m.

The model tests showed that increasing the roughness of the slope by varying the thickness of the blocks reduces the wave run-up, especially during moderate storm conditions. According to the stability calculations a structure with a slope 1:2 is stable during design conditions. Since the difference in calculated maximum uplift pressure and measured run-up with a 1:2 slope and 1:3 slope is only small, a 1:2 slope is preferred because less concrete has to be used. Figure 12 shows the adapted design.

A total of 11,420 m of this revetment had been built by September 1988.

References

- Terzaghi K., Peck R.B. Soil mechanics in engineering practice 2nd edition. Joh. Wiley & Sons 1967
- Stive. M.J.F., Dingemans M.W., Calibration and verification of 1-dimensional model for wave energy decay, Delft Hydraulics report. M1882 Dec. 1984.
- Burger A.M. Strength dikes along the Eastern Scheldt under concentrated wave attack (in Dutch). Delft Hydraulics Report. M2036 1985
- Hjortnaes-Pedersen, A.G.I., Bezuijen, A., Best, H. Non stationary flow under revetments using the F.E.M. Proc. 9th. Eur. conf. on Geotechnics and foundation Engineering Dublin. Sept. 1987.
- Bezuijen A., Klein Breteler, M, Bakker, K.J. Design criteria for block revetments and granular filters. Proc. 2nd Int. COPEDEC Beijing. Sept. 1987.
- den Adel A., Analysing permeability measurements with the Forchheimer relation (in Dutch). Delft Geotechnics report CO-272550/56 Nov.1987
- Klein Breteler M., Bezuijen A., The permeability of closely placed blocks on gravel. Proc. Int. SOWAS-symp. Delft Aug. 1988

CHAPTER 161

FULL-SCALE WAVE ATTACK OF UNIFORMLY SLOPING SEA DYKES

Alfred Führböter¹⁾ and Uwe Sparboom²⁾

ABSTRACT

Shock pressure phenomena due to breaking waves acting on sloping faces of sea dykes are focussed in this paper. The probability approach is pointed out and maximum shock pressure estimations are given for smooth and impermeable dyke slopes 1:4 and 1:6. An extension of the results to steeper and flatter slopes is proposed.

Results of full-scale stability tests on concrete block slope revetments are also reported in this paper. For various structural solutions with granular and geotextile filter layers stability numbers are recommended. Initial block lifting is explained physically by pressure measurements.

The full-scale experiments were carried out in the new research facility LARGE WAVE CHANNEL of the universities in Hannover and Braunschweig (Federal Republic of Germany).

1. INTRODUCTION

In the past dykes and revetments at the coastal zone of Germany were frequently destroyed by heavy wave attack during storm surge tides. Therefore, the most important objective of the new large scale facility LARGE WAVE CHANNEL is to investigate dykes and revetments with special reference to the German North Sea Coast (Führböter, 1982). The main reasons for dyke failures can be summarized as follows:

- shock pressures due to wave breaking,
- wave run-up and overtopping,
- up- and down-rush velocities,
- dyke construction (slope, cover layer, subsoil, etc) and
- local sea state characteristics.

First investigations of the fundamental research program dealt with shock pressure phenomena on dykes with uniformly sloping faces. Shock pressures due to plunging breaker types may cause very first damage of the cover layer and the subsoil (Führböter, 1966; Stephan, 1981). Comprehensive studies on this topic were firstly published by Bagnold (1939). Contributions by Skladnev and Popov (1969) dealt with impact forces and scale effects. Nearly full-scale test results on wave

1) Prof. Dr.-Ing., Full Professor, Leichtweiß-Institute, Division of Hydrodynamics and Coastal Engineering, Technical University of Braunschweig, Beethovenstraße 51a, 3300 Braunschweig, Fed. Rep. of Germany

2) Dr.-Ing., Senior Research Engineer, Large Wave Channel, Coastal Engineering Research Group SFB 205, University of Hannover, Merkurstraße 11, 3000 Hannover 21, Fed. Rep. of Germany

impacts acting on dyke slopes were reported by Stive (1984). Führböter (1986a) compared results of model and full-scale tests of wave impacts with reference to a 1:4 dyke slope.

Further full-scale investigations were focussed on the stability of concrete block slope revetments. Such permeable revetments must be designed in combination with filter layers if the dyke core exists of sand. The filter layer can be realized by a 3-dimensional granular layer, by a 2-dimensional geotextile mat (Heerten, 1984) or by a combination of both feasibilities. Stability criteria were often found by the extension of results from small-scale models to the prototype structure (Führböter et al., 1976; Whillock, 1980; Kostense and den Boer, 1984). This method is always affected by scale effects. A review on this topic was reported by Powell et al. (1985). From Dutch large-scale model tests stability numbers were published (den Boer et al., 1983; TAW/CUR-VB, 1984; Pilarczyk, 1987). Results of pressure measurements in the filter layer as well as results of numerical and analytical calculations were published by Bezuijen et al. (1986) and (1987). A theoretical treatment of the behaviour of loose blocks on slopes under wave action was given by Townson (1987). With reference to the bottom protection structure with loose blocks placed on granular sublayers at the EIDERDAMM storm surge barrier unexpected failure mechanisms were considered theoretically by Führböter (1986b).

The new research facility LARGE WAVE CHANNEL makes it possible to carry out full-scale investigations on dykes and revetments at German coastal regions. The main dimensions of the channel are: depth 7.0 m, width 5.0 m and length 324 m. Regular waves and random seas are produced mechanically by a wave generator. The maximum wave height is 2.5 m. Details about the LARGE WAVE CHANNEL were published by Grüne and Führböter (1975). Design criteria and technical works were reported by Grüne and Sparboom (1982).

2. PROTOTYPE DYKE STRUCTURES

The core profiles of the prototype dykes were constructed by sand. The compact cover layers were built by asphalt-concrete in a thickness of nearly 0.20 m. During the wave tests the core was drained to avoid dyke failures caused by positive water pressure below the impermeable cover layer.

With regard to modern dyke protection works the faces of the prototype dykes were constructed with uniform slopes 1:4 and 1:6 (Sparboom, 1987). The investigated asphalt dykes (Fig. 1) were supplied with measuring devices to obtain calibrated electrical signals for

- wave parameters at the toe of the dyke,
- wave impact pressures on the slope surface,
- wave run-ups on the slope and
- wave impact pressures in the subsoil.

The waves were generated regularly under absorption control. For each test nearly 200 waves were generated. Additionally, test series with narrow banded wave spectra were carried out.

A cross-section of the prototype revetment is given in Fig. 2. The area of the highest expected wave attack was subdivided into two testfields each of 10 m in length and 2.5 m in width. Out of the testfields the blocks were directly placed on a geotextile mat with a stabilization layer (needle punched fabric TERRAFIX 904 RS). The permeability of this filter was about $k_f \approx 3 \cdot 10^{-3}$ m/s⁻³ and ten times greater than the estimated sand permeability ($k_s \approx 3 \cdot 10^{-4}$ m/s).

There were tested four structural variants in the testfields (Fig. 3). In all cases the blocks were placed in stretcher-bond equivalently to practice.

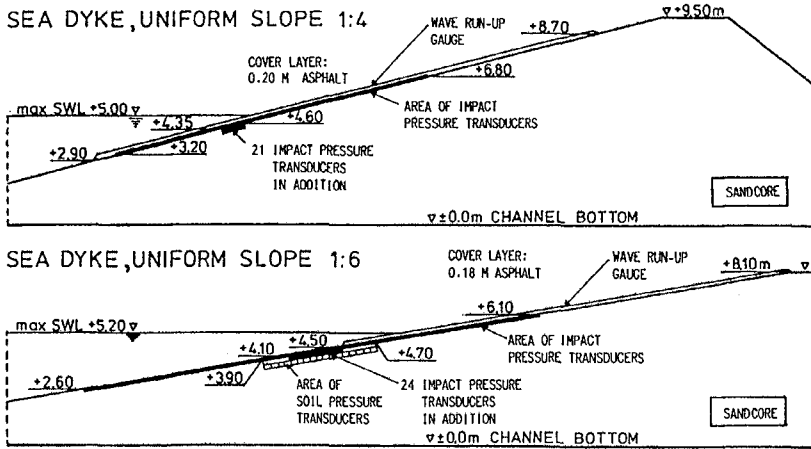


Figure 1. Investigated prototype sea dykes with impermeable top layers in the LARGE WAVE CHANNEL

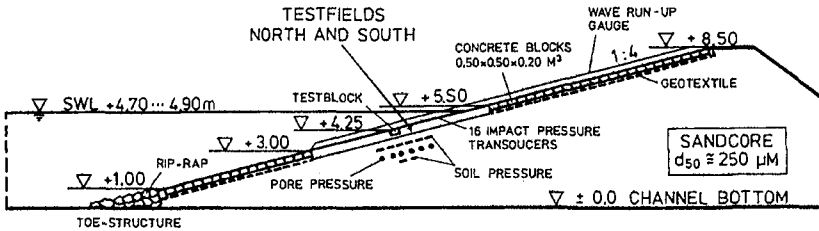


Figure 2. Prototype revetment in the LARGE WAVE CHANNEL

The measuring equipment (Fig. 2) was designed to registrate synchronous electrical signals for:

- wave parameters at the toe of the dyke revetment,
- wave impact pressures acting on the testblocks (top, bottom, each gap side),
- soil pressures beneath the top layer,
- pore pressures in the subsoil,
- block motions,
- wave run-ups on the slope and
- wave impact pressures on the slope between the testfields.

The waves were generated regularly applying an integrated absorption control system. The minimum wave number for each test was 200. After the first block failure the test was interrupted.

3. SHOCK PRESSURE INVESTIGATIONS

A typical record of a shock pressure (wave impact) due to wave breaking (plunging breaker type) on the slope can be seen in Fig. 4.

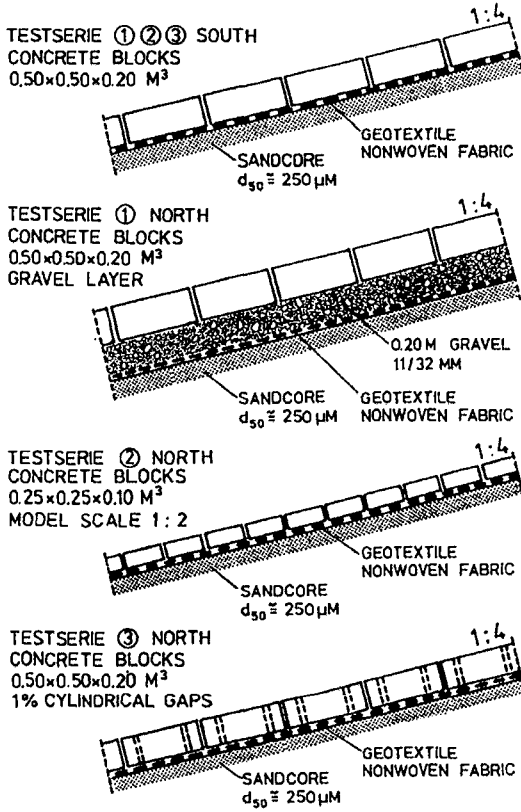


Figure 3. Cross-sections of investigated placed block revetments

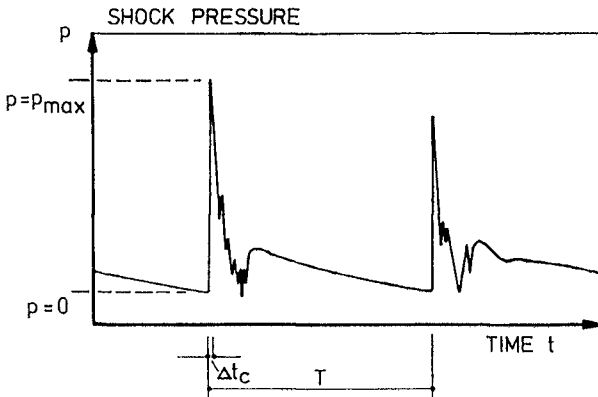


Figure 4. Typical shock pressure caused by breaking waves (plunging breaker type)

The peak pressure which is much higher than the wave or breaker height is highly effective during a relative short time. Due to the included airvolume by the plunging breaker the shock pressure occurrence can be explained by a compression phase. The time of compression Δt_c of all evaluated impacts lies between 10 and 60 milliseconds. The amplitude as well as the time history of shock pressures are strongly dependent on

- breaker process and aeration,
- angle of the sloping face,
- thickness of the backrush-water and
- wave characteristics (regular and random).

3.1 Probability theory

In the analysis of jet impacts (Führböter, 1966 and 1969) the maximum pressure p_{\max} is described by

$$p_{\max} = \delta \cdot \rho \cdot v \cdot c \cdot (c/v)^{1/3} \quad (1)$$

with $\delta = (E_a/E_w \cdot R/D)^{2/3}$

- E_a and E_w = elasticity of air and water
- R^w = hydraulic radius of impact area
- D = representative thickness of included air content
- δ = dimensionless impact number
- ρ = density of water
- v = impact velocity vertical to the wall
- c = sound velocity in water.

In this equation the air content term expressed by D (see Bagnold, 1939) is strongly stochastic and has an important influence on the impact as well as the hydraulic radius R of the impact area and the relation E_a/E_w . The following transformation of Eq. (1) yields:

$$p_{\max} = (E_a/E_w \cdot R/D)^{2/3} \cdot \rho \cdot v \cdot c \cdot (c/v)^{1/3} \quad (2)$$

stochastic \downarrow deterministic

$$\log p_{\max} = 2/3 \log E_a/E_w + 2/3 \log R - 2/3 \log D$$

(stochastic) (3)

+ $\log (\rho \cdot v \cdot c \cdot (c/v)^{1/3})$ (deterministic).

In this way a linear function is obtained for $\log p_{\max}$ and $\log D$. If the stochastic term is distributed after GAUSS, p_{\max} must consequently follow a Log-Normal distribution (Führböter, 1966; see also Weggel, 1971). Comparing results on jet impacts, wave impacts from 1:10 scaled model and from prototype (scale 1:1) in the LARGE WAVE CHANNEL Führböter (1986a) concluded that the Log-Normal distribution is valid for impact pressures in general as predicted by theory. Impact pressures due to breaking waves can therefore never be described deterministically but only probabilistically by the Log-Normal distribution.

With special reference to wave impacts on slopes Führböter (1986a) extended Eq. (1) to

$$p_{\max} = \epsilon \cdot \rho \cdot g \cdot H_B \cdot (y_B/H_B)^{1/3} \cdot ((1+2 \cdot n^2)/(1+n^2))^{1/3} \quad (4)$$

with $\epsilon = (c^2/2g \cdot E_a/E_w \cdot d_1/H_B \cdot 1/D)^{2/3}$

- ϵ = dimensionless impact number for breaking waves on slopes
- H_B = breaker height
- y_B = breaker crest above the bottom
- d_1 = length of the impact area on the slope

g = acceleration due to gravity

n = front slope 1:n .

Considering practical design methods of sea dykes the relation between wave height and impact pressure seems to be most convenient (Führböter, 1986a):

$$p_{max} = P_i = \text{const.} \cdot \zeta \cdot g \cdot H \tag{5}$$

with $i = 50, 90, 99, 99.9 \%$.

3.2 Shock pressure experiments

Maximum shock pressures were evaluated from each individual breaking wave. As already shown by Führböter (1986a) the maximum shock pressure values follow a Log-Normal distribution. In Fig. 5 and 6 the results for $i = 50, 90, 99, 99.9 \%$ are plotted as dimensionless relative impact pressures. Each line represents the results of a test serie with nearly 200 waves. For this wave number sufficient estimates were reached up to a level of 99.9 % probability.

In order to get informations about the spatial distribution of shock pressure occurrence the measured pressures (p_i) of each transducer at the slope were determined for each test cycle. $p_{i,max}$ Fig. 7 represents results of two test cycles. The length of the shock pressure area is strongly dependent on the wave parameters. The mean level of the highest maximum shock pressure, evaluated relatively to the wave height is drawn in Fig. 8 versus the relative shock pressure. The mean occurrence point for the slope 1:6 can be characterized by 0.5 H below SWL. The same value was found by Stive (1984) for steeper slopes 1:3 and 1:4.

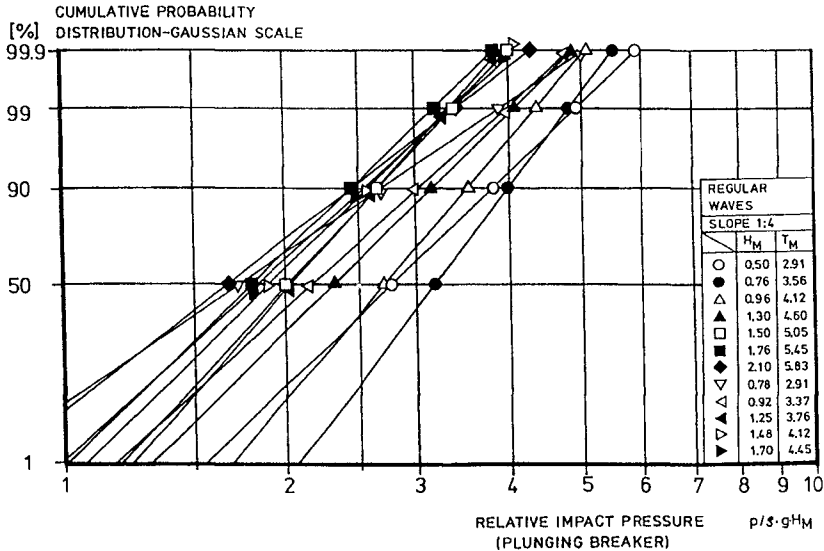


Figure 5. Shock pressure results, slope 1:4

Especially at the slope 1:6 shock pressures induced by simulated sea states were investigated. Representatively, in Fig. 9 relative shock pressures of a test with a significant wave height of 1.5 m and a peak period of 6.0 s are drawn against the well-known breaker number

(IRIBARREN-number). Maximum pressures occurred at breaker numbers from 0.6 to 1.8. The highest pressures were found at a breaker number of nearly 1.2.

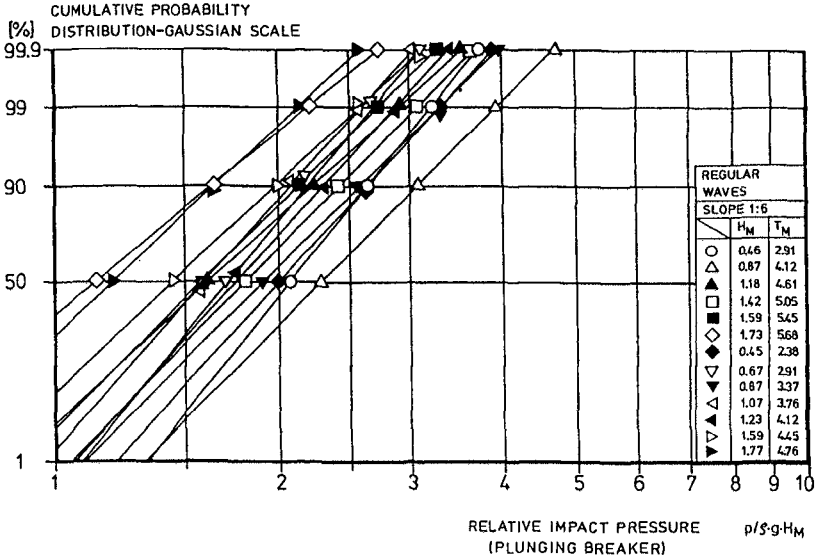


Figure 6. Shock pressure results, slope 1:6

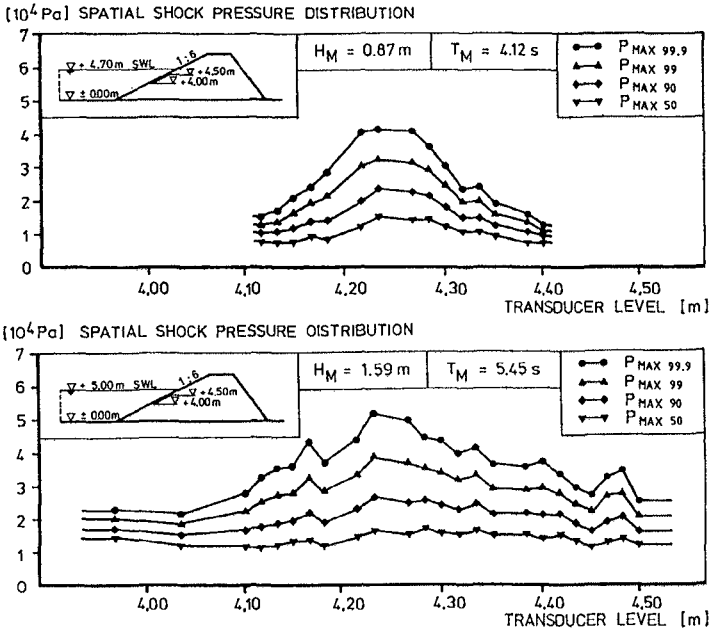


Figure 7. Spatial distributions of shock pressures on the slope 1:6

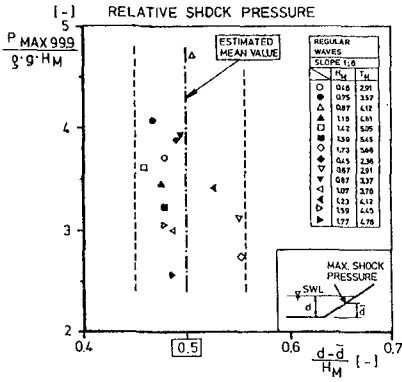


Figure 8. Area of maximum shock pressure occurrence for the slope 1:6

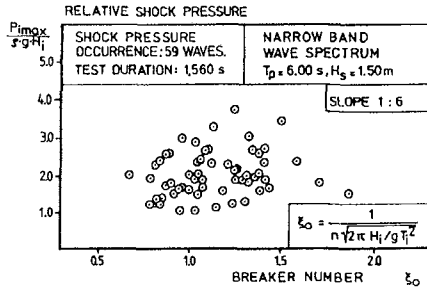


Figure 9. Random wave impact vs. breaker number, slope 1:6

3.3 Maximum shock pressure estimation

In Fig. 10 there are compared full-scale shock pressure results obtained by test cycles with regularly generated waves with those obtained by field measurements at the EIDERDAMM storm surge barrier and by test cycles with narrow banded wave spectra in the channel. Looking towards a practical approach of sea dyke design the maximum shock pressure distribution of the worst case is estimated with a tendency to the safe side (line with circled points).

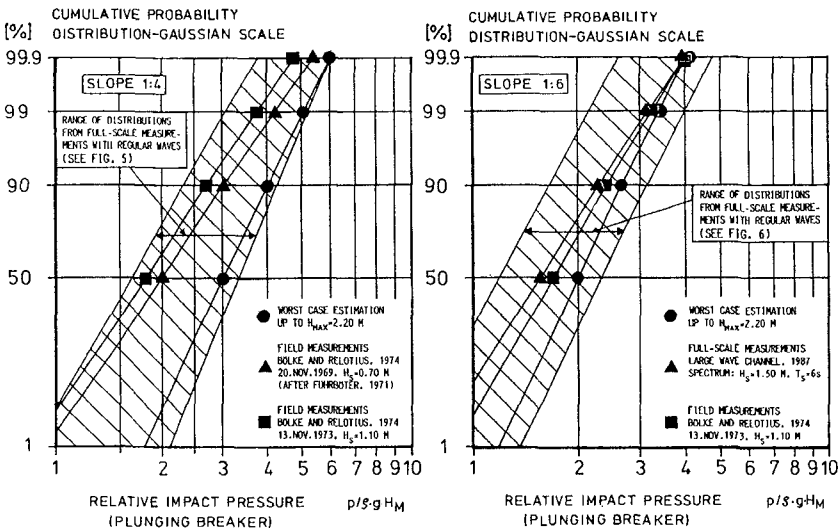


Figure 10. Full-scale shock pressure distributions

Based upon the worst case distributions (Fig. 10) for both slopes 1:4 and 1:6 it seems to be possible to establish a formula which contains the influence of the slope angle:

$$P_{max} = p_i = \text{const} \cdot 1/n \cdot f \cdot g \cdot H \quad (6)$$

with $i = 50, 90, 99, 99.9 \%$ and
 $n = \text{front slope } 1:n.$

The empirical Eq. (6) may be justified by the important damping influence of the backrush-water on the impact amplitude. The thickness of the backrush-water increases with flatter slopes and the impact pressure decreases proportionally. The application of this formula to slopes in general is proposed in Fig. 11. With respect to the real experiments with 1:4 and 1:6 slopes it should be considered that only for the range 1:3 to 1:8 a high reliability can be achieved. For the range 1:1 to 1:3 the values are extrapolated and should therefore be considered very cautiously. Based upon jet impact investigations Führbötter (1966) also determined relative impact pressures for the vertical wall. Expected values for breaker heights of 1.0 m are added in Fig. 11. Future full-scale investigations on very steep slopes up to the vertical wall could be useful to proof the proposed empirical formula.

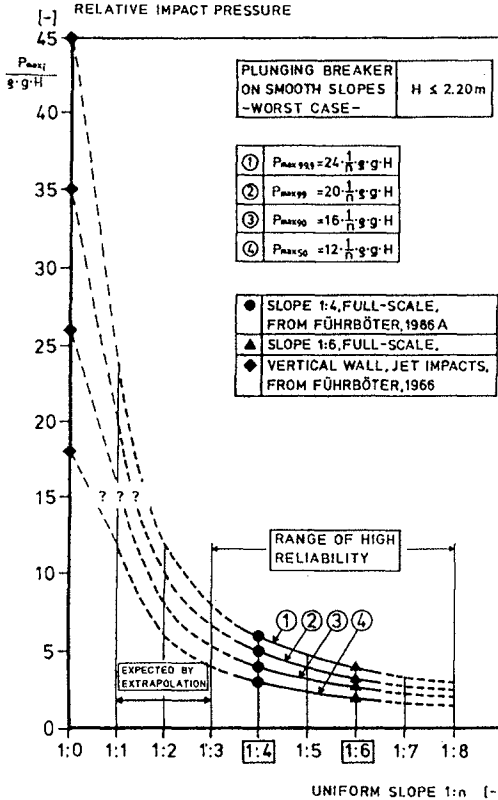


Figure 11. Generalized proposal for breaker-induced maximum shock pressures on smooth slopes

4. INVESTIGATIONS ON CONCRETE BLOCK SLOPE REVEITEMENTS

First experiments with permeable prototype revetments in the LARGE WAVE CHANNEL were used to explain statements of the following problems:

- Which real wave parameters (height and period) are responsible for the instability of natural revetments ?
- At which wave phase and in which location do very first failures occur ?
- How does a gravel layer (filter base) influence the stability of a revetment ?
- Which scale effects can be observed using a 1:2 model in revetment design ?
- How does an increase of the top layer permeability influence the stability of a revetment ?

4.1 Stability results

Usually, blocks or stones of seawalls are designed applying the HUDSON formula. The wave period is not considered in this approach. Recent investigations have shown clearly that the block stability depends on the breaker number ξ (Bruun, 1985). This parameter contains the influence of the wave period (or better wave steepness) and the slope angle.

Pilarczyk (1987) proposed a stability formula for concrete block revetments:

$$H_S / \Delta \cdot d_B = \gamma \cdot \cos \alpha / \xi_z^{1/2} \quad (7)$$

with H_S = significant wave height

Δ = relative block density

d_B = block thickness

α = slope angle

ξ_z = breaker number

$\tan \alpha / (2\pi H_S / g T_z^2)^{1/2}$

T_z = mean wave period

γ = Stability coefficient defined

for $\xi_z = 1$ in categories I to V.

Placed blocks which are treated in this paper should therefore be classified in categorie II ($3 < \gamma < 4$). The permeability of the top layer and of the filter layer as well as the horizontal dimensions of the single blocks are not taken into account. Special problems occur if the results of laboratory tests with regular waves are to be transferred to natural structures under real sea state conditions (wave spectra).

With regard to recent results on the block stability the parameters $H / \Delta \cdot d_B$ and ξ_o are considered here.

H = wave height (regularly generated)

Δ = relative block density

$\xi_b = \xi_w / \xi_w$

d_B = block thickness

ξ_o = breaker number in deep water

$\xi_o = 1 / (n \cdot (H / L_o)^{1/2})$

with $L_o = g \cdot T^2 / 2\pi$

n = front slope 1:n

L = wave length in deep water

T_o = wave period (regularly generated)

g = acceleration due to gravity.

Fig. 12 represents results of testseries ①, ② and ③. Safety is guaranteed up to $H/\Delta \cdot d_B = 4$. Comparing these results with those in Fig. 13 which refer to a 1:2 scaled model the same upper bound can be stated. But, failures seems to occur at higher ξ_0 - values. Probably only the unit of length should be scaled up and not the unit of time simultaneously. This problem due to scaling may necessitate more systematic tests in the future.

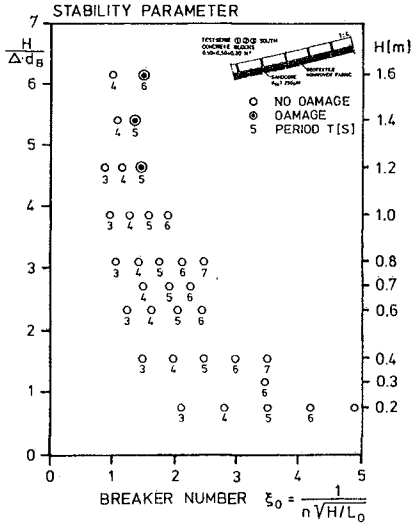


Figure 12. Stability numbers Testseries ①②③ South; Full-scale

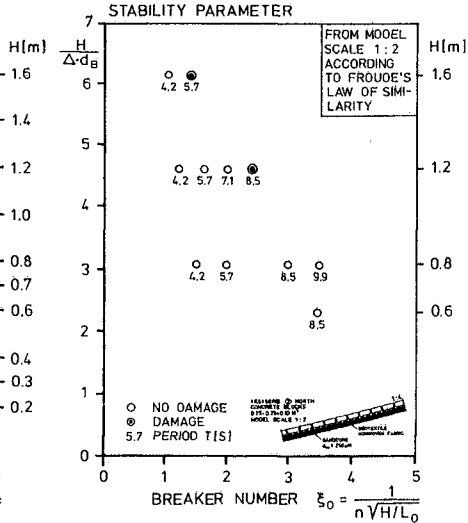


Figure 13. Stability numbers Testserie ② North; Model scale 1:2

In Fig. 14 there are plotted stability results for the structure with an added gravel layer. $H/\Delta \cdot d_B \approx 2.5$ is estimated as the maximum safe number. The influence on the stability by increasing the permeability of the top layer is seen in Fig. 15. Safe conditions can be expected for $H/\Delta \cdot d_B \approx 5.5$. In the last test vertical block motions in the range of 2 to 3 cm were observed. It was not possible to simulate the real failure because the revetment in the other testfield was totally damaged.

All observed failures occurred after about 65 to 110 waves. The location of the first block liftings can roughly be given with 0.5 H beneath SWL. Failures of the geotextile filter mats did not happen. Sandtightness was guaranteed over all test series (about 10,000 waves).

4.2 Initial block lifting

Placed block stability depends clearly on wave breaking characteristics. In the range $1 \leq \xi_0 \leq 1.5$ block failure was mainly observed. This is the same range in which Führböter (1986a) found the maximum wave impacts on an impermeable 1:4 sloping asphalt dyke. Wave impacts are of short duration (milliseconds) and therefore they can not cause block liftings out of the top layer. But wave impacts probably cause a strong reduction of friction contact (or friction stress) between the single blocks. Test observations have shown that first block liftings occurred just in front of the progressive wave before breaking. In order to study pressure variations, transducers were installed in special test-

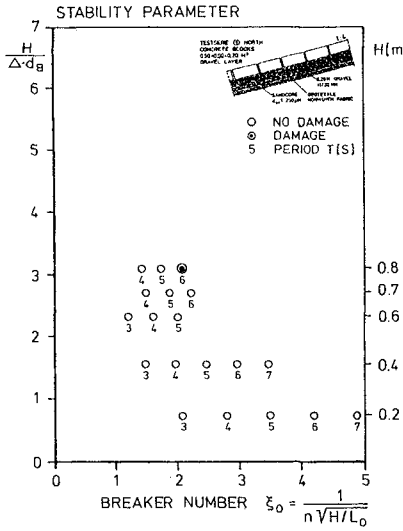


Figure 14. Stability numbers Testserie ① North; Full-scale

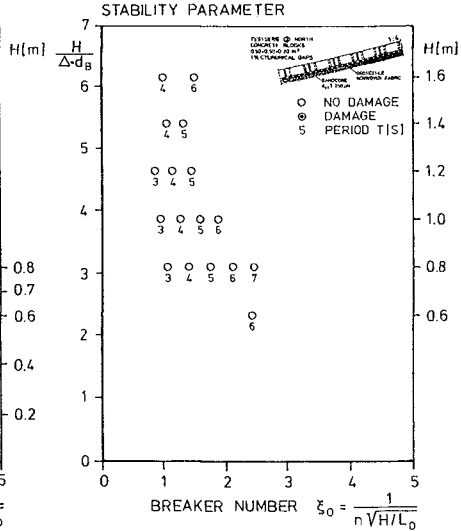


Figure 15. Stability numbers Testserie ③ North; Full-scale

blocks.

In Fig. 16 and in Fig. 17 synchronously measured pressures at top and bottom of a testblock are plotted. Additionally, the pressure difference is calculated. The positive sign indicates uplift pressures. The reaction time T_{up} is defined from the beginning of increase of Δp to the maximum of Δp before wave breaking. Dynamic impact pressures were not yet evaluated in detail. But nearly all impacts reacted in very short time and opposite to the uplift direction before wave breaking.

For about 35 waves of testserie ① ($H_s = 0.70$ to 0.80 m, measured at the toe of the dyke; $T = 4$ to 6 s) the reaction time T_{up} was evaluated (Fig. 18). The wave conditions correspond to the beginning of block liftings above the granular layer. Although a large scatter is obvious it can be seen that for both filter layers the uplift pressure amplitudes are of nearly equal amount but differ definitely in the reaction time. Increasing duration of the uplift pressure seems to be a most important phenomenon causing block failures.

In testserie ③ long reaction times were also found in the geotextile filter just before failure occurrence, but the waves were much higher. The reaction time can obviously be reduced by an increase of the top layer permeability. This was also demonstrated in testserie ③ (Fig. 15).

5. CONCLUDING REMARKS

As already stated by Führeböter (1986a) shock pressure phenomena due to breaking waves acting on dyke slopes can only be described probabilistically by the LOG-normal distribution.

The thickness of the backrush-water has an important influence on the shock pressure occurrence. Prototype and field investigations (slope 1:4 and 1:6) show that a proportionality exists for shock pressures and slope angles (Eq. 6). For mostly used sloping faces of sea

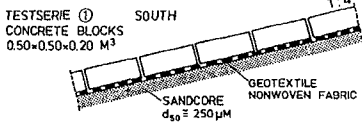
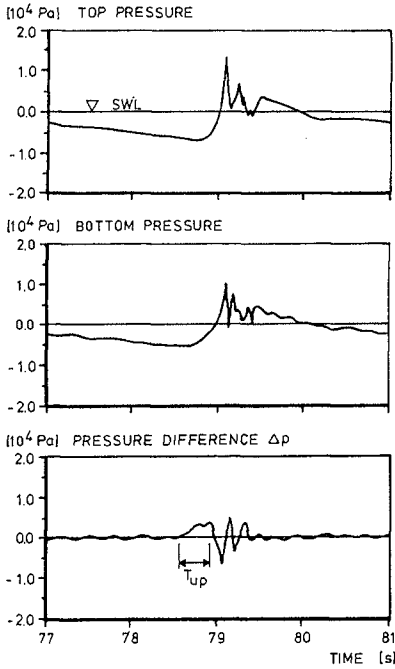


Figure 16. Block pressures Testserie ① South

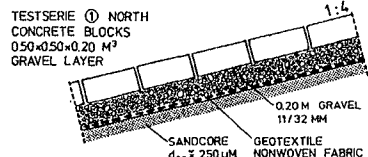
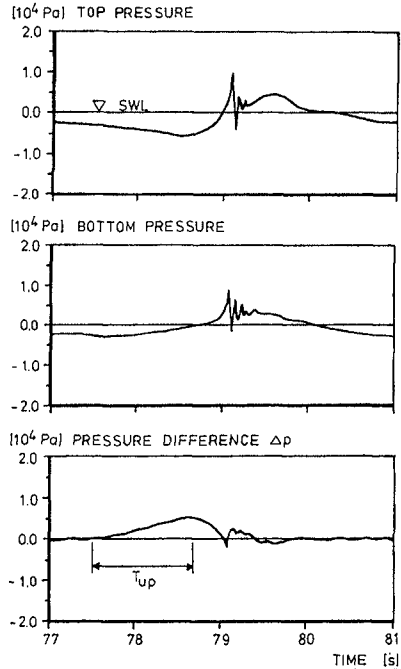


Figure 17. Block pressures Testserie ① North

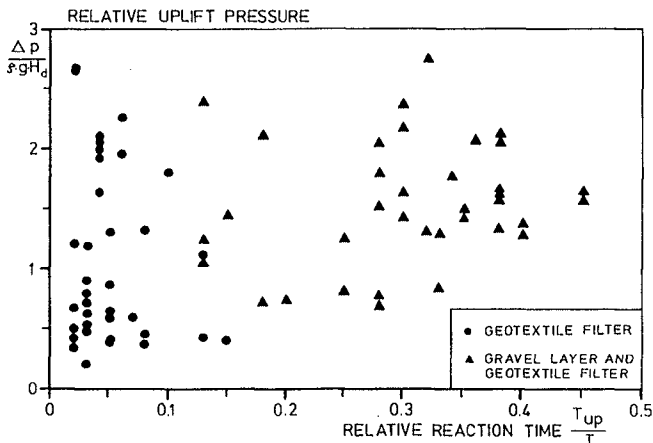


Figure 18. Relative uplift pressures versus relative reaction time (Testserie ①)

dykes in shallow water regions the following maximum shock pressures, acting nearly 0.5 H below SWL on the slope surface are to be expected:

$$\begin{array}{l} \text{SLOPE 1:4} \quad p_{\text{max}} \approx 6 \cdot \zeta \cdot g \cdot H, \\ \text{SLOPE 1:6} \quad p_{\text{max}} \approx 4 \cdot \zeta \cdot g \cdot H. \end{array}$$

Full-scale experiments on wave breaking phenomena are indispensable to avoid scale effects in small-scale modelling. Together with field investigations under real sea state conditions (Grüne, 1988) full-scale measurements guarantee highly reliable results for future design on sea dykes.

From the first analysis of the comprehensive full-scale measurements dealing with placed block revetments stability criteria are found. If the blocks are normally placed in stretcher-bond on a 2-dimensional geotextile filter, the stability parameter $H / \Delta \cdot d_B$ should not exceed 4. 1:2 scaled models can be used but variations in breaker characteristics should be considered carefully.

A 3-dimensional granular filter layer in a thickness equal to the block thickness reduces the stability considerably ($H / \Delta \cdot d_B \leq 2.5$).

Block failure occurs if the reaction time of the uplift pressure rises up to at least 1/3 of the wave period. Uplift pressure values roughly amount 2 to 3 times of the wave height measured at the toe of the dyke.

Better block stabilities can be reached by increasing the top layer permeability. For placed blocks on a geotextile filter the stability number $H / \Delta \cdot d_B \leq 5.5$ is obtained by uniformly distributed cylindrical gaps (1 % of the block surface).

Reported results can be applied to loose concrete blocks placed in stretcher-bond. Favourable stability effects due to block interlocking or connecting are not yet considered. It is proposed to carry out large-scale experiments for such block systems to find out most economical solutions.

ACKNOWLEDGEMENTS

The authors would like to acknowledge gratefully the German Research Foundation (DEUTSCHE FORSCHUNGSGEMEINSCHAFT) sponsoring the research program on safety and reliability of dykes and revetments for coastal protection (SFB 205 / A1).

REFERENCES

- Bagnold, R.A.: Interim Report on Wave Pressure Research. Journal of the Institution of Civil Engineers, Vol. 12, London, 1939
- Bezuijen, A.; Klein Breteler, M.; Pilarczyk, K.W.: Large-Scale Tests on a Block Revetment Placed on Sand with a Geotextile as Separation Layer. Proc. 3rd Int. Conf. on Geotextiles, Vienna, 1986
- Bezuijen, A.; Klein Breteler, M.; Bakker, K.J.: Design Criteria for Placed Block Revetments and Granular Filters. Proc. 2nd Int. Conf. on Coastal and Port Engineering in Developing Countries, Beijing, 1987
- Bölke, S. and Relotius, P.C.: Über die wellenerzeugten Druckschlagbelastungen von Seedeichen im Böschungsbereich zwischen 1:4 und 1:6. Mitt. Leichtweiß-Institut, Tech. Univ. Braunschweig, Heft 42, 1974 (in German)
- den Boer, K.; Kenter, C.J.; Pilarczyk, K.W.: Large Scale Model Tests on Placed Block Revetments. Proc. Coastal Structures '83, Arlington, 1983
- Brun, P.: Design and Construction of Mounds for Breakwaters and Coastal Protection. Elsevier, Amsterdam, 1985

- Führböter, A.: Der Druckschlag durch Brecher auf Deichböschungen. Mitt. Franzius-Institut, Tech. Univ. Hannover, Heft 28, 1966 (in German)
- Führböter, A.: Laboratory Investigations of Impact Forces. Proc. Symp. Research on Wave Action, Tech. Univ. Delft, Paper No. 6, Delft, 1969
- Führböter, A.: Zufallsprozesse bei der Belastung durch brechende Wellen. Jahresbericht 1970, Sonderforschungsbereich 79, Tech. Univ. Hannover, 1971 (in German)
- Führböter, A.: Die Forschungseinrichtung "GROSSER WELLENKANAL" (Hannover) und ihre Aufgaben. Berichtswerk Intermaritec '82, Hamburg, 1982 (in German)
- Führböter, A.: Model and Prototype Tests for Wave Impact and Run-Up on an Uniform 1:4 Slope. Coastal Engineering, Elsevier Science Publishers, 10, 1986a
- Führböter, A.: Hydrodynamische Belastungen der Sohlsicherung des Eidersperrwerkes. Bauingenieur 61, Springer-Verlag, 1986b (in German)
- Führböter, A.; Dette, H.H.; Grüne, J.: On the Response of Seadykes due to Wave Impacts. Proc. 15th Int. Conf. on Coastal Engineering, Honolulu, 1976
- Grüne, J.: Wave Induced Shock Pressure under Real Sea State Conditions. Proc. 21th Int. Conf. on Coastal Engineering, Malaga, Spain, 1988
- Grüne, J.; Führböter, A.: Large Wave Channel for "Full Scale Modelling" of Wave Dynamics in Surf Zones. Proc. Symp. on Modelling Techniques, San Francisco, 1975
- Grüne, J.; Sparboom, U.: Großer Wellenkanal-Problemstellung und Lösung aus versuchstechnischer und konstruktiver Sicht. Technischer Bericht, Sonderforschungsbereich 79, Universität Hannover, 1982 (in German)
- Heerten, G.: Geotextiles in Coastal Engineering—25 Years Experience. Geotextiles and Geomembranes, Vol. 1, Elsevier Applied Science, Amsterdam, 1984
- Kostense, J.K.; den Boer, K.: Effect of Model Scale on the Stability on Concrete-Block Slope Revetments. Proc. Symp. on Scale Effects in Modelling Hydraulic Structures, Esslingen, 1984
- Pilarczyk, K.W.: Dutch Guidelines on Dyke Protection. Report WB-NO-87110, Rijkswaterstaat, Delft, 1987
- Powell, K.A.; Allsop, N.W.H.; Owen, M.W.: Design of Concrete Block Revetments Subject to Wave Action—A Literature Review. Rep. No SR 54, Hydraulics Research Limited, Wallingford, 1985
- Skladnev, M.F. and Popov, J.Ya.: Studies of Wave Loads on Concrete Slope Protections of Earth Dams. Proc. Symp. Research on Wave Action, Tech. Univ. Delft, Paper No. 7, Delft 1969
- Sparboom, U.: Konzeption von Deicheinbauten im GROSSEN WELLENKANAL. Technischer Bericht, Sonderforschungsbereich 205, Universität Hannover, 1987 (in German)
- Stephan, H.J.: Über Schäden an Seedeichen durch Wellen- und Druckschlagbelastungen. Mitt. Leichtweiß-Institut, Tech. Univ. Braunschweig, Heft 70, 1981 (in German)
- Stive, R.J.H.: Wave Impact on Uniform Steep Slopes at Approximately Prototype Scale. Proc. Symp. on Scale Effects in Modelling Hydraulic Structures, Esslingen, 1984
- TAW/CUR-VB-Technische Adviescommissie voor de Waterkeringen/Stichting voor onderzoek, voorschriften en kwaliteitseisen op het gebied van beton: Leidraad cementbetonnen dijkbekledingen. Rapport 119, Betonvereniging, Zoetermeer, 1984 (in Dutch)
- Townson, J.M.: A Lower Bound for the Thickness of Revetment Blocks. Proc. Institution of Civil Engineers, Part 2, Vol. 83, 1987
- Weggel, R.L.: Discussion on "Shock Pressures on Coastal Structures (by Kamel)". ASCE, J. of the Waterways and Harbour Division, WW 3, 1971
- Whillock, A.F.: The Stability of Revetment Blocks under Wave Attack. Rep. No. IT 195, Hydraulics Research Station, Wallingford, 1980

CHAPTER 162

FLOATING BREAKWATER RESPONSE TO WAVE ACTION

Michael Isaacson¹, M.ASCE and Ronald Byres²

ABSTRACT

The present paper describes a study carried out to investigate floating breakwater behavior in waves. Components of the study include a field survey of floating breakwaters in British Columbia, Canada, the development of a numerical model of breakwater behavior and the experimental testing of a particular breakwater design. The numerical model has been developed to provide breakwater motions, transmission coefficients and mooring forces. The model combines linear diffraction theory for obliquely incident waves, a mooring analysis, the inclusion of viscous damping coefficients obtained from experimental or field data, and the inclusion of drag and wave drift forces for use in the static analysis of the moorings. The experiments were carried out with normally incident regular waves of different heights and periods. Preliminary results indicate that the numerical model should prove to be a useful tool in floating breakwater design.

INTRODUCTION

Floating breakwaters have found extensive application in many areas where relatively inexpensive protection from wind- and ship-generated waves is required and where open water wave conditions are not unduly severe and water depths are relatively large. The cost of traditional bottom-founded breakwaters increases significantly with water depth, so that a floating breakwater is a relatively attractive option in deeper water.

¹Professor, Department of Civil Engineering, University of British Columbia, Vancouver, B.C. Canada.

²Engineer, Sandwell Swan Wooster, 1190 Hornby Street, Vancouver, B.C. Canada.

A considerable literature on the subject has developed over the past decades, with the large variety of specific breakwater designs as well as the large number of areas of potential application having contributed to this wealth of information. Western Canada Hydraulics Laboratory (1981) carried out an extensive literature survey, covering topics ranging from analytical models of breakwater behavior to in-situ experiences with particular breakwater designs.

Numerical methods of describing breakwater response to waves have originated largely from ship hydrodynamics. Several authors have treated the two-dimensional problem of wave interaction with cylinders at or near the water surface by considering the corresponding potential flow problem and solving this to calculate the hydrodynamic coefficients necessary to determine the fluid forces on, and the motions of the cylinder. In particular, the case of oblique wave interaction with cylinders has been investigated by Bai (1975), Garrison (1969, 1984), Isaacson and Nwogu (1987) and others. Field studies involving prototype floating breakwaters are relatively uncommon. A number of authors have published field data including Nelson *et al.* (1983), Nece and Skjelbreia (1984) and Miller and Christensen (1984). Comparisons of field data with laboratory tests and numerical models have generally indicated that the response of breakwaters can be modeled quite well. However, one difficulty is that responses are lower than the inviscid theory predictions at frequencies near the resonant frequencies of the breakwater, primarily because of additional energy dissipation associated with flow separation.

The present paper describes a study carried out to investigate floating breakwater behavior in waves, with components of the study including a survey of floating breakwaters in British Columbia, Canada; the development of a numerical model of breakwater behavior which predicts transmission coefficients, breakwater motions and mooring forces for a specified breakwater/mooring system and specified incident wave conditions; and thirdly the experimental testing of a particular floating breakwater design.

FLOATING BREAKWATERS IN BRITISH COLUMBIA

British Columbia, Canada, contains relatively large areas of sheltered coastal waters, associated with protection from the open ocean provided by Vancouver Island and the presence of a large number of inlets and sounds. There is extensive use of pleasure craft in the region and a considerable number of floating breakwaters are located here. Locations of thirty more significant floating breakwaters presently in use in British Columbia are indicated in Fig. 1. In general, three categories of breakwater have been used:

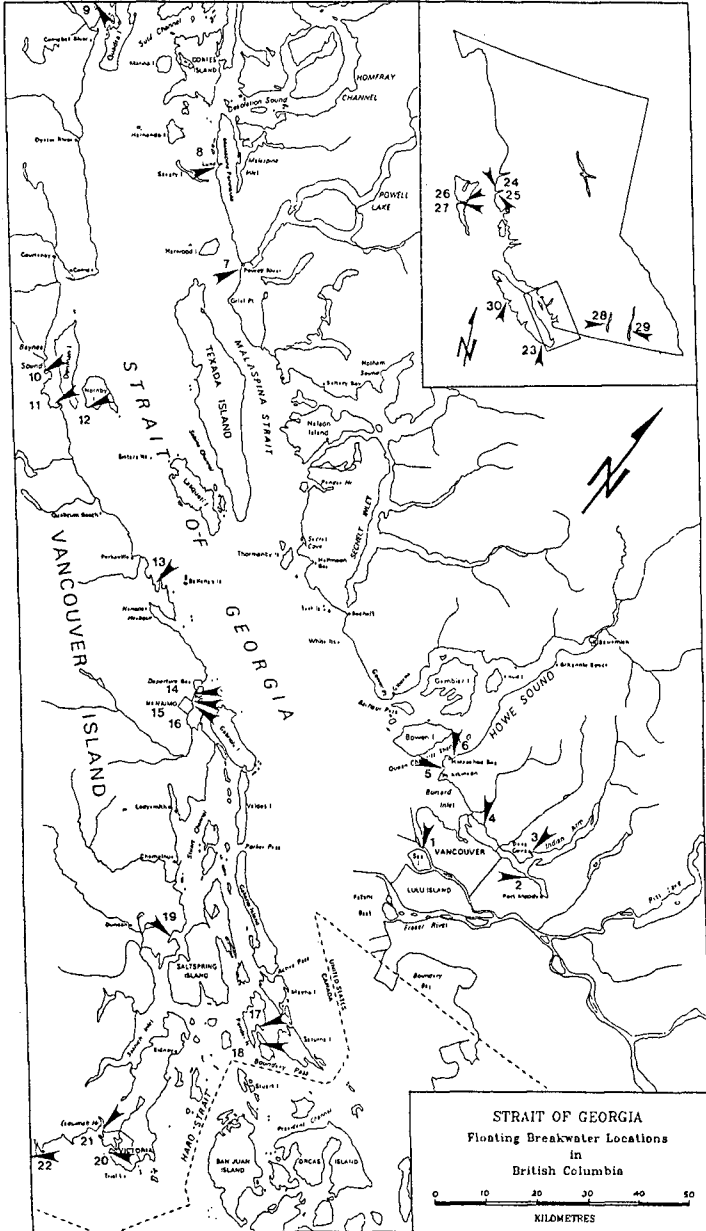


Fig. 1. Floating breakwater locations in British Columbia.

- concrete caisson breakwaters, which generally have a rectangular cross-section,
- log bundles, which generally have a circular or raft-like cross section,
- A-frame breakwaters, which generally include two pontoons and a central vertical plate.

These primarily rely on wave reflection to reduce transmitted wave heights. In addition, a scrap tire breakwater, which reduces the transmitted wave heights primarily by energy dissipation, is used at one location. Table 1 lists floating breakwaters in British Columbia corresponding to the locations shown in Fig. 1 and includes summary information on the fetch and principal wind direction for each location. Of the thirty breakwaters listed, eleven are caisson, fifteen are log and two are A-frame. Typical design wave conditions correspond to a wave period of about 4 sec and significant wave height of about 0.5 m. In addition, there is generally a large tidal range of up to about 5 m. The majority of breakwaters have generally provided quite satisfactory service. This is particularly true of the concrete caissons which tend to be more durable than the other designs and which are more amenable to secondary usage. Although they have an initially higher capital cost, the concrete breakwater systems have a lower incidence of structural damage and provide a greater degree of wave attenuation than either scrap tire breakwaters or log bundles.

As one example of a concrete caisson breakwater, a new three-module caisson breakwater was installed at Lund in May, 1987, replacing an earlier A-frame which had served at that location for 22 years. A photograph of the new breakwater during installation is shown in Fig. 2. Lund is perhaps exposed to the most severe wave climate of any caisson breakwater in the Strait of Georgia. The site is exposed primarily to waves from the southwest and northwest, with fetches of about 30 km and 12 km respectively. The layout of the breakwater is somewhat unusual in that the caisson sections are not inter-connected, but rather are staggered in the horizontal plane in an effort to avoid problems arising with inter-connections or collisions between units. The disadvantages of this arrangement include a reduction in the potential area of protection (because of the overlap of the sections), a reduction in the potential degree of protection because of wave diffraction through the gaps, and a relatively complicated mooring line arrangement.

Floating log bundles are used extensively throughout British Columbia, although in their simplest application - a mere boom of single logs - they are not particularly effective against any but the shortest period waves. An example at Reed Point Marina is shown in Fig. 3, and indicates wave reflection and diffraction around the end of the log bundle breakwater. In this case, the waves were caused by the passage of a tug and are estimated to have a height of 0.5 m and period of 3 sec.



Fig. 2. The new caisson breakwater at Lund during installation.



Fig. 3. The log bundle at Reed Point Marina, showing wave reflection and diffraction.

The A-frame breakwater at Lund which was in use until 1987 is shown in Fig. 4. The breakwater has steel pontoons of diameter 0.76 m, a beam of 7.6 m, and a draft of 3.7 m. The timber centerboard is connected to the pontoon with a steel space-frame, and extends upwards from the still water level approximately 2 m. The identical design has been used for the A-frame breakwater at Queen Charlotte City.

Only one breakwater in British Columbia involves scrap tires and is located at Eagle Harbor. The breakwater consists of two rows of cylindrical steel pontoons between which scrap tires are strung on conveyor belting.

A unique floating breakwater at Powell River comprises of ten old concrete-hulled ships and is shown in Fig. 5. This has been in use since about 1930, having been gradually expanded to the present configuration by the use of additional ships. The ships range in length from 102 m to 128 m and are anchored with eight to ten concrete anchors, each weighing up to 14.5 tonnes.

Although the breakwaters indicated in Table 1 have generally provided satisfactory service, possible difficulties which have been reported to arise with floating breakwaters have involved their inability to provide adequate wave protection, and possible damage or failure most often associated with connections between individual units of a breakwater or with its moorings.

NUMERICAL MODEL

A numerical model of floating breakwater behavior due to wave action has been developed. Linear diffraction theory is used for a two-dimensional breakwater section to provide the breakwater motions and transmission and reflection characteristics for a regular, obliquely incident wave train. The method has been described by Isaacson and Nwogu (1987) and is based on a boundary integral equation approach deriving from Green's theorem. The breakwater is treated as an infinitely long horizontal cylinder and the fluid is assumed incompressible and inviscid and the flow irrotational so that potential flow theory is used. The velocity potential Φ of the flow is considered to be made up of components associated with the incident waves ϕ_0 , the diffracted waves which would arise if the cylinder were fixed, ϕ_4 , both of these components being proportional to the incident wave height H , and forced waves associated with each of three modes of motions of the cylinder, ϕ_1 , ϕ_2 and ϕ_3 , corresponding to sway, heave and roll respectively. The latter potentials are proportional to the amplitude of the motion ξ_j of each mode. Thus the total velocity potential is expressed as:



Fig. 4. The A-frame breakwater at Lund (removed in 1987).



Fig. 5. The floating breakwater at Powell River, comprised of ship hulls.

$$\Phi = \left[\frac{-i\omega H}{2} (\phi_0 + \phi_4) + \sum_{j=1}^3 -i\omega \xi_j \phi_j \right] \exp[i(ky \sin \beta - \omega t)] \quad (1)$$

where $i = \sqrt{-1}$, ω is the wave angular frequency, y is the distance along the cylinder axis, β is the angle the incident wave crests make with the cylinder axis, k is the wave number, and t is time.

The equation of motion of the breakwater can be expressed in the usual way as:

$$\sum_{j=1}^3 [-\omega^2(m_{ij} + a_{ij}) - i\omega(b_{ij} + b'_{ij}) + c_{ij}] \xi_j = F_i \quad \text{for } i = 1, 2, 3 \quad (2)$$

where m_{ij} and c_{ij} are the mass and hydrostatic stiffness coefficients; and a_{ij} and b_{ij} are the added mass and damping coefficients associated with the hydrodynamic forces, and F_i are the exciting force amplitudes. b'_{ij} represents an empirical damping coefficient accounting for viscous effects which is used to modify motion predictions from those based solely on potential theory. The hydrodynamic coefficients a_{ij} , b_{ij} and F_i may be obtained in terms of the potentials ϕ_0, \dots, ϕ_4 . The transmission and reflection coefficients, defined as the ratio of transmitted or reflected wave heights to the incident wave height, are also of interest and are obtained by computing wave conditions on control surfaces upstream and downstream of the structure.

A suitable extension of this program provides the response to a random incident wave train, which may be obliquely incident, and which may be short-crested (see Isaacson and Nwogu, 1987). In particular, the program provides spectra of the transmitted wave train and of the component breakwater motions. These may be used to estimate the maximum transmitted wave heights and breakwater motions for a storm of specified duration.

The program may be used in conjunction with a three-dimensional mooring analysis program, which utilizes the predicted breakwater motions to provide maximum mooring line tensions.

EXPERIMENTAL STUDY

Laboratory experiments have been carried out to measure transmission coefficients and breakwater motions using two particular breakwater models subjected to normally incident, regular waves. One is a rectangular section breakwater, while the other is an A-frame breakwater. Measurements have been made of the breakwater motions and of the transmission coefficient for a range of incident wave conditions.

The experiments were carried out in the wave basin of the Hydraulics Laboratory at the University of British Columbia. This is 14 m long, 5 m wide and can accommodate water depths up to 0.45 m and wave periods ranging from about 0.5 to 1.5 sec. A variable speed electrically driven wave paddle at one end of the basin was used to provide regular long-crested waves, with the amplitude and period varied by adjusting the stroke and frequency of the paddle. A sloping beach consisting of a frame covered with artificial hair matting was located at the opposite end of the basin to reduce wave reflections. Capacitance type wave probes were used to measure the incident and transmitted wave heights. For all the tests, a vertical wall was installed in the basin to prevent waves reflecting from the model from interfering with the incident wave signal. The rectangular breakwater used was based on the concrete caisson breakwater employed in field tests reported by Nece and Skjelbreia (1984). This corresponds to a prototype beam of 4.8 m, a length of 23 m and a draft of 1.1 m, and the model was constructed to a scale of 1/15. Experiments were carried out at several different wave periods, with separate tests carried out at each wave period with waves of low and high steepnesses.

The transmission coefficient was measured by the use of wave probes, and the breakwater motions were measured by an optical system. Three reference markers were attached to the model at known positions vertically above the breakwater's center of gravity, with fixed scales located behind each target. The amplitudes of motion, but not the phases, were measured by sighting the targets and scales through a theodolite, and aligning the cross-hairs in turn on each target at its maximum horizontal or vertical excursion. Simple algebraic formulae were used to relate these motion amplitudes to those of the breakwater's center of gravity.

A preliminary comparison with numerical predictions for the case of the rectangular breakwater has been carried out and selected results are indicated in Figs. 6 and 7. In the figures, a is the half beam of the breakwater. Fig. 6 compares numerical results of the transmission coefficient with measured values, as well as with the field measurements reported by Nelson *et al.* (1983) and Nece and Skjelbreia (1984). There is considerable scatter in the measured values so that the comparison is somewhat inconclusive. The values obtained from field measurements are relatively high and relatively insensitive to wave frequency. Fig. 7 shows the heave response amplitude operator, with the numerical predictions based on various values of the viscous damping coefficient. The trend of the response to reduce with increasing wave frequency is apparent.

As expected, the numerical predictions confirm that the breakwater is most effective for higher frequency waves, corresponding approximately to $B/L > 0.3$, where B is the width of the rectangular section and L is the incident wave length. The roll and sway motions exhibit strong resonant peaks, which are quite sensitive to the value of the viscous damping

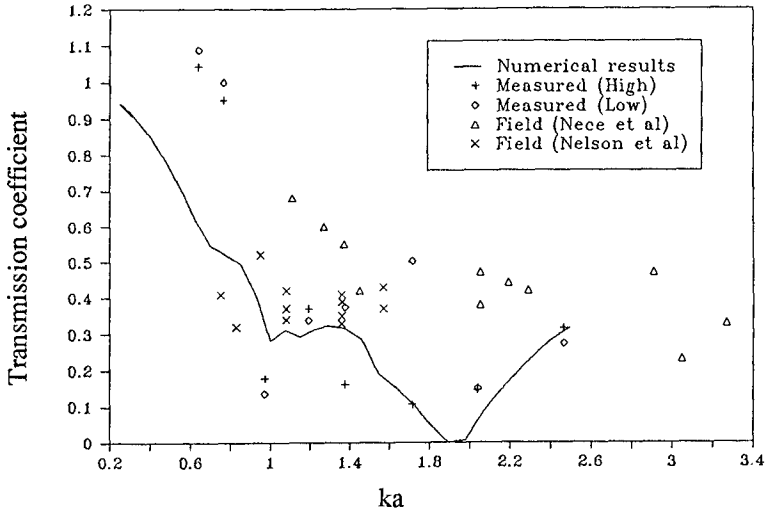


Fig. 6. Numerical, laboratory and field results of the transmission coefficient for the rectangular breakwater.

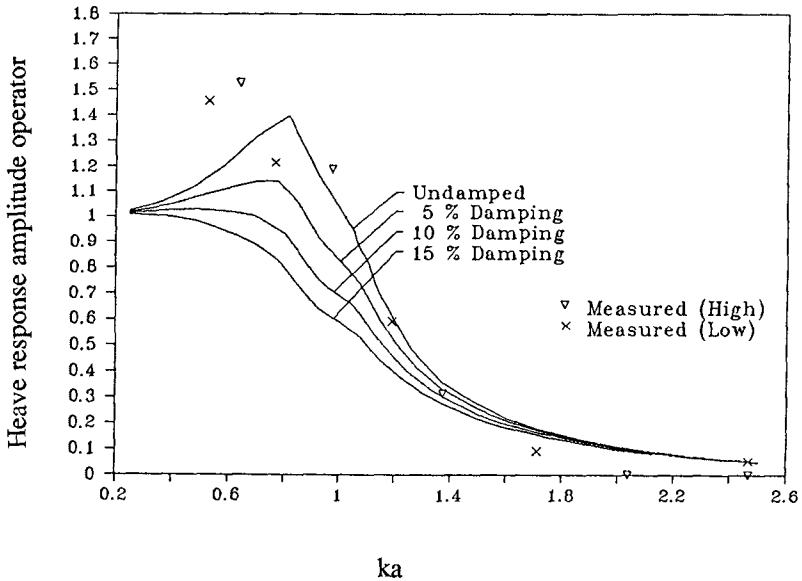


Fig. 7. Numerical and laboratory results of the heave response amplitude operator for the rectangular breakwater.

coefficient selected. With only 5% damping, these resonant peaks are all but removed, which is consistent with the observations of other studies (e.g. Miller and Christensen, 1984).

CONCLUSIONS

Floating breakwaters are a viable means of providing wave protection in areas where incident wave conditions are not too severe and water depths are relatively large. They have been widely used in British Columbia, Canada. Although experience in British Columbia has not revealed major difficulties in the use of floating breakwaters, other reported difficulties associated with their use include a possible inability to provide adequate protection from waves, and possible damage or failure most often associated with connections between individual units of a breakwater or with its moorings.

A numerical model based on linear diffraction theory and extended to include the effects of moorings, obliquely incident, random waves and additional damping has been developed. The program has been verified in part against laboratory measurements and should be quite viable for use in floating breakwater design. Laboratory tests have been carried out, but a comparison with numerical predictions is somewhat inconclusive.

APPENDIX - REFERENCES

- Bai, K.J. 1975. "Diffraction of oblique waves by an infinite cylinder," *Journal of Fluid Mechanics*, **68**, pp. 513-535.
- Garrison, C.J. 1969. "On the interaction of an infinite shallow-draft cylinder oscillating at the free surface with a train of oblique waves," *Journal of Fluid Mechanics*, **39**, pp. 227-255.
- Garrison, C.J. 1984. "Interaction of oblique waves with an infinite cylinder," *Applied Ocean Research*, **6** (1), pp. 4-15.
- Isaacson, M. and Nwogu, O. 1987. "Directional Wave Effects on Long Structures," *Journal of Offshore Mechanics and Arctic Engineering*, **109** (2), pp. 126 - 132.
- Miller, R.W., and Christensen, D.R. 1984. "Rigid body motion of a floating breakwater," *Proc. International Conf. on Coastal Engineering*, Houston, Texas, pp. 2663-2679.
- Nece, R.E., and Skjelbreia. 1984. "Ship-wave attenuation tests of a prototype floating breakwater," *Proc. International Conf. on Coastal Engineering*, Houston, Texas, pp. 2515-2529.

Nelson, E.E., Christensen, and Schuldt, A.D. 1983. "Floating breakwater prototype test program." *Proc. Conf. Coastal Structures '83*, ASCE, pp. 433-446.

Western Canada Hydraulics Laboratory. 1981. "Development of a manual for the design of floating breakwaters." *Canadian Manuscript Rept. of Fisheries and Aquatic Sciences*, No. 1629, Small Craft Harbors Branch, Dept. of Fisheries and Oceans, Ottawa, 228 pp.

Table 1. Summary of Floating Breakwaters in British Columbia

No.	Location	Type	Year	Fetch (km)	Dirn.
1	Richmond	Caisson	1979	1.7	W
2	Port Moody	Log Bundle	1976	0.8	NE
3	Deep Cove	Caisson	1976	5.5	NE
4a	Burrard YC	Caisson/barge	1977	3.1	E
4b	Burrard YC (Destroyed 1983)	Scrap tire	1977	3.1	E
5	Eagle Harbour	Pontoon / tire	1977	39.1	SW
6	Horseshoe Bay	Caisson / ship		9.0	N
7	Powell River	Ship Hull	1930+	28.7	SW
8a	Lund	Caisson	1987	29.6	SW
8b	Lund (Removed 1987)	A-frame	1963	29.6	SW
9	Brown Bay	Tank Car	1983	2.8	E
10	Fanny Bay	Log Bundle		2.6	NE
11	Deep Bay	Log Bundle		2.2	W
12	Ford Cove	Log Raft		6.5	NW
13	Northwest Bay (Destroyed 1980)	Log / Styrofoam	1975	37	
14	Nanaimo			0.2	E
15	Nanaimo	Caisson	1974	5.3	SE
16	Nanaimo				
17	Pt Browning	Log		2.1	SE
18	Bedwell Hbr	Log		3.0	NW
19	Maple Bay	Caisson	1977	4.3	NE
20	Victoria Hbr	Caisson		0.5	S
21	Esquimalt	Caisson		1.8	SW
22	Becher Bay	Log		1.5	SE
23	Sooke Basin	Log		1.9	SW
24	Prince Rupert	Log			
25	Prince Rupert	Log			
26	Qn Charlotte City	Log		4.4	
27	Qn Charlotte City	A-frame	1967	2.4	
28	Kelowna	Log Bundle	1978		W
29	Nakusp	Caisson	1986		
30	Tahsis	Log		2.8	SE

CHAPTER 163

SIMULATION OF WAVE FORCES ON A HORIZONTAL CYLINDER

SUSUMU TSUZUKI*
KIYOSHI HORIKAWA** F. ASCE
AKIRA WATANABE***

ABSTRACT

The characteristics of wave forces acting on a horizontal circular cylinder were investigated through numerical calculations as well as experimental findings. The laboratory data on wave forces were analyzed by the concept of wave force path and classified into two types. One is the circular type and the other one is the 8 - shaped type. In order to analyze the above phenomena, the discrete vortex method was applied with appropriate assumptions. The comparison between the numerically calculated results and laboratory data shows that the simulation model proposed in this paper seems to be favorable to predict the wave forces acting on a horizontal circular cylinder within a certain range of conditions.

1. INTRODUCTION

Prediction of wave forces acting on a circular cylinder has been investigated by number of researchers during the last thirty eight years since Morison et al. (1950) proposed their semi-empirical formula. The main interest of these researchers was to evaluate the hydrodynamic coefficients introduced in the stated formula (Koderayama et al., 1978). However, the formula cannot be applied to such a case that vorticies generated behind a circular cylinder are extremely unsymmetrical with respect to wave direction.

In the present paper, an analytical and numerical treatment was attempted to calculate the flow characteristics around a horizontal circular cylinder induced by gravity waves or oscillatory flows and the fluid forces acting on the body by using the discrete vortex

* Engineer, Tokyo Electric Co.

** Professor Emeritus, The University of Tokyo ;
Professor, Saitama University, Urawa, Japan.

*** Professor, Department of Civil Engineering, The
University of Tokyo, Japan.

method which was originally presented by Rosenhead (1931). The above treatment was carried out under such a restricted condition that the effects of free surface as well as of the bottom on fluid motion can be neglected. That is to say, it is assumed that the submerged cylinder is located in a certain range of water depth apart from the limited layers of both free surface and sea bed. The calculated results were compared with the experimental data reported by Sarpkaya (1975) in order to investigate the adaptability of the stated prediction method.

2. CHARACTERISTICS OF WAVE FORCES ACTING ON A HORIZONTAL CIRCULAR CYLINDER

2.1 Previous Studies

It is well known that the Morison formula is commonly applied to evaluate the wave forces acting on a cylinder, particularly on a circular cylinder. However, in the case of a submerged circular cylinder set horizontally at a certain water depth, the direction of wave force acting on the cylinder varies with time, the situation of which is different from that of a vertical cylinder. Hence the Morison formula was extended by Borgman (1958) to the vectorial form, under the assumption that the direction of drag force is the same to that of fluid velocity.

However the above assumption is not necessary to be true. Therefore Sawamoto et al. (1979) investigated the fluid force induced by oscillatory flows, and Tsuzuki et al. (1984) and Masuda et al. (1985) did by wave by introducing a phase difference. According to the result of flow visualization conducted at the University of Tokyo, it is realized that the Morison type formula can not be applied to the case in which the motion of vortices separated from the body surface is complicative.

As a theoretical approach, Sarpkaya (1968) applied the Blasius formula for unsteady flow to calculate the fluid force on a circular cylinder under uniformly oscillating flows. Detailed observations made by Sawamoto and Kikuchi (1979) in an oscillatory flume indicated that the pattern of vortex formation can be classified by using the Keulegan-Carpenter number as shown in Figure 1. The Keulegan-Carpenter number is defined by $K.C. = \bar{U}T/2R$, where \bar{U} is the amplitude of oscillatory flow velocity, T the period of oscillatory flow, and R the radius of the circular cylinder. From this diagram we can realize that the unsymmetrical vortices appear under the condition of $K.C. > 8$, causing nearly regular time variation of lift force.

2.2 Experimental Findings

In order to look at the above phenomena in an oscillatory flume more clearly, let us take the wave force path defined by the diagram illustrated in Figure 2. Here two kinds of typical laboratory data were picked up and drawn in Figure 3 for demonstration. The upper diagram indicates that the wave fore path for $K.C. = 4.24$ forms a

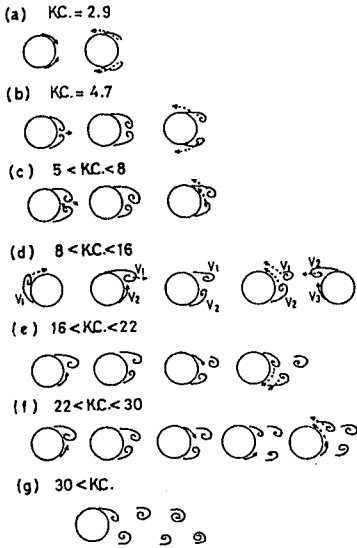


Fig.1 Vortex formation in an oscillatory flow (after Sawamoto and Kikuchi, 1979).

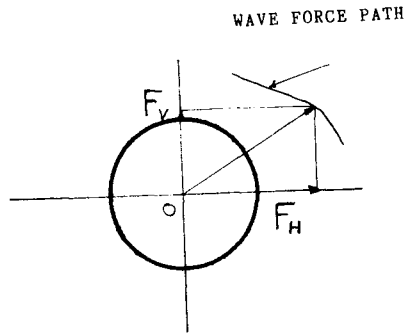
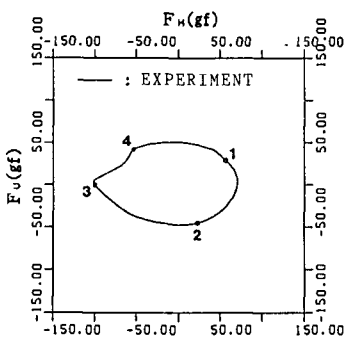
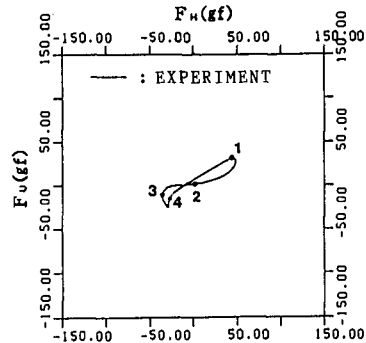


Fig.2 Definition of wave force path.



h=50.0 (CM) Y0=-10.0 (CM)
 T=1.00 (S) H=9.41 (CM)
 KC=4.24 $\hat{H}/\bar{U}=0.893$

(a) circular type



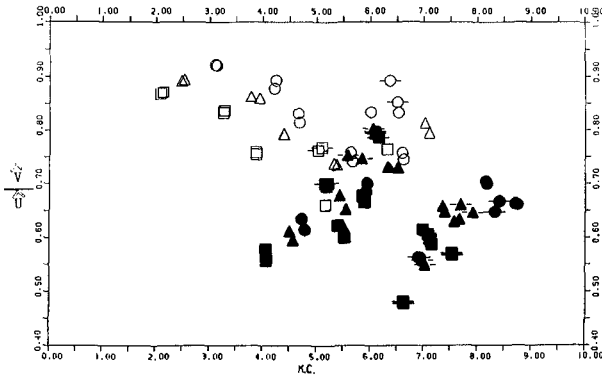
h=50.0 (CM) Y0=-10.0 (CM)
 T=1.90 (S) H=9.92 (CM)
 KC=8.75 $\hat{H}/\bar{U}=0.661$

(b) 8-shaped type

Fig.3 Typical examples of wave force path.

nearly circular curve, while the lower diagram indicates that the path for $K.C. \approx 8.75$ forms an 8 - shaped curve.

The situation of vortex formation in a wave field might be somewhat different from that in a uniformly oscillating flow. The laboratory data collected in a wave flume at the University of Tokyo were plotted as shown in Figure 4. The abscissa of this diagram is the K.C. number and the ordinate is the amplitude ratio between the vertical and horizontal fluid particle velocity amplitudes, \hat{v} and \hat{u} . The open marks are for the circular type wave force path, which is called C type, and the filled marks for the wave force path with the 8 - shaped curve, which is E type. The upper part of the ordinate in this diagram corresponds to the deeper water wave condition, while the lower part corresponds to the shallower water wave condition. A demarcation curve between these two types of wave force path can not be clearly drawn. However, it can be said that E type appears under the shallower water and larger K.C. number conditions.



C	E	y_0 (cm)	h (cm)
○	●	-10	60.0
△	▲	-13	
□	■	-16	
○	●	-10	50.0
△	▲	-15	
□	■	-20	

Fig.4
Wave force path data
obtained in a wave flume.

3. SIMULATION OF WAVE FORCES ACTING ON A HORIZONTAL CIRCULAR CYLINDER

3.1 Treatment for Simulation

(1) Discrete vortex method

The aim of this paper is to analyze the stated phenomena under appropriate conditions and assumptions. In the present treatment the discrete vortex method is applied. The following analysis is based on the potential flow theory in which the discrete vortices emitted from the horizontal circular cylinder surface are introduced. At first the Milne-Thomson circular theorem (Milne-Thomson, 1968) is used to determine the complex potential of the interested flow, however the free surface and bottom boundary make the analytical treatment extremely complex. According to Ogilvie (1963) and Chaplin (1981) it is concluded that the free surface effect on the boundary condition can be neglected when the ratio between the submerged water depth and the circular cylinder diameter is large enough, say 5. While Nath and Yamamoto (1974), and Uekita and Yamazaki (1980) investigated the effect of bottom boundary on the complex potential of the stated phenomena, and concluded that the bottom boundary effect can be neglected when the clearance between the lower portion of the cylinder and the bottom is larger than the circular cylinder diameter. Taking into account the above two results we will select an appropriate range of submergence of the circular cylinder in order to proceed the analysis in neglecting the surface and bottom boundary effects.

Now let us assume that the questioned complex potential, W , is the summation of those of potential flow surrounding a circular cylinder and of discrete vortices, W_p and W_v . That is to say,

$$W = W_p + W_v \quad (1)$$

(2) Determination of W_p

The term W_p can be expressed in the next equation by using the Milne-Thomson circular theorem,

$$W_p = W_{p0}(z) + \overline{W_{p0}(R^2/\bar{z})} \quad (2)$$

where $W_{p0}(z)$ is the complex potential for the flow field where the circular cylinder does not exist, and $z = x + iy$. In order to express the term explicitly, we are able to apply an appropriate wave theory such as the small amplitude wave theory, the finite amplitude wave theory, and the stream function theory. In case of the small amplitude wave theory

$$W_{p0} = \frac{\omega H}{2k \sinh kh} \sin(kz + iks_0 - \omega t) \quad (3)$$

where ω is the angular frequency, k the wave number, H the

wave height, h the water depth, s_0 the distance of the circular cylinder center from the bed, and t the time. While in case of the stream function theory (Dean, 1965)

$$W_{p0} = -A_0 z + \sum_n A_n \sin(k_n z + i k_n s_0 - \omega_n t - \beta_n) \quad (4)$$

where A_n , β_n are coefficient and phase lag appeared in the stream function theory, $k_n = nk$, and $\delta_n = n\delta$.

(3) Determination of W_v

The term W_v induced by discrete vortices can be expressed in the next equation by using again the Milne-Thomson circular theorem,

$$W_v = -\frac{i}{2\pi} \sum_k \Gamma_k \log(z - z_k) + \frac{i}{2\pi} \sum_k \Gamma_k \log(z - R^2/\bar{z}_k) \quad (5)$$

where Γ_k and z_k are the circulation and the complex position of each discrete vortex.

(4) Emission of a vortex and the vortex motion

In order to clarify the emission of a vortex from the circular cylinder surface, the location and the circulation of a vortex just before separating from the circular cylinder must be evaluated. From such a view point, the separation point is necessary to be determined by any appropriate way. As a first step, we calculated the velocity distribution within a laminar boundary layer developed along the surface of a circular cylinder. However, it is quite natural that the above treatment can not be applied to the case with large K.C. numbers and large Reynolds numbers. In order to determine the separation point in the above case, we decided to adopt the following two conditions. The first one is that the shear stress on the cylinder surface, τ_b , is zero at the separation point, the condition of which is commonly applied to the steady boundary layer flow. The second one is that the arcwise pressure gradient on the surface is zero at the separation point. The latter condition is adopted by the following reasons; that is, (1) the flow separation may appear in the vicinity of the point on the surface where the pressure reaches its maximum, and (2) the stated position can be easily determined by using the potential flow velocity outside the boundary layer.

In order to check which condition is more suitable for our purpose, we applied the above two to the uniformly oscillating flow and compared the evaluated time dependent separation point with the laboratory data obtained by Grass and Kemp (1979) as shown in Figure 5. The abscissa indicates the phase of flow and the ordinate indicates the location of flow separation point on the cylinder surface. Either of these two conditions is not adequate to predict precisely the location of flow separation, however the condition for pressure gradient is better than that for shear stress. Therefore we selected the condition of pressure gradient to determine the flow separation point in

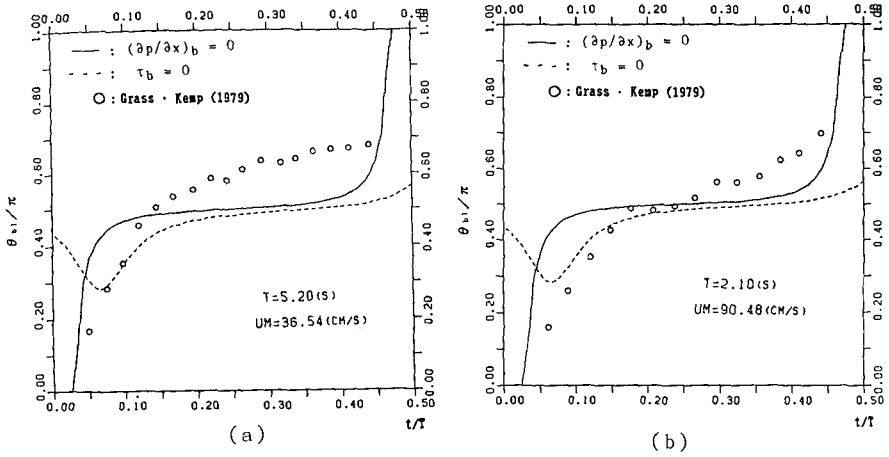


Fig.5 Comparison between predicted separation points and laboratory data

wave fields too.

The vortex flux, $\partial\Gamma/\partial t$, accumulated within the boundary layer in a unit time can be expressed by

$$\frac{\partial\Gamma}{\partial t} = \int_0^\delta \left(\frac{\partial v}{\partial x} - \frac{\partial u}{\partial y} \right) u dy \tag{6}$$

where δ is the thickness of boundary layer. Considering that the term $\partial v/\partial x$ is negligible comparing with the term $\partial u/\partial y$, we applied the following equation which was proposed by Sarpkaya (1968) as an approximate expression,

$$\frac{\partial\Gamma}{\partial t} = \frac{1}{2} U_B |U_B| \tag{7}$$

where U_B is the velocity just outside the boundary layer at the separation point.

Next we assumed that the discrete vortex separated from the cylinder surface is moving with the velocity (u_k, v_k) , which can be calculated by the following equation

$$u_k - iv_k = \frac{d}{dz} \left\{ W + \frac{i\Gamma_k}{2\pi} \log(z - z_k) \right\} \tag{8}$$

Therefore the position of the questioned vortex at the time step, $t + \Delta t$, can be determined as

$$z_k(t + \Delta t) = z_k(t) + (u_k, v_k) \Delta t \tag{9}$$

(5) Wave forces acting on a circular cylinder

The wave force components can be obtained by the Blasius formula for an unsteady flow by using the complex velocity potential. That is

$$F_H - iF_V = \frac{i\rho}{2} \oint_C \left(\frac{dW}{dz} \right)^2 dz + i\rho \frac{\partial}{\partial t} \oint_C \bar{W} dz \quad (10)$$

where C is an arbitrary closed curve surrounding the questioned cylinder section. Introducing Equations (1), (2) and (5) into Equation (10), we get the next equation,

$$\begin{aligned} F_H - iF_V = & 2\pi\rho R^2 \frac{\partial}{\partial t} \left(\frac{\partial W_{p0}}{\partial z} \right) + 2\pi\rho R^2 \frac{\partial W_{p0}}{\partial z} \frac{\partial W_{p0}}{\partial z} \\ & - i\rho \sum_k \Gamma_k (u_k - iv_k) - \rho \sum_k i \frac{\partial}{\partial t} (\Gamma_k R^2 / \bar{z}_k) \\ & + i\rho \sum_k \Gamma_k \frac{\partial^2 W_{p0}}{\partial z^2} (z_k - R^2 / \bar{z}_k) \end{aligned} \quad (11)$$

(6) Decay of vortex circulation

In the treatment of the discrete vortex method, it is assumed that the circulation of emitted vortex maintains its original value. However the above assumption can not treat the actual phenomena due to the decay of vortices by the fluid viscosity. Considering the above fact, we will introduce the decay of vortex in the following way to simulate the flow characteristics surrounding the horizontal circular cylinder. That is to say, we assume that the discrete vortex is represented by a Rankine vortex with a core, the radius of which, r_v , can be expressed by

$$r_v = 2.24 \sqrt{\nu t^*} \quad (12)$$

where t^* is the elapsed time since the vortex emitted from the cylinder surface and ν is the kinematic viscosity of fluid. The term r_v corresponds to the core radius of Stokes vortex. In addition to the above, we also assume that the elapsed time, t^* , has its upper value T_c , which represents a kind of decay time. Hence the limited core radius, r_c , is given by

$$r_{cr} = 2.24 \sqrt{\nu T_c} \quad (13)$$

(7) Calculation procedures

The flow chart of the numerical calculation is shown in Figure 6. That is to say, emit a discrete vortex at each time step, then calculate the velocity field, wave force acting on a cylinder and the translation of the above vortex. Repeat the above calculation processes until the time history of wave forces reaches its cyclic pattern. When two discrete vortices come in touch each other, let unite them to a single vortex in such a way to conserve the total angular momentum. When the vortex comes inside of the circular cylinder, return the vortex to the position where the vortex core comes in touch with the cylinder surface, and then let the vortex be convected by the induced flow velocity at the next time step.

3.2 Numerical Results and Verification

(1) Conditions of numerical calculations

Numerical calculations were made for the flow characteristics near the horizontally immersed circular cylinder 1) under a uniformly oscillating flow and 2) under progressive waves. Tables 1 and 2 give the various conditions of calculations for a uniformly oscillating flow and for progressive waves respectively.

Throughout the numerical calculations, the time histories of total wave force, fluid force induced by vortices, and circulation of emitted vortices were printed out in graphical forms for three to four wave cycles. In addition to these, streamlines at various time steps were illustrated to look at visually the behavior of vortices emitted from the cylinder surface.

(2) Wave forces

In case of uniformly oscillating flow, it is clearly observed from the calculated results that the vortex motion becomes unsymmetrical and induces the lift force, the magnitude of which is comparable to the drag force in the direction of flow with the increase of K.C. number.

While in the case of progressive waves, the following conclusions were obtained :

- 1) The lift force has the magnitude comparable to the drag force and is mainly induced by the vortex motion.
- 2) In general the time histories of wave forces are apt to be cyclic by the introduction of vortex decay.
- 3) Under the deep water wave condition, the wave force has a single modal peak. But under the intermediate water wave condition, the drag force has a single peak over one wave cycle, while the lift force has bimodal peaks due to the unsymmetrical behavior of emitted vortices.
- 4) In Case W-1, the flow pattern and calculated wave forces were not influenced by the strength of vortex decay. However in Cases W-2 and W-3, these strongly depend on the strength of vortex decay.

(3) Wave force path

In order to investigate the effect of vortex decay, the calculated wave force paths based on the stream function theory were compared with the laboratory data of Masuda et al. (1985) as shown in Figure 7. The solid lines are the experimental results, while the dotted lines are the calculated ones. The calculated curves in the upper

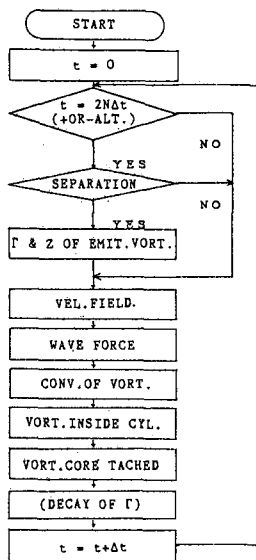


Fig. 6

Flow chart

Table 1 Conditions for a uniformly oscillating flow.

(a) Calculation conditions

Case	R (cm)	l (cm)	T (s)	U cm/s	K.C.	T/ Δt
S-1	2.5	20.0	1.0	20.5	4.1	60
S-2	2.5	20.0	1.4	22.9	6.4	80
S-3	2.5	20.0	1.9	21.8	8.3	120

R : circular cylinder diameter, l : cylinder length,
 T : oscillatory flow period, U : horizontal velocity
 amplitude, K.C. : Keulegan-Carpenter number,
 Δt : time step.

(b) Calculation runs for each case

Run	Flow pattern	Decay of vortex
1		Without
2	a) Symmetrical	With ($T_c = T$)
3		With ($T_c = T/2$)
4	b) Unsymmetrical	With ($T_c = T$)
5		With ($T_c = T/2$)

Table 2 Conditions for progressive waves.

(a) Calculation conditions

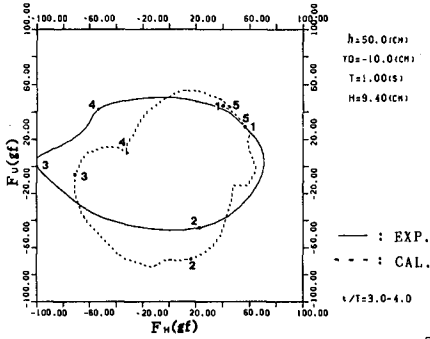
Case	R (cm)	l (cm)	h (cm)	Yo (cm)	T (s)	H (cm)	T/ Δt
W-1	2.5	20.0	50.0	10.0	1.0	9.4	60
W-2	2.5	20.0	50.0	13.0	1.4	11.0	80
W-3	2.5	20.0	50.0	10.0	1.9	9.9	120

h : water depth, Yo : cylinder center depth,
 H : wave height, others : same as in Table 1.

(b) Calculation runs for each case

Run	Decay of vortex
1	Without
2	With ($T_c = T$)
3	With ($T_c = T/2$)

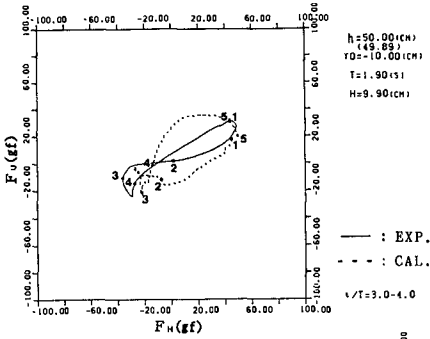
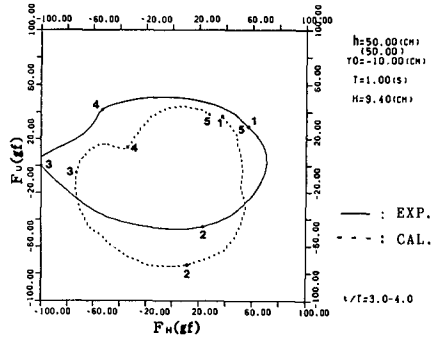
Note : Small amplitude wave theory and stream function
 theory were applied for calculations.



$T_c = T$

Fig.7 (a)

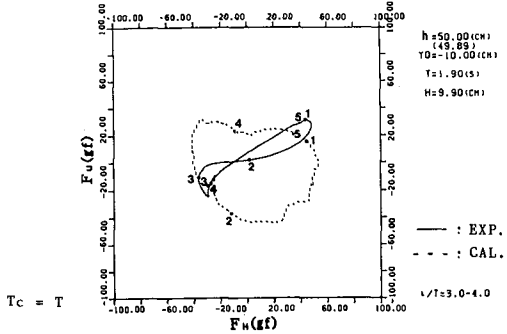
Comparison between calculated wave force path and laboratory data (C-type).



$T_c = T/2$

Fig.7 (b)

Comparison between calculated wave force path and laboratory data (E-type).



diagrams of Figures 7 (a) and (b) were obtained under the condition of $T_c = T$, and those in the lower diagrams were under the condition of $T_c = T/2$.

Looking at these diagrams, we can observe the following facts : 1) in the deeper water wave condition, the wave force path (C type) was simulated well under either conditions of $T_c = T$ or $T_c = T/2$, and 2) however in the shallower water wave condition, the 8-shaped type wave force path (E type) was reproduced well under the condition of $T_c = T/2$, but not under the condition of $T_c = T$. In order to make clear the reason why such a difference as stated in 2) happened, the calculated flow induced by the vortices in the vicinity of a circular cylinder for Case W-3 were displayed. From these diagrams, we could observe that the unsymmetrical vortex behavior was reproduced at the time step of $t/T = 3.6 \sim 3.8$ for $T_c = T/2$, but not for $T_c = T$. Therefore we can conclude that appropriate decay of vortex should be introduced to simulate the interested flow characteristics.

(3) Drag coefficient, inertia coefficient, and lift coefficient

By using the calculated time histories of horizontal wave force component in a uniformly oscillating flow, the drag coefficient, C_D , and the inertia coefficient, C_M , were calculated through the following equations

$$C_D = \frac{3}{8} \int_0^{2\pi} \frac{F \sin \theta}{\rho R \hat{U}^2 \ell} d\theta \quad (14)$$

$$C_M = \frac{\hat{U} T}{2\pi^2 R} \int_0^{2\pi} \frac{F \cos \theta}{\rho R \hat{U}^2 \ell} d\theta \quad (15)$$

The obtained data for the symmetrical flow cases were plotted and compared with the laboratory data of Sarpkaya (1975) as shown in Figure 8. The abscissa in these diagrams is the K.C. number. The agreement for C_M is fairly good, however the calculated values of C_D were underestimated. The main reason why the latter discrepancy appeared is in the condition applied for determining the separation point. In this treatment the potential flow velocity surrounding the circular cylinder with the effect of vorticities was used. That is to say, at the point where the velocity is zero flow separation does not occur at any time and this fact caused rapid migration of separation point. Due to the above circumstance the development of vortex is disturbed, hence the drag coefficient results in decrease.

On the other hand two kinds of lift coefficient were calculated by using the following equations,

$$C_{L(MAX)} = \hat{F}_L / \rho \hat{U}^2 R \ell \quad (16)$$

$$C_{L(RMS)} = \sqrt{\overline{F_L^2}} / \rho \hat{U}^2 R \ell \quad (17)$$

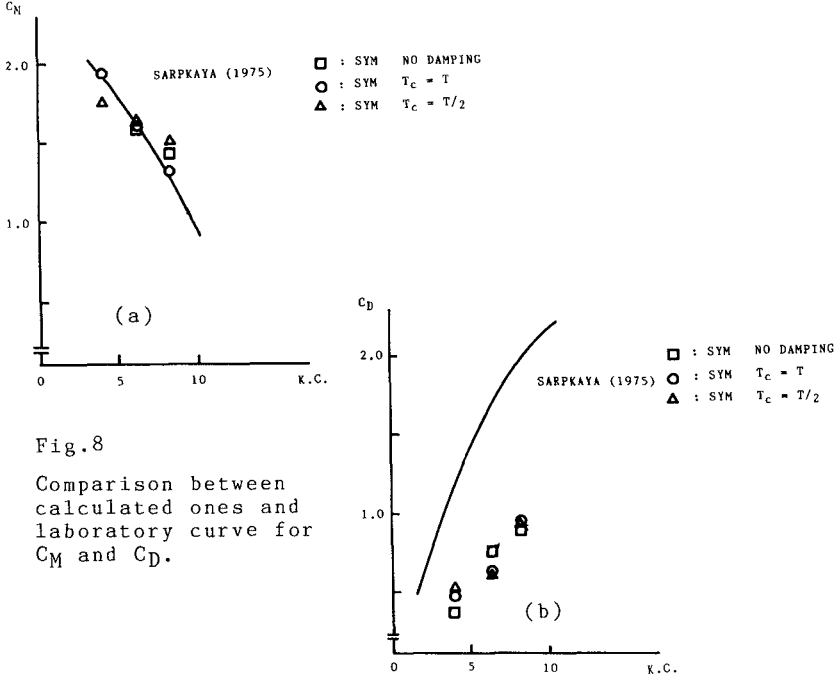


Fig. 8
Comparison between calculated ones and laboratory curve for C_M and C_D .

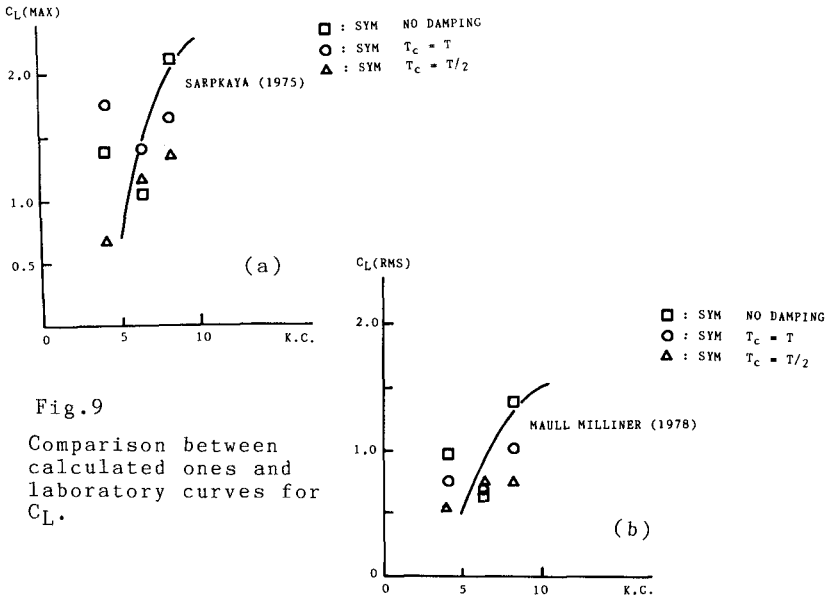


Fig. 9
Comparison between calculated ones and laboratory curves for C_L .

The former and latter data for symmetrical flow cases were compared with the laboratory data of Sarpkaya (1975), and that of Maull and Milliner (1978) as shown in Figures 9 (a) and (b) respectively. The abscissa of the diagrams is again the K.C. number. The tendency of scattered data agrees with the laboratory curve in both cases.

In the same way, these three coefficients for unsymmetrical flow cases were investigated. The unsymmetry of flow did not induce any strong influence on the coefficients of C_D and C_M , but induced a certain amount of influence on the coefficient of C_L .

4. CONCLUSIONS

In the present paper was presented the numerical calculation method for predicting the wave forces acting on a horizontal circular cylinder set in a certain range of water depth. The simulation model is based on the discrete vortex method. The adaptability of the present calculation method was checked by comparing the calculated results with available laboratory data. As a conclusion of the present treatment, we found that the method presented here is applicable by introducing appropriate decay of vortex circulation even to the cases where the emitted vortices induce strong unsymmetrical fluid motion.

Further study is needed to present a reasonable method to evaluate the vortex decay in the above treatment and to extend the capacity of the present simulation method for calculating the interested wave forces under more realistic or practical conditions.

REFERENCES

- Borgman, L.E. : Computation of the ocean-wave forces on inclined cylinders, Trans. Amer. Geophys. Union, Vol.39, pp.885-888, 1958.
- Chaplin, J.R. : On the irrotational flow around a horizontal cylinder in waves, Jour. App. Mech., Trans. ASME, Vol.46, pp.689-694, 1981.
- Dean, R.G. : Stream function representation of nonlinear ocean waves, Jour. Geophys. Res., Vol.70, pp.4561-4572, 1965.
- Grass, A.J. and P.H. Kemp : Flow visualization studies of oscillatory flow past smooth and rough circular cylinder, Mechanics of Wave-Induced Forces on Cylinders, Pitman, pp.406-420, 1979.
- Koderayama, W. and A. Tashiro : On the wave forces acting on a submerged horizontal circular cylinder, Jour. Japanese Society of Naval Architects, No.143, pp.134-144, 1978 (in Japanese).
- Masuda, S., A. Watanabe, and K. Horikawa : Wave forces acting on and velocity field of a circular cylinder set horizontally in wave, 40th Annual Conv. of JSCE, pp.II 541-542, 1985 (in Japanese).
- Maull, D.J. and M.G. Milliner : Sinusoidal flow past a

- circular cylinder, Coastal Eng., Vol.2, pp.149-168, 1978.
- Milne-Thomson, L.H. : Theoretical Hydrodynamics, 4th ed., McMillian, New York, 1968.
- Morison, J.R., M.P. O'Brien, J.W. Johnson, and S.A. Schaaf : The forces exerted by surface waves on piles, Petroleum Trans. AIME, Vol.189, pp.149-157, 1950.
- Nath, J.H. and T. Yamanoto : Forces from fluid around objects, Proc. 14th Coastal Engrg. Conf., pp.1808-1827, 1974.
- Ogilvie, T.F. : First- and second-order forces on a cylinder submerged under a free surface, J. Fluid Mech., Vol.16, pp.451-472, 1963.
- Rosenhead, L. : Formation of vorticies from a surface of discontinuity, Proc. Roy. Soc., A, Vol.134, pp.170-192, 1931.
- Sarpkaya, T. : An analytical study of separated flow about circular cylinders, J. Basic Engrg., Trans. of ASME, Vol.90, pp.511-518, 1968.
- Sarpkaya, T. : Forces on cylinders and spheres in sinusoidally oscillating fluid, J. App. Mech., Trans. of ASME, Vol.42 No.1, pp.32-37, 1975.
- Sawamoto, M., H. Oniwa, and J. Kashiwai. : A consideration on an expression of wave forces acting on a circular cylinder in an oscillatory flow, 34th Annual Conv. of JSCE, pp.II 579- 580, 1979 (in Japanese).
- Sawamoto, M. and K. Kikuchi : Uplift forces acting on a circular cylinder in an oscillatory flow, Proc. 26th Japanese Coastal Engrg. Conf., JSCE, pp.429-433, 1979 (in Japanese).
- Tsuzuki, S., A. Watanabe, and K. Horikawa : Wave forces acting on a horizontal circular cylinder, 39th Annual Conv. of JSCE, pp.II 303- 304, 1984 (in Japanese).
- Uekita, M. and H. Yamazaki : A study on inertia forces acting on a horizontal circular cylinder, Proc. 27th Japanese Coastal Engrg. Conf., JSCE, pp.358-362, 1980 (in Japanese).

CHAPTER 164

Water Wave Scattering by Rows of Circular Cylinders

Robert A. Dalrymple¹, M. ASCE, Seung Nam Seo², Paul A. Martin³

Abstract

The scattering of waves by a finite number of rows of circular cylinders is examined. Reflection and transmission coefficients are obtained and compared to Kakuno's experimental data. Following Twersky (1962), the scattering from a single row of cylinders (or the single grating problem) is numerically solved. The wide-spacing approximation is used to find the effect of multiple gratings.

1 Introduction

The reflection and transmission of waves through rows of vertical cylinders, corresponding to the use of rows of piling as breakwaters (Wiegel, 1961), is examined. The physical situation also could represent the effects of piers and other pile supported structures on the wave environment.

Hayashi *et al.* (1966) and Mei *et al.* (1974) have examined several methods to calculate the wave field in the vicinity of a single row of cylinders, taking into consideration the loss of energy by the flow between the closely spaced cylinders. Ozsoy (1977) has empirically examined the Mei *et al.* solution and finds reasonable agreement with the theory; however there is considerable scatter in the data. Spring and Monkmeyer (1975) assumed that the flow was potential and examined the pressures and forces on an infinite row of cylinders.

Kakuno (1984,1986) has examined the same problem, and also the problem of a double row of vertical cylinders. He also considered potential flow with two assumptions: (1) the wave length is long compared with the pile spacing in each row, and (2) the wave length is short compared to the row spacing. Because of (1) he was able to give an analysis similar to Lamb (1898) for the analogous problem of acoustic waves passing through a row of cylinders. However, it is known that Lamb's method is deficient for this case: the exact solution is composed of an odd (dipole) part and an even (monopole) part, whereas Lamb's method only gives the odd part correctly. Recently Martin and Dalrymple (1988)

¹Department of Civil Engineering, University of Delaware, Newark, Delaware 19716

²Korea Ocean Research and Development Institute, Ansan, Seoul 171-14, Korea

³Department of Mathematics, University of Manchester, Manchester, M13 9PL, U.K.

have shown how this deficiency can be rectified. Because of (2), Kakuno was able to use the "wide spacing approximation" for two rows of cylinders; see, e.g., Srokosz and Evans (1979).

In this paper, we eliminate assumption (1) by giving an (in principle) exact numerical solution for a single row of circular cylinders. (Note that the asymptotic methods of Lamb and of Martin and Dalrymple work for cylinders with any cross-section.) We combine these results with the wide-spacing approximation and give a comparison with Kakuno's data. Finally, scattering from several rows of cylinders is calculated.

2 Scattering by a cylindrical grating

We first consider scattering of water waves by an infinite grating of circular cylinders, located along the y -axis. A plane wave of frequency ω over a constant depth h is incident upon the grating with angle θ_o (See Fig. 1).

The velocity potential, which must satisfy the Laplace equation, can be written as

$$\Phi(x, y, z, t) = \text{Re} \left\{ \phi(x, y) \cosh k(h + z) e^{-i\omega t} \right\} \quad (1)$$

where Re denotes the real part and k is the wave number, determined from the dispersion relationship, $\omega^2 = gk \tanh kh$, which relates the angular frequency ω to the wave number, the water depth h , and the acceleration of gravity, g . Factoring out the time and depth dependency, the fluid motion is governed by the Helmholtz equation

$$(\nabla^2 + k^2)\phi = 0 \quad (2)$$

On the wall of each cylinder in the grating, the no-flux condition should be fulfilled:

$$\phi_n = 0 \quad (3)$$

where subscript n denotes the outward normal derivative. The scattered potential ϕ^{sc} , defined as the total potential ϕ minus the incident potential ϕ^{in} , must satisfy a radiation condition as $|x| \rightarrow \infty$.

Twersky (1962) used the method of separation of variables for solving scattered waves by an infinite grating of equally spaced identical circular cylinders with spacing d . (See Fig. 1) The total velocity potential by an incident wave $\phi^{in} = e^{i\vec{k} \cdot \vec{x}}$ can be expressed in cylindrical coordinates as,

$$\begin{aligned} \phi = & e^{ikr \cos(\theta - \theta_o)} + \sum_{n=-\infty}^{\infty} e^{in(\theta + \pi/2)} \left\{ A_n H_n^{(1)}(kr) \right. \\ & \left. + J_n(kr) \sum_{s=1}^{\infty} \sum_{m=-\infty}^{\infty} A_m H_{m-n}^{(1)}(skd) \left[e^{-iskd \sin \theta_o} + (-1)^{m-n} e^{iskd \sin \theta_o} \right] \right\} \end{aligned} \quad (4)$$

where J_n and $H_n^{(1)}$ denote the Bessel function of first kind order n and the Hankel function of order n . The multiple scattering coefficient A_n can be obtained by imposing no-flux condition at the cylinder wall ($r=a$).

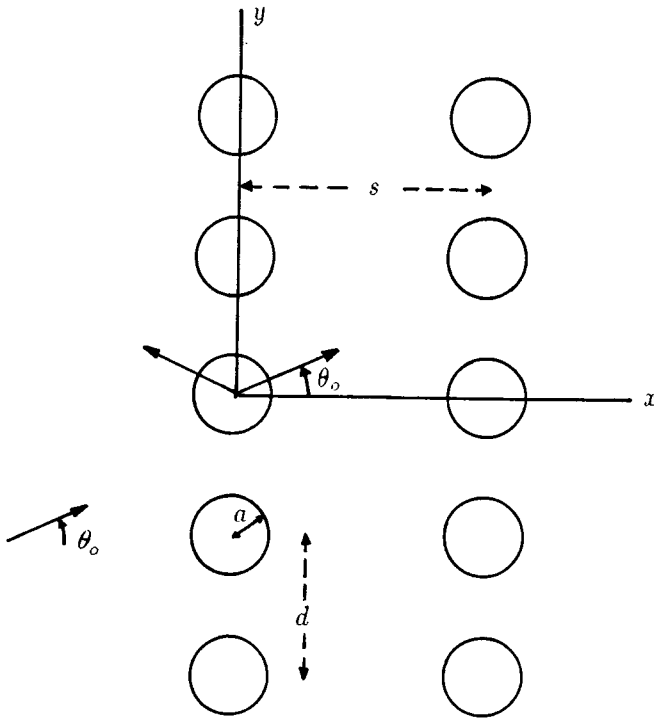


Figure 1: Schematic Diagram Showing Waves Incident on Two Rows of Cylinders

$$A_n = -\frac{J'_n(ka)}{H'_n(ka)} \left\{ e^{-in\theta_o} + \sum_{m=-\infty}^{\infty} A_m H_{n-m}^{(1)}(skd) \left[e^{-iskd \sin \theta_o} + (-1)^{m-n} e^{iskd \sin \theta_o} \right] \right\} \quad (5)$$

where prime denotes differentiation.

In order to calculate transmission coefficient K_T and reflection coefficient K_R , it is convenient to express the potential as a summation of plane wave modes in Cartesian, rather than polar coordinates. By Sommerfeld's integral representation of the Hankel functions and Poisson's summation formula, Twersky (1962) obtained the following representations: For the transmitted region ($x > 0$),

$$\phi_T = e^{i\vec{k}\cdot\vec{x}} + 2 \sum_{n=-\infty}^{\infty} A_n \sum_{\mu=-\infty}^{\infty} e^{in\theta_\mu} C_\mu e^{iky \sin \theta_\mu + ikx \cos \theta_\mu} \quad (6)$$

and for the reflected region ($x < 0$)

$$\phi_R = e^{i\vec{k}\cdot\vec{x}} + 2 \sum_{n=-\infty}^{\infty} A_n \sum_{\mu=-\infty}^{\infty} e^{in(\pi-\theta_\mu)} C_\mu e^{iky \sin \theta_\mu + ikx \cos \theta_\mu} \quad (7)$$

with

$$C_\mu = \frac{1}{kd \cos \theta_\mu} \quad \text{for } |Re \theta_\mu| \leq \frac{\pi}{2} \quad (8)$$

and the directions of the planar wave modes are given by

$$\sin \theta_\mu = \sin \theta_o + \frac{2\pi}{kd} \mu \quad \text{for } \mu = 0, \pm 1, \pm 2, \dots \quad (9)$$

It can be seen from Eq. 7 that when $|\sin \theta_\mu| < 1$, progressive waves exist, but when $|\sin \theta_\mu| > 1$ there are evanescent modes. If $kd < \pi$, therefore, only one progressive wave exists.

Introducing a multiple scattering amplitude $G(\theta_\mu) = \sum_{n=-\infty}^{\infty} A_n e^{in\theta_\mu}$, reflection and transmission coefficients for a mode μ are

$$K_{R\mu} = 2C_\mu G(\pi - \theta_\mu) \quad (10)$$

and

$$K_{T\mu} = \delta_{\mu o} + 2C_\mu G(\theta_\mu) \quad (11)$$

where δ denotes the Kronecker delta. From conservation of energy flux, we have

$$\sum_{\mu=\mu^-}^{\mu=\mu^+} \left(|K_{R\mu}|^2 + |K_{T\mu}|^2 \right) \frac{\cos \theta_\mu}{\cos \theta_o} = 1 \quad (12)$$

where

$$\mu^- = E\left[-(1 + \sin \theta_o) \frac{kd}{2\pi}\right] \quad (13)$$

$$\mu^+ = E\left[(1 - \sin \theta_o) \frac{kd}{2\pi}\right] \quad (14)$$

and $E[x]$ stands for the integer value of x .

Slow convergence of the series in Eq. (5), which is a family of Schlömilch series, leads to a difficulty in evaluating the multiple scattering coefficients. Twersky (1961) found a way to accelerate the convergence of the series. In the present method, Shanks transformation was used to evaluate the infinite series in Twersky's representation.

Scattering coefficients A_n were obtained by retaining up to the M^{th} harmonic in Eq. (5):

$$A_n = -\frac{J'_n(ka)}{H'_n(ka)} \left\{ e^{-in\theta_0} + \sum_{m=-M}^M A_m \sum_{s=1}^{\infty} H_{n-m}(skd) \left[e^{-iskd \sin \theta_0} + (-1)^{n-m} e^{iskd \sin \theta_0} \right] \right\} \quad (15)$$

for $n = -M, \dots, M$. (Care must be taken when Bessel function J_n is calculated using a recurrence formula, because of roundoff errors; see Abramowitz and Stegun, 1965, section 9.12.)

Twersky (1962) was able to get approximate solutions when there is only one propagating mode. Present numerical solutions of K_T and K_R were compared to Twersky's results in Figs. 2 and 3. The numerical solutions satisfied conservation of energy flux up to 10 digits for all the cases tested. Twersky's solutions (Eqs. 127 and 144) are valid only if $ka < a/d < 1$. As shown in Fig. 3, Twersky's solution does not agree to the numerical solution. For a fixed radius, longer waves propagate through the grating more easily. Normal incidence waves to the grating axis are more reflective.

3 Wide-spacing Approximation

We now move to wave scattering problems by multi-row gratings, where more than one length scale is involved. We further assume that the distance between gratings is large enough, so that gratings interact with each other via the propagating waves only; hence we can neglect the evanescent modes. For a longer wave train, ($kd < \pi$), only one wave transmits through the grating with the given incident angle.

In the case of two gratings, the interference can be explained physically. When an incident wave train, proportional to $e^{i\ell x}$, where $\ell = k \sin \theta_0$, strikes the first grating at $x = 0$, part of the wave train is transmitted and part is reflected. Upon seeing the grating at $x = s$, the transmitted wave undergoes the same scattering process; part of the wave is transmitted to $x > s$ and part is back-reflected toward the first grating. This back and forth process of transmission and reflection is repeated infinitely. (See Fig. 4). Mathematically, we have

$$K_R = R_1 + T_1^2 R_2 e^{i2\ell s} + T_1^2 R_1 R_2^2 e^{i4\ell s} + T_1^2 R_1^2 R_2^3 e^{i6\ell s} + \dots \quad (16)$$

$$= \frac{R_1 + R_2 e^{i2\ell s} (T_1^2 - R_1^2)}{1 - R_1 R_2 e^{i2\ell s}} \quad (17)$$

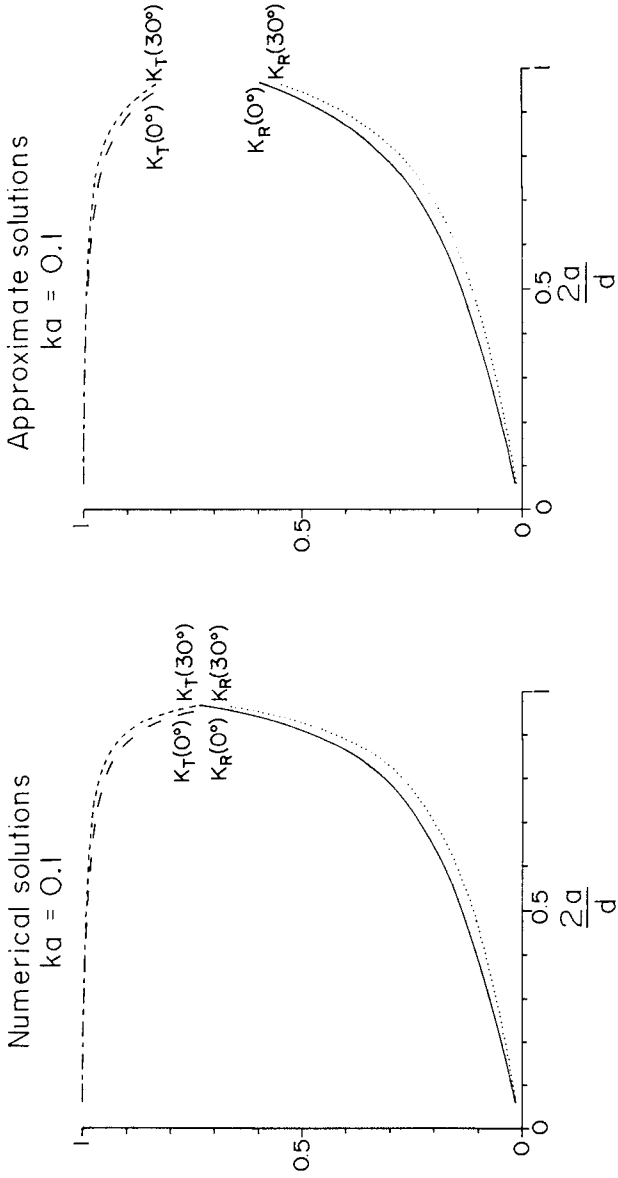


Figure 2: Comparison of Numerical and Approximate Solutions for Two Angles of Incidence for Small ka .

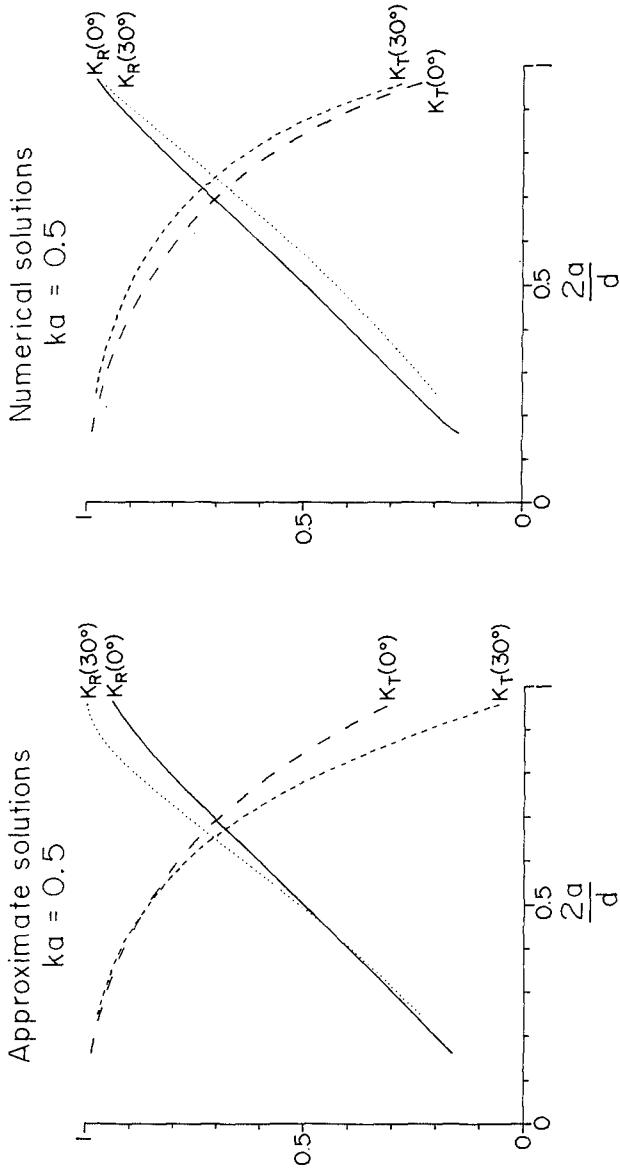


Figure 3: Comparison of Numerical and Approximate Solutions for Two Angles of Incidence for Larger ka .

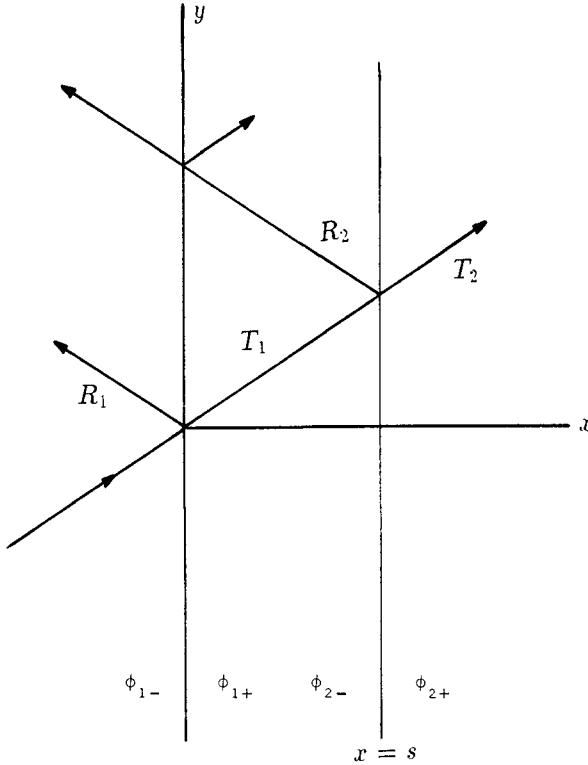


Figure 4: Reflection and Transmission by Two Gratings

$$\begin{aligned}
 K_T &= T_1 T_2 + T_1 T_2 R_1 R_2 e^{i2\ell s} + T_1 T_2 R_1^2 R_2^2 e^{i4\ell s} + \dots & (18) \\
 &= \frac{T_1 T_2}{1 - R_1 R_2 e^{i2\ell s}} . & (19)
 \end{aligned}$$

where T_i and R_i ($i = 1, 2$) are the transmission coefficient and reflection coefficient of the i^{th} grating, respectively. Stokes (1862) used this method to find light intensity in heterogeneous media. To generalize the formulation, we solve N-row grating problems using the wide-spacing approximation. Let the solution to scattering problem for the n^{th} grating by an incident wave $e^{i\ell(x-x_n)}$ with $\ell = k \cos \theta_0$ be ϕ_{n-} . We define transmission and reflection coefficients, T_{n-} and R_{n-} , respectively, by

$$\phi_{n-} \sim \begin{cases} e^{i\ell(x-x_n)} + R_{n-} e^{-i\ell(x-x_n)}, & \text{for } x \rightarrow -\infty \\ T_{n-} e^{i\ell(x-x_n)}, & \text{for } x \rightarrow \infty \end{cases} \quad (20)$$

Similarly, let ϕ_{n+} solve the scattering problem for the n^{th} grating by an incident wave from

the other direction, $e^{-i\ell(x-x_n)}$, and define T_{n+} and R_{n+} by

$$\phi_{n+} \sim \begin{cases} e^{-i\ell(x-x_n)} + R_{n+} e^{i\ell(x-x_n)}, & \text{for } x \rightarrow \infty \\ T_{n+} e^{-i\ell(x-x_n)}, & \text{for } x \rightarrow -\infty \end{cases} \quad (21)$$

Hence we can represent near field potential of the n^{th} grating by

$$\phi = C_n^- \phi_{n-} + C_n^+ \phi_{n+} \quad (22)$$

$$\sim \begin{cases} \left(C_n^- e^{-i\ell x_n} \right) e^{i\ell x} + \left(C_n^- R_{n-} e^{i\ell x_n} + C_n^+ T_{n+} e^{i\ell x_n} \right) e^{-i\ell x}, & \text{for } x \rightarrow -\infty \\ \left(C_n^- T_{n-} e^{-i\ell x_n} + C_n^+ R_{n+} e^{-i\ell x_n} \right) e^{i\ell x} + \left(C_n^+ e^{i\ell x_n} \right) e^{-i\ell x}, & \text{for } x \rightarrow \infty \end{cases} \quad (23)$$

where the C_n^\pm denote unknown complex constants to be determined.

We now require that the near field solutions be joined smoothly in intermediate regions. For a region between the $(n-1)^{th}$ and n^{th} gratings, we have

$$\left[C_{n-1}^- (T_{n-1})_- e^{-i\ell x_{n-1}} + C_{n-1}^+ (R_{n-1})_+ e^{-i\ell x_{n-1}} \right] e^{i\ell x} + \left[C_{n-1}^+ e^{i\ell x_{n-1}} \right] e^{-i\ell x} = \quad (24)$$

$$\left[C_n^- e^{-i\ell x_n} \right] e^{i\ell x} + \left[C_n^- (R_n)_- e^{i\ell x_n} + C_n^+ (T_n)_+ e^{i\ell x_n} \right] e^{-i\ell x}, \quad x_{n-1} < x < x_n \quad (25)$$

Hence

$$C_{n-1}^- (T_{n-1})_- e^{i\ell \Delta_{n-1}} + C_{n-1}^+ (R_{n-1})_+ e^{i\ell \Delta_{n-1}} - C_n^- = 0 \quad (26)$$

and

$$C_{n-1}^+ e^{-i\ell \Delta_{n-1}} - C_n^- (R_n)_- - C_n^+ (T_n)_+ = 0 \quad (27)$$

where $\Delta_n = x_{n+1} - x_n$. This near field matching gives $2(N-1)$ equations for $n = 2, N$.

On the other hand, the total velocity potential due to all the gratings can be expressed by

$$\phi \sim \begin{cases} e^{i\ell x} + K_R e^{-i\ell x}, & \text{for } x \rightarrow -\infty \\ K_T e^{i\ell x}, & \text{for } x \rightarrow \infty \end{cases} \quad (28)$$

Noting that $x_1 = 0$ and $C_1^- = 1$, and comparing Eqs. (23) and (28), we have

$$R_{1-} + C_1^+ T_{1+} = K_R \quad (29)$$

Since there is no wave incident on the N^{th} grating from the left, C_N^+ must be zero. Comparing Eqs. (23) and (28) gives

$$C_N^- (T_N)_- e^{i\ell x_N} = K_T \quad (30)$$

Finally, we have $2N$ unknown coefficients: $K_R, C_1^+, C_2^-, C_2^+, \dots, C_N^-, K_T$. Eqs. (26), (27), (29) and (30) give $2N$ linear equations, enough to solve $2N$ unknowns.

In Fig. 5, we tested the present method for two identical rows of cylinders against Kakuno's experimental data. In this case, $T_{n-} = T_{n+}$ and $R_{n-} = R_{n+}$ ($n = 1, 2$) because depth is constant. We introduce two nondimensional parameters associated with the grating geometry; spacing parameter $\alpha = s/d$ and grating parameter $\beta = 2a/d$. In the wide-spacing approximation, we can expect $\alpha \gg 1$ and shorter spacing between gratings increases

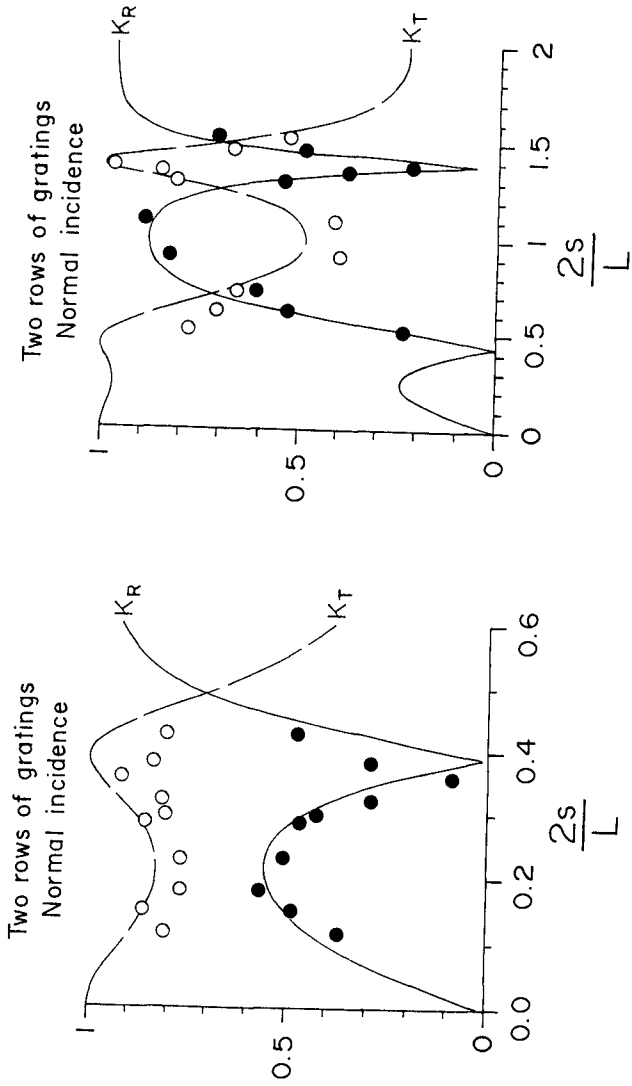


Figure 5: Comparison of Reflection and Transmission Coefficients with Kakuno's Data

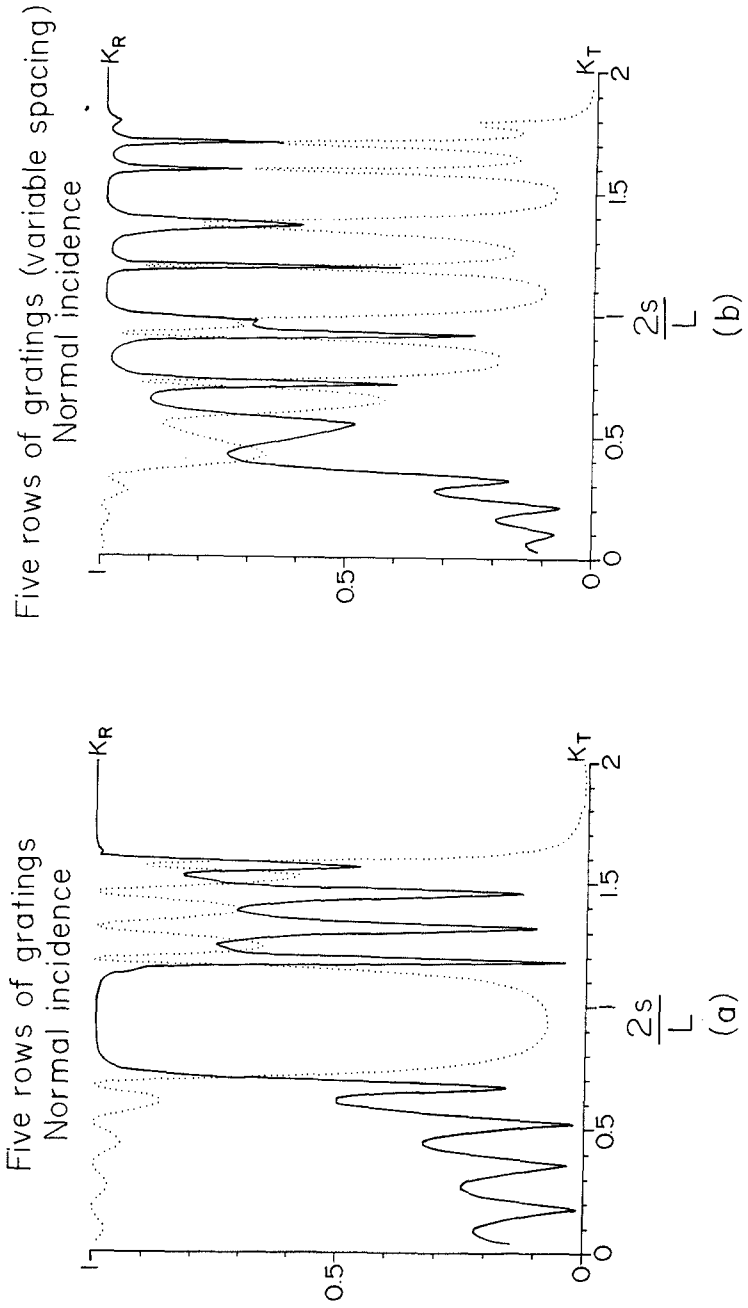


Figure 6: Reflection and Transmission Coefficients for Five Rows of Cylinders: Equal and Variable Spacing

the effect of evanescent modes. Fig. 5a shows this effect, which produces less agreeable results. For some values of α , a significant amount of waves are reflected. Under this condition, the phases of the reflected waves are the same, so that the reflected waves interfere constructively and the total amplitude is consequently the larger. This is referred to as Bragg scattering.

In Fig. 6, we presented K_R and K_T for five identical rows of cylinders. The interference of each grating is shown to be more complicated and total reflection can be observed for some values of α . In Fig. 6a, equally spaced gratings were used, while in Fig. 6b the spacing between the gratings increases from s for the first two gratings, by increments of $1.5s$, to $2.5s$. It is also interesting to note that some arrangements of gratings are essentially transparent to the waves.

4 Conclusion

Numerical results of wave scattering by N -row gratings are presented. Accurate numerical solutions for a single grating are constructed following Twersky (1962) procedure. For long waves ($ka \ll 1$), Twersky solution is identical to the numerical solution, but, as ka increases, Twersky's solution shows considerable deviation from the numerical solution. Using the wide-spacing approximation, reflection and transmission coefficients of long waves through N -row gratings are obtained.

For two identical rows of gratings, the present method shows good agreement with Kakuno's experimental data. Results for five rows of gratings are also presented.

5 Acknowledgments

Support for this research was provided by the NOAA Office of Sea Grant, Department of Commerce, under Grant NA87AA-D-SG040.

6 References

1. Abramowitz, M. and I.A. Stegun, 1965, **Handbook of Mathematical Functions**, Dover Publications, Inc., New York.
2. Hayashi, T., T. Kano and M. Shirai, 1966, "Hydraulic research on the closely spaced pile breakwater," Proc. 10th Intl. Conf. Coastal Engineering, ASCE, 873-884.
3. Kakuno, S. *et al.*, 1984, "Analysis of boundary value problems for hydraulic characteristics of vertically slotted breakwaters," Coastal Engineering in Japan (in Japanese).
4. Kakuno, S., 1986, Abstracts, 20th Int. Conf. Coastal Engineering, ASCE, Taiwan.
5. Lamb, H., 1898, "On the reflection and transmission of electric waves by a metallic grating," *Proc. London Math. Soc.*, Series 1, 29, 523-544.
6. Martin, P.A. and R.A. Dalrymple, 1988, "Scattering of long waves by cylindrical obstacles and gratings using matched asymptotic expansions," *J. Fluid Mechanics*, 188, 465-490.

7. Mei, C.C., P.L.-F. Liu, and A.T. Ippen, 1974, "Quadratic loss and scattering of long waves," *J. Waterways and Harbors Div.*, ASCE, 100, 217-239.
8. Ozsoy, E., 1977, "Dissipation and scattering by narrow openings," University of Florida, Coastal and Oceanographic Engineering Laboratory, UFL/COEL/TR-037, 137pp.
9. Spring, B.W. and Monkmeyer, P.L., 1975, "Interaction of plane waves with a row of cylinders," *Proc. Civil Engineering in the Oceans III*, ASCE, Newark, Delaware.
10. Srokosz, M.A. and Evans, D.V., 1979, "A theory for wave-power absorption by two independently oscillating bodies," *J. Fluid Mechanics*, 90, 337-362.
11. Stokes, G.G., 1862, "On the intensity of light reflected from or transmitted through a pile of plates," *Proc. Royal Society of London*, XI, 545-557.
12. Twersky, V., 1961, "Elementary function representations of Schlömilch series," *Arch. Rat. Mech. Anal.*, 8, 323-332
13. Twersky, V., 1962, "On the scattering of waves by the infinite grating of circular cylinders," *IRE Trans. Antennas Propag.*, 10, 737-765.
14. Wiegel, R.L., 1961, "Closely spaced piles as a breakwater," *Dock and Harbor Authority*, Sept. 1961, 150.

CHAPTER 165

WAVE TRANSMISSION THROUGH A DOUBLE-ROW PILE BREAKWATER

by

John B. Herbich, Ph.D., P.E., F.ASCE¹

and

Barry Douglas, B.S.²

Abstract

Several previous investigators have conducted experiments leading to expressions for predicting the transformation of waves passing through closely-spaced pile or large cylinder breakwaters. The present study extends the earlier experiments which used a single row of piles instead of a double row of piles forming a breakwater. The experiments using the double-pile breakwater were performed in the same facility as the experiments conducted on a single-pile breakwater and employed the same method of analysis for a more meaningful comparison.

The experiments consisted of allowing waves to pass through a pile array and measuring the incident and transmitted wave heights. The variables were: depth, period, diameter, monochromatic and random waves. The experimental matrix was three water depths, four wave periods, two pile diameters, two gap dimensions between piles and four random wave spectra: Darbyshire, I.T.T.C., Pierson-Moskowitz and JONSWAP, two pile diameters and two gap dimensions between piles.

The two-row breakwater had less wave transmission than the single-row breakwater, as expected. For a gap to a pile diameter ratio, or $b/D = 0.2$ (where b = gap spacing, D = pile diameter), the wave transmission was reduced by 15 percent, as compared with a single-row breakwater; for a gap ratio of $b/D = 0.1$, the wave transmission was reduced by 5 to 10 percent.

Introduction

In recent decades there has been a greater use of vertical face breakwaters, and consequently a considerable development in technology of caisson-type breakwaters.

¹Professor of Ocean and Civil Engineering, Texas A&M University, College Station, Texas 77843-3136, U.S.A.

²Graduate Student, Coastal and Oceanographic Engineering Department, University of Florida, Gainesville, FL 32611, U.S.A.

The first large cylinder-type breakwater was in all probability constructed in Hanstholm, Denmark in 1960. The cylindrical reinforced-concrete breakwater consisting of 12.5 m (41 ft) diameter units with a 0.25 m (0.8 ft) wall thickness was installed in 12 m (39 ft) of water. The breakwater at Marsa el Brega, Libya contains cylindrical shells in caissons that are 53.8 m (177 ft) long and 16 m (52 ft) wide.

A steel pipe breakwater was constructed in the Port of Osaka, Japan in 1966. The breakwater consists of 2 m (6.6 ft) diameter pipes. The spacings between adjacent steel pipes were 5 cm (0.16 ft) on the average.

A concrete pipe breakwater was constructed to protect a marina at Pass Christian, Mississippi to replace a breakwater destroyed by a hurricane. The breakwater consists of about 1.4 m (4.6 ft) diameter piles with approximately 15.2 cm (0.5 ft) spacings.

Laboratory Studies

Several laboratory investigations have been conducted to evaluate the transmission and reflection of waves from permeable-pile breakwaters. Published data include studies by Wiegel (1969), Hayashi, et al. (1966), Allsop and Kalmus (1985) and Truitt and Herbich (1987).

Hayashi, et al. derived an expression for wave transmission based on water jets discharging through the pile gaps:

$$\frac{H_t}{H_i} = 4 \left(\frac{d}{H_i} \right) E \left[-E + \sqrt{E^2 + \frac{H_i}{2d}} \right] \quad \dots \dots (1)$$

where H_t = height of transmitted wave,
 H_i = height of incident wave,
 d = water depth.

$$E = c \left(\frac{b}{D+b} \right) / \sqrt{1 - \left(\frac{b}{D+b} \right)^2} \quad \dots \dots (2)$$

where c = constant,
 b = spacing between piles,
 D = pile diameter.

Wiegel derived an expression for wave transmission based solely on geometry of the piles:

$$\frac{H_t}{H_i} = \frac{b}{D+b} \quad \dots \dots (3)$$

Model studies performed later showed that transmitted wave heights were larger (up to 25%) than the rate predicted by Equation 3.

Truitt and Herbich conducted experimental studies on wave transmission through a breakwater consisting of a single row of

piles employing both monochromatic and random waves. Earlier experiments of other investigators had been conducted with monochromatic waves. The results of experiments with random waves indicate that the relationships developed for monochromatic waves may be applicable to random waves. Very good agreement was observed between the values of wave transmission predicted by Hayashi's equation and experimentally-obtained values with random waves, provided the coefficient employed was equal to 0.9. It was also found that two dimensionless ratios affect the transmission coefficient:

- a) b/D , a ratio of breakwater spacing to pile diameter, and
- b) d/H_g , a ratio of water depth to wave height.

The influence of the second ratio on the transmission coefficient is more pronounced.

Experimental Studies

The breakwater consisted of two staggered rows of piles installed in a two-dimensional wave facility, 36.6 m (120 ft) long, 0.6 m (2 ft) wide and 0.91 m (3 ft) deep (Figures 1 and 2). The wave channel is glass-walled and is equipped with a programmable SEASIM wave generator. Either monochromatic or irregular wave spectra can be generated. Wave data were obtained using resistance-type, auto-compensating wave gauges in three water depths: 61 cm (24 in.), 51 cm (20 in.), and 41 cm (16 in.). Four wave spectra were also generated: Darbyshire, I.T.T.C., Pierson-Moskowitz, and JONSWAP.

The experiments consisted of passing waves through the pile breakwater and measuring both incident and transmitted wave heights. The models were built using steel conduit to assure rigid and uniform piles. Two sizes of conduit were used: 3.0 cm diameter (1-3/16 in.) and 2.4 cm diameter (15/16 in.). Four models were employed as shown in Table I.

TABLE I. Dimensions of Pile Breakwaters

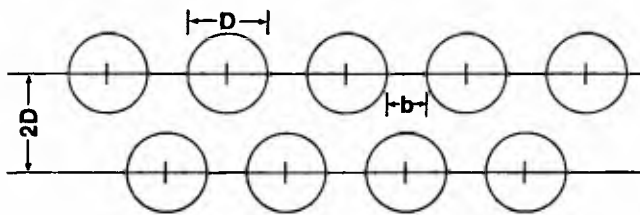
Pile Diameter (D)		b/D	Distance Between Rows	
(cm)	(in)		(cm)	(in)
2.4	15/16	0.1	2 (D) = 4.8	1-14/16
3.0	1-3/16	0.2	2 (D) = 6.0	2-3/8
2.4	15/16	0.1	2 (D) = 4.8	1-14/16
3.0	1-3/16	0.2	2 (D) = 6.0	2-3/8

Procedure and Analysis

Wave height measurements were made with auto-compensating wave gauges. One gauge was placed upstream of the pile array and another downstream of the breakwater. For tests with lower wave reflections, the carriage-mounted upstream gauge was moved through at least one wave length to delineate the envelope of incident and reflected waves. The incident wave height was computed from the recorded wave envelope. When high reflections occurred, the



Figure 1. Wave transmission through a pile breakwater in a glass-walled wave channel.



D - PILE DIAMETER

b - PILE SPACING

RATIO (b/D) CHOSEN TO BE 0.10, AND 0.20

Figure 2. Definition sketch for pile geometry.

significant wave height was computed from a stationary gauge using a record of 21 waves. All of the irregular wave spectra tests were measured with a stationary gauge. Significant wave heights were computed for direct comparison with results previously obtained for a single-row breakwater.

Results

Sample plots of dimensionless wave transmission (H_c/H_i) as a function of water depth to incident wave height ratio are shown in Figures 3 and 4. The increase of wave transmission with an increase in wave period and d/H ratio (up to 25) can be seen in these figures. As anticipated, the smaller the gap ratio, the lower the wave transmission. Reducing the gap space from 20 to 10 percent resulted in transmission for a gap ratio of b/D = 0.1 being reduced to 60-80 percent of the transmission for a gap ratio of b/D = 0.2. The wave transmission was reduced even more so at lower wave periods.

Plots of dimensionless wave transmission, (H_c/H_i), as a function of d/H were also prepared for random waves (Figures 5-8). Even though scatter occurred, data for the four wave spectra tended to plot together. The curves for the two sizes of pile were similar for the same gap ratios. The reduction in gap spacing from 20 to 10 percent reduced the values of wave transmission by approximately 30 percent.

A comparison was also made between wave transmission data for one row of piles (Truitt and Herbich) and two rows of piles. Both studies were conducted in the same facilities, using the same random waves and the same pile sizes and gap ratios. Figure 9 shows a comparison for a b/D ratio of 0.2 and Figure 10 for a b/D ratio of 0.1. For these plots all data points for the same gap ratio have been plotted together regardless of pile diameter. The data for one row of piles covered a very narrow range of d/H values and the resulting curve represents linear regression of the data. For a gap ratio of b/D = 0.2, wave transmission was reduced by about 15 percent, while for a gap ratio of b/D = 0.1 it was reduced by 5 to 10 percent.

The monochromatic wave data were also analyzed using the dimensionless parameter d/gT^2 where d is the water depth, g is the gravitational acceleration and T is the wave period. Figure 11 which is a plot of wave transmission as a function of d/gT^2 indicates that the wave transmission decreases as d/gT^2 increases. Values of wave steepness H_i/L are also shown next to the individual data points. The general trend is for the wave transmission to decrease as the wave steepness increases.

These data were also compared with a similar breakwater model consisting of one row of piles (Kilpatrick, 1984). This study was performed with slightly different pile diameters: 0.63 cm (4/16 in.) and 1.9 cm (12/16 in.) but with the same gap ratios (0.1 and 0.2). It has already been shown that pile diameter has a minimal effect on transmission and that the b/D (gap ratio) is the more important variable. Several plots of wave transmission as a function of d/gT^2 for the monochromatic waves present a comparison between the single- and double-pile breakwaters (Figures 12-15).

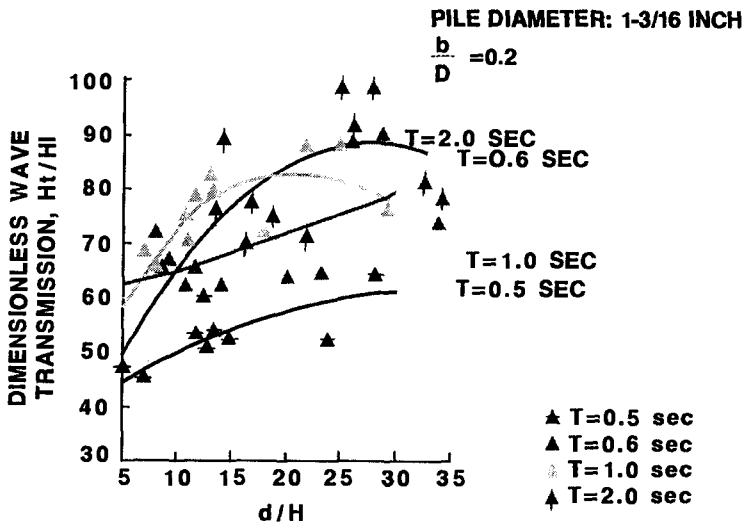


Figure 3. Dimensionless wave transmission as a function of depth to wave height ratio for four wave periods. $D = 3.0$ cm (1-3/16 in.), $b/D = 0.2$, two rows. Monochromatic waves.

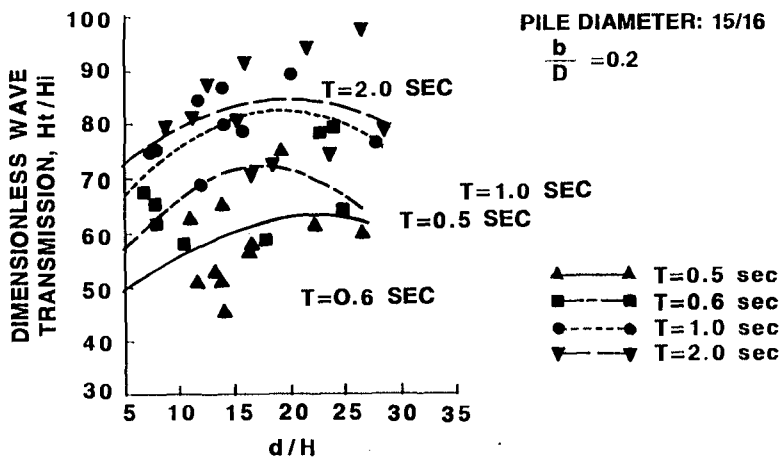


Figure 4. Wave transmission as a function of depth to wave height ratio for four wave periods. $D = 2.4$ cm (15/16 in.), $b/D = 0.2$, two rows. Monochromatic waves.

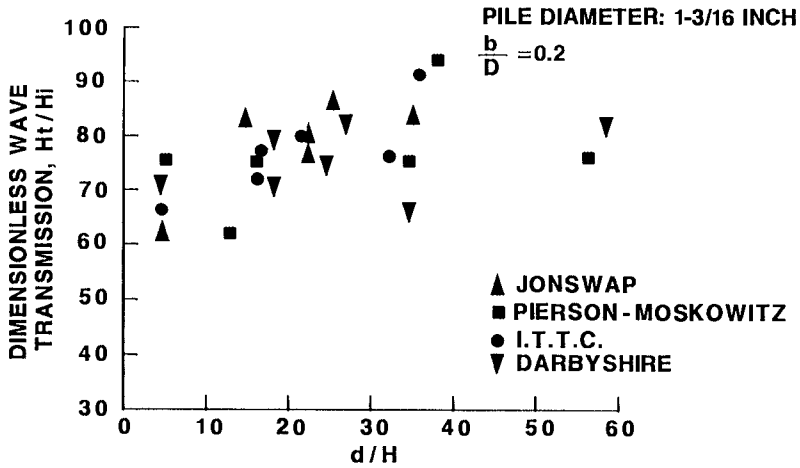


Figure 5. Wave transmission as a function of water depth to wave height ratio for random waves. $D = 3.0$ cm (1-3/16 in.), $b/D = 0.2$.

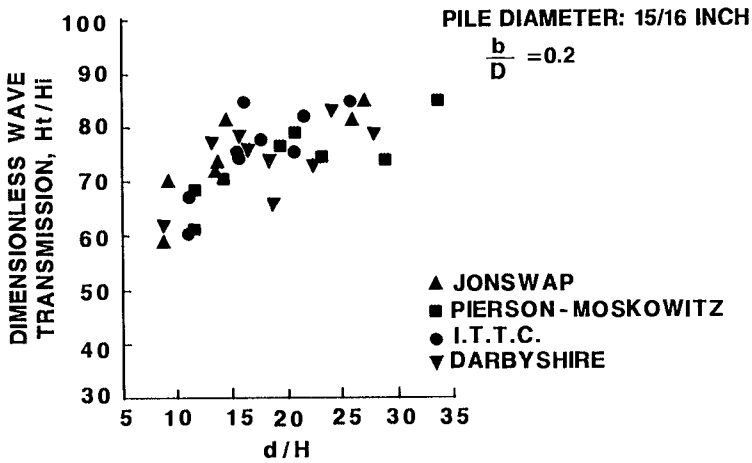


Figure 6. Wave transmission as a function of water depth to wave height ratio for random waves. $D = 2.4$ cm (15/16 in.), $b/D = 0.2$.

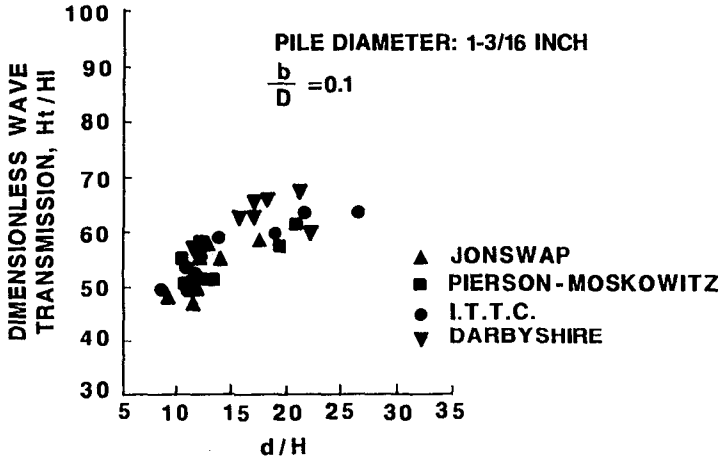


Figure 7. Wave transmission as a function of water depth to wave height ratio for random waves. $D = 3.0$ cm (1-3/16 in.), $b/D = 0.1$.

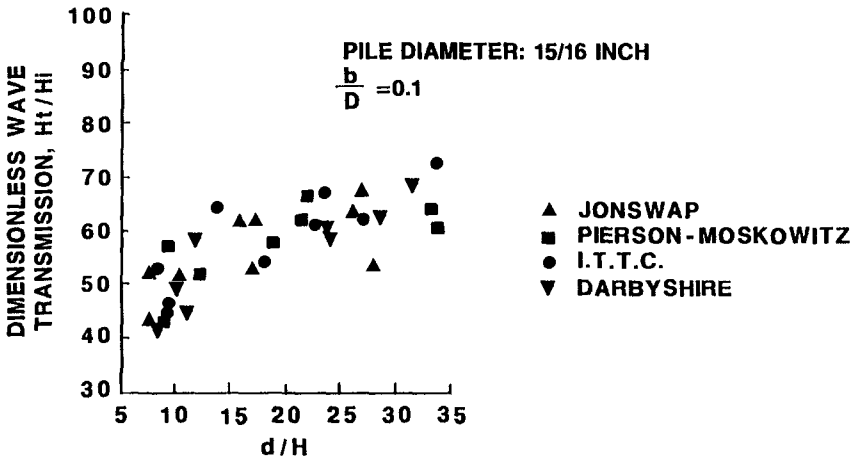


Figure 8. Wave transmission as a function of water depth to wave height ratio for random waves. $D = 2.4$ cm (15/16 in.), $b/D = 0.1$.

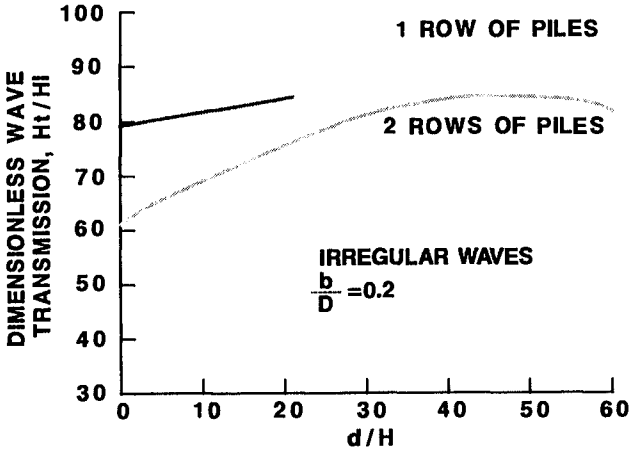


Figure 9. Wave transmission for one and two rows of piles. Random waves, $b/D = 0.2$.

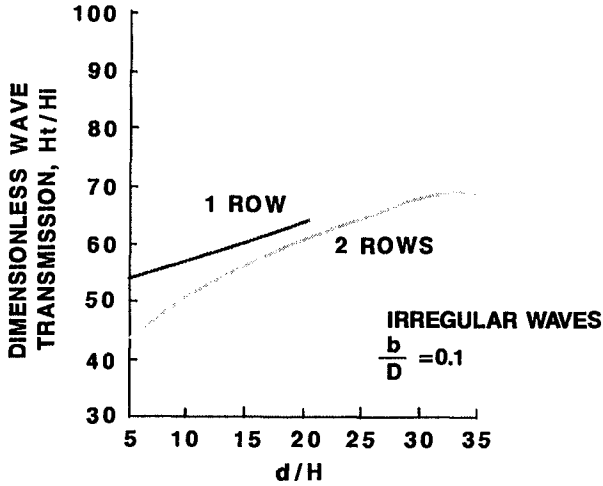


Figure 10. Wave transmission for one and two rows of piles. Random waves, $b/D = 0.1$.

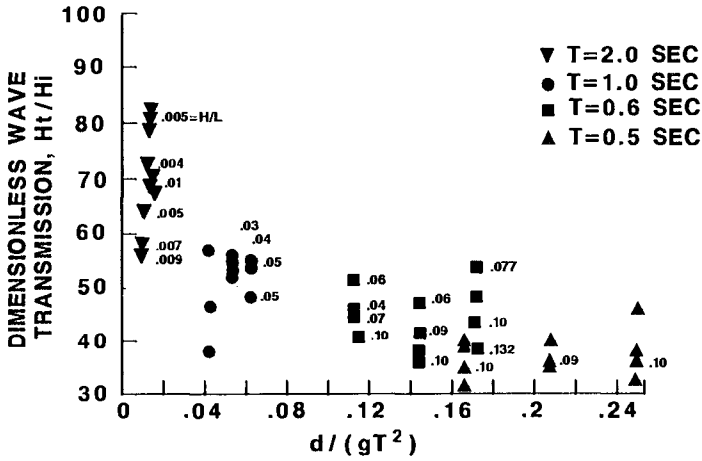


Figure 11. Wave transmission as a function of relative depth ratio for four wave periods. Monochromatic waves.
 $D = 3.0 \text{ cm (1-3/16 in.)}$, $b/D = 0.1$.

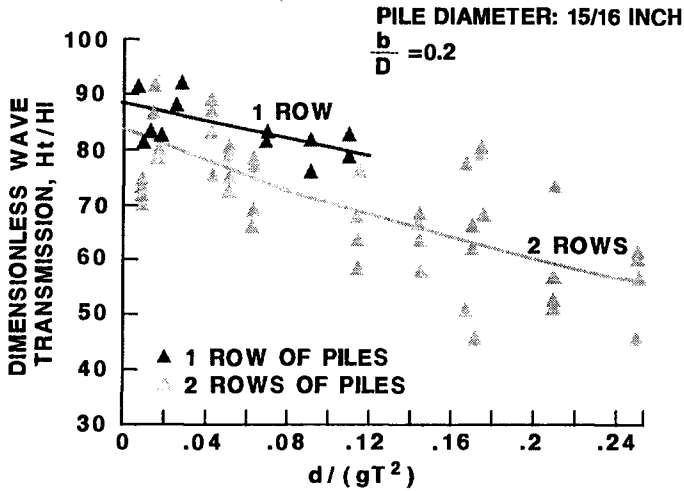


Figure 12. Wave transmission as a function of relative depth ratio for one and two rows of piles. Monochromatic waves.
 $D = 2.4 \text{ cm (15/16 in.)}$, $b/D = 0.2$.

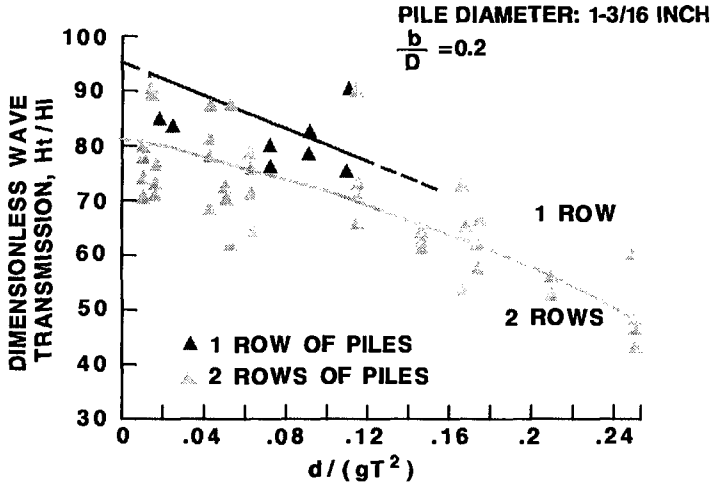


Figure 13. Wave transmission as a function of relative depth ratio for one and two rows of piles. Monochromatic waves. $D = 3.0$ cm (1-3/16 in.), $b/D = 0.2$.

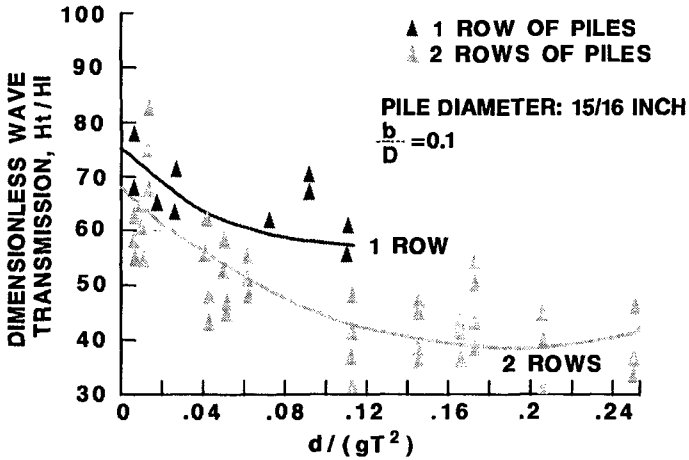


Figure 14. Wave transmission as a function of relative depth ratio for one and two rows of piles. Monochromatic waves. $D = 2.4$ cm (15/16 in.), $b/D = 0.1$.

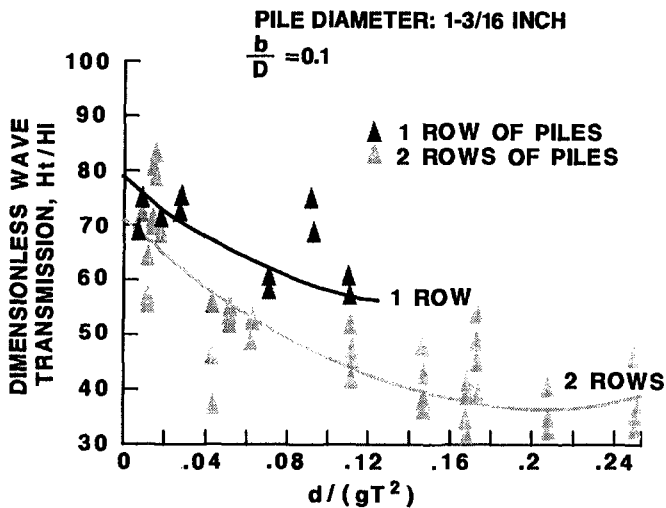


Figure 15. Wave transmission as a function of relative depth ratio for one and two rows of piles. Monochromatic waves. $D = 3.0$ cm (1-3/16 in.), $b/D = 0.1$.

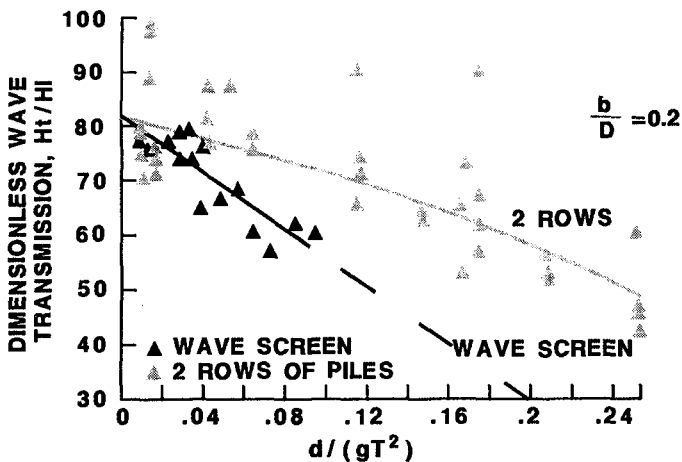


Figure 16. Wave transmission as a function of relative depth ratio. A comparison between two rows of piles and a wave screen.

The results were also compared with wave transmission data presented by Allsop and Kalmus (1985) for wooden wave screens. An arrangement of wooden wave screens was proposed to provide the wave protection for a new marina at Plymouth, United Kingdom. The wave screen breakwater consisted of vertical, rectangular slats with a gap ratio of 0.2. Experiments were performed with irregular wave spectra. The results were published for wave transmission as a function of wave frequency. These results could not be directly compared with the random wave pile experiments because the wave period was not measured for the random wave tests. However, the wave screen results were compared with the monochromatic wave pile experiments. Caution should be used when comparing these two sets of data. The wave screen experiments were conducted using irregular waves, a 8.6 meter water depth, 12 meter long slats and 3 to 12 second wave periods. The wave screen allowed less transmission than the pile breakwater. The results of both experiments agree better at smaller values of d/gT^2 and diverge as the value of d/gT^2 increases (Figure 16).

Conclusions

1. Wave transmission increases as d/H (water depth/wave height ratio) increases
2. Wave transmission for monochromatic waves increases as the wave period increases.
3. Wave transmission decreases as H/L (wave steepness) increases.
4. Wave transmission for monochromatic waves decreases as d/gT^2 (water depth/gravitational acceleration (wave period)²) values increase.
5. For a 10 percent gap ratio, the addition of a second row of piles reduced the wave transmission by 5 to 10 percent.

References

- ALLSOP, N.W.H. and KALMUS, D.C. (1985), Plymouth Marine Events Base: Performance of Wave Screens, Report No. Ex 1327, Hydraulics Research, Wallingford, U.K.
- HAYASHI, T., et al. (1966), Hydraulic Research on Closely Spaced Pile Breakwaters, Proceedings of the 10th Coastal Engineering Conference, Vol. II, Chapter 50, pp. 873-884.
- KILPATRICK, W.S. (1984), Wave Transmission Through a Row of Rigid, Vertical Piles, Unpublished report, Ocean Engineering Program, Texas A&M University.
- TRUITT, C.L. and HERBICH, J.B. (1987), Transmission of Random Waves Through Pile Breakwaters, Ch. 169, Proc. 20th International Conference on Coastal Engineering, ASCE, Taipei, Taiwan, pp. 2303-2313.
- WIEGEL, R.L. (1961), Closely Spaced Piles as a Breakwater, Dock and Harbour Authority, Vol. 42, No. 491.

CHAPTER 166

GEOHYDRAULIC INVESTIGATIONS OF RUBBLE MOUND BREAKWATERS

BÜRGER, W.; OUMERACI, H.; PARTENSKY, H.W.

Universität Hannover
Sonderforschungsbereich 205
Appelstrasse 9A, D-3000 Hannover 1, F.R.G.

1. Introduction

Due to the increase of ship sizes in recent decades a number of harbours and terminals have been built in deeper waters. Accordingly, the structures which have to provide protection against wave action become higher, too. In most cases, these protective structures are of the rubble mound type. Under such conditions the flow induced by waves within the breakwater and the related geotechnical behaviour of the rubble mound fill become more significant for the overall stability and should be considered in the design.

In addition, it is known that the scales usually adopted in hydraulic models (1:30 to 1:60) for investigating the stability of large rubble mound breakwaters generally lead to scale effects with respect to the flow field inside the breakwater. This means that small-scale model tests are not appropriate for investigating the internal flow patterns or for evaluating the pore pressure field induced by the incident waves in the core material.

Because of the uncontrolled conditions in the prototype, and since the actual permeability of the prototype rubble mound fill cannot be predicted (segregation, settlement, variation in grading, etc.), the use of large-scale physical models seems to be the most promising method for basic investigations of this kind. Moreover, the results of such large-scale model tests may be used to validate the usual smaller scale models and to calibrate numerical models.

Therefore, it is one of the objectives of our research programme on rubble mound breakwaters, which started in 1987, to concentrate on the evaluation of the wave-induced flow and pore pressure distribution within the breakwater.

The hydraulic model investigations have been essentially conducted in the Large Wave Channel in Hannover, F.R.G., and will be terminated in December 1988. It is the main purpose of this paper to present the first results of these model tests. However, a brief literature review related to the flow within rubble mound breakwaters and its effect on the overall stability is first given in order to show the necessity of developing reliable tools for the prediction of the actual internal flow field induced by storm waves.

2. Literature review

BARENDS et al. (1983) have demonstrated the importance of the internal flow field on the geotechnical stability of rubble mound breakwaters and applied a numerical model describing this flow for a number of existing breakwaters (BARENDS, 1985). Important improvements to this model were suggested by HANNOURA and Mc.CORQUODALE (1985). However, the reliability of such models is still limited, mainly due to the difficulties in simulating the complex phenomena involved, and to the lack of proper calibration. In this respect ALLSOP & WOOD (1987) have concluded from their most interesting and comprehensive literature review that there have been significant advances in the numerical modelling of the internal flow conditions in recent years, whereas measurements are extremely sparse.

On the other hand, measurements on small-scale model are not reliable because of the scale effects resulting from the lower permeability of the model core material. LE MEHAUTE (1957/1958) was the first to demonstrate the fundamental importance of a proper similitude of the rubble core permeability when investigating wave transmission aspects. The influence of core permeability on the stability of the armour layer has been demonstrated by BRUUN (1985), TIMCO et al. (1984) and VAN DER MEER (1985).

Although a number of investigations (LE MEHAUTE, 1957; DELMONTE, 1970; WILSON, 1971; KOGAMI, 1978) have been carried out on scale effects in modelling wave-induced flow within and through rubble mound structures, there is still no reliable method for the quantification and correction of these effects. The approach using scaling factors in the FROUDE modelling of the core material, as suggested for instance by LE MEHAUTE (1957/58), JENSEN & KLINTING (1983), and OUMERACI (1984), is very limited due to the unsteadiness of the actual internal flow; i.e. it is only valid for a specific hydraulic gradient.

In addition, it is known that slip-circle stability calculations according to BISHOP's method should include the excess pore pressure build-up induced by storm waves within the rubble mound structure and underneath the breakwater toe (BARENDS, 1984; BARENDS & CALLE, 1985). The most important characteristics needed for these calculations are the shear resistance parameters of the materials composing the foundation soil and the breakwater, as well as the maximum pore pressure distribution along a potential slip surface. Prototype measurements of the pore pressures within rubble mound breakwaters (HAKIMI et al, 1984) and underneath the breakwater (VAN IMPE, 1988) have also been performed.

However, a simple reliable method for assessing maximum pore pressure distribution under extreme wave loading and which is suitable for design purposes is not yet available. Such a method should include only the most relevant input parameters, i.e. the water depth and the incident wave parameters in front of the breakwater, the geometry of the structure and the hydraulic properties of the material composing the breakwater and the subsoil.

Well-calibrated numerical and hydraulic scale models may become reliable tools for developing simple relationships between these input parameters and the resulting excess pore pressure. Since the actual permeability of the prototype core and filter material cannot be predicted, the use of large-scale models as described below is most suitable for such calibration.

3. Experimental set-up

In the present research programme much effort has been concentrated upon the development of suitable instrumentation for measuring pore and soil pressure as well as the wave motion (wave run-up) directly at the interfaces between the various layers.

After small-scale tests were performed in the wave flume of the Franzius-Institut (110 m x 2.2 m x 2.0 m) with maximum wave heights up to 0.40 m, the same model was built in the Large Wave Channel in Hannover (320 m x 7.0 m x 5.0 m) in a scale 3.7 times larger. The tests are carried out by using monochromatic waves and JONSWAP-Spectra with $\gamma = 3.3$ and a Groupiness-factor of $GF = 0.77$. The wave maker is equipped with a SEASIM-wave absorption control. Maximum wave heights up to 2.5 m can be generated.

The waves are recorded in deeper water as well as in front of the structure by a 3 wave gauge-system in order to determine the incident and reflected wave energy. The position of the various wave gauges used is shown in Fig. 1.

In order to determine the variation of the wave-induced stress underneath the breakwater toe, three soil pressure cells and three pore pressure cells are installed in the sand bed layer. In addition, twenty pore pressure gauges are placed inside the rubble mound structure in such a way that the pore pressure distribution and the required boundary values for the calibration of numerical models can be gained with sufficient accuracy (Fig. 2).

One of the pore pressure gauges is shown in Figs. 3 and 4.

In order to follow the incident waves propagating in the armour and under-layer and penetrating into the core material three specially designed wave run-up gauges are also installed along the slope of the tetrapod armour, of the under-layer and of the core material (Fig. 2 and Fig. 6). The grain size distribution of the core material is shown in Fig. 5.

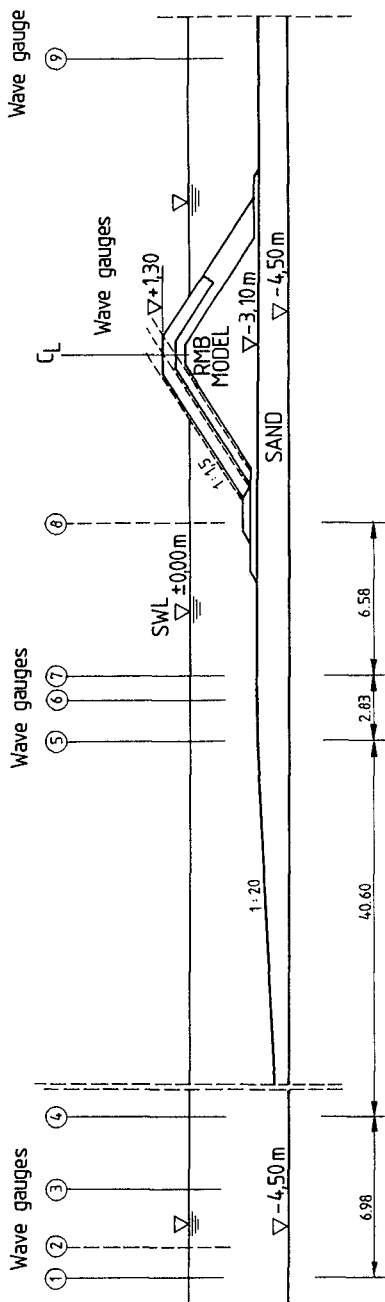


Fig. 1
Rubble mound breakwater model in the Large Wave Channel

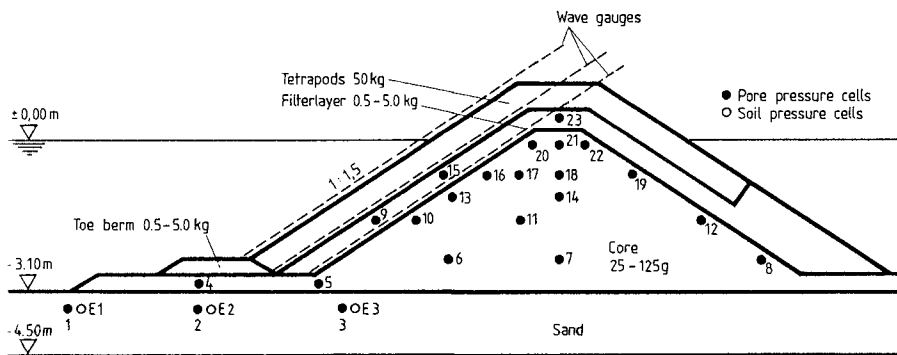


Fig. 2

Cross section of the instrumented large-scale model

4. First experimental results

Some of the first results of the performed model tests are presented in the following. A more detailed presentation and analysis of the final results will be published as soon as the test programme has been completed.

4.1 Wave reflection

Since wave reflection and energy dissipation are interrelated, and since little is known about the reflecting properties of tetrapod armours, the test results are first analysed with respect to wave reflection. For the range of wave conditions tested ($2.5 \leq \xi < 6.0$), the following formula has been derived for the reflection coefficient K_R :

$$K_R = \frac{H_I}{H_R} = \frac{0.6 \xi^2}{\xi^2 + 12} \quad (1)$$

in which:

H_I , H_R = incident and reflected wave height, respectively

ξ = surf similarity parameter

L = wave length

α = seaward slope angle of the breakwater

The surf similarity parameter is defined as follows:

$$\xi = \tan \alpha / \sqrt{H/L} \quad (2)$$

A reflection coefficient of $K_R = 0.20$ to 0.45 was obtained for the range of wave conditions tested.

These reflection coefficients are comparatively lower than those given by the relationship proposed by CERC (SEELIG, 1983) for natural stone armours.

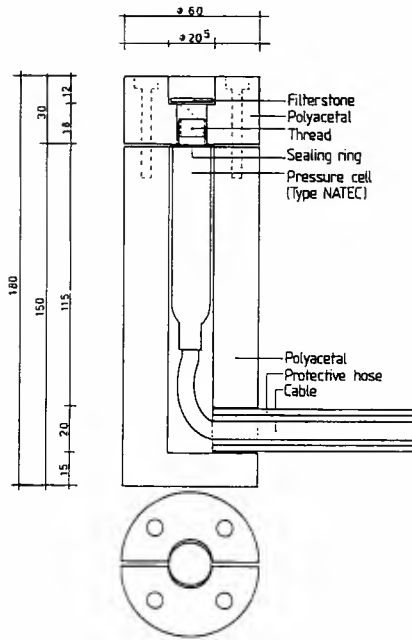


Fig. 3
Pore pressure gauge

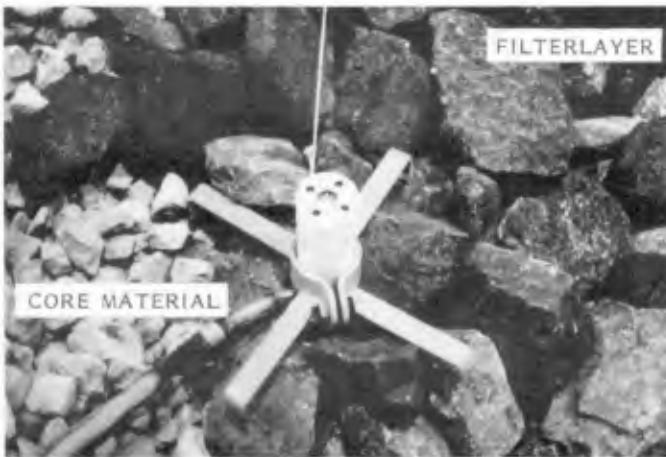


Fig. 4
Installed pore pressure gauge

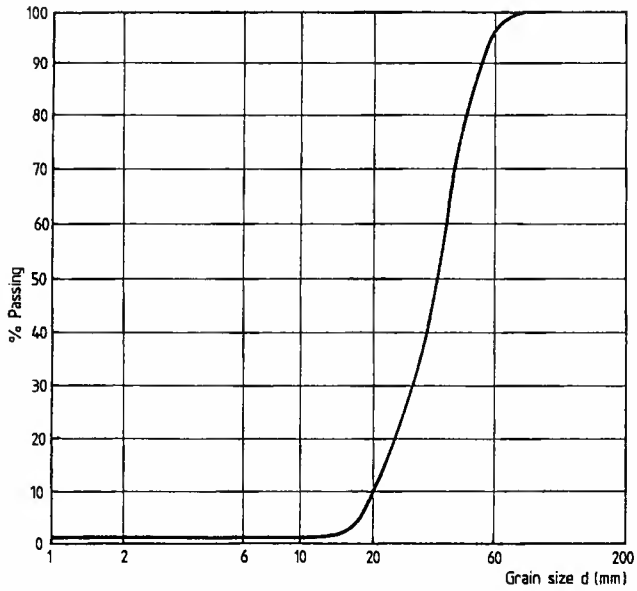


Fig. 5
Grain size distribution of the core material



Fig. 6
Pore pressure gauge and wave run-up gauge

4.2 Wave-induced pore pressure

One of the main objectives of the investigations by means of large-scale model tests is to measure and study the wave motion directly at the seaward face of the structure and the resulting wave-induced excess pore pressures inside the breakwater.

Typical examples of the waves simultaneously recorded by the 3 resistance-type wave gauges installed at the surface of the armour layer (WG 1), at the interfaces between the armour and filter layer (WG 2) and between the filter layer and the core material (WG 3), are given in Fig. 7 for incident waves with $H_s = 0.73$ m and $T_p = 4.5$ s in front of the breakwater. The corresponding pore pressure fluctuations induced in a horizontal plane and recorded at pressure cells PC 15-PC 19 (see Fig. 2 and 6) are shown in Fig. 8.

From these and further records it has been found that, in general:

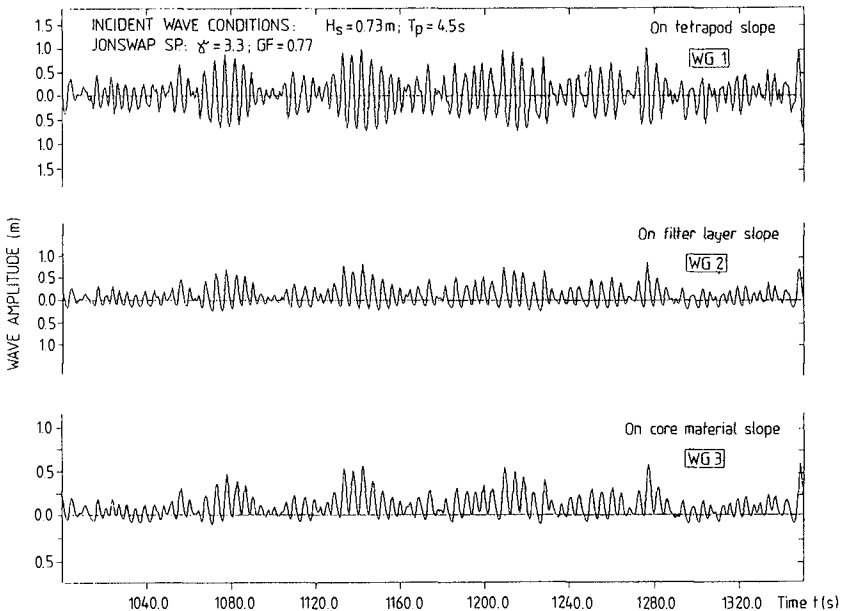


Fig. 7

Wave records at the interfaces
 sea-tetrapode slope, filter layer-core material
 (positions of WG 1, 2, and 3 see Fig. 2)

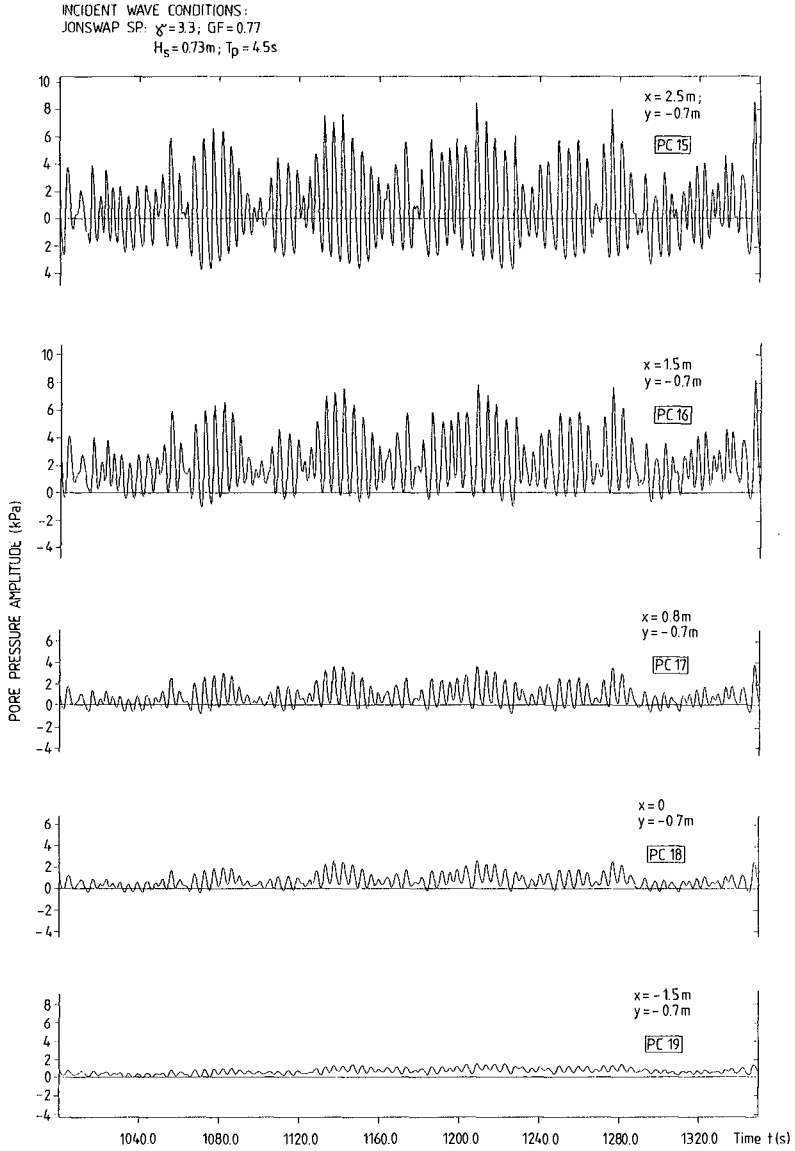


Fig. 8

Pore pressure fluctuations in a horizontal plane
inside the breakwater
(position of the pressure cells see Fig. 2)

- The frequency of the pore pressure fluctuations are of the same order of magnitude as the frequency of the incident storm waves;
- the incident waves induce a rise in the mean water level (setup) inside the rubble mound breakwater when compared with the sea water level outside the structure (10 - 20 % of the incident wave height);
- most of the incident wave energy is dissipated inside the armour and filter layer. The steeper the waves the more pronounced is this dissipation;
- the pore pressure amplitudes inside the breakwater decrease rapidly in the direction of wave propagation. This decay is more rapid for steeper waves.

The horizontal distribution of the maximum amplitudes of the excess pore pressure fluctuations induced by irregular waves at different elevations inside the breakwater and underneath the seaward toe is shown in Fig. 9. It can be seen that, particularly at elevations near the still water level, the maximum pore pressure amplitudes decay exponentially in the direction of wave propagation. Exponential decay of this kind has also been found theoretically by BIESEL (1950) for internal wave amplitudes. Fig. 9 and further similar results show that in deeper planes the amplitude decay becomes less pronounced.

Within the zone underneath the breakwater toe, however, the maximum pore pressure amplitudes tend to increase slightly in the direction of wave propagation. This is probably due to the more pronounced pressure build-up along the breakwater slope.

The distribution of the maximum pore pressure amplitudes at three different vertical profiles is shown in Fig. 10. From this and further results it is found that for the vertical profiles extending above still water level (SWL) the pore pressure amplitudes first increase and then slightly decrease with increasing depth. The maximum pressure amplitude is generally slightly below the still water level and depends upon the characteristics of the incident waves and the position of the vertical profile.

An interesting typical result is also shown in Fig. 11 for the distribution of the maximum pore pressure amplitudes along the slope of the core material and along another profile, parallel to the first, inside the core.

The results suggest, that:

- the pore pressure amplitudes do not decrease significantly in the direction normal to the slope;
- the position of the maximum value of the pressure amplitudes depends greatly on the depth of the profile considered.

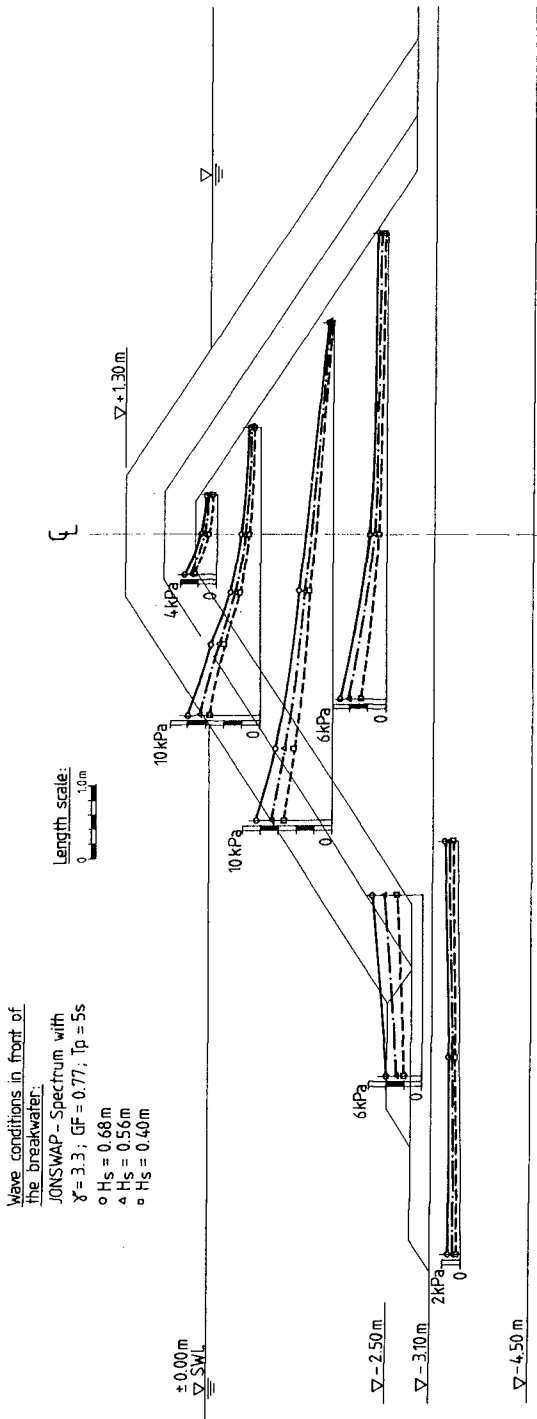


Fig. 9

Horizontal distribution of the maximum excess pore pressure amplitudes induced by irregular waves

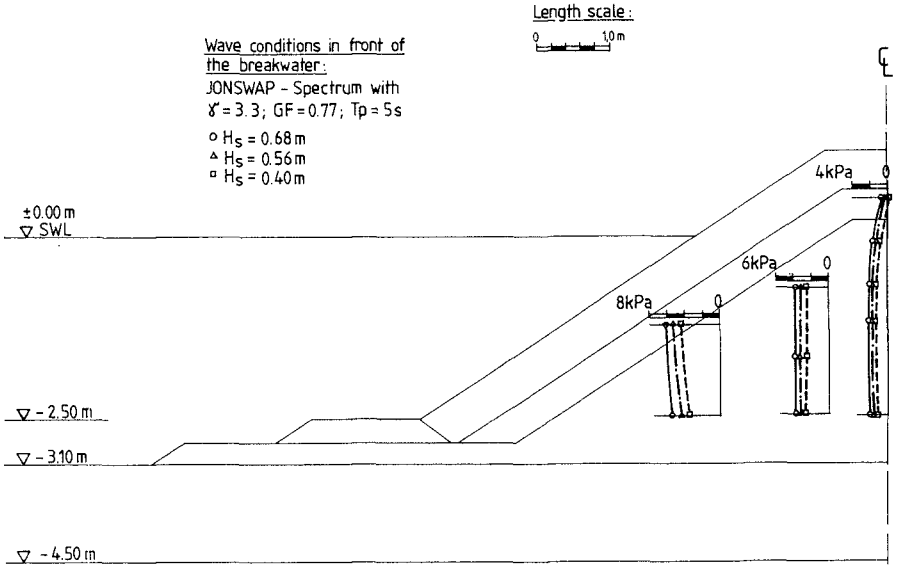


Fig. 10

Vertical distribution of the maximum excess pore pressure amplitudes induced by irregular waves

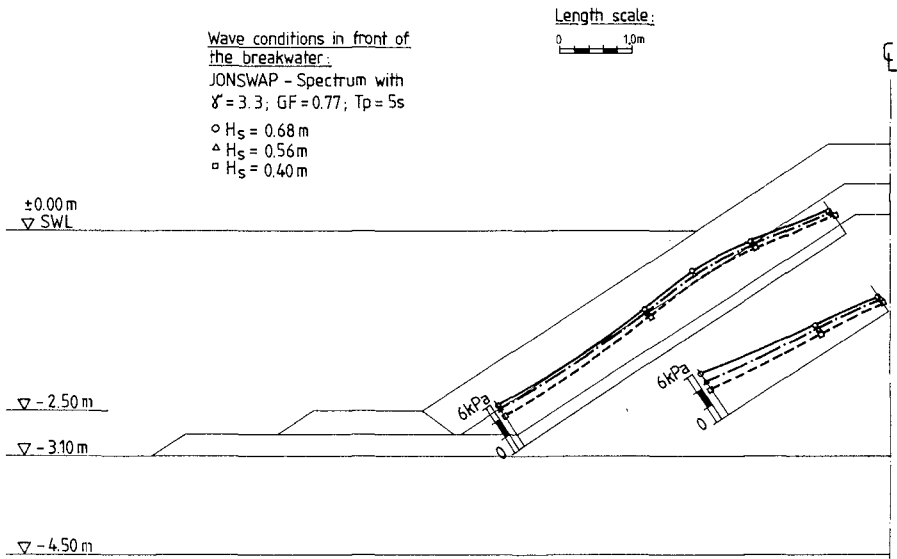


Fig. 11

Distribution of the maximum excess pore pressure amplitudes along the slope of the core material

5. Conclusion and perspectives

For the near future the problem of the wave-induced oscillatory flow inside rubble mound breakwaters will obviously not be amenable to an accurate analytical solution. This is due to a number of complex phenomena involved (breaking, air infiltration, unsteadiness and non-linear resistance of the flow, virtual mass effects, etc.) and uncertainties in the hydraulic properties of the porous media composing the breakwater.

Since a reliable method for quantifying and correcting scale effects in modelling wave-induced internal flow is still lacking and since an improvement and proper calibration of the existing numerical models by using results of large-scale model tests are needed, the analysis of the test results, which is underway, will focus particularly on these two aspects. Nevertheless, the first results and the literature review presented in this paper suggest that:

- Equation (1) for the reflection coefficient related to tetrapod armour layers would still be improved by including the results of small and large-scale model tests in the analysis;
- an empirical relationship between excess pore pressure and wave steepness (or surf similarity parameter) may be derived;
- an empirical or a semi-empirical equation for the decay of the pore pressure fluctuations within the breakwater in the direction of wave propagation should be formulated. For design application (slip-circle calculations), however, there is a need for simple formulae for approximately assessing the wave-induced pore pressures as a function of the water depth and the incident wave parameters in front of the breakwater. Unlike the approach in the hydraulic stability of armour layers, these formulae should be related to maximum wave loading;
- understanding of the interior process may be improved by including the transfer functions between wave and pore pressure fluctuations in the analysis. For the waves, use should be made of the recorded spectra at the interfaces sea-tetrapod slope and filter layer-core material.

6. Acknowledgements

This investigation is a part of a basic research programme in coastal engineering (SONDERFORSCHUNGSBEREICH 205) financed by the German Research Council (DFG). The authors are grateful to Dr. TAUTENHAIN and his staff at the Large Wave Channel, Hannover, for their help in the preparation and performance of the large-scale model investigations.

7. References

- Allsop, N.W.H.; Wood, L.A.: "Hydro-geotechnical performance of rubble mound breakwaters - A literature review". Hydraulics Research Ltd. Rep. SR 98, Wallingford March 1987
- Barends, F.B.T.; Kogel, H.; van der Uijtewall, F.J.; Haganaar, J.: "West-breakwater sines, dynamic-geotechnical stability of breakwaters". Proc. ASCE Conference Coastal Structures' 83, 1983
- Barends, F.B.T.: "Probability of wave induced seabed instability". International Symposium on Maritime Structures in the Mediterranean Sea, Athens, 1984
- Barends, F.B.T. & Calle, E.O.F.: "A method to evaluate the geotechnical stability of off-shore structures founded on a loosely packed seabed sand in a wave loading environment". Proc. of the 4th Intern. Conf. on Behaviour of Offshore Structures (BOSS' 85), Delft, 1985
- Barends, F.B.T.: "Geotechnical aspects of rubble mound breakwaters". Proc. Conf. Breakwaters' 85, ICE, London 1986
- Biesel, F.: "Equations de l'écoulement non lent en milieu perméable". La Houille Blanche, Mars-Avril 1950
- Bruun, P. (editor): "Design and construction of mounds for breakwaters and coastal protection". Elsevier, Amsterdam 1985
- Delmonte, R.C.: "Scale effects of wave transmission through permeable structures". ASCE Proc. of the 13th Conf. on Coastal Eng., Vancouver 1972
- Hakimi, A.; Diouri, A.; Kaissoum, A.: "Contribution empirique à l'étude de la propagation de la houle à l'intérieur des digues". La Houille Blanche No 5, 1984
- Hannoura, A.A.; Mc Corquodale, J.A.: "Rubble mounds: numerical modelling of wave motion". Proc. ASCE, Journal of Waterway, Port, Coastal and Ocean Engineering, Vol. 111, No. 5, Sept. 1985
- Jensen, O.J.; Klinting, P.: "Evaluation of scale effects in hydraulic models by analysis of laminar and turbulent flows". Coastal Engineering, Elsevier, Vol. 7, 1983
- Kogami, Y.: "Researches on stability of rubble mound breakwaters". Coastal Engineering in Japan, Vol. 21, 1978
- Le Mehauté, B.: "Permeabilité des digues en enrochements aux ondes de gravité périodiques". La Houille Blanche, No.6, 1957; No. 2 & 3, 1958
- Oumeraci, H.: "Scale effects in coastal hydraulic models". IAHR Symposium on Scale Effects in Modelling Hydraulic Structures, Esslingen, Sept. 1984
- Seelig, W.N.: "Wave reflection from coastal structures". ASCE Proc. Conf. Coastal Structures, 1983
- Timco, G.W.; Mansard, E.P.D.; Ploeg, J.: "Stability of breakwaters with variation in core permeability". ASCE Proc. 19th Conf. on Coastal Eng., Houston, 1984
- Van der Meer, J.W.: "Stability of rubble mound revetments and breakwaters under random wave attack". Proc. Conf. Breakwaters' 85, ICE, London, 1985

Van Impe, W.F.: " Geotechnische Probleme beim Bau des neuen Hafens Zeebrügge". Geotechnik, 1, 1988

Wilson, K.W.; Cross, R.H.: "Scale effects in rubble mound breakwaters". ASCE Proc. of the 13th Conf. on Coastal Eng., Vancouver, 1972

CHAPTER 167

IRREGULAR WAVE LOADING ON A CONICAL STRUCTURE

Wayne W. Jamieson, Etienne P.D. Mansard and
Geoffrey R. Mogridge¹

ABSTRACT

The horizontal forces, vertical forces and overturning moments exerted by waves on a fixed model of a 45° conical structure are presented. Irregular wave loading tests were conducted for a range of conditions described by base diameter on peak period wave length D/L_p from 0.31 to 1.76, water depth on peak period wave length h/L_p from 0.11 to 0.63, and significant wave height on peak period wave length H_{m0}/L_p up to 0.07.

Time series records, spectral densities and transfer functions for the irregular wave loading tests are used to illustrate the nonlinear nature of the measured wave loads. In most cases, similar trends in wave loading were observed for irregular and regular wave tests. For deep-water waves, the irregular and regular force measurements showed spectral peaks at the second harmonic of the wave frequency even though the waves themselves had relatively small second-order components. However, unlike the regular wave loading results, the fundamental spectral peak frequency for the irregular wave forces occurred at a frequency considerably lower than the peak frequency of the waves. Although linear diffraction theory provided a reasonable estimate of the wave forces for waves of low steepness, larger deviations were often present for higher wave steepness results. Comparison of theory and experiment for overturning moments was generally very poor for most wave conditions.

INTRODUCTION

In recent years numerous designs of offshore structures for drilling and production have been proposed for use in arctic regions. Buslov and Krahl (1983) have described sixty-one conceptual designs for arctic offshore platforms, some of which are currently being constructed, others of which are operational. Some of the designs incorporate large bottom-founded conical-shaped structures

¹ Research Officers, National Research Council of Canada, Hydraulics Laboratory, Montreal Rd., Bldg. M-32, Ottawa, Ontario, K1A 0R6, Canada.

which cause ice sheets to fail predominantly by bending rather than by buckling or crushing, in order to reduce ice loading. Of course, the relatively small area subjected to ice loading near the water surface also minimizes ice forces. The large hull of this type of gravity structure provides resistance against sliding and overturning at its base, but also provides sufficient buoyancy when deballasted so that it can be towed while floating on its hull to another site. Although none of these conical structures have yet been built, they are currently being considered for use in a range of water depths between 10 m and 80 m.

The wave loading on some of these proposed conical structures has been modelled both physically and numerically, but the results are for the most part proprietary and as a result, published data is very limited. Isaacson (1982) has published some results of numerical calculations for the case of a surface-piercing 45° conical structure utilizing the body's vertical axisymmetry to reduce considerably the computational effort required for bodies of arbitrary shape. Jamieson et al. (1985) have carried out regular wave loading measurements on a model of a surface-piercing 45° conical structure. The model was a simple axisymmetric structure which somewhat characterized the shape of proposed prototype conical structures, could easily be modelled both physically and mathematically and the results could be published without infringing on any proprietary designs. The tests indicated extremely nonlinear wave loading resulting in considerable differences between experiment and linear diffraction theory particularly for higher steepness waves. In this paper, the horizontal forces, vertical forces and overturning moments exerted by irregular waves on the same 45° conical model are presented. The irregular wave loading results are compared to those measured for regular waves and those computed by linear diffraction theory.

EXPERIMENTAL SETUP

Figure 1 shows a photograph of the conical model. It was constructed of 6 mm thick plexiglass in the shape of a 45° right circular cone, 125.5 cm in diameter at the base (see Figure 2). The model was tested in a water depth of 44.6 cm. Assuming a scale of approximately 1:100, the model corresponds to a full scale 45° conical gravity platform with a 126 m diameter at the base, resting in a water depth of 45 m. Model dimensions will be used throughout this paper. For structural considerations, the base of the model was slightly rounded rather than sharp-edged. Figures 3 and 4 show a photograph and schematic views respectively of the wave flume and the experimental setup. The model was installed 11 m from the wave generator in the centre of the 13 m wide portion of the wave flume. The outer circumference of the model base was sealed and the underside of the model was vented to atmospheric pressure so that no dynamic wave pressures were experienced underneath the model. This condition allowed the measurement of wave loading due to fluid pressures on the upper surfaces of the model, which is all that is of interest in the present study, because under full scale



Figure 1. Model of Conical Structure

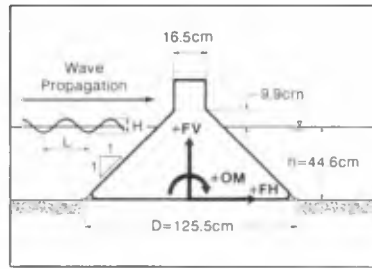


Figure 2. Model Dimensions and Sign Convention for Wave Loads

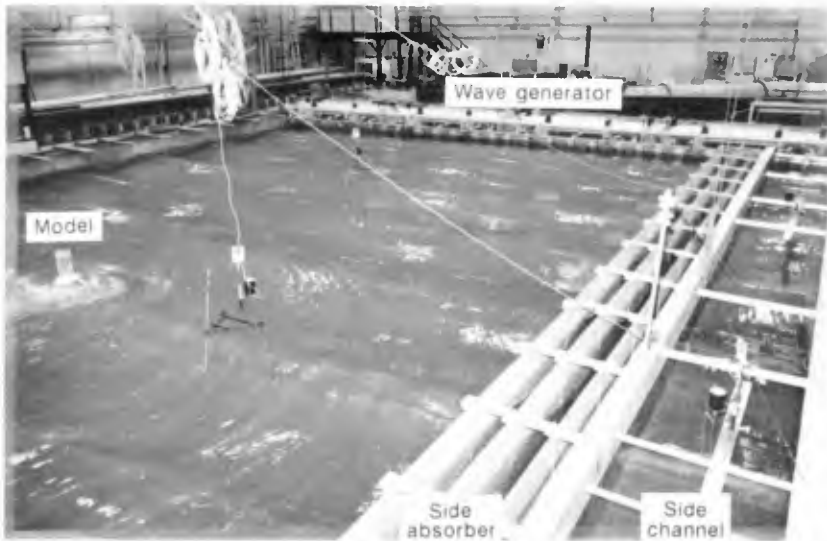


Figure 3. Photograph of Wave Flume and Experimental Setup

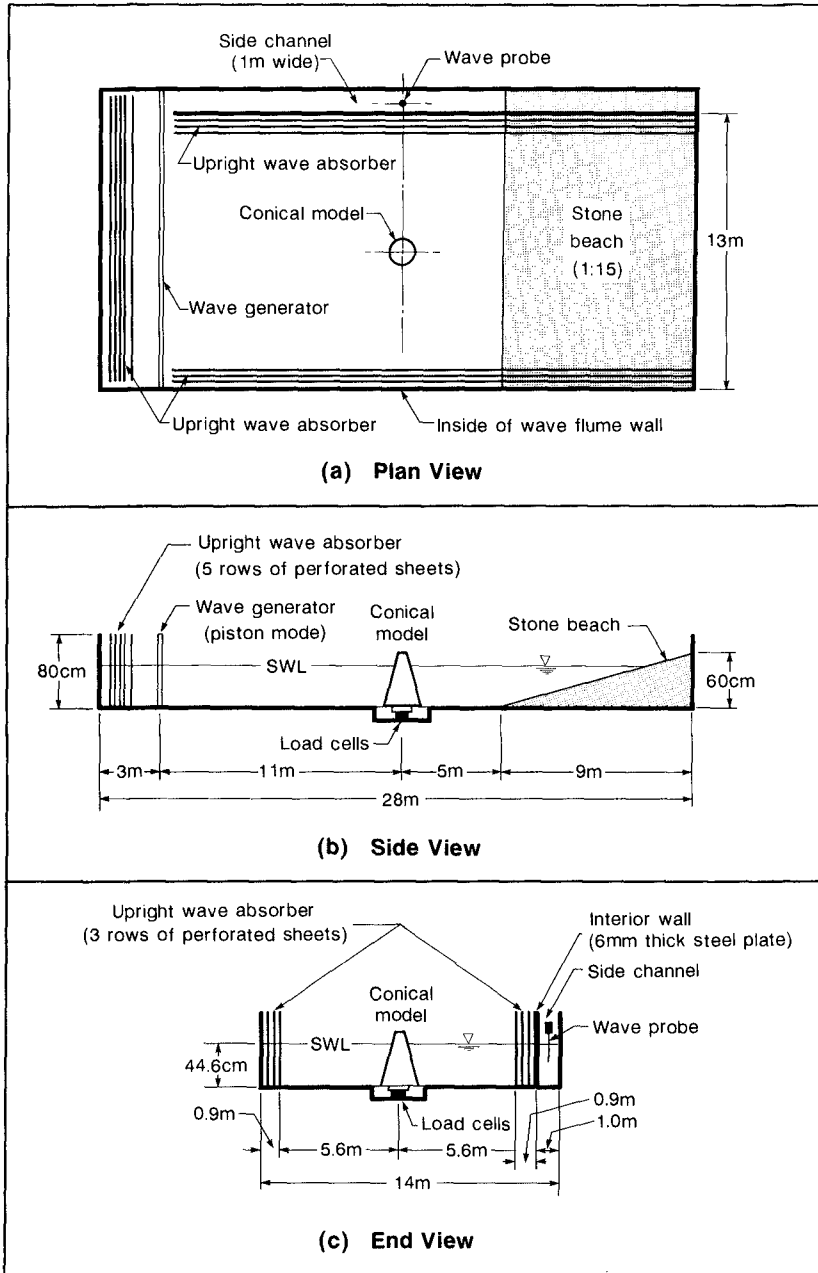


Figure 4. Schematic of Wave Flume and Experimental Setup

conditions the wave pressures underneath the structure propagate through a porous foundation rather than through an open gap as in a model study.

The base of the model was mounted to a three-component load cell dynamometer system which was in turn bolted to the bottom of a circular pit located below the concrete floor of the wave flume. The dynamometer system was designed so that three individual load cells could be bolted together in a configuration which allowed the measurement of horizontal force (FH), vertical force (FV) and overturning moment (OM). The three load cells were constructed of steel and designed by the Hydraulics Laboratory to have a very high stiffness-sensitivity product with only small cross-coupling errors. Each of the load cells used semiconductor strain gauges, which were thermally compensated and thoroughly waterproofed to minimize environmental problems caused by temperature changes and high humidity. They were initially calibrated individually in air on a calibration rig. Combined nonrepeatability, nonlinearity and hysteresis of the load cells were less than $\pm 0.5\%$. During the testing program, the load cell calibrations were checked once a day by applying known loads to the model by means of a system of low-friction pulleys. Natural frequencies of vibration of the total system were measured by applying a step load to the model in both vertical and horizontal directions, and recording the voltage outputs from each load cell sampled at a rate of 500 samples/second. With 44.6 cm of water in the wave flume, the natural frequencies of vibration were 30 Hz, 13 Hz and 30 Hz as measured by the horizontal and vertical force load cells, and the torque load cell, respectively.

In this paper, the measured wave forces and overturning moments on the conical model have been related to the incident wave conditions, that is, the waves that occur at the location of the model with the model removed. To eliminate the time required to regenerate the waves with the model removed, all incident waves were measured by a capacitive wire wave probe located alongside the conical model in the 1 m wide side channel (see Figures 3 and 4). The side channel was separated from the main channel by a 6 mm thick solid steel plate wall.

Voltage signals from the test instrumentation went to a high-speed data acquisition package consisting of programmable-gain differential amplifiers, a high-speed solid-state multiplexer and an analog-to-digital converter. The output from the wave probe required no amplification; however, the two force load cell signals and the torque load cell output were amplified 200 times. A mini-computer was used for the acquisition, processing, plotting and storage of experimental data.

The waves generated by the wave machine moved along the length of the flume past the model and were effectively absorbed by the 1 in 15 sloped stone beach at the end of the flume shown in Figure 4. Wave reflection coefficients (ratio of reflected wave height to incident wave height expressed as a percentage) for this beach were less than 5% for all wave conditions tested.

Figures 3 and 4 show the placement of upright wave absorbers along the side walls of the 13 m wide main channel. Each of these side absorbers consisted of three rows of perforated vertical sheets placed over a distance of 90 cm. The porosity of the rows of sheets decreased towards the rear of each absorber. The design is based on a new type of efficient upright wave absorber developed at the Hydraulics Laboratory of the National Research Council of Canada (Jamieson and Mansard (1987)). It is particularly suitable for laboratory wave basins where (1) limited space is available for the installation of absorbers, (2) testing at variable water depths is essential without having to make adjustments to the absorber, and (3) reflected wave energy from the absorber must be minimized for a wide range of water depths, wave heights and wave periods (wave reflection coefficients of less than 5%). The placement of the rows of perforated sheets in the side absorbers is such that the waves generated from the wavemaker moved along the length of the flume through the side absorbers quite freely but the waves radiated off the conical model were effectively absorbed. The attenuation of the waves as they propagated in the main channel was negligible, so that the side channel wave probe effectively measured the incident wave heights. After a test, the waves in the flume were attenuated in less than 5 minutes compared to a settling down period of more than 30 minutes if only solid side walls were used. An upright wave absorber was also used to provide effective wave absorption over a distance of 1.5 m between the rear of the wave generator and the back wall of the wave flume.

EXPERIMENTAL METHOD

The irregular waves generated in this study were synthesized using the random phase spectrum method. It is a technique which pairs the amplitude spectrum derived from a given target spectral density with a randomly selected phase spectrum, and creates a time series by inverse Fourier transformation (Funke and Mansard (1984)). JONSWAP spectral densities with a peak enhancement factor $\gamma = 3.3$ were used as target spectra. Each time series was synthesized with a record length of 300 s, resulting in approximately 150 waves for the lowest spectral frequency and about 450 waves for the highest.

A number of sea states with different spectral peak frequencies ($f_p = 0.48, 0.69, 0.80, 0.95, 1.02, 1.16, 1.33$ and 1.48 Hz) were generated. For each peak frequency, the significant wave height H_{m0} of the sea state was varied in order to evaluate the influence of nonlinearities due to wave steepness. This was achieved by rescaling the time series to match the desired variance. A minimum of four significant wave heights having wave steepnesses (H_{m0}/L_p) between 0.01 and 0.07 were run for each spectral peak frequency listed above. Since only the variance of the sea state was changed, other parameters such as groupiness factor, ratio of maximum to significant wave heights etc. were kept constant.

Sampling of the data was commenced three minutes after the first waves had passed the model. For each irre-

gular wave test, the incident wave profile in the side channel and the wave loads (FH, FV and OM) were sampled at a rate of 10 samples per second, for a total record length of 300 seconds. The water depth was maintained at 44.6 cm throughout the entire testing program. Total forces and overturning moments about the base of the model (see Figure 2) were computed and plotted along with the incident wave profile measured in the side channel.

Spectral analysis of the wave loads and the incident wave record was carried out for each test. The spectral analysis used in this study is an algorithm which performs a Fourier transform over the entire record length and computes the spectral ordinates by squaring and summing the complex Fourier coefficients. Smoothing of the spectrum was carried out by averaging the adjacent spectral estimates using a rectangular window.

Transfer functions of the irregular wave loads were calculated for each test as follows:

$$\text{TRF}(f) = [\text{S}_{\text{WL}}(f) / \text{S}_{\text{IW}}(f)]^{1/2}$$

where

TRF(f) = Transfer function of the wave load (FH, FV or OM)
 $\text{S}_{\text{WL}}(f)$ = Spectral density of the corresponding wave load
 $\text{S}_{\text{IW}}(f)$ = Spectral density of the incident wave (H).

Regular wave tests were carried out for the purpose of comparison with the irregular wave tests. Sampling of the data was commenced after ten waves had passed the model. For each regular wave test, the incident wave profile and the wave loads were sampled at a rate of 100 samples per second for a total record length of 50 s. Regular waves were generated for a wide range of frequencies ($f = 0.48, 0.60, 0.69, 0.80, 0.88, 0.95, 1.02, 1.16, 1.33$ and 1.48 Hz). A minimum of six wave heights having wave steepnesses (H/L) between 0.01 and 0.10 were generated for each wave frequency listed above.

EXPERIMENTAL RESULTS AND DISCUSSION

Time Series of Wave Loading

Figure 5 shows typical time series measurements of horizontal force (FH), vertical force (FV), overturning moment (OM) and the incident wave measured in the side channel (H) for two irregular wave tests of low wave steepness ($H_m/L_p = 0.02$). The time series results shown are representative of the tests carried out for intermediate-water depths ($h/L_p = 0.21$) and deep-water depths ($h/L_p = 0.51$). Only a 20 s portion of the 300 s record length is shown for each of the tests. The time series of the wave loading results for the intermediate-water depth ($h/L_p = 0.21$) results are smooth and one would expect the spectral analysis of the wave loading to give the same peak frequency as the waves. For the deep-water results ($h/L_p = 0.51$), a similar observation is evident for the overturning moment (OM). However, for the force records (FH and FV) both high and low frequency components are evident which are not identifiable in the wave record. Spectral

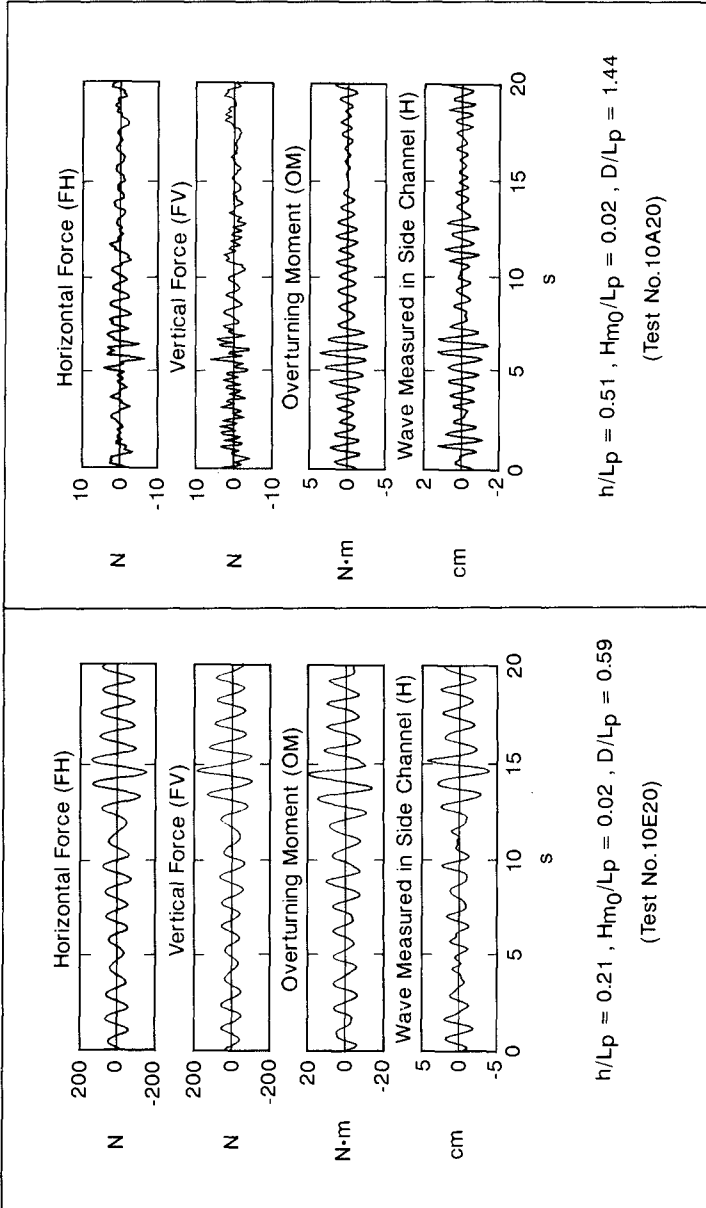


Figure 5. Typical Time Series Measurements for Irregular Wave Tests

analysis results of the data is discussed in the next section.

Spectral Densities of Wave Loading

Spectral density measurements for irregular and regular wave tests for a relative depth of 0.21 are shown in Figure 6. This illustrates the type of irregular wave loading commonly observed for intermediate-water depths, i.e. the peak frequency (0.80 Hz) of the wave forces (FH and FV) and the overturning moment (OM) is the same as that of the waves. In the time series for this test (shown in Figure 5) it can be seen that the frequency of the wave loads and the waves is about the same. The spectral density results for the regular wave test in Figure 6 also shows that for an intermediate-water depth, $h/L = 0.21$, the peak frequency of the wave loads coincides with that of the waves. The above examples are for low steepness waves for irregular and regular wave trains; the same general results occur for higher steepness waves.

Spectral density measurements for irregular and regular wave loading for deep-water waves (a relative depth of 0.51) in Figure 7 show the emergence of strong nonlinearities in the forces which are not present in the incident wave spectrum. The results for the regular wave test in Figure 7 are similar to those published previously for regular waves by Jamieson et al. (1985). For the horizontal and vertical forces, the spectral density plots show very little response at the fundamental frequency (1.34 Hz) of the incident waves; most of the response is at the second harmonic (2.68 Hz). Thus, it is not surprising that the irregular deep-water wave test ($f_p = 1.30$ Hz) results illustrated in Figure 7 indicate significant response in the spectra for the horizontal and vertical forces at frequencies approximately twice the peak frequency of the waves (2.60 Hz). However, it is not clear why the horizontal and vertical force spectral peaks for this irregular test do not occur at the same peak frequency as the waves (1.30 Hz) but at the slightly lower frequency of 1.04 Hz. It is not known why this occurs. Even though the magnitude of the wave loads for these conditions is quite small, it may still be important to understand the reason for this unusual nonlinear transfer of response. The regular wave loading results reported by Jamieson et al. (1985) for horizontal and vertical force, as well as the regular wave force results shown in Figure 7, do not show a similar shift of response because there is no interaction between frequency components. Indications of these two phenomena have already been observed in the time series plots (Figure 5). For the test results shown in Figure 7, the spectral peaks for the overturning moments occur at the same peak frequencies as the waves (1.30 Hz and 1.34 Hz for the irregular other wave conditions a significant amount of energy in the spectra for the overturning moment was measured at frequencies approximately twice the peak frequency of the waves.

In the previous paper by Jamieson et al. (1985) it was observed that for regular deep-water waves, the wave

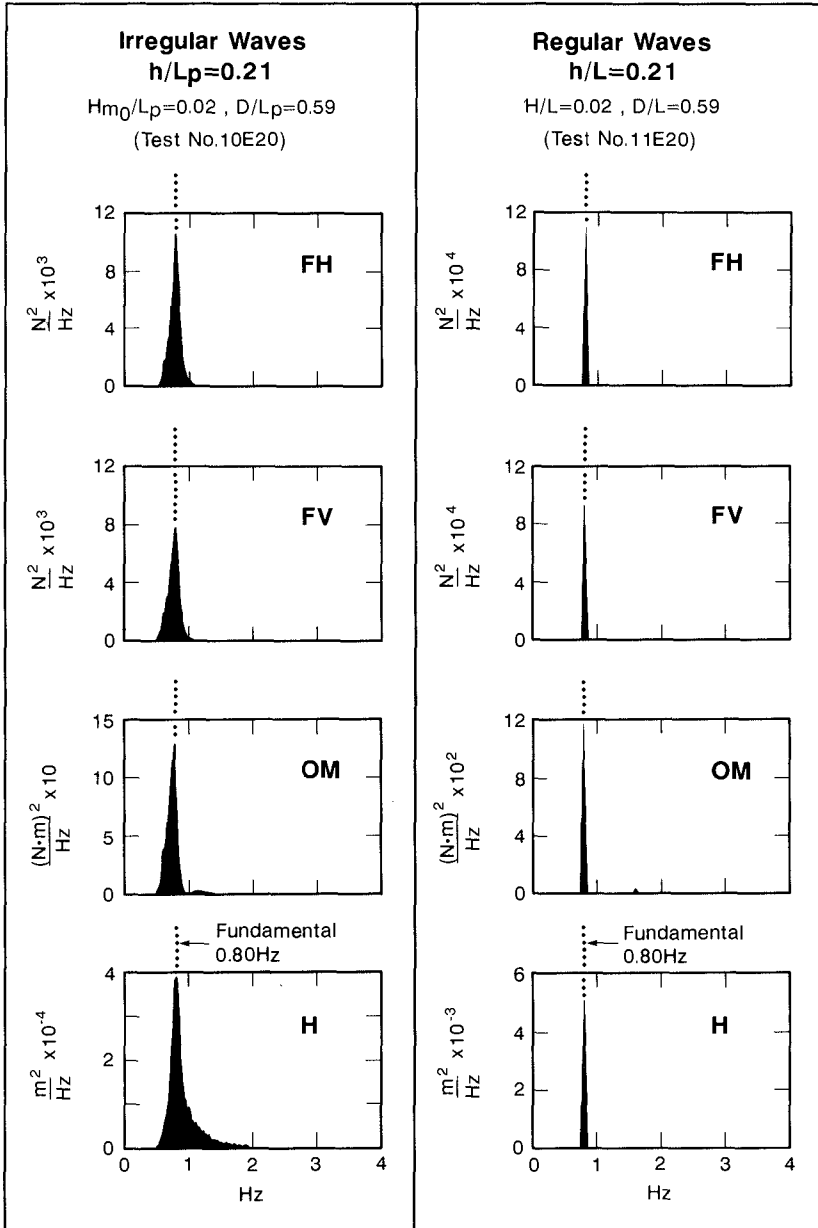


Figure 6. Typical Spectral Density Measurements for a Relative Depth of 0.21

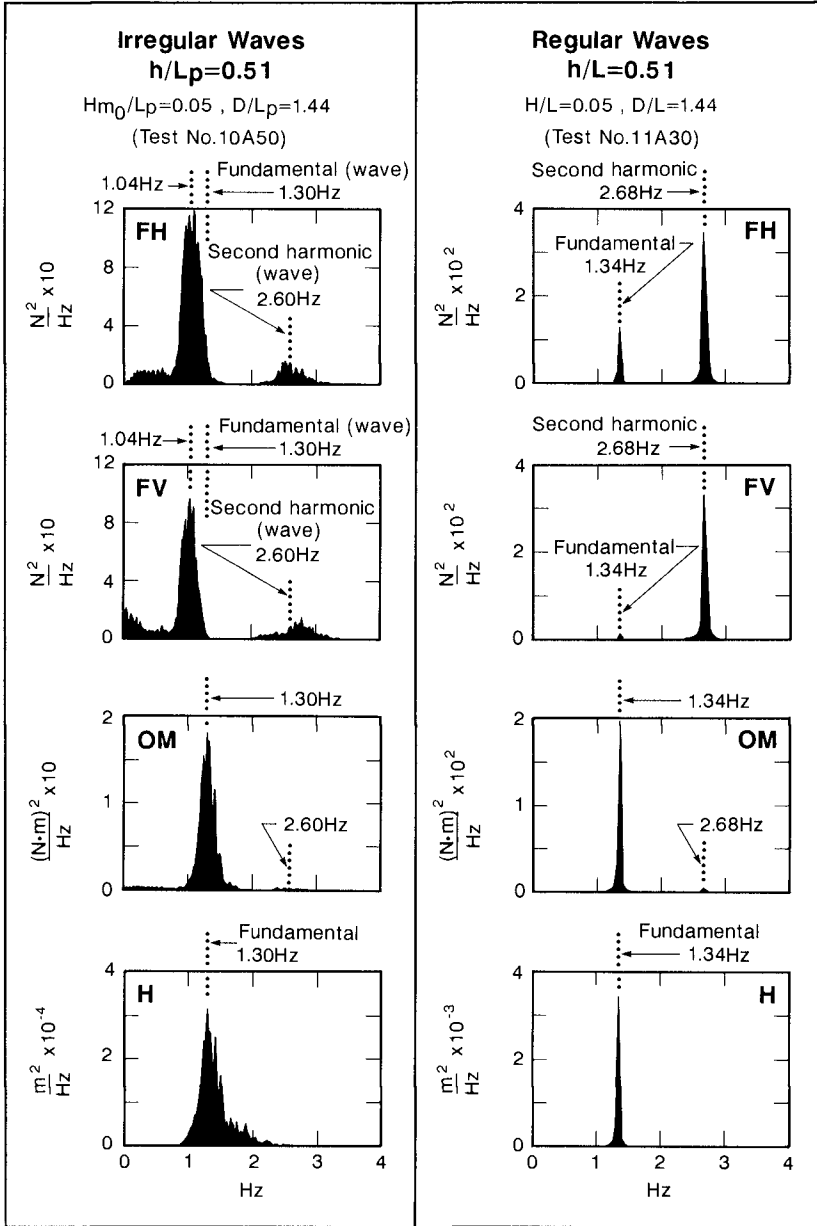


Figure 7. Typical Spectral Density Measurements for a Relative Depth of 0.51

loading was predominantly at the second-harmonic frequency of the waves (particularly for the horizontal and vertical wave forces). In that paper there was a brief discussion of previous reportings of second-order pressure fluctuations which do not attenuate with water depth, i.e. Longuet-Higgins (1950), Rundgren (1958), Hogben and Standing (1975). In the paper by Jamieson et al. (1985), it was observed that in addition to the wave frequency, the structural shape is important in determining whether second-harmonic forces and moments will appear. Thus, for a conical shape, the increasing diameter of the structure towards the bottom results in an increasing influence of the second-harmonic pressures where they are larger relative to the linear pressures. As far as the authors are aware, the shift in the irregular wave loading spectral peaks to a frequency lower than the wave excitation spectral peak frequency, has not been observed before.

Wave Load Transfer Functions

Transfer functions for horizontal force (FH), vertical force (FV) and overturning moment (OM) are plotted in Figure 8 for irregular wave tests having wave steepnesses, $H_{m0}/L_p = 0.02$ and 0.06 . Each of these transfer functions has only been calculated and plotted over the range of frequencies where there is significant energy in the incident wave spectrum for the given irregular wave test. Thus the nonlinear transfer of response in the wave loads from the wave frequency to lower or higher frequencies is not evident in the plotted results (shown in Figure 8) because the data has been truncated. The linear transfer function used here has large errors at frequencies where the energy of the wave excitation is small or negligible.

Transfer functions for eight tests with peak wave frequencies (as outlined in the experimental method) ranging from 0.48 Hz to 1.48 Hz each with a wave steepness of $H_{m0}/L_p = 0.02$ have been plotted on the left side of Figure 8 for each wave load (FH, FV and OM). For these low wave steepness results, all of the transfer functions fall on the same curve for each of the wave loads.

Transfer functions for seven tests with peak wave frequencies (as outlined in the experimental method) ranging from 0.69 Hz to 1.48 Hz each with a wave steepness of $H_{m0}/L_p = 0.06$ have been plotted on the right side of Figure 8 for the wave loads. For these higher steepness results, the transfer functions did not all fall on the same curves but showed some scatter as indicated by the wider lines used in plotting the curves. This is particularly evident for the plotted transfer functions of horizontal force and overturning moment.

If the wave loading results were linear, then the transfer functions would be the same for all wave steepness results. However, the results for the two wave steepnesses ($H_{m0}/L_p = 0.02$ and 0.06) in Figure 8 show a noticeable difference between the transfer functions for the different wave steepnesses. Although not shown here, the transfer

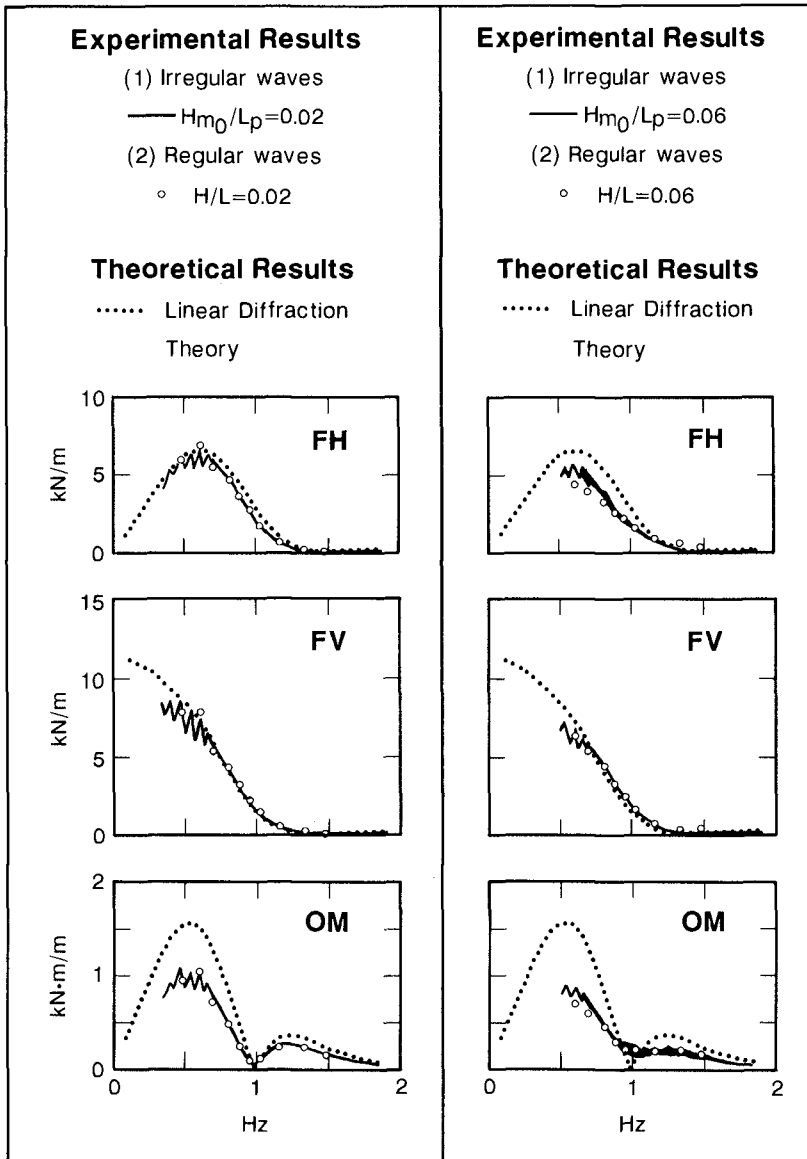


Figure 8. Comparison Between Experimental and Theoretical Wave Load Transfer Functions

functions for the other wave steepness results that were tested were also plotted and showed the same trends which are apparent in Figure 8. The variations in the transfer functions clearly indicate that the interaction between the conical structure and the incident waves is nonlinear.

Regular wave loading results are also included in Figure 8. Response amplitude operators (RAOs) were calculated for the regular wave tests previously described in the experimental method and are plotted for wave steepnesses $H/L = 0.02$ and 0.06 . The RAOs were calculated by adding the maximum positive wave load to the maximum negative wave load (since the absolute magnitudes were generally not equal) and dividing by the incident wave height. The RAOs for the regular waves are in good agreement with the transfer functions calculated for the irregular waves for all the wave loading conditions that were tested.

The theoretical wave load transfer functions shown in Figure 8 were calculated using the linear wave diffraction program (NPLWAVE) described by Hogben and Standing (1975). The lowest wave steepness results provided the closest agreement between theory and experiment, while the largest deviations between theory and experiment were measured for the highest wave steepness results. The transfer functions for vertical forces indicate very good agreement between linear diffraction theory and experiment for a wide range of frequencies and wave steepnesses. Extremely poor agreement between theory and experiment exists for the overturning moments. Other than in the vicinity of 1 Hz, the linear diffraction theory usually overestimates the measured overturning moments by more than 50%. For low steepness waves ($H_{m0}/L_p = 0.02$), linear diffraction theory slightly overestimates most of the horizontal force measurements; however, for higher steepness waves ($H_{m0}/L_p = 0.06$) such as those shown in Figure 8, the theory generally overestimates the measured results by more than 40%. For higher frequency results, the theoretical and experimental results are very similar although in this range of frequencies the wave forces are very small in magnitude compared to the higher loads measured for the lower frequency measurements.

CONCLUSIONS

1. Horizontal forces, vertical forces and overturning moments exerted by waves on a model of a surface-piercing 45° right circular conical structure have been measured.
2. Time series records, spectral densities and transfer functions for irregular wave loading tests have illustrated the nonlinear nature of the measured wave loads.
3. Similar trends in wave loading have been observed for irregular and regular wave tests.
4. For deep-water waves, the irregular and regular force measurements have shown spectral peaks at the second harmonic of the wave frequency even though the waves themselves had negligibly small second-order components. However, unlike the regular wave loading

results, the fundamental for the irregular wave forces occurs at a frequency considerably lower than the peak frequency of the waves.

5. Linear diffraction theory provides reasonable estimates of the wave forces for waves of low steepness; however, large deviations occur for waves of higher steepness. Linear diffraction theory generally provides very poor estimates of the overturning moments. Presently there is not a theoretical nonlinear method that provides an accurate solution of the wave loading on conical structures; thus, the overall wave loading must be determined by physical model tests.

REFERENCES

- Buslov, V.M. and N.W. Krahl. (1983). "Fifty-one New Concepts for Arctic Drilling and Production", Ocean Industry, Vol. 18 (1983), Parts 1, 2 and 3, Vol. 19 (1984), Parts 4, 5 and 6, 16 pp.
- Funke, E.R. and E.P.D. Mansard. (1984). "The NRCC 'Random' Wave Generation Package", National Research Council of Canada, Hydraulics Laboratory Technical Report, TR-HY-002.
- Hogben, N. and R.G. Standing. (1975). "Wave Loads on Large Bodies", International Symposium on the Dynamics of Marine Vehicles and Structures in Waves, edited by R.E.D. Bishop and W.G. Price, Mechanical Engineering Publications Limited, London, pp. 258-277, Authors' Replies, pp. 439-441.
- Isaacson, M. de St. Q. (1982). "Fixed and Floating Axisymmetric Structures in Waves", Proc. ASCE, Vol. 18, No. WW2, May, pp. 180-199.
- Jamieson, W.W., E.P.D. Mansard and G.R. Mogridge. (1985). "Wave Loading on a Conical Gravity Platform", Proc. 4th International Conference on Behaviour of Offshore Structures, Delft, The Netherlands, July, pp. 673-684.
- Jamieson, W.W. and E.P.D. Mansard. (1987). "An Efficient Upright Wave Absorber", ASCE Specialty Conference on Coastal Hydrodynamics, University of Delaware, Newark, Delaware, June 29-July 1, pp. 124-139.
- Longuet-Higgins, M.S. (1950). "A Theory of the Origin of Microseisms", Philosophical Transactions of the Royal Society of London, Series A, Vol. 243, No. 857, September, pp. 1-35.
- Rundgren, L. (1958). "Water Wave Forces: A Theoretical and Laboratory Study", Transactions of the Royal Institute of Technology, Stockholm, Sweden, Bulletin No. 54 of the Institution of Hydraulics, 123 pp.

NRCC, Hydraulics Laboratory Technical Reports are available upon request from the Hydraulics Laboratory, Bldg. M-32, National Research Council of Canada, Montreal Road, Ottawa, Ontario, K1A 0R6, Canada.

CHAPTER 168

EXPERIMENTAL STUDY OF IMMERSSED PLATES USED AS BREAKWATERS

Alain DROUIN* and Yvon OUELLET***

ABSTRACT

Under certain wave conditions, an immersed plate which is free to move horizontally produces what has already been called the oscillating water wall phenomenon. When this happens, the plate and the volume of fluid located under the plate move back and forth and then behave as a wave reflector. This type of breakwater was studied in a wave flume with monochromatic and irregular wave trains. Tests have provided a better understanding of the influence of certain parameters that define a plate and the hydraulic conditions under which the plate is used. Results show some interesting efficiencies and also transfert of the energy to harmonic frequencies.

1. INTRODUCTION

The reflective capacity of a freely moving and immersed plate has been shown in a recent study (Guevel et al., 1985). In this paper, it was demonstrated that under certain wave conditions, this kind of plate and the fluid located under it move back and forth. This movement generates in the rear part of the plate a radiation wave which interferes with the incident one; therefore, the plate behaves as a wave reflector (Figure 1). The French researchers developed a diffraction-radiation model which gave results similar to those obtained in their laboratory. However, when wave steepness was too high, the rear part of the plate became the seat of strong turbulence which seemed to generate harmonic waves, and, depending on the immersion depth of the plate, waves broke on its top. The numerical model did not account for these two phenomena.

* Research Assistant, Department of Civil Engineering, Laval University, Quebec, Canada, G1K 7P4.

*** Professor, Department of Civil Engineering, Laval University, Quebec, Canada, G1K 7P4.

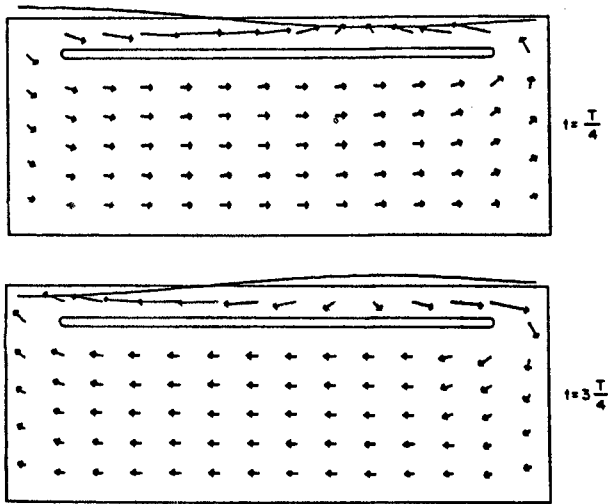


Figure 1 - Velocity distribution and free surface obtained with the oscillating water wall phenomenon (from Guevel et al., 1985)

The present work consists mainly of an experimental study on mobile and immersed plates (Drouin, 1988). The purpose was to determine if that kind of structure could be used as a breakwater under high steepness wave conditions. Plates were subjected to monochromatic and irregular waves, and some regular wave results were subsequently compared to those obtained with a fixed plate used in the same conditions. The fixed plates have been considered in many earlier studies which were well summarized in a paper written by Patarapanich in 1978.

2. EQUIPMENT AND DATA

The study was conducted in a 1.2 x 1.8 x 34.0 meter wave flume which was divided into three corridors of 0.45, 0.90 and 0.45 meters respectively. Studied structures were placed in the main corridor; therefore, the side flumes served essentially to dissipate waves reflected on breakwaters.

In order to maximize the information from the tests performed, time domain and frequency analyses were carried out. To reach the highest frequency of 4.0 Hz to which the spectrum would be evaluated, a data sampling interval of 0.125 second was chosen. In each case studied, eight records of 32 seconds were taken; therefore, the resulting increment in frequency between adjacent estimates of spec-

tral density was 0.03125 Hz, and the stability obtained for these estimates was satisfactory.

In the time domain, the zero down crossing method was used, while the basic frequency analysis was completed with Goda and Suzuki's algorithm (Goda and Suzuki, 1976) so as to account for multiple wave reflections. For that purpose, three groups of four probes permitted the defining of incident as well as transmitted waves; the assessment of incident waves was checked with measures taken in a side flume. Finally, measurement of the horizontal displacement of each structure was also done.

3. REGULAR WAVE TESTS

A first group of tests was performed using regular wave trains. The parameters of the plate studied in tests 1 to 12 were the width, the specific mass and the mobility (Table 1), while the plate thickness was constantly maintained at 5 cm. As illustrated in Figure 2, chains placed at corners kept the mobile plates immersed, and pieces of foam were added to avoid passage of water and friction along the flume walls. A rigid support was used to fix the immobile structure studied (plate 4); therefore, the specific mass of this plate is not indicated in Table 1 because it is not significant.

Table 1 - Definition of plates studied in tests 1 to 12

PLATE IDENTIFICATION	WIDTH (cm)	SPECIFIC MASS (g/cm ³)
1	100	0.27
2	150	0.27
3	150	0.42
4	150	-

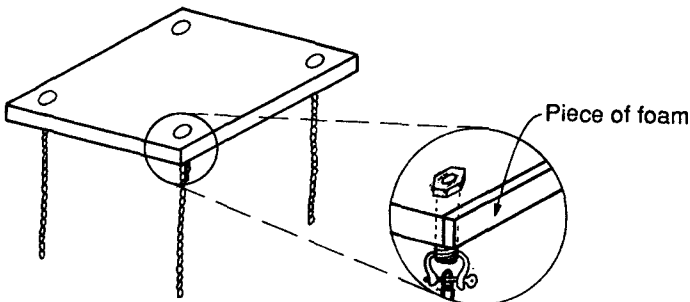


Figure 2 - Sketch of a typical mobile plate

For tests 1 to 12, plates were subjected to the fifteen wave conditions presented in Table 2, and each of these were considered with three different immersion depths of the plates (9.0, 13.5 and 18.0 cm). Water depth was kept at 75 cm; therefore, most of the waves were generated in intermediate water depth. In fact, only waves corresponding to the 0.95 second period were produced in deep water conditions.

Table 2 - Characteristics of regular waves used in tests 1 to 12

PERIOD (s)	HEIGHTS (cm)	WAVE LENGTH (cm)	WAVE STEEPNESSES
0.95	6.7, 5.3, 3.3	141	0.048, 0.038, 0.023
1.15	9.1, 7.0, 5.0	203	0.045, 0.034, 0.025
1.33	11.8, 8.8, 5.2	261	0.045, 0.034, 0.020
1.67	11.3, 8.1, 5.0	372	0.030, 0.022, 0.013
2.22	12.9, 9.9, 6.3	541	0.024, 0.018, 0.012

The effect of an increase in water depth was the object of tests 13 to 15, although it was not possible, considering the dimensions of the flume, to raise the water level already used. In order to obtain deeper water conditions, incident waves, immersion depths and dimensions of plate 2 were reproduced at scale 1:1.4 with respect to the Froude's similitude law. The use of this scale gave an equivalent water depth of 105 cm.

Incident waves generated in tests 13 to 15 are presented in Table 3. For those tests, which were performed with plate 5, deep water conditions resulted when the two smaller periods were used. The width of the plate was 107 cm, its thickness 3.6 cm, and the plate was immersed to depths of 6.4, 9.6 and 12.9 cm.

Table 3 - Characteristics of regular waves used in tests 13 to 15

PERIOD (s)	HEIGHTS (cm)	WAVE LENGTH (cm)	WAVE STEEPNESSES
0.80	4.8, 3.8, 2.4	100	0.048, 0.038, 0.023
0.97	6.5, 5.0, 3.6	146	0.045, 0.034, 0.025
1.12	8.4, 6.3, 3.7	193	0.044, 0.033, 0.019
1.41	8.1, 5.8, 3.6	288	0.028, 0.020, 0.013
1.88	9.2, 7.1, 4.5	437	0.021, 0.016, 0.010

Although incident waves were monochromatic, transmitted ones appeared to correspond to a superposition of waves at harmonic frequencies (Figure 3). Efficiencies of tests performed in regular wave conditions, obtained using equation (1), are given in Table 4.

With the equation (1), an efficiency value near zero indicates that almost all the incident energy has been transmitted behind the structure.

$$\text{Efficiency} = \left(1 - \frac{\text{transmitted energy}}{\text{incident energy}} \right) \times 100 \quad (1)$$

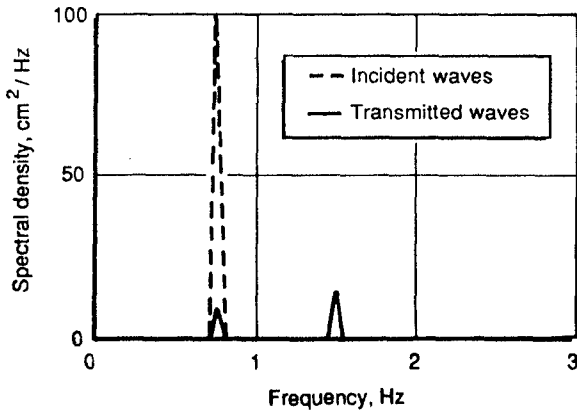


Figure 3 - Typical incident and transmitted waves spectra

Table 4 - Efficiencies obtained with regular waves

a) Immersion depth: 9 cm *

INCIDENT PERIOD (s)	WAVES HEIGHT (cm)	PLATE				
		1	2	3	4	5
0.95	6.7	67	86	77	77	85
	5.3	59	84	81	49	76
	3.3	23	41	36	30	53
1.15	9.1	85	77	80	79	73
	7.0	73	83	78	81	72
	5.0	44	85	76	73	68
1.33	11.8	77	87	87	87	85
	8.8	82	79	81	81	69
	5.2	68	72	72	69	54
1.67	11.3	78	96	95	91	91
	8.1	79	86	88	93	72
	5.0	55	62	61	79	55
2.22	12.9	51	75	69	79	84
	9.9	44	77	76	81	86
	6.3	76	77	80	85	83

b) Immersion depth: 13.5 cm *

INCIDENT PERIOD (s)	WAVES HEIGHT (cm)	PLATE				
		1	2	3	4	5
0.95	6.7	45	51	56	41	51
	5.3	25	49	37	28	53
	3.3	23	39	36	23	42
1.15	9.1	78	55	79	66	61
	7.0	48	54	67	49	57
	5.0	36	35	31	20	38
1.33	11.8	84	73	84	83	82
	8.8	69	57	62	61	73
	5.2	39	2	6	16	48
1.67	11.3	58	90	79	88	96
	8.1	44	82	82	75	74
	5.0	51	29	59	11	40
2.22	12.9	34	72	58	75	78
	9.9	64	69	54	81	80
	6.3	62	63	61	75	85

c) Immersion depth: 18.0 cm *

INCIDENT PERIOD (s)	WAVES HEIGHT (cm)	PLATE				
		1	2	3	4	5
0.95	6.7	10	28	38	25	30
	5.3	4	31	33	18	42
	3.3	0	35	44	14	26
1.15	9.1	56	37	40	50	43
	7.0	41	27	30	35	32
	5.0	38	31	29	32	21
1.33	11.8	80	69	91	74	77
	8.8	67	27	49	56	52
	5.2	47	27	23	41	26
1.67	11.3	61	79	74	83	74
	8.1	54	44	61	68	62
	5.0	54	23	49	16	52
2.22	12.9	32	62	38	47	74
	9.9	26	67	35	65	74
	6.3	25	61	66	83	83

* Frequencies, heights and immersion depths were reproduced at scale 1:1.4 for tests with plate 5.

Efficiencies obtained with plate 5 are illustrated in Figure 4 as a function of the kinematic energy per unit area of incident waves. Results shown in this way are representative of those obtained with other plates used.

The unusual choice of energy as a parameter to represent breakwater efficiencies can be understood by the implicit relationship between kinematic wave energy and an oscillating movement. This parameter was the only one which permitted the gathering of efficiency results in a relatively narrow range of values. Had adimensional parameters currently used, as the ratio of structure width to wave length or the wave steepness, been employed, efficiency results would have exhibited a significantly greater dispersion pattern.

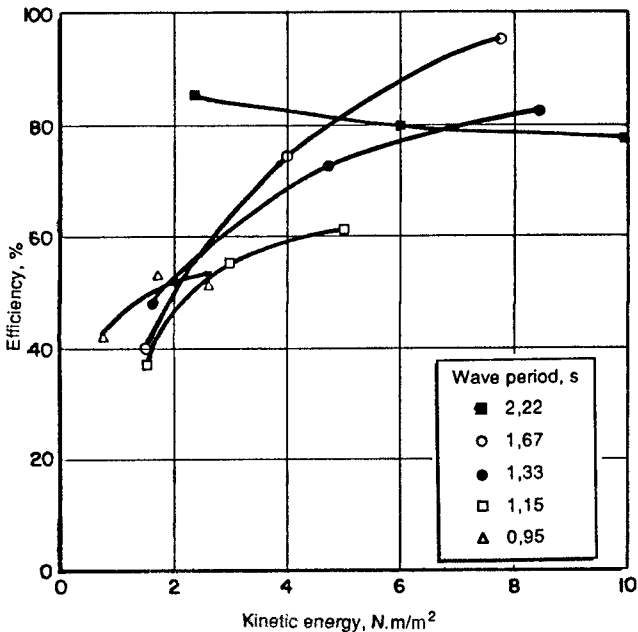


Figure 4 - Efficiencies of the plate 5 obtained with an immersion depth of 13.5 cm

4. DISCUSSION OF REGULAR WAVE RESULTS

The following analysis of results already given in Table 4, has been presented in such a way as to highlight the influence of wave and plate parameters studied.

Immersion depth

In almost all cases, efficiency decreased as the immersion depth became more important. This influence can be explained in two ways. When the immersion increased, there was less kinematic energy under the plate to initiate the water wall phenomenon as described by Guevel et al. Secondly, there was also less energy dissipated by wave breaking on the plate.

Wave height

As shown in Figure 4, with the exception of the higher period studied, the performance of plates increased as incident wave energy (proportional to height) also increased. As well as in the case of the immersion depth, results can be related to the dissipation of wave energy due to the wave breaking, and to the energy available under the plate to initiate the water wall phenomenon.

Plate width

With an immersion depth of 9 cm, plate 2 (width of 150 cm) performed better than plate 1 which was only 100 cm wide. When the plate 2 was immersed at 13.5 cm, efficiencies were equivalent to those of plate 1, except in certain cases including those with wave periods of 1.33 second. Finally, with a immersion depth of 18 cm, the second plate gave better results only with extreme wave periods studied (0.95 and 2.22 seconds); with other periods, smaller efficiencies were obtained with the larger plate.

Specific mass

With the smallest immersion depth, efficiencies calculated with plates 2 and 3 (specific masses of 0.27 and 0.42 g/cm³) were quite similar. With other immersion depths, an increase of the mass resulted in efficiencies similar or better, except with higher waves having a period of 2.22 s.

Plate mobility

Compared to the fixed plate, the efficiency of the mobile one was better when exposed to the lower energy waves of those described in Table 2. However, the fixed structure gave better results in higher wave energy cases. With both types of plate, a part of the transmitted energy had a harmonic relationship with incident wave frequency.

Water depth

Especially when highly immersed, plate 5, which was in deeper water, gave better results than plate 2. These results and the movement of the plates help, as it will be discussed next, to understand the effect of water depth on this kind of breakwater.

As described by Guevel et al, it was observed that an upward pressure was applied under the rear part of all mobile plates during their backward movement (Figure 5). If the pressure was important enough, it seemed to limit the horizontal displacement of these plates.

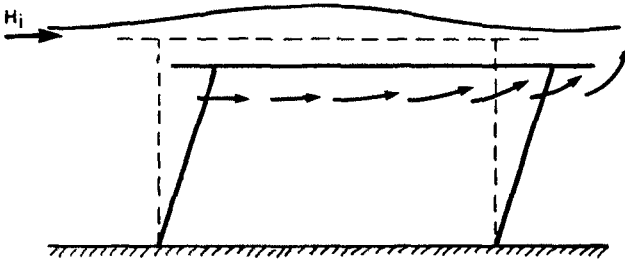


Figure 5 - Velocity distribution directly under the plate

When mobile plates 1, 2 and 3 were subjected to the longer wave periods (1.67 and 2.22 seconds), their movements were not as that described in Figure 6a, but rather like those illustrated in Figures 6b and 6c. However, when plate 5 was subjected to the same incident wave conditions, but in deeper water, its movements were as presented in Figure 6a. Especially with the two deeper immersions, the amplitude of plate 5 movements was, proportionally, bigger than those of plate 2 used in shallower water. Therefore, the horizontal displacement of the mobile plates was a function of the anchoring length.

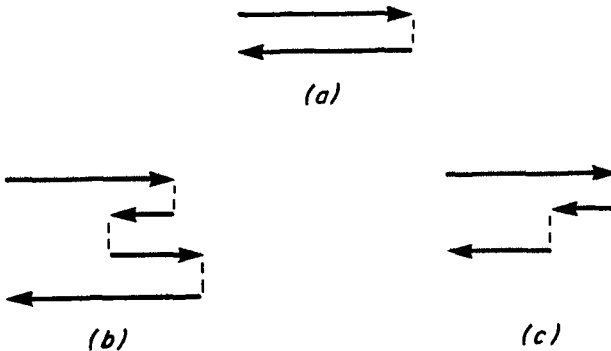


Figure 6 - Typical movements of the mobile plates

Considering geometric relations, it appears that a given horizontal displacement implies a larger vertical displacement of that structure when the anchoring length is shorter. Added to the efficiencies obtained, it seems to indicate that when a plate is limited in its horizontal oscillation, it cannot force as efficiently the horizontal displacement of the mass of water located under itself; therefore, the reflective capacity would be decreased.

It may be paradoxical to note that the fixed plate performed better than the mobile ones when subjected to the higher wave periods used. However, the mobile plates were agitated, in those cases, by strong vertical jolts which resulted, when added to the horizontal movement limitation, in lower efficiencies.

Finally, the movement of the plates described in Figures 6b and 6c seemed to create bigger strains in anchorings than that illustrated in Figure 6a; however, this assumption was not verified in tests performed, since no anchoring stresses were measured.

5. IRREGULAR WAVE TESTS

A limited amount of tests were performed using irregular incident waves. In order to permit direct comparison with regular wave tests, significant wave heights and peak periods were chosen such that they were equivalent to some of those used in monochromatic conditions. Spectra generated in the laboratory were based on the JONSWAP definition (Holmes, 1977). Efficiencies calculated with equation (1) and obtained with plates 1 and 2, already defined, are presented in Tables 5 and 6.

Considering the effect of the parameters studied, the results of irregular wave tests had a tendency to vary in the same manner as those obtained with regular wave trains. However, differences between extreme efficiencies were diminished, since lower and higher performances obtained with regular waves were more concentrated around mean values.

Table 5 - Efficiencies obtained in irregular wave conditions with plate 1

PEAK PERIOD (s)	SIGNIFICANT HEIGHT (cm)	IMMERSION DEPTH (cm)		
		9.0	13.5	18.0
1.15	9.1	65	58	50
	7.0	63	46	43
	5.0	40	34	41
1.67	11.3	74	65	51
	8.1	74	62	47
	5.0	67	57	49

Table 6 - Efficiencies obtained in irregular wave conditions with plate 2

PEAK PERIOD (s)	SIGNIFICANT HEIGHT (cm)	IMMERSION DEPTH (cm)		
		9.0	13.5	18.0
1.15	9.1	68	47	32
	7.0	67	42	35
	5.0	55	39	37
1.67	11.3	82	75	62
	8.1	76	66	45
	5.0	55	35	37

As well as with regular waves, transmitted energy was carried over to higher frequencies, especially to harmonics of the incident peak frequency (Figure 7).

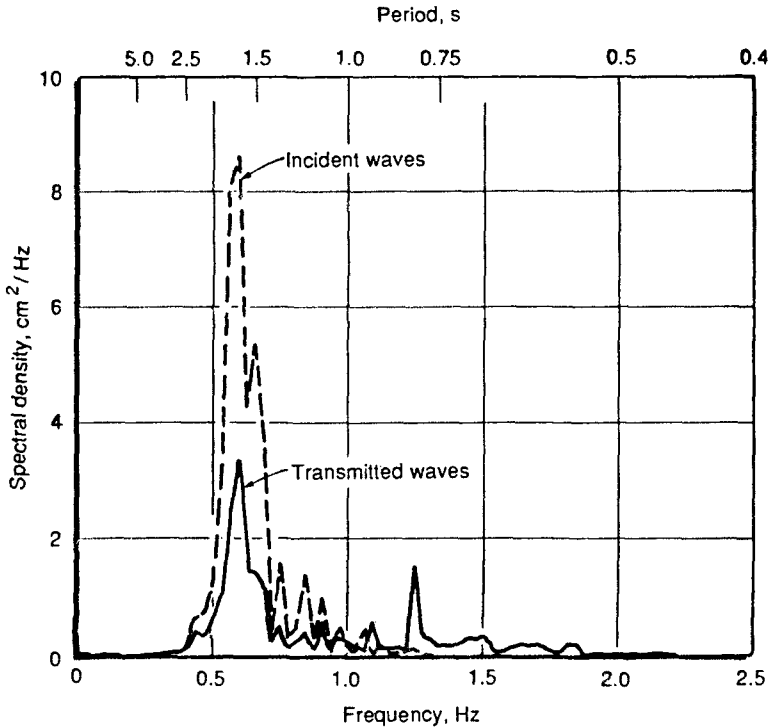


Figure 7 - Incident and transmitted waves spectra obtained with plate 1 immersed at 18.0 cm
Incident waves: $T_p = 1.67$ s, $H_{1/3} = 5.0$ cm

6. CONCLUSIONS

From tests performed, the plate width, the immersion depth and the distance between the plate and the bottom appeared to be the parameters having the most influence on the efficiency of a mobile plate used as a breakwater. Under severe wave conditions, horizontal displacement of the plate, and consequently its efficiency, were observed to be limited by the length of the anchoring chains (distance between the plate and the bottom) and the ascendant pressures on the rear part of the plate. In these cases, the rear part of the plate was agitated by strong vertical jolts. Under such conditions, a fixed plate of equivalent dimensions was found to be more effective.

Interesting efficiencies were obtained, even when ratios of plate width to wave length were small. These good performances occurred especially when plates were slightly immersed. With the exception of the higher wave periods studied, the efficiency of the plates as breakwaters increased as incident wave energy increased. Moreover, a variable part of this energy was carried over as a harmonic of the incident wave frequency.

More detailed studies should be done, using irregular wave conditions and variable incident wave angles, in order to better define the performance of the plates. The measurement of tensions on anchoring chains, when structures are subjected to these incident waves, will also give important information that must be known before considering the use of such mobile plates in the field as breakwaters.

REFERENCES

- DROUIN, A. (1988). «Étude expérimentale de plaques mobiles utilisées comme moyen de protection contre la houle». Thèse de maîtrise, Département de génie civil, Université Laval, 142 p.
- GUEVEL, P., LANDEL, E., BOUCHET, R. et MANZONE, J. M. (1985). «Le phénomène d'un mur d'eau oscillant et son application pour protéger un site côtier soumis à l'action de la houle». ATMA 1985, Principia Recherche Développement S.A. 18 p.
- GODA, Y. and SUZUKI, Y. (1976). «Estimation of Incident and Reflected Waves in Random Wave Experiments». Proceedings of 15th International Conference on Coastal Engineering, ASCE, pp. 828-845.
- HOLMES, P. (1977). «Wave Climate». Symposium on Design of Rubble Mound Breakwaters, Paper No 1, British Overcraft Corporation, 24 p.
- PATARAPANICH, M. (1978). «Wave Reflection from a Fixed Horizontal Plate». Proceedings of the International Conference on Water Resources Engineering, Bangkok, Thailand. pp. 427-446.

CHAPTER 169

ON 3-DIMENSIONAL STABILITY OF RESHAPING BREAKWATERS

by

H.F. Burcharth
Prof. of Marine Civil Engineering

Peter Frigaard
Research Associate

University of Aalborg, Denmark

INTRODUCTION

The paper deals with the 3-dimensional stability of the type of rubble mound breakwaters where reshaping of the mound due to wave action is foreseen in the design. Such breakwaters are commonly named sacrificial types and berm types. The latter is due to the relatively large volume of armour stones placed in a seaward berm. However, as also conventional armoured breakwaters sometimes do contain a berm it is assumed that a better and more ambiguous designation would be "reshaping" mound breakwaters.

The principle of reshaping breakwaters is to use relatively fine rock material which will then be eroded to S-shape profiles if sufficient amount of material is provided, Fig. 1. This type of breakwater can be constructed and maintained without the use of expensive specialized equipment. For a detailed discussion see Baird et al., 1984.

If sufficient material is provided to prevent the top of the mound to be eroded in its full width a reshaping breakwater will always be dynamically stable in head-on waves (2-dimensional case). This principle holds for all sizes of stone materials since even a sand beach stabilizes though with a very flat profile.

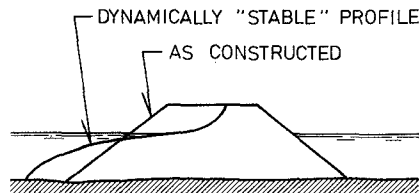


Fig 1. Reshaping breakwater.

However, in reality there are two important 3-dimensional effects which must be included in the design criteria, namely the rate of erosion (recession) of the roundhead and the rate of erosion of the trunk caused by oblique waves. The latter might cause unacceptable removal and transport of stones along the structure and thereby constitute a more restricting design criteria than head-on waves.

The paper discusses the trunk stability in oblique waves and the stability of berm round-heads and presents results from model tests.

The tests were conducted in a 3-dimensional model at The Hydraulics Laboratory, Department of Civil Engineering, University of Aalborg.

MODEL TEST SET-UP

Geometry of the model

Fig. 2 shows the cross sections of the model (before each test) and the lay-out of the model in the wave basin.

Two different lay-outs were used in order to examine the stability of breakwaters with different widths.

To avoid too many parameters a simple breakwater geometry and only one class of stones were used.

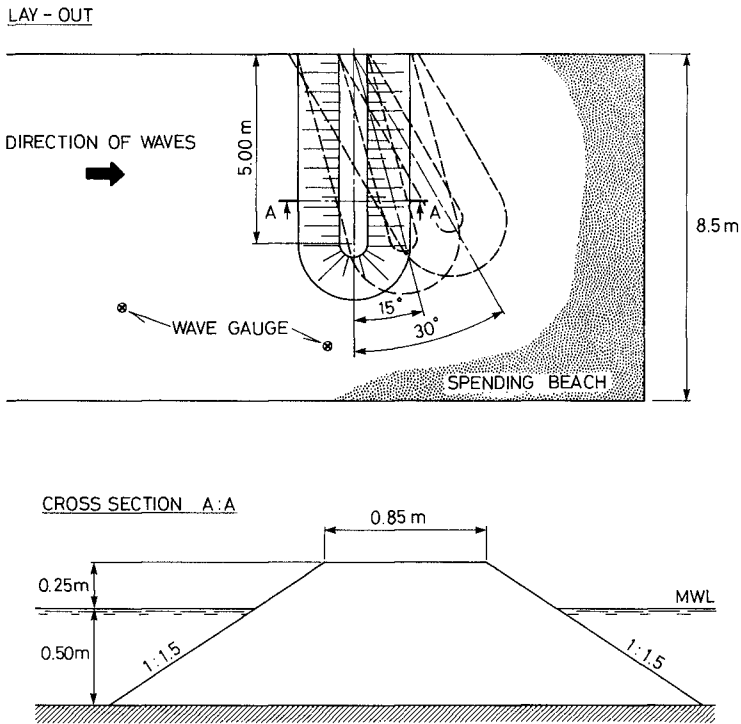
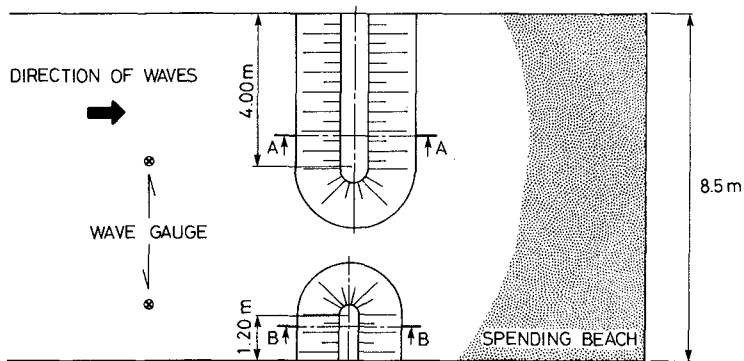


Fig 2. Lay-out and cross section of the model. (Continued on next page).

LAY - OUT



CROSS SECTION B · B

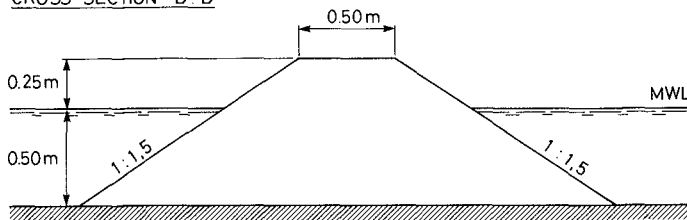


Fig 2. Lay-out and cross section of the model.

The stone material

The model consisted of one grading of crushed stones with a density $\rho_s = 2.65 \text{ t/m}^3$ (metric ton) and a gradation as given in Figs. 3 and 4. No special core material was used.

It was found that the relationship between the sieve diameter (quadratic sieve) d and the stone volume V and stone weight w is

$$V = 0.7d^3 = \frac{w}{\rho_s}$$

d is regarded a characteristic diameter of the stones.

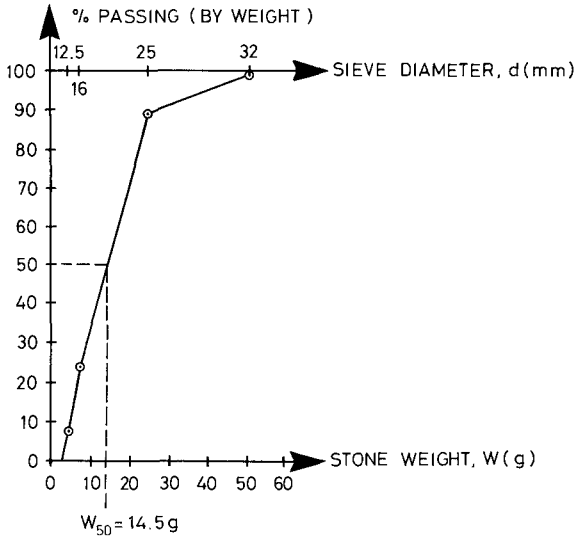


Fig 3. Gradation of model stones (Linear representation).

As seen from Fig. 3 w_{50} is found to be 14.5 g. However, it is most likely that an extra point on the gradation curve in the sieve interval 16-25 mm would have shifted the graph to the left and thereby given a w_{50} smaller than 14.5 g. This is investigated by Fig. 4.

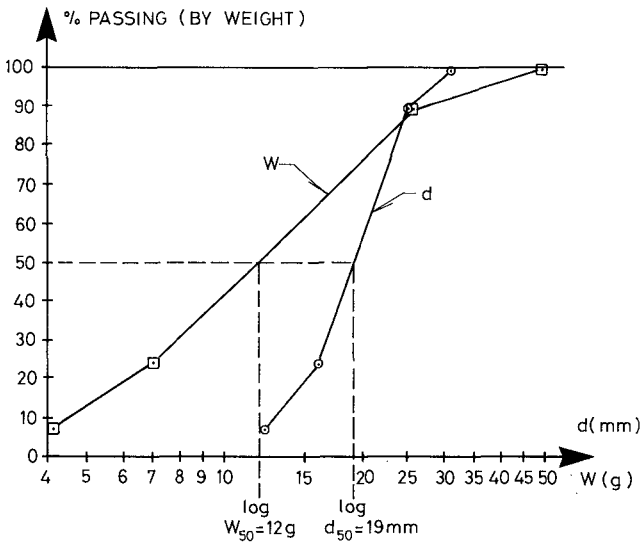


Fig 4. Gradation of model stones (Log-linear representation).

The stone weight corresponding to $d_{50}^{\log} = 19$ mm is $w_{d_{50}} = \rho_s \cdot 0.7d^3 = 2.65 \cdot 0.7 \cdot 1.9^3 = 12.7 \text{ g} \geq w_{50}^{\log} = 12$ g.

The log representation confirms that w_{50} is somewhat less than 14.5 g.

Based on the various figures a w_{50} of 12.7 g corresponding to $d_{50}^{\log} = 19$ mm is chosen as the most correct value.

D_{n50} is a nominal diameter defined as $D_{n50} = (w_{50}/\rho_s)^{1/3} = 16.9$ mm.

It should be noted that for the investigation of longshore transport in oblique waves samples of stones without diameters less than 16 mm were used. For these samples $d_{50}^{\log} = 22$ mm and $w_{d_{50}} = 20.3$ g.

Waves

All waves were irregular waves generated in accordance with a random phase JONSWAP-type spectrum (peakedness parameter $\gamma = 3.3$ and width parameters $\sigma_f = 0.10$ for $f \leq f_p$ and $\sigma_f = 0.50$ for $f > f_p$).

All tested sea states are stated in Tabel 1.

Spectrum no.	H_s (m)	T_p (sec.)	$H_s/\Delta \cdot D_{n50}$
A	0.10	1.50	3.5
B	0.10	2.00	3.5
C	0.15	1.80	5.4
D	0.15	2.50	5.4
E	0.20	2.50	7.1
F	0.10	1.70	3.5
G	0.13	1.80	4.6
H	0.13	2.50	4.6
I	0.15	2.00	5.4
J	0.15	2.20	5.4
K	0.15	2.50	5.4
L	0.175	2.50	6.3

Tabel 1. Tested sea states.

Two different methods of producing the wave generator control signals were used.

Control signals for the tests using spectrums A through E were calculated by use of FFT-transformation, while all other control signals were based on the method of filtering white noise.

The following three angles of wave attack were tested: $\alpha = 0^\circ$ (head-on waves), $\alpha = 15^\circ$, and $\alpha = 30^\circ$.

MODEL CONSIDERATIONS

The sea states were chosen in the range from very little erosion to fast erosion of the profile under oblique wave attack.

An indication of the relative stability of the profiles can be given by the dimensionless parameter $H_s/\Delta \cdot D_{n50}$, where $\Delta = \rho_s/\rho - 1$. It is seen that $H_s/\Delta D_{n50}$ equals the stability number $N_s \approx (K_D \cot \alpha)^{1/3}$, where K_D is the Hudson stability coefficient and α is the slope angle. (Note that the influence of the wave period is lacking in the parameter).

According to extensive testing of rock slopes in head-on waves by DHL(Pilarczyk and Van der Meer) the values of the dimensionless parameter can be related to various types of rock slopes as follows:

$H_s/\Delta D_{n50}$	
1 - 3	Conventional breakwater layer, start of damage
2 - 5	Conventional breakwater layer, failure
3 - 7	Reshaping breakwater (Berm breakwater)
5 - 50	Rock beaches

In the present tests we have

$$\Delta = \left(\frac{\rho_s}{\rho} - 1\right) = 1.65$$

$$D_{n50} \approx \left(\frac{12.7}{2.65}\right)^{1/3} = 1.69 \text{ cm}$$

$$\Delta \cdot D_{n50} = 2.79 \text{ cm}$$

and consequently the range of tests corresponds to

$$3.5 < H_s/\Delta \cdot D_{n50} < 7.1$$

which is the interval considered for reshaping breakwaters.

SCALE EFFECTS CONSIDERATIONS

Provided that the grading of the stones is not too wide, say $\frac{d_{85}}{d_{15}} < 3$, and provided that the amount of fine material cannot block the pores (which is usually the case if $\frac{d_{85}}{d_{15}} < 3$) it is

relevant to define a Reynolds' number with the characteristic length D_{n50}

$$Re = \frac{D_{n50} \sqrt{gH_s}}{\nu}$$

ν is the kinematic viscosity = 10^{-6} m²/s at 20°C.

With $H_s = 0.10 - 0.20$ m we get

$$1.7 \cdot 10^4 < Re < 2.4 \cdot 10^4$$

Juul Jensen and Klinting analysed the scale effects and found that no significant viscous scale effect is to be expected if in the outer part of the structure $Re > 0.6 \cdot 10^4$. Van der Meer found no scale effects for rock slopes with characteristic stone size of 20 mm, which is approximately the stone size in the present tests. This is also the experience of the Hydraulics Laboratory at the University of Aalborg.

However, although it is believed that a viscous scale effect is present it will be either negligible or will cause the results (in terms of amount of damage) to be on the safe side.

STABILITY OF ROUNDHEAD AND TRUNK IN HEAD-ON WAVES

Test procedure

The initial cross sections profiles of the model are shown in Fig. 2.

In the rough wave conditions only the model with the large crest width was used. In tests with calmer sea conditions both models were used.

The waves were recorded throughout all the tests. Wave height, wave period and shape of spectrum were controlled. The breakwater profile was measured after 3000 waves in all tests, and in most of the tests the waveseries were repeated once or twice and then the breakwater profile was measured again.

The wave basin was equipped with two cameras and contour plots of the breakwater was made after all tests using Photogrammetry.

Moreover, the characteristics of the stone movements were found from video recordings of the movements of coloured stones.

Test results for profiles in head-on waves

In agreement with results from several other authors, i.e. Van der Meer and Pilarczyk 1986, the shape of the profiles was found to be governed by the wave height and the wave period. The influence of the number of waves was found to be very little for profiles exposed to more than 3000 waves. After 6000 waves the profiles seem to have reached a "state of equilibrium".

Also, it was observed that most of the reshaping took place within approximately 200 waves.

It is characteristic that a very wide range of sea states (from mild to severe) produce only slightly different trunk profiles in head-on waves.

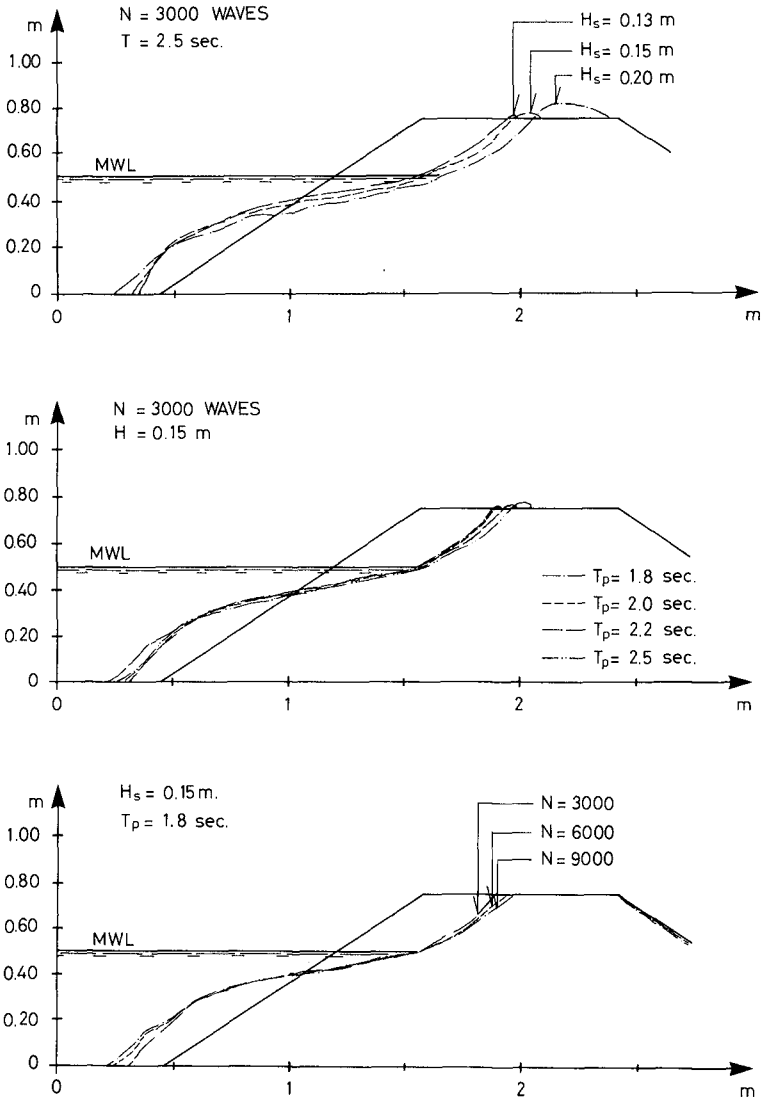


Fig 5. Examples of profiles in head-on waves
 - influence of wave height
 - influence of wave period
 - influence of number of waves

The material deficit is due to settlements caused by wave compaction and material transport across the crest.

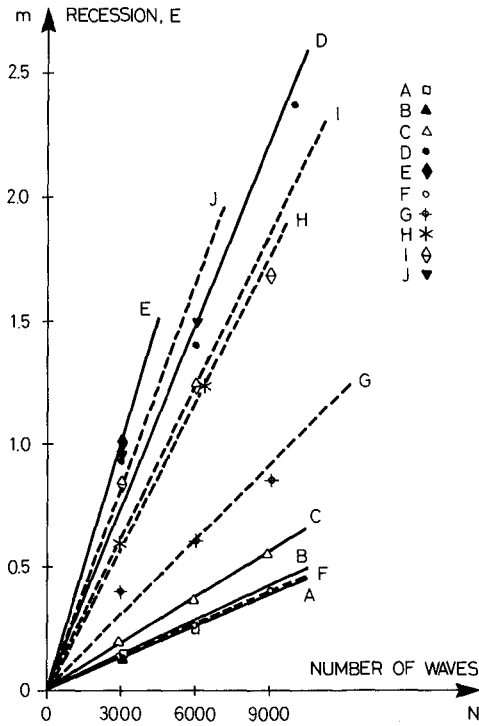


Fig 6. Recession (erosion) rate of the roundhead.

The erosion of the roundhead is expressed in terms of recession of the crest end measured along a longitudinal line parallel to the centerline of the breakwater, see Fig. 7.

Fig. 6 shows the recession as function of the number of waves. Note that the rate is almost constant for a certain sea state, i.e. a linear relationship between the recession of the central crest end and the time (or number of waves).

In spite of the almost linear relationship between the recession of the roundhead and the time for each sea state. Fig. 6 shows a large amount of scatter. Notice that wave spectrum G ($H_s = 0.13$ m and $T_p = 1.80$ sec.) gives larger erosion than spectrum C ($H_s = 0.15$ m and $T_p = 1.80$ sec.). It is believed that the scatter is due to different grouping in the waves caused by different methods of generating the wave control signals.

Fig. 6 shows that the roundhead erosion rate is small up to a certain sea state, characterized by both wave height and wave period. When this sea state is exceeded, erosion is fast and the sea state now seems to be characterized by the ability of practically every one of the waves to erode some of the stones from the roundhead and to displace (shift) them all the way across the roundhead.

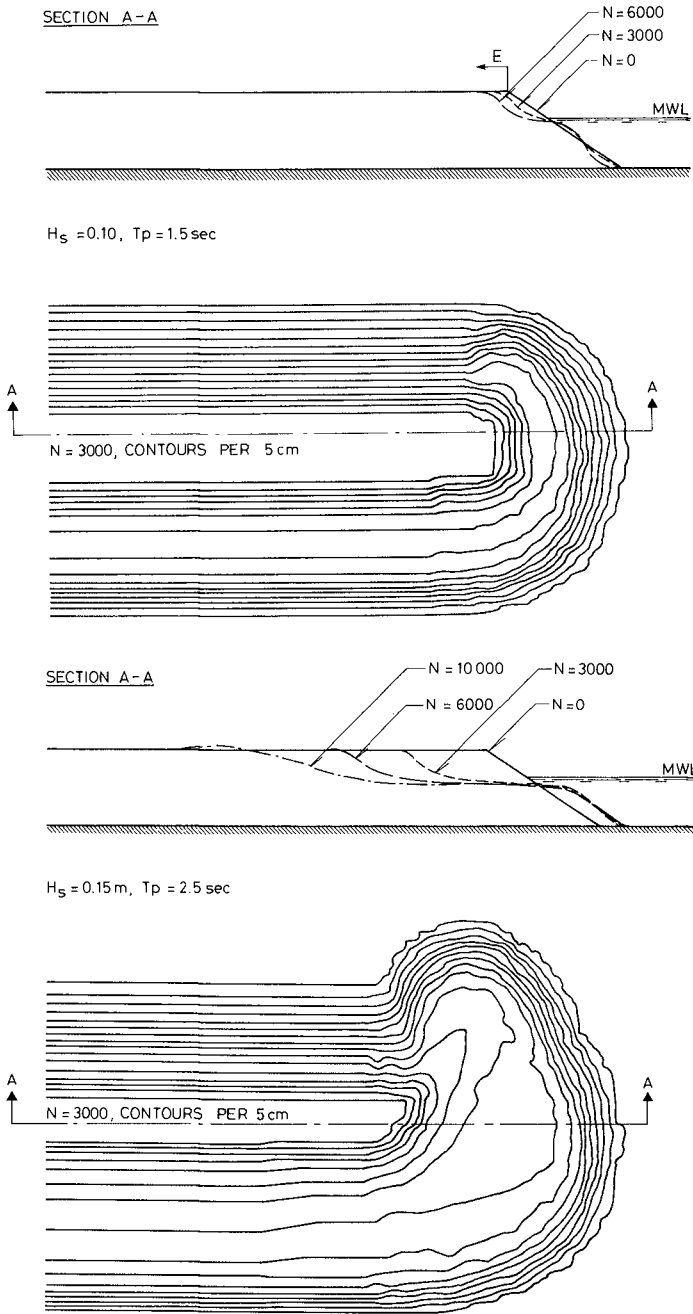


Fig 7. Examples of erosion of roundhead.

Simultaneous tests with the two lay-outs, Fig.2, indicate that erosion of the narrow breakwater will start at less severe sea states than for the wide breakwater.

Having observed in the tests that the erosion reached a level of approximately $H_s/2$ below the still water level the eroded cross sections can be evaluated.

The ratio of erosion of the breakwaters seems to have the same value as the ratio of the eroded cross sections until the sea state reaches the level where practically every one of the waves erodes some stones.

Seastate	H_s	T_p	Number of waves	Ratio cross section	Ratio recession
F	0.10	1.70	3000	1.5	1.7
F	0.10	1.70	6000	1.5	1.6
F	0.10	1.70	9000	1.5	1.5
G	0.13	1.80	3000	1.5	1.6
G	0.13	1.80	6000	1.5	1.5
H	0.13	2.50	2000	1.5	1.9
H	0.13	2.50	3000	1.5	> 2.0

Table 2. Ratio of recession between the narrow crested breakwater and the wide crested breakwater.

Fig. 8 shows that the maximum width of the eroded breakwater seems to be almost independent of the width of the non-eroded structure.

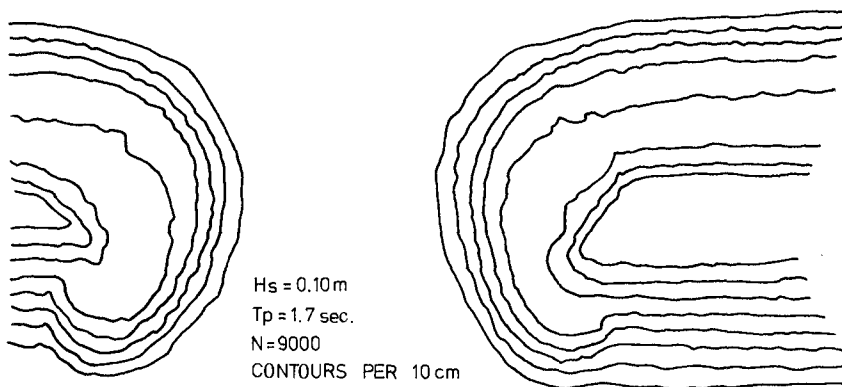


Fig. 8. Example of erosion of a narrow crested breakwater and a wide crested breakwater.

The area on the breakwater where the erosion starts was found to be on the seaward side of the roundhead. The location is different from what is observed for conventional breakwaters

where the erosion normally starts on the lee side of the breakwater, app. 135 degree angle with wave direction.

This difference might be explained by the larger width and larger roundhead diameter of the reshaping breakwater, which cause the stones on the leeward roundhead slope to be less exposed due to the diffraction of the waves along the relatively wide end of the roundhead. Moreover, the larger diameter provides a relatively better support of the stones in the direction of a wave attack.

Enlargement of the roundhead diameter has been used as a means of improving the stability of conventional breakwater roundheads, e.g. the Mohammedia breakwater in Morocco.

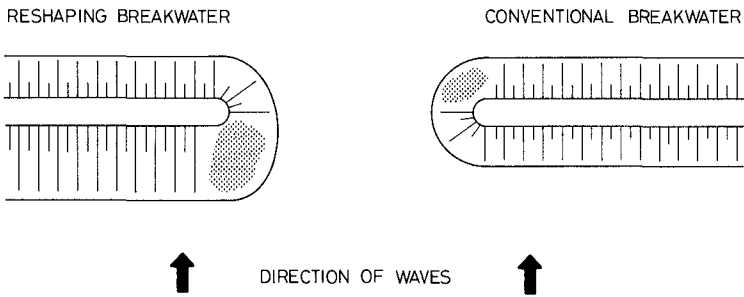


Fig 9. Area for start of erosion.

The breakwater develops into a characteristic banana shape as the erosion proceeds. Fig. 10 shows an example of the changing of the bathymetry of the roundhead.

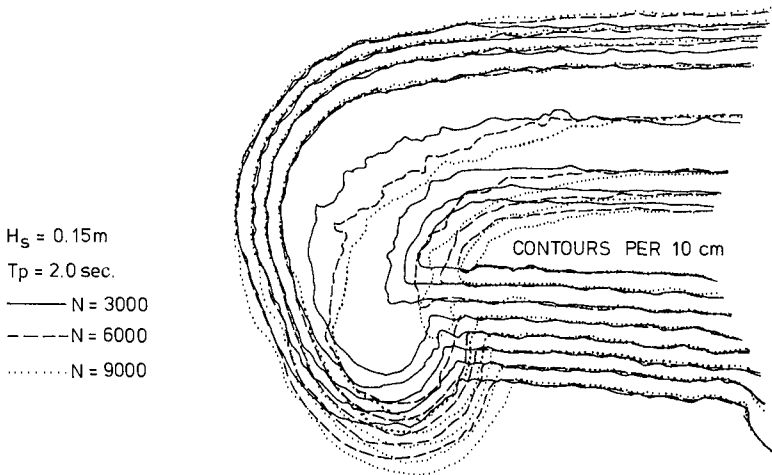


Fig 10. Time dependant development of roundhead.

STABILITY OF TRUNK AND LONGSHORE TRANSPORT IN OBLIQUE WAVES

In a trial test series it was found that for a given H_s , T_p the dynamically stable profiles in oblique waves within the tested range $\alpha \leq 30^\circ$, cf. Fig. 2, were almost identical to the profiles in head-on waves.

Thus in every test with oblique waves the initial profile was chosen as the one found after 3000 head-on waves.

The longshore transport was found from video recordings of the movements of coloured stones placed in three bands over the profile. Moreover, after a specific number of waves (or time) the number, the positions and the total weight of each type of coloured stones were recorded.

The band width and the number of waves N were adjusted to the sea state in such a way that within the test period the non-coloured stones upstream the coloured bands did not pass the downstream coloured band. In this way the average transport per second (or per wave) through a cross section could be found. Moreover, by studying the distribution of the coloured stones over the profiles the maximum erosion depth (i.e. the number of stone layers within which displacements take place) could be estimated. The number of waves in each test varied between 250 waves and 900 waves.

Test results

The steady state transport of stones along the trunk was studied for two angles of wave attack, $\alpha = 15^\circ$ and $\alpha = 30^\circ$, c.f. Fig. 2.

Sea state	H_s (m)	T_p (sec.)	Average mass transport, Q (g/sec.)	
			$\alpha = 15^\circ$	$\alpha = 30^\circ$
A	0.10	1.50	0.45	0.74
B	0.10	2.00	0.68	0.92
G	0.13	1.80	3.55	2.02
H	0.13	2.50	7.18	4.29
C	0.15	1.80	11.7	16.3
I	0.15	2.00	9.13	8.0
J	0.15	2.20	9.45	13.4
K	0.15	2.50	12.2	14.2
D	0.15	2.50	7.1	17.5
L	0.175	2.50	20.2	22.9
E	0.20	2.50	32.0	35.7

Table 3. Steady state mass transports along the trunk.

Notice that the sea states A and B only cause very small mass transports corresponding more or less to the onset of long-structure transport. Also notice that the more severe sea states L and E result in a significant transport, which in typical prototype situations will change the geometry of the structure significantly and might endanger the stability.

From the tests it is found that the average stone weight of the transported stones varied significantly. The range was from 14.3 g/stone (sea state H, $H_s = 0.13$ m, $T_p = 2.50$ sec., $\alpha = 15^\circ$) to 20.5 g/stone (sea state I, $H_s = 0.15$ m, $T_p = 2.00$ sec., $\alpha = 30^\circ$).

It was found that a small average stone weight corresponded to a relative large transport. Because the same stone sample was used in all the tests the observed sorting must be regarded as natural scatter of the process. The large scatter is a consequence of the relatively short duration of each test.

The results look homogeneous in the sense that the trend is that the transport increases with wave height, wave period and angle of incidence in the tested ranges. However, the large scatter in the results, makes it impossible to quantify the sediment transport accurately.



Fig 11. Example of the breakwater after longshore transport tests in oblique waves.

CONCLUSIONS

It is characteristic that a very wide range of sea states (from mild to severe) produce only slightly different trunk profiles in head-on waves, but very large differences in roundhead erosion and trunk erosion in oblique waves.

The roundhead erosion and the erosion of the trunk in oblique waves have a very strong non-linear dependency on the sea state. Below a certain sea state threshold value the erosion rates are very small, but excess of this value causes a drastic increase in the erosion. Consequently identification and consideration of this threshold value are of great importance in the design process.

Based on the presented model tests and the behaviour of some prototype breakwaters the

following somewhat premature recommendations valid for permanent designs with accepted moderate damage are proposed:

	$H_s/\Delta D_{n50}$
For trunks exposed to steep oblique waves	< 4.5
For trunks exposed to long oblique waves	< 3.5
For roundheads	< 3

These values should be used as guidelines *only* if no other more qualified information is available. This is because the parameters $H_s/\Delta D_{n50}$ is insufficient as among other things it does not contain the effect of wave length and the effect of the duration of the sea. Moreover, the influence of the breakwater geometry and the relative water depth are not included.

A study of a general parametric representation of the mass transport (erosion) based on a "shields approach" using characteristic wave parameters has been tried without much success.

It is believed that in additional investigations of erosion of reshaping breakwaters it will be necessary in principle to examine and summarize the respons from every single wave instead of using characteristic parameters like H_s to characterize the sea state. This is because the character of the flow kinematics in the erosion zones is strongly dependent on the size and the steepness of the single waves.

ACKNOWLEDGEMENT

The help of Mr. Van der Meer in estimating cross section profiles during the planning of the test is gratefully acknowledged. Also many thanks to the Laboratory for Photogrammetry and Surveying, University of Aalborg, for working out the photogrammetry and the contour plots of the bathymetry of the roundhead.

REFERENCES

- Van der Meer, J.W., Pilarczyk, K.W. *Dynamic stability of rock slopes and gravel beaches*. Published in proc. of the 20th Int. Conf. on Coastal Engineering, Taipei, 1986.
- Juul Jensen, O., Klinting, P. *Evaluation of scale effect in hydraulic models by analysis of laminar and turbulent flows*. Coastal Eng. vol. 7 no. 4, Nov. 1983, pp 319 - 329.
- Van Hijum, E., Pilarczyk, K.W. *Equilibrium profile and longshore transport of coarse material under regular and irregular attack*. Delft Hydraulics Laboratory. Publication no. 274, 1982.
- Bijker, E.W. *Littoral Drift as Function of Waves and Current*. Proc. 11th Coastal Eng. Conf., London, 1968.
- Baird, W.F. and Hall, K.R. *The design of Breakwaters using Quarried Stones*. Proc. of Offshore Technology Conf., Houston, Texas, 1984.
- Burcharth, H.F., Frigaard, P. *Reshaping breakwaters. On the stability of roundheads and trunk erosion in oblique waves*. Presented at Seminar for Unconventional Breakwaters, Ottawa, Canada, September 1987.

CHAPTER 170

ASSESSING THE EFFECT OF ARMOURSTONE SHAPE AND WEAR

John-Paul Latham*
Alan B. Poole**

ABSTRACT

Impacts, abrasion and physico-chemical weathering which sometimes result in rapid changes of armour shape and size can have disastrous consequences for armour stability. This paper draws together the background ideas and some new techniques which have been developed to tackle the prediction of weight loss and shape change of rock armourstone during the life of a coastal structure.

The framework proposed is to measure separately the wear resisting material properties of a rock type using a tumbling mill simulation of prototype block degradation. Time on the structure is then related to mill time by a factor which accounts for initial block size and the site specific environmental conditions. A field site in Scotland is used to demonstrate the new image analysis methods for measuring rounding of prototype blocks. The shape analysis results can also be used to calibrate the equivalent wear factor for conditions at that site. Discussion of this framework is extended to dynamically stable design concepts where abrasion losses are faster.

Preliminary flume testing in collaboration with H. R. Wallingford indicates that losses in stability due to rounding could be considerable.

INTRODUCTION

It is widely acknowledged that the occurrence of sources of rock with favourable geotechnical properties of rock in areas close to sites requiring slope protection against wave attack will guarantee the widespread use of rock armoured designs into the foreseeable future. By reviewing recent progress with techniques of measurement, this paper sets out to demonstrate that for natural armourstone, both block shape and the effect of wearing processes could be important design considerations and a way forward for taking these into account is suggested.

The paper is in three parts. The first provides the background, and presents the reasons for measuring shape and wear of armourstone. The second part summarizes the laboratory techniques for simulating prototype wear and measuring weight loss and shape changes, the details of which have been published elsewhere. In the third part, photography of block outlines from a Scottish case study are used to indicate abrasion rates. These form the basis of discussion of the implications for loss of stability of rounded rocks in the light

* Research Fellow: Geomaterials: School of Engineering, Queen Mary College, London, E1 4NS. U.K.

** Senior Lecturer, Geomaterials: School of Engineering, Queen Mary College, London, E1 4NS. U.K.

of recent flume experiments which were designed to investigate the effect of shape and rounding on stability.

BACKGROUND

Armourstone Degradation

The problem of rock degradation is not restricted to coastal engineering. In highway construction, (for example) to aid the selection of appropriate rock for road aggregate, Lees & Kennedy (1975) gave an account of mechanisms of degradation. In their paper, disintegration processes were considered according to the ratio of the size of the broken product to the size of the original particle. Although informative, their discussion is only partly applicable to the special demands of rock armourstone. Fookes et al. (1988) have recently attempted an extensive review of rock weathering in engineering time but again its applicability to armourstone wear is limited.

For riprap and armourstone, Lutton et al. (1981) reported details of project experience from 38 Corps of Engineers offices in the USA. The deterioration phenomena were classified as cracking, spalling, delaminating or splitting (of foliated rock), disaggregation (of granular poorly cemented rock), disintegration (due to unavoidable occurrence of shaly or weakened rock) and dissolution. Almost half the offices reported no degradation problems in the past 10 years to 1979 and, even though it was concluded that improved testing and geotechnical supervision could further reduce problems and achieve economies, degradation problems were generally considered relatively insignificant.

In recent years, with port expansion in areas where only poor quality rock is available, there has been growing interest in degradation problems. The mechanisms of wear and degradation of rock in the marine environment have been studied in Australia, the Middle East and the UK by Poole and various co-workers. Recommendations from their field and laboratory studies were reported by Fookes & Poole (1981), Dibb et al. (1983a,b), Poole et al. (1984) and Allsop et al. (1985). They identified catastrophic fracture, abrasion and spalling as the three classes of degradation mechanisms. The presence and nature of anisotropy, pre-existing cracks, joints and discontinuities in the rock fabric of an armour block are all important considerations, particularly since they may result in numerous block failures while handling during construction. However, further discussion, is concerned primarily with wear processes.

The disruptive forces driving the decay process which have a complex, often cyclic and stochastically varying time history, are set against the cohesive forces that the rock fabric can harness.

The static loads of the block weights give compressive and tensile stress concentrations depending upon block shapes, contact areas and settlements. With tensile strengths of rock at least ten times lower than compressive strengths, tensile cracking is much the commonest catastrophic failure mode under severe dynamic loads.

Abrasion due to attrition of suspended material is a type of high frequency dynamic indentation which leads to loosening of fragments along pre-existing cracks, cleavage planes and grain-boundaries and, to chipping resulting from lateral vent tensile cracks forming sub-parallel to the surface during unloading. It is not surprising therefore that Verhoef et al. (1984) were able to show a correlation of volume loss due to sand blasting with Brazilian tensile strength. On prototype armour, the size, velocity and hardness of the impactors and their density in the water jet will influence the attrition wear rates.

The larger dynamic forces occur during construction and while rocking, rolling and sliding during storms. These can result in major breakages creating new projectiles as well as shear and tensile mode cracking on all scales down to the rock grain size. In addition to impact forces, the more gradually varying wave forces produce a pulsating form of load

cycling. Both types promote the subcritical extension of tensile microcracks by the two mechanisms, stress corrosion and cyclic fatigue (see Costin and Holcomb, 1981).

The physico-chemical processes, whether salt crystallisation, hydration, differential thermal expansion or wetting and drying, can all induce cyclic pressure fluctuations which undoubtedly contribute to subcritical growth of tensile microcracks and eventual spalling of surface layers. Another cause of cracking and spalling could be the relaxation of residual tectonic stresses, an effect which can be measured using overcoring methods.

To summarize, it has been argued that wear processes at the armourstone surface, whether due to abrasion from external impacts or to disruptive pressures (e.g. from salt attack) within cracks and other surface openings, are essentially restricted by cohesive forces measured by the subcritical and critical indices of fracture toughness of the rock (which express its resistance to crack extension). Consider now the factors governing the rates of armourstone wear (i.e. weight losses) on coastal structures.

Rates of Wear

Rates of rounding were shown (Dibb et al., 1983a) to depend on the horizontal zone on the structure being considered because of the different energy associated with the various abrasion and physico-chemical forces at different positions relative to the still water level. The rates of armourstone wear as measured by the percentage of original weight remaining after a given number of years is likely to show a dependence on initial block dimensions since the rate of mass removal by abrasion is closely related to block surface area. The main factors governing wear rates on a new structure are:

- (i) size of armourstone;
- (ii) wave energy characteristics;
- (iii) zone on structure;
- (iv) size and type of water-borne attrition agents;
- (v) climatic influence on physico-chemical degradation mechanisms, e.g. temperature range, rainfall, humidity;
- (vi) local slope of armour layer - affects proportion of stone area exposed to attack;
- (vii) armourstone displacement tolerated in design concept;
- (viii) resistance of rock fabric to disaggregation under applied forces - a function of rock type and its degree of weathering.

Effects of Wear Processes

The effects of wear are to cause rounding, weight loss and some changes in void characteristics within the armourlayer surface. The number of point contacts with neighbouring blocks may even increase. The net effect will usually result in increased mobility of blocks and could possibly lead to instability. There may be a positive feedback here since increased mobility with significant rolling displacements of perhaps a few diameters per year, will further assist and accelerate wear.

Within the framework of Van der Meer's classification of rock slope structures (see Fig. 1), wear introduces two potential problems to the engineer. The first concern will be the reduction of interlock for conventional statically stable breakwaters. As the expected block mobility, crudely quantified by the dimensionless wave height parameter $H_s/\Delta D_{n50}$, is increased, a second concern becomes the weight loss. H_s is the significant wave height, Δ is the relative mass density and D_{n50} is the nominal diameter of the median armour weight. For structures with $H_s/\Delta D_{n50}$ approaching values as high as 20, seasonal profile adjustments can result in blocks moving up and down the slope depending perhaps on the timing of storms in relation to the tide cycle. The increased mobility that can result from rounding is not likely to be particularly threatening to the self-adjusting structure unless the weight losses due to size reduction and rounding become particularly marked and along-slope movements are considerable. As berm and S-shaped breakwaters and rock beach designs are increasingly being considered because of the possible economic advantages of their smaller block sizes, it

is important to consider whether the increased mobility is likely to affect the performance and integrity of the structure and, if so, in what time scale. Additionally, it should be noted that the overall rate of weight loss is faster for smaller armour blocks because in relation to their weight they have comparatively high surface area.

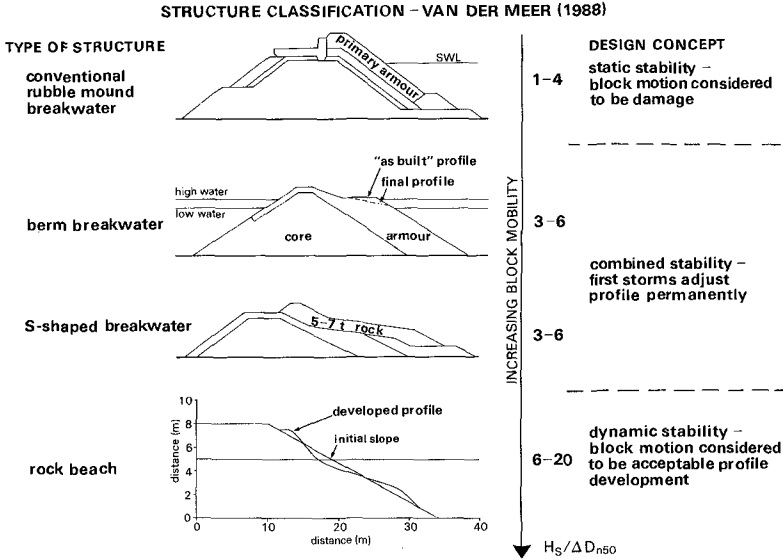


Figure 1: Types of rock armoured structures

Shape and its Controlling Factors

By shape, and in relation to armourstone, engineers will usually mean the gross shape which is often given by the axes of the enclosing cuboid. Most of the form indices such as flatness and sphericity are ratios of the X, Y and Z axes. In this paper, shape is taken to include the gross or overall shape but with details of the roundness of the corners together with the surface texture superimposed on and between the corners.

Factors at the quarry tend to govern the gross shape while those on the breakwater are a result of wear, and influence the roundness and surface texture.

The quarry may have been opened in a massive igneous intrusion yielding more equant blocks or alternatively, in a bedded sedimentary sequence giving more tabular blocks. If the rock is foliated or anisotropic, it may be impossible to obtain equant blocks with $X/Z < 2$. These are the geological controls. The structural geological setting which influences discontinuities and joint patterns as well as quarrying methods will also influence block shapes. The selection criteria (for example the exceedance value of the X/Z ratio) can also influence what is to be stockpiled and what rejected or re-blasted at the quarry.

Factors controlling block shape on the breakwater have already been discussed in relation to wear processes.

Design Implications of Block Shape

It should be stressed that it is placement technique in combination with block shape that is important in the performance of the breakwater.

For statically stable designs, interlock, macroporosity and thickness of the armour layer, which are all functions of shape are going to affect hydraulic stability. In fact, macroporosity and thickness both appear in Van der Meer's design equations through their influence on the permeability coefficient. The shape also influences hydraulic efficiency, i.e., reflection, transmission and run-up, although this may be of lesser significance.

Probably the main reason for rejecting rocks with higher X/Z ratios is a structural one. Tabular and elongate shapes, for example, have a lower resistance to fracture in bending because of the higher bending moments than for cubic blocks. However, there is some evidence emerging from the flume (see Table 1 and later discussion) that tabular blocks may have hydraulic advantages due to their higher resistance to rolling.

Purpose of Shape Quantification

To evaluate shape effects on static stability and hydraulic efficiency and thereby to improve specifications has been an overall objective of this current research. A related objective was to develop a laboratory simulation and a theory of abrasive wear in-service so that the wear during the life-time of a structure could be assessed for different rock types.

The whole question of shape effects could not be tackled with the conventional methods of shape quantification using the Krumbein/Wadell measure of roundness. The new techniques are described in a later section but first some of the evidence for the effect of rounding on static stability is reviewed.

Evidence of Shape Effects on Stability

Jensen (1984) presented two sets of results from random wave tests, one for 'quarystone' and one for rounded 'seastones'. A lower stability was noted for rounded tests although the two sets of test conditions appear to be different, making objective comparison difficult.

Bergh (1984) using an impermeable core, composite profile and irregular waves, found that for the start of damage $H_g/\Delta D_{n50}$ was 50% lower for rounded boulders than for cubic rock, implying an 8-fold increase in stone weight required for the rounded to achieve the same stability.

Van der Meer (1988) did not consider gross shape and roundness as test variables for static stability. However, significant abrasive rounding in his long test programme was suggested as a possible explanation of certain results. (For example, for surging waves, was generally 35% lower for the older and presumably rounded test material). These explanations have been vindicated by recent research to be reported in Latham et al. (1988).

The Shore Protection Manual suggests that a different stability coefficient K_D should be used for smooth rounded rock and rough angular quarystone. However, no clear guidance to the designer on shape effects is currently available.

It was noted that when, investigating dynamic stability, Van der Meer (1988) concluded that stone shape had no or only minor influence on the profile developed when for relatively permeable core conditions.

TECHNIQUES

Mill Abrasion Test

The mill abrasion test uses coarse aggregate pieces of crushed rock and was developed with the apparatus shown schematically in Fig. 2. For reasons set out in Latham & Poole (1987b) a number of features have been introduced which distinguish it from other tumbling mill abrasion tests used for aggregates. For example, there is a constant water level and throughput of water carrying fines and chippings away in suspension. The bulk volume

fraction of the mill cylinder is always kept between 0.5 and 0.4 as the successive increments of milling are followed by making up the weight losses with fresh material. The abrasion is relatively gentle and there are no steel balls in the mill. Keeping the abrasion/attrition environment relatively constant in this way means that any non-linear response of weight or shape with time in the mill is not an artefact of non-linear test conditions. Rather, it is a reflection of the behaviour of angular particles becoming rounded and smaller while they cascade across the dimetrical free surface on each revolution. It is these weight loss and shape change relationships that are of interest in the study of wear.

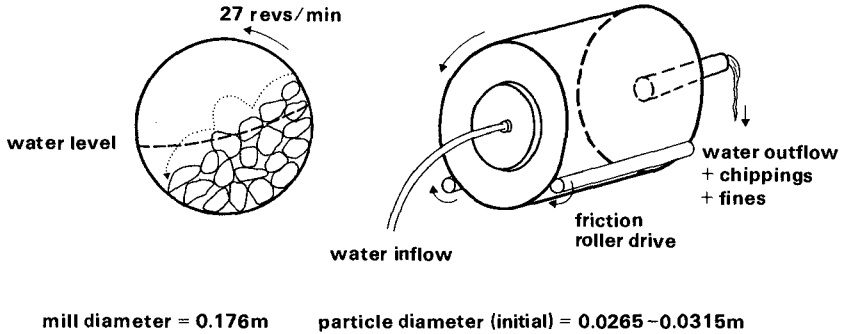


Figure 2: The tumbling mill abrasion test apparatus

The fraction of the original weight remaining when plotted against revolutions in the mill can be analysed to give two exponential coefficients, one of which is ideal for measuring and thus classifying the abrasion resistance of different rock types.

The experimental reproducibility was demonstrated using Carboniferous limestone aggregate in Latham & Poole (1988) and is reproduced in Fig. 3 together with the equation and coefficients describing the weight loss with time relationship. The coefficient k_s is the abrasion resistance index which can be used to describe the durability of the rock. The variation in test results for different rock types from a tough granite to a soft muddy limestone is indicated in Fig. 4. The values of k_s , indicated by the slopes, vary by about 2 orders of magnitude for the range of rock types likely to be encountered in coastal engineering works.

To examine the change in roundness or roughness of the blocks inside the mill, the image analysis techniques of the modern sedimentologist have proved invaluable.

Image analysis of block shape

The Fourier shape analysis methods of Ehrlich & Weinberg (1970) offer the best method for quantifying the rounding of blocks. Suppose the thin line in Fig. 5 is the outline given by the digitized coordinates (e.g. from a video camera). These coordinates can be represented by a Fourier series. The more terms or harmonics used in the series, the better the representation becomes. By the time the 10th term has been added see Fig. 5(d), the approximation, though quite good, is generally smoother than rough outlines with surface texture. To describe a rough irregular outline more precisely, the 11th to 20th harmonics are needed. In fact, the sum of the 11th to 20th harmonic amplitudes gives a very good measure of roughness, which was discussed with several other shape descriptors in Latham & Poole (1987a) and later given the name Fourier asperity roughness factor P_R where

$$P_R = (0.5 \sum_{n=11}^{20} C_n^2)^{0.5}$$

and C_n is the amplitude coefficient of the n th harmonic.

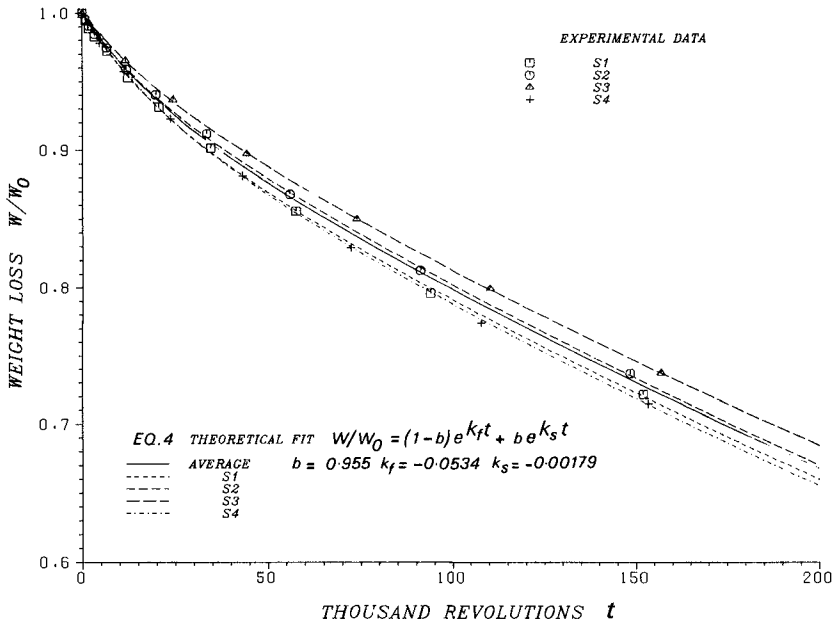


Figure 3: Reproducibility of mill abrasion test results from four limestone sample

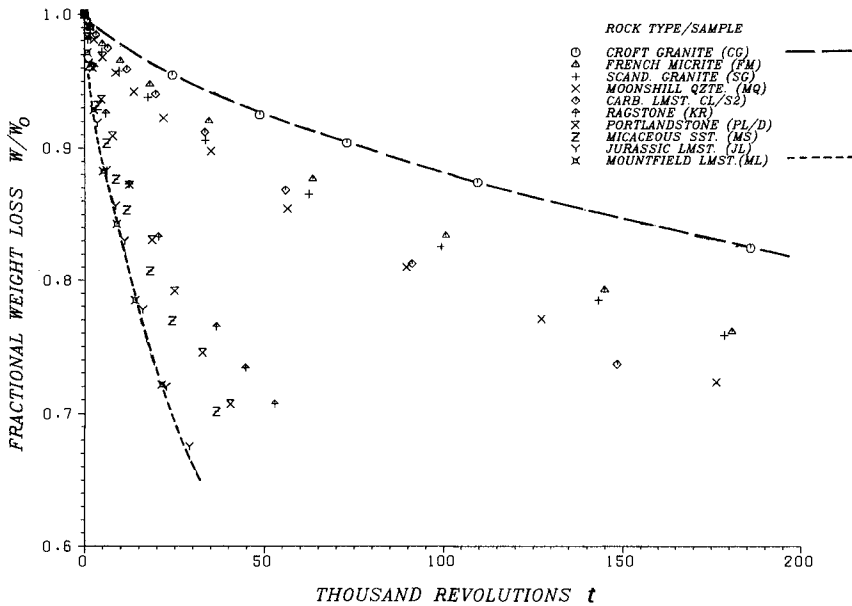


Figure 4: Variation of mill abrasion test results with rock type

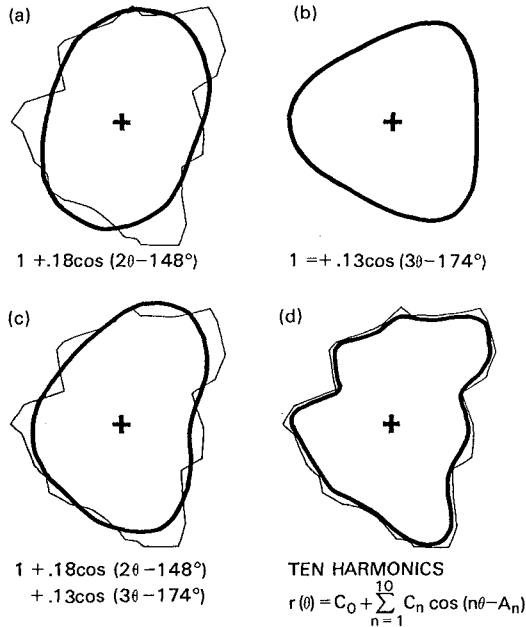


Figure 5: Contribution of Fourier harmonics to shape, after Ehrlich & Weinberg (1970)

AVERAGE SHAPE DESCRIPTOR VALUE	QMC/HR					DHL
	TABULAR	FRESH	EQUANT	S. ROUND	V. ROUND	EQUANT
Gross shape						
X/Z	3.23	2.22	1.82	2.19	1.92	1.7
P _C	2.67	1.88	1.43	1.89	1.55	
Roughness						
P _R	.0165	.0138	.0117	.0097	.0046	
V d Meer Coeff. surging formula	1.32 (7)	— (3)	1.19 (8)	1.10 (8)	0.95 (8)	1.0

$$H_s/\Delta D_{n50} = \underbrace{1.0}_{\text{COEFF}} P^{-0.13} (S/\sqrt{N})^{0.2} \sqrt{\cot\alpha} \frac{P}{\xi_m}$$

Table 1: Shape descriptor results for different armour shapes used in flume tests. A preliminary evaluation of a shape effect on stability is also shown.

A range of typical values of the Fourier shape descriptors is given in Table 1. The five shape classes were those tested for static stability in the flume at Hydraulics Research

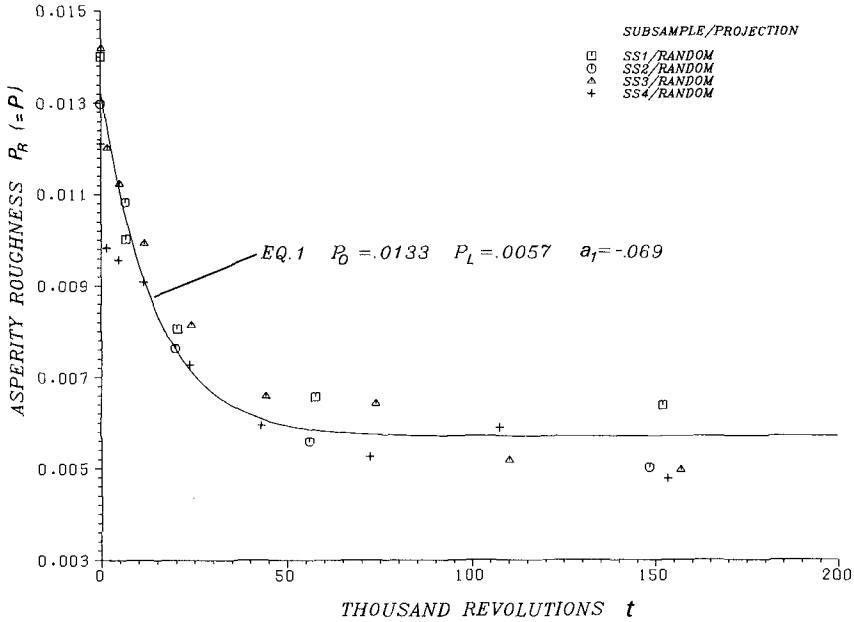


Figure 6: Roughness reduction during mill abrasion

Ltd. Each sample contained 48 blocks and the projections of the blocks were taken at random orientations to the video camera. Note P_C which indicates gross shape, is about 80% of the X/Z ratio for all 5 shapes. The asperity roughness P_R is very sensitive to the abrasive rounding. When FRESH material was put in the abrasion mill, after a 7% weight loss, P_R had fallen from 0.0138 to 0.0097 and after 23% weight loss, the VERY ROUND value was 0.0046.

Mill Abrasion Theory

To describe what is happening inside the mill, two assumptions are made. First, that a roughness parameter P will have the limiting exponential form

$$P - P_L = (P_0 - P_L) \exp(a_1 t) \tag{1}$$

during progressive abrasion where P_0 and P_L are initial and limiting (i.e. large t) values of P , a_1 is a constant and t is measured in thousands of revolutions of the mill. Second, that the instantaneous rate of weight loss is given by how much roughness there is left for removal and by the fraction of the original weight remaining, which yields the differential equation

$$\frac{d(W/W_0)}{dt} = a_2 (P - P_L) + a_3 (W/W_0) \tag{2}$$

The solution is $W/W_0 = \frac{a_2 (P_0 - P_L) \exp(a_1 t)}{(a_1 - a_3)} + \left\{ 1 - \frac{a_2 (P_0 - P_L)}{(a_1 - a_3)} \right\} \exp(a_3 t)$ (3)

which is the same form as the equation given in Fig. 3 for quantifying the abrasion resistance k_s from the weight loss results. It was expressed as follows

$$W/W_0 = (1 - b) \exp(k_f t) + b \exp(k_s t) \quad (4)$$

The consequence of equating these coefficients using experimental data and curve fitting to test the validity of the assumptions turns out to be favourable since a_f is approximately equal to k_f . It appears then, that the weight loss can be directly related to shape changes when the roughness P is described by the asperity roughness P_R . For the two exponential coefficients in equation (4), k_f is the smoothing resistance index which describes the rate of the fast process of removing asperities and k_s , the abrasion resistance index, describes the rate of the slow process of overall size reduction, (b is a mixing term). Eliminating t produces an equation for W/W_0 in terms of asperity roughness.

$$W/W_0 = (1 - b) \left(\frac{P - P_L}{P_0 - P_L} \right) + b \left(\frac{P - P_L}{P_0 - P_L} \right)^{k_s/k_f} \quad (5)$$

A more detailed theoretical development was given in Latham & Poole (1988). Fig. 6 has been taken from that paper to illustrate the fit of equation (1) to the abrasion mill data for four Carboniferous limestone samples.

A new concept is now introduced so that the laboratory information and theory of the mill abrasion test can be applied beyond simple rock durability assessment.

Equivalent Wear Factor

The great number of factors that affect the rate of wear on the prototype breakwater was indicated earlier in this paper. It is suggested that all the site specific and environmental factors should be combined together and kept separate from the rock durability and that the implicit assumption be made that the progress of prototype rounding, for a given rock type, is equivalent to that which occurs inside the mill for that same rock type but that it occurs at a different rate. The EQUIVALENT WEAR FACTOR X to relate these laboratory and prototype rates was defined (Latham & Poole, 1988) as the number of years of exposure at a particular zone on a given structure that is equivalent to 1000 revolutions in the tumbling mill test described in the reference. However, in that paper, the authors neglected to point out the need also to separate the initial block weight from the combined site specific factors. The effect that initial block size will have on rate of weight loss is conveniently taken into account assuming the volume to surface area relationship. For example, if the rate of removal of two different sized blocks with the same shape is initially governed by their surface areas, then for an 8-tonne block which after 1 year loses, say, 0.20 tonnes ($W/W_0 = 0.975$), a 1.0 tonne block loses 0.05 tonnes ($W/W_0 = 0.950$) which is a faster rate of fractional weight loss. For a given set of site specific factors, the equivalent wear factor x will depend on the size of the prototype blocks. In Latham & Poole (1988), the suggested values of x were based on observations of rounding where the armourstones were nominally 8 tonnes. To adjust for a different initial block weight W_n in tonnes, the equivalent wear factor x becomes $(W_n/8)^{1/3}$ times its value for an 8-tonne block. Clearly a suggested value of x should refer to a particular initial block weight.

From the data obtained on statically stable breakwaters in N.E. Queensland, the Middle East and the U.K., for the most aggressive environment in the intertidal zone, a value of $x = 0.5$ was suggested for 8 tonne armour. Table 2 shows how the mill abrasion test data for Carboniferous limestone can be used to predict wear rates (both weight loss and rounding) on statically stable structures built with 8-tonne Carboniferous limestone armour. For example, a 12% weight loss ($W/W_0 = 0.88$) would occur between 25 and 50 years in service for a relatively aggressive environment with $x = 0.5$ to 1. A smaller value of x implies a faster rate of wear.

Field evidence from West Bay, Dorset, reported by Clark (1988) is discussed in the report (Latham et al., 1988), where it was concluded that aggressive conditions with shingle attack corresponded to an x value of about 0.8 for 8-tonne armour.

The image analysis techniques can be applied to armour blocks from real structures. This allows for a direct measurement and comparison of the shapes and relative states of rounding of different armour blocks to be made. The results obtained can be used to help calibrate x for different site conditions as demonstrated below.

Weight loss W/W_0	Asperity roughness P_R	Revs in mill (thousand) t	Equivalent Wear Factor for $W_0 = 8$ tonnes		
			Mild $x = 5$	$x = 1$	Aggressive $x = 0.5$
Years on breakwater					
0.97	0.0102	10	50	10	5
0.94	0.0083	20	100	20	10
0.88	0.0062	50	250	50	25
0.80	0.0057	100	500	100	50

Table 2: Application of the equivalent wear factor concept to Carboniferous limestone armour

APPLICATIONS

Rounding of Whin Sill Dolerite from Buckhaven, Scotland.

This revetment structure was constructed in 1975 and was reported to have been designed at a 1 in 2 slope and built with 1 to 2-tonne armourstone quarried from the Whin Sill dolerite. It is underdesigned in that storms frequently cause rocks to roll down onto the foreshore. It is one of the only U.K. examples of a structure resembling a rock beach where block mobility and shingle attrition have combined to produce dramatic rates of wear against perhaps one of the most durable rock types in the U.K. A typical angular block and a well rounded block were shown in Allsop & Latham (1987). Digitized outlines of 8 upper blocks and 8 lower blocks are shown in Fig. 7.

Although these block outlines are not statistically representative samples, for illustration the upper block values may be equated with the initial condition during construction and the lower block values with 12 years' wear. The gross shape parameter P_C has hardly changed while the asperity roughness P_R has fallen from 0.0149 to 0.0062. Mill abrasion results were not available for this rock type but it is known to have a very high fracture toughness ($K_{Ic} \approx 3 \text{MPa.m}^{0.5}$) and density ($\approx 3.0 \text{tonnes/m}^3$).

On this basis and comparing with test results for the toughest granites, an estimate of the abrasion resistance index and other mill abrasion constants can be calculated. Applying the mill abrasion theory outlined above with the available measured and estimated data suggests that 50,000 revolutions in the mill would give the observed P_R value of 0.0062 and at a weight loss of 9%. The equivalent wear factor x for these semi-mobile blocks of about one tonne is therefore $12/50 = 0.25$. However, for 8-tonne blocks, the value would be 0.5.

It might be expected that equivalent wear factors on dynamic structures would be lower (i.e. faster wear) than for statically stable structures. It is possible then that the value of 0.5 for 8-tonne blocks which was suggested in Latham & Poole (1988) for extremely aggressive environments on statically stable structures is slightly too low and is more representative of a structure which has included some mobility in the design concept (e.g. $H_g/\Delta D_{n50} \approx 6$).

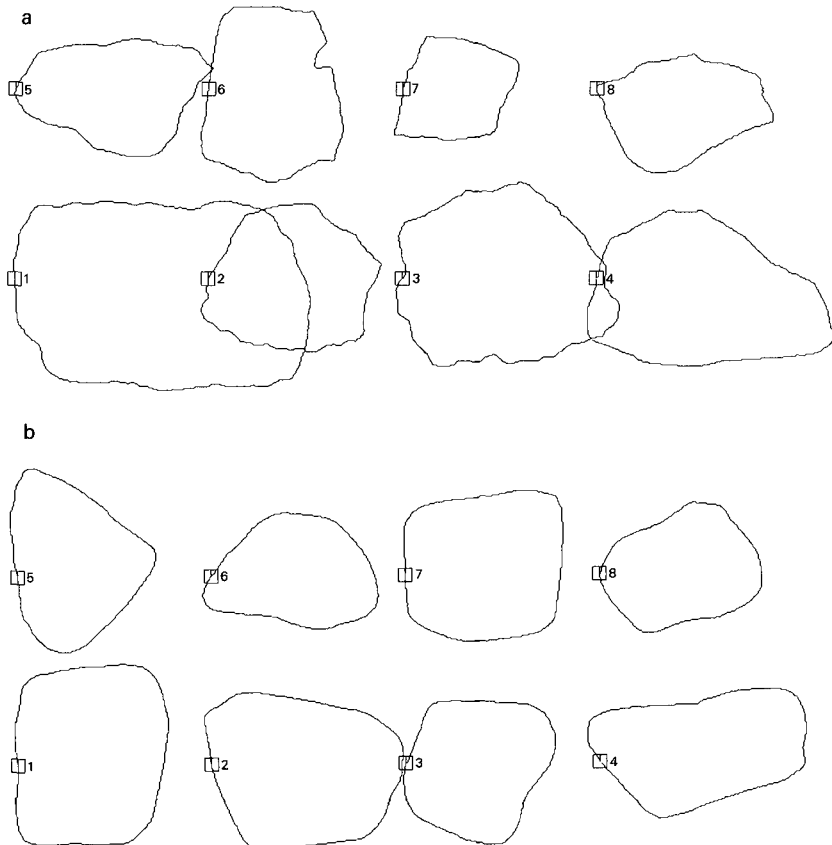


Figure 7: Digitized outlines of blocks from Buckhaven; a upper, b lower

Discussion

As a working hypothesis, it is reasonable to suggest that the material property measured by the resistance to weight loss inside the tumbling mill over, say, one day will rank different rock types correctly in terms of their weight loss performance over perhaps 10 years of episodic wear on a breakwater. The validity of the equivalent wear factor concept used in the prediction of in-service rates of wear is more tenuous and requires further validation in the future. The concept assumes that the non-linear equations (1) to (4) for mill abrasion also apply to prototype abrasion.

Two likely objections to this are (i) that wear mechanisms, particularly those of sub-critical crack growth, not properly represented in the abrasion mill may contribute to the form of the non-linear relationship on the prototype; (ii) that, while the work done per unit time is kept relatively constant in the mill, the average work done by disruptive forces on each armour block of a dynamic structure (where there is a gradual increase in block mobility due to rounding) may increase with time, thus having an accelerated effect on weight loss rates.

In response to these legitimate criticisms: (i) it was noted that the Allison and Savage (1976) prototype weight loss data gave essentially the same type of relationship observed for

abrasion inside the mill; (ii) the equivalent wear factor concept provides a framework which takes account of two of the most important reasons for relative differences in wear rates, namely material properties and initial block sizes. The framework can be refined and calibrated by future observations and tests; (iii) The relationship in equation (5) is time-independent so that, for blocks undergoing attack on all sides, it is possible to predict weight losses directly from shape changes measured on a prototype structure; (iv) for dynamic structures, the problem may be more complex although in some respects the mill simulation is more appropriate. It may be fruitful to consider Van der Meer's (1988) treatment of dynamically stable profile development in a search for the likely influence of armour block mobility on the choice of x . For structures with $H_g/\Delta D_{n50} \leq 6$, the acceleration effect of increasing mobility on wear rates may be negligible. For structures with $H_g/\Delta D_{n50} \geq 6$, a question to address is how many block diameters does the average block roll per year and does this distance depend on block shape?

Flume Test Results on Rounded and Angular Material

For static stability, the consequence of weight loss on armour stability can be calculated using Van der Meer's (1987) design equations. To predict the effect of rounding on static stability, the limited series of flume tests conducted in collaboration with Hydraulics Research Ltd, Wallingford, can provide some tentative guidance. The flume tests first reported by Bradbury et al. (1988) were intended as a preliminary series to evaluate shape effects on stability. For each different shape of rock tested, the results were fitted to Van der Meer's surging wave equation. Where Van der Meer obtained a coefficient value of 1.0, the flume tests found this coefficient, and therefore the stability, to be dependent on shape. For instance, the coefficients (see Table 1) suggest that the very round rock gives $(1.19/0.95)^5$ or 3 times more damage than the equant rock. The asperity roughness appears to account for the shape effect on stability reasonably systematically. For statically stable designs, the tests suggest that the loss of interlock due to rounding contributes more to instability than the weight loss itself accompanying the rounding. These aspects of the flume tests will be considered in detail in the report by Latham et al. (1988).

ACKNOWLEDGEMENTS

The authors wish to express their thanks to William Allsop for collecting photographs from Buckhaven and for his interest in this research. The paper has benefited from certain points raised during discussion by one questioner for which we are grateful. The research was funded by the Science and Engineering Research Council of Great Britain under grant GR/D/69921.

REFERENCES

- Allison, D. M. & Savage, R. P. (1976) Tests of low-density marine limestone for use in breakwaters. U.S. Army Corps of Engineers, Coastal Engineering Research Centre, Tech. Paper No. 76-4
- Allsop, N. W. H., Bradbury, A. P., Poole, A. B., Dibb, T. E. & Hughes, D. W. (1985). Rock durability in the marine environment. Hydraulic Research Ltd, Report No. SR11.
- Allsop, N. W. H. & Latham, J-P. (1987). Rock armouring to unconventional breakwaters: the design implications for rock durability. Seminar on Unconventional Rubble-Mound Breakwaters, NERC, Ottawa, Canada, Paper No. 2.
- Bergh, H. (1984). Riprap protection of a road embankment exposed to waves. Hydraulic Laboratory, Royal Institute of Technology, Stockholm, Sweden. Bulletin No. TRIA-VBI-123
- Bradbury, A. P., Allsop, N. W. H., Latham, J-P., Mannion, M. B. & Poole A. B. (1988). Rock armour for rubble mound breakwaters, sea walls and revetments: recent progress. Report no. SR 150, Hydraulics Research
- Clark, A. R. (1988). The use of Portland Stone rock armour in coastal protection and sea defence works. Q.J. Eng. Geol., London, Vol. 21, p.113-136.

- Costin, L. S. & Holcolm, D. J. (1981). Time-dependent failure of rock under cyclic loading. *Tectonophysics* Vol. 79, p.279-298.
- Dibbs T. E., Hughes, D. W. & Poole, A. B. (1983a). Controls of size and shape of natural armourstone. *Q.J. Eng. Geol.*, London, Vol. 16, p.31-42.
- Dibb, T. E., Hughes, D. W. & Poole, A. B. (1983b). The identification of critical factors affecting rock durability in marine environments. *Q.J. Eng. Geol.*, London Vol. 16, p.149-161.
- Ehrlich, R. & Weinberg, B. (1970). An exact method for characterizing grain shape. *Journal of Sedimentary Petrology*, Vol. 40 p.205-212.
- Fookes, P. G. & Poole, A. B. (1981). Some preliminary considerations on the selection and durability of rock and concrete materials for breakwaters and coastal protection works. *Q.J. Eng. Geol.*, London Vol. 14, p.97-128.
- Fookes, P. G., Gourley, C. S. & Ohikere, C. (1988). Rock weathering in engineering time. *Q.J. Eng. Geol.*, London Vol. 21, p.33-57.
- Jensen, O. J. (1984). A monograph on rubble mound breakwaters' Danish Hydraulic Institute, Denmark.
- Latham, J-P. & Poole, A. B. (1987a). The application of shape descriptor analysis to the study of aggregate wear. *Q.J. Eng. Geol.*, London Vol. 20, p.297-310.
- Latham, J-P. & Poole, A. B. (1987b). Pilot study of an aggregate abrasion test for breakwater armourstone. *Q.J. Eng. Geol.*, Vol. 20, p.311-316
- Latham, J-P. & Poole, A. B. (1988). Abrasion testing and armourstone degradation. *Coastal Engineering*, Vol. 12.
- Latham, J-P., Mannion, M. B., Poole, A. B., Bradbury, A. P. & Allsop, N. W. H. (1988). The influence of armourstone shape and rounding on the stability of breakwater armour layers. Coastal Engineering Research Group. Report 1, Queen Mary College, London University.
- Lees, G. & Kennedy, C. K. (1975). Quality, shape and degradation of aggregates. *Q.J. Eng. Geol.* Vol. 8, p. 193-209.
- Lutton, R. J., Houston, B. J. & Warriner, J. B. (1981). 'Evaluation of quality and performance of stone as riprap or armour. U.S. Army Corps of Engineers, Tech. Report GL-81-8.
- Poole, A. B., Fookes, P. G., Dibb, T. E. & Hughes, D. W. (1984). Durability of rock in breakwaters. *Breakwaters - design and construction*, p.31-43, Thomas Telford Ltd, London.
- Van der Meer, J. W. (1987). Stability of breakwater armour layers - Design formulae. *Coastal Engineering*, Vol. 11, p.219-239.
- Van der Meer, J. W. (1988). Rock slopes and gravel beaches under wave attack. PhD Thesis, Delft Hydraulics Communication No. 396.
- Verhoef, P. N. W., Kuipers, T. J. & Verwaal, W. (1984). The use of the sand blast test to determine rock durability. *Bulletin Int. Assoc. Eng. Geol.*, Vol. 29 PARIS, p.457-461.

Wave Uplift Forces on Platforms with Energy Absorbers

Jiin-Jen Lee, M. ASCE¹ & C.P. Lai, A.M. ASCE²

ABSTRACT

Interaction of large amplitude wave with platforms or docks in a variable depth medium has been studied theoretically and numerically. The underside of the platform is equipped with energy absorbing linear spring in order to study the energy absorbing effect for reducing the uplift forces on the platform or dock.

The flow is assumed to be inviscid, irrotational without current. Laplace equation with full non-linear free surface equations are solved by isoparametric mapping technique. A Galerkin finite element model is used to model the transformed equations. The adaptive line SOR (Successive-Over-Relaxation) technique is used.

The results indicate that uplift wave forces on platforms or docks can be significantly reduced by very soft springs. Wave profile history confirms the manifested mechanism of energy absorption. The results also indicate that larger uplift forces are easier to be damped out by the prescribed energy absorbing mechanism than the smaller uplift forces.

1. INTRODUCTION

It has been found that as a finite amplitude ocean wave strikes an offshore platform which is located above the still water surface, the platform will register a positive uplift force followed by a negative force if the clearance between the platform is smaller than the wave amplitude (see El Ghamry (1963), Wang (1967), French (1969), Lai (1986), Lee & Lai (1986), Lai & Lee (1988)). Such repeated wave actions constitute a serious dynamic loading to the marine platforms.

¹ Professor of Civil and Environmental Engineering, University of Southern California, Los Angeles, CA 90089-0231

² Project Engineer, Environmental and Ocean Technology, Inc. (E.O. Tech), Suite 885, 150 N. Santa Anita Ave., Arcadia, CA 91006

One of the ways to overcome this problem would be to place the platform at a distance significantly above the sea surface so as to ensure that no such dynamic uplift forces would occur. Such a design however, might place the platform in a height that could create other negative impacts. For example, the economic concern or the dynamic vibrations. Another approach would be to develop certain energy absorption mechanism on the platform allowing certain reasonable and moderate soffit clearance. In an earlier study by Lai (1986), Lee and Lai (1986), it has been found that this hydrodynamic force is strongly dependent on relative wave amplitude. As the relative amplitude of the wave increases, the maximum uplift force increases while the maximum negative forces decreases. From the point of view of the structure safety, the increase in maximum uplift force might create significant negative impacts on the structure.

The main objective of this study is to explore ways to reduce the maximum uplift forces when a large amplitude wave strikes a platform. To accomplish this the numerical model presented by Lai (1986) and Lee & Lai (1986) has been extended to allow the treatment of significantly large incident wave amplitude and to incorporate the energy absorption mechanism at the platforms.

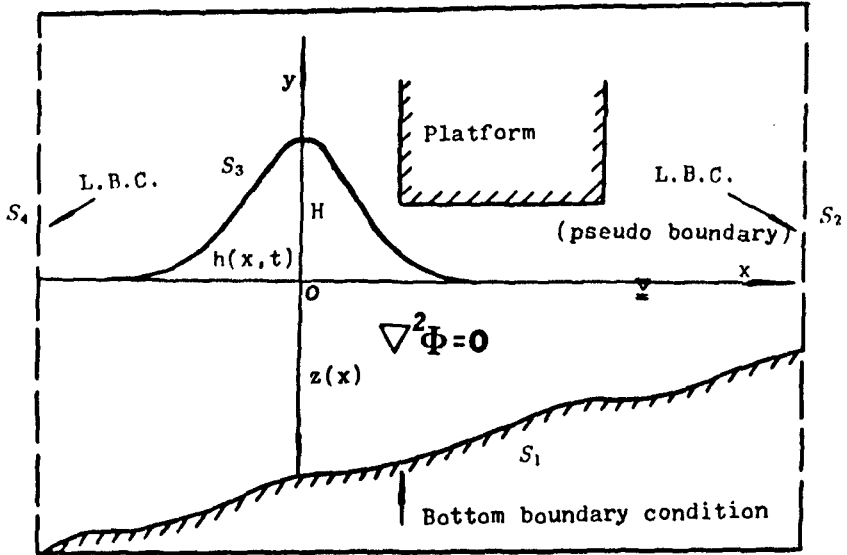
2. THEORETICAL DEVELOPMENT

For the mathematical model, the flow is assumed to be inviscid, incompressible, irrotational, and without ambient current. The wave-structure interaction can then be solved by making use of a potential flow theory, the velocity potential must satisfy the Laplace equation. A definition sketch is shown in figure 1. The dynamic free surface condition is that the pressure must be equal to the atmospheric pressure at the free surface. On the rigid boundaries, normal velocity is prescribed, for rigid bottom this velocity is zero, and for a body in motion the normal velocity of the fluid particle at the platform must be equal to that of the platform velocity. In the analysis, we allow physical domain to be long enough to have "no flow" conditions at both far field boundaries. This requires that the horizontal velocity be zero at lateral boundaries at infinity. Therefore, the governing equation and boundary conditions at free surface are:

$$\nabla^2 \phi = 0$$

$$h_t + \phi_x h_x - \phi_y = 0 \quad \text{on } y = h(x, t)$$

$$\phi_t + \frac{1}{2}(\phi_x^2 + \phi_y^2) + gh = 0 \quad \text{on } y = h(x, t)$$



L.B.C. = Lateral boundary condition

Figure 1 Definition Sketch for the Problem of a Wave Interacting with a Platform or a Dock

$$\phi_z = U = 0 \quad \text{on } S_2 \quad \text{and } S_4$$

$$\phi_n = 0 \quad \text{on } S_1$$

$$\phi_y = V = \frac{ds}{dt} \quad (\text{when wave hit the platform}) \quad \text{on } S_3$$

where S_1, S_2, S_3, S_4 are surface boundaries.

It is noted that the difference between the present formulation and the prior studies by the authors is to allow the underside of the platform to move at the velocity ds/dt . This motion is resisted by a distribution of linear springs assumed to exist just above the surface of the underside of the platform. A rigid platform would correspond to the case of spring constant being infinite. A softer spring therefore would yield a larger velocity of the underside of the platform.

The difficulty of the problem lies in the nonlinearity and the coupling of the boundary conditions at the free surfaces, which are time dependent. The free surface elevation is an unknown a priori and it must be a part of the solution of the problem along with the Laplace equation on the interior of the fluid region as well as the equations at the free surface. To handle a moving free surface and an irregular bottom topography, we adopt a mapping technique to transfer the fluid region and its boundaries into a regular geometry.

The physical domain is transformed into a regular computational domain by using isoparametric mapping. The transformed governing equations are more complicated than the original governing differential equations. However, the advantage is that the solution region has a regular rectangular shape in the parent plane. The nonlinearity of the moving free surface is no longer a serious problem in the transformed plane. The approximate solutions of the transformed equations are sought by using the Galerkin's finite element method. For a detailed discussion of the numerical procedure, the reader is referred to Lai (1986).

The finite element model is advanced in time by integrating the dynamic and kinematic free surface equations. The Runge-Kutta method is employed with mass lumping. The mass lumping technique can eliminate the coupling between the time derivatives of the unknowns at adjacent nodes and reduce the computer storage and computational steps with only a minor loss in accuracy.

A major difficulty in numerical integration of the free surface equations is the computational instability. Approximation of spatial derivatives by numerical methods introduces truncation errors.

These errors are amplified by nonlinear terms and as they accumulate for large time, would seriously affect the accuracy of the solution. Moreover, when a wave starts to hit a platform or a dock, run-up is created by the platform or the dock, and reflected wave can be formed at the frontal edge of the platform or dock. This discontinuity in the free surface profile causes a severe oscillation at the frontal face of the platform or dock for the large time. To avoid the instability of numerical integration, an artificial viscosity term has been introduced with their value determined by numerical experiments.

An adaptive line SOR algorithm is developed and used to speed up the repeated solution of linear algebraic equations resulting from finite element discretization of the transformed Laplace equation. The idea of adaptive line SOR method is to employ adaptive parameter of relaxation in LSOR to accelerate the convergence rate. It was found that the adapted line SOR algorithm could effectively reduce the error norm by several orders of magnitude for the similar number of iteration.

3. PRESENTATION AND DISCUSSION OF RESULTS

One of the simplest energy absorbing mechanisms which could be employed for numerical experiment is to place flexible spring just above the underside of the platform where wave could hit the platform. The spring allows the underside of the platform to deform upward as the positive uplift forces occur. It would also allow it to return to the original surface as the contact between the water surface and the underside of the platform ceases to exist. A variation of different spring constant has been experimented. It is noted that the case of rigid platform corresponds to the case of infinitely large spring constant K .

Figure 2 shows the numerical results of the hydrodynamic uplift force in platform with a 3 inch soffit clearance in a water depth of 15 inch. The relative wave amplitude is 0.24. The ordinate of the figure is the ratio of the total hydrodynamic uplift forces which is integrated from the computed uplift pressure over the entire platform divided by the total hydrostatic forces. The hydrostatic force is taken as the integrated weight of the water above the elevation of the platform. The computed forces based on the present numerical procedure is plotted as a function of the normalized time history. Three different spring constants are used for comparison. The rigid body would represent a spring constant of infinity. It is seen that the softer the spring the smaller the computed uplift forces. The wave amplitude used for this case is not too large, therefore the positive uplift forces differ only slightly from the hydrostatic forces. From the numerical result it is also clear that in order to meaningfully reduce the uplift force (either positive or negative) the flexible spring has to be quite

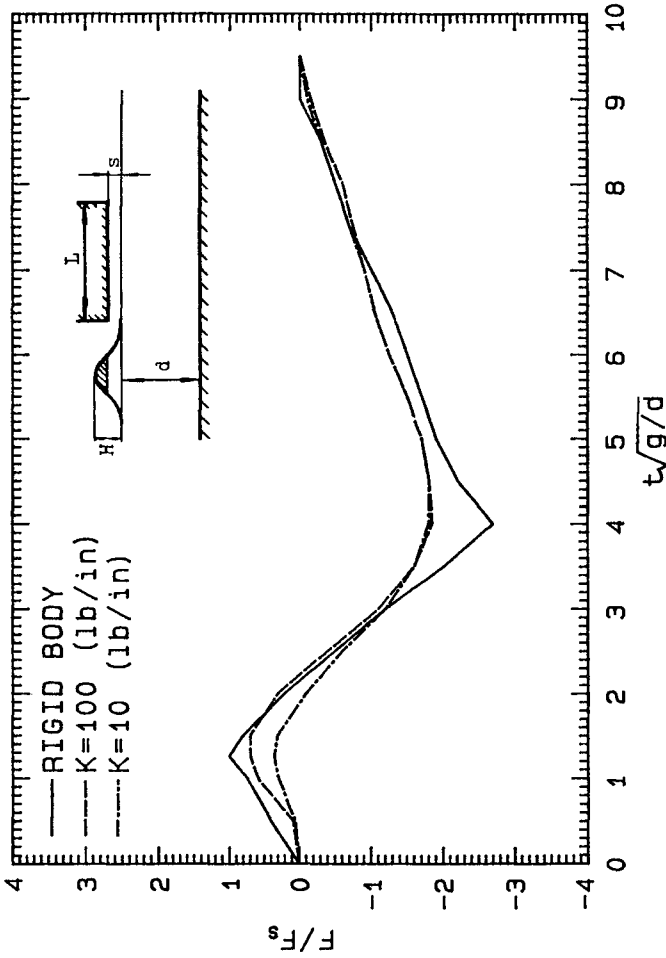


Figure 2 Normalized Total Hydrodynamic Force Per Unit Width.
 ($H/d = 0.24$, $s/d = 0.2$, $L/d = 4$, $d = 15$ in.)

soft.

Figure 3 presents the force history when the incident relative wave amplitude is increased to 0.32 keeping other parameters the same as that shown in Figure 2. In this case the positive uplift force is significantly increased, this phenomena has been shown in earlier studies by Lai (1986) and Lai and Lee (1988). Based on the numerical results it is surprising to find that for moderately stiff springs the magnitude of the forces can only be modified by a small amount. In order to reduce the maximum positive uplift forces by a significant degree the spring must be quite soft. A comparison of the results for $K=100$ lb/in and that for $K=10$ lb/in show that the magnitude of the positive uplift force is significantly reduced for $K=100$ lb/in the magnitude of uplift force is quite close to the case of rigid platform.

The normalized uplift force per unit width in a sloping bottom is shown in Figure 4 for a rigid platform and that with two different spring constants ($K=100$ lb/in and $K=10$ lb/in). The relative incident wave amplitude is 0.32 and that the platform is placed at the back wall allowing wave reflection from the back wall. As expected, the positive uplift force is drastically large than that shown in Figure 3 signifying the effect of wave reflection from the back wall. The effect of the energy absorbing spring to dampen the large uplift forces can clearly be seen from the numerical results.

It is interesting to learn how the wave form changes as the incident wave interact with the platforms or docks. Numerical result on the wave amplitude along the direction of wave propagation is shown in Figure 5. The parameters representing the wave channel, incident waves and the dock dimensions are the same as that shown in Figure 4. In Figure 5, wave profiles along the x axis at different time steps are shown for $K=100$ lb/in. It is seen that the wave crest have not reached the platform after 150 time steps thus the incident wave has been propagating unchanged toward the positive x direction. After 200 time steps portion of the incident wave hit the platform (as the soffit of the platform is smaller than the wave amplitude), thus wave form is changed accordingly and the relatively soft spring allow the underside of the dock to absorb energy by compressing the spring. This process continues through 250 time steps. At 300 time steps the travelling wave is reflected back from the back wall and is travelling away from the dock region. without the confinement of the underside of the dock platform, large amplitude oscillation is seen in the wave amplitude profile presented in the result for 300 time steps. This interesting phenomena is repeated in Figure 6 at 300 time steps for two different spring constants. For $K=100$ lb/in the maximum clearance between the still water level and the underside of the dock is less than 0.3 as shown in Figure 6. As portion of the wave travels back and moving away from the dock site, the wave (both positive

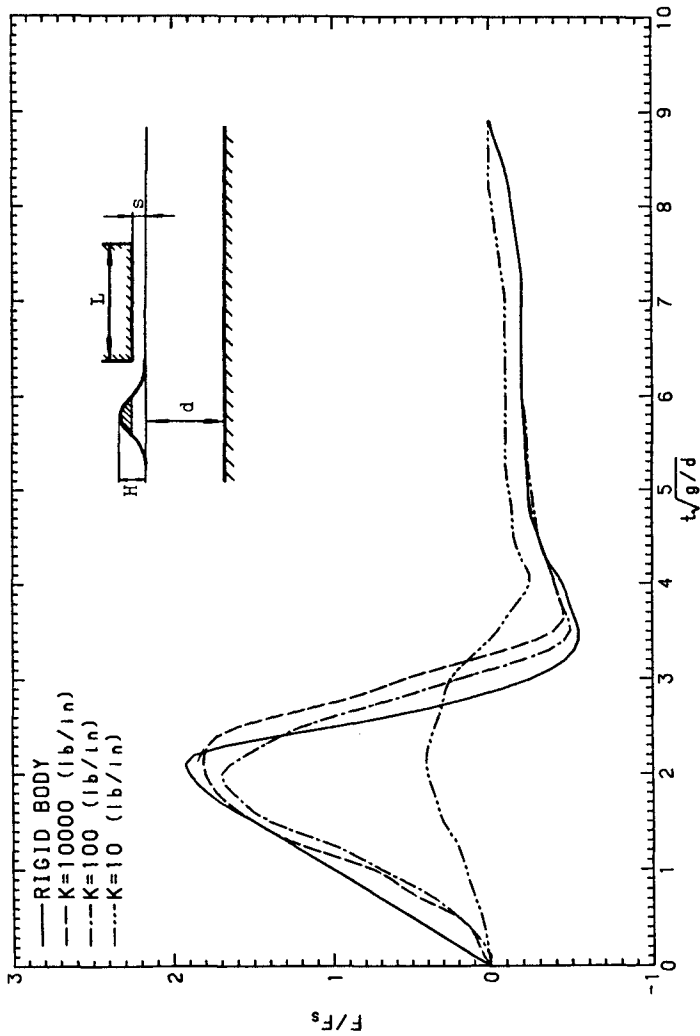


Figure 3 Normalized Total Hydrodynamic Force Per Unit Width.
 ($H/d = 0.32$, $s/d = 0.2$, $L/d = 4$, $d = 15$ in.)

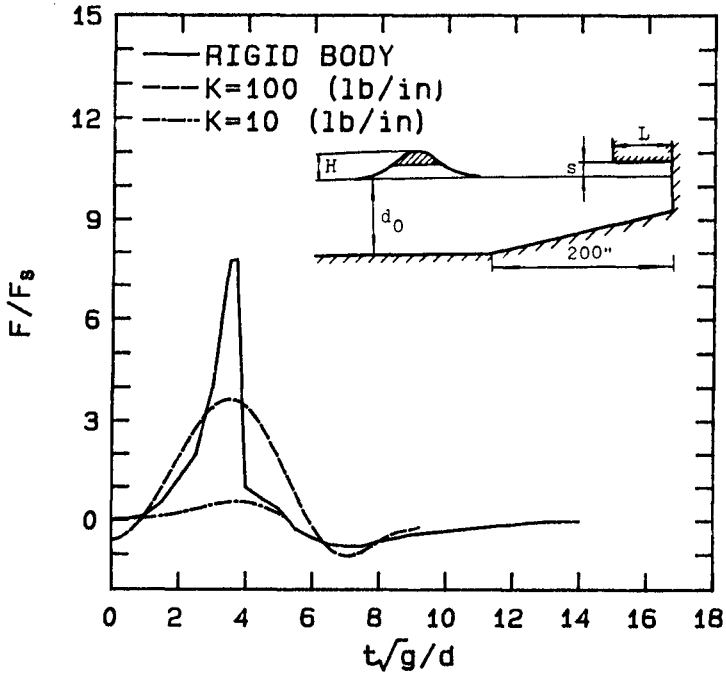


Figure 4 Normalized Uplift Force Per Unit Width
 ($H/d_0 = 0.32$, $s/d_0 = 0.2$, $L/d_0 = 4$,
 $d_0 = 15$ in.)

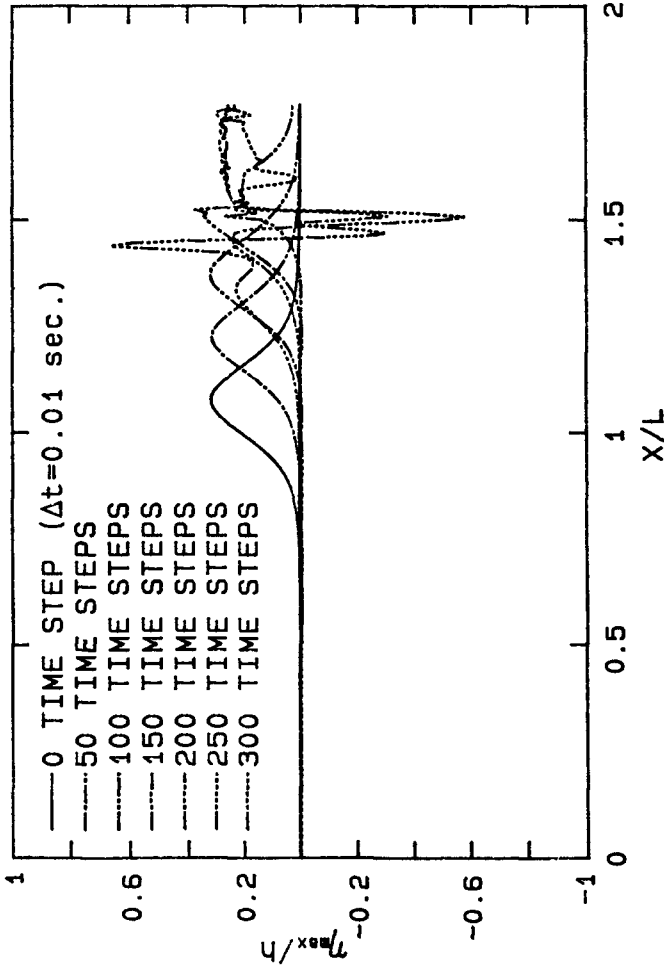


Figure 5 Wave Profiles at Different Time Step before and after Interacting with the Dock Placed at a reflecting Back Wall

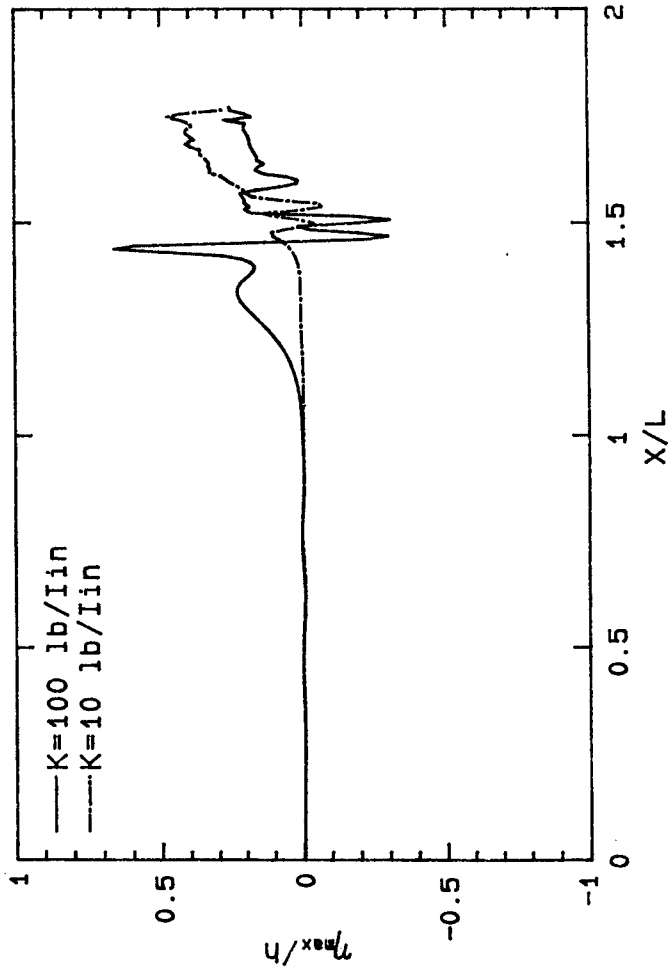


Figure 6 Wave Profile at 300 Time Steps Interacting with the Dock with Different Spring Constants Associated with the Energy Absorber

and negative) is significantly increased its amplitude. For a softer spring ($K=10$ lb/in) the underside of the dock is permitted to move upward thus the clearance is increased thereby absorbing a significant amount of wave energy. Therefore, wave profile for $K=10$ lb/in at 300 time steps is reduced. It is interesting to note the difference in wave phases for these cases for spring with $K=10$ lb/in, wave appears to travel at a slower speed.

4. CONCLUSION

The numerical experiments conducted in obtaining the effect of absorbing linear springs placed at the underside of the platform /or dock appears to be able to absorb certain wave energy and to reduce the positive uplift force induced by wave interacting with platforms /or docks. Significant reduction in this uplift force can only be achieved by very soft springs. For the dock problem (reflecting wall placed at the end of the dock) the energy absorbers appear to offer greater reduction in the uplift forces. The magnitude of the uplift forces experienced by the platform /or dock with spring attached at its underside can be computed using the present numerical model but can not be generalized by a simple formula due to the complexity of the problem.

5. ACKNOWLEDGMENTS

The authors appreciate the funding supports from the USC Foundation for Cross-Connection Control and Hydraulic Research (FCCCHR).

6. REFERENCES

1. El Ghamry, O. (1963), "Wave Forces on a Dock," Report No. HEL-9-1, University of California, Berkeley, California.
2. French, J.A. (1969), "Wave Uplift Pressure on Horizontal Platforms," Report NO. KH-R-19, W.M. Keck Laboratory of Hydraulics and Water Resources, California Institute Technology, Pasadena, California.
3. Lai, C.P. (1986), "Wave Interaction with Structure: Hydrodynamic Loadings on Platforms and Docks," Ph.D. thesis, University of Southern California.
4. Lai, C.P. & Lee, J.J. (1988), "Interaction of Finite Amplitude Waves with Platforms or Docks", Accepted for publication, ASCE,

Journal of Waterways Port, Coastal and Ocean Engineering Division.

5. Lee, Jiin-Jen & Lai, C.P., "Wave Uplift on Platforms or Docks in Variable Depth," Proceeding of the 20th International Conference on Coastal Engineering, November 9-14, 1986, Taipei, Taiwan, pp 2023-2034.
6. Wang, H. (1967), "Estimating Wave Pressure on a Horizontal Pier," Technical Report R546, Naval Civil Engineering Laboratory, Port Hueneme, California.

CHAPTER 172

A NEW TYPE OF BREAKWATER UTILIZING AIR COMPRESSIBILITY

Masaaki IKENO*

Naokatsu SHIMODA**

and

Koichiro IWATA***

ABSTRACT

This paper is to investigate both theoretically and experimentally the wave energy dissipation and air-pressure variation of a new type of breakwater having a pressurized air-chamber and two buoyancy tanks. The theoretical models are developed in this paper and they are shown to be in good agreement with experimental values. The new type of breakwater proposed in this paper is pointed out to attenuate the transmitted wave much better than the rectangular-shaped and concave-shaped breakwaters without the air-chamber.

1. INTRODUCTION

Development of a new type of breakwater having a high sea water exchange and wave energy dissipation is strongly required from environmental and disaster prevention viewpoints.

This paper deals with a new type of fixed breakwater which has one pressurized air-chamber and two buoyancy tanks. The great merit of the breakwater lies in the function that the resonant period can be easily adjusted only by changing the air pressure in the air-chamber without changing the geometrical shape of breakwater itself.

So far, Kiyokawa and Ohyama (1986) and Iwata et al. (1987) have discussed the wave attenuation of the breakwater with a pressurized air-chamber. There still remain, however, problems to be solved from theories and experiments.

* M.Eng., Research Engineer, Central Research Institute of Electrical Power Industry, Abiko, Chiba, Japan

** B.Eng., Vice-Head, General Technical Research Laboratory, Gikenkogyo Co. Ltd., Hachiohji, Tokyo, Japan

*** D.Eng., Professor, Dept. of Civil Eng., Nagoya Univ., Nagoya, Aichi 464, Japan.

First of all, two theoretical models based on the Dividing Region and Source Distribution Function Methods are newly developed, which take account of air compressibility in the air-chamber. Secondary, laboratory experiments are performed not only to examine the validity of the proposed theoretical models, but also to reveal the characteristics of wave energy dissipation and variation of air pressure in the air-chamber.

2. THEORETICAL MODELS

The Dividing Region Method and Source Distribution Function Method are employed to evaluate changes of wave and air pressure in the air-chamber. The wave treated here is a two-dimensional and irrotational small amplitude one. The fluid is assumed to be inviscid.

2-1. Dividing Region Method

The fluid domain is divided into five regions, as shown in Fig.1. The region I includes the incident and reflected waves and evanescent mode waves, and the transmitted wave exists in the region, V. The air pressure head R in the region III changes with wave motion. Extending the analytical treatment proposed by Iwata et al. (1986), velocity potentials in the five regions are expressed by the following:

$$\phi_1 = (A_0 e^{ik(x-\ell_2)} + B_0 e^{-ik(x-\ell_2)}) \frac{\cosh k(h+z)}{\cosh kh} + \sum_{n=1}^{\infty} B_n e^{-kn(x-\ell_2)} \frac{\cos k_n(h+z)}{\cos k_n h} \quad \text{--- (1)}$$

$$\phi_2 = C_0 x + D_0 + \sum_{s=1}^{\infty} (C_s \sinh \frac{s\pi x}{(1-q_1)}) + H_s \cosh \frac{s\pi x}{(1-q_1)} \cos \left(\frac{s\pi(h+z)}{(1-q_2)h} \right) \quad \text{----- (2)}$$

$$\phi_3 = (E_0 e^{ik'x} + F_0 e^{-ik'x}) \left(\frac{\cosh k'(h+z)}{\cosh k'h} \right) + \sum_{m=1}^{\infty} (E_m e^{k'_m x} + F_m e^{-k'_m x}) \left(\frac{\cos k'_m(h+z)}{\cos k'_m h} \right) + \frac{iP_0}{\rho\sigma} \quad \text{----- (3)}$$

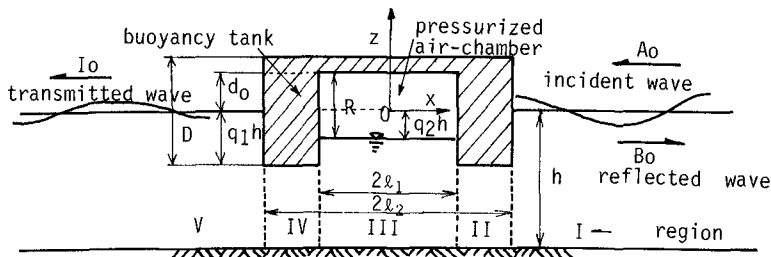


Fig.1 Schematic illustration of new type of breakwater with pressurized air-chamber and two buoyancy tanks and illustration of symbols

$$\phi_4 = G_0 x + H_0 + \sum_{s=1}^{\infty} (G_s \sinh \frac{s\pi x}{(1-q_1)h} + H_s \frac{s\pi x}{(1-q_1)h}) \cos(\frac{s\pi(h+z)}{(1-q_1)h}) \quad (4)$$

$$\phi_5 = I_0 e^{ik(x+\ell_2)} (\frac{\cosh k(h+z)}{\cosh kh}) + \sum_{n=1}^{\infty} (I_n e^{k_n(x+\ell_2)} (\frac{\cos k_n(h+z)}{\cos k_n h})) \quad (5)$$

Here, $\phi_1, \phi_2, \phi_3, \phi_4$ and ϕ_5 are, respectively, the velocity potentials in the regions, I, II, III, IV and V, A_0 the complex amplitude of incident wave ($=igH_I/2\sigma$); g the gravitational acceleration, H_I the incident wave height; i imaginary unit number; σ the angular frequency ($=2\pi/T$); T the wave period, B_0 the complex amplitude of reflected wave; I_0 the complex amplitude of transmitted wave; $B_n, C_s, D_s, E_m, F_m, G_s, H_s$ and I_n ($n=1, 2, 3, \dots, s=m=0, 1, 2, \dots$) complex unknown coefficients; h the still water depth; x the horizontal axis; z the vertical axis; k, k_{n1}, k' and k'_m the wave numbers satisfying the relationship of $\sigma^2/g = k \tanh kh = -k_n \tan k_n h = k' \tanh k'(1-q_2)h = -k'_m \tan k'_m(1-q_2)h$; ρ the density of water; P_0 the air pressure amplitude in the air-chamber; $2\ell_2$ the length of air-chamber; $2\ell_1$ the length of breakwater; $q_1 h$ the submerged depth of breakwater.

(b) Air pressure amplitude P_0

The 5th term, $iP_0/\rho\sigma$ in Eq.(3) is the pressure term added by compressibility of air in the air-chamber. In deducing Eq.(3), the air pressure, P_a in the air-chamber is expressed as

$$P_a = \bar{P}_0 + P_0 e^{i\sigma t}, \quad (\bar{P}_0 = \rho g q_2 h + P_{air}) \quad (6)$$

where, \bar{P}_0 is the initial air pressure and P_{air} the atmospheric pressure. The linearized dynamic boundary condition on the free surface in the air-chamber is

$$\eta = -i \frac{\sigma}{g} \phi_3 - \frac{P_a}{\rho g} \quad (7)$$

where, η is the free surface elevation from the still water level.

Substitution of Eqs.(3) and (6) into Eq.(7) and assumption of uniform rise and fall of water surface in the air-chamber yield

$$\eta = -q_2 h + \eta_0 e^{i\sigma t}, \quad \eta_0 = \frac{1}{2\ell_1} \int_{-\ell_1}^{\ell_1} (-i \frac{\sigma}{g} (E e^{ik'x} + F e^{-ik'x}) (\frac{\cosh k'(1-q_2)h}{\cosh k'h})) dx \quad (8)$$

The volume of air, V in the air-chamber is given by

$$V = V_0 - \eta_0 e^{i\sigma t}, \quad V_0 = d_0 + q_2 h \quad (9)$$

where, V_0 is the initial volume of air in the air-chamber and d_0 the clearance of the upper plate from the still water level at the region, I and V (see Fig.1).

Assuming the adiabatical change of air in the air-chamber, the air pressure P_a corresponding to air volume of V is given by

$$P_a = \bar{P}_0 (V_0/V)^r, \quad (r = 1.4) \quad (10)$$

Linearization after substitution of Eqs.(6) and (9) into Eq.(10) yields

$$P_o = r\bar{P}_o(\eta_o/do + q_2h) \quad \text{----- (11)}$$

(c) Matching condition

The continuity of pressure, P and horizontal particle velocity, u is employed as the matching condition at the boundary between two regions (i.e., $x = \ell_1, \ell_2, -\ell_1$ and $-\ell_2$). The pressure, $P_j, (j=1 - 5)$ and horizontal velocity of water particle, $u_j, (j=1 - 5)$ are estimated with

$$\left. \begin{aligned} P_j(x, z; t) &= -\rho g z - i\rho\sigma\phi_j(x, z)e^{i\sigma t} \\ u_j(x, z; t) &= \frac{\partial}{\partial x}(\phi_j)e^{i\sigma t} \end{aligned} \right\} \text{----- (12)}$$

where, subsuffix j indicates the region, j.

(i) $x = \ell_2$	$\begin{aligned} P_1(\ell_2, z; t) &= P_2(\ell_2, z; t) && ; (-h \leq z \leq -q_1h) \\ u_1(\ell_2, z; t) &= 0 && ; (-q_1h < z \leq 0) \\ &= u_2(\ell_2, z; t) && ; (-h \leq z \leq -q_1h) \end{aligned}$	}
(ii) $x = -\ell_2$	$\begin{aligned} P_5(-\ell_2, z; t) &= P_4(-\ell_2, z; t) && ; (-h \leq z \leq -q_1h) \\ u_5(-\ell_2, z; t) &= 0 && ; (-q_1h < z \leq 0) \\ &= u_4(-\ell_2, z; t) && ; (-h \leq z \leq -q_1h) \end{aligned}$	}
(iii) $x = \ell_1$	$\begin{aligned} P_3(\ell_1, z; t) &= P_2(\ell_1, z; t) && ; (-h \leq z \leq -q_1h) \\ u_3(\ell_1, z; t) &= 0 && ; (-q_1h < z \leq -q_2h) \\ &= u_4(\ell_1, z; t) && ; (-h \leq z \leq -q_1h) \end{aligned}$	}
(iv) $x = -\ell_1$	$\begin{aligned} P_3(-\ell_1, z; t) &= P_2(-\ell_1, z; t) && ; (-h \leq z \leq -q_1h) \\ u_3(-\ell_1, z; t) &= 0 && ; (-q_1h < z \leq -q_2h) \\ &= u_4(-\ell_1, z; t) && ; (-h \leq z \leq -q_1h) \end{aligned}$	}
----- (13)		

Since A_o is given as $igH_I/2\sigma$ (known value), the unknowns of $B_n, C_s, D_s, E_m, F_m, G_s, H_s$ and I_s ($n=s=m=0, 1, 2, 3, \dots$) are determined by solving Eq.(13) with help of Eqs.(1) through (12). The reflection coefficient, r_R and transmission coefficient, r_T are defined by $|B_o/A_o|$ and $|I_o/A_o|$, respectively.

2-2. Source Distribution Function Method

The velocity potential in the fluid, $\phi(x, z)$ is expressed by the sum of the incident wave velocity potential, ϕ_I and the scattered wave one, ϕ_D and ϕ_D is given by a function of the Green function, G and the source distribution function, f as follows (Nakamura et al.(1982));

$$\left. \begin{aligned} \phi(x, z) &= \phi_I(x, z) + \phi_D(x, z) \\ \phi_D &= \int_S f(X, Z) \cdot G(x, z; X, Z) ds(X, Z) \\ G &= \frac{(ik^2 - ko^2)e^{ik|x-X|}}{k(hk^2 - hko^2 + ko)} \cosh k(h+Z) \cosh k(h+z) \\ &\quad - i \sum_{n=1} \frac{(k_n^2 + ko^2)e^{-k_n|x-X|}}{k_n(hk_n^2 + hko^2 - ko^2)} \cos k_n(h+Z) \cos k_n(h+z) \end{aligned} \right\} \text{----- (14)}$$

where, ko is the wave number in deep water; k and k_n the

wave number satisfying the relationship of $\sigma^2/g = k_0 = k \tanh kh = -k_n \tan k_n h$; x the horizontal axis; z the vertical axis with origin at still water level; X and Z the source point; i the imaginary unit number; h the still water depth; s the boundary having the source points.

Once f is determined, P_0 , r_R and r_T are easily obtained. The detailed calculation technique is referred to reference 4). In this study, the source points were distributed at the interval of $\Delta s/L = 0.02$ along the submerged breakwater surface under water and along the water surface in air-chamber, where Δs is the element length between adjacent two source points and L the wavelength at the depth of h .

3. LABORATORY EXPERIMENTS

3-1. Equipment and procedure

In the experiments, two wave tanks were used. Main parts of experiments were performed in an indoor wave tank in 0.9m height, 0.7m width and 25m length at Nagoya University. A flap-type wave generator controlled by Oil-pressure servo was installed at one end of the tank. The water is perfectly shut out from the area behind the wave board. Therefore, the input electrical signal is smoothly converted to the wave motion. At the other end of wave tank, a wave absorbing slope constructed with crush stone and stainless steel chips was placed so as to reduce the wave reflection to a minimum. A large wave tank in 1.6m height, 1m width and 50m length of General Technical Research Laboratory at Gikenkogyo Co.Ltd. was also used to examine the scale effect of model breakwater to the air pressure variation in the air-chamber.

Two model breakwaters made of acrylic plate, as shown in Fig.2, were employed to investigate the wave energy dissipation and air pressure variation in the air-chamber. The other types of breakwater such as concave-shaped and rectangular-shaped ones were also employed in order to discuss the difference in wave attenuation among the three types of breakwater. The submerged depth, $q_1 h$ and pressurized head, $q_2 h$ adopted in this study are listed in Table 1, which also includes q_1 in case of the concave-shaped and rectangular-shaped breakwaters.

Water surface profiles were measured with three capacitance-type wave gauges and they were all recorded on a magnetic tape. The transmitted wave was measured with the wave gauge, No.3 which was located at about one wave length distance from back side of

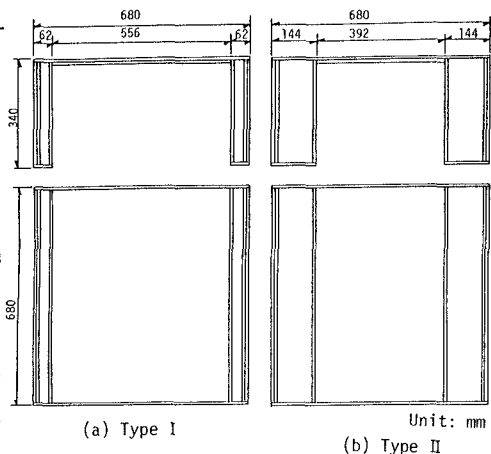


Fig.2 Geometrical scale of model breakwaters with pressurized air-chamber

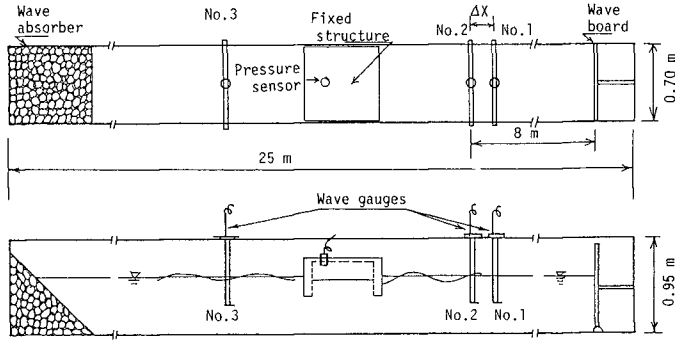


Fig.3 Schematic illustration of experimental set up

Type I pressurized-type		
	pressurized head q_2h (cm)	draft depth q_1h (cm)
 $\lambda_1/\lambda_2=0.82, 0.99$	1.1	29.3
	2.1	25.3
	4.0	17.7
	5.2	13.3
Type II		
	pressurized head q_2h (cm)	draft depth q_1h (cm)
 $\lambda_1/\lambda_2=0.58$	-1.7	17.7
	0.0	15.6
	1.8	13.3
Type I' concaved-shaped		
	pressurized head q_2h (cm)	draft depth q_1h (cm)
 $\lambda_1/\lambda_2=0.82$	1.1	29.3
	2.1	25.3
	4.0	17.7
	5.2	13.3
Type II'		
	pressurized head q_2h (cm)	draft depth q_1h (cm)
 $\lambda_1/\lambda_2=0.58$	-1.7	17.7
	0.0	15.6
	1.8	13.3

Table 1 Experimental condition for three types of breakwaters (pressurized-type, concave-shaped and rectangular-shaped breakwaters)

rectangular-shaped	
	draft depth q_1h (cm)
	29.5
	25.3
	17.7
	15.6
	13.3

the breakwater. The partial standing wave profiles were measured with two wave gauges, No.1 and No.2 in order to calculate the reflection coefficient, r_R . The distance, Δx between the two wave gauges was changed according to the wave period; that is, $\Delta x=(9/8)L$ for $T=0.5s$, $\Delta x=(7/8)L$ for $T=0.6s - 0.8s$ and $\Delta x=(3/8)L$ for $T \geq 1.0s$, where L is the wave length at the depth of h . The air pressure in the air-chamber was measured with a pressure gauge (Kyowa PGM-0.5) attached to the top plate in the air-chamber.

All the experimental waves generated in this study were regular ones. The wave period employed was $0.5s, 0.6s, 0.65s, 0.7s, 0.75s, 0.8s, 0.9s, 1.0s, 1.2s, 1.4s, 1.6s, 2.0s$, and $2.4s$. The wave steepness, H/L was 0.01 for $q_1=0.488$ and 0.02 for $q_1=0.222, 0.295$ and 0.422 in order to avoid wave breaking. The still water depth was $60cm$ throughout the experiments.

Total number of experimental runs was about 300. The experimental set-up and conditions performed in the large wave tank of GTRL at Gikenkogyo Co.Ltd. are not described here, due to limitation of paper. As mentioned above, experiments in the large wave tank were carried out to check the model scale effect to the air pressure in the air-chamber. Based on Froude similarity law, dimensions of model breakwaters, water depth and wave conditions were determined so as to correspond to experiments in small wave tank at Nagoya university. The geometrical scale in the large wave tank was selected as 1.7 times larger than that in the small wave tank. The number of experimental runs in the large wave tank was about 50.

3-2 Data analysis

The wave reflection coefficient, r_R was calculated with two-wave-gauges method (Goda & Suzuki (1976)), using the measured wave profiles at wave gauges No.1 and No.2. The transmission coefficient, r_T was calculated using measured wave height of wave gauge, No.3. The reflection and transmission coefficients, r_R and r_T are defined by H_R/H_I and H_T/H_I , respectively, where H_R , H_T and H_I are the reflected, transmitted and incident wave heights, respectively.

3-3 Results and discussion

Using Dividing Region Method (hereafter referred to as DRM) and Source Distribution Function Method (hereafter referred to as SDFM), theoretical values of wave transmission and reflection coefficients and air pressure variation in the air-chamber were evaluated to compare with experimental values. One example is shown in Fig.4, in which experimental values are also plotted for comparison. Theoretical calculations based on the two methods are in good agreement with experimental values. Difference between theoretical values estimated with DRM and those with SDFM is recognized very small in the range of $2\lambda_2/L \leq 0.6$, which is general feature in this study. Since DRM requires less computational time than

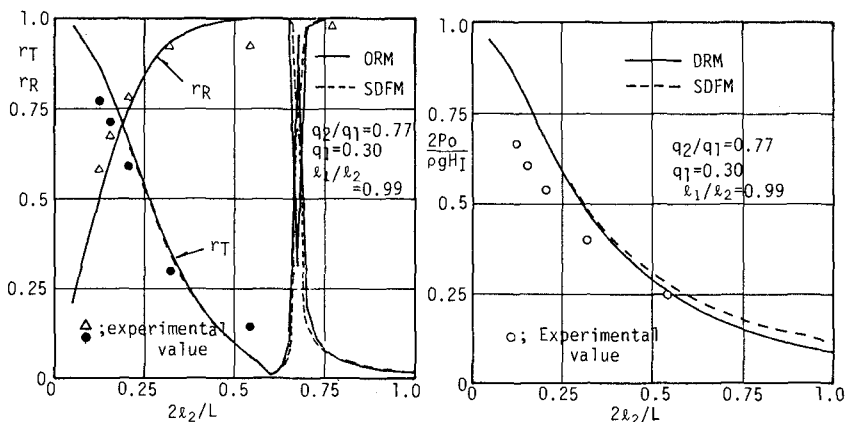


Fig.4 Comparison of theoretically estimated values between Dividing Region Method and Source Distribution Function Method.

SDFM. In addition, theoretical values of $P_o/\rho g H_I$ estimated with DRM seem to be in better agreement with experimental values, as shown in Fig.4. Therefore, hereafter, theoretical values evaluated with DRM are employed to compare theory with experiments.

Fig.5 shows changes of the transmission coefficient, r_T and the reflection coefficient, r_R with $2\lambda_2/L$. It is seen that the theoretical values agree well with experimental values. The transmission coefficient, r_T increases with decreasing of $2\lambda_2/L$ and q_1 . r_T is expected to be less than 0.25 for $2\lambda_2/L \geq 0.3$ in case of $q_1=0.422$, $q_2=0.035$ and $\lambda_1/\lambda_2=0.82$, as shown in Fig.5(c). On the other hand, the reflection coefficient, r_R decreases with a decrease of q_1 and $2\lambda_2/L$. r_R is almost equal to 1 in the range of $2\lambda_2/L \geq 0.8$, which is independent of q_1 , q_2 , d_0 and λ_2/λ_1 , as shown in Fig.4, in this study.

The effect of initial air pressure, \bar{P}_o to r_R and r_T is not clearly recognized. The effect of pressurized head, $q_2 h$ to r_R and r_T is not clear too, although r_T seems to become smaller as $q_2 h$ becomes larger, as shown in Fig.4. This may be due to the reason that the experimental range of the initial air pressure, \bar{P}_o and the pressurized head, $q_2 h$ was too narrow to affect r_R and r_T . Concerning the effect of initial air pressure or pressurized head to r_R and r_T , we will discuss later from theoretical calculations with DRM.

Fig.6 shows two examples of variations of the dimensionless air pressure amplitude, $P_o/\rho g H_I$ in the air chamber. It can be pointed out, from Fig.6, that theoretical values agree well with experimental values. $P_o/\rho g H_I$ increases monotonously as $2\lambda_2/L$ becomes smaller. This trend is different from those of r_R and r_T . $P_o/\rho g H_I$ measured in the small wave tank is quite equal to those measured in the large wave tank. Then, the model scale effect to $P_o/\rho g H$ is not recognized in the two laboratory experiments.

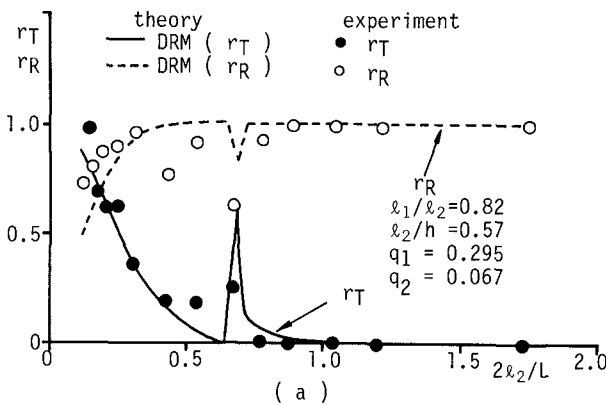


Fig.5 Comparison between theoretical values and experimental values of r_R and r_T .

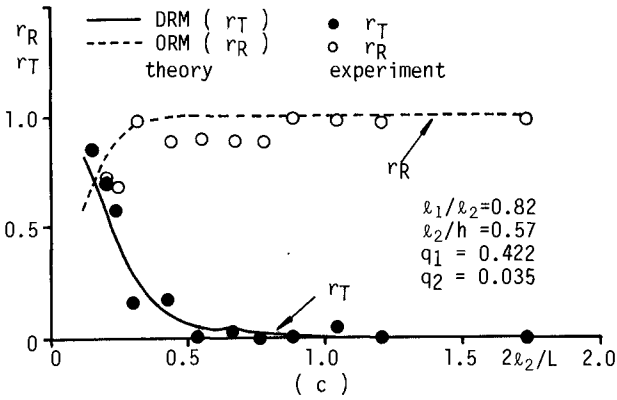
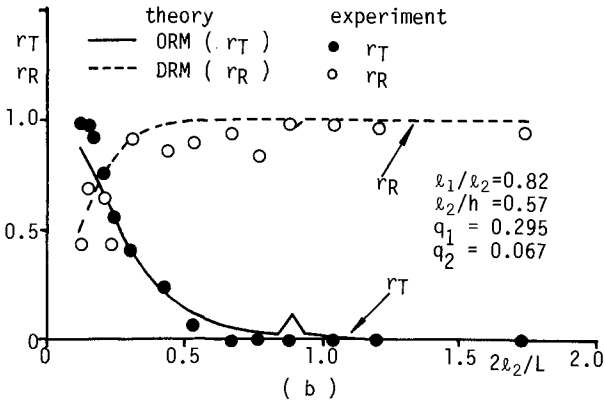


Fig.5 Comparison between theoretical values and experimental values of r_R and r_T .

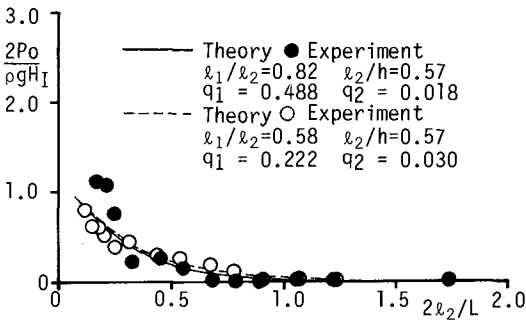


Fig.6 Comparison between theoretical values and experimental values of $P_o/\rho g H_l$

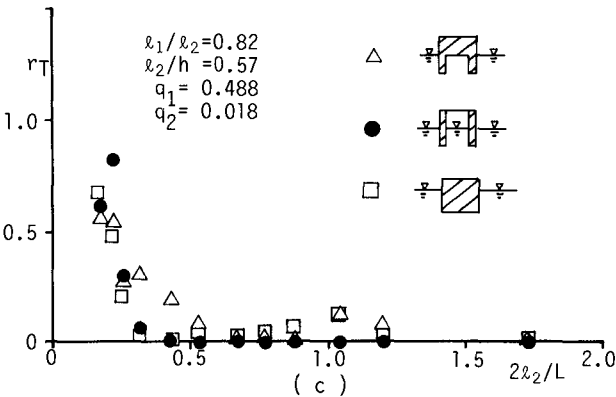
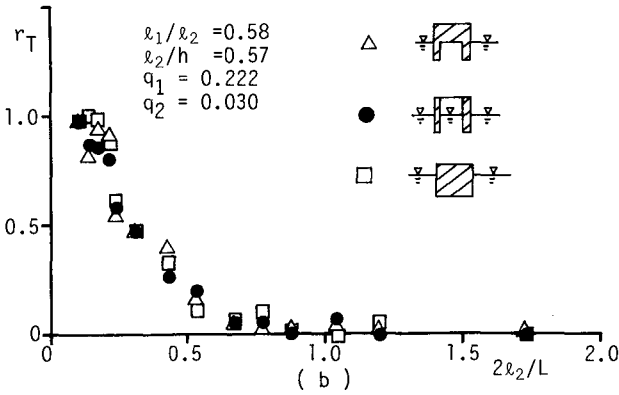
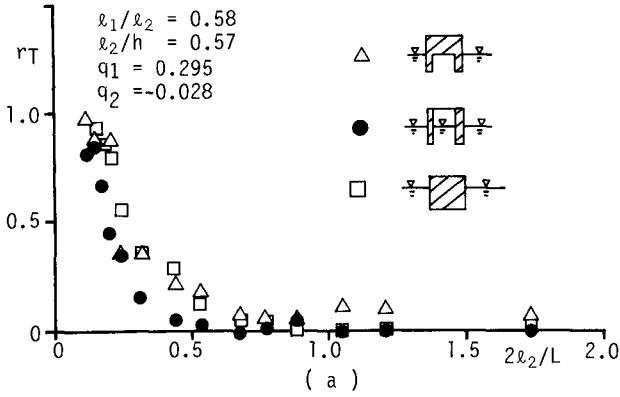


Fig.7 Comparison of transmission coefficient, r_T among pressurized-type, concave-shaped and rectangular-shaped breakwaters

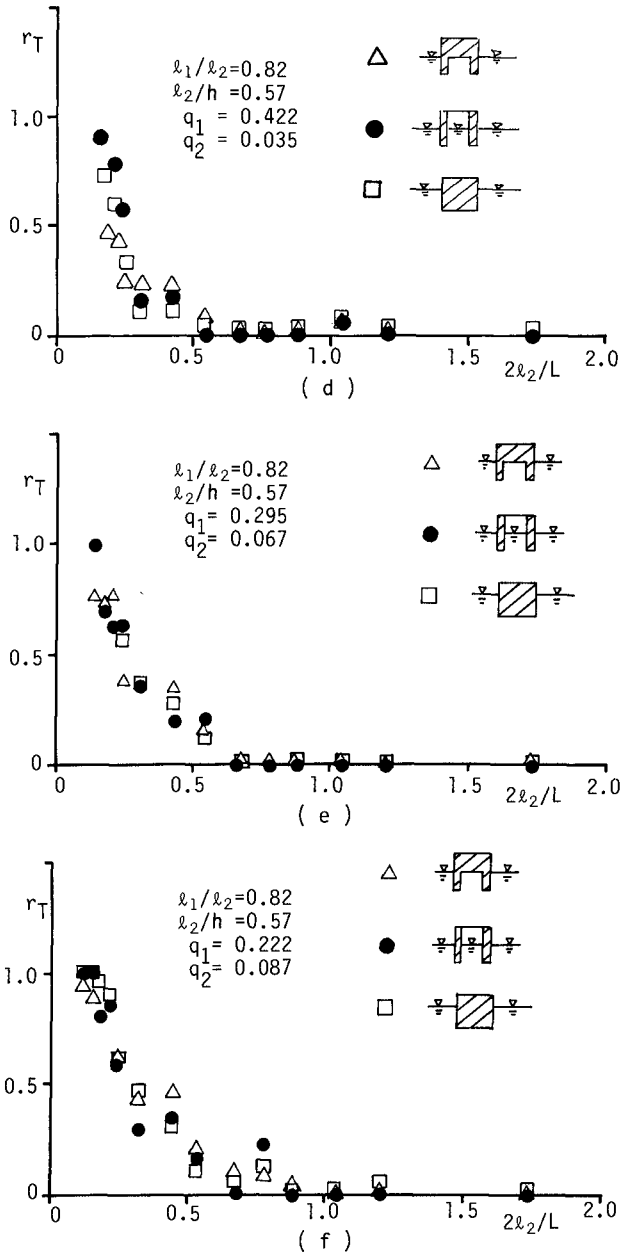


Fig.7 Comparison of transmission coefficient, r_T among pressurized-type, concave-shaped and rectangular-shaped breakwaters

Next, let us discuss the difference in the transmitted wave height due to the new type of breakwater (hereafter referred to as pressurized-type breakwater), and concave-shaped and rectangular-shaped breakwaters.

Figures 7(a)-(f) show experimental results of transmission coefficient, r_T due to the three different types of breakwaters. In each figure, the breakwater length, $2l_2$ and draft depth, $q_1 h$ are quite the same among the three different types of breakwaters. It is seen that the transmission coefficient, r_T increases largely with decreasing of $2l_2/L$ in the range of $2l_2/L \leq 0.5$. As shown in Figs.(a)-(f), there are no large difference in r_T due to the pressurized-type, concave-shaped and rectangular-shaped breakwaters. However, r_T of the pressurized-type breakwater are comparatively smaller than those of the concave-shaped and rectangular-shaped breakwaters (see Figs.(a),(b), (e) and (f)). Therefore, it can be pointed out that the pressurized-type breakwater proposed in this study is better than the concave- and rectangular-shaped breakwaters in order to attenuate the transmitted wave.

From engineering viewpoint, r_T is frequently requested to be less than 0.5 for $q_1 \leq 0.5$ and $2l_2/L \leq 0.4$. As stated above, since DRM evaluates well the experimental values of r_T due to the pressurized-type breakwater, we will further discuss here, based on theoretical calculations estimated with DRM, the effect of pressurized head, q_2 to r_T and geometrical dimensions of the pressurized breakwater which attenuate r_T less than 0.5 for $q_1 \leq 0.5$ and $2l_2/L \leq 0.4$.

Figure 8 indicates that r_T becomes smaller with increasing of the dimensionless pressurized head, q_2/q_1 and r_T becomes minimal at $q_2/q_1=1$. Then, it can be said that increase of the pressurized head is effective to decay the transmission coefficient.

Figures 9(a)-(c) show some cases of optimum geometrical dimensions of the pressurized-type breakwater which can attenuate r_T less than 0.5 for $q_1 \leq 0.5$ and $2l_2/L \leq 0.5$. It is said that r_T is also affected by $(1-l_1/l_2)$ and that r_T decreases as $(1-l_1/l_2)$ becomes smaller. From Fig.9, combinations of $(1-l_1/l_2)$, q_1 and $2l_2/L$ which attenuate r_T less than 0.5 are found out in case of $q_1/q_2=1.0$ for three relative water depth, $h/L=0.078, 0.131$ and 0.207 .

Figure 9(c) shows that r_T becomes 0.3 when $q_1=0.5$, $2l_2/L=0.28$ and $(1-l_1/l_2)=0.01$ in case of $q_1/q_2=1.0$ and $h/L=0.207$. Thus, it is possible for this type of breakwater to attenuate r_T less than 0.3 in the case of $q_1=0.5$ and $2l_2/L \leq 0.4$.

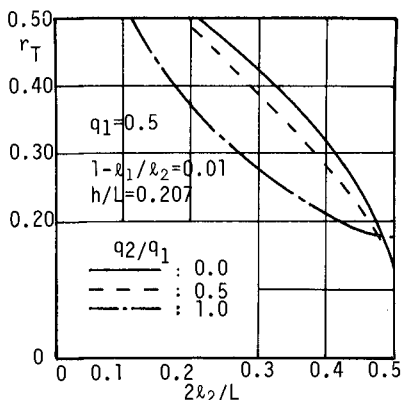


Fig. 8 Effect of pressurized head, q_2 to r_T

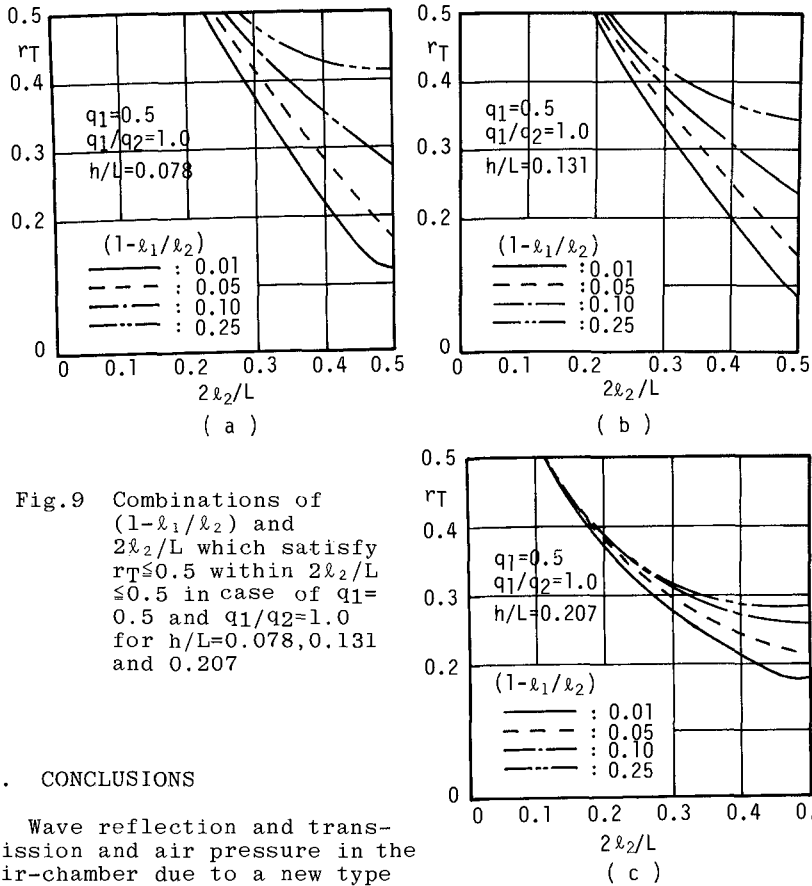


Fig.9 Combinations of $(1-l_1/l_2)$ and $2l_2/L$ which satisfy $r_T \leq 0.5$ within $2l_2/L \leq 0.5$ in case of $q_1=0.5$ and $q_1/q_2=1.0$ for $h/L=0.078, 0.131$ and 0.207

4. CONCLUSIONS

Wave reflection and transmission and air pressure in the air-chamber due to a new type of breakwater which has a pressurized air-chamber and two buoyancy tanks have been discussed from theory and laboratory experiments. The main results obtained in this study are summarized as follows:

- (1) The theory using the Dividing Region Method is newly developed in order to evaluate the reflection and transmission coefficients and air pressure variation in the pressurized air-chamber. The proposed theory estimates well experimental values.
- (2) Theoretical calculations show that the pressurized in the air-chamber plays an important role to attenuate the transmission coefficient, r_T . The transmission coefficient becomes smaller with increasing head in the air-chamber.
- (3) The transmission coefficient of the pressurized-type breakwater is comparatively smaller than those of the concave-shaped and rectangular-shaped breakwaters.
- (4) The effect of P_0 to the reflection and transmission coefficients becomes smaller as $2l_2/(d_0+q_1h)$ becomes larger.
- (5) Since the wave transmission coefficient due to the

proposed new type of breakwater can be attenuated less than 0.35 for $2\lambda_2/L \leq 0.3$ and $q_1 \leq 0.5$, there is high possibility that this pressurized-type breakwater will be put into practical use in the sea area where high water exchange and wave decay functions are simultaneously required.

REFERENCES

- 1) Goda, Y. and Y. Suzuki (1976): Estimation of incident and reflected waves in random wave experiments, Proc. 15th ICCE, Hawaii, pp. 828-845.
- 2) Iwata, K., Oki, M., Kitaura, S., Okuoka, T. and M. Ikeno (1986): Motion of floating structure with a pressurized air-chamber, Proc. 33rd Japanese Conf. on Coastal Eng., pp. 531-535 (in Japanese).
- 3) Iwata, K., Ikeno, M., Eguro, T. and K. Nakayama (1987): Wave deformation due to structure with a pressurized air-chamber, Abstracts of Ann. Conv., Chubu-Branch of JSCE, pp. 212-213 (in Japanese).
- 4) Iwata, K., Ikeno, M., Nakayama, K., Ueda, T. and H. Ishii (1988): Numerical programming of motions of structure with a pressurized air-chamber and two buoyancy tanks in floating, moored and fixed conditions, Technical Rept., Coastal and Ocean Eng. Labo, Dept. of Civil Eng., Nagoya Univ., pp. II-1 -II-53 (in Japanese).
- 5) Kiyokawa, S. and T. Ohyama (1986): Wave reflection and transmission due to structure with air-pressurized curtain-wall breakwater, Proc. JSCE, No. 375, pp. 271-280 (in Japanese).
- 6) Nakamura, T., Takahashi, K. and K. Nakayama (1982): Analytical method of wave deformation and forces around two-dimensional body using source distribution method, Proc. 29th Japanese Conf. on Coastal Eng., pp. 462-466 (in Japanese).

CHAPTER 173

WAVE-INDUCED SHOCK PRESSURES UNDER REAL SEA STATE CONDITIONS

by

Joachim Grüne¹

ABSTRACT

This paper deals with a study on shock pressures, which occur on sloping seadykes and revetments due to breaking waves. Results from field measurements are presented with respect to peak pressure values as well as to characteristics of pressure-time histories.

1. INTRODUCTION

Investigations on shock pressures, especially at vertical walls, have been done since 140 years. Tests mostly have been carried out in small scale models, only a few measurements have been done in field or in laboratory full-scale (for vertical walls see e.g. Blackmore, Hewson (1984), for sloping seadykes see e.g. Stive (1984), Führböter (1986), Führböter, Sparboom (1988).

Furthermore in laboratory tests mostly regular waves were used or irregular waves were not really related to the topographic relations in front of existing seadykes in nature.

The published data from the different investigations often show considerable differences especially with respect to maximum peak pressure values. It can be no doubt, that these differences mainly are a result of the different wave characteristic conditions. The wave characteristic conditions itself strongly influence the amount of air entrainment, therefore considerable scale effects can occur in small-scale models. Due to the more or less unsolved problems with these scale effects and due to the random characteristics of waves under real sea state conditions there still is a great need for detailed field data, to verify investigations in laboratory, even such in full scale.

2. FIELD MEASURING EQUIPMENT

The data presented in this paper, have been measured in field at two different locations at the coast of the German Bight during several storm surges (Grüne, 1982).

¹Dipl.-Ing., senior researcher, deputy operation manager of the joint institution LARGE WAVE CHANNEL of the University Hannover and the Technical University Braunschweig, Germany

At the EIDERDAMM location two different sections were used: the original adjacent dam of the Eider-storm-surge-barrier, which has a bended slope of 1:4 in the lower and 1:6 in the upper part, and additionally a testsection with a uniform slope of 1:4 (Fig. 1). On both sections upwards from $NN + 3.00m$ (which is roughly 1.5m above Mean High Tide) the cover layers are made from asphalt-concrete on a sand core. On these asphalt-covers the wave-induced pressures were measured synchronously on both slopes with up to 5 pressure cells, which had a vertical distance of roughly 25cm from each other (on both slopes).

The section used at the east-frisian island WANGEROOGE, has also a cover layer made from asphalt-concrete on a sand core with a nearly constant slope of 1:4. Up to 25 sensors with a vertical distance from each other of only 9cm have been used synchronously to measure the wave induced pressures on the surface.

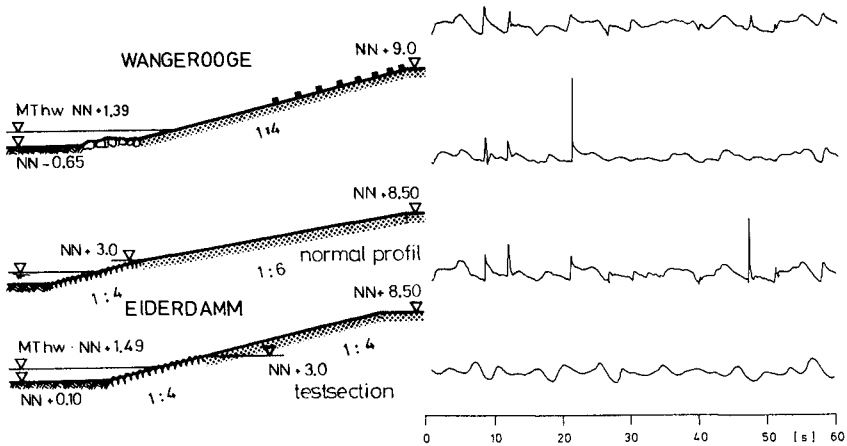


Fig. 1 Dyke profiles used for field measurements at both locations

Fig. 2 Example of a synchronous record from some pressure cells on slope 1 : 4 (EIDERDAMM location)

Waves at both locations were recorded also with pressure transducers. These pressure data have been transferred to surface elevations by means of correction factors for the statistical wave parameters in time domain, found in model tests and verified by field measurements (Grüne, 1982).

3. ANALYSIS OF WAVE-INDUCED SHOCK PRESSURES

The definition of shock pressures from field records of wave-induced pressures, especially measured on slopes, is more complicated than for laboratory data with idealized boundary conditions. Due to air entrainment of breakers and the occurrence of a waterfilm from the backflow of wave run-up the shock pressures under real sea state conditions are damped more frequently (compared to those on vertical walls) and they are mixed with pressures from waves and wave run-up (Fig. 2).

In previous reports results with respect to the pressure peak values are primarily predominant, but as to be seen in Fig. 2, 3 and 4, it is often difficult to distinguish

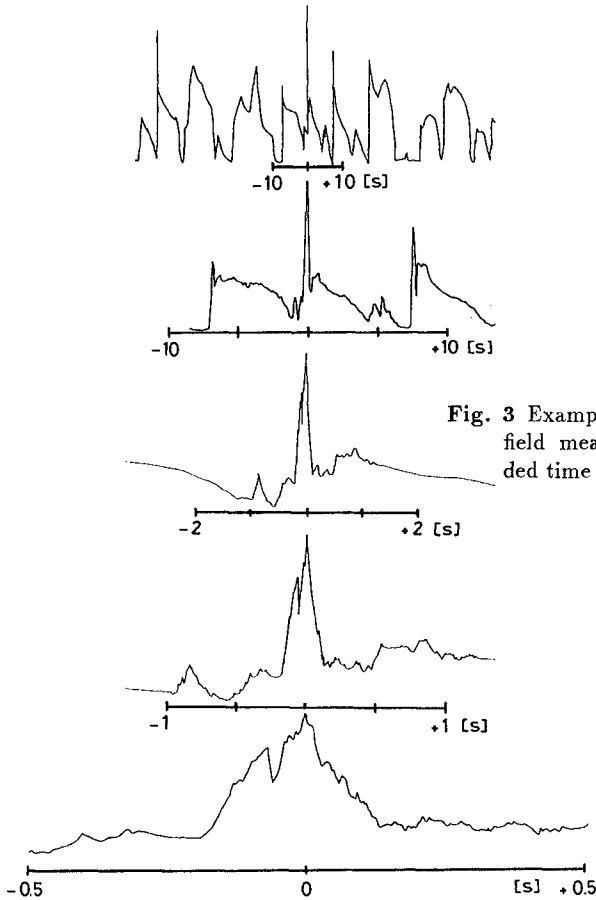


Fig. 3 Example of a record from field measurements with extended time disintegration

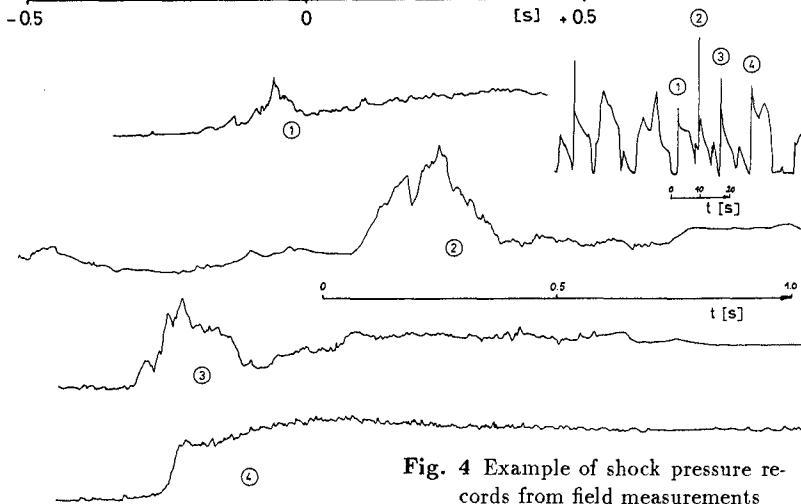


Fig. 4 Example of shock pressure records from field measurements

the real shock pressures from the steep wave fronts or the wave run-up fronts, using normal speed records. Furthermore a first review of some pressure-time histories from measured field data, which seem to fulfill classic shock pressure shapes on a normal speed record, pointed out a certain disagreement with common representations in former reports. This is illustrated in Fig. 3, where the time disintegration is extended in steps from top downwards up to 160 times. Fig. 4 demonstrates that even a series of four waves one by one produces four completely different pressure-time histories at same measuring point on the dyke surface.

Using normal speed records as shown in Fig. 2 for peak pressure analysis usually two main boundary conditions should be fulfilled to find out shock pressures:

1. the rising time up to the maximum peak pressure must be much shorter than the wave period (roughly less than 1/10 of the wave period).
2. the maximum peak value should exceed a certain multiple value of the wave height, that means a setting of a minimum value.

On the records as shown in Fig. 2, and on the top of Fig. 3 and 4 the first condition can be estimated only insufficiently. The second condition can result in neglecting real shock pressures with smaller peak values, but yet very short rising times, which might be important to the stability of seadykes. Furthermore the statistical values are affected by setting a minimum value.

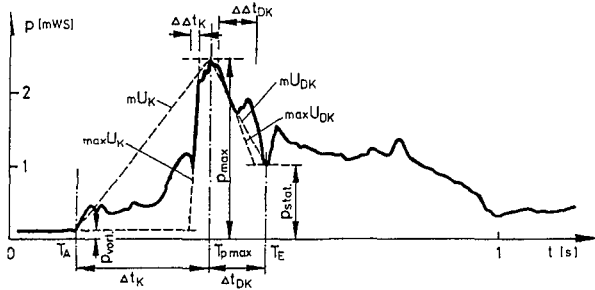


Fig. 5 Scheme for definition of shock pressure anatomy parameters

Table 1: List of shock pressure parameters

Symbol	Definition	Unit
p_{max}	total maximum (peak) pressure (at T_{pmax})	mWs (meter water column)
p_{vorl}	pressure before the occurrence of a shock pressure (at T_A)	mWs (meter water column)
p_{stat}	minimum pressure between the decompression term and the quasi-static term (at T_E)	mWs (meter water column)
T_A	starting time of shock pressure	s (second)
T_{pmax}	time at maximum pressure	s (second)
T_E	starting time of the quasi-static term	s (second)
Δt_k	total rising time of compression term, related to: $(p_{max} - p_{vorl})$	s (second)
$\Delta \Delta t_k$	minimum significant rising time of compression term, related to $(p_{max} - p_{vorl})$	s (second)
Δt_{ph}	time period to maximum pressure (at T_{pmax}), related to the first T_{pmax} of all pressure cells	s (second)
mU_k	mean rising velocity, related to Δt_k and $(p_{max} - p_{vorl})$	mWs/s (meter water column per second)
$max U_k$	maximum significant rising velocity, related to $\Delta \Delta t_k$ and $(p_{max} - p_{vorl})$	mWs/s (meter water column per second)

More detailed information on shock pressures (“anatomy”) can be obtained from high speed recorded pressure-time histories as shown in Fig. 3 and 4. To distinguish all these completely different pressure-time histories and to get a certain generalization, these complex shapes may be described suitable by parameters as shown in Fig. 5. The parameters in this example of a pressure-time history are separated for compression time (index K) and decompression time (index DK). The anatomy parameters, used in this paper, are listed in Table 1. It must be remarked, that in chapter 4.1 the peak pressure values p_{max} from Table 1 are defined as p .

An example of time-pressure histories of one individual wave event, recorded at WANGEROOGE location, is shown in Fig. 6. The local distribution of the anatomy parameters, determined from these pressure-time histories as listed in Table 1, are plotted in Fig. 7 in dependence of the waveheight related distance $\Delta d/H_{1/3}$ from stillwaterlevel. It should be noted that the recorded pressure-time histories mostly have more chaotic shapes than the classic ones in Fig. 6. More aspects on analyzing high speed recorded pressure-time histories are reported by Grüne, (1988).

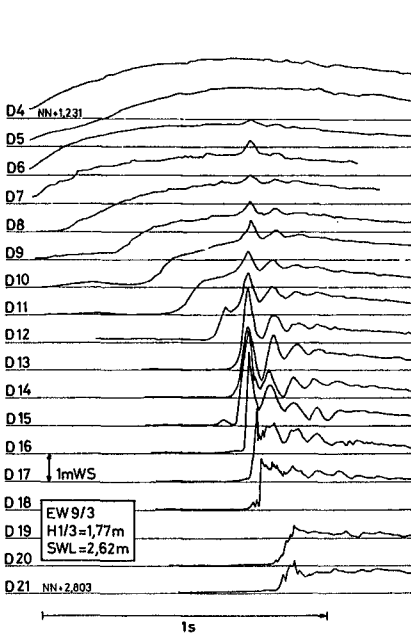


Fig. 6 Pressure-time histories for an individual breaking wave

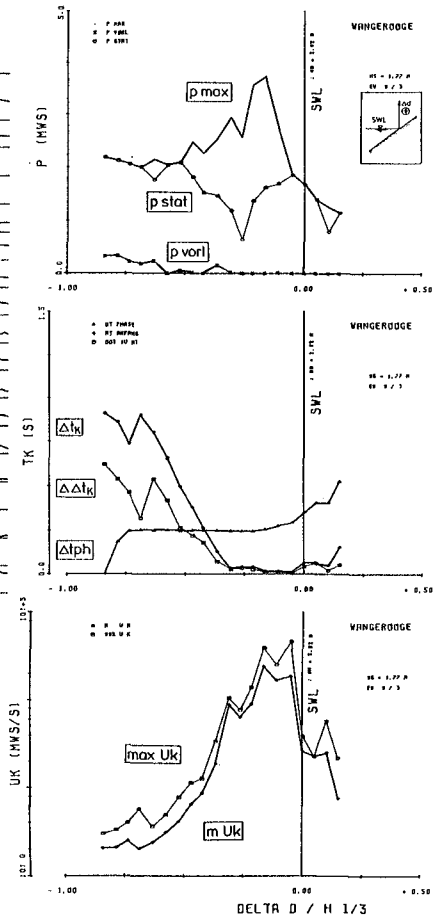


Fig. 7 Local distribution of anatomy parameters from the pressure-time histories in Fig. 6

4. RESULTS

The results, described in this paper, are analyzed from normal speed records (EIDERDAMM and WANGEROOGE location) with respect to peak pressure values as well as from high speed records (WANGEROOGE location) with respect to the anatomy of shock pressures.

4.1 Results of peak pressure values and their local distribution

Although the analysis of peak pressure values from normal speed records does not give detailed information on shock pressure characteristics as mentioned before, this method is useful to find the limited area of "worst case overall occurrence" of shock pressures on slopes, especially with respect to the local distribution.

An example of peak pressure data for one time interval, measured at Eiderdamm location on slopes 1 : 4, is given in Fig. 8. On the vertical axis, the statistical peak pressure values, which are determined directly from the peak pressure data, are related to significant wave height $H_{1/3}$. NP/NW gives the ratio of peak pressures to the number of individual waves (related frequency of occurrence). The horizontal axis gives the local distribution on the slope as a vertical waveheight related distance from the mean stillwaterlevel $\Delta d/H_{1/3}$ of the time interval. The data of the different pressure cells are used to form an linear interpolated envelope curve.

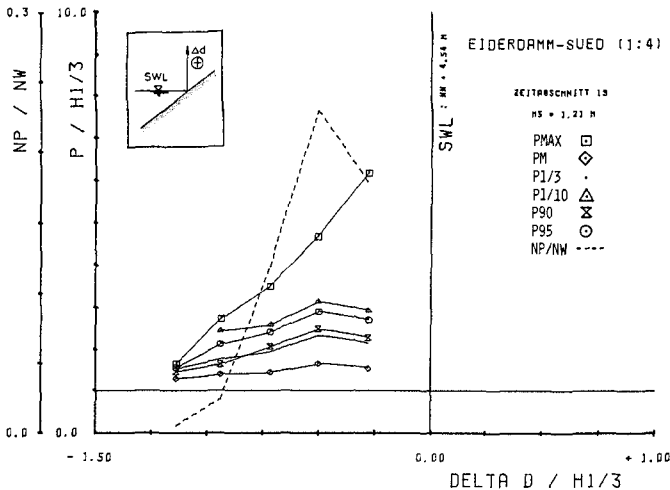


Fig. 8 Example of peak pressure data measured on slope 1 : 4 at EIDERDAMM location for one time interval

It must be remarked, that such summarized distributions of peak pressure values are influenced

- first by the measuring time, which is restricted for field measurements due to changing of stillwaterlevel
- second by the location of the pressure cells on the dyke referred to stillwaterlevel during storm surge events

third by the distance of pressure cells from each to another, which gives the local disintegration of the envelope curves.

Some further remarks should be made on statistical parameters, evaluated from calculated lognormal distribution. As shown in Fig. 9, the lognormal distribution of peak pressure values, measured with 23 pressure cells on the total dyke surface for one time interval, can be fitted by a least square method calculated lognormal distribution only moderate. It must be mentioned that this time interval has a length of 80 minutes with closely constant stillwaterlevel and significant wave height, which is rather rare for measurements during storm surge events.

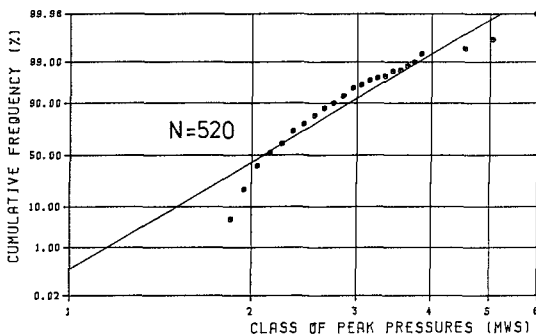


Fig. 9 Example of lognormal distribution of peak pressure values for one measured time interval

The local distributions of the statistical peak pressure parameters, evaluated from calculated lognormal distribution and related to mean peak pressure values, are plotted in the upper part of Fig. 10. It is obvious, that these parameters vary in dependance of the distance to stillwaterlevel. The local distributions of the waveheight related statistical parameters determined directly from the peak pressure values for this time interval are plotted in the lower part of Fig. 10. It is conspicuous, that the measured maximum peak pressures form the statistical values extensively and that they agree quite well with the corresponding calculated values $p_{99.9}$. This comes out more clearly in Fig. 11, where for each measured time interval at Wangerooze location the calculated statistical values $p_{99.9}$ from all shock pressures are plotted versus the measured maximum ones. Due to these results and additionally due to the fact, that the time for measuring shock pressures during storm surge events in field with nearly constant stillwaterlevel and waveheight parameters is limited, the measured maximum peak pressure values have been favoured for further considerations instead of calculated statistical values.

To get the "worst case occurrence area" with a certain approach to accuracy, the envelope curves for p_{max} of the different measured time intervals are superimposed to a summarized envelope curve, which is shown in Fig. 12 as an example for one storm surge event. For the same storm surge event the summarized envelope curves of the different statistical parameters are plotted in Fig. 13. It can be seen clearly, that the occurrence area spread over a wide range on the slope, but the intensity varies considerable in relation to distance from stillwaterlevel.

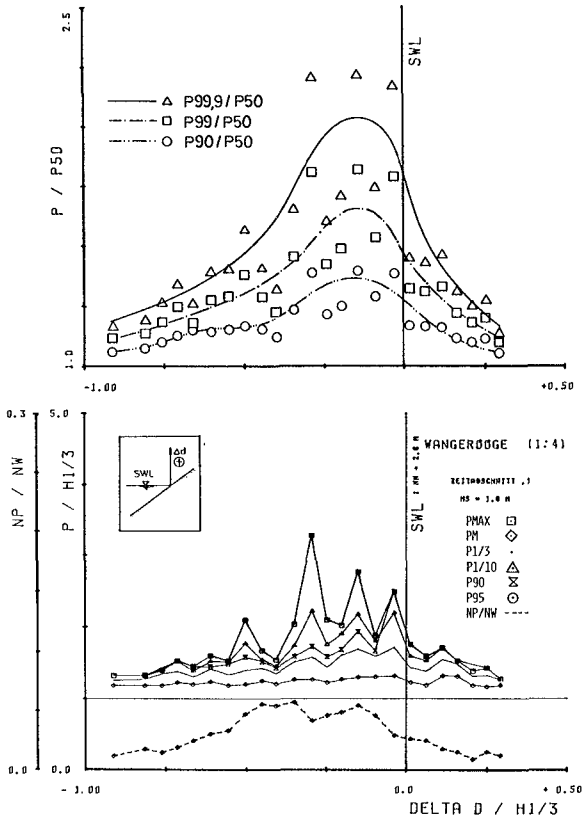


Fig. 10 Example of local distribution of statistical peak pressure values for one measured time interval

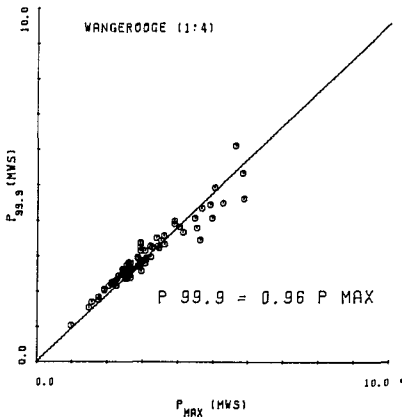


Fig. 11 Relation between statistical parameters $p_{99.9}$ and measured maximum pressure p_{max} for different time intervals, measured at WANGEROOGE location

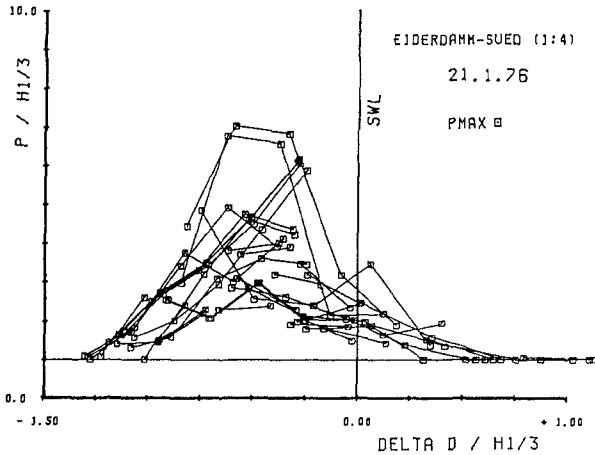


Fig. 12 Superimposed envelope curves for p_{max} of different time intervals, measured during one storm surge event at EIDERDAMM location 1 : 4

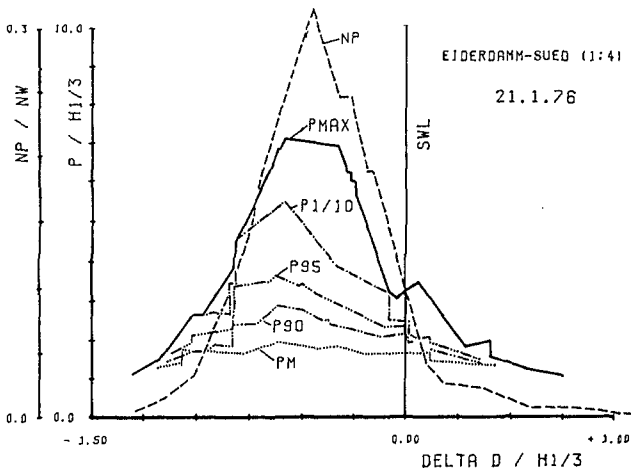


Fig. 13 Summarized envelope curves for different statistical parameters, measured during one storm surge event at EIDERDAMM location 1 : 4

The envelope curves for some parameters from all measured storm surge events at Eiderdamm location are compared in Fig. 14 for the both slopes 1:4 and 1:6. There is no significant difference of the total area of occurrence and of the mean pressure distribution between both slopes, but frequencies of occurrence and maximum peak pressures are lower on slope 1:6 due to the different wavebreaking and wave run-up characteristics.

A comparison of the peak pressure data between the two different locations with same slope 1:4 is given in Fig. 15. The total area of shock pressure occurrence is closely identical for both locations just as the mean pressure value distributions,

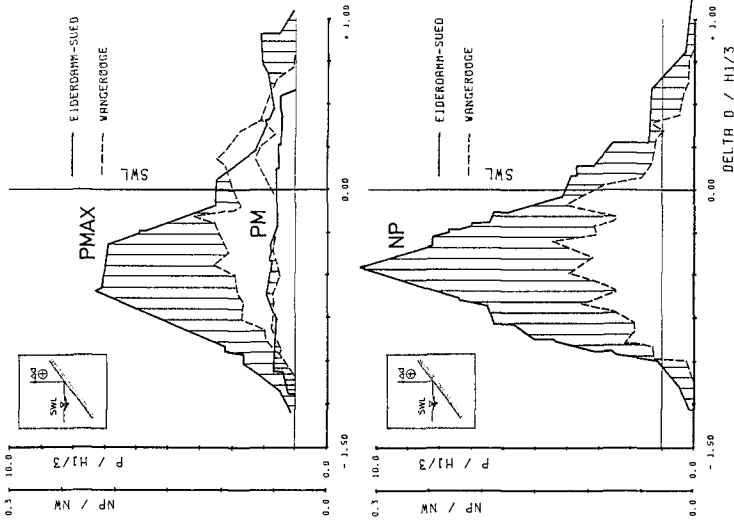


Fig. 14 Comparison of peak pressure parameters and their local distribution between 1 : 4 and 1 : 6 slope at EIDERDAMM location

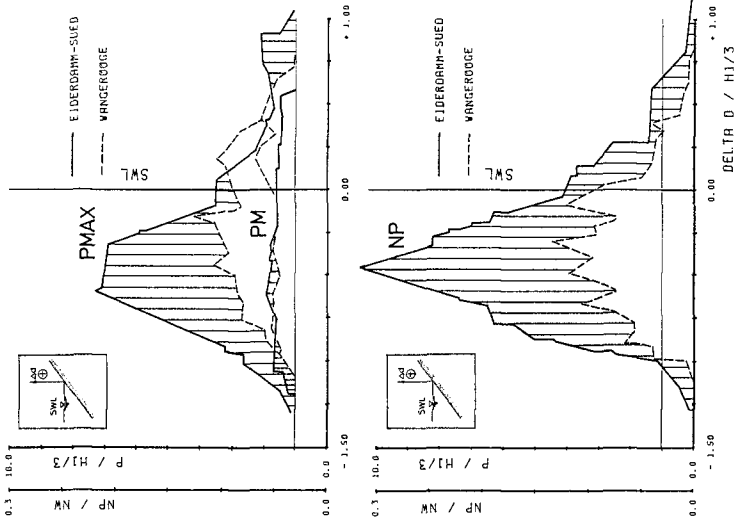


Fig. 15 Comparison of peak pressure parameters and their local distribution for slope 1 : 4 between the EIDERDAMM and WANGEROOGE location

but considerable differences occur for maximum peak pressure values and for the frequency. This is doubtless the influence of the different characteristic of local wave climate at both locations. Due to different waterdepth to waveheight relations in front of the slopes the plunger breaker type is predominant at Eiderdamm location, whereas at Wangerooge location the spilling breaker type is predominant. It should be noted, that similar effects from the wave characteristics were found also for wave run-up data, measured at both locations (Grüne, 1982).

4.2 Results of pressure-time history parameters (Anatomy parameters)

The results of parameters, evaluated from pressure-time histories as described in chapter 3, indicate very clearly, especially with respect to local distribution, that a certain gliding transition exists from the characteristics of steep wave front to those of shock pressure and then again to those of run-up front (see Fig. 7). This can be confirmed by the relations between some parameters independently from local distribution. Due to restricted place in this paper the following plots only should give an first overview of some summarized pressure-time history parameters from one storm surge event.

The relation between p_{vori} , which represents the thickness of watersheet before shock pressure occurrence, and peak pressure values p_{max} is given in Fig. 16. The solid line gives the upper limit of peak pressures with respect to watersheet thickness and indicate the damping effect of a possible watersheet from the backflow of the preceding wave. The mean rising time Δt_k is plotted versus the peak pressure value p_{max} in Fig. 17. The solid line represents the upper limit of the longest measured rising times, which decrease with increasing peak pressure values.

Fig. 18 gives the local distribution of the peak pressure values p_{max} . There is in fact no distinct tendency, but a broad spreading around stillwaterlevel. There is a clear tendency for the local distribution of the watersheet thickness p_{vori} in Fig. 19; the upper limit of the thickness decrease at higher levels on the surface. All data give an impression of the numberless different shapes of pressure-time histories.

A generalized scheme for the local distribution of the pressure-time history parameters is shown in Fig. 20. This scheme is a first evaluation from a part of analyzed individual wave events. These generalized shapes were found more or less exactly for all investigated significant shock pressure events, which indicates a certain deterministic characteristic of wave-induced pressures on slopes. The shapes may be roughly classified into five different local domains (circled in Fig. 20) with different trends (listed in the table):

- the first one represents the approaching steeped wave front
- at the second domain the steeped wave front has its maximum height, this can be seen as the breaker point
- the third domain represents the area between the breaking wave front and the point, where the breaker tongue hits on the dyke surface. In this area the most chaotic pressure-time histories were found due to the enclosed air pockets with high turbulence
- the fourth one represents the area, where the breaker tongue hits on the dyke surface and where significant shock pressures with classic shapes occur
- the fifth domain represents the very steep front of wave run-up.

It must be remarked, that due to definition these parameter-shapes do not represent the conditions at same time, therefore some further investigations were made to check the phase lag of these shapes. The results from these investigations indicated, that all maximum peak pressures can occur closely within a total time lag of 50 milliseconds, referred to the maximum peak pressure $max p_{max}$.

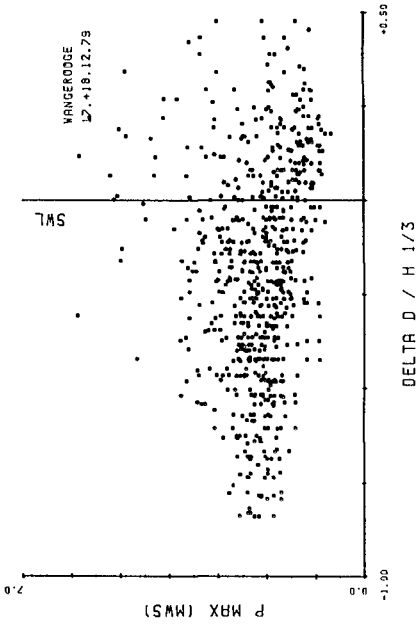


Fig. 18 Local distribution of p_{max}

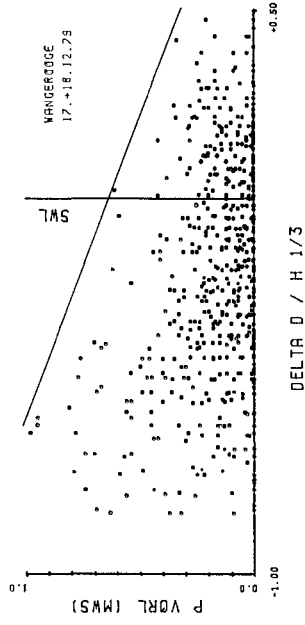


Fig. 19 Local distribution of p_{vorl}

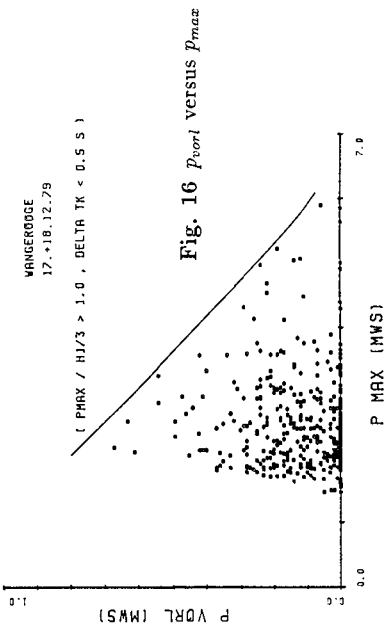


Fig. 16 p_{vorl} versus p_{max}

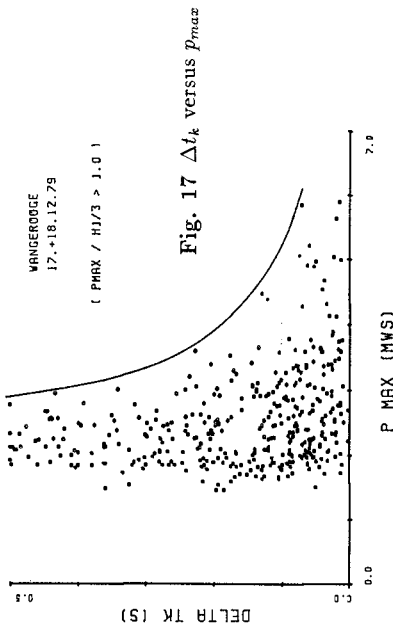


Fig. 17 Δt_k versus p_{max}

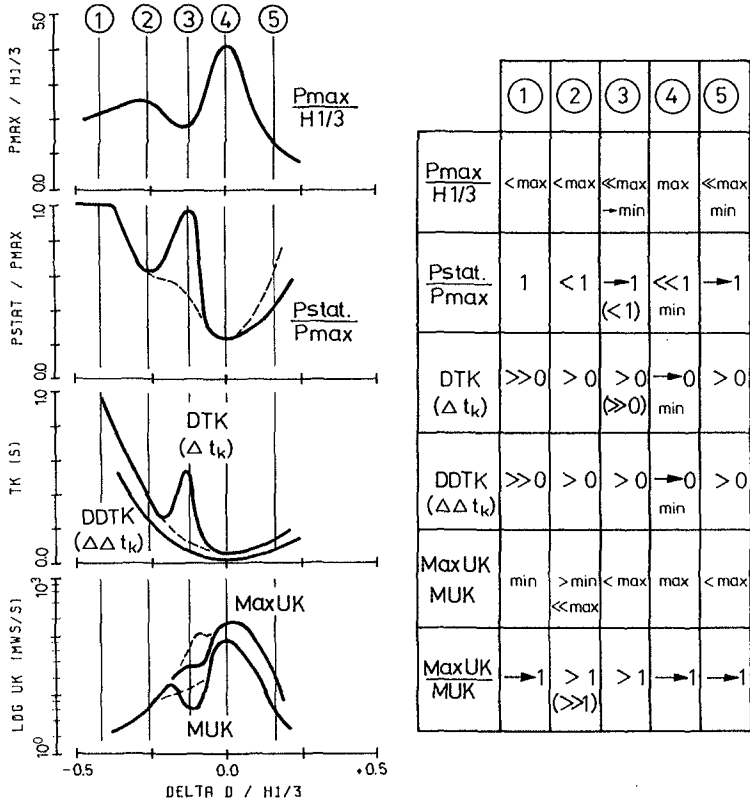


Fig. 20 Generalized scheme for local distribution of anatomy parameters

This leads to the first assumption, that anatomy parameter shapes, such as shown before, can give a realistic approximation of the synchronous worst-case loadings from individual breaking waves. Such a worst-case loading model for the synchronous pressure distribution is shown in Fig. 21. The thick line is evaluated from a part of the data from WANGEROOGE location. The thin line is extrapolated to the maximum peak pressure values measured at EIDERDAMM location. The local distribution is related to the true length on the surface with zeropoint at the maximum peak pressure. It must be mentioned, that this zeropoint varies considerable with respect to distance from stillwaterlevel as shown in Fig. 19. For application this loading model may be used as an input to a numerical model, to investigate for example the bending moments of an cover layer or the penetration of shock pressures into sandcore. To get the worst case, for different applications the following parameters of the loading model in Fig. 21 should be varied systematically with certain ranges:

- the waveheight related peak pressure $max p_{max}$ up to 10

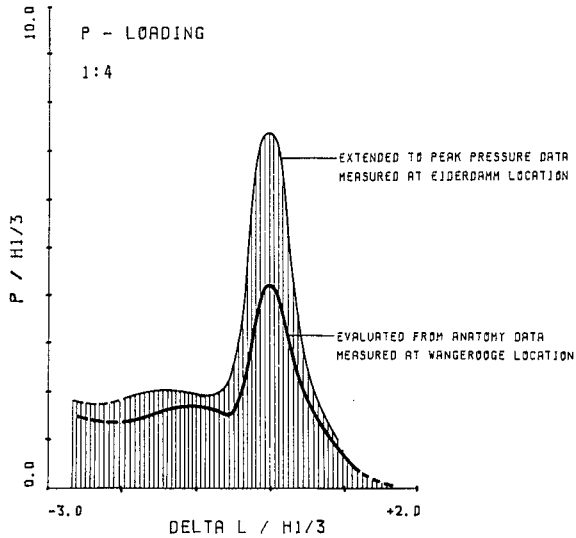


Fig. 21 Worst-case loading model (local peak pressure distribution)

- the duration time from 10ms up to 200ms
- the waveheight related vertical distance from stillwaterlevel of the local acting point of $max p_{max}$ from -0.75 up to $+0.5$

5. CONCLUSIONS

From the results of the measurements in field the following may be stated:

- The definition of shock pressures for field data, especially measured on slopes, is more complicated than for laboratory data with idealized boundary conditions.
- Analysis of peak pressure values from normal speed records are useful to get the local distribution of shock pressure occurrence on dyke surface.
- Shock pressures occur on slope 1:4 and 1:6 roughly within the same area on the slope, but have different magnitudes of pressure and frequency.
- The breaker type has a substantial influence on the magnitude and frequency of shock pressures, which was also found for wave run-up data. Waves with predominant spilling breaker type generate fewer and smaller shock pressures compared to waves with predominant plunging breaker type.
- The results may be described statistically, most sufficiently with a lognormal distribution, nevertheless the related ratio of the lognormal distributed pressure parameters, for example $p_{99.9}/p_{50}$, varies in dependence of the distance

from stillwaterlevel. The measured maximum peak pressure values of limited time intervals are well represented by the parameter $p_{99.9}$ from lognormal distribution.

- It has been demonstrated, that for detailed statements on the occurrence of shock pressures and the related loads on dykes an analysis of high speed pressure-time histories measured in field and in full-scale laboratory under real sea state conditions is necessary. On slopes shock pressures are damped more frequently compared to vertical walls and mixed with the pressures from waves and wave run-up, especially under real sea state conditions. Therefore the pressure-time histories mostly have very complex shapes. These complex shapes can be described suitable by parameters. If the pressure-transducers cover the area on the surface with a certain disintegration, the local distributions of these parameters for individual waves can be used for a loading model.

The research program on shock pressures will be continued with respect on combining the field data with different small-scale and full-scale laboratory data, especially those, measured in the "LARGE WAVE CHANNEL OF University Hannover and Technical University Braunschweig" (Grüne, Führböter 1975, Führböter 1986, Führböter, Sparboom 1988).

ACKNOWLEDGEMENTS

The research work partly was done by the SONDERFORSCHUNGSBEREICH 79/C4 - 205/A1 (supervision Prof. Dr.-Ing. A. Führböter) and has been supported by the GERMAN RESEARCH FOUNDTION (DFG). For their extensive and accurate help to analyze the field data the author is indepted expressly to Mr. S. Hecker and Mr. R. Kaiser.

REFERENCES

- Blackmore, Hewson (1984).** Experiments on full-scale wave impact pressures. Coastal Engineering, 8, pp. 331-346.
- Führböter (1986).** Model and prototype tests for wave impact and run-up on a uniform 1:4 slope. Coastal Engineering, 10, pp. 49-84.
- Führböter, Sparboom (1988).** Full-scale wave attack on uniformly sloping sea dykes. Proc. of the 21st Intern. Conf. on Coast. Eng., Malaga.
- Grüne, Führböter (1975).** Large wave channel for "full-scale modeling" of wave dynamics in surf zones. Proc. of Symp. on Modeling Techniques, San Francisco, pp. 82-100.
- Grüne (1982).** Wave run-up caused by natural storm surge waves. Proc. of the 18th Intern. Conf. on Coast. Eng., Kapstadt, pp. 785-803.
- Grüne (1988).** Anatomy of shock pressures (surface and sand core) induced by real sea state breaking waves. Proc. of the Intern. Symp. on Modeling Soil-water-structure interactions (SOWAS 88), Delft, pp. 261-270.
- Stive (1984).** Wave impact on uniformly steep slopes at approximately prototype scale. Proc. of Symp. on Scale Effects in Modeling Hydraulic Structures, pp. 7.11-1/7.11-12.

Measurements of Forces on Dolos Armor Units at Prototype Scale

Gary L. Howell

1 Introduction

In-situ measurements of the structural bending moments and torque about the shank-fluke interface of the dolos armor unit have been made for 42-ton (36-metric tonne) dolosse at Crescent City, California jetty. The measurements include the static loads on the dolosse as well as wave induced forces. The data were obtained from internal strain gages cast into the dolos during construction along with a special data acquisition system. The measurement system was also capable of capturing impact forces caused by dolos rocking or movement. Measurements were made during the winter storm seasons from January 1987 through May 1988.

Coincident with the structural measurements, wave height and period were measured at several water depths approaching the breakwater, including a site directly in front of the dolos test section.

The Crescent City jetty is a shallow water breakwater with depth limited waves in about 10 meters of water depth. The structural measurements were made from 14 dolos units arranged in a rectangular section on the top layer of the trunk portion of the jetty. Four of these dolosse are also instrumented with an accelerometer platform to measure motion with six degrees of freedom. In addition, there are three instrumented dolosse on the bottom layer of the breakwater. These dolosse measure the static stress due to the units placed on top of them, as well as pulsating forces.

The structural and wave measurements, reported here, are supplemented with hydrostatic pore pressure measurements in the core material of the breakwater, and by aerial photogrammetric motion analysis (Kendall, 1988), land based surveys, boundary condition surveys, hydrographic surveys, and side scan sonar surveys.

2 Instrumented Dolos Test Section

Unlike the physical model of instrumented dolosse, it is not practical to relocate instrumented dolosse within the breakwater. Selection of the test section was made after a careful evaluation of different proposed strategies. The Crescent City jetty dolosse section consists of a 100 meter trunk section wrapping in to a 90 degree

*Research Engineer, Coastal Engineering Research Center, Waterways Experiment Station, U.S. Army Corps of Engineers, Vicksburg, Ms.

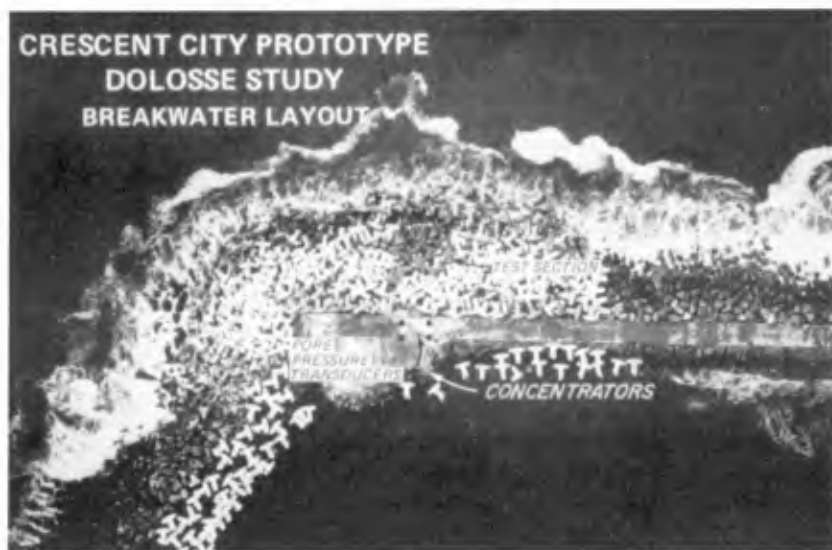


Figure 1: Crescent City Jetty Test Layout

turn to form a partial head section. Among the options considered were distributing the twenty instrumented dolosse throughout the structure, placing dolosse in three groups along the trunk and head section, purposely locating some dolosse in unstable positions, placing some dolosse on lower layers, and grouping all dolosse at a single location. Participants at the Workshop on Measurement and Analysis of Structural Response in Concrete Armor Units (Howell, 1985) discussed the trade-offs among the various options and arrived at a recommended consensus. Sixteen dolosse were placed in an approximate four by four matrix in the top layer, near the mean water line. The accelerometer equipped dolosse were in the center. The four remaining dolosse were placed in the bottom layer of dolosse under the upper instrumented units. The matrix was centered in the trunk section to permit all dolosse to receive, as much as possible, the same incident waves. The primary reason for selection of this test section was the concern that prototype measurements be useful to validate the physical model instrumentation and scaling laws. By placing the dolosse away from the head section and limiting the spatial variability of incident waves, statistical analysis of the prototype data will be comparable to the physical model. Figure 1 is an aerial photograph of the completed dolosse section and the instrumented test section. The darker colored dolosse are the instrumented units.



Figure 2: Instrumented Dolos and Chain Assembly

3 Measured Parameters

Implementation of the experiment required development of specialized instrumentation, data acquisition systems, and environmental protection (Howell, 1986). All dolos instrumentation is permanently sealed within the concrete armor unit. An internal microcomputer system for each dolos digitizes the strain at a 500 Hz sample rate, and accelerometer data at a 50 Hz sample rate. This rate is sufficient to capture all high energy modes resolvable with the strain gages located at the shank-fluke interface. Data from the dolos were retrieved by a cable connected to the underside of the unit. The cable was protected by a modified chain assembly as shown in Figure 2.

In order to gain maximum benefit from a minimum number of data channels, structural measurements were made from strain gages mounted on internal steel reinforcing bars, approximately 0.5 meters long. A rosette of these bars is located at the four faces of the section through the shank-fluke interface (Figure 3). The rosettes are 10 cm. below the surface of the concrete. Only the vertical shank-fluke interface was instrumented. Algebraic combinations of the strains allow estimates of the two bending moments, the axial thrust, and the torque about the shank-fluke interface. The data acquisition system selects any three of these estimates to be acquired simultaneously. Digital commands from the shore based computer allow

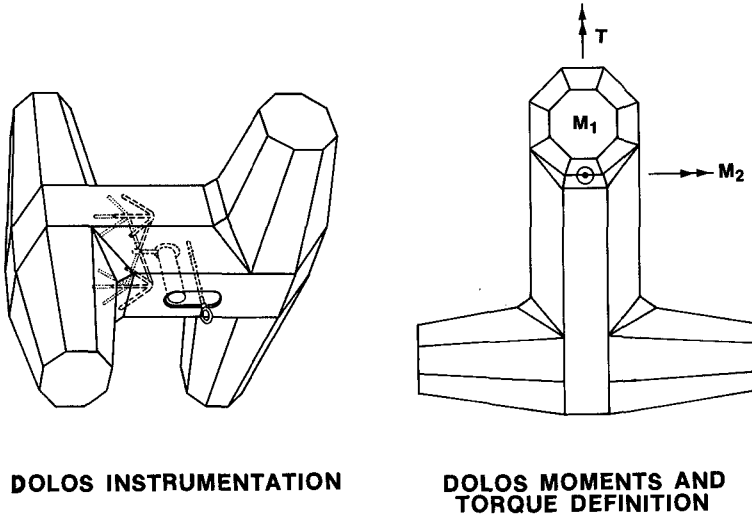


Figure 3: Internal Strain Gages and Moment and Torque Definitions

the selection of the signals as well as amplifier gain.

The steel bars were sized such that the strain in the bar could be assumed to approximate the strain in the surrounding concrete. The following relationships were then used to compute the moments and torques defined in Figure 3.

Labeling the rosettes clockwise, viewed from the horizontal fluke we have

- A, C ... upper and lower vertical rosettes,
- B, D ... right and left horizontal rosettes,
- m ... the rosette bar parallel to the dolos axis,
- t_1, t_2 ... the rosette bars at 45 deg angles,
- ϵ ... measured strain in the bar

then,

$$\epsilon_{AC} = \epsilon_{Am} - \epsilon_{Cm}$$

$$\epsilon_{BD} = \epsilon_{Bm} - \epsilon_{Dm}$$

$$\gamma_{AC} = \epsilon_{At_1} + \epsilon_{At_2} + \epsilon_{Ct_1} + \epsilon_{Ct_2}$$

and,

$$M_v = K_{vm} \epsilon_{AC} \dots \text{vertical moment}$$

$$M_h = K_{hm} \epsilon_{BD} \dots \text{horizontal moment}$$

$$T = K_{tor} \gamma_{AC} \dots \text{torque}$$

The K factors were obtained from Finite Element Method computations for a range of typical boundary conditions.

4 Time Domain Structural Response

During the experiment period the structure was exposed to numerous storms. The most severe storms occurred from Nov. 30 to Dec. 1, 1987. The characteristics of the observed structural response resemble those hypothesized by Burcharth (1984). There is a static response which varies with the tidal period, and a pulsating response which has periods similar to the waves. Figure 4 shows a typical raw data trace from all three channels, M_v , M_h , and T , from dolos M which is located in the center of the test section. The significant wave height in front of the structure was 3.8 meters with the spectral peak at 13 seconds.

Data from all dolosse are qualitatively similar, with the amplitude of the pulsating response proportional to the incident wave heights. Figure 5 shows an expanded trace of the M_v channel from Dolos M record along with a wave trace during the same time interval. A similar trace from Dolos H which is lower in the structure is shown in Figure 6. It would be desirable to show these traces with the waves time and celerity adjusted to coincide with the resulting moment trace, however software to permit this is not complete at this time. Therefore, the wave trace should be interpreted as only representative of the waves impacting the structure at the time of the moment trace.

The pulsating response shows a sharp peak followed by a drag-like relaxation. This response is qualitatively similar to results from physical scale model tests by Scott et al. (1986) and numerical wave force computations by McDougal et al. (1988). Dolos M and H show a double peak of the pulsating response. This feature is observed in many of the prototype dolos responses, but does not appear in the results of Scott or McDougal.

Burcharth and others predicted an impact response when dolos move and collide with each other. Although there has been dolos movement during the experiment (Kendall, 1988), no structural impact has yet been observed in the data. What has been observed are much slower changes in the mean stress such as can be seen in the M_h channel of Figure 4 and to a lesser extent in the other channels. The observations of Kendall have shown that dolos movement at Crescent City has tended to be sliding displacement upslope as would be expected from a shallow sloped (1:5) structure.

5 Static Response

Figure 7 shows mean values of T for Dolos P plotted with measured tide during the same period. Mean fluctuations of many of the dolos have been computed and show varying correlation with the tide depending on the boundary conditions or orientation of the unit in the matrix. A similar plot from Dolos H (Figure 8) demonstrates that static response is relative to the boundary condition and reference frame of the dolos. Since this record is also during a storm, the sharp bumps in the plot show the changes in the mean response mentioned previously. A somewhat surprising result is that dolosse well above the mean water level also show a static response related to tide. For example, Dolos P is located in the upper part of the test section, above the mean water level.

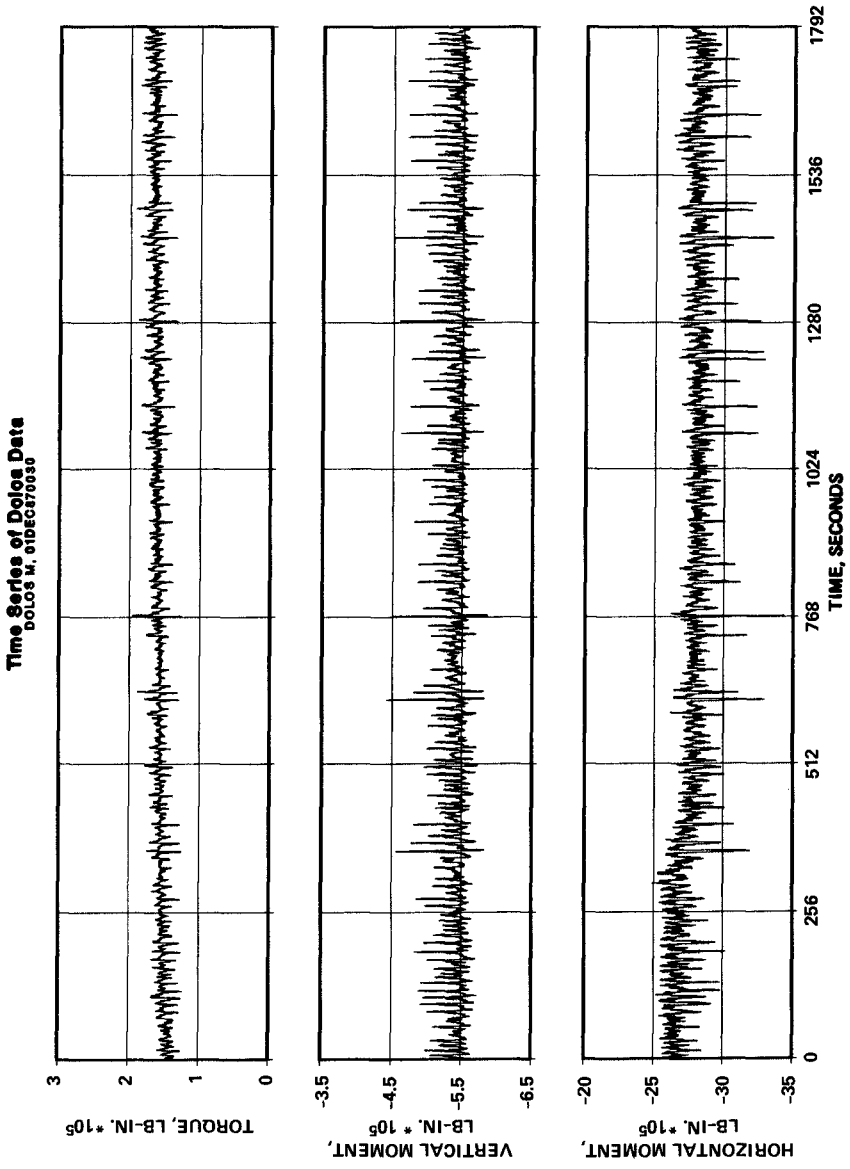


Figure 4: Raw Response Data from Dolos M

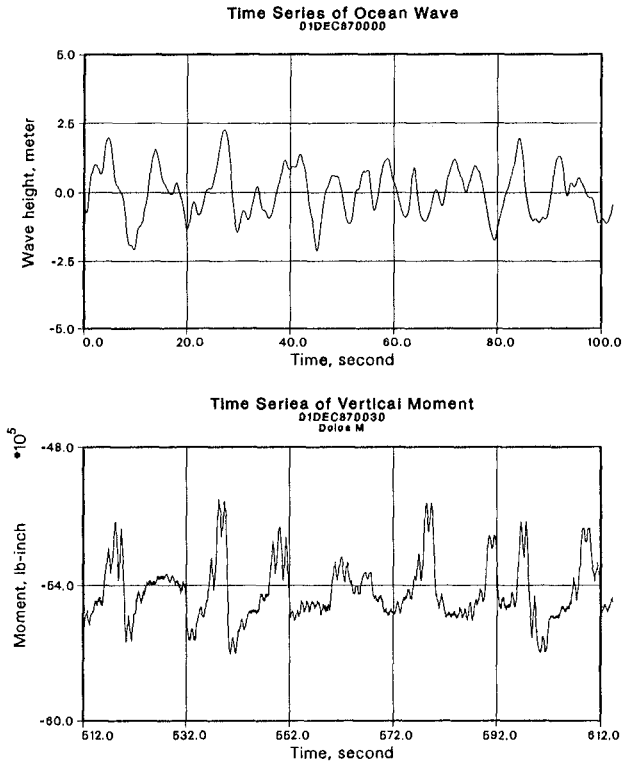


Figure 5: Dolos M Moment Response with Waves

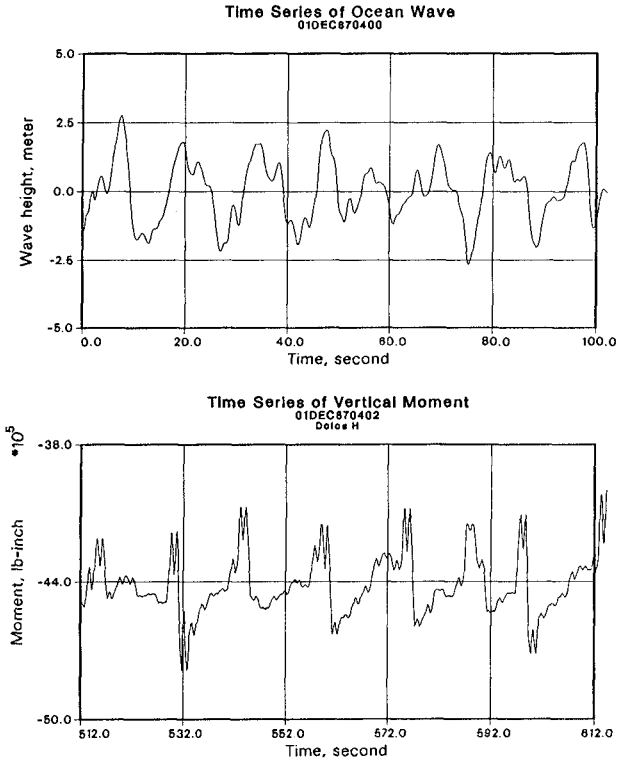


Figure 6: Dolos H Moment Response with Waves

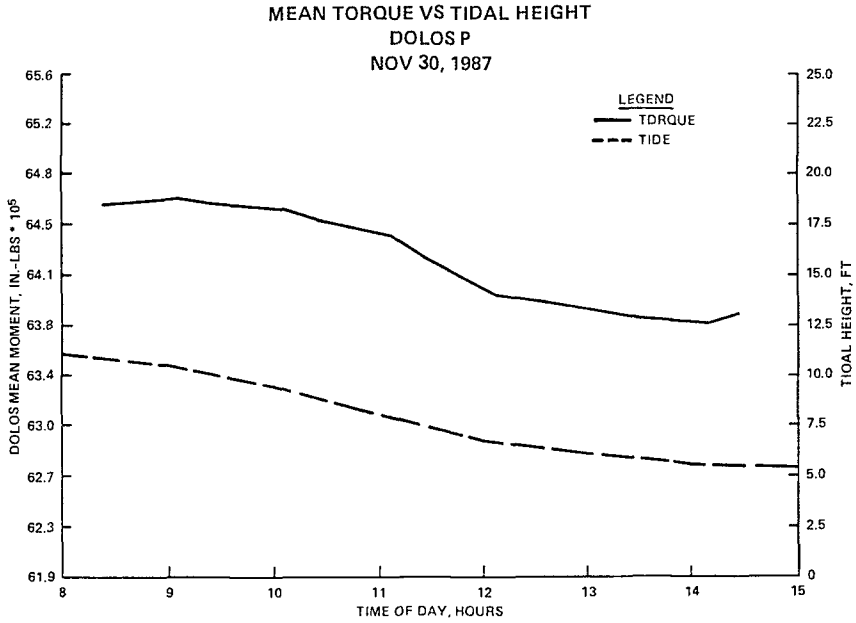


Figure 7: Dolos P Mean Response with Tide

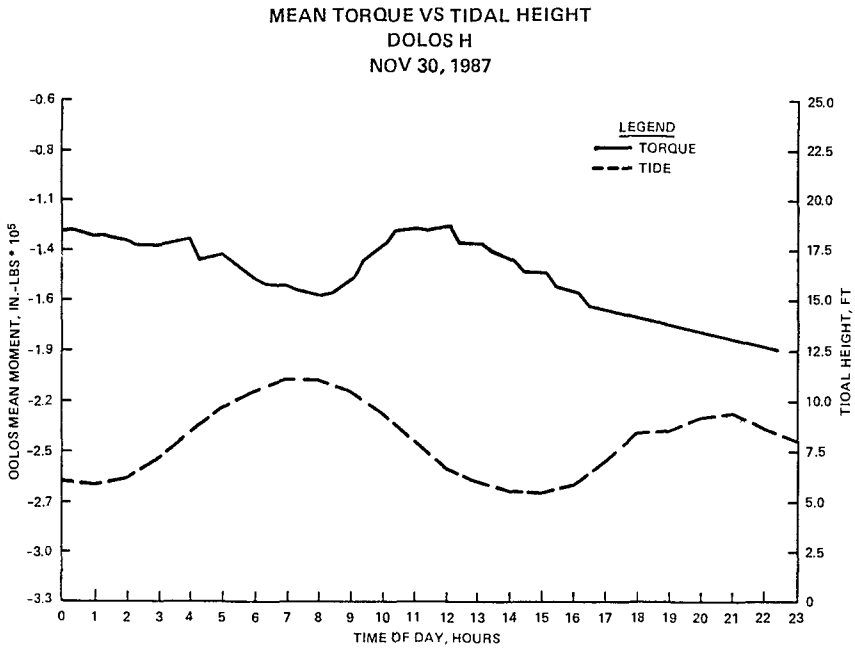


Figure 8: Dolos H Mean Response with Tide

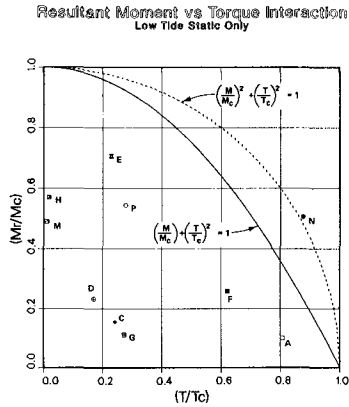


Figure 9: Static Moment-Torque Interaction Diagram

It is well known that static loads for large dolosse can be significant relative to breaking strength. However most estimates, to date, have been numerical computations based on a limited number of artificial boundary conditions. It is much more difficult to estimate static loads for individual units nested in an actual breakwater. Figure 9 shows the observed static load for 10 dolosse plotted on a moment-torque interaction diagram. The values are those observed at low tide, the case of maximum self weight load. The resultant moment and torque are normalized to the critical values, and two common design curves are plotted for the interaction breaking limit. As can be seen there is a wide distribution of loads, and all but one are within the design curves. This is consistent with the fact that none of these units are broken or cracked. The high value for dolos N is explained by its boundary condition. The vertical fluke is wedged downward into a hole with the horizontal fluke cantilevered, applying a large torque to the shank-fluke interface.

6 Pulsating Response

It is important for structural design of dolos armor units to determine the magnitude of loads due to wave attack. The details of the pulsating response are quite complex, however from a design engineer's point of view, the structural response is an extreme value problem. The characteristics of the stress are of little interest below breaking, but the likelihood of exceeding the breaking threshold must be predicted.

In order to develop a first look at the pulsating response, a large number of storm records from various dolosse were analyzed as follows. For a record 30 minutes long, the mean and trend were removed, and the absolute value of the maximum peak response for the record was found. For the same time period the largest wave was found. Figure 10 shows plots for Dolosse F and H which are both located on the lower portion of the test section. The horizontal axis is a wave power parameter H^2T where H is the height of the largest wave and T is its period. Although there

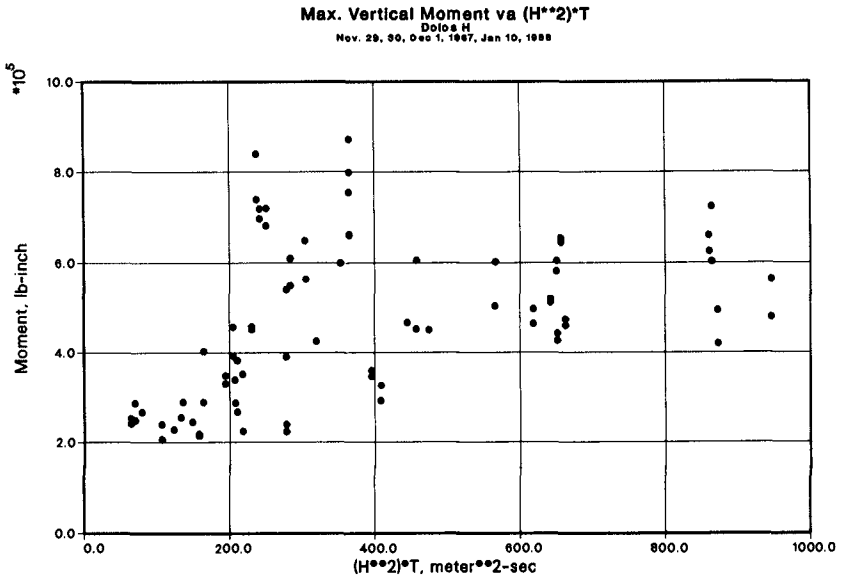
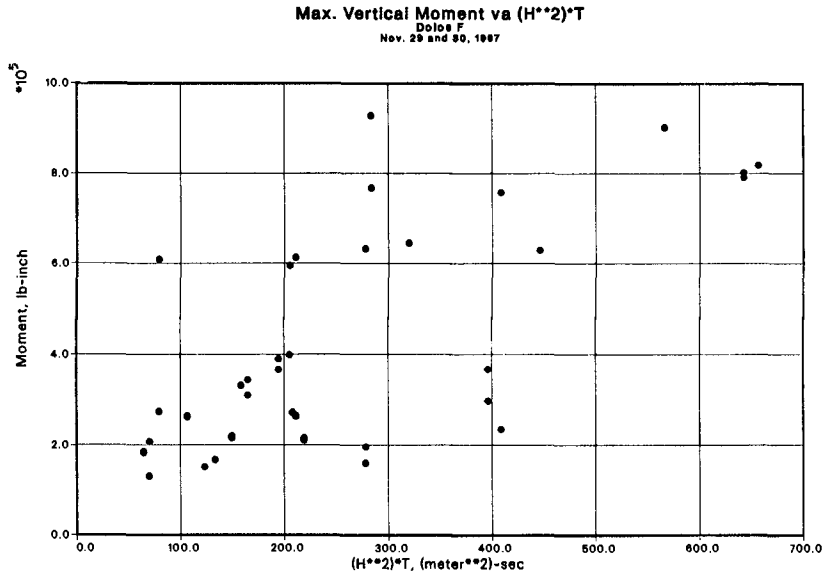


Figure 10: Maximum Pulsating Response vs. Maximum Wave Power

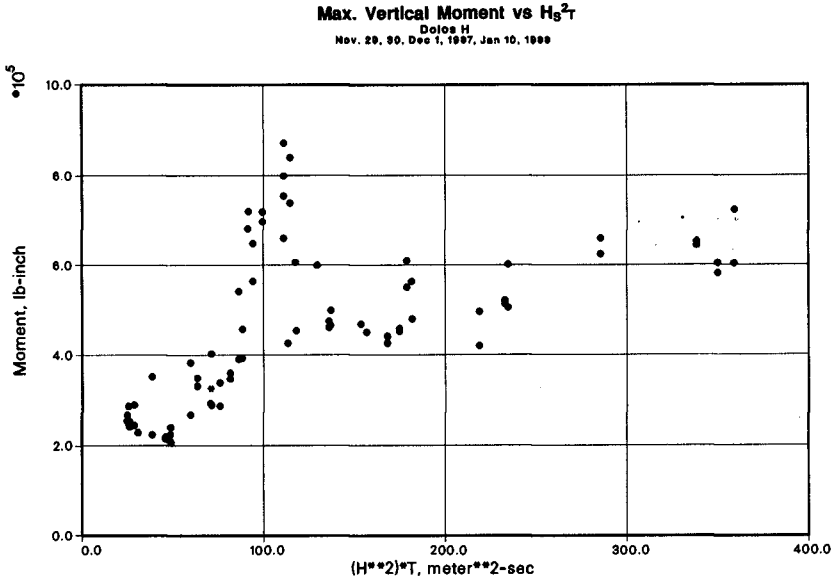
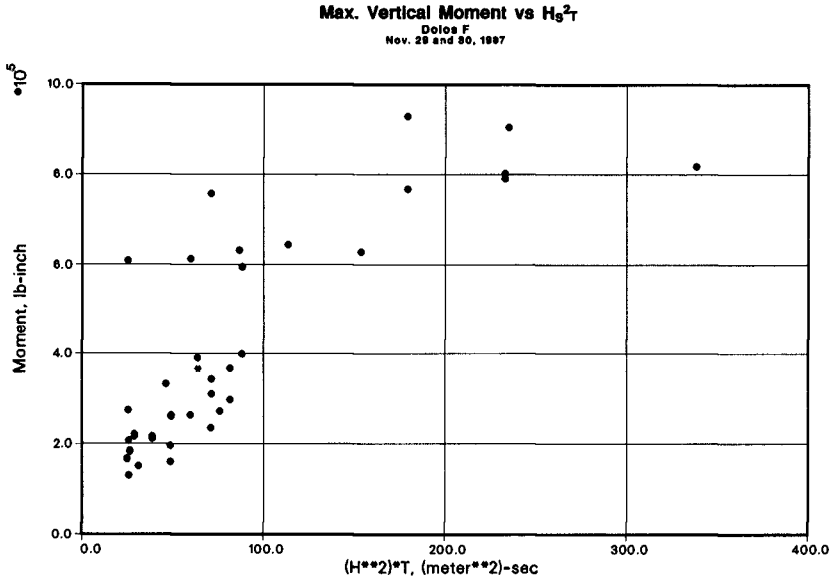


Figure 11: Maximum Pulsating Response vs. Significant Wave Power

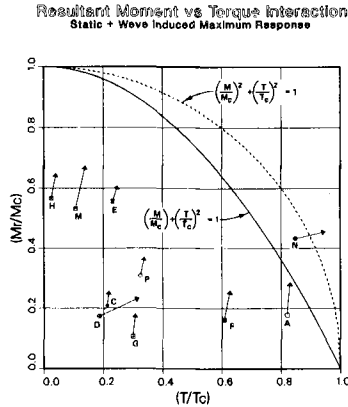


Figure 12: Combined Static and Maximum Pulsating Moment-Torque Interaction Diagram

is scatter to the data, both dolos can be plotted on the same linear scaled paper. Statistical variance can be reduced by using an averaging statistic such as $H_{1/10}$ or $H_{1/3}$ for the waves and a similar definition for the M_v . However to preserve the measured extreme value for the M_v , Figure 11 shows the same maximum M_v vs a wave power parameter computed from H_s and a T from the peak of the wave spectrum. As expected the scatter of the data is much less.

7 Preliminary results

Early in the investigation of the structural response of the dolos unit, most attention was focused on impacts as the most likely cause of dolosse breakage. It was generally assumed that wave forces would be much less important. However the magnitude of the pulsating forces observed at Crescent City are on the same order of magnitude as the static forces. It is easy to foresee an unfavorable combination of static forces and wave forces which could exceed the strength of the unit, causing failure without movement or impacts. Figure 12 shows a composite interaction diagram similar to the previous Figure 9. Here the static values are plotted at the time of the maximum pulsating response. Since this is generally at a higher water level, static forces are somewhat reduced from the low tide values shown previously. The absolute value of the maximum, resultant pulsating response is plotted as a vector extending from the base static value. The end of the arrow then represents the maximum combined static and pulsating response normalized to the breaking strength of the dolos. Dolos N is outside the conservative design range.

8 Conclusions

The work described here represents preliminary results from a unique set of measurements. Much remains to be done. However some general conclusions can focus the direction of future efforts:

- Static forces on dolosse in a real breakwater vary with mean water level and can be significant relative to the breaking strength of large dolosse.
- Wave (pulsating) forces are of the same order of magnitude as static forces.
- Wave forces compare qualitatively with scale model and numerical model results.
- Empirical relationships between wave energy and wave forces can be developed.

Acknowledgement

The work described in this paper was conducted as part of the Crescent City Prototype Dolosse Study of the Coastal Engineering Research Center, Waterways Experiment Station, US Army Corps of Engineers. Permission to publish this paper was granted by the Chief of Engineers.

Appendix - SI Unit Conversion

$$1 \text{ in.} \cdot \text{lb.} = 113 \text{ N} \cdot \text{mm} = 1.13 \times 10^{-4} \text{ KN} \cdot \text{m.}$$

References

- Burcharth, H.F.** (1984) Fatigue in Breakwater Concrete Armour Units. University of Aalborg, Denmark, Oct.
- Howell, G.L.** (1985), ed. *Proceedings of the Workshop on Measurement and Analysis of Structural Response in Concrete Armor Units*. January 23-24; Waterways Experiment Station, Coastal Engineering Research Center, Vicksburg, Mississippi. 421 pp.
- Howell, G.L.** (1986) A System for the Measurement of the Structural Response of Dolos Armour Units in the Prototype. *The Dock & Harbour Authority*, vol. 67, number 779, May. pp.6-10.
- Kendall, T.R.** (1988) Analysis of 42-ton Dolos Motions at Crescent City. *Proceedings, 21st International Conference on Coastal Engineering*, 20-25 June, Torremolinos, Spain, ASCE.
- McDougal, W.G.**, Melby, J.A., and Tedesco, J.W. (1988) Wave Forces on Concrete Armor Units. *Journal of Waterway, Port, Coastal, and Ocean Engineering*, vol. 114, no. 5, September, pp.582-598, ASCE.

Scott, R.D. , Turcke, D.J., Baird, W.F., (1986) A Unique Instrumentation Scheme For Measuring Loads In Model Dolos Units. *Proceedings, 20th International Conference on Coastal Engineering*, Taipei, Taiwan, ASCE.

CHAPTER 175

"Double U block" and "Iblock"
—the armour blocks of two new types

S. W. TWU*, S. C. LIN**, S.G. CHANG***

Abstract

A total of eleven new types of blocks are developed for this project. After performing a series of model tests for them and having a consideration of easy casting, two types of blocks are selected and presented here in this paper. They are named "Double U block" and "I block", respectively. The two have been compared with several existing types which have been widely used in Taiwan. It is shown that the Double U block is an excellent type of block with high stability and low reflection coefficient. The I block has an advantage of easy casting, although it is not outstanding in other characteristics.

I. INTRODUCTION

In the last two or three decades, concrete armour blocks have been commonly used in Taiwan for the construction of harbors and shore-protection structures. These blocks are usually Tetrapod, Dolosse, Holtripod and Shake. However, no matter what type of blocks are used, they are destroyed very often because the waves appearing around the coast of Taiwan are so awful, either in winter monsoon seasons or typhoon periods. Furthermore, when these damage occurs, it always extend to the block-covering structures or even to the back-side areas protected by them. The back-side areas are known as wharves, land or resident areas. Taiwan is a densely-populated area, naturally, the land is very valuable. Under this circumstance it is painful to tolerate any land loss due to wave attacks. So, it is reasonable to predict that the concrete armour blocks will be used more extensively for the shore-protection structures in the future. Consequently, we are looking forward to developing one or two types of armour blocks which are superior to those used currently in Taiwan.

* Prof., Hydraulics and Ocean Engineering Dept., Cheng-Kung University, Tainan, Taiwan, R.O.C.

** Assoc. Prof, Hydraulics and Ocean Engineering Dept., Cheng-Kung University, Tainan, Taiwan, R.O.C.

*** Research assistant, Tainan Hydraulic Laboratory, Cheng-Kung University, Tainan, Taiwan, R.O.C.

II. DESIGN PROCEDURE

A good concrete armour block should share a number of characteristics, such as good stability, good interlocking effect, low reflection coefficient and easy casting. Among them the stability is the most important. It is common thing that the coastal structures are covered with concrete armour blocks. Some of them, such as off-shore breakwaters, are even piled up entirely by concrete blocks. The primary function of these blocks is to dissipate the wave energy and to scatter the wave force, so that the structure might not be destroyed by waves. If the blocks slide down or move away from its place during the wave attacks, the structure will lose its protection layer. Afterward, a damage to the structure occurs. Hence, good stability takes priority of all other characteristics of the armour blocks.

The second required characteristic is the wave-energy-dissipation ability. If the blocks are placed inside a harbour, it is expected not to produce large amount of reflection waves to the water area. Generally speaking, the lower the reflection coefficient, the better the armour block.

In addition to the two characteristics mentioned above, there is another which is also very important, that is the casting feasibility. Good blocks should be easy to cast as they are being formed. So that the construction work can smoothly under way. Following the above rules, both the staffs of Tainan Hydraulic Laboratory and the Department of Hydraulics and Ocean Engineering start the design work for the new types of blocks. Finally, eleven types are finished.

III. TESTS FOR STABILITY

To pick the superior ones from these eleven types of blocks, a number of model tests have to be carried out. All of these tests are performed in a wave flume made of concrete, which has a length of 75 m with 1.0 m in width, and 1.2 m in height. One side of the flume is casted with sheets of glass with 36 m in length.

Among these tests the stability test is the most important, and is conducted first. In this test, all types of blocks have the same weight, 150 gm, and are placed on the same site with a slope of 1:1.5 and with water depth of 20cm. The inclined-face model is placed on a bed slope of 1:10, which is 4 m in length and ends in connection with the horizontal flume bed where is 52.9 m away from the wave maker. The sketch for this model is shown in Figure 1.

In this test a wave period of 2 sec is adopted. The wave height is adjusted so that they break and impact just on the tested blocks. For convenience of comparison, the stability situation of these blocks are divided into five degrees as follows: (Michael, 1974; Paul, 1971)

- (1) 1st degree: All the tested blocks stand still against wave attack.

- (2) 2nd degree: Part of the tested blocks shake with waves, but their final mean position never change.
- (3) 3rd degree: A few tested blocks are slightly moving, but the majority remains stable.
- (4) 4th degree: The tested blocks move slowly and continuously until the armour layer is destroyed.
- (5) 5th degree: The tested armour layer is destroyed in a short time.

For the 1st and 2nd degree, they are considered excellent in stability. In the 3rd degree a few blocks are removed at the start of the test, but later on nothing

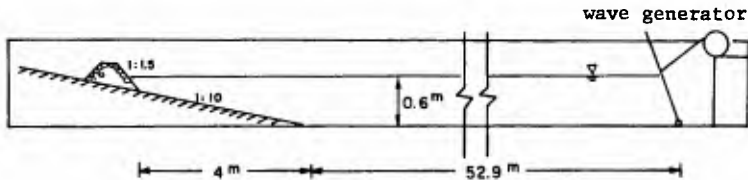


Fig 1. The sketch for the wave flume.

more happen. Therefore, the 3rd degree stability is still acceptable. If these definitions are compared with the percentage of damage. The 1st degree can be considered as zero percentage of damage. The zero percentage should fall on the transition between the 1st and 2nd degree. The 2nd degree will be equal to 0-2% damage, and the 3rd degree approximately 2-4% damage. In the 4th degree the damage percentage depends on time and therefore it will increase with increasing duration of wave attack. In the long run it will be totally destroyed. For the 5th degree total failure will occur in a short time. So, those types of blocks that reach the 4th or 5th degree in a short time are naturally not qualified. Based on the above criteria, four types of blocks are left for further tests that include tests for K_d value and reflection coefficients. After all these tests have been performed, a consultation with Chang-Ming Corporation, who financially supports this project, is held. In that meeting, we focused our attention on the stability and casting feasibility for selecting work. Consequently, two types of blocks, named "Double U block" as shown in Photo 1 and "I block" as shown in Photo 2,



Photo.1. Double U block



Photo.2. I block

are selected. To realize the superiority of the two new types, they are compared with a number of types which have been widely used in Taiwan, such as Holtripod, Dolosse and Shake. So, a number of additional tests for all these existing types have also been conducted. In case of uniform placing in two layers, Double U block and I block are compared with Holtripod and Shake in terms of the number of breaking waves needed to attack to reach the indicated stability degree. The results are shown in Figure 2. The case for uniform placing in one-layer is shown in Figure 3. For the case of pell-mell placing in two layers, the

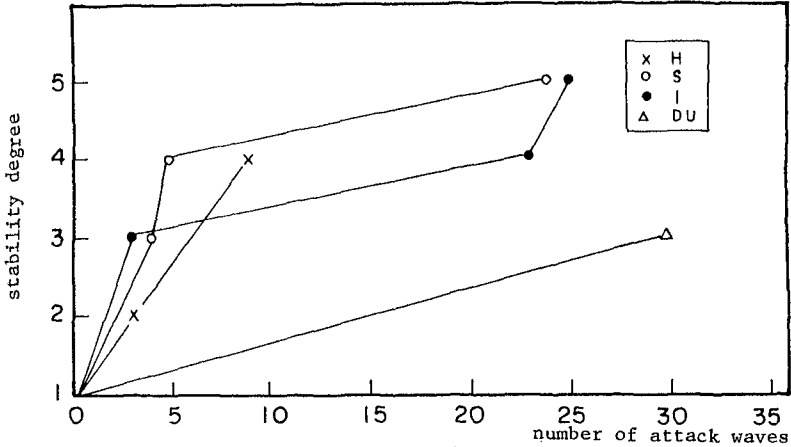


Fig 2. Relationship between stability degree and number of attack waves needed to reach that degree when blocks are uniformly placed in two layers.

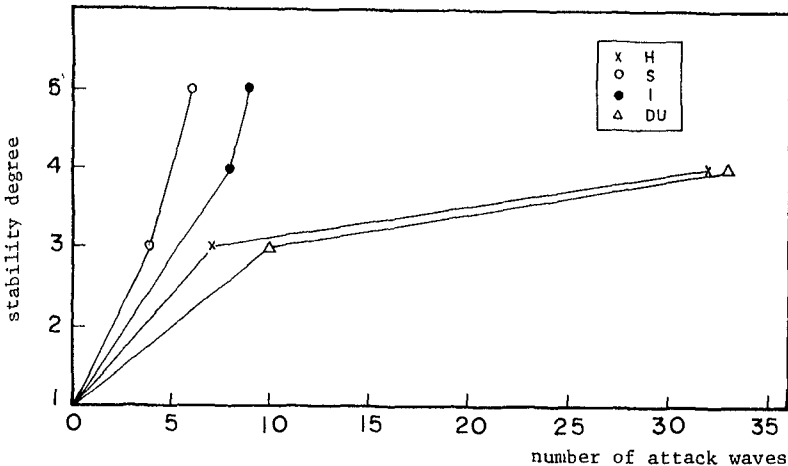


Fig 3. Relationship between stability degree and number of attack waves needed to reach that degree when blocks are uniformly placed in single layer.

new types are compared with Dolosse and the results are shown in Figure 4. It is found that Double U block is superior to all the compared ones. I block performs approximately the same as Shake and Holtripod if they are uniformly placed in two layers, and performs approximately the same as Dolosse if they are pell-mell placed in two layers. However, Figure 3 shows that I block is better than Shake but inferior to Holtripod as they are uniformly placed in single layer.

IV. TESTS FOR K_d VALUE

K_d values of armour blocks are usually calculated, by Hudson's formula

$$K_d = \frac{\gamma H^3}{W (S-1)^3 \cot \theta}$$

where W is the weight of individual armour block. γ and S are the specific weight and specific gravity of armour block, respectively. θ is the angle of armour-block slope with horizontal. H is the wave height.

Aside from the above-mentioned factors, K_d value for a given type of blocks is also closely related to the percentage of damage adopted for determining H in the Hudson's formula. In this study one percent of damage under the attack of nonbreaking waves is adopted. Two methods of placing are used for the test. One of them is uniform placing in two layers, and pell-mell placing in two layer is the another. In order to accurately measure the wave height the armour-block model is placed directly on the horizontal flume bed, rather than on an inclined bed, to keep the generated waves from shoaling effect. So, the water depth between the wave-maker and armour-block model is constant, i.e. 45cm. For a practical consideration, models of three armour-block slopes, i.e. 1:1.33, 1:1.5 and 1:2.0, are

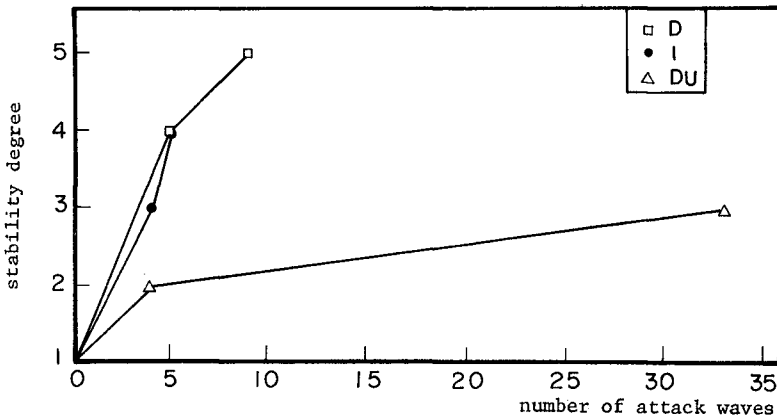


Fig 4. Relationship between stability degree and number of attack waves needed to reach that degree when blocks are pell-mell placed in two layers.

used. Wave periods of 1.5, 1.8, 2.0 sec are generated. The duration for each run is 30 mins. For a given type of blocks, the wave height in a run is adjusted by a little higher than that in the preceding run until one percent of damage to the mound of armour block meets. Dolosse has also been tested for Kd value in this study. So that they could be compared with each other under the same condition. The resulting Kd values are shown in Table 1. Five cases of them are crossed meaning that none of the waves generated in the wave flume could make any damage to them.

According to Hudson's formula, Kd is independent of wave period, but in this table it is found that Kd varies proportional to wave periods. It is indicated that Double U block has a Kd value higher than Dolosse, and I block is lower.

Table 1. Kd Value for the tested blocks.

block wave period method of armour-block slope placing		Double U block			I block			Dolosse		
		1.5	1.8	2.0	1.5	1.8	2.0	1.5	1.8	2.0
uniform placing in two layers	1:1½	20.9	29.5	30.4	18.8	23.3	26.2			
	1:1.5	18.3	24.7	31.1	21.1	24.7	28.1			
	1:2.0						22.9			
	average	25.8			23.6					
pell- mell placing in two layers	1:1½	17.8	22.2	26.2	13.9	21.1	23.8	13.4	21.4	24.1
	1:1.5	22.3	27.3	27.0	11.8	16.6	15.4	13.7	21.7	22.7
	1:2.0	14.4	19.8	20.0	13.9	14.5	14.5	13.5	21.2	17.2
	average	21.9			15.6			18.8		

The uniform placing method for Double U block shown in the table is a method named here as side-by-side method, and is shown in Photo.3. If another special uniform placing method named here as riding method, shown in Photo.4, is adopted, then the blocks would give a Kd value so high that we don't even know how high it is, because none of the waves generated in the flume can destroy them. Although the riding method could offer such a high stability, it would take much more amount of armour units to cover a given area, and produce much higher reflection coefficient, than the side-by-side method, which will be shown later.

V. TESTS FOR REFLECTION COEFFICIENT

Wave-energy-dissipation efficiency of a armour block is always indicated by the reflection coefficient and run-up value. A superior armour block should give a lower reflection coefficient and run-up value. Two armour-block slopes, 1:1.5 and 1:2.0, are used in this test to estimate

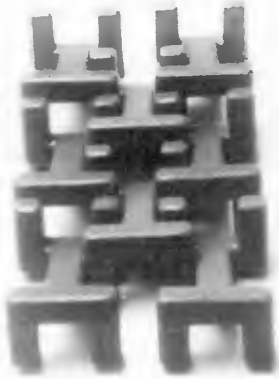


Photo.3. side by side method for Double U blocks



Photo.4. riding method for Double U blocks

the reflection coefficient. The wave periods include 1.0, 1.5 and 2.0 sec., and five varied wave heights are generated for each wave period. The water depth in the flume, as shown in Figure 1, is 60 cm in front of the wavemaker and 20 cm at the model toe. A technique developed by Goda (1979) to resolve the incident and reflected waves from the records of composite waves is used. Two simultaneous wave records are taken at adjacent locations in front of the armour-block model, and all the amplitudes of Fourier components are analyzed. From these Fourier components the amplitudes of incident and reflected wave components are estimated. According to Goda, as long as the spacings between the model and the wave gauges are kept in a proper range, the reflection coefficient can be accurately measured by the above incident and reflected wave heights. Goda suggested

$$L_{max} = \frac{\Delta \ell}{0.05} > L > \frac{\Delta \ell}{0.45} = L_{min} \quad \ell \geq 0.1 L$$

Where $\Delta \ell$ is the spacing between the wave gauges, ℓ is the spacing between model and the gauge adjacent to the model, L_{max} and L_{min} are the maximum and minimum wave length of the attack waves, respectively. In this test $\ell = 60\text{cm}$ and $\Delta \ell = 50\text{cm}$ are used, and they are in effective range as Goda suggested.

For convenience of comparison, three existing types of blocks have also been tested in addition to the new ones. Holtripod and Shake are compared with the new ones for the case of uniform placing, and Dolosse are for the case of pell-mell placing. The results are shown in Figure 5 to 10. In each case the reflection coefficients are calculated by taking average over five varied wave heights. The results are shown in Table 2. Both results of the side-by-side method and riding method for Double U block are all shown in Fig.5 and Fig.6, in which the side-by-side method is

Table 2. Reflection Coefficient

armour- block slope	wave period	uniform placing, one layer				uniform placing, two layers				pell-mell placing, two layers		
		Double U	I block	Shake	Holtripod	Double U	I block	Shake	Holtripod	Double U	I block	Dolosse
		1:1.5	1.0	0.232	0.213	0.214	0.318	0.195	0.270	0.219	0.227	0.131
	1.5	0.394	0.503	0.338	0.392	0.250	0.393	0.341	0.334	0.276	0.296	0.284
	2.0	0.603	0.657	0.591	0.492	0.544	0.637	0.565	0.564	0.512	0.420	0.507
1:20	1.0	0.243	0.349	0.259	0.250	0.180	0.301	0.294	0.198	0.178	0.175	0.161
	1.5	0.368	0.374	0.330	0.360	0.239	0.289	0.305	0.273	0.164	0.255	0.237
	2.0	0.487	0.584	0.504	0.575	0.474	0.584	0.543	0.514	0.546	0.530	0.519

indicated by DU without bracket, and the riding method by DU with bracket. In the remaining figures the results of riding method for Double U block are omitted. From these data it is found that Double U block, side-by-side method, has a reflection coefficient approximating to Shake and Holtripod as the blocks are uniformly placed in single layer. While I block has a little higher value. For uniform placing in two layers, Double U block, side-by-side method, is less than Shake and Holtripod. I block is a little higher. For pell-mell placing in two layers, Double U block and I block show approximately the same results as Dolosse. While the riding method for Double U block is adopted, it shows a reflection coefficient higher than all the compared ones.

VI. TESTS FOR RUN-UP VALUE

In this test the flume bed between the model and the wave generator is horizontal, and the water depth is 60cm. It is known that run-up value for a given type of block is primarily a function of wave steepness and armour-block slope. In addition to that, it is also related with the placing method for the blocks. With two armour-block slopes and three placing methods for the blocks, the test results are expressed as curves showing relationships between relative run-up value and wave steepness, as in Fig. 11-14. It is shown in this figures that the run-up values decrease with increasing wave steepness. And they are smaller in case of pell-mell placing than in case of uniform placing. These resulting run-up values may also be expressed by a formula, as follows

$$\frac{R}{H_0} = a - b \left(\frac{H_0}{L_0} \right)$$

where the coefficient a, b are shown in Table 3

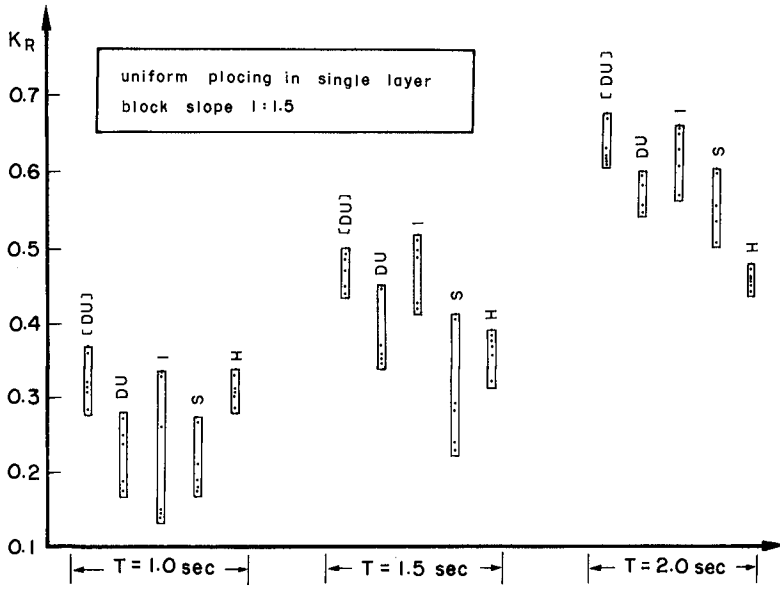


Fig.5. Experimental reflection coefficient

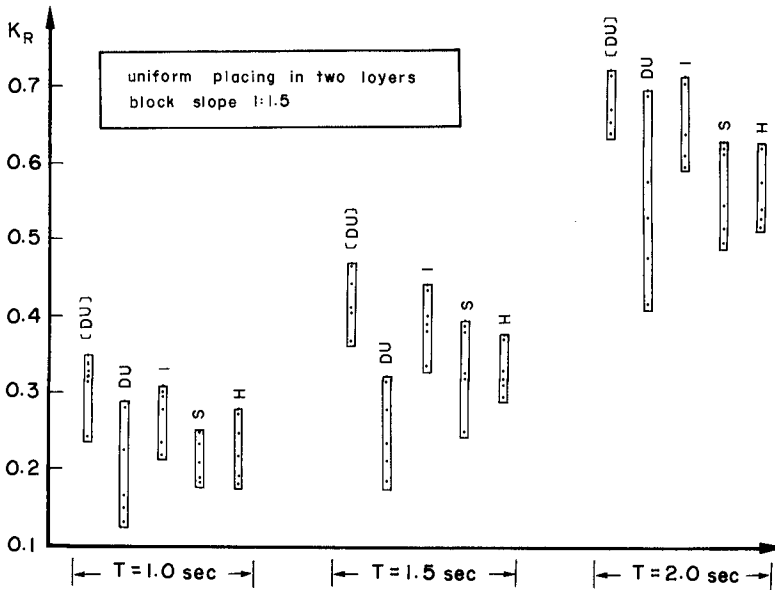


Fig.6. Experimental reflection coefficient

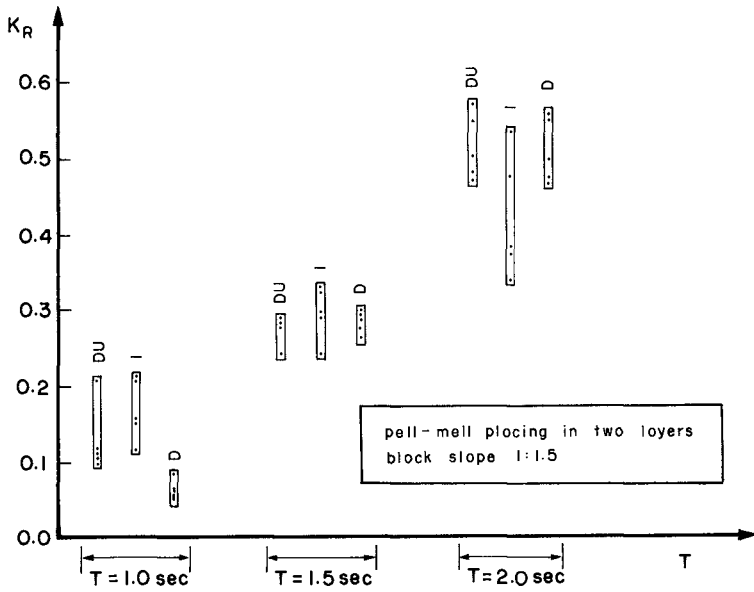


Fig.7. Experimental reflection coefficient

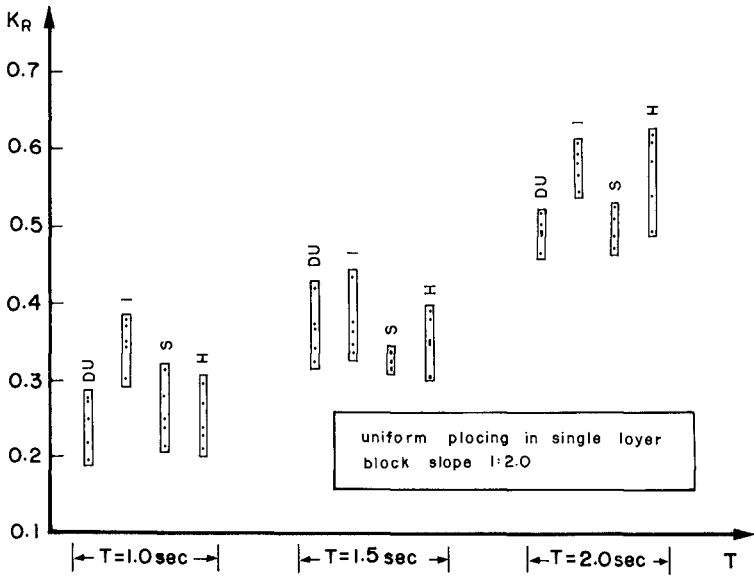


Fig.8. Experimental reflection coefficient

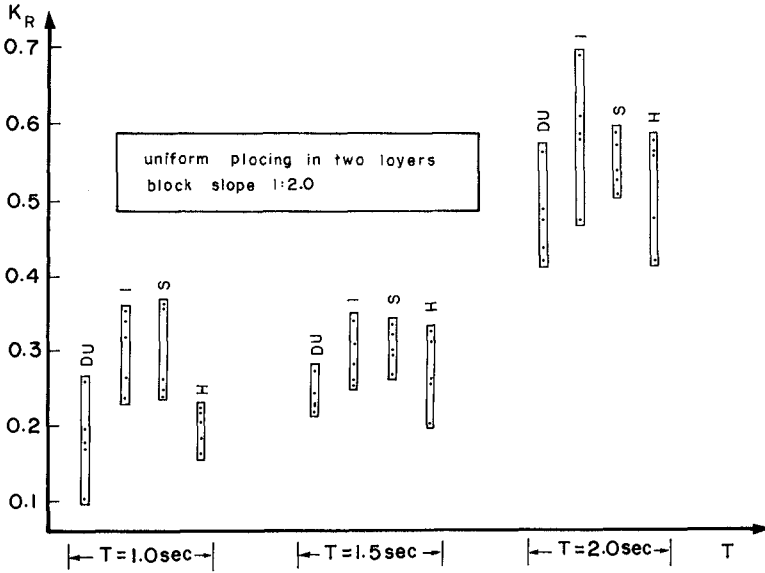


Fig.9. Experimental reflection coefficient

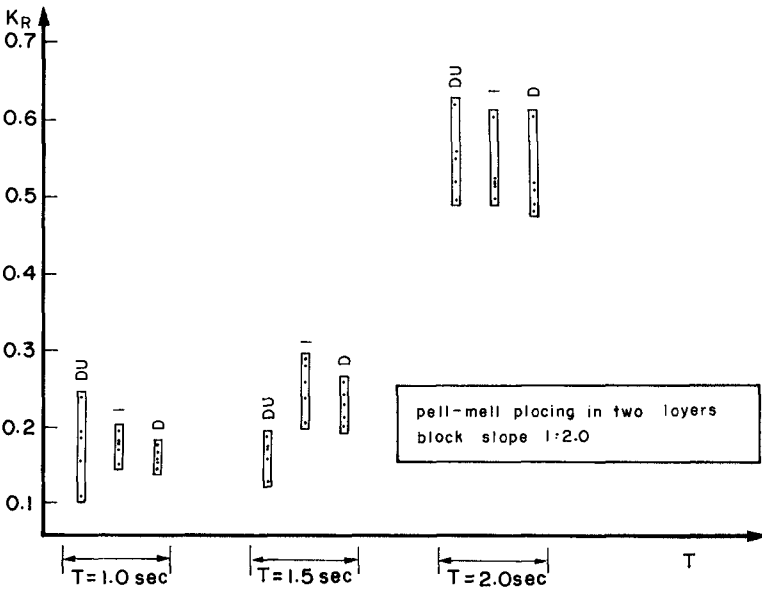
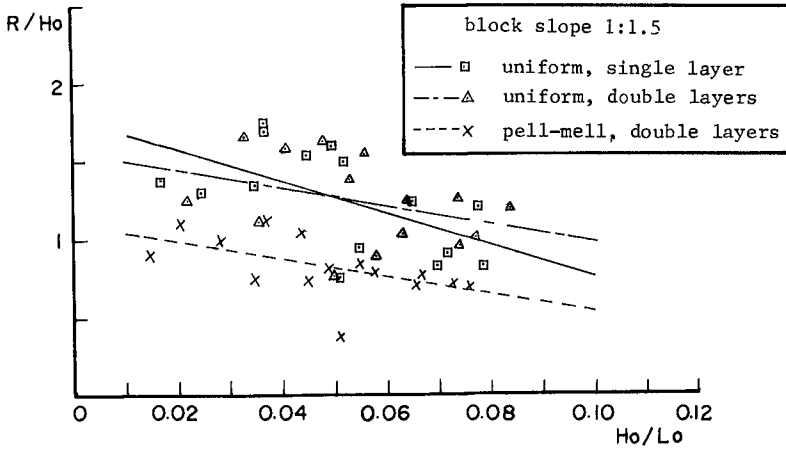
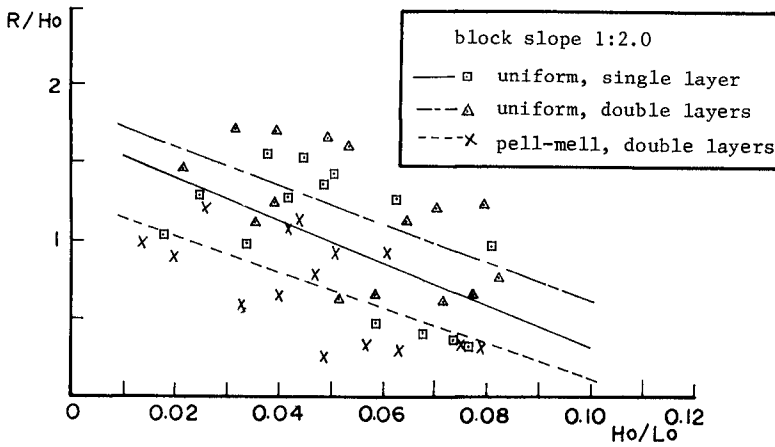


Fig.10. Experimental reflection coefficient

Fig 11. $R/Ho \sqrt{Ho/Lo}$ for I blockFig 12. $R/Ho \sqrt{Ho/Lo}$ for I block

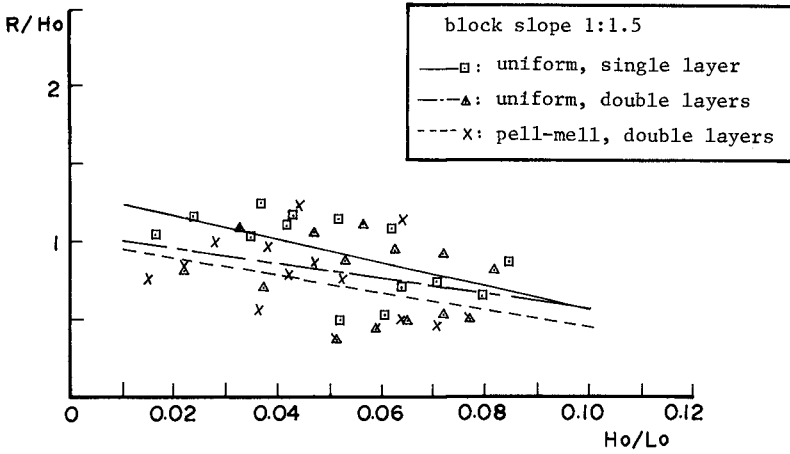


Fig 13. $R/H_o \sim H_o/L_o$ for Double U block

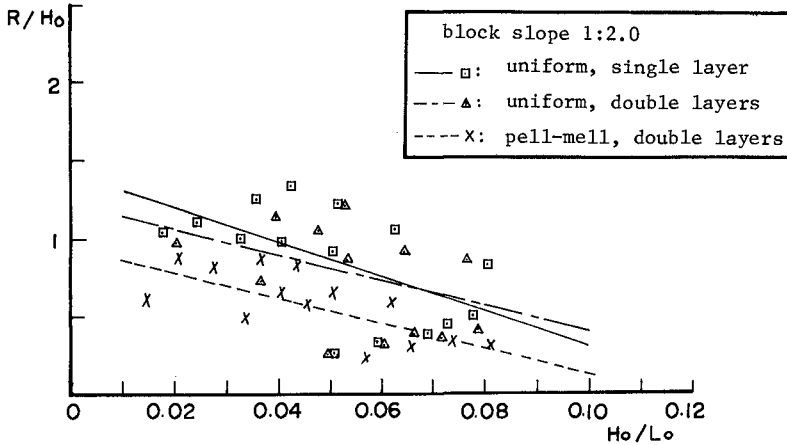


Fig 14. $R/H_o \sim H_o/L_o$ for Double U block

Table 3. a, b value for run-up

method of placing block for slope	type of block coefficient	Double U		I-block	
		a	b	a	b
1:1.5	uniform, one layer	1.319	7.52	1.775	10.19
	uniform, two layers	1.668	5.00	1.563	5.82
	pell-mell, two layers	1.017	5.69	1.100	5.72
1:20	uniform, one layer	1.408	10.90	1.677	13.52
	uniform, two layers	1.228	8.19	1.855	12.35
	pell-mell, two layers	0.947	8.15	1.259	11.41

VII. CONCLUSIONS

1. Double U block shows a stability superior to the existing blocks which have been commonly used in Taiwan. It gives a Kd value much higher than the existing types, no matter what method the blocks are placed.
2. If a riding method of placing is adopted, Double U block would give a very high Kd value, but it also produces a large reflection waves. Except that, with any other method of placing, it can always offer a low reflection coefficient in addition to the high stability.
3. Double U block is a newly developed block. The studies presented here are so far what we have done. It is easy to realize from the shape of the block that a good interlocking relation among blocks plays an important part in its high stability. Therefore, the block has to take large internal tension due to the interlocking effect. Under this circumstance, the Double U block has to be reinforced in actual field.
4. I block performs neither better nor worse than the existing blocks in stability and shows a little worse in reflection coefficient, however, it has an advantage of easy casting. So, I block is also an alternating type of block.

REFERENCE

1. Goda Yoshimi, Yasumasa Suzuki, Yasuharu Kishira, Osamu Kiruchi (1976), "Estimation of incident and reflected waves in random wave experiment." Proc. of the 15th

- Coastal Engr. Conf. p.828-845.
2. Michael Brorsen, H. F. Burcharth, Torben Larsen, (1974): "Stability of Dolos Slopes", Proc. of the 14th Coastal Engr. Conf. p.1691-1701.
 3. Paul, M.W., Baird, W.F. (1971): "Discussion on break-water armour units", Proc. of 1st int. conf. on port and ocean eng. under arctice conditions. Trondheim.

CHAPTER 176

ARMOUR UNIT STRUCTURAL RESPONSE - A PARAMETRIC STUDY

C. David Anglin*, Associate Member, William F. Baird*, Associate Member,
Etienne P.D. Mansard**, R. Douglas Scott*, Associate Member, David J. Turcke***

ABSTRACT

There is a general lack of knowledge regarding the nature and magnitude of loads acting on armour units used for the protection of rubblemound coastal structures. Thus, a comprehensive design procedure incorporating both the hydraulic stability and the structural integrity of the armour units does not exist.

This paper presents the results of a detailed parametric study of the structural response of armour units to wave-induced loading in a physical breakwater model. The effect of the following design parameters is investigated: breakwater slope, armour unit location, wave period and wave height.

This research has made a number of significant contributions towards the development of a comprehensive design procedure for concrete armour units. It has identified a linear relationship between the wave-induced stress in the armour units and the incident wave height. In addition, it has shown that the conditional probability of wave-induced stress given wave height can be estimated by a log-normal distribution. Finally, a preliminary design chart has been developed which incorporates both the structural integrity and the hydraulic stability of the armour units.

INTRODUCTION

Concrete armour units are often used for the protection of rubblemound coastal structures when wave conditions dictate the use of unreasonably large armour stones, or when armour stones of a sufficient size are not available. The design of these concrete armour units is primarily based on hydraulic stability, with little attention being given to the structural integrity of the individual units. The interaction between waves and rubblemound structures is a very complex process, and the wave forces acting on the armour units and the structural response of the units to these forces is poorly understood.

* W.F. Baird and Associates Coastal Engineers Ltd.
150-38 Antares Drive, Ottawa, Ontario, Canada K2E 7V2

* * Hydraulics Laboratory, National Research Council of Canada
Ottawa, Ontario, Canada K1A 0R6

* * * Department of Civil Engineering
Queen's University, Kingston, Ontario, Canada K7L 3N6

Current breakwater design procedures are based on empirical formulae, such as Hudson's equation (U.S. Army Corps of Engineers, 1977, 1984), or for larger structures, physical hydraulic modelling may be used. However, these approaches do not consider the structural integrity of the armour units themselves, but concentrate on the hydraulic stability of the armour layer. There is a general lack of knowledge regarding the nature and magnitude of loads on the armour units, and consequently a design procedure incorporating the structural integrity of the armour units does not exist.

The measurement of forces in a breakwater or stresses in an armour unit is a very complex task. However, a number of research groups have recently undertaken investigations of this nature, utilizing a variety of approaches. These have included prototype studies, physical and numerical modelling, and theoretical developments.

A number of researchers are making use of physical models to measure the structural response of armour units (for example, Scott et al, 1986a and b, Nishigari et al, 1986, Losada et al, 1988, Jensen and Juhle, 1988). In addition to these physical model investigations, a very extensive prototype study is being carried out at Crescent City, U.S.A. to measure dolos response in full scale situations (Howell, 1988), and a non-linear numerical model is being developed to determine the response of dolos in waves (Tedesco and McDougal, 1985, Tedesco et al, 1988). Other types of research, including both prototype studies (Burcharth, Feb. 1981, 1984) and physical modelling (Timco and Mansard (1982)) have also been carried out; however, these investigations have not measured the response of armour units under wave attack, but have tested units to failure. Finally, a number of investigators have utilized theoretical approaches to develop an understanding of the structural performance of armour units, and to establish design criteria (for example, Timco (1984), and Burcharth (May 1981)).

The Department of Civil Engineering at Queen's University, in co-operation with W.F. Baird and Associates Coastal Engineers Ltd., initiated a long term research and development program in 1980 to investigate the nature of forces acting on armour units in a breakwater, and ultimately to develop a comprehensive design procedure for concrete armour units. Initial investigations concentrated on a review of available instrumentation techniques for both model and prototype studies, and concluded that strain-gauging model armour units was the most viable approach (Baird, et al, 1983). Preliminary work, utilizing the concept of "strain distortion", was completed with model armour units constructed of an epoxy material and instrumented with surface-mounted strain gauges. However, the sensitivity of the instrumentation was insufficient to accurately measure the loads encountered in a typical hydraulic breakwater model (Scott, 1986). Further studies led to the development of a unique armour unit load cell, which utilizes the concept of "geometric distortion" to produce an extremely sensitive and accurate instrumentation system (Scott, 1986, Scott et al, 1986a and b).

A number of these load cells were manufactured for use in the present study, which is a parametric investigation into the structural response of armour units in a hydraulic breakwater model. The units were manufactured and calibrated at Queen's University, while the testing program was completed at the Hydraulics Laboratory of the National Research Council of Canada (NRCC). This paper describes details of the load cell, the testing program, and data reduction and analysis techniques, and finally presents a preliminary design chart which incorporates both the hydraulic stability and the structural integrity of the armour unit.

INSTRUMENTATION

The load cell, developed by Scott (1986) for his PhD degree, utilizes the concept of geometric distortion to produce an extremely sensitive and accurate instrumentation system. This force measuring device consists of a hollowed-out model armour unit (a

dolos in this study) and a thin-walled aluminum tube instrumented with strain gauges which is inserted in the shank of the dolos, as shown in Figure 1. The tube is instrumented with three full strain gauge bridges, which measure two orthogonal bending moments (M_1 and M_2) and the torque (T) at the mid-shank location of the dolos.

Calibration of the load cell was conducted by rigidly holding the unit in a test rig and applying known loads to the extremities of the unit's geometry. The output from the various strain gauge bridges was plotted against the applied load to produce a calibration curve of channel output versus applied load (either moment or torque). Thus, a load cell was created such that the output from the various strain gauge circuits could be directly converted into the two moments and the torque at the mid-shank location of the dolos. The accuracy of the instrumentation system was verified by comparing various test cases against theoretical and finite element model results.

The load cell is designed to accurately measure the response of the unit to static and quasi-static loads. The response to impact loads is not correctly measured; this would require considerable effort in correctly modelling the material properties of concrete at a selected model scale. This report focuses on the quasi-static (wave-induced) loads as measured in the breakwater model.

TEST PROGRAM

The tests were completed in a 2 m wide by 60 m long wave flume at the Hydraulics Laboratory of the National Research Council of Canada (NRCC). The breakwater cross-section was constructed in a 1 m wide section of the flume. The breakwater was a conventional multi-layer design, with a primary armour layer of dolos units (2 layers, dolos weight $W=482g$, dolos height $C=0.106m$, waist ratio $r=0.32$, random placement, with dimensionless packing density $\phi=NV^{2/3}=0.80$) placed over a filter layer of 30 to 100g crushed stone, as shown in Figure 2. The core consisted of a fine gravel.

Over 1000 tests were run to assess the effects of breakwater slope, unit location, wave period, and wave height, using both regular and irregular waves. Table 1 summarizes the range of parameters tested.

Table 1
Range of Parameters Tested

<u>Parameter</u>	<u>Range Tested</u>
Breakwater Slope	1:1.5, 1:2.0, 1:2.5
Load Cell Location	Number of Locations Tested Across Flume
elevation	+0.2m +0.1m 0 SWL* -0.1m -0.2m
top layer	2 4 4 4 2
bottom layer	2 2 2
Wave Period	regular waves $T = 1.25$ to 3.0 s irregular waves $T_p = 1.75$ to 2.5 s
Wave Height	regular waves $H = 0.05$ to 0.30 m irregular waves $H_s = 0.10$ to 0.25 m
Water Depth	0.80 m (non-breaking waves)
Crest Elevation	+0.40 m above water level (no overtopping)
*SWL = still water level	

A typical test series consisted of initializing and calibrating the instrumentation, placing the load cells (two) at selected positions in the breakwater model and running a short "burst" of waves, sampling the wave and load channels for 30 s. This procedure was repeated for numerous combinations of the various breakwater parameters, as summarized above. Data were sampled at a rate of 500 Hz using a NEFF analog to digital converter on an HP-1000 computer, and were stored on magnetic tape for later analysis.

The results presented in this paper are for a breakwater slope of 1:1.5 and regular waves only. The remainder of the data is currently being analysed.

DATA REDUCTION

Data reduction on the first series of tests (breakwater slope 1:1.5, regular waves, approximately 350 tests) has been completed using the NRCC GEDAP software system, and consisted of the following steps:

- (i) demultiplex the data into individual channels,
- (ii) removal of the static load component from the time series data,
- (iii) filtering to remove high frequency noise and dynamic events, which as noted earlier are not correctly measured by the load cell used in this study,
- (iv) calculation of combined moment, and normal, shear, and principal stresses using standard formulae (see below),
- (v) identification of data peaks in the various time series with a zero-crossing analysis, and calculation of the average peak values,
- (vi) calculation of mean, standard deviation, and root mean square values of the various time series,
- (vii) tabulation of the various input parameters (wave conditions and breakwater geometry) and output parameters (standard deviation and average peak values of moment, torque, and principal stress),
- (viii) plotting of various combinations of the input and output parameters, and regression analyses and estimation of confidence limits to identify trends.

The calculation of the various quantities is summarized below:

$$\text{longitudinal stress} = \sigma_x = Mc/I \quad (M = \text{combined moment} = \sqrt{M_1^2 + M_2^2})$$

$$\text{normal stress} = \sigma_y = 0 \quad (I = \text{moment of inertia of section})$$

$$\text{shear stress} = \tau = Tc/J \quad (J = \text{polar moment of inertia of section})$$

$$\text{principal stress} = 0.5(\sigma_x + \sigma_y) \pm \sqrt{[(\sigma_x - \sigma_y)/2]^2 + \tau^2} = 0.5\sigma_x + \sqrt{(\sigma_x/2)^2 + \tau^2}$$

average peak value = average of the highest "n" peaks, where n is the number of waves which occurred in the 30 s sample

$$\text{mean value} = \mu = (1/N)\sum x_i$$

$$\text{standard deviation value} = s = \sqrt{(1/N)\sum(x_i^2) - [(1/N)\sum x_i]^2}$$

$$\text{root mean square value} = \text{rms} = \sqrt{(1/N)\sum(x_i^2)} = \sqrt{s^2 + \mu^2}$$

A typical result from one of the tests is shown in Figure 3, which shows time series plots of the load cell response, including the combined moment (calculated from the two measured moments), the measured torque, and the calculated principal stress at the mid-shank location of the dolos. The corresponding wave time series is also shown.

DATA ANALYSIS

As mentioned earlier, only results from the first series of tests were available for presentation in this paper. These results consist of approximately 350 tests conducted with regular waves and a breakwater slope of 1:1.5. In addition, wave-induced quasi-static forces only are presented here; the static load component has been removed, while dynamic events were not measured by the load cell.

A series of parametric plots has been produced to investigate the influence of various input parameters on the measured armour unit response. The response parameters of average peak stress and standard deviation stress have been plotted against wave height (H) and the surf similarity parameter ($\xi = \tan \alpha / \sqrt{H/L}$). These plots have been produced with and without distinction of the individual wave periods and armour unit locations. In addition, various statistical analyses, including regression analyses, estimates of confidence limits, and estimates of data probability distributions have been completed to identify trends in the data. A review of the various plots leads to the following general observations, as demonstrated by the referenced figures:

- 1) wave-induced stresses increase approximately linearly with wave height, and scatter in the data tends to increase with increasing wave height; linear regression analyses at individual locations gave correlation coefficients (ρ) varying from 0.34 to 0.91 for individual wave periods, and from 0.62 to 0.77 for all wave periods considered together (Figure 4 shows typical results at a single location); quadratic regression analyses gave only slightly higher correlation coefficients - the curves tend to be concave down, showing a marginally decreasing stress with wave height.
- 2) wave-induced stresses tend to increase with wave period to a certain point, but may increase or decrease for $T > 2.25$ s depending on the load cell location (see Figures 4 and 5).
- 3) average peak and standard deviation wave-induced stress values show similar trends and scatter (results for standard deviation values are not presented here due to space limitations); the ratio of average peak to standard deviation stress values varies between approximately 1.8 and 3.9, but is typically around 3.2 (note that for a simple sinusoidal wave, this ratio is $\sqrt{2} = 1.414$).
- 4) wave-induced stresses tend to be higher in the bottom dolos layer than in the top dolos layer (see Figure 6).
- 5) for large waves, wave-induced stresses tend to be greatest above the still water level (SWL), while for small waves, stresses tend to be greatest at or just below the SWL (see Figure 7).
- 6) based on the available data, wave-induced stresses tend to be greatest for values of the surf similarity parameter between approximately 2.5 to 4 (see Figure 8); stresses tend to decrease for higher values of the surf similarity parameter, but no data is available below a value of approximately 2.2 for the 1:1.5 slope (data in this range was measured on the flatter breakwater slopes (1:2.0 and 1:2.5)); quadratic regression analyses of stress versus surf similarity gave correlation coefficients ranging from 0.37 to 0.96 for individual wave periods, and from 0.36 to 0.51 for all wave periods considered together.
- 7) results from all tests are presented in Figure 9, which shows the average peak wave-induced stress plotted against wave height; the conditional probability distribution of stress given wave height is skewed towards larger values, with the log-normal distribution giving a reasonable fit to the data (see Figure 10).

The trends described above tend to show up best at locations at or below the still water level (SWL), while positions above the SWL show less obvious trends and more scatter; this may be explained by the complexity of the wave-structure interaction during the wave breaking process against the structure, particularly above the swl where air entrapment and the air-water interface adds even more complexity.

These results show both consistencies and inconsistencies with previous research efforts. For example, it is widely recognized (for example, van der Meer and Pilarczyk (1987)) that armour unit stability is a minimum for values of the surf similarity parameter (ξ) in the order of 3 due to the nature of the wave breaking process. Thus, larger wave forces and wave-induced stresses in the armour units are to be expected under these conditions. This is confirmed by the results of this study, in which stresses in the armour units were largest for values of ξ between approximately 2.5 and 4, as shown in Figure 8. It is also generally accepted that forces on the armour layer reach a maximum just below the still water level, as shown by the concentration of damage at this location in prototype structures. In (apparent) contrast, the results of this study suggest that the largest wave-induced forces occur above the water level under severe wave conditions, as shown in Figure 7; however, it is important to note that these results do not include the static load component, which may be a significant factor in the total load acting on an armour unit. Clearly, the magnitude and distribution of static loads in the armour layer must be defined and incorporated in any design procedure. A detailed investigation of static loads in a breakwater armour layer is currently underway.

APPLICATIONS/DESIGN

The primary objective of this study was to complete a parametric investigation of wave-induced loading on breakwater armour units in order to establish statistically significant relationships between the stresses in the armour units and various design parameters. However, this study is also a major component in an ongoing long-term research effort with the overall objective of developing a design procedure for concrete armour units which incorporates both hydraulic stability and structural integrity. Towards this end, two applications for the presentation of the data have been developed, a moment-torque interaction diagram, and a preliminary design chart.

The moment-torque interaction diagram, shown in Figure 11, is based on an interaction equation relating failure in the dolos shank under the combined effects of bending and torsion, and was developed by Scott (1986). Based on the results of finite element modelling, moments measured at the mid-shank location of the dolos load cell are increased by a factor of 2.5 to account for the stress concentration at the fluke-shank interface. The resulting plot shows the location of the measured moments (factored) and torques relative to the theoretical failure line, and clearly shows the structural performance of the unit under the test conditions. This diagram is useful for the presentation of data from a specific breakwater study, for example, the assessment of an existing structure, or the design of a new structure. The interaction equation can be readily modified to account for unit design changes, such as size, geometry, reinforcement, and concrete strength.

The preliminary design chart, derived from the results of this study, is shown in Figure 12. This presentation consists of a plot of the maximum principal stress at the fluke-shank interface versus the dimensionless ratio H/C (wave height/dolos height) for various prototype dolos weights (W), thus allowing the designer to select the required concrete strength for a given application (H/C and W).

Data for all tests, encompassing all wave conditions and armour unit locations tested, was used to estimate the relationship between the maximum principal stress at the mid-shank location and the incident wave height. A linear regression analysis was completed, and the standard deviation of stress at a given wave height was calculated, as

shown in Figure 9, in order to derive a reasonable upper limit for the model data. For the purpose of this study, the upper limit was selected as a line one standard deviation above the linear regression line.

The model stress data, measured at the mid-shank location, was increased by a factor of 2.5 to represent stresses at the mid-shank location. This factor is based on the results of a series of finite element model analyses (Scott, 1986), in which the factor varied from approximately 1.7 to 2.7 depending on the loading and boundary conditions assumed. The factored model stresses were scaled to prototype based on the geometric scale of the model.

The hydraulic stability limit shown on the design chart was derived from Hudson's formula, and is defined by:

$$H/C = 0.537(Sr-1)(Kd \cot \alpha)^{1/3}$$

For example, with $Sr=2.4$, $Kd=25.0$ (77 SPM, trunk, non-breaking waves), and $\cot \alpha=1.5$, this results in a hydraulic stability limit of $H/C=2.52$. The Kd value used here is for presentation purposes only and does not reflect the state of the art concerning rubblemound breakwater design.

As mentioned, this design chart is preliminary in nature and is subject to a number of limitations, thus emphasizing the considerable research effort required to develop a design procedure incorporating both hydraulic stability and structural integrity. The following comments illustrate the major limitations:

- 1) The stresses are wave-induced only; static stresses are not included. Scott (1986) has shown that up to 50% of the internal strength of the dolos unit can be used up in resisting the static forces in the armour layer, depending on the concrete strength, unit size and unit location. Dynamic forces may also be significant due to unit motions and inter-unit impacts.
- 2) Concrete fatigue effects have not been included. Burcharth (1984) has shown that the "endurance limit" (ultimate stress range for n cycles/ultimate stress range for 1 cycle) is approximately 0.6 under quasi-static (pulsating) loads and 0.2 under impact loads.
- 3) The model data is based on regular waves only; as mentioned earlier, tests have been completed with irregular waves, but analysis of this data has not yet been completed.

CONCLUSIONS

This paper has described a parametric study of wave-induced loading on breakwater armour units. The effects of unit location, wave period, and wave height have been investigated and presented. Additional tests with different breakwater slopes and irregular waves have been completed, but the analysis of this data has not yet been completed. Applications of the data include an interaction diagram to demonstrate the structural performance of an armour unit under given conditions, and a preliminary design chart incorporating both hydraulic stability and structural integrity.

SUMMARY OF RESULTS

The following points summarize the results of this study :

- linear relationship between wave-induced stress and wave height
- wave-induced stress tends to increase with increasing wave period
- wave-induced stresses are greater in the bottom armour layer than the top armour layer

- wave-induced stresses are greatest above the still water level for large wave heights
- wave-induced stresses are greatest for values of the surf similarity parameter between 2.5 and 4
- the ratio of average peak stress to standard deviation stress values varies from approximately 1.8 to 3.9, but is typically around 3.2
- the conditional probability distribution of wave-induced stress given wave height can be described by a log-normal distribution

ONGOING AND FUTURE RESEARCH

The reduction and analysis of data from the remaining tests involving regular waves with breakwater slopes of 1:2.0 and 1:2.5 and irregular waves with a slope of 1:2.0 is currently underway. This will also involve a further examination of data distributions and confidence and tolerance limits. In addition, a series of static load tests is underway to provide additional data to the existing quasi-static results.

In the immediate future two issues will be addressed: (i) the relationship between the response of armour units subjected to regular and irregular waves, using the results of the tests currently being analyzed; and (ii) the relationship between mid-shank and fluke-shank stresses in the dolos unit, using both numerical and physical modelling.

In the more distant future it is planned to carry out a study on scale effects in measuring armour unit forces and to develop instrumentation to measure forces in more "current" armour units.

CONTRIBUTION OF THIS STUDY

Significant contributions of this study with respect to the development of a comprehensive design procedure incorporating both hydraulic stability and structural integrity are:

- (i) the identification of a linear relationship between wave-induced stress and wave height
- (ii) the identification of a log-normal conditional probability distribution of wave-induced stress given wave height

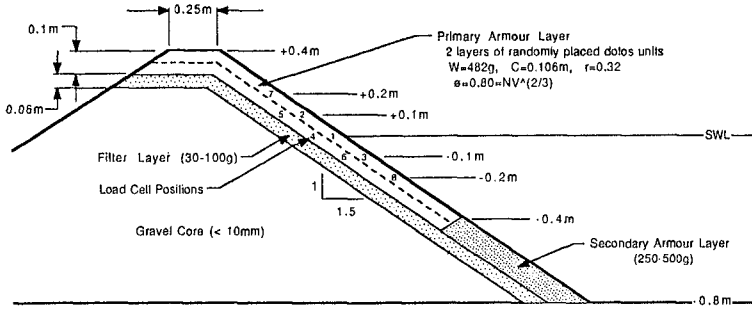
REFERENCES

- Baird, W.F., Hall, K.R., Turcke, D.J., and Chadwick, D.C., "Development of a Procedure for the Design of Concrete Armour Units for Rubble Mound Breakwaters", Report prepared for Public Works Canada, 1983.
- Burcharth, H.F., "Full Scale Dynamic Testing of Dolosse to Destruction", Coastal Engineering, Vol. 4, No. 3, pp. 229-251, Feb. 1981.
- Burcharth, H.F., "A Design Method for Impact-Loaded Slender Armour Units", Proceedings of the ASCE Convention, ASCE, New York, May 1981.
- Burcharth, H.F., "Fatigue in Breakwater Concrete Armour Units", Proceedings of the 19th International Conference on Coastal Engineering, pp. 2592-2607, Houston, Texas, Sept. 1984.
- Losada, M.A., Medina, R. and Alejo, M., "Wave Forces on Armour Blocks", 21st International Conference on Coastal Engineering, Spain, June 1988.
- Howell, G., "Measurements of Forces on Dolos Armour Units at Prototype Scale", 21st International Conference on Coastal Engineering, Spain, June 1988.

- Jensen, O.J., and Juhle, J., "Results of Model Tests on 2-D Breakwater Structure", Breakwaters 1988, Eastbourne U.K., May 4-6, 1988.
- Nishigari, W., Endo, I., and Shimada, A., "On Stress in Tetrapods under Wave Action", 20th International Conference on Coastal Engineering, pp. 2119-2132, Taipei, Taiwan, Nov. 1986.
- Scott, R.D., Baird, W.F., Readshaw, J.S., and Turcke, D.J., "A Procedure for the Analysis and Design of Concrete Armour Units", Proceedings of the 20th International Conference on Coastal Engineering, pp. 1739-1753, Taipei, Taiwan, Nov. 1986a.
- Scott, R.D., Turcke, D.J., and Baird, W.F., "A Unique Instrumentation Scheme for Measuring Loads In Model Dolos Units", Proceedings of the 20th International Conference on Coastal Engineering, pp. 2212-2223, Taipei, Taiwan, Nov. 1986b.
- Scott, R.D., The Analysis of Concrete Armour Units In a Breakwater, PhD Thesis, Queen's University, December 1986.
- Tedesco, J.W. and McDougal, W.G., "Non-linear F.E.M. Analysis of Concrete Armour Units", Presented at the Workshop on Measurement and Analysis of Structural Response in Concrete Armour Units, Vicksburg, Miss., Jan. 23-24, 1985.
- Tedesco, J.W., McGill, P.B., and McDougal, W.G., "Structural Response of Dolos in Waves", 21st International Conference on Coastal Engineering, Spain, June 1988.
- Timco, G.W., "On the Stability Criterion for Fracture in Dolos Armoured Breakwaters", Coastal Engineering, Vol. 8, No. 2, pp. 161-170, 1984.
- Timco, G.W., and Mansard, E.P.D., "Improvements In Modelling Rubblemound Breakwaters", Proceedings of the 18th International Conference on Coastal Engineering, pp. 2047-2061, Cape Town, S.A., Nov. 14-19, 1982.
- U.S. Army Corps of Engineers, Coastal Engineering Research Center, Shore Protection Manual, 3rd Edition, 1977.
- U.S. Army Corps of Engineers, Coastal Engineering Research Center, Shore Protection Manual, 4th Edition, 1984.
- van der Meer, J.W., and Pilarczyk, K.W., "Stability of Breakwater Armour Layers - Deterministic and Probabilistic Design", Delft Hydraulics Communication No. 378, February 1987.



Figure 1. THE LOAD CELL



Note: Positions 1,2,3 - four locations across flume at each position
 Positions 4,5,6,7,8 - two locations across flume at each position

Test Conditions: Regular waves, no overtopping
 $H = 0.05$ to $0.2m$
 $T = 1.25$ to $2.50s$

Figure 2. MODEL BREAKWATER CROSS-SECTION

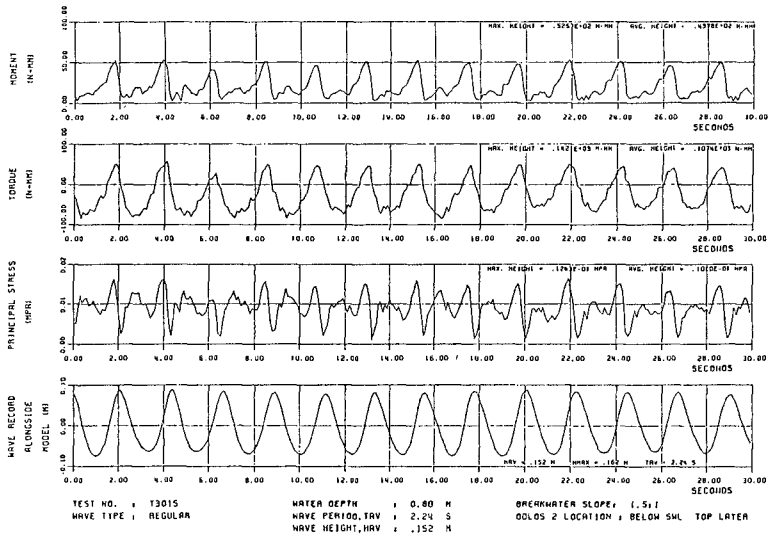


Figure 3. TYPICAL TEST RESULT SHOWING TIME SERIES RESPONSE OF THE LOAD CELL

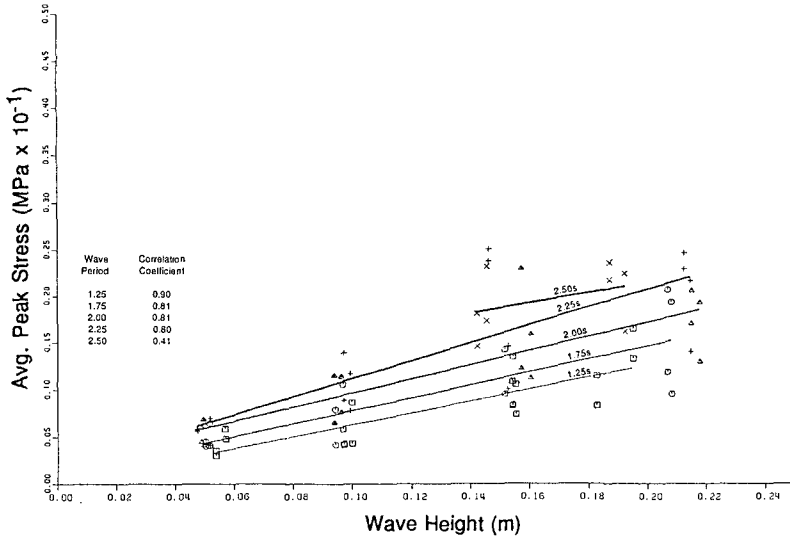


Figure 4. AVERAGE PEAK STRESS VS WAVE HEIGHT
Location 3 (0.1m below SWL, top layer)
Data Sorted by Wave Period

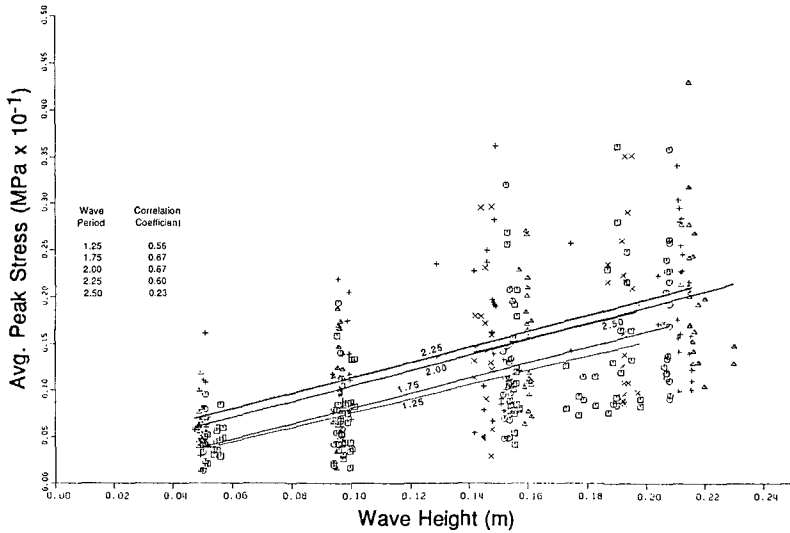


Figure 5. AVERAGE PEAK STRESS VS WAVE HEIGHT
All Locations and Wave Periods
Data Sorted by Wave Period

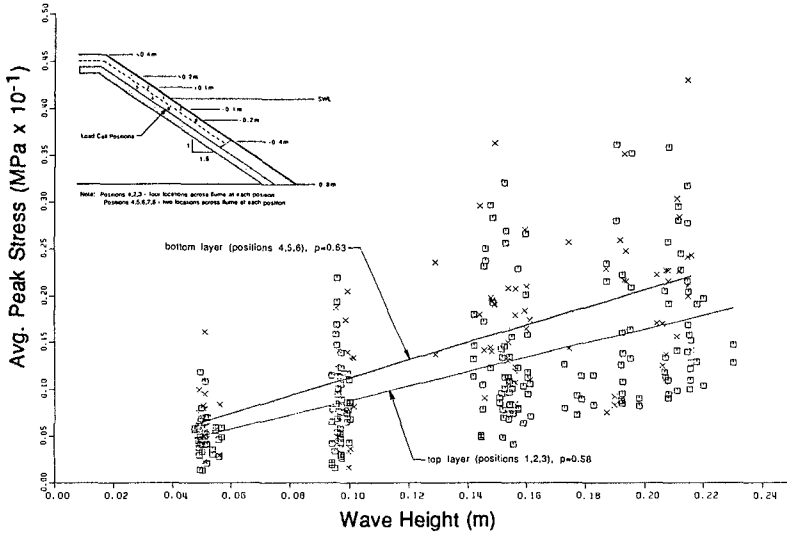


Figure 6. AVERAGE PEAK STRESS VS WAVE HEIGHT
All Locations and Wave Periods
Data Sorted by Layer

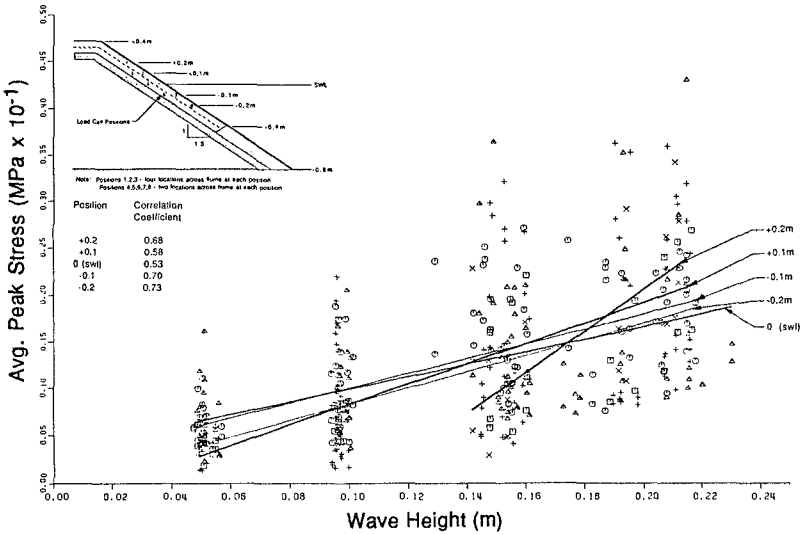


Figure 7. AVERAGE PEAK STRESS VS WAVE HEIGHT
All Locations and Wave Periods
Data Sorted by Position Relative to SWL

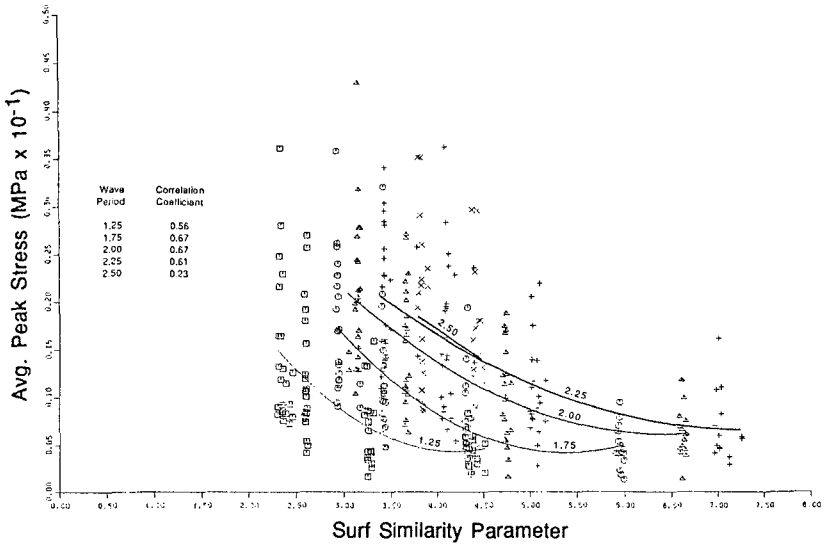


Figure 8. AVERAGE PEAK STRESS VS. SURF SIMILARITY PARAMETER
All Locations and Wave Periods
Data Sorted by Wave Period

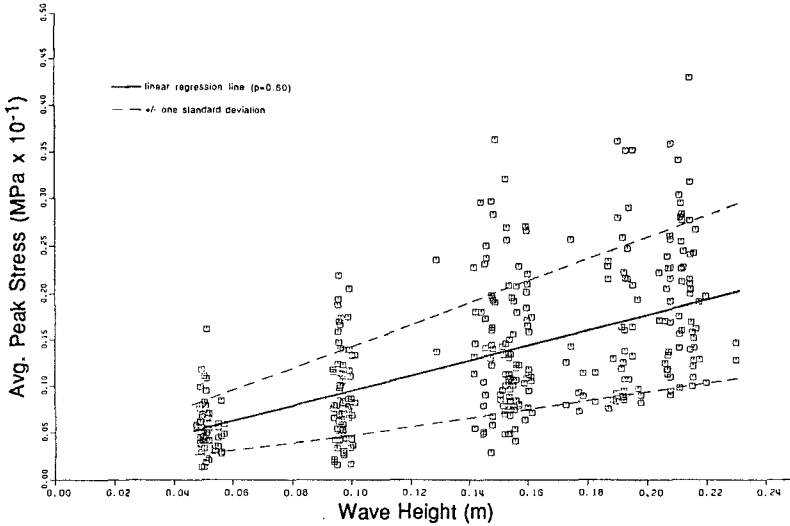


Figure 9. AVERAGE PEAK STRESS VS WAVE HEIGHT
All Locations and Wave Periods

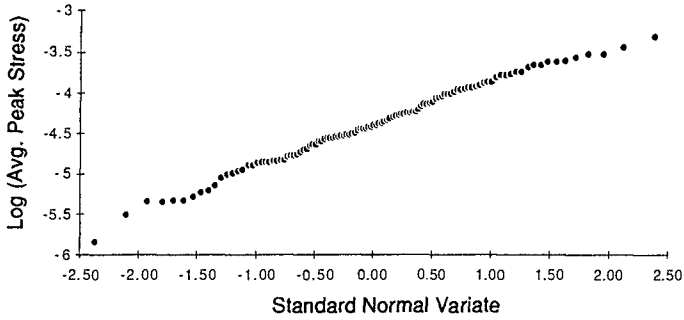


Figure 10. CONDITIONAL PROBABILITY DISTRIBUTION OF AVG. PEAK STRESS
H = 0.15m, All Locations and Wave Periods
Log-Normal Probability Paper

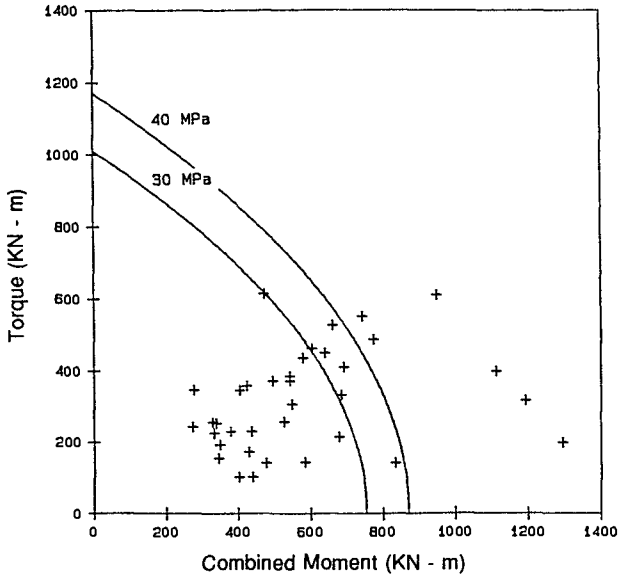
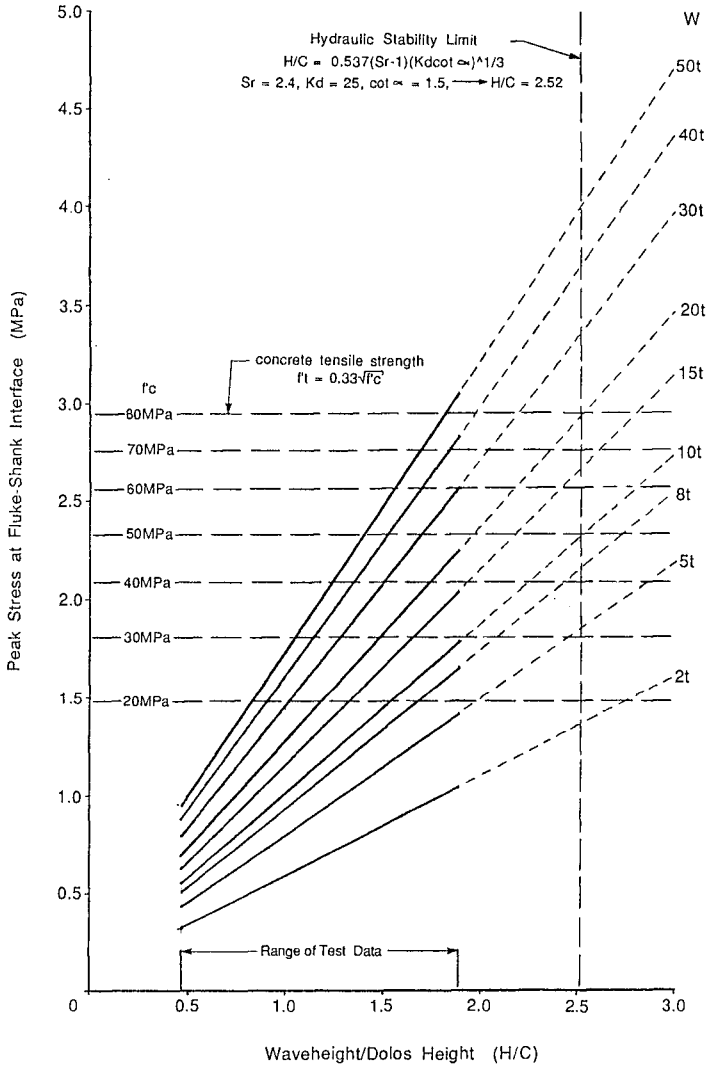


Figure 11. MOMENT TORQUE INTERACTION DIAGRAM
Avg. Peak Forces at Fluke-Shank Interface



- Notes: 1) stress values represent one standard deviation above the model data regression line.
- 2) stresses factored to mid-shank location by increasing by a factor of 2.5.
- 3) stresses scaled to prototype by model geometric (length) scale.
- 4) stresses are wave-induced only - no static stresses are included.
- 5) concrete fatigue effects have not been included.

Figure 12. PRELIMINARY ARMOUR UNIT DESIGN CHART
 Dolos Unit, Breakwater Slope 1:1.5

CHAPTER 177

ARTICULATED CONCRETE MAT SLOPE PROTECTION

Craig B. Leidersdorf, M. ASCE¹
Peter E. Gadd, M. ASCE¹
William G. McDougal, M. ASCE²

ABSTRACT

This paper provides guidance for the design, fabrication, and installation of articulated concrete mat slope protection. Although articulated mat armor has been utilized for many years in low-energy wave environments, it has been extended recently to accommodate intermediate wave energies and severe ice loads. The development of the concept is discussed, after which hydraulic design considerations, material design considerations, and fabrication and installation techniques are presented. Prototype performance is reviewed. It is concluded that articulated concrete mat armor is capable of providing effective slope protection in intermediate-energy wave environments, and that additional research is required relating to hydraulic stability and failure modes under wave and ice loading.

INTRODUCTION

Articulated concrete mats, consisting of precast blocks connected by flexible linkages, have been used for many years as an alternative to rubble armor in low-energy wave environments. During the past decade, however, the technology has been extended to accommodate intermediate wave energies and severe ice loads in response to the slope protection requirements of artificial islands constructed in the Alaskan Beaufort Sea.

The mat armor system which has evolved, an example of which is depicted in Plate 1, incorporates the findings of conceptual design studies, large-scale model tests, and prototype test sections. Based upon its performance to date, the concept appears promising not only for arctic applications, but also for use as slope and toe protection in temperate environments.

¹ Principal, Coastal Frontiers Corporation, 2193 Roosevelt Ave., Altadena, CA 91001-3510, U.S.A.

² Associate Professor, Department of Civil Engineering, Oregon State University, Corvallis, OR 97331, U.S.A.



Plate 1. Concrete Mat Panel

This paper provides guidance for the design, fabrication, and installation of articulated concrete mat armor based on experience gained over the past eight years. The sections which follow present information on the development of the mat concept, a discussion of hydraulic and material design considerations, a discussion of mat fabrication and installation, a review of prototype performance, and recommendations for future applications and additional research.

CONCEPT DEVELOPMENT

The primary advantages of the articulated mat concept, when compared with discrete-unit armor systems such as quarrystone or individually-placed blocks, include:

- enhanced stability, by virtue of the interconnection between adjacent blocks;
- the ability to accommodate changes in the subgrade without permitting catastrophic fill losses; and
- suitability for rapid installation in pre-assembled, modular panels (Ref. Plate 1).

Additional benefits with more limited applicability include resistance to displacement by ice, and the potential for modular removal at the end of the project life.

A potential disadvantage of the mat concept is the critical function performed by the linkage system. If the linkages are weakened by abrasion, corrosion, or fatigue, the ability of the mat to withstand wave and/or ice forces is significantly reduced. Other drawbacks include the relatively high runup elevations which occur on the smooth surface of the mat, the need for mild sea conditions during placement, and the lack of well-established design procedures which are based on prior experience. It is noteworthy, however, that considerable research has been devoted to concrete block revetments in recent years (Bakker and Meijers, 1988; Bezuijen, *et al.*, 1987; Bezuijen, *et al.*, 1988; Galvin, 1988; Klein Breteler, *et al.*, 1988; McDougal and Atkinson, 1987; Pilarczyk, 1988; Toyoshima, 1988). Although the majority of the research addresses placed block revetments, many of the findings are also relevant to the design of articulated mat armor.

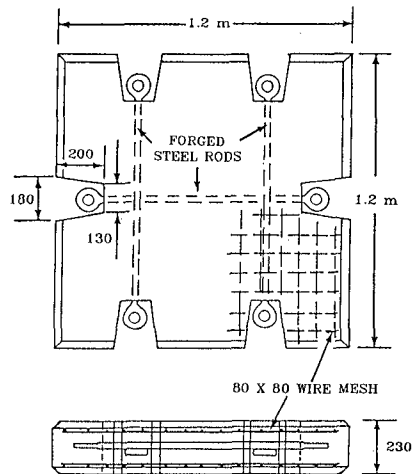
The concept of articulated concrete mat armor dates back to the early 1900's (Hawkes, 1907). Prior to the 1980's, however, its use was confined primarily to low-energy environments such as rivers, lakes, and estuaries, in which the design wave height was on the order of 1 m. A number of proprietary and non-proprietary designs were developed to address this application, typically utilizing square or rectangular blocks ranging from 0.3 to 0.6 m in maximum horizontal dimension and 0.15 to 0.3 m in height. In keeping with the relatively modest design loads anticipated, the blocks were not reinforced. Linkages consisted of wire rope, synthetic rope, steel rods, or attachment to a geotextile.

The advent of offshore oil operations in the Alaskan Beaufort Sea engendered slope protection requirements which were significantly more demanding than those of previous articulated mat applications. To support oil exploration and production activities, gravel islands were constructed in water depths to 15 m. Key design considerations included significant wave heights of 3 to 6 m, impact loads from moving ice features, and an extremely short open-water season (typically 75 days) in which to install the slope protection system. Although large sand bags were used to protect many of the initial islands (Gadd, 1988), the need for a more resilient armor system was apparent from the outset (Leidersdorf, *et al.*, 1982).

In view of the lack of quarystone and high cost of importing non-native materials to northern Alaska, articulated concrete mats emerged as a promising candidate for island slope protection. The linkage concept was attractive from the dual standpoint of reducing the weight of the armor layer and improving resistance to ice forces.

Three major design modifications were implemented to adapt the articulated mat concept to its intended use in the arctic: the provision of high-strength, corrosion-resistant linkages, the introduction of reinforcing steel into the blocks, and the use of larger block sizes. A representative example of the resulting design is presented in Figure 1. Developed for use on Northstar Island, an oil exploration island constructed in 1985 (Hayley, *et al.*, 1987), the mat is composed of 1.2 m square, precast concrete blocks which are reinforced with two layers of wire mesh. Linkage is provided by a combination of forged steel rods cast into each block, and interconnecting chains and shackles. Block thickness was adjusted in accordance with the design wave conditions; in this particular application, 230 mm was specified.

The selection of a 1.2 m square as the plan view outline of the block represents a compromise between the conflicting requirements of functional performance, fabrication, handling, and cost. Factors which favor a large block size include a reduced number of linkages per unit area, and an increased resistance to displacement by environmental forces. Factors which favor a reduced block size include ease of fabrication and handling, the ability to articulate into scour depressions rather than spanning across them, and a higher permeability to alleviate the hydraulic pressure differentials which may develop across the thickness of the mat and cause uplift.



NOTE: ALL DIMENSIONS IN MM EXCEPT AS NOTED
(AFTER HAYLEY, ET AL., 1987)

Figure 1. Concrete Block Design

Experience to date has indicated that the 1.2 m square block size approaches the upper bound for effective articulation. An additional benefit of this configuration is the fact that two blocks placed side-by-side are compatible with a standard 2.4-m (8-ft) wide truck bed. To improve the permeability of the mat system, as well as to protect the linkage components, recesses are provided in the perimeter of each block at the linkage points (Ref. Figure 1).

HYDRAULIC DESIGN

Stability

Although the current understanding of articulated mat stability is far from complete, significant insights have been gained from large-scale model testing. Based upon observations made at scales ranging from 1:6 to 1:3, the predominant hydraulic loads exerted on mat armor are as follows (Ref. Figure 2):

- (1) The time-dependent wave pressure, which tends to induce uplift by creating a pressure differential between the top of the mat and the subgrade;
- (2) The hydrostatic pressure head resulting from a setup of the water level in the structure core, which tends to induce uplift;
- (3) The shock pressure from the breaking wave, which can produce uplift forces on the blocks adjacent to the plunge point;
- (4) The shear forces from wave runup and especially wave rundown, which tend to displace the blocks in a downslope direction.

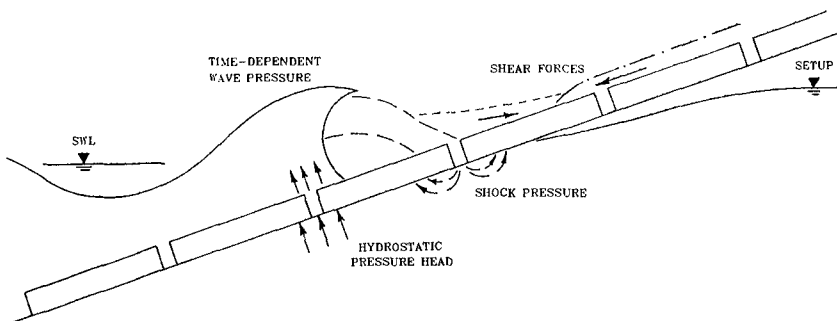


Figure 2. Hydraulic Loads on Articulated Mat Armor

The threshold wave height which initiates block uplift varies not only with the armor weight and slope steepness, but also with the wave period and the permeability of the mat and underlying filtration medium. The provision of adequate permeability is of particular importance in optimizing the performance of a selected mat thickness. In the absence of specific design guidelines, it is recommended that the permeability of each successive layer should increase from the structure core to the mat armor. For the artificial islands constructed to date in the Beaufort Sea, a minimum of 15% open area has been provided in the mat surface to accommodate the anticipated outflow from the permeable gravel core material.

A key feature of articulated mat armor is its ability to withstand wave conditions in excess of the threshold for block uplift. Although deformation of the subgrade will occur, catastrophic failure can be avoided provided that the linkage system and underlying filtration medium remain intact (Potter and Sun, 1983). Both model test and prototype experience have indicated that episodes of block uplift lead to the formation of an S-shaped slope profile, with flattening at the waterline and commensurate steepening above the limit of wave breaking and below the limit of wave rundown.

To resist the shear force exerted by wave rundown, as well as the tendency for blocks to migrate downslope during uplift episodes, the mat must be anchored at the top of the slope. Prototype experience has indicated that deadman anchors buried in the structure core material and linked to the upslope edge of the mat are an economical and effective means of fulfilling this requirement.

At present, there are no analytical models which accurately predict uplift thresholds and anchor loads for articulated mat armor. Large-scale model testing is therefore strongly recommended for the design of all major projects.

Wave Runup

The elevation of wave runup on concrete mat armor varies with the incident wave conditions, the structure slope, and the permeability of the mat and subgrade. In general, however, relatively high runup elevations are observed on the smooth surface of the mat.

Representative large-scale model test data reported by Gadd, *et al.* (1988), are reproduced in Figures 3 and 4. The data were acquired for breaking waves on a 3(H):1(V) gravel slope covered with a permeable geotextile and an articulated mat containing approximately 15% open area. Relative runup, R/H_0' , is displayed as a function of wave steepness, H_0'/gT^2 , for two values of relative water depth: $d_s/H_0' = 2$ in Figure 3, and $d_s/H_0' > 3$ in Figure 4. The notation is defined as follows:

- R = runup elevation relative to the prevailing still water level;
- H_0' = unrefracted deepwater wave height;
- g = gravitational acceleration;
- T = wave period; and
- d_s = water depth at structure toe.

Runup predictions for concrete blocks derived from the U.S. Army Corps of Engineers' Shore Protection Manual ("SPM"; 1984) are included in each figure. Although the predictions evidence good agreement with the model test

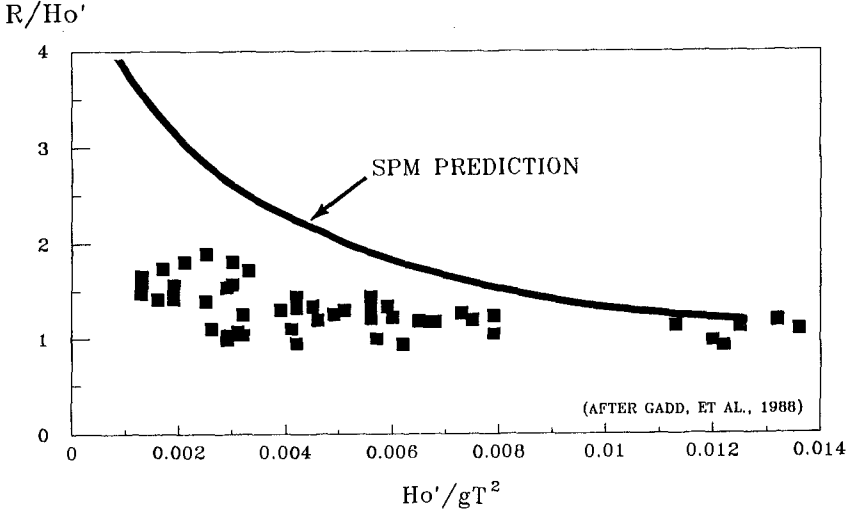


Figure 3. Wave Runup on 3(H):1(V) Slope, $d_s/H_o'=2$

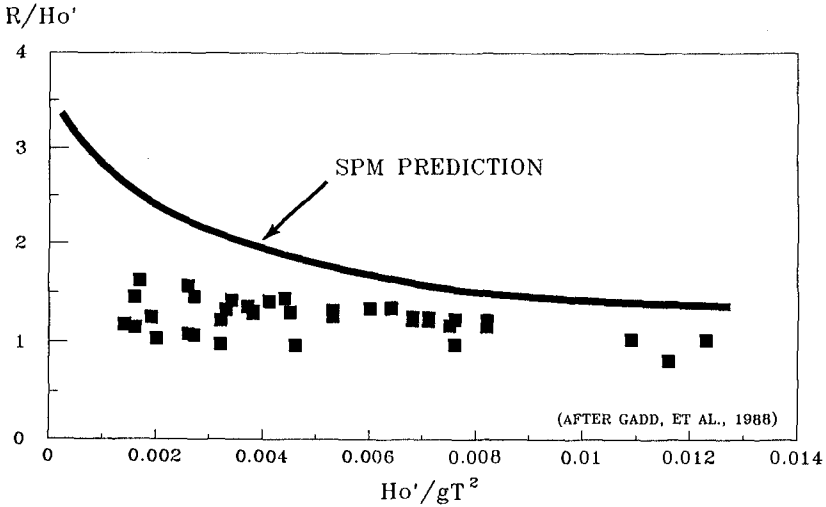


Figure 4. Wave Runup on 3(H):1(V) Slope, $d_s/H_o' \geq 3$

data at high values of wave steepness, they significantly overpredict the measured runup elevations at the lower steepness values. In consequence, the use of the SPM method to predict wave runup may be expected to yield conservative values in most instances. As in the case of hydraulic stability, large-scale model testing is recommended to evaluate the runup characteristics of all major projects.

Large-scale testing has also provided insight into measures which can reduce the runup elevations on articulated concrete mat armor. Increased roughness, as might be created by using blocks of different thicknesses, was found to have minimal effect in the region of wave breaking. If placed higher on the slope, however, in the zone of swash or sheet runup, the increased roughness significantly reduced the maximum runup elevation. Compound slope profiles which incorporated a bench near the waterline were also found to be effective. As reported in more detail by Leidersdorf, *et al.*, (1984), a bench width of 12 m typically decreased the runup elevation by 30 to 40% relative to a straight 3(H):1(V) slope.

MATERIAL DESIGN

Concrete Blocks

Because the concrete blocks in an articulated concrete mat must withstand impacts with both the subgrade and each other during uplift episodes, they must be more durable than those used for unlinked revetments. Additional material design considerations may include abrasion from littoral sediments, corrosion and fatigue of exposed steel, and, in the case of cold climates, ice impacts, ice abrasion, and freeze-thaw cycling.

As discussed previously, steel reinforcement was incorporated into the block design when the mat technology was adapted to the more severe wave and ice conditions of the arctic. Prototype experience to date suggests that a steel content of approximately 0.5% of the block cross-section is sufficient to maintain structural integrity except in the case of impact loads exerted by very large ice features. The reinforcement should extend throughout the plan view outline of the block, including the arms between the linkage recesses (Ref. Figure 1), to insure that the block will remain intact even if the concrete is fractured. Hot-dip galvanization of all steel is recommended to reduce its susceptibility to corrosion.

The concrete should be of high strength to resist cracking. In the case of the block design presented in Figure 1, a 28-day compressive strength of 27 MPa was specified (Hayley, *et al.*, 1987). Low permeability, which may be obtained through the use of a low water-cement ratio, a high cement factor, and the use of pozzolan or silica fume, is desirable to reduce chloride penetration.

Aggregate should be abrasion-resistant, especially when repeated exposure to littoral sediments and/or ice is anticipated. Additional design considerations for arctic service are presented by Leidersdorf (1988).

Linkage System

A properly designed linkage system will not only allow the mat to function under wave conditions which exceed the uplift threshold for individual blocks, but also facilitate rapid installation through the placement of large, pre-assembled panels. Both the placement loads and the in-place loads should be considered in determining the requisite strength of the linkage system. Additional design considerations include flexibility (to allow articulation), corrosion, abrasion, and fatigue over the design life of the armor system, and the ability to allow replacement of damaged blocks.

Kevlar rope, wire rope, and chain-and-shackle linkage systems have been tested at prototype scale with varying degrees of success. Although attractive from the standpoint of imperviousness to corrosion, Kevlar rope proved to be too elastic to permit accurate placement of large panels. Wire rope can be used for small panel sizes, but becomes difficult to handle at the large sizes required for heavy lifts. Additional disadvantages of wire rope include its susceptibility to corrosion (due to the large surface area of the component strands), and the difficulty associated with replacing individual blocks after the mat has been installed.

Chains and shackles, in conjunction with forged steel rods cast into the blocks, have emerged as the preferred linkage alternative (Ref. Plate 2). Connections between adjacent blocks are readily made, damaged blocks can be removed and replaced as needed, and corrosion is less problematical than with wire rope due to the reduced surface area. If the corrosion rate in the project area can be estimated, the linkage components can be oversized accordingly to provide for sufficient strength at the end of the design life. Hot-dip galvanization of all linkage hardware is also recommended.

Filtration Medium

The performance of an articulated mat armor system depends not only upon the characteristics of the mat itself, but also upon those of the underlying filtration medium. In addition to providing adequate permeability to relieve pore pressures in the structure core, the filter must be capable of retaining the core material during episodes of mat uplift.

The absence of suitable granular fill material has necessitated the use of geotextiles for filtration on all articulated mat armor installed in the Beaufort Sea to date. The advantages of fabric include the ability to



Plate 2. Chain-and-Shackle Linkage System

achieve a specified permeability, ease of installation, and low cost. The primary disadvantages relate to long-term performance: a susceptibility to abrasion by the concrete blocks, and progressive deterioration from exposure to the ultraviolet (UV) component of sunlight. Measures taken to ameliorate these effects have included the specification of UV-stabilized fabrics, the application of an abrasion-resistant resin coating, and the use of an overstrength fabric in anticipation of deterioration over the project life (Munday and Bricker, 1987). Although performance has been satisfactory to date, longer periods of service will be required to evaluate their long-term effectiveness.

In the absence of conclusive evidence regarding the long-term durability of geotextiles, their use is recommended for projects with a limited design life, or at which frequent mat uplift is not anticipated. When severe wave conditions and/or exposure to intense sunlight are expected, particularly over an extended design life, the use of graded stone or manufactured concrete rubble is recommended. Although rubble has not been used as a filtration medium for articulated mat armor at prototype scale, large-scale model tests have yielded satisfactory results (Leidersdorf, *et al.*, 1984). To prevent washout, the filter layer immediately beneath the mat should consist of rubble which is larger than the largest openings in the mat surface.

FABRICATION AND INSTALLATION

Both wet and dry casting techniques have been used to fabricate the individual concrete blocks which comprise the mat. In the case of dry casting, a block molding machine is utilized to inject concrete with a low

water-cement ratio into the forms. Although set-up of the molding machine and adjustment of the concrete mix can be time-consuming, the semi-automated block production process which results appears warranted for large projects. Fabrication rates of up to 20 blocks per machine-hour have been reported (Munday and Bricker, 1987).

When the blocks have cured sufficiently to be handled, they can be assembled into large panels in preparation for placement by crane. To minimize the number of underwater linkages required between panels, it is recommended that each panel extend from the lower terminus of the armor to the waterline. The width of the panel can be adjusted in accordance with the lifting capacity of the crane.

To insure that proper alignment is maintained during placement, the centerline position of each panel is monitored continuously using a theodolite. Any adjustments which are required are relayed to the crane operator. Once the panel has been lowered into position, a diver verifies that the desired side-by-side relation with the preceding panel has been achieved before releasing the mat from the crane. The diver then shackles the new panel to its predecessor, and the cycle is repeated. Based upon prototype experience to date, the underwater shackling is relatively straightforward, and is typically completed before the next panel has been lifted by the crane.

Continuous coverage of non-planar surfaces, such as island corners, can be achieved through the use of trapezoidally-shaped blocks (Ref. Plate 3). Fabrication and placement procedures are analogous to those for square blocks, although survey control of the placement operation assumes greater importance in maintaining proper alignment.

The maximum permissible wave height for mat installation depends not only upon the tolerance of the divers, but also upon the extent to which unevenness can be accepted in the finished grade. Because the mat represents a relatively thin veneer on the structure, any wave-cut scarps which develop prior to mat placement will be reflected in the mat surface.

Placement rates for articulated mat armor vary with crane capacity, wave conditions, water depth, and structure geometry. Reported rates have ranged from 44 m²/h for an exposed location with a maximum placement depth of 6 m (Hayley, *et al.*, 1987), to 110 m²/h for a more sheltered location with a maximum placement depth of 3 m (Munday and Bricker, 1987).

PERFORMANCE ASSESSMENT

Articulated concrete mat armor was first installed in the Alaskan Beaufort Sea in 1980 (Leidersdorf, *et al.*,

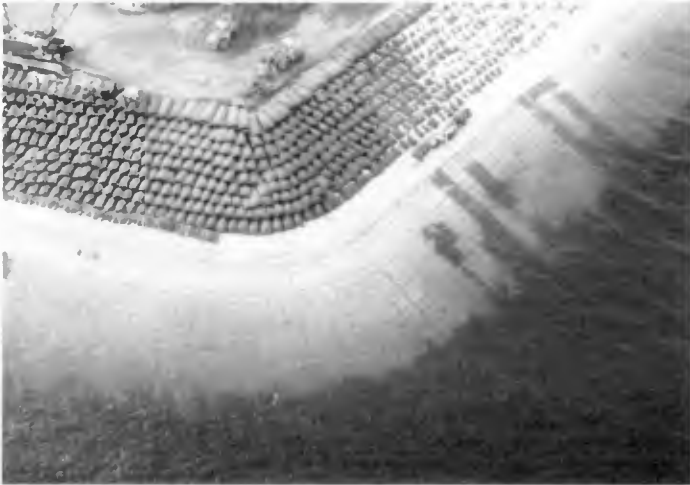


Plate 3. Island Corner Armored with Trapezoidal Blocks



Plate 4. Articulated Concrete Mat on the Endicott Project

1982). Subsequent projects have utilized more than 57,000 m² of mat armor in coastal and offshore locations. The primary application has been as slope protection for gravel islands, although mats have also been used as toe protection for seawall structures.

The most noteworthy projects to date which employ mat armor are the Endicott Project, an oil production facility consisting of two islands and a causeway in a maximum depth of 3.7 m, and Northstar Island, an oil exploration island located in a depth of 13.7 m. On the Endicott islands, approximately 40,000 m² of mat were installed from just above the waterline to the sea floor (Ref. Plate 4). To accommodate the anticipated design life of 25 years, a woven polyester filter fabric with an extremely high tensile strength of 2.1 kN/cm was specified (Munday and Bricker, 1987). Installation of the slope protection system was completed in 1986, one year ahead of schedule. Since that time, the mat has remained in sound condition.

Northstar Island, designed for a minimum service life of three years, is distinguished by its exposure to more extreme environmental conditions than the Endicott Project. A band of concrete mat was installed around the circumference of the hexagonal island from +1.5 to -6.1 m, the region most subject to wave and ice impacts (Hayley, *et al.*, 1987). In September, 1986, one year after the island was completed, it was exposed to a severe storm with estimated wave heights of 3 to 4.5 m. Although the mat experienced uplift, no significant adverse effects were noted. Damage was inflicted, however, by a late-1987 storm which drove large, deep-keeled multi-year ice features against the island. The damage consisted of block fractures and displacements in areas which received direct impacts from the ice.

CONCLUSIONS AND RECOMMENDATIONS

Based upon the experience gained to date, articulated concrete mat armor is capable of providing effective slope protection in intermediate-energy wave environments. Promising applications include not only the arctic projects for which it was developed, but also selected non-arctic uses such as:

1. Long-term slope protection against waves and ice in low-corrosion environments (such as the Great Lakes);
2. Rapidly-deployed emergency protection for coastal areas threatened by storm erosion; and
3. "Last Line of Defense" protection, in which the mat and an underlying geotextile are buried behind the beach face and exposed only during major storm events.

In the case of the last suggested application, the relatively thin nature of mat armor will facilitate its concealment in the backshore. If relocation becomes necessary to accommodate a moving shoreline (occasioned, for example, by long-term erosion or beach renourishment), the mat can be moved in modular panels.

Despite the promise demonstrated by the mat technology, additional research is required before a standardized design methodology can be elucidated. Areas which warrant further investigation include failure modes under wave and ice loading, quantification of hydraulic stability in terms of the primary design parameters, hydraulic stability on non-planar surfaces such as island corners, and geotextile performance over an extended design life or when frequent uplift is experienced. Until a more comprehensive understanding of mat performance is achieved, the final design process for all major projects should include large-scale hydraulic model testing, and, when feasible, observation of existing prototype structures.

REFERENCES

- Bakker, K.J., and P. Meijers, 1988, "Stability of Sliding of Flexible Revetments", Proceedings of Modelling Soil-Water-Structure Interactions, Delft, The Netherlands, pp. 163-172.
- Bezuijen, A., M. Klein Breteler, and K.J. Bakker, 1987, "Design Criteria for Placed Block Revetments and Granular Filters", Proceedings of 2nd International COPEDEC, Beijing, China.
- Bezuijen, A., J. Woulters, and C. Laustrup, 1988, "Block Revetment Design with Physical and Numerical Models", Abstracts Book, 21st International Conference on Coastal Engineering, Torremolinos, Spain, pp. 121-122.
- Gadd, P.E., 1988, "Sand Bag Slope Protection: Design, Construction, and Performance", in Chen, A.C.T., and C. B. Leidersdorf, Arctic Coastal Processes and Slope Protection Design, American Society of Civil Engineers, pp. 145-165.
- Gadd, P.E., V. Manikian, and J.L. Machemehl, 1988, "Wave Run-Up Prediction vs. Model Test Results: A Comparison", Proceedings of the 21st International Conference on Coastal Engineering, American Society of Civil Engineers.
- Galvin, C., 1988, "Stability of Tabular Concrete Revetments", Abstracts Book, 21st International Conference on Coastal Engineering, Torremolinos, Spain, pp. 163-164.

- Hayley, D.W., P.E. Gadd, and D.A. Horn, 1987, "Advances in Design and Construction of Slope Protection for Gravel Islands, Beaufort Sea, Alaska", Proceedings of the 9th International Conference on Port and Ocean Engineering under Arctic Conditions (POAC'87), Fairbanks, Alaska.
- Hawkes, F.W., 1907, "Riprap", Patent No. 869,566, United States Patent Office, Washington, D.C.
- Klein Breteler, M., A.M. Burger, L. Banach, and A. Bezuijen, 1988, "Analytical Design Method for Block Revetments", Abstracts Book, 21st International Conference on Coastal Engineering, Torremolinos, Spain, pp. 159-160.
- Leidersdorf, C.B., 1988, "Articulated Mat Slope Protection for Arctic Applications", in Chen, A.C.T., and C. B. Leidersdorf, Arctic Coastal Processes and Slope Protection Design, American Society of Civil Engineers, pp. 166-189.
- Leidersdorf, C.B., R.E. Potter, B.C. Gerwick, Jr., and Y.Y. Hsu, 1982, "Modular Slope Protection for the Arctic Environment", Proceedings of the 14th Annual Offshore Technology Conference, Houston, Texas, pp. 689-704.
- Leidersdorf, C.B., R.E. Potter, and C.J. Sonu, 1984, "Study of Slope Protection Works for the Arctic Ocean", Proceedings of the 31st Annual Coastal Engineering Conference, Japan Society of Civil Engineers, pp. 552-556.
- McDougal, W.G., and F.S. Atkinson, 1987, "Concrete Armor Mats: Large Scale Wave Tank Tests", Proceedings of Coastal Zone '87, American Society of Civil Engineers, pp. 1617-1629.
- Munday, J.P., and W.F. Bricker, 1987, "Endicott Slope Protection Design and Construction", Proceedings of the 6th International Conference on Offshore Mechanics and Arctic Engineering (OMAE '87), Houston, Texas, pp.47-54.
- Pilarczyk, K.W., 1988, "Design Aspects of Block Revetments", Abstracts Book, 21st International Conference on Coastal Engineering, Torremolinos, Spain, pp. 195-196.
- Potter, R.E. and J. Sun, , 1983, "Arctic Slope Protection Development", Proceedings of the 7th International Conference on Port and Ocean Engineering under Arctic Conditions (POAC '83), Helsinki, Finland.
- Toyoshima, O., 1988, "Gentle Slope Seawalls Covered with Armor Units", Abstracts Book, 21st International Conference on Coastal Engineering, Torremolinos, Spain, pp. 159-160.

U.S. Army Corps of Engineers, Department of the Army,
1984, Shore Protection Manual, Vols. I and II, U.S.
Government Printing Office, Washington, D.C.

CHAPTER 178

DESIGN AND CONSTRUCTION OF BERM TYPE BREAKWATERS

Rubble Mound Structures Committee
Waterways, Port, Coastal & Ocean Division,
American Society of Civil Engineers

Baird, William F., W.F. Baird & Associates, Ottawa, Canada
Davidson, D.D., Coastal Engineering Research Center, Vicksburg, MS, USA
Edge, Billy, Cubit Engineering Ltd., Charleston, S.C., USA
Magoon, Orville T., Committee Chairman, P.O. Box 279, Middleton, CA, USA
Rauw, Charles I., Winzler & Kelly, San Francisco, CA, USA
Treadwell, Donald, Geomatrix Consultants, San Francisco, CA, USA

The standard design for a rubble-mound breakwater as reported in recent text books and manuals has consisted of a core of rubble quarry-run that is protected from wave action by two layers of relatively large quarried stone or concrete units. Filter layers of intermediate size stone are recommended beneath the armour layer to prevent loss of the core material through the armour. The pioneering work of Hudson provides coefficients for a formula that allowed widespread use of this design concept throughout the world.

A breakwater of this form tends to require the smallest volume of stone; however, it may not represent the least cost structure for a specific location because of the cost and availability of local materials.

Recently, design engineers and hydraulic laboratories have given considerable attention to alternative forms of rubble mound structures. The objective of this work has been to minimize cost while maintaining the same or improved level of stability when the breakwater is subjected to extreme wave conditions.

Principally, emphasis has been given to the utilization of locally available quarried stone and to maximizing the use of the full yield of a local quarry. This has required the design of breakwaters using smaller armour stone and a wider range of sizes than was used in the more conventional breakwater. These designs have also given consideration to the realities of construction and the limitation of construction equipment on the assumption that cost savings will be achieved with relatively simple construction methods.

Clearly the use of smaller armour stones requires a change in other properties or characteristics of the armour layer, compared to a conventional design, in order to achieve the same stability. The principal characteristics of a berm breakwater are the high permeability of the armour-layer and the significantly larger volume of armour. Berm breakwaters generally consist of a relatively large and permeable mass of armour stone (of smaller size than required for a conventional design).

Breakwaters range from coarse sand barrier beaches to a more conventional breakwater protected by one layer of large armour stones. For the breakwaters using the smaller material, movement of the stone is an important consideration. For

breakwaters with larger stones where significant movement of stones does not occur the permeability of the mass of stones is an important consideration. In all structures the durability and strength of the armour stones is important.

The recent work towards "non-conventional" structures is based on extensive tests in hydraulic laboratories. Basically, a trial and error approach is undertaken and the success or failure of a structure is based on the observations of the model.

In September 1987, a two day workshop was held in Ottawa, Canada to discuss "non-conventional" breakwaters (1). Participants from Australia, Canada, Denmark, Netherlands, United Kingdom and the United States discussed design concepts, construction, materials and the performance of as-built structures. The workshop was sponsored by the American Society of Civil Engineers, Canadian Society for Civil Engineering and the National Research Council of Canada.

For the most part, the "non-conventional" breakwaters discussed consisted to a larger mass of smaller stone replacing the two layers of armour stone in a conventional breakwater. These breakwaters were referred to as mass armoured breakwaters or berm breakwaters.

Considerable discussion took place on the process by which a wave interacts with the mass of stone and processes by which stability is achieved.

It was concluded that very successful non-conventional breakwaters have been built in recent years. These structures have resulted in considerable cost savings to the owner while providing the required protection and stability when exposed to extreme waves.

However, these designs have all been supported by considerable engineering and model tests in a hydraulics laboratory. While numerical methods are being developed to assist with this process and to compare one design with another, it is unlikely that the site specific design work that can be undertaken with a physical model will be replaced by numerical methods in the near future.

Based on the results of the Ottawa workshop, it is concluded that properly designed and constructed Berm Type Breakwaters are an important and cost effective means of protecting exposed coastal harbors and locations from severe wave attack at specific locations.

The Rubble Mound Structures Committee acknowledges the contribution of Mr. Dave Willis and the Ottawa Hydraulic Research Laboratory of the National Research Council of Canada for assistance in providing the berm breakwater laboratory demonstration and venue for the workshop.

REFERENCES

- (1) Berm Breakwaters: Unconventional Rubble-Mound Breakwaters. Proceedings of a workshop at The Hydraulics Laboratory, National Research Council of Canada, Ottawa, Canada, September 15-16, 1987. Published by American Society of Civil Engineers.

CHAPTER 179

SIMPLIFIED MODELS FOR MEASURING ARMOUR UNIT FORCES

R.D. Scott*, D.J. Turcke**, C.D. Anglin*, W.F. Baird***

ABSTRACT

Damage of concrete armour units on a number of breakwaters around the world has brought into question the design methodology for these structures.

The interaction of waves with a rubblemound breakwater is a complex process typified by the random nature of the wave loadings and of the placement and orientation of the armour units.

The objective of this paper is to present the development of a more simplistic physical model for establishing a realistic upperbound for the forces occurring on concrete armour units, to more readily understand the response of the unit to various wave parameters, and to explore the effect of carrying out tests at different scales.

The results of these investigations demonstrate the applicability of employing simplified models to assist in understanding the response of armour in a breakwater and the consistency of the instrumentation at different scales.

INTRODUCTION

Damage of concrete armour units on a number of breakwaters throughout the world has brought into question the design methods of these structures. In certain cases, such as at the spectacular failure of the breakwater at Sines, Portugal, it is believed that damage of the structure may have been initiated by the structural failure of the individual concrete armour units. Generally, these breakwaters have been designed on the basis of physical model studies that assessed the hydraulic stability of the proposed breakwater but did not reproduce the mechanical strength of the concrete armour units. Recently, considerable research effort has been directed towards developing an understanding of the structural strength of armour units and of the environmental forces that act on these units.

* Senior Engineers, W.F. Baird and Associates, Coastal Engineers
38 Antares Drive, Suite 150, Ottawa, Ontario, Canada, K2E 7V2

* * President, W.F. Baird and Associates, Coastal Engineers
38 Antares Drive, Suite 150, Ottawa, Ontario, Canada, K2E 7V2

* * * Professor of Civil Engineering, Queen's University,
Kingston, Ontario, Canada, K7L 3N6

The interaction of waves with a rubblemound breakwater is a complex process typified by the random nature of the wave loadings and of the placement and orientation of the armour units. Recent work by the authors [Scott et al (1986), Anglin et al (1988)] has focused on the measurement of the response of concrete armour units to external forces using physical modelling. A considerable number of tests have been carried out using specially instrumented model dolos units placed in a model breakwater and subjected to simulated wave attack. This paper presents the results of some initial research work undertaken to:

1. Develop a more simplistic physical model that will establish a realistic upperbound for the forces occurring on concrete armour units.
2. Test the instrumented armour units under more simplified conditions so that the response of the armour unit to changes in various wave parameters may be more readily understood.
3. Provide further confidence in the use of such instrumentation by carrying out tests at various scales.

RECENT RESEARCH

Over the past few years a number of investigations have been initiated into the development of improved breakwater design procedures which incorporate both hydraulic stability and structural integrity.

In order to develop a more appropriate design procedure for concrete armour units, it is important to quantify the nature of the forces acting on the units in a breakwater. Although this represents a complex task at the present, prototype studies, physical and numerical modelling are all playing an important role in trying to solve this difficult problem. A number of researchers have made use of physical models to measure the force response of armour units. [Scott (1986), Scott et al (1986, 1987a, 1987b) Anglin (1988), Baird et al (1986), Endo (1985), Losada et al (1988), Jensen (1988)].

Attempts have been made to create design charts which can serve as preliminary tool for a design engineer. One such chart has been developed for a dolos unit in Baird et al (1986). In this work moment-torque interaction diagrams are developed which are graphical representations of the measured moments and torques scaled to prototype relative to a theoretically derived interaction equation describing failure of the concrete in the dolos shank. This type of representation of data is potentially useful for both the analysis and design of a breakwater armoured with concrete units.

More recently, a preliminary effort to provide a design chart which incorporates both the hydraulic stability and structural integrity was presented by Anglin (1988). This design chart is a plot of peak stress versus the ratio of wave height to dolos height for various dolos weight. It allows the designer to select an appropriate dolos size given the wave height and concrete strength.

In addition to the physical model studies, a very extensive prototype study is being carried out at Crescent City by the U.S. Coastal Engineering Research Council, to measure dolos response in an existing breakwater [Howell (1988)].

Finally, a non-linear numerical model is being developed to determine the response of dolos to waves [Tedesco and McDougal (1985)].

All of the above studies are extremely complex, time consuming and in most cases, very costly.

THE ARMOUR UNIT LOAD CELL

After extensive research [Scott, Turcke and Baird (1986), Scott (1986)] a unique armour unit "load cell" was developed for measuring the response of concrete armour units to forces in a breakwater. Utilizing the concept of geometric distortion, a thin walled aluminum tube instrumented with strain gauges was inserted at the mid-shank location of a dolos unit, as shown in Figure 1. The tube was extremely thin in order to maximize the strains so that they were measurable under even the smallest loads. By calibrating the output voltages of the strain gauge circuits against known loading conditions, an armour unit load cell was created which measured the internal forces at the mid-shank location of the dolos unit.

Subsequent to this earlier work, a number of significant improvements have been made to the unit. The major changes have been to the wiring system so as to minimize the effects of the lead wires on the accuracy of the load cell. The newer load cell has been designed to be of more modular construction so it can be rapidly disassembled. In addition, the unit was made more durable to withstand repeated testing in a hydraulic flume, particularly at the attachment points where the inner instrumentation tube connects with the armour unit itself.

Physical modelling of the behavior of concrete armour units in a breakwater subjected to wave attack is exceptionally difficult. The very nature of the environment presents difficult problems in the development of instrumentation to measure armour unit forces.

There are scaling problems in that both Froude and Cauchy scaling criteria cannot both be satisfied simultaneously by such a model using typical materials. The response of the model units to static and quasi-static forces may be readily determined but dynamic forces, particularly impact forces, are not easily measured or scaled to prototype.

Coupled with these difficulties is the random nature of the armour orientation and placement in the breakwater and the wave loading which, consequently, requires a large number of costly tests to be carried out in order that a statistical analysis of the data can be performed. This suggests the need for the development of a more simplified testing program.

SIMPLIFIED MODEL TESTS

Given the significant number of difficulties in determining forces in concrete armour units within a hydraulic model, an investigation was carried out to develop a simplified model for measuring these forces.

As a result, a model test that may be easily carried out has been developed which provides a realistic upper limit to the forces measured in a breakwater. The force measuring device selected was the dolos load cell as developed in Scott (1986), thoroughly described by Scott, Turcke and Baird (1986), and shown in Figure 2. The test set-up is presented in Figure 3. The instrumented dolos unit of height "d" is rigidly fixed on a plywood ramp. Both the position of the unit on the ramp represented by the parameter "h", and the ramp slope can be varied.

The tests reported here included three sets of regular waves with heights of 15, 18 and 24 cm and all having a period of 1.7 sec. The ramp was set at a slope of 1.5:1. Figure 5 illustrates a typical moment - time history plot which demonstrates good repeatability from one wave to another. Figures 5 and 6 show plots of the average peak moment versus the position of the unit on the slope for the 15 cm and 24 cm waves respectively. It is interesting to note that the results of these tests clearly demonstrated that the maximum moment occurs just below the still water level and as expected larger moments are experienced by the unit when subjected to the higher wave heights, independent of its position on the slope.



Figure 1 - Original "Load Cell"



Figure 2 - Current "Load Cell"

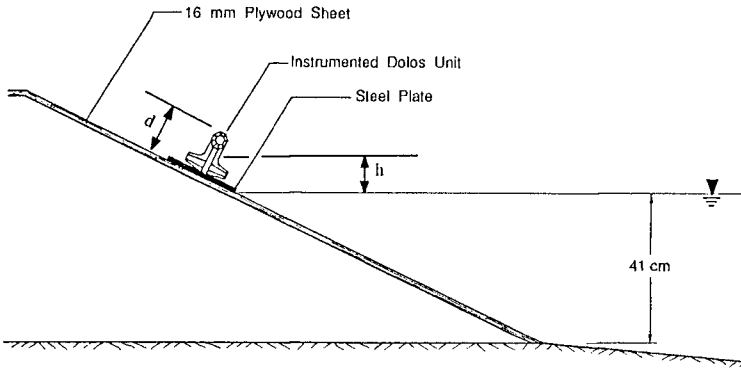


Figure 3 - Test Setup

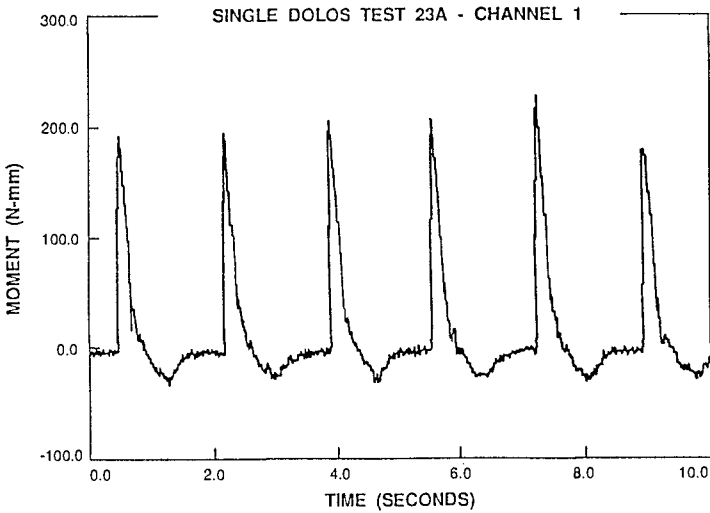


Figure 4 - Moment - Time Response History Plot

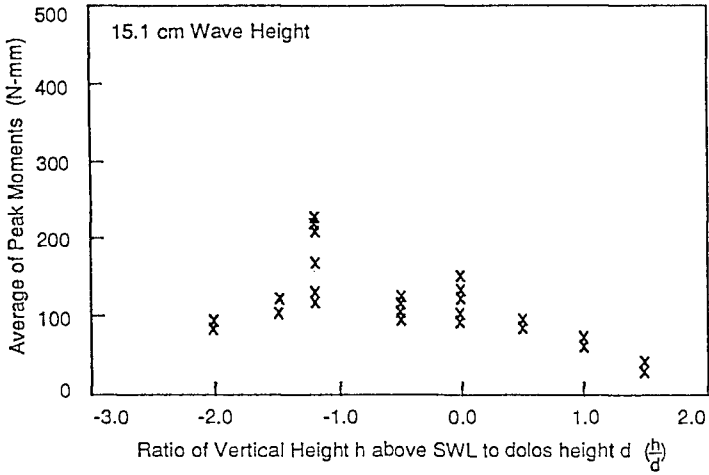


Figure 5 - Average Peak Mount versus h/d for 15.1 cm Wave Height

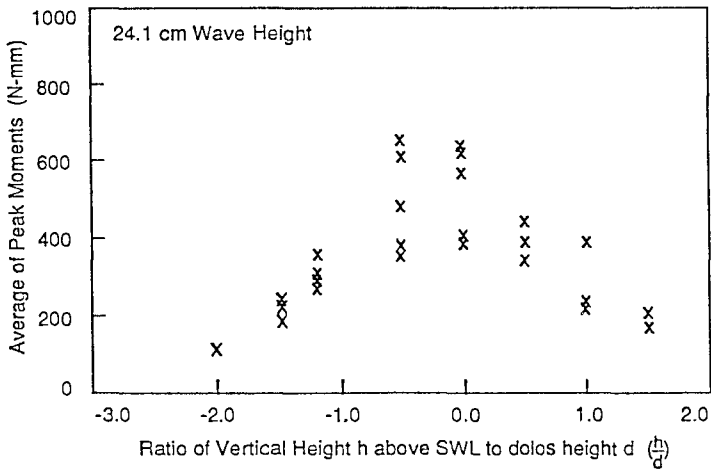


Figure 6 - Average Peak Moment versus h/d for 24.1 cm Wave Height

From these results the maximum stress considering all locations for a given wave height and period can be plotted against the ratio of wave height to dolos height, as shown in Figure 7. Even though a non-linear curve provided globally the best fit to the data, within the range of the measured data (H/d between 1.5 and 2.4), the results are strongly linear.

In order to see how well this result provides a realistic upperbound relationship, it can be compared to the research by Anglin (1988) in which an extensive parametric study of wave-induced loading on breakwater units was carried out. Over 1000 tests were performed and involved variable slopes, unit locations and wave periods and wave heights. Figure 8 shows the relationship developed here and put in a form so that it could be superimposed on the results of Anglin (1988). In this plot the average peak stress has been plotted against wave height. The data points represent the stresses in an armour unit at 22 different locations on a breakwater having a slope of 1.5:1 and subjected to waves with a period of 1.25 to 3.0 seconds and heights of 5 to 30 cm.

As presented in this figure, the simplified model has provided, with one simple test, a realistic upperbound to the set of 300 complex tests carried out by (Anglin 1988). This uncomplicated test can provide an indication of the maximum stress level in an armour unit and a global check on further more complex studies being carried out.

LARGER SCALE VERIFICATION TESTS

The purpose of this set of tests was to examine the repeatability and reproducibility of the load measurements with the instrumented armour units at various scales. Ideally, it would be useful to have data on prototype armour units tested under simplistic load and boundary conditions so that direct comparisons may be made with the physical model. Lacking this prototype data, some initial exploratory work was carried out utilizing model dolos unit load cells of three different sizes.

Three load cells were manufactured with total lengths of 106,203 and 305 mm. Each of the armour units was instrumented and calibrated so that the bending moment and shear in one plane of bending could be readily measured at the mid-shank location of the units.

A simple test was developed in which the instrumented unit was rigidly held to a steel plate then immersed below the still water level in a wave flume, as illustrated in Figure 9. The flume had an overall length of 26m, a large wave paddle capable of producing waves with a height in excess of 60 cm (depending on water depth and wave period) at one end and a series of wave absorbers at the opposite end of the flume. A series of five capacitance-type wave probes were used to measure the water surface elevation and a full wave reflection analysis was carried out.

Each of the mounted units was subjected to a series of regular waves during which the load cell output voltage was sampled at 500 Hz over a period of 30 seconds. The wave heights, wave periods and water depth were scaled exactly according to the overall lengths of the armour units. Table 1 provides a summary of the test conditions :

TABLE 1 - TEST CONDITIONS

DOLOS SIZE (cm):	10.6	20.3	30.5
DEPTH OF WATER (cm):	52	100	150
WAVE HEIGHTS (cm):	10-20	20-40	30-60
WAVE PERIODS (s):	1.44	2.04	2.50

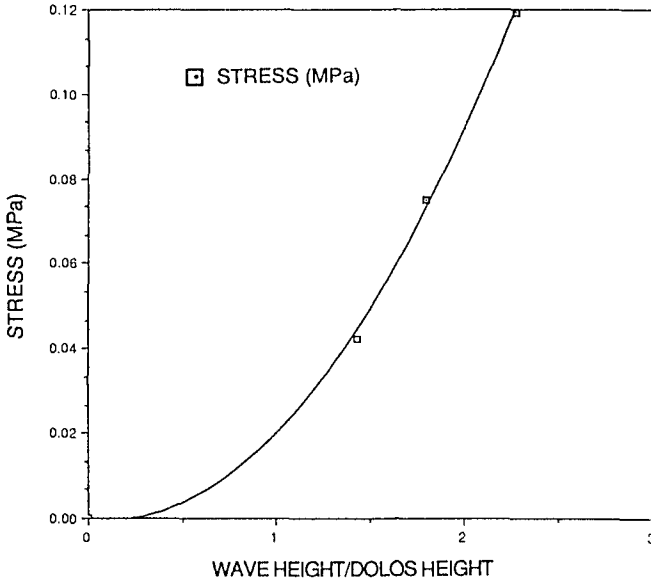


Figure 7 - Stress as a Function of H/d

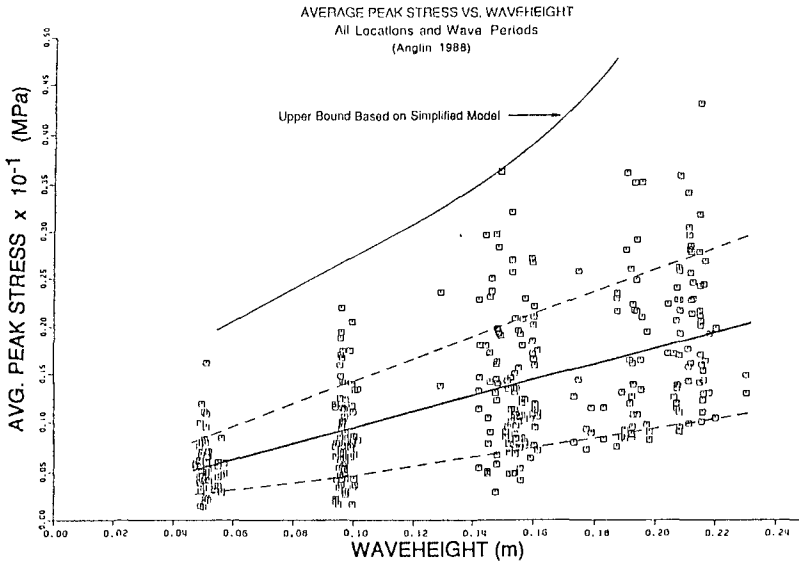


Figure 8 - UpperBound to Peak Stress Versus Wave Height Data

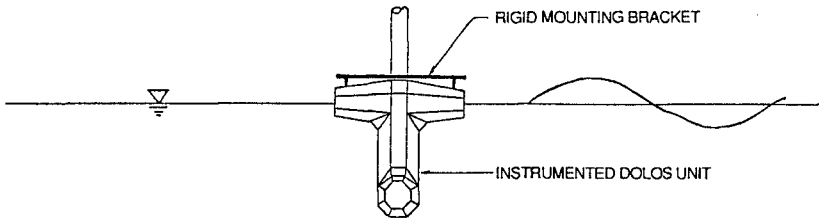


Figure 9 - Experimental Setup for Large Scale Verification Tests

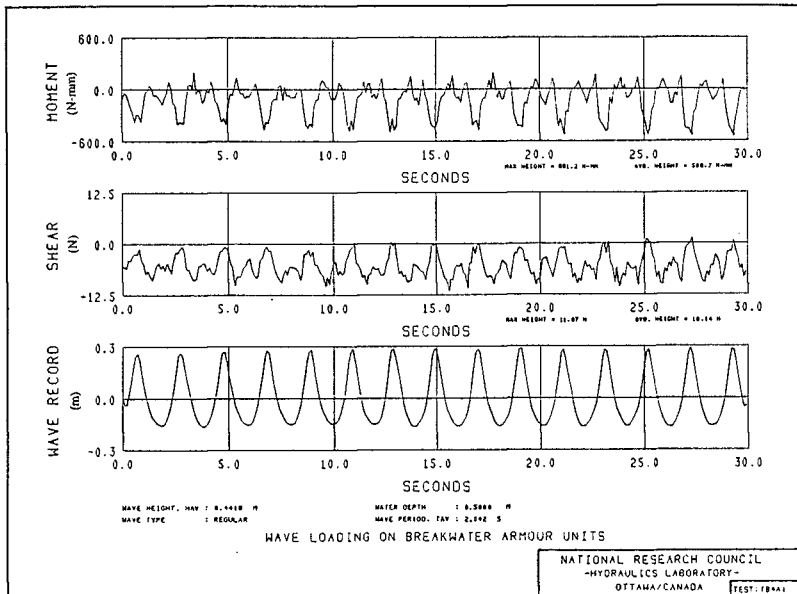


Figure 10 - Typical Response

Each test at a specific wave period and height was repeated three times. In one test series, the load cells were positioned so that the lower fluke was located at the still water level while in a second set of tests the armour units were immersed so that the still water level was at the upper fluke.

As three different sizes of dolos units were utilized in the test program, this provided three different scaling relationships for comparison of the measured responses of the load cells. That is, length scales of 1.5 (20.3 cm unit compared to 30.5 cm unit), 1.92 (10.6 cm and 20.3 cm units) and 2.88 (10.6 cm and 30.5 cm units) were used. Theoretically, the relationship between the measured bending moment of the units will vary with the fourth power of the length scale, or:

$$(M_L / M_S) = (d_L / d_S)^4 = \lambda^4$$

where, M_L is the bending moment in the larger unit having length d_L ; M_S , the amount in the smaller unit having a length of d_S ; and λ is the geometric length scale. The above scaling relationship indicates that, ideally, a log-log plot of moment ratio to geometric length scale will lie on a line of slope 4.

A typical response of a plot is presented in Figure 10 in which time histories of the measured bending moment, the shear and the water surface elevation are shown. The regularity of the load cell output as compared with the wave period may be noted in the figure.

In Figure 11, the average of the peak moments for each of the tests conducted on the 20.3 cm dolos unit with the upper fluke located at the still water level have been plotted against the wave height divided by the dolos length (H/d). A 3rd order polynomial was fit through the data points to examine the change in response with wave height.

In the final stage of the analysis, the peak moments measured for each of three tests repeats at a given wave height were averaged together and the ratios of bending moment and dolos length were compared. The log of the moment ratios was plotted versus the log of the geometric scales as given in Figure 12. A best fit line through the data points had a slope of 3.9 which compared remarkably well to the theoretical value of 4.0.

Further tests were carried out with waves of longer period but these tests gave inconsistent results. Subsequent analysis showed that considerable reflection within the flume was occurring with the longer waves leading to erroneous load cell measurements.

CONCLUSIONS AND RECOMMENDATIONS

This paper has presented the results of two sets of tests carried out using specially instrumented model armour units. These tests examined two issues that have arisen in the measurement of armour unit forces through physical modelling.

1. The development of a more simplified model of armour unit forces to compare with actual model breakwater tests.

Subjecting a single instrumented model armour unit positioned on a smooth slope to simulated prototype wave attack has been shown to provide a reasonable upper bound for the maximum quasi-static stress levels that may occur in a concrete armour unit. Additional research work is required to further refine this simplified test. Such refinement may include introducing porosity into the smooth slope to provide a more realistic simulation of fluid velocities in a rubblemound breakwater.

203 mm DOLOS - TOP FLUKE AT SWL

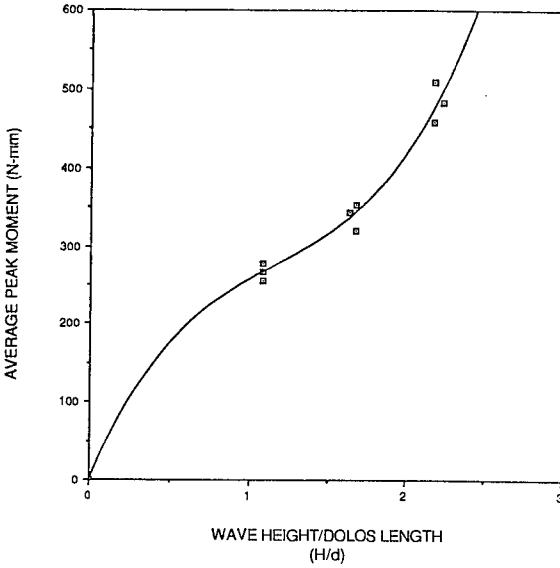


Figure 11 - Results for 203 mm Dolos Unit

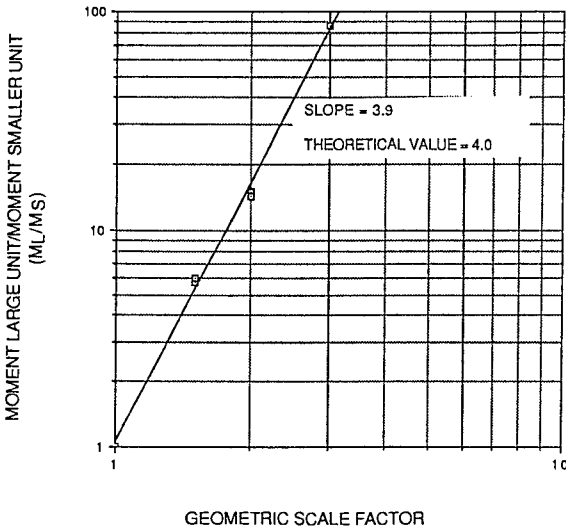


Figure 12 - Log-Log Plot of Moment Ratio to Scale Factor

2. The reliability of the instrumentation measurements if different model scales are employed.

The verification tests provided further confidence in the use of the load cell instrumentation for measuring static and quasi-static waves in physical models of concrete armour units. Three different sizes of dolos load cells were tested independently and all yielded similar results when appropriately scaled.

REFERENCES

- Anglin, C.D., Turcke, D.J., Scott, R.D., and Baird, W.F., "A Parametric Study of the Structural Response of Armour Units in a Breakwater", 21st Int'l. Conference on Coastal Engineering, Spain, June 1988.
- Baird, W.F., Scott, R.D., and Turcke, D.J., "An Analysis and Design of Armour Units", 20th International Conference on Coastal Engineering, Taiwan, Nov. 9-14, 1986.
- Endo, T., "Outline of our Studies on the Problems of Structural Strength of Armour Units", Presented at the Workshop on Measurement and Analysis of Structural Response in Concrete Armour Units, Vicksburg, Miss., Jan. 23-24, 1985.
- Howell, G., "Measurements of Forces on Dolos Armour Units at Prototype Scale. 21st Int'l. Conference on Coastal Engineering, Spain, June 1988.
- Jensen, O.J., and Juhle J., "Results of Model Tests on 2-D Breakwater Structure", Breakwaters 1988, Eastbourne, UK., May 4-6, 1988.
- Losada, M.A., Medina, R. and Alejo, M., "Wave Forces on Armour Blocks". 21st Int'l. Conference on Coastal Engineering, Spain, June 1988.
- Scott, R.D., "The Analysis of Concrete Armour Units in a Breakwater", Ph.D. Thesis, Queen's University, Kingston, Ontario, Canada, 1986.
- Scott, R.D., Turcke, D.J. and Baird, W.F., "A Unique Instrumentation Scheme for Measuring Loads in Model Dolos Units", 20th International Conference on Coastal Engineering, Taiwan, Nov. 9-14, 1986.
- Scott, D., Turcke, D.J., et al "The Design of Armour Units for Breakwaters", The Dock and Harbour Authority Journal, Vol. LXVII, No. 786, pp: 203-208, January 1987a.
- Scott, D., Turcke, D.J. and Baird, W.F., "Armour Protection for Rubble Mound Breakwaters", The Fifth Symposium on Coastal and Ocean Management, May 26-29, 1987b.
- Tedesco, J.W. and McDougal, W.G., "Non-linear F.E.M. Analysis of Concrete Armour Units", Presented at the Workshop on Measurement and Analysis of Structural Response in Concrete Armour Units, Vicksburg, Miss., Jan. 23-24, 1985.
- Tedesco, J.W., McGill P.B., and McDougal, W.G., "Structural Response of Dolos in Waves, 21st Int'l. Conference on Coastal Engineering, Spain, June 1988.

CHAPTER 180

Wave Force on a Curtain-Wall-Type Breakwater Due to Obliquely Incident Waves

by

Tsunehiro Sekimoto*, Kosuke Kondo**, Tetsunori Ohshimo*

ABSTRACT

Assessment of the characteristics of the wave force on the curtain-wall-type breakwater, due to obliquely incident waves, was conducted through numerical calculation, laboratory and field experiments. In the numerical calculations, the Boundary Integral Equation Method (BIEM) for obliquely incident waves was used. From the results of calculation and laboratory experiment, design graphs for estimating design wave force were established and the validity of the diagrams was verified through comparison with the results of laboratory and field experiments.

1. INTRODUCTION

The curtain-wall-type breakwater is a structure which has a vertical or inclined rigid thin barrier extending from above the water surface to some distance below. An example of the curtain-wall-type breakwater is shown in Fig. 1. The curtain-wall is supported by a jacket which is attached to the front side steel pile.

A curtain-wall-type breakwater is often selected as an inlet structure in the harbors of thermal or nuclear power plants in Japan, because they need to take in a great amount of water. The breakwater is also used as a simple wave eliminator in order to provide safe anchorage for vessels in large harbors or fishing ports. In these cases, the incident wave direction to the breakwater is usually restricted since breakwaters are constructed within the harbor. It is very important to know the characteristics of the wave force on the breakwater in relation to the direction of incident waves. However, little is known about the characteristics of the wave force.

In this study, two types of laboratory experiments and two series of field experiments were conducted and the numerical calculation based on Boundary Integral Equation Method was performed. Based on these experiments and calculation, the characteristics of wave force on the curtain-wall-type breakwater due to obliquely incident waves were discussed, and design graphs for estimating design wave force for a wide range of incident wave directions were established.

* Engineer, Design and Engineering Department, Penta-Ocean Construction Co., Ltd., 2-2-8 Koraku Bunkyo-ku Tokyo 112 Japan.

** Principal Engineer, Design and Engineering Department, Penta-Ocean Construction Co., Ltd.

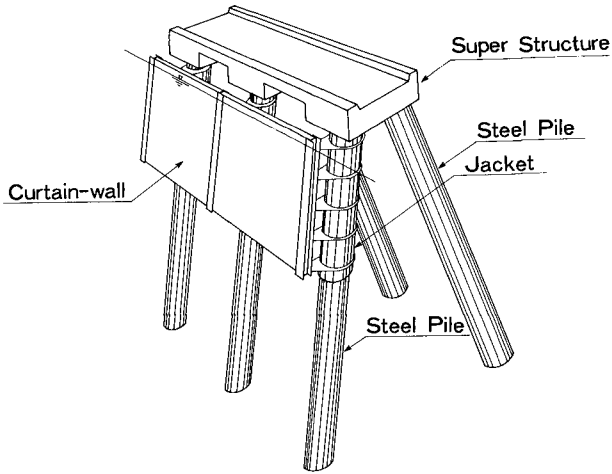


Fig. 1 A curtain-wall-type breakwater

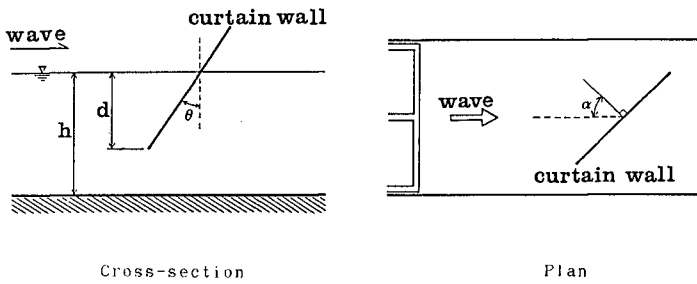


Fig. 2 Definition sketch of a curtain-wall-type breakwater

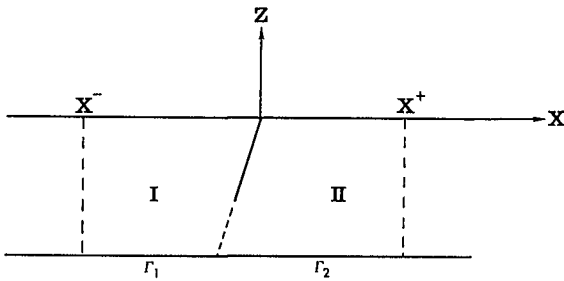


Fig. 3 Computational domain

2. NUMERICAL CALCULATIONS

Numerical calculations, which are based on the Boundary Integral Equation Method (BIEM) proposed by Liu and Abbaspour (1982), are extended to the cases of obliquely incident waves on the assumption that the length of the breakwater is infinitely long and its shape does not change along the breakwater.

A definition sketch of the curtain-wall is shown in Fig. 2. In these figures, α means incident angle, θ is curtain-wall inclined angle, d is the submerged curtain-wall depth and h means the water depth.

The sketch of the computational domain is shown in Fig. 3. Two auxiliary boundaries X^+ and X^- are introduced to utilize the BIEM technique. The procedure proposed by Liu and Abbaspour is characterized by two main points. One is the introduction of a velocity singularity at the tip of the breakwater, to aid accurate calculation. The second is the division of the calculation region into two subregions, Region I and Region II as shown Fig. 3, for simplification in the treatment of the thin barrier. The procedure of Liu and Abbaspour is as follows.

The boundary integral equation of the Laplace's Equation is

$$\frac{C_j}{2\pi} f(x_j, z_j) = \int_{\Gamma_j} \left[f^* \frac{\partial f}{\partial n} - f \frac{\partial f^*}{\partial n} \right] ds; \quad j=1,2 \quad (1)$$

Γ_j is the Boundary in each region. C_j is the interior angle at the base point (x_j, z_j) , $\partial/\partial n$ is the normal differential taken positive outwards, r is the distance between a base point to another point on the boundary. When the incident wave direction is normal to the Breakwater, f is the spatial variation of the velocity potential and f^* is defined by

$$\phi(x, y; t) = f(x, z) \exp[-i\sigma t] \quad (2)$$

Where ϕ is the velocity potential, σ is the angular frequency, x, z is the horizontal and vertical coordinates respectively and t is the time. The Green's function of the Laplace's Equation f^* is

$$f^* = \frac{1}{2\pi} \ln \frac{1}{r} \quad (3)$$

By discretizing and integrating equation (1) numerically and introducing the boundary conditions, the solutions can be obtained.

The boundary conditions are as follows
The condition on the surface;

$$\frac{\partial f}{\partial n} = \frac{\sigma^2}{g} f \quad (4)$$

The condition along the bottom and surface of the structure;

$$\frac{\partial f}{\partial n} = 0 \quad (5)$$

The condition along the auxiliary boundaries;

$$f = f^{\pm} \quad (6)$$

$$\frac{\partial f}{\partial n} = \frac{\partial f^{\pm}}{\partial n} \quad (7)$$

f^+ and f^- are presented by

$$f^+ = A_0^+ \frac{\cosh k(z+h)}{\cosh kh} \exp[ikx^+] + \sum_{n=1}^{\infty} A_n^+ \frac{\cos K_n(z+h)}{\cos K_n h} \exp[-Kn x^+] \quad (8)$$

$$f^- = A_0^- \frac{\cosh k(z+h)}{\cosh kh} \exp[-ikx^-] + \sum_{n=1}^{\infty} A_n^- \frac{\cos K_n(z+h)}{\cos K_n h} \exp[Kn x^-] + f_I \quad (9)$$

Where K_n is the n th imaginary root of the dispersion relationship, f_I is the velocity potential of the incident wave, A_0^{\pm} are the amplitude of the transmission and the reflection wave and A_n^{\pm} are the amplitude of the scattering waves.

Using a previous assumption, that the length of the breakwater is infinitely long and its shape does not change along the breakwater, the three dimensional Laplace's equation can be reduced to the two dimensional Helmholtz's equation. The boundary integral equation of Helmholtz's equation is also represented by equation (1). Assuming the y axis corresponds to the direction along the breakwater, f is defined by

$$\phi(x, y, z; t) = f(x, z) \exp[i(ky \sin \alpha - \sigma t)] \quad (10)$$

The Green's function of Helmholtz's equation is described by the modified Bessel's function.

$$f^* = \frac{1}{2\pi} K_0(kr \sin \alpha) \quad (11)$$

Introducing the boundary conditions previously used and using the equations (12) and (13) instead of equations (8) and (9), the solutions can be obtained in the case of obliquely incident waves.

$$f^+ = A_0^+ \frac{\cosh k(z+h)}{\cosh kh} \exp[ikx^+ \cos\alpha] \quad (12)$$

$$f^- = A_0^- \frac{\cosh k(z+h)}{\cosh kh} \exp[-ikx^- \cos\alpha] + f_I \quad (13)$$

The wave force and the water surface elevations were calculated from the potential f .

3. LABORATORY AND FIELD EXPERIMENTS

One of the experiments is a fundamental study with the curtain-wall in an uniform water depth. A wave-tank which has 34m length, 5m width and 1.2m depth was used. The incident and reflected waves, the transmission waves, the water surface elevation just in front of and just behind the curtain-wall and the wave pressure acting on the breakwater are measured using capacitance type wave gages and small size pressure gages. The models of the breakwater were made from a model unit which consists of steel frame and plywood curtain-wall. In order to reduce the effect of reflected waves from the side-wall and wave-paddle, the partition wall and the wave absorber were arranged for various conditions of incident wave angle. The experimental conditions are shown in Table 1. In the regular wave experiments, four kinds of wave period were used with three kinds of wave height. In the irregular wave experiments, three kinds of significant wave period were used with significant wave height of 8 cm only. Incident wave angle varied in six different directions from 0 to 90 degrees. Three kinds of inclined curtain-wall angle and two types of relative submerged depth d/h were tested. The water depth was set at 60cm in all cases. We carried out more than 200 runs using both regular and irregular waves.

Table-1 The experimental condition

	Regular wave	Irregular wave
Wave Period T, T _{1/3} (sec)	1.0, 1.5, 2.0, 2.5	1.0, 1.5, 2.0
Wave Height H, H _{1/3} (cm)	5.0, 8.0, 10.0	8.0
Incident wave angle α (deg)	0, 30, 45, 60, 75, 90	
Inclined angle θ (deg)	0, 20, 45	
Relative submerged depth d/h	0.4, 0.6	

The field experiments were carried out from January through March of 1985, and January through February of 1986, at the port of Kashiwazaki-Kariwa nuclear power plant, Niigata, Japan. Kashiwazaki-Kariwa is located on the Sea of Japan in central Niigata Prefecture and is shown in fig. 4.

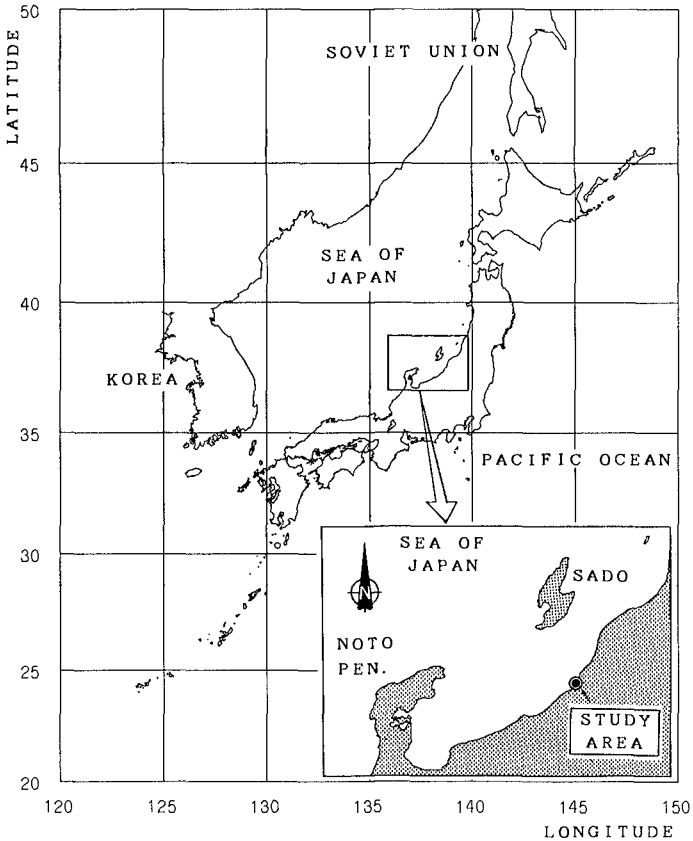


Fig. 4 The location of the investigation site

Fig. 5 is the shape of the port. The north breakwater and the north jetty are on the right hand side and the south breakwater and south jetty are on the left hand side of this figure. The curtain-wall-type breakwater is located in the middle of the south breakwater. The inclined angle and relative submerged depth of this curtain-wall are 15 degrees and 0.6 respectively. The water depth below the curtain-wall is 13 m. The water surface elevations just in front of and just behind the breakwater and the wave pressure on the breakwater are measured in the center section of this curtain-wall-type breakwater. The measurement of the water surface elevations and the wave pressures are performed using two capacitance type wave gages and eight pressure gages respectively.

Another experiment is an 1/80 scale model test of the port of Kashiwazaki-Kariwa nuclear power plant, in a 40 m length and 30 m width wave-tank. Both the water surface elevation and wave force were measured. In this experiment, unidirectional irregular waves, which have the Bretschneider-Mitsuyasu type power spectra, and JONSWAP Spectra, that approximate the field observed power spectra, were used. The water surface elevations were measured using capacitance type wave gages and the wave force measurement were performed by measuring the strain in the steel arm which supports the measuring part, when cut off from the other part of the curtain-wall.

The result of the calculations and the laboratory and field experiments were compared.

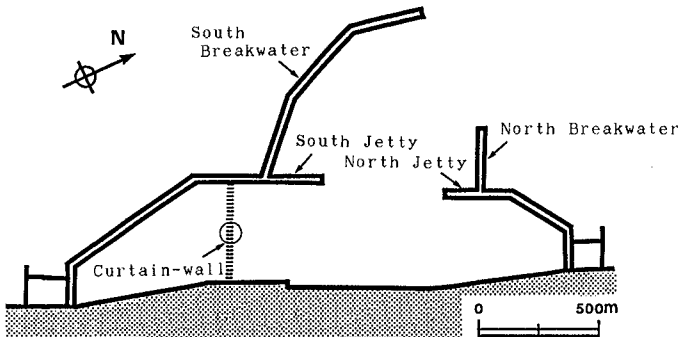


Fig. 5 Kashiwazaki-Kariwa port

4. COMPARISON BETWEEN RESULTS OF EXPERIMENT AND CALCULATION

Fig. 6 is the comparison of numerical predictions by BIEM with experimental results using regular waves for wave force coefficient as a function of the incident wave angle, with the condition that $h/L = 0.201$, $\theta = 20$ degrees and $d/h = 0.6$. The wave force coefficient is defined as the ratio between the wave force per unit curtain-wall length and the incident wave height. The experimental results agree with calculation results with the exception of the large value of α . One of the reasons for this anomaly is that the incident wave energy is transformed into a wave running along the curtain-wall.

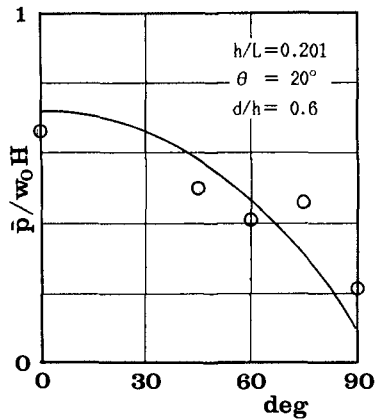


Fig. 6 The comparison between numerical and experimental results for wave force coefficient (regular wave)

The comparison results of irregular waves are shown in Fig. 7. The spectrum analysis is used for analysis of irregular waves. The wave force coefficient is defined as the transfer function of two times surface elevation of the incident wave to the wave force. The relative water depth is calculated from the wave length of each component wave. In the figures, a circle is the result using a wave with 1.5 sec significant wave period and a triangle means a wave of 2.0 sec. These are the results of plotting the wave force coefficient against the relative water depth in the case where $\theta = 20$ degrees and $d/h = 0.6$.

We obtain relatively good agreement between both, except for the lower range of h/L in the case where $\alpha = 30$ degrees. In this experiment, for the small incident wave direction, the distance between the edge of the model and the measuring point was short. Thus the effect of the scattering wave from the edge appeared in the result for the case where $\alpha = 30$ degrees.

For the case of inclined angle $\theta = 45$ degrees, agreement between results was not good because of the effect of the wave runup.

Fig. 8 are the figures showing the ratio of the wave force to the difference of the water level, on both sides of the curtain-wall, against h/L when $\alpha = 45$ degrees. The results from BIEM fit very well with the experiment results except for the case where $\theta = 45$ degrees. This is due to the effect of the wave runup. It is considered that the effective difference of the water levels is smaller than the measured difference. The ratio for different values of α lies almost on the same line. This fact was also confirmed in model tests and field experiments. Fig. 9 is the example of the result of an 1/80 model test and Fig. 10 is the result of field experiments. Good agreement between the calculation results and the experimental results is found in these figures. This implies that the wave force can be estimated accurately by BIEM if the difference of the water levels on both sides is given. And this fact also means the relations between the wave force and the difference of the water levels on both sides of the curtain-wall are hardly affected by the incident wave angle.

The difference of the water surface elevation on both sides can be separated into the amplitudes of the water surface elevation on both sides and the phase difference of both. Thus investigation followed on the phase difference and the ratio of the amplitude of the water surface elevation just behind the curtain-wall to the one just in front of it.

Fig. 11 shows the results of calculations and experiments on the phase difference between water levels as functions of h/L . It is found that the phase difference decreases as the incident angle of the waves increases. This is due to the increase in the apparent wave length. Agreement of the results of both calculation and experiment is good.

Fig. 12 shows the ratio of the water surface elevation just in front of to just behind the curtain-wall. When $\alpha = 30$ degrees, the experimental results agree well with the calculation results. However, as the incident wave angle increases, experiment results do not increase although the calculation result increases. This may be due to the fact that a part of the incident wave transformed into the wave running along the curtain-wall, although this is difficult to estimate quantitatively. However, it is found that the amplitude of the water surface elevation just in front of the curtain-wall decreases as the incident wave angle increases, and that the water surface elevation just in front of the curtain-wall and the ratio of the amplitudes of the both sides of the curtain-wall cancel the difference between calculation and experiment.

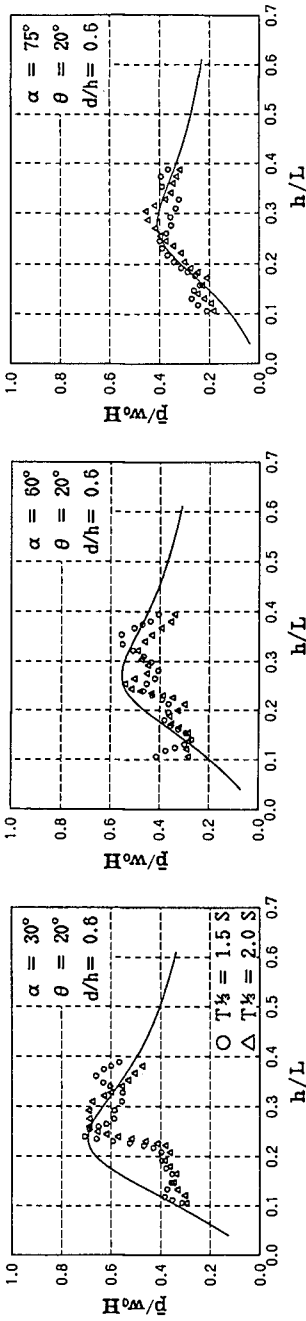


Fig. 7 The relation between wave force and incident wave height

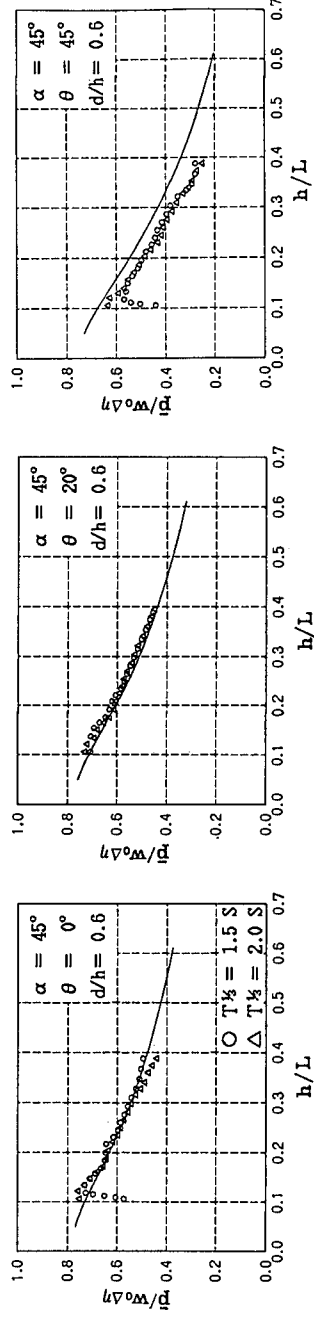


Fig. 8 The relation between wave force and the difference in water surface elevations

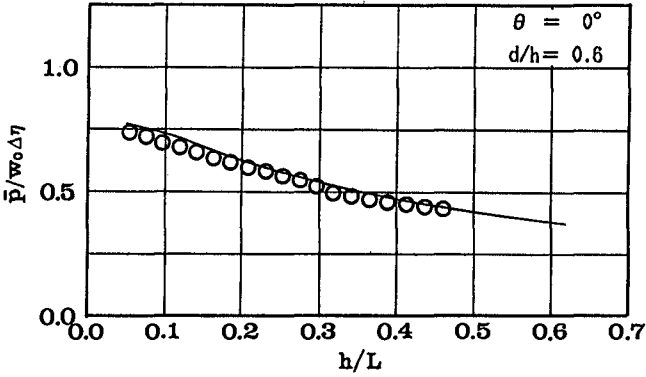


Fig. 9 The relation between wave force and the difference in water surface elevations (1/80 model test)

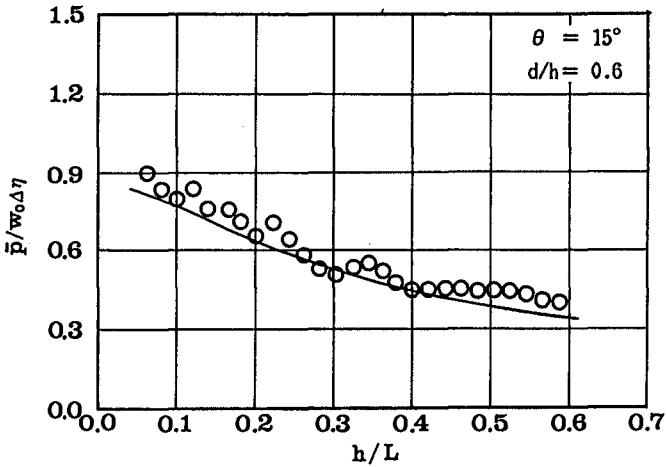


Fig. 10 The relation between wave force and the difference in water surface elevations (field experiment)

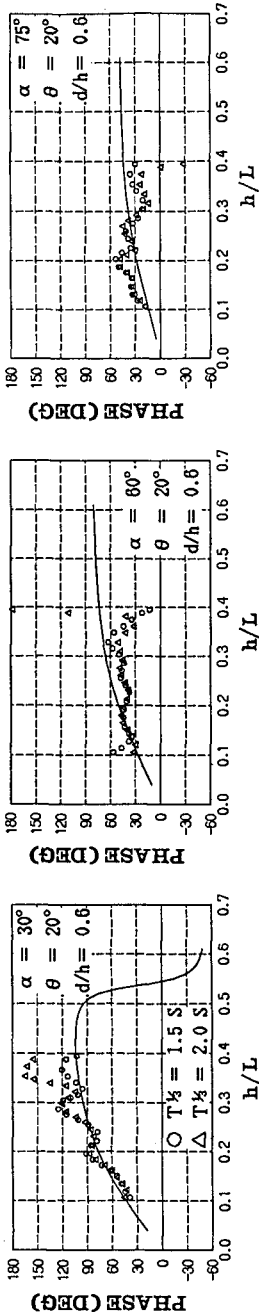


Fig. 11 The phase difference between the water surface elevations

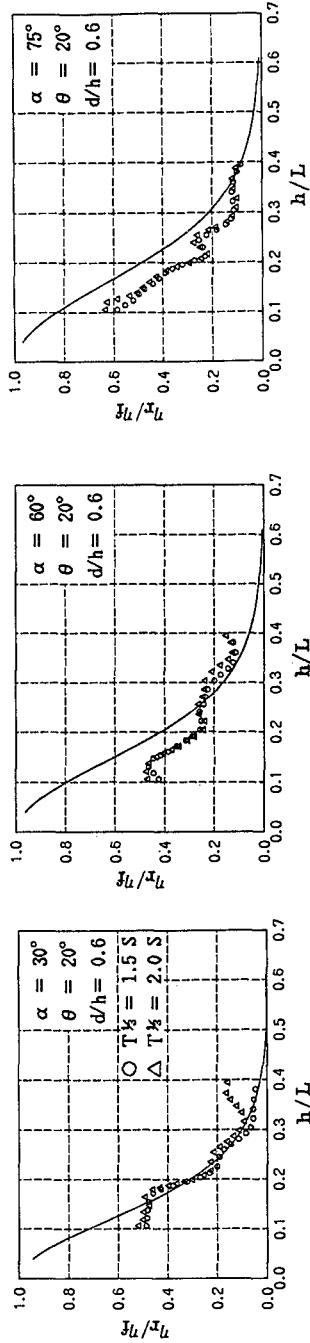
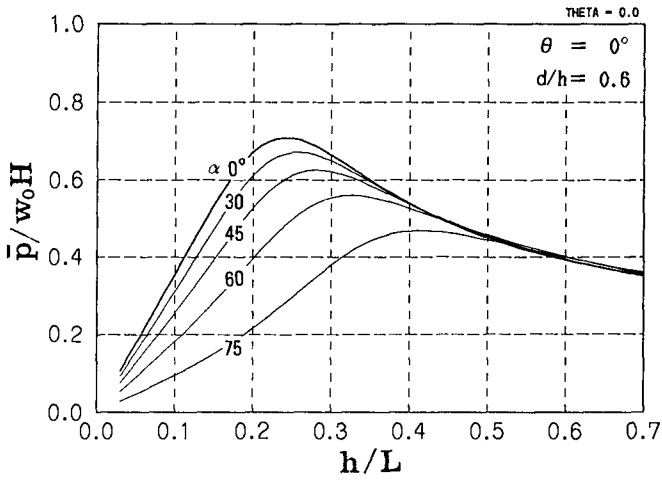
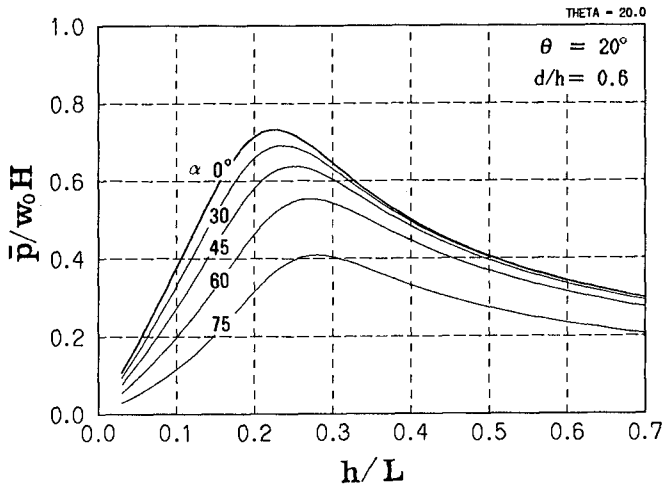


Fig. 12 The ratio between the amplitudes of water surface elevations



(a) $\theta = 0$ degree



(b) $\theta = 20$ degrees

Fig. 13 The diagram for estimation of design wave force

5. DESIGN WAVE FORCE

The wave force coefficient for irregular waves can be regarded as a transfer function. In the case of using the representative wave height as the design wave height, the moving weighted average of calculation results using BIEM, where 'weight' is a wave power spectra, is required. However, in consideration of the uncertainty about the mechanism of wave force and the accuracy of the calculation, BIEM results alone can be employed for estimation of design wave force. The diagrams for estimation of design wave force are shown in Fig. 13.

The comparison of numerical predictions with the experimental results of an 1/80 model test on wave force is shown in Fig. 14. In numerical predictions, Green's function method was used for calculation of directional spectra in a harbor [Kondo et al (1987)]. This is an extension of the procedure proposed by Gaillard (1984) in order to estimate the wave height and the wave direction at the measured point of the wave force. We obtained relatively good agreement between the calculation and the experimental results, even although the incident wave angle varied from 45 to 70 degrees.

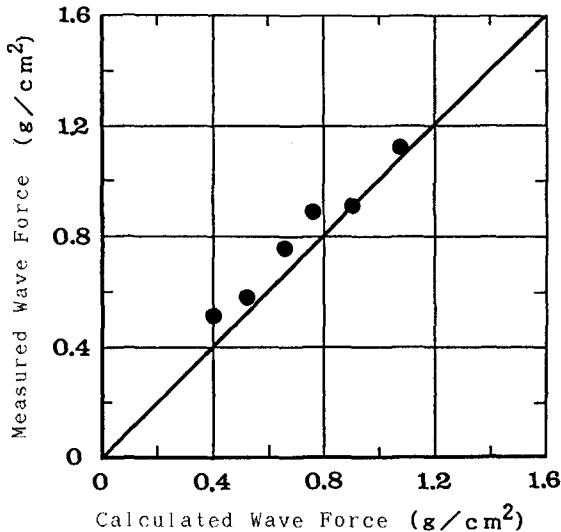


Fig. 14 The comparison of numerical predictions with the experimental results of an 1/80 model test on wave force

6. CONCLUSIONS

The characteristics of the wave force on the curtain-wall-type breakwater may be determined from the results of calculations based on BIEM and experiments. As a result, diagrams for estimating design wave force accurately for a wide range of incident wave direction were established. The applicability of this method are confirmed from the results of the 1/80 model test and field investigations.

ACKNOWLEDGMENTS

We would like to thank Mr. S. Imai of Tokyo Electric Power Co., Inc., and Mr. M. Nakamura of the Tokyo Electric Power Service Co., Ltd., for their support and cooperation.

REFERENCES

- [1] GAILLARD, P., Combined refraction-diffraction calculations with directional spectra, Proc. 19th Coastal Engineering., ASCE, pp.1040-1056, 1984.
- [2] KONDO, K., SHIMIZU, T. and YAMADA, K., Green function method for calculation of directional wave spectrum in a harbor, Proc. 34th Japanese Conf. on Coastal Eng., pp.106-110, 1987 (in Japanese).
- [3] LIU, P.L. and ABBASPOUR, M., A wave scattering by a rigid thin barrier, J. Waterway., Port, Coast and Ocean Engrg., ASCE, 108, PP.479-491, 1982.

CHAPTER 181

Structural Response of Dolos in Waves

Joseph W. Tedesco¹, A.M. ASCE, Preston B. McGill²,
Jeffrey A. Melby³, A.M. ASCE, and William G. McDougal⁴,
A.M. ASCE.

ABSTRACT

Several numerical models for estimating wave forces on dolosse are presented. These models are incorporated into a finite element method (FEM) analysis of a 42-ton unit. The results of the analysis permit identification of unit structural failure with respect to wave conditions.

INTRODUCTION

One means of protecting breakwaters and shorelines from wave-induced forces has been through the deployment of dolos concrete armor units. A typical dolos armor unit is shown in Figure 1. These randomly placed units form an interlocking yet porous armor layer providing a high degree of hydrodynamic stability. However, in the past, dolos armor units in severe wave environments, such as the breakwaters in Crescent City, California and Port Sines, Portugal, have experienced structural failures (Magoon, 1974, and Magoon and Baird, 1977). The unsatisfactory behavior of these units has prompted investigations into the wave loading on dolos armor units and an assessment of the subsequent dynamic structural response of the dolos unit.

This paper summarizes recent research conducted on the structural response of dolos armor units subject to wave forces. Several mathematical models (Tedesco and McDougal, 1985, and McDougal et al, 1988) developed for estimating wave forces on a single armor unit are presented. These wave force models were incorporated into a finite element method (FEM analysis of the dolos unit). Two types of analyses were conducted: 1) direct application of a critical wave to the armor unit restrained against rigid body motion, and 2) application of impact forces generated when wave-induced rigid body motion occurs causing dolos impacts.

SIMPLE WAVE-SLAMMING MODEL

In this model, the force on the dolos is estimated from the slamming of the wave with the structure. Only the horizontal component of

¹Assoc. Prof., Dept. of Civil Engr., Auburn University, AL 36849.

²Res. Asst., Dept. of Civil Engr., Auburn University, AL 36849

³Res. Hydr. Engr., Dept. of Army, Waterways Experiment Station, Corps of Engineers, P.O. Box 631, Vicksburg, MS 39180.

⁴Assoc. Prof., Ocean Engr. Program, Dept. of Civil Engr., Oregon State University, Corvallis, OR 97331.

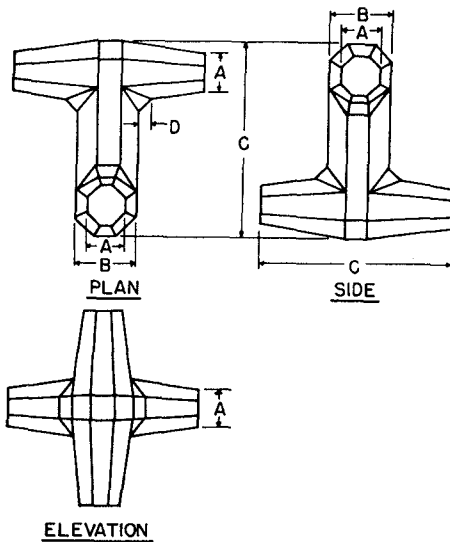


Fig. 1. Dolos Armor Unit.

this impact force is examined, which for the assumed geometry, is larger than the vertical component. Slamming is an important consideration in the design of ocean structures in the splash zone. As a result, a small body of information exists on wave-impact forces on horizontal cylinders. Kaplan (1979) and Kaplan and Silbert (1976) have developed models for both the horizontal and vertical forces due to impact. The models include the effects of buoyancy, pressure gradients, momentum flux (including added mass), and drag. Results are in reasonable agreement with measurements for the horizontal force but not for the vertical.

Experimental results suggest that the impact force, F , may be expressed in a simpler form

$$F = \frac{1}{2} C_s \rho d l U^2, \quad (1)$$

in which ρ is the fluid density; d is the diameter of the cylinder; l is the length of the cylinder; U is fluid velocity; and C_s is a slamming coefficient (Sarpkaya, 1978). The slamming coefficient is a function of the immersion depth of the cylinder and, therefore, a function of time. A time-dependent slamming coefficient has been empirically developed (Sarpkaya, 1978):

$$C_s = \frac{5.15}{1 + 19 \frac{Ut}{d}} + \frac{0.55 Ut}{d}. \quad (2)$$

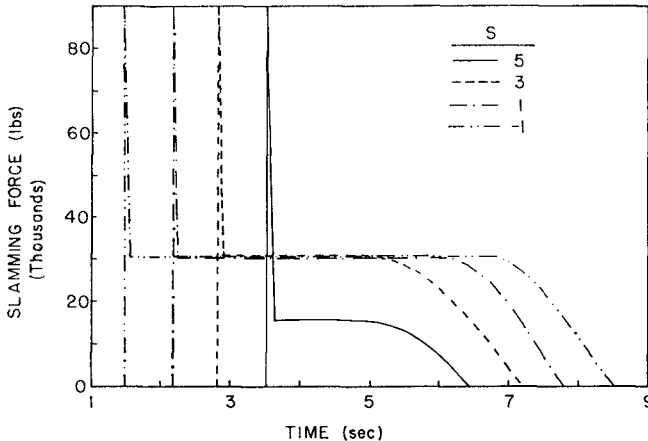
The maximum value for C_s at $t = 0$ is 5.15 and this value is appropriate if a static structural analysis is performed (Sarpkaya and Isaacson, 1981). For dynamic analyses, a value of 3.2 is suggested. Therefore, eq. (2) is accordingly scaled for use in the present dynamic analysis.

The foregoing formulation is, of course, only valid when some portion of the cylinder is immersed. However, when the cylinder is totally immersed, the formulation is inappropriate. Experimental results of Sarpkaya (1978) indicate that this formulation is only valid up to the point where the top of the cylinder is just below the free surface. Therefore, at this depth (when the slamming coefficient is at minimum)

the forces are assumed to no longer be impact dominated and a drag formulation is adopted.

$$F = \frac{1}{2} C_D \rho S d U^2, \quad (3)$$

in which S is the fraction of the cylinder which is immersed and C_D is a drag coefficient. It is noted in eq. (2) that the minimum value for the slamming coefficient is 0.5. This is of the same order as the drag coefficient for a smooth cylinder. Therefore, for purposes of calculation, this minimum value of C_S will be used for C_D . Several representative time histories of force are shown in Fig. 2. For a given wave and cylinder size, the duration of the force is a function of the position of the



cylinder relative to the stillwater level. The peak impact force is not a function of elevation because the horizontal velocity is assumed to be constant. The tailing off of the force depends upon the ratio of the cylinder diameter to the wave height.

Fig. 2. Time history of slamming force.
(S is height above SWL in feet)

An FEM (ADINA, 1984) analysis was conducted on three different sizes of dolosse subject to the simple wave slamming model. An isometric view of the model is depicted in Fig. 3. The analyses were performed for concrete compressive strengths, f'_c , of 5000 psi and 4000 psi for each model. The dolosse were assumed to be unreinforced, and the tensile strength of the concrete was assumed to be equal to the split cylinder strength, f_{ct} , of the concrete (where $f_{ct} = 6.7\sqrt{f'_c}$).

The failure of the dolosse depends on the maximum slamming load. This load, in the present analysis, is only a function of the wave conditions for a specific dolos unit. This load is calculated as discussed above and regions of structural stability are identified as a function of the wave conditions. These results are shown in Fig. 4 for a 42-ton dolos in which T is the wave period, T_c is the resonant period, H is the wave height, and H_H is the maximum stable wave height for the unit. Stable and failure regions are identified for 4000 psi and 5000 psi concrete. It is noted that structural failure would occur for the 4000 psi concrete at wave conditions for which the unit is hydrodynamically

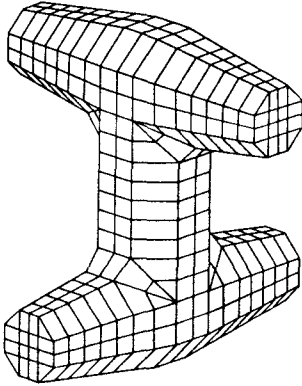


Fig. 3. Isometric view of FEM Model

stable. The higher strength concrete unit is very nearly at failure at these wave conditions.

MULTI-COMPONENT WAVE FORCE MODEL

The precise specification of the wave loads in the breaker zone is extremely difficult. However, there are many structures built in this zone and several approximate analysis methods have been developed. Kaplan (1979) and Kaplan and Silbert (1976) developed Morison type equations (Morison et al, 1950) for a horizontal cylinder in the "splash zone" where the structure is not in continuous contact with the wave. This model includes the slamming of the fluid on the structure as the structure penetrates the free surface. A primary assumption is that the wave

length is large with respect to the structure diameter. Kaplan and Silbert (1976) showed that the vertical force per unit length on a horizontal cylinder for a normally incident wave can be expressed as the sum of the buoyant, inertial, kinetic and drag forces as follows:

$$F_{VH} = \rho g A_1 + (m_3 + A_1) \ddot{\eta} + K_{HV} \frac{\partial m_3}{\partial z} \dot{\eta}^2 + \frac{\rho}{2} \dot{\eta} |\dot{\eta}| d \left(\frac{z}{r}\right) C_{DV} \left(\frac{z}{r}\right), \tag{4}$$

where the first subscript on F denotes the force direction and the second indicates the cylinder orientation. The force component notation is shown in Fig. 5. Also, K_{VH} is an empirical force coefficient, ρ is the mass density of the fluid, g is the acceleration of gravity, A_1 is the immersed area, $\ddot{\eta}$ and $\dot{\eta}$ are the vertical wave velocity and acceleration, respectively, $d(z/r)$ and $C_{DV}(z/r)$ are the depth dependent diameter and drag coefficient, respectively, and m_3 is the vertical added mass.

The horizontal force on a horizontal cylinder can similarly be stated as the sum of inertial, kinetic and drag forces:

$$F_{HH} = (m_2 + \rho A_1) \dot{u} + K_{HH} \frac{\partial m_2}{\partial z} \dot{u}^2 + \frac{\rho}{2} u |u| h \left(\frac{z}{r}\right) C_{DH} \left(\frac{z}{r}\right), \tag{5}$$

where K_{HH} is an empirical force coefficient, u and \dot{u} are the horizontal water particle velocity and acceleration, respectively, and m_2 is the horizontal added mass. For the case of a vertical cylinder, the previous equation for horizontal force can be directly applied to yield

$$F_{HV} = (M_4 + \rho A_1) \dot{u} + K_{HV} \frac{\partial m_4}{\partial z} \dot{u}^2 + \frac{\rho}{2} u |u| DC_{DH} \tag{6}$$

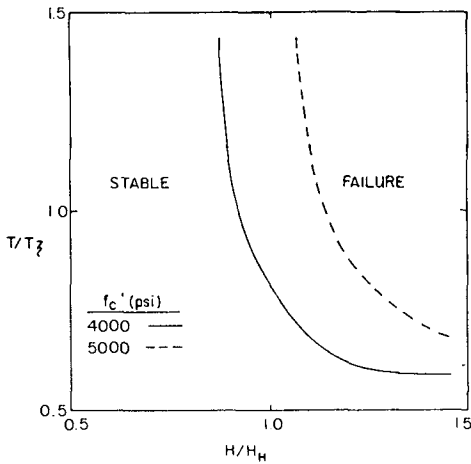


Fig. 4. Failure envelope for 42-ton dolos unit.

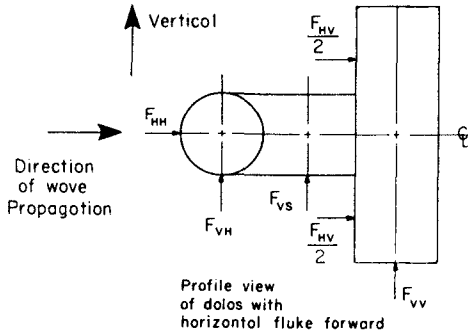


Fig. 5. Dolos orientation and wave force component notation.

in which K_{HY} is an empirical force coefficient. The vertical force on a vertical cylinder can be expressed as the sum of form drag and buoyancy acting on the lower end of the cylinder to yield

$$F_{VV} = \rho g \pi r^2 + \frac{\rho}{2} v |v| \pi r^2 C_D, \quad (7)$$

where v is the vertical water particle velocity at the cylinder base. Finally, the vertical force on a horizontal cylinder parallel to the direction of wave propagation is assumed to be buoyancy dominated and thus given by

$$F_{VS} = \rho g A_i. \quad (8)$$

These force equations are similar in form to the Morison equation. However, potential theory is employed to determine the kinetic term and the coefficients, m_2 , m_3 , m_4 and C_D , which are in terms of the geometric properties as well as flow and cylinder roughness characteristics.

for the design wave given in Table 1. The wave

In this study, linear wave theory was used to determine the values of wave variables to the maximum stable wave height for a 42-ton dolos on a 1V:2.5H slope as determined from Hudson's formula. The wave period was selected by choosing an Iribarren number of 2.5. The Iribarren number is the ratio of

Table 1. Wave and dolos specifications			
Wave		Dolos	
Height	33.4 ft	Elevation	12.0 ft
Period	12.77 sec	Fluke dia.	3.98 ft
Depth	42.8 ft	Fluke length	15.29 ft
		Shank dia.	4.89 ft
		Shank length	7.33 ft

the structure slope to the square root of the wave steepness. A value of 2.5 corresponds to a critical condition in which the wave breaks when rundown is at its lowest point (Bruun and Gunbak, 1977). The depth corresponds to the depth limited breaking for this wave height.

The dolos configuration is as shown in Fig. 5 with the horizontal fluke forward. The methodology developed for estimating wave forces is also applicable to the case with the vertical fluke forward. In both cases the shank is fixed in the horizontal plane and in line with the direction of wave propagation.

The multi-component wave force model was incorporated into an FEM analysis of a 42-ton dolos. In the analysis, the dolos unit was positioned among other units so that it is restrained only at the bottom of the vertical fluke which is perpendicular to the wave crest. The horizontal fluke is forward (seaward) and parallel to the wave crest.

For the specified wave loading and structure restraint conditions, the critical section in the dolos unit was located in the bottom portion of the vertical fluke, at the fluke-shank juncture, just below the fillet. The maximum tensile stress at the critical section was calculated to be 760 psi. This value exceeds the ultimate tensile strength of 743 psi (the modulus of rupture), thereby causing a structural failure.

IMPACT ANALYSIS

Damage to dolosse is primarily due to the impact forces resulting from the collision of units due to wave-induced rolling and rocking motions (Burchart, 1984). Knowledge of the rigid body motions is required for an appropriate design. Once the wave loads have been specified and the dolos orientation is known, the equations of motion can be solved numerically. The equations of motion for a dolos constrained as described in the previous section reduce to a single rotational degree of freedom. The equation of motion is (McDougal et al, 1988)

$$I\ddot{\theta}(t) + C\dot{\theta}(t) + K\theta(t) = M(t) \quad (9)$$

where θ , $\dot{\theta}$, and $\ddot{\theta}$ are the angular displacement, velocity, and acceleration, respectively, I is the mass moment of inertia, C is damping, K is stiffness, and M is the applied moment. In the analysis, $C = 0$ and the applied moment is given by the product of the time varying moment arms and the respective Kaplan forces. This equation was integrated using a fourth order Runge-Kutta algorithm.

In the present study, the case investigated is depicted in Fig. 6. The horizontal fluke is seaward and parallel to the wave crest. Under wave action, the dolos is permitted to pivot about the vertical fluke which is perpendicular to the wave crest. Damage to the unit occurs when the dolos falls back to its initial position and impacts another unit.

The FEM representation of the scenario is depicted in Fig. 7. The unit is assumed to impact a rigid contact surface at a contact velocity

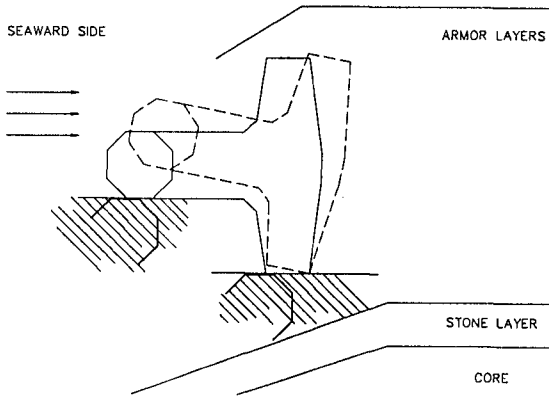


Fig. 6. Dolos orientation for impact analysis.

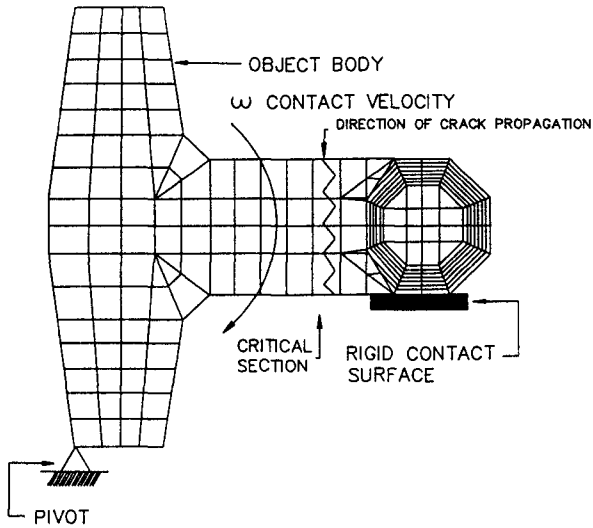


Fig. 7. FEM representation of impact analysis.

ω . The critical section in the unit is located on a vertical plane through the shank (Fig. 7). The dynamic stress history at the critical

section is presented in Fig. 8.

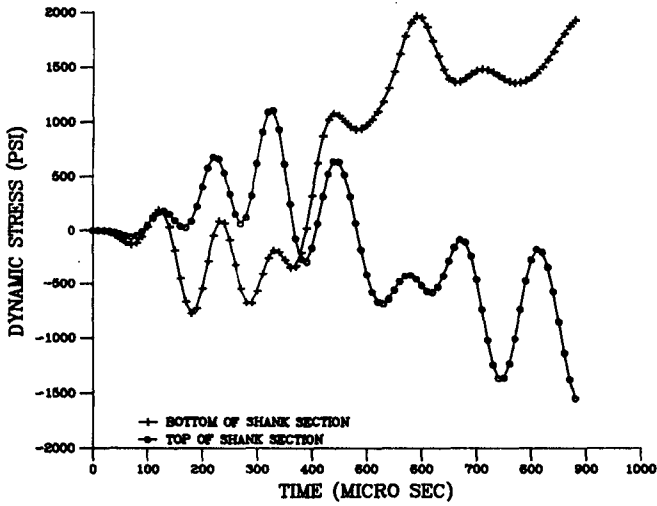


Fig. 8. Dynamic stress history for impact analysis.

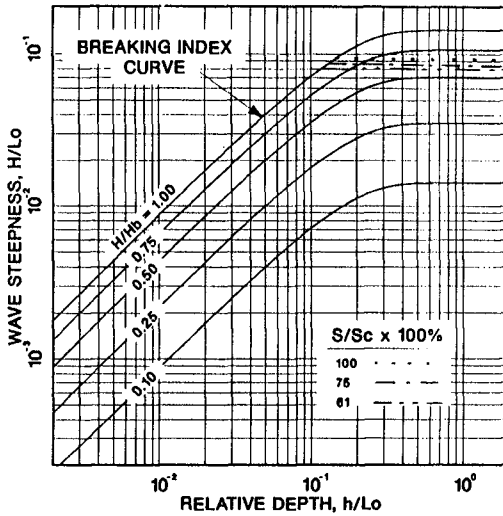


Fig. 9. Structural stability curves for a 42-ton dolos. (10 sec. wave period)

It is quite useful to be able to determine the wave conditions which induce a structural failure in the armor unit. Structural failure of a 42-ton dolos unit is depicted in Fig. 9 for a wide range of wave conditions at a constant period. Wave conditions producing 75% and 60% failure stresses are also presented in Fig. 9.

REFERENCES

- ADINA, (1984), "A Finite Element Computer Program for Automatic Dynamic Incremental Nonlinear Analysis," Report 84-1, ADINA R&D, Watertown, MA.
- Bruun, P. and Gumbak, A., (1977), "Stability of Sloping Structures in Relation to Risk Criteria Design," Coastal Engineering, 287-322.
- Burchart, H.F., (1984), "Fatigue in Breakwater Concrete Armor Units," Aalborg University, Denmark.
- Kaplan, P., (1979), "Impact Forces on Horizontal Members," Proceedings of Civil Engineering in Oceans IV, 716-731.
- Kaplan, P. and Silbert, M. N., (1976), "Impact Forces on Platform Horizontal Members in the Splash Zone," Proceedings of the Offshore Technology Conference, 169-176.
- Magoon, O. T., (1974), "Damages to Coastal Structures," Proceedings of the 14th Coastal Engineering Conference.
- Magoon, O. T. and Baird, W. F., (1977), "Breakage of Breakwater Armor Units," Proceedings of the Symposium on the Design of Rubble-Mound Breakwaters, Isle of Wright.
- McDougal, W. G., Melby, J. A., and Tedesco, J. W., (1988), "Wave Forces on Concrete Armor Units," Journal of the Waterway, Port, Coastal and Ocean Division, 114, 5:582-598.
- Morrison, J. R., O'Brien, M. P., Johnson, J. W., and Scaaf, S. A., (1950), "The Force Exerted by Surface Waves on Piles," Petroleum Trans., 189, TP 2846.
- Sarpkaya, T., (1978), "Wave Impact Loads on Cylinders," Proceedings of the Offshore Technology Conference, 169-176.
- Sarpkaya, T. and Isaacson, M., (1981), Mechanics of Wave Forces on Offshore Structures, Van Nostrand Reinhold, New York.
- Tedesco, J. W. and McDougal, W. G., (1985), "Nonlinear Dynamic Analysis of Concrete Armor Units," Computers and Structures, 21:189-201.

ACKNOWLEDGEMENT

The work described in this paper was conducted as part of the Crescent City Prototype Dolosse Study of the Coastal Engineering Research Center, Waterways Experiment Station, U. S. Army Corps of

Engineers. Permission to publish this paper was granted by the Chief of Engineers.

CHAPTER 182

LONG TERM EXPERIENCE WITH SEAWALLS ON AN EXPOSED COAST

by Orville T. Magoon¹, Joan L. Pope²,
Robert L. Sloan³, and Donald D. Treadwell⁴

Appropriately designed, constructed, and maintained rubble mound seawalls are an efficient and cost-effective means of protecting erodible sections of exposed coastline. This conclusion is supported by more than 25 years of satisfactory seawall performance along the Pacific Ocean coast of Santa Cruz County, California, U.S.A. Important factors in satisfactory seawall performance include a clear understanding of the oceanographic and geologic design parameters, a vigorous inspection program during construction, and continued observation and maintenance of the structures.

INTRODUCTION

The coastal city of Santa Cruz, in Santa Cruz County, California, U.S.A., is located about 75 miles south of San Francisco, along the northern shore of Monterey Bay (Figure 1). For more than a century, the beaches and shores in this area have served as a major recreational resource (Figure 2) for residents of the San Francisco Bay Area and the California Central Valley.

-
- 1 President, American Shore and Beach Preservation Association, P.O. Box 279, Middletown, California 95461
 - 2 Chief, Coastal Structures and Evaluation Branch, Coastal Engineering Research Center, U.S. Army Corps of Engineers, Waterways Experiment Station, Vicksburg, Mississippi 39180
 - 3 Program Manager, Planning Division, U.S. Army Corps of Engineers, South Pacific Division, 630 Sansome Street, San Francisco, California 94111
 - 4 President, Treadwell & Associates, Inc., 447 Battery Street, Suite 300, San Francisco, California 94111

The authors are Members of the American Society of Civil Engineers.

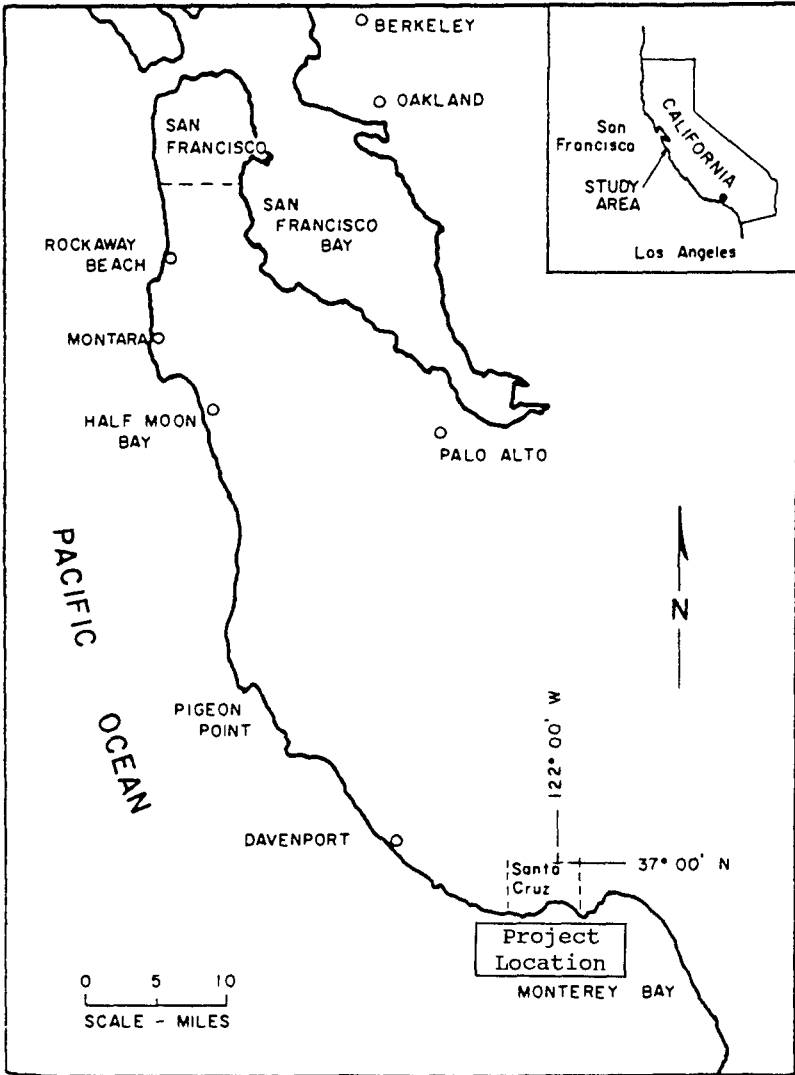


Figure 1 - Project Location



Figure 2 - Using the Beach at Capitola

The California coast in the Santa Cruz area is subject to very high waves, with maximum deep water waves often exceeding 50 feet in height. The water depths immediately seaward of the toe of the bluffs are sufficiently shallow to cause large waves to break well seaward of any protective structures under most conditions. The resulting waves at the shoreline are affected by both the depth of water as well as the complex bathymetry and topography immediately offshore.

The erosion of the beaches and cliffs on the northern side of Monterey Bay between the west limits of the City of Santa Cruz and New Brighton Beach State Park had been progressive for many years (Figure 3). The recession of the cliffs had cut through public streets, destroyed both public and private land, and threatened to destroy residences and other buildings. Individual efforts by local interests to combat the erosion problem were historically insufficient in scope or failed in their intended purpose.

GEOLOGIC SETTING

Coastal cliffs are a common landform along large sections of the geologically young California coast (Figure 4). The cliffs are the result of active erosion, being subject to periodic retreat during stormy periods. Many of the cliffs consist of relatively soft sandstones, siltstones, and shales, which are highly susceptible to erosion from wave action and surface runoff. The problem of coastal cliff erosion and retreat is well understood qualitatively and described in the literature. However, because the episodes of retreat are relatively infrequent and the overall rate is deceptively slow, property owners tend to develop a false sense of permanency and security.

The actual process and rate of cliff erosion and slope retreat depend to a large extent on the type of material involved. The weathering and erosion of the predominantly sandy rocks in California lead to the accumulation of talus and the formation of sandy beaches. The talus and the beach protect the toe of the slope from wave erosion between major storms. In areas underlain by stronger, more cohesive rocks, there is often not enough sandy material to form the beaches and the waves tend to lap directly at the toes of the cliffs. In both cases, however, the rates of cliff retreat tend to be relatively slow in the periods between large storms.

Failures, when they occur, tend to be the result of large episodic events such as major storms. For slopes protected by sandy beaches, the storm waves and tides must be sufficiently large to remove the protective sand before the waves can attach the slopes themselves. Once this occurs, the rate of cliff erosion can be very rapid. Cliffs that are not protected by beaches will obviously be exposed to significant wave action more often. Even



Figure 3 - Beaches and Cliffs near West Cliff Drive

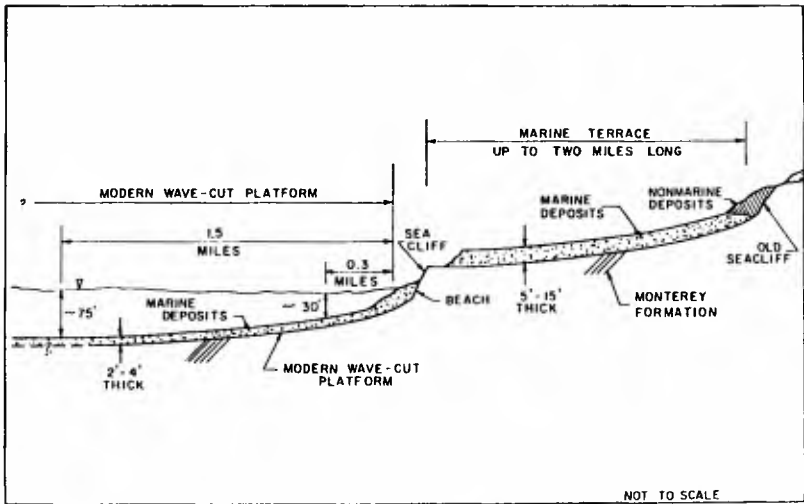


Figure 4 - Typical Profile Normal to Coastline

then, major failures will be relatively infrequent and more likely to occur during large storms. Overall, these infrequent failures result in a slow but steady average retreat of coastal cliffs, often at a rate of less than one foot per year. More important, a lack of erosion over a period of a few years is not evidence that the retreat of coastal cliffs has been halted.

Santa Cruz County lies along the northern coast of Monterey Bay in central California. Uplifted marine terraces flank most of the northern bay and also the open coast farther to the north. The seacliff varies in height from about 20 to 90 feet and is generally composed of Santa Cruz Mudstone and the Purisima Formation (siltstone and sandstone). These sedimentary rocks usually lie almost horizontal or dip gently seaward and are often capped by 6 to 20 feet of unconsolidated marine and non-marine terrace deposits.

The Santa Cruz Mudstone is predominantly a diatomaceous siliceous mudstone. It is thin-to-thick-bedded and individual beds vary from several centimeters to a meter in thickness. Joints and fractures give most outcrops a blocky appearance. The large number of rockfalls and block landslides which occur in the mudstone indicate its susceptibility to failure on steep slopes such as canyon walls and seacliffs. The Purisima Formation consists of thick bedded, poorly to moderately indurated siltstones and sandstones with occasional interbeds or lenses composed almost entirely of mollusk shells. This formation is jointed, faulted, and warped. The influence of individual stratigraphic units within the Santa Cruz Mudstone and in the Purisima Formation on local geomorphology and erosion rates is significant.

Coastal erosion or seacliff retreat is caused by both marine and terrestrial processes. Surf action is usually the dominant agent, producing both wave impact and abrasion. The rate of seacliff retreat is dependent upon the following natural factors: (1) available wave energy and exposure (including the presence or absence of a protective beach at the base of the cliff); (2) the lithology of seacliffs and their resistance to erosion; (3) geologic structure including joints, faults, and folding; and (4) the height and slope of the seacliff. Runoff and human activities are factors that can also add significantly to the rate of cliff retreat.

Within Monterey Bay, the seacliffs are generally protected from direct wave attack. The predominant waves from the west-northwest are refracted almost 90 degrees before striking the coast, and wide sandy protective beaches begin to appear. The coastal cliffs throughout most of the city of Santa Cruz are composed of erodible sediments of the Purisima Formation. Rapid erosion has cut back the cliffs, changing the trend of the coastline and creating the embayment known as northern Monterey Bay (Figure 5). Although the bay configuration protects this area from



Figure 5 - Monterey Bay (looking East)

direct wave attack, erosion rates in these sandstone and siltstone beds (Purisima Formation) are still greater than the rates in the Santa Cruz Mudstone along the open coast to the north. The erosion rate of the Purisima Formation is influenced by the varying hardness of different lithologic units within the formation, the orientation of well developed joint sets, and the presence of faults.

Cliff height sometimes exerts an indirect control on erosion rates. The quantity of material produced by a given amount of coastal retreat is a direct function of cliff height. For example, cliffs have been undercut and have subsequently failed, and large blocks have broken out along joint sets and fallen to the beach below. To the extent that this material remains in place at the foot of the cliff, it serves as temporary riprap to buffer the cliffs from direct wave attack. However, the large sandstone and siltstone blocks produced by breakdown of the Purisima Formation last only a few years in the surf zone.

PROJECT HISTORY

Studies of the beach and cliff erosion problem in Santa Cruz County were conducted in the mid to late 1950's by the U.S. Army Corps of Engineers in cooperation with the State of California, Santa Cruz County, and the City of Santa Cruz. These studies concluded that the most practicable plan for protection of the West Cliff Drive and Opal Cliffs-Capitola reaches would be rubble mound seawalls with top elevations ranging from 14.0 to 17.5 feet above Mean Lower Low Water (MLLW). It was further concluded that the irregular alignment and rocky nature of the shoreline would make

placement of beach fill economically infeasible. The numerous projecting points or minor headlands that function as groins do not impound sand in sufficient quantity to protect the cliffs, indicating that groins, either with or without fill, would not correct the problem.

In order to reconstruct and restore West Cliff Drive to serve the large public demand at this important resort, the City of Santa Cruz, the City of Capitola, the County of Santa Cruz, the State of California, and the U.S. Army Corps of Engineers cooperated in planning, designing, and constructing more than 4,000 feet of rubble-mound seawalls in about twenty sections. In their studies, they found that the cliffs in the area had been progressively eroded for many years.

Further south, the Opal Cliffs-Capitola reach, also about 2.5 miles long, is characterized by an irregular shoreline backed by cliffs ranging from 35 to 75 feet in height. Except for narrow beaches found during the summer in shallow embayments and at the mouth of Soquel Creek, the greater length of this section is devoid of beach material and the cliffs are exposed to wave attack all year. During the winter months, wave action strips the beaches of sand leaving the underlying bedrock exposed.

The beach erosion control project for these two reaches that evolved from the Federal studies was authorized by the River and Harbor Act of 1958. This act provided, in part, for Federal participation by contribution of funds toward the cost of construction of: (1) rubble mound seawall units with an aggregate length of 4,700 feet, along West Cliff Drive; and (2) rubble mound seawalls about 870 feet in length at Cliff Drive in the Opal Cliffs area of the City of Capitola, about 10 miles to the southeast.

The plan of protection for West Cliff Drive provided for rubble-mound, or riprap seawalls and/or revetments at critical reaches, totaling about 4,150 feet in length (Figures 6 and 7). These seawalls have a maximum width of 10 feet at an elevation of 17.5 feet above mean lower low water, and a seaward slope of 1 on 1-1/2 after anticipated settlement. The individual face or cap stones have a minimum weight of 4.5 tons so as to resist an anticipated wave 9.5 feet high. In accordance with then current design practices, the core of the seawalls consisted of quarry run stone from 10 to 1,000 pounds with 50 percent greater than 500 pounds. A stone filter blanket was placed prior to placement of larger stone when the thickness of the sand layer at the seaward toe of the seawalls exceeded one foot. The design was predicated on the premise that the (Federal) project could only protect the bluffs from that component of the erosion caused by direct wave action, and that erosion caused by other causes (i.e., surface runoff, wave splash erosion due to geologic causes, etc.) could not be a part



Figure 6 - Seawall during Construction (April 1962)



Figure 7 - Seawall Construction (May 1961)

of the Federal project. Erosion due to causes other than waves, currents and tides would thus be a non-Federal responsibility and were not included in these designs.

Because of funding considerations, the City of Santa Cruz chose to construct the shore protection improvements in stages over a three-year period. Stage one, accomplished in 1961, consisted of the construction of thirteen small units or sections totaling 1,950 feet in length. Stage two was completed in 1962 and consisted of seven units of a total length of 1,050 feet. Stage three was completed in 1964 and consisted of three sections aggregating 1,150 feet in length, a total of 4,150 feet.

RECENT OBSERVATIONS

An inspection of these rubble mound seawalls and revetments in early 1988 indicated that over ninety percent of them are in a very serviceable or nearly as-built condition (Figures 8 and 9). Damage or potential damage to the remaining five to ten percent appears to be caused by the following: (1) erosion and/or collapse of the bluff material landward of the seawalls with subsequent loss of backing or support which allowed rubble to be displaced; (2) erosion of the bluffs at the terminal ends of the seawall, allowing lateral movement, loss of core material, and subsequent damage; (3) erosion of material under the toe or foundation and subsequent settlement of wall (for relatively small displacements of the toe, remedial action of placing relatively minor quantities of additional armor stone appeared satisfactory); and (4) inadequate design wave height, related to difficulties in determining wave



Figure 8 - Seawall near Santa Cruz (May 1988)



Figure 9 - Seawall near Capitola (May 1988)

heights at the structure due to highly irregular bathymetry and topography immediately offshore.

The large majority of the Santa Cruz West Cliff seawalls were built as single armor layer revetments. Single armor layer structures have very little tolerance to any shifting or movement of the armor cover. The cover is not a "flexible" layer in the same manner as a multi-layer armor cover. Minor movement of the armor layer as the structure settles is not fatal in a two-layer armor where the shifting units can fall into the structure to heal gaps and still provide cover to the underlayer. With single layer construction any shifting or settling of the armor (even if there is no initial unit loss) may expose the underlayer to erosion.

Three distinctive modes of failure or structure unraveling were noted in those West Cliff sections where damage was observed. Even though the foundation material is bedrock, it is susceptible to erosion.

Flanking of the individual revetment sections can occur if the adjacent bluff continues to retreat; in these cases, the armor may slide toward the unsupported flank, exposing the core; minor losses of core material cause additional shifting of the armor layer and the revetment continues to unravel until enough of the crest armor collapses down to form a multiple layer flank which effectively seals off the core from wave action.

The toe of the seawall may not in all cases have been keyed down to the bedrock. Some of the revetments are built at the back of coves where a local pocket beach covers the bedrock with a thin veneer of sand; erosion of the pocket beach or possibly even some abrasion and scour of the bedrock may undermine the toe, causing stone to shift. In a multiple layer revetment, damage caused by the down-slope migration of the toe stone is usually minimized as an upper layer unit collapses into the lower layer. This may cause an apparent steepening of the toe but shifted units will often seal the cover without exposing underlayer further up slope. The multiple layer cover heals itself as it collapses. Not so with a single layer cover, where the displaced toe exposes the core and the downward migration of the cover continues without healing. Units can only migrate down slope by sliding on the core until there is enough loss of core to allow collapsing. In these cases, the revetment is reduced to a pile of armor which has collapsed into the void left as the core was eroded.

Erosion of the back bluff was observed in several cases. Runup and overtopping of the revetment or surface water runoff may have caused further retreat of the bluff behind the revetment and loss of support to the structure. Backward sliding crest stones again exposed the underlayer or core resulting in an unraveling of the structure from the top down. Sections exhibiting this type of

damage usually experienced only minor loss of the structure's integrity unless the retreat of the supporting bluff was significant.

Although several design limitations with single layer armor construction could be identified at this site, the satisfactory performance exhibited by most of the sections illustrates the acceptability of single layer construction in certain geologic settings. Single layer construction can be used in areas of a stable foundation where bedrock or erosion-resistant soil limits toe scour or retreat of the back support. However, if this shore protection system were to be designed and built today, advances in design standards and the information gathered from years of observation would lead to some differences in approach. These would include a more comprehensive investigation of foundation conditions, erosion rates, and the effects of extreme water levels and storm conditions. A formal operation and maintenance plan would also be prepared and implemented. And, double-layer construction with a filter fabric backing would probably be selected as the final design.

ACKNOWLEDGEMENTS

The authors gratefully acknowledge the cooperation of the City of Santa Cruz, the County of Santa Cruz, the State of California, and the U.S. Army Corps of Engineers in providing records of the original design and construction. The assistance of Jon A. Rosso of Treadwell & Associates during the final preparation of the paper is also appreciated.

SELECTED BIBLIOGRAPHY

- Bradley, W. G. and G. B. Griggs, 1976, Form, genesis, and deformation of central California wave cut platforms: *Bulletin Geological Society of America*, v. 87, p. 433-449.
- Dormurat, G., 1978, "Selected Coastal Storm Damage in California, Winter of 1977, 1978," *Shore and Beach* 46 (No. 3, July):15-20.
- Fitzgerald, D. M., D. Sullivan and A. D. Magee, 1981, "Effects of rip rap on onshore-offshore sediment transport," *Shore and Beach*, v. 49, No. 4, p 19.
- Griggs, G. B. and R. E. Johnson, 1976, Effects of the Santa Cruz Harbor on coastal processes of northern Monterey Bay; *Environmental Geology*, v. 1, p. 299-312.
- Griggs, G. B., and R. E. Johnson, 1979, "Coastal Erosion, Santa Cruz County," *California Geology* 32 (No. 4, April):67-76.
- Griggs, G. B. and R. E. Johnson, 1983. "Impact of 1983 storms on the coastline of northern Monterey Bay." *California Geology* v. 36, No. 8:163-174.

- Kuhn, C. G., and F. P. Shepard, 1981, "Should Southern California Build Defenses Against Violent Storms Resulting in Lowland Flooding as Discovered in Records of Past Century," Shore and Beach 49 (No. 4, October):3-11.
- Moffat and Nichol, Engineers, 1983. Construction materials for coastal structures. U. S. Army Corps of Engineers Coastal Engineering Research Center Special Rept. No. 10.
- National Marine Consultants, 1970, Wave statistics for seven deep water stations along the California coast: Report prepared for the U.S. Army Corps of Engineers, Los Angeles and San Francisco Districts, 20 p.
- Smith, A. W. and D. M. Chapman, 1982. The behavior of prototype boulder walls. Proc. ASCE 18th Coastal Engineering Conf. (Capetown) V.III:1914-1928.
- U. S. Army Corps of Engineers, 1956. Beach erosion control report on the cooperative study of the Santa Cruz Area, Serial No. 25, San Francisco, CA Jan. 20, 1956.
- U. S. Army Corps of Engineers, 1977, Coastal Engineering Research Center, Shore Protection Manual V.1 and 2, Third Edition.
- U. S. Army Corps of Engineers, 1983, Coastal Storm Damages: 1983, U. S. Army Corps of Engineers, Los Angeles District.
- U. S. Army Corps of Engineers and Dames and Moore, 1971, National shoreline study - California regional inventory, South Pacific Division, San Francisco, 103 p.

CHAPTER 183

DYNAMIC STUDIES ON CAISSON-TYPE BREAKWATERS

Gao Ming* Dai Guanying* Yang Jihua**

Abstract

In this paper, studies on dynamic characteristics and responses under waves of caisson-type breakwaters by field and model testings as well as dynamic analyses are described. It is found that the gravity-type structure-foundation system can be simplified as a rigid body on a linear or non-linear elastic foundation for evaluating its dynamic characteristics and responses. The dynamic displacements of the caisson are found related to the wave heights, the water depth as well as the foundation soil properties.

Introduction

Along with the increase of the ship tonnage, the construction of breakwaters, either for the development of a new port or for the extension of the existing port requires that the structures are to be built in deeper coastal areas, and these breakwaters are being subjected to severer wave actions. A problem is raised as to the dynamic behaviours of the breakwaters under the tough environmental conditions. Based on such needs, we performed a series of studies on the dynamic characteristics and responses under waves through field testing, model testing and numerical analyses for the caisson-type breakwater, either rectangular or cylindrical. This paper presents these investigations, mainly the test results and the comparison between the test results and the analytical results with different methods of analysis. (Gao et al 1988, Dai et al 1985,1987)

* Senior engineer, Nanjing Hydraulic Research Institute, Nanjing, China

** Engineer, Nanjing Hydraulic Research Institute, Nanjing, China

Field Test of the Rectangular-Caisson

The field testing site was chosen at a newly built port located in the southern part of Shandong province of China. The breakwater is one for composite use, i.e. with its inner side for ship berthing. Figure 1 shows the plane view and the profile of the breakwater. The rectangular caisson has a weight of 13,000t with a deck and a 2.1m high exterior parapet wall.

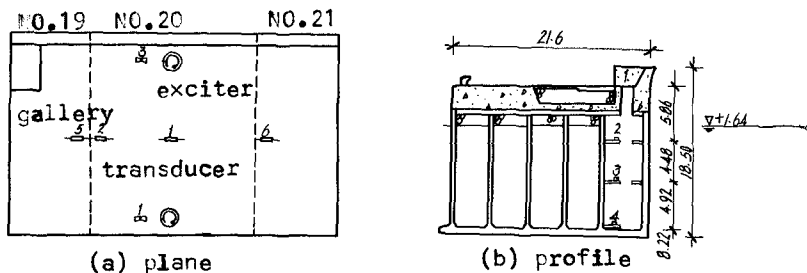


Fig. 1 Test Caisson

Two mechanical-type exciters of 6t capacity, with frequency range of 0-30Hz and frequency resolution of 0.01Hz, were adopted to excite the caisson. The exciters were placed on the top of the No.20 caisson, and the displacement transducers were fixed on the top surface of the three caissons and on the vertical gallery of the No. 19 caisson. The test results are listed in Table 1, and the mode shapes and amplitude-frequency curve are shown in Figure 2.

Table 1 Test results

Meas. pt. No.	Caisson No.	First order			2nd order	
		freq.(Hz)	phase	damp.	freq.(Hz)	phase
1	20	3.8	Ref.	.0579	8.01	Ref.pt.
2	20	3.8	same	.0592	8.48	same
3	19	3.8	same	.0329	8.48	same
4	21	3.8	same	.0619	8.48	same

From the tests, it shows that:

- Under the exciting force of 10-12KN, the three caissons have the same 1st and 2nd order natural frequencies and nearly the same values of damping ratio. It illustrates that due to the surface deck connection, the breakwater caissons vibrate simultaneously with good integrity.
- From the vibration modes measured, it illustrates that the vibration is coupled, with lateral vibration as the primary and rocking as secondary for the fundamental mode

and rocking as primary and lateral vibration secondary for the 2nd order mode.

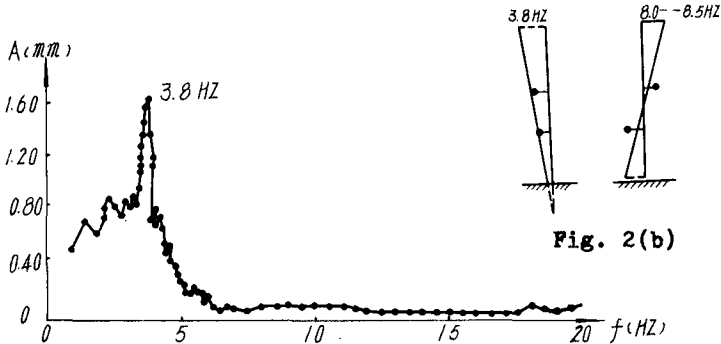


Fig.2(a) Resonance curve of pier caisson

It means that the vibration of caisson-type structure can be regarded as the vibration of a rigid body on elastic foundation, linear or nonlinear, for evaluating its dynamic characteristics and dynamic responses.

Using corresponding equations of vibration, it is feasible and easy to determine the compression and lateral coefficients of the subgrade by measuring the fundamental frequencies of the structure undergoing vertical or horizontal-rocking vibration and then to determine the bearing capacity of the subgrade.

Model Tests of the Rectangular-Caisson

The model tests were performed on a similar regular caisson-type composite breakwater at a model scale of 1 to 87. The model was not simulated exactly to the above existing structure but was for a new caisson-type breakwater in design stage. Plexiglass and weighted rubber were used as modelling materials for caisson structure and subgrade foundation. A portion of foundation, with a depth nearly equal to the height of the caisson and a width equal nearly to 3 times the width of the caisson was included in the model.

The models were tested for various restraint conditions. Table 2 shows the influence of the different foundation conditions of restraint and sizes on the natural frequency of caisson. The results given are in prototype scale.

Table 2

Foundation size M^3	Restraint condition of the foundation	Nat. freq. (Hz)	
		1st	2nd
71.3*62.3*26.1	Restricted on four side	1.18	1.85
71.3*62.3*26.1	Non-restraint	1.06	1.93
71.3*44.0*26.1	Non-restraint	0.93	2.02

Shown in Fig. 3 is the resonance curve and mode shapes of the rectangular caisson from model tests.

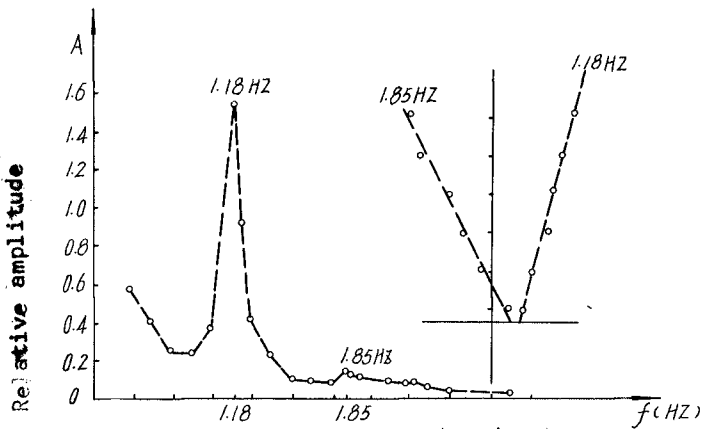


Fig. 3 Resonance curve and mode shapes

Tests for Different Water Levels

The model was tested for different water levels to investigate the added mass coefficient. Fig. 4 shows the response-frequency curves with various water levels. The natural frequency of the system lowers with the rise of water level. At the checking high water level the fundamental natural frequency lowered down about 9%. From this it can be estimated that the added mass coefficient of the water for the tested

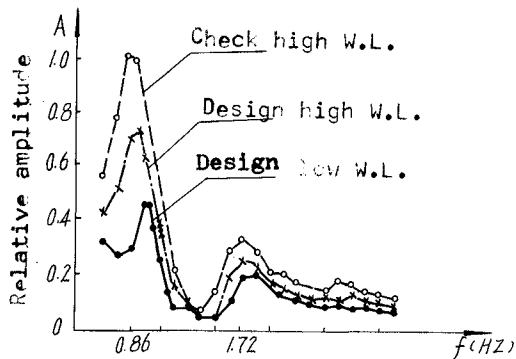


Fig. 4 Resonance curve for various water levels

caisson is around 0.6, about the same as that recommended by Dr. Hallam (Hallam 1977).

Table 3

Water level	Nat. Freq. (Hz)		Damping ratio	
	1st	2nd	1st	2nd
Without water	1.06	1.93	0.024-0.038	0.024-0.065
Design low w.l.	1.01	1.82	0.08	0.084
Design high w.l.	0.94	1.72	0.134	0.091
Check high w.l.	0.86	1.72	0.163	0.094

Dynamic Responses under Waves

The model with foundation was placed in a wave basin to test the dynamic responses under regular waves of various wave heights and wave periods with three different water levels. From these test results, it can be seen that the dynamic displacements increase with the increase of wave height as well as to water depth, the dynamic displacement is also increasing with the increase of wave period in general. The uplift forces measured show an evident linear relationship with wave heights.

Field Dynamic Experimental Studies on Cylindrical Caisson-type Breakwater

Field dynamic measurements were also carried out on cylindrical caisson of an island breakwater in the same port mentioned above. The caissons were 14m in diameter, 13.5m in height and connected together with a block at the top. Each caisson weighs 5000t. The same exciters as aforementioned were used, and the method of ambient vibration was also adopted for excitation. Fig. 5 shows the frequency-amplitude curve and the power spectra curve. The main results are listed in Table 4.

Table 4

Caisson No.	Ambient test freq. (Hz)		Reson. test freq. (Hz)	
	with cap	no cap	with cap	damping ratio
15	1.95		1.90	0.047-0.071
16	1.95			
40		2.18	2.20	0.032-0.075
41		2.18		

In order to determine the vertical dynamic characteristics, the caisson was also tested by the method of applying shock load vertically and the fundamental natural frequency for vertical vibration measured is 4.3-5 Hz..

Model Tests for Cylindrical Caisson-Type Breakwater

A model made of plexiglass for a cylindrical caisson of 14m in diameter and 26.5m in height was tested for a

practical pier design at a scale of 1 to 30, also with a portion of foundation included. The foundation is simulated to different compression stiffness. The model is tested

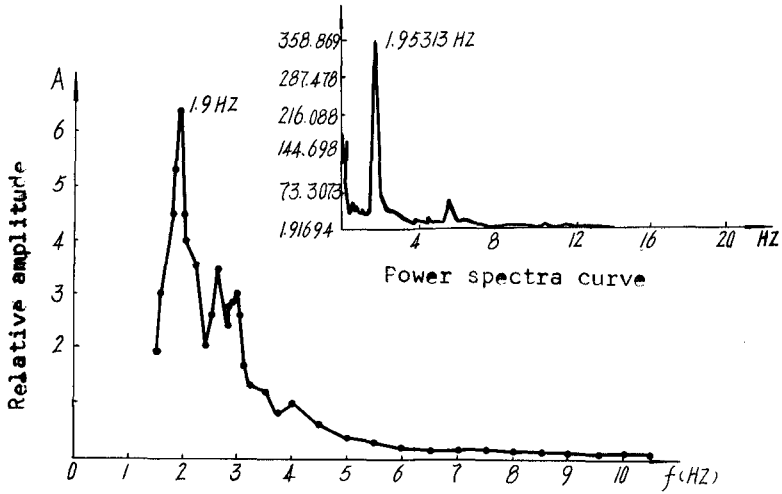


Fig. 5 Frequency-amplitude curve

in air by an actuator as well as by the method of hammering. The tested frequency-amplitude curve and the response spectrum, transfer function and coherence coefficient are shown in Figs. 6 and 7.

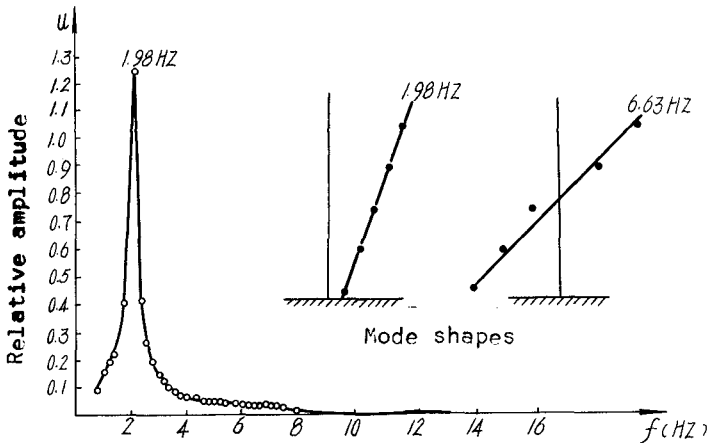


Fig.6 Frequency-amplitude curve

It agrees well with the results obtained from the field tests.

The model was then placed in a wave basin to test its responses under regular and irregular waves in different water depths. The irregular wave spectra used are the Pierson-Moskowitz spectrum and the local spectrum evaluated by Nanjing Hydraulic Research Institute. The input wave height spectrum as well as response spectrum are shown in Figs. 8(a), (b). Fig. 8(c) is the displacement response spectrum. The displacement of the caisson top versus wave height are plotted in Fig. 9 by solid line for various water depths and wave periods. The Tested results show that the displacement of the caisson is in nearly linear relation to the wave height and are much smaller than those for rectangular-caisson under the same wave condition. In Fig. 9 it also shows in dotted lines the calculated values of the responses without taking into account the dynamic effect. It can therefore illustrate that the dynamic effect can be neg-

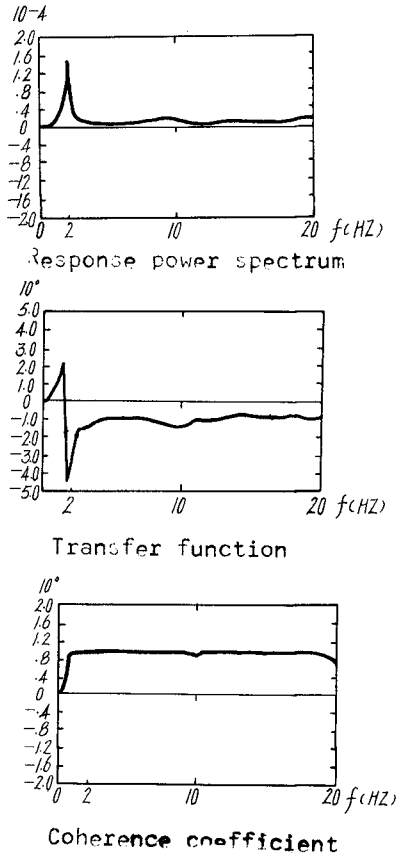


Fig. 7

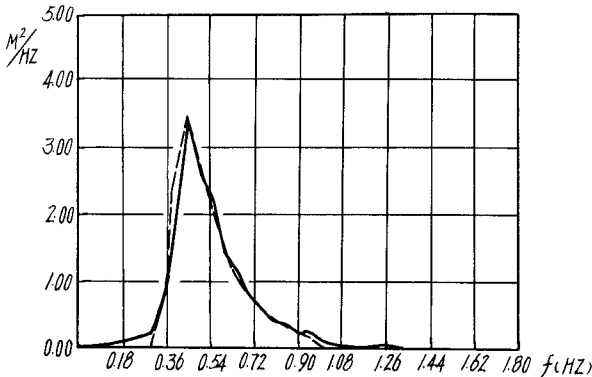


Fig. 8(a) Local wave spectrum

lected under ordinary wave condition.

Dynamic Analysis

The dynamic analysis for the caisson-type breakwater has been carried out. Two methods are adopted in the analysis; (1) The method of concentrated parameters; The system can be simplified as a 3 degree-of freedom rigid body

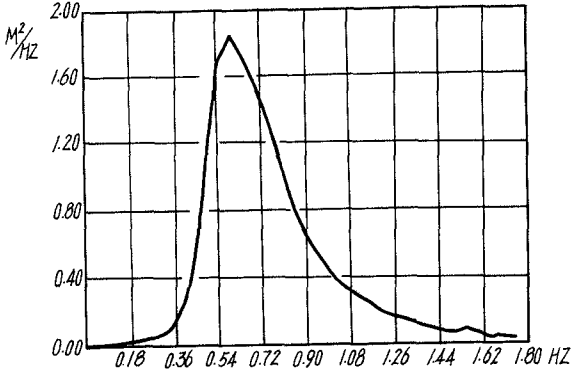


Fig.8(b) P-M wave spectrum

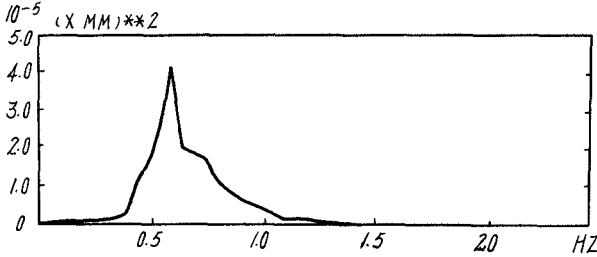


Fig.8(c) Displacement response spectrum

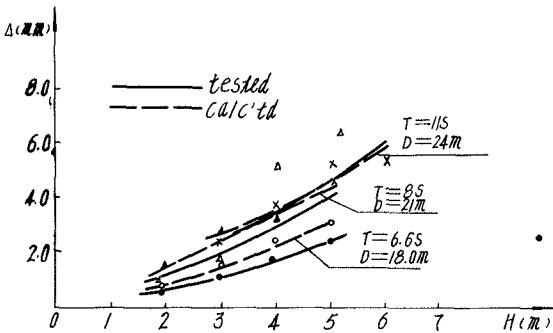


Fig. 9 Displacement versus wave height

on elastic foundation, treated as a series of vertical and lateral springs, with lateral, vertical and rocking spring constants denoted by C_x , C_z and C_ϕ respectively, as shown in Figure 10; (2) The finite element method; For the rectangular caisson, together with the foundation included, the system can be treated as a 2-dimensional problem. The calculated results for natural frequency are given in Table 5, and the test results are also listed for comparison. It can be seen from Table 5, that good agreements are reached by applying these methods.

In the finite element the dynamic responses of the rectangular caisson under different wave heights are evaluated, using the wave pressure formula recommended by Miche-Biesel and the results are shown in Table 6. It shows that, while the wave height ranges between 7 to 8m, the test results are also listed for comparison, and it can be found that the agreement is satisfactory.

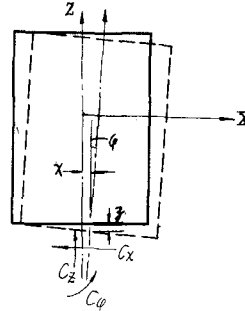


Fig. 10

Table 5

Caisson Type	Cz value of foundation (KN/M ³)	1st Nat. Freq. (Hz)			2nd Nat. Freq. (Hz)		
		Test	CPM	FEM	Test	CPM	FEM
Rect.	5,150	0.98-	0.95	1.07	1.83-	2.81	2.31
	68,000	1.06			1.93		
	102,000						
Cylind.	76,820	1.92	1.91		6.66	6.85	
	71,280	1.83	1.81			6.50	
	46,530	1.44	1.46			5.25	

C_z - the vertical compressive coefficient of the subgrade.

Table 6

D/H 0.766

Wave period height (s) (m)	8.0		10.0		12.0		14.0	
	test	cal.	test	cal.	test	cal.	test	cal.
6.86	3.05	2.96	3.48	3.65	5.22	4.18	6.00	4.70
7.76	3.57	3.39	3.74	4.34	5.48	4.96	6.79	5.66

D - water depth, Hc - height of caisson.

Concluding Remarks

Through the field testing, the model testing and the dynamic analysis using different methods, a quite thorough investigation of the problem of caisson-type breakwater has been made on its dynamic characteristics and dynamic responses to waves, and the following can be concluded:

1. The caisson-type breakwater, either rectangular or cylindrical, can be regarded as a system of rigid body on linear or nonlinear elastic foundation for evaluating its dynamic characteristics and dynamic responses.

2. The foundation stiffness has a great effect on the dynamic characteristics and responses, and any weak soft layer underlain should better be dredged out.

3. Under strong waves, the top displacement responses of the rectangular caisson will be much larger than those of the cylindrical caisson.

4. In general, the dynamic magnification factor under waves is very close to 1, and therefore, in the calculation of the stability of the caisson, it can be treated as a static problem.

References

1. Dai, G. Y. et al, 'The Dynamic Characteristics and Dynamic Responses of Gravity-type Caisson Port Structures', Jr. Nanjing Hydraulic Res. Inst., 1985, No.4 (in China)
2. Dai, G. Y. et al, 'Full Scale Dynamic Testing of Caisson Type Gravity Harbor Structures and the Determination of Load-bearing Capacity of the Foundation', Proc. of Symposium on Structural Assessment Based on Full and Large Scale Testing, Apr. 1987, London, U. K.
3. Gao, M., et al, 'The Dynamic Investigations and Aseismic Studies on Gravity-type Port Structures', 'Waterway Transportation Engineering', 1988 No. 2 (in China)
4. Hallam, M. G, et al, 'Dynamics of Marine Structures', CIRIA Underwater Engrg. Group, 1977

CHAPTER 184

Wave Forces on Armor Blocks

by

M.A. Losada*, R. Medina* and M. Alejo**

ABSTRACT

Experimental measurements of hydrodynamic forces on a cubic block near the bottom under solitary waves were carried out. Horizontal and vertical forces were recorded and instantaneous and averaged values of hydrodynamic coefficients C_D , C_M and C_L for different boundary conditions, gap between block and bottom, e , and two or three-dimensional flow, were obtained. Horizontal and vertical forces were found to depend strongly on e/D , where D is the block side. Instantaneous values of hydrodynamic coefficients vary considerably during the wave passage and differ appreciably from the averaged coefficients.

* Universidad de Cantabria. Spain.

** Universidad Politécnica de Las Palmas. Spain.

INTRODUCTION

In the last decades great efforts have been done to understand the causes of failure of sloped breakwaters with special attention to the "lift-out" of armor units from the slope by the uprush-downrush flow. Most of the research work has been oriented to evaluate the flow conditions on the slope. Minor contributions have been made in the analysis of pressure distribution around the block or resultant forces on the block. Recently Kobayashi et al., 1985, studied the stability conditions against sliding and lifting of rip-rap, expressing drag, inertia and lift forces in function of drag, C_D , inertia, C_M and lift, C_L , coefficients. This analysis similar to others presented in the past is a force equilibrium, based on Morison's equation.

The lift-out of armors (particularly in the case of cubes) generally starts with a rotation around a point or axle as experimentally may be checked. The moment equilibrium equation for an armor unit neglecting reactions by friction or interlocking and considering the flow forces applied in the gravity center of the block, can be expressed as follows:

$$W_a = \frac{1}{2} \int_w C_D D^2 u^2 \left[\left(1 + 2 \frac{C_M}{C_D} D \frac{du/dt}{u^2} + \frac{C_L}{C_D} \right) \right] \quad (1)$$

where W_a is the armor weight and u and du/dt the flow velocity and flow acceleration respectively.

Thus, if the flow characteristics (u and du/dt) and the hydrodynamic coefficients, C_D , C_M and C_L are known, the behavior of an isolated block under waves may be predicted. Kobayashi et al., 1985, used a similar equation in their rip-rap stability prediction, and adopted constant values of the hydrodynamic coefficients for all the wave cycle.

To study the evolution of the forces and the values of the hydrodynamic coefficients under a wave cycle a set of experiments in a wave flume were run. In the following, a general description of the experimental work and of the test results is given. It is clearly shown that boundary conditions strongly affect the evolution of forces on the block and that the values of the hydrodynamic coefficients vary considerably during the wave cycle.

EXPERIMENTAL WORK

The hydrodynamic behavior of isolated cubic units under wave action was analyzed. Smooth cubic blocks with side length, $D = 5$ cm, were subjected to the action of

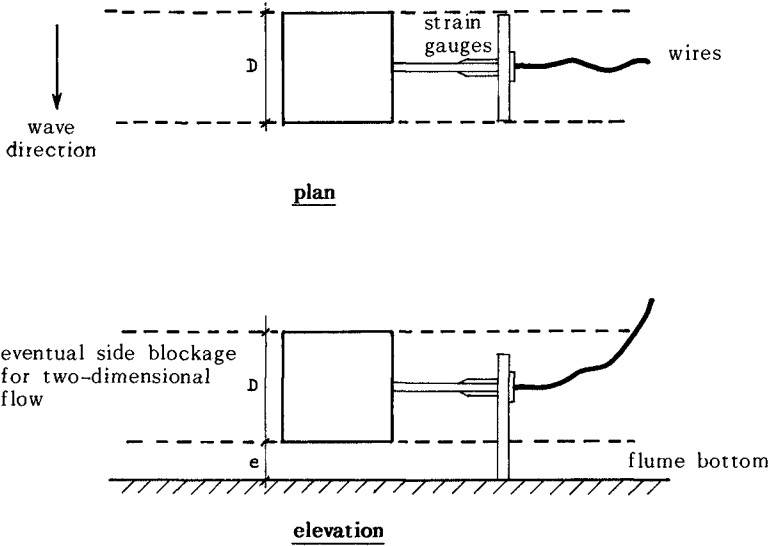


Fig. 1.- FORCE MEASURING DEVICE

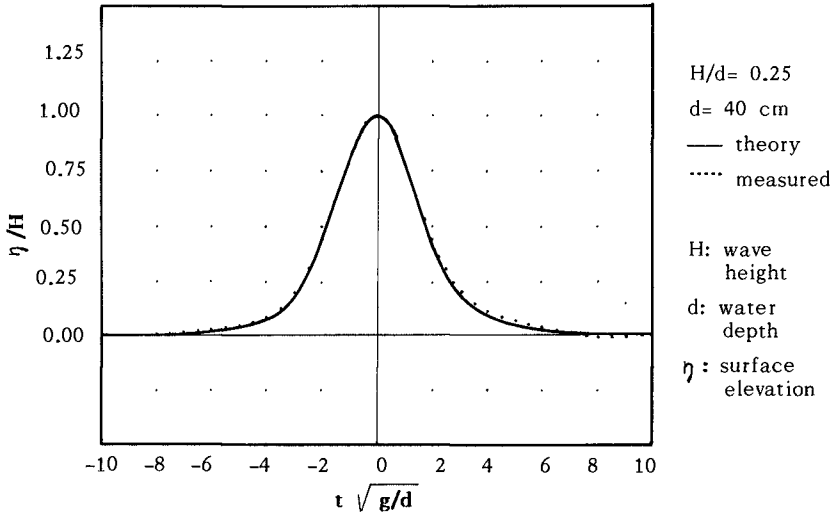


Fig. 2.- SOLITARY WAVE

solitary waves for the following conditions

$$e/D = \text{approx. } 0.0, 0.02, 0.1, 0.2 \text{ and } 0.4$$

where e = gap between cube and bottom (see fig. 1). Due to the force measuring technique the case of block resting on the flume bottom was not sealed. Some pressure transmission under the block might have occurred, "therefore" the indication approx. 0.0.

The type of waves considered were solitary waves (fig. 2). The distance of the test section to the paddle was approximately 45 m and the wave height varied in the range $2 < H(\text{cm}) < 20$, thus $10^3 < Re < 10^5$, where $Re = uD/\mu$ is a Reynolds number, μ = dynamic viscosity. The flow velocity was not recorded during the tests.

The cubes were placed horizontally and parallel to the main axes of the flume (fig. 1). Different test conditions were used, varying e , and establishing two or three-dimensional flow by incorporating the cubic block as a section of a square prism or not.

In all cases, cube size and gap were small when compared with water depth, in order to neglect the influence of the free water surface, and to allow the consideration of horizontal flow velocity.

Measurements of horizontal and vertical forces were made with pairs of strain gauges (see fig. 1). Maximum deviation expected in vertical and in horizontal force measurements is about seven per cent.

THREE-DIMENSIONAL FLOW UNDER SOLITARY WAVES

Figures 3, 4 and 5 show horizontal and vertical measured forces under a solitary wave for three cases: $e/D \approx 0, 0.1$ and 0.4 respectively. The most relevant characteristics are:

(1) The horizontal forces attain their maxima under the wave crest and take negative values (opposite to that of wave motion) associated to flow deceleration.

(2) Vertical forces are negative first (down to the bottom) and then positive for $e/D \neq 0$.

(3) For $e/D \approx 0$ vertical forces are always positive, showing two or more peaks. The first one is commonly much higher.

(4) For $e/D \geq 0.4$ the influence of the gap (indicated by the vertical force variation and magnitude) may be neglected.

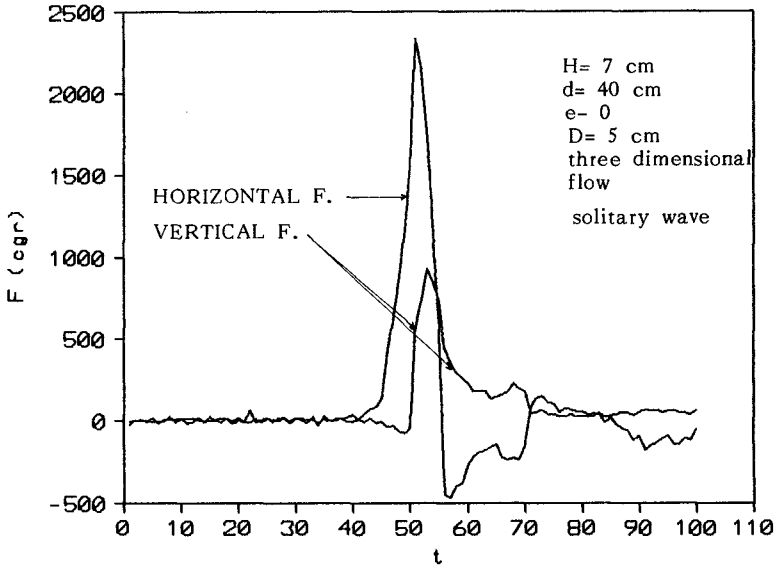


Fig. 3.- HORIZONTAL AND VERTICAL FORCES
 $e/D=0$. Free cube.

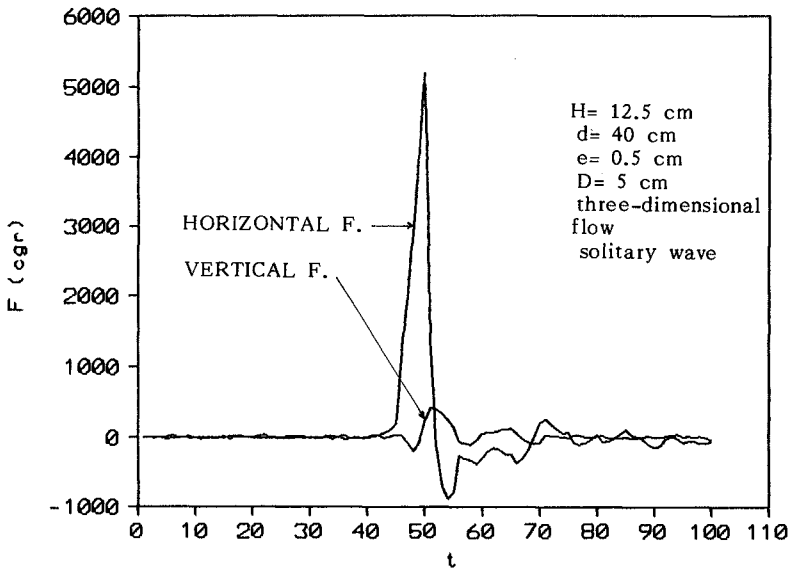


Fig. 4.- HORIZONTAL AND VERTICAL FORCES
 $e/D=0.1$. Free cube.

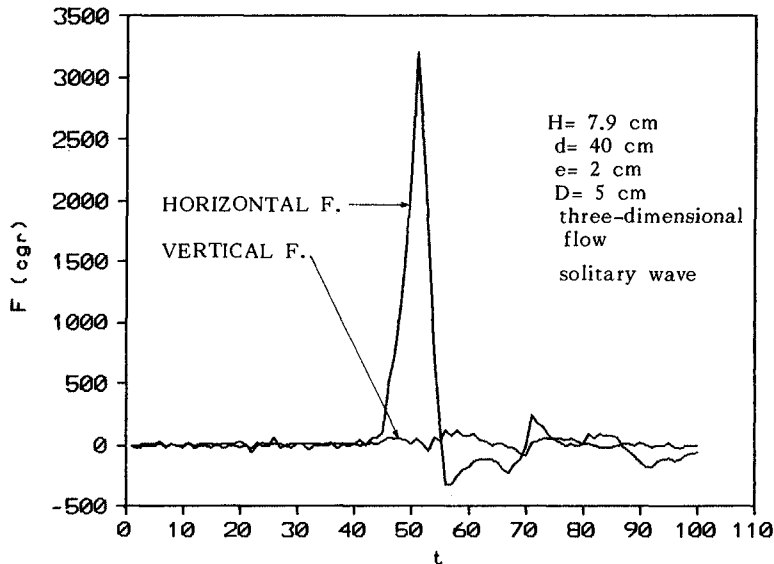


Fig. 5.- HORIZONTAL AND VERTICAL FORCES
 $e/D = 0.4$. Free cube.

TWO-DIMENSIONAL FLOW UNDER SOLITARY WAVES

Figures 6 and 7 show horizontal and vertical measured forces under a solitary wave for $e/D = 0.1$ and 0.4 respectively. The most relevant characteristics are:

(1) Maximum vertical and horizontal forces are almost in phase.

(2) Vertical forces are always larger than for three dimensional flow and present two or more peaks.

INSTANTANEOUS AND AVERAGED VALUES OF C_D , C_M AND C_L

Following Sarpkaya and Isaacson, 1981, from the measured horizontal forces the instantaneous values of C_D and C_M were obtained, solving from a set of Morison-type equations at two consecutive instants assuming that C_D and C_M remain constant in the time interval. Figure 8 shows C_D and C_M with the wave passage for $e/D = 0.1$. Several observations can be made, which agree with those given by Sarpkaya and Isaacson, 1981, for cylinders

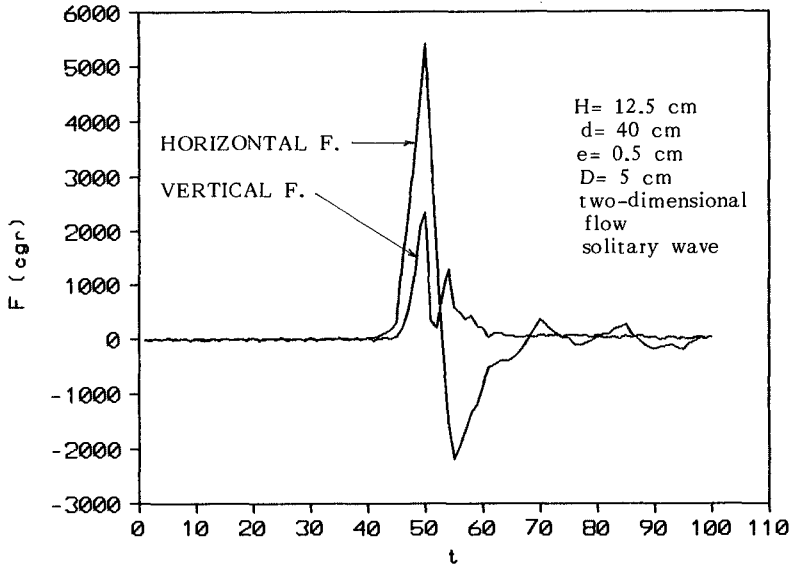


Fig. 6.- FORCES FOR TWO-DIMENSIONAL FLOW $e/D= 0.1$. Cube as a part of a prism.

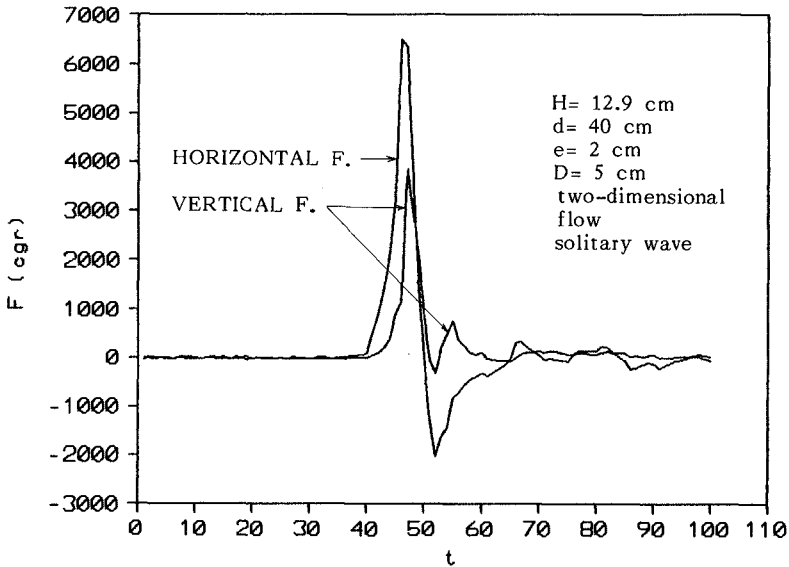


Fig. 7.- FORCES FOR TWO-DIMENSIONAL FLOW $e/D= 0.4$. Cube as a part of a prism.

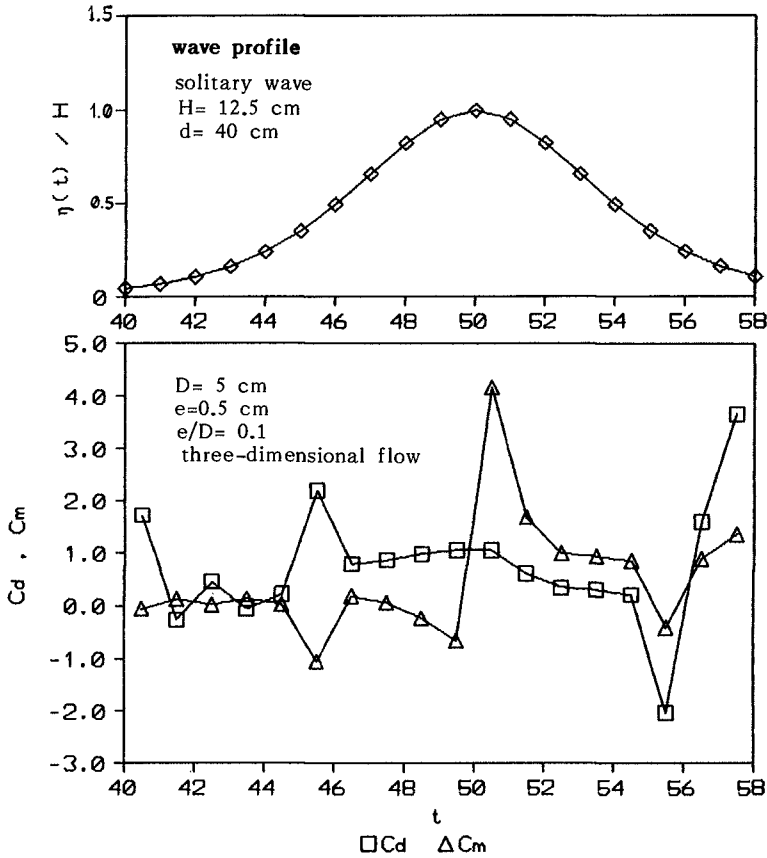


Fig. 8.- INSTANTANEOUS COEFFICIENTS Cd AND Cm

under oscillatory flows.

(1) The averaged C_M is less than unity and the added mass coefficient, C_A , is then negative, as $C_A = C_M - 1$.

(2) Neither C_M , C_D nor C_L are symmetrical with respect to the wave crest, showing a difference between accelerated and decelerated flow.

(3) C_M , C_D and C_L exhibit relative large variations during the wave passage.

From test results average hydrodynamic coefficients C_D , C_M and C_L were obtained. The average values of C_D , C_M and C_L were obtained through the use of the method of least squares by minimizing the square error between the measured and calculated forces. For a solitary wave 12.5 cm high, $e/D = 0.5$ and three-dimensional flow, the following values were calculated:

$$C_D = 0.65 \qquad C_M = 0.87 \qquad C_L = 4.7 \cdot 10^{-2}$$

When comparing these values with the instantaneous ones shown in fig. 8 it can be concluded that the former differs considerably from the latter.

CONCLUSIONS

In the present study an experimental investigation on wave forces exerted on an isolated armor unit was conducted. The experimental results lead to the following conclusions.

(1) The behavior of the instantaneous horizontal and vertical forces under solitary waves depend on e/D ratio, the relative distance from the block to the bottom. For $e/D \neq 0$ both the horizontal and vertical forces present a positive and a negative peak. For $e/D \approx 0$ the vertical force is always positive.

(2) The maximum positive forces for $e/D \neq 0$ and three-dimensional flow are out of phase. For $e/D \approx 0$ both forces are in phase, as well as for two-dimensional flows.

(3) The instantaneous hydrodynamic coefficients C_D , C_M and C_L vary considerably during the wave passage and differ appreciably from the averaged coefficients.

ACKNOWLEDGEMENTS

This research has been partially supported by the Comisión Asesora Científica y Técnica, project n° PA85-0176 and partially by the Dirección General de Puertos y Costas, M.O.P.U.

REFERENCES

Kobayashi, N. and B.K. Jacobs. Rip-rap stability under wave action. The Journal of Waterways, Port, Coastal and Ocean Engrg., ASCE, Vol. 111, No. 3, pp. 552-566.

Sarpkaya, T. and Isaacson, M., 1981. Mechanics of wave forces on offshore structures. Van Nostrand Reinhold Co., pp. 651.

CHAPTER 185

Hydrodynamic Characteristics of Wave-power-extracting Caisson Breakwater

Shigeo Takahashi*

ABSTRACT

The wave power extracting caisson breakwater can convert the wave energy into usable energy. The function and the stability of the caisson as a breakwater are investigated experimentally. It is found that wave reflection and wave transmission of the breakwater are relatively small and that the stability of the breakwater caisson against storm waves is high. The design method of the caisson is proposed considering the impact air pressure in the air chamber.

1. INTRODUCTION

Perforated wall caissons are increasingly adopted as the structures of seawalls and breakwaters since Jarlan (1961) invented the perforated wall caisson. This is because the perforated wall caissons have low wave reflection and overtopping characteristics, and is highly stable due to their wave absorbing capability. The wave power extracting caisson breakwater such as the one illustrated in Fig.1 is a kind of the perforated wall caisson because it can absorb the wave energy. However the wave power extracting caisson can actually convert the wave energy into usable energy. The converted energy can be used for many purpose in the sea and in the land near the breakwater.

This breakwater is consisted of the wave power extracting caisson on a rubble foundation. The caisson has an air chamber which is attached to the ordinary caisson. The waves enter into the air chamber from the opening under the front curtain wall, and cause the vertical oscillation of the water surface in the air chamber. Then the air in the upper half of the air chamber is



Fig.1 Wave Power Extracting Caisson Breakwater

* Chief of Maritime Structures Lab., Port and Harbor Res. Inst.,
3-1-1, Nagase, Yokosuka, Japan 239

compressed and is expanded. The air motion generates the high-velocity flow through the nozzle which activates the air turbine and generates electricity. Thus the caisson functions as a wave power converter. A combination of the wave power converter and the vertical breakwater is attractive from the viewpoint of economical feasibility of wave power extraction, because the construction cost can be jointly borne by the accounts for power generation and harbour protection.

The studies on the wave power conversion have been conducted and the design of the caisson as a wave power converter has already been established (Ojima 1984, Takahashi 1986, 1987). In the present paper, the function and the stability of the caisson as a breakwater are investigated.

2. THEORY OF WAVE POWER CONVERSION

The conversion efficiency from wave power to air power in the air chamber is the most important factor not only as a wave power converter but also as a breakwater, because the higher conversion efficiency yields the lower wave reflection and transmission coefficient, and probably yields the higher stability.

The theory of wave power conversion by the wave power extracting caisson was originally given by Ojima et al. (1984) and was extended by Takahashi et al. (1987). The theory was named as **the thermodynamics and wave kinematics method**. The theory comprises two thermodynamics equations in the air chamber and one wave-kinematics equation at the air chamber opening under the curtain wall as follows:

$$\frac{dp^*}{dt} = \gamma \frac{p^* + p_0}{D_0 - \eta} \left\{ \frac{d\eta}{dt} - c_d \varepsilon w_p \right\} \quad (1)$$

$$\frac{dT^*}{dt} = \frac{T^* + T_0}{D_0 - \eta} \left\{ -\frac{d\eta}{dt} + \frac{D_0 - \eta}{p^* + p_0} \frac{dp^*}{dt} + c_d \varepsilon w_p \right\} \quad (2)$$

$$2\eta_t = \frac{1}{\rho_w g} f(kh, kd_c) p^* + \frac{kB}{\tan kB} \eta + \frac{kB}{\sigma} \frac{d\eta}{dt} \frac{1}{\cos \theta_M} \quad (3)$$

The main unknown variables of the equations are

- p^* : oscillating fraction of the air pressure inside the air chamber
- η : oscillating fraction of the water surface elevation
- T^* : oscillating fraction of the air temperature inside the air chamber

The air flow velocity w_p in the air nozzle on the air chamber is defined by

$$w_p = \pm \varphi \sqrt{\frac{2}{\rho_a}} \sqrt{|p^*|} \quad (4)$$

The term $f(kh, kd_c)$ is given by

$$f(kh, kd_c) = \frac{2 \cosh kh \sinh k(h-d_c)}{\cosh k(h-d_c) \sinh k(h-d_c) + k(h-d_c)} \quad (5)$$

The above equations can be solved by step-by-step numerical calculations when the following dimensions and characteristics of the incident waves and the air chamber are given:

- η_I : incident wave profile
- σ : wave angular frequency for the significant wave period
- k : wave number for the significant wave period
- θ_M : instantaneous wave angle
- h : water depth
- B : width of the air chamber
- D_O : height of the air chamber above the still water level
- d_C : submerged depth of the front curtain wall
- A_w : nozzle opening area
- ϵ : nozzle opening ratio ($= A_w/l_B B$)
- l_B : length of air chamber in the breakwater direction
- c_d : contraction coefficient of the nozzle ($= 1.0$ in the calculations)
- φ : nozzle velocity coefficient

The constants in the equations are

- γ : specific heat ratio ($= 1.4$)
- ρ_w : density of water ($= 1030 \text{ kg/m}^3$ in salt water)
- g : gravity acceleration (9.8 m/s^2)
- ρ_a : density of air ($= 1.225 \text{ kg/m}^3$)
- T_a : temperature in open air ($15 \text{ C} = 288 \text{ K}$)
- p_a : pressure in open air ($1 \text{ atm} = 1.013 \times 10^5 \text{ N/m}^2$)

The wave power W_I is converted into air power. The instantaneous air power W_a , the average air power \bar{W}_a and the conversion efficiency \overline{EFF}_a are expressed by

$$W_a = p \cdot w, A_w \quad (6)$$

$$\bar{W}_a = \frac{1}{T_L} \int_0^{T_L} W_a dt \quad (7)$$

$$\overline{EFF}_a = \bar{W}_a / \bar{W}_I, \ell_s \quad (8)$$

where T_L is the time duration of the wave action.

The theory mentioned above describes only the conversion from wave power to air power by the air chamber with an air nozzle. When a turbine and a generator are installed instead of the nozzle an equation of motion of the turbine and generator should be given and the characteristics and dimensions of the nozzle should be replaced by those of the turbine. However only the conversion from wave power to air power is discussed in this paper.

3. EXPERIMENTS

A series of model experiments were conducted in a large wave

- flume. Four caisson breakwaters were tested in the experiments, namely,
- a) Wave power extracting caisson with a sloped front face as in Fig.2(a), (named as the S-type caisson and denoted by WPEC-S),
 - b) Wave power extracting caisson with a vertical front face as in Fig.2(b), (the V-type caisson , WPEC-V),
 - c) Ordinary caisson with a sloped front face, (the sloped front wall caisson, SFWC),
 - d) Ordinary caisson covered with wave dissipating blocks as in Fig.2(c), (the caisson with wave dissipating blocks, SFWC-B).

The S-type caisson was the main caisson in the experiments and the V-type caisson was employed to compare the function and the stability by the difference of the air chamber shape. The V-type caisson was used in the previous studies on the wave power conversion. The S-type caisson was designed to improve the characteristics of the V-type caisson. The two other caissons were also examined to compare the hydrodynamic characteristics with those of the wave power extracting caissons.

The S-type caisson has a width B_c of 135 cm, a crown height h_c of 55 cm, a caisson depth h of 80 cm and an air chamber width B of 35 cm. The front wall is inclined 45 degrees from the point 2.5 cm above the still water level. The armour units for the rubble foundation have a weight of 1.23 kgf each. The foot protection concrete block has a height of 7.5 cm and a width of 22.5 cm. The submerged depth d_c of the curtain wall of the caisson is 20 cm in the figure. The submerged depth was changed to 15 cm and 25 cm by changing the curtain wall plate. The caisson has an air nozzle with a diameter and length of 4.70 cm and 5.7 cm. The opening ratio ϵ of the nozzle to the horizontal area in the air chamber is 0.0075.

The air chamber width of S-type caisson is set at 13 % of the wavelength for $T = 1.34$ s. The air chamber width and the opening ratio are set to have a relatively high conversion efficiency with a small air chamber width. These values are dependent on the wave and other conditions and should be selected considering the whole wave conversion system. The submerged depth of the curtain wall is determined to be about $0.25 H_{max}$. The upper deck of the turbine room is design to be higher than $0.5 H_{max}$. The crown height of the caisson is designed to be $1.0 H_{1/3}$. The values of H_{max} and $H_{1/3}$ used in the design of model caisson are 75 cm and 55 cm. The submerged depth of the curtain wall is set so as not to receive severe impact air pressure. However, if the submerged depth is too large, the wave power conversion efficiency becomes small. The upper deck height of the turbine room is determined so as not to suffer from water intrusion from the nozzle. The crown height is set to be able to reduce the wave transmission as in conventional breakwaters. These values are determined by a preliminary study and should be examined further. Also, these values should be determined considering the entire wave power conversion system.

Six wave gauges (W1 -W6) were used in the experiments to measure the incident and reflected waves (W1 and W2), the water surface elevation in front of the air chamber (W3), the passing wave in the side flume (W4), the water surface elevation in the air chamber (W5),

and the transmitted waves (W6). Six pressure transducers (P1 - P6) were installed in the model caisson to measure the wave and air pressure. The transducers have a diameter of 10 mm and were fixed in the caisson walls. Only one pressure transducer (P1) was fixed in the front wall and five transducers (P2 -P6) were set in the air chamber. Among them transducers P2 and P3 usually measured the pure air pressure, and the others measured the air pressure plus the wave pressure. Ultrasonic displacement meters (D1 - D3) were also installed to measure the displacement of the caisson. These meters were newly developed to measure the displacement up to 1 m with a resolution of 0.1 mm and 100 Hz.

Irregular waves were used in the experiments. The target wave spectrum was the Bretschneider-Mitsuyasu spectrum (Goda 1985) and the target wave periods $T_x^{1/3}$ were 3.35, 2.24, 1.79, 1.57, and 1.34 s. The water depth h was 97.5 cm. Five wave groups A, B, C, D and E were prepared in the experiments for each significant wave period. Each wave group contained more than 450 waves. The relative water depth ranged from 0.10 to 0.356 and the ratio of the air chamber width to the wave length ranged from 0.036 to 0.128.

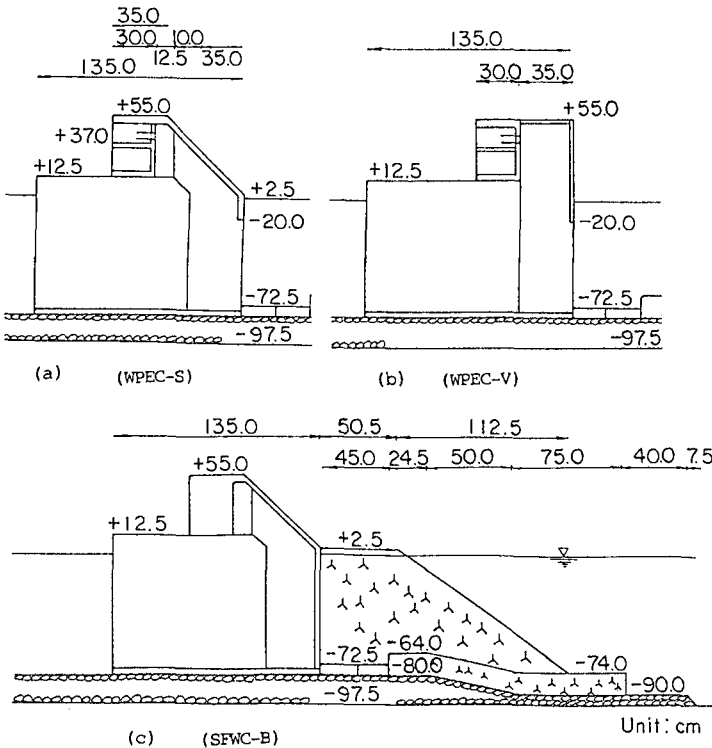


Fig. 2 Cross Sections of Model Caissons

4 FUNCTIONS OF CAISSONS

Conversion Efficiency of the Wave Power Extracting Caissons

The wave power is converted into air power in the air chamber with the nozzle opening ratio set at 0.0075. Figure 3 shows the conversion efficiency of the V-type wave power extracting caisson. The efficiency is from 0.55 to 0.7 where the significant wave height is less than 15 cm. The efficiency is relatively high in this region. The efficiency is lower than 0.5 where the significant wave height is larger than 25 cm, because the wavelength is relatively large and the air leaks from the opening under the curtain wall. The lines in the figure indicate the calculated results. The calculated results agree with the experimental results well.

Figure 4 shows the conversion efficiency for the S-type wave power extracting caisson. The conversion efficiency is changed by the submerged depth of the curtain wall. The efficiency increases with the decrease of the submerged depth clearly where the significant wave height is less than 20 cm. The efficiency of the S-type caisson of $d_c = 20$ cm is around 70 % where the significant wave height is less than 15 cm. The efficiency for the S-type caisson of $d_c = 20$ cm in the figure is larger than that for the V-type caisson in Fig 3.

Reflection Coefficient

Figure 5 shows the experimental results of the reflection coefficient of the S-type caisson together with those of the sloped front wall caisson and the caisson with wave dissipating blocks. The reflection coefficient of the S-type caisson is about 0.45 where the wave height is relatively small. The reflection coefficient is about 0.55 even when the wave height is large. The reflection coefficient of the S-type caisson is much smaller than the sloped front wall caisson, but larger than that of the caisson with wave dissipating blocks.

Wave Transmission and Overtopping

The wave transmission coefficients of the four caissons are compared in Fig. 6. For example, the wave transmission coefficient of the S-type caisson is 0.15 when the significant wave height is about 45 cm. The transmission coefficient of the V-type caisson is 0.13 for the same wave height. The transmission coefficient of the S-type caisson is a little larger than that of the V-type caisson. However, the transmission coefficient of the S-type caisson is lower than that of the sloped front wall caisson and is lower than that of the caisson with wave dissipating blocks. When the wave length and height are large, the waves climb up on the wave dissipating blocks. Therefore, the transmission coefficient of the caisson with the wave dissipating blocks is not less than that of the S-type caisson. The wave transmission in the experiments includes the wave transmission through the gap between the model caisson and the flume walls in addition to the wave transmission through the rubble foundation.

It is said that a sloped front wall caisson needs to have a crown

height of $1.0 H_{1/3}$ to reduce the wave transmission to a level as low as that by an ordinary vertical wall caisson with a crown height of $0.6 H_{1/3}$. The wave transmission of the S-type caisson with the crown height of $1.0 H_{1/3}$ is probably lower than that of the ordinary vertical caisson with the crown height of $0.6 H_{1/3}$. The wave transmission characteristics of the four caissons can be observed also by the wave overtopping rate although the experimental results are not shown here.

Water Surface Elevation

The maximum and the 1/3 highest values of the water surface elevation η^+ in the air chamber of the S-type caisson are plotted in Fig. 7. The maximum and the 1/3 highest values of $\eta^+/H_{1/3}$ increase with the increase of the significant wave period and decrease with the increase of the significant wave height. The maximum value ranges η^+ from 0.6 to $1.0 H_{1/3}$ and is above 37 cm when the significant wave

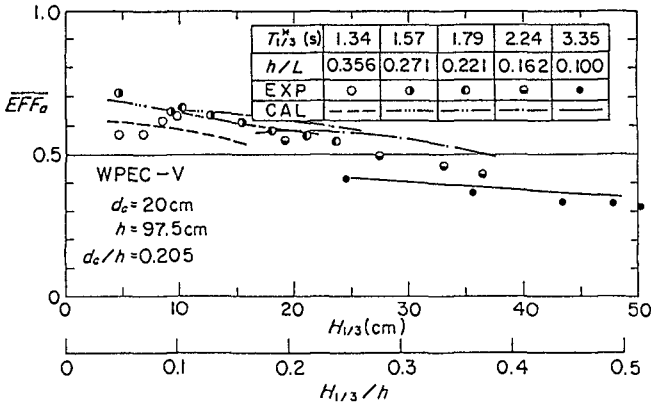


Fig.3 Conversion Efficiency of V-type Caisson

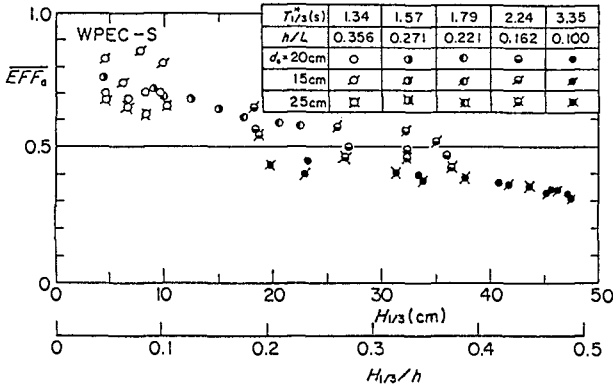


Fig. 4 Conversion Efficiency of S-type Caisson

period is 3.35 s and the significant wave height is larger than 40 cm. The upper deck of the machine room of the caisson is 37 cm above the still water level, which is designed to be $0.5H_{max}$. When the water level goes higher than the upper deck level, the water might intrude into the turbine opening. However, only the waves with a wave height near the maximum wave height can go up above the level and the velocity of the water surface elevation is very small when the water level reaches the upper deck level. It should be noted that the water surface elevation in the air chamber increases with the increase of the nozzle opening ratio.

$T_{1/3}^*$ (s)	1.34	1.57	1.79	2.24	3.35
h/L	0.356	0.271	0.221	0.162	0.100
WPEC	○	●	●	●	●
SFWC	△			△	△
SFWC-B	▽			▽	▽

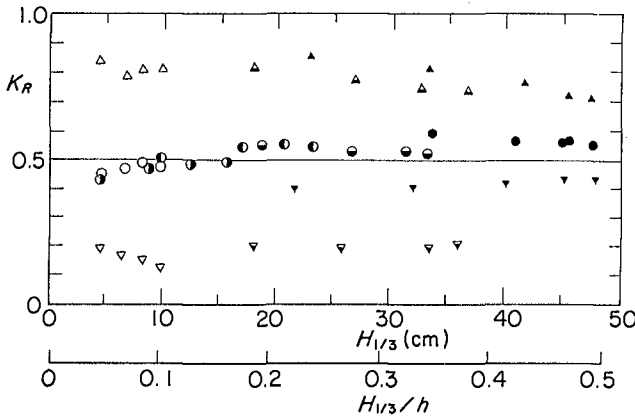


Fig. 5 Wave Reflection Coefficients

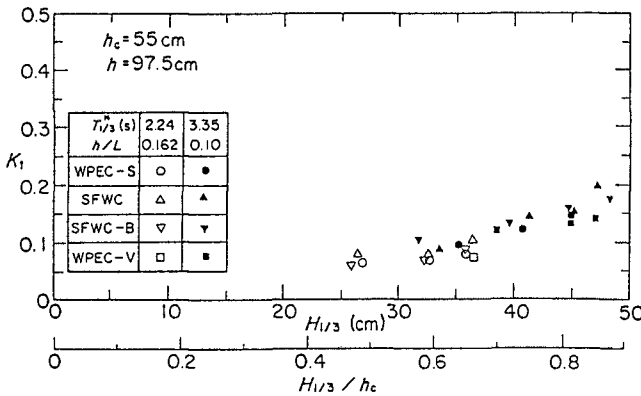


Fig. 6 Wave Transmission Coefficients

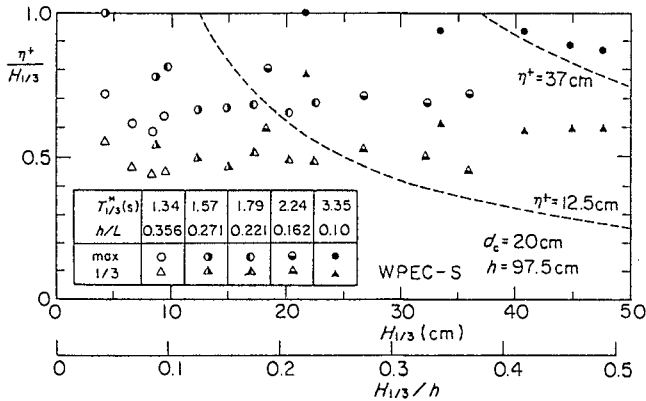


Fig. 7 Water Surface Elevation in the Air Chamber

5. WAVE PRESSURE AND WAVE-INDUCED AIR PRESSURE

Sample Analogue Data

Figure 8 shows sample analogue data when irregular waves of $T_{1/3} = 3.35$ s and $H_{1/3} = 47.8$ cm act on the S-type wave power extracting caisson. The water surface elevations η_F in front of the caisson, η_{pass} in the side channel and η in the air chamber are shown in the figure. The wave pressure p_1 on the sloped wall, the air pressure p_2 in the air chamber and the horizontal displacement R_g of the caisson are also shown in the figure. The air pressure becomes almost zero when the water surface elevation in the air chamber is below the curtain wall depth. Impact air pressure appears when the air in the air chamber is compressed by the uprising water surface. The impact air pressure occurs only when the water surface elevation in front of the chamber goes down significantly below the curtain wall depth. Impulsive pressure also appears on the sloped front wall. This pressure is generated by the direct impact of the water surface of waves and is characterized by its sharp rise and very short duration. Takahashi and Tanimoto (1983) named the air compression pressure Bagnold pressure and the direct wave impact pressure Wagner pressure. Bagnold (1939) and Wagner (1932) gave the theories on these pressures respectively.

Positive and Negative Peak Values of the Air Pressure

Figure 9 shows the positive peak values of the air pressure in the air chamber of the S-type caisson. The value of the air pressure p_{23}^+ is the average of the values obtained by the two pressure sensors P2 and P3. The 1/3 highest peak values and the maximum peak values which are divided by $w_0 H_{1/3}$ are plotted in the figure. The maximum and the 1/3 highest values of $p_{23}^+ / w_0 H_{1/3}$ increase with the increase of the significant wave height as a whole. However, the maximum value decreases where the significant wave height is larger than 40 cm. This is because the wave height is limited by the wave breaking. The maximum value fluctuates very significantly, and therefore additional

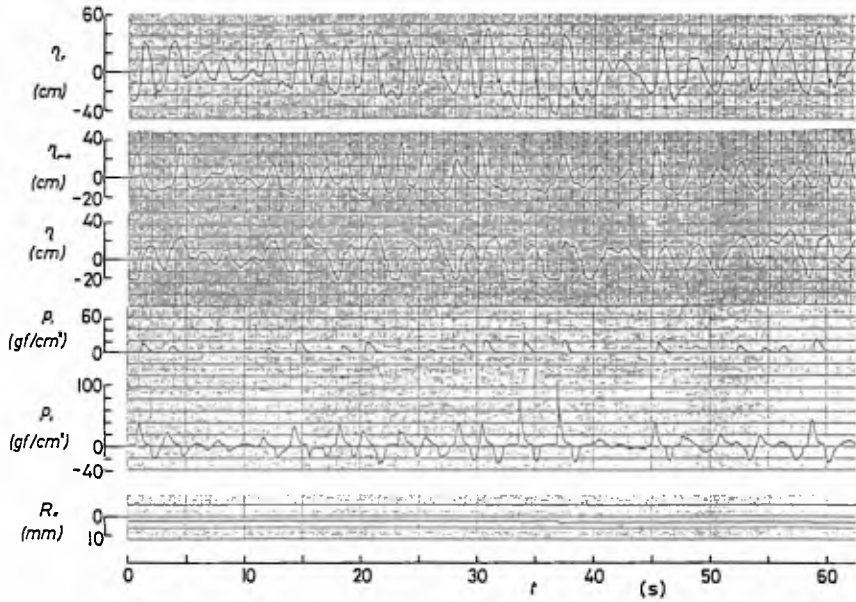


Fig. 8 Sample Analogue Data ($T_{1/3}^* = 3.35s$, $H_{1/3} = 47.8cm$, WPEC-S)

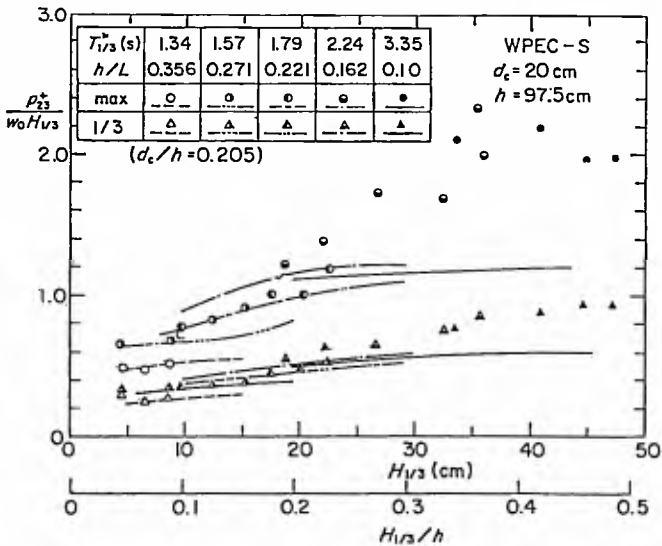


Fig. 9 Positive Air Pressure

measurements were conducted. Even though the incident wave train in the experiment is the same, the maximum value varies greatly. For example, the average of the maximum values for eight repeated measurements is 92.0 gf/cm² and their standard deviation is 10.4 gf/cm², while the average value of the significant wave height is 47.3 cm and the standard deviation is 0.6 cm. The average of the maximum values is 1.35 w₀H_{max} and equals 1.94 w₀H_{1/3}. The calculated value of the air pressure is also shown by the lines in the figure. The calculated value is much smaller when the impact air pressure occurs because the calculation cannot include the impact air compression.

Figure 10 shows the negative peak p⁻²³ of the air pressure. The maximum and the 1/3 highest absolute value of p⁻²³/w₀H_{1/3} increase with the increase of the significant wave height. However the maximum value decrease and the 1/3 highest value becomes constant when the significant wave height is larger than approximately 20 cm. This is because the water surface in front of the air chamber goes below the curtain wall and then the air pressure becomes the atmospheric pressure. The maximum absolute value of p₂₃⁻ is 0.50 w₀H_{max} when T^{*}_{1/3} = 3.35 s and H_{1/3} = 47.4 cm.

The measurement of the air pressure was also conducted for the V-type caisson. The air pressure of the V-type caisson shows almost the same tendency as that of the S-type caisson. The submerged depth of the curtain wall was changed in the experiments. It was found that the air pressure increases with the decrease of the submerged depth.

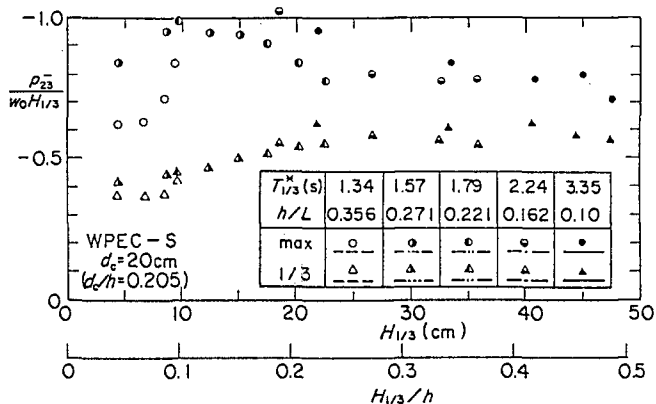


Fig. 10 Negative Air Pressure

Theory of the Impact Air Pressure

The uplift force on the ceiling slab of a wave dissipating caisson is generated by the compression of an air layer by the uprising water surface. This phenomenon is very similar to the impact air compression in the air chamber. The uplift force was investigated by Takahashi and Tanimoto(1985) employing the theory introduced by Bagnold(1939) and extended by Mitsuyasu(1966). The theory comprises

the equation of motion of the effective water mass which compresses the air and the equation of air pressure. The theory can be applied for the impact air compression in the air chamber.

The equation of the air pressure derived by Bagnold assumes an adiabatic air compression. However, the thermodynamic equations used in 2 can also describe the impact air compression even without the assumption of the adiabatic change. That is, Eqs.(1) and (2) express the thermodynamics in the air chamber. Then the water surface elevation can be expressed by the following equation:

$$\rho_w k_e \frac{d^2 \eta}{dt^2} = -p^* \quad (9)$$

where, k_e is the thickness of the effective water mass, which is given by

$$k_e = 0.25 \pi B \quad (10)$$

The initial conditions of the equations are given by

$$\left. \begin{aligned} \frac{d\eta}{dt} &= u_0 \\ \eta &= -d_c \end{aligned} \right\} \text{ at } t = 0 \quad (11)$$

where u_0 is the uprising velocity at $t = 0$ and $\eta = -d_c$. The initial thickness of the air layer is $d_c + D_0$. The equations mentioned above are almost the same as those in 2 but Eq.(9) instead of Eq.(3) is used. The equations can be solved by step-by-step numerical calculations.

Sample Calculations and Similitude Law

Sample calculations were made for the impact air pressure in the model air chamber. The value of the effective thickness of the water k_e is 27.5 cm, and the initial thickness $D_0 + d_c$ of the air layer is 65 cm. For example the peak value of the air pressure p_c becomes 95.8 gf/cm² when the uprising water surface speed is 194.4 cm/s and the nozzle opening ratio is 0.0075. The time t_p from the start of the compression to the peak is 0.0457 s in this case.

If the model scale is 1/20, the peak air pressure p_c is 787 gf/cm² when the uprising velocity u_0 is 8.96 m/s and $\epsilon = 0.0075$. This means that the peak air pressure becomes only 7.49 times that for the 1/20 model. The peak impact air pressure is 1/2.43 that predicted by the model experiments. That is, the correction factor λ of the experimental results is 2.43 in this case. This model scale effect comes from the compressibility of the air as described by Takahashi and Tanimoto(1985).

Prediction of the Impact Air Pressure

The impact air pressure for the prototype and model air chamber can be predicted by the calculation mentioned above. The effective thickness of the water mass k_e and the initial thickness of the air are evaluated by the dimensions of the air chamber. Estimation of the

uprising velocity of the water surface is very difficult. However the maximum value of the uprising velocity in the experiment can be roughly estimated by the following procedure:

a) The maximum absolute value of negative peak of water surface elevation $|\eta_{\text{pass}}^-|$ is given by the wave height $H_{1/3}$ for incident wave train as follows:

$$\left(\frac{\eta_{\text{pass}}^-}{H_{1/3}}\right)_{\text{max}} = -1.2 \frac{H_{1/3}}{h} + 1 : H_{1/3} < 0.417h \quad (12)$$

$$= 0.5 : H_{1/3} \geq 0.417h$$

b) The maximum absolute value of the water surface elevation in front of the air chamber $|\eta_{\text{F}}^-|$ is obtained from $|\eta_{\text{pass}}^-|$ as follows:

$$|\eta_{\text{F}}^-|_{\text{max}} = 1.4 |\eta_{\text{pass}}^-|_{\text{max}} : |\eta_{\text{pass}}^-|_{\text{max}} < d_c/1.4$$

$$= 3.5 |\eta_{\text{pass}}^-|_{\text{max}} - 30 : d_c/1.4 \leq |\eta_{\text{pass}}^-|_{\text{max}} < d_c \quad (13)$$

$$= 2.0 |\eta_{\text{pass}}^-|_{\text{max}} : |\eta_{\text{pass}}^-|_{\text{max}} \geq d_c$$

c) The maximum value of the uprising velocity u_0 is given by $|\eta_{\text{F}}^-|$ as follows:

$$u_0 = \sqrt{g |\eta_{\text{F}}^-|} \{1 - (d_c/|\eta_{\text{F}}^-|)^2\}^{1/2} \quad (14)$$

The calculated values by the above procedure agree with the experimental value as a whole. However, Eqs(11),(12) and (13) are only derived from the experimental results. Further study should be made to confirm the above procedure.

6. DESIGN OF CAISSON

Design of the Walls in the Air Chamber

The walls in the air chamber including the curtain walls should be designed against the wave and wave-generated air pressure. The following three phases should be considered in the design:

a) Peak of the positive air pressure

The impulsive air pressure can be calculated by the procedure described in 5. It should be noted again that the prototype value becomes much smaller than that predicted from the model value. If the impact air pressure is small, the slowly-varying air pressure is important for the design. The value $1.0 w_0 H_{\text{max}}$ in the figure is recommended for prototype air chambers of ordinary size and with an ordinary nozzle opening ratio. It should be noted that the impact pressure may exceed $1.0 H_{\text{max}}$ when the air chamber is small and the wave height is small.

b) Peak of negative air pressure

The value of $0.5 w_0 H_{\text{max}}$ is recommended for ordinary air chambers. This is a conservative value. The negative air pressure is not impulsive.

c) Peak of impulsive wave pressure

When the impulsive wave pressure acts on the front walls the air pressure is still positive. However the air pressure becomes relatively small for the prototype air chamber. Therefore, the air

pressure can be assumed to be zero when the impulsive air pressure acts. The value of $1.0 w_0 H_{\max}$ is recommended for the impulsive wave pressure on the front wall.

Stability Design of the Caisson

Goda proposed a wave pressure formula for the upright section of vertical breakwaters, which is now a standard formula for the caissons of composite breakwaters. The formula can be applied even for the wave power extracting caissons with a little modification. That is, the coefficient α_2 in the Goda formula is set to be zero for the wave power extracting caissons because the caissons absorb the wave energy. (For details, see Goda 1985 pp.107 - 144.)

When the front face of the caisson is inclined as the S-type caisson, the wave pressure on this part contributes to the forces in the horizontal direction and in the vertical direction. This vertical force acts downward and increases the stability of the caisson. The vertical force P_{SV} and the horizontal force P_{Sh} are usually defined as follows:

$$\begin{aligned} P_{Sh} &= P_s \sin^2 \theta_s \\ P_{SV} &= 0.5 P_s \sin 2 \theta_s \end{aligned} \quad (15)$$

where θ_s is the angle of the inclination of the sloped wall and P_s is the wave force above the beginning of the sloped wall.

Results of the Sliding Tests of the Caissons

Sliding Tests of the caissons were conducted to examine the pressure formula and to compare the stability of the caissons. The weight of the caisson was changed and the sliding distance of the caissons was measured. It can be concluded that the application of Goda's pressure formula with the modification is valid for the caissons examined in the experiments. The weight needed to stabilize the caisson changes greatly depending on the shape of the caisson. The S-type wave power extracting caisson requires less weight than the V-type wave power extracting caisson and than the sloped front wall caisson.

7. CONCLUSIONS

The functions and stability of the wave power extracting caisson breakwaters are investigated experimentally. Two wave power extracting caissons are tested in the experiments. One is the wave power extracting caisson with the sloped front wall (the S-type caisson) and the other is the caisson with the vertical front wall (the V-type caisson). However the S-type caisson is mainly discussed. Other caissons such as a sloped front wall caisson and a sloped front wall caisson with wave dissipating blocks are also tested in the experiments for comparison. Major conclusions are as follows:

- 1) The wave power extracting caisson can convert wave power into air power with relatively high efficiency, and the wave power extracting

- caisson has low wave reflection and low wave transmission characteristics.
- 2) Large impact air pressure occurs in the model air chamber of the wave power extracting caisson. The calculation method of the impact air pressure is presented. The impact air pressure in the prototype air chamber predicted by the calculation is much smaller than that evaluated with the Froude similitude law from the experimental result.
 - 3) The pressure distribution for the design of the walls of the air chamber is proposed. The pressure distribution for the stability design of the S-type wave power extracting caisson is proposed, which is confirmed by the sliding tests of the caisson.
 - 4) The stability of the S-type caisson against storm waves is high compared with other caissons.

The First Port Construction Bureau of the Ministry of Transport has decided to conduct field experiments of the wave power extracting caisson breakwater in Sakata Port from fiscal 1987 to 1991. A prototype wave power extracting caisson breakwater will be installed with a turbine and a generator.

The author wishes to express his deep appreciation to Dr. Y. Goda, Mr. T. Asada and Dr. K. Tanimoto for their precious comments on the present study.

REFERENCE

- Bagnold, M.R.A.(1939): Interim report on wave pressure research, Jour. of Institute of Civil Engineers, Vol.12, pp.201 - 226.
- Goda, Y.(1985): Random Seas and Design of Maritime Structures, Univ. of Tokyo Press.,322p.
- Jarlan, G.E.(1961): A perforated vertical wall breakwater, Dock and Harbour Authority, pp.394 - 398.
- Mitsuyasu, H.(1966): Shock pressure of breaking wave, Proc. of 10th Conference on Coastal Engineering, pp.268 -283.
- Ojima, R., Suzumura,S., and Goda, Y.(1984): Theory and experiments on extractable wave power by an oscillating water-column type breakwater caisson. Coastal Engg. in Japan, Vol.27, pp.315- 326.
- Takahashi, S.,Tanimoto, K., and Suzumura, S.(1983): Generation mechanism of impulsive pressure by breaking waves on a vertical wall, Rept. of Port and Harbour Res. Inst., Vol. 22, No.4. pp.3 - 31, (in Japanese).
- Takahashi, S., and Tanimoto,K(1985): Uplift forces due to compression of enclosed air layer and their similitude law, Coastal Engineering in Japan, Vol.28, pp.191 -206.
- Takahashi, S., Suzumura,S., and Myose, K.(1986): Turbine power by wave power extracting system with vertical breakwaters, Proc. of 5th OMAE Conference, ASME, pp.553-559.
- Takahashi, S.,Myose,K., Yoshimoto,Y., and Tanaka, S.(1987): Variation of wave power extraction due to incident angle and directional wave spreading. Rept. of PHRI, Vol.26, No.3. pp.3-39.
- Wagner, H.(1932): Über Stoss-und Gleitvorgänge and der Oberfläche von Flüssigkeiten, Zeishrift für Angewandte Mathematik und Mechnik, Band 12, Heft 4, pp.193 -215.

CHAPTER 186

DYNAMIC FORCES DUE TO WAVES BREAKING AT VERTICAL COASTAL STRUCTURES

by

Hans-Werner PARTENSKY

Franzius-Institute, University of Hannover, F.R.G.

1. Introduction

In the past 20 years, considerable effort has been devoted to replacing the widely used approaches of HIROI, MINIKIN, NAGAI, PLAKIDA and others /1,2,3,4/, for the design of vertical breakwaters under the impact of breaking waves, with improved and more exact calculation methods. However, almost all new theoretical and empirical approaches lacked the support of prototype measurements or test results from model measurements at a larger scale. The difference between the proposed design criteria and classical approaches is sometimes so great that engineers do not have a reliable method for the design of a vertical or composite breakwater. Figure 1 shows the resulting wave forces per unit width due to different theories as a function of the design wave height H .

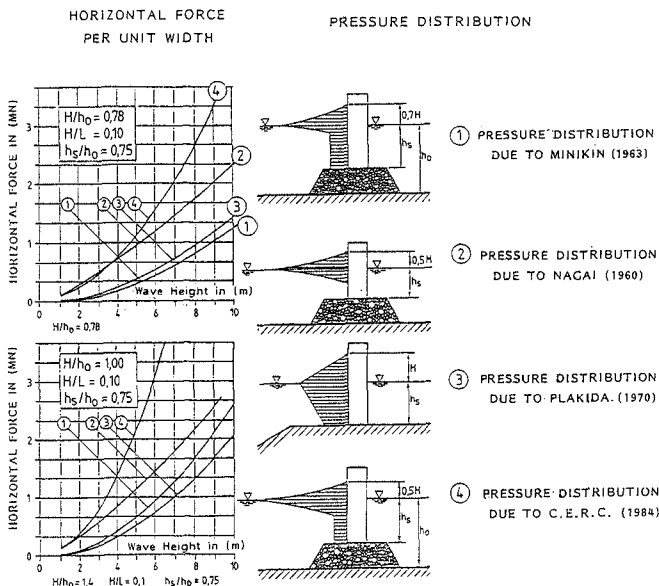


Fig. 1

Horizontal wave forces per unit width due to breaking waves according to different theories /5/

The results show clearly how much the different theories deviate from one another. Therefore, there seems to be an urgent need to re-examine the existing approaches and to support them by means of prototype or large-scale model measurements. The photos of Figures 2 and 3 show some classical examples of waves breaking against coastal structures.



Fig. 2

Impact of waves on the south west breakwater
of Colombo/Sri Lanka



Fig. 3

Wave breaking against Catania breakwater
on Sicily/Italy /4/

Although there have been no spectacular failures of vertical breakwaters in recent years, the existing and widely used design criteria fail to include some newly defined and recognized factors which may promote or cause damage to structures of this kind.

There factors include:

- the simplified assumption of the dynamic pressure distribution on the structure caused by breaking waves,

- the imprecise determination of the design wave height,
- the scale effects of past model tests with respect to the air entrainment of breaking waves, and
- incorrect dimensioning criteria for waves approaches the structure at an angle (Mach reflection).

There are basically three possible major failure modes for vertical and composite breakwaters (Fig. 4). These are sliding and overturning of the upright section as well as failure of the foundation.

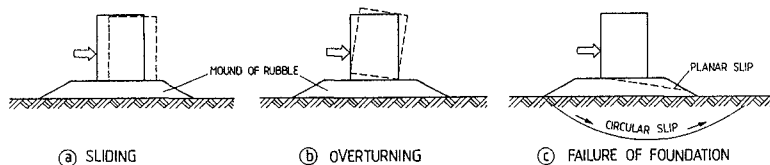


Fig. 4

Possible modes of failure of vertical and composite breakwaters

In all three cases, the impact of the breaking wave at the vertical face of the structure is one of the main causes for the damage. It is therefore extremely important to determine the instantaneous pressure distribution at the vertical wall due to the breaking wave.

2. Modes of wave impact

The resulting pressure distribution at the structure due to a breaking wave depends to a high degree on the mode in which the incoming wave collides with the wall. In this respect, two different cases must be distinguished.

In the first case, the wave begins to break in front of the wall and the tongue of the plunging breaker hits the vertical face enclosing a certain amount of air (Fig. 5).

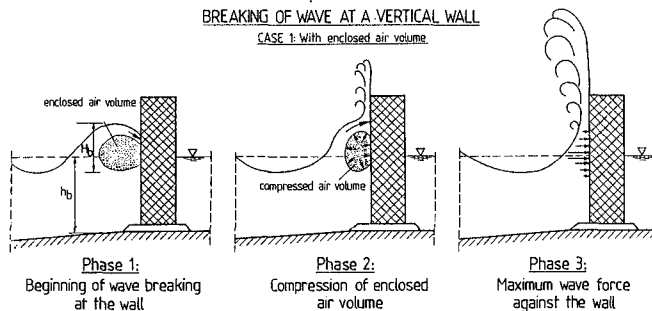


Fig. 5

Wave breaking against a vertical structure with an enclosed air volume

This air volume is quickly compressed during the impact process before the uprushing water carries it upward and away. Figure 6 shows the impact of breaking waves at the sea wall of Westerland/Sylt (F.R.G.) during the stormflood of January 4, 1976. In this case, a considerable amount of air is enclosed in the uprushing water mass which dampens the instantaneous wave pressure exerted at the wall.



Fig. 6

Impact of waves at the Westerland sea wall, Island of Sylt, F.R.G., during the stormflood of January 1976 /5/

In the second case, the wave collides with the structure with an almost vertical front face and only little air is enclosed between the wall and the wave front (Fig. 7).

BREAKING OF WAVE AT A VERTICAL WALL

CASE 2: Without enclosed air

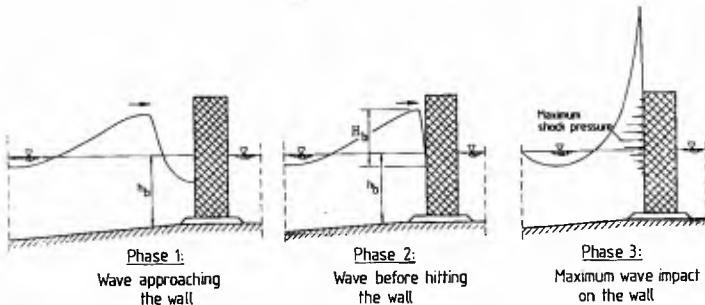


Fig. 7

Wave breaking against a vertical wall without enclosed air

In this case, the forward momentum of the impinging wave is fully transformed into a pressure force which acts on the vertical face of the structure. Measurements showed that the highest pressure values would be exerted at the wall in this case. Figure 8 shows

an example of a breaking wave with little air entrainment.



Fig. 8

Wave breaking against Catania breakwater in Sicily/Italy

Preliminary results of measurements obtained in the wave flume of the Franzius-Institut and in the Large Wave Channel showed that the force resulting from the instantaneous pressure distribution at the wall can rise to more than 10 times the hydrostatic pressure force corresponding to the breaker height. This result is in good agreement with observations made by GODA et al. /7,8/.

The peak pressure at the structure is exerted at some distance above the mean water level depending upon the breaker type. It is of very short duration (0.01 s to 0.03 s), and can easily reach values of several hundred kN/m², depending upon the height of the breaking wave and the amount of air entrapped.

According to OUMERACI /9/, the impact pressure depends essentially on the air content and can be determined by the following equation:

$$p_{\text{dyn}} = K_L \cdot \rho \cdot g \cdot H_b \quad (1)$$

in which: p_{dyn} = maximum dynamic pressure due to the wave impact (kN/m²)
 H_b = breaking height of the wave (m)
 ρ = density of the water (kN·s²/m⁴)
 g = acceleration of gravity (m/s²)

K_L is a kind of air content coefficient which is given by:

$$K_L = 5.4 \left(\frac{1}{\kappa_L} - 1 \right) \quad (2)$$

with κ_L = relative air content (Fig. 9).

Using equation (1), the dynamic pressure exerted at a vertical wall by a breaking wave of 1.5 m of height with an almost vertical front face (little air content, $\kappa_L = 0.1$ to 0.2) would amount to $p_{\text{dyn}} = 300$ to 700 kN/m², depending upon the volume of air enclosed. The order of magnitude of these values is in good agreement with the results of measurements obtained from tests in the Large Wave Channel in Hannover (see Table 1).

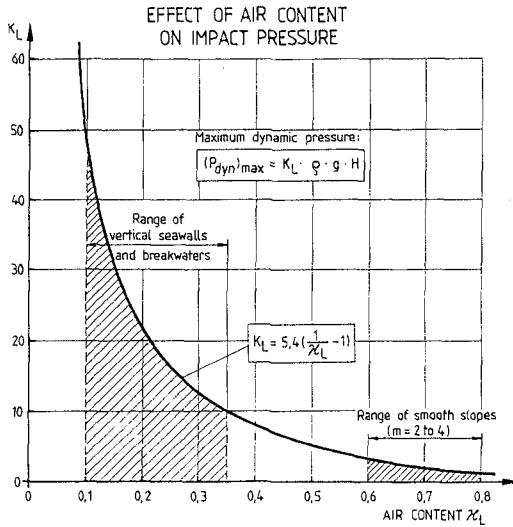


Fig. 9

Effect of air content on impact pressure due to breaking waves

3. Theoretical approach

In order to determine the instantaneous pressure distribution at a vertical wall due to a breaking wave (vertical face assumed), the momentum exchange between the water mass in motion and the rigid assumed structure must be determined. The resulting force per unit width is then given by (Fig. 10):

$$F = m \cdot du/dt = \int_{-h_s}^{h_c} \int_0^{t_1} p(z, t) \cdot dt \cdot dz \tag{3}$$

where m = participating water mass,

u = f(z) = velocity distribution under the breaking wave and

t₁ = duration of impact (0.013 s ≤ t₁ ≤ 0.02 s).

The difficulty is that none of the existing wave theories describes with a sufficient accuracy the velocity field under a breaking wave /10/. A simplified approach must therefore be used. For z ≤ 0, linear wave theory is applied for u₁(z), whereas for z > 0 an approximation is used for u₂(z) with u_c ≈ 0.5 c at the wave crest (Fig. 10). For waves just before breaking, this is in accordance with measurements carried out by LE MEHAUTE and al. /11/, by OCHI and TSAI /12/ and WATANABE, HARA and HORIKAWA /16,17/.

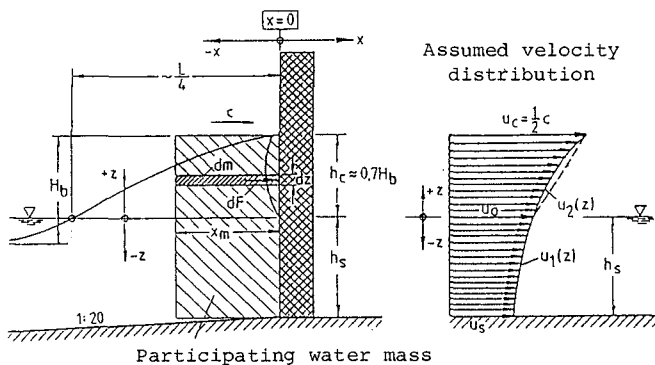


Fig. 10
Definition sketch

It is difficult to determine the exact water mass participating in the momentum exchange during the short duration of the wave impact. At the mean water level, the thickness of the water mass in motion can be approximated to be $x_m \approx 1/2 \cdot L/4 \approx H_B$. Although deeper lying water layers contribute less to the momentum exchange, for reasons of simplification the value of x_m was used over the entire water depth in the following calculations (Fig. 10).

The momentum exchange during the wave impact is of a very short duration with $t_1 \leq 0.02$ s (Fig. 11).

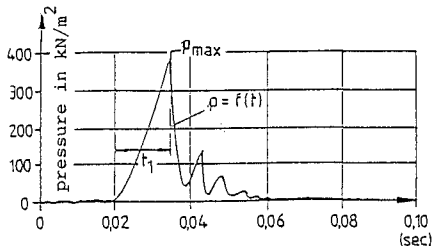


Fig. 11

Increase in pressure during the wave impact at a given location at the wall

Assuming a linear increase in pressure for $0 \leq t \leq t_1$ at a given location z on the wall, equation (4) holds:

$$p(z, t) = \frac{p(z)_{\text{max}}}{t_1} \cdot t \tag{4}$$

For the maximum pressure at a location z on the wall follows:

$$p(z)_{\max} = \frac{2\rho x_m}{t_1} \cdot u(z) \approx \frac{2\rho H_b}{t_1} \cdot u(z) = f(z) . \quad (5)$$

Using linear wave theory, the horizontal velocity components under the wave crest are obtained at the mean water level ($z = 0$):

$$u_0 = \frac{\pi \cdot H}{L} \cdot c \quad (6)$$

and at the bottom ($-z = h_s$):

$$u_s \approx \frac{\pi \cdot H}{L} \cdot \frac{c}{\cosh kh_s} . \quad (7)$$

At the wave crest ($z = h_c$), it is assumed (Fig. 10):

$$u_c = \frac{1}{2} c = \frac{1}{2} \sqrt{gh_s} . \quad (8)$$

By using the velocity distribution as shown in Figure 10, the instantaneous pressure distribution at the wall is obtained from equation (5). The peak pressure at $z = h_c$ can be determined by the following equation:

$$p_c = \frac{\rho \cdot H_b}{t_1} (gh_s)^{1/2} . \quad (9)$$

The pressure at $z = 0$ is obtained by:

$$p_0 = \frac{2\pi\rho \cdot H_b^2}{t_1 \cdot L} (gh_s)^{1/2} \quad (10)$$

and at the bottom ($-z = h_s$) by:

$$p_s = \frac{2\pi\rho \cdot H_b^2}{t_1 \cdot L \cdot \cosh kh_s} (gh_s)^{1/2} . \quad (11)$$

Figure 12 shows the resulting peak-pressure distribution at the wall due to the wave impact as well as the simplifying linear approxi-

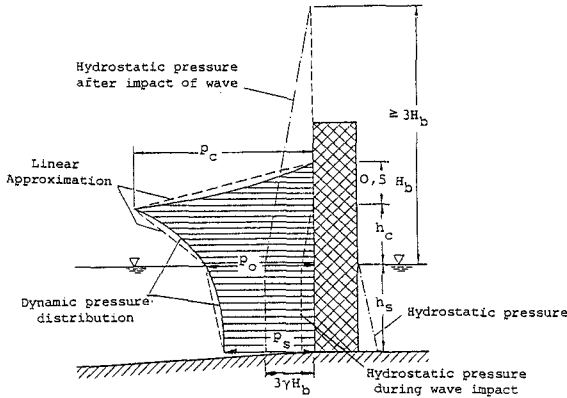


Fig. 12
Resulting peak-pressure distribution

mations. Measurements showed that the uprushing breaker tongue at the wall could reach a height of $3H_b$ or more after the wave impact (Fig. 12).

4. Research program of the Franzius-Institute

The research program of the Franzius-Institute concentrated on the impact of waves breaking against a vertical, solid structure. Portions of the systematic tests were performed in a smaller wave flume with significant wave heights of up to 0.40 m. The most important investigations, however, have been carried out in the Large Wave Channel of the Universities of Hannover and Braunschweig having an overall length of 320 m and a width of 5.0 m. This wave flume is equipped with an hydraulically driven wave maker by means of which monochromatic and random waves can be produced with wave heights up to 2.50 m.

In both flumes, the instantaneous pressure distribution at a vertical wall due to breaking waves was measured by means of a number of high sensitive pressure cells having a natural frequency of 28 kHz with an operating pressure range of up to 5 bar.

In the Large Wave Channel, the vertical wall was composed of seven stop logs, each with a height of 1.0 m and about 25 pressure gauges installed over the face of the wall (Fig. 13).

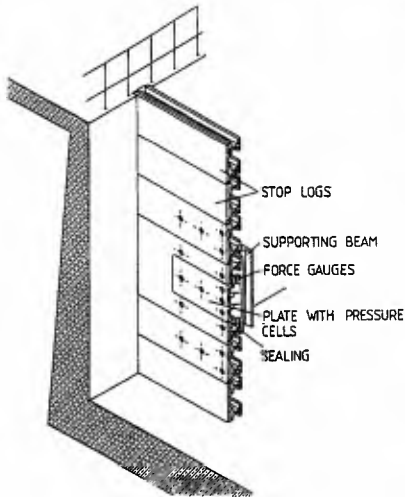


Fig. 13

Installation of vertical wall
in the Large Wave Channel



Fig. 14

Wave breaking against
vertical wall
in the Large Wave Channel

The measurements showed that the maximum dynamic pressure at the wall is exerted at a distance of $h_c \approx 0,7 H_b$. Above the mean water level, its value depending upon the breaker type and the amount of air enclosed. Figure 15 shows some time series of impact pressures obtained at different measuring points in the Large Wave Channel for a breaking wave height of 1.50 m.

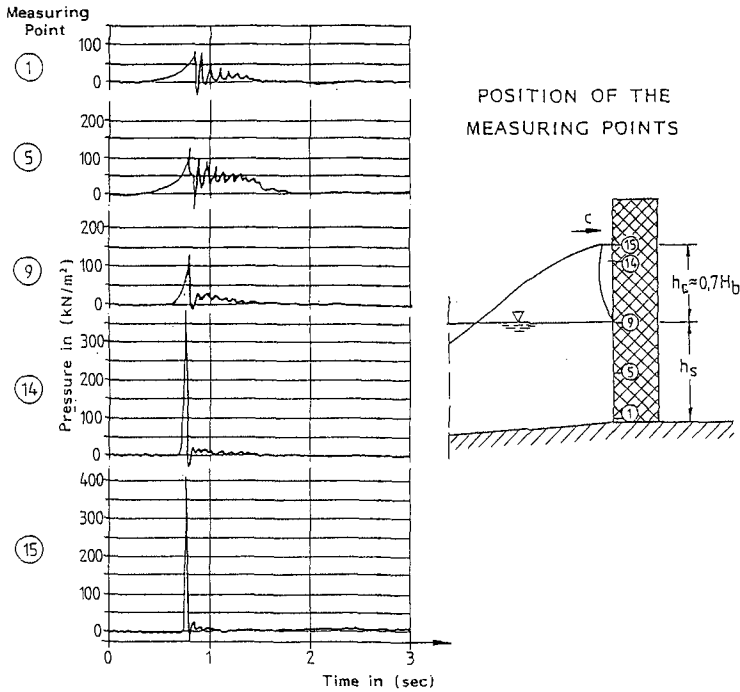


Fig. 15

Time series of impact pressures and location of measuring points

The evaluation of the measurements carried out in the Large Wave Channel is not yet finished. The first results, however, show clearly that the criteria used so far for the design of vertical breakwaters under the impact of breaking waves underestimate considerably the peak pressure and resulting wave forces.

Peak pressures at $z = h_c$ for a breaking wave height of $H_b = 1.50$ m measured in the Large Wave Channel exceeded, for example, the value resulting from the MINIKIN approach /13/ by a factor of 4 (Table 1). Based on the maximum pressure values obtained at different measuring points at the wall, the resulting force per unit width exceeded the corresponding CERC-value by a factor of 7.0 and the overturning moment about the toe of the wall was approximately

12 times greater than that obtained from the current design criteria (Table 1).

Peak pressures measured in the Large Wave Channel for given breaker heights were in good agreement with the distribution of maximum pressures as shown in Fig. 12 /5/.

In Table 1, a comparison of test results with existing theories and the new approach is made for a breaking wave height of $H_b = 1.50$ m. Based on the peak pressure values, the calculated wave force per unit width as well as the overturning moment about the toe of the wall were in good agreement with the theoretical values obtained by the new approach (Table 1).

Theoretical approach	Maximum dynamic pressure (kN/m ²)	Force per unit width (kN/m)	Overturning moment (kNm/m)
HIROI (1903)	23,0	124,6	191.2
NAGAI (1968)	20,0	45,7	62,6
PLAKIDA (1970)	23,0	80,3	117,6
C.E.R.C. (1984) (based on MINIKIN, 1950)	97,0	63,1	86,7
GODA (1985)	15,3	100,0	134,0
FRANZIUS-INSTITUTE (1987) (Measurements at Large Wave channel)	395,0	496,1*	1016,8*
PARTENSKY (1987) Based on maximum pressure values with $t_1 = 0,0167$ s:	361,0	541,0	1020,0
Based on maximum pressure values with $t_1 = 0,02$ s:	301,0	455,0	855,0
Recommended design values with $t_m = 0,04$ s:	75,2	130,0	230,0

* Calculation based on maximum pressure values

Table 1

Comparison of test results with existing theories and new approach (Example for breaking wave height of $H_b = 1.50$ m with $T = 7.8$ s)

5. Recommendations for the design of vertical coastal structures

As can be seen from the time series of impact pressures in Figures 11 and 15, the duration of the peak pressure at the different locations is extremely short ($t_1 < 0.02$ s). Due to its inertia, the coastal structure will therefore hardly show reactions during the short duration of the momentum exchange.

Prototype measurements at CAISSON-like breakwaters in Japan showed that the natural period of oscillation of these types of coastal structures lies between 0.1 and 0.3 s /14/, which is one order of magnitude higher than the duration of the peak pressure during the wave impact.

In addition, from the recorded pressure time series it can also be seen that the maximum pressures at the different locations along

the wall do not occur simultaneously, the phase shifts, however, are small.

The dimensioning of a coastal structure on the basis of the peak pressure distribution of Figure 12 therefore appears to be too conservative. It seems more realistic to replace the resulting peak pressure distribution by an averaged pressure distribution, in which the mean dynamic pressure $p_m = \bar{f}(z)$ over the total impact duration $t_m = t_1 + t_2$ is applied to each point of the structure (Fig. 16) /15/.

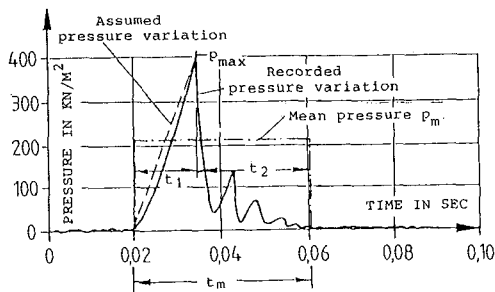


Fig. 16

Mean pressure p_m during the momentum exchange due to the wave impact

With the simplifying assumption of a linear increase and decrease of the pressure during the impact duration t_m , it follows for the mean pressure p_m that:

$$p_m(z) \approx \frac{1}{2} p_{max}(z) \tag{12}$$

By using this relationship, the following reduced pressure values result from equations (9), (10), and (11):

$$\text{At } z = h_c: \quad (p_c)_m = \frac{\rho \cdot H_b}{2 t_m} (gh_s)^{1/2} \tag{13}$$

$$\text{At } z = 0: \quad (p_o)_m = \frac{\pi \cdot \rho \cdot H_b^2}{t_m \cdot L} (gh_s)^{1/2} \tag{14}$$

$$\text{At } -z = h_s: \quad (p_s)_m = \frac{\pi \cdot \rho \cdot H_b^2}{t_m \cdot L \cdot \cosh kh_s} (gh_s)^{1/2} \tag{15}$$

The time series of the impact pressures recorded at the Large Wave Channel show that the impact duration is $t_m \approx 0.04$ s at and above the mean water level, whereas below the mean water level t_m increases with depth (Fig. 15).

Figure 17 shows the recommended distribution of average impact pressures which might serve as a new approach for the future design of vertical coastal structures subject to the impact of breaking waves.

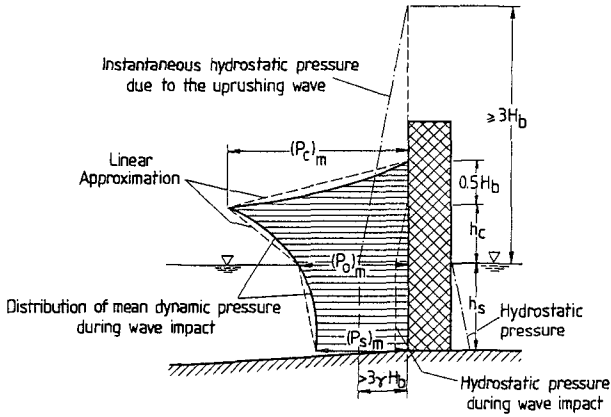


Fig. 17

Recommended pressure distribution for the design of coastal structures subject to the impact of breaking waves

In Figure 18 the dynamic pressure distributions at a vertical structure for a breaking wave height of $H_b = 1.50$ m are represented as they result from the classical MINIKIN-approach recommended in /13/ and from the new approach.

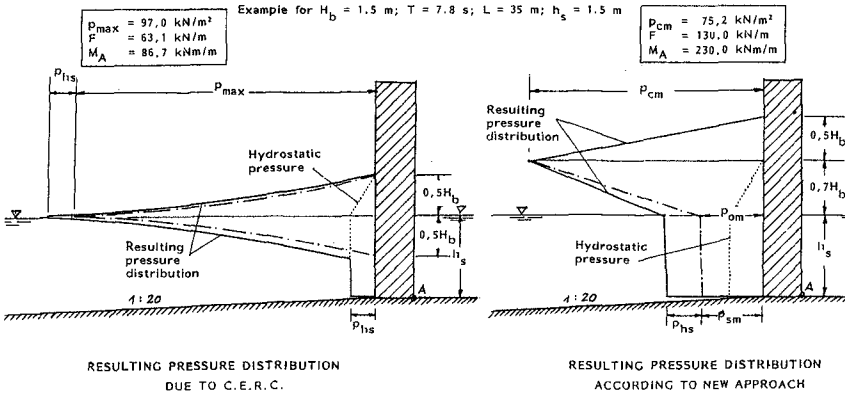


Fig. 18

Comparison of dynamic pressure distributions according to MINIKIN (C.E.R.C.) and the new approach

Although the recommended averaged peak pressure p_{CM} at the wave crest is somewhat smaller than that resulting from MINIKIN's theory, the effective wave force per unit width is twice as high and the overturning moment about the footpoint A of the structure is almost three times greater than that obtained from the classical theory (see also Table 1).

6. Conclusions

The results of the investigations show clearly that the design criteria used so far for the dimensioning of vertical coastal structures such as sea walls, vertical and composite breakwaters underestimate considerably the resulting wave forces.

The proposed pressure distribution of Figure 17 could therefore serve as a more realistic approach for the design of coastal structures under the impact of breaking waves.

To what extent the effect of structural elasticity as well as the type of foundation must be considered in the design and overall stability of the structure has not yet been investigated. It will, however, be the subject of further studies.

In addition, a numerical analysis of the impact process is planned in order to determine more precisely the time- and space-dependent phases of the momentum exchange at the coastal structure.

7. Acknowledgement

The research work described in this paper has been supported since 1983 by the German National Research Council (Deutsche Forschungsgemeinschaft) in Bonn, F.R.G. This support is highly appreciated by the Special Research Group (SFB 205) of the University of Hannover as well as by the author.

8. References

- /1/ Partenscky, H.W.: Breakwater design problems. Proc. of European Workshop on Coastal Zones, Techn. Univ. of Athens, 1985
- /2/ Nagai, S.: Shock pressures exerted by breaking waves on breakwaters. Trans. of ASCE, Vol. 126, No. 3261, 1961
- /3/ Plakida, M.E.: Pressure of waves against vertical walls. Proc. of 12th Coastal Eng. Conf. Vol. 3, 1970
- /4/ Minikin, R.R.: Wind, waves and maritime structures. Charles Griffin, London, 1963
- /5/ Partenscky, H.W.: Neue Bemessungskriterien für senkrechte und geschüttete Wellenbrecher, Jahrbuch der HTG, Band 42, 1987
- /6/ Partenscky, H.W.: New investigations on vertical and rubble mound breakwaters. Proceedings of the second Chinese-German-Symposium, Vol. II, University of Hannover, 1987

- /7/ Goda, Y.: Random seas and design of maritime structures. University of Tokyo Press, 1985
- /8/ Technical standards for port and harbour facilities in Japan, 1980
- /9/ Oumeraci, H.: Belastung von Betonplatten-Deckwerken und ihre Berücksichtigung bei der Bemessung. Dissertation, T.U. Dresden, 1981
- /10/ Longuet-Higgins, M.S.: The unsolved problem of breaking waves. Keynote address, Proc. of 17th Conf. on Coastal Eng., Sydney, 1980
- /11/ Le Méhauté, B., Divoky, D. and Lin, A.: Shallow waterwaves, a comparison of theories and experiments. Proc. of 11th Conf. on Coastal Eng., Vol. I, 1968
- /12/ Ochi, M.K. and Tsai, Chen-Han: Prediction of impact pressure induced by breaking waves on vertical cylinders in random seas. Appl. Ocean Research, Vol. 6, No. 3, 1984
- /13/ US-Army, Corps of Engineers: Shore protection manual, Vol. 2, Coastal Eng. Research Center, Vicksburg/Miss., 1984
- /14/ Muraki, Y.: Field investigation on the oscillation of break-water caused by wave action. Coastal Eng. in Japan, Vol. 9, 1966
- /15/ Partenscky, H.W.: Impact of waves breaking at vertical structures. Proceedings of the 21nd Conference on Coastal Engineering, Torremolinos/Spain, 1988
- /16/ Watanabe, A., Hara, T. and Horikawa, K.: Study on breaking conditions of compound wave trains. Coastal Engineering in Japan, Vol. 27, 1983
- /17/ Horikawa, K. (Editor): Nearshore dynamics and coastal processes. University of Tokyo Press, Tokyo, 1988



San Ciprian—Lugo

PART IV
COASTAL, ESTUARINE

Estarit—Gerona, costa Brava



CHAPTER 187

MIXING OF THERMAL DISCHARGES IN COASTAL WATERS

By N.M. Ismail⁽¹⁾ A.M. ASCE, R.L. Wiegel⁽²⁾ F.ASCE.
P.J. Ryan⁽³⁾, M. ASCE and S.W. Tu⁽⁴⁾, M.ASCE

ABSTRACT: Mixing of thermal effluents, being discharged from thermal power plants on coastlines and which head into surface waves was investigated by analyzing extensive field and laboratory data on plume and ocean ambient conditions. Emphasis was given on the effect of waves and surf zone currents on the modifications of plume surface area and vertical temperature profile in the near-field area.

The results of this investigation showed that large opposing waves increase the plume surface area, in the vicinity of the outfall, for all cases of tide level and wave direction. Moreover, waves focused cold bottom currents on the discharge outlet and consequently the temperature of the released warm water was decreased at the surface and near the bottom. Wave-induced cross flows decreased the plume cumulative surface area which corresponded to fractional excess temperature ranging between 0.8 and 0.5 normalized values. This decrease was shown to be contingent that there is no interaction between the far-field and near-field plume waters. Gradient of wave momentum flux across surf zone was found to be necessary parameter to characterize the incident wave field.

INTRODUCTION

The growing interest in recent times in the pollution of natural water bodies through the discharge of thermal effluents has advanced considerably the state-of-the-art knowledge on the mixing of surface buoyant jets in the aquatic environment. Thermal

-
1. Engineering Specialist, Enppi, Cairo, Egypt; formerly, Bechtel Inc., San Francisco, CA.
 2. Professor of Civil Engineering, University of California, Berkeley, CA.
 3. Chief Engineer, Hydraulics/Hydrology Group, Bechtel Civil, Inc., San Francisco, CA.
 4. Research Engineer, Department of Engineering Research, Pacific Gas and Electric Company, San Ramon, CA.

pollution studies usually involve a field survey in conjunction with either a physical and/or a mathematical model. When warmed water is discharged into the surf zone in the open sea, field surveys reveal that the thermal plume often shows a complicated horizontal shape. This phenomenon may be caused by the influence of waves in shoaling water and by nearshore currents. Such effects were reported by Grider (2) in 1973 to be important, based on the field survey of surface temperatures in the thermal plume discharged into the nearshore zone from the Encina Power Plant, Carlsbad, California. After examining the order of magnitudes of offshore currents and wind velocities, Grider concluded that heavy surf conditions play a major role in determining the size and the shape of the plume. Although a correlation between significant wave height and size, of the plume was shown to exist, some contradictory data were reported. Grider concluded that additional study of surface effects on horizontal surface plumes and detailed analysis of wave effects are warranted.

In 1974 (Wiegel et al., 1976) a 1:75 undistorted scale model of the Diablo Canyon Power Plant was constructed and used to predict the behavior of a 4000 cfs heated discharge into a shallow, rocky cove west of San Luis Obispo, California. In 1984-6 extensive field data were obtained for a wide range of plant operating and receiving water conditions. The data included horizontal and vertical temperature profiles and surface temperature isotherms for over 50 field tests. Key tests were selected, and the data used to calibrate and verify the physical model. The results demonstrated that a physical model is a reliable tool for prediction of prototype behavior as long as key parameters are simulated correctly in the model. Three parameters which are not normally emphasized in jet mixing models were found to be important, including details of the bottom topography, bottom roughness, and incident wave characteristics. The plant layout is shown in Fig. 1-a and an expanded view of the discharge cove is illustrated in Fig. 1-b. The latter figure shows the main features of the bottom bathymetry of Diablo discharge cove.

The field and model data showed that deep water-significant wave height and its associated period were sufficient parameters to characterize the incident wave field. An increase of height of waves, coming at 255° with north, from 4.5 to 6 ft destratified the south edge of the plume, and higher waves shifted the plume to the north. Further (Ismail et. al., 1987), it was found that the asymmetric distribution of the horizontal temperature profiles of the plume observed for all field tests conducted under large waves (> 6 ft), of 255° angle of approach, was due to a reverse eddy current. This eddy is generated in the discharge cove by wave breaking along the shallow plateau near the cove west entrance. These wave effects were similar at both low and high tides. Further it was observed that when the wave approach was changed in the model from 255° to 278° , there was a corresponding trend

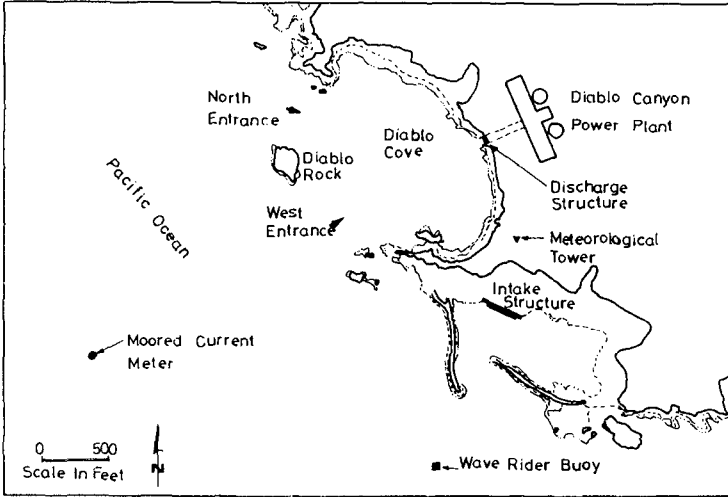


FIG 1-a DIABLO CANYON POWER PLANT AND RECEIVING WATER

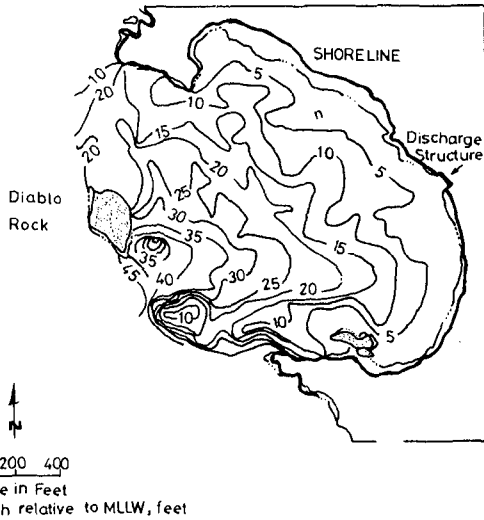


FIG. 1-b BOTTOM BATHYMETRY OF THE DISCHARGE COVE

of recirculation of warm water within Diablo Cove. The extent of this recirculation depended on the incident wave height and tide level. This recirculation had flattened the horizontal temperature profiles in the cove and increased the plume surface area within isotherms close to the discharge point. However, there was no attempt made to crystallize the effects of wave parameters and its induced-nearshore circulation on the plume surface area and the accompanied vertical temperature profiles.

Objective - The main purpose of the present work was to determine effects of wave parameters such as height, direction on the isotherm surface area in the near-field zone of thermal plumes discharged in coastal waters. In addition, the corresponding modifications of the plume vertical temperature profile will be determined. Emphasis was given to the effects induced by the interaction of the incident wave field with the nearshore bathymetry/topography. The results will be derived from examining the field data available on the thermal discharges from three power plants. Two of these plants; namely Fukushima in Japan and Encina in Calif. are located on straight long beaches. The third plant which is Diablo Canyon in Calif., is located on a partially closed embayment. The derived results from the field data will be supplemented with experimental prediction reduced from a systematic set of experiments which was conducted on the physical model of Diablo Canyon. This set of experiments will focus on effects of wave direction and modifications of vertical temperature profiles.

MIXING OF JETS/PLUMES IN WAVE-CURRENT FLOW

Most predictive models of thermal diffusion in the coastal zone consider an offshore current and/or tidal current, but do not consider the influence of surface waves and/or nearshore currents due to breaking waves. Among the few predictive models in the literature is the mathematical model developed by Tanaka and Wada (17) in 1982. Their evaluation of the numerical model was based on a comparison between the model predictions and data collected on a physical model. The authors came to the conclusion that in order to improve the capabilities of their model, it is necessary to acquire more field data on both the nearshore currents and diffusion patterns of large discharges of warm water under strong wave conditions. In addition, virtually all past hydraulic model studies of jet mixing problems have been performed in the absence of surface gravity waves.

The studies of Ismail and Wiegel (Ref. 4-7, 1980-83) which were performed for the case of non-buoyant jets were of considerable assistance in understanding the effect of waves during the analysis of the field and model data for Diablo Canyon thermal discharges. This is particularly valid in the zone close to the discharge area (near-field zone) where advection and free turbulence created by the shearing action, of the discharge causes

jet diffusion.

Ismail has found that the interaction of waves with jet driven flows modified the undisturbed coastal circulation of each and the combined bottom mass transport is always focused on the jet outlet (6, 1982). In addition, it was shown experimentally and theoretically that momentum jets expand at a greater rate than in the absence of waves (7, 1983). Also, velocity measurements at the jet-longitudinal-axis have shown that mean velocities of the current near the bottom are decreased with a tendency of the current shear near the water surface to increase as it is illustrated in Fig. 2. The effects of waves on jet spreading and bottom mass transport are shown in the sample photographs of Fig.3

FIELD DATA OF DIABLO CANYON

A total of 56 field tests were performed from late 1984 to mid 1986, including tests for a wide range of power levels (300-2280 Mwe), pump flows [500 - 4000 cfs (14.2 - 114 cms)] and ambient conditions. The ambient conditions included extreme low to extreme high tide, strong and weak currents both upcoast and downcoast, and low to high waves. Thirteen field tests, from the total of 56, were used to verify the model. The verification tests incorporated one unit, two unit and heat treatment operation, two and four pump flows (including co-flowing warm and cold jets), and a wide range of ambient conditions.

During each field test, temperature profiles were taken at 4 depths in the top 10 ft (3m), along 5 transect lines in Diablo Cove, ranging from approximately 400 ft (122m) from the discharge structure (Line 4) to just outside the west entrance [1400 ft (429m)] from the discharge (Line 14). Surface temperatures were measured outside Diablo Cove to approximately the 1°F (0.5°C) contour, typically a distance of 2-4 miles (3.2-6.5 km). Vertical temperature profiles were taken at 9-10 locations in the cove and 3-6 locations offshore. currents were measured both with drogues and moored current meters. Waves were measured with a wave rider buoy. The duration of each field test was 2-3 hours.

PHYSICAL MODEL OF DIABLO CANYON

The model is an undistorted densimetric Froude model with a scale of 1:75, and covers a prototype area 6400 ft (1960 m) along the coast by 4800 ft (1468 m) normal to the coast. The model basin is 85 ft by 64 ft by 2.5 ft deep (26 m x 19.6 m x 0.76 m). Model bathymetry was based on prototype hydrographic studies plus aerial photography. Coastal currents parallel to the coast were generated using a pump/manifold system. Dynamic tides were simulated using a computer controlled system. Monochromatic waves were generated using a piston-type wave maker. Temperature measurements were taken using a 45 sensor array, spaced at 50 ft (15.2 m) (prototype) centers in the horizontal, and 4 ft (1.2m) in the

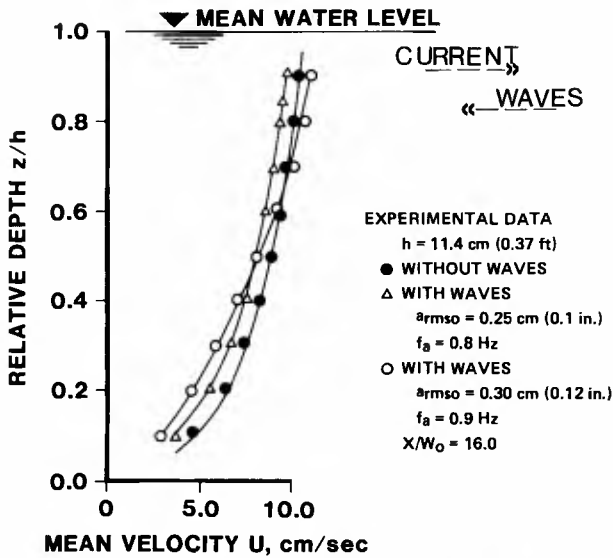


FIG.2 VELOCITY MODIFICAT. OF CURRENTS
Ismail(1980)

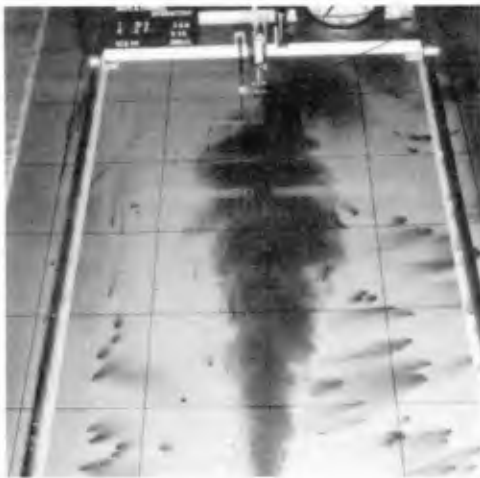
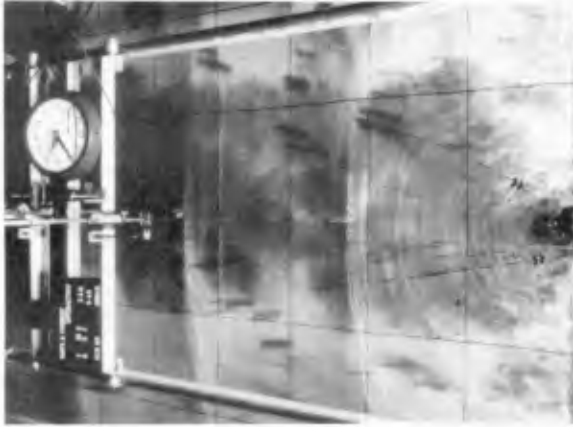


FIG.3A FLOW VISUALIZ. OF SURFACE JET

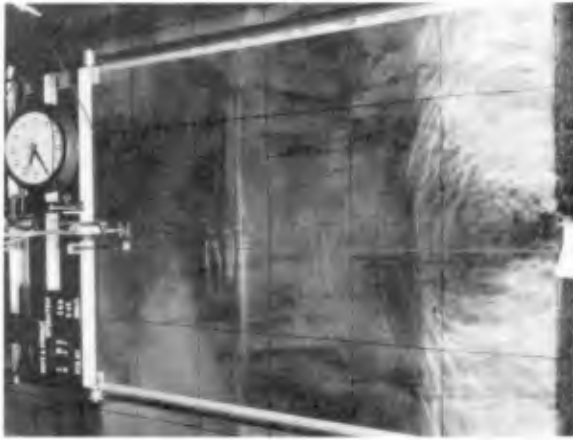
After ISMAIL (1981)



t = 3 sec



t = 15 sec



t = 45 sec

FIG.3.b MOMENTUM JET IN PRESENCE OF OPPOSING WAVES
 wave period 0.8 sec; wave height $a_0 \approx 0.9$ cm

vertical. The entire array could be moved in 3 directions, allowing the 3 dimensional plume field to be measured.

Experimental procedures- Detailed model operating procedures for the model were developed and strictly adhered to. Water level, currents and waves were established to simulate field conditions. Discharge flow conditions were established and temperature of the discharge was set so that the density difference in the model was the same as during the field test. Temperature probes and wave gages were calibrated prior to each test. The system was allowed to come to quasi-steady prior to taking any temperature measurements.

FIELD AND LABORATORY RESULTS

One the simplest methods of parameterizing plume spreading and decay is in terms of surface areas within isotherms. For Diablo Canyon surface temperature data in the field were used to develop isotherm contours. The far-field isotherm contours refer primarily to the area outside Diablo Cove. The near-field isotherms correspond to the area within Diablo Cove. The cumulative surface area for the complete field versus normalized temperature is shown on Fig. 4 for six field tests which reflect the effects of wave height and tide level. On the same figure the available field data for Encina and Fukushima power plants are plotted. To establish a comparative basis to examine wave effects on the thermal discharges from the three power plants, wave parameters in the surf zone were evaluated from deep water wave conditions. Figure 5 displays the shoreline configuration for the power plant sites. On the same figure, values of wave breaker height and surf zone width and flow pattern of surf zone currents are illustrated.

The results shown in Fig. 4 indicate that higher waves in general increase the plume total surface area in the near-shore zone. However, for Diablo Canyon and at low tide, the increase of surface area is limited close to its discharge structure. Thereafter, the initial region, entrainment is inhibited due to the restricted bottom bathymetry of the shallow plateau in the south cove. And further, the plume is shifted to the north by the induced offshore cool water ingress and circulation in the cove. This decrease of plume surface area in the presence of higher waves and at low tide was confirmed in the laboratory as it is illustrated in Fig. 6.

For extreme high tide, it is noticed on Fig. 4 that, under data for high waves, there is a slight trend of decline of the total surface area in the medium range of excess temperature. Examining this trend in the laboratory indicated that the decrease of the total surface area is mainly contributed by the action of the cool water return current. The extent of this decrease of the surface area depends greatly on the angle of wave incidence as it is demonstrated in Fig. 7. The corresponding modifications of the

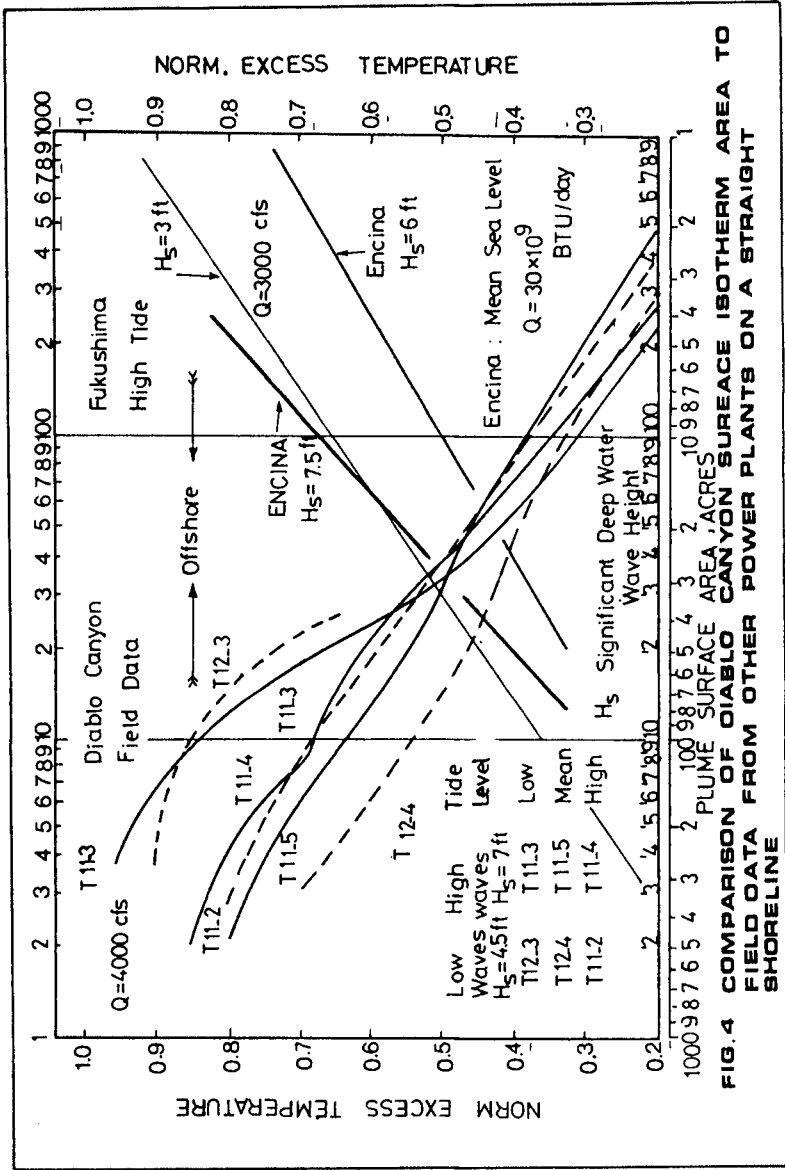
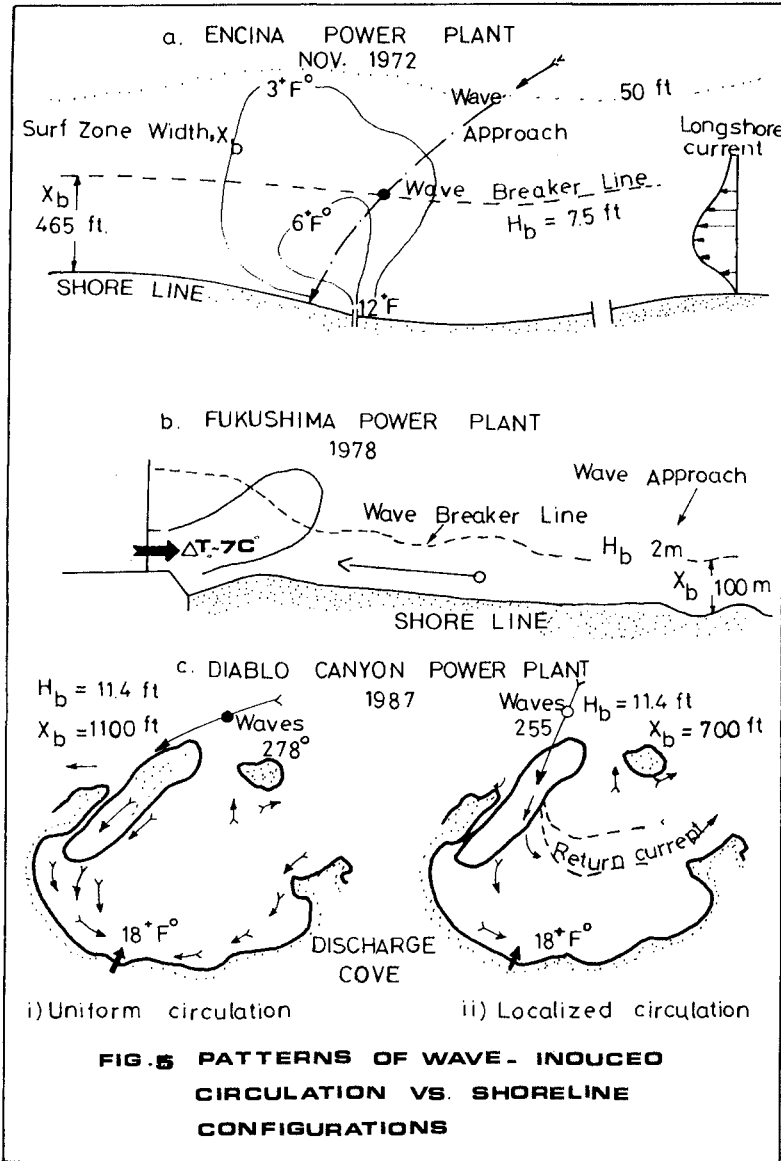


FIG. 4 COMPARISON OF DIABLO CANYON SURFACE ISOTHERM AREA TO FIELD DATA FROM OTHER POWER PLANTS ON A STRAIGHT SHORELINE



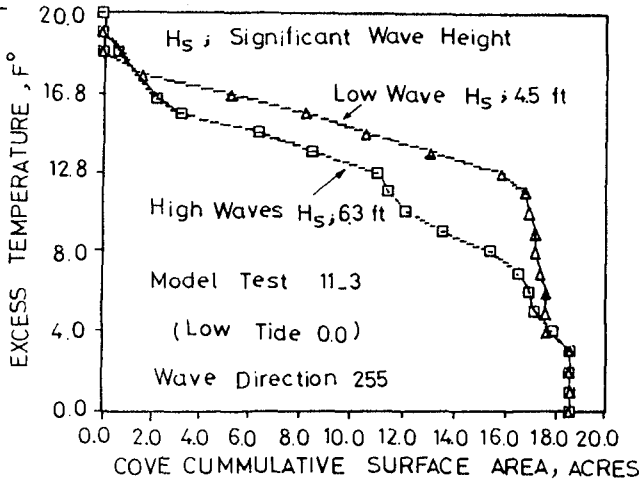


FIG. 6 PLUME SURFACE AREA VS. WAVE HEIGHT

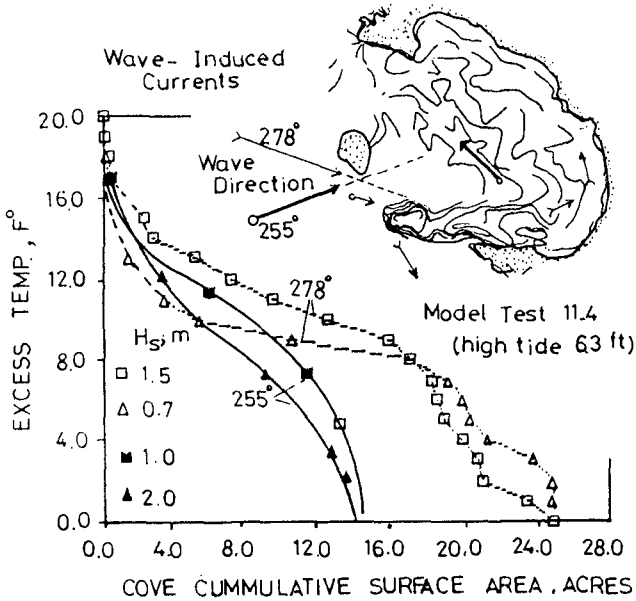


FIG. 7 WAVE PARAMETERS VS. PLUME SURFACE AREA

vertical temperature profile as a result of high waves are shown in Fig. 8 for cases of low and high tides.

The surface isotherm data for Diablo Canyon, obtained within Diablo Cove, and defined in terms of fractional excess temperature, are somewhat of less extent than surface areas for thermal discharges into open water. For thermal discharges on straight long beaches, it is possible to describe the surface area within the isotherms as it increases exponentially with decreasing relative excess as shown on Fig. 4. The slope of such a functional correlation was found to depend greatly on the gradients of wave momentum fluxes across the surf zone. Therefore, deepwater conditions of water waves are not generally sufficient parameters to characterize the incident wave field. Instead, wave characteristics in the surf zone and its associated currents should be evaluated from statistical wave data at deep water locations

CONCLUSIONS

Extensive field data on horizontal and vertical temperature distributions of thermal plumes, discharged horizontally from thermal electric power plants into coastal waters, were analyzed with a view to obtain basis of qualitative prediction of wave and currents effects on near-field mixing. Information on winds, swells/seas, currents, tide, shoreline configuration and sea bottom bathymetry were available for the analyzed data. Two of these plants Fukushima in Japan and Encina in southern California are located on straight long beaches. The third plant is Diablo Canyon and is located on a partially closed embayment. In addition, a series of sensitivity laboratory tests was conducted on the 1:75 physical model of Diablo Canyon to provide complementary data on the effect of waves and its induced currents on plume surface area and vertical temperature profiles. The results of the study lead to the following conclusions:

- (i) Cumulative surface area for the overall isotherm contours, of excess temperature ranges in the near field of thermal plumes, increases in the presence of opposing waves of finite height. This increase might be inhibited by restrictions due to water depth and side boundaries. Further, this trend of surface area increase might not apply uniformly over all ranges of excess temperature in the near field. This is due to the different mechanisms by which surface waves affect plume mixing in the surf zone and the plume densimetric Froude number.
- (ii) Within the upper range of normalized excess temperature, > 0.8 , opposing waves increase the plume surface area due to the excess longitudinal momentum flux of waves. Further it is also seen that the wave-induced cold bottom currents are entrained into the plume upper layer, close to the outfall, and thereby destratifies the vertical temperature profile.

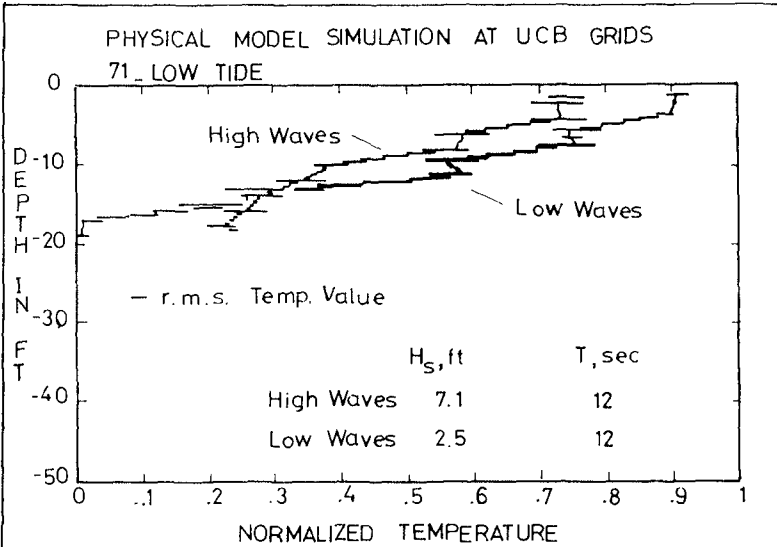


FIG 8-a MODIFICATION OF VERTICAL TEMP. PROFILES

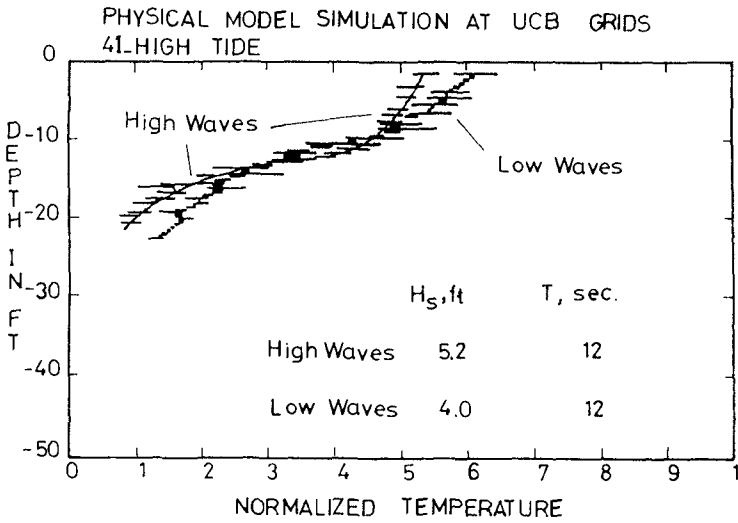


FIG8.b MODIFICATION OF VERTICAL TEMP. PROFILES

- Longshore or return rip currents, generated on straight long beaches and within shoreline embayments reduces plume surface area for the medium range of (0.8-0.5) normalized excess temperature in the near field zone.
- (iii) Interaction of incident oblique-wave field with a partially enclosed embayment induces a basin secondary circulation with an offshore wave-breaking current. This flow pattern forces a part of far-field plume warm water to return to the discharge area and be reentrained in the plume near-field. Thus waves under certain conditions may interact with the nearshore topography leading to a much higher effluent concentrations and larger surface areas for the high and medium ranges of excess temperature.
- (iv) Gradient of wave momentum flux across the surf zone is an important parameter in shaping the slope of functional relationship between plume surface area versus fractional excess temperature in coastal waters.

APPENDIX 1. REFERENCES

1. Adams, E.E., "Discussion of Reynolds Number Effects on Buoyant Surface Jets", ASCE, Journal of Hydraulic Engineering, Vol. III, No. 8, August 1985.
2. Grider, G.W., "Some Effects of Heavy Surf on a Horizontally Discharged Thermal Plume, Proc. Offshore Technology Conference, Paper 1721, Houston, TX, May 1973.
3. Horikawa, K., Lin, M-C and Sasaki, T.O., "Mixing of Heated Water Discharged in the Surf Zone", Proc. 16 th Int. Conf. Coastal Engineering, Ch. 155, Hamburg, Germany, Aug. 27-Sept. 3, 1978.
4. Ismail-Awadalla, N., "Wave-Current Interaction", Technical Report HEL 27-7, Hydraulic Engineering Laboratory, University of California, Berkeley, CA, October 1980.
5. Ismail, N.M., "Effects of Opposing Waves on the Mixing of a Horizontal Surface Momentum Jet", Technical Report HEL 27-9, Hydraulic Engineering Laboratory, University of California, Berkeley, CA, June 1981.
6. Ismail, N., "Effect of Wave-Current Interaction on Littoral Drift", Shore & Beach, Vol. 50, Jan. 1982.
7. Ismail, N.M., and Wiegel, R.L., "Opposing Wave Effect on Momentum Jets Spreading Rate", Journal of Waterways, Port, Coastal and Ocean Engineering, Vol. 109, No. 4, Nov. 1983.
8. Ismail, N.M., Ryan, P.J. and Tu, S.W. "Role of Wave Transformation on Mixing of Buoyant Jets", ASCE Speciality Conf. on Nearshore Hydrodynamics, Delaware, June 29-July 1, 1987.
9. Kuhlman, J.M., "Reynolds Number Effects on Buoyant Surface Jets". Journal of Hydraulic Engineering, ASCE, Vol. 110, No. 6, June 1984.
10. Leighton, J.P., Tu, S.W., Petrocetto, A.A., Eastman, L.K., "Characterization of Receiving Water Temperatures During Power Accension Testing of Unit 1 Diablo Canyon Power Plant", Report

- No. 420-85, Pacific Gas and Electric Company, Department of Engineering Research, March 1986.
11. Phillips, O.M., "The Dynamics of the Upper Ocean", Cambridge University Press, Cambridge, England, 1977.
 12. Porter, B.A., "Model Verification Study of the Thermal Plume Discharge Geometry and Temperature within Diablo Cove", Report No. UCB/HEL 27-14, U.C. Berkeley College of Engineering, June 1985.
 13. Ryan, P.J., Tu, S.W., Leighton, J.P., and Wiegel, R.L., "Hydraulic Model Tests for Unit 1, Diablo Canyon Power Plant, Report No. 420-86. 557, Department of Engineering Research, Pacific Gas and Electric Co., November 1986.
 14. Ryan, P.J., Ismail, N.M., Lou, R. Tu, S.W. and Wiegel, R.L., "Hydraulic Model Verification Tests for Units 1 and 2 Diablo Canyon Power Plant", Report No. 420-DC-87. 15, Department of Engineering Research, Pacific Gas and Electric Co., March 1987.
 15. Ryan, P.J., Kloepper R., Ismail, N., Tu, S.W., and Wiegel, R.L., "Hydraulic Model Tests for Heat Treatment Conditions at Diablo Canyon Power Plant", Report No. 420-DC-87.16, Department of Engineering Research, Pacific Gas and Electric Co., April 1987.
 16. Safaie, B., "Mixing of Buoyant Surface Jet Over a Sloping Bottom", Journal of Waterways, Harbors, and Coastal Engineering Division, Proc. ASCE, Vol. 105, No. WW4, 1979.
 17. Tanaka, H. and Wada, A., "Prediction of the Diffusion of Discharged Warm Water Influenced by Nearshore Currents", Coastal Engineering in Japan, Vol. 25, 1982.
 18. Tu, S.W., Leighton, J.P., White, C.O. Hsu, C.C. "Surface Buoyant Jet Characteristics of the Thermal Discharge Plume at Diablo Canyon Power Plant", Report No. 420-86, 475, Department of Engineering Research, Pacific Gas and Electric Company, November 1986.
 19. Wiegel, R.L., Harms, V.W., Safaie, B., Cumming, J.D., Della, R.P., C.B., Leidersdorf, and C. Young, "Report on Model Study of Cooling Water System of Pacific and Electric Company Nuclear Power Plant Located at Diablo Canyon, California", Technical Report HEL 27-2, Hydraulic Engineering Laboratory, University of California, Berkeley, CA, January 1976.

CHAPTER 188

STOCHASTIC ANALYSIS OF OFFSHORE CURRENTS

Michel K. Ochi* and Richard I. McMillen*

ABSTRACT

This paper presents the results of stochastic analysis of offshore currents. The purpose of this study is to clarify the stochastic properties of offshore currents, and to develop a method to predict the magnitude of the extreme currents and their direction from measured data. Statistical analysis as well as spectral analysis are carried out on current velocities measured over a period of several months off Newfoundland, Canada. The effect of water depth on the statistical characteristics of current velocity is also clarified. The extreme current velocity expected to occur in 4- months and its direction are estimated by applying order statistics and the results are compared with the measured data.

INTRODUCTION

Current velocity measured in offshore areas, in general, results from currents primarily related with astronomical tide and those induced by local wind. Current velocity associated with ocean circulation and storm surge, etc., may also be significant depending on geographical location. All of these components can exist simultaneously, and hence the measured data demonstrate that the magnitude of the current velocity fluctuates in a random fashion with frequencies covering a wide range from 0.0008 to 0.08 cycles per hour (period range from 12 to 1200 hours).

Furthermore, the direction of the current velocity changes with time; it rotates clockwise in the northern hemisphere due to the rotation of the earth and the coriolis force. The angular frequency of rotation, however, is random. It varies from 0.31 to 0.70 radians per hour. Thus, the current velocity is considered to be a random process with varying frequency and direction.

Several studies have been carried out on the fluctuating properties of offshore currents as listed, among others, in References [1] through [8]. The results demonstrated in these references suggest that currents may be considered as a stochastic process consisting of various frequency components; (a) a tidal component with a frequency of 1 cycle per day (cpd) or 2 cpd depending on the location, (b) a wind-induced component with frequencies ranging from 0.10 to 0.20 cpd, and (c) seasonal variations of extremely low-frequency.

* Coastal & Oceanographic Engineering Department
University of Florida, Gainesville, Florida, U.S.A.

The purpose of the present study is to clarify the stochastic properties of offshore currents, and to develop a method to predict the magnitude of the extreme currents and their direction from measured data. For this, a statistical analysis is carried out on current velocities measured over a period of several months off Newfoundland, Canada. Statistical analysis as well as spectral analysis are carried out and the relationship between the area under the spectral density function and the variance evaluated from the time history is clarified. An analysis is also made of the data to examine the effect that water depth has on the statistical characteristics of current velocity. Finally, the extreme current velocity expected to occur in 4-months, and its direction, are estimated by applying order statistics and the results are compared with the measured data.

OFFSHORE CURRENT DATA AND ANALYSIS PROCEDURE

Data

Statistical analyses are carried out on approximately four months of continuous current data. The current meter mooring was located in a water depth of 84 meters. The mooring had three current meters sampling at 10 minute intervals at depths of 26, 47 and 75 meters. The current meter data are hourly mean velocities obtained by removing the high-frequency noise with a digital filter and sub-sampling the resulting smoothed signal to hourly values.

A dominant hourly current direction was obtained for each hourly current velocity from the directional data which was obtained from compasses moored with the current meters at the three depths. Here, the current direction is defined as that to which the water is flowing.

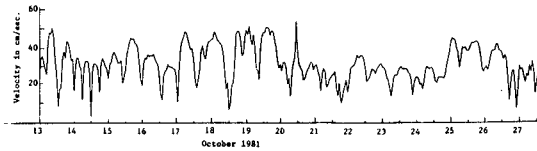
Analysis Procedure

The time history of the near-surface current velocity is first decomposed into an East-West and North-South direction. An example of the time history of hourly current velocities as well as the decomposed East-West and North-South time histories are shown in Figure 1. This example represents the data obtained for two weeks from October 13 to October 27, 1981.

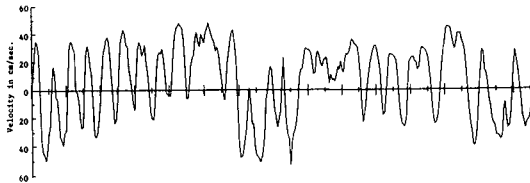
A statistical analysis is then performed on the East-West and North-South time histories in which the probability distributions applicable for deviations from the mean and the maximum (positive and negative variations) are obtained. After the statistical analysis is made for the East-West and North-South time histories, a Fast-Fourier-Transform (FFT) technique is used to obtain the energy spectrum for each time history.

In general, it is somewhat difficult to differentiate the measured current velocities into various components such as the wind-generated, tidal, and ocean current components, etc. Hence, it may be appropriate to decompose the measured currents into a high and low-frequency component. Here, the high-frequency component is considered to be the currents associated with tides, while the low-frequency components are those attributed to all other environmental conditions which may be called the residuals. The FFT is used to obtain the high-frequency (frequency > 0.035 cph) and the low-frequency (frequency < 0.035 cph) current velocity time histories in the East-West and North-South directions. These are called the tidal and residual currents, respectively, in the present study.

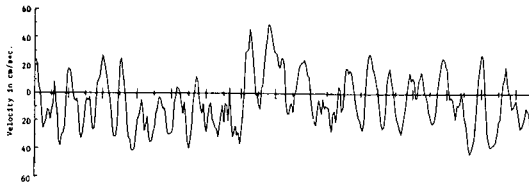
As an example, Figure 2 shows the time histories of the high-frequency (tidal) and the low-frequency (residual) current fluctuations for the East-West component which was shown in Figure 1.



Current velocity



East-west component of current velocity



North-south component of current velocity

Figure 1: Time histories of current velocity, and East-West, and North-South components of velocity.

RESULTS OF STATISTICAL ANALYSIS OF CURRENTS

Figure 3 shows an example of a polar diagram indicating the magnitude and direction of current velocity as a function of time. The data pertains to a 20-hour observation made on October 10th. The current velocities rotate clockwise in the Northern hemisphere through 360° in approximately 20 hours (a circular frequency of 0.31 radians per hour in this example). However, further analysis of the data indicates the circular frequency of the near-surface current is not constant, but instead varies from 0.31 to 0.70 radians per hour (9.0 to 20 hours). The circular frequencies of the current at 47 meter and 75 meter water depths are also examined. It is noted the preferred directions of motion water throughout the water column appears to be consistent with Ekman veering arguments.

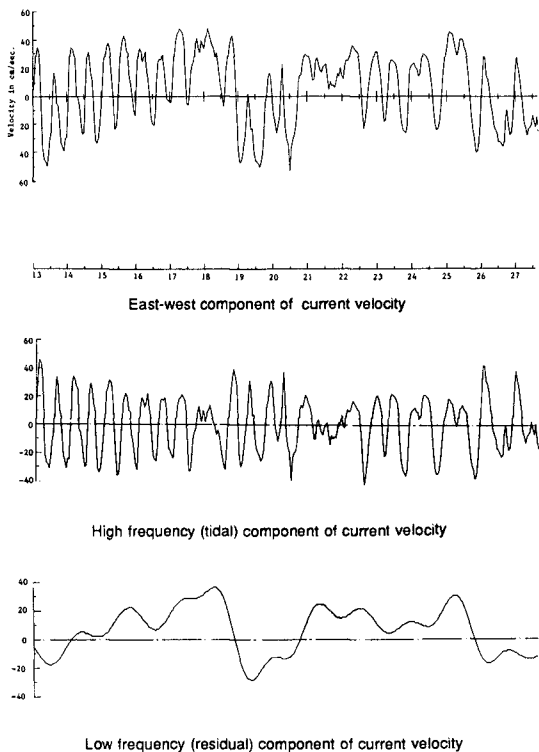


Figure 2: Time histories of East-West component of current velocity, and high frequency (tidal) and low-frequency (residual) components.

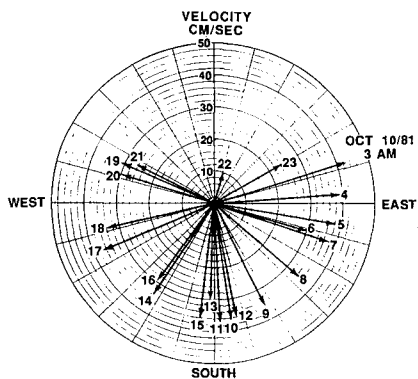


Figure 3: Current velocity magnitudes rotating in a clock-wise direction.

Distribution of Fluctuating Current Velocities

Figure 4 shows the histograms of the deviations from the mean constructed from the time history for the East-West components. The deviations include both tidal and residual velocity components.

Included also in the figures are the normal (Gaussian) and non-Gaussian distributions for comparison with the histograms. The non-Gaussian probability density function is given by the following form of a Gram-Charlier expansion (Edgeworth [9] and Longuet-Higgins [10]):

$$f(x) = \frac{1}{\sigma\sqrt{2\pi}} \exp\left\{-\frac{x^2}{2\sigma^2}\right\} \left[1 + \frac{\lambda_3}{3!} H_3\left(\frac{x}{\sigma}\right) + \frac{\lambda_3^2}{72} H_6\left(\frac{x}{\sigma}\right) + \frac{\lambda_4}{4!} H_4\left(\frac{x}{\sigma}\right) + \dots\right], \quad (1)$$

where σ^2 = variance of current velocity, λ_3 = skewness of the distribution, λ_4 = kurtosis - 3, $H_n\left(\frac{x}{\sigma}\right)$ = Hermite polynomial of degree n .

As can be seen in the figure, the distribution of the deviations from the mean value appears to follow a non-Gaussian probability distribution with parameter λ_4 which is associated with the kurtosis of the distribution. The same trend can also be observed for deviations from the mean in the North-South current component.

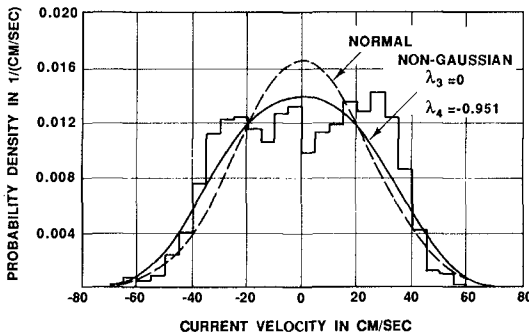


Figure 4:
Histogram of deviations
from the mean of East-
West current velocity.

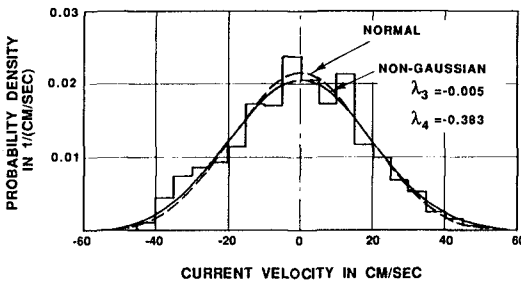


Figure 5:
Histogram of deviations
from the mean of tidal
current velocity in
East-West direction.

The correlation coefficient between two components (the East-West and North-South velocity components) is extremely small, on the order of 0.005. This implies that a statistical analysis of current velocities can be done independently in two directions.

Figures 5 and 6 show the histograms of deviations from the mean value for the tidal and residual components, respectively, in the East-West direction. Included also in these figures are the normal and non-Gaussian distributions for comparison with the histograms. As can be seen in these figures both the tidal and residual currents may be assumed to be Gaussian random processes. However, it will be shown later that the tidal component can be considered a narrow-band random process, while the residual component appears to be a non-narrow-band random process. This same trend can also be observed for currents in the North-South direction.

The results of computation show that the correlation coefficient between the tidal and residual currents is extremely small for both East-West and North-South directions. Therefore, it may safely be assumed that the tidal current and the residual current velocity components are statistically independent.

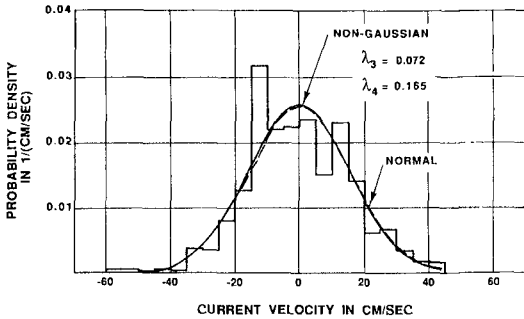


Figure 6: Histogram of deviations from the mean of residual current velocity in East-West direction.

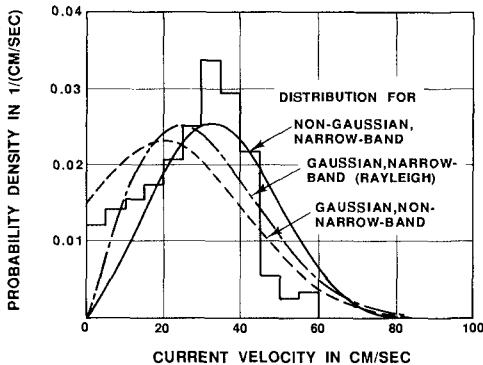


Figure 7: Histogram of maxima of current velocity in the East direction.

Distribution of Maxima

Figure 7 shows the histogram of the maxima in the East direction constructed from current velocities including both tidal and residual components. Included also in the figure are the probability distributions applicable for the maxima. These include the probability density functions of the maxima applicable for a (a) narrow-band Gaussian random process, (b) non-narrow-band Gaussian random process, and (c) narrow-band non-Gaussian random process given below (Ochi & Wang [11]):

$$f(\xi) = \frac{1}{L} \left[\frac{\xi}{\sigma^2} \exp \left\{ -\frac{\xi^2}{2\sigma^2} \right\} \left\{ 1 + \frac{\lambda_4}{4!} H_4 \left(\frac{\xi}{\sigma} \right) \right\} \right] \quad (2)$$

where σ^2 = variance of current deviation from the mean
 ξ = maxima, $0 < \sigma < \infty$, L = normalization factor.

As can be seen in the figure, the histogram of the maxima, as expected, is not represented by either of the two distributions associated with a Gaussian (normal) process. The representation of the histogram by the probability distribution of the maxima for a non-Gaussian random process is marginally acceptable. A possible explanation of this discrepancy between the histograms and the distribution for the maxima of a non-Gaussian random process is as follows:

The distribution applicable for the maxima of a non-Gaussian random process (Equation 2) is developed based on the assumption that the process is narrow-banded. However, the time history of offshore currents including both tidal and residual components encompasses an extremely wide range of frequencies (from 0.0008 to 0.08 cycles per hour). This indicates that the maxima of the offshore currents (including both tidal and residual components) may obey the distribution applicable for a non-narrow-band, non-Gaussian random process.

Spectral Analysis

Spectral analysis is carried out on measured current velocities to examine (a) frequency components which carry significant energy with the current flow, and (b) the relationship between spectral energy (area under the spectral density function) and the variance of the current fluctuations which can be evaluated from the time history of the current velocity. Figures 8 and 9 show the energy spectra for the tidal and residual components in the East-West direction, respectively. A Fast-Fourier-Transform technique is used to obtain the tidal and residual time histories in both the East-West and North-South directions. A cutoff frequency of 0.035 cycles/hour (28.4 hour period) is used to separate the time histories into their respective tidal and residual components.

The area under the spectral density function, denoted by m_0 , and the bandwidth parameter, denoted by ε , are evaluated from the spectra and tabulated in Table 1. Included also in the table are the variances, σ^2 , obtained from the time history of current velocity. It may be of interest to compare the variance, σ^2 , with the moment, m_0 . These should agree, in general for a weakly stationary, ergodic random process with zero mean. The offshore current velocity measured over a period of several months, however, cannot be considered as a stationary random process. Nevertheless, as can be seen in the table, the agreement between σ^2 and m_0 is reasonable in both the East-West and North-South directions. The

difference between them is approximately 8 percent in the East-West direction, and 4 percent in the North-South direction. The agreement between σ^2 and m_0 for the decomposed tidal and residual components is excellent. This is because the time histories of the tidal and residual components are obtained through FFT filtering techniques which retain the statistical properties of random phenomena including phase information as well.

The results obtained above substantiate the fact that the spectral density function of the current velocity in any direction is interrelated with the variance of current fluctuations. Hence, the probabilistic prediction of the magnitude of current velocity may be made through spectral analysis.

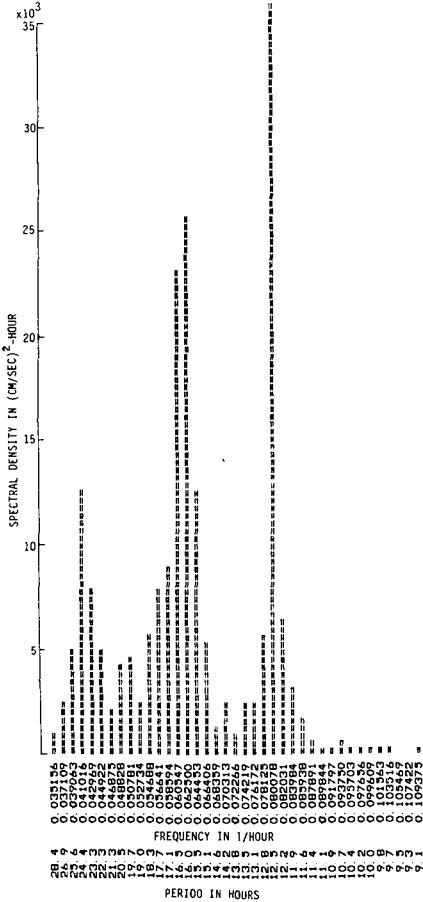


Figure 8:
Energy spectrum of tidal (High frequency) current velocity in East-West direction.

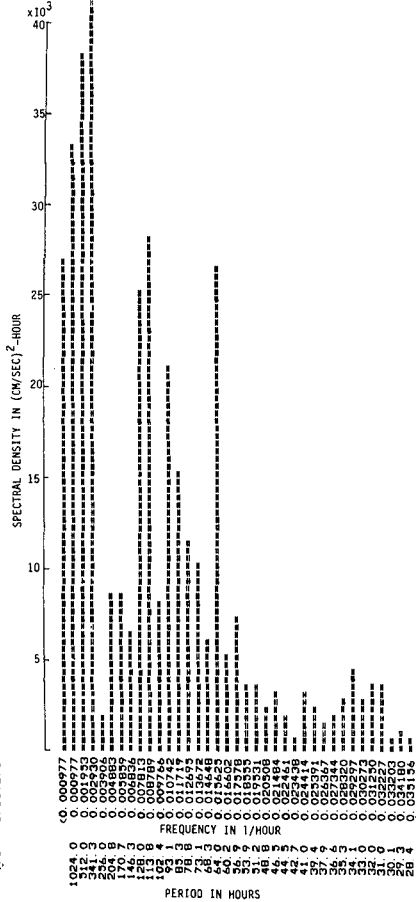


Figure 9:
Energy spectrum of residual (low frequency) current velocity in East-West direction.

Table 1: Variance evaluated from time history of current velocity, σ^2 , area under the current energy spectrum, m_0 , and spectrum band-width parameter, ϵ .

Current velocity components	Variance σ^2	Area under the spectrum m_0	Spectrum band-width parameter ϵ
East-West direction			
Total	627.5	583.2	0.735
Residual	248.6	248.7	0.845
Tidal	334.2	334.3	0.494
North-South direction			
Total	529.0	508.1	0.735
Residual	214.2	214.2	0.828
Tidal	293.6	293.7	0.505

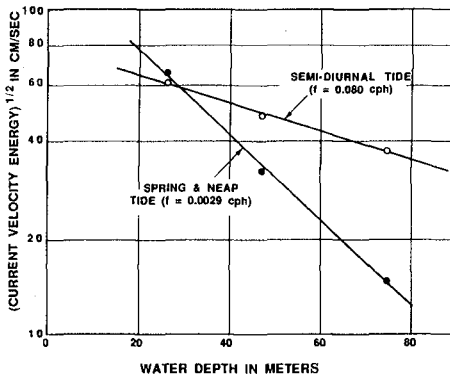


Figure 10: Square-root of current energy density for frequencies 0.080 cph (12.5 hour period) and 0.0029 cph (14.2 day period).

Effect of Water Depth

The same statistical analysis carried out on the near-surface current data was also made on data obtained at two deeper depths; 47 and 75 meters. These are called the mid-depth and near-bottom locations in the following analysis.

The results of the analysis indicate that almost all statistical properties of the fluctuating current velocity obtained from analysis of data at the deeper depths appear to be nearly the same as those obtained from the current velocities at the near surface. However, the severity of current fluctuations is drastically reduced with increase in depth, and the non-Gaussian random process characteristics observed for the near-surface current velocity are substantially less pronounced at deeper locations.

In order to examine the reduction of current velocity with increase in water depth, Figure 10 was prepared. The figure shows the square root of the current energy density (the vector sum of the East-West and North-South components) for the frequencies 0.080 cph (period 12.5 hours) and 0.0029 cph (period 341 hours) plotted on semi-log paper as a function of water depth. Here, the frequency 0.080 cph corresponds to that for the semi-diurnal tide, and the tidal current (high frequency) spectrum shows an extremely large energy density at this frequency. The frequency 0.0029 cph corresponds to that for the spring and neap tide, and the residual current (low frequency) spectrum shows considerable energy density at this frequency.

As can be seen in the figure, the square-root of current energy, which is proportional to the current velocity, reduces exponentially with increase in water depth. The reduction rate of the current velocity for the spring and neap tide (low-frequency) is much larger than that for the semi-diurnal tide (high-frequency component). This result indicates that the tidal and residual current energies both decrease substantially with increase in water depth. However, the rate of decrease for the residual currents is much larger than that for the tidal currents.

Estimation of Extreme Value

It was shown that the current velocity fluctuations can be considered as a non-Gaussian random process with the parameter λ_4 , and that the East-West component and the North-South component are statistically independent. This being the case, it can be proved that the current velocity for an arbitrary direction is also approximately a non-Gaussian random process as derived in the Appendix. That is, the probability density function of current velocity fluctuations (deviation from the mean) for an arbitrary direction θ can be given by Eq. (1) with $\lambda_3 = 0$ and with the following variance, σ^2 , and parameter, λ_4 , which are now a function of angle θ :

$$\begin{aligned}\sigma^2(\theta) &= \sigma_e^2 \sin^2 \theta + \sigma_n^2 \cos^2 \theta \\ \lambda_4(\theta) &= \frac{\lambda_{4e} \sigma_e^4 \sin^4 \theta + \lambda_{4n} \sigma_n^4 \cos^4 \theta}{(\sigma_e^2 \sin^2 \theta + \sigma_n^2 \cos^2 \theta)^2}\end{aligned}\quad (3)$$

where θ = angle measured from North to East, σ_e^2, σ_n^2 = variance of the East-West and North-South direction, respectively, $\lambda_{4e}, \lambda_{4n}$ = parameter λ_4 -value for the East-West direction and North-South direction, respectively.

This results in the probability density function of the maxima having the same form as shown in Eq. (2) but with the variance, $\sigma^2(\theta)$, and parameter, $\lambda_4(\theta)$, as given in Eq. (3). That is,

$$f(\xi, \theta) = \frac{1}{L} \left[\frac{\xi(\theta)}{\sigma^2(\theta)} \exp \left\{ -\frac{1}{2} \left(\frac{\xi(\theta)}{\sigma(\theta)} \right)^2 \right\} \left\{ 1 + \frac{\lambda_4(\theta)}{4!} H_4 \left(\frac{\xi(\theta)}{\sigma(\theta)} \right) \right\} \right] \quad (4)$$

where $L = 1 + \lambda_4(\theta)/3!$

Then, the extreme current velocity which is most likely to occur in n -peaks for a given angle θ , denoted by $\bar{\xi}(\theta)$, is given as the value which satisfies the following equation:

$$\int_0^{\bar{\xi}(\theta)} f(\xi, \theta) d\theta = F(\bar{\xi}(\theta)) = 1 - \frac{1}{n} \quad (5)$$

Numerical computations were carried out for various angles between 0 and 90 degrees, with variance $\sigma_z^2 = 583.2(\text{cm/sec})^2$ and $\sigma_n^2 = 508.1(\text{cm/sec})^2$, and $n = 175$ in a 4-month observation period.

Figure 11 shows the computed extreme current velocities for various directions plotted in polar coordinates. As can be seen in the figure, there is no substantial difference in the magnitude of the extreme current velocities in various directions for data used in the present analysis. The magnitudes of the extreme current velocities in the shaded domain in the figure are nearly equal (70.3 - 69.6 cm/sec). The magnitude of the extreme current velocity observed in the same time period is 74.0 cm/sec in the South-West direction.

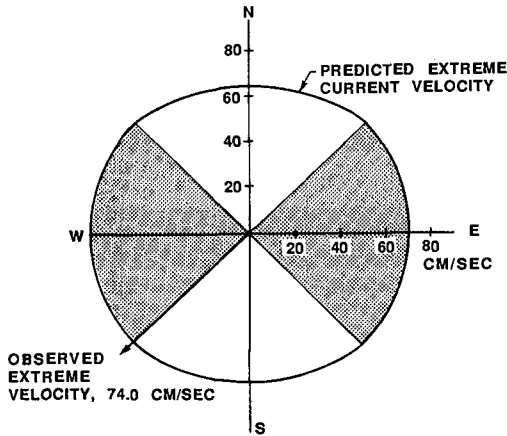


Figure 11:
Computed extreme current velocities expected in a four-month observation for various directions.

CONCLUSIONS

From the results of the stochastic analysis of offshore current data the following conclusions can be drawn:

(1) Deviations from the mean value of the current velocity for the East-West and North-South components (including both tidal and residual velocity components) obey a non-Gaussian probability distribution with parameter λ_4 which is associated with the kurtosis of the distribution.

(2) The correlation coefficient evaluated for the East-West and the North-South current velocity time histories is extremely small; hence they are considered to be statistically independent.

(3) When the East-West and North-South velocity components are decomposed into high-frequency (tidal) and low-frequency (residual) components, the tidal and residual components of the current velocity are found to be statistically independent. Both the tidal and residual currents may be assumed to be Gaussian random processes. In particular, the residual component appears to be a non-narrow-band Gaussian random process.

(4) Histograms of maxima (peak values) of fluctuating currents in all four directions (East, West, North, and South) indicate that the maxima (including both tidal and residual components) can be marginally represented by the distribution of the maxima for a narrow-band non-Gaussian random process. It appears that the maxima obey the distribution applicable for a non-narrow-band non-Gaussian random process.

(5) The area under the spectral density function agrees well with the variance obtained from the time histories for both the East- West and North-South velocity components.

(6) The statistical properties of current velocity obtained from analysis of current data at deeper depths are nearly the same as those obtained from near-surface current data. However, the non- Gaussian random process characteristics stated in Item (1) are substantially less pronounced at deeper depths.

(7) The square-root of the current energy, which is proportional to the current velocity decreases exponentially with an increase in water depth. The rate of decrease is much larger for the residual current velocity than that for the tidal current velocity.

(8) An approximate method for estimating the magnitude of extreme current velocity is developed by applying order statistics to the probability distribution of a non-Gaussian random process. The results of computations made for a 4-month observation period show satisfactory agreement with observed data.

ACKNOWLEDGEMENTS

This research was sponsored by the Office of Naval Research, Ocean Technology Program, through contracts N00014-86-k-0537 to the University of Florida. The authors would like to express their appreciation to Dr. E.A. Silva for his valuable technical discussions received during the course of this project. The authors are grateful to Dr. Max Sheppard for his kind help in obtaining the current data used in this study. The authors also wish to express their appreciation to Ms. Laura Dickinson for typing the manuscript.

APPENDIX: PROBABILITY DISTRIBUTION OF CURRENT VELOCITY FOR AN ARBITRARY DIRECTION

The standardized non-Gaussian probability density function with the parameter λ_4 can be written as

$$f(z) = \frac{1}{\sqrt{2\pi}} \exp\left\{-\frac{z^2}{2}\right\} \left[1 + \frac{\lambda_4}{4!} H_4(z)\right] \quad (\text{A.1})$$

where $H_4(z) = z^4 - 6z^2 + 3$.

mean, variance σ^2 , and parameter λ_4 becomes

$$\Phi_z(t) = \exp\left\{-\frac{\sigma^2 t^2}{2}\right\} \left(1 + \frac{\lambda_4}{4!} \sigma^4 t^4\right) \quad (\text{A.3})$$

Next, let us consider two statistically independent non-Gaussian random variables x_e and x_n , representing the East-West current velocity and the North-South current velocity, respectively. These are,

$$\begin{aligned} x_e &: \text{non-Gaussian}(0, \sigma_e^2; \lambda_{4e}) \\ x_n &: \text{non-Gaussian}(0, \sigma_n^2; \lambda_{4n}) \end{aligned} \quad (\text{A.4})$$

We may then write the current velocity for an arbitrary direction θ as

$$x(\theta) = x_e \sin \theta + x_n \cos \theta \quad (\text{A.5})$$

where θ = angle measured from North to East.

Since x_e and x_n are statistically independent, the characteristic function of $x(\theta)$ can be obtained by applying Eq.(A.3) as

$$\begin{aligned} \Phi_{x(\theta)}(t) &= \Phi_{x_e}(t \sin \theta) \cdot \Phi_{x_n}(t \cos \theta) \\ &\sim \exp\left\{-\left(\sigma_e^2 \sin^2 \theta + \sigma_n^2 \cos^2 \theta\right) \frac{t^2}{2}\right\} \\ &\quad \times \left[1 + \frac{1}{4!} (\lambda_{4e} \sigma_e^4 \sin^4 \theta + \lambda_{4n} \sigma_n^4 \cos^4 \theta) t^4\right] \\ &= \exp\left\{-\left(\sigma_e^2 \sin^2 \theta + \sigma_n^2 \cos^2 \theta\right) \frac{t^2}{2}\right\} \\ &\quad \times \left[1 + \frac{1}{4!} \frac{\lambda_{4e} \sigma_e^4 \sin^4 \theta + \lambda_{4n} \sigma_n^4 \cos^4 \theta}{(\sigma_e^2 \sin^2 \theta + \sigma_n^2 \cos^2 \theta)^2}\right. \\ &\quad \left. \times (\sigma_e^2 \sin^2 \theta + \sigma_n^2 \cos^2 \theta)^2 t^4\right] \end{aligned} \quad (\text{A.6})$$

From a comparison of Eqs.(A.3) and (A.6), it can be proved that the random variable $x(\theta)$ has approximately a non-Gaussian distribution with the following variance, $\sigma^2(\theta)$, and parameter, $\lambda_4(\theta)$:

$$\begin{aligned} \sigma^2(\theta) &= \sigma_e^2 \sin^2 \theta + \sigma_n^2 \cos^2 \theta \\ \lambda_4(\theta) &= \frac{\lambda_{4e} \sigma_e^4 \sin^4 \theta + \lambda_{4n} \sigma_n^4 \cos^4 \theta}{(\sigma_e^2 \sin^2 \theta + \sigma_n^2 \cos^2 \theta)^2} \end{aligned} \quad (\text{A.7})$$

REFERENCES

1. Beardlsey, R.C., and B. Butman, "Circulation on the New England Continental Shelf: Response to Strong Winter Storms," *Geophysical Research Letter*, Vol. 1, 1974, pp. 181-184.
2. Smith, R.L., "A Description of Current, Wind, and Sea Level Variations During Coastal Upwelling Off the Oregon Coast, July-August 1972," *Journal of Geophysical Research*, Vol. 79, 1974, pp. 435-443.
3. Lee, T.N. and D.A. Mayer, "Low-Frequency Current Variability and Spin-Off Eddies Along the Shelf Off Southeast Florida," *Journal Marine Res.*, Vol. 35, 1977, pp. 193-218.
4. Chuang, W-S., D-P. Wang and W.C. Boicourt, "Low-Frequent Current Variability on the Southern Mid-Atlantic Bight," *Journal of Physical Oceanography*, Vol. 9, 1979, pp. 1144-1154.
5. Hayes, S.P., "Variability of Current and Bottom Pressure Across the Continental Shelf in the Northeast Gulf of Alaska," *Journal of Physical Oceanography*, Vol. 9, 1979, pp.88-103.
6. Mayer, D.A., D.V. Hansen and D. Ortman, "Long-Term Current and Temperature Observations on the Middle Atlantic Shelf," *Journal of Geophysical Research*, Vol. 84, 1979, pp.1776-1792.
7. Noble, M. and B. Butman, "On the Longshelf Structure and Dynamics of Subtidal Currents on the Eastern United States Continental Shelf," *Journal of Physical Oceanography*, Vol. 13, 1983, pp. 2125-2147.
8. Butman, B. and R.C. Beardsley, "Long-Term Observations on the Southern Flank of Georges Bank. Part 1: A Description of the Seasonal Cycle of Currents, Temperature, Stratification, and Wind Stress," *Journal of Physical Oceanography*, Vol. 17, 1987, pp. 367-384.
9. Edgeworth, F.Y., "On the Representation of Statistical Frequency by a Series," *Journal, Royal Statistical Society Series A*, Vol 70, 1907, pp. 102-106.
10. Longuet-Higgins, M.S., "The Effect of Non-Linearities on Statistical Distribution in the Theory of Sea Waves," *Journal of Fluid Mechanics*, Vol. 17, Part 3, 1963, pp.459-480.
11. Ochi, Michel K. and W-C. Wang, "Prediction of Wave Height of Wind-Generated Seas in Infinite Water Depth," *Tech. Rep. UFL/COEL/TR-052*, University of Florida, 1984.

CHAPTER 189

Entrainment due to Mean Flow in Two-Layered Fluid

Masaru Ura*
and
Nobuhiro Matsunaga**

Abstract

The entrainment phenomena have been investigated across an interface between two-layered stratified flow induced by wind shear stress. The velocities of mean flow, turbulence and entrainment have been measured under three different conditions of water surface by using a wind-wave tank. When the entrainment velocity u_e is expressed on the basis of the turbulent quantities at the interface, the turbulent entrainment coefficient E ($\equiv u_e/u$) is given by $E = A \cdot (\epsilon g l / u^2)^{-3/2}$ ($A = 0.7$). Here ϵg , u and l are the effective buoyancy, the turbulence intensity and the integral lengthscale of turbulence at the interface, respectively. This result coincides with the relationship of entrainment due to oscillating grid turbulence, in which the mean flow does not exist. When, for the practical purpose, the estimation of u_e is made by using the mean velocity U_m and the depth h of mixed layer, E_m ($\equiv u_e/U_m$) $= A_m \cdot (\epsilon g h / U_m^2)^{-3/2}$ is derived from the transformation of $E = A \cdot (\epsilon g l / u^2)^{-3/2}$. There holds $A_m = A \cdot T_f$ between A_m and T_f , T_f being a turbulence factor given by $(u/U_m)^4 \cdot (l/h)^{-3/2}$. It has been found that this relationship is also valid in various types of two-layered stratified flows as well as the wind-induced two-layered flows.

Introduction

The density stratification is often observed in lakes or estuaries. When the wind blows over the surface of such a water body, the mixing phenomena occur frequently owing to turbulent flow induced by wind shear stress. Many laboratory studies on two-layered stratified flows have been made in order to understand this mixing phenomena. The mixing is characterized by entrainment process. Let us focus attention on the two-layered flows in which the shear stress τ is exerted on the water surface. The previous experimental works may be classified into four categories

* Professor, Department of Civil Engineering, Kyushu Institute of Technology, Tobata-ku Kitakyushu 804, Japan.

** Research Associate, Department of Civil Engineering, Kyushu University, Higashi-ku Fukuoka city 812, Japan.

as shown in Figure 1. They are as follows:

- (i) the case when flow near the interface has the same direction as that of action of τ and wind waves are present (Tsuruya et al., 1984),
- (ii) the case when shear-induced flow has the same flow pattern as the case (i) without the presence of wind waves (Kantha et al., 1975; Deardorff and Willis, 1982),
- (iii) the case when flow near the interface has the opposite direction to the surface shear stress and the wind waves are present (Wu, 1973; Kit et al., 1980; Ura, 1984; Kranenburg, 1985), and
- (iv) the case when flow pattern is the same as the case (iii) without the presence of wind waves (Kit et al., 1980).

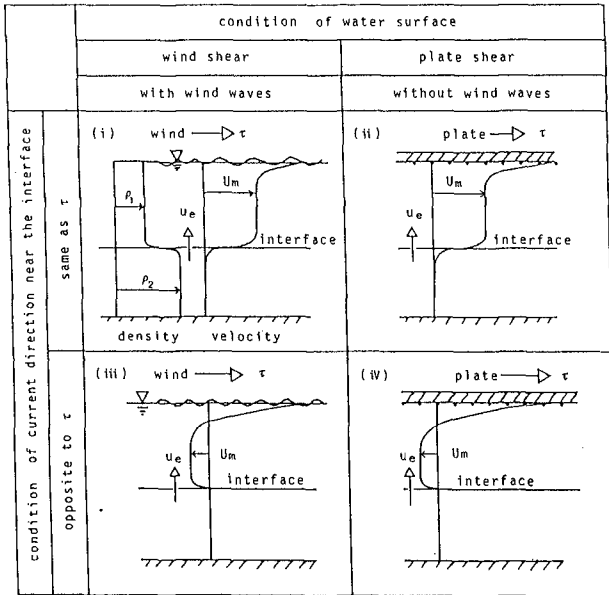


Figure 1. Classification of previous experimental works.

The researchers introduced in cases (i) to (iv) discussed the dependence of the entrainment coefficient E_* ($\equiv u_e/u_*$) on the Richardson number Ri_* ($\equiv \epsilon gh/u_*^2$). Here, u_e , u_* , ϵg and h are the entrainment velocity, the friction velocity acting on the water surface, the effective buoyancy and the water depth of mixed layer, respectively. Their results are plotted together in Figure 2. We can support the relationship of $E_* = A_* Ri_*^{-3/2}$, but the proportional factor A_* varies from 700 to 0.13 corresponding to cases (i) to (iv). This wide variation is closely related to whether mean flow direction near the interface is same or opposite to the surface shear stress and whether wind waves are present or not. Using u_* as a characteristic velocity may not be proper in order to explain consistently these data. This reason is that four

cases appear under a given magnitude of u_* at the least as far as referred here and that u_* includes no information about whether the reverse flow forms or not. Therefore, it seems appropriate to use the mean velocity U_m of uniform flow induced in the mixed layer rather than u_* .

On the other hand, it has been proposed by Ura et al. (1987b) that the entrainment process depends on the characteristic quantities of turbulence such as turbulence intensity u and integral lengthscale l of turbulence at the

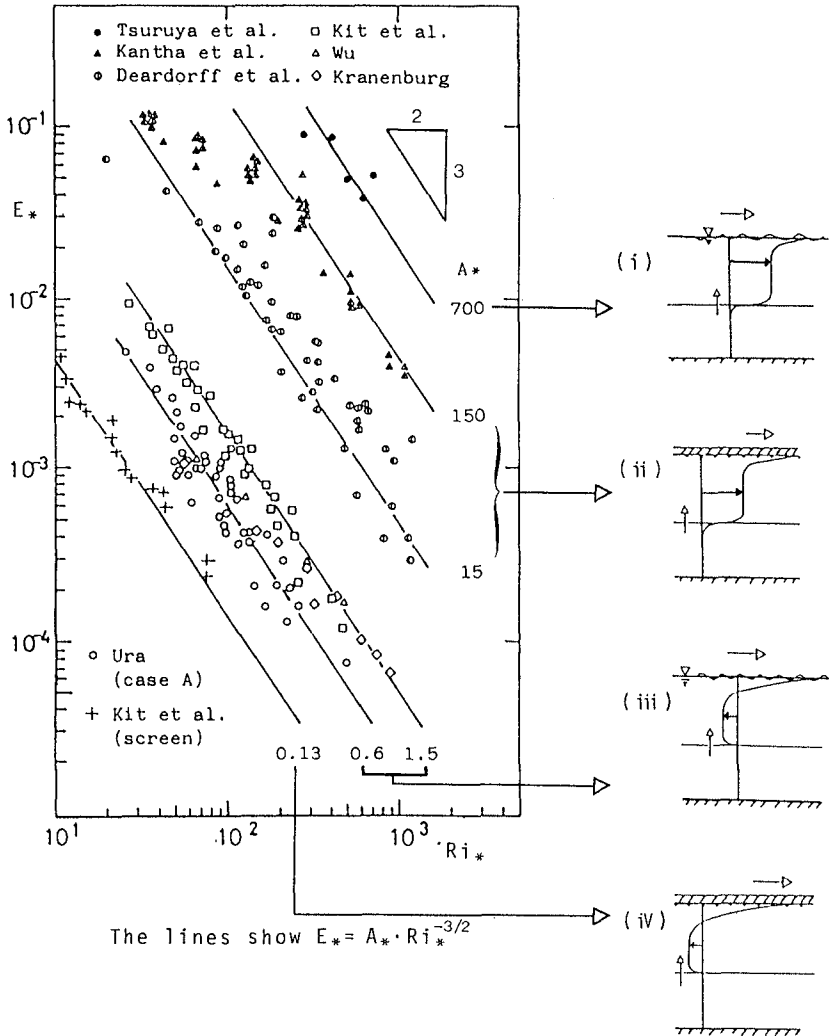


Figure 2. Ri_* - dependence of E_* .

interface. In fact, the turbulent entrainment coefficient E ($\equiv u_e/u$) is given by

$$E = A (\epsilon g l / u^2)^{-3/2} \quad (1)$$

for various types of two-layered stratified flows.

If equation (1) is rewritten by using h and U_m , the overall entrainment coefficient E_m ($\equiv u_e/U_m$) becomes

$$\begin{aligned} E_m &= (u_e/u) \cdot (u/U_m) \\ &= A [(\epsilon g l / u^2) \cdot (u/U_m)^2 \cdot (h/l)]^{-3/2} \cdot (u/U_m) \\ &= A (u/U_m)^4 \cdot (1/h)^{-3/2} \cdot (\epsilon g h / U_m^2)^{-3/2} \\ &= A_m \cdot Ri_m^{-3/2}, \end{aligned} \quad (2)$$

where

$$A_m = A \cdot (u/U_m)^4 \cdot (1/h)^{-3/2} \quad \text{and} \quad Ri_m = \epsilon g h / U_m^2.$$

It is seen from equation (2) that the proportional factor A_m is determined by the characteristic quantities of turbulence at the interface. Here, let us call $(u/U_m)^4 \cdot (1/h)^{-3/2}$ the 'turbulence factor', i.e.,

$$T_f = (u/U_m)^4 \cdot (1/h)^{-3/2}. \quad (3)$$

Equation (2) may also be applicable to general two-layered flows whose surface the shear stress does not act on.

The purpose of this paper is to explain consistently the entrainment coefficient of various types of two-layered flows on the basis of equation (2).

Experimental Methods

The wind-wave tank used in this experiment is schematically shown in Figure 3. It was 5.0m long, 0.2m wide and 0.59m high. The wind tunnel was 0.2m high with an approach section 1.0m long. A fetch of the wind on the water surface was 4.0m. The tank was filled with a two-layered fluid. The ordinate z is taken vertically downward from the mean water level.

A 4-pole conductivity probe has been used for the measurement of the fluid density. Density profiles were

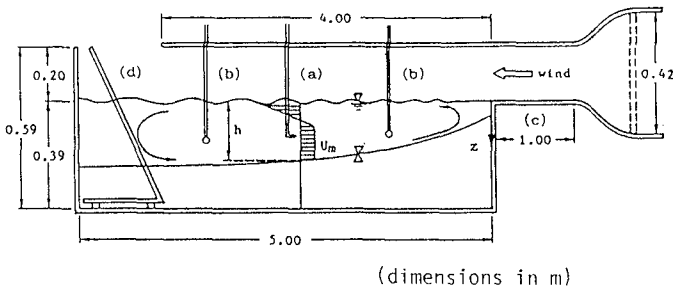


Figure 3. Experimental apparatus for wind-induced flow.

- (a) Hot-film anemometer; (b) conductivity probes;
(c) approach section; (d) wave absorber.

measured at the positions 1.42, 2.42 and 3.40m from the upstream end of the tank. The position of an interface is defined as the location where the mean density of fluid is equal to $(\rho_1 + \rho_2)/2$, where ρ_1 and ρ_2 are the fluid densities of upper and lower layers, respectively. Entrainment velocity u_e has been estimated from time variations of the depth h from the water surface to the interface level (i.e., $u_e = \partial h / \partial t$).

The wind shear stress, which induces a drift current and compensating return flow as sketched in Figure 3, acts on the free surface by blowing the wind into the tank. The vertical velocity distributions of the wind-induced flow were obtained at the middle of the tank in the longitudinal direction by using a single-component hot-film anemometer. The friction velocity u_* was evaluated from both the log-law profile of mean velocity under the water surface and the relation

$$\rho_1 u_*^2 = \gamma \rho_a u_{*a}^2,$$

where ρ_a is the density of air, u_{*a} is the air friction velocity and γ is a coefficient, which take a value between 1.0 to 0.9 (Ura, 1984). The intensity u and lengthscale l were calculated from the horizontal velocity fluctuation. The lengthscale was based on either the auto-correlation technique or the empirical formula proposed by Townsend (1976), i.e.,

$$l = 0.8 u^3 / \epsilon_d.$$

Here, ϵ_d is the rate of energy dissipation calculated from the $-5/3$ -power law of wavenumber spectrum.

Three kinds of experiments were conducted by changing the condition of water surface as shown in Figure 4.

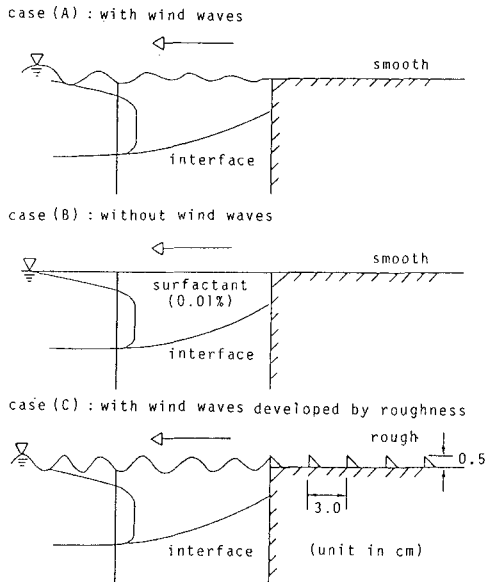


Figure 4. Experimental conditions of water surface.

- Case (A): the two-layered flow with wind waves, which developed gradually along the fetch because of the smooth approach section (i.e., case(iii)).
- Case (B): the formation of wind waves was suppressed by adding surfactant(sodium dodecyle sulfate, concentration $1.1 \times 10^{-2} \%$) in the water (similar to case(iv)).
- Case (C): the wind waves formed at the beginning of the fetch because of the existence of roughness elements on the approach section (i.e., case (iii)).

Flow Properties

Figures 5 (a) to (c) show vertical distributions of mean velocity, turbulence intensity and integral lengthscale, respectively for cases (A), (B) and (C). In these figures $z/h = 0$ indicates water surface and $z/h = 1.0$ the

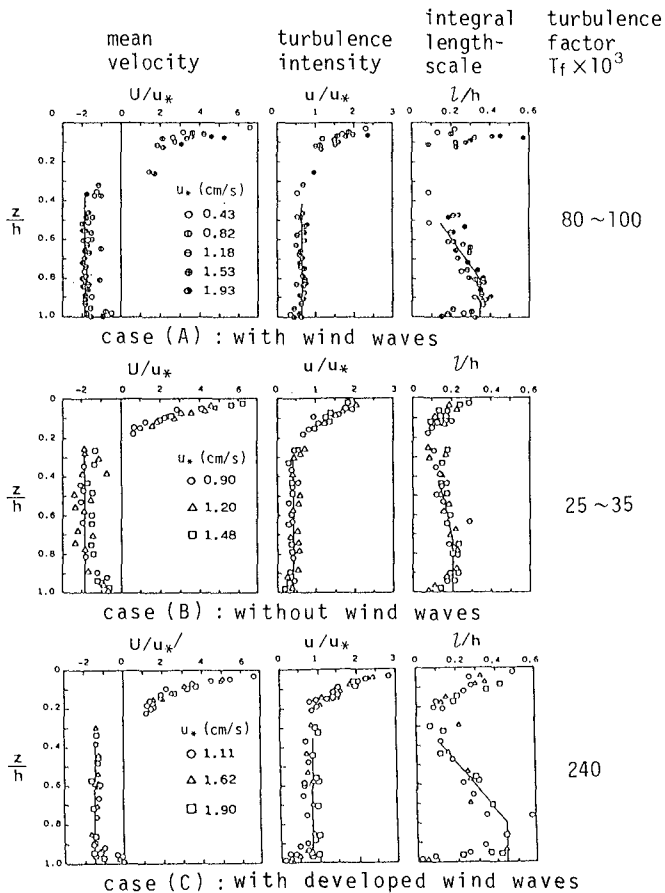


Figure 5. Vertical distributions of mean velocity, turbulence intensity and integral lengthscale.

interface. The values of these physical quantities at $z/h = 0.9$ are used as the representative values, because on the interface they are influenced significantly by the buoyancy effect. It is seen from the mean velocity profiles that a strong drift current occurs near the water surface by the wind, and that return flow with nearly uniform velocity forms in the range $1.0 > z/h > 0.25$. Denoting this uniform velocity by U_m , U_m/u_* equals about 1.85 in cases (A) and (B) and 1.50 in case (C). The relative turbulence intensities u/u_* have almost constant values in the return flow region and the intensities are approximately given by

$$u = 0.65u_* = 0.35U_m \quad \text{for case (A),}$$

$$u = 0.39u_* = 0.21U_m \quad \text{for case (B), and}$$

$$u = 0.82u_* = 0.52U_m \quad \text{for case (C).}$$

The integral lengthscales near the interface are given by

$$l \approx 0.35h \quad \text{for case (A),}$$

$$l \approx 0.20h \quad \text{for case (B), and}$$

$$l \approx 0.45h \quad \text{for case (C).}$$

From the results of these measurements, the values of the turbulence factor T_f are found to take $0.08 \sim 0.10$, $0.025 \sim 0.035$ and 0.24 in cases (A), (B) and (C), respectively. These results reveal that the condition of the water surface influences the value of T_f considerably.

Entrainment Coefficient

Figures 6 (a) and (b) are typical examples of the vertical density profiles, measured as the time proceeds, at the fetches F of 3.40 and 2.42m. The time-variations of h based on Figure 6 are shown in Figure 7. It is seen that the entrainment velocity $\partial h/\partial t$ is constant during the time of the measurement.

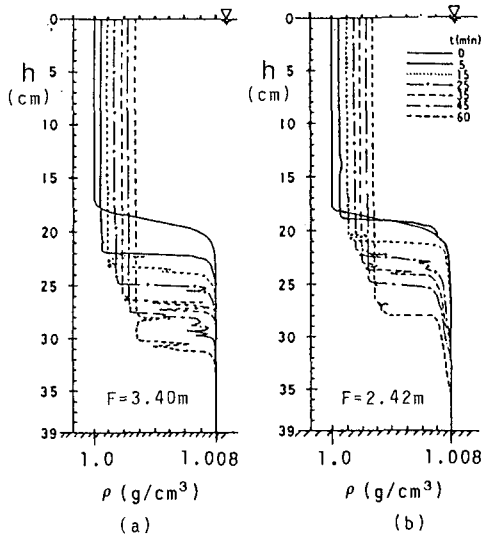


Figure 6. Time variations of vertical density profiles.

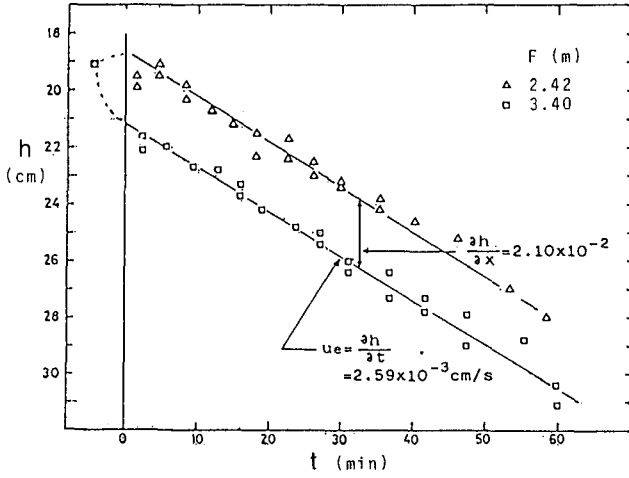


Figure 7. Time variations of the depth of the mixed layer.

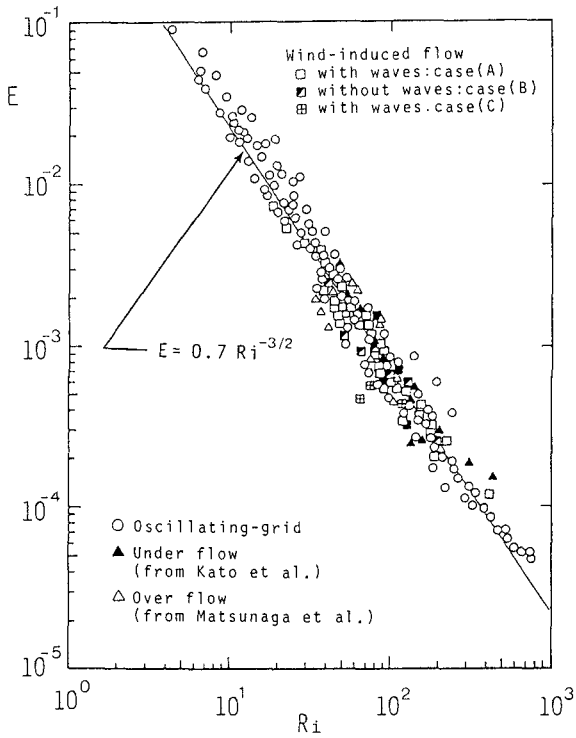


Figure 8. Ri - dependence of E .

In Figure 8, the turbulent entrainment coefficients $E = u_e/u$ are plotted against the local Richardson number $Ri = \epsilon g l / u^2$ for the three cases shown in Figure 4. The experimental results obtained from the oscillating grid turbulence (Ura et al., 1987a) and the over flow (Matsunaga et al., 1984) are also plotted in this figure. We confirm the unified expression of E based on Ri (Ura et al., 1987b), i.e.,

$$E = 0.7 \cdot Ri^{-3/2} \tag{4}$$

for various types of two-layered flows.

Figure 9 shows the relationships between bulk parameters E_m and Ri_m , which are obtained by many other researchers and authors. The values of T_f are also represented, being calculated on the basis of the data by the authors and Kato

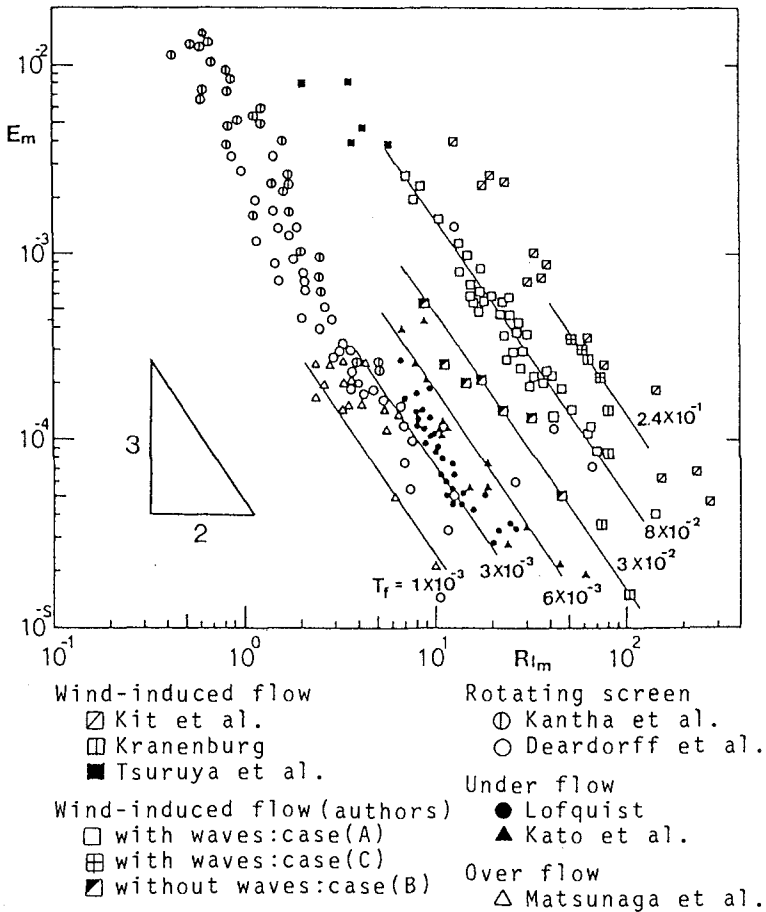


Figure 9. Relationships between E_m and Ri_m obtained by considering turbulence factor T_f .

et al. (1981). The values of T_f by the other researchers are unknown since they did not report the turbulence quantities. From this figure, however, we find that E_m is proportional to $Ri_m^{-3/2}$ and the proportional factor A_m consistently depends on T_f .

In order to confirm the validity of equation (2), it is necessary to show that A_m is proportional to T_f . Figure 10 shows the relationship between A_m and T_f . A_m is clearly proportional to T_f and the proportional constant takes 0.7. Therefore, we conclude that the entrainment relationship

$$E_m = A_m \cdot Ri_m^{-3/2} \quad ,$$

$$A_m = 0.7 \cdot T_f$$

holds for the various types of two-layered stratified flows.

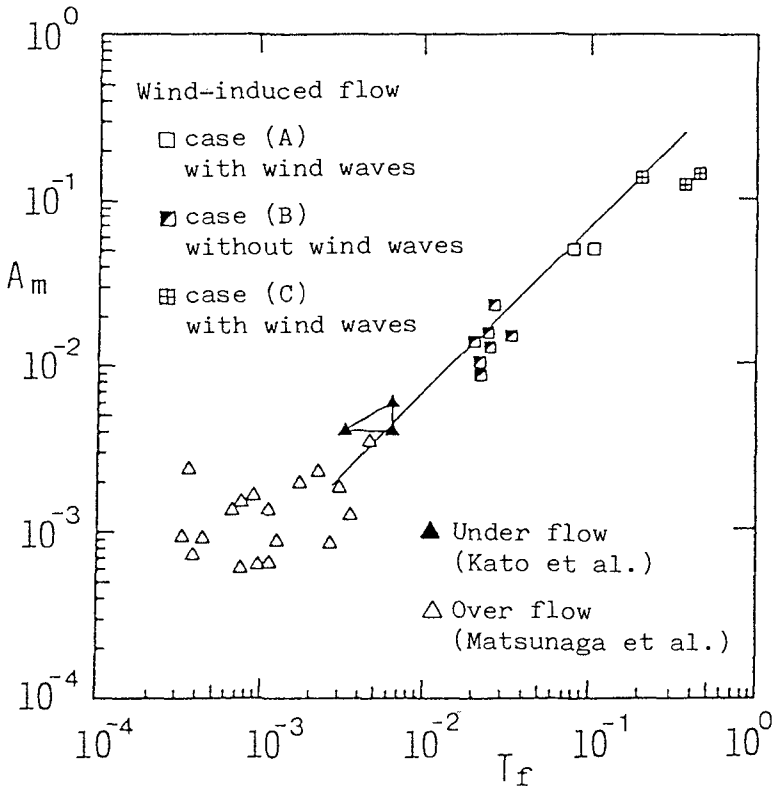


Figure 10. Relationships between A_m and T_f .

Acknowledgment

The authors thank Professors T. Tsubaki and T. Komatsu for stimulating discussions and Mr T. Awaya for technical help.

References

- Deardorff, J. W. and Willis, G. E. (1982). "Dependence of mixed-layer entrainment on shear stress and velocity jump." *J. Fluid Mech.*, 115, 123-149.
- Kantha, L. H., Phillips, O. M. and Azad, R. S. (1975). "On the turbulent entrainment at a stable density interface." *J. Fluid Mech.*, 79, 753-768.
- Kato, H. and Ikeda, T. (1981). "An experiment of lower density current(1)." *The 28th Japanese Conf. Coastal Eng.*, 520-524, (in Japanese).
- Kit, E., Berent, E. and Vajda, M. (1980). "Vertical mixing induced by wind and rotating screen in a channel." *J. Hydr. Res.*, 18(1), 35-58.
- Kranenburg, C. (1985). "Mixed-layer deepening in lakes after wind setup." *J. Hydr. Div., ASCE*, 111(HY9), 1279-1297.
- Lofquist, K. (1960). "Flow and stress near an interface between stratified liquids." *Phys. Fluids*, 3, 158-175.
- Matsunaga, N., Ura, M., Namikawa, T. and Tsubaki, T. (1984). "Flow properties near an interface in upper-layer flow." *Proc. 28th Japanese Conf. Hydr.*, 345-351 (in Japanese).
- Thompson, S. M. and Turner, J. S. (1975). "Mixing across an interface due to turbulence generated by an oscillating grid." *J. Fluid Mech.*, 67, 349-368.
- Townsend, A., A. (1976). *The structure of turbulence shear flow* (2nd ed.), Cambridge University Press. Cambridge, London.
- Tsuruya, H., Nakano, S. and Ichinohe, H. (1984). "Vertical mixing and turbulent characteristics of wind-driven two-layered flows." *Proc. 31st Japanese Conf. Coastal Eng.* 655-659, (in Japanese).
- Ura, M. (1984). "Interfacial waves and entrainment in a wind-induced stratified flow." *Proc. 4th Cong. APD- IAHR*, 403-417.
- Ura, M., Komatsu, T. and Matsunaga, N. (1987a). "Entrainment due to oscillating grid turbulence in two-layered fluid." *Turbulence Measurements and Flow Modeling*, Chen, C. J., Chen, L. D. and Holly, F. M. Ed. Hemisphere Publishing Corporation, New York, N.Y., 109-118.
- Ura, M., Tsubaki, T., Matsunaga, N. and Namikawa, T. (1987b). "A turbulence-based expression for the entrainment coefficient for two-layered stratified flows." *J. Hydroscience and Hydr. Eng.*, 5(1), 22-37.
- Wu, J. (1973). "Wind-induced turbulent entrainment across a stable density interface." *J. Fluid Mech.*, 61, 275-287.

CHAPTER 190

BOUNDARY CONDITIONS IN FINITE ELEMENT MODELING OF STRATIFIED COASTAL CIRCULATION

by George C. Christodoulou¹, M.ASCE
and George D. Economou²

ABSTRACT

The effect of boundary conditions on numerical computations of stratified flow in coastal waters is examined. Clamped, free radiation and sponge layer conditions are implemented in a two-layer finite element model and the results of simple tests in a two-layer stratified basin are presented.

INTRODUCTION

Numerical models of coastal circulation require the specification of boundary conditions at the sea boundaries, where the computational domain is artificially terminated. In 2-D depth-averaged models conditions are normally imposed on the vertical displacement of the free surface at the grid nodes located on the boundary. Most commonly, the surface displacements are prescribed in a desired manner, according to either a known tidal input or to an elevation time series available from field data. This type of b.c. is referred to as clamped, since the position of the surface at the boundary is absolutely defined a priori for the entire computation. Other types of b.c. often employed include the Sommerfeld free radiation conditions in various forms, which allow disturbances created within the domain to travel freely outwards, or sponging functions, which serve as filters absorbing outgoing waves. The importance of boundary conditions has been recognized in recent years and the development of improved formulations as well as their implementation in discretized form has been the subject of several investigations (Orlanski, 1976; Enquist and Majda, 1977; Miller and Thorpe, 1981; Roed and Cooper, 1986). Evidence from recent research (Blumberg and Kantha, 1985; Roed and Cooper, 1986) indicates

¹ Assoc. Prof., Dept. Civil Engrg., Natl. Tech. Univ. of Athens, Greece.

² Grad. Stud., Dept. Civil Engrg., Natl. Tech. Univ. of Athens, Greece.

that the type of boundary conditions used may have an appreciable influence on the computed circulation patterns, especially for transient problems.

During the summer, many coastal water bodies become stratified, primarily due to substantial temperature differences over the water column. Stratification may also develop in estuaries receiving large freshwater inflows, due to salinity differences. The simplest way to study such water bodies is by a two-layer idealization. However, in a two-layer system the problem of boundary conditions becomes more complicated, since conditions have to be specified not only for the free surface, but also for the interface, where data are usually lacking. The effect of the treatment of b.c. on the resulting circulation of layered systems has received little attention (Lorrenzzetti et al, 1985), although it may be at least as important as in the 2-D case.

In an effort to assess the importance of boundary conditions in hydrodynamic modeling of stratified coastal waters, the present paper examines the influence of some common types of b.c. on the wind-driven circulation of a two-layer stratified basin. In the following, the implementation of the various boundary conditions and the results obtained for some simple test problems are presented and discussed.

GOVERNING EQUATIONS AND NUMERICAL MODELING

For the purposes of this study an available two-layer finite element circulation model, code named CAFE-2 (Wang and Connor, 1975; Pagenkopf et al, 1976) was employed as a tool, after some suitable modifications for handling the various types of b.c. considered. It is felt, however, that the results obtained would be equally applicable, at least qualitatively, to other numerical models as well. The model used solves the following set of governing equations for the two-layer system, where the subscript 1 denotes the bottom layer and the subscript 2 the top layer (see Fig. 1):

$$\frac{\partial H_1}{\partial t} + \frac{\partial q_{1x}}{\partial x} + \frac{\partial q_{1y}}{\partial y} = q_{01} \quad (1)$$

$$\begin{aligned} \frac{\partial q_{1x}}{\partial t} + \frac{\partial}{\partial x} (\bar{u}_1 q_{1x}) + \frac{\partial}{\partial x} (\bar{u}_1 q_{1y}) - f q_{1y} = & - \frac{\partial F_{1p}}{\partial x} + \frac{\partial F_{1xx}}{\partial x} + \\ & + \frac{\partial F_{1xy}}{\partial y} + \frac{1}{\rho_1} (\tau_x^i - \tau_x^b) + \frac{1}{\rho_1} (p^i \frac{\partial \zeta_1}{\partial x} - p^b \frac{\partial \zeta_o}{\partial x}) \end{aligned} \quad (2)$$

$$\begin{aligned} \frac{\partial q_{1y}}{\partial t} + \frac{\partial}{\partial x} (\bar{u}_1 q_{1y}) + \frac{\partial}{\partial y} (\bar{v}_1 q_{1y}) + f q_{1x} = & - \frac{\partial F_{1p}}{\partial y} + \frac{\partial F_{1xy}}{\partial x} + \\ & + \frac{\partial F_{1yy}}{\partial y} + \frac{1}{\rho_1} (\tau_y^i - \tau_y^b) + \frac{1}{\rho_1} (p^i \frac{\partial \zeta_1}{\partial y} - p^b \frac{\partial \zeta_o}{\partial y}) \end{aligned} \quad (3)$$

$$\frac{\partial H_2}{\partial t} + \frac{\partial q_{2x}}{\partial x} + \frac{\partial q_{2y}}{\partial y} = q_{02} \tag{4}$$

$$\begin{aligned} \frac{\partial q_{2x}}{\partial t} + \frac{\partial}{\partial x}(\bar{u}_2 q_{2x}) + \frac{\partial}{\partial y}(\bar{v}_2 q_{2x}) - f q_{2y} = & - \frac{\partial F_{2p}}{\partial x} + \frac{\partial F_{2xx}}{\partial x} + \frac{\partial F_{2xy}}{\partial y} + \\ & + \frac{1}{\rho_2}(\tau_x^s - \tau_x^i) + \frac{1}{\rho_2}(p^s \frac{\partial \zeta_2}{\partial x} - p^i \frac{\partial \zeta_1}{\partial x}) \end{aligned} \tag{5}$$

$$\begin{aligned} \frac{\partial q_{2y}}{\partial t} + \frac{\partial}{\partial y}(\bar{u}_2 q_{2y}) + \frac{\partial}{\partial y}(\bar{v}_2 q_{2y}) + f q_{2x} = & - \frac{\partial F_{2p}}{\partial y} + \frac{\partial F_{2xy}}{\partial x} + \frac{\partial F_{2yy}}{\partial y} + \\ & + \frac{1}{\rho_2}(\tau_y^s - \tau_y^i) + \frac{1}{\rho_2}(p^s \frac{\partial \zeta_2}{\partial y} - p^i \frac{\partial \zeta_1}{\partial y}) \end{aligned} \tag{6}$$

where $\zeta_0, \zeta_1, \zeta_2$ are the elevations of the bottom, interface and free surface from an arbitrary datum, respectively.

- $H_1 = \zeta_1 - \zeta_0 =$ bottom layer thickness
- $H_2 = \zeta_2 - \zeta_1 =$ top layer thickness
- ρ_1, ρ_2 are the layer densities.
- \bar{u}_i, \bar{v}_i are the x,y components of the mean layer velocity (i=1,2)
- q_{xi}, q_{yi} are the x,y fluxes ($q_x = \bar{u}H, q_y = \bar{v}H$)
- q_{0i} is any external input, eg. rainfall
- $f = 2\omega \sin\phi$, is the Coriolis parameter
- p^s, p^i, p^b denote the pressure at the free surface, interface and bottom, respectively.
- τ^s, τ^i, τ^b denote the shear stress at the free surface, interface and bottom, respectively, which are modeled by quadratic laws.
- F_{pi} is the total pressure force over the layer thickness
- $F_{xxi}, F_{xyi}, F_{yyi}$ are the integrated internal stresses due to molecular viscosity, turbulent velocity fluctuations and spatial velocity nonuniformity over the vertical, which are modeled by the eddy viscosity approximation.

By employing linear triangular elements for the spatial discretization, the above partial differential equations are reduced to a system of ordinary differential equations, which is further discretized in time as follows (i=1,2):

$$\bar{M} \frac{H_i^{n+\frac{1}{2}} - H_i^{n-\frac{1}{2}}}{\Delta t} = P_i (H^{n-\frac{1}{2}}, Q^n) \tag{7}$$

$$\tilde{M}' \frac{Q_i^{n+1} - Q_i^n}{\Delta t} = \tilde{P}'_i (H^{n+1/2}, Q^n) \quad (8)$$

where \tilde{H}_i are the vectors of layer thickness at the nodes

$Q_i (q_{xi}, q_{yi})$ are the vectors of fluxes at the nodes

\tilde{M}, \tilde{M}' are matrices related to the geometry of the grid

and \tilde{P}, \tilde{P}' include all other terms, i.e. pressure gradient, friction, eddy viscosity, Coriolis, convective terms etc.

The time-stepping scheme employed solves for the dependent variables at alternate time levels, i.e. for the layer thicknesses \tilde{H}_1, \tilde{H}_2 at times $n+1/2, n+3/2$ and for the fluxes Q_1, Q_2 at times $n, n+1, n+2$ etc.

IMPLEMENTATION OF BOUNDARY CONDITIONS

For the numerical tests an idealized basin was considered, shown in Fig. 2. It has a rectangular shape, with dimensions about 40x60 Km, and an island near the center. The water depth was assumed constant, at 100 m, and the initial position of the interface was set at a depth of 35 m. The density difference between the layers was assumed to be 2%. As shown in the figure, a regular grid with 86 nodes and 129 triangular elements was established. Three types of boundary conditions were considered for the wind-driven circulation, as follows:

- (a) Clamped boundaries: Zero displacement was specified for both the free surface and the interface at all nodes on the sea boundary, so that the layer thicknesses were fixed:

$$H_1 = \bar{H}_1 = 65\text{m} \quad (9a)$$

$$H_2 = \bar{H}_2 = 35 \text{ m} \quad (9b)$$

- (b) Free radiation: Extending the well-known Sommerfeld radiation condition (Roed and Cooper, 1986) and considering as celerity that of long gravity waves, the following equations are applicable for the displacements of the free surface and the interface at the boundary nodes:

$$\frac{\partial \zeta_2}{\partial t} + \sqrt{g(H_1+H_2)} \frac{\partial \zeta_2}{\partial \eta} = 0 \quad (10a)$$

$$\frac{\partial \zeta_1}{\partial t} + \sqrt{g' \frac{H_1 H_2}{(H_1+H_2)}} \frac{\partial \zeta_1}{\partial \eta} = 0 \quad (10b)$$

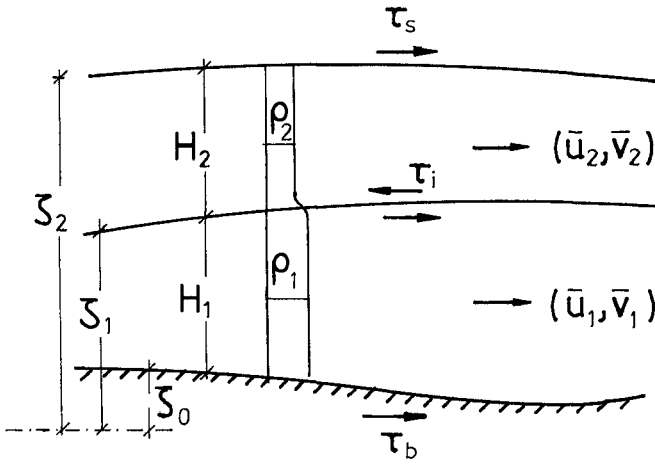


Figure 1. Notation sketch

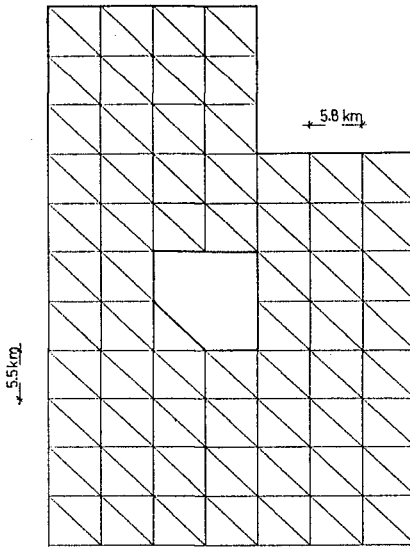


Figure 2. Idealized basin for the numerical tests

where $g' = g(\rho_1 - \rho_2) / \rho_1$

and η is the direction of the outward normal to the boundary.

To obtain the boundary values at each time step, the above equations were discretized by employing forward differences in time and backward in space, as follows.

$$\frac{\zeta_{2,b}^{n+1} - \zeta_{2,b}^n}{\Delta t} + \sqrt{g(H_{1,b}^n + H_{2,b}^n)} \frac{\zeta_{2,b}^n - \zeta_{2,a}^n}{\Delta \eta} = 0 \quad (11a)$$

$$\frac{\zeta_{1,b}^{n+1} - \zeta_{1,b}^n}{\Delta t} + \sqrt{g' \frac{H_{1,b}^n H_{2,b}^n}{(H_{1,b}^n + H_{2,b}^n)}} \frac{\zeta_{1,b}^n - \zeta_{1,a}^n}{\Delta \eta} = 0 \quad (11b)$$

where the subscript b denotes the boundary node, the subscript a refers to the adjacent node to the interior of the domain, and $\Delta \eta$ is the distance between these two nodes.

- (c) Sponge layer: The displacements of the boundary nodes were set to zero, as in case (a), but the elevation fields were sponged within a layer adjacent to the boundary, following the scheme proposed by (Lorrenzetti et al, 1985). To accommodate the sponge layer of a chosen thickness $L=2\Delta s$ the grid was locally refined in this case, so that four element were formed in this zone. The integration scheme (eq.7) was modified as follows:

$$\underset{\sim}{M} \frac{\underset{\sim}{H}_i^{n+\frac{1}{2}} - \underset{\sim}{H}_i^{n-\frac{1}{2}}}{\Delta t} + \underset{\sim}{K} \frac{\underset{\sim}{H}_i^{n-\frac{1}{2}} - \bar{\underset{\sim}{H}}_i^{n-\frac{1}{2}}}{\Delta t} = \underset{\sim}{P}_i \quad (12)$$

where $\bar{\underset{\sim}{H}}$ includes the specified depths at the boundary and $\underset{\sim}{K}$ is a damping function depending on the ordinate η normal to the boundary:

$$K(\eta) = A \left(\frac{\eta - \eta_0}{L - \eta_0} \right)^x \quad \text{for} \quad \eta_0 < \eta \leq L \quad (13a)$$

$$K(\eta) = 0 \quad \text{for} \quad \eta \leq \eta_0 \quad (13b)$$

The behaviour of the sponge layer depends to some extent on the values of the parameters A , x , in eq. (13a). The results shown below correspond to values of $A=1.0$ and $x=0.5$.

RESULTS AND DISCUSSION

The b.c. described above were used for studying the circulation in the rectangular basin of Fig. 2 under uniform wind forcing. For these tests, the non-linear convective terms and the Coriolis terms were omitted in the computations. Preliminary experiments indicated that considerable oscillations of the interface persist for several days after a sudden application of the wind field. Therefore to reduce the impact of sudden forcing, the wind was introduced gradually, using a linear increase from zero to 20 knots over a period of 90,000 sec; the wind speed was kept constant thereafter.

Figures 3, 4, 5 show the circulation patterns calculated at 360,000 sec for a 20-knot wind normal to the open boundary, directed inwards, for each of the three types of b.c. described previously. It is seen that in all cases an inflow is established in the top layer and outflow in the bottom layer, as expected for this particular wind direction. However, there are significant differences between the three cases. For the clamped boundaries, an anticlockwise gyre around the island forms in the top layer, with stronger velocities on the right side of the basin, and a reverse gyre in the bottom layer. Somewhat similar results are observed for the sponge layer conditions, but with comparable intensity of flow on both sides of the basin. However, the free radiation conditions generate a markedly different flow field, with nearly uniform inflow over the entire top layer and outflow at the bottom layer. Substantial differences are also noted in the displacement of the interface, which under the free radiation conditions descends much lower throughout the domain compared to the other two tests.

Fig. 6 presents the evolution of the differential volume of each layer relative to the initial position of the free surface and the interface. It is evident from the figure that under clamped or sponge boundary conditions, the resulting flow fields attain macroscopically nearly the same steady state after about 2 days of wind forcing, while no steady state is approached after 4 days for the free radiation conditions. In fact, there seems to be a gradual filling of the top layer and a corresponding emptying of the bottom layer. This result is qualitatively similar to that of Blumberg and Kantha (1985), who also observed in their 2-D model a continuous emptying of the domain when using free radiation conditions.

Figures 7, 8, 9 show the circulation pattern for a 20-knot wind parallel to the open boundary. Under clamped b.c., more intense currents are observed in this case. The flow generally tends to follow the wind direction on both sides of the island and in both layers, and outflow occurs on the opposite end of the sea boundary. Rather similar results are obtained under the sponge conditions. But again, the free radiation conditions yield a quite different flow pattern, where there is inflow along the entire opening in the top layer and outflow in the bottom layer. The behaviour of the differential volumes in this case is shown in Fig. 10.

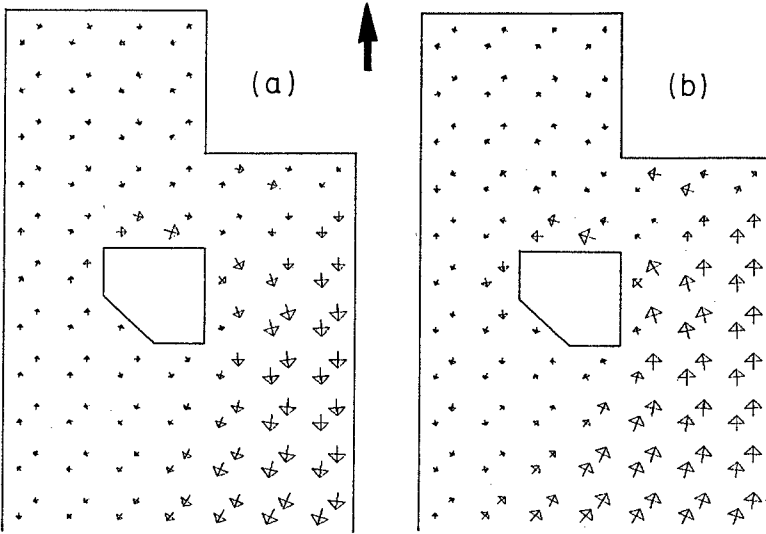


Figure 3. Flow field for wind normal to the open boundary, with clamped conditions: (a) Bottom, (b) Top layer

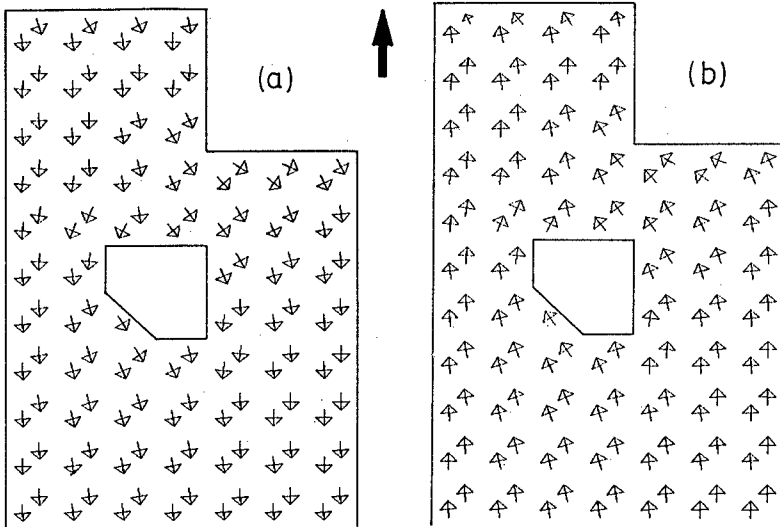


Figure 4. Flow field for wind normal to the open boundary, with free radiation conditions: (a) Bottom, (b) Top layer

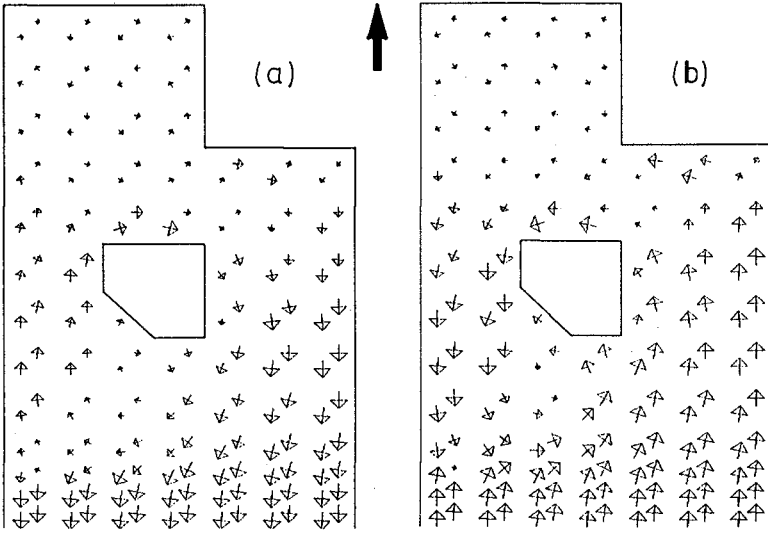


Figure 5. Flow field for wind normal to the open boundary, with sponge layer conditions: (a) Bottom, (b) Top layer

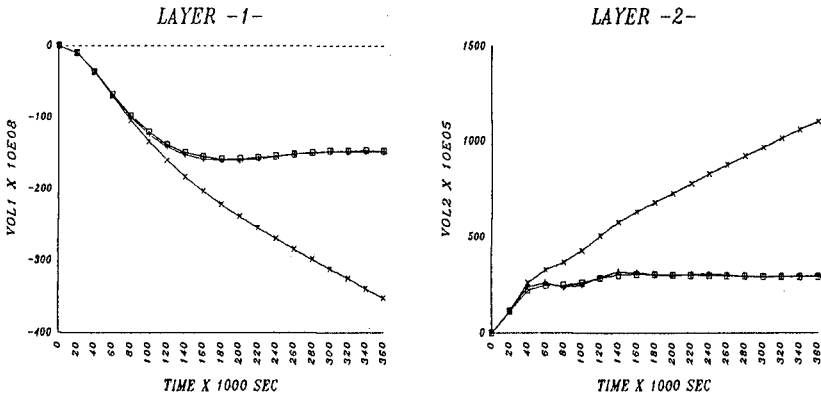


Figure 6. Time change of layer volumes for wind normal to the open boundary; + clamped conditions, x free radiation, \square sponge layer.

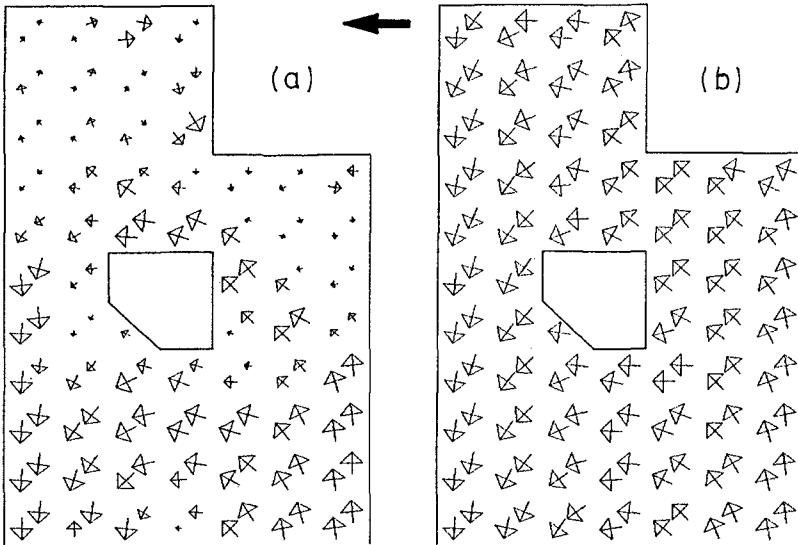


Figure 7. Flow field for wind parallel to the open boundary, with clamped conditions: (a) Bottom, (b) Top layer

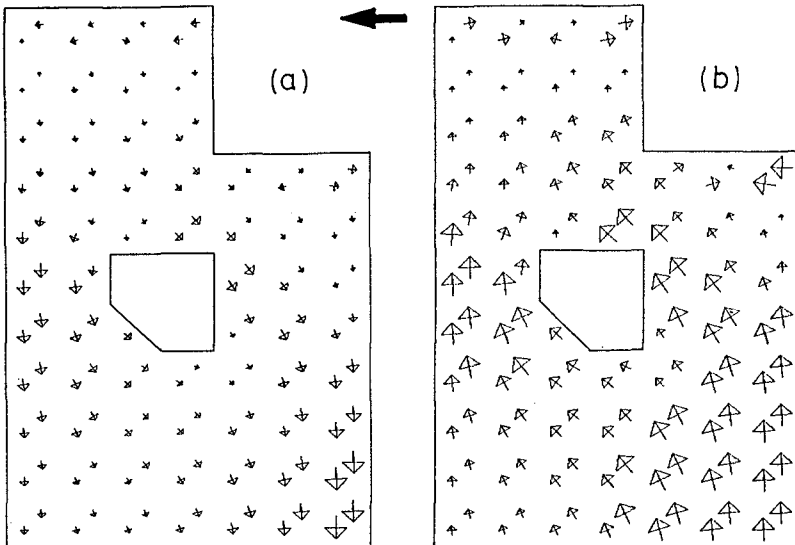


Figure 8. Flow field for wind parallel to the open boundary, with free radiation conditions: (a) Bottom, (b) Top layer

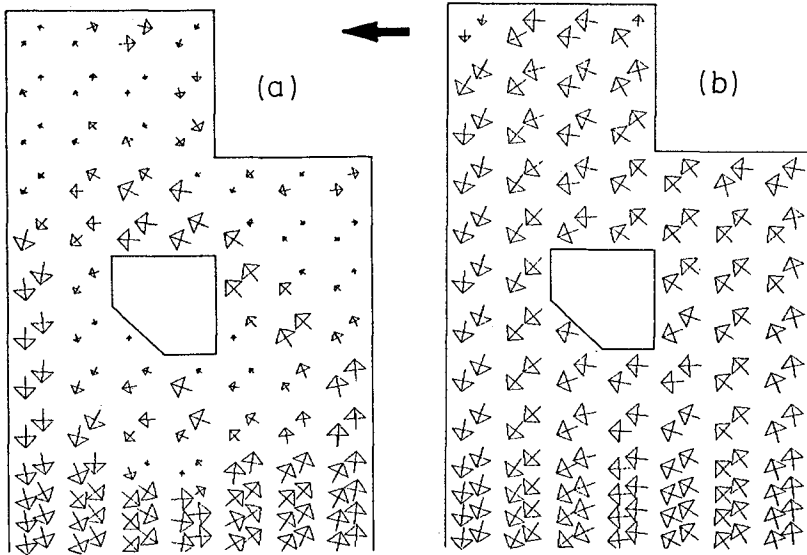


Figure 9. Flow field for wind parallel to the open boundary, with sponge layer conditions. (a) Bottom, (b) Top layer

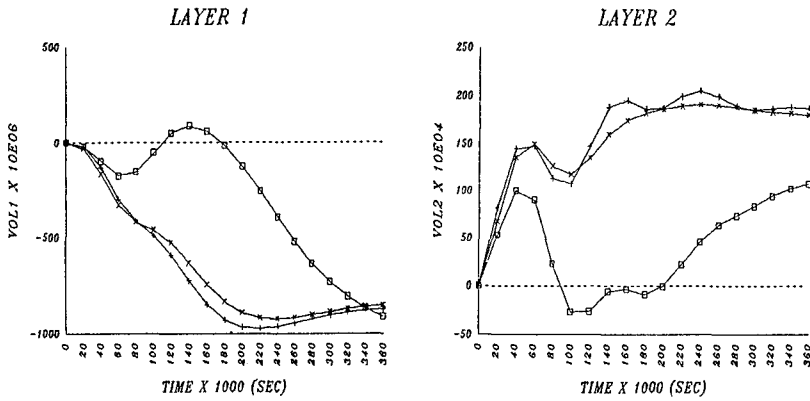


Figure 10. Time change of layer volumes for wind parallel to the open boundary: + clamped conditions, □ free radiation, x sponge layer

Substantial oscillations are observed for both layers, which under clamped conditions persist for almost 4 days, while stabilization occurs much earlier for the sponge conditions. Still, the results of these two types of b.c. are close to each other, both during transient and near steady state. On the contrary, the free radiation conditions yield much different global features and, after about 2 days of oscillatory transients, seem to establish again a progressive emptying of the lower layer and filling of the top layer.

It is evident from the above that the way of forcing has also some effect on the response of the two-layer system. Most boundary conditions are ideally designed to handle disturbances travelling normal to the opening. Thus, the enhanced oscillations observed in the second test are conceivably due to the wind direction being parallel to the boundary, indicating the difficulty of the system to accommodate the oblique incidence of waves.

The degree to which the above observations depend on the morphological features of the basin is currently being studied by additional tests made on a natural water body, namely the Saronic Gulf in Greece, which has dimensions of the same order of magnitude as those of the idealized basin but a variable bathymetry and complex geometry. Preliminary results obtained with the Coriolis terms included show also major differences for the wind-driven circulation under the three types of b.c., indicating qualitatively the same behaviour as above.

Therefore, it may be concluded that the clamped and sponge conditions give approximately the same results concerning the wind-driven circulation of a two-layer system. The former is simplest to implement, but the latter has the advantage of faster damping of the initial transient oscillations, so that the computation time to steady state is reduced. The free radiation conditions could be more appropriate for transient problems since they allow interior disturbances to exit, however they should not be used when a steady state solution is sought. Still, the computation of steady state might often be of academic rather than of practical interest. Taking into account the slow time response of a large stratified basin, it is practically impossible for a meteorological forcing to prevail for the duration necessary to create a steady flow field. In simulating events of finite duration, a combination of free radiation and clamped conditions of the form proposed in 2-D problems by Blumberg and Kantha (1985) may prove successful for stratified problems as well. In any case, the observed substantial influence of the b.c. on the computed flow patterns points out the need for further research into the subject.

CONCLUSIONS

Three different types of boundary conditions that may be specified along the sea boundaries of numerical models for stratified coastal circulation were examined, namely clamped, free radiation and sponge layer conditions. These boundary

conditions were implemented in an idealized two-layer basin and numerical experiments for wind forcing were carried out. It was found that the b.c. generally have a very pronounced effect on the flow field, not only close to the boundary, but essentially over the entire domain. Results obtained for clamped and sponge boundaries are to some extent similar, but free radiation conditions give very different patterns. Besides, in the latter case steady state is not reached for a long time, even after gradual introduction of the wind forcing.

ACKNOWLEDGMENT

Partial financial support by the Ministry of Environment, Planning and Public Works is gratefully acknowledged.

REFERENCES

- Blumberg, A.F., and Kantha, L.H. (1985), "Open boundary conditions for circulation models", *J. Hydr. Engrg., ASCE*, 111, (2), 237-255.
- Enquist, B. and Majda, A., (1977), "Absorbing boundary conditions for the numerical simulation of waves", *Math. Comp.*, 31, 629-651.
- Lorrenzetti, J.A., Wang, J.D., Lee, T.N., and Pietrafesa, L.J. (1985), "On the modeling of the summer circulation in the South Atlantic Bight by a two-layer finite element model", RSMAS Report No. 85002, Univ. Miami.
- Miller, M.J. and Thorpe, A.J. (1981), "Radiation conditions for the lateral boundaries of limited-area numerical models", *Quart. J.R. Met. Soc.*, 107, 615-628.
- Orlanski, I. (1976), "A simple boundary condition for unbounded hyperbolic flows", *J. Comp. Phys.*, 21, 251-269.
- Pagenkopf, J.R., Christodoulou, G.C., Pearce, B.R. and Connor, J.J. (1976), "A user's manual for CAFE-2, a two-layer finite element circulation model", R.M. Parsons Lab. Report No.220, Mass. Inst. of Tech., Cambridge, Mass.
- Roed, L.P. and Cooper, C.K. (1986), "Open boundary conditions in numerical ocean models", *Adv. Phys. Ocean. Modeling*, J.J. O'Brien (ed), Reidel.
- Wang, J.D. and Connor, J.J. (1975), "Mathematical modeling of near coastal circulation", R.M. Parsons Lab. Report No. 200, Mass. Inst. of Tech., Cambridge, Mass.

CHAPTER 191

A MODELING SYSTEM FOR COASTAL OIL SPILL RISK ANALYSIS

Shiao-Kung Liu and Jan J. Leendertse

INTRODUCTION

At present, the Prudhoe Bay oil field in Alaska contributes a substantial amount of the domestic oil production of the United States. Oil is also expected to be present on the continental shelf of Alaska, and it is estimated that approximately 28 percent of the total U. S. reserve is located beneath the shallow ice covered seas of the Alaskan continental shelf. To explore and to exploit these oil rich resources, engineers are confronted with hostile oceanographic conditions such as high tides, waves, strong currents and sea ice. The same area is also rich in fishery resources. Being one of the most productive fishing grounds in the northern Pacific, the potential ecological impact due to an oil spill is of a major concern. This paper describes the methodologies used for the development of a modeling system for the oil risk analysis. The system is designed with generality in mind so it can be used for other coastal areas.

The development of three dimensional models used in the modeling system described here have been published in the earlier International Coastal Engineering Conferences (Liu and Leendertse, 1982, 1984, 1986) and a report published recently by RAND (Liu and Leendertse, 1987). In the oil-spill risk analysis, these three dimensional hydrodynamic models are coupled to a two-dimensional stochastic weather model and an oil weathering model.

Before decisions are made concerning which specific offshore areas to lease for exploration or exploitation, the responsible government agency must balance orderly resources development against the protection of human, marine, and coastal environment, to ensure that the public receives a fair return for these resources. In studies made for this purpose, the impact of hypothetical oil spill are considered. Not only are oil spill pathways required for the impact analysis, in certain instances knowledge about the extent of oil spill is required as well as about the oil concentration that would occur in the water column. This paper presents an efficient way for making the risk analysis while maintaining the essential dynamics of the processes involved.

THE MODELING APPROACH FOR LONG DURATION WIND DRIVEN CURRENTS

As the three-dimensional models made of the different offshore areas of Alaska simulate the movements of water, and as a model is available to simulate wind sequences offshore, it would be logical to use these models in the computation of oil spill movements. To use these models effectively, we have developed a method to compute wind driven currents. This method retains the dynamic detail of the three-dimensional model and yet is approximately two orders of magnitude more efficient than the simulations with the three-dimensional model; it is called the "wind-driven response function method." In essence, the method extends the basic idea of the "drift ratio" between the wind speed and current speed except that the ratio changes in time and over space and is derived from the three-dimensional model.

The traditional, simple fixed drift-ratio method has many difficulties when applied in the Alaskan coastal waters. It is applicable only for cases of steady wind with constant speed blowing over water with finite depth and with no boundaries. However, the concept of the "drift ratio" is a good one—but we need to include more dynamics in it.

In examining the fundamental dynamics of wind-driven currents, even under the assumption of steady (in time), constant (over space) wind and an infinitely long straight coastline, wind-driven currents over water of finite depth do vary both in direction and speed at the surface and at different levels to satisfy the law of conservation of mass. Using information on the distance from shore, wind direction, and local depth, Ekman (1905) worked out the variabilities of drift currents by using highly simplified terms in the equations of motion. On the other hand, to include more terms would require the solution of the complete three-dimensional model.

In our study, time-varying response functions under various wind conditions were developed using wind stress associated with the marine wind speed. Reverse procedures (convolution) were then used during the oil trajectory simulation; therefore, they are not linear with respect to local wind speed. Since the response functions for all layers are derived from the three-dimensional model, time-varying effects (such as a moving storm, deepening of a mixed layer, and inertia components) are included in the oil spill trajectory computation. The method is very efficient, however, the oil spill trajectory model was programmed so that the drift ratio and deflection angle from field observations under various conditions over an entire area can, as an option, still be used for the computation of oil movement.

Wind driven currents over stratified waters vary with the degree of vertical stability associated with the stratification. To illustrate this point we use a simple case where the time series of water movement at two nearby locations in Norton Sound is plotted (Fig. 1), and wind from the east is applied for a duration of 12 hours (close to the inertial period) over the water. The response of surface water at two nearby locations is not the same to satisfy the continuity principle of water within a bay. Response functions over the water column of the entire modeled area are calculated by the three-dimensional model.

To generate the complete set of response functions, five computer simulation runs are needed. One computer run is without wind but with tide. The other four computer runs are with tides and with wind from each of four directions. The four response functions set are derived from the difference between them and the one with tide as the only forcing function. The level of tidal currents at different areas produces variable wind responses under the same wind, so the tide has to be included when deriving wind response functions, otherwise they will be overestimated. This is why in a coastal area with strong tidal currents the drift ratio would be lower than in the open ocean because of the quadratic nature of the bottom friction.

When response functions are saved in discrete time intervals (30 minutes was used) the drift velocity at a certain time is computed by numerical convolution.

$$U_{ij}(n \Delta t) = \Delta t \sum_{k=0}^n (W^2) h_{ij}(n \Delta t - k \Delta t) \quad (1)$$

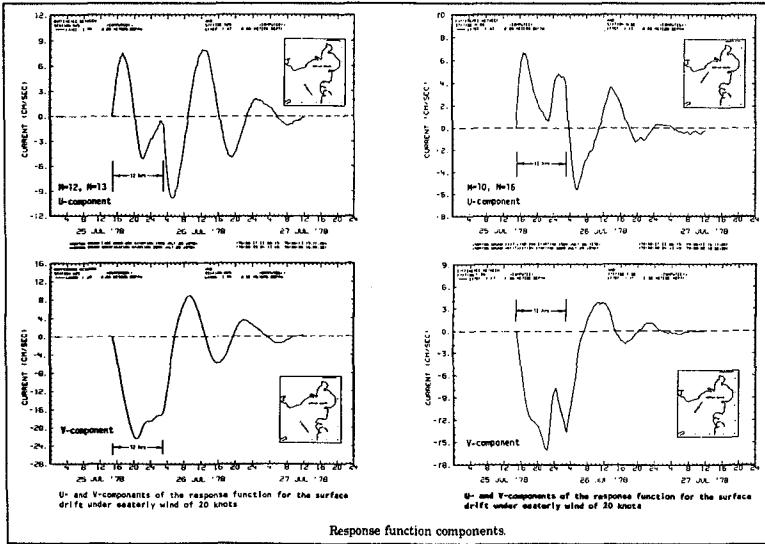


Fig 1

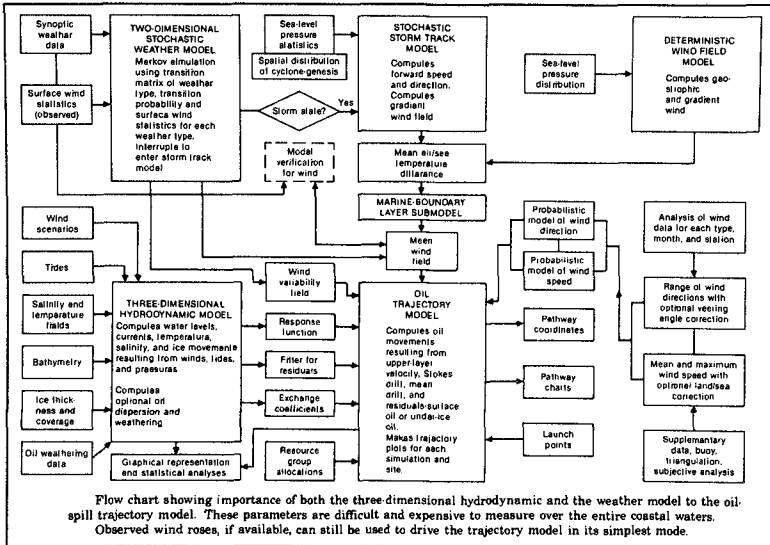


Fig 2

where W = wind speed from a certain direction,

U_{ijk} = velocity at a particular point (i, j, k), and

h_{ijk} = time domain response function between squared wind speed and velocity at point (k, j, k).

With this formula the velocity at point i, j, k can be determined if the wind speed from a specific direction is known, as well as the response function.

The same principle applies for complex wind scenarios, then the vectorial decomposition is involved.

COMPUTING OIL BEHAVIOR UNDER ICE

In the absence of a current, oil released in a water column will rise and be trapped underneath the ice. Under porous young ice during formation, oil will initially undergo a certain degree of vertical migration through the vertical brine channels. Most oil is initially in the form of droplets until a lateral slick is formed. The oil sheet tends to spread with an obtuse contact angle. For typical Alaska Prudhoe Bay crude oil, the average observed values of interfacial surface tension, density, and the contact angle are 31 dynes/cm, 0.911 g/cc, and 20°, respectively (Kovacs et al., 1980). The static thickness of the same oil is approximately 1.2 cm. Since the dynamic pressure exerted by a moving current on an oil slick of finite length tends to balance between the front and the back faces, the equilibrium thickness should be the same for both unaccelerated and static slicks.

The bottom roughness of ice not only determines the amount of oil that may be trapped beneath it, it also influences the speed of oil movement under moving currents. Using a radar echo sounding system, Cox et al. (1980) made extensive measurements of ice bottom morphology and found the standard variation of ice thickness to be 3.1 cm over a mean thickness of 1.53 m in an undeformed shore-fast ice zone near Prudhoe Bay. The thickness of ice was also found to be inversely proportional to the thickness of snow cover over it. The snow acts as an insulator that reduces heat exchange from the sea water through the ice to the atmosphere and thus retards the growth rate. Consequently, a substantial quantity of oil can be retained underneath the pack ice. Under weak currents, trapped oil will travel with the pack ice. The movement of oil under this condition would be identical to the computed movement of ice described above but the shear stress coefficients between water and ice are reduced.

Under strong "relative currents" (between water and ice), oil will travel at a speed different from the ice and currents. To compute the movement of oil under these conditions, in the three-dimensional model we adapted a method developed by Cox et al. (1980) with parameters evaluated from laboratory tests. This method involves the evaluation of a critical relative velocity between ice and water. Using ρ_w to represent the density of sea water in the surface layer of our computation, the critical velocity for the incipient motion with large roughness is approximately:

$$u_{\text{critical}} = 1.5 \left[\left(\frac{\rho_o + \rho_w}{\rho_o \rho_w} \right) \left(\sigma_{o/w} g (\rho_w - \rho_o) \right)^{1/4} \right]^{1/2} \quad (2)$$

in which ρ_o , $\sigma_{o/w}$ are, respectively, the density of oil and the surface tension at the oil/water interface. With the aforementioned typical values observed in the Beaufort Sea, this critical value is approximately 21 cm/sec.

Equation (2) is developed considering the formation of Kelvin-Helmholtz type instability, which exerts a limit on the thickness of an oil slick near the head region. A multiplier of 1.5 on the right-hand side of Eq. (2) was used considering the actual velocity that would cause droplet tearing. Ultimate slick failure occurs at about twice the critical velocity.

According to Cox et al. (1980), the critical velocity at which oil begins to move relative to the water when the relative velocity between ice and water is:

$$u_{oil} = u_{water} \left[1 - \left(\frac{\kappa}{A F_{\delta}^2 + B} \right)^{1/2} \right] \quad (3)$$

where κ is the amplification factor and F_{δ} is a slick densimetric Froude number defined by:

$$F_{\delta} = \frac{u_{water}}{\sqrt{[(\rho_w - \rho_o)/\rho_w] g \delta}} \quad (4)$$

in which δ represents the equilibrium slick thickness.

Equation (3) is derived from the momentum balance between form drag, oil/water interfacial shear stress, and the retarding of oil/ice frictional force. Constants A and B in the equation contain the effects of frontal shear and plane shear, as well as the normal force from oil's buoyance against the ice. For the field conditions of the model areas, the values of these coefficients are 1.75 and 0.115. The amplification factor κ equals unity for a hydrodynamic smooth region and is greater than zero for rough surfaces. For the field conditions in the model areas, the factor was given a value of 1.105. To determine the equilibrium oil slick thickness from the density of the oil, we used an empirical relation. The empirical difference is:

$$\delta = 1.67 - 8.5 (\rho_w - \rho_o)(cm) \quad (5)$$

In the three-dimensional model the local density of water is evaluated by the equation of state of sea water. The density of oil can be computed by a table look-up procedure.

In our computation, the local density of sea water associated with the ice formation/salt rejection and advection was evaluated and updated. The results of oil movement beneath the ice under various wind conditions, in the form of response functions computed from the three-dimensional simulation, were recorded on magnetic tape as subsequent inputs to the oil spill trajectory computation.

We found that oil will generally move with ice except under two conditions that cause it to travel at a different speed. The first condition is beneath the shore-fast ice in an area where tidal currents are strong. The second condition is when pack ice is located very close to a passing storm center, when drifting ice abruptly changes direction. Under this condition a high relative velocity between the water and ice can be reached.

Because of the pronounced nonlinear vertical shear coupling, and at high latitude, the direction of an oil movement appears to be extremely variable. Therefore, the vertical shear coupling should be included in the computation even though spilled oil beneath the ice may not seem to be in constant motion with appreciable magnitude.

MODELING OIL SPILL TRAJECTORIES

Oil spill trajectory computations involve two parts—the first part calculates the movement of oil mainly by advective transport, and the second part calculates the movement of dispersive mechanisms, including weathering, diffusion, and dissolution processes. In this section we will describe the modeling of advective transport only.

Oil transported by advective mechanisms contains several major components. The method used to compute each component is as follows:

Oil Transport by Mean Wind Drift. During this computational step, oil movement resulting from wind stress at the surface layer and at different levels in the water column is calculated by the response function technique. The response function represents local advective transient response to a given wind stress. If a three-dimensional model is used to develop these response functions, the effects of transient inertia, bottom, shoreline, and vertical stratification are all included. The computed movement using this response technique gives only the movement near the middle of the surface layer (typically 5 meters) schema-

tized in the 3D model. For the surface movement the results are extrapolated for speed and direction near the surface using an analytical solution of the Ekman type assuming constant density within that surface (mixed) layer.

Stokes' Transport. When wind blows over the water surface it generates Stokes' transport in addition to the mean wind-driven current. This transport is caused by the non-linear residual orbital motion associated with the local wind waves field. The magnitude of this transport is a function of the intensity and age of the wave field. The direction is nearly identical to the wave-propagating direction. In the oil spill trajectory model, a special sub-routine is used to compute the direction and speed of this transport. According to measurements in the field and in the laboratory, Stokes' transport is approximately 1.6 percent of the local wind speed if the wave field is not limited by wind duration and fetch length. The wind used to compute the Stokes' transport is obtained from the wind field model described in (Liu and Leendertse, 1987)

Tidal and Baroclinic Residual Component over the Alaskan Outer Continental Shelf Area. Because of the complex tidal regime and density field, tidal residual and baroclinic circulation components are quite essential. We have discussed their dynamics in great detail in (Liu and Leendertse, 1987)

To simulate a number of trajectories with the trajectory model, many data are needed from other models that we have previously described. Figure 2 gives an overview of the data flow between these models. As illustrated in the diagram, when computing the oil movement, the oil/trajectory model plays the role of data synthesizer. As physical parameters involved in calculating oil movements are difficult and expensive to measure over the entire Alaskan waters, the model is programmed with flexibility in mind, so that any field data, if available, can be used to drive the model in its simplest mode. On the other hand, the trajectory model would link results from the other models. To perform this task, it contains the basic physical parameters of the entire lease area as well as the grid network of the entire model and submodels within the system.

During the study period, spill trajectory analyses were made on a lease-area basis. For each lease sale, approximately 30 to 40 launch points were selected by the Minerals Management Service according to the potential petroleum resource. The movements of oil were then tracked for a period of time, typically a month during the summer period, to as long as six months during winter.

From each launch location 40 to 60 trajectories are computed under different weather scenarios. For each trajectory, half-hourly positions are computed and landfall locations are recorded where possible. As described above, the wind-driven component of the oil movements is computed using the wind-driven response function technique through the convolution procedure. To maintain accuracy, each response function has half-hourly weighting elements for each wind direction, each computational grid, each layer, and each season. One magnetic tape is required to store all response functions from each of four wind directions. For the computation of oil spill trajectories, this information is transferred to disk storage.

Results from a typical simulation are presented in Fig. 3. In the figure, the computational grid of the three-dimensional model of the Beaufort Sea is superimposed over the oil trajectory model, which also covers the eastern portion of the Chukchi Sea. The response functions and net-current field over that area are averages obtained from the two models.

On top of the graph, computed 12-hour wind vectors sampled at Point Barrow are plotted. The mean winds and half-hourly varying winds from the simulation are also presented in the form of wind roses for speed and direction, also at Point Barrow. The wind direction rose represents the frequency of occurrence of wind direction toward which wind is blowing. A wind speed rose represents the average marine wind speed associated with each of the 16 wind directions mentioned above. The plotting scale of the highest speed in the rose is 12 knots as indicated under the rose.

Each dot in the oil trajectory represents daily displacement originating from the launch point, which is marked by a number. When examining the trajectories one would notice the following interesting aspects:

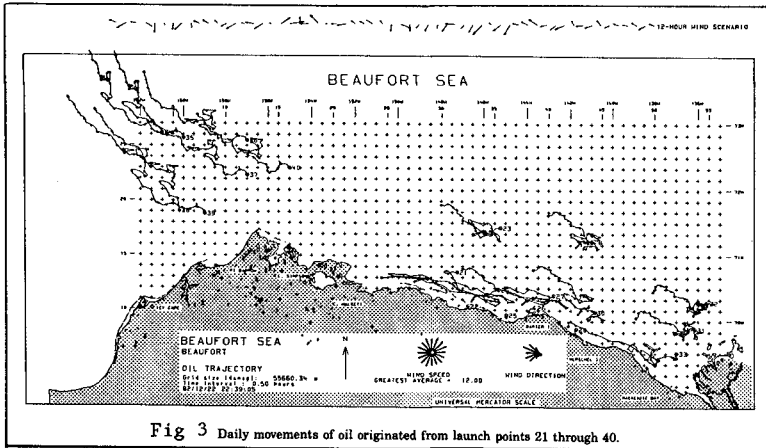


Fig 3 Daily movements of oil originated from launch points 21 through 40.

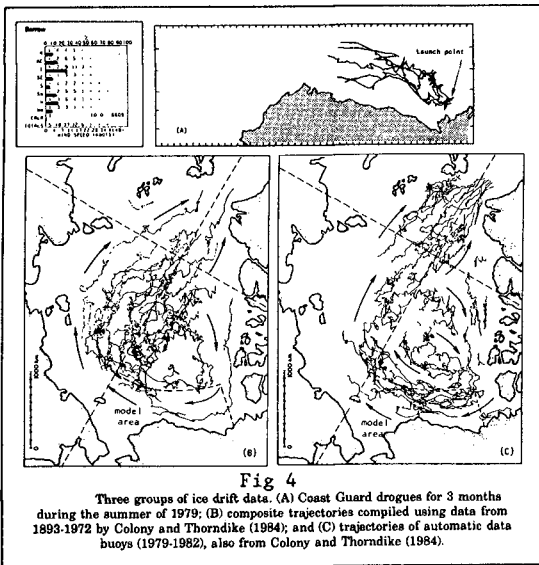


Fig 4

Three groups of ice drift data. (A) Coast Guard drogues for 3 months during the summer of 1979; (B) composite trajectories compiled using data from 1893-1972 by Colony and Thorndike (1984); and (C) trajectories of automatic data buoys (1979-1982), also from Colony and Thorndike (1984).

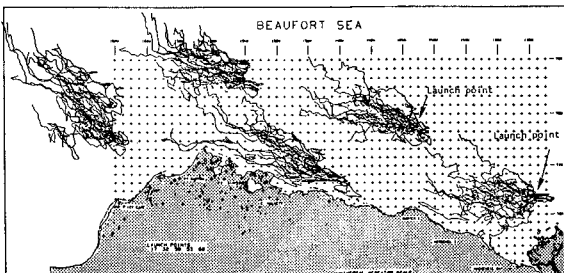


Fig 5 computed by the RAND oil trajectory model and the two-dimensional stochastic weather simulation model.

1. The predominant wind during a summer period is from the east-southeast.
2. Oil spilled closer to the shore travels faster, in a downwind position.
3. Oil spilled offshore moves in a more random direction and has a larger deflection angle. This can be attributed to the greater water depth and the existence of ice floes.
4. Oil spilled further offshore travels in a direction approximately the same as the Arctic Gyre (Colony and Thorndike, 1984, U.S. Coast Guard buoy data, Fig. 4). The simulation in Fig. 4 was made in December 1982.

The trajectories shown in Fig. 3 represent oil movements under a given 30-day weather scenario. In Fig. 5 comparison between satellite-tracked buoys (Murphy et al., 1981) and trajectories computed using the coupled trajectory-weather model is shown. During the summer period, the average observed movement of ice is approximately 140 nautical miles per month. The same is found in the computed monthly average displacement. The observed and the computed trajectory patterns in the Mackenzie Bay are quite irregular. This may be due, in part, to the cyclonic local eddy described above.

Without observed wind fields and the variability of winds, tracing the deterministic motion of a particular ice floe is not as desirable as comparing a group of observed trajectories to a group of computed trajectories using a weather model. The same weather model will be used for the statistical trajectory analyses below.

In the trajectories it can be seen that the impact of a moving storm can sometimes be seen as a loop in a trajectory. The size and shape of the loop vary because of their location relative to the moving storm.

The computed trajectories for the winter season have the similar direction of predominant movement. Figure 6 shows the general direction of movement launched from three selected points. The residence time within the modeled area is approximately two to three months. If all launch points for a given season are considered, one can assess the oil spill risk by counting the number of contact occurrences within each square area whose length is 10 nautical miles in the north-south direction (Fig. 7). In Fig. 7 the size of a circle represents the spatial distribution of landfall frequencies. If oil is trapped in a near-shore lagoon, a continuous contact is assumed for the remaining period. In preparing the map, analysis is made using two-hour counting method. Plotting scale for the circle is 21211, two-hour exposure periods equals one latitudinal grid spacing for the radius of the circle.

If the near-shore entrapments are excluded, a similar diagram (Fig. 8) gives the spatial distribution for the marine resource contact frequencies. In this case, each latitudinal grid spacing equals 1872 two-hour contact period for the radius of a circle. From graphs like Fig. 7 and 8, one would be able to obtain a general assessment of contact risk associated with the oil spill. However, sometimes it is more desirable to estimate the concentration of oil, if a contact is made.

DETERMINING THE OIL CONCENTRATION FIELD

When released in water, fresh crude oil will undergo major changes in its composition while being transported and dispersed. The spreading of oil at the surface is mainly due to mechanisms associated with viscosity, surface tension, and inertia. As time progresses the major process responsible for the spreading of spilled oil are advection and turbulent dispersion. While oil is being advected and dispersed, its concentration decreases as a result of evaporation, photochemical degradation, and biodegradation. These processes are called weathering.

In modeling an oil concentration field, advection, dispersion, and weathering are considered as well as the transport of oil. The rates of evaporation and the bio- and photochemical degradation were evaluated under field conditions by other investigators (Payne et al., 1983). The oil decay rates for the simulation were estimated by these investigators on the basis of turbulence levels determined by means of the three-dimensional models for the different areas.

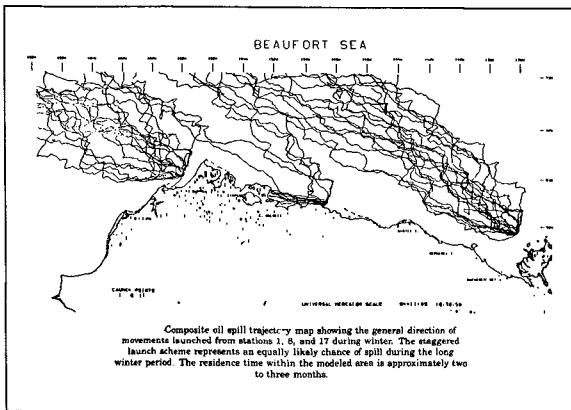


Fig 6

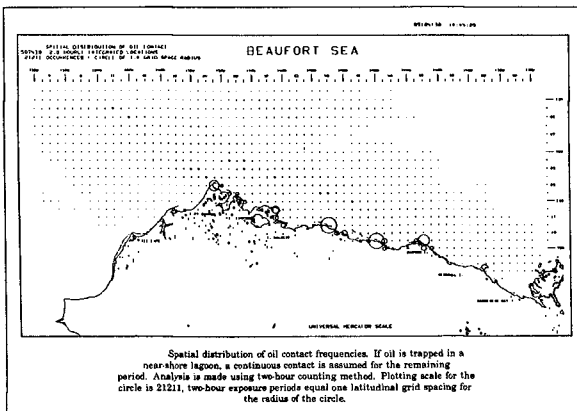


Fig 7

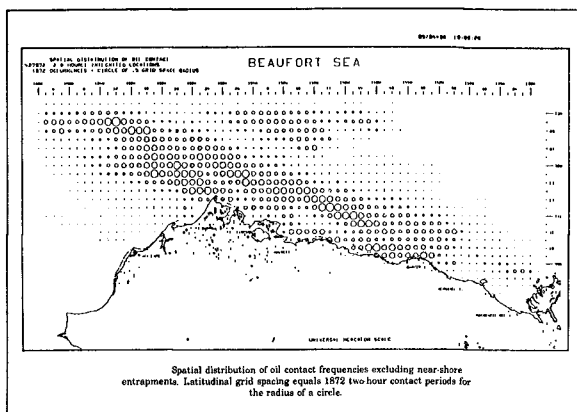


Fig 8

To illustrate the diffusion process induced by the turbulent oscillating flow, it is more convenient to demonstrate the magnitude of diffusion over the vertical plane in the absence of surface energy input from the wind. In other words, in this illustration the turbulence is generated primarily at the bottom by tide. To show the turbulent diffusion processes one hundred particles are released in each vertical layer near the Pribilof Island and half-hourly displacements are plotted there for a period of 24 hours (Fig. 9). The elevations for the eight layers are 2.5, 7.5, 12.5, 17.5, 25, 35, 85, and 240 meters, respectively.

In each layer the movements of particles are caused by advection and diffusion processes. For instance, the hourly displacement of the particle group in the first layer starts from the upper position, gradually moving with the tidal motion. As the group moves the distance between the particles increases because of the turbulent diffusion. In a stricter sense, the separation of particles is the combined result of diffusion and the nonuniformity of the current field. The combined process is called the turbulent dispersion. In shear flow, such as the one illustrated here, the major mechanism responsible for dilution of a soluble is dispersion. This is evident from the amount of dispersion experienced by the particle groups in the lower layers where the velocity gradient is much sharper than in the upper five layers. These five layers are located above the sharp pycnocline, which partially isolates the upward momentum transport.

Also of interest are the distances between the first and the last particle group within each layer. They represent the net displacement over a period of two days. The changes in net transport over the vertical are quite common in the coastal area, to satisfy the law of conservation of mass.

The example presented here illustrates the dispersion mechanism associated primarily with bottom stress and nonuniform velocity distribution. Dispersion effects can also be induced by shore line irregularity through the variability of the velocity field. For each of the large modeled areas, submodels are used to compute near-shore oil movements (Fig. 10). The turbulent diffusion coefficients averaged over ten tidal cycles, as computed by the three-dimensional model for each large area and for each layer, are stored on magnetic tapes. These diffusion coefficients became very useful for diffusion analysis in a limited near-shore area. Figure 11 represents the results of oil dispersion analysis in which crude oil is released instantaneously from five locations near the Bering Strait. Displacement of the one-part-per-billion concentration envelopes are plotted every five days. The influence of the shoreline and the variability of local advective/diffusive mechanisms (Fig. 11) are quite evident, as seen by the changing speed and direction of the oil movement.

Under a scenario of continuous release, the distribution of surface oil concentration is presented in Fig. 11. When oil moves through the Bering Strait, the strong local current tends to elongate the oil. Also notice the cumulation effects when the oil reaches the coastal area, where the on-shore current components drop and the along-shore currents strengthen. This near-shore effect tends to redirect the oil while slowing it down. The speed of an oil transport can be seen from the top diagram of Fig. 12, where daily displacements of the advancing plume are plotted. The daily traveling speed of oil is governed by the evolutionary weather state as well as the local circulation pattern.

To illustrate the effects of weather and local baroclinic circulation, a group of six trajectories are launched from five hypothetical spill locations in the Chukchi Sea/Barrow Arch lease area (Fig. 13). The net displacement for the northern trajectories during the eight-month period ranges between 3–5° latitude, which represents a daily movement of 1.4 to 2.31 km (Fig. 14). Oil launched near Point Hope travels substantially slower than its northern counterpart, which moves predominantly within the Arctic Gyre. The simulated direction and speed of ice movements within the Chukchi Sea agree with the observed values reported by Gordienko (1958), and Hibler (1979), who made computations using ice models including nonlinear plastic flow effects by means of viscous-plastic constitutive law.

Perhaps it is more illustrative to show and analyze a group of trajectories launched near an embayment so that the shore effects can be seen. The launch point is located between St. Lawrence Island and the Gulf of Anadyr, USSR (see the insert map of Fig. 15). Twenty-one

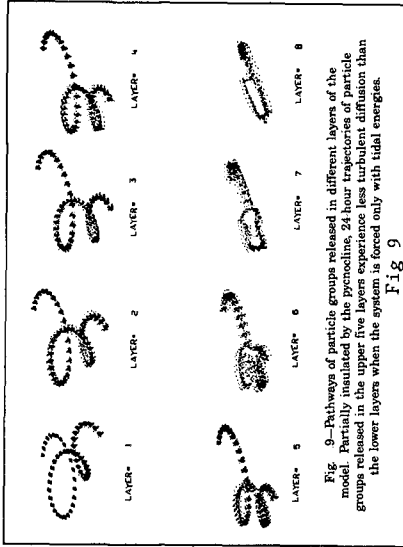


Fig. 9—Pathways of particle groups released in different layers of the model. Partially insulated by the pycnocline, 24-hour trajectories of particle groups released in the upper five layers experience less turbulent diffusion than the lower layers when the system is forced only with tidal energies.

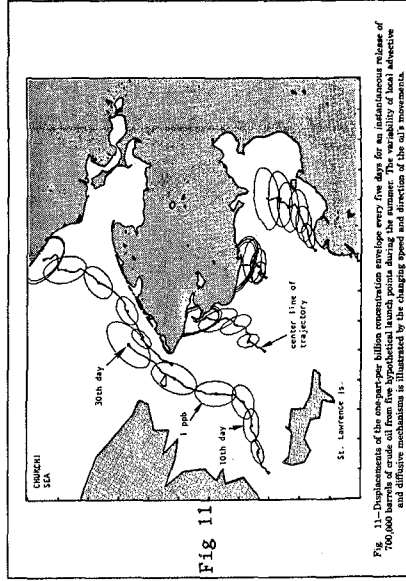


Fig. 11

Fig. 11—Displacements of the one-particle billion concentration envelope every five days for an instantaneous release of 700,000 barrels of crude oil from five hypothetical launch points during the summer. The variability of local advective and diffusive mechanisms is illustrated by the changing speed and direction of the oil's movements.

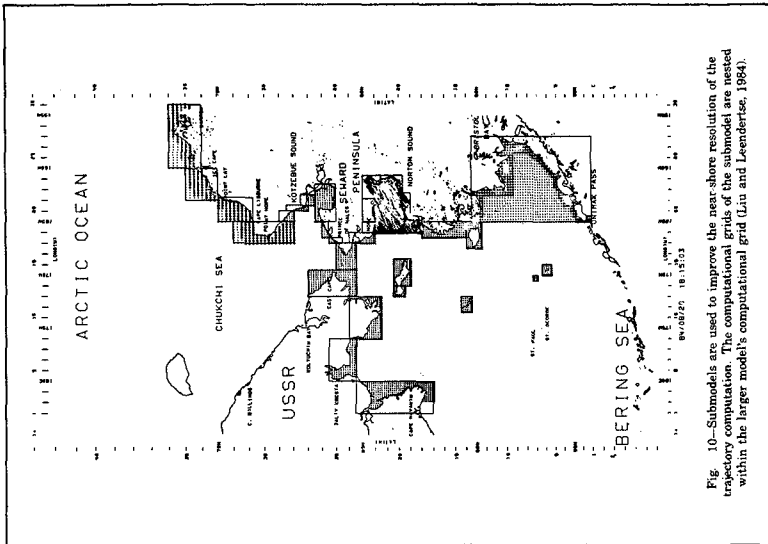


Fig. 10—Submodels are used to improve the near-shore resolution of the trajectory computation. The computational grids of the submodel are nested within the larger model's computational grid (Liu and Leendertse, 1984).

Fig 10

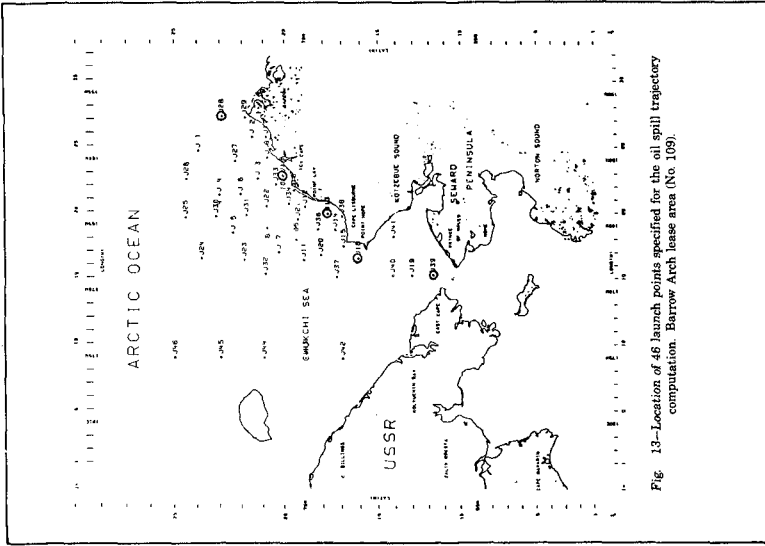


Fig. 13—Location of 46 launch points specified for the oil spill trajectory computation. Barrow Arch. lease area (No. 109).

Fig 13

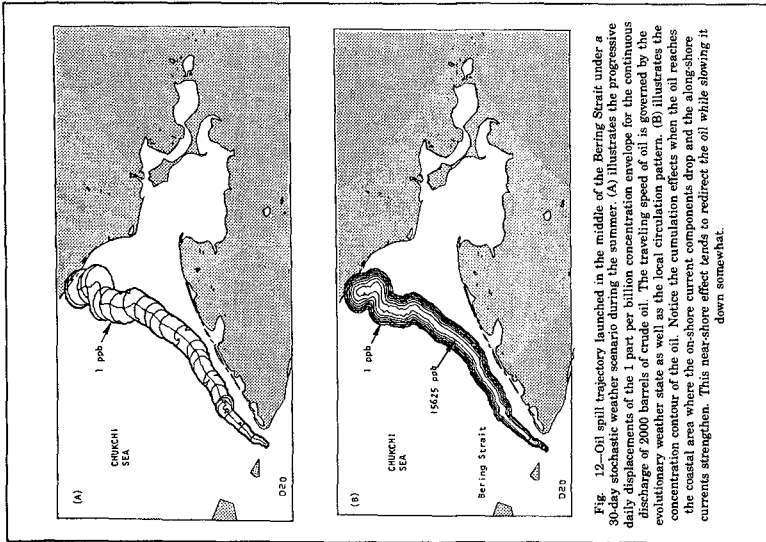


Fig. 12. Oil spill trajectory launched in the middle of the Bering Strait under a 30-day stochastic weather scenario during the summer. (A) illustrates the progressive daily displacements of the 1 part per billion concentration envelope for the continuous discharge of 2000 barrels of crude oil. The traveling speed of oil is governed by the evolutionary weather state as well as the local circulation pattern. (B) illustrates the concentration contour of the oil. Notice the cumulation effects when the oil reaches the coastal area where the on-shore current components drop and the along-shore currents strengthen. This near-shore effect tends to redirect the oil while slowing it down somewhat.

Fig 12

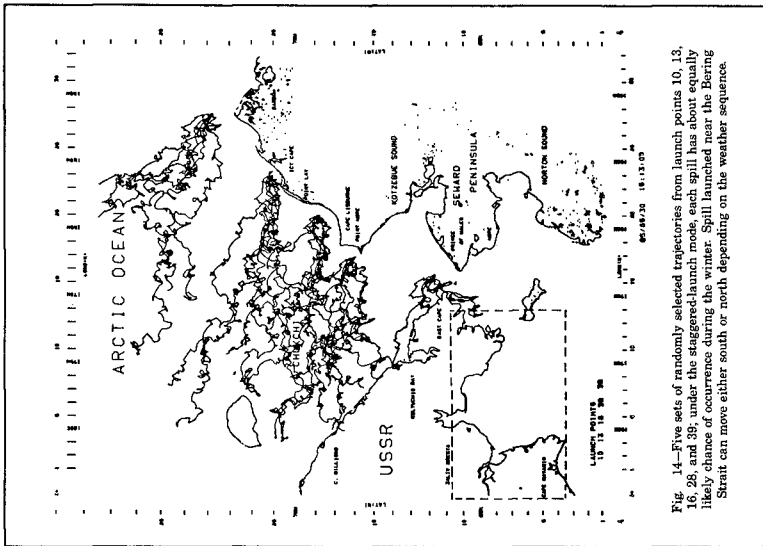


Fig. 14—Five sets of randomly selected trajectories from launch points 10, 13, 16, 23, and 39; under the staggered-launch mode, each spill has about equally likely chance of occurrence during the winter. Spill launched near the Bering Strait can move either south or north depending on the weather sequence.

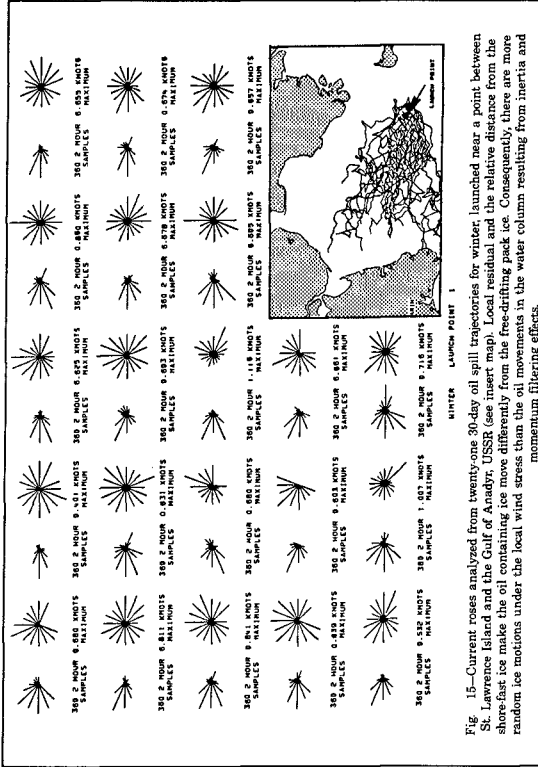


Fig. 15—Current roses analyzed from twenty-one 30-day oil spill trajectories for winter, launched near a point between St. Lawrence Island and the Gulf of Anadyr, USSR (see insert map). Local residual and the relative distance from the shore-fast ice make the oil containing ice move differently from the free-drifting pack ice. Consequently, there are more random ice motions under the local wind stress than the oil movements in the water column resulting from inertia and momentum filtering effects.

Fig 15

Fig 14

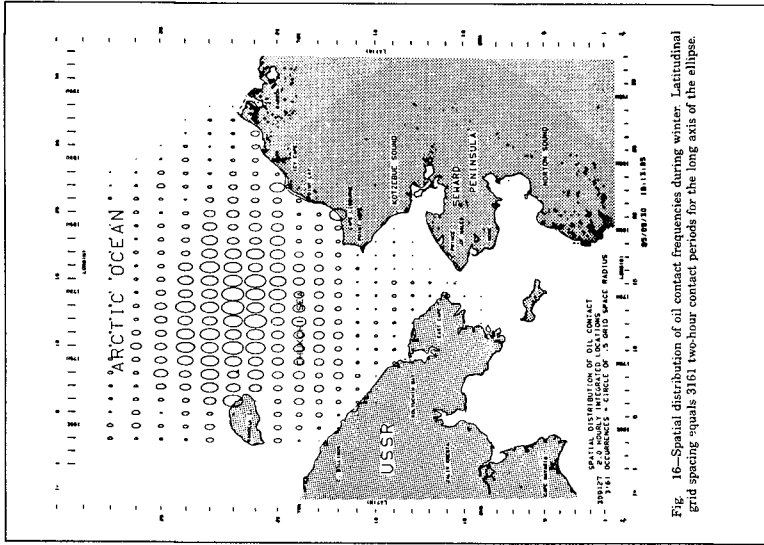


Fig. 16—Spatial distribution of oil contact frequencies during winter. Latitudinal grid spacing equals 3161 two-hour contact periods for the long axis of the ellipse.

Fig 16

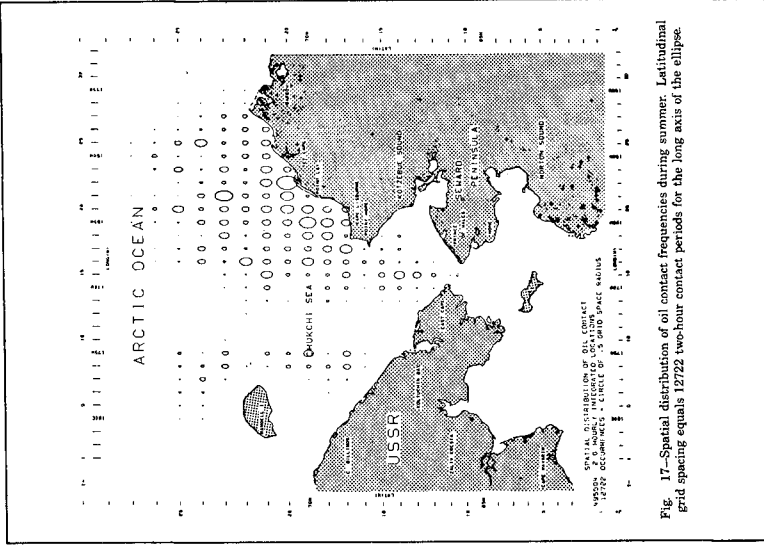


Fig. 17—Spatial distribution of oil contact frequencies during summer. Latitudinal grid spacing equals 12722 two-hour contact periods for the long axis of the ellipse.

Fig 17

groups of 30-day oil spill trajectories are sampled every two hours. These sampled data are then analyzed for their direction and speed. For a 30-day duration there are 360 two-hour samples for current directions and speeds. Since the directions and speeds of currents at every two hours are located over a different area, local residual circulation and the relative distance from the shore-fast ice make the movement of oil contained in ice different from that of free-drifting pack ice. Consequently, there are more random ice motions under the local wind stress than the oil movements in the water column resulting from inertia and momentum filtering effects.

Figure 16 indicates that most oil spill trajectories move in a predominantly northwesterly direction. For the summer period (Fig. 16), however, most contacts are closer to the eastern shore. It should be noted that the plotting scale of Fig. 17 is four times that of the one shown in Fig. 16. The western Chukchi Sea receives much less impact during the summer season than in the winter period. On the average, oil travels a shorter distance and moves more randomly under the summer winds. During summer, winds have higher variabilities and, as a consequence, the inertial current components have a substantial contribution toward the overall current direction. The area of greatest impact is located near Icy Cape.

REFERENCES

- Colony, R., and A. S. Thorndike, (1984): A estimate of the main field of the Arctic ice motion, *J. Geophys. Res.* Vol. 89, No. 6., pp. 10623-10629.
- Cox, J. C., L. A. Shultz, R. P. Johnson and R. A. Sheley, (1980): The transport and behavior of oil spilled in and under sea ice, *Arctic Pac. Rep. No. 460C.*
- Ekman, V. W. (1905): On the influences of the earth's rotation on ocean currents, *Ark. Math. Astr. Fysik. Kong. Su. Vetenskap. Akad., Stockholm*, Vol. 2, No. 11, p. 52.
- Gorgienko, P., (1958): Arctic ice drift, *Proc. Conf. on Arctic sea ice*, Published by the National Academy of Sciences and the National Research Council, Washington, D. C., pp. 210-220.
- Hibler, W. D., (1979): A dynamic thermodynamic sea ice model, *J. Phys. Oceano.* Vol. 9, No. 7., pp. 815-846.
- Kovacs, A., R. M. Morey, and D. Cundy, (1980): Oil pooling under sea ice, *Environmental Assessment of the Alaskan Continental Shelf*, Ann. Rep. Vol. 5, pp. 333-339.
- Liu, S. K., and J. J. Leendertse, (1982): A three-dimensional model of Bering and Chukchi Sea, *COASTAL ENGINEERING* Vol. 18, ASCE, N. Y.
- Liu, S. K., and J. J. Leendertse, (1984): A three-dimensional model of Beaufort Sea, *COASTAL ENGINEERING* Vol. 19, ASCE, N. Y.
- Liu, S. K., and J. J. Leendertse, (1986): A three dimensional model of the Gulf of Alaska, *COASTAL ENGINEERING* Vol. 20, ASCE, N. Y.
- Liu, S. K., and J. J. Leendertse, (1987): Modeling the Alaskan Continental Shelf Waters, *RAND R-3567-NOAA/RC*, 136 pages.
- Murphy, D. L., P. A. Tebeau, and L. M. Lissner, (1981): Long-term movements of satellite-tracked buoys in the Beaufort Sea, Office of Research and Development, U. S. Department of Transportation, CG-D-48-82.

CHAPTER 192

Bore front modeling in terms of Burgers equation and its numerical calculation method

Takao Yamashita ¹

Yoshito Tsuchiya ²

and

David R. Basco ³

Abstract

Bore front hydraulics are investigated in terms of Burgers equation to clarify the dynamics of a moving discontinuity in water flow. Burgers equation has been derived from the one dimensional open channel equation with the horizontal turbulent diffusion term. The derived equation system consists of Burgers with respect to dynamic characteristic and hyperbolic equation with respect to water surface elevation, which satisfies Jeffery-Vedernikov condition $F_r = 2$ through discontinuity. It has been verified from the experiments that the condition $F_r = 2$ is a good approximation of bore front dynamics. The numerical calculation method of Burgers equation employing Cole-Hopf transformation and QUICKEST algorithm was also proposed and confirmed its efficiency.

1. INTRODUCTION

Bores, which can often be observed in rivers, estuaries and coastal zones, i.e. hydraulic jumps, flood waves, breaking waves, tidal bores etc., are well known for their complicated flow structures consisting of typical time scales of order of mean flow, waves and turbulence. From the coastal engineering view point, developing our knowledge of bore dynamics may lead to a better understanding of breaker dynamics and flood wave hydraulics. From the view point of numerical calculation for bore front propagation on beaches, dry lands or rivers, more theoretical studies for its propagation speed and hydraulics are needed. Example numerical calculations include flooding simulation of tsunamis, storm surges and run-up of coastal waves. Sometimes an artificial (physically meaningless?) moving boundary condition is forced to apply to numerical models of this type. The so-called threshold depth is defined in the numerical cells in order to establish an artificial moving boundary.

1) Instructor, Disaster Prevention Research Institute, Kyoto University, Kyoto 611, Japan

2) Professor, Disaster Prevention Research Institute, Kyoto University, Kyoto 611, Japan

3) Professor of Civil Engineering and Director of Coastal Engineering Institute, Old Dominion University, Norfolk, VA 23529-0242, U.S.A.

The basic concept in treating this problem is made by employing the hydraulic jump analogy, where a weak solution of the physical conservation laws is allowed. There are, in general, three conservation laws, mass, momentum and energy, from which we get three sets of jump conditions. For the derivation of shallow water theory, the incompressible fluid approximation is assumed and only two conservation laws are used through the discontinuity.

On the other hand, the so-called Burgers equation is well known as an approximation for dissipative fluid systems, and has been used in analyzing shock-like fluid motions. In this equation, nonlinearity of propagation and diffusive effects are balanced. The main aim of this paper is to determine a method to apply this simple equation to the problem of modeling bore front propagating on the river and dryland.

It is also well known that the advantage in using Burgers equation is that it can be easily solved by transforming it into the linear heat equation by applying the Cole-Hopf transformation. In this paper, we attempt to describe bore front motion by application of Burgers equation, and we propose a solution method which is wiggle-free with no numerical viscosity. Consequently, the simple formulation of bore motion by Burgers equation, and its transformed linear version, advection/diffusion equation, can be solved accurately by the QUICKEST algorithm.

We carried out experiments of bore propagation as a dam-break problem. Our purpose was to examine the bore front profile while focusing on the criterion of undular bore creation in the relationship to bore amplitude and water depth, including extremely small depth (dry land condition). Furthermore, the derivation of Burgers equation, with respect to the propagation speed, is accomplished by using the equations of mass and momentum conservation, in which the Gardner-Morikawa (G-M) transformation is employed. Finally, we proposed an effective numerical calculation method for the Burgers equation by employing both the Cole-Hopf transformation and the QUICKEST numerical algorithm.

2. BORE FRONT PROPAGATION

2.1 Flood Wave Theories

Assuming a wide and rectangular channel, where the hydrostatic pressure law is valid, the 1-D open channel flow equations are,

$$h_t + (hu)_x = 0 \quad (1)$$

$$u_t + uu_x + g' h_x = g' S - C_f \frac{u^2}{h} \quad (2)$$

where subscripts indicate partial derivatives, $u(x,t)$ and $h(x,t)$ are depth-averaged current, and water depth, respectively, and $g' = g \cos \theta$, $S = \tan \theta$, θ is bottom slope angle (see Figure 1).

First of all, some consideration on flood waves with

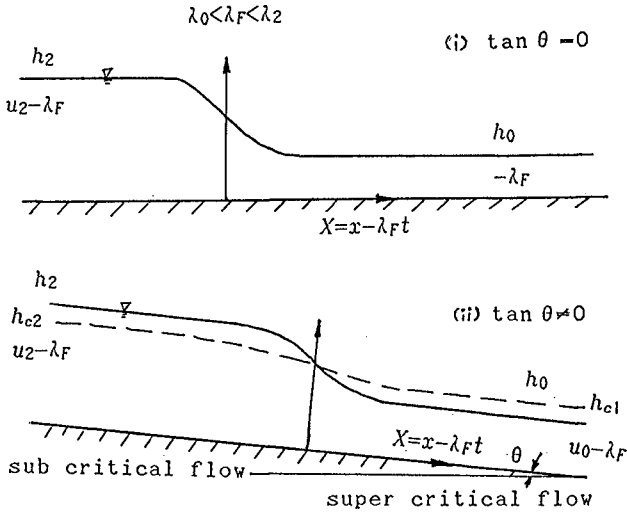


Figure 1. Coordinates and definition of variables

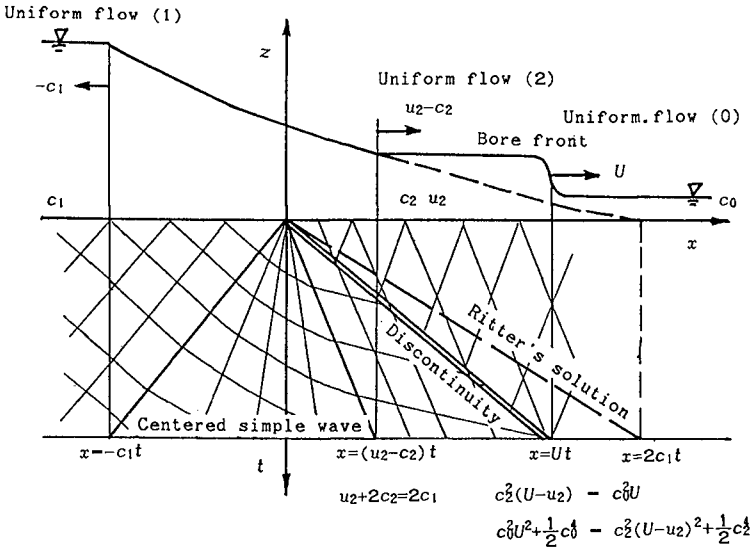


Figure 2. Characteristics of dam break problem.

smooth surface profile are made. If flow motion varies gradually, the kinematic wave approximation is derived, which is called Kleitz-Seddon formula.

$$h_{0t} + \frac{3}{2}u_0 h_{0x} = 0, \quad u_0 = \sqrt{\frac{g \cdot S h}{C_f}} \quad (3)$$

Whitham(1973) showed the monoclinal flood wave by assuming boundary conditions of kinematic approximation at both up and down stream ends, in the reference frame moving at the speed of λ_F as,

$$h = h(X), \quad u = v(X), \quad X = x - \lambda_F t \quad (4)$$

Eqs. (1) and (2) can be written by

$$\frac{dh}{dX} = -\frac{(Q - \lambda_F h)^2 C_f - g h^3 S}{g h^3 - Q^2} \quad (5)$$

where $Q = h_1(\lambda_F - u_1) = h_2(\lambda_F - u_2)$ is total discharge, subscripts 1 and 2 indicate the uniform state quantities in the up and down stream directions, respectively. The behavior of the solution of Eq. (5) depends on the sign of the denominator $g h^3 - Q^2$. The numerator must have roots of $h = h_1, h_2$ to be zero at both boundaries, which are the two roots of the cubic. The third root is

$$h_3 = \frac{C_f Q^2}{S g h_1 h_2} = \frac{h_1 h_2}{(h_1^{1/2} + h_2^{1/2})^2} \quad (6)$$

We are seeking the solution in the range of $h_1 < h < h_2$. Moreover, since $h_3 < h_1$ and $\lambda_F > u$, the sign of dh/dX depends on the denominator. At the stage of $h_2 \rightarrow h_1$, we get the front propagation speed as,

$$\lambda_F = \frac{3}{2}u_1 \quad (7)$$

This means the smallest amplitude flood wave is the kinematic wave, and a smooth surface solution (monoclinal flood wave) exists when the denominator is positive, which is satisfied in the condition of

$$\frac{3u_1}{2} < \lambda_F < u_1 + \sqrt{g h_1} \quad (8)$$

The smooth disturbance propagates faster than the kinematic wave but slower than the dynamic wave in the flow ahead.

When the disturbance's speed exceeds the downstream dynamic wave's

$$\lambda_1 = u_1 + \sqrt{g h_1} < \lambda_F < \lambda_2 = u_2 + \sqrt{g h_2} \quad (9)$$

no smooth surface solution exists. Flow changes from supercritical to subcritical in the reference frame (see Figure

1), which means the initiation of a breaking front (bore front).

Now we consider the higher order contribution of the advection term by introducing a small parameter ε perturbed from the kinematic solution of u_0, h_0 , and assuming constant S and C_f ,

$$\begin{aligned} u &= u_0 + \varepsilon u^{(1)} + \varepsilon^2 u^{(2)} + \dots \\ h &= h_0 + \varepsilon h^{(1)} + \varepsilon^2 h^{(2)} + \dots \end{aligned} \quad (10)$$

In the order of $O(\varepsilon)$, we get

$$h_t^{(1)} + u_0 h_x^{(1)} + h_0 u_x^{(1)} = 0 \quad (11)$$

$$u_t^{(1)} + u_0 u_x^{(1)} + g' h_x^{(1)} + g' S \left(\frac{2u^{(1)}}{u_0} - \frac{h^{(1)}}{h_0} \right) = 0 \quad (12)$$

From Eqs. (11) and (12) eliminating $u^{(1)}$, we get the single equation for $h^{(1)}$ in the form

$$\left(\frac{\partial}{\partial t} + c_{\pm} \frac{\partial}{\partial x} \right) \left(\frac{\partial}{\partial t} + c_{\pm} \frac{\partial}{\partial x} \right) h^{(1)} + \frac{2g'S}{u_0} \left(\frac{\partial}{\partial t} + \frac{3}{2} u_0 \frac{\partial}{\partial x} \right) h^{(1)} = 0 \quad (13)$$

where $c_{\pm} = u_0 \pm \sqrt{g' h_0}$. In Eq. (13) the first term indicates dynamic characteristics and the second term the kinematic one.

If the approximation of $\partial/\partial t \sim 3u_0/2 \partial/\partial x$ is applied in Eq. (13), we get the linear Burgers equation as,

$$h_t^{(1)} + \frac{3}{2} u_0 h_x^{(1)} = \frac{u_0}{2g'S} \left(g' h_0 - \frac{u_0^2}{4} \right) h_{xx}^{(1)} \quad (14)$$

The right hand side of Eq. (14) is the diffusion term. If its sign is a positive, solution of this equation is a diffusive type, and the negative sign leads to an explosive solution which means there is no solution balancing advection and diffusion. This criterion $F_r \cong 2$ is called Jeffery-Vedernikov condition, where F_r is Froude number defined as,

$$F_r = \frac{u_0}{\sqrt{g' h_0}} = 2 \quad (15)$$

In other words, this condition depicts the criterion of the balancing of nonlinearity and dissipation as well as the initiation of the bore front.

After the discontinuity appears, the weak solution is assumed to the conservation laws, such as the hydraulic jump analysis. However, we sometimes need information of flow quantities inside the discontinuity. For this we need a more complicated constitution equation system including turbulence dynamics.

On the other hand, the simplest equation which describes flow field inside the discontinuity is Burgers

equation. As long as the depth-averaged quantities are allowed, it might be easy-to-use the field equation. From the consideration of higher order effects in the flood wave, it is supposed that Burgers equation should describe the local balance of nonlinearity and dissipation effects through the discontinuity.

2.2 Dam break problem

To make sure the bore front propagation speed we considered here the dam break problem shown in Figure 2. Assuming the inviscid fluid flow with hydrostatic pressure distribution on the horizontal bottom, the open channel flow equations (1) and (2) can be rewritten by,

$$\left\{ \frac{\partial}{\partial t} + (u \pm c) \frac{\partial}{\partial x} \right\} (u \pm 2c) = 0 \quad (16)$$

where $c = \sqrt{gh}$, u is the depth-averaged flow velocity. If $c_0 = 0$ (dry land), the Ritter's solution is obtained, which consists of two regions, zone of silence and centered simple wave. In the case of $c_0 \neq 0$, the only possible configuration consists of three uniform flow regions and a centered simple wave, as shown in Figure 2. The discontinuity must occur in the region between uniform flow regions (0) and (2) shown in the figure. For determination of the unknown propagation speed of the discontinuity $\lambda_F = U$, c_2 and u_2 in the uniform flow region (2), we need additional conservation law. Other than mass conservation we could use the momentum or energy conservation law but both. Our choice for this problem is that of momentum.

One more relation can be obtained on the characteristic of $x = (u_2 - c_2)t$ where the Riemann invariant $u + 2c = 2c_1$ in the region of centered simple wave is given by the known quantity c_1 . Consequently we get three equations, as

$$u_2 + 2c_2 = 2c_1 \quad (17)$$

$$c_2^2 (U - u_2) = c_0^2 U \quad (18)$$

$$c_0^2 U^2 + \frac{1}{2} c_0^4 = c_2^2 (U - u_2)^2 + \frac{1}{2} c_2^4 \quad (19)$$

Combining Eqs. (18) and (19), third order polynomial equation with respect to U is obtained.

$$U^3 - 2u_2 U^2 + \{ (u_2)^2 - c_0^2 \} U + \frac{1}{2} u_2 c_0^2 = 0 \quad (20)$$

From Eqs. (17) and (18), the third order polynomial equation with respect to u_2 is derived.

$$u_2^3 - (4c_1 + U) u_2^2 + 4c_1 (c_1 + U) u_2 - 4U (c_1^2 - c_0^2) = 0 \quad (21)$$

To solve the above set of two equations, we consider Eq. (20), the second order polynomial equation with respect to u_2 and two its solutions $u_{2(\pm)}$ are

$$u_{2(\pm)} = \frac{1}{4U} \{ 4U^2 - c_0^2 \pm c_0 \sqrt{c_0^2 + 8U^2} \} \quad (22)$$

At the limit of $c_1 \rightarrow c_0$, u_2 should be zero. This condition is satisfied by $u_{2(-)}$. Substituting $u_{2(-)}$ into Eq.(22) and solving the resultant equation numerically in the range of $c_0 < U < 2c_1$, we get the configuration of solutions of U, u_2, c_2 as shown in Figure 3, where three regions of breaking front with undular component, strong bore front and Burgers front are zoned in terms of $\beta = c_0/c_1$. In addition to these other information such as $F_r = U/c_2$, $F_{r2} = u_2/c_2$ and U/c_0 are shown.

2.3 Experiment of bore front propagation

Experiments were conducted as a dam break problem by using a flume and gate system with dimensions of 0.7m in width and height (Figure 4). Surface profiles were measured by 5 wave gauges of capacitance type. Flow visualization techniques were employed for measuring the mean velocity fields near the bore front. The initial water depth in front of the gate was varied in order to examine the effects of downstream boundary condition to the bore propagation. The experimental conditions are presented in Table 1, where h_0, h_1 and h_2 are initial water depths of up/down-stream sides of the gate and water depth in the uniform region formed just after bore front, i.e. uniform flow (2) in Figure 2.

Table 1 Experimental conditions

Run No.	h_1 (cm)	h_0 (cm)	c_0/c_1	h_2 (cm) crest-mean	c_2/c_1 crest-mean
1	19.8	1.0	0.225	5.14	0.557
2	20.9	3.8	0.426	7.71-8.0	0.608-0.62
3	22.6	9.8	0.659	6.00-9.0	0.515-0.63
4	25.6	12.8	0.707	6.94-10.5	0.521-0.64
5	19.3	2.2	0.338	6.51	0.581
6	24.8	0.8	0.180	6.64	0.517
7	14.7	0.8	0.233	6.43	0.661
8	8.0	0.9	0.335	3.94	0.702

Figure 5 shows two typical examples of measured bore profiles above the initial still water level (Run No.3 and 6). It can be seen that undular bores are observed in the wave profiles of the case whose initial still water is deep, however there is no undular bore in the case of an extremely shallow initial depth. This fact can be explained by using the results shown in Figure 3. From the consideration of characteristics in the uniform region (2), the undular bore criterion is $u_2 = c_2$, which corresponds to the intersection of the curves c_2/c_1 and u_2/c_1 . Circles in Figure 3 indicate the experimental results of U/c_1 and c_2/c_1 . Numbers indicate Run No. in Table 1. Solid circles represent the cases of undular bores and white ones are strong bore fronts without undular components. Figure 6 shows Froude numbers F_{r2} calculated by measured currents and bore heights. It can be confirmed that Froude numbers exist in the range, $1 < F_{r2} < 2$.

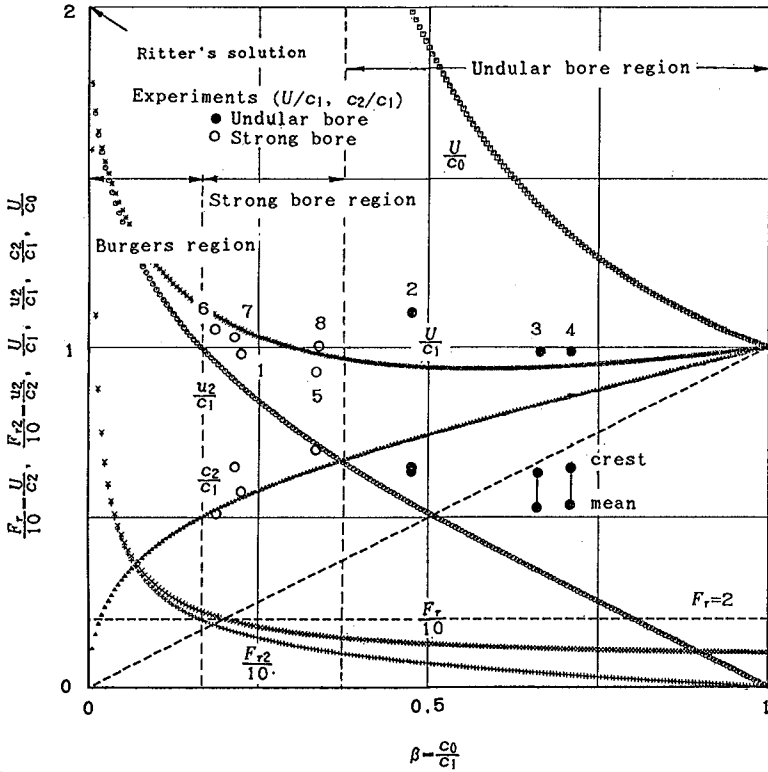


Figure 3. Solutions of dam break problem.

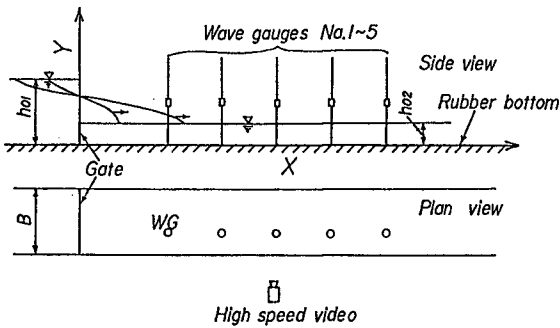


Figure 4. Set-up of experiment.

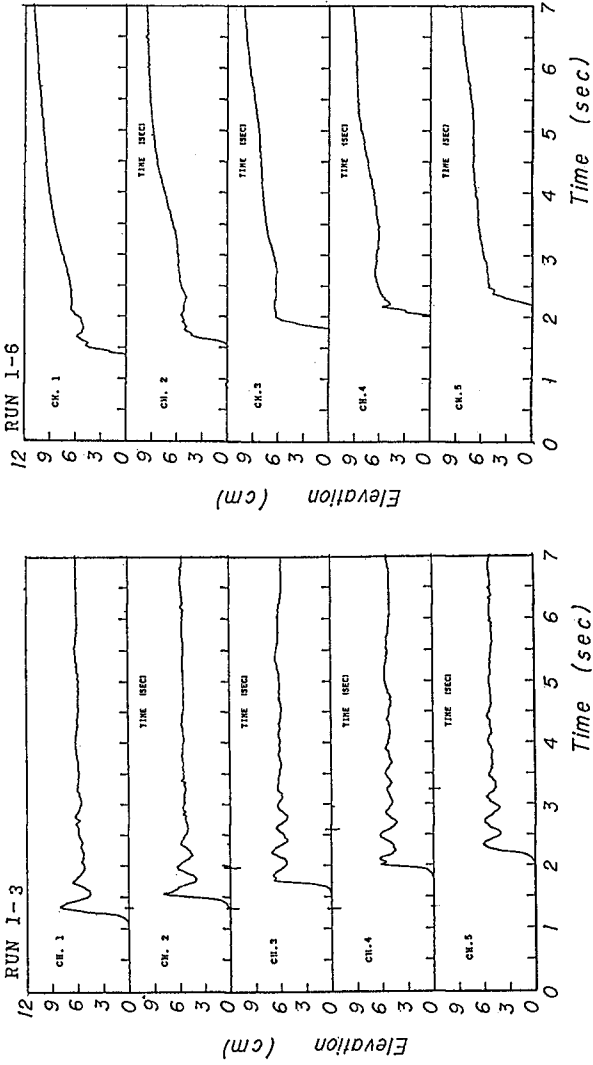


Figure 5. Examples of bore front surface profiles.
(above the still water level)

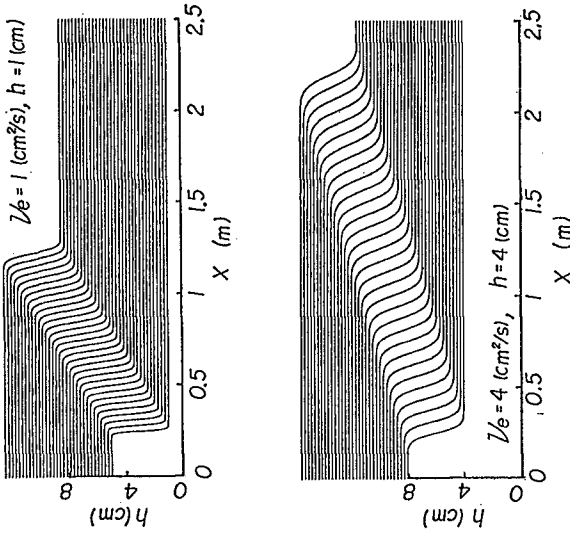


Figure 7. Test runs of numerical calculation of Burgers eq.

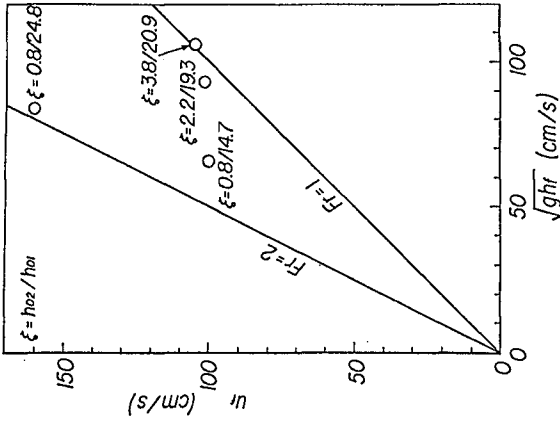


Figure 6. Experimental results of bore front Froude number.

In this figure it should be noted that bore propagating speed U/c_1 keeps almost constant up to the point of $F_{r2} = 2$, which is corresponding to Jeffery-Vedernikov condition. Furthermore experimental results of U/c_1 have good agreement with the curve calculated by nonlinear long wave theory, especially in the region of strong bore. Unfortunately there is no data in the region of $F_{r2} > 2$, however, it might be that the nonlinearity of the propagation and turbulent mixing effects balance each other to keep the relation of $F_{r2} = 2$ in this region. This is the basic conception of Burgers approximation which will be elaborated on in next section. It is also mentioned in the figure that the dispersion effect can not be neglected in the region of $F_{r2} < 1$, in which experimental results in c_2/c_1 are smaller than the theoretical one. This result indicates that undular bore components sustain their energy in the form of wave motion while some of them are transported in the backward direction.

3. BORE FRONT MODELING BY BURGERS EQUATION

3.1 Derivation of Burgers Equation

To introduce the balance effect of nonlinearity and dissipation, the horizontal momentum diffusive effect, $\nu_e u_{xx}$, is considered in the momentum equation (2).

$$u_t + uu_x + g' h_x = g' S - C_f \frac{u^2}{h} + \nu_e u_{xx}, \quad (23)$$

where ν_e is the horizontal turbulent eddy viscosity.

First of all, for the 0-th order (basic) flow condition, uniform flow, still water or dry land must be defined. For the open channel flow balancing between gravitational force and bottom friction the kinematic wave condition is the lowest order of the flood wave formulation called Kleitz-Seddon law. In addition to this it is possible to apply Burgers equation to the analysis of a discontinuity propagating on the 0-th order condition of still water or horizontal dry land. To achieve this aim the higher order effects of nonlinearity of propagation and turbulent diffusivity should be considered in the momentum equation, which should be described by Burgers equation. Employing the formulation of nonlinear long wave theory in terms of Riemann invariant, two variables of the propagation speed of disturbance defined by $c = \sqrt{gh}$ and the characteristic speed defined by $\lambda = u + c$ are chosen. The basic equations are rewritten using these variables as,

$$c_t + (\lambda - \frac{3}{2}c)c_x + \frac{1}{2}c\lambda_x = 0 \quad (24)$$

$$\lambda_t + (\lambda - \frac{1}{2}c)_x + \frac{3}{2}cc_x = g \tan \theta \frac{C_f u_0^2}{h_0} + \nu_e \lambda_{xx} + \nu_e c_{xx} \quad (25)$$

Based on the 0-th order solutions (kinematic waves or still water) 1-st order (Burgers discontinuity) and higher order components are introduced by

$$\begin{aligned}\lambda &= \lambda_0 + \varepsilon \lambda^{(1)} + \varepsilon^2 \lambda^{(2)} + \dots \\ c &= c_0 + \varepsilon c^{(1)} + \varepsilon^2 c^{(2)} + \dots\end{aligned}\quad (26)$$

where ε is defined by the parameter of magnitude of discontinuity, i.e. amplitude of discontinuity

$$\varepsilon = \frac{(\lambda_{-\infty} - \lambda_0)}{\lambda^{(1)}_{-\infty}}. \quad (27)$$

From the similitude of the Gardner-Morikawa transformation balancing equation, the nonlinearity of propagation and diffusivity are achieved by the following transformation (Taniuchi & Nishihara (1977)).

$$\xi = \varepsilon(x - \lambda_0 t), \quad \tau = \varepsilon^2 t \quad (28)$$

Applying the G-M transformation to the fundamental equations (24), (25) and substituting Eq(26), we get Burgers equation

$$\lambda_{\tau}^{(1)} + \lambda^{(1)} \lambda_{\xi}^{(1)} = \frac{2\nu_e}{3} \lambda_{\xi\xi}^{(1)} \quad (29)$$

and hyperbolic equation of $s^{(1)}$

$$c_{\tau}^{(1)} + \lambda^{(1)} c_{\xi}^{(1)} = 0, \quad \lambda^{(1)} = \frac{3}{2} u^{(1)} \quad (30)$$

These equations (29) and (30) are the Burgers equation system derived here for the problem of bore front propagation. Notice that discontinuity h or c propagates by the speed of $3u/2$ and the dynamic characteristic speed λ is described by Burgers equation (29). This also means that λ satisfies the Jeffery-Vedernikov condition which describes the intersection of the dynamic and kinematic characteristics through the discontinuity. As the discontinuity becomes greater, horizontal turbulent diffusivity increases in order to decrease the propagation speed, which is the balancing of effects of nonlinearity of propagation and horizontal diffusivity of momentum. The bottom friction does not contribute to the propagation of Burgers components.

For the practical purpose, we can calculate the front propagation speed $\lambda = \lambda_0 + \varepsilon \lambda^{(1)}$ and surface elevation h and current u by using the resultant set of equations when the up-stream boundary condition $\lambda_{-\infty}$ and 0-th order flow (basic flow) condition are given. If a bore propagates on the horizontal dry land and uniform flow exists in the up-stream region, $\xi = -\infty$, applying the basic flow condition, $\lambda_0 = 0$, the bore front speed can be given by $\lambda_F = \lambda_{-\infty}/2$.

The bore front formulation by using Burgers equation mentioned here might have following advantages.

- (1) Continuous flow structures through the discontinuity can be calculated by the depth-averaged quantities.
- (2) Bore front propagation speed and profile (front length) are also evaluated.
- (3) Burgers equation can be transformed into the linear

advection/diffusion equation by the nonlinear transformation, which makes the numerical calculation easy; this will be referred in the following section.

4. NUMERICAL CALCULATION METHOD OF BURGERS EQUATION

Burgers equation has an interesting property, in that it can be transformed into a linear equation (heat equation) by the Cole-Hopf transformation

$$h = -2\nu\phi_x/\phi, \quad \nu = \frac{2\nu_0}{3} \quad (31)$$

Applying this transformation to the derived Burgers equation (35) in the fixed coordinates, the advection/diffusion linear PDE is obtained

$$\phi_t + \lambda_0\phi_x = \mu\phi_{xx}, \quad \mu = \frac{2\nu_0}{3} \quad (32)$$

Leonard(1979) has developed a third order accurate numerical scheme for this equation called the QUICKEST algorithm. Basco(1984) has shown that using the quadratic upstream interpolation operator for the advection term of Eq.(5) along with a forward time operator and centered second derivative operator, is identically equal to a forward-time and centered advection operator (FTCS) plus removal of truncation error by employing a special technique. The resulting difference equation is

$$\begin{aligned} \phi_j^{n+1} = & \phi_j^n + \left\{ \rho(1-C_r) - \frac{C_r}{6}(C_r^2 - 3C_r + 2) \right\} \phi_{j+1}^n - \left\{ \rho(2-3C_r) - \frac{C_r}{2}(C_r^2 \right. \\ & - 2C_r - 1) \left. \right\} \phi_j^n + \left\{ \rho(1-3C_r) - \frac{C_r}{2}(C_r^2 - C_r - 2) \right\} \phi_{j-1}^n + \left\{ \rho C_r + \frac{C_r}{6}(C_r^2 \right. \\ & \left. - 1) \right\} \phi_{j-2}^n \end{aligned} \quad (33)$$

where $C_r = c_0 \Delta t / \Delta x$, $\rho = \mu \Delta t / \Delta x^2$ and $c_0 = \sqrt{gh_0}$. The abovementioned method of solving Burgers equation is wiggle-free, accurate and low cost.

Example testing of this method was performed by using propagation test of a bore whose profile was given by the kink solution of

$$h = h_0 + a \tanh \left\{ -\frac{a}{2\nu} (x - x_0) \right\} \quad (34)$$

where a is half amplitude x_0 is initial position of bore, and the corresponding transformed profile is given by

$$\phi = C \exp \left\{ -\frac{1}{2\nu} \int h dx \right\} \quad (35)$$

Using this initial condition and the boundary conditions of constant water depth in the far field, example solutions of Burgers equation were calculated as shown in

Figure 7.

5. CONCLUSIONS

Bore front hydraulics were investigated in terms of Burgers equation and experiments were carried out to make clear the dynamics of moving discontinuity of water flow. The main results obtained are:

(1) Burgers equation has been derived from the one dimensional open channel flow equation with horizontal momentum mixing term. The derived equation system consists of Burgers with respect to dynamic characteristic and hyperbolic equation with respect to water surface, which satisfies the Jeffery-Vedernikov relation $F_{r2} = 2$ through discontinuity.

(2) It is made clear from experiments that in the region of $1 < F_{r2} < 2$ nonlinear long wave theory has a good applicability for bore front propagation, however, in the region of $F_{r2} > 2$ turbulent diffusivity of momentum has to be considered in terms of Burgers equation. Moreover, in the region of $F_{r2} < 1$ the dispersion effect is not negligible in the observed undular bores.

(3) An accurate numerical calculation method to solve Burgers equation has also been proposed by employing the Cole-Hopf transformation and QUICKEST algorithm.

Acknowledgements

The authors would like to express their appreciation to Mr. M. Imashio, Civil Engineer of Kawasaki Steel Co. Ltd., for his help in the experiments. Part of this investigation were funded by a Grant-in-Aid for Scientific Research (No.59020023) from the Ministry of Education, Science & Culture of Japan.

References

- Basco, D.R.: An implicit wiggle-free and accurate upstream finite-difference algorithm for the one-dimensional advection-diffusion equation, USAE, Waterway Exp. Sta., M.P. EL-84, 49p., 1984.
- Leonard, B.P.: A stable and accurate convection modelling procedure based on quadratic upstream interpolation, Computer Meth. in App. Mech. Eng., vol.19, pp.59-98, 1979.
- Taniuchi, T and K. Nishihara: Nonlinear Wave Theory, Iwanami-shoten, p. , 1977.
- Whitham G.B.: Linear and Nonlinear Waves, John Wiley & Sons, p.636, 1974.

CHAPTER 193

Nearshore Circulations on a Wavy Coast

Ming-Chung Lin* and Sheng-Yeh Hwang**

1. Introduction

Nearshore circulations, produced by wave-induced radiation stress gradients, form different circulation patterns under different wave characteristics and topographical conditions. Although numerous studies of nearshore circulations, such as Bowen (1969), Miller and Barcilon (1978), Dalrymple & Lozano (1978) and so on, have been appeared in the literature, it seems that little attention is paid on the case of a non-straight shoreline. O'Rourke & Leblond (1972) have investigated the wave-induced longshore currents in a semicircular bay, while Uda (1982) has used the coordinate transformation to treat nearshore circulations on a circular-arc shaped coast. Lin and Lee (1982), introduced a small perturbation quantity of wave set-up and set-down, induced by the non-straight shoreline, into the mean total water depth to obtain a governing partial differential equation by which they investigated the nearshore circulations on a cusped coast. In Lin and Liou (1986), a more general equation was deduced on the orthogonal curvilinear coordinate system to unify the diversities among the related theories, and moreover, to investigate the rearshore circulations on the arc-shaped coast.

2. Mathematical formulation

With the wave field there will be associated a mean transport velocity which we will lump together with the secondary mean currents that we wish to describe under the velocity vector U , assumed horizontal and depth purely independent. The mean momentum density of a water column is

$$M = \rho dU \quad (1)$$

where ρ is the water density and d the total water depth. For a steady wave field the mean mass conservation equation reduces to

$$\nabla \cdot M = 0 \quad (2)$$

and then the linearized mean momentum equation is expressed as (O'Rourke and Leblond, 1972)

* Professor, Dept. of Naval Architecture, National Taiwan Univ., Taipei, Taiwan, Rep. of China.

** Graduate Institute of harbor and River Eng., National Taiwan College of marine Science and Technology, Keelung, Taiwan, Rep. of China.

$$\frac{1}{\rho d} \frac{\partial S_{ij}}{\partial X_i} = -g \frac{\partial \zeta}{\partial X_i} - \frac{fU_i}{\rho d} \quad (3)$$

where f is the friction coefficient, a function of total water depth and wave amplitude; S_{ij} is the radiation stress of the waves, g is the acceleration of gravity. In this equation, the lateral friction is neglected. Define

$$T_i = \frac{1}{\rho d} \frac{\partial S_{ij}}{\partial X_j}, \quad F_i = -\frac{fU_i}{\rho d} \quad (4)$$

then, in surf zone, equation (3) can be rewritten as

$$\nabla \times T = \nabla \times F \quad (5)$$

In linear model (O'Rourke and Leblond, 1972), in the outside surf zone:

$$\nabla \times F = 0 \quad (6)$$

and in the surf zone

$$\nabla \times T = \nabla \times F \quad (7)$$

The coordinate system used and the domain interested are duplicated as Fig. 1. in which ϕ is the angle of wave incidence, A and B, denote the region inside and outside the surf zone respectively. the shoreline is assumed as

$$Y = \alpha \cos kx, \quad k = 2\pi/L \quad (8)$$

where L is spatial wave length of shoreline, and α shoreline wave amplitude. Applying conformal mapping (Lyne, 1971)

$$z = x+iy, \quad \zeta = \mu_1 + i\mu_2 = z - i\alpha e^{ikz} \quad (9)$$

it yields, up to $O(\alpha k)$

$$\begin{aligned} \mu_1 &= x + \alpha e^{-ky} \sin kx \\ \mu_2 &= y - \alpha e^{-ky} \cos kx \end{aligned} \quad (10)$$

The continuity equation (2) then becomes

$$\frac{\partial}{\partial \mu_1} (J^{-1/2} du) + \frac{\partial}{\partial \mu_2} (J^{-1/2} dv) = 0 \quad (11)$$

where J is Jacobian:

$$J = \left| \frac{d\zeta}{dz} \right|^2 = 1 + 2\alpha k e^{-ky} \cos kx + (\alpha k)^2 e^{-2ky} \quad (12)$$

By equation (11) the velocity components u and v are

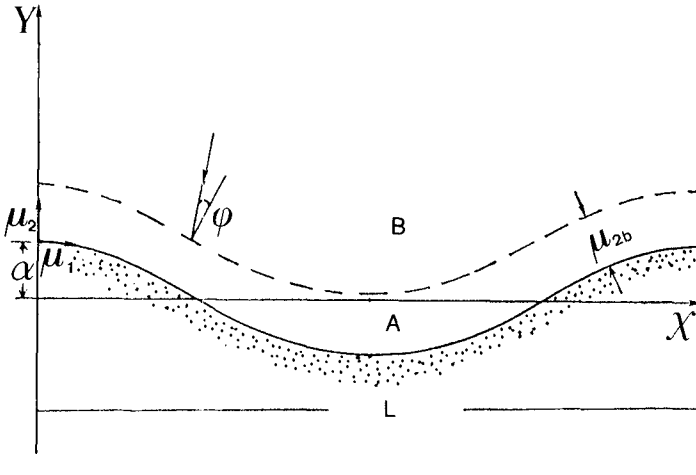


Fig. 1 Schematic diagram of coordinate system.

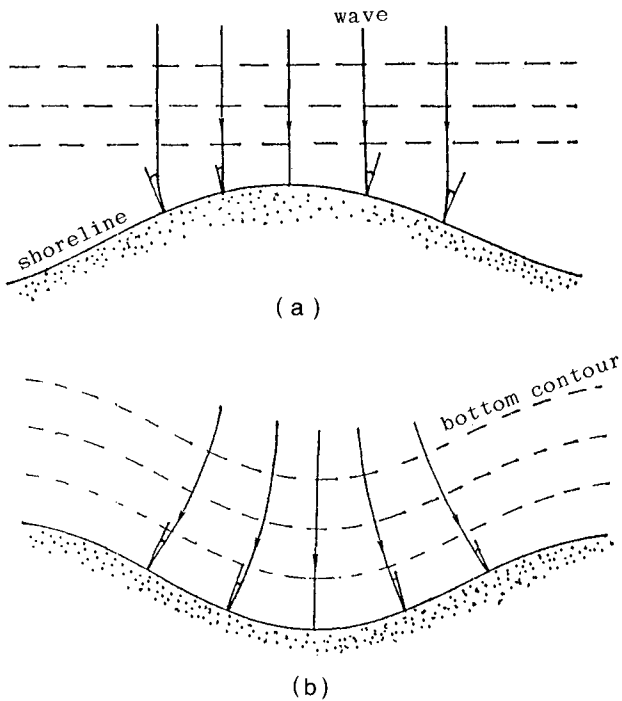


Fig. 2 Cases designed for calculations.

represented in terms of the transport stream function x as

$$u = \frac{J^{1/2}}{d} \frac{\partial x}{\partial \mu_2}, \quad v = \frac{J^{1/2}}{d} \frac{\partial x}{\partial \mu_1} \quad (13)$$

In surf zone, we express radiation stress components in (μ_1, μ_2) system to be $(T\mu_1, T\mu_2)$ then

$$\nabla \times T = J \left[\frac{\partial}{\partial \mu_1} (J^{-1/2} T\mu_2) - \frac{\partial}{\partial \mu_2} (J^{-1/2} T\mu_1) \right] \quad (14)$$

where $T\mu_1, T\mu_2$ are defined as

$$\begin{aligned} T\mu_1 &= \frac{J}{\rho d} \left[\frac{\partial}{\partial \mu_1} (J^{-1/2} S\mu_1\mu_1) + \frac{\partial}{\partial \mu_2} (J^{-1/2} S\mu_1\mu_2) \right] \\ T\mu_2 &= \frac{J}{\rho d} \left[\frac{\partial}{\partial \mu_1} (J^{-1/2} S\mu_2\mu_1) + \frac{\partial}{\partial \mu_2} (J^{-1/2} S\mu_2\mu_2) \right] \end{aligned} \quad (15)$$

Substituting equation (15) into equation (5), and expanding into Taylor's series, up to $O(\alpha k)$, we obtain

$$\begin{aligned} J \left[\frac{\partial}{\partial \mu_1} \left(\frac{f}{\rho d^2} \frac{\partial x}{\partial \mu_1} \right) + \frac{\partial}{\partial \mu_2} \left(\frac{f}{\rho d^2} \frac{\partial x}{\partial \mu_2} \right) \right] = \\ J \left\{ \frac{\partial}{\partial \mu_1} \left[\frac{J}{\rho d} \frac{\partial}{\partial \mu_1} (J^{-1/2} S\mu_1\mu_2) + \frac{J}{\rho d} \frac{\partial}{\partial \mu_2} \right. \right. \\ \left. \left. (J^{-1/2} S\mu_2\mu_2) \right] - \frac{\partial}{\partial \mu_2} \left[\frac{J}{\rho d} \frac{\partial}{\partial \mu_1} (J^{-1/2} S\mu_1\mu_1) \right. \right. \\ \left. \left. + \frac{J}{\rho d} \frac{\partial}{\partial \mu_2} (J^{-1/2} S\mu_2\mu_2) \right] \right\} \end{aligned} \quad (16)$$

where J_1 can be expanded by Taylor's series, up to $O(\alpha k)$

$$J^{-1/2} = 1 - \alpha k \epsilon k^{\mu_2} \cos k\mu_1 \quad (17)$$

In the region outside the surf zone, equation (6) can be similarly transformed to be

$$\begin{aligned} \nabla \times F = J \left[\frac{\partial}{\partial \mu_1} \left(\frac{f}{\rho d^2} \frac{\partial x}{\partial \mu_1} \right) + \frac{\partial}{\partial \mu_2} \left(\frac{f}{\rho d^2} \frac{\partial x}{\partial \mu_2} \right) \right] \\ = 0 \end{aligned} \quad (18)$$

we further assume that in the seaward zone the mean currents

do not reach to the bottom, but to about the water depth at the breaker line, as assumed by Liu and Lennon (1978). Thus the total water depth $d = \zeta + h_b$, where h_b is the water depth at the breaker line, will be taken as a constant. Assume $d = d_b$, we get

$$\frac{\partial^2 x}{\partial \mu_1^2} + \frac{\partial^2 x}{\partial \mu_2^2} = 0 \quad (19)$$

Let

$$\mu_1 = \frac{2\pi}{k} \xi, \quad \mu_2 = \frac{2\pi}{k} \eta \quad (20)$$

We can get the nondimensional equation:

$$\frac{\partial^2 x}{\partial \xi^2} + \frac{\partial^2 x}{\partial \eta^2} = 0 \quad (21)$$

3. General solution

In the seaward zone, the stream function satisfies $\nabla^2 X = 0$. We will label the stream function in each one of the two regions with a corresponding letter subscript. Now we consider some boundary conditions. The normal velocity at the shore line must vanish, that is

$$X_A(\xi, 0) = 0 \quad (22)$$

Further, the normal velocity must be matched at the boundaries between the two regions. By matching the stream function across those boundaries, this requirement is achieved:

$$\begin{aligned} X_A(\xi, 1) &= X_B(\xi, \delta) \\ X_{A,B}(0, \eta) &= 0 \\ X_{A,B}(1, \eta) &= 0 \\ X_B(\xi, \infty) &= X_\infty \end{aligned} \quad (23)$$

Set

$$X_A = X_1 + \delta X_2 \quad (24)$$

for δ is a small perturbation magnitude. In surf zone, we shall assume that the total mean depth is a linear function of the distance from shore

$$d = m(\xi) \cdot \eta \quad (25)$$

where $m(\xi) = m_0 (1 + p \cos 2\pi\xi)$, m_0, p are small quantity. Set a simple, but reasonable form for ϕ_b , we take

$$\phi_b = -\phi_0 \sin 2\pi\xi \quad (26)$$

Substituting equation (25) and (26) into equation (16) and make it nondimensional with

$$X_{A,B} = \frac{\pi g^{1/2} \gamma m_b^{5/2}}{C} \cdot X_{A,B}^* \quad (27)$$

we finally get the solutions for the region inside the surf zone:

$$\begin{aligned} X_A^* &= \frac{\phi_o}{6} (\sin 2\pi\xi + \frac{5}{4} p \sin 4\pi\xi) \cdot \eta^3 \\ &+ \frac{2\pi}{7} \delta p (\sin 2\pi\xi + \frac{3}{4} p \sin 4\pi\xi) \cdot \eta^{\frac{7}{2}} \\ &+ \frac{7\pi \phi_o^2}{24} \delta \cdot \sin 4\pi\xi \cdot \eta^4 + (\alpha k) \left\{ \frac{\phi_o}{4} (\sin 4\pi\xi \right. \\ &+ \frac{5}{4} p \sin 2\pi\xi + \frac{5}{4} p \sin 6\pi\xi) \cdot \left[\frac{\eta^3}{3} - \frac{k \mu_{2b}}{4} \cdot \eta^4 \right. \\ &+ \left. \left. \frac{(k \mu_{2b})^2}{10} \cdot \eta^5 \right] - \frac{5\pi}{4} \delta (\sin 2\pi\xi + \frac{5}{4} p \sin 2\pi\xi) \right. \\ &\cdot \left. \left[\frac{2}{7} \eta^{\frac{7}{2}} - \frac{2k \mu_{2b}}{9} \cdot \eta^{\frac{9}{2}} + \frac{(k \mu_{2b})^2}{11} \cdot \eta^{\frac{11}{2}} \right] \right\} \\ &+ \frac{\pi \delta p}{2} (\sin 4\pi\xi + \frac{3p}{4} \sin 2\pi\xi + \frac{3}{4} p \sin 6\pi\xi) \\ &\cdot \left[\frac{2}{7} \eta^{\frac{7}{2}} - \frac{2k \mu_{2b}}{9} \cdot \eta^{\frac{9}{2}} + \frac{(k \mu_{2b})^2}{11} \cdot \eta^{\frac{11}{2}} \right] + \pi \phi_o^2 \delta \\ &\cdot (\sin 2\pi\xi + \sin 6\pi\xi) \cdot \left[\frac{\eta^4}{6} - \frac{2k \mu_{2b}}{25} \cdot \eta^5 + \frac{(k \mu_{2b})^2}{42} \cdot \eta^6 \right] \\ &+ \frac{\pi \phi_o^2 \delta}{4} (\sin 2\pi\xi + \sin 6\pi\xi) \cdot \left[\frac{\eta^4}{4} - \frac{k \mu_{2b}}{5} \cdot \eta^5 \right. \\ &+ \left. \frac{(k \mu_{2b})^2}{12} \cdot \eta^6 \right] + \frac{\pi \phi_o \delta}{4} \cdot (\sin 4\pi\xi + \frac{5}{4} p \sin 2\pi\xi \\ &+ \frac{5}{4} p \sin 6\pi\xi) \cdot \left[\frac{\eta^4}{4} - \frac{k \mu_{2b}}{5} \cdot \eta^5 + \frac{(k \mu_{2b})^2}{12} \cdot \eta^6 \right] \quad (28) \end{aligned}$$

Equation (21) for the region outside the surf zone is the Laplace equation which can be solved easily. The final nondimensional form of the solution is

$$\begin{aligned}
 X_B^* = & e^{-2\pi(\eta-\delta)} \cdot \left\{ \frac{\phi_0}{6} \left[\sin 2\pi\xi + \frac{5}{4} p \sin 4\pi\xi \right. \right. \\
 & \cdot e^{-2\pi(\eta-\delta)} \left. \right] + \frac{2\pi}{7} \delta p \left[\sin 2\pi\xi + \frac{3}{4} p \sin 4\pi\xi \right. \\
 & \cdot e^{-2\pi(\eta-\delta)} \left. \right] + \frac{7\pi}{24} \delta \phi_0^2 \cdot \sin 4\pi\xi \cdot e^{-2\pi(\eta-\delta)} \\
 & + (\alpha k) \left\{ \frac{\phi_0}{4} \left[\sin 4\pi\xi \cdot e^{-2\pi(\eta-\delta)} \right. \right. \\
 & + \frac{5}{4} p \sin 6\pi\xi \cdot e^{-4\pi(\eta-\delta)} + \frac{5}{4} p \sin 2\pi\xi \left. \right] \\
 & \cdot \left[\frac{1}{3} - \frac{k \mu_{2b}}{4} + \frac{(k \mu_{2b})^2}{10} \right] - \frac{5\pi\delta}{4} \cdot \left[\sin 2\pi\xi \right. \\
 & + \frac{5}{4} p \sin 4\pi\xi \cdot e^{-2\pi(\eta-\delta)} \left. \right] \cdot \left[\frac{2}{7} - \frac{2}{9} k \mu_{2b} + \frac{(k \mu_{2b})^2}{11} \right] \\
 & + \frac{\pi}{2} \delta p \left[\sin 4\pi\xi \cdot e^{-2\pi(\eta-\delta)} + \frac{3}{4} p \sin 2\pi\xi \right. \\
 & + \frac{3}{4} p \sin 6\pi\xi \cdot e^{-4\pi(\eta-\delta)} \left. \right] \cdot \left[\frac{2}{7} - \frac{2 k \mu_{2b}}{9} \right. \\
 & + \frac{(k \mu_{2b})^2}{11} \left. \right] + \pi \phi_0^2 \delta \left[\sin 2\pi\xi + \sin 6\pi\xi \cdot e^{-4\pi(\eta-\delta)} \right] \\
 & \cdot \left[\frac{1}{6} - \frac{2}{25} k \mu_{2b} + \frac{(k \mu_{2b})^2}{42} \right] + \frac{\pi \phi_0^2 \delta}{4} \left[\sin 2\pi\xi \right.
 \end{aligned}$$

$$\begin{aligned}
& + \sin 6\pi\xi \cdot e^{-4\pi(\eta-\delta)} \cdot \left[\frac{1}{4} - \frac{k\mu_{2b}}{5} + \frac{(k\mu_{2b})^2}{12} \right] \\
& + \frac{\pi\phi_0\delta}{4} \cdot \left[\sin 4\pi\xi \cdot e^{-2\pi(\eta-\delta)} + \frac{5}{4}p \sin 6\pi\xi \right. \\
& \cdot e^{-4\pi(\eta-\delta)} + \left. \frac{5}{4}p \sin 2\pi\xi \right] \cdot \left[\frac{1}{4} - \frac{k\mu_{2b}}{5} \right. \\
& \left. + \frac{(k\mu_{2b})^2}{12} \right] \} \} \quad (29)
\end{aligned}$$

The solutions X_A and X_B (A indicates inside surf zone; B outside) finally obtained include two parts, one concerned with (αk) and the other independent on (αk) , where (αk) denotes the steepness of wavy shoreline.

4. Numerical results

If we neglect $O(\alpha k)$, then

$$\begin{aligned}
X^*_A = \eta^3 \left\{ \frac{\phi_0}{6} \left[\sin 2\pi\xi + \frac{5}{4}p \sin 4\pi\xi \right] + \right. \\
\left. \frac{2\pi}{7} \delta p \sin 2\pi\xi \cdot \eta^{1/2} + \frac{7\pi}{24} \delta \phi_0^2 \sin 4\pi\xi \cdot \eta \right\} \quad (30)
\end{aligned}$$

$$\begin{aligned}
X^*_B = e^{-2\pi(\eta-\delta)} \left\{ \frac{\phi_0}{6} \left[\sin 2\pi\xi + \frac{5}{4}p \sin 4\pi\xi \right] \right. \\
\left. \cdot e^{-2\pi(\eta-\delta)} \right\} + \frac{2\pi}{7} \delta p \sin 2\pi\xi + \frac{7\pi}{24} \delta \phi_0^2 \\
\sin 4\pi\xi \cdot e^{-2\pi(\eta-\delta)} \} \quad (31)
\end{aligned}$$

Set

$$\psi^*_{A,B} = X^*_{A,B} \times 10^2 \quad (32)$$

we take the term up to $O(\alpha k)$, in order to find the difference from that up to $O(\alpha k)^0$ done by Uda (1982). Two cases of topographical conditions, as shown in Fig. 2, are designed. In case A, we take $\phi_0 = 0.35$, $p = 1/3$; in case B, $\phi_0 = -0.35$ $p = 1/3$ are used. Then take the wave length of wavy shoreline $L = 1000\text{m}$, 500m and 300m in turns, the amplitude $\alpha = 50\text{m}$ and 80m , and $\mu_{2b} = 100\text{m}$. Some typical results are shown in Fig. 3-10. Table 1 shows the corresponding between those Figures and cases considered.

Table 1. Corresponding between Figures and Various Cases.

$\alpha = 50m$				
	up to $O(\alpha k)$		up to $O(\alpha k)^0$	
case L=	A	B	A	B
1000m ($\alpha k/2 = 0.05$)	Fig. 3	Fig. 6	Fig. 7	
500m ($\alpha k/2 = 0.1$)	Fig. 4			
300m ($\alpha k/2 = 0.16$)	Fig. 5		Fig. 8	
$\alpha = 80m$				
	up to $O(\alpha k)$		up to $O(\alpha k)^0$	
case L=	A	B	A	B
1000m ($\alpha k/2 = 0.08$)	Fig. 9	Fig. 10		

From Fig. 3, Fig. 4 and Fig. 5, we can find that the shorter the length of one wavy shoreline is, the smaller the magnitude of circulations are going to be; in similarity, from Fig. 3 and Fig. 9, only reducing the amplitude α , the magnitude of the scope of circulations are smaller. Consequently, we can indicate that the steepness of a giant cusped shoreline has influence to nearshore circulations. By comparing Fig. 3 with Fig. 7. It appears that term $O(\alpha k)$ has not much influence, while from Fig. 5 and Fig. 8, the term $O(\alpha k)$ has more influence. In addition it is supposed the positive values of $X^*_{A,B}$ denote counterclockwise of circulations, while minus values of $X^*_{A,B}$ mean that the circulations is in clockwise. Comparing to the definition of ϕ_0 , we get the results that in case (A), the direction of circulations are counterclockwise, while in case (B), it is in the clockwise, since we just take a half of one wave length of shoreline into account, with symmetry we can get the whole associated nearshore currents.

5. Concluding remarks

Although the situations considered here may be too simple, two important conclusions are made concerning with the effects of the steepness of a wavy shoreline on the nearshore circulations:

- (1) The smaller the steepness of a periodic shoreline, the larger the scope of the nearshore circulation.
- (2) It is common that there appear two even three circulations, when the steepness becomes larger to some

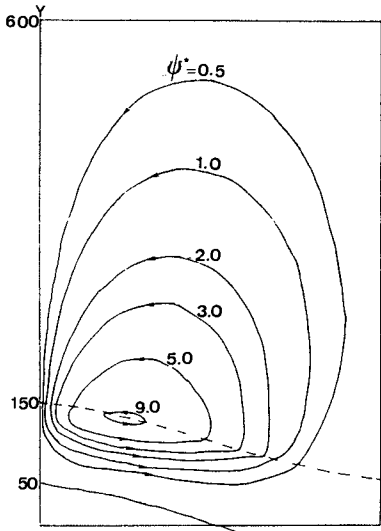


Fig. 3 Circulation pattern, Case(A), $\alpha k/2\pi=0.05$, $L=1000M$, $\alpha=50M$.

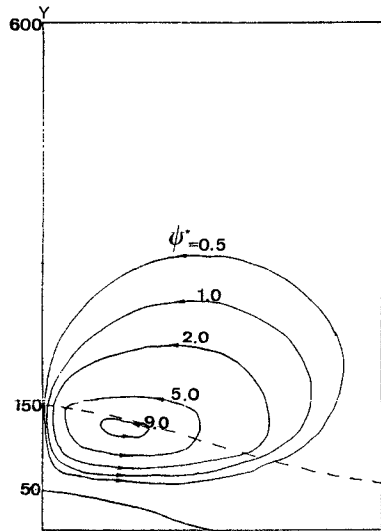


Fig. 4 Circulation pattern, Case (B), $\alpha k/2\pi=0.1$, $L=500M$, $\alpha=50M$.

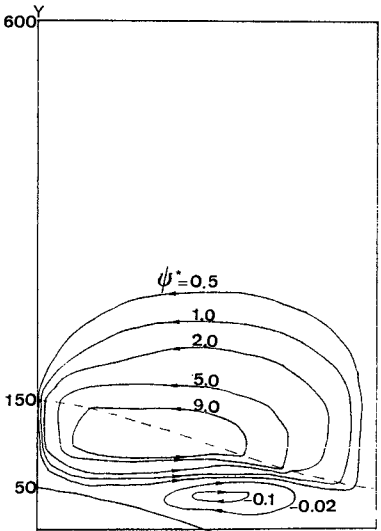


Fig. 5 Circulation pattern, Case(A), $\alpha k/2\pi=0.16$, $L=300M$, $\alpha=50M$.

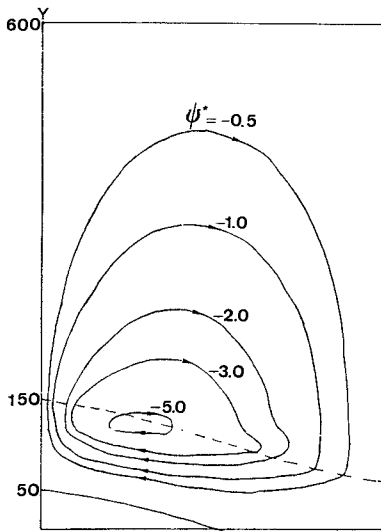


Fig. 6 Circulation pattern, Case(B), $\alpha k/2\pi=0.05$, $L=1000M$, $\alpha=50M$.

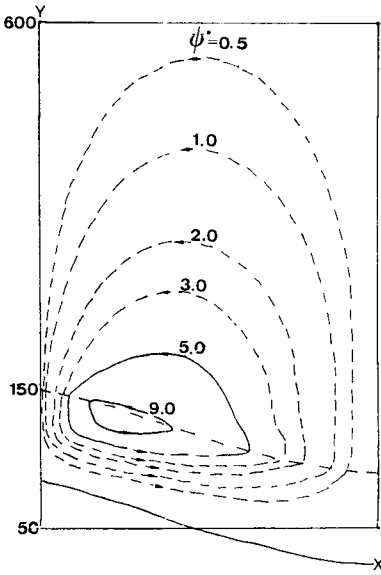


Fig. 7 Circulation pattern, Case(A), $O(\alpha k)$ term neglected, $\alpha k/2\pi=0.05$, $L=1000M$, $\alpha=50M$.

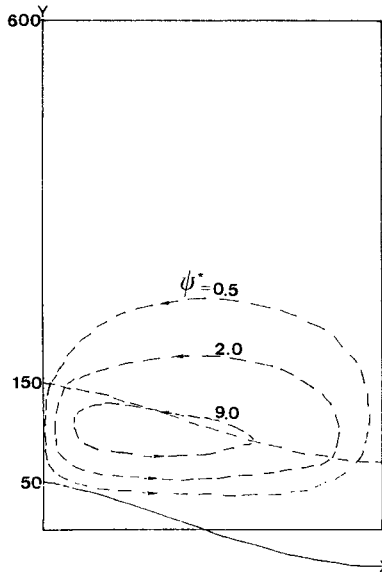


Fig. 8 Circulation pattern, Case(A), $O(\alpha k)$ term neglected, $\alpha k/2\pi=0.16$, $L=300M$, $\alpha=50M$.

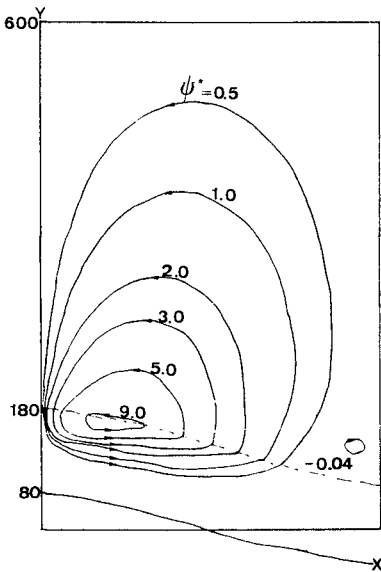


Fig. 9 Circulation pattern Case(A), $\alpha k/2\pi=0.08$, $L=1000M$, $\alpha=80M$.

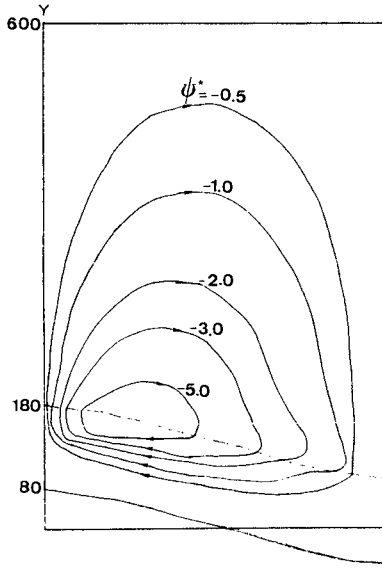


Fig. 10 Circulation pattern, Case(B), $\alpha k/2\pi=0.08$, $L=1000M$, $\alpha=80M$.

amount at extent.

6. Reference

1. Bowen, A.J. (1969) "Rip currents 1. theoretical investigations", *J. Geophys. Res.*, Vol. 74, No. 23, pp.5467-5478.
2. Dalrymple, R.A. and C.J. Lozano (1978), "Wave-current interaction models for rip currents", *J. Geophys. Res.* Vol.83, pp.6063-6071.
3. Lin, M.C. and Y.L. Lee (1982) "Nearshore circulations on a cuspidal coast" *Proc. 6th Conf. on Ocean Eng. in Taiwan*, pp.37-1-37-21. (in Chinese).
4. Lin, M.C. and J.Y. Liou (1986) "Analytical study of wave-induced longshore currents", *Journal of the Chinese Institute of Engineers*, Vol. 9, No.5, pp.437-449.
5. Liu, P.L.F. and G.P. Lennon (1978): "Finite element modeling of nearshore currents", *J. waterways, Port, Coastal and ocean Div., ASCE*, vol.103, pp.175-189.
6. Lyne, W.H. (1971): "Unsteady viscous flow over a wavy wall", *J. Fluid Mech.*, Vol.50. pp.33-48.
7. Miller, C and A. Barcilon (1978): "Hydrodynamic instability in the surf zone as a mechanism for the generation of horizontal gyre", *J. Geophys. Res.*, Vol. 83, No.C8, pp.4107-4116.
8. O'Rourke, J.C., and P.H. LeBlond (1972) "Longshore currents in a semicircular bay", *J. Geophys. Res.*, Vol.77, No.3, pp.444-452.
9. Uda. T. (1982): "Nearshore circulation around a circular spit and the cusped coast", *Proc. JSCE*, No.326, pp.63-72 (in Japanese).

CHAPTER 194

STUDY ON THE VARIATIONS OF AN EUTROPHIC ECOSYSTEM FROM THE SPANISH MEDITERRANEAN LITTORAL: DATA TO HAVE IN MIND IN THE NUTRIENT DUMPING TO THE SEA.

by

E. Soler T. (1); J.G. del Río (1) and J.J. Díez (2).

ABSTRACT:

Cullera Bay is a neritic ecosystem placed on the Spanish Mediterranean Littoral largely influenced by the Jucar River, that brings about lower salinities than surrounding waters, and broad variations of its values. An extensive research, with 9 samplings throughout the year, was carried out, measuring both physical and chemical parameters, and the planktonic communities. The trophic status of the ecosystem, the spatial and temporal variations of the nutrients and the planktonic communities were studied, evaluating the influence of the river loads and the littoral dynamics. Some essential basis to allow a suitable emplacement of waste waters disposals along the Valencian littoral are set up in order to minimize the gradual eutrophication of this coast.

INTRODUCTION:

According to the classic literature (until fifties), the incidence of human wastes on the trophic status of the littoral communities was almost negli-

(1) Biologist. Cát. Ing. Sanitaria, Dpto. Ing. Hidráulica y Medio Ambiente, E.T.S.I.C.C. y P., Univ. Politécnica, Valencia, SPAIN.

(2) Civil Engineer. Cát. Oceanografía, E.T.S.I.C.C. y P., Univ. Politécnica, Madrid. SPAIN.

geable. It was thus likely because of the lack of a systematic study of the waters from the continental shelf and the peculiar conditions of the ecosystems where these surveys were carried out. Nevertheless, after current studies, coastal ecosystems have appeared as much more complex and diverse than offshore ones.

Numerous processes of eutrophication caused by domestic waste waters have been monitored, and both politicians and scientists have found a lot of objections to standardize their study, monitoring and management, because of their broad variations according to local parameters -coastal shape, littoral dynamics, bulk and kind of loads, etc.

Thus, it is very important to keep in mind the particular characteristics of these areas where waste waters are dumped to the sea, and to conduct specific monitoring programmes to minimize their ecological consequences. In other wise, the uncontrolled spills may cause unpredictable and damaging consequences to the ecosystem. Regrettable examples are well known: the recent "red tides" generated by blooms of toxic phytoplankton species (Baltic Sea, Adriatic Sea, Galician Esuaries, etc.), the gradual degradation of benthic communities, the sanitary problems of beaches, etc.

In an extensive study carried out in Cullera Bay (eastern Spain), the combined effects on the neritic ecosystems caused both by the unpurified disposals of waste waters and the particular hydrodynamics conditions into the bay were evaluated throughout a year.

SAMPLING AREA:

Cullera Bay is placed on the Spanish Mediterranean Littoral (0 13'-0 15', W; 39 8'- 39 12', N), on the middle of the so called Valencian Oval (Figs.: 1A and 1B). A particular environmental problem is raised in this bay because of:

- The Jucar River's presence, which outflows at the southern beaches of the bay.
- The development of the tourism in this area, reaching more than 250.000 inhabitants in summer. The domestic waste waters are directly dumped into the bay through an insufficient marine outfall.
- The importance of the agriculture, involving a great amount of waste waters with high levels of nutrients, detritus, pesticides, etc. ,

The particular hydrodynamics within the bay, largely conditioned by some docks built in the mouth of the river and along the northern beaches. This allows the formation of a semi-enclosed area at the north, where the most serious environmental problems are noticed.

18 sampling stations were spread over the bay: 9 along the beaches and 9 within the bay (Fig.: 1C). 9 samplings were done throughout a year, from April-1983 to March-1984.

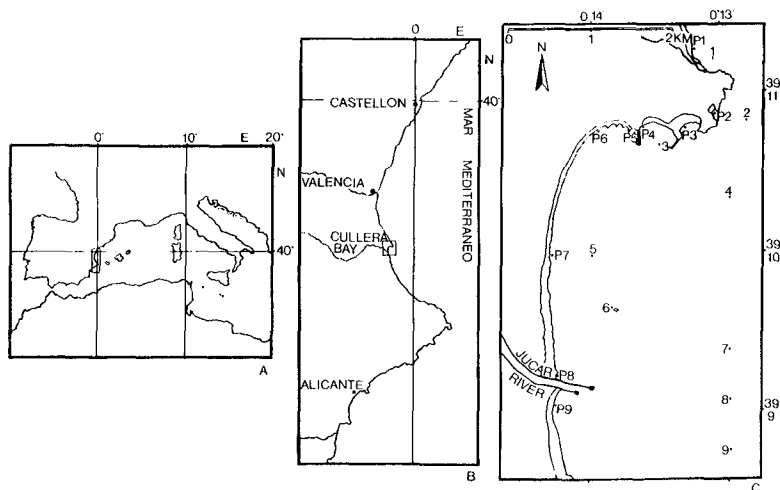


Fig.: 1.- Geographical location of Cullera Bay and sampling stations. A: Western Mediterranean Basin; B: Valencian Littoral (Valencian Oval); C: Cullera Bay with sampling stations (P=Beaches).

MATERIAL AND METHODS:

The parameters measured in each sample were:

- .- Quantitative and qualitative evaluation of phytoplankton communities.
- .- Sea temperature.
- .- Salinity.

.- Winds and waves.

.- Nutrients: NO₂, NO₃, NH₄, PSR and SiO₄.

Samplings were done with a Van Dorn bottles of 2x4 l, at 0 m depth at beach stations, and at 0 and 5 m depth at bay stations. Phytoplankton samples were fixed with lugol and studied at the laboratory according to Uthermöhl techniques. Salinity was also determined at the laboratory with a salinometer by induction GRUNDY ENVIRONMENTAL SYSTEMS, Inc., 6230 N (The International Oceanographic Tables Vol. I, UNESCO). Because of the broad temporal and spatial variations of surface salinities, the average values of the salinity at the stations placed at 5 m depth have been used in the present study, because they show more accurately the mean salinity values.

Nutrients were determined following basically the Strickland and Parsons' (1965) and Grashoff's (1975) methods, with some modifications by Solorzano (1969), Mullin and Riley (1955) and Murphy and Riley (1962).

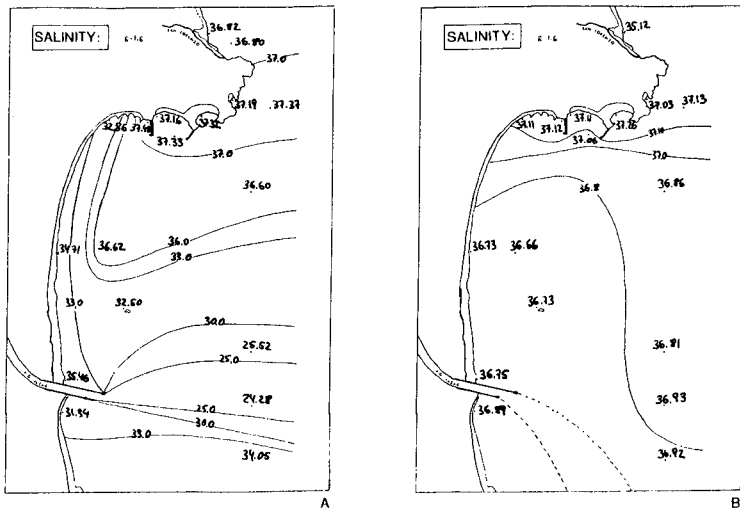


Fig.: 2.- Variations in surface salinities caused by changes in wind direction. A: North winds; B: South winds (G. del Río, 1987).

RESULTS:

The influence of the river gives rise to lower salinities than surrounding waters, with remarkable spatial and temporal variations. It is possible to differentiate between the variations caused by momentary changes of water direction and those originated by changes of average values in the water body. In the former, the local winds are the determinant factor, being less important the waves and the river flow.

These variations involve essentially to the upper layer, showing a bigger influence of freshwaters when the south wind prevails, and of offshore waters when it is the north or east wind the prevailing one (Figs.: 2A and 2B).

	S	P.S.R.	NH ₄ ⁺	NO ₂ ⁻	NO ₃ ⁻	SiO ₄ ⁻³	N.I.D.
	g/Kg	µatg/l	µatg/l	µatg/l	µatg/l	µatg/l	µatg/l
10-5-83	\bar{X}	37,90	0,36		0,07	11,3	0,7
	C.V.	0,2	41,7		42,9	61,9	57,1
4-7-83	\bar{X}	37,25	0,10	0,12	0,06	7,7	3,2
	C.V.	0,2	20,0	50,0	66,7	24,7	40,6
19-7-83	\bar{X}	37,43	0,03	1,26	0,08	1,9	2,1
	C.V.	0,2	66,7	70,6	12,5	52,6	23,8
25-8-83	\bar{X}	37,43	0,33	1,02	0,05	4,7	1,0
	C.V.	0,2	21,2	73,5	40,0	34,0	20,0
10-10-83	\bar{X}	37,61	0,30	15,97	0,34	7,8	5,6
	C.V.	0,6	16,7	96,3	20,6	73,3	41,1
29-11-83	\bar{X}	37,54	0,38	2,13	0,53	6,2	4,7
	C.V.	0,1	10,5	16,4	7,6	32,3	10,6
17-1-84	\bar{X}	38,03	0,23	1,67	0,12	3,4	0,7
	C.V.	0,1	26,1	20,4	16,7	88,2	28,6
31-1-84	\bar{X}						
	C.V.						
21-2-84	\bar{X}	38,09	0,14	1,42	0,37	14,9	3,2
	C.V.	0,3	35,7	20,9	59,5	59,7	75,0
28-3-84	\bar{X}	37,88	0,18	1,90	0,45	15,5	
	C.V.	0,8	44,4	57,9	64,4	34,2	17,47
							34,0

Table: 1.- Mean values (\bar{X}) and coefficient of variation (C.V.) of salinity and nutrients at 5 m depth (P.S.R. = Soluble Reactive Phosphorus; N.I.D. = Dissolved Inorganic Nitrogen) (G. del Río, 1987).

Several factors are involved in the mean salinity of the bay, being the most important:

- The river discharge.
- The evaporation.
- The littoral dynamics.

Attending to the first and second ones, and assuming a maximum evaporation in summer and a rainfall pattern with summer and winter as dry seasons and rains in spring and, mainly, in autumn, the highest salinity records should be expected in summer and the lowest ones in autumn. Nevertheless, our data do not agree with that pattern (Table: 1), showing that it is the littoral dynamics which is the essential factor to explain this kind of variation.

		FITOPLANCTON nº cél./l.x10 ⁶	CIANOFICEAS nº cél./l.x10 ⁶	COCOLITOFORIDOS nº cél./l.x10 ⁶	DIATOMEAS nº cél./l.x10 ⁶	DINOFITAGELADOS nº cél./l.x10 ⁶	EUGLENIALES nº cél./l.x10 ⁵	FLAGELADOS nº cél./l.x10 ⁶
10-5-83	\bar{X}	0,80	--	--	0,58	0,06	--	0,15
	C.V.	57,5	--	--	69,0	70,9	--	100,0
4-7-83	\bar{X}	0,61	0,16	--	0,22	0,05	0,02	0,16
	C.V.	54,1	106,3	--	18,2	9,3	150,0	243,8
19-7-83	\bar{X}	0,79	--	--	0,59	0,20	--	0,15
	C.V.	63,3	--	--	62,7	60,0	--	253,3
25-8-83	\bar{X}	2,55	0,03	--	2,38	0,06	--	0,09
	C.V.	30,5	133,3	--	32,8	50,0	--	77,8
10-10-83	\bar{X}	3,76	5,44	--	2,74	0,28	--	0,25
	C.V.	51,1	51,5	--	66,8	46,4	--	84,0
29-11-83	\bar{X}							
	C.V.							
17-1-84	\bar{X}	3,55	0,12	--	2,15	0,08	--	1,17
	C.V.	36,3	58,3	--	61,9	50,0	--	29,1
31-1-84	\bar{X}							
	C.V.							
21-2-84	\bar{X}	1,97	--	--	0,72	0,28	--	0,89
	C.V.	39,6	--	--	41,7	28,6	--	39,3
28-3-84	\bar{X}				0,95			
	C.V.				41,1			

Table: 2.- Mean values (\bar{X}) and coefficient of variation (C.V.) of phytoplankton community at 5 m depth (G. del Río, 1987).

The salinity of the bay results from the mixing of waters with different salt concentration. Firstly, the inshore waters from the bay, secondly the continental freshwaters from the river, and finally the more salted offshore waters. The ratio of each one of them is largely depending on the littoral dynamics.

Two levels in water mixing have to be distinguished between the effects caused by the waves. On the first hand, a low intensity level, which do not generate a quantitatively significant mixing in the water column within the bay. On the other hand, a level of higher intensity, when the autumn and winter storms produce the mixing not only of the water column, but also the dilution of the bay water in the large bulk of open sea waters removed by these storms; thus, an increase in the salinity is observed, reaching its maximum values in this period. The clear deviation from the average value of the sample taken on 29th November was on account of the intense storm and flood suffered some days before of sampling.

The waters taking part in the mixing have distinct salinities at the same time as very distinct trophic status. Those from the Jucar river are very eutrophicated, those from the bay have an intermediate eutrophication levels, and those coming from open sea are clearly less eutrophic and cleaner. According to the ratio of each one of them in the mixing a neat accumulation or a loss of nutrients will be produced, respectively.

Thus, it is possible to suppose that an accumulation of nutrients is taken place during summer and a loss in winter (Table: 1). This can be observed by comparing the samples on 10th October (before the storms) and on 17th January (at the height of winter); not only a higher phytoplankton standing stock (Table: 2), but also higher mean values of the nutrient concentrations (G. del Río, 1987). This winter loss is favoured by the bulk of offshore waters displaced by these storms to the bay, which release and redilute the benthic nutrients from the sediments.

Several dense phytoplankton blooms have been observed in Cullera throughout the year. This is a characteristic feature of eutrophic coastal ecosystems, where the shallowness of the waters allows the release of benthic nutrients in the water column with a low intensity mixing of waters, because no strong thermocline is formed. Only in calm waters like in the sampling of July, the flow of nutrients from sediment to water column ceases, and the ecological succession begins in

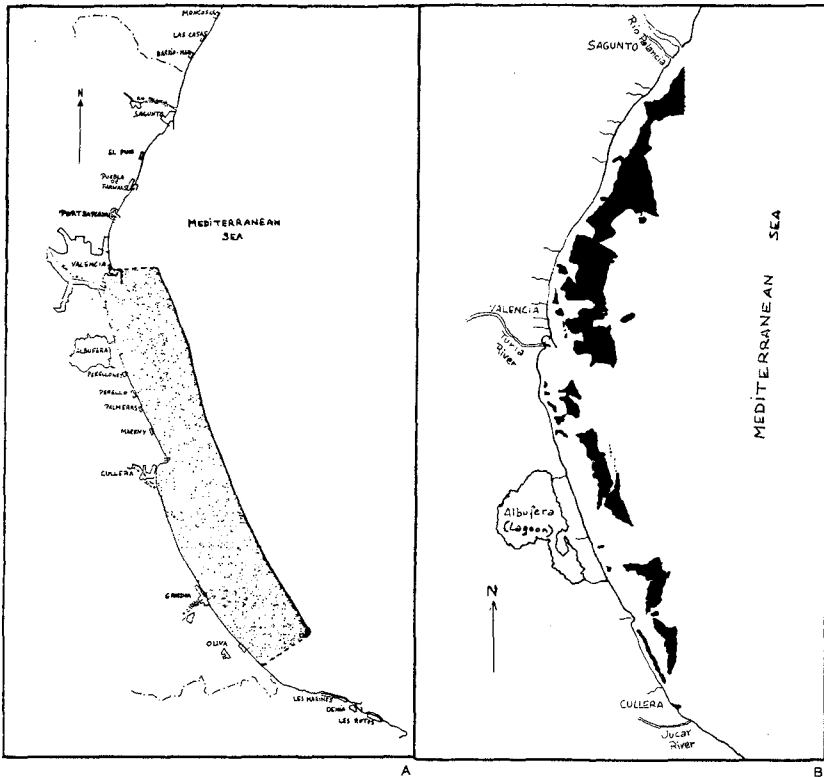


Fig.: 3.- Valencian littoral. A: Estimated eutrophicated area (dotted zone), where the Posidonia oceanica has almost disappeared and the plankton based ecosystem is the dominant one; B: Posidonia oceanica sea grasses over forty years ago spread over the Valencian coast (black zone).

plankton populations (G. del Río, 1987). Furthermore, the differences between the phytoplankton communities of the northern beaches are sharper in this period. similar phenomenons have been noticed in Kiel Bight (Smetacek, 1985), Rumanian coasts (Minhea and Cuingioglu), Narragansett Bay (Smayda, 1983), the estuaries of St. Lawrence (Sinclair, 1978) and Puget Sound (Winter, 1975), Anka Bay (Iverson et al., 1979) among others.

This kind of neritic ecosystems with highly

eutrophiced waters is not restricted to this place of the Valencian Oval. In a survey carried out that winter (1983-1984) between Valencia Harbour and Cullera Bay, very similar qualitatively and quantitatively phytoplankton communities appeared. But the area with a high eutrophic level is clearly delimited by the dramatic regression of the Posidonia oceanica sea grass. It comprises the coast between Valencia Harbour and the southern limit of the province (Fig.: 3A), where a very intense and fast industrialization and an increase of the resident and non-resident population have happened, and where vast sea grasses of this marine phanerogam spread over the coastal mobile bottoms of this section of littoral have disappeared in a few years (Fig.: 3B). Because of that, and an intense overfishing by trawling, an oligotrophic benthic based ecosystem has been transformed into an eutrophic and plankton based one, with limited diversity and very low economic profitability, and a drastic decrease in the number of benthic and demersal species.

This new and unbalanced situation makes possible the unpredictable and uncontrollable proliferation of opportunistic species, like the massive blooms of the benthic Rhodophyta Ceramium fastigiatum during several years along the Valencian Oval, accumulating large amounts of this red algae on the beaches, mainly in summer, owing to local hydrodynamic features (Cullera Bay, Puebla de Farnals, etc.), and causing sanitary and aesthetic problems in these tourist beaches. But in the same way as a non-toxic algae has proliferated, other toxic phytoplankton species can do it too, causing environmental problems as the "red tides".

The high richness of waters and, indirectly, the increase of water turbidity (phytoplankton blooms, suspended particles, detritus, etc.) seems to be the main reason for the regression of the sea grasses and the proliferation of the red algae in this littoral.

CONCLUSIONS:

Marine outfalls obviously can not be considered the definitive solution to the problem of the disposal of waste waters into the sea but, in any case, they must be contemplated as a suitable choice to mitigate the uncontrollable and unpredictable impact caused by the loads in the same shoreline. Nevertheless, not only sanitary aspects must be taken into account in the project and management of sea dumpings, but also the

eutrophic conditions of the ecosystem and the problems in regard to them. It seems hence suitable to consider as conclusions of the present work four suggestions in order to keep the Valencian coasts as clean and as healthy as possible.

- 1.- To preserve the Posidonia oceanica sea grasses of the northern part of the littoral, placing the disposal points as far away as possible from them.
- 2.- To assess the real spreading of the affected area by the eutrophication, and to evaluate the loss of benthic and demersal communities in regard to the volume and pollutant charge of the disposals, specially on P. oceanica.
- 3.- To favour the correct dilution of the nutrients in the open sea along the coast, removing them from the shoreline.
- 4.- To keep in mind that some coastal constructions (harbours, docks, etc.) are both sand traps and nutrient-organic matter too, because of the special hydrodynamic conditions generated around and inside of them, favouring hence mass blooms of opportunistic species, some of them of damaging effects for the ecosystem, like the "red tides".

REFERENCES:

- G. DEL RIO, J., 1987. Problemas de eutrofización litoral. El caso de la Bahía de Cullera. Ph. Thesis (unpubl.). Universidad de Valencia. 514 pp. and two attached vols.
- GRASSHOF, K., 1976. Methods of seawater analysis. Verlag Chemie. Weinheim. New York. 317 pp.
- IVERSON, R.L.; T.E. WHITLEDGE and J.J. GOERING, 1979. Chlorophyll and nitrate fine structure in the southeastern Bering Sea shelf break front. Nature, London. 281: 664-666.
- MINHEA, J.B. and E. CUINGIOGLU, 1982. Particularités des phénomènes de "floraison". Cercetari. Mar. 15: 27-57.
- MULLIN, J.B. and J.P. RILEY, 1955. The spectrophotometric determination of silicate-silicon in natural waters with special reference to seawater. Annal. Chem. Acta. 12: 162-170.
- MURPHY, J. and J.P. RILEY, 1962. A modified single solution method for the determination of phosphate in natural waters. Annal. Chem. Acta. 27: 31-26.
- SINCLAIR, M., 1978. Summer phytoplankton variability in the lower st. Lawrence Estuary. J. Fish. Res. Bd. Can. 35: 1171-1185.
- SMAYDA, T.J., 1983. The phytoplankton of estuaries. Estuaries. (ed. B.H. Ketchum). 65-102.
- SMETACEK, V., 1985b. The annual cycle of Kiel Bight plankton: a long-term analysis. Estuaries. 8: 145-157.
- SOLORZANO, L., 1969. Determination of ammonia in natural waters by the phenol hypochlorite method. Limnol. Oceanogr. 14: 799-803.
- STRICKLAND, J.D.H. and T.R. PARSONS, 1965. A practical handbook of seawater analysis. Bull. Fish. Res. Can. 167: 1-310.
- WINTER, D.F.; K. BANSE and C.G. ANDERSON, 1975. The dynamics of phytoplankton blooms in Puget Sound, a fjord in the northwestern United States. Mar. Biol. 29: 139-176.

CHAPTER 195

FLUSHING BEHAVIOUR OF A COASTAL MARINA

R. A. Schwartz * and J. Imberger **

Abstract

The flushing characteristics of a newly constructed marina were determined from a comprehensive field study which included a dye dilution experiment together with measurements of barotropic and baroclinic forcing parameters. The results to be presented show that the major exchange process in this particular marina is a baroclinic circulation, and that the exchange rate is controlled by the harbour entrance geometry.

1.0 Introduction

The continued growth of population centres along the Western Australian coast implies that the existing recreational and commercial boating facilities will not satisfy future demand. To increase the number of sheltered boat moorings, state and local authorities are constructing new marinas and enlarging the existing facilities. State regulations require that such projects be preceded by an Environmental Review and Management Planning (E.R.M.P.) report, wherein the potential impact on water quality must be assessed. Since the quality of the water in a coastal harbour largely depends on the natural ability of the harbour to flush out trapped pollutants, any water quality forecast requires an understanding of how the water is exchanged with the adjoining sea.

The circulation of water between a marine harbour and the connecting sea is generally the result of natural parameters such as the local tidal range, wave climate, meteorological conditions, and water density differences. Depending on the geographical location, one or more of these variables can dominate the exchange properties of a harbour. Pollutants such as pesticides, heavy metals, and organic compounds enter a marina basin via surface run-off, leaching from boats' anti-fouling paint, and spillages from service facilities located within the marina boundaries. If pollutant concentrations are allowed to increase above critical levels, then the result is sub-standard water quality as characterized by a reduction in dissolved oxygen and the presence of algal blooms. Detrimental water quality within a marine harbour can be avoided by reducing the potential sources of pollutants,

* Graduate student, Department of Civil Engineering,
University of Western Australia, Nedlands, W.A., 6009, Australia.

** Professor of Civil Engineering, and Director of the Centre for Water Research,
University of Western Australia, Nedlands, W.A., 6009, Australia.

Environmental Dynamics reference ED - 88 - 259

and by maintaining an optimal flushing rate. The water exchange rate is affected by factors such as the planform geometry, entrance dimensions and number of entrances (Nece, 1984). So, once the geometrical effects and locally dominant flushing parameters are understood, a marina can be designed to have an optimal water exchange rate.

To understand the flushing characteristics of a marine harbour situated on the Western Australian coastline, the Centre for Water Research (CWR) in conjunction with the State Department of Marine and Harbours conducted a series of field experiments in a newly constructed marina. The specific aims of this project were to quantify the flushing rate as a function of time and space, identify the dominant flushing mechanisms, and measure fine-scale dissipation rates of turbulent kinetic energy. The results will be used to develop a strategy for water quality monitoring in all marinas under the control of the Department of Marine and Harbours and aid in designing future marinas.

The marina chosen for the field experiments is known as Hillarys Boat Harbour. It is located on the southwest Australian coast approximately 26 km north of Fremantle. The tidally averaged depth of Hillarys Boat Harbour is approximately 5.5 m. With a water surface area of about $2.46 \times 10^5 \text{ m}^2$, its tidally averaged volume can be estimated as $1.3 \times 10^6 \text{ m}^3$. The harbour was designed to contain 1,000 boat moorings. It has a single asymmetric entrance which is 90 m wide by 5 m deep, and is oriented to the north as shown in Figure 1.

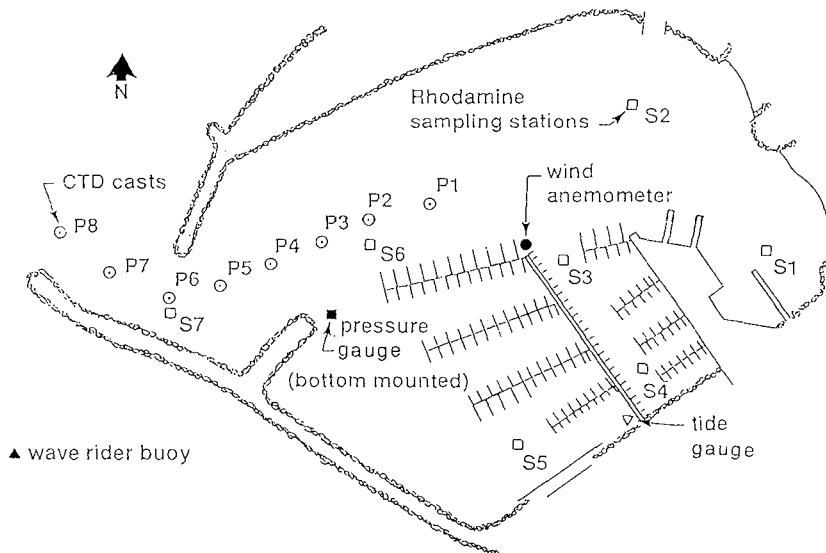


Figure 1 Hillarys Boat Harbour planform together and sampling sites.

The flushing time of Hillarys Boat Harbour was determined by uniformly seeding the harbour with a fluorescent dye and subsequently monitoring its dilution as a function of time and space. Simultaneous to the dye dilution experiment, vertical profiles of salinity and temperature were measured with Conductivity Temperature Depth (CTD) probes, and a microstructure probe was deployed to estimate the dissipation of turbulent kinetic energy. The *Djinnang III* was the largest of the two CWR research vessels used for

collecting data. Its onboard instruments included a CTD probe, a microstructure probe, and a mini-ranger system for establishing the coordinates of the sampling stations. The other research vessel, known as the *Trail Craft*, also had a CTD probe onboard and was outfitted with a fluorometer which measured the concentration of the fluorescent dye. These vessels and their respective instruments were used for three weeks to monitor the response of the water body to natural forcing conditions.

Wind speeds, tidal amplitudes, and wave statistics were measured with remotely operated devices positioned as shown in Figure 1. Wind directions were obtained from the Bureau of Meteorology's weather station at Ocean Reef, located approximately 5 km north of the harbour. A CWR mini-logger was installed to measure wind speeds. The mini-logger was attached to RIMCO® cup anemometer and recorded a sample every ten minutes. Other remote recording instruments were installed and monitored by the Department of Marine and Harbours. These included a float/counter-weight type tide gauge mounted within the marina, a bottom-mounted Weslog® logger for recording wave actions inside the marina, and a Datawell® series 6000 wave-rider buoy located outside the marina.

2.0 Experimental Programme

Early on 29 April 1987 (Julian day 119), 60 litres of a 20% Rhodamine WT aqueous solution were diluted with seawater and injected into the harbour from a small dinghy. The dye mixture was pumped through a diffuser end-pipe which was continuously raised and lowered while the dinghy slowly criss-crossed the interior of the harbour. Immediately following the injection of the dye, a monitoring cycle was initiated at seven interior stations (S1 - S7 shown in Figure 1) to determine the dilution rate of the Rhodamine WT tracer as a function of time and space. At each station, tracer concentrations were measured just below the surface, at mid-depth and 1 m from the bottom. Water was selectively withdrawn through a special disc inlet (Imberger and Berman, 1986) with an effective vertical resolution of 0.30 m, and pumped up to a debubbler mounted one metre above a Turner Designs® model 10 series fluorometer. A gravity outflow from the debubbler supplied the fluorometer with a bubble-free stream of water, which was analysed and recorded on a Multiterm® micro-computer before being discharged overboard. The natural fluorescence of the marina water was measured prior to injecting the dye, and the fluorometer was tuned to zero out this 'blank' concentration. Each station was initially sampled several times a day. However as the experiment progressed, it was only necessary to sample once a day or once every other day.

In conjunction with the dye dilution experiment, free-falling and rising probes were deployed from the *Djinnang III* and the smaller *Trail Craft* to obtain density, salinity and temperature profiles inside and outside of the harbour. The free-falling CTD probe (Fozdar, 1983) consisted of a pressure transducer for determining depth, a SEA-BIRD SBE-3 oceanographic thermometer for temperature measurements and a SEA-BIRD SBE-4 conductivity cell for determining salinities. Water parcels were sampled at 50 Hz as the probe descended to the bottom with a fall-rate of 1 ms^{-1} . This is equivalent to a spatial resolution of 2 cm. The vertically rising microstructure profiler (RMP) (Carter and Imberger, 1986) was used to measure fine-scale temperature gradients from which rates of turbulent kinetic energy dissipation were estimated. As the RMP rises at 0.1 ms^{-1} from a pre-set depth, its pressure transducer, two fast-response thermistors and two specially designed conductivity cells sample at 100 Hz. This results in a spatial resolution of 1 mm, which represents a 200% increase in resolution over the CTD probe.

3.0 Data Analysis

Profiles representing the measured dye concentrations at every sampling station for each circuit showed that a non-uniform dye distribution existed throughout the harbour for 24 hours after the dye was injected. This initial depth and spatial variation is primarily a reflection of the logistics involved in manually seeding such a large volume of water to obtain a uniform distribution. A well-mixed condition was eventually achieved on Julian day 120, one day after the dye was introduced into the system.

Dilution Rate

The rate at which the tracer concentration decreased with time is shown in Figure 2. The plotted data were best described by an exponential curve fit of the form

$$C = 169 \times 10^{-9} e^{-0.0917 t} \quad (1)$$

where C is the concentration value for a particular Julian day value t. Using an initial Rhodamine WT concentration of 1.35×10^{-9} on Julian day 120, an e-folding time was calculated as the time required for the initial concentration to drop to C/e. Solving equation (1) for t yielded a corresponding Julian day value of 125. Thus, the measured dilution rate of Rhodamine WT had an e-folding time of 5 days!

Rhodamine WT is quite stable with respect to photochemical decay, sediment absorption, and pH; however, salinity and temperature can significantly affect the fluorescence of Rhodamine WT. Smart and Laidlaw (1977) reported contradictory results from two independent tests which produced radically different decay rates for the fluorescence of Rhodamine WT with long-term exposure (~10 days) in saline environments. To evaluate the effect of salinity on the fluorescence of Rhodamine WT in the harbour, a laboratory experiment was conducted under controlled conditions in which samples with dye concentrations of 1×10^{-9} were monitored for two weeks. The results showed a 3% reduction in the initial dye fluorescence for a typical seawater chlorinity of 19 ‰ (salinity 35 ‰). The effect of temperature on fluorescence intensity was determined from an empirical equation of the form

$$F = F_0 e^{-0.027 t} \quad (2)$$

where F is the fluorescence at a standard temperature, F_0 is the fluorescence at the sample temperature, and t represents the difference between the standard and sample temperatures (°C). The error in fluorescence intensity which can be attributed to temperature variations was estimated to be less than 5%. Because the combined error in fluorescence intensity due to salinity and temperature was less than 8%, it was concluded that the observed dye loss in the harbour was caused by flushing actions and not chemical degradation.

Tidal Motions

The tides of the southwestern Australian coast are unusual because they are generally diurnal with amplitudes so small that astronomical and meteorological forces produce changes in the sea level of the same order of magnitude. Similar characteristics were exhibited in the sea level fluctuations measured during the three week field study, namely, an overriding diurnal pattern with amplitudes less than one metre.

The overall contribution to flushing from the oscillating sea level was determined by using the tidal prism method. This method assumes that the exchange flow is only a function of the tidal range, and any mass removed on the ebb tide does not return on the following flood tide. These assumptions were proven to be valid for Hillarys Boat Harbour by aerial photographs taken on Julian day 119. The photographs showed that wind-induced circulations outside the harbour quickly dispersed any dye which was flushed out with the ebbing tide. Given that the sea level prism is about 0.5 m, an e-folding time for the tidal flushing mechanism was calculated to be 11 tidal cycles. This corresponds to 11 days since the tidal cycle was primarily diurnal. A comparison between the analytical e-folding time of 11 days and the measured e-folding time of 5 days revealed a discrepancy which was too large to be attributed to experimental error. Therefore, the tide was not the dominant mechanism for driving an exchange flow between the harbour and the sea.

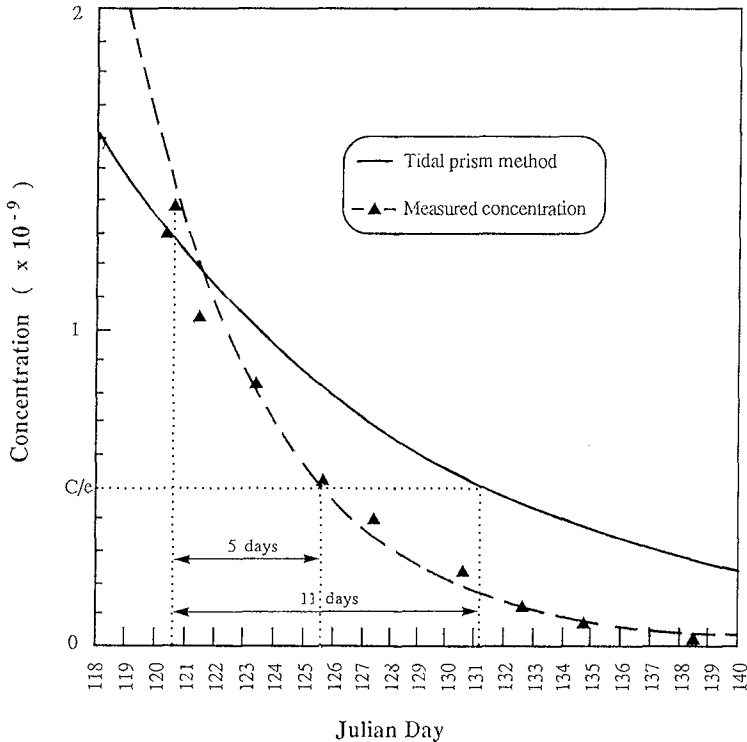


Figure 2 Comparison of the tidal prism method with the measured dilution rate.

Stratification

Hillarys Boat Harbour is situated on the coastal border of an inland freshwater mound which rises 70 m above sea level. Submarine groundwater discharges along the coast in this area were first reported by Johannes (1980). Freshwater patches were detected by the CTD probe near the bottom and along the shoreline inside the marina. The quantity of freshwater discharging into the marina was estimated to be about $2 \times 10^3 \text{ m}^3 \text{ day}^{-1}$.

Knowledge about the density structure of a water body is useful for quantifying the internal transport processes associated with advection, mixing and diffusion. The CTD and the vertically rising microstructure profiler (RMP) were deployed at various points in the vicinity of the harbour to measure conductivity and temperature characteristics. From these measurements, practical salinities and densities were calculated using the practical salinity scale and equations of state given in UNESCO (1981). The raw data were processed to account for the different response characteristics of the probes' sensors and their vertical separation. In this way, all the data relating to the same parcel of fluid were matched with each other. Failure to properly match the conductivity, temperature and depth signals results in unrealistic spiking in the salinity and density calculations. After the CTD and RMP data were adjusted for vertical separation, a recursive time series technique developed by Fozdar *et al.* (1985) was used to match the sensor response times.

Data collected from a series of equally spaced CTD drops were used to produce contour plots of salinity, temperature and density profiles. An interesting example of an isopycnal plot is shown in Figure 3. The density structure shown in this figure is indicative of a baroclinic circulation caused by a gravitational adjustment. Only a few of the isopycnal plots revealed such a pattern, while the remainder showed density structures characteristic of well-mixed to longitudinally stratified conditions. Thus, no single steady-state stratification condition existed within the harbour during this study. In Table 1, the various isopycnal plots were classified according to the degree of stratification exhibited along with measured wind speeds and tidal conditions. The noteworthy feature in this table is that an internal frontal structure resembling a standing wave was observed to occur under light wind conditions (less than 3 ms^{-1}) and predominantly on the ebb tide. This observation is supported by Simpson and Nunes (1981), who reported similar frontogenesis behavior occurring on the ebb tide in several different estuaries. Dyer (1973) also described frontal formations in a partially mixed estuary as a consequence of a distinct two-layer flow system.

Wind Effects

Air currents moving across an exposed body of water exert a drag force on the water surface in the form of a shear stress. This mechanism generates surface waves which act to transfer momentum and mechanical energy from the wind to the water surface, thereby contributing to the circulation dynamics of the water body. Effects such as topographic gyres, differential deepening of the mixed-layer and subsequent gravitational adjustments are all directly related to the input energy flux from the wind.

Imberger (1985) defined the surface mixed-layer in a stratified water body as that part of the water column which is directly influenced by the momentum and turbulence introduced by a surface wind stress. Production of turbulent kinetic energy (TKE) at the base and surface of the mixed-layer causes the mixed-layer depth to fluctuate. TKE produced at the base of the mixed-layer is known as "shear production" and is primarily caused by seiche motions. At the surface, TKE production is commonly referred to as "stirring". As the wind-induced TKE is dissipated down through the water column by viscous forces, heavier water from below the mixed-layer is entrained. The result is that the mixed-layer deepens, the potential energy of the water column increases, and a longitudinal density gradient is established. A subsequent reduction in TKE allows the density structure to "relax", thereby creating a gravitational current which further redistributes the mass within the water body.

Table 1 Classification of density contour plots.

Julian day	Time	Stratification	Wind Speed (ms ⁻¹)	Tide
119A	11:20 - 11:27	V.S.	< 3	Ebb
119B	13:12 - 13:27	V.S.	< 3	Ebb
119C	16:24 - 16:45	F	< 3	Ebb
119D	18:03 - 18:12	F	< 3	Ebb
119E	18:53 - 19:07	F	< 3	Ebb
120A	08:12 - 08:56	M	8	Flood
120B	12:44 - 12:59	M	10	Ebb
120C	14:28 - 14:59	M	12	Ebb
121A	08:38 - 09:19	L.S.	9	Flood
121B	14:40 - 15:09	L.S.	7	Ebb
123A	10:04 - 10:19	M - L.S.	4	Flood
123B	13:08 - 13:25	V.S.	4	Flood
123C	15:03 - 15:17	V.S.	5	Ebb
125A	11:01 - 11:14	V.S.	5	Flood
125B	17:29 - 17:43	F - V.S.	< 3	Ebb
127A	09:19 - 09:44	L.S.	6	Flood
127B	14:07 - 14:30	V.S.	5	Flood
130	11:44 - 12:00	F - L.S.	4 - 7	Ebb
132	11:19 - 11:38	F	3	Ebb
134	16:44 - 17:00	F	3	Ebb
135	00:16 - 00:38	F	< 3	Flood

V.S. = Vertically Stratified M = Well-mixed condition
L.S. = Longitudinally Stratified F = Frontal structure evident

The efficiency of the energy transfer process depends on the wind strength, the stability of the atmospheric boundary layer over the water surface, and the basin geometry relative to the wind direction. Of these influences, the wind speed is the dominant factor that determines the actual stress exerted on the water surface, and the response of the wind mixed-layer is a function of this kinematic shear stress.

Wave Actions

A Draper-Tucker wave analysis was performed to extract significant wave heights and periods from the data collected by the two Marine and Harbours wave recording instruments. The surface buoy, which was mounted outside the harbour in 8 m of water, measured an average significant wave height of 0.71 m and a mean period of 7.29 s. The bottom-mounted pressure transducer inside the harbour recorded an average significant wave height of 0.11 m and a 39.52 s mean period. The difference between the larger waves outside the harbour and the smaller waves inside is a measure of the protection provided by the breakwaters. The contribution to flushing by surface wave actions outside Hillarys Boat Harbour was considered to be negligible; however, the surface wave actions within the harbour were important for mixing.

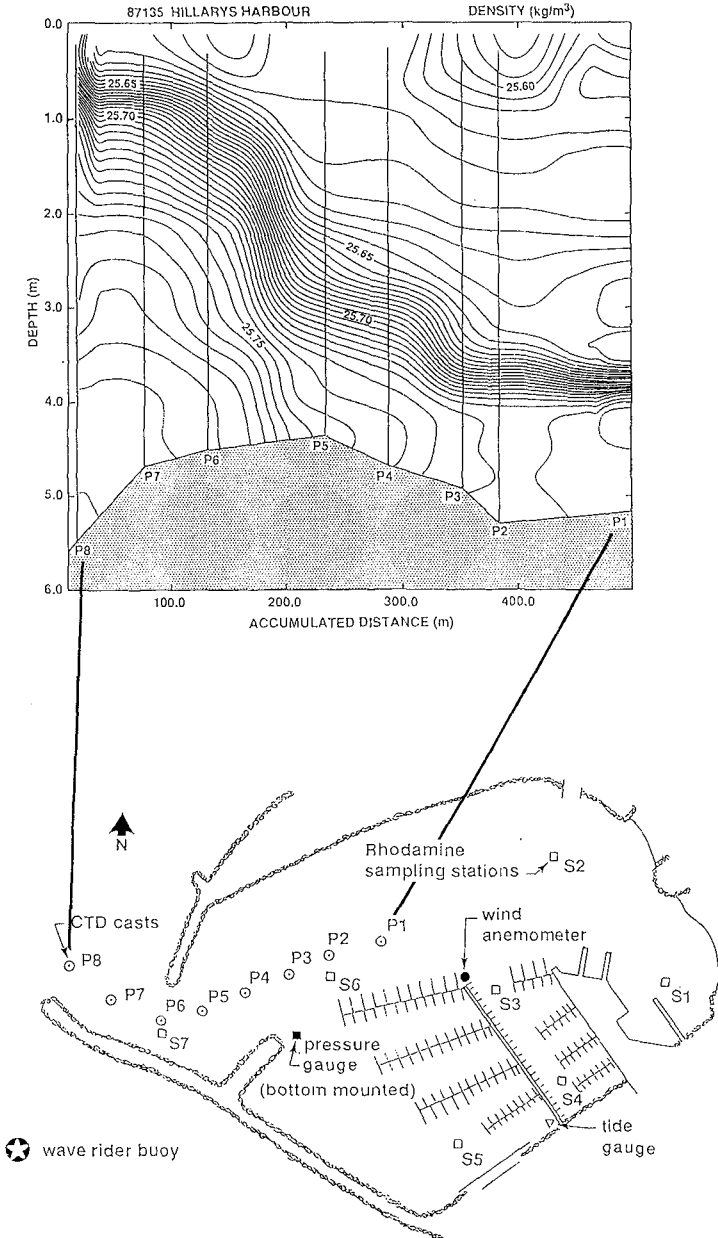


Figure 3 An isopycnal plot derived from 8 CTD casts (P1-P8) on Julian day 135.

Turbulent Mixing

It was necessary to assess the efficiency of turbulent mixing processes because the effectiveness of tidal flushing is dependent on the rate at which the tidal inflow is mixed with the harbour water. The transport of mass by turbulent motions is a function of the kinematic viscosity and the supply rate of kinetic energy. Energy enters a water body at large scales of motion which correspond to the basin dimensions, and it is transferred to smaller scales of motion by random velocity fluctuations and turbulent diffusion. In his universal equilibrium theory, Kolmogorov (1941 a,b) formulated the following expression for the smallest length scale which is characteristic of turbulent motion,

$$\eta = (\varepsilon^{-1} \nu^3)^{1/4} \quad (3)$$

where ε is the turbulent kinetic energy dissipation rate and ν is the kinematic viscosity. Typically, η is on the order of a few millimeters. At this level, viscosity becomes important and kinetic energy is dissipated into heat by internal friction forces. From knowing the rate at which kinetic energy is dissipated, the transport rate associated with the turbulent motions can be determined.

An estimate of the turbulent kinetic energy dissipation rate can be determined either directly from measurements of the velocity-shear spectrum, or indirectly from fine-scale temperature gradient measurements (Dillon and Caldwell 1980, and Oakey 1982). The current study made use of the latter approach, which is based on the premise that the spectrum of small-scale temperature variations is related to the energy spectrum by the same wavenumber. Batchelor (1959) used Kolmogorov's (1941) hypothesis to predict the existence of a length scale beyond which no further refinement of the temperature distribution can occur. The smallest length scale for temperature fluctuations is derived by balancing heat advection with thermal diffusion and is known as the Batchelor length scale. The reciprocal of the Batchelor length scale is the Batchelor wavenumber κ_B written as

$$\kappa_B = (\varepsilon \nu^{-1} D^{-2})^{1/4} \quad (4)$$

where D is the molecular diffusivity of heat. Gibson and Schwarz (1963) used Batchelor's results to derive the one-dimensional Batchelor wavenumber spectrum whose upper limit represents the onset of viscous or diffusive effects. Thus, equation (4) can be solved to give an estimate of the turbulent kinetic energy dissipation rate after the maximum Batchelor wavenumber has been identified.

To identify the maximum Batchelor wavenumber, a Wigner-Ville distribution was applied to the microstructure temperature gradient signal from the vertically rising microstructure profiler (RMP) instrument in accordance with the method described in Imberger and Boashash (1986). The Wigner-Ville transform method is an analysis technique whereby the energy content of a non-stationary signal, such as the microstructure temperature gradient, is distributed in a time-frequency domain. This technique yields the instantaneous and maximum frequencies of the energy spectrum. The maximum temperature fluctuation frequency is then converted by a dispersion relationship into a wavenumber representing the maximum Batchelor wavenumber.

The RMP probe was only used on Julian day 119 at two different locations within the harbour. The probe was deployed three times at each location to increase statistical

confidence in the collected data trends. The respective dissipation rates calculated from the temperature measurements are listed in Table 2 along with the corresponding times of deployment and wind speeds.

Table 2 Dissipation rate estimates from RMP temperature measurements.

Julian Day	Time	U_3 (ms^{-1})	ϵ ($\text{m}^2 \text{s}^{-3}$)
119A ₁	10:31	2.3	3.1×10^{-7}
119A ₂	10:41	2.3	4.4×10^{-7}
119A ₃	10:48	2.6	4.2×10^{-7}
119B ₁	12:08	3.1	3.8×10^{-7}
119B ₂	12:16	2.3	3.0×10^{-7}
119B ₃	12:30	3.0	3.7×10^{-7}

Scaling arguments were used to estimate a time scale for the turbulent diffusion process. The time scale associated with horizontal transport due to turbulent motions can be written as

$$T_x \sim (L_x)^2 / K_x \quad (5)$$

where K_x is a horizontal diffusion coefficient which represents the non-advective mixing processes; therefore, its real value is highly dependent on the magnitude of these non-linear processes. Fischer *et al.* (1979) depicted a unified diagram of patch diffusion (after Okubo, 1974) from which it is possible to estimate a diffusion coefficient given the size of a tracer cloud. Given that the width of the harbour is of order 1×10^4 cm, K_x was found to have a value of $1 \times 10^2 \text{ cm}^2 \text{ s}^{-1}$. Evaluating (5) with $K_x = 1 \times 10^{-2} \text{ m}^2 \text{ s}^{-1}$ and $L_x = 100$ m gives a value for a horizontal transport time scale of order 10 days, which was representative of the turbulent diffusion processes associated with wind speeds of about 2.5 ms^{-1} . However, it was shown that the harbour remained stratified when wind speeds were less than 3 ms^{-1} , and a baroclinic exchange existed under these conditions. Therefore, it was desirable to know the horizontal transport time scale for the diffusion mechanism under more turbulent conditions than those measured on Julian day 119.

A relationship between the dissipation rate of mechanical energy in the surface mixed-layer and the energy flux from the atmosphere was reported by Oakey and Elliott (1982). They recorded turbulence levels under a variety of wind-wave conditions at a site near Emerald Basin on the Scotian shelf. The correlation between their dissipation and atmospheric forcing data showed a linear relationship between ϵ_I and $(U_{10})^3$. Here, ϵ_I is an average value of the dissipation rate integrated over depth, and U_{10} is an average wind speed measured at 10 m above the water surface for the hour prior to the dissipation measurements.

For the data presented in Table 2, ϵ_I was equal to about $6 \times 10^{-6} \text{ m}^3 \text{ s}^{-3}$ and U_{10} cubed was equal to approximately $30 \text{ m}^3 \text{ s}^{-3}$. There was good agreement between these data and those presented by Oakey and Elliott (1982). It was therefore reasonable to assume that the dissipation rate in Hillarys Boat Harbour goes as the 10 m wind speed cubed. Given

that ϵ goes as $(U_{10})^3$, then doubling the wind speed halves the horizontal transport time scale associated with the diffusive mechanism. Thus, a wind speed equal to 6 ms^{-1} could introduce enough TKE for eddy-diffusion processes to disperse a tracer cloud the size of the harbour in a time of order 5 days. Since the time for dispersion by turbulent motions was greater than the diurnal period of the tide, this indicated that the contribution to flushing by barotropic forcing was limited by mixing and not the size of the tidal prism. Therefore, the 11 day flushing time derived from the tidal prism method was an optimal estimate, which means the actual barotropic flushing time was probably several days longer.

4.0 Discussion of Results

The interpretation of the processed data was simplified by viewing Hillarys Boat Harbour as a small estuary. A partially stratified estuary was defined by Imberger (1976) as "one which possesses a quite definite longitudinal salinity gradient from the mouth to the head of the estuary, but only a very weak vertical or transverse salinity structure". Such a stratification condition requires a fresh water source near the head of the estuary and a vertical mixing mechanism which will overcome the vertical stratification caused by the fresh water input.

It was shown that wind generated turbulence in Hillarys Boat Harbour was sufficient to break down the vertical structure caused by the groundwater seepage, thereby establishing a longitudinal density gradient. Such a density gradient causes a pressure gradient force which is directed from the mouth towards the head of the estuary. A second pressure gradient force results from a surface slope and is generally directed towards the mouth of the estuary. Consequently, a net circulation is established in which a barotropic force due to a surface slope drives a seaward flow in the upper layer, and a baroclinic force caused by a longitudinal density gradient drives a landward flow in the lower layer.

Two-Layer Flow

The concept of critical flow in a two-layer system was first studied by Stommel and Farmer (1952, 1953). They showed that the discharge at the mouth of an estuary can be limited by an interfacial Froude number F_i equal to unity. The interfacial Froude number was defined as

$$F_i = v_1 / (g' y_1)^{1/2} \quad (6)$$

where the subscript 1 refers to the upper layer. Critical flow occurs in the upper layer maintaining a critical depth so that the compensating inflow in the lower layer is restricted. Wood (1968) discovered that there are actually two points of control, one at the narrowest section and another at a neighbouring upstream location. The latter control point is called the virtual point of control, and its position is determined by the barotropic flow. The results by Wood (1968) were extended by Armi (1986), who parameterized the flows in terms of the internal Froude numbers in each layer and presented solutions to the non-dimensional continuity and energy equations in a Froude number plane. This approach parallels the specific energy method in that the conditions for critical flow in a two-layer system can be determined from a Froude number diagram just as unstratified critical flow conditions are determined from a specific energy diagram.

For a two-layer flow through a contraction, the non-dimensional continuity equation can

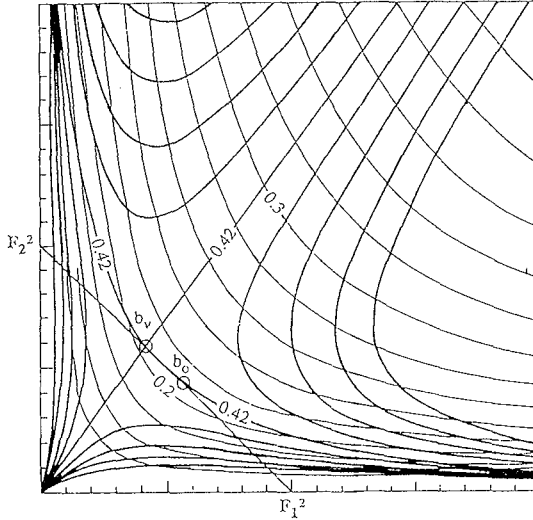


Figure 4 Critical flow conditions on Julian day 135 with $Q_r = 1.4$.

be written as

$$Q_r^{2/3} F_1^{-2/3} + F_2^{-2/3} = (Q_2' / b')^{-2/3} \tag{7}$$

where Q_2' is the non-dimensional lower layer discharge, b' is the width and $Q_r = Q_1 / Q_2$. The solutions to equation XX define the locus of possible Froude number pairs for any given Q_r and Q_2' / b' . For two-layer flow through a contraction, the non-dimensional energy equation in Froude number space is given by Armi (1986) as

$$\Delta H' = \frac{F_2^{-2/3} (1 + 0.5 F_2^2) - 0.5 Q_r^{2/3} F_1^{-2/3} F_1^2}{Q_r^{2/3} F_1^{-2/3} + F_2^{-2/3}} \tag{8}$$

where $\Delta H'$ is the dimensionless energy difference between the two layers. For small internal Froude numbers, $\Delta H'$ is the same as y_2' measured at the narrowest section. Armi and Farmer (1986) described all the flow properties for maximal two-layer exchange using nine dimensionless equations, nine unknowns and a non-dimensional barotropic flow.

The aforementioned method was applied to Hillarys Boat Harbour using data from Julian day 135 measurements. The barotropic flow for this case was calculated to be $2.85 \text{ m}^3\text{s}^{-1}$. Dividing this value by $(g')^{1/2} b_o (y_1 + y_2)_o^{3/2}$, where $g' = 0.0014 \text{ ms}^{-2}$, $b_o = 90 \text{ m}$, and $(y_1 + y_2)_o = 5 \text{ m}$, yielded a non-dimensional barotropic flow component $U_o' = 0.09$. This was used to solve for $y_2'_o \approx 0.42$, $b_v' \approx 1.05$, $Q_1' \approx 0.30$, $Q_2' \approx 0.21$, $v_1' \approx 0.56$, and $v_2' \approx 0.44$. The subscripts $_o$ and $_v$ refer to the narrowest section and location of the virtual control, respectively. The results are schematically shown in Froude number space in Figure 4. The line connecting (1,0) with (0,1) represents the locus of composite Froude numbers ($G^2 = F_1^2 + F_2^2 = 1$) that separate subcritical flow ($G^2 < 1$) from supercritical flow ($G^2 > 1$). On Julian day 135, a composite Froude number $G^2 = 0.64 + 0.40 = 1.04$ identified the existence of internal critical flow conditions with a normal control at $b_o = 90 \text{ m}$ and a virtual control at 94.5 m .

Flushing

The tidal prism method was used to calculate an optimal tidal flushing time on the order of 11 days. By superimposing the tidal prism decay rate onto the measured decay rate, it became apparent that at times the Rhodamine WT concentration was dropping at a rate similar to the tidal flushing rate; while at other times, the tracer concentration decayed much faster. This can be seen in Figure 2. An explanation for the variable flushing rate is that a baroclinic flushing mechanism was dominant during calm weather conditions, and the barotropic tide coupled with diffusion processes were responsible for flushing during active mixing periods. A similar case study was reported by Bienfang (1980) in which continual groundwater infiltration produced harbour flushing rates six to ten times those calculated for tidal flushing alone.

The flushing rate due to an internal flow driven by a density variation within Hillarys Boat Harbour was determined using $v_{1'o}$ & $v_{2'o}$ from Julian day 135. It was shown that $v_{1'} \approx 0.56$, and $v_{2'} \approx 0.44$. Dividing $v_{1'o}$ & $v_{2'o}$ by $[g'(y_1+y_2)]^{1/2}$ gives their dimensional form as an outflowing upper layer velocity $v_{1o} \approx 0.045 \text{ ms}^{-1}$, and an inflowing lower layer velocity $v_{2o} \approx 0.035 \text{ ms}^{-1}$. These values appeared to be consistent with drogue measurements conducted on Julian day 119. Defining the smaller of the two velocities as the baroclinic exchange rate, the time required for an uninterrupted baroclinic exchange flow to renew the $1.3 \times 10^6 \text{ m}^3$ harbour volume was calculated to be on the order of 2 days! However, it was shown that wind stirring was capable of destroying the vertical stratification, thereby inhibiting the flushing effectiveness of an established baroclinic circulation. Since the total flushing time and the barotropic component were known, it was possible to estimate the percentage of time for which a baroclinic circulation was active.

Substituting a measured total flushing time $T_f = 5$ days, a barotropic component of 11 days, and a baroclinic flushing time of 2 days into the expression

$$1/T_f = 1/T_{\text{Tide+Diffusion}} + X/T_{\text{Baroclinic}} \quad (9)$$

indicates that the baroclinic flushing mechanism was active during approximately 20% of the experimental period. It should be remembered that the barotropic flushing time used to solve equation (9) was an optimal estimate. Therefore, the baroclinic flushing process was probably active for a bit more than 20% of the time during the experiment.

5.0 Conclusions

The primary conclusion of this investigation is that within Hillarys Boat Harbour a baroclinic circulation caused by a fresh groundwater influx enhances the barotropic flushing. An overall flushing time of 5 days was measured during the experimental programme, and an optimal tidal flushing time of 11 days was calculated using the tidal prism method. The discrepancy was too large to be explained by experimental error, which meant that another process was accelerating the ongoing tidal exchange flow.

Fine-scale salinity and temperature measurements revealed a range of stratification conditions within the harbour due submarine groundwater discharges. When a vertical stratification condition existed, an internal two-layer flow was established. This flow was shown to be critical near the harbour entrance, which acted as a control on the

depth-discharge relationship. An uninterrupted flushing rate for the observed baroclinic exchange was calculated to be on the order of 2 days. However, a variable wind field was shown to be capable of destroying the gravitational circulation. As a result, the gravitational circulation was estimated to have been active during at least 20% of the experimental period, which was sufficient to cause a two-fold improvement over the tidal flushing time.

Acknowledgment

The Hillarys Boat Harbour flushing study was conducted by the Centre for Water Research, University of Western Australia on behalf of the Department of Marine and Harbours of Western Australia. The writers are grateful to the members of these two organizations for their financial support and cooperative assistance. The authors would also like to thank Dr. L. Armi for suggesting the baroclinic flushing as a possibly important mechanism.

References

- Armi, L. (1986) "The Hydraulics of Two Flowing Layers with Different Densities". *J. Fluid Mech.* **163**:27-58.
- Armi, L. and Farmer, D. M. (1986) "Maximal Two-Layer Exchange Through a Contraction with Barotropic Net Flow". *J. Fluid Mech.* **164**:27-51.
- Batchelor, G.K. (1959) "Small Scale Variation of Convected Quantities Like Temperature in Turbulent Fluid". *J. Fluid Mech.* **5**:113-133.
- Bienfang, P. (1980) "Water Quality Characteristics of Honokohau Harbor: A Subtropical Embayment Affected by Groundwater Intrusion". *Pacific Science*, **34**:279-291.
- Carter, G. D. and Imberger, J. (1986) "Vertically Rising Microstructure Profiler". *J. Atmospheric and Oceanic Tech.* **3**:462-471.
- Dillon, T. M. and Caldwell, D. R. (1980) "The Batchelor Spectrum and Dissipation in the Upper Ocean". *J. Geophys. Res.* **85**:1910-1916.
- Dyer, K. R. (1973) *Estuaries: A Physical Introduction*. John Wiley & Sons, pp. 133.
- Fischer H. B., List E. J., Koh R. C., Imberger J. and Brooks N. H. (1979) *Mixing in Inland and Coastal Waters*. Academic Press, New York.
- Fozdar, F. M. (1983) "Mixed Layer Probe Technical Report". *Env. Dyn. Ref. ED-83-039*, Univ. of Westn. Aust., 68 p.
- Fozdar F. M., Parker G. J., and Imberger J. (1985) "Matching Temperature and Conductivity Response Characteristics". *Amer. Meteor. Soc.* pp. 1557-1569.
- Gibson, C.H. and Schwarz W.H. (1963) "The Universal Equilibrium Spectra of Turbulent Velocity and Scalar Fields". *J. Fluid Mech.* **16**:365-384.
- Imberger, J. (1976) "Dynamics of a Longitudinally Stratified Estuary". *Proc. 15th Coastal Eng. Conf.* pp. 3108-3123.
- Imberger, J. (1985) "The Diurnal Mixed Layer". *Limnological Oceanogr.* **30**:737-488.

- Imberger, J. and Berman T. (1986) "An Optimized Pumping System for Vertical Profiling in Aquatic Environments". *Env. Dyn. Ref. EFM-1*, Univ. of Westn. Aust.
- Imberger, J. and Boashash, B. (1986) "Application of the Wigner-Ville Distribution to Temperature Gradient Microstructure: A New Technique to Study Small-Scale Variations". *J. Phys. Oceanography*, **16**:1997-2012.
- Johannes, R. E. (1980) "The Ecological Significance of the Submarine Discharge of Groundwater". *Marine Ecology Progress Series*, **3**:365-373.
- Kolmogorov, A. N. (1941a) "The Local Structure of Turbulence in an Incompressible Viscous Fluid for very Large Reynolds Numbers". *C.R. Acad. Sci., URSS*, **30**: 301.
- Kolmogorov, A. N. (1941b) "Dissipation of Energy in Locally Isotropic Turbulence". *C.R. Acad. Sci., URSS*, **32**: 16.
- Nece, N. E. (1984) "Planform Effects on Tidal Flushing of Marinas". *J. Waterway, Port, Coastal and Ocean Eng. Div., A.S.C.E.*, pp.251-269.
- Oakey, N. S. (1982) "Determination of the Rate of Dissipation Turbulent Energy from Simultaneous Temperature and Velocity Shear Microstructure Measurements". *J. Phys. Oceanography*, **12**:256-271.
- Oakey, N. S. and Elliott, J. A. (1982) "Dissipation Within The Surface Mixed Layer". *J. Phys. Oceanography*, **12**:171-185.
- Okubo, A. (1974) "Some Speculations on Oceanic Diffusion Diagrams". *Rapp. P. Reun. Cons. Int. Explor. Mer.* **167**:77-85.
- Simpson, J. H. and Nunes, R. A. (1981) "The Tidal Intrusion Front: An Estuarine Convergence Zone". *Estuarine and Coastal Shelf Science*, **13**:257-266.
- Smart, P.L. and Laidlaw, I.M.S. (1977) "An Evaluation of Some Fluorescent Dyes for Water Tracing". *Water Resources Research*, **13**:15-33.
- Stommel, H and Farmer, H. G. (1952) "Abrupt Change in Width in Two-Layer Open Channel Flow". *J. Mar. Res.* **11**(2):205-214.
- Stommel, H and Farmer, H. G. (1953) "Control of Salinity in an Estuary by a Transition". *J. Mar. Res.* **12**:13-20.
- UNESCO (1981) "The Practical Salinity Scale 1978, and the International Equation of State 1980". Tenth rep. of the joint panel on oceanographic tables and standards. UNESCO Tech paper in Mar. Sci. **36**:13-21.
- Wood, I. R. (1968) "Selective Withdrawal from a Stably Stratified Fluid". *J. Fluid Mech.* **32**:209-223.

CHAPTER 196

Steep Slope Seawater Supply Pipeline

Dr. Lloyd F. Lewis¹ Dr. Joseph Van Ryzin² Dr. Luis Vega³

Abstract

The State of Hawaii's Ocean Science and Technology (HOST) Park, the U.S. Department of Energy (DOE), and the Pacific International Center for High Technology Research (PICHTR) sponsored the construction and installation of an expanded seawater supply system at the Natural Energy Laboratory of Hawaii (NELH). This effort included the installation of a 1.0m diameter high density polyethylene pipe capable of delivering 840 l/s of cold seawater, representing the longest (2,060m) large diameter pipe traversing the steepest slope ever spanned. Acceptance testing of the system was completed in June 1988 and the design service life is 10 years.

Introduction

Since 1975, the State of Hawaii, DOE, and others have sponsored projects using relatively pristine seawater found adjacent to NELH at Keahole Point, Hawaii (Towill, 1976). Figure 1 illustrates the location of the NELH site. With the successful installation in 1981 of a bottom-mounted 0.3m diameter polyethylene pipe (PICHTR, 1988), experiments have had a constant supply of cold (7-8°C), nutrient-rich, pollution- and pathogen-free seawater as a resource. The State of Hawaii and others supported research in both warm and cold water mariculture (Daniel, 1985) and DOE has focused its support on both closed- and open-cycle ocean thermal energy conversion (OTEC) research (Penney, 1987). By 1985, with the formation of the High Technology Development Corporation and HOST Park adjacent to NELH, the State of Hawaii developed plans to increase the existing 130 l/s cold seawater supply and to install a 0.7m diameter pipeline to pump up to 430 l/s of cold seawater to several large-scale mariculture demonstration projects (HTDC, 1985). At the same time, DOE began designing a similar size line to supply up to 410 l/s of cold seawater (as well as a 0.7m line for 600 l/s of warm water) to a planned DOE-PICHTR net-power producing open-cycle OTEC experiment at NELH (SER1, 1985; Lewis, 1987). As plans and funding availability were evaluated, it became clear that a cost-effective solution would be to install a single line of 1.0m diameter to supply the required 840 l/s of cold seawater along with a 600 l/s warm seawater line.

1. U.S. Department of Energy, Washington, D.C. 20585
2. Makai Ocean Engineering, Kailua, HI 96734
3. Pacific Int'l. Ctr. for High Tech. Research, Honolulu, HI 96814

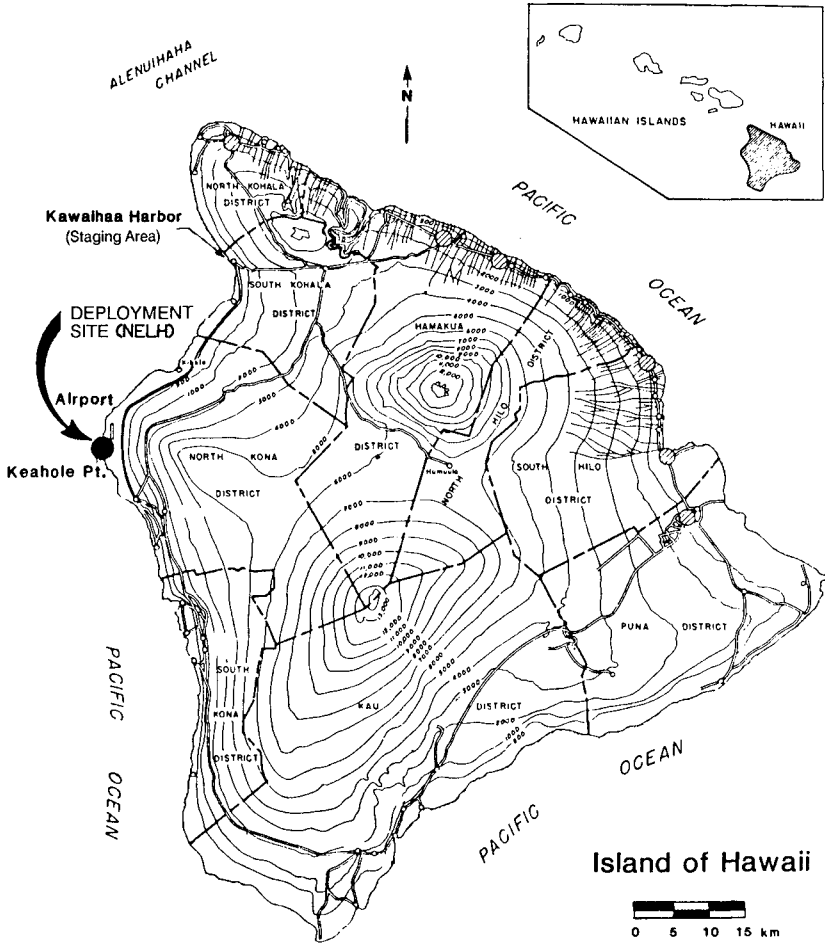


Figure 1. Seawater Supply System Deployment Site

Keahole Point Seawater Pipelines

The 0.3m diameter bottom-mounted cold ocean water pipe has been operating since 1981. In addition to the 1.0m seawater system described here, three other bottom-mounted polyethylene pipelines were installed at Keahole Point. Hawaiian Abalone Farms installed two 0.4m lines and the State of Hawaii installed a 0.5m line (PICHTR, 1988), all in 1987. These lines were small enough to be installed by a direct pull from shore. Pump installation and final inspection for all three lines were recently completed.

Site Conditions

Site-specific oceanographic, bathymetric, and environmental studies have been conducted at and near Keahole Point since 1975 in anticipation of OTEC and mariculture research (Bathen, 1975). Although Keahole Point is located on the leeward side of the Big Island of Hawaii relative to the predominant trade winds, during the November-March time frame there is a strong possibility of Kona storms (i.e., from the unprotected south and west) at the site (Rocheleau, 1979). Waves from those storms break suddenly on the very narrow island shelf and are known to move large boulders in the shoreline area. In addition, tsunami runup has been recorded at 3.7m (Cox, 1982) causing significant site inundation. Open ocean waves for the 100-year event have been estimated to exceed 14.3m (Bretschneider, 1978). Ocean currents off Keahole Point have been monitored by several researchers since 1975 (Bathen, 1975; Noda, 1979; Frye, 1981; Lobel, 1985; Noda, 1986). In the presence of a large-scale eddy often formed west of the Big Island, local currents can reach 2.6 m/s at the surface, 1.1 m/s at 150m depth, and 0.4 m/s at 300m depth. The bathymetry and sediment cover off Keahole Point have been studied in detail both with surface supported (Campbell, 1979) and submersible supported (Noda, 1979; Makai, 1983; Fornari, 1984) geophysical and geotechnical equipment. Although the distance offshore and therefore the pipe length to the cold water resource is less than 1.5 km, the slopes are very steep, occasionally exceeding 50°. In places, large outcroppings of irregular lava occur. Fig. 2 schematically illustrates the bottom slope and thin sediment condition. Environmental studies have pointed out that although there are no resident threatened or endangered species near Keahole Point, endangered marine mammals and sea turtles are known to migrate nearby in the winter months (HTDC, 1985; MSG, 1986; NELH, 1987).

Pipe Design

Considering the site-specific and environmental conditions described above, the design chosen for the 1.0m pipeline was the partially bottom-weighted and partially inverted buoyant catenary configuration shown in Figs. 2 and 3 (Horn, 1980; State of Hawaii, 1986; Vuillemot, 1988). Table 1 lists the principal design requirements of the pipeline for the DOE-PICHTR OTEC experiments (Lewis, 1987). In addition to the 410 l/s of cold seawater supplied to the OTEC experiments, another 430 l/s are simultaneously pumped to HOST Park for mariculture projects (Table 2). Additional design requirements included having only relatively inert surfaces contacting seawater and a design service life of 10 years.

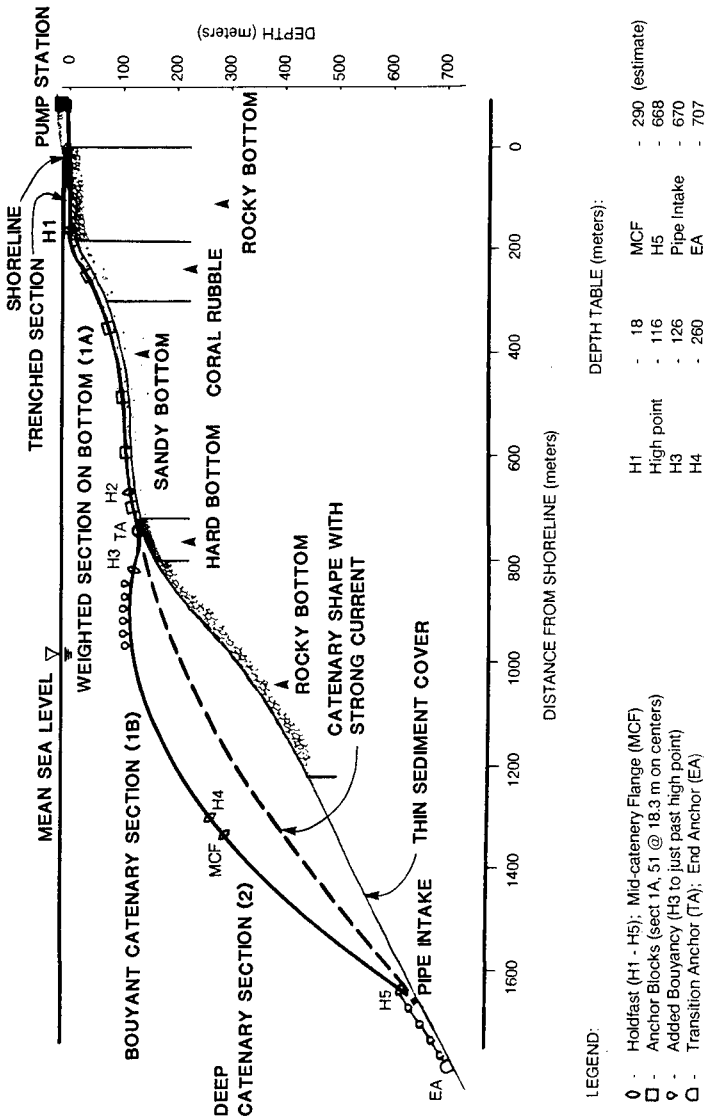


Figure 2. Profile View of Seawater Supply System

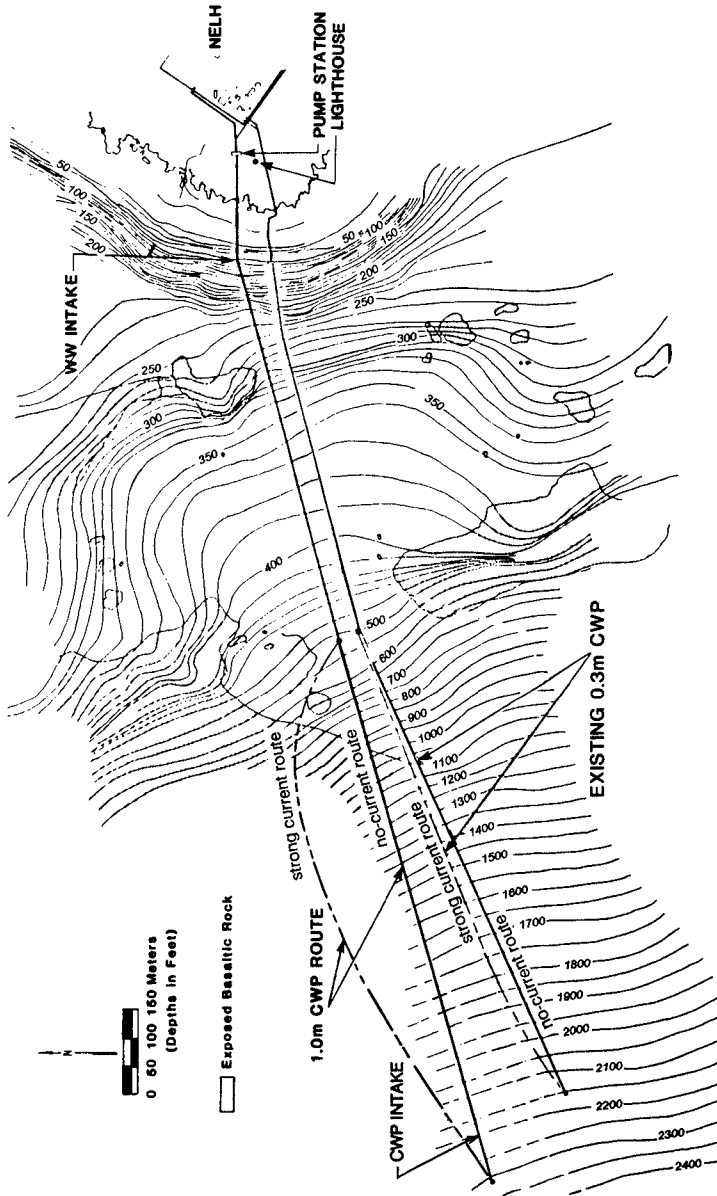


Figure 3. Plan View of Seawater Supply System

High density polyethylene was chosen as the pipe material for several reasons. Its natural buoyancy in seawater offers the option of reversibility in the deployment scenario. Its inertness satisfies the user requirements. It is sufficiently flexible yet strong in tension and bending in the chosen diameter and wall thickness to facilitate towing, controlled submerging, and long-term flexure in the deployed configuration. Fabrication is facilitated by thermal butt welding (Fig. 4) resulting in welds as strong as the extruded pipe. Finally, it has demonstrated success in prior bottom-laid configurations on steep and rugged slopes (PICHT, 1988).

The buoyant, inverted catenary prevents the pipe from contacting the rough and steep ocean floor that it spans. As illustrated in Figures 2 and 3, however, the catenary does allow the pipe to sway in the locally strong currents (as much as 150m horizontally and 75m vertically). An 18,000kg gravity anchor below the cold water intake fixes the seaward end of the catenary as shown in Fig. 5. At a depth of about 150m, the pipe transitions from the floating catenary to a bottom-weighted configuration through bridles and a sliding sleeve (Fig. 6). Another gravity anchor (36,000kg) restrains the shoreward end of the catenary through these bridles. Shoreward of this transition section, the slope is less steep and generally sediment-covered with only minor outcrops along the route. The weighted section of pipe is restrained from downslope movement by chain bridles linked to rock-bolted anchor plates installed at the shore end of the pipe. At a depth of 15m (just above the warm water intake), the cold water pipe enters a trenched and backfilled section (Fig. 7) along with the warm water pipe and two spare conduits, all of which continue to the onshore pumphouse invert at approximately 5.5m below sea level. Submersible pumps draw warm and cold water from the pumphouse sump and force these supplies through a distribution network to the NELH and HOST Park sites.

Makai Ocean Engineering (MOE) designed the ocean portion of the pipe system. R. M. Towill Corporation designed the land portion of the system and, assisted by MOE, also served as the resident engineer for the State of Hawaii during construction. Construction of the seawater system was done by Kiewit Pacific Company under contract to the State of Hawaii.

Site Preparations

The principal site preparation for installing the seawater system involved trenching for the nearshore, surf zone, and onshore pipe route. Other predeployment activities included installing the nearshore rock anchors and clearing the chain bridle paths to the pipeway. Blasting and excavation were precluded during the winter marine mammal migration period. Pre- and post-construction surveys were conducted to assess the impact on, and recovery time of, local nearshore aquatic biota. In addition, these diver surveys were coordinated with the National Marine Fisheries Service and Hawaii Department of Land and Natural Resources. A shore-based navigation and positioning triangulation system was installed along with visual range markers. Numerous radio frequencies were selected for voice communications among the deployment vessels and shore-based personnel.



Figure 4. Polyethylene Pipe Thermal Butt Welding

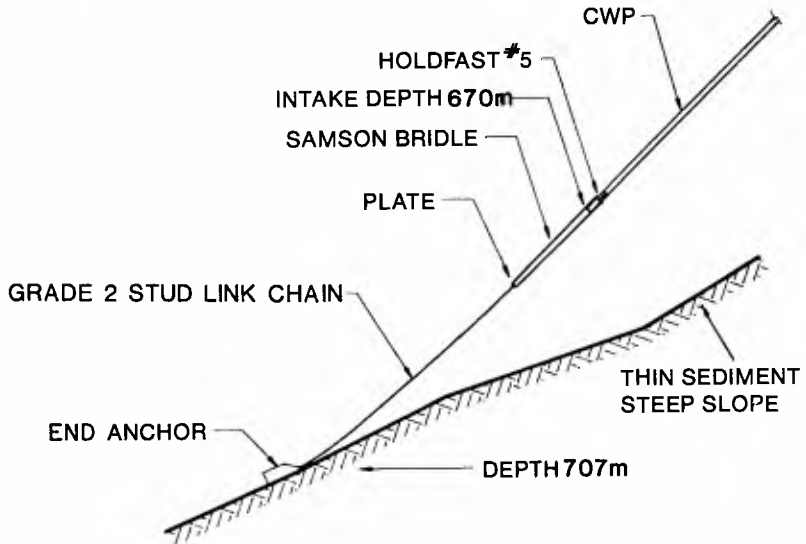


Figure 5. Pipe Intake Assembly

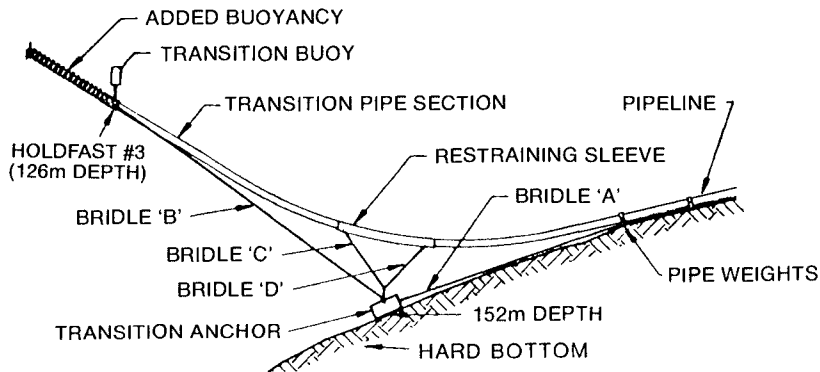


Figure 6. Pipe Transition Area

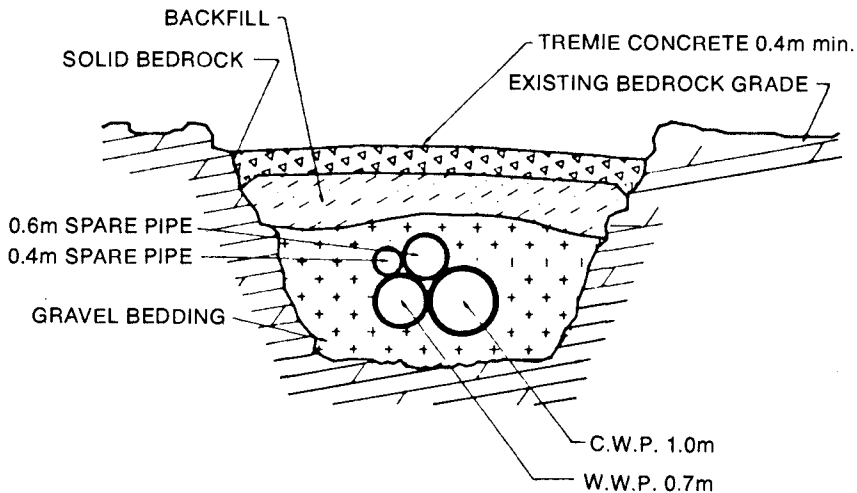


Figure 7. Section of Offshore Trench, Typical

Weather windows were selected with regard to each of the planned deployment operations. The deployment guideline (State of Hawaii, 1986) called for towing in sea states less than 4, pipe alignment in sea states less than 3 with surface currents less than 0.8 m/s, and pipe lowering in sea states less than 3 with currents less than 0.5 m/s. Weather conditions were monitored daily from the National Weather Service and by a Kiewit-employed meteorologist. An in situ telemetering current meter was monitored continually during critical phases of the deployment. None of the condition limits were exceeded during deployment.

Fabrication, Assembly, and Deployment

The high density polyethylene pipe was shipped by the manufacturer, DuPont of Canada, in 12m sections and off-loaded at the Kawaihae Harbor staging area. DuPont and Kiewit personnel then formed sections 1A, 1B, and 2 (Fig. 2) using a thermal welding machine (Fig. 4). Holdfasts, floats, weights, flanges, certain bridles, and other attachments (Fig. 2) were installed and the pipe sections floated into the harbor (Fig. 8). These sections were anchored to prevent movement due to winds and were also restrained to prevent twisting during holdfast installation. Sections 1A and 1B were pressure tested by running a pig through the pipe and pressurizing to 125% of the maximum expected deployment pressures (e.g. 620kPa) for 24 hours. Lights were attached at 60m intervals for night tows.

Deployment of the ocean portion of the seawater system off Keahole Point was initiated in late July, 1987. Sections 1A and 1B were mechanically flanged together (Fig. 9), pressurized to 140kPa, and towed as a unit to Keahole Point. The tow tug transferred holdfast 1 to the crane barge for controlled lowering and connection by divers to the nearshore anchor plate bridles. After aligning section 1 along its deployment corridor (Fig. 10), hoses were connected to the shoreward end, and the 36,000kg transition anchor and associated bridles were connected near holdfast 3 (Fig. 6). In order to cool the pipe and thus reduce bending strains, it was necessary to spray water on the floating pipe during this period. The pipe was pressurized to 350kPa to prevent pipe collapse during deployment. Then the pig was forced through the pipe by water pumped from the shore end, causing the pipe and concrete anchor blocks to sink; however, pressure equilibrium was maintained in case the pipe had to be raised during this period. The offshore tug, pulling up to 220kN tension, maintained the pipe alignment and acceptable bend radii. As the final anchor blocks were submerging, the crane barge lowered the transition anchor into place. After about 600,000 liters were pumped, lowering was stopped and holdfast 4 was kept on the surface.

The University of Hawaii's manned submersible PISCES V was launched to inspect the pipe from about anchor block 30 through the transition area to confirm placement of weights, condition of bridles, clearance from the existing 0.3m line, avoidance of rock outcrops, etc. After the inspection, pipe section 2 was towed from Kawaihae and connected to section 1 at the mid-catenary flange. The crane barge moved to the pipe intake, and the catenary end anchor and bridles were attached. Pumps were started again and the pig



Figure 8. Pipe Haul, Kawaihae Harbor



Figure 9. Connecting Pipe Sections 1A and 1B, Kawaihae Harbor



Figure 10. Aligning Pipe Section 1, Keahole Point

displaced air from the pipe while the barge lowered the end anchor. Since the distance between the two catenary anchors was critical in determining catenary shape, the end anchor was acoustically positioned into its touchdown location. A few days after this six-day pipe installation was completed, PISCES V made another dive to confirm the as-deployed condition of the pipe over its full length. The entire deployment was documented by helicopter-, surface-, and submersible-supported video taping and still photography.

Acceptance Testing

In June 1988, after completion of the surf zone and onshore pipes and pumphouse components, a full set of acceptance tests was successfully completed, including operation of the eight cold and four warm water pumps (Table 2). The stainless steel submersible pumps are rated for service to 20m depth. They have alarms and shutoffs for overheating, excessive motor current, vibration, and low water levels in the pumphouse sump. The pumps are rotated during low flow use periods to maintain uniform wear.

Additional Effort

The HOST Park portion of the system is presently operating with discharges into large capacity, deep injection wells. It is not anticipated that the NELH portion of the system will be fully used until 1990-1991 when the DOE-PICHTER large-scale, net-power producing open-cycle OTEC experiment is operational. Presently, a shallow trench is being designed and, when constructed, will serve to collect and disperse the OTEC discharges.

The pipe will be instrumented at holdfast 3 with recording depth gauges to monitor depth changes as a function of ocean currents, which will also be monitored on a separate nearby mooring. It is expected that this data will assist in verifying predictive pipe motion models and in designing future catenary pipe systems.

References

- Bathen, K.H. (1975). "A Further Evaluation of Oceanographic Conditions Found off Keahole Point, Hawaii." Department of Ocean Engineering, University of Hawaii, Honolulu, HI.
- Bretschneider, C.O. (1978). "An Evaluation of Extreme Wave Climates at Keahole Point, Hawaii." Proceedings, 16th International Conference on Coastal Engineering, Hamburg, Germany.
- Campbell, J.F. and Erlandson, D.L. (1979). "OTEC-1 Anchor Site Survey." HIG-79-C. Hawaii Institute of Geophysics, University of Hawaii, Honolulu, HI.
- Cox, D.C. (1982). "Tsunami Hazard at Keahole Point, Hawaii." Special Report. 0028, Environmental Center, University of Hawaii, Honolulu, HI.
- Daniel, T.H. (1985). "Aquaculture Using Cold Water." Proceedings, Marine Technology Society OCEANS '85, San Diego, CA.

- Fornari, D.J. (1982). "Deep Sea Vehicle TURTLE Dives off Keahole Point, Hawaii." ETEC N2B5-058ZKX. Energy Technology Engineering Center, Canoga Park, CA.
- Frye, D., Leavitt, K. and E.K. Noda (1981). "Current Data from the Keahole Point, Hawaii OTEC Benchmark Sites, June 1980-April 1981." DOE/NBM-2015777. National Technical Information Service, Springfield, VA.
- Gibbs & Cox (1985). "Seacoast Test Facility Upgrade Project Conceptual Design Study." ETEC STFU-XR-0002. Energy Technology Engineering Center, Canoga Park, CA.
- High Technology Development Corporation (1985). "Final Environmental Impact Statement and Development Plan for HOST Park and Expansion of NELH." High Technology Development Corp., Honolulu, HI.
- Horn, H.M. and Van Ryzin, J.C. (1980). "Deep Ocean Polyethylene Pipe Installations." Proceedings, International Pipeline Technology Exhibition and Conference, (Interpipe 80) Vol. 1, Houston, TX.
- Lewis, L.F., Trimble, L. and J.L. Bowers (1987). "Open-Cycle OTEC Seawater Experiments in Hawaii." Proceedings, Marine Technology Society OCEANS '87, Halifax, Nova Scotia, Canada.
- Lobel, P.S. and Robinson, A.R. (1985). "Summary of Wind and Ocean Current Patterns Along the Kona Coast, Hawaii." Marine Sciences Group, University of California, Berkeley, CA.
- Makai (1983). "Offshore Engineering Survey at Keahole Point, Hawaii, Using the Submersibles MAKALI'1 and TURTLE." Makai Ocean Engineering, for the Department of Business and Economic Development, State of Hawaii, Honolulu, HI.
- MSG (1986). "Environmental Report, Construction of an Expanded Facility for the Seacoast Test Facility, Stage 2 of NELH." Marine Sciences Group, University of California, Berkeley, CA.
- NELH (1987). "Final Supplemental Environmental Impact Statement, Alternative Methods of Seawater Return Flow Disposal." Natural Energy Laboratory of Hawaii, Honolulu, HI.
- Noda, E.K. and Brower, R.E. (1979a). "Bottom Current Survey, Keahole Point, Hawaii." Look Lab-79-47. University of Hawaii, Honolulu, HI.
- Noda, E.K. (1979b). "Manned Submersible Reconnaissance Survey, OTEC Seacoast Test Facility Proposed Pipeline Route, Keahole Point, Hawaii." UNIHI-SEAGRANT-TP-79-02, University of Hawaii, Honolulu, HI.
- Noda, E.K. (1986). "Oceanographic Criteria for the Design and Deployment of the Cold Water Pipe System." EKN-1071-R-1 E.K. Noda & Associates, Honolulu, HI.
- Penney, T.R. and Bharathan, D. (1987). "Power from the Sea." Scientific American, Vol. 256, No. 1, pp. 86-92.

PICHTER (1988). "Bottom Mounted OTEC Seawater System Workshop." Pacific International Center for High Technology Research, Honolulu, HI. (in press).

Rocheleau, R.E. (1979). "Evaluation of Extreme Wind and Wave Climate at Keahole Point, Hawaii." Sea Grant Working Paper 42, University of Hawaii, Honolulu, HI.

State of Hawaii (1986). "HOST Park, First Increment and Seacoast Test Facility Upgrade, Keahole, North Kona, Hawaii." Job. 01-26-8018 Plans and Specifications. Department of Accounting and General Services, State of Hawaii, Honolulu, HI.

Towill (1976). "Environmental Impact Statement, NELH, Keahole Point, Hawaii." R.M. Towill Corp. for the Research Corporation, University of Hawaii, Honolulu. HI.

Vuillemot, F.L., Van Ryzin, J.C. and A.M. Resnick (1988). "The HOST-Seacoast Test Facility (OTEC) Project in Hawaii, Planning, Design and Construction." Presented at Marine Technology Society Pacific Congress on Marine Science & Technology (PACON'88), Honolulu, HI.

TABLE 1

OPEN-CYCLE OTEC SEAWATER
SUPPLY SYSTEM CHARACTERISTICS

<u>Characteristic</u>	<u>Cold Water</u>	<u>Warm Water</u>
Primary Flow (l/s)	410	600
Secondary Flow (l/s)*	19	19
Head at Test Pad (m)	6.1	6.1
Intake Depth (m)	670	20
Particulates Screened (cm)	1	1

*continuous flow

TABLE 2

SEAWATER PUMP CHARACTERISTICS

<u>User</u>	<u>Type</u>	<u>Number*</u>	<u>Power</u> (kw)	<u>Flow</u> (l/s)	<u>Head</u> (m)
HOST	Cold	5	66	110	37
DOE/NELH	Cold	3	57	205	19
DOE/NELH	Warm	4	57	200	19

*each use has one redundant pump

CHAPTER 197

Coastal and Estuarine Hydrodynamic Modeling in Curvilinear Grids

by

Y. Peter Sheng¹, M. ASCE

T.S. Wu²

P.F. Wang²

ABSTRACT

A time-dependent three-dimensional numerical model of coastal and estuarine circulation, which allows the use of generalized curvilinear grids to resolve the complex shoreline geometry and bathymetry, has been developed. Model formulation is briefly presented, followed by example model applications to such water bodies as Lake Okeechobee, James River and Chesapeake Bay.

INTRODUCTION

Numerical models are routinely used for scientific investigations and management studies of circulation and transport processes in coastal and estuarine waters. However, a number of complexities are associated with the numerical modeling of coastal and estuarine circulation and transport. First of all, the geometry and bathymetry of water bodies are often quite complex (see, for example, Fig. 1). Secondly, circulation and transport in coastal and estuarine waters are generally turbulent and time-dependent, and often three-dimensional. Last but not least, circulation and transport are generally affected by wind, tide, wave, and often density stratification. A thorough discussion of these various aspects and a review of numerous existing hydrodynamic models were presented in Sheng (1986a). This paper focuses on the aspect of complex geometry and bathymetry, and highlights the recent development and application of a curvilinear linear-grid numerical model of coastal and estuarine circulation and transport.

¹Professor, Coastal and Oceanographic Engineering Department, University of Florida, Gainesville, Florida 32611

²Postdoctoral Associate, Coastal and Oceanographic Engineering Department, University of Florida, Gainesville, Florida 32611

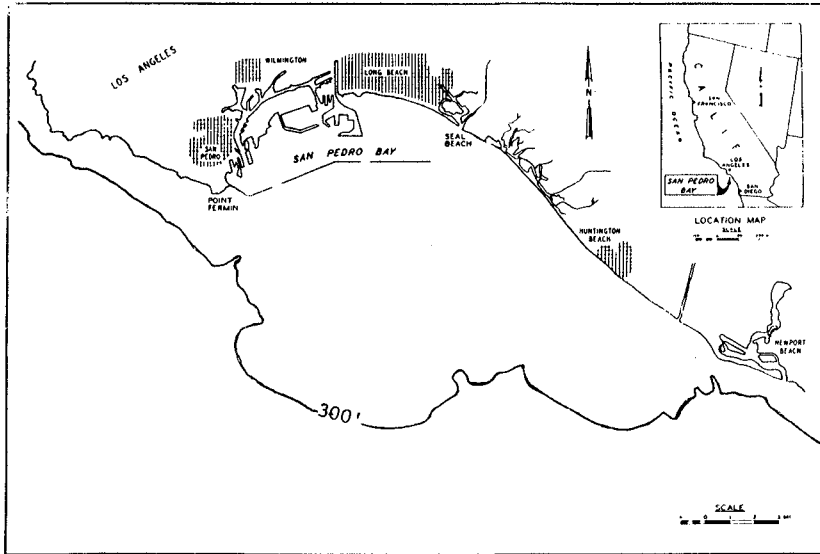


Figure 1. Los Angeles and Long Beach Harbor.

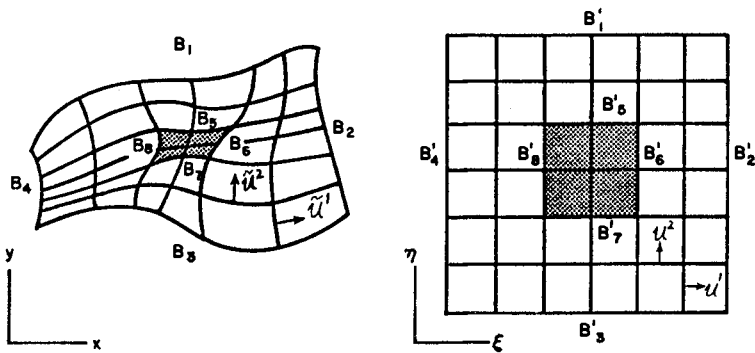


Figure 2(a). Generalized curvilinear (boundary-fitted) grid used in the horizontal directions of the 3-D model.

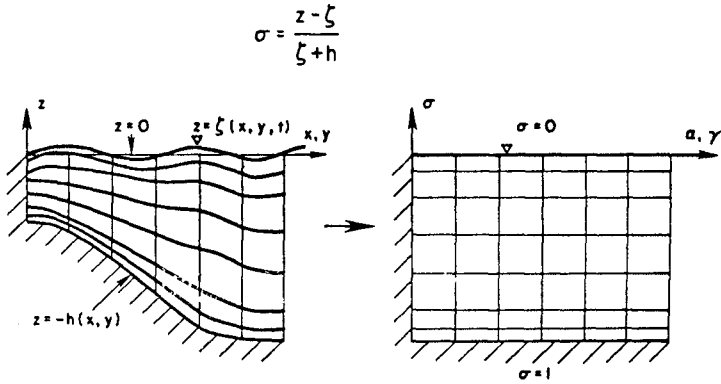


Figure 2(b). Vertical stretching of the coordinates in the 3-D model.

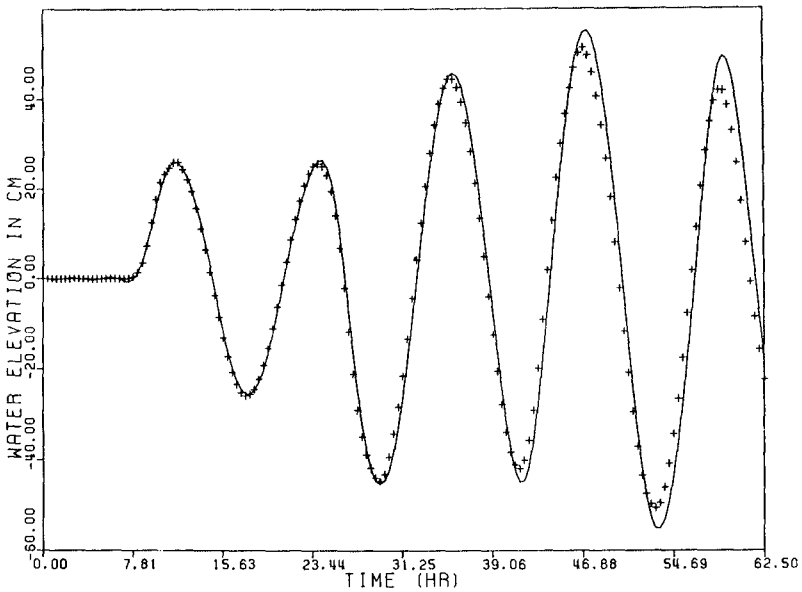


Figure 3. Transient response of water level near the closed end of an initially quiescent basin of 300 km x 29 km x 10 m, subject to a tidal forcing with 1 m amplitude and 12.5 hr period. (— model results, +++ analytical results)

Traditional finite-difference models use uniform or non-uniform rectangular grid to approximate the complex geometry of water bodies. Consequently, very fine grid is often required to resolve a shoreline or an internal feature such as a structure or navigation channel. As a larger number of rectangular grid points are employed, the "stair-step" model shoreline can better represent the actual shoreline, at the expense of much increased computational cost. To alleviate some of these problems, simple curvilinear grids such as conformal grid (Warnstrath, 1977) and orthogonal curvilinear grid (Bennett and Schwab, 1981) have been used for modeling water bodies where geometries are not so complex. Despite the relative simplicity of these curvilinear grid models, it is extremely difficult (if not impossible) to generate conformal or orthogonal curvilinear grids for most coastal and estuarine water bodies, such as the Los Angeles and Long Beach Harbors shown in Figure 1. Not only is the grid generation process extremely difficult, but the final grid may also be unnecessarily fine in some areas while very coarse in others. In addition, the final grid may not be very smooth. Thus, for coastal and estuarine applications, a hydrodynamic model that can resolve arbitrary shoreline and bathymetry must be developed. Numerical model must be able to accept not only conformal grids or orthogonal grids, but also generalized curvilinear grids which are often non-orthogonal. Such a numerical model will allow the modeler added flexibility in the design of numerical grids with optimal smoothness, resolution, and orthogonality.

This paper presents a generalized curvilinear-grid model for coastal and estuarine circulation and transport. The model resolves the contravariant components of horizontal velocity vectors, thus significantly simplifies the resulting equations of motion and boundary conditions in the transformed grid. In the limiting cases of conformal grids or orthogonal grids, the model equations become substantially simplified.

MODEL FORMULATION

Governing Equations in Curvilinear Grid

The basic circulation and transport model is developed in terms of the contravariant velocity components (u^1 and u^2) in the horizontal directions (x^1 and x^2) and the vertical velocity (ω) in the vertical direction of a σ -stretched (Sheng and Butler, 1982) curvilinear grid (Fig. 2). The basic equations of motion in dimensionless and tensor-invariant forms can be written as (Sheng, 1986b):

$$\dot{\zeta}^i + \frac{\beta}{\sqrt{g_\sigma}} \frac{\partial}{\partial x^k} (\sqrt{g_\sigma} H u^k) + H \frac{\partial \omega}{\partial \sigma} = 0 \quad (1)$$

$$\begin{aligned} \frac{1}{H} \frac{\partial H u^k}{\partial t} = & - \zeta^{!k} - g_{nj} \epsilon^{kj} u^n \\ & - \frac{Ro}{H} \left[(H u^\ell u^k)_{,\ell} + \frac{\partial H u^k \omega}{\partial \sigma} \right] \end{aligned} \quad (2)$$

$$\begin{aligned}
 &+ \frac{E_v}{H^2} \frac{\partial}{\partial \sigma} \left(A_v \frac{\partial u^k}{\partial \sigma} \right) + E_H A_H u_{,m}^k \text{!}^m \\
 &- \frac{Ro}{Fr_d^2} \left[H \int_{\sigma}^0 \rho^!^k d\sigma + H \text{!}^k \left(\int_{\sigma}^0 \rho d\sigma + \sigma \rho \right) \right]
 \end{aligned}$$

where $k = 1$ and 2 , $(x^1, x^2) = (\xi, \eta)$ represent the coordinates in the computational domain which is always consisted of uniformly spaced rectangular grid, $\partial/\partial x_k$ is the partial derivative, $g_{\epsilon n}$ is the metric tensor while g_o is the determinant of the metric tensor, ζ is the free surface displacement, $H = h + \zeta$ is the total depth, u^k is the contravariant velocity component, $\sigma = (z - \zeta)/(\zeta + h)$, $(\)_{,\epsilon}$ represents the covariant spatial derivative, !^k represents the contravariant spatial derivative, and ϵ^{kj} is the permutation tensor, $Ro = u_r/fXr$ is the Rossby number, $E_v = A_{vo}/fH^2$ is the vetical Ekman number, $E_H = A_{Ho}/fL^2$ is the lateral Ekman number, $Fr_d = u_r(gD\Delta\rho_o/\rho_o)^{0.5}$ is the densimetric Froude number, $\beta = (Ro/Fr)^2 = gD/f^2L^2$, f is the Coriolis parameter, and (u_r, D, L) represent the reference (velocity, depth, horizontal length).

The above Eq. (2) can be expanded into 2 equations for u^1 and u^2 . For example, denoting (u^1, u^2) by (u, v) , the following equation represents the momentum equation in the ξ direction (Sheng, 1986b):

$$\begin{aligned}
 \frac{1}{H} \frac{\partial Hu}{\partial t} = & - \left(g^{11} \frac{\partial \zeta}{\partial \xi} + g^{12} \frac{\partial \zeta}{\partial \eta} \right) + \frac{g_{12}}{\sqrt{g_o}} u + \frac{g_{22}}{\sqrt{g_o}} v \\
 & - \frac{Ro}{H} \left[\frac{\partial}{\partial \xi} (Huu) + \frac{\partial}{\partial \eta} (Huv) + (2D_{11}^1 + D_{12}^2)Hu \\
 & + (3D_{12}^1 + D_{22}^2)Huv + D_{22}^1Hvv + \frac{\partial Huw}{\partial \sigma} \right] \\
 & + \frac{E_v}{H^2} \frac{\partial}{\partial \sigma} \left(A_v \frac{\partial u}{\partial \sigma} \right) \\
 & - \frac{Ro}{Fr_d^2} \left[H \int_{\sigma}^0 \left(g^{11} \frac{\partial \rho}{\partial \xi} + g^{12} \frac{\partial \rho}{\partial \eta} \right) d\sigma \right. \\
 & \left. + \left(g^{11} \frac{\partial H}{\partial \xi} + g^{12} \frac{\partial H}{\partial \eta} \right) \left(\int_{\sigma}^0 \rho d\sigma + \sigma \rho \right) \right] \\
 & + E_H A_H \cdot (\text{Horizontal Diffusion of } u)
 \end{aligned} \tag{3}$$

where D_{jk}^i represents the Christoffel symbol of the second kind:

$$\begin{aligned}
 D_{jk}^i &= g^{in} D_{njk} \\
 &= \frac{1}{2} g^{in} (g_{nj;k} + g_{nk;j} - g_{jk;n})
 \end{aligned} \tag{4}$$

The above equation appears to be more complicated than the momentum equation in a Cartesian grid with (x, y, σ) or (x, y, z) as coordinates. Most of the terms are doubled, while nonlinear and lateral diffusion terms are more than doubled. However, if an orthogonal grid is used, the following equation will result from Eq. (3):

$$\begin{aligned} \frac{1}{H} \frac{\partial H u}{\partial t} = & - g^{11} \frac{\partial \xi}{\partial \xi} + \frac{g^{22}}{\sqrt{g_o}} v \\ & - \frac{R_o}{H} \left[\frac{\partial}{\partial \xi} (H u u) + \frac{\partial}{\partial \eta} (H u v) + \frac{\partial H u \omega}{\partial \sigma} \right] \\ & + \frac{E_v}{H^2} \frac{\partial}{\partial \sigma} \left(A_v \frac{\partial u}{\partial \sigma} \right) \\ & - \frac{R_o}{F r_a^2} \left[H \int_{\sigma}^0 g^{11} \frac{\partial \rho}{\partial \xi} d\sigma + g^{11} \frac{\partial H}{\partial \xi} \left(\int_{\sigma}^0 \rho d\sigma + \sigma \rho \right) \right] \\ & + E_H A_H \left(g^{11} \frac{\partial^2 u}{\partial \xi^2} + g^{22} \frac{\partial^2 u}{\partial \eta^2} \right) \end{aligned} \quad (5)$$

As indicated before, such simplified equation cannot be used unless the shoreline geometry is so simple such an orthogonal grid can be generated. Even then, the numerically computed metric coefficients, which represent the geometric effects in the transformed equations of motion, do not necessarily guarantee the satisfaction of conservation laws in the discrete system.

The transport equations for temperature, salinity, and sediment concentration are simpler and can be written as:

$$\begin{aligned} \frac{1}{H} \frac{\partial H \phi}{\partial t} = & \frac{E_v}{P r_v} \frac{\partial}{\partial \sigma} \left(K_v \frac{\partial \phi}{\partial \sigma} \right) \\ & - \frac{R_o}{H \sqrt{g_o}} \left(\frac{\partial \sqrt{g_o} H u \phi}{\partial \xi} + \frac{\partial \sqrt{g_o} H u \phi}{\partial \eta} + \frac{\partial \sqrt{g_o} H \omega \phi}{\partial \sigma} \right) \\ & + \frac{E_H K_H}{P r_H} \left(g^{11} \frac{\partial^2 \phi}{\partial \xi^2} + 2g^{12} \frac{\partial^2 \phi}{\partial \xi \partial \eta} + g^{22} \frac{\partial^2 \phi}{\partial \eta^2} \right) \end{aligned} \quad (6)$$

where ϕ can be temperature (T), salinity (S), or suspended sediment concentration (C), ($P r_v, P r_H$) represent the vertical and lateral turbulent Prandtl numbers, and (K_v, K_H) are the dimensionless vertical and horizontal turbulent diffusivities.

Other Model Features

The above system of equations are solved in conjunction with the proper boundary conditions at the free surface, the bottom, and the lateral boundaries. At the bottom, the velocity profile asymptotically approaches that of the law-of-the-wall, with a drag coefficient which depends on the bottom roughness.

Turbulence parameterization used in the present model is similar to the one described in Sheng (1987). While the horizontal turbulent eddy coefficients are prescribed as uniform values which decrease with the grid spacing, the vertical eddy coefficients are determined from simplified versions of a second-order closure model of turbulent transport (Sheng and Chiu, 1986; Sheng and Villaret, 1988).

Numerical Algorithm

To allow efficient solution of the 3-D model, the mode-splitting technique described in Sheng et. al. (1978) and Sheng and Butler (1982) is also used here. Vertically-integrated equations obtained by integrating Eqs. (1) and (2) represent the so-called "external mode", while the internal mode consists of equations obtained by subtracting the vertically-averaged equations from the u and v equations. An ADI scheme, which is somewhat more complicated than that for the Cartesian equations, is used for the external mode of the present model. Either two-time-level or three-time-level scheme can be used for the time integration of the 3-D model.

The numerical model described above constitutes the main body of a flow code, CH3D. In addition to CH3D, a grid generation code based on the elliptic grid generation technique (Thompson and Johnson, 1985) and a preprocessor code (Sheng, 1986) which computes the metric coefficients must also be used when solving practical problems.

At the present time, we do not adjust the grid during a particular model simulation. Adaptive grid technique, which allows the adjustment of grid resolution according to the evolution of dynamic flow, is being developed (Sheng and Luo, 1988).

Model Applications

Numerous model simulations have been performed. Model applications to a number of idealized basins were presented in Sheng (1987). Additional model sensitivity tests have been performed. For example, Figure 3 shows the transient response of an initially quiescent rectangular basin (300 Km x 29 Km x 10 m) to a suddenly imposed tidal forcing with 1 m amplitude and 12.5 hr period. Since no diffusion or bottom friction was used in the model, the model results faithfully simulated the analytically computed transient response which consists of higher harmonics in addition to the forcing harmonic.

Model application to the James River estuary (Fig. 4) produced mean tides which agreed well with data, both in terms of amplitude (Fig. 5) and phase shift (Fig. 6). Model application to the Chesapeake Bay (Fig. 7) produced results which compared well with mean tides. Significant spatial variation is found in the model computed velocity field, which is being compared with measured data now. The same basic model is being applied to the upper Chesapeake Bay (Johnson, 1988).

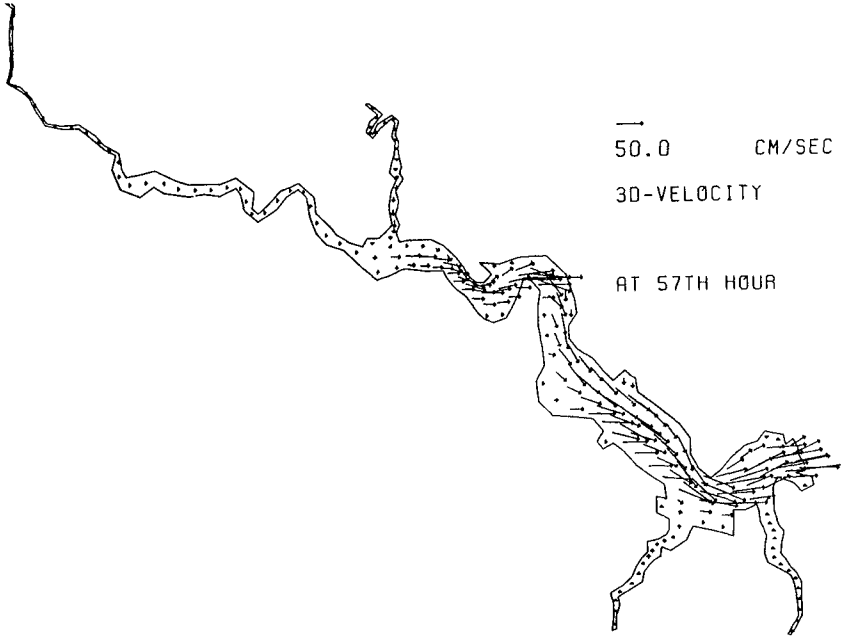


Figure 4. Near-surface current in the James River driven by a M_2 tide of 38 cm amplitude at the open boundary.

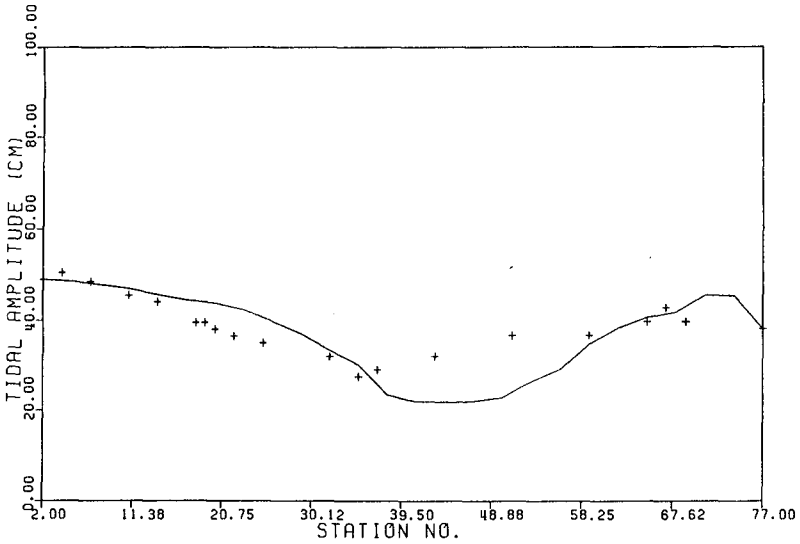


Figure 5. Mean M_2 tidal amplitude in the James River (— model results, +++ data). Amplitude at open boundary = 38 cm.

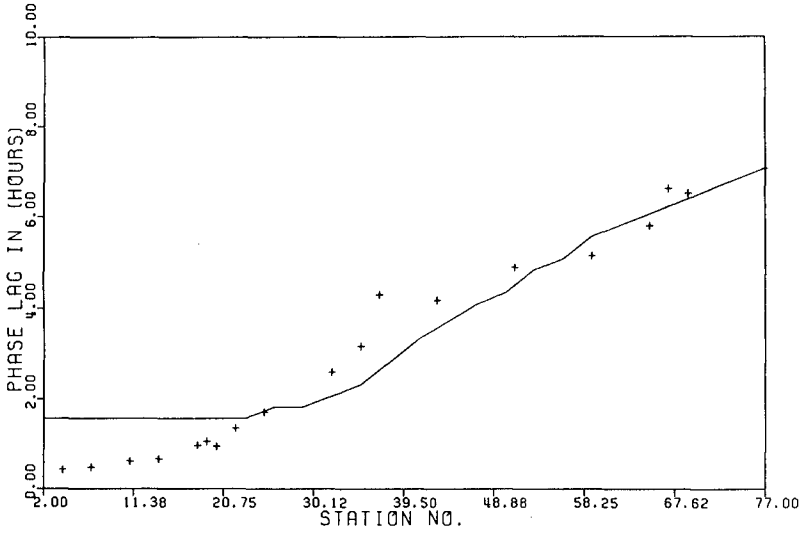


Figure 6. Mean M_2 tidal phase lag in the James River (— model results, +++ data).

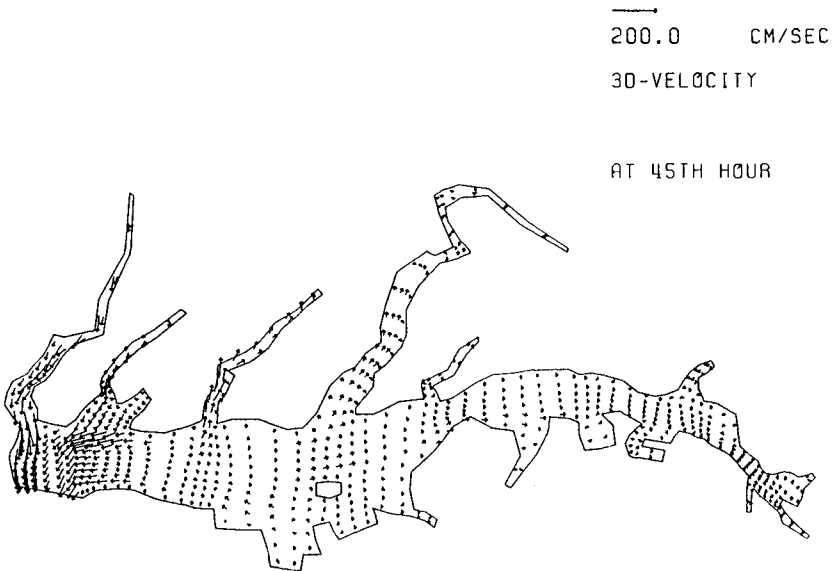


Figure 7. Near-surface current in the Chesapeake Bay driven by a M_2 tide of 60 cm amplitude.

Model application to Lake Okeechobee showed that, despite the shallowness of the lake (average depth of 3m), significant return flow is produced near the bottom due to a 5 ms^{-1} wind from the east (Figs. 8 and 9). The vertically-averaged velocity field clearly showed the existence of 2 topographically induced circulation gyres.

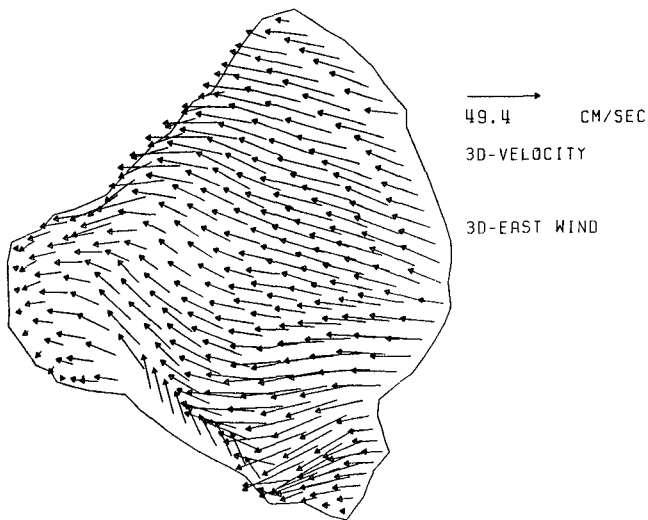


Figure 8. Near-surface wind-driven currents in Lake Okeechobee due to a wind of 5 m/sec from the east.

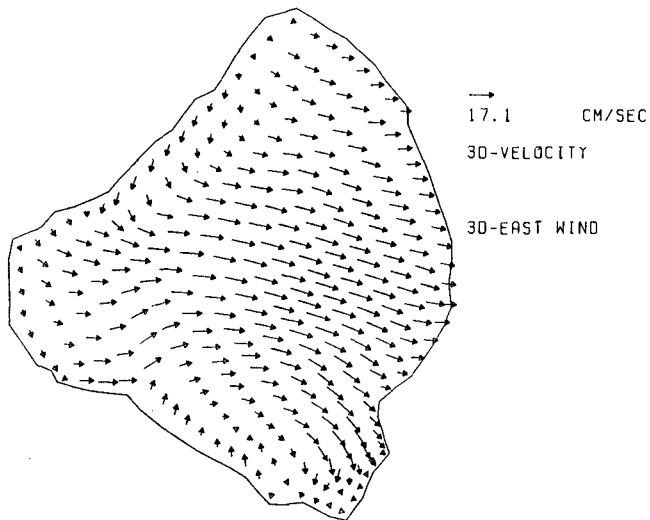


Figure 9. Near-bottom wind-driven currents in Lake Okeechobee due to a wind of 5 m/sec from the east.

ACKNOWLEDGEMENT

Supports from U.S. Army Engineer Waterways Experiment Station, Virginia Institute of Marine Science, and South Florida Water Management District are acknowledged.

REFERENCES

1. Bennett, J.R. and D.J. Schwab, 1981: "Calculation of the Rotational Normal Modes of Oceans and Lakes with General Orthogonal Coordinates", Journal of Comp. Phys., vol. 44, pp. 359-376.
2. Johnson, B.H., 1988: "An Approach for Modeling the Upper Chesapeake Bay", Proc. of the 1988 National Conference on Hydraulic Engineering, ASCE, pp. 588-93.
3. Sheng, Y.P., 1986a: "Finite-Difference Models for Hydrodynamics of Lakes and Shallow Seas", in Physics-Based Model of Lakes, Reservoirs, & Impoundments (W.G.Gray, ed.), ASCE, pp. 146-228.
4. Sheng, Y.P., 1986b: "A Three-Dimensional Mathematical Model of Coastal, Estuarine and Lake Currents Using Boundary-Fitted Grid", ARAP Technical Report No. 585, Aeronautical Research Associates of Princeton/California Research and Technology/Titan Systems, Princeton, N.J.
5. Sheng, Y.P., 1987: "On Modeling Three-Dimensional Estuarine and Marine Hydrodynamics", in Three-Dimensional Models of Marine and Estuarine Dynamics (J.C.J. Nihoul and B.M. Jamart, eds.), Elsevier Oceanography Series, Elsevier, pp. 35=54.
6. Sheng, Y.P., W. Lick, R.T. Gedney, and F.B. Molls, 1978: "Numerical Computation of Three-Dimensional Circulation in Lake Erie: A Comparison of a Free-Surface Model and a Rigid-Lid Model", J. Phys. Oceanog., Vol. 1, pp. 713-27.
7. Sheng, Y.P. and H.L. Butler, 1982: "Modeling Coastal Currents and Sediment Transport", Proc. of the 18th ICCE, ASCE, pp. 1127-48.
8. Sheng, Y.P. and S.S. Chiu, 1981: "Tropical Cyclone Generated Currents", Proc. of the 20th ICCE, ASCE, pp. 737-51.
9. Sheng, Y.P. and C. Villaret, 1988: "Modeling the Effect of Suspended Sediment Stratification on Bottom Exchange Processes", Submitted to the Journal of Geophysical Research.
10. Thompson, J.F. and B.H. Johnson, 1985: "Development of an Adaptive Boundary-Fitted Coordinate Code for Use in Coastal and Estuarine Areas", Misc. Paper HL-85-5, U.S. Army Engineer Waterways Experiment Station, Vicksburg, MS.
11. Warnstrath, J.J., 1977: "Nearshore Numerical Storm Surge and Tidal Simulation Model", T.R. H-77-17, U.S. Army Engineer Waterways Experiment Station, Vicksburg, MS.

CHAPTER 198

HYDRAULIC ASPECTS OF WETLAND DESIGN

James R. Walker¹, M. ASCE
Andrea Bertolotti², M. ASCE
Reinhard E. Flick³
C. Robert Feldmeth⁴

ABSTRACT

Tidal wetland preservation, restoration and creation have become requisites for coastal development projects in the United States. A basic approach to design of tidal wetlands is presented, stressing cooperation between regulatory agencies, biologists, engineers, and developers. Basic principles of wetland functions are explained and presented as criteria for engineering design. A description of wetlands is given to identify biological features relevant to design. Also, some key features of tides are summarized as they affect wetland design. A numerical model was used to demonstrate how tidal wetlands may be designed to conform with criteria developed by the agencies and biologists. This approach has been used on wetland designs in California, but the approach may be applicable to other areas of the world.

1.0 INTRODUCTION

Wetlands must be designed based on sound engineering principles to meet given biological requirements. Commercial and residential development along the coastal areas of the United States has increased pressure on many wildlife habitats. State and Federal wildlife agencies have been charged with preservation, enhancement and replacement of wetlands. Now, new developments in coastal areas must be done in conjunction with restoration or creation of wetlands.

The agencies must define the habitat type desired and biologists must define the conditions which will create the desired habitats. The objective is to create habitat that will support desired animal and plant life. After a site is

¹ Vice President, Moffatt & Nichol, Engineers, Long Beach, CA 90807

² Coast Engineer, Moffatt & Nichol, Engineers, Long Beach, CA 90807

³ Oceanographer, Cal. Dept. of Boating and Waterways, Scripps Institution of Oceanography, La Jolla, CA 92013

⁴ Professor of Biology, Joint Science Center, The Claremont Colleges, Claremont, CA 91711

selected, hydraulic studies are conducted in order to determine how best to achieve the desired biological setting. The wetland habitat depends in part on the tide elevations relative to the ground elevation. The ocean tide, which drives the water exchange in the wetland, has peculiar properties that influence the behavior of the water levels in the wetland. Tide control structures regulate the flow of water in and out of a wetland. Hydraulic models can simulate the flow regime in the wetland and through tide control structures. The effect of tide control structures to change wetland tide elevations relative to ground elevations is also an important design consideration.

2.0 BIOLOGICAL CHARACTERISTICS OF WETLANDS

Southern California coastal wetlands occur around bays and in estuaries and are generally restricted to narrow river valleys that were cut during periods of lower sea level in the Pleistocene era. Many of these wetlands are exposed to daily tidal action. The rise and ebb of water in tidal marshes produces a zonation of vegetation types determined by both physical and biotic factors. Other wetlands persist where the tidal range is muted by culverts or restricted by tide gates. Wetlands exist because the soils remain saturated throughout most of the year. These wetland areas are characterized by an assemblage of plants and animals, an ecological community, adapted to the particular conditions of this transition area between salt water and land.

At a particular ground elevation in a wetland, there is an associated duration of inundation by tides and salinity in the soil. Wetland plants grow in areas where they are best suited to resist the inundation by tides and soil salinity. Mahall and Park (1976) examined the transition between cordgrass (low wetland) and pickleweed (mid wetland) in wetlands in northern San Francisco Bay and found tidal inundation to be the most important factor determining their distribution.

A typical Southern California coastal wetland is composed of a low wetland community characterized by dense stands of cordgrass (*Spartina foliosa*). Cordgrass normally occurs between mean lower high water (MLHW) and mean higher high water (MHHW) (Zedler, 1982), as shown schematically in Figure 1. At lower elevations, mud flats may support eelgrass (*Zostera marina*) and often mats of various algal species such as sea lettuce (*Ulva*).

At elevations above the low wetland, a mid and high wetland vegetative association is present. Common pickleweed (*Salicornia virginica*) is by far the most important plant species in terms of biomass. It normally ranges from MHHW to about 0.6 meters (2 feet) above extreme high water (EHW). Common pickleweed is abundant down to the low wetland and can often occur with cordgrass in soils that are wet by each high tide.

Also present in the mid wetland association are a number of other plants such as saltwort (*Batis maritima*), annual pickleweed (*Salicornia bigeovii*) and *Jaumea carnosa*. High wetland associations include common pickleweed and sea blite (*Suaeda californica*). These assemblages extend up to an elevation of about 0.6 meters (2 feet) above MHHW.

The transition from mid wetland to high wetland is less distinct. Soil moisture decreases in the high wetland and soil salinity increases. Shoregrass, saltgrass, and glasswort appear to be more tolerant of the drier soils of this higher wetland zone. A summary of wetland vegetation with

respect to the elevation of the tide ranges is given in Table 1.

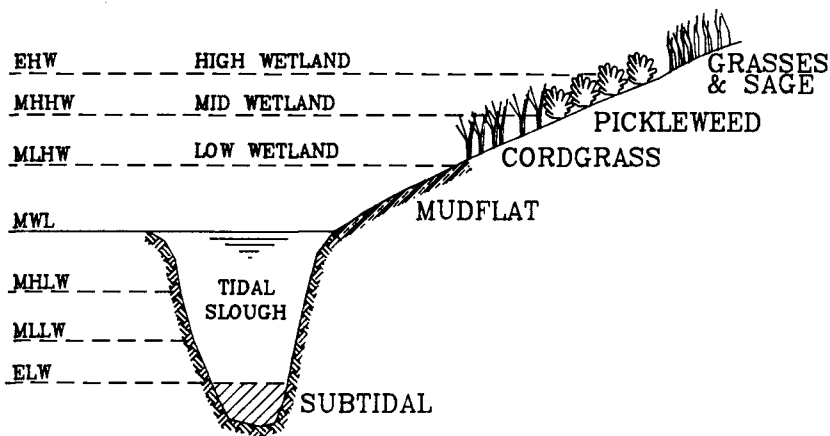


Figure 1 Typical Southern California Wetland

TABLE 1

Division of Wetland Vegetation by Elevations
of Tide Ranges

TIDE RANGE	HABITAT NAME	TYPE OF HABITAT
Above EHW	High Wetland	Grasses and Coastal Sage Scrubs
MHHW to EHW	Mid Wetland	Pickleweed, Salt Wort, Annual Pickleweed and Sea Blite
MLHW to MHHW	Low Wetland	Cordgrass
MSL to MLHW	Mudflat	Eelgrass, Algae and Sea Lettuce
Below MSL	Subtidal	Marine habitat

In the mid and high wetland areas, marsh plants provide cover and foraging material for many invertebrates. Birds, such as the Clapper Rail, also utilize this cover in order to forage on burrowing crustaceans. Small snails occur on the substrate surface. Crabs and shrimp burrow in the substrate within the vegetational cover.

At high tide, mudflats are a foraging area for fishes and large wading birds, such as herons and egrets. At low tide, the exposed mudflat becomes a

foraging area for shore birds. Fishes forage in the mudflat zone and up into the low wetland. These fishes form an important source of food for fish-eating birds, such as herons, egrets, and terns.

Horn (1976) showed that the fish species diversity for a bay or an estuary is proportional to its size. The relationship of bay size to species composition is shown in Figure 2. Fish diversity is an index of habitat quality; the more fish species present, the better the system is as an environment for bay-wetlands plants and animals. Other factors such as water depth, habitat diversity, pollution load are also important. Bay systems of various sizes, where the tidal regime is muted by culverts or other restrictions, can be evaluated in terms of their fish assemblages (Feldmeth, 1980 & 1986).

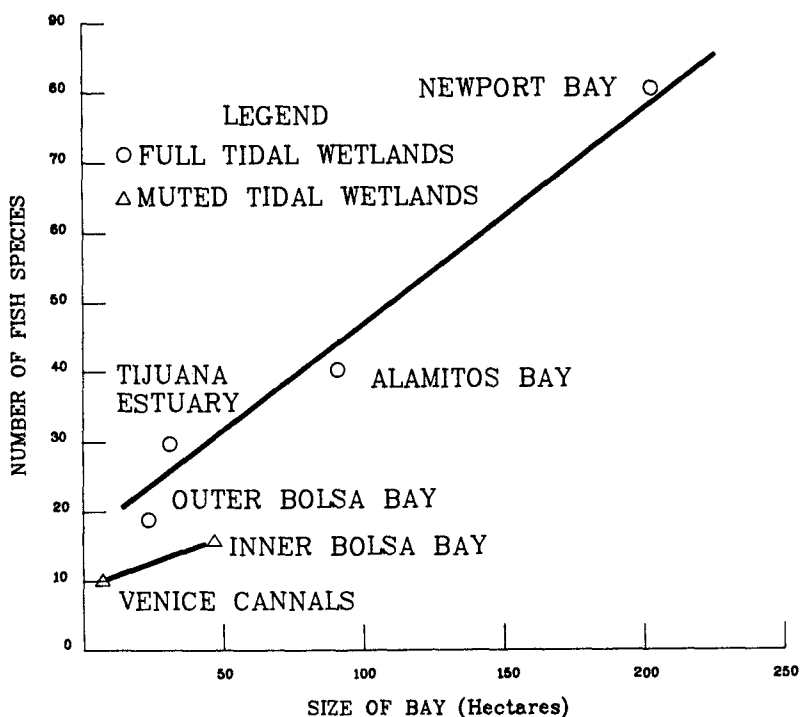


Figure 2 Number of Fish Species versus Area of Bay

3.0 TIDE CHARACTERISTICS

General tide characteristics in Southern California are presented to outline features relevant to the hydraulic design of wetlands. Tides are a well studied phenomenon and are only summarized here to illustrate their influence on design of wetlands.

Tides along the California coast are mixed semidiurnal and show a marked diurnal inequality and extreme tide ranges approach 3 meters (10 feet). A

common characteristic of California tides is that the lower-low water almost always follows the higher-high water after a time interval of about 7 hours. The semidiurnal peak breaks the rising tide such that there are about 17 hours between lower-low water and higher-high water. In Figure 3, the average rate of water elevation change is plotted versus the elevation change between high and low tide for the 1983 tide record at San Diego, California. As shown in the figure, the greatest water level changes and highest tide ranges occur during ebb period. The peak flow velocities in a bay entrance will be greater during ebb flows than flood flows. This may have an effect on sediment transport and on altering the water elevations in a wetland because of the non-linear nature of tidal hydraulics.

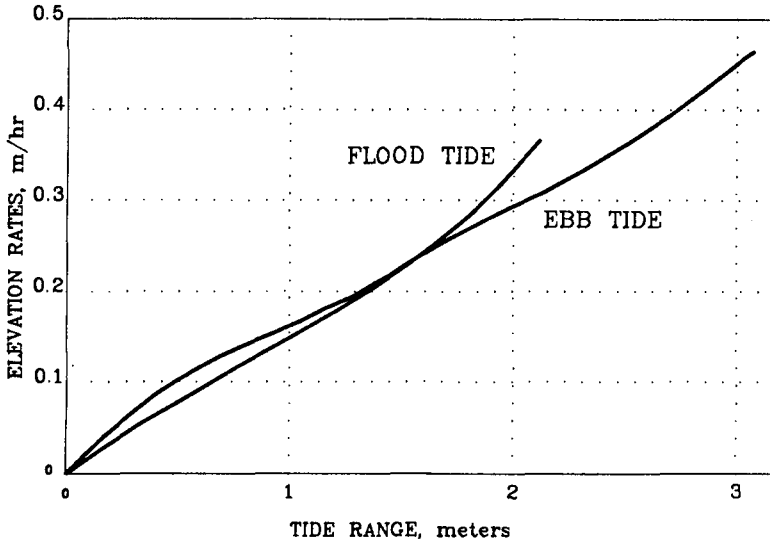


Figure 3 Water Elevation Change Rates versus Tide Range for Southern California

Variations in the tide also have a yearly cycle. Higher-high tides tend to occur in the morning during winter and in the evening during summer. Changes in the times of day of high and low tide during the year lead to significant changes in wetlands exposed to sunlight. Figure 4 shows monthly averages of the percentage of daylight hours (taken as the time from sunrise to sunset) the tide remains below MHHW, MSL and MLLW. Maximum intertidal exposure to sunlight occurs from February through April, with tide below MSL about 65% of daylight hours. There is a marked decrease in exposure to a minimum of about 25% during September.

Zetler and Flick (1985a, b) describe the cyclical variations of predicted maximum monthly high tides for the period 1983-2000. Besides the summer-winter cycle, they identify a 4.4 year variation and an 18.6 year cycle that characterize the west coast tides. The 4.4 year period arises from a modulation of the lunar perigee cycle while the 18.6 year variation is associated with the lunar node cycle. These periods increase the tide range about 0.3 and 0.15 meters (1 and 0.5 foot) respectively. During peak tides

within the 4.4 year cycle, the winter and summer maximum ranges can exceed the spring-autumn ranges by about one meter (3 to 4 feet). This effect also tends to obscure the variation in seasonal mean sea level which tends to be low in April and higher by about 0.15 meter (0.5 foot) in September (Flick and Cayan, 1984)

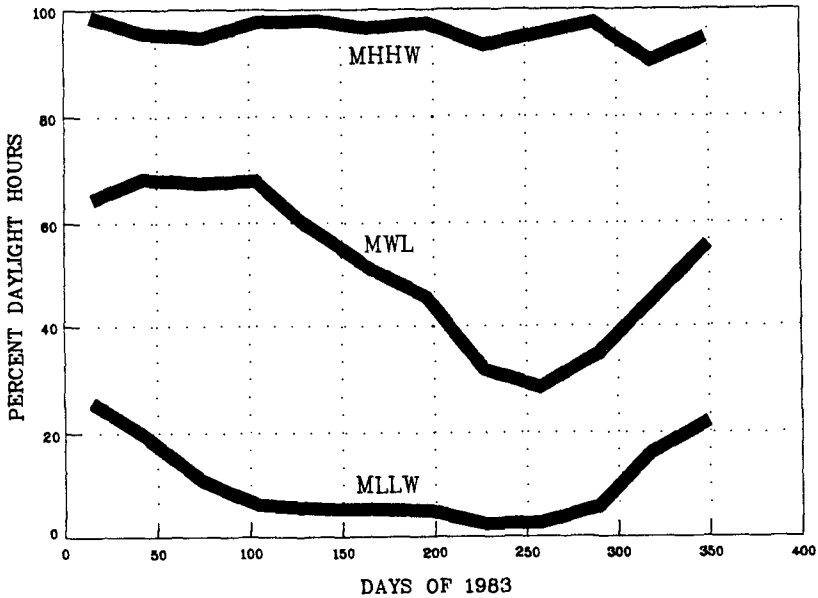


Figure 4 Percent of Daylight Hours that the Tide Remains below MHHW, MSL and MLLW.

4.0 DESIGN ANALYSIS AND METHODS

4.1 Principles

Perhaps the most important design consideration is the relationship of the tide range with respect to the ground elevation inside the wetland. Changing either the tide regime or the ground elevations can significantly effect the nature of the wetland. Scour and siltation of wetland channels is also an important design consideration that includes an evaluation of flow regimes and of soil types. In wetlands that have reduced tidal flushing or are near a source of pollutants, water circulation and quality need to be considered. Finally, in newly created wetlands, colonization or plantation of flora and fauna need to be evaluated in view of the particular restoration goals.

In California, wetland restorations are founded on goals specified by wildlife agencies such as the Department of Fish and Game, National Marine Fisheries and the Fish and Wildlife Service. Other agencies that can participate are the California Coastal Commission, the Audobon Society and

the Army Corps of Engineers. While no specific agenda exists for developing design goals and criteria, some guidelines can be followed such as those proposed by Smith (1983) and Williams and Harvey (1983).

As described previously, the relationship between tide range and ground elevations provides a zonation of vegetation that characterizes a wetland. Wetlands can have tide regimes and sea levels that are different from those in the open ocean. This is an essential consideration in wetland design. Friction and flow restrictions induce energy losses in tidal flow that give rise to reduced amplitudes and phase lags in the tides of inland water bodies. Some harbors or bays experience resonant conditions in which the amplitude of the tides is larger than in the ocean. In muted tidal wetlands, however, the energy dissipations at the tide control structure tend to suppress resonant oscillations and, in general, larger reductions in amplitude are accompanied by greater phase lags. Under some conditions, the mean water level in the wetland will be different than in the ocean.

The ground elevations in a wetland should be designed considering stable soil slopes and the possibility for scour and siltation of the channels. Myrick and Leopold (1963) applied the concept of equilibrium profiles developed for inland rivers to describe the hydraulic geometry of tidal channels. These equations relate the water surface width, mean depth and mean velocity to the discharge. Pestrong (1965) used the same equations to characterize the drainage patterns of tidal marshes in South San Francisco Bay, California. In the design of muted wetlands, channels that are initially sized close to the equilibrium profile can be expected to have less changes over time than channels that are of other sizes. Adding new wetland areas to existing wetland can induce scour in existing channels.

Wetlands with a small tidal prism in relation to the total water volume, or wetlands that are near a source of pollutants, can promote unfavorable water quality and circulation for the animal and plant communities. The accumulation of nutrients such as nitrogen and phosphorous used in fertilizers can promote undesirable algal blooms.

In newly created wetlands, the flora can be established by either natural colonization or by planting. The desired fauna, instead, can only be introduced by natural colonization. The type of hydraulic connection between the new wetland and the ocean should consider the passage of plant seeds and marine animals, such as fish and crustaceans. This is important were natural plant colonization is desired and were the wetlands are to function as spawning areas for fish.

4.2 Hydraulic Modeling

A numerical model based on work by Fisher (1977) was developed to analyze tide elevations and flow velocities in wetlands subject to an ocean tide. The hydraulic system is divided into a series of basins and channels. The water level in the basins and the flow velocity in the channels are related through the conservation of mass and conservation of momentum equations. These equations are solved for one-dimensional flow by the method of finite differences. The model performs a time domain simulation and calculates tide elevations and flow velocities at specified time step intervals.

The model, called Hydrodynamic Circulation Model (HCM), employs an implicit routine, where the water elevations and velocities are related to each

other and to their present values through a system of simultaneous non-linear equations. The equations are solved iteratively using a Newton-Raphson algorithm. One-dimensional differential equations are used to express the conservation of mass and momentum in an open channel. The equation are as follows:

$$\begin{aligned} \text{Mass:} & \quad b(dy/dt) + A(du/dx) = 0 \\ \text{Momentum:} & \quad du/dt + g(dy/dx) + gku|u| = 0 \end{aligned}$$

where:

- t = time
- x = horizontal distance
- y = water surface elevation
- u = velocity in x direction
- g = acceleration due to gravity
- b = surface width
- A = cross-sectional area
- k = friction coefficient

The convective acceleration term, $u(du/dx)$ which is part of the conservation of momentum equation, was omitted in the model. Including this term significantly increases the computation load and does not have a significant effect on the results.

The friction coefficient is derived from Manning's open channel equation and has been modified to include an entrance and exit energy loss term as follows:

$$\text{Friction Coefficient:} \quad k = K_x + K_e + (n/1.486R^{2/3})^2$$

where:

- $K_x = 1.0$ (common exit loss factor)
- K_e = entrance loss factor
- n = friction coefficient
- R = hydraulic radius

The hydraulic features of an area are included in the model through a number of user-selected parameters. These include the length, width and depth of channels, the friction associated with the type of channel bed, the slope of the channel banks, the storage curves of basins, the tide properties of the ocean or driving body of water, and the type and geometry of the tide control structure.

The friction of the channel beds and concentrated head losses of restrictions to flow can be derived from published values. However, calibration of these parameters with field measurements from a hydraulic area similar to that being modeled provides more reliable values. The HCM model has been used for design of Anaheim Bay and Bolsa Chica wetlands in California (Moffatt & Nichol, Engineers, 1987a and 1987b)

4.3 Tide Control Structures

Tide control structures can be used in wetland restoration projects to control the ocean tide and produce specific tide properties within the wetland. Tide control structures can vary from a simple pipe culvert through a dike to more complex systems that have flap gates and overflow weirs that require manual or automatic operation. Usually, the complexity of the tide control system is directly related to the amount and type of change induced to the

ocean tides.

A basic muted wetland comprises a dike, which separates the wetland from the source of ocean water and protects surrounding lowland areas from flooding, and one or more culverts, which allow for tidal flow between the ocean and the wetland. In this system, the flow area of the culverts and the invert elevations can be selected to produce the desired response. Check valves, typically in the form of flap gates, can be used in tide control structures to change the mean water elevation in the wetland. Flap gates can be installed on one or several culverts comprising the tide control structure depending on the amount of sea level control desired.

4.4 Maintenance of Tide Control Structures

Tide control structures are subject to gradual deterioration by being exposed to environmental conditions. The maintenance of tide control structures is important in order to keep the water elevations in the wetland within the desired range. Mussels, barnacles and other marine organisms will grow at the entrance as well as inside the culvert. This increases friction to flow and reduces the flow area. For culverts with flap gates, marine organisms can grow on the flap and culvert entrance, allowing water to leak when the flap gate should be closed. Flap gates have tendencies to restrict low flow out and to remain open with leaks for inward flow. Pinch check valves may be considered as an alternative with more positive control.

4.5 Determination of Tidal Elevations

Tidal elevations are measured by the National Oceanic and Atmospheric Administration (NOAA). Data are averaged over an 18.6-year tidal epoch to establish reference elevations such as MHHW, MLLW and MSL at the gauge station. Tide elevations in wetlands are a function of the connection with the ocean and can be different than tide elevations in the ocean.

A technique was developed to predict reference tide elevations in wetlands with tide ranges different than those in the ocean. The tide data for the Los Angeles station are used as an example. The distribution of tide elevations for a 18.6-year epoch was determined from data published by NOAA. The data was plotted as percent time of exposure versus tide elevation as shown in Figure 5; this format can be useful to wetland biologists. For the purpose of numerical modeling, a hypothetical 14-day mixed tide was developed so that it would reproduce the distribution of a 18.6-year tidal epoch. The mix between high and low tides as well as diurnal and semi-diurnal features was varied to achieve the desired distribution. This 14-day tide was used in the model analysis to determine the tidal distribution inside a wetland. In this manner, non-linearities with storage curves and hydraulic losses would be included in the prediction.

From the distribution of a 18.6-year period of tide elevations given by NOAA, it can be determined that ground at an elevation of MHHW is exposed 95 percent of the time, at MSL it is exposed 50 percent and at MLLW 5 percent. In a tidal wetland, these percentages give rise to the habitat zonations previously described.

The distribution of tide elevations inside a wetland can be defined using numerical models such as the HCM. The MHHW elevation inside a wetland is then identified as the elevation at which the ground is exposed

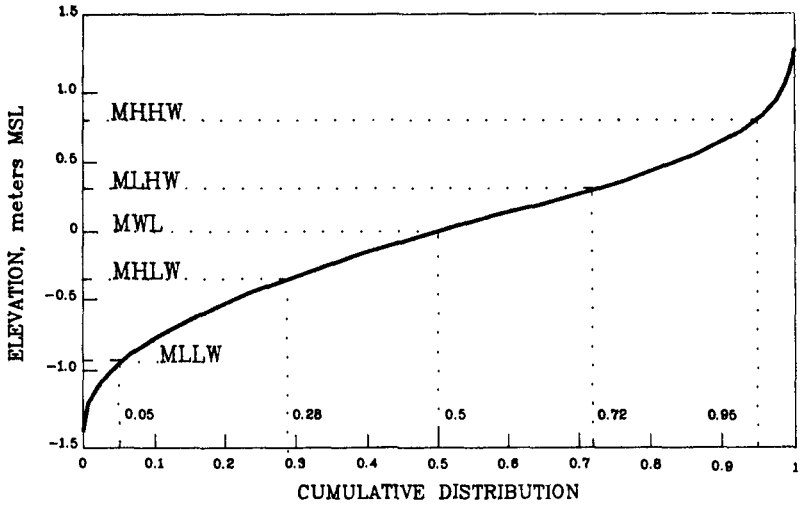


Figure 5 Percent Occurrence of Water Elevation At or Below a Given Level

95 percent of the time. The definitions of MWL and MLLW follow a similar form, where ground at MWL is exposed 50 percent of the time and at MLLW is exposed 5 percent of the time. In this method, shown in Figure 6, the tidal elevations in a wetland are related to the type of hydraulic connection between the wetland and the ocean.

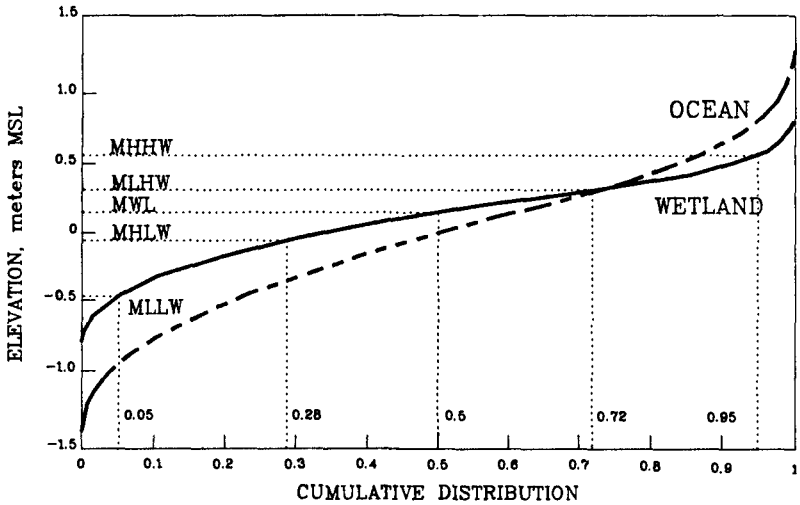


Figure 6 Method for Determining Tide Reference Elevations in a Wetland

4.6 Effects of Tide Control Structures

The numerical model HCM was applied to demonstrate the effects of changing control structure on wetland tides. The parameters of control structures investigated were culvert area, invert elevation, culvert roughness, entrance losses and use of flap gates.

A hypothetical wetland, connected to the ocean by a channel and tide control structure, was used in the simulations. The ground elevations and storage curve of the wetland were similar to those of an existing muted tidal wetland located at Bolsa Chica, 20 km south of Los Angeles, California.

4.6.1 Culvert Size

The flow area of a culvert connecting the ocean to the wetland was varied to evaluate the effects on wetland tides. The culvert height was kept constant, with an invert elevation low enough so that the culvert would always flow with a full section even at low tide. The width of the culvert was then changed to increase the flow area. The culvert used was 2 meters high, 10 meters long, an invert at -5.5 meters, with an entrance loss factor of 0.5 and a Manning's "n" of 0.05 to represent marine growth inside the culvert. The results, shown in Figure 7, indicate a strong effect of flow area on tide range in the wetlands. It can be noted that the mean water level inside the wetland is similar to that in the ocean and is not affected by the flow area of a culvert that is always submerged.

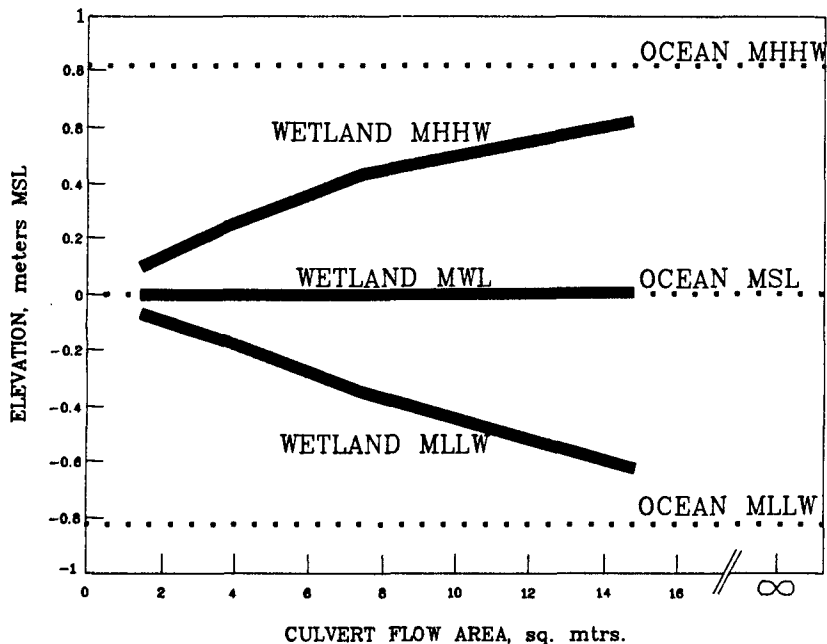


Figure 7 Effect of Culvert Flow Area on Wetland Tide Elevations

4.6.2 Invert Elevation of Culverts

The invert elevation of a culvert is the distance from the bottom of the flow area to the elevation datum. The invert elevation determines the minimum elevation that a wetland can drain and also whether a given culvert flows with a free surface. The effect of varying the invert elevation of wetland tide is shown in Figure 8. When the invert of the culvert is fairly deep, the culvert has a full flow section throughout the tide range. However, as the invert elevation is raised, the culvert will flow partially full with a free surface at low tide. The creation of a free surface affects first the elevation of the MLLW in the wetland by raising it higher than with a full section. The elevations of MWL and MHHW do not respond to changes in invert elevation as soon as MLLW. Further raising the invert elevation affects the MWL elevation in the wetland by raising it above MSL in the ocean. At higher invert elevations, the MHHW elevation in the wetland is reduced.

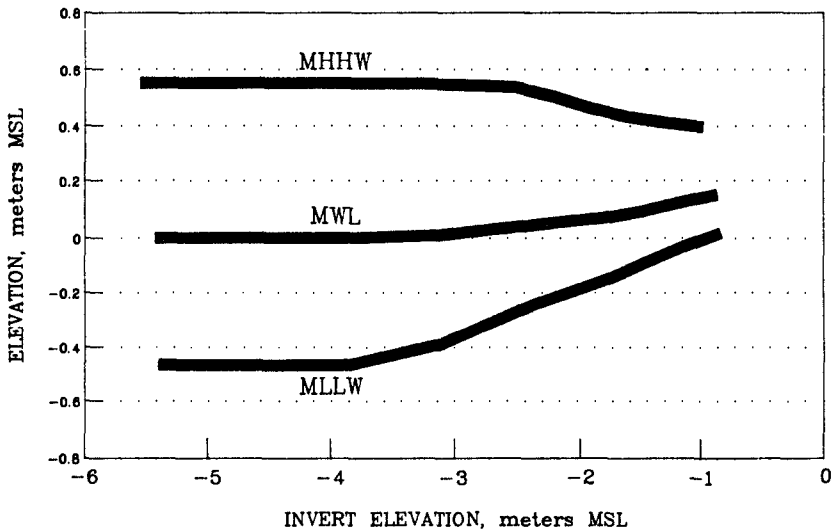


Figure 8 Effect of Culvert Invert Elevation on Wetland Tide Elevations

4.6.3 Culvert Roughness

The friction factor for a culvert depends on the type of material used in construction as well as on marine growth inside of the culvert. Values of friction factors for new culverts can be found in many references (such as Chow, 1959). However, increase in friction due to organic growth inside the culvert is more difficult to determine. An analysis of the effect of the friction factor on the wetland tide is shown in Figure 9. For a new concrete culvert, for example, Manning's "n" can vary from 0.011 to 0.013 (Chow, 1959). Experience with analysis of culverts colonized by marine growth indicated a friction factor of 0.04 to 0.06 (Moffatt & Nichol, Engineers, 1987b). The growth also reduces the culvert flow area which further restricts the flow.

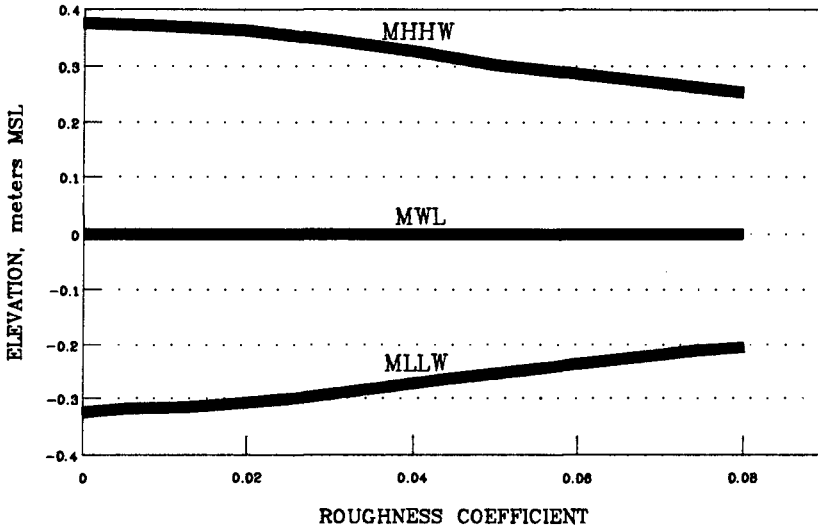


Figure 9 Effect of Culvert Roughness on Wetland Tide Elevations

5.0 FINDINGS

- o In wetland creation or restoration, the goals and criteria must be established by the agencies in charge. Then biological criteria and sound engineering principles can be used in the creation or restoration of wetlands.
- o Wetland creation or restoration goals should be defined by habitat type rather than by ocean tide ranges.
- o Wetland habitats can be defined by the relative tide and ground elevations as well as soil conditions.
- o Tide elevations inside a wetland can be defined from a water elevation distribution in the wetland. Ground at MHHW will be exposed 95 percent of the time, at MSL it will be exposed 50 percent of the time and at MLLW 5 percent of the time.
- o Hydraulic numerical models are an essential tool for the analysis of wetland projects. The models provide an accurate and cost-effective method for evaluation of tide ranges in wetlands with varying ground elevations and type of hydraulic connections and controls.
- o Tide characteristics should be evaluated to assess the impact of tide control structures on wetlands. In particular, during field survey and tide measurements, the various cycles of the tides should be considered to include seasonal and longer-term influences.

- o The size and invert elevation of culverts as well as the topography and channel dimensions are very important parameters in the design of muted tidal wetlands.
- o The long term effect of a wetland design should be investigated. Factors that will need to be considered include sea level rise, land subsidence or upheaval, sedimentation, and biofouling of tide control structures.

ACKNOWLEDGEMENTS

The design approach and model development presented in this paper came from designs of wetlands and field studies of existing wetlands. It is a summary of a larger wetland design study. The designs include the Anaheim Bay Mitigation Project for the Pier J expansion at the Port of Long Beach and the Bolsa Chica wetland development project for Signal Landmark. The authors extend their gratitude to Dr. Andrew Gram of Moffatt & Nichol, Engineers for his participation and development of the numerical model.

REFERENCES

- Feldmeth, C.R. "Survey of inner and outer Bolsa Bays: recolonization and recruitment study", Unpublished report submitted to Signal Bolsa Corp., 1980, 30pp.
- Feldmeth, C.R., "Biological resources of the Venice Canals", Report to Phillips Brandt Reddick for the City of Los Angeles Planning Department. 1986, 18pp.
- Fisher, H. B., "A Numerical Model of the Suisun Marsh, California", Proceedings from the 17th Congr. Int. Assoc. Hydraul. Res. held at Baden-Baden, Germany 1977.
- Flick, R.E. and D.R. Cayan, "Extreme Sea Levels on the California Coast", Proc. 19th Coastal Eng. Conf., Amer. Soc. Civil Eng., 1984, p. 886-898.
- Horn, M.H., "Numbers of species and faunal assemblage of marine fishes in California Bays and Estuaries", Bulletin of S. Calif. Acad. Sci., 1976, 75:159-170.
- Mahall, B.E. and R.B. Park, "The ecotone between Spartina foliosa Trin. and Salicornia virginica L. in salt marshes of northern San Francisco Bay. I. Biomass and production. II. Soil water and salinity. II. Soil aeration and tidal immersion", J. Ecol., 1986, 64:793-820.
- Moffatt & Nichol, Engineers, "Anaheim Bay Mitigation Project" prepared for the Port of Long Beach, March, 1987.
- Moffatt & Nichol, Engineers, "Bolsa Chica Project: Hydraulic Design Approach for Muted-Tide Wetlands", prepared for Signal Landmark, Inc., December, 1987.

Smith, David D., "A Practical Evaluative Procedure for the Design of Coastal Wetland Restoration Projects", Presented at the Coastal Zone 83 conference in San Diego, California, June, 1983, Vol II, pp. 1477-1487.

Williams, Philip B. and H. Thomas Harvey, "California Coastal Salt Marsh Restoration Design", presented at the Coastal Zone 83 conference in San Diego, California, June, 1983, Vol II, pp. 1444-1456.

Zedler, J.B., "The ecology of Southern California coastal salt marshes: A community profile", U.S. Fish and Wildlife Service, Biological Services Program. Washington D.C. FWS/OBS-81/54, 1982, 110pp.

Zetler, B.D. and R.E. Flick, "Predicted Extreme High Tides for California, 1983-2000", Jour. Waterway Port, Coastal and Ocean Eng., Amer. Soc. Civil Eng., 1985a, v. 111, n. 4, p. 758-765.

Zetler, B.D. and R.E. Flick, "Predicted Extreme High Tides for Mixed Tidal Regimes", Jour. Phys. Oceanog., 1985b, v. 15, n. 3, p. 357-359.

CHAPTER 199

A COMPARISON BETWEEN GERMAN AND NORTH AMERICAN TIDAL INLETS

REINHARD DIECKMANN *
MANUELA OSTERTHUN **
HANS WERNER PARTENSKY ***

ABSTRACT

Initial results are presented relating to an investigation of geomorphological parameters from 26 of a total of 28 tidal inlets and 11 coastal structures similar to inlets along the German Bight. The following parameters were investigated:

- tidal prism - inlet area relationship,
- cross-sectional form and depth,
- location of the channel within the cross-section,
- ebb tidal deltas and
- the structures of the back barrier regions.

The most important parameter governing the shaping process of these coastal structures is considered to be the tidal volume. The results of the investigations were compared with data from American publications. Despite the differences between the regions studied, in overall terms, surprisingly good agreement was obtained between the parameters investigated. Notable differences exist only in relation to the morphological structure of the back barrier regions (tidal flats, salt marshes, open water lagoons). In respect of the latter differences, a short account is given of the biological and climatological influencing factors.

1. INTRODUCTION

Barrier islands and inlets are one of the most commonly occurring coastal formations worldwide. In particular, the American barrier island - inlet systems are widely dealt

* Dr.-Ing., Wasser- und Schifffahrtsamt Bremerhaven, Am Alten Vorhafen 1, D-2850 Bremerhaven, West Germany

** Dipl.-Ing., Research Engineer,

*** Prof. Dr.-Ing. Dr.phys., Director,

both at

Franzius-Institut für Wasserbau und Küsteningenieurwesen der Universität Hannover, Nienburger Str. 4, D-3000 Hannover 1, West Germany

with in literature. In contrast, the corresponding inlets along the coast of the German Bight have not as yet been geomorphologically investigated in their entirety. An exception to this are three inlets on the southern North Sea coast (WALTHER, 1972; LUCK, 1976; FITZGERALD et.al., 1984).

Initial results will be presented concerning a comprehensive investigation of 26 from a total of 28 tidal inlets and 11 inlet-type structures along the coast of the German Bight between Den Helder in the Netherlands and Skallingen in Denmark.

Basic differences between the coast of the German Bight and the southeast American Atlantic coast are highlighted by NUMMEDAL and FISCHER (1978). In this context, it should be noted that the German Bight lies on the same latitude as the southern part of Hudson Bay (James Bay) in Canada.

2. TIDAL INLET SYSTEMS ALONG THE GERMAN BIGHT

2.1. COASTAL OVERVIEW

Over a length of 450 km, the inner part of the German Bight is bordered by a large tidal flat area of 7,500 km² (see Fig. 1) with a barrier island chain in front of it.

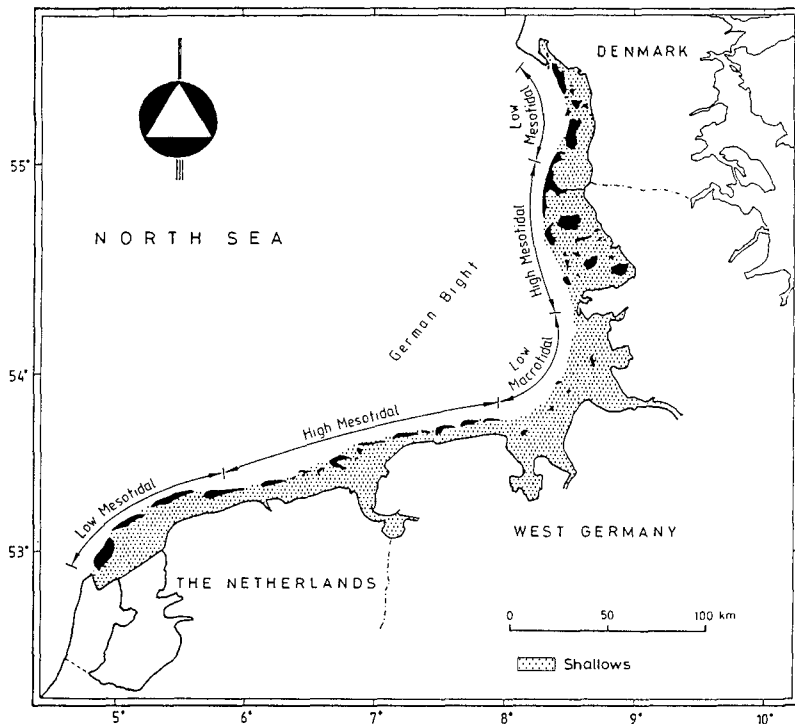


Fig. 1: Map of the German Bight

If one considers the investigations by HAYES (1979) concerning the relationships between coastal morphology, tidal range and wave climate, it becomes evident that the coast of the German Bight is a typical barrier island - inlet region.

According to the tidal and wave conditions, the majority of the German Bight region belongs to the "tidally dominated mixed energy coasts". The barrier islands on the south coast frequently have a well-defined drumstick shape with distinct ebb tidal deltas owing to the littoral drift. Flood tidal deltas, on the other hand, are not present as usual under meso- and macrotidal conditions. Along the south coast, a downdrift offset configuration is apparent, whilst in the case of the east coast, a negligible or small updrift offset is detectable.

The inlets on the south coast are strongly influenced by natural forces. Owing to the action of westerly winds, waves and currents parallel to the coastline, the islands and hence the inlets undergo continuous displacement from the west to the east. Since about 1890, the westerly heads of the islands have been fortified to avoid further drift. The east ends of the islands, however, remain exposed to natural forces and are thus in a continuous state of change. The currents in the inlets are so large as to prevent sedimentation and there are no jetties available which might reduce or alter the direction of the littoral drift.

On the east coast, the tidal inlets are less clearly defined and little is known concerning the barrier island - inlet systems on the east coast. Preliminary depth chart evaluations indicate however that these inlets are relatively stable. Consequently, the need to fortify or protect the heads of the islands has never arisen.

2.2. DATA COLLECTION

A total of 37 inlets and inlet-type coastal structures along the German Bight were investigated. For each inlets investigated, a data set containing the following information was established:

- tidal heights at MHW, MLW and the half-tide water level (HTWL),
- cross-sectional area of the inlet at MHW, MLW and HTWL,
- width of the inlet at MHW, MLW and HTWL,
- drainage area size at MHW, MLW and HTWL,
- maximum and mean depths of the inlet,
- tidal volume.

Since each inlet of the German Bight has a precisely defined drainage area, the mean tidal volumes (tidal prisms) could be obtained with high accuracy from the drainage basin hypsometric curves. The evaluation technique used for this purpose is described in detail in DIECKMANN & PARTENSCKY, 1985.

3. US AMERICAN TIDAL INLETS

In relation to US American tidal inlets, a vast amount of material has been published. A comprehensive review is given in the GITI Reports published by the US Army, Corps of Engineers and Waterways Experiment Station as well as in "Stability of Tidal Inlets" by PER BRUUN (1978). Further details will be given there.

4. COMPARISON OF RESULTS

4.1. TIDAL PRISM - INLET CROSS-SECTIONAL AREA RELATIONSHIP

Relationships between the minimum throat cross-sectional area below mean tide level and the tidal prism of an inlet were first reported by O'BRIEN (e.g. 1969). More recent evaluations were presented by JARRETT (1976). On the basis of such relationships, estimates may be made of the long-term changes in the inlet cross-section up to the point at which a mean state of equilibrium is attained.

In Fig. 2, data relating to the inlets of the German Bight are presented in the form of diagrams after JARRETT. All data points lie within the 95% confidence limits and very close to the regression curve given by JARRETT.

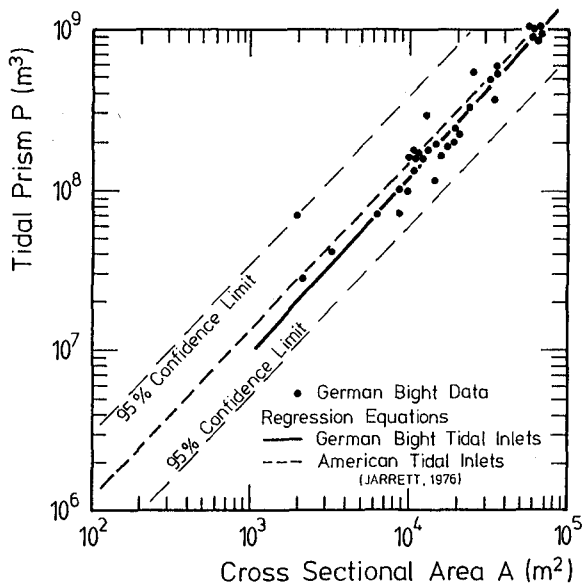


Fig. 2: Tidal prism vs. cross-sectional area for American inlets and inlets along the German Bight.

The corresponding regression equations in metric units are as follows:

$$\text{German Bight: } A_C = 3.720 \cdot 10^{-4} \cdot p^{0.915} \quad (1)$$

$$\text{Atlantic coast: } A_C = 3.039 \cdot 10^{-5} \cdot p^{1.050} \quad (2)$$

$$\text{Gulf coast: } A_C = 9.311 \cdot 10^{-4} \cdot p^{0.840} \quad (3)$$

$$\text{Pacific coast: } A_C = 2.833 \cdot 10^{-4} \cdot p^{0.910} \quad (4)$$

where:

A_C = minimum cross-sectional area below MSL = HTWL (m^2)

p = tidal prism (m^3)

As a result, the best agreement is achieved between the inlets of the German Bight and the Pacific coast as may be seen from the equations (1) to (4). The good agreement between the above relationships indicates that the minimum cross-sectional area of an inlet is primarily determined by the inflowing and outflowing tidal volume. For the German Bight no particular influence of the different coastal and tidal range regions could be detected. This result is surprising in so far as significant differences exist between the US American inlets and tidal flats and the corresponding regions in the German Bight.

4.2. GEOMETRIC PARAMETERS

4.2.1 SHAPE AND DEPTH OF THE INLET CROSS-SECTIONS

An inlet is characterized in the terms of its geometry by the shape of its cross-section and the mean or maximum depth. The cross-sectional shapes of the inlets in the German Bight may be subdivided into 3 groups (see Fig. 3):

- the wide synclinal profile will tend to form in the case of small tidal volumes in combination with relatively wide inlets,
- the triangular profile is characteristic of narrow inlets exposed to large tidal volumes and
- the composite profile may be taken to represent the normal case.

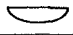

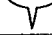
		shape of tidal inlet		
				
occurrence	-	5	12	20
width/depth ratio	-	>300	50-150	90-250
mean depth	m	3-8	>9	>7
maximum depth	m	5-16	12-48	10-37

Fig. 3: Different types of tidal inlet shape.

An account of American inlet cross-sections by VINCENT & CORSON (1980) indicates that the triangular shaped cross-

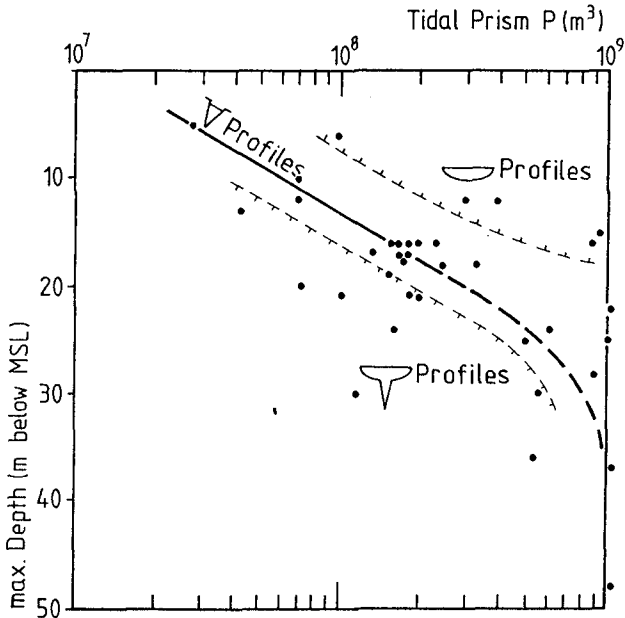


Fig. 4: Relationship between the tidal volume and the maximum depth of inlets in the German Bight.

section is clearly predominant whereas the synclinal shape seldom occurs.

The maximum water depth is also dependent upon the tidal volume. The corresponding relationship for the inlets of the German Bight is illustrated in Fig. 4.

Furthermore, a relationship also exists between the mean and maximum depth in an inlet cross-section. The data for the German Bight inlets have been added to another diagram of VINCENT & CORSON, as shown in Fig. 5. As may be seen in the Figure, the scatter in the latter data is much larger than that of the American data. On the whole, the German Bight inlets are characterized by larger maximum depths.

An interesting aspect concerns the ratio of the tidal volume to the inlet cross-sectional area which lies between $1.0 \cdot 10^4$ and $1.8 \cdot 10^4$, i.e. with a mean value of $1.4 \cdot 10^4$. From a total of 37 inlets investigated, only 5 showed a deviation from the latter ratio. Deviations above this value clearly characterize wide inlets with several channels, whilst deviations below are indicative of narrow inlets with a composite cross-section and a narrow, deep channel (> 20 m). Further investigations may quite possibly lead to the characterization of inlet cross-sections by simple numerical values.

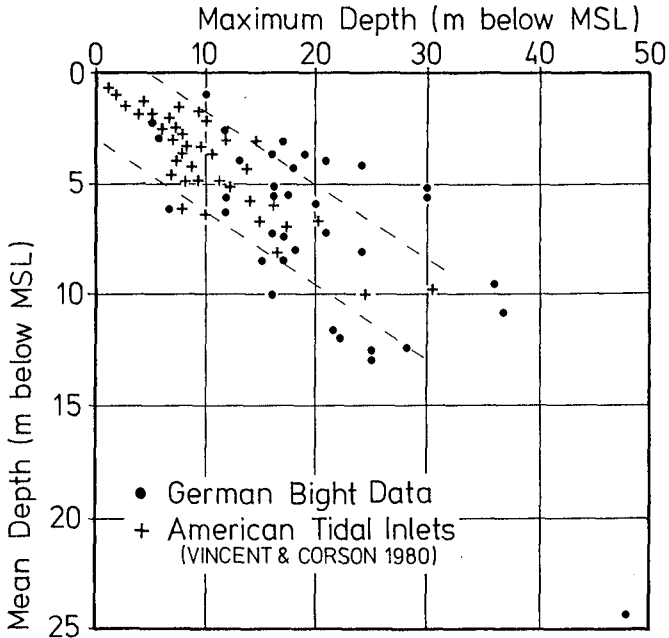


Fig. 5: Relationship between the mean and maximum depth in an inlet cross-section.

4.2.2. LOCATION OF THE CHANNEL WITHIN THE CROSS-SECTION

The geometry of the cross-sectional area and the location of the deep channel within the inlet cross-section in the region of the German Bight are different from the corresponding parameters arising from American investigations (FITZGERALD & FITZGERALD, 1977). In the case of the German Bight, these factors are less dependent upon meandering of the channel bed, the form of the coastline outside the inlet mouth and the dominant longshore transport direction, but are mainly governed by the shape of the drainage area and the location of the latter with respect to the inlet. These conditions are particularly noticeable along the south coast of the German Bight in the vicinity of the East Frisian islands. A distinction must be made between the following cases:

- a) The drainage area is located symmetrically behind the inlet and the deep channel lies in the middle of the inlet (symmetrical cross-section).
- b) The drainage area lies for the most part behind an island (barrier island), e.g. in the downdrift direction relative to the inlet, whilst the deep channel of the inlet is orientated in the updrift direction. This situation is due to the fact that the tidal water volume associated with the morphologically active ebb phase must flow behind the barrier island before the

tidal inlet is reached (non-symmetrical updrift cross-section).

- c) In the case of receding coastlines, two main channel arms often meet together within the inlet. One arm usually runs parallel to the barrier island whilst the other runs directly towards the inlet. If the tidal volume of the channel orientated at right angles to the inlet is sufficiently large, the channel running parallel to the island will be forced in a downdrift direction against the barrier island (non-symmetrical downdrift cross-section). The development of inlets with double channel systems is also possible.

On the east coast of the German Bight, the inlet drainage areas are orientated at right angle to the coastline. For this reason and also because of the lower degree of sediment transport, the channels extend a long way seawards and are located centrally within the inlet cross-section. In the water inlets, side channels frequently occur.

4.2.3. EBB TIDAL DELTAS

General forms of ebb tidal deltas, which develop due to differences in flow velocities and longshore sediment transport rates, have been compiled by OERTEL (1975) for the mesotidal coast of Georgia (Fig. 6).

Similar structures are also apparent in the German Bight. Of particular significance are the curved sand bars of the tidal inlets along the East Frisian chain of islands which have been dealt with in detail by LUCK (1976).

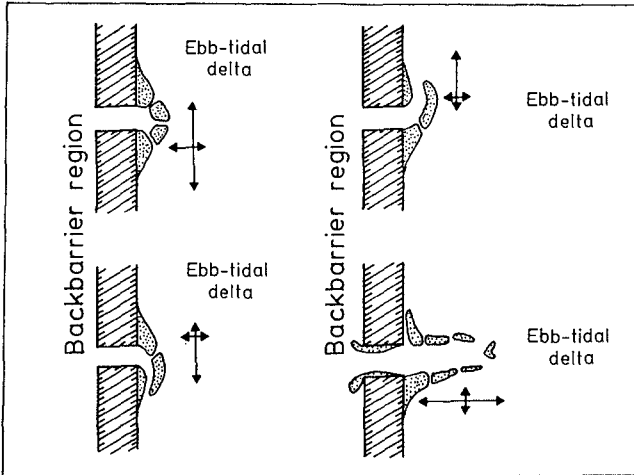


Fig. 6: Ebb tidal deltas of tidal inlets (with arrows indicating the relative magnitudes of onshore, longshore and offshore currents).

4.3. BACK BARRIER BATHYMETRY

The differences between the back barrier bathymetry of the American south coast and the German Bight were first pointed out by NUMMEDAL & FISCHER (1978). The American intertidal salt marshes are mainly comprised of areas overgrown with spartina; only about 20% of the total surface area consists of open water (tidal creeks). In contrast to this, the geomorphological structure of corresponding areas in the German Bight is totally different. Below the MHW line, no vegetation exists. The main factor which governs the morphological structure of the tidal flats is the tidal range (DIECKMANN & PARTENSKY, 1985). Hypsographic curves published in the literature for American coastal sections in the mesotidal range are presented in Fig. 7 together with curves for corresponding regions in the German Bight. As may be seen in Fig. 7, the differences are clearly apparent.

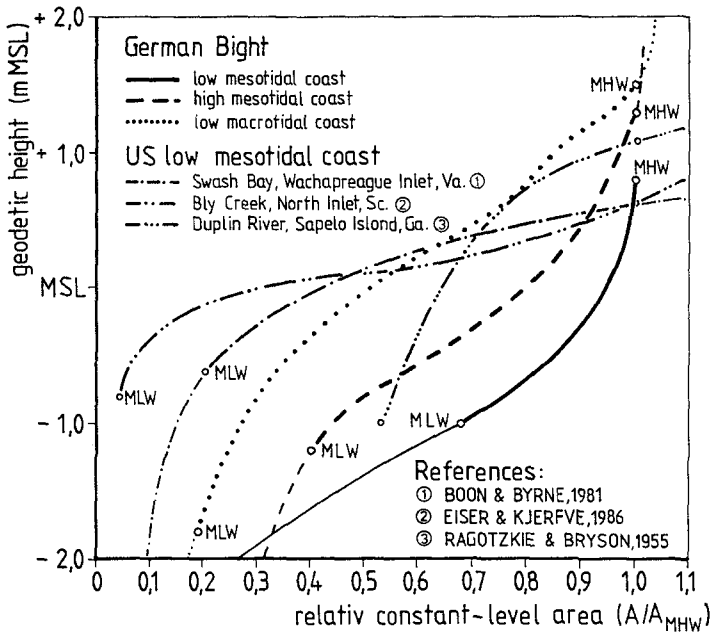


Fig. 7: Hypsographic curves for several American coastal sections (mesotidal range) and the basic types of different tidal range regions in the German Bight.

It should be noted that the given American hypsographic curves represent relatively small coastal sections (0.6 to 27.4 km²) whereas those for the German Bight are derived from larger regions (95 to 260 km²). Differences in the back barrier bathymetry do not govern the size and shape of the tidal inlets, which are themselves determined by the tidal volume, but rather the form of the flow velocity

profiles within the inlets.

4.4. OTHER PARAMETERS

In addition to the parameters mentioned above, there are no doubt other parameters worthy of comparison such as sediments, flows and biological effects relating to different climatic conditions.

For example, NUMMEDAL & FISCHER make mention of the fact that in inlets adjoining open water lagoons in the back barrier region, flood flow dominance is evident whereas for tidal flats and salt marshes in the back barrier region, ebb flow dominance is present. Similar conditions also appear to apply in the case of the German Bight region. For 3 inlets on the East Frisian coast with tidal flats in the back barrier region, a definite ebb flow dominance could be ascertained (PFENNIG, 1978).

5. CONCLUSIONS

From a comparison of American inlets with those in the German Bight, it was found that in the case of all parameters which describe hydrodynamic processes, good agreement exists. In contrast, significant differences were apparent in relation to the morphological structure of the tidal flat salt marshes as well as climatic influences (vegetation). In the context of coastal engineering science, however, these aspects are of no particular importance.

6. REFERENCES

- BOON, J.D.III; BYRNE, R.J.: On Basis Hypsometry and Morphodynamic Response of Coastal Inlet Systems. *Marine Geology*, vol. 40, p. 27 - 48, 1981.
- BRUUN, P.: Stability of Tidal Inlets. Theory and Engineering. Developments in Geotechnical Engineering no. 23, Elsevier Scientific Publishing Company, Amsterdam, 1978.
- DIECKMANN, R.; PARTENSKY, H.W.: Quantitative Geomorphology of Tidal Flat Areas. In: SIGBJARNARSON, G. (ed.): Proc. Iceland Coastal and River Symposium, Reykjavik/Iceland, p. 53 - 62, 1985.
- EISER, W.C.; KJERFVE, B.: Marsh Topography and Hypsometric Characteristics of a South Carolina Salt Marsh Basin. *Estuarine, Coastal and Shelf Science*, vol. 23, p. 595 - 605, 1986.
- FITZGERALD, D.M.; FITZGERALD, S.A.: Factors Influencing Tidal Throat Geometry. Proc. Coastal Sediments '77, publ. by ASCE, p. 563 - 581, 1977.
- FITZGERALD, D.M.; PENLAND, S.; NUMMEDAL, D.: Control of Barrier Island Shape by Inlet Sediment Bypassing: East Frisian Island, West Germany. *Marine Geology*, vol. 60, p. 355 - 376, 1984.

- HAYES, M.O.: Barrier Island Morphology as a Function of Tidal and Wave Regime. In: LEATHERMAN, S.P. (ed.): Barrier Islands. Academic Press, New York, 1976.
- JARRETT, J.T.: Tidal Prism - Inlet Area Relationship. General Investigations on Tidal Inlets (GITI), report no. 3, US Army Engineer Waterways Experiment Station, Vicksburg/Miss., 1976.
- LUCK, G.: Inlet Changes of the Eastfrisian Islands. Proc. 15th Int. Conf. on Coastal Eng., Honolulu/Hawaii, p. 1938 - 1957, 1976.
- NUMMEDAL, D.; FISHER, I.A.: Process Response Models for Depositional Shorelines: The German and the Georgia Bights. Proc. 16th Int. Conf. on Coastal Eng., Hamburg/West Germany, p. 1215 - 1231, 1978.
- O'BRIEN, M.P.: Equilibrium Flow Areas of Inlets on Sandy Coasts. Jour. of the Waterways and Harbors Div., ASCE, no. WW1, p. 43 - 52, 1969.
- OERTEL, G.F.: Ebb Tidal Deltas of Georgia Estuaries. In: CRONIN, L.E. (ed.): Estuarine Research, vol. II: Geology and Engineering. Academic Press, New York, p. 267 - 276, 1975.
- PFENNIG, A.: Bewertungsmodelle zur Untersuchung transportwirksamer Reststromsysteme. Sonderübung, Franzius-Institut, University of Hannover/West Germany, unpubl., 1978.
- RAGOTZKIE, R.A.; BRYSON, R.A.: Hydrography of the Duplin River, Sapelo Island/Georgia. Bull. of Marine Science of the Gulf and Caribbean, vol. 5, p. 297 - 314, 1955.
- VINCENT, C.L.; CORSON, W.D.: The Geometry of selected US tidal inlets. GITI Report no. 20, US Army Engineer Waterways Experiment Station, Vicksburg/Miss., 1980.
- WALTHER, F.: Zusammenhänge zwischen der Größe der ostfriesischen Seegaten mit ihren Wattgebieten sowie den Gezeiten und Strömungen. Forschungsstelle Norderney der niedersächsischen Wasserwirtschaftsverwaltung, vol. 23, 1972.

CHAPTER 200

FLOW DEPENDENCY OF BOTTOMSTRESSES IN TIDAL MODELS

Jan J. Leendertse ¹
A. Langerak ²

In modeling studies the bottomstress parameter may not be taken as a constant for making predictions. This is particularly true when large changes are being made in the water bodies. Engineering judgement is than necessary as studies to a relation between the bottomstress parameter and tidal flow velocity are not conclusive.

Introduction to the project

In 1976 the Netherlands Rijkswaterstaat embarked on constructing the final stage of the Deltaplan with the Eastern Scheldt-project. Three structures had to be built: a 3 kilometer long stormsurge barrier in the mouth of the estuary - to be closed during storms - and two so-called compartimentation dams (fig. 1). The dams, which created a lake in part of the estuary, had to provide (a) a tide-free shipping lane from the city of Antwerp to the river Rhine, and b) storage of fresh water flowing into the estuary. The latter was necessary to maintain high salinity in the estuary without large fluctuations for the ecological system as the stormsurge barrier reduced the tidal currents and thus the mixing.

The Deltaplan as a whole (fig. 2) enhanced the protection from the stormsurges in the Rhine-Meuse delta. The plan comprised closure of all estuary branches except for the New Waterway, which is the shipping lane to Rotterdam, and the Western Scheldt, which is the shipping lane to Antwerp. In 1976, the Deltaplan was completed except

¹ The RAND Corporation, Santa Monica, California, USA

² Tidal Waters Division, Rijkswaterstaat, Zierikzee, The Netherlands

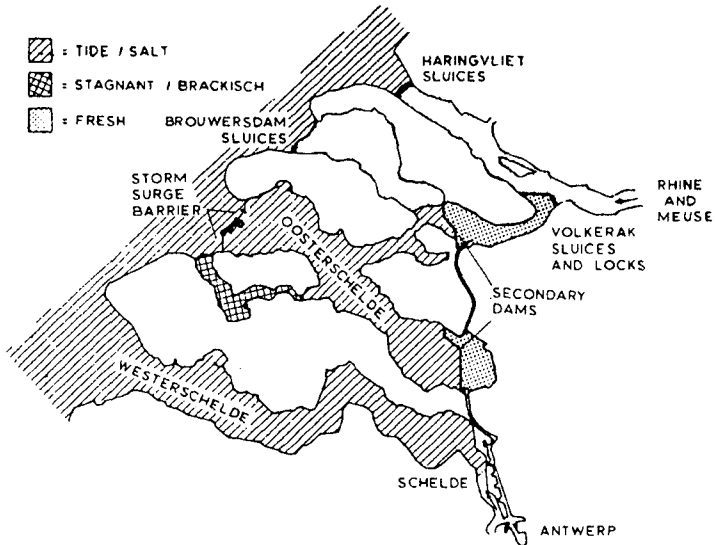


Fig. 1 Overview of the Eastern Scheldt project with location of the Stormsurge Barrier and Compartmentation Dams.

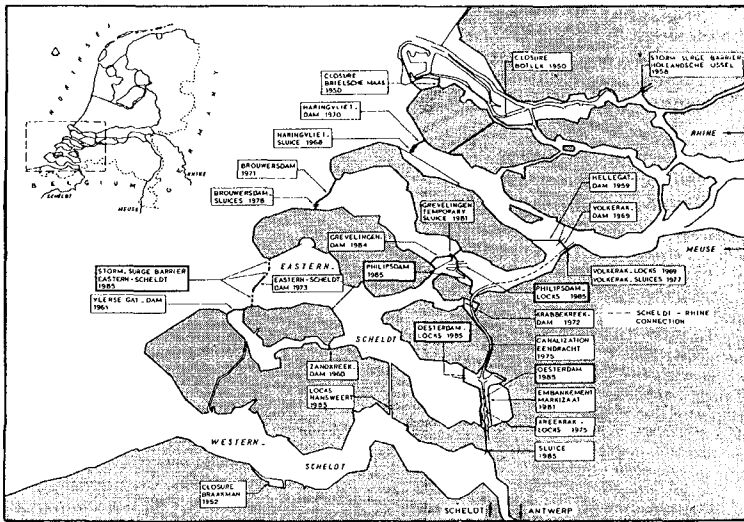


Fig. 2 View of the Deltaplan, including the Eastern Scheldt project.

for the most difficult part, namely the construction of the storm-surge barrier and the compartmentation dams in the Eastern Scheldt.

Function of the models

Large hydraulic engineering projects like the construction of the storm-surge barrier and the compartmentation dams require reliable short term predictions of the weather and of the currents and water-levels. The predictions are needed to schedule and adjust the progress of the construction. Predictions over longer periods are also required to evaluate different options in the design and the construction methods.

The contract between the government and the construction-consortium for the project contained a clause which required the Rijkswaterstaat to provide the consortium with accurate tide and surge predictions. If the predictions deviated from observed values by a certain amount, extra payments were due for expected damages. As a result, the required accuracy of the models was high. The waterlevels had to be predicted within 5% of the observed values on an average, and currents had to be predicted within 10% of the observed values on an average. The prediction period ranged from 24 hrs.- for predictions of the combined tide and surge - to 4 yrs., the latter for predictions of tide only.

For the short term predictions, a one-dimensional model was used. This model was based on the numerical solution of the St. Venant-equations (fig. 3). For the long term predictions of tidal heights and currents, the one-dimensional model was also used, as the computation time on a HP1000-A was only one minute for every 24 hrs. real time. However, for the prediction of current distributions and intensities to be used in the design and construction planning, the one-dimensional model had insufficient resolution and a family of depth averaged two-dimensional models (fig. 4) was used with a spatial solution ranging from 45 m. for the detail models to 400 m. for the overview model. Some of the high resolution simulations required 20 hours on a main frame computer.

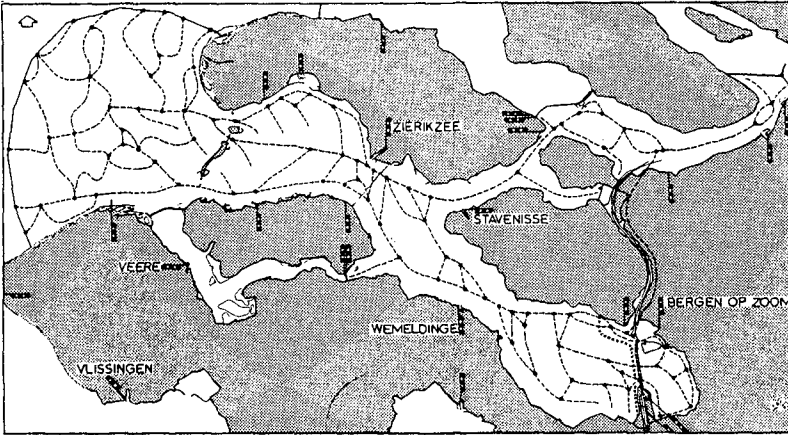


Fig. 3 One-dimensional tidal model used to make long and short term predictions.

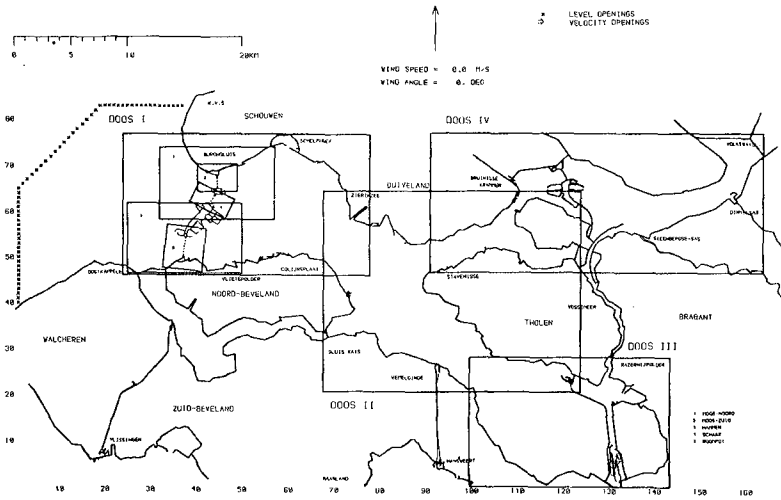


Fig. 4 Two-dimensional tidal models used in the evaluation of the design and construction methods.

In the beginning of the planning and execution of the project, hydraulic scale models were used together with numerical models. But after comparing hydraulic scale model results and numerical model results with observed data it was shown that numerical model results were more accurate (Leendertse 1984). As a numerical model was also more flexible and cost-effective, during the final construction phases of the project the design, the preparation and the actual construction depended completely on the use of numerical models.

Importance of the bottomstress representation

To fulfill the requirements of accuracy, all aspects of the models like the boundary conditions, bottom-schematisation and friction factors were carefully reviewed. A large number of experiments were made in a two-dimensional model of the estuary (Leendertse, 1988) to investigate the effects of the advection term approximation in the hydrodynamic equations and to investigate the comparative importance of the timestep size, the gridsize, the depth accuracy, the roughness estimates, and the horizontal momentum exchange. Similar experiments were made for the one-dimensional model.

From these experiments, it was concluded that the depth approximation, the boundary conditions and the bottomstress coefficients were the most significant factors to obtain accurate predictions. For the depth approximation about a man-year's effort was expended to present the geometry of the estuary with high accuracy in the models. For the depth approximation, extensive use was made of computer programs which accessed the huge bathymetric data files. To verify the accuracy of the approximation, graphs were prepared with the depth in every cross-section of the model in comparison with the data of the bathymetric files. For the boundary conditions, a new technique was developed for estimating boundary tide levels from existing waterlevel recording stations in the vicinity of the boundary. A high accuracy of the estimates of these boundary conditions was obtained, but it appeared more expedient to measure the waterlevels at the model seaward boundary by installing off-shore recording stations and transmitting the data to the computer which made

all the predictions. For verification purposes of the one-dimensional model, measurements of levels and currents were made at many locations in the estuary and these were also available on-line for verification.

The bottomstress parameters were found by adjusting the model for existing conditions. After making verification simulations, a project review indicated that all required standards were met for the existing conditions. However, as the flow conditions in the estuary would change due to the construction of the barrier and the dams, it was to be expected that the bottomstress parameters would change also. Thus for the long term predictions, considerable uncertainty was introduced particularly as the tidal amplification in the estuary is very sensitive to the bottomstress.

Bedforms and tidal systems

If significant changes in a hydraulic system of an estuary with a sandbottom are made, then such changes have an impact on the bedform. However, little is known about bedform changes in estuaries. This is in contrast to rivers where estimates are available on the impact of discharge changes on the bedform and the frictional losses. For estuaries where the changes in flow are much more rapid such estimates are not yet possible as the research directed toward establishing relations between flow and bottomstress is not conclusive. However, a relationship between flow and bottom roughness for quasi stationary systems can, under certain conditions, be used to obtain an insight in the behaviour of the bedform and bottomstress in an estuary.

The key parameter in this case is the bed response time to hydraulic changes. The bed-response time will be short if the bottom consists of loose packed fine sands and the currents are strong. The bed is then easily erodable and new bedforms appear in a matter of hours. In such a case, the relationships for quasi stationary flow can be expected to be applicable. However, if the bottom consists of densely packed sands or consists of coarse sands or gravel, the development of new bedforms can be a matter of months. In the first

case, with loose packed fine sands and relatively strong currents, the tidal currents will have a direct one to one relationship with the bedform and the full cycle of bedforms depicted in Fig. 5 might be seen during a springtide/neaptide cycle or even during one tidal cycle. In the second case, the tidal currents have an impact on bedforms, but the extent of the changes can not yet be predicted.

The Eastern Scheldt estuary resembles more or less to the first case as it consists for a large part of the fine (D50 is 300 μ or less) loose packed sands and the currents are strong. Thus, we may expect a "rapid" response to changes in the hydraulic system.

Effect of the stormsurge barrier on bottomstress parameters

An extensive analysis of field data and a very extensive modeling effort permitted an accurate prediction of the modification of the tidal amplification in the Eastern Scheldt due to the construction of the stormsurge barrier.

Part of the modification was due to the obstruction of the flow by the barrier, in part it was due to modification of the bottomstress. In engineering investigations, it is common to assume that the bottomstress parameters are invariant, but before the barrier was constructed, it was noted from comparisons of one- and two-dimensional model results with observed tidal heights and currents that the bottomstress parameters depended on the flow conditions during previous tidal cycles. For example, if the model was adjusted for average tide conditions then the computation of a springtide would show too much tidal amplification and computations for neaptide would underestimate the tidal heights (Leendertse 1988).

To analyze the phenomena, the amplification of the tide in the estuary was determined from observations at two stations. One station was located at the seaward extremity of the estuary, the other far inland. The tidal amplification was determined by cross-spectral analysis from records of about 100 hours during springtide, during neaptide, and during average tide. The tidal amplification of the semi-diurnal tide appeared strongly dependent on the tidal heights.

For example, during neap tide amplification is 1.31, but during spring tide the amplification is only 1.17. The phase lag is also influenced by the tidal amplification.

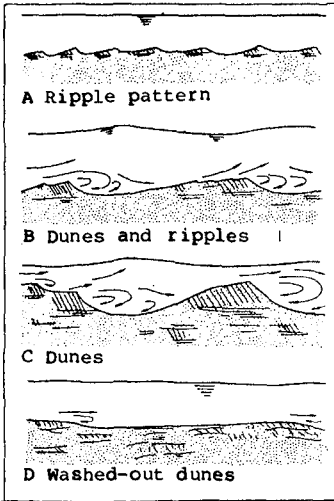


Fig. 5 various bedforms at increasing velocity.

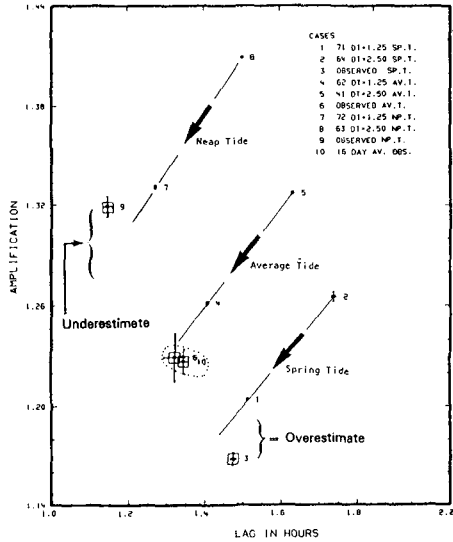


Fig. 6 Computed and observed amplification and phase lag of the semi-diurnal tide over the estuary.

The amplification and phase-shift of the tide in a model may depend on one hand on the resolution in space and time of such a model and on the other hand on the bottomstress parameters such as the Chézy- or Manning's-value found during calibration of the model. In the numerical experiments with a two-dimensional model the three mentioned tide conditions were simulated and the tidal amplifications were determined by cross-spectral analysis. Two sets of experiments were performed, one with a time-step of 1.25 min. and the other with a time-step of 2.5 min.

As in numerical models, the time-step influences the propagation speed and amplitude of the tide, the two sets of experiments determined the influence of the resolution in time upon the results. The results of the analysis are summarized in fig. 6. The arrows in the graph show the effect of the reduction of the time-step. Increased resolution brings the amplification of tide in the model within the confidence band of the observations of the average tide, but this is not the case for the simulations of the springtide and the neap tide.

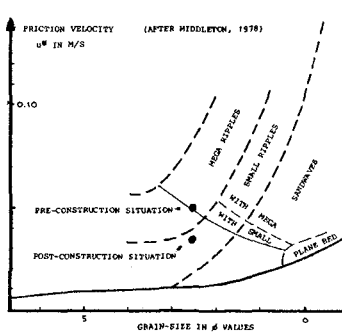


Fig. 7 Bedforms during the pre-construction and the post-construction period.

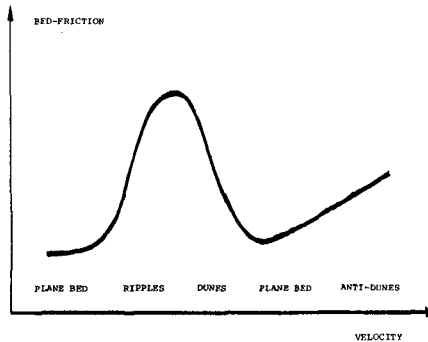


Fig. 8 Bedforms and their impact on bed friction.

From the experiments with the two-dimensional model and similar experiments with the one-dimensional model, it was concluded that the magnitude of the tidal flow reduction due to the barrier had to be taken into account in determining the bottomstress parameter. The impact of the structure as a whole on the hydraulic system was considerable as a decrease of the tidal currents at least to 70% of the original value was predicted; thus not only needs the bottomstress parameter to be adjusted for neap- and springtide, but also for the long term predictions.

From literature for stationary systems, it was evident that the bed forms for fine sands like in the Eastern Scheldt (D_{50} is 200 μ) would vary with the flow speed according to the following ranges:

- flat bed 0,00 to 0,40 m/s
- bed with small ripples 0,40 to 0,70 m/s
- bed with mega-ripples or dunes 0,70 to 3,00 m/s

The friction is deemed to vary accordingly and a literature study indicated that the bedform with the highest bottomfriction is centered around the transition from mega-ripples to small ripples.

If the Eastern Scheldt would be a stationary system or a system with a very short response time, the bedforms before the construction should be a transition from mega-ripples to small ripples (fig. 7). Side looking sonar surveys showed indeed small ripples on top of mega-ripples as the dominant bedform in the non-stationary Eastern Scheldt.

As this bedform has the highest bedfriction (fig. 8), lower frictions could be expected when the construction proceeded. The tidal velocities during construction would drop at least to 70% of their original value, leading to a predominant bedform with small ripples and thus a smaller bedfriction.

Two different approaches were used to predict the modification of the bottomstress parameter. In the first approach, the Chézy-coefficient in the numerical model was adjusted for neap tide and for spring tide and a relation was established between the Chézy-coefficient and the tidal range. The next step was to extrapolate the available data on the neap tide/spring tide cycle to the future situation after the construction of the storm surge barrier. We assumed a linear relation between the tides and the change in bedfriction and so an extrapolation was made for the future situation with lower tidal amplitudes, lower velocities and thus a lower bedfriction. A 12% higher Chézy-value (12% lower bedfriction factor) based on this analysis was expected.

For the second approach to predict the modification of the bottomstress parameter, we used the results of experiments in a sand flume of the Delft Hydraulics Laboratory. The Netherlands Rijkswaterstaat had commissioned the Laboratory to study the interaction between

sand and flowing water. The studies resulted in a relation between velocity and bedfriction for stationary systems at different grain sizes. The results (Van Rijn 1982) are depicted on a prototype scale in fig. 9.

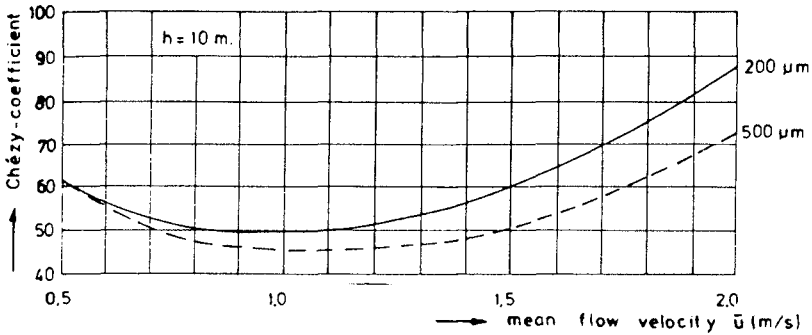


Fig. 9 Relation between the velocity and the Chézy-value in a flume at constant velocity for two grainsizes.

As fine and loose packed sands are present in the Eastern Scheldt, we assumed the bed-response time of this estuary to be short and certainly shorter than the construction time of the barrier. The results of the flume investigation indicated that the velocities which were present before the construction would generate mega-dunes with small ripples, and these were indeed present. As from numerical model studies, the tidal changes after construction were as a first estimate known, we could derive from fig. 9 that the Chézy-values would increase by 10 to 12%.

As both approaches indicated about the same increase, we estimated that a 10 to 12% higher Chézy-value was to be expected after the construction of the storm surge barrier. This modification was then used for the post-construction predictions. After the barrier was constructed, a comparison was made again between observed tidal heights and currents and those obtained from the one- and two-dimensional models.

The agreement was excellent and this confirmed that the Chézy-value had indeed increased by 12% because of the construction of the barrier. We found it somewhat remarkable to achieve such a good estimate, because predicting changes in morphology is still more an art than a science.

Effect of dam construction on bottomstress parameters

The two dams near the inland extremities of the estuary were constructed to form two lakes (Fig. 1). These two lakes were connected by a ship channel. The dams were not constructed at about the same time, but the tidal openings in the dams were closed in sequence.

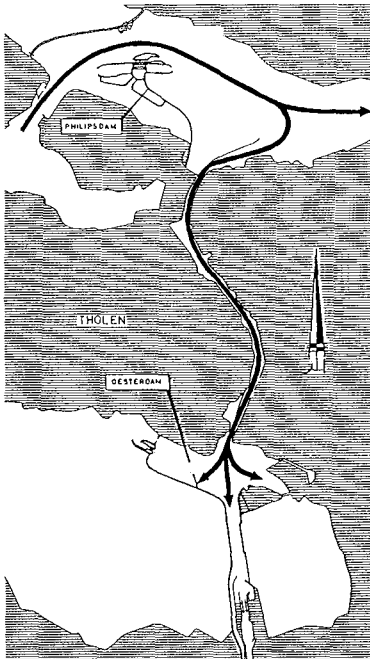


Fig.10 Flooding of the (southern) lake via the adjoining ship-channel.

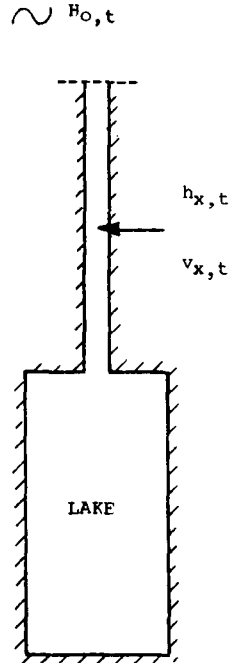


Fig.11 Schematic representation of the southern lake and the adjoining channel.

First the opening in the southern dam was closed and about a half year later the remaining opening in the northern dam was closed. Before the dam construction and also before the openings in the dams were closed, the tidal amplitudes and phases were about the same at the northern and southern end of the channel. As the surface area of the channel is fairly small, the tide generated only weak currents in the channel. During flood, water flowed southward in the northern part of the channel and northward in the southern part. Near the middle currents were very weak and variable (slack). This rather unusual situation precluded estimation of the bottomstress parameter with adjusted numerical models.

It was to be expected that after closure of the southern dam, the tidal flow in the channel would change very significantly. The area behind the southern dam would then receive its ebb and flood waters through the channel (Fig. 10). To predict the currents in the channel and the tidal heights in the area behind the southern dam for the condition with one dam closed, a series of model experiments were made. In the simulations the same bottomstress parameter as in other tidal channels with similar bottom material and currents was used, but shortly after the closure of the southern dam, it appeared that the measured currents were about 20% larger than predicted. Apparently, the bedfriction in the channel was reduced significantly. These high currents introduced erosion at several locations and required the installation of more revetments and bottom protection devices than originally expected. The high currents impeded shipping also.

After the closure, the tidal system consisted of a basin connected by a narrow channel to the tidal waters at the northern end of the channel (Fig. 11). In the channel, the velocities would reach their maximum value about 10 minutes after high water or low water slack and the maximum velocity remained constant until 10 minutes before the next change of tide.

Further analysis indicated that the tidal flows (maximum velocities) and the bedform were in a weak unstable equilibrium. If the maximum

velocities increase temporarily because of a passing storm, then the bottom roughness could be reduced slightly by a feed back system as depicted in fig. 12 and in following tidal cycles higher velocities could occur. If the relation between bedform (flow resistance) and maximum velocities was taken into account in the analysis, it appeared that the velocities would increase gradually until the velocities would exceed 1,65 m/s.

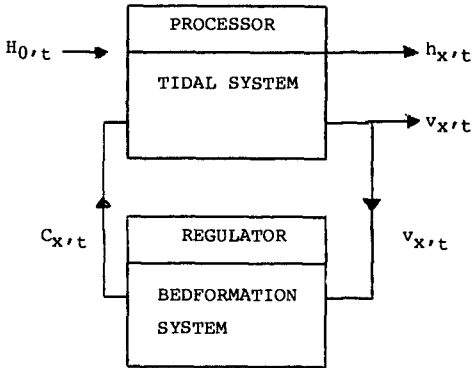


Fig. 12 The ship channel depicted as a control system

If then an increase would occur by a storm, the bottom roughness might be reduced significantly and the velocities would become very high. However, a stable equilibrium would finally be attained with maximum velocities of 2.0 m/s. From measurements in the channel just before the closure of the northern dam, it appeared that the maximum velocities were 1.60 m/s. This just below the critical transition.

Fortunately, the very high velocities of 2,0 m/s were not observed. It is not clear if the gradual increase had not reached the critical transition of about 1,65 m/s or that the relations used in the analysis were not valid. For example the analysis used a relation between velocity and bottomstress obtained from data which show considerable deviations from the mean. Also the sediment of the channel

contained some clay, thus the bottom material was not exactly the same as used in the analysis. Furthermore, the installation of revetments and bottom protection, which all have rough surfaces, might have increased the flow resistance locally.

A significant change in an estuary due to a temporarily unstable flow/bedform equilibrium can not often be observed. However, it is expected that such temporarily unstable bedform conditions are occurring quite often in estuaries. The instabilities are, however, mostly not obvious as the changes in the tidal system occur gradually. The "unstable" system then adapts itself by increased sedimentation or erosion till a new equilibrium is reached. The occurrence of such events may by the way be one reason for the deviations between observed and computed water levels and currents of a well adjusted model.

Conclusions

In modeling studies, the bottom stress parameter may not be taken as a constant for making predictions. This is particularly true when large changes are being made in the water bodies that are modeled.

References

- Leendertse, J.J., "Verification of a model of the Eastern Scheldt"; The Randcorporation; R-3108-NETH; april 1984.
- Leendertse, J.J., "A summary of experiments with a model of the Eastern Scheldt"; The Randcorporation; R-3611-NETH; juni 1988.
- Van Rhijn, L.C., "The Prediction of Bedforms, Alluvial Roughness and Sediment Transport"; The Delft Hydraulics Laboratory; S 487; oktober 1982.

CHAPTER 201

NUMERICAL MODELLING OF SUSPENDED SEDIMENT TRANSPORT IN THE LOIRE ESTUARY

TEISSON Ch. *, FRITSCH D. *

ABSTRACT

In order to evaluate silt displacements and deposits in the outer part of the Loire Estuary over one year, a two-dimensional depth-integrated model of suspended sediment transport has been carried out. It takes into account transport and dispersion of suspended sediment by tidal currents, and processes of erosion, deposition and bed consolidation. Erosion laws and consolidation laws are specific of the Loire Estuary and come from laboratory experiments.

Representative tidal conditions and river Loire flowrates have been identified : results of the model for these typical cases will be tentatively extrapolated to a one year evolution.

1. INTRODUCTION

As part of environmental studies involved in a future nuclear power plant near the mouth of the Loire Estuary, the Laboratoire National d'Hydraulique has been commissioned to look into hydraulic and sediment problems and to focus on silt displacement in the outer part of this estuary, located on the west coast of France (fig. 1).

The main feature of this estuary is a turbidity maximum which lies most of the time in the inner part ; but every year, during flood discharge, about one million tons of suspended sediments are partially expelled seawards (fig. 1).

It is therefore of great interest to know if a silt particle, coming from the inner part of the estuary and possibly polluted with radionuclide, will be either quickly ejected seawards or trapped off the mouth of the estuary in one of the sensitive bays devoted to tourism or oyster farming.

* Research Engineers, Laboratoire National d'Hydraulique. Electricité de France, 6 quai Watier - 78400 CHATOU, FRANCE

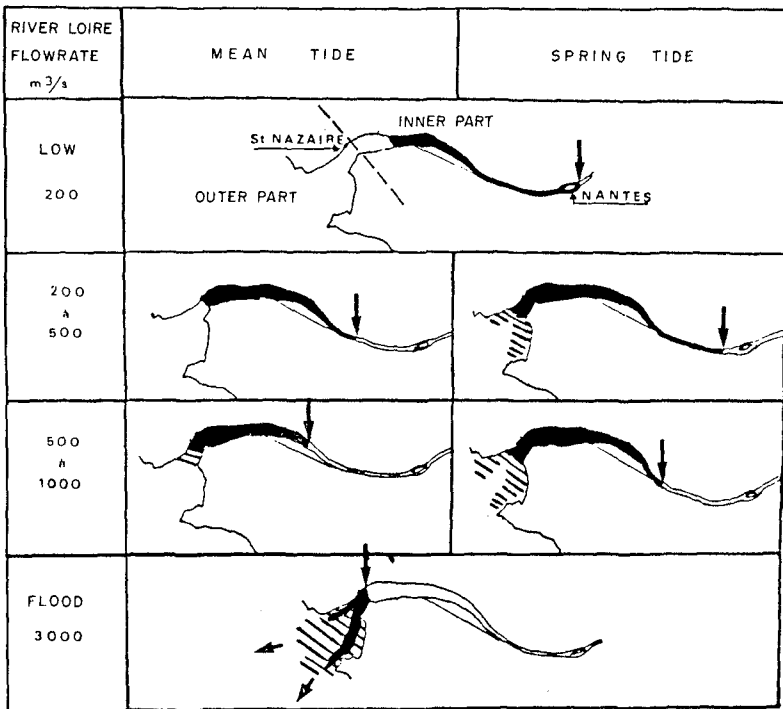
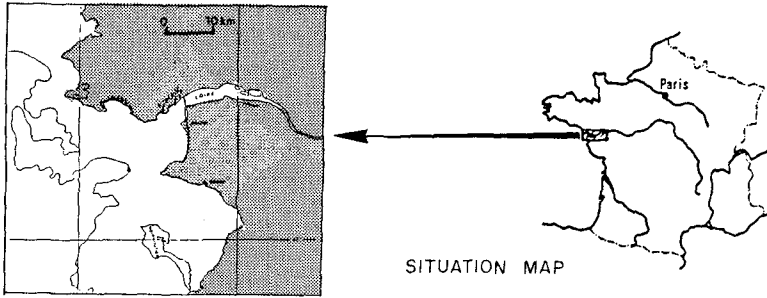


Figure 1 - OSCILLATIONS OF THE TURBIDITY MAXIMUM IN THE LOIRE ESTUARY, ACCORDING TO RIVER FLOWRATES AND TIDAL RANGE (after GALLENNE 1974) -

After a presentation of the sediment model and processes of mud involved, hydrodynamic results, turbid plume extent, bed evolution are shown and lead to a better understanding of sediment dynamic.

2. SEDIMENT MODEL

2.1 The depth-averaged equation and its hypothesis

Flow structure and sediment circulations in coastal waters and estuaries are complex phenomena and need often a three-dimensional model in order to simulate really accurately their motions and patterns. In fact, in case of morphological computations as maintenance of navigation facilities, a prediction over a period of several months or years is asked and a three-dimensional model is not well adapted due to prohibitive computational work.

Fortunately, it is not always necessary to model the complete structure of the flow. Provided the transport quantity is well mixed throughout the water depth, it can be sufficient to consider depth-averaged equations : this approximation is particularly appropriate for a wash-load which consists of fine cohesive particles with very low settling velocities, and when sediment concentration remains moderate. Such depth-integrated models have been extensively developed in the past years (ARIATHURAI and al, 1977 ; HAYTER, 1983 ; THOMAS and MC ANALLY, 1985).

In this way the use of a monodimensional vertical model of suspended sediment transport developed at LNH has enabled to outline first criteria concerning the vertical homogeneity allowing depth integration : advection time scale (linked to the fall velocity) has to be at least twice the diffusion time scale, and furthermore must be much larger than the slack duration (TEISSON, 1984).

The bidimensional depth-averaged equation for transport of suspended sediment is then the following :

$$\frac{\partial C}{\partial t} + u \frac{\partial C}{\partial x} + v \frac{\partial C}{\partial y} = \frac{1}{h} \frac{\partial}{\partial x} \left[hK_x \frac{\partial C}{\partial x} \right] + \frac{1}{h} \frac{\partial}{\partial y} \left[hK_y \frac{\partial C}{\partial y} \right] + \frac{S}{h} \quad (1)$$

in which :

C = depth-integrated concentration of the suspended sediment

u, v = depth-integrated components of velocity

Kx, Ky = dispersion coefficients

h = water depth

S = source - sink term accounting for erosion or deposition

The main hypothesis of the numerical modelling of suspended sediment transport is the decoupling between hydrodynamic and sedimentology. In the equation for transport of suspended sediment, hydrodynamic conditions - i.e. velocity and water depth fields (U , V , h) - are known, being previously computed by a numerical model solving the equations of tide propagation. It is assumed that sediment transport does not affect the hydrodynamic behaviour of the flow ; a new computation of velocity components occurs only if bottom evolution is relevant, due to erosion or deposition.

2.2 Mud processes

2.2.1) Settling velocity

For very low concentration, the settling velocity W_c is assumed constant. For higher concentration the settling velocity can depend on the concentration, in the range $C = 1 - 10$ g/l, as for example :

$$W_c = K C^{4/3} \quad (2)$$

where K is a constant about 10^{-5} (S.I. units), depending on sediment characteristics (from measurements in the Loire Estuary made in 1969).

2.2.2) Deposition rate

The deposition rate can be given by the KRONE's formulation (1962).

$$Q_d = P_d W_c C \quad (3)$$

in which P_d is the probability of particles sticking to the bed and not being reentrained by the flow, given by :

$$P_d = 1 - \left[\frac{u_*}{u_{*d}} \right]^2 \quad \text{for } u_* < u_{*d} \quad (4)$$

where u_* is the shear velocity and u_{*d} the critical shear velocity under which deposition occurs.

2.2.3) Erosion rate

Erosion rate is represented by an experimental formulation obtained for the Gironde Estuary (CORMAULT, 1971) :

$$Q_e = M \left[\left(\frac{u_*}{u_{*e}} \right)^2 - 1 \right] \quad \text{for } u_* > u_{*e} \quad (5)$$

where u_{*e} is the critical shear velocity above which erosion occurs and M is determined experimentally :

$$M = 0.55 \left(\frac{C_s}{1000} \right)^3 \quad \begin{array}{l} C \text{ in g/l} \\ M^S \text{ in kg/m}^2/\text{s} \end{array} \quad (6)$$

where C_s is the concentration of the outcropping deposit.

Other formula of erosion rate depending of soil consolidation (MEHTA et al, 1982) may also be tested.

2.2.4) Bed profile

Consolidation of the bed is simulated at each node in the numerical model by a pile of ten layers of increasing concentration, each layer of various thickness being characterized by a maximum residence duration (after which mud of the layer goes into the underlocated more concentrated layer) and a critical shear stress for erosion related to the layer density.

The duration stay accounts for consolidation and is based upon experiences of MIGNIOT (1980) (fig. 2).

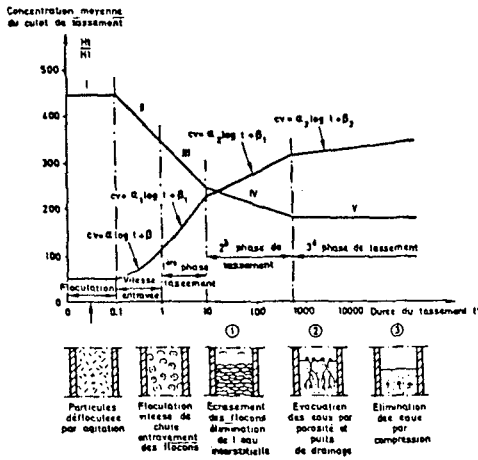


Fig. 2 - Graphical representation of bedding-down phases

For instance, for the Loire Estuary, the mean concentration of settled sediment in g/l is given by :

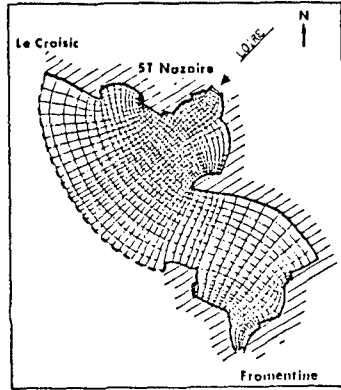
$$C(t) = 136.2 \log_{10}(t + 5.42) \quad 0 < t < 24h \quad t \text{ in hours} \tag{7}$$

$$C(t) = 200 + 70 \log_{10}(t) \quad t > 1 \text{ day} \quad t \text{ in days}$$

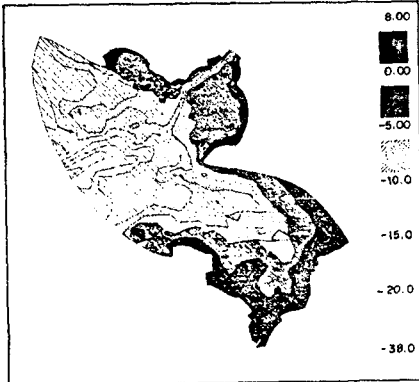
Furthermore MIGNIOT (1981) has related the critical shear for erosion to the concentrations of deposit. For the Loire Estuary :

$$\text{for partially consolidated deposits} \quad (C_s < 240 \text{g/l}) : u_{*e} = 3.2 \cdot 10^{-5} (C_s)^{1.175} \tag{8}$$

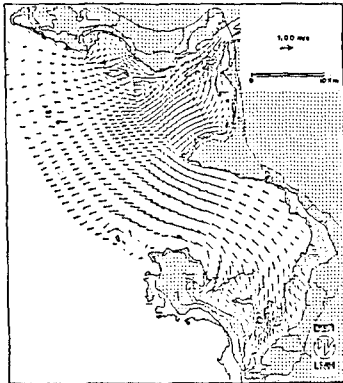
$$\text{for consolidated deposits} \quad (C_s > 240 \text{g/l}) : u_{*e} = 5.06 \cdot 10^{-8} (C_s)^{2.35}$$



a) Curvilinear Grid _



b) Bathymetry _



c) Current Field (Ebb)

Figure 3 _ MODEL OF THE RIVER LOIRE ESTUARY, SPRING TIDE .
LOIRE FLOWRATE : $1000 \text{ m}^3/\text{s}$.

With these data, and for a type of mud corresponding to the one of the Loire Estuary, the bed has been modelled as shown in table 1 :

n° Layers	Concentration (g/l)	Duration stay (h)	u_{*e} (cm/s)
1	100	2	0.72
2	118.6	2	0.88
3	132.7	2	1.00
4	144.1	4	1.10
5	161.8	6	1.26
6	181.3	8	1.44
7	200	16	1.62
8	215.5	32	1.77
9	233.4	54	1.94
10	250.4	infinite	2.19

Table 1 : Layer characteristics for bed modelling

When deposition occurs, the deposit always goes into the first layer, the thickness of which increases consequently. After 2 hours, if no erosion occurs, the content of the first layer goes into the underlocated more consolidated layer and is added to the existing content (the same operation is repeated for other layers).

When bed shear exceeds critical shear velocity of the top layer, then erosion occurs ; each successive layer is similarly tested for potential erosion.

Finally at each time step, the source - sink term is computed :

$$S = Q_d + Q_e$$

from the formulations (3) and (5) above.

2.3 Numerical solution

Given the hydrodynamic data, the numerical model of suspended sediment transport computes horizontal advection and dispersion by the current by means of a time splitting method.

The first intermediary step solves the advection terms on the left hand of equation (1), with a characteristics method.

The second and third intermediary steps solve dispersion in the x and y direction by means of an implicit scheme which takes into account the source term S (TEISSON, 1985).

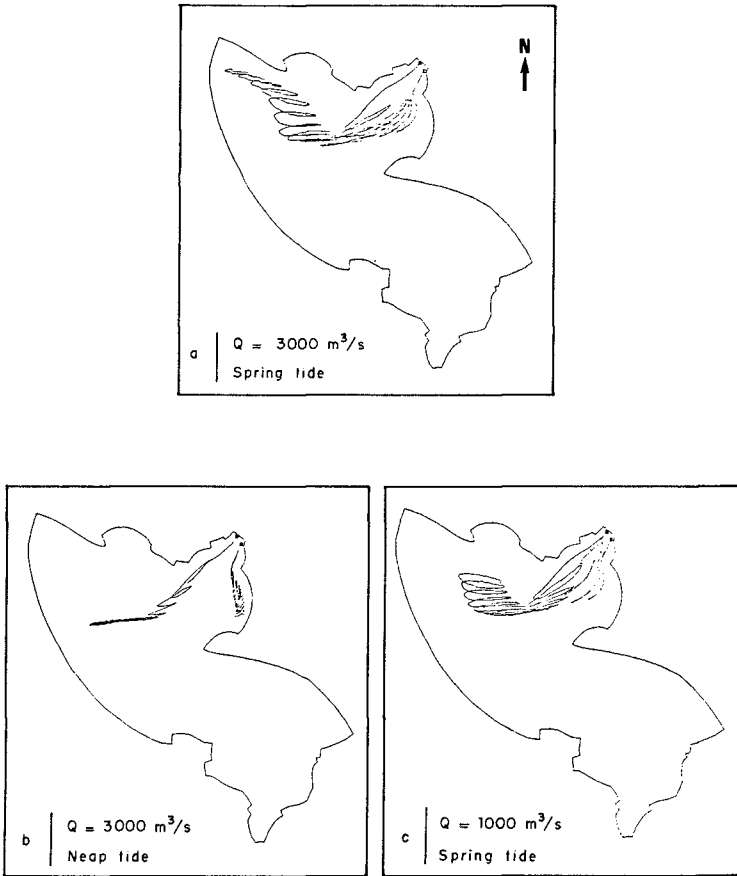


Figure 4 — INFLUENCE OF THE TIDAL RANGE (a - b) AND OF THE LOIRE FLOWRATE (a - c) ON LAGRANGIAN DRIFTS .

Every 2 hours the residence times of deposits are compared to the duration stay of the corresponding layers : when this duration stay is reached, the contents of the layer go into the underlocated more consolidated layer and the total thickness of deposit is reduced consequently.

Both hydrodynamic and sediment depth-integrated models use rectangular or curvilinear orthogonal grid, finite difference scheme, time - splitting method.

3. APPLICATION TO THE LOIRE ESTUARY

Running of the hydrodynamic and sediment models have been performed for various tidal conditions and discharge flows of the Loire river. Assuming that the most interesting phenomena for suspended sediment occur for strong discharge flows (see fig. 1), two flow rates have been chosen - $1000 \text{ m}^3/\text{s}$ and $3000 \text{ m}^3/\text{s}$ - associated to three different tidal range - spring tide, neap tide and mean tide - in order to obtain six representative environmental conditions.

The curvilinear grid comprises 1146 nodes ; the size of the mesh varies from less than 300 meters in refined areas (navigation fairway) to 2500 m for the largest (fig. 3). Bathymetry has been very accurately represented, taking into account navigation fairway, intertidal flat, isolated islands. Time step is 240 s, both for hydrodynamic and sediment model.

3.1 Results of the hydrodynamic model

The hydrodynamic modelling is performed using the two-dimensional, depth-integrated flow model CYTHERE ES1 (BENQUE and al., 1982). This model solves the classical St-Venant equation for tide propagation and incorporates intertidal flats.

The corresponding fields of current and water depth (u, v, h) have been calculated for the six environmental conditions, and calibrated against natural measurements (TEISSON and al., 87). The results are good and do account with the complex problem of intertidal flats : these flats take up 10% of the area at low water.

As an example figure 3 presents current field during the ebb of a spring tide for a Loire flowrate of $1000 \text{ m}^3/\text{s}$.

Lagrangian calculations have also been made and keeping tracks of floats during 10 tides from hydrodynamic result displays an offshore drift, magnified in flood, which saves the bays (fig. 4).

3.2 Input data for the sediment model

In addition to velocity and water depth fields at each time step, the model requires values for sediment parameters derived from consolidation, deposition and erosion laws already presented in Section 2.2, as also boundaries and initial conditions.

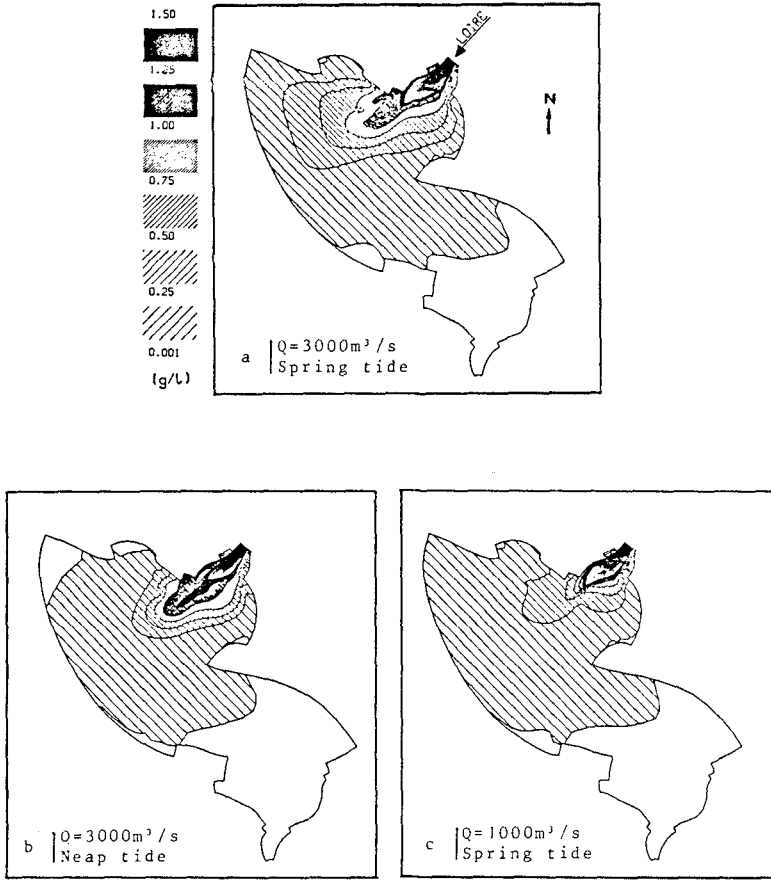


Figure 5 - INFLUENCE OF THE TIDAL RANGE (a-b) AND OF THE LOIRE FLOWRATE (a-c) ON THE PLUME EXTENT (Low Water)

At the upstream boundary, extensive fields surveys have been made in four stations in the narrowest section, and provide suspended sediment concentrations throughout the tide period for various tidal range and river flowrate : these concentrations can reach up to several grams per liter. At the seaward boundary, suspended sediment concentration varies from 0 to 5 mg/l from scarce measurements.

Initial conditions are the following : there is no sediment in suspension or at the bottom, as the aim is to investigate silt displacement coming from the inner part of the estuary.

3.3 Results of the sediment model

Numerous model runs, constituting a sensitivity analysis, have been conducted in order to evaluate the influence of various parameters as horizontal dispersion coefficient, critical shear stress for deposition, dependance of fall velocity upon suspended sediment concentration. For each typical case, representative of one tidal range and one river flowrate, computations were performed over a period of ten identical tides in order to load the model and reach an equilibrium state.

The fig. 5 presents the influence of the tidal amplitude (compare a - b) and of the Loire flowrate (a - c) on the suspended concentration : the flowrate appears to be the main parameter for plume extent. The plume extent is canalized by the navigation fairway where the highest concentrations of suspended sediment are found : this is a feature common to the prototype.

Although suspended sediment concentration is governed by the river flowrate, sediment deposition appears to be controlled by tidal range : thicknesses of deposit are 8 times greater in neap conditions than in spring conditions (compare a-c on fig. 6). Bed evolutions throughout the tide can be followed : deposit that occurs in the fairway during slack at high water is swept out by strong currents during ebb conditions (a-b, fig. 6). Beside the navigation fairway, the first results show good qualitative results ; the difficulty is the lack of reliable and evenly distributed in situ measurements to accurately assess the results for deposit.

3.4 Modelling of a typical year evolution

As it would be computer time consuming to represent the whole year (705 tides), modelling of a typical year evolution is attempted by use of the six typical environmental conditions of the hydrodynamic model. A fortnightly tidal cycle is schematized by a succession of the three basic tidal ranges, for a constant Loire flowrate (either 1000 or 3000 m³/s). The typical year evolution is approached by the combination and extrapolation of various fortnightly tidal cycles results, with or without mud injection at the upstream boundary depending on season (winter-summer).

This stage of the experimentation is going on at the present time : results after fortnightly tidal cycles are available but it remains to combine and extrapolate these results to one year.

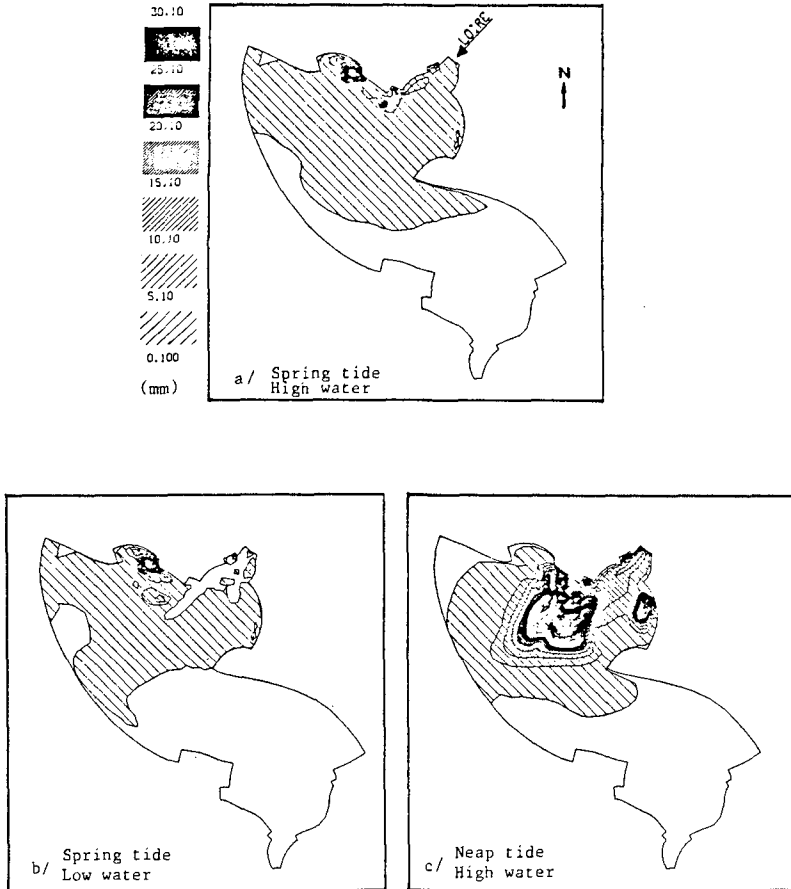


Figure 6 - TOTAL THICKNESS OF DEPOSIT

$$Q = 3\,000 \text{ m}^3/\text{s}$$

CONCLUSION

The objective of the study was to evaluate silt displacement and deposit in the outer part of Loire estuary in an attempt to represent typical year's evolution.

The hydrodynamic model CYTHERE ESI has enabled to compute very satisfactorily six typical current and water depth fields related to different tides and flowrates of the Loire River.

For each of these six typical cases, the 2D numerical model of suspended sediment transport has led to a better understanding of the processes which govern sediment dynamic. Suspended sediment concentration is under the influence of river Loire flowrate, while deposit is controlled by tidal range. Importance of spring-neap tidal cycle has been pointed out, and this fortnightly cycle has been chosen as an intermediary step before the extrapolation to one year's evolution which is currently under progress.

REFERENCES

ARIATHURAI R., MAC ARTHUR R.C, KRONE R.B. (1977 : Mathematical model of estuarial sediment transport. T.R. D77.12 - U.S. Army Engineer - Waterways Exp. Station P.O. Box 63 Vicksburg, Miss 39180.

BENQUE J.P., CUNGE J.A., FEUILLET J., HAUGUEL A., HOLLY F.M. Jr. (1982) : "New Method for Tidal Current Computation", Journal of the Waterway, Port, Coastal and Ocean Div., ASCE, vol 108, No. WW3, Aug. 1982.

CORMAULT P. (1971) : "Détermination expérimentale du débit solide d'érosion des sédiments fins cohésifs", 14e Congrès de l'A.I.R.H., Paris.

GALLENNE B. (1974) : "Les accumulations turbides de l'estuaire de la Loire. Etude de la crème de vase. Thèse de 3ème cycle. Université de Nantes.

HAYTER E.J. (1983) : Prediction of cohesive sediment movement in estuarial waters PHD Thesis UFL/COEL-83/010 Coastal and Oceanographic Engineering Department. University of Florida, Gainesville, Florida 32611.

KRONE R.B. (1962) : "Flume studies of the Transport Sediment in Estuarial Shoaling Process", Tech. Resp., Hydr. Eng. Lab., University of California at Berkeley.

MEHTA A.J., PARCHURE T.M., DIXIT J.G., ARIATHURAI R. (1982) : Resuspension potential of deposited cohesive sediment beds Estuarine comparison, U.S. Kennedy, Ed, Acad. Press. New York pp. 591-609.

MIGNIOT Cl. (1980) : "Dynamique sédimentaire estuarienne - Matériaux cohésifs et non cohésifs", Oceanis, vol. 6, Fasc. 4, pp. 359-432.

MIGNIOT Cl. (1981) : "Erosion et sédimentation en mer et en rivière" in "La Pratique des Sols et des Fondations", Edition Moniteur 1981, 103 p.

TEISSON Ch. (1984) : "Transport en suspension en mer ouverte. Modélisation bidimensionnelle verticale", LNH HE/42/84.30.

TEISSON Ch. (1985) : "Transport en suspension en mer ouverte - Modélisation bidimensionnelle horizontale", LNH HE/42/85.57.

TEISSON Ch., GRAFF M., FRITSCH D. (1987) : "Etudes hydrosédimentaires de l'estuaire externe de la Loire liées au projet de Centrale du Carnet - 1ère partie : Modèle hydrodynamique", LNH HE/42/87.15.

THOMAS, W.A., and W.H. Mc ANALLY (1985) : A generalized numerical modeling system for open channel flow and sedimentation, TABS-2, "IR HL-85-1, U.S.A. WES, Vicksburg, Miss.



Puerto de Barcelona

PART V

CASE STUDIES

San Ciprian—Lugo



CHAPTER 202

ENGINEERING STUDY FOR A NEW SEAWATER INTAKE SYSTEM

Billy L. Edge* and Roger S. Schlueter**

ABSTRACT

Environmental assessment, engineering studies and designs were completed for a new 26.5 m³/s seawater intake system in the Persian Gulf. The original intake facility consisted of a curved, 60m breakwater with one end attached to the shoreline, a settling basin immediately adjacent to the shoreline and dredged to a maximum depth of approximately 5m, and a pumphouse structure located on shore such that the seaward wall formed one side of the settling basin. The facility located on an island in the Gulf, which served multiple seawater uses, had experienced both structural and operational problems, the latter consisting principally of excessive ingestion of sediment and seaweed. These factors plus the requirement for additional demands for seawater beyond plant capacity caused the owner to initiate a study of alternative intake systems, produce a design for the most effective solution and construct the new intake system.

INTRODUCTION

The intake system supplies cooling water primarily to a large LNG processing facility. Cooling water enters from the Gulf on the north side of the island through a small 5m deep sedimentation basin into the front bay of a large pump station with seven pumps. The cooling water circulates through the condensers and then back into the Gulf on the east side of the island. The site location is shown on Figure 1. Through field studies and numerical analysis it was shown that the heated discharge did reach the intake at some stages of the tide causing poor cooling performance.

A second problem has occurred seasonally for several years. In particular, at certain times of the year *Colpomenia cf. sinuosa* (a macro algae) appear in great quantity and clog the cooling water intake. In front of the pump bays, a rotating screen operates behind a bar screen. On several occasions the quantities of macro algae were so great as to totally clog the system and to cause the plant to shut down for several days. The economic consequences of this are obvious.

The third problem which required solution was the identification of the source and elimination of the sediments being ingested into the plant. These sediments were not only filling in the deposition basin but were also going through the pumps causing excessive wear on the cooling system.

Lastly, there was a desire to increase the capacity of the intake plant by 50% to include increased cooling requirements as well as fire water and desalination needs.

*Cubit Engineering, 4431 Embarcadero Drive, West Palm Beach, FL

**AMI Systems Inc., Santa Barbara, CA

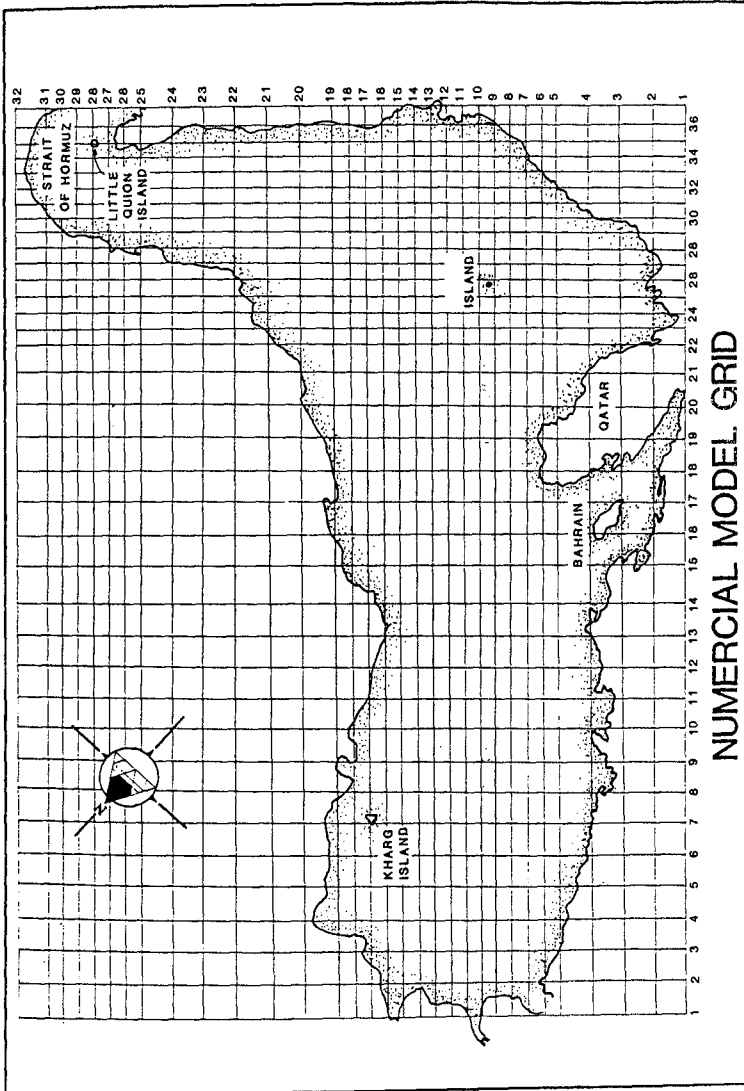


Figure 1. Location of project site in Persian Gulf.

A program was developed to analyze the problem, to identify appropriate solutions and to carry those solutions through design to construction. The study and analysis included:

- o Field data collection and analysis covering site physical oceanography, meteorology, coastal geomorphology, biofouling, and thermal dispersion;
- o Engineering studies including thermal recirculation, bio-fouling control, and development of design criteria;
- o Formulation and evaluation of alternative conceptual layouts for a new intake facility with particular attention directed to construction and operational integration with the existing plant;
- o Recommendations for any additional field studies and hydraulic modeling prior to initiation of the final design process;
- o Preparation of final design and tender documents and completion of construction.

FIELD AND ENGINEERING STUDIES

Winds

Winds are of primary concern in the design of virtually any coastal or offshore structure because of the direct influence they have upon the wave climate, current circulation, and storm surge phenomena. The dominant extreme wind regime in the Persian Gulf is the winter "shamal", characterized by strong northwesterly winds which generally persist for a period of several days. A statistical analysis of wind velocity maxima was made on the basis of continuous speed and direction measurements during the period 1958 to 1967 (IMCOS Marine, 1969). The analysis indicates that about 50 percent of the time winds are from the northwest. Return probabilities of storm wind occurrence at the site were estimated from this data and are shown below:

Table 1. Extreme wind statistical analysis

Return Period (years)	6-hr Mean Velocity (m/sec)
100	23
25	21
10	19

In support of these figures it should be noted that ship observations in the southern Persian Gulf tabulated by the U.S. Naval Weather Service Command (USNWS, 1971) indicate that during the period 1963 to 1971 no winds occurred that were in excess of 24 m/sec from any direction.

A recent study performed for ARAMCO (Ocean Weather, Inc., 1983) reviewed the storm meteorology of the Persian Gulf since 1963. Historical wind data were compiled, annotated, and reduced to 15 extreme events over the study period. This data base was used to develop design wave and water level criteria.

Waves

A statistical definition of storm-generated wave heights and periods was required to determine (1) the degree of attenuation necessary to protect shoreline pump bays and (2) the structural requirements necessary to ensure the survival of intake structures and breakwaters during adverse weather conditions. Design wave parameters have been previously prepared by A.H. Glenn Associates (1982).

Long-term records of wave data directly relevant to the site are virtually non-existent. Consequently, a description of the design wave condition were made through hindcast techniques. In this analytical technique, the more extensive wind data over the Gulf region is used to reconstruct historical storms of record. Numerical and empirical models are then employed to calculate or "hindcast" the corresponding wave characteristics at the point of interest.

Table 2. Predicted wave heights

Return Period (years)	Water Depth (m ISLW)	Sig. Wave Ht. (m)	Sig. Wave Per. (sec)	Max. Wave Ht. (m)	Max. Wave Per. (sec)
10	4.7	3.4	7.3	---	---
	13.5	4.2	7.4	7.9	8.2
	25.0	4.4	7.4	8.2	8.2
100	6.0	4.4	8.6	4.6	9.6
	13.5	5.4	8.7	10.0	9.7
	25.0	5.7	8.7	10.7	9.7

Based upon 15 extreme wind events compiled in a recent study for ARAMCO (Oceanweather, Inc., 1983), a storm considered to be the largest event over the last 25 years was analyzed for wave incidence at the intake site. This shamal occurred over the period January 19 to 21, 1964 and is estimated to represent a 25-yr event. Hindcast analysis of this storm using the discrete spectral model of Resio (Resio et al., 1981), which has been calibrated for this region of the Persian Gulf, gave a peak significant wave height of 4.5 m and a spectral peak period of 10 seconds.

Wave refraction analysis was performed to evaluate the transformation of deeper water waves to the near shore region on the northern side of the island. Wave behavior for waves with periods of 6, 8, 10 and 12 seconds approaching the site from the northwest, north and northeast sectors was analyzed. These conditions were chosen as representative of those generated by the shamals.

Water Levels

Anticipated extreme water levels over the design life of the intake system determine requirements for pump machinery protection. Furthermore, they govern the maximum wave height which can propagate to the intake. Conversely, the minimum water level to be expected at the site is an important

consideration in terms of insuring enough water depth to maintain the design cooling water flow rate. Astronomical tidal information relative to the site is summarized below:

Table 3. Astronomical tide summary
(elevations in meters relative to Chart Datum)

Level	Elevation (m)	Reference
Highest astronomical tide	1.7	A.H. Glenn, 1982
Mean Higher High Water	1.2	U.S. NOS, 1980
Mean Tide Level	.8	A.H. Glenn, 1982
Mean Lower Low Water	.5	U.S. NOS, 1980
Lowest Astronomical tide	-.1	A.H. Glenn, 1982

Storm surge and seiche resulting from sustained winds blowing over the Gulf can create an additional rise or fall of the water level. The northwesterly shamal is capable of generating storm surges via wind stress effects over the axis of the Gulf. IMCOS Marine (1969) predicted a still water level of +3.05 m and it is assumed that this value represents a 100-yr event.

To confirm this value, one and two-dimensional numerical storm surge models were run over the entire Persian Gulf using hindcast wind fields obtained from Oceanweather, Inc. Surge was assumed to be coincident with a Mean Higher High Water tide and results indicated that a maximum still water level on the order of +2.76m and possibly lower may be a more likely expectation over the project design life.

Southerly winds which persist for some duration are capable of lowering the still water level at the southern end of the Persian Gulf. A simplified one-dimensional drawdown calculation was made using bathystrophic storm tide theory. Preliminary and uncalibrated results indicate that drawdown on the order of 0.75 m may be expected over the project life of the intake structures.

Currents

Determination of predominant flow characteristics provides important operational design information related to net flow rates of fouling organisms or other material toward the intake as well as thermal plume recirculation. No historical, site specific data were available on currents in the vicinity of the site. Consequently, a brief field measurement study to record in situ current speed and direction was undertaken.

Thermal Recirculation

The hydrodynamic and thermal characteristics of the LNG intake and discharge structures are reasonably complex due to the poorly defined advection and mixing conditions and complex bathymetry. The discharge volumes and velocities of the proposed new discharge channel are large as is the temperature difference between the discharge and ambient waters. The

discharge is into shallow waters which are subject to complete current reversal as the tide sweeps around the island.

The field study results of the vertical profiles of temperature and the synoptic temperature plots indicate that the discharge plume remains attached to the surface and shows relatively little vertical dispersion. Field studies also indicate that during conditions of tidal cycle which carries the discharge plume towards the intake, the observed temperature rise was primarily confined to the upper water layer.

Because of the complexities stated above it was decided to divide the analyses into two phases, the first analyzing the near-field plume and the second the far-field effects. The near-field is defined as that region in which the discharge plume characteristics are dominant. The far-field is defined as the region in which the larger scale oceanic forces dominate.

Modeling of the far-field, where tidal and wind forces are dominant, poses different problems from the near-field. Due to the location of the site, a conventional hydrodynamic modeling effort is complicated by the difficulties to determine appropriate boundary conditions. With the surface plume stratification, use of a three-dimensional or stratified model would be desirable. However, given the lack of information regarding vertical mixing and the far greater amount of boundary information required by a three-dimensional model, such an approach is not justifiable. Therefore, it was decided to use a depth averaged model and apply various sets of assumptions which would bound the extreme case conditions. Boundary conditions were determined by running a two-dimensional model for the entire Gulf as schematized in Figure 1.

Sediments

Required seawater quality in terms of undissolved solids for the new intake system were defined as 1.5 ppm for calm conditions and 5 ppm for storm conditions. In addition, it was stated that water for the new firewater system should not contain solids which will block a 3.5-mm diameter spray nozzle. These requirements essentially define the limitations on sediment ingestion by the new seawater intake system.

Significant sedimentation within the existing pump forebay area was reported but no quantitative information adequately delineated the problem. Therefore, it was necessary to conduct an investigation to determine the origin and magnitude of this sedimentation problem.

While the rate of intake of sediments rises during storms, it is reported to be a minor problem. The sediments appearing just on the outside of the breakwater are not in sufficient quantity to create an ongoing problem. In addition, because of their coarseness, they are not readily mobilized and do not appear to be moving toward the mouth of the intake at a rate to create a problem. Moreover, these sediments do not appear to have been transported into this area from a remote distance.

Field studies determined that the breakwater was responsible for the majority of sediment build-up. Improperly graded filter stone was placed beneath the 15-ton tetrapod armor units and significant leaching of the core material occurred. Furthermore, poor stone materials, including breccia from

the island, were used and a breakdown toward fine material began via water induced deterioration and wave generated abrasive stresses.

Geotechnical Factors

The site is one of a number of diapiric structures which occur in the Persian Gulf and which are part of a major province of salt diapirism centered in southern Iran. During the early Pleistocene epoch, tectonic pressures within the crustal rocks at depth beneath the Gulf initiated a redistribution of a major evaporite horizon within the Cambrian Hormuz series. The low specific gravity and viscosity of this evaporite as compared with the surrounding rock types resulted in the upward movement of the evaporite mass through the overlying strata forming a salt plug.

The northern part of the island is the gypsum cap of the salt plug. Severe disturbance of surrounding rocks occurred during the upward movement of the evaporites. Large masses of rock have been detached and reoriented and a wide variety of rock fragments were mixed into a gypsum matrix. The subsequent dissolution of the salt plug by seawater has resulted in a chaotic aggregation of evaporite, sedimentary and igneous rocks around numerous domes of gypsum and gypsum breccia, and today, no orderly geological sequence can be established within the rocks. However, it is estimated at this time that the near shore region sub-bottom most likely consists of a layer of coral rock underlying breccia or sandstone.

From an engineering standpoint, offshore excavation will be difficult and require powerful dredging equipment as some of the coral and breccia can be moderately strong (unconfined compressive strengths for coral and breccia reaching values of up to 5 MN/m² and 17 MN/m², respectively). Breakwater protection can most likely be placed directly on the sea bottom without any risks for a base type failure. The rock will need to be imported to the island.

EVALUATION OF ALTERNATIVE SYSTEMS

Several onshore and offshore alternative cooling water intake system concepts were evaluated during the course of this study. Each concept was formulated to satisfy the following basic design requirements:

1. Provide the necessary cooling water volume
2. Eliminate sediment ingestion
3. Eliminate entrainment of biological foulants
4. Not interfere with the existing intake during construction
5. Afford practical construction methodology
6. Minimize thermal recirculation of discharge water.

In developing alternative system configurations, the primary concern was system reliability since the present facilities provide unacceptable levels of downtime associated with fouling and unacceptable rates of wear and high maintenance due to sediment ingestion.

Because of the large expense associated with shutdowns of the seawater system, a more reliable system having a higher initial construction cost may

provide a more economical long-term solution when total costs are considered. Consequently, hydraulic performance and antifouling characteristics were heavily weighed evaluating the alternatives. Secondly, construction logistics were considered in terms of the ease of building the various schemes at this site in the Persian Gulf.

Table 4. Cooling water intake alternatives

Onshore Concepts

1. Extension of West Breakwater to create a calming zone and construction of new intake pump chamber near existing structure.
2. Porous dike.

Offshore Concepts

3. Offshore pipeline and intake; pipeline laid on bottom surface.
4. Offshore pipeline and intake; pipeline buried below bottom surface.
5. Offshore tunnel and intake.
6. Offshore pipeline trestle and suction riser.

Onshore Concepts

An onshore intake withdraws seawater from the entire nearshore water column because of the relatively shallow entry depth compared to the large pumping demand. Any onshore system will be exposed to the same loading stresses which the existing pump station has experienced. Therefore, facility improvements are required so that sand entrainment, biological fouling, and pollution contamination can be handled with no loss of plant efficiency.

Two onshore concepts were reviewed. The first concept is shown in Figure 2 and is essentially an extended modification of the existing intake layout with the breakwater running parallel to the shoreline. The stilling basin would be designed to provide sufficient wave protection and a sufficiently low current that sediments would be induced to settle out in the deepened basin. This would allow a longer accumulation time between maintenance dredging.

Entrained Colpomenia and other biota would still require mechanical screen removal. However, it is possible that some improvement over the present design could be obtained through careful specification of filter systems and screen wash management.

The second onshore alternative incorporates the use of a porous dike--a rubblemound structure constructed of highly permeable material--to completely enclose the onshore pump station. In this scheme, seawater filters through the structure's voids en route to the pump station and undesired foulants and sediments are virtually precluded from entry.

The principal drawback to porous dikes are their uncertain history regarding long-term clogging. The structure must be designed to anticipate a degradation of porosity. Calculations were made to determine the length of

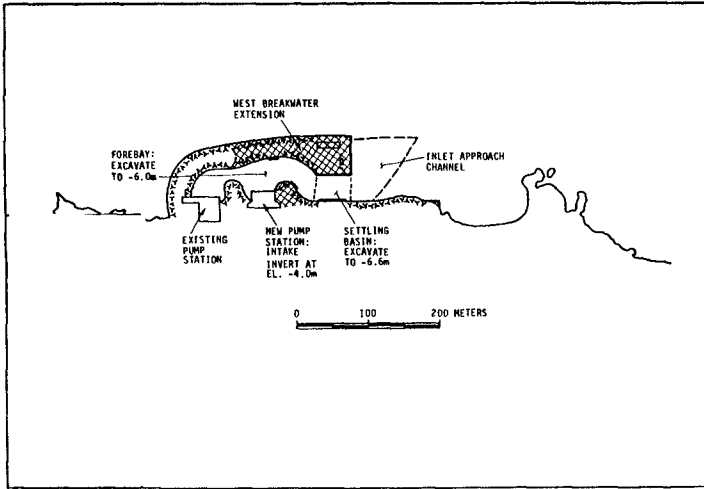


Figure 2. Onshore intake with parallel breakwater.

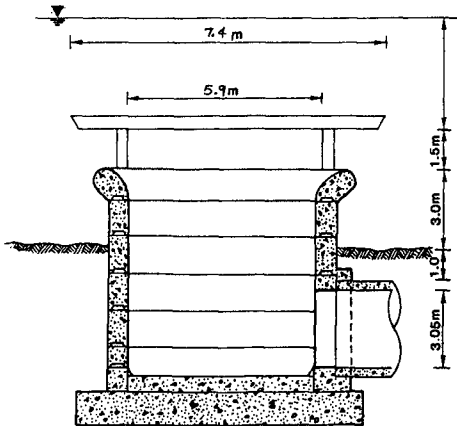


Figure 3. Offshore submerged intake riser.

dike needed to provide the design flow rate. Assuming a cross section constructed with fine gravel, a dike length of at least 1,200 m would be required. Furthermore, the ability of the system to prevent infiltration of floating pollutants is unknown. For these reasons, the concept was rejected.

Offshore Concepts

An offshore intake is often employed to withdraw large quantities of water when onshore intakes are not acceptable. Furthermore, an offshore intake can be used to access ambient water with cooler temperature characteristics. Consequently, this concept has important, attractive features that allow it to meet the design specification for the cooling water system.

Offshore intakes have been successfully used in a variety of marine cooling water applications. By submerging the point of water withdrawal sufficiently below still water level, operation can continue uninterrupted even during severe storm wave activity.

Based on available information, the offshore intake concept was recommended for design. Because of its proven operating capabilities, it offers the highest potential for alleviating the problems which are presently being experienced at the existing onshore intake.

The cooling water intake for an offshore system consists of three components:

1. The pump station and forebay;
2. The seawater intake; and
3. The connecting corridor between the pump forebay and seawater intake.

The following sections discuss desirable design features of each component in formulating a complete offshore system.

Pump Station and Forebay

The pump station should be designed so that the area is sufficiently protected from destructive waves, affords the opportunity to clarify the intake water prior to pump suction, and prevents fouling from nearshore waters. All three objectives can be met by completely enclosing the pump station within a small stilling basin. Little difference is expected between the design for the pump station with an offshore intake and that for an onshore intake.

Of primary importance, incorporation of a stilling basin provides a quiescent area for settling of any sand ingested at the offshore intake. This settling basin limits the entrainment of particles to sizes and concentrations required by design requirements. Construction of the settling basin can be achieved by extending the west breakwater to the east or building an entirely new breakwater for the new pump station. This will also preclude oil pollution, wave action, sediments, and seaweed from directly entering the basin. In short, the enclosed forebay greatly enhances pump station efficiency and reduces maintenance activity.

Seawater Intake

The primary function of the intake is to eliminate ingestion of large quantities of foulant which would overload pump station screens or harm internal cooling water components. The intake should be located in areas which exhibit reduced concentrations of Colpomenia populations and minimal sediments.

Offshore seawater intakes are simple structures which rest on the sea bottom and are elevated sufficiently above the seabed to minimize entrainment of sediment or bottom dwelling organisms. Figure 3. illustrates the chosen concept. The intake consists of prefabricated annular sections, normally of reinforced concrete, which are pieced together onsite. The assembled structure is then floated to the site and sunk into position. The horizontal velocity cap atop the structure induces lateral inflow of seawater thereby minimizing vortex generation and entrainment of bottom or surface floating material. The entrance slot is sized so that the velocity through the intake is no greater than .3 m/sec to minimize fish entrainment.

Intake Corridor

The most standard scheme is an offshore buried pipe. In this design, shown schematically on Figure 5, a trench is excavated to accommodate a large diameter conduit which is then covered for wave protection purposes. The diameter of the pipe must be sufficient to maintain velocities and hydraulic head losses within reasonable limits. A single conduit with a 4.27 m internal diameter (ID) would be required to satisfactorily convey the required flow from the offshore intake structure to the nearshore forebay.

Burial of a large diameter pipe involves extensive excavation of the marine bottom. The trench must then be lined with a gravel bedding to provide uniform foundation support for the heavy pipe segments. Select backfill is then placed to the crown elevation of the pipe and the trench is capped with suitable armor material.

An unburied pipe section would be fully exposed to the hydrodynamic loadings of storm generated waves and currents. Estimated wave forces would be of such magnitude that they could not be resisted by conventional pipeline anchors. An exposed conduit is therefore not recommended for further consideration.

Because of the hard bottom material found at the site and a sensitivity to the use of explosives to aid in excavating such strata, a tunneled conduit was considered. A tunnel can be considerably less disruptive to the marine environment and operation of the present intake. The total length requirement of 200m for the tunnel proved too costly for implementation of this alternative.

The third alternative, an over-water pipe system, is one in which water is drawn from an offshore location and pumped/siphoned via several smaller conduits to the depressed forebay. The siphon would be elevated over water by a conventional trestle-type structure as depicted on Figure 4. This concept can make use of smaller, lightweight, and hydraulically smooth Fiberglas reinforced pipe. Based on the flow requirements of the site, three 2.44-m ID pipes would satisfactorily deliver the cooling water from the intake to the

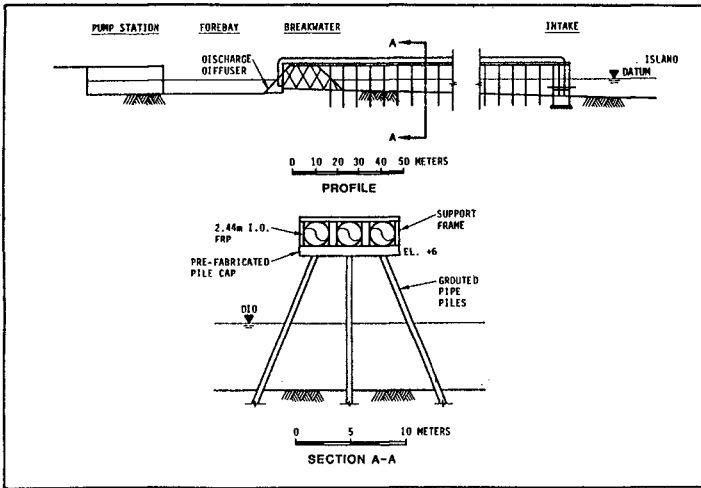


Figure 4. Pump/siphon water intake on trestle.

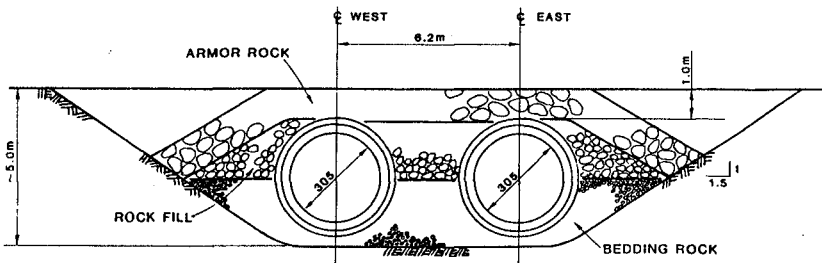


Figure 5. Buried concrete pipe design with backfill.

forebay. Additional advantages include ease of construction and an exposed pipe which facilitates operational maintenance. The elevated trestle allows waves to pass beneath it such that only the piling requires wave force design.

ENGINEERING DESIGN

Based on the above criteria, an intake system comprised of an onshore pumping facility and an offshore intake structure best met all relevant criteria and provided a proven, workable system. Key characteristics of the recommended system are given below.

Intake Design

1) Two partially buried, cylindrical offshore intake structures 5.88m in diameter are located approximately 175m offshore at the 8m contour. Each riser structure including velocity cap is approximately 9m high with the intake gap protruding 3.5m above the seabed.

2) Each riser is connected to a shoreline stilling basin via a buried concrete pipe 3.05m in diameter as shown in Figure 5.

3) The stilling basin is formed by a horseshoe shaped breakwater designed around the new pump station. The entrance to the 30m long stilling basin is a 20m long concrete diffusor structure which transitions the flow from the concrete pipe(s) into quiescent flow in the stilling basin. The enclosed stilling basin provides the desired water quality and protects all shoreline structures from surge and waves.

4) The intake stilling basin is dredged to -5.0m and will require only infrequent dredging for maintenance purposes.

5) Construction of the system can be achieved through positive isolation of nearly all of the new facilities from the present operating facility. Changeover from the old facility to the new is required to be achieved in a smooth transition period without loss of cooling water service to the island.

Hydraulic Model and Design Criteria

As part of the preliminary design, an extensive series of two and three dimensional model tests were conducted at the Delft Hydraulics Laboratory. Horizontal and vertical loadings on the intake risers were measured and the required pipeline armor stone size was determined. The wave tests were also used to confirm the design horseshoe breakwater. Separate model tests were conducted for the stilling basin diffusor and pump bay.

The allowable damage for the breakwater was 3% for $T_r = 50$ years. The allowable damage for the armor cover and the pipeline was 1% for $T_r = 100$ years. Damage was defined as movement of an armor unit more than 1.5 units away. One of the interesting results of the model tests was that the breakwater responded best to the placement of a berm at the toe as shown in Figure 6. This allowed the tetrapod layer to be reduced from 15 ton to 10.6 ton units and eliminate the observed Mach stem effect at wave breaking.

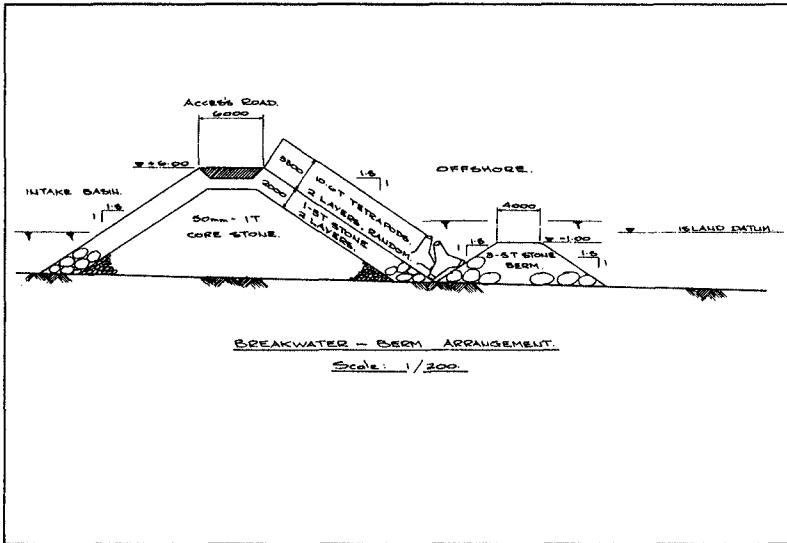


Figure 6. Breakwater cross-section showing berm and tetrapods.

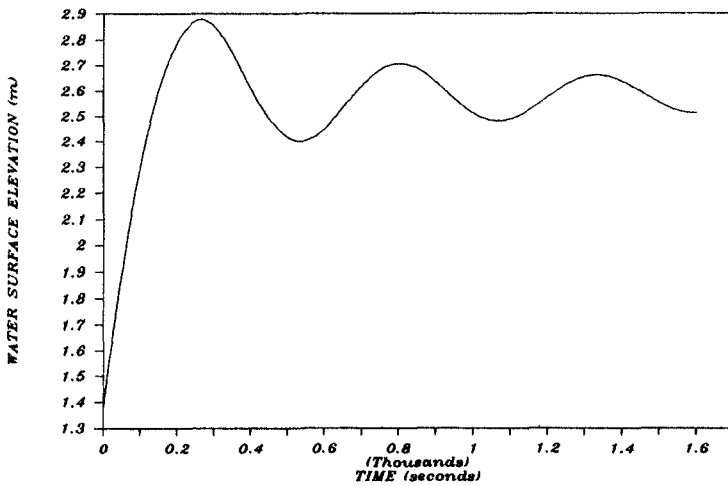


Figure 7. Surge analysis for pump shut-down conditions.

In addition to the above there were several additional specific criteria which were used in the design and the model studies. In the two and three dimensional wave tank tests a Jonswap spectrum was used having the following characteristics:

$$\begin{aligned} \gamma &= 3.3 \\ \lambda_a &= 0.07 \\ \lambda_b &= 0.09 \end{aligned}$$

Hydraulic performance of different components of the system were tested at different design water levels. For example, the breakwater was tested at a HWL of +2.67 representing a 50 year event whereas the pipeline armor was tested at a HWL of +2.76 representing a 100 year event. The significant wave height for the breakwater is $H_{sd} = 5.23\text{m}$ for a return period of $T_r = 50$ years.

During the hydraulic performance tests three discharges were applied:

- half normal flow: 13.25 m³/s through 1 pipe
- normal flow: 26.5 m³/s through both pipes
- maintenance flow: 25.4 m³/s through 1 pipe

Both numerical and physical tests were performed to ensure that the settling basin would not be subject to surging problems due to external wave conditions.

SUMMARY

No difficult or insurmountable final design, construction or operation issues were revealed in the selected alternate for this replacement of the cooling water intake. Nevertheless, there were a series of critical design issues which required satisfaction in the final design.

Construction of this facility is currently proceeding to completion. The offshore parts of the new intake system is expected to be completed in 1988.

CHAPTER 203

ACCRETION - EROSION IN THE BEACHES OF THE CANARY ISLANDS (SPAIN).

JESUS MARTINEZ MARTINEZ

Member of the Spanish Geological Society

Facultad de Ciencias del Mar. Apartado 550. Las Palmas. España.

ABSTRACT

In the beaches under study on the island of Grand Canary, we are identifying and measuring the intertidal annual cyclic processes of accretion and erosion, starting from the topographical movements of the strand.

These processes:

a) We are analyzing and interpreting these in the framework of the physical and geographical interdependences, and as responses to the more internal evolutions of the morphodynamics, in the sedimentary environments in question,

b) and permitting the definition and calculation of some indices of sedimentary gains and losses, of interest to coastal planning and management.

INTRODUCTION AND OBJECTIVES

In the opinion of Charlier (1987), the mathematical calculation and management of the sedimentary volumes, through observation of the topographical movements is, actually, the optimum method for the identification, measurement, and interpretation of the accretion and erosion processes (gains and losses) in sandy beaches.

If the topographical movements refer to the intertidal zones, as it happens in this work, we are obtaining answers to the more internal evolutions of the beach environment morphodynamics, in agreement with the outline of Wright and Short (1983).

The sedimentary dynamics of the beaches develop, to a very important proportion, between the shoreline and the breaker line. With a range of the astronomical tide of up to 2.82 m. (as is the case in the Canaries), the intertidal zones have sufficient amplitude to support truly valid investigations, referring to the accretion - erosion processes, in the beaches under study.

The accretion - erosion processes represent effects resulting from some determined causes. Knowing and understanding the "effect - cause" duality, we can predict "causes - effects" through the numerical model.

The modelling of these processes develops various conceptual stages. We will order these from bottom to top, depending on the best level of abstraction and generalization:

a) In the first phase, the works in the field aimed at identifying a physical model, in which predominates the selection of basic qualitative characteristics.

b) The translation of qualitative data to quantitative data constitutes a complex process, which passes through intermediate partial modeling steps. The representation of the selected descriptive parameters, of adequate scale, culminates in the establishment of a quantitative stage.

c) And in the quantitative phase, we apply, essentially, the mathematical method. This establishes an abstract problem which serves, preferentially, for the analysis of general questions.

The actual work, in the framework described, is situated between the qualitative phase and an intermediate semi-quantitative phase.

On the other hand, the estimations and indices of the sedimentary gains and losses in the beaches are useful, in the present form, in coastal planning and management. Nevertheless, the making of decisions needs to be based on an analysis of the whole of the physical processes and handicaps which appear in these situations.

GEOGRAPHICAL SETTING

The sandy beaches under study (figure 1) are located on the island of Grand Canary (Spain). The descriptions of the same are presented in condensed form in table 1.

ACTUAL TECHNIQUES

The study is based on the following techniques:

1. Elevation of the topographical profiles of the monthly studies, mostly in 1986. We are using the method of geometric levelling (by altitudes), as developed and described by Martínez et al (1987 a, 1987 b, and 1987 c).

2. Calculation of the relative volume of the sands, by the trapezoidal method, in agreement with Puig Adam (1979). The volumes correspond to an intertidal strip, previously determined, and from a convenient base level. The contrast of the series of relative volumes, in relation to the lowest value, measures the sand gains or losses.

3. Oceanographical analysis of the annual gains and losses of the beach sand. For this we have recourse to:

- the surface meteorological predictions
- and visual observations of the surf from ships "en route", in the Canary environment. The data is taken from the "Oceanographic Atlas of the North Atlantic Ocean", in its successive revisions.

With observations of the surf we analyze, for the greatest part of the Grandcanary coast:

- the maximum possibility of presentation/altitude, indefinite depth, of the significant "swell" and "sea" waves in a certain direction (pattern of the directional surf),

Beach	Location	Morphology	Approximate dimensions		Genetic classification after Suárez Bores (1980)
			Length in m.	Maximum width in m.	
Sardina del N.	Costa N. (Gáldar)	in cove	85	45	$G_{0,0}^0$
Las Cantarás	Costa N. (Las Palmas)	subcoves in a large cove	3100	90	$GDDGGDDG_{0,0}^1$
El Hombre	Costa Oriental. (Teide)	in cove	224	91	$G_{0,0}^0$
El Burrero	Costa Oriental. (Agüimes)	in cove	205	30	$G_{0,0}^0$
El Inglés	Costa Meridional (S. Bartolomé)	rectilinear	2700	100	$G_{0,0}^0$ (2)
La Rajeta	Costa Meridional (S. Bartolomé)	convex towards the ocean	470	100	$8_{0,2}^1$
Maspalomas	Costa Meridional (S. Bartolomé)	rectilinear	2103	50	$8D_{0,2}^2$

Table 1

Descriptions of the beaches of Grand Canary (Spain) under study.

- as well as the annual percentages.

Once the annual processes of accretion and erosion have been measured and interpreted, we can define two operative indices:

- estimation of the sedimentary support capacity,
- and the sedimentary variability.

INDEX OF SEDIMENTARY SUPPORT CAPACITY (S.S.C.I.)

This index defines the difference between the actual and potential volumes, derived from topographical profile levelling in situ and theory, respectively, for unity of the observed intertidal surface, and in a certain period of the annual cycle. This is expressed with the formula:

$$\text{S.S.C.I.} = \frac{\text{Cr} - \text{Cp}}{\text{Su}}$$

in which:

Cr = actual volume
 Cp = potencial volume
 Su = observed surface

The theoretical topography is calculated based upon the slope, obtaining:

a) In agreement with:

- the median diameter and densities of the beach sand,
- and the surf characteristics.

Formulas of the type of Sunamura (1984) are considered.

b) Or by employing empirical curves of the equilibrium between beach-face slope and the median diameter of sand.

Among others, Bascom (1959), Komar (1976), and Martínez (1986) describe curves of this type.

Using this method the estimation error is larger.

The potential volume for the operative total of a sandy beach, are deduced, in immediate form, with the equation:

$$\text{Cp} = \text{L A} \left(\text{H} - \frac{\text{A}}{2} \text{tag } a \right)$$

in which:

Cp = potential volume
 L = operative length of the beach
 A = amplitude of the observed strand
 H = average vertical length from the head of the profiles till reference basis
 a = beach - face slope.

The index in question qualifies the beaches according to:

- equilibrium,
- deficiencies
- or in surplus,

as is shown in table 2.

INDEX OF SEDIMENTARY VARIABILITY (S.V.I.)

This index is defined as the estimate of the average altitude of erosion to accretion, in an annual cycle, that overtakes the surface of an intertidal delimited strip, in a sector of or in all of the beach. To sum up, it evaluates the maximum "effective" sedimentary deposition during the annual cycle under study.

In the calculation of this index:

- for a determined transverse profile, with a convenient length and width,
- or for the whole of the intertidal delimited strip of the beach;

we divide the volume of the sand into increments, during the period of significant accretion, for the basic profile section area, or for the operative strip.

The index of sedimentary variability qualifies the beaches as:

- changing attenuatedly (with low indices),
- changing moderately (with intermediate indexes)
- or changing strongly (with high indices),

as shown in table 3.

This index allows us to represent the longitudinal topographic movements of the beaches quantitatively, in scale block diagrams.

A third index that may be fundamental in temporal series analysis of the strand volumes, with data from successive campaigns during a significant number of years under study. The beaches are classified as stable, hyper-stable, and unstable, after the work of Suárez Bores (1980).

All of these indices need to be considered:

- in the design of projects, for the optimization and recuperation of sandy beaches, with maritime works and/or artificial sustenance,
- and in the continueing analysis of these beaches, when we have already had experience with the same, for verifying the conduct of the sedimentary process, and to adapt, in each case, the necessary corrective measures.

RESULTS

Table 4 shows the sand gains, in cubic meters, of the beaches under stu

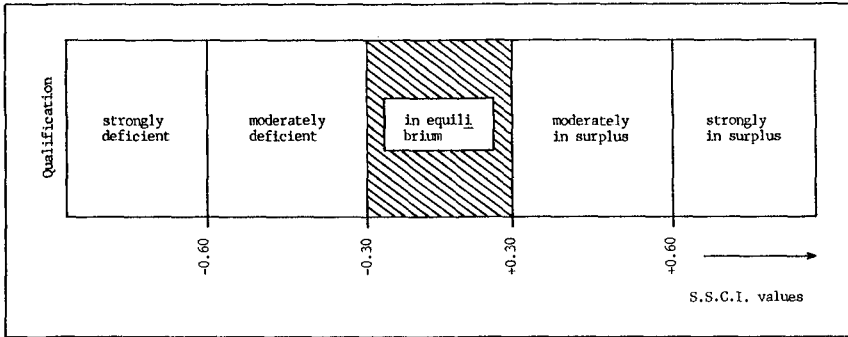


Table 2

Tentative scale for qualifying the sandy beaches according to the index of sedimentary support capacity.

S.V.I. values	Qualification
of 0.00 to 0.75	changing attenuatedly
of 0.75 to 1.50	changing moderately
> 1.50	changing strongly

Table 3

Tentative scale for qualifying the sandy beaches, according to the index of sedimentary variability.

beach		Sand gains, in m ³ , in relation to the significant erosion of the annual cycle under study							
		Sardina del N	Las Canteras	El Hombre	El Burrero	El Inglés	La Bajeta	Maspalomas	
Date		D:66.869.0	D:2169.0x10.0	0:200.6x10.0	D:97.1x12.0	0:2111.0x15.0	D:471.5x15.0	0:2102.5x15.0	
1985/12	303.14	05745.23	3285.30	689.49	32642.96	10680.09	04192.74		
1986/1	272.50	03816.09	3585.86	334.70	35704.79	12365.50	06562.86		
1986/2	038.38	04095.64	2893.17	313.86	40266.28	12024.72	00000.00		
1986/3	100.58	00000.00	0271.30	300.93	38369.33	13671.17	01729.70		
1986/4	000.00	03511.69	0000.00	166.31	35401.32	12476.15	01829.60		
1986/5	070.63	05861.03	2779.44	292.80	29423.33	11574.44	04696.84		
1986/6	266.69	09953.13	3434.31	251.82	17331.43	10148.07	14806.72		
1986/7	494.01	09075.08	2686.86	226.63	16042.21	06671.15	16841.51		
1986/8	489.18	10687.70	2959.49	132.51	14070.81	04225.79	28591.80		
1986/9	327.72	09794.63	3192.79	091.71	12653.42	05070.47	30345.58		
1986/10	444.91	04845.50	3096.40	000.00	08796.16	04499.33	37778.00		
1986/11	343.37	---	3347.16	023.23	01338.24	02208.58	28671.13		
1986/12	445.95	---	3051.68	---	00000.00	00000.00	10215.95		

D = dimensions, in meters, of the intertidal delimited strip

Table 4

Sedimentary balances, during an annual cycle, in various sandy beaches on the island of Grand Canary (Spain).

dy, in relation to the most extreme erosion of the same. This corresponds to an annual cycle (1986).

In the Canaries are presented, habitually, certain surface meteorological situations. These form three groups, depending on the prevailing wind direction:

1. Atlantic anticyclones (trade winds), in combination with the occasional influence of Saharic thermal depressions, during the spring and summer. These involve winds from the N-NE.

2. Deep Atlantic storms with a nucleus over the Gulf of Vizcaya, and at times Atlantic anticyclones greatly displaced to the south, during the autumn and the end of winter-beginning of spring. These involve winds from the W-NW.

3. North-african and South-european anticyclones, Saharic thermal depressions, and Atlantic storms displaced to the south, from autumn to the beginning of spring. These involve winds from the E-S.

In figure 2 are recompiled the directional components and the frequency of these winds, depending on the aforementioned situations, that provoke the dominant and prevailing surfs on the Canary Island coasts.

In the selected beaches. The values of the sedimentary indices are recorded in table 5.

DISCUSSIONS

1. The beaches of Grand Canary are classified based on:

- their geographical location
- and the seasonal incidence of the surf.

We propose the following groups:

Group I:

- beaches in the north cornice, under the influence of diffracted trade wind surf (from the N-NE), and exposed to storms from the W-NW,
- beaches of the south, protected from the trade wind surf.

Group II:

- beaches in the north cornice, directly exposed to the trade wind surf,
- beaches on the east coast, exposed to the trade winds.

Group III:

- beaches on the east coast, protected from the trade winds and open to the SE.

Group IV:

- beaches on the west coast.

We would like to present these transitional cases.

Beach	Period under study	S.S.C.I. (accretion)	Qualification	S.V.I. (annual)	Qualification
Sardina del N. (Galdar)	1985-86	-0.13	in equilibrium	0.82	changing moderately
Las Canteras S. (Las Palmas)	1985-86	+0.15	in equilibrium	0.84	changing moderately
Playa Chica (Las Canteras)	1985-86	+0.24	in equilibrium	0.62	changing attenuatedly
Las Canteras N. (Las Palmas)	1985-86	+0.46	moderately in surplus	0.58	changing attenuatedly
El Hombre (Telde)	1985-86	+0.01	in equilibrium	1.79	changing strongly
El Burrero (Ingenio)	1985-86	-0.01	in equilibrium	0.59	changing attenuatedly
El Inglés (S. Bartolomé)	1985-86	+0.89	strongly in surplus	1.27	changing moderately
Punta de La Bajeta (S. Bartolomé)	1985-86	+0.74	strongly in surplus	1.93	changing strongly
Maspalomas (S. Bartolomé)	1985-86	+0.20	in equilibrium	1.20	changing moderately

Table 5

Estimations of the sedimentary support capacity and of the annual intertidal sedimentary variability, in various beaches under study in the Grand canary environment.

2. The significant accretions and erosion (table 4) of the beaches under study, inside of a yearly cycle, have a strong dependence on the proposed beach groups.

In the Group I sandy beaches the erosion takes place preferably during the winter and spring months, and the accretion during the summer and the first part of autumn.

In the Group II beaches the erosion culminates in summer, and the maximum accumulations occur at the end of autumn-beginning of winter.

In the Group III beaches the erosion develops, above all, during autumn, while the accretion takes place from the end of autumn until the beginning of spring.

The Group IV beaches are under actual study at this time.

Figures 3 and 4 show the performance described.

3. At this time we establish a correlation between:

- The most frequent of the different surface winds (figure 2), corresponding to the period of taking the beach data.
- The greatest probability of presentation and the highest maximums, to indefinite depth, of the surf in relation with these winds (with data from visual observations of ships en route).
- And the significant erosion processes in the beaches open to the surf in question (table 4).

In the correlations:

a) During the dominant time of the trade winds, in the summer, we see the greatest probability of the presentation of the "swell" surf from the N-NE.

In this period, and in the north, east and southern coasts, predominate, with various exceptions, wave heights between 1.83 and 3.66 m. Also are presented, although in low percentages, waves with heights greater than 3.66 m.

b) On the north coast, the maximum probability of the presentation of the "sea" surf, from the N-NE, coincides with the dominance of the trade winds. In this case the dominant waves are of little height, less than 0.91 m. They do not surpass a height of 2.44 m.

c) On the east and southern coasts, the maximum probabilities of the presentation of the "swell" and "sea" surfs from the E, SE and S take place during the autumn and winter and coincide with the most frequent winds determined by:

- South-european or North-african anticyclones,
- Saharic storms,
- or Atlantic storms displaced to the south.

The "sea" surf from the NE does not depend on the trade winds, but on the first two meteorological conditions mentioned above.

In this period waves of low height are predominate; smaller than or equal to 1.83 m. With the exception of "sea" surfs from the NE, they do not ap

proach 3.66 m.

d) When the winds come from the W-NW, from autumn to spring, we observe the maximum probabilities of the presentation of the "swell" and "sea" surf from the NW.

During this period prevailing waves of heights between 1.83 and 3.66 m., and a few others that are higher, come to the northern coast, which is directly affected.

4. In agreement with the described previous aspects, the physical model of the accretion - erosion processes, designed for the sandy beaches of Grand Canary, is formulated as follows:

a) When the trade wind surf predominates and takes its main energy (in the summer season).

- This produces the most extreme erosion in Group II beaches.
- And develops the most important accretions in Group I beaches.

b) During the decline of the trade winds:

- The Group II beaches attain the process of accretion (autumn-winter).
- Surfs from the E, SE, and S make their appearance. The dominant and most energetic of these, in autumn, are connected with Group III beach erosion.
- And the Atlantic storms come from the W - NW (from autumn to spring). These same do not impede the most important accretions in the Group III beaches (winter) and determine, in those situations of high surf energy, the significant erosion in the Group I beaches (winter-spring).

5. The index of sedimentary support capacity qualifies for all the beaches under study between in equilibrium and strongly in surplus (table 5).

Forthwith, aside from anomalous very energetic oceanographic situations, and if we do not wish to enlarge the surface in use, the beaches do not have the capacity to accept artificial sustenance for the optimization of these sedimentary environments.

6. The annual sedimentary variations of the beaches are adjusted by a continuity function:

- the "net" processes of erosion are determined by the seasonal impact energies of the surf,
- and the "effective" sedimentary contributions (predominately gains over losses) occur when these impacts subside.

With respect to the dominant trade wind surf, the exposed beaches under study (El Hombre and Punta de La Bajeta) have higher indices of sedimentary variability than the protected ones (Sardina del Norte, Las Canteras, El Burrero, El Inglés and Maspalomas), as we see in table 5. The first group takes the title of "attenuating" and "moderately changing" while the second group takes the title "strongly changing".

From this we deduce that, on the island of Grand Canary, the surf from the N-NE is the most erosive in relation to the others.

On a single beach (Las Canteras for example), the sector most exposed to

the indicated surf shows the largest sedimentary variation (Las Canteras South).

In a single beach or a sector of the same, with an important annual sedimentary variation, the construction of an adequate breakwater, nevertheless determines a reduction in the contributions, would produce a considerable reduction in the erosion processes. The result of the above conveys a net sand gain, with consequent growth of the dry-intertidal area.

CONCLUSIONS

The Grand Canary beaches are classified into four groups. For this we take into account:

- their geographic location,
- and the seasonal incidence of the surf.

The annual accretion and erosion processes are different for each beach group.

In the analysis of the sedimentary balances, we satisfactorily establish correlations between the selected significant variables.

The beaches under study are situated, for the one part, between in equilibrium and strongly in surplus, and for the other part, between attenuating and strongly changing, depending on the scales proposed for the sedimentary indices here defined.

ACKNOWLEDGMENT

The author wishes to express his appreciation to Dr. José M. Pacheco Castalao, the Dean of the Facultad de Ciencias del Mar (Universidad Politécnica de Canarias), for his critical reviewing and contribution of suggestions in the development of this work.

REFERENCES

- Bascom, W.N. 1959. The relationship between sand size and beach-face slope. *Am. geophys. union trans.*, 32 (6), 866-874.
- Charlier, R.H. 1987. General discussion and round table. *European Intensive Course on Land-use Problems, Planning and Management in the Coastal zone*. Bilbao (Spain), October, 8-17.
- Enriquez, F. y Berenguer, J.M. 1986. Evaluación metodológica del impacto ambiental en las obras de defensa de costas. *Publicación del CEDEX. Madrid*.
- Komar, P.D. 1976. *Beach processes and sedimentation*. Ed. Prentice-Hall. Englewood Cliffs, New Jersey.
- Martínez, J. 1986. Estabilidad-inestabilidad en los depósitos de arenas de las playas canarias: Relaciones entre pendientes topográficas y

- granulométricas. Boletín del Instituto Español de Oceanografía, 3(2), 87-96.
- Martínez, J.; Sastre, J.; Alemán, G.; Castro, J.; Martín, A. y Robayna, D. 1987a. Los movimientos de las superficies topográficas en las playas de arena: método de investigación e interpretación. Revista de Obras Públicas, julio-agosto, 469-483.
- Martínez, J. y Cárdenas, M. 1987b. Los cambios topográficos y sedimentológicos en las playas arenosas de El Inglés y Maspalomas (Gran Canaria-España). Actas de la VII Reunión sobre el Cuaternario, AEQUA, 223-226.
- Martínez, J.; Navarro, T.; Roldán, A. y Rosario, M. Del. 1987c. Cuantificación e interpretación de los procesos de acreción-erosión, en la playa arenosa de El Hombre (Gran Canaria-España). Actas de la VII Reunión sobre el Cuaternario, AEQUA, 227-230.
- Puig Adam, P. 1979. Cálculo Integral. Editorial Gómez Puig. Madrid.
- Suárez Bores, P. 1980. Formas Costeras. Publicación de la Escuela Técnica Superior de Ingenieros de Caminos, Canales y Puertos de Madrid.
- Sunamura, T. 1984. Quantitative predictions of beach-faces slopes. Geological Society of America Bulletin, 95, 242-245.
- US Naval. 1970. Oceanographic Atlas of the North Atlantic Ocean. S. Naval Oceanographic Office. Washington.
- Wright, L. y Short, A. 1983. Morphodynamics of beaches and surf zones in Australia. In: P.D. Komar (Editor), C.R.C. Handbook of Coastal Processes and Erosion, C.R.C. Press, Boca Raton, Fla., pages 35-64.

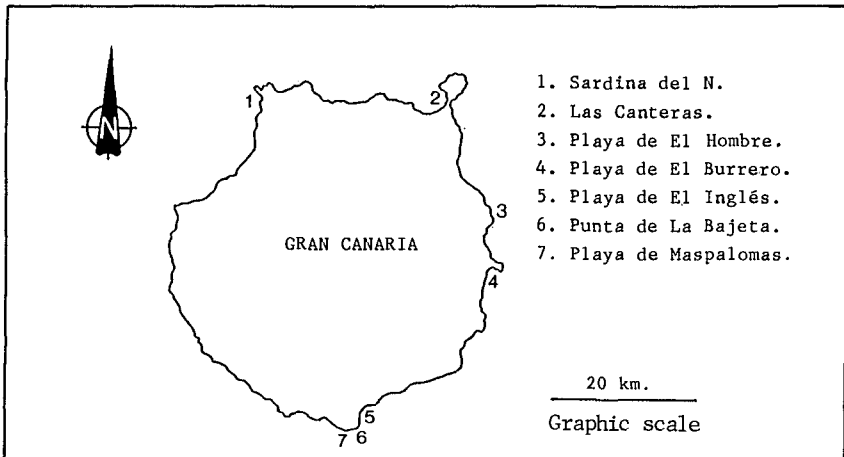


Figure 1

Geographical location of the Grandcanary beaches under study.

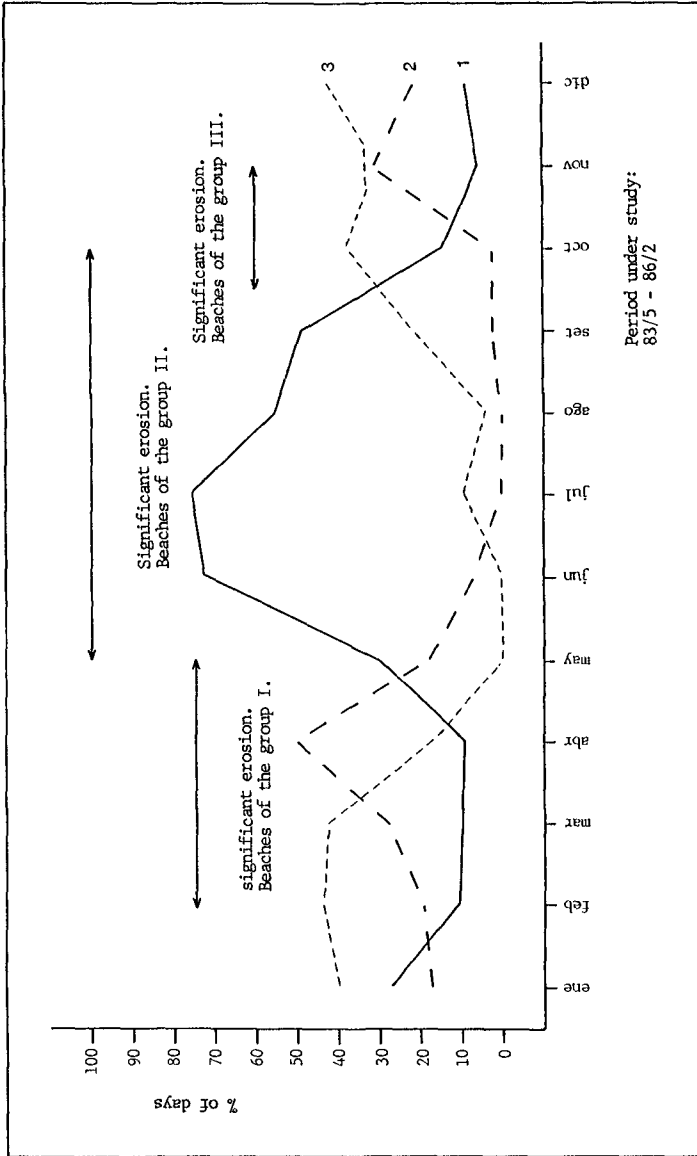


Figure 2

Frequency of the winds in the environment of the island of Grand Canary (Spain). 1: winds from the N - NE,, 2: winds from the W - NW,, 3: winds from the E - S.

Period of year	Group of beach	I	II	III	IV
		Winter	↕		
Spring		↕			
Summer			↕		
Autumn				↕	

Figure 3

Localization of the extreme processes of annual erosion in the sandy beaches of Grand Canary.

Period of year	Group of beach	I	II	III	IV
		Spring			
Summer		↕			
Autumn		↕			
Winter			↕	↕	

Figure 4

Localization of the most important annual accretion processes in the sandy beaches of Grand Canary.

CHAPTER 204

SUBMARINE SIPHONS FOR ATHENS SEWERAGE SYSTEM

Y. Eisenberg, M.ASCE
Th. C. Gofas, M.ASCE
R. A. Fasano, M.ASCE
F. S. Hindes

ABSTRACT

The submarine siphons with an overall length of almost 1300 meters and an ultimate capacity of 27 cubic meters (m^3) per second (about 600 million gallons per day) will be a major element of the new wastewater conveyance and treatment system presently under construction in Athen, Greece. This will help alleviate the present condition where an average of more than $6 m^3$ per second (130 million gallons per day) of untreated domestic and industrial wastewater are discharged into the sea near Athens. Construction of the submarine siphon pipes started in late 1984 and was completed in early 1987.

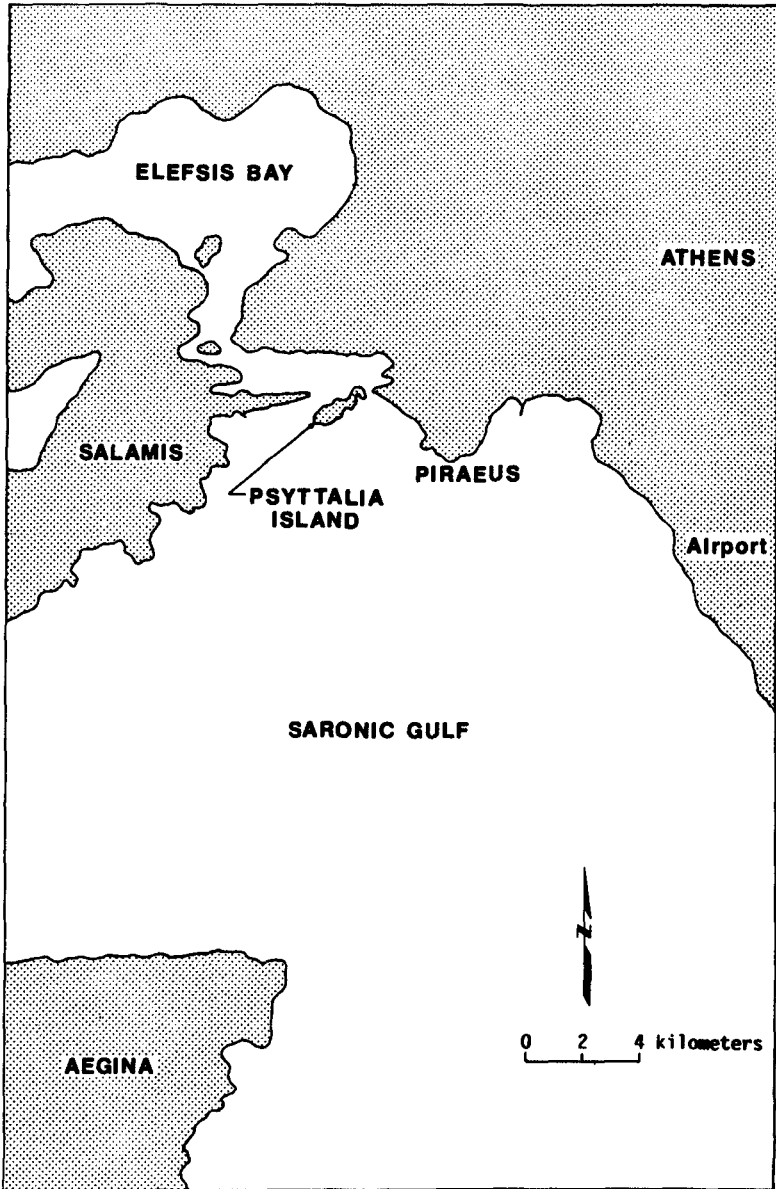
Description of the data collection for and the design, manufacture and construction of these submarine siphons are presented in this paper.

INTRODUCTION

In 1983, the Greek Government undertook a \$100 million program dealing with the collection, transportation, treatment, and disposal of sewage of the greater Athens area serving a population of over three million people. The program involves the collection of sewage from the mainland and its transportation to the small island of Psyttalia through two 1300 meter long submarine siphon pipelines with an inside diameter of 2.8 meters. A treatment plant on Psyttalia will process the sewage prior to its ultimate disposal through a 1600 meter long diffuser outfall into the 60 meter deep water of the Gulf of Saronikos.

The submarine siphon pipelines, whose design and construction are described in this paper, have a hydraulic design capacity of 27 cubic meters per second (about 600 million gallons per day). They traverse a shipping channel carrying heavy traffic to Elefsis Bay near Piraeus Harbor (see figure 1 - Vicinity Map and figure 2 - Project Site) through a troublesome layer of sludge created by previous sewage dumping and are placed in a protective trench at depths reaching almost 50 meters below sea level (see figure 3).

Y.Eisenberg, Parsons Brinckerhoff, San Francisco, California, U.S.A.
Th.C.Gofas, Th. Gofas and Partners Ltd., Athens, Greece
R.A.Fasano, AWD Technologies, Wayne, New Jersey, U.S.A.
(formerly with Woodward-Clyde Consultants, Wayne, NJ, U.S.A.)
F.S.Hindes, Lafayette, California U.S.A.



VICINITY MAP

Figure 1

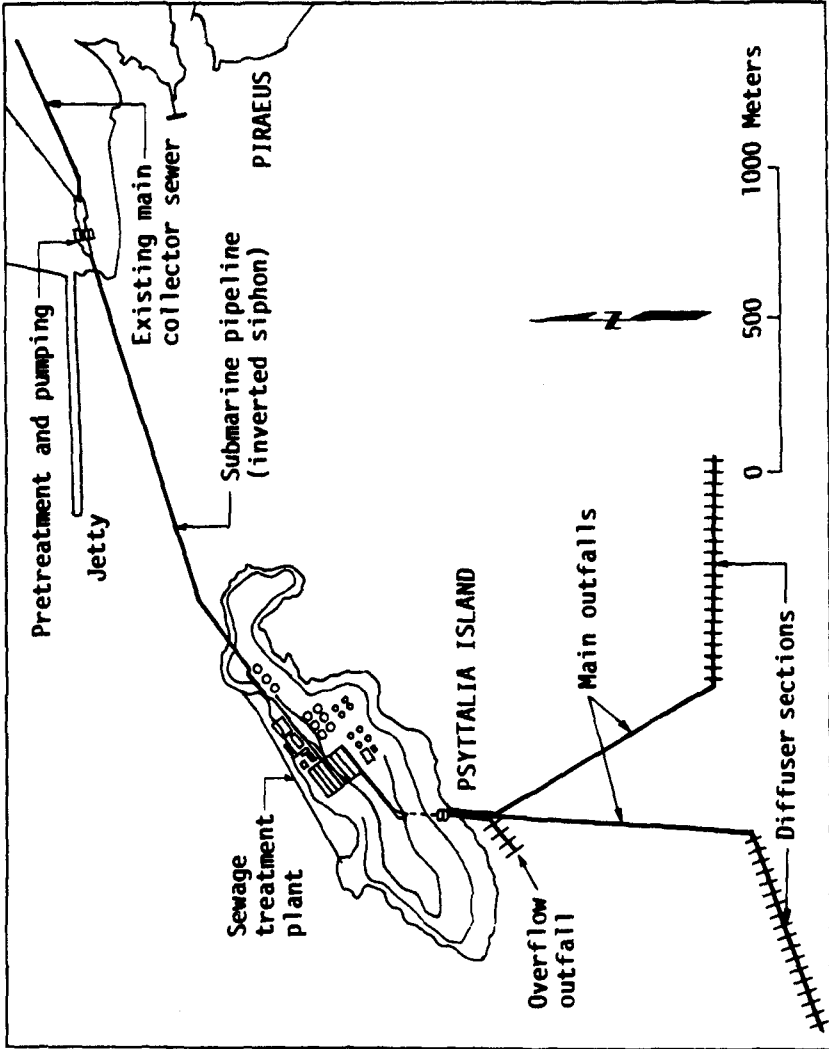


Figure 2

SITE PLAN

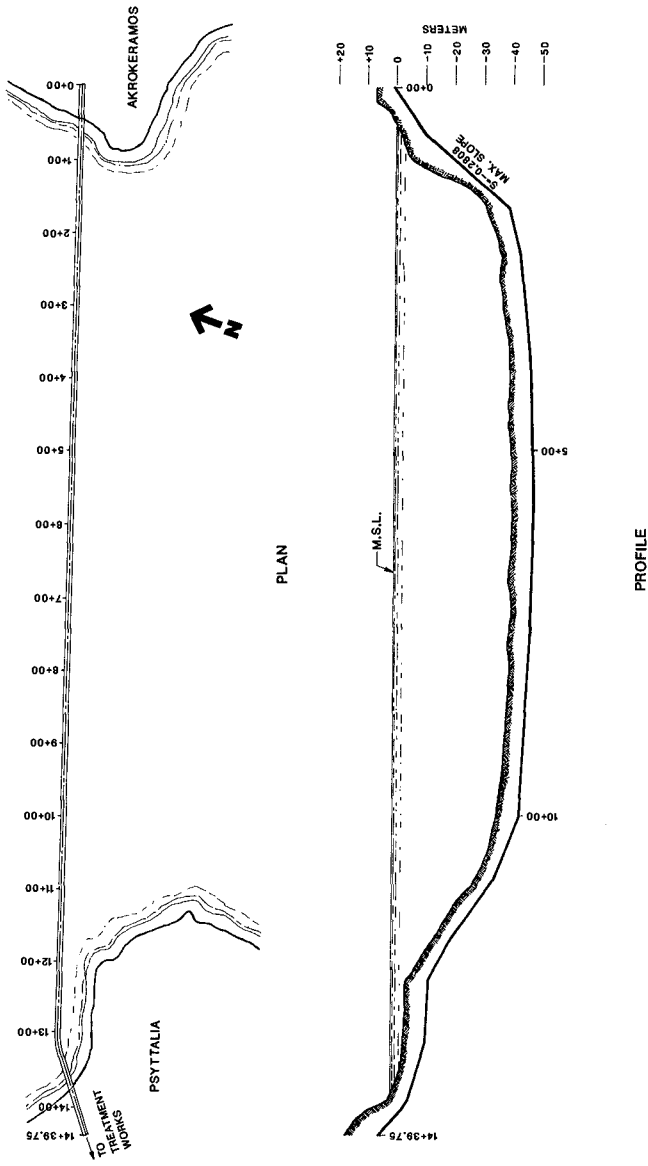


Figure 3

DATA COLLECTION

The geotechnical conditions along the route of the pipeline were investigated by a combination of borings, probes, and marine geophysics.

A total of 14 borings were made at 100 meter intervals to depths of approximately 15 meters below the sea bottom. The borings were supplemented by a total of 30 probes driven to "firm" conditions below the sea bottom. The purpose of the probes was to provide additional information on the depth, extent, and consistency of the sewage sludge discharged into the sea from the main interceptor sewer, and the thickness of loose natural sediments lying on the sea bottom.

Marine geophysical methods included bathymetric surveys and an attempt at sub-bottom profiling. The bathymetric surveys, combined with depth measurements from the borings and probes, were sufficient to map the surface of the sea bottom in an approximately 500 meter wide corridor along the route of the pipeline. Sub-bottom profiling was not successful over most of the alignment due to the presence of methane gas bubbles in the sewage sludge. The gas bubbles tended to cause absorption of the acoustic energy of the signal, rather than having it reflected back to the sensor by successive harder layers below. The results of the geotechnical investigation indicated that the sewage sludge covered the sea bottom over approximately two-thirds of the pipeline route from the discharge of the interceptor sewer on the east side of the channel to near the end of a jetty on the north side of the channel. The sludge varied in consistency from very loose or "liquid" near the surface to medium stiff at its deepest point. The gain in consistency with depth is attributed to consolidation of the lower, older portions of the sludge under the weight of more recently deposited sludge near the surface. The thickness of sludge varied from 0 near the edges of the deposit to approximately 6 meters near the center of the deposit.

The natural sea bottom consists of loose to medium dense marine sand with a high silt and clay content. The sand exhibited some natural cementation which varied in location and depth. The thickness of the sand varied from 0 near the shorelines to greater than 15 meters near the center of the channel.

Beneath the marine sand is rock which is classified as Neogene limestone. Based on inspection of cones and observations of outcrops of rock on the mainland and on Psyttalia Island, the rock is characterized by the presence of solution cells and cavities. Some of the smaller cells are filled with calcite. As observed on land, the dimensions of cavities vary from 1 to 2 cm up to a few meters. The formation of these cavities is attributed to the existence of joints and faults in the limestone and to solution activity. It was the presence of these cavities which lead to the decision to transport the sewerage from the mainland to Psyttalia Island via siphon pipes laid in a trench in the sea bottom, rather than via a sewer tunnel in rock beneath the sea bottom.

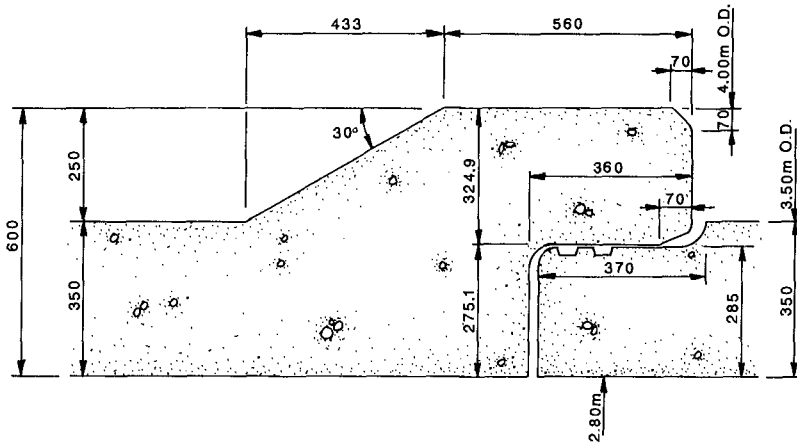
DESIGN

The submarine siphon pipelines are situated in a seismically active zone. More than 40 seismic events with intensities exceeding 5.0 on the Richter scale have been recorded in the last 80 years. This ground shaking as well as seismically induced liquefaction were among the major design concerns. The siphon pipelines location under a major shipping channel with all the attendant risks such as anchor dragging required special remedial protective measures.

The siphon pipelines were designed to withstand all forces to which they may be subjected during manufacture, transportation, installation, testing, backfilling and operation.

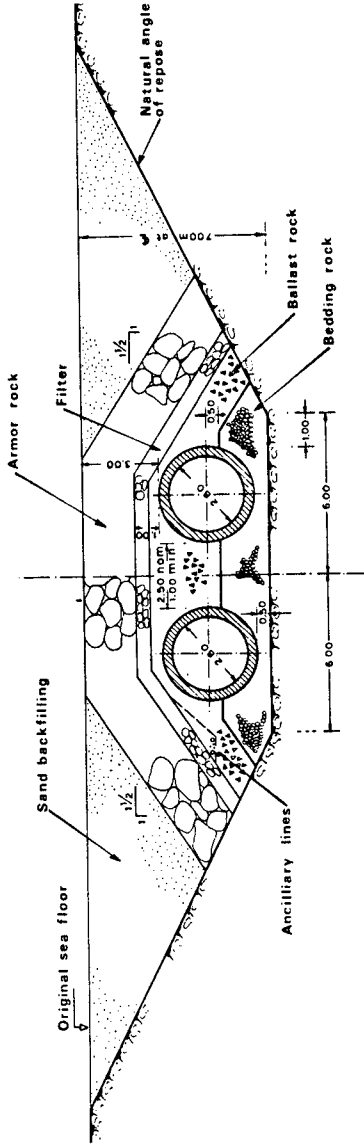
The pipe finally selected has 2.80 meter inside diameter, was made of reinforced concrete with an upset bell and spigot. The pipe has a wall thickness of 350 millimeters (mm) and a spigot 370 mm long. All pipe spigots contain two grooves for 32 mm diameter O-ring gaskets (see figure 4). The two gaskets allow the pipe joint to be tested under water for integrity. The long spigots will minimize the likelihood of a pipe pull-out during a seismic event. All pipes were coated with coal tar epoxy, both internally and externally. In order to protect the siphons from the twin hazards of dragging ship anchors and seismically induced liquefaction, they were placed in a 7 meter deep protective trench and covered with rock (see figure 5). Specially designed double bell sections were designed for the lowest point of the siphons and pipe laying proceeded from the double bells in both directions (see figure 6 and figure 7).

One unique feature of the siphon design was the requirement that they be able to withstand an evacuation test, allowing for a visual inspection of the pipes after the completion of construction.



BELL AND SPIGOT DETAIL

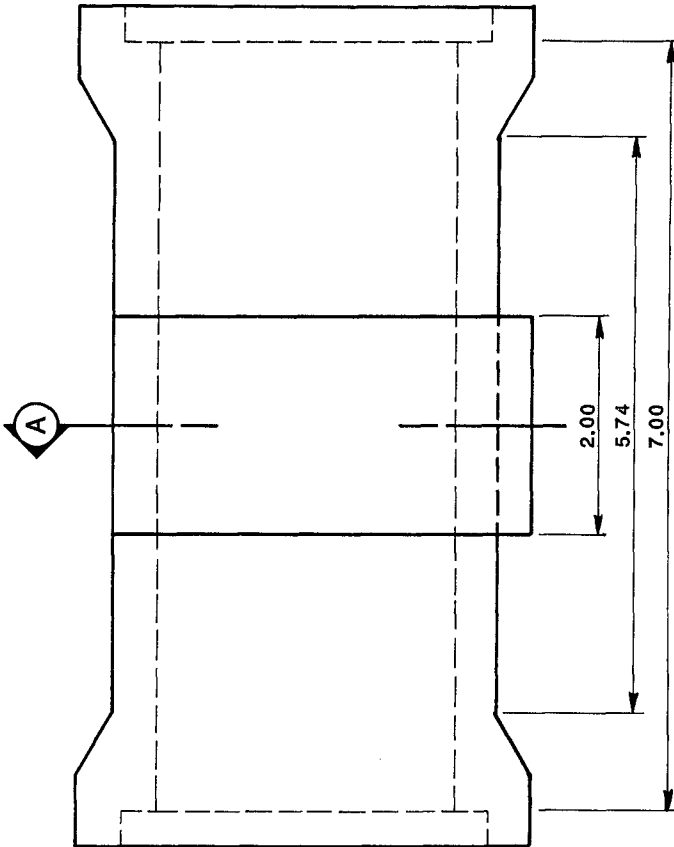
Figure 4



- Bedding rock : 9 to 60 m.m
- Ballast rock : 90 to 240 m.m
- Filter : 150 to 250 kg
- Armor rock : 1.5 to 2.5 tonnes

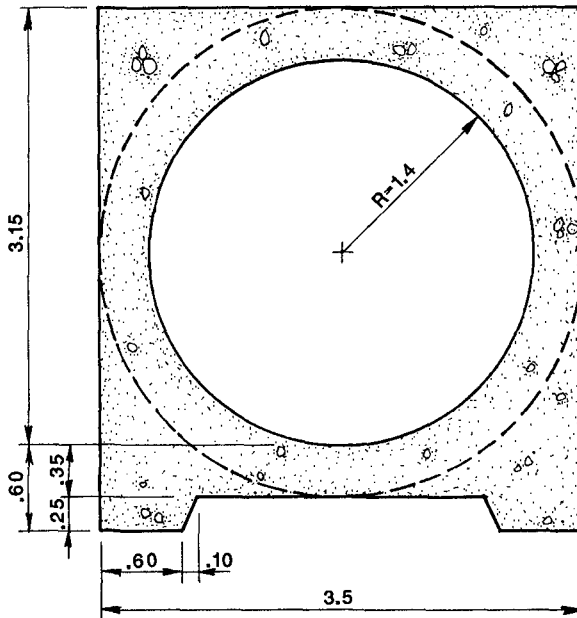
Figure 5

BACKFILL DIAGRAM



DOUBLE BELL PIPE AT STATION 5+43

Figure 6



(A) SECTION OF DOUBLE BELL PIPE

Figure 7

PIPE MANUFACTURE (See Figures 8, 9, 10 & 11)

The 8-meter lengths of pipe were cast at the jobsite. PIPE, Inc. of Tacoma, Washington, were retained as consultants to the Contractor and were vital in minimizing the problems that did occur. Casting large Reinforced Concrete Pipe is a much more sophisticated operation with unique skills than would appear on the surface to the uninitiated.

The pipe was cast-in-place vertically with the raised bell down. Three sets of forms were fabricated locally with some of the problems which should be expected. The tolerances on the bell and spigot

machined rings are critical in order to have interchangeability between pipe cast in different forms with the very close dimensional clearances in the joint design.

The double reinforcing cages were fabricated at the jobsite using PIPE's imported machine, which they had used on San Francisco's Southwest Ocean Outfall Project.

The spigot is the "tenderest" part of the pipe, and any spalling or cracking of the front edge usually results in a test failure at installation, which is a costly expense to the Contractor. Unfortunately, due to the nature of the spigot being cast up, this concrete has the least consolidation, most segregation, air entrapment and laitence formation requiring extraordinary care in concrete placement, vibration and finishing. Unfortunately, this lesson is not appreciated until major problems are encountered with the laying, at which time a considerable amount of defective pipe has already been cast.

Another problem arose when the too-small crane used to strip the too-tight fitting and untrue interior form would rock back and forth as the form would break loose and then stick, resulting in a non-vertical pull on the form, which in turn had a prying effect on the spigot end, invariably resulting in spalling the spigot. The result was that every pipe spigot had to be patched. The O-ring grooves required extensive finishing work ending up with every spigot epoxy-coated to provide the necessary crack-free, smooth, uniform surface and uniform groove depth which varied due to lack of attention in maintaining the forms.

Every pipe was internally hydrostatically tested, revealing very few cracks and giving a good check on the sealing configuration of the spigot. Additionally, after months of unexplained joint test failures during field installation, each pipe was joined with what was going to be its mate, and the joint was hydrostatically tested in the yard before being sent out for installation.

The epoxy painting of the interior and exterior was an unusual requirement and made for a very high-quality finish, which should more than pay for itself in increased longevity and flow characteristics. A side benefit was that the light sandblast prior to application of the paint revealed many air-entrapped pockets under the grout surface, particularly on the interior of the pipe, including high porosity conditions at the rebar chairs. These areas were epoxy patched before painting.

The concrete was batched on the job into ready mix trucks and then craned into place. As the local aggregates are not high strength, the Contractor elected to use generous proportions of cement, resulting in exceedingly high compressive strengths. The Greek Ministry of Public Works maintained a complete and competent inspection force at the jobsite.



PIPE PLANT

Figure 8



PIPE SPIGOT DETAILS

Figure 9



DOUBLE BELL SECTION

Figure 10



COAL-TAR EPOXY FINISH ON PIPE

Figure 11

CONSTRUCTION

The construction of the submarine siphon described below was divided into the following components:

1. Excavation
2. Pipe Laying and Bedding
3. Rock Backfill
4. Surveying
5. Utility Line Installation
6. Final System Leakage Tests

1. Excavation (See Figure 12)

The trench was dredged in its entirety using three 2400 Lima barge-mounted cranes clamming into small dump scows (i.e., 250 m³) and disposing of the material a short distance away.

The first order of business was to remove the sewer sludge which overlay a third of the alignment on the mainland side and varied up to 7 meters in thickness. This material was the deposited result of the many, many years of discharge of Athen's raw sewage at the shoreline adjacent to the project and was only diverted 100 meters away for the convenience of construction. The material consisted of very low shear strength "black mud" and posed no problem in excavation other than its odorous nature. However, due to the long delay (1-½ years) between the initial excavation and pipe placement in the excavated trench, the sludge crept back into the trench, which required extensive clean up before pipe installation and again before cover rock placement.

The 7-meter deep trench in the seabed was founded generally in hard clayey sand, posing considerable problems for the Contractor. One-half of the material lies below a 40-meter depth and almost three-quarters below 30 meters.

The dredging was conducted in two shifts, six days a week, and the average production was in the range of 250-300 m³ per dredge per shift.

Rock was encountered on both ends of the alignment, and after unsuccessful attempts at drilling and shooting, the rock was removed using chiseling and scraping with the buckets.

Upon experiencing the hardness of the seabed material, the Contractor elected to help offset the adversities by excavating the trench to the minimum width (12 meter) with the side slopes standing competently at near vertical. This, of course, minimized the quantity of material to be excavated and the quantity of manufactured rock backfill to be produced and placed. The minimum width combined with the vertical side slopes did cause some difficulty in trying to maintain adequate clearances for the pipe laying, as one can imagine the difficulties in trying to clam a 12 meter-wide groove 40 plus meters below you in the blind!

In total, the excavation of the 7 meter deep trench entailed the removal of 125,000 m³ of sludge overburden in addition to 200,000 m³ of other material.



PIPE TRENCH EXCAVATION

Figure 12

2. Pipe Laying and Bedding (See Figures 13, 14, 15, 16 & 17)

The pipe was lowered into the trench, mated with the previously laid joint and held in alignment while being bedded in the conventional manner using a "Horse" (see Figure 14). This device is like a four-legged table under which the pipe is strapped, and, once set on the trench bottom, is independent of the barge-mounted 4600 Ringer lowering crane above. The four legs telescope independently such that grade and slope can be controlled. The pipe is fastened to a carriage within the "table", allowing for longitudinal (2 meters) translation for joining and independent transverse movement (± 1 meter) of either end of the pipe for alignment. The hydraulic controls for these movements are all on the surface and directed via communication link from a diver on the bottom. The station positioning of the "Horse" during lowering and setdown was controlled by an inhaul winch on the beach. The cable was marked at 8-meter intervals, which allowed the "Horse" to be positioned at just the right place so as not to set on the previously laid pipe nor too far away to be "out-of-stroke" for joining. The inhaul winch also held the "Horse" from sliding down the 25% slopes on the shore ends of the alignment.

As there was no visibility on the bottom due to the existing sewage discharge and/or silt from the bedding operation, all pipe laying and jointing was done "in-the-dark" by feel.

The dual pipelines were laid concurrently with the joints of one line, staggered a half-length (4 meters) from the adjacent line in order to give the maximum clearance at the raised bells. The narrowness of the trench gave surprisingly few problems to the laying operation, and, in fact, forced the Contractor down the "straight and narrow" such that he didn't get into any steering/gap tolerance problems.

The bedding was accomplished by bringing an anchored gravel barge with a long tremie pipe over the top of the "Horse" once the pipe was joined. A 1-½ m³ rubber-tired loader would dump gravel into an overboard hopper which fed the tremie pipe. The tremie was "spotted" over the centerline of the pipe and gravel was fed down bedding the leading end of the previously placed pipe and about ¾ of the one being laid and held in position by the "Horse". Transport of the gravel under the bottom of the pipe was aided by divers using a hand-held water jet and later by a jetting system plumbed into the "Horse" itself. The water was provided by a small diesel-powered jet pump on board the derrick barge.

Adequate placement and consolidation of the bedding under the barrel of the pipe is always one of the more controversial aspects of pipe laying, and this job was no exception. If the bedding is not adequately placed and consolidated under the pipe, voids can exist which may cause differential settlement when the pipe is covered with rock, resulting in the joints articulating.

3. Rock Backfill

The remainder of the ballast rock, that above the springline and covering the pipe, was placed similarly to the bedding portion by tremie pipe fed by a front end loader on the rock barge. The section was controlled by leadline sounding and later proofed with fathometer readings. Low spots were later supplemented with rock placed with a clamshell derrick.

The ½-meter cover of filter rock was placed using the "bombing" method -- discharged from a split-hull dump scow. In the deep water this method worked fairly satisfactorily, as the material has a chance to disperse on the way down. However, the material, if discharged too rapidly, will have a tendency to "blow away" from the center of impact leaving highs on the edges and lows in the middle.

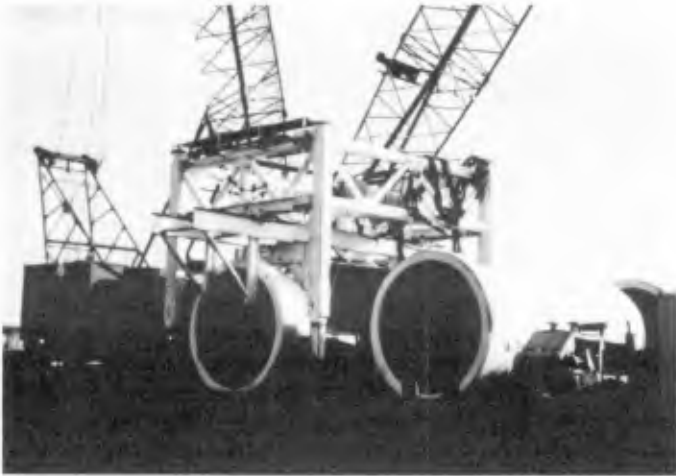
The armor rock was very laboriously placed using the 2400 Lima clamshell rigs -- up to four rigs operating at a time, which in the end ran the rock quarry dry.

In total, the backfill operation entailed the placement of 30,000 m³ of ballast, 10,000 m³ of filter material and 40,000 m³ of armor rock.



PIPE CARRIER

Figure 13



PIPE LAYING "HORSE"

Figure 14



PIPE LAYING BARGE

Figure 15



BACKFILL BARGE

Figure 16



ON-SHORE TERMINUS
OF SIPHON PIPES

Figure 17

4. Surveying

Alignment for all the operations was controlled by normal vertical-fan shore mounted lasers. As almost all of the marine work was on a tangent, this system worked satisfactorily.

Grade was controlled strictly by manual tide gages. The tide gages (floats) were housed in stilling wells which negated the influence of the short period waves (chop). The grade on the pipe laying was similarly monitored by attaching a floating tide gage, also in a stilling well, by cable to the center of the frame on the leading end of the pipe. Given the low tidal currents in the area, this tensioned leg gage also served for monitoring the transverse position of the pipe.

Due to the steep-sidedness of the trench excavation, meaningful fathometer readings were unobtainable so lead line soundings were used for the dredging cross-sectioning.

5. Utility Line Installation

A multi-utility line bundle consisting of one 12" water line, one 6" gas line, two fiber optic cables and one electrical power line was placed in the trench. The water line and gas line were cement-coated at the jobsite to provide proper ballast for the pull. The bundle was prefabricated into 100-meter lengths with a continuous timber plant bottom. The bundle was pulled across the 1400 meters by a winch placed on the opposite shore. The electric cable required one mid-pull splice, which required a two-day delay in the pull.

6. Final System Leakage Tests

Both siphons successfully passed the system-wide leakage tests which were completed in May 1987. No pipe evacuation tests were carried out as of the writing of this paper (June 1988). They are presently scheduled to take place during the summer of 1988.

ACKNOWLEDGEMENTS

The Owner of the facility is "The Special Service for the Sewerage and Sewage Treatment Authority of Greater Athens" (E.Y.D.E.) of the Greek Ministry of Environment, Regional Planning and Public Works. Consultants to E.Y.D.E. is a Joint-Venture of Th. Gofas and Partners, Athens, Greece; Haiste International, Leeds, U.K. and Woodward-Clyde Consultants, San Francisco, California, U.S.A. Parsons Brinckerhoff, San Francisco, California, U.S.A. is under subcontract to Woodward-Clyde Consultants.

The Contractor was a Joint-Venture of Athena Hellenic Engineering, Industrial and Touristic Co. S.A., Athens, Greece, and Raymond International, Houston, Texas, U.S.A.

REFERENCES

Theofanis C. Gofas, Yiannis Tselentis, Hugh A. Allan, Ralph A. Fasano, Yair Eisenberg and Donald D. Treadwall. Athens Siphon and Outfall - Coastal Zone '87, ASCE, Seattle, Washington, U.S.A., May 1987.

CHAPTER 205

Quantification of Longshore Sand Transport and Sand Bypassing at South Lake Worth Inlet Palm Beach County, Florida

John S. Yeend, P.E.¹
Darryl J. Hatheway, E.I.²

1.0 INTRODUCTION

1.1 Abstract

The intent of this paper is to express the quantities of sand bypassed by a sand transfer facility and transported in the littoral drift at the South Lake Worth Inlet, Palm Beach County, Florida. Discussion on littoral transport volumes will include estimates of the annual average drift from 1948 to 1987, and discussions of sand bypassing quantities will include improvements in the estimation of pumping rates.

1.2 History

The South Lake Worth Inlet District was established by the Florida Legislature in 1915 (Ref. 1), for the purpose of creating an Inlet flushing canal from the Atlantic Ocean to help alleviate serious pollution in freshwater (slightly brackish) Lake Worth, resulting from rapid development of the area after the turn of the century.

The United States Army Corps of Engineers (COE) issued a permit in April of 1924, authorizing the District to construct and maintain the Inlet, including stone jetties on each side of the Inlet and allowing for the construction of a fixed bridge across the Inlet (Ref. 2). The Inlet was completed in July 1927.

Substantial improvements resulted from a 1964 model study by the University of Florida (Ref. 3). These included a new Inlet configuration with curved north and south jetties extended from their original lengths and a widening of the Inlet by removing a bridge abutment. Also, a training wall was constructed west of the bridge to improve the flow and self-maintenance of the Inlet channel and to redirect the suspended sediment flow into a sand trap area. The Sand Transfer Facility was relocated approximately 100 feet seaward of the MHW line on the north jetty (Fig.1).

1) Manager, Coastal Engineering Group, GEE & JENSON
Engineers-Architects-Planners, Inc., West Palm Beach, FL

2) Coastal Engineer, GEE & JENSON Engineers-Architects-
Planners, Inc., West Palm Beach, FL



Fig. 1 **Aerial Photo of South Lake Worth Inlet (photo circa 1984)**

The STF's function is to transfer the sand as it reaches the north side of the north jetty to the downdrift beaches. Sand not transferred, generally flows around the Inlet in the ebb tidal shoal, acting as a conveyor belt, and is deposited on the downdrift beach to the south (Fig. 2).

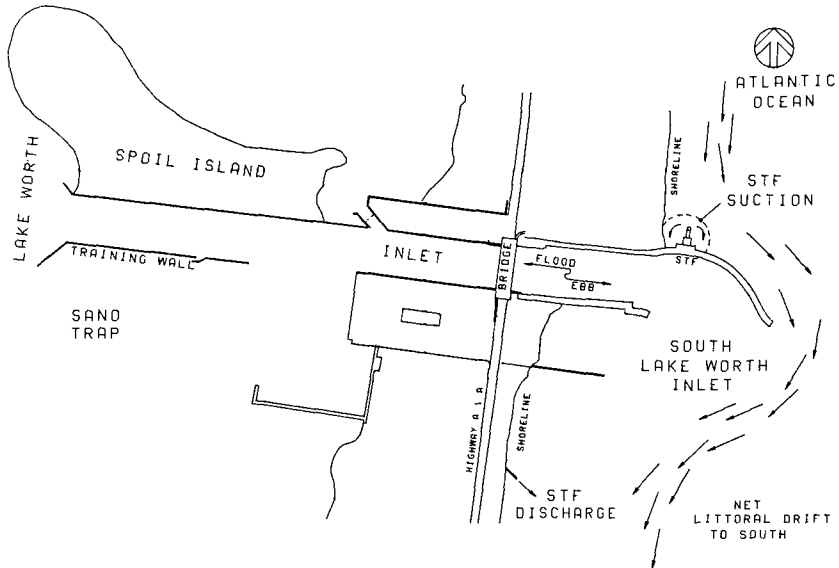


Fig. 2 Present Configuration of South Lake Worth Inlet, Palm Beach County, Florida

2.0 QUANTIFICATION OF LITTORAL TRANSPORT

2.1 Littoral Environment Observations

In October 1984, monitoring of the littoral environment was initiated utilizing the (COE) Littoral Environment Observation (LEO) Data Collection Program (Ref. 4). The LEO beach monitoring site is located about 1,000 feet north of the South Lake Worth Inlet. The LEO Program was developed by the Coastal Engineering Research Center (CERC) branch of COE. The purpose of the LEO Program is to record visual observations of breaker conditions (height, angle of approach, and tides), local winds, longshore currents, rip currents and beach geometry on a daily basis for at least one year or more (Ref. 5). The reliability and credibility of the LEO observation results and analysis depend on the number of observations taken and the availability of trained observers.

The application of the LEO data at the South Lake Worth Inlet is for the purpose of predicting longshore sand transport rates utilizing observed waves breaking at a recorded angle to the shoreline. The quantities of sand transported along the shore are a result of waves creating a longshore current and the breaking wave turbulence that suspends the sediment. Empirical equations in the Shore Protection Manual (Ref. 6) utilize LEO data in the empirical relationship to relate the longshore transport to wave conditions. Using a second method in 1980, Todd L. Walton Jr. (Ref. 5) applied LEO current observations to compute the longshore transport. The annual summary of

LEO data by CERC uses these two separate, although not completely independent, methods for determination of sediment transport rates.

The data summary in Table 1 presents two years of LEO longshore transport estimates. Review of the annual estimated littoral transport rates clearly show the net movement of sand is to south, but a true determination of the annual rate will need more years of data collection and observations. The LEO estimates for 1987 have been deleted due to data collection errors resulting in inaccurate transport rates.

TABLE 1

A. CERC LEO estimated annual net southerly sediment transport volumes (Jan-Dec.)		
	<u>Method 1</u>	<u>Method 2</u>
1985	379,731 cy	110,987 cy
1987	385,168 cy	126,996 cy
B. South Lake Worth Inlet average annual estimated sand bypassing volumes (dredge years 1968-87)		
Based on 100 CY per hr of pump operation		50,140 CY
Based on 125 CY per hr of pump operation		62,675 CY
Based on 160 CY per hr of pump operation		80,224 CY
Based on 200 CY per hr of pump operation		100,280 CY
C. South Lake Worth Inlet average annual measured sand bypassing volumes (1985-88)		
		74,409 CY

2.2 Annual Average Drift

There have been many estimates of the annual average drift for the purpose of determining the net littoral drift to the south (Table 2). In 1948, the COE did a study which concluded that during the fourteen (14) year period immediately following completion of the Inlet and the jetties, material was impounded at a rate averaging 150,000 to 225,000 cubic yards (CY) per year (Ref. 7). In a 1953 study by the COE, an estimate of 200,000 CY per year was used as the "southward drift at the South Lake Worth Inlet to the 27 ft. depth" (Ref. 8). In 1964, the University of Florida Coastal Engineering Department, by contract for the South Lake Worth Inlet District, used an estimate of 200,000 CY as the net drift to the south (Ref. 3).

In 1966, Per Bruun's book entitled "Inlets and Littoral Drift" (Ref. 9), credited the COE, Jacksonville District for its determination of the predominant drift at the South Lake Worth Inlet as being 150,000 to 200,000 CY per year. In a later report dated July 21, 1965, Per Bruun, assumed that the normal rate of drift at the Inlet is 225,000 CY per year (Ref. 10).

TABLE 2
Estimates of Annual Average Drift

<u>Year</u>	<u>Agency/Individual</u>	<u>Rate (Net to South)</u>
1948	U.S. Army Corps of Engineers (COE)	150,000 to 225,000 cy/yr. Drift to south at area of South Lake Worth Inlet
1953	COE	200,000 cy/yr.
1964	University of Florida	200,000 cy/yr.
1965	Per Bruun	225,000 cy/yr.
1966	Per Brunn	150,000 to 200,000 cy/yr.
1985	COE/WES	270,000 cy/yr. based on wave data collected in Atlantic Wave Information Study (1956- 1975)
1987	Olsen	270,000 cy/yr.

The COE Waterway and Experiment Station (WES) in Vicksburg, Mississippi utilized twenty (20) years of wave hindcast data (1956 to 1975) to determine the potential average annual net southerly littoral transport rate of 270,000 CY in the area of South Lake Worth Inlet, which was later reported in the 1985 General Design Memorandum for Beach Erosion Control Projects in Palm Beach County (Ref. 11). The wave data utilized in the determination was supplied by the 1976 Atlantic Ocean Wave Information Study (Ref. 12). In 1987, Olsen & Associates prepared a report for Palm Beach County entitled "Guidelines for the Review and Consideration of Coastal Permits" and utilized the same 1985 WES estimate (Ref. 13).

2.3 Sediment Transport Rates

Most of the above annual littoral transport quantities are based on estimates rather than the observed data interpretation that the LEO Program attempts to correlate. The LEO Program allows for the variation in weather conditions (i.e., calm periods, when less sand will be moving, as opposed to the very active northeastern and hurricane periods, with the larger sand movement). It would be erroneous to expect any value of estimated net littoral drift to be constant year after year.

As stated in CETA 81-5 (Ref. 4) "the usefulness of the LEO program is best expressed in the statistical descriptions of the environment, often in areas where no other data exists, and in the inexpensive estimation of longshore transport rates."

2.4 Discussion

The estimates of net littoral transport have a common flaw in that there is an assumption of no interruption in the littoral transport system. The nearest interruption to the South Lake Worth Inlet littoral drift system is located fourteen (14) miles to the north at the Lake Worth Inlet. The Lake Worth Inlet, at its present location, was cut in the Barrier Island in 1917 and currently has a project depth of 35 ft. and channel width of 400 ft.

In a reference to maintenance dredging by Robert Dean (Ref. 14), it was suggested that the placement of sand in water deeper than 12 ft. does not allow for the sand to re-enter the longshore system by natural forces. This would mean that any sand naturally bypassed by the Lake Worth Inlet around the north jetty would have entered the wide channel where depths are greater than 12 ft., or deposited in the channel to be carried offshore with the ebb tide currents, or into the channel during the flood tide currents and deposited in the Intracoastal areas.

Therefore, since 1958 when the sand transfer plant was constructed on the north jetty of the Lake Worth Inlet, the only constant littoral drift across the Lake Worth Inlet was the approximately 70,000 CY per year pumped by the sand transfer plant.

All of the above information presented would make estimates of the net littoral drift at the South Lake Worth Inlet questionable. It would appear that the only way the South Lake Worth Inlet has been able to maintain the transferring, both artificially and naturally, of large quantities of sand is by tapping the supply between the two inlets. Therefore, there is a range of uncertainty in all of the above estimates.

3.0 QUANTIFICATION OF SAND BYPASSING

3.1 History

Prior to 1937, the South Lake Worth Inlet configuration with stone jetties extending perpendicular from the center line of Ocean Boulevard, approximately 350 ft. in length, allowed large quantities of sand to drift into Lake Worth through the Inlet (Ref. 15). In order to mitigate these sand losses, a sand transfer plant was constructed on the north jetty through a cooperative effort between the Inlet District and private property owners. This sand transfer plant is believed to have been the first of its kind in the United States.

Because of the fuel shortage during World War II, the plant did not operate between the years 1942 and 1945. Even though resumption of the plant operation following the war significantly restored the beaches to the south of the Inlet, it was found that a considerable amount of sand was still being trapped inside the Inlet in Lake Worth. Accordingly, the sand transfer plant was enlarged in 1948. This pump remained in operation until major renovations were made in 1967 in response to the physical model study

and recommendations by the University of Florida, Coastal Engineering Lab (Ref.3) and previously discussed.

The primary purposes for these modifications were to prevent the loss of sand to the interior shoals of the Inlet, improve the sand transfer capabilities of the Inlet, and to make the Inlet channel self-flushing.

3.2 STF Quantities

The sand transfer facility today is a fixed hydraulic suction dredge with a rotating boom and 12 in. diameter suction intake line and 10 inch diameter discharge line. The dredge pump is driven by a 400 hp. diesel Caterpillar engine rated to pump 4,000 gpm with 20 percent solids in suspension. The discharge line extends west from the sand transfer facility to the road, then south across the bridge to the discharge location approximately 700 feet south of the south jetty.

Records of the quantities of sand bypassed and dredged at the South Lake Worth Inlet date back to the 1960's. For this paper, the review of quantities of sand bypassed will be for periods following the 1967 renovations and newly constructed inlet configuration. The estimated quantities of sand bypassed by hydraulic dredge have been based on rates varying from 100 to 200 CY per hour of pump operation from dredge years 1968 to 1988 (Ref. 16). Current sand bypassing estimates of 125 CY per hour of pump operation were determined by comparing estimated quantities with the measured quantities from a nuclear density measuring unit and Doppler flow meter combination that comprises the production monitor unit at the South Lake Worth Inlet.

The production monitor is a liquid slurry density system developed by Kay-Ray Inc. Industrial Process Control Equipment. The unit was installed in late 1985 to work with the Taylor Disk Pressure Recording System installed in the pumphouse of the sand transfer facility. The measuring unit was placed inside the engine room on the 10 in. discharge line and linked to the recording and equipment panels located in the room above. The control panel and lever room are located in the upper level where a digitized readout for production monitor measured quantities can be recorded by the dredge operator. The system is calibrated to read out in cubic yards of dredged material discharged through the system.

3.3 Discussion

The production monitor data indicated that during peak pumping periods, typically September to March, a larger volume of sand was being bypassed than previously estimated. It was in October of 1986 that the conversion of sand bypassing estimated cubic yards per hour of operation was increased from 100 to 125. Data in Table 1 for measured quantities reflect adjusted totals to account for periods when the production monitor was not operating due to repairs.

Prior to the introduction of the production monitor, the method of determining the dredge volumes bypassed by the sand transfer facility were to assume a constant quantity per unit of time. Changes in the estimated cubic yard per hour totals for plant operation have varied from 100 to 200 cubic yards from 1968 to 1988.

The graph (Fig. 3) presents the data collected from the production monitor since 1985. The vertical axis of sand transfer operating hours per week and the horizontal axis of measured cubic yards per week from the production monitor system illustrates the variation of weekly available material for bypassing.

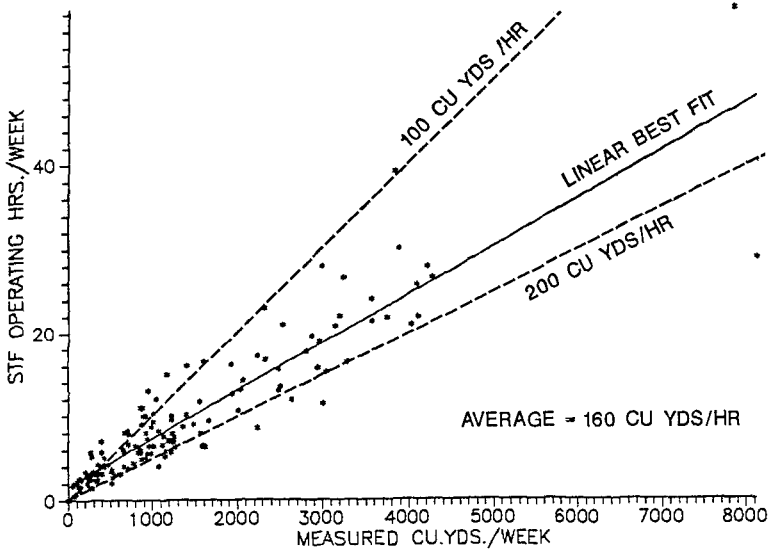


Fig. 3 Weekly Production Monitor Quantities (1984-1988)

During less active weather climates and operating conditions typical of summer and southeast winds and waves, the average measured bypassing totals are near an estimated 75 cubic yards per hour of plant operation. During active transport periods, with maximum sand availability, the plant has shown the capability to pump at a higher capacity for longer periods of time. Totals of measured bypassing in excess of 250 cubic yards per hour of plant operation have been recorded. The data in Table 3 lists the three peak periods of operation and the bypassing quantities measured during that dredge week from 1984-1988.

TABLE 3
Peak Measured Bypassing Volumes
(1984-1988)

<u>Weekly Hours</u>	<u>Total Volume</u>	<u>Hourly Rate</u>
39.2	3,832 CY	98.75 CY/Hr.Operation
58.6	7,816 CY	133.39 CY/Hr.Operation
28.9	8,113 CY	280.73 CY/Hr.Operation

Dashed lines on Fig. 3 represent the estimated rates of 100 and 200 cubic yards per hour to show the variation of measured bypassing rates around the upper and lower previously estimated rates of the sand transfer facility.

With a computerized linear best fit line, interpretation of the line was accomplished by averaging the data for operating periods of 10, 20 and 40 hours per week. The resulting average rate (based on these measured dredge rates) would be approximately 160 cubic yards of material per hour of plant operation.

The quantities of dredged material will vary depending upon the weather climate in the area of the South Lake Worth Inlet. As reported in an earlier paper, "Inlet Dredging Production as a Function of Sea State" (Ref. 17), a correlation was made between wave height and direction and the estimated quantities of material that could be dredged per hour of plant operation. It was determined that the problem was much more complex than simply averaging volumetric quantities for varying weather conditions.

In this paper, we also present the average annual estimates of sand bypassing volumes from 1968 to 1988 based on four (4) different estimates for bypassing: 100, 125, 160 and 200 CY per hour of pump operation (Table 1).

The graph (Fig. 4) shows that annual variations in the operating time for the sand transfer facility are apparent. The period of 1982-83 had 1,140 hours of operation and the period of 1971-72 had 231.5 hours of operation.

The graph shows a decrease in annual operating hours since 1982. This reflects a change in operation procedures and better efficiency in pumping as a result of the production monitor data (measured data) being available.

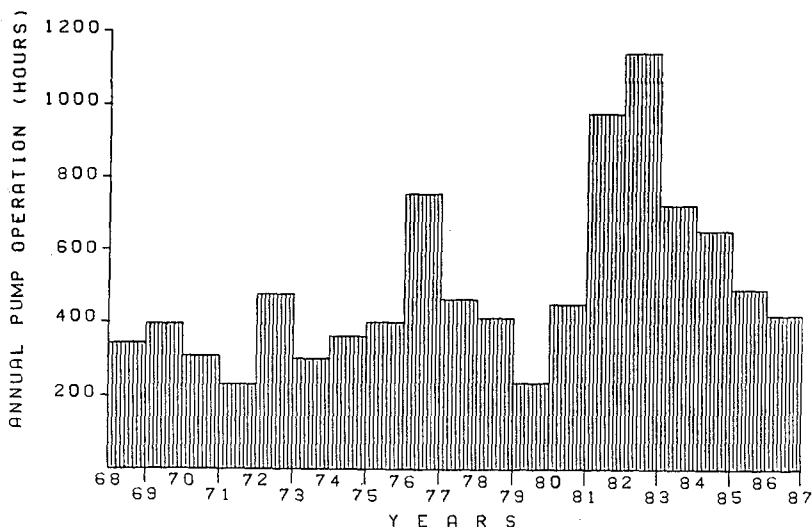


Fig. 4 Sand Transfer Facility Annual Operating Hours (1968-1987)

4.0 SUMMARY

4.1 Littoral Transport

Littoral transport is generally defined as the movement of sediments in the near shore zone by action of waves and currents. The Longshore Sand Transport component of the littoral transport is the volume of sand moving parallel to the shore. The review of the littoral drift and estimated sediment transport rates and associated volumes as presented in this paper were based on estimates, wave hindcast data, and LEO's two Shore Protection Manual methods.

The variations in the estimates of wave angle, surf zone width, and weighting of calm wave height observations in the littoral transport rate determination produce a wide range of estimated annual volume totals. As stated earlier, there is a range of uncertainty in all of the above estimates. The past estimates of littoral drift presented here documents the longshore transport rates variability.

4.2 Sand Bypassing

The sand bypassing operations at the sand transfer facility of the South Lake Worth Inlet show a great variability in the total annual volumes of material pumped from the north beach to the south beach. The combined presentation of the bypassing data and estimated LEO transport rates illustrates the variation in the dredge volumes due to the seasonal fluctuations of the wave and wind climate that create the transport events.

REFERENCES AND BIBLIOGRAPHY

1. Chapter 7080, Laws of Florida, 1915
2. War Department Permit to Construct Inlet, Executed 30 April 1924
3. Coastal Engineering Laboratory, University of Florida, Coastal Engineering Study of South Lake Worth Inlet, Gainesville, Florida, May 1964
4. Schneider, C., "The Littoral Environment Observation (LEO) Data Collection Program," CETA 81-5, U.S. Army, Corps of Engineers, Coastal Engineering Research Center, Ft. Belvoir, Virginia, March 1981
5. Walton, TL, Jr., "Computation of Longshore Energy Flux Using LEO Current Observations," CETA 80-3, U.S. Army, Corps of Engineers, Coastal Engineering Research Center, Ft. Belvoir, Virginia, March 1980
6. U.S. Army, Corps of Engineers, "Shore Protection Manual," Coastal Engineering Research Center, 1977.
7. House Document No. 772 - 80th Congress, 2nd Session, December 1948
8. Watts, G.M., A Study of Sand Movement at South Lake Worth Inlet, Florida - Beach Erosion Board, Corps of Engineers TM-42, October 1953
9. Per Bruun, Tidal Inlets and Littoral Drift, Stability of Coastal Inlets, Vol. 2, 1966
10. Bruun, P., The Effect of South Lake Worth Inlet and Its Bypassing Plant on Adjacent Shores, Present and New Installations for the T11F, University of Florida, July 1965
11. U.S. Army, Corps of Engineers, Jacksonville District, "Beach Erosion Control Projects for Palm Beach County, General Design Memorandum with Environmental Impact Statement," April 1987
12. U.S. Army, Waterways Experiment Station, "Atlantic Coast Hindcast, Shallow-Water, Significant Wave Information," 1976
13. Olsen Assoc., Inc., Guidelines for the Review and Consideration of Coastal Permits, for Palm Beach Beaches and Shores Council, October 1987
14. Dean & O'Brien, Florida's East Coast Inlets Shoreline Effects and Recommended Action, December 1987, for Florida Department of Natural Resources, Division of Beaches and Shores.

15. Caldwell, J.M., Bypassing Sand at South Lake Worth Inlet, Florida, Proceedings of First Conference on Coastal Engineering, October 1950
16. South Lake Worth Inlet Dredging Records, 1960 to Present
17. Yeend, J.S. and Hatheway, D.J., "Inlet Dredging Production as a Function of Sea State," Proceedings of the Fifth Symposium on Coastal and Ocean Management, Coastal Zone '87, American Society of Civil Engineers, 1987

CHAPTER 206

The beach of Vinaroz. Its origin, evolution and future

JOSE SERRA PERIS*
JOSE JAVIER DIEZ GONZALEZ**

INTRODUCTION

The great physiographical unity named "Ovalo Valenciano" is outstanding in Western Mediterranean. The Oval is limited by River Ebro, in the North, and Cape San Antonio in the South. On its Northern, margined by River Cenia, in the north, and Tomboło of Peñiscola in the South, is the subunity called Peñiscola and there stand the beach of Vinaroz, extending itself from the harbour of Vinaroz to river Cervol mouth.

COASTAL EVOLUTION

The beach lies on a steep coast, the cliff being higher all around River Cenia mouth and disappearing on the border line between Benicarló and Peñiscola districts the steep rock is composed of conglomerates made from multi-sized pebbles, cemented together in a matrix of finer materials, even clays. Sea action has given shape to a littoral where small bays, having pebbly and sandy beaches, alternate with relict debris cones (Figure, 1)

Cavanilles, giving us an extremely clear description, writes: Una descripción muy clara la encontramos en Cavanilles, quien dice: "En estas costas las olas por lo comun baten contra un terreno duro pocas veces de piedra, y muchas de un hormigón endurecido, compuesto de chinás, cantos y marga arcillosa roxa con algunas arenas. A fuerza de los choques de las olas y de renovarse la humedad, se ablanda la base que sostiene el cortezón y se descarna: presenta al principio hacia el mar excavaciones y cuevas; cayendo después al agua por su propio peso masas considerables. Mientras permanecen allí caídas, sirven de parapeto a las furias de las olas, y defienden por algún tiempo la porción con la cual estuvieron unidas; pero

*University Titular Professor. Escuela Técnica Superior de Caminos Canales y Puertos de Valencia. Camino de Vera s/n, 46071 VALENCIA. Spain.

**Professor of University. Escuela Técnica Superior de Caminos Canales y Puertos de Madrid. Ciudad Universitaria, 28040 MADRID. Spain.

cediendo en fin quedan expuestas a igual suerte las que en otros siglos existieron sin riesgos, y de este modo va haciendo el mar lentas conquistas en la costa" (Cavanilles, 1975)

The beach of Vinaroz, born backing on the harbour breakwater, developed itself beneath a low cliff which constitutes now the foundation of the maritime promenade. It receives materials mainly from nearby sources: River Cervol, Rambla Barbiguera, River Cenia and erosive materials coming from cliffs located on River Cenia shores. River Ebro, being a further source, supplies fines to be deposited on the submerged beach; they are easily removed and conveyed southward to settle on more receptive beaches. The beach of Vinaroz has been defined as a typical gravel one because of the local character of its sources of materials and the grain size characteristics of the stuff.

SEDIMENT TRANSPORT

The medium yearly direction of the littoral dynamic is North-South, seasonally being South-North sometimes. Carriage ability moves from 170.000 m³ to 510.000 m³ per year (Serra, J., 1986), Figure, 2).

The beach of Vinaroz has enveloped in accordance with its genesis; the harbour breakwater acted partially as a barrier to conveyance and so allowed a backed up beach to be born, no longer than one kilometer but well dimensioned in width. An aggregates exploitation was set beside River Cervol which cut off stuff supply towards the littoral. Even when the exploitation came to an end, River Cervol is no longer a source of materials because of its few functionalism; adding to this scarce mobility of products coming from cliff's erosion and the decrease of Rivers Cenia and especially Ebro's apports, the result is a recessive shore.

Even when it only brought thin stuff River Ebro allowed the existence of a submerged beach trending to a profile of equilibrium with heterogeneous materials sand and gravels which formed a somerhour stable beach. As in the earlier paragraph has been told, the conjunction of all the afore mentioned aspects brings forth as a result a recessive beach whose characteristics are a weak accumulation by the harbour dyke (breakwater) and strong erosion in the rest of the berm sand and in the whole of the submerged beach (see figures 3 and 4).

CONCLUSIONS

Two actions trending to regenerate the beach have been undertaken in the last years: building a T-groin in the Northern end of the beach and artificial feeding.

A T-groin was built in 1985, giving birth to a sheltered beach leeward, but this came to accentuate erosion in the central stretch of the beach as

materials gravitate towards sheltered zones in the break-water and in the harbour causing a natural selection of sediments, the coarses swelling the backed up beach and the media and fine ones going to the sheltered beach. The results of these conditions had they been maintained, would have been a sandy beach sheltered by the break water; the birth of a pebbly beach backed up to the harbour; and strong erosion in the center of the beach which would endanger the stability of the maritime promenade.

Erosion in the central stretch of the beach has been palliated since 1986 by artificial feeding but this caused two serious objections: in the first place, since their origin was pounding, material used nailed into bathers' feet, the water getting a peculiar colour because of high contents of clays and for the same reason the beach "swallowed" bathers beside the shore. Secondly, the beach retained very few materials, due to high contents in thin ones, the rest escaping to the sheltered zone, besides off-shore loses of media and coarses stuff caused by steep slopes proper from pebbly beaches.

Several solutions can be adopted in order to regenerate the beach of Vinaroz. Among them, two are to be mentioned:

Exclusive artificial feeding; the united effect of the T-groin and artificial feeding would be satisfactory, provided that a series of permits come together. Apports should be grain-size distribution appropriate, with periodical reloading in amounts to be predetermined. Feeding with natural, not pounded, sand should be required as we cannot hypothesize that because of surge action might get typical round shape proper from marine sediments after one year stay in the shore.

Isolated breakwaters; artificial apports can be retained by means of isolated breakwaters, since they act as reducers of surging energy, diminishing its ability to convey and avoiding deposits gravitation towards the harbour or the T-groin, and so helping to the maintenance of apported materials. It would be not necessary that these breakwaters we propose obey to classical conceptions such as emergent or semi-emergent dykes; as a solution could be adopted that of the artificial reef, according to express wishes of the area fishermen whom by means of the afore mentioned system intend to protect and strengthen their fishing reservoir. This solution requires artificial feeding too, in the same qualitative conditions said in the former paragraph.

REFERENCES

- Cavanilles, A.J., 1795-1797. "Observaciones sobre la historia natural, geografía, agricultura, poblaciones y frutos del Reyno de Valencia". Imprenta Real. Madrid.
- Copeiro, E., 1980. "Sobre la progresiva ruina de nuestras

costas arenosas". Rev. de Obras Públicas. Madrid, pp 307-319.

-Diez, J.J., Arenillas, M., Serra, J., 1982. "Shore protection in Almazora coast" (Castellón, Spain). 4th Inter. Congress I.A.E.G. New Delhi.

-Serra, J., Esteban, V., Díez, J.J., 1984. "The performance of different shore protection systems in the East-Spanish Mediterranean coasts". Inter. Sym. on maritime struc. in the Mediterranean Sea. Athenas.

-Serra, J., 1986 "Procesos litorales de las costas de Castellón". Tesis Doctoral Universidad Politécnica de Valencia.

-Serra, J., Medina, J.R., 1987. "Arrecifes artificiales en el litoral español. Experiencia valenciana." Rev. de Obras Públicas. En prensa.

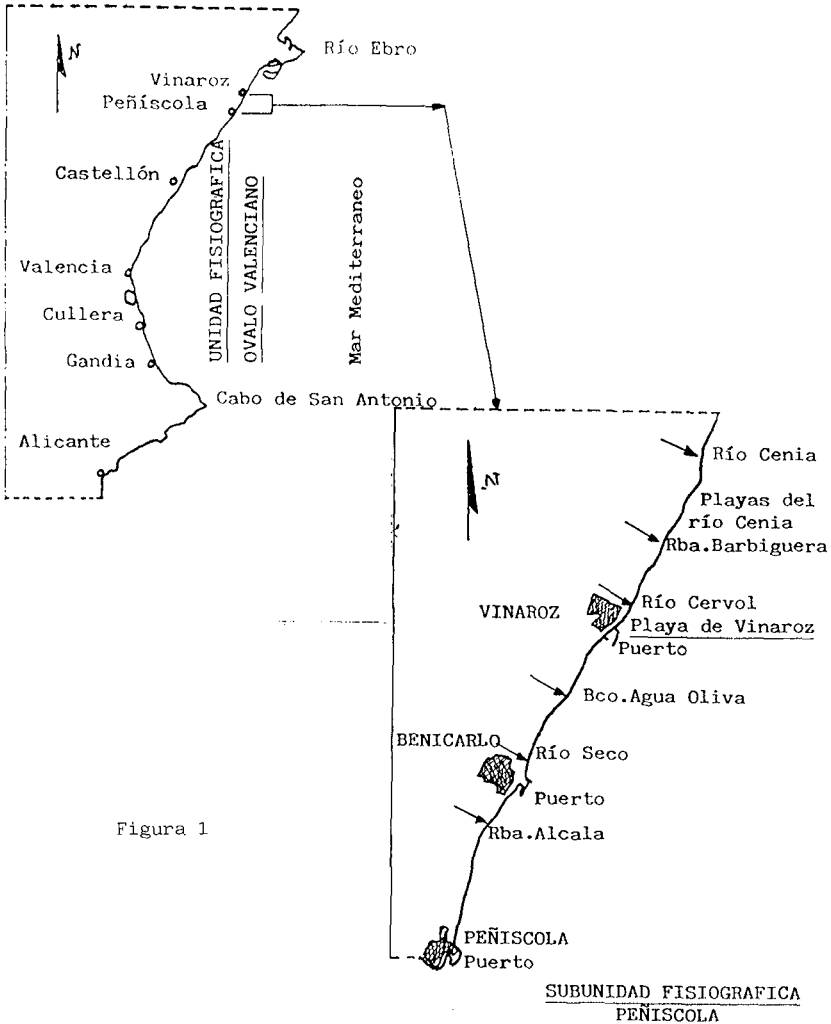


Figura 1

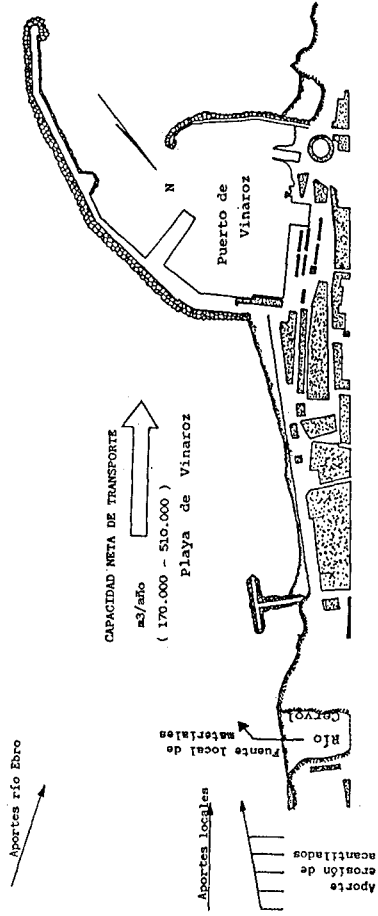


Figura. 2

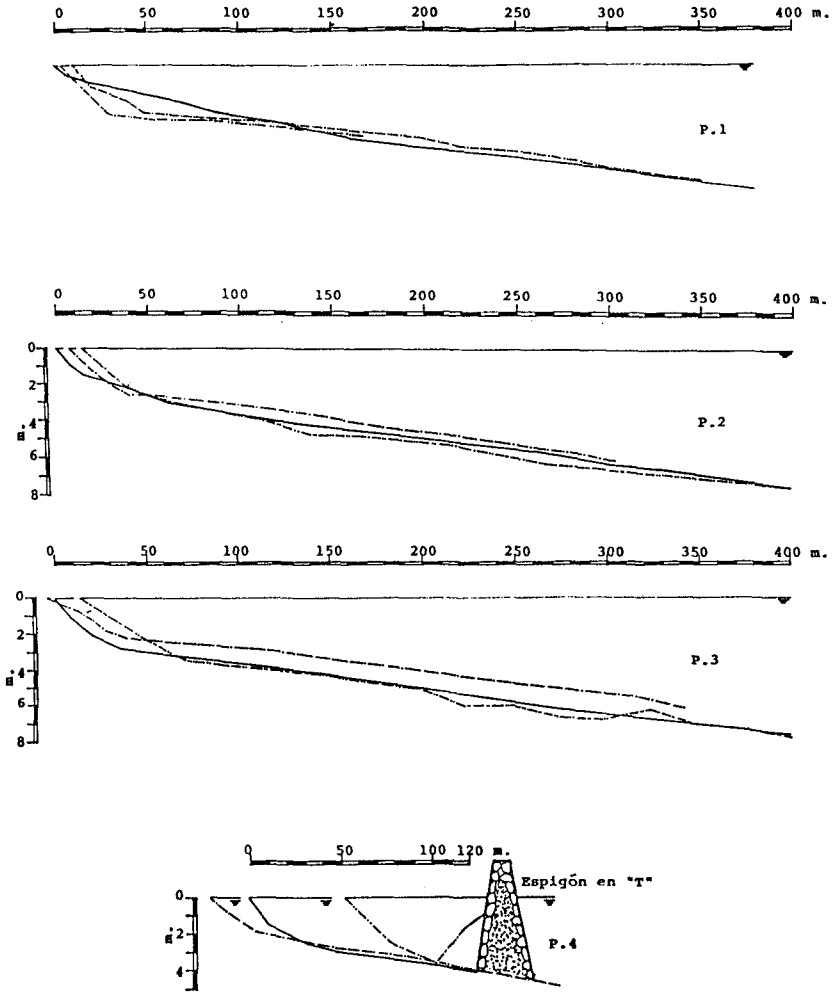


Figura 3

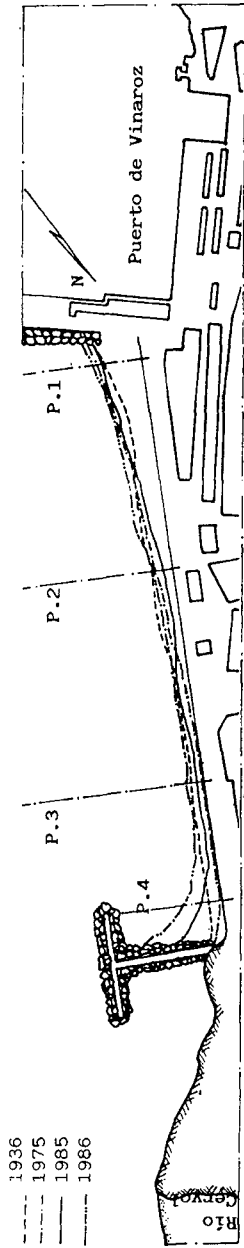


Figura 4

CHAPTER 207

STABILIZATION OF COAST BY CONSTRUCTION OF HEADLANDS ON THE KASHIMANADA COAST, JAPAN

Uda, T.*, M. Sumiya**, and H. Sakuramoto***

ABSTRACT

Eleven artificial headlands were constructed on the Ohno-Kashima Beach facing the Pacific Ocean to prevent further extension of beach erosion and to form the dynamically stable beach. This paper summarizes the results of the follow-up study of the new works applied on the actual coast. Field investigations such as bottom sounding around headlands and aerial photographing were conducted. It was found that the periodic changes of the shoreline configuration corresponding to seasonal change of the wave direction exist on this coast and these variations of the shoreline position can be reduced by the effect of these headlands.

I. INTRODUCTION

In recent years beach erosion has been considerably severe along Japan's coasts, so that various types of coastal protective measures have been carried out; seawalls, wave-dissipating breakwaters, groins or detached breakwaters have been constructed. Most of these facilities are constructed continuously or with small intervals along the shoreline. As a result of these works natural sandy beaches decrease year by year. Natural beach possesses not only prominent function of disaster prevention but also great advantages in view of landscape. Therefore, it is desirable for preventive works to be carried out while maintaining natural sandy beaches as much as possible.

Along the Kashimanada Coast in Ibaraki Prefecture, beach erosion has been severe in recent years (Uda et al., 1986 a,b). For a measure against beach erosion, construction of the artificial headland was planned by the Ibaraki Prefectural Government since 1983 on the

-
- * Dr. Eng., Head, Coastal Eng. Div., Public Works Res. Inst., Ministry of Construction, Ibaraki 305, Japan.
 - ** River Div., Public Works Dep., Ibaraki Pref. Office, Ibaraki 310, Japan.
 - *** INA Civil Eng. Consultants Co., Ltd., Tokyo 162, Japan.

Kashimanada Coast facing the Pacific Ocean, and a group of 11 headlands have already been constructed up to the present. Artificial headlands have been applied in Japan for the first time, and at present there remain some problems to be solved in its applications. This paper summarizes the results of the follow-up study of the new works applied on the actual coast. Present headlands have not been completed up to its final design, but further field investigations are to be conducted to attain the reasonable form of the headland system through actual field tests.

Regarding the headland system for the beach stabilization method some previous studies have been already conducted by Silvester (1976) or Tsuchiya (1984). These methods can be applied to the beach where waves obliquely approach to the shoreline with large angle. On the coasts in Ibaraki Prefecture, however, the direction of wave approach varies seasonably and periodically, so that their methods are not applicable. One of the authors has proposed a shoreline control method --artificial headland-- for the field with periodic changes of the incident wave direction (Uda et al., 1987). Since both methods have similar meaning with respect to a point that a long extensive beach is changed stable by separating into several segments by these works, the measures carried out in this study will be called by the same name-headland.

II. OVERALL FEATURES OF BEACH CHANGES ALONG THE KASHIMANADA COAST

The study site (the Ohno-Kashima Beach) is located on the north side of Kashima Port in the middle of the Kashimanada Coast (Fig. 1). On this beach the direction of longshore sediment transport is changing according to the seasonal changes of incident wave directions, but

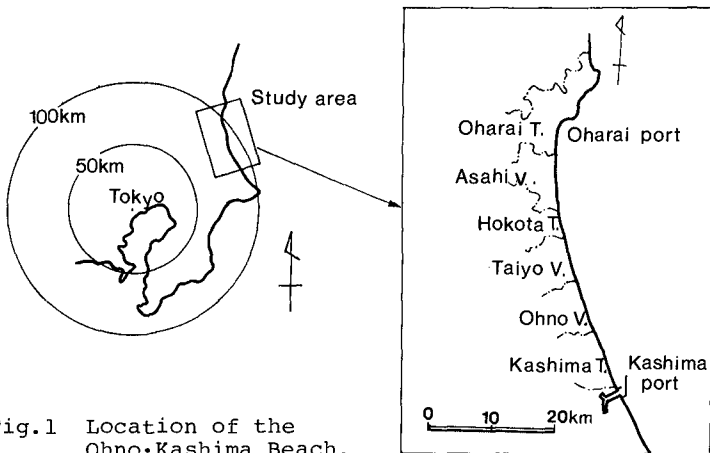


Fig.1 Location of the Ohno-Kashima Beach.

northward component of the wave energy flux dominates, so that severe beach erosion is observed on the north side of the Kashima Port, obstructing northward longshore sand transport (Uda et al., 1986).

The longshore distribution of the shoreline change, median diameter of beach materials and foreshore slope are shown in Fig. 2, illustrating the shoreline change until 1985 and 1987 with reference to the one measured in October, 1984. The abscissa is the longshore distance from the origin located at Oharai Port (refer to Fig. 1). In addition, median diameter and foreshore slope were measured both in 1985 and 1987. It is clearly understood that the shoreline has retreated considerably in recent years on the Ohno-Kashima Beach 25km to 39km south of the origin, and also beach materials and foreshore slope have become

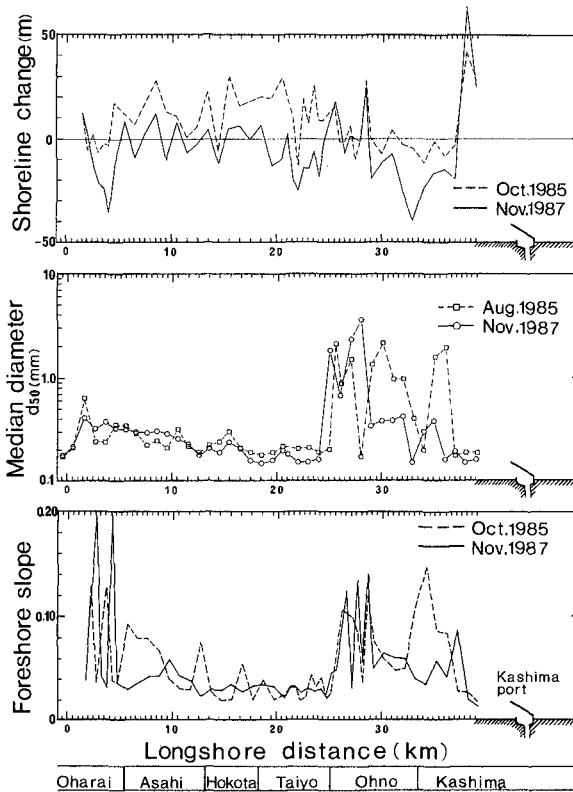


Fig. 2 Longshore distribution of shoreline change, median diameter of the foreshore materials and foreshore slope along the Kashimanada Coast.

coarser and steeper at the same locations, respectively. The same characteristics as mentioned above are found on the south beach adjacent to Oharai Port. In order to prevent these beach erosions and to form stable beaches on this coast the construction of headlands was proposed.

III. CONSTRUCTION OF HEADLANDS

Headlands were constructed at the interval of about 1km based on the aerial photographs taken in August, 1984, assuming that the shoreline retreat should be less than about 30m, because the original shoreline width at the planning time had already been narrow enough and the shoreline retreat over 30m was not permissible for the stability of various coastal facilities. The construction sites of headlands were decided, based upon the simulation of the shoreline evolution by using one-line theory with the present shoreline data. The arrangement of each headland is shown in Fig. 3. Eleven headlands have already been constructed up to the present and the two are to be set in future. The construction of No. 1 and No. 4 headlands out of 11 headlands began in December, 1985 and were completed in March, 1986. The construction period of the remains is presented in Table 1. In addition, Fig. 4 represents details of headland plan; the crown width is 6m, the crown height is +2.2m above the M.S.L., its length is 100m and it was built by natural stones over 1 ton. The length of headland is about 80m at present.

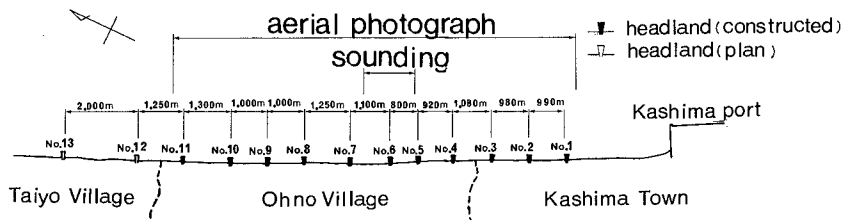


Fig. 3 Location of construction site of headlands on the Ohno-Kashima Beach.

Table 1 Dates of measurement of the bottom sounding and aerial photographs.

Date Kind	1986				1987												1988				
	Sep.	Oct.	Nov.	Dec.	Jan.	Feb.	Mar.	Apr.	May	Jun.	Jul.	Aug.	Sep.	Oct.	Nov.	Dec.	Jan.				
Sounding	○			○	○	○		○				○		○		○		○			
Aerial Photo		○		○	○	○		○				○	○		○			○			
Construction Period of Headlands	← No. 3, No. 5~7				← No. 8 ~10																← No. 2, No. 11

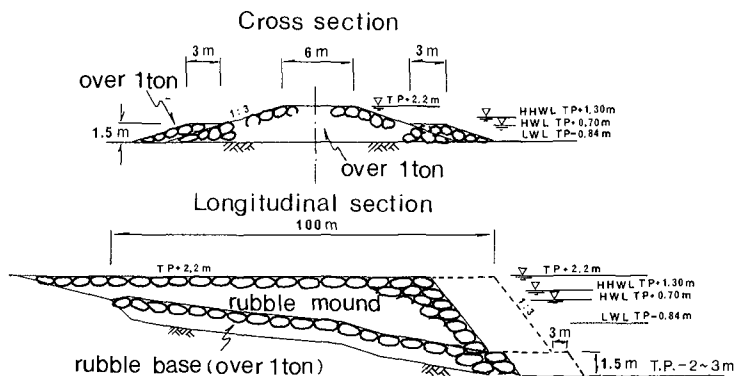


Fig. 4 Configuration of headland.

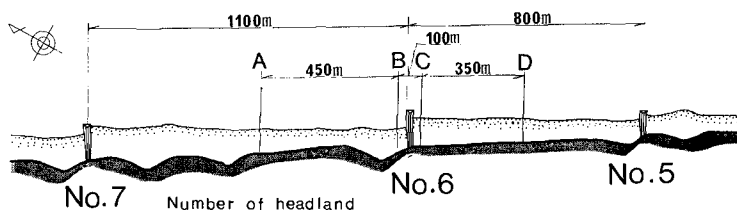


Fig. 5 Arrangement of survey lines of bottom sounding.

IV. METHOD OF FIELD INVESTIGATIONS

Field investigations consist of bottom soundings and aerial photographing, whose schedules are summarized in Table 1. Bottom soundings were carried out 9 times in total. Both observations were tried to be conducted at the same day, but there was a little time lag in execution due to the weather conditions.

The soundings were carried out along 20 survey lines of 200m in length, covering the sites of No. 5 to No. 7 headlands. The investigation of the profile changes were conducted in detail only with the representative 4 survey lines such as the north lines (A, B) and the south ones (C, D) of No. 6 headland as shown in Fig. 5, because beach changes caused by the construction of headlands can be well examined by the comparison of beach profiles near the structure with those far from that. Comparison with the beach profiles along the survey lines B and C near the structure enables to evaluate the influences of the headland for the surrounding beach topography.

Figure 6 represents the wave data during the field survey in terms of significant wave height ($H_{1/3}$) and wave

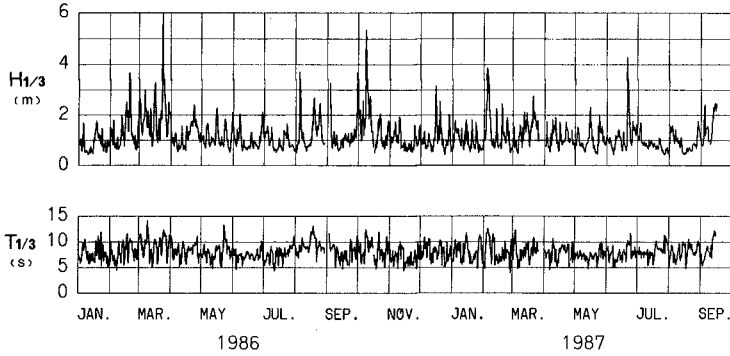


Fig. 6 Temporal changes of significant wave height and wave period off Oharai Port.

period ($T_{1/3}$) observed at a location of 21m deep off Oharai Port in January, 1986 through September, 1987. Wave condition of this coast is usually rough in February, March and October. On the contrary, from April to August calm sea condition generally prevails. There exists a weak correlation between significant wave height and wave period as shown in Fig. 6, and wave period tends to be longer with the increase of wave height.

At Oharai Port wave directions have been observed. The joint distribution of significant wave height and wave direction is summarized in Table 2, in which the data are summed up separately in 1986 and 1987. On both tables four predominant direction with high wave energy level are apparent, and in addition these wave directions are roughly divided into two groups of NE, ENE and SE, SSE. Assuming the same wave incidence at a location off the Ohno-Kashima Beach, the longshore sediment transport on this site

Table 2 Joint distribution of significant wave height and wave direction.

Jan, 1986 ~ Dec, 1986												(%)
$H_{1/3}$ (m)	Direction	N	ENE	NE	ENE	E	ESE	SE	SSE	S	Total	
0.00 ~ 0.49												
0.50 ~ 0.99		0.6	9.0	11.3	4.8	0.3	1.0				27.0	
1.00 ~ 1.49		0.6	7.7	15.1	1.9	2.3	6.9	3.9			36.3	
1.50 ~ 1.99		1.0	4.2	7.1	2.9		5.8	1.3			22.2	
2.00 ~ 2.49		0.3	0.6	1.6	1.3	0.6	2.6	0.3			7.4	
2.50 ~ 2.99					0.6	1.3	0.6	0.3			2.9	
3.00 ~ 3.49					0.3	0.3		1.0			1.6	
3.50 ~ 3.99								0.3			0.3	
4.00 ~				0.3							0.3	
Total		2.6	21.5	36.3	12.5	3.9	17.7	5.5			100.0	

Jan, 1987 ~ Sep, 1987												(%)
$H_{1/3}$ (m)	Direction	N	ENE	NE	ENE	E	ESE	SE	SSE	S	Total	
0.00 ~ 0.49					0.6				0.6	0.6	1.7	
0.50 ~ 0.99		1.1	8.0	10.9	2.3				1.1	5.1	29.1	
1.00 ~ 1.49			14.3	9.7	1.7				1.7	10.9	38.9	
1.50 ~ 1.99			5.7	5.7						7.4	18.9	
2.00 ~ 2.49			1.7	1.1						4.0	6.9	
2.50 ~ 2.99				1.1						0.6	1.7	
3.00 ~ 3.49										1.1	1.1	
3.50 ~ 3.99				0.6							0.6	
4.00 ~												
Total		1.1	31.4	28.0	4.0				3.4	30.9	100.0	

dominates southward by wave incidence from NE, and northward from SE or SSE, respectively because the direction normal to the mean shoreline is ENE. As is mentioned, this coast is characterized by seasonal changes of wave direction and to this reason typical changes of the beach configurations can be seen around coastal structures.

V. RESULTS OF INVESTIGATION

5.1 Shoreline Evolution

Shoreline changes around headlands between September 8, 1986 through January 7, 1988 are expressed in Fig. 7. In this figure comparisons are made with subsequent shoreline configurations. The locations of No. 1 through No. 7 headlands are also shown at the bottom of the figure. From September 8 to October 28, the shoreline retreated on almost all area except adjacent part north of No. 1 and No. 4 headlands which had been already constructed at that time. This recession of the shoreline is thought to be caused mainly by the cross-shore sediment transport by high waves which attacked the beaches with the significant wave height over 5m on October 9 as shown in Fig. 6. On the other hand, the local advance on the north part of No. 1 and No. 4 headlands may be caused by the accretion due to the southward longshore transport by waves approaching from counterclockwise direction

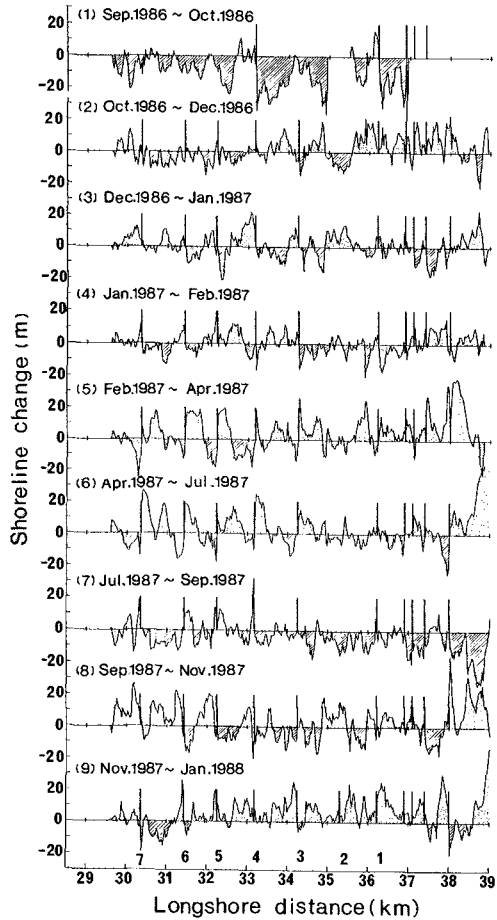


Fig. 7 Shoreline change between September, 1986 and January, 1988 measured from the aerial photographs.

to the normal of the shoreline. Between October 28 and December 24, any typical feature of shoreline evolution did not appear, only accompanying with some local erosion or accretion. From December 24 to January 17, as seen especially around No. 3, No. 4 and No. 7 headlands, the shoreline retreated on the south side in contrast to the advance on the north side of these headlands. These phenomena of the shoreline change were induced by the southward longshore sediment transport resulting from the wave incidence from the counterclockwise direction to the normal of the shoreline, corresponding to the wave approach from NE to ENE on the study coast. On the contrary, the shoreline changes occurred between February 13 and April 13, and between April 13 and July 23 are entirely reversed to the above, i.e., the shorelines advanced greatly on the south (right) side but retreated on the north side of each structure. This is due to the wave approach from the predominant direction of SE to SSE through spring to summer. Then, remarkable changes of the shoreline did not appear between July 23 and September 12, but from September 12 to November 6 the shoreline advanced again on the north side and retreated on the south side of each structure. These characteristics of shoreline changes are the same as the ones between December 24, 1986 and January 17, 1987. Consequently, it is found that the shoreline between headlands are dynamically stable with periodic fluctuations of the amplitude of about 40m.

The above-mentioned periodic fluctuations of shoreline configuration between headlands are recognized on the north coast in the same Ibaraki Prefecture (Uda et al., 1986 a,b). Taking into consideration of these facts, it is considered that this shoreline evolution represents a general features along the Ibaraki Coast facing the Pacific Ocean.

A reversal mode was observed on south and north sounding lines near a certain headland. This change is due to the periodic change of incident wave direction. In the following these phenomena will be examined in detail on the basis of temporal change of shoreline position on both survey lines of 25m away from No. 6 headland (Fig. 8). In the figure solid and open circles represent the shoreline positions on the south and north lines, respectively, including the shoreline position before the construction plotted as a broken line. There is little difference in the shoreline change before the construction on both lines, whereas the shoreline position advanced on the north side and retreated on the south side between January and February, 1987 after the construction of the headland. Then, the opposite mode of the shoreline change was observed until August resulting in large advance of the shoreline on the south side. Moreover, between August and December appeared again the recession of the shoreline position on the south side. The reasons of above mentioned cyclic shoreline changes could be explained as follows; from autumn to winter the southward longshore sand

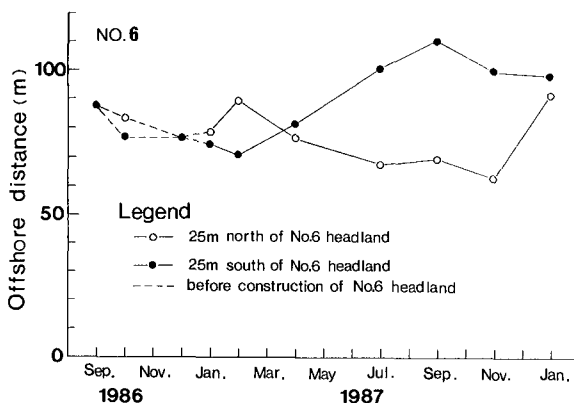


Fig. 8 Temporal change of shoreline position in the vicinity of No.6 headland.

transport prevails by the incident waves approaching from NE or ENE to this coast and then the obstruction of longshore sediment transport by the structures produces the progression of the shoreline on the north side. On the contrary, from spring to summer northward longshore sediment transport is caused by the predominant waves from SE or SSE, which is clockwise to the normal of the coastline. Then shoreline position progrades on the south side of the structure.

5.2 Comparison of Aerial Photographs Around Headlands

Shoreline configurations will be investigated in detail, selecting No. 7 headland as a typical example. Aerial photographs were taken five times between January 17 and September 12, 1987 around No. 7 headland.

The shoreline on January 17, 1987 is shown in Photo 1. Taking into account of the headland length of about 80m, it is seen that the sea is very calm and the surf zone width is narrow. This calm wave condition coincides with the characteristics observed in Fig. 6. Comparing the shoreline configuration on both sides of the headland, the shoreline on the right (south) side retreats a little more than that on the left (north) side. It shows a resultant beach change caused by the weakly-oblique wave incidence from the counterclockwise direction to the normal of the shoreline. On February 13 wave conditions turned rough and the whole picture were covered by the surf waves (Photo 2). This photograph is thought to represent a typical rough wave condition in winter, because wave height in February is high as shown in Fig. 6. In addition, the shoreline south of the headland retreats greatly compared with that north of headland. This fact indicates the same feature



Photo 1 Aerial photo of
No.7 headland
(January 17, 1987)



Photo 2 Aerial photo of
No. 7 headland
(February 13, 1987)

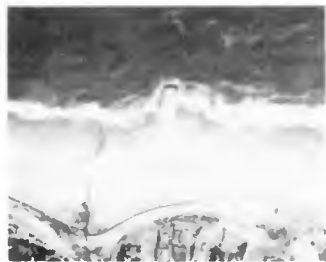


Photo 3 Aerial photo of
No.7 headland
(April 13, 1987)



Photo 4 Aerial photo of
No.7 headland
(July 23, 1987)



Photo 5 Aerial photo of
No.7 headland
(September 12, 1987)

observed in Photo 1. In other words, incident wave approaches from counterclockwise direction to the normal of the shoreline.

Two month later (Photo 3), the shoreline configuration on both sides became almost symmetry to the headland, and there disappeared the distinct shoreline retreat on the south side in Photo 2. It shows that the direction of incident wave turned clockwise with respect to the normal to the shoreline during these two months. In addition, low waves are supposed to be approaching to the coast judging from the occurrence of narrow surf zone. Actually low wave conditions appeared in April as shown in Fig. 6, so that Photo 3 is thought to show the typical state of the shoreline form in this season. On the other hand the shoreline on July 23, 1987 (Photo 4) represents remarkable changes; great advance on the south side and recession on the north side. The characteristics of the shoreline changes on this date are totally opposite to those on February 13. Furthermore, the wave conditions are also calm and the swell waves are clearly noticeable to approach in the offshore zone of the headland from a clockwise direction. Finally it is found that morphological changes between April and July are caused by the clockwise wave incidence.

Photo 5 represents the beach circumstances on September 12. Entire region of the photograph is covered by the surf waves, thereby high waves were clearly incoming to the beach at that time. Also in the offshore of the headland the waves approach clockwise at an angle of about 12° to the normal of the shoreline and even the tip of the headland locates within the surf zone. Since the northward longshore sediment transport dominates under the wave climate, the shoreline advanced on the south side, whereas the shoreline retreated on the north side of the structure. Consequently, it is concluded that the periodic variations of the incident wave direction throughout a year determine the direction of the longshore transport on this coast. This means that the seasonal changes of wave directions are the most important factor to consider beach deformation on this coast. Having seen in Photos 2 and 5, the tip of the headland becomes contained occasionally within the surf zone under high wave conditions. It is, therefore, possible for the longshore sediment to turn around the tip of the structures to the adjacent beaches. This means that the headland of present dimension can reduce the rate of sediment, but can not prevent from the decrease of sand volume between headlands. Taking the present situation into account, it is necessary to elongate the headlands in future.

5.3 Beach Profile Changes

Here will be described time series of the beach profile changes based on the data surveyed almost at the same time as the shoreline changes as shown in Fig. 7. Figure 9

expresses the beach profiles along the section A, where the influence of the existence of the headlands is minimum because it is located in the middle of No. 6 and No. 7 headlands. Since this section is located far from the structure, the characteristics of topographic changes due to cross-shore sediment transport can be investigated in detail.

First, from September 8 to December 24, 1986 the foreshore was eroded to form a bar-trough topography off the coast. According to Fig. 6, very high waves beyond $H_{1/3} = 5\text{m}$ attacked the coast on October 9, so that the bar-trough topography might be formed due to the offshore sand movement. Thereafter the beach had not changed so greatly until April 14, but changed remarkably between April 14 and July 8; offshore bar receded as well as sand accumulated on the foreshore. This topographic change has a reverse mode against the pattern occurred between September 8 and December 24. Furthermore the critical depth to which the erosion or accretion occurs near the foreshore agrees well with about 3m in both cases. During the period between April and July mainly calm sea conditions continued with the significant wave height less than about 2m except on June 19 with the height of $H_{1/3} = 4.3\text{m}$. Considering these calm wave conditions, it may be concluded that the profile change illustrated in the figure was caused by the onshore sand transport. After that, the whole beach profiles tend to retreat slightly until November 6.

Comparing the profile on September 8, 1986 with the one on September 10, 1987, both shoreline positions and beach profiles are almost the same each other and therefore it is found that the eroded beach retrieved into the previous state after one year. It should be noted that on this

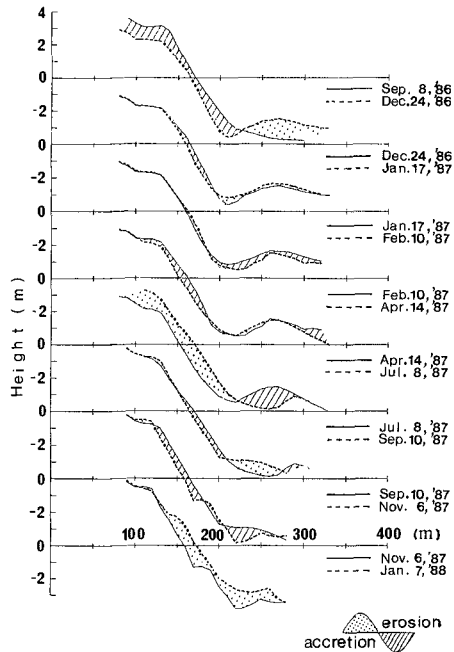


Fig. 9 Temporal profile change along section A.

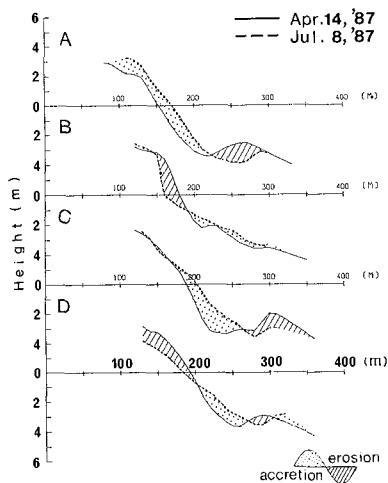


Fig. 10 Spatial and temporal profile changes along section A through D measured between April and July in 1987.

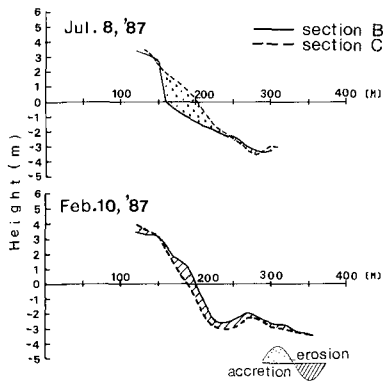


Fig. 11 Comparison of beach profiles on both sides of No.6 headland between February and July in 1987.

coast the following two types of sand movement can be observed; the variation of the longshore sediment transport caused by the periodic changes of wave direction and the change of cross-shore sediment transport due to wave climate change.

As shown in Fig.7, the shoreline on the north side of the structure retreated between April 13 and July 23, 1987. The typical profile changes in this period are illustrated in Fig. 10. On the section C just south of the headland of No. 6, sand accumulated near the shoreline to form the gentle slope of the foreshore, and in addition the accreted area extends to the depth of about 3m. On the contrary, on the section B located in the symmetric position with respect to the headland, the area shallower than the water depth of 1m was eroded to form a steep slope of the foreshore, whereas beach slope of the offshore zone becomes mild. These accretion-erosion pattern of topographic changes having opposite features on both sides of the headlands indicate that the beach changes are caused mainly by the longshore transport. On the other hand, on the section D, 375m south from No. 6 headland, the foreshore was eroded to form a gentle slope similar to the section C.

In order to examine the extent of the obstruction of longshore sand transport by the headlands, it is preferable to compare the spatial profiles on both sides of the structure rather than to examine the temporal changes of profiles as shown in Fig. 10. Because the influences of

the structure to surrounding topography can be well understood by superimposing each others, since the two sections next to the headland should have the same profile before the construction of the headlands.

Figure 11 represents the superimposed profiles the sections B and C measured on February 10 and July 8, 1987. The former date is in the period when the southward longshore sediment prevails as shown in Fig. 7. The shoreline position on the section B north of the headland advances more than that on the section C, and the sand obviously accumulates in the region shallower than the depth of 3m deep, but at further offshore zone both profiles nearly coincide with each other. Taking the tip depth of about 2m into account, the above accretion shows that the effect of the headland extends to the region somewhere offshore from the tip of headland.

The similar comparison will be made with regard to the profiles on July 8, when the northward longshore transport was predominant. The shoreline position on the section C south of the structure is located further offshore than that on the section B, resulting in the quite opposite to the case of February 10. The foreshore slope on the section B is steeper than that on the section C, and also the region shallower than 2m deep is eroded, but almost coincides with the section C in further offshore zone.

Consequently, it is concluded that the headlands on this coast are effective for controlling sediment movement in a zone shallower than 2m because the tip of the headland is about 2m, although sediment may pass through around the tip of the headland. Nevertheless, it can be said that this headland is useful at present stage in reducing the longshore sediment transport rate.

VI. CONCLUSIONS

- (1) Eleven headlands were constructed in order to prevent further extension of beach erosion and to form the dynamically stable beach on the Ohno-Kashima Beach. The variation of the shoreline position can be reduced by the effect of the construction of these headlands in the field where seasonal change of the wave direction dominates.
- (2) The periodic changes of the shoreline configuration corresponding to seasonal change of the wave direction have been observed along the other coast facing Pacific Ocean in Ibaraki Prefecture such as the Joban Coast or the Ajigaura Beach. From these facts, the characteristics mentioned above may be considered as a typical example of the beach changes along the Eastern Coast of Japan.
- (3) The depth at the tip of the headland is about 2m. Comparing beach profiles on both sides of headland, there exist differences in the region shallower than about 3m. Therefore the region where longshore sediment transport is remarkably obstructed by the

headlands is thought to be the region up to a location of about 3m deep.

ACKNOWLEDGEMENT

The authors wish to express their gratitude to Ibaraki Prefectural Sanpin Port Office with offering the wave data.

REFERENCES

- Silvester, R. (1976): Headland defense of coasts, Proc. 15th Coastal Eng. Conf., ASCE, pp.1394-1406.
- Tsuchiya, T. (1986): Beach erosion control, Coast, Vol.24, pp.100-109. (in Japanese)
- Uda, T., M. Sumiya and Y. Kobayashi (1986 a): Beach change along the Ibaraki Coast, Japan, Trans. Japan. Geomorphological Union, Vol.7, No.3, pp.141-163. (in Japanese)
- Uda, T., M. Sumiya and Y. Kobayashi (1986 b): Analysis of beach erosion around large-scale coastal structures, Proc. 20th Coastal Eng. Conf. ASCE, pp.2329-2343.
- Uda, T. and K. Yamamoto (1987): On the beach stabilization method of sandy beach, Civil Eng. Jour., Vol.29, No.9, pp.21-26. (in Japanese)

CHAPTER 208

Results from the Atlantic City, NJ Beach Nourishment Monitoring Program

R. M. Sorensen* F. ASCE
S. L. Douglass** M. ASCE
J. R. Weggel*** F. ASCE

Abstract

A beach nourishment project was carried out at Atlantic City, NJ during the summer of 1986. One million cubic yards of sand was dredged from adjacent Absecon Inlet and placed over a 9000 foot long section of the beach. The authors monitored the fill for a period of eighteen months, including two winters, after placement of the fill.

This paper briefly summarizes the fill project and monitoring program. Key results of the monitoring program are presented and compared with results of the monitoring program for previous nourishment projects at the site in 1963 and 1970. Differences in the behavior of the 1986 fill vis-a-vis the 1963 and 1970 fills are discussed and possible reasons for these differences are given.

Introduction

It is still difficult to fully predict the behavior of a planned beach nourishment project. Season to season variations in wave climate, the impact of existing structures and proposed structure modifications, and the frequency and mode of fill placement can have a significant impact on the behavior of beach fill. Monitoring of completed beach nourishment projects will hopefully increase our understanding of fill behavior and continue to improve our ability to design such projects. The 1986 beach nourishment project at Atlantic City, NJ was monitored and results of the monitoring program are compared with the behavior of earlier fill projects at Atlantic City.

Project Site

Atlantic City is situated on the northern third of Absecon Island, a barrier island located 40 miles north of the southern tip of the Jersey coast. It is separated from Brigantine by the jettied Absecon Inlet (Figure 1). The shoreline has a general northeast-

-
- * Professor, Department of Civil Engineering, Lehigh University, Bethlehem, PA 18015
 - ** Project Engineer, Pare Engineering Corporation, Pawtucket, RI 02860
 - *** Professor, Department of Civil Engineering, Drexel University, Philadelphia, PA 19104

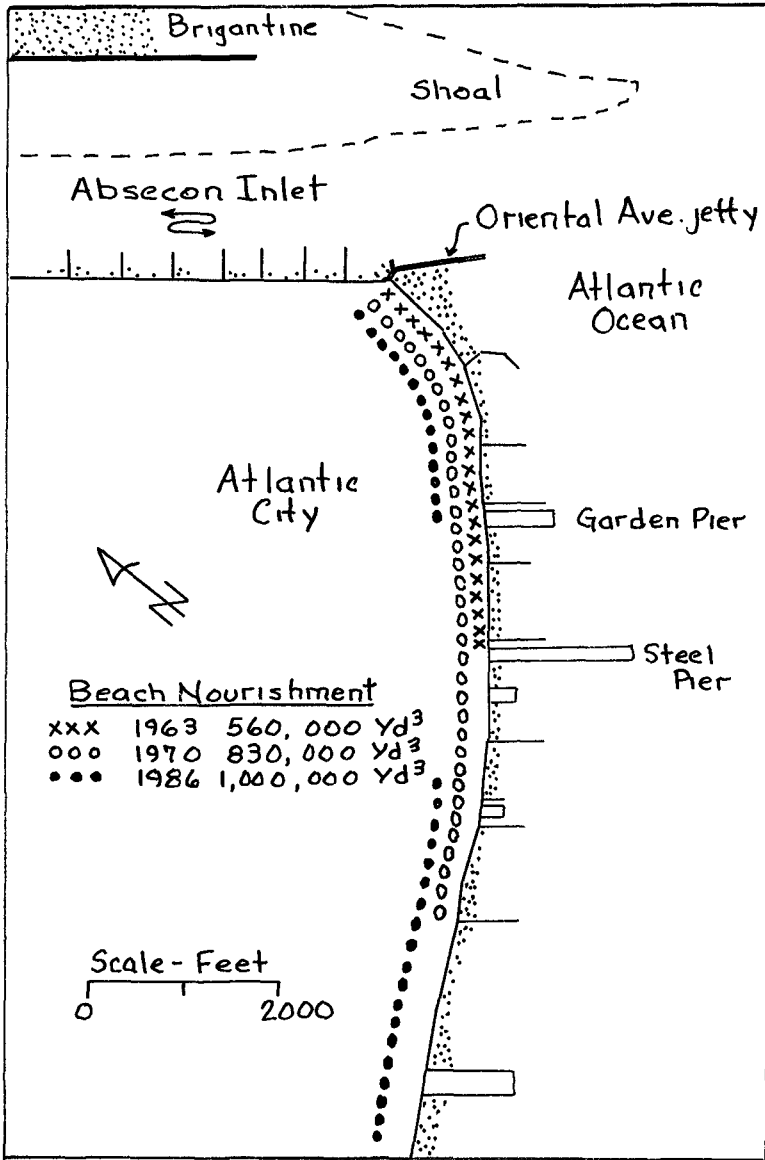


Figure 1 - Project site

southwest orientation.

The beach at Atlantic City is backed by wooden bulkheading and a boardwalk. There are five commercial piers which act as permeable groins as well as nine wood and stone groins varying from 100 ft to 800 ft (but typically 500-600 ft) in length. Beach berm widths vary from zero up to 500 feet (at Oriental Avenue jetty) out from the boardwalk. However, along several important beach segments, the berm width is typically fifty feet or less.

The U.S. Army Corps of Engineers (1974) estimates that there is a net southwestward transport of 150,000 cu.yd./yr. at Atlantic City (from a gross transport of 250,000 cu.yd./yr. northeastward and 400,000 cu.yd./yr., southwestward). Visual wave observations indicate dominant southwestward transport throughout the year except for some months during the summer. The dominant southwestward transport drives the Absecon Inlet Channel up against the Atlantic City side of the inlet. And it causes a large shoal to form on the Brigantine side of the inlet and extending over a thousand yards seaward of the head of the Brigantine jetty (Figure 1).

Although there is a general net southwesterly longshore transport in the study area, there is a local reversal of transport on the Atlantic City shore near the inlet. Observations of beach offsets at the groins taken from historic air photos and from onsite observations at different times of the year (Sorensen and Weggel, 1985) showed a diverging nodal zone that is consistently located between Carden Pier and Steel Pier (Figure 1). The nodal zone was generally located around Carden Pier during the spring to fall months, but it shifted to the vicinity of Steel Pier during the winter to early spring months.

Beach Nourishment Projects

Major beach nourishment projects were carried out at Atlantic City in 1948, 1963 (February-May), 1970 (June-July) and 1986 (April-June). The fill volumes and locations for the 1963, 1970 and 1986 projects are shown on Figure 1. The gap in the 1986 fill placement was due to ongoing construction work in the vicinity of Steel Pier.

The borrow area for all of the fill projects was the shoal area on the north side of Absecon Inlet. Sand was hydraulically dredged from various points along the channel side of the shoal and carried to the fill areas by pipeline. The four fill projects were essentially bypassing operations.

1963, 1970 Nourishment Projects

As a direct outcome of the damaging "five high" storm in March 1962, the U.S. Army Corps of Engineers established a beach monitoring program at Atlantic City which lasted from October 1962 to May 1973. Beach profiles, to wading depth, were measured at seven locations (Figure 2) on approximately a monthly basis (more frequently in winter, less frequently in summer). Note that profiles 1-3 are in the 1963 fill area; profiles 1-4 are in the 1970 fill area. The profile data are presented by McCann (1981) and discussed by Everts et al. (1974) in relation to the 1963 and 1970 fill projects. Owing to the truncation of profiles at wading depths, changes discussed by Everts et al. (1974) refer only to the portion of the beach profile above MSL.

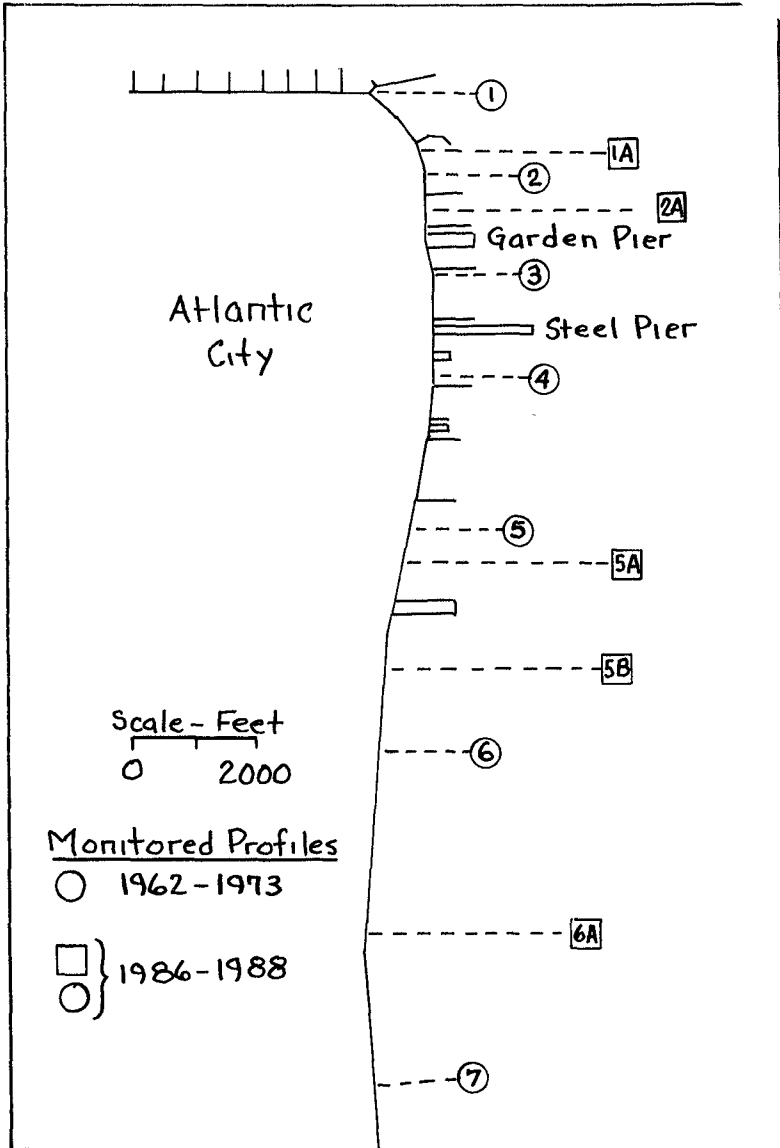


Figure 2 - Monitoring program profile locations

At profile 1, which is adjacent to the inlet, there was a rapid and constant loss of sand until the profile returned to its pre-fill volume. Ninety percent of the fill volume was lost in the first six months in 1963 and within eight months in 1970 (i.e. by December 1963 and February 1971 respectively). At profile 2, located about 1500 feet south of the inlet, there was an initial rapid loss similar to profile 1; but, when the volume loss reached seventy percent of the fill volume, the rate of loss dropped sharply to less than half the initial rate. Still, essentially all of the fill placed above MSL at profile 2 was removed during the first year of both fill projects. On profile 3, the loss rate was uniformly lower and large natural recoveries were observed during following summers. Four years passed before ninety percent of the 1963 fill volume above MSL was lost at profile 3. The profile lines south of the 1963 fill (lines 4-7) showed initial net erosion but within a period of one to three years after the fill, they showed net accumulation.

The trend in beach sediment losses at the successive profiles (1 to 7) indicated that sand moved alongshore to the southwest from the inlet (as well as having a net movement offshore). This was consistent with wave observations (1962-1967) which showed that the mean direction of wave approach during all months (except April when there was a reversal) was from the northeast.

Based on their evaluation of the profile data for the two fill projects, Everts, et al. (1974) offered the following interpretations and recommendations:

- 1) Predominant offshore loss of sand appears to occur between September and March, so fill should be placed in the spring for optimum residence time for the fill. Also, the larger the volume of fill placed at a given location, the faster it is lost; smaller volumes of fill placed more frequently would increase total fill residence time.
- 2) Fill should be placed in a localized feeder beach adjacent to the inlet (vicinity of profile 1) - because fill from that area moves along the shore to the southwest to nourish down-drift beaches and because that area requires the shortest pumping distance for fill material taken from the inlet.
- 3) Placement of fill in a localized feeder beach adjacent to the inlet should be done after April, when longshore current reversals are at a minimum and all of the fill material that moves alongshore can be expected to nourish beaches to the southwest.

Shore Structure Modifications, 1983-1984

During 1983 and 1984 four of the shore structures at Atlantic City were modified. These modifications, which are summarized in Figure 3, appear to have had an impact on the behavior of the 1986 fill project vis-a-vis the 1963 and 1970 fill projects.

The Oriental Avenue jetty, which had an original seaward crest elevation of +7 feet MLW and which had deteriorated some since its construction during 1946-1961 was rehabilitated with a raised crest elevation of +11 feet MLW. The first groin to the south was extended 200 feet (to yield a C rather than just a dog-leg alignment) and

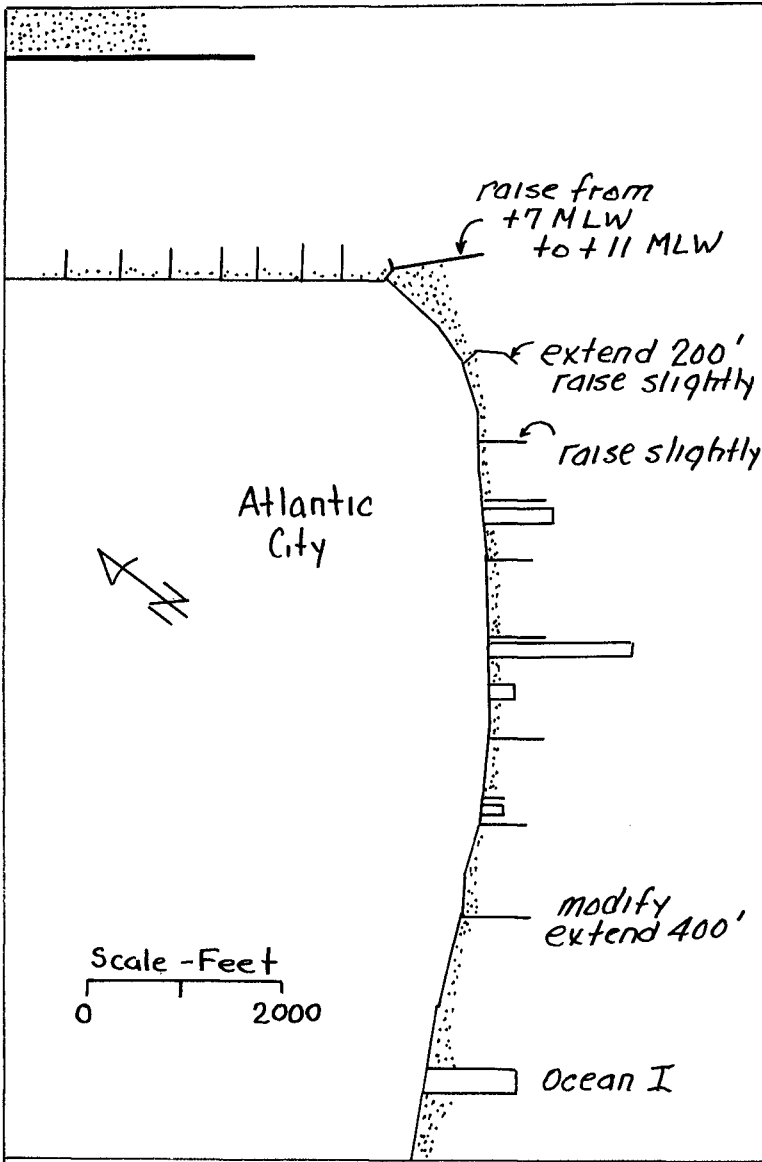


Figure 3 - Structure modifications: 1983 - 1984

raised slightly; and the second groin was raised slightly. A groin further to the southwest, which had been a timber groin, was reconstructed 400 feet longer with a stone seaward section. Also, in the early eighties, the Million Dollar Pier was removed and replaced with a new structure - Ocean I. Ocean I has a high density of relatively small support piles and, consequently, acts as a permeable groin.

Monitoring Program, 1986 Nourishment Project

The 1986 beach nourishment project was funded by the State of New Jersey and conducted through the New Jersey Department of Environmental Protection. NJDEP contracted with the authors to monitor the project for a year and a half period following completion of the fill. The monitoring program ran from August 1986 to March 1988, and included the collection of sand samples, visual wave observations, and beach profile data.

Sand samples were taken from the dredge discharge line and from the beach face during and after the nourishment operation. LEO visual wave observations (Schneider, 1981) were taken at a site in the fill area and at a site southwest of the fill area. Beach profiles (to wading depth) were taken at the seven profile locations used by the Corps of Engineers during 1962 and 1973, plus an additional five profile lines added by the authors. The locations of these twelve profile lines are shown in Figure 3. Profiles were taken on approximately a monthly basis from August 1986 to March 1988.

An NJDEP nearshore hydrographic survey was conducted in December 1985, approximately four months prior to the start of the nourishment project. Data from this survey do not cover all of the twelve profile lines, but data were taken sufficiently close to profile lines 1 through 6 to define the profile depths at these locations. Since the NJDEP survey was conducted four months prior to the start of the nourishment project, an allowance for this four month interval must be made when looking at the profile data.

1986 Monitoring Program Results/Discussion

The beach profile data were analyzed to determine sequential volumetric changes between profiles. Key results are summarized in the Table where volumetric changes are given in cubic yards per yard of beach and in percent change from the volume tabulated in column two.

The second column in the Table gives the profile volume changes between the December 1985 NJDEP survey and the end of the fill in August 1986, when the first monitoring program profiles were obtained. This column thus gives the fill volume plus changes in the beach profile during the previous four months. Fill was placed at profiles 1, 1A, 2, 2A, 5 and 5A; and some of the fill may have been placed in the vicinity of profile 3. Thus, the accumulation of between 40 and 65 cu.yd./yd. at profiles 4, 5B and 6 gives an indication of the natural change from December 1985 to August 1986. The accumulations at profiles 1, 1A, 2, 2A, 5 and 5A should be reduced by about that amount to give a truer indication of the fill placed at each profile line. This yields values of between 400 and 500 cu.yd./yd.

The third column gives the volume changes during the first year after fill placement (and the percentage of the second column). Note that both gains and losses occurred at the unfilled profiles. The

Table - Profile Unit Volume Changes - Yd³/Yd and (%)

Profile No.	Fill* (12/85 - 8/86)	Change Yr 1 (8/86 - 8/87)	Change Yr 2 (8/87 - 3/88)	Σ (%)
1	465.0	-39.0 (-8.4)	-105.0 (-22.6)	(-31.0)
1A	460.0	-200.0 (-43.5)	-20.0 (-4.3)	(-47.8)
2	505.0	-200.0 (-39.6)	-5.0 (-1.0)	(-40.6)
2A	437.2	-81.5 (-18.6)	-51.3 (-11.7)	(-30.3)
3	162.9	-21.4 (-13.1)	-55.6 (-34.1)	(-47.2)
4	43.2	+54.4 (+125.9)	-18.8 (-43.5)	(+82.4)
5	561.2	-72.4 (-12.9)	-30.0 (-5.3)	(-18.2)
5A	567.3	-95.4 (-16.8)	-40.9 (-7.2)	(24.0)
5B	65.7	-15.0 (-22.8)	-7.5 (-11.4)	(-34.2)
6	50.0	-84.3 (-168.6)	-51.3 (-102.6)	(-271.2)
6A	-	+24.5	-21.8	-
7	-	+62.2	-72.2	-

* Includes any natural profile changes between 12/85 and end of fill project in 8/86.

fourth column gives the volume change for the remainder of the monitoring program - essentially these values represent changes that occurred during the second winter season after fill placement. The final column gives the percent change during the monitoring program compared to the approximate fill volume (in the second column).

The major difference in the behavior of the 1986 fill and the 1963 and 1970 fills is the greatly reduced rate of loss of material above MSL, north of the nodal point. Profiles 1 through 2A lost a total of 30 to 40 percent of their volume after two winters compared to a loss of essentially all of their volume during the first winter during 1963 and 1970. Four possible reasons for the improved behavior of the fill in this area are: improved quality of sand fill, less fill placed at a given location (less berm extension and beach face steepening), milder wave climate, and the structure modifications. Each is discussed below.

Pipeline outfall sand samples showed very little difference in median particle diameter from the contemporary native sand on the beach face. Earlier studies (McMaster, 1954, Ramsey and Galvin, 1977 and Sorensen and Weggel, 1985) showed that there is very little difference in the range of sand sizes at the inlet borrow area and on the beach face.

Making allowances for the nonfill changes included in the tabulated values in column 2 of the Table and for differences in the profile volume analyses techniques for the 1963/1970 fills and the 1986 fill, it appears that the volume of fill placed at profile lines 1 and 2 was approximately the same during all three nourishment projects. Comparison of the volumes of fill and the lengths of beach filled for the three projects (see Figure 1) confirms that the volumes of fill per unit length of beach were about the same.

It appears that differences in the wave climate partially account for the observed differences in beach fill behavior. No uniform set of wave data is available for the year following the 1963 and 1970 fills and the two years following the 1986 fill, from which a definite comparison can be made. Hindcast wave data (Jensen, 1983) are available for Atlantic City for the period 1956-1975. From these data, the winters of 1963-1964 and 1970-1971 can be compared to the average 1956-1975 data to see how relatively mild or severe they were. This can then be compared with the experience of the authors and others active along the New Jersey shore during 1986-1988.

Comparing mean monthly significant wave heights for September through April in 1963-1964, 1970-1971, and 1956-1975 (Figure 4) indicates that the winters following the 1963 and 1970 beach fills were essentially average for the twenty year period. Also shown on Figure 4 are the average significant wave heights for March and April of 1962 when the major beach scour that instigated the 1963 fill occurred. These monthly averages are significantly higher than any of the monthly averages in 1963-1964 or 1970-1971. The 1986-1987 winter had two big storms that were coincident with unusually high astronomical tides. Overall, however, this winter was average or slightly milder than average. The winter of 1987-1988 had essentially no major storms until April which was just after the last beach monitoring profiles were taken. Comparison of the first and second year changes in the Table confirms the comparatively milder conditions in 1987-1988 versus 1986-1987.

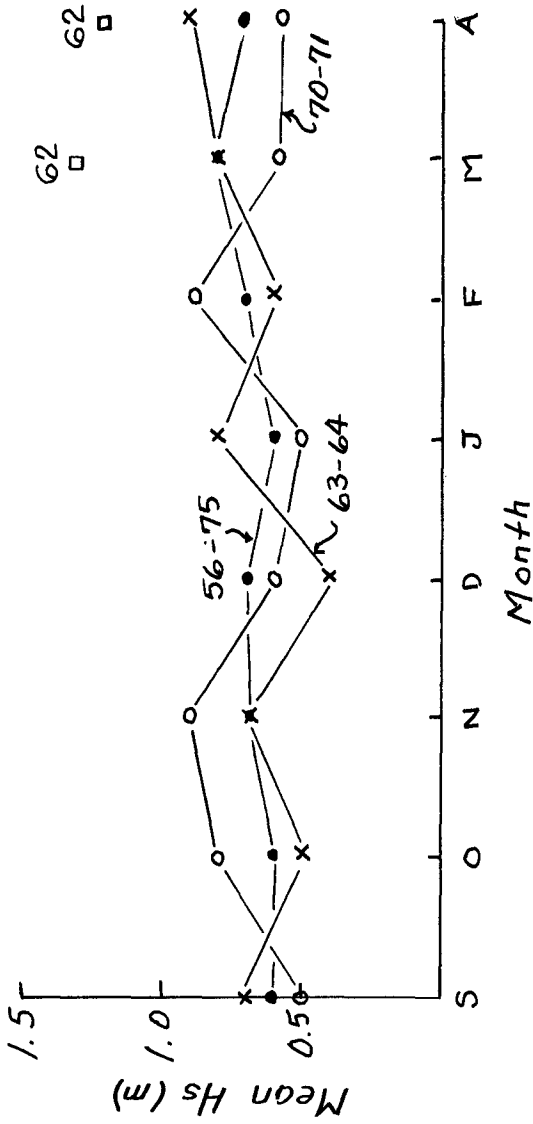


Figure 4 - Atlantic City wave hindcast data

Thus, it appears that the winters following the 1986 fill were somewhat milder than those following the 1963 and 1970 fills. However, there is another cause for the improved behavior of the 1986 fill versus the fills in 1963 and 1970, in the vicinity of profiles 1 and 2. That is the structure improvements made in 1983-1984.

Although Everts et al. (1974) suggest that beach fill placed between the Oriental Avenue jetty and Garden Pier (see Figure 1) moves to the southwest (and offshore), the observed nodal zone position suggests otherwise. Much of the fill place in this region in 1963 and 1970 probably moved toward the northeast, over and around the jetty, and into the inlet. The 1983-1984 structure modifications (Figure 3) limited this movement and subsequent loss. Everts et al. (1974) also suggest that after April dominant transport each month is to the southwest. However, LEO observations made in 1987 showed north-eastward littoral transport to dominate in June.

The fill placed at profiles 5 and 5A suffered an immediate and consistent but small rate of loss. The rate of loss was about half that which occurred at profiles 1 through 2A. In 1963, no fill was placed at profile 5 which showed little net change after the first year and then showed a net accumulation (over the condition at the time of fill) for the next several years - likely because of the transport of sand from upcoast. Compared to the post-1986 fill behavior at profiles 1 through 2A and to the post-1963 behavior at profile 5, the post-1986 fill behavior at profiles 5 and 5A was excellent. Again, the probable causes for this behavior were the milder wave climate and the structure modifications.

Summary and Conclusions

Overall, the 1986 beach nourishment project at Atlantic City has been successful to date. Comparison of beach fill behavior at the six fill profile lines during the first and second winters after the fill (see Table) shows the importance of the milder wave climate during the second winter. Part of the reduced rate of loss is due to the typical exponential loss rate that occurs for beach fills; however, most of the difference is likely due to the milder wave climate.

Comparison of the behavior of the 1963 fill and the 1986 fill (given the differences in wave climate) demonstrates the improvement in fill behavior owing the improvement of some of the shore structures, which reduced the loss of sand alongshore to the inlet and to the southwest. The jetty, groins and piers do significantly improve the behavior of any beach fill placed at Atlantic City.

As Everts et al. (1974) recommend, future fills should be placed as often as possible rather than in larger volumes at longer intervals. Beach nourishment at Atlantic City should be thought of as a sand by-passing operation. The shore stabilization structures should not be allowed to deteriorate, and the fill should be placed over the entire beach length northeast and southwest of the nodal zone.

References

- Everts, C. H., A. E. DeWall and M. T. Czerniak (1974), "Behavior of Beach Fill at Atlantic City, New Jersey" Proceedings, 14th International Conference on Coastal Engineering, Copenhagen, Denmark, June 1974.
- Jensen, R. E. (1983), "Atlantic Coast Hindcast, Shallow-Water Significant Wave Information", U.S. Army Waterways Experiment Station, WIS Report 9, January 1983.
- McCann, D. P. (1981), "Beach Changes at Atlantic City, New Jersey (1962-73)" Misc. Report 81-3, U.S. Army Coastal Engineering Research Center, Ft. Belvoir, VA, March 1981.
- McMaster, R. L. (1954), "Petrography and Genesis of the New Jersey Beach Sands", Bulletin 63, Geologic Series, New Jersey Department of Conservation and Economic Development, Trenton, 1954.
- Ramsey, M. D. and C. J. Calvin (1977), "Size Analysis of Sand Samples from Southern New Jersey Beaches", Miscellaneous Report No. 77-3, U.S. Army Coastal Engineering Research Center, Ft. Belvoir, VA, March, 1977.
- Schneider, C. (1981), "The Littoral Environment Observation (LEO) Data Collection Program", CETA 81-S, U.S. Army Coastal Engineering Research Center, Ft. Belvoir, VA, March 1981.
- Sorensen, R. M. and J. R. Weggel (1985), "Evaluation of Beach, Behavior and Coastal Structure Effects at Atlantic City, NJ" Fritz Engineering Lab Report, Lehigh University, April 1985.
- U.S. Army Corps of Engineers (1974), "New Jersey Coastal Inlets and Beaches, Barnegat Inlet to Longport", Interim Report, Philadelphia District, September 1974.

CHAPTER 209

BERM BREAKWATER FAILURE AT ST. PAUL HARBOR, ALASKA

Javier Weckmann,⁽¹⁾ Associate Member, ASCE
George M. Watts,⁽²⁾ Fellow Member, ASCE

1.0 INTRODUCTION

St. Paul Island, Alaska, is located at 50°10'N latitude and 170°15'W longitude in the south central Bering Sea. It is the most northward and largest island of the Pribilof Island group. The area of the island is about 70 square miles (180 square kilometers), with the city and harbor of St. Paul located at a cove (Village Cove) on the southern coastline. The Pribilof Islands are of volcanic origin and are generally hilly with much of the coastline consisting of precipitous rocky cliffs. Moderate to strong winds are characteristic throughout the year, causing the island to be treeless. It is predominantly covered with grasses, sedges, and wild flowers.

The Pribilofs are a natural haven for a variety of flora and fauna. More than a quarter of a million seabirds nest each year along the coastal cliffs. About two-thirds of the world's population of northern fur seals migrate annually to the Pribilofs for mating purposes. The Pribilof Island area of the Bering Sea is also one of the most abundant and richest seafood grounds in the world. Due to a recent moratorium, the harvest of fur seals in the Pribilofs has been discontinued. In order to maintain existing cultural and economic resources, the City of St. Paul has elected to construct a harbor facility at Village Cove to provide services to commercial fishing vessels operating in the central Bering Sea. The maximum natural water depth in the Village Cove area is 26 feet (7.9m) relative to mean lower low tide datum (MLLW=0.0). Mean higher high tide level is 3.2 feet (1m) above MLLW, with extreme high tide during storm periods being estimated at between 5.0 and 6.0 feet (1.5 to 1.8m) above MLLW. Waves approaching from the southwest sector have the most effect on St. Paul Harbor. During the winter months, breaking waves with heights of 25 feet (7.6m) and 13-16s periods can be expected at Village Cove several times each year.

-
- (1) Senior Engineer, Tetra Tech, Inc., 630 N. Rosemead Blvd., Pasadena, CA, 91107, U.S.A.
(2) Director, Tetra Tech, Inc., 1911 Fort Myer Dr., Arlington, VA, 22209, U.S.A.

2.0 1984 BREAKWATER CONSTRUCTION

2.1 ORIGINAL DESIGN

The St. Paul Harbor was to be constructed in Village Cove using a shore-connected breakwater commencing at the base of Village Hill, and extending approximately 2,000 feet (600m) in a north-northwest direction. The original design of the rubblemound breakwater followed a conventional 3 layer system. This consisted of a quarry stone core protected by 2 layers of 8-17 ton stone (Class II). The seaward slope of this structure would have been 1 vertical to 2.5 horizontal and have a crest elevation of +30 feet (9m) MLLW. The head section was to be constructed using a heavier armor layer of 17-24 ton stone (Class I) with a slope of 1:3. A typical cross-section is illustrated in Figure 1.

Due to a low and insufficient production of Class I and II armor stone at the selected island quarry sites, the contractor and engineer agreed to redesign the breakwater to better suit the quarry stone production. The modified design was then based on the berm breakwater concept, hereby referenced to as the "A-B" design. In theory, this approach to breakwater design would have maximized the use of all quarry stone by minimizing stone by-product, and therefore resulting in a more economical unit stone production cost. The breakwater was then completed to a length of approximately 870 feet (260m) by early October of 1984 using the "A-B" design.

2.2 MODIFIED BREAKWATER DESIGN ("A-B" DESIGN)

The "A-B" design called for an outer layer of "A" stone which ranged from 0.75 tons to 8 tons with a median stone size of 1.5 tons. A 60-foot (18.2m) wide berm was placed on the seaward side. The core material ("B" stone) also composed an outer berm section, with a gradation similar to the original Class V core stone. The crest height of the "A-B" breakwater was +28 feet (8.5m) MLLW (see Figure 1). This design was based on 2-D tests conducted at the Danish Hydraulic Institute (DHI). The tests used wind, wave, and storm parameters developed in a Pribilof Island wave study prepared by DHI in June 1982.

The breakwater was completed with a temporary head section consisting of "A" and "B" stone only. No armor stone of the Class I or II type was placed on the head as an armor layer. It was assumed at that time that construction would continue the following year.

2.3 BREAKWATER PERFORMANCE WITH "A-B" DESIGN

Substantial damage to the breakwater resulted from storms occurring on 13 November and 7 December 1984. A hindcast analysis showed that the first storm produced a deepwater significant

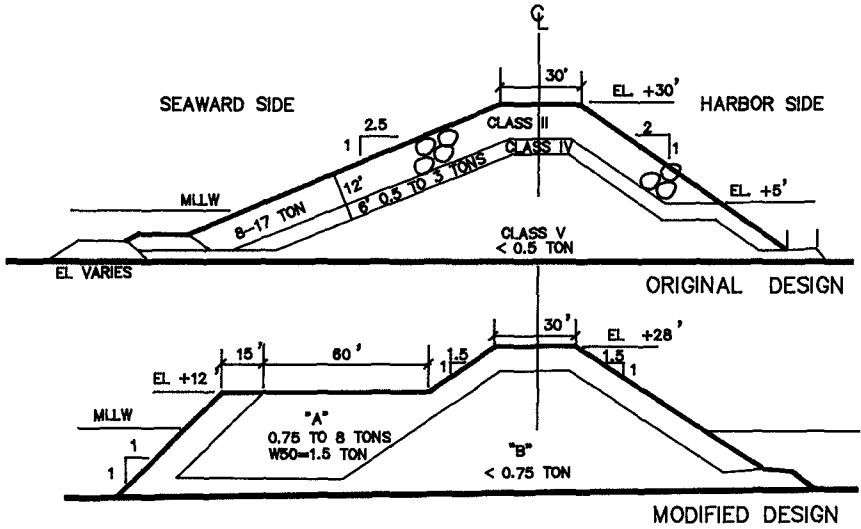


FIGURE 1 BREAKWATER CROSS SECTIONS

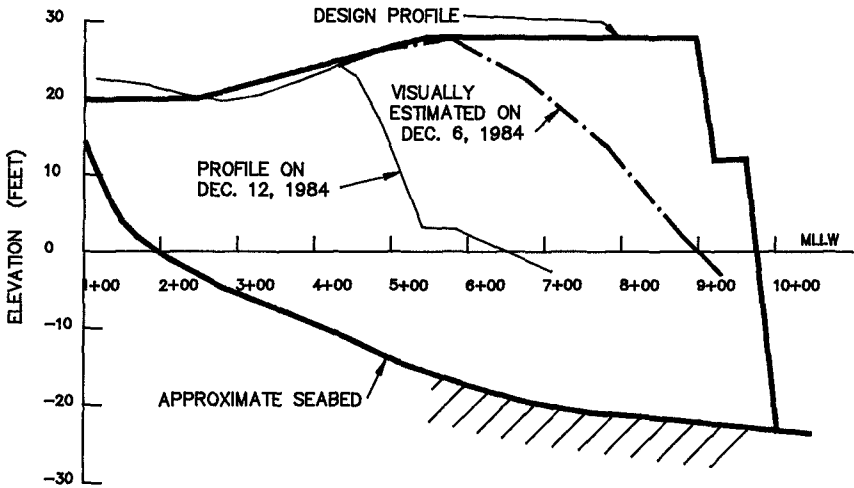


FIGURE 2 COMPARISON OF CENTERLINE PROFILES

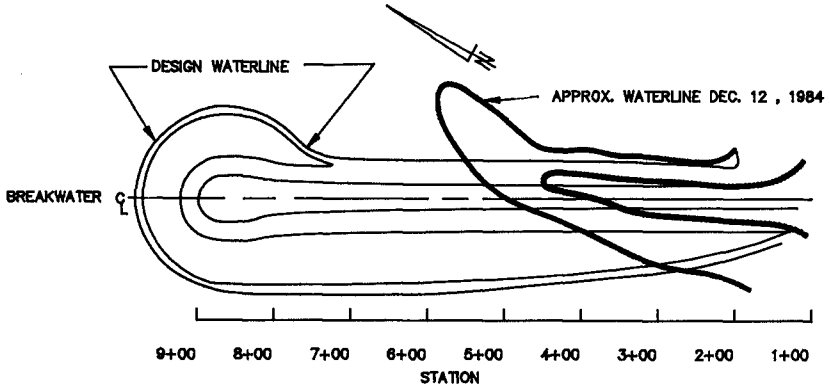


FIGURE 3 BREAKWATER PLANVIEW

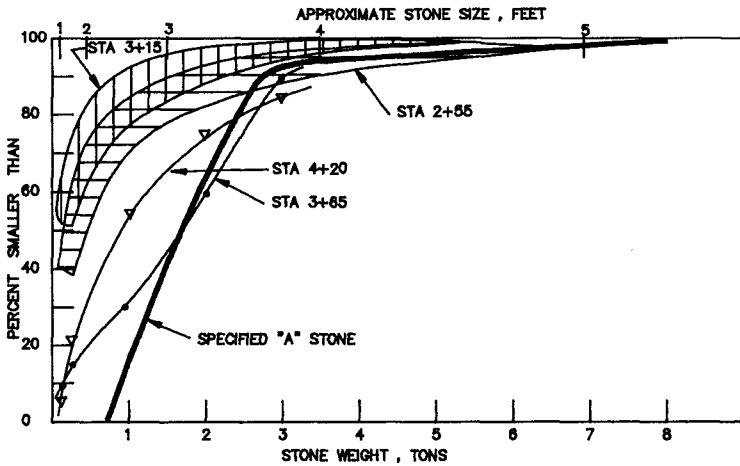


FIGURE 4 ESTIMATED GRADATION OF "A" STONE

wave height, H_s , of 30 feet (9.1m) with peak periods of 16 seconds, and the second storm had an H_s of 22 feet (6.7m) with 13 second peak periods. Storms of these magnitudes can be expected to occur several times a year in the Bering Sea. Tide levels were estimated at +3.5 to +4.0 feet (1.1 to 1.2m) MLLW for both storms. The 13 November storm resulted in considerable redistribution of the "A" stone along the entire structure length. Approximately 300 feet (91m) of the original crest and 100 feet (30m) at the waterline were lost. Data gathered after the 7 December storm indicated that an additional 200 feet (60m) of crest and 250 feet (75m) of waterline were lost, for a total damage of 500 feet (150m) of crest and 350 feet (100m) at the waterline. A comparison of centerline profiles before and after the storms is shown in Figure 2. It was evident that material at the head section was transported into the harbor area and formed a low, wide underwater mound east of the initial centerline, producing a reef type structures. Plan views of the before and after structure are shown in Figure 3.

Independent gradation estimates were made at various locations along the breakwater above the waterline. The results of this work showed that the in-place "A" stone outer layer was generally finer than the specified gradation for "A" stone (see Figure 4). Some signs of slumping on the harbor side south of STA 4+50 slope were also visible.

2.4 DISCUSSION OF DAMAGE

During the field investigation, slope measurements indicated substantial adjustment of the outer "A" stone layer, similar to that experienced in the DHI 2-D tests. However, north of STA 4+50 and with respect to the construction of the head section, the excessive damage was due to the fact that the "A" stone size used was inadequate for the design wave conditions of 20-25 foot (6-7.6m) breaking waves with periods ranging from 13-16 seconds. At the head, the direction of wave attack will be at an angle which will cause displaced stones to travel laterally and into the harbor and entrance channel. The head then receded until the water depth limited the wave height to less than 10 feet (3m), where a 1.5-2 ton stone on a 1:5 slope can be stable.

Breaching of the breakwater trunk was also witnessed by City of St. Paul officials during the 13 November 1984 storm. The reduced porosity of an extremely well-graded material, such as "A" stone in combination with "B" stone, probably increased the run-up potential of the design wave conditions. This, in turn, resulted in excessive overtopping, and finally breaching of the "A-B" breakwater.

3.0 BERM BREAKWATER DESIGN CONSIDERATIONS

The investigation on the construction of this berm breakwater, as well as the events and circumstances that culminated in its

completion, have raised various items of concern when designing and constructing these types of structures. Several of these items are presented below.

1. The procedures for production and inspection of armor stone for any rubblemound type structure are extremely important. It may be more difficult to determine if an armor stone class with a wide gradation meets design specifications, as compared to conventional armor stone with a narrow gradation. The performance of a berm breakwater, as well as the potential degree of damage, would also have to be assessed if the median stone size in the berm armor stone is less than that specified. Does a small reduction in median stone size or skewed gradation result in a disproportionate degree of damage under design conditions?
2. The determination of potential long shore movement of material along a berm type structure should be addressed in order to evaluate its long-term maintenance needs, and consequently estimate the annualized maintenance costs. A design with a significant savings in capital costs may not be the most economical if the maintenance costs are excessive.
3. Due to the inherent capability for the seaward slope of berm type structures to adjust in direct relation to the impinging sea state, some guidelines need to be established for the definition and assessment of potential damage.

These are a few of the items that need to be addressed by the engineer and planner when evaluating berm type breakwaters.

4.0 BREAKWATER - 1985 TO PRESENT

Following the "A-B" breakwater damage in 1984, the Alaska Department of Transportation hired Tetra Tech, Inc. to develop a breakwater damage assessment. The City then retained Tetra Tech, Inc. to provide assistance in re-designing the breakwater, designing a 200-foot (60m) length dock, preparing plans and specifications, and advertising and awarding construction contracts. A 25-foot (7.6m) breaking wave was selected for the re-design, which required armor stone of 14-ton on the breakwater trunk section and 18-ton on the head section. Seaside trunk slope was 1:2.5 and 1:3 for the head. This redesign also incorporated the criteria of near-zero percent annualized maintenance (minimum 50 year design life). Since the 200-foot (60m) dock, and future extension thereof to 1000 feet (300m) in length, would be positioned along the harbor side of the breakwater, the breakwater crest elevation was designed for no wave over-topping and established at +37 feet (10.1m) MLLW. The 200-foot (60m) long by 40 feet (12m) wide dock was a pre-stressed, pre-cast concrete caisson design. The caisson was constructed in Tacoma, Washington, towed to St. Paul Island, Alaska and placed on a

specially constructed foundation. During the period May 1985 to January 1986, the breakwater was constructed. The concrete caisson/dock was installed, and a 200-foot (60m) wide, 300-foot (90m) long channel dredged in the summer of 1986.

The breakwater with armored head has been subjected to the design wave a number of times during the 1985, 1986 and 1987 winter seasons. Visual inspections indicate no armor stone displacement along the trunk or head of the breakwater. The dock system has been utilized extensively for vessel off-loading of cargos which previously had to be lightered. St. Paul Harbor is a Federally Authorized Project and since December 1986, the U.S. Army Corps of Engineers (Alaska District) and the City of St. Paul have been carrying out further studies of the existing design for the St. Paul Harbor Project. This has included 2 and 3 dimensional hydraulic model studies, and complete re-evaluation of economic benefits for the project. At this time, findings of the hydraulic model tests indicate the seaward slope of the breakwater can be steepened to 1:2 using 18-ton armor stone. Presently it is planned to construct additional navigation features in 1989. This includes the extension of the breakwater length to Station 18+00, adding 700 feet (210m) of dock, constructing a 1000-foot (300m) second detached breakwater and final excavation of a mooring basin.

CHAPTER 210

COASTAL GENESIS

J.H. de Vroeg *, E.S.P. Smit *, W.T. Bakker **

ABSTRACT

In order to investigate the effect of enhanced sea level rising (greenhouse effect), of sand mining in the North sea and the large-scale effects of beach nourishment, the Rijkswaterstaat (Governmental Board for Ways, Waterways and Harbours) started the project "Coastal Genesis". This paper deals about research, carried out at the Delft University of Technology in the scope of this project.

The behaviour of the Holland coast at three timescales, i.e. 15 years, 1000 years and 6000 years is considered. Use is made of line models. New techniques are developed for finding the coastal constants of these models (the use of Kalman filtering) and for simulating the effect of sea level rise on coastal accretion and erosion. An extensive set of data on coastal topography, the JARKUS dataset is analyzed.

It is concluded that the effect of cross-shore transport becomes more and more dominant compared to the longshore transport when the time scale increases. A physical conception is displayed, which explains more or less the accretion of the Dutch coast between 4000 Before Christ and the Roman times, and the erosion later on.

I. INTRODUCTION

The coastal management of Rijkswaterstaat requires a strategy of overall coastal defence, starting from the general idea that the Netherlands should be kept in shape, however not against unlimited expense. According to a statement of the Dutch queen "the coast is safe" since the storm surge barrier in the Eastern Scheldt came in operation. What should be done to keep it safe and how should aspects of increasing importance of nature preservation and conservation of areas needed for water purification and recreation be encountered? How to cope with enhanced sea level rise?

Good predictions are necessary. Understanding of how the present was generated from the past might be of help, and for this goal Dutch geologists, geographers and civil engineers of Rijkswaterstaat, Delft Hydraulics Laboratory and a number of universities are collaborating in the project "Coastal Genesis". For a further description may be referred to Vellinga and Zitman (1988).

This paper deals with research at the Delft University of Technology carried out in the scope of this project. The behaviour of the

*) Researchers, Faculty of Civil Engineering, Delft University of Technology, The Netherlands.

***) Principal scientific officer, Faculty of Civil Engineering, Delft University of Technology, and coastal specialist Rijkswaterstaat (Public Works Department), the Hague, The Netherlands.

uninterrupted central part of the Dutch coast in 6000 years is considered. Although "the" truth never will be found, it will be seen, that the effect of onshore-offshore transport dominates more and more the effect of longshore transport when larger time scales are considered. In this paper the general conception is captured by the use of line models. Constants occurring in these models are found from hindcasting coastal behaviour. Another paper (Bakker et al., 1988) also gives the relations between these constants and the wave characteristics. Ch.II gives a description of the Dutch coast in the last 15 years and ch.III describes a newly developed way of finding the coastal constants. In ch.IV a one-line model concerning the behaviour in the last 1000 years is given, leading to constants, comparable with the ones for the last 15 years. In ch.V the qualitative effects of sea level rise are modelled (only considering cross-shore transport) and finally ch.VI contains some conclusive remarks.

II. 15 YEARS

Coastal behaviour during the last two decennia can be investigated rather accurately due to the Jarkus dataset, which contains yearly measurements of coastal profiles along the entire dutch coast, up to a depth of 5 a 6 m below MSL. The distance between the ranges is 200 m. A more detailed description is given by Bakker and de Vroeg (1987, 1988^{a, b}).

This dataset can be used to study the bottom topography and changes of the coastal profile. Also, the measurements provide a useful source for verification and calibration of coastal models.

First the bottom topography is considered. Fig 9^a shows the situation. Fig 1^a shows a three-dimensional picture of the coastal area between Den Helder and IJmuiden (see also fig 9^a), as measured in the year 1984. The scales are distorted: the distance between Den Helder and IJmuiden is 55 km, while the width of the considered coastal zone is 800 m. The landward boundary is chosen near the dune foot. In the north, at Den Helder, the influence of the Texel inlet is visible. At Petten a large seawall prevents the coast from moving landward. Due to a structural regression of this part of the coast the wall is now situated seaward compared to the rest of this region. At IJmuiden there is a physical boundary, formed by large harbour moles.

The picture clearly shows the coast is not uniformly shaped. Not only differences in the slope of the profile are visible, but also shape and number of breaker bars vary along the coast. It appears that a gentle beach slope results in a great number of bars. The same can be concluded from fig 1^b, which shows the coastal area south of IJmuiden over a distance of 59 km. (At the harbour of Scheveningen no measurements were available).

As a result of the breaker bars the coast is constantly transforming, which can be derived from fig 2^{a, b, c}. These figures show "3-D-time diagrams" in which the changing of one coastal profile during 15 years is displayed by plotting the profile in successive years next to each other, thus resulting in three-dimensional figures, however, with the time instead of the distance along the coast as third dimension. These diagrams enable the investigation of the migration of breaker bars. It appears that the bars are moving in a seaward direction, however, with strongly varying velocities. In the north, between Den Helder and Callantsoog, the bars are very stable (fig 2^a). Between Callantsoog and IJmuiden a seaward velocity of 15 a 20 m/year is found (fig 2^b). South of IJmuiden the bars are moving very fast: 50 m/year (fig 2^c). No correlation is found between the structural movement of the coast and the migration of the bars.

The changes of the profile due to the breaker bars can be expressed as a fluctuating cross-shore transport within the surfzone. In fig 3 this transport is compared to other sources of transverse transport. Without any doubt some interaction between the tidal zone and the inshore exists, however according to present estimates it is of no great importance where the behaviour of the beach on a time scale of decennia is concerned. On this time scale gradients in the wave induced longshore transport give a possible explanation of the development of the curved Dutch coastline (although not the only possibility). Fig 4 shows an estimate of the magnitude of this transport, based upon Bakker (1971) and Bakker and de Ras (1971). Some simple models based on this longshore transport exist, and will be discussed in this paper.

Though many of the observed characteristics are not yet fully understood, knowledge derived from this "phenomenological approach" can be made of use for statistical purposes. The 3-D-time diagrams in fig 2 show it is difficult to determine any structural movement of the profile. This structural movement is small compared to the fast movement of large amounts of sand due to the breaker bars. This is a problem when trying to use the Jarkus dataset for the calibration of models. One can treat the motions of the bars as a periodical feature or as a random noise, each treatment giving its specific problems (Bakker and de Vroeg (1987,1988^D)). Kalman filtering appears to be a tool for finding the vital characteristics.

III. THE LINEAR KALMAN FILTER

The Kalman filter combines the advantages of the deterministic and the statistical approach, and has proven to be very suitable for recursively updating parameter estimates or time-varying model coefficients, based on the latest data information. It is an algorithm which uses measurements, a physical model of the system, and knowledge of the inaccuracy (noise) of both the measurements and the model, in order to achieve an optimal estimate of system behaviour (Kalman,1969). The method is based on two linear equations:

$$\text{System Equation} \quad : \quad \underline{x}(t) = F(t) \underline{x}(t-1) + \underline{w}(t) \quad (1)$$

$$\text{Measurement Equation} \quad : \quad \underline{z}(t) = H(t) \underline{x}(t) + \underline{v}(t) \quad (2)$$

where $\underline{x}(t)$ is the system state at time t .

$\underline{z}(t)$ is a measured state, not necessarily the same as the system state, however, it has to be linearly related to the system state (in the linear filter).

$F(t)$ is a transformation matrix, transforming the system state at time $t-1$ to the state at time t .

$H(t)$ is a transformation matrix, describing the linear relation between the system state and the measured state.

$\underline{w}(t)$ is the white noise, affecting the state $\underline{x}(t)$.

$\underline{v}(t)$ is the white noise, affecting the observations $\underline{z}(t)$.

$F(t)$ and/or $H(t)$ contain the physics of the system. Both $\underline{w}(t)$ and $\underline{v}(t)$ refer to additional noise, generated during one time step.

Using the system equation it is possible to estimate the system state $\underline{x}(t-1)$ one time step ahead (- denotes an estimate before the measurements are taken into account). The term $\underline{w}(t)$ is added because the transformation through $F(t)$ is not perfect: an error will occur which is not known at every time. Only the statistical characteristics of this error are known or can be estimated. Assuming a Normal distribution of this noise with mean 0 and variance $Q(t)$, this can be denoted as $\underline{w}(t) \approx N(0, Q(t))$. This variance $Q(t)$ is used in the filter

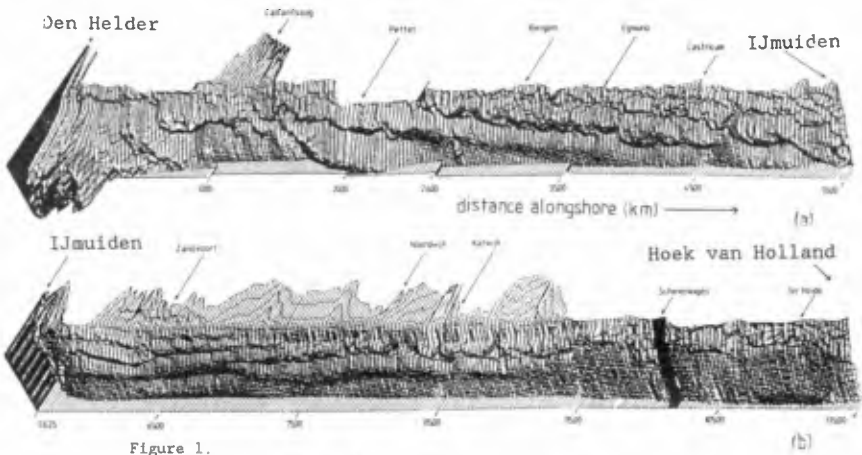


Figure 1.
Three dimensional picture of the coast between
(a) Den Helder and IJmuiden (b) IJmuiden and Hoek van Holland
(see fig 9^a for situation Holland coast)



Figure 2.
3-D-time diagram of profile between (a) Den Helder and Petten
(b) Petten and IJmuiden (c) IJmuiden and Scheveningen

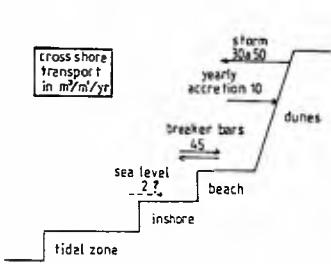


Figure 3.
Estimated cross-shore transport
along the central coast of Holland
(storm erosion is balanced by on-
shore windtransport during quiet
conditions)

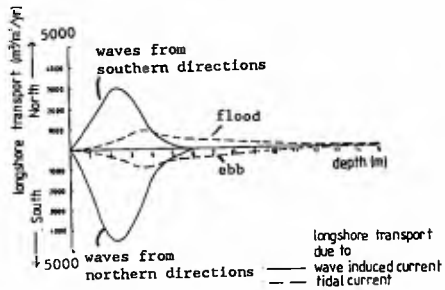


Figure 4.
Longshore transport,
along the coast of Holland
as a function of depth.

algorithm. Like all other noise terms it is used in the form of a covariance matrix, so it is possible to take into account not only variances but also noise covariances.

Applying the measurement equation (disregarding the noise) results in an expectation of the measured state at the considered time. This equation is also affected by errors, which are characterized by $\underline{v}(t) \approx N(0, R(t))$. The variance $R(t)$ will appear in the filter algorithm. When the measurements $\underline{z}(t)$ actually become available, these are taken into account to get an improved estimate $\underline{x}(t+)$, using the equation:

$$\underline{x}(t+) = \underline{x}(t-) + K(t) \{ \underline{z}(t) - H(t) \underline{x}(t-) \} \quad (3)$$

where $\underline{x}(t+)$ is the optimal estimate.
 $\underline{x}(t-)$ is the estimate of the state at time t before the measurements are taken into account.
 $\underline{z}(t) - H \underline{x}(t-)$ is the difference between the measurements and their expected value.

$K(t)$ is the "gain matrix", the essence of the Kalman filter. It has two functions: $\underline{1}$: it re-transforms the correction on \underline{z} to a correction on \underline{x} , and $\underline{2}$: it gives a weight to the importance of the correction, varying from zero (perfect theory not to be disturbed by sorted measurements) to one (What You See is What You Get). The expressions for $K(t)$, depending on $H(t)$, $Q(t)$ and $R(t)$ are given in the Appendix, which may be written more or less symbolically as:

$$K(t) = \frac{\underline{1}}{H(t) \{ 1 + \text{noise in latest estimate} \}} \quad (4)$$

The method has been applied to parts of the Dutch coast, using as physical model the line-theory and estimating the model coefficients. The physical conception involved is the existing of a (set of) coastal constant(s) \underline{s} , stationary in time. This means that $F(t)$ in (1) should be the unit (identity) matrix. Improved estimates of \underline{x} are made by checking a calculated coastline (or for the two-line theory: lines of beach and inshore) against measured values $\underline{z}(t)$. This application is best demonstrated by the following example, based on the single-line model which is described in the next chapter, see equation (8). The successive steps of the procedure are shown in fig 5.

In order to find the coastal constant s in (8) the system equation (1) becomes:

$$s(t) = s(t-1) + w(t) \quad (5)$$

with inaccuracy characterized by $w(t) \approx N(0, Q)$

Due to the noise $w(t)$ this "constant" is given the opportunity to change a bit each time step. This noise is thought to have a Normal distribution (Gaussian) with mean 0 and variance Q . In this particular case Q is assumed to remain stationary and uniform along the coast.

Using the Jarkus dataset "measured coastlines" can be determined in each year, giving in each range the mean of the positions of the various contourlines between NAP -5m and NAP +15m (fig 8) (NAP \approx MSL). The measurement equation (2) provides the link between $s(t)$ and these measured coastlines, using an explicit difference scheme for the Pelnard-Considère equation (8). This can be rewritten as

$$y_i(t) = y_i(t-1) + B \{ y_{i-1}(t-1) - 2y_i(t-1) + y_{i+1}(t-1) \} s \quad (6)$$

where y denotes the seaward coordinate of a coastline (fig 8).
 i denotes the distance along the coast, t the time.

$$B = h \frac{\Delta t}{\Delta x^2}; \Delta x = \text{distance between two adjacent ranges.}$$

Thus for the one-line theory the measurement equation (2) becomes:

$$\begin{bmatrix} y_2 \\ y_3 \\ \vdots \\ y_{n-1} \end{bmatrix}_t = \begin{bmatrix} B (y_1 - 2y_2 + y_3) & y_2 \\ B (y_2 - 2y_3 + y_4) & y_3 \\ \vdots & \vdots \\ B (y_{n-2} - 2y_{n-1} + y_n) & y_{n-1} \end{bmatrix}_{t-1} \begin{bmatrix} s \\ 1 \end{bmatrix}_t \quad (7)$$

with inaccuracy characterized by $\underline{y}(t) \approx N(0, R)$

$H(t)$ (the matrix $[\dots]_{t-1}$ in (7), see equation (2)) is derived from the measured coastlines at time $t-1$.

$\underline{y}(t)$ is the Gaussian noise with mean 0 and variance R , in this particular case containing two sources of error: measurement errors and inaccuracy of the model. It appears that it is difficult to determine this variance on physical grounds. So this noise is estimated after study of the measurements and assumed to remain constant with time. This variance can be of magnitude of several tens of m^2 to several hundreds of m^2 .

If the matrices Q and R and an initial estimate of s are known the filter procedure can be started, resulting in a "time history" for the observed model coefficient s . The result shown in fig 6 ($s = 1$ a $1.2 * 10^6 m^3/year$) is based on measurements for the coast between IJmuiden and Scheveningen. Results for the two-line model and the use of those coastal constants for making hindcasts and predictions will be exposed by Bakker et al. in another paper (1988).

IV. 1000 YEARS

Fig 7 shows the accretion and erosion of the coast of Holland, as follows from ancient registrations of the site of the dune foot in the last 100 years according to Edelman (1961). Edelman considers the coast as principally accreting, however with "sinks" at the Northern and Southern boundary. A possible explanation for the coastal behaviour, as indicated already by Edelman and Eggink (1963) is based upon the conception of Pelnard-Considère (1954). This involves that a concave coast accretes and a convex coast erodes. The ruling equation is:

$$\frac{\partial y}{\partial t} = s - \frac{\partial^2 y}{\partial x^2} \quad (8)$$

where x, y are the coordinates of the coastline (x in longshore direction, y in seaward direction), t is the time, h is the thickness of the layer of the coast, which is supposed to participate in the process of accretion and erosion (fig 8) and s is the rate of change of coastal transport ($m^3/year/radian$) as function of the coastal direction. Equation (8) is based on the continuity equation and a transport equation, which read respectively:

$$h \frac{\partial y}{\partial t} + \frac{\partial S}{\partial x} = 0 \quad (9) \quad S = S_0 - s \frac{\partial y}{\partial x} \quad (10)$$

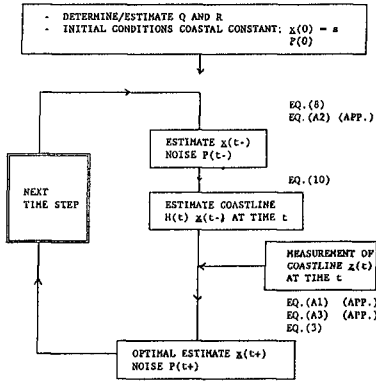


Figure 5. Procedure Kalmanfiltering.

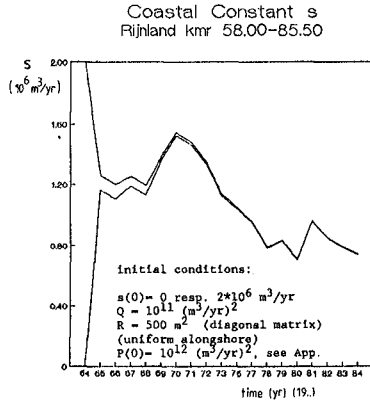


Figure 6. Value of coastal constant s , found by Kalman filtering

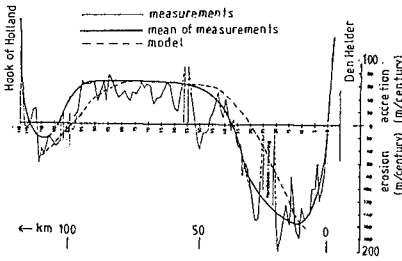


Figure 7. Accretion and erosion of the coast of Holland during the last 100 years, after Edelman (1961)

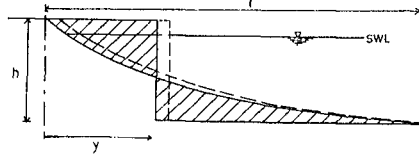


Figure 8. Line schematization of a coastal profile

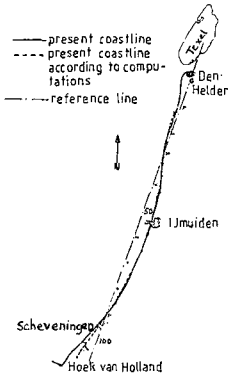


Figure 9^a. Model-computed coastline, compared with real coastline

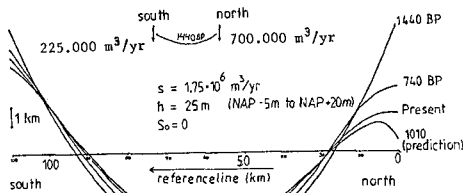


Figure 9^b. Result line-model and used constants on a 1000 years time scale

where S is the littoral transport and S_0 is the littoral transport along a coast, parallel to the x-axis.

This physical concept allows for a simplified one-line model concerning the behaviour of the Holland coast in the last 1000 years (between km 10 and km 100) starting from the following initial and boundary conditions (fig 9^b):

a. the initial coast is assumed to have a parabolic shape;
 b. at the boundaries the coast is assumed to erode according to \sqrt{t} following the Pelnard-Considère solution for a "negative delta" (1954). This implies, that the coastal development is schematized according to a parabolic shape, stretching itself, combined with two "negative delta's" on both sides.

Implicit assumptions are a constant subtraction of material at the boundaries, starting more or less abruptly. Physically, this can be justified at the Northern side because of the developing Texel inlet, leading to the Wadden shallows and, at the Southern side, sand subtraction by the emerging outlet of the river Rhine. Development of the Texel inlet was triggered because of the burning and dewatering of existing peat layers (Edelman, 1974) which caused the strong development of this inlet, starting about a millenium ago. Since then, the Wadden shallows tend to keep themselves at mean sea level (despite sea level rise). The reason for this is a subtle mechanism of sand, being brought to this shoals during flood tide with rather high flood velocities and coming to rest on this shoals during the ebb with rather low velocities. Already in 1949 Van Bendegom reported about this so-called "sand hunger" of the Wadden shallows.

Fig 9^a shows the present coastline according to the line model and in reality. Fig 9^b gives constants used in the applied model. A value of $s/h = 71 * 10^3 \text{ m}^2/\text{year}$ is found, leading with a depth h of 25 m (20 m dune height + 5 m water depth) to $s = 1.75 * 10^6 \text{ m}^3/\text{year}$. The dashed line in fig 7 gives the present coastal erosion/accretion according to the model, compared with the Edelman data. Details are given by Bakker and Smit (1987).

However, the following objection against the model can be made. It appears (Ligtendag en Borger, 1987) that the middle part of the dutch coast showed erosion from 1600 A.D. to 1800 A.D. instead of accretion, as found in the last century. Probable cause is wind erosion which is not taken into account in the Pelnard-Considère theory. Only since the 19th century the dune front is protected by planting marram grasses etc.

V. 6000 YEARS

Where for "short" terms longshore transport (only) can provide some explanation of coastal behaviour, for a 6000 year period sea level rise and cross-shore transport become vitally important.

Fig 10 shows the sea level rise in the course of time since 10000 Before Present (BP) according to Jelgersma (1979). Fig 11, from Jelgersma et al. (1985), shows the submerging of the North Sea in the last millennia. Fig 12 shows the development of the Dutch coast according to Jelgersma et al. (1985). Apart from a regression during the period of fast sea level rise a transgression took place between ca. 5500 BP and 3000 BP (van Straaten (1965), Zagwijn (1974), Jelgersma et al. (1985), Roep (1984)). Afterwards, erosion started again.

Is it possible to make a conceptual model of this process of sea level rise? A good model should be able to reproduce as well the coastal transgression from 5500 to 3000 BP as the erosion afterwards. In the present preliminary stage, it has only been attempted to make a

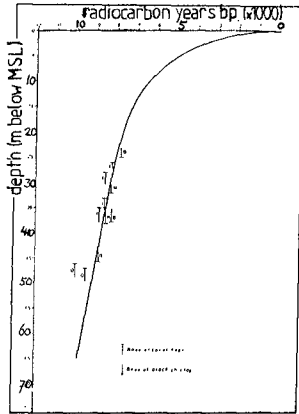


Figure 10.
Sea level rise during
the last millennia,
after Jelgersma (1979)

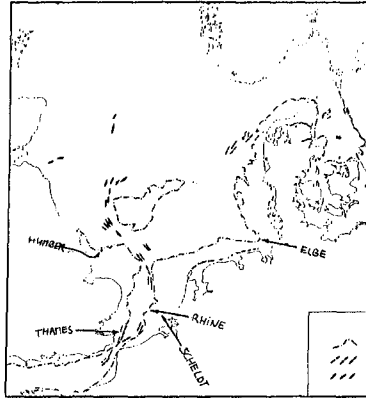


Figure 11.
The submerging of the North Sea
in the last millennia,
after Jelgersma et al. (1985).
--- Coastline 8000 B.P.
sealevel 30m below present
level.
/// Old sediment ridges

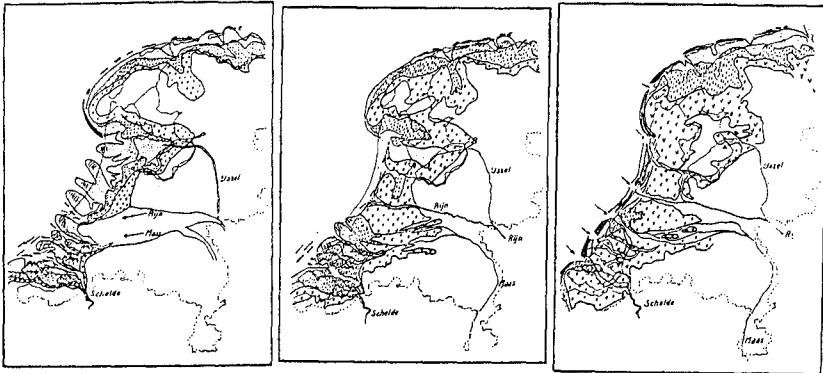


Figure 12.
Development of the Dutch coast according to Jelgersma et al. (1985)
Time (years Before Present) : (a) 5500 (b) 4600 (c) 2000
Sealevel (m Below Present Level) : 7 3.5 1

model which gives qualitative agreement, without paying too much attention to quantitative accuracy. Before explaining this model, some literature concerning this subject will be reviewed.

A very simple model for the response of a coast on sea level rise is provided by Bruun ((1983) and earlier papers) (fig 13). He starts from the assumption, that the sea level rise is so slow, that the upper part of the coast - up to a certain so-called "closure depth" - will always be able to adjust itself and will keep a cross-section according to an equilibrium profile. From simple geometry and continuity it shows, that the coastal erosion will be equal to the cotan of the mean slope (l/h in fig 13) times the mean sea level rise a . Here h denotes the so-called "closure depth", i.e. the depth up to which eroded material settles itself.

According to the authors it will always cost time to attain the equilibrium profile. They agree with Wright et al. (1984), that short-term processes take place with a small closure depth, where a larger part of the profile will be involved in long-term processes; the time necessary to reshape the profile to an equilibrium profile will be longer. Fig 14, after Wright et al. elucidates this idea.

The time-dependent adapting of a coastal profile to its equilibrium profile is simulated mathematically by Bakker (1968) and Swart (1974). These authors schematized the coastal profile essentially to two areas, a beach and an inshore, each represented by a line in plan view (fig 15). Beach and inshore are separated by a horizontal flat between. The region seaward of the inshore is assumed to be horizontal; here no cross-shore transport takes place. According to their schematization and according to experiments of Swart, if longshore transport plays no role, the line of beach and inshore will tend to reach an equilibrium distance W in a negative-exponential way.

The model starts from the assumption, that the cross-shore transport S_y depends on the overall coastal slope:

$$S_y = s_y (y_1 - (y_2 - W)) \quad (11)$$

where S_y is positive in seaward direction, y_1 and y_2 denote the position of the line of beach and inshore (fig 15, i.e. the mean of the positions of the equidistant contourlines of the beach and the inshore respectively) and W denotes the equilibrium distance.

Basic physical thought behind the model is, that a slope determines the cross-shore transport; that two counteracting mechanisms determine this slope, where one mechanism increases the offshore transport when the slope increases (gravity mostly) and the other determines the onshore transport and increases, when the slope becomes flatter (for instance the asymmetry of the orbital motion). Making a Taylor series of the transport in the vicinity of the equilibrium slope gives a dynamical equation of the kind as given by (11). Implicitly it is assumed that the cross-shore transport is not affected by local changes in slope of beach and inshore separately, as long as the mean position of the beach, c.q. the inshore remains the same. Some motivation for this assumption can be found from fig 2: like a huge rake the breaker bars correct differences in large-scale slope every three to four years and the local slope is a very short-term feature, effected by the breaker bars and has no essential importance.

This philosophy also more or less determines the lower edge of the inshore, which can be considered as a kind of "closure depth" as well. The theory only holds when the profile of beach and inshore respectively can adapt itself much faster to changes than at the time scale of the coastal process to be schematized by the two-line theory. Looking to fig 3 it might be expected that cross-shore transport below the level, where the breaker bars decay (say 5 m below MSL) will be

much smaller than above this level. Therefore, this provides a logical closure depth. The characteristic time scale T_0 for exponential decay according to the two-line theory equals:

$$T_0 = (h_1 h_2)/(s_y h) \quad (12)$$

where h_1 and h_2 are the thickness of the layer of beach and inshore respectively and h equals $h_1 + h_2$.

In the case of sea level rise, cross-shore transport will take place between the inshore and the layer below, however at a larger time scale (slower) than between beach and inshore. Furthermore, it might be expected that the slope between the inshore and this lower layer to a great extent determines the cross-shore transport between those layers. In other words; the local slope will be more of importance than the overall slope and therefore a two-line approach will not be sufficient. The ideas of Wright (variable closure depth) and of Bakker and Swart (negative-exponential tending to an equilibrium profile) can be combined in the following way. To simulate sea level rise, a 6-line program has been made, starting from 6 layers with seaward distance with respect to a reference point of y_1, y_2, \dots, y_6 , each layer having a height of 3 m; the cross-shore transport $S_{y1}, S_{y2} \dots S_{y5}$ between the first and the second, the second and the third... etc. layer is related to y_1-y_2, y_2-y_3, \dots in the following way:

$$S_{yn} = s_{yn} ((y_n - L_n) - (y_{n+1} - L_{n+1})) \quad (13)$$

where $n = 1$ to 5 and L_n denote the position of y_n in an equilibrium position. The characteristic time T_n is defined accordingly:

$$T_n = (h_n h_{n+1})/s_{yn} \quad (14)$$

Fig 16 shows the schematization and the assumed time scales T_n . The values of T_4 and T_5 are pure guesses: for some justification of the values of T_1 to T_3 is referred to Bakker and Delver (1986).

It is assumed, that the present profile is an equilibrium profile (fig 17^a) and that 6000 BP the rising of the sea level was so fast, that no time was available to bring the profile in an equilibrium shape; the profile of 6000 years ago is assumed to be the present profile, in which the water level is 6 m lowered (fig 17^c); the water level at 6000 BP was 6 m lower than the present level (fig 17^b). This "sudden" exposure of the present coastal area to the waves is caused also for a large part by the degradation and erosion of former coastal barriers in the North Sea, which became submerged. With respect to this conception is referred to Niederoda et al. (1985) for the behaviour of coastal barriers in general and to van Straaten (1985) for the behaviour of the Holland coast. Fig 18^a (in which the third dimension denotes the time) shows how, according to the model, the coast would have been accreted, if the sea level had not risen since 6000 BP; in fig 18^b this sea level rise has been taken into account. In fig 18^a the coast accretes, because the profile of fig 17^c is much flatter than the equilibrium profile; in fig 18^b erosion starts again because the upper part of the profile has formed nearly an equilibrium profile and erodes according to the Bruun conception (see above). For details concerning the way of computation is referred to Smit (1987).

Thus it shows, that the model gives qualitative agreement with the features, found in nature.

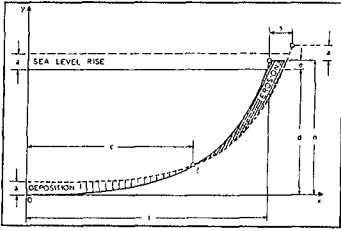


Figure 13. The Bruun model, translation of coastal profile due to sea level rise.

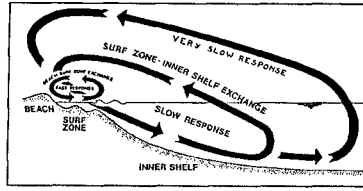


Figure 14. Interaction of different parts of the profile, after Wright et al. (1984)

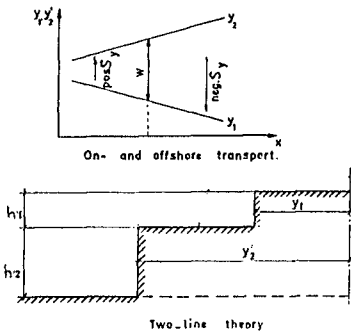


Figure 15. Schematization in beach and inshore according to Bakker and Swart.

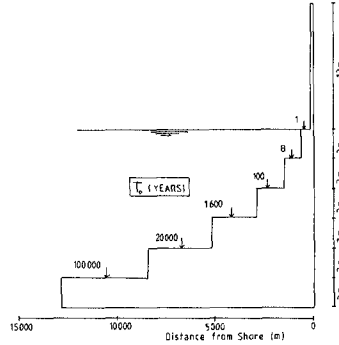


Figure 16. Schematization n-line model and time scales.

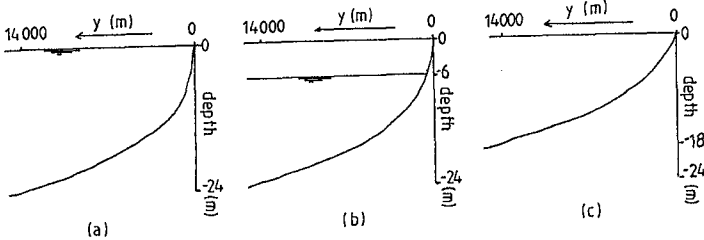


Figure 17. Initial profile of the coast.
 (a) Present profile
 (c) Assumed profile of 6000 BP

VI. CONCLUSION

If coastal behaviour is considered at increasing time scales, beginning at a time scale of decennia and going to millennia, the effect of sea level rise and cross-shore transport becomes more and more pronounced. Line models may provide (a rough) insight at every time scale.

For the coast of Holland, coastal constants derived on one hand from data concerning the last 15 years (with the aid of Kalman filtering) and on the other hand from data with regard to the last 100 to 1000 years are not contradictory. For larger time scales, a schematization of the coast in one or two layers (one- or two-line model) will not be sufficient. Small amounts of cross-shore transport from deeper water to the inshore, as well as the local slope of these deeper regions become important at this time scale. In this paper, for a case like this the use of for instance a six-line model is proposed. This simulates as well a closure depth dependent on the time-scale of the feature, corresponding to the measurements of Wright (1984) as a negative-exponential trend to an equilibrium profile according to ideas and experiments of Bakker (1968) and Swart (1974). The method is more sophisticated than the Bruun rule (1983). Accretion of the Holland coast between 4000 years and the Roman times and erosion later on can be simulated this way.

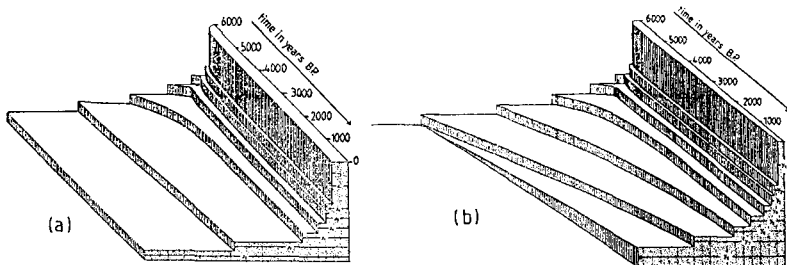


Figure 18.
Development of the profile of 6000 BP,
(a) if no sea level rise is taken into account.
(b) taking sea level rise into account.

APPENDIX

The equation for the Kalman gain matrix $K(t)$ is

$$K(t) = P(t-) H^T(t) \{ H(t) P(t-) H^T(t) + R(t) \}^{-1} \quad (A1)$$

Where

$$P(t-) = F(t) P((t-1)+) F^T(t) + Q(t) \quad (A2)$$

is the inaccuracy (variance) belonging to $\underline{x}(t-)$ (The righthand side of (A2) denotes old noise + new noise, so $P(t-)$ involves the total noise as a result of all preceeding time steps) and

$$P(t+) = (I - K(t) H(t)) P(t-) \quad (A3)$$

is the inaccuracy belonging to $\underline{x}(t+)$.

I denotes the unit (identity) matrix.

H^T and F^T denote the transposed of H and F respectively.

By thinking of the matrices as scalars (notation small letter instead of capital) equation (A1) can be rewritten as:

$$k(t) = \frac{1}{\frac{1}{h} r(t) p(t-)} = \frac{1}{h(1 + \text{noise in latest estimate})} \quad (A4)$$

So the Kalman gain matrix $K(t)$ contains the inverse of the matrix $H(t)$, thus transforming $\underline{z}(t)$ to $\underline{x}(t)$, and a matrix of weight-factors (derived from system- and measurement noise, through $P(t-)$ and $R(t)$ respectively), determining the weight given to the physics relative to the measurements.

Kalman proved that this algorithm results in an optimal estimate $\underline{x}(t+)$ in least squares sense on time t (Kalman, 1969).

Present estimates are computed in a recursive way, meaning that all previous measurements are taken into account in a sequential way (filtering by a "moving window"). Unlike batch processing of measurements, in this recursive filter there is no need to store past measurements (Gelb, 1974). The weight given to the previous measurements depends on the noise characteristics of the model and the measurements.

REFERENCES

- Bakker, W.T. (1968), The dynamics of a coast with a groyne system, Proc. 11th Conference on Coastal Engineering, London, ch. 31, pp 492-517
- Bakker, W.T. (1971), Computation of the wave-induced littoral drift according to the Svasek-method, adapted to parallel depth contours, Rijkswaterstaat, Dept. for coastal res., Rep. WWK71-2
- Bakker, W.T., de Ras, M.A.M. (1971), Computation of sand transport by waves and tide, using an adapted Bijker method (in Dutch), R.W.S., Dept. for coastal res., Rep. WWK71-4
- Bakker, W.T., Delver, G. (1986), Coastal changes caused by a shallow sanddam in front of the Delfland coast (in Dutch), Delft Univ. of Techn., Hydraulic Engineering Group
- Bakker, W.T., Smit, E.S.P. (1987), Possible truth in coastal behaviour (in Dutch), R.W.S. nota GWA0-87.004

- Bakker, W.T., de Vroeg, J.H. (1987), Coastal modeling and coastal measurements in the Netherlands, Proc. seminar Sogreah: Prototype Measurements to validate Numerical Models of Coastal processes, Grenoble, Oct 14-15
- Bakker, W.T., de Vroeg, J.H. (1988^a), Looking at the Holland coast (in Dutch), de Ingenieur (mei)
- Bakker, W.T., de Vroeg, J.H. (1988^b), Is the coast safe ? (in Dutch), R.W.S. Tidal Waters Dept., Report GWA088.017
- Bakker, W.T., v.d. Kerk, C., de Vroeg, J.H. (1988), Determination of coastal constants in mathematical line models, 2nd European workshop on coastal zones as related to physical processes and coastal structures, Loutraki, Greece
- van Bendegom, L. (1949), Considerations of the fundamentals of coastal defence (in Dutch), R.W.S., Dir. ben.riv.
- Bruun, P. (1983), Review of conditions for uses of the Bruun rule of erosion, Coastal engineering 7, pp 77-89
- Edelman, T. (1961), Erosion and accretion of the coast between Den Helder and Hoek van Holland (in Dutch), R.W.S., WWK61-1
- Edelman, T., Eggink, D.N. (1963), Some characteristics of the Dutch coast, Proc. 8th Conf. on Coastal Eng., Mexico, ch41 pp 756-764
- Edelman, T. (1974), Historical geography of the Dutch coastal area, R.W.S., Dept. of Water Management and Hydr. Res., publication 14
- Gelb, A. (1974), Applied optimal estimation, T.A.S.C., Massachusetts Institute of Technology
- Jelgersma, S. (1979), Sea-level changes in the North Sea basin, The quaternary history of the North Sea, pp 233-248
- Jelgersma, S., Beets, D., Schuttenhelm, R. (1985), A Geological view on the coast (in Dutch), kustmorfologie in ontwikkeling, pt/Civ.Techn. nr 11, pp 3-8
- Kalman, R.E. (1969), A new approach to linear filtering and prediction problems, J. Basic Eng., pp. 35-46
- Ligtendag, W.A. (1987), From Yzer to Jade (reconstruction of the Southern North Sea coast in the years 1600 and 1750), Univ. of Amsterdam, Hist. Geograph. Seminarium
- Niederoda, A.W., Swift, D.J.P., Figueredo (jr), A.G., Freeland, G.L. (1985), Barrier island evolution, middle Atlantic shelf, U.S.A., part 2: evidence from the shelf floor, Marine Geology, 63, pp 363-396
- Pelnaud-Considère, R. (1954), Essai de théorie à l'évolution des formes de rivages en plages de sable et de galets, Quatrième Journées de l'Hydraulique, Paris, Les énergies de la mer, question III
- Roep, T.B. (1984), Progradation, erosion and changing coastal gradient in the coastal barrier deposits of the Western Netherlands, Geol. en Mijnb. nr 3, vol.63, pp 225-336
- Smit, E.S.P. (1987), The role of cross-shore transport in the development of the dutch coast (in dutch), Delft univ. of Techn., Hydraulic Engineering Group
- van Straaten, L.M.J.U. (1965), Coastal barrier deposits in South- and North-Holland, Mededelingen Geologische Stichting, nr 17, pp 41-75
- Swart, D.H. (1974), Offshore sediment transport and equilibrium beach profiles, Ph.D. thesis
- Vellinga, P., Zitman, T.J. (1988), Coastal zone response to an increasing sea level rise, Proc. 21st Conf. on Coastal Eng., Malaga, Spain
- Wright, L.D., May, S.K., Short, A.D., Green, M.O. (1984), Beach and surf zone equilibria and response times, Coastal Engineering
- Zagwijn, W.H. (1974), The paleo-geographic evolution of the Netherlands during the Quaternary, Geologie en mijnbouw 53, pp 369-385

CHAPTER 211

ARTIFICIAL BEACH UNITS ON LAKE MICHIGAN

K.J., MacIntosh,* Associate Member, C.D. Anglin,* Associate Member
ASCE

ABSTRACT

High water levels on Lake Michigan during 1985 and 1986 created substantial erosion of the shoreline and reduced the size and recreational potential of many of the parks and beaches. To prevent further erosion, protect existing properties and structures, and to create and improve recreational areas along the Lake Michigan shoreline, four coastal engineering projects were designed and constructed during this time. Artificial beach units stabilized by offshore breakwaters were used as the main component of each project.

Physical hydraulic model studies were used to determine the orientation, size, and spacing of breakwaters and artificial beach units. Model predictions of beach profiles and plan shapes compare closely with prototype surveys. Surveys completed since construction demonstrate the stability of the beaches and support their use as effective, low maintenance shoreline protection.

Prototype experience has shown that these projects are extremely successful both in their ability to withstand storms on the Great Lakes and to attract people for recreational activities.

INTRODUCTION

Four coastal projects were constructed on the west shore of Lake Michigan during 1985 and 1986 to prevent excessive erosion during a period of record high water levels. Of the four projects discussed in this paper, two are located in Lake Forest, Illinois and the other two are located in Milwaukee, Wisconsin.

Each project has a combination of offshore breakwaters and artificial beaches as the basic component providing both shoreline protection and new recreational areas. In assessing the attributes of various shoreline protection schemes it was evident that the benefits of creating new recreational areas outweighed the additional costs in comparison to the costs associated with simply providing basic shoreline protection.

Physical hydraulic models were used in all four projects to design the shoreline protection, determine optimum beach fill profiles, and to assess the impact of design storms on these projects.

* Senior Engineers, W.F. Baird and Associates, Coastal Engineers, 38 Antares Drive, S-150, Ottawa, Ontario, Canada, K2E7V2

The final designs are unique to each project depending on the particular recreational requirements and environmental conditions specific to each site. Varied combinations of breakwaters, groins, shoreline revetments, and sand fills have been used. Specific items which were varied between projects are discussed in further detail below:

- The type of beach fill material varies from a coarse sand (D₅₀=2.6mm) to waste rock from a tunneling project. Criteria for selection of beach fill materials included:
 - 1) beach stability -grain size must be sufficiently large to provide stable, low maintenance beaches.
 - 2) aesthetics and recreation -the material had to be acceptable for pedestrian traffic.
 - 3) cost -the total cost of material per unit length of shoreline had to be reasonable relative to providing other forms of basic shoreline protection.
- The length, height , and orientation of steel sheet pile groins between the individual beach cells was varied in all four projects. The groins were used to control the amount of alongshore sediment transport behind the breakwaters. In two of the projects the groins were tapered to match the stable beach profiles estimated from hvdraulic model studies. This allows native sand to bypass the projects by moving between the breakwaters and artificial beach. Alongshore currents and waves overtopping the breakwaters move the sand through the projects to the downdrift shoreline.
- The constructed plan and profile shapes of the artificial beaches varied significantly between projects. Depending on the cost of the beach fill and room available for beach profile development, physical models were used to determine the most effective elevations and shapes of the beaches, breakwaters and revetments.
- Breakwater design details including both layout and cross-section (for example, the distance that the breakwaters were constructed offshore, breakwater crest heights, and breakwater gap widths) were varied depending on the bathymetry at the site, size of recreational area required, and environmental conditions.

Literature Review

The large grain size of beach fill materials used in the projects discussed in this paper create stable beaches with unique profiles and plan shapes and make direct comparisons to other projects discussed in the literature generally inappropriate. However, a number of papers dealing with related topics have been published. Most of the published information deals with the construction of offshore breakwaters along coastlines with significant littoral drift. In the majority of cases described in the literature the breakwaters are used to trap sand.

For example, Toyoshima (1974 and 1982), and Nir (1982) discuss offshore breakwaters and their effect on coastlines in Japan, and Israel and Sinai respectively. Both authors report rapid formation of large tombolos behind the structures; the tombolo shape tends to stabilize after several years, following which only seasonal fluctuations occur.

Chew et al (1974) and Silvester et al (1980) discuss the use of offshore breakwaters to provide artificial headland control along beaches with substantial littoral drift. In these cases, construction of the structures is followed by the development of pocket or log-spiral beaches, also known as zeta bays, between the offshore breakwaters.

Theoretical aspects of sedimentation behind offshore breakwaters is discussed by Dean (1978). Dean presents a procedure for calculating beach planforms behind closely spaced offshore breakwaters. Perez and Fernandez (1988) also provide a method of predicting beach planforms based on the analysis of data collected from 33 beaches on the Mediterranean coast of Spain.

Model studies assessing the sedimentological influences of offshore breakwaters were discussed in a number of papers, including Shinohara and Tsubaki (1966), Rosen (1982) and Noda (1984).

Curren and Chatham (1977, 1980) describe model investigations undertaken to assess the performance of various schemes of protecting eroding beaches at Imperial Beach, California, and Oceanside Harbor, California. Both offshore breakwater and groin systems were tested.

The most recent information available on the use of detached breakwaters for shore protection is found in Dally and Pope, 1986. The authors review existing systems in the United States, including four single detached breakwaters and six segmented breakwater systems.

The papers described above generally discuss depositional effects behind an offshore breakwater, assuming a suitable source of sand, such as net alongshore drift. Several other papers discussing the use of offshore breakwaters to protect an artificial beach were also reviewed. These included Tourman (1968) (Larvotto Bay, Monte Carlo), Sato and Tanaka (1980) (Suma and Ito Beaches, Japan) and to a limited extent, Walker et al (1980) (Lakeview Park, Ohio). In addition, information on an artificial beach system, constructed near Cannes, France was obtained from the engineering firm Sogreah in France.

ENVIRONMENTAL CONDITIONS

Environmental conditions specific to each site were determined prior to the preparation of designs. The data has been summarized below for the projects discussed in this paper to allow a general comparison of the environmental conditions to other locations.

Water Levels

The maximum and minimum water levels recorded by the U.S. Army Corps of Engineers for Lake Michigan are summarized in Table 1:

Table 1

Lake Michigan	International Great Lakes Datum (IGLD)	Low Water Datum (LWD)
Record high water level	177.30m (October 4, 1986)	+1.5m
Record low water level	175.18m	-0.63 m

Lake Michigan low water datum (LWD) = 175.8m IGLD

The projects described in this paper were designed for maximum water levels of +1.4 m to +2.5 m. These values include an allowance for storm surge, which may increase water levels up to approximately 1m along the west shore of Lake Michigan. For example, a storm surge of 0.88 m occurred at Milwaukee on February 8, 1987 during a severe winter storm. However, it is unlikely that the maximum storm surge levels will ever occur during the summer months which generally correspond with the period of highest water levels on Lake Michigan.

In summary , it was appropriate to design the structures and land based facilities so that severe damage will not occur with water levels in the order of +1.4 to+2.5 m above LWD. These water levels account for extreme water levels plus storm surge. In addition, the facilities are designed to be functional for recreational purposes with both high and low water levels.

Wave Climate

Table 2 provides the range of maximum offshore significant wave conditions estimated using a 20 year parametric wind-wave hindcast. These results represent typical maximum offshore wave climates for the projects described in this paper.

Direction	Maximum Deepwater Significant Wave Height (m)	Peak Period Tp (s)
N	4.0 to 5.0	8 to 10
NE	4.0 to 4.6	8 to 10
E	3.0 to 3.3	6 to 8
SE	3.0 to 3.3	7 to 8
S	2.7 to 3.0	6 to 7

In all of the projects discussed in this paper the breakwaters are constructed in depths ranging from -1.5 m to -3.5 m LWD. Therefore, the wave climate incident on the breakwaters and beaches is depth limited during storms. For each project the inshore refracted wave climate was estimated and model tests were completed for the range of incident wave directions and water levels. This procedure provided sufficient information to estimate the possible range of beach profiles and plan forms. It also provided data on the effects of storms from different directions.

Beach Materials

Two types of primary beach fill materials were used in the projects discussed in this paper. Waste material from a tunnelling project was used as the main source of material for beach fills in the two Milwaukee projects and a coarse sand was used as the primary fill material in the two Lake Forest projects. Figure 1 provides a gradation curve for the tunnel spoil material used in the Milwaukee projects and the coarse sand fill used in all the projects.

The waste material used in the Milwaukee projects consisted of limestone fragments ranging in size from 0.1mm to approximately 80mm in the largest dimension. The D₅₀ was approximately 3mm. The material is very angular as shown in Figure 2 but stone quality tests and prototype experience since construction indicate that the majority of sharp edges will be removed as wave action continues to move the beach materials in the swash zone. The areas above the swash zone have compacted since construction was completed and can be comfortably walked on by pedestrians.

The two Lake Forest projects used a coarse sand fill referred to as Bird's Eye sand as the primary source of beach fill material. This sand consists of a well sorted natural source of sand with a D₅₀ of 2.6mm. Other finer materials were used in the initial stages of filling the beach cells in areas where it was predicted that the coarse sand would not be removed from the outer face of the beach. Several other types of sand were considered however, model study results and cost/benefit analyses indicated that the Bird's Eye sand provided the optimum solution. The Bird's Eye sand provided a stable beach profile which allowed maximum development of land based facilities without having to construct the offshore breakwaters in deep water.

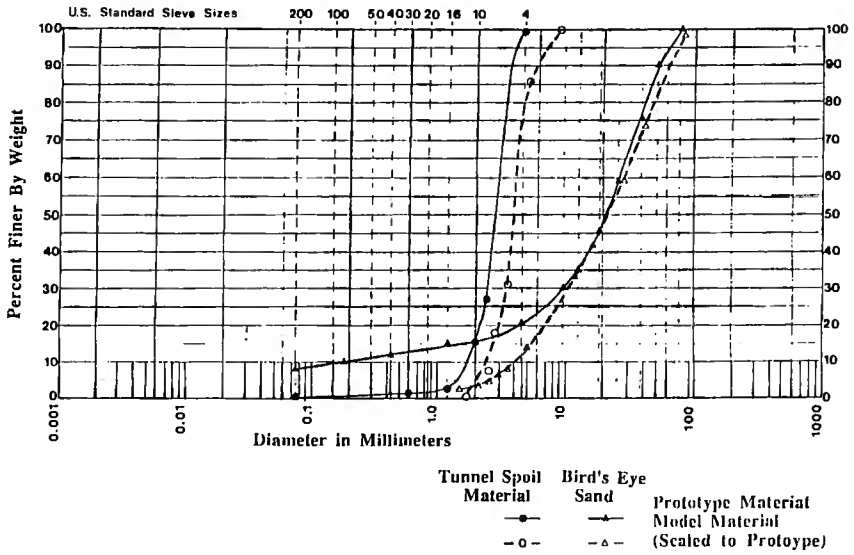


Figure 1

BEACH MATERIAL GRADATION CURVES



Figure 2 TUNNEL SPOIL BEACH FILL MATERIAL

PROJECT SUMMARIES

Of the projects discussed below one was completed in 1986, one in 1987 and the other two in 1988. Information available at this time is provided below. This includes: photographs of prototype structures; survey results of the 'as-built' projects and surveys completed since construction; and photographs showing the public's perspective.

Forest Park Beach Development, Lake Forest, Illinois

The shoreline development at Forest Park extends approximately 1067 m along the Lake Michigan shoreline, and consists of a series of four individual beach cells contained by detached offshore rubblemound breakwaters and shore connected steel sheet pile groins. The project also includes a protected boat launch basin, a shoreline revetment, and considerable greenspace and land based development as shown in Figure 3. Construction of the project started in the spring of 1986, and was completed approximately one year later.

The Lake Forest project was designed using a three dimensional hydraulic model study at a geometric scale of 1:20. Figure 4 shows the Forest Park model study in progress. During the hydraulic model tests it was demonstrated that it would be necessary to separate the beach cells with groins and to use a coarse sand as the artificial beach fill. The selected beach fill consists of sand with a D₅₀ of approximately 2.6 mm. The coarse sand was necessary to reduce the amount of material transported between beach cells during storms, and to provide stable beaches within the limited area available.

An extensive review of the history of the shoreline and coastal processes was completed at this site prior to construction. It concluded that the project would have no negative impacts on the shoreline, since the alongshore sediment transport is negligible. A comparison of surveys taken in late April and August 1988 supports this conclusion. Cross sections were surveyed every 15m (50 ft) along the beach and indicate a total net accretion of 178m³ for the project. Considering the accuracy of the surveys, the net accumulation of sand within the project is considered to be negligible. Figure 5 shows the project in plan view including the locations of the breakwaters, design and August 1988 plan forms, and locations where beach cross sections were completed.

Beach cross sections are presented in Figures 6 and 7 for the following conditions: original beach profile, the as-built profile, April 1988 survey, and August 1988 survey. Profiles 2+00 to 3+00 indicate a net accumulation of sand whereas profiles 12+00 through 14+00 show a net loss between the as-built and August surveys. The elevation of the groins, +2.4 m LWD, is insufficient to prevent movement to the south as evidenced by the net accumulation of sand in beach cell 1.

The project was subjected to several severe storms during the winters of 1986-87 and 1987-88. It was noted during the model studies and during the first winter following construction that the storm profiles included development of a sand berm up to elevation +3.7m LFD. The comparison between model and actual beach plan and profile development under storm conditions was excellent as shown in Figure 8.

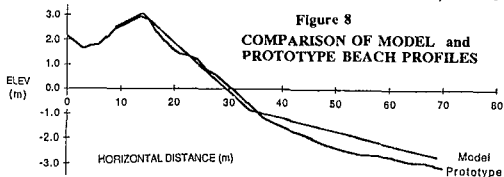




Figure 3 COMPLETED FOREST PARK PROJECT



Figure 4 FOREST PARK MODEL STUDIES IN PROGRESS

FIGURE 5 FOREST PARK PLAN SURVEYS
and LOCATION OF PROFILES

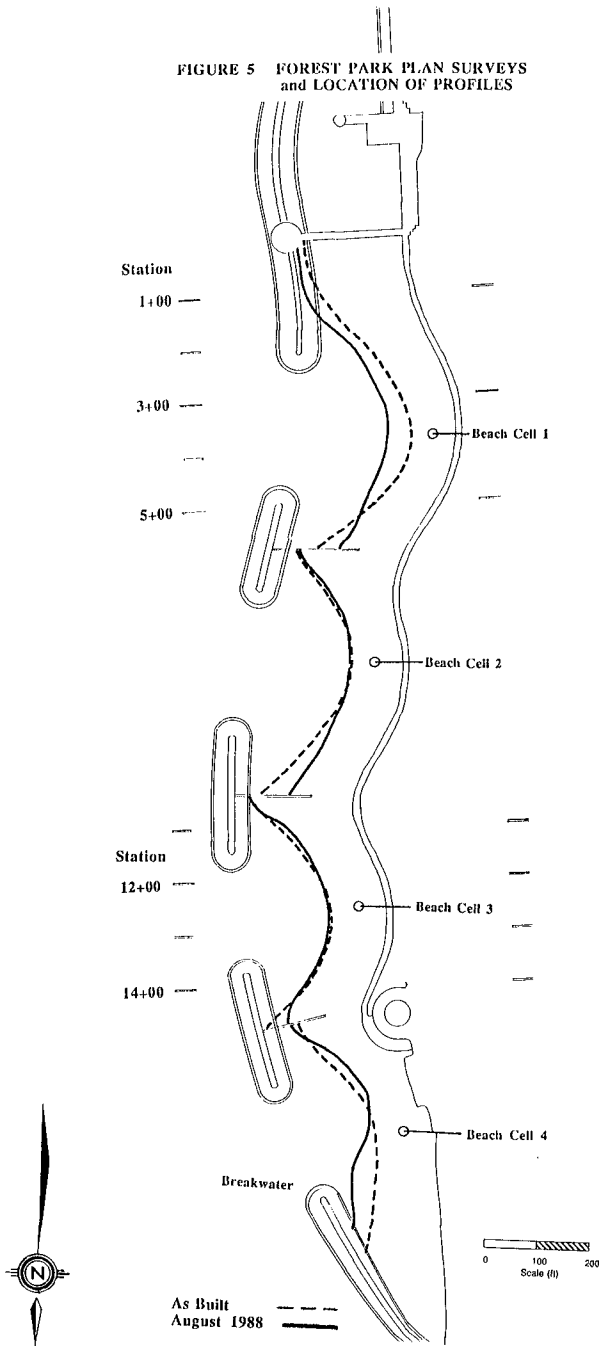
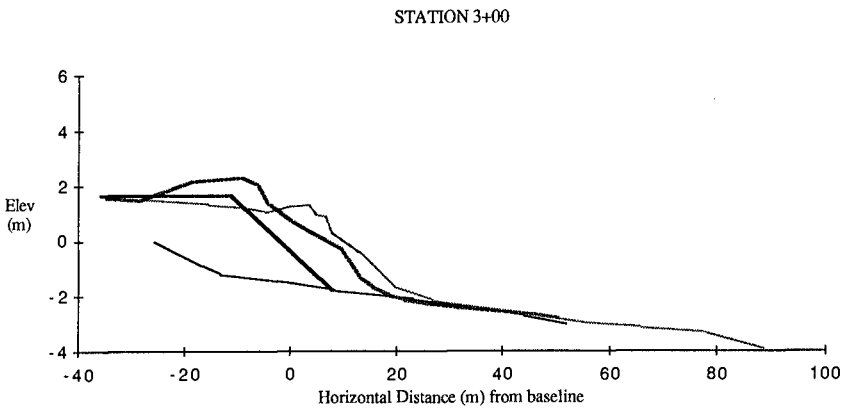
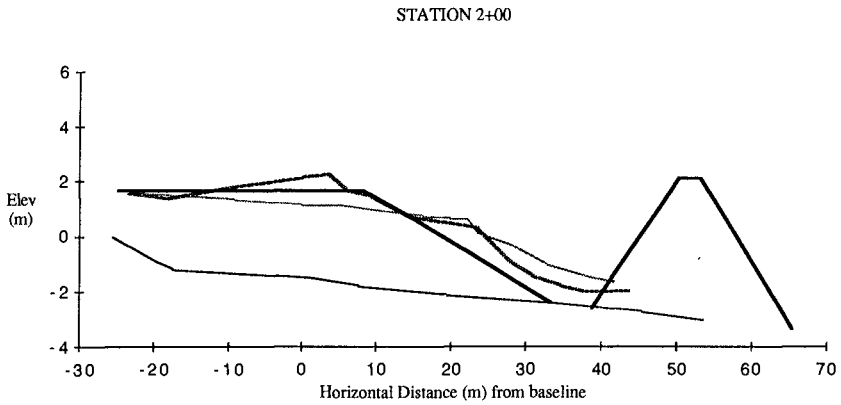
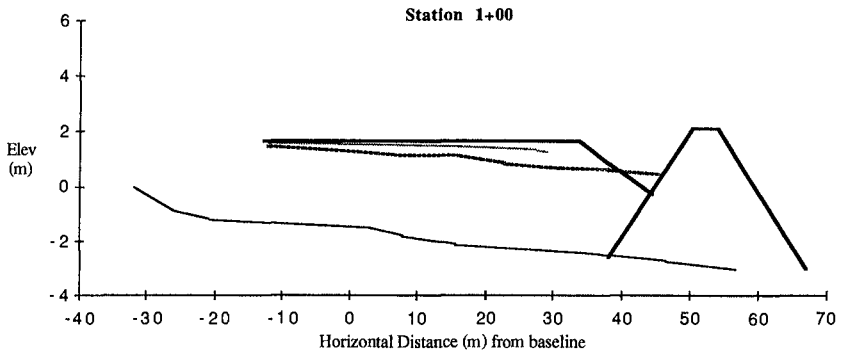
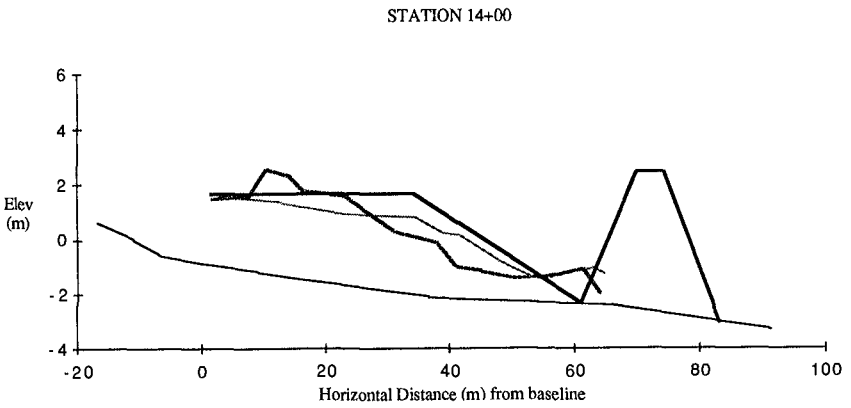
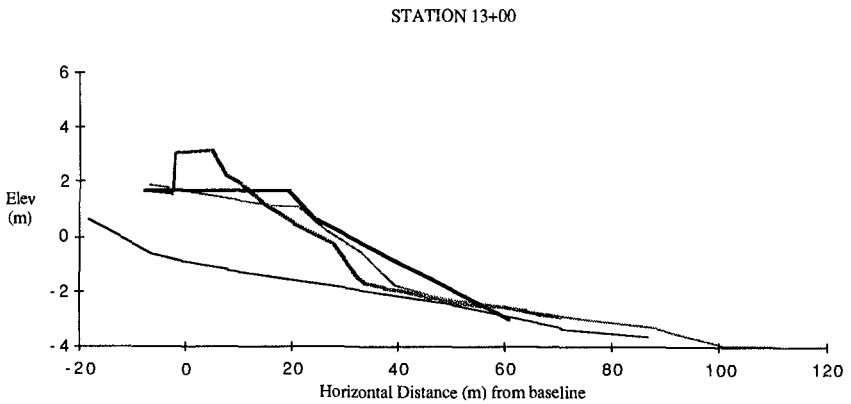
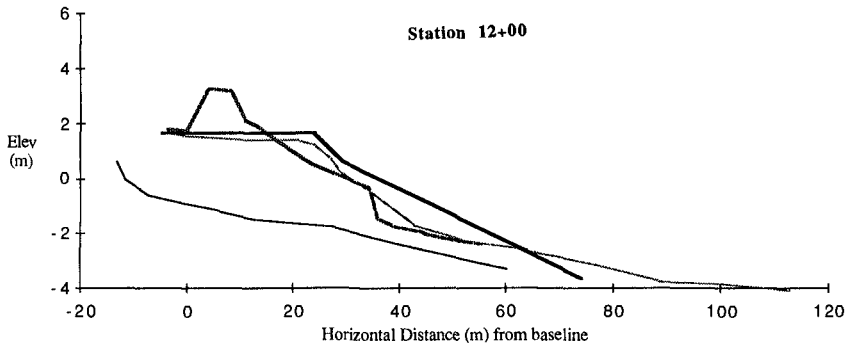


Figure 6 FOREST PARK BEACH PROFILES



— original (y) - - - Apr 88 - - - Aug 88 - - - As Built (y) — Breakwater

Figure 7 FOREST PARK BEACH PROFILES



— original (y) — Apr 88 — Aug 88 — As Built (y) — Breakwater

The prototype berm profile is also evident in Figures 6 and 7 in profiles 3+00,12+00 and 13+00 which are located primarily in the center of the beach cells. The berm is now constructed each fall by pushing the existing beach sand up into the storm profile. This protects the land based facilities behind the beach during fall and winter storms, and each spring the berm is levelled to provide a clear view of lake from the walkways for the summer season.

The Forest Park project has been extremely successful since its completion. Thousands of people visit the beach each day during the summer and the facility is also used for cross country skiing in the winter.

McKinley Park Shoreline Restoration, Milwaukee, Wisconsin

A design to protect a 762m long section of shoreline at McKinley Park was developed using a combination of desk and model studies. The project is located along a main commuter roadway which was frequently flooded during major storms.

The project consists of a series of rubblemound groins, revetments, and offshore breakwaters to contain landfill, a stone beach, and a coarse sand beach. Alongshore sediment transport was not a concern at this site, as the project is immediately north of Milwaukee harbor, which extends much further out into Lake Michigan.

The landfill and stone beach fill consist of crushed limestone produced by a large sewer tunnelling project underway in Milwaukee during construction of the McKinley Park project. This material is very angular, and ranges in size from 0.1 to 80 mm, as mentioned previously. The material was delivered to the site at no cost making it an extremely attractive product to be used as beach fill.

Figure 9 provides a photograph of a 180m wide beach cell which was filled with tunnel material. The photograph was taken in the fall of 1987 immediately following construction. A vertical edge is visible near the top of the beach which was removed during winter storms leaving a smooth beach face as shown in Figure 2.

Figure 9 McKinley Park Beach



There have been no obvious changes in the plan form shape of the tunnel spoil beach since construction. As evidenced in Figure 9 the beach has a very flat plan profile along the majority of its length.

Since construction was completed the McKinley project has prevented flooding and damage to the roadway in addition to adding a significant recreation area for the public's enjoyment. By taking advantage of the free tunnel material it was possible to construct this project for a total sum estimated to be similar to the cost of a conventional revetment using quarried armour stone.

Klode Park Beach Development, Whitefish Bay, Wisconsin

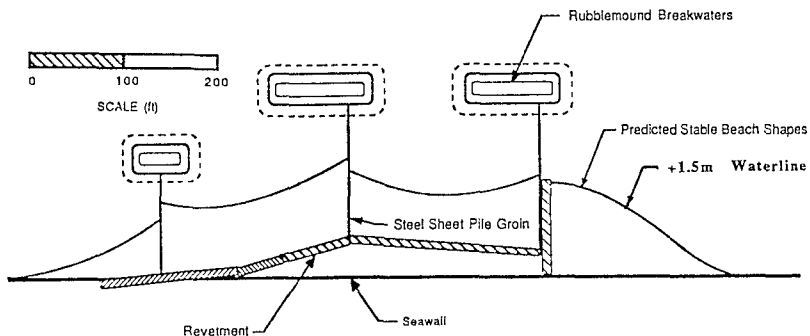
A three dimensional hydraulic model study conducted at a geometric scale of 1:20 was completed to develop a design for a shoreline restoration project to protect the Klode Park shoreline (approximately 200 m long), and to provide increased recreational space. The shoreline at Klode Park has a bluff with a height of approximately 20m. At the time the project was initiated the bluffs and shoreline had been steadily eroding to the point that slope failures were occurring which were threatening a water filtration plant located within the park.

Due to the existence of alongshore sand transport in this area it was necessary to limit the extent to which the project extended out into the lake and to account for sand bypassing the project. This was accomplished by constructing the offshore breakwaters within 60m of the original shoreline and by tapering the steel sheet pile groins which separated the beach cells. The groins were tapered to match the beach profiles to minimize the loss of beach fill during severe storms. The tapered groins also allowed native sediments to bypass the project behind the breakwaters. Because the distance from the offshore breakwaters to the permanent land based facilities is substantially shorter in this park as compared to Forest Park it was necessary to significantly modify the design of the beaches and other shoreline protection measures.

Variations over the Forest Park project include significantly reducing the breakwater gap width, tapering the groins, increasing the breakwater crest height, and adding stone revetments to the upper beach area. The revetments are buried and not noticeable to the public, but become exposed during severe storms at extreme water levels providing protection to the land based facilities and water filtration plant.

The final design, shown in Figure 10, consists of three offshore rubblemound breakwaters, which contain artificial beaches. The beaches consist of either all tunnel material similar to the McKinley project or tunnel material covered with coarse sand fill. The coarse sand has a D50 of approximately 2.6 mm placed over a general fill consisting of tunnel material similar to the McKinley project.

FIGURE 10 KLODE PARK FINAL DESIGN



Public's perspective from the park down onto the beach and from the beach looking down the adjacent shoreline are provided in Figure 11.



FIGURE 11 PUBLIC PERSPECTIVES



Pesch Property Shoreline Protection, Lake Forest, Illinois

Similar to the other projects the high Lake levels in 1985 and 1986 had caused considerable shoreline erosion and bluff retreat along this section of the Lake Michigan shoreline. The project was required to prevent further erosion of a 130 m long privately owned section of shoreline where erosion was threatening the stability of the bluff and the property owner's house.

The project was completed in the winter of 1986 and consists of two offshore rubblemound breakwaters and two steel sheet pile groins which contain small pocket beaches filled with a coarse sand as shown in Figure 12. Rubblemound revetments provide additional protection along the shoreline behind the breakwater gaps where the beach fill is not sufficient to protect the bluff during storms. A physical model study was used to design the combination of offshore breakwaters, steel sheet pile groins and sand beaches.

This project was subjected to several severe storms during the winters of 1986-87 and 1987-88 and similar to the Forest Park project performed as predicted by the model investigation.

FIGURE 12 PESCH PROPERTY ARTIFICIAL BEACH

**SUMMARY**

Shoreline protection was the basic goal of each of the projects described above. In assessing the attributes of various shoreline protection schemes it was evident that the benefits of incorporating recreational areas into the projects outweighed the additional costs associated with creating them. Prototype experience has shown that these projects are extremely successful both in their ability to withstand storms on the Great Lakes and to attract people for recreational activities. Therefore each of these projects meets the basic criteria of providing effective shoreline protection while also providing excellent recreational areas, and demonstrates the numerous advantages associated with choosing artificial beach units versus standard protection measures.

REFERENCES

- Bascom, W.N., (1951) from King, C.A.M., *Beaches and Coasts*, published by Edward Arnold Ltd., London, 1972.
- Chew, S.Y., Wong, P.P., and Chin, K.K., "Beach Development Between Headland Breakwaters", Proceedings of the 14th Coastal Engineering Conference, Copenhagen, June 1974, pp. 1300-1418.
- Clark, G., Personal Communication, January 1986.
- Curren, C.R. and Chatham, C.E., Jr., "Imperial Beach, California, Design of Structures for Beach Erosion Control", TR H-77-15, U.S. Army Engineer Waterways Experiment Station, Vicksburg, Mississippi, August 1977.
- Curren, C.R. and Chatham, C.E., Jr., "Oceanside Harbour and Beach, California, Design of Structures for Harbour Improvement and Beach

- Erosion Control", TR HL-80-10, U.S. Army Engineer Waterways Experiment Station, Vicksburg, Mississippi, June 1980.
- Dally, W.R. and Pope, J., "Detached Breakwaters for Shore Protection", draft report TR CERC-86-1, U.S. Army Engineer Waterways Experiment Station, Vicksburg, Mississippi, January 1986.
- Dean, R.G., "Diffraction Calculations of Shoreline Planforms", Proceedings of the 16th Coastal Engineering Conference, Hamburg, August 1978, pp. 1903-1917.
- Noda, H., "Depositional Effects of Offshore Breakwater Due to Onshore-Offshore Sediment Movement", Proceedings of the 19th Coastal Engineering Conference, Houston, September 1984, pp. 2009-2025.
- Perez, J.M.B, and Fernandez, J.E., "Design of Pocket Beaches. The Spanish Case", Proceedings of the 21st Coastal Engineering Conference, Torremolinos, Spain, June 1988, pp. 463-464, Abstracts.
- Rosen, D.S., and Vajda, M., "Sedimentological Influences of Detached Breakwaters", Proceedings of the 18th Coastal Engineering Conference, Cape Town, November 1982, pp. 1930-1949.
- Sato, S. and Tanaka, N., "Artificial Resort Beach Protected by Offshore Breakwaters and Groins", Proceedings of the 17th Coastal Engineering Conference, Sydney, March 1980, pp. 2003-2022.
- Seeling, W.N. and Walton, T.L., Jr., "Estimation of Flow Through Offshore Breakwater Gaps Generated by Wave Overtopping", CETA 80-8 U.S. Army Corps of Engineers, Coastal Engineering Research Center, Fort Belvoir, Virginia, December 1980.
- Shinohara, K. and Tsubaki, T., "Model Study of the Change of Shoreline of Sandy Beach by the Offshore Breakwater", Proceedings of the 10th Coastal Engineering Conference, Tokyo, September 1966, pp. 550-563.
- Silvester, R., Tsuchiya, Y. and Shibano, Y., "Zeta Bays, Pocket Beaches, and Headland Control", Proceedings of the 17th Coastal Engineering Conference, Sydney, March 1980, pp. 1306-1319.
- Tourman, L., "The Creation of an Artificial Beach in Larvotto Bay - Monte Carlo Principality of Monaco", Proceedings of the 11th Coastal Engineering Conference, London, September 1968, pp. 558-569.
- Toyoshima, O., "Design of a Detached Breakwater System", Proceedings of the 14th Coastal Engineering Conference, Copenhagen, June 1974, pp. 1419-1431.
- Toyoshima, O., "Variation of Foreshore Due to Detached Breakwaters", Proceedings of the 18th Coastal Engineering Conference, Cape Town, November 1982, pp. 1873-1892.
- Walker, J.R., Clark, D. and Pope, J., "A Detached Breakwater System for Beach Protection", Proceedings of the 17th Coastal Engineering Conference, Sydney, March 1980, pp. 1968-1987.

CHAPTER 212

THE BEACH REHABILITATION PROJECT AT OSTEND-BELGIUM

ir. R. SIMOEN*
ir. H. VERSLYPE**
ir. D. VANDENBOSSCHE***

Abstract

Steady erosion has occurred on the beaches at Ostend, Belgium, especially on the section between the Casino and the Harbour Entrance. The gravel beach supported by a sandfill core has been proven to be a feasible and cost effective flood protection alternative, the first objective of the long term beach enhancement programme. Secondary goals are also met such as : new beach recreational facilities in safe conditions for the public ; the economic incentive for the needed redevelopment of this part of down-town Ostend and the beach front ; the conservation of the present sea-view from the promenade.

1. Introduction

Since the end of the 19th century the beaches at Ostend, Belgium have been popular holiday resorts. However, steady erosion has occurred, especially on the beach section between the Casino-Kursaal and the Harbour entrance (see fig. 1). Indeed, the beach front promenade was constructed along the line of the 17th century fortifications of the city, which protrude into the sea beyond the natural coastline over ca. 150 m. A system of huge perpendicular groynes, ca. 200 m long could only slow down the erosion process.

- * Inspector General, Ministry of Public Works, Coastal Service, Administratief Centrum, Vrijhavenstraat 3, B-8400 Oostende, Belgium
- ** Chief Engineer - Director, Ministry of Public Works, Coastal Service, Administratief Centrum, Vrijhavenstraat 3, B-8400 Oostende.
- *** Technical Director, HAECON (Harbour and Engineering Consultants) N.V., Deinsesteenweg 110, B-9810 Gent.

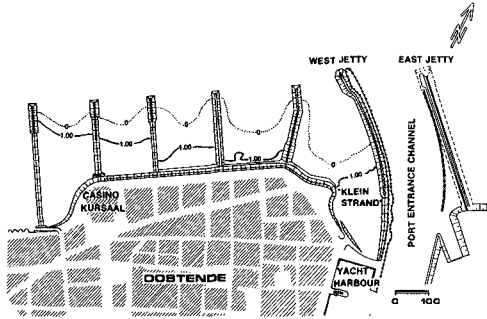


Figure 1. Existing situation

At that time, the coastal protection consisted of :

- a seawall up to $Z + 9.80$ at the promenade level, with a slope revetment of natural stone masonry on $10/4$ slope ;
- a sandy beach with a gentle slope of $1:60$, the level at the seawall toe is around $Z + 2.80$ to 3.00 m, almost the Mean Sea Level (MSL). As the beach had reached this rather low level, the main functions of the coastal defence, as depicted on cross-section (fig. 2) became progressively inadequate e.g. :

- * flood protection : during storm surges Ostend's lower downtown became more frequently flooded by waves over-topping the seawall. During extreme storm surges as in February 1953, the seawall was even partially destroyed.
- * recreation : remained only viable on the "Klein Strand" beach section (fig. 1). The remainder being flooded at mean sea level up to high water. Practical use of the beach is limited to only a brief period at low-water. Compared with other similar beach fronts at Ostend and elsewhere along the Belgian Coast the real estate properties are consequently less developed to modern age standards.

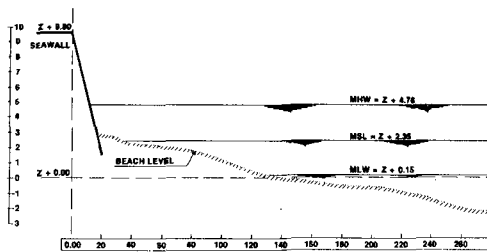


Figure 2. Typical cross-section existing beach

A flood protection enhancement programme, realized after the dramatic storm surge of February 1953 and extended after the winter storms of January 1976, resulted in a small storm surge barrier wall on top of the seawall up to level

Z+10.20 and associated storm surge sewer system. This programme gives results but only in the short term.

2. The beach rehabilitation project

The National Ministry of Public Works, Coastal Service entrusted HAECON, Consulting Engineers of Ghent, to elaborate a beach enhancement programme in order to provide in the long term :

- flood protection by preventing storm surge waves overtopping the seawall ;
- additionally the realization of a recreational beach potential by both a dry sun beach, and to a lesser extent a bathing beach.

3. Physical design data

3.1. Beach and shore morphology has been analyzed from beach profiles and bathymetry soundings from '71 up to '82.

The beach in the project area although at a low level is compared to other sections stabilized on a typical average slope of 1:60. The beach foot is situated at the Z-5.00 contour. From this to the LW-line the depth contours are almost parallel to the coast. Off-shore to deep water the wave attenuation is influenced by the system of banks (ca. Z-6.00) and channels (Z-8.00 to Z-10.00) of the Flemish Bank area.

3.2. Hydrographic data

A comprehensive set of data was available concerning : tides, currents, surges and waves.

3.2.1. Tides : the high and low water characteristics at spring tide are : MHWS = Z+4.75 ; MLWS = Z+0.15. The period of the semi-diurnal tide is : 12 h 17 min.

3.2.2. Surges : the exceedance frequency of high waters were established by linear regression of the tide observations of the Ministry of Public Works' Hydrographic Service from 1952 to 1967 (see fig. 4). From this the decennial surge level has been estimated at Z + 6.00 m ; the centennial level at 6.40 m.

3.2.3. Waves : from deepwater wave data, measured from 1977 to 1980 at the lightship Westhinder. The near-shore exceedance frequency of significant waves was established with mathematical refraction analysis. The annual significant wave height is estimated at $H_s = 4.00$ m ; the centennial significant wave height 4.80 m is depth limited. From this data the frequency of occurrence of wave periods was also established. The peak period of the wave energy spectrum is around 6 to 6.5 sec.

3.3. Beach and beach fill materials

The existing beach sand is a rather fine material, on average characterized by : $D_{50} = 173 \mu$ and $D_{90} = 688 \mu$.

The typical grain size distribution of the beach fill sand from the Kwintebank and the gravel to be found off Dieppe, Wisant and Wight, Thames, is given on fig. 3. One should note that the sand quantity in the gravel load can reach 30 % by weight.

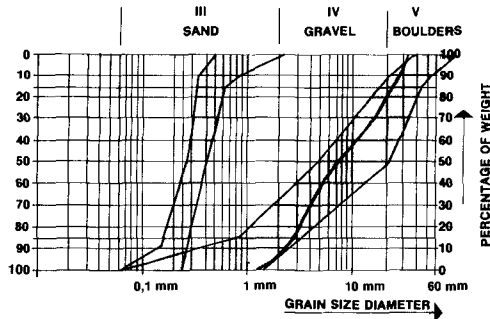


Figure 3. Grain size distribution tolerances of beach fill sand and gravel

4. Planning and design

4.1. For the beach rehabilitation, a straight sand fill solution was technically unfeasible because of the adjoining access-channel to the Port of Ostend. Indeed, in order to prevent higher sedimentation in this channel, the beach replenishment should be limited within the confines of the existing groyne system and the western harbour jetty.

4.2. The main conceptual design alternatives were assessed :

- Figure 4 - the spending beach concept : consisting of a beachfill from HW-level ($Z+4.75$) at the seawall down to LW-level whereas the beach foot is supported by a low crested rubble mound at level $Z+0,75$ parallel to the coast. The slope of the replenished beach is designed at 1:50.
- Figure 5 : the concept of a gravel beach supported by a 50 m wide sandfill core with the gravel beach crest at $Z+6.00$, the sand level at the seawall up to $Z+7.00$. Based on literature data the gravel slope has been designed at 1:7 and the required gravel layer thickness estimated around 3.00 m, for gravel with size distribution $D_{50} = 12 \text{ mm}$ / $D_{90} = 30 \text{ mm}$, $H_o = 4.00 \text{ m}$ and $T = 6 \text{ sec}$.

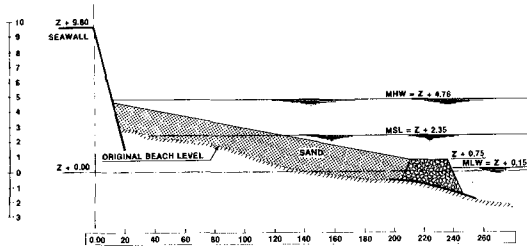


Figure 4. The spending beach concept

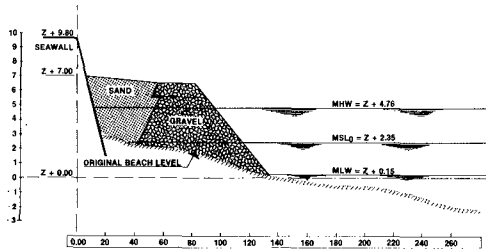


Figure 5. The gravel beach concept

Both the designs, together with the existing beach seawall configuration were evaluated for the occurrences of wave overtopping, transport capacity of beach material, accomplishment of design functions and other related aspects.

4.3. The results of the wave overtopping calculation are given in the table below.

	Average occurrence of wave overtopping (N/year)
* Existing situation (fig. 2)	21
* Spending beach	
- at designed level (fig. 4)	1.8×10^{-2}
- at assumed eroded level (-1.00 m)	2
* Gravel beach (fig. 5)	1.24×10^{-5}

TABLE : Estimated wave overtopping rate.

The results in the existing situation fit well with those experienced on site.

4.4. The morphological aspects have been assessed mainly by evaluating the longshore transport capacity especially the eastbound component towards the Port Entrance Channel.

4.4.1. Present situation : Longshore transport is to a large extent blocked by the groynes. The eastbound transport capacity for $D_{50} = 173 \mu$ / $D_{90} = 242 \mu$ can be estimated at 400,000 m³/year. The resultant longshore transport is up to 180,000 m³/year eastbound.

4.4.2. Spending beach : The longshore transport capacity for a beach fill of $D_{50} = 371 \mu$ / $D_{90} = 600 \mu$ has been estimated on 140,000 m³/yr (eastbound component) and 20,000 m³/year (resultant eastbound). The resultant longshore transport may be caught in the "Klein Strand" beach section near the West Harbour jetty. Consequently, a higher sedimentation risk in the access-channel is to be excluded.

Despite the decreased transport capacities, compared with the present situation, increased losses due to the higher turbulence caused by wave reflection on the seawall and breaking waves at the rubble mound toe, giving rise to concern about the long-term flood protection efficiency of the concept. Indeed, a lowering of only 1.00 m brings the wave overtopping almost to the same order of magnitude as the present situation ! (See table : from 1.8×10^{-2} tides/yr designed to 2 tides/yr, cfr. the present 21 tides/year).

The rubble mound structure prevents the normal exchange of beach material between the replenished upper beach and the foreshore. A prerequisite for a profile in dynamic equilibrium is therefore not met.

As all waves will break on the rubble mound the erosion pits near the structure would create a dangerous situation for the public. Bathing and swimming should not be tolerated.

4.4.3. Gravel beach : The longshore transport capacity will decrease as the beach material is increased by grain size. The resultant is lower than 200 m³/yr and the eastbound component less than 8,000 m³/yr.

The gravel beach and the foreshore represents a natural beach system both in morphology and in grain size distribution. A dynamic equilibrium can be expected with greatly reduced cross-sectional transport losses.

Compared with a sandy beach the gravel beach would not be the preferred choice for a bathing beach, however, by no means create dangerous situations for the public.

5. Detailed design

5.1. The retained gravel beach concept (fig. 5) has been designed in detail based on extensive physical scale model

testing in the wave flume and wave tank facilities of the Ministry of Public Works' Hydraulic Research Station at Antwerp.

5.2. The aims of the test programme were :

- 1) the definition of the equilibrium slope and active layer thickness as a function of the waves ;
- 2) the study of wave overtopping by defining the water quantities overwashing the seawall ;
- 3) the study of some construction phases of the gravel mound in order to establish guidelines for construction.

5.3. The studies on items 1) and 2) were realized on the wave flume in a 2-dimensional model. The 3-dimensional model has been used for item 3).

The wave flume measures $63.5 \times 4.08 \times 1.45 \text{ m}^3$ and is equipped with a Arenfield wave generator and a hydraulic system to simulate the tidal changes of the water levels. Maximal tidal difference can be set up to 1.20 m. The geometric scale of the models was $1/12$, time scale $1/3.464$.

The model tides schematization was calibrated around a spring tide ($LW = Z - 0.10$, $HW = Z + 4.00$ and $T = 12 \text{ h } 30$).

The irregular model waves correspond to the Pierson Moskowitz Spectrum, the theoretical spectrum best fitting with the shallow water wave conditions off the Belgian Coast.

The grain size distribution of the model gravel is given on fig. 3.

5.4. Equilibrium slope and required layer thickness

5.4.1. The results of the tests regarding equilibrium slopes as a function of H_s and active layer thickness are summarized in fig. 6.

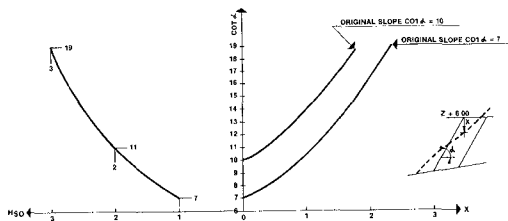


Figure 6. Equilibrium slopes ($\cotg \alpha$) and active layer thickness (x) in function of significant design wave (H_s)

The behaviour of the gravel beach under a schematic annual wave climate is reported on fig. 7.

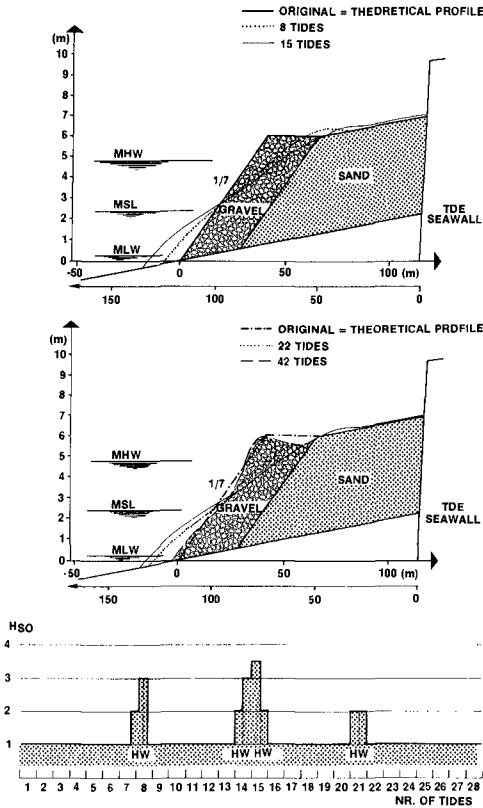


Figure 7. Behaviour of gravel beach profile line under schematic annual wave action

5.4.2. From the test series one determines that :

- the equilibrium slopes range from 1:7 over 1:11 to 1:19 for wave classes $H_{s0} = 1.00, 2.00$ and 3.00 m respectively ;
- the equilibrium slopes are found roughly by a rotation of the slope around MSL.

5.4.3. For the design of the gravel beach following conclusions could be retained :

- 1) the theoretical design slope should be 1:8, because :
 - * this slope corresponds with a wave of $H_s = 1.25$ which is exceeded 10% of the tides ;
 - * with the slope of 1:7 the gravel beach crest at $Z+6.00$ could be eroded over the whole width of 25.00 m during one storm with $H_s = 3.00$ to 3.50 m (ca. 2 times/year) ;
 - * for the schematic annual wave climat test the final slopes were : 1:7.50 to 1:9.

- 2) the theoretical design crest width may be 25.00 m with a slope of 1:8. Two consecutive tides of $H_s = 3$ to 3.50 m are needed to erode this width ;
- 3) the active layer thickness with a slope of 1:8 for $H = 3$ to 3.50 m is at equilibrium 2.00 m. A layer thickness of 2.50 to 3.00 m seems adequate, depending on the safety margin needed.

5.5. Wave overtopping

5.5.1. The test series on wave overtopping have been conducted starting from the equilibrium profile resulting from the annual wave climate test serie. With consecutive constant water levels of $Z+4.75$ m ; $Z+5.75$, $Z+6.25$ and 6.75 m the water quantities have been measured from irregular overtopping wave fields with $H_s = 3.00$, $H_s = 3.50$ and $H_s = 4.00$ m.

5.5.2. In the existing situation wave overtopping starts when $HW = 4.75$ m (ca. 100 times/year) and $H_s = 2.00$ m (ca. 25 times/year) or 3.4 tides per year. The same quantity of water (ca. 60 l/m'/min.) will pass by the gravel beach concept when $HW = 6.25$ m (1 time/25 years) and $H_s = 4.00$ m (1 time/year) or 5.5×10^{-5} tides per year.

As the beach level of the gravel beach design is lowered by between 0.5 and 1.00 m the quantities of overtopping water will only be increased by ca. 10 times. The long term flooding protection efficiency is thus well demonstrated.

5.5.3. Upon completion of all the wave overtopping test series the remaining profile is measured. The test record is given on fig. 8.

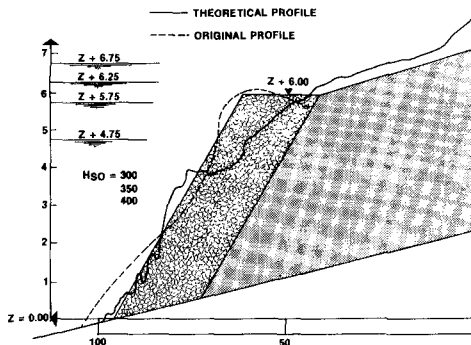


Figure 8. Gravel beach slope after wave overtopping test series ("crash-storm" surges)

The wave overtopping test series can be also used as "crash tests" for the design of wave stability. For the very unlikely event of combined surge waterlevels, wave action and duration, we observe that under no

circumstances is the sandlayer touched. The beach, at worst, will only be covered by a gravel layer. After such a "crash-storm" the beach needs only be cleaned of the overwashed gravel.

5.6. Construction phases

5.6.1. In the wave flume two provisional round heads - one at level $Z+5.00$, the other at level $Z+3.50$ - have been tested under orthogonal irregular wave action. The test cycles consisted each time of 7 tides with $H_s = 1.00$ m, 1 tide with $H_s = 2.00$ and 1 tide with $H_s = 3.00$ m.

As shown on fig. 9, using a cross section taken 10.00 m out from the round head, some material will be transported towards the sea-wall mainly from $H_s = 1.00$ m, exceedance frequency ca. 10 % of the tides.

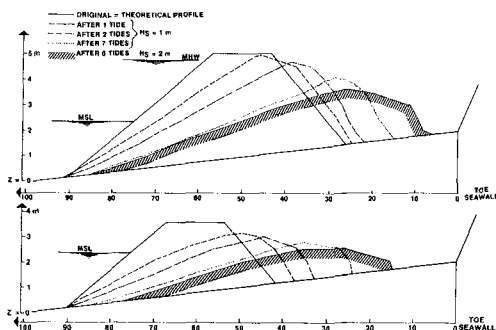


Figure 9. Construction phases - test series

5.6.2. The following guidelines for the construction could be formulated from these tests .

- the gravel beach structure should be constructed (at a maximum) in a calm wave season to avoid waves exceeding $H_s = 1.00$ m ;
- the gravel mound should be first constructed to a level above HW ($Z+4.76$) in order to decrease the amount of material out of the gravel profile and so as to redress the incurred damages during construction from a dry work level ;
- a gravel mound running section of that nature will probably resist waves of between $H_s = 1.00$ m and 1.50 m. At the round head some damage will occur which can be repaired.

5.6.3. Finalizing the detailed design : taking into account the construction constraints and guidelines several execution methods have been identified and analyzed. The final choice will be that of the successful contractor in accordance with the job-specifications.

5.6.4. The detailed design has been finalized as shown on fig. 10 and 11. The construction phases anticipate the possible gravel losses towards the sandfill section. The project covers ca. 850 m of beach front. At both ends some minor works had to be conceived to finish the gravel beach. The volumes of material are : sea sand : 300,000 m³ ; sea gravel : 180,000 m³. The works have been estimated at 260 M BF or some 7,5 M US\$. A construction time of 3 months inclusive down-time is thought feasible.

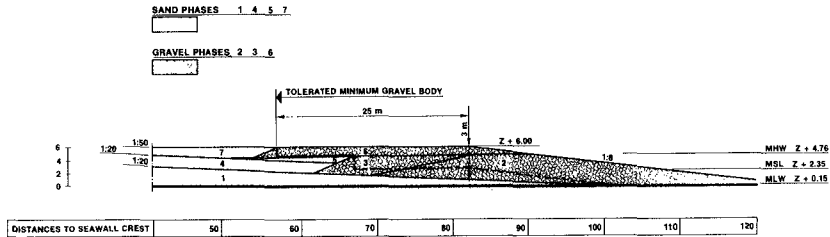


Figure 10. Final design cross section gravel mound and sandfill beach construction phases

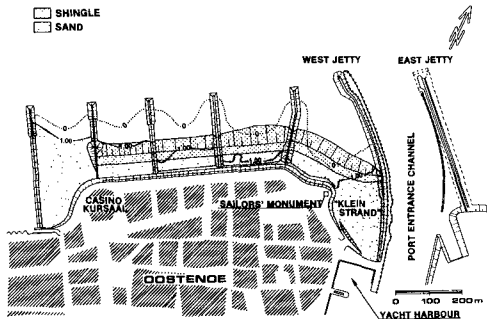


Figure 11. Final layout beach rehabilitation project depicted on the existing bathymetry, the groynes system and jetties are existing and will remain

6. Conclusion

6.1. The gravel beach supported by a sandfill core has been proven to be a feasible and cost effective flood protection alternative, the first objective of the scheme.

6.2. The following secondary goals have also been met :

- new beach recreational facilities in safe conditions for the public ;
- the economic incentive for the much-needed redevelopment of this part of down-town Ostend and the beach front ;
- the conservation to a large extent of the present sea-view from the sea promenade.

REFERENCES

- HAECON Gent, various planning and design reports (in dutch).
- Hydraulic Research Station Antwerp : Reports on the physical model testseries of the gravel beach concept (in dutch).

CHAPTER 213

AN ENGINEERING STUDY OF OCEAN CITY'S BEACHES, NEW JERSEY, USA

J. Richard Weggel, F ASCE (1)
Scott L. Douglass, AM ASCE (2)
Robert M. Sorensen, F ASCE (3)

INTRODUCTION

Ocean City, New Jersey is a major coastal resort in the heavily populated northeastern part of the United States. It is located on a 13 km-long barrier island about 13 km south of Atlantic City and 48 km north of Cape May, the southernmost point in New Jersey. See Figure 1. The barrier island, called Peck's Beach, is bounded on the north by Great Egg Harbor Inlet and on the south by Corsons Inlet.

Because wide recreational beaches are important to Ocean City's economy, an engineering study of the beaches was undertaken: a) to quantify natural and man-made shoreline changes, b) to quantify tides, sea level changes, waves, longshore sand transport rates, seasonal variations in beach width and Great Egg Harbor Inlet processes and incorporate them into a sediment budget for Ocean City, c) to determine why past attempts to maintain wide recreational beaches were only partially successful, and d) to recommend a plan to establish and maintain wide beaches.

EXISTING CONDITIONS

The northerly end of Ocean City is the most densely developed part of the city. Here the barrier island is at its widest at about 1.4 km. Heavily used commercial development and tourist facilities are also located in this area. Further southward the island narrows to about 0.9 km and development consists primarily of single and multiple family dwellings. The streets in Ocean City are numbered from north to south with 9th Street being about the commercial and tourist center. A boardwalk extends from First Street in the north, southward to 23rd Street. Timber sheet-pile bulkheading parallels the shoreline behind much of Ocean City's beach. In some areas, e.g. south of 47th

-
- (1) Professor & Head, Department of Civil & Architectural Engineering, Drexel University, Philadelphia, PA, USA.
 - (2) Senior Project Engineer, PARE Engineering, Inc., Lincoln, RI, USA.
 - (3) Professor, Department of Civil Engineering, Lehigh University, Bethlehem, PA, USA.

Street, the bulkhead is fronted by rubble toe protection and the high water shoreline is up against the bulkhead. At the heavily used northern end of Peck's Beach the shoreline has been stabilized by a number of long, high, impermeable rubble-mound groins. Groin crest elevations vary but average about 2.5 m above the local mean low water datum which is 0.58 m below the mean sea level of 1929 (National Geodetic Vertical Datum, NGVD). There are 18 groins between the terminal groin at Great Egg Harbor Inlet and 21st Street. Groin spacing ranges from 225 m to 370 m and averages about 300 m. In addition, there is a terminal groin at 59th Street, the southern end of the developed part of the island. There are no groins between 21st Street and 59th Street. South of 59th Street the shore is characterized by natural sand dunes on the sand spit which comprises the northern boundary of Corson's Inlet.

HISTORICAL SHORELINE CHANGES

Historical shoreline changes at Ocean City were studied by analyzing 21 sets of controlled, vertical, aerial photographs taken between April 1952 and September 1984. Most photos had a scale of 1:4800. The "wet line" or the interface between the wet and dry beach was identified at 46 stations along Ocean City's shoreline. This line is easily identifiable and is close to the limit of wave runup during the preceding high tide and to the berm line. The location of the wet line relative to a local baseline, usually the centerline of a shore-parallel street, was noted. Most of the 46 stations were located close together along the more northerly beaches to define shoreline changes within the groin compartments there. Stations were spaced further apart along the southerly beaches where spatial variations were smaller. Linear regression lines were fitted to the plots of wet line location as a function of time.

Interestingly, with only minor exceptions, the analysis found that the shoreline in 1984 was in almost the same location as it had been 32 years earlier in 1952. In addition, the regression lines showed that the time-averaged erosion rate was small or nearly zero even though there had been significant fluctuations of the shoreline about the average. In at least two locations, narrowing of the beach was due to encroachment from the landward side rather than by beach erosion.

The air photo analysis incorporated into it the effect of beach nourishment activities carried out by the Corps of Engineers and the City of Ocean City between 1952 and 1984. During that time, 6.4 million cu m (8.4 million cu yd) of sand were placed on Ocean City's beaches in three major beach fills in 1952, 1959 and 1982 and in numerous smaller fills between 1970 and 1981. Watts (1956) documented the performance of the relatively successful 1952 fill, one of the earliest beach fills ever undertaken, in which 1.95 million cu m (2.6 million cu yd) of sand was placed on the beach. During the 11 year period from 1970 to 1981, the City of Ocean City operated a dredge behind the barrier island and pumped an average of 166,000 cu m (217,000 cu yd)

of relatively fine sand onto the beaches each year. Thus the average rate of beach filling from all sources between 1952 and 1984, the period covered by the air photo analysis, was 198,000 cu m/yr (259,000 cu yd). While the 1952 fill was relatively successful, the 1982 fill, placed during September and October, was short-lived and most of it was lost during that first winter. The winter of 1982-83 was marked by 18 storms out of the northeast which contributed to the rapid loss of fill (Farrell & Inglin, 1988).

Ocean City's beaches are relatively stable, but only at the expense of placing an average of 200,000 cu m (262,000 cu yd) of fill per year on them. However, the problem is beaches that are too narrow rather than beaches that are experiencing excessive erosion. The solution is to initially widen Ocean City's recreational beaches and then to stabilize and maintain these wider beaches.

SEASONAL BEACH PROFILE CHANGES

Quarterly surveys of 17 beach profile lines were made in September 1985, December 1985, May 1986 and June 1986 to determine what seasonal changes might be typical of Ocean City's beaches. Horizontal movements of 25 m at the mean sea level shoreline were not unusual during this period. In fact, changes of about 35 m occurred near the center of the island between 14th and 22nd Streets. See Figure 2. Most changes occurred between the September survey and the December survey with a further, less dramatic, shoreline recession between December and May. In general, there was little change between May 1986 and June 1986. A dramatic loss of sand occurred along the Great Egg Harbor Inlet shoreline between September and December 1985. The wide beaches and large sand dunes in the inlet area were eroded during two storms that occurred in late September and October. Shortly after the September survey, hurricane "Gloria" threatened the New Jersey coast. While most of Ocean City's beaches were spared major damage because the hurricane was too far offshore, the Great Egg Harbor Inlet beaches of Ocean City were severely eroded. Large volumes of sand, stockpiled in dunes along the inlet shoreline, disappeared and two groins, which had been constructed in 1979 and buried beneath the sand, were exposed. See Figure 3.

WAVE AND POTENTIAL LONGSHORE TRANSPORT ENVIRONMENT

The wave and longshore sand transport environment in the vicinity of Ocean City were investigated using the hindcast wave data developed under the Corps of Engineers' Wave Information Study (WIS) (Jensen, 1983). WIS Station 62, Peck Beach, is located approximately offshore of 40th Street and best represents the average wave conditions in Ocean City. The next station to the north (Station 61) is at Atlantic City while the next station to the south (Station 63) is at Seven Mile Beach. Maximum offshore wave heights in 10 meters of water for Station 62 are given in Figure 4 along with an estimate of their return period.

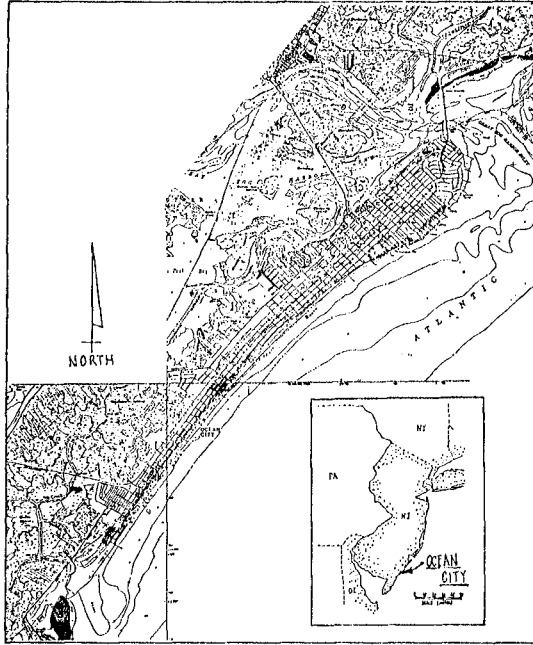


Figure 1 Location Map, State of New Jersey and Ocean City, New Jersey

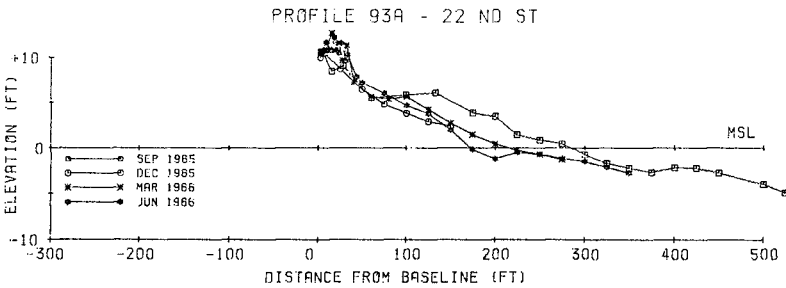


Figure 2 Beach Profiles at 22nd Street Showing Seasonal Shoreline Movement

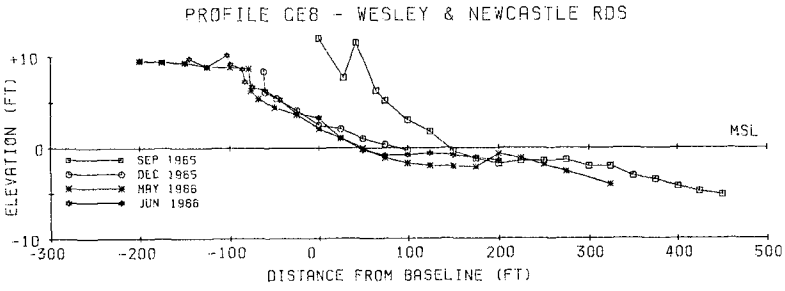


Figure 3 Beach Profiles at Great Egg Harbor Inlet Shoreline Showing Sand Losses between September and December attributable to Hurricane "Gloria"

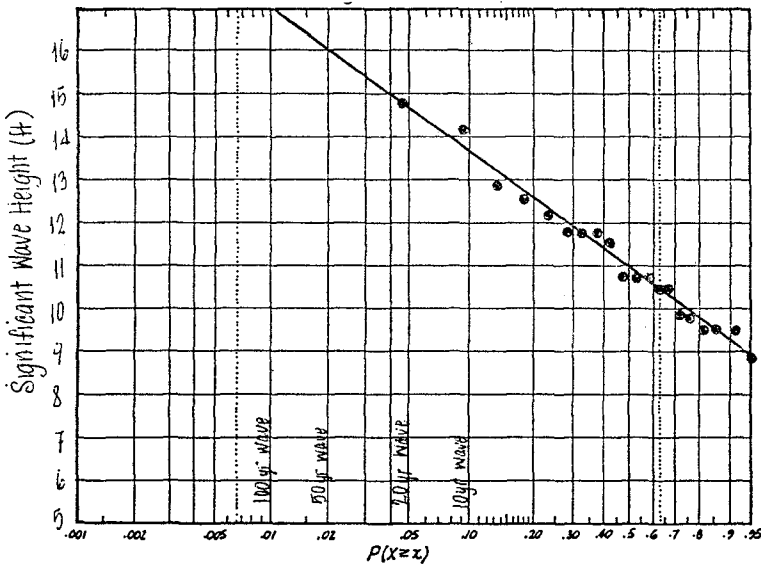


Figure 4 Frequency of Occurrence of High Waves in 10 Meters of Water at Station 62, Peck Beach (WIS Hindcast Data)

The WIS tabulated wave heights, periods and directions were used with the CERC formula to calculate potential longshore sand transport rates. In most cases calculated transport rates represent only potential transport because of: a) the effect of groins on transport, b) local reorientation of the shoreline, and c) the limited amount of sand available for transport in some areas. Transport rates calculated from the Station 62 WIS data were analysed statistically to determine how often given levels of transport are exceeded. The calculated transport rates were separated into two populations: positive transport (transport to the right for an observer looking seaward) and negative transport. Each data set was then listed in rank from the highest transport rate to the lowest. The number of hours that each transport rate prevailed was accumulated to obtain two frequency plots, one for positive transport and one for negative transport. The resulting longshore transport frequency data was plotted on log-normal probability paper to obtain the plots shown in Figure 5. Thus the longshore transport environment can be summarized by six parameters, the mean and variance of each of the two log-normal distributions (a positive transport distribution and a negative transport distribution) and the fractions of time the transport is positive, negative or calm (Weggel & Perlin, 1988; Weggel, Douglass & Tunnell, 1988). Driven by waves out of the northeast, sand moves southwestward only about 38% of the time at Station 62, Ocean City. Sand moves northeastward about 60% of the time. While northeastward transport occurs over a greater fraction of time, it is at a lower rate since it is driven by the relatively smaller waves out of the southeast during the summer months. Episodes of southwestward transport (northeasters), while less frequent, are more intense and carry more sand in the course of a year. This results in a net southwestward longshore transport. The potential net southwestward transport is estimated to be 56,000 cu m/yr (73,000 cu yd/yr). The northeastward transport is estimated at 540,000 cu m/yr (706,000 cu yd/yr) and the southwestward transport is 596,000 cu m/yr (779,000 cu yd/yr) for an annual gross transport rate of 1,136,000 cu m/yr (1,485,000 cu yd/yr). Obviously, these net and gross transport rates vary from year to year. The numbers given here are estimates of the 20-year average conditions summarized in the WIS hindcast data.

Similar analyses were performed for WIS Stations 61 and 63. Analysis of the Station 61 data, Atlantic City, predicts a northward net longshore transport on Absecon Island. This is contrary to evidence obtained from observations of sediment accumulation at structures on Absecon Island, particularly the terminal groin on the Longport side of Great Egg Harbor Inlet; consequently, Station 61 data was not used in the present analysis. This discrepancy between predicted and observed net transport rates shows that care must be exercised in interpreting transport rates computed from the WIS data and that other evidence to confirm or deny transport predictions should be sought. Quite often, as is the present case, net transport rates are the difference between large upcoast and large downcoast transport rates.

Small errors in estimating either the upcoast or downcoast rate can result in a large error in the net rate.

GREAT EGG HARBOR INLET PROCESSES

Great Egg Harbor Inlet has a significant effect on Ocean City's beaches, particularly those beaches adjacent to the inlet at the north end. However, even the beaches exposed to the ocean in the vicinity of the inlet are influenced by the effect of the inlet's ebb tidal shoal on incident waves. The prevailing southerly longshore sediment transport in the area causes the ebb tidal shoal to elongate so that it frequently extends southward from the inlet in the form of a shore-parallel offshore bar. This bar affords some protection from high waves to these beaches and thus influences the magnitude and direction of longshore transport near the inlet. In addition, Great Egg Harbor Inlet serves as a sediment trap for sand carried into it from both Longport's beaches to the north and Ocean City's beaches to the south. Historically, before construction of the stabilizing terminal groin/jetty on the Longport side of the inlet, the inlet was migrating northward. See Figure 6. Following construction of the jetty, the inlet's location stabilized but Ocean City's inlet shoreline has since been subjected to alternating periods of accretion and erosion as the channel thalweg moves back and forth in response to the influx and trapping of sand.

An analysis was made of the sedimentation patterns and of the volume of sediment trapped within the inlet. Extensive hydrographic surveys of the inlet had been made by the U.S. Army Corps of Engineers in 1965 and 1984. These two surveys coincided with the time period for which a sediment budget of the area was developed. Contours of the differences in depth between the two surveys were constructed as shown in Figure 7. The resulting contours show areas within the inlet where accretion occurred (solid lines) and areas where scour occurred (dashed lines). The figure demonstrates the southward movement of the channel thalweg since the accretion contours on the northeasterly side show filling of the old channel thalweg and the scour contours on the southwesterly side show the scouring of a new channel thalweg. The southward migration of the thalweg is also shown in Figure 8 which is a profile through the inlet's throat.

In addition to the southward migration of the inlet channel, there was an net increase of the volume of sand within the inlet. Between 1965 and 1984 the inlet accumulated approximately 3.6 million cubic meters (4.7 million cubic yards) of sand, presumably stripped from the Longport beaches to the north and Ocean City beaches to the south. This corresponds to an annual rate of trapping of 179,000 cu m/yr (234,000 cu yd/yr).

SEDIMENT BUDGET

A sediment budget for Ocean City's beaches was developed for the 19 year, 9 month period between 1964 and 1983. These

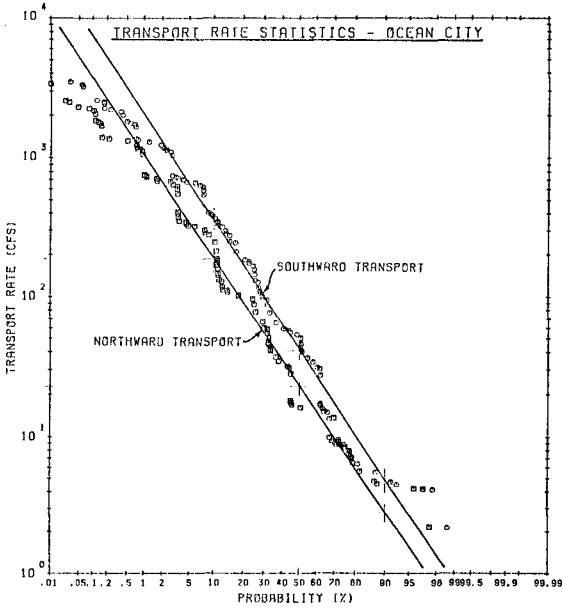


Figure 5 Log-Normal Probability Distributions for Positive and Negative Potential Longshore Sand Transport Rates at Station 62, Peck Beach (Computed from WIS Hindcast Data)

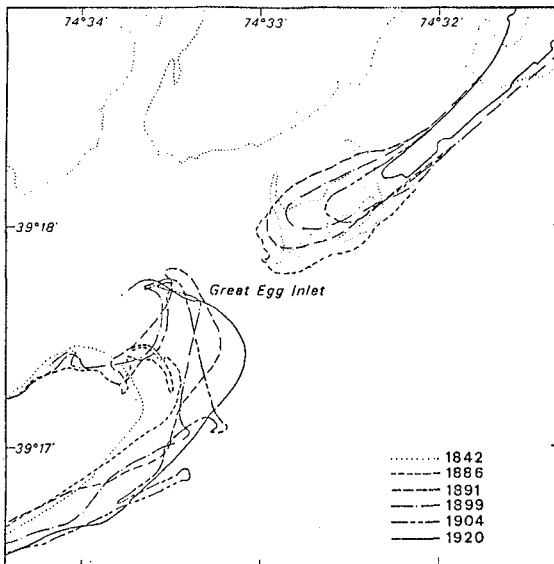


Figure 6 Historical Locations of Great Egg Harbor Inlet Showing Northward Migration Prior to Construction of Terminal Groin at Longport

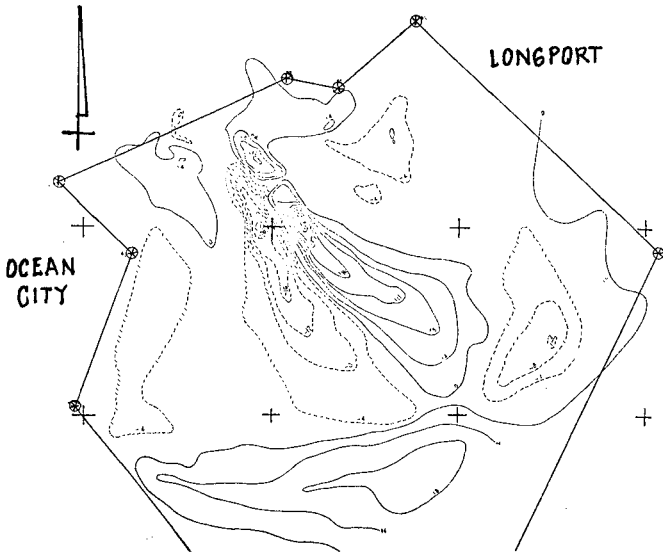


Figure 7 Bathymetric Changes Occurring within Great Egg Harbor Inlet Between 1965 and 1984

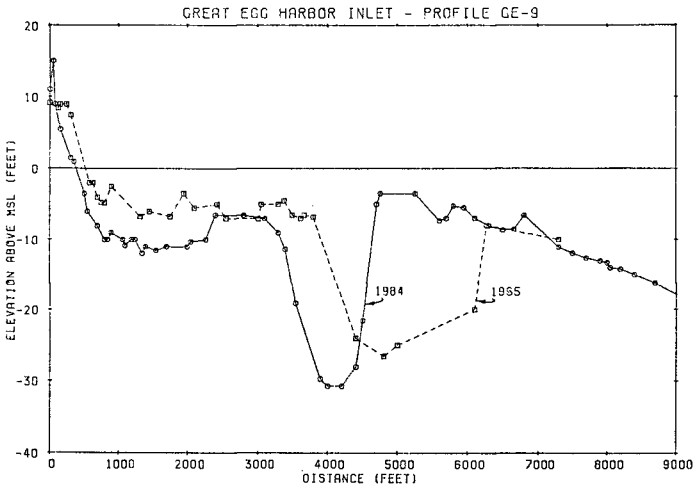


Figure 8 Profiles Through Throat of Great Egg Harbor Inlet Showing Southward Migration of Channel Thalweg

dates were dictated by the times for which both inlet bathymetric data and beach profile data were available. The area was divided into three cells and the transport of sediment into and out of each cell was balanced against the change in sediment volume within the cell. The three cells were: Ocean City's beaches from the inlet south to about 40th Street, Great Egg Harbor Inlet, and Longport's beaches on the southern end of Absecon Island just north of the inlet. See Figure 9. Sand volume changes on both Longport's beaches and Ocean City's beaches were determined from beach profile surveys obtained by the Philadelphia District of the Corps of Engineers. Sand volume changes in the inlet were obtained from two bathymetric surveys obtained in 1964 and 1983 by the Corps. Offshore losses were assumed to be caused by the long term increase in relative sea level as measured at Atlantic City. This rate is about 0.01 foot/year and is believed to be one-half due to sea level rise and one-half to local subsidence. Offshore losses were determined using the Bruun rule (Bruun, 1962) with the closure depth determined by the semi-logarithmic profile methodology outlined in Weggel (1979). The closure depth was estimated at about 7.9 to 8.5 meters (26 to 28 feet) below mean low water and erosion rates were estimated at between 7.0 and 9.3 cu m/m/yr (75 to 100 cu ft/ft/yr) yielding a shoreline recession rate of about 0.96 m/yr (2.5 ft/yr).

The results of a simplified sediment budget are shown in Figure 9. The three cells are shown schematically along with the contributions to and losses from each cell. Units on the figure are in thousands of cubic meters per year. The 7,000 m (23,000 ft) long Longport cell lost 47,400 cu m/yr (62,000 cu yd/yr) offshore, gained an unknown amount of sand from Atlantic City's beaches to the north and lost an unknown amount of sand to Great Egg Harbor Inlet to the south. The annual rate of increase in sand volume on Longport's beaches was 40,500 cu m/yr (53,000 cu yd/yr). The inlet lost an estimated 17,600 cu m/yr (23,000 cu yd/yr) offshore and gained unknown amounts of sand from Longport's and Ocean City's beaches. The net accumulation of sand in the inlet was at a rate of 178,900 cu m/yr (234,000 cu yd/yr). The Ocean City cell lost an unknown amount of sand to the inlet, 79,500 cu m/yr (104,000 cu yd/yr) offshore and 55,800 cu m/yr (73,000 cu yd/yr) to the beaches at the south end and the spit at Corsons Inlet. Ocean City gained 141,100 cu m/yr (195,000 cu yd/yr) through beach nourishment; however, there remained a net loss of 100,900 cu m/yr (132,000 cu yd/yr) from the beaches. Solving the three simultaneous equations that result, yields values for the three unknown transport rates: the transport into the Longport cell from Atlantic City is 169,700 cu m/yr (222,000 cu yd/yr), transport into the inlet from Longport is 81,800 cu m/yr (107,000 cu yd/yr), and transport into the inlet from Ocean City is 114,700 cu m/yr (150,000 cu yd/yr). Obviously, these results are sensitive to the quality of the data used to determine them. The longshore transport rates are most suspect; in fact, longshore transport into the Longport cell from Atlantic City should be known from the WIS wave hindcast longshore sand transport analysis. However, because the magnitude and direction of this longshore rate

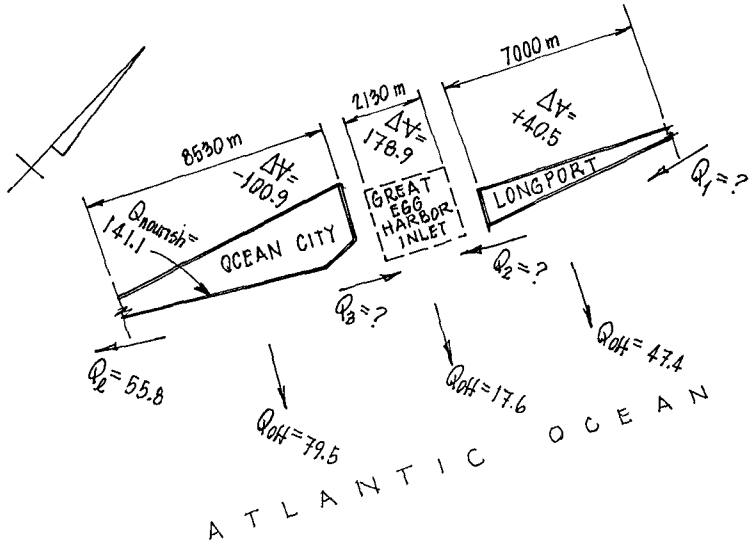


Figure 9 Schematic of Sediment Budget Analysis Showing Longport Cell, Great Egg Harbor Inlet Cell, and Ocean City Cell

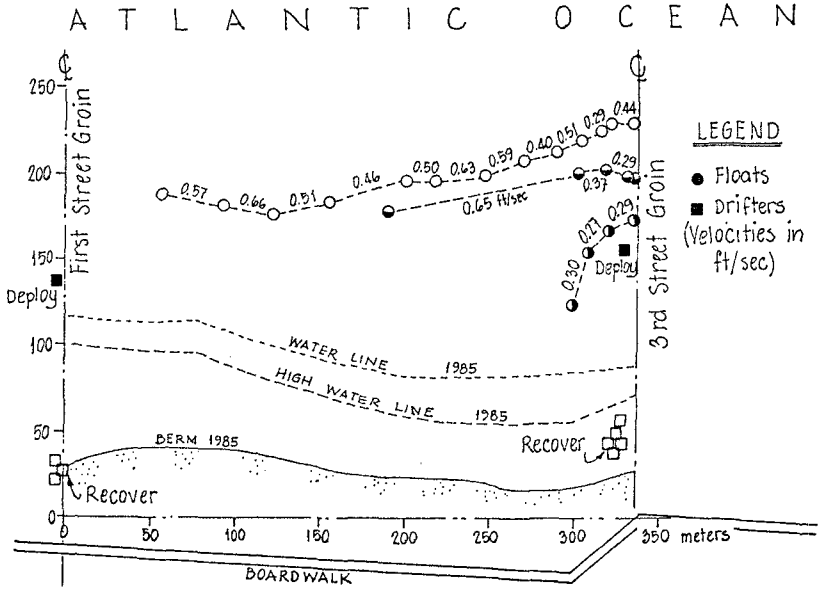


Figure 10 Current Patterns in Compartment Between Groins at First and Third Streets, Ocean City, New Jersey, 2 November 1986

is questionable, it was taken to be an unknown in the analysis. Actually, the rate of sand loss to the beaches south of Ocean City might also differ from the 55,800 cu m/yr (73,000 cu yd/yr) assumed here. Larger losses to downdrift beaches would result in larger transport rates into the Longport cell at the northern end of the analysis; smaller losses would result in smaller transport rates into the Longport cell.

CIRCULATION STUDY IN GROIN COMPARTMENT BETWEEN FIRST AND THIRD STREETS

The groin compartments along the northerly beaches of Ocean City are believed to induce circulation cells that exacerbate the loss of beach fill during storms. Even during high storm water levels, the high rubble mound groins block longshore transport and divert sand offshore in rip currents that form adjacent to the groins. A field study was undertaken offshore of the beach compartment formed by the groins at First and Third Streets to evaluate the circulation patterns that might arise within the groin compartments. Surface currents were measured by tracking plywood surface floats equipped with a small flag. (In subsequent tests, plastic milk bottles partially filled with sand and water were used instead of plywood floats. These proved easier to deploy and always floated with the flag upward since the body of the bottle was submerged.) The floats were released from the groins and followed using two surveyor's transits set up a known distance apart along a shore-parallel baseline. Simultaneous recording of the angle between the float's location and the baseline by the two transits along with the time of the observation allowed the pathlines of the floats to be plotted and their average velocity between observations calculated.

The results of a field test conducted on 2 November 1986 are shown in Figure 10. During that test, transport was northward with current velocities averaging about 0.15 m/sec (0.5 ft/sec). The wave period was about 8.5 sec and breaker heights averaged about 0.55 m (1.8 feet). Longshore current speeds, measured by throwing dye into the surf, were about 0.2 m/sec (0.66 ft/sec). Figure 10 shows no evidence of rip current development along the First Street groin; however, initial observations made with floats released from the First Street groin showed offshore movement. Unfortunately, the floats often became trapped within the rocks of the groin. The floats also capsized and could not be seen with the transits.

FINDINGS AND RECOMMENDATIONS

Ocean City's beaches have been relatively stable, at least over the period of observation covered by this study. In 1984 the beaches were in essentially the same location as they were in 1953. This is believed in part to be due to the high, impermeable, rubble-mound groins constructed to stabilize the northerly beaches, and in part to the occasional renourishment of the beaches. Over the 32 year period between 1952 and 1984, more than 6.4 million cu m

(8.4 million cu yd) of sand were placed on the beaches. Some of these beach nourishment projects were relatively successful, e.g. the 1952 fill, while others, such as the 1982 fill, were very short-lived. Between 50% and 90% of the beach fill placed late in 1982 was lost before the following summer (Farrell & Inglin, 1988). The existing beaches are not wide enough to accommodate the many beach users during the summer months. Also, in the commercially developed areas along Ocean City's narrow northerly beaches, the beach affords little protection to the area behind it. The problem is to widen the beach and to stabilize it in a new, equilibrium position that is farther seaward than the present equilibrium position.

The long, high, impermeable groins contribute a level of stability to the beaches by sheltering a length of the shoreline from northeast storms; however, they probably also contribute to the rapid loss of sand during storms by inducing the formation of rip currents. Following the placement of a beach fill, groin compartments are full of sand and the more-seaward, less-protected shoreline is exposed and vulnerable to wave attack during storms. During storm periods with high water levels and swift longshore currents, the longshore currents are deflected seaward as rip currents form along the groins. The rip currents quickly transport beach fill sand offshore. After the shoreline has eroded back to approximately its pre-fill location, it is again sheltered by the groins and a dynamic, near-equilibrium condition is again established.

Lowering and lengthening the existing groins was recommended to increase the residence time of future beach fills. Lower groins would allow sand to spill over them during high storm water levels rather than have the sand diverted seaward by rip currents. While the sand might not remain in the groin compartment in which it was placed, it would at least remain on the beach rather than be diverted offshore. The modified groin profiles would approximate the natural beach profile from about the +2.4 m (+8 foot) berm elevation out to the mean high water line; from here, the groin crest would extend seaward horizontally. See Figure 11. Stone removed by lowering the groins will be used to lengthen and extend them seaward. Also, several existing groin spurs (rock extensions to the groins that extend perpendicular to the groin axis) would be lowered or removed and the stone used to lengthen the groins.

Approximately 1.1 million cu m (1.4 million cu yd) of beach fill is required to provide at least a 30.5 m (100 ft) wide berm having an elevation of +3.0 m (+10 ft) between the northern end of the barrier island and about 20th Street. The Corps of Engineers has recommended a more extensive beach fill extending from the inlet southward to 59th Street. The fill proposed by the Corps will require about 3.8 million cu m (5 million cu yd) of sand. Construction of the groin modifications is scheduled to begin in late 1988 or early 1989 and the Corps of Engineers beach fill project is scheduled for 1990.

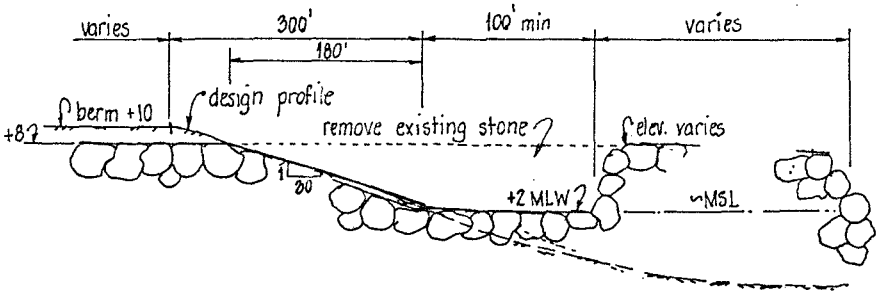


Figure 11 Proposed Modified Groin Profile

ACKNOWLEDGEMENTS

The authors wish to acknowledge the contributions to this paper made by Monica Ippolito, Michael Strzelecki, Craig Young, Sherrerd Steel, Steve Kemp, David Weggel, Ted Wilson, Juan Carlos Escajadillo, and Dave Givler, all of whom, at one time or another were involved in data collection and/or analysis. In addition, John Carey, Joseph Kane, John Gideonse, Jack Schreiner, Jr. of Ocean City; Bernard Moore and John Garofolo of the Bureau of Coastal Engineering, and Jeff Gebert of the Philadelphia District of the Corps of Engineers were all helpful in providing information used in the course of this study.

LITERATURE CITED

BRUUN, P. (1962) "Sea Level Rise as a Cause of Shore Erosion," Journal of the Waterways and Harbors Division, ASCE, Vol. 88, No. 1, pp 117-130

FARRELL, S.C. & D.C. INGLIN (1988) "A Summary of Beach Survey Data from the 1982-83 Ocean City, NJ Beach Fill Administered by the NJ Department of Environmental Protection," prepared for the NJ Division of Coastal Resources, Coastal Research Center, Stockton State College, Pomona, NJ, September 1988.

JENSEN, R.E. (1983) "Atlantic Coast Hindcast, Shallow Water, Significant Wave Information," WIS Report 9, U.S. Army Waterways Experiment Station, Vicksburg, MS 39180.

WATTS, G.M. (1956) "Behavior of Beach Fill at Ocean City, New Jersey," U.S. Army Corps of Engineers, Beach Erosion Board, Technical Memorandum 77, February 1956.

WEGGEL, J.R. (1979) "A Method for Estimating Long Term Erosion Rates from a Long Term Rise in Water Level," CETA 79-2, U.S. Army Coastal Engineering Research Center, Fort Belvoir, VA 1979.

WEGGEL, J.R. & M. PERLIN (1988) "Statistical Description of Longshore Transport Environment," Journal of Waterway, Port, Coastal and Ocean Engineering, ASCE, Vol. 114, No. 2, March 1988.

WEGGEL, J.R., S.L. DOUGLASS & J. TUNNELL (1988) "Sand Bypassing Simulation Using Synthetic Longshore Transport Data," Journal of Waterway, Port, Coastal & Ocean Engineering, ASCE, Vol. 114, No. 2, March 1988.

CHAPTER 214

SHORE PROTECTION OF KAOHSIUNG HARBOR OUTER BREAKWATER

Kuo, Shih-Duenn *

ABSTRACT

As shown in Fig.1 the main fairway of Port of Kaohsiung is running from north to south with a length of 12 kilometers. To the west, there is a sand bar served as a natural breakwater, the so called outer Breakwater, to provide the port and resident's property the necessary safety and security. Recently, due to rapid growth of container traffic and bulk cargo transportation, Port of Kaohsiung has developed some parts of the outer breakwater near the 2nd Harbor Entrance as Container Terminal No.4 with seven 14-meter-deep, 320-meter-long container berths and about 100 hectares container yard on northern side, and coal Terminal with 16-meter-deep, 320-meter-long berth and a huge storage yard on southern side. Therefore, the shore protection along the area become more and more important year by year. So far, some 6-kilometer seawall and 20 groynes have built successively, and already played a very important role for the shore protection there.

INTRODUCTION

Port of Kaohsiung is the largest port in Taiwan, R.O.C. and handles more than two-thirds of the Island's total imports and exports, over 100 million tons of cargo annually. It is expected to become one of the top international seaports in the world in terms of freight handled and physical size resulting from the huge expansion projects which have completed, now under construction or in planning stage.

Starting from 1967, Port of Kaohsiung come to a new era due to the construction of 2nd Harbor Entrance to navigate ships under 100,000 D.W.T. and to bring city of Kaohsiung to a international industrial metropolis. Since then, the outer breakwater between 1st Harbor Entrance and 2nd Harbor Entrance has been isolated. It not only influenced the development of the bar area, but also affected the stability of the shore line. Anyway, no protection is done until a blue-print for developing that area was made in 1970's by the Harbor Bureau to meet the overall expansion project of the whole harbor area. Further, following the completion of Cross Harbor Tunnel in 1984 to pave the way for the transportation between city of Kaohsiung and the island, the pace of development of the bar area, including construction of Container Terminal No.4 and seawall or groynes, is accelerated. So far, all projects go on well and in good performance, As a result, its container

* Senior Civil Engineer & Section Chief of Engineering Affairs of
Engineering Dept, Kaohsiung Harbor Bureau, Taiwan, R. O. C.

throughput of about 2.8 million TEUs in 1987 has put Port of Kaohsiung in third place in the world. This tremendous achievement is, no doubt, attributed to the perfect shore protection of the outer breakwater.

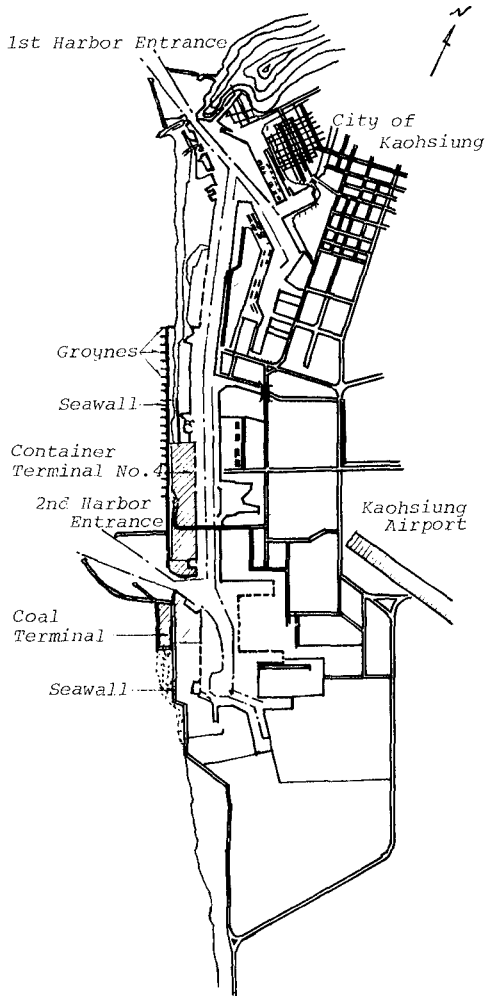


Fig. 1 Port of Kaohsiung

NATURAL CONDITIONS

(1) Sea bed condition:

The sea bed condition off the sand bar is very flat and homogeneous. Most of the 12 kilometers coastal area is distributed with fine sand of $D_m=0.15m/m$, and in a slope ranging from 1:30 to 1:100, as shown in Fig.2

except section F5 which located near 2nd Harbor Entrance has D_m value of about 0.30-0.35m/m at depth of 15m-20m, (see Fig.3).

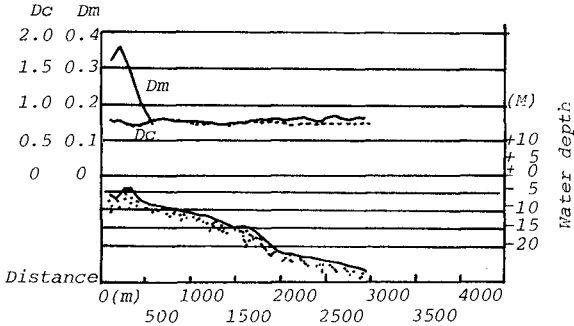


Fig. 2 Typical section of sand size VS sea bed gradient

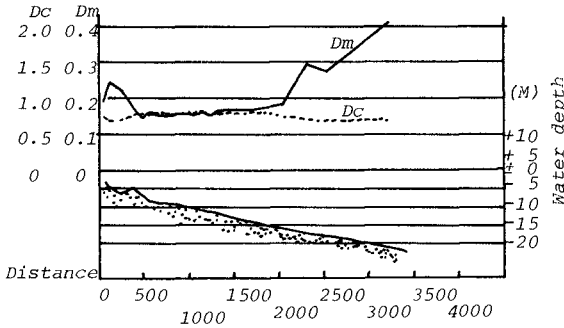


Fig.3 F5 section

(2) Wind condition:

Due to different paths of typhoon and different seasons of monsoon, the transport of sediment along the sea shore will be changed for different periods.

- a) Every year, typhoon (cyclone) from May through October occasionally packs wind of 11-65 m/sec to hit the area and to cause a lot of sediment transport along the coastal area. Among the paths which are probable to pass the area, path D is the main one to influence the coast area as shown in Fig.4 due to its big wave height & high wind velocity. Fig.5 shows the actual example of typhoon path D and its corresponding wave height and wind velocity.
- b) Winter monsoon, appearing mostly in NNE, N, NNW directions with wind speed of about 0.3-10 m/sec, is longer in duration, but less in unit sediment transport, as shown in Fig.6.
- c) Summer monsoon, prevailing in SE, SSE, S directions with 5.5-13.8 m/sec wind speed, performed in a different way as winter monsoon does (see the same figure as b.)

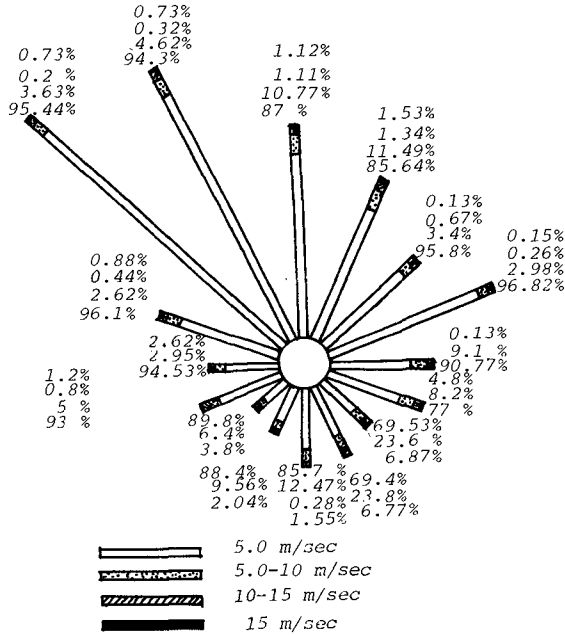


Fig. 6. Typical wind rose for Kaohsiung Harbor outer breakwater area

(3) Wave condition:

The wave condition in the area will depend largely on the magnitude and duration of typhoon and monsoon. A statistical wave data is shown in Table. 1. The max. wave height is some thing like 5-6 meters in 12 years from 1966-1977, while the corresponding max. significant wave height is about 4 meter.

Year	1966	1967	1968	1969	1970	1971	1972	1973	1974	1975	1976	1977	
Wave direction (S.W.)	63	56	53	50	48	49	47	49	50	52	55	57	
Max. wave	Wave height (M)	7.00	3.13	6.96	5.30	4.20	4.60	4.31	9.09	6.00	8.50	5.10	6.80
	Mean (M)	2.54	1.52	2.90	2.64	2.64	3.05	2.95	3.63	3.11	2.70	1.60	2.90
	Period (sec)	7.4	8.1	11.0	9.5	7.7	9.4	10.2	8.1	9.0	8.6	8.11	11.0
Sig. wave	Wave height (M)	5.24	1.67	4.95	3.70	2.04	3.85	2.96	6.29	4.01	6.40	3.10	4.10
	Mean (M)	1.71	0.99	1.75	3.09	1.51	1.98	2.95	2.78	3.90	2.98	1.90	1.71
	Period (sec)	7.7	8.5	9.3	10.8	7.8	5.7	10.5	8.8	10.1	8.3	8.4	10.0

Table. 1. Max. wave height and significant W. H.

(4) Others:

Such as tide, current etc. will also play an important factor to the shore protection. Tide in the area is about 0.7 meter in range as shown in Table. 2 and current is about 0.25 m/sec or 0.5 knots (nautical mile). But it will be changed depending on the wave height.

YEAR TIDE	1966	1967	1968	1969	1970	1971	1972	1973	1974	1975	1976	1977	M.V.
H.H.W.L.	1.60	1.55	1.75	2.60	1.53	1.60	1.63	1.62	1.60	1.51	1.56	1.56	1.60
L.L.W.L.	2.02	0.04	0.03	0.02	0.06	0.05	0.16	0.10	0.15	0.10	0.13	0.02	0.03
M.H.W.L.	1.09	1.14	1.10	1.11	1.16	1.11	1.12	1.13	1.14	1.15	1.14	1.16	1.15
M.L.W.L.	0.37	0.42	0.39	0.41	0.42	0.41	0.42	0.42	0.44	0.46	0.49	0.53	0.49
M.S.L.	0.69	0.74	0.71	0.71	0.76	0.73	0.75	0.74	0.76	0.77	0.78	0.78	0.76
H.W.O.S.T.	1.20	1.25	1.19	1.21	1.24	1.20	1.22	1.22	1.21	1.24	1.24	1.25	1.24
L.W.O.S.T.	0.32	0.40	0.32	0.35	0.37	0.36	0.38	0.37	0.39	0.41	0.47	0.49	0.43
H.W.O.N.T.	0.94	0.99	0.99	0.98	1.05	1.02	1.02	1.04	1.05	1.05	1.03	1.00	1.01
L.W.O.N.T.	0.42	0.44	0.44	0.44	0.47	0.47	0.48	0.48	0.49	0.51	0.54	0.56	0.51
Sprang Tide Range	0.89	0.85	0.88	0.86	0.87	0.84	0.84	0.85	0.82	0.81	0.75	0.78	0.81
Neap Tide Range	0.54	0.55	0.55	0.55	0.58	0.55	0.54	0.56	0.55	0.52	0.51	0.46	0.50
Mean Tide Range	0.72	0.71	0.70	0.70	0.73	0.70	0.70	0.71	0.70	0.69	0.67	0.63	0.66

Table. 2. Tide levels surveyed from 1966-1977

SEDIMENT TRANSPORT AND SHORE CHANGE

Through long term observation, the change of shore profile near 2nd Harbor Entrance is quite similar with the results of model test which carried out during construction of the 2nd Harbor Entrance.

- (1) Transport of sediment before construction of 2nd Harbor Entrance

- a) In winter season, sediment transport, from north to south, was governed by winter monsoon NNW, N, NNE. etc. and shore line appeared in an accretion condition along the whole area. While in summer, typhoon and summer monsoon SE, S, SSE etc. dominated the process of sediment transport, and shore line was eroded by the north-bound wave force (current). But finally the processes of accretion and erosion would come to balance, and return to it original state unless in abnormal condition such as being hit by super typhoon, and if so, the shore line would be scoured until next cycle. The contour line of water depth in the coastal area before 2nd Harbor Entrance being constructed is shown in Fig. 7.

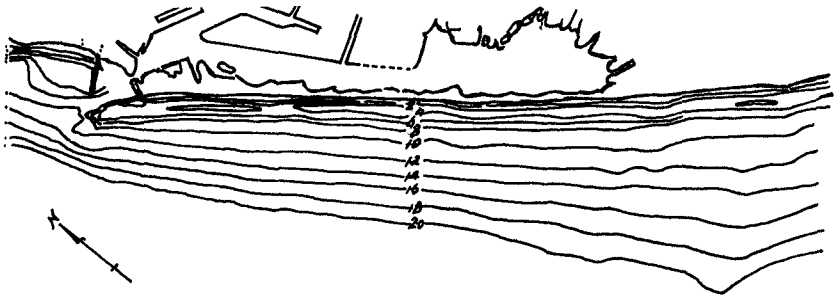


Fig. 7. Shore contours before construction of 2nd Harbor Entrance

- b) Due to the southern breakwater of 1st Harbor Entrance being constructed almost to parallel the shore line, the channel near the Entrance will be silted in summer time, and will be scoured in winter season, as shown in Fig. 8 and Fig. 9.

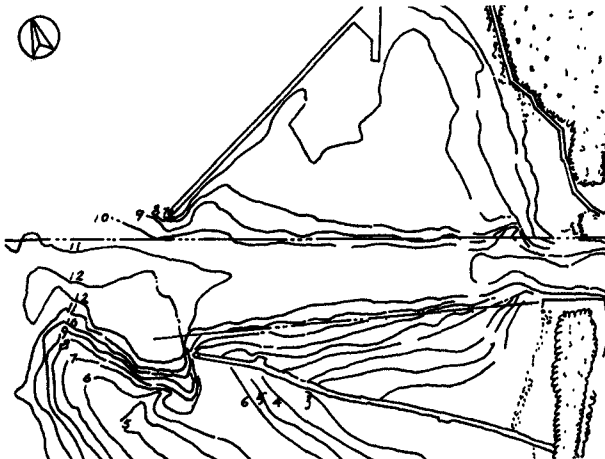


Fig. 8. Depth data of 1st Harbor Entrance surveyed in Sep-Dec. 1969



Fig. 9. Depth data of 1st Harbor Entrance surveyed in April-July 1970

(2) Transport of sediment after construction of 2nd Harbor Entrance:

Due to the prevention of the breakwater of 2nd Harbor Entrance, the change of shore line on both sides of the entrance has different result under the same conditions as described above, that is:

- a) In winter season, the northern shore of the entrance is a creative beach, while the southern shore is an erosive one, and vice versa in summer time. The contour line of water depth in the coastal area after 2nd Harbor Entrance being constructed is shown in Fig. 10.

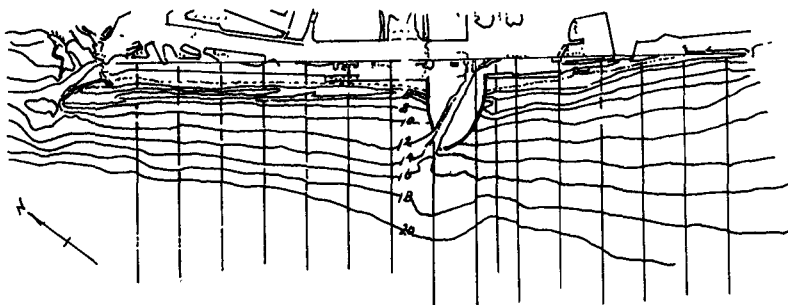


Fig. 10. Shore contours after construction of 2nd Harbor Entrance

- b) Due to the source of littoral drift being cut by the breakwater of 2nd Harbor Entrance, the shore line between 1st Entrance and 2nd Entrance may draw a sharp change toward the land area during typhoon season.
- c) Although, the channel of 1st Harbor Entrance is unable to totally free from silting or scouring, but it already has a great improvement to compare with the condition of which before construction of 2nd Harbor Entrance. It said from 50,000 m³/year decreasing to less than 10,000 m³/year.

PROTECTIVE METHOD

In addition to providing the port and residents the protective function, the outer breakwater of Kaohsiung Harbor is also to be considered as an integral part of port facility. Therefore, the protective facilities are designed as permanent structure as following.

(1) Parallel seawall:

Parallel seawall was built on the land area about 30 meters far from the shore line to parallel to the quay wall of container berth as a result of making up the required space of about 450m * 320m of back-up area in each berth to cope with the development of Container Terminal No.4 in northern side of the 2nd Harbor Entrance as shown in Fig. 1. In the south, the seawall was located about 300-meter off the shore line to constitute a big coal storage yard for the Coal Terminal, also shown in Fig. 1. So far, totally, some 6 kilometers of this seawall has been built to form the main structure for shore protection of the outer breakwater of Kaohsiung Harbor. For the seawall, besides the concrete parapet and wall itself, it also includes a earth dike planting with tropic trees to serve as a wind shield for the port area, and some side ditches to collect rainfall and overtopping salt water, if any, as shown in Fig. 11.

(2) Perpendicular groynes:

Perpendicular groynes, being constructed on every other 200 to 300 meter interval with each a length of about 90 meters, are perpendicular to the parallel seawall with a view to stabilizing the shore line and keeping the approach channel of the entrance from silting. In order to meet the attack of 6-meter height wave force, the groynes are designed as rubble mound type structure with 2 tons of modified Tetrapod for the armored layer as the conventional breakwater does, as shown in Fig. 12. From an engineer point of view, it sounds to cost too much, but for the point view of safety and security, it's worth-while to do so and perhaps it's the best choice for the long-range-project consideration.

(3) Artificial beach nourishment

In addition to the protective facilities mentioned above, the erosive beach between 1st and 2nd Entrances has been nourished with good material occasionally to prevent the shore from further scouring. From 1968 to 1982, the total spoil disposed to the area was about 34 million m³, But no headland is formed due to typhoon reason.

RESULT

Referring to the purpose as many other protective works do, the design of shore protective facility should take both direct function and indirect function into account, the former is aimed at protecting the shore and facility itself from eroding and damaging under the normal

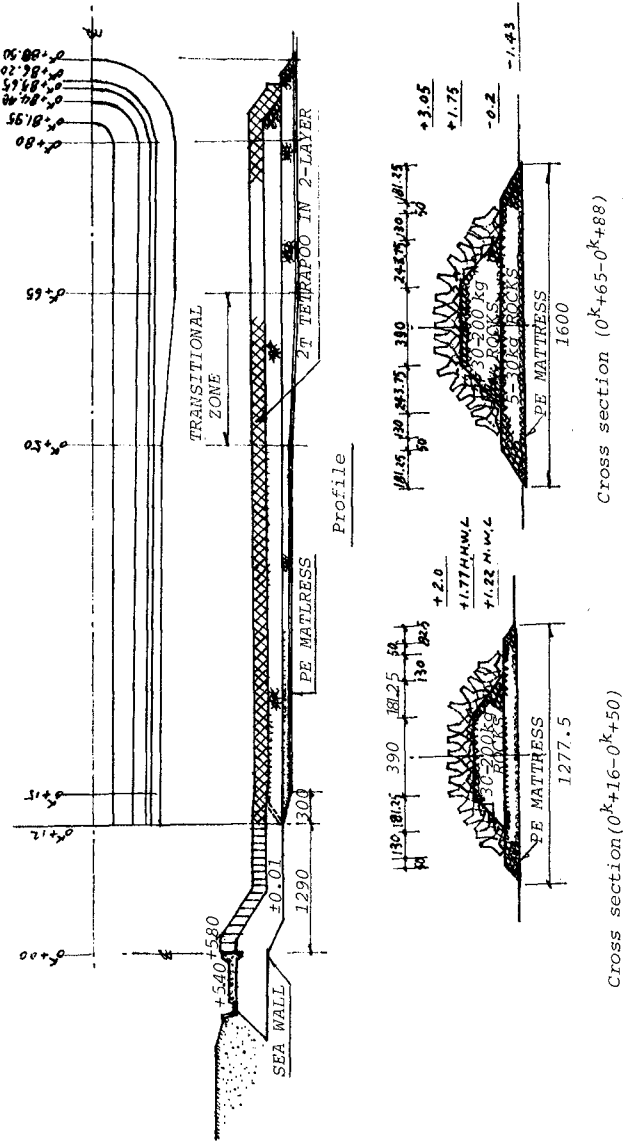


Fig. 12. Typical cross section & profile of groyne

condition. While the latter is emphasized on the function of durability from which the structure can still provide a retard action to decrease the loss to a minimum, should the facility once has been damaged in extraordinary conditions.

Basically, the protective facilities in Kaohsiung Harbor have followed the above-said guiding principle in design and construction. Therefore the shore protection of the outer breakwater has performed well up to now since its completion for about 13 years during which a number of big typhoons have experienced. Fig. 13. shows the field results of seawall & groynes and beach erosive conditions after being attacked by a great of big typhoons. Though, the seawall and groynes keep no damage at all, while the beach in between the groynes presents some different extend erosion due to different width(w) between the groynes and different length(L) of the groynes. Normally, for normal wave $w=4L$ is the best solution and for inclined wave, 35° - 50° against shore line, the best solution will be $w=3L$.



Fig. 13. Field results of shore protection of Kaohsiung Harbor outer breakwater

CONCLUSION

(1) For the protective structure, the rubblemound groyne (jetty) may be the most effective and reliable means in using against big wave force, should the layout and design method be right in principle. The case in Kaohsiung is a good example as the groyne built there have brought function into fully play up to now.

(2) The width between every two groynes is a main factor to beach control, it also means best result comes to perfect layout, from the field results got in Kaohsiung Harbor outer breakwater, we found that the width between every two groynes designing as 3 times and 4 times of the groyne length (length from shore line to head) for inclined wave (angle from 35° - 50° against shore line) and normal wave respectively, will be the solution for shore protection.

(3) Taking eroded beach into account, artificial beach nourishment is a very important approach to the shore protection. For instance, the northern shore of the 2nd entrance of Kaohsiung Harbor is something like an erosive beach for long term consideration, due to the source of sediment transport being cut by the breakwater. But, through artificial beach nourishment management, occasionally by disposing the good material of sand from channel dredging, the shore, however, has maintained in a stable condition year by year. It means that to the erosive shore line the best salution is to do beach nourishment and protective work simultaneously, if possible.

(4) Due to the breakwater of the 1st Entrance of Kaohsiung Harbor being laid in a way, almost, to parallel to the shore line, the channel near the Entrance was, frequently, to be silted by sand drift from the shore area between 1st and 2nd Entrance before shore protection in the area was done. While conditions have been improved since the completion of parallel seawall and perpendicular groynes. It means that shore protective management can play a multifunction role depending on what the case needs. The successful method in Kaohsiung Harbor, no doubt, has set a good example in this field.

(5) No headland or other simple methods can be used for shore protection like Kaohsiung Harbor outer Breakwater since it will resist the big wave up to 6-meter height and it left no tracks after disposing about 34 million M^3 spoil in the area in last 14 years from 1968-1982.

REFERENCES

- (1) Report on study of construction planning of Kaohsiung 2nd Harbor Entrance (1968), Kaohsiung 2nd Harbor Entrance Construction Department, Kaohsiung Harbor Bureau.
- (2) Gong. C. I. et all (1976), Report on Improvement study of Kaohsiung 1st Harbor Entrance.

*Listing of key words to index the paper entitled SHORE PROTECTION OF
OF KAOHSIUNG HARBOR OUTER BREAKWATER is:*

Kuo, Shih-Duenn,

CHAPTER 215

RIA DE FOZ: SOLUTION FOR A HARBOUR AND COASTAL PROBLEM

Jose Javier Díez González*
Victor A. Escobar Paredes
José Aguilar Herrando

SITUATION.-

The ría of Foz is located in the Northwestern part of the Ibérica - Península, inside the Rías Altas group, in the Eastern extrem of Lugo/ province. It is placed on the natural form known as Golfo of Masma, - topographical accident that takes its name from the river that flows - into the ría.

From the point of view of the materials that constitute the environ- ment, they are mainly composed by slaters and quarzites, with some le- vels of carbonates from the Low Paleozoical period. To the West, the - granitic materials are predominant.

The ría is limited in its margens by some little slope and relative- ly low cliffs. Its bounds have a little depth, due to the filling pro- cess, natural in the Rías Altas. The materials that refill the ría, - come from the sea erosion of the cliffs (1), and the refilling is due/ to the sea waves action that produces in the tidal flow and ebb an - - asymmetrical capacity of erosion and transport (2). That is a natural - situation, but the human action, building some channeling constructions has accelerated this refilling process.

The traditional economic development on this zone, has been based - on some principal activities: fishing and agriculture, but nowadays - turistic use rounds off the others. This situation and the evolution - of sailing necessities on the ría, has been a conflict reason, which - is a consequence of the competition between these uses.

In these terms, the first problem to the possible feasibility of - Foz harbour was its accesibility, and that depended on the stability - of the main tidal channel. Therefore, the harbour authorities developed a planning design to fix the position of the entry channel, by the - - construction of a couple of jetties; however only one of them was built up to the date. In a certain phase of the construction, when the inlet gorge was affected, the sandy barrier was destroyed. Since then, seve- ral erosion problems have affected to the neighbour littoral and bea- - ches. And the aim of this study is to regenerate the coast without - - decreasing the harbour availability. We might not forget that the natu- - ral tendence of the ría is to refill itself; and that means a hight - variability of channel, trying to adapt themselves to the new condi - - tions and distribution of materials that refill the ría.

The light was built because of the risks derived of the existence -
*Universidad Politecnica de Madrid, Ciudad Universitaria, Madrid 3, SPAIN

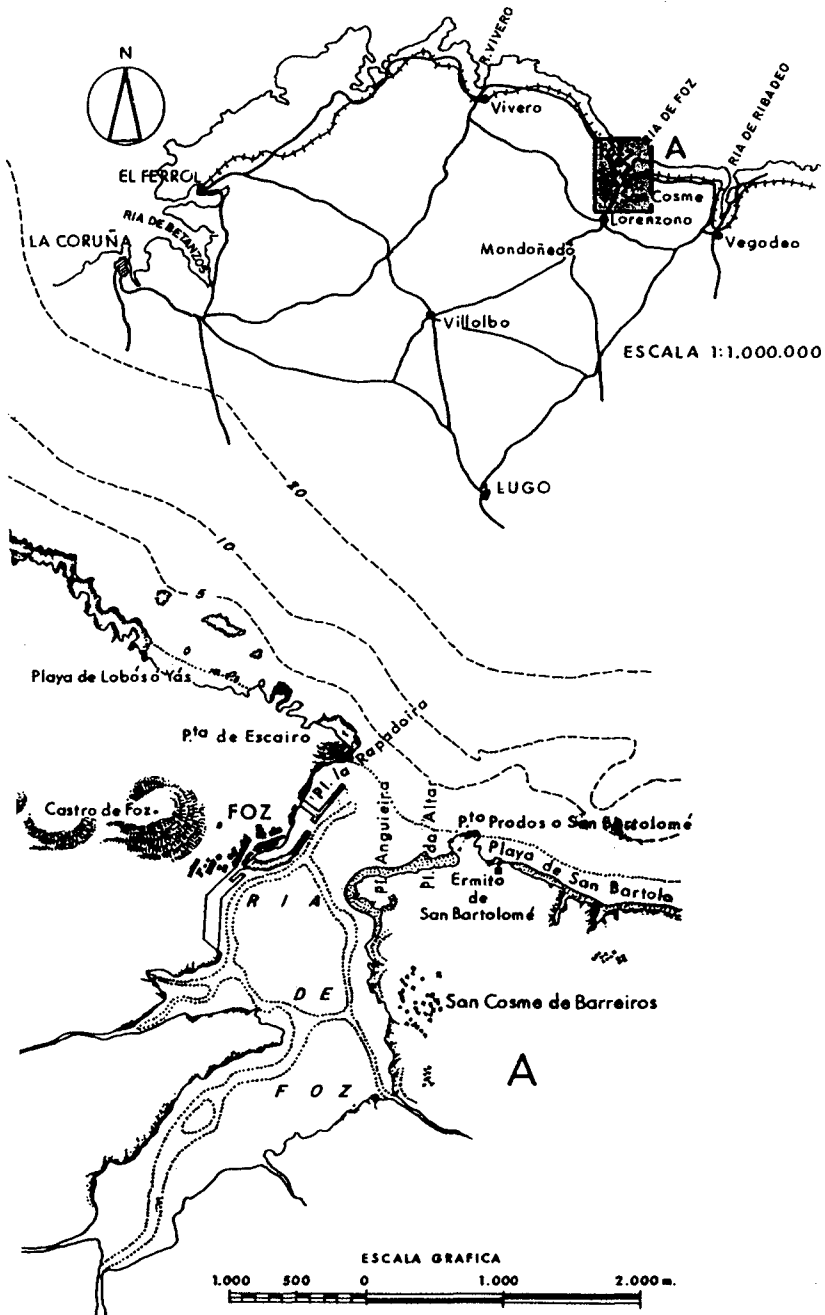


FIG. 1 Situation

of a dangerous rocky system (shoals and rocks of the Rapadoira). This/light caused degeneration of a little beach on the left hand of the - mouth and stabilized in a certain way the barrier on the inlet. Nevertheless, in this brief note, we have explained the situation we - have to face up, which is derived from the general development of the/ fishing activity that requests every day bigger depths and safety.

So the objective was to define the necessary works to protect the - coast considering the natural conditions of littoral dynamics, in such a way that the conditions of the harbour entrance and exploitation do - not suffer additional problems.

ELEMENTS OF LITTORAL DYNAMICS.-

Relating to the processes that affect to the mouth, the determinant elements are tides and sea waves, and, in a minor order, winds and - - fluvial contribution.

Tides: They introduce some flow and ebb currents that carry the - - solid materials. The net component of this transport is to the basin./ The main high water appears in equinox (but it is little out of phase). The M.H.W. has an amplitude of 4'50 m. approximately₃ The tidal prism - considered in the project is between 1'7 and 7 hm.

Waves: Due to the special morphology and topography of the exterior part of the ría, the littoral currents induced by wind waves have a - quasy permanent sense from E. to W. in Angueira and Altar beaches; on the opposite, out of the ría mouth and along all Masma Gulf, currents/ have a variable direction, related to the wind wave direction, but the dominant currents and littoral transport are there from W. to E..

The special direction of currents and drifts in the beaches is the/ most important reason of the shaping of the lock barrier as a spit, - what may be checked by observing the distribution of materials in the/ tombolos produced by the Peña do Altar.

Winds: They are responsible of the formation of dunes on the lock - barrier before it were demolished. They are also responsible of the - filling of some marginal zones. Winds effect can be considered as a - second order action.

Fluvial waters: Their effect can be compared to the tides only in - extraordinary floods. But they are not so important in normal condi -- tions. In₃ the project it is considered a flow between 10 and 110 m³/s. and 170 m³/s. in extraordinary floods.

MATERIALS.-

From the point of view of the materials, Masma Gulf can be conside- red as a morphodynamic unity, with some located differences, but the - materials are generally very similar.

Several samples have been obtained and analized in their grain size distribution and mineralogy. A group of the samples were obtained from the different sandy formations of the ría, but other group corresponds to different beaches along Masma Gulf. The analysis of sediments shows that the anterior afirmation is all right, and that is proved with a - high certainty between Foz and Ribadeo.

On the other hand, the mineralogical analysis show that in broad - outline, materials in this zone proceed from the erosion of the cliffs principally, and that the sands from the beaches around ría mouth and/ from the ría sandbanks are completely similar.

The similarity of the sediments showing in the analysis of sands - from Angueira and Altar beaches and from the sandbanks in the interior of the ría allows the use of the last for refilling of beaches with - them.

PRELIMINARY CONCLUSIONS.-

Some historic and recent cartographic and topographic documentation has been analyzed and it is possible to propose some reflexions that - can help to puzzle out the present situation of the inlet-outlet system:

-Based on the available documentation before the building of the - channeling jetty, the location of the exterior tidal channel was very/ variable. This situation was foreseen to reappear (2) and is now - - reappearing, but in the extrem of the jetty; therefore the entry pro-- blems have not been definitively solved.

-Though the spit seemed to be stabilized, its morphology was adap-- ting itself to the new hydrodynamic situation, changing its orientation Northwestward and modifying its relative dimensions, its anterior - - cyclic evolution, however seems to have been broken, after the cons -- truction of the light and before the building of the channeling jetty, dunes and vegetables colonization grew up; this situation went down - during the construction of the channeling jetty, but in 1.978 the lock barrier disappeared, just when the interior stretch of the jetty was - constructed.

-The accretion in Rapadoira beach was following on the growing of - the jetty.

-After destruction of the barrier, the erosion on the right hand - beaches began to occur and with some little delay the erosion of the - beaches Eastern towards Ribadeo began too.

-Since then, the inner channel suffers quicker changes in a dialectic relationship with the cyclic regeneration and demolishing of the - lock barrier. The successive growths of the spit has been permitted by/ the erosion of Angueira and Altar beaches and by the mentioned permanent Western littoral drift along them. Finally the successive destruc-- tions of the spit became quicker. These variations depends on the sea-- sonal changes of the conditions of the sea dynamics; it will mean that the variations of the channel are now very quick in this zone.

-The monthly variations of the tidal prism (due to the tide compo-- nents in this area) produce a very high mutability of the channel - - depths and breadths. And the increased filling process of the ría - - after the first demolishing of the spit increases the sailing difficul-- ties.

SOLID TRANSPORT ON THE OUTLET.-

The values of the littoral transport contained in a first numeri-- cal study based on hindcasting methodology are very important, for the net as for the gross transports. However these values correspond to a/

potential transport and do not mean the same importance in the littoral drift, which is limited by the existence of materials. In any case, the littoral drift is important enough to impose a very high variability of the tidal channel, even seasonally, following the motions of the transported solids.

In the exterior mouth of the ría, like in other cases, the natural/mechanism of by-passing of materials is established. In this way, the bars that exist in front of the ría, with their net movements to the SE., catch up their aim of solid transport when they arrive to the sandbanks next to the Punta de St. Bartolomé; in this moment the channel opens again suddenly in the Northwest end. The changes of the position of the outlet are so progressive towards the East up to the sudden openings.

In terms of the transport of solids to the inner basin, it becomes smaller when the effect of the lock barrier is efficient; in this way, before 1.978, when the lock barrier was demolished, the net transport was less than it is possible to observe nowadays.

In the exterior beaches, the transport has a special direction, due to the intrinsic characteristics of this zone. The bay which is open between Escairo and St. Bartolomé headlands, stays widely emerged in low tide; therefore the transport only occurs in mid and high tide there.

If we observe the materials in the shelter formed in the Peña do Altar, and we accept that the disposition of materials should respect the orientation of predominant waves in term of their main annual resultant (recognizing the seasonal variations), we can conclude that the disposition and growth of the lock barrier is logical, in spite of the fact that out of the mouth of the ría the transport has frequently the opposite direction. We should not forget that in the bay of the ría it is necessary to wait for high water to observe solid transport and in this moment the refraction, the diffraction in the Escairo headland and even the reflexion on the St. Bartolomé headland and Altar Rock are important. The tide currents help this current direction too. We have proved that the solid transport is from E. to W. along the bay beaches; so the genesis and orientation of the lock barrier may be perfectly explained as a spit.

CONSTRUCTIONS: EVOLUTION.-

The morphologic changes, as an evolution of the materials distribution in relationship with the construction which are made along the time, are analyzed as follows:

-Between 1.931-1.953 it is built a little transversal jetty, for giving access to the light in the Rapadoira Rocky shoals. Leaned and supported on this jetty a little beach was formed; that system seems to have operated as a stabilizer of the lock barrier which moved innerward and became wider allowing an increasing colonization of dunes.

-In 1.969 it began the construction of the jetty which starting from the light and parallel to the left margin, tried to stabilize the position of the main tidal channel. The response of the lock barrier materials was fast; the spit began to take a progressive orientation Northward with evident lengthening and lost of thickness/

in its extrem head due to the following processes:

- . The stabilization of the tidal channel caused a reduction of its - - curvature in the interior zone, and so, it began to erode the lock - - barrier from the internal side.
- . In the area extended between the jetty and the original shoreline - the Rapadoira beach became progressively wider what supposed a bleeding of a part of the materials that constituted the feed of the spit, Altar beach and beaches further to the East.

-Between 1.975-1.977 the construction of the last exterior of the - channeling jetty was ended. These buildings supposed the outer prolongation of the jetty in the left margen to the present position. Its - inner prolongation began then producing a subsequent reduction of the/ gorge.

-The effects were immediate and spectacular; in March 1.978 the - - lock barrier had disappeared. It is possible to observe a faster - - filling of the ría and an increasing of the exterior bars since then,/ and also Altar beach began to be eroded, trying the materials to feed/ the lock barrier that was demolished every time by the littoral dyna-- mics. But this process was not immediately evident in the regression - of the shoreline up to three years later; initially the erosion only - affected to the intertidal beach (depth erosion).

-In 1.981-1.982, we could confirm a very important backward move -- ment of the coast-line due to the processes we have explained.

-Since 1.983, we could observe a relative important erosion (changes in the transversal profiles) of the beaches East from ría of Foz.

OBJECTIVES.-

The most adjusted solution to the problem we have exposed, might - accomplish therefore the following objective:

1. Regeneration and stabilization of the shore between Angueira - and St. Bartolomé headlands. This is the principal objective; the - - follows are secondary and act as limitant conditions.
2. Preservation and improvement of Foz harbour facilities, so that/ particularly the sailing conditions in the access channel do not worsen.
3. To avoid negative impacts in the ría and its environment.
4. To respect the natural conditions of littoral drift Eastward - - from the ría.

Securing theses objectives it will be possible to obtain an inte -- gral solution to Foz coastal and harbour problem. And a discussion of/ the possible element of the solution will be done previous to the - - analysis and definition of the complete solution.

A. Artificial filling with sand.-

The level of the regression process of the Altar beach is so impor-- tant and the risk of damages so high that it seemed necessary an arti-- ficial refilling on this beach. But that decision planned two suplemen-- tary problems: the source of sands and their stabilization.

- In relation to the sand source the sedimentological analysis have shown that the sands from the bay and from the channel as the ones - - from the banks of the ría have the same characteristics than the sand/ of the beaches; the use of them is, in consequence, allowed. We have - also test the materials of Rapadoira beach; these sediments have not - the same characteristics but they can be used too. Nevertheless the Ra padoira beach has become too wide and now it needs a bleeding because/ the sediments are in the way to overstep the jetty, bringing some nave gability problems in the exterior end of the channel.

-Nowadays, due to the natural processes that the littoraz dynamics impose in Altar and Anguieira beaches, the balance of sediments is - - negative; that means an evident erosion of them. This erosion has some immediate consequences: the acceleration of filling speed in the ría,/ and the lost of the materials that feeded the beaches, further to the/ East from the ría. Therefore, in relation with the stabilization of - materials, it would be necessary some kind of artificial shelter, - - barrier or protection. Taking into account both problems. Two different types of solutions may be considered:

. A continuous feeding after an adequately great first reclamation - what should interrupt the actual rythm of filling in the inner basin./ The simple reclamation surely would be not enough; it is also neccesa- rry to feed periodically with, to counteract the deficit that imposes - the natural eroding tendence.

. Construction of a kind of element that allows the stabilization of - sands, by support, shelter or protection. These elements are analized/ in the following discussion.

B. Transversal jetties.-

It is a parcial solution that should allow the defence of shore - and buildings (apartments and hotels) in the zone of Altar beach, - - where the erosion has been stronger, attacking the quaternary cliffs/ over what these constructions are located. They behave principally as barriers or supports. Nevertheless this solution has some important - disadvantages:

-On the one hand, it does not resolve all the problem because it - does not give a really solution to the accessibility to Foz harbour.

-On the other, the traspassing of materials to the beaches Eastern from Foz is not favoured and possibly, if the barrier was long enough, it would be even not allowed; so there the erosion process should - - increased.

-In addition, this kind of jetties would produce undesirable visual impacts.

C. Free jetties.-

Though they behave a shelter works, like in the previous case, it - is a parcial solution if they are not complemented with other channe- ling constructions and by-passing disposal.

D. Channeling constructions.-

The only way to complay with the demands of Foz harbour is to sta-- blish a channeling element on the right margen that completes the old/ jetty. The old channeling project defined two parallel jetties already.

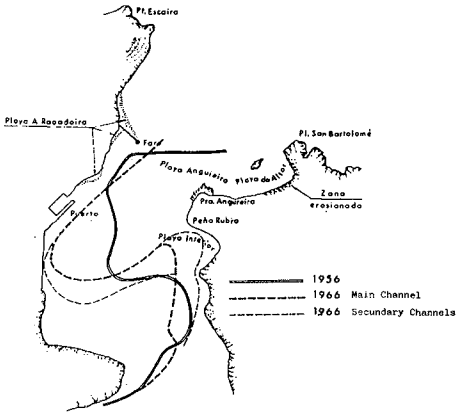


FIG. 2
Evolution of the inner channel-1956-1966

FIG. 3
Evolution of the inner channel-1975-1978

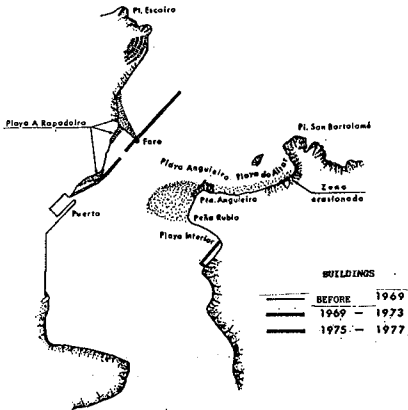
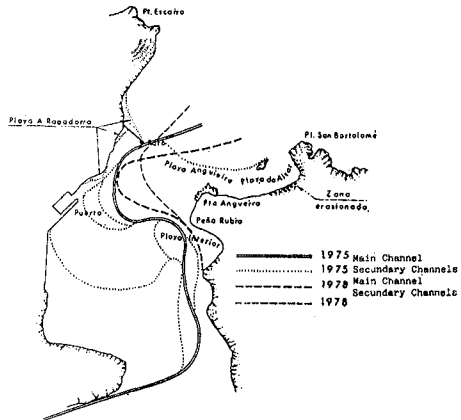


FIG. 4
Schedule of the channeling constructions

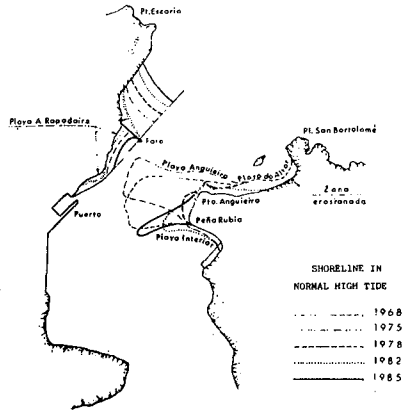


FIG. 5
Changes in shoreline

But only the one of the left margen was built. That was other reason - of the posterior erosion happened. At present the second jetty is also necessary for channeling, however nowadays it is necessary to regenerate the lock barrier too.

There is a difficulty derived from the shortage of complete studies about bathymetric and hydrodynamic conditions, and in consequence, - - there are not dates enough to assure the success of the solution, - - because the definition of the exact cross section of the tidal channel, that would be necessary to improve the accessibility conditions of Foz harbour needed a wider research.

The channeling works on the right margen made behave as bracket and protection against the waves and tidal erosion of the spit that may be regenerated in base of an artificial filling. This is, in consequence, the most complete and economic solution in relationship with all the - planned objectives. It has the advantage of beeing the less detectable visually because the jetty stays sumerged under the lock barrier, - - except on the tide channel side.

ADOPTED SOLUTION.-

The adopted solution is composed of the following elements:

1. Artificial filling with sand.

2. Extraction of sand from the ría increasing the tidal prism and - reconstituting the primitive condition. It is possible to take out the sands from Rapadoira beach too. We have explained that Rapadoira beach needs a bleeding to avoid both posterior problems of accessibility to/ Foz harbour and risks in the own beach.

3. Construction of a bracket-channeling jetty that starting from - Angueira headland approaches enough to Foz light to allow a breadth - compatible with the final tidal prism. This jetty should stabilize the tidal channel on one hand, and avoid the breaking and eroding of the - spit due to the tidal and wave actions on the other hand. The following conditions must be observed:

-The jetty would be short enough to be sure that the distance from/ its head to the Rapadoira jetty exceeds the theoric channel breadth, - to make easier the foreseen construction of its extension as the right margen channeling jetty; but at the same time it must be as long as - possible to favour the natural inlet-outlet stability.

-It might adopt in the ground plane a compatible form with the - - tidal ebb channel eroding action.

In abstract, the solution can be defined as the artificial settle-- ment of a lock barrier, stabilized by a channeling and bracket jetty,/ in such a way that this may constitute the first stretch of the complete right side channeling jetty.

THE JETTY.-

1. The ground plane will be conditioned by two kind of considera--- tions: fluent circulation and constructive facility.

They have been taking into account three different layouts which -

are shown in figure 3. The following discussion was carried on:

The hydrodynamical conditions improved for number 1 to number 3; - number 3 allows better the evacuation of water in the ebb, and the - - changes of direction are less than in number 1; the curvature is minor in number 3 too. At the same time, solution number 1 corresponds to - the maximum increasing of the lock barrier. Therefore, all these consi- derations select layout number 3. However the easiness decreases from/ number 1 to number 3; while the number 3 layout supposes a construction through the presently flattened lock barrier sandbanks, demanding to - pump out a great quantity of sand, number 1 layout demands a minor - - previous sandy pumping. This need for pumping sandy out is imposed by/ the necessity of getting an adequate level for jetty foundation. Never- theless on the other hand, solution number 3 has the advantage of - - being shorter than the others; so, the anterior disadvantages are - - partially balanced. Therefore, solution number 3 has been selected, - taking into account other motives:

-The present changes of the tidal channel do not allow a clear defi- nition of the jetty based on the present morphology and other condi- tions in the moment of the design, which undoubtedly will be some - - different from the ones of the unforeseeable moment of the construc- tion.

-The jetty number 3 has the advantage of starting from the rocky - massif known as Peña Rubia, what means a good stability in the star- ting point.

-This solution guarantees the best stability of depths in the har- bour access channel.

2. Referring to the jetty cross section, its double function as a - channeling and bracket jetty may allow the construction of an asymetri- cal section. The channel zone demands bigger slopes to decrease the - roughness and in consequence to improve the evacuation of waters in - ebb tide. On the other hand, the right slope is going to be covered by the sands of the supported lock barrier.

OTHER ACTIONS.-

As it has been pointed out before in this paper, it is possible to/ observe some changes in the natural transversal profiles of the bea - ches Eastern from the ría of Foz. These changes forseably mean some - erosion of the shore and therefore it is recomended to refill the - shortage of sands of those beaches. It is also proposed to carry the - sands out of the inner ría for this reclamation in order to increase - its tidal prism.

ECOLOGICAL ASPECTS.-

The proposed sandy extraction from the ría may affect the ecosystem, but this affection may be considered positive, because it is just the/ acceleration of the speed of filling of the ría and the variability in the position of the internal sandbanks (and channels), the factors - - that more ecological impact have represented in the past.

On the other hand, the bentonic fauna and flora needs a certain - - stability of bounds and this project forseably will favour this stabi- lity, and the ecological impact for sandy extraction is not so important

as the stabilization of bounds.

SOME INTERESTING RESULTS.-

The construction of the jetty has begun on the beginning of 1.987 - and as early in summer of that year was still possible to observe as - an interesting result, the advance from the near shore of an important sandbank towards the beach all along the Altar and Angueira beaches./ Besides it was the first summer without erosions in Altar beach since/ 1.978. By then, the artificial refilling was still scarce. It is a - - good prove of the correct behaviour of the jetty as a support for the/ lock barrier. The work will foreseeably be finished in summer of 1.988.

POST CONCLUSIONS.-

Since 1.987, based on the results of the measurements of currents - speed and tidal levels, we are working in the sense of determining the hydrodynamics of the ría. Periodically we make some bathymetrics cam-- paigns, to allow us to discern the changes of the volume of materials/ that come into the ría in relation to the volume that entered before - the construction of the jetty.

On the other hand it is foresight to make a pursuit for the project to verify the grade of adjusting of it to the foreseen behaviour.

In other term, we are measuring the relationship between the tidal/ prism and the cross section of the gorge. We have not forget that soon in the future it will be necessary to determine the breadths and the - depths to the definitive stabilization of the harbour entrance and it/ has been previously exposed.

All these works in the future can serve to elaborate some conclu -- sions about ría of Foz hydrodynamics to extrapolate them to other - - analogous outlets.

BIBLIOGRAPHY.-

- (1) Asensio Amor
- (2) Díez J. Introducción al Estudio Geomorfológico y de los proce--
 sos Litorales en la Ría de Foz. Rev. O. P. 1.980.
 Madrid.
- (3) P. Bruun. Stability in tidal inlets.



Puerto de la Coruna

PART VI
SHIP MOTIONS

"Camino II," —puerto de Cadiz



CHAPTER 216

WAVE-INDUCED SHIP MOTIONS IN HARBOUR APPROACH CHANNELS

A C VAN WYK* and J A ZWAMBORN**

ABSTRACT

The results of scale-model simulation of wave-induced hull motions of large bulk carriers under conditions representative of those for coastal ports are presented and discussed to illustrate their usefulness in studies aimed at evaluating the optimum depth requirements for port approach channels.

1. INTRODUCTION

Port accessibility, particularly with regard to safe underkeel clearance for deep-draught vessels, is receiving close attention at South Africa's major export harbours. Saldanha Bay harbour on the west coast provides for ships up to about 270 kt deadweight and Richards Bay harbour, on the east coast, for ships up to 180 kt deadweight. Model studies are at present being carried out to determine the conditions under which ships of 270 kt deadweight could be considered in the future.

The CSIR has been engaged in an extensive programme of research including field measurements and physical and mathematical model simulations to study the behaviour of these deep-draught ships in port approaches of limited depth and exposed to waves, particularly long-period swell.

This paper deals mainly with the ship responses as function of the wave direction and water depth.

2. APPROACH

Fundamental model simulation studies were conducted to determine the responses of two models, the M150 (draught = 17 m) and the M270 (draught = 21 m), representing typical 150 and 270 kt deadweight bulk carriers in terms of their

* Research Engineer, Maritime and Hydraulic Structures, CSIR, P O Box 320, Stellenbosch, 7600, South Africa.

**Programme Manager: Maritime and Hydraulic Structures, CSIR, P O Box 320, Stellenbosch, 7600, South Africa.

vertical hull motions resulting from heaving, pitching and rolling in waves from various directions and in different depths of water. The primary test conditions were selected to represent, in broad outline, the range of conditions most likely to influence ship behaviour at the major South African ports.

The ship model responses to these conditions were determined by physical modelling to a 1:100 scale as well as by mathematical simulation using a 3-D source method.

Subsequent to these fundamental studies the physical model tests were extended to cover the operational conditions characteristic of the approach channel to Richards Bay harbour. During these tests due account was taken of the spatial variations in the wave conditions due to the local wave refraction for different deep-sea swell directions. Prior to and also during the course of these model studies, a comprehensive field monitoring study was conducted at Richards Bay harbour to record the behaviour of prototype vessels presently using the entrance channel to this port. The results of these field measurements primarily served to validate the results obtained with the model studies for the 150 kt deadweight class ship.

3. TECHNIQUES AND FACILITIES

The techniques and facilities used for both the field monitoring and scale-model studies were described in detail by Van Wyk (1982) and Van Wyk and Zwamborn (1984).

The field monitoring basically comprised the photographic recording of the behaviour of ships while transiting the approach channel to Richards Bay harbour during both entry and departure. The photographic records were processed to derive the time series of the wave-induced hull motions of the ships during the selected channel transits and wave conditions.

The scale model tests were conducted in a 23 x 28 m flat-bottomed basin with variable water-depth and in a scaled model of the Richards Bay harbour entrance channel. A bank of programmable wave generators, of the modular paddle type, was used for simulating typical swell conditions.

The hull geometries for the two 1-in-100 scale model ships were determined from line drawings of existing prototype vessels. The propulsion and steering systems were designed in accordance with the scale model laws to ensure realistic steerability. The required loading conditions were obtained by the proper distribution of lead weights, both horizontally and vertically, to ensure correct metacentric heights and radii of gyration for both rolling and pitching. These determine the natural periods for the two rotational modes of movement.

Four ultrasonic sensors fitted at relevant positions on the hulls of these models served to measure the instantaneous distances between these hull points and the basin floor

(underkeel clearances). These sensors had a measuring resolution of about 2 mm and could sample at 0,2 s intervals. The models' horizontal excursions were monitored by two remote-controlled overhead cameras. Three flashing lights on the decks, triggered at 3 s intervals, were time-exposed on film and served to position the models relative to their intended course.

Both the propeller revolutions and rudder movement were remote radio-controlled. The propeller speed, rudder angle and underkeel clearances were sampled at 0,2 s intervals and were transmitted by six-channel telemetry equipment to a data acquisition system linked to an in-house mini computer. Three additional channels were used for recording wave conditions in the test basin.

During testing each model was run along a straight course at the appropriate angle to the waves, covering a distance of about 20 m (2 km prototype). Each test condition was repeated between 20 and 30 times to obtain sufficient data for reliable statistical analysis.

During a time-domain analysis the recorded motion time series were used to derive time series of roll, pitch and heave and these principal motions were then used to calculate the vertical motion time series at the perpendiculars, shoulders and quarters of the models for each individual run.

These time series together with the recorded waves were spectrally analyzed individually and averaged over the number of runs during the test. The averaged spectra were then used to calculate the significant wave height and significant motion amplitudes (defined as twice the standard deviation of the motion time series) for roll, pitch and heave and for the vertical motions at the six hull points (i.e. the perpendiculars, shoulders and quarters). The data were also reduced to amplitude response functions for the said principal and hull motions using the encountered wave spectra derived from the incident wave spectra, average angle of wave incidence and average ship speed during the test.

4. SCALE-MODEL TEST PROGRAMME

A test programme was devised to enable coverage of as wide a range of test variables as possible in the available time. The test conditions were selected to represent, in broad outline, the range of conditions most likely to influence ship behaviour at the major South African ports.

In this respect only swells ranging from 1 to 4 m in height and with spectral periods of 12 to 16 s and longer would have to be considered. The angles of wave incidence relative to the models could, depending on their sailing directions, vary from following waves, through beam waves, to heading waves.

Overdepths could range from as little as 10 per cent to as much as 50 (to 75) per cent of the draughts of the model ships.

Ship speeds in and around ports would probably not exceed about 6 m/s (12 kn).

In planning a justifiable test programme, the following assumptions, based on earlier literature surveys, were first made:

- (i) The irregular nature of both waves and wave-induced ship motions could be described by a linear superpositioning of sinusoidal components of different frequencies, these frequency compositions being fully described by one-dimensional energy density spectra.
- (ii) In a given water-depth and for a given ship speed, the wave-induced ship motion amplitudes were assumed to be linearly related to wave amplitudes for each frequency of wave encounter with the result that the model's motion responses could be expressed in terms of frequency response functions for each angle of wave incidence.

Based on the above assumptions, the initial tests were done with one spectral shape (fixed wave height and spectral peak period) and one ship speed. Thus, only the angle of wave incidence and the relative water-depth were varied which were expected to be the most important variables.

A typical swell spectral shape, based on field measurements, was used to reconstruct a swell spectrum with a significant wave height of 3 m and a spectral peak period of 14 s. An appropriate ship speed of advance of 4 m/s (8 kn) was chosen to run the models in the specified swell conditions with the angles of wave incidence relative to the models to be incremented in steps of 15°. These tests were all done in a relative water-depth (depth-to-draught ratio) of 1,3.

The influence of different relative water depths, ranging from 1,1 to 1,5 in steps of 0,1 was studied for the primary angles of wave incidence, that is, following ($\alpha = 0^\circ$), heading ($\alpha = 180^\circ$), beam ($\alpha = 270^\circ$) and stern- and bow quartering waves ($\alpha = 315^\circ$ and 135°).

In addition to the primary tests, secondary test programmes were devised to serve both for checking the validity of the above assumptions and for studying the influence of additional factors such as the absence/presence of bilge keels on the models, different loading conditions and different spectral shapes.

On completion of the fundamental model tests, a series of tests were planned to simulate typical port entries and departures with both models in a scale model of the Richards Bay harbour approach channel for comparison with

data collected during the field monitoring study as well as for determining port accessibility for the deeper draught (21 m draught) model ship.

5. TEST RESULTS

5.1 Wave-induced Hull Motions Versus Angle Of Wave Incidence And Depth Of Water

The significant motion responses, A_{moz}/H_{mo} , versus angle of wave incidence, α , are shown for the perpendiculars, shoulders and quarters of the two models for the case with a relative water-depth, d/D , of 1,3 in Figures 1a and b.

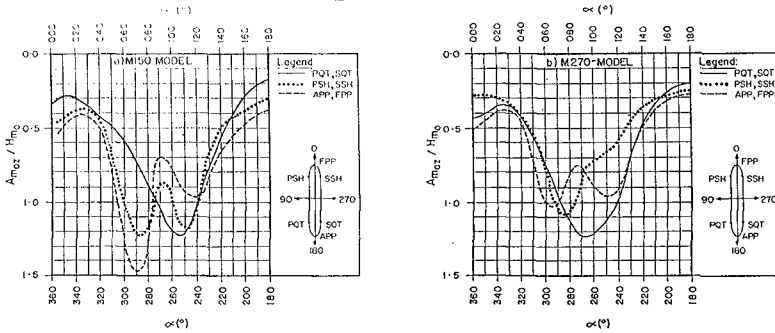


Figure 1a & b. Significant motion response at critical hull points versus angle of wave incidence for $d/D = 1,3$ and $H_{mo} = 3m$, $T_p = 14s$

The maximum significant motion responses are given by the lower limits of the envelopes described by these trend curves.

The effect of the relative water-depth (depth-to-draught ratio, d/D) on these maximum significant hull motions was studied for following ($\alpha = 0^\circ$), heading ($\alpha = 180^\circ$), beam ($\alpha = 270^\circ$) and bow and stern quartering ($\alpha = 135^\circ$ and 315°) waves. The results for the M270 model are shown in Figure 2.

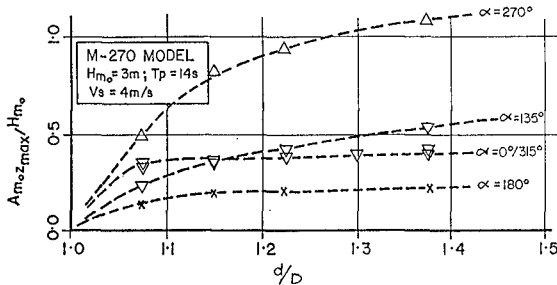


Figure 2. Maximum significant motion amplitude versus water depth

The dependence on water-depth is most noticeable (for both models) in beam and quartering waves indicating a gradual reduction in motion with decrease in underkeel clearance.

The maximum significant motion responses versus angle of wave incidence and relative water-depth, based on the above data, are shown for the two models in Figures 3a and b.

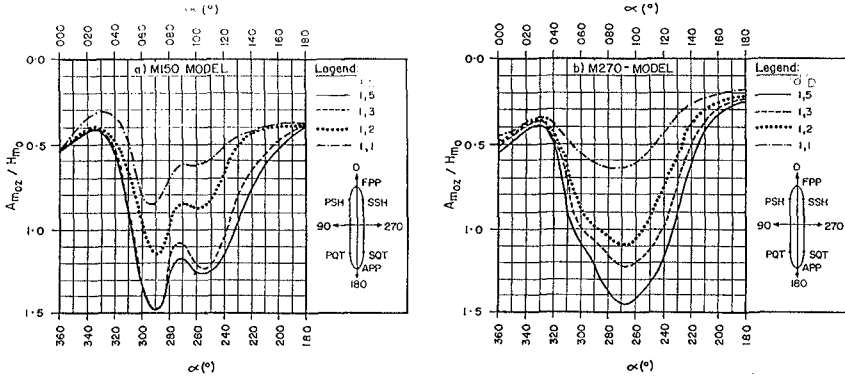


Figure 3a & b. Maximum significant motion response versus angle of wave incidence and relative water depth for $H_{m0} = 3\text{m}$, $T_p = 14\text{ s}$

Figures 1 and 3a and b show significantly different responses for the two models in equal wave conditions and relative water-depths. The most severe motions, for the M150 model, occurred at the perpendiculars for values of α around 70° (or 290°) and were caused mainly by pitching. Fairly severe motions were, however, also recorded at the quarters and shoulders for values of α between 90° and 120° (or 270° and 240°).

In the case of the M270 model the motions were largest at the quarters during rolling in beam waves ($\alpha = 90^\circ$ or 270°). Motions were also quite severe at the shoulders for values of α around 75° (or 285°) and at the perpendiculars around 65° and 110° (or 295° and 250°).

The least vertical motions, for both models, occurred during heading waves ($\alpha = 180^\circ$) and were usually largest at the perpendiculars.

Motions in following waves ($\alpha = 0^\circ$) were generally larger than those in heading waves particularly for the M270 model where these were almost twice the magnitude of those in heading waves.

The differences in the motion responses for the two models can be ascribed to the differences in their principal dimensions and loading conditions as well as to the differences in absolute underkeel clearances for equal relative water-depths (e.g. with $d/D = 1.3$ the underkeel

clearance for the M150 model ($D = 17$ m) was 5,1 m while that for the M270 model ($D = 21$ m) was 6,3 m).

Recorded maximum significant motion responses for both models are compared with mathematically predicted responses (using the VESDYN model) in Figures 4a and b.

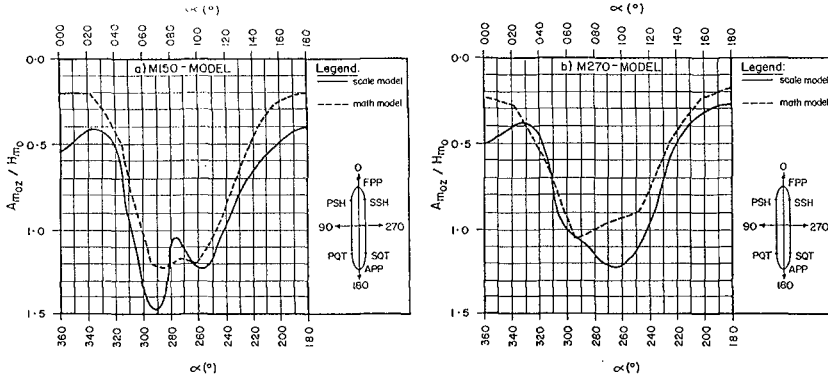


Figure 4a & b. Measured versus predicted significant motion response for $d/D = 1,3$ and $H_{m0} = 3$ m, $T_p = 14$ s

Measured motions were generally larger than those predicted particularly in following and heading waves and for angles of wave incidence where extreme motions were recorded.

5.2 The Effect Of Wave Height

The effect of wave height on the vertical motion response of the model ships was studied for the primary angles of wave incidence, namely heading ($\alpha = 180^\circ$), following ($\alpha = 0^\circ$), beam ($\alpha = 270^\circ$), bow quartering ($\alpha = 135^\circ$) and stern quartering ($\alpha = 315^\circ$) waves. These tests were all done in a relative water-depth of 1,3 and in a 14 s peak period swell with the models advancing at 4 m/s. Wave heights were varied between about 1 m and 5 m.

Figure 5 illustrates the effect of wave height on the maximum significant motion amplitudes for the M270 model for the different angles of wave incidence. Similar trends were also obtained for the M150 model.

The significant motion amplitudes showed an almost linear increase with increase in wave height for all test conditions except those in following waves ($\alpha = 0^\circ$). During this latter conditions the maximum motions were recorded at the aft perpendiculars of the models and would therefore have resulted from a combination of heaving and pitching.

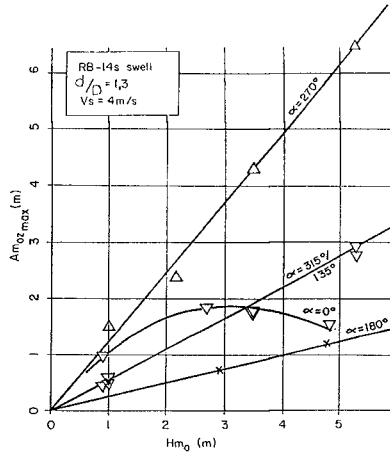


Figure 5. Maximum significant motion amplitude versus wave height for M270 Model

5.3 Sensitivity To Wave Spectral Shape, Peak Period And Ship Speed

Sensitivity tests were conducted to study the influence on wave-induced motion response for different wave spectral shapes, spectral peak wave periods and ship speeds.

The tests confirmed the assumption of linearity in response with respect to the above variables in the sense that hull motion response amplitude operators (RAOs) show only insignificantly small changes for the range of conditions tested.

As would be expected significantly large differences were, however, recorded in the resulting significant hull motions for different spectral shapes, peak periods and ship speeds for different angles of wave incidence. The differences primarily result from the differences in the distribution of wave energy with frequency of wave encounter and emphasize the need for using measured (or calculated) RAOs (response amplitude operators) as functions of angle of wave incidence and relative water-depth together with the operating condition, determined by the ship speed, angle of wave incidence and wave spectrum, to determine the resulting hull motion response. Sample RAOs as function of angle of wave incidence for the M270 model in a relative water-depth of 1,3 are shown in Figure 6.

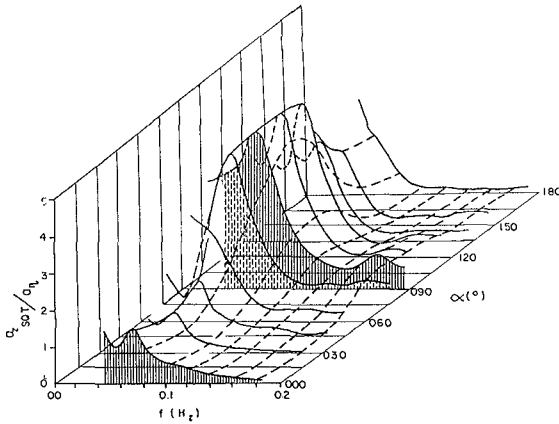


Figure 6. Motion amplitude response function for M270 Model

5.4 Maximum Versus Significant Vertical Hull Motions

The most probable maximum motion amplitude can be approximated by the mean of maxima obtained for the number of repeat runs for each test condition. This mean value, A_{max} , is shown versus A_{moz} for a representative number of tests with the M150 model in different relative water-depths and with different significant wave heights and angles of wave incidence in Figure 7.

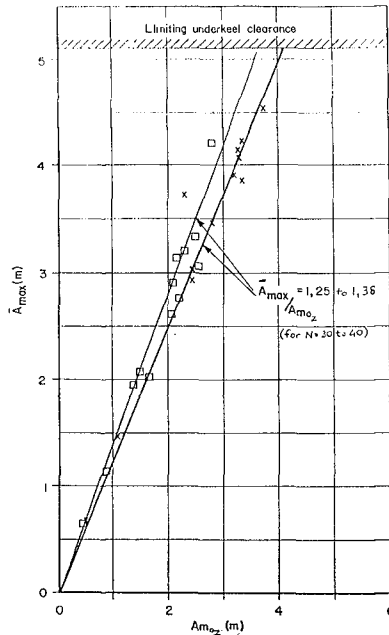


Figure 7. Maximum motion amplitude versus significant motion amplitude

The data indicate ratios of A_{max}/A_{moz} of between 1,25 and 1,38 for motion time series resulting in, on average, 30 to 40 motion oscillations. The apparent linearity of this relationship implies that extreme hull motions are also not affected by the limited underkeel clearances. The data of Figure 7 also appear to confirm the assumption that ship motions are approximately Rayleigh distributed.

The data of Figure 7 also appear to confirm the assumption that ship motions are approximately Rayleigh distributed. This assumption implies that the most probable maximum motion amplitude, μ (A_{max}) can be found from the relationship

$$\mu (A_{max}) = \frac{1}{\sqrt{2}} (\ln N)^{0,5} \cdot A_{moz}$$

where N is the average number of oscillations of the ship for the duration of the tests. For values of N of 30 to 40 the theoretical most probable maxima show good agreement with the means of maxima obtained from the model data (Figure 7).

5.5 Ship Motions in the Richards Bay Harbour Entrance Channel

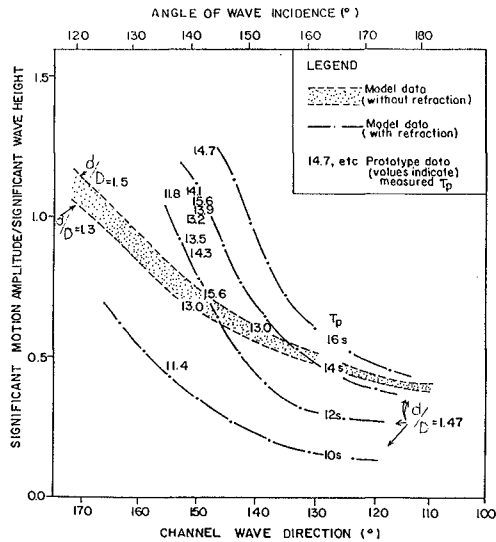


Figure 8. 150kt deadweight (17 m draught) ship: model and prototype response in Richards Bay harbour entrance channel and comparison with model response in unidirectional waves

Figure 8 presents the results of the model tests with the M150 model during departure in the Richards Bay harbour approach channel together with those obtained from the field measurements and the model tests in the flat-bottomed basin.

The significant hull motions of the model in the channel were significantly larger than those obtained from the tests in the flat-bottomed basin. This phenomenon is explained by the fact that the wave energy, having accounted for wave directionality due to refraction for any given incident wave spectrum, was much more concentrated at frequencies of wave encounter close to the natural frequencies of motion of the model.

Good agreement was also found between the M150 model results and the prototype data and thus gave confidence in the model study approach and results also for the larger ship model.

CONCLUSIONS

The tests with the two model ships showed that there are significant differences in their vertical motion responses even with identical wave conditions and identical relative water-depths.

For both models the water-depth appeared to have effected the vertical motions for relative depths less than about 20 to 30 per cent of their draughts. This resulted in a non-linear reduction in motion with decrease in water-depth.

Vertical motions at any given depth of water appeared to have increased almost linearly with wave height except during following waves in which case the hull motions appeared to be relatively insensitive to wave height.

The amplitude response functions were found to be insensitive to ship speeds ranging from 0 to about 5 m/s. The amplitude response functions also were not affected by the spectral shape (peak period) although the significant motion amplitudes as such could differ appreciably.

In this respect use should rather be made of the actual amplitude response functions versus angle of wave incidence for given ships and of the wave spectra (accounting for directional spreading and refraction) to be encountered by these ships to determine their significant motion response for operating conditions other than those used during the tests.

The study further showed that local wave conditions in a harbour entrance can cause large differences in ship behavior. In the case of Richards Bay, vertical motion predictions based on the fundamental study results (flat-bottomed basin tests) were considerably less than those recorded by prototype ship monitoring at Richards Bay. Only after carrying out detailed tests in an accurately scaled model of the entrance area of Richards Bay and by reproducing correctly refracted directional swells could the recorded prototype motions be adequately reproduced.

The results of these studies, in general, are believed to offer a significant contribution to the state-of-the-art

knowledge of wave-induced ship behaviour in limited depths of water. Since the model results could be verified by prototype measurements, these can be applied with more confidence in the determination of optimum depths for safe harbour approaches.

ACKNOWLEDGEMENT

The permission of South African Transport Services to publish this paper is gratefully acknowledged.

REFERENCES

VAN WYK, AC (1982). Wave-induced ship motions in harbour entrances. Proceedings of 18th ICCE, Cape Town.

VAN WYK, AC and ZWAMBORN, JA (1984). The effect of wave direction on ship motions in harbour entrance channels - model study approach. Proceedings of 19th ICCE, Houston.

CHAPTER 217

DYNAMIC BEHAVIOR OF A MOORING BUOY INSTALLED IN OPEN SHORE

TOSHIYUKI SHIGEMURA*, M.ASCE
AND
KENJIRO HAYASHI**

Abstract

To investigate the dynamic behavior of a mooring buoy installed in an open shore, a simplified simulation model is developed, which consists of the surging and heaving motions of a mooring buoy.

A series of the model tests is performed to examine the reliability of the developed model. The model tests verify that the developed model can predict the dynamic motion of a mooring buoy satisfactorily.

Finally, simulation is made for the buoy installed in the west shore of Iwo-jima which failed during a stormy weather. This simulation indicates that the external loads enough to cause the failure has been loaded on the buoy at the moment of the failure.

Introduction

A mooring buoy is normally installed inside a port or a bay where it is well protected against severe wind and wave loads. However, on some shores where a port can't be built for some reason, it has to be installed in the open shore where it is fully exposed to severe environmental condition. Iwo-jima is an example of this.

Iwo-jima is an isolated small volcanic island located in the Pacific Ocean about 1250 kilometers south of Tokyo. Because of the continuous upheaval of the island, no port has been built there yet. Instead, four single point mooring buoys have been installed off the west shore of the island, to moor the tankers or cargo ships which occasionally come to the island. The problem experienced by these mooring buoys is the frequent failures of the buoy systems during a period of stormy weather although no ship is moored to the buoys. In fact, the mooring buoys installed in Iwo-jima often fail during the typhoon season, which causes a lot of trouble for the supplying operation to the island.

Thus, to insure efficient operation of the mooring buoys installed in the open sea, it is important to clarify the

*Professor, Department of Civil Eng., National Defense Academy, 1-10-20 Hashirimizu, Yokosuka, Kanagawa 239, Japan.

**Assistant Professor, Department of Civil Eng., National Defense Academy.

dynamic behavior of the mooring buoys to which no ship is moored. This paper intends to investigate the dynamic behavior of a single point mooring buoy when no ship is moored to it. The investigation will be performed by putting the emphasis on the research of tensile stress induced on a mooring line as follows:

- (1) Development of a simplified simulation model of a single point mooring buoy subject to severe environmental loads.
- (2) Examination of the adequacy of the developed model through the model tests.
- (3) Investigation of the possible causes of a failure which occurred in Iwo-jima through the simulation done by using the developed model.

Motion Equations of a Mooring Buoy

When a ship is not moored to a buoy, the buoy may experience the translational motions called surging, swaying and heaving and the rotatory motions called rolling, pitching and yawing due to the environmental loads. Thus, six equations should be developed and solved simultaneously to clarify the dynamic behaviors of the mooring buoy. However, it is difficult at the present stage to get reliable equations which represent each of these six motions. Further, one of the aims of this paper is to develop a simplified simulation model which can predict the dynamic behaviors of the tensile stress induced on a mooring line satisfactorily. Thus, the following assumptions were made to derive the motion equations:

- (1) A mooring buoy doesn't take any rotational motions but takes the translational motions of surging and heaving.
- (2) Dynamic motion of the mooring line is not taken into account in the derivation of the simulation model.
- (3) A buoy is moored to the sea floor by an open link chain of uniform size which is elastically extensible.
- (4) Only the wind and wave loads act on a buoy as the external loads.
- (5) Tensile stress induced on the line by external loads can be substituted for the static tensile stress evaluated by an available formula.

Assumption (1) means that the motion of a mooring buoy can be treated as a two dimensional motion. Figure 1 shows the coordinate system used for deriving the motion equations.

Here, each notation in figure 1 indicates the following:

- a =draft of the buoy
- b =freeboard of the buoy
- F_{wd} =wind load acting on the buoy
- T =tensile stress induced on the mooring chain
- T^x =horizontal component of T
- T^z =vertical component of T
- F^x =horizontal component of the wave load acting on the buoy
- F^z =vertical component of the wave load acting on the buoy
- η =elevation of wave surface

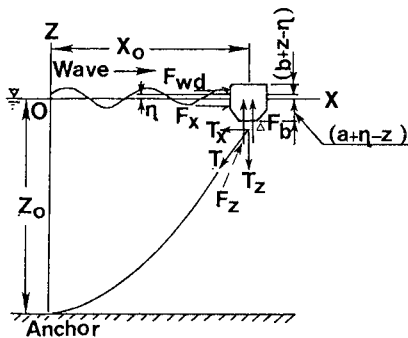


Figure 1. Coordinate system used for the analysis.

X_0 = original position of the model buoy on X axis

Z_0 = original position of the model buoy on Z axis

Suppose the model buoy moved to (X_0+x, Z_0+z) from its initial position (X_0, Z_0) for time t due to the wind and wave load. Then, basing on the assumptions together with the coordinate system provided, the following two equations can be derived as the motion equations of a mooring buoy:

$$(m+m'_x)\ddot{x} = F_{wd} + F_x - T_x - C_x \dot{x} \quad \dots\dots(1) \text{ (for surging)}$$

$$(m+m'_z)\ddot{z} = F_z - T_z + \Delta F_b - C_z \dot{z} \quad \dots\dots(2) \text{ (for heaving)}$$

where

m = mass of a buoy

m'_x, m'_z = horizontal and vertical components of virtual mass of model buoy

C_x, C_z = horizontal and vertical components of damping coefficient of a buoy system

ΔF_b = dynamic buoyance of model buoy

X = horizontal displacement of a buoy from the origin

x = horizontal displacement of a buoy from its initial position

Z = vertical displacement of a buoy from the origin

z = vertical displacement of a buoy from its initial position

The former equation includes the horizontal components of wind load F_{wd} and wave load F_x , both acting on a buoy, tensile force induced on a chain T_x , and a damping force of the buoy system $C_x dx/dt$. The latter includes the vertical components of the wave load F_z , tensile stress T_z , damping force of the buoy system $C_z dz/dt$, and the dynamic buoyance of the buoy ΔF_b . However, values of these components together with the coefficient values are all unknown and should be somehow determined at an arbitrary time to solve eqs.(1) and (2) simultaneously.

Evaluation of Tensile Stress and External Loads

The catenary theory is generally used to calculate the static tensile stress induced on a mooring line. However, the value of the tensile stress T varies due to the hanging state of a mooring line under the water. The hanging state is usually classified into three states as follows:

- (1) State I in which a part of the mooring line is hanging down vertically from a buoy to the sea floor and the rest of it is resting on the sea floor.
- (2) State II in which the most part of the mooring line is hanging in the water forming a catenary curve although the rest of the chain is resting on the sea bed near the anchor.
- (3) State III in which all of the mooring line is suspended in the water and no part of the line is resting on the sea bed near the anchor.

Figure 2 shows these states of the hanging of a mooring line. The notations in this figure indicates the following:
 X_1 = limiting displacement of a buoy from its origin in which the hanging state of the mooring line stays in state I.
 X_2 = limiting displacement of a buoy from its origin in which the hanging state of the mooring line stays in state II.
 X_3 = limiting displacement of a buoy from its origin in which the hanging state of the mooring line stays in state III.

a_r = length of the mooring line resting on the sea floor.
 θ_a = directional angle of the tangential line to the mooring line at the anchoring point measured from the sea floor.

Calculation of the tensile stress is then made for each of these three states separately. Shoji(1975) introduced the effect of the elasticity of a mooring line to the catenary theory and derived three approximate polynomials expanded into a power series of T_x . However, there is some

uncertainty in his equation for the line in state II. Further, there is some difficulty in finding the real value of T_x among the solutions of the polynomials. Thus, the authors developed new equations for each of the three states (1987), following Shoji's deriving method. Table 1 summarizes these equations developed for each state of hanging.

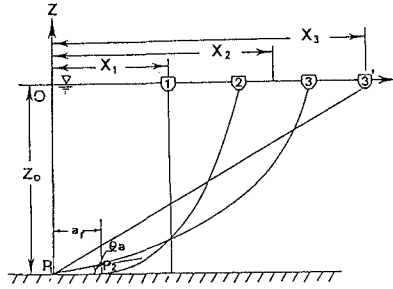


Figure 2. Hanging states of a mooring lines.

Table 1. Summary of the equations for evaluating the tensile stress induced on a mooring line and other related terms

Equations for a mooring line in State I

$$T_x = 0 \dots\dots\dots(3)$$

$$T_z = W Z_0 - W Z_0^2 / (2EA) \dots\dots\dots(4)$$

$$X_1 = S - Z_0 + W Z_0^2 / (2EA) \dots\dots\dots(5)$$

Equations for a mooring line in State II

$$X = S(1 + T_x / EA) - (S - a_r) + T_x / W \left\{ \ln W / T_x (S - a_r) + \sqrt{[W(S - a_r) / T_x]^2 + 1} \right\} \dots\dots(6)$$

$$Z_0 = \sqrt{[T_x / W]^2 + (S - a_r)^2} - T_x / W + W(S - a_r)^2 / (2EA) \dots\dots(7)$$

$$T_z = W(S - a_r) \dots\dots\dots(8)$$

$$X_2 = T_x S / EA + T_x / W \left\{ \ln WS / T_x + \sqrt{(WS / T_x)^2 + 1} \right\} \dots\dots(9)$$

Equations for a mooring line in State III

$$X = T_x S / EA + T_x / W \left\{ \ln [\tan \theta_a + WS / T_x + \sqrt{(\tan \theta_a + WS / T_x)^2 + 1}] - \ln [\tan \theta_a + \sqrt{\tan^2 \theta_a + 1}] \right\} \dots\dots(10)$$

$$Z_0 = T_x / W \left\{ \sqrt{(\tan \theta_a + WS / T_x)^2 + 1} - \sqrt{\tan^2 \theta_a + 1} + WS(\tan \theta_a + WS / 2T_x) / EA \right\} \dots\dots(11)$$

$$T_z = T_x \tan \theta_a + WS \dots\dots\dots(12)$$

$$X_3 = \sqrt{S^2 - Z_0^2} \dots\dots\dots(13)$$

In this table, several new notations appear. These notations indicate the following:

S=total length of a mooring line before getting deformation

W=weight of a mooring line per unit length under the water

A=sectional area of a mooring line

a_r' =original length of a_r before getting a deformation

Using these equations developed above, we can determine the static tensile stress and its components induced on a mooring line for any location of buoy if the physical properties of the mooring line are given. Namely, the values of T_2 and X_1 are determined immediately from eqs.(4) and (5) because every variable in the equations is known. In case of State II, values of T and T' can be determined from eqs.(7) and (8) if a_r' is given. Once the value of T' is determined, the corresponding X_2 is also determined from eq.(6). In case of State III, the values of T and T' are determined similarly from eqs.(11) and (12) if the value of $\tan\theta$ is given. The corresponding value of X is then determined from eq.(10) easily.

Next, let's derive the equations for wind and wave loads, referring to figure 1. It was decided to evaluate the wind load F_{wd} by a conventional type formula as shown below.

$$F_{wd} = 1/2 \rho_a C_d D (b+Z-\eta) V^2 \dots\dots\dots(14)$$

where ρ_a is air density, C_d is drag coefficient of a buoy, D is diameter of a buoy, b is freeboard of a buoy, η is the elevation of wave surface, z is the elevation of the gravity center of the buoy and V is the mean velocity of wind. Further, it was assumed that wave load can be evaluated by the following formulas derived from the Morison equation:

$$F_x = 1/2 \rho_w C_{dx} D (a+\eta-z) u |u| + 1/4 \rho_w C_{mx} D^2 (a+\eta-z) \dot{u} \dots\dots(15)$$

$$F_z = 1/8 \rho_w C_{dz} D^2 v |v| + 1/4 \rho_w C_{mz} D^2 (a+\eta-z) \dot{v} \dots\dots\dots(16)$$

where

ρ_w =water density

u =horizontal component of water particle's velocity at still water level

\dot{u} =horizontal component of water particle's acceleration at still water level

C_{dx} =drag coefficient of a buoy for horizontal flow

C_{mx} =mass coefficient of a buoy for horizontal flow

v =vertical component of water particle's velocity at still water level

\dot{v} =vertical component of water particle's acceleration at still water level

C_{dz} =drag coefficient of a buoy for vertical flow

C_{mz} =mass coefficient of a buoy for vertical flow

Finally, it was decided to evaluate the dynamic buoyancy ΔF_b by the following equation:

$$\Delta F_b = 1/4 \rho_w D^2 (a+\eta-z) \dots\dots\dots(17)$$

Using the equations developed above, respective terms in the righthand sides of eqs.(1) and (2) could be evaluated once we get the values of respective coefficients, flow field induced by the wave, physical properties of the buoy

and mooring line, and other values of the related terms.

Model Tests of a Single Point Mooring Buoy

As described previously, a mooring buoy installed off the west shore of Iwo-jima often fail during the typhoon season. Photo 1 shows the failure which occurred at Iwo-jima on August 4, 1986. In this case, the mooring chain was parted due to the severe environmental loads caused by the typhoon and the buoy was cast on the west coast of the island.



Photograph 1. Buoy cast on the west coast of Iwo-jima.

Thus, it was decided to perform a series of model tests in light of the buoy systems and their surrounding environmental conditions at the west shore of Iwo-jima. The following basic principles were established for performing the model tests:

- (1) Model tests are to be performed in a two dimensional wave tank with a constant depth of water.
- (2) Regular waves of various size will be used as the waves acting on the buoy.
- (3) A constant weight will be loaded on the buoy horizontally instead of blowing wind at the buoy.
- (4) An open link chains will be used as the mooring line because of its availability, although stud link chains are used in Iwo-jima.

The geometric scale of the test model was set to be 1/35 of the prototype and the time scale was determined by referring to the Froude law of similarity. Table 2 summarizes the detail of the test conditions.

Table 2. Details of the model tests

Dimension of the model buoy	
Diameter	7.9 cm(2.76 m)
Height	5.2 cm(1.83 m)
Draft	2.4 cm(1.0 m)
Weight in the air	70.0 grf(3.0 tonf)
Dimension of the model chain	
Diameter	1.9 mm(68.0 mm)
Weight under the water	0.7 grf/cm(86.5 kgf/m)
Length	57.1 cm(20.0 m), 68.6 cm(24.0 m), 91.4 cm(32.0 m), 114.3 cm(40.0 m)
Type	Open link(Stud link)
Range of the test conditions	
Water depth	45.7 cm(16.0 m)
Wave height	3.0--16.5 cm(1.0--5.8 m)
Wave period	0.7 --2.0 s(4.1--11.8 s)
Steepness	0.01--0.10
Wind load	12.9 grf(55.0 m/s)
Scope of the mooring line	1.25, 1.50, 2.0 and 2.5

In this table, the numerical figures in parentheses indicate the corresponding values for the prototype in Iwo-jima.

The model buoy was made of aluminum. Chains of four different length were prepared to use as mooring line. The length of these chains was determined so that the scope of the line may become the respective values shown in table 2. Here, the scope is a parameter defined as the ratio of line length to the depth of water.

A 39.6m long, 0.6m wide and 0.8m high wave channel was used for the model tests. Around the middle portion of this channel, a model buoy was moored to the channel bottom by one of the four chains shown in table 2. Figure 3 shows the setup of the model test. A waterproof tension meter was placed on the line at the position just below the bottom of the model buoy, and string-pully system was provided upon the upper structure of wave channel so that constant weight may be loaded to the buoy horizontally through that system.

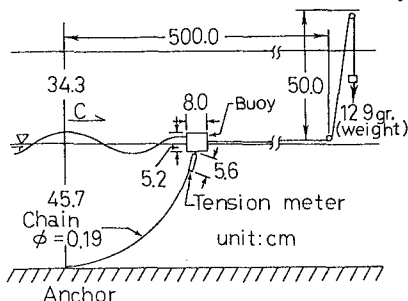


Figure 3. Setup of the model test

Beside the initial position of the buoy a capacitance type wave meter was installed and both the tension and wave meters were connected to a data recorder. Further, a video camera was placed in front of the buoy 2m from the glass wall to record the motion of buoy.

Regular waves of 24 kinds were chosen as the external waves acting on the buoy. Their characteristic values are shown in table 2. In addition, it was decided to load a constant weight of 12.9grf to the buoy horizontally as the substitute for the wind load. This weight of 12.9grf corresponds to the wind load which might be generated on the buoy by a wind having a speed of 55m/s. Here, the wind speed of 55m/s is the maximum one which was recorded in Iwo-jima for the past 20 years.

Prior to starting the model tests, performance of tension meter was examined statically. Tests were made in another small channel, changing both water depth and size of weight loaded on the model buoy horizontally through the string-pully system. The position of the model buoy, the size of the loaded weight, the hanging state of the mooring chain, and the tensile stress detected by the tension meter were all recorded. These tests were repeated a couple of times for three of the four chains prepared. The main tests were conducted for the model buoy moored by each of the four chains mentioned previously. This was done by exerting regular waves of 24 kinds one after another. In each run, both waves and tensile stress were recorded on the data recorder and the motion of the model buoy was recorded by video recorder.

Results of the Model Tests

To check the reliability of equations developed for evaluating the static tensile stress induced on the mooring line,

measured values of the horizontal components of tensile stress T_x were compared with the corresponding values calculated by the equations shown in table 1, using the physical properties of mooring line shown in table 2. Further, it was assumed in the calculation that modulus of elasticity E_0 of the mooring line is 2.1×10^6 kgf/cm^2 .

Figure 4 shows the results of this comparison. In this figure, CL means the length of the mooring line and D means the water depth at which the tests were made. As can be seen from this figure, calculated values of tensile stress agree quite satisfactorily with the measured ones within the range of the expected position of model buoy. This fact clearly verified that the developed equations would be quite reliable for evaluating the statical tensile stress induced on the mooring line.

It was assumed previously that tensile stress induced on the mooring line dynamically could be substituted for the static tensile stress evaluated by some available equations. Thus, tensile stress T and its components T_x and T_z were all calculated similarly by the equations shown in table 1 by varying the position of the buoy every one centimeter within the expected range of the buoy's movement. This calculation was made for each of the four chains and the results were stored on floppy disks. Next, results of the model tests were analyzed. From the recorded data of tensile stress T , the extreme values of it were extracted from the record over 20 cycles, and their mean value T_m was determined by simply averaging them.

Photograph 2 is a picture of the orbital motion of model buoy. Similar pictures were taken at every run shading the laboratory from the sun light. At the same time, motion of the model buoy was recorded on a video recorder. Based on these data, the authors read the data such as horizontal and vertical displacements of model buoy x_m and z_m , the length of both m major and m minor axes of the inclined orbit of model buoy a and b , inclination of the m major axis against the horizontal axis θ_{am} and the inclination of the mooring chain at the bottom of model buoy θ_{cm} . This data was analyzed using the steepness H_0/L_0 , ratio of wave height to water depth H/h of the

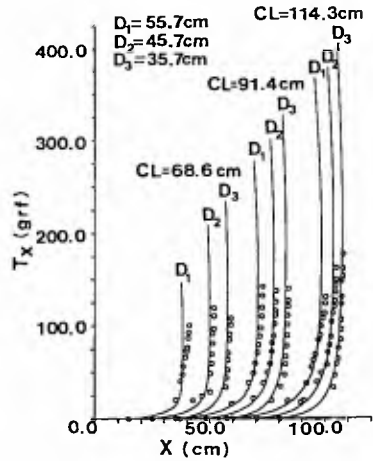
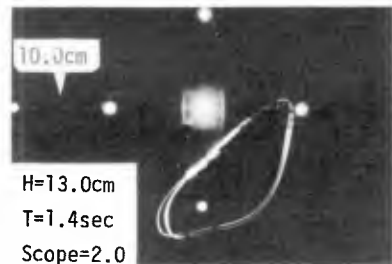


Figure 4. Reliability of the equations for evaluating the static tensile stress.



Photograph 2. Orbital motion of a buoy moored by a chain.

incident wave and scope of the mooring line as the controlling variables.

Figure 5 shows the relationship between T_m/W and H'_0/L_0 plotted introducing the scope as a parameter. Here, W is the dead weight of model buoy. As can be seen from this figure, quite a high correlation exists between both variables. Further, it can be seen that the gradient between two variables decreases almost linearly as the value of scope increases.

Next, it was determined how the displacement of the buoy varies with the variation of external loads and mooring conditions. Figures 6 shows the relationship between x_m/L_0 and H'_0/L_0 . In this figure scope of the mooring line is taken as a parameter. From this figure, it can be seen that both x_m/L_0 increases almost linearly as H'_0/L_0 increases although the effect of the scope to the distribution is not clear. Similar distribution was also found between z_m/L_0 and H'_0/L_0 . Further, figure 7 shows the relationship between z_m/x_m and H'_0/L_0 taking the scope as a parameter. Data scatters considerably. However, we can see that the ratio of both displacements tends to increase as H'_0/L_0 increases in the range of H'_0/L_0 less than approximately 0.3 and that it tends to have a constant value surrounding 1.0 in the range of H'_0/L_0 greater than nearly 0.3. Effect of the scope is also not clear in this case.

Similar analyses were also made for the axial length of the inclined orbit of the buoy. Figure 8 shows the relationship between a_m/L_0 and H'_0/L_0 . From this figure,

it can be seen that there exists a firm correlation between a_m/L_0 and H'_0/L_0 although the effect of the scope to this relationship is not seen clearly. Relationship between b_m/L_0 and H'_0/L_0 was also checked similarly. However, cor-

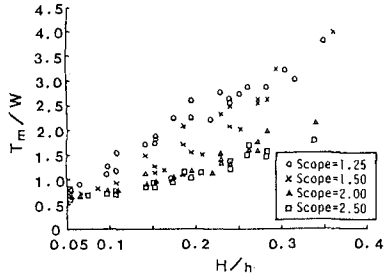


Figure 5. Relationship between T_m/W and H'_0/L_0 .

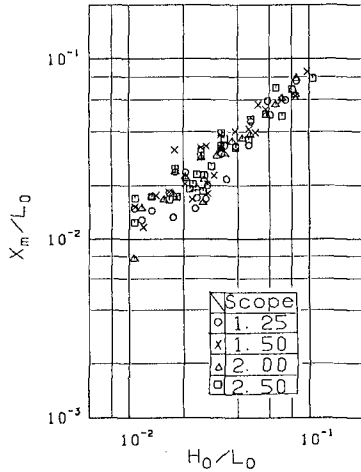


Figure 6. Relationship between x_m/L_0 and H'_0/L_0 .

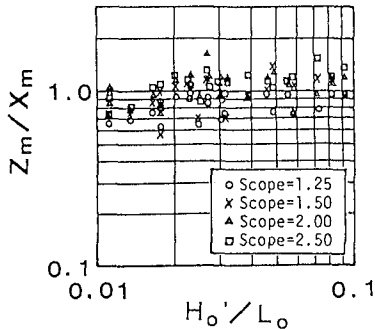


Figure 7. Relationship between z_m/x_m and H'_0/L_0 .

relation between b_m/L_o and H_o'/L_o was not as high as that found for a_m/L_o . Especially, in the range of H_o'/L_o less than 0.03, data of b_m/L_o scattered considerably against the corresponding values of H_o'/L_o .

Figure 9 shows the relationship between the ratio of both axial length a_m/b_m and H_o'/L_o . This figure shows that b_m/a_m tends to increase as H_o'/L_o increases in the range of H_o'/L_o less than nearly 0.4 although data scatters considerably. Further, this ratio tends to converge to a constant value of nearly 0.05 in the range where H_o'/L_o is greater than approximately 0.05.

Finally, let's review the inclination of the mooring line at the bottom of model buoy. Figure 10 shows the relationship between θ_{cm} and H_o'/L_o . In this case, scope of the mooring buoy is also taken as a parameter. As can be seen from this figure θ_{cm} tends to decrease almost linearly as the value of H_o'/L_o increases in the range of H_o'/L_o less than 0.25. This figure further indicates that θ_{cm} tends to keep a constant value of approximately 45 degrees in the range of H_o'/L_o greater than 0.25.

Adequacy of the Simulation Model

The following assumptions were made prior to starting the numerical analysis:

- (1) virtual mass of the model buoy m'_x and m'_z in eqs.(1) and (2) are both equal to the mass of water displaced by the model buoy.
- (2) drag coefficients of model buoy C_{dx} and C_{dz} in eqs.(15) and (16) are both equal to 1.0.
- (3) mass coefficients of model buoy C_{mx} and C_{mz} in eqs.(15) and (16) are both equal to 2.0.
- (4) velocity and acceleration fields of the wave induced flow can be evaluated by the theory of small amplitude wave.
- (5) damping coefficients of the buoy system C_x and C_z can be determined by trial and error method in the process of numerical analysis although the coefficient values determined

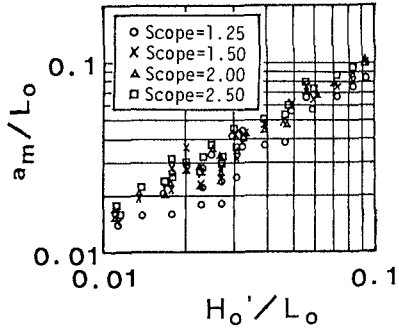


Figure 8 Relationship between a_m/L_o and H_o'/L_o .

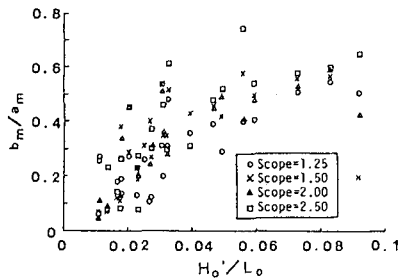


Figure 9. Relationship between a_m/b_m and H_o'/L_o .

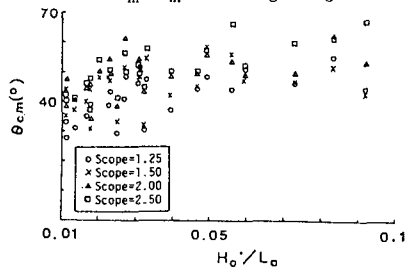


Figure 10. Relationship between θ_{cm} and H_o'/L_o .

by Shoji(1975) through his tests of similar size are used as the initial values of them.

Based on these assumptions, we can now calculate the wave load and dynamic buoyance included in eqs.(1) and (2), for any time and location of model buoy. Further, wind load has been set to be 12.9grf and tensile stress and its components induced on the mooring line have been calculated for any location of model buoy. Thus, we are ready to solve eqs.(1) and (2) simultaneously. Numerical analyses were made for every case of the model tests by using the Runge-Kutter-Gill method. In the actual analyses, time interval was set to be 0.01 second and the analyses were proceeded until the calculated orbit of the model buoy reached almost stable state.

Figure 11 shows some examples of the numerical analyses. Namely, tensile stress T_c induced on the line and orbit of the model buoy both obtained from the analyses are compared in this figure with the corresponding ones measured in the model tests. The solid lines indicate the results obtained from the analyses and the dotted lines indicate the results measured in the model tests. From this figure, we can see that eqs(1) and (2) can simulate the dynamic motion of model buoy fairly well although the developed model tends to give a slight overestimation.

To see the adequacy of the simulation model more quantitatively, the maximum values of the calculated tensile stress T_c , horizontal and vertical displacements of model buoy x_c and z_c , and inclination of the mooring chain θ_{cc} were compared with the corresponding values measured through the model tests.

Figures 12 shows the distribution of T_c/T_m plotted against H'_0/L_0 for the scope greater than 2.0. From this figure, we can see that developed model can predict the dynamic tensile stress induced on the mooring line quite satisfactorily when the scope value is greater than 2.0 and steepness of the acting wave is less than approximately 0.04. Further, the value of T_c/T_m scatters considerably when H'_0/L_0 is greater than approximately 0.04. Similar analysis was made for the case whose scope is less than 1.5. In such a case, the developed model has a tendency to considerably overestimate the ten-

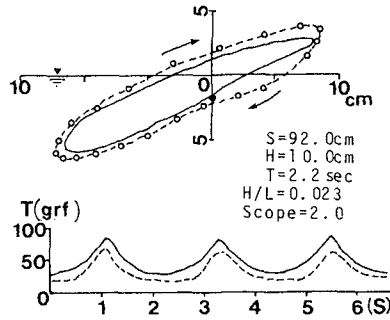


Figure 11. Example of the simulation of buoy's motion.

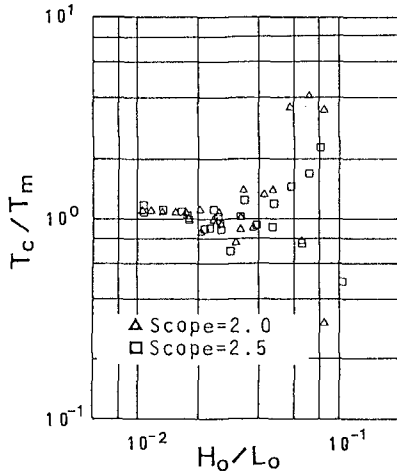


Figure 12. Relationship between T_c/T_m and H'_0/L_0 .

sile stress.

Figures 13 shows the distribution of z_c/z_m plotted against H_o'/L_o . This figure indicates that z_c/z_m agrees quite satisfactorily with z_m in the whole range of H_o'/L_o used in this model test. However, the model still has a tendency to overestimate the respective displacements of the model buoy when the scope of the line is 1.25. Analysis done for x_c/x_m also indicates a similar distribution for the values of H_o'/L_o .

Figure 14 shows the distribution of θ_{cc}/θ_{cm} plotted against H_o'/L_o . From this figure, we can see that θ_{cc}/θ_{cm} scatters around the value of 1.2 in the whole range of H_o'/L_o although the model has a tendency to overestimate θ_{cc} .

These comparisons indicate that the developed model can trace the dynamic behaviors of the mooring buoy fairly well when scope of the mooring line is greater than 2.0 and the steepness of the acting waves is less than nearly 0.04. Further, these comparisons may indicate the possibility that the developed model can be improved more when some modifications are made on the values of respective coefficients and the formulae to evaluate wind and wave load.

Application of the Developed Model to a Real Buoy

To determine whether the developed model can be applied to simulate the dynamic behaviors of a real buoy, and further to see whether the simulation done by this model can serve to find any possible causes for the failures of buoy systems which have often occurred in Iwo-jima, it was decided to choose a failure incident which occurred in Iwo-jima on May 23, 1982, as an object of the simulation, and to simulate the dynamic behaviors of the buoy just before its failure.

This incident occurred during a stormy weather which was caused by the typhoon No.4 which had been hitting the island since the day before the failure. In this incident, the harp shackle was distorted seriously due to a huge tensile force induced on it by the severe environmental loads, and was pulled out through the chain hole of the buoy. As a result, the buoy was cast away on the west coast of the island. Figure 15 is the side view of a harp shackle of the

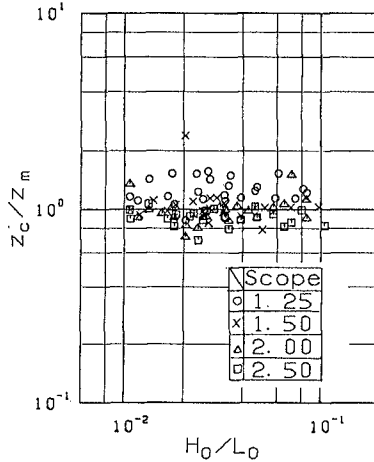


Figure 13. Relationship between z_c/z_m and H_o'/L_o .

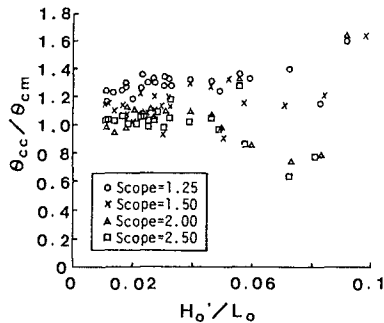


Figure 14. Relationship between θ_{cc}/θ_{cm} and H_o'/L_o .

same size as that used at the island. As can be seen from this figure, it is clear that a huge tensile force strong enough to squash the shackle's width from 420 mm into 352 mm was loaded on it at the moment of the failure.

Soon after the incident, the harp shackle was recovered by members of the Japan Maritime Self Defense Force (JMSDF) stationed there, and it was reported later that the width of the harp shackle was 364 mm and that several scratches were found on the inner wall of the chain hole of the recovered buoy. Further, the Engineering Office of JMSDF

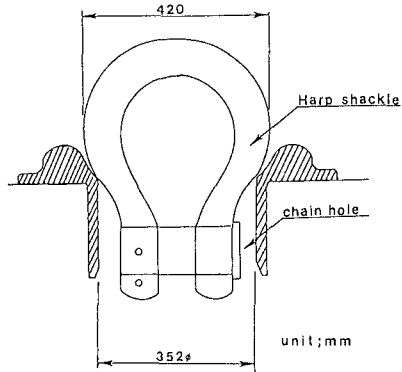


Figure 15. Side view of a harp shackle used in Iwo-jima in 1982.

made a series of static pulling test of harp shackles in a laboratory and concluded that external loads of approximately 110 tonf were loaded on the harp shackle at the moment of the failure(1982). This buoy was one of four buoys installed off the west coast of Iwo-jima, and it had been just swapped two months before the incident. The depth of installation was 16m and, and the buoy had been moored by a 20 m long mooring chain with a diameter of 68mm. Thus, the scope of mooring line was 1.25. Just two weeks before the failure incident, the authors had installed a supersonic wave meter about 450 m off the west coast of Iwo-jima at a depth of 12 m(1984). This site is about 500 m south of the installation site of the four mooring buoys. Fortunately, the wave meter recorded the wave data for ten minutes every two hours during this typhoon although the wave meter was washed away by typhoon No.17 which hit the island in November, 1983.

Through the analysis of this record, it was found that the maximum wave height was nearly 7 m and the significant wave period was approximately 10 second. The JMSDF on Iwo-jima has a meteorological station which is built near the center of the island and whose elevation is approximately 110 m above the mean sea level. At 6 a.m. of May 23, 1982, the station recorded the instantaneous maximum wind speed of 26.0 m/s. However, wind data around the installation site of the buoy is unknown. Thus, it was decided to use the wind of 55m/s which is the maximum wind speed recorded on the island for the

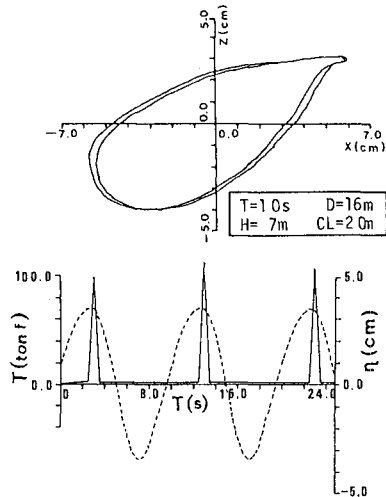


Figure 16. Results of the numerical analysis done for the buoy failed in Iwo-jima.

past 20 years. Further, it was decided to use the value of 1200 kgf.s/m for the damping coefficient C_1 and the value of 560 kgf.s/m for the damping coefficient C_2 , respectively. These values were determined by applying the Froude law of similarity to the corresponding coefficient values obtained through the model tests. Numerical analysis was made for the conditions stated above.

Figure 16 shows the analytical results. Namely, the upper figure shows the orbit of the buoy, and the lower one shows the time variations of both wave profile and tensile stress T . This figure clearly indicates that tensile stress exceeding 110 tonf may possibly be induced on the mooring line if the buoy is subject to as large external loads as those used for the numerical analysis.

Concluding Remarks

A rather simplified model was developed for simulating the dynamic behavior of a simple point mooring buoy which is installed in the open sea and the adequacy of the model was examined through the model tests. Further, using the developed model, numerical analysis was made for the dynamic motion of a real buoy in Iwo-jima whose system failed during a stormy weather caused by a typhoon. As a result, it was verified that the developed model can satisfactorily predict the dynamic behavior of a mooring buoy in the open sea.

References

1. Engineering Office of JMSDF, "Investigation report on the failure of No.1 buoy in Iwo-jima", p.13, June 1982.
2. Shigemura, T. and Komiya, Y., "Formation of tombolo at the west coast of Iwo-jima", Proc. of the 19th Conf. on Coastal Eng., Chap.96, pp.1403-1419, 1984.
3. Shigemura, T., Hayashi, K and Kouzaki, T., "Dynamic behavior of a single point mooring buoy installed in open shore", Proc. of the 34th Japanese Conf. on Coastal Eng., pp.621-625, 1987.
4. Shoji, K., "Study on the motion of a moored buoy and tension of mooring lines", Journ. of the Society of Naval Architects of Japan, Vol.138, pp.233-246, 1975.

CHAPTER 218

The Fundamental Study to Reduce The Settled Area of The Fish Aggregation Devices on The Sea Floor Thrown from A Ship

by Yoshiharu Matsumi* and Akira Seyama**

ABSTRACT

This study aims at clarifying the effective method to set up the fish aggregation device (FAD) thrown down from a ship on the designed position most accurately. The numerical simulation technique is developed to analyzed the behavior of the settling FAD in consideration of the effect of vortices generated behind it. From the systematic calculations for the change of the initial condition on the posture of the FAD at throwing, the effective initial posture of the FAD which reduces the settled area on the sea floor most is investigated. Furthermore, the added-mass coefficient of the settling FAD is numerically analyzed from the kinetic energy of the fluid induced by the settling FAD. The FAD treated in this study is the structure to gather fishes.

1. INTRODUCTION

The fish aggregation device is usually placed on the sea floor of a depth from about 30m to 100m to gather fishes. The most common shape of the FAD is the cubic type of 2mx2mx2m with a hollow inside and a gap in individual surfaces as shown Fig.1. Although the reason why and how the FAD can gather fishes has not been enough clarified yet, vortices formed at the FAD and their shedding behind the FAD have been pointed out to be the major reason to gather fishes around it. The FAD supplies for fishes not only a hiding place but also nourishing materials which are flung up from the sea bed by the vortex induced. The multi-FAD system in which the FADs are arrayed with a constant interval along a dominant flow in planned sea area has been adopted to activate the mentioned properties of the FAD. The multi-FAD system is mainly constructed by throwing them down from a ship to lay out on the fishing ground. It is difficult to set up the FAD in the fluid is consisted by following three complex motions (i.e. an oscillatory motion in horizontal direction, a rotational motion and vertical

* Research Associate Dept. of Ocean Civil Engg. Faculty of Engineering, Tottori University, Tottori, Japan.

** Prof. Dept. of Ocean Civil Engg. Faculty of Engineering, Tottori University, Tottori, Japan.

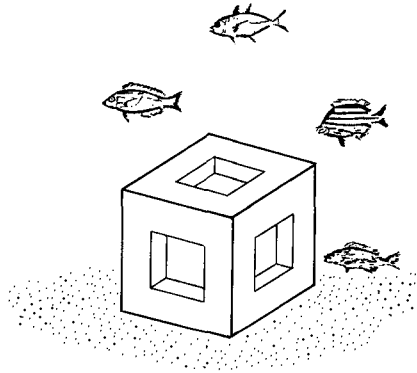


Fig.1 Illustration of fish aggregation device

drop). As a result of the position errors induced in the set up, the work of the system on gathering fishes may not be demonstrated sufficiently. Hence, to make it clear the settling behaviors of the FAD becomes urgent to carry out their accurate settling on the designed position. On the other hand, from the strength point of view, the impulsive force exerted on the FAD at landing on the sea bottom must be evaluated accurately. The impulsive force F is given by

$$\int_{\Delta t} F dt = (M + C_{MA} M') v_0 (1 + e) \quad (1)$$

where M and M' are the mass of the FAD and the liquid displaced by FAD respectively, C_{MA} is the coefficient of the added-mass coefficient, v_0 is the speed of the settling FAD at immediate time before landing, e indicates the repulsion factor between the FAD and the sea bottom. In general, the added-mass coefficient of the settling body is affected by the distance between the body and the bottom. Therefore, in order to evaluate the stability of the FAD against the impulsive force at landing efficiently, the affection of the sea bottom on the added-mass coefficient should be taken into account when we determine the design impulsive force on the FAD.

This study aims to clarify the following points; (1) the numerical simulation technique to analyze the behaviors of the settling FAD considering the effect of vortices generated behind it, (2) the initial condition of posture of the FAD at throwing to set up the FAD thrown down from a ship on the designed position most accurately, (3) the change of the added-mass coefficient of the settling FAD.

2. NUMERICAL SIMULATION TECHNIQUE OF THE SETTLING FAD

The oscillatory motion of the settling FAD in a periodic wave is induced by the instantaneous fluctuations of the pressure distribution around it, which is induced by the vortices generated from it and the wave motion. Hence, in the present numerical simulation technique, the fluid resistance exerted on the settling FAD is estimated firstly

by integrating the pressure distribution around its surface. This surrounding pressure distribution is numerically analyzed with both the discrete vortex approximation method (see Sarpkaya 1968, Clements 1973) for the simulation of the vortex formation behind the FAD and the source-sink points method (see Chakrabarti 1987) for the formulation of the boundary condition on the surface of it. Secondly, the oscillatory motion of the settling FAD at every moment is numerically calculated from the equation of horizontal, vertical and rotational motion for the settling FAD.

2-1 DESCRIPTION OF THE FLUID FIELD AROUND THE SETTLING FAD

In the case of two-dimensional wave field as shown in Fig.2, applying the small amplitude wave theory to the incident wave, the free surface in the wave field can be approximately replaced by the fixed rigid surface. Then, the appropriate complex velocity potential for the flow around the settling FAD can be determined by using the Schwartz-Christoffel transformation to project the interior region

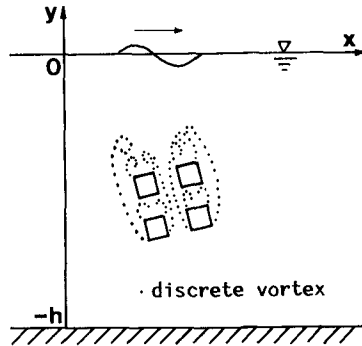


Fig.2 Schematic figure of flow field around the settling FAD

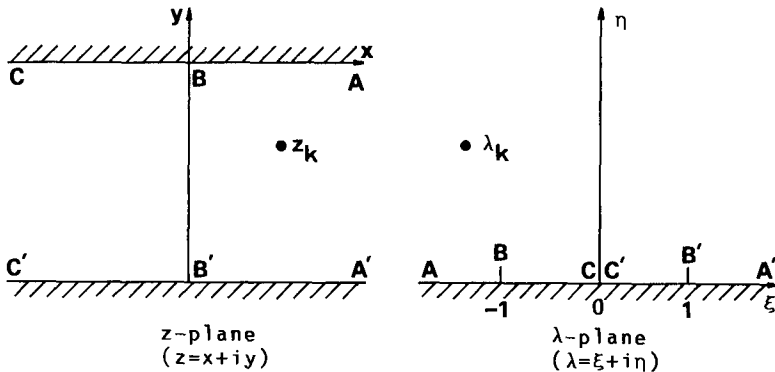


Fig.3 (a) physical plane z ; (b) transformed plane λ

between the boundaries in the z -plane into an upper half of the λ -plane with the boundary along the real axis (see Fig.3). The λ -plane is transformed into the physical z -plane by the function

$$z = x+iy = K \log(-\lambda) + C \quad (2)$$

where K is the constant determined by the water depth, and C is a integral constant. Since $\lambda=-1$ at $z=0$ and $\lambda=1$ at $z=-ih$ in which $i=\sqrt{-1}$ and h is the water depth, Eq.(2) is rearranged in term of z as,

$$\lambda = -\exp(C_0 z) \quad (C_0 = \pi/h) \quad (3)$$

The complex velocity potential ($\omega_{V\lambda k}$) of the discrete vortex (λ_k) in λ -plane (see Fig.3) is given by the following equation in terms of the imaginary discrete vortex which is necessary to maintain the boundary condition of zero flow across the real axis in λ -plane.

$$\omega_{V\lambda k} = \frac{i\Gamma_k}{2\pi} [\log(\lambda - \lambda_k) - \log(\lambda - \bar{\lambda}_k)] \quad (4)$$

where Γ_k and λ_k are the circulation and the complex coordinate of the vortex respectively, the circulation is defined as positive being clockwise, and the over bar denotes the complex conjugate. Substituting Eq.(3) into Eq.(4), the complex velocity potential (ω_{Vzk}) in z -plane is introduced as

$$\omega_{Vzk} = \frac{i\Gamma_k}{2\pi} [\log(e^{C_0 z k} - e^{C_0 z}) - \log(e^{C_0 \bar{z} k} - e^{C_0 z})] \quad (5)$$

where z_k is the complex coordinate of the vortex in z -plane. With the same way that used for the discrete vortex (Eq.(5)), the complex velocity potential (ω_{Rz_c}) of the source point in z -plane is given by

$$\omega_{Rz_c} = \frac{D(z_c)}{2\pi} [\log(e^{C_0 z_c} - e^{C_0 z}) + \log(e^{C_0 \bar{z}_c} - e^{C_0 z})] \quad (6)$$

where z_c and $D(z_c)$ are a location and a strength of the source point respectively.

When the flow around the settling FAD in z -plane consists of a periodic wave, N discrete vortices with some circulations generated from P separation points and the flow from the source points on the FAD surface, the complex velocity potential ω_z at the point z in z -plane is given by

$$\omega_z = \phi_z + i\psi_z = \omega_W + \omega_V + \omega_R \quad (7)$$

where ϕ_z and ψ_z are the velocity potential and the stream function for the total flow in the z -plane respectively, ω_W , ω_V and ω_R are the complex velocity potential of the incident wave, the discrete vortices and the source points, these are derived as follows with Eq.(5) and Eq.(6).

$$\omega_W = \frac{\sigma H}{2k \sinh kh} \sin[k(ih+z) - \sigma t] \tag{8}$$

$$\omega_V = \frac{i}{2\pi} \sum_{j=1}^P \sum_{k=1}^N \Gamma_{jk} [\log(e^{C_0 z_j k - e^{C_0 z}}) - \log(e^{C_0 \bar{z}_j k - e^{C_0 z}})] \tag{9}$$

$$\omega_R = \frac{1}{2\pi} \oint_c D(z_c) [\log(e^{C_0 z_c - e^{C_0 z}}) + \log(e^{C_0 \bar{z}_c - e^{C_0 z}})] dc \tag{10}$$

Here H , σ and k are a wave height, angular frequency and wave number respectively, \oint_c represents the contour integral along the surface c of the settling FAD. In the numerical calculation of Eq.(10), the surface c of the FAD is divided into M sections of length ΔC_m ($m = 1 \sim M$) and the source point is set on the center of the each section. Then the corner of the FAD is approximated with a circular arc of a radius $0.02a$, in which a is the side length of the FAD. The integration in Eq.(10) is evaluated as

$$\omega_R = \frac{1}{2\pi} \sum_{m=1}^M D(z_m) [\log(e^{C_0 z_m - e^{C_0 z}}) + \log(e^{C_0 \bar{z}_m - e^{C_0 z}})] \Delta C_m \tag{11}$$

The strength of the individual source point in Eq.(11) is determined by the boundary condition on the FAD surface (i.e. the fluid velocity normal to the FAD surface is equal to the settling velocity normal to the FAD surface). When the FAD is settling with speed (u_C, v_C) and with an angular velocity ω_r as shown in Fig.4, the identical equation of the strength $D(z_m)$ of the source point becomes as

$$R \left[\frac{\partial \omega_W}{\partial n} \right] + R \left[\frac{\partial \omega_V}{\partial n} \right] + R \left[\frac{\partial \omega_R}{\partial n} \right] = (u_C + u_r) n_x + (v_C + v_r) n_y \tag{12}$$

(on the surface of the FAD)

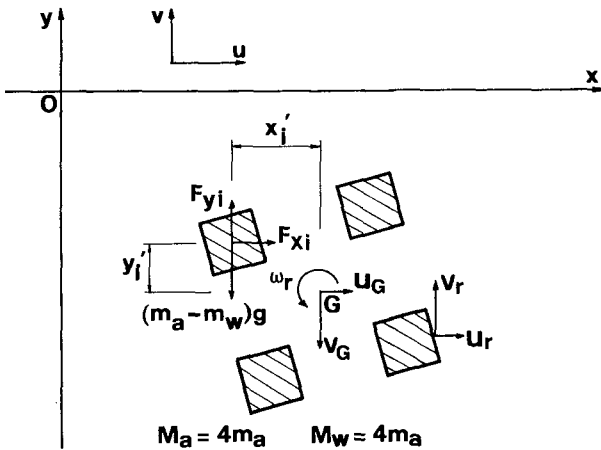


Fig.4 Fluid resistance on the settling FAD

where $\partial/\partial n$ denotes the derivative taken normal to the surface of the FAD, n_x and n_y are the x and y components of the unit vector taken outward normal to the FAD surface respectively, u_r and v_r are the x, y components of the velocity induced by the FAD rotation with angular velocity ω_r , $R[\]$ denotes the real part.

In Eq.(9), the velocities of the vortices are decided from the kinematic condition for the discrete vortices (i.e. a marked vortex is affected only from the incident wave, the other vortices and the source points on the FAD surface). Therefore, the velocity components u_{jk} , v_{jk} of the j-th vortex generated from the k-th separation point are expressed as

$$u_{jk} - iv_{jk} = \frac{d}{dz} \left[\omega_z - \frac{i\Gamma_{jk}}{2\pi} \log(e^{C_0 z_{jk}} - e^{C_0 z}) \right] \Big|_{z=z_{jk}} \quad (13)$$

If there are PN pieces of discrete vortices simultaneously around the settling FAD, a set of PN ordinary differential equations are derived as equations of the kinematic conditions for the discrete vortices.

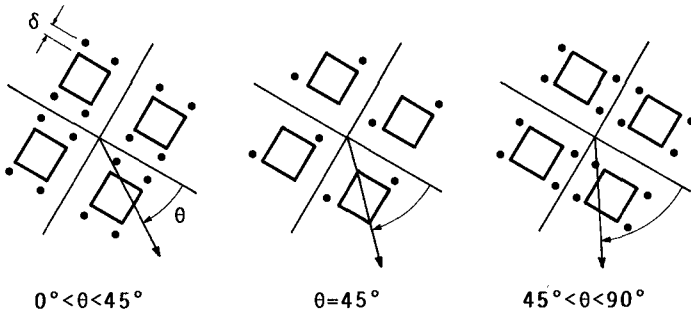


Fig.5 Initial positions of nascent vortices

In Eq.(13), the unknown initial position of the nascent vortex and the circulation of the vortices are included. There have been no established method, however, to calculate the initial position of a nascent vortex, its position has been determined with (A) the Kutta condition at the edge of the body or (B) the boundary layer thickness. In this study, (B) is adopted, and the initial positions are located at the distance of δ (boundary layer thickness which is determined by $\delta = \sqrt{\nu T/\pi}$ in which ν is the kinematic viscosity coefficient and T is the period of the wave) from the edges of the settling FAD as shown in Fig.5. Each initial position of the nascent vortex is changed with the relation between the angle of the FAD and the settling direction. The three separation patterns are treated in this study as shown in Fig.5. Secondly, the circulation of the nascent vortex is calculated with the Roshko's approximate equation (Roshko 1954). Taking the direction of the rotation of vortices into consideration, the circulation of the nascent vortex is given by

$$\partial\Gamma/\partial t = U_s |U_s|/2 \quad (14)$$

where U_s is a fluid velocity at the initial position of the nascent vortex. Although some vortices induce large velocities when they approach each other because we neglect the viscosity, this phenomenon is avoided by replacing the distributed discrete vortices with the Rankine vortex. The core radius of the Rankine vortex is given by $|\Gamma_{jk}|/2\pi U_s$ (Stansby 1977) in this study.

2-2 FLUID RESISTANCE ON THE SETTLING FAD

The fluid resistance exerted on the settling FAD can be obtained by integrating the pressure distributions around it, which is given in terms of $\partial\phi_z/\partial t$, u and v on the FAD surface ($z=z_p$) as

$$P(z_p) = -\rho \left[\frac{\partial\phi_z}{\partial t} + \frac{1}{2}(u^2+v^2) \right] \Big|_{z=z_p} \quad (15)$$

where ρ is the fluid density. Since the position z_{jk} of the discrete vortices, the strength $D(z_m)$ and the location z_m of the source points; and the position z_p on the FAD surface are functions of time, the first term of Eq.(15) is given by

$$\begin{aligned} \frac{\partial\phi_z}{\partial t} \Big|_{z=z_p} = & \left[R \left[\frac{\partial\omega_W}{\partial t} \right] + R \left[\frac{\partial\omega_W dz}{\partial z dt} \right] + R \left[\frac{\partial\omega_V}{\partial z_{jk}} \frac{dz_{jk}}{dt} \right] + R \left[\frac{\partial\omega_V}{\partial z_{jk}} \frac{dz_{jk}}{dt} \right] \right. \\ & \left. + R \left[\frac{\partial\omega_V dz}{\partial z dt} \right] + R \left[\frac{\partial\omega_R dz_m}{\partial z_m dt} \right] + R \left[\frac{\partial\omega_R dz_m}{\partial z_m dt} \right] + R \left[\frac{\partial\omega_R dz}{\partial z dt} \right] + R \left[\frac{\partial\omega_R dD}{\partial D dt} \right] \right] \Big|_{z=z_p} \quad (16) \end{aligned}$$

In Eq.(16), dD/dt can be calculated by differentiating Eq.(12) with respect to time t , the differentiated equation is analyzed in the same manner as the above-mentioned method for the strength of the source point. The horizontal and the vertical fluid resistance F_x , F_y exerted on the settling FAD are given as follows lastly

$$F_x = - \sum_{p=1}^M P(z_p) n_{xp} \Delta C_p \quad , \quad F_y = - \sum_{p=1}^M P(z_p) n_{yp} \Delta C_p \quad (17)$$

2-3 THE EQUATIONS OF MOTION OF THE SETTLING FAD

Referring to Fig.4, the equations of horizontal, vertical and rotational motion for the settling FAD are give as

$$\begin{aligned} M_a \frac{du_G}{dt} &= \sum_{i=1}^4 F_{xi} \quad , \quad M_a \frac{dv_G}{dt} = \sum_{i=1}^4 F_{yi} - (M_a - M_w)g \\ I_r \frac{d\omega_r}{dt} &= \sum_{i=1}^4 (x_i ' F_{yi} - y_i ' F_{xi}) \quad (18) \end{aligned}$$

where M_a is a mass of the FAD per unit thickness, M_w is the liquid (per unit thickness) displaced by the FAD, g is the gravity acceleration, and I_r is an inertia moment of the FAD around the gravitational center axis of the FAD. x_i' and y_i' are the distance from the center of the FAD cross section to the center of an i -th piece in the x and y direction as illustrated in Fig.4.

3. APPLICATION OF THE NUMERICAL SIMULATION TECHNIQUE

The application of the numerical simulation technique for the settling behavior of the FAD was investigated by comparing the calculated and experimented results. The experiments were carried out by using the wave tank of 30m long, 60cm wide and 1m depth to observe the behaviors of the settling FAD. The FAD model used in the experiments was consisted of four pieces of slender rectangular (1cmx1cm in the cross section) bodies. This study restricted the FAD motion on the vertical plane. Therefore, to prevent the FAD from 3-dimensional motion, a long model which had the same cross section was used in the experiments. Size of the model section is 3cmx3cm, length is 56cm, the void ration per unit thickness is 55.6%. The photographs of the settling figures of the FAD model were taken on a same film by using a strobe flash, the interval time of the flash is 0.2s. 2-dimensional motion is strictly inspected through the experiments. Since the behaviors of the settling FAD model were very irregular in the experiments, it was difficult to compare the simulated FAD behaviors with the measured behaviors. Therefore, we compared the simulated and measured horizontal fluctuation of FAD and the angular velocity of the rotational motion of the settling FAD.

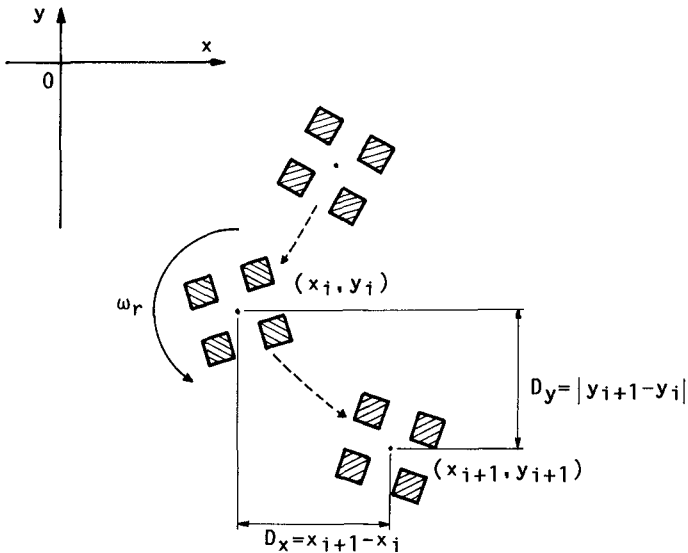
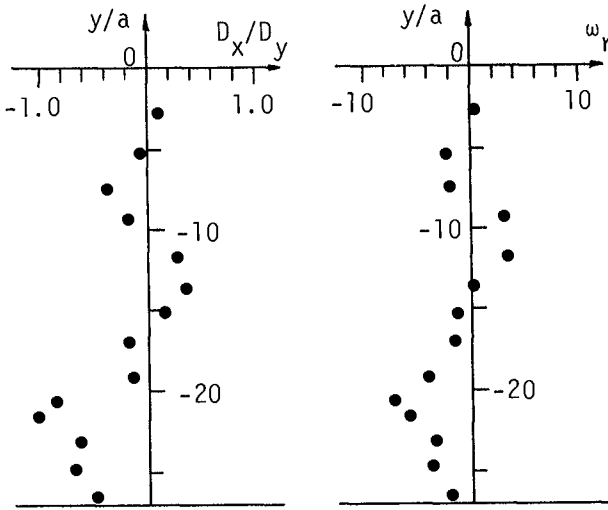
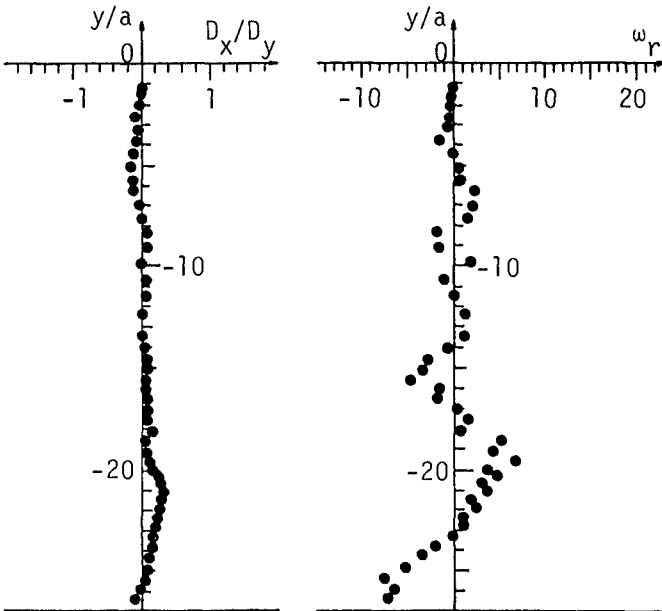


Fig.6 Definition of the fluctuation of the settling FAD



(A) Experiment



(B) Calculation

Fig.7 Measured and calculated oscillatory motion of the settling FAD

Fig.6 shows the definitions of the fluctuation of the settling FAD, D_x and D_y are the horizontal fluctuation and the settling distance from the simulated position. The angular velocity ω_r is defined as positive being anti-clockwise. When ω_r is positive, since the FAD moves in the positive direction of horizontal axis in Fig.6, the relative horizontal fluctuation to the settling distance D_x/D_y becomes positive.

Fig.7 shows examples of the experimented and calculated oscillatory motions of the settling FAD, x/a and y/a are the normalized x , y positions of the center of the FAD cross-section at each measured and calculated position. From the experiment (Fig.7(A)), the dominant behaviors of the settling FAD are the fluctuation in the horizontal direction which corresponds to a change in the rotational direction and the time lag between the inflection points of D_x/D_y and ω_r . This time lag may come from the change in the direction of the horizontal fluctuation which can not instantly correspond to the change in the rotational direction, because a motion of the settling FAD is the inertia motion. On the other hand, in the calculated results (Fig.7(B)), the present simulation technique can simulate also the dominant settling behaviors which are recognized in the experiments, i.e., the fluctuation of the settling FAD in horizontal direction and the change of its direction of rotation, the points of inflection. From these investigations, we may conclude that the settling behavior of the FAD can be evaluated with this numerical simulation technique.

4. RELATION BETWEEN INITIAL ANGLE OF FAD AT THROWING AND SETTLING BEHAVIOR

To investigate the effective initial posture of the FAD at throwing to reduce the settled area on the sea floor most, the systematic calculations for the change of the initial angle from the still water surface at throwing were carried out by using the present simulation technique.

Fig.8 shows the calculated behaviors of the settling FAD for three kinds of the initial angles, $\theta_0=0^\circ$, 22.5° , 45° . In these cases, wave period of $T=1s$ is applied. From the settling figures, it is found that the fluctuation of the settling FAD in the horizontal direction has close relation to the initial angle of the FAD at throwing. Therefore, the initial angle is the important factor to dominate the scatter range of the landing FAD on the sea floor. In Fig.8(A) and (B), the ω_r takes the positive value for the major part of water depth, D_x/D_y also takes the positive values. From these results, it can be seen that the FAD settles in the positive direction of the horizontal axis. When θ_0 is 45° , the period of the change in the rotational direction is shortest among these three cases, and the horizontal fluctuation becomes very small. This situation for the settling FAD becomes the most stable, i.e., less oscillation may take place. From this result, it may be estimated that this situation reduces the settled area on the sea floor most. Furthermore, Fig.9 shows the calculated behaviors of the settling FAD in the case of $T=1.5s$. When θ_0 is 45° (Fig.9(C)), the period of the change in ω_r becomes the shortest, and the most stable situation for the settling

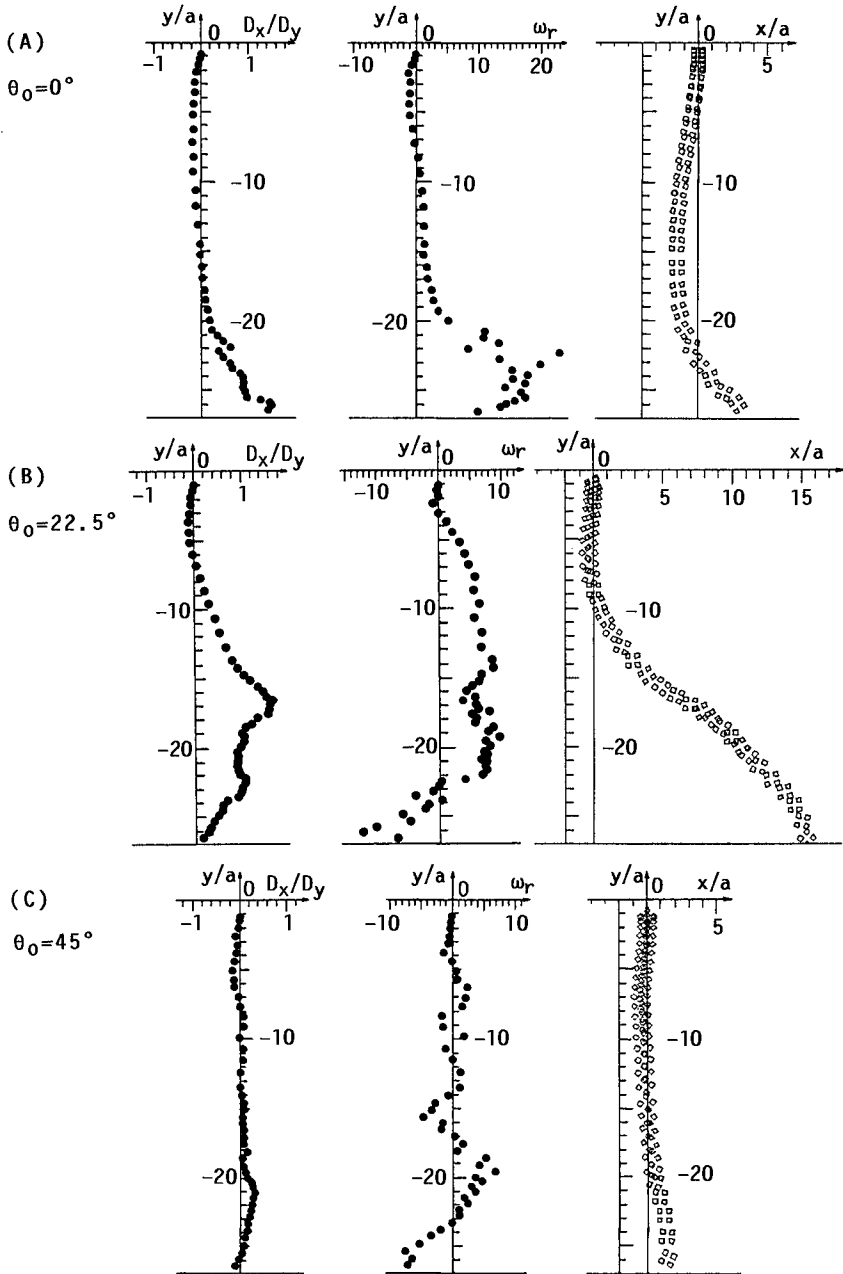


Fig. 8 D_x/D_y , ω_r and behaviors the settling FAD with respect to the initial angle θ_0 ($T=1s$)

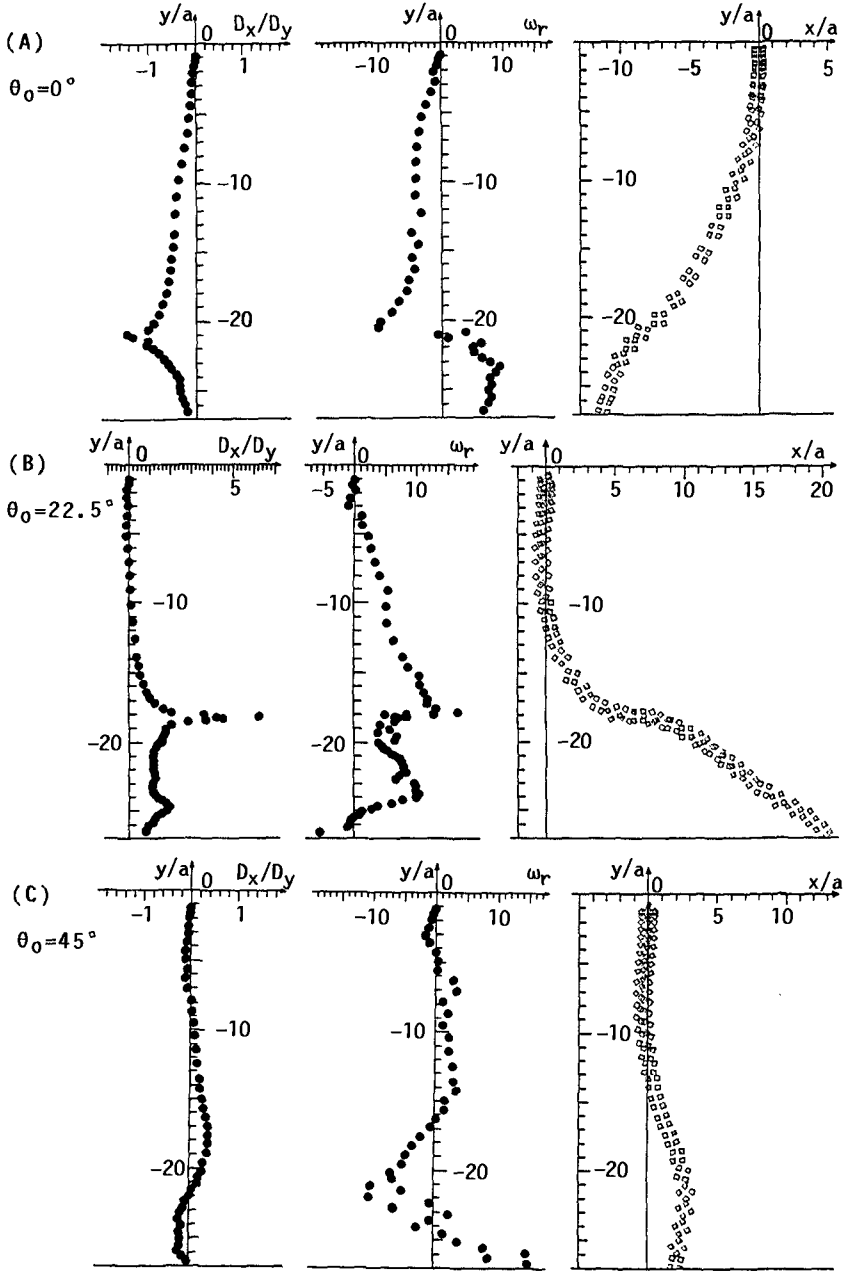


Fig.9 D_x/D_y , ω_r and behaviors the settling FAD with respect to the initial angle θ_0 ($T=1.5s$)

FAD can be observed again. From these investigations, it can be concluded that the initial posture of the FAD at throwing with the angle of 45° from the still water surface reduces the settled area on the sea floor most.

5. ADDED-MASS COEFFICIENT OF THE SETTLING FAD

The added-mass coefficient of the settling FAD is evaluated from the kinetic energy of the fluid induced by the settling FAD (see Milne-Thomson 1968). The kinetic energy T_w of the flow induced by the settling FAD is given by

$$T_w = -\frac{1}{2} \rho \oint_c \phi \frac{\partial \phi}{\partial n} dc \quad (19)$$

where ϕ is the velocity potential. If V is the volume (per unit thickness) of the FAD, the kinetic energy E_w of the fluid replaced by the settling FAD is

$$E_w = \frac{1}{2} C_{MA} \rho V v_0^2 \quad (20)$$

Since the added-mass $C_{MA} V$ is defined as the mass such that the kinetic energy E_w becomes equivalent to the kinetic energy T_w , the added-mass coefficient C_{MA} becomes from Eq.(19) and Eq.(20) as

$$C_{MA} = -\frac{\oint_c \phi \frac{\partial \phi}{\partial n} dc}{(V v_0^2)} \quad (21)$$

In the numerical calculation technique of the added-mass coefficient, the source-sink points method is adopted for the formulation of the boundary condition on the surface of the settling FAD. The velocity potential of flow around the settling FAD is given by

$$\phi = R \left[\frac{1}{2\pi} \oint_c D(z_c) [\log(e^{C_0 z_c} - e^{C_0 \bar{z}_c}) + \log(e^{C_0 \bar{z}_c} - e^{C_0 z_c})] dc \right] \quad (22)$$

The second term of Eq.(22) is the imaginary part which is necessary to maintain the bottom boundary condition of zero flow across the sea floor. The calculations are carried out for the settling FAD in a still water, the horizontal and the rotational motion for the settling FAD are neglected for simplicity.

Fig.10 shows the change of the added-mass coefficient of the settling FAD with respect to the relative distance h_q/a from the sea bottom. When $h_q/a > 4$, C_{MA} is less affected by h_q/a . When $h_q/a < 4$, however, C_{MA} is affected by the "bottom" effect, and in the region of $h_q/a < 1$ the shorter the relative distance becomes, C_{MA} starts to increase very quickly in spite of the void ratio of the FAD. Furthermore, from Table-1 which shows the C_{MA} at landing on the sea bottom ($h_q/a=0.5$) and that in the infinite fluid field ($h_q/a=\infty$), it

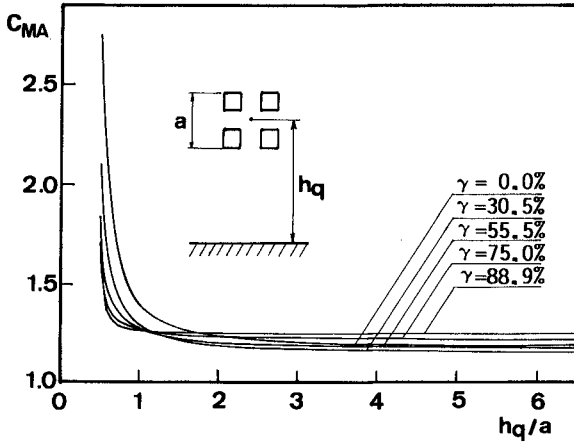


Fig.10 Change of the added-mass coefficient of the FAD with settling

Table-1 C_{MA} at landing and C_{MA} in the infinite field

γ (%)	0	30.5	55.5	75.0	88.9
C_{MA} at $h_q/a = \infty$	1.19	1.15	1.18	1.22	1.24
C_{MA} at $h_q/a = 0.5$	2.74	2.08	1.84	1.82	1.78

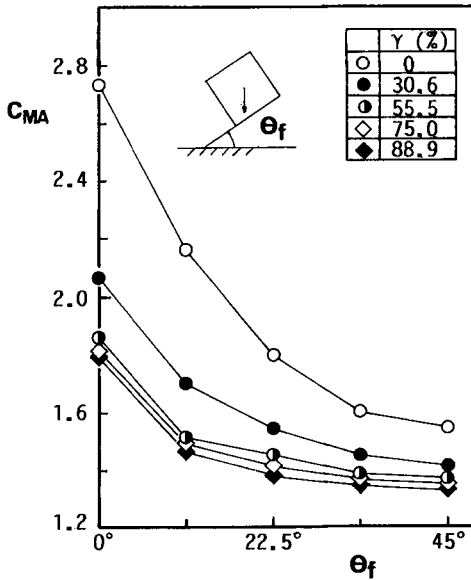


Fig.11 Relation between C_{MA} and the posture of the FAD at landing on the sea bottom

can be found that C_{MA} at landing on the sea bottom reaches about 1.4 to 2.3 times of that in the infinite fluid field. Fig.11 shows the relation between the C_{MA} and the posture of the FAD at landing on the sea bottom, θ_f is the angle between the FAD surface and the bottom, C_{MA} is the value at landing on the sea bottom. From this figure, it is seen that the added-mass coefficient of the settling FAD is affected by θ_f and C_{MA} in the case of $\theta_f=0^\circ$ becomes the largest among these five angles.

6. CONCLUSION

Concluding remarks are as follows.

(1) The present simulation technique for the settling behaviors of the FAD can successfully simulate the dominant behaviors of the settling FAD in the experiments (i.e. the fluctuation of the settling FAD in the horizontal direction corresponding to the change of its rotational direction, the time lag between the inflection points in the relative horizontal fluctuation to the settling distance and those in the angular velocity in the rotational motion).

(2) The fluctuations of the settling FAD in the horizontal direction are closely related to the initial angle of the FAD at throwing. The most stable situation for the settling FAD is achieved when the initial posture of the FAD is thrown with the angle of 45° from the still water surface. This situation may reduce the settled area on the sea floor most.

(3) The added-mass coefficient of the settling FAD may be evaluated through the calculation of the kinetic energy of the flow around the settling FAD using the potential theory with a sufficient accuracy. The added-mass coefficient at landing on the sea bottom reaches about 1.4 to 2.3 times of that in the infinite field. When the settling FAD lands on the sea bottom with zero angle, the added-mass coefficient becomes the largest.

REFERENCES

- Chakrabarti S.K.(1987): Hydrodynamics of Offshore Structures, Springer-Verlag, pp.286-324.
Clements R.R.(1973): An Inviscid Model of Two-Dimensional Vortex Shedding, J. F. Mech. Vol.57, Part 2, pp.321-336.
Milne-Thomson L.M.(1968): Theoretical Hydrodynamics, Macmillan Education LTD, pp.240-268.
Roshko A.(1952): On The Development of Turbulent Wakes from Vortex Street, NACA TN 2913.
Sarpkaya T.(1968): An Analytical Study of Separated Flow about Circular Cylinders, J. Basic Engg., TRANS., ASME, Series D, Vol.90, pp.511-518.
Stansby P.K.(1977): An Inviscid Model of Vortex Shedding from A Circular Cylinder in Steady and Oscillatory Far Flow, Proc. Instn Civ. Engrs, Part 2, pp.865-880.

CHAPTER 219

THE TIME DOMAIN ANALYSIS ON MOORED SHIP MOTIONS

Masayoshi KUBO*
M.JSCE, Dr.Eng., Associate Professor

Naokatsu SHIMODA**
M.JSCE, B.Eng., Vice-Head

Shunsaku OKAMOTO***
B.Sc.

ABSTRACT

The ship refuge inside a harbor in storm requires the analysis of moored ship motions along a quay wall. In this case the time domain analysis with the convolution integral method becomes effective. But the calculation accuracy is not enough and must be improved to analyze actual moored ship motions. In this paper some methods of the improvement are proposed and their efficiency is verified by comparing the calculation results with the experimental ones.

1. INTRODUCTION

Recently, many developments in the coastal zone are planned in Japan, for example the construction of artificial islands and so on. Since the reclamations of the sea narrow the anchoring areas outside a harbor in storm, the ship refuge inside a harbor in storm has been investigated by the Ministry of Transport.

When moored ship motions along a quay wall are considered, the time domain analysis with the convolution integral method becomes effective. But the papers with this method are very few¹⁾²⁾ and moreover the calculation accuracy for actual moored ship motions does not seem to be satisfactory. In this paper, some calculation methods are proposed to improve the accuracy and their efficiency is verified by comparing the calculation results with the experimental ones.

* Associate Professor, Kobe University of Mercantile Marine
1-1, 5-Chome, Fukae-Minami-Machi, Higashinada-Ku, Kobe
658, Japan

** Vice-Head, Technical Laboratory, Giken Kogyo Co., LTD.
1540, Kawaguchi-Cho, Hachiohji 193, Japan

*** Technical Laboratory, Giken Kogyo Co., LTD.
1540, Kawaguchi-Cho, Hachiohji 193, Japan

2.ON HYDRODYNAMIC COEFFICIENTS

2.1 Calculation Method

a) Equations of Ship Motions in the Time Domain

The calculations and the experiments are carried out by using the model ship shown in Fig.-1. The model is a rectangular floating body moored symmetrically along a quay wall. The incident wave angle θ is 60 (deg). The equation of ship motions in the time domain and the coefficients are given by,

$$\sum_{i=1}^6 \{M_{ij} + m_{ij}(\infty)\} \ddot{x}_i(t) + \sum_{i=1}^6 \int_{-\infty}^t \dot{x}_i(\tau) L_{ij}(t-\tau) d\tau + \sum_{i=1}^6 (C_{ij} + G_{ij}) x_i(t) = F_j, \quad (1)$$

(j=1,2,...,6)

$$L_{ij}(t) = \frac{2}{\pi} \int_0^{\infty} B_{ij}(\omega) \cos \omega t d\omega, \quad (2)$$

$$m_{ij}(\infty) = A_{ij}(\omega) + \frac{1}{\omega} \int_0^{\infty} L_{ij}(t) \sin \omega t dt, \quad (3)$$

where $x_i(t)$ =displacement, M_{ij} =mass or moment of inertia, $m_{ij}(\infty)$ =constant added mass or constant added moment of inertia, $L_{ij}(t)$ =retardation function, C_{ij} =hydrostatic restoring force coefficient, G_{ij} =mooring force coefficient, F_j =external force, t =time, τ =integral variable, $A_{ij}(\omega)$ =added mass or added moment of inertia (which is called added mass hereafter) and $B_{ij}(\omega)$ =damping coefficient which correspond to the angular frequency ω . The subscripts i and j describe the mode of ship motions, namely, 1:Sway, 2:Surge, 3:Heave, 4:Pitch, 5:Roll and 6:Yaw. The coefficients with the subscript ij show the effect on the i -th mode from the motion of the j -th mode.

As is obvious from the above, the hydrodynamic coefficients in Eq.(1) are decided by calculating the

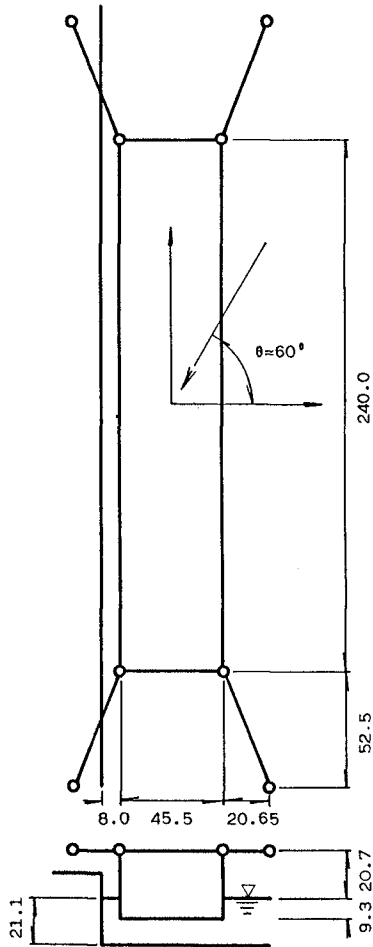


Fig.-1 The model ship (unit:cm)

frequency dependent added mass and the damping coefficient.

b) Calculation of Added Mass and Damping Coefficient

The added mass and the damping coefficient are calculated by the method of Green's function. Then the length of the mesh must be divided into less than a quarter of the wave length, so that the meshes represent the wave profile. In the case shown in Fig.-1, there are 18 coupling terms of $A_{ij}(\omega)$ and $B_{ij}(\omega)$ as shown in Table-1 because of the influence of the reflected waves. Further, the number of coupling terms is decreased to 12 by confirming the symmetry of the hydrodynamic coefficients, $A_{ij}(\omega)=A_{ji}(\omega)$ and $B_{ij}(\omega)=B_{ji}(\omega)$.

c) Calculation of Retardation Function

Since the damping coefficients in the whole angular frequency are required to calculate the retardation functions by Eq.(2), the damping coefficients must be approximated in the higher frequency than the maximum calculation angular frequency. In the two dimensional case the approximating formula for the higher frequency is given by Takagi and Saito³⁾ as follows,

$$B_{ij}(\omega)=k_{ij} \omega^{-n}, \quad (4)$$

where k_{ij} is a coefficient for joining calculated values to approximated ones and n is a multiplier. It's considered that the same approximation can be possible in the three dimensional case, then the values of n are given as shown in Table-2.

As mentioned above, the retardation functions are given by substituting Eq.(4) into Eq.(2).

Table-1 The coupling between each motion mode

		i					
		1	2	3	4	5	6
j		Sway	Surge	Heave	Pitch	Roll	Yaw
1	Sway	o	x	o	x	o	x
2	Surge	x	o	x	o	x	o
3	Heave	o	x	o	x	o	x
4	Pitch	x	o	x	o	x	o
5	Roll	o	x	o	x	o	x
6	Yaw	x	o	x	o	x	o

o = coupling term

x = no coupling term

Table-2 The values of n in Eq.(4)

i \ j		1	2	3	4	5	6
		Sway	Surge	Heave	Pitch	Roll	Yaw
1	Sway	3	-	5	-	5	-
2	Surge	-	3	-	5	-	3
3	Heave	5	-	7	-	7	-
4	Pitch	-	5	-	7	-	5
5	Roll	5	-	7	-	7	-
6	Yaw	-	3	-	5	-	3

$$L_{ij}(t) = \frac{2}{\pi} \left\{ \int_0^{\omega_e} B_{ij}(\omega) \cos \omega t d\omega + k_{ij} \int_{\omega_e}^{\infty} \omega^{-n} \cos \omega t d\omega \right\}, \tag{5}$$

where ω_e is the maximum calculation angular frequency. The analytical integral in the second term of the right hand side can be carried out by using the integration by parts and cosine integral.

d) Calculation of Constant Added Mass

The retardation functions are also required in the whole time domain to calculate the constant added masses in Eq.(3). On the other hand, the retardation functions show the decreasing oscillatory curve, so they are approximated by the next Eq.,

$$L_{ij}(t) = r e^{-pt} \cos(qt + \epsilon), \tag{6}$$

where r, p, q and ϵ are arbitrary constants. And the damping coefficients are given by applying the inversion formula of Fourier transform to Eq.(2),

$$B_{ij}(\omega) = \int_0^{\infty} L_{ij}(t) \cos \omega t dt. \tag{7}$$

Substituting Eq.(6) into Eq.(7) and carrying out the integrations by parts in the right hand side, then Eq.(8) is obtained,

$$B_{ij}(\omega) = \frac{r}{2} \left\{ \frac{p \cos \epsilon - (q + \omega) \sin \epsilon}{p^2 + (q + \omega)^2} + \frac{p \cos \epsilon - (q - \omega) \sin \epsilon}{p^2 + (q - \omega)^2} \right\}, \tag{8}$$

where the constants r, p, q and ϵ are decided by comparing the values obtained from Eq.(6) and (8) with ones from the numerical integral calculation. The truncation error S_p which is occurred from the halfway end of the infinite integral Eq.(7) is defined by using these constants and the

end time of the integral t_e , namely,

$$Sp = \frac{\int_0^{t_e} e^{-pt} \cos(qt + \epsilon) \sin \omega t dt}{A_{ij}(\omega) + \frac{1}{\omega} \int_0^{t_e} L_{ij}(t) \sin \omega t dt} \quad (9)$$

Since both the numerator and the denominator in Eq.(9) can be calculated analytically, t_e for the enough accuracy can be decided by Eq.(9). Eventually, the infinite integral in Eq.(3) is changed to the finite integral from 0 to t_e .

2.3 Calculation Results

a) Added Mass and Damping Coefficient

The length of the mesh is decided as the value which makes the maximum calculation angular frequency ω_e 10.0 ($2\pi/\text{sec}$). To confirm the symmetry of the hydrodynamic coefficients, the added masses and the damping coefficients in the case of $i=1, j=5$ and $i=5, j=1$ are shown in Fig.-2. In the figure the dotted line shows the case of $i=1, j=5$, the broken line shows the case of $i=5, j=1$ and the solid line shows the average values of them. Good agreements between the results of the two cases are obtained but there are a little difference. So the average values are used in the cases of $i \neq j$ hereafter.

In Fig.-2, there is a discontinuous value at $\omega=7.9$ ($2\pi/\text{sec}$). In particular, the value of the damping coefficient is negative at this frequency, therefore, the calculation of ship motions diverges. So we use the smoothed value at the angular frequency as shown in Fig.-3.

b) Retardation Function

The damping coefficients are shown in Fig.-4. The solid line shows the calculation results and the dotted line shows the approximate curve by Eq.(4). The results in the range from 10.0 to 14.0 ($2\pi/\text{sec}$) become valid by shortening the mesh length to a half and the converging tendency proves the validity of the approximation. The converging tendency of all damping coefficients in the high angular frequency is completed by the results of B22.

The retardation functions by Eq.(5) are shown in Fig.-5. The abscissas show the elapsed time.

c) Constant Added Mass

As an example, the value of t_e will be shown in the case of $i=5, j=5$. The approximate results of the retardation functions and the damping coefficients by Eq.(6) and (8) are shown as the solid line in Fig.-6. The dotted line shows the damping coefficients by the numerical calculation, when $r=1.6 \times 10^8$ ($\text{g} \cdot \text{cm}^2/\text{sec}^2$), $p=0.416$ ($1/\text{sec}$), $q=5.153$ ($1/\text{sec}$) and $\epsilon=0$. The relation between t_e and Sp is shown in Fig.-7. Since Sp is less than 0.01 at $t_e=20$ (sec), t_e is decided 60 (sec) to secure the calculation accuracy.

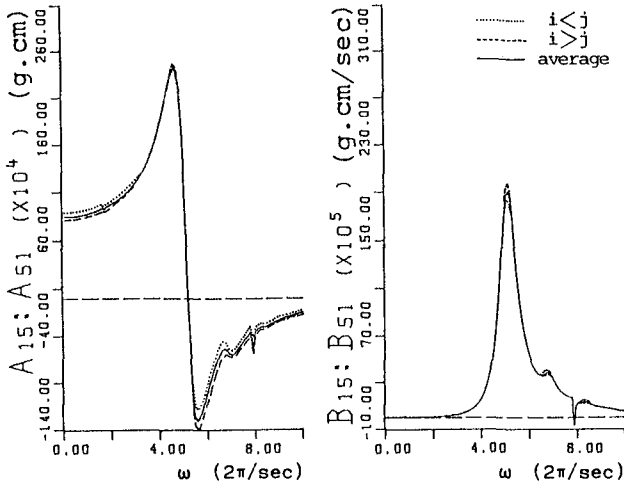


Fig.-2 The added mass and the damping coefficient

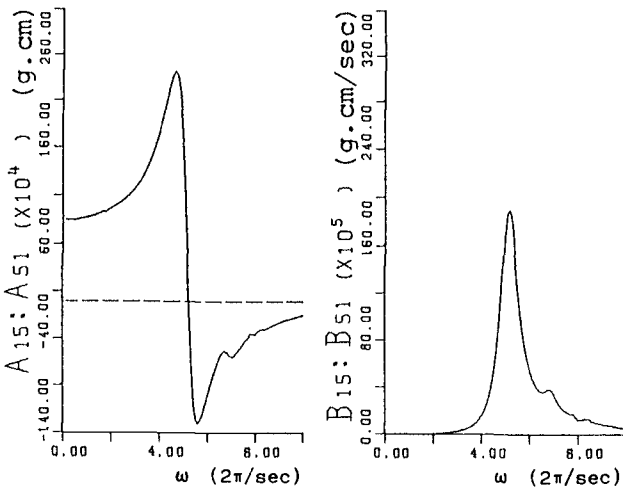


Fig.-3 The smoothed added mass and the damping coefficient

Next, the constant added masses calculated by using the t_e and Eq.(3) are shown as the thick lines in Fig.-8. The thin lines show the average values of them and the two-dot-dash-lines show the added masses which correspond to the angular frequency ω . It can be considered that the constant added masses show the constancy on the angular frequency.

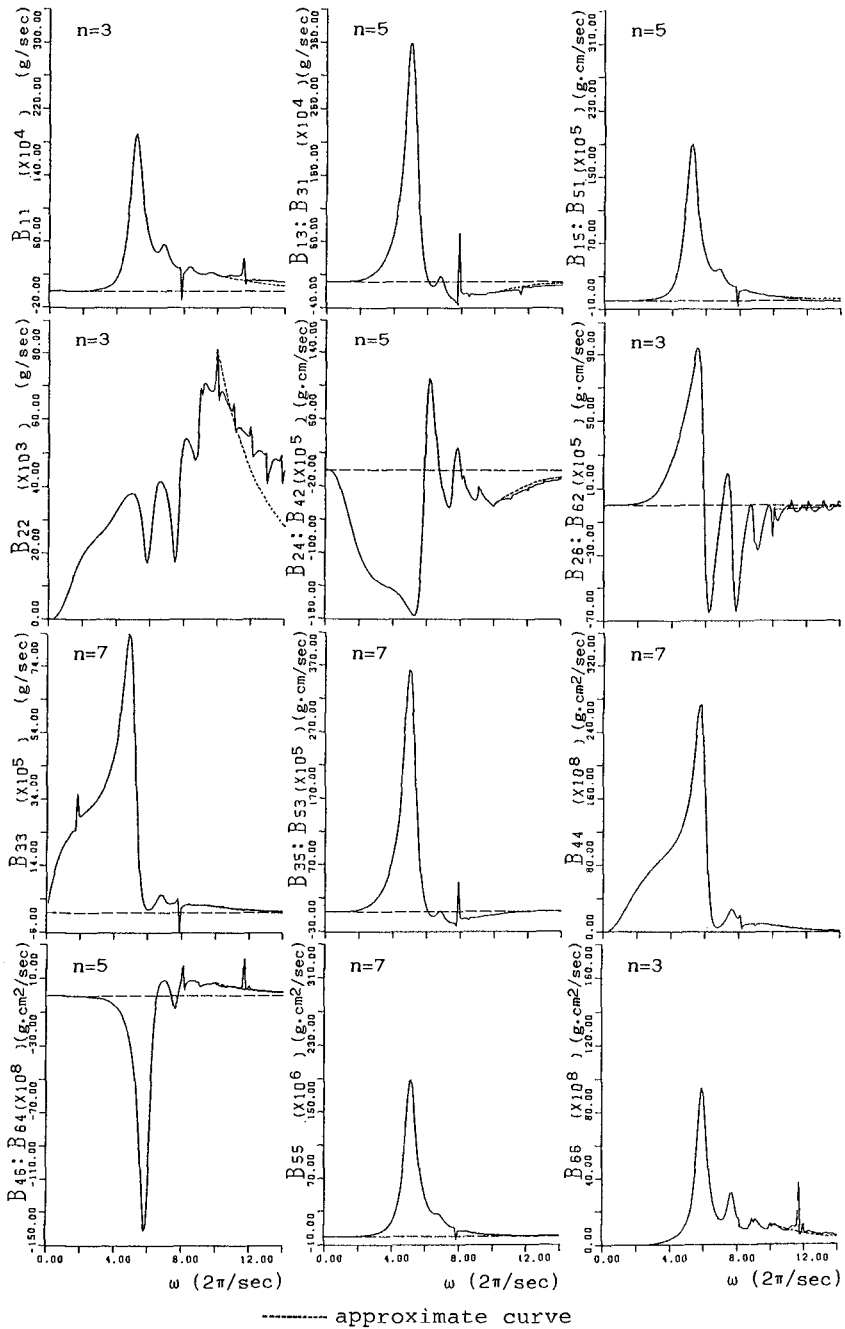


Fig.-4 The approximate curves of the damping coefficients

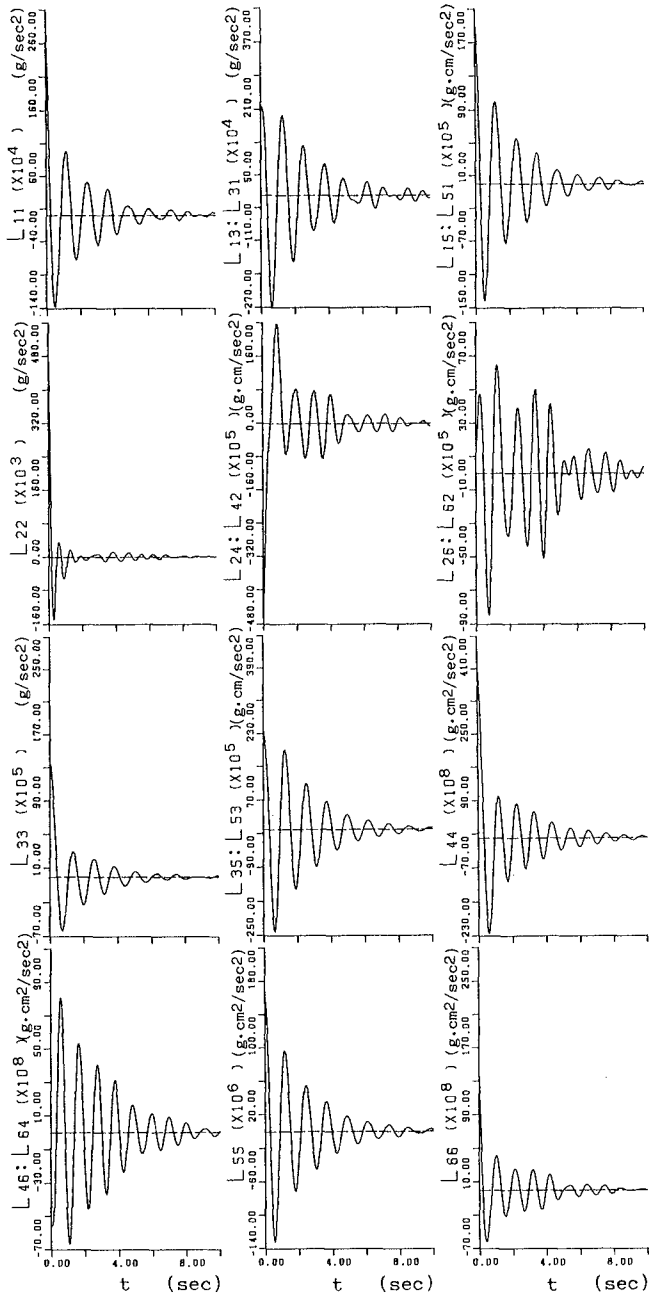


Fig.-5 The retardation functions

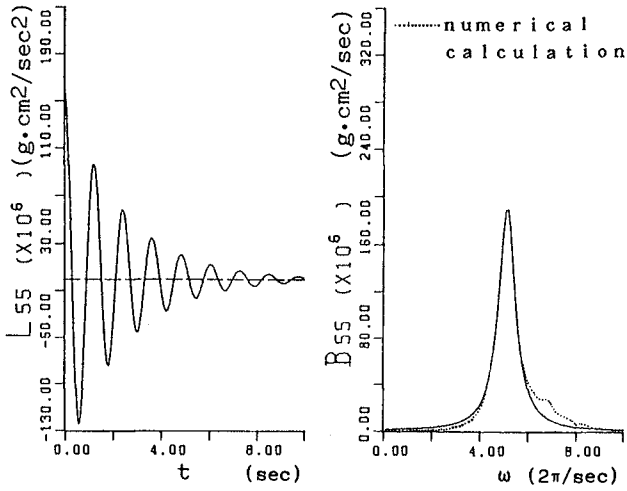


Fig.-6 The approximate results of the retardation function and the damping coefficient

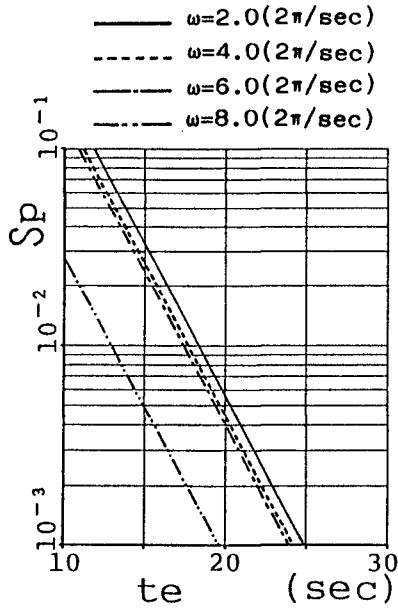


Fig.-7 The relation between t_e and Sp

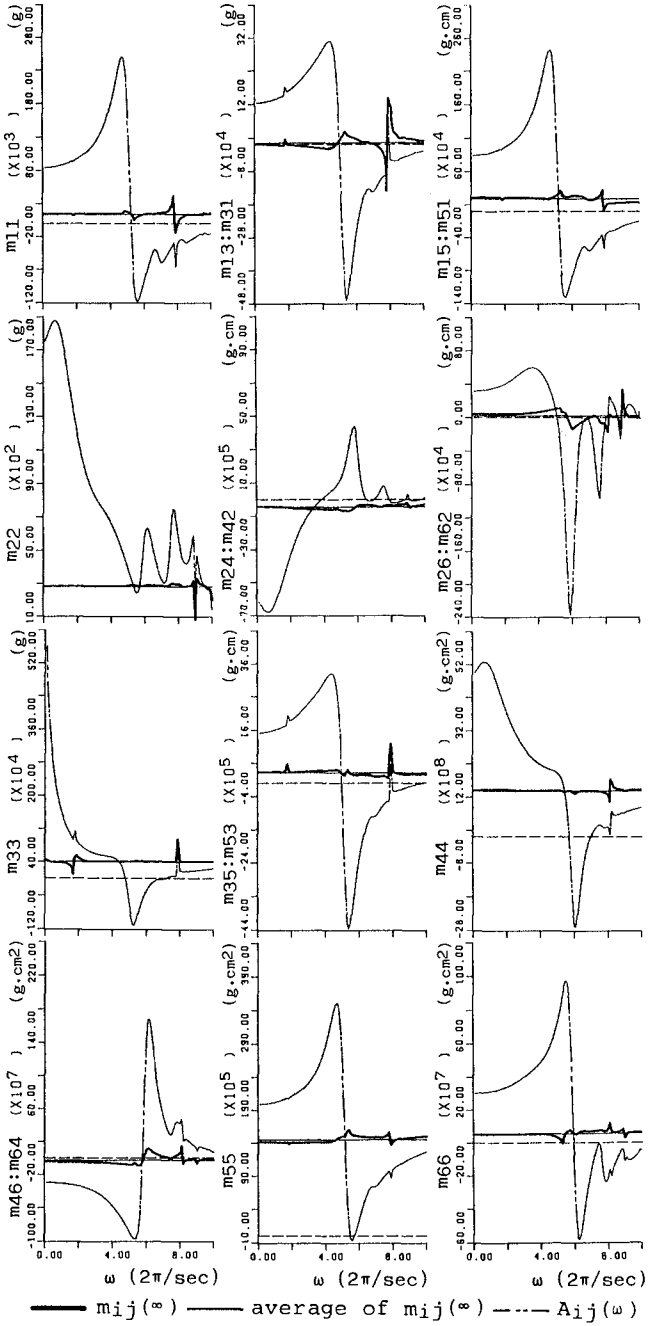


Fig.-8 The constant added masses

3. TIME DOMAIN ANALYSIS

3.1 Calculation Method

A time domain analysis can be carried out by calculating Eq.(1) with the obtained results. But the attention should be paid to the following matters.

a) Natural Period

Since the potential theory dose not give the viscosity term, the amplitude of ship motions is overestimated at the natural period because of the lack of damping force. Therefore, the existence of the natural period must be investigated within the range of used period. The natural period is obtained from the calculation of the free oscillations by giving an initial displacement in Eq.(1).

b) Introduction of Viscosity Term

The calculations are corrected by introducing the viscosity term $N_i \cdot x_i(t)$ to the second term of the left hand side in Eq.(1). The coefficient N_i is decided so that the calculated amplification factors of ship motions coincide with the experimental ones at the natural periods.

3.2 Calculation Results

a) Natural Period

The calculation results of the free oscillations are shown in Fig.-9. Each natural period is 10.1 (sec) in Sway, 3.8 (sec) in Surge, 0.8 (sec) in Heave, 0.8 (sec) in Pitch, 1.4 (sec) in Roll and 9.6 (sec) in Yaw.

b) Ship Motions in Beam Seas

The calculations are carried out in the range of the incident wave period from 0.6 to 2.4 (sec) and the results are compared with the experimental ones. The viscosity terms are introduced in Heave and Roll which have the natural periods in the above wave period range. The viscosity damping are evaluated by the logarithmic damping coefficient λ . The calculated free oscillations and the experimental ones are shown in Fig.-10. The ordinates, α , show the ratio of the displacement to the initial one. λ of Heave is varied widely because of the considerable change of the neighboring wave amplitude ratio. In Roll, 0.58 of λ is suitable for the calculations of ship motions, but 0.26 of λ is adequate for the above free oscillations. That is to say, the viscosity coefficient in ship motions is bigger than the one in the free oscillations. The difference may be modified by considering that the viscosity force is in proportional to the velocity squared.

Both results of the experiments and the calculations with and without the viscosity terms are shown in Fig.-11.

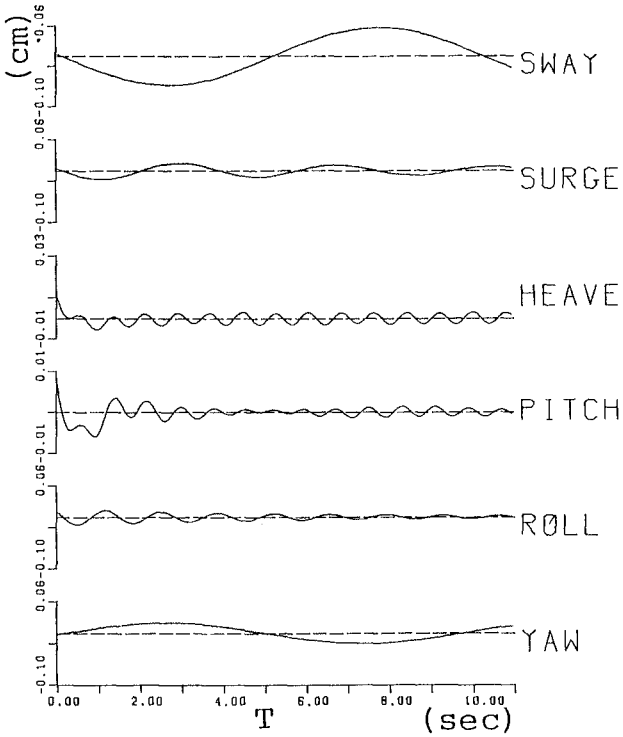


Fig.-9 The free oscillations

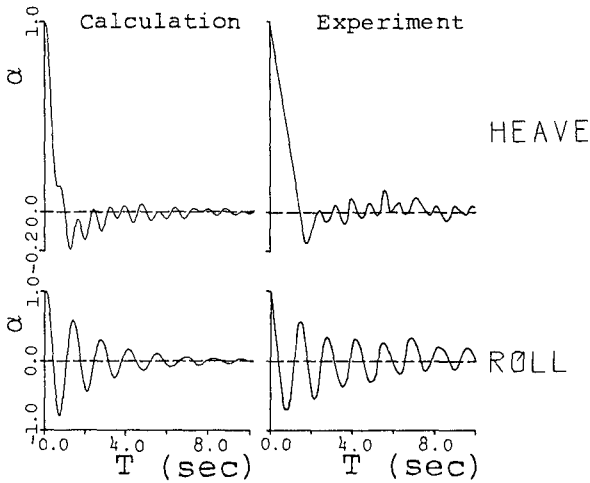


Fig.-10 The experiments and the calculated free oscillations with the viscosity terms

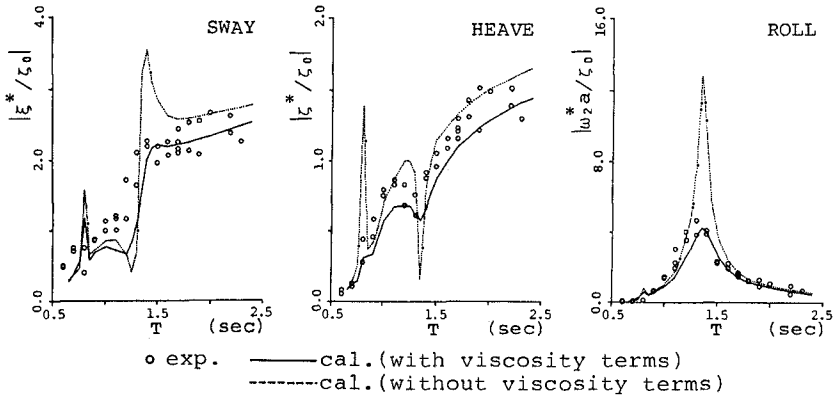


Fig.-11 The calculations and the experiments in the beam sea

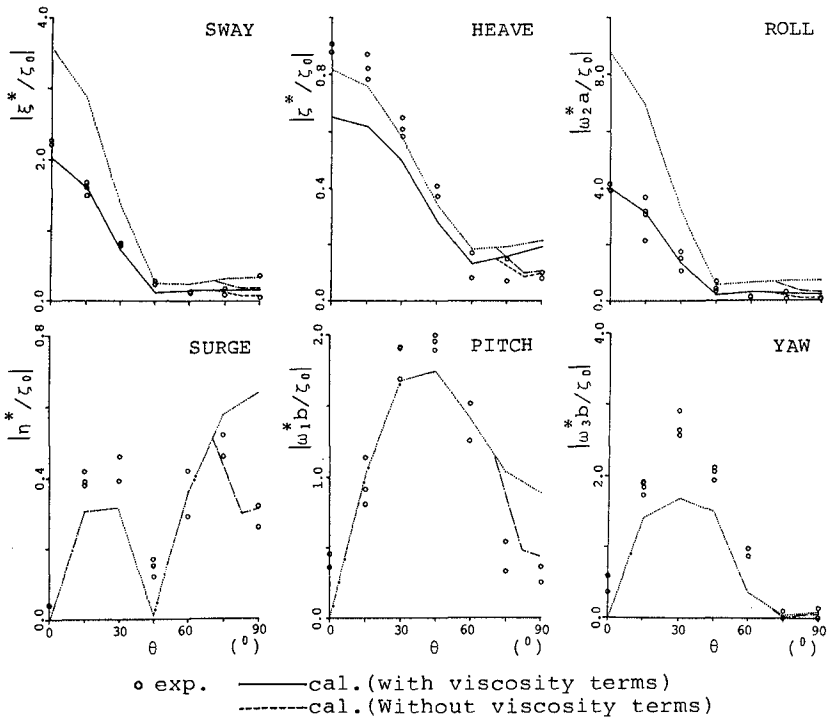


Fig.-12 The calculations and the experiments when the incident wave period is fixed at 1.4 (sec) and the incident wave angle is changed.

The ordinates show the amplification factor of ship motions. ξ^* , ζ^* and ω_2^* correspond to the complex amplitudes of Sway, Heave and Roll. ζ_0 is the incident wave amplitude and a is a half ship width. On Sway and Roll, the correction by the viscosity term is effective, but on Heave the correction tends to be overestimated except in the vicinity of the natural period.

c) Ship Motions in Oblique Waves

When the incident wave period is fixed at 1.4 (sec) and the incident wave angle θ is changed, the results are shown in Fig.-12. The ordinates show the amplification factor of ship motions. The abscissas θ show the incident wave angle and $\theta=0$ (deg) corresponds to the beam sea. η^* , ω_1^* and ω_3^* correspond to the complex amplitudes of Surge, Pitch and Yaw. b is a half ship length and the others are the same in Fig.-11. The viscosity terms are not introduced into Surge, Pitch and Yaw because of the disagreement between the wave period and the natural periods. The dotted line and the one-dot-dash-line show the results corrected by considering the effect of the finite length of a quay wall when θ is bigger than 75 (deg). It can be seen from Fig.-12 that there is a little error in the modes except Sway and Roll.

4. CONCLUSION

It is confirmed that the calculation accuracy is advanced by the improvement of the calculation methods on the retardation functions, the constant added masses and the introduction of the viscosity terms into equation of ship motions. But the introduction of the viscosity terms into the other modes where the viscosity forces are not considered in this paper must be discussed hereafter. They will be a main problem when the long period ship motions are calculated.

REFERENCES

- 1) Swaragi, T., M. Kubo and S. Aoki: New mooring system to reduce ship motions and berthing energy, Coastal Engineering in Japan, pp.303-313, Vol.27, 1984.
- 2) Oortmerssen, G. Van: The motions of a moored ship in waves, Publication No.510, Netherlands Ship Model Basin, Wageningen, The Netherlands, 1976.
- 3) Takagi, M. and K. Saito: On the description of non-harmonic wave problems in the frequency domain (5-th report), Journal of the Kansai Society of Naval Architects, Japan, pp.51-59, No.191, 1983 (in Japanese).

CHAPTER 220

FENDER SELECTION CRITERIA

F. Vasco Costa*

F. ASCE

ABSTRACT

Fenders are to be selected taking into account two quite distinct functions they have to fulfill:

- During berthing manoeuvres fenders have to avoid damage to the ship and to the berthing structure;
- After ships are already berthed and moored, fenders have to keep them quiet during loading and unloading operations.

To fulfill the first function fenders have to be able, while deflecing, to absorb a very large amount of energy.

To fulfill the second function fenders need to be able, while recovering their form, to dissipate a large amount of energy. Besides, they have to contribute to reduce or to increase the natural period of oscillation of already moored ships, depending on their tendency to oscillate in phase or out of phase with waves reaching the berths.

INTRODUCTION

The dimensions of ships have increased very rapidly in the last thirty years. The power of tugboats and the strength of ropes needed to assist the ships during berthing manoeuvres did not increase as fast as the dimensions of the ships. Besides, because they are larger, ships have now, at least in some harbours, to be moored in where ships will possibly be brought to move in ressonance with very stable long waves reaching such berths.

For these reasons fenders need to be selected taking into account that they will have not only to be able to absorb large amounts of energy during risky berthing operations but, as well, to be able to oppose, working as dash-pots, the tendency of moored ships to oscillate in ressonance with waves reaching their berths.

*Rua Borges Carneiro 6, 2o, Lisboa 1200, PORTUGAL

Just by passing ashore several strong ropes and keeping them tight, it is possible to keep small ships quiet at their berths, independently of the periods of the waves reaching the berths. But to prevent large ships from starting to move in resonance with long waves it is preferable, in most cases, to just use a few soft long mooring ropes passed not very tightly, so as to bring the natural periods of oscillation of the moored ships well above the periods of the waves reaching the berths.

THE FIRST IMPACT DURING A BERTHING MANOEUVRE

Berthing manoeuvres are very risky operations, especially when the ships are to be berthed in locations exposed to the action of waves, of currents and of wind.

A sudden change in the magnitude or in the direction of the wind or current, a rope that breaks, a deficient evaluation of the velocity of the point of the ship about to contact the first fender, an order to a tugboat which is not well understood or not promptly obeyed, and the ship will hit the fender moving at a too high velocity (Fontijn 1987, Svensen 1970 and Tryde 1987).

The cost of a fender is just a small fraction of the cost of a repair in the ship's hull or in the berthing structure. Preference is therefore to be given to fenders that are not only able to absorb a large amount of energy without being damaged but that, in case of something going wrong during the berthing manoeuvre, will keep absorbing an extra amount of energy while being damaged and having afterwards to be substituted.

Fenders that just "bust" in case of being overloaded, are to be avoided.

Berthing manoeuvres, which must always be planned and performed with the greatest care, are usually accomplished in the following phases:

- Placing the ship in front of the berth in a position parallel to the berth;
- Bringing the ship by a rotation, or a translation at a small angle, into contact with a first fender;
- Rotation of the ship around the first point of contact until she touches a second fender at the other end, becoming again parallel to the berthing surface.

In case of the velocity and the direction of the translation being known, the amount of the energy to be absorbed during the impact of the ship with the first contacted fender can be evaluated by the expression (see fig. 1)

$$E = \frac{mu^2}{2} \times \frac{k^2 + r^2 \cos^2 \gamma}{k^2 + r^2} \tag{1}$$

where

m is the mass of the ship plus the added mass;

u is the ship's velocity of translation;

r is the ship's radius of gyration;

k is the distance from the center of mass of the ship to the point of contact;

γ is the angle of the velocity direction with the line connecting the center of mass of the ship with her point of contact with the fender.

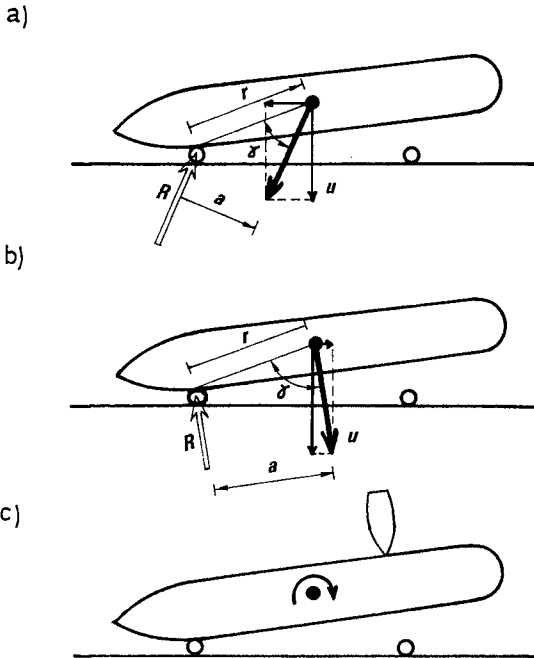


Fig. 1 - The berthing manoeuvre

In order to render the first impact of the ship as smooth as possible, the ship has to be moved in such a way as to render both the distance r and the angle γ as large as possible (Vasco Costa, 1964).

In case of $r/k = 1,6$, the making of $\gamma = 90^\circ$ instead of $\gamma = 70^\circ$ will permit the amount of energy to be absorbed by the fender during the first impact to be halved.

The bringing of the ship not in a perpendicular but in an oblique direction towards the berth will imply the risk of her hull sliding on the fender surface. If this happens, part of the ship's kinetic energy will be dissipated overcoming the friction between hull and fender. If the fender is not damaged in the process, nor the neighbouring ships affected, the sliding contributes to the reduction of the amount of energy to be absorbed by the deflection of the fender.

What is to be avoided is the bringing of the ship to berth moving in a direction with a tangential component oriented towards the point of contact, as indicated in the British Standard Code of Practice for Maritime Structure BS 6349, Part 4, and in fig. 1a. The bringing the ship as represented in fig. 1b, will not only imply a reduction on the amount of energy to be absorbed by the fender but, as well, a reduction on the magnitude of the fender reaction on the ship's hull. The only inconvenient of the recommended procedure is the increase on the amount of energy to be absorbed later, when a second fender is contacted at the other end of the ship.

If the ship enters in contact with the fender while moving in a simple rotation, instead of a translation, the amount of energy to be absorbed can still be evaluated by expression (1) by making $\gamma = 0$. The rotation permits, therefore, the minimization of the energy to be absorbed for a given velocity of the point of the ship's hull entering into contact with the first fender.

THE SECOND IMPACT

When a ship about to contact a first fender is moving at an excessive velocity, there is a tendency to apply on her, through ropes or tugboats, a force at the other end of the ship, in order to reduce the velocity of the point about to hit the first fender (see fig. 1c). In this way the risk of an accident during the first impact is, no doubt, reduced, but at the cost of increasing the amount of energy to be absorbed at the other end of the ship during the second impact (see fig. 1c). This must be the reason why second impacts are usually harder than the first (Jamm and Russman 1966). As second impacts take place after the motion of the ship is already under control, serious accidents never happen during the second impact.

The bringing of the ship to berth moving in a direction with a tangent oriented as represented in fig. 1b, and applying on a berthing ship torques that will reduce the velocity of the point of the hull about to contact the first fender, are practices to be recommended. Although implying an increase on the amount of energy to be absorbed during the second impact, they will permit to reduce the risk of accidents during the first impact.

It is customary practice to assume, in the evaluation of the energy to be absorbed by the fender, that a certain amount of water, to be denoted as added or hydrodynamic mass, is moving solidary with the ship, contributing to increase the amount of energy to be absorbed by the fender. In fact most of the water in the vicinity of the ship has to move in a direction opposed to that of the ship, not in the direction the ship is moving, in order to give room for the ship to move.

Much has been written about the elusive concept of added mass. For the purpose of fender selection the suggestion is advanced to evaluate the mass to be decelerated just by multiplying the mass of the ship by a coefficient

$$1 + 2 D/B$$

where D is the draught and B the beam of the ship (Vasco Costa, 1964).

To reduce the influence of the added mass, and therefore the amount of energy the fenders will be required to absorb, the suggestion is advanced to stop the ship, or at least to reduce her velocity, just before the ship contacts the fender. In this way the inertia of the water will keep for a while the water moving faster than the ship. When the ship is brought again into motion, the water that has overtaken the ship will contribute to reduce her velocity during the impact with the fender.

MOORED SHIPS AS OSCILLATING SYSTEMS

It has been found in some harbours, by trial and error, that the most convenient way to keep moored ships quiet at some berths is by reducing the number of mooring lines and making them longer and slacker, while at some other berths it is better to make them shorter and to keep them very tight (Khanna and Bert 1977, Kilner 1960, Vasco Costa 1983 and Wilson 1970).

Why does it so happen?

Just because some waves, of so small height as to pass unnoticed, but of such great length as to render them very stable, succeed in reaching berths far inside harbours and in bringing the ship to oscillate in resonance with the periodic forces they exert on the ship.

These long waves, with periods of 30 seconds and longer, may have been generated by long/lasting violent storms in far-off places, or be the result of the interference of distinct trains of shorter waves.

If the basins they reach inside a harbour happen to have good reflective walls, and natural modes of oscillation coincident with any of the periods of the incoming waves, stationary waves will be formed inside the basins, their height possibly becoming larger than that of the waves in the open seas (Martinez and Naverac 1988, Oortmerssen 1987, and Portela 1970).

The periods of the distinct modes of oscillation of a closed rectangular basin can be evaluated by the expression

$$T = \frac{2 \ell}{n \sqrt{gd}} \quad (2)$$

where

- ℓ is the length of the basin;
- d is the depth of the water;
- n is an integer defining the mode of oscillation.

In table 1 are given the natural periods of oscillation of closed basins with rectangular form. For the evaluation of periods of oscillation of basins with other simple geometrical forms see Wilson (1970).

The natural period of oscillation of a moored ship of mass m being held at berth, without clearances, by mooring lines and fenders that deflect proportionally to the forces to which they are submitted, is to be evaluated by the expression

$$T = 2 \pi \sqrt{m/K} \quad (3)$$

where

K is the spring factor of the moorings (see table 2).

The smaller the mass of a ship, the stiffer the fenders and shorter her mooring lines, the shorter will be her natural period of oscillation. The larger the mass of a ship the softer the fenders and the longer her mooring lines, the longer will be the natural period of oscillation of the moored ship.

Small ships, namely pleasure and fishing boats, have natural periods of oscillation that are in general much shorter than the natural periods of oscillation of the basins in which they are moored. For that reason they oscillate in phase with the periodic forces exerted on their hulls by the waves. To reduce the amplitude of their motions after being moored, the spring factors of

TABLE 1
Periods of oscillation of closed basins

$$T = \frac{2L}{n \sqrt{gh}}$$

Dimensions of basin		Periods of oscillation				
Length	Depth	Uninodal	Binodal	Trinodal	Quadri-nodal	Quinui-nodal
500 m	5 m	2min23s	1min12s	48s	36s	29s
	8 m	1min53s	56s	38s	28s	23s
1 000 m	8 m	3min46s	1min53s	1min15s	56s	45s
	15 m	2min45s	1min22s	55s	41s	33s

TABLE 2
Periods of oscillation of ships moored without clearances

$$T = 2 \pi \sqrt{m/K}$$

Mass of ship m	Spring factor of moorings K				
	200 kN/m	500 kN/m	1000 kN/m	2000 kN/m	5000 kN/m
100 t	4.4s	2.8s	2.0s	1.4s	0.9s
500 t	9.9s	6.3s	4.4s	3.1s	2.0s
1 000 t	14.0s	8.9s	6.3s	4.4s	2.8s
5 000 t	31.4s	19.9s	14.0s	9.9s	6.3s
10 000 t	44.4s	28.1s	19.9s	14 s	8.9s
50 000 t	1min40s	1min3s	44.4	31.4s	19.9s
100 000 t	2min20s	1min29s	1min3s	44.4s	28.1s
500 000 t	5min14s	3min19s	2min20s	1min40s	1min3s

their moorings are to be increased by resort to a large number of shorter, stiffer and tighter ropes, as well to stiffer fenders.

Large ships, especially if moored in basins of relatively small dimensions, present natural periods of oscillation that are larger than the natural periods of oscillation of such basins. As a consequence, they will tend to oscillate out of phase with the periodic excitation forces exerted in them by the waves. To reduce the amplitude of their movements after being moored it is convenient to increase their natural periods of oscillation by holding them with just a few very long ropes, to be kept not too tight, and by resort to soft fenders.

Unfortunately, large moored ships never have well-defined natural periods of oscillation. This is not only because surge, sway, yaw, heave, pitch and roll motions interfere with each other but, besides, because mooring ropes, instead of having elongations proportional to the forces to which they are submitted, become stiffer when the forces applied on them increase in magnitude, the same happening to some types of fenders. When mooring ropes and fenders become stiffer, the natural period of oscillation of the moored ship decreases, this implying a greater risk of her starting to move in resonance with shorter waves.

The places where the consequences of moored ships starting to move in resonance with stationary waves in a basin can be more serious are the nodes of such waves. At the anti-nodes a moored ship will only be made to move up and down a few centimeters, while at the nodes the vertical movements will be almost non-existent, but the slope of the water surface will keep changing all the time. The larger the slope of the water surface the larger will be the force tending to bring the ship to slide down the water surface.

A stationary wave with a length of 1 500 m and a height of 0.5 m will cause the water slope to reach every half period a value of

$$\pi \frac{H}{L} = \pi \frac{0,5 \text{ m}}{1500 \text{ m}} \cong \frac{1}{1000} \quad (4)$$

Such slope will pass unnoticed to visual observation. Notwithstanding, a ship with a displacement of 300 000 t will be submitted to an horizontal force of 300 t, which every half period will change direction (see fig. 2).

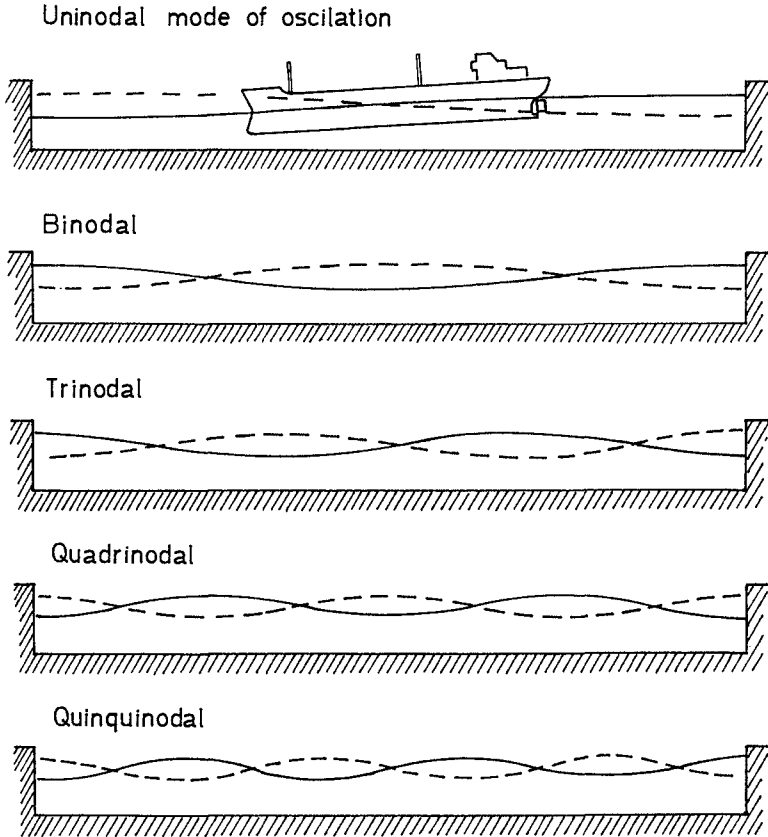


Fig. 2 - Modes of oscillation of a closed basin

Such periodic force will bring the moored ship to have oscillatory motions whose amplitude will increase from motion to motion if the natural period of oscillation of the moored ship happens to be coincident, or near coincident, with that of the wave. In such case not only loading and unloading operations will have to be suspended but the ship will possibly break her mooring ropes or damage the fenders.

What can be done to avoid such situations?

Confronted with the difficulty of keeping ships quiet at their berths, some entities just prefer to ignore the nature of problem. This is the reason why, in the book "Guidelines and Recommendations for the Safe Mooring of Large Ships at Pier Piers and Sea Islands", published by the Oil Companies International Marine Forum, is stated on page 3: The design mooring conditions do not include wave conditions able to cause significant dynamic loadings in mooring.

Let us present some considerations on how to deal with the oscillation of moored ships in resonance with long waves reaching their berths.

First of all the possible modes of oscillation of the water in front of the berth must be identified. Just by throwing a few pieces of cork along a quay berth it will be possible to find out if stationary waves are present, which are their periods, and where are located their nodes and anti-nodes. But equipment is already available to study the motion of the water in front of a berth. In case of basins with simple geometrical forms, it will be possible to find the main forms of oscillation of a basin just by resort to simple analytical expressions (Kubo et al, 1988).

Once the periods of stationary waves in the basin and the natural periods of oscillation of the moored ship have been found, an option has to be made between two alternative ways of reducing the risk of the ship starting to move in resonance with the waves. Are the stiffnesses of mooring ropes and of fenders to be increased in order to reduce the natural period of oscillation of the moored ship, or are their stiffnesses to be decreased in order to increase her natural period of oscillation?

In general, as referred, small ships are to be held by stiff mooring cables and stiff fenders while large ships, especially when berthed in small basins, are to be held by just a few, soft, long mooring cables and relatively soft fenders.

It must be pointed out that the avoidance of resonance by increasing the natural period of oscillation of a moored ship implies the risk of the ship starting to move with undetected longer waves, that can be the occasional result of the superposition of trains of long waves with different lengths. For such reason, resort to soft moorings and soft fenders should only be adopted when the occurrence of very long waves is not to be feared.

When selecting fenders having in view the keeping of moored ships quiet at berth, one has to take into account that fenders, besides contributing to increase or decrease their natural periods of oscillation, will also have to act as dash-pots, dissipating as much energy as possible while recovering their form after deflection (see fig. 3).

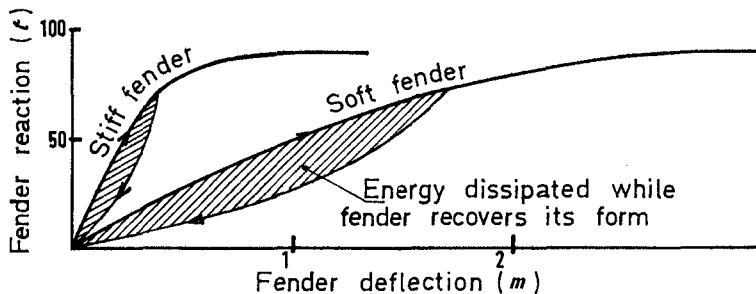


Fig. 3 - Stiff versus soft fenders

RECOMENDATIONS

In order to reduce not only the frequency of accidents during berthing manoeuvres but also their consequences, fenders need to be able to absorb very large amounts of energy when something goes wrong during such operations. Preference is to be given to fenders that, instead of just "busting" when overloaded, will keep absorbing energy while being damaged.

In order to reduce "down time" during loading and unloading operations, the fact has to be faced that moored ships are oscillating systems, and that the problems they pose are to be studied and solved, just as similar systems have been studied and solved, namely the suspension of automobiles. For such purpose the modes and periods of oscillation of the water inside harbour basins and the location of nodes and anti-nodes of stationary waves have to be identified. Spring factors of mooring ropes and fenders and of their combinations are to be evaluated, in order to find out if the natural periods of oscillation of the moored ships are to be increased or decreased.

When selecting fenders having in view the quietness of moored ships, preference has to be given to fenders which present deflections proportional to the forces they are being submitted to, because such fenders permit moored ships to present well defined natural periods of oscillation. Preference has also to be given to fenders that dissipate a large amount of energy while recovering their original form after being deflected.

Great progress in the study of modes of oscillation of water basins and of moored ships has been made in the last twenty years.

In the Proceedings of the NATO-ASI on "Advances in Berthing and Mooring of Ships and Offshore Structures", held in 1987 in Trondheim, reference is made to most recent publications on the subject.

ACKNOWLEDGEMENTS

Tanks are due for valuable comments by Eugene H. Harlow and by Bela Komman, both of Soros Associates, on the original version of this contribution.

REFERENCES

Bruun, Per [1986], "Can we save on breakwaters by providing better mooring-fendering?" PIANC Bolletín № 53, Brussels.

Fontijn, H. L. [1987], "On the prediction of fender forces on berthing structures" NATO-ASI on Advances in Berthing and Mooring of Ships, Trondheim, Norway.

Jamm and W. Russman [1965], "Measurement of tankers berthing manoeuvres" Hamburg, Report submitted to the Int. Oil Tankers Commission of PIANC.

Khanna, J. and C. Brit [1977], "Soft mooring systems at exposed terminals", Ports 77.

Kilner, F. A. [1960], "Model tests on the motion of moored ships placed on long waves". Proc. VII Conf. on Coastal Eng., Den Haag.

Kubo, M. N. Shinoda and S. Okamoto [1988], "The time domain analysis on moored ship motions", 21st Int. Conf. Coastal Eng., Torremolinos.

Martinez, F. and V. S. Naverao [1988], "An experimental study of harbours resonance phenomena" 21st Int. Conf. Coastal Eng., Torremolinos.

Oortmerssen, G. Van [1987], "Forces related to motions of moored ships - Analytical methods of moored ship motions" NATO-ASI on Advances in Berthing and Mooring Ships, Trondheim, Norway.

Oumeraci, H., O. Burkhardt and S. Kohlhasse [1987], "Influence of ship motions on the optimum design of ports layouts" 2nd Conf. Coastal and Port Eng. in Developing Countries. Beijing, China.

Scheffer, Hans-Joachim, and Sosen Kohlhasse, "On the vertical motion of ships at berth" 2nd Conf. Coastal and Port Eng. in Developing Countries, Beijing, China, 1987.

Svensen, I. A. [1970], "Measurement of impact energies on

fenders" The Dock and Harbour Authority, Oct. 1970.

Tryde, P. [1987], "Use of statistical data and methods in impact evaluation of fender design" NATO-ASI on Advances in Berthing and Mooring of Ships, Trondheim, Norway.

Ueda, Shigeru, Satorn Shiraishi and Mazakasu Yoshimi, "Estimation of Port Operation Rate by use of numerical simulation method of moored ship motions", 2nd Conf. Coastal and Port Eng. in Developing Countries, Beijing, China, 1987.

Vasco Costa, F. [1964], "The berthing ship" The Dock and Harbour Auth. May, June & July 1964, also published in booklet form by Foxlow Publications, London. U.K.

Vasco Costa, F. [1973], "Selection of fender performance", Proc. NATO-ASI on Analytical Treatment of Problems in the Berthing and Mooring of Ships, Wallingford, England.

Vasco Costa, F. [1983], "Moored ships as oscillating Systems" The Dock & Harbours Auth. Feb.

Wilson, Basil W. [1968], "The threshold of surge damage for moored ships" Proc. Inst. Civil Eng. Vol. 40, London.

Wilson, Basil W. [1965], "Seiches and other causes of the motion of ships already moored" Proc. of a NATO-ASI on Analytical Treatment of Problems of Berthing and Mooring Ships, Lisbon, published by the ASCE 1970.

Wyk, A. C. Van, and J. A. Zwanborn [1988], "Wave-induced ship motions in harbours approach channels", 21st Int. Conf. Coastal Eng., Torremolinos.

CHAPTER 221

UTILIZATION OF MOORED VESSELS IN HYDRAULIC MODELS OF HARBORS.

Dr. Ing. Rafael Guarga (IAHR member)*
Ing. Eduardo Goldsztejn**
Ing. Fernando Puntigliano**

Abstract

The behavior of the model of a moored vessel in a harbor's hydraulic model (Froude's model) is studied, taking into account the difficulties arising from the fact that modelling a moored vessel requires to incorporate the Reynolds number. Experiments made with the model of a large grain carrier at a 1/175 scale are shown. The horizontal motions of this ship due to the waves were measured when it is moored in a zone in which the length scale along the vertical axis was modified (vertical distortion), and the influence of different depths on these motions was studied.

This study was performed in order to be able to use this ship model for the evaluation of different alternatives of harbor design, in the building of new facilities at a port placed in the Atlantic coast of Uruguay.

*Director, Institute of Fluid Mechanics and Environmental Engineering, J. Herrera y Reissig 565, Montevideo, Uruguay

**Assistant Professors, Institute of Fluid Mechanics and Environmental Engineering

Introduction

The amount of agitation in the hydraulic model of a harbor is a main fact to be taken into account when decisions about harbor design are to be made. The traditional way for the evaluation of agitation is directly measuring wave heights in those places of the berth which are considered important for its performance. Comparison between two harbor designs is done by comparing the wave heights associated to each design, and frequently, design criterium is not reaching certain values of wave height which are accepted as maximum for a safe and economical development of the port's activities. Nevertheless, this method, though useful to compare two harbor designs, does not provide an absolute criterium for the evaluation of the port. The port's ability to fulfill performance requirements must be based on experience about the influence of the action of waves. An absolute criterium for the evaluation of a harbor design must provide the prediction, by means of the model, of the motions to be experienced by the ships which will be moored to the prototype's docks. A good design will be that in which these motions allow cargo handling to be safe and economical. These motions shall also be safe to all the port's facilities. References related to the behavior of vessels' physical models and their utilization to harbor design is found in bibliography about harbor design [2,3,4,5].

Stating the problem

When harbor's modelling is performed to study the behavior of a moored vessel, a similitude problem arises. The harbor's hydraulic models are Froude's models with length scales e_L roughly varying from 1/100 to 1/200, and the modelling of a moored vessel makes it necessary to introduce the Reynolds number. Simulation of the motion of a body subjected to external forces produced by the fluid, the mooring lines and the fenders system must be performed. Oscillatory flows between the ship's hull, the sea bottom and the docks take place and in such flows, power dissipation per unit of surface area is a function of the Reynolds number of the flow. Reynolds number scale (e_{Re}) in a Froude's model is $e_{Re} = e_L^{3/2}$. Considering, for example, $e_L = 1/100$, it results $e_{Re} = 1/1000$. Reynolds number reduction from prototype to model is then very important, and therefore there will be no similitude between the model of a moored ship in an agitation hydraulic model, and its prototype.

As an exact theoretical solution for the complex dissipative process which takes place in the turbulent boundary layer placed between the ship's hull, the sea bottom and the docks, is still not available, the problem must be tackled experimentally. This will be performed taking into account recent results related to the turbulent boundary layer created by a wave. Following Blondeaux [1], it is seen that the dimensionless mean power D dissipated by the boundary layer generated by the wave,

per unit of surface area, usually decreases with the Reynolds number. D is defined as $D = D^*/\rho U_b^{*3}$, D^* being the mean power dissipated by the boundary layer per unit of surface area, and ρ is the water density. The Reynolds number is defined as $U_b^* a_b / \nu$, being U_b^* the maximum velocity of the irrotational wave in the bottom, $a_b = U_b^* t / 2\pi$, t being the period of the wave, and ν the kinematic viscosity of water. In the referred paper it is stated that in hydraulically smooth regime, D can be calculated, by means of the relationship: $D = 0.14 Re^{-0.23}$. Considering now the average total power per unit of surface area in a simple harmonic progressive wave, E^* , this power can be expressed as $E^* = H^2 \gamma / 8t$, where H is the wave amplitude, and t the wave period. Therefore $D^*/E^* = 8U_b^{*3} D / gH^2 T$. If model's and prototype's D^*/E^* values are compared and a D^*/E^* scale is defined it is obtained

$$e_{D^*/E^*} = (D^*/E^*)_m / (D^*/E^*)_p = e_v^3 e_t e_L^{-2} e_{Re}^{-0.23} = e_L^{-0.345},$$

being e_t the time scale, and e_v the velocity scale. Then

$$d(e_{D^*/E^*}) / d(e_L) < 0$$

If this result is applied to a ship moored in a harbor, the conclusion is that the D^*/E^* value in the model is higher than in the prototype. The precedent reasoning shows that if dissipation in the model is not reduced, results obtained about angular and linear displacements of a moored vessel in a hydraulic model of a harbor will be smaller, at prototype's scale, than real displacements.

Experimental solution of the problem.

The installations:

The experiments described in the paper were performed in a hydraulic agitation model*. The ship which was modelled is the largest grain carrier that will be able in the future to operate in the new facilities to be built at this port. The model is shown in figure 1, in working position, with the mooring lines and fenders system described later in this paper. The length scale was $e_L = 1/175$. The main dimensions of the ship's model are:

*built in the Institute of Fluid Mechanics and Environmental Engineering, of the Faculty of Engineering of Uruguay.



Figure 1. Ship's model moored in harbor's hydraulic model.

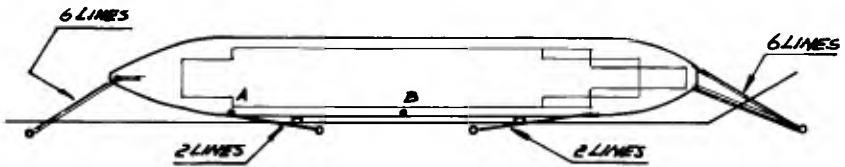


Figure 2. Arrangement of mooringlines in ship's model.

Length between perpendiculars:.....Lppm =1.41m
 Maximum moulded breadth:.....Bm =0.184m
 Displacement (maximum):.....Dm =146N
 Draught (maximum):.....Tm =0.071m
 Displacement (ballast condition):...D'm =75.2N
 Draught (ballast condition):.....T'm =0.039m
 Block coefficient:.....Cb=0.84

In addition to the hull's shape, longitudinal distribution of the weight (longitudinal position of the center of gravity, LCG) was simulated. The model's behavior was studied in ballast condition, and for this case, transverse distribution of weight, and metacentric radius were simulated. Being the time scale $e_t = e_l^{1/2}$, as it happens in Froude's models, the natural period of roll, which is of 8s in the prototype, resulted of 0.605s in the model.

This model was built to study the new breakwaters location in the port adjacent to the city of La Paloma, in the Atlantic coast of the country.

Mooring of the model and fenders system

Figure 2 shows the mooring of the vessel. The lines in the bow and in the stern simulate six synthetic-fibres lines of 80 mm diameter in each case, as required for this kind of ships. The lines on the sides simulate the behavior of two of these 80mm diameter lines, for each mooring. In order to measure the motions of the ship's model, the moorings of bow and stern were pretensioned with a force of 0.137 N, correspondent to 1.23×10^5 N for each line in the prototype. Forces on the lines were measured in the model by joining them to two force transducers which operate with strain-gages. In these transducers, a variable current is obtained when a horizontal force, perpendicular to them, is exerted. When forces vary from 0 to 0.98 N, the intensity of this current vary from 4 to 20 mA, and the variation is linear. Pretensioning of the lines meant therefore an increase of 2.24 mA in the intensity of the current generated at each transducer. The simulation of the mooring lines was performed using textil fibres which have a force-deformation law reproducing, at model's scale, the behavior of real mooring lines. The force-deformation law of several 80 mm diameter lines are shown in figure 3, as function of a reference force F_0 of 0.98×10^5 N in the prototype. In this figure, δ is a relative deformation, expressed in percentage ($100 \times \Delta L/L$), and δ_0 is the relative deformation corresponding to F_0 . With regard to the fenders system, simulation was achieved by using two force transducers of the same kind used to measure the forces on the mooring lines. Two springs were added in parallel to these transducers (figure 4). The elasticity constant of the device formed by each transducer and its spring is 1.23×10 N/m, so that both of them, when placed in the model's docks simulate the behavior of a fenders system adequate for the reception of ships of the size of the one which was modelled.

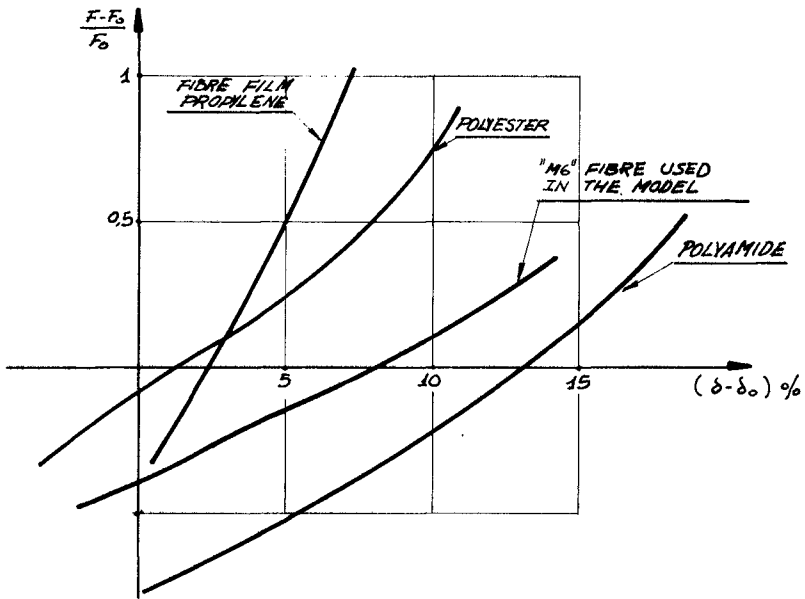


Figure 3. Force-deformation laws of 80 mm diameter lines, and of line used in the experiments.

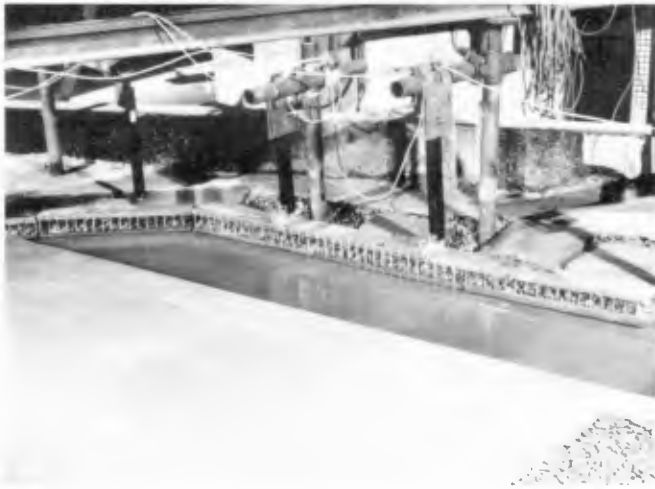


Figure 6. View of the distorted zone.

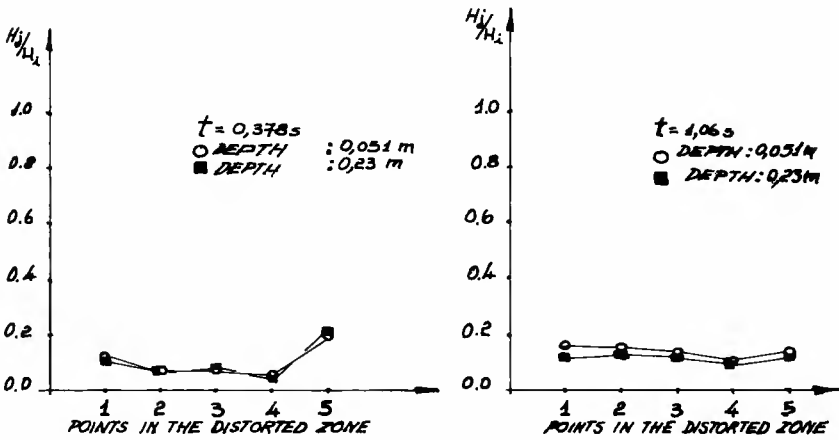


Figure 7. Measurement of wave heights in the distorted for different depths.

Horizontal motions of points A and B (figure 2), were measured visually with the aid of graduated scales

With the aim of reducing power dissipation in the model, and taking into account that power transfer from the mean flow to turbulent fluctuations is proportional to the magnitude of the components of the mean deformation velocities tensor [6], the harbor's model depth in the ship's neighborhood was distorted. The distortion was made in a zone in which reception of large vessels is planned. The area of this distorted zone is 3.72% of the total area of the port, and with regard to wave heights, no change in the behavior of the hydraulic model of the port was detected, either inside or outside the distorted zone, when measuring these wave heights with resistive devices.

In figure 5, the location of this zone is shown, and in figure 6 an overall view of it is provided. In figure 7, wave heights in five points named 1,2,3,4 and 5, in the distorted region are shown. Wave heights are referred to the amplitude of the wave in the generation zone, and they were measured with the normal depth of the port design (without any distortion), and with a depth of 0.23 m in the model, correspondent to the maximum distortion made. In both cases, wave periods in the model were 1.06s, and 0.378s. In figure 8, location of the points above mentioned in the distorted zone, is indicated.

The vertical distortion proportionally reduces the vertical gradients of mean velocities, which are the most important in this case, for turbulent dissipation. The effect of different depths in the distorted zone, on the motions of points A and B of the ship's model was studied. The depths used were $d = 0.051\text{m}$, $d = 0.15\text{m}$, and $d = .23\text{m}$, and referring these depths to the model's draught in ballast condition, values of d/T' were 1.32, 3.9 and 5.88. In figure 9 (a,b), results of the measurement of horizontal motions' magnitudes at points A and B (denoted as HA and HB) are summarized. In order to make comparison possible, HA and HB were divided by the height H_i of the generated wave in the hydraulic model of the harbor. Wave periods utilized were $t_1 = 1.06\text{s}$, $t_2 = 0.907\text{s}$, $t_3 = 0.756\text{s}$, $t_4 = 0.605\text{s}$ and $t_5 = 0.454\text{s}$, which are correspondent to periods of 14s, 12s, 10s, 8s and 6s in the prototype. In figure 10 (a,b), the ratios HA/H_i and HB/H_i are plotted against increasing values of L_w/L_{ppm} , L_w being the wave longitude in the generation zone, and, as already stated, L_{ppm} is the length between perpendiculars of the ship's model.

It is found that when depth increases in the distorted zone, the amplitudes of oscillations of the ship's model also increase. It's found also that the effect of depth on these amplitudes diminishes when distortion is increased, and that a condition is reached in which, beneath the appreciation of the measurements performed, no more effects on these motions are observed when depth is increased. the same behavior was observed by Giraudet [4], when studying berthing speeds in vessels' models, and energy transfer from ships to the fenders system.

These results are interpreted as a limit situation in which power transfer from mean flow to turbulent

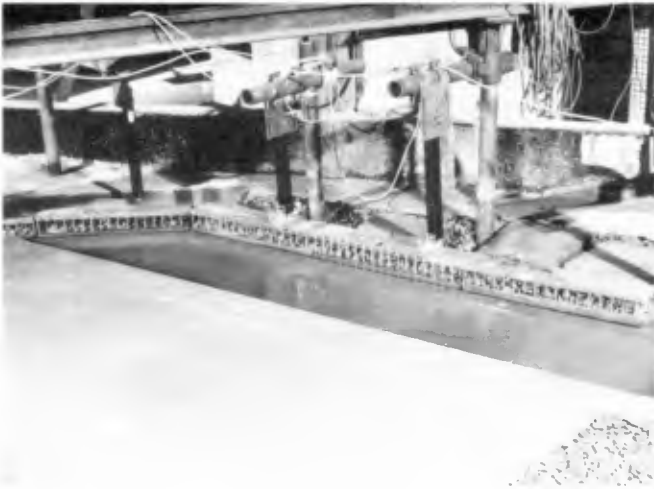


Figure 6. View of the distorted zone.

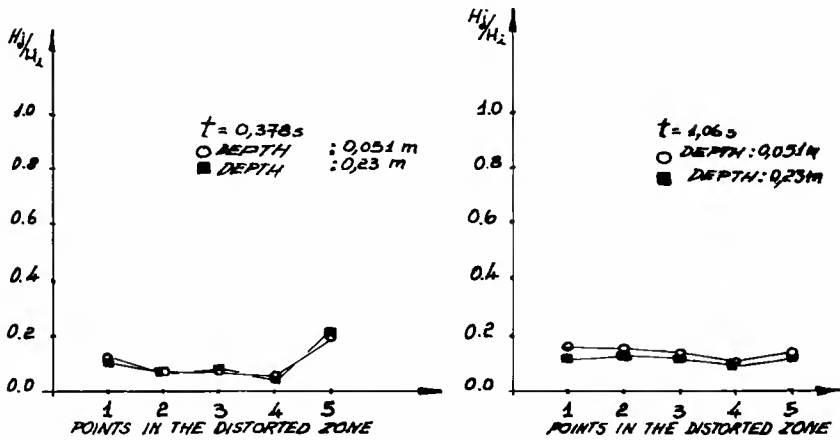


Figure 7. Measurement of wave heights in the distorted for different depths.

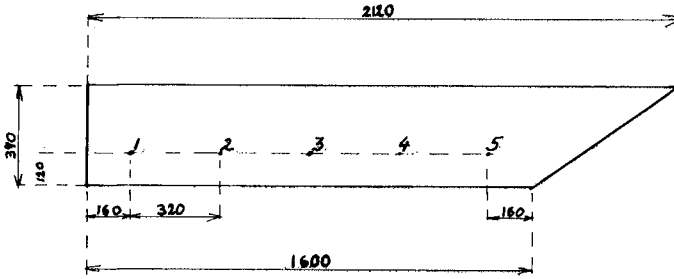


Figure 8. Location of points 1 to 5 in the distorted zone.

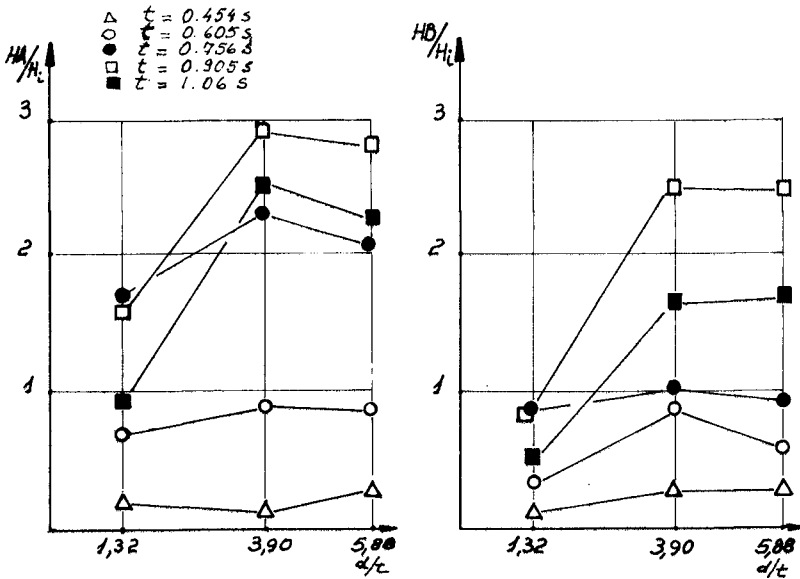
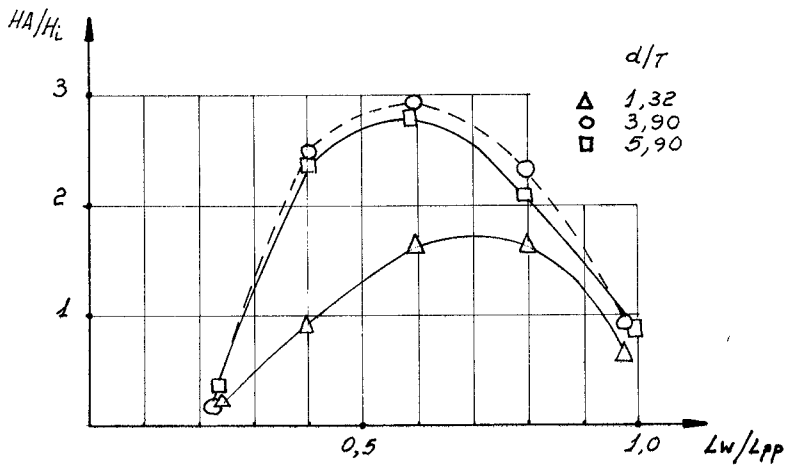
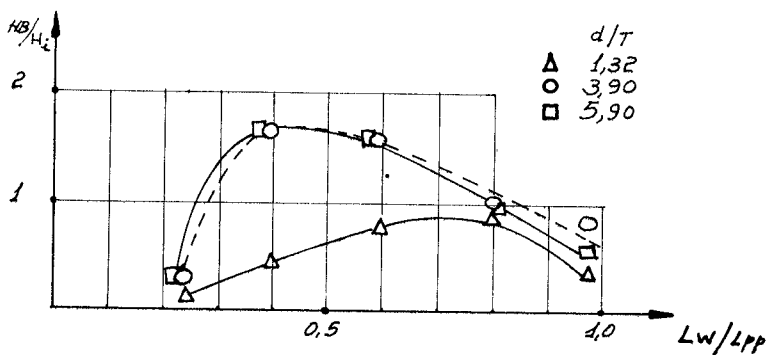


Figure 9(a,b). Displacement of the ship's model for different depths.



a



b

Figure 10(a,b). Displacement of ship's model as function of incident wave length.

fluctuations does not depend now on geometry, and, thus on the Reynolds number. Therefore the model operates in an "automodelling condition" with regard to Reynolds number. As the magnitude of the motions increases with depth, this condition places the model in a situation in which these motions will not be of less magnitude, at model's scale than those of the prototype, and results related to harbor's agitation by means of these ship's motions are on the safety side.

Conclusions

A method for evaluating agitation in harbors' hydraulic models is studied, which is more representative of port operation than measuring only wave heights in a mesh of points of the berth. It is shown that by using this method, safety factors are introduced if the bathymetry of the model is modified in a reduced area, which in view of it's small size, does not change the behavior of the port.

BIBLIOGRAPHY

1 - Blondeaux, P., "Turbulent layer at the bottom of gravity waves", Journal of Hydraulic Research, N° 4, vol 25, 1987 p. 447-464.

2 - Giraudet, P., "Recherches expérimentales sur l'énergie d'accostage des navires", Annales des Ponts et Chaussées, Mars-Avril 1966, N° II p. 103-127.

3 - Keith, J. and Murphy, E., "Harbor Study for San Nicolás Bay, Perú", Journal of the Waterways and Harbors Division, vol 2, May 1970 p. 251-273.

4 - Kim, C.H., "The influence of water depth on ship motions in oblique waves", Civil Engineering in the Oceans, vol.1, 1975, p.653-667.

5 - Schaeffer, H. and Kolhase, S., "Functional harbor design under consideration of ship motions", International Conference on Numerical and Hydraulic Modelling of Ports and Harbors, BHRA Birmingham, England, April 1985, p.221-229.

6 - Tennekes, H. and Lumley, J., "A first course in turbulence", MIT Press, 10th edition, 1985, Chapter 3.

7 - Van Wart, T. "Model testing a LNG terminal at Bintulu, Malasia", Civil Engineering in the Oceans, vol.1, 1979.

CHAPTER 222

A NUMERICAL WAVE PREDICTION MODEL FOR PERSONAL COMPUTERS¹

David J. Schwab²

ABSTRACT

A two-dimensional wave prediction model suitable for use on personal computers is described. The model requires the two-dimensional time-dependent wind field as input. Output consists of wave height, wave period, and wave direction estimates at all grid points on a computational grid representing an enclosed or semi-closed basin. Model predictions compare favorably with observations from a wave research tower in Lake Erie. A formula is provided to estimate how long a model simulation would take on a personal computer given the surface area of the computational domain, the grid size, and the computer clock speed.

1. Introduction

Numerical wave prediction models have been categorized in various ways according to their development as one-dimensional or two-dimensional, parametric or spectral, discrete or hybrid, and first, second, or third generation. The SWAMP Group, 1985, provides a summary and intercomparison of the various model types. The simple empirical formulas for wave height and period estimation such as the SMB formulas (Bretschneider, 1970) or JONSWAP relations (Hasselmann et al., 1973) are basically one-dimensional in that they depend only on local wind speed and upwind fetch distance. Two-dimensional models take account of advective effects on the wave field by predicting the spatial distribution of wave energy over an entire two-dimensional domain. Until recently, the two-dimensional prediction models have only been implemented on multi-user mainframe or minicomputers while microcomputer (PC) users were limited to using empirical, one-dimensional wave prediction formulas for wave estimation. With improvements in the capabilities of the personal computers, it is now

1

GLERL Contribution number 632.

2

National Oceanic and Atmospheric Administration
Great Lakes Environmental Research Laboratory
2205 Commonwealth Blvd.
Ann Arbor, Michigan 48105 USA

possible to make practical use of some two-dimensional models with relatively inexpensive computing machines.

This paper describes the formulation and implementation of a particular two-dimensional wind wave prediction model (Donelan, 1977, Schwab et al., 1984a and Liu et al., 1984) for use on personal computers. The model is a parametric type that numerically solves a local momentum balance equation on a computational grid covering a closed or semi-closed basin. Only actively generated wind waves are predicted, swell is not included. The model is driven by the two-dimensional, time-dependent wind field. Output includes estimates of significant wave height, peak energy period, and wave propagation direction at each grid point. The fact that the model is a parametric model and only needs to retain a few parameters describing the wave spectrum at each grid point instead of a complete spectral description makes it practical for use on personal computers.

2. Techniques

The basic model equations relate the time rate of change of wave momentum and the divergence of the wave momentum flux to wind forcing as follows:

$$\begin{aligned} \frac{\partial M_x}{\partial t} + \frac{\partial T_{xx}}{\partial x} + \frac{\partial T_{xy}}{\partial y} &= \frac{\tau_w^x}{\rho_w} \\ \frac{\partial M_y}{\partial t} + \frac{\partial T_{yx}}{\partial x} + \frac{\partial T_{yy}}{\partial y} &= \frac{\tau_w^y}{\rho_w} \end{aligned} \quad (1)$$

The x and y momentum components are defined as

$$\begin{aligned} M_x &= g \int_0^\infty \int_0^{2\pi} \frac{F(f, \theta)}{c(f)} \cos \theta \, d\theta \, df \\ M_y &= g \int_0^\infty \int_0^{2\pi} \frac{F(f, \theta)}{c(f)} \sin \theta \, d\theta \, df. \end{aligned} \quad (2)$$

$F(f, \theta)$ is the wave energy spectrum as a function of frequency, f , and direction, θ . $c(f)$ is the phase speed. T_{xx} , T_{xy} , T_{yx} , and T_{yy} are the components of the momentum flux tensor defined as:

$$T_{xx} = \frac{g}{2} \int_0^{\infty} \int_0^{2\pi} F(f, \theta) \cos^2 \theta \, d\theta \, df$$

$$T_{xy} = T_{yx} = \frac{g}{2} \int_0^{\infty} \int_0^{2\pi} F(f, \theta) \cos \theta \sin \theta \, d\theta \, df \quad (3)$$

$$T_{yy} = \frac{g}{2} \int_0^{\infty} \int_0^{2\pi} F(f, \theta) \sin^2 \theta \, d\theta \, df$$

If we assume that deep water linear theory applies and that wave energy is distributed about the mean wave direction as cosine squared, i.e.,

$$F(f, \theta) = \frac{2}{\pi} E(f) \cos^2(\theta - \theta_0) \quad \text{for } |\theta - \theta_0| \leq \frac{\pi}{2} \quad (4)$$

then the momentum fluxes can be expressed as (Schwab et al., 1984a)

$$\begin{aligned} T_{xx} &= \frac{g\sigma^2}{4} \left[\cos^2 \theta_0 + \frac{1}{2} \right] \\ T_{xy} = T_{yx} &= \frac{g\sigma^2}{4} \left[\cos \theta_0 \sin \theta_0 \right] \\ T_{yy} &= \frac{g\sigma^2}{4} \left[\sin^2 \theta_0 + \frac{1}{2} \right] \end{aligned} \quad (5)$$

where σ^2 is the variance

$$\sigma^2 = \int_0^{\infty} \int_0^{2\pi} F(f, \theta) \, d\theta \, df. \quad (6)$$

In the numerical model, only the two components of the wave momentum vector (M_x , M_y), the wave phase speed at the peak of the spectrum (c_p), and the total energy in the spectrum (σ^2) are calculated at each grid point. To calculate the wave momentum vector components, the time derivatives in (1) are represented by central differences. An upwind difference scheme is used for the momentum flux advection terms. The time step is determined dynamically as

$$\Delta t = \Delta s / \sqrt{2} c_m \quad (7)$$

where c_m is either the maximum wind speed during that time step or the maximum wave phase velocity calculated at the previous time step, whichever is greater and Δs is the grid interval. The wave momentum fluxes in (4) are calculated using the approximate relation

$$\sigma^2 = \frac{c_p |M|}{g} \quad (8)$$

Although this relation between variance (or energy), peak energy frequency ($f_p = g/2\pi c_p$), and integrated wave momentum is basically empirical, it applies quite well over a wide range of conditions.

The numerical model is based on a wave momentum conservation equation rather than wave energy conservation so that the following formula can be used for the wind input source function:

$$\frac{\tau_w}{\rho_w} = 0.028 c_d \vec{u} - 0.83 c_p |\vec{u} - 0.83 c_p| \quad (9)$$

where \vec{u} is the 10 m wind vector and c_d is the form drag coefficient defined as

$$c_d = [0.4 / \ln(50/\sigma)]^2 \quad (10)$$

with σ in meters. This formula for the drag coefficient is based on a logarithmic atmospheric boundary layer profile with a surface roughness height of $\sigma/5$. Note that when the wind and waves are travelling in the same direction, the momentum input function goes to zero when $\vec{u} = 0.83 c_p$ or $c_p = 1.2 \vec{u}$ (full development). This form of wind input is useful in describing the relative amounts of atmospheric momentum being expended on wave generation and the amount going into the water column to generate currents (see Donelan, 1977).

In the numerical scheme, after the new wave momentum vector is calculated from (1), peak energy frequency is found from the empirical relation

$$\frac{g^2 \sigma^2}{u^4} = 6.23 \times 10^{-6} \left(\frac{f_p u}{g} \right)^{-10/3} \quad (11)$$

By using (8) this relation can also be written as

$$f_p = 0.0179 \left(\frac{u^2}{|M/g|^3} \right)^{1/7} \quad (12)$$

It should also be pointed out, however, that other values of the coefficient and exponent in the empirical relation (11) between nondimensional energy and nondimensional peak energy frequency could be used and, in fact, are currently being evaluated in the model.

3. Results

The numerical model has been implemented on an IBM-XT type personal computer with an 8087 numeric coprocessor running at a clock rate of 4.77 MHz. With this configuration, a thirty day hindcast for a 10 km grid covering Lake Erie (253 grid squares) takes about one hour. Because the time step (7) in the numerical model is proportional to the grid interval, the total computation time is proportional to the cube of the grid interval, i.e., doubling the resolution of the computational grid (halving the grid interval) increases computation time by a factor of eight. Model tests on several different types of mainframe and microcomputers using various lake grids led to the development of a rough formula for the expected computation time. As shown in (7), the total computation time in seconds for one day of simulation, T , is going to depend on the maximum phase speed of the waves predicted during a run, but for typical wind speeds of $5-10 \text{ m s}^{-1}$, T can be estimated for a lake of surface area A with a computational grid of grid interval Δs and a computer running at a CPU clock rate of R Mhz as

$$T = \frac{1.7 \times 10^4 A}{(\Delta s)^3} \left(\frac{4.77}{R} \right) \frac{\text{m-sec}}{\text{day}} \quad (13)$$

For Lake Erie with $A=2.54 \times 10^{10} \text{ m}^2$, Table 1 shows some typical expected run times on a 4.77 Mhz machine with various grid intervals.

Table 1. Typical PC run times for various grid sizes on Lake Erie

Δs (km)	T (sec/day)
15	128
10	432
5	3456

In September and October of 1981, a solar-powered wave research tower was deployed in the eastern part of the central basin of Lake Erie (see Schwab et al., 1984b for the details). The tower was 6 km offshore in 14 m of water. Instruments on the tower measured wave height, wave period, and wave direction at hourly intervals. The numerical model was run for this entire period using the wind measured

at the tower for the forcing function (9). The results from the model are compared to observed wave parameters in Fig. 1.

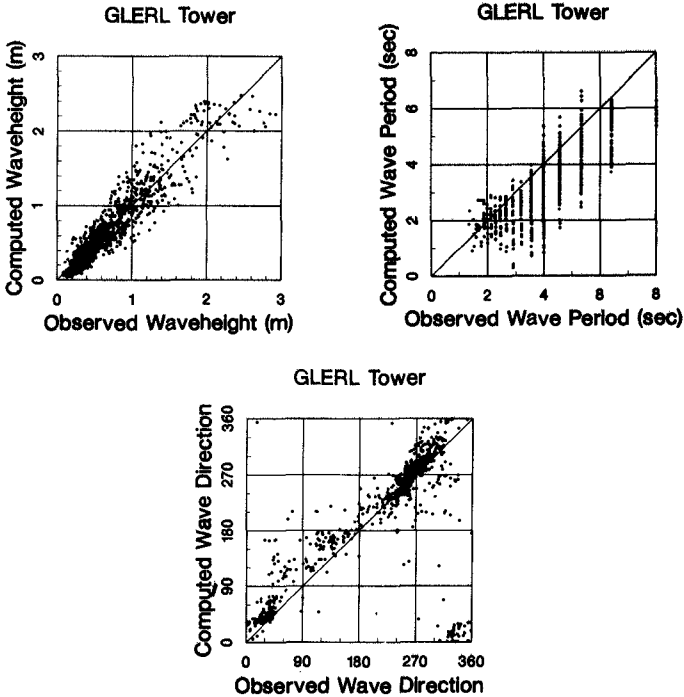


Figure 1. Comparison of observed and computed wave height, period, and direction in Lake Erie for September and October, 1981.

The agreement for wave height is quite good, with a root mean square error of 0.20 m and a correlation coefficient of 0.93 between computed and observed values. The computed wave periods, however, tend to underestimate the observed wave period. This may be due to using (12) to estimate wave period. Other formulas of the general form of (14) are currently being tested. Wave direction is modeled quite well, except for waves travelling in the 90-180° range. These are small waves generated from winds coming directly offshore (6 km fetch) so that it is very difficult to measure dominant wave direction accurately.

The model has also been extensively tested against other field data from the Great Lakes (typical fetch distances 100-300 km) and has been applied to Puget Sound, Hudson's Bay and the Beaufort Sea. Calibration and verification runs from deep and intermediate water depths show typical accuracies of 10-20% for wave height and 20-30% for wave period. The model is currently being used operationally by the National Weather Service for routine wave forecasting for the Great Lakes.

4. Conclusions and Recommendations

Although this type of model applies only to active wave generation, it can provide practical estimates of design waves for lakes, bays, estuaries, and semi-enclosed coastal areas. The main limitations of the model are that the wave spectrum is assumed to be single-peaked (no swell or multiple wind seas) and that shallow water effects are ignored. It is possible to extend the parametric formulation of the model to finite depth water by incorporating depth-dependent phase speed and depth-dependent spectral shape functions in the model equations along with a bottom dissipation term. Experiments with a shallow water model and comparisons of the results with field measurements are currently underway.

REFERENCES

- Bretschneider, C. L., 1970: Wave forecasting relations for wave generation. Look Lab, Hawaii, Vol. 1, No. 3.
- Donelan, M.A., 1977: A simple numerical model for wave and wind stress prediction. Report, Nat. Water Res. Inst., Burlington, Ontario.
- Hasselmann, K.D., T.P. Barnett, E. Bouws, H. Carlson, D.E. Cartwright, K. Enke, J.A. Ewing, H. Cienapp, D.E. Hasselman, P. Kruseman, A. Merrburg, P. Muler, D.J. Olbers, K. Richter, W. Sell, and H. Walden, 1973: Measurements of wind-wave growth and swell decay during the joint North Sea wave project (JONSWAP). Deutsh. Hydrogr. Zeit., Sup. A, Vol. A, No. 12, 95pp.
- Liu, P.C., D.J. Schwab and J.R. Bennett, 1984: Comparison of a two-dimensional wave prediction model with synoptic measurements in Lake Michigan. J. Phys. Oceanogr., 14(9), 1514-1518.
- Schwab, D.J., J.R. Bennett, P.C. Liu and M.A. Donelan, 1984a: Application of a simple numerical wave prediction model to Lake Erie. J. Geophys. Res., 89(C3), 3586-3592.
- Schwab, D.J., C.A. Meadows, J.R. Bennett, H. Schultz, P.C. Liu, J.E. Campbell, and H.H. Dannelongue, 1984b: The response of the coastal boundary layer to wind and waves: analysis of an experiment in Lake Erie. J. Geophys. Res., 89(C5), 8043-8053.
- The SWAMP Group, 1985: Ocean Wave Modeling. Plenum Press, New York, 256 pp.

SUBJECT INDEX

Page number refers to first page of paper.

- Accretion, 2738
Aeration, 166
Air chambers, 2326
Alaska, 2574, 2818
Altimeters, 1508
Analysis, 2952
Approximation methods, 2144, 2927
Armor units, 644, 2063, 2075, 2102, 2116, 2129, 2284, 2299, 2355, 2370, 2385, 2416, 2418, 2445, 2479
Armored units, 2144
Armour units, 1983
Australia, 2626

Barrier islands, 2681
Bars, riverine, 1167
Bathymetry, 2655
Bayesian analysis, 62
Beach erosion, 1, 121, 322, 1197, 1253, 1330, 1411, 1426, 1437, 1482, 1493, 1508, 1558, 1721, 1818, 1857, 1882, 1911, 1937, 1983, 2028, 2090, 2738, 2791, 2840, 2855, 2896, 153501543
Beach nourishment, 1323, 1411, 1482, 1558, 1882, 1922, 2806, 2825, 153501543
Beaches, 32, 77, 136, 151, 219, 292, 539, 553, 705, 807, 1182, 1238, 1295, 1338, 1396, 1618, 1631, 1676, 1736, 1763, 1959, 2116, 2784, 2867
Bed load movement, 1774, 1803
Bed ripples, 1748, 1868
Bed roughness, 492, 1842, 2692
Bedforms, 849, 1868, 2692
Belgium, 2855
Berms, 1997, 2284, 2416, 2818
Berths, 2966
Blocks, 2159, 2479
Boundary conditions, 181, 393, 624, 2561
Boundary element method, 624
Boundary layer, 234, 743, 914, 1129, 1280, 1603
Boundary layer flow, 492
Brazil, 261
Breaking waves, 234, 292, 350, 377, 393, 419, 478, 539, 578, 632, 682, 871, 1020, 1035, 1058, 1113, 1167, 1212, 1238, 1368, 1646, 1721, 2174, 2272, 2340, 2504
Breakwaters, 47, 121, 166, 246, 281, 624, 782, 1073, 1573, 1997, 2013, 2028, 2075, 2129, 2229, 2272, 2326, 2355, 2430, 2469, 2479, 2489, 2504, 2840, 2882
Buoys, 2923

Caissons, 2469, 2489
Calibration, 2013
California, 2129, 2455
Caribbean, 1618
Case reports, 756, 1265
Channels, waterways, 2896, 2911
Cnoidal waves, 219, 553, 588
Coastal engineering, 1, 204, 350, 363, 463, 858, 871, 884, 929, 941, 999, 1011, 1045, 1058, 1152, 1323, 1411, 1437, 1452, 1631, 1788, 1842, 1882, 1911, 1922, 2144, 2589, 2603, 2626, 2641, 2666, 2818, 2855, 2952
Coastal environment, 2574, 2615
Coastal management, 1, 2090, 2738, 2896
Coastal morphology, 1, 322, 1084, 1295, 1330, 1618, 1689, 1736, 1788, 1818, 1857, 2825
Coastal processes, 32, 181, 743, 1084, 1152, 1227, 1253, 1265, 1323, 1330, 1338, 1382, 1396, 1426, 1437, 1452, 1544, 1603, 1618, 1631, 1646, 1661, 1676, 1704, 1774, 1803, 1922, 1937, 1952, 1974, 2655, 2772, 2784, 2825, 2867
Coastal structures, 1, 166, 281, 655, 756, 782, 1020, 1310, 1482, 1573, 2043, 2053, 2090, 2174, 2189, 2299, 2370, 2385, 2400, 2455, 2504, 2681, 2791, 2840
Coastal zone, 2028
Coefficients, 47
Comparative studies, 644, 2681
Composite materials, 1588
Computation, 292, 1974
Computer aided drafting (CAD), 463
Computer applications, 463
Computer models, 2991
Computerized design, 463
Concrete blocks, 2043, 2053, 2144, 2174, 2370, 2400
Concrete construction, 2102, 2385, 2418
Conical bodies, 2257
Construction, 2416, 2723, 2753, 2791
Cost minimization, 2416
Currents, 77, 136, 363, 971, 1035,

Volume 1 – 1-998

Volume 2 – 999-1980

Volume 3 – 1981-2998

- 1140, 1212, 1368
Curtain walls, 2430
Cylinders, 914, 2201, 2216
- Damage assessment, 2818
Damage prevention, 1558
Damping, 2952
Data collection, 2753
Deformation, 393
Deltas, 1323
Design, 655, 782, 1280, 1997, 2043, 2063, 2159, 2174, 2299, 2326, 2385, 2416, 2489, 2666, 2723, 2753, 2979
Design criteria, 756, 1020, 1197, 1411, 2129, 2284, 2504
Design data, 770
Design events, 756
Design waves, 822, 899, 2504
Differential equations, 2603
Diffusion coefficient, 166
Dikes, 335, 1897, 2174, 2340
Discharge, 1573, 2521
Displacement, 1464
Distribution functions, 899
Docks, 2313
Dolos, 2075, 2129, 2355, 2385, 2418, 2445
Dunes, 1197, 1426, 1588, 1721, 1857, 2090
Dye studies, 2626
Dynamic analysis, 2469
Dynamic response, 1763, 2189, 2469, 2923
- Ecology, 2574, 2615
Economic factors, 1558
Eddie viscosity, 492
Eddies, 234, 1646
Eddy viscosity, 408, 478, 505, 1661
Effluents, 2521
Energy absorption, 2313, 2966
Energy conversion, 2489
Energy dissipation, 292, 363, 408, 492, 578, 1045, 1113, 1833, 2326
Energy losses, 1842, 2216
Energy transfer, 999
Entrainment, 2550
Environmental factors, 1238
Environmental impacts, 1330, 2574
Equations of motion, 419
Equilibrium, 1045
Equilibrium profile, 1396, 1618
Erosion, 1197, 1368, 1897, 2299
Erosion control, 1588
Estimating, 2445
Estimation, 62
- Estuaries, 1212, 1573, 1788, 2655, 2692, 2707, 2784
Eutrophication, 2615
Experience, 2455
Experimental data, 270, 153501543
- Failures, 1897, 2053, 2063
Failures, investigations, 2818, 2923
Fenders, 2966
Field investigations, 524, 539, 1522, 1618, 1833, 2430, 2626
Field tests, 47, 136, 1588, 1763
Finite difference method, 1129
Finite element method, 32, 2313, 2445
Finite elements, 2561
Fishing, 2927
Floating breakwaters, 2189
Flood control, 2855
Flood forecasting, 1197
Florida, 2772
Flow characteristics, 2201
Flow patterns, 505
Flow visualization, 234
Fluid dynamics, 718
Fluid-structure interaction, 17
Flumes, 448, 612, 770, 835, 871, 1140, 1763, 1803
Flushing, 2626
Forecasting, 566, 602, 667
Fourier transform, 246, 307
France, 2707
Frequency analysis, 2272
Friction, 505, 849, 1073
Friction factor, 363, 492, 2013
- Geomorphology, 2681
Grain size, 1952, 1959
Grain size analysis, 1129
Grains, 718
Gravel, 2116
Gravity foundations, 2469
Gravity waves, 512, 667, 2201
Grid systems, 2655
Groins, structures, 2882
- Harbor engineering, 463, 782, 984, 1997, 2896
Harbors, 32, 47, 270, 463, 1227, 2242, 2784, 2818, 2882, 2911, 2979
Head loss, 270
Hurricanes, 1098
Hydraulic design, 2400
Hydraulic models, 770, 2242, 2840, 2979
Hydraulic performance, 795

- Hydraulics, 2589, 2666
Hydrodynamics, 463, 505, 1058,
1382, 1974, 2189, 2479, 2655
Hydrostatics, 682
- Ice loads, 2400
In situ tests, 2355
Inlets, waterways, 433, 2681
Innovation, 2326
Intake structures, 2723
Islands, 322, 2738
- Japan, 2028, 2063, 2791
Jetties, 1911, 2896
- Kinematics, 377, 448, 871
- Laboratory tests, 91, 612, 632, 795,
835, 849, 1646, 1748, 1763, 1842,
1897, 1983, 1997, 2430
Lakes, 2840
Land fill, 2806, 2855
Linear functions, 884
Littoral current, 408, 1182
Littoral currents, 77, 234, 393, 705,
1113, 1238, 1396, 1689, 1736, 1959,
1974, 2521, 2603
Littoral drift, 1152, 1182, 1238, 1253,
1330, 1382, 1396, 1437, 1452, 1603,
1676, 1818, 1937, 1959, 1974, 2772,
2825
Loading, 2257
Long waves, 91, 219, 270, 984
- Marinas, 2626
Markov process, 956
Mathematical models, 246, 281, 566,
1129, 1603, 1689, 1897
Mats, 2400
Measuring instruments, 77
Mediterranean Sea, 566
Methodology, 884, 899, 1857
Mineralogy, 1338
Mixing, 2521
Model accuracy, 566
Model studies, 2692
Model tests, 644, 770, 984, 1265,
2075, 2257, 2923
Model verification, 433
Modeling, 121, 261, 335, 718, 956,
1952, 2418, 2589
Models, 270, 492, 698, 743, 795, 807,
822, 1098, 1212, 1253, 1676, 1736,
1818, 1833
Monitoring, 2806
Monte Carlo method, 899
- Mooring, 2189, 2923, 2952, 2979
Movable bed models, 1227, 1544
- Nearshore circulation, 106, 393, 408,
578, 1058, 1113, 1452, 1522, 1704,
2561, 2603, 2626, 2655
Netherlands, 2825
New Jersey, 2806, 2867
Nonlinear differential equations, 732
Nonlinear response, 1803
North Sea, 322, 956, 1788
Norway, 1997
Numerical analysis, 743
Numerical calculations, 307, 624,
2430, 2589
Numerical models, 350, 393, 433,
463, 512, 578, 588, 602, 858, 929,
941, 1113, 1167, 1265, 1295, 1426,
1437, 1911, 1937, 2013, 2159, 2189,
2445, 2561, 2655, 2666, 2707
Nutrient loading, 2615
- Ocean disposal, 2521
Ocean engineering, 2927
Ocean environments, 2536
Ocean thermal energy conversion,
971
Ocean waves, 204, 335, 602, 655,
1464
Oceanography, 602
Offshore engineering, 2536
Offshore pipeline, 2641
Offshore platforms, 62, 261, 956,
2257, 2313
Offshore structures, 914, 1280, 2257
Oil spills, 2574
Oregon, 1338
Oscillations, 151, 270, 2952, 2966
Oscillatory flow, 718, 743, 1140
Outfall sewers, 2615
Outwash, 1922
Overtopping, 335, 770, 795, 1983
- Perturbation theory, 705
Physical properties, 941
Phytoplankton, 2615
Piers, 1310
Pile tests, 1368
Piles, 1310, 2229
Plastic pipes, 2641
Plates, 2272
Plunging flow, 632, 682
Polyethylene, 2641
Polymers, 1588
Pore pressure, 1011
Pore pressure measurement, 2242

- Pore water pressure, 1842
- Porous materials, 1073
- Ports, 756, 1997, 2882, 2911
- Potential flow, 17
- Predictions, 644, 698, 871, 1098, 1167, 1253, 1396, 1426, 1508, 1676, 1803, 1857, 2201, 2536, 2692
- Pressure distribution, 682, 2504
- Probabilistic methods, 2063
- Probabilistic models, 1352
- Probability density functions, 524, 807, 822
- Probability distribution, 655, 822
- Probability theory, 1011, 2053
- Profiles, 1482, 1493, 1631, 1676, 1882, 2806, 153501543
- Project evaluation, 2806
- Prototype tests, 718, 1265, 1721, 2355
- Pump intakes, 2723
- Pumped storage, 1897

- Quality assurance, 2102
- Quantitative analysis, 2772

- Radar, 667
- Random waves, 91, 770, 807, 835, 941, 1736, 1748, 1763, 1911, 2257
- Recreational facilities, 1558, 2840, 2867
- Reefs, 335
- Regeneration, 1437
- Rehabilitation, 2855
- Reliability, 2063
- Reliability analysis, 2053
- Remote sensing, 667
- Repairing, 2075
- Research needs, 1
- Resonance, 270
- Restoration, 1411
- Return flow, 448
- Revetments, 281, 782, 795, 2043, 2116, 2159, 2174, 2340
- Reviews, 377, 2784
- Reynolds number, 2979
- Reynolds stress, 478
- Rip current, 408
- Rip currents, 32, 1603
- Risk analysis, 2574
- Rivers, 1573
- Rock properties, 2299
- Rock structures, 2116
- Roughness coefficient, 644
- Rubble-mound breakwaters, 770, 2053, 2063, 2102, 2116, 2144, 2242, 2284, 2385, 2416, 2418, 2455, 2818
- Sand, 718, 1588, 1882
- Sand transport, 1152, 1182, 1212, 1238, 1280, 1295, 1338, 1382, 1721, 1748, 1868, 1897, 2772
- Sand waves, 1748
- Sandbars, 2882
- Scale effect, 153501543
- Scale models, 2159, 2911
- Scattering, 2216
- Scour, 1310, 1368
- Scouring, 1280
- Sea floor, 1035, 1352, 1464, 1748, 1868, 2927
- Sea flow, 1842
- Sea level, 2825, 2867
- Sea state, 322, 655, 667, 956, 2340
- Sea walls, 281, 335, 782, 795, 1493, 1882, 1983, 2090, 2455, 2882
- Sea water, 2641, 2723
- Sediment, 849
- Sediment concentration, 1661, 2738
- Sediment control, 2723
- Sediment deposits, 1573
- Sediment transport, 234, 1084, 1140, 1152, 1167, 1182, 1227, 1280, 1338, 1368, 1382, 1396, 1452, 1493, 1508, 1522, 1544, 1676, 1689, 1704, 1721, 1736, 1774, 1803, 1818, 1868, 1882, 1911, 1952, 1959, 2707, 2772
- Sediment yield, 2867
- Selection, 2966
- Sensitivity analysis, 1959
- Service life, 2102
- Settlement analysis, 2927
- Sewage treatment plants, 2753
- Shallow water, 612, 807, 929, 1020, 1035, 1310
- Shaoling, 632
- Shear stress, 77, 1084, 1140, 2550
- Ship motion, 2911, 2952, 2966
- Ships, 2979
- Shoaling, 106, 419, 588, 807, 1035, 1212
- Shock, 2340
- Shore protection, 644, 1482, 1493, 1788, 2028, 2090, 2370, 2455, 2840, 2882
- Shoreline changes, 539, 1253, 1265, 1295, 1426, 1544, 1937, 2791, 2825, 2867
- Simulation, 91, 835, 858, 899, 941, 2299, 2911
- Simulation models, 106, 505, 1857, 2201, 2923
- Siphons, 2753
- Skewness, 1508

- Slope stability, 2116, 2400
Slopes, 281, 419, 2641
Soil analysis, 1352
Soil layers, 1352
Soil liquefaction, 1352
Soil mechanics, 1011
Soil stabilization, 1588
Soil stresses, 1352
Solitary wave, 219, 624, 1073, 2479
Sonar, 1508
Spain, 204, 858, 984, 1323, 1330,
1411, 2784, 2896
Spectral analysis, 524, 2536
Stability, 1997, 2028, 2053, 2075,
2174, 2284, 2299, 2370, 2489
Stability criteria, 2043
Stabilization, 2791
Standing waves, 151
State-of-the-art reviews, 971, 2043
Statistical analysis, 91, 756, 835,
1011, 1522, 2028, 2536
Statistical data, 655, 956
Statistics, 106
Steady flow, 1140
Steady state models, 929
Stochastic processes, 292, 941, 2536
Stoke's law, 17
Storm surges, 999, 1493
Storms, 566, 756, 956, 984, 1197,
1426, 1464, 1482, 1508, 1544, 1558
Stratified flow, 2550, 2561
Stress, 2418, 2692
Structural behavior, 2075, 2355
Structural design, 2129
Structural failures, 2445
Structural response, 2385, 2445
Structural strength, 2102
Submarine pipelines, 1464
Surf beat, 1058, 1167
Surf zone, 77, 151, 292, 377, 408, 419,
478, 539, 578, 612, 632, 705, 807,
999, 1058, 1167, 1182, 1295, 1382,
1646, 1661, 1704, 1774, 1833, 1959,
153501543
Surface waves, 246, 512
Suspended load, 1897
Suspended sediments, 1129, 1452,
1603, 1646, 1661, 1704, 1842, 2707

Taiwan, 1152, 2370, 2882
Technology assessment, 971
Theories, 181, 307, 588, 1073
Thermal pollution, 2521
Thermal power plants, 2521
Three-dimensional analysis, 1689,
2284
Three-dimensional flow, 705
Three-dimensional models, 667, 858,
2574
Tidal bores, 2589
Tidal currents, 433, 858, 1227, 1508,
2536, 2666, 2707
Tidal flats, 1788
Tidal marshes, 2666
Tidal power plants, 971
Tidal waters, 2681, 2692, 2896
Tides, 512, 2867
Time series analysis, 350
Topography, 1937, 2603, 2738
Tracers, 1338, 1774
Trends, 1
Turbulence, 478, 743, 2550
Turbulent boundary layer, 1661
Turbulent diffusion, 1661, 1704, 2589
Turbulent flow, 1646
Two-dimensional models, 350, 505,
2991

Uncertainty analysis, 1045
Undertow, 705, 1833
Undertown, 478
Underwater structures, 2753
United Kingdom, 1922
Unsteady flow, 624, 914
Uplift pressure, 2313

Velocity distribution, 1661
Velocity profile, 682, 743, 1368
Vertical cylinders, 17
Vortex shedding, 1310
Vortices, 914, 2927

Waste heat, 2521
Wastewater treatment, 2753
Water depth, 307, 419, 2469, 2911,
2979
Water flow, 2013, 2589
Water level, 999
Water levels, 539
Water pollution, 2615
Water purification, 166
Water supply systems, 2641
Water tunnels, 718, 1084
Water waves, 246, 433, 448, 682, 705,
732, 743, 1129, 1508, 1842, 2216
Wave action, 166, 281, 782, 1113,
1464, 1482, 1631, 1803, 1868, 1911,
2189, 2242, 2284, 2340, 2370, 2400,
2469, 2603
Wave attenuation, 363, 478, 492, 849
Wave climatology, 204, 261, 2806,
1535 1543

- Wave crest, 17, 307, 871, 1020
Wave defraction, 393, 2189
Wave diffraction, 17, 47, 121, 433, 732, 929, 2216
Wave dispersion, 578, 612
Wave energy, 62, 106, 261, 292, 971, 1721, 1833, 2272, 2326, 2489, 2991
Wave equations, 181
Wave forces, 77, 914, 1084, 1140, 1227, 1280, 1295, 1310, 2144, 2201, 2257, 2313, 2355, 2418, 2430, 2445, 2479, 2504, 2784, 2911, 2966
Wave generation, 91, 448, 612, 667, 698, 835, 941, 1098, 1544, 2991
Wave groups, 204, 884, 984
Wave height, 106, 136, 151, 307, 363, 419, 524, 553, 588, 667, 732, 807, 822, 871, 884, 899, 956, 1182, 1197, 1983, 2229, 2469, 2504
Wave measurement, 47, 62, 136, 204, 322, 377, 524, 588, 667, 1152, 2229, 2355, 2991
Wave pressure, 2159, 2340, 2489
Wave propagation, 32, 62, 181, 350, 363, 377, 419, 512, 553, 929, 999, 1073, 2229
Wave propagation, 246, 433
Wave reflection, 47, 136, 219, 393, 553, 782, 1073, 1493, 1763, 1983, 2013, 2216, 2272, 2489
Wave refraction, 121, 393, 433, 588, 732
Wave runup, 17, 151, 219, 553, 644, 655, 795, 1167, 1763, 1857, 1922, 1983, 2013, 2053, 2129, 2370
Wave spectra, 47, 62, 91, 261, 350, 492, 602, 612, 849, 929, 999, 1011, 1045, 2229
Wave tanks, 632, 1482, 1588, 1952, 2550
Wave velocity, 151, 377, 448, 524
Waves, 2991
Weirs, 335
West Germany, 1788
Wetlands, 2666
Wind direction, 602
Wind forces, 77, 261, 433, 632, 698, 929, 2550
Wind velocity, 1098
Wind waves, 512, 566, 602, 698, 1011, 1045, 1098, 2550

AUTHOR INDEX

Page number refers to first page of paper.

- Acinas, Juan R., 698
Aguilar Herrando, José, 1323, 2896
Aguilar, Jose, 1974
Ahrens, John P., 795
Alejo, M., 2479
Allsop, N. W. H., 281, 782
Aminti, Pierluigi, 770
Andersen, Ole Holst, 1603
Anglin, C. D., 2418, 2840
Anglin, C. David, 2385
Arcilla, A. S., 350
Arcilla, A. S., 463, 1382
Arenillas Parra, Miguel, 1330
Armanini, Aronne, 1129
Asano, Toshiyuki, 743
Auerbach, M. H., 1588
Awaya, Yoichi, 234
- Backhaus, J. O., 858
Baird, W. F., 2418
Baird, William F., 2385, 2416
Bakker, W. T., 718, 2825
Banno, Masato, 1868
Barnett, Michael R., 1493
Basco, David R., 682, 2589
Beil, N. J., 1482
Bendykowska, Genowefa, 612
Berenguer, José Ma, 1411
Bertolotti, Andrea, 2666
Bertotti, Luciana, 566
Bezuijen, A., 2159
Bijker, E. W., 1368
Bijker, Eco W., 2090
Blázquez, Rafael, 1352
Bodge, Kevin R., 1396
Boon, John D., 1508, 1618
Borden, G. W., 1588
Bowen, A. J., 1452, 1522
Bowen, Anthony J., 136
Bryden, I. G., 1020
Burcharth, H. F., 2284
Bürger, W., 2242
Burrows, R., 956
Byres, Ronald, 2189
- Campello Chorro, José L., 1323
Castel, David, 1676
Cavaleri, Luigi, 566
Chang, Jo Y. -H., 1464
Chang, S. G., 2370
Christodoulou, George C., 2561
Claassens, H., 2075
Clemens, Karen E., 1338
- Cooker, Mark, 624
Cortés Gimeno, Rafael, 1330
Costa, F. Vasco, 2966
Crowley, J. B., 181
- Daemrich, Karl-Friedrich, 322
Dai, G., 835
Dai, Guanying, 2469
Dally, William R., 807
Dalrymple, Robert A., 246, 2216
Davidson, D. D., 2416
Davis, Gregory A., 539
de Bruyn, C. A., 1368
De Luis, Jose E., 566
de Reus, J. H., 433
De Rouck, J., 2102
de Souza, Maria Helena Severo, 261
de Vriend, H. J., 1689
de Vroeg, J. H., 2825
Dean, Robert G., 807, 1558
Deb, Manas Kumar, 553
Dedeyne, R., 2102
Deguchi, Ichiro, 335, 1573
Deigaard, Rolf, 1603
del Río, J. G., 2615
Dette, H. H., 1721
Dette, Hans-Henning, 292
Dibajnia, Mohammad, 578
Dieckmann, Reinhard, 2681
Diez González, J. Javier, 1323, 1330
Diez Gonzalez, Jose Javier, 2784
Diez González, Jose Javier, 2896
Díez, J. J., 2615
Diez, Jose Javier, 1974
Dingemans, Maarten W., 32
Dodd, N., 732
Doering, J. C., 1452
Douglas, Barry, 2229
Douglass, S. L., 2806
Douglass, Scott L., 632, 2867
Drouin, Alain, 2272
- Easson, W. J., 1020
Easson, William J., 871
Economou, George D., 2561
Edge, B. L., 1588
Edge, Billy, 2416
Edge, Billy L., 2723
Egozcue, J. J., 350
Eisenberg, Y., 2753
Endo, Taiji, 2053, 2063, 2144
Enriquez, Javier, 1411
Escobar Paredes, Víctor A., 2896

- Esteban Chapapria, Vicent J. de, 1323, 1330
 Fasano, R. A., 2753
 Feldmeth, C. Robert, 2666
 Fenaish, T. A., 1426
 Fisher, J. S., 1426, 1857
 Flick, Reinhard E., 2666
 Foda, Mostafa A., 1464
 Franco, Leopoldo, 770
 Fredsøe, Jørgen, 1603
 Frigaard, Peter, 2284
 Fritsch, D., 2707
 Führböter, Alfred, 2174
 Funke, E. R., 91, 106, 835

 Gadd, Peter E., 644, 2400
 Gao, Ming, 2469
 Gingerich, Kathryn J., 1182
 Girard, R. K., 106
 Goda, Yoshimi, 899
 Godo, Hitomi, 743
 Gofas, Th. C., 2753
 Goldsztejn, Eduardo, 2979
 Graber, Hans C., 492
 Grass, Anthony J., 363
 Gravens, Mark B., 1265
 Greated, C. A., 1020
 Greated, Clive A., 871
 Green, Malcolm O., 1508, 1618
 Griffiths, Matthew W. P., 871
 Grüne, Joachim, 2340
 Guarga, Rafael, 2979

 Haines, J. W., 1522
 Hallermeir, Robert J., 1197
 Hands, Edward B., 1911
 Hanson, Hans, 1265
 Hardy, Thomas A., 588
 Hashimoto, Noriaki, 62
 Hatheway, Darryl J., 2772
 Hattori, Masataro, 2144
 Hayashi, Kenjiro, 2923
 Hayashi, Kenjiro, 914
 Hedegaard, Ida Brøker, 1603
 Heimbaugh, Martha S., 795
 Herbich, John B., 2229
 Hettiarachchi, S. S. L., 782
 Hides, F. S., 2753
 Hirayama, Ken-ichi, 1035
 Holthuijsen, L. H., 602
 Horikawa, Kiyoshi, 478, 1748, 2201
 Hosoi, Yoshihiko, 166
 Hotta, Shintaro, 151
 Hou, Ho-Shong, 1152
 Howell, Gary L., 2355

 Hsu, Tai-Wen, 121, 1631
 Huang, Jianwei, 1227
 Hudspeth, Robert T., 884
 Huntley, David A., 136
 Hwang, Sheng-Yeh, 2603

 Ifuku, Makoto, 1661
 Igarashi, Tatsuyuki, 1646
 Ikeno, Masaaki, 2326
 Imberger, J., 2626
 Inagaki, Keiji, 2144
 Instanes, Arne, 1997
 Isaacson, Michael, 2189
 Ismail, N. M., 2521
 Isobe, Masahiko, 393, 524
 Ito, Masahiro, 1544
 Iwagaki, Yuichi, 743
 Iwata, Koichiro, 2326

 Jamieson, Wayne W., 2257
 Jensen, Ole Juul, 756

 Kaczmarek, L., 1011
 Kakinuma, Tadao, 1661
 Katoh, Kazumasa, 1253
 Katsui, Hidehiro, 1280
 Kawata, Yoshiaki, 1310
 Kendall, Thomas R., 2129
 Kim, Young C., 971
 Kimura, Akira, 419, 655
 Kinose, Koichi, 1212
 Kjeldsen, Søren Peter, 667
 Klinting, P., 756
 Kobayashi, Nobuhisa, 1167
 Kobune, Koji, 62
 Komar, Paul D., 1238, 1338
 Kondo, Kosuke, 47, 2430
 Kostense, Jan K., 32
 Kraus, Nicholas C., 588, 1182, 1265, 1295
 Kriebel, David L., 17
 Krogstad, Harald Elias, 667
 Kröhn, J., 858
 Kubo, Masayoshi, 2952
 Kubota, Susumu, 151
 Kuo, Shih-Duenn, 2882
 Kyriacou, Andreas, 363

 Lai, C. P., 2313
 Langerak, A., 2692
 Larson, Magnus, 1295
 Latham, John-Paul, 2299
 Lastrup, C., 2159
 Law, Andrian W. -K., 1464
 Lee, Jiin-Jen, 2313
 Leendertse, Jan J., 2574, 2692

- Lee-Young, J. S., 1140
 Leidersdorf, Craig B., 2400
 Lewis, Lloyd, 971
 Lewis, Lloyd F., 2641
 Lin, Ming-Chung, 2603
 Lin, S. C., 2370
 Lionello, Piero, 566
 List, Jeffrey H., 1508
 Liu, Paul C., 1045
 Liu, Philip L. -F., 1911
 Liu, Shiao-Kung, 2574
 Lo, Jen-Men, 999
 Lorenz, Rene S., 705
 Losada, M. A., 1073, 2479

 McCormick, Michael E., 971
 McDougal, William G., 2400, 2445
 McGill, Preston G., 2445
 Machemehl, Jerry L., 644
 MacIntosh, K. J., 2840
 McMillen, Richard I., 2536
 Madsen, Ole Secher, 492, 849
 Madsen, P. A., 505
 Maeno, Yoshi-Hiko, 1842
 Magoon, Orville T., 2416, 2455
 Manikian, Victor, 644
 Mansard, E. P. D., 106, 835
 Mansard, Etienne P. D., 2257, 2385
 Marón, Adolfo, 204
 Martin, Paul A., 2216
 Martinez, F. M., 270
 Martínez, Felipe M., 1352
 Martinez Martinez, Jesus, 2738
 Massel, S. R., 1011
 Mather, D., 1020
 Matsumi, Yoshiharu, 2927
 Matsunaga, Nobuhiro, 234, 2550
 Medina, Josep R., 884, 941
 Medina, R., 1073, 2479
 Melby, Jeffrey A., 2445
 Miles, M. D., 91
 Mizuguchi, Masaru, 151
 Mizumura, Kazumasa, 2053, 2063
 Mogridge, Geoffrey R., 2257
 Möller, J. P., 1882
 Monso, J. L., 350
 Monsó, J. L., 463
 Moutzouris, C. I., 1959
 Murakami, Hitoshi, 166
 Murakami, Y., 1937

 Nadaoka, Kazuo, 1646
 Naeæss, Steinar, 1997
 Nairn, Robert B., 1818
 Nath, John H., 448
 Naverac, V. S., 270

 Negro Valdecantos, Vicente, 1437
 Nicholls, Robert, 1922
 Nielsen, Peter, 539, 1952
 Noguchi, Yuuji, 2144

 Ochi, Michel K., 2536
 Oelerich, Johannes, 292
 Ohishi, H., 1937
 Ohnaka, Susumu, 393
 Ohshimo, Tetsunori, 47, 2430
 Okamoto, Shunsaku, 2952
 Okayasu, Akio, 478
 Okushima, Shuji, 1212
 Olsen, Richard Bjarme, 667
 Osterthun, Manuela, 2681
 Ou, Shan-Hwei, 121, 1631
 Ouellet, Yvon, 2272
 Oumeraci, H., 2242
 Overton, M. F., 1426, 1857
 Ozaki, Akira, 408

 Papanicolaou, Panos, 377
 Park, San-Kil, 335
 Partenscky, H. W., 2242
 Partensckv. Hans Werner, 2681
 Partenscky, Hans-Werner, 2504
 Peregrine, D. H., 732
 Peregrine, Howell, 624
 Pilarczyk, K. W., 2043, 2116
 Pina, Gregorio Gómez, 984
 Poole, Alan B., 2299
 Poon, Ying-Keung, 492
 Pope, Joan L., 2455
 Pous, J., 1382
 Powell, K. A., 1763
 Pruszk, Zbigniew, 1774
 Puntigliano, Fernando, 2979

 Quecedo Gutierrez, Manuel, 1437

 Radder, A. C., 433
 Raichlen, Fredric, 377
 Ramsden, Jerald D., 448
 Rauw, Charles I., 2416
 Readshaw, J. S., 106
 Ren, Rushu, 153501543
 Resio, Donald T., 929
 Rhodes, Perry E., 1197
 Ribberink, J. S., 1689
 Ribeiro, Carlos Eduardo Parente,
 261
 Rodriguez, I., 858
 Roelvink, J. A., 1736
 Rosati, Julie Dean, 1182
 Rosengaus, Moises Michel, 849
 Rossouw, J., 822

- Rubio, J., 1073
 Rugbjerg, M., 505
 Ruol, Piero, 1129
 Ryan, P. J., 2521
- Saeki, Hiroshi, 408, 1035
 Sakai, Shigeki, 1035
 Sakuramoto, H., 2791
 Salih, B. A., 956
 Sánchez-Carratala, Carlos R., 941
 Santás López, Jose C., 984
 Sasaki, Mikio, 408
 Sato, Shinji, 1748
 Sawaragi, Toru, 335, 1573
 Sayao, Otavio J., 1818
 Schade, Daniel, 322
 Schäffer, Hemming A., 1058
 Schlueter, Roger S., 2723
 Scholtz, D. J. P., 2075
 Schwab, David J., 2991
 Schwartz, R. A., 2626
 Scott, R. Douglas, 2385
 Scott, R. D., 2418
 Seikmoto, Tsunehiro, 47
 Sekimoto, Tsunehiro, 2430
 Seo, Seung Nam, 2216
 Serra Peris, Jose, 2784
 Seyama, Akira, 419, 2927
 Seymour, Richard J., 1676
 Sheng, Y. Peter, 2655
 Shibayama, Tomoya, 478
 Shigemura, Toshiyuki, 914, 2923
 Shimoda, Naokatsu, 2326, 2952
 Shiraishi, Naofumi, 2053, 2063
 Siefert, Winfried, 1788
 Sierra, J. P., 350, 463
 Simoen, R., 2855
 Simons, Richard R., 363
 Skyner, D., 732
 Sleath, J. F. A., 1140
 Sloan, Robert L., 2455
 Slotta, Larry S., 971
 Smallman, J. V., 281
 Smit, E. S. P., 2825
 Snook, M. W. G., 1020
 Sobey, Rodney J., 307
 Soler, E., 2615
 Sorensen, R. M., 1482, 2806
 Sorensen, Robert M., 2867
 Sparboom, Uwe, 2174
 Stephens, R. V., 281
 Stiassnie, M., 732
 Stive, Marcel J. F., 1736
 Strzelecki, Michael S., 1167
 Suh, Kyung Duck, 246
 Sumiya, M., 2791
- Sunamura, Tsuguo, 1295
 Svendsen, Ib A., 705, 1058
 Swart, D. H., 181, 1882
 Synolakis, Costas Emmanuel, 219, 553
- Taerwe, L., 2102
 Takahashi, Shigeo, 2489
 Takehara, Kosei, 234
 Takezawa, Mitsuo, 151
 Tallent, James R., 1833
 Tanaka, Hitoshi, 1803
 Tatavarti, Rao V. S. N., 136
 Tedesco, Joseph W., 2445
 Teisson, Ch., 2707
 Thompson, Alex C., 2013
 Thornton, E. B., 77
 Tickell, R. G., 956
 Tolman, Hendrik L., 512
 Tørum, Alf, 1997
 Toue, Takao, 1280
 Toyoshima, Osamu, 1983
 Treadwell, Donald, 2416
 Treadwell, Donald D., 2455
 Tsuchiya, Yoshito, 1310, 1544, 1833, 1868, 2589
 Tsuru, Masahito, 1212
 Tsuzuki, Susumu, 2201
 Tu, S. W., 2521
 Turcke, D. J., 2418
 Turcke, David J., 2385
 Twu, S. W., 2370
 Tzang, Shiao-Yih, 121
- Uda, T., 2791
 Uda, Takaaki, 2028
 Uda, T., 1937
 Ueno, Seizo, 1646
 Uliczka, K., 1721
 Ura, Masaru, 2550
- Van Damme, L., 2102
 van de Graaff, Jan, 2090
 Van den Bosch, Peter, 32
 van der Meer, J. W., 2116
 van Kesteren, W. G. M., 718
 Van Ryzin, Joseph, 2641
 van Vledder, G. Ph., 602
 Van Wyk, A. C., 2911
 Vandenbossche, D., 2855
 Vega, Luis, 2641
 Verslype, H., 2855
 Vidal, C., 1073
 Vidoar, A., 1382
 Visser, Paul J., 1897
 Vogel, J. A., 433

- Vold, Svein, 1997
Vongvisessomjai, Suphat, 1084
- Walker, James R., 2666
Walton, Todd L., Jr., 1911
Wang, Hsiang, 1493
Wang, Liang, 153501543
Wang, P. F., 2655
Warren, I. R., 505
Watanabe, Akira, 393, 578, 2201
Watanabe, M., 1937
Watts, George M., 2818
Webber, Norman, 1922
Weckmann, Javier, 2818
Weggel, J. R., 2806
Weggel, J. Richard, 632, 2867
Werner, Gosta, 612
Whitford, D. J., 77
Wiegel, R. L., 2521
- Wiegel, Robert L., 1
Wouters, J., 2159
Wright, L. Don, 1508
Wu, T. S., 2655
Wurjanto, Andojo, 1167
- Yamaguchi, Masataka, 1113
Yamamoto, Masato, 2053, 2063
Yamashita, Takao, 682, 1833, 2589
Yanagishima, Shin-ichi, 1253
Yang, Jihua, 2469
Yeend, John S., 2772
Yen, Kai, 153501543
Young, Ian R., 1098
Yu, Z. H., 718
- Zeidler, Ryszard B., 1704, 1774
Zwamborn, J. A., 2075, 2911
Zyserman, Julio A., 1603